



VOLUME 1

Edited by Billy L. Edge

# Coastal Engineering 1994

Proceedings of the  
twenty-fourth international conference

VOLUME 1

RAO

# Coastal Engineering 1994

Proceedings of the  
twenty-fourth international conference

October 23-28; 1994  
Kobe, Japan

Conference held under the auspices of the  
Coastal Engineering Research Council of the  
American Society of Civil Engineers

Organized by the Japan Society of Civil Engineers

Edited by Billy L. Edge



Published by the  
American Society of Civil Engineers  
345 East 47th Street  
New York, New York 10017-2398

## ABSTRACT

This proceedings contains over 200 papers presented at the 24th International Conference on Coastal Engineering which was held in Kobe, Japan, October 23-28, 1994. The book is divided into six parts: 1) Characteristics of coastal waves and currents; 2) long waves and storm surges; 3) coastal structures; 4) coastal processes and sediment transport; 5) coastal, estuarine and environmental problems; and 6) case studies. The individual papers include such topics as the effects of wind, waves, storms and currents as well as the study of sedimentation and beach nourishment. Special emphasis is given to case studies of completed engineering projects. With the inclusion of both theoretical and practical information, these papers provide the civil engineer and related fields with a broad range of information on coastal engineering.

Coastal engineering 1994: proceedings of the twenty-fourth international conference, October 23-28, 1994, Kobe, Japan  
edited by Billy L. edge.

p. cm.

"Conference held under the auspices of the Coastal Engineering Research Council of the American Society of Civil Engineers; organized by the Japan Society of Civil Engineers (JSCE)." Papers presented at the 24th International Conference on Coastal Engineering.

Includes index.

ISBN 0-7844-0089-X

1. Coastal engineering—Congresses. 2. Ocean waves—Congresses. 3. Shore protection—Congresses. I. Edge, Billy L. II. Coastal Engineering Research Council (U.S.) III. Doboku Gakkai. IV. International Conference on Coastal Engineering (24th: 1994: Kobe, Japan)

TC203.5.C6184 1995  
627'.58—dc20

95-18653  
CIP

The Society is not responsible for any statements made or opinions expressed in its publications.

Photocopies. Authorization to photocopy material for internal or personal use under circumstances not falling within the fair use provisions of the Copyright Act is granted by ASCE to libraries and other users registered with the Copyright Clearance Center (CCC) Transactional Reporting Service, provided that the base fee of \$2.00 per article plus \$.25 per page copied is paid directly to CCC, 222 Rosewood, Drive, Danvers, MA 01923. The identification for ASCE Books is 0-7844-0089-X/95 \$2.00 + \$.25. Requests for special permission or bulk copying should be addressed to Permissions & Copyright Dept., ASCE.

Copyright © 1995 by the American Society of Civil Engineers,  
All Rights Reserved.  
Library of Congress Catalog Card No: 95-18653  
ISBN 0-7844-0089-X  
Manufactured in the United States of America.

## FOREWORD

The 24th International Conference on Coastal Engineering was held in Kobe, Japan. The 24th ICCE, like the ones before it, was organized and managed by volunteers from within Japan representing private, industrial and governmental contributors. This Conference represented an opportunity to share scientific and engineering information and provided a forum for interaction with other engineers and scientists working on similar coastal problems. The time and effort contributed to the development and organization of each conference becomes more complex and difficult as they continue to grow in size and content. The Local Organizing Committee worked on the planning for this Conference for four years. The 24th ICCE was a tremendous success in every way. The **Proceedings** of this Conference will represent a major step forward in the field of coastal engineering.

The chapters in this **Proceedings** have been prepared by the authors who were selected to make presentations at the 24th International Conference on Coastal Engineering. The authors were asked to make presentations at the Conference based upon review of the abstracts which were submitted well in advance of the Conference. The Technical Review Committee included six professionals who are active in the field of coastal engineering. One of the members is a representative of the Local Organizing Committee; the other five members were selected for their broad understanding and recognition in the field. The papers included in this volume are eligible for discussion in the **Journal of the Waterways, Port, Coastal and Ocean Division** of the ASCE. All papers are eligible for ASCE awards.

Venues for the upcoming conferences are listed below:

25th ICCE - Orlando, FL USA	1996
26th ICCE - Copenhagen, Denmark	1998
27th ICCE - Sydney, Australia	2000

Coastal engineers who would desire to host a future conference in their country should contact the Secretary of the Coastal Engineering Research Council to receive information about submitting a proposal.

The continuing coordination of the International Conferences on Coastal Engineering is through the Coastal Engineering Research Council of the ASCE. The Research Council began at the instigation of Professor Boris Bakhmeteff who as chairman of the Research Committee of the Engineering Foundation suggested the formation of the Council on Wave Research. The Council was established in June 1950 under the Engineering Foundation. In 1963 the Council was transferred from the Foundation to the ASCE and was renamed the Coastal Engineering Research Council which better described its expanded function.

Members of the coastal engineering community recognized that the problems they faced required broad based research to better define the coastal and ocean phenomena with which they dealt. The Foundation felt that it was important that all disciplines working in the coastal area should have an opportunity and be encouraged to communicate with one another through the mechanism of interdisciplinary conferences.

The first conference was held in Long Beach, CA in 1950. The papers which were delivered at the conference were published and became the first coastal engineering conference **Proceedings**. Although the conferences began with a national focus they quickly became international in scope. After planning and conducting 24 conferences on coastal engineering the Series has been established as the principal conference on coastal engineering in the world. Contributors to the conference represent nearly all coastal nations and the numbers of abstracts which are submitted for consideration are generally twice as large as the available opportunity for presentations. The **Proceedings** of the conferences are all available from the ASCE.

Billy L. Edge, Secretary  
Coastal Engineering Research Council  
American Society of Civil Engineers

# ACKNOWLEDGMENTS

## LOCAL ORGANIZING COMMITTEE

Chairman:

K. Sasayama - Mayor of Kobe

Vice Chairman:

Y. Iwagaki - Professor, Meijo University

K. Horikawa - President, Saitama University

N. Shiraishi - Nippon Tetrapod Co., Ltd. (deceased)

T. Sawaragi - Professor, Osaka University

Y. Tsuchiya - Professor, Meijo University

## EXECUTIVE COMMITTEE

Co-Chairman:

T. Sawaragi - Professor, Osaka University

Co-Chairman:

Y. Tsuchiya - Professor, Meijo University

M. Hattori - Professor, Chuo University

M. Inoue - Professor, Kansai University

K. Oda - Professor, Osaka City University

A. Watanabe - Professor, University of Tokyo

T. Sakai - Professor, Kyoto University

Y. Kawata - Professor, Kyoto University

I. Deguchi - Professor, Osaka University

## SUPPORTING ORGANIZATIONS

International Association for Hydraulic Research

Japanese Association for Coastal Zone Studies

Japan Society for Natural Disaster Science

The Society of Naval Architects of Japan

Architectural Institute of Japan

Meteorological Society of Japan

The Oceanographic Society of Japan

The Ministry of Agriculture, Forestry and Fisheries

The Ministry of Transport

The Ministry of Construction

## FINANCIAL SUPPORT

City of Kobe  
Hyogo Prefectural Government  
Osaka Prefectural Government  
Wakayama Prefectural Government  
City of Osaka  
City of Himeji  
City of Sakai  
Japan Ocean Development Construction Association  
The Federation of Electric Power Companies  
Japan Association for Wave-Dissipating and Foot Protection Blocks  
Japan Iron and Steel Foundation  
The Japan Port and Harbor Association  
Osaka Bay Regional Offshore Environmental Improvement Center  
All Japan Fishing Ports Association  
Fishery Infrastructure Development Center  
The Japanese Institute of Technology on Fishing Ports and Communities  
Japan Consulting Engineers Cooperation  
Osaka Gas Co., Ltd.  
The Portopia 81 Foundation  
The Kajima Foundation  
Commemorative Association for the Japan World Exposition (1970)  
International Exchange Fund, JSCE

## COASTAL ENGINEERING RESEARCH COUNCIL (ASCE)

Chairman:

R. G. Dean

Vice Chairman:

O. T. Magoon

Secretary:

B. L. Edge

Members:

K. Horikawa

T. Saville, Jr.

R. M. Noble

J. W. Kamphuis

R. A. Dalrymple

K. d'Angremond

S. A. Hughes

# CONTENTS

## PART I

Plenary Session THE PRESENT AND FUTURE OF COASTAL ENGINEERING IN JAPAN.....	1
<i>Yuichi Iwagaki</i>	
Chapter 1 ON THE CHARACTERISTICS OF ONE-DIMENSIONAL SPECTRA AND NON-DIMENSIONAL PARAMETERS OF WIND WAVES.....	12
<i>Toshio Aono, Chiaki Goto</i>	
Chapter 2 SWASH MOTION DUE TO OBLIQUELY INCIDENT WAVES.....	27
<i>Toshiyuki Asano</i>	
Chapter 3 LABORATORY COMPARISON OF DIRECTIONAL WAVE MEASUREMENT SYSTEMS AND ANALYSIS TECHNIQUES .....	42
<i>Michel Benoit, Charles Teisson</i>	
Chapter 4 ACCURACY OF WIND AND WAVE EVALUATION IN COASTAL REGIONS.....	57
<i>Luciana Bertotti, Luigi Cavaleri</i>	
Chapter 5 A SPECTRAL MODEL FOR WAVES IN THE NEAR SHORE ZONE .....	68
<i>R.C. Ris, L.H. Holthuijsen, N. Booij</i>	
Chapter 6 WIND VARIABILITY AND EXTREMES STATISTICS.....	79
<i>Luigi Cavaleri, Luciana Bertotti</i>	
Chapter 7 MEAN FLUX IN THE FREE SURFACE ZONE OF WATER WAVES IN A CLOSED WAVE FLUME.....	86
<i>Witold Cieslikiewicz, Ove T. Gudmestad</i>	
Chapter 8 VERTICAL VARIATIONS OF FLUID VELOCITIES AND SHEAR STRESS IN SURF ZONES .....	98
<i>Daniel T. Cox, Nobuhisa Kobayashi, Akio Okayasu</i>	



Chapter 9	
VORTICITY EFFECTS IN COMBINED WAVES AND CURRENTS .....	113
<i>I. Cummins, C. Swan</i>	
Chapter 10	
WAVES IN AN ANNULAR ENTRANCE CHANNEL .....	128
<i>Robert A. Dalrymple, J.T. Kirby</i>	
Chapter 11	
WAVE DAMPING BY KELP VEGETATION .....	142
<i>Alfonse Dubi, Alf Tørum</i>	
Chapter 12	
NONLINEAR COUPLING IN WAVES PROPAGATING OVER A BAR .....	157
<i>Y. Eldeberky, J.A. Battjes</i>	
Chapter 13	
AN ABSORBING WAVE-MAKER BASED ON DIGITAL FILTERS .....	168
<i>Peter Frigaard, Morten Christensen</i>	
Chapter 14	
WAVE CLIMATE STUDY IN WADDEN SEA AREAS .....	181
<i>Ralf Kaiser, Günther Brandt, Joachim Gärtner, Detlef Glaser, Frerk Jensen, H.D. Niemeyer, Joachim Grüne</i>	
Chapter 15	
FALSE WAVES IN WAVE RECORDS AND NUMERICAL SIMULATIONS .....	192
<i>Marcos H. Giménez, C.R. Sánchez-Carratalá, J.R. Medina</i>	
Chapter 16	
MEASURING WAVES WITH MANOMETER TUBES .....	207
<i>David J. Hanslow, P. Nielsen, K. Hibbert</i>	
Chapter 17	
QUANTITY OF SPRAY TRANSPORTED BY THE STRONG WIND OVER BREAKING WAVES .....	219
<i>Nobuhiro Matsunaga, Misao Hashida, Hiroyuki Mizui, Yuji Sugihara</i>	
Chapter 18	
EXTENSION OF THE MAXIMUM ENTROPY PRINCIPLE METHOD FOR DIRECTIONAL WAVE SPECTRUM ESTIMATION .....	232
<i>Noriaki Hashimoto, Toshihiko Nagai, Tadashi Asai</i>	

Chapter 19	
A REGRESSION MODEL FOR ESTIMATING SEA STATE PERSISTENCE .....	247
<i>Yoshio Hatada, Masataka Yamaguchi</i>	
Chapter 20	
THE MAXIMUM SIGNIFICANT WAVE HEIGHT IN THE SOUTHERN NORTH SEA .....	261
<i>L.H. Holthuijsen, J.G. de Ronde, Y. Eldeberky, H.L. Tolman, N. Booij, E. Bouws, P.G.P. Ferier, J. Andorka Gal</i>	
Chapter 21	
IMPROVED BOUNDARY CONDITIONS TO A TIME-DEPENDENT MILD-SLOPE EQUATION FOR RANDOM WAVES .....	272
<i>Toshimasa Ishii, Masahiko Isobe, Akira Watanabe</i>	
Chapter 22	
TIME-DEPENDENT MILD SLOPE EQUATIONS FOR RANDOM WAVES .....	285
<i>Masahiko Isobe</i>	
Chapter 23	
MODELLING MOVEABLE BED ROUGHNESS AND FRICTION FOR SPECTRAL WAVES .....	300
<i>L.M. Kaczmarek, J.M. Harris, B.A. O'Connor</i>	
Chapter 24	
DIFFERENCE BETWEEN WAVES ACTING ON STEEP AND GENTLE BEACHES .....	315
<i>Kazumasa Katoh</i>	
Chapter 25	
WAVE BREAKING UNDER STORM CONDITION .....	330
<i>Yoshiaki Kawata</i>	
Chapter 26	
APPLICATION OF MAXIMUM ENTROPY METHOD TO THE REAL SEA DATA .....	340
<i>Taerim Kim, Li-Hwa Lin, Hsiang Wang</i>	
Chapter 27	
PROBABILITY OF THE FREAK WAVE APPEARANCE IN A 3-DIMENSIONAL SEA CONDITION .....	356
<i>Akira Kimura, Takao Ohta</i>	

Chapter 28	
ON THE JOINT DISTRIBUTION OF WAVE HEIGHT, PERIOD & DIRECTION OF INDIVIDUAL WAVES IN A 3-DIMENSIONAL RANDOM SEAS.....	370
<i>J.G. Kwon, Ichiro Deguchi</i>	
Chapter 29	
SPECTRAL WAVE-CURRENT BOTTOM BOUNDARY LAYER FLOWS .....	384
<i>Ole Secher Madsen</i>	
Chapter 30	
TIME DOMAIN MODELLING OF WAVE BREAKING, RUNUP AND SURF BEATS .....	399
<i>Per A. Madsen, O.R. Sørensen, H.A. Schäffer</i>	
Chapter 31	
ORTHONORMAL WAVELET ANALYSIS FOR DEEP-WATER BREAKING WAVES .....	412
<i>Nobuhito Mori, Takashi Yasuda</i>	
Chapter 32	
A FULLY DISPERSIVE-NONLINEAR WAVE MODEL AND ITS NUMERICAL SOLUTIONS .....	427
<i>Kazuo Nadaoka, Serdar Beji, Yasuyuki Nakagawa</i>	
Chapter 33	
A GENERALIZED GREEN-FUNCTION METHOD FOR WAVE FIELD ANALYSIS .....	442
<i>Hitoshi Nishimura, Michio Matsuoka, Akira Matsumoto</i>	
Chapter 34	
COUPLED VIBRATION EQUATIONS FOR IRREGULAR WATER WAVES.....	455
<i>Masao Nochino</i>	
Chapter 35	
NONLINEAR EVOLUTION OF DIRECTIONAL WAVE SPECTRA IN SHALLOW WATER .....	467
<i>Okey Nwogu</i>	
Chapter 36	
NON-GAUSSIAN PROBABILITY DISTRIBUTION OF COASTAL WAVES .....	482
<i>M.K. Ochi, K. Ahn</i>	

Chapter 37	
PROBABILITY CHARACTERISTICS OF ZERO-CROSSING WAVE HEIGHT .....	497
<i>Takao Ohta, Akira Kimura</i>	
Chapter 38	
NUMERICAL SIMULATION AND VALIDATION OF PLUNGING BREAKERS USING A 2D NAVIER-STOKES MODEL.....	511
<i>H.A.H. Petit, P.Tönjes, M.R.A. Van Gent, P. Van Den Bosch</i>	
Chapter 39	
WAVE VELOCITY FIELD MEASUREMENTS OVER A SUBMERGED BREAKWATER .....	525
<i>Marco Petti, Paul A. Quinn, Gianfranco Liberatore, William J. Easson</i>	
Chapter 40	
VELOCITY FIELD MEASUREMENTS AND THEORETICAL COMPARISONS FOR NON-LINEAR WAVES ON MILD SLOPES .....	540
<i>Paul A. Quinn, Marco Petti, Michele Drago, Clive A. Greated</i>	
Chapter 41	
THE CONCEPT OF RESIDENCE TIME FOR THE DESCRIPTION OF WAVE RUN-UP, WAVE SET-UP AND WAVE RUN-DOWN.....	553
<i>Holger Schüttrumpf, Hendrik Bergmann, Hans-Henning Dette</i>	
Chapter 42	
BOTTOM SHEAR STRESSES UNDER RANDOM WAVES WITH A CURRENT SUPERIMPOSED.....	565
<i>Richard R. Simons, Tony J. Grass, Wameidh M. Saleh, Mehrdad M. Tehrani</i>	
Chapter 43	
EFFECTS FROM DIRECTIONALITY & SPECTRAL BANDWIDTH ON NON-LINEAR SPATIAL MODULATIONS OF DEEP-WATER SURFACE GRAVITY WAVE TRAINS .....	579
<i>Carl Trygve Stansberg</i>	
Chapter 44	
SHEAR STRESSES AND MEAN FLOW IN SHOALING AND BREAKING WAVES .....	594
<i>Marcel J.F. Stive, Huib J. De Vriend</i>	

Chapter 45	
PREDICTION OF THE MAXIMUM WAVE ON THE CORAL FLAT .....	609
<i>Dede M. Sulaiman, Shigeaki Tsutsui, Hiroshi Toshioka,</i>	
<i>T. Yamashita, S. Oshiro, Y. Tsuchiya</i>	
Chapter 46	
DEVELOPMENT OF A SUBMERGED DOPPLER-TYPE DIRECTIONAL	
WAVE METER .....	624
<i>Tomotsuka Takayama, Noriaki Hashimoto, Toshihiko Nagai,</i>	
<i>Tomoharu Takahashi, Hiroshi Sasaki, Yoshiki Ito</i>	
Chapter 47	
BRAGG SCATTERING OF WAVES OVER POROUS RIPPLED BED .....	635
<i>Hijime Mase, Ken Takeba</i>	
Chapter 48	
NON-REFLECTIVE MULTI-DIRECTIONAL WAVE GENERATION	
BY SOURCE METHOD .....	650
<i>Masahiro Tanaka, Takumi Ohyama, Tetsushi Kiyokawa, Kazuo Nadaoka</i>	
Chapter 49	
THE GROWTH OF WIND WAVES IN SHALLOW WATER .....	665
<i>L.A. Verhagen, I.R. Young</i>	
Chapter 50	
ESTIMATION OF TYPHOON-GENERATED MAXIMUM WAVE	
HEIGHT ALONG THE PACIFIC COAST OF JAPAN BASED ON	
WAVE HINDCASTING .....	674
<i>Masataka Yamaguchi, Yoshio Hatada</i>	
Chapter 51	
RUN-UP OF IRREGULAR WAVES ON A GENTLY SLOPING BEACH .....	689
<i>Yoshimichi Yamamoto, Katsutoshi Tanimoto, Karunaratna Harshinie</i>	
Chapter 52	
SOLITON-MODE WAVEMAKER THEORY AND SYSTEM FOR	
COASTAL WAVES .....	704
<i>Takashi Yasuda, Takeshi Hattori, Seirou Shinoda</i>	
Chapter 53	
ON A METHOD FOR ESTIMATING REFLECTION COEFFICIENT	
IN SHORT-CRESTED RANDOM SEAS .....	719
<i>Hirumune Yokoki, Masahiko Isobe, Akira Watanabe</i>	

Chapter 54	
THE DIRECTIONAL WAVE SPECTRUM IN THE BOHAI SEA.....	731
<i>Yuxiu Yu, Shuxue Liu</i>	

Chapter 55	
IRREGULAR WAVES OVER AN ELLIPTIC SHOAL.....	746
<i>Xiping Yu, Hiroyoshi Togashi</i>	

Chapter 56	
PERFORMANCE OF A SPECTRAL WIND-WAVE MODEL IN SHALLOW WATER.....	761
<i>Gerbrant Ph. van Vledder, John G. de Ronde, Marcel J.F. Stive</i>	

## PART II

Chapter 57	
THE GENERATION OF LOW-FREQUENCY WAVES BY A SINGLE WAVE GROUP INCIDENT ON A BEACH.....	776
<i>Gary Watson, Timothy C.D. Barnes, D. Howell Peregrine</i>	

Chapter 58	
INFLUENCE OF LONG WAVES ON SHIP MOTIONS IN A LAGOON HARBOUR.....	791
<i>Volker Barthel, Etienne Mansard</i>	

Chapter 59	
RESONANT FORCING OF HARBORS BY INFRAGRAVITY WAVES.....	806
<i>Gordon S. Harkins, Michael J. Briggs</i>	

Chapter 60	
NUMERICAL SIMULATION OF THE 1992 FLORES TSUNAMI IN INDONESIA: DISCUSSION ON LARGE RUNUP HEIGHTS IN THE NORTHEASTERN FLORES ISLAND.....	821
<i>Fumihiko Imamura, Tomoyuki Takahashi, Nobuo Shuto</i>	

Chapter 61	
A COMPARATIVE EVALUATION OF WAVE GROUPING MEASURES.....	832
<i>É.P.D. Mansard, S.E. Sand</i>	

Chapter 62	
RELATIONSHIP OF A MOORED VESSEL IN A HARBOUR AND LONG WAVE CAUSED BY WAVE GROUPS.....	847
<i>Toshihiko Nagai, N. Hashimoto, T. Asai, I. Tobiki, K. Ito, T. Toue, A. Kobayashi, T. Shibata</i>	

Chapter 63	
COHERENT STRUCTURE OF TIDAL TURBULENCE IN A ROTATING SYSTEM OF OSAKA-BAY .....	861
<i>Tsakasa Nishimura, Tomonao Kobayashi, Goichi Furuta</i>	

Chapter 64	
DEVELOPMENT OF A PARTIALLY THREE-DIMENSIONAL MODEL FOR SHIP MOTION IN A HARBOR WITH ARBITRARY BATHYMETRY .....	871
<i>Takumi Ohyama, M. Tsuchida</i>	

Chapter 65	
THE MEASURED AND COMPUTED HOKKAIDO NANSEI-OKI EARTHQUAKE TSUNAMI OF 1993 .....	886
<i>Tomoyuki Takahashi, Nobuo Shuto, Fumihiko Imamura, Hideo Matsutomi</i>	

Chapter 66	
QUASI-THREE-DIMENSIONAL MODEL FOR STORM SURGES AND ITS VERIFICATION .....	901
<i>Takao Yamashita, Yoshito Tsuchiya, Hiroshi Yoshioka</i>	

### PART III

Chapter 67	
ANALYSIS OF PRACTICAL RUBBLE MOUNDS .....	918
<i>N.W.H. Allsop, R.J. Jones, P. Besley, C. Franco</i>	

Chapter 68	
FRICTION AND CLAMPING FORCES IN WAVE LOADED PLACED BLOCK REVETMENTS .....	932
<i>Adam Bezuijen</i>	

Chapter 69	
A FIELD EXPERIMENT ON THE INTERACTION WAVES-REFLECTING WALL .....	945
<i>Paolo Boccotti</i>	

Chapter 70	
THE APPLICATION OF LOAD-CELL TECHNIQUE IN THE STUDY OF ARMOUR UNIT RESPONSES TO IMPACT LOADS .....	958
<i>Hans F. Burcharth, Zhou Liu</i>	

Chapter 71	
STEEP WAVE DIFFRACTION BY A SUBMERGED CYLINDER.....	973
<i>J.T. Aquije Chacaltana, A.F.T. da Silva</i>	
Chapter 72	
WAVE STRESSES ON RUBBLE-MOUND ARMOUR .....	986
<i>Andrew M. Cornett, Etienne Mansard</i>	
Chapter 73	
DAMAGE ANALYSIS FOR RUBBLE-MOUND BREAKWATERS .....	1001
<i>Michael H. Davies, Etienne P.D. Mansard, Andrew M. Cornett</i>	
Chapter 74	
NUMERICALLY MODELING PERSONNEL DANGER ON A PROMENADE BREAKWATER DUE TO OVERTOPPING WAVES .....	1016
<i>Kimihiko Endoh, Shigeo Takahashi</i>	
Chapter 75	
WAVE OVERTOPPING ON VERTICAL AND COMPOSITE BREAKWATERS.....	1030
<i>L. Franco, M. de Gerloni, J.W. van der Meer</i>	
Chapter 76	
AN INVESTIGATION OF THE WAVE FORCES ACTING ON BREAKWATER HANDRAILS.....	1046
<i>Atsushi Hujii, Shigeo Takahashi, Kimihiko Endoh</i>	
Chapter 77	
RUBBLE MOUND BREAKWATER STABILITY UNDER OBLIQUE WAVES: AN EXPERIMENTAL STUDY .....	1061
<i>J.-C. Galland</i>	
Chapter 78	
WAVE LOADS ON SEADYKES WITH COMPOSITE SLOPES & BERMS .....	1075
<i>Joachim Grune, Hendrik Bergmann</i>	
Chapter 79	
COMPUTERISED METHODOLOGY TO MEASURE RUBBLE MOUND BREAKWATER DAMAGE.....	1090
<i>Bruno Chilo, Franco Guiducci</i>	



Chapter 80	
WAVE BREAKING OVER PERMEABLE SUBMERGED BREAKWATERS .....	1101
<i>Masataro Hattori, Hiroyoki Sakai</i>	
Chapter 81	
WAVE FORCES ACTING ON A VORTEX EXCITED VIBRATING	
VERTICAL CYLINDER IN WAVES .....	1115
<i>Kenjiro Hayashi, Futoshi Higaki, Koji Fujima,</i>	
<i>Toshiyuki Sigemura, John R. Chaplin</i>	
Chapter 82	
OVERTOPPING OF SEA WALLS UNDER RANDOM WAVES .....	1130
<i>D.M. Herbert, N.W.H. Allsop, M.W. Owen</i>	
Chapter 83	
STABILITY OF HIGH-SPECIFIC GRAVITY ARMOR BLOCKS .....	1143
<i>Masahiro Ito, Y. Iwagaki, H. Murakami, K. Nemoto, M. Yamamoto,</i>	
<i>M. Hanzawa</i>	
Chapter 84	
ROCK ARMoured BEACH CONTROL STRUCTURES ON	
STEEP BEACHES .....	1157
<i>R.J. Jones, N.W.H. Allsop</i>	
Chapter 85	
EFFECT ON ROUGHNESS TO IRREGULAR WAVE RUN-UP.....	1169
<i>Jea-Tzyy Juang</i>	
Chapter 86	
WAVE OVERTOPPING OF BREAKWATERS UNDER OBLIQUE WAVES.....	1182
<i>Jørgen Juhl, Peter Sloth</i>	
Chapter 87	
CONSTRUCTION OF OFFSHORE FISHING PORT FOR PREVENTION	
OF COASTAL EROSION .....	1197
<i>Takeshi Kawaguchi, O. Hashimoto, T. Mizumoto, A. Kamata</i>	
Chapter 88	
TOPOGRAPHICAL CHANGE AROUND MULTIPLE LARGE	
CYLINDRICAL STRUCTURES UNDER WAVE ACTIONS.....	1212
<i>Chang-Je Kim, Koichiro Iwata, Yoshihito Miyaike, Hong-Sun Yu</i>	

Chapter 89	
STABILITY OF RUBBLE MOUND FOUNDATIONS OF COMPOSITE BREAKWATERS UNDER OBLIQUE WAVE ATTACK .....	1227
<i>Katsutoshi Kimura, Shigeo Takahashi, Katsutoshi Tanimoto</i>	
Chapter 90	
ANALYSIS OF NONLINEAR COEFFICIENTS OF REFLECTION AND TRANSMISSION OF WAVES PROPAGATING OVER A RECTANGULAR STEP .....	1241
<i>Wudhipong Kittitanasuan, Yoshimi Goda</i>	
Chapter 91	
OSCILLATORY MOTIONS AND PERMANENT DISPLACEMENTS OF CAISSON BREAKWATERS SUBJECT TO IMPULSIVE BREAKING WAVE LOADS.....	1255
<i>P. Klammer, H. Oumeraci, H.-W. Partenscky</i>	
Chapter 92	
HYDRAULIC CHARACTERISTICS AND FIELD EXPERIENCE OF NEW WAVE DISSIPATING CONCRETE BLOCKS (ACCROPODE) .....	1269
<i>Masanori Kobayashi, Sumio Kaihatsu</i>	
Chapter 93	
EXPERIMENTAL STUDY ON DEVELOPING PROCESS OF LOCAL SCOUR AROUND A VERTICAL CYLINDER.....	1284
<i>Tomonao Kobayashi, Kenji Oda</i>	
Chapter 94	
WAVE-INDUCED UPLIFT LOADING OF CAISSON BREAKWATERS .....	1298
<i>Andreas Kortenhaus, Hocine Oumeraci, Søren Kohlhase, Peter Klammer</i>	
Chapter 95	
LINEAR AND NONLINEAR WAVE FORCES EXERTED ON A SUBMERGED HORIZONTAL PLATE.....	1312
<i>Haruyuki Kojima, A. Yoshida, T. Nakamura</i>	
Chapter 96	
MODERN FUNCTIONAL DESIGN OF GROIN SYSTEMS .....	1327
<i>Nicholas C. Kraus, Hans Hanson, Sten H. Blomgren</i>	
Chapter 97	
RESHAPING BREAKWATERS IN DEEP AND SHALLOW WATER CONDITIONS.....	1343
<i>A. Lamberti, G.R. Tomasicchio, F. Guiducci</i>	

Chapter 98	
DESIGN OF BREAKWATERS AND BEACH NOURISHMENT .....	1359
<i>Christian Laustrup, Holger Toxvig Madsen</i>	
Chapter 99	
CIRCULAR CHANNEL BREAKWATER TO REDUCE WAVE OVERTOPPING AND ALLOW WATER EXCHANGE .....	1373
<i>Dal Soo Lee, Woo Sun Park, Nobuhisa Kobayashi</i>	
Chapter 100	
INCREASED DOLOS STRENGTH BY SHAPE MODIFICATION .....	1388
<i>S.A. Luger, D.T. Phelp, A. Van Tonder, A.H. Holtzhausen</i>	
Chapter 101	
INFLUENCE OF WAVE DIRECTIONALITY ON STABILITY OF BREAKWATER HEADS.....	1397
<i>Y. Matsumi, E.P.D. Mansard, J. Rutledge</i>	
Chapter 102	
COST-EFFECTIVENESS OF D-ARMOR BREAKWATER.....	1412
<i>Josep R. Medina</i>	
Chapter 103	
THE CORE-LOC: OPTIMIZED CONCRETE ARMOR.....	1426
<i>Jeffrey A. Melby, George F. Turk</i>	
Chapter 104	
STABILITY OF ARMOR STONES OF A SUBMERGED WIDE-CROWN BREAKWATER .....	1439
<i>Norimi Mizutani, Teofilo Monge Rufin, Jr., Koichiro Iwata</i>	
Chapter 105	
WAVE INDUCED FLOW AROUND SUBMERGED SLOPING PLATES.....	1454
<i>Hitoshi Murakami, Sadahiko Itoh, Yoshihiko Hosoi, Yoshiyuki Sawamura</i>	
Chapter 106	
SECOND-ORDER WAVE INTERACTION WITH ARRAYS OF VERTICAL CYLINDERS OF ARBITRARY CROSS SECTION .....	1469
<i>Keisuke Murakami, Akinori Yoshida</i>	
Chapter 107	
HYDRODYNAMIC FORCES ON BOTTOM-SEATED HEMISPHERE IN WAVES AND CURRENTS.....	1484
<i>Hidenori Nishida, A. Tada, F. Nishihira</i>	

Chapter 108	
THE PRESSURE FIELD DUE TO STEEP WATER WAVES INCIDENT ON A VERTICAL WALL .....	1496
<i>D.H. Peregrine, M.E. Topliss</i>	
Chapter 109	
RESULTS OF EXTENSIVE FIELD MONITORING OF DOLOS BREAKWATERS.....	1511
<i>D. Phelps, S. Luger, A. Van Tonder, A. Holtzhausen</i>	
Chapter 110	
FAILURE OF RUBBLE MOUND STRUCTURES DUE TO THE STORM DURATION AND THE IRREGULARITY OF OCEAN WAVES .....	1526
<i>Cheong-Ro Ryu, Hyeon-Ju Kim</i>	
Chapter 111	
BLOCK SUBSIDENCE UNDER PRESSURE AND FLOW .....	1541
<i>T. Sakai, H. Gotoh, T. Yamamoto</i>	
Chapter 112	
STABILITY OF ROCK ON BEACHES.....	1553
<i>Gerrit J. Schiereck, Henri L. Fontijn, Wout V. Grote, Paul G.J. Sijstermans</i>	
Chapter 113	
SHORT TERM WAVE OVERTOPPING RATE OF BLOCK ARMORED SEAWALL .....	1568
<i>Tsunehiro Sekimoto, Hiroshi Kunisu, Tsuyoshi Yamazaki</i>	
Chapter 114	
ESTIMATING THE SLIDING DISTANCE OF COMPOSITE BREAKWATERS DUE TO WAVE FORCES INCLUSIVE OF IMPULSIVE FORCES .....	1580
<i>Kenichiro Shimosako, S. Takahashi, K. Tanimoto</i>	
Chapter 115	
BED SHEAR STRESS AND SCOUR AROUND COASTAL STRUCTURES .....	1595
<i>B.M. Sumer, J. Fredsøe, N. Christiansen, S.B. Hansen</i>	
Chapter 116	
LABORATORY MEASUREMENT OF OBLIQUE IRREGULAR WAVE REFLECTION ON RUBBLE-MOUND BREAKWATERS.....	1610
<i>Charles Teisson, Michel Benoit</i>	

Chapter 117	
STONE MOVEMENT ON A RESHAPED PROFILE .....	1625
<i>G. Roberto Tomasicchio, A. Lamberti, F. Guiducci</i>	
Chapter 118	
THE LARGE SCALE DOLOS FLUME STUDY.....	1641
<i>George F. Turk, Jeffrey A. Melby</i>	
Chapter 119	
H <sub>0</sub> PARAMETER FOR PRELIMINARY DESIGN OF CONVENTIONAL BREAKWATER STRUCTURAL HEAD: DATA ANALYSIS OF SPANISH NORTH COAST HARBOURS .....	1657
<i>Vincente Negro Valdecantos, Ovidio Varela Carnero</i>	
Chapter 120	
NUMERICAL MODELLING OF BREAKING WAVE IMPACTS ON A VERTICAL WALL .....	1672
<i>N.T. Wu, H. Oumeraci, H.-W. Partenscky</i>	
Chapter 121	
WIND EFFECTS ON RUNUP AND OVERTOPPING .....	1687
<i>Donald L. Ward, Christopher G. Wibner, Jun Zhang, Billy L. Edge</i>	
Chapter 122	
MODELLING OF WAVE OVERTOPPING OVER BREAKWATER.....	1700
<i>F. Zhuang, C. Chang, J.J. Lee</i>	
Chapter 123	
STRESSES IN TETRAPOD ARMOR UNITS INDUCED BY WAVE ACTION.....	1713
<i>Kees d'Angremond, J.W. van der Meer, C.P. van Nes</i>	
Chapter 124	
PORE PRESSURES IN RUBBLE MOUND BREAKWATERS.....	1727
<i>M.B. de Groot, H. Yamazaki, M.R.A. van Gent, Z. Kheyruri</i>	
Chapter 125	
WAVE ACTION ON AND IN PERMEABLE STRUCTURES.....	1739
<i>M.R.A. van Gent, P. Tönjes, H.A.H. Petit, P. Van Den Bosch</i>	
Chapter 126	
PROBABILISTIC CALCULATIONS OF WAVE FORCES ON VERTICAL STRUCTURES.....	1754
<i>J.W. van der Meer, K. d'Angremond, J. Juhl</i>	

## PART IV

Chapter 127	
VELOCITY AND PRESSURE BOUNDARY CONDITIONS FOR FLOW OVER THE PERMEABLE BOUNDARY OF A POROUS MEDIUM.....	1770
<i>Ismail Aydin</i>	
Chapter 128	
PHYSICAL EXPERIMENTS ON THE EFFECTS OF GROINS ON SHORE MORPHOLOGY.....	1782
<i>Peyman Badiei, J. William Kamphuis, David G. Hamilton</i>	
Chapter 129	
LINE-MODELING OF SHOREFACE NOURISHMENT .....	1797
<i>Willem T. Bakker, Nico F. Kersting, Hanz D. Niemeyer</i>	
Chapter 130	
STATISTICAL VARIATIONS IN BEACH PARAMETER CHANGE RATES FOR WALLED & NON-WALLED PROFILES AT SANDBRIDGE, VA.....	1812
<i>John M. Hazelton, David R. Basco, D. Bellomo, G. Williams</i>	
Chapter 131	
A BOTTOM BOUNDARY LAYER SEDIMENT RESPONSE TO WAVE GROUPS .....	1827
<i>J. Lee, S. O'Neil, K. Bedford, R. Van Evra</i>	
Chapter 132	
GEOMORPHOLOGICAL ANALYSIS OF A BEACH AND SANDBAR SYSTEM.....	1837
<i>Chen-Shan Kung, Marcer Stive, Geffery Toms</i>	
Chapter 133	
SUSPENDED SEDIMENT TRANSPORT IN INNER SHELF WATERS DURING EXTREME STORMS.....	1849
<i>O.S. Madsen, T.A. Chisholm, L.D. Wright</i>	
Chapter 134	
SEA BED STABILITY ON A LONG STRAIGHT COAST.....	1865
<i>E. Christensen, R. Deigaard, J. Fredsoe</i>	
Chapter 135	
THE RESPONSE OF GRAVEL BEACHES IN THE PRESENCE OF CONTROL STRUCTURES .....	1880
<i>T.T. Coates, N. Dodd</i>	

Chapter 136	
THE ROLE OF ROLLERS IN SURF ZONE CURRENTS .....	1895
<i>William R. Dally, Daniel A. Osiecki</i>	
Chapter 137	
THREE DIMENSIONAL MORPHOLOGY IN A NARROW WAVE TANK: MEASUREMENTS AND THEORY .....	1906
<i>Robert G. Dean, Tae-Myoung Oh</i>	
Chapter 138	
NUMERICAL SIMULATION OF FINITE AMPLITUDE SHEAR WAVES & SEDIMENT TRANSPORT .....	1919
<i>Rolf Deigaard, Erik Damgaard Christensen, Jesper Svarrer Damgaard, Jørgen Fredsøe</i>	
Chapter 139	
BEACH NOURISHMENT AND DUNE PROTECTION .....	1934
<i>Hans H. Dette, Arved J. Raudkivi</i>	
Chapter 140	
PROFILE CHANGE OF A SHEET FLOW DOMINATED BEACH .....	1946
<i>Mohammad Dibajnia, Takuzo Shimizu, Akira Watanabe</i>	
Chapter 141	
A NONLINEAR SURF BEAT MODEL .....	1961
<i>Zhili Zou, Nicholas Dodd</i>	
Chapter 142	
PIV MEASUREMENTS OF OSCILLATORY FLOW OVER A RIPPLED BED....	1975
<i>H.C. Earnshaw, T. Bruce, C.A. Greated, W.J. Easson</i>	
Chapter 143	
SHEAR INSTABILITY OF LONGSHORE CURRENTS: EFFECTS OF DISSIPATION AND NON-LINEARITY .....	1983
<i>Albert Falqués, Vicente Iranzo, Miquel Caballería</i>	
Chapter 144	
INTERPRETATION OF SHORELINE POSITION FROM AERIAL PHOTOGRAPHS .....	1998
<i>John S. Fisher, Margery F. Overton</i>	

Chapter 145	
SETTLING COLUMNS PARAMETRIC TESTS APPLIED TO COASTAL SEDIMENT CONSOLIDATION.....	2004
<i>Stephane Gallois, Alain Alexis, Pierre Thomas</i>	
Chapter 146	
SEDIMENT-CLOUD BASED MODEL OF SUSPENSION OVER RIPPLE BED DUE TO WAVE ACTION .....	2013
<i>Hitoshi Gotoh, Tetsuro Tsujimoto, Hiroji Nakagawa</i>	
Chapter 147	
WAVE OVERTOPPING AND SEDIMENT TRANSPORT OVER DUNES.....	2028
<i>Mark W. Hancock, Nobuhisa Kobayashi</i>	
Chapter 148	
SEDIMENT TRANSPORT OVER RIPPLES IN WAVES AND CURRENT .....	2043
<i>Gilles Perrier, Erik Asp Hansen, C. Villaret, Rolf Deigaard, Jorgen Fredsøe</i>	
Chapter 149	
IN-SITU DETERMINATION OF THE CRITICAL BED-SHEAR STRESS FOR EROSION OF COHESIVE SEDIMENTS.....	2058
<i>Erik-Jan Houwing, Leo C. van Rijn</i>	
Chapter 150	
CONTROL OF CROSS-SHORE SEDIMENT TRANSPORT BY A DISTORTED RIPPLE MAT .....	2070
<i>Isao Irie, N. Ono, S. Hashimoto, S. Nakamura, K. Murakami</i>	
Chapter 151	
HOW MUCH VELOCITY INFORMATION IS NECESSARY TO PREDICT SEDIMENT SUSPENSION IN THE SURF ZONE? .....	2085
<i>Bruce E. Jaffe, David M. Rubin, Asbury Sallenger, Jr.</i>	
Chapter 152	
BEACH PROFILE SPACING: PRACTICAL GUIDANCE FOR MONITORING NOURISHMENT PROJECTS.....	2100
<i>Timothy W. Kana, Christopher J. Andrassy</i>	
Chapter 153	
WATERTABLE OVERHEIGHT DUE TO WAVE RUNUP ON A SANDY BEACH.....	2115
<i>Hong-Yoon Kang, P. Nielsen, D.J. Hanslow</i>	



Chapter 154	
A MODEL FOR CROSS SHORE SEDIMENT TRANSPORT .....	2125
<i>Irene Katopodi, Nikos Kitou</i>	
Chapter 155	
NUMERICAL MODELLING OF FLOW OVER RIPPLES USING SOLA METHOD.....	2140
<i>Hyoseob Kim, Brian A. O'Connor, Youngbo Shim</i>	
Chapter 156	
SWASH DYNAMICS UNDER OBLIQUELY INCIDENT WAVES .....	2155
<i>Nobuhisa Kobayashi, Entin A. Karjadi</i>	
Chapter 157	
WAVE RUN-UP AND SEA CLIFF EROSION .....	2170
<i>S.-M. Shih, P. Komar, K.J. Tillotson, W.G. McDougal, P. Ruggiero</i>	
Chapter 158	
MEASUREMENT OF PARAMETERS, DIRECTION AND RATE OF BEDFORM MIGRATION .....	2185
<i>Ruben D. Kos'yan, I.S. Podymov</i>	
Chapter 159	
BREACH-GROWTH RESEARCH PROGRAMME AND ITS PLACE IN DAMAGE ASSESSMENT FOR A POLDER.....	2197
<i>Arie W. Kraak, W.T. Bakker, J. van de Graaff, H.J. Steetzel, P.J. Visser</i>	
Chapter 160	
SWASH ZONE WAVE CHARACTERISTICS FROM SUPERTANK .....	2207
<i>David L. Kriebel</i>	
Chapter 161	
MORPHOLOGICAL MONITORING OF A SHOREFACE NOURISHMENT NOURTEC EXPERIMENT AT TERSCHELLING, THE NETHERLANDS.....	2222
<i>Aart Kroon, Piet Hoekstra, Klass Houwman, Gerben Ruessink</i>	
Chapter 162	
NUMERICAL MODEL FOR LONGSHORE CURRENT DISTRIBUTION ON A BAR-TROUGH BEACH .....	2237
<i>Yoshiaki Kuriyama</i>	

Chapter 163	
PREDICTION OF BEACH PROFILE CHANGE AT MESOSCALE UNDER RANDOM WAVES .....	2252
<i>Magnus Larson</i>	
Chapter 164	
A QUASI-3D SURF ZONE MODEL .....	2267
<i>Jung Lyul Lee, Hsiang Wang</i>	
Chapter 165	
QUANTIFICATION OF LONGSHORE TRANSPORT IN THE SURF ZONE ON MACROTIDAL BEACHES .....	2282
<i>Franck Levoy, Olivier Monfort, Helene Rousset, Claude Larssonneur</i>	
Chapter 166	
A THREE DIMENSIONAL MODEL FOR WAVE INDUCED CURRENTS .....	2297
<i>Bin Li, Roger J. Maddrell</i>	
Chapter 167	
INFLUENCE OF OFFSHORE BANKS ON THE ADJACENT COAST .....	2311
<i>N.J. MacDonald, B.A. O'Connor</i>	
Chapter 168	
WAVE RUNUP ON COMPOSITE-SLOPE AND CONCAVE BEACHES .....	2325
<i>Robert H. Mayer, D.L. Kriebel</i>	
Chapter 169	
SIMULATION OF NEARSHORE WAVE CURRENT INTERACTION BY COUPLING A BOUSSINESQ WAVE MODEL WITH A 3D HYDRODYNAMIC MODEL .....	2340
<i>Roberto Mayerle, Andreas Schröter, Werner Zielke</i>	
Chapter 170	
EXPERIMENTAL RESULTS OF WAVE TRANSFORMATION ACROSS A SLOPING BEACH.....	2350
<i>Constantine D. Memos</i>	
Chapter 171	
A RELATIVE INTERCOMPARISON BETWEEN VARIABLE WAVE SHOALING, BREAKING AND TRANSITION ZONE FORMULATIONS .....	2365
<i>G.P. Mocke, F. Smit</i>	

Chapter 172	
ANALYSIS OF COASTAL PROCESSES AT TORONTO ISLANDS.....	2380
<i>R.B. Nairn, R.D. Scott, C.D. Anglin, P.J. Zuzek</i>	
Chapter 173	
STABILITY AND MANAGEMENT OF AN ARTIFICIAL BEACH.....	2395
<i>Naofumi Shiraishi, Hoiku Ohhama, Taiji Endo,</i> <i>Patricia G. Pena-Santana</i>	
Chapter 174	
SUSPENDED SEDIMENT PARTICLE MOTION IN COASTAL FLOWS.....	2406
<i>Peter Nielsen</i>	
Chapter 175	
LONG-TERM MORPHODYNAMICAL DEVELOPMENT OF THE EAST FRISIAN ISLANDS AND COAST .....	2417
<i>Hanz D. Niemeyer</i>	
Chapter 176	
FIELD OBSERVATION AND NUMERICAL SIMULATION OF BEACH AND DUNE SCARPS.....	2434
<i>Ryuichiro Nishi, Michio Sato, Hsiang Wang</i>	
Chapter 177	
EFFECTS OF CONTROLLED WATER TABLE ON BEACH PROFILE DYNAMICS .....	2449
<i>Tae-Myoung Oh, R.G. Dean</i>	
Chapter 178	
LABORATORY EXPERIMENTS ON 3-D NEARSHORE CURRENTS AND A MODEL WITH MOMENTUM FLUX BY BREAKING WAVES.....	2461
<i>Akio Okayasu, Koji Hara, Tomoya Shibayama</i>	
Chapter 179	
SUSPENDED SEDIMENT CAUSED BY WAVES AND CURRENTS .....	2476
<i>Masanobu Ono, Kyu Han Kim, Toru Sawaragi, Ichiro Deguchi</i>	
Chapter 180	
DEVELOPMENT OF A DUNE EROSION MODEL USING SUPERTANK DATA.....	2488
<i>Margery F. Overton, John S. Fisher, Kyu-Nam Hwang</i>	

Chapter 181	
NUMERICAL MODELLING OF THREE-DIMENSIONAL WAVE-DRIVEN CURRENTS IN THE SURF-ZONE.....	2503
<i>Philippe P��chon, Charles Teisson</i>	
Chapter 182	
SEDIMENT TRANSPORT IN VARIOUS TIME SCALES .....	2513
<i>Zbigniew Pruszk, Ryszard B. Zeidler</i>	
Chapter 183	
SEDIMENT TRANSPORT UNDER (NON)-LINEAR WAVES AND CURRETNS .....	2527
<i>Jan S. Ribberink, Irene Katopodi, Khaled A.H. Ramadan, Ria Koelewijn, Sandro Longo</i>	
Chapter 184	
WAVES AND CURRENTS AT THE EBRO DELTA SURF ZONE: MEASUREMENTS AND MODELLING .....	2542
<i>A. Rodriguez, A. S��nchez-Arcilla, F.R. Collado, V. Gracia, M.G. Coussirat, J. Prieto</i>	
Chapter 185	
A NUMERICAL SIMULATION OF BEACH EVOLUTION BASED ON A NONLINEAR DISPERSIVE WAVE-CURRENT MODEL .....	2557
<i>Shinji Sato, Michael B. Kabiling</i>	
Chapter 186	
AN EXPERIMENTAL STUDY ON BEACH TRANSFORMATION DUE TO WAVES UNDER THE OPERATION OF COASTAL DRAIN SYSTEM.....	2571
<i>Michio Sato, Sadakatsu Hata, Masahiro Fukushima</i>	
Chapter 187	
WAVE BREAKING AND INDUCED NEARSHORE CIRCULATIONS .....	2583
<i>Ole R. S��rensen, Hemming A. Sch��ffer, Per A Madsen, Rolf Deigaard</i>	
Chapter 188	
ACCURACY AND APPLICABILITY OF THE SPM LONGSHORE TRANSPORT FORMULA.....	2595
<i>J.S. Schoonees, A.K. Theron</i>	

Chapter 189	
FIELD VERIFICATION OF A NUMERICAL MODEL OF BEACH TOPOGRAPHY CHANGE DUE TO NEARSHORE CURRENTS, UNDERTOW AND WAVES .....	2610
<i>Takuzo Shimizu, Masahito Tsuru, Akira Watanabe</i>	
Chapter 190	
AN ATTEMPT TO MODEL LONGSHORE SEDIMENT TRANSPORT ON THE CATALONIAN COAST .....	2625
<i>J.P. Sierra, A.I. Presti, A. Sánchez-Arcilla</i>	
Chapter 191	
EROSION AND OVERTOPPING OF A GRASS DIKE LARGE SCALE MODEL TESTS .....	2639
<i>G.M. Smith, J.W.W. Seijffert, J.W. van der Meer</i>	
Chapter 192	
CALCULATION OF TOMBOLO IN SHORELINE NUMERICAL MODEL.....	2653
<i>Kyung Duck Suh, C. Scott Hardaway, Jr.</i>	
Chapter 193	
BEACH IMPROVEMENT SCHEMES IN FALSE BAY .....	2668
<i>D.H. Swart, J.S. Schoonees</i>	
Chapter 194	
BEACH EROSION IN KUTA BEACH, BALI & ITS STABILIZATION .....	2683
<i>Abdul R. Syamsudin, Yoshito Tsuchiya, Takao Yamashita</i>	
Chapter 195	
FUNDAMENTAL CHARACTERISTICS OF A NEW WAVE ABSORBING SYSTEM UTILIZING SAND LIQUEFACTION .....	2698
<i>Shigeo Takahashi, S. Yamamoto, H. Miura</i>	
Chapter 196	
LABORATORY STUDY OF SURF-ZONE TURBULENCE ON A BARRED BEACH .....	2712
<i>Francis C.K. Ting</i>	
Chapter 197	
BEACH EROSION AROUND A SAND SPIT—AN EXAMPLE OF MIHONO-MATSUBARA SAND SPIT .....	2726
<i>Takaaki Uda, Koji Yamamoto</i>	

Chapter 198	
SHORECIRC: A QUASI 3-D NEARSHORE MODEL .....	2741
<i>A.R. Van Dongeren, F.E. Sancho, I.A. Svendsen, U. Putrevu</i>	
Chapter 199	
A MODEL FOR BREACH GROWTH IN SAND-DIKES.....	2755
<i>Paul J. Visser</i>	
Chapter 200	
SCALING EFFECTS ON BEACH RESPONSE PHYSICAL MODEL .....	2770
<i>Xu Wang, Li-Hwa Lin, Hsiang Wang</i>	
Chapter 201	
A NUMERICAL MODEL OF BEACH CHANGE DUE TO SHEET-FLOW .....	2785
<i>Akira Watanabe, Kazuhiko Shiba, Masahiko Isobe</i>	
Chapter 202	
FIELD TESTS OF RADIATION-STRESS ESTIMATORS OF LONGSHORE SEDIMENT-TRANSPORT .....	2799
<i>Thomas E. White</i>	
Chapter 203	
SUSPENDED SEDIMENT CONCENTRATION PROFILES UNDER NON-BREAKING AND BREAKING WAVES .....	2813
<i>Rattanapitikon Winyu, Tomoya Shibayama</i>	
Chapter 204	
MASS TRANSPORT AND ORBITAL VELOCITIES WITH LAGRANGEIAN FRAME OF REFERENCE .....	2828
<i>Stefan Woltering, Karl-Friedrich Daemrich</i>	
Chapter 205	
CROSS-SHORE PROFILE MODELLING UNDER RANDOM WAVES.....	2843
<i>Yongjun Wu, H-H Dette, H. Wang</i>	
Chapter 206	
MULTIPLE BAR FORMATION BY BREAKER-INDUCED VORTICES: A LABORATORY APPROACH.....	2856
<i>Da Ping Zhang, Tsuguo Sunamura</i>	
Chapter 207	
IDENTIFICATION OF SOME RELEVANT PROCESSES IN COASTAL MORPHOLOGICAL MODELLING.....	2871
<i>Hakeem Johnson, Ida Brøker, Julio A. Zyserman</i>	

Chapter 208	
EXPERIMENTAL SHOREFACE NOURISHMENT, TERSCHELLING, (NL) .....	2886
<i>J.P.M. Mulder, J. van de Kreeke, P. van Vessem</i>	

## PART V

Chapter 209	
IMPORTANCE OF PERMEABILITY IN THE SEDIMENTATION CONSOLIDATION PROCESS.....	2902
<i>Alain Alexis, P. Thomas</i>	

Chapter 210	
WAVE-CURRENT INTERACTION WITH MUD BED .....	2913
<i>Nguyen Ngoc An, T. Shibayama</i>	

Chapter 211	
ON RESIDUAL TRANSPORT IN SHALLOW TIDAL BASINS .....	2928
<i>Andrea Balzano</i>	

Chapter 212	
THE EXTENT OF INLET IMPACTS UPON ADJACENT SHORELINES .....	2943
<i>Kevin R. Bodge</i>	

Chapter 213	
THE SPREADING OF DREDGING SPOILS DURING CONSTRUCTION OF THE DENMARK-SWEDEN LINK.....	2958
<i>Ida Brøker, John Johnsen, Morten Lintrup, Anders Jensen, Jacob Steen Møller</i>	

Chapter 214	
EXPERIMENTAL STUDIES ON THE EFFECT OF THE DREDGING ON CHANG-HWA RECLAMATION AREA, TAIWAN .....	2972
<i>Tai-Wen Hsu, Hsien-Kuo Chang</i>	

Chapter 215	
OSCILLATIONS INDUCED BY IRREGULAR WAVES IN HARBOURS .....	2987
<i>C.R. Chou, W.Y. Han</i>	

Chapter 216	
MECHANISM AND ESTIMATION OF SEDIMENTATION IN BANGKOK BAR CHANNEL.....	3002
<i>Chiro Deguchi, Toru Sawaragi, Masanobu Ono, Sucharit Koontanakulvong</i>	

Chapter 217	
TURBIDITY & SUSPENDED SEDIMENT ASSOCIATED WITH BEACH NOURISHMENT DREDGING .....	3016
<i>Daniel M. Hanes</i>	
Chapter 218	
SOIL MECHANICS OF SHIP BEACHING .....	3030
<i>N.-E. Ottesen Hansen, B.C. Simonsen, M.J. Sterndorff</i>	
Chapter 219	
THE DILUTION PROCESSES OF ALTERNATIVE HORIZONTAL BUOYANT JETS IN WAVE MOTION .....	3045
<i>Hwung-Hweng Hwung, Jih-Ming Chyan, Chen-Yue Chang, Yih-Far Chen</i>	
Chapter 220	
STUDY ON THE BEHAVIORS OF THE COHESIVE SEDIMENT IN THE YANGTZE ESTUARY .....	3060
<i>Xiaochuan Zeng, Yixin Yan, Kai Yen</i>	
Chapter 221	
DISPERSION OF POLLUTION IN A WAVE ENVIRONMENT .....	3071
<i>R. Koole, C. Swan</i>	
Chapter 222	
MODEL OF BIVALVE ON/OFFSHORE MOVEMENT BY WAVES .....	3086
<i>Hisami Kuwahara, Junya Higano</i>	
Chapter 223	
INITIAL GAP IN BREAKOUT OF HALF-BURIED SUBMARINE PIPE DUE TO WAVE ACTION .....	3099
<i>Adrian W.K. Law, M.A. Foda</i>	
Chapter 224	
ANALYTICAL SOLUTION FOR THE WAVE-INDUCED EXCESS PORE-PRESSURE IN A FINITE-THICKNESS SEABED LAYER.....	3111
<i>Waldemar Magda</i>	
Chapter 225	
RESPONSE CHARACTERISTICS OF RIVER MOUTH TOPOGRAPHY IN WIDE TIME SCALE RANGE.....	3126
<i>A. Mano, M. Sawamoto, M. Nagao</i>	



Chapter 226	
HALF-LIFE PERIOD OF SEDIMENTATION—MODEL TEST ON A SCALE 1:1 .....	3139
<i>Helmut Manzenrieder</i>	
Chapter 227	
RISK ASSESSMENT FOR COASTAL AND TIDAL DEFENCE SCHEMES.....	3154
<i>I.C. Meadowcroft, P.H. von Lany, N.W.H. Allsop, D.E. Reeve</i>	
Chapter 228	
WATER OXYGENATION IN THE VICINITY OF COASTAL STRUCTURES DUE TO WAVE BREAKING .....	3167
<i>C.I. Moutzouris, E.I. Daniil</i>	
Chapter 229	
ENVIRONMENTAL ASSESSMENT OF HYPOTHETICAL LARGE-SCALE RECLAMATION IN OSAKA BAY, JAPAN.....	3178
<i>Keiji Nakatsuji, Toshiaki Sueyoshi, Kohji Muraoka</i>	
Chapter 230	
FLOOD AND EROSION CONTROL IN THE CONTEXT OF SEA-LEVEL RISE.....	3193
<i>E. Bart Peerbolte, Herman G. Wind</i>	
Chapter 231	
OFFSHORE BREAKWATERS VERSUS BEACH NOURISHMENTS— A COMPARISON.....	3208
<i>M. Pluijm, J.C. van der Lem, A.W. Kraak, J.H.W. de Ruig</i>	
Chapter 232	
MORPHOLOGICAL MODELLING OF KETA LAGOON CASE .....	3223
<i>J.A. Roelvink, D.J.R. Walstra, Z. Chen</i>	
Chapter 233	
COST-BENEFIT ANALYSIS OF SHORE PROTECTION INVESTMENTS.....	3237
<i>L. Felipe Vila Ruiz, Fernando Bernaldo de Quirós</i>	
Chapter 234	
PARAMETRIZATION FOR CONCEPTUAL MORPHODYNAMIC MODELS OF WADDEN SEA AREAS .....	3251
<i>Ernst Schroeder, R. Goldenbogen, H. Kunz</i>	

Chapter 235	
MUD TRANSPORT AND MUDDY BOTTOM DEFORMATION BY WAVES .....	3266
<i>Daoxian Shen, Masahiko Isobe, Akira Watanabe</i>	
Chapter 236	
WAVE-INDUCED SEDIMENT RESUSPENSION AND MIXING IN SHALLOW WATERS.....	3281
<i>Y. Peter Sheng, X. Chen, E.A. Yassuda</i>	
Chapter 237	
A NUMERICAL MODEL FOR BEACH DEFORMATION AROUND RIVER MOUTH DUE TO WAVES AND CURRENTS.....	3295
<i>Tomoya Shibayama, Akiko Yamada</i>	
Chapter 238	
DEVELOPMENT OF A NUMERICAL SIMULATION METHOD FOR PREDICTING THE SETTLING BEHAVIOR & DEPOSITION CONFIGURATION OF SOIL DUMPED INTO WATERS .....	3305
<i>Kazuki Oda, Takaaki Shigematsu</i>	
Chapter 239	
PLANE DESIGN OF “SPAC”; COUNTERMEASURE AGAINST SEABED SCOUR DUE TO SUBMERGED DISCHARGE AND LARGE WAVES .....	3320
<i>Takao Shimizu, Masaaki Ikeno, Hisayoshi Ujite, Kazuaki Yamauchi</i>	
Chapter 240	
MODELLING AND ANALYSIS TECHNIQUES TO AID MINING OPERATIONS ON THE NAMIBIAN COASTLINE .....	3335
<i>G.G. Smith, G.P. Mocke, D.H. Swart</i>	
Chapter 241	
ENGINEERING APPROACH TO COASTAL FLOW SLIDES .....	3350
<i>Theo P. Stoutjesdijk, Maarten B. de Groot, Jaap Lindenberg</i>	
Chapter 242	
EROSION OF LAYERED SAND-MUD BEDS IN UNIFORM FLOW.....	3360
<i>Hilde Torfs</i>	
Chapter 243	
STANDING WAVE INDUCED SOIL RESPONSE IN A POROUS SEABED .....	3369
<i>Ching-Piao Tsai, Tsong-Lin Lee</i>	

Chapter 244	
EROSION CONTROL BY CONSIDERING LARGE SCALE COASTAL BEHAVIOR .....	3378
<i>Yoshito Tsuchiya, Takao Yamashita, Tatsuhisa Izumi</i>	
Chapter 245	
SHORELINE EROSION DUE TO OFFSHORE TIN MINING.....	3393
<i>Suphat Vongvisessomjai</i>	
Chapter 246	
BEHAVIORS OF FLUID MUD UNDER OSCILLATORY FLOW .....	3408
<i>Hiroyuki Yamanishi, Tetsuya Kusuda</i>	
Chapter 247	
FORMATION OF HABITATS FOR BIVALVES BY PORT AND HARBOR STRUCTURES .....	3420
<i>Kenji Yano, S. Akeda, Y. Miyamoto, S. Kuwabara</i>	
Chapter 248	
USE OF THREE-DIMENSIONAL HYDRODYNAMICS MODEL FOR TIDAL INLETS STUDIES .....	3432
<i>E.A. Yassuda, Y.P. Sheng</i>	
Chapter 249	
STUDY OF UPWELLING PHENOMENA OF ANOXIC WATER “A-OSHIO” ....	3447
<i>Jong Seong Yoon, Keiji Nakatsuji, Kouji Muraoka</i>	
Chapter 250	
SEA LEVEL RISE AND COAST EVOLUTION IN POLAND.....	3462
<i>Ryszard B. Zeidler</i>	

## PART VI

Chapter 251	
FORMATION OF DYNAMICALLY STABLE SANDY BEACHES ON AMANOHASHIDATE COAST BY SAND BYPASSING .....	3478
<i>Ikuo Chin, Minoru Yamada, Yoshito Tsuchiya</i>	
Chapter 252	
THE RECONSTRUCTION OF FOLLY BEACH .....	3491
<i>Billy L. Edge, Millard Dowd, Robert G. Dean, Patrick Johnson</i>	

Chapter 253	
THE COMPLEMENTARY INTERACTION BETWEEN BEACH NOURISHMENT AND HARBOUR MANAGEMENT: FOUR CASES IN SPAIN .....	3507
<i>Gregorio Gómez-Pina, Jose L. Ramírez</i>	
Chapter 254	
WAVE IMPACTS ON THE EASTERN SCHELDT BARRIER EVALUATION OF 5 YEARS FIELD MEASUREMENTS .....	3522
<i>Leo Klatter, Hans Janssen, Michiel Dijkman</i>	
Chapter 255	
SALINITY & WATER LEVELS IN THE WESER ESTUARY DURING THE LAST HUNDRED YEARS—ANTHROPOGENIC INFLUENCES ON THE COASTAL ENVIRONMENT .....	3533
<i>Hans Kunz</i>	
Chapter 256	
REVIEW OF SOME 30 YEARS BEACH REPLENISHMENT EXPERIENCE AT DUNGENESS NUCLEAR POWER STATION, UK .....	3548
<i>Roger Maddrell, Bill Osmond, Bin Li</i>	
Chapter 257	
PROJECT, WORKS AND MONITORING AT BARCELONA OLYMPIC BEACHES .....	3564
<i>Carlos Peña, Manuel F. Covarsi</i>	
Chapter 258	
SANTA CRISTINA BEACH NOURISHMENT WORKS AND MONITORING PROGRAM .....	3579
<i>Eduardo Toba, G. Gomez-Pina, J. Alvarez</i>	
Chapter 259	
DESIGN & CONSTRUCTION OF AN EXTENDED BERM BREAKWATER AT PORT OF HAINA, DOMINICAN REPUBLIC .....	3594
<i>David W. Yang, Mark H. Lindo, Edward J. Schmeltz, Joaquin Fernandez, Daniel Gomez</i>	
Chapter 260	
REHABILITATION OF THE WEST BREAKWATER— PORT OF SINES .....	3608
<i>Orville T. Magoon, J.R. Weggel, B.L. Edge, E. Mansard, R.W. Whalin, W.F. Baird</i>	

Subject Index .....	3615
Author Index .....	3621

## The Present and Future of Coastal Engineering in Japan

Yuichi Iwagaki<sup>1</sup>

The subject I am going to talk on is the present and future of Coastal Eng. in Japan, which is rather large-scale topics both in time and space. Because of the limits of my abilities and time appointed for this speech, I should like to scale down the subject in space, and focus on the present and future of Coastal Eng. in Kansai and Chubu regions, mainly in Osaka Bay Area including here, City of Kobe.

### Change in Coastal Engineering in Japan

I should like to start with describing very briefly a change in Coastal Eng. in Japan. As you all may know, the 1st International Conference on Coastal Eng. took place at Long Beach in 1950. Four years later, in 1954, the 1st Japanese Conference on Coastal Eng. was held here at Kobe. At this stage, we experienced frequent attacks of Typhoon that caused serious disasters. That is, if we count Typhoons that caused more than 100 death and missing for every ten years, 13 Typhoons occurred during the period from 1945 to 1954. But the number reduced very drastically to 5 from 1955 to 1964, and 4 from 1965 to 1974 (see, Table 1). This change reflected our research topics as shown in Table 2. Until 1964, Japanese Conference on Coastal Eng., which takes place every year, covered mainly the topics and problems of waves, storm surge, tsunami and coastal disasters. Around 1965, new study fields were introduced in the Conference; those include tidal currents, density currents, and sea water exchange. These new fields were motivated by the increased demand for reclamation in the coastal zone. At this stage, Japan was just entering a high-growth period of the economy. Eventually, the high level of

Table 1 Typhoon which generated over one hundred of killed and missing (after 1945)

date of occurrence	name of typhoon	killed and missing (persons)
1945. 9. 17	Makurazaki	3,756
1945. 10. 10	Akune	877
1947. 9. 13	Catharine	1,930
1947. 9. 15	Ion	838
1949. 6. 15	Delia	468
1949. 8. 15	Judith	179
1949. 8. 31	Kitty	160
1950. 9. 3	Jane	509
1951. 10. 13	Ruth	943
1952. 6. 22	Dinah	135
1953. 9. 24	No. 13	478
1954. 9. 10	No. 12	107
1954. 9. 25	Toyamaru	1,761
1958. 9. 26	Kanogawa	1,175
1959. 8. 12	No. 7	235
1959. 9. 26	Isewan	5,041
1961. 9. 15	Daini Muroto	202
1961. 10. 25	No. 26	114
1966. 9. 17	No. 24, 26	314
1968. 8. 10	Hidagawa	135
1971. 8. 27	No. 23, 25, 26	147
1974. 5. 29	No. 8	143
1975. 8. 5	No. 5, 6	143
1976. 9. 7	No. 17	169
1979. 10. 14	No. 20	111

<sup>1</sup> Dean, Faculty of Science and Technology, Meijo University, Shiogamaguchi 1-501, Tempaku-ku, Nagoya 468, Japan

Table 2 Change in topics of Coastal Engineering in Japan

Period	Special topics in Proc. of Coastal Eng., JSCE
1954 - 1964	Coastal disaster, Waves, Storm surge, Tsunami
1965 - 1979	Tidal current, Density current, Sea water exchange, Heated water discharge
1980 - at present	Water pollution, Environmental problem, Sea level rise

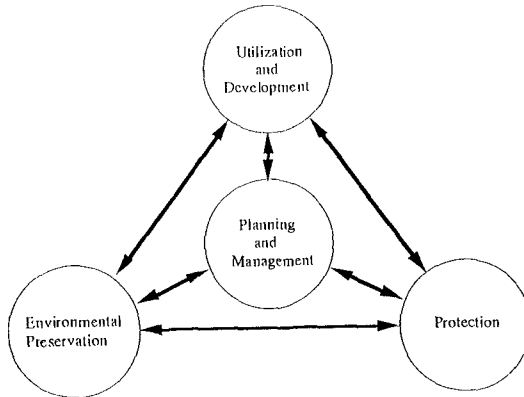


Fig.1 Mutual relation between coastal activities

economic growth brought various pollution problems. Water pollutants are one of the coastal problems. In 1976, we started to carry out study on the water quality, for example, the problems connected with dissolved oxygen. Since then, about 20 percent of the papers presented at the Japanese conference aims at the improvement of the water quality. I looked over the 93's proceedings, and found that 50 out of 236 papers, that comes up to 21 percent, still treats the environmental problems including the water pollution. The ratio seems to be unchanged for the last 25 years.

For the last 15 years, the preservation of coastal environments is highlighted. Global environment issues, especially sea level rise and its impact on the coastal zone become our problems. In addition, we become more and more aware of conservation of ecosystem and natural environment. Future coastal works have to be undertaken in a coordinated manner with the nature conservation. Fig.1 shows a conception of the coastal management. Further utilization of coastal resources has to be carefully planned satisfying the sometimes conflicting requirements of protection, development and conservation.

### Coastal Protection

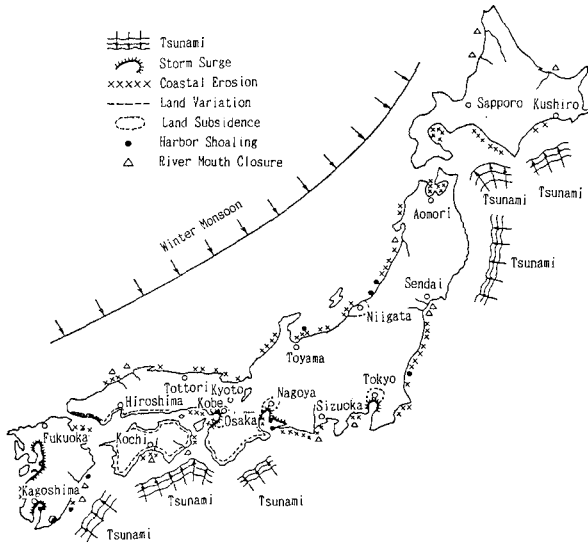


Fig.2 Illustrative map of usual coastal disaster places in Japan

Table 3 Storm surges of over 2m anomaly by typhoons during 1900-1987

date	place	max. anomaly (m)	cause
1917. 10. 1	Tokyo Bay	2.1	Typhoon
1930. 7. 18	Ariake Bay	2.5	Typhoon
1934. 9. 21	Osaka Bay	3.1	Ty. Muroto
1938. 9. 1	Tokyo Bay	2.2	Typhoon
1950. 9. 3	Osaka Bay	2.4	Ty. Jane
1956. 8. 17	Ariake Bay	2.4	Ty. No. 9
1959. 9. 26	Ise Bay	3.5	Ty. Isewan
1961. 9. 16	Osaka Bay	2~2.5	Ty. Daini Muroto
1964. 9. 25	Osaka Bay	2	Ty. No. 20
1965. 9. 10	East of Seto Island Sea	2.2	Ty. No. 23
1970. 8. 21	Tosa Bay	2.4	Ty. No. 10
1972. 9. 16	Ise Bay	2.0	Ty. No. 20

Next we will look briefly at the respective fields; coastal protection, utilization and environmental preservation in Japan, first at the coastal protection. Natural conditions surrounding the nation are very severe as one can tell from the geographical location of Japan. There is constant danger of the tsunami attack due to earthquake, the storm surge due to Typhoon, and the erosion due to waves (see, Fig.2). Since Japan belongs to Circum-Pacific earthquake belt, earthquakes and tsunamis associated with large earthquakes often occur. Many earthquakes caused severe damage, and tsunamis sometimes caused still more loss of life and property damage along the coastline. Japan also lies on the course of Typhoon born in Southern Ocean, and so suffers various disasters. The average number of Typhoons is 25 to 30 per year, 31 for this year up to



Table 4 Some examples of design waves

Name of Coast	Prefecture	Design Waves		note
		Wave Height (m)	Wave Period (sec)	
Tsugaru	Aomori	5.70	-	monsoon
Sakata	Yamagata	8.30	12.0	monsoon
Kaetsu	Fukui	8.30	14.0	monsoon
Kochi	Kochi	10.10	15.2	model Typhoon
Fuji-Yoshihara	Sizuoka	20.00	20.0	model Typhoon

now, and about 4 out of them strike Japan. Major coastal disasters caused by Typhoon are due to storm surges. Storm surge disasters often occur especially when Typhoon passes on the western side of large bay opening south, for example, Tokyo Bay, Ise Bay, Osaka Bay, Ariake Bay and Kagoshima Bay. Table 3 shows the area of storm surge and the name of Typhoon for period of 1900 through 1987 for the cases where the maximum meteorological tide anomaly exceeds 2 m. The largest anomaly was observed at the Nagoya Port due to the Ise Bay Typhoon in September 1959. It was recorded 3.5 m. Until now, for the past 90 years, this record is the largest. I myself carried out statistical analysis on the return period using the observed data for the past 42 years. My analysis gives that the return period of the value of 3.5m is 200 to 400 years.

By contrast, the coast of Japan Sea is most threatened with attack of the monsoon during winter. According to the record at Hajikizaki in Sado Island, the maximum velocity of the wind was 31.7 m/s, and the north-northwest wind continued to blow at more than 10m/s for 21 hours. High wind waves are generally developed, and thus the design wave height adopted for coastal dikes and revetments is typically 8 to 9 m and the period of 12 to 14 s. The design waves for the Pacific coast are generally based on the waves generated by Typhoons. For example, the design wave height and period for the Kochi Coast is 10.1m and 15.2s, and 20m and 20s for the Yoshihara Coast in Suruga Bay which is the maximum design wave in Japan (see, Table 4). Problems caused by action of such high waves are the beach erosion. Coastal erosion is influenced by various factors, but chiefly caused by a shortage of beach material supplied from the river, and by blocking the movement of the coastal sediment with the construction of port and harbor structures, and the reclamation. In other words, the beach erosion is a fatal problem associated with the utilization and the development of river and coastal zone.

We now look at the social environment of the coastal zone in Japan. There are 47 Prefectures in Japan. Among them, only 8 Prefectures, are not adjacent to the sea. These account for 14 percent in the total area and 15 percent in the total population. That is to say, 85 percent of the Japanese people are adjacent to the sea and receive benefit from the sea. The total population of Tokyo, Chiba and Kanagawa Prefectures along Tokyo Bay accounts for 20 percent, Aichi and Mie Prefectures occupy 7 percent in the total population, and Osaka, Hyogo and Wakayama Prefectures occupy 12 percent as summarized in Table 5. The total population of these three major bay areas comes up to 39 percent of the national population. A large city which has a population of more than one million is also distributed along these major bay areas; Tokyo, Yokohama and

Table 5 Concentration of population and cities in three bays

Name of bay	Population (million)	Name of city (over 1 million)
Tokyo	25.11 (20%)	Tokyo, Yokohama, Kawasaki
Ise	8.41 ( 7%)	Nagoya
Osaka	15.01 (12%)	Osaka, Kobe
Total	48.53 (39%)	

Kawasaki along Tokyo Bay, Nagoya along Ise Bay, and Osaka and Kobe along Osaka Bay. The population highly concentrates along these three bay areas. Major ports are also located along these bays; Port of Kobe, Chiba, Nagoya, Yokohama and Kawasaki. The volume of cargo handled at these five ports ranks top five in Japan. The ports along three major bays handle 75 percent of the total exports and 60 percent of the total imports.

Measures against storm surges were well planned and taken in three major bays, Tokyo Bay, Ise Bay and Osaka Bay where population and industry highly concentrate. Coastal dikes, seawalls and watergates were constructed to prevent sea water penetration. In designing these structures, the most disastrous Ise Bay Typhoon is generally used to determine the sea level and wave height assuming the typhoon route which generates the worst effect at the location of interest.

Tsunami countermeasures are very difficult to establish because the tsunami frequently attacks small towns located at the back of a deeply indented rias bay. The past highest tsunami record at the location of interest is used to determine the design sea level. Tsunami seawall 10m in height was constructed at Taro-cho in Iwate Prefecture, and tsunami breakwaters were constructed at Ofunato Bay in Iwate Prefecture and elsewhere. Recent tsunami disaster occurred in Okusiri Island due to the South West off Hokkaido in July 1993, however, indicates that even after the experience of the tsunami disaster due to the 1983 Japan Sea earthquake we were not able to prevent the disastrous damage and lost 200 lives. I believe that the best measures are to establish a speedy refuge system and a speedy and accurate warning system.

Needless to say, the forecasting and observation of incoming waves are essential to the coastal protection. As we all realize, ocean waves are not monochromatic but random, so in designing coastal structures the theory for monochromatic waves cannot be always applied to random wave transformation, random wave forces, random wave runup and overtopping. Dr. Yoshimi Goda, professor of Yokohama National University, has been investigating this problem for a long time, and successfully established a method for introducing the random wave property; for example, he introduced the directional spectrum into the design forces for port and harbor structures. His works on this problem should be recognized as a great success in coastal, port and harbor engineering

research in Japan. We are indeed proud of Dr. Goda. Recently, the coastal engineering committee of JSCE organized the subcommittee for the purpose of reviewing existing papers on the coastal waves, including the computing techniques of wave transformation, tsunami transmission, storm surge generation, wave-structure interaction and wave-soil interaction. The first work of the subcommittee was done and the result was published, in this July but unfortunately in Japanese.

I think that one of the most difficult problem we are faced with is beach erosion. As I said before, the beach erosion is mostly fatalistic in retaliation for revolution of nature by human. As countermeasures for the beach erosion, we used to adopt jetties, offshore breakwaters, sand nourishment works, bypassing works, artificial reefs, headland works and so on. These measures are, however, not permanent but temporal in most cases, which means we just gain time. We should try to enlarge time and space in our view, and reconsider the human activity once more. I believe that a fundamental countermeasure is tightly connected with our philosophy of nature in the human life.

### Utilization and Development of the Coastal Zone

There is not enough time to go into details, but I like to call your attention now to the utilization and development of the coastal zone. Japan extends 2,600 km from northern Hokkaido to southern Okinawa. Four islands, Hokkaido, Honsyu, Shikoku and Kyushu are connected each other by the long-span bridges and or submarine tunnels. At present, we have the vision of the national land axis, which is defined as the

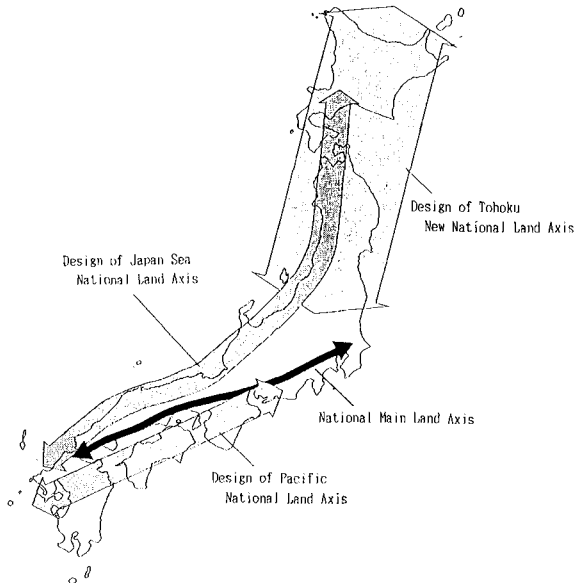


Fig.3 Proposed designs of New National Land Axis

common space providing information and communication, and the extensive economical area as sketched in Fig.3 . Along this axis, highways, railways, cities and industries are planned to develop. More recently, in addition to the main axis, various designs of new national land axis are proposed as shown in Fig.3 . Among the proposed axes, the most expected one is the Pacific new national land axis, which runs 800km from the western Kyushu to Chukyo Area through the central Kyushu, Shikoku, Awaji Island and Kii Peninsula. If this new design axis will be put into practice in the next century, long-span bridges across the channels or submarine tunnels will be constructed at Irako channel of the Ise Bay mouth, Tomogashima channel of the Osaka Bay mouth, and Hayasui channel between Kyushu and Shikoku Islands. These big projects will make coastal engineering researches more active , and contribute the further development of the coastal zones along the new axis.

One of the large-scale utilization at the coastal zone is by a man-made island. A typical example is an offshore airport. The first one in Japan is the Nagasaki Airport in Ohmura Bay, which was constructed on the small island, Minoshima, but needed some reclamation works. Nagasaki Airport was opened with the runway of 3,000m length in 1980. The second offshore airport is the Kansai International Airport, which many of you arrived at for this conference. The airport was open on September 4th of this year as the nation's first airport available for 24 hours. The present airport was constructed on the basis of the first stage plan. The construction of man-made island of 511ha needed seven years since starting the work. The expense was as much as 1 trillion 5 hundred billion yen and the soil for reclamation was as much as 180 million cubic meters. The airport is located 5km off the coast to keep the craft noise on the land less than a critical value 70 according to the WECPNL index (see, Fig.4) . The average water depth of the airport site is 18m . The geological survey of the seabed showed the alluvial clay layer of 20m thick, and below that, the Pleistocene clay layer. So, the foundation improvement was necessary to accelerate the consolidation settlement. The improvement by using over one million sand piles was actually performed for the alluvial clay layer. Expected average settlement of the whole airport is estimated 10m at the time of opening and 11.5m in 50 years as shown in Fig.5 . For the time being, additional reclamation of the offshore side is being investigated for the overall plan for 3 runways and 1,200 ha. area. As the currently planned offshore airports, we have Chubu International Airport in Ise Bay (see, Fig.6) , which is expected open in 2005, Kobe Airport expected open in 2003, and New Kitakyushu Airport in 2005. At the site of the Chubu International Airport, the Observation

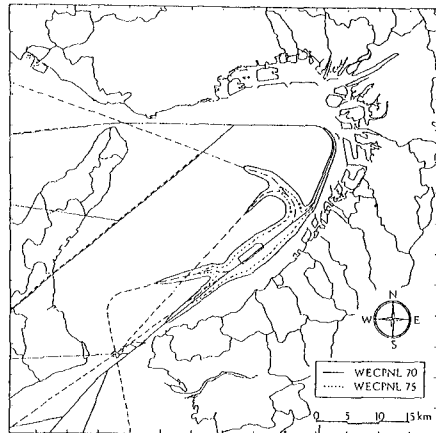


Fig.4 Aircraft noise estimation  
[WECPNL:Weighted Equivalent Continuous  
Perceived Noise Level]

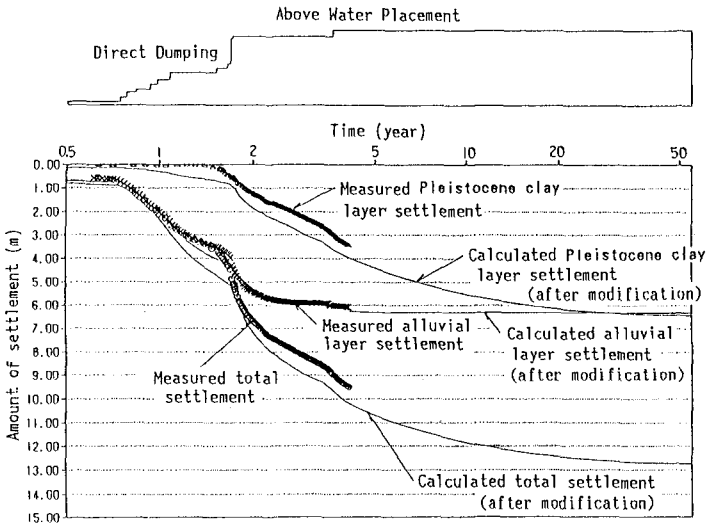


Fig 5 Comparison of calculated and observed settlement in the pilot area of the airport island (After Kansai International Airport Project, JSCE, Sept. 1992)

Tower for measuring various environmental factors has been already constructed and in operation.

I should like to make special mention of enactment of the special law for Osaka Bay Area Development in 1992. By this law, Osaka Bay Area is expected to develop greatly in the 21st century, and at present a grand design of the development by 2025 is under review.

Environmental Preservation

There are some other facilities for the utilization of coastal zone, such as reclamation for the waterfront industrial area and for the agricultural farm, electric power stations, oil storage station, seaports, fishery ports, waste disposal facilities, marinas and so on. The

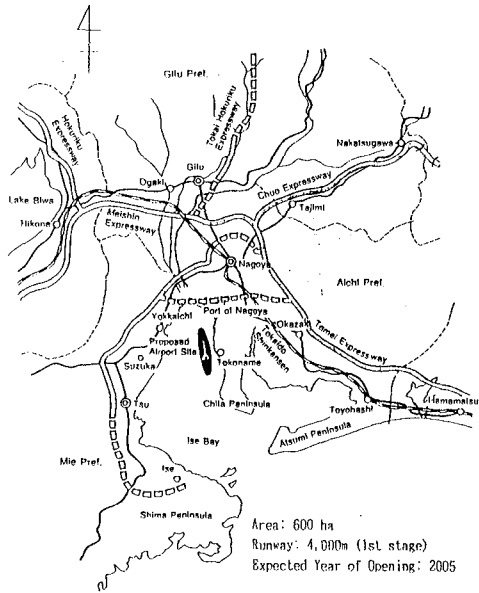


Fig.6 Proposed site of Chubu International Airport

The

construction of such facilities has much possibility of destroying natural environment and worsening living environment. The plan for the projects for the coastal zone is sometimes stopped and withdrawn by the opposition of residents, fishermen and nature-conservation groups. Whenever a big civil engineering project is planned, the environmental impact assessment has to be generally made by law. The further advancement of coastal engineering is definitely required to make a more precise assessment. For Seto Inland Sea including Osaka Bay, the special law named as Act on Special Measures for the Seto Inland Sea Environmental Conservation was enacted in 1978, which covers the various regulations concerning the environmental conservation. The development of Osaka Bay Area is subject to the regulations by this special law.

As for the improvement of water quality and landscape of the coastal zone, the methods of artificial beach nourishment, sand banking on the sea bottom, artificial formations of tideland and seaweed bed have been proposed. The effects of these improvement methods for the sea water quality have not been cleared yet.

More global environment issues arise from the fact that the atmospheric concentration of carbon dioxide has increased rapidly since the industrial revolution in the second half of the 18th century, and is still increasing at the rate of 1.5ppm per year. The rapid concentrations induce the greenhouse effect and warm the surface temperature of the earth. The mass added to oceans due to deglaciation and the thermal expansion of oceans' volume due to heat diffusion will result in the global sea level rise. According to IPPC, the sea level rise reaches 0.3m to 1.1m, in average 0.65m by the end of the 21st century. This problem is very important to coastal engineers. Recently, the subcommittee under the coastal engineering committee of JSCE has investigated the possible effects of sea level rise on the coasts in Japan and the possible countermeasures. The final report was published in July of this year. I think this report will stimulate the further progress of coastal engineering research.

### Concluding Remarks

In closing my speech, I should like to summarize my opinion to promote a sustainable development of the coastal zone. First of all, in planning coastal projects we should consider the harmony of mutual relations between the utilization and development, the protection and preservation, and the environmental conservation. This means Harmony with Nature, the key word of this conference. Secondly, from a viewpoint of the paradigm of coastal engineering, we should include not only the field based on the mechanics but also the field related to environmental problems in the research topics. Third, in planning coastal zone projects, we should consider the multifarious values, that is, not only the economical value but also the environmental and the social-cultural values. Finally, we should establish the mitigation engineering in the near future.



# **PART I**

## **Characteristics of Coastal Waves and Currents**





## CHAPTER 1

### On The Characteristics of One-Dimensional Spectra and Non-Dimensional Parameters of Wind Waves

Toshio Aono\*    Chiaki Goto\*\*

#### Abstract

Similarity relationship among non-dimensional significant wave parameters are discussed which is based upon the  $3/2$  power law. The characteristics of the wind wave spectra in deep water are investigated by using the parameters of JONSWAP spectrum and the  $3/2$  power law. From theoretical and empirical arguments, it is confirmed that a  $f^{-4}$  power law exists at high frequency range, that JONSWAP spectrum parameter  $\gamma$  and  $\sigma$  are varied with fetch, and that parameter  $\alpha$  and  $\gamma$  satisfied a  $-1/3$  power law. In shallow water region, spectral form of wind waves is varied with the shoaling coefficient. Through the analysis of the wind wave spectra, a new spectral formula is obtained.

#### 1. Introduction

Relationship between the marine surface wind and wind waves gives us the basic knowledge in field as diverse as air-sea interaction, wave hindcasting and engineering design of maritime structures.

Many researchers pointed out that the frequency spectra of wind-generated gravity waves shows similarity. It is well known that a similarity law is applicable to the spectral form of wind waves. Phillips (1959) derived the  $f^{-5}$  power law using the similarity and dimensional analysis argument. Many functional forms of the wind wave spectrum have been proposed in the past, such as Pierson-Moskowitz (1964), Bretshneider-Mitsuyasu (1970) and JONSWAP (1973). However, such spectral forms represent the fully developed condition of wind waves, except the

---

\* Senior Research Engineer, Technical Research Institute, Toa Corporation, 1-3 Anzen-cho, Tsurumi-ku, Yokohama 230, Japan

\*\* Professor, Department of Civil Engineering, Tokai Univ., 1117 Kitakaname, Hiratsuka city, Kanagawa 259-12, Japan

JONSWAP, so that in the case of rapid development of wind waves by typhoon, observed and calculated spectral forms do not show good agreement, especially near the peak frequency. Recently, Toba(1973) derived the  $f^4$  power law based on  $3/2$  power law. This argument of spectral gradient was related to the resistance law between the wind and the wind waves.

These characteristics of wind waves are investigated in deep water, but field observation data is limited at shallow water region, especially under high wave condition. The standard form of shallow water spectrum is proposed by Thornton (1977) and Bouse et. al (1985). These spectrum is based upon the  $f^5$  power law.

The present work reveals the quantitative relationship linking marine surface wind and wind waves. The paper discusses the significant wave parameters and the frequency spectrum of wind waves by using the  $3/2$  power law relation.

## 2. Observation of wave data

In this study, field observation wave data are used. To get long fetch wave data, 13 wave observation points around the coasts of Japan are used, and to get short fetch wave data, Meteorological station or MT station at Osaka bay is used.

### (1) Ocean wind waves

Figure. 1 shows the wave observation system called as NOWPHAS operated by Port and Harbour Research Institute, Ministry of Transport. There are 41 wave observation points. In this study, ocean wave data obtained at 13 major points around the Japan coast are used. These points are located at relatively deep water and there are no topography effects. Table 1 shows the observation systems and

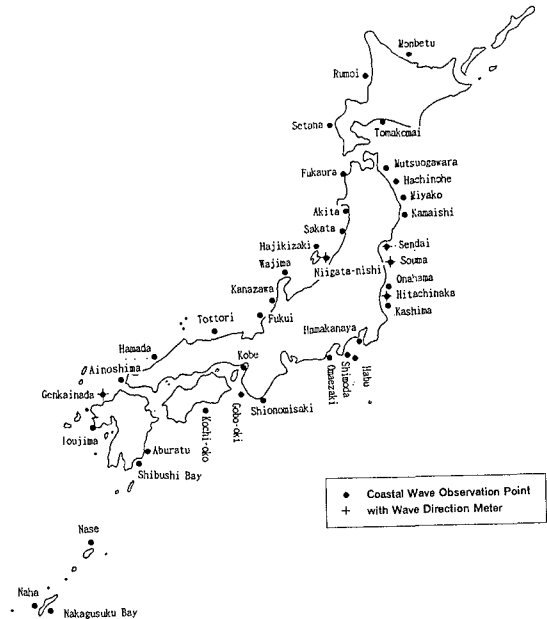


Fig. 1 The NOWPHAS system

Table 1 Observation points

Location	Waveage Type	Depth(m)	Latitude	Longitude
Hajikizaki	U S W	- 5 . 4	38° 20' 39" N	138° 30' 25" W
Wajima Port	U S W	- 5 . 0	37° 25' 40"	136° 54' 19"
Fukaura Port	U S W	- 4 . 9 . 6	40° 39' 25"	139° 54' 57"
Mutuogawara Port	U S W	- 4 . 9	40° 55' 20"	141° 25' 40"
Hitachinaka Port	U S W	- 3 . 0	36° 23' 24"	140° 39' 36"
Habu Port	U S W	- 4 . 9	34° 40' 23"	139° 27' 18"
Kouchi-oki	A W	- 1 . 2 . 0	33° 15' 24"	133° 30' 06"
Hamada Port	U S W	- 5 . 1	34° 54' 07"	132° 02' 21"
Aburatu Port	U S W	- 4 . 6 . 5	31° 33' 27"	131° 26' 32"
Setana Port	U S W	- 5 . 2 . 9	42° 26' 30"	139° 49' 16"
Monbetu Port	U S W	- 5 . 2	44° 24' 58"	143° 26' 00"
Naha Port	U S W	- 5 . 1	26° 15' 19"	127° 38' 56"
Nakagusuku Bay	U S W	- 5 . 0	26° 14' 15"	127° 58' 10"

condition of each points. The sampling frequency of wave data is 2 Hz. Waves are defined by using the zero up crossing method. Frequency spectra are calculated by using the FFT method. The number of total observation cases are 2546.

These observation points have no wind profile. Thus, a data of the wind waves are determined by using the following criteria.

- a) From the time series of significant parameters, significant wave height should be in its developed stage.
- b) The swell component is not included in wave data clearly. Thus, a spectral form should be a single peak spectrum.
- c) The JONSWAP spectrum parameter  $\gamma$  should be greater than 1.

## (2) Wind waves of short fetch

Short fetch waves are obtained at MT station in Osaka Bay. Figure 2 shows the location of MT station. The water depth is 17m. The wave data and wind velocity at 10m high from sea surface are measured at MT station. Sampling frequency is 10 Hz. The analysis method is the same as for ocean waves. The duration of observation used is from 1984 to 1991. The FFT analysis is applied

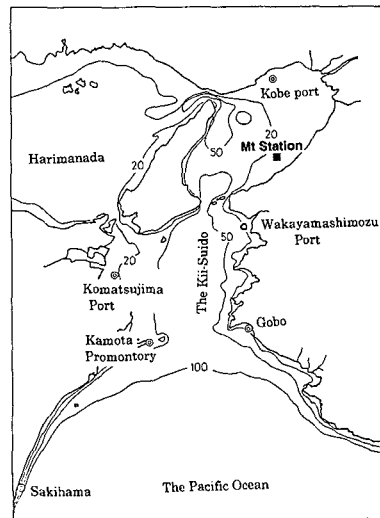


Fig. 2 Location of MT station

to the duration of storm or typhoon. The number of total observation data is 70080 and the data analyzed by FFT is 246.

**3. Non-dimensional parameters of wind waves**

The non-dimensional parameters that describe the characteristics of wind waves are as follows.

$$\frac{gH_{1/3}}{u_*^2}, \frac{gT_{1/3}}{u_*}, \frac{g^2E}{u_*^4}, \frac{gF}{u_*^2}, \frac{f_m u_*}{g}, \frac{C}{u_*}, \frac{H_{1/3}}{L_{1/3}} \tag{1}$$

where  $H_{1/3}$  is the significant wave height,  $T_{1/3}$  the significant wave period,  $E$  the wave energy,  $F$  the fetch,  $f_m$  the peak frequency of spectrum,  $C$  the wave celerity,  $L_{1/3}$  the wave length corresponding to the significant wave period,  $u_*$  the friction velocity of wind, and  $g$  the gravity acceleration. Equation (2) is the 3/2 power law relation of Toba (1972):

$$\left(\frac{gH_{1/3}}{u_*^2}\right) = B \left(\frac{gT_{1/3}}{u_*}\right)^{3/2}, B = 0.062 \tag{2}$$

Goto (1990) modified the coefficient  $B$  to 0.067. Toba (1992) also showed that if wind waves include components of swell, the exponent of the power law is changed from 3/2 to 2. The friction velocity of wind is calculated by using Eq. (3):

$$u_* = \sqrt{C_D} U_{10} \tag{3}$$

where  $U_{10}$  is wind speed at a 10m high from the sea surface. To determine the drag coefficient  $C_D$  of sea surface, the following Mitsuyasu's formula (1980) is applied:

$$C_D = \begin{cases} (1.290 - 0.024U_{10}) \times 10^{-3} & (U_{10} < 8m/s) \\ (0.581 + 0.063U_{10}) \times 10^{-3} & (U_{10} \geq 8m/s) \end{cases} \tag{4}$$

Figure 3 shows the relation of  $gH_{1/3}/u_*^2$  and  $gT_{1/3}/u_*$  by using the data at MT station. The solid line shows Toba's 3/2 power law while the dotted line shows the Goto's. The deviation of the data from the corresponded line represents the effects of swell components. It is confirmed that the measured wind waves data satisfied the 3/2 power law.

If the relationship linking non-dimensional fetch and energy, significant wave height and wave energy, peak frequency and significant

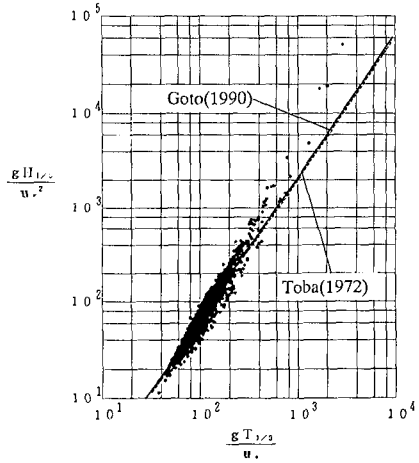


Fig. 3 3/2 power law relation

Table 2 Relationship among the non-dimensional parameters  
( $Y = aX^n$ )

X	$gH/U^2$		$gT/U$		$g^2E/U^4$		$gF/U^2$		C/U		$f_m U/g$		H/L	
	$\alpha$	$n$	$\alpha$	$n$	$\alpha$	$n$	$\alpha$	$n$	$\alpha$	$n$	$\alpha$	$n$	$\alpha$	$n$
$gH/U^2$	1	1	B	3/2	a	1/2	$aA^{1/2}$	1/2	$(2\pi)^{3/2}B$	3/2	$\frac{B}{b^{3/2}}$	-3/2	$(2\pi)^3 B^4$	-3
$gT/U$	$\frac{1}{B^{2/3}}$	2/3	1	1	$\frac{a^{2/3}}{B^{2/3}}$	1/3	$\frac{a^{2/3}A^{1/3}}{B^{2/3}}$	1/3	2 $\pi$	1	$\frac{1}{b}$	-1	$(2\pi)^2 B^2$	-2
$g^2E/U^4$	$\frac{1}{a^2}$	2	$\frac{B^2}{a^2}$	3	1	1	A	1	$\frac{(2\pi)^3 B^2}{a^2}$	3	$\frac{B^2}{a^2 b^3}$	-3	$(2\pi)^6 \frac{B^8}{a^2}$	-6
$gF/U^2$	$\frac{1}{a^2 A}$	2	$\frac{B^2}{a^2 A}$	3	$\frac{1}{A}$	1	1	1	$\frac{(2\pi)^3 B^2}{a^2 A}$	3	$\frac{B^2}{b^3 a^2 A}$	-3	$(2\pi)^6 \frac{B^8}{a^2 A}$	-6
C/U	$\frac{1}{2\pi B^{2/3}}$	2/3	$\frac{1}{2\pi}$	1	$\frac{a^{2/3}}{2\pi B^{2/3}}$	1/3	$\frac{a^{2/3}A^{1/3}}{2\pi B^{2/3}}$	1/3	1	1	$\frac{1}{2\pi b}$	-1	$2\pi B^2$	-2
$f_m U/g$	$\frac{B^{2/3}}{b}$	2/3	$\frac{1}{b}$	-1	$\frac{B^{2/3}}{ba^{2/3}}$	-1/3	$\frac{B^{2/3}}{ba^{2/3}A^{1/3}}$	-1/3	$\frac{1}{2\pi b}$	-1	1	1	$\frac{1}{(2\pi)^2 b B^2}$	2
H/L	$2\pi B^{4/3}$	-1/3	2 $\pi B$	-1/2	$\frac{B^{4/3}}{a^{1/3}}$	-1/6	$\frac{B^{4/3}}{a^{1/3}A^{1/6}}$	-1/6	$(2\pi)^{1/2}B$	-1/2	2 $\pi b^{1/2}B$	1/2	1	1

wave period are revealed, all non-dimensional parameter are related to each other by using 3/2 power law.

Table 2 shows the relationship among the non-dimensional parameters. In this table, a is the coefficients of the relationship between wave height and wave energy (Fig. 4), A the coefficients of the relationship between fetch and energy (Fig. 5), b the coefficients of the relationship between peak frequency and wave periods (Fig. 6), and B the coefficient of 3/2 power law. These relation indicate that if the friction velocity and other only one parameter of wind waves are determined, all significant wave parameters can be calculated. The coefficients determine from observed data, are as follows:

$$A = 0.00016, a = 3.86, B = 0.067, b = 1.13 \tag{5}$$

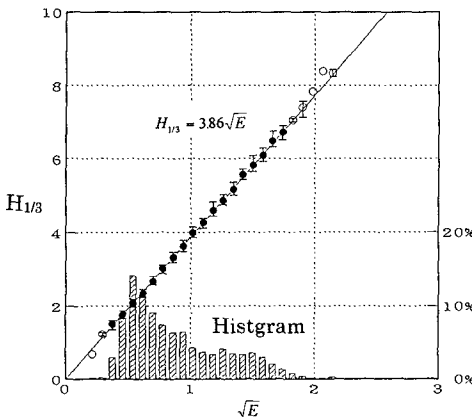


Fig. 4 Relationship between  $H_{1/3}$  and E

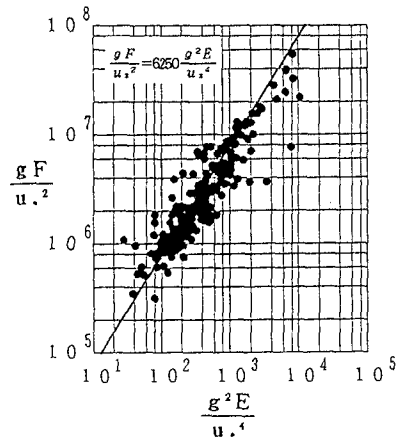


Fig.5 Relationship between E and F

Table 3 Comparison between observed and calculated results

X \ Y		$gH/u.^2$	$gT/u.$	$g^2E/u.^4$	$gF/u.^2$	$C/u.$	$f_w u./g$	$H/L$
$gH/u.^2$	observed		0.067	3.86	0.0475	1.0675	0.0628	0.006
	calculated		0.067	3.86	0.0518	1.0552	0.0556	0.005
	ratio			1.	0.9170	1.0117	1.1295	1.2
$gT/u.$	observed	6.091		14.97	0.7941	6.281	0.949	0.185
	calculated	6.062		14.91	0.8098	6.283	0.883	0.177
	ratio	1.005		1.004	0.9806	0.999	1.0747	1.0452
$g^2E/u.^4$	observed	0.0676	$3.10 \times 10^{-4}$		$1.6 \times 10^{-4}$	0.0786	$2.74 \times 10^{-4}$	$1.46 \times 10^{-4}$
	calculated	0.0671	$3.01 \times 10^{-4}$		$1.6 \times 10^{-4}$	0.0747	$2.07 \times 10^{-4}$	$1.68 \times 10^{-4}$
	ratio	1.0075	1.0299		1	1.0522	1.3237	0.8690
$gF/u.^2$	observed	523	2.2267	6250		551	1.9214	0.0136
	calculated	419	1.8830	6250		467	1.2964	0.0105
	ratio	1.25	1.1825	1		1.18	1.4821	1.2952
$C/u.$	observed	0.9696	0.1592	2.3840	0.1264		0.1510	0.0295
	calculated	0.9648	0.1590	2.3741	0.1289		0.1405	0.0282
	ratio	1.0050	1.0013	1.0042	0.9806		1.0747	1.0461
$f_w u./g$	observed	0.1575	0.9489	0.0640	1.2191	0.1511		5.6241
	calculated	0.1457	0.8830	0.0592	1.0904	0.1405		4.9829
	ratio	1.0810	1.0746	1.0811	1.1180	1.0754		1.1287
$H/L$	observed	0.1745	0.4259	0.1113	0.4755	0.1700	0.4377	
	calculated	0.1710	0.4210	0.1090	0.4678	0.1679	0.4480	
	ratio	1.0205	1.0116	1.0211	1.0165	1.0125	0.9770	

Table 3 shows the comparison between observed and calculated results. The results show good agreement. Thus, table 2 shows similarity of wind waves parameter.

**4. Wave spectrum in deep and shallow water**

On the basis of the non-dimensional significant wave parameter, frequency spectra of wind waves in the deep and shallow water region are discussed and a new functional form of wind wave spectrum is proposed.

The JONSWAP spectrum is an extension form of Pierson-Moskowitz spectrum and is applicable to cases ranging from developing wave to fully developed wave. Equation (6) is the generalized JONSWAP spectrum.

$$S(f) = \alpha(2\pi)^{-m+1} g u_*^{5-m} f^{-m} \exp\left\{-\frac{m}{4}\left(\frac{f}{f_m}\right)^{-4}\right\} \gamma^\beta \tag{6}$$

$$\beta = \exp\left\{-\left(1 - f/f_m\right)^2 / 2\sigma^2\right\}$$

where  $\alpha$  is scale factor,  $\gamma$  the peak enhancement factor,  $\sigma$  the band width near peak frequency. By using this equation, the similarity and the characteristics of slope of high frequencies and parameter of spectrum are dis-

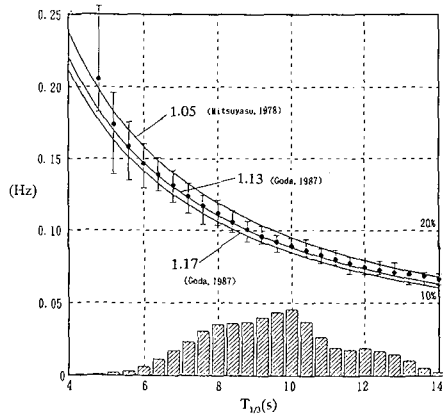
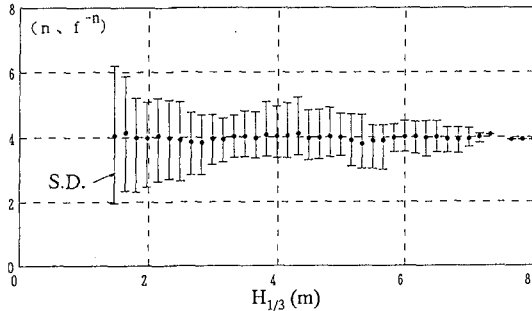


Fig. 6 Relationship between  $f_m^*$  and  $T_{1/3}$

cussed.

Figure 7 shows the slope of wind wave spectra at high frequencies by using least-squares estimation. The high frequency range is the same as Donelan's (1985). The x-axis is significant wave height. In this figure, the vertical lines are the standard deviations of the data to



indicate the amount of scatter. From Fig. 7, the mean slope of wind wave spectra at high-frequency range is approximated by  $f^4$  power law. The amount of scatter decreases with increasing wave height. This fact implies that the  $3/2$  power law is applicable in the frequency domain and the development of the wind waves is essentially a strongly nonlinear phenomenon. Hence, the JONSWAP spectrum follows the  $f^4$  law, expressed as follows:

$$S(f) = \alpha(2\pi)^{-3} g u_* f^{-4} \exp\left\{-(f/f_m)^4\right\} \gamma^\beta \tag{7}$$

The functional forms of the peak enhancement factor  $\gamma$  are proposed by Donelan (1985) and Mitsuyasu (1980). They use the non-dimensional peak frequency as variable. Figure 8 shows the relationship linking  $\gamma$  and non-dimensional peak frequency  $f_m^* = f_m u_* / g$ . The vertical lines are standard deviations. There is a large scatter in  $\gamma$ , but the mean value is increasing with non-dimensional peak frequency and has logarithmic relation. It means the spectral form is change to Pierson-Moskowitz spectrum with the increase of the fetch. Hence, the following empirical formula for  $\gamma$  is obtained:

$$\gamma = 6 f_m^{*0.15} \tag{8}$$

The scale factor  $\alpha$  is varied with spectral form. In this study, the relationship between  $\alpha$  and  $\gamma$  is discussed. The total energy of JONSWAP spectrum is

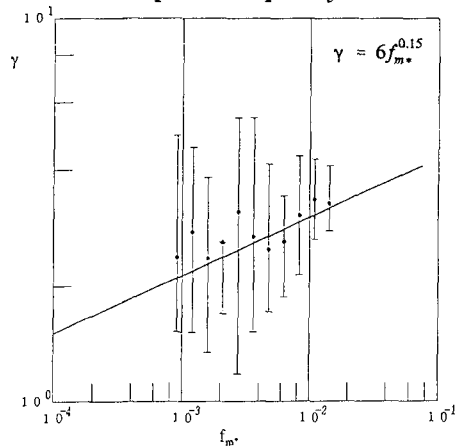


Fig. 8 Relationship between  $\gamma$  and  $f_m^*$

$$E = \alpha(2\pi)^{-3} g u_* f_m^{-4} M_0 \tag{9}$$

where,  $M_0$  is expressed as Eq. (10)

$$M_0 = \int_0^\infty \left(\frac{f}{f_m}\right)^{-4} \exp\left\{-\left(\frac{f}{f_m}\right)^{-4}\right\} \gamma^6 df \tag{10}$$

therefore,  $M_0$  is approximated by (Goto and Aono, 1993)

$$M_0 = 0.30\gamma^{1/3} \tag{11}$$

By using this approximate formula for  $M_0$  and the relation of non-dimensional energy and peak frequency, and the 3/2 power law, this equation is derived:

$$\alpha \approx \gamma^{-1/3} \tag{12}$$

From Eq. (12),  $\alpha$  is related to  $\gamma$ . Table 4 shows the relationship linking  $\alpha$  and  $\gamma$  derived using the 3/2 power law for various spectral forms.

Table 4 Relationship between  $\alpha$  and  $\gamma$

Power	Pierson-Moskowitz	JONSWAP
-4	Const.	$\alpha \sim \gamma^{-1/3}$
-5	$\alpha \sim \left[\frac{g^2 E}{u_*^4}\right]^{-1/3}$	$\alpha \sim \gamma^{-1/3} \left[\frac{g^2 E}{u_*^4}\right]^{-1/3}$

Figure 9 shows the relation of  $\alpha$  and  $\gamma$ , while solid line correspond to the least squares estimate. The coefficient is determined from the line and yields

$$\alpha = 0.17\gamma^{-1/3} \tag{13}$$

Figure 10 and Fig. 11 show the relation of  $\sigma_1$ ,  $\sigma_2$ , and the non-dimensional peak frequency. The symbol  $\sigma_1$  is low frequency side while  $\sigma_2$  is high frequency side. Because the low frequency side include the weak swell components, there are no trends in  $\sigma_1$ . In the high frequency side,  $\sigma_2$  varies inversely as the non-dimensional frequency on a log-log axis. This means the spectral form near peak frequency is varied from sharp to mild in the case of developing wind waves. Hence the band width near peak frequency is determined:

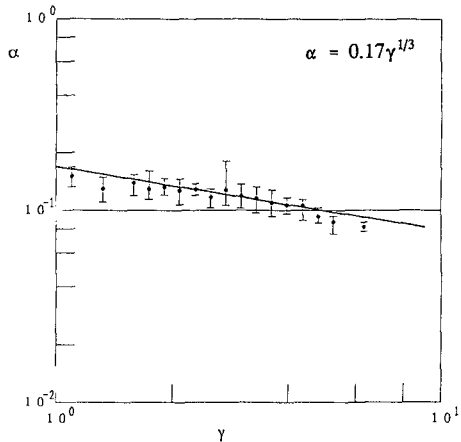


Fig. 9 Relation between  $\alpha$  and  $\gamma$



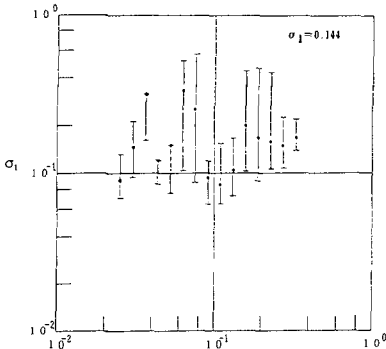


Fig. 10 Relation of  $\sigma_1$  and  $f_m^*$

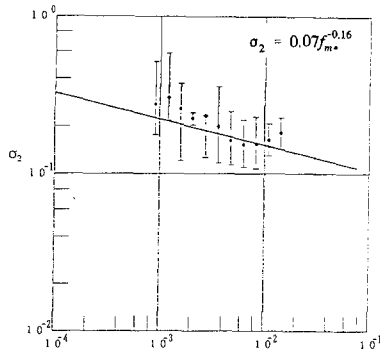


Fig. 11 Relation of  $\sigma_2$  and  $f_m^*$

$$\sigma_1 = 0.144, \quad \sigma_2 = 0.07 f_m^{*-0.16} \tag{14}$$

These characteristics of spectral parameters are in deep water region. Next, the spectrum in shallow water region is discussed.

Figure 12 show the change of the coefficient of 3/2 power law in shallow water. The x-axis is relative depth, the shaded bar is the histogram of observed data and the solid line is the linear shoaling coefficient  $K_s$ . The mean value of  $B/B_0$  shows good agreement with  $K_s$ . The 3/2 power law is also extended in a shallow water region by using the shoaling coefficient.

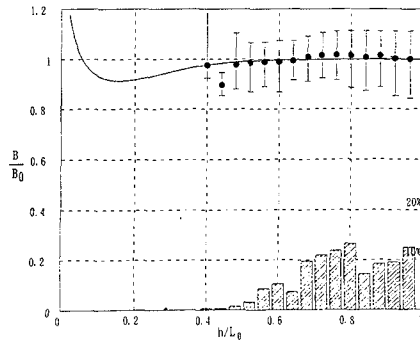


Fig. 12 Relation of  $B$  and  $h/L_0$

The spectral form in shallow water is derived by using 3/2 power law. In this derivation, subscript 0 indicates values in deep water and s indicates there in shallow water. The integrated form of the JONSWAP spectrum is

$$E_0 = \alpha_0 g u_* f_m^{-3} M_1 \tag{15}$$

where  $M_1$  is

$$M_1 = \int_0^\infty \left(\frac{f}{f_m}\right)^{-4} \exp\left\{-\left(\frac{f}{f_m}\right)^{-4}\right\} \gamma_0^\beta d\left(\frac{f}{f_m}\right) \tag{16}$$

From the analogy of  $M_0$ ,  $M_1$  is approximated by Eq. (17)

$$M_1 = c \gamma_0^{1/3} \tag{17}$$

Thus, Eq. (15) is expressed as

$$E_0 = c\alpha_0 u_* \gamma_0^{1/3} f_m^{-3} \tag{18}$$

Using the relationship of  $u_* f_m/g$  and  $gT_0/u_*$  and the relationship of  $gH_0/u_*^2$  and  $g^2 E_0/u_*^4$ , Eq. (19) is derived.

$$\left[ \frac{gH_0}{u_*^2} \right] = a \left[ \alpha_0 b^{-3} c \gamma_0^{1/3} \right]^{1/2} \left[ \frac{gT_0}{u_*} \right]^{3/2} \tag{19}$$

Equation (19) is the 3/2 power law which derived from the spectral form. The coefficient  $B_0$  of 3/2 power law in deep water region is expressed as Eq. (20).

$$B_0 = \left[ ab^{-3/2} \right] \left[ \alpha_0 c \gamma_0^{1/3} \right]^{1/2} \tag{20}$$

If the coefficients a, b and  $B_0$  is constant, the relationship between  $\alpha_0$  and  $\gamma_0$  is

$$\alpha_0 = \left[ \frac{B^2}{ab^{-3}} \right] \frac{1}{c \gamma_0^{1/3}} \tag{21}$$

The same argument applies in shallow water. The total energy and the coefficient of 3/2 power law in shallow water is expressed by the following equations:

$$E_s = c\alpha_s \gamma_s^{1/3} u_* f_m^{-3} \tag{22}$$

$$\left[ \frac{gH_s}{u_*^2} \right] = a \left[ \alpha_s b^{-3} c \gamma_s^{1/3} \right]^{1/2} \left[ \frac{gT_s}{u_*} \right]^{3/2} \tag{23}$$

The coefficient of 3/2 power law is

$$B_s = B_0 K_s = a \left[ \alpha_s b^{-3} c \gamma_s^{1/3} \right]^{1/2} \tag{24}$$

The combination of Eq. (20) and Eq. (24) lead to Eq. (25).

$$\left[ \frac{\gamma_s}{\gamma_0} \right]^{1/6} = K_s \quad \alpha_0 = \alpha_s \tag{25}$$

Equation (25) determine the spectral form in shallow water. Figure 13 shows the change of  $\gamma$  with relative depth  $h/L_0$ . The mean value of  $\gamma$  and  $K_s$  show good agreement.

The characteristics of the wind waves spectrum in deep water are invest-

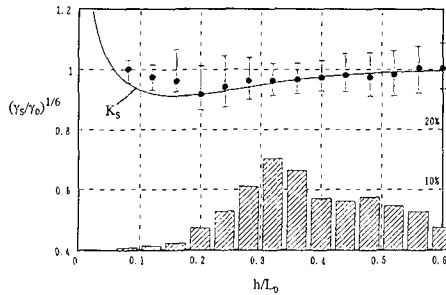


Fig. 13 Change of  $\gamma$  with  $h/L_0$ .

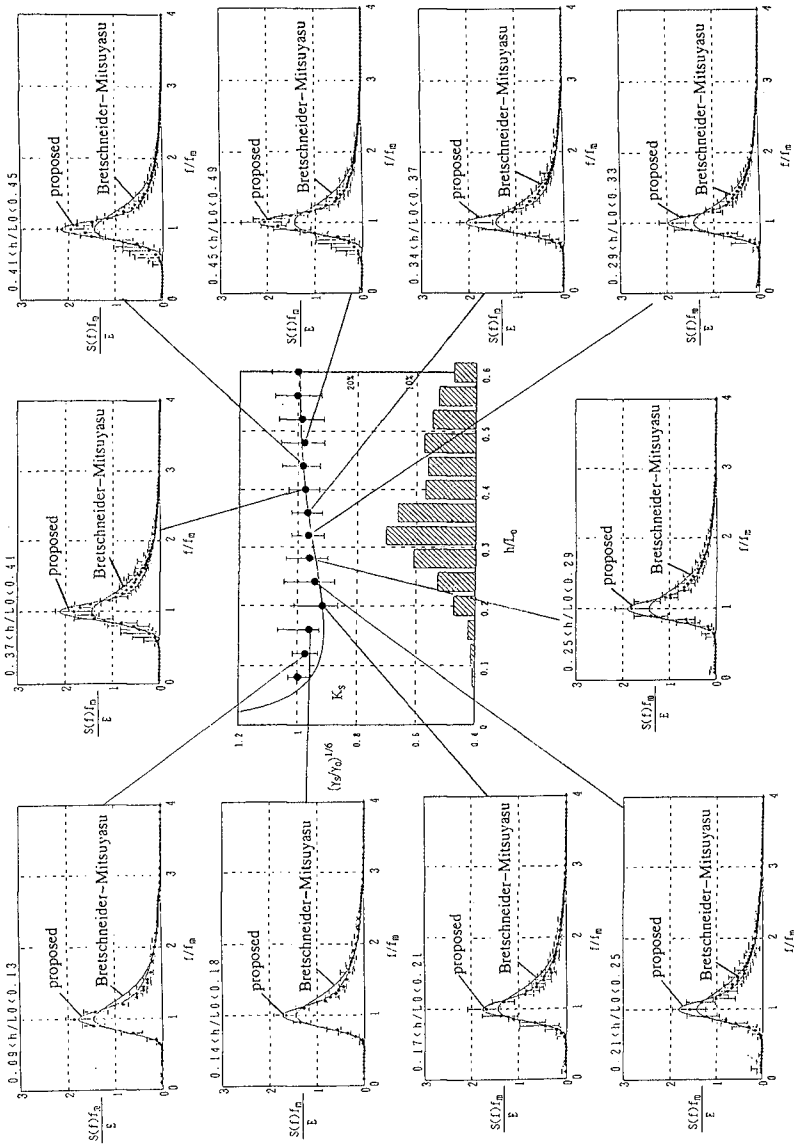


Fig. 14 Change of the spectral form with  $h/L_0$ .

gated by using the parameters of JONSWAP spectrum. From theoretical and empirical arguments, it is confirmed that a  $f^4$  power law exists at high frequency range, that  $\gamma$  and  $\sigma$  are varied with fetch, and that a  $-1/3$  power law, based on  $3/2$  power law, also exists in relation between  $\alpha$  and  $\gamma$ . Wave energy is concentrated near the peak frequency during the development stage, and approaches the Pierson-Moskowitz spectrum gradually with the increase of fetch. In shallow water region, the spectral form of wind waves varies with the shoaling coefficient. From these characteristics of the wind wave spectrum, the following new spectral formula is obtained:

$$S(f) = \alpha(2\pi)^{-3} g u_* f^{-4} \exp\left[-(f / f_m)^{-4}\right] \gamma^\beta \left. \begin{array}{l} \\ \beta = \exp\left[1 - (f / f_m)^2 / 2\sigma^2\right] \end{array} \right\} \quad (26)$$

$$\left. \begin{array}{l} \gamma = 6 f_m^{0.15}, \quad \alpha = 0.17 \gamma^{-1/3}, \quad f_m = 1 / 1.136 T_{1/3} \\ \sigma_1 = 0.144, \quad \sigma_2 = 0.07 f_m^{-0.16}, \quad f_m^* = f_m u_* / g \\ u_* = H_{1/3}^2 / g B^2 T_{1/3}, \quad B = 0.067 \end{array} \right\} \quad (27)$$

In shallow water region, the spectral form of wind waves is expressed as  $S_s(f) = K_s^{6\beta} S(f)$  (28)

In this spectrum, the input variables are significant wave height and period only. Figure 14 shows the comparison of the newly-proposed spectral model with the observed spectral data and Bretshneider-Mitsuyasu spectrum. The spectral form varies with  $h/L_0$  and the proposed model and observed data show good agreement.

**5. Discussion**

Table 4 shows the relationship between non-dimensional wave height and period derived from selected spectral forms. Where  $B$  is coefficients and  $\beta_1$  is power. It is confirmed that  $3/2$  power law relation applies to  $f^4$  power law and 2 power law relation applies to  $f^5$  power law. 2 power law relation is revealed under the condition that the swell components are included in the wind waves. This is the reason of such change of power.

Table 4 Relationship between  $H$  and  $T$  derived from spectral forms.

	<i>Pierson · Moskowitz</i>		<i>JONSWAP</i>	
<i>Power</i>	B	$\beta_1$	B	$\beta_1$
-5	$a b^{-2} [0.2 \alpha]^{1/2}$	2	$a b^{-2} [0.2 \alpha \gamma^{1/3}]^{1/2}$	2
-4	$0.5 a [\alpha b^{-3}]^{1/2}$	$3/2$	$a [\alpha b^{-3} c \gamma^m]^{1/2}$	$3/2$

The 3/2 power law is not dependent on the fetch and shows local equilibrium between wind and wind waves. In the frequency domain, such local equilibrium is revealed by the  $f^4$  power law. It implies that the spectral form depends on the characteristics of the high frequency range. However, spectral parameters depend on the fetch, so that the spectral form cannot be determined from the 3/2 power law directly. The implication in the case of developing wind waves is that  $\alpha$  varies with  $\gamma$ , which depends on the fetch, in order to satisfy the 3/2 power law.

To apply Eq. (28) for actual work, it is necessary to investigate the error between the observed data and Eq. (28). The error of the calculated spectrum is defined as

$$E_r = \frac{\int_0^\infty |S_c(f) - S_o(f)|df}{\int_0^\infty S_o(f)df} \quad (29)$$

Figure 15 shows the characteristics of the error of proposed spectrum and Bretschneider-Mitsuyasu spectrum. The horizontal axis is the  $U_{10}$  calculated by using the 3/2 power law and Mitsuyasu's  $C_D$  law. The error of the proposed spectrum is relatively small in the entire range of wind velocity. The error is being

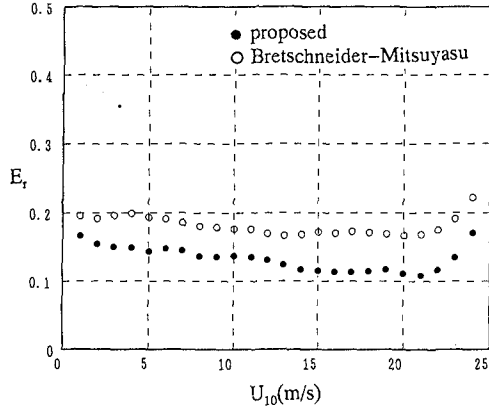


Fig. 15 Error of the spectrum

large in the range of low wind velocity and the wind velocity is greater than the 22m/s. These characteristics of error indicates the mixture of wind waves and swell at low wind velocity range. The increase of error at high wind velocity range suggest the change of the wind resistance law, but there is not enough the data such high wind velocity range.

Figure 16 shows the results of comparison of the observed and proposed spectra. The spectrum of Bretschneider-Mitsuyasu is given in this figure for reference. Observation data was taken from Kochi-Oki on July, 1981. Time series of  $H_{1/3}$ ,  $T_{1/3}$ ,  $h/L_0$ , and error which defined by Eq. (29) is also shown in Fig. 16. It can be seen that the proposed spectrum shape agrees well with the observed one.

**6. Conclusions**

The major conclusions of this study are as follows:

- (1) It was confirmed that the measured wind waves data satisfied the 3/2

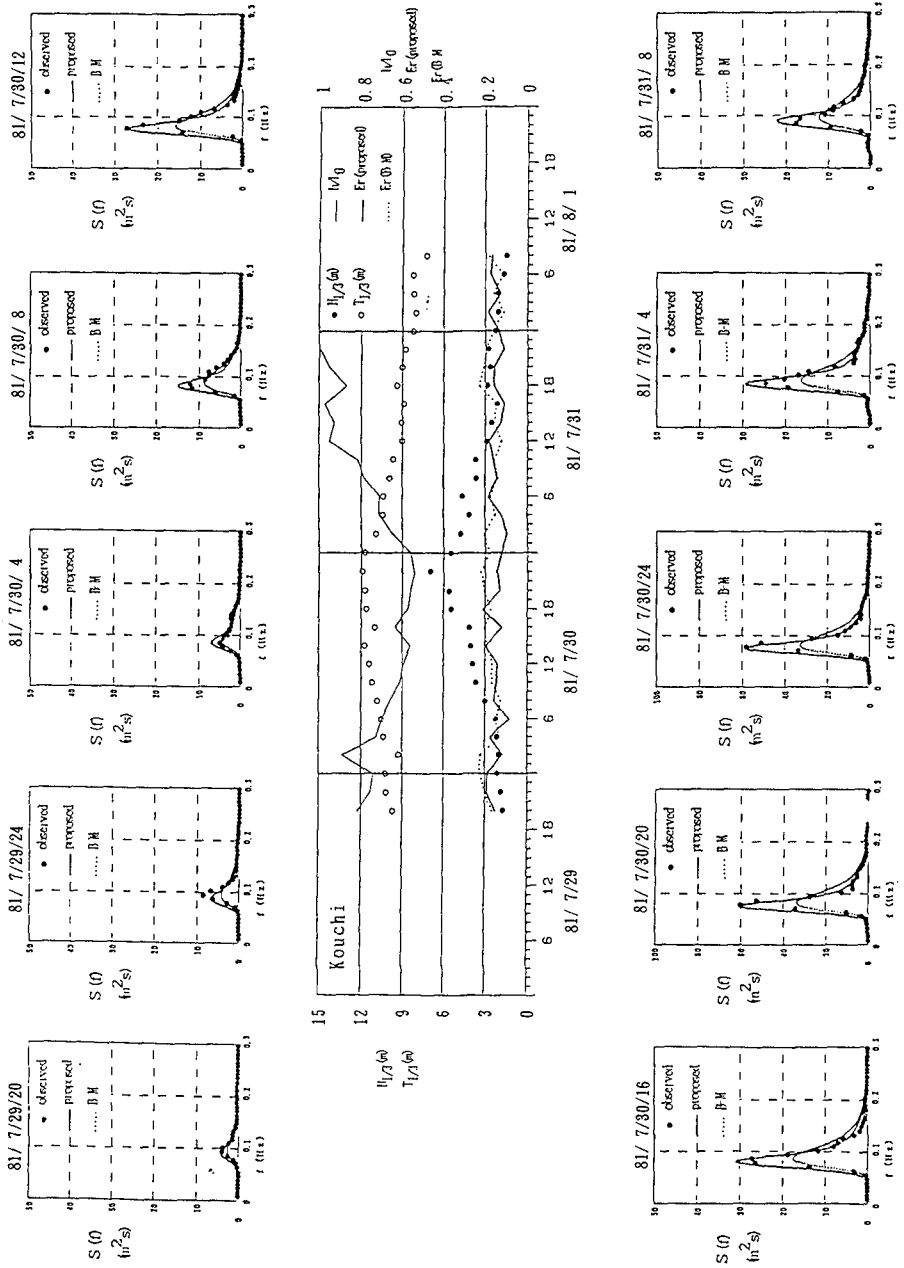


Fig. 16 Results of the comparison of the observed and proposed spectra.

power law which is an empirical formula between non-dimensional wave height and period.

- (2) By using the 3/2 power law relation, non-dimensional parameters of wind waves are all related.
- (3) The new spectral model, which is based on the 3/2 power law, is proposed. This spectral model is evaluated from  $H_{1/3}$  and  $T_{1/3}$ , and calculated result is very accurate. The applicability of this new spectrum is very wide, ranging from the case of developing wind to that of fully developed wind, and from deep to shallow water region.

### Reference

- (1) Bouws, E., H. Gunther, W. Rosenthal and C. L. Vincent (1985): Similarity of the wind wave spectrum in finite depth water 1. Spectral form, *J. Geophys. Res.*, Vol.90 No.C1, pp.975-986.
- (2) Donelan, M.A., J. Hamilton and W. H. Hui (1985): Directional spectra of wind-generated waves, *Phil. Trans. R. Soc. Lond.* A315, pp.509-562.
- (3) Ebuchi, N., Y. Toba and H. Kawamura (1992): Statistical study on the local equilibrium between wind and wind waves by using data from ocean data buoy stations, *J. Oceanogr.*, Vol.48, pp.77-92.
- (4) Goto, C., K. Suetsugu and T. Nagai (1990): Wave Hindcast Model for Short Fetch Sea, *Rep. of P.H.R.I.* Vol.29, No.3, pp. 3-26.
- (5) Goto, C. and T. Aono (1993) : On the Characteristics of One-Dimensional Spectra and Non-Dimensional Parameters of Wind Waves - Wave Hindcast Model Using the Hybrid-parameter Methods (2nd report) -, *Rep. of P.H.R.I.*, Vol. 32, No.1, pp. 53-99 (in Japanese)
- (6) Hasselman, K. et. al(1973): Measurements of wind wave growth and swell decay during the Joint North Sea Wave Project (JONSWAP), *Deut. Hydrgr. Z.*, Suppl. 8, pp.1-95.
- (7) Mitsuyasu, H (1968): On the growth of the spectrum of wind generated waves (1), *Rep. Res. Inst. Mech. Kyushu Univ.*, Vol.16, pp.459-482.
- (8) Mitsuyasu, H., R. Nakamura and T. Komori (1971): Observation of the wind and waves in Hakata Bay, *Rep. Res. Inst. Mech. Kyushu Univ.*, Vol.19, pp.37-74.
- (9) Phillips, O. M. (1958): The equilibrium range in the spectrum of wind-generated waves, *J. Fluid Mech.*, 4, pp. 426-434.
- (10) Pierson, W. J. and L. Moskowitz (1964): A proposed spectral form for fully developed wind seas based on the similarity theory of S. A. Kitaigorodskii, *J. Geophys. Res.*, 69, pp.5181-5190.
- (11) Thornton, E. B. (1977): Rederivation of the saturation range in the frequency spectrum of wind-generated gravity waves, *J. Phys. Oceanogr.*, Vol.7, pp.137-140.
- (12) Toba, Y. (1972): Local balance in the air-sea boundary processes, I. On the growth process of wind waves, *J. Oceanogr Soc. Japan*, 28, pp. 109-120.
- (13) Toba, Y. (1973): Local balance in the air-sea boundary processes, III. On the spectrum of wind waves, *J. Oceanogr. Soc. Japan*, 29, pp. 209-220.

## CHAPTER 2

# SWASH MOTION DUE TO OBLIQUELY INCIDENT WAVES

Toshiyuki Asano<sup>1</sup>

### abstract

A numerical model is developed to predict the flow characteristics in a swash zone for obliquely incident wave trains. The two-dimensional shallow water equations are de-coupled into independent equations each for on-off shore motion and for longshore motion. A front of swash wave train is treated as a moving boundary which makes the solution predictable for landward zone of the still water level. The results show non-vanishing longshore velocities and volume flux at the still water shoreline. These quantities are found to increase with the beach slope. The two-dimensional uprush and downrush motion near the front of swash waves shows skew figures, which may cause zig-zag longshore sediment transport inherent in swash zone.

### 1.INTRODUCTION

Swash zone is the most familiar area that we can easily observe its motion while walking along a sandy beach, but it is one of the unsolved area from the hydrodynamic point of view. The difficulty lies on that waves in swash zone are highly nonlinear and show such a unique behaviour that the seabed is immersed during run-up and dried during run-down alternatively. Lately, the swash motion has received much attention because the sediment process in this zone provides the important boundary condition for the beach evolution. And also, recent studies have reported an important new finding that longshore sediment transport takes two major peaks located at the breaking point and on the foreshore in the swash zone(Bodge - Dean, 1987; Kamphuis, 1991;b).

Under obliquely incident waves, sediment near shoreline moves in a zig-zag way which results in the inherent longshore transport in the swash zone.

---

<sup>1</sup>Dept. of Ocean Civil Engrg., Kagoshima Univ., Korimoto, Kagoshima, 890, JAPAN



Intensive turbulence generated in the uprush and backwash waves causes a large volume of sediment to be suspended. Moreover, infragravity wave motion might be more influential on the sediment dynamics in this very shallow water region (Thornton - Abdelrahman, 1991).

Although such complicated dynamics needs to be investigated for full descriptions, this study, as the first step, focuses on the velocity field as a basic forcing function of the sediment motion under obliquely incident monochromatic waves. The horizontally two-dimensional water particle velocities are computed based on Ryrie(1983)'s analysis. Moreover, the velocity measurements in the swash zone under obliquely incident waves are conducted using tracer method. Through comparisons between the numerical and experimental results, the hydrodynamic properties related to longshore sediment transport are discussed.

## 2. NUMERICAL ANALYSIS

### 2.1 Formulation of Shallow Water Wave Equations

Based on Ryrie's formulation, the following two dimensional wave and topographic system is assumed. The incident monochromatic waves with straight parallel crests are assumed to arrive at the seaward boundary with an angle  $\theta_B$  (Fig. 1). The  $x'$  - and  $y'$  - axis, in which the prime indicates the dimensional variables, is chosen to be in the normal and the parallel direction to the shoreline, respectively. The  $z'$  - axis is taken positive upward with  $z' = 0$  at the still water level(SWL). The beach slope  $S'$  is herein restricted to be uniform and its contours are assumed to be straight and parallel to the shoreline. The water depth at the toe of the slope is given as  $d'_B$  where the offshore boundary conditions for the incident waves are provided. The free surface is located at  $z' = \eta'$ , so that the instantaneous water depth  $h'$  is given by  $h' = \eta' + (d'_B - S'x')$ .

The governing equations for the mass and momentum conservations may be expressed as

$$\frac{\partial h'}{\partial t'} + \frac{\partial}{\partial x'}(h'u') + \frac{\partial}{\partial y'}(h'v') = 0 \quad (1)$$

$$\begin{aligned} \frac{\partial}{\partial t'}(h'u') + \frac{\partial}{\partial x'}(h'u'^2) + \frac{\partial}{\partial y'}(h'u'v') = \\ -gh' \frac{\partial \eta'}{\partial x'} - \frac{1}{2} f' |u'| u' \end{aligned} \quad (2)$$

$$\begin{aligned} \frac{\partial}{\partial t'}(h'v') + \frac{\partial}{\partial x'}(h'u'v') + \frac{\partial}{\partial y'}(h'v'^2) = \\ -gh' \frac{\partial \eta'}{\partial y'} - \frac{1}{2} f' |v'| v' \end{aligned} \quad (3)$$

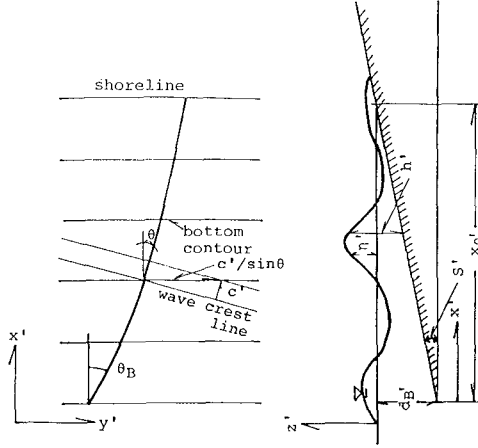


Fig. 1: Two dimensional plane wave on a uniform beach

in which,  $t'$  is the time,  $u'$ ,  $v'$  is the on-offshore and longshore velocity respectively,  $g$  is the gravitational acceleration and  $f'$  is the bottom friction factor. Eqs.(2) and (3) are the two dimensional nonlinear shallow water equations, where the vertical pressure distribution is assumed to be hydrostatic.

According to Kobayashi et al.(1987), the following dimensionless variables using the characteristic period  $T'$  and height  $H'$  associated with the incident wave train are introduced.

$$\begin{aligned}
 u &= \frac{u'}{\sqrt{gH'}}; \quad \eta = \frac{\eta'}{H'}; \quad h = \frac{h'}{H'}; \quad t = \frac{t'}{T'}; \\
 x &= \frac{x'}{T'\sqrt{gH'}}; \quad c = \frac{c'}{\sqrt{gH'}}; \quad f = \frac{1}{2}\sigma f'; \\
 S &= T'\sqrt{\frac{g}{H'}}S'; \quad d_B = d'_B/H'; \quad \sigma = T'\sqrt{g/H'};
 \end{aligned} \tag{4}$$

in which,  $S$  is expressed by the surf similarity parameter  $\xi$  as  $S = \sqrt{2\pi}\xi$ ,  $d_B$  corresponds to the inverse number of relative water depth at the offshore boundary and  $\sigma/h$  means the ratio of wave length to water depth  $L'/h'$ .

Since we have assumed that the wave crest is straight parallel and bottom topography does not vary in the  $y$ -direction, the observed wave motion moving along the alongshore direction at the speed  $C'/\sin\theta$  (which remains constant throughout the surf zone by Snell's law) becomes independent in the  $y$ -direction. Consequently, a new independent variable referred to "pseudotime"  $\hat{t}'$  is introduced to unify two independent variables  $t'$  and  $y'$ .

$$\hat{t}' = t' - \frac{\sin\theta_B}{C'_B}y' \tag{5}$$

Providing the incident wave angle  $\theta_B$  is small, the following small parameter  $\epsilon$  can be used for the scaling of the governing equations

$$\epsilon = \frac{\sin \theta_B}{C'_B} \sqrt{gH'} \quad (6)$$

Since the length scale of variations in the  $y'$  direction is much greater than that in the  $x'$  direction and also the velocity  $v'$  is much smaller than  $u'$ , we introduce the following transformations in order to make these variables of order unity

$$v = \frac{v'}{\epsilon \sqrt{gH'}}; \quad y = \frac{\epsilon y'}{T' \sqrt{gH'}} \quad (7)$$

Using the above scaling parameters and transformations, the normalized pseudotime is given by,

$$\hat{t} = t - y \quad (8)$$

and the differentiations with the dimensional variables are replaced by as follows.

$$\frac{\partial}{\partial t} = \frac{\partial}{\partial \hat{t}} \quad \frac{\partial}{\partial y} = -\frac{\partial}{\partial \hat{t}} \quad (9)$$

After these deductions, the original equations (1) ~ (3) are considerably simplified into the following non-dimensional form.

$$\frac{\partial h}{\partial \hat{t}} + \frac{\partial(uh)}{\partial x} = \epsilon^2 \frac{\partial(vh)}{\partial \hat{t}} \quad (10)$$

$$\frac{\partial u}{\partial \hat{t}} + u \frac{\partial u}{\partial x} + \frac{\partial h}{\partial x} + S + \frac{fu |u|}{h} = \epsilon^2 v \frac{\partial u}{\partial \hat{t}} \quad (11)$$

$$\epsilon \left\{ \frac{\partial v}{\partial \hat{t}} + u \frac{\partial v}{\partial x} - \frac{\partial h}{\partial \hat{t}} + \frac{f |u| v}{h} \right\} = \epsilon^3 v \frac{\partial v}{\partial \hat{t}} \quad (12)$$

If we neglect higher terms than  $O(\epsilon^2)$ , that is, the right hand sides of Eqs. (10), (11) are set to be zero, the resultant equations are the same as the usual one dimensional shallow water wave equations normally incident to the shoreline. If we consider Eq. (12) in the order  $O(\epsilon)$ , the equation becomes as

$$\frac{\partial v}{\partial \hat{t}} + u \frac{\partial v}{\partial x} - \frac{\partial h}{\partial \hat{t}} + \frac{f |u| v}{h} = 0 \quad (13)$$

After all, the leading order in  $\epsilon$  of perturbation equations yields decoupled equations each for on-offshore motion and for longshore motion. Thus, the longshore velocity  $v(x, \hat{t})$  can be solved like one-dimensional analysis once  $h(x, \hat{t})$  and  $u(x, \hat{t})$  is known.

## 2.2 Numerical Method

The basic equations were solved using an explicit Lax-Wendroff finite difference method. To attenuate numerical oscillations in the vicinity of wave front, a so-called artificial-viscosity term was included (Hibberd-Peregrine, 1979). The computational domain in the cross shore direction was discretized into 100 grid points so that one wave length can be represented at least 20 grid points. The time discretization was set as  $\Delta t = T/4000$ .

The initial condition for free water surface  $\eta$  is still water condition;  $\eta = 0$ . Accordingly, the flow velocities  $u$  and  $v$  are set to be zero for all the computational domain. The offshore boundary was set at around one wave length offshore from the breaking point so that the boundary value for time averaged longshore velocity  $V$  may be given by zero. The offshore boundary should be devised to make the reflected waves from the on-shore side transmit through the boundary freely. The total water depth at the offshore boundary is expressed as

$$h_B = d_B + \eta_i(t) + \eta_r(t), \quad \text{at } x = 0 \quad (14)$$

in which,  $\eta_i$ ,  $\eta_r$  denotes the water surface fluctuation due to the incident and reflected waves, respectively. The time variation  $\eta_r$  was evaluated using the retreat characteristic variable  $\beta$  as follows (Kobayashi et al., 1987)

$$\eta_r(t) = \sqrt{d_B \beta(t)/2} - d_B, \quad \text{at } x = 0 \quad (15)$$

The offshore boundary condition for  $u_B$  is easily determined by the boundary values of  $\beta$  and  $h_B$ , and that for  $v_B$  was assumed to be  $u_B \tan \theta$ . The onshore boundary was treated as a moving boundary in which the front of wet waterline node was determined as such a location that the total water depth is less than a given threshold small depth (Hibbert-Peregrin, 1979).

## 2.3 Numerical Results

Calculations were carried out under similar conditions of Kamphuis's experiments(1991; a, b); that is , the water depth at the offshore boundary  $d_B' = 0.50\text{m}$ , the incident wave height  $H' = 12.4\text{cm}$ , wave period  $T' = 1.15\text{s}$ , incident wave angle  $\theta_B = 10^\circ$ , beach slope  $S' = 1/10$ .

Fig. 2 shows the computed spatial variations of free surface elevation  $\eta'$  (bottom), on-offshore velocity  $u'$  (middle) and longshore velocity  $v'$  (top). Fig. 2(a) and (b) shows the results under the bottom friction factor  $f' = 0.01$  and  $f' = 0.10$ , respectively. Comparison of these figures indicates that the results of free surface elevation  $\eta'$  and on-offshore velocity  $u'$  are little affected by the change of the friction factor, whereas the results of the longshore velocity  $v'$  shows the considerable difference by  $f'$  especially around the still water shoreline(S.W.S.L.).

Fig. 2(c) and (d) are the results when the beach slope  $S'$  is changed from the original input condition. Although, Eq. (13) for the longshore velocity  $v'$  does not include  $S'$  term, the effects of beach slope are indirectly involved in  $v'$

through the alterations of  $h'$  and  $u'$  by  $S'$ . Under the mild slope case  $S' = 1/20$ , the longshore velocity around S.W.S.L. takes small value as shown in Fig. 2(c). On the other hand, under steep slope case  $S' = 1/5$ , the longshore current velocity becomes large even in the landward region of S.W.S.L. The longshore velocity  $v'$  near S.W.S.L. is found to be positive not only up-rush phase but also down rush phase.

In order to discuss the properties of calculated longshore velocity, the following characteristics are investigated; the peak value of temporal velocity fluctuation at a specific point;  $v'_{peak}$ , the time average value;  $v'_{mean}$  and the volume flux of longshore velocity;  $Q'$ , defined as

$$Q' = \frac{1}{T} \int_0^T h' v' dt \quad (16)$$

Fig. 3 illustrates the on-offshore variations of the above characteristics. As the beach slope  $S'$  becomes steeper, all the characteristics increase and the peaks of the distributions move toward S.W.S.L. (Fig. 3(a)). Non-vanishing velocities and volume flux are found at the still water shoreline and in further landward region. Fig. 3(b) indicates the effect of incident wave period  $T'$ , where the increase of  $T'$  has the same effects as the increase of  $S'$ . Fig. 3 (c) illustrates the results when the friction factor  $f'$  is varied. The characteristics decrease with the friction factor, but the differences are not so significant.

Fig. 4 shows the temporal variations of free surface elevation  $\eta'$  (bottom), velocity vector  $\mathbf{v}'$  (middle) and volume flux vector  $\mathbf{Q}'$  (top) at the locations from offshore to onshore. In order to stress the difference between run-up and downwash motion, this calculation was carried out under relatively steep slope  $S' = 1/5$  and large wave incident angle  $\theta_B = 20^\circ$ . The stick-diagrams of  $\mathbf{v}'$  show that the water mass runs up on the beach with a certain angle to the shoreline, then runs down approaching the right angle. The diagram of volume flux  $\mathbf{Q}'$  shows more predominant difference in magnitude between run-up and run-down phases, because the water depth  $h'$  becomes larger in run-up phase than in run-down phase. This property is more evident as the location  $(x - x_0)/x_0$  ( $x_0 = d'_B/S'$ : the position of still water shoreline) is in the direction of landward. These properties seem to be useful to explain the zig-zag sediment transport in a swash zone. The velocity vector  $\mathbf{v}'$  or the volume flux vector  $\mathbf{Q}'$  may govern the sediment movement corresponding whether the transport mode is bed load or suspended load, respectively.

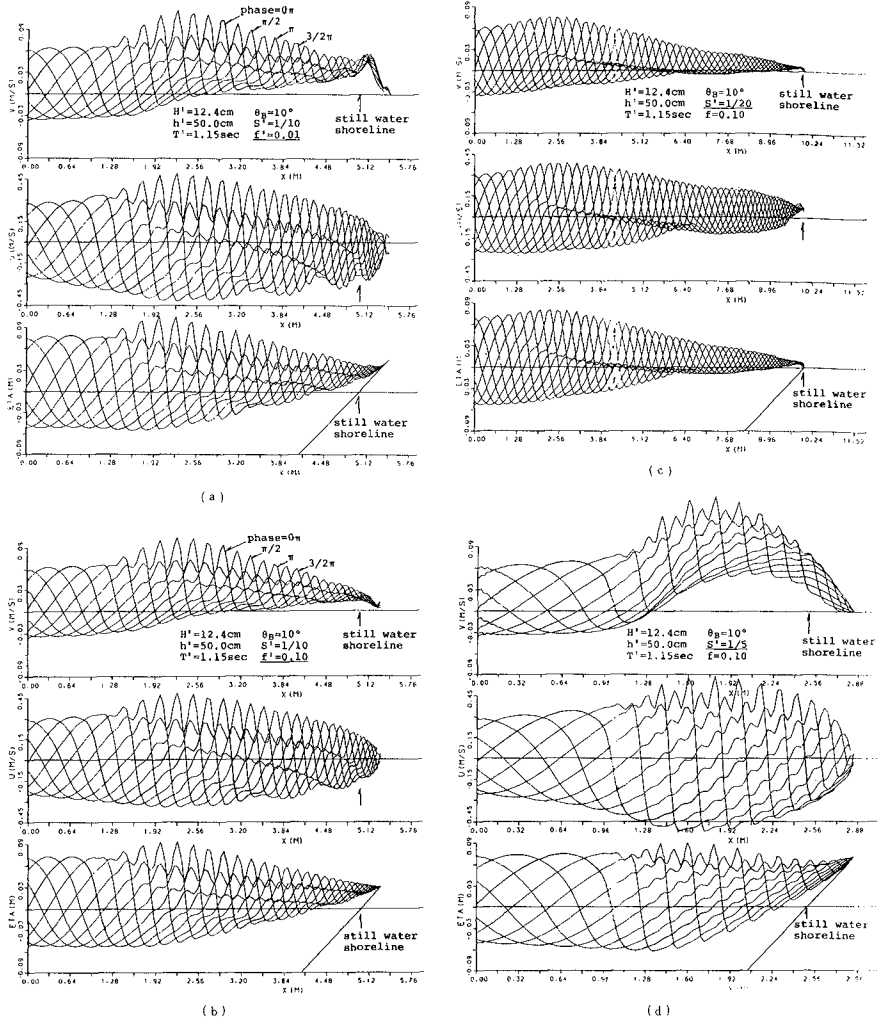


Fig. 2: Spatial variations of longshore velocity  $v'$  (top), on-offshore velocity  $u'$  (middle) and free surface elevation  $\eta'$  (bottom)

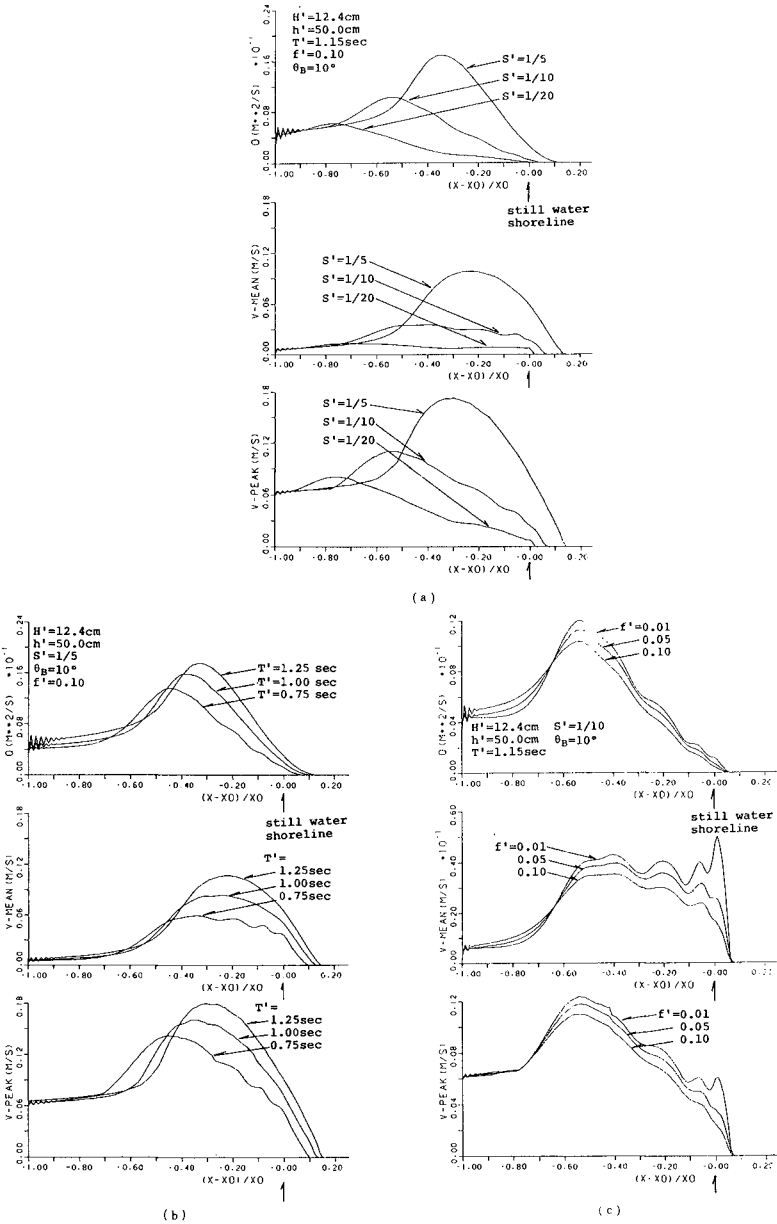


Fig. 3: On-offshore variations of the peak longshore velocity  $v'_{peak}$  (bottom), time averaged longshore velocity  $v'_{mean}$  (middle) and time averaged longshore volume flux  $Q'$  (top)

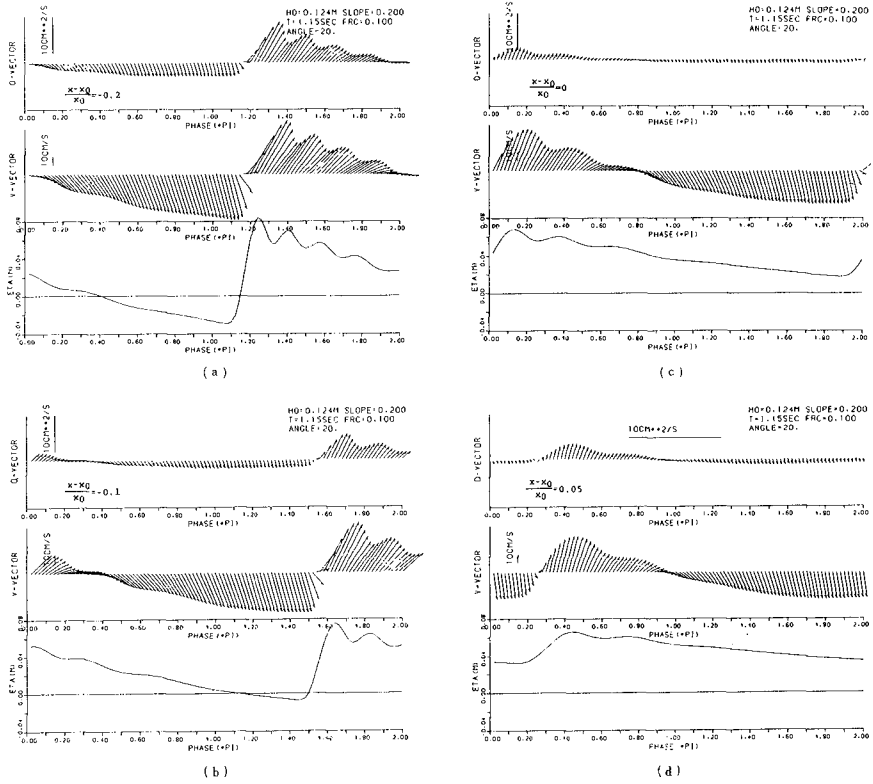


Fig. 4: Temporal variations of free surface elevation  $\eta'$  (bottom), velocity vector  $v'$  (middle) and longshore volume flux vector  $Q'$  (top)



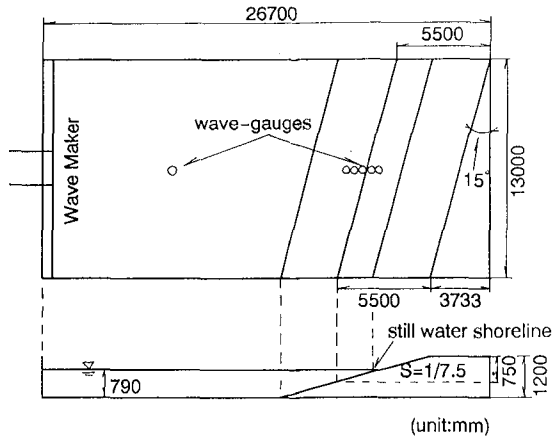


Fig. 5: Wave basin and experimental set-up

### 3. EXPERIMENTAL STUDY

#### 3.1 Experimental Arrangements and Procedure

A wave basin of 26.7m long, 13m wide and 1.2m deep was used. A uniform plane slope of the gradient  $S=1/7.5$  was set up at an angle  $\theta = 15^\circ$  with a wave generator which was equipped at the other end of the basin. The slope was carefully built up by covering 30mm thick concrete mortar with reinforced mesh over a sandy mound. The water depth in the offshore uniform depth region was kept at 79cm constant throughout the experiments. Water surface fluctuations were measured with an array of five capacitance type wave gauges at 12.5cm interval on the slope. The experimental set-up is illustrated as Fig. 5.

In order to measure very shallow flows in a swash zone including landward region of the still water shoreline, tracer method was adopted. An important demand for the tracer is to represent the fluid velocity accurately in the swash zone. Another demand is visibility because the tracer movements were recorded with a bird's-eye video camera locating 5 ~ 6 m above the water surface. After several trials, the following three type tracers were chosen: a fluorescent color sphere float of styrene form with 3cm in diameter(type-A), a 2.5mm thick circular plate made of plywood with 110mm diameter(type-B) and a 6.6mm thick octagonal plate made of plywood with 93mm in diagonal length(type-C). A small electro-magnetic current meter with a cylindrical shape sensor 16mm in length and 5mm in diameter was also used in the preliminary measurements.

For each test run, the velocity measurement was started two minutes after the start of wave generation to attain the steady state condition. The velocity measuring area for the tracer method should be chosen where the uniformity of the longshore current is confirmed. In order to detect the position of a moving tracer throughout the surf zone and swash zone, a 20cm-mesh reference

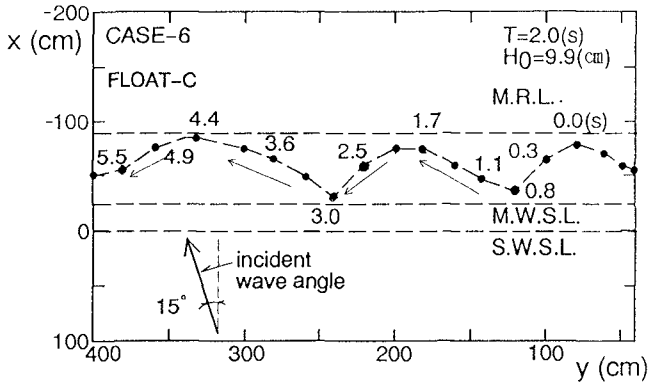


Fig. 6: Trajectories of tracers

frame of  $3.6\text{m} \times 3.6\text{m}$  was installed. The trajectories of the tracers over the reference frame were recorded at an interval of  $1/30$  second. Frame by frame analysis of the video film yields Lagrangian velocities both in on-offshore and alongshore directions. For the detailed descriptions of the experiment, see Asano et al.(1994).

### 3.2 Experimental Results on Longshore Velocity in Surf and Swash Zone

Fig. 6 shows examples of plane trajectories of tracers. Each tracer runs up obliquely on the slope, then tends to run-down vertically. This property corresponds to the numerical results illustrated in Fig. 4.

The longshore velocity of a fluid particle was herein evaluated from the alongshore displacement of the tracer during one wave cycle. Fig. 7 shows an example of the on-offshore distributions of longshore current velocity  $V$ . In plotting the data  $V$ , the  $x$ -position was determined by the central point of a tracer over one wave cycle. Some data which the position after one wave cycle were clearly shifted in the on-offshore direction were discarded. Fewer data are obtained in the negative  $x$ -region because the plate type tracers (type-B and C) are frequently thrown up on the slope. Also fewer data are available slightly onshore of the breaking point because white-caps generated by breaking waves often make tracer invisible. Since no obvious differences by the tracer types are noticed in Fig. 7, results will be shown without distinguishing the tracer types in the following. One important point in this result is that the longshore current velocity at the still water shoreline  $x=0$  has the same order of magnitude as that in the surf zone.

Fig. 8 shows the results where the incident wave heights are almost the same. Here, the measured longshore current velocities including the case shown in Fig. 7 are averaged over every 10cm segment in the on-offshore direction, then plotted in the non-dimensional form  $V/V_{max}$  against normalized alongshore

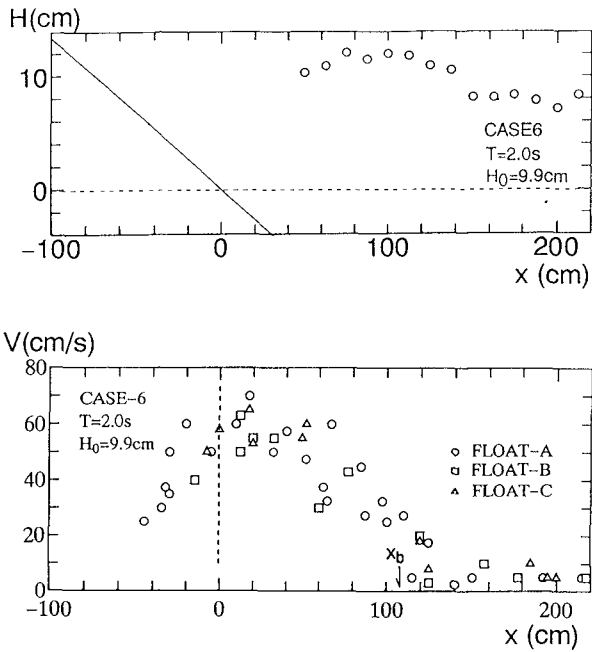


Fig. 7: On-offshore distributions of wave height and longshore current velocity

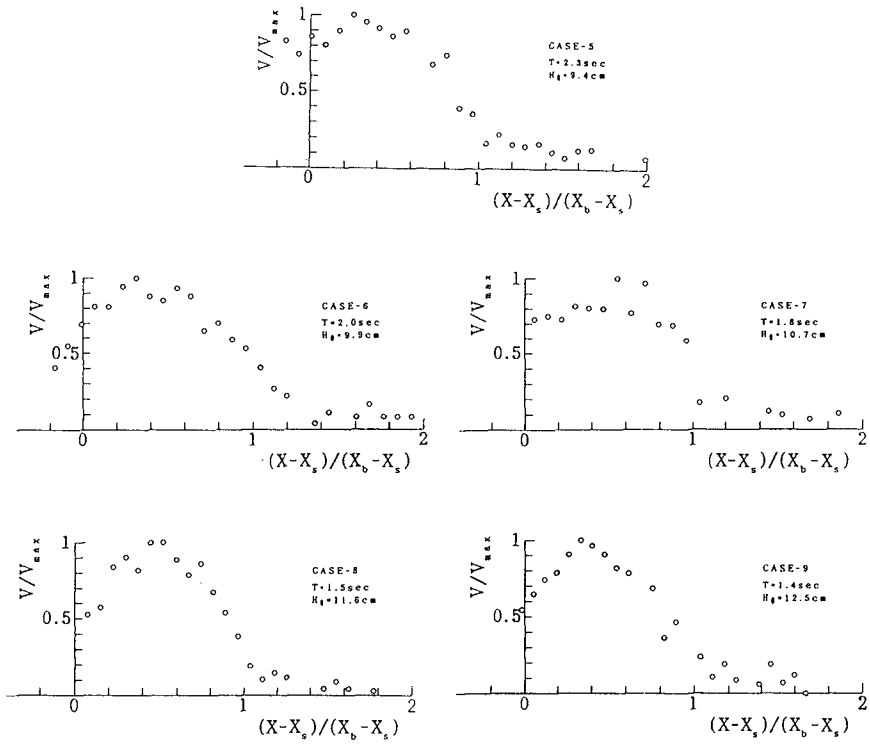


Fig. 8: On-offshore distributions of longshore current velocity

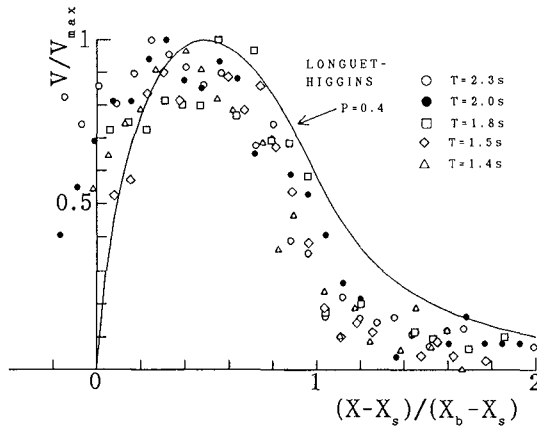


Fig. 9: On-offshore distributions of longshore current velocity and comparison with Longuet-Higgins'(1970) analytical solution

position.

Fig. 9 shows the comparison of all the data shown in Fig. 8 with Longuet-Higgins'(1970) analytical solution, in which the ratio between the horizontal mixing term and the friction term  $P$  is given by 0.4. It should be noted that little attention has been paid on the longshore current velocity at and beyond the shoreline landward, and conventional time averaged models inevitably predict the longshore current at the shoreline  $V_s$  as 0. Whereas, Fig. 8 and Fig. 9 show that  $V_s$  has a substantial value even at the mean water shoreline  $x = x_s$  after wave set-up. It is also noticed that the longshore velocity at the mean water shoreline  $V_s$  increases with the incident wave period. This property agrees with the numerical results shown in Fig. 3 (b).

Further investigation reveals that the present results as well as a part of Visser(1991)'s results on  $V_s/V_{max}$  are well arranged by the surf similarity parameter (See Asano et al.(1994)).

#### 4. CONCLUSIONS

A numerical model is developed to predict the flow characteristics in a swash zone for obliquely incident wave trains. The two dimensional shallow water equations are de-coupled into independent equations each for on-off shore motion and for longshore motion. The numerical results on the longshore velocity in a swash zone are compared with measured results by the tracer method. Both the numerical and experimental studies reveal the following properties.

- (1) Substantial longshore velocities have been obtained even in the landward region of the still water shoreline.
- (2) The magnitude of the longshore current velocities at the mean water shoreline is found to increase with the beach slope and incident wave period.

(3) The swash wave which rushed up obliquely on a slope tend to run down approaching to the right angle with the shoreline. The property may cause zig-zag longshore sediment transport inherent in swash zone.

Quantitative comparison between numerical and experimental results should be conducted with considering the effects of the vertical velocity profiles and turbulence in swash waves.

## REFERENCES

- Asano T., H. Suetomi and J. Hoshikura (1994): Velocity measurements in swash zone generated by obliquely incident waves, Coastal Engineering in Japan (in Printing).
- Asano T. and T. Nakano (1992): Numerical Analysis on obliquely incident run-up waves, Proc. of Coastal Engrg., JSCE, Vol. 39, pp.26-30 (in Japanese).
- Bodge K. R. and R. G. Dean (1987): Short-term impoundment of longshore transport, Proc. of Coastal Sediment '87, pp.468-483.
- Hibberd, S. and Peregrine, D.H. (1979): Surf and run-up on a beach; A uniform bore, J. of Fluid Mech., Vol.95, pp.323-345.
- Kamphuis J. W. (1991, a): Wave transformation, Coastal Engineering, Vol.15, pp.173-184.
- Kamphuis J. W. (1991, b): Alongshore sediment transport rate distribution, Proc. of Coastal Sediment '91, pp.170-183.
- Kobayashi N., A. K. Otta and I. Roy (1987): Wave reflection and run-up on rough slopes, J. of Waterway, Port, Coastal and Ocean Div., ASCE, Vol.113, No.3, pp.282-298.
- Longuet-Higgins, M. S. (1970) : Longshore current generated by obliquely incident sea waves, J. Geophys. Res. , Vol.75, pp.6778-6801.
- Ryrie S. C. (1983): Longshore motion generated on beaches by obliquely incident bores, J. Fluid Mech., Vol.129, pp.193-212.
- Thornton E. B. and S. Abdelrahman (1991): Sediment transport in the swash due to obliquely incident wind-waves modulated by infragravity waves ; Proc. Coastal Sediment '91, pp. 100-113.
- Visser, P. J.(1991) : Laboratory measurements of uniform longshore currents, Coastal Engineering, Vol. 15, pp.563-593.

## CHAPTER 3

# LABORATORY COMPARISON OF DIRECTIONAL WAVE MEASUREMENT SYSTEMS AND ANALYSIS TECHNIQUES

Michel BENOIT<sup>1</sup> and Charles TEISSON<sup>2</sup>

### Abstract

In order to define a directional wave sensor for laboratory experiments, three measuring systems as well as seven directional analysis methods are combined, applied and compared on three different tests performed in a directional wave basin. "Single-point" gauges are found to accurately analyse unimodal spectra when associated to advanced methods (Fit to bimodal model, Iterative Maximum Likelihood Method, Maximum Entropy Method, Bayesian Method). The heave-pitch-roll gauge used in this study is in particular very simple and shows promising capabilities. For bimodal spectra (two directional peaks at same frequency) however, only the wave probe array combined with the Maximum Entropy Method or the Bayesian Method appears to be able to produce reliable estimates.

### 1. INTRODUCTION — SCOPE OF THE STUDY

The measurement of directional wave spectrum may be performed through various systems, including co-located gauges (directional buoys, pressure sensor combined with a 2D currentmeter,...), arrays of gauges (wave probe arrays or mixed instruments arrays) or remote-sensing systems (satellite synthetic aperture radar, aerial stereo-photography techniques,...). Each of these measuring devices delivers a rather limited amount of information and the estimation of directional wave spectrum is then an awkward inverse problem, mathematically speaking. In order to get an estimate from the data anyway, various directional analysis methods have been proposed : Fourier Series Decomposition, Fit to parametric models, Maximum Likelihood Methods, Maximum Entropy Methods, Bayesian Methods,...

From practical point of view these methods exhibit different behaviours and characteristics for instance in mathematical complexity, directional accuracy, directional spectrum shape dependency, computing time, numerical convergence,... A good number of these methods have recently been implemented at Laboratoire National d'Hydraulique (LNH) and tested quite extensively on numerical simulations using heave-pitch-roll data (Benoit, 1992) as well as gauge array data (Benoit, 1993). The present study aims to proceed a step further in this comparative analysis by evaluating the capabilities of the methods on laboratory data.

1 Research Engineer — Maritime Group

2 Head of Maritime Group

EDF - Laboratoire National d'Hydraulique, 6, quai Watier 78400 CHATOU, FRANCE

We briefly recall that the main unknown of the problem is the directional wave spectrum  $S(f,\theta)$ , a function of wave frequency  $f$  and direction of propagation  $\theta$ . The following conventional decomposition is used :  $S(f,\theta) = E(f).D(f,\theta)$

$E(f)$  is the classical variance or 1D-spectrum that may be estimated by a single record of free-surface elevation. and  $D(f,\theta)$  is the Directional Spreading Function (DSF) satisfying two important properties :

$$D(f,\theta) \geq 0 \text{ over } [ 0 , 2\pi ] \quad \text{and} \quad \int_0^{2\pi} D(f,\theta) d\theta = 1$$

The directional analysis procedure may be roughly decomposed into three steps :

- a. record simultaneously one or several wave properties (elevation, velocities, pressure, slopes,...) at one or more locations :  $X_1(t), \dots, X_N(t)$  ( $N \geq 3$ )
- b. compute the cross-spectra between each pair of recorded signals :

$$G_{ij}(f) = \int_{-\infty}^{+\infty} R_{ij}(\tau) e^{-i2\pi f\tau} d\tau \quad \text{with} \quad R_{ij}(\tau) = \lim_{T \rightarrow \infty} \frac{1}{T} \int_0^T X_i(t).X_j(t+\tau) dt$$

- c. estimate the directional spectrum by inverting the following set of equations :

$$G_{ij}(f) = \int_0^{2\pi} H_i(f,\theta). \bar{H}_j(f,\theta).S(f,\theta) .\exp(-\vec{k}.\vec{x}_{ij}) d\theta$$

In this study, three measuring systems are set up in LNH directional wave basin (see section 2) and seven directional analysis methods are selected (see section 3). The experimental lay-out is described in section 4 and the three test-cases are presented in section 5. The comparative analysis of results is reported in section 6.

**2. DIRECTIONAL MEASURING DEVICES**

Three measuring systems are considered for laboratory measurements (figure 1) :

— a wave probe array : the array is composed of five probes (numbered from 1 to 5) laid out on the same configuration as the one used by Nwogu (1989). The wave probes are resistive-type wires mounted on a frame that allows a precise positioning. The radius  $R$  of the array is 0.40 m. As it will be presented in section 5, the wavelength corresponding to peak frequency is  $L_p = 2.42$  m, and thus the ratio  $R/L_p$  is about 16 %.

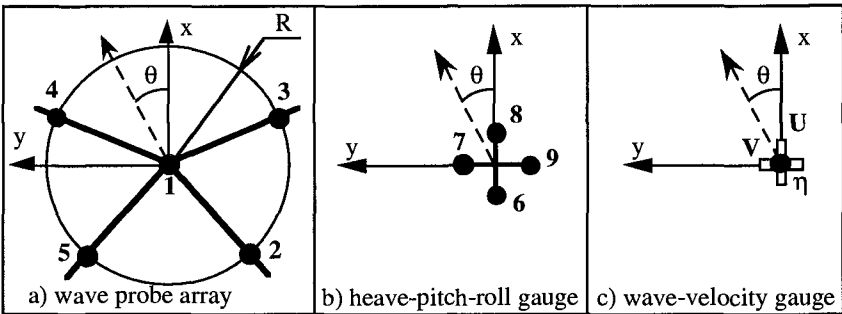


**Figure 1 :** the three directional measuring devices used for experiments.



— a "heave-pitch-roll" gauge : this gauge aims to deliver the same type of signals as the heave-pitch-roll buoy used in the field. To that extent, four wave probes are set up close to each other in a very simple way (see figure 1-b). From the four recorded free-surface elevation time series, the elevation and two orthogonal slopes of free-surface at the center of the gauge are computed :

$$\eta(t) = (\eta_6 + \eta_7 + \eta_8 + \eta_9)/4.$$

$$\frac{\partial \eta}{\partial x}(t) = \frac{\eta_8(t) - \eta_6(t)}{d_{6,8}}$$

$$\frac{\partial \eta}{\partial y}(t) = \frac{\eta_7(t) - \eta_9(t)}{d_{7,9}} \quad \text{with : } d_{6,8} = 11.4 \text{ cm} \quad \text{and} \quad d_{7,9} = 13.2 \text{ cm}$$

— a wave-velocity gauge : as the previous one, this gauge is also a "single-point" gauge, recording at the same location the free-surface elevation (through a wave probe) and the two horizontal components of velocity (through a 3D acoustic velocimeter, from which only the two velocity signals U and V are kept).

### 3. DIRECTIONAL ANALYSIS METHODS

Among the methods available at LNH, the seven following ones are considered, because each of them may be used both for "single-point" systems and arrays :

— **Weighted Fourier Series (WFS)** : the directional spreading function is expressed as a truncated Fourier series whose first coefficients are computed from the cross-spectra (Borgman, 1969). A weighting function is used to avoid possible negative values taken by this estimate (Longuet-Higgins *et al.*, 1963).

— **Fit to bimodal Gaussian model (2MF2)** : A bimodal parametric model obtained from linear combination of two unimodal Gaussian-type models is used. Its five unknown parameters are determined from the cross-spectra. In the case of "single-point" systems, the problem becomes awkward because there are only four information available and additional constraints are thus needed (Benoit, 1992).

— **Maximum Likelihood Method (MLM)** : By this method the directional spectrum is regarded as a linear combination of the cross-spectra. The weighting coefficients are calculated with the condition of unity gain of the estimator in the absence of noise (Oltman-Shay and Guza, 1984 ; Krogstad, 1988). Recently, Haug and Krogstad (1993) proposed a modified version of MLM (the constrained MLM) for gauge arrays which is not taken into account here.

— **Iterative Maximum Likelihood Method (IMLM2)** : The estimate obtained from the former method is not consistent with the measured cross-spectra. It may be iteratively modified to let its cross-spectra become closer to the ones obtained from the data (Oltman-Shay and Guza, 1984).

— **Maximum Entropy Method (MEM2)** : The method is based on the

definition of Shannon for entropy :

$$\chi = - \int_0^{2\pi} D(f, \theta) \cdot \ln(D(f, \theta)) \, d\theta .$$

This entropy is maximized under the constraints given by the cross-spectra. The application to single-point systems or gauge arrays is described by Kobune and Hashimoto (1986), Nwogu *et al.* (1987) and Nwogu (1989).

This entropy definition is different from the one used by other authors (e.g. Lygre and Krogstad, 1986) which generally appears to be less powerfull.

— **Bayesian Directional Method (BDM)** : No *a priori* assumption is made about the spreading function which is considered as a piecewise-constant function over  $[0, 2\pi]$ . The unknown values of  $D(f, \theta)$  on each of the  $K$  segments dividing  $[0, 2\pi]$  are obtained by considering the constraints of the cross-spectra and an additional condition on the smoothness of  $D(f, \theta)$  (Hashimoto *et al.*, 1987).

— **Variational Fitting Technique - Long-Hasselmann Method (LHM)** : Long and Hasselmann (1979) developed this method by which an initial simple estimate is iteratively modified to minimize a "nastiness" function that takes into account the various conditions on the spreading function. The application to buoy data is described in detail by Long (1980).

When referring to previous LNH numerical comparative surveys (Benoit, 1992), the Fit to unimodal model method (e.g. Borgman, 1969) and the Eigenvector Method (Mardsen and Jusko, 1987) have been dropped. The former is definitely unable to analyse bimodal cases and the latter has not been applied to gauge arrays.

#### 4. EXPERIMENTAL LAY-OUT

The LNH multirectional wave facility is a rectangular wave basin of 50 m by 30 m used for coastal studies. The segmented wavemaker is composed of 56 piston-type paddles. The width of the paddles is 0.40 m. The total wavemaker length is thus 22.4 m. It is movable along the main side of the basin. The maximum water depth in the basin is 0.80 m. The facility is equipped with numerous mobile upright progressive wave absorbers. Each absorber unit measures 2.8 m by 2 m, allowing variable and adaptable absorber configurations in the basin. Tidal currents may also be simulated in addition to waves.

For the present experiments only the eastern part of the basin was used as there was a breakwater model set up in the remaining part of the basin. Only the first 30 paddles were activated, giving an effective wavemaker length of 12 m. The test area was then a rectangle of 12 m by 25 m (figure 2) limited by wave absorbers. Fully reflective sheets over a length of 6 m were set-up at each side of the wavemaker in order to increase the work area through the corner reflection method. The bottom was flat over the whole test area. The water depth was kept constant at 0.60 m.

The three measuring devices were located 6 m apart from the wavemaker. They were set up every 0.40 m on a line parallel to the wavemaker (see figure 2).

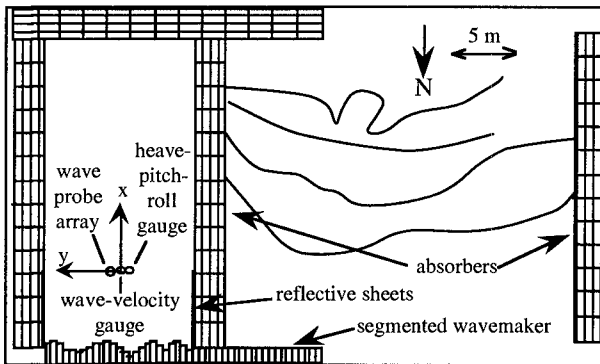


**Figure 2 :** definition sketch of experimental setup.

**5. CHARACTERISTICS OF LABORATORY TEST-CASES**

5.1 Wave simulation characteristics

The directional wave simulation is achieved by using a "single summation" method (also called "single direction per frequency method") (Miles, 1989) :

$$\eta(x,y,t) = \sum A_n \cos(2\pi.f_n.t - k_n(x.\cos \theta_n + y.\sin \theta_n) + \phi_n)$$

The sea surface elevation is obtained through a linear superposition of numerous elementary components. The amplitude of each component is related to the target spectrum through :  $A_n = \sqrt{2 S(f_n, \theta_n) \Delta f_n \Delta \theta_n}$

The phases are uniformly and randomly distributed over  $[0, 2\pi]$ . The directions  $\theta_n$  are of the form  $k.\Delta\theta$ , but randomly distributed over  $[0, 2\pi]$ .

The frequency spectrum  $E(f)$  is a classical JONSWAP spectrum with a significant wave height of 0.10 m, a peak period of 1.3 s and a peak-factor  $\gamma = 5$ . The simulated directional spreading function (DSF) is frequency independent :

$$\Pi_{s1,\alpha1,s2,\alpha2,\lambda}(\theta) = \lambda.\Pi_{s1,\alpha1}(\theta) + (1-\lambda).\Pi_{s2,\alpha2}(\theta) \quad \text{with } 0 \leq \lambda \leq 1$$

$$\text{with : } \Pi_{s,\alpha}(\theta) = \Delta(s) \cos^{2.s}[(\theta - \alpha)/2] \quad \text{if } \theta - \alpha \in [-\theta_m ; \theta_m] \quad (\theta_m = 60^\circ)$$

Three DSF are simulated with the following characteristics (see figure 3) :

Test	Description	s1	$\alpha1$	s2	$\alpha2$	$\lambda$
A1	Unimodal Broad DSF	1	0.			1.
A3	Unimodal sharp DSF	15	0.			1.
A5	Bimodal DSF	25	-40.°	5	30.°	0.5

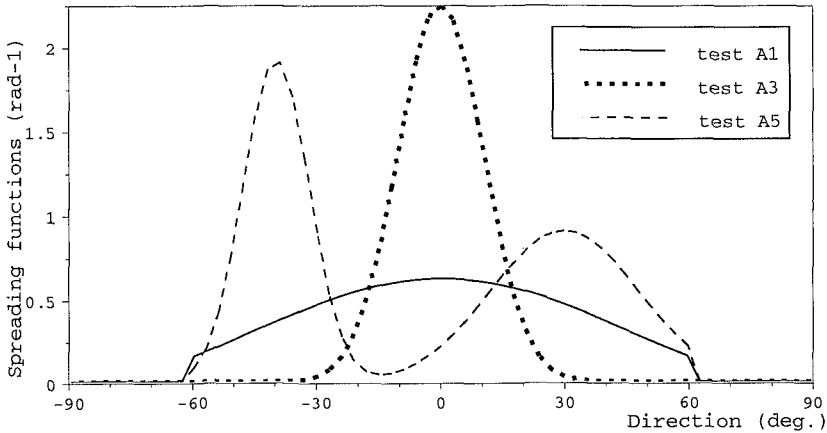


**Figure 3 : The three simulated directional spreading functions.**

5.2 Signal recording characteristics

The signals are recorded with a time step of 0.05 s over a duration of 819.2 s.

5.3 Cross-spectral analysis characteristics

The spectral analysis procedure is based on the technique of the averaged periodogram on the whole recorded signals partitioned in segments of 512 points. An overlapping of 25% between adjacent segments is used. The resulting frequency resolution is 0.039 Hz. Directional analysis is carried out between 0.5 and 1.25 Hz.

## 6. PRESENTATION AND DISCUSSION OF LABORATORY TESTS RESULTS

The directional spectra analysed on the three laboratory test-cases are presented using 2D-plots on figures 4-a and 4-b (test A1), 5-a and 5-b (test A3), 6-a and 6-b (test A5). Figure 7 gives a 3D-view of directional spectra analysed by MEM2 and BDM for the three measuring devices on test A5.

### 6.1 Analysis of test A1 — Unimodal broad spectrum — Figures 4-a and 4-b :

— Wave probe array : Reliable estimates are obtained by the BDM and MEM2 methods only. The WFS, MLM and LHM estimates are broader than the target spectrum. The 2MF2 and IMLM2 estimates are either too sharp or quite bimodal and reveal some unstable behaviour of the methods.

— Heave-pitch-roll gauge : Very accurate and similar estimates are obtained from the 2MF2, IMLM2, MEM2 and BDM methods. This similarity allows a certain confidence in the results of this gauge. The spectra analysed by the WFS, MLM and LHM methods are too broad.

— Wave-velocity gauge : the behaviour of analysis methods is very similar to the heave-pitch-roll gauge, but the estimated spectra are a little bit sharper than the former ones. Correct estimates are again obtained from the 2MF2, IMLM2, MEM2 and BDM methods.

### 6.2 Analysis of test A3 — Unimodal sharp spectrum — Figures 5-a and 5-b :

— Wave probe array : Best estimates are obtained from MEM2 method. The BDM and IMLM2 methods produce acceptable results, but the latter one shows some numerical instabilities out of peak region. The 2MF2 method also exhibits some numerical instabilities, resulting in spurious peaks of the spectrum. The WFS, MLM and LHM methods are unable to model the sharpness of the spectrum and appear to be unefficient for sea-states with narrow angular spreading of energy.

— Heave-pitch-roll gauge : the best estimates are given by IMLM2, BDM and MEM2 methods. The spectrum analysed by the 2MF2 method is clearly too sharp, while the spectra analysed by the WFS method especially, but also by the MLM and LHM methods, are far too broad.

— Wave-velocity gauge : As for test A1, the observations for this measuring device are very close to the ones of heave-pitch-roll gauge. Again the most accurate estimates are achieved by the IMLM2, BDM and MEM2 methods. On this second case however the directional widths of the estimates are very close to those obtained from heave-pitch-roll gauge.

### 6.3 Analysis of test A5 — Bimodal spectrum — Figures 6-a, 6-b and 7 :

— Wave probe array : Reliable estimates are obtained from the 2MF2, MEM2 and BDM methods. For these three methods the bimodal nature of the sea-state (with a difference in the shapes of the two peaks) is clearly reproduced. On figure 7 it may be seen that the spectra given by MEM2 and BDM agree quite well with the theoretical spectrum. One must emphasize that this bimodal case with two peaks at the same frequency only separated by 70 degrees is very severe. Bimodality of spectrum is hardly detected by the LHM and the IMLM2. The WFS and MLM methods only produce a unimodal and very broad spectrum.

— Heave-pitch-roll gauge : The results given by the various methods are definitely worse than for the wave probe array. The quite low number of information recorded by the single point-system undoubtedly limits here the resolution capability of the analysis methods. The bimodal nature of the spectrum is

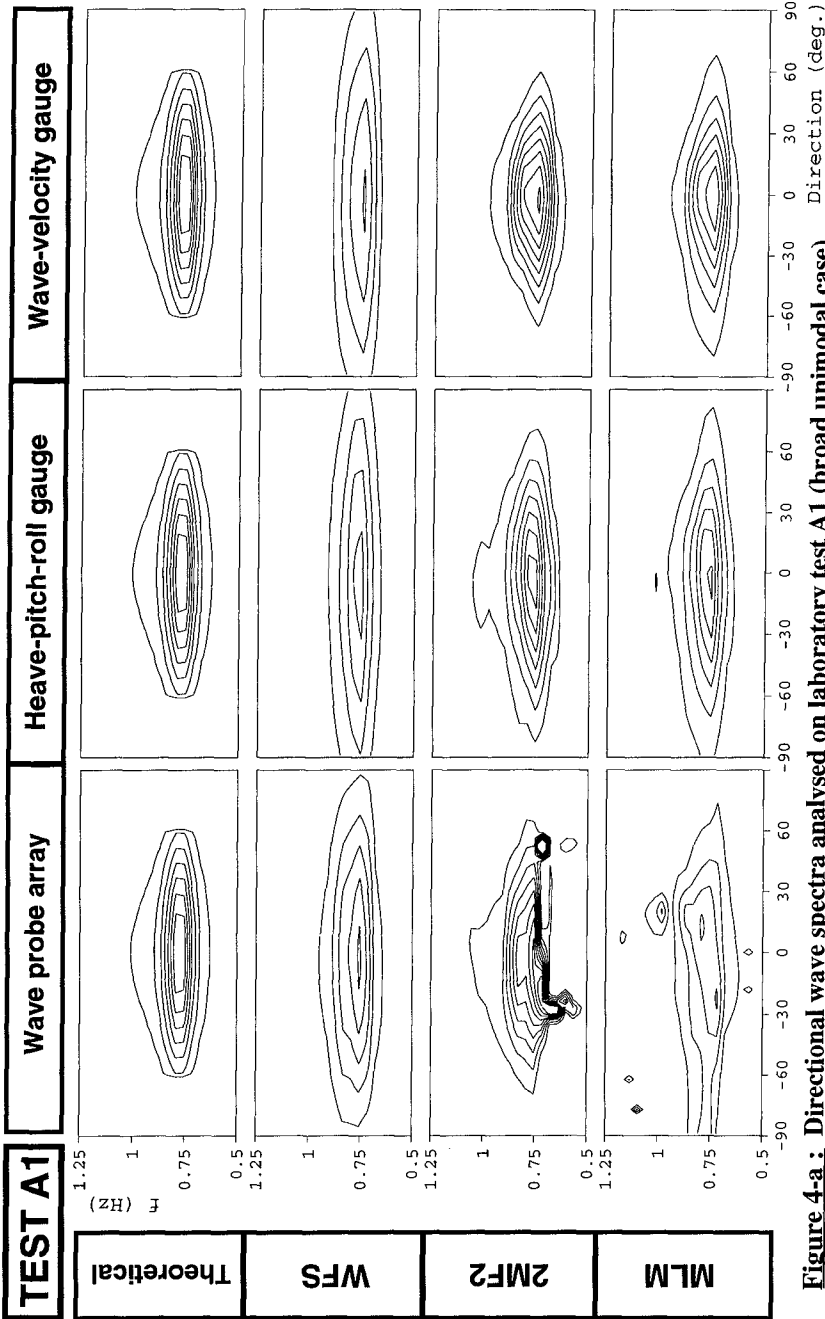
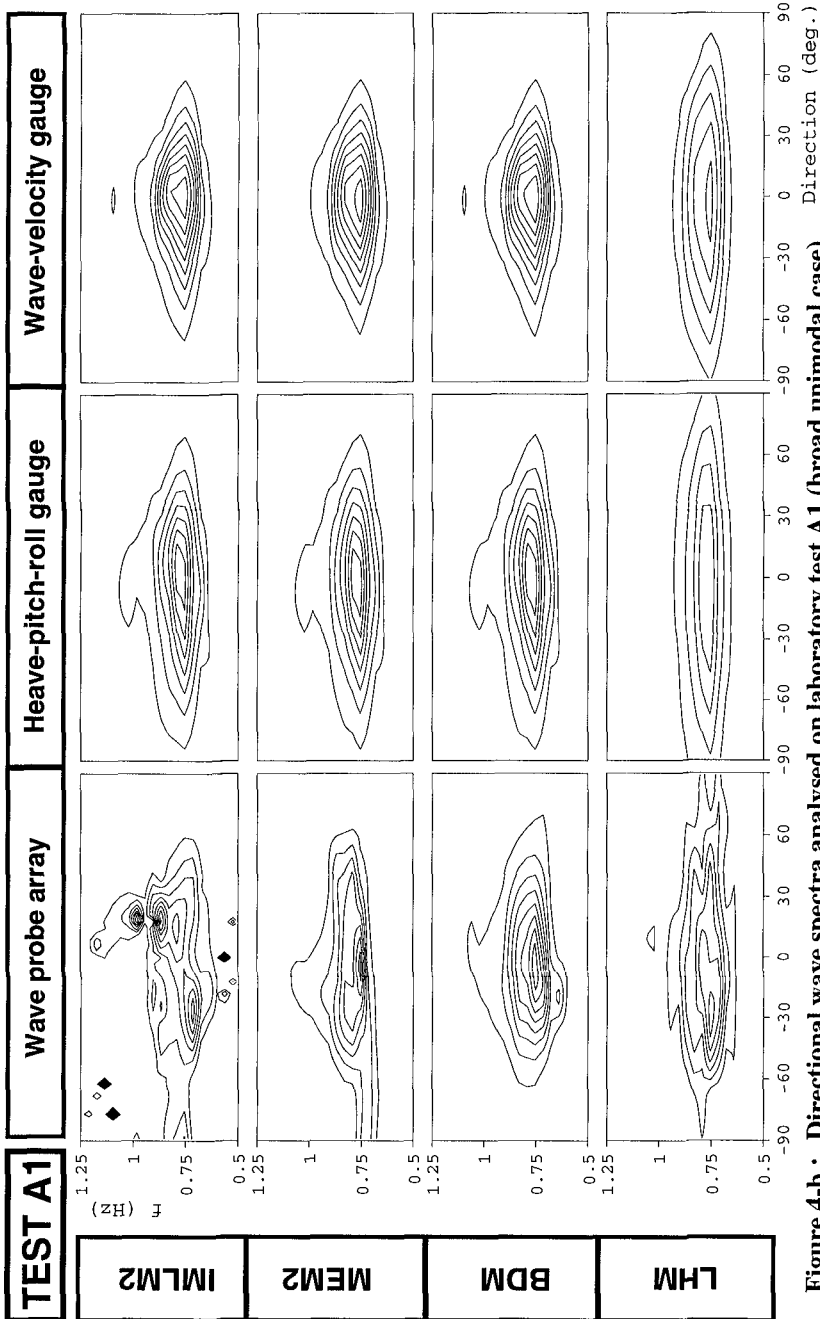
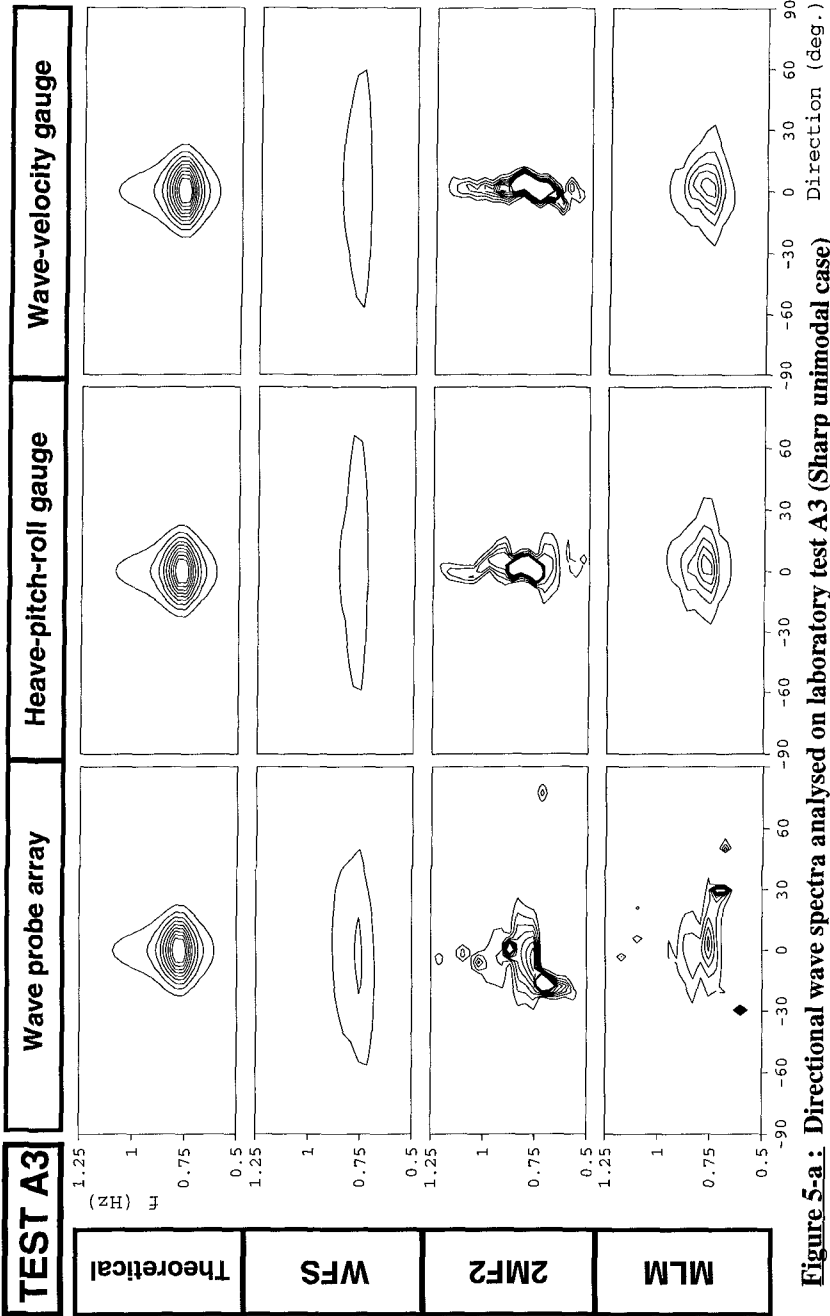


Figure 4-a: Directional wave spectra analysed on laboratory test A1 (broad unimodal case)  
 Comparison of measuring systems and analysis methods (WFS, 2MF2, MLM)



**Figure 4-b:** Directional wave spectra analysed on laboratory test A1 (broad unimodal case)  
 Comparison of measuring systems and analysis methods (IMLM2, MEM2, BDM, LHM)



**Figure 5-a :** Directional wave spectra analysed on laboratory test A3 (Sharp unimodal case)  
 Comparison of measuring systems and analysis methods (WFS, 2MF2, MLM)

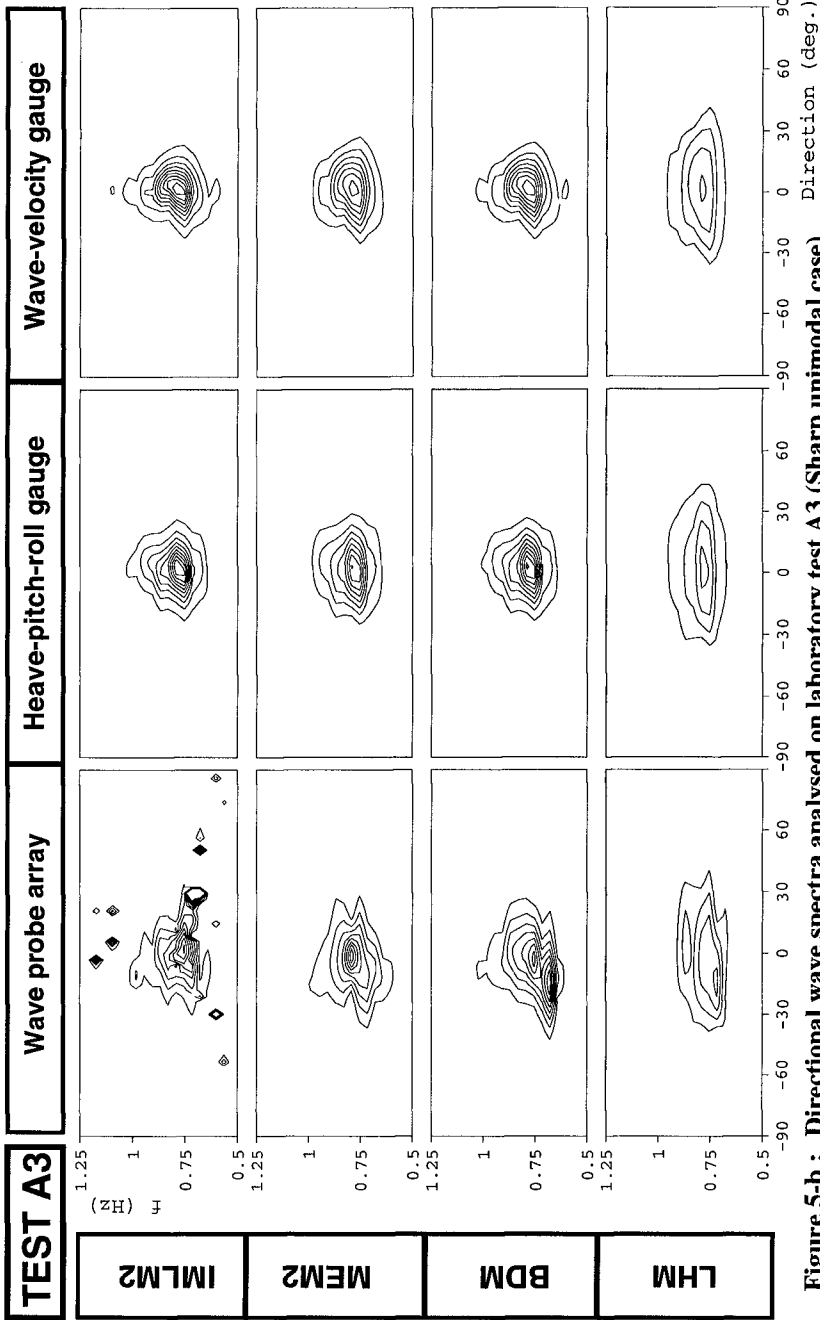


**Figure 5-b :** Directional wave spectra analysed on laboratory test A3 (Sharp unimodal case)  
 Comparison of measuring systems and analysis methods (IMLM2, MEM2, BDM, LHM)



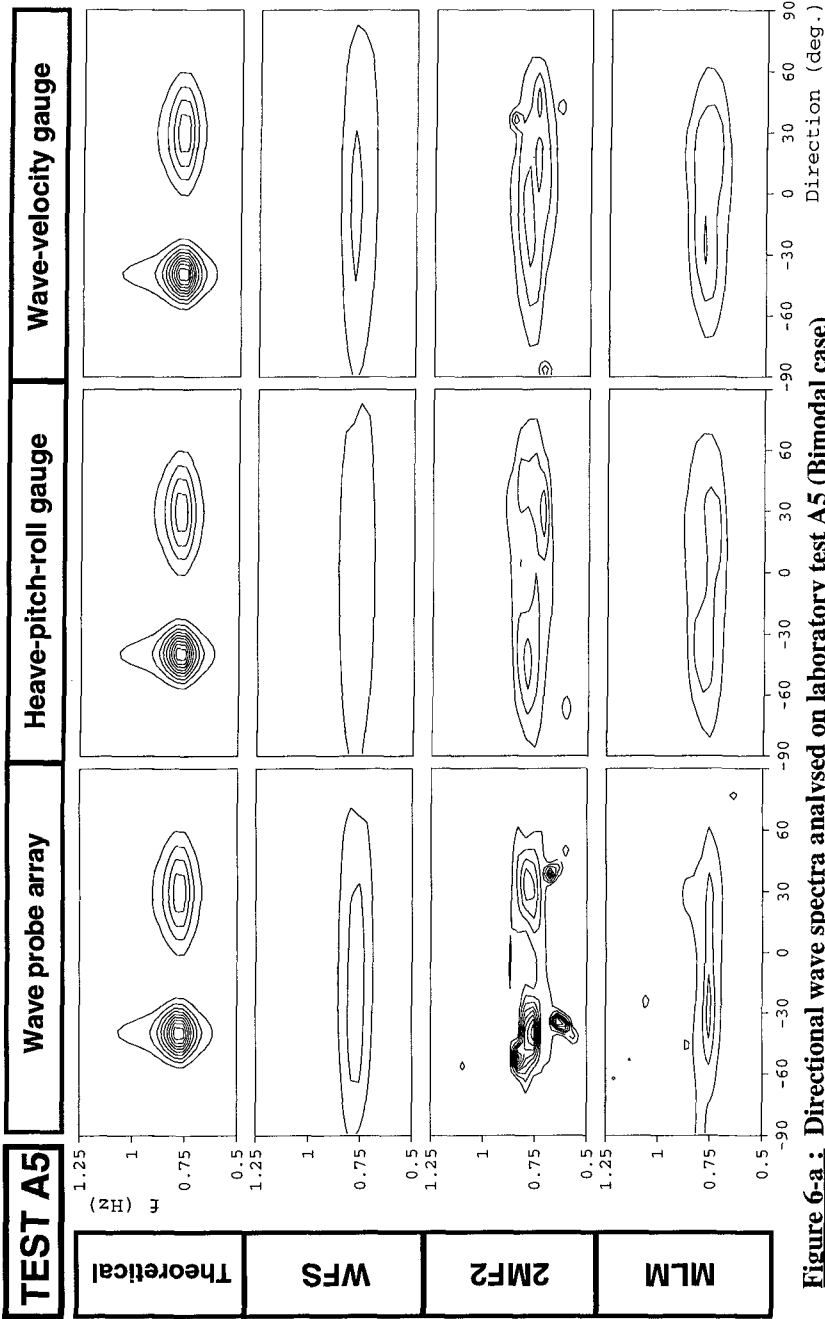


**Figure 6-a:** Directional wave spectra analysed on laboratory test A5 (Bimodal case)  
 Comparison of measuring systems and analysis methods (WFS, 2MF2, MLM)

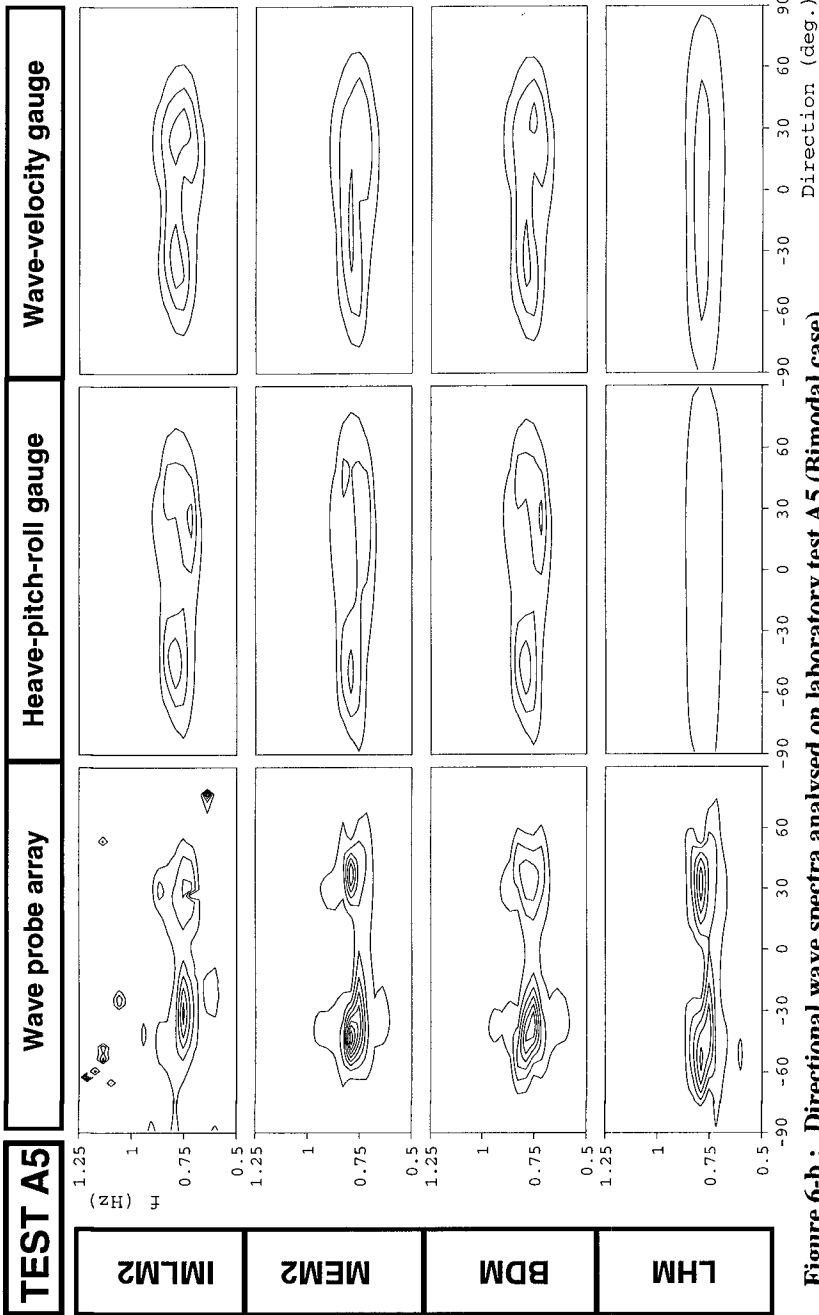


**Figure 6-b :** Directional wave spectra analysed on laboratory test A5 (Bimodal case)  
 Comparison of measuring systems and analysis methods (IMLM2, MEM2, BDM, LHM)

slightly noticeable for the 2MF2, IMLM2, MEM2 and BDM methods, but it is almost impossible to get detailed information about the relative shapes of the two peaks. Again these four methods give very similar and concordant results.

— Wave-velocity gauge : Most of the estimates are of same quality —and generally even a little bit worse— than the ones obtained from the heave-pitch-roll gauge. An exception is maybe the IMLM2 method which shows some better results than for the heave-pitch-roll gauge. Figure 7 however indicates that on this test-case the heave-pitch-roll gauge is superior to the the wave-velocity gauge when associated with sophisticated methods (MEM2 and BDM).

## 7. CONCLUSIONS — FUTURE WORK

Based on the comparative analysis of the various laboratory experiments carried out during this study, the following conclusions may be expressed :

- Great care should be given to the preliminary steps of signal recording and spectral analysis. There is a strong need to record rather long time series in order to get minimum variance spectral estimates. It seems worthwhile to increase the number of degrees of freedom of the cross-spectra as much as possible.
- The analysis of unimodal directional sea-states may be quite efficiently achieved by "single-point" (or "co-located") measuring systems, recording only three wave signals : heave-pitch-roll gauge or wave-velocity gauge.
- Each of these gauges usually produces concordant estimates from the 2MF2, IMLM2, MEM2 and BDM methods. When associated to one of these analysis methods, the "single-point" gauges exhibit good resolution capabilities for unimodal spectra, whatever the directional spreading of energy is.
- In addition, the comparison of tests results seems to indicate that the heave-pitch-roll gauge is somewhat superior to the wave-velocity gauge. This point needs however to be confirmed on more extensive experiments with velocity measurement at various depths. Furthermore, the heave-pitch-roll gauge used for these laboratory experiments is very simple and may be set up at moderate cost. Although these performances have to be confirmed on additional test-cases, the present experimental results indicate promising capabilities for operational laboratory measurements.
- For complex bimodal sea-states, the "single-point" systems usually fail to reproduce the shape of the target spectra. The bimodal nature of sea-state is hardly detected by these systems, even by using sophisticated analysis methods (MEM2, IMLM2, BDM). The output resolution seems too low to allow physical interpretation of results. For such bimodal cases, the amount of input information must be extended (up to five or more). The gauge array composed of five wave probes used in these experiments has proven to be able to produce reliable estimates on the three tests.
- The gauge array however usually requires more refined and complex numerical treatment because of the additional assumption it needs about spatial homogeneity of sea-state. For this type of measuring system, one must emphasis the need of advanced methods (MEM2 or BDM) in order to get reliable results .

Additional laboratory experiments with differents conditions will be performed in order to confirm or modify the present conclusions. The extension of these methods for the measurement of directional wave spectra close to a reflective structure is also a major research field for the next future.

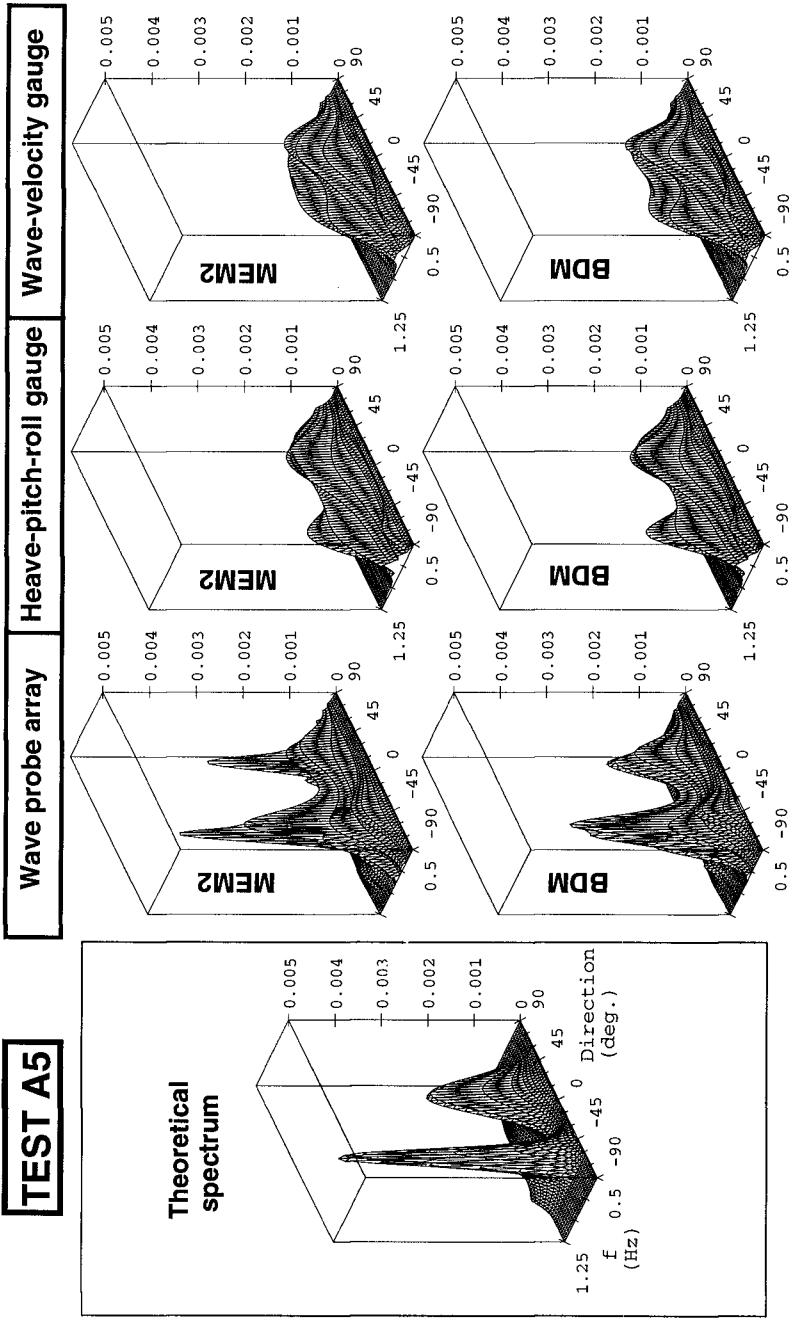


**Figure 7 :** Directional wave spectra analysed on laboratory test A5 (Bimodal case)  
 Comparison of measuring systems and analysis methods (MEM2, BDM)

## 8. ACKNOWLEDGEMENTS

This study is a joint research program between EDF-Laboratoire National d'Hydraulique and the French Ministry of the Sea (Service Technique de la Navigation Maritime et des Transmissions de l'Équipement — STNME).

## 9. REFERENCES

- BENOIT M. (1992) : Practical comparative performance survey of methods used for estimating directional wave spectra from heave-pitch-roll data. *Proc. 23rd Int. Conf. on Coastal Eng. (ASCE)*, pp 62-75, Venice (Italy).
- BENOIT M. (1993) : Extensive comparison of directional wave analysis methods from gauge array data. *Proc. 2nd Int. Symp. on Ocean Wave Measurement and Analysis (ASCE)*, pp 740-754, New-Orleans (USA).
- BORGMAN L.E. (1969) : Directional spectra models for design use. *Offshore Technology Conference, Houston, Texas*
- HASHIMOTO N., KOBUNE K., KAMEYAMA Y. (1987) : Estimation of directional spectrum using the Bayesian approach and its application to field data analysis. *Report of the Port and Harbour Research Institute.*, vol 26, pp 57-100.
- HAUG O., KROGSTAD H. E. (1993) : Estimation of directional spectra by ML/ME methods. *Proc. 2nd Int. Symp. on Ocean Wave Measurement and Analysis (ASCE)*, pp 394-405, New-Orleans (USA).
- KOBUNE K., HASHIMOTO N. (1986) : Estimation of directional spectra from maximum entropy principle. *Proc. 5th OMAE Symp.*, pp. 80-85, Tokyo (Japan).
- KROGSTAD H.E. (1988) : Maximum likelihood estimation of ocean wave spectra from general arrays of wave gauges. *Modelling, Identification and Control*, vol 9, pp 81-97
- LONG R.B., HASSELMANN K. (1979) : A variational technique for extracting directional spectra from multicomponent wave data. *J. Phys. Ocean.*, vol 9, pp 373-381.
- LONG R.B. (1980) : The statistical evaluation of directional estimates derived from pitch/roll buoy data. *J. Phys. Oceanogr.*, vol 10, pp 944-952.
- LONGUET-HIGGINS M.S., CARTWRIGHT D.E., SMITH N.D. (1963) : Observations of the directional spectrum of sea waves using the motions of a floating buoy. *Ocean Wave Spectra, Prentice-Hall*, pp 111-136.
- LYGRE A., KROGSTAD H.E. (1986) : Maximum entropy estimation of the directional distribution in ocean wave spectra. *J. Phys. Oceanogr.*, vol 16, pp 2052-2060.
- MARDSSEN R.F., JUSZKO B.A. (1987) : An eigenvector method for the calculation of directional spectra from heave, pitch and roll buoy data. *J. Phys. Oceanogr.*, vol 17, pp 2157-2167.
- MILES M.D. (1989) : A note on directional random wave synthesis by the Single Summation Method. *Proc. 23rd IAHR Congress, Vol C*, pp243-250, Ottawa (Canada).
- NWOGU O.U., MANSARD E.P.D., MILES M.D., ISAACSON M. (1987) : Estimation of directional wave spectra by the maximum entropy method. *Proc. 17th IAHR Seminar - Lausanne (Switzerland)*.
- NWOGU O.U. (1989) : Maximum entropy estimation of directional wave spectra from an array of wave probes. *Applied Ocean Research*, vol 11, N°4, pp 176-182
- OLTMAN-SHAY J., GUZA R.T. (1984) : A data-adaptative ocean wave directional-spectrum estimator for pitch-roll type measurements. *J. Phys. Oceanogr.*, vol 14, pp 1800-1810.

## CHAPTER 4

### Accuracy of Wind and Wave Evaluation in Coastal Regions

Luciana Bertotti<sup>1</sup> and Luigi Cavaleri<sup>1</sup>

#### Abstract

We have made a critical analysis of the processes and the parameters that affect the accuracy with which wind and waves can be evaluated close to coast. For each process we quantify the possible error, whenever possible complementing this with numerical tests and practical cases.

#### 1. Introduction

The standard evaluation of the performance of a wave model is usually done off the coast, in the open sea. Typically the analysis fields (wave fields obtained using as input the wind provided by the analysis of 3-D meteorological models) are compared with the measured data available at certain locations. This provides a fair estimate of the overall performance. More detailed analyses, possibly referred to some test cases, can provide information on specific aspects of the model. The forecast fields are compared with the analysis fields to assess the reliability of the results in the forecast mode (in doing so we effectively check the forecast wind fields).

The related statistics are commonly available (see e.g., Günther et al., 1992 and Komen et al., 1994). Particularly during the last three years, with most meteorological centers moved to high resolution meteorological models, the results are quite satisfactory. The average bias for the significant wave height  $H_s$  is about 0.10-0.15 m or less, the rms error is limited to a few tens of centimeters.

However, the condition is not similarly satisfactory in coastal areas. Here a number of problems arise. First, the orography of the coast strongly affects the wind field, hence the local evolution of the wave fields. Then, the shallow waters bring to relevance a number of processes, some of them being of difficult evaluation, but

---

<sup>1</sup>Istituto Studio Dinamica Grandi Masse-CNR, San Polo 1364, 30125 Venice, Italy

The practical application of wave modeling in coastal areas requires therefore a careful analysis of the local conditions, to assess, even if only on a qualitative basis, the relevance of each process. This will tell us where to focus our attention, following the principle of "larger corrections first".

We have done an evaluation of the potential relevance of the processes active in coastal areas and of the model parameters that affect the accuracy of the results. Whenever possible, this has been done with numerical tests, supporting the results with wave measurements at suitable locations. In section 2 we discuss the evaluation of the wind field and the related consequences on the evaluation of the wave fields. Then (section 3) we analyze the relevance of the conservative processes arising from the interaction of the waves with the bottom. The dissipative processes are analyzed in section 4. In 5 we turn our attention to the resolution of the grid and of the wave model. Interactions with currents are briefly mentioned in 6. The overall results are summarized and commented in the final section 7.

## 2. Wind in Coastal Areas

The wind is the source of the whole energy present in the sea in the wind wave frequency range. The sensitivity of waves to even limited variations imply a careful attention to the modifications of the wind fields in coastal areas.

Wind can be modified both at large and local scales. Analyzing a very severe storm in the Mediterranean Sea, Cavaleri et al. (1991) report an increase of the wind speed of about 30% by increasing the resolution from 150 to 70 km. In another case in the same area (Cavaleri et al., 1993), a further increase of resolution to 40 km succeeded in revealing an otherwise unnoticed local turn of the wind, strictly associated to the local orography, that produced a 5 m significant wave height in the Gulf of Genoa, duly found in the measured data. It is not possible to specify the characteristics of a meteorological model that are required for a sufficient accuracy. As a practical rule, we can say that, given a characteristic length  $D$  of the local orography (the dimension of a bay, or of an island or a promontory), a good wind requires a resolution of  $D/5$  or better. The same applies if  $D$  is the minimal distance from a coast with a complicated orography at which we want to evaluate the fields.

## 3. Wave Conservative Bottom Processes

We discuss the following processes: refraction, shoaling, bottom scattering. While the first two are a standard part of any shallow water wave model, the third one is rarely considered, but it can become dominant in certain conditions.

*Refraction.* Well established, both with grid and ray techniques. If no particular complication arises (e.g., caustics), the accuracy for the single spectral component is of the order of a few percents and a few degrees in direction.

More care is required when dealing with a full 2-D spectrum, from which we extract the mean direction (we anticipate here a result connected to the subject of section 5). Hubbert and Wolf (1991) have considered a narrow swell approaching at

60° with respect to the isobaths a one-dimensional 1:10<sup>4</sup> sloping coast. Figure 1 shows the resulting turning of the swell mean direction while approaching the beach, as a function of the directional resolution used in the model. While all the results are good, and excellent for a resolution of 15° or better, we need to go down at 5° before being able to reproduce the result obtained with Snel's law (note: Komen et al., 1994, p. 345, point out that, contrarily to the common use, the correct spelling of this Dutch mathematician requires a single "l").

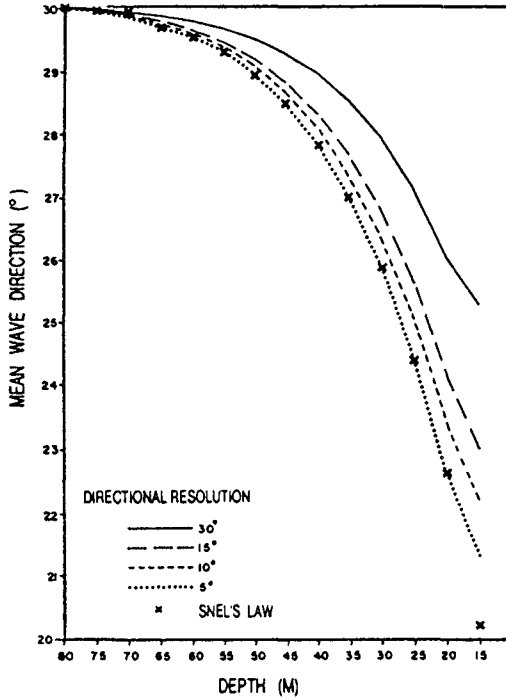


Figure 1. Refraction on a sloping bottom as a function of directional resolution (after Hubbert and Wolf, 1991).

*Shoaling.* When shoaling a wave spectrum towards the coast, two basic approaches are possible: to use linear theory for each component separately, or to summarize the spectrum into a representative wave of given height and period, and to use one of the several nonlinear theories available. To our knowledge no general method to deal with nonlinear shoaling of the whole 2-D spectrum has been published. We expect some substantial improvement not far in the future. For the time being we call the attention to one result of strong interest for the coastal engineer. Starting from recorded data and by numerical integration of the KdV equation, Osborne (1993) has analyzed the shoaling of a heavy swell case in the Northern Adriatic Sea,



shows the same system of waves at 6 meters of depth. The relevant point is the development by nonlinear interactions of long period components, formally appearing as a train of solitons. These long components are important for beach shaping and harbor management. They appear for large Ursell numbers in the field. In this case the results of standard theories should be taken with care.

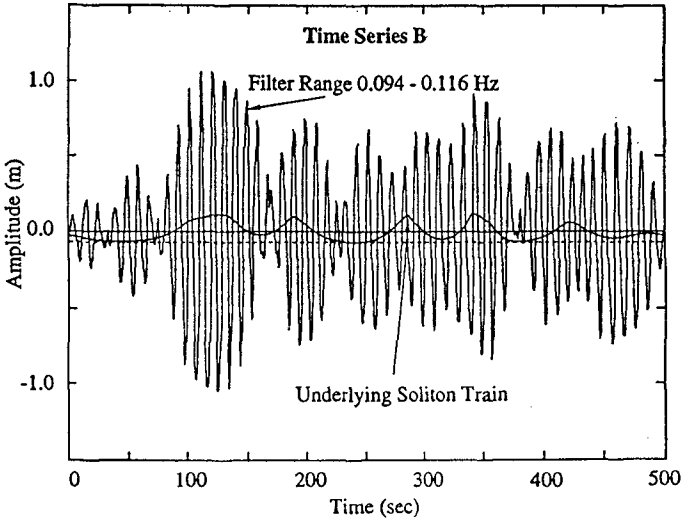


Figure 2. Non linear shoaling of a heavy swell case in the Northern Adriatic Sea. Surface profile evaluated at 6 m of depth. Note the development of long period wave components.

*Bottom-scattering.* We refer here to the interaction of a surface wave spectrum with the oscillations of the bottom. The theory is well established (see Long, 1973), but it has rarely been applied for the practical difficulty to have the necessary data available (the 2-D spectrum of the depth variations is required) and because of the very large computer power requirements. However, some laboratory experiments have clearly confirmed the theory and provided spectacular results. Davies and Heathershaw (1983) have shown that four oscillations of the bottom (wavelength half of that of the surface wave) are sufficient to reflect in the opposite direction 80% of the incoming wave height. Ten oscillations reflect 90%.

The wavelength is critical, which makes the application problematic. However, because of its potential dominant role, this process should be kept in mind whenever a series of transversal parallel bars or reefs is present in front of a coast.

#### 4. Dissipative Bottom Processes

We discuss bottom friction, percolation, breaking and bottom elasticity.

*Bottom friction.* It can be evaluated with both linear and nonlinear (fully spectral) approaches. The non linearity leads to more correct evaluations, but this is paid with two orders of magnitude in computer power. A rather comprehensive treatment of the subject is given by Weber (1991). The linear approach suffices till water particles velocity at the bottom of about 0.15 m/s, above which it underestimates the energy loss at an increasing rate. A first hand estimate of the expected wave conditions at a given location and of the associated orbital velocity will tell the user which approach is to be followed.

A good example of the possible difference between the two approaches is given in figure 3, showing a 1-D spectrum at an oceanographic tower located on 16 m of depth at the far north of the Adriatic Sea, in front of Venice (Cavaleri et al., 1989). The tower is at the upper end of a long, slowly sloping continental platform, and the swell represented in the figure has been propagating in shallow water for many tens of kilometers. Clearly, the linear approach (WAM in the figure) fails to dissipate the low frequency energy at a sufficiently high rate.

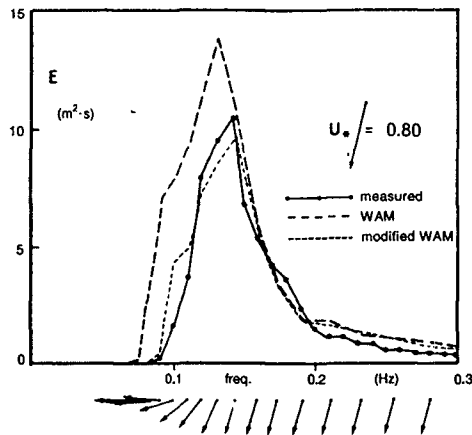


Figure 3. Comparison between measured and evaluated 1-D spectra in the Northern Adriatic Sea. WAM, evaluated with linear theory for bottom friction; modified WAM, with non linear theory (after Cavaleri et al., 1989).

*Percolation.* Of little importance offshore, it becomes important when the bottom is composed of shingles or very coarse sand, which are usually found close to the beach. Its role is never dominant. If to be considered, its proper evaluation requires laboratory tests to measure the transmission coefficient necessary for the estimate of the related energy budget (see, e.g., Shemdin et al., 1978).

*Breaking.* It is the most dominant factor for wave height in shallow water. Its consideration is essential whenever  $H_s > 0.4$  depth.

The breaking is not fully understood. Notwithstanding this, well-devised approaches provide very good results (see Battjes and Beji, 1993, for a clear example). In general, also simple methods provide acceptable results, simply because all of them essentially follow the basic principle of limiting the wave height to a certain percentage of depth. Larger differences, in percent terms, are found very close to shore.

*Bottom elasticity.* This phenomenon is rarely considered because in the very large majority of cases the energy involved is negligible. Besides, the bottom material (e.g., sand) is practically elastic, with a negligible absorption of energy. In a few special cases (the Mississippi Delta and the Bay of Bengal are the best known examples), the bottom is locally composed of viscoelastic mud. In this case tremendous absorptions of energy can be experienced in heavy storm. Figure 4 shows the evolution of a shoaling wave spectrum during hurricane Frederic (Forristall et al., 1990). In 30 km the wave height passed from 8.6 m (in deep water) to 2.4 m (in 19 m of depth), a loss of energy of more than 90%. It is obvious then, whenever present, this process must be considered and it is going to be the dominant one.

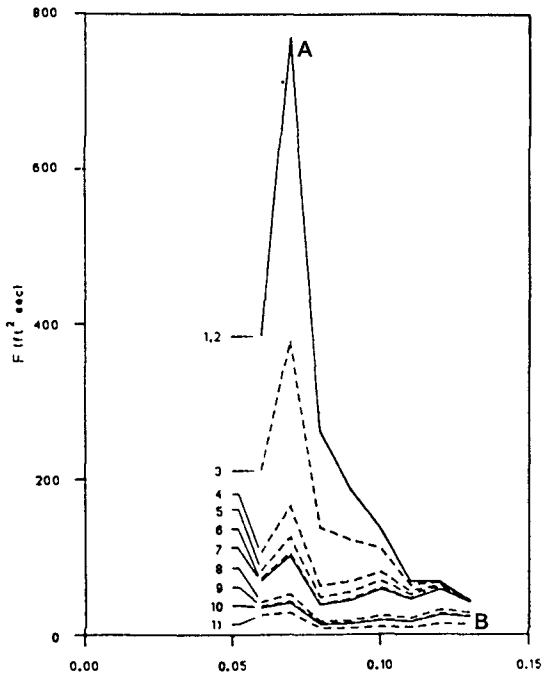


Figure 4. Attenuation of the wave spectrum during hurricane Frederic in the Gulf of Mexico. A and B locations are only 30 km apart (after Forristall et al., 1990).

## 5. Grid and Model Resolution

*Grid resolution.* It is essential in establishing the scale at which we want to analyze the phenomenon. The resolution affects the results of a wave model, particularly when strong gradients are present in the field. In this case a doubling of the resolution (say from 40 to 20 km) can increase the estimate of the peak wave height by 10-20%.

The grid resolution establishes also the accuracy with which we describe the coast. An uncertainty of half the grid step size on the actual position of the coast must be considered. This becomes critical in slanting fetch conditions or, e.g., with waves coming towards the coast after going around a promontory enclosing a gulf. To avoid errors larger than 10%, the point of interest should be at a distance from the coast at least five times the uncertainty in its exact location.

The overall effect of the grid resolution is exemplified in Figure 5. A very severe storm in the Mediterranean Sea ( $H_s > 11$  m between Tunisia, Sardinia and Sicily, 8 m in the Sicily Channel) has been hindcast using the same input wind, but two different resolutions, namely  $0.5^\circ$  and  $0.25^\circ$  (see Cavaleri et al., 1991). The figure shows the differences (with 0.5 m isolines) between the two fields, at the peak of the storm. They are partly due to a better description of the wave generation, and partly to coastal effects.

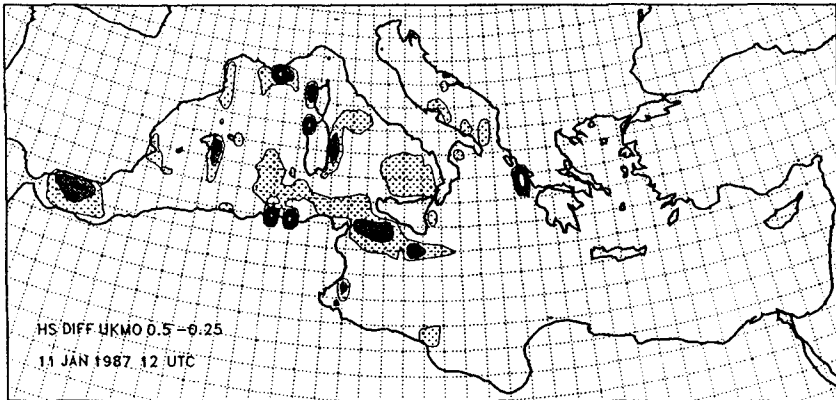


Figure 5. Wave height comparison between the hindcasts of a severe storm in the Mediterranean Sea done with different grid resolution. The differences are indicated as isolines at 0.5 m interval (after Cavaleri et al., 1991).

*Model resolution.* The integration time step  $\Delta T$  is connected to the grid step size and to the time scale of the phenomenon we want to describe. Therefore  $\Delta T$  must be equal or smaller than the time required by the minimal change we want to detect in the evolution of the storm. If larger, the phenomenon will be smoothed, and we must expect a likely underestimate of the peak conditions.

The resolution in frequency is usually not a problem. We have formerly discussed in section 3 the implications for refraction. Some particular cases, e.g., the proper evaluation of swell on the Pacific Ocean, can require an extension towards the low frequency range. De La Heras (1990) gives a nice example of this.

A more critical aspect for coastal engineers is the resolution in direction. The usual 24 or 30 degree resolution suffices for most of the cases. However, when approaching a complicated shallow water topography or a winding coastal shape, an increased resolution will provide a substantially better description of the wave distribution. Errors of 15-20% on Hs can easily be found at some location, if a coarse resolution in direction is used.

## 6. Interactions with Current

The wave-current interactions are usually neglected by the wave modeller for two reasons. First, in the large majority of cases the currents are not strong enough to affect a developed wave field in an appreciable way. Second, very rarely a detailed distribution of the current field is available. In any case many wave models (see Tolman, 1991 and Komen et al., 1994) are built to face the problem.

In practical terms, till when the current speed is below a few tens of centimeters per second, there is no strict need of taking it into consideration. Rather the problem for the coastal engineer is the eventual, if necessary, availability of a detailed description of the current field. Particularly in coastal areas, with a strong spatial variability, this can be a serious problem that deserves a particular attention. Besides, to properly evaluate the interactions, the grid resolution of the wave model must be better than that required for a proper description of the current field.

## 7. Summary

In the previous sections we have highlighted the possible relevance of each single process and model parameter in the modeling of wind waves in coastal areas. The difficulty in so doing is that the influence of the single factor can span a wide range of values, depending on the conditions in the area of interest.

Some processes, like bottom scattering and bottom elasticity, require special conditions for their appearance. They are usually not considered. However, when the conditions are present, their role becomes dominant.

Even if only on a qualitative basis, we have summarized in figure 6, the relevance of the single physical processes. The figure provides an "expected" level of influence at 20 m of depth, at 5 m of depth, and the maximum possible relevance of each process in the local energy budget.

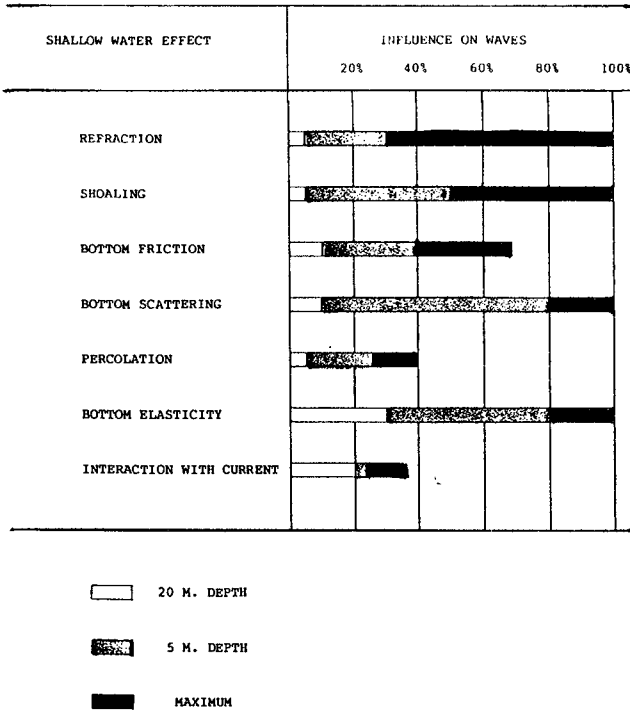


Figure 6. Possible influence of the single physical processes affecting waves in shallow water.

Acknowledgments

This research has been partially funded by the *Progetto Salvaguardia Laguna Venezia*.

References

Battjes J.A. and S. Beji, 1993. Breaking waves propagation over a shoal, ICCE 1992, **3**, 42-51.

- Cavaleri, L., L. Bertotti and P. Lionello, 1989. Shallow water application of the third generation WAM wave model, *J. Geophys. Res.*, **C94**, 8111-8124.
- Cavaleri, L., L. Bertotti and P. Lionello, 1991. Wind wave-cast in the Mediterranean Sea, *J. Geophys. Res.*, **C96**, 10739-10764.
- Cavaleri, L., L. Bertotti, C. Koutitas, S. Christopoulos, G. Komen, G. Burgers, K. Mastenbroek, J.M. Lefevre, A. Guillaume, J.C. Carretero, A. Guerra, L. Iovenitti and P. Cherubini, 1993. MAST Contract 0042, Final Report, 211 pp.
- Davies, A.G. and A.D. Heathershaw, 1983. Surface wave propagation over sinusoidally varying topography: Theory and observation, I.O.S. Report no. 159, Part 1, Wormley (UK), 88 pp.
- Forristall, G.Z., E.H. Doyle, W. Silva and M. Yoshi, 1990. Verification of a soil interaction model (SWIM), p. 41-68, In: *Modeling Marine Systems, II*, A.M. Davies (ed), CRC Press, Boca Raton, Florida (USA).
- Günther, H., P. Lionello, P.A.E.M. Janssen, L. Bertotti, C. Brüning, J.C. Carretero, L. Cavaleri, A. Guillaume, B. Hanssen, S. Hasselmann, K. Hasselmann, M. de las Heras, A. Hollingworth, M. Holt, J.M. Lefevre and R. Portz, 1992. Implementation of a third generation ocean wave model at the European Centre for Medium-Range Weather Forecasts, Final Report for EC Contract SC1-0013-C(GDF), ECMWF, Reading (UK).
- Heras, M. de las, 1990. WAM hindcast of long period swell, KNMI Afeling Oceanografisch Onderzoek Memo, OO-90-09, De Bilt (NL), 10 pp.
- Hubbert, K.P. and J. Wolf, 1991. Numerical investigation of depth and current refraction of waves, *J. Geophys. Res.*, **C96(C2)**, 2737-2748.
- Komen, G.J., L. Cavaleri, M. Donelan, K. Hasselmann, S. Hasselmann and P.A.E.M. Janssen, 1994. *Dynamics and Modelling of Ocean Waves*, Cambridge University Press, 532 pp.
- Long, R.B., 1973. Scattering of surface waves by an irregular bottom. *J. Geophys. Res.*, **78**, 7861-7870.
- Osborne, A.R., 1993. Behavior of solitons in random-function solutions of the periodic Korteweg-de Vries equation, *Physical Review Letters*, **71** (19), 3115-3118.
- Shemdin, P., K. Hasselmann, S.V. Hsiao and K. Herterich, 1978. Non-linear and linear bottom interaction effects in shallow water, p. 347-372, In: *Turbulent*

*Fluxes Through the Sea Surface, Wave Dynamics and Prediction*, A. Favre and K. Hasselmann (eds.), Plenum Press, New York, 677 pp.

Tolman, H.L., 1991. A third-generation model for wind on slowly varying, unsteady and inhomogeneous depths and currents, *J. Phys. Oceanogr.*, **21**, 782-797.

Weber, S.L., 1991. Eddy-viscosity and drag-law models for random ocean wave dissipation, *J. Fluid Mech.*, **232**, 73-98.



## CHAPTER 5

### A SPECTRAL MODEL FOR WAVES IN THE NEAR SHORE ZONE

*R. C. Ris<sup>1</sup>, L.H. Holthuijsen<sup>1</sup> and N. Booij<sup>1</sup>*

#### **Abstract**

The present paper describes the second phase in the development of a fully spectral wave model for the near shore zone (SWAN). Third-generation formulations of wave generation by wind, dissipation due to whitecapping and quadruplet wave-wave interactions are added to the processes of (refractive) propagation, bottom friction and depth-induced wave breaking that were implemented in the first phase (Holthuijsen et al., 1993). The performance and the behaviour of the SWAN model are shown in two observed cases in which waves are regenerated by the wind after a considerable decrease due to shallow water effects. In the case of the Haringvliet (a closed branch of the Rhine estuary, the Netherlands) reasonable results in terms of significant wave heights were obtained. In the case of Saginaw Bay (Lake Huron, USA), the SWAN model underestimates the significant wave height deep inside the bay (as did two other models). Due to the absence of triad wave-wave interactions in the model the mean period is not properly shifted to the higher frequencies in shallow water. Adding these triads is planned for the next phase of developing the SWAN model.

#### **Introduction**

In conventional wave models (at least in coastal engineering) wave components are traced from deep water into shallow water along wave rays to obtain realistic estimates of wave parameters in coastal areas, lakes and estuaries. However, this technique often results in chaotic wave ray patterns which are difficult to interpret. Moreover, nonlinear processes cannot be calculated efficiently. Using a spectral wave model that represents the evolution of the waves on a grid is superior in several respects. The inherent spatial smoothing of such a model ensures a realistic smooth representation of the wave pattern, and it allows an efficient representation of the random, short-crested waves with their generation and dissipation. Models of

---

<sup>1</sup> Delft University of Technology, Department of Civil Engineering, Stevinweg 1, 2628 CN, Delft, The Netherlands.

this type are fairly common for oceans and shelf seas. However in coastal applications several orders of magnitude more computer effort is required due to the very high spatial resolution that is needed and the numerical techniques that are used. We reduced the required computer effort greatly by considering stationary situations only and by developing an unconditionally stable propagation scheme. The model is described and results are shown of tests for observed conditions in the Haringvliet and in Saginaw Bay with effects of wind, whitecapping, quadruplet wave-wave interactions, bottom friction and depth-induced wave breaking included.

### Model formulation

The SWAN model (Simulation of Waves in Near shore areas) is conceived to be a third-generation, stationary wave model that is discrete spectral in both frequencies and directions. The qualification "third-generation" implies that the spectrum in the model evolves free from any a priori restraints (Komen et al., 1994). The model is formulated in terms of action density  $N$  (energy density divided by relative frequency:  $N = E/\sigma$ ). From the possible representations of the spectrum in frequency, direction and wave number space, we choose a formulation in terms of relative frequency  $\sigma$  and direction of propagation  $\theta$  (normal to the wave crest of a wave component). This is convenient for two reasons. Because of efficiency and accuracy, an implicit numerical scheme should be chosen for energy transport across the directions (refraction) and an explicit scheme for energy transport across the frequencies or wave numbers (frequency or wave number shift). The latter is subject to a Courant stability criterion which is more restrictive for the wave number formulation than the formulation in terms of frequency. Choosing the relative frequency  $\sigma$  rather than absolute frequency  $\omega$  has the advantage that the relationship between the relative frequency and wave number remains unique when currents are added.

In general the evolution of the spectrum can be described by the spectral action balance equation (e.g., Phillips, 1977):

$$\frac{\partial}{\partial t} N(\sigma, \theta) + \nabla_{x,y} \cdot [(c_g + \underline{U}) N(\sigma, \theta)] + \frac{\partial}{\partial \sigma} [c_\sigma N(\sigma, \theta)] + \frac{\partial}{\partial \theta} [c_\theta N(\sigma, \theta)] = \frac{S(\sigma, \theta)}{\sigma} \quad (1)$$

The first term in the left-hand side is the rate of change of action density in time, the second term is the rectilinear propagation of action in geographical  $x, y$ -space. The third term describes the shifting of the relative frequency due to currents and unsteadiness of depths with propagation velocity  $c_\sigma$  in  $\sigma$ -space. The fourth term represents the propagation in  $\theta$ -space (depth and current induced refraction) with propagation velocity  $c_\theta$ . This action balance equation implicitly takes into account the interaction between waves and currents through radiation stresses. The term  $S(\sigma, \theta)$  at the right hand side of the action balance equation is the source term representing the growth by wind, the wave-wave interactions and the decay by bottom friction, whitecapping and depth-induced wave breaking.

To reduce computer time, we removed time from the action balance equation (i.e.,  $\partial/\partial t = 0$ ). This is acceptable for most coastal conditions since the residence time of the waves is usually far less than the time scale of variations of the wave boundary condition, the ambient current or the tide. For cases in which the time scale of these variations becomes important, i.e., variable incoming waves at the boundary, or variable winds or currents, a quasi-stationary approach can be taken by repeating the computations for predefined time intervals. For the wind effects the formulations of Cavaleri and Malanotte-Rizzoli (1981) and Snyder et al. (1981) are used. For the bottom friction effects the formulation from JONSWAP (Hasselmann et al., 1973; WAMDI group, 1988) is taken with the friction coefficient  $\Gamma$  equal  $0.067 \text{ m}^2\text{s}^{-3}$  (wind sea conditions; Bouws and Komen, 1983). Whitecapping is represented by the formulation of Hasselmann (1974) and Komen et al. (1984) in which the dissipation is controlled primarily by the steepness of the waves. Depth-induced wave breaking is modelled by a spectral version of the Battjes/Janssen wave breaking model (Battjes and Janssen, 1978) resulting in a dissipation which does not affect the shape of the spectrum itself (Beji and Battjes, 1993; Battjes et al., 1993). For the breaking coefficient in this model we use  $\gamma=0.73$  which is the average value in the field experiments summarized in Table 1 of Battjes and Stive (1985). The quadruplet wave-wave interactions of Hasselmann (1962) are calculated with the Discrete Interaction Approximation (DIA) of Hasselmann et al. (1985) as in the WAM model (WAMDI group, 1989). A complete version of the SWAN model is planned to include triad wave-wave interactions. In very shallow water these triad wave-wave interactions transfer energy to higher frequencies. However, the triad interactions are still poorly understood and no suitable expression in terms of energy density has yet been derived (only for non-dispersive waves, Abreu et al., 1992). Efforts are presently being made to model the triad interactions based on the work of other authors, e.g., Beji and Battjes (1993), Battjes et al. (1993) and Madsen et al. (1991).

### **The numerical algorithm**

In coastal wave models it is customary to propagate waves from deeper water towards the shore. In the HISWA model (Holthuijsen et al., 1989) this is exploited by propagating the waves line by line roughly parallel with the crests from deeper water to shallower water over a regular grid. This is computationally very efficient and unconditionally stable from a numerical point of view but waves can only propagate within a directional sector of about  $120^\circ$ . Complicated wave conditions with extreme refraction, reflections or initial cross seas cannot be properly accommodated. In the SWAN model we retain the unconditionally stable character of this technique but we expand it to accommodate these complicated conditions (wave from all directions). This modified version of the technique of the HISWA model (which in turn was borrowed from parabolic refraction/diffraction models) is a forward marching scheme in geographic  $x,y$ -space in a sequence of four  $90^\circ$  sectors of wave propagation (quadrants). In the first quadrant the state in a gridpoint  $(x_i, y_j)$  is determined by its up-wave gridpoints  $(x_{i-1}, y_j)$  and  $(x_i, y_{j-1})$ .

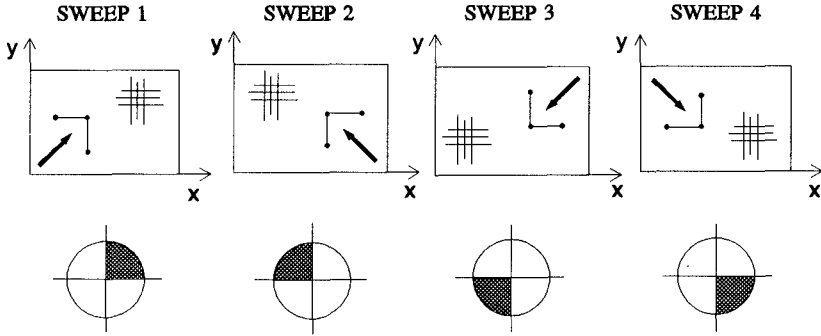


Fig. 1 Numerical scheme for wave propagation in geographic space in SWAN with the appropriate directional quadrant indicated per sweep for which the waves are propagated.

The computation is therefore unconditionally stable for all wave propagation directions in the  $90^\circ$  quadrant between the up-wave  $x$ - and  $y$ -direction because the wave characteristics lie within this quadrant. The waves in this quadrant are propagated with this scheme over the entire geographical region on a rectangular grid (sweep 1, Fig. 1). By rotating the stencil over  $90^\circ$ , the next quadrant ( $90^\circ$ - $180^\circ$ ) is propagated (sweep 2). Rotating the stencil twice more ensures propagation within all four quadrants. This allows waves to propagate from all directions with an unconditionally stable scheme. In cases with current- or depth induced refraction, action density can shift from one quadrant to another. This is taken into account through the boundary conditions of the directional quadrants and by repeating the computations with converging results. Hence the method is characterized as an iterative four-sweep technique (Holthuijsen et al., 1993). Typically we choose a change of less than 1% in significant wave height and mean wave period in 99% of the wetted geographic gridpoints to terminate the iteration. The propagation in  $\theta$ -direction (refraction) is computed with an implicit scheme to achieve numerical stability for large bottom gradients (central second-order scheme). The corresponding tri-diagonal matrix is solved with a Thomas algorithm (Abbott and Basco, 1989). Preliminary results of propagation tests (also with currents induced wave blocking) for analytical and real cases show an accurate and stable behaviour of the wave model. In all of the next cases, however, no currents are present.

The integration of the source terms is straightforward for all frequencies of the discretized spectrum (the prognostic part of the spectrum,  $\sigma < \sigma_{\max}$ ). For frequencies higher than  $\sigma_{\max}$ , a diagnostic spectral tail is added to the spectrum. To ensure a stable integration of the source terms we have used explicit schemes for the input

source terms and semi-implicit and fully implicit schemes for the sink terms. To suppress the development of numerical instabilities, the maximum growth of energy density per sweep in a spectral bin is limited to a fraction of 10% (Tolman, 1992) of the fully developed equilibrium level (Phillips, 1958). Decay is not similarly limited to allow realistic rapid decrease near the shore. In SWAN the frequency  $\sigma$  is exponentially distributed ( $\sigma_{i+1} = \alpha\sigma_i$ , with  $\alpha$  constant) so that the calculation of the nonlinear transfer scales with frequency and can be integrated economically.

### Field measurements: the Haringvliet and Saginaw bay

We will concentrate on a comparison with observations in two observed cases in which regeneration after decay is dominant. Both cases are in shallow water with an initial decrease of wave energy due to dissipation and refraction and a subsequent increase of wave energy due to wind. One is taken from the Haringvliet in the Netherlands (a closed branch of the Rhine estuary; Holthuijsen et al. 1989; Holthuijsen et al., 1993). Here a shoal protects the branch (5 km length scale) from the open sea (see Fig. 2). The computations have been carried out for a situation which occurred on October 14, 1982 at 23:00 h (1.95 m depth over the top of the shoal). The waves are locally generated in the southern North Sea and approach the estuary from NW direction and travel across and around the shoal. The observations show that a considerable fraction of wave energy is dissipated over the shoal. Behind the shoal the waves are regenerated by the wind. The wind speed was 16.5 m/s from NW. During this period currents were practically absent. The other case is taken from Saginaw Bay (USA; Bondzie and Panchang, 1993). Here a shallow region with an island protects the bay (25 km length scale) from Lake Huron (see Fig. 3). During a storm event in May, 1981 wave conditions were recorded with wave gauges at three locations (A, B and C). The wind velocity was 11.2 m/s, blowing along the main axis of the bay from Lake Huron. The observed wave height initially decreases between location A and B and then increases between location B and C.

### Model results for the Haringvliet

The resolution of the bottom grid for the Haringvliet is  $\Delta x = 500$  m and  $\Delta y = 500$  m. The directional resolution in the spectrum is  $\Delta\theta = 10^\circ$  and the frequency resolution is  $\Delta f = 0.1045 \cdot f$  between 0.055 Hz and 0.66 Hz. The observed wave boundary conditions at location 1 (see Fig. 2) are a significant wave height  $H_s = 3.54$  m and a peak period  $T_p = 8.3$  s. A JONSWAP spectrum is assumed at this up-wave boundary with a  $\cos^2(\theta)$  directional distribution since the observed width of the directional energy distribution is about  $31^\circ$ . We carried out two calculations with the SWAN model to show the effects of the regeneration of wave energy by wind: one with and one without wind. Fig. 2 shows the pattern of the significant wave height. The results indicated in Table 1 as "wind" are obtained with all mechanisms of generation and dissipation activated (the same station identification as in Holthuijsen et al. (1989) is used). Note that no measurements are available for location 2 at

23.00 h. The significant wave height thus computed agrees fairly well with the observations. The results indicated in Table 1 as "no wind" are obtained with only depth-induced breaking and bottom friction activated.

Table 1 Measurements and SWAN results at various locations in the Haringvliet and Saginaw Bay of significant wave height  $H_s$  and mean wave period  $T_M$ .

Location	Measurements		SWAN results			
	$H_s$ (m)	$T_M$ (s)	"wind"		"no wind"	
			$H_s$ (m)	$T_M$ (s)	$H_s$ (m)	$T_M$ (s)
<b>Haringvliet</b>						
1	3.54	6.6	3.54	6.6	3.54	6.6
2	—	—	3.22	6.8	3.32	6.6
3	2.63	6.4	2.85	6.9	2.85	6.8
4	2.71	6.3	2.82	6.9	2.81	6.8
5	0.79	3.2	0.95	6.0	0.82	6.8
6	1.41	4.9	1.54	6.5	1.42	6.8
7	1.84	6.0	1.77	6.7	1.66	6.9
8	1.08	3.7	1.00	5.2	0.65	6.4
<b>Saginaw Bay</b>						
A	1.90	7.3	1.91*	7.3*	1.92*	7.3*
B	0.94	4.2	0.80	3.7	0.23	6.9
C	1.30	—	0.78	3.5	0.07	5.3

\* fitted.

A comparison of the significant wave height between "wind" and "no wind" shows the relative importance of wind effects on the significant wave height deep inside in the branch (1.00 m versus 0.65 m at location 8). It is obvious that the added wind input, whitecapping and the quadruplet wave-wave interactions were essential to obtain the better results ("wind") deep inside the Haringvliet. The regeneration of waves is clearly visible as a second, high frequency peak in the spectrum (see Fig. 4). This secondary peak shifts the mean frequency to higher values but not sufficiently (compare the computed and observed mean wave period  $T_M$  in Table 1), most probably because the triad interactions are absent in the present version of SWAN.

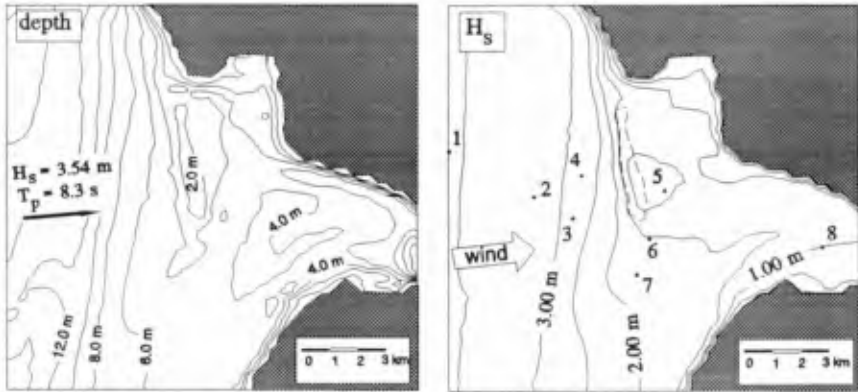


Fig. 2 Left-hand panel: the bathymetry of the Haringvliet area (contour line interval 2 m). Right-hand panel: results of the SWAN computation in terms of significant wave heights (all mechanisms activated) and location of the eight buoys. The dashed line indicates the location of the shoal.

### Model results for Saginaw Bay

We carried out the calculations for Saginaw Bay using the same bottom grid resolution of 1200 m by 1200 m as used by Bondzie and Panchang (1993). To assume an up-wind boundary that is as homogeneous as possible, we choose this boundary at a line just outside the bay (the right-hand boundary of Fig. 3). Since the observations were taken during a storm, we assume a  $\cos^2(\theta)$  distribution and a JONSWAP spectrum at this up-wave boundary. For such conditions, a directional resolution of  $\Delta\theta=10^\circ$  is sufficient. We used a frequency resolution  $\Delta f=0.1225 \cdot f$  between 0.555 Hz and 1. Hz. The significant wave height and peak period at the up-wave boundary was chosen such that at location A the model reproduces the observed wave height and period (Table 1). The calculated pattern of the significant wave height is shown in Fig. 3. The wave height gradually decreases between the up-wave boundary and the entrance of the bay. Due to depth effects, more wave energy penetrates into the deeper entrance than into the shallower entrance of the bay (roughly 20 % lower wave height near location A than in the other entrance). As the waves penetrate into the bay they refract laterally to the shallower parts of the bay. The calculated significant wave heights and mean periods at the three wave gauges are shown in Table 1. In contrast with the observations, the calculated wave height shows no growth between gauge B and C at all. Calculations with a 25% higher wind speed, which is fairly realistic since the wind speed was recorded on land, also did not show the observed growth (similarly for a 50% higher wind speed). Additional computations with another third-generation wave model

(WAVEWATCH; Tolman, 1991, 1992) also failed to reproduce the observed net growth. Also the HISWA model failed in this (Bondzie and Panchang, 1993; who used an uniform wave boundary condition along a straight line across the entrance through location A). Still the effect of wind on the significant wave height deep inside the bay is clearly visible in the model as shown in Table 1 (0.78 m versus 0.07 m at location C) and Fig. 4. Apparently the decay of the low-frequency part of the spectrum is compensated by the growth of the high-frequency part.

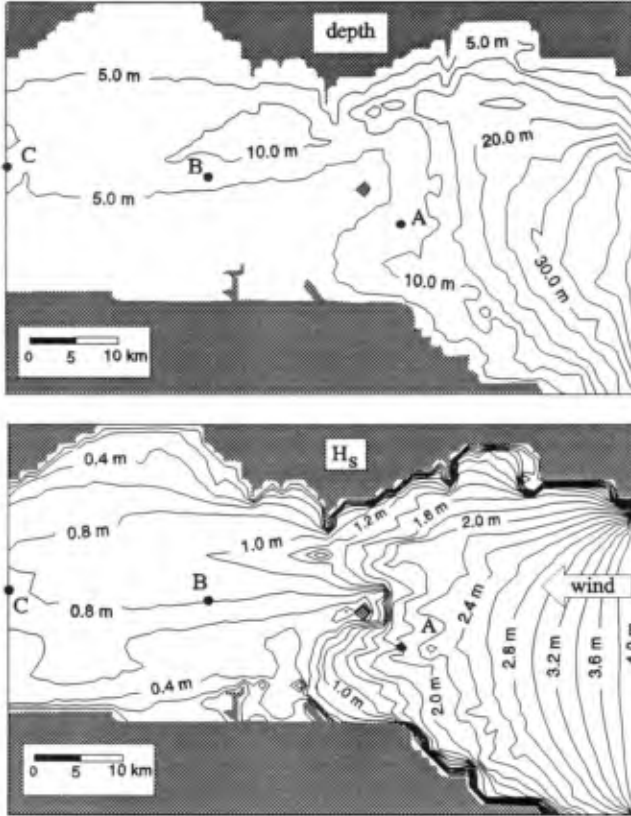


Fig. 3 Top panel: the bathymetry of Saginaw Bay (contour line interval 5 m). Bottom panel: results of the SWAN computation in terms of significant wave heights (all mechanisms activated) and the locations of the three wave gauges.



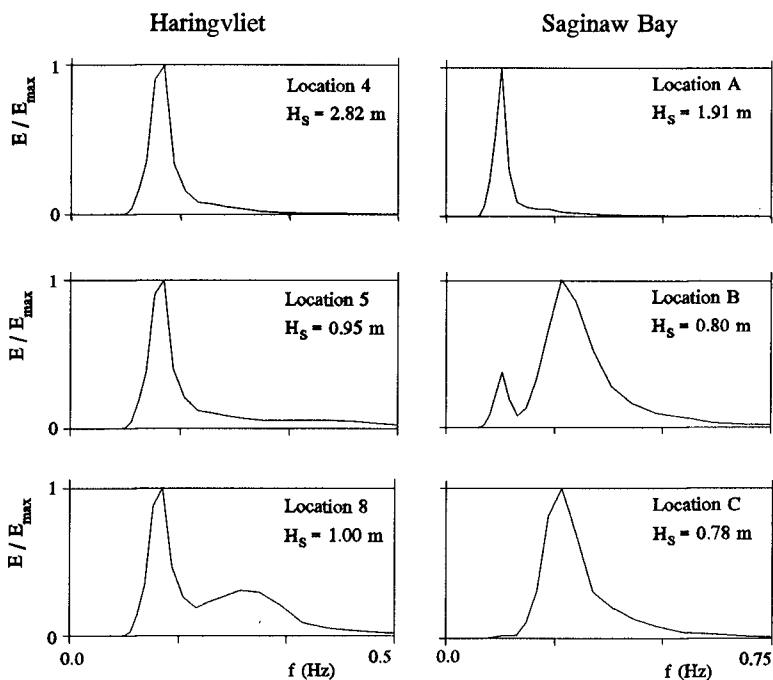


Fig. 4 Left-hand panels: Computed, normalized frequency spectra at location 4, 5 and 8 of the Haringvliet. Right-hand panels: Computed, normalized frequency spectra at locations A, B, and C of Saginaw Bay.

### Conclusions and future work

We have described the second phase in the development of a third-generation fully spectral wave model for near-shore applications (SWAN) that is stationary and unconditionally stable. This permits economically feasible, high-resolution computations with all relevant effects of propagation, generation and dissipation included without a priori restraints on the development of the wave spectrum. The present version includes refractive propagation (currents included), wind generation, quadruplet wave-wave interactions, whitecapping, bottom friction, depth-induced breaking and wave blocking.

We have performed a number of computations with the SWAN model in two cases: the Haringvliet and Saginaw Bay. In the Haringvliet case the agreement of the computed significant wave heights with the observations is reasonable in spite of the absence of the triad interactions. We have found in Saginaw Bay a significant

difference between the calculated and observed wave heights deep inside the bay. Although the effect of regeneration of waves by wind is clearly visible in the model, we could not reproduce the observed wave growth between location B and C, even when we increased the wind speed. The wave periods are not properly computed, in particular in the Haringvliet case. This underscores the importance of the next phase in the development of the SWAN model in which a parameterized formulation for the triad wave-wave interactions will be implemented.

### Acknowledgements

We thank our colleagues C. Bondzie and V.G. Panchang of the University of Maine for providing us with the data of Saginaw Bay. We also thank H.L. Tolman for his permission to use the WAVEWATCH II model for the Saginaw Bay computation.

### References

- Abbott, M.B. and D.R. Basco (1989). *Computational Fluid Dynamics*, Jonh Wiley & Sons, Inc., New York, 425 p.
- Abreu, M., A. Larraza and E. Thornton (1993). Nonlinear transformation of directional spectra in shallow water. *J. Geophysical Res.*, 97 (C10), 15,579-15,589.
- Battjes, J.A. and J.P.F.M. Janssen (1978). Energy loss and set-up due to breaking of random waves. *Proc. 16<sup>th</sup> Int. Conf. Coastal Engineering*, Hamburg, 569-587.
- Battjes, J.A., Y. Eldeberky and Y. Won (1993). Spectral Boussinesq modelling of random, breaking waves. *Proc. of 2<sup>nd</sup> Int. Symposium on Ocean Wave Measurement and Analysis*, New Orleans, 813-820.
- Beji, S and J.A. Battjes (1993). Experimental investigation of wave propagation over a bar. *Coastal Engineering*, 19, 151 - 162.
- Bondzie, C. and V.G. Panchang (1993). Effect of bathymetric complexities and wind generation in a coastal wave propagation model. *Coastal Engineering*, 21, 333-366.
- Bouws, E. and G.J. Komen (1983). On the balance between growth and dissipation in an extreme depth-limited wind-sea in the southern North sea. *J. Phys. Oceanography*, 13, 9, 1653-1658.
- Cavaleri, L. and P. Malanotte-Rizzoli (1981). Wind wave prediction in shallow water: Theory and applications. *J. Geophys. Res.*, 86, No. C11, 10, 961-973.
- Hasselmann, K. (1962). On the non-linear energy transfer in a gravity wave spectrum. Part 1. General theory. *J. Fluid Mech.*, 12, 481-500.
- Hasselmann, K. (1963). On the non-linear energy transfer in a gravity wave spectrum. Part 2. Conservation theorems; wave-particle analogy; irreversibility. *J. Fluid Mech.*, 15, 273-281.

- Hasselmann, K., T.P. Barnett, E. Bouws, H. Carlson et al. (1973). Measurements of wind-wave growth and swell decay during the Joint North Sea Wave Project (JONSWAP). *Ergänzungsheft zur Deutschen Hydrographischen Zeitschrift*, 12.
- Hasselmann, K. (1974). On the spectral dissipation of ocean waves due to whitecapping. *Boundary-Layer Meteorology*, Vol. 6, No. 2, 200-228.
- Hasselmann, K. and S. Hasselmann (1985). Computations and parameterizations of the nonlinear energy transfer in a gravity-wave spectrum. Part I: A new method for efficient computations of the exact nonlinear transfer integral. *J. Phys. Oceanography.*, 15, 1369-1377.
- Holthuijsen, L.H., N. Booij and T.H.C. Herbers (1989). A prediction model for stationary, short crested waves in shallow water with ambient currents. *Coastal Engineering*, 13, 23 - 54.
- Holthuijsen, L.H., N. Booij and R.C. Ris (1993). A spectral wave model for the coastal zone. *Proc. of 2<sup>nd</sup> Int. Symposium on Ocean Wave Measurement and Analysis*, New Orleans, 630-641.
- Komen, G.J., S. Hasselmann and K. Hasselmann (1984). On the existence of a fully developed wind-sea spectrum. *J. Phys. Oceanography.*, 14, 1271-1285.
- Komen, G.J., L. Cavaleri, M. Donelan, K. Hasselmann, S. Hasselmann and P.A.E.M. Janssen (1994). *Dynamics and modelling of ocean waves*. Cambridge University Press, UK, 560 p.
- Madsen, P.A., R. Murray and O.R. Sørensen (1991). A new form of the Boussinesq equations with improved linear dispersion characteristics. *Coastal Engineering*, 15, 4, 371-388.
- Phillips, O.M. (1958). The equilibrium range in the spectrum of wind-generated waves. *J. Fluid Mech.*, 4, 426-434.
- Phillips, O.M. (1977). *The dynamics of the upper ocean*, 2<sup>nd</sup> edition, Cambridge University Press, 261 p.
- Snyder, R.L., F.W. Dobson, J.A. Elliott and R.B. Long (1981). Array measurements of atmospheric pressure fluctuations above surface gravity waves. *J. Fluid Mech.*, 102, 1-59.
- Tolman, H.L. (1991). A third-generation model for wind waves on slowly varying unsteady, and inhomogeneous depths and currents. *J. Phys. Oceanography.*, 21, no. 6, 782-797.
- Tolman, H.L. (1992). Effects of numerics on the physics in a third generation wind-wave model. *J. Phys. Oceanography.*, 22, no. 10, 1095-1111.
- WAMDI group (Hasselmann et al.), 1988, The WAM model - a third generation ocean wave prediction model, *J. Phys. Oceanography*, 18, 1775-1810.

## CHAPTER 6

### Wind Variability and Extremes Statistics

Luigi Cavaleri<sup>1</sup> and Luciana Bertotti<sup>1</sup>

#### Abstract

Continuous records of wind speed and direction show a high variability both in the high and low frequency ranges. This variability is usually not considered in the numerical hindcast of a storm. We discuss the related implications for the maximum wave heights and for the values from the statistics of extremes.

#### 1. Introduction

Extremes statistics at a given location are based on the availability of extended time series of the parameter of interest. Notwithstanding the recent increase in their number, measured wave data are still scarce and not sufficiently representative closer to coast where the wave conditions exhibit a strong variability. If proper data are not available at the location of interest, the usual solution is the hindcast, with suitable mathematical models, of all the relevant storms of the last 10 or 20 years, using their output as a basis for the extremes statistics. In this paper we analyze one aspect of this reconstruction relevant for the final results.

Meteorological models provide a smooth description of the atmosphere, their filtering characteristics depending on the grid step size and on the time integration step. In a model, the representation of the passage of a storm at a given location is characterized by a smooth growth of the wind speed and a similarly smooth decay. This is not what is experienced in the field. Cavaleri and Burgers (1992, henceforth referred to as CB) point out that levels of turbulence with rms percentage variability  $\sigma = 0.10$ , up to values  $\sigma = 0.30$ , are common in nature. This turbulence leads to a substantial increase of the maximum significant wave height  $H_s$  in a storm.

In this paper, first we briefly describe (in section 2) the physics of the process and the effects on the evolution of a storm. Then (section 3) we focus on the statistics of the extremes, showing how the related results are affected by data derived from "turbulent" storms. The overall findings are summarized in section 4.

---

<sup>1</sup>Istituto Studio Dinamica Grandi Masse-CNR, San Polo 1364, 30125 Venice, Italy

## 2. Turbulent Wave Growth

Figure 1 shows four records of wind speed  $U$  with different degrees of turbulence taken from an oceanographic platform located in the Northern Adriatic Sea (Cavaleri, 1979). The turbulence ranges from periods of seconds, where it interacts with the basic wave generation process, till one hour and beyond, shifting gradually into the synoptic variability. Here we focus our attention on the part from one minute upwards. In practice we do not deal with the frequency range connected to the pure generation.

Within its range of variability, the wind speed happens to be for part of the time lower than the phase speed of part of the spectral frequencies. CB show that, through a rectification of the Miles generation process (1957), the relatively fast turbulence (i.e., with period approximately between one and twenty minutes) leads to an enhancement of the actual significant wave height  $H_s$ , the enhancement increasing with the level  $\sigma$  of the turbulence. A second order effect, but acting also on the low speed waves, i.e., on the high frequency range of the wave spectrum, is associated with the non linear relationship between friction velocity and wind speed.

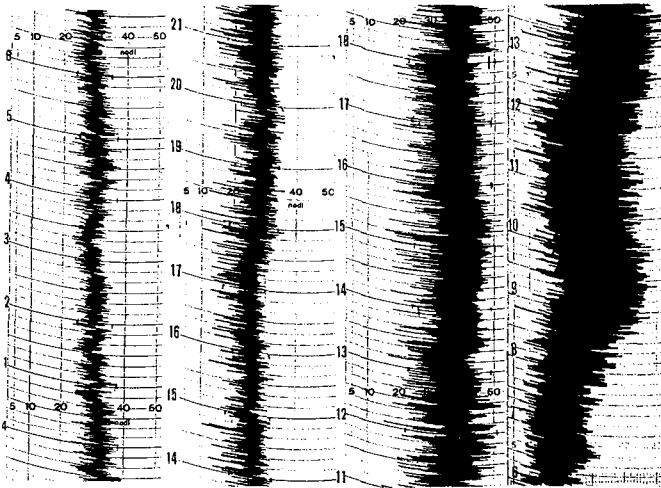


Figure 1. Records of wind speed with different degrees of turbulence.  
Wind speed in knots. Time in hours (after Komen et al., 1994).

Figure 2 shows the classical case of time limited wave growth, with different turbulence  $\sigma$  ranging from 0.0 (uniform wind) till 0.30 (very strong turbulence). We see that the latter value leads to an increase of the final  $H_s$  of more than 30%.

A further increase of the maximum wave height in a storm derives from the relatively long period of turbulence of the wind field (periods from twenty minutes till several hours). These oscillations are clearly recognizable by direct inspection of a record lasting one day or more. Obviously the wave field reacts to this variability with a related  $H_s$  variability throughout the field. To simulate such a variability we need first to simulate the turbulent wind. CB show that this can be done with a Markov chain, where, for a given  $\sigma$ , the time scale of the turbulence is dictated by the correlation  $\alpha$  between the sequential  $U$  values. Actual turbulent records seem to be well reproduced by this approach, provided the correct  $\sigma$  and  $\alpha$  are used. The  $\alpha = 0.90$  seems to be a good value for data taken at one minute intervals. CB have introduced a Markov chain turbulence with these characteristics in a uniform wind field, then repeating the test of figure 2. The results are shown in figure 3, where the test has been extended also to the cases of  $\alpha = 0.95$  and  $0.99$ . The  $\sigma$  was equal to  $0.25$ . The effect of air turbulence is clear. The "turbulent" growth curve follows the smooth one (already enhanced by fast turbulence, compare with figure 2), waving around it. Note that in figure 3 each couple of lines has been shifted up by 2 meters for the sake of clarity.

By direct inspection of the diagram in figure 3 (but similar results are often found in recorded  $H_s$  time series, even if obscured by the usual 3-hour intervals), we recognized immediately the further increase of the maximum  $H_s$  value, the increase being directly dependent on  $\sigma$  and  $\alpha$ .

We can summarize the present situation as follows. Standard numerical wave hindcasts are based on wind fields obtained from meteorological models. Turbulence is usually not considered, and the field evolves smoothly in time. The introduction of wind turbulence affects the wave field in two ways. On one hand, it increases the actual  $H_s$  values. On the other, it forces the wave field to oscillate around the otherwise smooth growth curve, reaching in the process still higher wave heights. Note that, while the first effect is fully determined by  $\sigma$ , and it can therefore be correctly evaluated, for the latter we come across statistics. The highest  $H_s$  in a turbulent storm is crudely a matter of chance. The consequence of this on the statistics of the extreme wave heights is the subject of the next section.

### 3. The Uncertainty in the Extremes Statistics - The Probability of a Probability

The classical procedure of extremes statistics starts from a long term time series of the parameter of interest, typically available as a regular sequence of single values at 3-hour intervals. Then, a subset of values is selected, according to one of two principles: pick up (a) all the values above a certain threshold, (b) the highest value for each pre-established time interval (for wave height a month, a semester, or, one year are a regular choice). If an extended time series is not available, the wave hindcast of a large number of storms is performed, retaining as input information for the extremes statistics the highest  $H_s$  in each storm. The selected data are then best-fitted by some extremal distribution, Weibull, Gumbel or FT-1, exponential being among the common ones. Given the distribution and the number of data in the subset, we can then estimate the probability to overcome a given value at the next event or

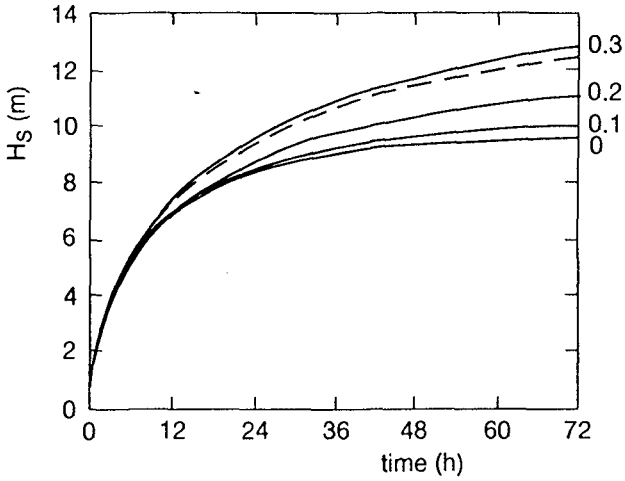


Figure 2. Time growth of the significant wave height under a 20 m/s wind with different degree of turbulence (after Komen et al., 1994).

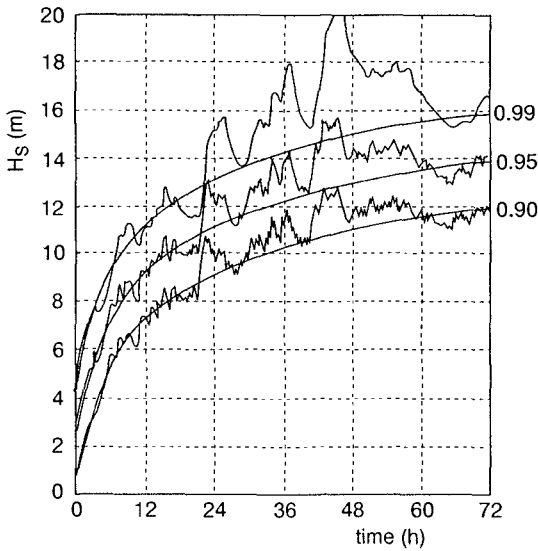


Figure 3. Oscillations of the significant wave height in the time growth curve as a function of the degree of correlation in the sequential wind values (after Komen et al., 1994).

during the next time interval, depending on how the data have been selected. Given the period covered by the input time series, the statistics can be usefully referred to time. In practice, we can reply to the following question. What is the probability  $P^+$  to overcome a certain value  $H$  within  $T$  years? More generally, given two of the quantities  $P^+$ ,  $H$ ,  $T$ , we can immediately deduce the third one.

The analytical expression relating the three quantities is

$$P^+ = 1 - [p^-(H)]^{nT} \quad (1)$$

where  $p^-$  is the no-exceeding probability at the next event deduced from the extremal distribution, and  $n$  is the average number of storms per year. A full discussion of the subject is found in Gumbel (1958) and practical applications illustrated in Cavaleri et al. (1986).

The graphical representation of the results is particularly enlightening. Figure 4 shows the exceedance probability for a certain area of the Tyrrhenian Sea (see Cavaleri et al. 1986). The enhancement of the wave height  $H$  due to the somehow more efficient generation described in the previous section means that we are dealing with higher wave heights. This crudely shifts all the lines in figure 4 to the right, the shift depending on the  $\sigma$  of turbulence typical of the area and on the kind of storms we are considering.

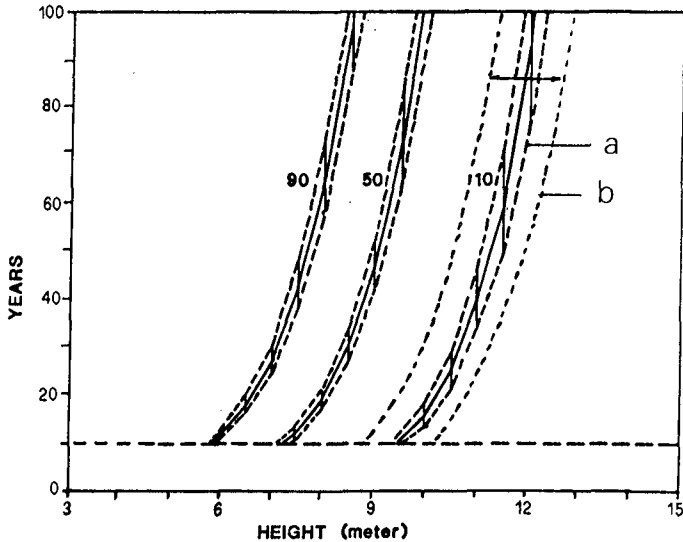


Figure 4. Exceedance probability (given by the number close to each continuous curve) with respect to wave height and elapsed period. The broken lines represent the corresponding confidence limits due to a) choice of the storms and b) wind turbulence.



Three points must be stressed. First, Resio (1978) warns that an extremal statistic produces meaningful results only if applied to a consistent data set, i.e., including only data of the same kind. We cannot mix data associated with substantially different kinds of storms, e.g., southern swell and extra-tropical storms in the North Atlantic Ocean. Clearly the presence of turbulence stresses further this point.

Second, the confidence we have in our input data must depend on the actual source. If derived from a hindcast, we must be aware that they are likely to be underestimated (if turbulence is likely to be present and it has not been considered). But also recorded data have problems. Our usual 20 minute sample chosen for the record is just a random choice in a waving time series as the ones in figure 3. As such, the confidence limits on the actual average representative value (the smooth growth curves in figure 3) are much larger than those associated only to the sampling variability connected with the randomness of the surface, typically 15% instead of 6-8%.

Third, after estimating, by means of diagrams as the one in figure 4 or the related expression (1), the extremal conditions, i.e., a certain  $H_e$ , we must warn the user of our results that the maximum  $H$  he will be likely to come across in such conditions is going to be higher than  $H_e$ . Our numerical results suggest an increase between 5 and 10%. Starting from the extremes in figure 4, we have evaluated the associated confidence limits by a combined use of the Jack-knife and Montecarlo techniques.

A full description of the Jack-knife technique can be found in Cavaleri et al. (1986) who also describe practical applications. Basically, given a subset of  $N$  data and the extremal distribution fitted to them, the technique estimates the reliability of the results by checking how much they depend on the single datum. This is done by excluding in turn each datum and getting a new extremal fit on the remaining  $N-1$  data. This produces  $N$  new estimates of the extremes that are statistically analyzed to provide an estimate of the confidence limits of the overall extremal evaluation. Acting on the extremes shown in figure 4, we have so obtained the limits given by the two (a) curves lying close to the original ones.

This procedure does not account for the uncertainty on the single data due to sampling variability and/or turbulence effects. This can be obtained by Montecarlo technique. Each datum has been left oscillating randomly around its original value, following a Gaussian distribution with  $\sigma=10\%$ , and the fitting procedure repeated for each realization. Similarly to the Jack-knife technique, the results have been statistically analyzed providing a new estimate of the confidence limits. These are given in figure 4 by the wider (b) limits associated with each extremal curve. It is obvious that the turbulence introduces into the estimate of the extremes an uncertainty much larger than derived from the sampling of the input data.

#### 4. Conclusions

We summarize here the relevant points for extremes statistics when dealing with measured or hindcast data.

#### Measured data.

- enhancement of wave height: naturally present in the data, hence automatically considered.
- confidence limits for choice of input data: to be evaluated by Jack-knife technique (or similar one).
- enhancement of estimated extreme values, because of oscillations in the growth curve, estimated to be 5-10%.

#### Hindcast data.

- enhancement of wave height: its consideration requires introduction of turbulence into the input wind data.
- confidence limits for choice of input data to be evaluated by the Jack-knife technique (or similar one).
- confidence limits for turbulent records: not required.
- enhancement of estimated extreme values, because of oscillations in the growth curve, estimated to be 5-10%.

#### Acknowledgments

This research has been partially supported by the *Progetto Salvaguardia Laguna Venezia*.

#### References

- Cavaleri, L., 1979. An instrumental system for detailed wind wave study, *Il Nuovo Cimento*, Serie 1, 2C, 288-304.
- Cavaleri, L. and G.J.H. Burgers, 1992. Wind gustiness and wave growth, KNMI Afdeling Oceanografisch Onderzoek Memo, 00-92-18, De Bilt, 38 pp.
- Cavaleri, L., P. De Filippi, G. Grancini, L. Iovenitti and R. Tosi, 1986. Extreme wave conditions in the Tyrrhenian Sea, *Ocean Engng.*, 13, 2, 157-180.
- Gumbel, E.J., 1958. *Statistics of Extremes*, Columbia University Press, NY, 375 pp.
- Komen, G., L. Cavaleri, M. Donelan, K. Hasselmann, S. Hasselmann and P.A.E.M. Janssen, 1994. *Dynamics and Modelling of Ocean Waves*, Cambridge University Press, 532 pp.
- Miles, J.W., 1957. On the generation of surface waves by shear flows, *J. Fluid Mech.*, 3, 185-204.
- Resio, D.T., 1978. Some aspects of extreme waves prediction related to climatic variations, In: Proc. 10th Offshore Technology Conference, Houston, Texas, 3, 1967-1980.

## CHAPTER 7

# MEAN FLUX IN THE FREE SURFACE ZONE OF WATER WAVES IN A CLOSED WAVE FLUME

Witold Cieřlikiewicz<sup>1</sup> and Ove T. Gudmestad<sup>2</sup>

### Abstract

This paper presents some results of research relating to the theoretical predictions of mass-transport velocity within the free surface zone of water waves in intermediate water depth. The theoretical results are compared with measurements made in a wave flume.

The theoretical estimate of a mean drift has allowed for a better estimation of the return flow in the wave flume. Examples of such estimation are given and graphically presented in the paper. Finally, the stability of the obtained mean velocity profiles through the experiments is examined.

### Introduction

The occurrence of a second-order mean drift is one of the more interesting, and by the same time, important non-linear features of a progressive water gravity wave. This drift, an apparent mass transport, influences such a phenomena like migration of sediments and pollutant particles in the water, and it can also result in the pilling up of water at a beach, with an associated increase in the local mean water level.

---

<sup>1</sup> Institute of Hydroengineering, Polish Academy of Sciences, Kořcierska 7, 80-953 Gdańsk, Poland. Presently at British Maritime Technology, 7 Ocean Way, Ocean Village, Southampton SO14 3TJ, England

<sup>2</sup> Statoil, P.O. Box 300 Forus, 4001 Stavanger, Norway

The formulae for the mass-transport velocity and the total mean flux are usually derived in the Lagrangian frame. The total mean flux in Eulerian frame was developed by Starr (1947) for a small-amplitude wave train and by Phillips (1960) for a random wave field. These traditional approaches, in the Eulerian frame, allow us only to treat the total flux like a physical quantity "existing on a subset of zero measure," namely, *exactly* at the free surface of the wave. Within such an approach we are not able to discuss the distribution of the mean horizontal velocity in the free surface zone. We would then have the artificial situation that the mean velocity along the vertical is everywhere equal to zero except at the free surface.

Tung (1975) has shown a positive mean value of the horizontal orbital velocity of random waves in the near surface zone, but to the authors' knowledge, this has not been discussed and interpreted as a current induced by waves until the works of Cieřlikiewicz and Gudmestad (1993, 1994). In those works the modified particle velocity  $\bar{\mathbf{u}}$  of a wave field is introduced by following the approach of Tung (1975):

$$\bar{\mathbf{u}}(\mathbf{x}, z, t) = \begin{cases} \mathbf{u}(\mathbf{x}, z, t) & \text{for } z \leq \zeta(\mathbf{x}, t) \\ \mathbf{0} & \text{for } z > \zeta(\mathbf{x}, t) \end{cases} \quad (1)$$

in which  $\mathbf{u}$  is unmodified water wave orbital velocity,  $\zeta$  is the free surface elevation,  $\mathbf{x}$  is the location vector on the horizontal plane,  $z$ -axis is directed vertically upwards and  $t$  is the time.

### Random waves

Tung (1975) had derived the probability density function and the first three statistical moments of this modified velocity. The mean value of the horizontal velocity component  $u$  is given as

$$\langle \bar{u}(z) \rangle = r(z) \sigma_u(z) Z(z') \quad (2)$$

where  $Z(\gamma) = (2\pi)^{-1/2} \exp(-\gamma^2/2)$ ,  $\sigma_\zeta$  and  $\sigma_u$  are the standard deviations of  $\zeta$  and  $u$ , respectively, and  $z' = z/\sigma_\zeta$ . Assuming that the wave is unidirectional and denoting the frequency spectrum by  $S(\omega)$ , the cross-correlation coefficient of  $u$  and  $\zeta$  is given as

$$r(z) = \frac{1}{\sigma_u(z)\sigma_\zeta} \int_0^\infty \frac{gk}{\omega} \frac{\cosh k(z+h)}{\cosh kh} S(\omega) d\omega \quad (3)$$

in which  $g$  denotes the gravitational acceleration,  $h$  is the water depth, and the wavenumber  $k$  is related to the angular frequency  $\omega$  by the dispersion relation.

Cieřlikiewicz and Gudmestad (1993) developed the formula for total mean flux of random waves using the modified velocity (1) in the following form:

$$q = \int_0^{\infty} \frac{gk}{\omega \cosh kh} W(-h; \sigma_{\zeta}, k) S(\omega) d\omega \quad (4)$$

where the function  $W$  is defined as

$$\begin{aligned} W(z_a; \sigma, k) &= \int_{z_a/\sigma}^{\infty} \cosh k(z+h) Z(z) dz \\ &= \frac{1}{2} \exp\left[\frac{\sigma^2 k^2}{2}\right] \left\{ e^{kh} Q(z/\sigma + k\sigma) + e^{-kh} Q(z/\sigma - k\sigma) \right\} \end{aligned} \quad (5)$$

and where  $Q(z) = \int_z^{\infty} Z(\gamma) d\gamma$

The approximation of that formula leads to the result obtained by Phillips (1960). Phillips' formula for total mean flux,  $q = \int_{-h}^{\infty} \langle u(z) \rangle dz$ , may be easily obtained by using the modified velocity (1) and formulae (2) and (3) (see Cieřlikiewicz 1994):

$$\begin{aligned} q &= \frac{1}{\sigma_{\zeta}} \int_{-h}^{\infty} Z(z') \left[ \int_0^{\infty} \frac{gk}{\omega} \frac{\cosh k(z+h)}{\cosh kh} S(\omega) d\omega \right] dz = \\ &\quad \int_0^{\infty} \frac{gk}{\omega} S(\omega) \left[ \int_{-h}^{\infty} \frac{\cosh k(z+h)}{\cosh kh} Z(z') dz' \right] d\omega \approx \\ &\quad \int_0^{\infty} \frac{gk}{\omega} S(\omega) \left[ \int_{-h}^{\infty} Z(z') dz' \right] d\omega \end{aligned} \quad (6)$$

since we assume in practice that  $h \gg 3\sigma_{\zeta}$ , then for  $|z| < 3\sigma_{\zeta}$  we obtain in the above integral an approximation  $\cosh k(z+h)/\cosh kh \approx 1$ . A large error in this approximation outside the region  $|z| < 3\sigma_{\zeta}$  is nonessential since the value of  $Z(z')$  is close to zero here. As we have assumed  $h \gg 3\sigma_{\zeta}$ , we have  $\int_{-h}^{\infty} Z(z') dz' \approx \int_{-\infty}^{\infty} Z(z') dz' = 1$ . Thus

$$q \approx \int_0^{\infty} \frac{gk}{\omega} S(\omega) d\omega \quad (7)$$

Note that for deep water waves above formula can be rewritten as  $q = \int_0^{\infty} \omega S(\omega) d\omega$  which is the value of the spectral moment of the first order  $m_1$ .

### Deterministic wave

In the paper of Cieslikiewicz and Gudmestad (1994), the same approach as described above for random waves, is adapted to deterministic small-amplitude waves. The result for the total mean flux  $q^{(d)}$  in the unidirectional wave case is equal to

$$q^{(d)} = \frac{ga}{\omega} I_1(ak) \quad (8)$$

where  $I_1(\cdot)$  is the modified Bessel function of the first order. The above formula in approximation gives a result first obtained by Starr (1947):  $M^{(d)} = \rho q^{(d)} = E/C$  where  $E$  is the average energy per unit surface area and  $C$  is the phase velocity. It should be emphasised that this approximation may be easily obtained by assuming that

$$\frac{\cosh k(z+h)}{\cosh kh} \approx 1 \quad \text{for } |z| \leq a \quad (9)$$

where  $a$  is the wave amplitude. Consider a unidirectional progressive small-amplitude wave of the form

$$\zeta(x, t) = a \cos(kx - \omega t) \quad (10)$$

The associated horizontal velocity under the wave is given by

$$u(x, z, t) = \frac{gak}{\omega} \frac{\cosh k(z+h)}{\cosh kh} \cos(kx - \omega t) \quad \text{for } z \in [-h, \zeta(x, t)] \quad (11)$$

Introduce the extension of  $u$  on the  $z$ -domain  $[-h, \infty)$  by the definition

$$\bar{u}(x, z, t) = \begin{cases} u(x, z, t) & \text{for } z \leq \zeta(x, t) \\ 0 & \text{for } z > \zeta(x, t) \end{cases} \quad (12)$$

The mean value of  $u$  over a wave period  $T$  of a deterministic wave is

$$m_{\bar{u}}^{(d)}(z) = \langle \bar{u}(x, z, t) \rangle^{(d)} = \frac{1}{T} \int_{-T/2}^{T/2} \bar{u}(x, z, t) dt \quad (13)$$

In view of (11) and (12)

$$m_{\bar{u}}^{(d)}(z) = \begin{cases} \frac{1}{T} \int_{t_1(z)}^{t_2(z)} u(x, z, t) dt & \text{for } |z| \leq a \\ 0 & \text{for } |z| > a \end{cases} \quad (14)$$

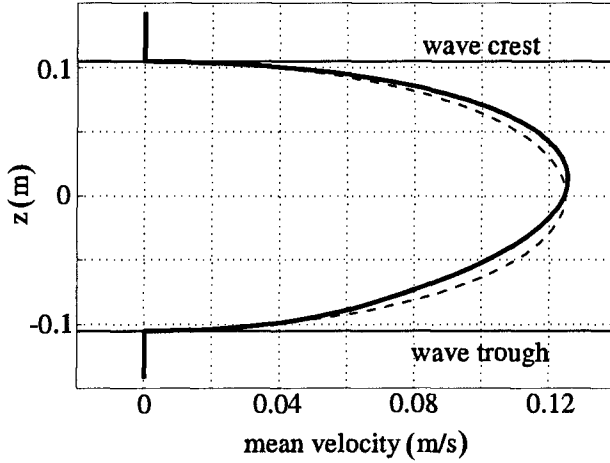


Fig. 1. Theoretical Eulerian mean velocity profile for deterministic small-amplitude wave (solid line) and its approximation (dashed line).

where  $t_1$  and  $t_2$  are such that

$$\begin{cases} z = \zeta(x, t_1) = \zeta(x, t_2) \\ z \leq \zeta(x, t) \quad \text{for } t_1 \leq t \leq t_2 \end{cases} \quad (15)$$

Carrying out the integration in (14) yields

$$m_{\bar{u}}^{(d)}(z) = \begin{cases} \frac{g a k}{\pi \omega} \frac{\cosh k(z+h)}{\cosh k h} \sin\left(\arccos \frac{z}{a}\right) & \text{for } |z| \leq a \\ 0 & \text{for } |z| > a \end{cases} \quad (16)$$

Taking into account the approximation (9) we obtain

$$m_{\bar{u}}^{(d)}(z) \approx \begin{cases} \frac{g a k}{\pi \omega} \sin\left(\arccos \frac{z}{a}\right) & \text{for } |z| \leq a \\ 0 & \text{for } |z| > a \end{cases} \quad (17)$$

The mean horizontal velocity profiles according to above expressions are presented in Fig. 1.

To obtain the total mean flux  $q^{(d)}$  at a fixed position  $x$  (Eulerian frame) we perform the following integration

$$q^{(d)} = \int_{-h}^{\zeta(x,t)} m_{\bar{u}}^{(d)}(z) dz \quad (18)$$

In view of (17)

$$q^{(d)} \approx \int_{-a}^a \frac{g a k}{\pi \omega} \sin\left(\arccos \frac{z}{a}\right) dz \quad (19)$$

By substituting  $\theta = \arccos(z/a)$  we obtain

$$q^{(d)} \approx \frac{g a^2 k}{\pi \omega} \int_0^\pi \sin^2 \theta d\theta = \frac{g a^2 k}{2 \omega} \quad (20)$$

Therefore, the flow of mass  $M^{(d)}$  in approximation is equal to

$$M^{(d)} = \rho q^{(d)} \approx \frac{\rho g a^2 k}{2 \omega} = \frac{E}{C} \quad (21)$$

which is the well-known result usually derived in the Lagrangian frame. The quantitative understanding of mass transport and return flow in the closed wave flume plays an important role in experimental studies of water wave kinematics. A review of recent research relating to the problem of return flow may be found in Gudmestad (1993).

### Return flow

A theoretical prediction of the mean horizontal velocity (in the Eulerian frame) allows for a better estimation of the return flow in the wave flume. We suggest in the present study that the difference between the predicted and the measured mean values of mean horizontal velocity gives an estimate of the return current in the wave flume. Figs. 2, 3, and 4 show the results of such calculations applied to laboratory data. These data were collected in the Norwegian Hydrotechnical Laboratories' 33 m long, 1.02 m wide and 1.8 m deep wave channel by a two-component Laser Doppler Velocimeter (LDV). The LDV allowed wave velocity measurements from wave crest down to tank bottom but at one point in space only during one run. In order to obtain the distributions for the statistical properties of the velocity along the vertical axis it was necessary to repeat the experiment with exactly the same free surface elevation spectrum but locating the LDV station at different vertical positions. The first series I18, consisting of 12 runs is given by the significant wave height  $H_S = 0.21$  m and peak period  $T_p = 1.8$  s, while the second series I24 consisting of 13 runs is given by the significant wave height  $H_S = 0.25$  m and peak period  $T_p = 2.4$  s. The third series R15B consisting of 10 runs represents a deterministic wave given by the value of wave height  $H = 0.26$  m and period  $T = 1.5$  m. Digitisation of the free surface elevation and velocity time series was carried at a rate of 40 Hz and



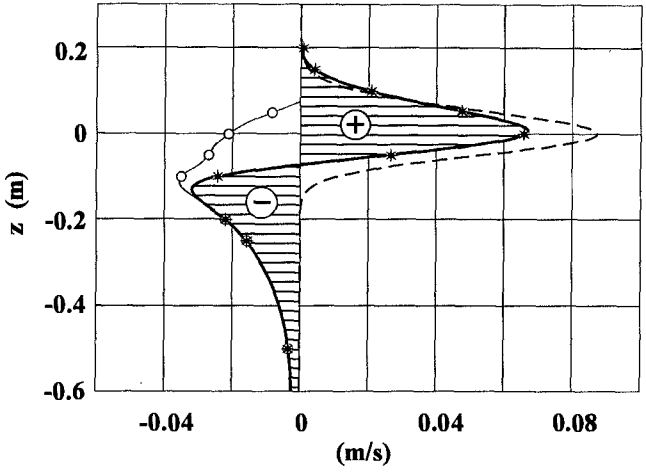


**Fig. 2.** Mean value of horizontal velocity and estimate of return flow: \* observed mean values, ---- theoretical mean drift, o estimated return flow. Wave case I18.

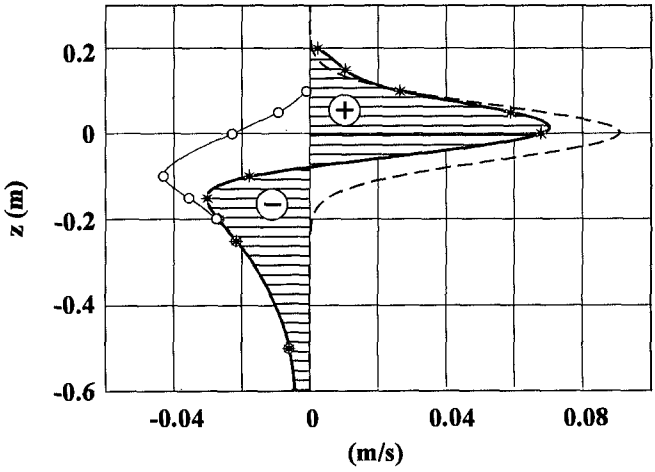


**Fig. 3.** Mean value of horizontal velocity and estimate of return flow: \* observed mean values, ---- theoretical mean drift, o estimated return flow. Wave case I24.

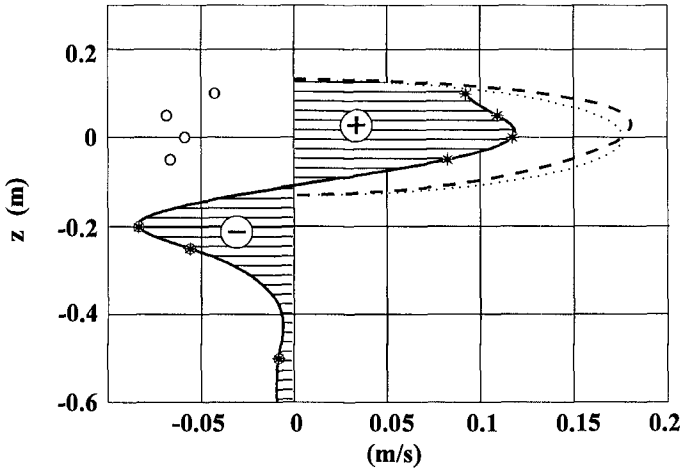


**Fig. 4.** Mean value of horizontal velocity and estimate of return flow for regular wave: \* observed mean values, - - - theoretical mean drift and its approximation (dotted line), o estimated return flow.

samples of 32,768 measuring points were collected. The water depth was 1.3 m. The experimental arrangement is described in detail in papers by Skjelbreia *et al.* (1989, 1991).

In Figs. 2 and 3 the measured mean horizontal velocity is marked with stars for the irregular wave cases I18 and I24, respectively, from Skjelbreia's measurements. The dashed line presents the theoretical mean value of the modified (according to equation (1)) horizontal velocities. Open circles show the estimated values of the return flow.

Data for a deterministic case have been examined through analysis of data series R15B from Skjelbreia's experiments. The full line in Fig. 4 presents the measured (in the Eulerian frame) mean flow for this deterministic wave case.

The return flow profiles presented in Figs. 2, 3, and 4 were averaged over the whole velocity data collected during each run. In order to examine the stability of the mean velocity profiles obtained, each time series has been divided into four equal parts. We believe that all resulting sub-series were long enough for calculation of a statistical estimate of their mean values and standard deviations. We believe also that a comparison of those four mean values provides us with at least an indication of the stability of the mean velocity profiles. The results of

these estimations are presented on Figs. 5 and 6 for the wave cases I18 and I24, respectively. It can be noted that the mean values as well as standard deviations of horizontal velocity calculated for each of four parts of time series are very much the same. Closer examination of the plots shows some similarities between I18 and I24 wave cases indicating that some trends in the mean horizontal velocity may exist. For example in both cases, for elevations below  $z = -0.4$  m the mean values in the first quarter of the experiment series have the smallest values, while, on the other hand, above that level it has the largest values.

## Conclusions

In the approach of Cieřlikiewicz and Gudmestad (1993) we are able, in the Eulerian frame, to discuss the distribution of the mean velocity along the vertical axis—the mean horizontal velocity is “stretched out” from the exact location at the surface onto the free surface zone. Moreover, we are able to calculate not only the total mean water flux but also the flux between two given  $z$ -elevations. The theoretical results relating to the current in the direction of the wave advance can be used for better estimation of a return current in the wave flume.

## REFERENCES

- Cieřlikiewicz, W. and Gudmestad, O. T., (1993). Stochastic characteristics of orbital velocities of random water waves. *J. Fluid Mech.*, 255, 275-299.
- Cieřlikiewicz, W. and Gudmestad, O. T., (1994). Mass transport within the free surface zone of water waves. *Wave Motion*, 19, pp. 275-299.
- Cieřlikiewicz, W., (1994). Influence of free surface effects on wave kinematics. *Schriftenreihe des Vereins der Freunde und Förderer des GKSS-Forschungszentrums Geesthacht e.V. Heft Nr. 5*, Geesthacht.
- Gudmestad, O. T., (1993). Measured and predicted deep water wave kinematics in regular and irregular seas. *Marine Structures*, 6, 1-73.
- Phillips, O. M., (1960). The mean horizontal momentum and surface velocity of finite-amplitude random gravity waves. *J. Geophys. Res.*, 65, No. 10, 3473-3476.
- Skjelbreia, J., Tørum, A., Berek, E., Gudmestad, O. T., Heideman, J. and Spidsøe, N., (1989). Laboratory measurements of regular and irregular wave kinematics. E&P Forum Workshop on Wave and Current Kinematics and Loading IFP, Rueil Malmaison, France, 45-66.

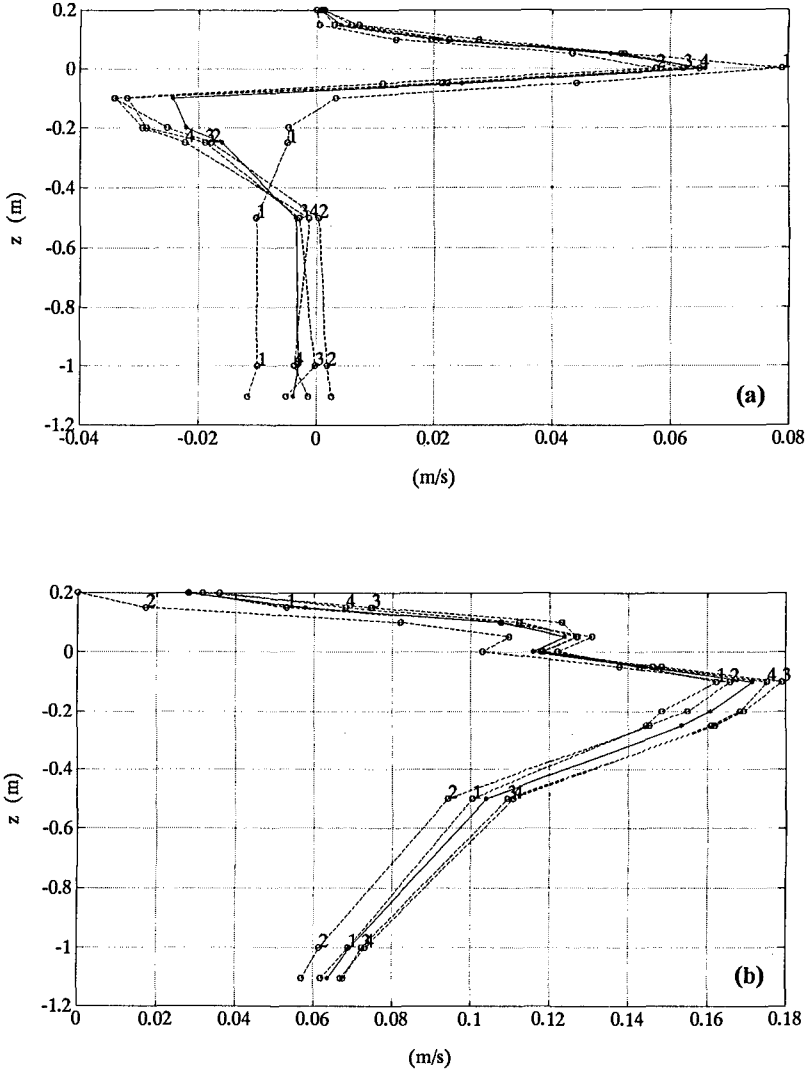


**Fig. 5.** Mean values (a) and standard deviations (b) of horizontal velocity calculated for each sub-series (dashed lines with circles) against the one calculated for the whole data series (solid line with stars). Wave case I18. The numbers of successive quarters of the experiment series are indicated.

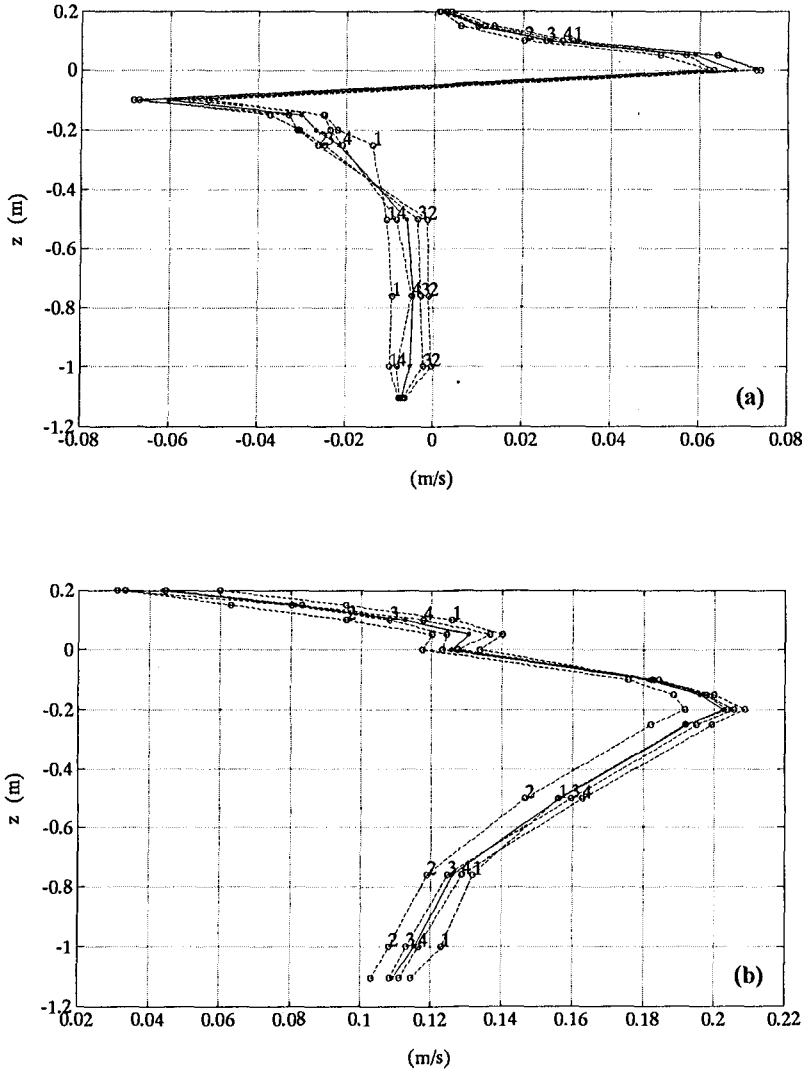


**Fig. 6.** Mean values (a) and standard deviations (b) of horizontal velocity calculated for each sub-series (dashed lines with circles) against the one calculated for the whole data series (solid line with stars). Wave case I24. The numbers of successive quarters of the experiment series are indicated.

Sjelbreia, J. E., Berek, E., Bolen, Z. K., Gudmestad, O. T., Heideman, J. C., Ohmart, R. D., Spidsøe, N. and Tørum, A., (1991). Wave kinematics in irregular waves. Proc. 10th Intern. Conf. on Off-shore Mech. and Arctic Engng., Stavanger, Norway, 223-228.

Starr, V. P., (1947). A momentum integral for surface waves in deep water. *J. Marine Res.*, 6, No. 2, 126-135.

Tung, C. C., (1975). Statistical properties of the kinematics and dynamics of a random gravity wave field. *J. Fluid Mech.*, 70, 251-255.

## CHAPTER 8

# Vertical Variations of Fluid Velocities and Shear Stress in Surf Zones

Daniel T. Cox<sup>1</sup>, Nobuhisa Kobayashi<sup>2</sup>, and Akio Okayasu<sup>3</sup>

**ABSTRACT:** Detailed laboratory measurements are made of the velocity fluctuations to investigate the processes of the turbulence generation, advection, diffusion and dissipation in the surf zone. An order of magnitude analysis of the transport equation of the turbulent kinetic energy using the normalization adopted by Kobayashi and Wurjanto (1992) indicates an approximate local equilibrium of turbulence for shallow water waves in the surf zone. Estimates are found for common surf zone turbulence parameters. The calibrated values are used to show that the eddy viscosity varies gradually over depth and is nearly time-invariant and that the local equilibrium of turbulence is a reasonable approximation for spilling waves in the inner surf zone.

## INTRODUCTION

The spatial and temporal variations of fluid velocities, shear stress, and turbulence intensity are required for a detailed analysis of sediment transport in the surf zone (Deigaard *et al.*, 1986). Field measurements of turbulent velocity fluctuations in the surf zone are difficult due to the harsh conditions for hot film anemometers and problems of calibration and voltage drift (George *et al.*, 1994). Laser-Doppler anemometry has been used in the laboratory (e.g., Stive, 1980; Nadaoka and Kondoh, 1982) to measure turbulent velocity fluctuations. However, no detailed analysis has been made of the turbulent kinetic energy transport equation in the nearshore region with laboratory data. Turbulence measurements in the surf zone are presented herein and are used to show that the local equilibrium of turbulence is a reasonable approximation for spilling waves in the inner surf zone. In addition,

---

<sup>1</sup>Graduate Student, Center for Applied Coastal Research, University of Delaware, Newark, DE 19716 USA. Email: dtc@coastal.udel.edu Tel: +1 302 831 8477

<sup>2</sup>Professor and Associate Director, Center for Applied Coastal Research, University of Delaware, Newark, DE 19716 USA. Email: nk@coastal.udel.edu

<sup>3</sup>Assistant Professor, Department of Civil Engineering, Yokohama National University, 156 Tokiwadai, Yokohama 240, Japan. Email: okayasu@coast.cvg.ynu.ac.jp

the present analysis will be used to calibrate coefficients for the simple turbulence model for the surf zone.

### TURBULENCE MODEL

The transport equation of the turbulent kinetic energy,  $k$ , is normally written as

$$\frac{\partial k}{\partial t} + u_j \frac{\partial k}{\partial x_j} = \nu_t \left( \frac{\partial u_i}{\partial x_j} + \frac{\partial u_j}{\partial x_i} \right) \frac{\partial u_i}{\partial x_j} + \frac{\partial}{\partial x_j} \left( \frac{\nu_t}{\sigma_k} \frac{\partial k}{\partial x_j} \right) - C_d^{3/4} \frac{(k)^{3/2}}{\ell} \quad (1)$$

where use is made of the repeated indices,  $i = 1, 2$ ;  $t$  is time,  $x_1 = x$  is the onshore directed horizontal coordinate;  $x_2 = z$  is the vertical coordinate, positive upward with  $z = 0$  at the still water level (SWL);  $u_1 = u$  and  $u_2 = w$  are the horizontal and vertical velocities; and  $\sigma_k$  is an empirical constant associated with the diffusion of  $k$ . The turbulent eddy viscosity,  $\nu_t$ , may be expressed as (e.g., ASCE, 1988)

$$\nu_t = C_d^{1/4} \ell \sqrt{k} \quad (2)$$

in which  $\ell$  is the turbulent mixing length, and  $C_d$  is an empirical coefficient.

The typical values of  $C_d$  and  $\sigma_k$  for *steady turbulent flow* are  $C_d \simeq 0.08$  and  $\sigma_k \simeq 1.0$  (Lauder and Spalding, 1972). The value of  $C_d$  is determined herein for normally incident waves on a rough, impermeable slope under the assumption of the approximate local equilibrium of turbulence. The equation for the dissipation rate of  $k$  might be used to estimate the turbulence length scale ( $k$ - $\epsilon$  model) but this equation is more empirical than (1) and gives only slightly better results for the case of bed shear stress calculations (Fredsoe and Deigaard, 1992). Alternatively, the mixing length  $\ell$  in (2) may be specified simply as

$$\ell = \begin{cases} \kappa(z - z_b) & \text{for } z < (\overline{C_\ell} h / \kappa + z_b) \\ \overline{C_\ell} h & \text{for } z \geq (\overline{C_\ell} h / \kappa + z_b) \end{cases} \quad (3)$$

where  $\kappa$  is the von Karman constant ( $\kappa \simeq 0.4$ );  $z_b$  is the bottom elevation;  $h$  is the instantaneous water depth; and  $\overline{C_\ell}$  is an empirical coefficient related to the eddy size.  $\overline{C_\ell}$  is written with an overbar to show that it is time-invariant and to differentiate it from  $C_\ell$  used later. Eq. (3) is similar to that used by Deigaard *et al.* (1986) for their analysis of suspended sediment in the surf zone in which use was made of  $\overline{C_\ell} = 0.07$  and the mean water depth,  $\bar{h}$ , instead of the instantaneous depth,  $h$ . The use of  $h$  should be more appropriate in the swash zone in light of the limited field data of Flick and George (1990). Svendsen (1987) suggested  $\overline{C_\ell} = 0.2$ – $0.3$  for the steady undertow. The value of  $C_\ell$  for the *unsteady* flow and the time-averaged value,  $\overline{C_\ell}$ , will also be determined for the present data.

The dimensionless variables are introduced following Kobayashi and Wurjanto (1992):

$$t' = \frac{t}{T}; \quad x' = \frac{x}{T\sqrt{gH}}; \quad z' = \frac{z}{H}; \quad u' = \frac{u}{\sqrt{gH}}; \quad w' = \frac{w}{H/T} \quad (4)$$



$$p' = \frac{p}{\rho g H}; \quad \nu_t' = \frac{\nu_t}{H^2/T}; \quad k' = \frac{k}{gH/\sigma}; \quad \ell' = \frac{\ell}{H/\sqrt{\sigma}}; \quad \sigma = \frac{T\sqrt{gH}}{H} \quad (5)$$

where the primes indicate dimensionless quantities,  $T$  and  $H$  are the characteristic wave period and height of the shallow water waves, and  $\sigma$  is the ratio between the horizontal and vertical length scales. The order of magnitude of  $k$ ,  $\ell$ , and  $\nu_t$  is estimated such that the resulting normalized equations become consistent with the measured data as explained later.

Substitution of (4) and (5) into (1) under the assumption of  $\sigma^2 \gg 1$  yields

$$\sigma^{-1} \left( \frac{\partial k'}{\partial t'} + u' \frac{\partial k'}{\partial x'} + w' \frac{\partial k'}{\partial z'} \right) = \tau' \frac{\partial u'}{\partial z'} + \sigma^{-1} \frac{\partial}{\partial z'} \left( \frac{\nu_t'}{\sigma_k} \frac{\partial k'}{\partial z'} \right) - C_d^{3/4} \frac{k'^{3/2}}{\ell'} \quad (6)$$

where the first and third terms on the right-hand-side are the production and dissipation terms, respectively. For their analysis of suspended sediment in the surf zone, Deigaard *et al.* (1986) used (6) in which the advection terms were neglected and the production of  $k'$  was estimated empirically. In short, they attempted to predict the variation of  $k'$  without analyzing  $u'$ ,  $w'$  and  $\tau'$ . Eq. 6 indicates that the production and dissipation of  $k'$  are dominant under the assumption of  $\sigma^2 \gg 1$ . This is qualitatively consistent with the findings of Svendsen (1987) who concluded that only a very small portion of the energy loss in the breaker (2-6% for the cases considered) was dissipated below trough level.

Considering the empirical nature of (6) with the coefficients  $\sigma_k$  and  $C_d$  as well as the uncertainty of the free surface boundary condition of  $k'$  even for steady turbulent flow (Rodi, 1980), (6) may be simplified further by neglecting the terms of the order  $\sigma^{-1}$  and the resulting equation is expressed in dimensional form as

$$\frac{\tau}{\rho} \frac{\partial u}{\partial z} \simeq C_d^{3/4} \frac{k^{3/2}}{\ell} \quad (7)$$

which implies the local equilibrium of turbulence. Substitution of  $\tau/\rho = \nu_t \partial u / \partial z$  and (2) into (7) yields

$$k = |\tau| / (\rho \sqrt{C_d}) \quad (8)$$

$$\nu_t = \ell^2 \left| \frac{\partial u}{\partial z} \right| \quad (9)$$

With these assumptions, (8) is used to determine the appropriate value of  $C_d$ . Eq. (9) corresponds to the standard mixing length model (ASCE, 1988) and is used with (2) to determine  $C_\ell$  and  $\overline{C}_\ell$  in (3). The degree of the local equilibrium of turbulence is assessed using (7) with the calibrated coefficients  $C_d$  and  $\overline{C}_\ell$ .

## EXPERIMENT and DATA REDUCTION

The experiment was conducted in the 33 m long, 0.6 m wide and 1.5 m deep wave flume at the University of Delaware. A hydraulically actuated piston wavemaker

with a 1 m stroke was at the far end; and a rough, uniform 1:35 slope was emplaced at the near end of the flume. The water depth was 0.4 m in the constant depth section. Regular cnoidal waves were specified at the wavemaker, and the waves broke by spilling on the impermeable slope. The rough slope consisted of a layer of natural sand grains with median diameter  $d_{50}=1$  mm glued to Plexiglas sheets and mounted on the entire slope. This was used to increase the bottom boundary layer thickness for estimating the bottom shear stress. A detailed analysis of the bottom shear stress outside and inside the surf zone is given in Cox, *et al.* (1995).

The free surface elevations were measured using capacitance-type wave gages with a sampling rate of 100 Hz. The velocities were measured using a two-component laser-Doppler anemometer with a pair of burst spectrum analyzers. The effective sampling rate was in excess of  $1 \times 10^3$  data points per second, and the sampling rate was later reduced by band averaging to 100 Hz before the phase averaging procedure described below. The free surface and velocity fluctuations were measured at six vertical lines and are denoted L1, L2, . . . , L6 for brevity. The horizontal spacing of the measuring lines was on the order of 1 m, and the vertical spacing of the measuring points was on the order of 1 cm except near the bottom where measurements were made on the order of a fraction of the grain height, i.e. less than 1 mm. Details of the experiment are provided in Okayasu and Cox (1995).

The free surface and velocity measurements were reduced by a standard phase averaging procedure over 50 waves. The sampling interval was  $\Delta t = 0.01$  s and the wave period was  $T = 2.2$  s which gave  $J = T/\Delta t = 220$  as the number of data points or phases per wave. The phase-averaged free surface elevations,  $\eta_a$ , were computed from the measured free surface,  $\eta_m$ , where the subscripts  $a$  and  $m$  refer to the phase-averaged and measured quantities. The variance of the free surface elevation,  $\sigma_\eta^2$ , and the standard deviation,  $\sigma_\eta$ , were also computed. For the figures presented here, the phases are aligned with zero-upcrossing of the free surface elevation at  $t = (T/4) = 0.55$  for the six measuring lines (Cox, 1995).

The normalization parameters for the turbulent quantities in (5) are given in Table 1 with the range of values for the measured data as explained later. The range is found by taking the minimum and maximum values for the phase-averaged quantities between the trough level and the bottom boundary layer which is defined simply as 1 cm above the impermeable bottom and consistent with the analysis of Cox (1995). The ranges given in parentheses are for the bottom boundary layer. The cross-shore locations of the measuring lines are given in Table 2 and are characterized as follows: L1 is seaward of the break point; L2 is at the break point which is defined as the start of aeration in the tip of the wave; L3 is in the transition region where the wave form goes from organized motion to a turbulent bore; and L4, L5, and L6 are in the inner surf zone where the saw-toothed wave shape is a well-developed turbulent bore (Cox, 1995). Table 1 indicates that the scaling of  $k$ ,  $\ell$ , and  $\nu_i$  in (5) is appropriate inside the surf zone for L3 to L6.

Table 1: Range of  $k$ ,  $\ell$ , and  $\nu_t$  for L1 to L6 and Normalization Quantities.

Line No.	$k$ ( $\text{cm}^2/\text{s}^2$ )	$gH/\sigma$ ( $\text{cm}^2/\text{s}^2$ )	$\ell$ (cm)	$H/\sqrt{\sigma}$ (cm)	$\nu_t$ ( $\text{cm}^2/\text{s}$ )	$H^2/T$ ( $\text{cm}^2/\text{s}$ )
L1	0.2 – 2.8 (0.3 – 18.8)	684	0.60 – 1.20 (0.01 – 0.40)	3.04	0.11 – 0.61 (0.00 – 0.27)	79.4
L2	0.4 – 3.8 (0.4 – 35.9)	1007	0.60 – 1.91 (0.01 – 0.40)	4.19	0.17 – 1.03 (0.01 – 0.28)	132.9
L3	14.4 – 297 (4.9 – 45.6)	645	0.60 – 3.23 (0.01 – 0.40)	2.89	0.65 – 18.4 (0.01 – 0.76)	73.4
L4	20.7 – 559 (6.8 – 65.7)	337	0.61 – 4.26 (0.02 – 0.41)	1.68	0.81 – 34.8 (0.01 – 0.68)	30.9
L5	17.4 – 206 (4.1 – 35.6)	268	0.60 – 2.64 (0.01 – 0.40)	1.39	0.97 – 12.9 (0.01 – 0.60)	22.8
L6	13.9 – 179 (4.4 – 76.7)	162	0.61 – 2.00 (0.02 – 0.41)	0.91	0.81 – 11.1 (0.02 – 0.83)	11.6

Table 2 lists the free surface statistics for L1 to L6 where  $x$  is the onshore directed horizontal coordinate with  $x = 0$  cm at L1;  $d$  is the distance below the still water level to the top of the Plexiglas sheet, i.e. the bottom of the 1 mm sand layer;  $H$  is the local wave height given by  $H = [\eta_a]_{max} - [\eta_a]_{min}$  where the subscripts  $min$  and  $max$  indicate the minimum and maximum values of a phase-averaged quantity;  $\bar{\eta}_a$  is the setup or setdown;  $\bar{\sigma}_\eta$  is the time-average of the standard deviation of  $\eta_a$ ; and  $[\sigma_\eta]_{min}$  and  $[\sigma_\eta]_{max}$  are the minimum and maximum of the standard deviation values over the wave period. The cross-shore variations of  $\bar{\eta}_a$ ,  $[\eta_a]_{min}$ , and  $[\eta_a]_{max}$  have been well studied; however, less mention has been made of  $\bar{\sigma}_\eta$ ,  $[\sigma_\eta]_{min}$ , and  $[\sigma_\eta]_{max}$ . From Table 2,  $[\sigma_\eta]_{max}$  is very small for L1 indicating repeatability of the wave form. For L2,  $[\sigma_\eta]_{max}$  increases slightly due to irregularities of wave breaking. For L3 in the transition region,  $[\sigma_\eta]_{max}$  is at a maximum. For L4 to L6,  $[\sigma_\eta]_{max}$  decreases with increasing distance to the shore. It is interesting to note the cross-shore variation of  $[\sigma_\eta]_{max}$  because it could be used to better quantify the transition region of the surf zone (e.g., Nairn *et al.*, 1990 and references therein).

The signal dropouts are excluded in the phase averaging of the measured horizontal and vertical velocities. The phase-averaged horizontal and vertical velocities are denoted  $u_a$  and  $w_a$ , and the horizontal and vertical velocity variances are denoted  $\sigma_u^2$  and  $\sigma_w^2$ . The turbulent normal stresses may be assumed to be equal to  $-\rho\sigma_u^2$  and  $-\rho\sigma_w^2$  in the horizontal and vertical directions, where  $\rho$  is the fluid density. The phase-averaged covariance of the measured horizontal and vertical velocities is denoted  $\sigma_{uw}$ , and the turbulent shear stress,  $\tau$ , may be assumed to

Table 2: Phase-Averaged Free Surface Statistics for L1 to L6.

Line No.	$x$ (cm)	$d$ (cm)	$H$ (cm)	$\bar{\eta}_a$ (cm)	$[\eta_a]_{min}$ (cm)	$[\eta_a]_{max}$ (cm)	$\bar{\sigma}_\eta$ (cm)	$[\sigma_\eta]_{min}$ (cm)	$[\sigma_\eta]_{max}$ (cm)
L1	0	28.00	13.22	-0.30	-3.88	9.34	0.10	0.05	0.22
L2	240	21.14	17.10	-0.44	-3.60	13.50	0.14	0.06	0.98
L3	360	17.71	12.71	-0.05	-2.82	9.89	0.41	0.19	2.06
L4	480	14.29	8.24	0.20	-2.33	5.91	0.38	0.17	1.37
L5	600	10.86	7.08	0.75	-1.60	5.48	0.28	0.15	1.03
L6	720	7.43	5.05	1.13	-0.82	4.23	0.22	0.11	0.92

be equal to  $-\rho\sigma_{uw}$ .

Figure 1 compares the vertical variation of the Froude-scaled time-averaged horizontal turbulent intensity for the present measurements L3 to L6 with the data of George *et al.* (1994), Stive (1980), and Nadaoka and Kondoh (1982). The data of George *et al.* (1994) from their Figure 8a are for the natural surf zone and include random waves of both plunging and spilling type. The frozen turbulence assumption was used to extract the turbulent signal. The middle curve of George *et al.* (1994) indicates the mean value in several vertical bins and the envelope is this mean  $\pm 1$  standard deviation plus the uncertainty in the data reduction. The data of Nadaoka and Kondoh (1982) from their Figure 7 are for Case 1, spilling waves on a 1:20 slope, and include only the measuring lines inside the surf zone, i.e. P1 to P5. A frequency filter was used to extract the turbulent signal. It is noted that these data are plotted in Figure 1 using  $d$  rather than  $\bar{h}$ . The data of Stive (1980) are also taken from Figure 8a of George *et al.* (1994) and are presumably for Test 1, spilling waves on a 1:40 slope, and include the measuring lines in the transition region as well as the inner surf zone. Phase-averaging was used to extract the turbulent signal.

Only the data of George *et al.* (1994) are for multidirectional random waves measured in the field. The other three data sets are for normally incident, regular waves measured in the laboratory. The comparison of the present data set with that of Stive (1980) shows that the phase averaging method gives consistent results for laboratory waves of similar type. The comparison with Nadaoka and Kondoh (1982) indicates that the frequency filter may underestimate the turbulent signal as noted by other researchers (e.g., George *et al.*, 1994). Nevertheless, it would be useful to have a simple relation between the turbulent signals from the two methods since phase averaging cannot be used for random waves in a natural surf zone. Interpretation of the data of George *et al.* (1994) is difficult

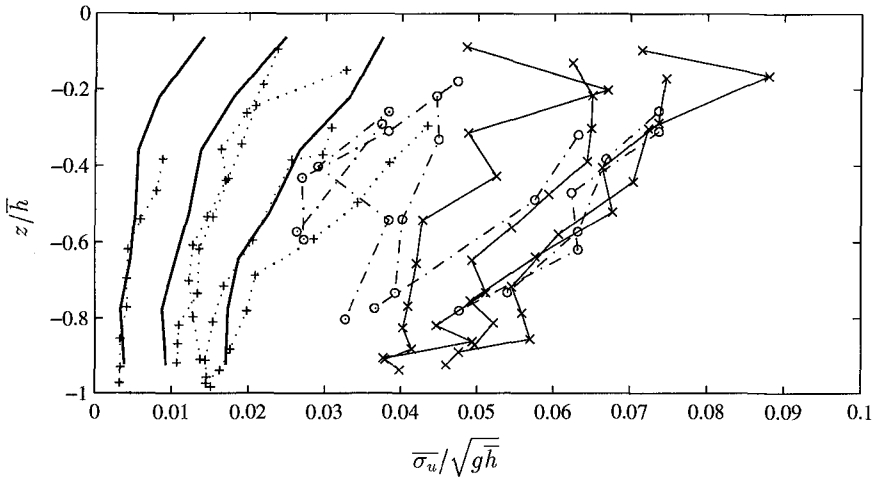


Figure 1: Comparison of Vertical Variation of Froude-Scaled Horizontal Turbulence Intensity with George *et al.* (1994) (—); Stive (1980) (o - - -); Nadaoka and Kondoh (1982) (+ ····); Present Data L3 to L6 (× —).

because of the method used to extract the turbulent signal and because the waves were random and multidirectional. Clearly, more work is necessary in this area.

Figure 2 shows the temporal variations of the phase-averaged horizontal and vertical velocity variances,  $\sigma_u^2$  and  $\sigma_w^2$ , and velocity covariance,  $\sigma_{uw}$ , for five vertical elevations for L2. The five vertical locations for L2a to L2e are  $-5.04$ ,  $-13.04$ ,  $-17.04$ ,  $-20.04$ , and  $-20.94$  cm, respectively, where the still water level is  $z = 0.0$  cm and the still water depth is  $d = 21.14$  cm. Figure 2 shows almost no turbulence in the interior, and the turbulence seems to be confined to the bottom boundary layer. Also, as indicated in the caption, the proposed scaling may not be appropriate in the boundary layer outside the surf zone. The same quantities of Figure 2 for L2 are shown in Figure 3 for L4. The five vertical locations for L4a to L4e are  $-2.19$ ,  $-6.19$ ,  $-10.19$ ,  $-13.19$ , and  $-14.09$  cm, respectively, where the still water depth is  $d = 14.29$  cm. This figure shows the spread and decay of turbulence generated by wave breaking. Also, the peak of the turbulence shifts downward. For L4a, the horizontal velocity variance is greater than the vertical variance over most of the wave period except at  $t = 0.6$  s when the phase-averaged horizontal and vertical velocities are approximately the same (Cox, 1995). The proposed scaling indicated in the caption seems appropriate here. For L4c, the horizontal and vertical variances are approximately the same since the turbulence becomes more isotropic even though the vertical velocity is much smaller than the horizontal velocity at this elevation. For L4e, the horizontal variance is again

greater than the vertical variance since the vertical turbulent fluctuations may be limited by the solid boundary. Also, the covariance is negative for L4a to L4c.

Figure 4 shows the detail of the cross-shore variations of time-average horizontal and vertical variances,  $\overline{\sigma_u^2}$  and  $\overline{\sigma_w^2}$ , and the time-averaged covariance,  $\overline{\sigma_{uw}}$ . Comparison of  $\overline{\sigma_u^2}$  and  $\overline{\sigma_w^2}$  for L3 to L6 shows that they are about the same magnitude below trough level and decay linearly downward except in the lower portion of the water column where  $\overline{\sigma_u^2}$  remains approximately constant over depth and  $\overline{\sigma_w^2}$  tends to zero near the bottom.

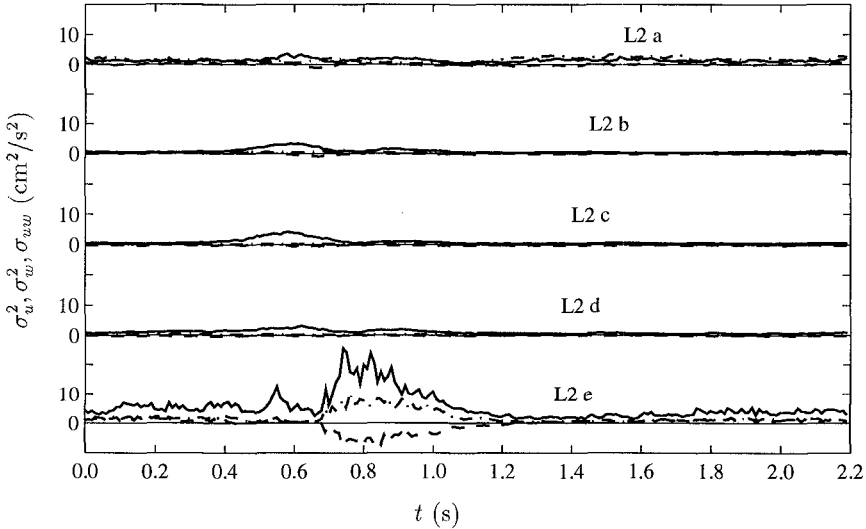


Figure 2: Temporal Variations of Phase-Averaged Horizontal Velocity Variance,  $\sigma_u^2$  (—); Vertical Velocity Variance,  $\sigma_w^2$  (---); and Covariance,  $\sigma_{uw}$  (- -) for Five Vertical Elevations for L2 with  $gH/\sigma = 1007 \text{ cm}^2/\text{s}^2$ .

## ANALYSES OF WAVE GENERATED TURBULENCE

The dimensional shear stresses,  $\tau_{ij}$ , are written in tensor notation as (e.g., Rodi, 1980)

$$\tau_{ij} = \rho \left[ \nu_t \left( \frac{\partial u_i}{\partial x_j} + \frac{\partial u_j}{\partial x_i} \right) - \frac{2}{3} k \delta_{ij} \right] \quad (10)$$

where  $\delta_{ij}$  is the Kronecker delta and  $k$  is the turbulent kinetic energy per unit mass which can be expressed in terms of the normal stresses as

$$k = -\frac{1}{2\rho} (\tau_{11} + \tau_{22} + \tau_{33}) \quad (11)$$

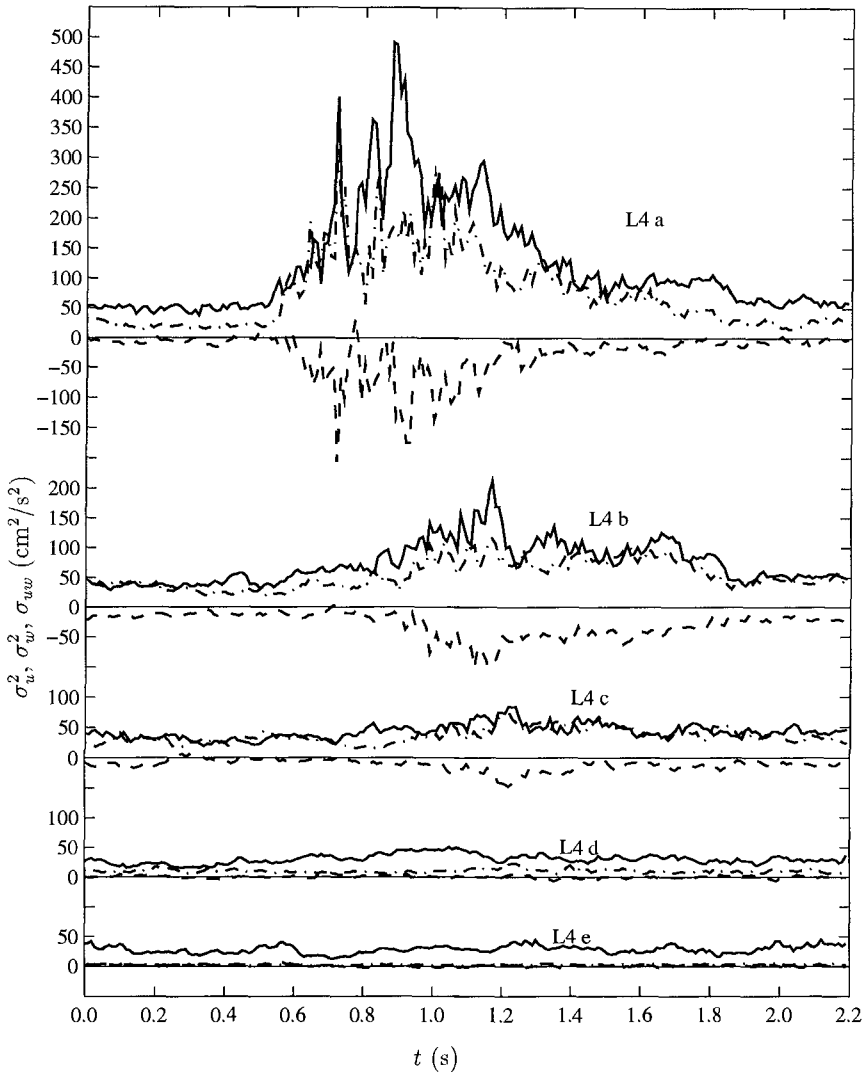


Figure 3: Temporal Variations of Phase-Averaged Horizontal Velocity Variance,  $\sigma_u^2$  (—); Vertical Velocity Variance,  $\sigma_w^2$  (-.-); and Covariance,  $\sigma_{uw}$  (- -) for Five Vertical Elevations for L4 with  $gH/\sigma = 337 \text{ cm}^2/\text{s}^2$ .

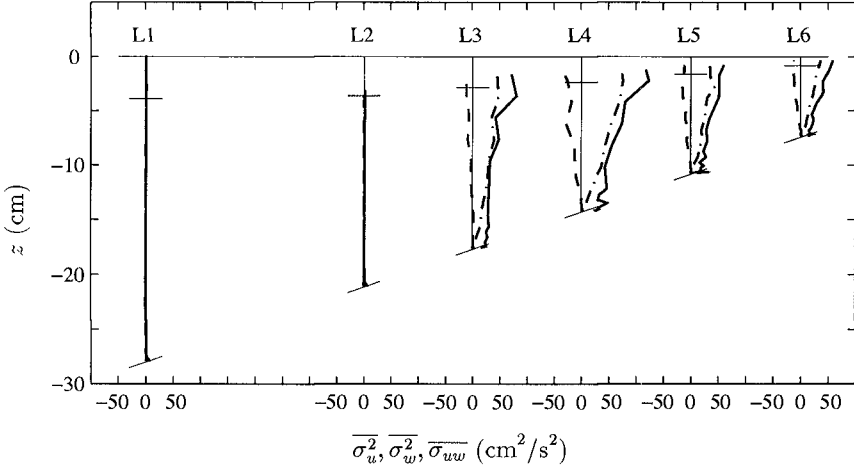


Figure 4: Cross-Shore Comparison of Mean Horizontal and Vertical Velocity Variances and Mean Covariance with  $\sigma_u^2$  (—);  $\sigma_w^2$  (---); and  $\sigma_{uw}$  (- -) for L1 to L6.

Assuming that Reynolds averaging is the same as the phase averaging used here, the standard definition of  $k$  in terms of the variances is given as

$$k = \frac{1}{2} (\sigma_u^2 + \sigma_w^2 + \sigma_v^2) \quad (12)$$

The transverse velocity variance,  $\sigma_v^2$ , was not measured for this experiment.

For idealized two-dimensional turbulent flow,  $\partial u_3 / \partial x_3 = 0$  so that  $\tau_{33} = -\frac{2}{3} \rho k$  and then  $\sigma_v^2 = \frac{2}{3} k$ . This reduces (12) to

$$k = -\frac{3}{4\rho} (\tau_{11} + \tau_{22}) = \frac{3}{4} (\sigma_u^2 + \sigma_w^2) \quad (13)$$

The use of (10) results in  $\frac{1}{2}(\sigma_v^2/k) = \frac{1}{3}$ , corresponding to homogeneous isotropic turbulence. For steady turbulent flow, the ratios of the normal stresses to the turbulent kinetic energy have been tabulated by Svendsen (1987). This table indicates that the range is  $0.21 \leq \frac{1}{2}(\sigma_v^2/k) < \frac{1}{3}$  so that  $\sigma_v^2$  may be overestimated slightly here.

Having measured  $\sigma_u^2$  and  $\sigma_w^2$  directly, Cox (1995) determined whether the ratio of the vertical to horizontal velocity variance,  $C_w = \sigma_w^2 / \sigma_u^2$ , is constant over a wave period. The results show that the values lie in the range  $0.06 \leq C_w \leq 0.86$  for the variances below trough level whereas the range for the types of flows listed in Svendsen (1987) is  $0.16 \leq C_w \leq 1.00$ . For L3 to L6,  $C_w$  is fairly constant



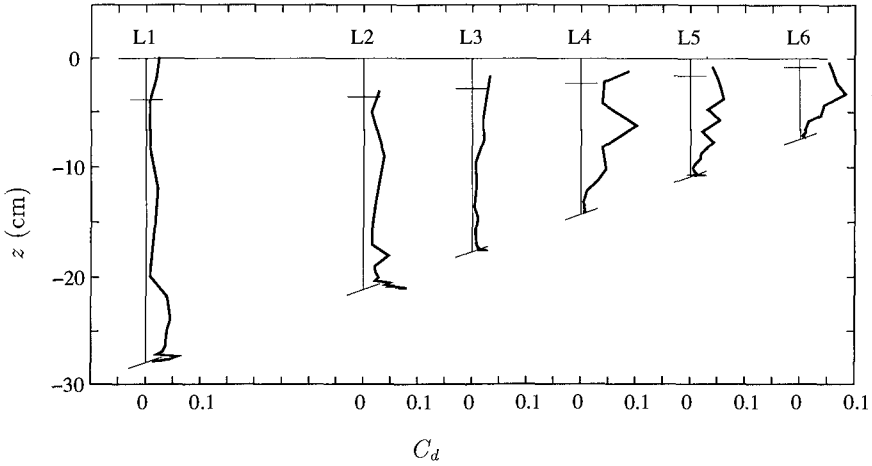


Figure 5: Cross-Shore Variation of  $C_d$  for L1 to L6.

over depth with  $C_w \simeq 0.7$  until the lower portion of the water column where it decreases linearly toward the rough bottom. Further comparisons of the temporal variations of  $C_w \sigma_u^2$  and  $\sigma_w^2$  similar to Figures 2 and 3 show that it is appropriate to assume that  $C_w$  is constant over a wave period in the boundary layer outside the surf zone and below trough level inside the surf zone (Cox, 1995).

A least-squares error method is used to calibrate  $C_d$  following (8). Assuming that  $C_d$  is independent of time, the least-squares equation is

$$\sqrt{C_d} = \frac{\sum_{j=1}^J |\sigma_{uw}|_j k_j}{\sum_{j=1}^J k_j^2} \tag{14}$$

where  $j$  indicates the phase out of  $J = 220$  phases. Figure 5 shows the cross-shore variation of  $C_d$  for L1 to L6 using (14). The vertical variation of  $C_d$  is distinctly different for the three regions: L1 and L2 seaward of breaking, L3 in the transition region, and L4 to L6 in the inner surf zone. For L1 and L2,  $C_d \simeq 0.06$  in the bottom boundary layer whereas a similar value  $C_d = 0.08$  has been used for steady flows and for oscillatory flows in nonbreaking waves. Above the bottom boundary layer for L1 and L2, the values on the right-hand-side of (14) are near zero so that the estimated values in this region are not useful. For L3 in the transition region, the magnitude of  $C_d$  is less than 0.03 over most the water column even though the values for  $k$  and  $\sigma_{uw}$  are non-zero. For L4 to L6, a typical value is  $C_d \simeq 0.05$  below trough level except in the lower portion where it decreases to a small value.

Eqs. (9) and (2) with the calibrated values of  $C_d$  are used to determine  $C_\ell$  in

(3). For this procedure, an error term is computed for a range of  $C_\ell$  by summing the absolute value of the difference of (9) and (2) over the water column at each of the 220 phases. The error term is given as

$$Err(j) = \frac{1}{I} \sum_{i=1}^I \left| (\ell^2 \left| \frac{\partial u}{\partial z} \right|) - (C_d^{1/4} \ell \sqrt{k}) \right|_i, \quad j = 1, 2, \dots, 220 \quad (15)$$

where the index  $i$  refers to points in the vertical measuring line. The ranges of  $C_\ell$  were  $0.01 \leq C_\ell \leq 0.20$  for L1 and L2 and  $0.05 \leq C_\ell \leq 0.45$  for L3 to L6. The value of  $C_\ell$  that gave the least error in (15) was adopted at that phase. Figure 6 shows the temporal variation of the adopted value of  $C_\ell$  at each of the 220 phases for L4. This figure shows the amount of scatter expected for the calibrated  $C_\ell$  and shows that there is a slight variation over the wave period. The bore arrives at  $t \simeq 0.6$  s (see also Figure 8 for the relative phases of the free surface elevation in the inner surf zone). The time-average values,  $\overline{C_\ell}$ , computed for all the measuring lines L1 to L6 are  $\overline{C_\ell} = 0.032$  (.021); 0.055 (.041); 0.117 (.065); 0.211 (.105); 0.162 (.081); and 0.172 (.089), respectively, where the standard deviation is given in parentheses (Cox, 1995). This gives an overall value of  $\overline{C_\ell} \simeq 0.04$  (0.03) outside the surf zone, and  $\overline{C_\ell} \simeq 0.12$  (0.07) in the transition region, and  $\overline{C_\ell} \simeq 0.18$  (0.09) for the inner surf zone.

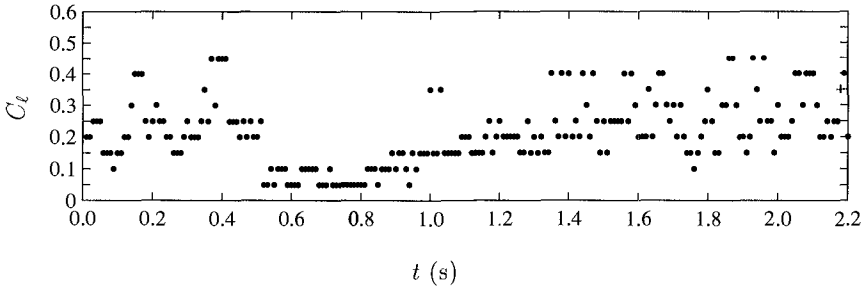


Figure 6: Temporal Variation of Adopted  $C_\ell$  Value at Each of 220 phases for L4 with  $\overline{C_\ell} = .211$ .

Figure 7 shows the vertical and temporal variations of the eddy viscosity,  $\nu_t$ , given in (2) computed using the calibrated values of  $C_d$  and  $\overline{C_\ell}$  for L4. The light vertical lines in the upper figure indicate the extent of the water column at the given phase. The two light horizontal lines in the lower left corner of the top figure indicate the vertical range plotted in detail in the bottom figure. In the bottom figure,  $z_m$  is the vertical coordinate from the bottom where  $z_m = 0$  on the top of the Plexiglass sheet, i.e. the bottom of the 1 mm sand layer. From both figures, it is clear that  $\nu_t$  at a given phase increases gradually from the bottom until about the middle of the water column where it is more or less constant

over depth. Also, it is reasonable to assume that  $\nu_t$  is time-invariant except near trough level with the passing of the bore.

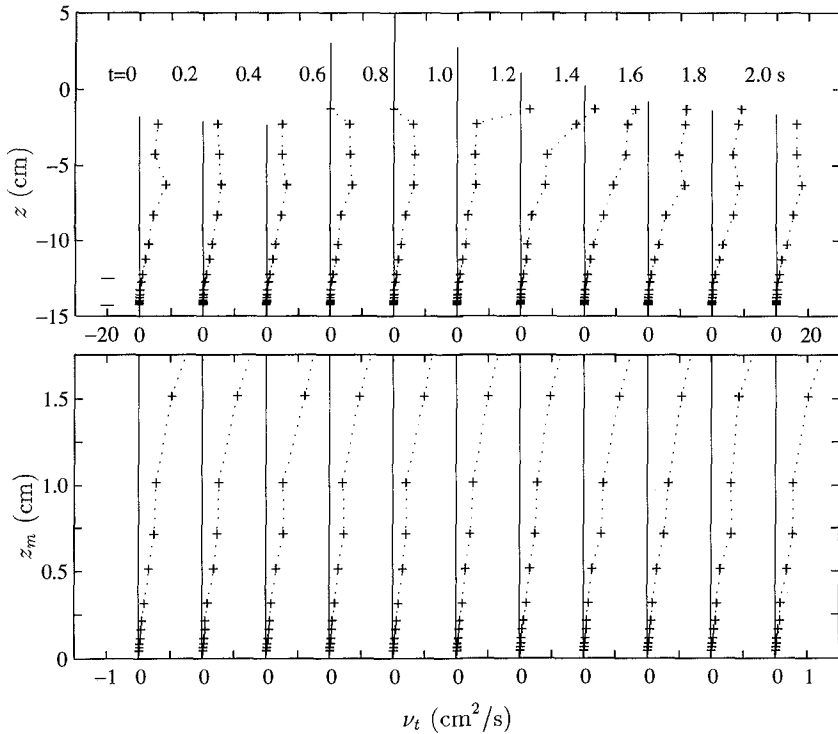


Figure 7: Vertical Variations of Eddy Viscosity,  $\nu_t$ , at Eleven Phases for L4 with  $H^2/T = 30.9 \text{ cm}^2/\text{s}$ .

Figure 8 shows the temporal variation of the dissipation term  $C_d^{3/4}(k^{3/2}/\ell)$  and the production term  $\tau(\partial u/\partial z)$  using the calibrated  $C_d$  and  $\overline{C}_\ell$  values for L5. Smoothing was used for the final plot since the contour lines of the unsmoothed values are difficult to discern in black and white (Cox, 1995). Also, only the measuring points above the bottom boundary layer are plotted. This figure shows that the approximate local equilibrium of turbulence is a reasonable assumption for spilling waves in the inner surf zone. It is noted that the numerical derivatives for additional terms in the dimensional equivalent of (6) were computed and that the noise level was on the same order as the quantities of interest.

## CONCLUSIONS

Turbulence measurements of spilling waves were presented and used to show that

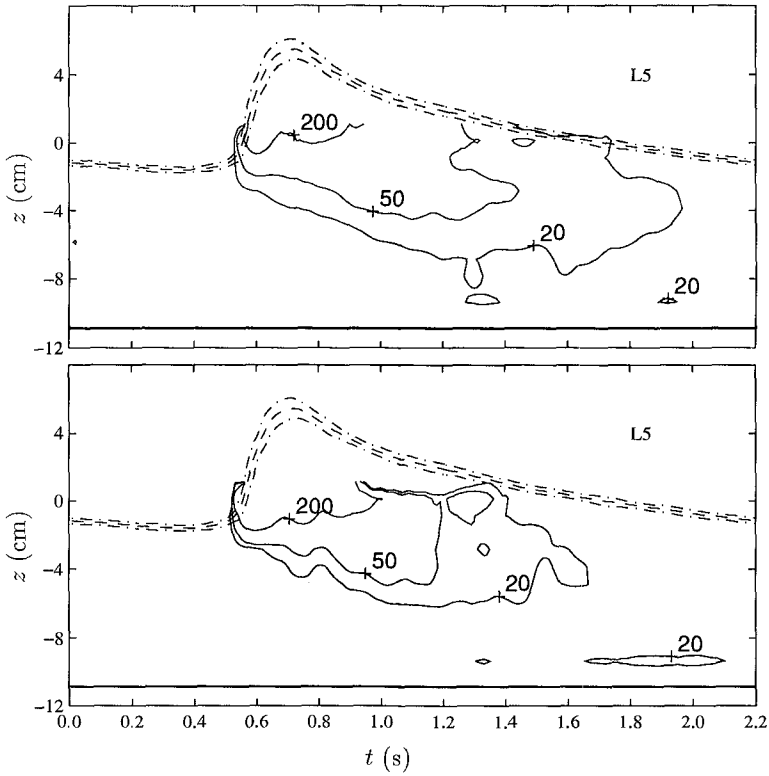


Figure 8: Contour Plot of Temporal Variation of Dissipation Term,  $C_d^{3/4}(k^{3/2}/\ell)$ , (Top) and Production Term,  $\tau(\partial u/\partial z)$ , (Bottom) using Calibrated  $C_d$  and  $\overline{C}_\ell$  with  $\eta_a$  (—) and  $\eta_a \pm \sigma_\eta$  (---) for L5.

the local equilibrium of turbulence is a reasonable approximation for spilling waves in the inner surf zone. Further, the empirical coefficient for the mixing length was shown to be roughly constant over the wave period but varied in the cross-shore direction. The typical values were of  $\overline{C}_\ell \simeq 0.04$  (0.03) outside the surf zone, and  $\overline{C}_\ell \simeq 0.12$  (0.07) in the transition region, and  $\overline{C}_\ell \simeq 0.18$  (0.09) for the inner surf zone. The coefficient related to the dissipation of  $k$  was found to be  $C_d \simeq 0.06$  in the bottom boundary layer outside the surf zone. In the transition region, the magnitude of  $C_d$  was less than 0.03 over most of the water column. In the inner surf zone a typical value was  $C_d \simeq 0.05$  over most of the water column except in the lower portion where it decreased to a small value. The eddy viscosity was also shown to increase approximately linearly from the bottom to the middle of the water column where the value became more or less

constant over depth. The eddy viscosity was fairly constant over the wave period except near trough level with passing of the bore.

### ACKNOWLEDGMENTS

This work was sponsored by the U.S. Army Research Office, University Research Initiative under contract No. DAAL03-92-G-0116 and by the National Science Foundation under grant No. CTS-9407827. Dr. Okayasu was supported by the Foundation for International Exchanges, Yokohama National University, during his stay at the University of Delaware.

### REFERENCES

- ASCE Task Committee on Turbulence Models in Hydraulic Computations (1988). "Turbulence modeling of surface water flow and transport: Part I to V." *J. Hydraulic Engrg.*, ASCE, 114(9), 970-1073.
- Cox, D. T. (1995). "Experimental and numerical modeling of surf zone hydrodynamics." Ph.D. Dissertation, University of Delaware, Newark.
- Cox, D. T., Kobayashi, N. and Okayasu, A. (1995). "Bottom shear stress in the surf zone." in preparation for *J. Geophys. Res.*
- Deigaard, R., Fredsøe, J. and Hedegaard, I. B. (1986). "Suspended sediment in the surf zone." *J. Wtrway. Port Coast. and Oc. Engrg.*, ASCE, 112(1), 115-127.
- Flick, R. E. and George, R. A. (1990). "Turbulence scales in the surf and swash." *Proc. 22nd Coast. Engrg. Conf.*, ASCE, 557-569.
- Fredsøe, J. and Deigaard, R. (1992). *Mechanics of Coastal Sediment Transport*, Advanced Series on Ocean Engineering, Volume 3, World Scientific, New Jersey.
- George, R. A., Flick, R. E. and Guza, R. T. (1994). "Observations of turbulence in the surf zone." *J. Geophys. Res.*, 99(C1), 801-810.
- Launder, B. E. and Spalding, D. B. (1972). *Mathematical Models of Turbulence*. Academic Press, New York, NY.
- Nadaoka, K. and Kondoh, T. (1982). "Laboratory measurements of velocity field structure in the surf zone by LDV." *Coast. Engrg. in Japan*, 25, 125-145.
- Nairn, R.B, Roelvink, J.A. and Southgate, H.N. (1990). "Transition zone width and implications for modelling surfzone hydrodynamics." *Proc. 22nd Coast. Engrg. Conf.*, ASCE, 68-81.
- Okayasu, A. and Cox, D. T. (1995). "Laboratory study on turbulent velocity field in the surf zone over a rough bed." in preparation for *Coast. Engrg. in Japan*.
- Kobayashi, N. and Wurjanto, A. (1992). "Irregular wave setup and run-up on beaches." *J. Wtrway. Port Coast. and Oc. Engrg.*, ASCE, 118(4), 368-386.
- Rodi, W. (1980). *Turbulence Models and Their Application in Hydraulics*. Int'l. Assoc. for Hydraul. Res., Delft, The Netherlands.
- Stive, M. J. F. (1980). "Velocity and pressure field of spilling breakers." *Proc. 17th Coast. Engrg. Conf.*, ASCE, 547-566.
- Svendsen, I. A. (1987). "Analysis of surf zone turbulence." *J. Geophys. Res.*, 92(C5), 5115-5124.

## CHAPTER 9

### Vorticity effects in combined waves and currents.

I. Cummins<sup>1</sup> & C. Swan<sup>2</sup>.

#### Abstract.

This paper concerns the interaction of waves and currents, and in particular the effect of the time-averaged vorticity distribution associated with a sheared current. Laboratory data describing both the "initial interaction" of waves and currents, and the "equilibrium" conditions arising within an established wave-current combination are presented. These results are compared to both the existing irrotational solutions and a multi-layered numerical model capable of describing an arbitrary current profile. The interaction of regular waves and sheared currents is shown to be in good agreement with this latter solution. However, a similar description of random waves on sheared currents is limited by the wave-induced changes in both the mean current profile and the associated turbulent structure.

#### 1. Introduction.

In general, the interaction of waves and currents may be sub-divided into two distinct stages. The first corresponds to the "initial interaction" which arises when a given wave train (specified in the absence of a current) propagates onto a pre-determined current profile. This stage is usually solved in terms of a "gradually varying flow", and describes the initial changes in the wave height, the wave length, and (under some circumstances) the current profile. In contrast, the second stage concerns the description of the so-called "equilibrium conditions" arising from an established wave-current combination. It is this stage which seeks to define the fluid motion appropriate to the wave height, the wave period, the water depth, and the current profile determined in stage 1.

---

<sup>1</sup> Research student & <sup>2</sup> Lecturer. Department of Civil Engineering, Imperial College of Science Technology and Medicine, London, United Kingdom. SW7 2BU.

In its simplest form the combination of waves and currents involves a series of regular waves propagating on a depth-uniform current. In this case the current has no associated vorticity, and laboratory measurements (Thomas, 1990 and Swan, 1990) suggest that the "initial interaction" is well defined by the conservation of wave action and the "equilibrium conditions" are in good agreement with a Doppler shifted solution (Fenton, 1985). Although this case appears very simplistic it is, in fact, valid for a wide range of flow conditions. For example, in the case of a logarithmic current profile (typical of many tidal flows) the vorticity distribution is largely confined to a lower layer adjacent to the sea bed. In this case the vorticity has little effect beyond the near-bed region, and an approximate uniform current provides a reasonable description of both the "initial interaction" and the resulting oscillatory flow. Furthermore, if the current profile is weakly sheared, an "equivalent uniform current" based upon the flow conditions at the water surface (Hedges and Lee, 1992) may be sufficient to define the resulting flow field.

Unfortunately, the success of these simplistic solutions, and in particular the ease with which they can be incorporated within large-scale coastal models, has tended to detract from those situations in which a uniform approximation is inappropriate. For example, in the case of a wind generated current (or, indeed, a wind modified current) offshore measurements suggest that the current profile is strongly sheared in the vicinity of the water surface. In this case a non-uniform vorticity distribution arises (ie. the current is not linearly sheared), and consequently the wave motion may be very different to that which is predicted by the existing irrotational wave-current solutions. Indeed, Tsao (1959) suggested that the wave motion would itself become rotational; while Swan (1992) provided explicit analytical calculations (within a truncated series expansion), and confirmed that the near-surface vorticity distribution altered the wave kinematics over the entire water depth.

The present paper will consider the interaction of waves with depth varying currents, and will examine the importance of the vorticity distribution. Section 2 commences with a brief outline of the experimental apparatus. Laboratory measurements describing the interaction of regular waves and random waves with a variety of current profiles are presented in sections 3 and 4. Section 3 concerns the "equilibrium conditions" and compares the measured data with a variety of solutions including a five-layered numerical model similar to that outlined by Dalrymple and Heideman (1989) and previously discussed by Cummins and Swan (1993). In section 4 this model is, in turn, used within an iterative procedure to solve the energy transfer equation first outlined by Longuet-Higgins and Stewart (1960). Although this latter approach is computationally intensive, it is applicable to both regular and random waves, and (unlike the conservation of wave action) provides an explicit description of the spectral changes arising when random waves propagate onto strongly sheared currents. This is of particular importance from a practical point of view. Finally, some concluding remarks concerning the importance of the vorticity distribution and the applicability of the various solutions are made in section 5.

## 2. Laboratory apparatus.

The experimental measurements were undertaken in a purpose built wave flume which allows the simultaneous generation of waves and co-linear currents. This facility is 25m long, 0.3m wide, and has a working depth of 0.7m. It is equipped with a numerically controlled random wave paddle located at one end of the wave flume, and a large passive absorber (consisting of poly-ether foam) at the other. The current is introduced via three loops of re-circulating pipework which are pumped individually to give a total volume flow of  $0.45\text{m}^3/\text{s}$ . Each loop is fully reversible, and the inlets and outlets are adjustable (in height) to give a variety of both "favourable" (in the same direction as the phase velocity) and "adverse" (in the opposite direction to the phase velocity) current profiles. With this arrangement it is possible to generate a uniform current of approximately  $0.2\text{m/s}$ , or a highly sheared current in which the near-surface velocities may be as large as  $0.6\text{m/s}$ . A sketch showing the layout of this apparatus is given on figure 1.

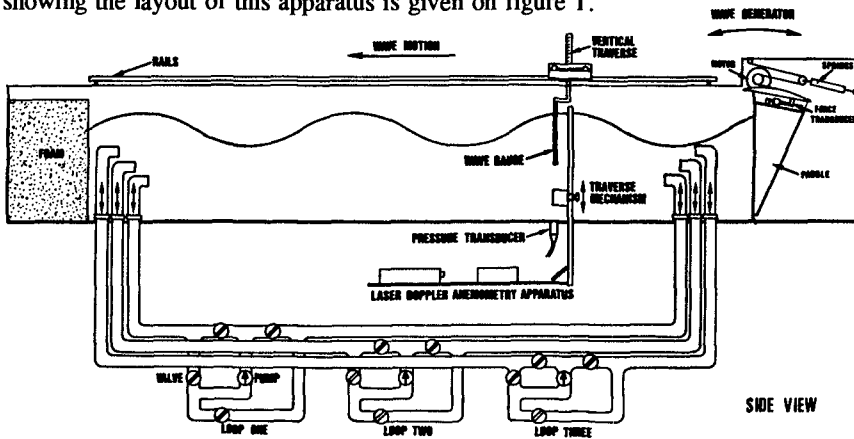


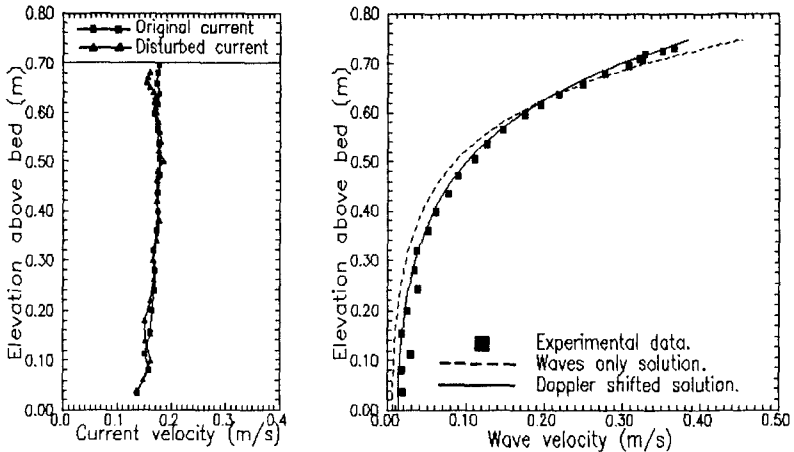
Figure 1. Laboratory apparatus.

Within this study measurements of the water surface elevation were obtained from surface piercing wave gauges which were mounted above the wave flume. Each gauge consists of two vertical wires and provides a time history of the water surface elevation at one point fixed in space. These probes cause a minimal disturbance of the water surface, and have a measuring accuracy of  $\pm 1\text{mm}$ . The velocity field was measured using laser Doppler anemometry. This was based upon a  $35\text{mW}$  helium-neon laser, used to create a three beam arrangement with cross polarisation. The intersection of the beams was located along the centre-line of the wave flume, and produced a measuring volume which was estimated to be  $0.5\text{mm}^3$ . This intersection was observed in forward scatter using two photomultipliers positioned on the opposite side of the wave flume. This arrangement provides the optimal signal to noise ratio, with no disturbance of the flow field. After seeding the flow with milk, added in the ratio of  $100\text{ppm}$ ., a data rate of  $2.5\text{kHz}$  was achieved with a measuring accuracy of  $\pm 2\%$ .



### 3. Equilibrium conditions.

The interaction of regular waves ( $T=0.75\text{s}$  and  $H=0.083\text{m}$ ) with a "favourable" uniform current is considered on figures 2a and 2b. The first of these figures describes the current profile measured both before and after the interaction with the wave train; while the second figure describes the depth variation in the horizontal component of the wave velocity measured beneath a wave crest. In this case, and indeed in all other cases with zero vorticity, there is virtually no change in the current profile, and the measured wave kinematics are in good agreement with the fifth order Doppler shifted solution proposed by Fenton (1985).

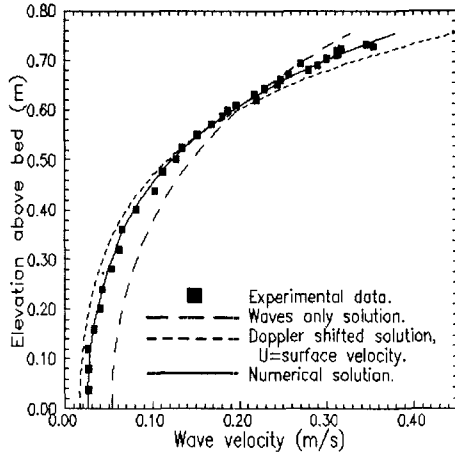
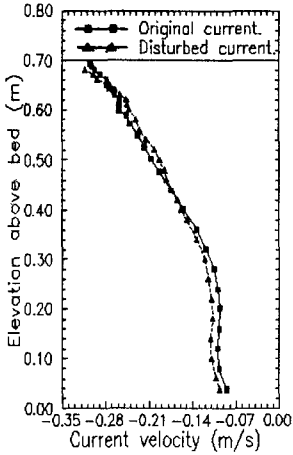


Figures 2a-2b. Regular waves on a "favourable" uniform current.

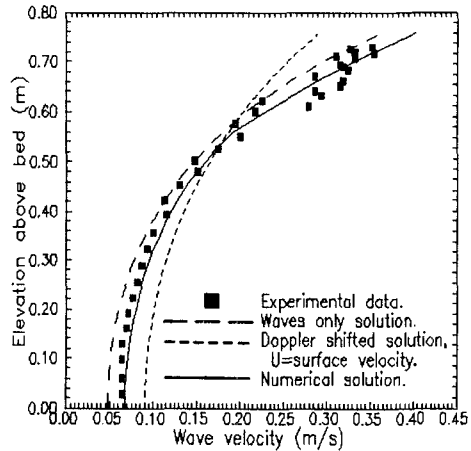
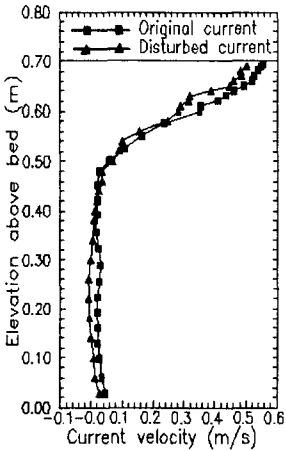
Figures 3a-3b present a similar sequence of results describing the interaction of regular waves on an "adverse" sheared current; while figures 4a-4b correspond to waves on a "favourable" sheared current. In both of these cases there is some evidence of a change in the current profile ( $\Delta U$ ). This is particularly apparent in the "favourable" case (figure 4a) where the interaction with the wave motion appears to reduce the time-averaged near-surface vorticity (ie. the current becomes less sheared). In contrast, figure 3a suggests that in an "adverse" current the magnitude of the near-surface vorticity increases.

If the disturbed current profile (or that measured in the presence of waves) is used to calculate the wave-induced kinematics, a Doppler shifted solution based on the magnitude of the near-surface current is in poor agreement with the laboratory data (figures 3b and 4b). However, a non-linear numerical model, which incorporates the effects of the vorticity distribution, provides a good description of the measured data. The numerical solution referred to in figures 3b and 4b is based upon a five layered approximation in which the measured current profile is described by five linear segments of variable depth. This approach represents an extension of the bi-linear

model originally proposed by Dalrymple (1974), and provides a satisfactory compromise between the description of the current profile (particularly the vorticity distribution) and the computational effort required for convergence. This model has been rigorously tested against other wave-current models (Chaplin, 1990), and is described in detail by Cummins and Swan (1993). Figures 3b and 4b confirm the importance of the vorticity distribution, and suggest that this must be taken into account if the wave kinematics are to be correctly predicted.



Figures 3a-3b. Regular waves on an "adverse" sheared current.



Figures 4a-4b. Regular waves on a "favourable" sheared current.

Previous work by Hedges and Lee (1992) suggests that the interaction of waves with sheared currents may be described by an "equivalent uniform current". This is defined as the uniform current which produces the same wave number as the measured current for a given wave period, wave height, and water depth. In other words, it ensures that the dispersive characteristics of the waves are correctly modelled. However, this does not imply that the underlying kinematics will be correctly predicted. Indeed, Hedges and Lee comment that the solution may be inappropriate if there are regions of very strong shear; while Swan (1992) suggests that if this is indeed the case, an additional rotational term arises within the description of the wave kinematics. The measured data appears to confirm this effect. Figure 5 compares the measured kinematics on a "favourable" sheared current with the numerical model (discussed above), and a Doppler shifted solution based upon an "equivalent uniform current". In this case (and indeed, in several other cases involving layers of strong current shear) the "equivalent uniform current" does not provide a good description of the wave kinematics.

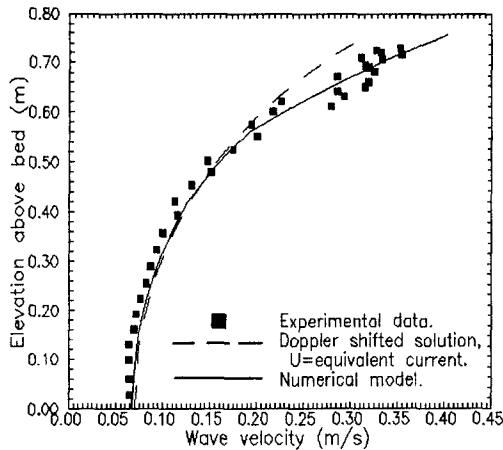


Figure 5. Comparison with an "equivalent uniform current".

#### 4. Initial interaction.

When a wave train first propagates onto a current there are changes in the wave number ( $k$ ), the wave height ( $H$ ), and under some circumstances the current profile,  $U(z)$ . The numerical model (discussed above) is able to predict the wave number for a given wave period, wave height, water depth, and current profile. If we assume that the water depth is known, and (at present) that the current profile remains unchanged, the energy transfer equation first identified by Longuet-Higgins and Stewart (1960) may be applied in conjunction with the numerical model to define an iterative solution for the overall change in the wave train (ie.  $\Delta k$  and  $\Delta H$ ).

If  $R$  defines the mean rate of energy transfer across a fixed surface ( $S$ ), Longuet-Higgins and Stewart (1960) give:

$$R = \int_S \left( P + \frac{1}{2} \rho U^2 + \rho g z \right) \underline{u} \cdot \underline{n} \, dS \quad (1)$$

where  $\underline{u}$  is the velocity vector,  $P$  is the pressure,  $\rho$  is the density,  $g$  is the gravitational constant and  $\underline{n}$  a unit vector normal to the surface  $S$ .

If we consider a control volume, and assume that there is no reflection of wave energy, then the sum of the mean energy transfer rates due to the current (acting alone) and the wave train (also acting alone), must exactly balance the total mean rate of energy transfer associated with the combined wave-current motion. This approach is entirely consistent with the original analysis outlined by Longuet-Higgins and Stewart (1960) in which they introduced the concept of radiation stress. Indeed, Longuet-Higgins and Stewart suggested in a footnote (page 574) that the vorticity may be taken into account by supposing  $U$  to be dependent upon  $z$  (ie.  $U(z)$ ). This is exactly what we have done in the present analysis.

### *Regular waves.*

Having coupled the energy transfer equation with the numerical model the interaction of regular waves with a uniform current was considered. In this case the present calculations were shown to be in good agreement with the fifth order solution (based upon the conservation of wave action) proposed by Thomas (1990). In a second test-case the interaction of regular waves with a linearly sheared current was considered, and the results compared with the second order solution outlined by Jonsson et al. (1978). In this case there was again good agreement between the two solutions provided (as one might expect) the comparisons were restricted to small amplitude waves. However, in those cases involving larger wave amplitudes, the difference between these solutions emphasises the importance of the higher order non-linear interactions. These results appear to be consistent with the laboratory observations presented by Swan (1990) and, in particular, the comparison with the third order kinematics predicted by Kishida and Sobey (1988). Further comments concerning the importance of the non-linear interactions are provided by Cummins and Swan (1993).

The experimental measurements presented on tables 1a and 1b concern a total of seven cases involving the interaction of regular waves and depth varying currents. Cases 1-4 correspond to a "favourable" sheared current (table 1a); while cases 5-7 correspond to an "adverse" sheared current (table 1b). In each case the initial wave properties (measured in the absence of a current) are denoted by  $H_0$  and  $T_0$ ; while the wave height measured in the presence of a current is indicated by  $H$ . Three comparative solutions are also presented. The first corresponds to a uniform current based upon the near surface velocity ( $U=U_s$ ); the second corresponds to an "equivalent uniform current" ( $U=U_e$ ); and the third represents the present solution. In each case the numerical model provides the best description of the measured data.

Initial state.		Lab. data	Predicted wave height		
$T_0$	$H_0$	H	$U=U_s$	$U=U_c$	Model.
.75	.083	.079	.051	.061	.077
.90	.088	.082	.055	.066	.081
1.1	.102	.096	.065	.083	.091
1.2	.107	.104	.071	.093	.096

Table 1a: Wave height change on a "favourable" sheared current.

Initial state.		lab. data	Predicted wave height		
$T_0$	$H_0$	H	$U=U_s$	$U=U_c$	Model.
0.9	.075	.086	.107	.111	.094
1.0	.075	.096	.111	.110	.098
1.1	.075	.097	.113	.108	.098

Table 1b: Wave height change on an "adverse" sheared current.

In figures 6a-6b the wave lengths associated with cases 1-7 are again compared to three potential solutions. The first corresponds to a waves only solution and thus describes the waves in the absence of the current. The second corresponds to a Doppler shifted solution based upon the near surface current ( $U=U_s$ ), while the third represents the present numerical results. In each case the latter solution provides the best description of the measured data. In general, the measured changes in both the wave height and the wave length suggest that the vorticity distribution acts to reduce the effect of the Doppler shift associated with the surface current. This is consistent with the second order approximation presented by Swan (1992), but because of the non-linearity of the wave-current interaction a higher order numerical solution is required to provide a good fit to the measured data.

#### **Random waves.**

Having demonstrated that the present approach is able to describe the changes in a regular wave train propagating onto a strongly sheared current, a similar approach will be applied to investigate the spectral changes in a random wave train. The laboratory apparatus described in section 2 was used to generate a random wave train with a Pierson-Moskowitz input spectrum. Both the water surface elevation ( $\eta(t)$ ) and the horizontal velocity component ( $u(t)$ ) at  $z=-0.1m$  were sampled at 25Hz for 200 minutes, and the resulting data was analysed using a ten point moving average. Figures 7a-7b concern the interaction with a "favourable" uniform current. In figure 7a the uppermost curve (indicated by a dashed line) describes the spectrum of the

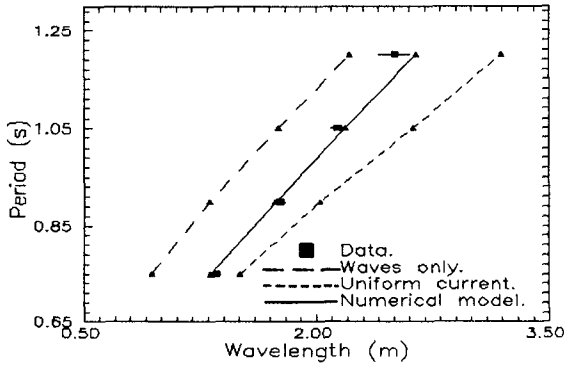


Figure 6a. Wave length on a "favourable" sheared current.

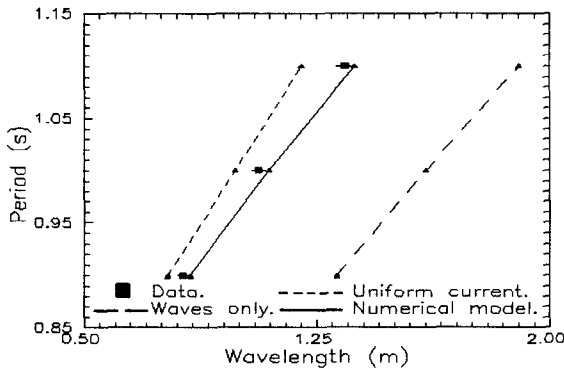
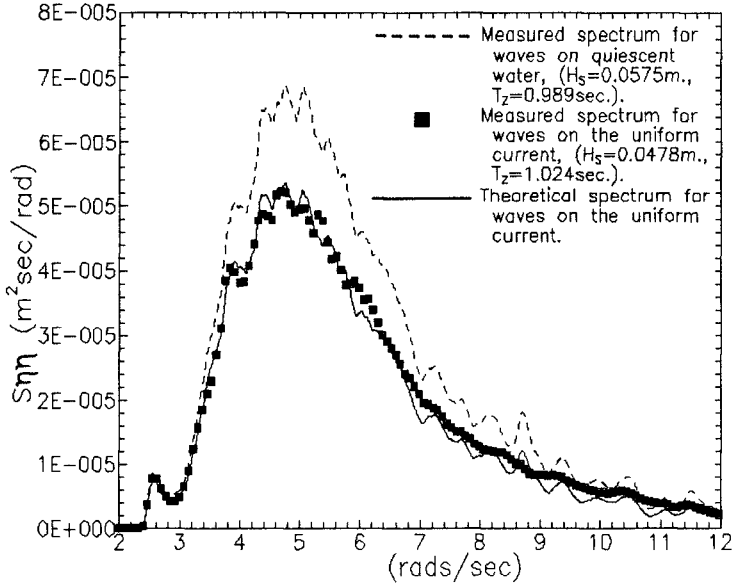


Figure 6b. Wave length on an "adverse" sheared current.

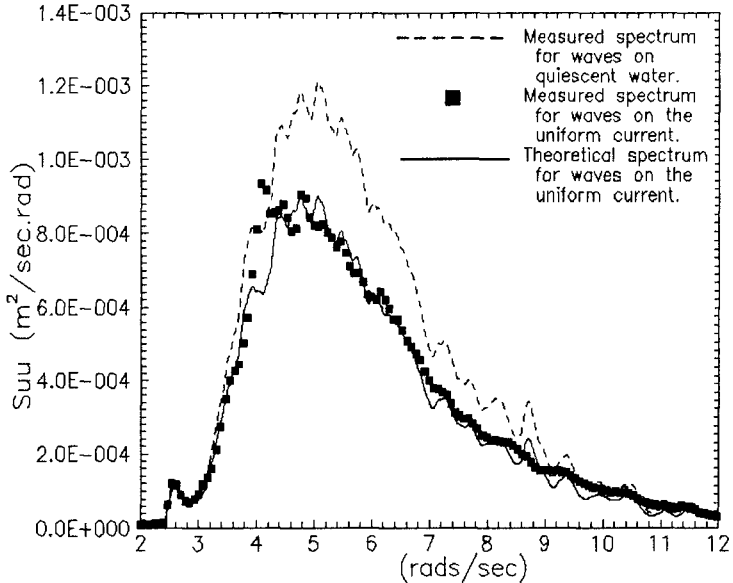
water surface elevation ( $S\eta\eta$ ) measured in the absence of a current; the solid squares represent the data measured in the combined wave-current motion; and the solid line corresponds to the present numerical model. A similar sequence of results is presented on figure 7b, but in this case they correspond to the spectrum of the measured horizontal velocity ( $Suu$ ) at  $z=-0.1m$ . Together, these figures suggest that the proposed numerical model provides a good description of the changes in both the water surface elevation and the underlying kinematics.

Figures 8a-8b present a similar sequence of plots concerning the interaction with an "adverse" uniform current. In this case the steepening of the high frequency components induces wave breaking, and consequently the experimental measurements within the range ( $\omega > 7$  rad/s) diverge from the predicted behaviour. This result was also noted by Hedges et al. (1985), and an experimental correction (referred to as the equilibrium range constraint) was proposed. Having incorporated this correction, the present model once again provides a good description of the laboratory data.

(a) Water surface elevation.

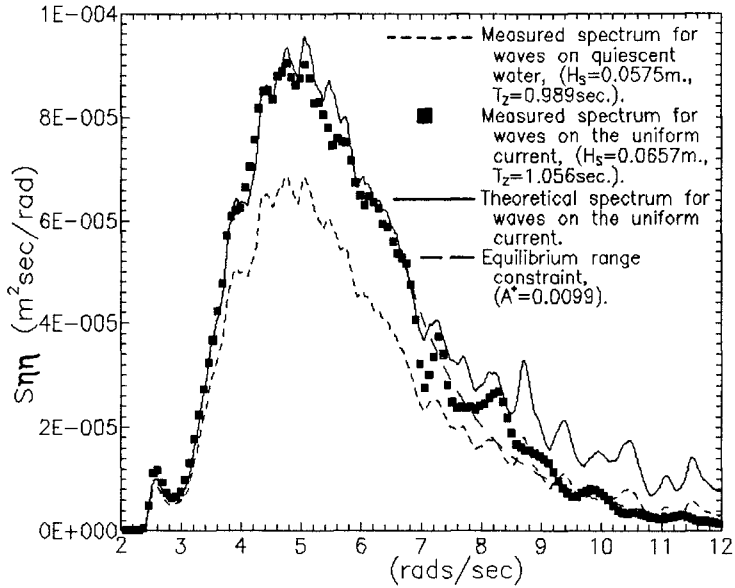


(b) Horizontal kinematics ( $z=-0.1\text{m}$ .)

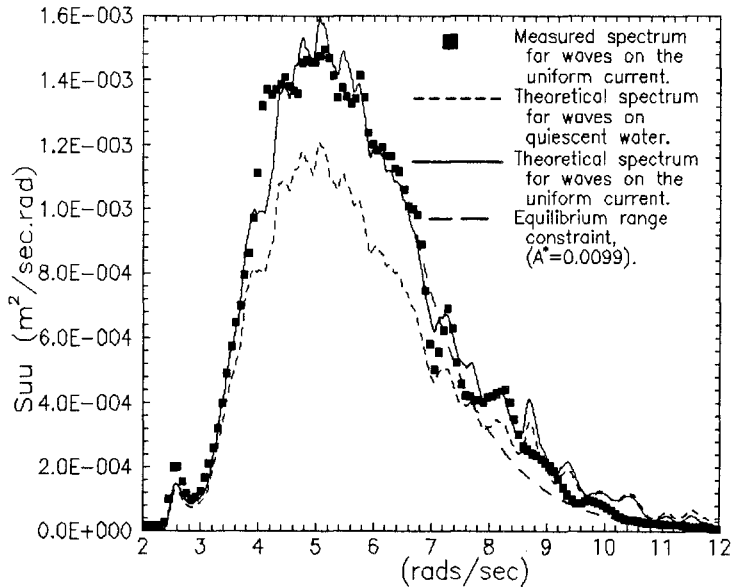


Figures 7a-7b. Interaction of random waves with a "favourable" uniform current.

(a) Water surface elevation.



(b) Horizontal kinematics ( $z=-0.1\text{m}$ ).



Figures 8a-8b. Interaction of random waves with an "adverse" uniform current.

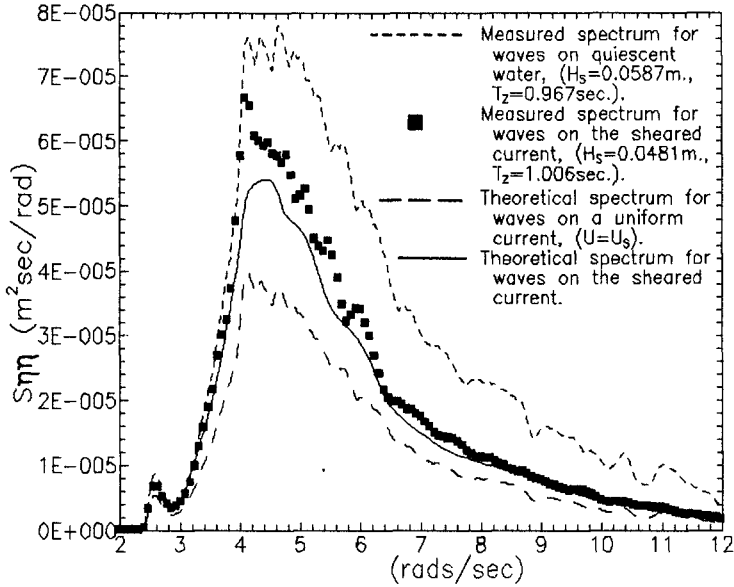


These examples (involving the interaction with a uniform current) provide further validation of the proposed numerical scheme. However, in practice, the existing analytical solutions are also appropriate to these cases, and provide a simpler calculation procedure. Indeed, if the individual waves are linear, the first order approximation originally proposed by Longuet-Higgins and Stewart (1960) may be applied. Alternatively, if the waves are steeper (and, in particular, if the interaction involves an "adverse" current) the fifth order solution proposed by Thomas (1990) will be appropriate.

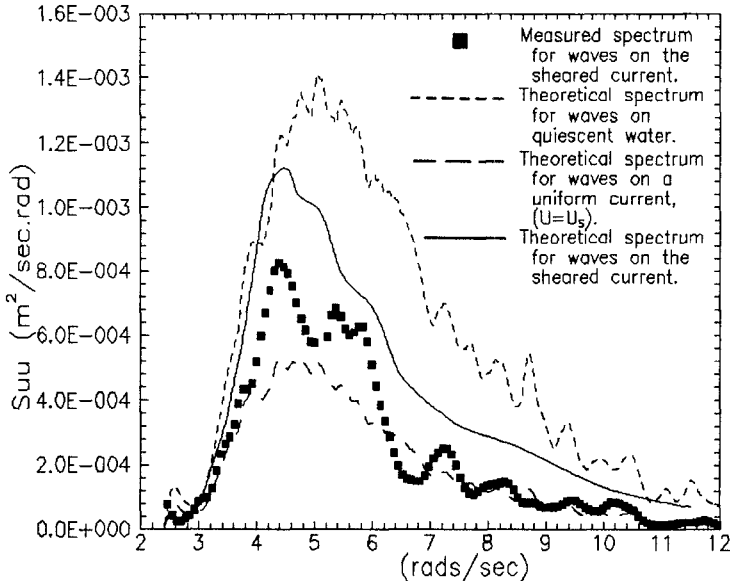
In contrast, if the current profile is strongly sheared and involves a non-uniform vorticity distribution, the analytical solutions are invalid. In this case the present numerical scheme provides the only method of determining the change in the wave spectra. Figures 9a-9b concern exactly this case and compare the measured data with both a uniform current approximation and the numerical solution. The power spectrum of the water surface elevation ( $S_{\eta\eta}$ ) is considered in figure 9a. Although, in this case, the numerical model provides the best description of the measured data, there remain significant differences between the observed and predicted behaviour. These discrepancies are probably associated with a change in the current profile similar to that noted on figures 3a and 4a. The present formulation assumes that the current velocity is unchanged by the wave-current interaction. Indeed, if the fluid is inviscid and the flow laminar, the vorticity must remain constant along a streamline. However, in the present investigation the turbulent intensity (or the root-mean-square velocity fluctuations expressed as a ratio of the mean current velocity) was of the order of 8-10%. This provides an effective transport mechanism capable of redistributing the vorticity profile. Without a detailed description of the turbulent structure, the change in the current profile remains indeterminate. This represents an important limitation to the present model. Nevertheless, figure 9a suggests that the numerical calculations provide a significant improvement over the uniform current approximation based upon the near-surface velocity.

Figure 9b describes the spectrum of the horizontal velocity at  $z=-0.1\text{m}$ . In this case the measured data, including an apparent bi-modal peak, does not correspond to either of the existing solutions. Indeed, the data lies mid-way between the uniform current approximation ( $U=U_c$ ) and the numerical predictions. These results may, once again, reflect the importance of the current change ( $\Delta U$ ). However, the wave spectrum indicated on figure 9b, has been derived by subtracting the power spectrum of the turbulent fluctuations (measured in the absence of waves) from the total velocity spectrum measured in combined waves and currents. If, as discussed above, the interaction of waves and currents produces a modification of both the vorticity distribution and the turbulent structure, the present results may also reflect the uncertainty in the turbulence spectrum arising in combined waves and currents.

(a) Water surface elevation.



(b) Horizontal kinematics ( $z=-0.1\text{m}$ ).



Figures 9a-9b. Interaction of random waves with a "favourable" sheared current.

## 5. Concluding remarks.

The present paper has considered the interaction of waves and currents, and has presented the results of a new experimental study. This has considered both regular and random waves, and has sought to identify the importance of the time-averaged vorticity distribution. Preliminary measurements concerning the interaction with a uniform current (zero vorticity) confirm that the initial changes in both the wave height and the wave length are consistent with the fifth order solution proposed by Thomas (1990). Furthermore, in the absence of vorticity, the underlying kinematics are in good agreement with the Doppler shifted solution proposed by Fenton (1985).

In contrast, if the current profile is strongly sheared, and in particular if there is significant vorticity at the water surface, the present data suggest that the resulting flow field cannot be predicted by an "equivalent uniform current". However, a multi-layered numerical model, capable of describing an arbitrary current profile, provides a good description of the kinematics beneath a regular wave train. Furthermore, if the solution is coupled with an energy transfer equation the initial change in both the wave height and the wave number can be satisfactorily predicted. Finally, a similar approach was applied to the propagation of random waves on a strongly sheared current. In this case the predicted power spectrum of the water surface elevation was in reasonable agreement with the laboratory data. However, there were important differences between the observed and predicted spectrum of the underlying wave motion. At present, these discrepancies are believed to reflect the wave-induced changes in both the mean current profile and its associated turbulent structure. Until these changes are clarified, the exact nature of these important wave-current interactions will remain indeterminate.

## Acknowledgements.

The authors gratefully acknowledge the financial support provided by the Engineering and Physical Sciences Research Council (EPSRC) and The Royal Society.

## References.

- Chaplin, J.R. (1990) Computation of non-linear waves on a current of arbitrary non-uniform profile. OTH 90 327, HMSO.
- Cummins, I. & Swan, C. (1993) Non-linear wave-current interactions. Soc. for Underwater Tech., 29, 35-51.
- Dalrymple, R.A. (1974) Water waves on a bi-linear shear current, Proc. 14th. Int. Conf. Coastal Eng., 1, 626-641.

- Dalrymple, R.A. & Heideman, J.C. (1989) Non-linear water waves on a vertically sheared current. Proc. I.M.P. Forum. Paris, 1989.
- Fenton, J.D. (1985) A fifth-order Stokes theory for steady waves. *J. Waterway, Port, Coastal and Ocean Eng.*, 111, 216-234.
- Hedges, T.S., Anastasiou, K. & Gabriel, D. (1985) Interaction of random waves and currents. *J. Waterway, Port, Coastal and Ocean Eng.* ASCE 111(2), 275-288.
- Hedges, T.S. & Lee, B.W. (1992) The equivalent uniform current in wave-current computations. *Coastal Eng.*, 16, 301-311.
- Jonsson, I.G., Brink-Kjaer, O. & Thomas, G.P. (1978) Wave action and set-down for waves on a shear current. *J. Fluid Mech.* 87, 227-250.
- Kishida, N. & Sobey, R.J. (1988) Stokes theory for waves on linear shear current, *J. Eng. Mech.*, ASCE, Vol. 114, 1317-1334.
- Longuet-Higgins, M.S. & Stewart, R.W. (1960) Changes in the form of short gravity waves on long waves and tidal currents, *J. Fluid Mech.*, 8, 565-583.
- Swan, C. (1990) An experimental study of waves on a strongly sheared current profile. Proc. 22nd. Int. Conf. Coastal Eng. Delft (1990). 1, 489-502.
- Swan, C. (1992). A stream function solution for waves on a strongly sheared current. Proc. 23rd. Int. Conf. Coastal Eng. Venice (1992). 1, 684-697.
- Thomas, G.P. (1990) Wave-current interactions: An experimental and numerical study. Part 2. Non-linear waves. *J. Fluid Mech.*, 216, 505-536.
- Tsao, S. (1959) Behaviour of surface waves on a linearly varying flow. *Moskow. Fiz.-Tech. Inst. Issl. Mekh. Prikl. Mat.*, 3, 66-84.

## CHAPTER 10

# Waves in an Annular Entrance Channel

Robert A. Dalrymple, F. ASCE and James T. Kirby, M. ASCE<sup>1</sup>

### Abstract

Waves propagating in a curved channel are examined analytically and with a variety of parabolic and spectral models. The results show that the wide angle parabolic method is reasonably robust, but not exact, while a spectral method based on trigonometric functions is superior to a Chebyshev polynomial method. Angular spectrum models are discussed and shown to be equivalent to an eigenfunction expansion in the cross-channel direction.

### Introduction

Waves propagating in curved narrow (with respect to the wave length) channels behave as if the channel were straight. However, when the curved channel is wide, then wave reflection from the outer wall and the diffraction of waves around the channel bend at the inner wall lead to a complicated sea state within the channel.

The prediction of the transmission of waves into harbors with curved entrance channels and the use of annular wave tanks (in small laboratories) depend on our ability to model waves in curved domains. Here waves propagating in a curved channel, taken to be a section of a circular annulus, are studied. An analytical and three different types of numerical solutions are obtained and compared. The analytical solution is used to verify the validity of the numerical techniques developed in a conformally mapped domain, resulting from mapping the curved channel into a straight channel.

An annular channel can be classified as narrow or wide with respect to the incident wave depending on the dimensionless width, defined by Dalrymple, Kirby, and Martin (1995) as  $k(r_2 - r_1) = kw$ , where  $r_2$  is the outer radius of the channel,  $r_1$  is the inner radius,  $w$  is the width of the channel, and  $k$  is the wavenumber of the progressive wave train found from the dispersion equation,

$$\sigma^2 = gk \tanh kh$$

---

<sup>1</sup>Center for Applied Coastal Research, Ocean Engineering Laboratory, Univ. Delaware, Newark, DE 19716

where the angular frequency of the wave is  $\sigma = 2\pi/T$ , the wavenumber  $k = 2\pi/L$ ,  $h$  is the water depth, and  $g$  the acceleration of gravity. The parameter  $kw$  is  $2\pi$  times the number of waves that fit across the channel width; wide channels can fit numerous waves across their widths.

In acoustics, the problem of sound propagation in curved ducts has been studied by Rostafinski in a variety of papers (see References). The mathematical problem is analogous, although now the computing tools make the problem much simpler.

### Analytical Solution

For linear wave theory, with irrotational motion and an incompressible fluid, the governing equation for the velocity potential of the wave motion is the Laplace equation. The Laplace equation is written conveniently for this problem in polar form; therefore, we will take the velocities to be given by

$$u = -\frac{\partial\Phi}{\partial r} \tag{1}$$

$$v = -\frac{1}{r}\frac{\partial\Phi}{\partial\theta} \tag{2}$$

$$w = -\frac{\partial\Phi}{\partial z} \tag{3}$$

and the Laplace equation is:

$$\frac{\partial^2\Phi}{\partial r^2} + \frac{1}{r}\frac{\partial\Phi}{\partial r} + \frac{1}{r^2}\frac{\partial^2\Phi}{\partial\theta^2} + \frac{\partial^2\Phi}{\partial z^2} = 0 \tag{4}$$

Figure 1 shows a layout of an annular channel with a maximum  $\theta$  value of  $\pi$ , corresponding to the positive  $y$  axis.

Taking the depth  $h$  as constant, we assume  $\Phi(r, \theta, z) = \phi(r, \theta) \cosh k(h + z)$ , where the wavenumber  $k$  is fixed from the dispersion relationship. Substituting into (4), gives the polar form of the Helmholtz equation:

$$\frac{\partial^2\phi}{\partial r^2} + \frac{1}{r}\frac{\partial\phi}{\partial r} + \frac{1}{r^2}\frac{\partial^2\phi}{\partial\theta^2} + k^2\phi = 0 \tag{5}$$

The boundary conditions for vertical no-flow channel sidewalls are

$$\frac{\partial\phi}{\partial r} = 0, \text{ at } r = r_1, \text{ the inner wall} \tag{6}$$

$$\frac{\partial\phi}{\partial r} = 0, \text{ at } r = r_2, \text{ the outer wall.} \tag{7}$$

The general solution for  $\phi$  that satisfies these boundary conditions is

$$\phi = \sum_{n=0}^N a_n \left[ Y'_{\gamma_n}(kr_1)J_{\gamma_n}(kr) - J'_{\gamma_n}(kr_1)Y_{\gamma_n}(kr) \right] e^{i\gamma_n\theta} \tag{8}$$

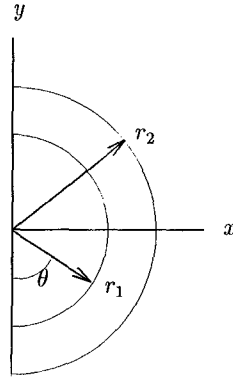


Figure 1: Schematic Diagram of Circular Channel

$$= \sum_{n=0}^N a_n F_n(r) e^{i\gamma_n \theta} \quad (9)$$

where  $k$  is the wavenumber of the incident wave,  $r_1$  is the inner radius of the channel, and  $\gamma_n$  must satisfy

$$Y'_{\gamma_n}(kr_1)J'_{\gamma_n}(kr_2) - J'_{\gamma_n}(kr_1)Y'_{\gamma_n}(kr_2) = 0, \quad n=1, 2, \dots, N$$

to enforce a no-flow boundary condition on the outer wall ( $r = r_2$ ) (see, e.g. Kirby *et al.*, 1994). There are only  $N$  real values of  $\gamma_n$  that satisfy this equation, which are ranked in descending order of magnitude. The largest  $\gamma_n$  is less than  $kr_2$ .

Each of the terms in the summation (Eq. 9) is a wave mode, propagating in the  $\theta$  direction with  $1/\gamma_n$  waves per  $2\pi$  radians, and a cross-channel variation given by the radial term  $F_n(r)$ . These terms are orthogonal to each other with weight  $(1/r)$  from the Sturm-Liouville theorem and provide a method for determining the  $a_n$  values.

The values of the unknown coefficients  $a_n$  in Eq. 9 are found from the initial condition at  $\theta = 0$ , which is prescribed as a function of  $r$ . Here we assume that the wave height is uniform across the mouth of the channel. In actuality, there is an interaction between the channel and the ocean that leads to variations across the channel. These are assumed to be small. For  $\phi(r, 0) = 1$ , we use the expression for the velocity potential (9) and the orthogonality of the  $r$  terms to find the  $a_n$ .

$$a_n = \frac{\int_{r_1}^{r_2} r^{-1} \phi(r, 0) F_n(r) dr}{\int_{r_1}^{r_2} r^{-1} F_n^2(r) dr} \quad (10)$$

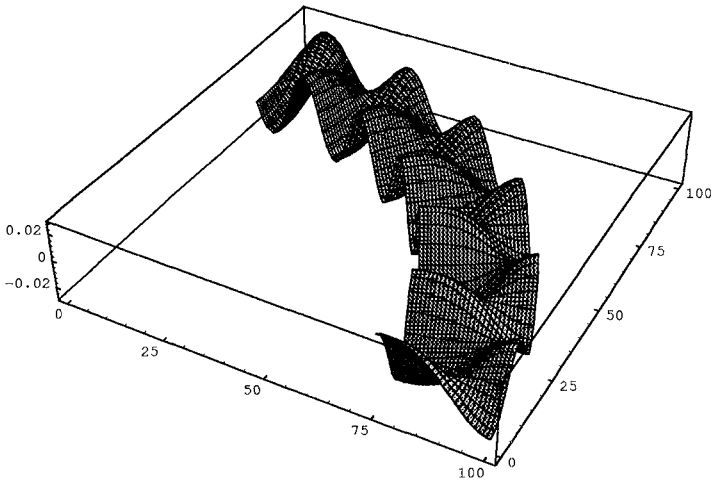


Figure 3: First Mode of Analytical Solution

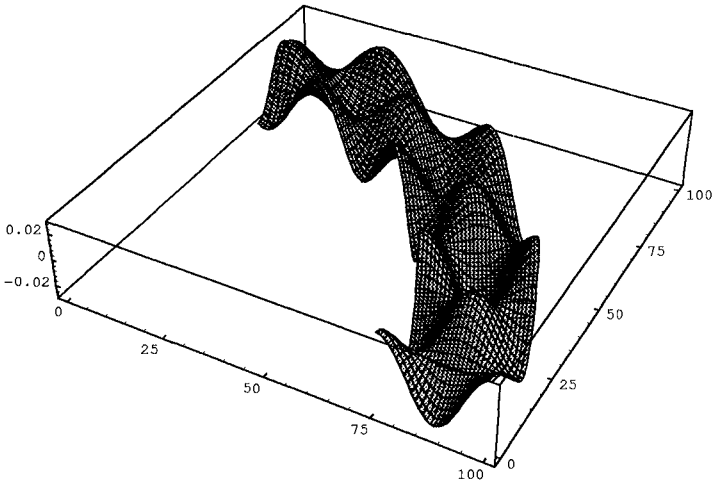


Figure 4: Second and Last Mode for Analytical Solution



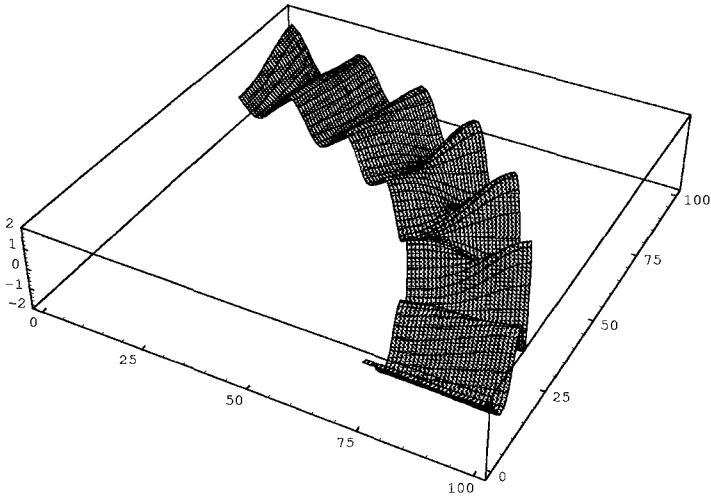


Figure 5: Analytic Solution (Sum of All Three Modes)

seiching problem was studied by Campbell (1953), who had to deal with waves in a circular (ship) testing channel.

### Parabolic Modelling

A simple parabolic model can be easily derived from the Helmholtz equation (5). Since the waves will travel in the azimuthal direction (particularly for narrow channels), most of the oscillation in the wave form can be described by a periodic function in  $\theta$  and we write

$$\phi(r, \theta) = A(r, \theta) e^{i\Gamma\theta} \quad (11)$$

where  $\Gamma$  is a dimensionless constant and  $A$  is likely to vary slowly in the  $\theta$  direction. Substituting into the Helmholtz equation, we find, after neglecting a second derivative of  $A$  with respect to  $\theta$  (assumed to be small).

$$2ikr_0 \frac{\partial A}{\partial \theta} + (k^2 r^2 - k^2 r_0^2)A + r \frac{\partial}{\partial r} \left( r \frac{\partial A}{\partial r} \right) = 0 \quad (12)$$

The value of  $\Gamma$  was taken as  $kr_0$ , where  $r_0$  is a reference radius arbitrarily taken as the mid-point of the channel,  $\bar{r}$ , or  $r_0 = \bar{r} = (r_1 + r_2)/2$ . This model will work for narrow channels.

We can obtain more correct values of  $r_0$  by comparing to the  $\gamma_1$  angular wavenumbers from the analytical solution. By comparing to a number of cases, we find an approximate linear trend (with unit slope) between  $(r_0 - \bar{r})/\bar{r}$  with the relative width of the channel  $k(r_2 - r_1)$ . Therefore for narrow channels,  $r_0 = \bar{r}$ , but for wide channels,  $r_0 = \bar{r}(1 + k(r_2 - r_1))$ .

Kirby, Dalrymple, and Kaku (1994) provide a general form for small and large angle parabolic models in arbitrary mapped and conformal domains. Here we need only the mapping for conformal domains.

The constant depth Helmholtz equation with constant coefficients is conformally mapped into a variable coefficient Helmholtz equation:

$$\frac{\partial^2 \phi}{\partial u^2} + \frac{\partial^2 \phi}{\partial v^2} + k^2 J(u, v) \phi = 0 \quad (13)$$

Here,  $J(u, v)$  is the Jacobian of the transformation. Assuming that  $\phi(u, v)$  varies rapidly in the propagation direction  $u$ , we write

$$\phi(u, v) = \text{Re} \left\{ A(u, v) e^{i \int k_0 J_0^{1/2} du} \right\} \quad (14)$$

where  $k_0 = k(u, v_0)$  and  $J_0 = J(u, v_0)$  and  $v_0$  is a fixed reference distance. Substituting into Eq. 13 and neglecting a second derivative of  $A$  with respect to  $u$ , Kirby *et al.* find a small angle parabolic model:

$$2ik_0 J_0^{1/2} \frac{\partial A}{\partial u} + i \frac{\partial (K_0 J_0^{1/2})}{\partial u} A + (K^2 J - K_0^2 J_0) A + \frac{\partial^2 A}{\partial v^2} = 0 \quad (15)$$

In wide channels, the turning of the channel leads to large angle discrepancies between the assumed azimuthal propagation direction and the actual wave direction. To allow for these wave directions differing from the azimuthal direction to a greater extent than permitted by the small angle parabolic model, a wide angle model was developed:

$$\begin{aligned} 2ikJ^{1/2} \frac{\partial A}{\partial u} + 2kJ^{1/2} (kJ^{1/2} - k_0 J_0^{1/2}) A + i \frac{\partial (kJ^{1/2})}{\partial u} A + \left\{ \frac{3}{2} - \frac{1}{2} \left( \frac{k_0^2 J_0}{k^2 J} \right)^{1/2} \right\} \frac{\partial^2 A}{\partial v^2} \\ - \frac{3i}{4k^2 J} \frac{\partial (kJ^{1/2})}{\partial u} \frac{\partial^2 A}{\partial v^2} + \frac{i}{2kJ^{1/2}} \frac{\partial^3 A}{\partial u \partial v^2} = 0 \end{aligned} \quad (16)$$

Kirby *et al.* use a conformal mapping to convert a circular channel into a straight channel in the  $(u, v)$  domain. One such map is  $w = u + iv = \pi/2 - i \ln(z/r_m)$ , where  $r_m = \sqrt{r_1 r_2}$ . For this case, the  $kJ_0^{1/2}$  is not a function of  $u$  and the equations simplify. For the small angle parabolic models, it is easily shown that Eq. 12 and 15 are equivalent. They compared their models to the exact solution for a wide angle case; the simple parabolic began to fail 60° from the channel mouth, while the wide angle model compared reasonably

well for the full 180° test channel. They also went further, adding nonlinear effects to the models.

## Spectral Modelling

### Fourier-Galerkin Modelling

Angular spectrum modelling has been used to model waves propagating over sloping and irregular bathymetry in regions which are bounded by a rectangular box (cf. the review by Dalrymple and Kirby, 1992). The angular spectrum model was defined by Booker and Clemmow (1950) in a Cartesian coordinate system as the decomposition of the initial condition into progressive plane waves. The subsequent wave field is found by summing the plane waves within the computational domain. In an  $(x, y)$  coordinate system, the angular spectrum corresponds to a Fourier-Galerkin spectral method of solution, as the plane waves in this system are described by trigonometric functions. In the polar coordinate system, the angular spectrum model corresponds to a modal decomposition, based on the analytical modes shown above. Therefore the angular spectrum model in any coordinate system corresponds to an eigenfunction expansion for that coordinate system.

The Fourier-Galerkin model (using trigonometric functions in the cross-channel (radial) direction) is a natural extension of the angular spectrum model in Cartesian coordinates (e.g., Dalrymple *et al.*, 1989): it is based on the Fourier transform of the wave field in the lateral direction. In the Fourier domain, the wave equations are split into forward and backward propagating waves. Only the forward waves are kept as back-reflection is assumed to be negligible.

Dalrymple, Kirby and Martin (1995) have used Fourier-Galerkin modelling to examine waves in conformally mapped channels. In the  $(u, v)$  conformal domain, the Fourier transform pair is:

$$f_n(u) = \mathcal{T}_F[\phi(u, v)] = \frac{1}{2v_b} \int_{-v_b}^{v_b} \phi(u, v) \cos[\lambda_n(v + v_b)] dv, \quad n = 0, 1, 2, \dots \quad (17)$$

$$\phi(u, v) = \mathcal{T}_F^{-1}[f(u)] = \sum_{n=0}^{\infty} \epsilon_n f_n(u) \cos[\lambda_n(v + v_b)] \quad \text{for } -v_b < v < v_b. \quad (18)$$

where  $v_b = \frac{1}{2} \ln(r_2/r_1)$ , which is half the channel width in the conformal domain.

Defining

$$\overline{k^2 J}(u) = \frac{1}{2v_b} \int_{-v_b}^{v_b} k^2 J(u, v) dv. \quad (19)$$

and substituting this into the governing Helmholtz equation gives

$$\frac{\partial^2 \phi}{\partial u^2} + \frac{\partial^2 \phi}{\partial v^2} + \overline{k^2 J} (1 - \nu) \phi = 0, \quad (20)$$

where

$$\nu(u, v) = 1 - k^2 J / \overline{k^2 J} \quad (21)$$

Fourier transforming the above Helmholtz equation yields

$$\frac{d^2 f_n}{du^2} + \gamma_n^2 f_n - \overline{k^2 J} \mathcal{T}_F[\nu \mathcal{T}_F^{-1}[f]] = 0, \quad n = 0, 1, 2, \dots, \quad (22)$$

where

$$\gamma_n^2(u) = \overline{k^2 J} - \lambda_n^2 \quad \text{and} \quad \lambda_n = \frac{1}{2}n\pi/v_b.$$

Splitting the problem into forward and backward propagating modes, they find the following equation for the forward propagating modal amplitudes,  $f_n$ , in the Fourier-transformed conformal domain:

$$\frac{df_n(u)}{du} = i\gamma_n f_n - \frac{i \overline{k^2 J}}{2\gamma_n} \mathcal{T}_F[\nu \mathcal{T}_F^{-1}[f]], \quad n = 0, 1, 2, \dots \quad (23)$$

where

$$\overline{k^2 J} = \frac{k^2 (r_2^2 - r_1^2)}{2 \ln(r_2/r_1)} \quad \text{and} \quad \nu(v) = 1 - \frac{2 \ln(r_2/r_1) r_1 r_2 e^{-2v}}{r_2^2 - r_1^2},$$

This set of first order ordinary differential equations is solved numerically.

After the conformal mapping, the cosines used in the Fourier transform are no longer an optimal basis, as the forms of the lateral eigenfunctions  $F_n(r)$  are far more complicated, as shown in Eq. 9. The errors increase with the width of the channel. This has implications also for application of the angular spectrum model for open coast cases where the bathymetry is varying significantly in the longshore direction.

### Chebyshev-tau Modelling

Chebyshev polynomials provide another set of orthogonal bases with which to expand the wave potential across the channel. Panchang and Kopriva (1989) have used these polynomials for the solution of the mild-slope equation. Here a cross-channel Chebyshev transform is used to develop the governing equation in the transform domain, which must be scaled to be in the range of -1 to 1, so we define  $\zeta = v/v_b$ , so that the lateral boundaries are located at  $\zeta = \pm 1$ . The appropriate Chebyshev-transform pair is:

$$c_n(u) = \mathcal{T}_C[\phi(u, v)] = \frac{c_n}{\pi} \int_{-1}^1 \frac{\phi(u, v_b \zeta) T_n(\zeta)}{\sqrt{1 - \zeta^2}} d\zeta, \quad n = 0, 1, 2, \dots, \quad (24)$$

$$\phi(u, v) = \mathcal{T}_C^{-1}[c(u)] = \sum_{n=0}^{\infty} c_n(u) T_n(\zeta) \quad \text{for } -1 < \zeta < 1. \quad (25)$$

As the Chebyshev polynomials do not satisfy the lateral boundary conditions, the tau method, which forces the Chebyshev sum to satisfy these conditions, is used.

Introducing  $\overline{k^2 J}$  and  $\nu$ , defined by (19) and (21), respectively, we find that the Chebyshev transform of (20) is

$$\frac{d^2 c_n(u)}{du^2} + \overline{k^2 J} c_n(u) + \frac{1}{v_b^2} c_n^{(2)} - \overline{k^2 J} T_C[\nu T_C^{-1}[c]] = 0.$$

The splitting in the transform domain yields:

$$\frac{dc_n^+}{du} = i\gamma_0 c_n^+(u) + \frac{i}{2\gamma_0} \left( \frac{1}{v_i^2} c_n^{(2)} - \overline{k^2 J} T_C[\nu T_C^{-1}[c^+]] \right) = 0. \quad (26)$$

There are significant disadvantages of the Chebyshev approach. First all modes are progressive, while for the Fourier-Galerkin method, only those modes for which  $\gamma_n$  are positive propagate (thus reducing the number of simultaneous differential equations to solve). Also, the splitting of the Chebyshev transformed equation introduces an error, which does not occur with the Fourier-Galerkin model; it in fact reduces the Chebyshev method to an equivalent of the small angle parabolic model (Dalrymple *et al.*, 1995).

## Results

For narrow channels, all of the methods, parabolic and spectral, work well. As the channel width  $kw$  increases, then the errors begin increase for all the methods. As an example of these errors, we increase the width in the previous example to  $w = 125$  m ( $r_1 = 75$  m,  $r_2 = 200$  m); now  $kw = 37.625$ , or almost 6 wavelengths can fit across the channel.

The exact solution, given by the analytical model, is shown in Figure 6. The waves entering the channel from the right, begin to diffract around the channel bend and to reflect from the outer radius. At about  $120^\circ$ , the wave field is dominated by reflected waves from the outer side wall. Finally at  $180^\circ$ , the wave field is reasonable complex, indicating that a  $180^\circ$  bend in a laboratory wave channel will not result in planar waves.

The surface elevations along the outer wall ( $r = r_2$ ) predicted by the exact solution and the small and wide angle parabolic models are shown in Figure 7. The wide angle parabolic model does a reasonable job for the  $180^\circ$  length of channel shown, while the small angle begins to fail at  $50^\circ$ . Note that the phase of the waves is well predicted by the parabolic model.

For the Fourier-Galerkin model, a comparison to the exact solution for water surface elevations at the outer radius is shown in Figure 8 for  $90^\circ$ , while the Chebyshev result is shown in Figure 9. Both have problems with the phase speed of the wave as evidenced by the mis-matching of the wave crests. The Fourier-Galerkin results have the biggest discrepancy about  $52^\circ$ , but the Chebyshev model fairs worse, with mismatches over the entire sector from  $50$ - $90^\circ$ .

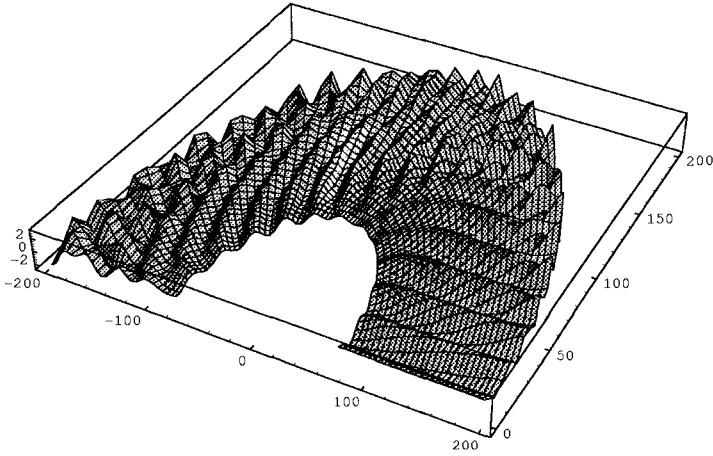


Figure 6: Exact Solution for Waves in a Wide Circular Channel

## Conclusions

Waves propagating in curved channels are shown for constant depth channels that are annular in planform. For a given wave height at the mouth of the channel, the wave field within the channel is predicted by an analytic solution and parabolic and spectral (Fourier-Galerkin and Chebyshev-tau) methods.

The analytic solution, by separation of variables, shows the modal structure of the wave field. The lowest mode, with no zero crossings across the channel, combines with higher order modes to form the total wave field. The wider the channel the more modes are present with the largest mode having an angular wavenumber  $\gamma_1$  less than  $kr_2$ . Higher modes have smaller values of angular wavenumber.

All of the numerical models work well for narrow channels (say  $kw < 8$ ) and become more inaccurate as the dimensionless width of the channel increases, with the wide-angle parabolic model doing better than the Fourier-Galerkin model, which out-performed the Chebyshev-tau model for the wide channel case ( $kw = 37.6$ ).

## Acknowledgments

Both authors were supported in part by the NOAA Office of Sea Grant,

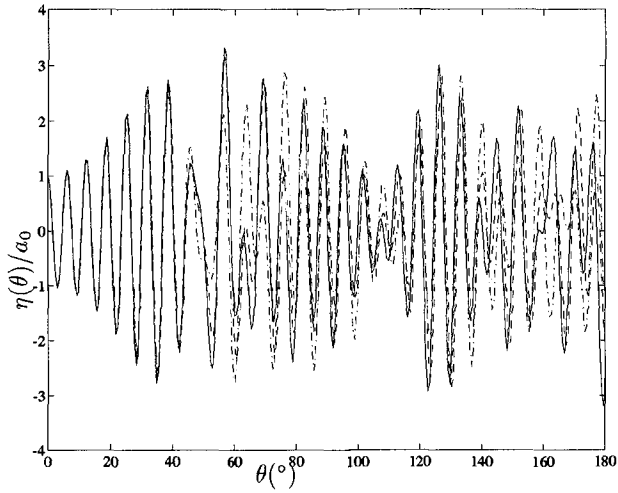


Figure 7: Parabolic model Results. Analytical solution is the solid line; dashed line, wide angle parabolic model and the dashed dot line is the small angle parabolic model.

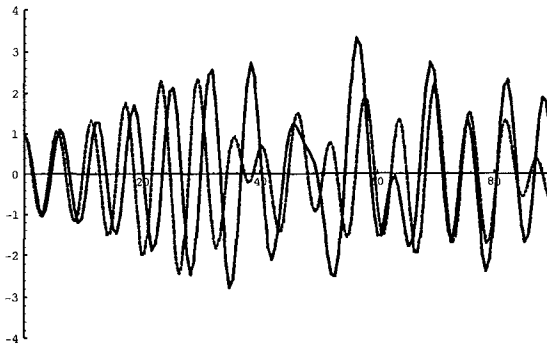


Figure 8: Comparison of the Water Surface Variation Along Outer Wall Between the Exact Solution (solid line) and the Fourier-Galerkin Model (dashed line)

As an example, Figures 4, 4, 2 show the only three wave modes that comprise the total solution shown in Figure 5. The first mode ( $n = 0$ ) has no zero crossing across the channel and the wave action is confined to the outer channel wall. This is the equivalent “whispering gallery” mode. The next mode ( $n = 1$ ) has one zero crossing and a longer angular wave length (defined as  $2\pi/\gamma_2$  radians). The last mode has two zero crossings across the channel and an even longer angular wave length. For this case, the channel radii are  $r_1 = 75$  m,  $r_2 = 100$  m. The channel depth is 4 m and the wave period is 4 s. The corresponding wavenumber  $k$  is  $0.301 \text{ m}^{-1}$ , and therefore the dimensionless channel width is  $kw = 7.53$ , or 1.2 wave lengths fit across the channel. It is neither a narrow nor a very wide channel. The three values of  $\gamma_n$  are 27.6676, 22.8667, 14.2745 from the gravest to the highest mode.

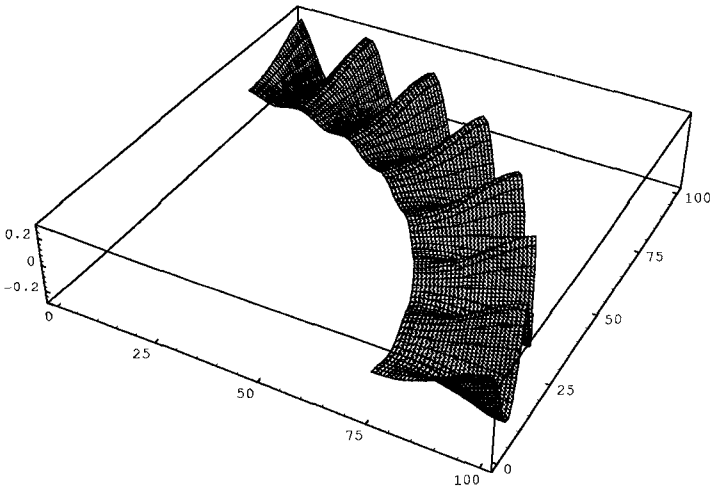


Figure 2: Zeroth (Whispering Gallery) Mode for Analytical Solution

One interesting phenomena of wide channels is the ‘loss’ of waves within the channel. Since the length of the outer circumference is greater than the inner, there are more waves around the outer circumference than the inner, which means that waves become short-crested across the channel and singular points in the wave phase occur, similar to that discussed by Nye and Berry (1974), Radder (1992), and Dalrymple and Martin (1994).

This problem of progressive waves entering the channel with a given wavenumber  $k$  is different than the seiching problem in an annular channel where an integer number of waves fit along the centerline of the circular channel. The



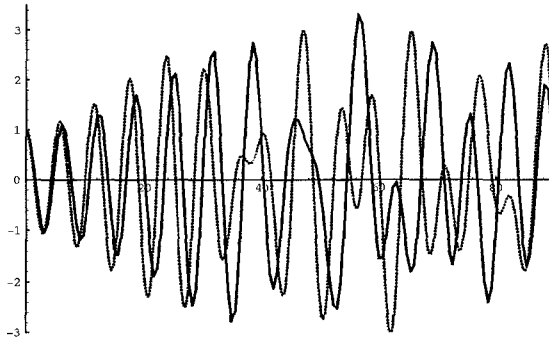


Figure 9: Comparison of the Water Surface Variation Along Outer Wall Between the Exact Solution (solid line) and the Chebyshev-tau Model (dashed line)

Department of Commerce, under Award No. NA 16 RG 0162 (University of Delaware). The U.S. Government is authorized to produce and distribute reprints for government purposes notwithstanding any copyright notation that may appear herein.

## References

- Booker, H.G. and Clemmow, P.C., "The Concept of an Angular Spectrum of Plane Waves, and its Relation to that of Polar Diagram and Aperture Distribution," *Proc. Inst. Electr. Engineering*, 3, 97, 11, 1950.
- Campbell, I.J., "Wave Motion in an Annular Tank," *Phil. Magazine*, Series 7, 44, 355, 845-853.
- Dalrymple, R.A. and J.T. Kirby, "Angular Spectrum Modelling of Water Waves," *Reviews in Aquatic Sciences*, CRC Press, 6, Iss. 5 and 6, 383-404, 1992.
- Dalrymple, R.A., K.D. Suh, J.T. Kirby, and J.W. Chae, "Models for Very Wide Angle Water Waves and Wave Diffraction. Part 2. Irregular Bathymetry," *J. Fluid Mechanics*, 201, 299-322, 1989.
- Dalrymple, R.A., J.T. Kirby and P.A. Martin, "Spectral Methods for Forward Propagating Water Waves in Conformally-mapped Channels," *Applied Ocean Research*, in press.
- Kirby, J.T., R.A. Dalrymple, and H. Kaku, "Parabolic Approximations for Water Waves in Conformal Coordinate Systems,"

*Coastal Engineering*, 23, 185-213, 1994.

Nye, J. F. and M. V. Berry, "Dislocations in wave trains," *Proc. Roy. Soc. London*, A, 336, 165-190, 1974.

Martin, P.A. and R.A. Dalrymple "On Amphidromic Points," *Proc. Roy. Soc. London*, A, 444, 91-104, 1994.

Panchang, V.G. and D. A. Kopriva, "Solution of two-dimensional water-wave propagation problems by Chebyshev collocation," *Mathl. Comput. Modelling*, 12, 625-640, 1989.

Radder, A. C., "Efficient elliptic solvers for the mild-slope equation using the multigrid technique, by B. Li and K. Anastasiou: comments" *Coastal Engineering*, 18, 347-350, 1992.

Rostafinski, W., "On Propagation of Long Waves in Curved Ducts," *J. Acoustical Soc. of America*, 52, 5, Pt. 2, 1411-1420, 1972.

Rostafinski, W., "Analysis of Propagation of Waves of Acoustic Frequencies in Curved Ducts," *J. Acoustical Soc. of America*, 56, 1, 11-15, 1974.

Rostafinski, W., "Transmission of Energy in Curved Ducts," *J. Acoustical Soc. of America*, 56, 3, 1005-1007, 1974.

Rostafinski, W., "Acoustic Systems Containing Curved Duct Sections," *J. Acoustical Soc. of America*, 60, 1, 23-28, 1976.

## CHAPTER 11

### WAVE DAMPING BY KELP VEGETATION

<sup>1</sup>Alfonse Dubi and <sup>2</sup>Alf Tørum

#### 1. INTRODUCTION

Aquatic vegetation, like seagrasses, macroalgae and trees whether submerged or subaerial are an important feature of a coastal ecosystem. In addition to the structural and functional aspects to the environment, they are known to reduce wave and current energies propagating through them. The reduction of energy would then influence sediment motion and thus render an impact on coastal sediment transport. The dissipative character of large stands of kelp has been studied for instance by Jackson and Winant, (1983), Dalrymple et al. (1984) and for artificial seaweed as material for shore protection Price et al. (1968).

Kelp is a macroalga which grows on hard rock and stone and extracts all of its nutrients from the water column. The plant consists of a root-like holdfast organ, a stipe and a frond (Fig.1). The general properties of a fully grown (4-8 years) kelp are summarized as follows:

Length of stipe: 1-2 meters. Fronds have the same length as the stipe.

Specific gravity: 1.18 kg/cu. m; Biomass: 10-30 kg/sq. m

Growth density: 10-15 per sq. meter of horizontal area

---

<sup>1</sup>Dept. of Structural Engineering, The Norwegian Inst. of Technology, (NTH), N-7034 Trondheim, Norway

<sup>2</sup>Dept. of Structural Engineering, NTH/SINTEF-NHL, N-7034 Trondheim, Norway

Specimen found at water depths 2-20 metres.

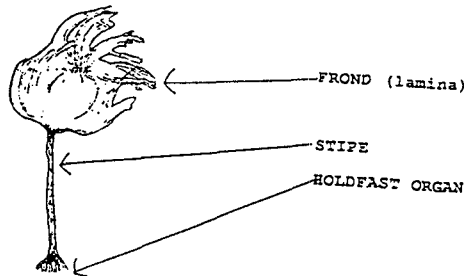


Figure 1: Kelp *Laminaria hyperborea*

Kelp is harvested at several places along the Norwegian coast and is used as a raw material for the manufacturing of various chemicals. In some areas the harvesting of the seaweed has become a controversial issue in which there is suspicion among coastal zone managers that the harvesting results in beach erosion. This study is actually a consequence of the controversy.

Basing on the most recent work by Asano et al. (1992), a new analysis is developed for the flow model and the vegetation motion using field and experimental results carried out on kelp fronds and kelp plant models. The theoretical model is compared with experimental results. The influence of kelp vegetation on beach erosion is not included in this paper because of space limitation.

## 2. BASIC FORMULATION FOR THE FLOW MODEL

Let us consider small amplitude waves propagating in the  $x$ -direction in water of depth  $h$  above submerged vegetation of mean height  $d$ . We employ cartesian coordinates  $(x, z)$  fixed on the mean free surface,  $z=0$ , where  $z$  is positive upwards (see Fig.2). The surface displacement at the free surface is given by  $\eta_1 = a_0 e^{i(kx - \omega t)}$  and displacement at the interface is  $\eta_2 = b_0 e^{i(kx - \omega t)}$ . Let us assume flat bottom, potential flow in the water layer, frictional flow in the vegetation zone. At the interface the viscous shear stresses and the corresponding layer,  $\delta$ , are initially neglected. The bottom shear stress is considered to be negligible in comparison with the frictional resistance of the vegetation. Further, let us assume known a priori the wave amplitude  $a_0$ , the angular frequency  $\omega = 2\pi/T$  both of which are real and positive.  $k$  is a wave number and  $T$  is the wave period.

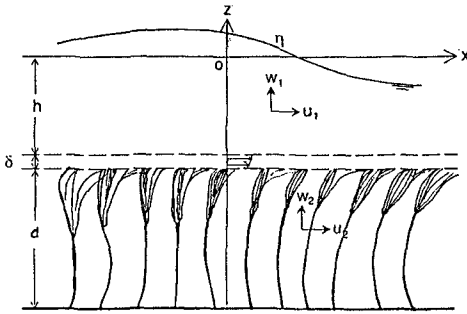


Figure 2: Definition sketch of the flow model

The equations of motion employed are the linearized momentum equations for the water and vegetation zones. For a unit volume

$$\frac{\partial U_1}{\partial t} = -\frac{1}{\rho} \nabla P_1 \tag{1}$$

$$\frac{\partial U_2}{\partial t} = -\frac{1}{\rho} \nabla P_2 - F \tag{2}$$

and the equation of continuity

$$\nabla U = 0 \tag{3}$$

where the subscripts 1 and 2 denote the water and the vegetation zones respectively;  $t$  = time;  $U = (u, w)$  = water particle velocity vector;  $\rho$  is the fluid density and  $P$  is the dynamic pressure.  $F = (F_x, F_z)$  = force vector acting on vegetation given as

$$F_x = \frac{\rho}{2} N [C_{Dx} A]_e |u_2 - \dot{\xi}| (u_2 - \dot{\xi}) + \rho N [C_{ax} V]_e (\dot{u}_2 - \ddot{\xi}) \tag{4}$$

and

$$F_z = \frac{\rho}{2} N [C_{Dz} A]_e |w_2| w_2 + \rho N [C_{az} V]_e \dot{w}_2 \tag{5}$$

where  $N$  is the number of vegetation per unit horizontal area,  $C_{Dx}$  and  $C_{Dz}$  are drag force coefficients in the  $x$ - and  $z$ - directions respectively;  $C_a$  is the added mass coefficient,  $u_2$  and  $w_2$  are the horizontal and vertical velocities of the fluid particles.  $\xi$  is the horizontal displacement of the vegetation stipe with the dot denoting the derivative with respect to time. The subscript  $e$

indicates the equivalent value taking into account of both the stipe and the frond.  $A$  and  $V$  are the total projected area and volume of the plants in this unit volume. More details on the equivalent values are given in the section on the solution for the vegetation motion.

Let us assume that the particle velocities and the dynamic pressure are sinusoidal such that

$$U = U(z) e^{i(kx - \omega t)} \quad (6)$$

and

$$P = P(z) e^{i(kx - \omega t)} \quad (7)$$

where  $i^2 = -1$ .

Substituting equations (4), (5), (6) and (7) into equations (1) and (2) we get a new set of equations. For the upper layer we have

$$\frac{\partial u_1}{\partial t} = -\frac{1}{\rho} \frac{\partial P_1}{\partial x} \quad (8)$$

$$\frac{\partial w_1}{\partial t} = -\frac{1}{\rho} \frac{\partial P_1}{\partial z} \quad (9)$$

and for the lower layer we have

$$\frac{\partial P_2}{\partial x} = -\rho \omega f_x u_2 \quad (10)$$

$$\frac{\partial P_2}{\partial z} = -\rho \omega f_z w_2 \quad (11)$$

where  $f_x$  and  $f_z$  are the horizontal and vertical force components due to the presence of vegetation and expressed by

$$f_x = f_{Dx} + i f_{Ix} \quad (12)$$

and

$$f_z = f_{Dz} + if_{Iz} \quad (13)$$

in which the horizontal and vertical drag force terms are defined by

$$f_{Dx} = \frac{1}{2} [C_{Dx} A]_e \left| 1 - \frac{\dot{\xi}}{u_2} \right| \left( 1 - \frac{\dot{\xi}}{u_2} \right) |u_2| / \omega \quad (14)$$

and

$$f_{Dz} = \frac{1}{2} [C_{Dz} A]_e |w_2| / \omega \quad (15)$$

The inertial force terms are expressed by

$$f_{Ix} = [C_{mx} V]_e \left| 1 - \frac{\dot{\xi}}{u_2} \right| \quad (16)$$

Here  $C_{mx} = 1 + C_{ax}$

$$f_{Iz} = - [C_{mz} V]_e \quad (17)$$

We impose the following linearized boundary conditions at the free surface, interface and bottom boundaries on the momentum equations (8), (9) (10) and (11) :

$$\eta(x,t) = \frac{1}{g} \frac{\partial \phi_1}{\partial t} \quad \text{at } z = 0 \quad (18)$$

$$\frac{\partial^2 \phi_1}{\partial t^2} + g \frac{\partial \phi}{\partial z} = 0 \quad \text{at } z = 0 \quad (19)$$

$$\rho \frac{\partial \phi_1}{\partial t} = P_1 = P_2 \quad \text{at } z = -h \quad (20)$$

$$-\frac{\partial \phi_1}{\partial z} = w_1 = -\frac{1}{\rho \omega f z} \frac{\partial P_2}{\partial z} = w_2 \quad \text{at } z = -h \quad (21)$$

$$-\frac{1}{\rho \omega f z} \frac{\partial P_2}{\partial z} = 0 \quad \text{at } z = -(h+d) \quad (22)$$

$$\frac{\partial P_2}{\partial z} = 0 \quad \text{at} \quad z = -(h+d) \tag{23}$$

where  $\eta = a_0 e^{i(kx-\omega t)}$  is the free surface elevation at SWL ,  $a_0$  is the wave amplitude at the origin,  $g$  is the acceleration due to gravity.  $k$  is complex =  $k_r + k_i$  in the subscripts  $r$  and  $i$  denote real and imaginary values. Substituting  $k$  into the surface elevation , the local wave amplitude is found to decay exponentially as  $a = a_0 \exp(-k_i x)$ .

The solutions for the flow model can be shown to be

$$\Phi_1 = i \frac{C}{\omega} [\cosh(\alpha kd) \cosh(k(h+z)) - \frac{i}{\alpha fx} \sinh(\alpha kd) \sinh(k(h+z))] \exp[i(kx-\omega t)] \tag{24}$$

$$P_2 = \rho C \cosh(\alpha k(h+d+z)) \exp[i(kx-\omega t)] \tag{25}$$

where

$$C = \frac{ga_0}{\cosh(\alpha kd) \cosh(kh) [1 - \frac{i}{\alpha fx} \tanh(\alpha kd) \tanh(kh)]} \tag{26}$$

and

$$\alpha = \sqrt{\frac{|fz|}{|fx|}} \leq 1 \tag{27}$$

is the force ratio. In the upper layer a velocity potential  $\Phi_1$  exists which satisfy Laplace equation

$$\nabla^2 \Phi = 0 \tag{28}$$

where the particle velocities are expressed as

$$u_1 = -\frac{\partial \Phi_1}{\partial x}; \quad w_1 = -\frac{\partial \Phi_1}{\partial z} \tag{29}$$



In the vegetation zone, however, the particle velocities can be obtained by substituting equation (25) into equations (10) and (11) to give

$$u_2 = -i \frac{Ck}{\omega fx} \cosh(\alpha k(h+d+z)) \exp[i(kx - \omega t)] \quad (30)$$

$$w_2 = -\frac{Ck}{\omega fx} \sinh \alpha k(h+d+z) \exp[i(kx - \omega t)] \quad (31)$$

We remark that the horizontal and vertical wave numbers in the upper layer are the same when the fluid is inviscid and homogeneous. In the vegetation zone they are different due to the different horizontal and vertical resistance forces. At the interface, the horizontal particle velocities are discontinuous, i.e.  $u_1 \neq u_2$ , thus a shear stress is present which is accounted for by a boundary-layer type of solution.

Finally, from the combined kinematic and dynamic free surface boundary conditions we derive the dispersion relationship given by

$$\omega^2 = gk \frac{\tanh kh - \frac{i}{\alpha fx} \tanh \alpha kd}{1 - \frac{i}{\alpha fx} \tanh \alpha kd \tanh kh} \quad (32)$$

For given  $\alpha$ ,  $\omega$ ,  $h$ ,  $d$  and  $fx$  the unknown complex wave number  $k$  can be found by solving equation (32) by iteration. This is done in the coming section on calculated results.

### 3. SOLUTION FOR THE VEGETATION MOTION

In order to solve the flow field described above we need the knowledge of the kelp motion. The basic approach is the Morison equation in which the forces resisting the fluid flow are the sum of the drag and inertial forces. Following Asano et al. (1992), the motion of the vegetation is regarded as a forced vibration with one degree of freedom. Let the horizontal displacement of a single kelp plant be denoted by  $\xi$  while the differentiation with respect to time  $t$  be denoted by the over dot. For a unit length of kelp, the equation of motion is given by

$$m_0 \ddot{\xi} + c_1 \dot{\xi} + k_0 \xi = \frac{1}{2} \rho C_{Dx} A |u_2 - \dot{\xi}| (u_2 - \dot{\xi}) + \rho V \dot{u}_2 + \rho V C_{ax} (\dot{u}_2 - \dot{\xi}) \quad (33)$$

where  $m_0$  = mass of kelp per unit length,  $c_1$  = structural damping,  $k_0$  = spring constant,  $C_{Dx}$  and  $C_{ax}$  are drag and added mass coefficients respectively,  $A$  is the projected area and  $V$  is the volume per unit length of kelp. Neglecting the structural damping on the assumption that it is small compared to the frictional forces and rearranging we get

$$m \ddot{\xi} + \frac{1}{2} \rho C_{Dx} A |u_2 - \dot{\xi}| \dot{\xi} + k_0 \xi = \frac{1}{2} \rho C_{Dx} |u_2 - \dot{\xi}| u_2 + \rho (1 + C_{ax}) \dot{u}_2 \quad (34)$$

The general solution of equation (34) requires iterations involving volumetric integration of unknown variables. For our particular case of kelp we shall simplify the equation of motion before attempting to solve the coupled system. The kelp plant consists of a stipe and a frond which together make a total height  $d$ . The stipe can be represented as a slender vertical cylinder of height  $d - l_k$  with uniformly distributed mass and the frond is taken as a concentrated mass at the top of the stipe. Here  $l_k$  is the half length of the frond. Integrating over depth gives the equation that represents the integrated effect over the water column by the motion at the top of the stipe. Now the equation of motion (34) becomes

$$m_e \ddot{\lambda} + \frac{1}{2} \rho [C_{Dx} A]_e |u_\lambda - \dot{\lambda}| \dot{\lambda} + k_0 \lambda = \frac{1}{2} [C_{Dx} A]_e |u_\lambda - \dot{\lambda}| u_\lambda + \rho [C_{mx} V]_e \dot{u}_\lambda \quad (35)$$

where we have assumed that the velocities of both the stipe and fluid can be treated as varying linearly from the bottom to the top of the stipe, that is

$$\dot{\xi} = \frac{h+d+z}{d-l_k} \dot{\lambda} ; \quad u_2 = \frac{h+d+z}{d-l_k} u_\lambda \quad (36)$$

where  $\lambda$  refers to the level at the top of the stipe and the subscript  $e$  stands for equivalent values for the stipe and frond such that

$$m_e = \frac{1}{2} m_0 + m_f + \rho \left( \frac{1}{2} C_{as} V_s + C_{af} V_f \right) \quad (37)$$

Here subscripts  $s$  and  $f$  denote the stipe and frond properties respectively. The mass per unit length,  $m_0$ , of the stipe and its equivalent added mass is weighted by  $\frac{1}{2}$  to imply the conversion of the entire kelp motion to the top. This is valid also for the drag and inertial force coefficients which are given by

$$[C_{Dx} A]_e = \frac{1}{2} C_{Ds} A_s + C_{Df} A_f \quad (38)$$

$$[C_m V]_e = \frac{1}{2}(1+C_{as})V_s + (1+C_{af})V_f \quad (39)$$

Prior to linearization of equation (35) we need to establish the relationship between the drag forces and the flow velocity. One complication with kelp is that the projected area of the frond varies in a flow field. When the velocity (or the relative velocity as the case may be) is zero, the kelp will assume an upright position and the projected area is largest. As the velocity increases, the plant tends to bend over and the fronds tend to streamline in the direction of the flow thereby reducing the projected area. A field experiment has been carried out by the authors in collaboration with prof. Martin Mork and dr. scient. student Kjersti Sjøtun of the University of Bergen (UiB) using a research vessel "Hans Brattstrøm" belonging to UiB. Drag forces were measured on 7 fronds of different sizes of the Norwegian kelp by ship towing. In the laboratory, the forces have been measured using a shear plate on which 95 model kelp plants were fixed. Details of the procedure follow in the section on experimental set-up. Results from the two experiments as shown in Fig.3 show that the drag force does not follow the normal quadratic relationship with velocity, instead, the force is linearly proportional to the velocity.

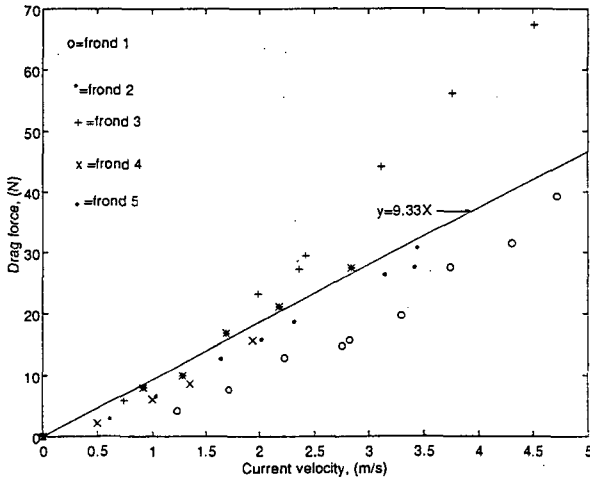


Figure 3: Variation of the drag force on kelp fronds with current velocity

Basing on the two experiments, the following general relationship is proposed between the projected area and the flow velocity:

$$\frac{\rho}{2}[C_{Dx}A]_e = F_\lambda |u_\lambda - \dot{\lambda}|^{-m} = \text{constant} \quad (40)$$

where  $F_\lambda$  = equivalent drag force coefficient evaluated at elevation  $\lambda$ , or at

$z = -(h + l_k)$ . Substituting equation (40) into equation (35) gives

$$m_e \ddot{\lambda} + N_D \dot{\lambda} + k_0 \lambda = N_D u_\lambda + N_I \dot{u}_\lambda \quad (41)$$

where

$$N_D = F_\lambda |u_\lambda (1 - \frac{\dot{\lambda}}{u_\lambda})|^{1-m} \quad (42)$$

Both  $F_\lambda$  and  $m$  are empirically determined constants. The experimental results shown in figure 3, suggest that  $m=1$  and  $F_\lambda=9.3$  and  $30.9$  for currents and waves (fig. 7) respectively. With this information we can now proceed with the linearization of equation (35) to get an analytical solution.

Assuming small amplitudes for the vegetation and fluid particle motion and that the particle velocity amplitude is much greater than the maximum velocity amplitude of vegetation, equation (35) now becomes

$$m_e \ddot{\lambda} + \frac{1}{2} \rho [C_{Dx} A]_e |u_\lambda| \dot{\lambda} + k_0 \lambda = \frac{1}{2} \rho [C_{Dx} A]_e |u_\lambda| u_\lambda + \rho [C_{mx} V]_e \dot{u}_\lambda \quad (43)$$

which represents a linear system provided  $k_0$  is also constant. The solution to this equation gives a ratio known as the velocity amplification factor

$$A_m = \frac{\dot{\lambda}}{u_2|_{z=-(h+l_k)}} = \frac{1 - i\omega \frac{N_I}{N_D}}{1 + i\omega \left(\frac{\omega_n^2}{\omega^2} - 1\right) \frac{m_e}{N_D}} \quad (44)$$

where  $\omega_n = \sqrt{(k_0/m_e)}$  in which  $k_0$  is the spring constant which was determined experimentally to be  $20 \text{ N/m}$  for deflections up to  $55 \text{ cm}$  at the top of the plant. From equation (44) we can derive the quantity

$$|1 - A_m| = \frac{\omega \left[ \left(\frac{\omega_n^2}{\omega^2} - 1\right) + N_I \right]}{\sqrt{N_D^2 + \omega^2 \left(\frac{\omega_n^2}{\omega^2} - 1\right)^2}} \quad (45)$$

The linearized damping force coefficient used in the solution for the flow model can be established by applying the principle of equivalent work which the energy dissipation of the actual system to that of a linear system (Wang and Tørum,1994). The time averaged work done by the actual system per unit surface area is given by

$$W_a = \alpha_k N F_\lambda (1 - \frac{\lambda}{u_\lambda}) \overline{u_\lambda^2} \quad (46)$$

where  $N$  is the number of plants per unit surface area,  $\alpha_k$  is a force reduction factor due to group effect and the over bar denotes the time averaging. For the linearized flow system

$$W_L = \rho f_{Lx} \int_{-(h+d)}^{-(h+l_k)} \overline{u_2^2} dz \quad (47)$$

Equating equation (46) and (47) gives

$$f_{Lx} = \frac{\alpha_k N F_\lambda (1 - A_m) \overline{u_\lambda^2}}{\rho \int_{-(h+d)}^{-(h+l_k)} \overline{u_2^2} dz} \quad (48)$$

Substituting equation (30) into equation (48) gives

$$f_{Lx} = \frac{\alpha_k N F_\lambda (1 - A_m) \cosh^2 k_s (d - l_k)}{\rho \left( \frac{1}{2} + \frac{\sinh 2k_s d}{4k_s d} \right)} \quad (49)$$

where  $k_s = \alpha k$ . Then the linearized damping force coefficient becomes

$$f_x = \frac{f_{Lx}}{\omega} + [C_m V]_e (1 - A_m) \quad (50)$$

## 4. EXPERIMENTAL RESULTS AND DISCUSSION

### 4.1 Experimental setup

The experiment was carried out in a 33 m long, 1 m wide and 1.6 m high wave tank as shown in Fig.4. Five thousand models (scale 1:10) of typical Norwegian kelp plants were fixed in the wave flume bottom over a span of 9.3 meters. This represented a density of about 12 plants per horizontal square meter in the field. Eight capacitance wave gauges were used to measure surface elevations, one shear plate to measure the horizontal force

and a mini current meter was inserted in the plants 4 centimeters above the shear plate. One of the wave gauges was fixed above the shear plate. The shear plate was fixed flush with the bottom. The location of the first wave gauge, taken to be  $x=0$  and the last taken to be  $x = 7\text{m}$  were fixed about 1.2 meters inward from the outer boundaries. In total, 50 tests were carried out for different wave periods (6-14 s, full scale) and wave heights in water depth of 60 cm. Analysis of the results is done within  $0 \leq x \leq 7\text{ m}$ .

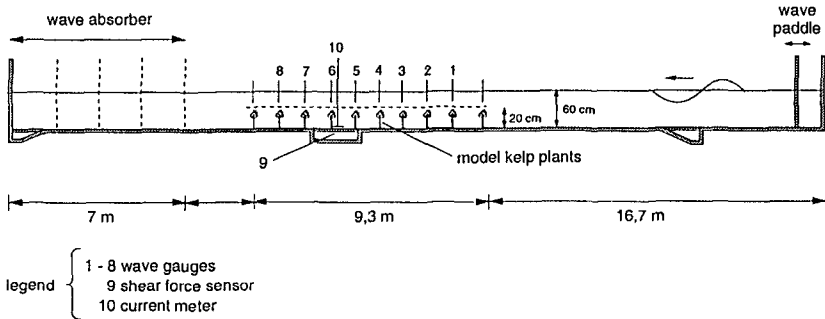


Figure 4: Test setup

### 4.2 Comparison of theoretical and experimental results

The wave heights measured at the eight locations along the wave channel are fitted to an exponential decay curve  $H/H_0 = \exp(-0.00327X)$  as shown in Fig. (5) whereby  $H$  is the local wave height and  $H_0$  is the incident wave height measured at  $x=0$ ,  $k_i = 0.00327/\text{m}$  was found by regression based on the least squares in the MATLAB environment.

Basing on the relationship proposed in equations (40) and (42), the force can then be generalized as

$$F = F_\lambda |1 - A_m| u_\lambda \tag{51}$$

where  $|1 - A_m|$  is given by equation (45). Fig. 6 shows this function fitted to the measured force for given wave heights. Fig. 7 and Fig. 8 show the linear

variation of the measured force with the horizontal particle velocity and wave height respectively.

Finally, inserting equation (50) into the dispersion relationship given by equation (32) for a given water depth  $(h+d)$  wave period,  $T$ , and number of vegetation per unit surface area, the damping coefficient,  $k_i$ , is found by iteration in the MATLAB environment . This solution, however, does not include the contribution of the shear stress to damping.

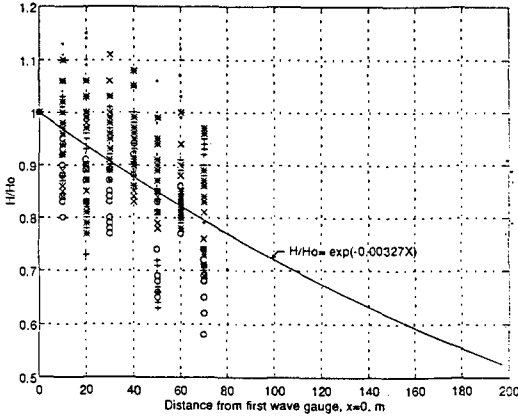


Figure 5. Exponential decay model fitted to data

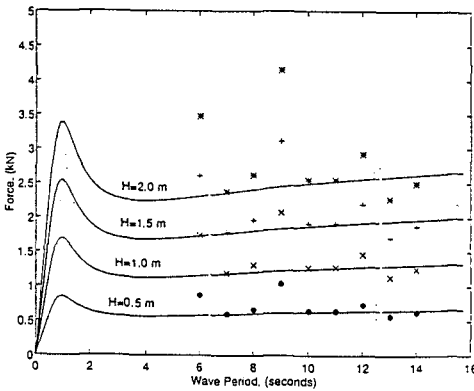


Figure 6. Theoretical force model (Eq. (51)) fitted to measured force

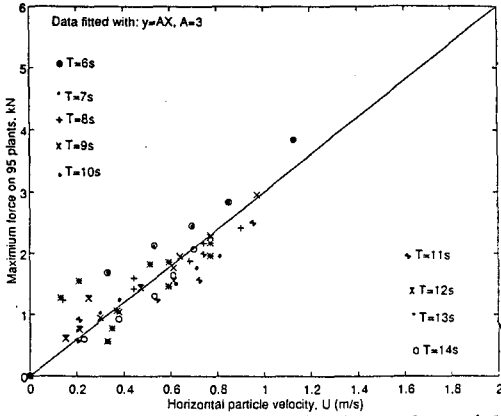


Figure 7: Variation of force with horizontal particle velocity amplitude

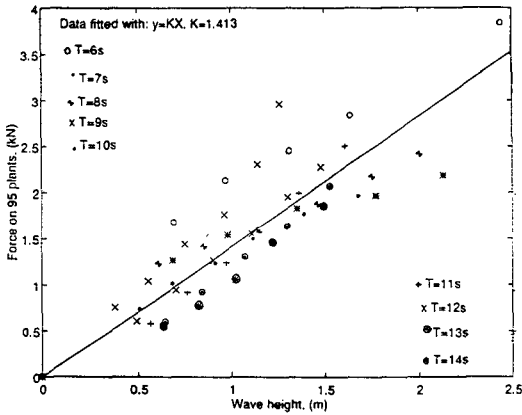


Figure 8: Variation of force with wave height

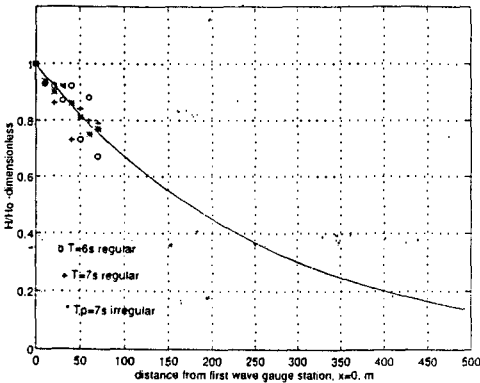


Figure 9: Comparison of scatter for regular and irregular waves



## 5. CONCLUSION

The present study has given an analytical solution for water waves propagating over submerged vegetation taking account of the vegetation motion using the field experimental results. The linear relationship of the damping force with velocity has been applied effectively to obtain an analytical solution for the otherwise iterative equation of the vegetation motion. The average damping coefficient has been found to be  $k_i=0.00327/m$  for the type of kelp we considered. However there has been a large scatter of about 30% which may have been due to reflection of the waves from the wave absorber (Fig. 4). A trial run with irregular waves has revealed a smaller scatter (Fig.9). In this study only regular waves were used. It is our intention to use irregular waves to investigate further on the damping force and the damping coefficient.

## 6. ACKNOWLEDGEMENT

We acknowledge the financial support granted to us by The Norwegian Directorate of Nature Management and The Norwegian Universities Committee for Development, Research and Education (NUFU).

## 7. REFERENCES

1. Asano, T., Deguchi, H., and Kobayashi, N. (1992): Interaction between water waves and vegetation. *Proc. 23rd International Conference on Coastal Engineering, Venice, Italy*
2. Dalrymple R.A., Kirby, J.T., and Hwang, P.A. (1984): Wave diffraction due to areas of energy dissipation. *Journal of Waterway, Port, Coastal and Ocean Engineering*. ASCE, Vol.110(1)
3. Jackson, G.A., and Winant, C.D. (1983): NOTE Effect of a kelp forest on coastal currents. *Continental Shelf Research*, 2(1), pp75-80
4. Price, W.A., Tomlinson, K.W., and Hunt, J.N., (1968): The effect of artificial seaweed in promoting the build up of beaches. Proc. 11th International Conference on Coastal Engineering, London, pp 570-578
5. Wang, H and Tørum, A. (1994): A numerical model on beach response behind coastal kelp. SINTEF-NHL Report No. STF60 A 94092

## CHAPTER 12

### NONLINEAR COUPLING IN WAVES PROPAGATING OVER A BAR

Y. Eldeberky<sup>1</sup> and J.A. Battjes<sup>2</sup>

#### Abstract

The degree of nonlinear coupling in a random wavefield propagating over and beyond a bar is examined using a physical wave flume as well as numerical simulations based on time-domain extended Boussinesq equations and their frequency-domain counter-part. The nonlinear phase speed is computed from the evolution of the nonlinear part of the phase function inherent in the frequency-domain model. Over the bar, the phase speeds of the higher harmonics are larger than the linear estimates due to the nonlinear couplings, resulting in virtually dispersionless propagation, while beyond the bar crest, nonlinear effects on the phase speed vanish rapidly, implying full release of bound harmonics. Quantitative measures of nonlinearity such as the skewness and asymmetry have also been determined. They have near-zero values in the deep-water region on either side of the bar and a pronounced peak over the bar. On the downwave side, the random wave field is found to be spatially homogeneous. This implies that it can be fully described by the energy density spectrum without additional phase information related to the bar location.

#### 1. Introduction

The research described in this contribution deals with the propagation of nonbreaking waves over a shallow bar. It is aimed at investigating the degree of nonlinear coupling as waves evolve over and beyond a bar region. It is a continuation of previous related work by the authors on this subject (Eldeberky and Battjes, 1994).

---

<sup>1</sup>Research Assistant, <sup>2</sup>Professor at Delft University of Technology, Department of Civil Engineering, Section Hydraulics, Stevinweg 1, P.O. Box 5048, 2628 CN Delft, Netherlands

The conventional viewpoint is that on the seaside, the harmonics, bound to the primary, are amplified because of the increasing nonlinearity in the shoaling region, and that they are released on the shoreside, at least partially, because of the decreasing nonlinearity in the deepening region. Strictly speaking, however, even in the shoaling region free components are generated as a result of the nonhomogeneity, whereas conversely some degree of phase coupling may remain in the deepening region.

The phenomena mentioned above can with reasonable accuracy be modelled with Boussinesq-type equations, but these are unwieldy in applications involving wave propagation over large distances, for which phase-averaged, energy-based models with linear propagation are better suited. It is then convenient to switch to such a model at some distance downwave from the bar. Two questions then arise:

(1) How far downwave do the nonlinearities extend with non-negligible intensities? The answer to this question determines whether and from where the switch to a linear propagation model is justified.

(2) Are the fixed phase relations between harmonics, which are induced in the bar region, noticeable on the downwave side of the bar? If so, the wavefield on the downwave side of the bar would be spatially nonhomogeneous, with a "memory" of what happened over the bar (although the local nonlinear exchanges may already have vanished). This phenomenon is to be expected for wavefields with a discrete spectrum of only a few harmonics, but we expect that these effects cancel out in case of a continuous spectrum. If this is indeed the case, the wavefield shoreward of the bar would again be statistically homogenous. Knowledge of the energy spectrum on the downwave side (including the harmonics generated over the bar) would then be sufficient to characterize the wave field in a statistical sense, without additional phase information from "upwave" regions expressing the distance downwave from the bar.

The purpose of this paper is to investigate the questions raised above in a quantitative manner. This is done by determining the values and spatial distributions of the nonlinear contributions to the phase speed and of the skewness and asymmetry parameters, which are quantitative measures of nonlinearity.

The paper is arranged as follows. In section 2, the experimental arrangement is described. In section 3, the model equations used in the numerical simulations are presented. The analyses using the measures of nonlinearity followed by some results are given in section 4. Finally, section 5 presents the summary and conclusions.

## **2. Experimental Approach**

Experiments with random waves reported by Beji and Battjes (1993) have yielded time series of surface elevation at a number of stations over a bar (still-water

depth 0.10 m) and on either side of it (still-water depth 0.40 m) (Fig. 1). A mechanical wave maker was used to generate wave signals according to a prescribed spectrum. The target spectrum was narrow-banded with peak frequency of 0.40 Hz and variance of  $0.35 \text{ cm}^2$ . At the downwave side, a beach with 1:20 slope was used as an absorbing boundary. Surface elevations were measured at stations 1 to 8 (the other stations refer to the numerical simulations). Station 1 is at the beginning of the upslope side of the bar, station 2 is 5.0 meters from station 1, and stations 3 to 8 are positioned every 1.0 meter.

These measurements have been analyzed to address the questions raised above. The analyses are mainly in the frequency-domain. Power spectra for these observations indicated significant transfer of energy from the spectral peak to higher frequencies (Beji and Battjes, 1993). Bispectral analysis showed the intensity and the spectral distribution of nonlinear couplings (Eldeberky and Battjes, 1994). Here we focus on the total measures of nonlinearity such as the skewness and asymmetry in order to investigate the spatial variation in the intensity of nonlinear couplings.

Due to the fact that the spatial coverage of the experimental data (up to station 8) is not enough to examine nonlinearity beyond the bar, a numerical "wave flume" has been employed to obtain results farther downwave. This is done using the time- and frequency-domain extended Boussinesq equations. The model equations are presented in the next section.

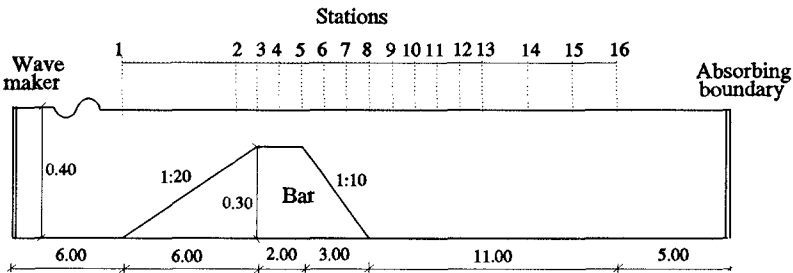


Fig. 1. Definition sketch of wave flume and location of wave gauges. All distances are expressed in meters

### 3. Numerical Approach

#### 3.1 Time-domain model

Numerical simulations were performed using a 1-D extended Boussinesq model (Beji and Battjes, 1994) with improved dispersion characteristics, as in Madsen and Sørensen (1992), describing relatively long, small amplitude waves

propagating in water of slowly varying depth:

$$\frac{\partial u}{\partial t} + u \frac{\partial u}{\partial x} + g \frac{\partial \xi}{\partial x} = \frac{2}{5} h^2 \frac{\partial^3 u}{\partial x^2 \partial t} + h \frac{\partial h}{\partial x} \frac{\partial^2 u}{\partial x \partial t} + \frac{1}{15} g h^2 \frac{\partial^3 \xi}{\partial x^3}, \quad (1)$$

$$\frac{\partial \xi}{\partial t} + \frac{\partial}{\partial x} [(h + \xi)u] = 0 \quad (2)$$

Here,  $\xi$  is the surface displacement,  $u$  the depth-averaged horizontal velocity,  $h$  the still water depth, and  $g$  the gravitational acceleration. This set of equations has been integrated numerically using a difference scheme as described by Beji and Battjes (1994).

In the computation, the initial condition used is the unperturbed state. At the upwave boundary (station 1), the surface elevation is set equal to the experimental values; velocity values are derived from these using the long-wave approximation. At the outgoing boundary, an absorbing boundary condition has been used to ensure that the disturbances leave the computational domain without reflection.

### 3.2 Frequency-domain model

Numerical simulations were also performed using the frequency-domain counter part of the extended Boussinesq equations mentioned above. For one-dimensional propagation considered so far, the time ( $t$ ) variation of the surface elevation ( $\xi$ ) at each location ( $x$ ) is expanded in a Fourier series as in

$$\xi(t;x) = \sum_{p=-\infty}^{\infty} A_p(x) \exp\{i(\omega_p t - \psi_p(x))\} \quad (3)$$

with  $A_p$  denoting a complex amplitude,  $p$  indicating the rank of the harmonic,  $\omega_p = p\omega_1$ , and  $d\psi_p/dx = k_p$ , the wave number corresponding to  $\omega_p$  according to the dispersion equation for the linearised Boussinesq equations. By substituting (3) into the time-domain Boussinesq equations, and by neglecting certain higher-order terms on the assumption of a sufficiently gradual evolution of the wave field, Madsen and Sørensen (1993) develop a set of coupled evolution equations for the set of complex amplitudes  $A_p$  which in abbreviated form can be written as

$$\frac{dA_p}{dx} = L_p \frac{dh}{dx} A_p + \sum_{m=1}^{p-1} Q_{m,p}^+ A_m A_{p-m} + \sum_{m=1}^{\infty} Q_{m,p}^- A_m^* A_{p+m} \quad (4)$$

The first term on the right represents linear shoaling, proportional to the bottom slope  $dh/dx$ , the second term the triad sum interactions and the third the triad difference interactions. Complete expressions for the coefficients  $L$ ,  $Q^+$  and  $Q^-$  can be found in Madsen and Sørensen (1993). For the numerical integration of the evolution equation (4) and the applications to random waves with a given energy spectrum refer to Battjes *et al.* (1993).

## 4. Analysis

### 4.1 Phase speed

The evolution equation of the frequency-domain model is formulated in terms of complex Fourier amplitudes that contain the nonlinear part of the phase function. This equation (4) is used to obtain an evolution equation for the nonlinear part of the phase function in order to derive and evaluate a nonlinear correction to the linear phase speed. To this end, we express the complex amplitude  $A_p(x)$  in its magnitude  $a_p(x)$  and its phase  $\alpha_p(x)$ :

$$A_p(x) = a_p(x) e^{i\alpha_p(x)} \quad (5)$$

After straightforward algebra, we obtain the following phase evolution equation for each harmonic after omitting the  $x$ -dependency for abbreviation,

$$a_p \frac{d\alpha_p}{dx} = \Im \left[ \frac{dA_p}{dx} \right] \cos \alpha_p - \Re \left[ \frac{dA_p}{dx} \right] \sin \alpha_p \quad (6)$$

The values of  $a_p$ ,  $\alpha_p$ , and  $dA_p/dx$  at each location can be obtained from the numerical integration of equation (4). The phase speed of each harmonic, linear  $(c_p)_l$  and nonlinear  $(c_p)_{nl}$ , can be obtain as follows

$$(c_p)_l = \frac{\omega_p}{(k_p)_l} = \frac{\omega_p}{d\psi_p/dx} \quad (7)$$

$$(c_p)_{nl} = \frac{\omega_p}{(k_p)_{nl}} = \frac{\omega_p}{d\psi_p/dx + d\alpha_p/dx} \quad , \quad (8)$$

where  $(k_p)_l$  and  $(k_p)_{nl}$  are the linear and nonlinear phase change per unit length.

To examine the intensity of nonlinear coupling, the nonlinear phase speeds are compared to the linear predictions obtained from the extended Boussinesq equations.

For random incident waves, assumed to have independent, random phases at station 1, Fig. 2 shows the spectral densities, the linear and the nonlinear phase speeds at different locations over the bar. Over the upslope of the bar (station 2), the nonlinear phase speeds of the higher harmonics are larger than the linear estimates due to the nonlinear couplings to the primary. Over the bar crest (station 4), the nonlinear phase speeds are nearly constant and equal to  $\sqrt{gh}$  (nondispersive shallow-waves). Beyond the bar (station 8), the nonlinear predictions of phase speed agree with the linear estimates, implying full release of bound harmonics. The results farther beyond the bar (not shown here) did not show any deviation in the nonlinear phase speeds from the linear predictions, implying the absence of nonlinear couplings. Likewise, the energy spectrum of

the waves did not evolve in the region beyond the bar. This in turn means that nonlinear models are not needed to characterize the wavefield beyond the bar.

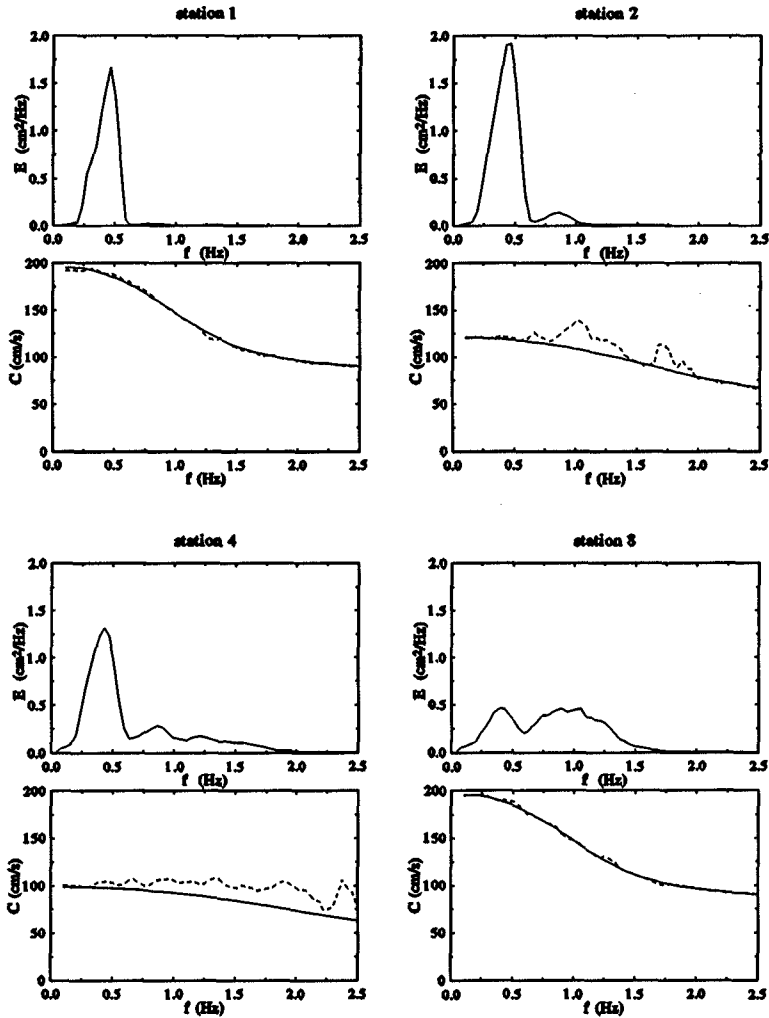


Fig. 2. Computed energy density spectra (upper panels), linear (solid line) and total (dashed line) phase speeds (lower panels) at stations 1, 2, 4, and 8

## 4.2 Skewness and Asymmetry

To measure the nonlinearities associated with the nonlinear couplings, higher-order moments are needed such as the skewness and asymmetry. These are measures of asymmetry of the wave profile around the horizontal (crest to trough asymmetry) and the vertical (front to back asymmetry) plane respectively. Skewness and asymmetry values have been computed according to the definitions given by Hasselmann *et al.* (1963) and Elgar and Guza (1985) respectively.

### The original wave flume and its numerical simulation

The skewness and asymmetry have been computed for both the measured and time-domain computed surface elevations at various locations over the bar. Their variations are given in Fig. 3. The comparison shows the ability of the numerical model to reproduce the nonlinear evolution of waves propagating in varying water depth with sufficient accuracy for the present purpose.

The variations indicate a significant increase on the upslope to a maximum over the bar. To the lee of the bar crest, the skewness and asymmetry decrease rapidly to near-zero values, comparable to those on the exposed side of the bar. (For skewness values less than 0.2, Ochi and Wang (1984) found virtually no deviation from the Gaussian probability density of the sea surface elevation.) This in turn means absence of significant nonlinear interactions at the downwave side of the bar. We expect that for random waves with a continuous spectrum, this will imply spatial homogeneity. This is checked below by using computed signals in the region beyond that of the measurements.

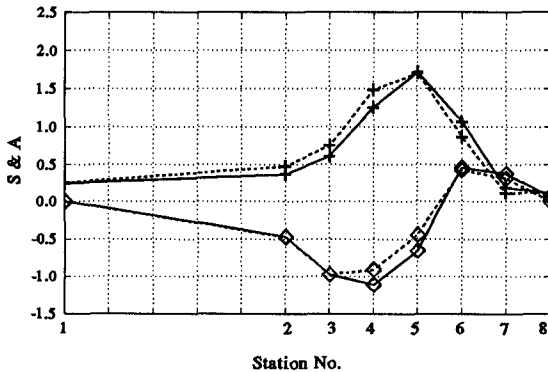


Fig. 3. Skewness (+) and asymmetry (◇): comparison between results from the physical wave flume (solid lines) and the numerical wave flume (dashed lines)



### Numerical simulation for extended region

Time-domain numerical computations have been performed extending to distances farther downwave in order to examine the homogeneity of the wavefield in that region. The computational domain now extends to station 16; the distances between stations 9 to 13 are 1.0 m and those between stations 14 to 16 are 2.0 m.

Computations are done for two different upwave boundary conditions, corresponding to sinusoidal and irregular waves. The former is to demonstrate the spatial nonhomogeneity associated with the interference between a primary wave and its harmonics. The latter is to investigate the matter for the case of a continuous spectrum, where the innumerable interferences are expected to cancel, resulting in a homogeneous wavefield.

To demonstrate the contrast between the two cases, the nonlinearity parameter ( $a/h$ ) is kept constant by imposing the same surface elevation variance at the upwave boundary. The computations are performed for the same record duration as in the physical experiment, and the computed signals at stations 1 to 16 have been analyzed in the frequency-domain in the same manner as the experimental records.

#### *Sinusoidal waves*

Fig. 4 shows the spatial variations of the amplitudes of the primary wave and its harmonics. Over the bar, a significant energy transfer takes place into the second, third and fourth harmonics. Beyond the bar, the amplitudes do not vary because of absence of nonlinear interactions.

The corresponding variations in the skewness and asymmetry are shown in Fig. 5. They indicate a significant increase on the upslope to a maximum over the bar as a result of harmonic generation. On the downslope side of the bar, the skewness and asymmetry decrease rapidly to values between  $\pm 0.5$ . Beyond the bar, although the amplitudes of the harmonics are nearly constant, the skewness and asymmetry vary significantly as a result of the varying phase lags between the freely propagating component-waves, resulting in a spatially nonhomogenous wavefield.

#### *Irregular waves*

Fig. 6 shows the variations of skewness and asymmetry over the upslope, the bar crest, the downslope and farther downwave; the latter is of particular interest here. It shows that over the horizontal region, and in contrast to the case of sinusoidal waves, the skewness and asymmetry remain at near-zero values (less than 0.2), comparable to those on the exposed side of the bar, without any significant spatial variations. This implies that there is no memory of the bar location, in contrast to the discrete case. The practical implication of this is that the waves downwave from the bar can again be assumed to have independent, random phases.

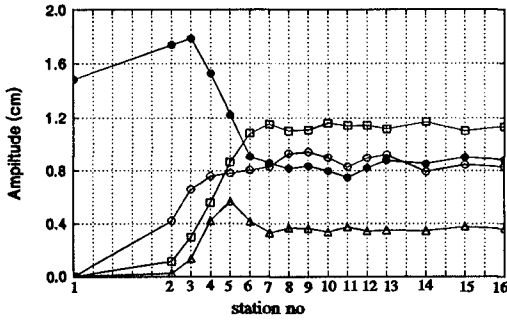


Fig. 4. Spatial variations of the amplitudes of the primary wave and its harmonics primary wave (●), second harmonic (○), third harmonic (◻), and fourth harmonic (△)

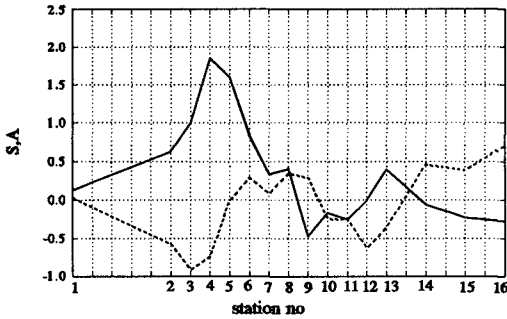


Fig. 5. The spatial variations of skewness (solid line) and asymmetry (dashed line) for sinusoidal incident waves (at station 1)

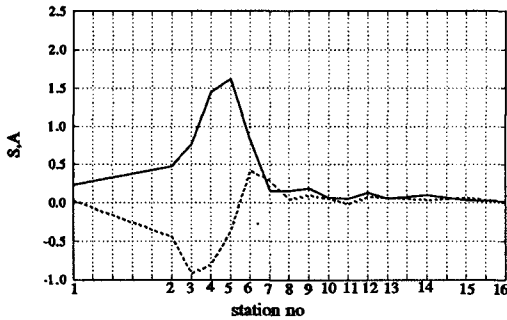


Fig. 6. The spatial variations of skewness (solid line) and asymmetry (dashed line) for irregular waves

## 5. Summary and Conclusions

The degree of nonlinear coupling as waves evolve over and beyond a bar is examined. The extended Boussinesq equations that had shown success in this kind of application are used in this investigation together with experimental data. The situation considered was such that significant harmonic generation took place on the upslope leading to the bar crest. The following indicators of nonlinearity were used: the nonlinear phase speed, the skewness and asymmetry. Inspection of their spatial variations has led to the following conclusions.

- The comparison between linear and nonlinear estimates of the phase speeds indicates that over the bar, the bound harmonics travel faster than their corresponding free waves that have linear phase speeds. Beyond the bar, they propagate with the linear phase speed implying that they are fully released.
- The skewness and asymmetry have near-zero values in the deep-water region on either side of the bar and a pronounced peak over the bar. On the downwave side, the wavefield is found to be spatially homogeneous for irregular waves without memory of the phase couplings which existed over the bar crest. This is in contrast to the case of a discrete, finite set of wave components.

Summarizing, the wavefield on the downwave side is virtually linear and statistically homogeneous. It can be fully described by the energy density spectrum with linear propagation, and without the need for additional phase information reflecting the site-dependent distance downwave from the bar.

## Acknowledgements

The work presented here is part of a project sponsored by the National Institute for Coastal and Marine Management and the Road and Hydraulics Engineering Division of Rijkswaterstaat, the Dutch Department of Public Works.

## References

- Beji, S., and Battjes, J.A. (1993). Experimental investigation of wave propagation over a bar. *Coastal Eng.*, 19, 151-162.
- Beji, S., and Battjes, J.A. (1994). Numerical simulation of nonlinear waves propagating over a bar. *Coastal Eng.*, 23, 1-16.
- Battjes, J.A., Eldeberky, Y., and Won, Y. (1993). Spectral Boussinesq modelling of breaking waves. *Proc. Int. Conf. WAVES '93*, New Orleans, ASCE, pp. 813-820, New York.
- Eldeberky, Y., and Battjes, J.A. (1994). Phase lock in waves passing over a bar. *Proc. Int. Sym. WAVES-PHYSICAL AND NUMERICAL MODELLING*

- '94, Vancouver, pp. 1086-1095.
- Elgar, S. and Guza, R.T. (1985). Observations of bispectra of shoaling surface gravity waves. *J. Fluid Mech.*, Vol. 161, 425-448.
- Hasselmann, K., Munk, W., and McDonald, G. (1963). Bispectra of ocean waves. In: *Time Series Analysis* (edited by M. Rosenblatt), 125-139, Wiley, New York.
- Madsen, P.A., and Sørensen, O.R. (1992). A new form of the Boussinesq equations with improved linear dispersion characteristics. Part 2: a slowly-varying bathymetry. *Coastal Eng.*, 18, 183-205.
- Madsen, P.A., and Sørensen, O.R. (1993). Bound waves and triad interactions in shallow water. *J. Ocean Eng.*, 20 (4), 359-388.
- Ochi, M.K. and Wang, W.C. (1984). Non-Gaussian characteristics of coastal waves. *Proc. 19th Int. Conf. on Coastal Eng.*, Houston, Vol.1, pp.516-531

## **CHAPTER 13**

### **AN ABSORBING WAVE-MAKER BASED ON DIGITAL FILTERS**

Peter Frigaard and Morten Christensen  
Hydraulics & Coastal Engineering Laboratory  
Aalborg University, Sohngaardsholmsvej 57, DK-9000 Aalborg, Denmark

#### **ABSTRACT**

An absorbing wave maker operated by means of on-line signals from digital FIR filters is presented.

Surface elevations are measured in two positions in front of the wave maker. The reflected wave train is separated from the sum of the incident and rereflected wave trains by means of digital filtering and subsequent superposition of the measured surface elevations. The motion of the wave paddle required to absorb reflected waves is determined and added to the original wave paddle control signal.

Irregular wave tests involving test structures with different degrees of reflection show that excellent absorption characteristics have been achieved with the system.

#### **INTRODUCTION**

Coastal engineering problems are often solved by means of physical models. Physical modelling of coastal engineering phenomena requires the capability of reproducing natural conditions in the laboratory environment.

One of the problems associated with the physical modelling of water waves in laboratory wave channels is the presence of rereflected waves.

In nature the sea constitutes an open boundary which absorbs waves reflected by the coastal system.

A wave channel is a closed system: waves reflected from a model structure will be rereflected at the wave paddle, thus altering the characteristics of the wave train incident to the model structure. Consequently, the reproduction of a specified

incident wave train will often be impossible when a reflective structure is being tested.

The problem of rereflection can be reduced by applying a so-called absorbing wave maker: a combined wave generator and active wave absorber, which, in addition to generating incident waves, absorbs waves reflected from the test structure.

The construction of an absorbing wave maker requires (Gilbert (1978)):

1. A means of detecting reflected waves as they approach the wave maker
2. A means of making the paddle generate waves that are, in effect, equal and opposite to the reflected waves so that the reflected waves are cancelled out as they reach the paddle. This requirement is over and above the need to generate the primary incident waves.

Milgram (1970) presented a system in which waves in a channel were absorbed by means of a moving termination at the end of the channel. The motion of the termination needed for absorption was determined by analog filtering of a surface elevation signal measured in front of the termination. This active wave absorber was not used in a combined generation and absorption mode.

Bullock and Murton (1989) described the conversion of a conventional wedge-type wave maker to an absorbing wave maker. The system developed by Bullock and Murton was based on analog filtering of a surface elevation signal measured on the face of the wave paddle. Good absorption characteristics were achieved with a less-than-perfect circuit design.

Recently, an absorbing wave maker has been installed in a wave channel at Aalborg Hydraulic Laboratory, Aalborg University.

In the following the design of this absorbing wave maker is presented and its performance is evaluated based on the results of physical model tests.

**PRINCIPLE**

The absorbing wave maker is operated by digital FIR filters working in real time. The relation between the input  $\eta$  and the output  $x$  of a digital FIR filter of length  $N$  is given by the discrete convolution integral:

$$x^k = \sum_{i=-M}^{i=M} h^i \eta^{k-i} \quad , \quad M = \frac{N-1}{2} \tag{1}$$

where  $h$  denotes the filter impulse response (filter operator). Given a desired frequency response, the corresponding FIR filter operator is obtained by computing the inverse discrete Fourier transform of the complex frequency response function, see e.g. Karl (1989). Notice, that the filter output is delayed  $\frac{N-1}{2}$  time

steps relative to the input. For FIR filters operating in real time, this time delay must be removed.

The paddle displacement correction signal needed for absorption of reflected waves is determined by means of digital filtering and subsequent superposition of surface elevation signals measured in two positions in front of the wave maker (fig. 1).

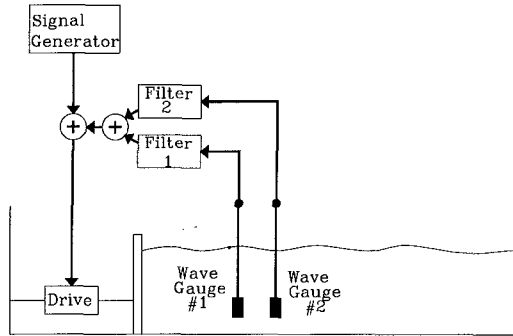


Figure 1: Principle of absorbing wave maker.

When active absorption is applied, the paddle displacement correction signal is added to the input paddle displacement signal read from the signal generator, causing the wave maker to operate in a combined generation/absorption mode. Having outlined the principle of the system, the only remaining problem in the design process is to specify the frequency response of the FIR filters applied.

### FREQUENCY RESPONSE OF FIR FILTERS

In fig. 2, a wave channel equipped with two wave gauges is shown.

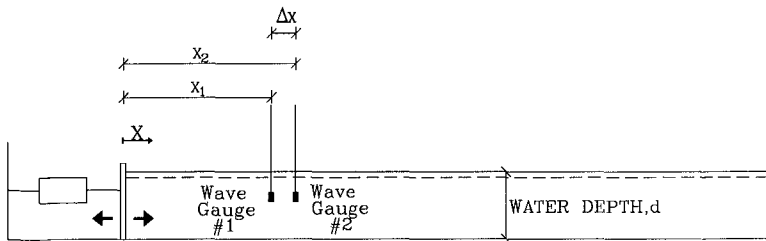


Figure 2: Wave channel with piston-type wave maker.

The surface elevation signal at a position  $x$  may be regarded as a sum of harmonic components. Considering an isolated component of frequency  $f$ , the surface elevation arising from this component may be written as the sum of the corresponding incident and reflected wave components:

$$\begin{aligned} \eta(x, t) &= \eta_I(x, t) + \eta_R(x, t) \\ &= a_I \cos(2\pi ft - kx + \phi_I) + a_R \cos(2\pi ft + kx + \phi_R) \end{aligned} \quad (2)$$

where

$$\begin{aligned} f &: \text{frequency} \\ a = a(f) &: \text{wave amplitude} \\ k = k(f) &: \text{wave number} \\ \phi = \phi(f) &: \text{phase} \end{aligned}$$

and indices  $I$  and  $R$  denote incident and reflected, respectively.

Provided a linear relation exists between a given paddle displacement signal and its corresponding surface elevation signal, the paddle displacement correction signal,  $X_{corr}(t)$ , which cancels out the reflected component without disturbing the incident component, is given by

$$X_{corr}(t) = B \cdot a_R \cos(2\pi ft + \phi_R + \phi_B + \pi) \quad (3)$$

where

$$\begin{aligned} B &: \text{piston stroke/wave height relation} \\ \phi_B &: \text{phaseshift between paddle displacement and surface} \\ &\quad \text{elevation on the face of the paddle} \end{aligned}$$

In the following it is shown that it is possible to amplify and phase shift the surface elevation signals from the two wave gauges in such a way that their sum is identical to the paddle correction signal corresponding to absorption of the reflected component as given by eq. (3).

At the two wave gauges (fig. 2) we have:

$$\begin{aligned} \eta(x_1, t) &= a_I \cos(2\pi ft - kx_1 + \phi_I) + a_R \cos(2\pi ft + kx_1 + \phi_R) \\ \eta(x_2, t) &= a_I \cos(2\pi ft - kx_2 + \phi_I) + a_R \cos(2\pi ft + kx_2 + \phi_R) \\ &= a_I \cos(2\pi ft - kx_1 - k\Delta x + \phi_I) + \\ &\quad a_R \cos(2\pi ft + kx_1 + k\Delta x + \phi_R) \end{aligned} \quad (4)$$

where  $x_2 = x_1 + \Delta x$  has been substituted into eq. (5).

An amplification of  $C$  and a theoretical phase shift  $\phi^{theo}$  are introduced into the expressions for  $\eta(x, t)$ . The modified signal is denoted  $\eta^*$ . For the  $i$ 'th wave gauge signal the modified signal is defined as:

$$\begin{aligned} \eta^*(x_i, t) &= C a_I \cos(2\pi ft - kx_i + \phi_I + \phi_i^{theo}) + \\ &\quad C a_R \cos(2\pi ft + kx_i + \phi_R + \phi_i^{theo}) \end{aligned} \quad (6)$$



This gives at wave gauges 1 and 2:

$$\eta^*(x_1, t) = Ca_I \cos(2\pi ft - kx_1 + \phi_I + \phi_1^{theo}) + Ca_R \cos(2\pi ft + kx_1 + \phi_R + \phi_1^{theo}) \quad (7)$$

$$\eta^*(x_2, t) = Ca_I \cos(2\pi ft - kx_1 - k\Delta x + \phi_I + \phi_2^{theo}) + Ca_R \cos(2\pi ft + kx_1 + k\Delta x + \phi_R + \phi_2^{theo}) \quad (8)$$

The sum of  $\eta^*(x_1, t)$  and  $\eta^*(x_2, t)$ , which is denoted  $\eta^{calc}(t)$ , is:

$$\begin{aligned} \eta^{calc}(t) &= \eta^*(x_1, t) + \eta^*(x_2, t) \\ &= 2Ca_I \cos\left(\frac{k\Delta x + \phi_1^{theo} - \phi_2^{theo}}{2}\right) \\ &\quad \cos\left(2\pi ft - kx_1 + \phi_I + \frac{-k\Delta x + \phi_1^{theo} + \phi_2^{theo}}{2}\right) + \\ &\quad 2Ca_R \cos\left(\frac{-k\Delta x + \phi_1^{theo} - \phi_2^{theo}}{2}\right) \\ &\quad \cos\left(2\pi ft + kx_1 + \phi_R + \frac{k\Delta x + \phi_1^{theo} + \phi_2^{theo}}{2}\right) \end{aligned} \quad (9)$$

It is seen that  $\eta^{calc}(t)$  and  $X_{corr}(t) = Ba_R \cos(2\pi ft + \phi_R + \phi_B + \pi)$  are identical signals in case:

$$2C \cos\left(\frac{k\Delta x - \phi_1^{theo} + \phi_2^{theo}}{2}\right) = B \quad (10)$$

$$kx_1 + \frac{k\Delta x + \phi_1^{theo} + \phi_2^{theo}}{2} = \phi_B + \pi + n \cdot 2\pi, \quad n \in (0, \pm 1, \pm 2, \dots) \quad (11)$$

$$\frac{k\Delta x + \phi_1^{theo} - \phi_2^{theo}}{2} = \frac{\pi}{2} + m \cdot \pi, \quad m \in (0, \pm 1, \pm 2, \dots) \quad (12)$$

Solving eqs. (10)-(12) with respect to  $\phi_1^{theo}$ ,  $\phi_2^{theo}$  and  $C$  with  $n = m = 0$  gives

$$\phi_1^{theo} = \phi_B - k\Delta x - kx_1 + 3\pi/2 \quad (13)$$

$$\phi_2^{theo} = \phi_B - kx_1 + \pi/2 \quad (14)$$

$$C = \frac{B}{2\cos(-k\Delta x + \pi/2)} \quad (15)$$

Eqs. (13)-(15) specify the frequency responses, i.e. the amplification factors and phase shifts, of FIR filters 1 and 2 in fig. 1.

Even though the theoretical frequency response of the filters easily can be calculated from the eqs. (13)-(15) one should notice that an actual realization of such

a theoretical frequency response in FIR filters might be rather difficult to obtain. The aim of this paper is not to describe design of Fir filters, but notice that the actual frequency response of the filters (read: performance of the absorbing system) are strongly dependent upon: Type of wave-maker, water depth, location of wave gauges, number of filter coefficients, sample frequency in filter etc.

**PHYSICAL MODEL TEST**

In order to determine the performance of the active absorption method described above, the method was implemented in the control system of a piston-type wave maker placed in a small laboratory wave channel at Aalborg Hydraulic Laboratory, Aalborg University and the method was implemented in the control system of the wedge type wave maker placed in the CIEM at LIM/UPC, Catalonia University of Technology.

The geometry of the Aalborg Hydraulics Laboratory wave channel and the wave gauge positions are given in fig. 3.

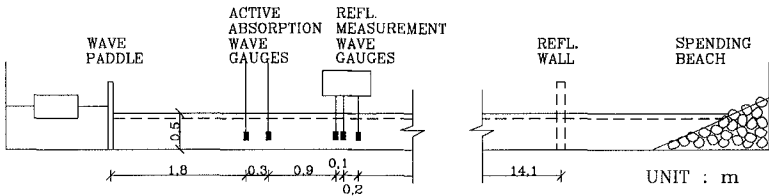


Figure 3: Wave channel and wave gauge positions.

The active absorption system was based on surface elevation measurements obtained in wave gauges positioned at distances of  $x_1 = 1.80$  m and  $x_2 = 2.10$  m from the wave paddle. The phase  $\phi_B$  and gain  $B$  (see eq. (3)) were determined using the linear transfer functions derived by Biesel (1951).

When active absorption was applied, the surface elevation time series were recorded and digitized by means of a PC equipped with an A/D-D/A-card, digital filtering and superposition were performed, and the resulting paddle displacement correction signal was added to the input signal read from the signal generator.

At the far end of the channel, a spending beach was situated. In order to be able to perform tests with different degrees of reflection from the channel termination, provision was made for mounting a vertical reflecting wall in front of the spending beach.

The channel is equipped with three pairs of wave gauges mounted on a beam at distances of 3.0 m, 3.1 m and 3.3 m from the wave paddle. These gauges are used for reflection measurements.

A water depth of  $d = 0.5$  m was maintained throughout the test series.

In order to evaluate the efficiency of the absorbing wave maker when applied to irregular wave tests involving test structures with different degrees of reflection, tests covering all four permutations of the alternatives

- Either with or without active absorption applied
- Either with the spending beach or the reflecting wall at the far end of the channel

were performed.

All tests were performed with exactly the same input from the signal generator: a wave paddle displacement signal corresponding to a JONSWAP-spectrum with significant wave height  $H_s = 0.04$  m, peak frequency  $f_p = 0.6$  Hz and peak enhancement factor  $\gamma = 3.3$  sampled at a frequency of  $f_s = 40$  Hz and generated by means of digital filtering of Gaussian white noise in the time domain. In each test the incident and reflected spectra were resolved as described by Mansard and Funke (1980). The incident spectra are given in fig. 4.

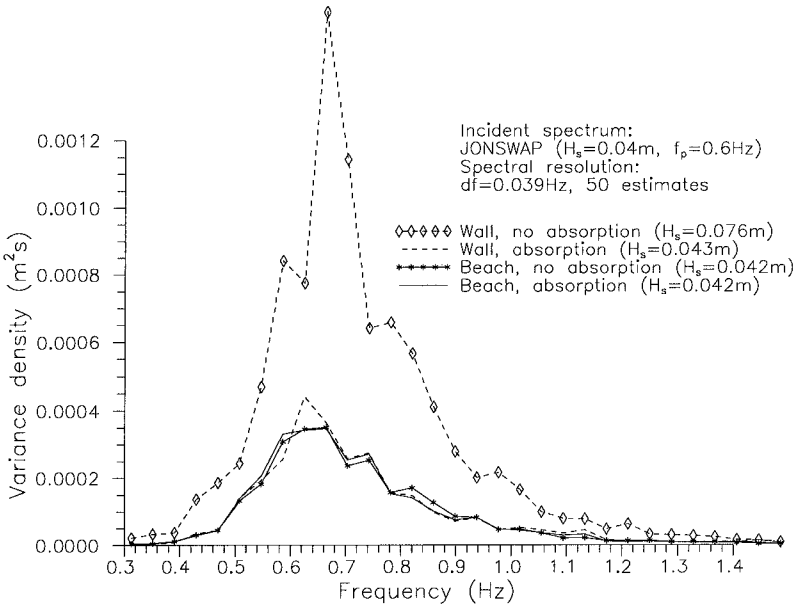


Figure 4: Incident wave spectra.

The tests showed that the spending beach reflected only 5-10% of the incoming wave energy in the frequency range of the input spectrum. Consequently, the "beach, no absorption" incident spectrum in fig. 4 may be regarded as the target spectrum: the disturbances introduced by rereflection are negligible.

The "beach, absorption" incident spectrum is almost identical to the target spectrum. This implies, that applying the active absorption system to tests involving test structures with little reflection will not introduce disturbances in the incident spectrum.

The efficiency of the active absorption system is demonstrated by the test results obtained with the reflecting wall installed at the far end of the channel. When active absorption is applied, the incident spectrum is in excellent agreement with the target spectrum, whereas the incident spectrum obtained without active absorption is significantly distorted by rereflection (see fig. 4.).

In order to visualize the effect of active absorption in the time domain, the following test was performed: the reflecting wall was installed in the far end of the channel, and irregular waves were generated. After 60 seconds, wave generation was terminated, and active absorption was applied. A surface elevation time series recorded at  $x = 3.0$  m is given in fig. 5 a.

For comparison, a time series recorded in a similar test in which active absorption was not applied is given in fig. 5 b.

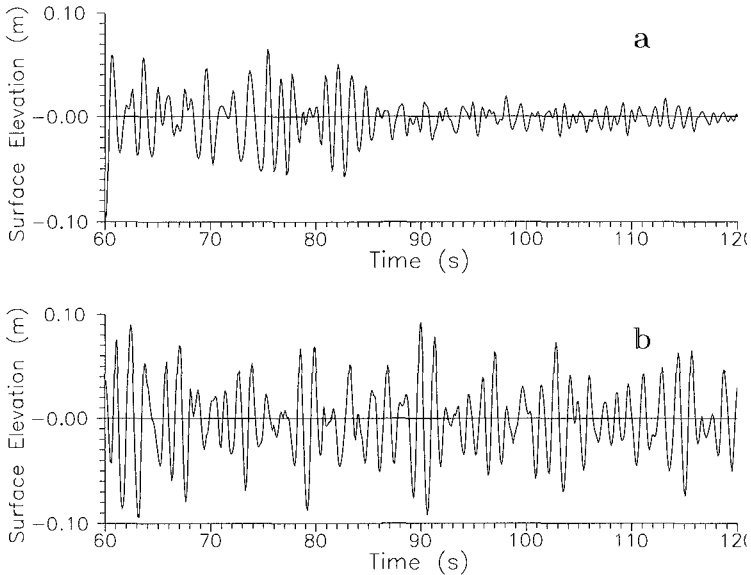


Figure 5: Time series obtained with (a) and without absorption (b).

Furthermore, the stability of the system was tested.

Again, the reflecting wall was mounted at the far end of the channel. The active absorption system was applied, and a paddle displacement time series of length  $T = 51.2$ s was generated, and sent repeatedly to the wave maker.

Two surface elevation time series of length  $T$  were recorded starting from  $t = T$  and  $t = 25T$ , respectively, and the incident and reflected spectra were resolved. The resulting incident spectra are given in fig. 6.

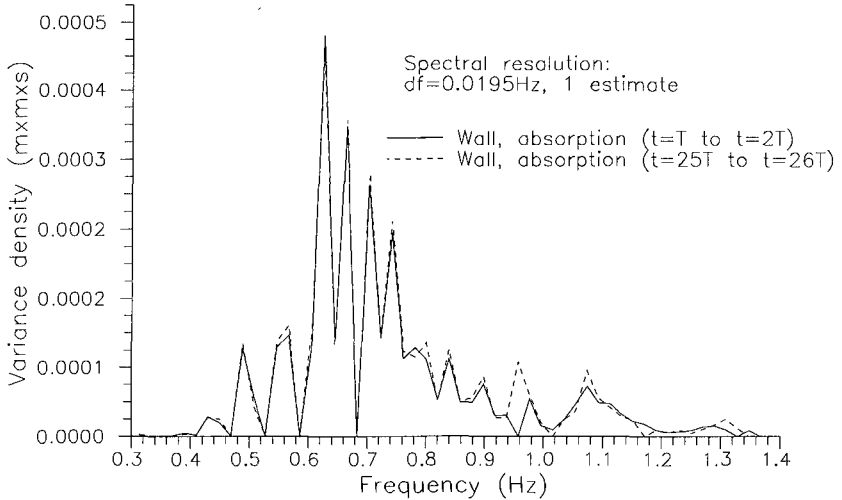


Figure 6: Incident wave spectra.

Fig. 6 indicates that the system is stable. Apparently, 25 repetitions of the input signal (approx. 20 minutes of wave generation) have not caused significant disturbance in the incident spectrum despite reflection from the wall at the channel termination.

The geometry of the wave channel in the CIEM at LIM/UPC and the wave gauge positions are given in fig. 7.

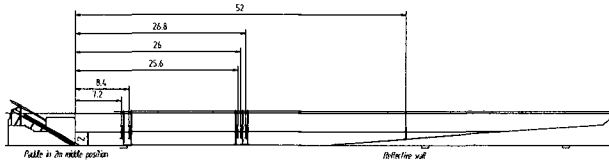


Figure 7: Wave channel and wave gauge positions.

In this test, the reflection compensation system was based on surface elevation measurements obtained in wave gauges positioned at distances of  $x_1 = 7.20m$  and  $x_2 = 8.40m$  from the wave paddle. The phase  $\phi_B$  and gain  $B$  were determined using the linear transfer functions derived by Biesel (1951). An additional phase shift was introduced in order to compensate for a measured time delay of  $0.1s$  between demand and feedback signals in the wave maker control system.

When reflection compensation was applied, the surface elevation time series were recorded and digitised by means of a PC equipped with an A/D-D/A-card, digital filtering and superposition was performed, and the resulting paddle displacement correction signal was added to the input signal read from the signal generator.

At the far end of the channel, a spending beach was situated. In order to be able to perform tests with different degrees of reflection from the channel termination, a vertical reflecting wall could be placed in front of the spending beach.

The channel was equipped three wave gauges mounted at distances of  $25.6m$ ,  $26.0m$  and  $26.8m$  from the wave paddle. These gauges were used for reflection measurements.

A water depth of  $d = 2.0m$  was maintained throughout the test series.

All tests were performed with exactly the same input from the signal generator: a wave paddle displacement signal corresponding to a JONSWAP-spectrum with significant wave height  $H_s = 0.25m$ , peak period of  $T_p = 3s$  and peak enhancement factor  $\gamma = 3.3$  sampled at a frequency of  $f_s = 20Hz$  and generated by means of digital filtering of Gaussian white noise in the time domain.

In each test, the incident and reflected spectra were resolved as described by Mansard and Funke (1980).

The spending beach had a reflection coefficient of only 6-8 % in the frequency range of the input spectrum. Consequently, the incident spectrum measured with the spending beach at the far end of the channel and no reflection compensation applied may be regarded as the target spectrum: the disturbances introduced by rereflection are negligible.

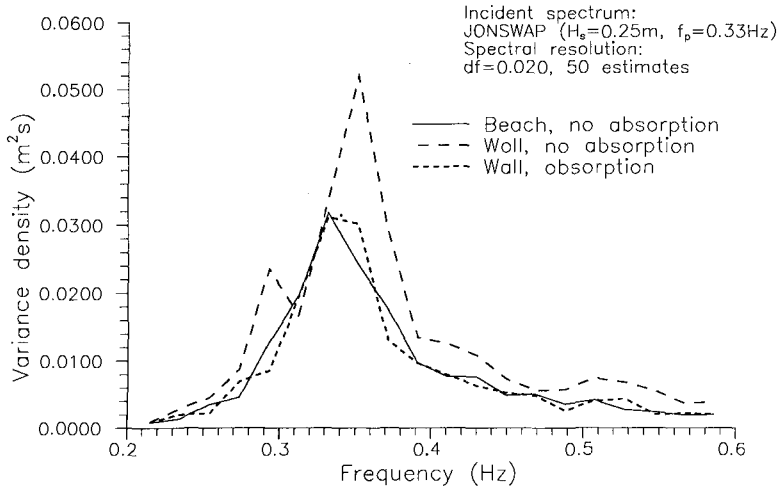


Figure 8: Incident wave spectra.

In fig. 8 the efficiency of the active absorption system is demonstrated. The figure shows that the tests in the large flume are very comparable to the tests in the small flume.

The performance of the reflection compensation system developed at Aalborg University (AU) appears to be excellent. When the system is applied to the test with a spending beach at the channel termination, the measured incident spectrum is almost identical to the target spectrum (fig. 4 and fig. 8). This implies, that applying this reflection compensation system to tests involving test structures with little reflection will not introduce disturbances in the incident spectrum.

LONG WAVES

Laboratory tests with irregular waves often give problems with absorption of long waves. Absorption of long waves requires an enormous stroke of the paddle. This means, that the designer of the filters always have to limit the low frequent performance of the system in order to have enough stroke in the wave maker system. Fig. 9 shows the performance of the system used in the tests at Aalborg Hydraulics Laboratory. Even though the figure indicates a rather poor performance of the system for long waves, it should be noted that as long as the system absorbs a part of the re-reflected waves it will prevent the growth of long waves.

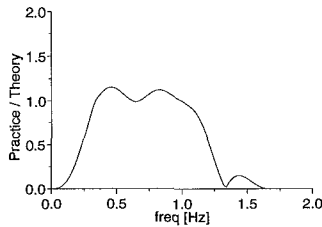


Figure 9: Performance of system.

CONCLUSION

A method for active absorption of reflected waves in wave channels by means of an absorbing wave maker has been presented. (Notice, that the system also can be very usefull in numerical models).

The motion of the wave maker, which is needed for absorption, is determined by means of digital filtering and subsequent superposition of surface elevations measured in two fixed positions in front of the wave maker.

The method has been implemented in the control system of a piston-type wave maker installed in a wave channel, and irregular wave tests involving test structures with different degrees of reflection have been carried out in order to determine the performance of the absorbing wave maker.

The tests performed imply that excellent absorption characteristics have been achieved. The absorbing wave maker is capable of reducing the problem of rereflection considerably even at very high levels of reflection. Furthermore, the active absorption system appears to be stable.

Converting a conventional wave maker to an absorbing wave maker based on the method presented above is relatively inexpensive considering the improvements achieved: the only requirements are two conventional wave gauges and a PC



equipped with an A/D-D/A-card. These facilities will normally already be available in most laboratory environments (if a PC equipped with an A/D-D/A-card is used as signal generator for the wave maker, the wave gauges can be connected to this computer, allowing the computer to perform signal generation and correction signal calculation simultaneously).

## ACKNOWLEDGEMENTS

The authors would like to thank the Danish Technical Research Council for financial support and the LIM/UPC for the use of the large flume.

## REFERENCES

- Biesel, F., 1951. Les Appareils Generateurs de Houle en Laboratoire. *La Houille Blanche*, Vol. 6, nos. 2, 4 and 5.
- Bullock, G.N. and Murton, G.J., 1989. Performance of a Wedge Type Absorbing Wave Maker. *Journal of Waterway, Port, Coastal and Ocean Engineering*, Vol. 115, No. 1.
- Christensen, M. and Høgedal, M., 1994. Reflection Compensation in the CIEM, LIM/UPC – Test Report. Aalborg University
- Frigaard, P. and Brorsen, B., 1993. A Time Domain Method for Separating Incident and Reflected Irregular Waves. To be published in *Coastal Engineering*.
- Gilbert, G., 1978. Absorbing Wave Generators. Hydr. Res. Station notes, Hydr. Res. Station, Wallingford, Oxon, United Kingdom, 20, 3-4.
- John H. Karl, 1989. *An Introduction to Digital Signal Processing*. Academic Press, San Diego.
- Mansard, E. and Funke, E., 1980. The Measurement of Incident and Reflected Spectra Using a Least Squares Method. *Proceedings, 17th International Conference on Coastal Engineering*, Vol. 1, pp 154-172, Sydney, Australia.
- Milgram, J.S., 1970. Active Water-Wave Absorbers. *J. Fluid Mech.*, 43(4), 845-859.

## CHAPTER 14

### Wave Climate Study in Wadden Sea Areas

Ralf Kaiser<sup>1</sup>, Günther Brandt<sup>1</sup>, Joachim Gärtner<sup>2</sup>, Detlef Glaser<sup>1</sup>,  
Joachim Grüne<sup>3</sup>, Frerk Jensen<sup>4</sup>, Hanz D. Niemeyer<sup>1</sup>

#### Abstract

Significant features on Wadden Sea wave climate are evaluated in respect of the state of the art. Main emphasis was laid on an analysis of the governing boundary conditions of local wave climate in island sheltered Wadden Sea areas with extensions being sufficient for local wind wave growth. Explanatory for significant wave heights a reliable parametrization of local wave climate has been evaluated by using generally available data of water level and wind measurements.

#### Introduction

In the German Bight comprehensive wave climate investigations in six distinct Wadden Sea areas have been carried out in recent years (fig. 1). Each of them represents a significant type of Wadden Sea coastal areas: Mesotidal barrier island coasts where the protective islands are seaborne or remnants of former mainland and macrotidal estuarine coasts [NIE-

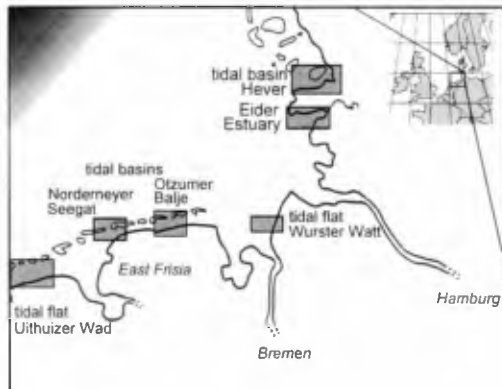


**Fig. 1:** Investigation areas on Wadden Sea Wave climate in the German Bight

<sup>1</sup>Coastal Research Station of the Lower Saxonian Central State Board for Ecology, Nordemeyer/East Frisia, Germany

<sup>2</sup>Regional Board for Water Management (ALW), Heide, Germany

<sup>3</sup>Joint Research Facility Large Wave Channel, Hannover, Germany

<sup>4</sup>Regional Board for Water Management (ALW), Husum, Germany

MEYER 1990]. The measuring locations within each of these typical areas have been chosen in such a way, that each location itself represents the conditions of a significant part of the total area in respect of the typical morphological boundary conditions. Main aim of these investigations was to establish a parametrization for local wave climate in dependence of the distinct types of morphological boundary conditions of each area as a basis for a more general approach.

Wave climate in Wadden Seas is characterized by strong hydrodynamical-morphological interactions due to restriction of water depths and an often very complex three-dimensional underwater topography. Waves propagating from the offshore shelf via ebb deltas towards the flats break partly or completely experience significant energy dissipation. The generation of strong waves by local windfields on the intertidal flats depends remarkably on tidal elevation and on the wind-induced surge set-up. Therefore this effect is restricted to those limited time intervals for which these necessary boundary conditions occur. On the one hand a reliable forecasting of wave parameters is mostly not achievable by using generally known forecasting procedures, which have been evaluated in areas for less differentiated boundary conditions. On the other hand as useful field data are still very poor the need for such data is tremendous.

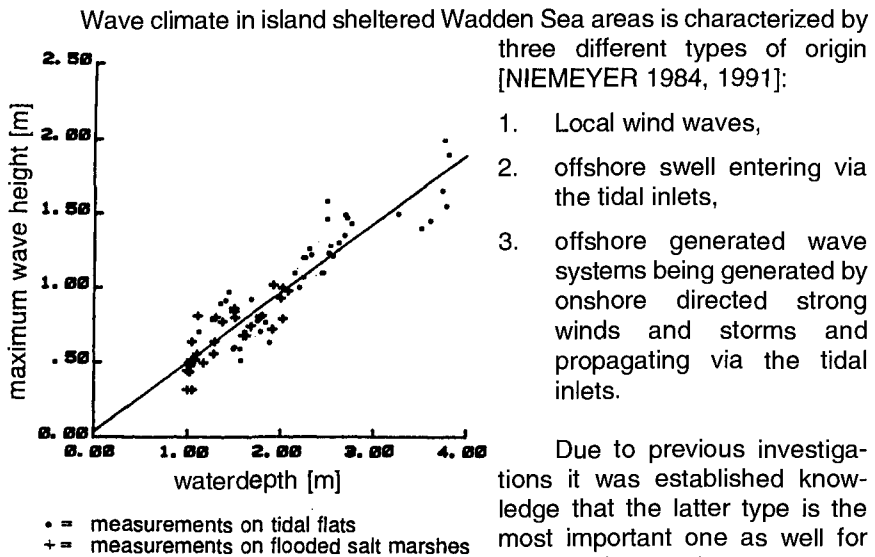


**Fig. 2:** Wave height/water depth relation for island sheltered tidal flat areas and salt marshes at the East Frisian coast [NIEMEYER 1991]

Due to previous investigations it was established knowledge that the latter type is the most important one as well for design of coastal structures as for impacts on tidal flat and salt marsh morphology [NIEMEYER 1983]: The dynamical equilibrium

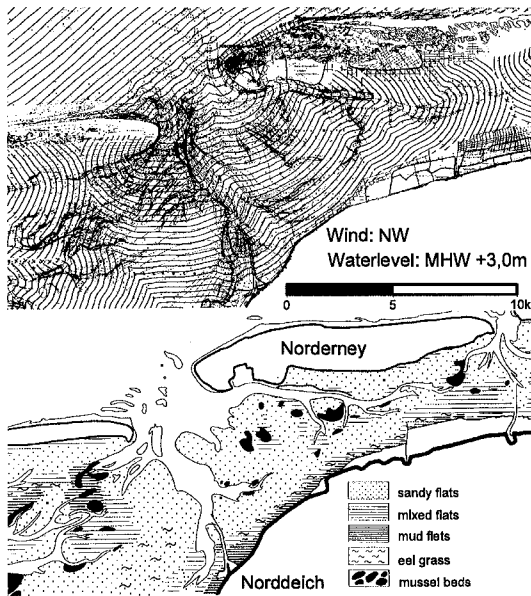


**Fig. 3:** Combination of refraction diagram and map of surface sediments for the Norderneyer Seegat [NIEMEYER 1987b]; map of surface sediments by RAGUTZKI [1982]

succession of sandy, mixed and muddy flats follows the wave propagation from the inlet to the main land. The sector of wave propagation with only modest refraction coincides with the smallest band of mixed and muddy flats in front of the mainland. Due to the dominant changes the wave climate experiences on the tidal inlet bar [NIEMEYER 1987a], wave propagation landward of the inlet is mainly independent from offshore wind direction and setup above mean high water level [NIEMEYER 1986]. There are also small muddy and sandy flats landwards in wave direction of the mussel beds.

Although the data of Wadden Sea waves for the areas above MSL fits generally to the linear relationship  $H_w/h$  one has to be aware that different boundary conditions generate distinct spectral energy distributions which is evident by examples of wave spectra (fig. 4) taken from NIEMEYER et al. [1992]. For spectrum No. 107 the still water level is about 1m above MHW and there are wind velocities of 11 m/s from NNW. Energy is distributed over the range from 15-3 seconds, with even higher energy for lower frequencies. For the same water level occurring in coincidence with higher wind velocities from more westerly directions spectrum no. 43 shows a more pronounced peak energy concentration, but its total energy is only about 20% higher than that

between morphologically stable tidal flats above mean sea-level and waves of type 3 is characterized by a strong linear relationship of local wave heights and water depths which is also valid for adjacent supratidal salt marshes (Fig. 3). The relationship is strictly fitting for onshore directed strong winds and storm but is only valid for areas above MSL.

A combination of refraction diagram and a map of surface sediments has been used by NIEMEYER [1987b] in order to demonstrate the interaction of waves and morphology and the resulting surface sediment distribution for the tidal basin of the tidal inlet Norderneyer Seegat (Fig. 3). The landward

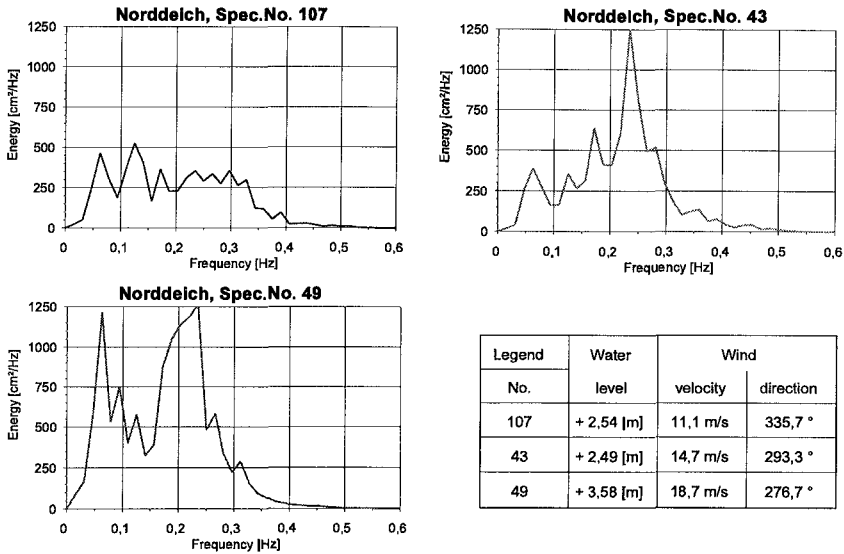


**Fig. 4:** Wave spectra for station Norddeich (see fig. 3) for different boundary conditions [NIEMEYER et al. 1992]

one of no. 107. Waterdepth and fetch for the spectrum No. 107 were more convenient in respect of generating higher waves. The high peak in spectrum No. 43 is due to waves entering from the North-Sea experiencing an energy shift to higher frequencies. An increase in water level of about 1m and higher wind velocities from west produced perform the boundary conditions for spectrum No. 49 with a significant low frequent high peak. For water levels with this height even longer waves with periods of about 15 s can penetrate into the Wadden Sea.

Regional characteristics of Wadden Sea wave climate

An detailed study on wave climate in distinct German Wadden Sea areas [NIEMEYER et al. 1992] reflects their remarkable morphodynamical features in the different regions causing specific characteristic interactions everywhere. Regional wave climate in a particular Wadden Sea area is therefore often very remarkably distinct from that one occurring in another one. Explanatory a comparison of the wave climate in the Hever tidal basin (fig. 1 + 5) and the East Frisian Wadden Sea coast is carried out in order to make differences evident as explained before. The East Frisian Wadden Sea is protected by sea built barrier islands and with relative small tidal basins. The Hever tidal basin has comparatively larger extensions (e. g. width up to 25 km), a wider spreaded tidal inlet and a lower ebb delta with shoals laying 3m below MSL.

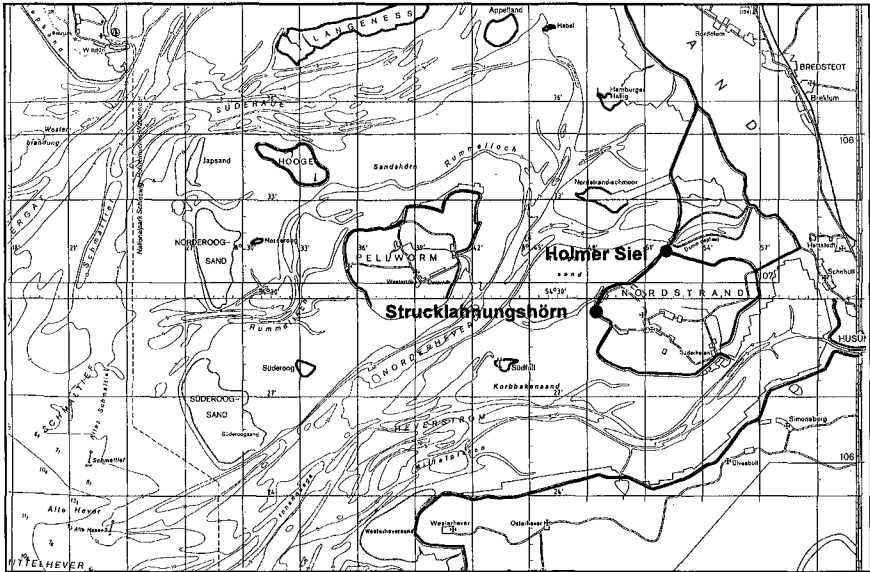


**Fig. 5:** Hever tidal basin with measuring locations Strucklahnungshörn and Holmer Siel

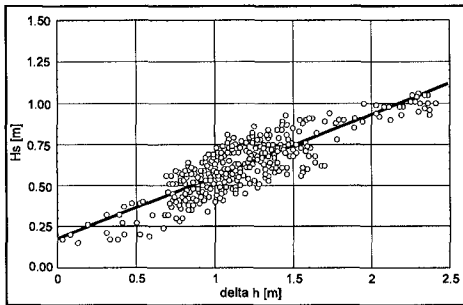


**Fig. 6:** Norddeich [ $H_s=0.177+0.378*\Delta h$ ]

The islands in this system are remnants of the former mainland. According to the hydrodynamical classification of tidal inlets [HAYES 1979] both areas are mesotidal and characterized by mixed energy, tide dominated [NIEMEYER 1990, NIEMEYER et al. 1992].

In the figures 6 to 8 significant wave heights versus wind-induced set-up is plotted for the stations Norddeich (fig. 3) at the mainland coast of the tidal basin of the Norderneyer Seegat and the stations Strucklahnungshörn in the tidal basin of the Hever (fig. 5). At the station Norddeich data represent strictly fitting linear relationship for the whole range of positive  $\Delta h$ -values with relative small scattering. The data of the station Strucklahnungshörn (fig. 7) reflect a more differentiated correlation of both parameters: There is no pronounced relationship between significant wave height and smaller values of  $\Delta h$ . With increasing  $\Delta h$  two distinct values of both parameters can be distinguished which identify

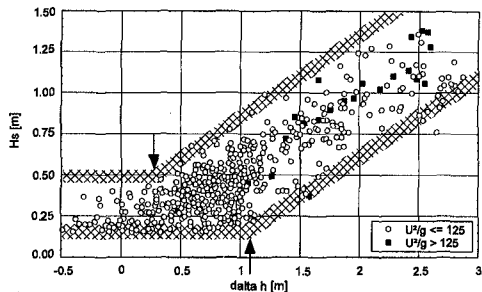


**Fig. 7:** Significant wave height as function of wind-set-up; Strucklannungshörn

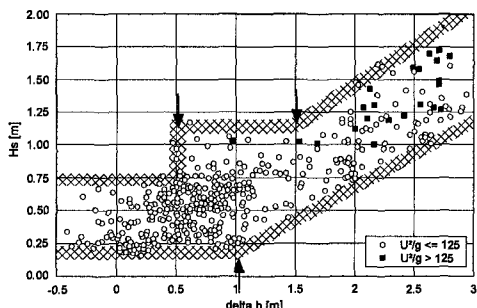


**Fig. 8:** Significant wave height as function of wind-set-up; Holmer Siel

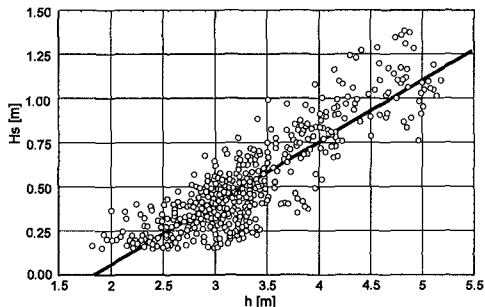


**Fig. 9:** Strucklannungshörn [Model:  
 $H_s = -0.633 + 0.347 h$ ]

the transition to a relationship for an upper and a lower value. Higher waves increase already for a lower  $\Delta h$ . Smaller waves need a larger critical value of  $\Delta h$  in order to fulfill the same linear relationship. The scattering of the data is significantly higher than for that one of the station Norddeich, which is also valid if only higher wind velocities are taken into consideration.

The station Holmer Siel (fig. 8) is situated landward of Strucklannungshörn. Regarding the correlation of the same parameters three distinct values of  $\Delta h$  mark significant changes. Similar to the data from Strucklannungshörn the significant wave heights cover a certain range of values for set-ups in the same order of magnitude. For a wind-set-up of about 0.5 m a rapid increase of the upper value of significant wave height variation is obvious but it remains constant for increasing  $\Delta h$  until the value of 1.5 m. Beyond that figure as well the upper limit as the lower limit of significant wave height variation increase with the set-up whereas the lower one starts already to increase from a set-up of about 1.0 m.

It is of great importance to find a reliable parametrization of local wave climate in order to make the results of field data analysis for a broader range of applications suitable and easily adaptable for coastal managers. Therefore relations are

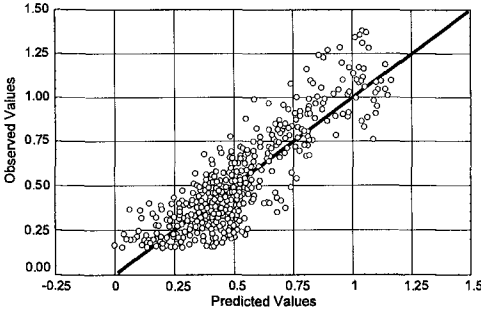


**Fig. 10:** Strucklahnungshörn [Model:  $H_s = -0.633 + 0.347 h$ ];  $r = 0.859$

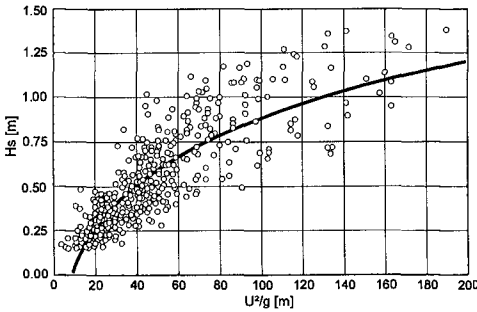


**Fig. 11:** Strucklahnungshörn [Model:  $H_s = 1.757 + 1.231 (U^2/g)^{0.166}$ ]

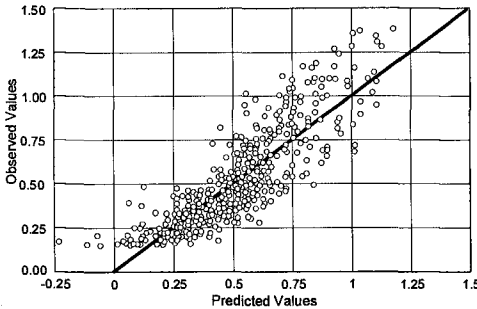


**Fig. 12:** Strucklahnungshörn [Model:  $H_s = -1.76 + 1.23 (U^2/g)^{0.166}$ ];  $r = 0.84994$

required which on the one hand vary only to a small extent and can on the other derived from a small number of parametrized boundary conditions. Comparing the correlation of the significant wave-height and local water depth for the station Strucklahnungshörn (Fig. 9) with the same one island sheltered tidal flat areas and salt marshes at the East Frisian coast, it becomes evident that the first one in respect of its statistical quality must be regarded as insufficient for a reliable parametrization of local wave climate in the basin of the Hever inlet. Correlating significant wave heights with local water-depths and plotting observed against predicted values (Fig. 10), there are deviations of more than  $\pm 35\%$ . The strength of the relationship given by the coefficient of determination is  $r^2 = 0.74$ . Doing the same for significant wave heights and local wind velocities (Fig. 11) for the station Strucklahnungshörn the relationship is in agreement with the physical process nonlinear. The results of the nonlinear regression model scatter as well as that one for the linear wave height / water-depth regression (fig. 9) in relation to measured data. Evaluating the fit of the model by the correlation of predicted versus observed values there

are also large deviations and the coefficient of determination has a similar value:  $r^2 = 0.72$  (Fig. 12).



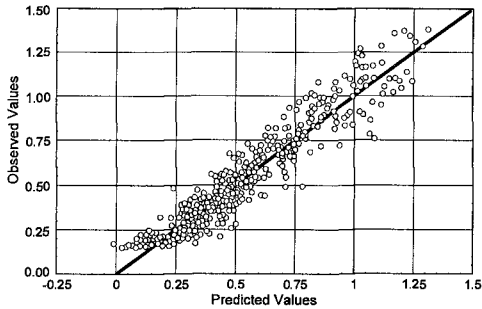


**Fig. 13:** Struckklahnungshörn [Model:  $H_s = -0.81 + 0.21 h + 0.16 (U^2/g)^{0.372}$ ];  $r = 0.950$

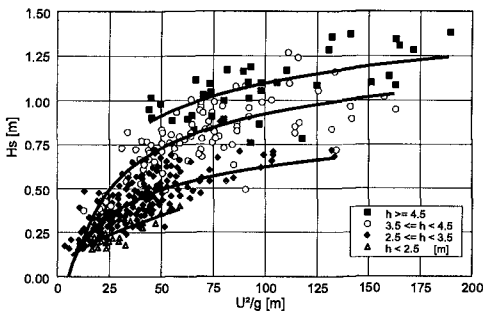


**Fig. 14:** Struckklahnungshörn, Models:  $H_s = f(U^2/g)$  differentiated for four ranges of water depth

The boundary conditions waterdepth and local windfields effect the local wave climate interactively by superimposing each other. These combined effects are described by the following equation:  $H_s = f(h, U)$ . According to the physical background the model for the estimation of the relationship has a linear term for waterdepth and a nonlinear one for the wind velocity (fig. 13). The scatterplot of values predicted by this model versus observed wave heights show much smaller deviations of about 25% in comparison with those ones which estimate significant wave heights by considering only one boundary condition. The coefficient of determination is  $r^2 = 0.903$  which can directly be compared with those ones gained previously, because they are calculated for the same data set. But for a reliable parametrization of local wave

climate this result is still insufficient. In order to improve the empirical relationship by a more differentiated consideration of boundary conditions we have to break down the data of water levels and wind into different groups. The creation of four data subsets for different ranges of water depths allow a deeper insight into the processes governing local Wadden Sea wave climate (fig. 14): The significant wave heights are plotted versus the local wind velocities for four distinct water level subsets. Incorporated are additionally the nonlinear regression models for the different groups, but the scattering is significantly large. Due to the limiting condition of the water depth even higher wind velocities result in lower wave heights for lower water depth. The limitation of local wave heights due to water depth are stronger than could be expected in respect of the shallow water breaking criteria. This effect has already been detected for East and West Frisian Wadden Sea areas [NIEMEYER 1983] and is obviously a typical feature of wave climate in island sheltered Wadden Sea areas.

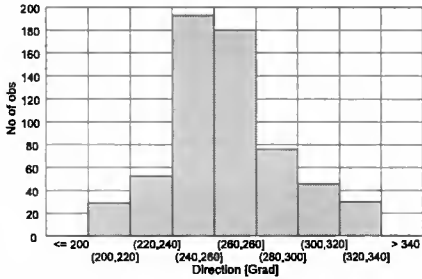


**Fig. 15:** Wind Strucklahnungshörn; numbers of observations for wind directions from 200° to 340°

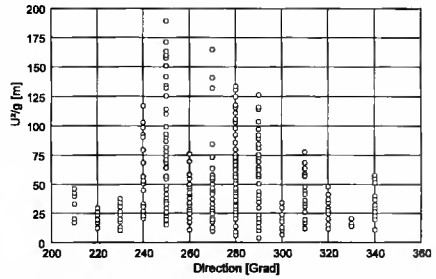


**Fig. 16:** Wind Strucklahnungshörn; distribution of velocities in respect of directions

For coastal areas and particularly regions like the Wadden Sea with their complex morphology the orientation to the open sea and the wind direction are of great importance because they determine both wave growth and energy dissipation. Therefore a differentiation in respect of wind directions seems to be an appropriated approach. The distribution of both the numbers of observations and the wind velocities in respect of the relevant sectors for the Hever inlet are documented in the figures 15 and 16. Due to measurement procedures the distribution of wind observations in these graphs is dependent of wave measurements, because these measurements were triggered by distinct wave height or water depth exceedence levels and reflect therefore situations with higher water levels and higher waves. Highest waves could be expected in the Hever tidal basin for wind from the sector South-West to North-West. Grouping the data sets for the wind directions from 240° to 290° for sectors of 10° is used to produced differentiated data sets for the nonlinear model  $H_s = f(h, U)$ . The fit of the nonlinear model  $H_s = f(h, U)$  after grouping for different wind directions has generally improved (fig. 17-22). Particularly for the sectors 240°, 250° and 270° the relationship has a very high significance.

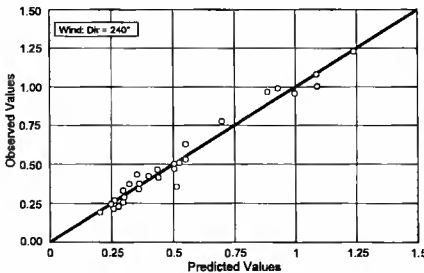


**Fig. 17:** Strucklahnungshörn [Model:  $H_s = -1.32 + 0.27 h + 0.27 (U^2/g)^{0.34}$ ]  $r = 0.98453$

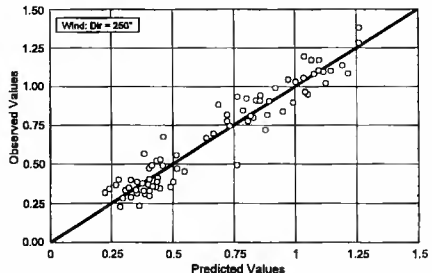


**Fig. 18:** Strucklahnungshörn [Model:  $H_s = -1.84 + 0.27 h + 0.93 (U^2/g)^{0.13}$ ]  $r = 0.96238$

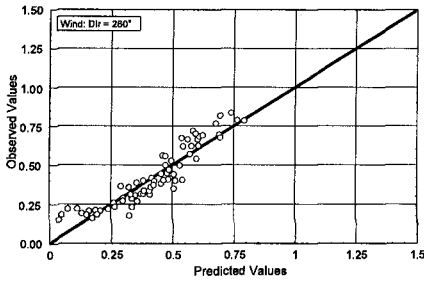


**Fig. 19:** Strucklauhningshörn [Model:  $H_s = 1.25 + 0.22 h + (-2.58) (U^2/g)^{-0.16}$ ]  
 $r = 0.92363$

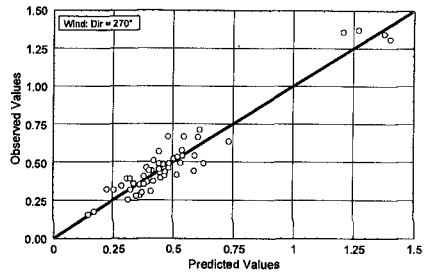


**Fig. 20:** Strucklauhningshörn [Model:  $H_s = -0.24 + 0.16 h + 0.003 (U^2/g)^{1.09}$ ]  
 $r = 0.95980$

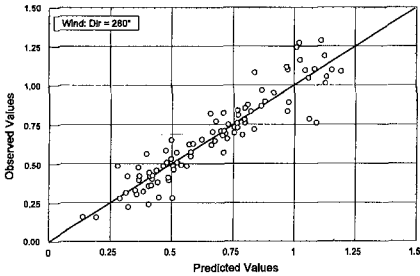


**Fig. 21:** Strucklauhningshörn [Model:  $H_s = -0.63 + 0.23 h + 0.06 (U^2/g)^{0.50}$ ]  
 $r = 0.93208$

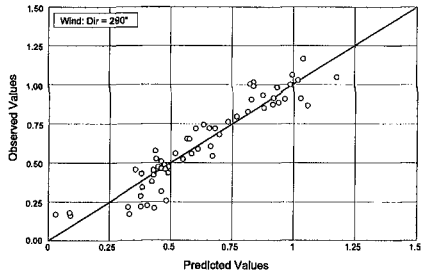


**Fig. 22:** Strucklauhningshörn [Model:  $H_s = -0.76 + 0.24 h + 0.11 (U^2/g)^{0.40}$ ]  
 $r = 0.93705$

### Conclusions:

- In island sheltered Wadden Sea areas with large onshore-offshore extensions local wind effects on wave climate cannot be neglected. The simple wave height / waterdepth relation is therefore no longer sufficient for a parametrization of Wadden Sea wave climate.
- The maximum wave heights in Wadden Sea areas are limited by water depths by a critical value below the shallow water breaking limit. They are independent from wind velocities beyond a certain level but depend on wind direction in respect of both wave growth and energy dissipation.

References

- HAYES, M.O. [1979]:** Barrier island morphology as a function of tidal and wave regime. in: S. P. Leatherman: Barrier islands, Academic Press, New York, pp. 1-27
- NIEMEYER, H.D. [1983]:** On the Wave Climate at Island Sheltered Wadden Sea Coasts (in German). BMFT-Forschungsbericht MF 0203
- NIEMEYER, H.D. [1984]:** Hydrographische Untersuchungen in der Leybucht zum Bauvorhaben Leyhörn. Jber. 1983 Forsch.-Stelle f. Insel- u. Küstenschutz, Bd. 35
- NIEMEYER, H.D. [1986]:** Ausbreitung und Dämpfung des Seegangs im See- und Wattengebiet von Norderney. Jber. 1985 Forsch.-Stelle Küste, Bd. 37
- NIEMEYER, H.D. [1987a]:** Changing of wave climate due to breaking on a tidal inlet bar. Proc. 20th Intern. Conf. o. Coastal Eng. Taipei, ASCE, New York
- NIEMEYER, H.D. [1987b]:** Seegang und Biotopzonierung in Wattgebieten. in: Niedersächsischer Umweltminister: Umweltvorsorge Nordsee - Belastungen - Gütesituation - Maßnahmen -. Hildesheim
- NIEMEYER, H.D. [1990]:** Morphodynamics of tidal inlets. Civ. Eng. Europ. Course Prog. o. Cont. Educ. Coast. Morph., Syll. Delft Univ. o. Tech. Int.-Int. Civ. Eng.
- NIEMEYER, H.D. [1991]:** Case study Ley Bay: an alternative to traditional enclosure. Proc. 3<sup>rd</sup> Conf. Coast & Port Eng. i. Devel. Countr., Mombasa/Kenya
- NIEMEYER, H.D. ; GÄRTNER, J. & GRÜNE, J. [1992]:** Naturuntersuchungen von Wattseegang an der deutschen Nordseeküste. Schlußbericht zum BMFT-Forschungsvorhaben MTK 464 B
- RAGUTZKI, G. [1982]:** Verteilung der Oberflächensedimente auf den niedersächsischen Watten. Jber. 1980 Forsch.-Stelle f. Insel- u. Küstenschutz, Bd. 32

## CHAPTER 15

# FALSE WAVES IN WAVE RECORDS AND NUMERICAL SIMULATIONS

Marcos H. Giménez<sup>1</sup>, Carlos R. Sánchez-Carratalá<sup>2</sup> and Josep R. Medina<sup>3</sup>

### ABSTRACT

It is common practice to consider the random waves as a succession of discrete waves characterized by individual amplitudes and periods. The zero-up-crossing criterion isolates some discrete waves that are not physical waves. The orbital criterion avoids these "false waves". As a result, the orbital criterion proves to be more consistent and robust, and to have a less variability. The selection of the discretization criterion results in some significant differences in the wave statistics, which are analyzed. As an example, while the mean period for the zero-up-crossing criterion is  $T_{0z}$ , the mean period for the orbital criterion is  $T_{0o}$ .

### INTRODUCTION

Regular waves can be characterized by amplitude and period, and random waves may be described by the energy spectrum. However, it is common practice to consider the random waves as a succession of "discrete waves" characterized by individual amplitude and period.

---

<sup>1</sup> Ass. Prof., Dept. of Applied Physics, EUITI, Universidad Politécnica de Valencia, Camino de Vera s/n, 46022, Valencia, SPAIN.

<sup>2</sup> Ass. Prof., Dept. of Applied Physics, ETSICCP, Universidad Politécnica de Valencia, Camino de Vera s/n, 46022, Valencia, SPAIN.

<sup>3</sup> Professor, Director of the Lab. of Ports and Coasts, Dept. of Transportation, ETSICCP, Universidad Politécnica de Valencia, Camino de Vera s/n, 46022, Valencia, SPAIN.

Unfortunately, a variety of reasonable criteria for discretizing waves have been proposed by different authors. In fact, any method used to define a discrete wave in regular waves could be extended to the case of random waves.

A number of papers are related to wave statistics and may be affected by the wave discretization procedure. Moreover, a variety of subjective criteria are used for neglecting small waves in the analysis.

Giménez et al. (1994) have proposed an orbital criterion for discretizing waves. Using numerical simulations, the authors have proved that this method is more consistent and robust than the zero-up-crossing criterion. These results are in good agreement with the observations given by Pires-Silva and Medina (1994) analyzing wave records off the coast of Portugal.

This paper describes first the most common wave discretization methods, and summarizes the concepts and properties of "orbital wave" and "false wave". The advantages of the orbital criterion are presented, including consistency, robustness and a less variability. Finally, the influence of the wave discretization criteria on the wave statistics is analyzed using numerical simulations.

## WAVE DISCRETIZATION CRITERIA

The more commonly used wave discretization criteria are the following:

### \* The ZUC criterion

In the zero-up-crossing criterion, a discrete wave is limited by two consecutive up-crossings of the mean level. Following Rice (1954), Longuet-Higgins (1958) showed that for linear random waves the mean period using the ZUC criterion is  $T_{02}$ , where  $T_{ij}$  is given by:

$$T_{ij} = \sqrt[j-i]{\frac{m_i}{m_j}} \quad (1)$$

where  $m_n$  is the  $n$ th moment of the energy spectrum  $S(f)$ ,

$$m_n = \int_0^{\infty} f^n S(f) df \quad (2)$$

### \* The ZDC criterion

In the zero-down-crossing criterion, a discrete wave is limited by two consecutive down-crossings of the mean level. For linear random waves, the ZUC and the ZDC criteria are statistically equivalent. Therefore, the mean period using the ZDC criterion is also  $T_{02}$ .

\* The crest-to-crest criterion

In the crest-to-crest criterion, a discrete wave is limited by two consecutive maxima of the surface displacement function. From Rice (1954), it can be proved that the mean period using the crest-to-crest criterion is  $T_{2\alpha}$ .

**THE ORBITAL CRITERION**

For linear waves, the free surface elevation in a fixed point,  $\eta(t)$ , can be modeled by:

$$\eta(t) = \sum_{i=1}^M c_i \cos(2\pi f_i t + \varphi_i) \quad (3)$$

where the frequencies  $f_i$  are  $i\Delta f$ , the phases  $\varphi_i$  are random variables distributed uniformly over the interval  $[0, 2\pi[$ , and the amplitudes  $c_i$  are such that over any frequency interval  $[f_i, f_i + \Delta f[$  is:

$$\frac{1}{2} c_i^2 = \int_{f_i}^{f_i + \Delta f} S(f) df \quad (4)$$

The Hilbert transform of  $\eta(t)$  is:

$$\hat{\eta}(t) = \sum_{i=1}^M c_i \sin(2\pi f_i t + \varphi_i) \quad (5)$$

The functions  $\eta(t)$  and  $\hat{\eta}(t)$  can be taken as the real and the imaginary part, respectively, of the analytical function  $AF(t)$ :

$$AF(t) = \sum_{i=1}^M c_i \exp[j(2\pi f_i t + \varphi_i)] = \eta(t) + j\hat{\eta}(t) \quad (6)$$

where  $j = \sqrt{-1}$  is the imaginary unit.  $AF(t)$  can be expressed in the form:

$$\left. \begin{aligned} AF(t) &= A(t) \exp[j\theta(t)] \\ A(t) &= \sqrt{\eta^2(t) + \hat{\eta}^2(t)} \\ \theta(t) &= \arctan \frac{\hat{\eta}(t)}{\eta(t)} \end{aligned} \right\} \quad (7)$$

where  $A(t)$  is the wave envelope and  $\theta(t)$  is the phase angle. As noted by Medina and Hudspeth (1987),  $AF(t)$  represents the orbital movement of a point floating on the sea surface.

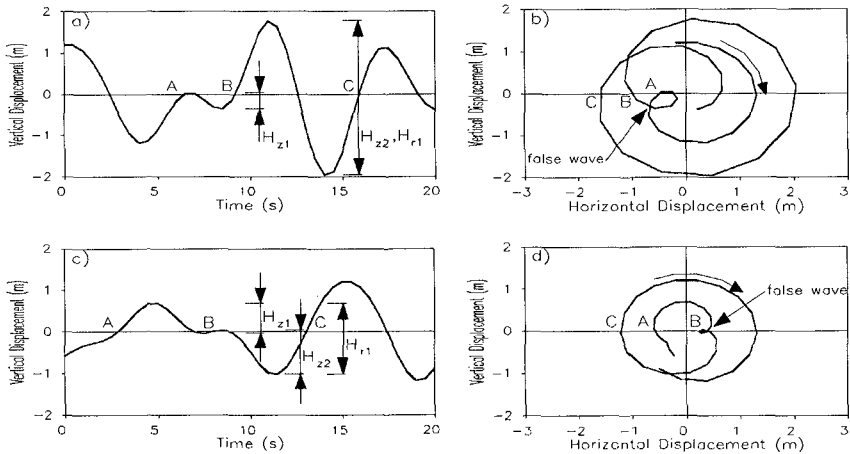


**Figure 1.-** ZUC criterion vs. orbital criterion: (a) example of time series; (b) orbital analysis of a); (c) example of time series; (d) orbital analysis of c).

According to Giménez et al. (1994), the orbital criterion defines a discrete wave as corresponding to a  $2\pi$  advance of the phase angle in the complex plane. Figures 1(a) and 1(c) show two pieces of numerical simulation from a JONSWAP spectrum. Figures 1(b) and 1(d) represent the corresponding analytical functions  $AF(t)$ . The ZUC and the orbital waves are denoted by  $H_z$  and  $H_o$ , respectively. In both pieces two ZUC waves (AB and BC), but only one orbital wave (AC), are present. The first small wave in Figure 1(a) is not considered by the orbital criterion. Furthermore, the two ZUC waves in Figure 1(c) are only one, and higher, wave in the orbital criterion.

Giménez et al. (1994) define false wave as any discrete wave that does not correspond to a  $2\pi$  advance in the complex plane. Examples of these false waves are shown in Figures 1(b) and 1(d). In the same reference, the authors prove (both, mathematically and numerically) that the mean period using the orbital criterion is  $T_{o1}$ . Furthermore, the discrepancy between  $T_{o1}$  and  $T_{o2}$ , is completely due to the presence of false waves.

## ADVANTAGES OF THE ORBITAL CRITERION

Because of its dependence of  $m_4$ , the crest-to-crest criterion is very sensitive to the cut-off frequency. On the other hand, the ZUC and the ZDC are statistically equivalent for linear random waves. Therefore, the ZUC criterion has been used as reference for analyzing the advantages of the orbital criterion. Giménez et al. (1994) have carried out that comparison, and have come to the next conclusions:



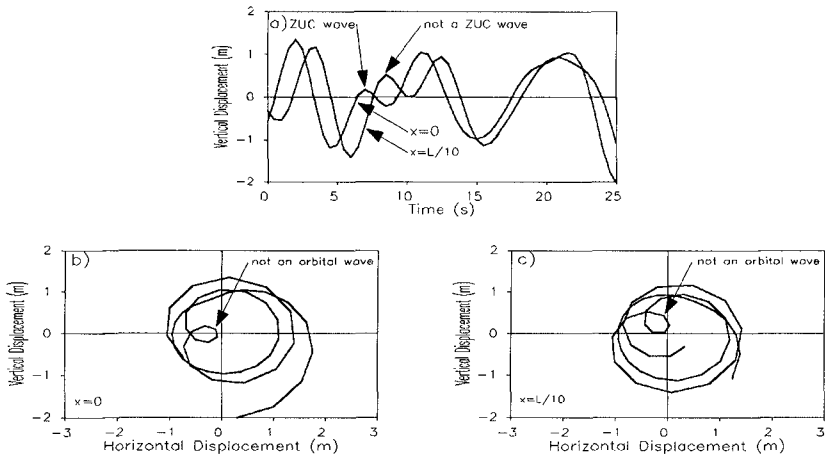


**Figure 2.-** ZUC criterion vs. orbital criterion: (a) time series of two close points; (b) orbital analysis of the first point; (c) orbital analysis of the second point.

#### \* Consistency

Figure 2(a) shows a numerical simulation of two time series corresponding to two points in the sea surface separated by 10% of the mean wavelength  $L$ . There is a perturbation that is a ZUC wave in  $x=0$ , but not in  $x=L/10$ . This physical inconsistency can be solved using the orbital criterion. Figures 2(b) and 2(c) show that the perturbation is a false wave.

Another problem of the ZUC criterion is the wide variety of subjective thresholds for neglecting small invalid waves (see Rye, 1974; van Vledder, 1983; Thompson and Seeling, 1984; Mansard and Funke, 1984; Mase and Iwagaki, 1986). For the orbital criterion, any wave that does not correspond to a  $2\pi$  advance of the phase angle is not an actual wave. No additional thresholds are required.

#### \* Robustness

Figure 3(a) shows a piece of simulation, and the same record when a 5% of white noise is added. Additional ZUC waves appear due to the presence of noise. However, Figure 3(b) shows that these waves are not orbital waves. In fact, most of the additional ZUC waves due to noise are false waves. Therefore, the ZUC criterion is more sensitive to noise than the orbital criterion.

Giménez et al. (1994) have analyzed the sensitivity to noise using numerical simulations. The mean period of orbital waves is underestimated about 2% when a 2% of white noise is added. On the contrary, the resulting error in the mean period of ZUC waves is about 10%. The underestimations with a 5% of white noise are about 5% for orbital waves, and 20-25% for ZUC waves.

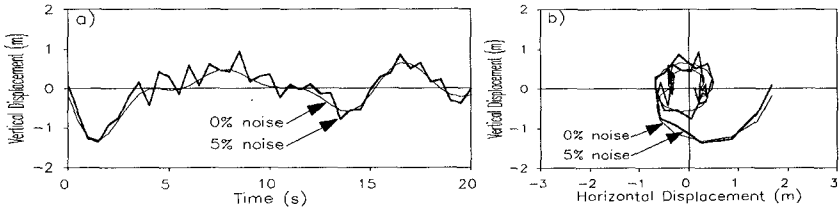


Figure 3.- Influence of white noise: (a) time series; (b) orbital analysis.

\* Less variability

As proved in Appendix A, the variabilities of the mean periods  $T_{01}$  and  $T_{02}$  are:

$$CV^2[T_{01}] = \frac{\int_0^\infty S^2(f) [T_{01}f - 1]^2 df}{m_0^2 T_R} \tag{8}$$

$$CV^2[T_{02}] = \frac{\int_0^\infty S^2(f) [(T_{02}f)^2 - 1]^2 df}{4m_0^2 T_R} \tag{9}$$

where  $CV[.]$  is the coefficient of variation and  $T_R$  is the length of the record. The result depends on the spectral shape. Table 1 shows the variability for JONSWAP type spectra (see Goda, 1985) with a peak frequency of 0.1 Hz and different values of the peak enhancement parameter  $\gamma$ . The mean period  $T_{01}$  proves to have a less variability than  $T_{02}$ .

$\gamma$	$CV[T_{01}]$	$CV[T_{02}]$
1	$0.677/\sqrt{T_R}$	$0.695/\sqrt{T_R}$
2	$0.686/\sqrt{T_R}$	$0.744/\sqrt{T_R}$
3.3	$0.678/\sqrt{T_R}$	$0.771/\sqrt{T_R}$
5	$0.655/\sqrt{T_R}$	$0.776/\sqrt{T_R}$
7	$0.623/\sqrt{T_R}$	$0.762/\sqrt{T_R}$
10	$0.577/\sqrt{T_R}$	$0.728/\sqrt{T_R}$

Table 1.- Variability of  $T_{01}$  and  $T_{02}$ .

## DISTRIBUTIONS OF WAVE HEIGHTS AND PERIODS

The mean period is not the only statistical parameter that is affected by the selected wave discretization criterion. The parameters related with discrete waves are altered in two ways. First of all, the presence of false waves varies significantly the number and characteristics of small waves. As a second effect, the total number of orbital waves in a record is less than the number of ZUC waves. Therefore, the relative number of higher waves is slightly greater in the orbital criterion than in the ZUC criterion.

A comparison between the statistics for orbital and ZUC waves has been developed using numerical simulations. These simulations were obtained using a DSA-FFT algorithm (see Tuah and Hudspeth, 1982) and a JONSWAP type spectrum (see Goda, 1985) with  $N=8192$  points and a time interval  $\Delta t=0.2$  sec. 1000 simulations were carried out for different values of the peak enhancement parameter ( $\gamma=1,2,3,3.3,5,7,10$ ). The number of simulated ZUC waves varies from about 180000 (for  $\gamma=10$ ) to 210000 (for  $\gamma=1$ ). The results for all the indicated values of  $\gamma$  have been analyzed, and figures corresponding to the extremal values  $\gamma=1$  and  $\gamma=10$  are included in this paper.

The methodology developed by Sobey (1992) was used for the statistical analysis of the simulations. Therefore, the wave periods were obtained by linear interpolation in the neighborhood of the zero-up-crossings. The wave heights were determined from quadratic interpolation at the crest and the trough. The wave heights were normalized by  $H_{ms}$ , and the wave periods by  $T_{01}$ . Finally, the waves were aggregated, according to their normalized height and period, into a joint histogram in  $0.025 \times 0.025$  dimensionless bins.

Figures 4(a) and 4(b) show the joint distributions of wave heights and periods, for  $\gamma=1$ , corresponding to the orbital and the ZUC criteria respectively. Figures 5(a) and 5(b) show the same distributions for  $\gamma=10$ . For both criteria, the distribution is bimodal. The external contour corresponds to points with a probability of 0.01. The other contours correspond to probabilities of 0.20, 0.40, 0.60 and so on. The values in the thicker lines are 0.01, 1.00 and 2.00.

A maximum is located near the point corresponding to  $H_{ms}$  and  $T_{01}$ . This maximum becomes higher for narrower spectra, and is slightly greater in the orbital criterion. On the other hand, the maximum corresponding to small waves has a less value for orbital waves.

Figures 6(a) and 6(b) show the distributions of wave heights for  $\gamma=1$  and  $\gamma=10$  respectively. The probability of both the orbital and the ZUC waves is underestimated by the Rayleigh distribution near its mode, and overestimated in the ranges of small and high waves. As expected according to the narrow band assumption, the fitting is slightly better for narrower spectra.

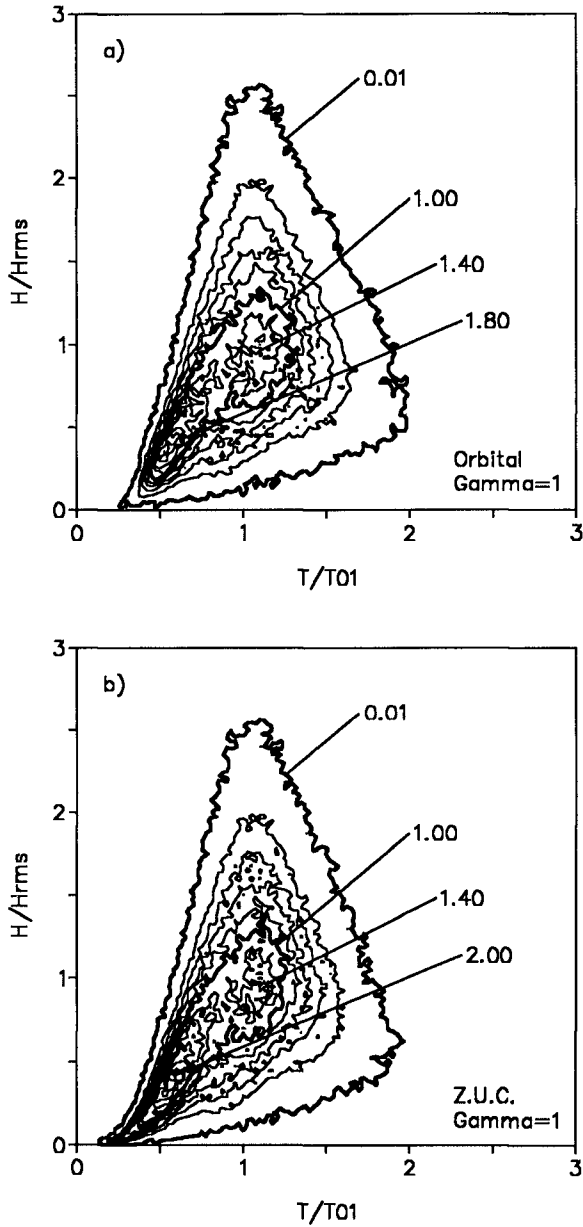


**Figure 4.-** Joint distributions of wave heights and periods for  $\gamma=1$ : (a) orbital waves; (b) ZUC waves.

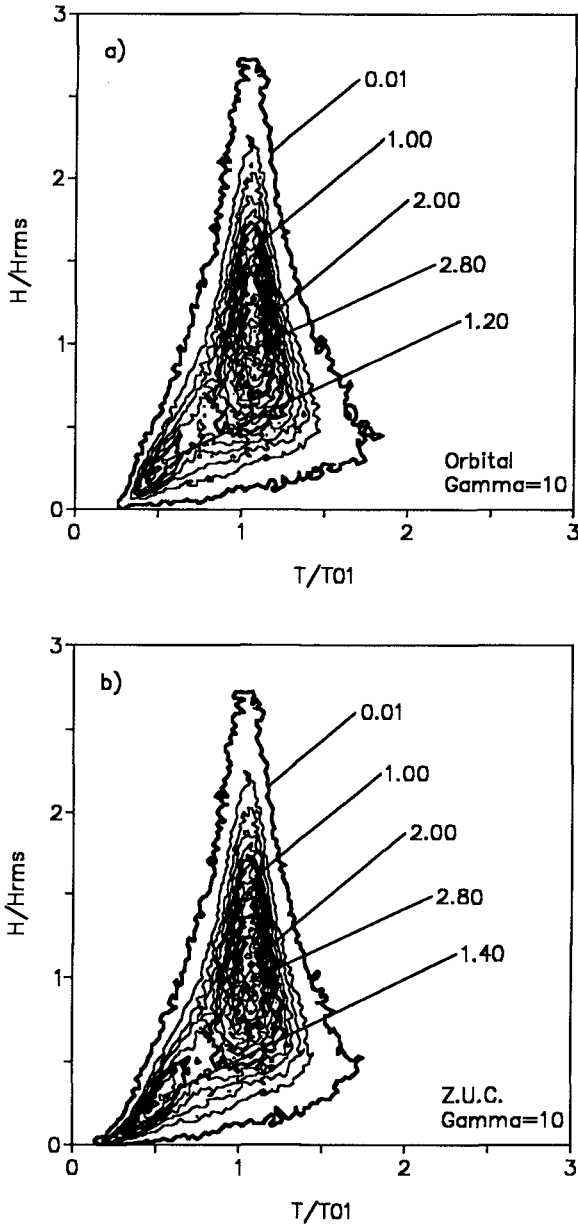


Figure 5.- Joint distributions of wave heights and periods for  $\gamma=10$ : (a) orbital waves; (b) ZUC waves.

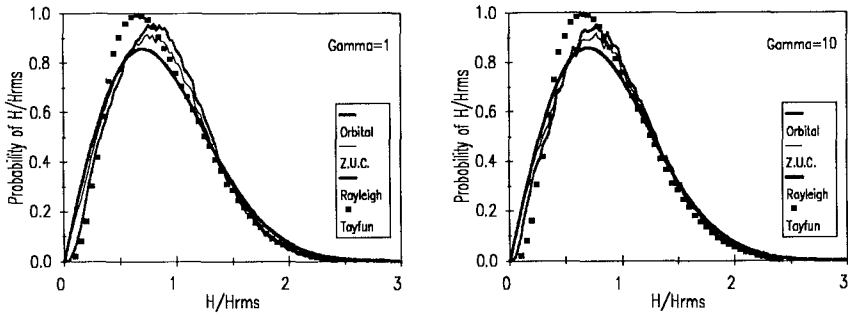


Figure 6.- Distributions of wave heights: (a)  $\gamma = 1$ ; (b)  $\gamma = 10$ .

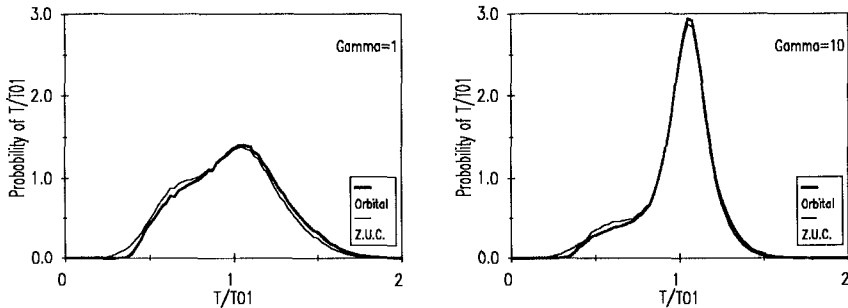
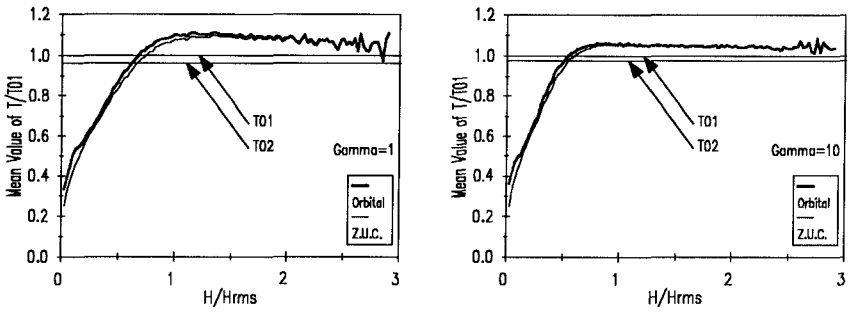


Figure 7.- Distributions of wave periods: (a)  $\gamma = 1$ ; (b)  $\gamma = 10$ .

A comparison between the distributions of orbital and ZUC wave heights leads to the next conclusions: in the orbital criterion, the probability is less in the range of small waves, greater around the mode, and nearly the same in the range of high waves. This behaviour could be expected due to the presence of false waves in the ZUC criterion.

Figures 6(a) and 6(b) also show the distribution of Tayfun (1981) corresponding to  $\nu=0.2$ . This distribution is based on the values of the envelope with a lag of  $T_{01}/2$ , and therefore is supposed to be more appropriate for orbital waves than for ZUC waves.

Figures 7(a) and 7(b) show the distributions of wave periods for  $\gamma=1$  and  $\gamma=10$  respectively. As noted above, the mean period is  $T_{01}$  for orbital waves and  $T_{02}$  for ZUC waves. It can be concluded from these distributions that the orbital waves have higher periods than the ZUC waves, as expected.



**Figure 8.-** Variation of the mean wave period as a function of the wave height: (a)  $\gamma=1$ ; (b)  $\gamma=10$ .

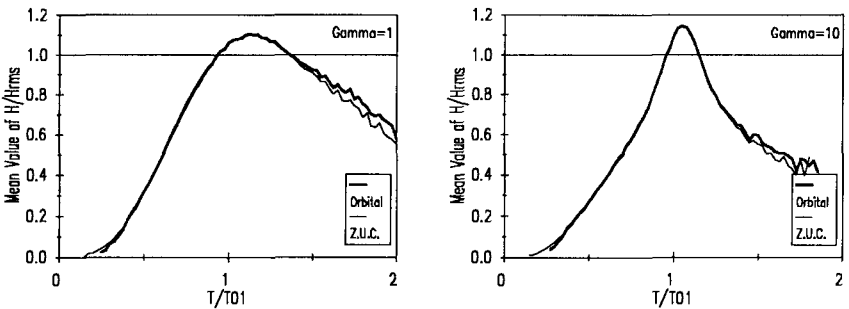


**Figure 9.-** Variation of the mean wave height as a function of the wave period: (a)  $\gamma=1$ ; (b)  $\gamma=10$ .

Figures 8(a) and 8(b) show the variation of the mean wave period for  $\gamma=1$  and  $\gamma=10$ , respectively, as a function of the wave height. The mean value of the orbital waves is greater for every wave height, especially in the range of small waves. Waves with  $H/H_{rms} > 0.5-0.7$  have a mean period over  $T_{01}$ , with a certain tendency to this value for higher waves.

Figures 9(a) and 9(b) show the variation of the mean wave height for  $\gamma=1$  and  $\gamma=10$ , respectively, as a function of the wave period. The greatest mean wave heights correspond to periods around  $T_{01}$ . The orbital waves have a larger mean wave height than the ZUC waves in the range of high periods.

## CONCLUSIONS

The ZUC criterion commonly used to discretize wave records generates discrete waves that do not correspond to physical waves. The orbital criterion avoids these "false waves", and proves to be more consistent and robust, and to have a less variability. Finally, the wave statistics are altered by the selection of the wave discretization criteria. The differences are basically located in the range of small waves, but some slight variations are also found for larger waves.

## ACKNOWLEDGEMENTS

The authors gratefully acknowledge the financial support provided by the Dirección General de Investigación Científica y Técnica (PB92-0411).

## APPENDIX A: VARIABILITY OF THE MEAN PERIODS

Random waves, taken as a Gaussian ergodic stochastic process, are described by the energy spectrum  $S(f)$ . When this spectrum is estimated from records of finite length  $T_R$ , the resulting  $M$  components are independent random variables. If  $T_R$  is large enough, then every component is distributed as a chi-squared law with two degrees of freedom. The mean and variance of this distribution are:

$$\left. \begin{aligned} E[S_{m,R}] &= S_m \\ \sigma^2[S_{m,R}] &= S_m^2 \end{aligned} \right\} \quad (A.1)$$

where  $S_m = S(m\Delta f)$  with  $\Delta f = 1/T_R$ , and  $S_{m,R}$  is the corresponding estimation. The  $i$ th moment of the estimated spectrum is:

$$m_{i,R} = \sum_{m=1}^M f_m^i S_{m,R} \Delta f \quad (A.2)$$

From (A.1) and (A.2), it can be proved that the mean of the random variable  $m_{i,R}$  is:

$$E[m_{i,R}] = m_i \quad (A.3)$$

and the covariance between the moments  $m_{i,R}$  and  $m_{j,R}$  is:

$$C[m_{i,R}, m_{j,R}] = \frac{1}{T_R} \int_0^\infty f^{i+j} S^2(f) df \quad (A.4)$$

The square of the coefficient of variation of  $m_{i,R}$  is:



$$CV^2[m_{i,R}] = \frac{C[m_{i,R}, m_{i,R}]}{E^2[m_{i,R}]} = \frac{1}{m_i^2 T_R} \int_0^\infty f^{2i} S^2(f) df \quad (A.5)$$

The period  $T_{ij} = (m_i/m_j)^k$ , where  $k = 1/(j-i)$ , cannot be determined when  $S(f)$  is unknown. On the other hand,  $T_{ij,R} = (m_{i,R}/m_{j,R})^k$  can be obtained from the estimated spectrum. However,  $T_{ij,R}$  is a random variable, and presents a certain variability. The objective of this appendix is to obtain an expression for that variability.

A Taylor expansion of  $T_{ij,R}$  and an integration lead to:

$$\begin{aligned} E[T_{ij,R}] &= \int_0^\infty \int_0^\infty T_{ij,R} p(m_{i,R}, m_{j,R}) dm_{i,R} dm_{j,R} \approx \\ &\approx T_{ij} \left[ 1 + \frac{k(k-1)}{2} CV^2[m_{i,R}] + \frac{k(k+1)}{2} CV^2[m_{j,R}] - k^2 \frac{C[m_{i,R}, m_{j,R}]}{m_{i,R} m_{j,R}} \right] \end{aligned} \quad (A.6)$$

The same method leads to:

$$\begin{aligned} E[T_{ij,R}^2] &= \int_0^\infty \int_0^\infty T_{ij,R}^2 p(m_{i,R}, m_{j,R}) dm_{i,R} dm_{j,R} \approx \\ &\approx T_{ij}^2 \left[ 1 + k(2k-1) CV^2[m_{i,R}] + k(2k+1) CV^2[m_{j,R}] - 4k^2 \frac{C[m_{i,R}, m_{j,R}]}{m_{i,R} m_{j,R}} \right] \end{aligned} \quad (A.7)$$

Therefore:

$$CV^2[T_{ij,R}] = \frac{E[T_{ij,R}^2] - E^2[T_{ij,R}]}{E^2[T_{ij,R}]} \approx k^2 \left[ CV^2[m_{i,R}] + CV^2[m_{j,R}] - 2 \frac{C[m_{i,R}, m_{j,R}]}{m_{i,R} m_{j,R}} \right] \quad (A.8)$$

From (A.4) and (A.5), if  $T_R$  is large enough, then  $CV[m_{i,R}]$ ,  $CV[m_{j,R}]$  and  $C[m_{i,R}, m_{j,R}]$  are much smaller than one, and, according to (A.6):

$$E[T_{ij,R}] = T_{ij} \quad (A.9)$$

Therefore, the random variable  $T_{ij,R}$  can be used for estimating  $T_{ij}$ , and the expression (A.8) gives the variability of the estimation. For  $T_{02}$  the result is:

$$\begin{aligned}
CV^2[T_{02,R}] &= \frac{1}{4} \left[ CV^2[m_{0,R}] + CV^2[m_{2,R}] - 2 \frac{C[m_{0,R}, m_{2,R}]}{m_{0,R} m_{2,R}} \right] = \\
&= \frac{1}{4} \left[ \frac{1}{m_0^2 T_R} \int_0^\infty S^2(f) df + \frac{1}{m_2^2 T_R} \int_0^\infty f^4 S^2(f) df - \frac{2}{m_0 m_2 T_R} \int_0^\infty f^2 S^2(f) df \right] = \quad (A.10) \\
&= \frac{1}{4 m_0^2 T_R} \int_0^\infty S^2(f) \left[ 1 + \frac{m_0^2}{m_2^2} f^4 - 2 \frac{m_0}{m_2} f^2 \right] df = \frac{1}{4 m_0^2 T_R} \int_0^\infty S^2(f) [(T_{02} f)^2 - 1]^2 df
\end{aligned}$$

This expression was obtained by Cavanié (1979). On the other hand, the variability of the estimation of  $T_{01}$  is:

$$\begin{aligned}
CV^2[T_{01,R}] &= CV^2[m_{0,R}] + CV^2[m_{1,R}] - 2 \frac{C[m_{0,R}, m_{1,R}]}{m_{0,R} m_{1,R}} = \\
&= \frac{1}{m_0^2 T_R} \int_0^\infty S^2(f) df + \frac{1}{m_1^2 T_R} \int_0^\infty f^2 S^2(f) df - \frac{2}{m_0 m_1 T_R} \int_0^\infty f S^2(f) df = \quad (A.11) \\
&= \frac{1}{m_0^2 T_R} \int_0^\infty S^2(f) \left[ 1 + \frac{m_0^2}{m_1^2} f^2 - 2 \frac{m_0}{m_1} f \right] df = \frac{1}{m_0^2 T_R} \int_0^\infty S^2(f) [T_{01} f - 1]^2 df
\end{aligned}$$

## REFERENCES

- Cavanié, A.G. (1979).** Evaluation of the Standard Error in the Estimation of Mean and Significant Wave Heights as well as Mean Period from Records of Finite Length. *Proc. Int. Conf. Sea Climatology*, 73-88.
- Giménez, M.H., Sánchez-Carratalá, C.R. and Medina, J.R. (1994).** Analysis of False Waves in Numerical Sea Simulations. *Ocean Engineering*, 21 (8), 751-764.
- Goda, Y. (1985).** *Random Seas and Design of Maritime Structures*. University of Tokyo Press.
- Longuet-Higgins, M.S. (1958).** On the Intervals between Successive Zeros of a Random Function, *Proc. Roy. Soc., Ser.A*, 246, 99-118.
- Mansard, E.P.D. and Funke, E.R. (1984).** Variabilité Statistique des Paramètres des Vagues, *Proc. Int. Symp. Marit. Struct. in the Mediterranean Sea*, Athens, Greece, 1.45-1.59.
- Mase, H. and Iwagaki, Y. (1986).** Wave Group Analysis from Statistical Viewpoint, *Proc. Ocean Struct. Dynamics Symp.*, Corvallis, Oregon, 145-157.
- Medina, J.R. and Hudspeth, R.T. (1987).** Sea States Defined by Wave Height and Period Functions, *Seminar on Wave Analysis and Generation in Laboratory Basins*, 22nd IAHR Congress, Lausanne, Switzerland, 249-259.
- Pires-Silva, A.A. and Medina, J.R. (1994).** False Waves in Wave Records. *Ocean Engineering*, 21 (8), 765-770.

- Rice, S.O. (1954).** Mathematical Analysis of Random Noise, *Selected Papers on Noise and Stochastic Processes*, Nelson Wax, ed., Dover Publications, Inc., New York.
- Rye, H. (1974).** Wave Group Formation among Storm Waves, *Proc. 14th ICCE*, Copenhagen, Denmark, 164-183.
- Sobey, R.J. (1992).** The Distribution of Zero-Crossing Wave Heights and Periods in a Stationary Sea State. *Ocean Engineering*, 19 (2), 101-118.
- Tayfun, M.A. (1981).** Distribution of Crest-to-Trough Wave Heights. *Journal of the Waterway, Port, Coastal and Ocean Division*, 107 (WW3), 149-158.
- Thompson, E.F. and Seeling, W.N. (1984).** High Wave Grouping in Shallow Water, *J. Waterway, Port, Coastal and Ocean Engng.*, 110 (2), 139-157.
- Tuah, H. and Hudspeth, R.T. (1982).** Comparisons of Numerical Random Sea Simulations, *J. Waterway, Port, Coastal and Ocean Division*, 108 (WW4), 569-589.
- van Vledder, G.Ph. (1983).** Verification of the Kimura Model for the Description of Wave Groups, Part 2, M.Sc. Thesis, Tech. Univ. Delft.

## CHAPTER 16

### MEASURING WAVES WITH MANOMETER TUBES

David J Hanslow<sup>1</sup>, Peter Nielsen<sup>2</sup> & Kevin Hibbert<sup>1</sup>

#### **Abstract**

A new type of wave gauge has been developed for the measurement of waves near a beach or near an existing coastal structure. It consists of a nylon tube with diameter between 0.5 and 1cm and length up to 500m. The seaward end of the tube is open so that the wave induced pressure fluctuations can be transmitted through the water in the tube. The landward end, which is conveniently above the water, is fitted with a pressure transducer. This is simple and reliable technology well suited for use in developing countries. Maintenance and running costs are also very low. The frequency response function of the system is somewhat complicated but a workable formula is presented and "once and for all" calibration of the system can be done very easily.

#### **Background**

The authors were prompted to look for a new type of nearshore wave gauge by the difficulty encountered with getting representative wave data for the Brunswick Heads field site during storm conditions. The problem with that particular site is that the nearest offshore waverider, which is off Cape Byron, tends to go a drift during "interesting" weather conditions. This leads to increased difficulty with interpreting the most interesting data.

The above mentioned example is not isolated. There is a considerable general need for a simple, inexpensive method of measuring nearshore wave heights, i.e. within 50 to 500 metres of a beach or an existing structure.

The existing devices for nearshore wave measurements include surface piercing gauges, "Schwartz poles", and bottom mounted current meters and pressure transducers. All of these are well proven but not without problems.

---

1) Coast and Floods Branch, New South Wales Public Works Department, Po Box 5280 Sydney 2001, Australia.

2) Department of Civil Engineering, University of Queensland, Brisbane, Australia 4072. Fax +61 7 365 4599, e-mail: nielsen@civil.uq.oz.au.

Not all locations allow the installation of a "Schwartz pole" because the supporting structure becomes very expensive with increasing depth and it may present a navigation hazard.

One problem with bottom mounted pressure transducers/current meters is that they tend to get lost to trawlers etc. Secondly, the fact that it is impossible to check their performance during the deployment has led to many disappointments when the instruments, upon recovery, have been found to contain no useful data. The tubes of the present system are usually buried in the sand and thus protected from "trawler attack", see Figure 1.

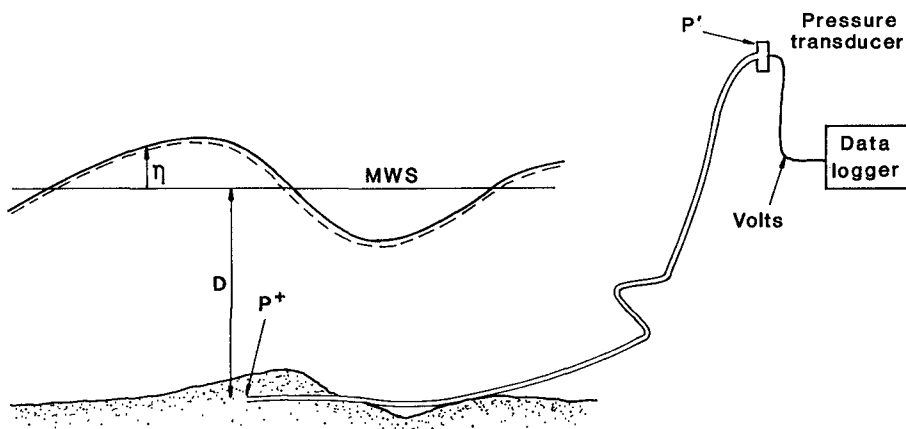


Figure 1: The idea is to estimate the water surface elevation time series  $\eta(t)$  on the basis of measured pressure fluctuations  $p'(t)$  at the landward end of a water filled nylon tube.

#### **A new type of cheap and reliable nearshore wavegauge**

The present study has investigated the possibility of measuring waves by monitoring the pressure fluctuations  $p'(t)$  at the landward end of nylon tubes of 10mm OD and lengths between 50 and 500 metres. The seaward ends of the tubes are exposed to the wave induced pressure fluctuations  $p^+(t)$ , See Figure 1.

The main problem addressed here is that of estimating of  $p^+$  on the basis of  $p'$ . However, the second step in the process of getting wave data from  $p'$ , namely determining the surface elevation  $\eta$  from  $p^+$  is also discussed briefly.

### **Initial field testing**

Initial field testing has been performed with the new tube-transducer system in order to assure that the transmitted pressure signal  $p'(t)$  is of adequate strength and that the system is easy to operate in the field. The system performed very satisfactorily in these tests. The transducer connected to the tubes which are permanently installed at Brunswick Heads. Connection and evacuation of the system takes only a few minutes.

The pressure signal was initially recorded by a chart recorder in the field. The  $p'(t)$ -signal has a low noise level and is of adequate strength to be recorded with the chart recorders 0-50mV range. The transducers applied in the present study are Model AB Pressure Transducers from Data Instruments Inc, Ma, USA. In later field tests the data was recorded in digital form on a portable PC. Various combinations of pressure transducers and recording equipment can be used but it should be noted that the working range for the pressure transducer should be about 0.5 - 1 atmosphere absolute, i.e., the working pressure is below atmospheric pressure.

### **Pressure transducer on the bed**

Relationships between the dynamic bottom pressure  $p^+$  ( $p(t) = \bar{p} + p^+(t)$ ) and the surface elevation  $\eta$  may be taken from linear wave theory for monochromatic small amplitude waves

$$\eta = \frac{p^+}{\rho g} \cosh kh \quad (1)$$

where  $k$  is the wave number  $2\pi/\lambda$ ,  $\lambda$  is the wave length and  $h$  is the water depth.

For irregular, non-linear waves, local approximations may be used. Nielsen (1989) recommended the formula

$$\eta_n = \frac{p_n^+}{\rho g} \exp \left\{ \frac{2}{3} \frac{-p_{n-1}^+ + 2p_n^+ - p_{n+1}^+}{p_n^+ g \delta_t^2} \left( h + \frac{p_n^+}{\rho g} \right) \right\} \quad (2)$$

based on a measured time series  $p_1^+, p_2^+, p_3^+, \dots$ .

As an alternative to the local approximations approach, the classical spectrum transformation approach may be applied. With this method a Fourier transform is applied to the pressure record. Then each spectral estimate is transformed in accordance with Equation (1). Finally, the inverse Fourier transform is applied to the transformed spectral estimates to obtain an estimate of the surface elevation time series. The relative merits of the two methods has been discussed by Nielsen (1989).

### **Transducer buried in the bed**

It is possible that a layer of sand on top of the "open" end of the tube can cause extra

damping. Most likely however, the effect is negligible for typical beach sand and typical wave frequencies.

Sleath (1970) and Maeno & Hasagawa (1987) measured pore pressures inside the bed simultaneously with pressures at the bed surface. The pressure amplitude ratios agreed reasonably with the formula

$$|p^+| = \rho g \frac{H}{2} \frac{\cosh k(z+h_1)}{\cosh kh \cosh kh_1} \quad (3)$$

where  $z$  is the transducer elevation measured from the sand surface  $h$  is the water depth and  $h_1$  is the thickness of the sand bed, see e.g. Sleath (1984).

According to this formula it makes very little difference whether a transducer, at a fixed depth below the water surface, is covered with sand or not. Consider for example, the situation in Figure 2.

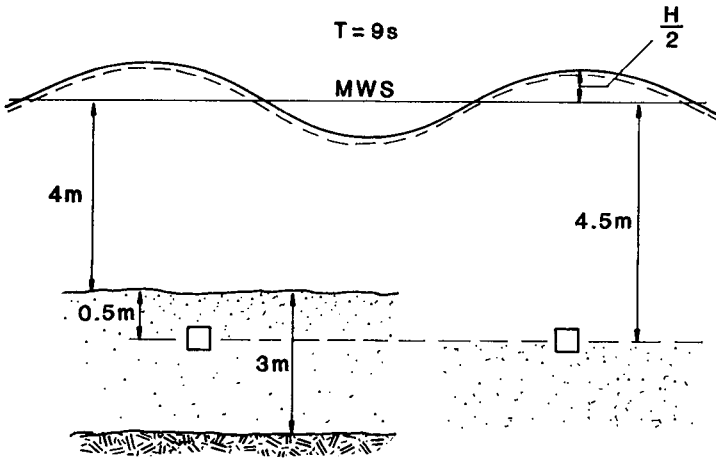


Figure 2: The pressure felt by a transducer 4.5m below the MWS under a 9s wave changes very little due to a sand cover of 0.5m.

A pressure transducer is placed 4.5m below the MWS. The wave period is 9s, and we consider the situation where the sand level is at the transducer level as well as the situation where the sand level is 0.5m above the transducer. The bed is assumed impermeable below -7m.

Linear wave theory plus Equation (3) gives  $|p^+| = 0.889\rho gH/2$  for the "uncovered case" and  $|p^+| = 0.885\rho gH/2$  for the "covered" case. This difference is negligible compared to the accuracy of linear wave theory. It should be noted however that finer material like silt or mud will provide a stronger damping of the pressure signal than 0.2mm sand.

### **The speed of pressure waves in a flexible tube**

The frequency response of the tube-transducer system in Figure 1 depends critically on the speed of pressure waves in the tube. This speed, in turn, is a function of the compressibility of the water, the rigidity of the tube walls and, if air bubbles are present, of the bubble concentration.

In an infinite fluid, the speed  $c$  of a plane sound wave is determined by the density  $\rho$  and the compressibility  $K$

$$c = \frac{1}{\sqrt{\rho K}} \quad (4)$$

The speed of sound in sea water is approximately 1500m/s, corresponding to a compressibility  $K$  of  $4.4 \cdot 10^{-10} Pa^{-1}$ .

If the fluid is contained in a flexible tube, the speed of sound will be reduced in accordance with the formula

$$c = \frac{1}{\sqrt{\rho (K + D)}} \quad (5)$$

where the distensibility  $D$  of the tube is defined in terms of the normal cross sectional area  $A_o$  and the excess pressure  $p_e$  by

$$D = \frac{1}{A_o} \left. \frac{dA}{dp_e} \right|_{p_e=0} \quad (6)$$

If the tube cross section is circular, the distensibility can be due to stretching of the wall only. However, if the normal tube cross section is not circular a greater distensibility may be partly due to this non-circularity. In this case, an area increase may be obtained by bending the wall towards the circular shape. Thus, the speed of sound in an oval shaped tube will be lower than in a perfectly circular tube for the same wall thickness.

### **Experimental determination of the distensibility**

Experiments were performed to determine the distensibility of 10mmOD Nylex tubing



by monitoring the volume increase in  $60m$  of tube as function of excess pressure.

The results are shown in Figure 3 and the best-fit distensibility  $(\frac{1}{V_0} \frac{dV}{dp})$  was found to be  $2.0 \cdot 10^{-8} Pa^{-1}$ . We note that the behaviour of the tube material is linear up to excess pressures of at least  $120 kPa$ , corresponding to  $12m$  excess head of water.

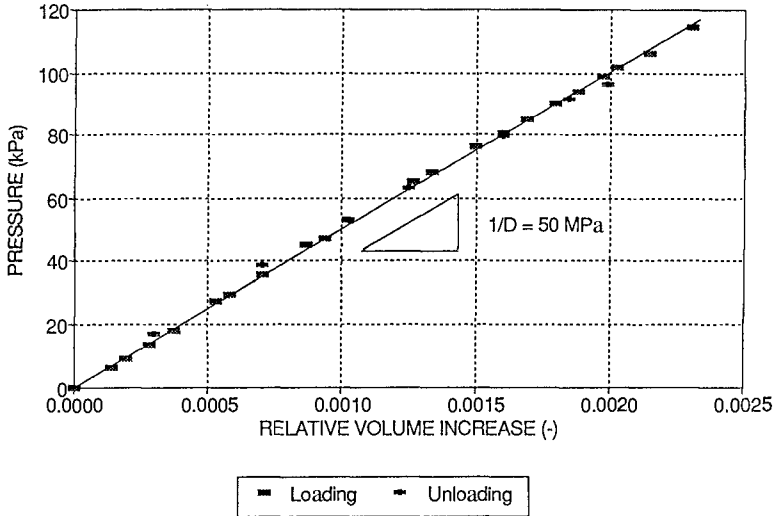


Figure 3: Expansion test data for  $10mm$  OD Nylex pressure tubing (standard).

According to Equation (5) this corresponds to the speed of sound  $c = 224m/s$  for a  $10mm$  OD Nylex tube with no air bubbles.

A complementary stretching test was performed on a short ( $150mm$ ) length of tube to determine Young's modulus  $E$  for the tube material. Based on a measured ID of  $6.7mm$  and wall thickness  $\delta$  of  $1.67mm$  the result was  $E = 2.03 \cdot 10^8 Pa$ .

Through the simple relationship

$$D \approx \frac{d}{\delta E} \quad (7)$$

this gives a distensibility of  $1.95 \cdot 10^{-8} Pa^{-1}$  in close agreement with the directly measured value above. The manufacturer's value for  $E$  is  $35kg/mm^2$  corresponding to  $3.4 \cdot 10^8 Pa$  for standard tubing (all colours) and  $100kg/mm^2$  (They must be thinking in terms of "kg force") corresponding to  $9.8 \cdot 10^8 Pa$  for "semi rigid tubing (only black)". The discrepancy (3.4 versus 2.0) being due to uncertainty of tube dimensions in test and to variable humidity. The laboratory tests were performed with fully wet tubes.

### **The effect of air bubbles on the speed of sound**

Small, isolated air bubbles can also slow down the pressure waves in the tube. They do this by effectively increasing the distensibility. To quantify this effect, consider for simplicity an air bubble of volume  $V_o$  at the ambient pressure  $p_o$ , which is compressed isothermally. Its volume is then given by  $V(p) = V_o p_o/p$  and hence,

$$\frac{dV}{dp} = -V_o \frac{p_o}{p^2} \approx -\frac{V_o}{p_o} \quad (8)$$

The presence of air bubbles with concentration  $C_{air}$  (vol/vol) will therefore increase the distensibility by the amount

$$D_{air} \approx \frac{C_{air}}{p_o} \quad (9)$$

leading to the reduced speed of sound

$$c = \frac{1}{\sqrt{\rho (K + D + C_{air}/p_o)}} \quad (10)$$

### **Test for linearity with regular waves**

A series of measurements were conducted at the University of Queensland in the period August to October 1993 to establish the possible existence and importance of nonlinearity of the systems response to regular waves.

Regular but not quite simple harmonic pressure waves with "heights" in the range  $0.5m < H < 4.5m$  and periods in the range  $2s < T < 7s$  were generated by moving a small reservoir with mercury up and down in a quasi simple-harmonic fashion. The test tube was approximately  $100m$  of  $10mm$  OD Nylex standard tubing.

The data indicate that the gain is only weakly dependent upon the amplitude and hence, the use of a linear frequency response model (Equation (15)) developed below for the system is reasonably well justified.

### **Frequency response for the tube-transducer system**

As a working hypothesis, it was assumed that the tube-transducer system can be modelled in analogy with a dampened "quarter length resonator". That is, it has resonant pressure wave modes of the form indicated in Figure 4. Such a system has the approximate frequency response function

$$F(f) = \frac{1}{\cos\left(\frac{\pi f}{2 f_o}\right) + i D_E \left(\frac{f}{f_o}\right)} \quad (11)$$

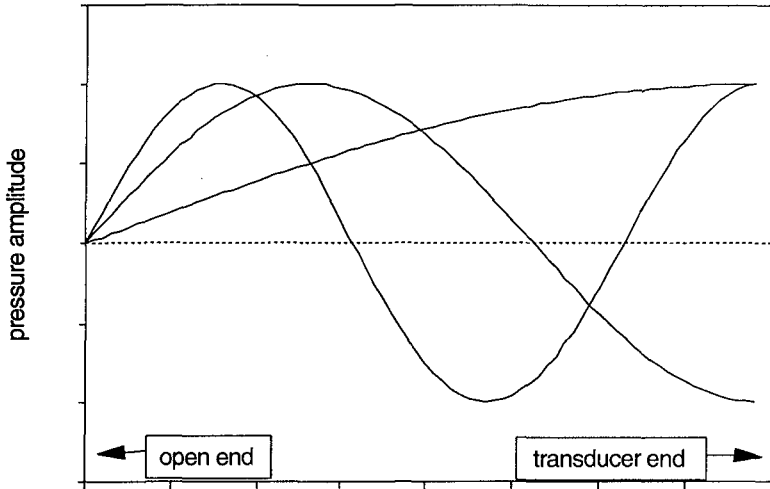


Figure 4: Assuming that the pressure transducer forms a hard, reflecting boundary, the tube/transducer system will behave as a dampened quarter length resonator and have infinitely many resonant wave modes of which the first three are shown here.

where  $D_E(f/f_o)$  is an energy dissipation function. The corresponding gain function is

$$G(f) = |F(f)| = \frac{1}{\sqrt{c \cos^2 \left( \frac{2f}{\pi f_o} \right) + D_E^2 \left( \frac{f}{f_o} \right)}} \quad (12)$$

In these expressions,  $f_o$  is the lowest resonance frequency corresponding to the resonance period  $T_o$ . It is seen from Equation (12) that the gain function has peaks for all odd multiples of the resonance frequency  $f_o$ . This model is in reasonable agreement with experiments see Figure 5

The experiments show the first two peaks of the gain function rather clearly.

The mode of resonance has a pressure antinode at the transducer end and a node at the open end of the tube, see Figure 4. Hence, the resonant pressure wave in the tube resembles a seiche in a bay. The length of the tube must in that case be 1/4 of the wavelength of the first mode:  $L = \lambda_o/4 = c T_o/4$ , corresponding to the resonance frequency

$$f_o = \frac{c}{4L} \quad (13)$$

the frequencies of the higher resonant modes are all the odd multiples of  $f_o$ .

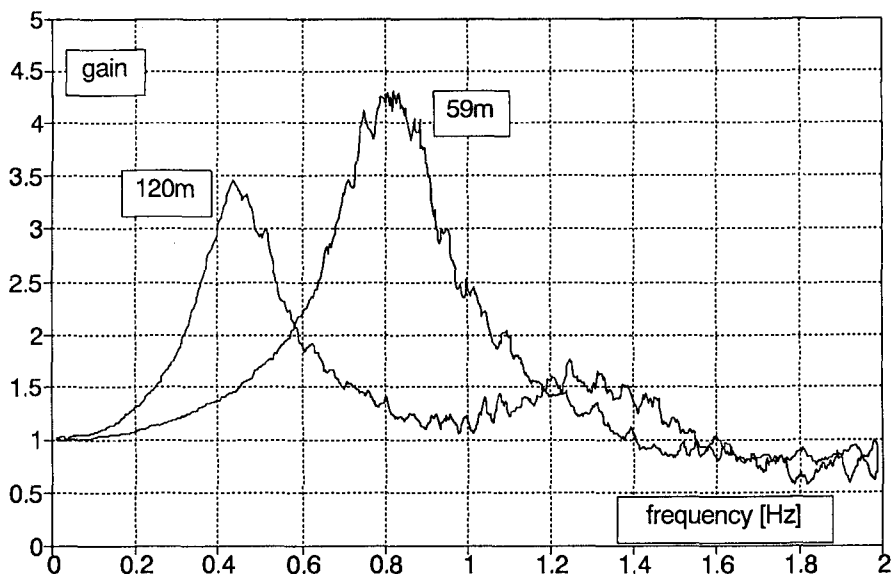


Figure 5: Gain functions measured in the laboratory for a 120m and a 59m OD10mm tube (Nylex standard pressure tubing). The frequency response data was obtained by comparing the output of two transducers. One at the closed end of the tube and one at the "open" end where irregular pressure forcing was provided by moving a water filled open ended tube up and down,

### **Energy dissipation and damping**

The maximum gain values observed with 10mm Nylex tubes of lengths 60m to 120m are of the order 4.5 and 3.5 respectively, see Figure 4.

These finite gain values indicate some damping in the system. The nature of this damping i e, the loss of energy is not completely understood. - The energy may be turned into heat in the fluid and in the tube walls. Alternatively, it may be radiated away. Radiation may occur along the full length of the tube or mainly from the open end.

Energy loss in the form of heating of the fluid is caused by the viscosity  $\nu$  and may be estimated as follows. The rate of heat generation in a boundary layer is  $\overline{u_{\infty} \tau}$  where  $u_{\infty}$  is the velocity at the edge of the boundary layer and  $\tau$  is the wall shear stress. The wall shear stress may, under the assumption  $\sqrt{\nu T} \ll d$ , be estimated by the formula  $|\tau| = \rho \sqrt{2\pi f \nu} |u_{\infty}|$  which holds for a plane, oscillatory boundary layer, see e g Nielsen 1992, p 21. The velocity amplitude  $|u_{\infty}|$  is related to the pressure amplitude by  $u = p/\rho c$ , see Lighthill 1978, p 4. Hence the energy dissipation due to fluid viscosity in a tube of length  $L$  and diameter  $d$  over one period can be estimated by

$$DE_{fluid} \approx \rho u^2 \sqrt{2\pi f v} L d T.$$

The loss of energy as heat in the tube walls may be estimated as follows. For a given pressure amplitude  $|p|$ , the deformation of the tube wall is of the magnitude  $\frac{|p| d^2}{\delta E}$  where  $\delta$  is the wall thickness and  $E$  is Young's modulus for the tube material.

Hence, the work done on the tube wall per unit length through one cycle is of the magnitude  $\frac{|p|^2 d^3}{\delta E}$  and the work done on a tube of length  $L$  in one period is  $\frac{|p|^2 d^3}{\delta E} L$ . Since the general magnitude of  $|p|$  along the tube is  $|p^+|$ , this may be written

$$DE_{wall} \sim \frac{|p^+|^2 d^3}{\delta E} L \approx \frac{|p^+|^2 L d^2}{\rho c^2}, \text{ since } \rho c^2 \approx E \frac{\delta}{d} \text{ for relatively flexible tubes,}$$

cf Equations (5) and (7).

The energy flux through the tube cross section is of the order  $|p|cd^2$  corresponding to an energy input of  $|p^+| c d^2 T$  at the open end during one wave period.

Based on these considerations, and with  $p' = G p^+$ , we find that the relative energy loss  $D_E$  can be quantified approximately by

$$D_E = \frac{\text{energy loss}}{\text{energy input}} \sim \frac{\frac{|p^+|^2 d^2 L}{\rho c^2} + \frac{|p^+|^2 \sqrt{2\pi f v} T d L}{\rho c^2}}{|p^+| c d^2 T}$$

$$D_E = \frac{\text{energy loss}}{\text{energy input}} = G \frac{|p^+| L}{\rho c^2 c} [C_1 f + C_2 \frac{\sqrt{v}}{d} \sqrt{f}] \quad (14)$$

where  $C_1$  and  $C_2$  are dimensionless coefficients.

### **A semi empirical gain function**

Based on the analysis above, which indicates the existence of some damping terms proportional to the square root of the frequency and some which are proportional to the frequency it seems reasonable to suggest a semi empirical gain function of the form

$$G = \frac{1}{\sqrt{\cos^2\left(\frac{\pi f}{2 f_0}\right) + [B_1 \frac{f L}{c} (1 + B_2 \sqrt{\frac{v}{f d^2}})]^2}} \quad (15)$$

Based on the data shown in Figure 5 the values of the dimensionless constants were found to be  $(B_1, B_2) = (0.58, 5.0)$ . The fact that  $B_2 \gg B_1$  indicates that the loss

due to fluid viscosity is dominant compared to the loss due to deformation of the tube walls for these tubes. The formula (15) with these values of  $B_1$  and  $B_2$  is compared with the data in Figure 6.

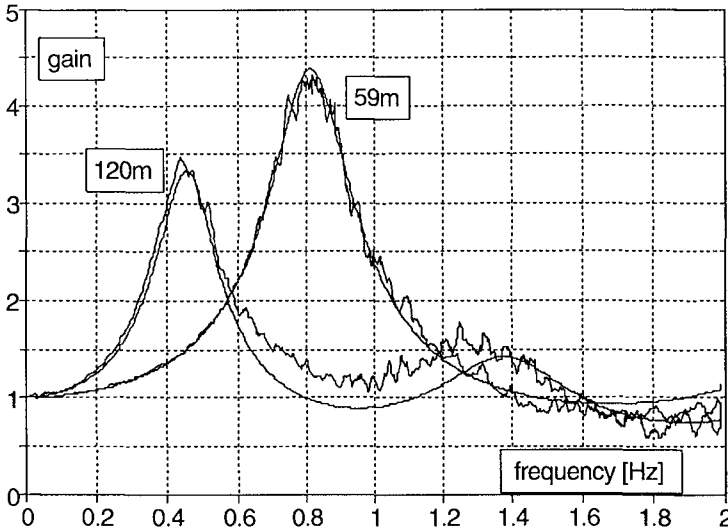


Figure 6: The semi empirical gain function (15) compared with laboratory measurements.

The matching of the shape of the gain function is not perfect, but the discrepancies seem to be due to the cosine function not having the right shape.

### **Calibration**

The values of the constants  $B_1$  and  $B_2$  which were determined on the basis of the data in Figure 5 may not be universal. Hence, when working with systems with different lengths, diameters and tube materials it would be wise to calibrate the system before deployment. This calibration is best done in the way described in connection with Figure 5.

### **Evaluation of the system**

The indication of the tests carried out so far is that the new wave gauge offers a cheap and reliable alternative to existing gauges for measuring the wave conditions in shallow ( $< 5\text{-}6\text{m}$ ) depths near ( $0\text{-}500\text{m}$ ) beaches or existing structures. The main advantages of the new system are that it is cheap and easy to service and interrogate

because all electronics are kept "high and dry".

Based on the field, it can be concluded that using the system in the field with tubes which are already in place is easy (installation time about 5 minutes in fair weather). Earlier tests also show that deployment of the tubes for a one or two day experiment on a beach is manageable, provided a 4 wheel drive vehicle is at hand to help pull the tubes back ashore.

The pressure signal is of adequate strength, and the noise level is very low provided the tubes are prevented from moving with the waves. This is normally achieved by tying the tubes to an 8mm steel chain.

Variable degrees of sand cover over the seaward end of the tube seem not to cause problems with the translation of dynamic bottom pressures into water surface elevations. However, thick layers of silt or mud may have a very strong dampening effect.

The frequency response function for the system is fairly complicated. It has several peaks and the dampening is non-linear. However, with the use of Nylex standard pressure tubing the second peak of the gain function will generally be well outside the frequency range of ocean waves. For example, a 600m 10mmOD tube system will have its second peak at  $f = 0.45\text{Hz}$  ( $f_0 = 0.15\text{Hz}$ ) and most of the energy in the pressure spectra from wind waves on a beach lies at frequencies below 0.25Hz.

### **References**

- Lighthill, M J (1978): *Waves in fluids*. Cambridge University Press.
- Maeno, Y & T Hasegawa (1987): In situ measurements of wave induced pore pressure for predicting properties of seabed deposits. *Coastal Engineering in Japan, Vol 30, No 1*, pp 99-115.
- Nielsen, P (1989): Analysis of natural waves by local approximations. *J Waterway, Port, Coastal and Ocean Engineering, Vol 115, No 3*, ASCE, pp 384-396.
- Nielsen, P (1992): *Coastal bottom boundary layers and sediment transport*. World Scientific, 324pp.
- Sleath, J F A (1970): Wave induced pressures in beds of sand. *J Hydraulics Division A S C E, Vol 96, No Hy2*, pp 367-378.
- Sleath, J F A (1984): *Sea Bed Mechanics*, John Wiley and Sons, UK, 335pp.

## Quantity of Spray Transported by Strong Wind over Breaking Waves

Nobuhiro Matsunaga<sup>1</sup>, Misao Hashida<sup>2</sup>, Hiroyuki Mizui<sup>3</sup> and Yuji Sugihara<sup>4</sup>

### Abstract

The quantity of spray transported by strong wind has been measured experimentally when the wind blows over waves propagating on a sloping bed. The leeward variation of spray concentration is much smaller than that in the vertical direction because of the quasi uniform supply of spray from the water surface. In the theoretical development, therefore, the balance has been analyzed between the upward flux of the concentration by turbulent diffusion and the downward flux due to the spray precipitation. Three characteristic quantities introduced in the analysis have been obtained by superposing the experimental data on the theoretical solutions. They are related to the wave and wind parameters to predict quantitatively the spray concentration supplied from sea to shore.

### 1. Introduction

Japan is well known as a country which many typhoons pass through every year. Two big typhoons hit successively the western

- 
1. Associate Professor, Department of Earth System Science and Technology, Kyushu University, Kasuga 816, Japan
  2. Professor, Department of Civil Engineering, Nippon Bunri University, Oita 870-03, Japan
  3. Civil Engineering Department, Nagoya Regional Office, Fujita Corporation, Nagoya 460, Japan
  4. Research Associate, Department of Earth System Science and Technology, Kyushu University, Kasuga 816, Japan



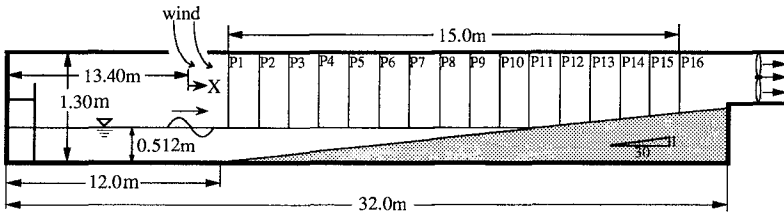


Fig. 1. Schematic diagram of experimental set-up.

part of Japan on September 1991. They gave extensive severe damages along the coastal region, such as the stoppage of electric current over more than four days and poor harvest of crops. A report of the investigation showed that a large quantity of spray of sea water distributed over a wide area and it caused these disasters. To predict the magnitude of the salt damage, it is necessary to evaluate how much the quantity of spray is transported from sea to shore. Some studies (e. g., Toba, 1959; Toba & Tanaka, 1967; Hama & Takagi, 1970) have been already made on the generation and transport of sea-salt particles. However, many fundamental problems have been left unsolved.

In this study, the quantity of spray which is transported when strong wind blows over breaking waves has been measured experimentally, and the discussion has been made about vertical and leeward profiles of the spray concentration.

## 2. Experimental arrangements

Experiments were carried out by using a wave tank. It was equipped with an inhalation-typed wind tunnel. Its schematic diagram is shown in figure 1. The tank was 32 m long, 0.60 m wide and 1.30 m high. It was covered with a semicircular cylindrical ceiling whose radius was 0.37 m. As a model beach, a sloping flat bed of 1/30-grade was fixed at one side of the tank. The mean depth of water was 0.52 m at the horizontal bed section. Spilling breakers were formed by making two-dimensional regular waves propagate on the sloping bed. The wave parameters are given in table 1, where  $T$  is the wave period and  $H_0$ ,  $L_0$  and  $C_0$  are the wave height, wavelength and wave velocity in deep water, respectively.

The wind was taken into the tank by opening a part of the ceiling. Water spray entrained into the air was captured by arranging vertically ten or twelve cylindrical containers filled with cotton. Their diameter and length were 3.0 m and 5.0 cm, respectively. The vertical interval

Table 1. Experimental parameters.

Run	T(s)	H <sub>0</sub> (cm)	L <sub>0</sub> (cm)	C <sub>0</sub> (m/s)	U <sub>m</sub> (m/s)	H <sub>0</sub> /L <sub>0</sub>	U <sub>m</sub> /C <sub>0</sub>	γ
1					12.0		6.15	
2	1.25	11.6	243.7	1.95	16.8	0.048	8.63	0.2
3					19.4		9.95	
4					12.0		7.69	
5	1.00	10.9	156.0	1.56	16.9	0.070	10.8	0.4
6					17.5		11.2	
7					12.1		7.76	
8	1.00	14.0	156.0	1.56	16.9	0.090	10.8	0.6
9					19.1		12.2	

between the containers was 5.0 cm. As shown in figure 1, the test section was 15.0 m long. The positions from p1 to p16 were data-taking stations. Their leeward interval was 1.0 m except for Run 6, in which it was 1.2 m. At each station, wave height, wave set-up and spray quantity were measured. The concentration of spray in the air  $C$  ( $\text{g}/\text{cm}^3$ ) was obtained by dividing the mass of spray transported per square centimeter and second by the cross-sectionally averaged wind velocity  $U$ . The wind velocities  $U_m$  given in table 1 are ones obtained by averaging  $U$  in the leeward direction. The values of non-dimensional parameters  $H_0/L_0$ ,  $U_m/C_0$  and  $\gamma$  are also given in table 1. The parameter  $\gamma$  will be mentioned in §3.2 and 3.3.

In the following discussion, the horizontal coordinate axis  $x$  is taken in the leeward direction from the center of the wind intake. The vertical axis  $z$  is taken upwards from wave crest at each data-taking station.

### 3. Results and discussion

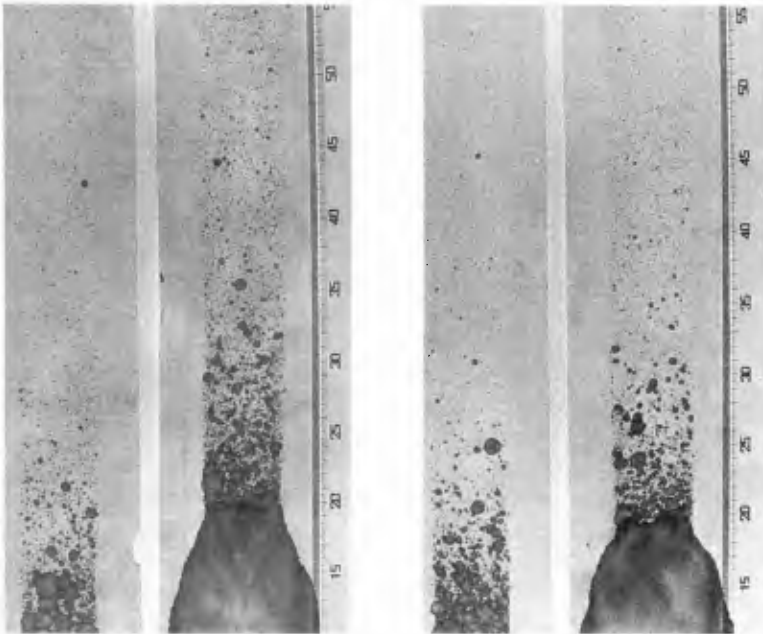
#### 3.1 Transport of spray by wind

Photo 1 shows the generation of spray from a spilling breaker under strong wind. It was taken at  $x = 10$  m in Run 6. A large amount of spray is occurring from the breaking crest.

Photos 2(a) and (b) show vertical profiles of spray size obtained by using droplet sampling paper,  $t$  being the time for which the paper had been exposed to spray. The paper is made of filter paper, and a solution of aniline blue dye in benzene is applied to it. From these profiles, it is seen that the spray size decreases remarkably in the



Photo 1. Generation of spray from spilling breaker under strong wind.



$t = 3.7 \text{ s}, \quad t = 24 \text{ s.}$   
 (a)  $x = 10.2 \text{ m.}$

$t = 6.3 \text{ s}, \quad t = 28 \text{ s.}$   
 (b)  $x = 15.0 \text{ m.}$

Photo 2. Vertical profiles of spray size.

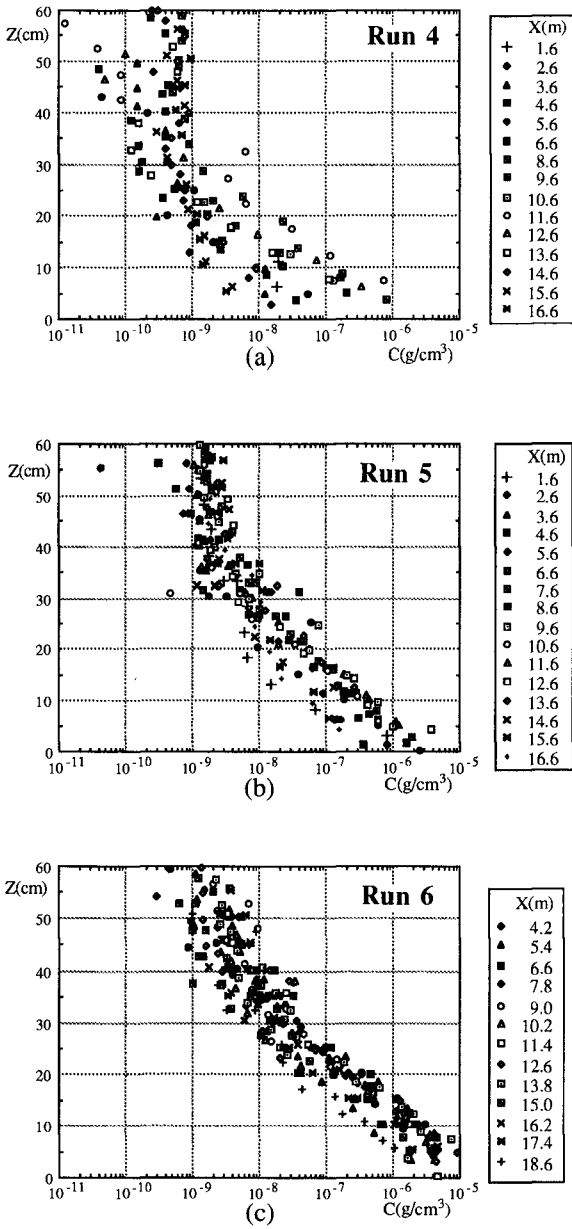


Fig. 2. Vertical profiles of spray concentration.

vertical direction but the vertical profiles do not change so rapidly in the leeward direction.

Figures 2 (a) to (c) show some examples of vertical profiles of spray concentration  $C$ . The values of  $C$  increase with the increase of  $x$ . The rate of increase in the leeward direction is one or two orders of magnitude over ten and several meters. On the other hand, the change in the vertical direction is much larger than that in the leeward direction. The values of  $C$  decrease vertically upwards to three or four orders of magnitude over about 40 cm. It means that the supply of spray from the water surface is almost uniform in the leeward direction.

### 3.2 Theoretical development

The following assumptions have been made in the theoretical development.

- The field is steady and two-dimensional.
- The leeward variation is much smaller than the vertical one.
- Vertical mean velocity is nearly equal to zero.

Under these assumptions, the governing equation for the spray concentration becomes

$$\frac{\partial}{\partial z} \left( D \frac{\partial C}{\partial z} \right) + \frac{\partial}{\partial z} (w_0 C) = 0, \quad (1)$$

where  $D$  is the coefficient of turbulent diffusion and  $w_0$  the settling velocity of spray. Boundary conditions are given by

$$C = C^*(x, 0) \quad \text{at } z = 0 \quad (2)$$

$$\text{and } C \rightarrow 0 \quad \text{as } z \rightarrow \infty$$

Let us introduce the dimensionless quantities defined by

$$f(\tilde{z}) = C/C^*(x, 0), \quad g(\tilde{z}) = D/w_0 l^*(x, 0) \quad \text{and} \quad \tilde{z} = z/l^*(x, 0), \quad (3)$$

where  $l^*(x, 0)$  is a characteristic length scale defined as a value of  $D/w_0$  at  $z = 0$ . Substituting equation (3) into equation (1), we obtain

$$df/d\tilde{z} + g^{-1}f = 0 \quad (4)$$

Considering that the diffusion coefficient increases generally with  $z$ ,  $w_0$  decreases oppositely because of the decrease of the spray size with  $z$  and  $g(0)=1$ , we can assume the form of  $g$  as follows.

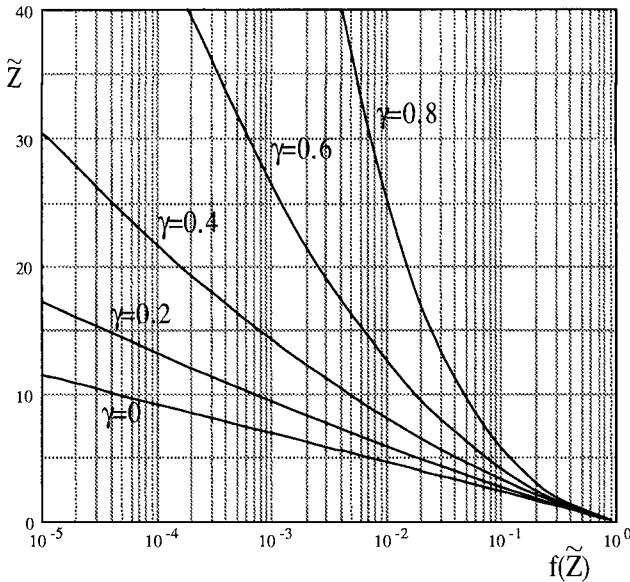


Fig. 3. Vertical profiles of theoretical solutions for various values of  $\gamma$ .

$$g = (1 + \tilde{z})^\gamma . \quad (\gamma > 0) \tag{5}$$

Substituting equation (5) into equation (4) and using  $f(0) = 1$ , we obtain the solution

$$f(\tilde{z}) = \exp \left[ \frac{1}{1 - \gamma} \left\{ 1 - (1 + \tilde{z})^{1 - \gamma} \right\} \right] . \tag{6}$$

Since  $f(\infty) \rightarrow 0$ ,  $\gamma$  must take a value from 0 to 1.

Figure 3 shows the vertical profiles of the theoretical solutions for various values of  $\gamma$ . As  $\gamma$  increases, spray diffuses to higher elevation and the vertical profile  $C$  becomes uniform. Therefore, it is the result which can be accepted easily.

### 3.3 Quantification of spray concentration

To predict quantitatively the spray concentration, the quantities introduced in the theoretical development,  $C^*$ ,  $l^*$  and  $\gamma$  should be related with the wave and wind parameters. For their evaluations, the method

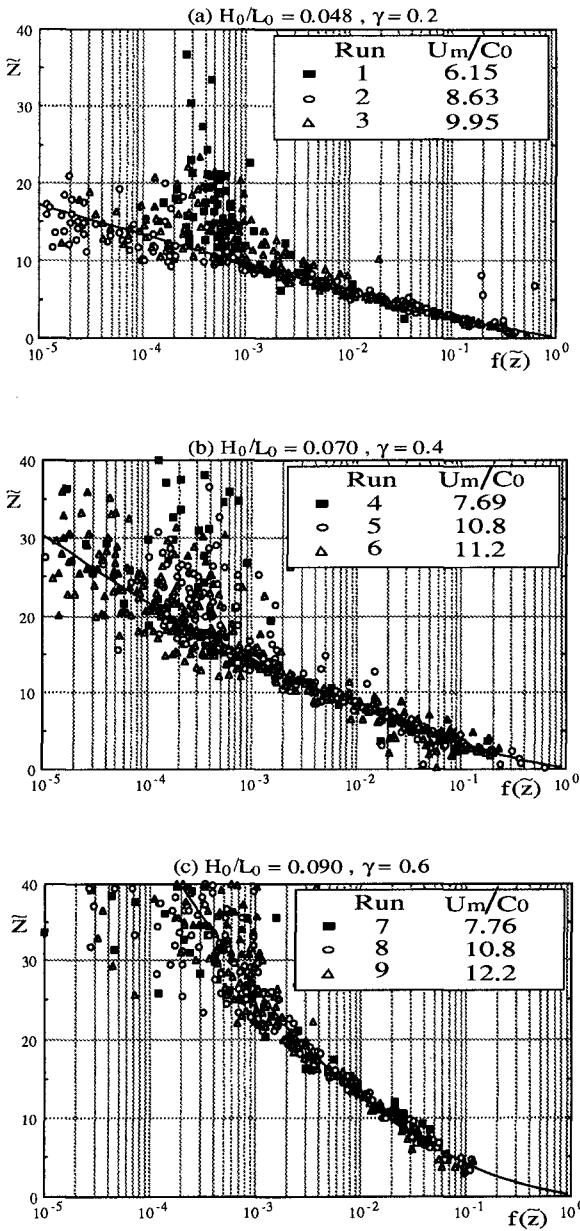


Fig. 4. Degree of agreement between the non-dimensionalized experimental data and theoretical solutions.

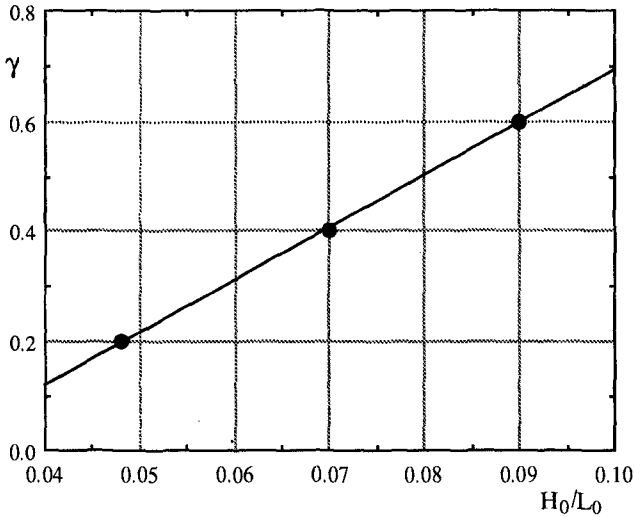


Fig. 5. Relation between  $\gamma$  and  $H_0/L_0$ .

was used of superposing the experimental data on the theoretical solutions in log-log graph paper, and the theoretical curve fitting best to the experimental data was determined by the method of trial and error. The values of  $\gamma$  determined by this method are given in table 1. Figures 4 (a) to (c) show the degree of agreement between the experimental data and theoretical curves. Though some scattering can be seen in the upper region, the agreement between the both is very good in the lower region. From table 1, it is seen that  $\gamma$  does not depend on  $U_m/C_0$  but  $H_0/L_0$ . In figure 5, the values of  $\gamma$  are plotted against  $H_0/L_0$ . The values of  $\gamma$  increase linearly with the increase of  $H_0/L_0$ .

The leeward variations of  $C^*(x, 0)$  are given in figures 6 (a) to (c). The values of  $C^*$  increase gradually with  $x$ . After reaching the maximum value  $C^*_{max}$ , it decrease rapidly. It results from the decrease of the supply of spray due to the wave propagation into a swash zone.  $C^*_{max}$  is an important quantity to evaluate the maximum quantity of spray transported from sea to shore. In figure 7, the values of  $C^*_{max}/\rho_0$  are plotted against  $U_m/C_0$ , where  $\rho_0$  is the density of water. They increase exponentially with the wind velocity.

Figures 8 (a) to (c) give the leeward variations of  $l^*$ . The values



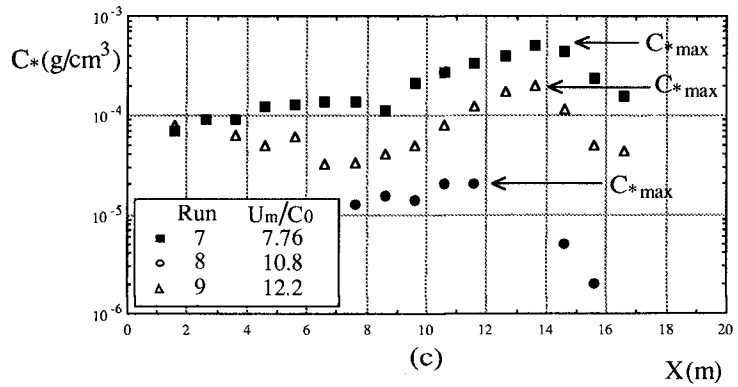
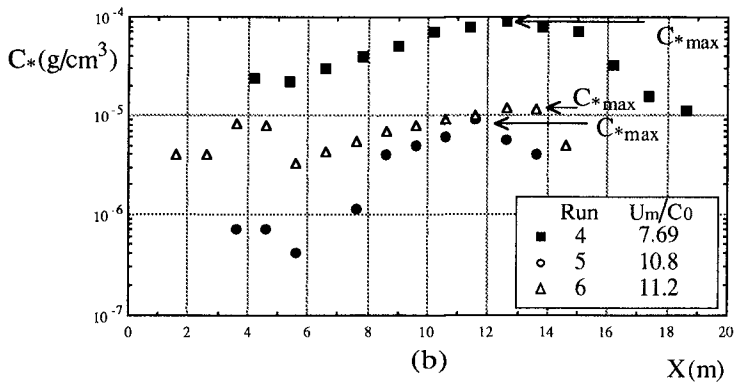
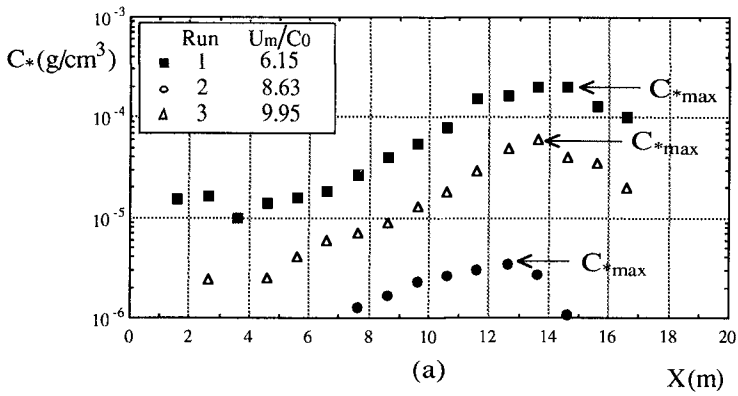


Fig. 6. Variations of  $C^*$  in the leeward direction.

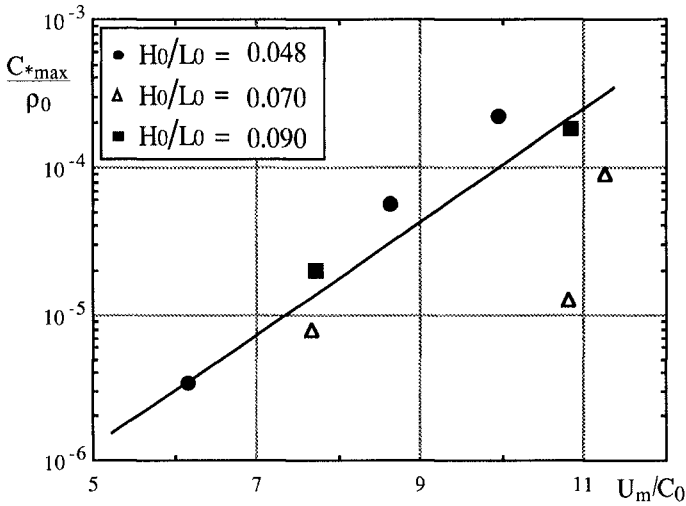


Fig. 7. Relation between  $C_{*max}/\rho_0$  and  $U_m/C_0$ .

of  $l^*$  are approximately constant in the leeward direction and tend to decrease with the increase of the wave steepness. Here, let us define  $\bar{l}^*$  as a value of  $l^*$  averaged in the leeward direction. Figure 9 shows the relation between  $\bar{l}^*/H_0$  and  $H_0/L_0$ . The values of  $\bar{l}^*/H_0$  decrease linearly with the increase of  $H_0/L_0$  without depending on  $U_m/C_0$ .

It should be noted that the relatively small leeward-variations of  $C^*$  and  $l^*$  guarantee the validity of the second assumption made in §3.2.

#### 4. Conclusions

In the case when strong wind blows over breaking waves, the vertical and leeward profiles of spray concentration are investigated experimentally and theoretically. The leeward variation is much smaller than that in the vertical direction. The non-dimensional vertical profile is expressed by an exponential function. The three characteristic quantities to determine the spray concentration supplied from sea to shore, i. e., the maximum concentration at the elevation of wave crest  $C_{*max}$ , a characteristic length scale of the vertical profiles  $\bar{l}^*$  and the non-dimensional parameter determining the vertical profile of the ratio of the diffusion coefficient to the settling velocity  $\gamma$  are related to the wave and wind parameters. The values of  $C_{*max}$  increase exponentially with the increase of wind velocity. The values of  $\gamma$

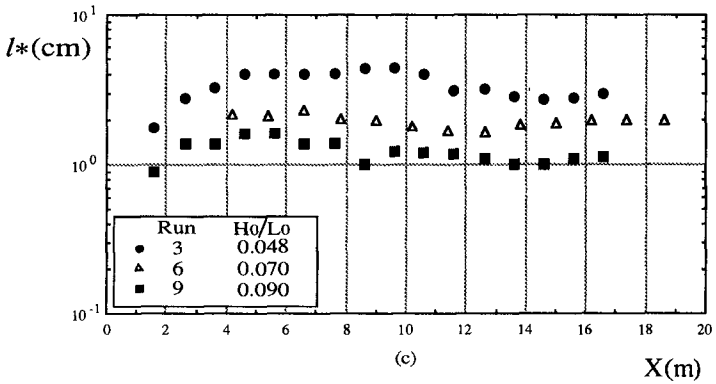
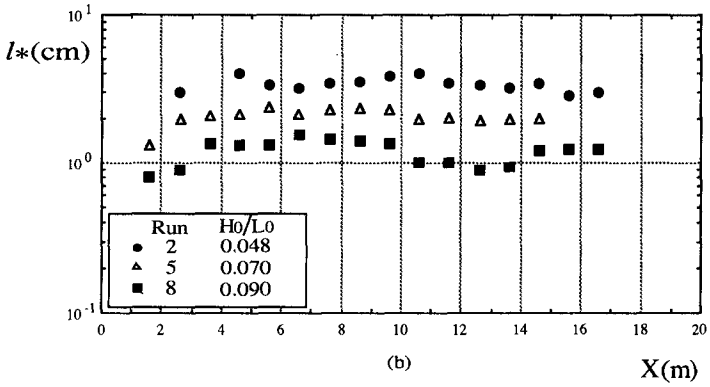
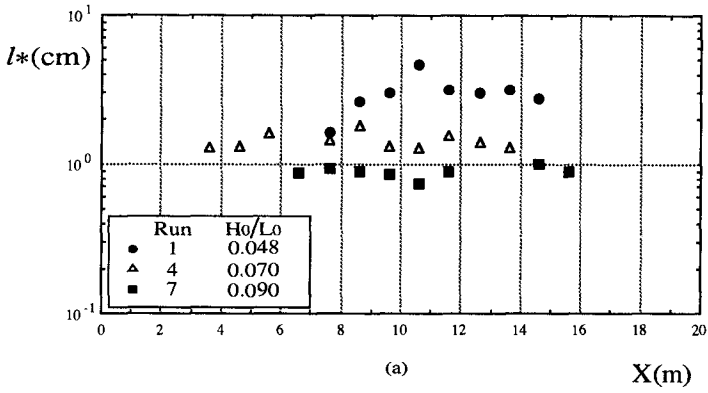


Fig. 8. Variations of  $l^*$  in the leeward direction.

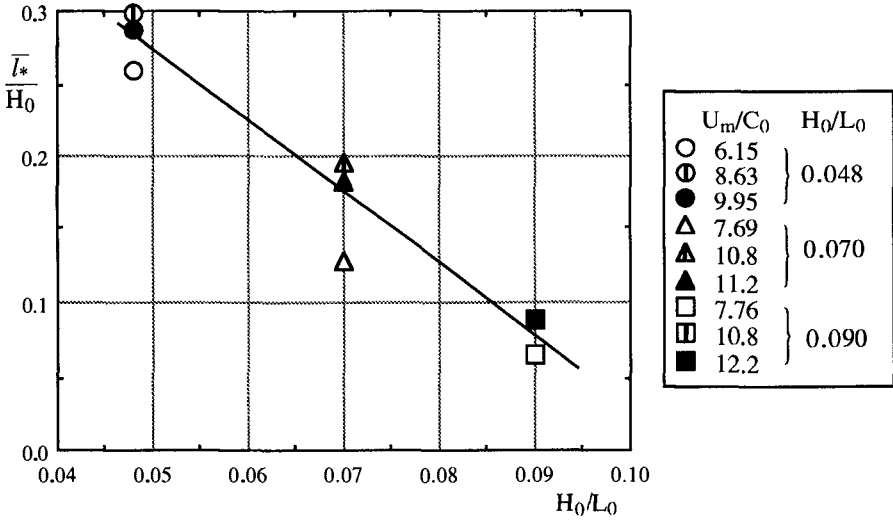


Fig. 9. Relation between  $\bar{l}^*/H_0$  and  $H_0/L_0$ .

depend only on the wave steepness and increase with its increase. On the other hand, the ratios of  $\bar{l}^*$  to the wave height decrease linearly as the wave steepness increases. The non-dimensional vertical profile of spray concentration and the evaluation of  $C^*_{max}$ ,  $\bar{l}^*$  and  $\gamma$  enable us to know how much the spray concentration is supplied from sea to shore. It offers us the boundary condition on the sea side in calculating the spray concentration on land.

The authors are grateful to Ms Y. Arizumi and K. Uzaki for their help.

REFERENCES

HAMA, K. and TAKAGI, N. (1970) Measurement of sea-salt particles on the coast under moderate winds. Papers in Meteorology and Geophysics, **21**, 449-458.  
 TOBA, Y. (1959) Drop production by bursting of air bubbles on the sea surface (II): Theoretical study on the shape of floating bubbles, J. Oceanogr. Soc. Japan, **15**, 121-130.  
 TOBA, Y. and TANAKA, M. (1967) Basic study on salt damage (I): Production sea-salt particles and a model of their transport inland, Disaster Prevention Research Institute Annuals, **10**, 331-342 (in Japanese).

## CHAPTER 18

# Extension of the Maximum Entropy Principle Method for Directional Wave Spectrum Estimation

Noriaki Hashimoto<sup>1</sup>, Toshihiko Nagai<sup>2</sup> and Tadashi Asai<sup>3</sup>

### Abstract

This paper presents an extension of the maximum entropy principle method (MEP), named the extended MEP (EMEP), as a general and practical method for estimating directional wave spectra. Since the EMEP is formulated to consider errors in the cross-power spectra, it proves to be an accurate, reliable, and robust method against such errors. In addition, we also examine the EMEP using numerical simulation and field wave data, with its validity being subsequently discussed.

### 1. Introduction

The directional spectrum of ocean waves expresses their fundamental properties by describing the energy distribution as a function of wave frequency and wave propagation direction. Many methods have been proposed for estimating the directional spectra of various types of ocean wave measurements, e.g., the direct Fourier transformation method (DFTM), parametric method, maximum likelihood method (MLM), extended maximum likelihood method (EMLM), maximum entropy principle method (MEP), and Bayesian directional spectrum estimation method (BDM).

The MEP (Hashimoto and Kobune, 1985) can estimate the directional spectra using three simultaneously measured quantities related to random wave motion, for instance, pitch, roll, and heave data, and when applied as such, estimates of directional spectra have better directional resolution than other existing methods. On the other

---

<sup>1</sup> Chief, Ocean Energy Utilization Laboratory, Hydraulic Engineering Division.

<sup>2</sup> Chief, Marine Observation Laboratory, Marine Hydrodynamics Division.

<sup>3</sup> Member, Environmental Hydraulics Laboratory, Marine Hydrodynamics Division.

Port and Harbour Research Institute, Ministry of Transport,  
1-1 Nagase 3-chome, Yokosuka 239, Japan

hand, the MEP is not a general method because it is restricted to applications involving three-quantity measurements.

In comparison, the BDM (Hashimoto, 1987) can handle more than three arbitrary-mixed instrument array measurements and has the highest resolution among existing methods for estimating the directional spectrum under such conditions. This method is a robust method for estimating the directional spectrum using cross-power spectra contaminated by estimation errors, though it is also a general method and requires the use of time-consuming iterative calculations.

Consequently, a method needed to be developed that can be applied to arbitrary general measurements, while at the same time easily yielding an accurate and reliable estimate of the directional spectrum.

The present paper discusses inherent drawbacks of several existing methods for estimating the directional spectrum, and then describes a new method, the Extended MEP (EMEP), which correspondingly functions as a general yet practical method. Since the EMEP is formulated in the same manner as the BDM, i.e., considering errors in the cross-power spectra, it demonstrates both robustness and reliability. Here we also examine the EMEP using numerical simulation and field wave data, with its validity being subsequently discussed.

## 2. Fundamental Equation Related to Directional Spectrum

The general relationship between the cross-power spectrum for a pair of wave properties and the wave-number frequency spectrum was introduced by Isobe et al. (1984) as follows:

$$\Phi_{mn}(\omega) = \int_k H_m(k, \omega) H_n^*(k, \omega) \exp\{-ik(x_n - x_m)\} S(k, \omega) dk, \quad (1)$$

where  $\omega$  is the angular frequency,  $\mathbf{k}$  the wave number vector,  $\Phi_{mn}(\omega)$  the cross-power spectrum between the  $m$ -th and  $n$ -th wave properties,  $H_m(\mathbf{k}, \omega)$  the transfer function from the water surface elevation to the  $m$ -th wave property,  $i$  the imaginary unit,  $\mathbf{x}_m$  the location vector of the wave probe for the  $m$ -th wave property,  $S(\mathbf{k}, \omega)$  the wave-number frequency spectrum, and " \* " denotes the conjugate complex. The wave number  $k$  is related to the frequency  $f$  by the following dispersion relationship:

$$\omega^2 = (2\pi f)^2 = gk \tanh kd, \quad (2)$$

hence, the wave-number frequency spectrum can be expressed as a function of the frequency  $f$  and wave propagation direction  $\theta$ . Equation (1) can therefore be rewritten as

$$\begin{aligned} \Phi_{mn}(f) = \int_0^{2\pi} H_m(f, \theta) H_n^*(f, \theta) [\cos\{k(x_{mn} \cos\theta + y_{mn} \sin\theta)\} \\ - \sin\{k(x_{mn} \cos\theta + y_{mn} \sin\theta)\}] S(f, \theta) d\theta, \end{aligned} \quad (3)$$

where  $x_{mn} = x_n - x_m$ ,  $y_{mn} = y_n - y_m$ , and  $S(f, \theta)$  is the directional spectrum.

The directional spectrum is commonly expressed as a product of the frequency spectrum  $S(f)$  and the directional spreading function  $G(\theta|f)$ , i.e.,

$$S(f, \theta) = S(f)G(\theta|f), \quad (4)$$

with  $S(f, \theta)$  taking a non-negative value and satisfying the following relationship:

$$\int_0^{2\pi} S(f, \theta) d\theta = S(f). \quad (5)$$

Substitution of Eq. (4) into (5) yields

$$\int_0^{2\pi} G(\theta|f) d\theta = 1. \quad (6)$$

The transfer function  $H_m(f, \theta)$  in Eq. (3) is generally expressed as

$$H_m(f, \theta) = h_m(f) \cos^{\alpha_m} \theta \sin^{\beta_m} \theta, \quad (7)$$

where the function  $h_m(f)$  and parameters  $\alpha_m$  and  $\beta_m$  obtained from small amplitude wave theory are specified for each measured quantity in Isobe et al. (1984).

Equations (1) and (3) are the fundamental equations for estimating the directional spectrum on the basis of simultaneous measurements of various wave properties. If the function  $S(k, \omega)$  or  $S(f, \theta)$  is determined which respectively satisfies Eq. (1) or (3), and it has a non-negative value, then this function is termed as the directional spectrum.

### 3. Existing Methods for Estimating the Directional Spectrum

If an infinite number of wave properties are measured, i.e., the cross-power spectra are known for infinite pairs of  $m$  and  $n$  in Eq. (1) or (3), the directional spectrum can be uniquely determined. However, only a limited number of wave properties can actually be measured at a limited number of locations; thus, the directional spectrum cannot be uniquely determined since the number of component waves is infinite. Existing methods for directional spectral estimation therefore attempt to determine the unique function by introducing some type of idea and/or trick, and as a result, their advantages and disadvantages depend on the employed concept. The most prominent methods and their advantages/disadvantages are briefly discussed as follows.

#### (1) Direct Fourier Transformation Method (DFTM)

This method was first proposed by Barber (1961) and uses the following estimation equation:

$$\hat{S}(f, \theta) = \alpha \sum_m \sum_n \Phi_{mn}(f) \exp\{ik(x_n - x_m)\}, \tag{8}$$

where  $\alpha$  is a proportionality constant such that the estimate of the directional spectrum satisfies Eq. (5). Although the method's computation is easy, the directional resolution is low and a negative energy distribution sometimes occurs.

(2) Parametric Method

Parametric methods employed by Longuet-Higgins et al. (1963), Panicker and Borgman (1974), and Hasselman et al. (1980) assume a specific formulation for the directional spectrum, such the following truncated Fourier series or a cosine-powered function:

$$S(f, \theta) = a_0(f) + \sum_{n=1}^N \{a_n(f) \cos \theta + b_n(f) \sin \theta\} \tag{9}$$

$$S(f, \theta) = S(f) \sum_n \alpha_n(f) \cos^{2s_n(f)} \left\{ \frac{\theta - \theta_n(f)}{2} \right\}. \tag{10}$$

It should be realized that these methods are only able to approximate the real directional spectrum when it suitably fits the model.

(3) Extended Maximum Likelihood Method (EMLM)

This method was proposed by Isobe et al. (1984) who extended the maximum likelihood method (MLM) developed by Capon (1969) so as to handle an arbitrary combination of wave properties. The EMLM formula is derived using a window theory, namely,

$$S(\mathbf{k}, \omega) = \alpha / \left[ \sum_m \sum_n \Phi_{mn}^{-1}(\omega) H_m^*(\mathbf{k}, \omega) H_n(\mathbf{k}, \omega) \exp\{ik(x_n - x_m)\} \right], \tag{11}$$

where  $\Phi_{mn}^{-1}(\omega)$  is the  $mn$  element of inverse matrix  $\Phi^{-1}(\omega)$ , while  $\alpha$  is a proportionality constant such that the directional spectrum  $\hat{S}(\mathbf{k}, \omega)$  satisfies Eq. (5).

The EMLM has high-directional resolution and versatility, and consequently, has been widely employed in directional wave analysis. On the other hand, when the layout of the probe array is not proper or the cross-power spectra are contaminated by errors, this method sometimes estimates erroneous peaks or negative values, while also in some cases failing to yield a smooth and continuous estimation of the directional spectrum.

(4) Maximum Entropy Principle Method (MEP)

We previously developed the MEP (Hashimoto and Kobune, 1985), which provides a powerful means for estimating the directional spectrum when three-quantity point measurements are available. Such data can be obtained, for example,



using a disc buoy or a two-axis current meter and a wave gauge. The estimation equation of the MEP's directional spreading function is expressed by maximizing the entropy with an assumption that the directional spreading function is a type of probability density function, i.e.,

$$G(\theta|f) = \exp[a_0(f) + \sum_{n=1}^2 \{a_n(f) \cos n\theta + b_n(f) \sin n\theta\}], \quad (12)$$

where the coefficients  $a_n$  and  $b_n$  are the Lagrange multipliers. The advantage of this expression is that even though the Fourier series in the power of the exponential function is truncated by  $n = 2$ , it has non-negative values and yields a wide range of shapes for  $G(\theta|f)$ .

It should be noted that although the MEP was originally developed to be used with three-quantity point measurements, Nwogu (1989) expanded it for application to array measurements. Since this expansion was carried out using the same procedure as the original one, the directional spreading function results in a complex form including Bessel functions; thereby making the computation more difficult than the original MEP.

#### (5) Bayesian directional spectrum estimation method (BDM)

The BDM (Hashimoto, 1987) provides an accurate and reliable estimate of the directional spectrum for array measurements consisting of more than three arbitrary quantities. The assumed estimation equation of the BDM's directional spreading function is not a formal mathematical function, instead being a piece-wise constant function expressed as

$$\hat{G}(\theta|f) = \sum_{k=1}^K \exp\{x_k(f)\} I_k(\theta), \quad (13)$$

where

$$x_k(f) = \ln\{G(\theta_k|f)\} \quad (14)$$

$$I_k(\theta) = \begin{cases} 1 & : (k-1)\Delta\theta \leq \theta < k\Delta\theta \\ 0 & : \text{otherwise} \end{cases} \quad (15)$$

$(k = 1, \dots, K).$

Equation (13) can be determined by minimizing Akaike's Bayesian information criterion (ABIC) (Akaike, 1980) and applying an additional condition that the directional spreading function be smooth and continuous, namely,

$$\{x_k - 2x_{k-1} + x_{k-2}\}^2 \rightarrow \text{small} \quad (16)$$

$(k = 1, \dots, K \text{ and } x_0 = x_K, x_{-1} = x_{K-1}).$

The advantage of Eq. (13) is that even though the additional condition of Eq. (16) is

imposed, it generates non-negative values and yields a wide range of arbitrary shapes for  $G(\theta|f)$ . However, since it consists of many unknown parameters  $x_k(f)$ ; ( $k = 1, \dots, K$ ), the BDM involves the use of time-consuming iterative calculations.

After reviewing the various methods, it is clear that each formulates a tailored model for approximating the directional spectrum, being characterized by some unknown parameters. Though the principle and method of deriving each model are different, inherent advantages and disadvantages arise due to the model's different characteristics. When considering the MEP and BDM, since they are characterized by an exponential function incorporating a power function, an advantage exists in that these models result in non-negative values and flexibly yield a wide range of arbitrary shapes of the directional spectrum.

**4. Formulation of Extended Maximum Entropy Principle Method (EMEP)**

To simplify the nomenclature in the equations, Eq. (3) is rewritten using the upper triangular components of the hermitian matrix  $\Phi(f)$ , such that

$$\phi_i(f) = \int_0^{2\pi} H_i(f, \theta)G(\theta|f)d\theta \quad (i = 1, \dots, K), \tag{17}$$

where  $K$  is the number of equations, and

$$H_i(f, \theta) = H_m(f, \theta)H_n^*(f, \theta)[\cos\{k(x_{mn} \cos\theta + y_{mn} \sin\theta)\} - \sin\{k(x_{mn} \cos\theta + y_{mn} \sin\theta)\}] / W_{mn}(f) \tag{18}$$

$$\phi_i(f) = \Phi_{mn}(f) / \{S(f)W_{mn}(f)\} \tag{19}$$

$$G(\theta|f) = S(f, \theta) / S(f), \tag{20}$$

with  $W_{mn}(f)$  being a weighting function introduced for normalizing and non-dimensionalizing the errors of the cross-power spectra. This function is represented by the following equation (standard deviations of error of co-spectrum and quadrature-spectrum, Bendat and Pirsol, 1986) for the real and imaginary part of Eq. (17), respectively:

$$\sigma[\hat{C}_{mn}(f)] \approx [ \{ \Phi_{mn}(f)\Phi_{mn}(f) + C_{mn}(f)^2 - Q_{mn}(f)^2 \} / 2N_a ]^{1/2} \tag{21}$$

$$\sigma[\hat{Q}_{mn}(f)] \approx [ \{ \Phi_{mn}(f)\Phi_{mn}(f) - C_{mn}(f)^2 + Q_{mn}(f)^2 \} / 2N_a ]^{1/2}, \tag{22}$$

where  $\Phi_{mn}(f) = C_{mn}(f) - iQ_{mn}(f)$  and  $N_a$  is the number of the ensembled average.

The directional spreading function normally takes values greater than or equal to zero. However, in the EMEP, the function is treated as a function which always takes positive values. Then, as a general expression for  $G(\theta|f)$ , we can extend Eq. (12) (or simplify Eq. (13)) to obtain

$$G(\theta|f) = \frac{\exp\left[\sum_{n=1}^N \{a_n(f) \cos n\theta + b_n(f) \sin n\theta\}\right]}{\int_0^{2\pi} \exp\left[\sum_{n=1}^N \{a_n(f) \cos n\theta + b_n(f) \sin n\theta\}\right] d\theta} \quad (23)$$

where  $a_n(f)$ ,  $b_n(f)$ ; ( $n = 1, \dots, N$ ) are unknown parameters.

For the sake of convenience, the complex values  $\phi_i(f)$  and  $H_i(f, \theta)$  are rewritten as

$$\left. \begin{aligned} \phi_i &= \text{Re}\{\phi_i(f)\} & \phi_{K+i} &= \text{Im}\{\phi_i(f)\} \\ H_i(\theta) &= \text{Re}\{H_i(f, \theta)\} & H_{K+i}(\theta) &= \text{Im}\{H_i(f, \theta)\} \end{aligned} \right\} \quad (24)$$

so that  $\phi_i(f)$  and  $H_i(f, \theta)$  are real. For simplicity, the frequency  $f$  is omitted on the LHS of Eq. (24), and is also omitted hereafter.

When Eq. (17) is applied to the observed data, the errors contained in the cross-power spectra must be taken into account. Thus, after making the substitution of Eq. (23) into (17), it can be modified by considering the existence of errors  $\epsilon_i$ , i.e.,

$$\epsilon_i = \frac{\int_0^{2\pi} \{\phi_i - H_i(\theta)\} \exp\left\{\sum_{n=1}^N (a_n \cos n\theta + b_n \sin n\theta)\right\} d\theta}{\int_0^{2\pi} \exp\left\{\sum_{n=1}^N (a_n \cos n\theta + b_n \sin n\theta)\right\} d\theta} \quad (25)$$

$(i = 1, \dots, M)$

where  $M$  is the number of independent equations left after eliminating the meaningless equations such as the zero co-spectrum and zero quadrature-spectrum.

Now, if  $\epsilon_i$ ; ( $i = 1, \dots, M$ ) are assumed to be independent of each other, and the probability of their occurrence is expressed by the normal distribution having a zero mean and variance  $\sigma^2$ , the optimal  $G(\theta|f)$  is one which minimizes  $\sum \epsilon_i^2$ . However, Eq. (25) is nonlinear with respect to  $a_n$ ,  $b_n$ ; ( $n = 1, \dots, N$ ), and is therefore difficult to solve. Consequently, let us apply Newton's technique of local linearization and iteration to solve the problem.

If approximate solutions  $\tilde{a}_n$ ,  $\tilde{b}_n$ ; ( $n = 1, \dots, N$ ) are known, the solution  $a_n$ ,  $b_n$ ; ( $n = 1, \dots, N$ ) can be written as

$$\left. \begin{aligned} a_n &= \tilde{a}_n + a_n' \\ b_n &= \tilde{b}_n + b_n' \end{aligned} \right\} \quad (26)$$

where  $a_n'$ ,  $b_n'$  are the residuals between the solution  $a_n$ ,  $b_n$  and the approximate solution  $\tilde{a}_n$ ,  $\tilde{b}_n$ .

Substitution of Eq. (26) into (25) and rearranging yields the following linearized equation with respect to  $a_n'$ ,  $b_n'$ :

$$\epsilon_i = Z_{N,i} - \sum_{n=1}^N (a_n' X_{n,i} + b_n' Y_{n,i}) \quad (i = 1, \dots, M), \quad (27)$$

where

$$Z_{N,i} = \frac{\int_0^{2\pi} \{\phi_i - H_i(\theta)\} F_N(\theta) d\theta}{\int_0^{2\pi} F_N(\theta) d\theta} \quad (28)$$

$$X_{n,i} = Z_{N,i} \left\{ \frac{\int_0^{2\pi} F_N(\theta) \cos n\theta d\theta}{\int_0^{2\pi} F_N(\theta) d\theta} - \frac{\int_0^{2\pi} \{\phi_i - H_i(\theta)\} F_N(\theta) \cos n\theta d\theta}{\int_0^{2\pi} \{\phi_i - H_i(\theta)\} F_N(\theta) d\theta} \right\} \quad (29)$$

$$Y_{n,i} = Z_{N,i} \left\{ \frac{\int_0^{2\pi} F_N(\theta) \sin n\theta d\theta}{\int_0^{2\pi} F_N(\theta) d\theta} - \frac{\int_0^{2\pi} \{\phi_i - H_i(\theta)\} F_N(\theta) \sin n\theta d\theta}{\int_0^{2\pi} \{\phi_i - H_i(\theta)\} F_N(\theta) d\theta} \right\} \quad (30)$$

$$F_N(\theta) = \exp\left\{ \sum_{n=1}^N (\tilde{a}_n \cos n\theta + \tilde{b}_n \sin n\theta) \right\}. \quad (31)$$

Equation (27) can be solved iteratively by assuming a proper approximate solution  $\tilde{a}_n$ ,  $\tilde{b}_n$ ; ( $n = 1, \dots, N$ ).

Minimizing  $\sum \epsilon_i^2$  for a particular data set also introduces an additional problem of choosing the optimal finite order  $N$  for the model (Eq. (23)); hence to overcome this, the minimum Akaike's Information Criterion (AIC) procedure (Akaike, 1973) is incorporated into the above iterative calculations to yield a reasonable and smooth estimate of  $G(\theta|f)$ . The AIC is given by

$$\text{AIC} = M(\ln 2\pi + 1) + M \ln \hat{\sigma}^2 + 2(2N + 1), \quad (32)$$

where  $M$  is the number of independent equations (Eq. (27)) and  $\hat{\sigma}^2$  is the estimate of the variance of  $\epsilon_i$ ; ( $i = 1, \dots, M$ ).

## 5. Numerical computation of the EMEP

To estimate the directional spectrum using the EMEP, the computation must be performed from lower ( $N = 1$ ) to higher orders. During the iterative computation, however, the computation occasionally becomes unstable in special cases. If so, a control parameter  $\delta$  is introduced into Eq. (26) to under-relax the iterative computation:

$$\left. \begin{aligned} a_n &= \tilde{a}_n + \delta \alpha_n' \\ b_n &= \tilde{b}_n + \delta b_n' \end{aligned} \right\} \quad (33)$$

that is, when the iterative computation is unstable, the control parameter  $\delta$  is changed to a smaller value, followed by  $\delta = (0.5)^k : (k = 0, \dots, 4)$ .

The numerical computation procedure including the minimization of the AIC is summarized as follows:

- 1) Select the lowest model order  $N = 1$  and compute  $X_{n,i}$ ,  $Y_{n,i}$ , and  $Z_{N,i}$  of Eq. (28)  $\sim$  (30) assuming the initial approximate solutions of  $\tilde{a}_1$  and  $\tilde{b}_1$  being equal to zero. Then, to obtain solutions  $a_1$  and  $b_1$ , carry out the iterative computation of Eq. (27) and perform the least square method for  $\sum \epsilon_i^2$  until the absolute values of residuals  $|\alpha'_1|$  and  $|b'_1|$  become small enough ( $|\alpha'_1|, |b'_1| < 0.01$ ).
- 2) Compute the AIC by Eq. (32).
- 3) Substitute  $a_1$  and  $b_1$  obtained in step 1) into Eq. (31) vice  $\tilde{a}_1$  and  $\tilde{b}_1$ , leaving  $\tilde{a}_2$  and  $\tilde{b}_2$  equal to zero, and carry out the same procedure as step 1) to obtain the solutions  $a_i, b_i : (i = 1, 2)$  of the 2nd order model ( $N = 2$ ). If during the iterative computation one of the absolute values of residuals  $|\alpha'_i|, |b'_i| : (i = 1, 2)$  has a value greater than 30, terminate the computation and adopt  $N = 1$  as the optimal model order, with the values  $a_1$  and  $b_1$  obtained in step 1) being chosen as the solutions. If the iterative computation does not converge after 100 iterations, terminate the computation and similarly choose the solutions obtained in step 1). If  $|\alpha'_i|, |b'_i| : (i = 1, 2)$  become less than 0.01, compute the AIC using Eq. (32) and proceed to the next step.
- 4) If the AIC obtained in step 3) is greater than that of step 2), or if the absolute value of the difference between the two AICs is much less than 1, adopt  $N = 1$  as the optimal model order and choose the values  $a_1$  and  $b_1$  of step 1) as the solutions. If the above cases do not hold, proceed to the next step.
- 5) Change the model order into a higher one (3rd, 4th, ..... ) and repeat in the same manner as steps 3) and 4).
- 6) During the computation of step 5), if the AIC of the model order  $N+1$  is greater than that of the previous order  $N$ , or when the absolute value of the difference between the AIC of the model order  $N+1$  and that of the previous order  $N$  is much less than 1, or when the iterative computation does not converge at the model order  $N+1$ , then terminate the computation and choose the model order

$N$  and  $\alpha_i, b_i : (i=1, \dots, N)$  as the optimal solutions.

7) Substitute the optimal solutions  $\alpha_i, b_i : (i=1, \dots, N)$  into Eq. (23) to get the optimal directional spreading function  $\hat{G}(\theta|f)$ .

In addition, since the number of unknown parameters should be less than or equal to the number of independent equations, i.e.,  $2N \leq M$ , steps 1) ~ 6) should be performed at most within this order.

**6. Examination of EMEP by Numerical Simulation**

Here we will employ numerical simulation to examine the validity of using the EMEP to estimate the directional spectrum. The procedure is the same as that used for examining the EMLM (Isobe et al., 1984), where the employed directional spreading function is a cosine-powered type function expressed as

$$G(\theta) = \sum_i \alpha_i \cos^{2S_i} \left( \frac{\theta - \theta_i}{2} \right). \tag{34}$$

When  $i=1$  only, Eq. (34) yields a unimodal directional spreading function, while a bimodal function is formulated by the superposition of two unimodal directional spreading functions, i.e.,  $i=1$  and 2, having a different coefficient  $\alpha_i$ , mean direction  $\theta_i$ , and spreading parameter  $S_i$ . The cross-power spectra utilized for the numerical simulation are obtained by numerically integrating Eq. (3).

**Figure 1** compares the given directional spreading function (TRUE) and the estimated ones by the EMEP, MEP, BDM, and EMLM, where the three measured quantities (sea surface elevation and two orthogonal slopes on the surface at the same location) are assumed to be the simulated observation condition. The ordinate is normalized by dividing the value of the directional spreading function by the maximum value of the TRUE directional spreading function. As indicated, the EMEP yields the same estimate as the MEP and can detect the small peak in proper direction in **Fig. 1(e)** and **(f)**, though it overestimates the main peak and underestimates the

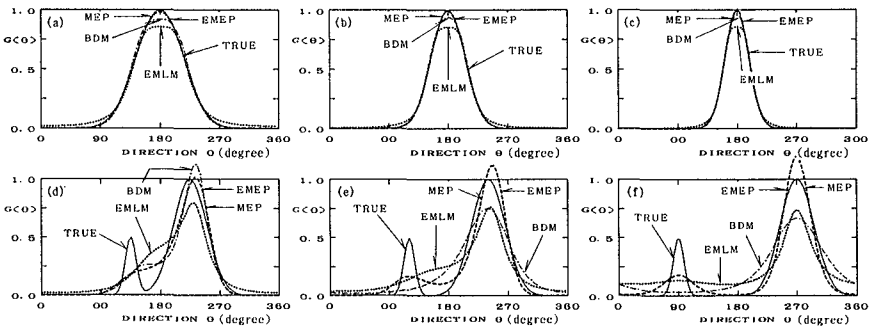


**Fig. 1** Comparison of EMEP, MEP, BDM and EMLM (Three-quantity measurement)

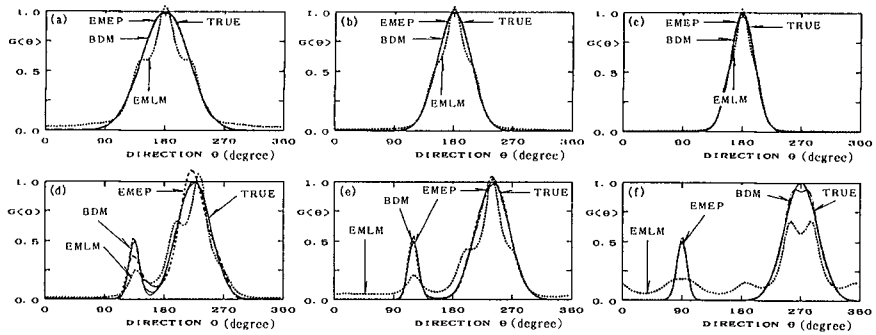


**Fig. 2** Comparison of EMEP, MEP, BDM and EMLM (Star array measurement)

small peak. Also note that the EMEP (MEP) shows the minimum leakage of the wave energy into neighboring directional bands. On the other hand, the EMLM appears to recognize the existence of the small peak in **Fig. 1(e)**, but its estimated direction is not proper, while the BDM does not even recognize the small peak.

**Figure 2** shows results when a star array consisting of four wave gauges is assumed as the simulated observation condition. The minimum distance  $D$  between the wave gauges is assumed as  $D/L=0.2$ , where  $L$  is the wave length. In comparison with **Fig. 1**, the directional resolution of the EMEP, BDM, and EMLM is improved in **Fig. 2(d)**, **(e)**, and **(f)**. In particular, the EMEP is very close to the BDM and shows good agreement with TRUE. In contrast, the EMLM underestimates the small peak and shows some energy leakage around the peaks, especially in **Fig. 2(e)** and **(f)**.

## 7. Field Data Analysis

Here we apply the EMEP to analyze wave records acquired at an offshore oil rig (Iwaki-oki Station) located 42 km off the Iwaki coast, the northeastern coast of the main island of Japan (**Fig. 3**), where the water depth is 155 m. **Figure 4** shows the oil rig, which has installed on its legs, four step-resistance wave gauges, a two-axis ultrasonic current meter, and a pressure sensor (**Fig. 5**). The simultaneous measurement of seven elements is performed over 20 min every 2 h. The Onahama Port Construction Office, Second Port Construction Bureau, Ministry of Transport, has been conducting this multi-element measurement of directional waves since 1986.

**Figure 6** shows typical directional spectra of a swell having a significant wave height  $H_{1/3} = 3.81$  m, period  $T_{1/3} = 12.3$  s, and directional spreading parameter  $S_{\max} = 75$ , which are estimated by the EMEP, BDM, and EMLM. Note that the shape of the EMEP estimate is very similar to that of the BDM, but different from the EMLM's. The major difference between them is that the EMLM is more diffuse and does not show a concentration around the peak. In addition, the peak of the EMLM is obviously much lower than that of the EMEP and BDM.

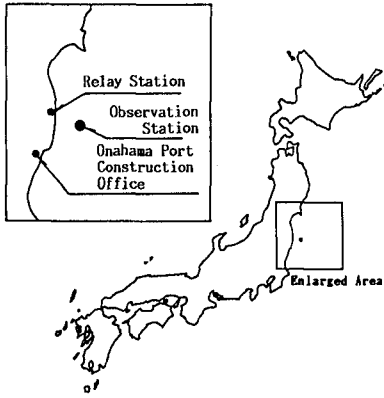


Fig. 3 Location of the wave observation station.

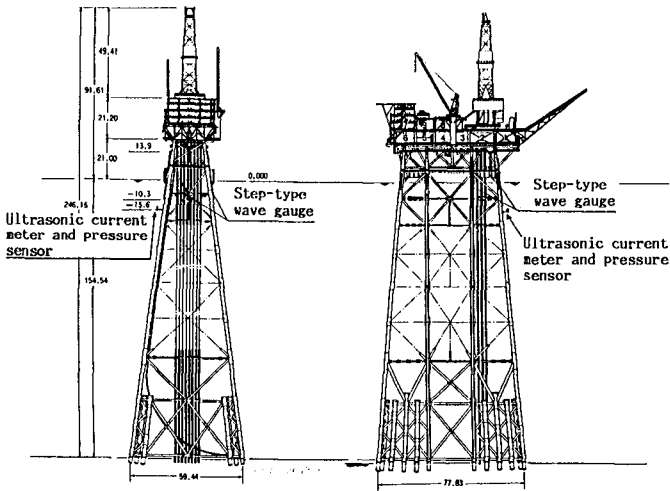


Fig. 4 Offshore oil rig and the location of wave instruments.

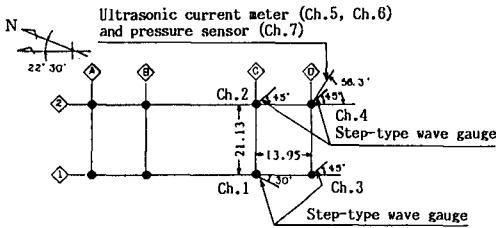


Fig. 5 Wave instrument array.



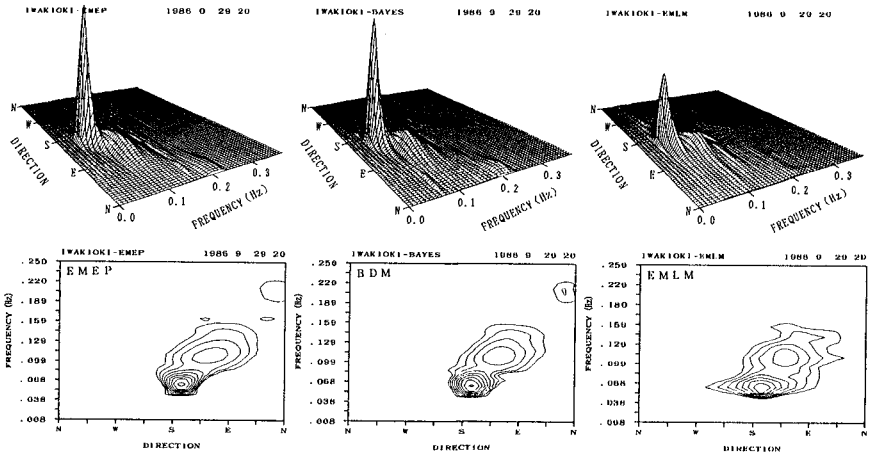


Fig. 6 Typical directional spectra of a swell estimated by EMEP, BDM and EMLM

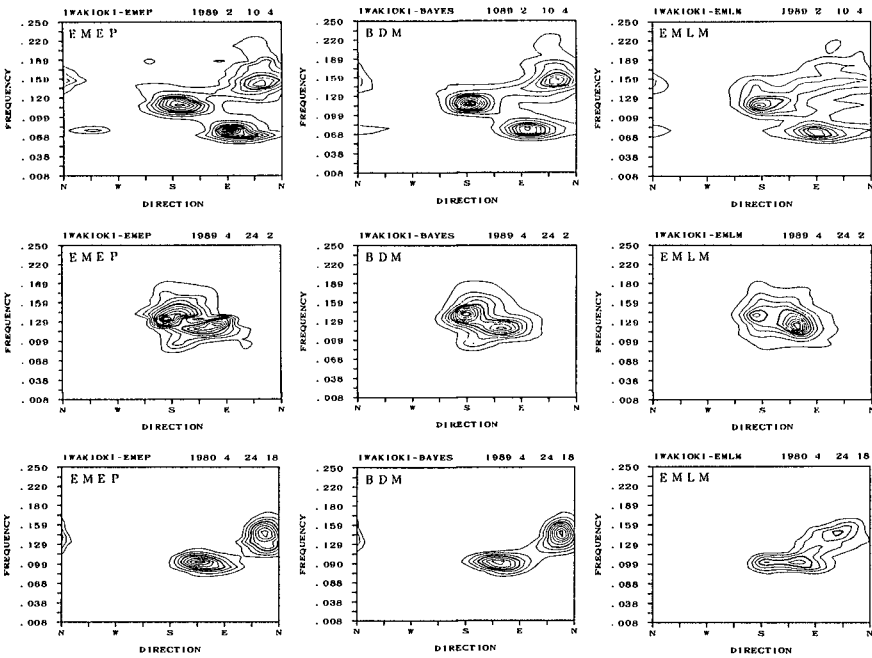


Fig. 7 Typical directional spectra of multiple wave systems estimated by EMEP, BDM, and EMLM.

Sometimes several wave systems exist from different sources, with Fig. 7 showing such an example measured at the Iwaki-oki Station for the EMEP, BDM, and EMLM. The contour lines of the relative spectral density are plotted by direction versus frequency domain. The upper figures show directional spectra having  $H_{1/3} = 2.18$  m and  $T_{1/3} = 9.0$  s, while the middle ones are  $H_{1/3} = 2.02$  m and  $T_{1/3} = 8.2$  s and the lower ones  $H_{1/3} = 3.94$  m and  $T_{1/3} = 8.8$  s. In the EMEP and BDM, several wave groups can be clearly seen coming from different directions with different peak frequencies, whereas some of the EMLM energy peaks are diffused and not as clear.

## 8. Conclusions

Precise determination of the directional spectral characteristics of ocean waves is an essential step in planning and designing of coastal and offshore structures. Since field measurements of directional wave spectra require deployment of multiple sensors, all of which must be maintained in good condition for successful data recording, the obtained data must be analyzed using an accurate, reliable, and robust method to estimate the directional wave spectrum. We believe the proposed EMEP meets these criteria and can be successfully employed for carrying out research on directional seas.

Our major conclusions are as follows:

- 1) The EMEP can be applied to handle arbitrary-mixed instrument array measurements.
- 2) When the EMEP is applied to three-quantity measurements, it yields the same estimate as the MEP and has higher resolution than the EMLM.
- 3) When the EMEP is applied to more than three arbitrary-mixed instrument array measurements, it yields almost the same estimate as the BDM and has the highest resolution among other existing methods.
- 4) A personal computer can be used to perform the EMEP; thereby obtaining real-time estimation of directional spectra.

## References

- Akaike, H. (1973): Information theory and an extension of the maximum likelihood principle, 2nd Inter. Symp. on Information Theory (Petrov, B. N. and Csaki, F. eds.), Akademiai Kiado, Budapest, pp. 267–281.
- Akaike, H. (1980): Likelihood and Bayes procedure, Bayesian statistics (Bernardo, J. M., De Groot, M. H., Lindley, D. U., and Smith, A. F. M. eds.), University Press, Valencia, pp. 143–166.
- Barber, N. F. (1961): The directional resolving power of an array of wave detectors, *Ocean Wave Spectra*, Prentice Hall, Inc., pp. 137–150.
- Bendat, J. S. and A. G. Piersol (1986) : *Random Data Analysis and Measurement Procedures*, 2nd ed., John Wiley & Sons, 566 p.
- Capon, J. (1969): High-resolution frequency-wavenumber spectrum analysis, *Proc. IEEE*, Vol. 57, pp. 1480–1418.
- Hashimoto, N. and K. Kobune (1985): Estimation of directional spectra from the

- Maximum Entropy Principle, Rept. of P.H.R.I., Vol. 23, No. 3, pp. 123 – 145 (in Japanese); or Kobune, K. and N. Hashimoto (1986): Estimation of directional spectra from the Maximum Entropy Principle, Proc. 5th Inter. OMAE Symp., Tokyo, pp. 80–85.
- Hashimoto, N. (1987): Estimation of directional spectra from a Bayesian approach, Rept. of P.H.R.I., Vol. 26, No. 2, pp. 97 – 125 (in Japanese); or Hashimoto, N., K. Kobune and Y. Kameyama (1987): Estimation of directional spectrum using the Bayesian Approach, and its application to field data analysis, Rept. of P.H.R.I., Vol. 26, No. 5, pp. 57 – 100; or Hashimoto, N. and K. Kobune (1988): Directional spectrum estimation from a Bayesian approach, Proc. 21st ICCE, Spain, Vol. 1, pp. 62 – 76.
- Hashimoto, N. and K. Kobune (1987): Estimation of directional spectra from a Bayesian approach in incident and reflected wave field, Rept. of P.H.R.I., Vol. 26, No. 4, pp. 3 – 33 (in Japanese).
- Hasselmann, D. E., M. Dunckel, and J. A. Ewing (1980): Directional wave spectra observed during JONSWAP 1973, Journal of Physical Oceanography, Vol. 10, pp. 1264 – 1280.
- Isobe, M., K. Kondo and K. Horikawa (1984): Extension of MLM for estimating directional wave spectrum, Proc. Symp. on Description and Modeling of Directional Seas, Paper No. A-6, 15 p.
- Longuet-Higgins, M. S., D. E. Cartwright, and N. D. Smith (1963): Observation of the directional spectrum of sea waves using the motions of a floating buoy, Ocean Wave Spectra, Prentice Hall Inc., New Jersey, pp. 111 – 136.
- Nwogu, O. (1989): Maximum Entropy estimation of directional wave spectra from an array of wave probes, Applied Ocean Res., Vol. 11, No. 4, pp. 176 – 193.
- Panicker, N. N. and L. E. Borgman (1974): Enhancement of directional wave spectrum estimate, Proc. 13th ICCE, Copenhagen, pp. 258 – 279.

## CHAPTER 19

### A Regression Model for Estimating Sea State Persistence

Yoshio Hatada<sup>1</sup> and Masataka Yamaguchi<sup>2</sup>

#### Abstract

This paper deals with regression models for estimating probability distributions of long term wave height, sea state persistence above a wave height threshold and peak wave height during a storm, and yearly-averaged occurrence rate of peak wave height event. The models, in which input condition is the variance of long term wave height at a concerned sea area, were constructed on the basis of statistical analysis of the long term wave height data obtained around the Japanese coast. First, the effect of observation interval on the above-mentioned wave climate statistics was investigated and a method to remove the effect by use of FFT was proposed. Second, Applicability of each regression model was confirmed from close agreement between estimation and observation for the wave climate statistics. Finally, return periods of extreme wave height with prescribed sea state persistence and wave height threshold at wave observation points around the Japanese coast were estimated with a combination of the present regression models.

#### 1. Introduction

Sea state persistence is an important factor to be considered in maritime activity and design of coastal structures. Although many studies on its statistical properties (Lawson and Abernethy, 1975; Graham, 1982; Takahashi et al., 1982; Kuwashima and Hogben, 1984; Smith, 1988; Yamaguchi et al., 1989, 1993; Teisson, 1990; Mathiesen, 1994) have been conducted using the observed

---

1 Research Assistant, Dept. of Civil and Ocean Eng., Ehime Univ., Bunkyocho 3, Matsuyama 790, Ehime Pref., Japan

2 Prof., Dept. of Civil and Ocean Eng., Ehime Univ., Bunkyocho 3, Matsuyama 790, Ehime Pref., Japan

wave data, probability distribution of sea state persistence of high waves which is crucial to the design of coastal structures and a statistical model for estimating sea state persistence of high waves still remain open to question, because of the lack of long term observed wave data with good quality.

The aim of this study is to present a regression model for estimating return period of extreme wave height with prescribed sea state persistence and wave height threshold on the basis of statistical analysis for distributions of significant wave height and sea state persistence and peak wave height during a storm using long term data of coastal waves around Japan acquired over several years by the Japan Meteorological Agency and the Bureaus of Harbor Construction, Ministry of Transport.

## 2. Wave Data and Analysis Method

Wave data used in the analysis are those measured for 20 minutes every 1 to 3 hours with a sonic-type wave gauge installed in water of 30 to 50 m depth. Fig. 1 shows location of 14 wave observation points around the Japanese coast. The longest and shortest observation periods are 14 years at Irouzaki in the Pacific coast and Kyougamisaki in the Japan Sea coast and 5 years at Shirihamisaki in the Pacific coast of North Japan. The



Fig. 1 Location of wave observation points.

most prominent feature of the wave data is that breaks in the data record are rare, in which even the highest ratio of breaks is less than 5 % of the total run at Sakihama in the Pacific coast. One or two missing data points in the time series of wave height were filled using linear interpolation but larger gaps due to breaks were not filled.

Fig. 2 illustrates the definitions of sea state persistence  $\tau$  and peak wave height  $H_p$ . Individual sea state persistence  $\tau$  is defined as linearly-interpolated time span above a wave height threshold  $H_{1/3c}$ . Wave height threshold is prescribed every 0.25 m for the range of 0.5 to 5 m. Peak wave height  $H_p$  is obtained by fitting of parabolic curve to the three largest wave height data to recover the reduction of wave height associated with observation of discrete interval and application of FFT.

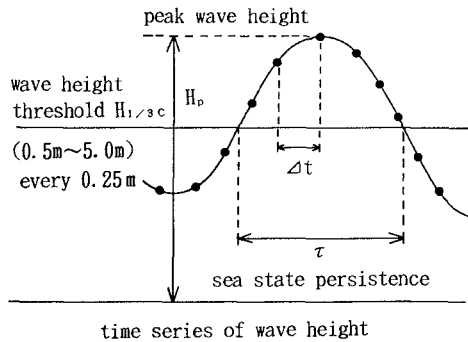


Fig. 2 Definitions of sea state persistence and peak wave height.

### 3. Fitting of Probability Distribution to Wave Data

Four kinds of probability distributions such as 3-parameter and 2-parameter Weibull distributions, 3-parameter lognormal distribution and hypergamma distribution (Suzuki, 1964) or generalized gamma distribution (Ochi, 1992) were used for data fitting. As a result of goodness of fit test, the 3-parameter Weibull distribution was chosen for fitting to the long term wave height data and peak wave height data, and the 2-parameter Weibull distribution was used for fitting to persistence data above a wave height threshold given every 0.25 m. The method applied for the estimation of the parameters is the maximum likelihood method. Each parameter is distinguished with suffix "H", or " $\tau$ " or "e". Non-exceedance probability of the 3-parameter Weibull distribution

F(x) is written as

$$F(x) = 1 - \exp\left[-\left\{\frac{(x-b)}{(x_0-b)}\right\}^k\right], \quad (1)$$

in which k, b and  $x_0$  are the shape parameter, location parameter and scale parameter respectively. If the location parameter b is set to zero, Eq. (1) reduces to 2-parameter Weibull distribution.

Fig. 3 shows an example of the probability distributions fitted to the wave height data. Goodness of fit of the 3-parameter Weibull distribution to the wave height data is satisfactory in this case. The other distributions produce poor fit in the higher or lower wave height region and the parameters estimated for hypergamma distribution are not always statistically stable.

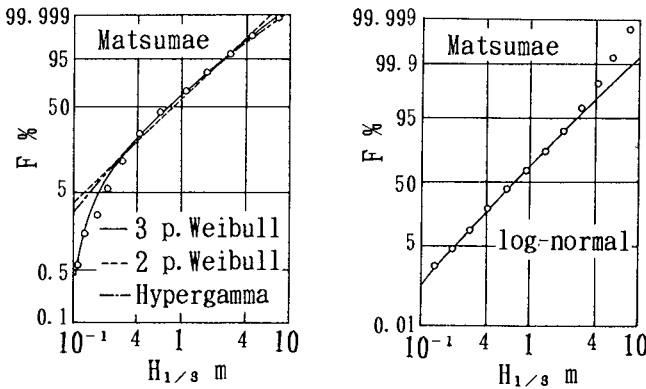


Fig. 3 Fitting of probability distributions to wave height data.

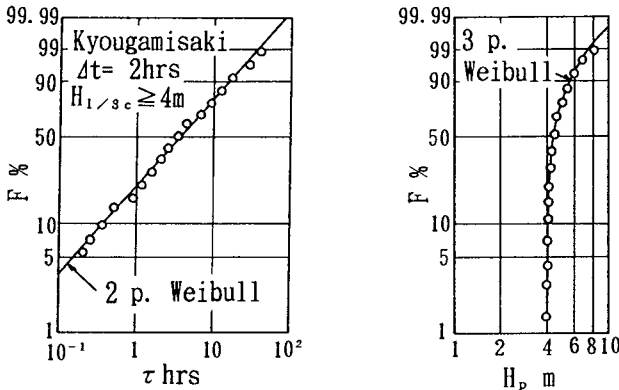


Fig. 4 Fitting of 2-parameter Weibull distribution to sea state persistence data and fitting of 3-parameter Weibull distribution to peak wave height data.

Examples of the fitting of the 2-parameter Weibull distribution to the persistence data and the fitting of the 3-parameter Weibull distribution to the peak wave height data are indicated in Fig. 4. Goodness of fit of these distributions is satisfactory. When sea state persistence data are well approximated with the 2-parameter Weibull distribution, use of the 2-parameter distribution rather than the 3-parameter distribution is preferable, because the estimates of parameters in this case are statistically more stable.

#### 4. Effect of Sampling Interval on Wave Climate Statistics

In order to investigate the effect of sampling interval on wave climate statistics, time series of wave height data were resampled with sampling intervals of 2, 3, 4, 5, 6, 8, 10 and 12 hours from those observed every 1 hour and with sampling intervals of 4, 6, 8, 10 and 12 hours from those observed every 2 hours. Then, wave climate characteristics were analyzed using the above-mentioned methods. The left side of Fig. 5 shows an example of the relation between shape parameter  $k_\tau$  of the 2-parameter Weibull distribution fitted to sea state persistence data and wave height threshold  $H_{1/3c}$  in the case of sampling time of  $\Delta t=2$  hours, and the right side of Fig. 5 is the relation between shape parameter  $k_e$  of the 3-parameter Weibull distribution fitted to peak wave height data and wave height threshold  $H_{1/3c}$ . Relations between the Weibull parameters and wave height threshold are approximated well with power functions such as  $k_\tau = a_{k_\tau} (H_{1/3c})^{b_{k_\tau}}$  and  $k_e = a_{k_e} (H_{1/3c})^{b_{k_e}}$ . These results hold for the other parameters  $x_{0\tau}$ ,  $b_e$  and  $x_{0e}$  of the Weibull distribution.

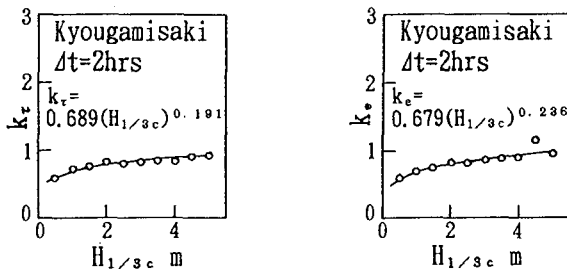


Fig. 5 Relation between Weibull parameter and wave height threshold.

The relations between the coefficients  $a_{k_\tau}$ ,  $a_{k_e}$  in the power function and sampling interval  $\Delta t$  are indicated in Fig. 6. These coefficients, and consequently, the



probability distributions of sea state persistence and peak wave height are strongly dependent on sampling interval  $\Delta t$ . But the parameters of the 3-parameter Weibull distribution fitted to long term wave height data are almost independent of sampling interval.

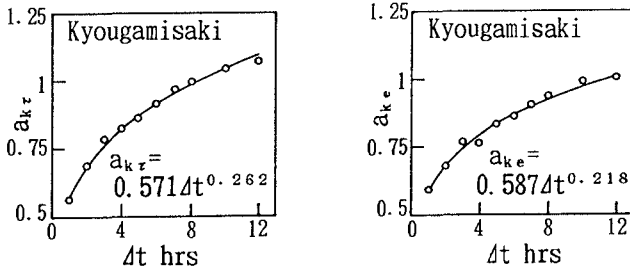


Fig. 6 Dependence of coefficient in power function on observation interval.

In order to remove the effect of the sampling interval on wave climate statistics, higher frequency components in time series of wave height data were filtered out by making use of FFT, and then the same methods as before were applied for the estimation of the wave climate statistics. Fig. 7 describes the effect of cut-off period on the coefficient in the power function, and an almost constant value of the coefficient can be found for the range of sampling interval shorter than half of a prescribed cut-off period. But it should be noted that filtering of time series of wave height data produces longer sea state persistence data and lower peak wave height data. In the following analysis, the cut-off period of  $\Delta t=6$  hours is chosen in order to avoid the smoothing effect as much as possible and to make quality of wave height data similar with respect to the sampling interval, when the sampling interval used in actual observation is taken into account.

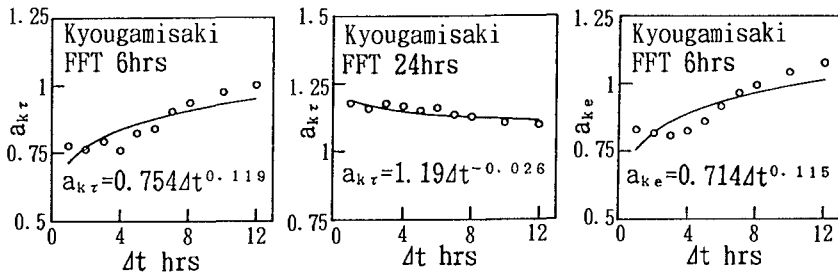


Fig. 7 Effect of cut-off period on coefficient in power function.

5. Construction of Regression Models

(1) Regression model for wave height distribution

Fig. 8 shows the relations between parameters of the 3-parameter Weibull distribution fitted to long term wave height data and variance  $H_{\sigma}^2$  of wave height data in each wave observation point. The relations are approximated well by power functions such as

$$\begin{aligned}
 k_H &= 1.10(H_{\sigma}^2)^{-0.246}, & b_H &= 0.088(H_{\sigma}^2)^{-0.894}, \\
 x_{0H} &= 1.19(H_{\sigma}^2)^{0.088}
 \end{aligned}
 \tag{2}$$

These relations are approximate ones, because the parameters of the Weibull distribution theoretically depend on mean, variance and skewness of the population. But long term wave height distribution can be approximately estimated from these regression equations by giving wave height variance in the sea area as an input condition.

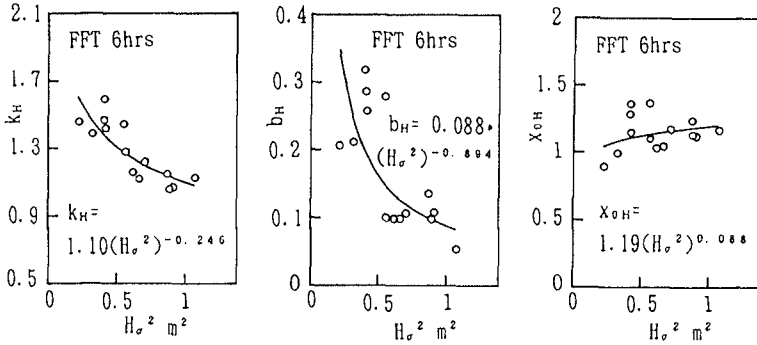


Fig. 8 Relation between Weibull parameter for wave height distribution and variance of wave height.

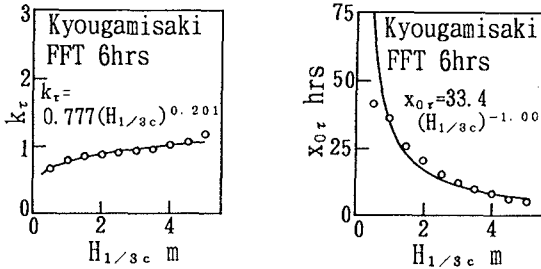


Fig. 9 Relation between sea state persistence parameter and wave height threshold.

(2) Regression model for sea state persistence

Relations between sea state persistence parameters and wave height threshold are indicated in Fig. 9. The relations are approximated well by regression equations such as

$$k\tau = a(H_1/3c)^b, \quad x_0\tau = c(H_1/3c)^d \quad (3)$$

Fig. 10 shows the relations between coefficients in the above regression equations and variance of wave height at 14 wave observation points around the Japanese coast. Relatively high correlation is found between these variables and the relations are approximated with power functions such as

$$\begin{aligned} a &= 0.778(H_\sigma^2)^{0.088}, & b &= 0.205(H_\sigma^2)^{-0.284} \\ c &= 35.1(H_\sigma^2)^{0.555}, & d &= 0.955(H_\sigma^2)^{0.324} \end{aligned} \quad (4)$$

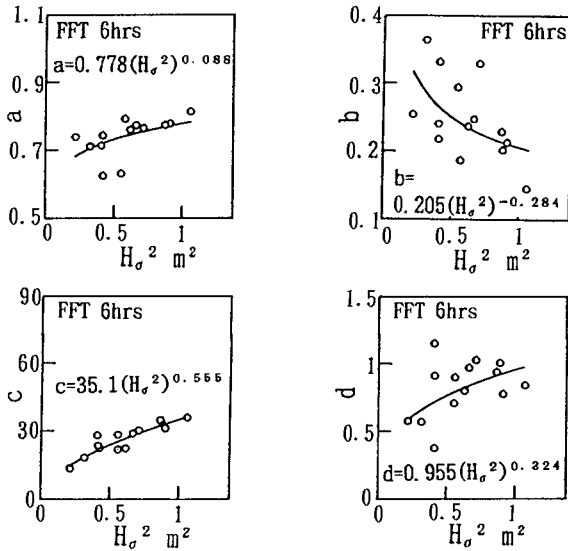


Fig. 10 Relation between coefficient in regression equation and variance of wave height.

Thus, probability distribution of sea state persistence above a prescribed wave height threshold can be estimated by using these regression models, when wave height variance in the sea area is given as an input condition. Fig. 11 illustrates the comparison between estimation and observation for mean  $\bar{\tau}$  and standard deviation  $\tau_\sigma$  of sea state persistence and probability distribution. Good correspondence is observed between estimation and observation.

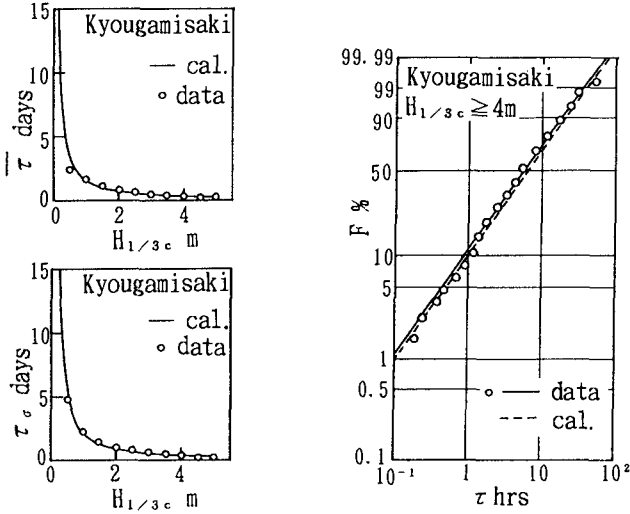


Fig. 11 Comparison between estimation and observation for sea state persistence.

(3) Regression models for peak wave height and its occurrence rate

Fig. 12 shows the relation between peak wave height parameters in the Weibull distribution  $k_e$ ,  $b_e$ ,  $x_{0e}$  and yearly-averaged occurrence rate of peak wave height  $N$ , and wave height threshold  $H_{1/3c}$ . The former three relations are approximated with power functions such as

$$k_e = a(H_{1/3c})^b, \quad b_e = c(H_{1/3c})^d, \quad x_{0e} = e(H_{1/3c})^f \quad (5)$$

and the last relation is approximately expressed with exponential function as

$$N = p \cdot \exp\{-q(H_{1/3c})^{1.5}\} \quad (6)$$

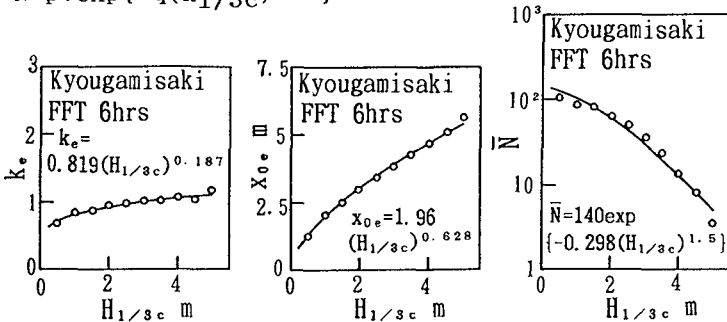


Fig. 12 Relation between peak wave height parameters and occurrence rate, and wave height threshold.

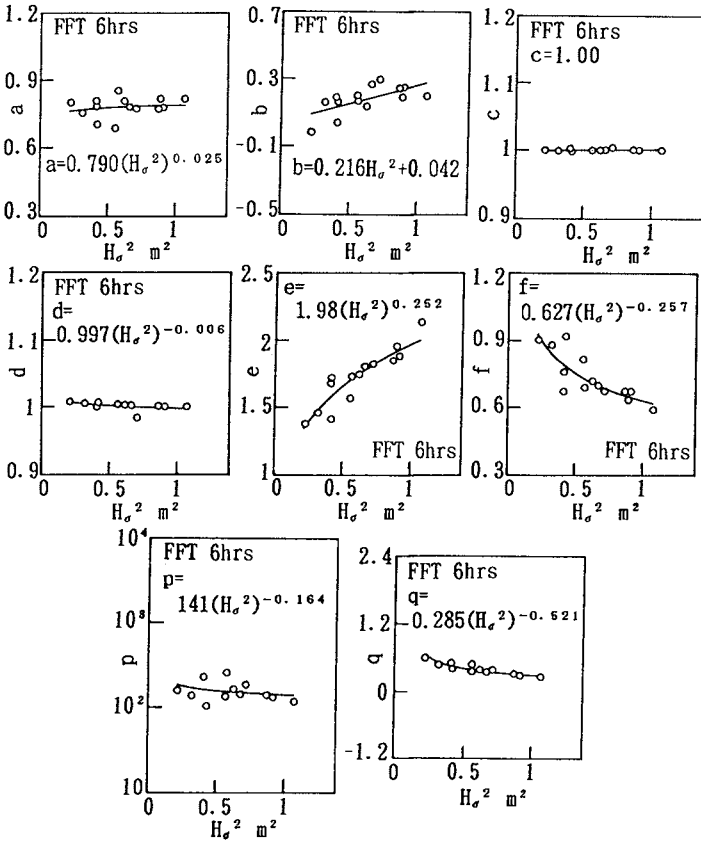


Fig. 13 Relation between coefficients in regression equations and wave height variance.

Then relations between coefficients in regression equations and variance of wave height estimated individually at 14 wave observation points are shown in Fig. 13. These relations are also well approximated with power functions as

$$\begin{aligned}
 a &= 0.790(H_\sigma^2)^{0.025}, & b &= 0.216H_\sigma^2 + 0.042 \\
 c &= 1.000, & d &= 0.997(H_\sigma^2)^{-0.006} \\
 e &= 1.98(H_\sigma^2)^{0.252}, & f &= 0.627(H_\sigma^2)^{-0.257} \\
 p &= 141(H_\sigma^2)^{-0.164}, & q &= 0.285(H_\sigma^2)^{-0.521}
 \end{aligned}
 \tag{7}$$

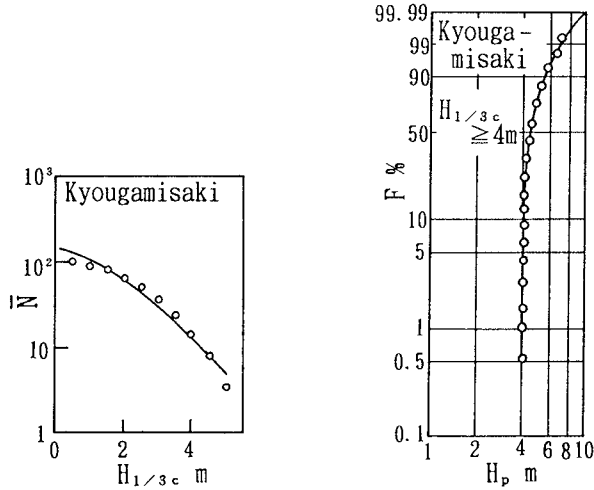


Fig. 14 Comparison between estimation and observation for yearly-averaged occurrence rate of peak wave height and probability distribution of peak wave height.

Probability distributions of peak wave height and yearly-averaged occurrence rate of peak event at a prescribed wave height threshold can be estimated by using these regression models for given wave height variance. Fig. 14 is an example of the estimation for yearly-averaged occurrence rate of peak wave height and probability distribution of peak wave height. High correlation between estimation and observation can be seen.

## 6. Estimation of Return Period of Extreme Wave Height

Assuming independence between sea state persistence and peak wave height, return period  $R$  of peak wave height  $H_p$  with prescribed sea state persistence  $\tau$  above a wave height threshold  $H_{1/3c}$  can be estimated from the following equation

$$1/R = N(H_{1/3c}) \{1 - F(H_p; H_{1/3c})\} \{1 - F(\tau; H_{1/3c})\} \quad (8)$$

in which  $F(H_p; H_{1/3c})$  and  $F(\tau; H_{1/3c})$  are non-exceedance probabilities of peak wave height  $H_p$  and sea state persistence  $\tau$  above a wave height threshold  $H_{1/3c}$ . When variance of long term wave height at a location around

the coastal area of Japan is given as an input condition, the Weibull parameters and yearly-averaged occurrence rate of peak event above a prescribed wave height threshold required in Eq. (8) are determined by using all regression equations mentioned before.

Table 1 illustrates examples of return periods of peak wave height  $H_p=8$  m with sea state persistence  $\tau=12$  hours above a wave height threshold  $H_{1/3c}=4$  m which are estimated around the coastal area of Japan. The return periods of extreme wave height under these conditions range from about 160 to 270 years. The longest return period is obtained at Atsumi facing Northern Japan Sea. This is due to low exceedance probability of a prescribed extreme wave height and the resulting longer return period. The second longest return period is evaluated at Satamisaki facing Western Pacific Ocean. This is due to geographical situation around Satamisaki. That is to say, two islands, Tanegashima Island and Yakushima Island are located near Satamisaki, which tends to be sheltered from incoming waves by these islands.

Table 1 Return period R for peak wave height  $H_p$  with sea state persistence  $\tau$  above wave height threshold  $H_{1/3c}$  for  $H_p=8$  m,  $\tau=12$  hours and  $H_{1/3c}=4$  m.

location	$H_\sigma^2$ ( $m^2$ )	$\bar{N}(H_{1/3c})$	$1-F(\tau)$	$1-F(H_p)$	R (years)
Matsumae	.620	8.2	.246	.0029	169
Atsumi	1.067	15.4	.276	.0009	269
Kyougamisaki	.885	12.7	.268	.0014	211
Kashima	.663	9.0	.251	.0026	173
Fukuejima	.565	7.2	.240	.0035	165
Shirihamisaki	.406	4.3	.214	.0066	165
Enoshima	.555	7.0	.239	.0036	164
Irouzaki	.407	4.3	.215	.0066	164
Sakihama	.320	2.7	.194	.0105	179
Satamisaki	.216	1.1	.157	.0223	249
Kiyanmisaki	.415	4.4	.216	.0064	164
Wajima	.869	12.4	.267	.0015	207
Kanazawa	.906	13.0	.269	.0013	216
Tottori	.708	9.8	.255	.0023	178

## 7. Conclusions

Main results obtained in this study are summarized as follows;

(1) Effects of wave observation interval on the distributions of sea state persistence and peak wave height during a storm are relatively strong, whereas the effect on the long term wave height distribution is negligibly weak.

(2) Effect of observation interval on wave climate statistics can be removed by use of FFT.

(3) Probability distribution of sea state persistence above a prescribed wave height threshold can be estimated with a proposed regression model, when variance of long term wave height is given as an input condition.

(4) At the coastal sea area of Japan, return period of extreme wave height with prescribed sea state persistence and wave height threshold can be estimated with a combination of regression models for probability distributions of sea state persistence and peak wave height, and yearly-averaged occurrence rate of peak wave height, when wave height variance in the sea area is given as an input condition.

## 8. Acknowledgment

The authors thanks the Japan Ocean Data Center of Maritime Safety Agency, the Maritime Section of Japan Meteorological Agency and the Bureaus of Harbor Construction, Ministry of Transport for kindly offering the valuable wave data. Thanks are also due to Mr. M. Ohfuku, Technical Officer of Civil and Ocean Engineering, Ehime University and Mr. Arai, former student of Department of Ocean Engineering, Ehime University for their sincere assistance during the study.

## References

Graham, C.(1982): The parameterization and prediction of wave height and wind speed persistence statistics for oil industry operational planning purposes, Coastal Eng., Vol. 6, pp.303-329.

Kuwashima, S. and N. Hogben(1984): The estimation of persistence statistics from cumulative probability of wave height, Rept. No. R183, NMI Ltd., 72p..



Lawson, N. V. and C. L. Abernethy(1975): Long term wave statistics off Botany Bay, Proc. 2nd Austr. Conf. on Coastal and Ocean Eng., pp. 167-176.

Mathiesen, M.(1994): Estimation of wave height duration statistics, Coastal Eng., Vol. 23, pp.167-181.

Ochi, M. K.(1992): New approach for estimating the severest sea state from statistical data, Proc. 23rd ICCE, Vol. 1, pp.512-525.

Smith, O. P.(1988): Duration of extreme wave condition, J. Waterway, Port, Coastal, and Ocean Eng., ASCE, Vol. 114, No. 1, pp. 1-17.

Suzuki, E.(1964): Hypergamma distribution and its fitting to rainfall data, Papers in Meteorol. and Geophys., Vol. 15, pp.31-51.

Takahashi, T. et al.(1982): Statistical properties of coastal waves, Proc. 29th Japanese Conf. on Coastal Eng., pp.11-15 (in Japanese).

Teisson, C.(1990): Statistical approach of duration of extreme storms, Consequences on break water damages, Proc. 22nd ICCE, Vol. 111, pp.1851-1860.

Yamaguchi, M. et al.(1989): Analysis of wave climate around the coastal area of Japan, Natural Disas. Sci., 8-2, pp.23-45 (in Japanese).

Yamaguchi, M. et al.(1993): Statistics of duration of severe sea state and its evaluation model, Proc. Coastal Eng., Vol. 40, pp.116-120 (in Japanese).

## CHAPTER 20

### THE MAXIMUM SIGNIFICANT WAVE HEIGHT IN THE SOUTHERN NORTH SEA

*L.H. Holthuijsen<sup>1</sup>, J.G. de Ronde<sup>2</sup>, Y. Eldeberky<sup>1</sup>, H.L. Tolman<sup>3</sup>, N. Booij<sup>1</sup>,  
E. Bouws<sup>4</sup>, P.G.P. Ferrier<sup>1</sup>, J. Andorka Gal<sup>2</sup>*

#### **Abstract**

The maximum possible wave conditions in the southern North Sea are estimated with synthetic storms and a third-generation wave model. The storms and the physics in the wave model have been chosen within the uncertainty of the state-of-the-art to have maximum effect. The wave conditions appear to be limited by the presence of the bottom and to some extent by the assumed maximum wind speed of 50 m/s. The maximum significant wave height thus determined for the southern North Sea is about 0.4 times the local water depth.

#### **Introduction**

Extrapolations of observations usually provide fair estimates of extreme conditions as long as the physical regime of the waves does not change dramatically. Such a change may occur because the wind speed is limited and in shallow seas the water depth is limited. An extrapolation of the significant wave height should take this into account, possibly as an upper limit of the significant wave height. In the present study, the existence of such an upper limit in the southern North Sea is investigated.

Although the maximum wind speed in the North Sea is not well known, consultation with meteorologists suggested the 50 m/s wind speed as an upper limit. We investigate the sensitivity of our results for this assumption. The physical phenomena of waves in these conditions are not well known either but we use a state-of-the-art wave model. For deep water this type of model has shown to be reliable in hurricane conditions.

---

<sup>1</sup> Delft University of Technology, the Netherlands, <sup>2</sup> Ministry of Public Works and Transport, the Netherlands, <sup>3</sup> NOAA, National Meteorological Center, USA, <sup>4</sup> Royal Netherlands Meteorological Institute, the Netherlands

## The wave model

We use the numerical wave model WAVEWATCH II (Tolman, 1991, 1992). It is based on the discrete spectral action balance equation with a number of optional formulations for wave generation and dissipation. First we use it with initial choices for these formulations and then we investigate the alternatives.

### The wave model

The action balance equation is a generalization of the energy balance equation in the presence of currents (e.g., Phillips, 1977). In the model this balance is formulated for propagation over a sphere with coordinates longitude  $\lambda$  and latitude  $\phi$ :

$$\frac{\partial N(\omega, \theta)}{\partial t} + (\cos \phi)^{-1} \frac{\partial C_{\phi} \cos \phi N(\omega, \theta)}{\partial \phi} + \frac{\partial C_{\lambda} N(\omega, \theta)}{\partial \lambda} + \frac{\partial C_{\omega} N(\omega, \theta)}{\partial \omega} + \frac{\partial C_{\theta} N(\omega, \theta)}{\partial \theta} = S(\omega, \theta)$$

in which  $N(\omega, \theta)$  is the action density of the waves, defined as the energy density  $E(\omega, \theta)$  divided by the relative frequency  $\sigma$ , as function of absolute frequency  $\omega$  and direction  $\theta$ . The left-hand-side represents the local rate of change of the action density, propagation along great circles, shifting of the absolute frequency due to time variations in depth and currents, and refraction. The expressions are taken from linear wave theory (e.g. Mei, 1983). We will not consider currents in the present study. The right-hand-side of the above balance (the net production of wave action) represents all effects of generation and dissipation of the waves. The processes which are included in the model are: wave generation by wind, nonlinear quadruplet wave-wave interactions and dissipation (white-capping and bottom friction). The WAVEWATCH II model incorporates more than one formulation for each of these processes except for depth-induced wave breaking, which we added. For this we used the formulation of Battjes and Janssen (1978) and Battjes et al. (1993). As an alternative for Battjes and Janssen (1978) we added the formulation of Roelvink (1993).

In discretizing the spectrum we used a logarithmic frequency distribution from .022 Hz (a rather low frequency, chosen to cover extreme conditions) to .75 Hz with a 10% resolution. The directional resolution is 15°. From the numerical options in WAVEWATCH II (see Tolman, 1992) we choose to use the up-wind propagation scheme with either the static integration of the source terms (constant-wind cases) or dynamic integration (all other cases). The spatial resolution of the bottom grid is about 8 km except near the Dutch coast where it is 3 km. The bathymetry is indicated in Fig. 1. In view of the type of storms that we will consider, we imposed a uniform increase of 5 m in water depth to simulate the corresponding storm surge. We verified with sensitivity computations that the wave conditions at the northern boundary of the model (at 62° N) are not relevant for the southern North Sea in the extreme conditions considered here.

### Maximum wave physics

We initially use formulations that are identical to those of the published WAM model (WAMDI group, 1988; to investigate the sensitivity of the results for the assumed maximum wind speed). However, we replaced the bottom friction

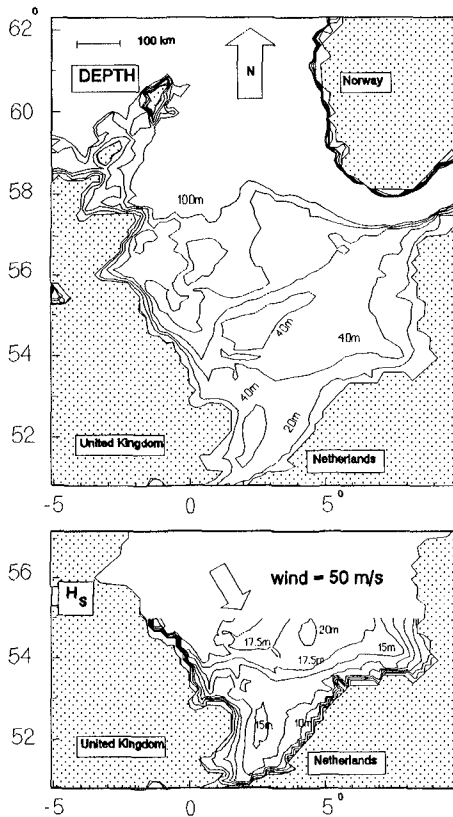


*Fig. 1 The bathymetry of the North Sea (8 km resolution; upper panel) and the maximum significant wave height in the southern North Sea computed with 16 km resolution in a uniform wind field (50 m/s from 330°; lower panel). Physics selected for maximum effect.*

formulation of Hasselmann et al. (1973) with the formulation of Madsen et al. (1988) and we added the depth-induced breaking of Battjes and Janssen (1978) and Battjes et al. (1993). This setting of the physics is summarized in Table 1 under the heading "initial".

The maximum significant wave height in given wind conditions is achieved by minimizing the effect of dissipation and maximizing the effects of generation

(within the uncertainty of the state-of-the-art). We therefore varied the formulations of the physics in the model to each of the available options in WAVEWATCH II (Table 1).

WAVEWATCH II		
physics	initial	options
wind input	Snyder et al. (1981) + Komen et al. (1984)	Janssen (1991)
wave-wave interactions	Hasselmann and Hasselmann (1985)	-
white-capping	Komen et al. (1984)	Komen et al. (1984) + Janssen (1991)
bottom friction	Madsen et al. (1988)	Hasselmann et al. (1973)
depth-induced breaking	Battjes and Janssen (1978) + Battjes et al. (1993)	Roelvink (1993) + Battjes et al. (1993)

Table 1. *The formulations of the physics of wave generation and dissipation in WAVEWATCH II (Tolman, 1991, 1992). The formulations that generate the maximum significant wave height are indicated with shading.*

We hindcasted for each variation independently the significant wave height at all stations indicated in Fig. 4 for wind speed 50 m/s from direction 330°. After all variations were considered and selected (as indicated in Table 1), we hindcasted the significant wave height in the southern North Sea with the selected formulations of the physics combined. The results are shown in Fig. 1. The significant wave height thus obtained is typically 1 m higher than obtained with the initial model setting.

### Verification

We verified results of the model with the selected formulations for generation and dissipation (Table 1) with WAVEC buoy observations in a severe storm (December 12, 1990). The time series of the significant wave height for the station with best agreement between observed and computed maximum significant wave height and the station with the worst agreement are given in Fig. 2. The maximum significant wave height at these and other stations is given in Table 2. The agreement between observation and computation is generally reasonable except at station SON which is planned to be investigated further (the buoy seems to be located between two ship wrecks).

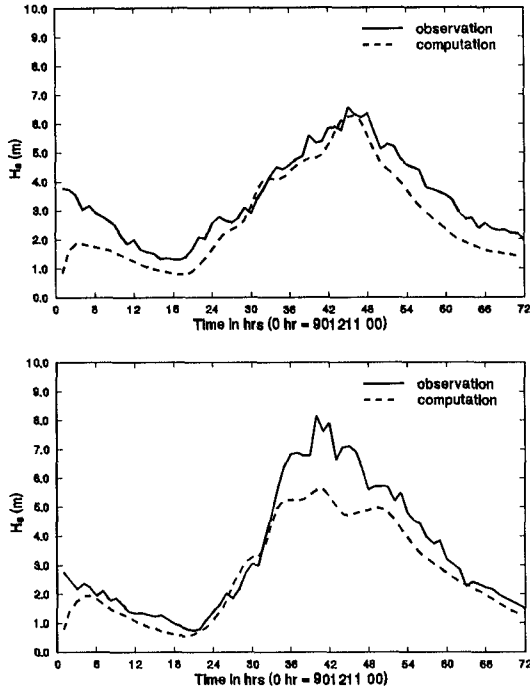


Fig. 2. The observed and measured time series of the significant wave height in the storm of December 12, 1990 at stations EUR (top panel) and SON (bottom panel).

station	observations	computations	difference
AUK	12.20 m	12.47 m	-0.27 m (2%)
SON	7.70 m	5.60 m	+2.10 m (26%)
ELD	7.70 m	7.25 m	+0.45 m (6%)
K13	7.70 m	7.60 m	+0.10 m (1%)
YM6	6.70 m	6.40 m	+0.30 m (4%)
EUR	6.25 m	6.30 m	-0.05 m (1%)
LEG	6.00 m	5.42 m	+0.58 m (10%)

Table 2. Observed and computed maximum significant wave height at various locations in the storm of December 12, 1990.

### The wave model for the parametric storms

To find the storm that would generate the maximum significant wave height in the southern North Sea, we used a search procedure with a large number of synthetic storms (see below). For economic reasons these hindcasts were carried out with the second-generation wave model DOLPHIN-B described by Holthuijsen and de Boer (1988). This wave model has been adapted for shallow water and tuned to resemble the behaviour of the WAVEWATCH II model (initial setting) at station K13 in the storm of Feb. 1953. Dedicated computations showed that the storms that generated the largest significant wave heights at station K13 also generated the largest values at the other locations along the Dutch coast. The computations for the selected synthetic storm were repeated with the WAVEWATCH II model.

### **The wind field**

In search for the existence of a physical upper-limit of the significant wave height we assume, in consultation with meteorologists of the Royal Netherlands Meteorological Institute, a wind speed of 50 m/s to be the maximum realizable sustained wind speed over the North Sea (at 10 m elevation). This is only a crude estimate and we will therefore determine the sensitivity of the maximum significant wave height for this assumption.

### Uniform wind

The waves are hindcasted in a uniform wind field over the entire North Sea until a stationary situation is achieved for various wind speeds and directions. For these hindcasts a 16 km spatial resolution was used (sensitivity tests showed practically no effect of refining the resolution to 8 km). Fig. 3 shows that between northerly and westerly wind directions the significant wave height is weakly dependent of the direction with most (but not very pronounced) maxima at wind direction 330°. To find the sensitivity for the wind speed, we repeated these hindcasts for wind speeds in this direction increasing from 20 m/s to 60 m/s. As shown in Fig. 3 the sensitivity is rather weak (practically absent at the shallower stations) around the assumed maximum wind speed of 50 m/s.

### *Results*

To obtain high resolutions results along the Dutch coast, we refined the computations in the southern North Sea with nested computations (from a 16 km via an 8 km to a 3 km grid resolution). The results are shown in Fig. 4.

### Synthetic storm

To investigate whether the maximum wave conditions found in the above constant wind field are physically realizable, we hindcasted the waves in an extreme storm that we synthesized from historic storms. We selected this storm with search procedures involving wave hindcasts in a large number of synthetic storms.

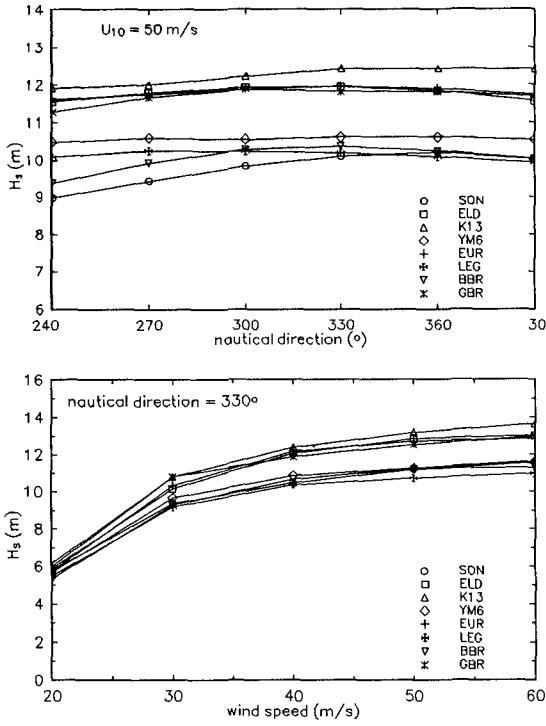


Fig. 3 The significant wave height as a function of wind direction (50 m/s) at various stations (top panel). The significant wave height as a function of wind speed from 330° at various stations (bottom panel).

**Storm parameterization**

To represent the atmospheric pressure in the synthetic storms we used a spatial Gaussian distribution with the radius to maximum wind different along the four major (orthogonal) axes of the storm. This created an elliptical asymmetric pressure field. From this pressure field we computed the geostrophic wind which we reduced to 65% and turned counter-clockwise by 15° to estimate the surface wind at 10 m elevation. Storms with surface wind speeds exceeding 50 m/s were removed from the search (due to the incremental nature of the search, small overshoots of about 2 m/s were permitted). The parameters of these synthetic storms were all assumed to vary linearly in time, characterized by one value at the moment when the centre of the storm is located at 10° W and one value 72 hours later.

We varied these time histories in the following search procedure within limits



obtained from historic storms. To that end we analyzed five storms that are considered by meteorologists to be the severest storms in the southern North Sea over the last decennia.

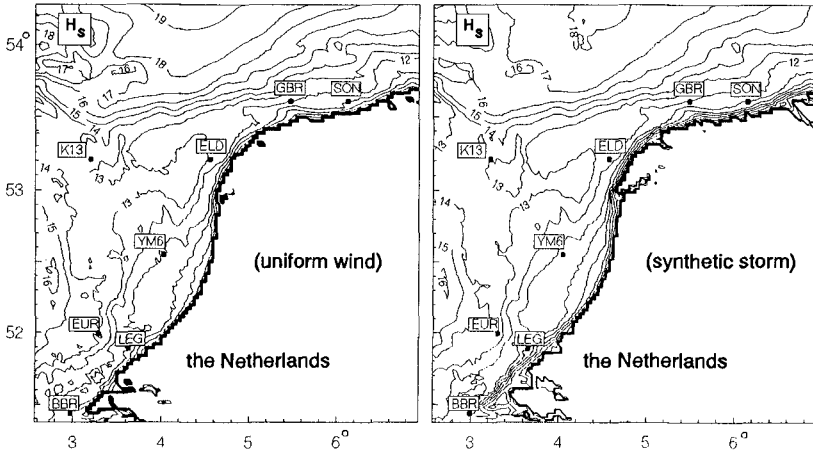


Fig. 4 The maximum significant wave height along the Dutch coast computed with 3 km resolution in a uniform wind field (wind speed = 50 m/s from 330°) and in a synthetic storm (maximum wind speed = 51.8 m/s).

These are all storms from westerly or north-westerly directions: 1st Feb '53, 21st Dec '54, 3rd Jan '76, 19th-25th Nov '81 and 26th Feb - 2nd March '90. (We verified with extra hindcasts that storms with tracks from more northerly directions were irrelevant.) We followed these storms on standard weather maps after they passed 10° W longitude and we visually estimated as a function of time: the forward speed, the central pressure, the orientation of the major axes and the radii along these axes. We thus obtained for each of these parameters five time histories. By roughly approximating the upper and lower envelope of these time histories with straight lines. From this we estimated the limits of the parameter values at the start of the storm and 72 hours later. For the start and end positions of the storms we used the results of an earlier and more extensive analysis of historic storms by Zwart (1993).

#### *The search procedure*

To determine which synthetic storm would lead to the largest significant wave height in the southern North Sea, we have used a sequential binary search with the storm parameters varying within the limits obtained from the above analysis of historic storms. First a reference hindcast is carried out with the value of all storm parameters (start and end values considered separately) set at their mid-range value. In sequence each storm parameter is then investigated: it is set at

two values, one at the centre of the upper half-range and one at the centre of the lower half-range. All other parameters retain their reference value. Two hindcasts then decide which of these two values produces the largest significant wave height. The reference value of this parameter is then replaced by this selected value (it retains this value during the continuation of the search). Then the next storm parameter is modified similarly. After all storm parameters are thus investigated and selected the procedure is repeated twice, each time cutting the range of the storm parameter in half and centering it at the last selected reference value (three iterations in all). To increase the probability that the proper storm has been selected, we also carried out a synoptic binary search (replacing the reference values only after each of the three iterations has been completed) and a random search (shifting the mean to the selected value and reducing the widths of the assumed distributions by 50% after each of three iterations). A total of about 800 hindcasts was thus carried out. As the searches are carried out with three iterations, the resolution of the result is 1/8 of the original parameter range.

### *Results*

The storm with the maximum significant wave height was selected by the sequential binary search. It is a fairly small but intense storm (300 to 400 km radius) tracking across the southern North Sea from a westerly direction. An inspection of the results suggests that to achieve the extreme wave heights, the wave field in the southern North Sea requires a locally high wind speed to compensate for local, bottom-induced dissipation (particularly breaking). Within the permitted range of atmospheric pressure, this locally high wind speed can be achieved only with a fairly small radius of the storm. The results of the other searches (synoptic binary and random) were storms that were similar in pattern to the one found with the sequential binary search but with somewhat lower significant wave heights.

To obtain the results with third-generation formulations, we carried out the hindcast for the selected synthetic storm with the WAVEWATCH II model with the formulations selected for maximum effect of the physics. This hindcast was nested to 3 km along the Dutch coast. The resulting maximum significant wave height (at each location) is given in Fig. 4.

### **Discussion**

Comparing the two wave fields in Fig. 4, it is obvious that the maximum significant wave height obtained with a uniform wind field is practically equal to that obtained with the extreme synthetic storm. Apparently the wave field in these conditions (maximum wind speed of about 50 m/s) is dominated by the local water depth. This is supported by the similarity between the pattern of the maximum significant wave height and the water depth (Figs. 1 and 4). In fact, in the region considered with depth between 10 and 55 m, the ratio between

maximum significant wave height and depth varies only between 0.35 and 0.45. This suggests a local equilibrium between generation on the one hand (for 50 m/s wind speed) and dissipation on the other. An uncertainty analysis based on sensitivity computations and on the uncertainty range of the coefficients in the selected formulations of the physics of wave generation and dissipation (not presented here) indicates that (a) the mechanism of bottom-induced breaking dominates the estimate of the maximum significant wave height and (b) the uncertainty of the estimated maximum significant wave height is about 5% upward and 25% downward.

## Conclusions

The significant wave height in the southern North Sea seems to be limited by the local water depth and to some extent by an upper limit of the wind speed. The physics of wave generation and dissipation in these extreme conditions are not well known but with the available formulations selected for maximum effect, an estimate of the physical maximum of the significant wave height has been made. This has been done for selected wind fields using the third-generation model WAVEWATCH II (Tolman, 1991, 1992). The wind speed was limited to 50 m/s.

The results in a uniform wind field over the entire North Sea and in a selected extreme synthetic storm (based on historic information) are almost equal, indicating a local balance between wind generation and bottom induced dissipation. The local ratio between maximum significant wave height and water depth is nearly constant in the southern North Sea and equal to about 0.4.

## References

- Battjes, J.A. and J.P.F.M. Janssen, 1978, Energy loss and set-up due to breaking of random waves, *Proc. 16th Int. Conf. Coastal Engineering*, Hamburg, 569 - 587
- Battjes, J.A., Eldeberky, Y., and Won, Y., 1993, Spectral Boussinesq modelling of random, breaking waves, *Proc. Int. Symposium WAVES '93*, New Orleans, ASCE, pp.813-820, New York
- Hasselmann, K., T.P. Barnett, E. Bouws, H. Carlson, D.E. Cartwright K. Enke, J.A.Ewing, H. Gienapp, D.E. Hasselmann, P. Kruseman, A. Meerburg, P. Müller, D.J. Olbers, K. Richter, W. Sell and H. Walden, 1973, Measurements of wind-wave growth and swell decay during the Joint North Sea Wave Project (JONSWAP). *Ergänzungsheft zur Deutschen Hydrographischen Zeitschrift*, Reihe A (8) Nr. 12, 95 pp.
- Hasselmann, S. and K. Hasselmann, 1985, Computations and parameterizations of the nonlinear energy transfer in a gravity-wave spectrum, Part I: A new method for efficient computations of the exact nonlinear transfer integral, *J. Phys. Oceanogr.*, 15, 1369-1377
- Holthuijsen, L.H., and de Boer, S., 1988, Wave forecasting for moving and

- stationary targets, In: *Computer Modelling in Ocean Engineering*, Eds. B.Y. Schrefler and O.C. Zienkiewicz, Balkema, Rotterdam, 231-234
- Janssen, P.A.E.M., 1991, Quasi-linear theory of wind-wave generation applied to wave forecasting, *J. Phys. Oceanogr.*, 21, 1631 - 1642
- Komen, G.J., S. Hasselmann and K. Hasselmann, 1984, On the existence of a fully developed wind-sea spectrum. *J. Phys. Oceanogr.*, 14, 1271-1285.
- Madsen, O.S., Y.-K. Poon and H.C. Graber, 1988b, Spectral wave attenuation by bottom friction: theory. *Proc. 21st Int. Conf. Coastal Eng.*, ASCE, Malaga, 492-504.
- Mei, C.C., 1983, *The applied dynamics of ocean surface waves*, Wiley, New York
- Phillips, O.M., 1977, *The dynamics of the upper ocean*, Cambridge University Press
- Roelvink, J.A., 1993, Dissipation in random wave groups incident on a beach, *Coastal Engineering*, 19, 127 - 153
- Snyder, R.L., F.W. Dobson, J.A. Elliott and R.B. Long, 1981, Array measurements of atmospheric pressure fluctuations above surface gravity waves. *J. Fluid Mech.*, 102, 1-59.
- Tolman, H.L., 1991, A third-generation model for wind waves on slowly varying, unsteady, and inhomogeneous depths and currents, *J. Phys. Oceanogr.*, 21 (6), 782 -797
- Tolman, H.L., 1992, User manual for WAVEWATCH-II, NASA/GSFC, Laboratory for Oceans
- WAMDI group, 1988, The WAM model - a third generation ocean wave prediction model. *J. Phys. Oceanogr.*, 18, 1775-1810.
- Zwart, B., 1993, De stormvloed van 1 februari 1953, Memorandum KNMI, VEO 93 -01, pp. 20, in Dutch

## CHAPTER 21

# Improved Boundary Conditions to a Time-Dependent Mild-Slope Equation for Random Waves

Toshimasa Ishii<sup>1</sup>, Masahiko Isobe<sup>2</sup>, and Akira Watanabe<sup>2</sup>

## Abstract

The offshore and side boundary conditions to a time-dependent mild slope equation for random waves are improved to introduce given incident waves into and extract reflected waves from the computational domain with reduced computational time and storage size. The resulting numerical model is applied to calculate the wave field, nearshore current, and bottom topography change around a detached breakwater.

## 1 Introduction

A time-dependent mild-slope equation for random waves was derived from the mild slope equation by approximating frequency-independent expressions to the frequency-dependent coefficients (Kubo *et al.*, 1991; Kotake *et al.*, 1992). In the numerical solution, however, the peripheral region for absorbing the outgoing wave energy becomes large in comparison with the calculation domain of interest. In addition, because the velocity potential due to the incident waves must be calculated at each point in the peripheral region, extensive computational time is required.

The present study deals with the incident wave boundary condition and the open boundary condition in more detail and improves them, so that the deformation of multi-directional irregular waves may be calculated with much less computational time and storage size. The numerical model developed is applied to calculate the wave field, nearshore current, and bottom topography change around a detached breakwater on a uniform slope.

---

<sup>1</sup>Tokyo Electric Power Co., Ltd.

<sup>2</sup>Dept. of Civil Eng., Univ. of Tokyo, Bunkyo-ku, Tokyo 113, Japan

## 2 A time-dependent mild-slope equation for random waves

A time-dependent mild-slope equation for random waves (Kubo *et al.*, 1992) is given by

$$\nabla(\bar{\alpha}\nabla\tilde{\eta}) + i\nabla\left[\bar{\beta}\nabla\left(\frac{\partial\tilde{\eta}}{\partial t}\right)\right] + \bar{k}^2\bar{\alpha}(1 + if_D)\tilde{\eta} + i\bar{\gamma}(1 + if_D)\frac{\partial\tilde{\eta}}{\partial t} = 0 \quad (1)$$

$$\bar{\alpha} = \bar{C}\bar{C}_g \quad (2)$$

$$\bar{\beta} = \frac{\bar{C}}{k}[-2(1 - \bar{n}) + \frac{1}{2\bar{n}}(2\bar{n} - 1)\{1 - (2\bar{n} - 1)\cosh 2\bar{k}d\}] \quad (3)$$

$$\bar{\gamma} = \bar{k}\bar{C}[2\bar{n} + \frac{1}{2\bar{n}}(2\bar{n} - 1)\{1 - (2\bar{n} - 1)\cosh 2\bar{k}d\}] \quad (4)$$

$$\bar{n} = (1/2)(1 + 2\bar{k}d/\sinh 2\bar{k}d) \quad (5)$$

where  $\bar{C}$  is the wave celerity,  $\bar{C}_g$  the group velocity,  $k$  the wave number,  $d$  the water depth,  $t$  the time,  $\nabla$  the horizontal gradient operator,  $i$  the unit of imaginary number, and  $f_D$  an energy absorbing coefficient. The symbol  $\bar{\quad}$  denotes quantities at the representative frequency  $\bar{\omega}$ . The relation between  $\tilde{\eta}$  and the temporal water surface variation  $\eta$  is :

$$\eta = Re[\tilde{\eta}e^{-i\bar{\omega}t}] \quad (6)$$

## 3 Improvement of boundary condition for incident waves

### 3.1 Layer boundary method

In the numerical solution of horizontal two-dimensional problems, we introduce the incident waves at the offshore and side boundaries. In addition, the outgoing waves should propagate out at the boundaries without reflection.

Kubo *et al.* (1992) presented a method that satisfies the above conditions, whereby the incident waves are introduced through a layer boundary. This technique is illustrated in Figure 1. The energy of the outgoing waves is absorbed in the energy absorbing layer of a sufficient width, and the incident irregular waves must be prescribed as an excitation force at all grid points in the layer by a superposition of component waves. Consequently, the method requires considerable computational time and large storage, and therefore the number of component waves is restricted to about 200. Also, as seen from results of computations

performed by Kubo *et al.* (1992) and the authors for multi-directional irregular waves around a detached breakwater, the distribution of the wave height was asymmetrical due to the statistical variation.

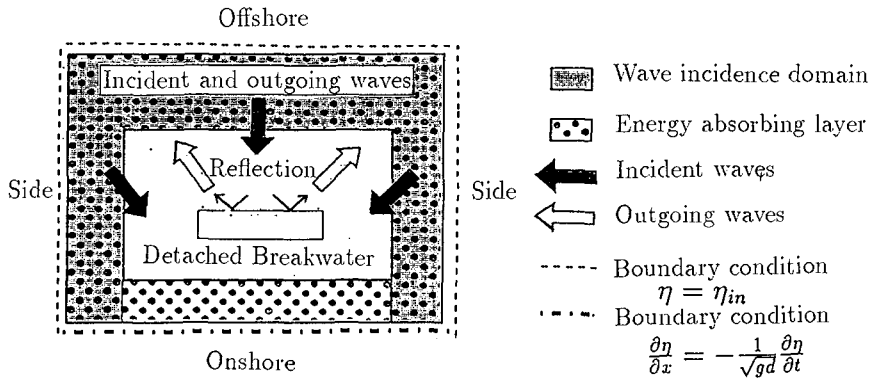


Fig.1: Method for introducing incident waves through a layer boundary (Kubo *et al.*, 1992)

### 3.2 Line boundary method

The incident wave boundary condition is improved in the present study by introducing the incident waves through a line boundary as shown in Figure 2. The incident wave potential is only specified along the line boundary, which significantly reduces computational time and storage. With the new method wave transformation can be calculated for irregular incident waves even with as many as 1,000 components, whereas the previous method has a practical limit of about 200 components. As a result, the deformation of multi-directional irregular waves can be calculated with a much higher accuracy because the statistical variation is reduced.

The method is summarized in the following. First we set up a line boundary where the incident waves are introduced. Inside the line boundary, incident and outgoing waves are to be dealt with, whereas only outgoing waves exist outside the line boundary as shown in Figure 2. For this purpose, we only have to adjust the incident wave component  $\tilde{\eta}_{in}$  in the finite difference equation for which the central grid point is located adjacent to the line boundary. The incident waves are introduced into the calculation domain through this operation.

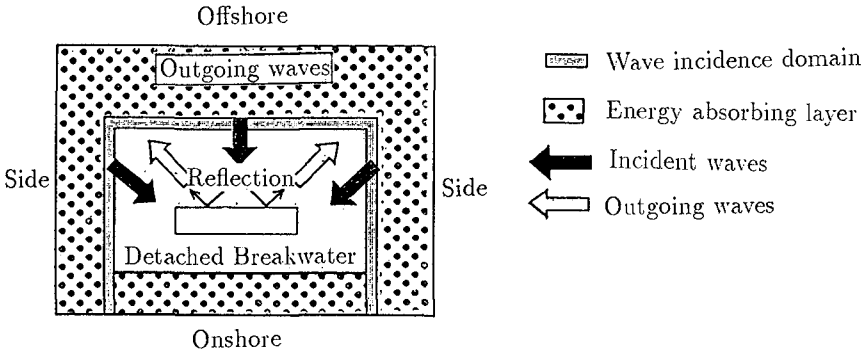


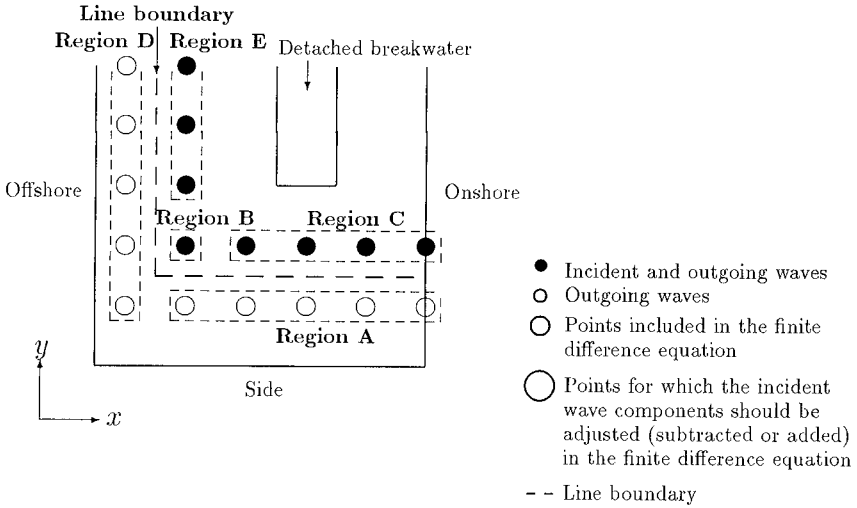
Fig.2: Method for introducing incident waves through a line boundary

To describe the method in more detail, we apply it to a horizontal two-dimensional problem. The ADI method is employed in the numerical calculations to solve the present equation. The calculations are carried out alternately in the  $x$  and  $y$  directions, implying that the application of the present method must be considered separately for each direction. Figure 3 shows the application in the  $x$  direction. For a horizontal two-dimensional model on a uniform slope, the finite difference equation of the time-dependent mild-slope equation for random waves in the  $x$  direction is written

$$\begin{aligned}
 & \frac{\bar{\alpha}_{i+1} - \bar{\alpha}_{i-1}}{2\Delta x} \left\{ \frac{\tilde{\eta}_{i+1,j}^{t+1} - \tilde{\eta}_{i-1,j}^{t+1}}{2\Delta x} \right\} \\
 & + \bar{\alpha}_i \left\{ \frac{\tilde{\eta}_{i-1,j}^{t+1} - 2\tilde{\eta}_{i,j}^{t+1} + \tilde{\eta}_{i+1,j}^{t+1}}{\Delta x^2} + \frac{\tilde{\eta}_{i,j-1}^t - 2\tilde{\eta}_{i,j}^t + \tilde{\eta}_{i,j+1}^t}{\Delta y^2} \right\} \\
 & + i \frac{\bar{\beta}_{i+1} - \bar{\beta}_{i-1}}{2\Delta x} \left\{ \frac{(\tilde{\eta}_{i+1,j}^{t+1} - \tilde{\eta}_{i-1,j}^{t+1}) - (\tilde{\eta}_{i+1,j}^t - \tilde{\eta}_{i-1,j}^t)}{2\Delta x \Delta t} \right\} \\
 & + i \bar{\beta}_i \left\{ \frac{(\tilde{\eta}_{i-1,j}^{t+1} - 2\tilde{\eta}_{i,j}^{t+1} + \tilde{\eta}_{i+1,j}^{t+1}) - (\tilde{\eta}_{i-1,j}^t - 2\tilde{\eta}_{i,j}^t + \tilde{\eta}_{i+1,j}^t)}{\Delta x^2 \Delta t} \right. \\
 & \left. + \frac{(\tilde{\eta}_{i,j-1}^t - 2\tilde{\eta}_{i,j}^t + \tilde{\eta}_{i,j+1}^t) - (\tilde{\eta}_{i,j-1}^{t-1} - 2\tilde{\eta}_{i,j}^{t-1} + \tilde{\eta}_{i,j+1}^{t-1})}{\Delta y^2 \Delta t} \right\} \\
 & + \bar{k}^2 \bar{\alpha}_i (1 + i f_D) \frac{\tilde{\eta}_{i,j}^{t+1} + \tilde{\eta}_{i,j}^t}{2} + i \bar{\gamma}_i (1 + i f_D) \frac{\tilde{\eta}_{i,j}^{t+1} - \tilde{\eta}_{i,j}^t}{\Delta t} = 0 \tag{7}
 \end{aligned}$$

By rearranging the equation under the condition that  $\Delta x = \Delta y = \Delta l$ , the left-hand side contains only unknown values (time step  $t + 1$ ) and the right-hand side





	Region A	Region B	Region C	Region D	Region E
$t+1$ Step	No operation $j+1$ ● ● ● $j$ ○ ○ ○ $j-1$ ○ ○ ○ $i-1$ $i$ $i+1$	$+\tilde{\eta}_{i-1,j,in}^{t+1}$ $j+1$ ○ ● ● ● $j$ ○ ● ● ● $j-1$ ○ ○ ○ $i-1$ $i$ $i+1$	No operation $j+1$ ● ● ● ● $j$ ● ● ● ● $j-1$ ○ ○ ○ ○ $i-1$ $i$ $i+1$	$-\tilde{\eta}_{i+1,j,in}^{t+1}$ $j+1$ ○ ○ ○ ● $j$ ○ ○ ○ ● $j-1$ ○ ○ ○ ● $i-1$ $i$ $i+1$	$+\tilde{\eta}_{i-1,j,in}^{t+1}$ $j+1$ ○ ● ● ● $j$ ○ ● ● ● $j-1$ ○ ● ● ● $i-1$ $i$ $i+1$
$t$ Step	$-\tilde{\eta}_{i,j+1,in}^t$ $j+1$ ● ● ● ● $j$ ○ ○ ○ ○ $j-1$ ○ ○ ○ ○ $i-1$ $i$ $i+1$	$+\tilde{\eta}_{i-1,j,in}^t$ $j+1$ ○ ● ● ● $j$ ○ ● ● ● $j-1$ ○ ○ ○ ○ $i-1$ $i$ $i+1$	$+\tilde{\eta}_{i,j-1,in}^t$ $j+1$ ● ● ● ● $j$ ● ● ● ● $j-1$ ○ ○ ○ ○ $i-1$ $i$ $i+1$	$-\tilde{\eta}_{i+1,j,in}^t$ $j+1$ ○ ○ ○ ● $j$ ○ ○ ○ ● $j-1$ ○ ○ ○ ● $i-1$ $i$ $i+1$	$+\tilde{\eta}_{i-1,j,in}^t$ $j+1$ ○ ● ● ● $j$ ○ ● ● ● $j-1$ ○ ● ● ● $i-1$ $i$ $i+1$
$t-1$ Step	$-\tilde{\eta}_{i,j+1,in}^{t-1}$ $j+1$ ● ● ● ● $j$ ○ ○ ○ ○ $j-1$ ○ ○ ○ ○ $i-1$ $i$ $i+1$	$+\tilde{\eta}_{i,j-1,in}^{t-1}$ $j+1$ ○ ● ● ● $j$ ○ ● ● ● $j-1$ ○ ○ ○ ○ $i-1$ $i$ $i+1$	$+\tilde{\eta}_{i,j-1,in}^{t-1}$ $j+1$ ● ● ● ● $j$ ● ● ● ● $j-1$ ○ ○ ○ ○ $i-1$ $i$ $i+1$	No operation $j+1$ ○ ○ ○ ○ $j$ ○ ○ ○ ○ $j-1$ ○ ○ ○ ○ $i-1$ $i$ $i+1$	No operation $j+1$ ○ ● ● ● $j$ ○ ● ● ● $j-1$ ○ ● ● ● $i-1$ $i$ $i+1$

Fig.3: Illustration of the method of introducing incident waves through a line boundary for the case of calculation in the  $x$  direction

only known values (time steps  $t$  and  $t-1$ ), and the above equation can be written

$$\begin{aligned}
 & A1_i \tilde{\eta}_{i-1,j}^{t+1} + A2_i \tilde{\eta}_{i,j}^{t+1} + A3_i \tilde{\eta}_{i+1,j}^{t+1} \\
 & = B1_i \tilde{\eta}_{i-1,j}^t + B2_i \tilde{\eta}_{i,j}^t + B3_i \tilde{\eta}_{i+1,j}^t + B4_i \tilde{\eta}_{i,j-1}^t + B5_i \tilde{\eta}_{i,j+1}^t \\
 & \quad + C1_i \tilde{\eta}_{i,j-1}^{t-1} + C2_i \tilde{\eta}_{i,j}^{t-1} + C3_i \tilde{\eta}_{i,j+1}^{t-1}
 \end{aligned}
 \tag{8}$$

where  $(i, j)$  is the grid number in the  $(x, y)$  coordinate system,  $t$  the time,

$A1_i \sim A3_i$ ,  $B1_i \sim B5_i$  and  $C1_i \sim C3_i$  the coefficients determined by  $\bar{\alpha}_i, \bar{\beta}_i, \bar{\gamma}_i$  etc. Equation (8) includes grid points indicated with a double circle in Figure 3. There are three such points at time  $t + 1$ , five points at time  $t$  and three points at time  $t - 1$  around the central grid point  $(i, j)$ . These grid points are divided into two types according to their position relative to the line boundary. In the first type incident and outgoing waves coexist, and these grid points are shown with solid circles. In the second type only outgoing waves exist, which is indicated by empty circles. As an illustration, let us consider region A. The point  $(i, j + 1)$  at times  $t$  and  $t - 1$  are points including both incident and outgoing waves whereas the double circle points are points with outgoing waves only. Hence, we apply an operation which subtracts the incident wave term  $\tilde{\eta}_{i,j+1,\text{in}}^t, \tilde{\eta}_{i,j+1,\text{in}}^{t-1}$  from point  $(i, j + 1)$  at times  $t$  and  $t - 1$ . For this particular case, the finite difference equation (8) applied to outgoing waves may be written

$$\begin{aligned}
 & A1_i \tilde{\eta}_{i-1,j}^{t+1} + A2_i \tilde{\eta}_{i,j}^{t+1} + A3_i \tilde{\eta}_{i+1,j}^{t+1} \\
 = & B1_i \tilde{\eta}_{i-1,j}^t + B2_i \tilde{\eta}_{i,j}^t + B3_i \tilde{\eta}_{i+1,j}^t + B4_i \tilde{\eta}_{i,j-1}^t + B5_i \tilde{\eta}_{i,j+1}^t \\
 & + C1_i \tilde{\eta}_{i,j-1}^{t-1} + C2_i \tilde{\eta}_{i,j}^{t-1} + C3_i \tilde{\eta}_{i,j+1}^{t-1} \\
 & - B5_i \tilde{\eta}_{i,j+1,\text{in}}^t - C3_i \tilde{\eta}_{i,j+1,\text{in}}^{t-1}
 \end{aligned} \tag{9}$$

In regions B to E, the incident waves are introduced along the line boundary using the same method. In the case of the  $y$  direction, the position of the double circles at  $t + 1$  and  $t - 1$  time step should be reversed.

The computational time required by the present method was compared with the previous method for the case of a calculation region with  $80 \times 100$  grid points, 100 component waves, and 3000 time steps. Multi-directional irregular waves were expressed using the single summation method. In this case, the computational time required by the present method was one-third that of the previous method.

## 4 Improvement of open boundary condition

### 4.1 One-dimensional open boundary condition

The boundary condition at the outer edge of the energy absorbing layer used in the numerical calculations presented by Kubo *et al.* (1992) is shown in Figure 1. The one-dimensional Sommerfeld radiation condition is employed at the onshore boundary with the celerity  $C$  approximated by the long wave celerity in the same way as Ohyama *et al.* (1990). This condition is motivated by the fact that the wave direction becomes perpendicular to the onshore boundary due to wave refraction. The condition at the offshore and side boundary is that the water

surface elevation is equal to that of the incident waves. This condition is based on the assumption that the outgoing waves are absorbed perfectly in the energy absorbing layer. In the numerical calculation presented by Kubo *et al.* (1992), a wide energy absorbing layer was needed to achieve perfect absorption.

In the present study, a new open boundary condition is derived from the Sommerfeld-type boundary condition by applying a Taylor expansion in terms of the angular frequency and wave direction. The aim is to reduce the energy absorbing layer. We present the result for the one-dimensional case first and then for the two-dimensional case.

The new open boundary condition for the one-dimensional case may be written

$$\eta(x_b, t + \Delta t) = \eta(x_b - \bar{C}\Delta t, t) + \bar{C}(1 - \bar{n})\Delta t \left[ \frac{\partial \eta(x_b - \bar{C}\Delta t, t)}{\partial x} - i\bar{k}\eta(x_b - \bar{C}\Delta t, t) \right] \quad (10)$$

where  $\eta(x_b, t + \Delta t)$  is the water surface elevation at the outer edge of the energy absorbing layer, and  $\bar{C}$ ,  $\bar{n}$  and  $\bar{k}$  the wave celerity, shallowness factor and wave number at the representative frequency, respectively.

Equation(10) consists of coefficients which are independent of the frequency of component waves as a result of applying the Taylor expansion to the wave celerity  $C$ , which is a coefficient in the Sommerfeld-type boundary condition. Equation (10) is, therefore, applicable to irregular waves. The physical meaning of equation (10) is illustrated in Figure 4.

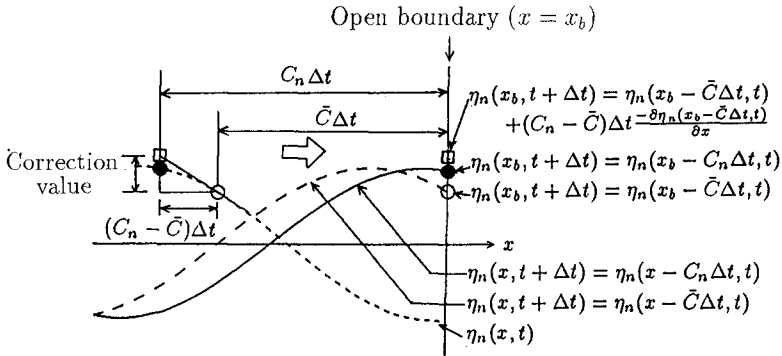


Fig.4: Physical interpretation of the improved Sommerfeld-type boundary condition for the one-dimensional case

The first term on the right-hand side of equation (10) expresses that the water

surface elevation of the wave at time  $t$  and at a point which is  $\bar{C}\Delta t$  away from the outer edge of the energy absorbing layer is equal to that at the outer edge after  $\Delta t$ , because the wave moves to the outer edge.  $\bar{C}$  is the wave celerity at the representative angular frequency, however, the wave celerity of irregular waves is different from  $\bar{C}$ . This is because irregular waves consist of many component waves with various angular frequencies. The second term on the right-hand side is a correction for the phase of the water surface elevation at the outer edge of the absorbing layer due to the difference in wave celerity.

Equation(10) is derived as follows. First we have

$$\eta(x_b, t + \Delta t) = \eta_n(x_b - \bar{C}\Delta t, t) - (C_n - \bar{C})\Delta t \frac{\partial \eta(x_b - \bar{C}\Delta t, t)}{\partial x} \quad (11)$$

Expanding  $C_n$  into a Taylor series of  $\Delta\omega_n$  and truncating the series at the first order gives

$$C_n = \bar{C} + \left( \frac{d\bar{C}}{d\omega} \right) \Delta\omega_n \quad (12)$$

where  $\left( \frac{d\bar{C}}{d\omega} \right)$  and  $\Delta\omega_n$  are written as

$$\left( \frac{d\bar{C}}{d\omega} \right) = \frac{1}{\bar{k}} \left( 1 - \frac{1}{\bar{n}} \right) \quad (13)$$

$$\Delta\omega_n = \left( \frac{d\omega}{dk} \right) \Delta k_n = \bar{n}\bar{C}\Delta k_n \quad (14)$$

Next, we assume that  $\eta_n(x, t)$  in equation (11) is expressed as  $\eta_n(x, t) = a_n e^{i(k_n x - \omega_n t)}$  and differentiate  $\eta_n(x, t)$  with respect to  $x$ . Expanding  $k_n$  in  $\eta_n(x, t)$  into a Taylor series and truncating it at the first order gives

$$\frac{\partial \eta_n(x - \bar{C}\Delta t, t)}{\partial x} = i(\bar{k} + \Delta k_n)\eta_n(x - \bar{C}\Delta t, t) \quad (15)$$

Substituting equations (12) to (15) into the second term of equation (11) and neglecting second-order terms of the resulting equation yield

$$- (C_n - \bar{C})\Delta t \frac{\partial \eta_n(x - \bar{C}\Delta t, t)}{\partial x} = i\bar{C}(1 - \bar{n})\Delta t \Delta k_n \eta_n(x - \bar{C}\Delta t, t) \quad (16)$$

Equation (15) is rewritten as

$$i\Delta k_n \eta_n(x - \bar{C}\Delta t, t) = \frac{\partial \eta_n(x - \bar{C}\Delta t, t)}{\partial x} - i\bar{k}\eta_n(x - \bar{C}\Delta t, t) \quad (17)$$

Substituting equation (17) into equation (16) gives

$$\begin{aligned} & - (C_n - \bar{C})\Delta t \frac{\partial \eta_n(x - \bar{C}\Delta t, t)}{\partial x} \\ &= \bar{C}(1 - \bar{n})\Delta t \left( \frac{\partial \eta_n(x - \bar{C}\Delta t, t)}{\partial x} - i\bar{k}\eta_n(x - \bar{C}\Delta t, t) \right) \end{aligned} \quad (18)$$

Equation (18) consists only of coefficients that are independent of the frequency and hence determined only by the representative frequency. Superposition of equation (18) for an infinite number of component waves gives the second term on the right-hand side of equation (10). The present open boundary condition combines equation (10) and the energy absorbing layer where the energy absorbing coefficient  $f_D$  is increased linearly towards the outer edge of the layer in the same way as Ohyama *et al.* (1990).

In the present study, we determine the width of the energy absorbing layer and the coefficients  $\bar{C}$ ,  $\bar{n}$ , and  $\bar{k}$  in equation (10) as follows. The width is given as  $0.6L_1$ , where  $L_1$  is the longest wavelength in the irregular waves. This width is chosen because reflection due to friction of the energy absorbing layer begins to increase rapidly at a width of  $0.6L$  for a regular wave with wavelength  $L$  as obtained from the numerical calculations. Moreover, the coefficients  $\bar{C}$ ,  $\bar{n}$ , and  $\bar{k}$  in equation (10) are determined from the component wave having the longest wavelength. The energy absorption in the layer is the lowest for this component wave, implying that the energy at the outer edge of the layer is the highest. The behavior of the open boundary condition is shown in Figure 5.  $f_{Dmax}$  is the

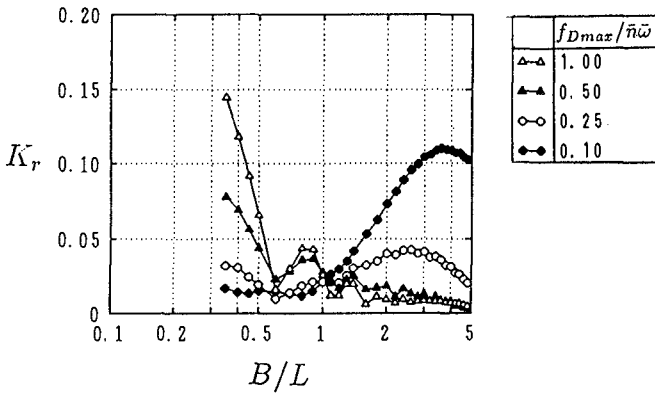


Fig.5: Reflection coefficient for the improved open boundary condition in the one-dimensional case

maximum value of the energy absorbing coefficient, given at the outer edge of the layer. Figure 5 displays the reflection coefficient for component waves in an irregular wave field at a water depth of 10m that has a representative period of 6s and a longest period of 12s. It is seen that if  $B/L$  is greater than 0.6 and a proper value of  $f_{Dmax}$  is selected, the reflection coefficient becomes sufficiently small. The

previous method needed a width of  $2L$  for a regular wave of wavelength  $L$ . Thus, a significant improvement is achieved with the present method.

### 4.2 Two-dimensional open boundary condition

In the horizontal two-dimensional case, it is necessary to approximate both the wave angle and the angular frequency by expanding them in Taylor series. For the two-dimensional case, equation (10) is written

$$\begin{aligned} & \eta_n(x, y, t + \Delta t) \\ = & \eta_n(x - \bar{C}\Delta t \cos \theta_n, y - \bar{C}\Delta t \sin \theta_n, t) \\ & + \bar{C}(1 - \bar{n})\Delta t \cos \theta_n \frac{\partial \eta_n(x - \bar{C}\Delta t \cos \theta_n, y - \bar{C}\Delta t \sin \theta_n, t)}{\partial x} \\ & + \bar{C}(1 - \bar{n})\Delta t \sin \theta_n \frac{\partial \eta_n(x - \bar{C}\Delta t \cos \theta_n, y - \bar{C}\Delta t \sin \theta_n, t)}{\partial y} \\ & - i\bar{C}(1 - \bar{n})\Delta t \bar{k} \eta_n(x - \bar{C}\Delta t \cos \theta_n, y - \bar{C}\Delta t \sin \theta_n, t) \end{aligned} \tag{19}$$

The wave angle  $\theta_n$  is expressed as the sum of a representative angle  $\bar{\theta}$  and a deviation  $\Delta\theta_n$  :

$$\theta_n = \bar{\theta} + \Delta\theta_n \tag{20}$$

We then substitute equation (20) into equation (19) and apply the additional theorem. Neglecting second order terms gives

$$\Delta t \cos \theta_n = \Delta t \cos \bar{\theta} \tag{21}$$

$$\Delta t \sin \theta_n = \Delta t \sin \bar{\theta} \tag{22}$$

Substituting equations (21) and (22) into equation (19) gives an equation in which the coefficients are independent of component angular frequencies and wave angles. Superimposing the equation gives an improved Sommerfeld-type boundary condition for the two-dimensional case.

$$\begin{aligned} & \eta(x, y, t + \Delta t) \\ = & \eta(x - \bar{C}\Delta t \cos \bar{\theta}, y - \bar{C}\Delta t \sin \bar{\theta}, t) \\ & + \bar{C}(1 - \bar{n})\Delta t \cos \bar{\theta} \frac{\partial \eta(x - \bar{C}\Delta t \cos \bar{\theta}, y - \bar{C}\Delta t \sin \bar{\theta}, t)}{\partial x} \\ & + \bar{C}(1 - \bar{n})\Delta t \sin \bar{\theta} \frac{\partial \eta(x - \bar{C}\Delta t \cos \bar{\theta}, y - \bar{C}\Delta t \sin \bar{\theta}, t)}{\partial y} \\ & - i\bar{C}(1 - \bar{n})\Delta t \bar{k} \eta(x - \bar{C}\Delta t \cos \bar{\theta}, y - \bar{C}\Delta t \sin \bar{\theta}, t) \end{aligned} \tag{23}$$

where the representative wave angle  $\bar{\theta}$  is determined from the gradient of the water surface elevation in the  $x$  and  $y$  directions at the outer edge of the energy-absorbing layer :

$$\bar{\theta} = \tan^{-1} \left( \frac{\partial \eta(x, y, t) / \partial y}{\partial \eta(x, y, t) / \partial x} \right) \quad (24)$$

## 5 Calculation of wave field, nearshore current and bottom topography change

With the boundary conditions developed above, we carried out the calculation of deformation of multi-directional irregular waves around a detached breakwater on a uniform slope. The waves consisted of 958 components and were given by the single summation method. Also, the nearshore current and the bottom topography change were calculated by using the results of the calculation of the wave field. These results were compared with calculations for regular waves.

The method of calculating the nearshore current and the bottom topography change was similar to that of Kubo *et al.* (1992). Figure 6 shows the distribution of wave height for multi-directional irregular waves ( $(H_{1/3})_0 = 1\text{m}$ ,  $T_{1/3} = 6\text{s}$ ,  $(\theta_p)_0 = 0^\circ$ ) around the breakwater, and Figure 7 shows the distribution for regular waves ( $H_0 = 0.706\text{m}$ ,  $T = 6\text{s}$ ) which has the same wave energy as the irregular waves. In the results for regular waves, a node and antinode occur in front of the detached breakwater, but for the multi-directional irregular waves, the variation in the wave height is small except just in front of the breakwater. This is because the multi-directional irregular waves consist of component waves with various wave direction and frequency, which affects the position of the node and antinode. Furthermore, the unreasonable value on the wave height due to the statistical variation that can be seen in the front of the breakwater in the results of Kubo *et al.* (1992) does not appear in the results of the present study. Figures 8 and 9 show the calculation results for the nearshore current under the above wave field. Overall, the current shows almost the same tendency, but the current velocity due to the multi-directional irregular waves is smaller than that due to the regular waves. This is because the radiation stress gradients become smaller around the average break point due to the variability in the break-point location and the large width of the surf zone for multi-directional irregular waves. In addition, in front of the breakwater the variation in the wave height, and hence the radiation stress, is large, however, a current does not occur since the gradients of the radiation stress and the mean water level are balanced here. Figure 10 shows the result of the calculation of the bottom topography change after 24 hours, computed by using the wave field in Figure 6 and the nearshore current

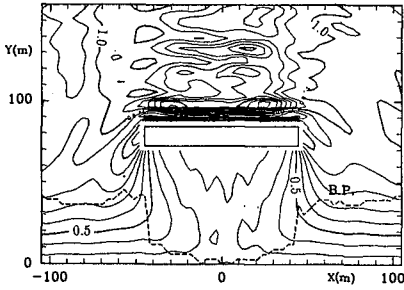


Fig.6: Wave height distribution  
(Multi-directional irregular waves)

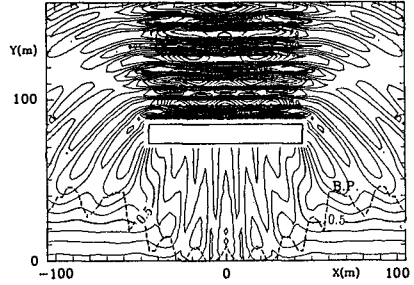


Fig.7: Wave height distribution  
(Regular waves)

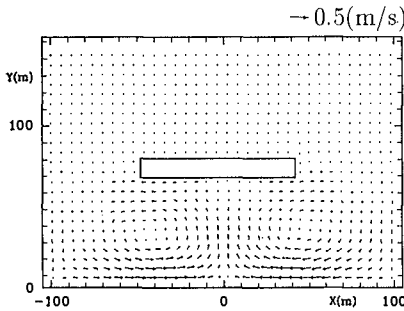


Fig.8: Velocity distribution of  
nearshore current  
(Multi-directional irregular waves)

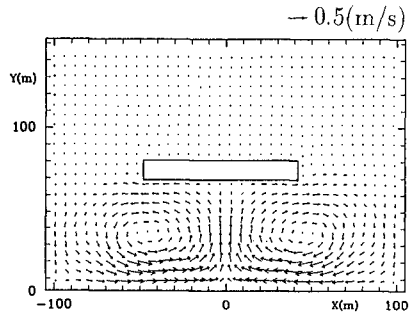


Fig.9: Velocity distribution of  
nearshore current  
(Regular waves)

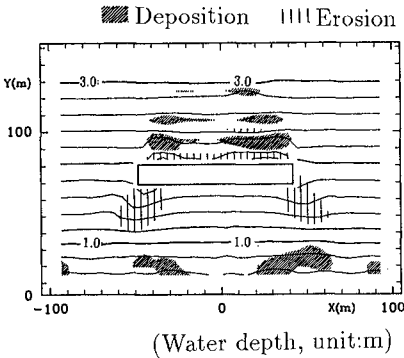


Fig.10: Bottom topography change  
(Multi-directional irregular waves)

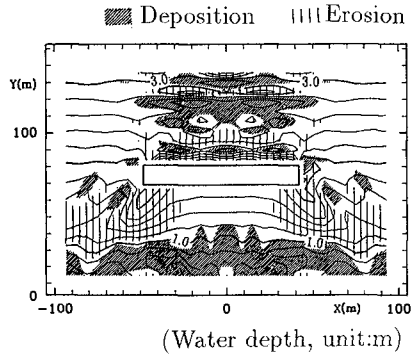


Fig.11: Bottom topography change  
(Regular waves)



field in Figure 8 as a steady external force. Figure 11 shows the result of the calculation of the bottom topography change after 24 hours for regular waves. By comparing these two figures, it is seen that the bottom topography change due to multi-directional irregular waves is smaller than that caused by regular waves with equal energy. This is because the bottom wave velocity and nearshore current are smaller for the multi-directional irregular waves.

## 6 Conclusion

A new incident wave boundary condition which is more efficient than that proposed previously is presented. In addition, the width of the energy absorbing layer is reduced by improving the non-reflective boundary condition for irregular waves. As a result, the accuracy in predicting the wave height distribution was considerably improved by reducing the statistical variation of the wave characteristics. The numerical model developed was applied to calculate the wave field, nearshore current and bottom topography change around a detached breakwater on a uniform slope. The results from calculations with regular and irregular waves were compared.

## Acknowledgement

The authors wish to thank Dr. Larson, Associate Professor, University of Lund, Sweden for his assistance in improving the English expressions of this paper.

## References

- Berkhoff, J. C. W.(1972) : Computation of combined refraction-diffraction, Proc. 13th Int. Conf. on Coastal Eng., pp. 191-203.
- Kotake, Y., M. Isobe and A. Watanabe (1992): On the high-order time-dependent mild-slope equation for irregular waves, Proc. 39th Japanese Conf. on Coastal Eng., pp. 91-95 (in Japanese).
- Kubo, Y., Y. Kotake, M. Isobe and A. Watanabe (1992) : Time-dependent mild-slope equation for random waves, Proc. 23rd Int. Conf. on Coastal Eng., ASCE, pp. 419-431.
- Ohyama, T. and N. Nadaoka (1990) : Modeling the transformation of nonlinear waves passing over a submerged step, Proc. Japanese Conf. on Coastal Eng., JSCE, Vol. 37, pp. 16-20 (in Japanese).

# CHAPTER 22

## Time-dependent mild-slope equations for random waves

Masahiko Isobe<sup>1</sup>

### Abstract

Linear and nonlinear governing equations are derived to calculate the time evolution of random waves subject to refraction and diffraction.

In the linear theory, the frequency-dependent coefficients in the mild-slope equation (Berkhoff, 1972) are approximated by a rational function of the frequency, and then a time-dependent and frequency-independent expression of the mild-slope equation is derived. The resulting equation is applicable to simulate the transformation of random waves in the nearshore zone. Results of numerical calculation agree well with experimental results for random wave shoaling in the offshore zone.

A set of nonlinear governing equations is also derived to simulate the nonlinear wave transformation. The velocity potential for the wave motion is expressed as a series in terms of a given set of vertical distribution functions. Then, the Lagrangian is integrated vertically and the variational principle is applied to yield a set of nonlinear, time-dependent, two-dimensional governing equations for the nonlinear random wave transformation. Comparison between the results of numerical calculation and flume experiment shows good agreement for the random wave shoaling near the breaking point and for wave disintegration due to a submerged breakwater.

## 1 Introduction

The mild-slope equation derived by Berkhoff (1972) has widely been used in the numerical calculation of refraction and diffraction of regular waves. However, the randomness of sea waves has a significant effect on the wave transformation especially due to refraction and diffraction. In this paper, linear and nonlinear governing equations are derived to calculate the time evolution of random waves subject to refraction and diffraction. In the linear equation, a term for the energy dissipation due to breaking is added to simulate the random wave field in the near shore zone. Results of numerical calculations are compared with those of laboratory experiments in wave flumes.

## 2 Linear Theory

### 2.1 Derivation

#### 2.1.1 rational approximation

The mild-slope equation derived by Berkhoff (1972) is written as

$$\nabla(cc_g \nabla \hat{\eta}) + k^2 cc_g \hat{\eta} = 0 \tag{1}$$

---

<sup>1</sup>Dept. of Civil Eng., Univ. of Tokyo, Tokyo 113, Japan.

where  $\hat{\eta}$  is the complex amplitude of the water surface elevation,  $c$  the wave celerity,  $c_g$  the group velocity and  $k$  the wave number, and  $\nabla$  denotes the differential operator in the horizontal two directions. To simplify the equation, the transformation by Radder (1979) is employed:

$$\hat{\phi} = \hat{\eta} / \sqrt{cc_g} \quad (2)$$

Then, within the accuracy up to the first order in the bottom slope, the resultant equation becomes a Helmholtz equation:

$$\nabla^2 \hat{\phi} + k^2 \hat{\phi} = 0 \quad (3)$$

The time-dependent quantity,  $\phi$ , corresponding to  $\hat{\phi}$  is expressed as

$$\phi = \hat{\phi} e^{-i\omega t} \quad (4)$$

where  $\omega$  is the angular frequency and  $t$  the time. For the random wave analysis,  $\phi$  is composed of an infinite number of component waves and the angular frequency differs from component to component; however, a unique value must be chosen to express  $\phi$  of random waves. Thus a slowly varying amplitude,  $\tilde{\phi}$ , is defined from  $\phi$  as

$$\phi = \tilde{\phi} e^{-i\bar{\omega} t} \quad (5)$$

where  $\bar{\omega}$  is a certain representative angular frequency such as the average frequency. Comparison between Eqs. (4) and (5) gives

$$\tilde{\phi} = \hat{\phi} e^{-i\omega' t} \quad (6)$$

where  $\omega'$  is the deviation from the representative frequency and defined as

$$\omega' = \omega - \bar{\omega} \quad (7)$$

Equation (6) implies that  $\tilde{\phi}$  is a slowly varying function of time.

Since the Helmholtz equation (3) is independent of time, the governing equation for  $\tilde{\phi}$  has the same form. When an energy dissipation term which is expressed in terms of the energy dissipation coefficient,  $f_D$ , is added, the equation is expressed as

$$\nabla^2 \tilde{\phi} + k^2 (1 + i f_D) \tilde{\phi} = 0 \quad (8)$$

Equation (8) cannot be used to calculate  $\tilde{\phi}$  of random waves directly since the coefficients included vary with the frequency. Linear approximation (Kubo *et al.*, 1992) and parabolic approximation (Kotake *et al.*, 1992) to the coefficients were employed in the previous studies. To improve the accuracy of approximation, a rational function is used in the present study.

Consider the following approximation to Eq. (8):

$$\nabla^2 \tilde{\phi} - i a_1 \nabla^2 \left( \frac{\partial \tilde{\phi}}{\partial t} \right) + (b_0 + i c_0) \tilde{\phi} + i (b_1 + i c_1) \frac{\partial \tilde{\phi}}{\partial t} - b_2 \frac{\partial^2 \tilde{\phi}}{\partial t^2} = 0 \quad (9)$$

where the coefficients  $a_1$ ,  $b_0$ ,  $b_1$ ,  $b_2$ ,  $c_0$  and  $c_1$  are constants and independent of the frequency. Theoretical consideration on stability condition requires that the highest orders of approximation for  $b$  and  $c$  should be second and first, respectively. The order

for  $a$  is lower than that for  $b$  so that the ADI method may be available in the numerical calculation.

For monochromatic progressive waves expressed as

$$\tilde{\phi} = ae^{i(\hat{k}x \cos \theta + \hat{k}y \sin \theta - \omega't)} \tag{10}$$

Eq. (9) becomes

$$-\hat{k}^2 + a_1\hat{k}^2\omega' + (b_0 + ic_0) + (b_1 + ic_1)\omega' + b_2\omega'^2 = 0 \tag{11}$$

from which the approximated dispersion relation is obtained as

$$\hat{k}^2 = (b_0 + b_1\omega' + b_2\omega'^2)/(1 - a_1\omega') \tag{12}$$

The values of the coefficients should be determined so that the error in the approximation (12) may become minimum without causing numerical instability.

**2.1.2 determination of coefficients**

Equation (11) can be solved for  $\omega'$  as

$$\omega' = \{-(a_1\hat{k}^2 + b_1 + ic_1) \pm \sqrt{(a_1\hat{k}^2 + b_1 + ic_1)^2 - 4b_2(-\hat{k}^2 + b_0 + ic_0)}\}/(2b_2) \tag{13}$$

To avoid numerical divergence,  $Im\{\omega'\} \leq 0$ . This requires that the magnitude of the imaginary part for  $\sqrt{\quad}$  should not exceed  $c_1$ . Let the real and imaginary parts in the  $\sqrt{\quad}$  be denoted by  $X$  and  $Y$ , respectively, then the condition is written as

$$X \geq 0 \tag{14} \quad (c_1 = 0)$$

$$X \geq (Y/2c_1)^2 - c_1^2 \tag{15} \quad (c_1 > 0)$$

The above condition should be satisfied for an arbitrary  $\hat{k}$ , which yields

$$b_1^2 - 4b_0b_2 \geq 0, \quad c_0 = 0 \quad (c_1 = 0) \tag{16}$$

$$\left(\frac{c_0}{c_1}\right)^2 - \left(\frac{b_1}{b_2}\right)\left(\frac{c_0}{c_1}\right) + \left(\frac{b_0}{b_2}\right) \leq 0 \quad (c_1 > 0) \tag{17}$$

Within the above restrictions, we take the equal sign for the sake of convenience. Then,

$$b_1 = 2\sqrt{b_0b_2} \tag{18}$$

$$c_1 = (2b_2/b_1)c_0 \tag{19}$$

By considering the above two equations, independent parameters are  $a_1, b_0, b_2$  and  $c_0$ .

When we determine the values of these parameters, we compensate for the error included in the finite difference form of the equation. For waves progressive in the  $x$ -direction, the central finite difference expressions for each term in Eq. (9) are related with the corresponding derivatives as

$$\left. \begin{aligned} \left. \begin{aligned} \frac{\partial^2 \tilde{\phi}}{\partial x^2} \Big|_{\text{F.D.}} &= \alpha_2 \beta_0 \frac{\partial^2 \tilde{\phi}}{\partial x^2}, & \frac{\partial^2}{\partial x^2} \left( \frac{\partial \tilde{\phi}}{\partial t} \right) \Big|_{\text{F.D.}} &= \alpha_2 \beta_1 \frac{\partial^2}{\partial x^2} \left( \frac{\partial \tilde{\phi}}{\partial t} \right), & \tilde{\phi} \Big|_{\text{F.D.}} &= \beta_0 \tilde{\phi} \end{aligned} \right\} \\ \left. \begin{aligned} \frac{\partial \tilde{\phi}}{\partial t} \Big|_{\text{F.D.}} &= \beta_1 \frac{\partial \tilde{\phi}}{\partial t}, & \frac{\partial^2 \tilde{\phi}}{\partial t^2} \Big|_{\text{F.D.}} &= \beta_2 \frac{\partial^2 \tilde{\phi}}{\partial t^2} \end{aligned} \right\} \end{aligned} \tag{20}$$

where  $|_{F,D}$  denotes the finite difference expressions and

$$\left. \begin{aligned} \beta_0 &= (2/3) \cos \omega' \Delta t + (1/3), & \beta_1 &= \{(\sin \omega' \Delta t)/(\omega' \Delta t)\}^2 \\ \beta_2 &= \left\{ \left( \sin \frac{\omega' \Delta t}{2} \right) / \left( \frac{\omega' \Delta t}{2} \right) \right\}^2, & \alpha_2 &= \left\{ \left( \sin \frac{\hat{k} \Delta x}{2} \right) / \left( \frac{\hat{k} \Delta x}{2} \right) \right\}^2 \end{aligned} \right\} \quad (21)$$

are correction factors. Then, instead of Eq. (11), the finite difference equation for Eq. (9) implies

$$-\alpha_2 \hat{k}^2 \beta_0 + a_1 \alpha_2 \hat{k}^2 \beta_1 \omega' + b_0 \beta_0 + b_1 \beta_1 \omega' + b_2 \beta_2 \omega'^2 = 0 \quad (22)$$

for  $c_0 = c_1 = 0$ . Three independent parameters can be determined from three sets of  $\omega'$  and  $k$  which satisfy the dispersion relation exactly:

$$-b_2^* \alpha_2 k_l^2 \beta_0 + a_1^* \alpha_2 k_l^2 \beta_1 \omega'_l + \xi^2 \beta_0 + 2\xi \beta_1 \omega'_l + \beta_2 \omega_l'^2 = 0 \quad (l = 1, 2, 3) \quad (23)$$

where

$$b_2^* = 1/b_2, \quad \xi = \sqrt{b_0/b_2}, \quad a_1^* = a_1/b_2 \quad (24)$$

Since Equations expressed by (23) are linear in  $b_2^*$  and  $a_1^*$ , these parameters can be eliminated to yield a parabolic equation in terms of  $\xi$ . After solving for  $\xi$ , we can determine  $b_2, b_0, a_1$  and  $b_1$  by Eqs. (18) and (24).

### 2.1.3 breaking wave model

Breaking wave model used is the same as Isobe (1987). First, the relative wave amplitude is defined by

$$\gamma = |\eta|/h \quad (25)$$

The critical relative amplitude,  $\gamma_b$ , for breaking of an individual wave in the random wave train is given as

$$\gamma_b = 0.8 \times \gamma'_b \quad (26)$$

$$\gamma'_b = 0.53 - 0.3 \exp(-3\sqrt{h/\bar{L}_o}) + 5 \tan^{3/2} \beta \exp\{-45(\sqrt{h/\bar{L}_o} - 0.1)^2\} \quad (27)$$

After breaking, the energy dissipation coefficient is introduced as follows:

$$f_D = \frac{5}{2} \tan \beta \sqrt{\frac{1}{k_o h}} \sqrt{\frac{\gamma - \gamma_r}{\gamma_s - \gamma_r}} \quad (28)$$

$$\gamma_s = 0.4 \times (0.57 + 5.3 \tan \beta) \quad (29)$$

$$\gamma_r = 0.135 \quad (30)$$

From  $f_D$  determined at the representative frequency,  $c_0 = \bar{k}^2 f_D$  and  $c_1$  is calculated by Eq. (19). Thus all the coefficients in Eq. (9) are determined and  $\tilde{\phi}$  can be calculated.

### 2.1.4 water surface elevation

In Eq. (2) which determines the water surface elevation from the calculated  $\tilde{\phi}$ , the coefficient  $\sqrt{cc_g}$  is also a function of frequency but can accurately be approximated by a second-order polynomial function. Therefore, Eq. (2) is approximated by

$$\tilde{\eta} = d_0 \tilde{\phi} + d_1 \frac{\partial \tilde{\phi}}{\partial t} + d_2 \frac{\partial^2 \tilde{\phi}}{\partial t^2} \quad (31)$$

where the constants,  $d_0, d_1$  and  $d_2$ , are determined from the values of  $\sqrt{cc_g}$  at three different frequencies:

$$d_0 + d_1 \beta_1 \omega'_l + d_2 \beta_2 \omega_l'^2 = (1/\sqrt{cc_g})_l \quad (l = 1, 2, 3) \quad (32)$$

2.2 Error evaluation

Since  $1/\sqrt{cc_g}$  is constant for low frequency and proportional to the frequency for high frequency, the second-order approximation has a high accuracy. On the other hand, since  $k^2$  is proportional to  $\omega^2$  and  $\omega^4$  for low and high frequency, respectively, even the rational approximation may not have a sufficient accuracy.

Figure 1 shows the interval from  $\omega_{\min}$  to  $\omega_{\max}$  within which the relative error of  $k^2$  is less than 1%. The three frequencies for determining the coefficients are denoted

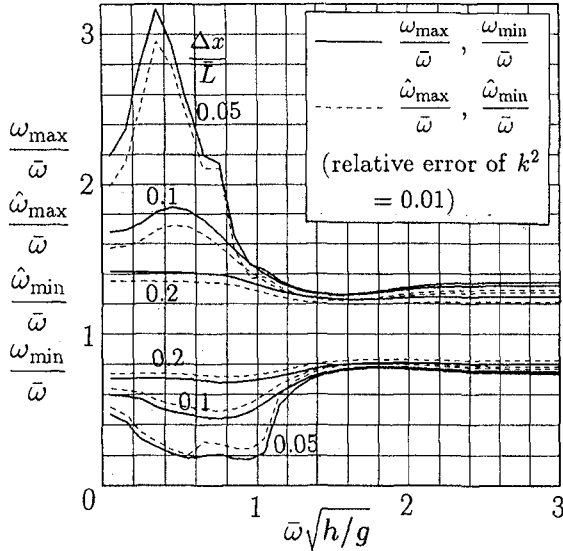


Figure 1: Frequency intervals within which the maximum relative error of  $k^2$  is 1%

by  $\hat{\omega}_{\min}$ ,  $\bar{\omega}$  and  $\hat{\omega}_{\max}$ , and therefore  $\omega'_1$ ,  $\omega'_2$  and  $\omega'_3$  in Eq. (23) are  $\hat{\omega}_{\min} - \bar{\omega}$ , 0 and  $\hat{\omega}_{\max} - \bar{\omega}$ , respectively. The horizontal axis is the nondimensionalized representative angular frequency  $\bar{\omega}\sqrt{h/g}$  ( $h$ : the water depth;  $g$ : the gravitational acceleration). Lines are drawn for various relative grid size  $\Delta x/L$  ( $L$ : the wavelength at  $\bar{\omega}$ ). Figure 2 shows the same interval for various relative errors. From these figures, the interval becomes narrowest at about  $\bar{\omega}\sqrt{h/g} = 1.4$ . Finally, Fig. 3 shows the narrowest interval as a function of the relative error. The relative grid size,  $\Delta x/L$ , is assumed to be 0.1 but does not have much influence.

From Fig. 3, if the relative error of  $k^2$  is permitted up to 10%, most of the energy in random waves will be included in the interval and therefore the transformation of random waves can be analyzed by Eq. (9). This may usually be the case because the wave energy at the frequency far different from the representative frequency is usually small. However, for random waves with a very wide banded spectrum and a small relative error of  $k^2$ , the frequency interval have to be divided into several sections and the results of calculation for each section are superimposed.

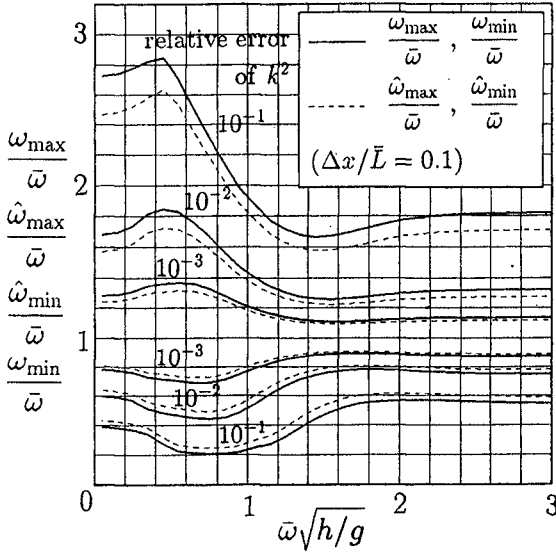


Figure 2: Frequency intervals for various maximum relative errors of  $k^2$

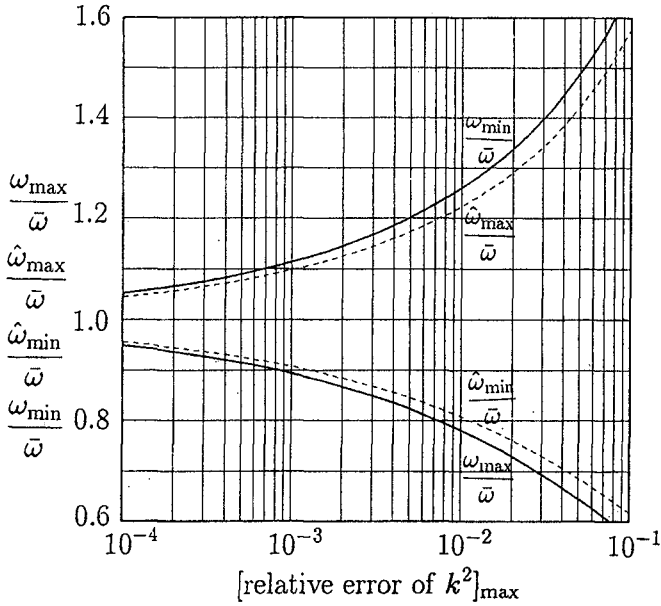


Figure 3: Frequency intervals in terms of the allowable relative error of  $k^2$

2.3 Sample calculations

Once the representative frequency and the grid size are fixed, the grid size to wavelength ratio may become large for high frequency. Figure 4 examines the effect of grid size for analyzing wave shoaling on a uniformly sloping bottom. The angular frequency,  $\omega$ , of the waves analyzed is  $0.8\bar{\omega}$  for which the error of  $k^2$  becomes almost maximum. In the upper figure, the agreement with the analytical solution is very good. Even in the lower figure for which the relative grid size is as large as 0.321, the agreement is not bad, which may be acceptable in analyzing far side frequency band component.

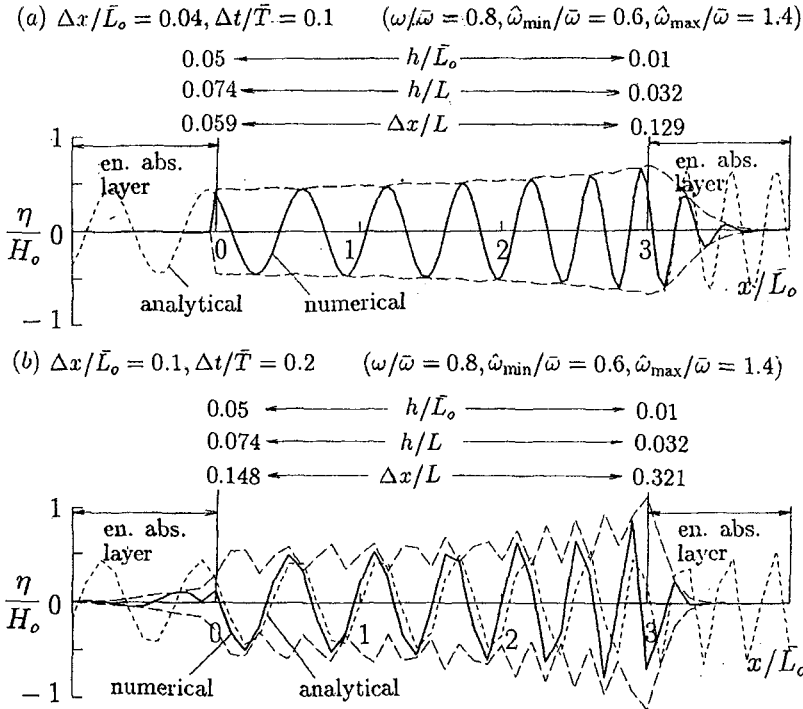


Figure 4: Effect of grid size and time interval on the accuracy

Figure 5 compares calculated and measured water surface elevation due to shoaling random waves. The incident wave profile which is shown in the upper figure was measured on a horizontal bottom with water depth of 40cm. From the point, a horizontal bottom with 0.4m in length, a 1/10 slope with 1m, and a 1/30 slope are installed. The onshoreward measuring point is located 2.6m from the beginning of the 1/30 slope and the water depth there is 21cm. The frequency interval was divided into four sections in the numerical calculation. The agreement is seen to be very good. However, near the breaker zone where nonlinearity of waves is strong, steepening of wave crests can not be reproduced by the present linear theory, even though energies of wave groups are fairly well reproduced. This implies that the present linear theory can be used to



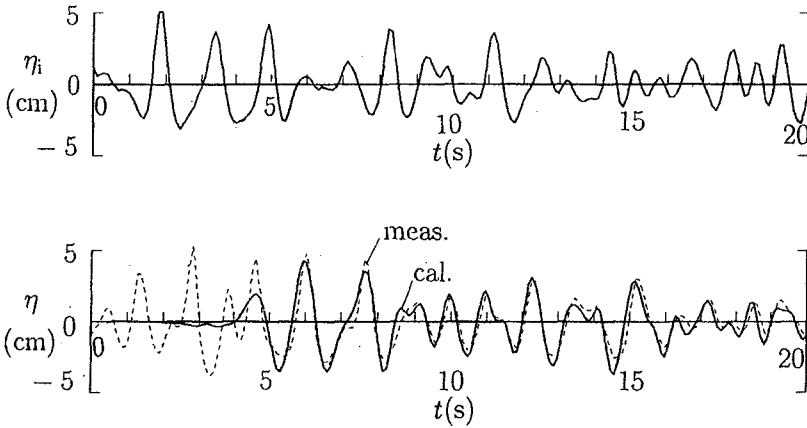


Figure 5: Comparison between calculated and measured water surface elevation in shoaling water

predict the distribution of integral properties such as the wave energy and radiation stress. To predict the wave profile in the nearshore zone, nonlinear theory must be employed.

### 3 Nonlinear Theory

#### 3.1 Derivation

##### 3.1.1 definition of Lagrangian

A Lagrangian  $L$  which is equivalent to the basic equation and boundary conditions for water surface waves is given as follows (Luke, 1967):

$$L[\phi, \eta] = \int_{t_1}^{t_2} \iint_A \int_{-h}^{\eta} \left\{ \frac{\partial \phi}{\partial t} + \frac{1}{2}(\nabla \phi)^2 + \frac{1}{2} \left( \frac{\partial \phi}{\partial z} \right)^2 + gz \right\} dz dA dt \quad (33)$$

where unknown functions are the velocity potential  $\phi$  and the water surface elevation  $\eta$ , and  $t_1$  and  $t_2$  denote the beginning and end of time,  $A$  the area of concern in  $(x, y)$  plane,  $h$  the water depth,  $g$  the gravitational acceleration,  $\nabla = (\frac{\partial}{\partial x}, \frac{\partial}{\partial y})$  the differential operator in the horizontal directions,  $(x, y) = \mathbf{x}$  the horizontal coordinates,  $z$  the vertical coordinates, and  $t$  the time.

The variation of  $L$  due to small variations of  $\phi$  and  $\eta$  is obtained from Eq. (33):

$$\begin{aligned} \delta L = & - \int_{t_1}^{t_2} \iint_A \int_{-h}^{\eta} \left( \nabla^2 \phi + \frac{\partial^2 \phi}{\partial z^2} \right) \delta \phi dz dA dt \\ & - \int_{t_1}^{t_2} \iint_A \left[ \left\{ \frac{\partial \phi}{\partial t} + \frac{1}{2}(\nabla \phi)^2 + \frac{1}{2} \left( \frac{\partial \phi}{\partial z} \right)^2 + g\eta \right\} \delta \eta \right]_{z=\eta} \\ & + \left\{ \frac{\partial \eta}{\partial t} + \nabla \eta \nabla \phi - \frac{\partial \phi}{\partial z} \right\} \delta \phi \Big|_{z=\eta} + \left\{ \nabla h \nabla \phi + \frac{\partial \phi}{\partial z} \right\} \delta \phi \Big|_{z=-h} \Big] dA dt \end{aligned}$$

$$+ \int_{t_1}^{t_2} \oint_C \int_{-h}^{\eta} \frac{\partial \phi}{\partial n} \delta \phi \, dz \, ds \, dt + \iint_A \int_{-h}^{\eta} [\delta \phi]_{t_1}^{t_2} \, dz \, dA \tag{34}$$

where  $C$  denotes the boundary of  $A$ . To terminate  $L$  for small variations of  $\phi$  and  $\eta$  in an arbitrary point, all the integrands in the above equation must vanish. The Laplace equation for  $\phi$  can be obtained from the first integral, and the dynamic and kinematic free surface boundary conditions and the bottom boundary condition, respectively, from the first, second and third terms in the second integral. Therefore the application of the variational principle to  $L$  results in the basic equation and boundary conditions for water surface waves. The third and fourth integrals are, respectively, related with the lateral and initial conditions which are given in each specific problem.

**3.1.2 vertical distribution functions**

Wave equations such as the mild-slope equation and Boussinesq equation are two-dimensional equations which are obtained by integrating vertically the governing three-dimensional equations. For the integration, vertical distribution functions are introduced theoretically or a priori. Massel (1993) derived an extended mild-slope equation by introducing a vertical distribution function of hyperbolic cosine type and integrating the governing equation. A clear and generalized concept of this procedure was proposed by Nadaoka and Nakagawa (1993) and Nadaoka *et al.* (1994) in deriving a strongly-nonlinear, strongly-dispersive wave equation by applying the Galerkin method to the Euler equations of motion. Nochino (1994) used another set of vertical distribution functions to derive a nonlinear dispersive equation. The present theory also introduces vertical distribution functions and integrate the Lagrangian to yield a nonlinear mild-slope equation.

First, the three-dimensional dependent variable,  $\phi$ , is expanded into a series in terms of a certain set of vertical distribution functions,  $Z_{\alpha}(z)$ , given a priori:

$$\phi(\mathbf{x}, z, t) = \sum_{\alpha=1}^N Z_{\alpha}(z; h(\mathbf{x})) f_{\alpha}(\mathbf{x}, t) \equiv Z_{\alpha} f_{\alpha} \tag{35}$$

where the function,  $Z_{\alpha}$ , may change according to the water depth  $h$ , and  $f_{\alpha}$  is the coefficient for  $Z_{\alpha}$  and a function of  $\mathbf{x}$  and  $t$  but not of  $z$ . The summation convention will be applied hereafter.

Then, after substituting Eq. (35) into Eq. (33), the integration is carried out in the vertical direction:

$$L[f_{\alpha}, \eta] = \int_{t_1}^{t_2} \iint_A \xi(f_{\alpha}, \frac{\partial f_{\alpha}}{\partial t}, \eta, \frac{\partial \eta}{\partial t}) \, dA \, dt \tag{36}$$

$$\begin{aligned} \xi(f_{\alpha}, \frac{\partial f_{\alpha}}{\partial t}, \eta, \frac{\partial \eta}{\partial t}) &= \frac{g}{2}(\eta^2 - h^2) + \tilde{Z}_{\beta} \frac{\partial f_{\beta}}{\partial t} + \frac{1}{2} A_{\gamma\beta} \nabla f_{\gamma} \nabla f_{\beta} + \frac{1}{2} B_{\gamma\beta} f_{\gamma} f_{\beta} \\ &+ C_{\gamma\beta} f_{\gamma} \nabla f_{\beta} \nabla h + \frac{1}{2} D_{\gamma\beta} f_{\gamma} f_{\beta} (\nabla h)^2 \end{aligned} \tag{37}$$

where

$$\tilde{Z}_{\alpha} = \int_{-h}^{\eta} Z_{\alpha} \, dz \tag{38}$$

$$A_{\alpha\beta} = \int_{-h}^{\eta} Z_{\alpha} Z_{\beta} dz \quad (39)$$

$$B_{\alpha\beta} = \int_{-h}^{\eta} \frac{\partial Z_{\alpha}}{\partial z} \frac{\partial Z_{\beta}}{\partial z} dz \quad (40)$$

$$C_{\alpha\beta} = \int_{-h}^{\eta} \frac{\partial Z_{\alpha}}{\partial h} Z_{\beta} dz \quad (41)$$

$$D_{\alpha\beta} = \int_{-h}^{\eta} \frac{\partial Z_{\alpha}}{\partial h} \frac{\partial Z_{\beta}}{\partial h} dz \quad (42)$$

The above coefficients,  $\tilde{Z}_{\alpha}$ ,  $A_{\alpha\beta}$ ,  $B_{\alpha\beta}$ ,  $C_{\alpha\beta}$  and  $D_{\alpha\beta}$ , are obtained from given vertical distribution functions and then the Lagrangian is expressed by Eq. (36) as an integral in the horizontal two-dimensional plane.

### 3.1.3 variational principle

Application of the variational principle to Eq. (36) in terms of  $\eta$  and  $f_{\alpha}$  yields Euler equations which are expressed in general forms:

$$\frac{\partial \xi}{\partial f_{\alpha}} = \frac{\partial}{\partial t} \left[ \frac{\partial \xi}{\partial (\partial f_{\alpha} / \partial t)} \right] + \nabla \left[ \frac{\partial \xi}{\partial (\nabla f_{\alpha})} \right] \quad (43)$$

$$\frac{\partial \xi}{\partial \eta} = \frac{\partial}{\partial t} \left[ \frac{\partial \xi}{\partial (\partial \eta / \partial t)} \right] + \nabla \left[ \frac{\partial \xi}{\partial (\nabla \eta)} \right] \quad (44)$$

Substituting Eq. (37) into Eqs. (43) and (44), a set of nonlinear partial differential equations is obtained for analyzing nonlinear water wave transformation:

$$Z_{\alpha}^{\eta} \frac{\partial \eta}{\partial t} + \nabla (A_{\alpha\beta} \nabla f_{\beta}) - B_{\alpha\beta} f_{\beta} + \nabla (C_{\beta\alpha} f_{\beta} \nabla h) - C_{\alpha\beta} \nabla f_{\beta} \nabla h - D_{\alpha\beta} f_{\beta} (\nabla h)^2 = 0 \quad (45)$$

$$\begin{aligned} g\eta + Z_{\beta}^{\eta} \frac{\partial f_{\beta}}{\partial t} + \frac{1}{2} Z_{\gamma}^{\eta} Z_{\beta}^{\eta} \nabla f_{\gamma} \nabla f_{\beta} + \frac{1}{2} \frac{\partial Z_{\gamma}^{\eta}}{\partial z} \frac{\partial Z_{\beta}^{\eta}}{\partial z} f_{\gamma} f_{\beta} + \frac{\partial Z_{\gamma}^{\eta}}{\partial h} Z_{\beta}^{\eta} f_{\gamma} \nabla f_{\beta} \nabla h \\ + \frac{1}{2} \frac{\partial Z_{\gamma}^{\eta}}{\partial h} \frac{\partial Z_{\beta}^{\eta}}{\partial h} f_{\gamma} f_{\beta} (\nabla h)^2 = 0 \end{aligned} \quad (46)$$

where

$$Z_{\alpha}^{\eta} = Z_{\alpha}|_{z=\eta} \quad (47)$$

The above equations includes terms up to the second order in the bottom slope; however, vertical distribution functions given will usually be consistent only with a horizontal or mild-slope bottom. Therefore, on assuming that the bottom slope is mild, the terms of the second order are neglected to yield a set of nonlinear mild-slope equations:

$$Z_{\alpha}^{\eta} \frac{\partial \eta}{\partial t} + \nabla (A_{\alpha\beta} \nabla f_{\beta}) - B_{\alpha\beta} f_{\beta} + (C_{\beta\alpha} - C_{\alpha\beta}) \nabla f_{\beta} \nabla h + \frac{\partial Z_{\beta}^{\eta}}{\partial h} Z_{\alpha}^{\eta} f_{\beta} \nabla \eta \nabla h = 0 \quad (48)$$

$$g\eta + Z_{\beta}^{\eta} \frac{\partial f_{\beta}}{\partial t} + \frac{1}{2} Z_{\gamma}^{\eta} Z_{\beta}^{\eta} \nabla f_{\gamma} \nabla f_{\beta} + \frac{1}{2} \frac{\partial Z_{\gamma}^{\eta}}{\partial z} \frac{\partial Z_{\beta}^{\eta}}{\partial z} f_{\gamma} f_{\beta} + \frac{\partial Z_{\gamma}^{\eta}}{\partial h} Z_{\beta}^{\eta} f_{\gamma} \nabla f_{\beta} \nabla h = 0 \quad (49)$$

The total number of equations is  $(N + 1)$  since Eqs. (48) and (49) contain 1 and  $N$  components, respectively. On the other hand, the total number of unknowns,  $\eta$  and  $f_\alpha$  ( $\alpha = 1$  to  $N$ ), is  $(N + 1)$ . Therefore, with appropriate boundary conditions, the equations can be solved numerically. Then, the velocity is obtained through the velocity potential expressed by Eq. (35).

### 3.2 Sample vertical distribution functions

A set of vertical distribution functions should be selected so that the velocity potential may accurately be expressed by Eq. (35) with a small number of terms. As understood from the small amplitude wave theory, hyperbolic cosine functions may be effective for deep to intermediate water, whereas polynomial functions for very shallow water. Here, for the sake of simplicity, polynomial functions are chosen and analytical expressions for the coefficients are shown.

As inferred from shallow water wave theory, we select a set of even-order polynomial functions:

$$Z_\alpha = \left( \frac{h+z}{h} \right)^{2(\alpha-1)} \tag{50}$$

Then, Eqs. (47) and (39) to (41) give

$$Z_\alpha^\eta = \zeta^{2\alpha_1} \tag{51}$$

$$A_{\alpha\beta} = h \frac{\zeta^{2(\alpha_1+\beta_1)+1}}{2(\alpha_1 + \beta_1) + 1} \tag{52}$$

$$B_{\alpha\beta} = \frac{4\alpha_1\beta_1}{h} \frac{\zeta^{2(\alpha_1+\beta_1)-1}}{2(\alpha_1 + \beta_1) - 1} \tag{53}$$

$$C_{\alpha\beta} = -2\alpha \left[ \frac{\zeta^{2(\alpha_1+\beta_1)+1}}{2(\alpha_1 + \beta_1) - 1} - \frac{\zeta^{2(\alpha_1+\beta_1)}}{2(\alpha_1 + \beta_1)} \right] \tag{54}$$

where

$$\zeta = (h+z)/h \tag{55}$$

$$\alpha_1 = \alpha - 1 \tag{56}$$

$$\beta_1 = \beta - 1 \tag{57}$$

To check the effectiveness of the polynomial functions, the dispersion relation of the linearized equation is examined for a horizontal bottom. In the linear theory, the coefficients expressed by Eqs. (51) to (53) are evaluated at  $z = 0$  instead of  $z = \zeta$ . By denoting the quantities at  $z = 0$  by superscript  $^\circ$ , the following equation can be obtained by eliminating  $\eta$  from the linearized forms of Eqs. (48) and (49) on a horizontal bottom:

$$-\frac{1}{g} Z_\alpha^\circ Z_\beta^\circ \frac{\partial^2 f_\beta}{\partial t^2} + \nabla(A_{\alpha\beta}^\circ \nabla f_\beta) - B_{\alpha\beta}^\circ f_\beta = 0 \tag{58}$$

where from Eqs. (51) to (53)

$$Z_\alpha^\circ = 1 \tag{59}$$

$$A_{\alpha\beta}^\circ = h / \{2(\alpha_1 + \beta_1) + 1\} \tag{60}$$

$$B_{\alpha\beta}^2 = 4\alpha_1\beta_1/[h\{2(\alpha_1 + \beta_1) - 1\}] \tag{61}$$

For progressive waves,

$$f_\alpha = a_\alpha e^{i(k-\omega t)} \tag{62}$$

By substituting the above expression into Eq. (58), the following homogenous equations are obtained:

$$\sum_{\beta=1}^N \left( \frac{\omega^2}{g} - \frac{1}{h} \frac{4\alpha_1\beta_1}{2(\alpha_1 + \beta_1) - 1} \right) a_\beta = \hat{k}^2 \sum_{\beta=1}^N \frac{h}{2(\alpha_1 + \beta_1) + 1} a_\beta \tag{63}$$

For a given  $\omega$ ,  $\hat{k}^2$  is obtained as an eigenvalue which gives a non-trivial solution to the above equations. At least up to  $N = 4$ , it was confirmed numerically that only one eigenvalue is positive and the others are negative. A positive value of  $\hat{k}^2$ , *i.e.*, a real value of  $k$ , corresponds to progressive waves, and a negative value to evernescent waves. The relationship between the frequency and wave celerity of the progressive waves is shown in Fig. 6 for various  $N$ . As can be seen, agreement with the linear wave theory

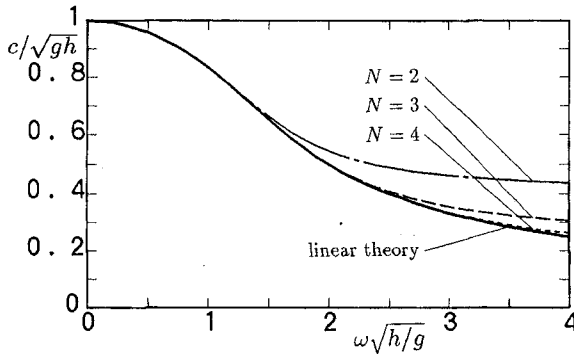


Figure 6: Dispersion relation for vertical distribution functions of even-order polynomials

is good for shallow to deep water even with small  $N$ .

### 3.3 Sample calculations

Figure 7 compares calculated and measured water surface elevation  $\eta$  and bottom velocity  $w_b$  in shoaling water. Even for Case 2-2 in which nonlinearity is strong at the measuring point, agreement is good for the bottom velocity as well as the water surface elevation.

Figure 8 compares calculated and measured water surface elevation around a submerged breakwater. Nonlinearity and dispersion are significant on the breakwater and on the horizontal bottom, respectively. Agreement is good even with a small number of  $N$  ( $N = 3$ ).

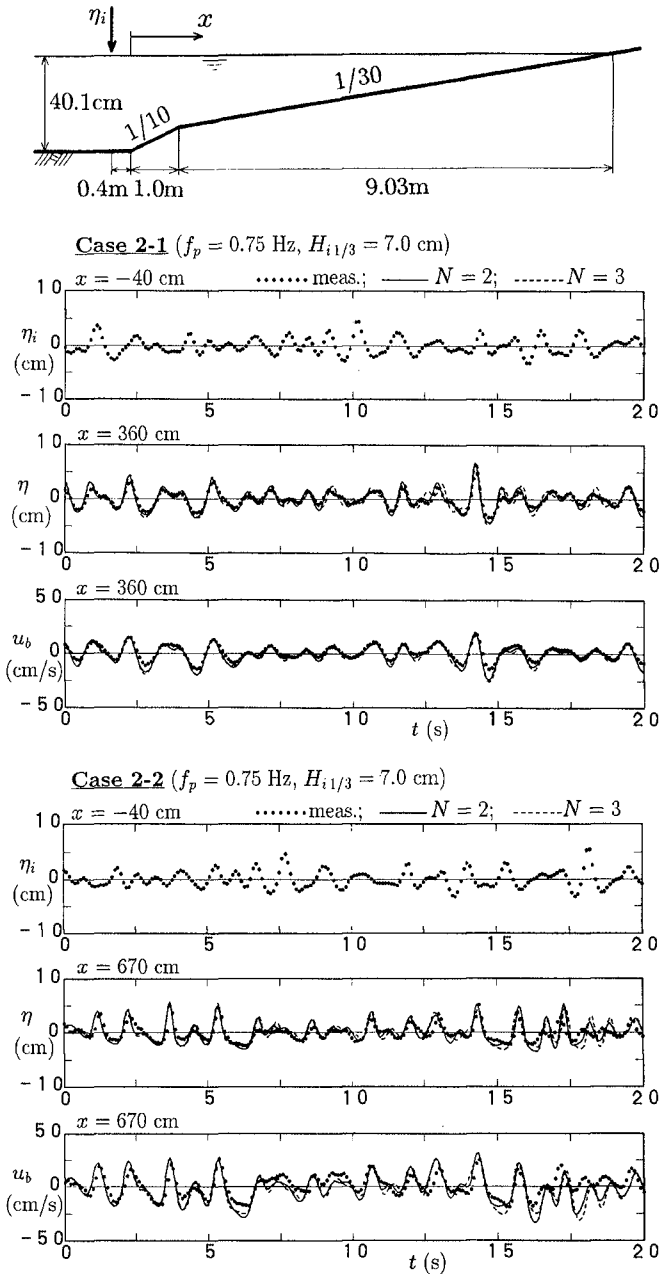
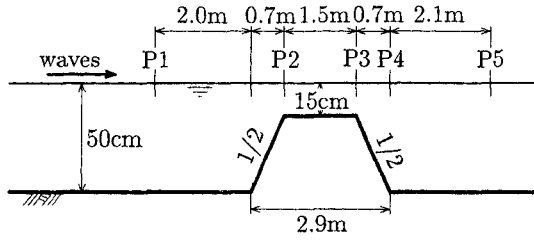


Figure 7: Comparison between calculated and measured water surface elevation and bottom velocity in shoaling water



**Case 4** ( $T = 2.01$  s,  $H_o = 5.0$  cm)

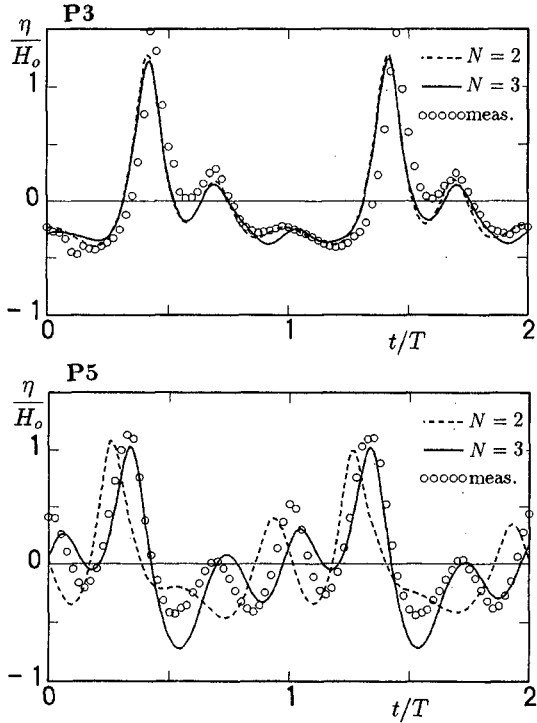


Figure 8: Comparison between calculated and measured water surface elevation on and behind the submerged breakwater

## 4 Conclusions

A time-dependent mild-slope equation for random waves is derived from the mild-slope equation by approximating rational function to the frequency-dependent coefficients. This equation allows to simulate the time evolution of short-crested random waves in the nearshore area. Agreement between calculated and measured water surface elevation in the offshore zone is good because wave nonlinearity is not essential.

A nonlinear mild-slope equation is derived by expanding the velocity potential into a series in terms of vertical distribution functions and then applying the variational principle to a Lagrangian. Comparison between calculated and measured quantities confirms the validity of the theory even for a strongly nonlinear and dispersive wave field.

## References

- [1] Berkhoff, J. C. W. (1972): Computation of combined refraction-diffraction, Proc. 13th Int. Conf. on Coastal Eng., ASCE, pp. 471-490.
- [2] Isobe, M. (1987): A parabolic equation model for transformation of irregular waves due to refraction, diffraction and breaking, Coastal Eng. in Japan, Vol. 30, pp. 33-47.
- [3] Kotake, Y., M. Isobe and A. Watanabe (1992): On a high-order approximation of the time-dependent mild-slope equation for irregular waves, Proc. 39th Japanese Conf. on Coastal Eng., pp. 91-95 (in Japanese).
- [4] Kubo Y., M. Isobe and A. Watanabe (1992): Time-dependent mild slope equation for random waves, Proc. 23rd Int. Conf. on Coastal Eng., pp. 419-431.
- [5] Luke, J. C. (1967): A variational principle for a fluid with a free surface, J. Fluid Mech., Vol. 27, pp. 395-397.
- [6] Massel, S. R. (1993): Extended refraction-diffraction equation for surface waves, Coastal Eng., Vol. 19, pp. 97-126.
- [7] Nadaoka, K. and Y. Nakagawa (1993): Simulation of nonlinear wave fields with the newly derived nonlinear dispersive wave equations, Proc. 40th Japanese Conf. on Coastal Eng., pp. 6-10 (in Japanese).
- [8] Nakaoka, K., S. Beji, Y. Nakagawa and O. Ohno (1994): A fully-dispersive nonlinear wave model and its numerical solution, Proc. 24th Int. Conf. on Coastal Eng., ASCE (in press).
- [9] Nochino, M. (1994): Coupled oscillation equation for strongly nonlinear random wave field and its basic characteristics, Proc. 41st Japanese Conf. on Coastal Eng., pp. 11-15 (in Japanese).
- [10] Radder, A. C. (1979): On the parabolic equation method for water-wave propagation, J. Fluid Mech., Vol. 95, pp. 159-176.



## CHAPTER 23

### Modelling Moveable Bed Roughness and Friction for Spectral Waves

Kaczmarek, L.M.<sup>1</sup>, Harris, J.M.<sup>2</sup>, O'Connor, B.A.<sup>2</sup>

#### Abstract

The present paper is concerned with the simulation of turbulent boundary layer dynamics over a moveable seabed in random waves. A new theoretical approach for the evaluation of moveable bed roughness in spectral waves based on the grain-grain interaction idea is presented and tested against data from the laboratory and field. The new approach is combined with the methodology which assumes that the spectral wave condition can be represented by a monochromatic representative wave. Good results have been obtained, although further testing against data gathered in the North Sea is required.

#### 1. Introduction

For a moveable sandy bed, one may distinguish three general seabed conditions due to the action of surface gravity waves: a flat bed, rippled bed and sheet flow. If we consider the latter condition, the need to study sediment transport under wave-induced sheet flow conditions is necessary in the understanding of beach profile changes in the surf zone. The understanding of nearbed sediment dynamics is also of great importance for the mathematical description of cross-shore sediment transport.

To understand the effect of changing bed roughness by the hydrodynamic forces requires knowledge of the dynamic behaviour of sand grains in the collision-dominated, high concentration nearbed region. At high shear stresses and sediment transport intensities, the nearbed sediment transport appears to take place in a layer with a thickness that is large compared to the grain size. It is therefore not possible to properly describe flow in this layer by conventional engineering models which assume

---

<sup>1</sup> Polish Academy of Sciences, Institute of Hydro-Engineering, IBW PAN, 7 Koscierska, 80-953, Gdansk, Poland.

<sup>2</sup> Department of Civil Engineering, University of Liverpool, Brownlow St., P.O. Box 147, Liverpool L69 3BX. UK.

that bed load transport occurs in a layer that has a thickness of the order of one or two grain diameters.

The present paper is concerned with developing an iterative procedure for the estimation of the effective bed roughness for a monochromatic wave, as characterised by the roughness parameter  $k_s$ , and extending this to the case of a spectral sea. The nearbed sediment dynamics are modelled in two regions with continuous profiles of stress and velocity. Namely (i) a granular fluid region and (ii) a wall bounded turbulent fluid shear region.

In sheet flow conditions it is assumed that the external drag produced by the boundary layer flow is related to the particle interactions within the sub-bed layer and hence to the effective roughness at the boundary.

**2. The sheet flow model**

**2.1 Formulation of the problem**

A typical velocity distribution with depth of a rough bed is supposed to be characterised (Kaczmarek & O'Connor 1993a,b) by a sub-bottom flow and a main or outer flow, as shown in Figure 1.

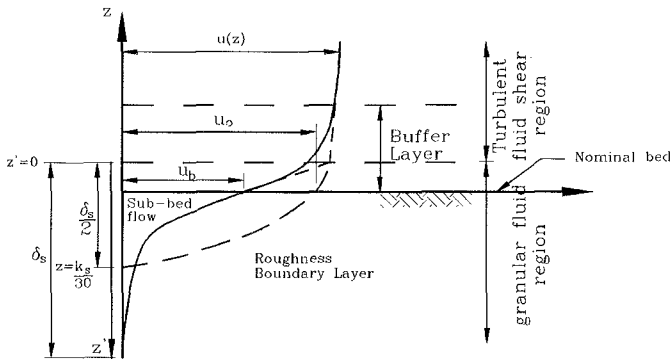


**Figure 1: Definition sketch of turbulent flow over a moveable bed.**

The velocity distribution is supposed to be continuous. Its intersection with the nominal bottom is the apparent slip velocity  $u_b$ . The downward extension of the velocity distribution in the outer zone of the main flow yields a fictitious slip velocity,  $u_o$  at the nominal bed, which is necessarily larger than  $u_b$  because of the supposed asymptotic transition in the buffer layer between the sub-bed flow and the fully turbulent flow in the turbulent-fluid shear region.

The velocity distribution in the roughness layer depends on the type of geometric roughness pattern and the bed permeability. There must be some transition between both parts of the velocity distribution bridged by the buffer zone. However, for present

purposes it is assumed that the velocity distribution in the turbulent-fluid shear region can be determined by parameters dependent on the geometric roughness properties of the bed and the outer flow parameters, such as the free-stream orbital velocity. It is proposed to extend the sub-bed granular-fluid flow region to the matching point with the velocity distribution in the turbulent-fluid shear region. Thus, shear stress velocities in the two layers are set equal at the theoretical bed level, as it is shown in Figure 1, point A.

The sub-bed flow region has a high sediment concentration. For sheet flow conditions in this layer, chaotic collisions of grains are the predominant mechanism. In this case water does not really transfer shear stresses at all. The dynamic state of such a mixture is characterised by stresses  $\sigma_{ij}$  which are the sum of dynamic  $\sigma^*_{ij}$  and plastic  $\sigma^o_{ij}$  stresses.

The first problem, therefore, is to determine the velocity profile distribution in the upper turbulent layer, which means determining the effective roughness height of the bed  $k_s$ , as well as the lower grain-fluid flow. The intersection of these two profiles will determine point A (See Figure 1).

## 2.2 Mathematical description of flow in the turbulent upper region

It is assumed that flow in the upper layer is governed by the simplified equation of motion:

$$\frac{\partial u}{\partial t} = \frac{\partial U}{\partial t} + \frac{1}{\rho} \frac{\partial \tau}{\partial z} \quad (2.1)$$

in which  $u(z,t)$  is, in general, a combined wave-period-averaged "steady" current and wave velocity and  $U(t)$  is the free-stream wave velocity at the top of the wave boundary layer.

The present work uses an eddy viscosity model, which is an extension of Kajiura's (1968) and Brevik's (1981) model. Thus the eddy viscosity over the flow depth is assumed to be given by the equations.

$$v_t(z) = \kappa u_{fmax} z \quad \text{for} \quad \frac{k_s}{30} \leq z \leq \frac{\delta_m}{4} + \frac{k_s}{30} \quad (2.2)$$

$$v_t(z) = \kappa u_{fmax} \left( \frac{\delta_m}{4} + \frac{k_s}{30} \right) \quad \text{for} \quad \frac{\delta_m}{4} + \frac{k_s}{30} < z \leq 2\delta_m + \frac{k_s}{30} \quad (2.3)$$

in which  $\kappa$  is von Karmen's constant;  $u_{fmax}$  is the maximum value of bed shear velocity ( $u_b(\omega t)$ ) during the wave period that is  $\max [u_b(\omega t)]$ ;  $\delta_m$  is the maximum value of  $\delta_1$  and  $\delta_2$ , that is,  $\max (\delta_1, \delta_2)$  where  $\delta_1$  and  $\delta_2$  are the boundary layer thickness at the moments corresponding to maximum and minimum velocity (of the combined wave and current flow) at the top of the turbulent boundary layer.

The quantities  $u_{fmax}$ ,  $\delta_m$  are determined from the solution of the integral equation derived from equation (2.1) as used by Fredsøe (1984):

$$\frac{\tau(\delta)}{\rho} - \frac{\tau_o}{\rho} = - \int_{\frac{k_s}{30}}^{\delta + \frac{k_s}{30}} \frac{\partial}{\partial t} (U - u) dz \tag{2.4}$$

Fredsøe (1984) assumed a logarithmic velocity profile in the boundary layer

$$\frac{u}{u_f} = \frac{1}{\kappa} \ln \frac{30z}{k_s} \tag{2.5}$$

The solution of equation (2.4) using Fredsøe's (1984) approach enables the value of  $u_{fmax}$  to be determined, if  $k_s$  is specified. Equation (2.1) can then be solved to provide the velocity distribution in the wave boundary layer.

### 2.3 Mathematical description of the flow in the granular-fluid region

Particle interactions in the shear-grain-fluid flow are assumed to produce two distinct types of behaviour. The Coulomb friction between particles gives rise to rate-independent stresses (of the plastic type) and the particle collisions give rise to stresses that are rate-dependent (of the viscous type). We assume the co-existence of both types of behaviour and the stress tensor is divided into two parts.

$$\sigma_{ij} = \sigma_{ij}^0 + \sigma_{ij}^* \tag{2.6}$$

Where  $\sigma_{ij}^0$  is the plastic stress and  $\sigma_{ij}^*$  is the viscous stress.

For two-dimensional deformation in the rectangular Cartesian co-ordinates  $x'$  and  $z'$  the Coulomb yield criterion is satisfied by employing the following stress relations:

$$\sigma_{x'x'}^0 = -\sigma'(1 + \sin \phi \cos 2\psi) \tag{2.7}$$

$$\sigma_{z'z'}^0 = -\sigma'(1 - \sin \phi \cos 2\psi) \tag{2.8}$$

$$\sigma_{x'z'}^0 = -\sigma' \sin \phi \cos 2\psi \tag{2.9}$$

Where  $\phi$  is the quasi-static angle of internal friction, while  $\psi$ , denoting the angle between the major principal stress and the  $x'$ -axis is equal to:

$$\psi = \frac{\pi}{4} - \frac{\phi}{2} \tag{2.10}$$

For the average normal stress:

$$\sigma' = - \left( \frac{\sigma_{x'x'}^0 + \sigma_{z'z'}^0}{2} \right) \tag{2.11}$$

we employ the following approximate expression (Sayed and Savage 1983).

$$\sigma' = \alpha^0 \left( \frac{c - c_0}{c_m - c} \right) \quad (2.12)$$

where  $\alpha^0$  is a constant and  $c_0$  and  $c_m$  are the solid concentrations corresponding to fluidity and closest packing respectively.

The viscous part of the stress tensor according to Sayed and Savage (1983) is assumed to have the following form:

$$\sigma_{x'x'}^* = \sigma_{z'z'}^* = -(\mu_0 + \mu_2) \left( \frac{\partial u}{\partial z'} \right)^2 \quad (2.13)$$

$$\sigma_{x'z'}^* = \sigma_{z'x'}^* = \mu_1 \left| \frac{\partial u}{\partial z'} \right| \frac{\partial u}{\partial z'} \quad (2.14)$$

in which the viscous stress coefficients  $\mu_0$ ,  $\mu_1$  and  $\mu_2$  are functions of the solids concentration  $c$ :

$$\frac{\mu_1}{\rho_s d^2} = \frac{0.03}{(c_m - c)^{1.5}} \quad (2.15)$$

$$\frac{\mu_0 + \mu_2}{\rho_s d^2} = \frac{0.02}{(c_m - c)^{1.75}} \quad (2.16)$$

Considering steady fully developed two-dimensional shear-grain-flow, the balance of linear momentum according to Kaczmarek & O'Connor (1993a,b) yields:

$$\alpha^0 \left[ \frac{c - c_0}{c_m - c} \right] \sin \phi \sin 2\psi + \mu_1 \left[ \frac{\partial u}{\partial z'} \right]^2 = \rho u_f^2 \quad (2.17)$$

$$\alpha^0 \left[ \frac{c - c_0}{c_m - c} \right] (1 - \sin \phi \cos 2\psi) + (\mu_0 + \mu_2) \left[ \frac{\partial u}{\partial z'} \right]^2 = \left[ \frac{\mu_0 + \mu_2}{\mu_1} \right]_{c=c_0} \rho u_f^2 + (\rho_s - \rho) g \int_0^{z'} c dz \quad (2.18)$$

where  $\rho$  is the density of the fluid.

Eliminating  $(\partial u / \partial z')$  from equations (2.16) and (2.17) allows the calculation of the profiles of the sub-bed sediment concentration  $c$  and velocity  $u$  in relation to known maximum shear stress  $(\rho u_{f \max}^2)$  at the theoretical bed level ( $z'=0$ ).

In Kaczmarek & O'Connor (1993a,b) equation (2.18) was solved for  $c$  as a function of depth ( $z'$ ) by using an iteration method in conjunction with numerical integration. Integration started at the theoretical bed level ( $z'=0$ ) with  $c=c_0$ . Proceeding downwards at each step the iteration method was used to evaluate  $c$ . The integration was stopped

when  $c$  was equal to  $c_{ms}$ . For the calculations the following numerical values were recommended for the various sand beds.

$$\frac{\alpha^0}{\rho_s g d} = 1 ; c_0 = 0.32 ; c_m = 0.53 ; c_{ms} = 0.50 ; \phi = 24.4^\circ$$

### 3. Results for monochromatic waves

#### 3.1 Plane bed

The above procedure was used to compare computations for the model with the experimental results of Horikawa *et al.* (1982). The conditions for Horikawa *et al.*'s test 1 were used for the model calculations:  $d = 0.2\text{mm}$ ,  $s = \rho_s / \rho = 2.66$ ,  $\phi = 24.4^\circ$ ,  $T = 3.64\text{s}$  and  $U = 127\text{ cm/s}$ . A value of  $k_s = 7.3\text{mm}$  was found for the roughness parameter.

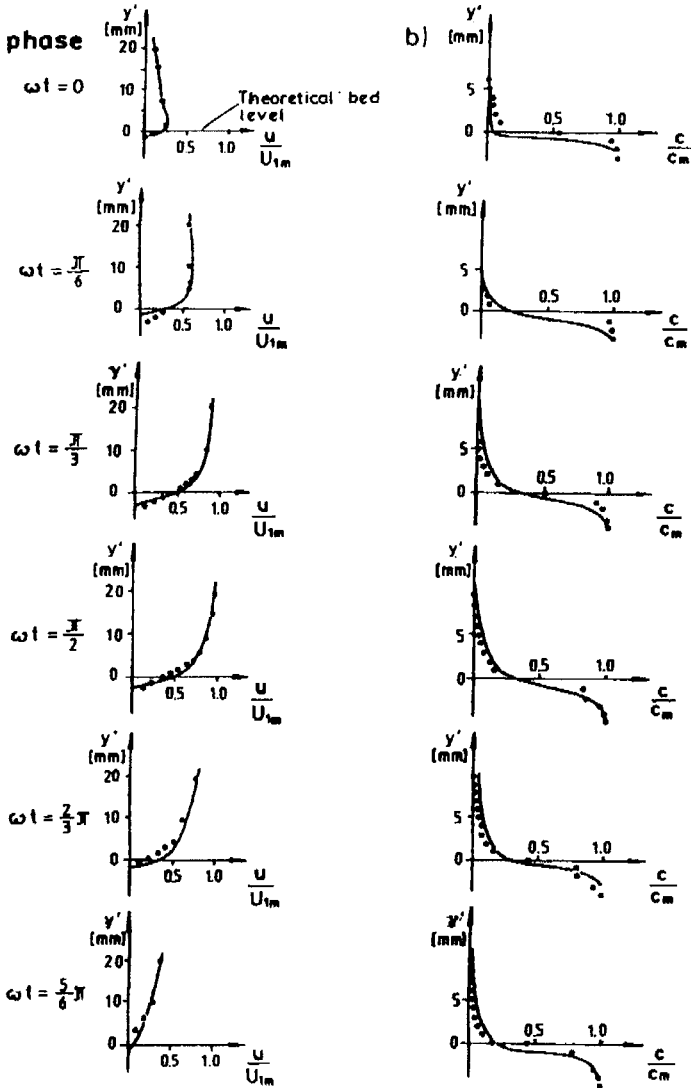
Having obtained the roughness parameter it is then easy to obtain the instantaneous profiles both in the turbulent layer and the sub-bottom flow zone without reference to empirical formulas of any kind. Knowing  $u_r$  and solving equations 2.17 and 2.18 the velocity and concentration distributions at any time inside the entire sub-bottom layer can be found.

The results are shown in Figure 2. A reasonable agreement is obtained between the model and the laboratory data.

The model was then run for a range of conditions including those outside its range of application. The results of these tests are shown in Figure 3. The calculations were obtained using the simplified iteration procedure to determine  $k_s$  by introducing a simple logarithmic distribution (2.5) instead of the numerical solution of equation (2.1). Such a simplification makes the calculations much more efficient. It is seen that the roughness parameter,  $k_s$ , decreases with increasing dimensionless bed shear stress  $\theta_{max}$  and  $k_s$  is seen to attain its greatest value for small dimensionless shear stresses where  $\theta \approx 1$  (the transition from plane bed to ripples).

The trend shown in the present results, that is, that the roughness parameter increases drastically with decreasing dimensionless maximum shear stress, is similar to that shown by Nielsen (1992). Nielsen (1992) showed that the hydraulic roughness for equilibrium ripple formations is of the order  $100d_{50}$  to  $1000d_{50}$ . However, for artificial flat beds where measurements were taken before ripples had time to form Nielsen (1992) found that the hydraulic roughness decreased with decreasing grain roughness Shields parameter.

Next, calculations were carried out for a moveable sandy bed ( $d = 0.2\text{mm}$ ,  $s = 2.66$ ,  $\phi = 24.4^\circ$ ) with a variety of wave heights with a mean water depth of  $5.0\text{m}$ . The wave period was kept constant at  $T = 3.6\text{s}$ . The maximum shear stresses were calculated on the basis of equation (2.4) and using the simplified iteration procedure to determine  $k_s$ .



— present model  
 ○ measurements by Horikawa et al. (1982)

Figure 2: Theoretical and experimental distributions of velocity (a) and concentration (b) below and above the bed.

The results of the analysis of friction for wave-induced sheet flow, shown in Figure 4, suggest that the present approach restricted to the sheet flow regime may be extended to lower flow regimes and on the basis of analogy used to investigate lower flow conditions involving bed ripples.

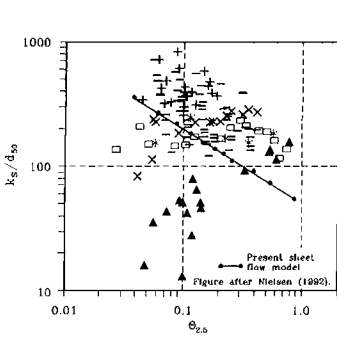


Figure 3: Nikuradse sand roughness by present theory along with results of Nielsen .

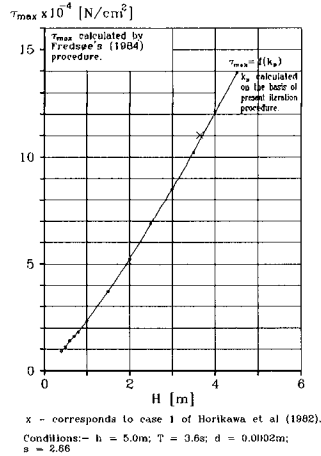


Figure 4: Calculation of maximum shear stresses

### 3.2 Rippled bed

Calculations for a rippled bed were performed for two different sediment sizes (0.2mm and 0.12mm diameter quartz sands). The calculations were carried out in two steps. Firstly, the values of the bed roughness  $k_s$  were obtained using the proposed iterative scheme. Then, the friction factors were calculated on the basis of an adjusted version of the semi-empirical formula of Jonsson and Carlsen (1976) in order to include the effects of the vortices formed in the lee of the roughness element crest due to turbulent mixing.

The theoretical results are shown in Figure 5. Presented alongside these results are the experimental results over a moveable bed reported by Madsen *et al.* (1990). The values of wave friction factor  $f_w$  are plotted against the representative value of a fluid-sediment interaction parameter, defined as:

$$S_r = \frac{\theta'}{\theta_c} \tag{3.1}$$

in which the skin Shields parameter is defined for a monochromatic wave as:



$$\theta' = \frac{u_{f \max}^2}{(s-1)gd} \tag{3.2}$$

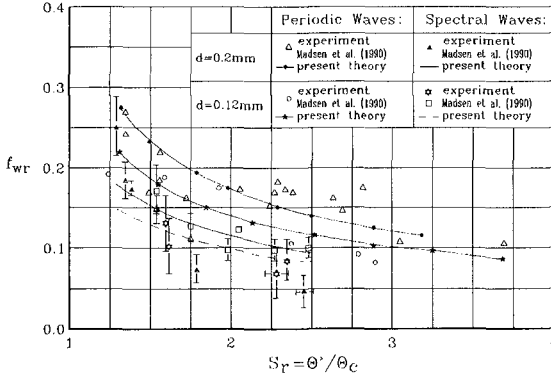


Figure 5: Moveable bed friction factors.

The agreement between theoretical and experimental results appears quite reasonable. It therefore appears that the sheet flow model can be used to investigate rippled bed conditions.

If the model can be used to investigate rippled bed conditions then it might also be possible to extend the analogy to include spectral wave conditions.

#### 4 Spectral sheet flow model

##### 4.1 Introduction

In the real world the Sea’s motion is a random process. To describe a real sea it is usual to use spectral methods. However, it is possible to simplify the process by using appropriate representative values for the spectral components (See O’Connor *et al.* 1992).

The effect of random waves on bed roughness needs to be studied, since it is known that the bed friction changes between mono-frequency and random wave conditions. It is hypothesized by Madsen *et al* (1990) that the larger waves in a spectral simulation shave off the sharp ripple crests thereby causing the observed reduction in dissipation and friction factors for spectral waves. In an attempt to explain this reduction of spectral wave friction factors a new theoretical approach for predictive evaluation of moveable bed roughness for spectral waves is proposed. The new approach is based on the methodology which assumes that the spectral wave condition can be represented by a monochromatic wave and is combined with the theoretical grain-grain interaction ideas.

**4.2 Modified iterative method**

Following on from the iterative method used for monochromatic waves, a modified iterative procedure to evaluate the moveable bed roughness under spectral waves is proposed as shown in Figure 6.

Representative values are used in the calculation routine for the free stream velocity and the angular frequency. Previously for monochromatic waves, the maximum value of shear stress was the maximum value of shear stress during a wave period. For spectral waves the maximum value of the random shear stress time series is used:

$$\tau_{\max} = \frac{3\tau_{\text{rms}}}{\sqrt{2}} = 3\sigma_{\tau} \tag{4.1}$$

The choice of this maximum value of the random shear stress time series was checked using the simple Rayleigh Method as well as a through running a more sophisticated one dimensional through depth (1DV) k-ε boundary layer model.

**4.3 Spectral shear stress**

Using the Rayleigh method, it is possible to quickly determine a value for the shear stress for a random time series. Assuming a Rayleigh distribution then:

$$\frac{\tau_{\max}}{\tau_{\text{rms}}} = [\ln(N)]^{\frac{1}{2}} = R \tag{4.2}$$

T <sub>z</sub> /sec	10	10	10
Time /min	10	20	40
N	60	120	240
R	2.02	2.18	2.34

The assumed value of R is:

$$3/\sqrt{2} = 2.12$$

The 1DV k-ε boundary layer model provides a method to directly simulate a random from shear stress from a known random velocity field. The method is based on the previous work of O’Connor *et al.* (1992) where a zero equation mixing length model was used to simulate a random sea.

The two equation k-ε model uses the standard equations to represent the momentum, the turbulent energy, k and the dissipation rate , ε.

Momentum:

$$\frac{\partial \mathbf{u}}{\partial t} = \frac{\partial \mathbf{u}_f}{\partial t} + \frac{\partial}{\partial \mathbf{z}} \left( \nu_t \frac{\partial \mathbf{u}}{\partial \mathbf{z}} \right) \tag{4.3}$$

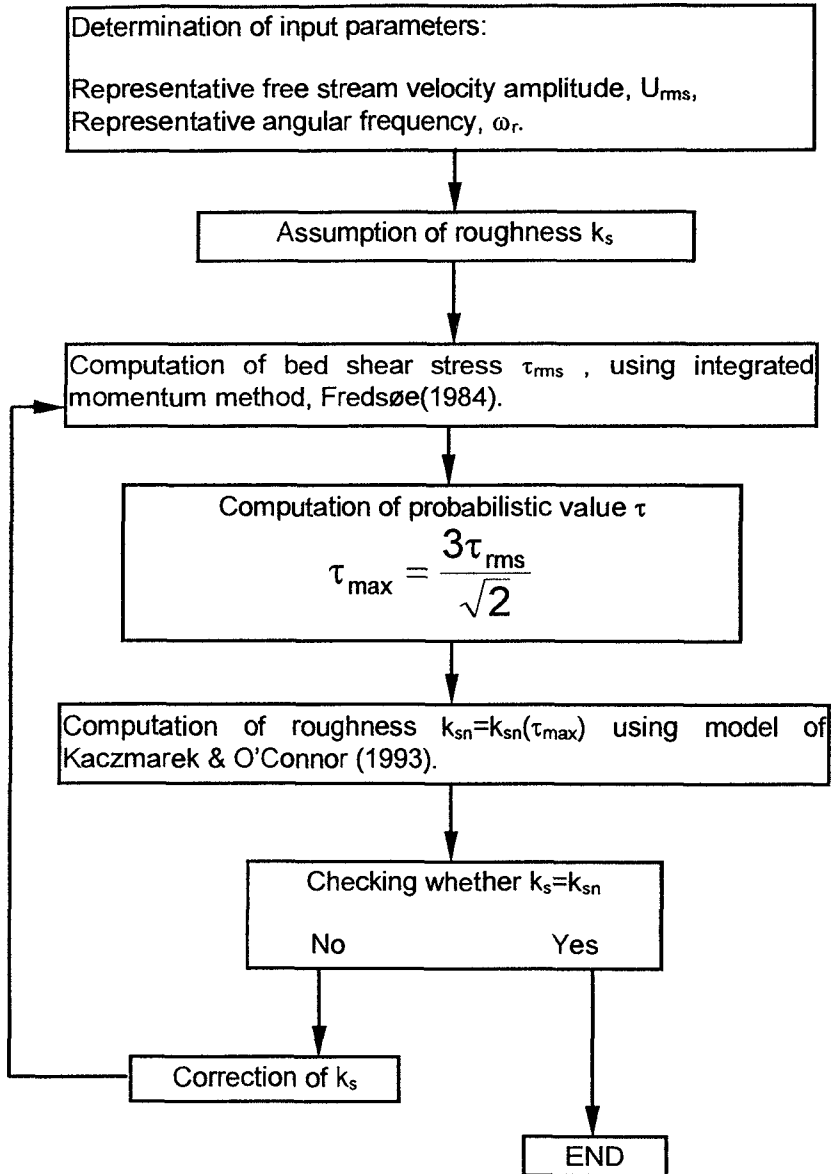


Figure 6: Modified iteration scheme for spectral waves.

Turbulent Energy,  $k$ :

$$\frac{\partial k}{\partial t} = \frac{\partial}{\partial z} \left( \frac{v_t}{\sigma_k} \frac{\partial k}{\partial z} \right) + v_t \left( \frac{\partial u}{\partial z} \right)^2 - \varepsilon \quad (4.4)$$

Dissipation Rate,  $\varepsilon$ :

$$\frac{\partial \varepsilon}{\partial t} = \frac{\partial}{\partial z} \left( \frac{v_t}{\sigma_\varepsilon} \frac{\partial \varepsilon}{\partial z} \right) + c_{1\varepsilon} \frac{\varepsilon}{k} v_t \left( \frac{\partial u}{\partial z} \right)^2 - c_{2\varepsilon} \frac{\varepsilon^2}{k} \quad (4.5)$$

Turbulent Eddy Viscosity,  $v_t$ :

$$v_t = c_1 \frac{k^2}{\varepsilon} \quad (4.6)$$

The upper boundary condition for the  $k$ - $\varepsilon$  model is given by :-

$$u_o(t) = \sqrt{\frac{2M_{oc}}{N}} \sum_{n=1}^N \left( \frac{\omega_n}{\sinh(k_n d)} \right) \cos(-\omega_n t + \delta_n) \quad (4.7)$$

Results from the model appear to indicate that the shear stress time series is not necessarily Rayleigh in its distribution. A typical model value for  $R$  was 2.6.

## 5. Results

### 5.1 Spectral bed roughness

The ability of the present iteration procedure, shown in Figure 6 to evaluate moveable bed roughness,  $k_s$ , under spectral waves was checked for a sandy bed:  $s = \rho_s / \rho = 2.66$   $\varphi = 24.4^\circ$  with different grain size and various wave conditions. The results of the computations plotted in Figure 7 are for both irregular and regular waves.

In an attempt to explain the reduction of spectral wave friction factors the present theoretical approach was compared with Madsen *et al.* (1990) laboratory data. The results are shown in Figure 5 with the previous results for a monochromatic wave. The parameters are defined as before except that for spectral waves as the skin Shields parameter is given by:

$$\theta' = \frac{u_{fr}'^2}{(s-1)gd} = \frac{\tau'_{rms}}{\rho(s-1)gd} \quad (5.1)$$

The calculation of the friction factors were carried out in two steps. First, the values of the bed roughness  $k$ , were obtained using the modified iterative scheme (Figure 6) with Fredsøe's (1984) model used to determine the bed shear stress,  $\tau_{rms}$ . Then the friction factors were calculated on the basis of adjusted the semi-empirical formula of Jonsson

& Carlsen (1976) , as for monochromatic waves, in order to include the contribution of vortex formation in the lee of the roughness crests on the shear stress. Here, Jonsson & Carlsen's (1976) formulae were proposed for the calculations of both the friction factors and the dimensionless skin shear stresses.

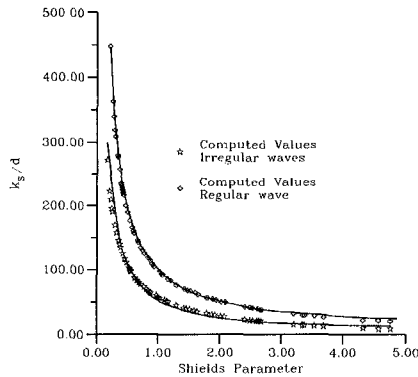


**Figure 7: Results of sheet flow model for regular and random waves.**

Similarly as for monochromatic waves, the calculations were performed for two different sediments (0.2mm and 0.12mm diameter quartz sands). Again the agreement between theoretical and experimental results appears quite satisfactory.

## 6. Conclusions

The sheet flow model appears to produce reasonable results for the conditions tested. However further testing is required.

The use of the model for a range of flow conditions and grain sizes produces a trend of large bed roughnesses at low flow regimes. According to this trend it is suggested that the sheet flow model provides a simple method, or rather an analogy, for the investigation of rippled bed conditions.

Using  $\tau_{rms}$  to represent mono-frequency waves and  $\tau_{max}$  to represent spectral waves produces a reasonable agreement with laboratory data.

The simple model results for  $k_s / d$  may be of use in preliminary engineering estimates although further testing is required. The present findings can be summarized for both the plane and rippled bed by the equation:

$$\tau_{rms1,2} = F_{1,2} \left[ U_{rms}, T_p, k_s = f \left( \frac{3\tau_{rms1}}{\sqrt{2}}, s, d \right) \right] \quad (6.1)$$

The subscripts 1 and 2 refer to the plane and rippled bed respectively.

The function  $f$  is described by the proposed iterative procedure and may be represented by the approximating formula:

$$\log \left[ \frac{k_s}{d} \right] = -1.05 \log [\theta_{rms1}] + 4.00 \quad (6.2)$$

where the Shields parameter is calculated using Fredsøe's (1984) model.

The above approximation differs from that given for monochromatic waves due to the largest waves causing a reduction in the roughness parameter.

To calculate the function  $F$  in the case of a plane bed, Fredsøe's (1984) model is recommended ( $F_1 \rightarrow \tau_{rms1}$ ). For the rippled bed case, the empirical formula of Kamphuis (1975) or semi-empirical formula of Jonsson & Carlsen (1976) have been used ( $F_2 \rightarrow \tau_{rms2}$ ) in order to include the effects of the vortices formed in the lee of the roughness crest on the turbulent mixing.

Based on experimental data, it was found that the representative period equals the peak period. It appears as though the proposed method of predicting bed roughness in spectral waves by using ideas derived for sheet-flow modelling and a representative design wave is capable of providing realistic values for effective bed roughness height. Further work is in progress on the application of the model to additional North Sea data.

## 7. References

Brevik, I. (1981). 'Oscillatory rough turbulent boundary layers.' *J. Waterways, Port, Coastal and Ocean Eng. Div., ASCE*, Vol. 107, No. WW3, pp175-188.

Fredsøe, J. (1984). 'The turbulent boundary layer in combined wave and current motion.' *J. Hydraulic Eng., ASCE*, Vol. 110, No. HY8, pp1103-1120.

Horikawa, K., Watanabe, A. and Katori, S. (1982). 'Sediment transport under sheet flow condition.' *Proc. 18th Int. Conf. on Coastal Eng., ASCE, Cape Town, South Africa*, pp1335-1352.

Jonsson, I.G. and Carlsen, N.A. (1976). 'Experimental and theoretical investigations in an oscillating turbulent boundary layer.' *J. Hydr. Res.*, Vol. 14, No. 1, pp45-59.

Kaczmarek, L.M. and O'Connor, B.A. (1993a). 'A new theoretical approach for predictive evaluation of wavy roughness on a moveable-flat bed.' Part I, Report No. CE/14/93, Department of Civil Engineering, University of Liverpool, 31pp.

Kaczmarek, L.M. and O'Connor, B.A. (1993b). 'A new theoretical approach for predictive evaluation of wavy roughness on a moveable-rippled bed.' Part II, Report No. CE/15/93, Department of Civil Engineering, University of Liverpool, 29pp.

Kamphuis, J.W. (1975). 'Friction factor under oscillatory waves.' *J. Waterways, Port, Coastal and Ocean Eng. Div., ASCE*, Vol. 101, No. WW2, pp135-144.

Kajiura, K. (1968). 'A model of the bottom boundary layer in water waves.' *Bull. Earthq. Res. Inst., Univ. Tokyo*, Vol. 46, pp75-123.

Madsen, O.S., Mathison, P.P. and Rosengaus, M.M. (1990). 'Moveable bed friction factors for spectral waves.' *Proc. 22nd Int. Conf. on Coastal Eng., ASCE*, pp420-429.

Nielsen, P. (1992). 'Coastal bottom boundary layers and sediment transport'. *Advanced Series on Ocean Engineering*, Vol. 4, World Scientific, Singapore, 324pp.

O'Connor, B.A., Harris, J.M., Kim, H., Wong, Y.K., Oebius, H.U. and Williams, J.J. (1992). 'Bed boundary layers.' *Proc. 23rd Int. Conf. on Coastal Eng., ASCE*, pp2307-2320.

Savage, S.B. (1984). 'The mechanics of rapid granular flows.' *Advances in Applied Mechanics*, Vol. 24, pp289-367.

Sayed, M. and Savage, S.B. (1983). 'Rapid gravity flow of cohesionless granular materials down inclined chutes.' *J. Applied Mathematics and Physics (ZAMP)*, Vol.34, pp84-100.

## CHAPTER 24

### Difference between Waves Acting on Steep and Gentle Beaches

Kazumasa KATOH<sup>1)</sup>

#### Abstract

The physical difference of beach erosions between on the steep and on the gentle beaches has been discussed, based on the field data and the theory of generation of the infragravity waves. As a result, it is shown that the incident waves are predominant in the wave run-up phenomena on the steeper beach, while on the gentler beach the infragravity waves are predominant.

#### Dear Prof. Dalrymple,

Based on the data obtained at the Hazaki Oceanographical Research Facility (**HORF**), I reported at the 23rd ICCE held in Venice, Italy, that the foreshore erodes under the action of infragravity waves of one to several minutes in a period (Katoh and Yanagishima, 1992). This conclusion, however, was distressed with the question made by one of participants, you Prof. Dalrymple, in the conference. Your question was; "There are many examples of beach erosion in experimental flumes with the regular waves, where the infragravity waves cannot exist. How do you explain away the experimental facts of erosion with your conclusion?". Your question was very excellent, because I could not answer on that time.

Since then, I have been studying on the physical difference between the beach erosions in the experimental flume and in the field. Here, I am going to explain the advanced conclusion on the role of the infragravity waves in the process of beach erosion, in the following.

---

1) Chief of Littoral Drift Laboratory, Port and Harbour Research Institute, Ministry of Transport, 3-1-1, Nagase, Yokosuka, 239 JAPAN



### Critical Level of Foreshore Profile Change

At the HORF which is located on the sandy beach facing to the Pacific Ocean, Katoh and Yanagishima(1990) carried out the field observations on the foreshore berm erosion and formation. By analyzing the small scale sand deposition on the higher elevation when the berm eroded (see Figure 1), Katoh and Yanagishima (1992) presented that the critical levels of foreshore profile change in the processes of both erosion and accumulation are expressed by the significant wave run-up level,  $R_{max}$ ;

$$R_{max} = (\bar{\eta})_o + 0.96(H_L)_o + 0.31 \quad (\text{m}), \quad (1)$$

where  $(\bar{\eta})_o$  is the mean sea level and  $(H_L)_o$  is the height of infragravity waves at the shoreline, respectively, and the third constant term is considered to represent the run-up effect of incident wind waves.

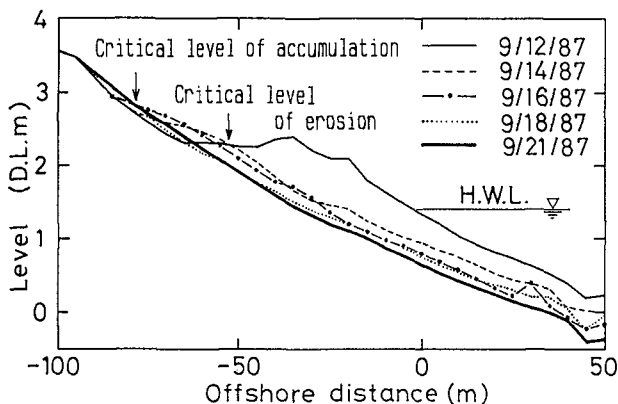


Figure 1 Typical example of berm erosion.

Equation (1) is the empirical relation which has been derived from the field data. The observation spans wide range of incident waves (offshore significant wave heights 0.39–5.11 m and significant wave periods 4.5–15.6 s),  $(H_L)_o = 0.15$ –1.23 m, and  $(\bar{\eta})_o = 0.79$ –1.88 m. There is, however, a serious problem due to a fixation of observation site, that is to say, the constancy of profile slope. Namely, the effect of beach slope is excluded from equation (1), which restricts its general application.

For making up for this insufficiency of excluding the effect of slope, the empirical equation (1) has been compared with the previous results of experimental

and theoretical studies. As the comparison of the results of field observation at the HORF with the Goda's theory (1975) has been already done in regard to the wave set-up at the shoreline (Yanagishima and Katoh,1990), the run-up heights of incident waves and the heights of infragravity waves at the shoreline have been examined in this study.

### **Run-up Heights of Incident Waves**

Mase and Iwagaki (1984) carried out experiments as to the run-up of irregular waves on the uniform slope ( 1/5 to 1/30 ). As a result, they showed the relationship between the run-up height and the Iribarren number  $\xi$ , or a surf similarity parameter, as follow;

$$\frac{R_{1/3}}{H_{1/3}} = 1.378 \xi^{0.702}, \quad (2)$$

$$\xi = \tan\beta / \sqrt{H_{1/3} / L_o},$$

where  $R_{1/3}$  is the significant run-up height which is defined by the crest method,  $H_{1/3}$  and  $L_o$  are a significant wave height and a wavelength in deep water respectively, and  $\tan\beta$  is a bottom slope. As Mase *et al.* used a still water level as a reference level for the wave run-up height, the effect of wave set-up is included in the run-up height in their analysis. On the other hand, as the reference level in equation (1) is a mean water level at the shoreline under the action of waves on beach, the wave set-up is included in  $(\bar{\eta})_o$ , not in the wave run-up height. In short, a direct comparison of equation (1) with equation (2) is impossible. Then, a magnitude of wave set-up at the shoreline,  $\bar{\eta}_{max}$ , has been estimated from the data of offshore significant waves by using the Goda's theory (1975). In the calculation, the bottom slope is 1/60, which is the mean slope in the surf zone at the HORF. By adding  $\bar{\eta}_{max}$  to the third constant term in equation (1), the run-up height above the still water level,  $R_s$ , is evaluated as follow;

$$R_s = 0.31 + \bar{\eta}_{max}, \quad (m) \quad (3)$$

Figure 2 shows the relation between the non-dimensional run-up height normalized by the offshore significant wave height and  $\xi$ , where the bottom slope is fixed to be 1/60. The data plotted by circles and by triangles are obtained in the processes of berm erosion and berm formation respectively (Katoh and Yanagishima, 1993,1993). From this figure, we have a linear relationship between two parameters as

$$\frac{R_s}{H_{1/3}} = 2.50 \xi, \quad (4)$$

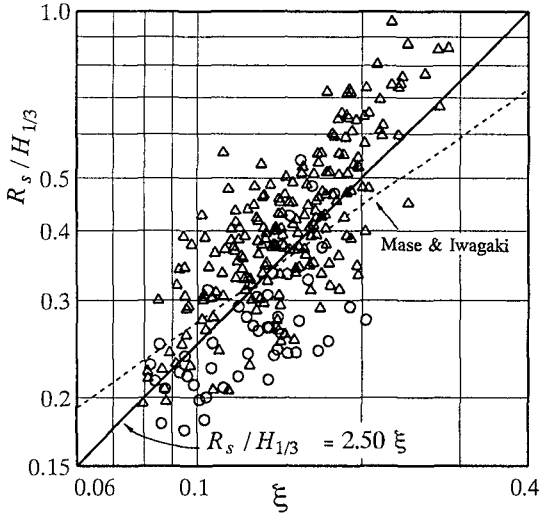


Figure 2 Relation between  $\xi$  and run-up heights of incident waves.

which is shown by a solid line closed to the equation (2).

Equation (2) proposed by Mase *et al.* is the significant run-up height by the crest method, while equation (3) is the critical run-up height where the significant profile change occurs. Although the physical meaning are different each other, it can be said that both run-up heights depend on  $\xi$ . Here, I have to give a supplementary explanation concerning equation (4). Since the data plotted in Figure 2 do not include the effect of bottom slope which is fixed to be 1/60 in analysis, it must be properly said that the non-dimensional run-up height is inversely proportional to the square root of wave steepness. However, equation (4) is the similar form to equation (2) which is based on the experimental data obtained on the bottom slope from 1/10 to 1/30. By taking this similarity into account, it can be concluded that the non-dimensional run-up height is proportional to  $\xi$ .

It is recognized in Figure 2 that the data plotted by the triangles, in the process of berm formation, are scattered mainly above the solid line, while the circles in the process of berm erosion are below the line. The leading cause of these inclined properties is considered to be due to the disregard of the effect of bottom slope in the area from the shallow water depth to the foreshore. If we consider the profile changes in the processes of berm formation, being steeper, and berm erosion, being gentle, the data by the triangles are shifted to the right and the data by circles to the left. As a result, all data will be plotted closer to the solid line.

## Heights of Infragravity Waves at the Shoreline

### Statistics of infragravity waves

In order to observe the waves near the shoreline, an ultra-sonic wave gauge was installed to the pier deck at the location where the mean water depth was about 0.4 meter in M.W.L. The wave measurement was carried out during 20 minutes of every hour with the sampling interval of 0.3 seconds (Katoh and Yanagishima, 1990). By utilizing the wave profile data, the wave heights and periods of infragravity waves were calculated by the following equations based on the result of spectra analysis;

$$H_L = 4.0 \sqrt{m_0} \quad , \quad (5)$$

$$T_L = \sqrt{m_0 / m_2} \quad , \quad (6)$$

$$m_n = \int_0^{f_c} f^n S(f) df, \quad (7)$$

where  $H_L$  and  $T_L$  are the wave height and the period of infragravity waves respectively,  $f$  is the frequency,  $S(f)$  is the spectral energy density,  $f_c$  is the threshold frequency of 0.33 Hz. The wave height of infragravity waves at the shoreline where the water depth was zero,  $(H_L)_0$ , has been estimated by the following transformation equation (Katoh and Yanagishima, 1990);

$$(H_L)_0 = H_L \sqrt{(1 + h / H_{1/3})} \quad , \quad (8)$$

where  $h$  is the water depth at the observation point which can be evaluated from the bottom level and the mean water surface level.

A statistical analysis has been done for the data obtained during 4 years from 1989 to 1990, provided that some data have been excluded according to the following criteria;

- (a) The data obtained when the water depth was shallower than 0.5 meter should be excluded, because the sea bottom sometimes emerged when the waves ran down offshoreward.
- (b) The data obtained when the water depth was deeper than 1.1 meters is not preferable, because the relative distance from the observation point to the shoreline was large.

Figures 3 and 4 show the frequency distributions of the heights and the periods of infragravity waves at the shoreline, respectively. The highest frequency of wave heights is in the rank of 0.2 to 0.3 meter, while the mean height is 0.38 meter. The number of cases is 45 ( 4.1% ) for the waves higher than 0.8 meter, and 15 (

1.4% ) for the waves higher than 1.0 meter. The maximum wave height is 1.34 meters. The wave periods distribute in the range from 40 to 100 seconds, being 62.4 seconds in average.

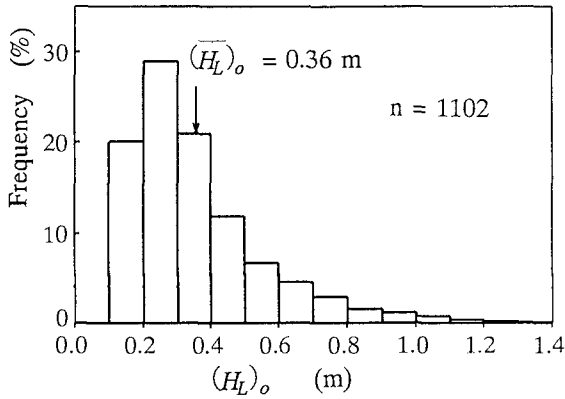


Figure 3 Frequency distribution of heights of infragravity waves.

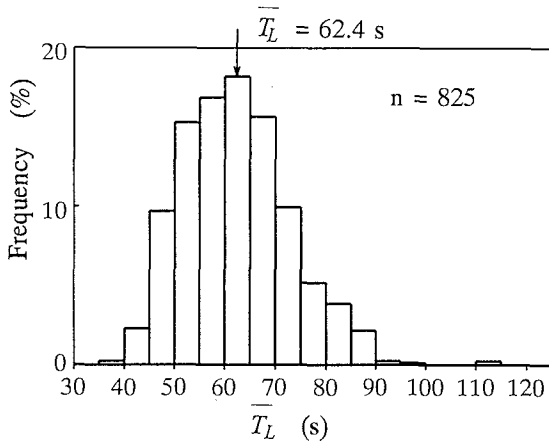


Figure 4 Frequency distribution of periods of infragravity waves.

Figure 5 shows the relation between the heights of infragravity waves at the shoreline and the offshore wave energy flux. On the upper, the significant wave height is shown as an indicator for the case that the wave period is 8.2 seconds. Although there is a little scattering of data, by means of the least square method we have a following relation;

$$(H_L)_o = 0.23 E_f^{0.51} \tag{9}$$

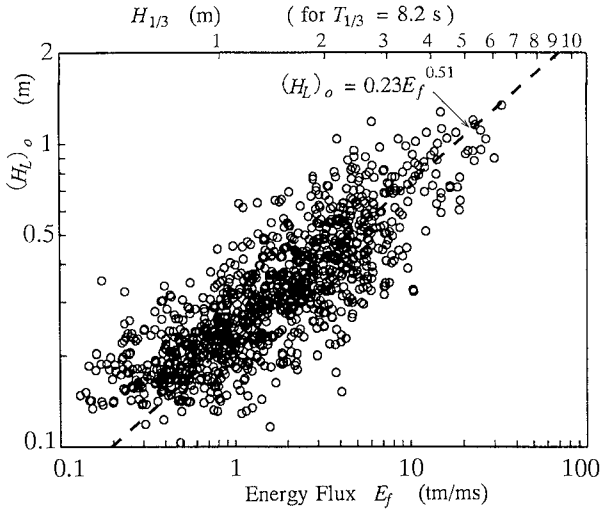


Figure 5 Relation between offshore wave energy flux and the height of infragravity waves at the shoreline.

where  $E_f$  is the offshore wave energy flux. Yanagishima and Katoh(1990) reported that the wave set-up at the shoreline,  $\bar{\eta}_{\max}$ , at the HORF can be well explained only by the offshore wave energy flux,

$$\bar{\eta}_{\max} = 0.14 E_f^{0.4} \tag{10}$$

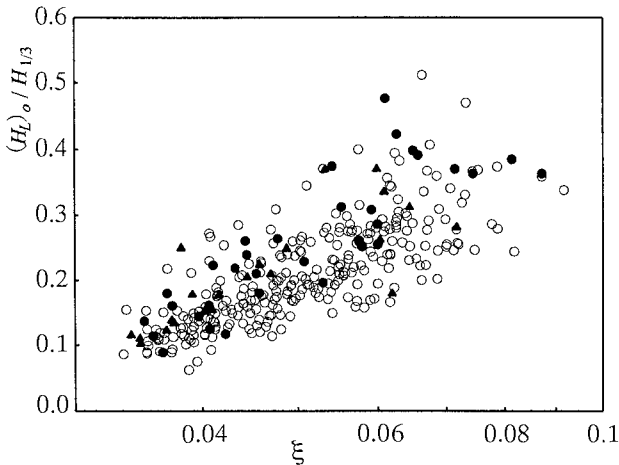


Figure 6 Relation between  $\xi$  and height of infragravity waves.

By substituting equations (9) and (10) into the first and second terms of equation (1) respectively, the critical level of foreshore change is expressed only by the wave energy flux. This result corresponds to another result that the daily changes of shoreline position can be well predicted by the offshore wave energy flux (Katoh and Yanagishima, 1988).

Figure 6 shows the relation between the non-dimensional height of infragravity waves at the shoreline, which are normalized by the offshore significant wave heights, and the Iribarren number  $\xi$ , provided that the mean slope in the area of 5 to 8 meters in depth where the incident waves break in a storm is utilized, which is 1/140. In this figure, the data obtained when the offshore significant wave height was larger than 2 meters is plotted. The closed triangles and the closed circles are the data which have been analyzed with respect to the berm formation and erosion (Katoh and Yanagishima, 1992). Figure 6 shows that the non-dimensional height of infragravity waves increases with  $\xi$ . However, since the bottom slope is fixed to be 1/140 in the analysis, it must be properly said that the non-dimensional height increases with a decrease of wave steepness.

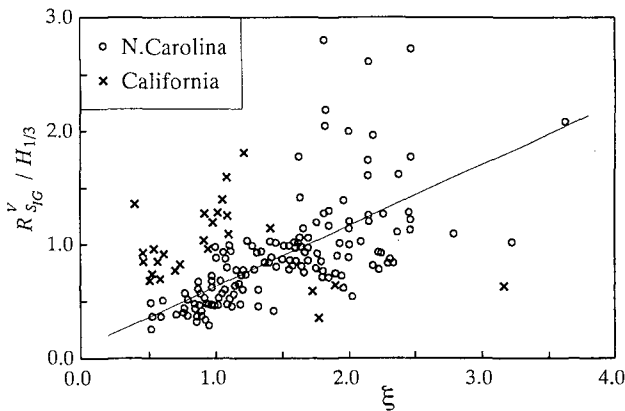


Figure 7 Relation between  $\xi$  and significant vertical swash excursion of infragravity waves ( $\xi$  is defined with the foreshore slope, from Guza *et al.*, 1984).

In the same way, Guza *et al.* (1984) analyzed the two sets of wave run-up data, which were obtained on the beaches facing to the Pacific Ocean and the Atlantic Ocean. Figure 7 shows their result, where  $R_{SIG}^V$  is the significant vertical swash excursion of infragravity waves. We should remark that the foreshore slope was considered in their calculation of  $\xi$ . Figure 7 shows that two data sets are systematically different in this parameter space. While the data obtained in the

Carolina beach show a clear trend as shown by the best fit solid line, the data obtained in the California beach show no significant slope when  $\xi$  is large. Guza *et al.*(1984) said that the apparent discrepancy between the data sets lay in the rather arbitrary choice of a cutoff frequency for the infragravity band. However, I think as explained later that it depends on the difference of bottom slope in the wave breaking zone.

**Effect of bottom slope on the infragravity waves**

As the dependence of infragravity waves at the shoreline on  $\xi$  is different from beach to beach, the theory on the generation of infragravity waves by Symonds *et al.*(1982) has been examined. They used the non-dimensional, depth-integrated, and linearized shallow water equations, that is,

$$x \frac{\partial U}{\partial t} + \frac{\partial \zeta}{\partial x} = - \frac{\partial (a^2)}{2x \partial x} \tag{11}$$

$$\frac{\partial \zeta}{\partial t} + \frac{\partial (xU)}{\partial x} = 0 \tag{12}$$

$$x = \frac{\sigma^2 X}{g \tan \beta}, \quad U = \frac{2U'}{3\gamma \sigma X}, \quad t = \sigma t', \tag{13}$$

$$\zeta = \frac{2\zeta'}{3\gamma^2 X \tan \beta}, \quad x = \frac{x'}{X}, \quad a = \frac{a'}{\gamma X \tan \beta},$$

where  $\sigma = 2\pi / \overline{T_R}$ ;  $\overline{T_R}$  is a repetition period of wave group,  $x'$  is a distance offshore with the origin at the shoreline,  $X$  is the mean position of break point,  $g$  is the gravitational acceleration,  $U'$  is the depth-integrated velocity,  $\gamma$  is the ratio of the incident wave height to the water depth in the surf zone,  $t'$  is the time,  $\zeta'$  is the level of sea surface, and  $a'$  is the amplitude of incident waves.

Nakamura and Katoh(1992) pointed out that the Symonds' theory overestimates the height of infragravity waves in comparison with the field data. They modified the Symonds' theory by taking a time delay of small wave breaking due to propagation into consideration, which well predicts the wave height of infragravity waves. According to the modified theory, the non-dimensional wave profile of infragravity waves at the shoreline,  $\zeta_o$ , is as follow ( see, Nakamura and Katoh, 1992 );

$$\zeta_o = \sum_{n=1} C_n \sin( n t + \epsilon_n ), \tag{14}$$

where  $C_n$  are the coefficients which have been expressed in complicated forms, and  $\epsilon_n$  are the phase lags.



In order to examine the characteristic of wave profile expressed by equation (14), relatively simple, but acceptable, assumptions will be introduced, although they make a little sacrifice of quantity. By assuming that the ratio of the wave amplitude to the water depth,  $\gamma$ , is constant, we have,

$$X = \frac{\bar{H}}{2\gamma \tan\beta} \quad , \quad (15)$$

where  $\bar{H}$  is the mean wave height which is correlated with  $H_{1/3}$  as

$$H_{1/3} = 1.6 \bar{H} \quad . \quad (16)$$

Next, let us assume that the height of incident waves in groups varies sinusoidally ( Nakamura and Katoh,1992 ), that is,

$$H = \bar{H} + \sqrt{2} H_{1/3} \cos(\sigma t) / 3. \quad (17)$$

By utilizing equations (15),(16), and (17), the ratio of the amplitude of wave break point varying to  $X$  is 0.75 ( =  $\Delta a$  ).

Figure 8 shows the theoretical relation between  $C_n$  ( ; n=1 to 4 ) and  $\chi$  , which have been obtained based on the above assumption. In Figure 8, the amplitude of infragravity waves at the shoreline is also shown, which is calculated by means of  $\sqrt{2} (\zeta_0)_{ms}$  from the wave profile composed by equation (14) for n=1 to 4.

In regard to  $\chi$  , an interesting rewriting will be possible. By referring the empirical relation between  $T_R$  and  $T_{1/3}$  (  $T_R = 9.24T_{1/3}$ , Nakamura and Katoh, 1992), we have

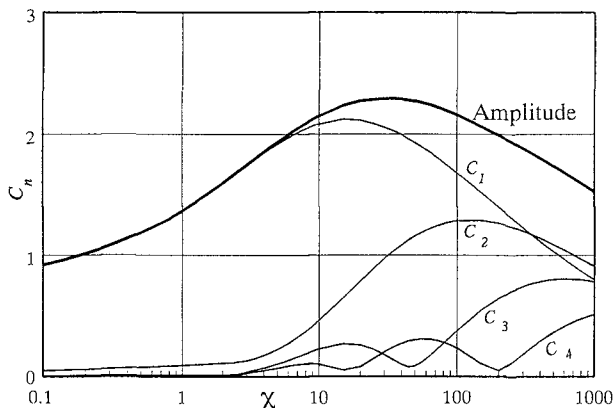


Figure 8 Relation between  $\chi$  and  $C_n$  or amplitude of infragravity waves at the shoreline.

$$\sigma = \frac{2\pi}{9.24 T_{1/3}} = \frac{1}{9.24} \sqrt{\frac{2\pi g}{L_o}} \tag{18}$$

Then, by substituting equations (15),(16), and (18) into equation (13), we have

$$\chi = \frac{0.023}{\gamma} \frac{H_{1/3} / L_o}{\tan^2 \beta} = \frac{0.023}{\gamma \xi^2} \tag{19}$$

that is to say,  $\chi$  is the function of  $\xi$ . Furthermore, another relation in equation (13) can be rewritten for the condition at the shoreline as follow;

$$\sqrt{2} (\zeta_o)_{rms} = \frac{(H_L)_o}{3\gamma^2 X \tan \beta} \tag{20}$$

According to the parameter definitions, we have

$$\bar{H} = 2\gamma X \tan \beta \tag{21}$$

By substituting equation (21) into equation (20) and taking equation (16) into account, we finally have

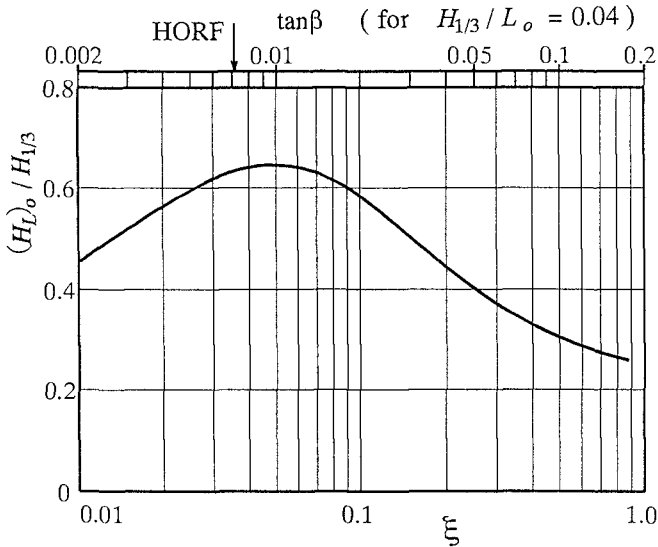


Figure 9 Relation between  $\xi$  and height of infragravity waves at the shoreline ( theory ).

$$\frac{(H_L)_o}{H_{1/3}} = \frac{3\gamma}{3.2} \sqrt{2} (\zeta_o)_{rms} . \tag{22}$$

By utilizing equations (19) and (22), Figure 8 can be represented by using new parameters.

Figure 9 is the transformed relation between new parameters, by assuming  $\gamma = 0.3$ . On the upper side, a scale is marked for the bottom slope when the mean value of offshore wave steepness at the HOLF, 0.04, is adopted. The mean bottom slope in the area of wave breaking in a storm is 1/140 at the HOLF, which is indicated by an arrow on the upper side. In a range of bottom slope up to 0.01 (=1/100), the non-dimensional wave height increases with  $\xi$ , of which tendency is the similar as that shown in Figure 6. On the other hand, it decreases with  $\xi$  in a range of bottom slope steeper than 0.01.

In the analyses by Guza *et al.*(1984), they defined  $\xi$  by the foreshore slope, not by the bottom slope in the wave breaking area. Then, I have inspected the bottom slopes of two beaches in literature. The mean bottom slope in the area from -2 to -6 meters is 1/127 in the North Carolina beach (Holman and Shalenger,1985), which is too much gentler than the foreshore slope. The bottom slope in the Torrey Pines Beach, California, is almost constant up to the water depth of 7 meters, being 1/45 (Guza and Thornton,1985). By utilizing these slopes, the values of  $\xi$  have been calculated, provided that the foreshore slopes are 6 degrees

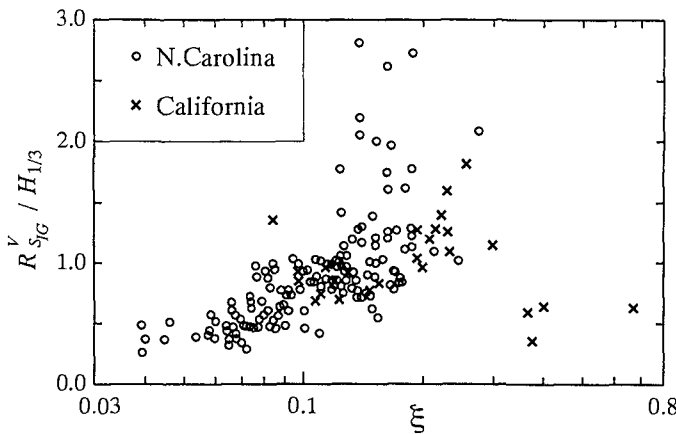


Figure 10 Relation between  $\xi$  and significant vertical swash excursion of infragravity waves ( $\xi$  is defined with the mean bottom slope in the wave breaking area ).

in both the beaches. Figure 10 is the result of calculation, in which the data are rearranged to give the qualitative agreement with the theoretical relation in Figure 9.

**Discussion and Conclusions**

Figure 11 shows the result of present study. A thick line is the theoretical relation between the non-dimensional height of infragravity waves at the shoreline and  $\xi$ , which has been qualitatively verified with three sets of field data. The linear relationship between the non-dimensional run-up height of incident waves and  $\xi$ , equation (4), is superimposed on this figure by a thin line, which is curved in a semi-log space. There is an intersection of two lines, which is roughly corresponding to the bottom slope of 1/25 when the wave steepness is 0.04. In the right-hand side from the intersection, on the steeper beach, the incident waves are predominant in the wave run-up phenomena, while on the gentler beach the infragravity waves are predominant.

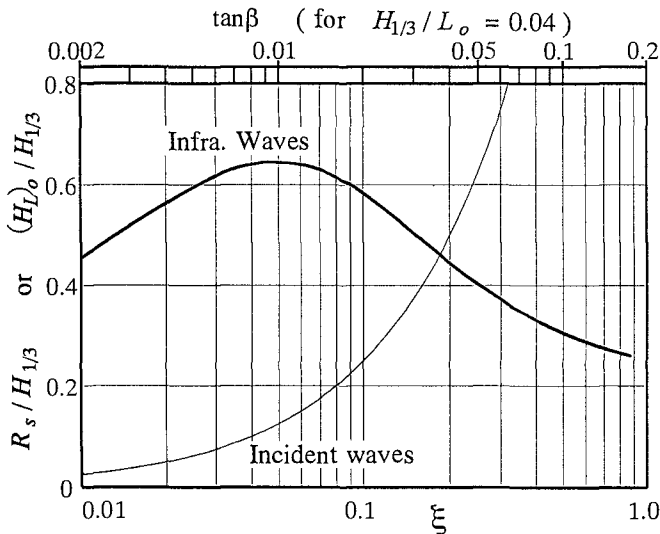


Figure 11 Dependences of infragravity waves and incident waves on  $\xi$ .

Almost all of the model experiments were conducted on the model beach steeper than 1/30, probably due to the limited length of flume. Under this condition, the dominating external force for profile changes is the incident waves. Then, the foreshore erodes even though only the incident waves are reproduced in the experiment. On the other hand, the infragravity waves exist on the gentle

beach in the field. However, the evidences which show the cross relation between the beach erosion and the infragravity waves are scarce. One of reasons is that many field observations in connection with the wave run-up were carried out on the steep beach ( according to literature survey by Kubota ;1991). Another reason is that many field observations were done in the relatively calm wave conditions. The smaller waves break closer to the beach where the bottom slope is steeper because the profile of nearshore topography is usually concave upward. In short, the development of infragravity waves is weak when the incident waves break on the steep bottom. Therefore, in order to have quantitative information on the relation between the infragravity waves and the beach erosion, the further field observations are required concerning the phenomena on the gentle beaches in storms.

Finally, the author is grateful to Mr. Satoshi Nakamura, a member of the littoral drift laboratory, for his courtesy in using the computer program which he developed to predict the height of infragravity waves in the surf zone.

### **References**

- Goda,Y.(1975):Deformation of irregular waves due to depth controlled wave breaking, Rep. of PHRI, Vol.14, No.3, pp.56-106( in Japanese, see Goda, 1985).
- Goda,Y.(1985):Random seas and design of maritime structures, University of Tokyo Press, 323p.
- Guza,R.T., E.B.Thornton and R.A.Holman(1984):Swash on steep and shallow beaches, Proc. of 19th ICCE, pp.708-723.
- Guza,R.T. and E.B.Thornton(1985):Observation of surf beat, J.G.R., Vol.90, No.C2, pp.3161-3172.
- Holman,R.A. and A.H.Sallenger(1985):Setup and swash on a natural beach, J.G.R., Vol.90, No.C1, pp.945-953.
- Katoh,K. and S.Yanagishima(1988):Predictive model for daily changes of shoreline, Proc. of 21st ICCE, pp.1253-1264.
- Katoh,K. and S.Yanagishima(1990):Berm erosion due to long period waves, Proc. of 22nd ICCE, pp.2073-2086.
- Katoh,K. and S.Yanagishima(1992):Berm formation and berm erosion, Proc. of 23rd ICCE, pp.2136-2149.
- Katoh,K. and S.Yanagishima(1993):Beach erosion in a storm due to infragravity waves, Rep. of PHRI, Vol.31, No.5, pp.73-102.
- Kubota,S.(1991):Dynamics of field wave swash and its prediction, a doctor's thesis, Chuo University, 232p.(in Japanese)
- Mase,H. and Y.Iwagaki(1984):Run-up of random waves on gentle slopes, Proc. of 19th ICCE, pp.593-609.

- Nakamura,S. and K.Kato(1992):Generation of infragravity waves in breaking process of wave groups, Proc. of 23rd ICCE, pp.990-1003.
- Symonds,G., D.A.Huntley and A.J.Bowen(1982):Two-dimensional surf beat:Long wave generation by a time-varying breakpoint, J.G.R., Vol.87, No.C1, pp.492-498.
- Yanagishima,S. and K.Kato(1990):Field observation on wave set-up near the shoreline, Proc. of 22nd ICCE, pp.95-108.

## CHAPTER 25

### Wave Breaking under Storm Condition

Yoshiaki Kawata, M.ASCE<sup>1</sup>

#### Abstract

The effects of strong wind on wave breaking were discussed with the field data. At around  $U = 23\text{m/s}$  the maximum wave steepness of 0.034 was obtained. At the wind velocity of more than 23m/s, the wave steepness becomes small once because reformed waves which were already broken at the offshore were measured. This corresponds with the changes of the ratio of wave breaking. The relationship between the mean period of SIWEH and significant wave period was made clear. It was found that pulsating behavior of undertow influences wave breaking in a shallow water.

#### Introduction

In spite of many trials to explain the mechanism of wave transformation and wave breaking, in a shallow water, we have still obscure phenomena in the nearshore zone. For example, under high wind, it is very difficult to predict the location of breaking points of incoming waves. Most of coastal structures have been designed to avoid impulsive shock pressure due to wave breaking, but usually breaker index has been developed on the basis of experimental data conducted under no wind condition. Some coastal disasters have been generated by underestimation or miscalculation of wave forces due to wave breaking.

On a mild sloping beach, high waves under strong wind break two or more times in the crossshore direction. In the shoaling process, we observed frequently that a lower wave just after a higher wave breaks easily. This mechanism was not well understood yet. Moreover, at the wind velocity of more than 20m/s, the applicability of breaker index and plausible maximum wave steepness have not made clear due to lack of field data. Moreover, high wind waves usually come to the shore in accompany with high wind.

The effects of strong wind on wave breaking were discussed with some traditional methods. Firstly, changes of wave steepness and ratio of wave breaking with wind velocity were studied. Secondly, applicability of breaker index was investigated. In order to make clear the effect of undertow on wave breaking, the relationship between the dominant period of SIWEH and significant wave period was also justified. The measurement was conducted on 18 November, 1981 on which developing low pressure moved eastward in the Japan Sea and high wind blew around the coast.

---

<sup>1</sup> Professor, Disaster Prevention Research Institute, Kyoto University  
Gokasho, Uji, Kyoto 611, Japan

### Field Observation Site and Method

The field experiments were conducted on the Ogata coast which is a straight sandy beach of 20km long facing the Japan Sea. At the measuring site (water depth:7m, bottom slope:1/130, offshore distance:200m), capacitance wave gauges were installed as shown in Fig. 1. Two wave gauges were set respectively in the crossshore direction at the distances of 12.9m landward and 19.6m seaward from the measuring site. A unit of data is each 100 sec in length and 40 units were analyzed as every averaged data. VTR systems focused on sea surface at Ch. 1. Wind characteristics were measured with the anemometer installed at the 35m offshore from Ch. 1 and its height was 15m above mean sea level (tidal range is about 30cm). At the observatory, the anemometer was installed at the height of 10m above ground level. Dominant wave direction was determined through the analysis of directional spectra with the data obtained by eleven wave gauges. The undertow was measured with the ultrasonic type current meters at the height of 1m above the bottom.

### Observation Results

Firstly, we analyzed the data with surf similarity parameter  $\xi$  to divide into breaking and non-breaking waves. The wave length was calculated with small amplitude wave theory and second-order Stokes wave theory. Figure 2 shows one of the results in which  $\eta_d$  means the distance between mean sea level and wave trough. From this figure, it was found that it is impossible to clarify breaking and non-breaking with the traditional expression. In the similar expression such as  $\eta_u / \eta_d$  ( $\eta_u$ : distance between mean sea level and wave crest),  $H / \eta_d T$  ( $T$ : wave period), the combination of and the variables defined here can not express the criterion of breaking and non-breaking. In these relationship, we introduced the wind velocity as the parameter, but we could not get good results to explain wave breaking phenomena.

### Effects of High Wind on Wave Breaking

In this chapter, we firstly tried to justify the applicability of breaker index and changes of wave steepness and rate of wave breaking with wind velocity. On the Ogata coast, wind waves develop in accompany with the movement of low pressure and the wave direction changes from west, northwest to east sequentially. It is generally

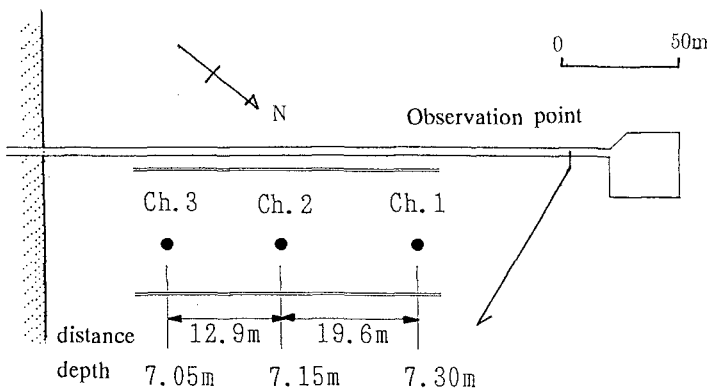


Fig. 1 Observation pier and point on the Ogata coast



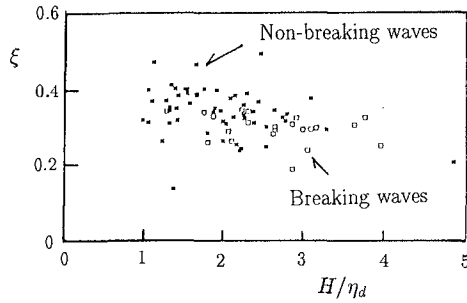


Fig. 2 Relationship between  $H / \eta_d$  and surf similarity parameter

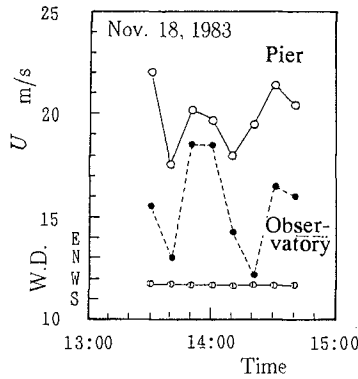
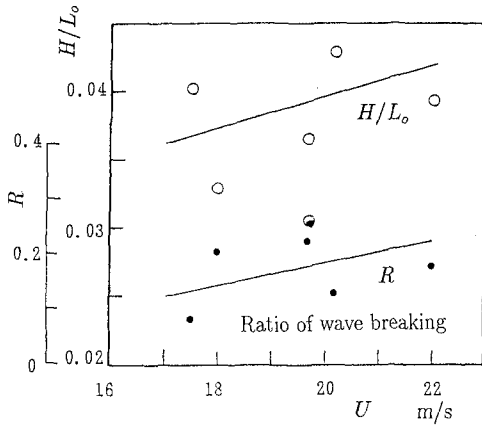


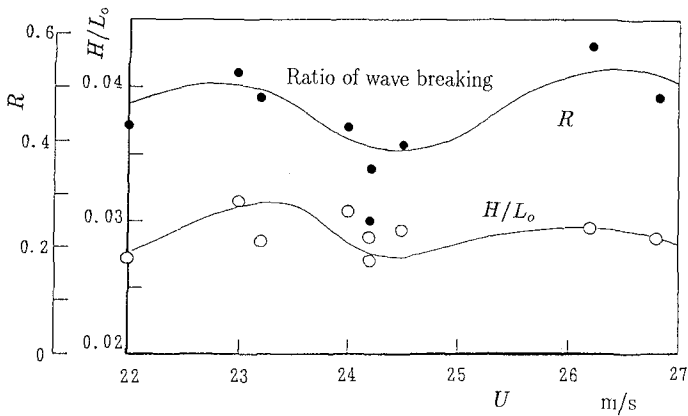
Fig. 3 Changes of wind characteristics

recognized that wave height increases until wave direction becomes northwest. After this stage, waves change to swell.

Figure 3 shows an example of sequential changes of wind characteristics. Every point is 10 min. averaged data. At the pier, we had very high wind and wave breaking with spilling type frequently occurred. Figure 4 shows the changes of the wave steepness  $H/L_0$  and ratio of wave breaking  $R$  with wind velocity  $U$ . Wave steepness was measured at the point of Ch. 3. Individual wave steepness is calculated and averaged in the period of 10 min. The ratio  $R$  is defined as the number of wave breaking divided by the total wave number. In the case of (a) (wind direction :WSW) the increase of wave steepness with wind velocity is clear and also the increase of  $R$  show same tendency. On the contrary, in the case of (b)(wind direction:WNW), the following results were observed: At around  $U = 23\text{m/s}$  the maximum wave steepness of 0.034 was obtained and at the wind velocity of more than 23m/s, the wave steepness becomes small once because reformed waves which were already broken at the offshore were measured. Furthermore, more than 26m/s, the reformed waves also begin to break. The difference of wind velocity of



(a) wind direction: WSW



(b) wind direction: WNW

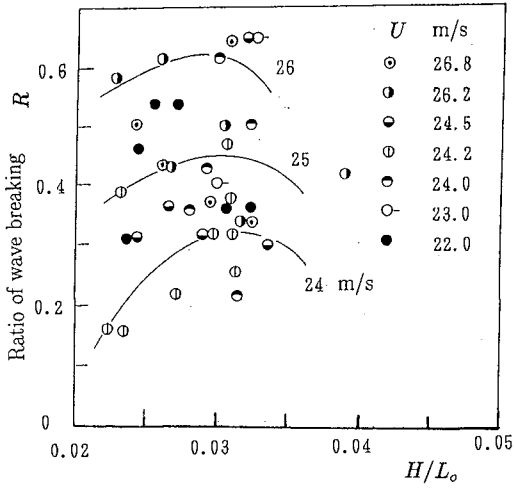
Fig. 4 Changes of wave steepness and ratio of wave breaking with wind velocity

only 3m/s is correspond to the enlargement of width of breaker zone. The effect of wind direction on the changes of wave steepness is reflected the difference not only fetch and duration of wind waves but also of wave refraction characteristics. For example, the westerly waves changes from long crested to short crested waves due to wave refraction.

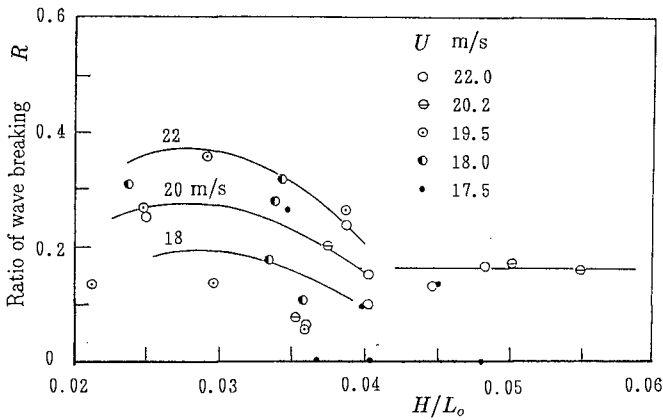
The changes of the rate of wave breaking is similar to that of wave steepness as follows:

- a) wind velocity is less than 23m/s, the ratio  $R$  increases up to 0.5
- b) 23 to 25m/s,  $R$  decreases to 0.4.
- c) more than 25m/s,  $R \approx 0.5$

They correspond well with the changes of wave steepness under high wind conditions.



(a) wind velocity is more than 22m/s



(b) wind velocity is less than 22m/s

Fig. 5 Changes of ratio of wave breaking and wave steepness

Figure 5 shows the relationship between wave steepness and ratio of wave breaking. The following remarks were observed:

- a) wind velocity is less than 22m/s, ratio of wave breaking increases with wind velocity. When wave steepness becomes more than 0.04, ratio of wave breaking keeps 0.16.
- b) wind velocity ranges from 22 to 24m/s, ratio of wave breaking slightly decreases.
- c) more than 24m/s, waves whose steepness is more than 0.04 can not be found.

Figure 6 shows the applicability of breaker index proposed by Goda(1970). The data were recorded at  $U = 26.7\text{m/s}$  and  $R = 0.457$ . It was found that the breaking height was classified into some groups in each wave age and the breaker index was the upper limit of the field data.

**Effect of Undertow on Wave Breaking**

In the field, a following lower wave behind a higher wave is sometimes prone to breaking. The following mechanism may be related with the wave breaking phenomena on a mild slope in a shallow water:

- a) high waves have low trough level, therefore, following low waves may break.
- b) undertow due to high wave breaking promotes breaking of following waves.

Under storm wave condition on the Ogata coast, wave grouping is clearly formed and trough level of carrier waves is almost constant in every storm conditions as shown in Fig. 7. This may be only applicable to the shallow water at the depth of 7m, but the If

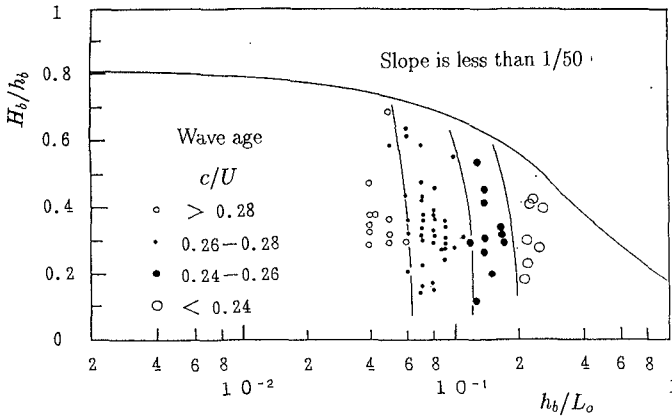


Fig. 6 Applicability of breaker index

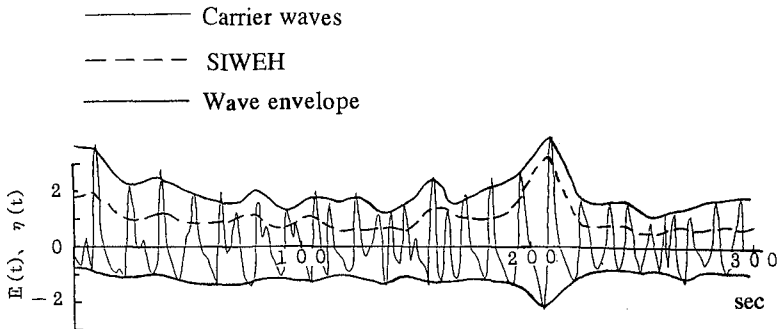


Fig. 7 Wave grouping

hypothesis a) is inadequate. Secondly, we discuss about the plausibility of hypothesis b). If we assume the control volume whose rectangular frame includes one wave length in the crossshore direction and one wave height above the bottom with moving coordinate, the bore model gives undertow due to energy dissipation at the moment of wave breaking. In this case, local water level changes due to changes of radiation stress and its gradient. However, a shoreline is the fixed boundary and flow structure can not be described without consideration about conservation of momentum or energy. Moreover, time scale in the analysis has to be comparable to spatial scale of width of nearshore zone. Therefore, formation of wave grouping and its related phenomena are focused on explanation of wave breaking.

As already pointed out, traditional methods can not predict the wave breaking. The reason of the pulsating occurrence of wave breaking is firstly discussed. If the pulsation exists, the oscillation of wave energy level with nearly same period should be found. Figure 8 shows the changes of wave height along Chs. 1, 2 and 3. The increase of wave height depends on wave transformation or existence of reverse flow. The averaged data show that the increase of wave height is larger than that predicted by wave transformation with small amplitude theory (in the calculation, wave height of 2m and wave period of 8s). In order to make wave height twice, it is necessary to add the reverse flow at the velocity of 2.75m/s. This is very large, but in the field the breaking phenomena is unsteady and the increase of wave height due to breaking also exist, this result suggests that the reverse flow may influence the wave breaking process.

#### Long Period Fluctuation of Current Velocity

Figure 9 shows the power spectrum of current velocity in the Northwest direction (it is almost in the crossshore direction) at the height of 1m above the bottom (water depth is about 6m)(Tsuchiya et al., 1989). In this figure, the first peak with the frequency of about 0.1Hz responds to that of incoming dominant waves. In the low frequent range, it is found to be some primary peaks.

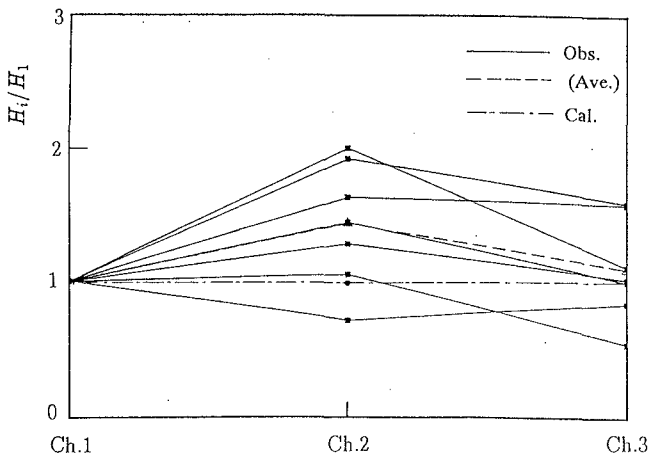


Fig. 8 Changes of wave height in the crossshore direction

Figure 10 shows the long period fluctuation of the current velocity in which the higher frequent component were cut off with the low pass filter of 0.03Hz. The current was recognized with the amplitude of 50cm/s. By this pulsating fluctuation, bursting of the bottom sediment were observed as shown in Fig. 11. The optical suspended sediment sensors are mounted in a vertical steel pipe of 3cm in diameter by 4m long. The lowest sensor was set at the height of 10cm above the bottom.(kawata et al., 1989). This bursting occurred at the moment of the concurrence of undertow and maximum water particle velocity in the offshore direction. The results reveals the importance of undertow to control bottom sediment concentration.

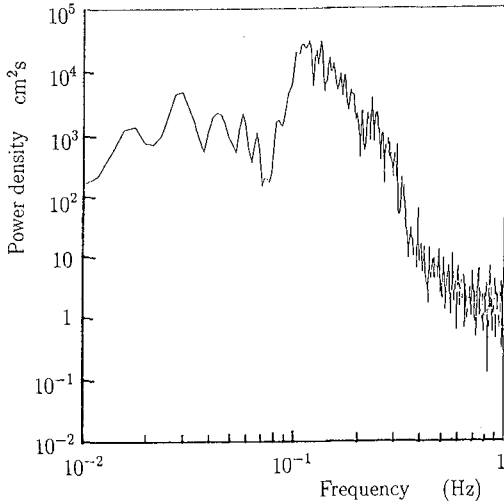


Fig. 9 Power spectrum of current velocity in the crossshore direction

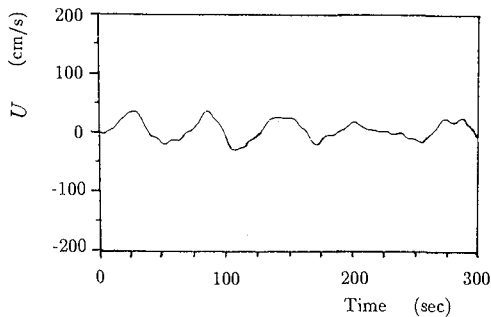


Fig. 10 Long period oscillation of undertow

### Correspondence of Undertow and Wave Breaking

It is necessary to make clear the generation mechanism of undertow whose period is several to around ten times of those of incoming waves. Firstly, we checked the wave energy levels of wave grouping on the Ogata coast. Figure 12 shows that the mean period of SIWEH is proportional to that of significant wave period. This figure shows that the increase of wave period well correlate to the long period variation in wave grouping. Secondly, we checked the relationship between the time variation of undertow and the occurrence of wave breaking. The procedure is as follows:

- a) In every 200 waves recorded at Chs. 1, 2 and 3, significant wave height and its period are calculated. We get a series of them during 600 waves.
- b) In every breaking wave, the period  $T_{sh}$  ( the period of SIWEH in Fig. 12, given by  $5.81 T_{1/3} + 1$ ) is shifted behind it and check the certain wave breaking or not.
- c) This checking is applied to every individual 30 waves.

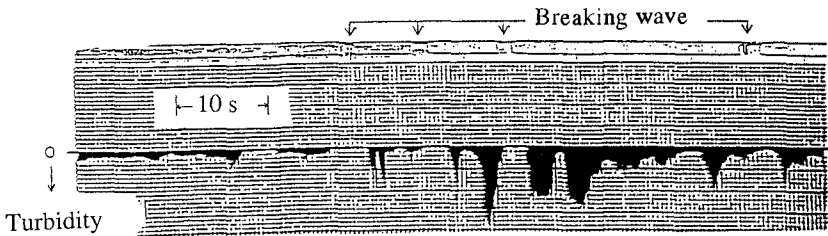


Fig. 11 Suspended sediment bursting due to wave breaking

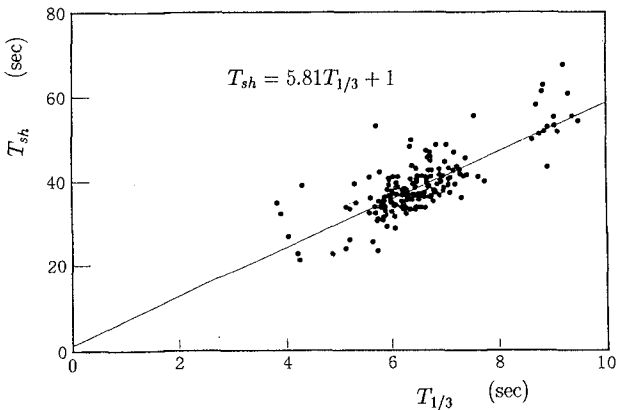


Fig. 12 Relationship between mean period of SIWEH and significant wave period

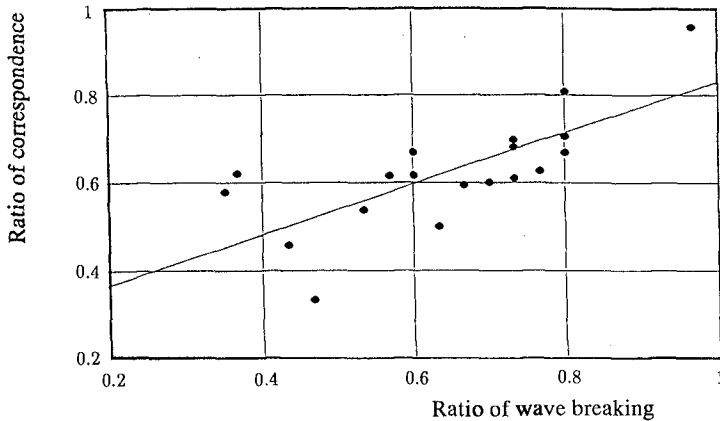


Fig. 13 Changes of ratio of correspondence with ratio of wave breaking

Figure 13 shows the relationship the ratio of correspondence and the ratio of wave breaking. It was found that the increase of the former is roughly predicted by the increase of the latter. Therefore, it was concluded that wave breaking in a shallow water is well depend on the pulsation of the energy level of wave grouping.

### Conclusions

The effects of high wind on wave breaking in a shallow water were discussed with the field data. In rough sea state under strong wind, the wave breaking conditions in the nearshore zone can not be predicted with some traditional expressions. At around  $U = 23\text{m/s}$  the maximum wave steepness reaches to 0.034. At the wind velocity of more than 23m/s, the wave steepness becomes small once because reformed waves which were already broken at the offshore site were measured. This corresponds with the changes of the ratio of wave breaking. The relationship between the mean period of variation of SIWEH and significant wave period was made clear. It was found that pulsating behavior of undertow influences wave breaking in a shallow water.

### References

- Goda, Y. : A synthesis of breaking indices, Trans. JSCE, Vol. 2, Part 2, 1970, pp. 227-230.
- Kawata, Y. et al.: Field observation of sediment transport under storm wave conditions, Proc. Coastal Engineering, JSCE, Vol. 36, 1989, pp. 269-273 (in Japanese).
- Tsuchiya, Y. et al.: Longterm nearshore current observation in surf zones with ultra-sonic current meters, Annuals, DPRI, Kyoto University, No. 32B-2, 1989, pp. 847-879 (in Japanese).



## CHAPTER 26

### APPLICATION OF MAXIMUM ENTROPY METHOD TO THE REAL SEA DATA

Taerim Kim<sup>1</sup>, Li-Hwa Lin<sup>2</sup>, and Hsiang Wang<sup>3</sup>

#### Abstract

Two different versions of maximum entropy methods(MEM) were compared with two conventional methods for analyzing directional ocean wave spectra. The two MEMs were originally proposed by Lygre and Krogstad (1986) and Kobune and Hashimoto (1986), respectively, and the two conventional methods are the truncated Fourier series method(TFS) and Longuet-Higgins parametric model(LHM). The comparisons included hypothetical idealized cases and actual measured data. For the hypothetical cases, the MEM by Kobune and Hashimoto clearly performed better, particularly for dual-peaked spectra. As for the comparisons from measured data, the MEM generally yielded narrower directional spreading than the two conventional methods but all methods gave nearly identical main direction information. However, this MEM does have occasional convergence problem in real sea data analysis. The problem is removed with the aid of an approximation scheme. This modified scheme is employed in the automated directional spectral analysis of measured sea data.

#### Introduction

In coastal engineering applications, directional ocean wave information becomes increasingly important owing to the advancement of technology and the demand of better design information. In order to acquire more accurate information of the directional sea waves, much efforts have been devoted to the development of measuring system and the method of analyzing the data. There are several different measuring systems utilized today. For instance, a heave/pitch/roll buoy has been used in the open ocean while wave gage array or pressure transducer and bi-axial current meter are often deployed in coastal water to collect directional wave data. Since ocean waves can be treated as random signals in both time and space, the information derived from all these measuring systems are truncated partial statistical properties, such as in the

---

<sup>1</sup>Graduate Assistant, <sup>2</sup>Research Scientist, <sup>3</sup>Professor, Coastal and Oceanographic Engineering Department, University of Florida, Gainesville, FL 32611, USA.

form of moments or in the expression of a finite number of Fourier coefficients. Based on the limited information, different methods have been developed to estimate the true ocean wave properties which were often expressed as directional ocean wave spectra. The most direct method clearly is to express the directional spectrum by a finite Fourier series presentation known as truncated Fourier series (TFS) method. However, this method is found to often produce the unreasonable results of negative energy components in the directional domain. When this situation occurs, the estimate is evidently badly biased. For other methods which were developed to analyze directional spectrum, the Longuet-Higgins' parametric model(LHM) is presently the most popular one owing to its concise form and the guaranteed non-negative spectral values. However, the model always gives symmetrical single-peaked directional distribution for each frequency band. Hence, LHM is not suitable for waves with frequency bands containing multi-directional peaks. The maximum entropy directional spectrum estimator developed recently has a major improvement. The method is capable of showing both multiple peaks and asymmetric distribution in direction (Kim, *et al.*, 1993). Therefore, the MEM is particularly useful for shallow water application where waves can be very asymmetric in nature.

Two different entropy definitions have been utilized in finding the corresponding maximum entropy directional spectra. One is from Lygre and Krogstad (1986) who applied MEM under the assumption of a complex Gaussian, stationary process of directional waves and the other is from Kobune and Hashimoto (1986) regarding the directional distribution of wave spectrum as a probability density function. The maximum entropy estimator derived by Lygre and Krogstad was designated here as MEM I and the one by Kobune and Hashimoto as MEM II. Benoit (1992) compared twelve different methods for estimating the directional wave spectrum based on numerical simulations and showed that MEM II gives more reliable estimates but the computational time is rather long. Brissette *et al.* (1992) also compared several methods and pointed out that MEM I often overpredicts the energy at the distribution peaks. Kim *et al.* (1993) tested TFS, LHM, MEM I, and MEM II using three different types of target spectrum and concluded that MEM II is more reliable than the other methods compared. They also suggested an approximation scheme of MEM II to avoid the occasional problem in MEM II and, hence, to significantly reduce the computational time for the practical use. Up to the present, most of the tests for the reliability of the directional spectrum estimator were done based on either artificially simulated target spectra or just one sample set of data. However, simulation test of different directional methods may also be influenced by the target spectra chosen and, therefore, does not provide sufficient evidence for the better method.

In this paper, MEM II was compared and evaluated with two classical methods, TFS and LHM, using two sets of real time series data. The comparisons include the spectral pattern and statistical parameters of dominant frequency peak direction and mean direction, which are important for many different applications in the coastal and ocean engineering.

### Methods Estimating Directional Spectrum

Mathematically, a true directional spectrum  $E(\sigma, \phi)$ , with  $\sigma$  and  $\phi$  denoting the frequency and direction, respectively, can be expressed in terms of an infinite Fourier series as

$$E(\sigma, \phi) = \frac{A_0(\sigma)}{2} + \sum_{n=1}^{\infty} [A_n(\sigma) \cos(n\phi) + B_n(\sigma) \sin(n\phi)], \quad |\phi| \leq \pi,$$

where  $A_0$ ,  $A_n$  and  $B_n$  are the frequency dependent Fourier coefficients, which can be determined based on the measured or simulated sea data. Although several different techniques analyzing the directional spectrum have been developed in the past, only two classical and two versions of MEM methods are discussed here. The two classical methods are the truncated Fourier series (TFS) and the Longuet-Higgins' parametric model (LHM). The two MEM methods (MEM I and II) have different entropy definitions. To be consistent, the four methods are summarized below based upon the first five Fourier coefficients,  $A_0$ ,  $A_1$ ,  $B_1$ ,  $A_2$ , and  $B_2$ .

#### (1) TFS (truncated Fourier series)

The directional estimator expressed by the truncated five-term Fourier series is

$$E(\sigma, \phi) = \frac{A_0(\sigma)}{2} + \sum_{n=1}^2 [A_n(\sigma) \cos(n\phi) + B_n(\sigma) \sin(n\phi)] \quad |\phi| \leq \pi.$$

#### (2) LHM (Longuet-Higgins parametric model)

The parametric model proposed by Longuet-Higgins (1963) is

$$E(\sigma, \phi) = E(\sigma) \frac{2^{2s-1} \Gamma^2(s+1)}{\pi \Gamma(2s+1)} \cos^{2s} \frac{\phi - \phi_o}{2}, \quad |\phi_o| \leq \pi, \quad s > 0,$$

where  $\Gamma$  denotes the Gamma function,  $s = s(\sigma)$  and  $\phi = \phi_o(\sigma)$  are the directional spreading parameter and the symmetric center direction, respectively. As a first order approximation, the parameters  $s$  and  $\phi_o$  can be determined from

$$s = \frac{C_1}{1 - C_1}, \quad \phi_o = \tan^{-1} \frac{B_1}{A_1}, \quad C_1 = \frac{\sqrt{A_1^2 + B_1^2}}{A_0}.$$

#### (3) MEM I (Maximum Entropy Approach, Method I)

By defining the entropy of directional sea as

$$M = - \int_0^{2\pi} \ln H(\sigma, \phi) d\phi.$$

and maximizing  $M$ , Lygre and Krogstad(1986) showed that

$$E(\sigma, \phi) = E(\sigma)H(\sigma, \phi), \quad H(\sigma, \phi) = \frac{1 - d_1 c_1^* - d_2 c_2^*}{2\pi |1 - d_1 e^{-i\phi} - d_2 e^{-2i\phi}|^2},$$

with

$$c_1 = \frac{A_1}{A_0} + i \frac{B_1}{A_0}, \quad c_2 = \frac{A_2}{A_0} + i \frac{B_2}{A_0}, \quad d_1 = \frac{(c_1 - c_2 c_1^*)}{(1 - |c_1|^2)}, \quad d_2 = c_2 - c_1 d_1,$$

where  $H(\sigma, \phi)$  is the directional distribution function and the asterisk indicates a complex conjugate.

(4) MEM II (Maximum Entropy Approach, Method II)

By maximizing the entropy defined as

$$M = - \int_0^{2\pi} H(\sigma, \phi) \ln H(\sigma, \phi) d\phi,$$

Kobune and Hashimoto (1986) showed that

$$H(\sigma, \phi) = \exp[- \sum_{j=0}^4 \lambda_j(\sigma) \alpha_j(\phi)],$$

where  $\alpha_0(\phi) = 1$ ,  $\alpha_1(\phi) = \cos \phi$ ,  $\alpha_2(\phi) = \sin \phi$ ,  $\alpha_3(\phi) = \cos 2\phi$ ,  $\alpha_4(\phi) = \sin 2\phi$ , and  $\lambda_j$ 's are the Lagrange's multipliers. The  $\lambda_j$ 's are determined by iteration method solving a set of nonlinear equations:

$$\int_0^{2\pi} [\beta_i(\sigma) - \alpha_i(\phi)] \cdot \exp[- \sum_{j=1}^4 \lambda_j(\sigma) \alpha_j(\phi)] d\phi = 0, \quad i = 1, 2, 3, 4$$

with

$$\lambda_0 = \ln \{ \int_{-\pi}^{\pi} \exp[\sum_{j=1}^4 \lambda_j(\sigma) \alpha_j(\phi)] d\phi \},$$

where  $\beta_1(\sigma) = A_1/A_0$ ,  $\beta_2(\sigma) = B_1/A_0$ ,  $\beta_3(\sigma) = A_2/A_0$ , and  $\beta_4(\sigma) = B_2/A_0$ . It is noted here that, based upon the first five Fourier coefficients measured, the directional spreading function  $H(\sigma, \phi)$  determined from both MEM I and II can have at most two directional peaks, which can be understood by taking  $\partial H/\partial \phi = 0$ . Using the maximum entropy technique to estimate the directional spectrum is also attractive in that the wave spectrum computed does not have to be symmetrical in direction. This certainly indicates a better approach than the conventional LHM method of which the directional distribution is modelled by a symmetrical function. On the other hand, the TFS is known to often yield a biased estimate to the directional spectrum and the computed directional spectrum may have negative energy components.

Fig. 1 displays several comparisons of four methods shown above for the simulated directional spectra which include unimodal, bimodal, and asymmetric distributions. It is seen that TFS can result in non-positive spectral densities, LHM always gives a symmetric, single-peaked distribution, and MEM I generally produces two peaks and overestimates the peak. The overall comparisons show that MEM II generates the closest estimates to the target spectra for all cases tested.

# WAVE DIRECTIONAL SPECTRUM

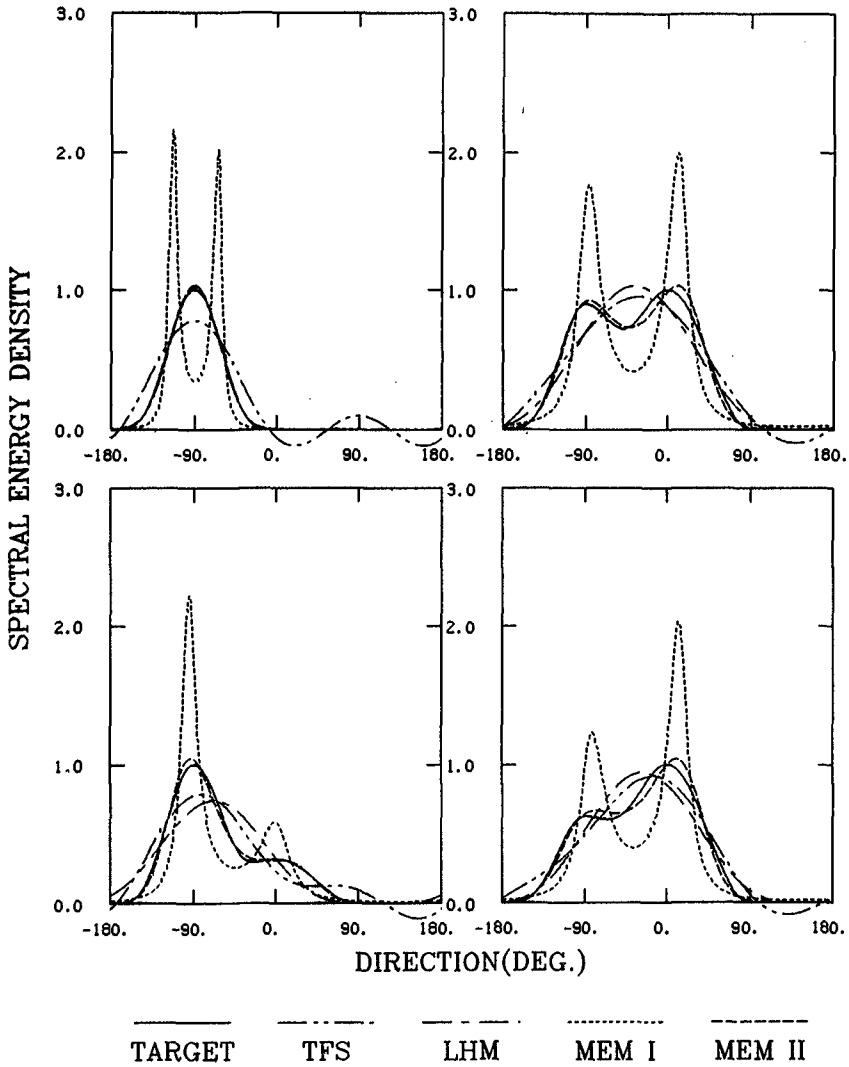


Figure 1: Comparison of simulation results with target spectra.

Application of MEM II

In general, there are no difficulties in computation of directional spectra based on TFS, LHM, and MEM I. However, when MEM II is applied, a nonconvergence problem may occur due to numerical iterations. This problem can be overcome by using an approximation scheme for solving the Lagrange's multipliers. It can be shown that by expanding the exponential term appearing in the nonlinear equations solving for  $\lambda_j$ 's to the second order as

$$\int_0^{2\pi} [\beta_i(\sigma) - \alpha_i(\phi)] \cdot \left\{ 1 - \sum_{j=1}^4 \lambda_j(\sigma) \alpha_j(\phi) + \frac{[\sum_{j=1}^4 \lambda_j(\sigma) \alpha_j(\phi)]^2}{2} \right\} = 0,$$

an approximation of solutions of  $\lambda_i$ ,  $i = 1, 2, 3, 4$ , can be obtained as

$$\begin{aligned} \lambda_1 &= 2\beta_1\beta_3 + 2\beta_2\beta_4 - 2\beta_1(1 + \sum_{i=1}^4 \beta_i^2), \quad \lambda_2 = 2\beta_1\beta_4 - 2\beta_2\beta_3 - 2\beta_2(1 + \sum_{i=1}^4 \beta_i^2), \\ \lambda_3 &= \beta_1^2 - \beta_2^2 - 2\beta_3(1 + \sum_{i=1}^4 \beta_i^2), \quad \lambda_4 = 2\beta_1\beta_2 - 2\beta_4(1 + \sum_{i=1}^4 \beta_i^2). \end{aligned}$$

This approximation scheme is designated as MEM AP2 in the present paper. Fig. 2 shows some numerical simulations comparing the original MEM II and MEM AP2 spectra along with the target spectra. Although the MEM AP2 is not identical to MEM II, it generally yields reasonably good result to the unimodal, bimodal, and asymmetric target spectra.

Extended MEM II

As an extension of the MEM II based on the five Fourier coefficients measured, the directional distribution function may be also estimated by combining the first and any  $J$ -th directional modes as

$$H(\sigma, \phi) = \exp[-\lambda_0 - a_1 \cos(\phi - \phi_1) - a_J \cos J(\phi - \phi_J)].$$

For example, when  $J = 3$ ,

$$H(\sigma, \phi) = \exp[-\lambda_0 - \lambda_1 \cos(\phi) - \lambda_2 \sin(\phi) - \lambda_5 \cos(3\phi) - \lambda_6 \sin(3\phi)].$$

The solution of  $\lambda_j$ 's from the above equation can be obtained either by iteration method or from an approximation scheme as followings:

$$\begin{aligned} \lambda_1 &= -\beta_1 \frac{2 \sum_{i=1}^4 \beta_i^2 + 2.5[\sum_{i=1}^4 \beta_i^2 - (\sum_{i=1}^4 \beta_i^2)^2]^2}{\beta_1^2 + \beta_2^2 + 2\beta_1\beta_2\beta_4 + \beta_1^2\beta_3 - \beta_2^2\beta_3}, \quad \lambda_2 = \lambda_1\beta_2/\beta_1, \\ \lambda_5 &= \frac{\lambda_1(3\beta_2^2 - \beta_1^2) - 4(\beta_1\beta_3 - \beta_2\beta_4)}{2(\beta_1^2 + \beta_2^2)}, \quad \lambda_6 = \frac{\lambda_2(\beta_2^2 - 3\beta_1^2) - 4(\beta_3\beta_2 + \beta_1\beta_4)}{2(\beta_1^2 + \beta_2^2)}. \end{aligned}$$

The above approximation scheme is designated here as MEM AP3. Fig. 3 shows some comparisons between the MEM II and MEM AP3 with the target spectra. It is seen that MEM AP3 can still generate good estimate to the target spectrum and

## WAVE DIRECTIONAL SPECTRUM

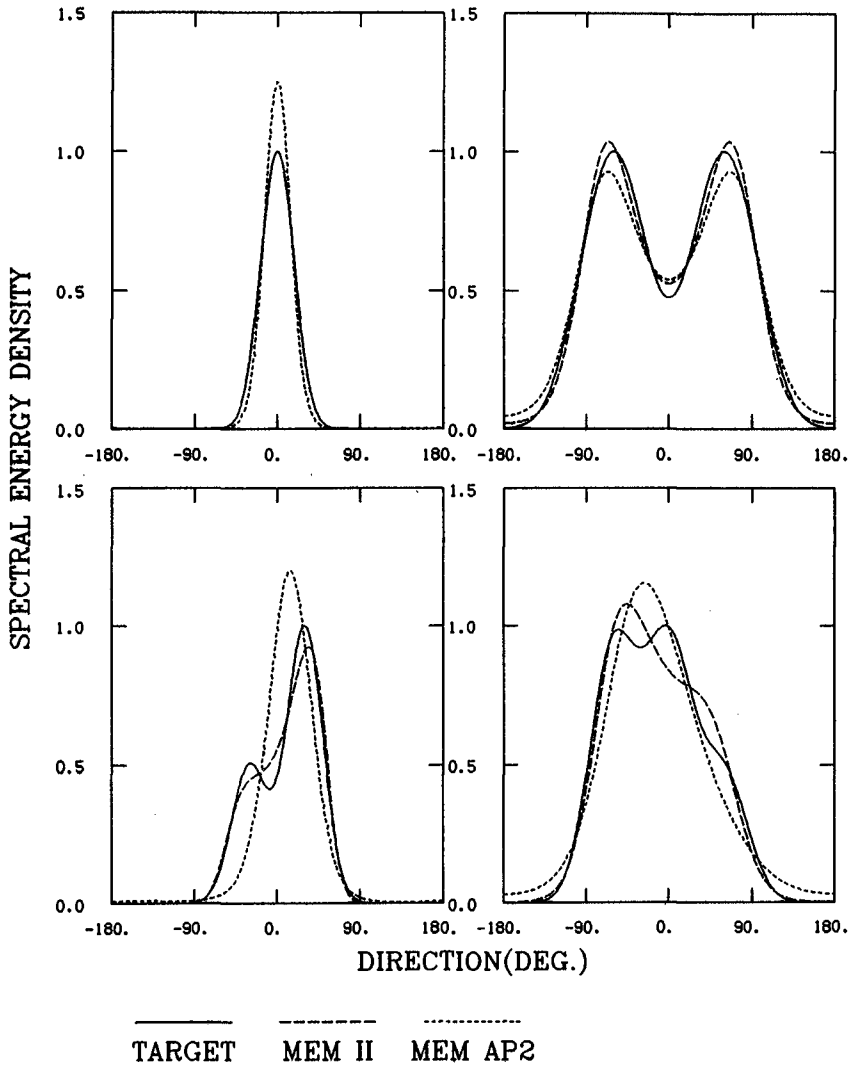


Figure 2: Comparison of the MEM II and MEM AP2 with target spectra.

WAVE DIRECTIONAL SPECTRUM

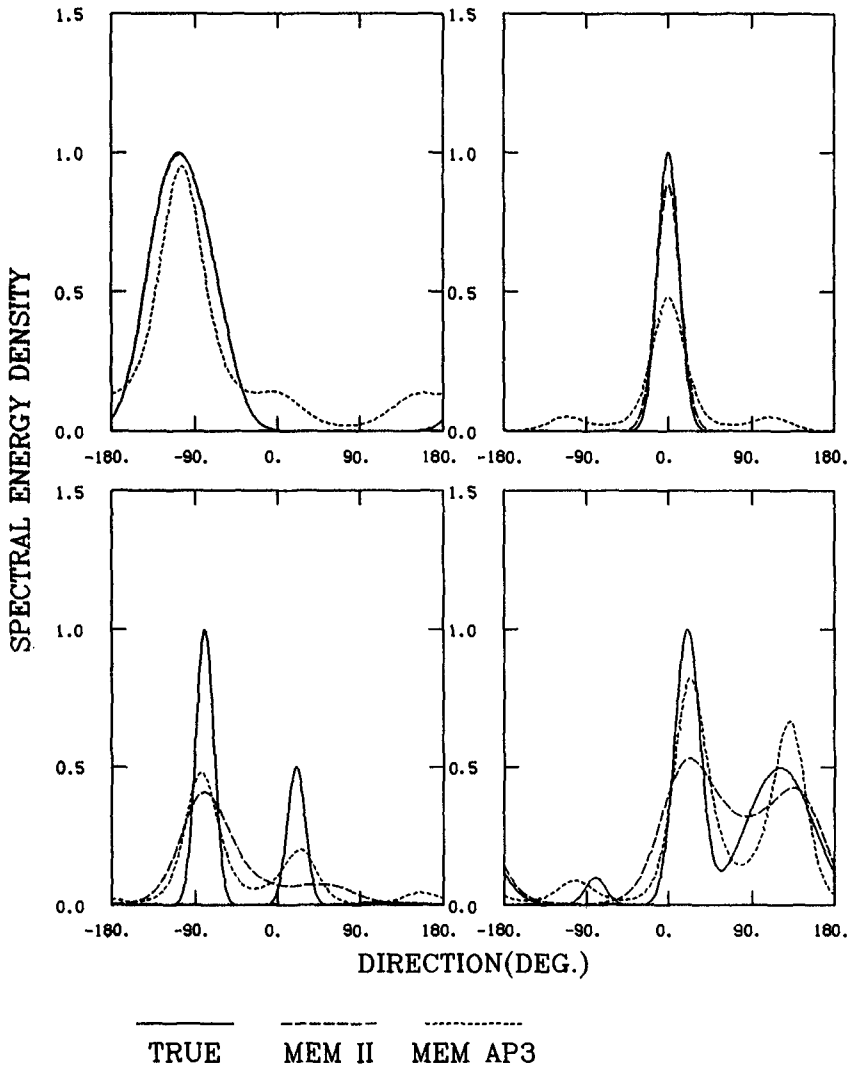


Figure 3: Comparison of the MEM II and MEM AP3 with target spectra.



sometimes show better result than MEM II depending on the target spectrum tested. However, similar to MEM II, the extended model combining the first and limited higher directional modes can result false, although small, side lobe(s) in directions.

### Real Sea Data Analysis

Although MEM II shows attractive advantage in simulation test over TFS, LHM, and MEM I, it is more important to see how the method corresponds when applied to the real sea data. The effort here was to test MEM II for the measured time series sea data and compare the results with those from TFS and LHM. Two sets of real data representing two different sea states near coast were chosen for the test. One is a typical storm event of high wind and large waves. The other is for an event of combined swell and local waves due to moderate wind. Both data sets composed of two-day time series. In addition to the wave data, the wind information was also collected from the nearby coastal weather station. In most cases, the computations in MEM II converged rapidly after about five iterations. When they did not converge, the approximation scheme of MEM AP2 automatically took over the calculation.

Fig. 4 shows the computed results of directional spectra for the large wind and wave event which occurred at the Perdido Key, Florida, in the Gulf of Mexico from January 16th to 17th, 1994. The results displayed that new short waves were developed in the beginning when small wind started over the calm sea. As the wind strengthened, the waves were seen to grow steadily and, meanwhile, extend the spectral pattern toward the low frequency region. During the high wind stage, the waves appeared to have reached a state of equilibrium as the spectral pattern remained nearly stationary. As the wind gradually died out, spectra exhibited energy dissipation near the high frequency end. The spectral estimates for this case mostly have single directional peak. The estimates from TFS and MEM II occasionally yielded asymmetric distribution with two peaks, but mostly in frequency bands with little energy content. In terms of the directional dispersion, the directional spectra computed by MEM II displayed much narrower distribution than the results from TFS and LHM methods. Since the MEM II is deemed to predict better directional properties than TFS and LHM, the narrow distribution of directional spectra as estimated by MEM II shall be more representative to the real sea waves.

Fig. 5 shows the results for the event of combined swell and moderate wind waves. The measurement was taken at Cape Canaveral on the Atlantic coast from December 20th to the 21st, 1993. In this event, westbound sea swell was observed throughout the two-day time data used in analysis. At first, only small short waves in scattered directions were observed as the wind was nearly absent. Later on as a moderate southerly wind started, local waves were rapidly developed heading to the north. It was noticed that although local wind waves and existing swell have different directions, as the local wind waves grew, the directions of wind waves and swell began to merge in the middle frequency region. This result seems to suggest that interaction took place between wind waves and swell in this frequency range. Again, the general pattern of directional distribution is narrower as obtained from MEM II than the other two methods.

Ideally, if both wind waves and swell are present at sea, there may be good chance

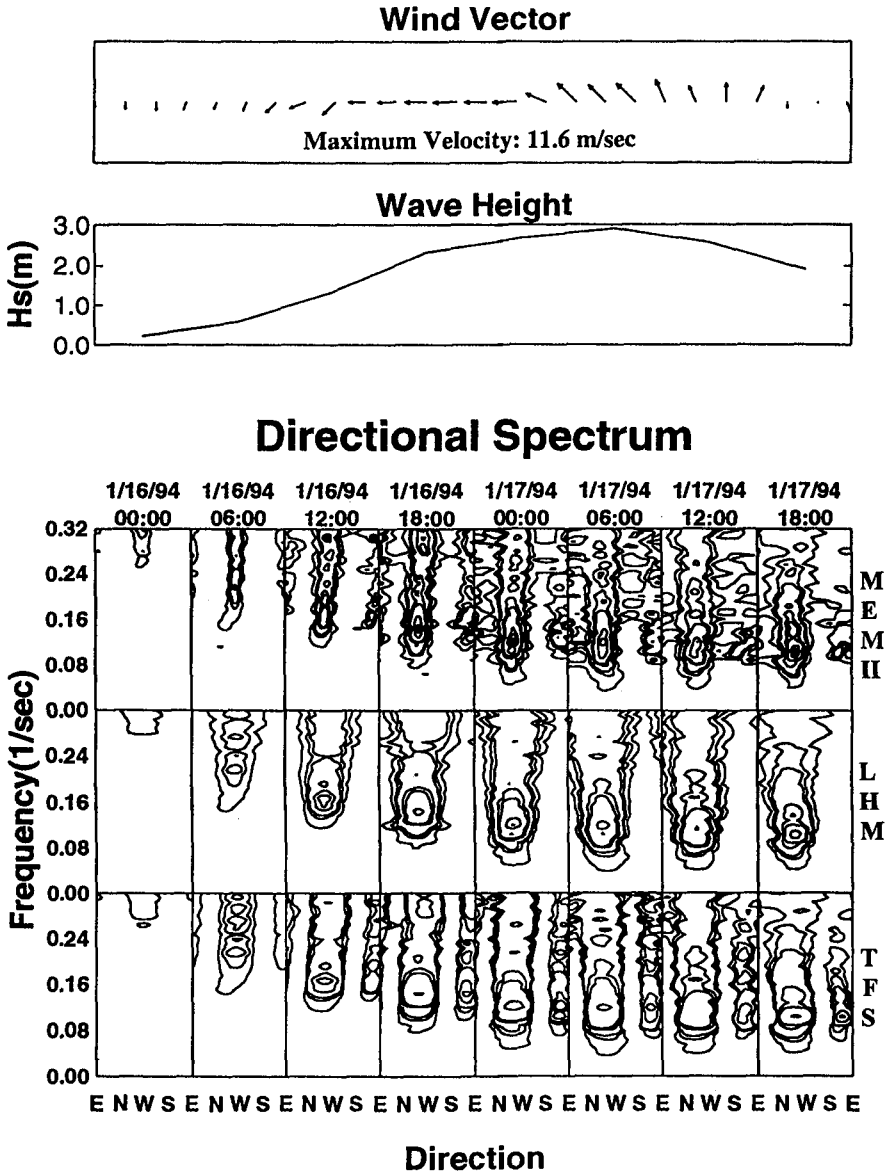


Figure 4: Comparison of MEM II, TFS, and LHM with real time series sea data measured at Perdido Key, Florida (contours in log scale).

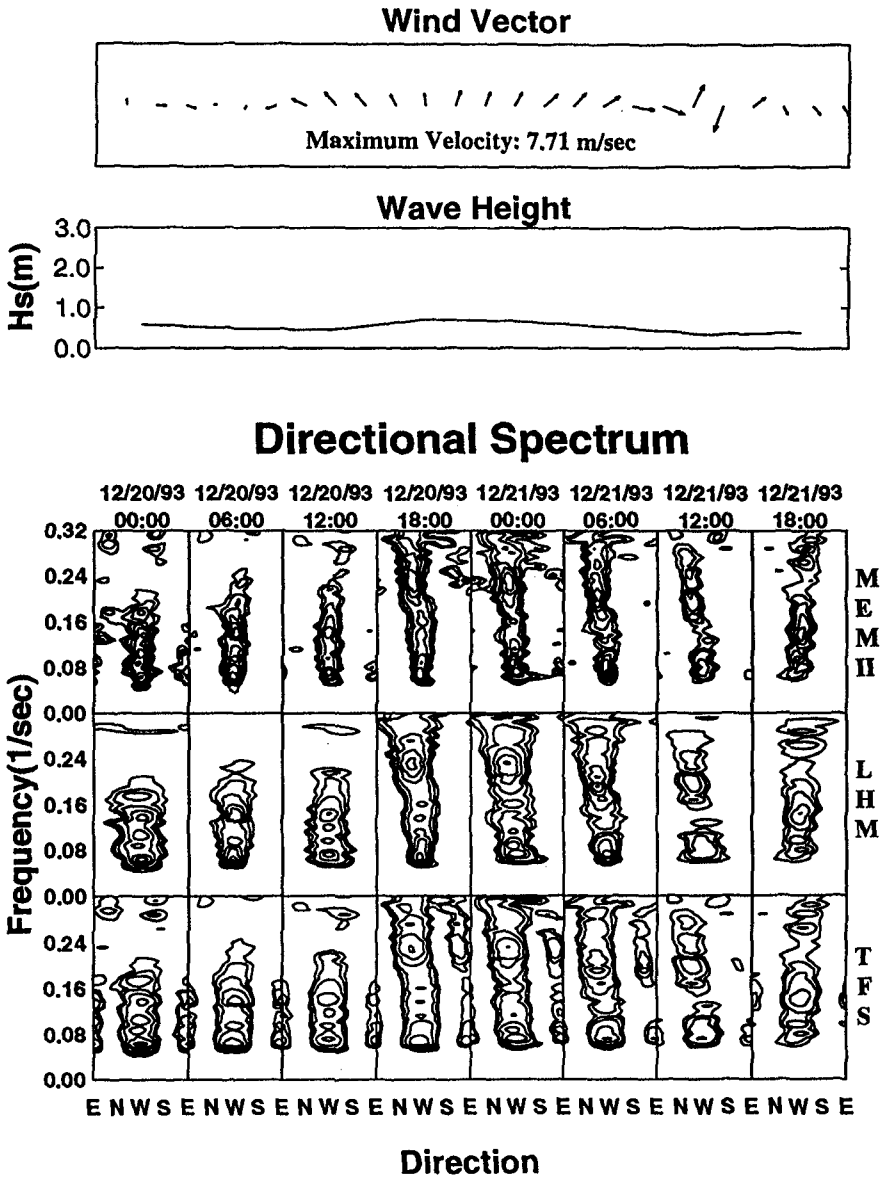


Figure 5: Comparison of MEM II, TFS, and LHM with real time series sea data measured at Cape Canaveral, Florida (contours in log scale).

to have two peaks in directional distribution at the same frequency. However, based on the results of real sea data from MEM II, two directional peaks at the same frequency were rare events, excluding the cases with false secondary peak which usually occurred in the opposite direction of the main peak direction. One possible explanation is the interaction between wind wave and swell components in the same frequency band. However, outside the main energy content range where spectral energy is relatively low, a few cases with two directional peaks were found. A few examples with the presence of directional spectra with dual peaks or asymmetric distribution from the combined wind sea and swell event are shown in Fig. 6.

In order to compare the different methods more specifically for real sea data analysis, three statistical parameters, namely, the peak direction, the mean direction, and the standard deviation at the dominant frequency, which corresponds to the largest spectral energy in frequency domain, were computed. Figs. 7 and 8 show the three parameters computed for the two sets of real sea data tested earlier. For the peak direction at the dominant frequency, all the LHM, TFS, and MEM II results are almost identical. For the mean direction at the dominant frequency, the LHM gives the same direction as the peak direction but both the TFS and MEM II show different directions from the peak directions because of the asymmetry of the directional distribution. In terms of standard deviation, the MEM II exhibits much narrower distribution than both LHM and TFS. In other words, wave energy is more concentrated around the main peak direction as resulted by MEM II.

### Conclusions

Four different methods analyzing directional wave spectrum were compared using numerical simulation and actual measured sea data. The four methods include the Truncated Fourier series(TFS), the Longuet-Higgins parametric model(LHM), two different maximum entropy methods (MEM I and II) that utilize different definitions of entropy. The numerical simulation consisted of a variety of target spectra with different properties. And the test results showed that the maximum entropy method with the entropy defined as a statistical probability density function, named here as MEM II, is clearly performed better than the other methods in estimating the target spectra. From the real sea data analysis, it is also concluded that MEM II is most suitable as the method could differentiate dual peaks in the same frequency component and detect the evolution of directional interactions of each frequency component.

The specific findings from the study were summarized below:

- (1) For the four different methods compared as candidates for analyzing the measured directional waves, the LHM is restricted to a symmetrical single peak distribution, the TFS has the disadvantage producing negative energy component, the MEM I often overestimates the peak, and the MEM II may have a convergence problem.
- (2) For applications to both simulated and real sea data, the MEM II is considered superior to the other methods compared in the paper. The convergence problem of the MEM II in numerical iterations can be overcome by using an approximation scheme.

# Wave Directional Spectrum

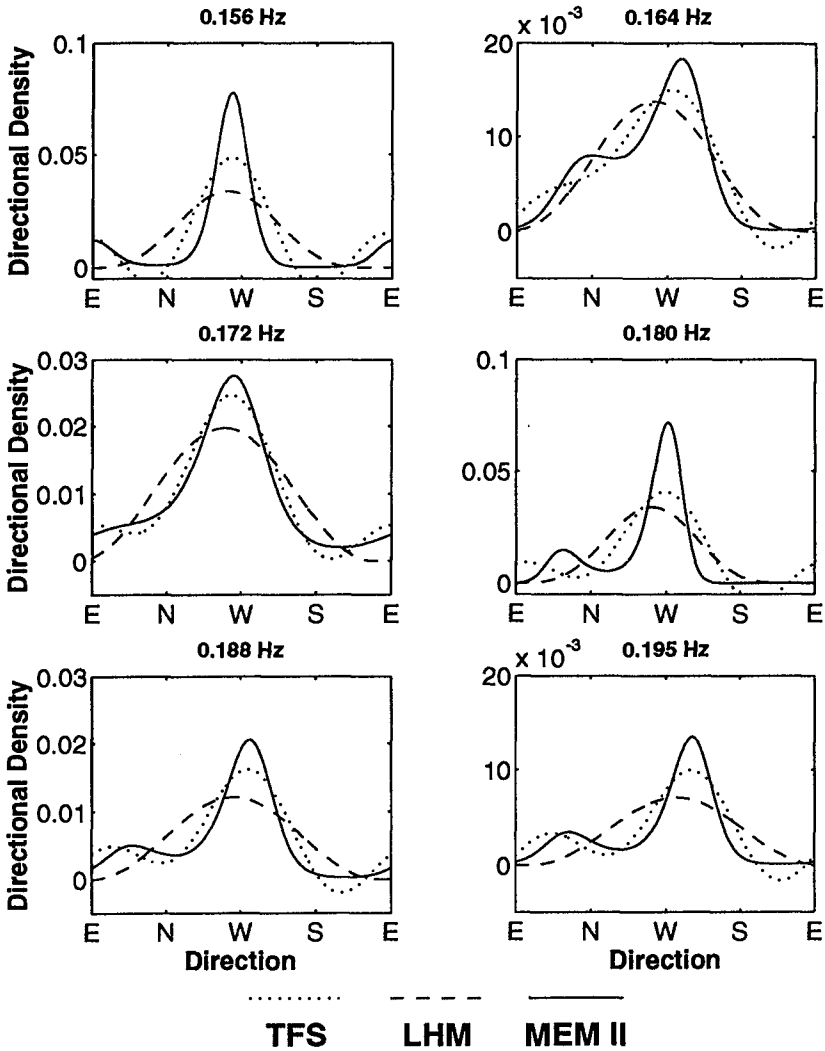


Figure 6: Examples of bimodal and asymmetric directional spectra computed by MEM II along with those from LHM and TFS, based on measured real sea data.

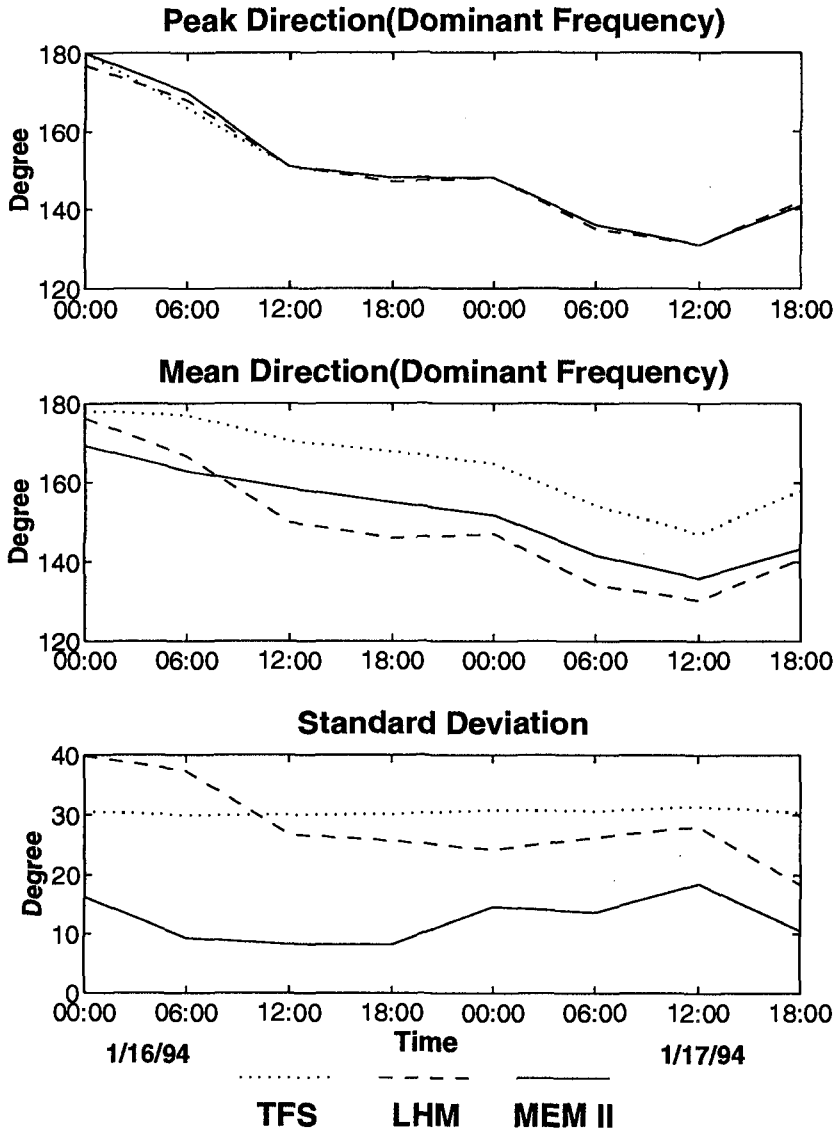


Figure 7: Comparison of dominant frequency peak and mean directions with standard deviations computed based on Perdido Key data.

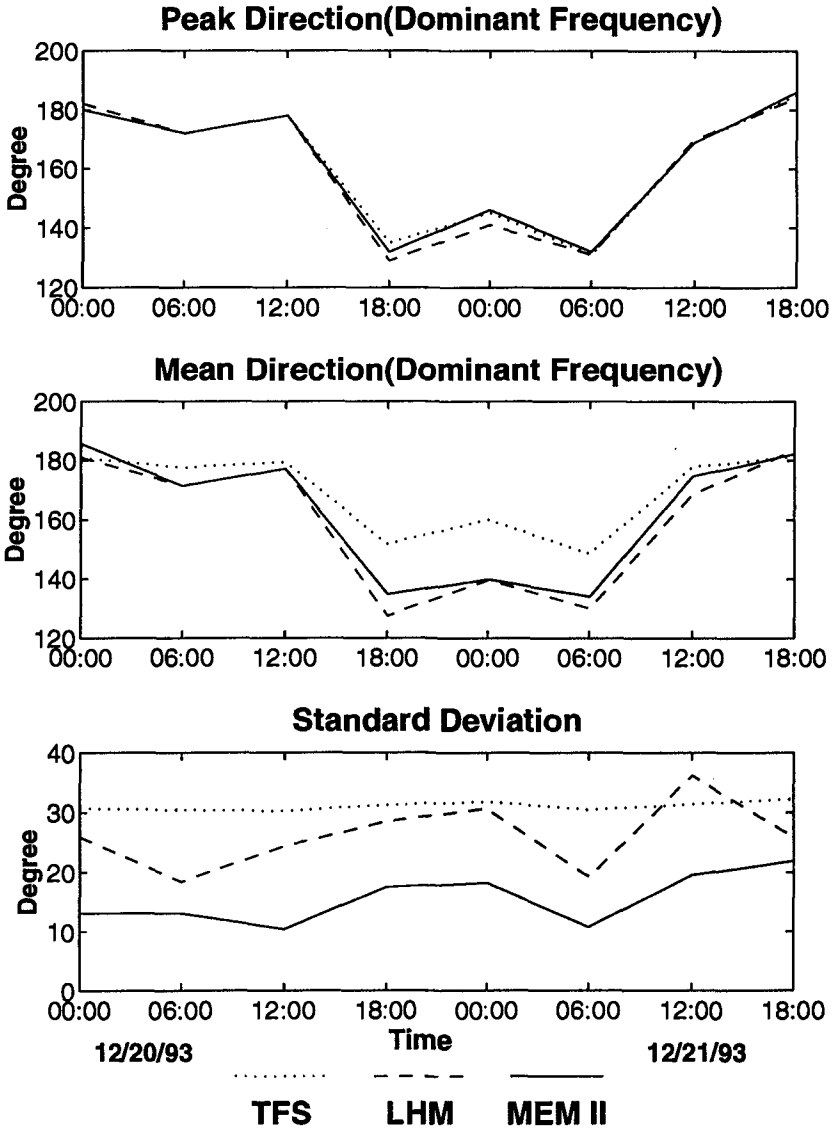


Figure 8: Comparison of dominant frequency peak and mean directions with standard deviations computed based on Cape Canaveral data.

(3) Applying TFS, LHM, and MEM II to the real sea time series data shows similar patterns of directional spectrum. The TFS, LHM, and MEM II are all seen to result almost identical peak direction for the dominant frequency component. However, they all yield different mean directions for dominant frequency component. This is because LHM produces symmetrical directional distribution whereas TFS and MEM II give asymmetrical distribution of directional spectrum. The MEM II, in general, produces narrower directional distribution than the other two methods.

(4) Even with the presence of both local wind waves and swell, it is generally rare to have two distinguished directional peaks at the same frequency. It appears that in the mid frequency range that contains most of the wave energy, the directional components from wind waves and swell tend to merge.

(5) With the aid of an approximation scheme, the MEM II can be programmed for practical applications such as automated directional spectrum analysis from real time data with significant reduction of computational time.

### References

- Benoit, M., 1992, "Practical Comparative Performance Survey of Methods Used for Estimating Directional Wave Spectra from Heave-Pitch-Roll Data.", Proc. 23rd ICCE, ASCE, pp.62-75.
- Brissette, F.P. and Tsanis, I.K., 1992, "Estimation of Wave Directional Spectra from Pitch-Roll Buoy Data.", J. WPCOE, ASCE, Vol. 120, No. 1., pp 93-115.
- Krogstad, H.E., 1989, "Reliability and Resolution of Directional Wave Spectra from Heave, Pitch, and Roll Data Buoys", Directional Ocean Wave Spectra, The Johns Hopkins University Press, Baltimore and London, pp.66-71.
- Longuet-Higgins, M. S., Cartwright, D. E., and Smith, N. D., 1963, "Observations of the Directional Spectrum of Sea Waves Using The Motion of a Floating Buoy", in Ocean Wave Spectra, Prentice Hall, Englewood Cliffs, N. J., pp.111-136.
- Kim, T., Lin, L. W., and Wang, H., 1993, "Comparisons of Directional Wave Analysis Methods.", Ocean Wave Measurement and Analysis, Proc. of the Second International Symposium, New Orleans, pp.554-568.
- Kobune, K., and Hashimoto, N., 1986, "Estimation of Directional Spectra from the Maximum Entropy principle", in Proc. 5th International Offshore Mechanics and Arctic Engineering (OMAE) Symposium, Tokyo, pp.80-85.
- Lygre, A., and Krogstad, H. E., 1986, "Maximum Entropy Estimation of the Directional Distribution in Ocean Wave Spectra", J. Phys. Oceanogr. 16, pp.2052-2060.



## CHAPTER 27

### Probability of the freak wave appearance in a 3-dimensional sea condition

Akira Kimura<sup>1</sup> and Takao Ohta<sup>2</sup>

#### Abstract

In this study, the appearance probability of the freak waves is theoretically introduced applying the definitions by Klinting and Sand (1987). Their three conditions are formulated theoretically applying the probability distributions for the run of wave heights (Kimura, 1980) and the distance of a mean point of the zero-crossing wave crest and trough from mean water level (Kimura and Ohta, 1992b). Its appearance probability in a uni-directional irregular wave condition is studied first, the theory is extended then to the 3-dimensional wave condition, and the definition is discussed in terms of the probability in the last.

#### 1. Introduction

The term "freak waves" may be used to express a huge wave in height. Freak waves have been seen and reported in many places in the world. Many fishing boats, even a man of wars have been destroyed by exceptionally huge waves. And the possibilities have been pointed out that the recent disasters on break waters at port of Sines (Portugal), Bilbao (Spain), (per Bruun, 1985) are also due to the freak waves. Although a common recognitions "what is the freak wave" may not have been established yet, it may have following properties as described by per Bruun (1985).

It is a single "mammoth" short crested wave with, apparently, little relation to its neighboring waves. It has a high crest but not necessarily a corresponding pronounced trough. It does not stay long but break down in small waves.

In 1987, clear definition was made by Klinting and Sand as,

---

<sup>1</sup> Professor and <sup>2</sup> Research associate of the Faculty of Eng., Tottori Univ., Koyama Minami 4-101, Tottori, 680, Japan

- (1) it has a wave height higher than twice the significant wave height,
- (2) its wave height is larger than 2 times of the fore-going and the following wave heights,
- (3) its wave crest height is larger than 65% of its wave height.

Recently, only the first condition may be used for the definition (Sand, 1990). However very large appearance probability is given if only the first condition is used. Furthermore the idea that there is a big jump in wave heights, is not realized in the recent definition. The present study applies three all conditions by Klinting and Sand theoretically in the cases of uni-directional and directional random sea conditions. The importance of the conditions is compared and examined through the individual probability.

2. Definition for freak wave

Three conditions given by Klinting and Sand (1987) are as follows.

If we have a following time series of wave height,

$$\dots, H_{j-1}, H_j, H_{j+1}, \dots$$

and if  $H_j$  is the freak wave (Fig.1), the definition by them is expressed as,

- |     |                       |                |
|-----|-----------------------|----------------|
| (1) | $H_j > H_{1/3},$      | (Condition 1 ) |
| (2) | $H_j > 2H_{j-1},$     | (Condition 2A) |
|     | and $H_j > 2H_{j+1},$ | (Condition 2B) |
| (3) | $\eta_j > 0.65H_j,$   | (Condition 3 ) |

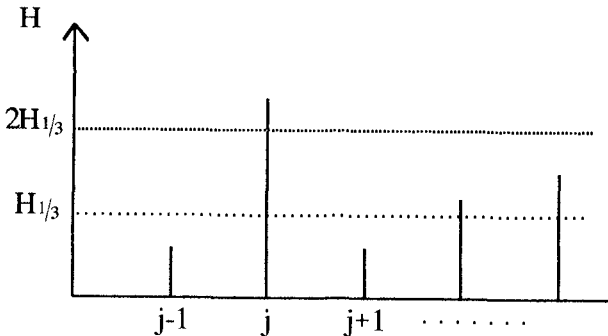


Fig.1 Time series of wave heights. ( $H_j$  is the freak wave)

in which  $H_{1/3}$  is a significant wave height and  $\eta_j$  is a crest height of  $H_j$ .

### 3. Probability distribution of wave heights

The wave height distribution for the zero-crossing deep water irregular waves agrees well with the Rayleigh distribution. However the agreement of data and distribution in a very large part of wave height has not been sufficiently investigated yet. Goda (1985) reported the measured data show slightly larger probability of appearance than the Rayleigh distribution in a large part of the distribution. Kimura (1981), Mase (1986) reported that increasing non-linearity on wave profiles brings narrower wave height distribution. However Yasuda (1992) showed the non-linearity brings about no significant difference on wave height distribution when the waves are those of fully saturated in a deep sea condition.

If a physical mechanism in which the freak waves are brought about differs from other wind waves, there is a possibility that the freak waves do not follow the statistical law for irregular wave heights. Per Bruun (1985) pointed several phenomena such as orthogonal crossing of waves, overtaking of waves. However numerical simulations for the waves from two separate wind wave sources showed no significant difference in the wave height distribution from the Rayleigh distributions. Therefore we apply the Rayleigh distribution for the wave height distribution in this study. Further assumption used in this study was that waves are those of fully saturated in deep water condition.

### 4. Formulation of the condition 2A and 2B by Klinting and Sand

If the time series of wave height,

$$\dots, H_{j-1}, H_j, H_{j+1}, \dots$$

forms a Markov chain and its transition probability is given by the normalized 2-dim. Rayleigh distribution (Kimura, 1980), the probability for the condition 2A is given as follows.

The probability of the first "jump" from  $H_{j-1}$  to  $H_j$  ( $H_j > 2H_{j-1}$ ) is given as

$$p_{12}(H_j) dH = \frac{\int_0^{H_j/2} dH_1 \int_{H_j}^{H_j + dH} p(H_1, H_2) dH_2}{\int_{H_j}^{H_j + dH} p(H_1) dH_1}, \quad (1)$$

in which  $p(H_1, H_2)$  is the 2-dim. Rayleigh distribution and

$p(H_1)$  is the Rayleigh distribution which are given by

$$p(H_1, H_2) = \frac{\pi^2}{4(1-\kappa^2)} H_1 H_2 \exp\left(-\frac{\pi}{4(1-\kappa^2)}(H_1^2 + H_2^2)\right) I_0\left(\frac{\pi\kappa H_1 H_2}{2(1-\kappa^2)}\right), \quad (2)$$

and

$$p(H_1) = \frac{\pi}{2} H_1 \exp\left(-\frac{\pi}{4} H_1^2\right). \quad (3)$$

$H$  is a normalized wave height by the mean wave height. Correlation parameter ( $\kappa$ ) between  $H_1$  and  $H_2$  is correlated to the wave spectrum (Battjes and van Vledder, 1984) as,

$$\kappa = (\rho^2 + \lambda^2)^{1/2} / m_0, \quad (4)$$

where

$$\begin{aligned} \rho &= \int_{f_d}^{f_u} S(f) \cos(2\pi(f-f_m)T_m) df, \\ \lambda &= \int_{f_d}^{f_u} S(f) \sin(2\pi(f-f_m)T_m) df, \\ f_m &= m_1 / m_0, \\ T_m &= 1 / f_m, \\ m_n &= \int_{f_d}^{f_u} f^n S(f) df, \\ f_d &= (-0.186 / r + 0.735) f_p \quad : (4 \leq r \leq 20) \\ f_u &= (1.61 / r + 1.62) f_p \quad : (4 \leq r \leq 20) \end{aligned} \quad (4)'$$

in which  $S(f)$  is a power spectrum,  $f_p$  is its peak frequency,  $r$  is a shape factor of the spectrum.

$$S(f) = (f/f_p)^{-r} \exp\left[\left(\frac{r}{4}\right)\left\{1 - (f/f_p)^{-4}\right\}\right]. \quad (5)$$

Narrow integration range from  $f_d$  to  $f_u$  instead of 0 and  $\infty$  respectively, in the calculations for  $\rho$ ,  $\lambda$  and  $m_n$  is used to improve the value of correlation parameter (Kimura and Ohta, 1992a).

The probability of the second jump from  $H_j$  to  $H_{j+1}$  ( $H_j > 2H_{j+1}$ ) is also given by

$$p_{21}(H_j) dH = \frac{\int_0^{H_j/2} dH_2 \int_{H_j}^{H_j+dH} p(H_1, H_2) dH_1}{\int_{H_j}^{H_j+dH} p(H_1) dH_1} \tag{6}$$

in which  $P(H_1, H_2)$  and  $p(H_1)$  are given by eqs.(2), (3) respectively. Combining eqs.(1) and (6), the condition 2A and 2B is given as

$$p_{f1}(H) dH = p_{12}(H) dH p_{21}(H). \tag{7}$$

5. Formulation of the condition 3

Two waves in Fig.2 have the same zero-down-cross wave height and period but different crest heights. To clarify the difference between these two waves, Kimura and Ohta (1992b) introduced the new parameter : the mean point between wave crest and trough (Fig.2). Applying this parameter, the condition 3 is formulated as,

$$d/H_* > 0.15 , \tag{8}$$

in which  $d$  is a distance from the mean water level to the mean point between wave crest and trough,  $H_*$  is a wave height.

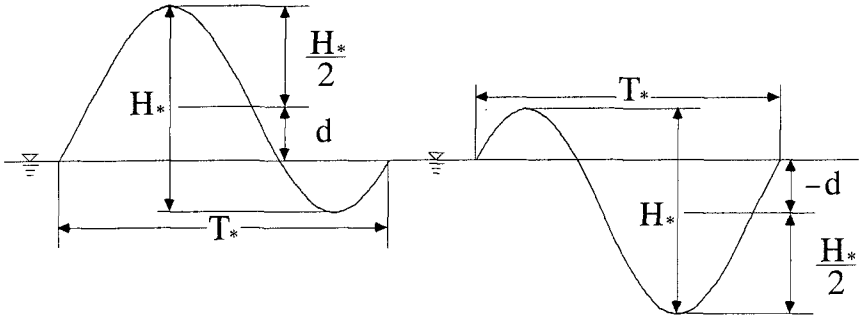


Fig.2 Zero-crossing waves with the same wave height and period but different crest heights.

Probability of eq.(8) is theoretically given as follows. Putting  $\epsilon = d/H_*$ , combined distribution of  $\epsilon$  and  $H$  is given as (Kimura and Ohta, 1992b),

$$p(\epsilon, H) = \frac{\pi^2 H^3 (1 - 4\epsilon^2)}{1 - \kappa_2^2} \exp\left(-\frac{\pi H^2 (1 - 4\epsilon^2)}{2(1 - \kappa_2^2)}\right) I_0\left(-\frac{\pi \kappa_2 H^2 (1 - 4\epsilon^2)}{2(1 - \kappa_2^2)}\right) \tag{9}$$

in which  $H$  is the normalized wave height with its mean ( $H=H_s/H_m$ ). The condition 3 (eq.8) is also expressed as

$$p_{fz}(H) = \int_{0.15}^{0.5} p(\epsilon|H) d\epsilon, \tag{10}$$

in which  $p(\epsilon|H)$  is determined as

$$p(\epsilon|H) = p(\epsilon, H) / p^*(H), \tag{11}$$

where

$$p^*(H) = \int_0^{2H} p(A_1, H) dA_1, \tag{12}$$

and

$$p(A_1, H) = \frac{\pi^2 A_1 (2H - A_1)}{2(1 - \kappa_2^2)} \exp\left(-\frac{\pi\{A_1^2 + (2H - A_1)^2\}}{4(1 - \kappa_2^2)}\right) I_0\left(\frac{\pi\kappa_2 A_1 (2H - A_1)}{2(1 - \kappa_2^2)}\right). \tag{13}$$

In eqs.(9) and (13),  $\kappa_2$  is the correlation parameter. This value is calculated using the values 0,  $\infty$  and  $T_m/2$  instead of  $f_d$ ,  $f_u$  and  $T_m$  respectively in eqs.(4), (4)'.

Solid line in Fig.3 shows the calculated  $p_{fz}$  (for a fully saturated sea condition, for example,  $r=5$ ).

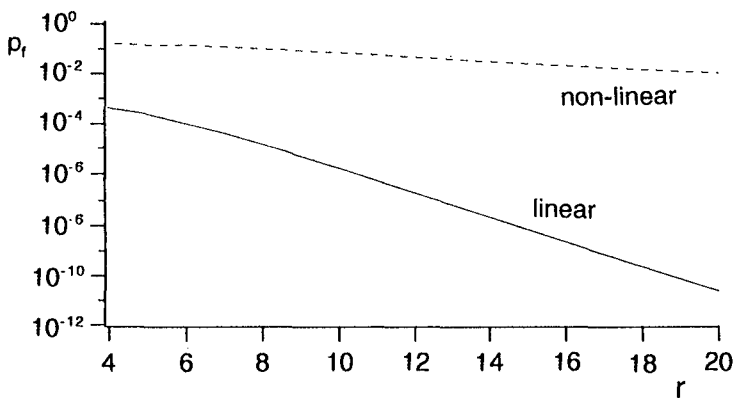


Fig.3  $p_{fz}$  with non-linearity (dotted line) without non-linearity (solid line)

If we take the non-linearity of wave profile into account,  $p_{fz}$  increases considerably as follows.

In a deep sea condition, the 3rd order wave profile is

given as,

$$\eta = a \cos(2\pi\theta) + \frac{\pi a^2}{L} \cos(4\pi\theta) + \frac{3\pi^2 a^3}{2L^2} \cos(6\pi\theta), \quad (14)$$

in which  $\theta$  is a phase,  $L$  is a wave length and the relation between wave height  $H_s$  and  $a$  is given by

$$H_s = 2a + 3 \frac{\pi^2}{L^2} a^3. \quad (15)$$

Wave steepness of a significant wave for fully saturated wind waves is about 0.04 ~ 0.05 (Goda, 1975). Since  $H_\epsilon > 2H_{1/3}$  ( $H_\epsilon$ : freak wave height), wave steepness of the freak wave may be larger than 0.1, and  $d/H_s$  may be approximately,

$$\pi a^2 / LH_s = \pi / 4 \cdot H / L. \quad (16)$$

Putting  $H/L$  in eq.(16) equals to 0.1, we obtain  $\epsilon$  to be about 0.08. Therefor taking the non-linearity into account, the condition 3 may be able to change as,

$$p_{f2}(H) = \int_{0.15-0.08}^{0.5} p(\epsilon|H) d\epsilon. \quad (17)$$

## 6. Formulation of the condition 1

Assuming the conditions 2A and 2B and the condition 3 to be independent, the condition 1 together with 2A, 2B and 3 is formulated as,

$$p_f = \int_{2H_{1/3}}^{\infty} p_{f1}(H) p_{f2}(H) dH \quad (18)$$

## 7. Result of the calculation

Result of the calculations are listed in Table-1. If we apply eq.(10) for the condition 3,  $p_f$  is about  $0.155 \times 10^{-4}$  when  $r=5$  in eq.(5). Narrower spectrum brings far smaller value for  $p_f$ . The effect of non-linearity on the condition 3 is compared in Fig.3. Broken line show  $p_f$  from eqs.(17) instead of eq.(10).  $p_f$  with non-linearity gives a far larger value.  $\epsilon$  does not distribute widely when wave height is very large (Kimura and Ohta, 1992b) and large waves have non-linearity on their profiles, the condition 3 may not be important.

Furthermore, the second jump ( $H_j > H_{j+1}$ ) in the condition 2 may not be an important also. To realize only a hazardous property of the freak wave, consecutive wave height after the freak wave may not be important.

Table-1 Appearance probability of the freak waves

Conditions considered	uni-directional	directional
1	$0.321 \times 10^{-3}$ (1/3,100)	$0.477 \times 10^{-3}$ (1/2,100)
1, 2A, 2B, 3	$0.155 \times 10^{-4}$ (1/65,000)	-
1, 2A, 2B	$0.106 \times 10^{-3}$ (1/9,400)	-
1, 2A	$0.198 \times 10^{-3}$ (1/5,000)	$0.278 \times 10^{-3}$ (1/3,600)

The calculated result is listed in Table-1 when the conditions 2B and 3 are neglected.

8. 3-dimensional sea condition

If we use a single wave gauge in the measurements, the wave gauge can not always record the local maximum in a directional sea condition as shown in Fig.4. If wave gauges can selectively record wave profiles at the local maxima of short crested waves, we may have larger appearance probability of large waves. In this section, the change in the appearance probability of the freak wave is introduced when the maximum

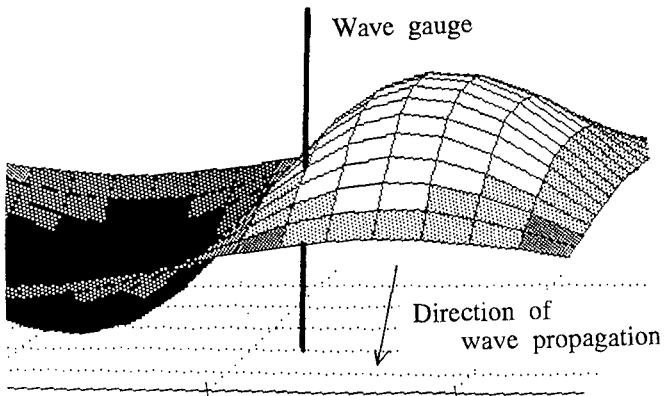


Fig.4 Short crested wave and wave gauge



wave height within a certain distance from a fixed point is applied.

We place a plane Q which is vertical to the horizontal still water plane ( $x' - y'$ ) and is perpendicular to the dominant wave direction.  $x'$  is taken in the dominant direction of waves and  $y'$  is taken on Q. Figure 5 shows schematically a wave envelope for the cross section of short crested wave profile on Q at a certain instance. A wave gauge is placed at point A and this point is taken as an origin ( $x'=0, y'=0$ ). Using the Taylor series expansion, the envelope  $R(y')$  is expanded around A as,

$$R(y') = R_A + R'_A(y') + R''_A(y')^2/2 + \dots \quad (19)$$

$R'_A$  and  $R''_A$  are the first and second derivatives of  $R$  at point A. Since we only discuss the wave height in the vicinity around A, we apply three terms in eq.(19) :  $R$  is approximated with a quadratic function around A. The value of  $R$  at the local maximum ( $R_B$ ) is given as

$$R_B = \left\{ 2R_A R''_A - R'^2_A \right\} / 2R''_A \quad (20)$$

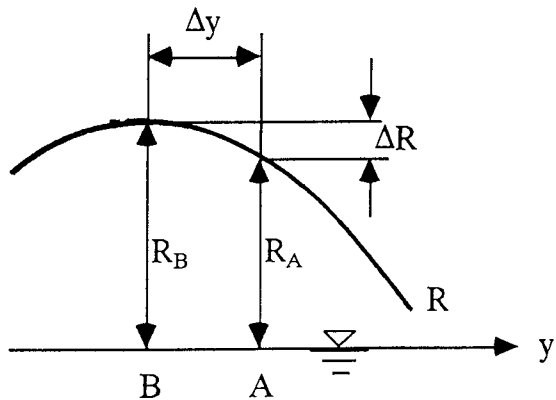


Fig.5 Wave envelope on Q

A distance from A to B is given as

$$\Delta y = \left| R'_A / R''_A \right| \quad (21)$$

The probability that the value  $R_B - R_A$  exist within  $\Delta R \sim \Delta R + dR$  is given by

$$P_F = \int_S P(R', R''; R_A) dR' dR'' \quad (22)$$

in which  $P(R_A', R_A''; R_A)$  is the conditional probability distribution of  $R_A'$  and  $R_A''$  for the given value of  $R_A$ .  $S$  is the region of integration. Figure 6 shows the region  $S$  schematically. Solid lines shows the relations,

$$\Delta R = -R_A'^2 / 2R_A'' \quad (23)$$

and

$$\Delta R = -R_A'^2 / 2R_A'' + dR \quad (24)$$

respectively where  $\Delta R = R_B - R_A$ . Dotted line shows the relation,

$$\Delta y = |RA' / RA''| = const. \quad (25)$$

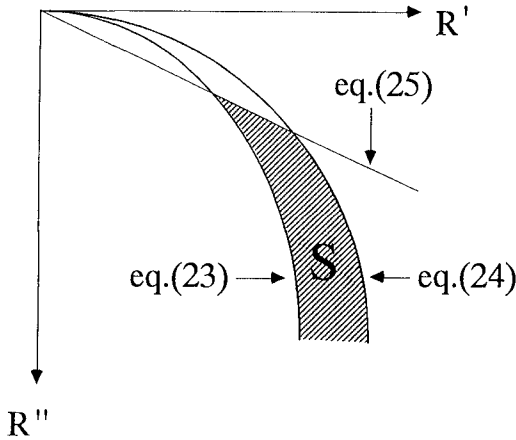


Fig.6 Region of integration  $S$

If the shadowed part is taken as a region  $S$ , eq.(22) gives a probability of  $R_B - R_A = \Delta R \sim \Delta R + dR$  within a distance  $\Delta y$  on  $Q$  from  $A$ .

$P(R_A', R_A''; R_A)$  is introduced as follows. The combined distribution of  $R_A', R_A'', R_A$  :  $P(R_A', R_A'', R_A)$ , is derived theoretically by Rice(1945) as

$$p(R, R', R'') = 2\alpha \int_0^\infty \exp(-\beta\phi'^4 - \gamma\phi'^2) d\phi' \quad (26)$$

in which

$$\alpha = \frac{R^2}{(2\pi)^{3/2} \sqrt{B_4}} \exp \left\{ -\frac{1}{2B^2} (B_0 R^2 - 2B_2 R R'' + B_{22} R'^2 + B_4 R''^2) \right\}, \quad (27)$$

$$\beta = B_4 R^2 / 2B^2,$$

$$\gamma = (B_{22} R^2 - 2B_4 R R'' + 2B_2 R'^2) / (2B^2),$$

where

$$B = b_0 b_2 b_4 + 2b_1 b_2 b_3 - b_2^3 - b_0 b_3^2 - b_4 b_1^2 \quad (28)$$

$$B_0 = (b_2 b_4 - b_3^2) B, \quad B_{22} = (b_0 b_4 - b_2^2) B,$$

$$B_1 = -(b_1 b_4 - b_2 b_3) B, \quad B_2 = (b_1 b_3 - b_2^2) B,$$

$$B_3 = -(b_0 b_3 - b_1 b_2) B, \quad B_4 = (b_0 b_2 - b_1^2) B.$$

$b_i$  ( $i=0,1,2,3,4$ ) is given as follows,

$$b_0 = \frac{\overline{(l'_{c1})^2}}{\overline{(l'_{s1})^2}}, \quad b_1 = \frac{\overline{(l_{c1} l'_{s2})}}{\overline{(l_{c2} l'_{s1})}}, \quad (29)$$

$$b_2 = \frac{\overline{(l'_{c2})^2}}{\overline{(l'_{s2})^2}}, \quad b_3 = \frac{\overline{(l_{s2} l'_{c3})}}{\overline{(l_{c2} l'_{s3})}},$$

$$b_4 = \frac{\overline{(l'_{c3})^2}}{\overline{(l'_{s3})^2}},$$

where

$$l_{c1} = \sum_{n=1}^{\infty} C_n \cos \left( u'_n x' - u'_m x' + \epsilon_n \right)$$

$$l_{s1} = \sum_{n=1}^{\infty} C_n \sin \left( u'_n x' - u'_m x' + \epsilon_n \right) \quad (30)$$

and

$$l_{c2} = (l_{c1})', \quad l_{s2} = (l_{s1})', \quad l_{c3} = (l_{c1})'', \quad l_{s3} = (l_{s1})''. \quad (31)$$

$()'$  and  $()''$  are the first and the second derivatives,  $C_n$  is calculated by the relation (Longuet-Higgins, 1957),

$$\sum_{u,v} \frac{u+du, v+dv}{2} \frac{C_n^2}{2} = E(u,v) du dv, \quad (32)$$

where  $E(u, v)$  is the directional wave spectrum in which  $u$  and  $v$  are the wave number of component wave in  $x'$  and  $y'$  directions respectively.  $\Sigma$  means to take the total of  $C_n^2/2$  in the region  $u \sim u+du$  and  $v \sim v+dv$ . The conditional distribution  $P(R'_\lambda, R''_\lambda; R_\lambda)$  is given as,

$$P(R', R''; R_\lambda) = P(R', R'', R) / P(R) \Big|_{R=R_\lambda}, \quad (33)$$

in which  $p(R)$  is the Rayleigh distribution.

Rice (1945) gave a theoretical expression for eq.(26), the integration was made numerically, for the simplicity.

In the calculation of  $E(u, v)$ , Bretschneider-Mitsuyasu spectrum with the significant wave of  $H_{1/3} = 5.5m$ ,  $T_{1/3} = 10s$  is used. For the directional function, Mitsuyasu type directional function (Goda,1985) with  $S_{max} = 10$  is used. When the sea is in a fully saturated condition, above value for  $S_{max}$  is recommended (Goda,1985). The power spectrum and the directional function is multiplied and transformed into  $E(u, v)$ , applying the dispersion relation of component waves. Above power spectrum brings same statistical properties of freak waves when  $r=5$  and directionarity is ignored.

Figure 7 shows the probability that  $R_b$  exceed 2 times of  $R_{1/3}$  (1/3 highest amplitude) in terms of  $R_A/(2R_{1/3})$ . Considerable probability exists in the region  $R_A/(2R_{1/3}) > 0.85$ .

If we take the waves of  $R_A < 2R_{1/3}$  but  $R_b > 2R_{1/3}$  into account as freak waves, appearance probability of the freak wave can be calculated as follows.

When only the condition 1 is used for the freak wave definition,

$$p = \int_0^{\infty} p_F p(H) dH , \tag{34}$$

in which

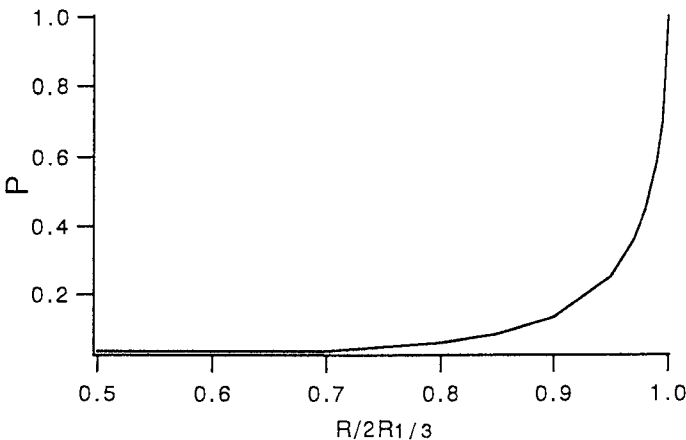


Fig.7 Appearance probability of the freak wave within the vicinity  $0.1 L_{1/3}$ .

$$P_F = \begin{cases} p_F & : 0 < R < 2R_{1/3} \\ 1 & : R > 2R_{1/3} \end{cases} \quad (35)$$

$p_F$  is given by eq.(22).

If the conditions 2B and the 3 are neglected, the appearance probability is given by,

$$p = \int_0^{\infty} p_F p_{12}(H) dH \quad (36)$$

Equation (35) is also applied in eq.(36) for  $p_F$ .

The results from eqs.(34) and (36) are also listed in Table-1. If we take the directional property of waves into account, the appearance probability increases about 45% when the sea condition is fully saturated and the condition 1 and 2A are applied in the freak wave definition.

## 9. Conclusion

If only the conditions 1 and 2A given by Klinting and Sand are applied, the appearance probability of the freak wave is about  $2.78 \times 10^{-4}$ . This means a freak wave appears once every 3,600 waves on the average. Considering the extremely disastrous properties of this wave, this is slightly too frequent. We may have to use a higher wave height for the freak wave. We also have to continue looking for the possibility that freak wave may not follow the ordinary statistical law but comes from other physical mechanism.

## References

- Battjes, J. A. and G. Ph. van Vledder (1984) : Verification of Kimura's theory for wave group statistics, Proc. 19th ICCE, pp.642-648.
- Goda, Y. (1985) : Random seas and design of maritime structures, Univ. of Tokyo Press, 323p.
- Kimura, A. (1980) : Statistical properties of random wave groups, Proc. 17th ICCE, pp.2974-2991.
- Kimura, A. (1981) : Joint distribution of the wave heights and periods of random sea waves, Coastal Eng. in Japan, Vol.24 pp.77-92.
- Kimura, A. and T. Ohta (1992a) : On probability distributions of the zero-crossing irregular wave height, Proc. 6th Intl. Symp. on Stochastic Hydraulics, pp.291-298.
- Kimura, A. and T. Ohta (1992b) : An additional parameter for the zero crossing wave definition and its probability distribution, Proc. 23rd ICCE, pp.378-390.
- Klinting, P. and S. Sand (1987) : Analysis of prototype freak wave, Coastal Hydrodynamics (Ed. Darlymple), ASCE, pp.618-632.

- Longuet-Higgins, M.S. (1957) : The statistical analysis of a random, moving surface, *Phil. Trans. Roy. Soc. London, Ser.A* (966), Vol.249, pp.321-387.
- Mase, H., A. Matsumoto and Y. Iwagaki (1986) : Calculation model of random wave transformation in shallow water, *Proc. JSCE, No.375/II-6*, pp.221-230. (in Japanese)
- per Bruun (1985) : Design and construction of mounds for breakwater and coastal protection, Elsevier, 938p.
- Rice S.O. (1945) : Mathematical analysis of random noise, reprinted in selected paper on noise and stochastic processes, Dover Pub. Inc. pp.133-294.
- Sand, S. (1990) : Report from the working group on breaking and freak waves, *Water wave kinematics* (Ed. Torum and Gudmestad), NATO ASI series, pp.17-21.
- Yasuda, T., K. Ito and N. Mori (1992) : Non-linearity effect on the statistical property of uni-directional irregular waves, *Proc. JSCE, No.443*, pp.83-92. (in Japanese)

## CHAPTER 28

### On the Joint Distribution of Wave Height, Period and Direction of Individual Waves in a Three-Dimensional Random Seas

J.G.Kwon<sup>1</sup> and Ichiro Deguchi<sup>2</sup>

#### Abstract

A theoretical expression for the joint distribution of wave height, period and direction is derived based on the hypothesis that sea surface is a Gaussian stochastic process and that a band-width of energy spectra is sufficiently narrow. The derived joint distribution is found to be an effective measure to investigate characteristics of three-dimensional random wave fields in shallow water through field measurements.

#### I. Introduction

A variety of studies has been conducted on the sediment transport in shallow water regions and a lot of formula has been proposed on the rate of sediment transport. However, these formulas do not always predict the same estimation of the rate of sediment transport even under the same conditions. This discrepancy can be explained by the following reasons: i) the dynamics and kinematics of sediment movement are not fully understood yet and each formula contains empirical coefficients which have to be fixed through experiments or field measurements, and ii) the accurate measurement of sediment transport rate is extremely difficult. In the case of applying these formula to the sediment transport in the fields, further difficulties such as how to take into account the effect of irregularities in wave heights, periods and directional spreading of incident waves arise.

On the other hand, a wave transformation including wave breaking in the shallow water region is a

---

<sup>1</sup> Assistant Professor, Dept. of Environmental Eng., Pusan Univ., Changjun-dong, Kumjeoung-ku, Pusan, 609-735, Korea

<sup>2</sup> Assistant Professor, Dept. of Civil Eng., Osaka Univ., 2-1 Yamadaoka, Suita City, Osaka 565, Japan

non-linear and discontinuous phenomenon. Therefore, a so-called individual wave analysis (or a wave-by-wave analysis) rather than spectral approach seems to be adequate to investigate the wave transformation in such regions.

In this study, a joint distribution of wave height, period and direction of zero-down crossing waves which is required in the individual wave analysis in the shallow water region is derived theoretically. The applicability of the derived joint distribution, which is hereafter referred to as H-T- $\theta$  joint distribution, to the shallow water waves in the fields is examined through field observations.

## II. Derivation of H-T- $\theta$ Joint Distribution

---

### 2.1 Expression of Waves in Three-dimensional Random Seas

In a deep water region where a dispersive property of wave is strong, three-dimensional random seas waves are expressed by a directional spectrum. A transformation of irregular waves is also analyzed as the transformation of directional spectrum. While wave transformations in the shallow water region, where a significant sediment transport takes place, are usually investigated by applying the individual wave analysis (or the wave-by-wave analysis) of zero-down(or up)-crossing waves due to the non-linearity and discontinuity caused by wave breaking. The applicability of this approach has already been verified through experiments in two-dimensional wave tanks (for example, Mase et al., 1982).

The authors aim at applying the individual wave analysis to the three-dimensional random sea waves in shallow water with directional spreading. To do so, the joint distribution of wave height, period and direction of individual zero-down(or up)crossing waves has to be given.

Theoretical investigations on the joint probability density functions of H-T and H- $\theta$  have been conducting assuming that the band width of the frequency spectra of surface displacement  $\eta(t)$  is sufficiently narrow so that  $\eta(t)$  can be expressed by the envelope function. In this paper, referring to these results, the joint distribution of H-T- $\theta$  is derived from envelope functions of surface displacements  $\eta(t)$ , bi-directional water particle velocities  $u(t)$ ,  $v(t)$  and time derivatives of surface displacements  $\dot{\eta}(t)$ .

The surface displacement in three-dimensional



random sea is usually expressed by the sum of an infinite number of sine-waves of amplitudes  $a_{ij}$  and periods  $T_i$ , each of which has different wave direction  $\theta_j$ , in the following form :

$$\eta(t) = \sum_{i=1}^{\infty} \sum_{j=1}^{\infty} a_{ij} \cos \phi_{ij} \quad (1)$$

$$\phi_{ij} = k_i(x \cos \theta_j + y \sin \theta_j) - 2\pi f_i t - \varepsilon_{ij} \quad (2)$$

where  $k_i$  are the wave numbers and  $f_i$  are the frequencies, both of which correspond to the periods  $T_i$ ,  $\theta_j$  are the wave directions and  $\varepsilon_{ij}$  represent the phase differences of the waves whose amplitudes are  $a_{ij}$ . A coordinate system used in this study is shown in Fig.1 .

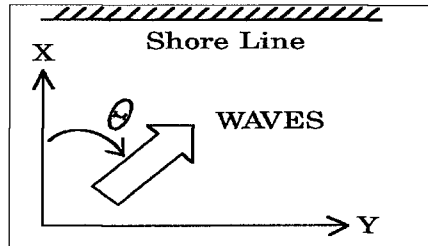


Fig. 1 Coordinate system

In the same way, water particle velocities in x- and y-directions  $u(t)$ ,  $v(t)$  are expressed as follows :

$$u(t) = \sum_{i=1}^{\infty} \sum_{j=1}^{\infty} b_i \cos \theta_j a_{ij} \cos \phi_{ij} \quad (3)$$

$$v(t) = \sum_{i=1}^{\infty} \sum_{j=1}^{\infty} b_i \sin \theta_j a_{ij} \cos \phi_{ij} \quad (4)$$

$$b_i = 2\pi f_i \frac{\cosh k_i z}{\sinh k_i h} \quad (5)$$

where,  $z$  is the height from the bottom where water particle velocities were measured..

Besides these three time series, a time derivative of the surface elevation  $\dot{\eta}(t)$  which is expressed by Eq.(6) is required to obtain the H-T- $\theta$  joint distribution.

$$\dot{\eta}(t) = \sum_{i=1}^{\infty} \sum_{j=1}^{\infty} 2\pi f_i a_{ij} \sin \phi_{ij} \quad (6)$$

## 2.2 Envelope Functions

To express envelopes of time series of the quantities given by Eqs.(1), (3), (4) and (6), the phase function given by Eq.(2) is rewritten by using a representative frequency  $\bar{f}$  as,

$$\dot{\phi}_{ij} = k_i(x \cos \theta_j + y \sin \theta_j) - 2\pi(f_i - \bar{f})t - \varepsilon_{ij} \quad (7)$$

Substituting Eq.(7) into Eqs.(1), (3), (4) and (6), the following envelope functions of time series of  $\eta(t)$ ,  $u(t)$ ,  $v(t)$  and  $\dot{\eta}(t)$  are obtained :

$$\begin{aligned} \eta(t) &= \eta_c(t) \cos 2\pi \bar{f} t + \eta_s(t) \sin 2\pi \bar{f} t \\ \dot{\eta}(t) &= \dot{\eta}_c(t) \cos 2\pi \bar{f} t + \dot{\eta}_s(t) \sin 2\pi \bar{f} t \\ u(t) &= u_c(t) \cos 2\pi \bar{f} t + u_s(t) \sin 2\pi \bar{f} t \\ v(t) &= v_c(t) \cos 2\pi \bar{f} t + v_s(t) \sin 2\pi \bar{f} t \end{aligned} \quad (8)$$

where,

$$\begin{aligned} \eta_c(t) &= \sum_{i=1}^{\infty} \sum_{j=1}^{\infty} a_{ij} \cos \dot{\phi}_{ij} \\ \eta_s(t) &= \sum_{i=1}^{\infty} \sum_{j=1}^{\infty} a_{ij} \sin \dot{\phi}_{ij} \\ \dot{\eta}_c(t) &= \sum_{i=1}^{\infty} \sum_{j=1}^{\infty} 2\pi(f_i - \bar{f}) a_{ij} \sin \dot{\phi}_{ij} \\ \dot{\eta}_s(t) &= \sum_{i=1}^{\infty} \sum_{j=1}^{\infty} 2\pi(f_i - \bar{f}) a_{ij} \cos \dot{\phi}_{ij} \\ u_c(t) &= \sum_{i=1}^{\infty} \sum_{j=1}^{\infty} b_i \cos \theta_j a_{ij} \cos \dot{\phi}_{ij} \\ u_s(t) &= \sum_{i=1}^{\infty} \sum_{j=1}^{\infty} b_i \cos \theta_j a_{ij} \sin \dot{\phi}_{ij} \\ v_c(t) &= \sum_{i=1}^{\infty} \sum_{j=1}^{\infty} b_i \sin \theta_j a_{ij} \cos \dot{\phi}_{ij} \\ v_s(t) &= \sum_{i=1}^{\infty} \sum_{j=1}^{\infty} b_i \sin \theta_j a_{ij} \sin \dot{\phi}_{ij} \end{aligned} \quad (9)$$

The amplitude of each carrier wave and the phase relation between carrier waves and water particle velocities are determined by these envelope functions.

### 2.3 Joint Probability Density Function of Envelope Amplitudes

As can be understood from Eq.(8), these eight envelope amplitudes are stationary Gaussian stochastic processes with zero mean by virtue of the central limit theorem. Therefore, the probability density function for eight envelope amplitudes is expressed as :

$$\begin{aligned}
 P(\eta_c, \eta_s, u_c, u_s, v_c, v_s, \dot{\eta}_c, \dot{\eta}_s) &= \frac{1}{(2\pi)^4 [M]^{1/2}} \text{EXP} \left[ -\frac{1}{2} \sum_{i=1}^8 \sum_{j=1}^8 \frac{M_{ij}}{[M]} \zeta_i \zeta_j \right] \\
 &= \frac{1}{(2\pi)^4 (m_{00} m_{02} m_{20} m_{22})} * \text{EXP} \left[ -\frac{1}{2 * \Delta} * \left\{ A_{11} \left( \frac{\eta_c^2 + \eta_s^2}{m_{00}} \right) \right. \right. \\
 &\quad + A_{22} \left( \frac{u_c^2 + u_s^2}{m_{20}} \right) + A_{44} \left( \frac{\eta_c^2 + \eta_s^2}{m_{22}} \right) + A_{33} \left( \frac{v_c^2 + v_s^2}{m_{02}} \right) + \\
 &\quad 2A_{12} \left( \frac{\eta_c u_c + \eta_s u_s}{\sqrt{m_{00} m_{20}}} \right) + 2A_{13} \left( \frac{\eta_c v_c + \eta_s v_s}{\sqrt{m_{00} m_{02}}} \right) + 2A_{23} \left( \frac{u_c v_c + u_s v_s}{\sqrt{m_{02} m_{20}}} \right) + \\
 &\quad \left. \left. 2A_{14} \left( \frac{\eta_c \dot{\eta}_s + \dot{\eta}_c \eta_s}{\sqrt{m_{00} m_{22}}} \right) + 2A_{24} \left( \frac{u_c \dot{\eta}_s - u_s \dot{\eta}_c}{\sqrt{m_{22} m_{20}}} \right) + 2A_{34} \left( \frac{v_c \dot{\eta}_s - v_s \dot{\eta}_c}{\sqrt{m_{22} m_{02}}} \right) \right\} \right]
 \end{aligned} \tag{10}$$

where,

$$[M] = \begin{pmatrix} M_0 & 0 \\ 0 & M_0' \end{pmatrix}, \quad M_0 = \begin{pmatrix} m_{00} & m_{10} & m_{01} & 0 \\ m_{10} & m_{20} & m_{11} & m_{12} \\ m_{01} & m_{11} & m_{02} & m_{21} \\ 0 & m_{12} & m_{21} & m_{22} \end{pmatrix},$$

$$M_0' = \begin{pmatrix} m_{00} & m_{10} & m_{01} & 0 \\ m_{10} & m_{20} & m_{11} & -m_{12} \\ m_{01} & m_{11} & m_{02} & -m_{21} \\ 0 & -m_{12} & -m_{21} & m_{22} \end{pmatrix}$$

is the determinant of covariance matrix whose elements  $\langle \zeta_i, \zeta_j \rangle$  are defined as :

$$\begin{aligned}
 \langle \eta_c \eta_c \rangle &= \langle \eta_s \eta_s \rangle = \langle \eta^2 \rangle = m_{00}, \quad \langle \eta_c v_c \rangle = \langle \eta_s v_s \rangle = \langle \eta v \rangle = m_{01} \\
 \langle u_c u_c \rangle &= \langle u_s u_s \rangle = \langle u^2 \rangle = m_{20}, \quad \langle u_c v_c \rangle = \langle u_s v_s \rangle = \langle uv \rangle = m_{11}
 \end{aligned} \tag{11}$$

$$\begin{aligned}
 \langle v_c v_c \rangle &= \langle v_s v_s \rangle = \langle v^2 \rangle = m_{02}, \quad \langle \dot{\eta}_c \dot{\eta}_c \rangle = \langle \dot{\eta}_s \dot{\eta}_s \rangle = \langle \dot{\eta}^2 \rangle = m_{22} \\
 \langle \eta_c u_c \rangle &= \langle \eta_s u_s \rangle = \langle \eta u \rangle = m_{10}, \quad \langle u_c \dot{\eta}_s \rangle = -\langle u_s \dot{\eta}_c \rangle = m_{12} \\
 \langle v_c \dot{\eta}_s \rangle &= -\langle v_s \dot{\eta}_c \rangle = m_{21}
 \end{aligned}
 \tag{11}$$

$M_{ij}$  is the co-factor of  $\langle \zeta_i, \zeta_j \rangle$  and

$$\begin{aligned}
 \Delta &= (1 + 2\gamma_{11}\gamma_{12}\gamma_{21} - \gamma_{12}^2 - \gamma_{21}^2 - \gamma_{11}^2 - \gamma_{10}^2 - 2\gamma_{01}\gamma_{10}\gamma_{12}\gamma_{21} \\
 &\quad + 2\gamma_{10}\gamma_{01}\gamma_{11} + \gamma_{10}^2\gamma_{21}^2 + \gamma_{01}^2\gamma_{12}^2 - \gamma_{01}^2) \\
 A_{11} &= (1 + 2\gamma_{11}\gamma_{12}\gamma_{21} - \gamma_{12}^2 - \gamma_{21}^2 - \gamma_{11}^2) \\
 A_{12} &= (\gamma_{21}^2\gamma_{10} + \gamma_{01}\gamma_{11} - \gamma_{10} - \gamma_{01}\gamma_{12}\gamma_{21}) \\
 A_{13} &= (\gamma_{10}\gamma_{11} + \gamma_{12}^2\gamma_{01} - \gamma_{10}\gamma_{12}\gamma_{21} - \gamma_{01}) \\
 A_{14} &= (\gamma_{10}\gamma_{12} + \gamma_{01}\gamma_{21} - \gamma_{10}\gamma_{11}\gamma_{21} - \gamma_{01}\gamma_{11}\gamma_{12}) \\
 A_{22} &= (1 - \gamma_{21}^2 - \gamma_{01}^2) \\
 A_{23} &= (\gamma_{01}\gamma_{10} + \gamma_{12}\gamma_{21} - \gamma_{11}) \\
 A_{24} &= (\gamma_{11}\gamma_{21} + \gamma_{01}^2\gamma_{12} - \gamma_{12} - \gamma_{10}\gamma_{01}\gamma_{21}) \\
 A_{33} &= (1 - \gamma_{12}^2 - \gamma_{10}^2) \\
 A_{44} &= (1 + 2\gamma_{10}\gamma_{01}\gamma_{11} - \gamma_{01}^2 - \gamma_{11}^2 - \gamma_{10}^2)
 \end{aligned}$$

where,

$$\begin{aligned}
 \gamma_{10} &= m_{10}/\sqrt{m_{00}m_{20}}, \quad \gamma_{01} = m_{01}/\sqrt{m_{00}m_{02}}, \quad \gamma_{11} = m_{11}/\sqrt{m_{20}m_{02}} \\
 \gamma_{12} &= m_{12}/\sqrt{m_{20}m_{22}}, \quad \gamma_{21} = m_{21}/\sqrt{m_{02}m_{22}},
 \end{aligned}
 \tag{12}$$

Among these nine covariances from  $m_{00}$  to  $m_{21}$  of preceding description, seven covariance except for  $m_{12}$  and  $m_{21}$  can be directly calculated from the time series of surface elevation  $\eta(t)$  and horizontal water particle velocities  $u(t)$  and  $v(t)$ . While,  $m_{12}$  and  $m_{21}$  can be calculated from the directional spectra  $s(f, \theta)$  as :

$$\begin{aligned}
 m_{12} &= - \int_0^\infty \int_{-\pi}^\pi 2\pi b(f)(f - \bar{f}) \cos \theta s(f, \theta) d\theta df \\
 m_{21} &= - \int_0^\infty \int_{-\pi}^\pi 2\pi b(f)(f - \bar{f}) \sin \theta s(f, \theta) d\theta df
 \end{aligned}
 \tag{13}$$

## 2.4 Joint Probability Density Function of Wave Height , Period and Direction

To derive the joint probability density function for wave height, period and direction, the following series of variable transformation are carried out :

- 1) Normalization of the envelope functions.

$$\begin{aligned} N_c &= \eta_c / \sqrt{m_{00}}, N_s = \eta_s / \sqrt{m_{00}}, V_c = v_c / \sqrt{m_{02}}, V_s = v_s / \sqrt{m_{02}}, \\ U_c &= u_c / \sqrt{m_{20}}, U_s = u_s / \sqrt{m_{20}}, \dot{N}_c = \dot{\eta}_c / \sqrt{m_{22}}, \dot{N}_s = \dot{\eta}_s / \sqrt{m_{22}}, \end{aligned} \quad (14)$$

- 2) Introduction of the amplitude R and phase angle  $\delta$  of carrier waves.

$$N_c = R \cos \delta, \quad N_s = R \sin \delta \quad (15)$$

$$\dot{N}_c = \dot{R} \cos \delta - R \dot{\delta} \sin \delta, \quad \dot{N}_s = \dot{R} \sin \delta + R \dot{\delta} \cos \delta$$

$$\text{where, } R^2 = N_c^2 + N_s^2, \quad \delta = \tan^{-1}(N_s / N_c) \quad (16)$$

- 3) Transformation of the phase angle of water particle velocities so that the phase of the surface displacement becomes a standard and introduction of the polar coordinate system after defining the wave direction of each wave  $\theta$  (after Isobe, 1987).

$$\begin{aligned} U_c &= u_p \cos \delta - u_q \sin \delta, & U_s &= u_p \sin \delta + u_q \cos \delta \\ V_c &= v_p \cos \delta - v_q \sin \delta, & V_s &= v_p \sin \delta + v_q \cos \delta \end{aligned} \quad (17)$$

$$\begin{aligned} \theta &= \tan^{-1}(v_p / u_p) \\ u_p &= W \cos \theta, & v_p &= W / \Gamma \sin \theta \end{aligned} \quad (18)$$

After conducting these transformation of variables of Eq.(10), the following joint probability density function for R,  $\delta$  and  $\theta$  is obtained by integrating with respect to  $u_q, v_q, \dot{R}, \dot{\delta}$  and W which have nothing to do with H-T- $\theta$  joint distribution :

$$\begin{aligned} P(R, \theta, \delta) &= \frac{1}{2\pi^{3/2} * \Gamma} * R^2 * \text{EXP} \left[ \frac{R^2}{2A} * (A_{11} + A_{44} \delta^2 + 2A_{14} \delta) \right] * \\ &\quad \left[ \frac{\sqrt{A}}{A} + \frac{RB}{A^{3/2}} * \frac{\sqrt{\pi}}{\sqrt{2}} * \text{EXP} \left\{ \frac{R^2 B^2}{2AA} \right\} * \left( 1 - \text{Pr} \left( -\frac{RB}{\sqrt{AA}} \right) \right) \right] \end{aligned} \quad (19)$$

where,  $\Gamma = \sqrt{m_{02} / m_{20}}$  is a longcrestedness parameter and

$$\begin{aligned} \text{Pr}(\xi) &= \frac{1}{\sqrt{2\pi}} * \int_{-\infty}^{\xi} \exp\left(-\frac{t^2}{2}\right) dt \\ A &= (A_{22} \cos^2 \theta + A_{33} \sin^2 \theta / \Gamma^2 + 2A_{23} \cos \theta \sin \theta / \Gamma) \\ B &= -(A_{12} \cos \theta + A_{13} \sin \theta / \Gamma + A_{24} \delta \cos \theta + A_{34} \delta \sin \theta / \Gamma) \end{aligned}$$

When the spectral bandwidth is sufficiently narrow,  $R$  and  $\delta$  in Eq.(19) can be related to the wave height  $\bar{H}$  and the period  $\bar{T}$  (Longuet - Higgins, 1975) as :

$$R = H/2, \quad \delta = 2\pi(\bar{f} - f) = 2\pi(1/\bar{T} - 1/T) \quad (20)$$

By using these relations together with the zero-th and first special moments  $m_0$  and  $m_1$ , wave heights and periods are normalized as follows :

$$\begin{aligned} \tau &= T/\bar{T} = 2\pi / (2\pi\bar{f} - \delta) * m_1 / m_0 \\ x &= H/\bar{H} = 2R / (2\pi m_0)^{1/2} \end{aligned} \quad (21)$$

Substituting, Eq.(21) into Eq.(19), the following joint probability density function for wave heights( $x$ ), period ( $\tau$ ) and direction ( $\theta$ ) is obtained :

$$\begin{aligned} P(x, \tau, \theta) &= \frac{x^2 * \bar{\sigma}}{2^3 * \Gamma * \tau^2} * \text{EXP} \left[ -\frac{\pi}{4A} * x^2 (A_{11} + A_{44} \bar{\sigma}^2 (1 - 1/\tau)^2 \right. \\ &\quad \left. + 2A_{14} \bar{\sigma} (1 - 1/\tau)) \right] * \left[ \frac{\sqrt{A}}{A} + \frac{B'}{A^{3/2}} * \frac{\sqrt{\pi}}{\sqrt{2}} * x * \frac{\sqrt{\pi}}{\sqrt{2}} \right. \\ &\quad \left. \text{EXP} \left\{ \frac{B'^2 \pi}{4AA} x^2 \right\} * \left\{ 1 - \text{Pr} \left( -B' \frac{\sqrt{\pi}}{\sqrt{2AA}} x \right) \right\} \right] \end{aligned} \quad (22)$$

where,  $\bar{\sigma} = 2\pi m_1 m_0$  and

$$\begin{aligned} B' &= -\{A_{12} \cos \theta + A_{13} \sin \theta / \Gamma + A_{24} \bar{\sigma} (1 - 1/\tau) \cos \theta \\ &\quad + A_{34} \bar{\sigma} (1 - 1/\tau) \sin \theta / \Gamma\} \end{aligned}$$

Akai et al.(1988) also derived the joint distribution of wave height, frequency and direction. They omitted cross correlation term( $\gamma_{21}$ ) for influence of the asymmetrical property of directional spreading, but in our derivation, all correlation are taken into account.

### III. H-T- $\theta$ Joint Distribution of Measured Waves in Shallow Water

#### 3.1 Field Observation

Field observation were carried out at two coasts to verify the proposed joint probability density function for wave height, period and direction under the condition of wind waves in a winter. One observation site was the Keinomatsubara Beach located in the west coast of the Awaji Island and the other was the Nishikinohama Beach on the southern part of OSAKA Bay. These locations are shown in Fig. 2.

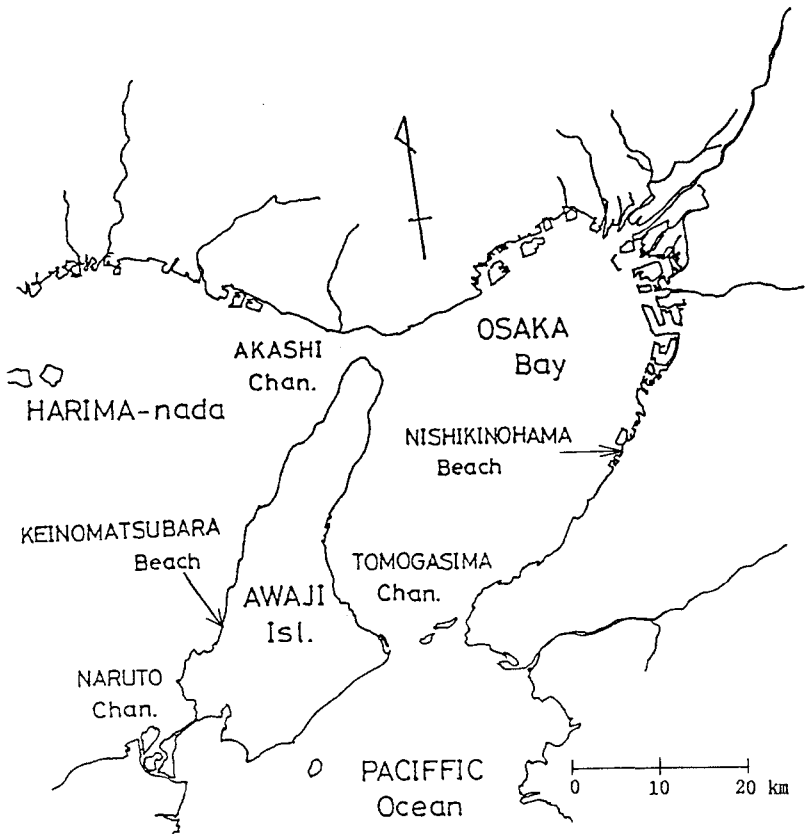


Fig. 2 Location of observation sites

Wave heights were measured by capacitance type wave gages. Longshore and cross-shore water particle velocities were measured by bi-directional electromagnetic current meters at the same place of wave gauges and about 25cm above the bottom to consist a so-called 3-element array. Analogue data from these installments were first recorded by an analogue data recorder and then digitized by an A-D converter at a sampling time of 0.1sec for the data processing. Very small waves whose frequencies were greater than  $4 \cdot f_p$  ( $f_p$  : peak frequency) were disregarded in the data processing.

### 3.2 Characteristics of Measured Waves

Before discuss the joint distribution, characteristics of measured waves are examined briefly. Table 1 shows the statistical characteristics obtained from the time series in which more than 500 waves were recorded at the two coasts. In the following analysis, the x-axis is rotated to be the principle direction of incident waves.

Table 1 Statistical characteristics of measured waves

Case No.	Dep. (cm)	$r_{10}$	$r_{01}$	$r_{11}$	$r_{12}$	$r_{21}$	$\gamma$	$U_r$	Ku-rt.	Skew.	$Q_p$
1-1	82	0.806	0.103	-0.004	0.042	0.204	0.305	21.4	3.19	0.162	2.37
1-2	48	0.827	0.101	-0.021	0.148	0.717	0.257	30.7	3.14	0.193	1.84
1-3	97	0.821	0.037	-0.015	0.003	0.412	0.301	6.0	3.27	0.048	2.04
1-4	115	0.819	0.103	-0.020	0.051	0.632	0.392	2.6	2.94	0.023	2.32
1-5	121	0.693	0.161	-0.020	0.019	0.163	0.317	4.6	3.36	0.052	1.90
1-6	134	0.783	0.125	-0.012	0.066	0.680	0.355	4.3	3.07	0.033	1.89
1-7	67	0.596	0.142	-0.022	-0.020	0.656	0.296	24.7	2.71	-0.251	2.72
1-8	113	0.808	0.115	-0.009	-0.291	-0.009	0.299	9.4	2.95	0.016	2.22
2-1	80	0.933	0.026	-0.003	-0.000	0.649	0.307	66.6	3.32	0.144	3.46
2-2	1320	0.906	-0.006	0.000	0.276	0.433	0.431	10.0	2.99	0.107	2.39

Results of Case-number from 1-1 to 1-6 and Case-number from 2-1 to 2-2 correspond to the data obtained at Nishikinohama Beach and Keinomatsubara Beach, respectively.  $r_{ij}$  in the table is the covariance defined by Eqs. (11) and (12),  $\gamma$  is the longcrestedness parameter,  $\nu$



is the band width parameter and  $Q_p$  is the peakedness parameter. Ursell number  $U_r$  is calculated by using the significant wave height and the period. The integration of the directional spectrum, which was estimated by EMLM(Isobe et al., 1984), was carried out between  $0.5 f_p$  and  $3 f_p$  to obtain  $m_{12}$  and  $m_{21}$ .

It is found from Table 1 that a large part of measured waves has a significant non-linear property ( $U_r = 2.6-66.6$ , Kurtosis = 2.939-3.266, skewness = -0.251-0.193) and had a wide directional spreading ( $\gamma = 0.2565-0.4306$ ). The value of  $r_{21}$  which represents asymmetrical property of directional spreading of incident waves is relatively large when compared with other covariances in the table. However, any correlation between parameters of directional spreading of incident waves ( $r_{10}$  and  $\gamma$ ) and those of asymmetry of directional spreading ( $r_{12}$  and  $r_{01}$ ) can not be seen.

### 3.3 Joint Distribution of Wave Height, Period and Direction

In this paper, Case 2-1 whose significant wave height and  $r_{21}$  are relatively large and more than 1000 waves were recorded is analyzed as an example to examine the applicability of theoretical joint distribution for  $H$ ,  $T$  and  $\theta$  derived in this study.

Figure 3 (a)~(c) shows nondimensional scatter diagram of wave period ( $T/\bar{T}$ ) and direction ( $\theta$ ) of measured 1000 waves (Case 2-1) under the condition of wave height shown in the figure. The class bands of nondimensional wave heights and directions are 0.25 and  $22.5^\circ$ , respectively. Numerals in the figure show the frequency of zero-down crossing waves. In the figure, predicted isolines of frequency obtained from multiplying the integrated probability density (Eq.(21) between the range of wave height shown in the figure by the total number of measured waves (1000) are also illustrated by solid lines.

Figure 4 is the joint distribution of non-dimensional wave height and directions under the conditions of  $0.25 < T/\bar{T} < 0.75$  (Fig(a)),  $0.75 < T/\bar{T} < 1.25$  (Fig(b)) and  $1.25 < T/\bar{T} < 1.75$  (Fig(c)). Solid lines in the figures are the predicted isolines of frequency calculated in the same way as those in Fig.3.

In Fig. 3, the predicted isolines exhibit almost symmetric profile with respect to the direction when

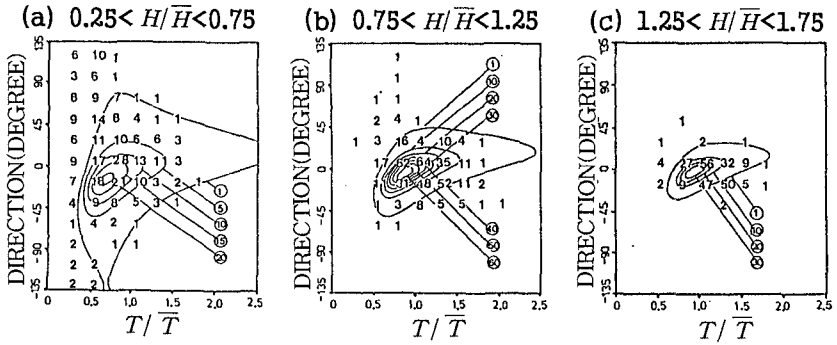


Figure 3 Joint distribution of wave directions and periods

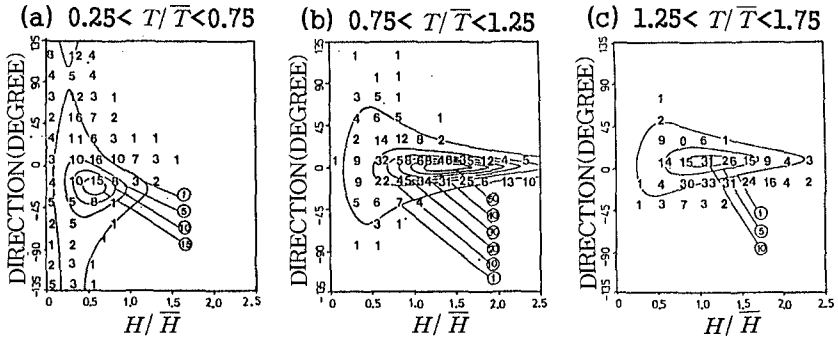


Figure 4 Joint distribution of wave directions and heights

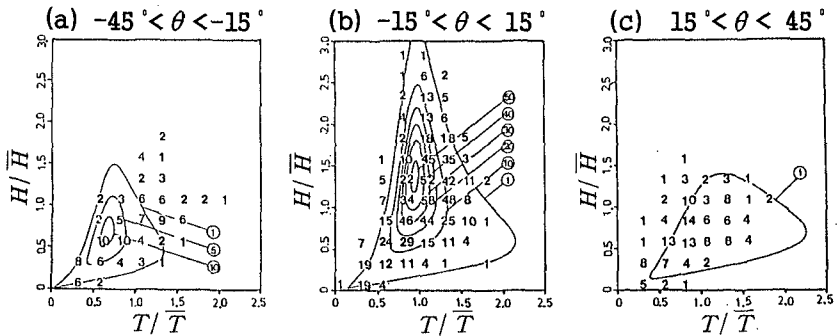


Figure 5 Joint distribution of wave heights and periods

$T/\bar{T} < 0.75$ . On the other hand, the predicted isolines in Fig.4 show asymmetry around the principle direction ( $\theta = 0.0^\circ$ ), ie, wave periods distribute asymmetrically around the principle direction. This difference is partly explained by the fact that wave refraction does not depend deeply on wave heights but mainly on wave periods. It is also found from Figs. 3 and 4 that the predicted isolines do not coincide well with the measured frequency in the region where  $T/\bar{T} < 0.5$  or  $H/\bar{H} < 0.5$  or  $|\theta| > 45^\circ$ . However, in the region of  $H/\bar{H} > 0.75$ ,  $T/\bar{T} > 0.75$  and  $|\theta| < 15^\circ$ , where a large part of measured waves is included, a relatively good agreement is seen.

Figure 5 is a scatter diagram of non-dimensional wave heights and periods under the conditions of  $-45^\circ < \theta < -15^\circ$  (Fig(a)),  $-15^\circ < \theta < 15^\circ$  (Fig (b)) and  $15^\circ < \theta < 45^\circ$  (Fig(c)). Solid lines in the figures are the isolines of frequency calculated in the same way as the former two figures. In the region of  $-15^\circ < \theta < 15^\circ$ , which is shown in Fig.(b), the predicted isolines coincide well with the measured frequency indicating the tail toward the origin in the regions of  $T/\bar{T} < 0.75$  and  $H/\bar{H} < 0.75$  due to the correlation between the wave heights and periods. The correlation coefficient between wave heights and periods of Case 2-1 is 0.57.

Although the tail can be seen in Figs.(a) and (c), the agreement between the predicted and measured frequency is not good in these regions. It is also found that the joint distribution of wave heights and periods is not symmetrical with respect to the wave direction by comparing Figs.(a) and (c).

#### IV. CONCLUSIONS

Summing up the results of the study described above, the followings are the major conclusions:

- (1) The joint propability density function of wave height, period and direction is derived by using time series of surface displacement  $\eta(t)$ , its time derive  $\dot{\eta}(t)$ , and horizontal two component water particle velocities  $u(t)$ ,  $v(t)$  assuming that  $\eta(t)$  is a Gaussian process with a narrow band power spectra. It is found that the marginal joint distribution of wave heights and direction has less influence of the asymmetrical property of directional spreading (directional spectra) than that of wave period and direction.
- (2) The derived joint distribution are compared with the measured joint distribution in the field of shallow

water. In the region where the appearance frequency of waves is high (ie.  $T/\bar{T} > 0.75$  ,  $H/\bar{H} > 0.75$  ,  $|\theta| < 15^\circ$  ) , a relatively high agreement is obtained between measured and predicted frequencies. Especially, the marginal distribution of wave heights and periods in the region of  $|\theta| < 15^\circ$  , the predicted frequency coincides fairly well with the measured one. However, in the region of low appearance frequency, both of them do not agree well with each other.

The measured waves had a strong asymmetric property of directional spreading with respect to the principle direction. They also exhibited wide directional spreading and a little nonlinearity.

### References

- Akai, S., et al., (1988), Joint distribution of wave height, frequency and direction in multi-directional wave fields, Proc. Japanese Conf. on Coastal Engineering, pp. 142~147, in Japanese.
- Isobe, M., K. Kondo and K. Horikawa, (1984), Extension of MLM for estimating directional wave spectrum, Proc. Sympo. on Dispersion and Modeling of Directional Seas, Paper No. A-6, 15p.
- Isobe, M., (1988), On the joint distribution of wave heights and directions, Proc. 21st Conf. on Coastal Eng., pp. 524~538.
- Longuet-Higgins, M. S., (1975), On the joint distribution of the periods and amplitudes of sea waves, Jour. Geophysical Res. Vol. 80, No. 18, pp. 2688~2694.
- Mase, H. and Y. Iwagaki, (1982), Wave heights distribution and wave grouping in surf zone, Proc. 18th Conf. on Coastal Eng., pp. 58~76.

## CHAPTER 29

# Spectral Wave-Current Bottom Boundary Layer Flows

Ole Secher Madsen<sup>1</sup>

### Abstract

Based on the linearized governing equations, a bottom roughness specified by the equivalent Nikuradse sand grain roughness,  $k_N$ , and a time-invariant eddy viscosity analogous to that of Grant and Madsen (1979 and 1986) the solution is obtained for combined wave-current turbulent bottom boundary layer flows with the wave motion specified by its near-bottom orbital velocity directional spectrum. The solution depends on an *a priori* unknown shear velocity,  $u_{*r}$ , used to scale the eddy viscosity inside the wave boundary layer. Closure is achieved by requiring the spectral wave-current model to reduce to the Grant-Madsen model in the limit of simple periodic plane waves. To facilitate application of the spectral wave-current model it is used to define the characteristics (near-bottom orbital velocity amplitude,  $u_{br}$ , radian frequency,  $\omega_r$ , and direction of propagation,  $\phi_{wr}$ ) of a representative periodic wave which, in the context of combined wave-current bottom boundary layer flows, is equivalent to the wave specified by its directional spectrum. Pertinent formulas needed for application of the model are derived and their use is illustrated by outlining efficient computational procedures for the solution of wave-current interaction for typical specifications of the current.

### Introduction

Over the past couple of decades several theoretical models for turbulent bottom boundary layers associated with combined wave-current flows have been proposed. In view of the vastly different levels of sophistication with which these different models represent turbulence, their end result, most

---

<sup>1</sup> R.M. Parsons Laboratory, Massachusetts Institute of Technology, Cambridge, MA 02139 USA

notably their predicted effect of the presence of waves on the current, is surprisingly similar. Thus, in the absence of solid experimental evidence as to which of the many models is truly *the* best, choosing a particular model for applications becomes a matter of personal preference and convenience. However, since all existing wave-current interaction models have been derived for a wave motion corresponding to a simple periodic plane progressive wave, one additional choice – the choice of simple periodic wave characteristics to represent a wave motion which more realistically is described by its directional spectrum – must be made prior to model applications.

The objective of this study is therefore to derive a simple theoretical model for turbulent wave-current bottom boundary layer flows for a wave motion described by its directional spectrum and to use this model to determine the characteristics of the periodic wave which, in the context of wave-current interaction, is equivalent to the directional sea.

Theoretical Model

The theoretical model for spectral wave-current boundary layer flows is based on the linearized boundary layer equation which, in standard notation, reads

$$\frac{\partial \mathbf{u}}{\partial t} = -\frac{1}{\rho} \frac{\partial p}{\partial x_i} + \frac{\partial}{\partial z} \left[ \nu_t \frac{\partial \mathbf{u}}{\partial z} \right] \tag{1}$$

in which the turbulent eddy viscosity,  $\nu_t$ , is assumed to be scaled by an *a priori* unknown shear velocity,  $u_{*r}$ , which inside the wave boundary layer,  $z < \delta_{wc}$ , reflects the combined wave-current flow and outside the wave boundary layer is a function of only the average, *i.e.* the current, shear velocity,  $u_{*c}$ . To keep the analysis relatively simple and because the universally made *assumption* of a *single* roughness scale, the equivalent Nikuradse sand grain roughness,  $k_N$ , for currents and waves alone as well as for combined wave-current flows has been experimentally validated (Mathisen and Madsen, 1993) only for this model, we adopt the Grant-Madsen (1979 and 1986) eddy viscosity

$$\nu_t = \begin{cases} \kappa u_{*r} z & \text{for } z < \delta_{wc} \\ \kappa u_{*c} z & \text{for } z > \delta_{wc} \end{cases} \tag{2}$$

Assuming  $u_{*r}$  and therefore  $\nu_t$  to be time-invariant, resolving velocity and pressure into their mean and time-varying components, *i.e.*

$$\mathbf{u} = \bar{\mathbf{u}} + \tilde{\mathbf{u}} = \mathbf{u}_c + \mathbf{u}_w \quad ; \quad p = \bar{p} + \tilde{p} = \bar{p} + \tilde{p}_b \tag{3}$$

and introducing these expressions in the governing equation, two separate equations are obtained. One for the wave motion

$$\frac{\partial(\mathbf{u}_w - \mathbf{u}_b)}{\partial t} = \frac{\partial}{\partial z} \left[ \nu_t \frac{\partial(\mathbf{u}_w - \mathbf{u}_b)}{\partial z} \right] \quad (4)$$

in which the relationship between  $\tilde{p}_b$  and the near-bottom velocity  $\mathbf{u}_b$ , predicted by potential theory, has been invoked; and another equation for the current

$$\nu_t \frac{\partial \mathbf{u}_c}{\partial z} = \tau_c / \rho = u_{*c}^2 \{ \cos \phi_c, \sin \phi_c \} \quad (5)$$

in which the law-of-the-wall arguments have been used, and  $\phi_c$  denotes the current angle with the x-axis.

### Wave Solution

For the wave solution only the eddy viscosity formulation assumed for  $z < \delta_{wc}$  is pertinent. Hence, the wave portion of the wave-current problem is completely analogous to the pure wave boundary layer problem discussed and solved by Madsen *et al.* (1988) for a wave motion described by its directional spectrum, *i.e.* the solution to (4) may be written as a sum of wave components, each being the real part of

$$\mathbf{u}_{wnm} = \left[ 1 - \frac{\ker 2\sqrt{\zeta_n} + i\text{kei} 2\sqrt{\zeta_n}}{\ker 2\sqrt{\zeta_{no}} + i\text{kei} 2\sqrt{\zeta_{no}}} \right] \mathbf{u}_{bnm} e^{i\omega_n t} \quad (6)$$

in which the velocity is related to the directional near-bottom orbital velocity spectrum,  $S_{u_b}(\omega, \theta)$ , through,

$$\mathbf{u}_{bnm} = \sqrt{2S_{u_b}(\omega_n, \theta_m) d\theta d\omega} \{ \cos \theta_m, \sin \theta_m \} \quad (7)$$

ker and kei denote the zeroth order Kelvin functions and

$$\zeta_n = z\omega_n / (ku_{*r}) \quad (8)$$

with  $\zeta_{no}$  denoting the value of  $\zeta_n$  at  $z = z_o = k_N/30$  where  $k_N$  is the equivalent Nikuradse sand grain roughness of the bottom.

### Current Solution

The solution for the current, obtained from (5) and (2), is for  $z < \delta_{wc}$

$$\mathbf{u}_c = \frac{u_{*c}u_{*c}}{u_{*r}\kappa} \ell n \frac{z}{z_o} \{\cos \phi_c, \sin \phi_c\} \tag{9}$$

and for  $z > \delta_{wc}$

$$\mathbf{u}_c = \frac{u_{*c}}{\kappa} \ell n \frac{z}{z_{oa}} \{\cos \phi_c, \sin \phi_c\} \tag{10}$$

in which  $z_{oa}$  – the apparent bottom roughness experienced by the current in presence of waves – is obtained by matching the current velocities at  $z = \delta_{wc}$ , *i.e.*

$$\ell n \frac{\delta_{wc}}{z_{oa}} = \frac{u_{*c}}{u_{*r}} \ell n \frac{\delta_{wc}}{z_o} \tag{11}$$

Closure

In the preceding analysis we have formally obtained the solution for the near-bottom turbulent flow associated with a wave motion described by its directional frequency spectrum and a superimposed steady current. However, the solution can be evaluated only when the value of the representative wave-current shear velocity,  $u_{*r}$ , is known. To determine this unknown, *i.e.* to close the problem, we obtain the bottom shear stress for each wave component from

$$\begin{aligned} \tau_{wnm} &= \rho \kappa u_{*r} z \left. \frac{\partial \mathbf{u}_{wnm}}{\partial z} \right|_{z=z_o} = \\ &= \rho \kappa u_{*r} \sqrt{\zeta_n} \left. \frac{\partial \mathbf{u}_{wnm}}{\partial (2\sqrt{\zeta_n})} \right|_{\zeta_n=\zeta_{no}} = \\ &= \rho \kappa u_{*r} \sqrt{\zeta_{no}} \frac{-\text{ker}'2\sqrt{\zeta_{no}} - i \text{kei}'2\sqrt{\zeta_{no}}}{\text{ker}2\sqrt{\zeta_{no}} + i \text{kei}2\sqrt{\zeta_{no}}} \mathbf{u}_{bnm} e^{i\omega_n t} \end{aligned} \tag{12}$$

in which “prime” denotes the derivative of the zeroth order Kelvin function with respect to its argument, and  $\mathbf{u}_{bnm}$  is given by (7).

This equation may alternatively be interpreted as an expression for the directional spectrum of the wave-associated bottom shear stress

$$S_{\tau_w}(\omega, \theta) = K^2(\omega) S_{u_b}(\omega, \theta) \tag{13}$$



$$K(\omega) = \rho \kappa u_{*r} \sqrt{\zeta_o} \left| \frac{-\ker' 2\sqrt{\zeta_o} - i \ker 2\sqrt{\zeta_o}}{\ker 2\sqrt{\zeta_o} + i \ker 2\sqrt{\zeta_o}} \right| \quad (14)$$

is a function of  $\omega$  since

$$\zeta_o = \frac{z_o \omega}{\kappa u_{*r}} = \frac{k_N \omega}{30 \kappa u_{*r}} \quad (15)$$

From (13) we may obtain the representative amplitude of the bottom shear stress of a simple harmonic wave with the same variance as the spectral representation, *i.e.* the root-mean-square amplitude,

$$\tau_{wr}^2 = 2 \iint S_{\tau_w}(\omega, \theta) d\theta d\omega = \int_0^\infty \int_0^{2\pi} K^2(\omega) [2S_{u_b}(\omega, \theta)] d\theta d\omega \quad (16)$$

with a direction given by

$$\tan \theta_{wr} = \frac{\iint S_{\tau_w}(\omega, \theta) \sin \theta d\omega d\theta}{\iint S_{\tau_w}(\omega, \theta) \cos \theta d\omega d\theta} \quad (17)$$

In principle (16) and (17) may be evaluated if the bottom roughness,  $k_N$ , and the near-bottom orbital velocity spectrum,  $S_{u_b}(\omega, \theta)$ , are known. This would lead to a representative wave-associated bottom shear stress amplitude vector

$$\tau_{wr} = \tau_{wr} \{ \cos \theta_{wr}, \sin \theta_{wr} \} \quad (18)$$

which depends on the unknown representative wave-current shear velocity,  $u_{*r}$ .

Final closure is obtained by requiring the spectral wave-current solution to reduce to that of Grant and Madsen (1986) in the limit of simple periodic waves, *i.e.*

$$u_{*r}^2 = \frac{1}{\rho} |\tau_{wr} + \tau_c| \quad (19)$$

The bottom shear stress in (12) is evaluated at  $z = z_o = k_N/30$  rather than by taking the limit  $z \rightarrow 0$ , which was used in Madsen *et al.* (1988). For small values of  $\zeta_o$  which, by (15), is seen to correspond to small values of the bottom roughness, this difference is of negligible importance. However,

for larger roughness values and hence larger values of  $\zeta_0$  this difference has important implications that will be discussed in Appendix A.

The Representative Periodic Wave

Actual application of the theoretical spectral wave-current model as presented in the preceding section would be extremely cumbersome, particularly since the evaluation of the integrals in (16) and (17) presumes  $u_{*r}$  to be known. For this reason a further simplification is achieved by introducing the concept of a representative periodic wave which, in the context of wave-current interaction, is equivalent to the spectral wave representation.

This representative periodic wave is characterized by its near-bottom orbital velocity amplitude,  $u_{br}$ , radian frequency,  $\omega_r$ , and direction of propagation,  $\phi_{wr}$ . To obtain the representative wave characteristics we start by writing (16) in the form

$$\begin{aligned} \tau_{wr}^2 &= 2 \int_0^\infty K^2(\omega) \int_0^{2\pi} S_{u_b}(\omega, \theta) d\theta d\omega = \\ &\int_0^\infty \left[ K^2(\omega_r) + \frac{\partial K^2}{\partial \omega} \Big|_{\omega=\omega_r} (\omega - \omega_r) + \dots \right] \int_0^{2\pi} 2S_{u_b}(\omega, \theta) d\theta d\omega \quad (20) \end{aligned}$$

Neglecting higher order terms in the expansion of the transfer function  $K^2(\omega)$  around  $\omega = \omega_r$ , the expression given by (20) reduces to that for a simple periodic wave

$$\tau_{wr} = \tau_{wm} = K(\omega_r)u_{br} \quad (21)$$

in which  $\tau_{wm}$  is the maximum bottom shear stress of the periodic wave with the representative wave orbital velocity amplitude given by

$$u_{br} = \sqrt{2 \iint S_{u_b}(\omega, \theta) d\omega d\theta} \quad (22)$$

and the representative wave radian frequency taken as

$$\omega_r = \frac{\iint \omega S_{u_b}(\omega, \theta) d\omega d\theta}{\iint S_{u_b}(\omega, \theta) d\omega d\theta} \quad (23)$$

Finally, the direction of propagation of the representative periodic wave may be obtained from (17) as

$$\tan \phi_{wr} = \frac{\iint S_{ub}(\omega, \theta) \sin \theta d\omega d\theta}{\iint S_{ub}(\omega, \theta) \cos \theta d\omega d\theta} \quad (24)$$

when it is assumed either that  $K(\omega)$  is sufficiently accurately represented by  $K(\omega_r)$  or that the directional spreading function for  $S_{ub}(\omega, \theta)$  is independent of radian frequency.

For completeness it is noted that the expression for  $\omega_r$ , (23), differs from that obtained by Madsen *et al.* (1988). Since Madsen *et al.* (1988) based their representative radian frequency on rather intuitive arguments whereas (23) is based on more rigorous considerations the expression given here should be considered the correct definition of  $\omega_r$ . The effects of small variations of  $\omega_r$  on the predicted wave-current interaction are, however, insignificant compared to other uncertainties so this point is made primarily to avoid confusion.

### Application of Spectral Wave-Current Model

#### Pertinent Formulas

To illustrate the application of the spectral wave-current model we assume that the current is specified and that the characteristics of the representative periodic wave are known.

We first define the angle between current direction,  $\phi_c$ , and direction of wave propagation,  $\phi_{wr}$ , as

$$\phi_{cw} = \phi_c - \phi_{wr} \quad (25)$$

With this definition, the representative shear velocity is obtained from (19) as

$$u_{*r}^2 = \frac{1}{\rho} \left| \tau_{wr} \{1, 0\} + \tau_c \{ \cos \phi_{cw}, \sin \phi_{cw} \} \right| = C_\mu u_{*wm}^2 \quad (26)$$

in which  $u_{*wm} = \sqrt{\tau_{wr}/\rho}$  is the shear velocity based on the maximum representative wave-associated shear stress,

$$C_\mu = (1 + 2\mu |\cos \phi_{cw}| + \mu^2)^{1/2} \quad (27)$$

and

$$\mu = \tau_c / \tau_{wr} = \left( \frac{u_{*c}}{u_{*wm}} \right)^2 \quad (28)$$

expresses the ratio of current and wave bottom shear stresses; a ratio which generally is much smaller than unity and therefore results in values of  $C_\mu$ , given by (27), close to unity.

To obtain the maximum wave shear stress, we introduce the wave friction factor concept in the presence of a current through the definition

$$\frac{1}{\rho}\tau_{wr} = u_{*wm}^2 = \frac{1}{2}f_{wc}u_{br}^2 \tag{29}$$

Introducing (14) and (15), with  $\omega = \omega_r$ , in (21) and using (29) with (26) to replace shear stresses and shear velocities lead to an implicit equation for the wave friction factor in the presence of a current

$$\sqrt{f_{wc}/C_\mu} = \kappa\sqrt{2\zeta_{ro}} \left| \frac{-\ker'2\sqrt{\zeta_{ro}} - i\text{kei}'2\sqrt{\zeta_{ro}}}{\ker2\sqrt{\zeta_{ro}} + i\text{kei}2\sqrt{\zeta_{ro}}} \right| \tag{30}$$

in which

$$\zeta_{ro} = \frac{k_N\omega_r}{30\kappa u_{*r}} = \frac{(k_N\omega_r)/(u_{br}C_\mu)}{(30\kappa/\sqrt{2})\sqrt{f_{wc}/C_\mu}} \tag{31}$$

Written in this form clearly brings out the feature that the wave friction factor, in the presence of a current, is a function of the relative magnitude of the current shear stress, expressed through the factor  $C_\mu$  defined by (27) and (28), and the bottom roughness,  $(C_\mu u_{br}/\omega_r)/k_N = C_\mu A_{br}/k_N$ , relative to the representative wave near-bottom orbital excursion amplitude,  $A_{br} = u_{br}/\omega_r$ , modified by the factor  $C_\mu$  to account for the presence of a current. It is particularly interesting to note that (30) and (31) reduce to the pure wave case in the absence of any current since then  $C_\mu = 1$ . Thus, (30) and (31) may be regarded as the generalized wave friction factor relationship valid both in the presence and absence of a current.

To evaluate the wave friction factor as a function of relative roughness, series expansions for zeroth order Kelvin functions and their derivatives, given in Abramowitz and Stegun (1972, Chapter 9), are used to obtain  $\sqrt{f_{wc}/C_\mu}$  from (30) with von Karman's constant  $\kappa = 0.4$  for a chosen value of  $\zeta_{ro}$ . Once  $\sqrt{f_{wc}/C_\mu}$  is obtained from (30) the corresponding relative roughness,  $C_\mu u_{br}/(\omega_r k_N)$ , is obtained from (31). The resulting relationships between wave friction factor and relative roughness is shown in Figure 1, and may be approximated by the following explicit formulas

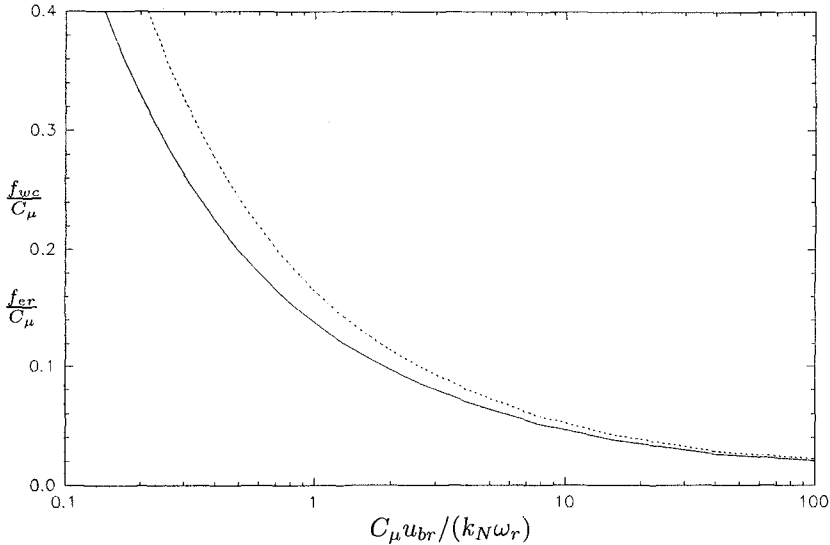


Figure 1: Generalized Friction Factor Diagram for Waves in the Presence of a Current. Wave Friction Factor,  $f_{wc}$ , (dashed line), Wave Energy Dissipation Factor,  $f_{er}$  (full line), for the Representative Periodic Wave.

$$f_{wc} = C_\mu \exp \left\{ 7.02 \left( \frac{C_\mu u_{br}}{k_N \omega_r} \right)^{-0.078} - 8.82 \right\} \quad (32)$$

$$\text{for } 0.2 < C_\mu u_{br} / (k_N \omega_r) < 10^2;$$

and

$$f_{wc} = C_\mu \exp \left\{ 5.61 \left( \frac{C_\mu u_{br}}{k_N \omega_r} \right)^{-0.109} - 7.30 \right\} \quad (33)$$

$$\text{for } 10^2 < C_\mu u_{br} / (k_N \omega_r) < 10^4.$$

These expressions are accurate to within about 1% for the indicated ranges of relative roughness and are far superior to the approximate implicit friction factor equations that may be derived from (30) and (31) under the assumption of small values  $\zeta_{ro}$ , *i.e.* large values of  $C_\mu u_{br} / (k_N \omega_r)$ . Thus the wave-current friction factor equation given *e.g.* by Madsen *et al.* (1988) is not only far more cumbersome to use but it is also less accurate than (33)! The author is indebted to Prof. Stephen R. McLean (U.C. Santa Barbara, personal communication) for pointing out the advantages of friction factor formulas of this type (originally suggested by Swart, 1974).

The Wave Boundary Layer Thickness,  $\delta_{wc}$ 

The matching level for the current profile, here referred to as the wave boundary layer thickness and denoted by  $\delta_{wc}$ , has up to this point not been defined in quantitative terms.

Considerations of  $\delta_{wc}$  as the level required for the wave orbital velocity to approach its free stream value within a certain percentage were used by Grant and Madsen (1979 and 1986) to arrive at

$$\delta_{wc} = \alpha \frac{\kappa u_{*r}}{\omega_r} \quad (34)$$

with  $\alpha$ -values in the range of 1 to 2. Madsen and Wikramanayake (1991) concluded from a comparison of current velocity profiles predicted by the Grant-Madsen model with limited experimental result as well as predictions afforded by more sophisticated turbulence closure models that reasonable agreement was obtained for  $\alpha$ -values in the range of 1 to 1.5.

If therefore one accepts (34) as the appropriate expression for  $\delta_{wc}$  one is faced with the problem of predicting a wave boundary layer thickness smaller than the equivalent Nikuradse sand grain roughness,  $k_N$ , when the roughness is large. This apparent inconsistency of the wave-current theory may be removed by requiring that  $\delta_{wc}$  should be at least some fraction of the Nikuradse roughness,  $k_N$ . Choosing, somewhat arbitrarily,  $\delta_{wc} \geq k_N$  for the current profile matching level leads to a limiting value of (34) given by

$$\frac{k_N \omega_r}{\kappa u_{*r}} = 30 \zeta_{ro} \leq \alpha \quad (35)$$

in which (31) was used.

Choosing, in honor of Bill Grant,  $\alpha = 2$  use of (35) in (30) and subsequent use of (31) leads to a limiting value of the relative roughness for which  $\delta_{wc}$  is determined from (34), and results in the following definition:

$$\delta_{wc} = \begin{cases} 2\kappa u_{*r}/\omega_r & \text{for } C_\mu u_{br}/(k_N \omega_r) > 8 \\ k_N & \text{for } C_\mu u_{br}/(k_N \omega_r) < 8 \end{cases} \quad (36)$$

Whereas there is evidence in support of (34) for small relative roughness, the "prediction" of  $\delta_{wc} = k_N$  should be regarded as tentative (at best). Since large roughness values, for naturally occurring wave-current flows over a movable bed, generally are associated with ripples and since  $k_N \simeq 4 \times$  (ripple height) for two-dimensional equilibrium-range ripples, *e.g.* Grant

and Madsen (1982), the prediction from (36) of  $\delta_{wc} = 4 \times$  (physical scale of two-dimensional roughness features) does, however, appear reasonable.

### Application

Assuming the bottom roughness ( $k_N = 30z_o$ ) and the representative periodic wave characteristics ( $u_{br}$ ,  $\omega_r$ , and  $\phi_{wr}$ ) known the method of solution depends on the specification of the current.

*Current Specified by  $u_{*c}^2$  and  $\phi_c$ .* This specification may physically arise in near-shore waters with a strong wind-driven shore-parallel velocity. In this situation the bottom shear stress may be approximated by the shore-parallel wind stress.

Obtaining  $\phi_{cw}$  from (25), solution is started by initially taking  $\mu = \mu^{(0)} = 0$  in (28), to obtain  $C_\mu = C_\mu^{(0)} = 1$  from (27). With  $C_\mu = C_\mu^{(0)}$  and known wave and bottom roughness conditions  $f_{wc} = f_{wc}^{(0)}$  is obtained from (32) or (33), whichever is appropriate. Now,  $f_{wc}^{(0)}$  and (29) provide a first estimate of  $u_{*wm}^{(0)}$ , so that (28) may be revisited to obtain an improved estimate of  $\mu = \mu^{(1)}$ . With  $\mu = \mu^{(1)}$  the procedure is repeated and iteration is terminated when  $f_{wc}^{(n+1)} = f_{wc}^{(n)}$  within 1%.

Convergence is generally achieved within a few iterations and from knowledge of  $u_{*c}$  and  $u_{*wm}$  the representative shear velocity,  $u_{*r}$ , is obtained from (26). The current velocity profile may now be evaluated from (9) and (10) with  $\delta_{wc}$  specified by (36) and the apparent bottom roughness,  $z_{oa}$ , may be determined from (11).

*Current Specified by  $\phi_c$  and  $u_c(z_r) = u_{cr}$ .* This specification of the current corresponds to a current velocity and direction measured at a given elevation,  $z_r$ , above the bottom. (It is assumed that  $z_r > \delta_{wc}$ .)

For this specification of the current the solution procedure is somewhat more cumbersome. Again, after use of (25) the iterations are started by  $\mu = \mu^{(0)} = 0$  in (28) and  $C_\mu = C_\mu^{(0)} = 1$  from (27) resulting in  $f_{wc} = f_{wc}^{(0)}$  from (32) or (33) and then  $u_{*wm} = u_{*wm}^{(0)}$  from (29) followed by  $u_{*r} = u_{*r}^{(0)}$  from (26). Since it is assumed that  $z_r > \delta_{wc}$ , the specified current velocity is given by (10), which with the aid of (11) may be written as a quadratic equation in the current shear velocity,  $u_{*c}$ ,

$$u_c(z_r) = u_{cr} = \frac{u_{*c}}{\kappa} \ln \frac{z_r}{\delta_{wc}} + \frac{u_{*c}^2}{\kappa u_{*r}} \ln \frac{\delta_{wc}}{z_o} \quad (37)$$

Since  $\delta_{wc}$  is given by (36) this equation, with  $\kappa = 0.4$ ,  $z_o = k_N/30$  and the latest value of  $u_{*r}$  may be solved to give

$$u_{*c} = \frac{u_{*r} \ell n(z_r/\delta_{wc})}{2 \ell n(\delta_{wc}/z_o)} \left( -1 + \sqrt{1 + \frac{4\kappa \ell n(\delta_{wc}/z_o)}{(\ell n(z_r/\delta_{wc}))^2} \frac{u_{cr}}{u_{*r}}} \right) \quad (38)$$

For the initial iteration  $u_{*r} = u_{*r}^{(o)}$  in (36) and (38) yields the first approximation for the current shear velocity  $u_{*c} = u_{*c}^{(o)}$ . With  $u_{*c} = u_{*c}^{(o)}$  and  $u_{*wm} = u_{*wm}^{(o)}$  the value of  $\mu$  may be updated by use of (28) and the procedure may be repeated until convergence is achieved ( $f_{wc}^{(n+1)} = f_{wc}^{(n)}$  within 1%). Again, convergence is generally achieved after a couple of iterations and the current velocity profile is determined from (9) and (10) with the apparent bottom roughness obtained from (11).

Discussion and Conclusions

Based on the linearized governing equations and adopting a simple time-invariant eddy viscosity a solution for combined wave-current turbulent bottom boundary layer flows was obtained for a wave motion specified by its near-bottom orbital velocity directional spectrum,  $S_{u_b}(\omega, \theta)$ . Closure was achieved by requiring the model to reduce the Grant-Madsen model in the limit of simple periodic plane waves. The spectral wave-current interaction model was used to determine the characteristics of a representative periodic wave which, in the context of combined wave-current bottom boundary layer flows, was equivalent to the directional sea. This representative periodic wave is specified by  $u_{br}$ , its near-bottom orbital velocity amplitude,

$$u_{br} = \iint 2S_{u_b}(\omega, \theta) d\omega d\theta,$$

*i.e.* the root-mean-square bottom velocity amplitude of the directional sea;  $\omega_r$ , its radian frequency,

$$\omega_r = \frac{\iint \omega S_{u_b}(\omega, \theta) d\omega d\theta}{\iint S_{u_b}(\omega, \theta) d\omega d\theta},$$

*i.e.* the mean frequency of the directional sea; and  $\phi_{\omega_r}$ , its direction of propagation,

$$\phi_{\omega_r} = \arctan \frac{\iint \omega S_{u_b}(\omega, \theta) \sin \theta d\omega d\theta}{\iint S_{u_b}(\omega, \theta) \cos \theta d\omega d\theta},$$

*i.e.* the mean direction of the directional sea.



Although based on the simple Grant-Madsen eddy viscosity formulation it is believed that the representative periodic wave characteristics determined here can be adopted with any wave-current interaction model to determine the effect of a directional sea on the near-bottom flow associated with a superimposed current. This transferability of the present results to any model that is based on a time-invariant eddy viscosity is assured on theoretical grounds and is not likely to seriously affect the practical significance of results obtained from elaborate numerical turbulent-closure models.

The most severe limitation of the spectral wave-current model's ability to predict current velocity profiles in the presence of waves is associated with the uncertainty in the determination of matching level for the current profile segments, *i.e.* the wave boundary layer thickness,  $\delta_{wc}$ , for large values of the equivalent bottom roughness. This limitation is not unique to the class of models presented here. It is inherent in all theoretical formulations of turbulent boundary layer flows that apply the turbulent no-slip condition at  $z = z_o$ , and may, for large roughness, lead to the nonsensical result of a boundary layer thickness less than the physical scale of bottom roughness elements. Clearly, when  $\delta_{wc}$  is not large relative to the physical scale of the bottom roughness, assuming a horizontally uniform flow is a poor assumption. This issue is particularly important in the context of wave-current interaction in the coastal environment where wave-generated bottom bedforms (ripples) create a large bottom roughness. Theoretical and especially experimental studies are required to shed some light on this problem whose existence is acknowledged here by tentatively suggesting  $\delta_{wc} \geq k_N$ .

In retrospect these characteristics of the representative periodic wave can hardly be considered surprising. The most important wave characteristic in terms of wave-current interaction is the magnitude of the bottom orbital velocity since this has the greatest effect on the bottom shear stress which, in turn, dominates the turbulence intensity within the wave boundary layer. Since the wave-associated bottom shear stress is proportional to the square of the near-bottom orbital velocity amplitude,  $u_{bm}^2$ , with the "constant" of proportionality, the wave friction factor, being "essentially constant" it follows directly that the near-bottom velocity of a representative periodic wave should be  $(\overline{u_{bm}^2})^{1/2}$ , *i.e.* exactly the form of  $u_{br}$  that we obtained through laborious, albeit theoretically rigorous, considerations. Despite the "intuitively obvious" nature of our rigorously derived expression for the representative periodic wave's bottom orbital velocity amplitude it is interesting to note that several investigators have chosen to represent a random sea by a "significant" bottom velocity amplitude, *i.e.* greater than our  $u_{br}$  by a factor of  $\sqrt{2}$ . The theoretically rigorous derivation of the representative periodic wave characteristics presented here therefore firmly

establishes the *significance* of the root-mean-square near-bottom wave orbital velocity (and the *insignificance* of the “significant” velocity) in the context of combined wave-current bottom boundary layer flows.

### Acknowledgements

The research presented in this paper was sponsored by the MIT Sea Grant College Program under Grant NA90-AA-D-SG424 from the Office of Sea Grant of NOAA during the early stages, and continued under sponsorship from NSF’s Marine Geology and Geophysics Program Grant Nos. OCE-9017878 and 9314366 and NSF’s Ocean Sciences CoOP Grant No. OCE-9123513.

### References

- Abramowitz, M., I.A. Stegun (1972) *Handbook of Mathematical Functions*. National Bureau of Standards Applied Math Series, No. 55, pp. 379-509.
- Grant W.D., O.S. Madsen (1979) Combined wave and current interaction with a rough bottom. *Journal of Geophysical Research* 84(C4):1979-1808.
- Grant, W.D., O.S. Madsen (1982) Moveable bed roughness in oscillatory flow. *Journal of Geophysical Research* 87(C1):469-481.
- Grant, W.D., O.S. Madsen (1986) The continental shelf bottom boundary layer, In *Annual Review of Fluid Mechanics* (M. Van Dyke, ed.), 18:265-305.
- Kajiura, K. (1968) A model of the bottom boundary layer in water waves. *Bulletin of the Earthquake Research Institute* 46:75-123.
- Madsen, O.S., Y.-K. Poon, H.C. Graber (1988) Spectral wave attenuation by bottom friction: Theory. *Proceedings 21st International Conference on Coastal Engineering*, ASCE, Torremolinos. 1:492:504.
- Madsen, O.S., P.N. Wikramanayake (1991) Simple models for turbulent wave-current bottom boundary layer flow. U.S. Army Corps of Engineers, WES, Report No. DRP-91-1.
- Mathisen, P.P., O.S. Madsen (1993) Bottom roughness for wave and current boundary layer flows over a rippled bed. MIT Sea Grant College Program. Tech. Rept. MITSG93-27.
- Swart, D.H. (1974) Offshore sediment transport and equilibrium beach profiles. Delft Hydraulic Laboratory. Publication No. 131.

### Appendix A: Spectral Wave Energy Dissipation

As mentioned earlier the effect of evaluating the bottom shear stress at  $z = z_o$  ( $\zeta = \zeta_{ro}$ ) rather than by taking the limit  $z \rightarrow 0$  ( $\zeta \rightarrow 0$ ) has pronounced effects for larger roughness values. Thus the wave friction factors predicted by (32) are significantly lower than those obtained if the limit  $z \rightarrow 0$  were used to define the bottom shear stress. Furthermore, the phase difference,  $\varphi_\tau$ , between bottom shear stress and free stream wave orbital velocity, which is important for the computation of wave energy dissipation in the wave bottom boundary layer, is extremely sensitive to the choice of definition,  $z = z_o$  or  $z \rightarrow 0$ , used to evaluate the bottom shear stress for large values of the bottom roughness.

The phase difference,  $\varphi_\tau$ , is given by the argument of the complex fraction of Kelvin functions and their derivatives in (12), (14) and (30). The phase difference,  $\varphi_{\tau r}$ , for the representative periodic wave, obtained from (30), may be approximated by the explicit relationship

$$\varphi_{\tau r}^\circ = 33 - 6.0 \log_{10} \frac{C_\mu u_{br}}{k_N \omega_r} \quad \text{for } 0.2 < C_\mu u_{br} / (k_N \omega_r) < 10^3 \quad (39)$$

which is accurate within  $1^\circ$  for the range indicated.

For each wave component the rate of energy dissipation in the bottom boundary layer,  $D_{nm}$ , is obtained from Kajjura (1968) with bottom shear stress given by (12) and free stream velocity by (6), evaluated for  $\zeta_n \rightarrow \infty$ . The resulting formula is written in compact form by using (26) and (29) to express  $u_{*r}$  and generalizing (30) and (39) for arbitrary choice of  $\omega$ . The end result is

$$D_{nm} = \overline{\tau_{wnm} \cdot (\mathbf{u}_{wnm})}_{\zeta_n \rightarrow \infty} = \frac{1}{4} \rho \sqrt{f_{wc}} \sqrt{f_{wc,n}} \cos \varphi_{\tau n} u_{br} \mathbf{u}_{bnm}^2 \quad (40)$$

in which  $f_{wc,n}$  and  $\varphi_{\tau n}$  are obtained from (32) or (33) and (39), respectively, with  $\omega_r$  replaced by  $\omega_n$  and  $\mathbf{u}_{bnm}$  is given by (7).

Madsen *et al.* (1988) used the  $z \rightarrow 0$  definition to obtain the wave friction factor and neglected the influence of the phase difference,  $\varphi_\tau$ , in the evaluation of the energy dissipation rate. Strictly speaking this limits the applicability of their results to the range of relative roughness associated with (33). For this range  $f_{wc,n}$  and  $\cos \varphi_{\tau n}$  depend weakly on  $\omega_n$  and may be replaced by their values for  $\omega_n = \omega_r$ . In this way (40) becomes equivalent to Eq. (26) in Madsen *et al.* (1988) if their " $f_{wr}$ " is replaced by  $f_{er} =$  "the representative wave energy dissipation factor"  $= f_{wc} \cos \varphi_{\tau r}$ . For small bottom roughness  $\cos \varphi_{\tau r} \simeq 1$  and  $f_{er} = f_{wc}$  makes (40) identical to Eq. (26) of Madsen *et al.* However, as seen in Figure 1,  $f_{er}$  may be significantly different from  $f_{wc}$  for large bottom roughness.

## CHAPTER 30

### TIME DOMAIN MODELLING OF WAVE BREAKING, RUNUP, AND SURF BEATS

P.A. Madsen\*, O.R. Sørensen\* and H.A. Schäffer\*

#### Abstract

In this paper we study wave breaking and runup of regular and irregular waves, and the generation of surf beats. These phenomena are investigated numerically by using a time-domain primary-wave resolving model based on Boussinesq type equations. As compared with the classical Boussinesq equations the ones adopted here allow for improved linear dispersion characteristics, and wave breaking is incorporated by using a roller concept for spilling breakers. The swash zone is represented by incorporating a moving shoreline boundary condition and radiation of short and long period waves from the offshore boundary is allowed by the use of absorbing sponge layers. The model results presented include wave height decay, mean water setup, depth-averaged undertow, shoreline oscillations and the generation and release of low frequency waves.

#### Introduction

Previous work on the modelling of surf beats and low frequency waves in the surf zone has mainly been based on the wave-averaged approach for the primary waves combined with linear or nonlinear equations for the long waves (Symonds et al., 1982; Schäffer, 1993; Roelvink, 1993).

In the analytical work of Symonds et al. (1982) a sinusoidal variation of the break point was assumed corresponding to weakly modulated short waves. Inside the surf zone the modulation or groupiness of these waves was assumed to vanish and the wave height was taken to be a fixed proportion of the local water depth. The low frequency waves were described by the linear shallow water equations driven by radiation stresses according to linear wave theory. Incoming bound long waves and frictional effects were neglected.

-----  
\* International Research Centre for Computational Hydrodynamics (ICCH). Located at the Danish Hydraulic Institute, Agern Alle 5, DK-2970 Hørsholm, Denmark

Schäffer (1990, 1993) improved this analytical work in a number of ways of which the inclusion of the incoming bound long waves and their transformation on a sloping beach turned out to be most important for the results. He also considered different types of surf zone models for the incident modulated short waves: The first one was the saturation approach by Symonds et al. (1982), neglecting groupiness inside the surf zone. The second one assumed a fixed break point position but allowed for full transmission of groupiness into the surf zone. The model finally adopted was a hybrid between the two allowing the transmission of groupiness to be zero, partial, full or even to be reversed.

Roelvink (1993) developed a numerical model using a nonlinear description of the low frequency waves based on the nonlinear shallow water equations including bottom friction and radiation stress terms. The primary waves were described by a wave energy balance equation including dissipation terms similar to the formulation by Battjes and Janssen (1978).

As an alternative to the wave-averaged approaches Watson and Peregrine (1992) used the nonlinear shallow water (NSW) equations to resolve the short wave motion as well as the long wave motion. A shock-capturing method allowed for an automatic treatment of bores and shocks without the need for any special tracking algorithm. The drawback of this method is, however, the lack of frequency dispersion, which forces the high frequency waves to move with shallow water celerities and to steepen into bores at a certain distance from the seaward boundary. Another problem is the prediction of the fluctuating surf zone width. It is well known that the NSW equations are not able to predict the break point position in regular waves. Hence it is unlikely that they should be able to give a good estimate of the time varying break point in wave groups and irregular waves.

In the present work we have studied and modelled the nonlinear interaction processes described above on the basis of a special type of Boussinesq equations. The equations were derived by Madsen et al. (1991) and Madsen and Sørensen (1992) and have proved to incorporate improved linear dispersion characteristics and shoaling properties, which are important for a correct representation of the nonlinear energy transfer (Madsen and Sørensen, 1993). Incorporation of wave breaking is an essential part of the model complex and it is based on the concept of surface rollers following the formulation by Schäffer et al. (1992,1993). The model has proved to be able to represent a variety of processes such as the initiation and cessation of spilling wave breaking, and the evolution of wave profiles before, during and after wave breaking.

The present paper presents a further extension of the Boussinesq model by including the swash zone and the moving shoreline. The new extension of the model makes it possible to simulate wave breaking and runup of irregular waves and to study the generation of surf beats and low frequency waves induced by short-wave groups.

Only 1D results will be presented in this paper, while the extension to 2D horizontal problems is described by Sørensen et al. (1994).

## A Simple Model for Spilling Breakers

The incorporation of wave breaking for spilling breakers in the Boussinesq model is based on the concept of surface rollers as described by Schäffer et al. (1992,1993). A brief summary of the concept will be given in the following. First of all it can be split up into two parts:

- Determination of the spatial and temporal variation of surface rollers.
- Determination of the effect of the rollers on the wave motion.

The determination of the rollers is based on the heuristic geometrical approach by Deigaard (1989). First of all wave breaking is initiated when the local slope of the surface elevation exceeds a critical value,  $\tan\phi$ . Due to the transition from initial breaking to a bore-like stage in the inner surf zone this angle,  $\phi$ , is assumed to vary in time. Breaking is assumed to be initiated for an angle of 20 Degrees, which then gradually changes (with an exponential decay) to a smaller terminal angle of 10 Degrees. Locally, the roller is defined as the water above the tangent of  $\tan\phi$  and wave breaking is assumed to cease when the maximum of the local slope becomes less than  $\tan\phi$ .

The determination of the effect of the surface rollers on the wave motion is inspired by the simple model suggested by Svendsen (1984). The basic principle is that the surface roller is considered as a volume of water being carried by the wave with the wave celerity and this is assumed to result in the vertical distribution of the horizontal particle velocity shown in Fig 1. Although this is a very simple approximation it allows for the description of some important physical phenomena:

- It leads to additional convective terms in the depth-integrated momentum equations. This results in a conversion of potential energy into forward momentum flux immediately after breaking and while the wave height starts to decay the radiation stress may keep constant for a while. This leads to the well known horizontal shift between the break point and the point where the setup in the mean water level is initiated.
- The inclusion in the mass balance of the net mass transport due to the roller has a significant effect on the time-average of the depth-averaged particle velocities and improves the prediction of the depth-averaged undertow in the surf zone.

These two features are illustrated in the following by Fig 2, dealing with wave height decay and setup, and by Fig 3 dealing with wave height decay and undertow.

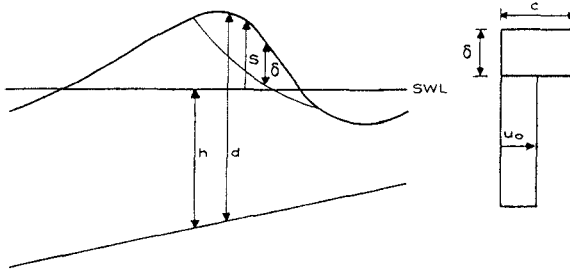
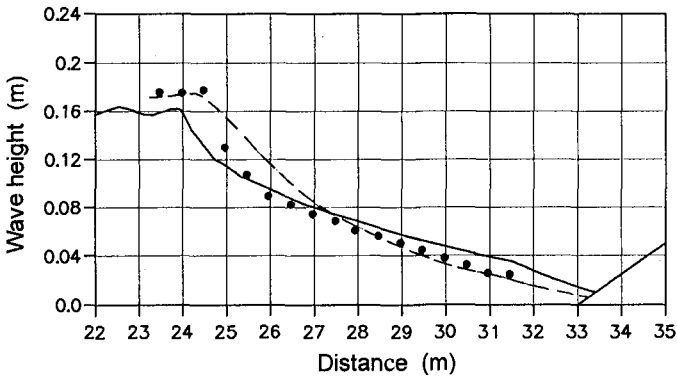


Figure 1 Cross-section and assumed velocity profile of a breaking wave with a surface roller.  
 Definitions:  $S$ =elevation,  $d$ =total water depth,  $\delta$ =roller thickness,  $c$ =wave celerity,  $U_0$ =particle velocity.

Fig 2 shows a comparison with the measurements of test 1 presented by Stive (1980). In this test incident monochromatic waves shoal and break as spilling breakers on a plane slope of 1:40. The wave period is 1.79 s and at the seaward boundary the depth is 0.70 m and the wave height is 0.145 m. From the variation in wave heights wave breaking is seen to occur at a distance of 24.5 m from the wavemaker, while the setup in mean water level starts at 25.5 m. The numerical results obtained by the present Boussinesq model are slightly underestimating the last part of the shoaling, breaking occurs at 24.0 m and setup starts at 24.7 m. Except for the discrepancy near the break point the overall agreement with the measurements of wave height and setup is acceptable.

a)



b)

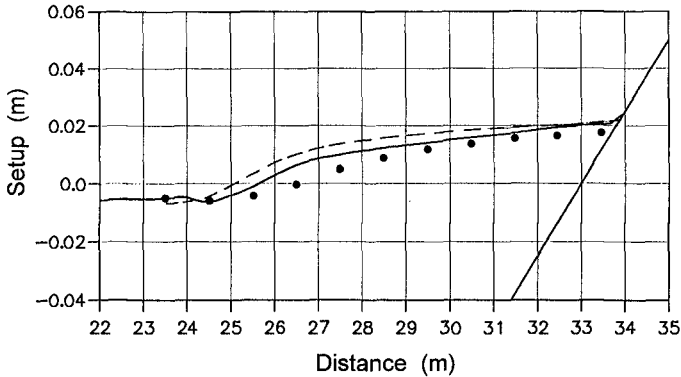


Figure 2 Monochromatic waves on a mild slope  
 a) Computed and measured variation of the wave height  
 b) Computed and measured variation of MWL  
 — Present model --- Kobayashi et al. (1989)  
 • Measurements by Stive (1980)

Kobayashi et al. (1989) solved the nonlinear shallow water NSW equations by using a dissipative shock-capturing method in which bores or shock fronts are frozen to cover only a few grid points. Due to the lack of dispersion this type of model will predict breaking to occur very near the seaward boundary. For this reason the NSW calculations were started very near the observed breaking point at a depth of 0.2375 m with an incoming wave height of 0.172 m. From Fig 2 we notice that for the computed results the positions of the break point and the start of setup coincide. Furthermore, the wave height decay is clearly underestimated initially. However, the overall performance of the NSW model is very good.

Fig 3 shows a comparison with the measurements by Hansen and Svendsen (1984). In this test incident monochromatic waves shoal and break as spilling breakers on a plane slope of 1:34.25. The wave period is 2.0 s and at the seaward boundary the depth is 0.36 m and the wave height is 0.12 m. The Boussinesq model was started at the toe of the slope with a cnoidal input. The variation of the wave height is shown in Fig 3a. We notice that the position of the break point is quite well predicted, and also the rate of energy decay after breaking is satisfactory. However, again the maximum wave heights occurring just before breaking are underestimated in the simulation. The depth-averaged undertow is obtained by determining the time-average of the particle velocity  $U_0$ , defined in Fig. 1. In Fig. 3b this is compared to the measurements of Hansen and Svendsen (1984). The agreement is seen to be much improved as compared with the NSW results by Kobayashi et al. (1989).



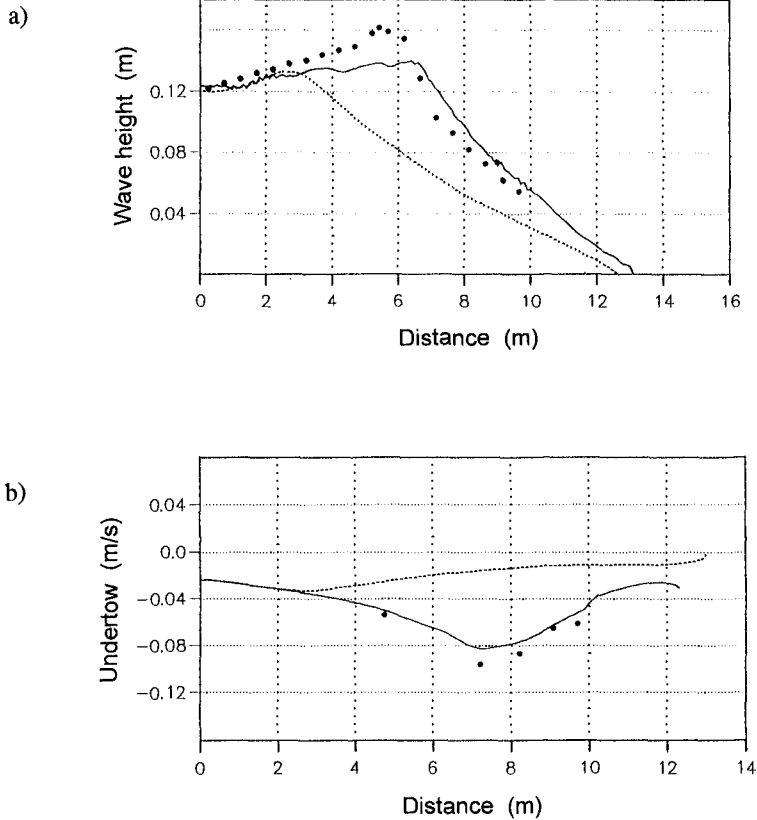


Figure 3 Monochromatic waves on a mild slope  
 a) Computed and measured variation of the wave height  
 b) Computed and measured depth-averaged undertow  
 — Present model    ---- Kobayashi et al. (1989)  
 • Measurements by Hansen and Svendsen (1984)

For this case measured wave profiles immediately seaward of the observed break point were not available, and consequently the NSW model was started at the toe of the slope. This position being quite far from the break point makes it a very difficult test for the NSW model. Clearly, the NSW model fails to predict the break point and the wave height starts decaying much too early. This generally leads to a significant underestimation of the wave height. Also, the undertow is clearly underestimated, partly due to the discrepancy in the wave height and partly due to the fact that the NSW equations do not include the important net mass transport in the rollers.

## Swash Oscillations and Runup

One of the difficult points in simulating runup of regular and irregular waves is the treatment of the moving shoreline. In the present work we have adopted a modified version of the slot-technique described by Tao (1983). A brief summary of this concept will be given in the following.

First of all the computational domain is extended artificially to cover the solid beach by introducing narrow channels or slots in which the waves can propagate. The width of the slot will enter the depth-integrated mass and momentum equations in two ways:

- Generally the water depth will be replaced by a cross sectional area which will include the slot area.
- The time derivative of the surface elevation will be multiplied by the slot width.

The artificial slots have to be very narrow to avoid a distortion of the mass balance and a disturbance of the flow in the physical domain. On the other hand, the numerical solution will break down when the width becomes too small. In practice the width is chosen in the interval between 0.01 and 0.001 times the grid size. An alternative way to interpret this technique is to consider the solid beach to be replaced by a porous beach with a very low porosity factor (the relative slot width).

In order to make this technique operational in connection with Boussinesq type models a couple of problems call for special attention:

- The Boussinesq terms are switched off at the still water shoreline where their relative importance is extremely small anyway.
- The convective terms are treated by central differences in the physical flow domain and by upwind differences inside the slots.
- An explicit filter is introduced near the still water shoreline to remove short wave instabilities during uprush and downrush.

Some of the advantages of the method is that it works very well in combination with implicit numerical schemes and it is quite easy to generalize and implement in two horizontal dimensions. The drawback is that the method will always introduce minor errors in the mass balance and these will generally lead to an underestimation of the maximum uprush and downrush on impermeable slopes.

To check the accuracy of the method we have tested the numerical model against the analytical solution for non-breaking shallow water waves on a sloping beach (Carrier and Greenspan, 1958). The analytical solution is based on the nonlinear shallow water equations, hence for this test case we have switched off the Boussinesq terms everywhere.

The test case considered is an initial water depth of 0.5 m, a wave period of 10 s, a slope of 1/25, and a wave height of 50% of the limiting value (giving breaking at rundown). Fig 4 shows the horizontal motion of the shoreline computed with three different values of the relative slot width (0.01, 0.005 & 0.001). The numerical solution is clearly converging towards the analytical solution, but even for a value of 0.001 the maximum runup is still underestimated by 8%. The reason

is that the upper part of the swash zone is containing only a thin film of water and this is quite sensitive to even small portions of water entering the porous beach.

Further testing and a more complete description of the technique will appear in Madsen et al. (1995).

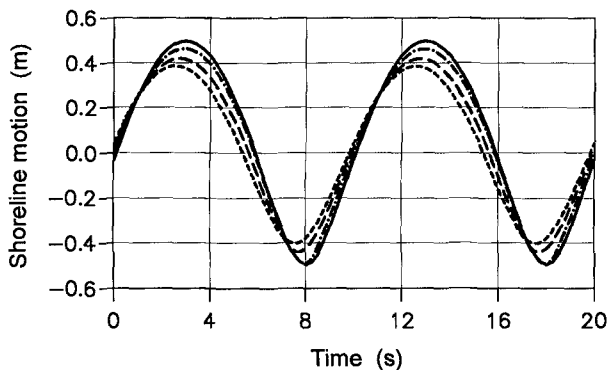


Figure 4 Horizontal motion of the shoreline  
 — Analytical solution by Carrier & Greenspan (1958)  
 - - - Present model with a slot width of 0.01  
 - . - - " - " slot width of 0.005  
 . . . " - " slot width of 0.001

### Low Frequency Waves in the Surf Zone

The extension of the Boussinesq model to include wave breaking of spilling breakers and a moving shoreline formulation makes it possible to simulate the generation of surf beats due to shoaling, breaking and runup of irregular waves. The simplest possible study of this phenomenon can be made with a bichromatic wave group composed of a superposition of two sine waves with slightly different frequencies.

For simplicity we consider a test case where linear boundary conditions can be applied at the seaward boundary. The bathymetry consists of a horizontal section of 40 m with a water depth of 2.0 m and a section of 75 m with a constant slope of 1/34.25 (Fig 5). Waves are generated internally and re-reflection of waves from the seaward boundary is avoided by using a 5 m wide sponge layer. As input we apply linear bichromatic waves with frequencies of 0.4 hz and 0.5 hz and with amplitudes of 0.03 m on both frequencies. This leads to a *linear* wave group in the horizontal section of the flume, and it has several advantages: One is that higher order boundary conditions are not necessary and the other is that the determination of the amplitude of the outgoing free low frequency wave due to the surf beat can be determined accurately by simple means. This is not the case if the seaward

boundary is placed in shallow water. In order to resolve the superharmonics in shallow water we use a grid size of 0.1 m and a time step of 0.02 s.

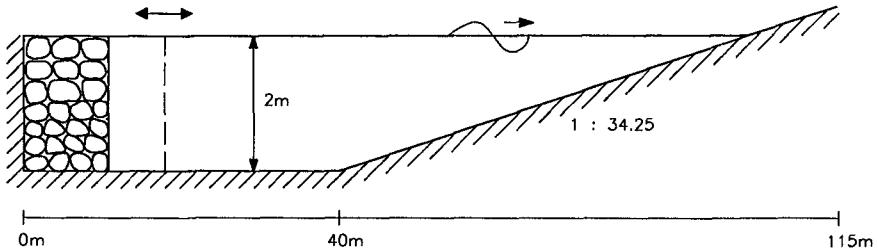


Figure 5 Bichromatic waves on a mild slope. Sketch of model setup.

Fig 6 shows the instantaneous surface elevation as a function of the distance from the seaward boundary. The individual waves can be seen to steepen and break in shallow water. The figure also contains two curves, showing the maximum and minimum elevation obtained during the last two wave groups of the simulation. The maximum curve has three spikes indicating three different break points. The outermost point is seen to be at 101 m and the envelope drops steeply landwards of this point due to the roller dissipation. The second break point occurs at 102.5 m and a new steep descent follows. This pattern indicates that the highest waves decay to become smaller than the second highest waves before the latter start decaying. In other words, the modulation of the primary waves or the groupiness is reversed inside the surf zone. This phenomenon was also discussed by Schäffer (1993).

Fig 7 shows the resulting surf beat obtained by low-pass filtering the surface elevation time series in each grid point with a cutoff at 0.1 hz. The envelope plot shows a combination of bound and free long waves running in the onshore direction and reflected free waves running in the offshore direction. Furthermore, the stationary setup is included in the plot. An almost perfect nodal point is occurring at 94 m, but further offshore the nodes become more and more open indicating that the outward free long waves become dominant compared to the inward bound long waves. The overall picture for the long waves shows the same behaviour as the analytical solution by Schäffer (1993) for weakly modulated primary waves.

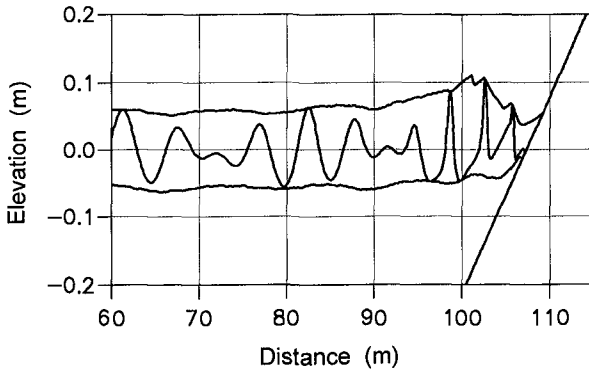


Figure 6 Bichromatic waves on a mild slope. Spatial variation of the surface elevation.

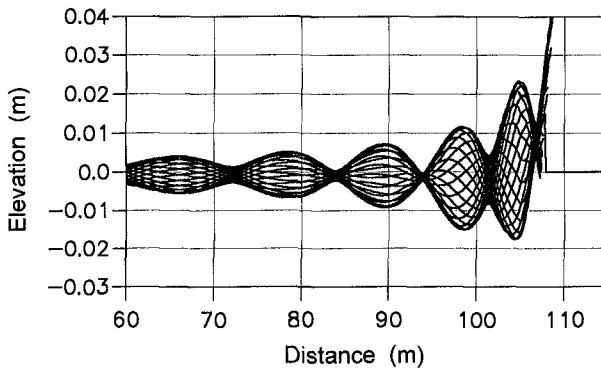


Figure 7 Bichromatic waves on a mild slope. Envelope of lowpass filtered surface elevations.

Fig 8 shows the temporal variation of the shoreline and the spatial and temporal evolution of the individual rollers identified by the model. The outermost break point is again spotted at 101 m and we clearly see how the break point changes in time. The slope of the trajectories of the rollers indicate the local speed of the breaking waves and especially close to the shoreline this is clearly influenced by the swash oscillations. The temporal variation of the shoreline shows a low frequency variation superimposed by individual swash oscillations. Unfortunately, the use of the slot-technique for handling the moving boundary has the undesired effect, that the individual wave runups disappear too rapidly due to the thin film of water penetrating the porous beach. In reality we expect the shoreline motion to be less spiky because the thin film of water will stay on the slope until the next wave arrives. This aspect requires further investigation.

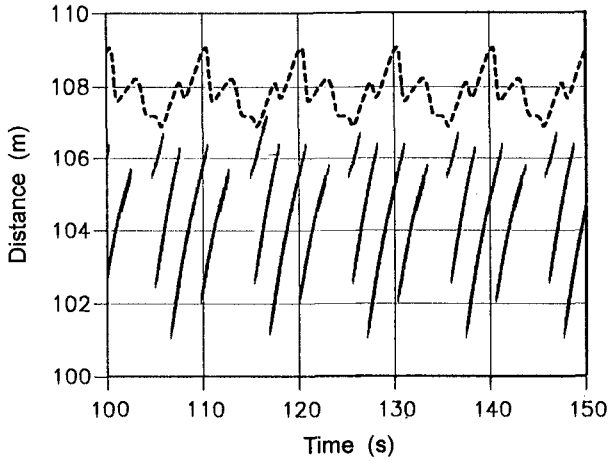


Figure 8 A time-space plot of the horizontal motion of the shoreline ( ---) and the tracks of detected surface rollers (—).

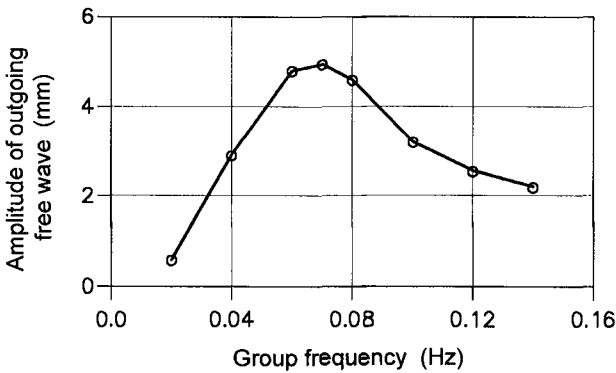


Figure 9 The amplitude of the outgoing free long wave as a function of the group frequency,  $\Delta f$ .

To investigate the sensitivity of the surf beat to the variation of the group frequency a number of simulations were made with different fully modulated bichromatic wave inputs: The first frequency was fixed to be 0.5 hz while the second was varied in the range of 0.36 hz - 0.48 hz, leading to group frequencies in the interval of 0.14 hz to 0.02 hz. Input amplitudes of 0.03 m on both frequencies were used in all cases. Fig 9 shows the amplitude of the resulting outgoing free long wave as a function of the group frequency,  $\Delta f$ . A clear local maximum is obtained for a value of 0.07 hz indicating that the surf beat mechanism is indeed sensitive to the ratio between the surf zone width and the wave length of the low

frequency waves. The local maximum in the resulting amplitude occurs when the long waves reflected from the shoreline are in phase with the long waves generated to move in the offshore direction by the oscillating break point. This confirms the mechanism first described by Symonds et al. (1982).

Further investigations and comparisons with e.g. the measurements by Kostense (1984) will appear in Madsen et al. (1995).

## Conclusion

A Boussinesq type model with improved linear dispersion characteristics and with a roller concept for spilling breakers is extended to include the swash zone and the moving shoreline. The model is capable of representing a variety of processes such as the initiation and cessation of breaking, and the evolution of wave profiles before, during and after wave breaking. In this work we have concentrated on resulting wave-averaged quantities such as wave height decay, mean water setup and depth-averaged undertow.

The new extension of the model to include the swash zone makes it possible to simulate wave breaking and runup of irregular waves and to study the generation of surf beats and low frequency waves induced by short-wave groups. The test cases presented in this paper are only first examples of what can be achieved by the use of the Boussinesq model. The results obtained so far are qualitatively correct and most promising. However, further work is necessary to quantify the accuracy of the results.

## Acknowledgement

This work has been financed mainly by the Danish National Research Foundation and partly by the Commission of the European Communities, Directorate General for Science, Research, and Development under MAST contract No. MAS2-CT92-0027. Their financial support is greatly appreciated.

## References

- Battjes, J.A. and J.P.F.M. Janssen (1978), "Energy loss and setup due to breaking in random waves". Proc. 16th Int. Conf. on Coastal Eng., ASCE, pp 569-587.
- Carrier, G.F. and H.P. Greenspan (1958), "Water waves of finite amplitude on a sloping beach". Journal of Fluid Mechanics, Vol 4, pp 97-109.
- Deigaard, R. (1989), "Mathematical Modelling of waves in the surf zone". Prog. Report 69, pp 47-59, ISVA, Technical University, Lyngby, Denmark.
- Hansen, J.B. and I.A. Svendsen (1984), "A theoretical and experimental study of undertow", In Proc. of the 19th Coastal Eng. Conf., pp 2246-2262.
- Kobayashi, N., G.S. De Silva and K.D. Watson (1989), "Wave transformation and swash oscillation of gentle and steep slopes". Journal of Geophysical Research, Vol. 94, No. C1, pp 951-966.
- Kostense, J.K. (1984), "Measurements of surf beat and set-down beneath wave groups". In Proc. of the 19th Coastal Eng. Conf., pp 724-740.

Madsen, P.A., R. Murray and O.R. Sørensen (1991), "A new form of the Boussinesq equations with improved linear dispersion characteristics. Part 1", *Coastal Engineering*, Vol 15, pp 371-388.

Madsen, P.A. and O.R. Sørensen (1992), "A new form of the Boussinesq equations with improved linear dispersion characteristics. Part 2: A slowly-varying bathymetry", *Coastal Engineering*, Vol 18, pp 183-204.

Madsen, P.A. and O.R. Sørensen (1993), "Bound waves and Triad Interactions in shallow water", *Ocean Engineering*, Vol 20, pp 359-388.

Madsen, P.A., O.R. Sørensen and H.A. Schäffer (1995), "Wave breaking, swash oscillations and surf beats simulated by a Boussinesq type model". Submitted for publication.

Roelvink, J.A. (1993), "Surf beat and its effect on cross-shore profiles". Technical University of Delft, 117 pp.

Schäffer, H.A. (1990), "Infragravity water waves induced by short-wave groups". Technical University of Denmark, Series paper 50, 168 pp.

Schäffer, H.A., R. Deigaard and P.A. Madsen (1992), "A two-dimensional surf zone model based on the Boussinesq equations". In Proc. of the 23th Coastal Eng. Conf., Chapter 43, pp 576-590.

Schäffer, H.A. (1993), "Infragravity waves induced by short-wave groups". *J. Fluid Mech.* (1993), vol. 247, pp. 551-588.

Schäffer, H.A., P.A. Madsen and R. Deigaard (1993), "A Boussinesq model for waves breaking in shallow water". *Coastal Engineering*, Vol 20, pp 185-202.

Stive, M.J.F. (1980), "Velocity and pressure field of spilling breakers". In Proc. of the 17th Coastal Eng. Conf., pp 547-566.

Svendsen, I.A. (1984), "Wave Heights and setup in a surf zone". *Coastal Engineering*, Vol 8 (4), pp 303-329.

Symonds, G., G.A. Huntley and A.J. Bowen (1982), "Two dimensional surf beat: Long wave generation by a time-varying break point". *J. Geophys. Res.*, 87, C1, pp 492-498.

Sørensen, O.R., H.A. Schäffer, P.A. Madsen and R. Deigaard (1994), "Wave breaking and induced nearshore circulations modelled in the time domain". In Proc. of the 24th Coastal Eng. Conf., Kobe.

Tao, J. (1983). "Computation of wave run-up and wave breaking". Internal Report, 40 pp, Danish Hydraulic Institute.

Watson, G. and D.H. Peregrine (1992), "Low frequency waves in the surf zone". In Proc. of the 23th Coastal Eng. Conf., Chapter 61, pp 818-831.



## CHAPTER 31

# Orthonormal Wavelet Analysis for Deep-Water Breaking Waves

Nobuhito MORI \* and Takashi YASUDA †

### ABSTRACT

This study aims to develop a method using wavelet transform to detect wave breaking event from temporal water surface elevation data. Sudden surface jump associated with breaking wave is regarded as shock wave and shock wavelet spectrum is defined to detect the occurrence of the surface jump. The visual observation of breaking wave crest shows that this method can almost completely detect the occurrence of breaking wave in random wave trains.

### 1. INTRODUCTION

Wave breaking plays important roles in numerous aspects of horizontal and vertical momentum transfer from surface waves to current and mixing of surface layer. Since breaking waves are associated with steep and giant waves, wave breaking is very important phenomenon to estimate their upper limit and the occurrence probability of their wave height. Furthermore, breaking waves exert the strong wave induced force, which occasionally bring about impact pressure to structures.

A great deal of effort has been made on direct observations of wave breaking in the ocean. One of them is direct visual observation of white caps to detect the breaking waves [Holthuijsen & Herbers(1986)], because the wave breaking is related to some sort of instability near the crests. Since they required much efforts, the visual observations are not adequate to ordinary routine observation. Another approach is to detect the breaking events in the time series of surface elevation, directly. Longuet-Higgins & Smith(1983) observed breaking waves by using a surface jump meter. Recently, Su & Cartmill(1993) developed a

---

\*Graduate student, Graduate School of Gifu University, Yanagido, Gifu 501-11, Japan.

†Professor, Dept. of Civil Eng., Gifu University, Yanagido, Gifu 501-11, Japan.

new detection method of breaking wave by a void fraction technique. These direct measurement methods are quite well but require special and sophisticated instrument, so that they are not also in general use. Weissman *et al.*(1984) measured energy backscattering of the high frequency components due to wave breaking with the running Fourier spectrum method. Their detection method is empirical and has not objectivity, nevertheless their method need not any special instruments. They use the Fourier spectrum analysis that is generally effective to analyze an energy change, periodicity and a power law of data. However, it is not suitable to use unsteady process such as breaking. The reason why the Fourier analysis has not temporally or spatially local information on data is that its integral basis consists of periodic function.

Recently, a new method of aperiodic and unsteady data analysis which has a locally confined integral basis, so-called '*wavelet analysis*', is getting well known[for example, Meyer(1991) and Farge(1992)]. Shen *et al.*(1994) studied local energy characteristics of wind generated waves using a continuous wavelet transform. Since the continuous wavelets, however, have overcomplete basis which causes formal relations among expansion coefficients, they are not suitable to analyze local energy properties. Meyer(1989) studied and formulated the orthogonal analyzing wavelet system. This orthogonal wavelet transform is known as adequate analysis of the local energy characteristics of the data[Mori *et al.*(1993)].

In this study we make a rational breaking wave detection scheme to indicate and to measure small jumps and discontinuities in surface elevation associated with breaking waves. Further, we check the validity of the method by experimental data and analyze the local energy properties of breaking wave using the orthonormal wavelet analysis.

## 2. PRINCIPLE OF MEASUREMENT

### 2.1 Orthonormal wavelet expansion

Since the kernel functions of continuous wavelet transforms are not mutually orthogonal, we have the redundancy of wavelet coefficients independent of data. The excellent mathematical formulation of orthogonal analyzing wavelet, *multi-resolution analysis*, was developed by Mallat(1989). Accordingly, in this paper, we employ the orthonormal wavelet expansion to analyze a water surface elevation.

The orthogonal wavelet expansion of an arbitrary function  $\eta(t)$  is written as

$$\eta(t) = \sum_{j=1}^{\infty} \sum_{k=1}^{\infty} \alpha_{j,k} \psi_{j,k}(t), \quad (j, k \in Z) \quad (1)$$

in which  $\alpha_{j,k}$  ( $j, k \in Z$ , where  $Z$  is the set of all integers) is an expansion coefficient and  $\psi_{j,k}(t) \in L(\mathbf{R}^2)$  is a complete orthonormal set of wavelets generated from an analyzing wavelet, which is sometimes called mother wavelet, by discrete translations  $k$  and is corresponding to temporal position of time  $k/2^j$ , and discrete dilations  $j$  corresponds to frequency. It is conventional to take the discrete dilation as

$$\psi_{j,k}(t) = 2^{\frac{j}{2}} \psi(2^j t - k), \quad (j, k \in Z) \quad (2)$$

with the orthonormality condition. From the orthogonality, the wavelets allow us to obtain the expansion coefficient  $\alpha_{j,k}$  in Eq.(1) by taking the innerproduct of  $\eta(t)$  and  $\psi_{j,k}^*(t)$  as

$$\alpha_{j,k} = \int_{-\infty}^{\infty} \eta(t) \psi_{j,k}^*(t) dt. \quad (3)$$

There are typically three types of the orthonormal analyzing wavelets as Meyer's, Daubechies' and Battle-Lemariés's. To investigate the complete relation to the Fourier analysis for the purpose of this study, we follow Meyer's method(1989) which has the properties that; i)  $\psi(t)$  is a real analytic function, ii)  $\psi(t)$  and its derivatives of any order are rapidly decreasing functions, iii) the moments of any order are zero, and iv) the Fourier transform of  $\psi(t)$  has a compact supported in the Fourier space.

We define the mother function  $\tilde{\phi}(\omega)$  of analyzing wavelet that is an infinitely differentiable real function satisfying the following conditions,

$$a) \left. \begin{aligned} \tilde{\phi}(\omega) &\geq 0, \\ \tilde{\phi}(\omega) &= \tilde{\phi}(-\omega), \\ \tilde{\phi}(\omega) &\text{ is monotonically decreasing for } \omega \geq 0, \end{aligned} \right\} \quad (4)$$

$$b) \left. \begin{aligned} \tilde{\phi}(\omega) &= 1 \quad (|\omega| \leq 2\pi/3), \\ &= 0 \quad (|\omega| \geq 4\pi/3), \end{aligned} \right\} \quad (5)$$

$$c) \{ \hat{\phi}(\omega) \}^2 + \{ \hat{\phi}(\omega - 2\pi) \}^2 = 1 \quad (2\pi/3 \leq |\omega| \leq 4\pi/3). \quad (6)$$

The conditions of a) to c) do not uniquely determine  $\tilde{\phi}(\omega)$ , so that we can make arbitrary functions  $\tilde{\phi}(\omega)$ , if  $\tilde{\phi}(\omega)$  satisfies the above conditions of a) to c). We employ here the mother function  $\tilde{\phi}(\omega)$  defined as

$$\tilde{\phi}(\omega) = \sqrt{g(\omega)g(-\omega)}, \quad (7)$$

where

$$g(\omega) = \frac{h(4\pi/3 - \omega)}{h(\omega - 2\pi/3) + h(4\pi/3 - \omega)}, \quad (8)$$

$$h(\omega) = \begin{cases} \exp(-1/\omega^2), & (\omega > 0) \\ 0, & (\omega \leq 0) \end{cases} \quad (9)$$

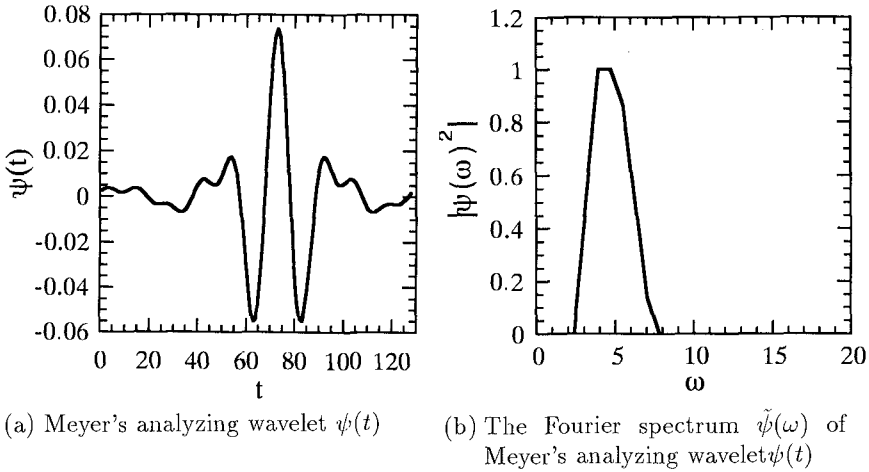


Figure 1: Illustrations of Meyer's analyzing wavelet.

which is the same definition of Yamada & Ohkitani(1990).

From the conditions of a) to c) and Eqs.(7) to (9), the Fourier coefficients of analyzing wavelet  $\tilde{\psi}(\omega)$  are defined as

$$\tilde{\psi}(\omega) = e^{(-i\omega/2)} \sqrt{\{\tilde{\phi}(\omega/2)\}^2 - \{\tilde{\phi}(\omega)\}^2}. \tag{10}$$

Note that  $\tilde{\phi}(\omega)$  has a compact support in  $\{\omega \mid 2\pi/3 \leq |\omega| \leq \pi/3\}$ . Therefore, the wavelet coefficient is directly connected to the Fourier coefficient.

The inverse Fourier transform of  $\tilde{\psi}(\omega)$  gives the following desired analyzing wavelet,

$$\psi(t) = \frac{1}{2\pi} \int_{-\infty}^{\infty} \tilde{\psi}(\omega) e^{i\omega t} d\omega. \tag{11}$$

Fig.1 shows Meyer's analyzing wavelet and its Fourier spectrum. The analyzing wavelet is very regular. However, it is not very well localized in physical space but is supported compact in the Fourier space. The fast algorithm for wavelet transform with Meyer's analyzing wavelet using FFT algorithm is formulated by Yamada & Ohkitani(1991).

### 2.2 Relation between the wavelet and the Fourier spectra

It could be worth pointing out that the relations between the wavelets and the Fourier spectra. Meyer's analyzing wavelet has a useful property that is the compactness of the support in the Fourier space. Eq.(6) shows that  $\tilde{\psi}(\omega)$  is only included in  $[-2^{j+3}\pi/3, -2^{j+1}\pi/3] \cup [2^{j+1}\pi/3, 2^{j+3}\pi/3]$ . Since the square of wavelet coefficient is corresponding to the energy, the direct relation between

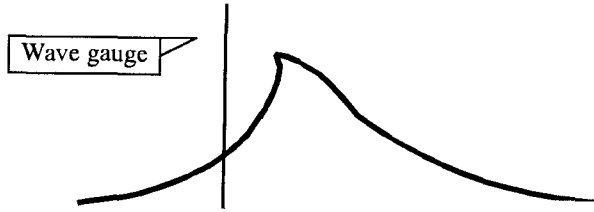


Figure 2: Illustration of breaking wave passing a wave gauge.

the wavelet and the Fourier spectrum is expected as

$$E_j = \sum_{k=1}^{\infty} |\alpha_{j,k}|^2 \sim \omega S(\omega) \quad (\omega \sim 2^{j+2} \pi/3) \quad (12)$$

where  $\omega$  is angular frequency,  $S(\omega)$  the Fourier spectrum and  $E_j$  the wavelet spectrum. Particularly, the relationship of a power law of the energy spectrum between the wavelet and the Fourier spectrum can be expressed as

$$E_j \sim 2^{-j(p-1)} \iff S(\omega) \sim \omega^{-p}. \quad (13)$$

Eq.(13) gives the relation that  $\omega^{-p}$  in the Fourier spectrum is equivalent to  $2^{-j(p-1)}$  in the wavelet spectrum.

### 2.3 Local and shock wavelet spectra

The purpose of this study is to detect jumps in water surface elevation associated with breaking. We suppose that the sea surface elevation  $\eta(t)$  is measured as a function of time  $t$  with a discrete sampling time  $\Delta t$  at a fixed horizontal position as illustrated in Fig.2. The wave passing the sensor will generally show a smooth rise  $\partial\eta/\partial t$ . But, if a just breaking wave passes the sensor, we can expect a sudden jump of the surface elevation. The magnitude of the sudden jump is associated with the scale of breaker type: *i.e.* for a plunging breaker this is relatively large and it is smaller for spilling breaker.

The Fourier series of shock wave represented as

$$y(t) = \begin{cases} At, & t \leq 0.5, \\ A(t-1), & t \geq 0.5, \end{cases} \quad (0 \leq t \leq 1) \quad (14)$$

where  $A$  is the height of shock is easily given by  $\sum(-4/n) \sin(n\omega t)$ . Therefore, a power law of the energy spectrum of the breaking wave with the sudden jump is expected to  $\omega^{-2}$  or  $2^{-j}$ .

To investigate the local energy information among the scale, we define the local wavelet spectrum  $L_{j,k'}$  for the scale  $j \geq j_s$  as

$$L_{j,k'} = \sum_{k'} |\alpha_{j,k}|^2, \quad (0 \leq k' \leq 2^{j_s}) \quad (15)$$

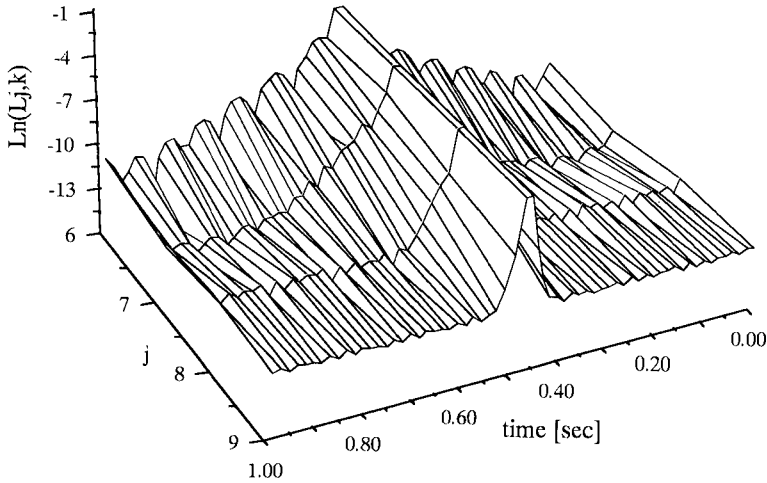


Figure 3: The local wavelet spectrum  $L_{j,k'}$  of shock wave given by Eq.(14).

where,  $j_s$  is minimum dilation mode of the local wavelet spectrum which determine the resolution and  $\sum$  denotes the special summation over  $k$  satisfying:  $(k/2^{j_s} \leq k'/2^j \leq (k+1)/2^{j_s})$ . The local wavelet spectrum  $L_{j,k'}$  can analyze characteristics of microscopic or local energy properties for data. Besides, we introduce the shock wavelet spectrum to detect the surface jump of the shock wave described by Eq.(14). The shock wavelet spectrum  $M_{j,k'}$  is defined by following as

$$M_{j,k'} = 2^j \times \sum_{k'} |\alpha_{j,k}|^2. \quad (0 \leq k' \leq 2^{j_s}) \tag{16}$$

Since power law of shock wave is  $2^{-j}$  for the wavelet spectrum, that is corresponding to power law of  $\omega^{-2}$  for the Fourier spectrum, the shock wavelet spectrum detects the shock as a constant power whenever jumps observed in the surface elevation.

Fig.3 shows the local wavelet spectrum( $j_s=6$ ) for the shock wave given by Eq.(14). The number of points to discretize the shock wave is 512. The local wavelet spectrum shows the energy distribution of *time-frequency* space and indicates existence of the high crest corresponding the time of shock at  $t=0.5$ . This result implies the effectiveness of the local wavelet spectrum for local energy analysis. To make clear the local energy properties of the shock wave, the shock wavelet spectrum( $j_s=6$ ) for shock wave of Eq.(14) is shown in Fig.4. We can easily detect the shock from the characteristic structures of shock wavelet spectrum  $M_{j,k'}$  both of the occurrence time and their magnitudes.

To say nothing of the accuracy of detection of shock depend on discretization of data. The relation sampling frequency  $\Delta t$  and the local power law is shown

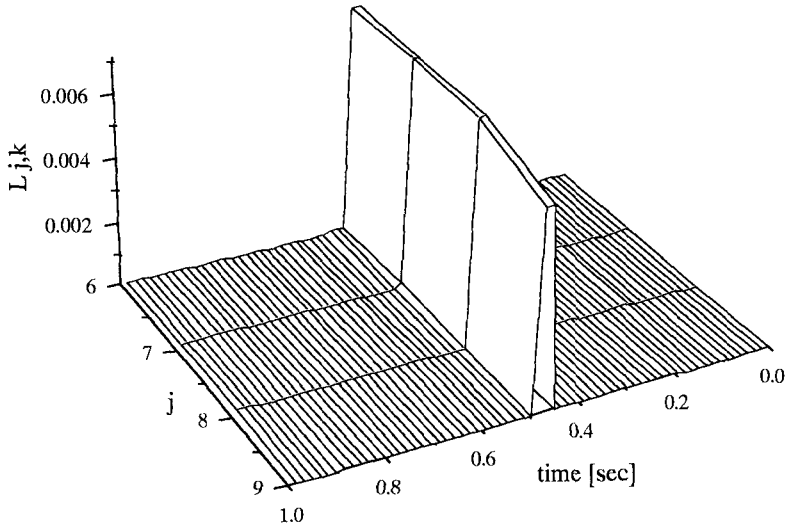


Figure 4: The shock wavelet spectrum  $M_{j,k}$  of shock wave given by Eq.(14).

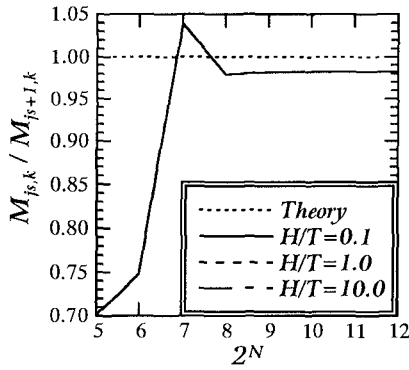


Figure 5: Comparison of the local power law of shock wave between the numerical and analytical one.

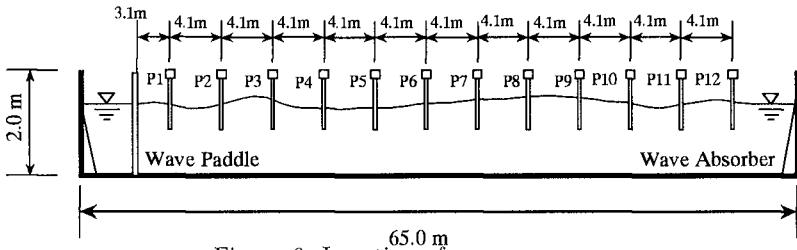


Figure 6: Location of wave gages.

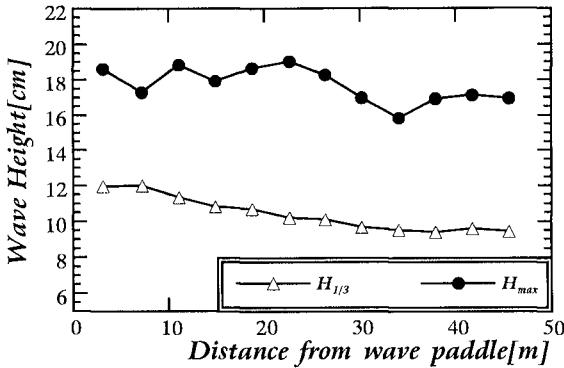


Figure 7: Spatial variation of the wave height statistics.

in Fig.5, where  $H$  is the height of the shock wave and  $T$  is the wave period. The value of  $j_s$  is set equal to  $j_{max}-2$  and the local power law of the wavelet spectra are calculating the scales between the  $j_s$  and  $j_s + 1$ . The error of estimating of power law is 2.7% for  $N=256$  to 4096, 4% for  $N=128$ , 25% for  $N=64$  and 30% for  $N=32$ . We conclude that the number of point  $N \geq 64$  or 128 per one wave is required to accurate estimation the jump from the data. Note that the accuracy of estimation is independent of the amplitude of the shock wave.

### 3. EXPERIMENTS

#### 3.1 Experimental condition

The experiments were conducted in the glass channel installed at Technical Research & Development Institute of Nishimatsu construction Co.,Ltd. The channel is 65m long, 1m wide, 2m high and was filled to a depth of 0.98m. Waves were generated by computer-controlled piston type wave paddle. The initial spectra of the surface elevations are composed of the Wallop type spectra with the band width  $m=10$  and the peak frequency  $f_p=1\text{Hz}$ , giving a wavenumber  $k_p=4.072\text{m}^{-1}$  and characteristic water depth  $k_p h=3.99$ , so that the waves



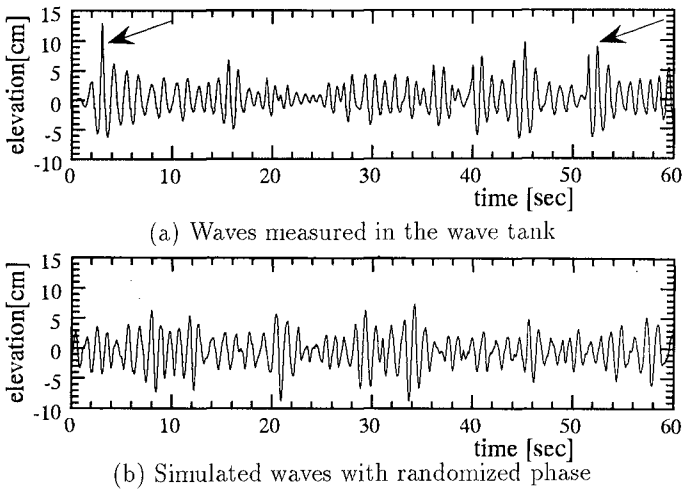


Figure 8: Water surface elevations of the random wave trains.

were deep water waves. Water surface displacements were measured with twelve capacitance type wave gages as shown in Fig.6. The measurements were performed at a sampling frequency of 100Hz for over 100sec. At the same, spatial surface profiles were recorded by video camera to examine the breaking event.

Figure 7 shows the spatial variation of  $H_{max}$  and  $H_{1/3}$ . Although, the value of  $H_{max}$  is fluctuated, the spatial variation of  $H_{1/3}$  shows that there is some energy dissipation due to the wave breaking. In the following, we only focus the surface elevations at P5.

### 3.2 Local energy characteristics of nonlinear wave

The values of skewness and kurtosis at P5 are 0.245 and 3.473, so that the waves are found to have weakly nonlinear characteristics. For comparison with the experimental data, we calculate artificial random phase wave data(linear waves) which is obtained by the inverse Fourier transform of the original surface elevations of P5 after randomizing their phases uniformly over  $[0, 2\pi]$  with their amplitudes unchanged. The surface elevations of experimental data and simulated wave with randomized wave are shown in Fig.8, respectively. The two arrows in the Figure indicate the time when breaking event just occurs.

Weissman *et al.*(1984) developed the detection method of breaking waves based on the singularities of the high frequencies, which is the intrinsic frequency of gravity-capillary waves, by a trial and error method with the running Fourier transform. The wave profile band-passed of high frequencies(10-12Hz) shown in Fig.8(a) is illustrated in Fig.9. The bursts of energy in the high frequency com-

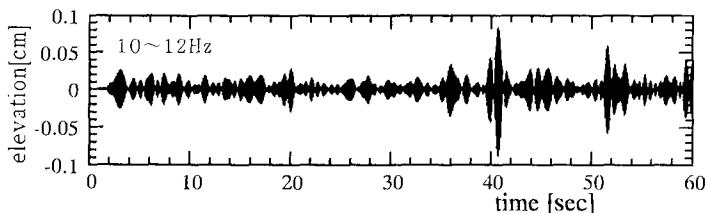


Figure 9: Water surface profile of band-pass filtered wave with the high frequency components(10-12Hz) of Fig.8(a).

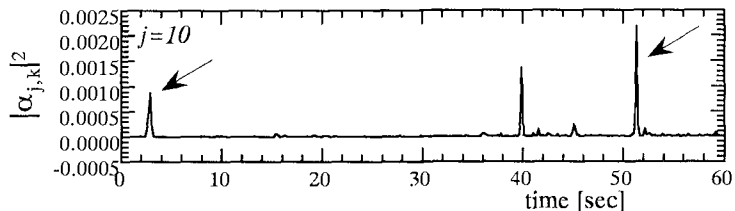
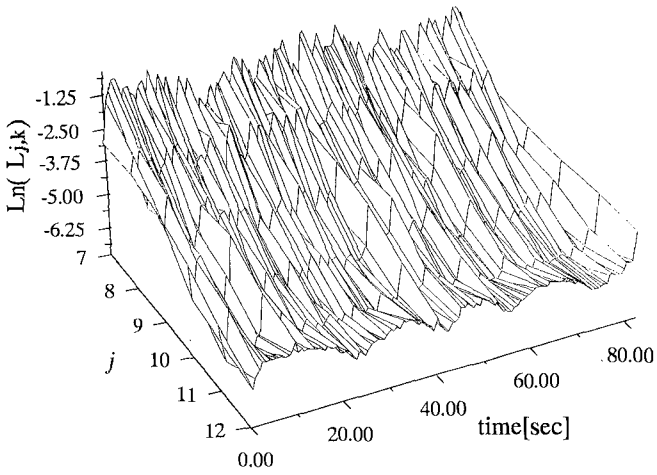


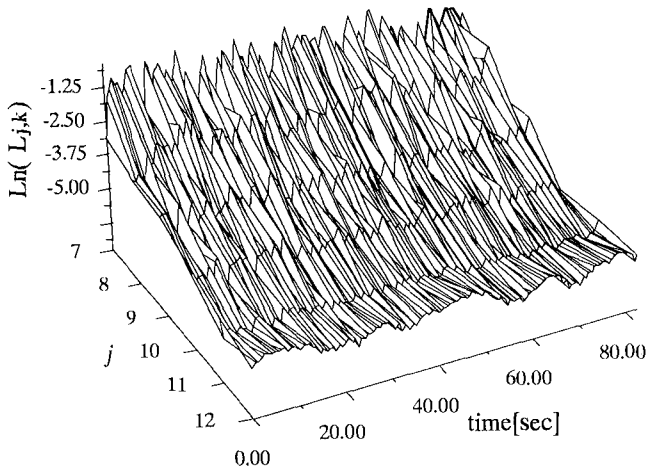
Figure 10: Temporal distribution of the square value of wavelet coefficient,  $|\alpha_{j,k}|^2$ , of the experimental wave

ponents are indicative of breaking events. He detected wave breaking from burst of the temporal energy distributions in this frequency band. Fig.10 shows the square value of wavelet coefficients  $\alpha_{j,k}$  at the scale  $j=10$  which is corresponding to about 8Hz. The distributions of square values of  $\alpha_{j,k}$  clearly indicate the singularities of the high frequencies, which are corresponding to the time of breaking waves, in comparison with the result of the Fourier band filtered method(Fig.9). The same empirical method to detect the breaking waves can be applied by the wavelet analysis and will be given better result rather than the running Fourier transform, but let us then considered here the energy structure and energy cascade process among lower and higher frequency components.

It was already shown that the local wavelet spectrum is effective to analyze the temporal energy structures in previous section. Fig.11 shows the local wavelet spectra with  $j_s=7$  for the experimental wave and the simulated wave, respectively. The experimental data indicate that characteristic structure of energy distribution is shown running in parallel with the  $j$ -axis. Particularly, some big crests can be observed at the large scale into small scale. Although the Fourier spectrum is the same as experimental wave, there is no pattern or structure in the local wavelet spectrum as the experimental wave in the simulated wave(b) and they seem to distributing uniformly. This implies that the high frequency components of experimental wave, nonlinear wave, are not constant in amplitude and that there are sharp peaks sporadically distributed along the time series. In other words, the high frequency components are intermittent in



(a) Waves measured in the wave tank



(b) Simulated waves with randomized phase

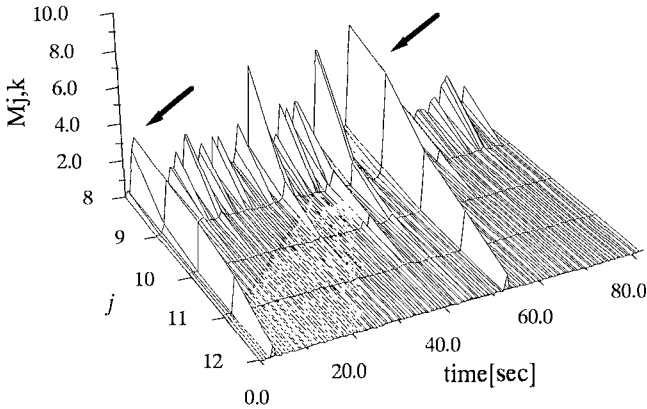
Figure 11: Local wavelet spectra for the measured and simulated waves.

the nonlinear wave.

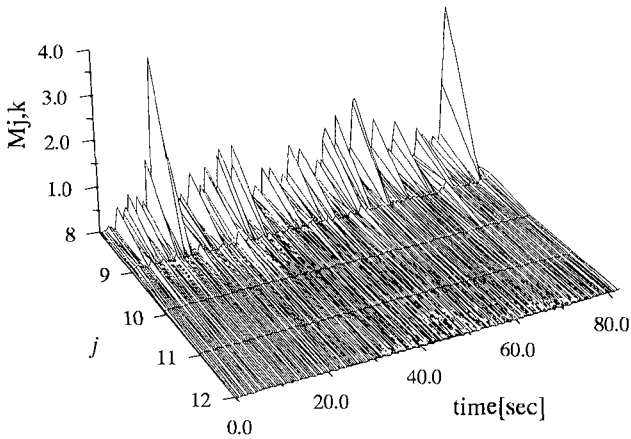
The sharp peaks and structures in wavelet space( $j, k$ ) are related with nonlinear wave-wave interaction but we may leave the details to further studies.

### 3.3 Detection of breaking wave

The nonlinear waves have the local energy characteristics as already shown in Fig.11. This will lead us further into a consideration of detection of breaking



(a) Waves measured in the wave tank



(b) Simulated waves with randomized phase

Figure 12: Shock wavelet spectra for the measured and simulated wave.

wave by shock wavelet spectra. The shock wavelet spectra of experimental wave and simulated wave are shown in Fig.12. The sharp peaks are shown intermittently in the experimental wave, corresponding to the time when breaking wave passes. Therefore, we need some detector function to judge whether they break or not. Thus, we define the detector function  $a_i$  is calculated as

$$a_i = \frac{M_{j_s+m,k_i}}{M_{j_s,k_i}}, \tag{17}$$

where subscript  $i$  denotes temporal position ( $0 \leq k^i \leq 2^{j_s}$ ),  $j_s$  is resolution of scale parameters and  $m$  is distance between the  $j_s$ . The illustration of the

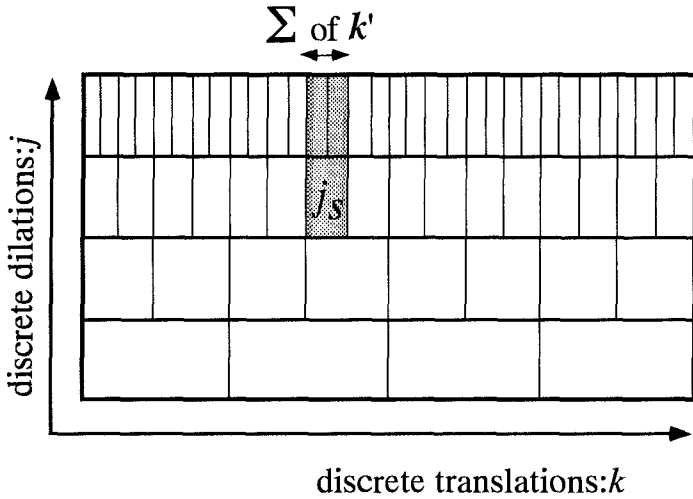


Figure 13: Illustration of wavelet space and relationship with parameters

Table 1: Accuracy of the present detection method

$a \setminus n$		$j_s=7$	$j_s=7$	$j_s=8$	$j_s=8$
		$m=1$	$m=2$	$m=1$	$m=2$
0.9	(-1)	<b>2</b>	1	3	<b>2</b>
0.8		3	1	4	<b>2</b>
0.6		4	1	5	<b>2</b>
0.5	(-2)	5	1	5	3

wavelet space and the relationship with parameter is shown in Fig.13. The experimental result of detection of the method for the experimental wave is shown Table 1 ( $j_s=7$  is corresponding peak frequency of the spectrum). The actual number of breaking waves is two, therefore,  $j_s=8$ ,  $m=2$ ,  $a_i=0.9$  and 0.8, 0.6 and  $j_s=7$ ,  $m=1$ ,  $a_i=0.9$  gives quite nice value when we selected. The fine resolution scale of  $j_s=8$  accurately detect the breaking waves rather than  $j_s=7$  and the  $m=2$  gives more accurate results than  $m=1$ . The reason for this result is sampling frequency of shock and fluctuation of the local power law due to the external noise of data.

It could be concluded that the present method can detect the breaking wave from the temporal water surface elevation data, if the adequate parameters  $a$  and  $m$  are selected as  $a_i \geq 0.8$  and  $m=2$ .

#### 4. CONCLUSION

We applied the orthonormal wavelet expansion to the water surface elevations of random waves and studied their local characteristics. It is found that the sudden surface jumps associated with the breaking waves were well reflected in the shock wavelet spectra. Thus, we developed the rational detection method of breaking wave as following procedure:

- 1.The wavelet coefficients  $\alpha_{j,k}$  of the surface elevations are calculated Eq.(3).
- 2.The appropriate resolution with the scale  $j_s$  is selected.
- 3.The shock wavelet spectra are calculated with Eq.(16).
- 4.The local power law of the surface elevations are calculated Eq.(17).
- 5.Breaking waves are expected to have the local power a law  $2^{-j}$  of the wavelet spectrum

Furthermore, the sudden surface jumps can be well detected, if they are described by using sufficiently many discretized points. We demonstrated the validity of the method by comparing with the experimental data. Note that this method can be applied to not only deep water waves but also shallow water.

#### ACKNOWLEDGEMENT

The authors are grateful to Dr.Yamada at University of Tokyo for valuable advice and wish to thank Technical Research & Development Institute of Nishimatsu construction Co.,Ltd. for their cooperation. One of the authors is supported by fellowships of the Japan Society for the Promotion of Science for Japanese Junior Scientists. Further, this research is supported in part by Grant-in-Aid for Scientific Research(JSPS-0440), The Ministry of Education, Science and Culture.

#### REFERENCES

- Farge, M. (1992) Wavelet transforms and their applications to turbulence, *Annual.Review.Fluid Mech.*, 24, pp.395-457.
- Holthuijsen, L.H. & T.H.C.Herbbers(1986) Statistics of breaking waves observed as whitecaps in the open sea, *J.Phys.Oceanogr*, 16, pp.290-297.
- Kennedy, R.M. & Snyder, R.L.(1983) On the formation of whitecaps by threshold mechanism Part II: Monte Carlo experiments, *J.Phys.Oceanogr*, 13, pp.1493-1504.
- Longuet-Higgins, M.S. & N.D.Smith(1983) Measurement of breaking waves by a surface jump meter, *J.Geo.Res.*, 88, C14, pp.9823-9831.

- Mallat, S.(1989) Multiresolution approximations and wavelet orthonormal bases of  $L^2(R)$ , *Tans.Am.Math.Soc.*, 315, pp.69-89.
- Meyer, Y.(1989) Wavelets, eds. J.M. Combes *et al.*, (Springer).
- Meyer, Y.(1991) Wavelets and Applications, (Masson-Springer).
- Mori, N., T.Yasuda & M.Yamada(1993) Orthonormal wavelet expansion and its application to water waves, *Proc.40th Coastal Eng.Conf., JSCE*, 40-1, pp.141-145(in Japanese).
- Shen, Z., W.Wang & K.Mei(1994) Finestructure of wind waves analyzed with wavelet transform, *J.Phys.Oceanogr.*, 24, pp.1085-1094.
- Su, M.Y. & J.Cartmill(1993) Breaking wave measurement by a void fraction technique, *WAVE'93*, pp.951-962.
- Weissman, M.A., S.S.Ataktürk and K.B.Katsaros(1984) Detection of breaking events in a wind-generated wave field, *J.Phys.Oceanogr*, 14, pp.1608-1619.
- Yamada, M. & K.Ohkitani(1990) Orthonormal wavelet expansion and its application to turbulence, *Prog.Theor.Phys.*, 83, No.5, pp.819-823.
- Yamada, M. & K. Ohkitani(1991) An identification of energy in turbulence by orthonormal wavelet analysis, *Prog.of Theoretical Phys.*, 86, No.4, pp.799-815.

## CHAPTER 32

# A Fully-Dispersive Nonlinear Wave Model and its Numerical Solutions

Kazuo Nadaoka<sup>1</sup>, Serdar Beji<sup>2</sup> and Yasuyuki Nakagawa<sup>3</sup>

### Abstract

A set of fully-dispersive nonlinear wave equations is derived by introducing a velocity expression with a few vertical-dependence functions and then applying the Galerkin method, which provides an optimum combination of the vertical-dependence functions to express an arbitrary velocity field under wave motion. The obtained equations can describe nonlinear non-breaking waves under general conditions, such as nonlinear random waves with a wide-banded spectrum at an arbitrary depth including very shallow and far deep water depths. The single component forms of the new wave equations, one of which is referred to here as "*time-dependent nonlinear mild-slope equation*", are shown to produce various existing wave equations such as Boussinesq and mild-slope equations as their degenerate forms. Numerical examples with comparison to experimental data are given to demonstrate the validity of the present wave equations and their high performance in expressing not only wave profiles but also velocity fields.

### INTRODUCTION

Although evolution of non-breaking waves is principally governed by their nonlinearity and dispersivity, there exist no wave equations which can express these two effects under general conditions. For example, the Boussinesq-type equations are *weakly* nonlinear-dispersive equations and can describe only shallow water waves. Although several successful attempts for extending their applicable range in relative water depth have been reported (Madsen, et al., 1991; Nwogu, 1993, etc.), even such an improved model cannot be relied on if the depth becomes comparable with the wave length or more.

---

<sup>1</sup> Department of Civil Engineering, Tokyo Institute of Technology, 2-12-1 O-okayama, Meguro-ku, Tokyo 152, Japan

<sup>2</sup> Faculty of Naval Architecture and Marine Technology, Istanbul Technical University, Maslak 80626, Istanbul, Turkey

<sup>3</sup> Hydrodynamics Laboratory, Port and Harbour Research Institute, Nagase 3-1-1, Yokosuka 239, Japan



The mild-slope equation of Berkhoff (1972) has no restriction on depth; but it can be used only for linear monochromatic (and hence *non-dispersive*) waves. The time-dependent forms of the mild-slope equation (e.g., Smith and Sprinks, 1975) can describe the dispersive evolution of linear random waves; but their band-width of spectrum is restricted to be narrow. (In this sense, they may be called "*narrow-banded mild-slope equations*".)

To break through all these restrictions, in the present study, new fully-dispersive nonlinear wave equations have been developed. Unlike the Boussinesq equations, which are derived with an asymptotic expansion procedure, the new equations are obtained by introducing a velocity expression with a few vertical-dependence functions and then applying the Galerkin method, which provides an optimum combination of the vertical-dependence functions to express an arbitrary velocity field of waves. The derived equations can express nonlinear non-breaking waves under general conditions, such as nonlinear random waves with a *wide-banded* spectrum at an *arbitrary depth* including very shallow and far deep water depths.

In the following sections, the principal idea and derivation procedure of the new wave equations\* as well as their simplified forms are presented with some numerical examples and their comparison to experimental data to demonstrate the validity of the equations and the performance especially in expressing velocity fields. Besides theoretical relationships of the present theory to various existing wave equations such as Boussinesq and mild-slope equations are also shown.

## THEORY

### Principal Idea :

Generally speaking, any mathematical procedure to obtain a water-wave equation is a conversion process from original basic equations defined in a 3-D  $(x,y,z)$  space to wave equations to be defined in a horizontal 2-D  $(x,y)$  space. For this conversion, we must introduce an assumption on the vertical dependence of the velocity field.

For example, the Boussinesq equations are obtained by introducing the following expression with polynomials of  $z$  on the velocity potential  $\Phi$  (e.g., Mei, 1983):

$$\Phi(x,y,z,t) = \sum_{m=0}^{\infty} \Phi_m(x,y,t)(z+h)^m, \quad (1)$$

where  $h$  is the water depth and the vertical coordinate  $z$  is taken upward from the still water level. With the Laplace equation of  $\Phi$  and the boundary condition at the horizontal bottom, the above equation may be expressed as

$$\Phi(x,y,z,t) = \Phi_0 - \frac{(z+h)^2}{2!} \nabla^2 \Phi_0 + \frac{(z+h)^4}{4!} \nabla^2 \nabla^2 \Phi_0 - \dots, \quad (2)$$

where  $\nabla = (\partial/\partial x, \partial/\partial y)$ . Usually only the first two terms in the above equation are retained to derive the Boussinesq equations.

This procedure is a kind of asymptotic expansion of  $\Phi$  around the long wave limit,

---

\* The fundamental idea of the present theory and numerical examples only for linear random waves with wide-band spectrum have been given in Nadaoka and Nakagawa (1991, 1993a,b). The extension to nonlinear waves but in more complicated form of equations has been reported in Nadaoka and Nakagawa (1993c).

and hence the Boussinesq equations can be applied only to shallow water waves. This restriction is related to the fact that the asymptotic approximate form of eq.(2) is not enough to express a velocity field under deeper waves. This in turn suggests that derivation of new wave equations with much wider applicability may be achieved by providing a more reasonable way to express the vertical dependence of a velocity field for more general cases including random waves in deep water.

In the present study, the following assumption is introduced to express the horizontal velocity vector,  $q = (u, v)$ :

$$q(x, y, z, t) = \sum_{m=1}^N U_m(x, y, t) F_m(z), \tag{3}$$

where

$$F_m(z) = \frac{\cosh k_m(h+z)}{\cosh k_m h}. \tag{4}$$

The choice of cosh functions in the above as the vertical-dependence functions is based on the general 2-D solution of Laplace equation of  $\Phi$  on the horizontal bottom (e.g., Nadaoka and Hino, 1983),

$$\Phi(x, z, t) = \int_{-\infty}^{\infty} A(k, t) \frac{\cosh k(h+z)}{\cosh kh} \exp(ikx) dk, \tag{5}$$

where  $k$  is the wavenumber and  $A(k, t)$  is a time-varying wavenumber spectrum. It should be noted that eq.(5) is valid also for nonlinear waves and hence the use of eq.(4) as the vertical-dependence function  $F_m(z)$  is not restricted to linear waves.

In the discrete form of eq.(5),

$$\Phi(x, z, t) \cong \sum_{i=1}^{i \max} A(k_i, t) \exp(ik_i x) \Delta k \frac{\cosh k_i(h+z)}{\cosh k_i h}, \tag{6}$$

we need a large number of the spectral component  $A(k_i, t)$  in case of broad-banded random waves. However this fact does not necessarily mean that  $N$  in eq.(3) should be a large number, in spite of the resemblance between eqs.(3) and (6). This is true if each function,  $\cosh k_i(h+z)/\cosh k_i h$ , in eq.(6) can be expressed by eq.(3) with a few prescribed  $F_m(z)$ .

### Galerkin Expression of a Velocity Field :

To examine this, the following approximation has been attempted:

$$\frac{\cosh k(h+z)}{\cosh kh} \cong \sum_{m=1}^N Q_m F_m(z), \tag{7}$$

where  $k$  is an arbitrary wavenumber and  $F_m(z)$  is as defined in (4). For this approximation we need a mathematical procedure to determine the unknown coefficients  $Q_m$  ( $m = 1, \dots, N$ ). For this purpose, in the present study, the Galerkin method has been employed.

Figure 1 shows the results of the approximation for five values of  $kh$ , covering very shallow to deep water depths. The number of components in eq.(7),  $N$ , is only 4 in this case and the prescribed values of  $k_m h$  for  $F_m(z)$  are 1.6, 3.5, 6.0, 10.5, respectively. The fact that the remarkably good agreements between the exact and approximated values are obtained for any arbitrary  $kh$  means that the

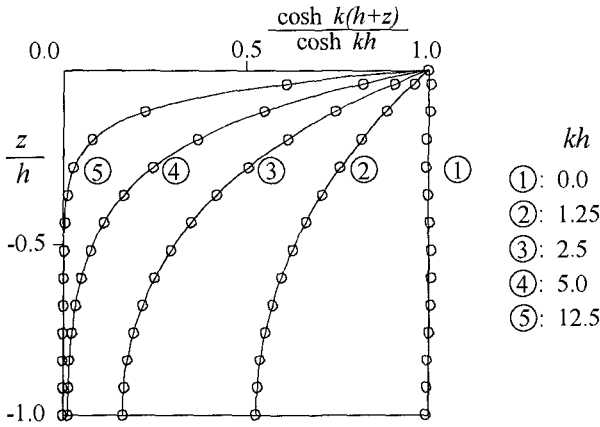


Fig. 1 Comparisons of the exact and approximated vertical distribution functions.

velocity expression by eqs.(3) and (4) with a small  $N$  may be applied to wave field under general conditions, such as random waves at an arbitrary depth including very shallow and far deep water depths. This is the most important finding to provide a basis of the new formulation of wave equations described in what follows.

**Derivation of Fully-Dispersive Nonlinear Wave Equations :**

With this basis of formulation, we are now ready to proceed to the derivation of new wave equations (for details, see Nadaoka et al., 1994).

The basic equations defined in 3-D  $(x,y,z)$  space are the continuity equation,

$$\nabla \cdot \mathbf{q} + \frac{\partial w}{\partial z} = 0, \tag{8}$$

and an alternative exact form of the Euler equation for irrotational flow (Beji,1994),

$$\frac{\partial \mathbf{q}}{\partial t} + \nabla \left[ g\eta + \int_z^\eta \frac{\partial w}{\partial t} dz + \frac{1}{2} (\mathbf{q}_s \cdot \mathbf{q}_s + w_s^2) \right] = 0, \tag{9}$$

where  $\mathbf{q}_s$  and  $w_s$  are the velocity components at the free surface  $z=\eta$ .

The vertical velocity  $w$  is obtained from the continuity equation (8) by substituting eqs.(3) and (4) and integrating from the bottom to an arbitrary depth  $z$ :

$$w(x,y,z,t) = - \sum_{m=1}^N \nabla \cdot \left[ \frac{\sinh k_m (h+z)}{k_m \cosh k_m h} U_m(x,y,t) \right]. \tag{10}$$

The vertical integration of the continuity equation (8) over the entire depth gives

$$\frac{\partial \eta}{\partial t} + \nabla \cdot \left( \int_{-h}^\eta \mathbf{q} dz \right) = 0, \tag{11}$$

which then with the substitution of eqs.(3) and (4) yields

$$\frac{\partial \eta}{\partial t} + \sum_{m=1}^N \nabla \cdot \left[ \frac{\sinh k_m (h + \eta)}{k_m \cosh k_m h} \mathbf{U}_m \right] = 0. \quad (12)$$

To obtain the evolution equations of  $\mathbf{U}_m$  ( $m = 1, \dots, N$ ), on the other hand, we may apply the Galerkin method to the momentum equation (9). Namely, after substituting eqs.(3) and (4) into eq.(9), the resulting equation is multiplied by the depth dependent function  $F_m(z)$  and vertically integrated from  $z = -h$  to  $\eta$ . Since the depth-dependence function has  $N$  different modes, we obtain a total of  $N$  vector equations corresponding to each mode:

$$\sum_{m=1}^N a_{nm} \frac{\partial \mathbf{U}_m}{\partial t} + b_n \nabla \left[ g \eta + \frac{1}{2} (\mathbf{q}_s \cdot \mathbf{q}_s + w_s^2) \right] = \sum_{m=1}^N \left[ c_{nm} \nabla (\nabla \cdot \mathbf{U}_m)_t + \mathbf{d}_{nm} \cdot (\nabla \cdot \mathbf{U}_m)_t \right], \quad (n = 1, 2, \dots, N) \quad (13)$$

where

$$a_{nm} = a_{mn} = \frac{1}{2 \cosh k_m h \cosh k_n h} \left\{ \frac{\sinh(k_m + k_n)(h + \eta)}{k_m + k_n} + \frac{\sinh(k_m - k_n)(h + \eta)}{k_m - k_n} \right\},$$

$$b_n = -g \frac{\sinh k_n (h + \eta)}{k_n \cosh k_n h},$$

$$c_{nm} = c_{mn} = \frac{1}{k_m^2 \cosh k_m h \cosh k_n h} \left[ \frac{\cosh k_m (h + \eta) \sinh k_n (h + \eta)}{k_n} \right. \quad (14)$$

$$\left. - \frac{1}{2} \left\{ \frac{\sinh(k_m + k_n)(h + \eta)}{k_m + k_n} + \frac{\sinh(k_m - k_n)(h + \eta)}{k_m - k_n} \right\} \right].$$

The coefficients  $\mathbf{d}_{nm}$  in eq.(13) have rather complicated mathematical forms, but may be evaluated as being nearly equal to  $\mathbf{D}_{nm}$  shown in eq.(19) later. In this evaluation the neglected terms are  $O(\varepsilon \cdot \nabla h)$ .

Equations (12) and (13) constitute a solvable set of equations for  $2N+1$  unknowns,  $\eta$ ,  $\mathbf{U}_m$  ( $m = 1, \dots, N$ ), and describe their evolution as wave equations. It should be noted that no approximation has been introduced on the nonlinearity and that the full-dispersivity can be attained by taking only a few components, as demonstrated later; hence eqs.(12) and (13) may be referred to as "fully-dispersive nonlinear wave equations".

It should be further noted that  $k_m$  in eqs.(12) and (14) are *not* the wavenumbers in a usual sense like the spectral wavenumbers  $k_i$  in eq.(6), but they are the parameters to prescribe  $F_m(z)$  so as to approximate a velocity field well enough. The wavenumber parameters  $k_m$  ( $m = 1, \dots, N$ ) are to be specified with the linear dispersion relation,  $\omega_m^2 = g k_m \tanh k_m h$ , by prescribing the angular frequencies  $\omega_m$  ( $m = 1, \dots, N$ ) as a set of input data for the computation to properly cover the wave spectrum concerned. Therefore  $k_m$  must be treated as spatially varying quantities, according to the variation in  $h(x, y)$ .

**Weakly Nonlinear Version of Fully-Dispersive Wave Equations :**

Although equations (12) and (13) may express both full nonlinearity and dispersivity, they have disadvantages in computational aspects; i.e., the coefficients (14) includes many hyperbolic functions, besides the arguments of them have the unknown variable  $\eta$ . These points are undesirable in terms of computational time and robustness of the numerical algorithm.

Therefore, in the present study, a simplified version of eqs.(12) and (13) has been also developed by introducing a weakly-nonlinear formulation. By invoking a Taylor series expansion of  $q$  around  $z=0$ , and keeping only the first-order nonlinear contributions both in eqs.(9) and (11), we obtain

$$\frac{\partial \eta}{\partial t} + \nabla \cdot \left( \int_{-h}^0 q dz + \eta q_0 \right) = 0, \tag{15}$$

$$\frac{\partial q}{\partial t} + \nabla \left[ g\eta + \int_z^0 \frac{\partial w}{\partial t} dz + \eta \frac{\partial w_0}{\partial t} + \frac{1}{2} (q_0 \cdot q_0 + w_0^2) \right] = 0, \tag{16}$$

in which  $q_0$  and  $w_0$  are the velocities at the still water level  $z=0$ .

With the corresponding change of the upper limit of the vertical integration from  $\eta$  to 0 in the Galerkin procedure, we get the following simultaneous equations as the weakly-nonlinear version of eqs. (12) and (13).

$$\frac{\partial \eta}{\partial t} + \sum_{m=1}^N \nabla \cdot \left[ \left( \frac{C_m}{g} + \eta \right) U_m \right] = 0, \tag{17}$$

$$\begin{aligned} \sum_{m=1}^N A_{nm} \frac{\partial U_m}{\partial t} + B_n \nabla \left[ g\eta + \eta \frac{\partial w_0}{\partial t} + \frac{1}{2} (q_0 \cdot q_0 + w_0^2) \right] = \\ \frac{\partial}{\partial t} \sum_{m=1}^N [C_{nm} \nabla (\nabla \cdot U_m) + D_{nm} (\nabla \cdot U_m)], \quad (n = 1, 2, \dots, N) \end{aligned} \tag{18}$$

where,

$$\begin{aligned} A_{nm} &= \frac{\omega_n^2 - \omega_m^2}{k_n^2 - k_m^2}, & A_{mm} &= \frac{g\omega_n^2 + h(g^2 k_n^2 - \omega_n^4)}{2gk_n^2}, & \omega_m^2 &= gk_m \tanh k_m h, \\ B_n &= \frac{\omega_n^2}{k_n^2}, & C_{nm} &= \frac{B_n - A_{nm}}{k_m^2}, & D_{nm} &= \nabla C_{nm}, \\ D_{nm} &= \frac{2}{k_m^2 - k_n^2} \left[ \frac{2\nabla k_m}{k_n} \{ A_{nm} - (k_m^2 - k_n^2) C_{nm} \} + \frac{g\nabla h}{\cosh k_n h \cdot \cosh k_m h} \right], \end{aligned} \tag{19}$$

$q_0$  and  $w_0$  in eq.(18) may be evaluated as

$$q_0 = \sum_{m=1}^N U_m, \quad w_0 = - \sum_{m=1}^N \nabla \cdot \left( \frac{B_m}{g} U_m \right). \tag{20}$$

As shown in (19), the coefficients of the weakly nonlinear version of the equations are considerably simplified as compared with those defined in (14).

**Linear Dispersion Characteristics of New Wave Equations :**

The linear dispersion characteristics of the present wave equations can be examined by solving the eigenvalue problem defined with the linearized equation of the fully-dispersive equations and with the prescribed values of  $k_m h$  ( $m=1, \dots, N$ ). An example of the computed dispersion curve is shown in Fig. 2, where  $N=4$  and the same values as those for Fig. 1 are assigned to  $k_m h$  ( $m=1, \dots, N$ ). The computed values show perfect agreements with the theoretical linear dispersion curve over wide wavenumber domain extending from very shallow to far deep water. This remarkable feature of the present wave equations becomes more prominent by comparing with the dispersion curves of the classic Boussinesq equations and of the improved Boussinesq equations (Madsen et al. 1991), as shown in Fig. 2.

The reason why the present equations can possess fully dispersive characteristics may be found by examining the dispersive characteristics of the linearized single-component ( $N=1$ ) equation. In this case, the following analytical expression of the

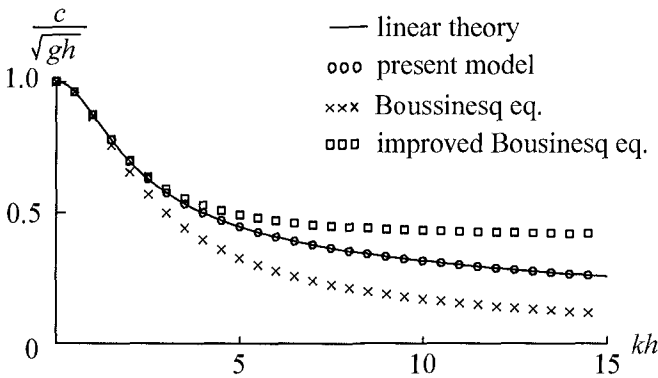


Fig.2 Linear dispersion characteristics of the fully-dispersive equations.

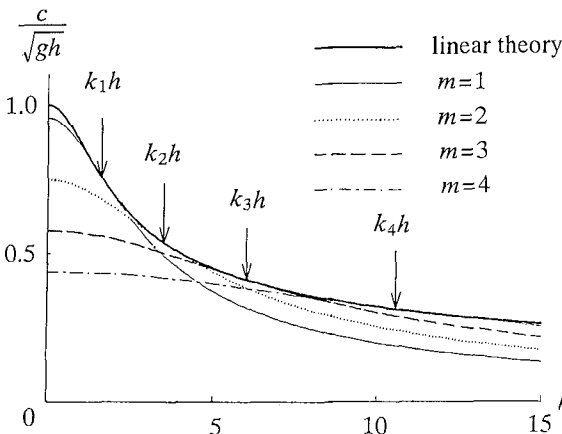


Fig.3 Dispersion curves of the single-component equation with each  $k_i h$  for Fig.2.

dispersion relation can be obtained by solving the corresponding eigenvalue problem :

$$C^2 = \frac{C_p^3}{C_g + \frac{k^2}{k_p^2}(C_p - C_g)}, \quad (21)$$

where  $C_p$  and  $C_g$  are the theoretical linear phase and group velocities corresponding to the prescribed wavenumber  $k_p$ , while  $k$  and  $C$  denote an arbitrary incident wavenumber and the corresponding phase celerity dictated by the dispersion relation (21). Figure 3 depicts the dispersion curves described by eq.(21), in which one of the values of  $k_m h$  ( $m=1, \dots, N$ ) for Fig.2 is given respectively for each curve as  $k_p h$ . As it is seen, each selected component describes a dispersion curve which is tangent to the exact curve at the selected wavenumber  $k_p$ . Hence combining all these contributions by the Galerkin procedure, we obtain the perfect agreement in the expression of the dispersive characteristics as shown in Fig.2.

### Single-Component ( $N=1$ ) Forms :

#### "Narrow-banded nonlinear wave equations"

The fact that as shown in Fig.3 each selected component describes a dispersion curve which is tangent to the exact curve at the selected wavenumber  $k_p$  means that if the waves in concern have a narrow-band spectrum centered at  $k_p$ , the single-component ( $N=1$ ) versions of the wave equations (12) and (13) or (17) and (18) may be employed as "narrow-banded nonlinear wave equations".

For example, the single-component forms of eqs.(17) and (18) may be written as:

$$\frac{\partial \eta}{\partial t} + \nabla \cdot \left[ \left( \frac{C_p^2}{g} + \eta \right) \mathbf{q}_0 \right] = 0, \quad (22)$$

$$\begin{aligned} C_p C_g \frac{\partial \mathbf{q}_0}{\partial t} + C_p^2 \nabla \left[ g \eta + \eta \frac{\partial w_0}{\partial t} + \frac{1}{2} (\mathbf{q}_0 \cdot \mathbf{q}_0 + w_0^2) \right] = \\ \frac{\partial}{\partial t} \left\{ \frac{C_p (C_p - C_g)}{k_p^2} \nabla (\nabla \cdot \mathbf{q}_0) + \nabla \left[ \frac{C_p (C_p - C_g)}{k_p^2} \right] (\nabla \cdot \mathbf{q}_0) \right\}, \quad (23) \end{aligned}$$

where  $C_p$  and  $C_g$  denote the phase and group velocities corresponding to  $k_p$  as defined by the linear theory.

By specifying  $C_p$  and  $C_g$  in these equations, we can show that various existing wave equations may be reproduced as the degenerate forms. For example, Airy's shallow water equations and Boussinesq equations can be obtained as follows.

(1) Airy's shallow water equations:  $C_p = C_g = \sqrt{gh}$

$$\frac{\partial \eta}{\partial t} + \nabla \cdot [(h + \eta) \mathbf{q}_0] = 0, \quad (24)$$

$$\frac{\partial \mathbf{q}_0}{\partial t} + \nabla \left( g \eta + \frac{1}{2} \mathbf{q}_0 \cdot \mathbf{q}_0 \right) = 0. \quad (25)$$

(2) Boussinesq equations:

$$C_p = \sqrt{gh} \left( 1 - \frac{k_p^2 h^2}{6} \right), \quad C_g = \sqrt{gh} \left( 1 - \frac{k_p^2 h^2}{2} \right)$$

$$\frac{\partial \eta}{\partial t} + \nabla \cdot [(h + \eta) \mathbf{q}_0] + \frac{h^3}{3} \nabla^2 (\nabla \cdot \mathbf{q}_0) = 0, \tag{26}$$

$$\frac{\partial \mathbf{q}_0}{\partial t} + \nabla \left( g\eta + \frac{1}{2} \mathbf{q}_0 \cdot \mathbf{q}_0 \right) = 0, \tag{27}$$

where all the higher-order terms have been neglected.

**Combined Form of the Single-Component Equations :**

*"Time-dependent nonlinear mild-slope equation"*

The single-component equations (22) and (23) may be combined, with the introduction of the mild-slope assumption, to give the following equation of  $\eta$  (Beji and Nadaoka, 1994):

$$C_g \eta_{tt} - C_p^3 \nabla^2 \eta - \frac{(C_p - C_g)}{k_p^2} \nabla^2 \eta_{tt} - C_p \nabla (C_p C_g) \cdot (\nabla \eta) - \frac{3}{2} g C_p \left( 3 - 2 \frac{C_g}{C_p} - \frac{k_p^2 C_p^4}{g^2} \right) \nabla^2 (\eta^2) = 0. \tag{28}$$

By further manipulations, the linearized equation of (28),

$$C_g \eta_{tt} - C_p^3 \nabla^2 \eta - \frac{(C_p - C_g)}{k_p^2} \nabla^2 \eta_{tt} - C_p \nabla (C_p C_g) \cdot (\nabla \eta) = 0, \tag{29}$$

can be found to lead to the time-dependent (or "narrow-banded") mild-slope equation proposed by Smith and Sprinks (1975),

$$\eta_{tt} + \omega_p^2 \left( \frac{C_p - C_g}{C_p} \right) \eta - \nabla (C_p C_g \nabla \eta) = 0, \quad (\omega_p = C_p k_p) \tag{30}$$

and also to Berkhoff's (1972) elliptic equation as an original steady form of the mild-slope equation,

$$k_p^2 C_p C_g Z + \nabla \cdot (C_p C_g \nabla Z) = 0, \tag{31}$$

in which  $Z$  denotes a spatially varying wave amplitude. Therefore, eq.(28) can be regarded as an extension of the mild-slope equations to nonlinear waves. In this sense, eq.(28) may be called "time-dependent nonlinear mild-slope equation". However its linear dispersion characteristics are not the same as those of the time-dependent mild-slope equation (30), since the latter equation approximates more limited region around  $\omega_p$  in the dispersion curve (Beji and Nadaoka, 1994). This means that even in the linear version of eq.(28), eq.(29), the new mild-slope equation has an advantage as compared with the conventional one.



### Unidirectional Simplified Form of Nonlinear Mild-Slope Equation :

Equation (28) may be further elaborated for case of unidirectional propagation of waves in the positive  $x$ -direction only. The reason of taking up the analysis of such a simplified case lies in the attractive form of the KdV equation, which will be recovered as a special case. Skipping the derivation procedure (see Beji and Nadaoka, 1994) the equation we obtain is

$$C_g \eta_t + \frac{1}{2} C_p (C_p + C_g) \eta_x - \frac{(C_p - C_g)}{k_p^2} \eta_{xxt} - \frac{C_p (C_p - C_g)}{2k_p^2} \eta_{xxx} + \frac{1}{2} [C_p (C_g)_x + (C_p - C_g)(C_p)_x] \eta + \frac{3}{4} g \left( 3 - 2 \frac{C_g}{C_p} - \frac{k_p^2 C_p^4}{g^2} \right) (\eta^2)_x = 0, \quad (32)$$

which describes the weakly-nonlinear wave evolution of a narrow-banded unidirectional wave field centered at the primary wave frequency  $\omega_p = k_p C_p$ .

The specification of  $C_p$  and  $C_g$  in eq.(32) yields again some degenerate forms. For weakly-dispersive shallow water waves, the specification,

$$C_p = \sqrt{gh} \left( 1 - \frac{k_p^2 h^2}{6} \right), \quad C_g = \sqrt{gh} \left( 1 - \frac{k_p^2 h^2}{2} \right)$$

leads to the KdV equation for a gently varying depth :

$$\eta_t + C_0 \left[ \eta_x + \frac{h_x}{4h} \eta + \frac{h^2}{6} \eta_{xxx} + \frac{3}{4h} (\eta^2)_x \right] = 0, \quad (33)$$

in which  $C_0 = \sqrt{gh}$ .

For deep water, on the other hand,  $C_p = \sqrt{g/k_p}$ ,  $C_g = C_p/2$ , then we have

$$\eta_t + \frac{3}{2} C_p \eta_x - \frac{1}{k_p^2} \eta_{xxt} - \frac{C_p}{2k_p^2} \eta_{xxx} + \frac{3}{2} \frac{g}{C_p} (\eta^2)_x = 0, \quad (34)$$

which can be shown to admit the second-order Stokes' waves in deep water as an analytical solution.

### NUMERICAL EXAMPLES

The forms of the single-component equations are in perfect correspondence with those of the Boussinesq equations. This is an important advantage because it allows the adoption of an efficient implicit scheme which has been developed for solving the Boussinesq equations. The numerical schemes for the combined forms of the single-component equations, (28) and (32), are of course much simpler and need shorter computational time.

The fully-dispersive equations, on the other hand, require a more complicated scheme to solve the  $N$  momentum equations. In the present study, a generalized Thomas algorithm, or the so-called block elimination method, is used for solving the linear algebraic equations resulting from an implicit three-time-level, centered discretization of the momentum equations (Nadaoka, et al., 1994). The values of

$U_m$  ( $m=1, \dots, N$ ) at the boundary may be prescribed by applying a Galerkin procedure similar to that for eq.(7). The angular frequencies  $\omega_m$  to specify the corresponding  $k_m$  ( $m=1, \dots, N$ ) are chosen so as to properly cover the frequency spectrum concerned. It has been found through various numerical computations, some of which will be shown later, that  $N$  required is usually no more than 3 and the use of slightly different set of  $\omega_m$  ( $m=1, \dots, N$ ) yields no appreciable difference in the computational results and hence the apparent ambiguity in selecting  $\omega_m$  ( $m=1, \dots, N$ ) does not affect the validity of the present model.

The following parts are devoted to show some typical numerical examples.

### (1) Linear random waves

To examine the fundamental performance of the fully-dispersive equations, their linearized equations were applied to a case of linear random waves in deep water with a Bretschneider-type spectrum, which has a broad band-width in comparison with, e.g., JONSWAP. The relative water depth to the wave length corresponding to the mean period  $T_m$  is one ( $h/L_m=1$ ). Figure 4 shows the comparisons with the predictions of linear theory for surface displacement and horizontal velocity at two different depths after 20 wave periods elapsed over a distance of five wavelengths. Good agreement with the theory is observed for both the surface displacement and velocity profiles. In the computation three components were used:  $k_1h=2\pi$ ,  $k_2h=3\pi$ ,  $k_3h=5\pi$  with  $\Delta x=L_m/90$  and  $\Delta t=T_m/90$ . The relatively fine resolutions were deemed necessary for the accurate representation of higher frequency components with shorter wavelengths and periods. No sponge layer was needed to improve the absorption at the outgoing boundary; the computational domain was not longer than shown. Good absorption of the radiating waves is attributable to the fact that the outgoing waves are radiated at three different wavenumbers instead of one. This is an important advantage especially in long time simulation of random waves.

### (2) Nonlinear regular and irregular waves propagating over a bar

Further examinations on the fully-dispersive equations have been made through the comparisons with the laboratory data obtained by the experiment on the nonlinear wave deformation over a submerged trapezoidal bar as shown in Fig.5, which is similar to that of Beji and Battjes (1994). The two-component form of eqs. (17) and (18) was used for the computation by selecting the corresponding angular frequencies as  $\omega_1=2\pi/T$  and  $\omega_2=4\pi/T$ . The experimental data compared is that for which the incident wave height  $H$  and period  $T$  are 2.0cm and 1.5s, respectively. Note that in this case the largest relative depth  $h/L$  observed was 0.35 at most. Figure 6(a) shows the comparisons for the water surface profiles at station 3, 5 and 7, while Fig.6(b) represents the velocity comparison at three depths at station 7, where an appreciable wave-decomposition phenomenon was observed. On the other hand, Figs.7(a) and (b) show the comparisons in which the improved Boussinesq equations of Madsen et al. (1991) were used for the computation. From these results, it is found that in the water surface profiles the present wave equations show good but nearly the same degree of agreements as compared with the improved Boussinesq equations. In the velocity profiles, on the contrary, the agreements for the improved Boussinesq equations deteriorate, although for the present equations the agreements are comparable to those in the surface profiles.

As a test for nonlinear random waves traveling over a submerged trapezoidal bar, the experimental data of Beji and Battjes (1994) was compared with the computational results by the two-component wave equations (17) and (18). The incident wave field has a JONSWAP type random wave spectrum with a peak period  $T_p=2s$ . The first four stations are in the upslope region where the nonlinear shoaling takes place. The remaining three stations are in the downslope region,

where harmonic wave decomposition becomes appreciable. In the computations  $k_1$  and  $k_2$  for each component are selected to be  $k_p$  and  $\pi k_p$ , respectively, where  $k_p$  denotes the wavenumber corresponding to the peak period  $T_p$ . Figure 8 shows the results of the comparison at six different stations, indicating good agreements at all the stations. (It has been also found that even in case of using the simplest single-component equation (32) for the computations the agreements are slightly worse but still comparable to those indicated in Fig.8.)

### (3) Stokes and cnoidal waves

The comparisons with the theories of steady nonlinear wave train have been also conducted by using the various versions of the present wave equations. The wave theories compared are of Stokes, cnoidal and solitary waves. As an example, Fig.9 show the comparisons with the second-order Stokes and cnoidal wave theories. The computations were carried out with the unidirectional simplified form of the nonlinear mild-slope equation (32). It is found that even this simplest version of equations can describe steady nonlinear wave trains with remarkably good accuracy under wide conditions including very shallow and far deep water waves. Solitary waves are also found to be well predicted by the present models, although the results are not presented here (see Nadaoka, et al.,1994; Beji & Nadaoka, 1994).

## CONCLUSIONS

The major conclusions of the present study are summarized as follows :

1. Fully-dispersive nonlinear wave equations are presented which can express nonlinear non-breaking waves under general conditions, such as nonlinear random waves with *wide-spectrum* at an *arbitrary depth* including very shallow and far deep water depths.
2. The single-component forms of the new wave equations, one of which is referred to as "*time-dependent mild-slope equation*", are shown to produce various existing wave equations like Boussinesq and mild-slope equations as their degenerate forms.
3. Even under relatively shallow wave condition, present wave model can evaluate more precisely the velocity field than the improved Boussinesq equations.

## Acknowledgement

The authors would like to thank Prof. J.A. Battjes for his permission to use the experimental data and a graduate student O. Ohno for his helpful cooperation in laboratory works.

## References

- Beji, S.(1994): Note on conservation equations for nonlinear surface waves. *Submitted to Coastal Eng.*
- Beji, S. and Battjes, JA.(1994): Numerical simulation of nonlinear wave propagation over a bar, *Coastal Eng.*, Vol.23, pp.1-16.
- Beji, S. and Nadaoka, K.(1994): A time-dependent nonlinear mild-slope equation. *Submitted to Proc. Roy. Soc. London A*
- Berkhoff, J.C.W.(1972): Computation of combined refraction-diffraction. Proc. 13th Int. Conf. Coastal Eng., ASCE, pp.471-490.
- Madsen, P.A., Murray, R. and Sørensen, O.R.(1991): A new form of the Boussinesq equations with improved linear dispersion characteristics, *Coastal Eng.*, Vol.15, pp. 371-388.
- Mei, C.C.(1983): *The applied dynamics of ocean surface waves*, John Wiley & Sons, 740pp.
- Nadaoka, K. and Hino, H.(1984): Conformal mapping solution of a wave field on the

arbitrary shaped sea bottom, Proc. 19th Int. Conf. Coastal Eng., ASCE, pp.1192-1208.

Nadaoka, K. and Nakagawa, Y.(1991): A Galerkin derivation of a fully-dispersive wave equation and its background, Tech. Rep. No.44, Dept. Civil Eng., Tokyo Inst. of Tech., pp.63-75. (in Japanese)

Nadaoka, K. and Nakagawa Y.(1993a): Fully-dispersive wave equations derived by a Galerkin formulation, *Meet'n '93*, ASCE/ASME/SES Abstracts, p.724.

Nadaoka, K. and Nakagawa, Y.(1993b): Derivation of fully-dispersive wave equations for irregular wave simulation and their fundamental characteristics, *J. Hydraulics, Coastal and Environmental Eng.*, JSCE, No.467, pp.83-92. (in Japanese)

Nadaoka, K. and Nakagawa, Y.(1993c): Simulation of nonlinear wave fields with the newly derived nonlinear dispersive wave equations, Proc. Coastal Eng., JSCE, Vol.40, pp.6-10. (in Japanese)

Nadaoka, K., Beji, S. and Nakagawa, S.(1994): A fully-dispersive weakly-nonlinear wave model. *Submitted to Proc. Roy. Soc. London A*

Nwogu, O.(1993): Alternative form of Boussinesq equations for nearshore wave propagation, *J. Waterway, Port, Coastal, and Ocean Eng.*, ASCE, Vol.119, No.6, pp.618-638.

Smith, R. and Sprinks, T.(1975): Scattering of surface waves by a conical island, *J. Fluid Mech.*, Vol.72, pp.373-384.

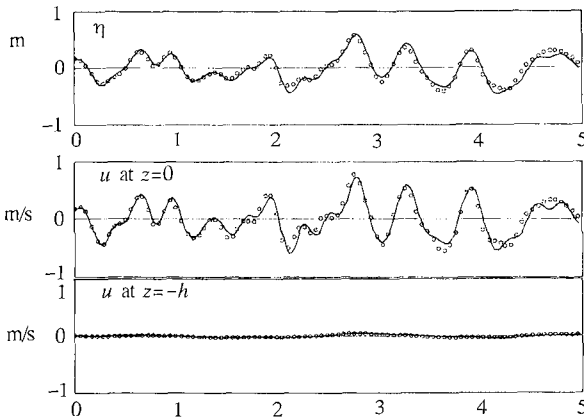


Fig.4 Linear random wave simulation ; linear theory (—) vs. computational results (O).

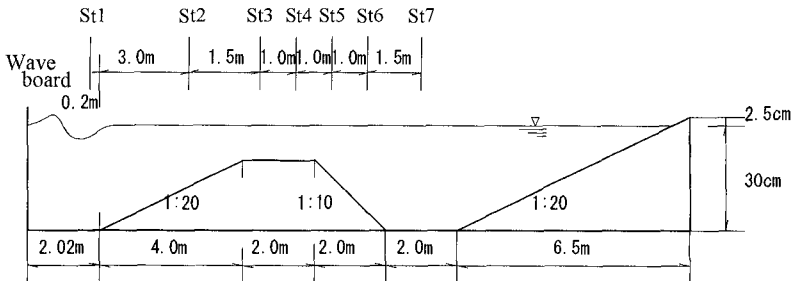
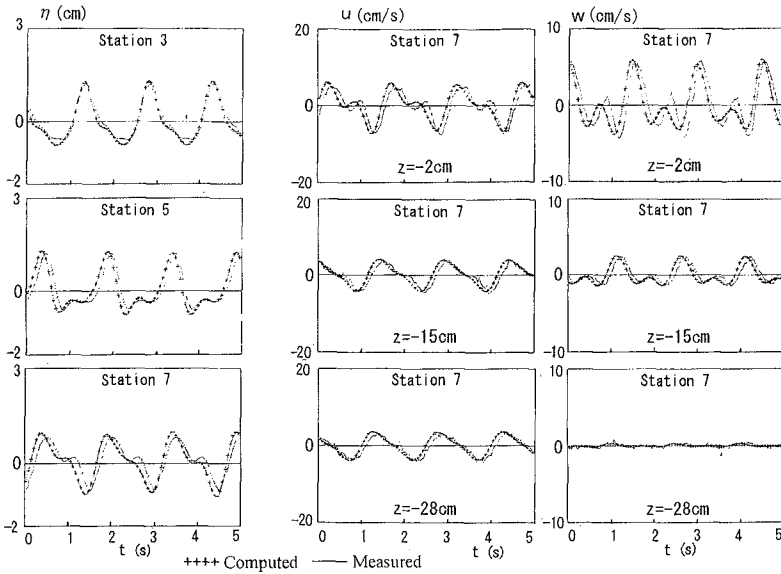
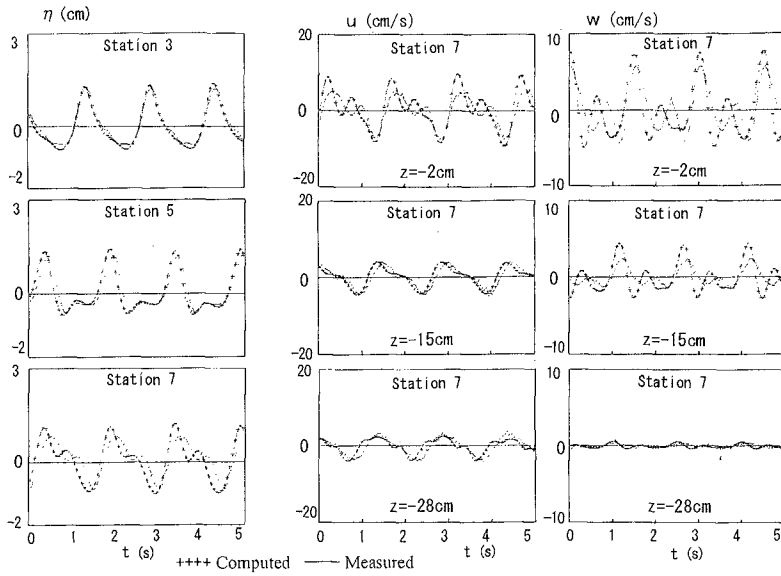


Fig.5 Definition sketch of wave flume and locations of wave gauges.



(a)  $\eta$  (b)  $u$  and  $w$   
 Fig. 6 Comparisons in  $\eta$ ,  $u$  and  $w$  for the present fully-dispersive equations.



(a)  $\eta$  (b)  $u$  and  $w$   
 Fig. 7 Comparisons in  $\eta$ ,  $u$  and  $w$  for the improved Boussinesq equations.

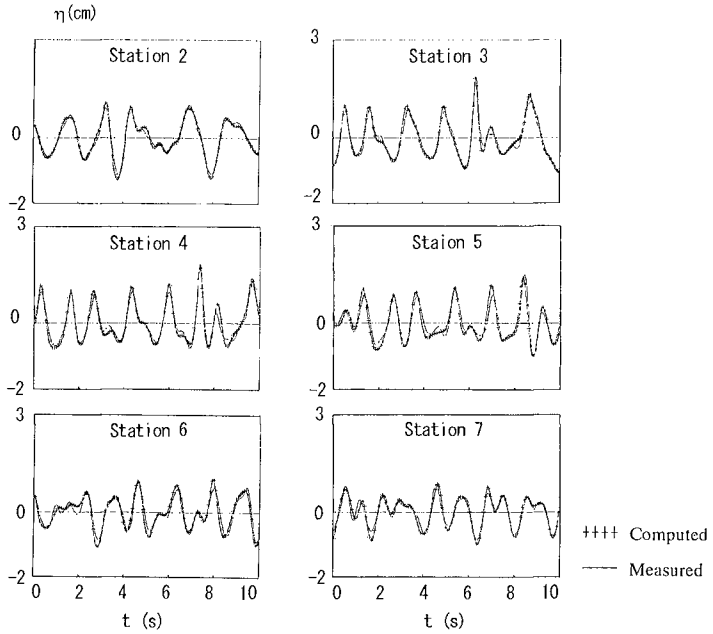


Fig. 8 Comparison with laboratory data for nonlinear random waves propagating over a bar.

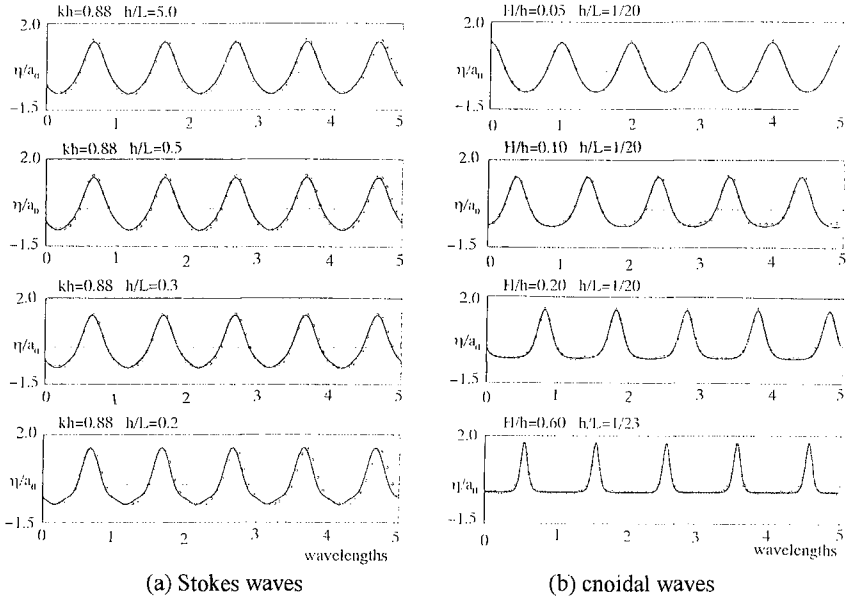


Fig. 9 Comparison with Stokes and cnoidal wave theories; theory (—) vs. computed (O).

## CHAPTER 33

### A Generalized Green-Function Method for Wave Field Analysis

Hitoshi Nishimura <sup>1</sup>, Michio Matsuoka <sup>2</sup> and Akira Matsumoto <sup>3</sup>

#### Abstract

The Green-function method for analyzing wave refraction, diffraction and reflection is improved by deriving rational explicit formulations of boundary conditions. Possibilities and limitations of the method are discussed. Trial computations and their comparisons with experiments demonstrate the validity and usefulness of the numerical model.

#### Introduction

To analyze refraction, diffraction and reflection of simple sinusoidal waves is one of the very fundamental problems in the field of coastal engineering. If an accurate and simple method is provided for this purpose, deformation of irregular waves may also be analyzed through superposition of solutions for constituent waves. In this context, numerical modeling based on the Green-function method is quite promising since it describes the diffraction and multiple reflection of waves more accurately than any other methods. This kind of numerical model was first proposed by Barailler and Gaillard (1967), and has been widely used in particular for simulation of waves in semi-closed sea basins. In numerical models presently used, however, continuation of solutions are often insufficient at artificial boundaries.

In the following sections, rational explicit formulations of boundary conditions is derived for more rigorous computation of two-dimensional wave fields. Validity of the numerical model thus improved is examined through trial computations and their comparisons with experiments.

---

<sup>1</sup>Professor, Inst. of Eng. Mech., Univ. of Tsukuba., Tsukuba, Ibaraki, 305, Japan.

<sup>2</sup>Senior Researcher, Applied Hydraulic Laboratory, Nippon Tetrapod Co., Ltd., 2-7 Nakanuki, Tsuchiura, Ibaraki, 300, Japan.

<sup>3</sup>Ditto.

Principle of the Green-Function Method

If we express the wave profile  $\zeta(x, y, t)$  in a water area with a uniform depth as

$$\zeta = f(x, y) \cdot e^{i\omega t} \tag{1}$$

the complex amplitude  $f(x, y)$  satisfies the following Helmholtz equation:

$$\frac{\partial^2 f}{\partial x^2} + \frac{\partial^2 f}{\partial y^2} + k^2 f = 0 \tag{2}$$

where  $(x, y)$  is the Cartesian coordinate in a horizontal plane,  $t$  is the time,  $\omega$  is the angular frequency, and  $k$  is the wave number.

Suppose the existence of a perfectly reflective wall along the x-axis and a wave source at a point  $(\xi, \eta)$ , as shown in Fig.1. It is well known that the resulting wave field in the semi-finite region of  $y > 0$  is then

$$f(x, y) = -\frac{i\Gamma}{4} [H_0^{(1)}(kr^+) + H_0^{(1)}(kr^-)] \tag{3}$$

$$r^\pm = \sqrt{(x - \xi)^2 + (y \mp \eta)^2} \tag{4}$$

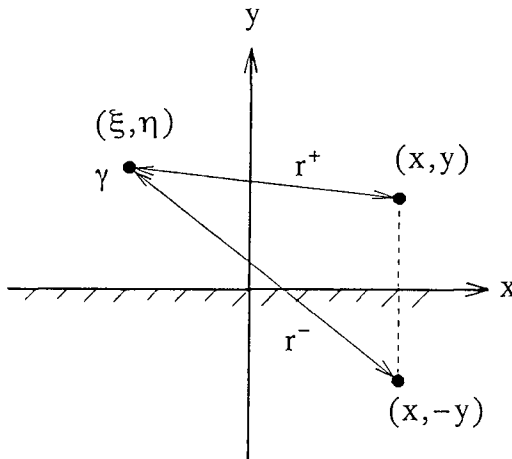


Figure 1: Definition sketch.



in which  $H_0^{(1)}$  denotes the zeroth-order Hankel function of the first kind. Note that the complex source intensity  $\Gamma$  represents the wave phase as well as the amplitude. The solution (3) satisfies the basic equation (2) and, at the same time, the boundary condition  $\partial(f_1 + f_2)/\partial y = 0$  along the  $x$ -axis. It also satisfies Sommerfeld's radiation condition toward the infinity.

For a particular case that the wave source is located on the  $x$ -axis ( $\eta = 0$ ), the expressions (3) and (4) are simplified as follows:

$$f(x, y) = -\frac{i\Gamma}{2} H_0^{(1)}(kr) \quad (5)$$

$$r^{\pm} = \sqrt{(x - \xi)^2 + y^2} \quad (6)$$

Distribution of such wave sources along the boundary of a water area will cause a composite wave field, which is expressed by the integration of the unit solution:

$$f(x, y) = \int_C \gamma(s) \cdot H_0^{(1)}(kr) ds \quad (7)$$

where  $s$  is the coordinate taken along the boundary  $C$ ,  $r$  is the distance from the boundary point ( $s$ ) to the point ( $x, y$ ), and  $\gamma(s)ds$  corresponds to the wave source intensity  $\Gamma$  in Eq.(5). The wave source distribution has to be determined so that the resulting wave field satisfies all the boundary conditions imposed, as correctly suggested by Lee (1969, 1971) for harbor oscillation analysis.

#### Relationship between the Source Intensity and Wave Amplitude on a Boundary

Consider the situation that wave sources in the semi-infinite region of  $y > 0$  produce a wave field  $f_1(x, y)$ . As to the waves propagating across the  $x$ -axis, the following relationship proves from Green's theorem between the complex amplitude and its gradient in the  $y$ -direction:

$$f_1(x, 0) = -\frac{i}{2} \int_{-\infty}^{\infty} \frac{\partial f_1(\xi, \eta)}{\partial \eta} \Big|_{\eta=0} \cdot H_0^{(1)}(k|x - \xi|) d\xi \quad (8)$$

On the other hand, a similar relationship is obtained for a wave field  $f_2(x, y)$  which is produced in the same region by the source distribution  $\gamma_2(x)$  along the  $x$ -axis:

$$f_2(x, y) = -\frac{i}{2} \int_{-\infty}^{\infty} \frac{\partial f_2(\xi, \eta)}{\partial \eta} \Big|_{\eta=0} \cdot H_0^{(1)}(kr) d\xi \quad (9)$$

It can thus be concluded that the source intensity is directly proportional to the local gradient of resulting wave amplitude in the normal direction to the boundary:

$$\gamma_2(\xi) = -\frac{i}{2} \frac{\partial f_2(\xi, \eta)}{\partial \eta} \Big|_{\eta=0} \quad (10)$$

### Condition of Reflective Boundary

If  $x$ -axis is a perfectly reflective boundary in the above discussion, then the incident waves  $f_1(x, y)$  and reflected waves  $f_2(x, y)$  appear in the semi-infinite region. The boundary condition in this case is

$$\frac{\partial(f_1 + f_2)}{\partial y} \Big|_{y=0} = 0 \quad (11)$$

which leads to the following simple expression of the source intensity:

$$\gamma_2(\xi) = -\frac{i}{2} \frac{\partial f_2(\xi, \eta)}{\partial \eta} \Big|_{\eta=0} \quad (12)$$

In rigorously formulating a condition of partial reflection, hydraulic mechanism of wave reflection has to be known. A conventional method for simulating the partial reflection is to simply reduce the source intensity by multiplying the reflection coefficient  $\beta$  as follows:

$$\gamma_2(\xi) = -\frac{i\beta}{2} \frac{\partial f_1(\xi, \eta)}{\partial \eta} \Big|_{\eta=0} \quad (13)$$

### Continuation of Solutions along an Open Boundary

For the convenience of numerical computation, the whole region in question is often divided into subregions by supposing imaginary boundaries between them. A breakwater gap illustrated in Fig.2 is a typical example of such a boundary. In the figure, waves  $f_I(x, y)$  are incident to the imaginary boundary  $C$  on the  $x$ -axis. Note that  $f_I(x, y)$  represents all the incident waves to  $C$  including those from the boundaries immediately beside  $C$ .

If the boundary is either finite or semi-infinite, waves are partly reflected as they are transmitted across the boundary. In other words, two kinds of wave sources are in general to be distributed along a transmissive boundary. On one side of the boundary, the reflected waves  $f_R(x, y)$  is superposed on the incident waves  $f_I(x, y)$ , whereas only transmitted waves  $f_T(x, y)$  propagate on the other side. It is thus feasible for these two wave fields to coincide in terms of both the amplitude and its gradient along the boundary  $C$ :

$$(f_I + f_R) \Big|_C = f_T \Big|_C \quad (14)$$

$$\frac{\partial(f_I + f_R)}{\partial y} \Big|_C = \frac{\partial f_T}{\partial y} \Big|_C \quad (15)$$

These conditions lead to the following integral equations for the source intensities  $\gamma_R$  and  $\gamma_T$  for reflected and transmitted waves respectively:

$$2 \int_C \gamma_R(\xi) \cdot H_0^{(1)}(k|x - \xi|) d\xi = f_I^*(x, 0) - f_I(x, 0) \quad (16)$$

$$2 \int_C \gamma_T(\xi) \cdot H_0^{(1)}(k|x - \xi|) d\xi = f_I^*(x, 0) + f_I(x, 0) \quad (17)$$

where

$$f_I^*(x, 0) = -\frac{i}{2} \int_C \frac{\partial f_I(\xi, \eta)}{\partial \eta} \Big|_{\eta=0} \cdot H_0^{(1)}(k|x - \xi|) d\xi \quad (18)$$

and

$$f_R(x, y) = \int_C \gamma_R(\xi) \cdot H_0^{(1)}(kr) d\xi \quad (19)$$

$$f_T(x, y) = \int_C \gamma_T(\xi) \cdot H_0^{(1)}(kr) d\xi \quad (20)$$

For solution of the above equations, they are discretized by dividing the boundary into a number of segments. The problem is then ascribed to linear systems of simultaneous equations, and the source intensities are obtained through matrix operations. Since the coefficient matrices of the systems are fixed for each boundary of this type regardless of wave conditions, inverse matrices once calculated can be repeatedly used throughout the computation.

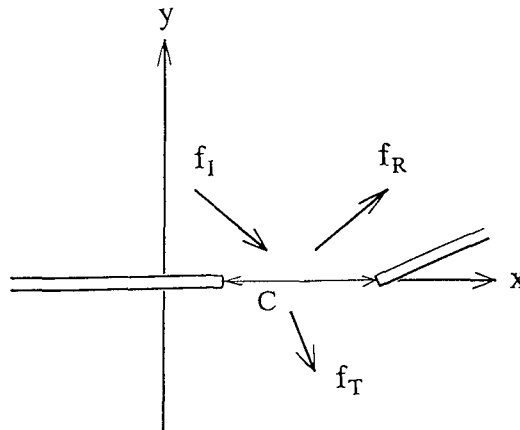


Figure 2: Imaginary boundary.

In the actual computation, it is not necessary to solve both the above equations. After solving one of them for  $\gamma_R$  or  $\gamma_T$ , we can easily evaluate the other from the following relationship:

$$\gamma_I(x) + \gamma_R(x) + \gamma_T(x) = 0 \quad (21)$$

Even if incident waves with uniform amplitude are incident to the boundary, wave sources thus obtained are not uniform with high peaks at the boundary ends. These peaks represent the singularity of the boundary ends, reproducing fields of diffracted waves with good approximation. It is important to note here that the source intensity cannot necessarily be related to the local energy density of incident waves.

### Outline of the Numerical Model

When the configuration of a sea area in question is complicated, the whole region for computation is divided into several convex polygonal subregions. A semi-infinite open sea area is regarded as one of the subregions. The other subregions are totally enclosed by boundaries, at least one of them being transmissive. All the boundaries are subdivided into a number of segments and the effect of each segment is represented by a wave source. A transmissive boundary serves as two boundaries at once for two subregions on its both sides, where two sources defined are for either reflected or transmitted waves depending on the subregion currently treated.

The distribution of source intensities is calculated for each boundary. The flow of computation starts from the the subregion of wave incidence. It moves from one subregion to the next, and from one boundary to another in a subregion. Since the source intensities are interdependent, these boundarywise calculations over the whole region are repeated until all the intensities reach an equilibrium.

It is somewhat difficult to formulate the condition of a partially transmissive boundary. Such a boundary may be reasonably regarded as a fully reflective boundary in evaluating reflected waves, and as a fully open boundary for transmitted waves. Prior to these calculations, the incident wave amplitudes are to be reduced by multiplying reflection or transmission coefficient. In this case, the source intensities for reflected and transmitted waves have to be memorized separately on both the sides of the boundary.

The present method for wave field analysis can be applied even to a water area with arbitrary bathymetry by numerically obtaining unit solutions to replace the Hankel function. For the calculation of unit solutions, a relatively simple method for analyzing wave refraction may be employed, since the main part of wave diffraction is included in principle in the process of superposition of point source waves. Nonlinear wave deformation, however, can never be analyzed by means of the Green-function approach as it is essentially based on the superposition of unit solutions.

### Physical Model Experiments

A series of experiments on waves in a harbor were conducted (Photo 1) to provide wave distribution data to examine performance of the numerical model described above. The model harbor configuration shown in Fig.3 and experimental conditions listed in Table 1 were determined along one of the model cases specified for trial simulation works by a subcommittee of the Coastal Engineering Conference, JSCE. The model was installed on a horizontal bed in a narrow wave basin. Gaps between the harbor and basin walls were filled by wave absorbing material to avoid the elevation of the mean water level.

In some cases of the experiments, tetrapod mounds were arranged on the outer sea sides of the breakwaters, but all the other walls were vertical walls. As a matter of fact, arrangement of absorbing facility inside the harbor significantly narrows the harbor area in such a small-scale model. The reflection coefficient for each part of the model was separately estimated by applying Healy, Goda (1976) and Isaacson's (1991) methods, as summarized in Table 2.

Wave heights were measured using servo-type gauge array at every 10cm grid point over the whole area near and inside the harbor. The measurements were repeated more than twice for each case, but no significant scattering was observed in the data obtained. The incident wave heights listed in Table 1 were obtained at the location of the harbor entrance prior to the model installation.



Photo 1: Experimental setup.

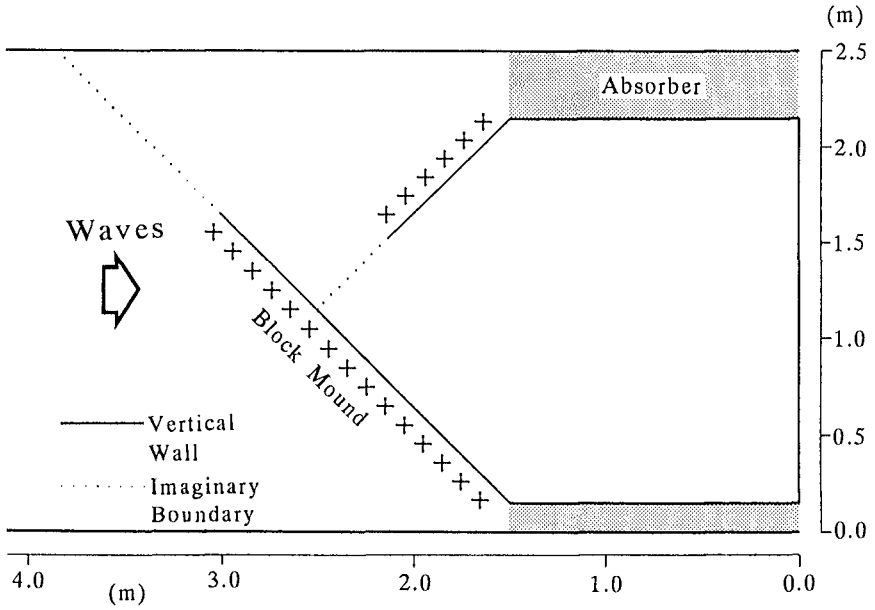


Figure 3: Experimental setup.

Table 1: Experimental conditions.

Case	Water depth (cm)	Period (s)	Incident wave height (cm)	Breakwaters
1	12.0	0.70	2.62	with block mounds
2	12.0	0.72	2.06	with block mounds
3	12.0	0.70	1.96	without block mounds

Table 2: Reflection coefficient.

	Measured value	For computation
Vertical wall	0.95-1.00	0.95
Block mound	0.35-0.40	0.40
Wave absorber	0.30-0.35	0.30

### Comparison of Numerical Computations and Experiments

In the numerical computations, the whole region was divided into four subregions. Two imaginary boundaries are shown in by dotted lines in Fig.3. Another boundary for wave incidence was assumed at 4m from the outer breakwater tip, and further offshore area was treated as a semi-infinite region. All the boundaries were divided into segments with length of roughly  $1/20$  wavelength. The reflection coefficient values used are also shown in Table 2, and the boundarywise computations were repeated until the relative accuracy of  $1/1000$  at maximum was attained.

Figure 4 compares measured and calculated distributions of relative wave heights normalized with the incident wave height for Case-1 with a period of 0.70s. The numerical model well simulates the field of standing waves formed inside the harbor, although the wave heights calculated are somewhat smaller than those measured. The incident wave height may have been substantially increased involving reflected waves from the wave generator. In numerical analyses, waves in the innermost area of the harbor are apt to be underestimated as they are subject to multiple diffractions. This sort of tendency, however, is not apparent at all here.

Figure 5 presents a similar comparison for Case-2 with a slightly longer period of 0.72s. It is seen that the wave period sensitively affect the wave field in such a system of multiple reflection, as is well simulated by the numerical model. These periods may be close to one of the resonant oscillation periods of the harbor water.

The effects of the absorbing mounds on the breakwater fronts first appears on the wave height distribution outside the harbor. Then the change in wave heights along the harbor entrance indirectly influences the wave field inside the harbor. Figure 6 shows wave fields for Case-3, where the block mounds were eliminated. The computation again reasonably reproduces significant differences in the wave height distribution which is noticed through comparison with Fig.4 for the Case-1 experiment.

### Concluding Remarks

The Green-function method provides a powerful tool for analyzing wave diffraction and multiple reflection of coastal and harbor waves. The rational treatment of imaginary boundaries allows the arbitrary division of water area with a complicated configuration without deteriorating the accuracy of total computation. The present model is rather simple and minimizes empirical factors for its actual application.

Since computer memory and computational labor required are not so large, even irregular waves can be treated so far as the linear superposition of constituent waves are acceptable. The model may be extended for arbitrary bathymetry, but cannot contribute to analyses of nonlinear wave deformation.

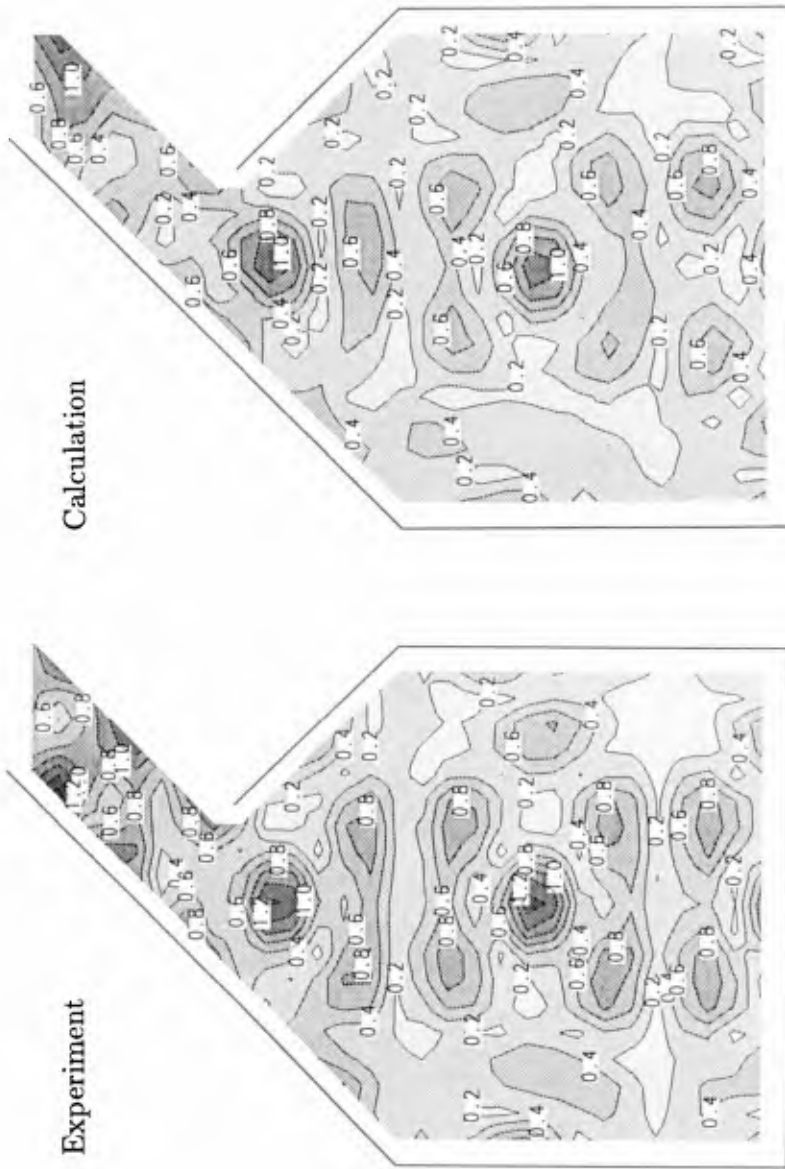


Fig. 4: Relative wave height distribution (Case 1, period: 0.70s).



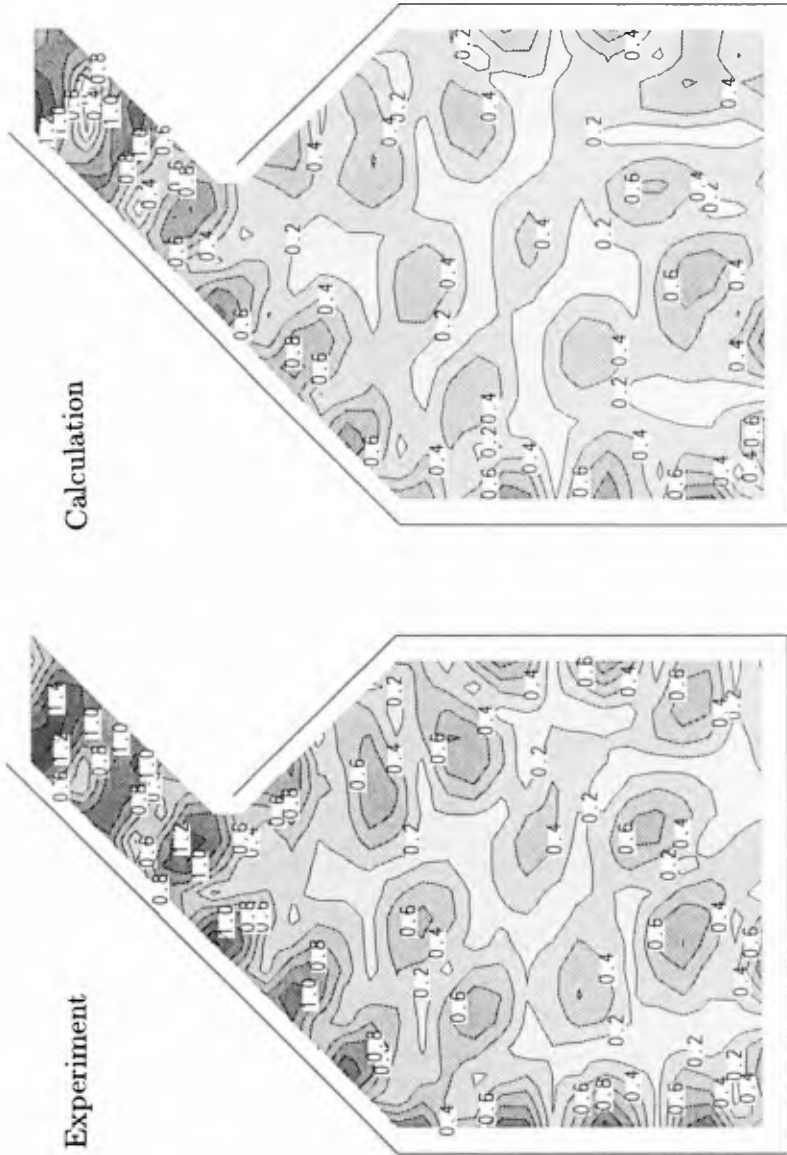


Fig. 5: Relative wave height distribution (Case 2, period: 0.72s).

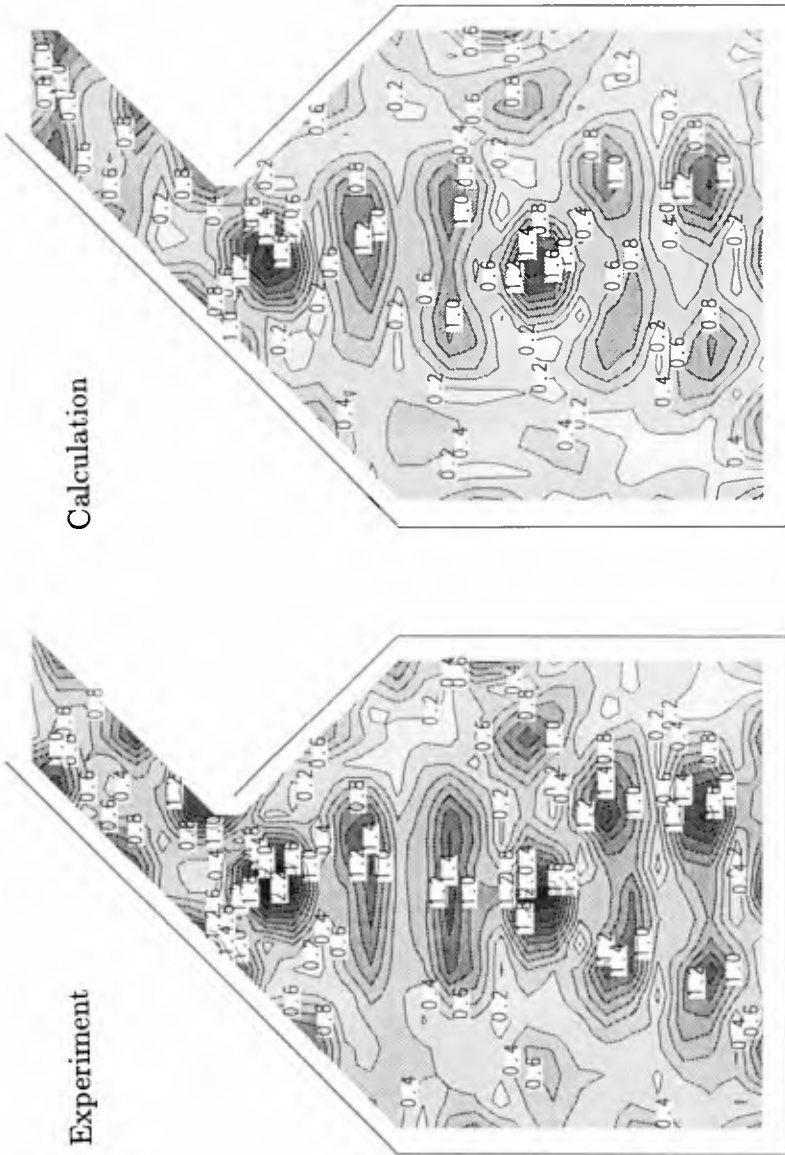


Fig. 6: Relative wave height distribution (Case 3, period: 0.70s, without block mounds).

### Acknowledgment

The authors' gratitude is due to Mr. Nobumasa Shinoda, Toyota System Research Co., for his good help in the computer work for this study.

### References

- Barailler, L., and P. Gaillard (1967). Évolution récente des modèles mathématiques dagitation due à la houle. La Houile Blanche, Vol.22, No.8, pp.861-869.
- Goda, Y. (1976). Estimation of incident and reflected waves in random wave experiments. Tech. Note of Port and Harbour Res. Inst., Min. of Transport, Japan, No.248, 24p. (in Japanese)
- Isaacson, M (1991). Measurement of regular wave reflection, J. Waterway, Port, Coastal and Ocean Eng., ASCE, Vol.117, pp.553-509.
- Lee, J.-J., and F. Raichlen (1969). Wave induced oscillations in harbors of arbitrary shape. W. M. Keck Lab., Calif. Inst. of Tech., Rep. No.KH-R-20, 266p.
- Lee, J.-J., and F. Raichlen (1971). Wave induced oscillations in harbors with connected basins. W. M. Keck Lab., Calif. Inst. of Tech., Rep. No.KH-R-26, 135p.

## CHAPTER 34

# COUPLED VIBRATION EQUATIONS FOR IRREGULAR WATER WAVES

Masao Nochino\*

### Abstract

A new system of equations is proposed for calculating wave deformation of irregular waves under the assumption of small amplitude wave and of mild slope of bottom configuration. The system is composed of a vibration equation for water surface elevation and three elliptic equations defined in horizontal plane. These equations are coupled each other. The coupled vibration equations are capable of calculating water surface elevation of irregular waves in a time domain.

## 1 Introduction

Some equations have been proposed for the deformation of water waves; the mild slope equation by Berkhoff(1972), the unsteady mild slope equation considering wave-current interaction by Liu(1983), Boussinesq equation by Pregrine(1978). The mild slope equations are able to apply only for a simple harmonic wave. The Boussinesq equation is derived for nonlinear long waves. The equation to calculate the deformation of irregular waves including long waves is expected for the coastal structure design and the analysis of coastal process.

Kubo et. al.(1992) modified the time-dependent mild slope equation by applying the Fourier expansion technique to the coefficient in the mild slope equation. The modified mild equation is capable of simulating random waves without long waves. Nadaoka et. al.(1993) proposed the fully-dispersive wave equation capable of simulating random waves with long waves.

In this paper, a new system of equations is proposed for calculating the deformation of the linear and irregular water waves including long waves. The waves are expressed as motions of coupled vibrations. The system of equations are applicable for the waves in the range of deep water depth to very shallow water depth.

---

\*Associate Professor, Osaka Institute of Technology, Department of Civil Engineering  
5-16-1 Omiya Asahi-ku, Osaka, 565, Japan

## 2 Theory

### 2.1 Basic equation

The motion equations and the equation of continuity are expressed as follows under the assumption that the motion due to waves be small and the nonlinear terms in the motion equations be negligible.

$$\frac{\partial u}{\partial t} + \frac{\partial \tilde{p}}{\partial x} = 0 \quad (1)$$

$$\frac{\partial v}{\partial t} + \frac{\partial \tilde{p}}{\partial y} = 0 \quad (2)$$

$$\frac{\partial w}{\partial t} + \frac{\partial \tilde{p}}{\partial z} = 0 \quad (3)$$

$$\frac{\partial u}{\partial x} + \frac{\partial v}{\partial y} + \frac{\partial w}{\partial z} = 0 \quad (4)$$

where,  $\tilde{p}$ ; the fluctuating pressure defined as

$$\tilde{p} = p/\rho + gz, \quad (5)$$

$x, y$ ; the coordinates in horizontal axes,  $z$ ; the vertical coordinate in upward direction with the origin at still water surface,  $p$ ; the pressure,  $\rho$ ; the water density,  $g$ ; the gravitational acceleration,  $u, v, w$ ; the water particle velocity in  $x, y, z$  direction, respectively. Taking divergence of the motion equation, the Laplace equation of the fluctuating pressure  $\tilde{p}$  are given as follows.

$$\Delta \tilde{p} = 0 \quad (6)$$

In this paper, Equation(6) is treated as the basic equation and  $\tilde{p}$ , the main variable as same as the water surface elevation  $\eta$ .

### 2.2 Boundary conditions

There are three boundary conditions; two boundary conditions at free surface and one at bottom. These boundary conditions should be expressed by the main variable and linearized as the motion equations are linearized.

The dynamic and kinematic free surface boundary conditions are expressed as follows.

$$\tilde{p} = g\eta \quad \text{at } z = 0 \quad (7)$$

$$\frac{\partial \eta}{\partial t} = w \quad \text{at } z = 0 \quad (8)$$

The motion equation should be satisfied at free surface. Eliminating the vertical velocity  $w$  in above equation by using the motion equation in vertical direction, Eq. (3), the kinematic boundary condition, Eq.(8), can be expressed as follow.

$$\frac{\partial^2 \eta}{\partial t^2} = -\frac{\partial \tilde{p}}{\partial z} \quad \text{at } z = 0 \quad (9)$$

The boundary condition at bottom ( $z = -h$ ) is commonly expressed as follow.

$$u \frac{\partial h}{\partial x} + v \frac{\partial h}{\partial y} + w = 0 \quad \text{at } z = -h \tag{10}$$

where,  $h = h(x, y)$  indicates the water depth. Derivating above equation with respect to time and applying the motion equations (1)-(3), the following equation is given as the boundary condition at bottom expressed by the fluctuation pressure.

$$\left( \nabla \tilde{p} \cdot \nabla h + \frac{\partial \tilde{p}}{\partial z} \right) = 0 \quad \text{at } z = -h \tag{11}$$

where  $\nabla = (\partial/\partial x, \partial/\partial y)$  indicate the differential operator in horizontal plane.

### 2.3 Expansion series of fluctuating pressure

The fluctuating pressure  $\tilde{p}$  is expanded by using the series of Legendre's Polynomials  $P_n(z)$  as follows.

$$\tilde{p} = \sum_{m=1}^{\infty} q_m P_{2(m-1)}(\tilde{z}) \tag{12}$$

where  $q_m = q_m(x, y, t)$  is the coefficient of  $m$ th term, and

$$\tilde{z} = 1 + z/h. \tag{13}$$

The variable  $\tilde{z}$  is defined in the interval of  $[0, 1]$  as the coordinate  $z$  is defined in  $[-h, 0]$  for the linearized theory. The Legendre's Polynomials  $P_m(\tilde{z})$  are defined as follows.

$$P_0(\tilde{z}) = 1, \quad P_m(\tilde{z}) = \frac{1}{2^m m!} \frac{d^m}{d\tilde{z}^m} (\tilde{z}^2 - 1)^m, \quad m = 1, 2, \dots \tag{14}$$

For example,

$$P_2(\tilde{z}) = \frac{1}{2}(3\tilde{z}^2 - 1), \quad P_4(\tilde{z}) = \frac{1}{8}(35\tilde{z}^4 - 30\tilde{z}^2 + 3), \quad \text{etc.} \tag{15}$$

The series of Legendre's Polynomials  $P_{2(m-1)}(z)$  have the property of the series of the orthogonal functions.

$$\int_0^1 P_{2(m-1)}(z) P_{2(n-1)}(z) dz = \begin{cases} 0, & \text{for } m \neq n \\ \frac{1}{4m-3}, & \text{for } m = n \\ (m, n = 1, 2, \dots) \end{cases} \tag{16}$$

The above relation implies that all coefficients  $q_m$  in Eq.(12) be uniquely determined.

The expression by the infinite series in Eq.(12) is not suitable for a numerical calculation. Let's suppose, in this paper, that the fluctuating pressure  $\tilde{p}$  be expressed by the series of the first 4 terms in the right side of Eq.(12), such as

$$\tilde{p} = q_1 P_0(\tilde{z}) + q_2 P_2(\tilde{z}) + q_3 P_4(\tilde{z}) + q_4 P_6(\tilde{z}). \quad (17)$$

The dynamic and kinematic boundary condition at free surface are rewritten as follows by substituting Eq.(17) into Eqs.(7) and (9).

$$g\eta = q_1 + q_2 + q_3 + q_4 \quad (18)$$

$$\frac{\partial^2 \eta}{\partial t^2} = -\frac{1}{h}(3q_2 + 11q_3 + 21q_4) \quad (19)$$

## 2.4 Depth integrated equation

There are five unknown variables;  $\eta(x, y, t)$ ,  $q_m(x, y, t)$ , ( $m = 1, 2, 3, 4$ ). All variables are the functions defined in horizontal plane. There are two equations, Eqs.(18) and (19) which relate the five unknown variables. Therefore, three more new equations are required in order to solve the five unknown variables, instead of Eq.(6) defined in three dimensional space.

The Galerkin method is applied to Eq.(6) to make up the three new equations.

$$\int_{-h}^0 P_{2(m-1)}(\tilde{z}) \Delta \tilde{p} dz + P_{2(m-1)}(0) \left( \nabla h \cdot \nabla \tilde{p} + \frac{\partial \tilde{p}}{\partial z} \right) \Big|_{z=-h} = 0 \quad (20)$$

(for  $m = 1, 2, 3$ )

The second term in left hand side of the above equation is added so that the boundary condition at bottom, Eq.(11) is satisfied. Integrating the above equation and eliminating the coefficient  $q_4$  by using Eq(18), the following equations are given.

$$\begin{aligned} \nabla^2 q_1 + \frac{\nabla(88q_1 + 24q_2 - 88q_3)}{128h} \nabla h - \frac{21q_1 + 18q_2 + 11q_3}{h^2} \\ = \frac{40g\nabla\eta\nabla h}{128h} - \frac{21g\eta}{h^2} \end{aligned} \quad (21)$$

$$\begin{aligned} \nabla^2 q_2 + \frac{\nabla(-190q_1 + 258q_2 + 330q_3)}{128h} \nabla h - \frac{90q_1 + 90q_2 + 55q_3}{h^2} \\ = -\frac{130g\nabla\eta\nabla h}{128h} - \frac{90g\eta}{h^2} \end{aligned} \quad (22)$$

$$\begin{aligned} \nabla^2 q_3 + \frac{\nabla(99q_1 - 693q_2 - 205q_3)}{128h} \nabla h - \frac{99q_1 + 99q_2 + 99q_3}{h^2} \\ = \frac{333g\nabla\eta\nabla h}{128h} - \frac{99g\eta}{h^2} \end{aligned} \quad (23)$$

When deriving the above equations, the assumption for the mild slope of the bottom configuration is applied; the terms related  $\nabla^2 h$  and  $|\nabla h|^2$  are neglected.

The Eq(19) can be rewritten as follows by eliminating  $q_4$  in a same manner.

$$\frac{\partial^2 \eta}{\partial t^2} = -\frac{1}{h}(21g\eta - 21q_1 - 18q_2 - 10q_3) \tag{24}$$

Eq.(24) shows the form of a vibration equation for the water surface elevation  $\eta$  with the exciting force as a function of  $q_1, q_2$  and  $q_3$ . The variables  $q_1, q_2$  and  $q_3$  are determined by the Eqs. (21)-(23) which has the form of the elliptic equation defined in the horizontal plane with the exciting term as a function of  $\eta$ . Eqs.(21)-(24) are coupled each other. The variables  $\eta$  and  $q_m$  are in phase. Therefore, the system of Eqs.(21)-(24) expresses the water waves as the system of motions of the coupled vibrations, not as a system of wave equations.

The system of coupled vibration equations are expressed by the water depth  $h$  and the constant coefficients. The system is independent to both the wave frequency and the wave length  $L$ .

### 3 Dispersion Relation of Coupled Vibration Equation

The system of coupled vibration equations satisfy the dynamic and kinematic boundary condition which are linearized. Applying the coupled vibration equations for water waves, the dispersion relation of the coupled vibration equation should be coincide with the one of the small amplitude theory (Airy's wave theory).

Suppose the monochromatic wave progressing in the  $x$  direction with angular frequency of  $\sigma$ , wave number of  $k$  on the water of uniform depth  $h$ . The water surface elevation  $\eta$  and the coefficients  $q_m$  can be expressed as follows,

$$\eta = \Re \left\{ \hat{\eta} e^{i(kx - \sigma t)} \right\} \tag{25}$$

$$q_m = \Re \left\{ \hat{q}_m e^{i(kx - \sigma t)} \right\} \quad m = 1, 2, 3, 4 \tag{26}$$

as  $\eta$  and  $q_m$  are in phase, where,  $\Re$  denotes the real part and  $\hat{\phantom{x}}$  the complex amplitude. Substituting above equations to Eqs.(21)-(23), the coefficients  $q_m$  are obtained as function of  $\eta$ .

$$q_1 = \frac{21g\eta(495 + 60(kh)^2 + (kh)^4)}{10395 + 4725(kh)^2 + 210(kh)^4 + (kh)^6} \tag{27}$$

$$q_2 = \frac{45g\eta(kh)^2(77 + 2(kh)^2)}{10395 + 4725(kh)^2 + 210(kh)^4 + (kh)^6} \tag{28}$$

$$q_3 = \frac{99g\eta(kh)^4}{10395 + 4725(kh)^2 + 210(kh)^4 + (kh)^6} \tag{29}$$

$$q_4 = \frac{g\eta(kh)^6}{10395 + 4725(kh)^2 + 210(kh)^4 + (kh)^6} \tag{30}$$



Substituting the above equations into Eq.(24), the relation between the angular frequency  $\sigma$  and the wave number  $k$  is finally obtained as follows.

$$\frac{\sigma^2 h}{g} = \frac{21(kh)^2(495 + 60(kh)^2 + (kh)^4)}{10395 + 4725(kh)^2 + 210(kh)^4 + (kh)^6} \quad (31)$$

This relation is the dispersion relation for the system of coupled vibration equations and corresponds to the one in the Airy's wave theory.

$$\frac{\sigma^2 h}{g} = kh \tanh kh \quad (32)$$

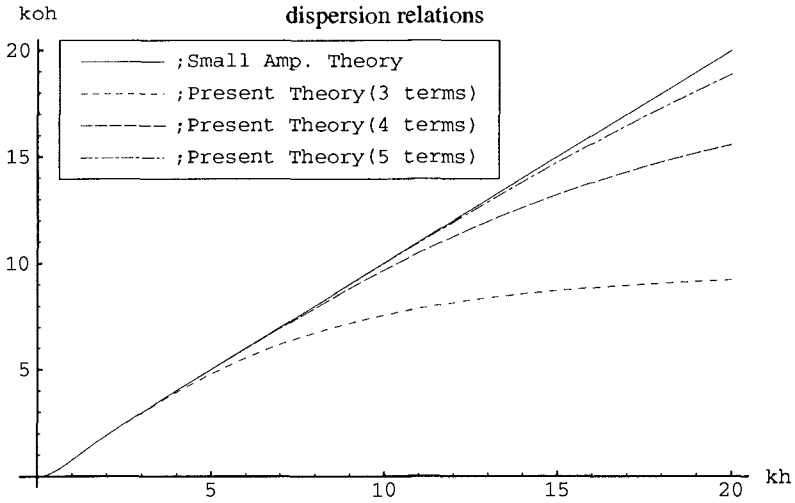


Figure 1: Comparison of dispersion relations

Figure 1 shows the relation of Eq.(32) by the solid line and of Eq.(31) by the broken line. The left hand side of these equations  $\sigma^2 h/g$  are expressed by  $k_0 h$  in the figure. The left two lines in the figure indicate the dispersion relation in the case that the first 3 and 5 terms are adopted in the Eq.(12)( see Appendix).

The dispersion relation of Eq.(31) coincide very well with the one of Airy's wave theory in the range of  $kh$  less than  $7(h/L \simeq 1)$ . This results implies that the system of coupled vibration equations be capable of expressing the waves on the very shallow water depth to the deep water depth.

Group velocity is important factor for waves deforming in a shallow water region and wave groups progressing in a deep water region. The group velocity  $C_g$  is defined by the gradient of the angular frequency  $\sigma$  with respect to the wave number  $k$ , that is,

$$C_g = \frac{\partial \sigma}{\partial k}. \quad (33)$$

The Eq.(31) gives the  $C_g/C$  of the coupled vibration equation by differentiating the equation with respect to  $k$ , where  $C$  denotes the phase velocity.

$$\frac{C_g}{C} = \frac{30}{495 + 60kh^2 + kh^4} \frac{343035 + 83160kh^2 + 14049kh^4 + 564kh^6 + 10kh^8}{10395 + 4725kh^2 + 210kh^4 + kh^6} \quad (34)$$

The Figure-2 shows the  $C_g/C$  due to the Airy's wave theory and to the present

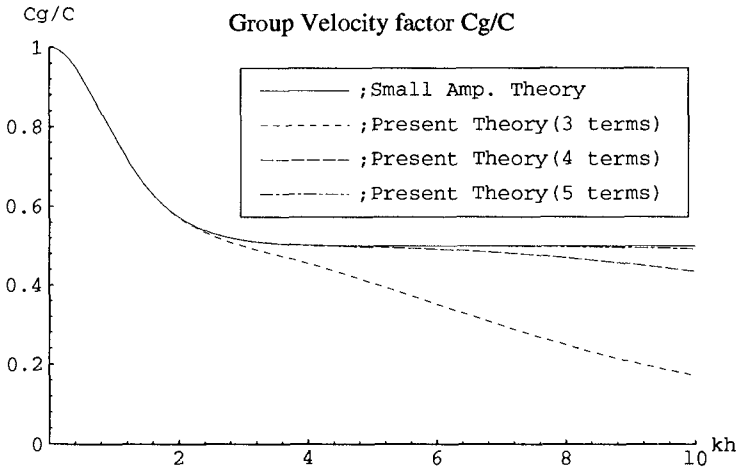


Figure 2: Comparison of group velocity

theory with the first 3, 4 and 5 terms as same as Figure-1. The group velocities due to the present theories in Figure-2 show less accuracy as comparing to the Airy's theory than the dispersion relation in Figure-1. This decrease of the accuracy is caused by differential calculus of the dispersion relation, Eq.(31) in order to obtain the group velocity.

Eq.(31) indicates the form of a *Padé* approximation for the right side of Eq.(32). The accuracy of differential coefficient of the approximated function is generally less than of the approximated function.

## 4 Calculation Method and Results

### 4.1 Incident boundary

The time series of water surface elevation is commonly measured in both field measurement and laboratory test. The position at measuring point of off-shore waves is generally treated as the incident boundary in most of calculations. In the calculation of the coupled vibration equations for irregular water waves,

the water surface elevation  $\eta$  and the coefficients  $q_m$  should be given at the incident boundary. The measured data give the water surface elevation  $\eta_{in}$  at incident boundary. The coefficient  $q_m$  is calculated by Eqs.(27)-(30) when the wave number  $k$  is given.

The wave number  $k$  is determined by the following method. The wave number  $k$  and the angular frequency  $\sigma$  for irregular waves are assumed to be a function of time and satisfy the following equations.

$$\{\sigma(t)\}^2 = gk(t) \tanh k(t)h \quad (35)$$

$$\frac{d^2\eta_{in}}{dt^2} = -\{\sigma(t)\}^2 \eta_{in} \quad (36)$$

The second equation gives the angular frequency changing with time and the wave number is determined by the first equation. The angular frequency, however, becomes infinity when the  $\eta_{in}$  is nearly equals to zero in the computer calculation. In order to avoid this problem, the complex water surface elevation  $\zeta$  is used instead of  $\eta$ . the complex water surface elevation  $\zeta$  is defined as

$$\zeta(t) = \eta_{in} + i\tilde{\eta}_{in}, \quad (37)$$

where,  $\tilde{\eta}_{in}$  is the Hilbert transform of  $\eta_{in}$  and  $i$  is the imaginary unit.  $\tilde{\eta}_{in}$  is calculated by the following relation.

$$i\tilde{H}(\omega) = \begin{cases} H(\omega) & , \text{ for } \omega > 0 \\ 0 & , \text{ for } \omega = 0 \\ -H(\omega) & , \text{ for } \omega < 0 \end{cases}, \quad (38)$$

where  $H(\omega)$  and  $\tilde{H}(\omega)$  are the complex Fourier transforms of  $\eta_{in}$  and  $\tilde{\eta}_{in}$ , respectively. Finally, the angular frequency  $\sigma(t)$  is redefined by the complex water surface elevation  $\zeta(t)$ .

$$\{\sigma(t)\}^2 = -\Re \left\{ \frac{d^2\zeta/dt^2}{\zeta} \right\} \quad (39)$$

## 4.2 Calculation results

Eqs.(21)-(24) are applied to the waves progressing in one direction on the constant water depth,  $7m$ . The waves is composed of the two wave groups; WAVE-A of which the dominant wave period is  $9s$  and WAVE-B,  $3s$ . Each wave group has a very narrow spectra, but is not monochromatic waves. That is, the waves calculated in this paper are parts of the components of the uni-directional irregular waves.

The finite difference method is applied for the equations. The time interval is  $0.183s$ , the distance of calculation nodes;  $0.73m$ , the number of nodes; 2800. The water channel is  $2km$  long and one end of the channel is a reflection boundary.

The calculated results are shown in Figure 3 as the snapshots of the water surface elevation per  $37.5s$ . In the Figure, each wave group progresses with the

each group velocity. Each wave group stretches with progress because of the frequency dispersion. The WAVE-A started later catches up with, passes the WAVE-B started earlier, then, reflects at the end, again meets with, and passes through the WAVE-B.

These results are a matter of course as the liner wave theory. A point is that the results are calculated in the time domain by the system of the coupled vibration equations.

## 5 Discussion

In the present theory, the fluctuation pressure  $\tilde{p}$  is expanded to 4 terms in Eq.(17) with the coefficients from  $q_1$  to  $q_4$ . There is, however, no  $q_4$  appeared in the final form of the coupled vibration equation in Eqs.(21)-(24). The evolution problem is calculated without  $q_4$ .

The vertical distribution of fluctuation pressure  $\tilde{p}$  in Airy's theory is given as follows.

$$\tilde{p} = g\eta \frac{\cosh k(h+z)}{\cosh kh} = g\eta \frac{\cosh kh\tilde{z}}{\cosh kh} \tag{40}$$

The right side of above equation can be expressed by the Taylor expansion.

$$\tilde{p} = \frac{g\eta}{\cosh kh} \left( 1 + \frac{(kh)^2}{2!} \tilde{z}^2 + \frac{(kh)^4}{4!} \tilde{z}^4 \right) + O\left( g\eta \frac{(kh)^6}{6!} \right) \tag{41}$$

Comparing Eq.(17) and above equation, the coefficient  $q_4$  corresponds to the resident term in the right side of above equation. The coefficient  $q_4$  indicates the truncation error of the coupled vibration equations.

The combined kinematic-dynamic free surface boundary condition is given as

$$\frac{\partial^2 \Phi}{\partial t^2} = -g \frac{\partial \Phi}{\partial z} \tag{42}$$

in the linear water wave problem based on the velocity potential theory. Assuming that the velocity potential  $\Phi(x, y, z, t)$  is expressed as the following form,

$$\Phi = \phi(x, y, t) \frac{\cosh k(h+z)}{\cosh kh}, \tag{43}$$

Eq.(42) is rewritten as follow.

$$\frac{\partial^2 \phi}{\partial t^2} = -gk \tanh kh \phi \tag{44}$$

This equation has the form of a vibration equiton. Expressing water waves as the form of vibration equation is a traditional and natural method. The coupled vibration equations, however, express the any shape of vertical distribution of the fluctuating pressure instead of an unique shape of vertical distribution such like the velocity potential in Eq.(43).

## 6 Conclusion

The system coupled vibration equations is derived for water waves progressing on the water with mild slope of the bottom configuration. The motion of water surface elevation is expressed by the vibration equation with the coupled exciting force. The new system of equations is able to be applied for the random waves composed by the monochromatic waves whose relative depth  $h/L$  is less than 1.

### REFERENCES

- Berkhoff, J. C. W.(1972): Computation of combined refraction diffraction. *Proc. 13th ICCE*, ACSE, New York, pp.471-490.
- Kubo, Y. , Y. Kotake, M. Isobe and A. Watanabe(1992): Time dependent mild slope Equation for random waves., *Proc. 23rd ICCE*, pp.419-431.
- Nadaoka, K. and Y. Nakagawa(1993): Fully nonlinear-dispersive wave equations derived by a Galerkin formulation., *Meet'n '93, ASCE/ASME/SES Abstracts*, p.724
- Liu, P. L.-F.(1983): Wave-current interactions on a slowly varying topography. *J. Geophys. Res.*, Vol.88(C7), pp4421-4426.
- Pregrine, D. H.(1967). Long waves on a beach. *J. Fluid Mech.*, Vol.27, pp.815-827

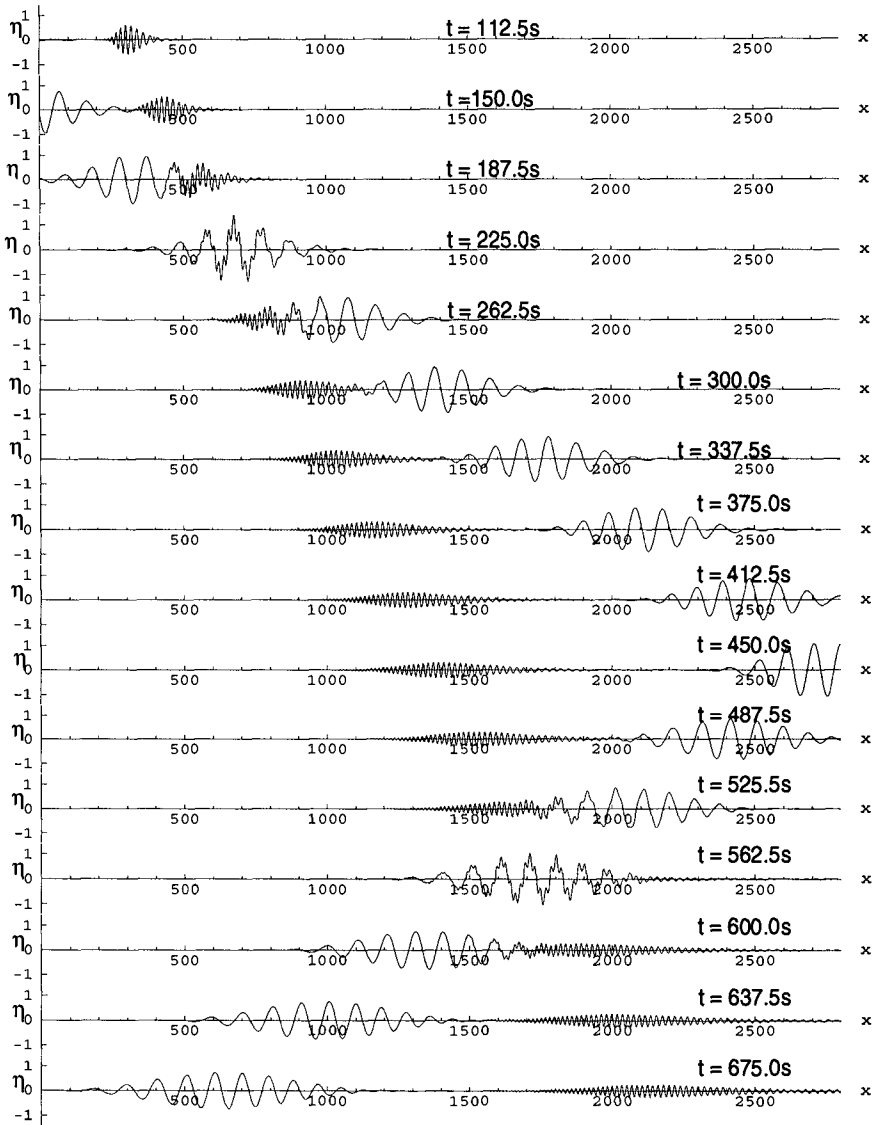


Figure 3: Propagation of two wave groups

## APPENDIX

## Equations for 3 Terms

$$g\eta = q_1 + q_2 + q_3 \quad (45)$$

$$\nabla^2 q_1 + \frac{\nabla(3q_1 + 7q_2)}{4h} \nabla h - \frac{10q_1 + 7q_2}{h^2} = \frac{3g\nabla\eta\nabla h}{4h} - \frac{10g\eta}{h^2} \quad (46)$$

$$\nabla^2 q_2 + \frac{\nabla(-10q_1 - 11q_2)}{4h} \nabla h - \frac{35q_1 + 35q_2}{h^2} = -\frac{5g\nabla\eta\nabla h}{2h} - \frac{35g\eta}{h^2} \quad (47)$$

$$\frac{\partial^2 \eta}{\partial t^2} = -\frac{1}{h}(10g\eta - 10q_1 - 7q_2) \quad (48)$$

## Equations for 5 Terms

$$g\eta = q_1 + q_2 + q_3 + q_4 + q_5 \quad (49)$$

$$\nabla^2 q_1 + \frac{\nabla(35q_1 + 99q_2 - 13q_3 + 75q_4)}{64h} \nabla h - \frac{36q_1 + 33q_2 + 26q_3 + 15q_4}{h^2} = \frac{35g\nabla\eta\nabla h}{64h} - \frac{36g\eta}{h^2} \quad (50)$$

$$\nabla^2 q_2 + \frac{\nabla(-95q_1 - 111q_2 + 65q_3 - 210)}{64h} \nabla h - \frac{165q_1 + 165q_2 + 130q_3 + 75q_4}{h^2} = -\frac{95g\nabla\eta\nabla h}{64h} - \frac{165g\eta}{h^2} \quad (51)$$

$$\nabla^2 q_3 + \frac{\nabla(639q_1 + 351q_2 + 571q_3 + 1575q_4)}{256h} \nabla h - \frac{234q_1 + 234q_2 + 234q_3 + 135q_4}{h^2} = \frac{639g\nabla\eta\nabla h}{256h} - \frac{234g\eta}{h^2} \quad (52)$$

$$\nabla^2 q_4 - \frac{\nabla(1222q_1 + 1066q_2 + 1794q_3 + 1291q_4)}{256h} \nabla h - \frac{195q_1 + 195q_2 + 195q_3 + 195q_4}{h^2} = -\frac{1222g\nabla\eta\nabla h}{256h} - \frac{195g\eta}{h^2} \quad (53)$$

$$\frac{\partial^2 \eta}{\partial t^2} = -\frac{1}{h}(36g\eta - 36q_1 - 33q_2 - 26q_3 - 15q_4) \quad (54)$$

## CHAPTER 35

### NONLINEAR EVOLUTION OF DIRECTIONAL WAVE SPECTRA IN SHALLOW WATER

Okey Nwogu<sup>1</sup>

#### ABSTRACT

Nonlinear aspects of the transformation of a multidirectional wave field in shallow water are investigated using Boussinesq-type equations. Second-order interactions between different frequency components in an irregular sea state produce lower and higher harmonic components at the sum and difference frequencies of the primary waves. For water of constant depth, expressions are derived from the Boussinesq equations for the magnitude of the second-order waves induced by bidirectional, bichromatic waves. These are used to investigate the effect of the direction of wave propagation on the near-resonant interactions that occur in shallow water. For waves propagating in water of variable depth, a numerical model based on a time-domain solution of the governing equations is used to predict the spatial evolution of the directional wave spectrum. The results of the numerical model are compared to experimental results for the propagation of bidirectional, bichromatic waves and irregular, multidirectional waves on a constant slope beach.

#### 1. INTRODUCTION

Surface waves in the ocean are short-crested or multidirectional with components of different amplitudes and frequencies, propagating in different directions. As surface waves propagate from deep to shallow water, the directional wave spectrum is transformed due to both linear and nonlinear processes. Linear refraction leads to a narrower directional distribution in shallow water, with the principal direction more closely aligned to the beach contours. Changes to the directional spectrum due to linear effects can be accurately predicted by linear refraction models (e.g. Longuet-Higgins, 1957). However, Freilich *et al.* (1990) found that linear theory could not predict the amplitudes and directions observed in certain frequency bands in field studies. This is due to the near-resonant amplification of wave components induced at the sum and difference frequencies of the primary waves. These wave harmonics could also propagate in directions quite different from those of the primary waves, resulting in substantial changes to the frequency and directional distribution of wave energy.

---

<sup>1</sup>Institute for Marine Dynamics, National Research Council, Ottawa, Canada K1A 0R6



In shallow water depths, Boussinesq-type equations (e.g. Peregrine, 1967) are able to describe the near-resonant quadratic interactions that occur in shoaling multidirectional waves. Various time and frequency domain methods have been used to solve the two-dimensional form of the Boussinesq equations. Liu *et al.* (1985) developed a parabolic model for the shoreward propagation of individual wave components while Kirby (1990) proposed an angular spectrum model. Abreu *et al.* (1992) developed a shallow water spectral model in which near-resonant interactions were only considered between colinear waves. In intermediate water depths, third-order interactions become the dominant nonlinear mechanism for the cross-spectral transfer of energy. Suh *et al.* (1990) have developed an angular spectrum model of the mild-slope equation for Stokes waves which includes cubic interactions.

In this paper, the Boussinesq model of Nwogu (1993) is used to investigate the effect of near-resonant nonlinear wave-wave interactions on the transformation of directional wave spectra in shallow water. Compared to the Boussinesq model of Peregrine (1967), the model proposed by Nwogu (1993) can be applied over a wider range of water depths due to improved frequency dispersion characteristics obtained by changing the velocity variable from the depth-averaged velocity to the velocity at an arbitrary distance from the still water level. Analytical expressions are derived from the Boussinesq equations for the bidirectional quadratic transfer function of the second-order waves induced in water of constant depth. These are used to evaluate the effect of the direction of propagation of the wave components on the near-resonant quadratic interactions that occur in shallow water. For irregular multidirectional waves propagating in water of variable depth, a numerical model based on a time domain solution of the equations is used to predict the spatial evolution of the directional wave spectrum. The results of the numerical model are compared to experimental results for the shoaling of multidirectional waves on a constant slope beach.

## 2. THEORETICAL MODEL

### 2.1 Governing Equations

Boussinesq equations represent the depth-integrated equations for the conservation of mass and momentum for weakly nonlinear and mildly dispersive waves, propagating in water of variable depth. By assuming a quadratic variation of the velocity potential over depth, the governing equations of fluid motion can be integrated over the depth, reducing the three-dimensional problem to a two-dimensional one. The continuity and momentum equations can be expressed in terms of the water surface elevation,  $\eta(\mathbf{x}, t)$ , and the horizontal velocity,  $\mathbf{u}_\alpha(\mathbf{x}, t)$ , at an arbitrary distance  $z_\alpha$  from the still water level as (see Nwogu, 1993):

$$\eta_t + \nabla \cdot [(h + \eta)\mathbf{u}_\alpha] + \nabla \cdot \left[ \left( \frac{z_\alpha^2}{2} - \frac{h^2}{6} \right) h \nabla (\nabla \cdot \mathbf{u}_\alpha) + \left( z_\alpha + \frac{h}{2} \right) h \nabla [\nabla \cdot (h\mathbf{u}_\alpha)] \right] = 0 \quad (1)$$

$$\mathbf{u}_{\alpha t} + g\nabla\eta + (\mathbf{u}_\alpha \cdot \nabla)\mathbf{u}_\alpha + \left[ \frac{z_\alpha^2}{2} \nabla(\nabla \cdot \mathbf{u}_{\alpha t}) + z_\alpha \nabla[\nabla \cdot (h\mathbf{u}_{\alpha t})] \right] = 0 \quad (2)$$

where  $\nabla = (\partial/\partial x, \partial/\partial y)$ ,  $h(\mathbf{x})$  is the water depth and  $g$  is the gravitational acceleration. The elevation of the velocity variable  $z_\alpha$  is a free parameter and is chosen to minimize the differences between the linear dispersion characteristics of the Boussinesq model and linear theory. An optimum depth for the velocity variable,  $z_\alpha = -0.53h$ , gives errors of less than 2% in the phase speed from shallow water depths up to the deep water depth limit.

### 2.2 Second-Order Forced Waves

As surface waves propagate, the different frequency components interact to produce wave components at the harmonics of the primary wave frequencies. The simplest example of this nonlinear phenomenon is the combination of two wave trains with different frequencies. The nonlinear boundary conditions at the free surface result in the generation of forced waves at the sum and difference frequencies of the primary waves,  $\omega_1 \pm \omega_2$ . The forced waves are bound or phase-locked to the primary waves or wave groups, and propagate in directions given by the sum and difference of the wavenumber vectors,  $\mathbf{k}_1 \pm \mathbf{k}_2$ . The magnitude of the forced harmonics can be determined by solving the governing equation of motion, with the free surface boundary condition satisfied at second-order in wave steepness. Starting from the Laplace equation, Dean and Sharma (1981) derived expressions for the magnitude of the forced harmonics for bidirectional, bichromatic waves, i.e. two waves with different frequencies, propagating in different directions. We shall now derive corresponding expressions from the Boussinesq equations. Consider a wave train consisting of two periodic waves with frequencies,  $\omega_1$  and  $\omega_2$ , amplitudes,  $a_1$  and  $a_2$ , propagating in directions,  $\theta_1$  and  $\theta_2$  respectively. The water surface elevation is given by:

$$\eta^{(1)}(\mathbf{x}, t) = a_1 \cos(\mathbf{k}_1 \cdot \mathbf{x} - \omega_1 t) + a_2 \cos(\mathbf{k}_2 \cdot \mathbf{x} - \omega_2 t), \quad (3)$$

where  $\mathbf{k} = (k \cos \theta, k \sin \theta)$ . The angle,  $\theta$ , is defined relative to the positive  $x$  axis. The individual waves are assumed to satisfy the first-order or linearized form of the Boussinesq equations, i.e.

$$\eta_t^{(1)} + h\nabla \cdot \mathbf{u}_\alpha^{(1)} + \left( \alpha + \frac{1}{3} \right) h^3 \nabla \cdot [\nabla(\nabla \cdot \mathbf{u}_\alpha^{(1)})] = 0, \quad (4)$$

$$\mathbf{u}_{\alpha t}^{(1)} + g\nabla\eta^{(1)} + \alpha h^2 \nabla(\nabla \cdot \mathbf{u}_{\alpha t}^{(1)}) = 0, \quad (5)$$

where  $\alpha = (z_\alpha/h)^2/2 + (z_\alpha/h)$ . The wavenumber,  $k$ , is thus related to the wave frequency by the following dispersion relation:

$$\frac{\omega^2}{k^2} = gh \left[ \frac{1 - \left( \alpha + \frac{1}{3} \right) (kh)^2}{1 - \alpha(kh)^2} \right] \quad (6)$$

The first-order horizontal velocities corresponding to the water surface elevation given by equation (3) can be determined from equations (4) and (5) as:

$$v_{\alpha}^{(1)}(\mathbf{x}, t) = \frac{\omega_1}{k_1' h} \cos \theta_1 a_1 \cos(\mathbf{k}_1 \cdot \mathbf{x} - \omega_1 t) + \frac{\omega_2}{k_2' h} \cos \theta_2 a_2 \cos(\mathbf{k}_2 \cdot \mathbf{x} - \omega_2 t), \quad (7)$$

$$v_{\alpha}^{(1)}(\mathbf{x}, t) = \frac{\omega_1}{k_1' h} \sin \theta_1 a_1 \cos(\mathbf{k}_1 \cdot \mathbf{x} - \omega_1 t) + \frac{\omega_2}{k_2' h} \sin \theta_2 a_2 \cos(\mathbf{k}_2 \cdot \mathbf{x} - \omega_2 t), \quad (8)$$

where  $k' = k[1 - (\alpha + 1/3)(kh)^2]$ . At second-order in wave steepness, the surface elevation and velocities have to satisfy the following set of equations:

$$\eta_t^{(2)} + h \nabla \cdot \mathbf{u}_{\alpha}^{(2)} + \left( \alpha + \frac{1}{3} \right) h^3 \nabla \cdot [\nabla(\nabla \cdot \mathbf{u}_{\alpha}^{(2)})] = -\nabla \cdot (\eta^{(1)} \mathbf{u}_{\alpha}^{(1)}) \quad (9)$$

$$\mathbf{u}_{\alpha t}^{(2)} + g \nabla \eta^{(2)} + \alpha h^2 \nabla (\nabla \cdot \mathbf{u}_{\alpha t}^{(2)}) = -(\mathbf{u}_{\alpha}^{(1)} \cdot \nabla) \mathbf{u}_{\alpha}^{(1)} \quad (10)$$

The second-order wave will consist of a sub-harmonic at the difference frequency,  $\omega_1 - \omega_2$ , and super-harmonics at the sum frequencies,  $2\omega_1$ ,  $2\omega_2$  and  $\omega_1 + \omega_2$ . It can be written as:

$$\begin{aligned} \eta^{(2)}(\mathbf{x}, t) &= \frac{a_1^2}{2} G_+(\omega_1, \omega_1, \theta_1, \theta_1) \cos(2\mathbf{k}_1 \cdot \mathbf{x} - 2\omega_1 t) \\ &+ \frac{a_2^2}{2} G_+(\omega_2, \omega_2, \theta_2, \theta_2) \cos(2\mathbf{k}_2 \cdot \mathbf{x} - 2\omega_2 t) \\ &+ a_1 a_2 G_{\pm}(\omega_1, \omega_2, \theta_1, \theta_2) \cos(\mathbf{k}_{\pm} \cdot \mathbf{x} - \omega_{\pm} t), \end{aligned} \quad (11)$$

where  $\mathbf{k}_{\pm} = \mathbf{k}_1 \pm \mathbf{k}_2$ , and  $G_{\pm}(\omega_1, \omega_2, \theta_1, \theta_2)$  is a bidirectional quadratic transfer function that relates the amplitude of the second-order forced wave to the first-order amplitudes. The quadratic transfer function can be determined by substituting equations (3), (7) and (8) for the first-order surface elevation and velocities into the second-order equations (9) and (10), and solving for the amplitudes of the second-order surface elevation and velocities. This leads to:

$$\begin{aligned} G_{\pm}(\omega_1, \omega_2, \theta_1, \theta_2) &= \frac{\omega_1 \omega_2 (k_{\pm} h)^2 \cos \Delta \theta [1 - (\alpha + \frac{1}{3})(k_{\pm} h)^2]}{2\lambda k_1' k_2' h^3} + \\ &\frac{\omega_{\pm} [1 - \alpha(k_{\pm} h)^2] [\omega_1 k_2' h [k_1 h \pm k_2 h \cos \Delta \theta] + \omega_2 k_1' h [k_1 h \cos \Delta \theta \pm k_2 h]]}{2\lambda k_1' k_2' h^3}, \end{aligned} \quad (12)$$

where  $\Delta \theta = \theta_1 - \theta_2$ ,

$$k_{\pm} = |\mathbf{k}_1 \pm \mathbf{k}_2| = \sqrt{k_1^2 + k_2^2 \pm 2k_1 k_2 \cos \Delta \theta}, \quad (13)$$

and

$$\lambda = \omega_{\pm}^2 [1 - \alpha(k_{\pm} h)^2] - g k_{\pm}^2 h [1 - (\alpha + 1/3)(k_{\pm} h)^2]. \quad (14)$$

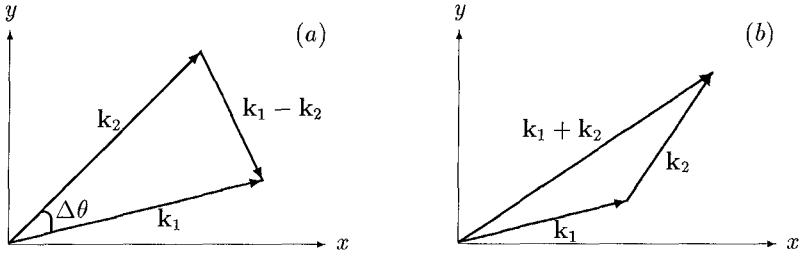


Figure 1. Directions of the sum and difference of the wavenumber vectors.

$\lambda = 0$  is actually the dispersion relation for first-order free waves in the Boussinesq model (Eqn. 6). The second-order forced waves do not satisfy the linear dispersion relation because of the forcing terms on the right hand side of equations (9) and (10), unlike second-order free waves that satisfy the homogeneous part of the equations. The second-order interactions could be resonant ( $\lambda \rightarrow 0$ ) if the frequency and wavenumber of the forced wave corresponds to that of a free wave. This occurs to unidirectional wave trains in shallow water depths where the phase velocities of the forced waves are nearly equal to the phase velocities of free waves, leading to a near-resonant amplification of the second-order waves. Wave breaking and cross-spectral energy transfers, however, limit the amplitude of the second-order waves in shallow water.

We shall now examine in detail, the differences between the magnitudes and directions of propagation of the sub-harmonics and super-harmonics in unidirectional and bidirectional seas. The sub-harmonic component, which is commonly referred to as the set-down component, travels at the velocity of the wave group,  $\omega_-/k_-$ , along a direction defined by the difference of the wavenumber vectors as shown in Figure 1(a). This direction could be quite different from the direction of propagation of the primary waves. If  $k_1$  is nearly equal to  $k_2$ , the second-order long wave would travel in a direction almost perpendicular to the average direction of the first-order short waves. On a sloping beach, this might excite the edge (transverse) wave modes as discussed by Gallagher (1971). In contrast, the super-harmonics travel in a direction nearly coincident with the average direction of the primary waves as shown in Figure 1(b).

The quadratic transfer function was evaluated for bidirectional waves with different angles of separation between the individual wave components. The transfer function of the sub-harmonic wave component is plotted in Figure 2 for an example where the frequency difference,  $\Delta\omega/\omega = 0.1$ , with  $\omega_1 = \omega - \Delta\omega/2$  and  $\omega_2 = \omega + \Delta\omega/2$ . Three crossing angles,  $\Delta\theta = 0^\circ$ ,  $10^\circ$  and  $20^\circ$  were considered. Also shown in Figure 2 are results obtained from expressions based on a second-order solution of the Laplace equation, derived by Dean and Sharma (1981).

A number of interesting observations can be made from Figure 2. The first one is that for unidirectional waves, the Boussinesq model underestimates the magnitude of the set-down wave, particularly in intermediate water depths. However, for bidirectional

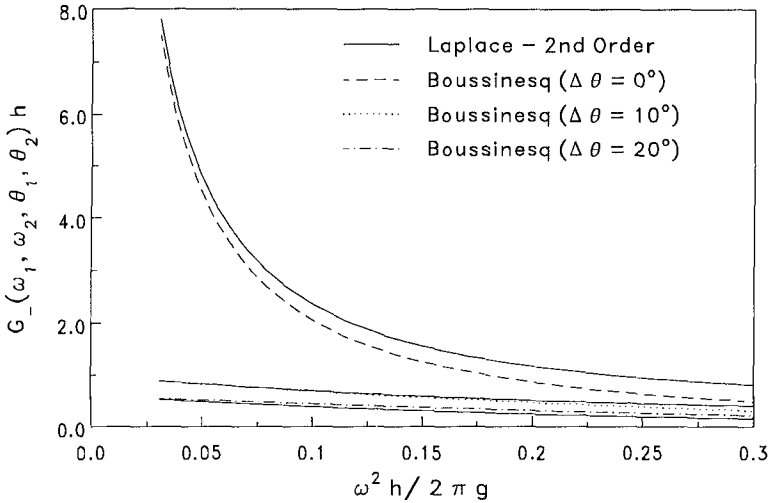


Figure 2. Bidirectional quadratic transfer function for the sub-harmonic component ( $\Delta\omega/\omega = 0.1$ ).

waves, the differences between the Boussinesq and Laplace models becomes negligible. The second one is that the directionality of the waves leads to a significant reduction of the set-down wave, as was noted by Sand (1982). In shallow water with  $\omega^2 h/2\pi g < 0.05$ , the amplitude of the forced long wave for  $\Delta\theta = 10^\circ$  is reduced by at least a factor of 5. This is because forced long waves in directional wave fields are not resonantly amplified in shallow water. Near-resonant amplification occurs for unidirectional waves because the wavenumber of the forced long wave  $|k_1 - k_2|$  is nearly equal to that of a free long wave  $k(\omega_-)$ , or equivalently,  $\omega_-$  and  $|k_1 - k_2|$  nearly satisfy the linear dispersion relation with  $\lambda \rightarrow 0$  in equation (12). In bidirectional seas, the magnitude of the wavenumber vector of the forced long wave,  $|k_1 - k_2|$ , is significantly larger than that of the corresponding free wave  $k(\omega_-)$  for small angles of separation. The forced waves are, thus, no longer close to satisfying the dispersion relation for free waves.

The quadratic transfer function for the super-harmonics is plotted in Figure 3 for an example with  $\Delta\omega/\omega = 0.1$ , and  $\Delta\theta = 0^\circ$  and  $40^\circ$ . The forced higher harmonics are slightly reduced in bidirectional waves, but not as significantly as the sub-harmonic component. For  $\omega^2 h/2\pi g = 0.05$  and  $\Delta\theta = 20^\circ$ , the super-harmonic component is reduced by 12%, compared to 90% for the sub-harmonic component. In contrast to the sub-harmonics, the super-harmonics in directional wave fields are resonantly amplified in shallow water. This is because with the addition of the wavenumber vectors, the magnitude of the wavenumber vector of the forced super-harmonic is closer to that of the corresponding free wave. The directional wave transformation model proposed

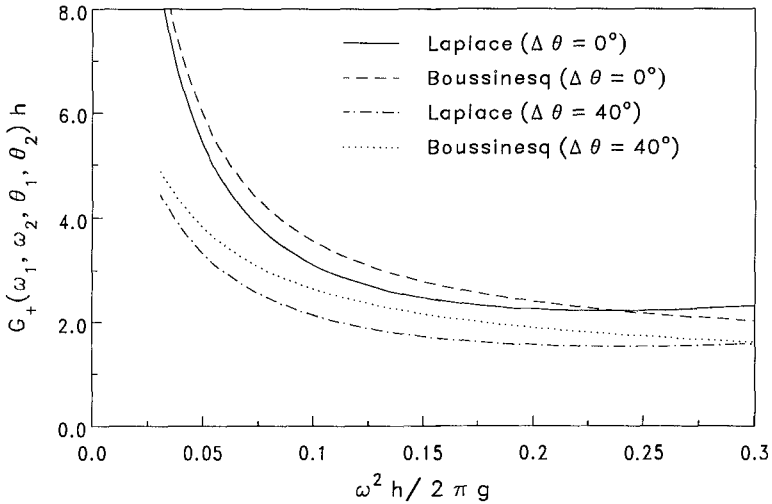


Figure 3. Bidirectional quadratic transfer function for the super-harmonic component ( $\Delta\omega/\omega = 0.1$ ).

by Abreu *et al.* (1992) assumes that near-resonant, second-order interactions only occur between colinear waves in shallow water. The present analysis, does, however, show that second-order interactions between non-colinear waves in shallow water are near-resonant for the super-harmonic component, although the strength of the interaction decreases with increasing angular separation.

### 3. Time Domain Solution

For waves propagating in water of variable depth, free second and higher-order waves are generated in addition to the forced waves. The bidirectional quadratic transfer function (Eqn. 12) can no longer be used to determine the amplitude of the wave harmonics. In this paper, we employ the time-domain model of Nwogu (1995) for irregular multidirectional wave propagation in water of variable depth. The model solves the governing set of Boussinesq-type equations using an iterative Crank-Nicolson finite difference method, with a predictor-corrector scheme used to provide the initial estimate. The computational domain is discretized using a rectangular grid, with the dependent variables  $\eta$ ,  $u_\alpha$  and  $v_\alpha$  defined at the grid points in a staggered manner. The numerical solution procedure consists of solving an algebraic expression for  $\eta$  at all grid points, tridiagonal matrices for  $u_\alpha$  along lines in the  $x$  direction and tridiagonal matrices for  $v_\alpha$  along lines in the  $y$  direction at every time step. Details of the third-order accurate scheme can be found in Nwogu (1995).

The boundaries of the computational domain may be specified as wave input boundaries or solid walls. Along incident wave boundaries, time series of  $u_\alpha$ ,  $u_{\alpha,xx}$  and  $v_{\alpha,xy}$  or  $v_\alpha$ ,  $v_{\alpha,yy}$  and  $u_{\alpha,xy}$ , corresponding to regular or irregular, unidirectional or multidirectional sea states are input at the grid points. The time histories may be derived from target directional wave spectra using the random phase, single direction per frequency model of wave synthesis (see Miles and Funke, 1987). Waves propagating out of the domain are artificially absorbed in damping regions placed next to solid wall boundaries. Artificial damping of wave energy is accomplished by introducing terms out of phase with the water surface velocity and fluid acceleration into the continuity and momentum equations respectively (see Nwogu, 1995). The output of the numerical model are time histories of  $\eta$ ,  $u_\alpha$  and  $v_\alpha$  at desired grid points in the computational domain. Directional wave spectra estimates are obtained from the time records by using the high resolution, maximum entropy method (Nwogu *et al.*, 1987)

#### 4. NUMERICAL AND EXPERIMENTAL RESULTS

Laboratory experiments were also conducted to investigate the propagation of multidirectional waves on a constant slope beach. The experiments were carried out in the three-dimensional wave basin of the Hydraulics Laboratory, National Research Council of Canada. The basin is 30 m wide, 20 m long and 3 m deep and is equipped with a 60-segment directional wave generator. The individual wave boards are 0.5 m wide and 2 m high. Wave energy absorbers made of perforated metal sheets are installed along the other sides of the basin not occupied by the wave generator. A 1:25 constant slope beach with an impermeable concrete cover was constructed in the basin, parallel to the wave generator. The toe of the slope was located 4.6 m away from the wave boards. Bidirectional bichromatic waves and irregular multidirectional sea states were generated in the basin. The water depth in the constant depth portion of the basin was 0.56 m. The water surface elevation along the centerline of the basin was measured with a linear array of 23 water level gauges. The experimental set-up is discussed in greater detail in Nwogu (1993).

##### 4.1 Shoaling of Bidirectional, Bichromatic Waves

Consider the shoaling of a bichromatic wave train with component wave periods,  $T_1 = 1.65$  s,  $T_2 = 1.5$  s, and heights,  $H_1 = 0.041$  m,  $H_2 = 0.037$  m. The tests were carried for both a unidirectional version with  $\theta_1 = \theta_2 = 0^\circ$ , and a bidirectional version with  $\theta_1 = 30^\circ$  and  $\theta_2 = -15^\circ$ . The spectral density of the measured surface elevation time history at location ( $h = 0.134$  m) is shown in Figure 4 for the bidirectional wave train. In addition to second-order wave harmonics at  $2f_1$ ,  $2f_2$  and  $f_1 \pm f_2$ , third-order wave components are also observed at  $2f_1 \pm f_2$ ,  $2f_2 \pm f_1$ ,  $3f_1$ , and  $3f_2$ , as well as some fourth-order components.

The numerical model was used to simulate the propagation of the unidirectional and

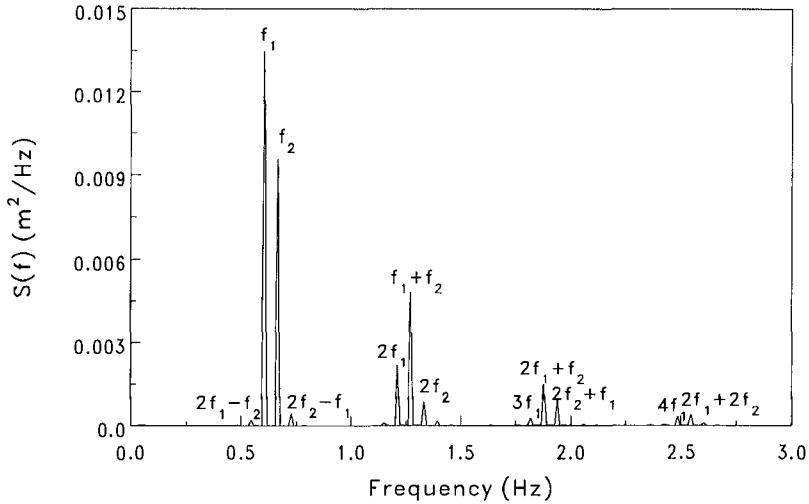


Figure 4. Measured spectral density in shallow water for a bidirectional bichromatic wave train ( $\Delta\theta = 45^\circ$ ,  $h = 0.134$  m).

bidirectional wave trains on the 1:25 beach. The simulations were carried out using a time step size  $\Delta t = 0.05$  s, and spatial grid sizes  $\Delta x = 0.1$  m and  $\Delta y = 0.2$  m. A contour plot of the instantaneous water surface elevation in the basin for the bidirectional wave train is shown in Figure 5. The variation in amplitude of a select number of wave harmonics along the centerline of the basin are plotted in Figure 6 for the unidirectional wave train, and Figure 7 for the bidirectional wave train. The experimental results are also shown in the figures. The Boussinesq model is observed to reasonably predict the measured variation in amplitude of the first-order waves and higher harmonics. The model, however, underestimates the magnitude of the set-down component for the unidirectional wave in shallow water. The simulated set-down wave has an amplitude of 0.003 m at  $h = 0.134$  m, while the measured wave has an amplitude of 0.006 m. The numerical model underestimates the magnitude of the long period wave partly because it does not simulate the reflected free waves that are generated after wave breaking and runup.

The ability of the numerical model to predict the change in wave direction between the deep and shallow water depths was also examined. The maximum entropy method, described by Nwogu *et al.* (1987), was used to estimate the directional distributions at different frequency bands from the simulated  $\eta$ ,  $u_\alpha$  and  $v_\alpha$  time series. The directions in the deep ( $h = 0.56$  m) portion of the basin are  $\theta(f_1) = 30^\circ$  and  $\theta(f_2) = -15^\circ$ . At  $h = 0.134$  m, the Boussinesq model predicts  $\theta(f_1) = 18^\circ$  and  $\theta(f_2) = -13^\circ$  while Snell's law predicts  $\theta(f_1) = 27^\circ$  and  $\theta(f_2) = -13^\circ$ . Good agreement is observed for the  $-15^\circ$  wave but not the  $30^\circ$  wave. The differences are primarily due to diffraction



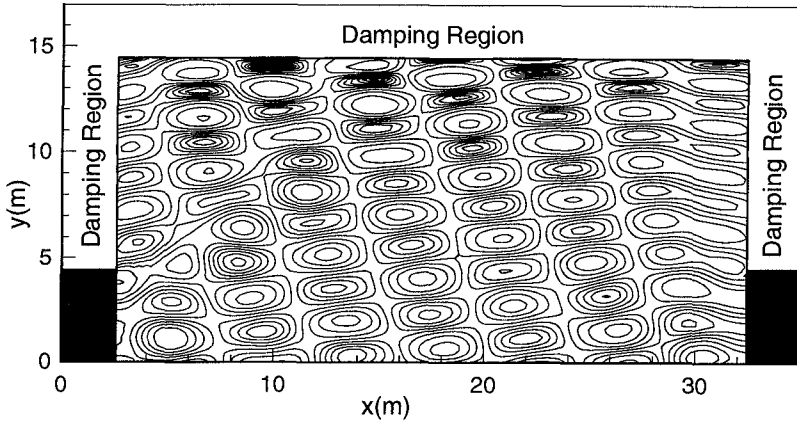


Figure 5. Contour plot of instantaneous water surface elevation for a bidirectional bichromatic wave train shoaling on a 1:25 beach ( $\theta_1 = 30^\circ, \theta_2 = -15^\circ$ ).

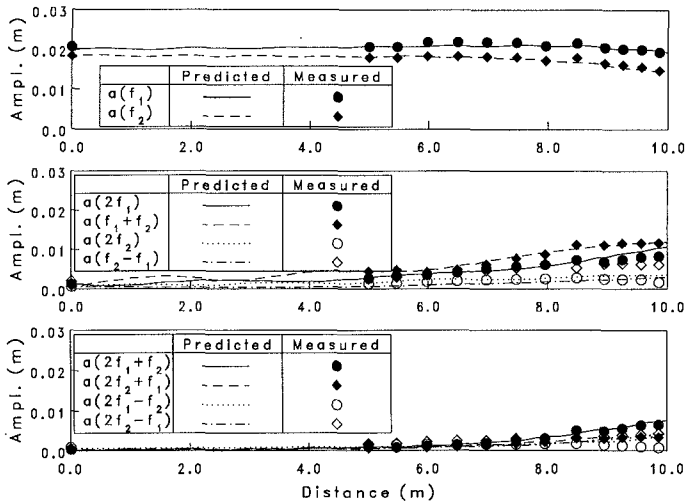


Figure 6. Variation in amplitude of wave harmonics for a unidirectional bichromatic wave train shoaling on a 1:25 beach ( $\Delta\theta = 0^\circ$ ).

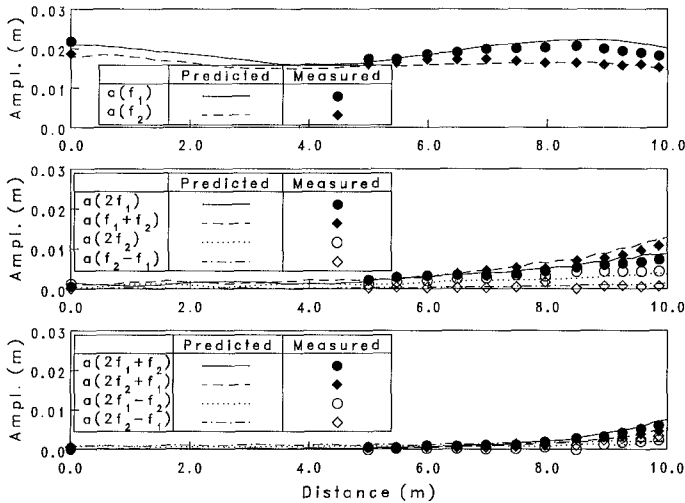


Figure 7. Variation in amplitude of wave harmonics for a bidirectional bichromatic wave train shoaling on a 1:25 beach ( $\Delta\theta = 45^\circ$ ).

effects caused by the finite width of the wave generator. The effect of diffraction is more important in the shallow portion of the basin for oblique waves with large angles of incidence. For the second-order higher harmonics, the numerical model predicts  $\theta(2f_1) = 19^\circ$ ,  $\theta(f_1 + f_2) = 2^\circ$ , and  $\theta(2f_2) = -12^\circ$ . The predicted direction for the sum frequency component is within  $2^\circ$  of that determined from the sum of the wavenumber vectors.

#### 4.2 Shoaling of Irregular Multidirectional Waves

Consider the shoaling of a bimodal sea state with local sea and swell components on the 1:25 beach from deep ( $h = 0.56$  m) to shallow water ( $h = 0.18$  m). The incident sea states were synthesized using the random phase, single direction per frequency model of wave synthesis (see Miles and Funke, 1987). The JONSWAP spectrum was used to describe the frequency distribution of wave energy while the parametric cosine power function was used for the directional distribution. The local sea component has a significant wave height,  $H_{mo} = 0.062$  m, peak period,  $T_p = 1.5$  s, peak enhancement factor,  $\gamma = 3.3$ , and a directional distribution defined by  $D(\theta) = \cos^{12}(\theta - 22.5^\circ)$ . The swell component is characterized by  $H_{mo} = 0.068$  m,  $T_p = 2$  s,  $\gamma = 10$ , and  $D(\theta) = \cos^{44}(\theta + 22.5^\circ)$ . The incident directional wave spectrum is shown in Figure 8.

The Boussinesq model was used to simulate the shoaling of the bimodal sea state with

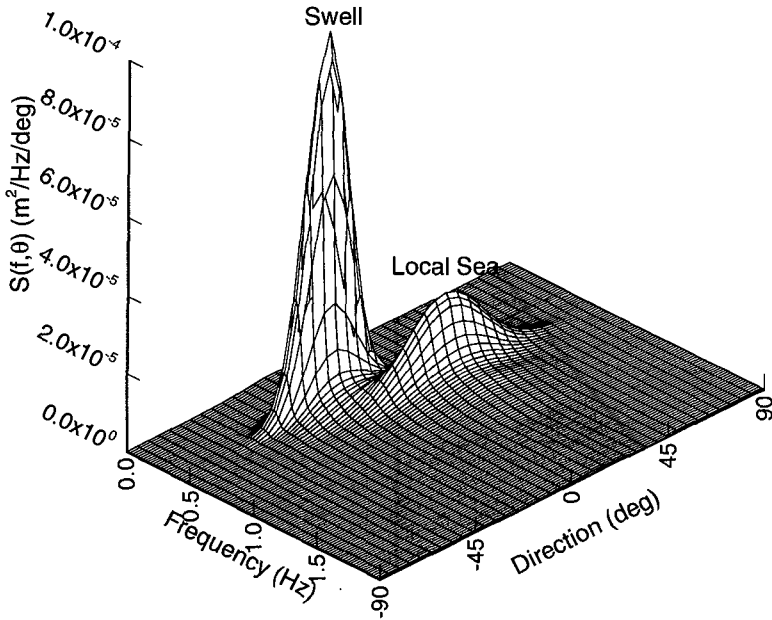


Figure 8. Numerically simulated directional spectrum of a bimodal sea state in deep water ( $h = 0.56$  m).

time step size,  $\Delta t = 0.05$  s and spatial grid sizes,  $\Delta x = 0.1$  m,  $\Delta y = 0.2$  m. Figure 9 shows a comparison of the wave spectrum at  $h = 0.56$  m with the measured and predicted spectral densities at  $h = 0.18$  m. Reasonably good agreement is observed between the measured and predicted wave spectra. Directional spectral estimates were also obtained from the simulated  $\eta$ ,  $u_\alpha$  and  $v_\alpha$  time histories using the maximum entropy method (Nwogu *et al.*, 1987). The predicted directional spectrum at  $h = 0.18$  m is shown in Figure 10. Nonlinear wave-wave interaction effects in the shoaling process substantially change the directional wave spectrum, with the transfer of energy across frequency and direction bands. There is a growth of the second, third and fourth harmonics of the swell component, and the generation of components at the vector sum of the local sea and swell components, and the vector sum of the local sea and second harmonic of the swell component. Such modifications of the directional wave spectrum can only be obtained with the use of a model that simultaneously treats nonlinearity and directionality in shoaling waves.

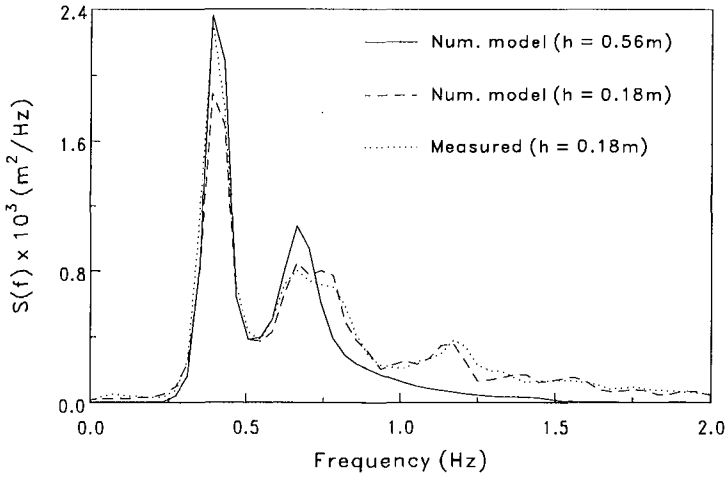


Figure 9. Surface elevation spectral densities at different water depths for bimodal sea state.

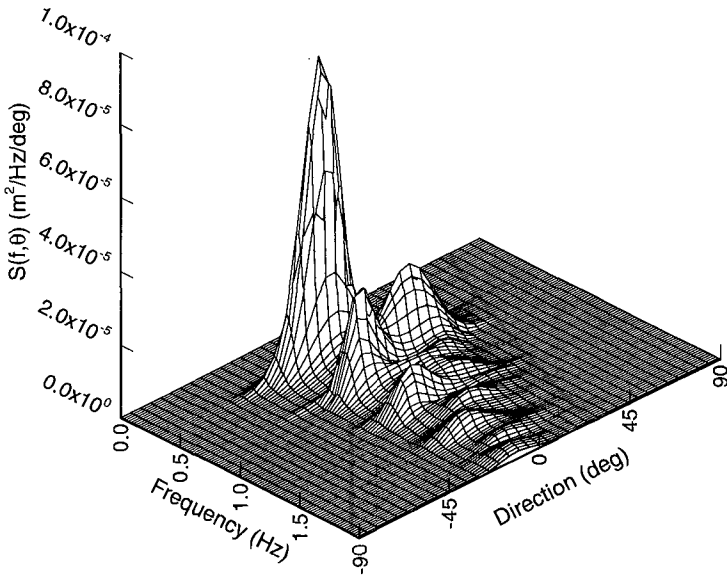


Figure 10. Numerically simulated directional spectrum of a bimodal sea state in shallow water ( $h = 0.18\text{ m}$ ).

## 5. CONCLUSIONS

A Boussinesq model has been used to investigate the effect of near-resonant nonlinear interactions on the transformation of directional wave spectra in shallow water. The amplification of second-order components induced at the sum and difference frequencies of the primary waves is near-resonant for unidirectional waves in shallow water. In multidirectional sea states, however, the second-order interactions are near-resonant for the higher harmonics but non-resonant for the lower harmonics. This leads to a significant reduction in magnitude of the long period waves induced by shoaling multidirectional waves. The spatial evolution of the directional wave spectrum in water of variable depth was predicted using a time domain Boussinesq model, and the maximum entropy method for directional wave analysis. The numerical model, which includes the effects of shoaling, refraction, diffraction and reflection, was able to predict a substantial modification of the directional wave spectrum in shallow water due to near-resonant nonlinear interactions.

## REFERENCES

- Abreu, M., Larraza, A., and Thornton, E. 1992. Nonlinear transformation of directional wave spectra in shallow water. *Journal of Geophysical Research*, **97**, 15579-15589.
- Dean, R.G., and Sharma, J.N. 1981. Simulation of wave systems due to nonlinear directional spectra. *Proc. Int. Symposium on Hydrodynamics in Ocean Engineering*, Trondheim, Norway, 1211-1222.
- Freilich, M.H, Guza, R.T., and Elgar, S.L. 1990. Observations of nonlinear effects in directional spectra of shoaling gravity waves. *Journal of Geophysical Research*, **95**, 9645-9656.
- Gallagher, B. 1971. Generation of surf beat by non-linear wave interactions. *Journal of Fluid Mechanics*, **49**, 1-20.
- Kirby, J.T. 1990. Modelling shoaling directional wave spectra in shallow water. *Proc. 22nd Int. Conference on Coastal Engineering*, Delft, The Netherlands, 109-122.
- Liu, P.L.-F., Yoon, S.B., and Kirby, J.T. 1985. Nonlinear refraction-diffraction of waves in shallow water. *Journal of Fluid Mechanics*, **153**, 185-201.
- Longuet-Higgins, M.S. 1957. On the transformation of a continuous spectrum by refraction. *Proc. Cambridge Phil. Soc.*, **53**, 226-229.
- Miles, M.D., and Funke, E.R. 1987. A comparison of methods for the synthesis of directional seas. *Proc. 6th Int. Offshore Mechanics and Arctic Engineering Symposium*, Houston, II, 247-255.

- Nwogu, O. 1993. Alternative form of Boussinesq equations for nearshore wave propagation. *Journal of Waterway, Port, Coastal and Ocean Engineering*, ASCE, **119**(6), 618-638.
- Nwogu, O. 1995. Time domain simulation of shoaling multidirectional waves. *submitted to Coastal Engineering*.
- Nwogu, O., Mansard, E.P.D., Miles, M.D, and Isaacson, M. 1987. Estimation of directional wave spectra by the maximum entropy method. *Proc. IAHR Seminar on Wave Analysis and Generation in Laboratory Basins*, XXII IAHR Congress, Lausanne, 363-376.
- Peregrine, D.H. 1967. Long waves on a beach. *Journal of Fluid Mechanics*, **27**, 815-827.
- Sand, S.E. 1982. Long waves in directional seas. *Coastal Engineering*, **6**, 195-208.
- Suh, K.D., Dalrymple, R.A., and Kirby, J.T. 1990. An angular spectrum model for propagation of Stokes waves. *Journal of Fluid Mechanics*, **221**, 205-232.

## CHAPTER 36

### NON-GAUSSIAN PROBABILITY DISTRIBUTION OF COASTAL WAVES

M.K. Ochi\* and K. Ahn\*\*

#### Abstract

This paper presents the development of a probability density function applicable to waves in finite water depth (which can be considered to be a nonlinear, non-Gaussian random process) in closed form. The derivation of the density function is based on the Kac-Siegert solution developed for a nonlinear mechanical system, but the parameters involved in the solution are evaluated from the wave record only. Further, the probability density function is asymptotically expressed in closed form. Comparisons between the presently developed probability density function and histograms constructed from wave records show good agreement.

#### Introduction

The wind-generated wave profile observed in a sea of finite water depth is significantly different from that observed in deep water in that there is a definite excess of high crests and shallow troughs in contrast to those of waves in deep water. This is attributed to nonlinear wave-wave interaction (energy transfer) between component waves, and such waves are considered to be a typical non-Gaussian random process.

Probability distributions applicable for presenting non-Gaussian random waves have been derived through three different approaches; (a) application of the orthogonal polynomials to the probability density function [Longuet-Higgins 1963], (b) application of Stokes wave theory [Tayfun 1980, Huang, et al., 1983], and (c) application of the Kac-Siegert solution [Langley 1987].

Derivation of the non-Gaussian probability density function by applying the concept of orthogonal polynomials is well-known as the

---

\* Professor, Coastal and Oceanographic Engineering Department, 336 Weil Hall, University of Florida, Gainesville, Florida, 32611, U.S.A.

\*\* Assistant professor, Civil Engineering Department, Handong, University, Pohang City, Korea.

Gram-Charlier series probability density function. The probability density function, however, is given in series form. Therefore, the density function usually has a negative value at some part of the distribution caused by the finite number of waves used in computing the density function.

The probability density function derived based on the application of Stokes waves imposes a preliminary form on the wave profile such that the individual waves are expressed as a Stokes expansion to the 2nd or 3rd order components. It is highly desirable to justify the validity of the assumption involved for random waves, particularly waves in shallow water. On the other hand, the probability density function derived by application of the Kac-Siebert solution appears to be pertinent for waves in finite water depth, since the solution represents a nonlinear, non-Gaussian random process. The probability density function, however, cannot be presented in closed form. Hence, it is not possible to develop a probability density function applicable to wave height therefrom.

This paper presents a probability density function applicable to waves in finite water depth which can be considered to be a nonlinear, non-Gaussian random process. The density function is derived based on the Kac-Siebert solution through spectral analysis. During the course of analysis, the wave spectrum is decomposed into linear and nonlinear components in order to clarify the degree of nonlinearity involved in shallow water waves. Furthermore, the probability density function is derived in closed form so that it can be used for derivation of the distribution functions applicable to peaks and troughs of waves in finite water depth.

### Basic Concept

The basic concept of the analysis applied in the present study is that the stochastic characteristics of waves in finite water depth may be considered to be the same as those of the output of a nonlinear mechanical system. In order to elaborate on this concept, let us examine the variation of wave profiles observed from deep to shallow water.

Figure 1 shows portions of wave records obtained by the Coastal Engineering Research Center, US Army, during the Atlantic Ocean Remote Sensing Land-Ocean Experiment (ARSLOE) project in 1980 at Duck, North Carolina. Included in each figure is the distance from the shoreline at the location where data were taken. As can be seen, the wave profile recorded by Gage 710 (obtained at the deepest of the three locations) is almost the same as that observed in deep water waves. As the water depth decreases, the wave profile shows a definite excess of high crests and shallow troughs which is a typical feature of a non-Gaussian random process. In other words, the wave profile transforms from a Gaussian random process to a non-Gaussian random process as they move from deep to shallow wave areas.

Let us compare the transformation of wave profiles from deep to shallow water with the output of a nonlinear mechanical system having a Gaussian random input with various degrees of nonlinearity. The



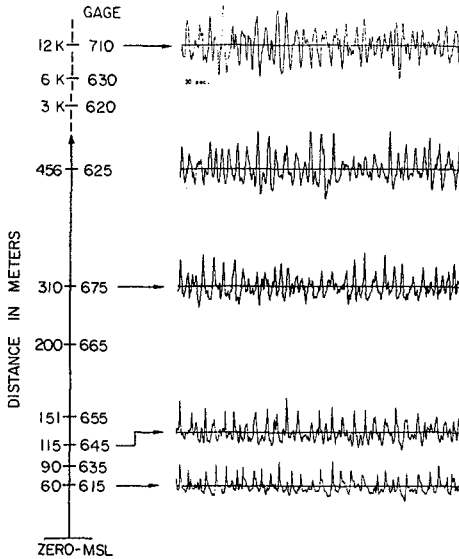


Figure 1:  
Portion of wave records obtained during ARSLOE Project at locations Gage 710, 625, 675 and 615.

output of a system with very weak nonlinearity may be considered as a Gaussian random process. However, the statistical properties of the system's output show increasing non-Gaussian characteristics with increase in the intensity of system's nonlinearity. Thus, we may consider the augmentation of the non-Gaussian characteristics of waves with decreasing water depth to be analogous to that observed in the output of a nonlinear system as its nonlinearity increases.

With this basic concept in mind, we may apply the unique solution of the output of a nonlinear system developed by Kac-Siegert [1947] to nonlinear waves. That is, the output (response) of a nonlinear system which can be presented by Volterra's stochastic series expansion can be presented in terms of the standardized normal random variable as follows:

$$y(t) = \sum_{j=1}^N (\beta_j Z_j + \lambda_j Z_j^2) \quad (1)$$

where  $y(t)$  = output of a nonlinear system  
 $Z_j$  = standardized normal variate.

The parameters  $\beta_j$  and  $\lambda_j$  are evaluated by finding the eigenfunction and eigenvalues of the integral equation given by

$$\int K(\omega_1, \omega_2) \psi_j(\omega_2) d\omega_2 = \lambda_j \psi_j(\omega_1) \quad (2)$$

where  $K(\omega_1, \omega_2) = H(\omega_1, \omega_2) \sqrt{S(\omega_1) S(\omega_2)}$

$\psi_j(\omega)$  = orthogonal eigenfunction

$H(\omega_1, \omega_2)$  = 2nd order frequency response function

$S(\omega)$  = output spectral density function.

As can be seen, knowledge of the 2nd order frequency response function,  $H(\omega_1, \omega_2)$  is necessary in order to solve the integral equation given in Eq.(2), but there is no way to evaluate it for random waves. Recently, however, the authors developed a probability density function applicable to the response of a nonlinear mechanical system in closed form based on Kac-Siebert's solution without knowledge of the second order frequency response function [Ochi and Ahn 1994]. Based on the analogy between the nonlinear mechanical system and transformation of wave profiles as they move from deep to shallow water, this paper presents the application of the authors' method in the above reference to the analysis of waves in finite water depth.

An approach to evaluate the nonlinear properties of random waves by applying the Kac-Siebert solution was considered earlier by Langley [1987]. Our approach, however, differs from Langley's approach in that (i) the wave spectrum is decomposed into linear and nonlinear components in order to examine how notably the nonlinearity increases with decreasing water depth, (ii) spectral analysis methodology instead of wave potential theory is applied in evaluating the parameters  $\beta_j$  and  $\lambda_j$ , and (iii) the probability density function applicable to wave profile  $y(t)$  is presented in closed form.

#### Presentation of Nonlinear Waves

Let us write the surface profile of nonlinear waves as follows:

$$y(t) = \text{Re} \sum_{k=1}^N c_k e^{i(\omega_k t + \varepsilon_k)} + \text{Re} \sum_{k=1}^N \sum_{\ell=1}^N c_k c_\ell \left[ q_{k\ell} e^{i\{(\omega_k + \omega_\ell)t + \varepsilon_+\}} + r_{k\ell} e^{i\{(\omega_k - \omega_\ell)t + \varepsilon_-\}} \right] \quad (3)$$

where  $\omega$  = frequency,  $\varepsilon$  = phase lag.

$q_{k\ell}$  is a coefficient associated with  $(\omega_k + \omega_\ell)$  which is the sum of the interaction between two frequency components  $\omega_k$  and  $\omega_\ell$ , while  $r_{k\ell}$  is associated with the interaction differential between  $\omega_k$  and  $\omega_\ell$ . Since there is a phase shift between the frequencies,  $\omega_k$  and  $\omega_\ell$ , in general, these interaction coefficients are complex numbers.

Equation (3) has often been considered for simulation studies as well as for analysis of nonlinear ocean waves in which the interaction coefficients are evaluated from second order nonlinear wave

theory [Hasselmann 1962, Hudspeth and Chen 1979, Sharma and Dean 1979, Anastasiou et al. 1982, etc.].

Let us write the first term of Eq.(3) as follows:

$$y_1(t) = \sum_{k=1}^N c_k e^{i(\omega_k t + \varepsilon_k)} = \sum_{k=1}^N c_k \{ \cos(\omega_k t + \varepsilon_k) + i \sin(\omega_k t + \varepsilon_k) \} \quad (4)$$

We assume that the linear component  $y_1(t)$  is a narrow-band Gaussian random process. By ignoring the factor  $\rho g$ ,  $(1/2)c_k^2$  represents the spectral density,  $S_L(\omega_k)\Delta\omega$ , where the subscript  $L$  stands for the spectral density of the linear wave components. That is, the spectral density at  $\omega = \omega_k$  is written by

$$s_k = \{S_L(\omega_k)\Delta\omega\}^{1/2} = \left\{ \int_{\omega_k - (\Delta\omega/2)}^{\omega_k + (\Delta\omega/2)} S_L(\omega) d\omega \right\}^{1/2}. \quad (5)$$

Then by defining

$$c_k \cos(\omega_k t + \varepsilon_k) = s_k \cdot u_k, \quad \text{and} \quad c_k \sin(\omega_k t + \varepsilon_k) = s_k \cdot v_k, \quad (6)$$

the linear component can be written as

$$y_1(t) = \text{Re} \sum_{k=1}^N s_k (u_k + i v_k). \quad (7)$$

The second term of Eq.(3) can be similarly written as

$$y_2(t) = \text{Re} \sum_{k=1}^N \sum_{\ell=1}^N s_k s_\ell \left\{ q_{k\ell} (u_k + i v_k) (u_\ell + i v_\ell) + r_{k\ell} (u_k + i v_k) (u_\ell - i v_\ell) \right\}, \quad \text{where} \quad s_\ell = \{S_L(\omega_\ell)\Delta\omega\}^{1/2} \quad (8)$$

Then, by taking the real-part of Eqs.(7) and (8), the nonlinear wave profile can be presented as follows:

$$y(t) = y_1(t) + y_2(t) = \sum_{k=1}^N s_k u_k + \sum_{k=1}^N \sum_{\ell=1}^N \left\{ s_k s_\ell (q_{k\ell} + r_{k\ell}) u_k u_\ell + s_k s_\ell (q_{k\ell} - r_{k\ell}) v_k v_\ell \right\} \quad (9)$$

Separation of Linear and Nonlinear Components of Wave Spectrum

Several methods for decomposing a wave spectrum into linear and nonlinear components have been developed to date. These include Tick [1959, 1961], Hamada [1965], Hudspeth and Chen [1979], Masuda, et al. [1979] and Anastasiou et al. [1982], among others. Almost all of these methods for evaluating the nonlinear part are based on the second order interaction kernel of a weakly nonlinear solution. Kim and Power [1979], on the other hand, have developed a method using the bicoherent spectrum to separate the nonlinear wave-wave interaction of coherent waves in plasma fluctuation data. Their method may be applied for separation of the spectral energy density of a random process with strong nonlinear characteristics.

Since the Kim-Power method was developed to evaluate the wave-wave interaction associated with two arbitrarily chosen constant frequencies, the method is extended in the present study so that any two frequencies associated with wave-wave interaction are not constant; instead they are variables. This implies that the nonlinear component of the spectral density at a frequency  $\omega_m$  is equal to the accumulation of nonlinear interaction associated with various pairs of frequency components  $\omega_k$  and  $\omega_l$  under the condition that  $\omega_k + \omega_l = \omega_m$ . Furthermore, we consider the interaction not only at the frequency  $(\omega_k + \omega_l)$  but also at the frequency  $(\omega_k - \omega_l)$ , where  $\omega_k > \omega_l$ . The latter is equivalent to the sum interaction between  $\omega_l$  and  $(\omega_k - \omega_l)$ . In evaluating the interaction at the frequency  $(\omega_k - \omega_l)$ , it is assumed that the spectral energy density at frequencies smaller than the minimum frequency of the main energy density in the spectrum ( $\omega_s$  in Figure 2) is due to nonlinear interaction associated with the difference between various combinations of the two frequency components at  $\omega_k$  and  $\omega_l$ . The spectral density for frequencies greater than  $\omega_s$  is due to the nonlinear interaction associated with the sum of various combinations of two frequency components.

Let us evaluate the interaction due to the sum of two frequency components. We may write the Fourier transform of  $y(t)$  at the frequency  $\omega_m$  as follows:

$$Y(\omega_m) = Y_L(\omega_m) + \sum_{\omega_k + \omega_l = \omega_m} A_L(\omega_k, \omega_l) Y_L(\omega_k) Y_L(\omega_l), \quad (10)$$

where  $Y_L(\omega_j) =$  Fourier transform of the linear component  $y_1(t)$  at the frequency  $j$ ,

$$A_L(\omega_k, \omega_l) = \text{coupling coefficient.}$$

The summation in Eq.(10) is for various combinations of components at  $\omega_k$  and  $\omega_l$  where  $\omega_k + \omega_l = \omega_m$ , and that the second term is a convolution in discrete form. The coupling coefficient  $A_L(\omega_k, \omega_l)$  can be obtained by multiplying each side of Eq.(10) by the product of the conjugates of  $Y_L(\omega_k)$  and  $Y_L(\omega_l)$ ,  $Y_L^*(\omega_k) Y_L^*(\omega_l)$ , and by taking the expected value. That is,

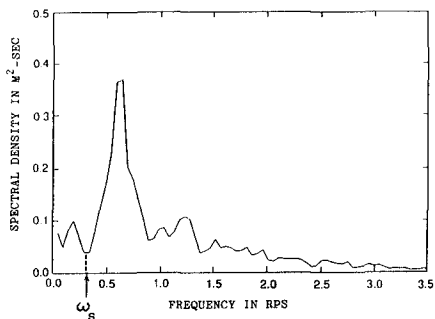


Figure 2: Definition of frequency  $\omega_s$ .

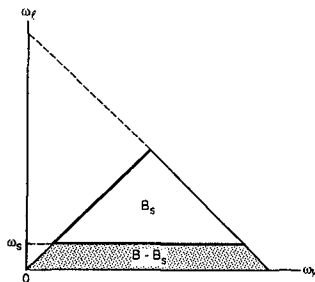


Figure 3: Domains for computing bispectra  $B(\omega_k, \omega_\ell)$  and  $B(\omega_\ell, \omega_k - \omega_\ell)$ .

$$A_L(\omega_k, \omega_\ell) = \frac{B^*(\omega_k, \omega_\ell)}{E \left[ |Y_L(\omega_k) Y_L(\omega_\ell)|^2 \right]}, \tag{11}$$

where  $B^*(\omega_k, \omega_\ell)$  = conjugate of the bispectrum  $B(\omega_k, \omega_\ell)$ . It should be noted that the domain of the bispectrum in this case is limited to that in  $B_s$  as indicated in Figure 3.

The spectral density function at the frequency  $\omega_m$  can be obtained from Eqs.(10) and (11) as

$$\begin{aligned} S(\omega_m) &= E \left[ |Y_L(\omega_m)|^2 \right] + \sum_{\omega_k + \omega_\ell = \omega_m} |A_L(\omega_k, \omega_\ell)|^2 \cdot E \left[ |Y_L(\omega_k) Y_L(\omega_\ell)|^2 \right] \\ &= E \left[ |Y_L(\omega_m)|^2 \right] + \sum_{\omega_k + \omega_\ell = \omega_m} \{b(\omega_k, \omega_\ell)\}^2 \cdot S(\omega_m), \end{aligned} \tag{12}$$

where 
$$b(\omega_k, \omega_\ell) = \left\{ \frac{|B(\omega_k, \omega_\ell)|^2}{E \left[ |Y_L(\omega_k) Y_L(\omega_\ell)|^2 \right] E \left[ |Y(\omega_m)|^2 \right]} \right\}^{1/2}. \tag{13}$$

The second term of Eq.(12) represents the accumulation of energy densities associated with interactions which occur at the frequency  $\omega_k + \omega_\ell$ . It is noted that  $E \left[ |Y_L(\omega_k) Y_L(\omega_\ell)|^2 \right]$  in Eq.(12) is unknown in advance; hence we may evaluate  $E \left[ |Y(\omega_k) Y(\omega_\ell)|^2 \right]$  for a given spectrum, and use it as an initial value in finding  $b(\omega_k, \omega_\ell)$  by iteration.

For the nonlinear components which occur at the frequency  $(\omega_k - \omega_\ell)$ ,  $B^*(\omega_k, \omega_\ell)$  as well as  $B(\omega_k, \omega_\ell)$  in Eq.(12) are replaced by

$B^*(\omega_\ell, \omega_k - \omega_\ell)$  and  $B(\omega_\ell, \omega_k - \omega_\ell)$ , respectively. Note that the domain of the bispectrum  $B(\omega_\ell, \omega_k - \omega_\ell)$  is limited to that in  $(B - B_s)$  as illustrated in Figure 3.

As an example of application of the method for separating the spectrum into linear and nonlinear components, Figures 4 through 6 show the results of computations carried out on three wave records, Gages 710, 625 and 615; a portion of each record is shown in Figure 1. It can be clearly seen in these figures that the ratio of nonlinear energy to total energy increases as water depth decreases. That is, for the Gage 710 wave record (depth 21.4 m), there exists no appreciable nonlinear energy component in its spectrum. On the other hand, for the Gage 625 record (depth 9.94 m), an appreciable amount of nonlinear energy exists at low and high frequencies, and the same trend can be observed on the Gage 615 wave record (depth 2.28 m) with substantial increase of nonlinear energy. It is noted that no nonlinear component exists in the neighborhood of the frequency where the spectrum peaks irrespective of sea severity.

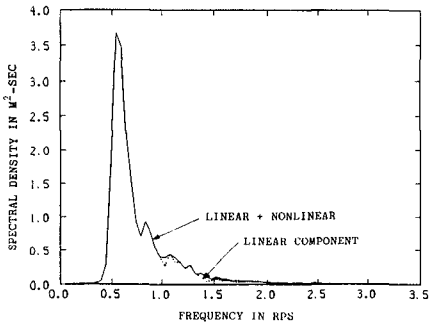


Figure 4: Separation of linear & nonlinear components of spectrum for wave record Gage 710.

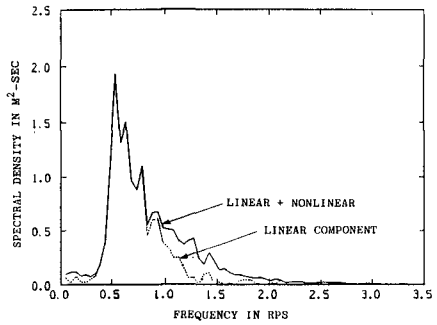


Figure 5: Separation of linear & nonlinear components of spectrum for wave record Gage 625.

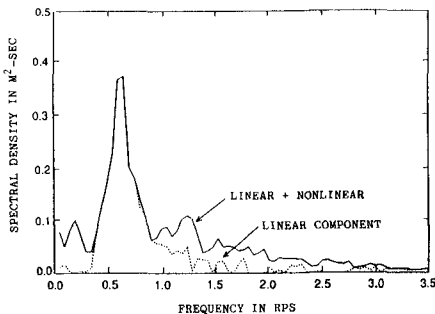


Figure 6: Separation of linear and nonlinear components of spectrum for wave record Gage 615.

Evaluation of Interaction Coefficients  $q_{k\ell}$  and  $r_{k\ell}$

The interaction coefficients  $q_{k\ell}$  and  $r_{k\ell}$  in Eq.(9) can be evaluated through bispectral analysis of the wave  $y(t)$ .

The bispectrum  $B(\omega_k, \omega_\ell)$  is most commonly evaluated in the fundamental region, which is the octant, the domain defined by  $0 \leq \omega_\ell \leq \omega_k$  and  $0 \leq \omega_k \leq \infty$  as shown in Figure 3. The volume under the bispectrum is equal to the 3rd moment of  $y(t)$  if the mean value of  $y(t)$  is zero. That is,

$$E \left[ \{y(t)\}^3 \right] = 6 \sum_{k=1}^N \sum_{\ell=1}^N \text{Re} \{B(\omega_k, \omega_\ell)\}. \quad (14)$$

On the other hand, the 3rd moment of  $y(t) = y_1(t) + y_2(t)$  can be obtained as

$$E \left[ \{y(t)\}^3 \right] = 3 E \left[ \{y_1(t)\}^2 y_2(t) \right] + E \left[ \{y_2(t)\}^3 \right]. \quad (15)$$

Note that  $y_1(t)$  is a normal distribution with zero mean, therefore  $E[\{y_1(t)\}^3]$  and  $E[y_1(t)\{y_2(t)\}^2]$  are zero.

Since the linear component  $y_1(t)$  is usually much greater than the nonlinear component  $y_2(t)$ , the second term of Eq.(15) may be neglected in comparison with the first term. Hence, we have from Eq.(9)

$$E \left[ \{y(t)\}^3 \right] = 3 E \left[ \{y_1(t)\}^2 y_2(t) \right] = 6 \sum_{k=1}^N \sum_{\ell=1}^N s_k^2 s_\ell^2 (q_{k\ell} + r_{k\ell}). \quad (16)$$

Then, Eqs.(14) and (16) yield

$$\sum_{k=1}^N \sum_{\ell=1}^N (q_{k\ell} + r_{k\ell}) = \sum_{k=1}^N \sum_{\ell=1}^N \frac{\text{Re} \{B(\omega_k, \omega_\ell)\}}{s_k^2 s_\ell^2}. \quad (17)$$

As stated in earlier, the domain of the bispectrum applicable for the interactions associated with the sum of two frequency components is  $B_s$  as shown in Figure 3. Therefore, from Eq.(17), the interaction coefficient  $q_{k\ell}$  can be obtained as

$$q_{k\ell} = \frac{1}{s_k^2 s_\ell^2} B_s(\omega_k, \omega_\ell). \quad (18)$$

Similarly, the interaction coefficient  $r_{k\ell}$  can be evaluated as

$$r_{k\ell} = \frac{1}{s_k s_\ell} \{B(\omega_\ell, \omega_k - \omega_\ell) - B_s(\omega_k, \omega_\ell)\}. \tag{19}$$

Application of the Kac-Siegert Solution

The functional relationship between parameters  $\beta_j$  and  $\lambda_j$  in the Kac-Siegert solution and the spectral densities of the linear wave components,  $s_k$  and  $s_\ell$ , as well as the interaction coefficients  $q_{k\ell}$  and  $r_{k\ell}$  are presented by Langley [1987] in a concise matrix form. Although our methods of deriving the linear wave component as well as the interaction coefficients are quite different from Langley's methods, the functional relationship between  $(\beta_j, \lambda_j)$  and  $(s_k, s_\ell, q_{k\ell}, r_{k\ell})$  can still be applied to the present problem. That is, Langley presents Eq.(9) as follows:

$$y(t) = \underline{s}' \underline{u} + \underline{u}' (\underline{Q} + \underline{R}) \underline{u} + \underline{v}' (\underline{Q} - \underline{R}) \underline{u}. \tag{20}$$

where  $\underline{Q}$  and  $\underline{R}$  are real symmetric matrices whose  $k\ell$ -th components are  $s_k s_\ell q_{k\ell}$  and  $s_k s_\ell r_{k\ell}$ , and  $\underline{s}$ ,  $\underline{u}$  and  $\underline{v}$  are vectors whose  $k$ -th components are  $s_k$ ,  $u_k$  and  $v_k$ , respectively. We may write the two matrices in Eq.(20) as

$$\begin{aligned} \underline{Q} + \underline{R} &= \underline{w}'_1 \underline{\Lambda}_1 \underline{w}_1 \\ \underline{Q} - \underline{R} &= \underline{w}'_2 \underline{\Lambda}_2 \underline{w}_2 \end{aligned} \tag{21}$$

where the column vectors of  $\underline{w}_j$  ( $j = 1, 2$ ) are normalized eigenvectors. They are orthonormal vectors satisfying the condition  $\underline{w}'_j \underline{w}_j = \underline{I}$ , where  $\underline{I}$  is the identity matrix. The elements of the diagonal matrices  $\underline{\Lambda}_j$  ( $j = 1, 2$ ) are eigenvalues of matrix  $\underline{Q} + \underline{R}$  and  $\underline{Q} - \underline{R}$ , respectively. Since  $\underline{Q} + \underline{R}$  and  $\underline{Q} - \underline{R}$  are  $N$  by  $N$  symmetric matrices, there is a total of  $2N$  eigenvalues.

Let us write

$$z_j = \begin{cases} (\underline{w}'_1 \underline{u})_j, & j = 1, 2, \dots, N \\ (\underline{w}'_2 \underline{u})_{j-N}, & j = (N+1), \dots, 2N \end{cases} \tag{22}$$

where  $z_j$  are independent standardized Gaussian random variables. Then, Langley has shown that Eq.(20) can be reduced to the Kac-Siegert formulation given in Eq.(1) with the following relationships:

$$\beta_j = \begin{cases} (\underline{s}' \underline{w}_1)_j, & j = 1, 2, \dots, N \\ 0 & j = (N+1) \dots, 2N \end{cases}$$



$$\lambda_j = \begin{cases} (\Delta_1)_j, & j = 1, 2, \dots, N \\ (\Delta_2)_j, & j = (N+1), \dots, 2N \end{cases} \quad (23)$$

Since the parameters of the Kac-Siebert solution are obtained through spectral analysis, the probability density function applicable to nonlinear, non-Gaussian waves can be derived numerically with the aid of the characteristic function as suggested by Kac-Siebert.

As an example, the method is applied to the Gage 615 wave record which indicates strong nonlinear characteristics. A comparison between the probability density function and the histogram constructed from the data is shown in Figure 7. Excellent agreement between them can be seen in the figure. This result implies that the Kac-Siebert solution evaluated from the time history of waves yields a probability density function representing the statistical properties of waves in finite water depth which have strong nonlinear characteristics. It is unfortunate, however, that the probability density function cannot be obtained in closed form.

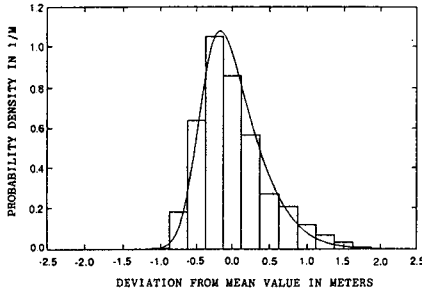


Figure 7:  
Comparison of probability density function obtained from the Kac-Siebert solution and histogram constructed from data for wave record Gage 615.

#### Asymptotic Probability Distribution for Non-Gaussian Waves

One method for deriving the probability density function in closed form is to present the Kac-Siebert solution (Eq.1) as a function of a single random variable instead of the summation of the standardized normal distribution and its squared quantity. For this, let us present Eq.(1) as

$$Y = U + aU^2 \quad (24)$$

where "a" is a constant (unknown) and U is a normal variate with mean  $\mu_*$  and variance  $\sigma_*^2$ , both of which are also unknown. The value of these unknowns will be determined from the following three equations which are derived by equating the cumulant generating function of Eq.(24) with that of Kac-Siebert's solution given in Eq.(1) (see Ochi and Ahn 1994).

$$\left\{ \begin{array}{l} a\sigma_*^2 + a\mu_*^2 + \mu_* = 0 \\ \left( \sum_{j=1}^{2N} \beta_j^2 \right) + 2 \left( \sum_{j=1}^{2N} \lambda_j^2 \right) = \sigma_*^2 - 2a^2\sigma_*^4 \\ 3 \left( \sum_{j=1}^{2N} \beta_j^2 \lambda_j \right) + 4 \left( \sum_{j=1}^{2N} \lambda_j^3 \right) = 3a\sigma_*^4 - 8a^3\sigma_*^6. \end{array} \right. \quad (25)$$

It should be noted that the left side of Eq.(25) can be presented in terms of cumulants,  $k_1$ ,  $k_2$  and  $k_3$ . If we have a wave record obtained for a sufficiently long time (on the order of 20 minutes) and if we let the mean value be the zero line, we have  $k_1 = 0$ , and thereby  $k_2$  and  $k_3$  are equal to the sample moments  $E[y^2]$  and  $E[y^3]$ , respectively. Thus, we can determine the unknown parameters  $a$ ,  $\mu_*$  and  $\sigma_*^2$  by simply evaluating the sample moments from the wave record  $y(t)$  and by applying the following relationship:

$$\begin{aligned} a\sigma_*^2 + a\mu_*^2 + \mu_* &= 0 \\ \sigma_*^2 - 2a^2\sigma_*^4 &= E[x^2] \\ 2a\sigma_*^4 (3 - 8a^2\sigma_*^2) &= E[x^3]. \end{aligned} \quad (26)$$

Since the random variable  $U$  in Eq.(24) is now a normal variate with known mean  $\mu_*$  and variance  $\sigma_*^2$ , the probability density function of  $Y$  can be derived by applying the technique of change of random variables from  $U$  to  $Y$ . Unfortunately, however, the density function thusly derived vanishes at a point  $y = -(1/4a)$  due to a singularity involved in the density function.

In order to circumvent this drawback, let us present the functional relationship between  $Y$  and  $U$  given in Eq.(24) inversely such that the random variable  $U$  is expressed as a function of  $Y$  as follows:

$$U = \frac{1}{\gamma a} \left( 1 - e^{-\gamma a Y} \right), \quad (27)$$

where  $\gamma$  is a constant; 1.28 for  $y \geq 0$  and 3.00 for  $y \leq 0$ . Justification for selecting these constant values of  $\gamma$  is given in Ochi and Ahn 1994. It may suffice here to say that these constants are valid even for a random process with very strong nonlinear characteristics.

It is noted that the values of  $\gamma$  are different for positive and negative  $y$ -values. This results in a slight difference in the slope of the probability density function at  $y = 0$ , although the density function is continuous at this point.

By using the functional relationship given in Eq.(27), we may derive the probability density function of Y from the random variable U which obeys the normal distribution with mean  $\mu_*$  and variance  $\sigma_*^2$ . The change of random variables technique yields the probability density function of Y as follows:

$$f(y) = \frac{1}{\sqrt{2\pi}\sigma_*} e^{-\frac{1}{2(\gamma a \sigma_*)^2} (1 - \gamma a \mu_* - e^{-\gamma a y})^2 - \gamma a y} \quad , \quad (28)$$

where  $\gamma = \begin{cases} 1.28 & y \geq 0 \\ 3.00 & y < 0. \end{cases}$

By applying the method for determining the limit of an indefinite function, it can be easily proved that Eq.(28) reduces to a normal probability density function with mean  $\mu_*$  and variance  $\sigma_*^2$  if  $a = 0$ ; namely, for a linear system.

Figure 8 shows a comparison of the newly developed asymptotic probability density function with the histogram of the Gage 615 wave record. The parameters  $a$ ,  $\mu_*$  and  $\sigma_*^2$  are determined from Eq.(26). Included also in the figure is the normal probability density function with zero mean and the variance evaluated from the record. As can be seen in the figure, the histogram deviates from the normal density function to a great extent; but, the agreement between the histogram and the newly developed probability density function is excellent.

Figures 9 and 10 show comparisons between the probability density function given in Eq.(28) and histograms for the Gage 625 (water depth 9.94 m) and the Gauge 710 (water depth 21.4 m), respectively. In the latter case, the probability density function is normally distributed and agrees very well with the histogram.

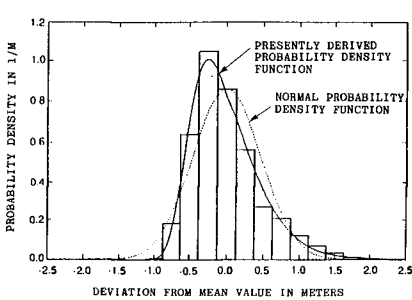


Figure 8: Comparison of presently developed probability density function and histogram constructed from data for wave Gage 615.

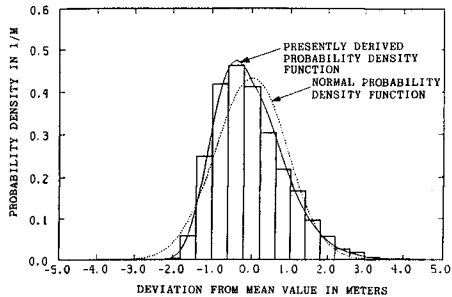


Figure 9: Comparison of presently developed probability density function and histogram constructed from data for wave Gage 625.

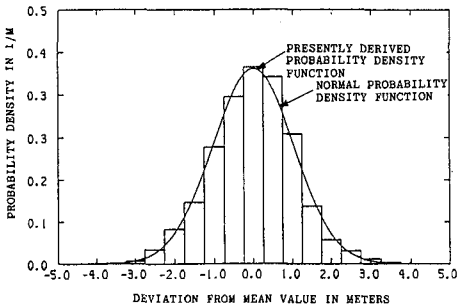


Figure 10:  
Comparison of presently developed probability density function and histogram constructed from data for wave record Gage 710.

From the results of these comparisons, it can be concluded that the probability density function covers the non-Gaussian distribution observed for random waves in shallow water as well as the Gaussian distribution observed for random waves in deep water, and that the probability density function agrees very well with the histograms constructed from wave data.

### Conclusions

This paper presents the results of a study on a probability density function applicable to waves in finite water depth developed based on the concept of Kac-Siegert's solution for the output of a nonlinear mechanical system. Although the Kac-Siegert solution requires knowledge of the second order frequency response function of the system, we developed a method to evaluate the parameters involved in the solution only from measured waves through spectral analysis. Further, the probability density function associated with the Kac-Siegert solution is asymptotically expressed in closed form (Eq.28). The presently developed probability density function covers the non-Gaussian distribution observed for random waves in shallow water as well as the Gaussian distribution observed for random waves in deep water. Comparison between the probability density function and histograms constructed from wave records show good agreement.

### Acknowledgements

This study was carried out in connection with the project on probability functions of nonlinear systems sponsored by the Naval Civil Engineering Laboratory through contract N 47408-91-C-1204 to University of Florida. The authors would like to express their appreciation to Mr. Paul Palo for his valuable discussions received during the course of this project. The authors are also grateful to Ms. Laura Dickinson for typing the manuscript.

References

- Anastasiou, K., et al. (1982), The non-linear properties of random wave kinematics, Proc. 3rd Int. Confer. on Behaviour Offshore Struct., pp.493-515.
- Hamada, T. (1965), The secondary interactions of surface waves, Rep. Port and Harbor Res. Inst., No.10, pp.1-28.
- Hasselmann, K. (1962), On the nonlinear energy transfer in a gravity wave spectrum, part I, general, J. Fluid Mechanics, Vol.12, pp.481-500.
- Huang, N.E., Long, S.R., Tung, C.C. and Yuan, Y. (1983), A non-Gaussian statistical model for surface elevation of nonlinear random wave fields, J. Geophys. Res., Vol.88, No.C12, pp.7597-7606.
- Hudspeth, R.T. and Chen, M-C. (1979), Digital simulation of nonlinear random waves, J. Waterway, Port, Coastal & Ocean, Vol.105, No.WW1, pp.67-85.
- Kac, M. and Siegert, A.J.F. (1947), On the theory of noise in radio receivers with square law detectors, J. Applied Physics, Vol.8, pp.383-397.
- Kim, Y.C. and Powers, E.J. (1979), Digital bispectral analysis and its applications to nonlinear wave interactions, IEEE Trans. Plasma Science, Vol.PS-7, No.2, pp.120-131.
- Langley, R.S. (1987), A statistical analysis of non-linear random waves, Ocean Eng., Vol.14, No.5, pp.389-407.
- Longuet-Higgins, M.S. (1963), The effect of non-linearities on statistical distribution in the theory of sea waves, J. Fluid Mech. Vol.17, Part 3, pp.459-480.
- Masuda, A., Kuo, Y. and Mitsuyasu, H. (1979), On the dispersion relationship of random gravity waves. Part 1, Theoretical framework, J. Fluid Mech., Vol.92, Part 4, pp.717-730.
- Ochi, M.K. and Ahn, K. (1994), Probability distribution applicable to non-Gaussian random processes, J. Prob. Eng. Mechanics, Vol.9, No.4, pp.255-264.
- Sharma, J.N. and Dean, R.G. (1979), Second order directional seas and associated forces, Proc. 11th Offshore Tech. Confer., Paper OTC 3645.
- Tayfun, M.A. (1980), Narrow-banded nonlinear sea waves, J. Geoph. Res., Vol.85, No.C3, pp.1548-1552.
- Tick, L.J. (1959), Nonlinear probability models of ocean waves I, J. Math and Mech., Vol.8, pp.184-196.
- Tick, L.J. (1961), Nonlinear probability models of ocean waves, Proc. Conf. Ocean Wave Spectra, pp.163-169.

## CHAPTER 37

### PROBABILITY CHARACTERISTICS OF ZERO-CROSSING WAVE HEIGHT

by T. Ohta<sup>1</sup> and A. Kimura<sup>2</sup>

#### Abstract

This study deals with the probability distribution of zero-crossing wave height applying the definition of the zero-up(down)-cross method faithfully. In this study, gap between wave crest or trough and the envelope at the same location, which has been neglected in the ordinary studies is taken into account in the wave height definition. Its probability distribution is approximated with the Weibull distribution. The probability distribution of the zero-crossing wave height is, then, introduced theoretically together with the theory by modified Tayfun Method and the statistical properties of the gaps. The numerically simulated irregular wave height distributions agree well with the theoretical distribution.

#### Introduction

The Rayleigh distribution has been used as a probability distribution of zero-crossing wave height. Although this distribution agrees very well for the almost irregular wave height distributions, it was derived theoretically as a probability distribution of "wave amplitude" in the case of narrow band spectrum by Longuet-Higgins(1952). Therefore, the Rayleigh distribution is not the theoretical probability distribution for "wave height", even when the wave spectrum is narrow. Tayfun(1981,1983) tried to derive the probability distribution of the zero-crossing wave height on the basis of its definition faithfully. However, his distribution is considerably different from the Rayleigh distribution when the wave spectrum is wide. We know the Rayleigh distribution

-----

- 1 Research Associate, Dept. of Social Systems Eng., Faculty of Eng., Tottori Univ., 4-101 Koyama Minami Tottori, Japan
- 2 Prof., Dept. of Social Systems Eng., Faculty of Eng., Tottori Univ., 4-101 Koyama Minami Tottori, Japan

can be applied to the probability distribution of zero-crossing "wave height" sufficiently. The agreements of the theory and data are mainly around its mean. Very few studies examined the wave height distribution in the very large part, larger than twice the mean wave height, for example. In the design of structural durability and reliability, however, reliable probability in a range over 2.5 times of the mean wave height may become necessary. This study aims at deriving the probability distribution of zero-crossing "wave height", applying the basic definition for the zero-crossing wave height and considering small errors which is inevitably introduced in the ordinary theory.

#### Definition of Zero-Crossing Wave Height

In a spectrum theory, the envelope for irregular wave profile has been used instead of the amplitude at crest and trough of zero-crossing wave. Fig.1 shows irregular wave profile  $\eta$ , its envelope  $R$  and their enlargements around  $t=t_2$ .  $\eta(t_1)$ ,  $\eta(t_2)$  and  $\eta(t_3)$  show maxima or minima of  $\eta$ .  $R_{m_1}$ ,  $R_{m_2}$  and  $R_{m_3}$  are the simultaneous envelope amplitudes respectively. The zero-crossing wave height is defined, in principle, as a sum of consecutive maximum and minimum of  $\eta$  between two zero-up or down-crossing points. For example, the wave height of the first zero-down-crossing wave in fig.1 is described as  $H_1 = \eta(t_1) + \eta(t_2)$ . In the ordinary theory, maxima and minima of zero-crossing waves are approximated by the simultaneous envelope amplitudes, then  $H_1$  is given by eq.1.

$$H_1 = R_{m_1} + R_{m_2} \quad (1)$$

When the wave spectrum is very narrow, the envelope changes gradually. Longuet-Higgins(1952) assumed that wave amplitudes are equal to the envelope amplitudes, and we have been applying the Rayleigh distribution as the probability distribution of zero-crossing "wave height", putting  $H_1 = 2R_{m_1}$ . However, if the wave spectrum is wide, this assumption brings considerable errors. On the basis of eq.1, Tayfun(1981) derived probability distributions of zero-crossing wave height. Since the gaps between  $\eta(t_j)$  and  $R_{m_j}$ , which are shown by  $\delta_j$  in fig.1, are order of  $v^2$  (Tayfun, 1989,  $v^2 = m_0 m_2 / m_1^2 - 1$ ,  $m_n$ : n-th order spectral moment), he neglected them. However the zero-crossing wave height should be defined, in principle as

$$H_1 = (R_{m_1} + R_{m_2}) - (\delta_1 + \delta_2) \quad (2)$$

To derive the probability distribution of zero-crossing wave height which basis on eq.2, it is necessary to make clear the additional probability distribution for  $R_{m_j}$  and  $\delta_j$ . The envelope

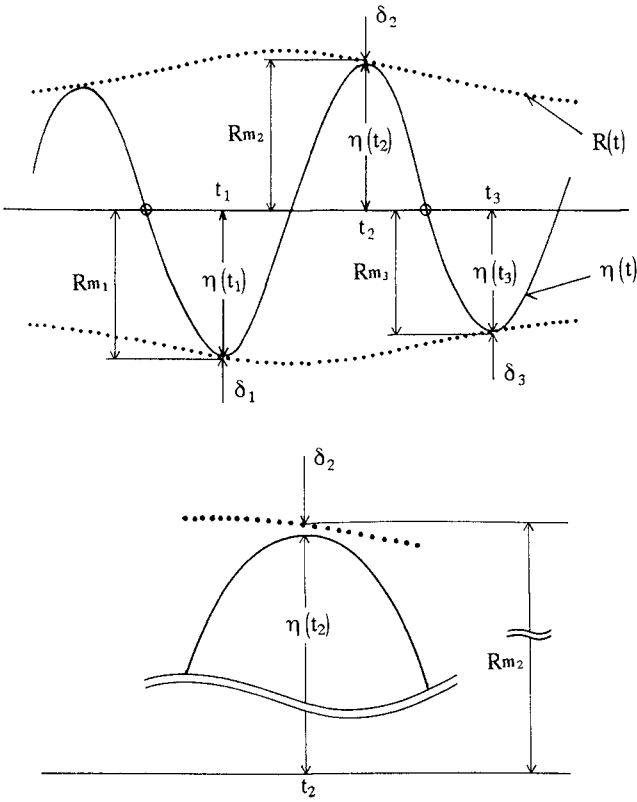


Fig. 1 Components of wave height

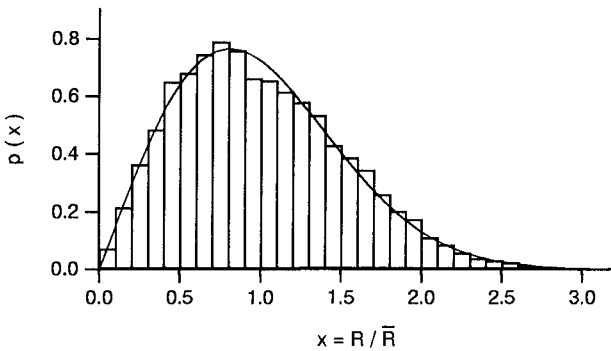


Fig. 2 Probability distribution of  $R$  ( $r=5$ )



amplitudes  $R(t)$  follow the Rayleigh distribution, however,  $R_{m_j}$  is not statistically uniform samples from the population of envelope amplitude. In other words, because of the uneven interval between consecutive  $R_{m_j}$ , its distribution may be depart from the Rayleigh distribution. And there is no theoretical probability distribution for  $\delta_j$ . In this study, the probability distribution for  $R_{m_j}$  and  $\delta_j$  are investigated experimentally through numerical simulations.

### Numerical Simulations

The irregular wave profiles  $\eta$  were simulated by FFT method (8192 points,  $\Delta t=0.05s$ ). Next wave spectrum  $S(f)$  with variable shape factor  $r$  ( $r=4,5,6,7,8,9,10,15,20$ ) is used in the simulations.

$$S(f) = \left( \frac{f}{f_p} \right)^{-r} \exp \left[ \frac{r}{4} \left\{ 1 - \left( \frac{f}{f_p} \right)^{-4} \right\} \right] \quad (3)$$

where,  $f_p$  is a peak frequency of  $S(f)$ . The envelope  $R(t)$  was calculated by the following equation.

$$R(t) = \sqrt{\eta^2(t) + \hat{\eta}^2(t)} \quad (4)$$

where,  $\hat{\eta}$  is the Hilbert transformation of  $\eta$ . The histogram in fig.2 shows the frequency distribution of  $R(t)$ . The theoretical probability distribution for  $R(t)$  is the Rayleigh distribution, however, we attempted to apply the Weibull distribution as a more general distribution (eq.5).

$$p(x) = \frac{\alpha}{2\gamma} x^{\alpha-1} \exp \left( -\frac{x^\alpha}{2\gamma} \right) \quad (5)$$

where,  $x = R/\bar{R}$

$$\gamma = \frac{1}{2} \left[ \Gamma \left\{ (1+\alpha)/\alpha \right\} \right]^{-\alpha}$$

$\alpha$  is the shape parameter,  $\gamma$  is the scale parameter and  $\Gamma$  is the Gamma function. In fig.2, the solid line shows the Weibull distribution whose shape parameter  $\alpha=2.027$  and scale parameter  $\gamma=0.639$ . In the case of  $\alpha=2.0$  and  $\gamma=0.637$ , it is the Rayleigh distribution. Therefore the probability distribution for  $R(t)$  agrees well with the Rayleigh distribution. The histogram in fig.3 illustrates the frequency distribution of  $R_{m_j}$ . In this case, the spectral shape parameter  $r$  is 5. Applying the Weibull distribution to this frequency distribution, we obtained a result that the shape parameter  $\alpha_2=1.864$  and the scale parameter  $\gamma_2=0.697$ . The solid line in fig.3 shows that Weibull distribution. In fig.4, the histogram

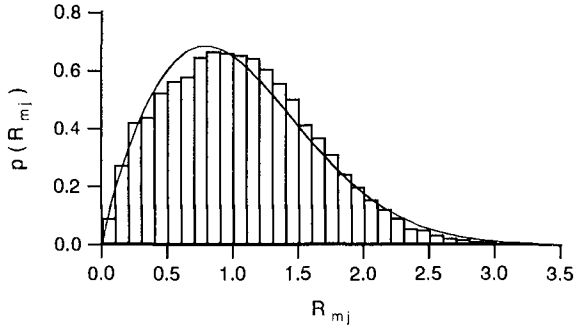


Fig. 3 Probability distribution of  $R_{mj}$  ( $r=5$ )

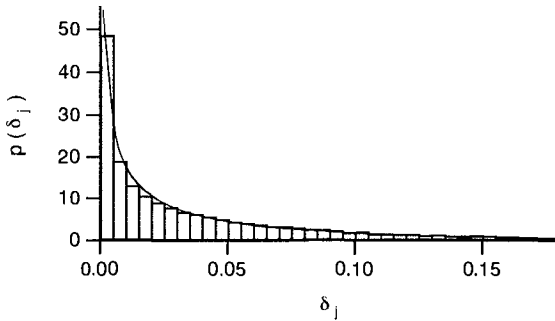


Fig. 4 Probability distribution of  $\delta_j$  ( $r=5$ )

Tab. 1 Parameters for Weibull distribution

$r$	$v$	$\alpha_1$	$\gamma_1$	$\alpha_2$	$\gamma_2$	$\bar{\delta}_j$	$\bar{R}_{mj}$
4	0.5571	0.6325	0.08649	1.829	0.8065	0.08469	1.154
5	0.4041	0.6394	0.06427	1.864	0.6975	0.05435	1.062
6	0.3247	0.6418	0.05081	1.898	0.6223	0.03802	0.9959
7	0.2768	0.6430	0.04274	1.939	0.5666	0.02891	0.9459
8	0.2444	0.6394	0.03767	1.975	0.5193	0.02356	0.9037
9	0.2205	0.6467	0.03262	1.921	0.4792	0.01955	0.8677
10	0.2018	0.6546	0.02900	1.941	0.4495	0.01701	0.8395
15	0.1514	0.6690	0.01988	1.941	0.3548	0.01043	0.7432
20	0.1256	0.6942	0.01462	1.988	0.2999	0.00775	0.6854

shows the frequency distribution of  $\delta_j$  when the spectral shape parameter  $r$  is 5. Solid line shows the Weibull distribution with shape parameter  $\alpha_1=0.639$  and scale parameter  $\gamma_1=0.0643$ . The results for other spectral shape parameters, whose range

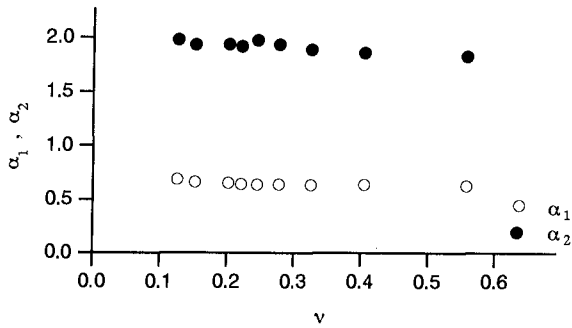


Fig. 5 Shape parameters of Weibull distribution

is from 4 to 20, are given in tab.1. Fig.5 shows shape parameters of the Weibull distribution. The open circles show the shape parameters of the Weibull distribution for  $\delta_j$  and the closed circles show those for  $R_{m_j}$ . Horizontal axis shows the spectral band width parameter  $\nu$ . As  $\nu$  increases, the shape parameter of the Weibull distribution has tendency to decrease. The distributions obtained become a little flatter shape compared with the Rayleigh distribution. We concluded that uneven sampling from the population of  $R(t)$  causes this deviation from the Rayleigh distribution.

#### Probability Distribution of Wave Height

It is confirmed so far that the probability distributions for  $R_{m_j}$  and  $\delta_j$  are well approximated by the Weibull distribution. To derive the probability distribution of wave height with the definition as eq.2, it is necessary to investigate the following points.

1. The joint probability distribution between consecutive envelope amplitudes  $R_{m_j}$  and  $R_{m_{j+1}}$  ;  $p(R_{m_j}, R_{m_{j+1}})$
2. The joint probability distribution between  $\delta_j$  and  $\delta_{j+1}$  ;  $p(\delta_j, \delta_{j+1})$
3. The joint probability distribution between  $R_m = (R_{m_j} + R_{m_{j+1}})$  and  $\delta = (\delta_j + \delta_{j+1})$  ;  $p(R_m, \delta)$

First of all, the probability distribution for  $R_{m_j}$  and  $R_{m_{j+1}}$  are also approximated by the Weibull distribution. The shape parameter is denoted by  $\alpha_2$ . Since the interval between  $R_{m_j}$  and  $R_{m_{j+1}}$  is about half of the mean period,  $R_{m_j}$  and  $R_{m_{j+1}}$  must have correlation. With only above limited conditions, however, it is not possible to determine the joint probability distribution theoretically. In this study, we use the 2-dimensional Weibull distribution (Kimura, 1981) as the joint probability distribution

for the consecutive envelope amplitudes,  $p(R_{m_j}, R_{m_{j+1}})$ .

$$p(R_{m_j}, R_{m_{j+1}}) = \frac{\alpha_2^2}{4(\gamma_2^2 - \rho^2)} R_{m_j}^{\alpha_2 - 1} R_{m_{j+1}}^{\alpha_2 - 1} \cdot \exp\left\{-\frac{\gamma_2}{2(\gamma_2^2 - \rho^2)} (R_{m_j}^{\alpha_2} + R_{m_{j+1}}^{\alpha_2})\right\} \cdot I_0\left(\frac{R_{m_j}^{\alpha_2/2} R_{m_{j+1}}^{\alpha_2/2}}{\gamma_2^2 - \rho^2} \rho\right) \quad (6)$$

where,  $I_0$  is the modified Bessel function of the first kind (0-th order),  $\rho$  is the correlation parameter between  $R_{m_j}$  and  $R_{m_{j+1}}$ .

$$\rho = \kappa \gamma_2 \quad (7)$$

and  $\kappa$  is given as following (Kimura and Ohta,1992).

$$\kappa = \sqrt{\mu_{13}^2 + \mu_{14}^2} / m_0 \quad (8)$$

$$\mu_{13} = \int_{f_d}^{f_u} S(f) \cos\{2\pi(f - \bar{f})t_m\} df$$

$$\mu_{14} = \int_{f_d}^{f_u} S(f) \sin\{2\pi(f - \bar{f})t_m\} df$$

$$f_d = (-0.186/r + 0.735) f_p \quad (4 \leq r \leq 20)$$

$$f_u = (1.61/r + 1.62) f_p \quad (4 \leq r \leq 20)$$

$$\bar{f} = m_1 / m_0, \quad t_m = \sqrt{m_0 / m_2}$$

Because  $R_{m_j}$  is not normalized by its mean, the scale parameter  $\gamma_2$  is given as follows.

$$\gamma_2 = \frac{1}{2} \left[ \Gamma\left\{(1 + \alpha_2) / \alpha_2\right\} \right]^{-\alpha_2} \overline{R_{m_j}}^{\alpha_2} \quad (9)$$

Fig.6 shows that the 2-dimensional Weibull distribution agrees well with the simulated joint frequency distribution between  $R_{m_j}$  and  $R_{m_{j+1}}$ . Three cases of  $r=5, 10$  and  $20$  were shown in fig.6. Similar agreements are obtained in other cases ( $r=4, 6, 7, 8, 9, 15$ ).

Second, the probability distribution for  $\delta_j$  and  $\delta_{j+1}$  are also approximated by the Weibull distribution. The shape parameter is described by  $\alpha_1$ . Open circles in fig.7 show the correlation coefficients between  $\delta_j$  and  $\delta_{j+1}$ , and fig.8 illustrates the distribution of  $\delta_j$  and  $\delta_{j+1}$  in the case  $r=5$ . Although calculated

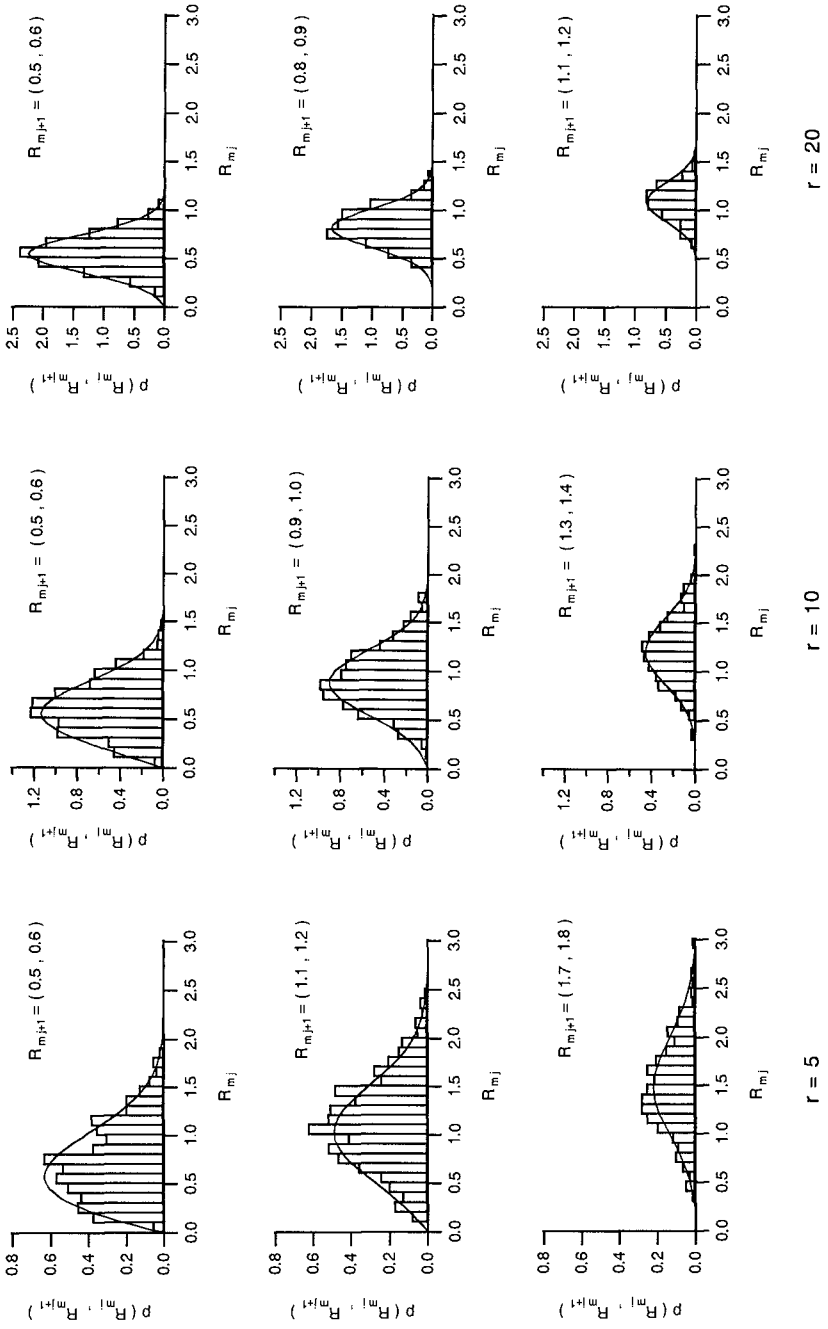


Fig. 6 Joint probability distribution of  $R_{m,j}$  and  $R_{m,j+1}$

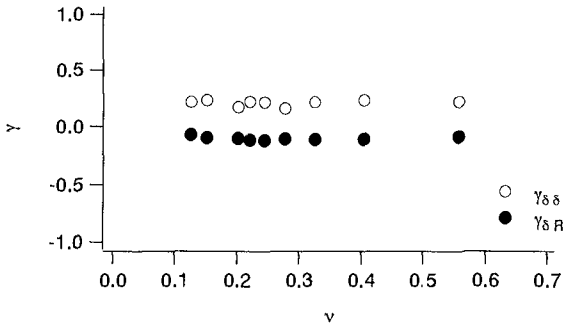


Fig. 7 Correlation coefficients

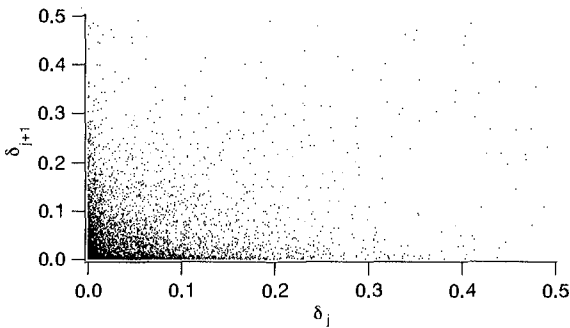


Fig. 8 Distribution of  $\delta_j$  and  $\delta_{j+1}$  ( $r=5$ )

correlation coefficient is about 0.2 in this case, we can not see apparent correlation as shown in fig.8. Considering  $\delta_j$  and  $\delta_{j+1}$  are independent, then, we tried to apply the product of Weibull distribution as a joint probability distribution between  $\delta_j$  and  $\delta_{j+1}$ ,  $p(\delta_j, \delta_{j+1})$ .

$$p(\delta_j, \delta_{j+1}) = \frac{\alpha_1^2}{4\gamma_1^2} \delta_j^{\alpha_1-1} \delta_{j+1}^{\alpha_1-1} \exp\left\{-\frac{1}{2\gamma_1}(\delta_j^{\alpha_1} + \delta_{j+1}^{\alpha_1})\right\} \quad (10)$$

Since  $\delta_j$  is not normalized by its mean, the scale parameter  $\gamma_1$  is given as

$$\gamma_1 = \frac{1}{2} \left[ \Gamma\left\{\frac{1+\alpha_1}{\alpha_1}\right\} \right]^{-\alpha_1} \bar{\delta}_j^{\alpha_1} \quad (11)$$

Fig.9 illustrates a comparison between the product of the Weibull distribution and the simulated joint frequency distribution of  $\delta_j$  and  $\delta_{j+1}$  in the cases of  $r=5, 10$  and  $20$ .

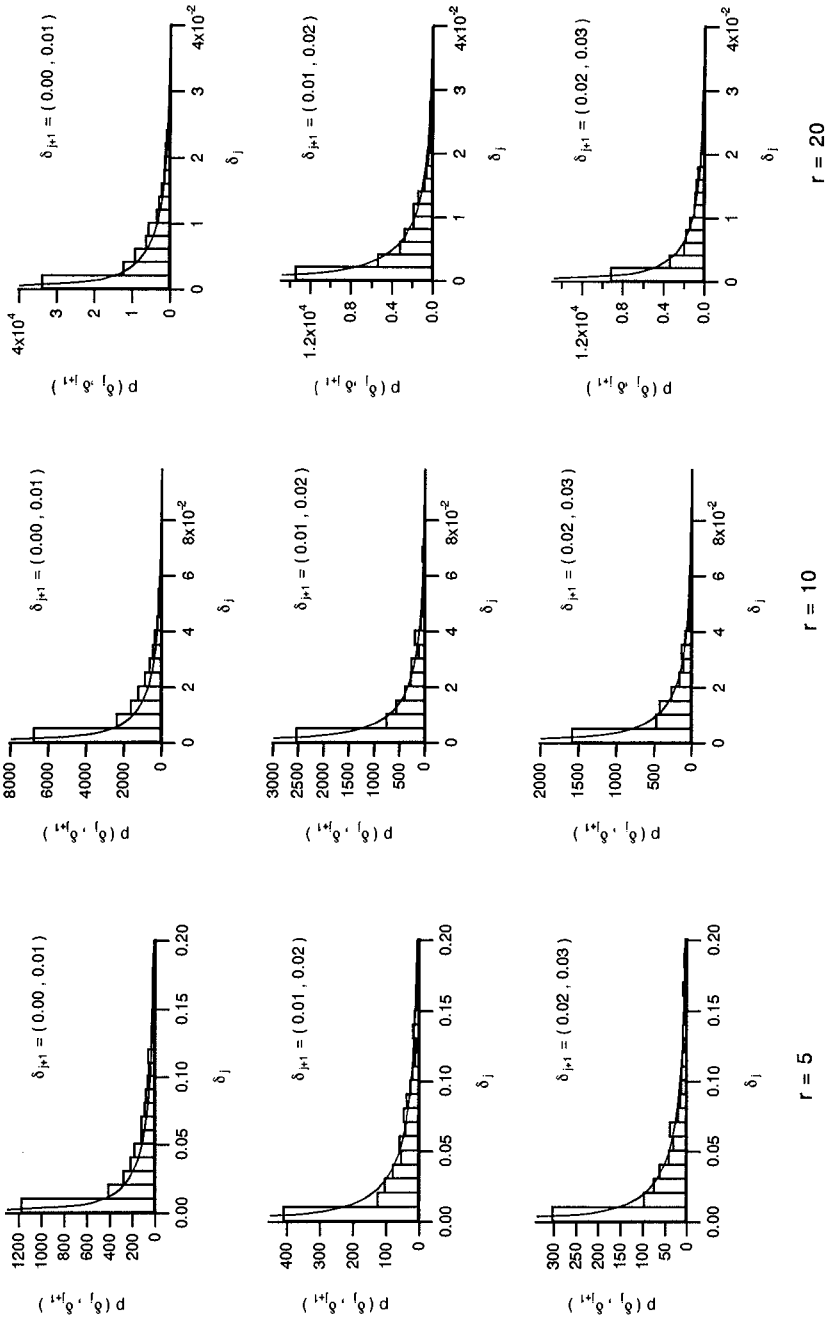


Fig. 9 Joint probability distribution of  $\delta_j$  and  $\delta_{j+1}$

Third, the joint probability distribution between  $R_m=(R_{m_1}+R_{m_{j+1}})$  and  $\delta=(\delta_j+\delta_{j+1})$  is determined by using above results. Closed circles in fig.7 show the correlation coefficients between  $R_m$  and  $\delta$ . Although the calculated values are about  $-0.1$ , we consider  $R_m$  and  $\delta$  to be independent. Therefore, the joint probability distribution between  $R_m$  and  $\delta$  is given by the product of the probability distribution for  $R_m$  and it for  $\delta$ .

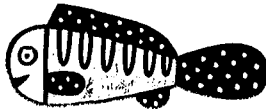
Using above results, we derive the probability distribution of zero-crossing wave height. First, the probability distribution for  $R_m$ , which is denoted by  $p(R_m)$ , is given as eq.(12).

$$\begin{aligned}
 p(R_m) = & \int_0^{R_m} \frac{\alpha_2^2}{4(\gamma_2^2 - \rho^2)} R_{m_j}^{\alpha_2 - 1} (R_m - R_{m_j})^{\alpha_2 - 1} \\
 & \cdot \exp \left[ -\frac{\gamma_2}{2(\gamma_2^2 - \rho^2)} \left\{ R_{m_j}^{\alpha_2} + (R_m - R_{m_j})^{\alpha_2} \right\} \right] \\
 & \cdot I_0 \left[ \frac{R_{m_j}^{\alpha_2/2} (R_m - R_{m_j})^{\alpha_2/2}}{\gamma_2^2 - \rho^2} \rho \right] dR_{m_j}
 \end{aligned}
 \tag{12}$$

Second, the probability distribution for  $\delta$ , which is described by  $p(\delta)$ , is given as following.

$$\begin{aligned}
 p(\delta) = & \int_0^\delta \frac{\alpha_1^2}{4\gamma_1^2} \delta_j^{\alpha_1 - 1} (\delta - \delta_j)^{\alpha_1 - 1} \\
 & \cdot \exp \left[ -\frac{1}{2\gamma_1} \left\{ \delta_j^{\alpha_1} + (\delta - \delta_j)^{\alpha_1} \right\} \right] d\delta,
 \end{aligned}
 \tag{13}$$

The zero-crossing wave height is defined as  $H=R_m-\delta$ , and the probability distribution of  $H$  can be obtained by



**TROPICAL FISH**  
 184. Orinda Pacific Oil Company is  
 one of the most beautiful tropical  
 spheres. Mexico is what Ace.



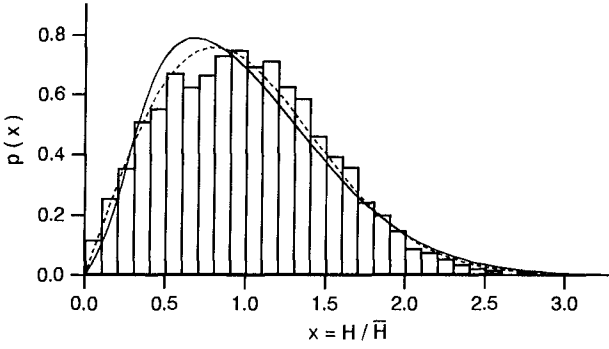


Fig.10 (a) Wave height distribution ( $r = 5$ )

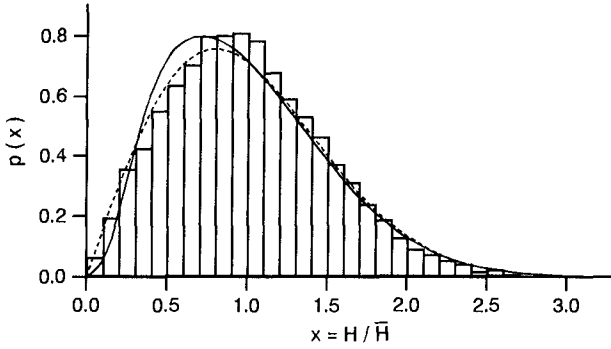


Fig.10 (b) Wave height distribution ( $r = 10$ )

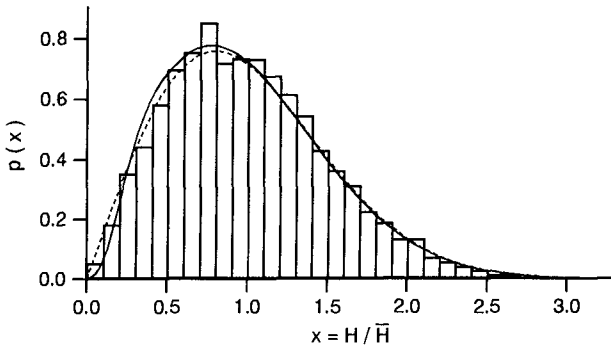


Fig.10 (c) Wave height distribution ( $r = 20$ )

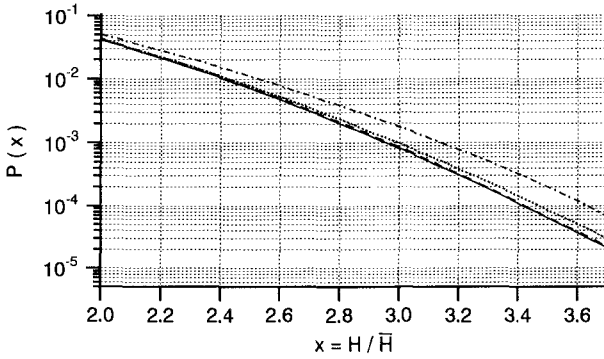


Fig.11 Exceedance probability  
(chain line : r=5, dotted line : r=10, broken line : r=20, solid line : Rayleigh)

$$\begin{aligned}
 p(H) = & \int_H^\infty \int_0^{R_m} \frac{\alpha_2^2}{4(\gamma_2^2 - \rho^2)} R_{m_j}^{\alpha_2 - 1} (R_m - R_{m_j})^{\alpha_2 - 1} \\
 & \cdot \exp \left[ -\frac{\gamma_2}{2(\gamma_2^2 - \rho^2)} \left\{ R_{m_j}^{\alpha_2} + (R_m - R_{m_j})^{\alpha_2} \right\} \right] \\
 & \cdot I_0 \left[ \frac{R_{m_j}^{\alpha_2/2} (R_m - R_{m_j})^{\alpha_2/2}}{\gamma_2^2 - \rho^2} \rho \right] dR_{m_j} \\
 & \cdot \int_0^{R_m - H} \frac{\alpha_1^2}{4\gamma_1^2} \delta_j^{\alpha_1 - 1} (R_m - H - \delta_j)^{\alpha_1 - 1} \\
 & \cdot \exp \left[ -\frac{1}{2\gamma_1} \left\{ \delta_j^{\alpha_1} + (R_m - H - \delta_j)^{\alpha_1} \right\} \right] d\delta_j \quad dR_m
 \end{aligned}
 \tag{14}$$

As results of the numerical calculation of eq.(14), the probability distributions of zero-crossing wave height are obtained as shown in fig.10(a)-(c). (a) is the case when the spectral shape parameter r=5, (b) r=10 and (c) r=20. The solid line shows the present theory and the broken line shows the Rayleigh distribution. Fig.11 shows the exceedance probability of wave height. The chain line, dotted line and broken line show the distribution when r=5,10 and 20, and

solid line shows the Rayleigh distribution respectively. We can see considerably larger probability than the Rayleigh distribution when  $r=5$ .

### Conclusion

The probability distributions of zero-crossing wave height, when the gap between maximum (minimum) of wave profile and the simultaneous envelope amplitude is taken into account, were derived. As the result, larger probability of exceedance than the Rayleigh distribution was obtained in the range of larger wave height, when the spectrum is wide.

### References

- Kimura, A. (1981): Joint distribution of the wave heights and periods of random sea waves, Coastal Eng. in Japan, Vol.24, pp.77-92.
- Kimura, A. and T. Ohta (1992): On probability distributions of the zero-crossing irregular wave height, Proc. 6th IAHR Int'l Symp. on Stochastic Hydr., pp.291-298.
- Longuet-Higgins, M.S. (1952): On the statistical distributions of the heights of sea waves, J. Marine Res., Vol.11, No.3, pp.245-265.
- Tayfun, M.A. (1981): Distribution of crest-to-trough wave height, J. Wtrway., Port, Coast. and Oc. Eng., ASCE, 107(WW3), pp.149-156.
- Tayfun, M.A. (1983): Effects of spectrum band width on the distribution of wave heights and periods, Ocean Eng., Vol.10, No.2, pp.107-118.
- Tayfun, M.A. (1989): Envelope, phase, and narrow-band models of sea waves, J. Wtrway, Port, Coast., and Oc. Eng., ASCE, Vol.115, No.5, pp.594-613.

## CHAPTER 38

### NUMERICAL SIMULATION AND VALIDATION OF PLUNGING BREAKERS USING A 2D NAVIER-STOKES MODEL

H.A.H. Petit<sup>1)</sup>, P. Tönjes<sup>2)</sup>, M.R.A. van Gent<sup>3)</sup>, P. van den Bosch<sup>1)</sup>

#### ABSTRACT

The numerical model SKYLLA, developed for simulation of breaking waves on coastal structures is described. The model is based on the Volume Of Fluid method and solves the two-dimensional (2DV) Navier-Stokes equations. Weakly reflecting boundary conditions allow waves to enter and leave the computational domain. Impermeable boundaries can be introduced to simulate a structure. A two-model approach can be used to simulate overtopping over a low crested structure. Results obtained with the model are compared with those obtained with physical model tests for waves on a 1:20 slope of a submerged structure.

#### INTRODUCTION

Traditionally, wave motion on coastal structures was studied by means of physical small-scale model tests. Some phenomena can be studied quite well on a small scale whereas others, like those which involve effects of viscosity, cannot. Numerical models do not have the disadvantage of scaling however, they have the disadvantage that the equations they solve represent a simplification of reality. Most models used to simulate wave motion on structures either solve the shallow water equations or potential flow formulations. For examples of the first we refer to Kobayashi et al.(1987) and Van Gent (1994). For examples of methods based on potential flow we refer to Klopman (1987) for the two dimensional case and to Broeze (1993) for a solver for three-dimensional flow. The shallow water equation

---

<sup>1)</sup> Delft Hydraulics, P.O.Box 152, 8300 AD, Emmeloord, The Netherlands.

<sup>2)</sup> Ministry of Transport, Public Works and Water Management. Directorate-General of Public Works and Water Management (Rijkswaterstaat), Road and Hydraulic Engineering Division, P.O. Box 5044, 2600 GA, Delft, The Netherlands.

<sup>3)</sup> Delft University of Technology, Dept. Civil Engrg., P.O. Box 5048 GA Delft, The Netherlands.

solvers cannot directly simulate wave breaking but need to add extra dissipation to simulate the wave height reduction caused by breaking. The potential flow solvers can solve the flow very accurately up to the moment where the flow domain becomes multiply connected as a result of the breaking process. After that moment these methods become unstable and the calculation breaks down. Solvers based on the MAC (Marker And Cell) or the VOF (Volume Of Fluid) method can solve the Navier-Stokes equation for breaking waves.

## THE 2D-NAVIER-STOKES MODEL

The Volume Of Fluid method (Hirt and Nichols, 1981) has been made applicable for simulation of wave and flow phenomena on coastal structures (Petit & Van den Bosch, 1992 and Van der Meer et al., 1992). The model solves the two-dimensional incompressible Navier-Stokes equations with a free surface.

For the treatment of the free surface a redistribution of water contained in the cells of the computational grid has to take place once the velocity is known. The method called FLAIR (Ashgriz and Poo, 1991) has been adopted for this purpose. Arbitrary free-slip boundaries can be introduced in the model to simulate breaking waves on impermeable coastal structures. The numerical simulation of the breaking process is not limited to the moment where the fluid domain becomes multiply connected.

## IMPROVEMENTS

Recent improvements of the model involve the use of weakly reflecting boundary conditions that allow nonlinear waves based on a Rienecker and Fenton (1981) (R&F) formulation to enter the domain. Further improvements allow the simulation of overtopping at a dike, not only with respect to the volume of water, but also a detailed simulation of water running down the rear of the dike (Petit et al. 1994). Furthermore, the simulation of flow through permeable structures has been made possible for the model (Van Gent et al. 1993) which, however, is beyond the framework of this paper.

## WEAKLY REFLECTING BOUNDARY CONDITIONS

In Figure 1 we show a situation where weakly reflective boundary conditions are needed at both sides of the model.

The waves are assumed to enter the domain at the left. They are given by the free surface elevation  $\eta_{in}(x_0, t)$ , and the velocity components  $u_{in}(x_0, y, t)$  and  $w_{in}(x_0, y, t)$  in x- and y direction respectively. At the right boundary the incoming waves are set to zero, although the model allows waves to be sent in from both sides. The equations which prescribe the weakly reflecting boundary conditions at the left boundary are:

$$\frac{\partial}{\partial t}(\eta - \eta_{in}) - C \frac{\partial}{\partial x}(\eta - \eta_{in}) = -r(\eta - \bar{\eta}) \quad (1)$$

$$\frac{\partial}{\partial t}(u - u_{in}) - C \frac{\partial}{\partial x}(u - u_{in}) = -r(u - \bar{u}) \tag{2}$$

$$\frac{\partial}{\partial t}(w - w_{in}) - C \frac{\partial}{\partial x}(w - w_{in}) = 0 \tag{3}$$

Here, it is assumed that at the boundary the free surface elevations and the velocity components can be decomposed as the sum of a wave travelling to the right and a wave travelling to the left. For the surface elevation at the left boundary this becomes:

$$\eta(x,t) = \eta_{out}(x+Ct) + \eta_{in}(x-Ct)$$

In the case where  $r=0$  this signal satisfies the weakly reflecting boundary condition (1) perfectly. If, again for the case of  $r=0$ ,  $\eta$  is replaced by  $\eta + d$  where  $d$  is a constant, equation (1) will still be satisfied. This means that a change in the time averaged water level caused by inaccuracies in the code will not be corrected by the boundary conditions. The same problem occurs for the weakly reflective boundary condition for the x- velocity component (2). We

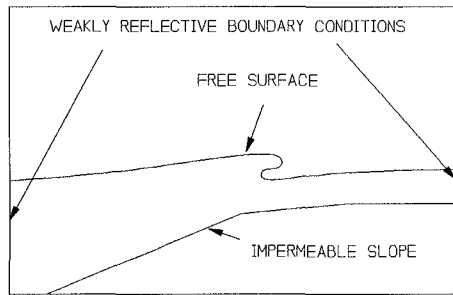


Figure 1 Model application with two weakly reflective boundary conditions

have experienced that in using free slip boundary conditions at the bottom unrealistic average velocities can develop during lengthy computations. By choosing  $r$  equal to a small positive constant a time averaged value for the free surface elevation  $\eta$  and for the velocity in x direction  $\bar{u}$  can be prescribed. Although the amplitude of the incoming signals will be reduced for positive values of  $r$ , small values like  $r = \omega/5$  which theoretically reduce the amplitude by a factor of 0.995 prove to work quite well.

In order to test the quality of the weakly reflecting boundary conditions with incoming nonlinear waves, the velocities and the free surface elevation from the R&F solutions were used. At the left boundary of a numerical wave flume with a constant water depth, these waves were generated using a weakly reflecting boundary condition. At the right boundary again a weakly reflecting boundary condition was used to allow the waves to leave the domain undisturbed. At both boundaries of the Navier-Stokes model the velocities and the surface elevation were calculated and compared with the incoming signal. For a flume with the length of one wave length (wave height 0.2 m, period 3.0 s) the time series of the free surface elevation at the right and the left boundary are shown in Figure 2. Here we can see that, once the

initial disturbances have left the domain, incoming and outgoing signals match nicely.

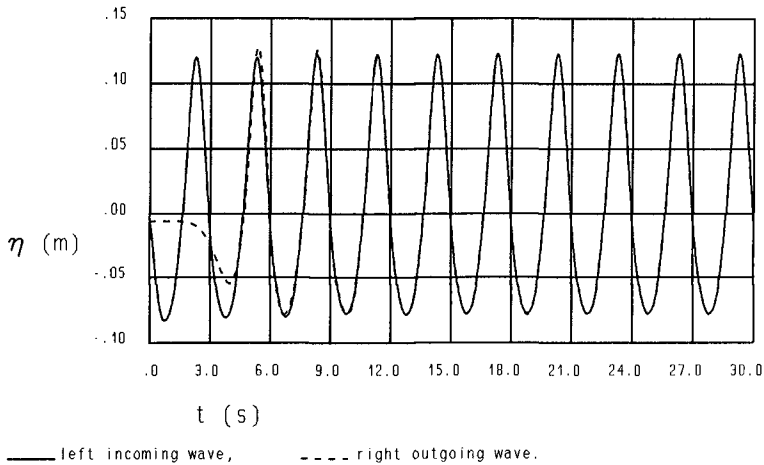


Figure 2 Time series of free surface elevation in a numerical wave flume in order to test the weakly reflecting boundary conditions at both sides

### IMPERMEABLE BOUNDARIES

The velocity components used in the VOF method are defined at the centres of the cell faces. In order to discretize the spacial derivatives in the Navier-Stokes equations, velocity components at several locations are used. They are indicated by the arrow in Figure 3 for the case of the momentum equations in the horizontal direction.

In order to model an impermeable boundary as indicated by the line, one could choose to change the stencil of velocity components such that none of the velocity components needed in the discretization is beneath the impermeable boundary. The disadvantage of this approach is that on a vector computer the vectorization of the computational process would be frustrated by the different treatment of the equations inside the fluid and at the boundaries. We wanted to avoid this problem and decided to define virtual velocities at those positions beneath the impermeable boundary. They are indicated by the dotted vectors in Figure 3. In Figure 4 an example of a submerged structure is shown where only the virtual velocities are given. The virtual velocities which are to be defined beneath the surface of the structure are determined by the boundary conditions at the surface.

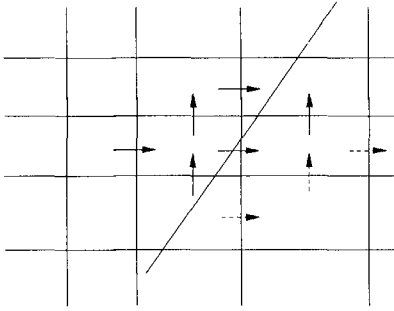


Figure 3 Velocity components needed to discretize the horizontal momentum equations

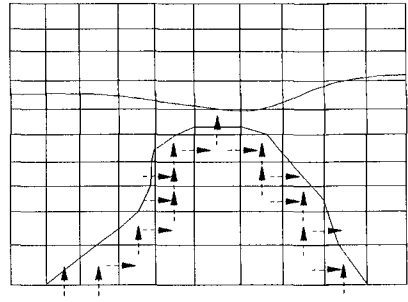


Figure 4 Virtual velocity components beneath the surface of the structure

In the program only the free slip boundary condition was implemented. Both conditions at the impermeable surface now become:

$$\frac{\partial u_{\tau}}{\partial n} = 0 \tag{4}$$

$$u_n = 0 \tag{5}$$

where  $u_n$  is the velocity component in normal direction to the impermeable surface,  $n$  the coordinate in this direction and  $u_{\tau}$  the velocity component along the surface.

The 14 cell categories which are identified in the program are shown in Figure 5. As can be seen here the impermeable boundary is to be modelled as a straight line inside each cell. For the case of category 4 we will examine how the virtual velocities can be determined. The velocity components shown in this figure are those which are used to discretize the impermeability and free slip condition.

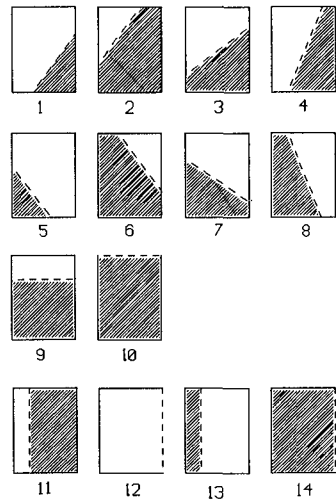


Figure 5 Examples of cell categories used in SKYLLO



By using the components of the normal unit vector at the part of the slope in this cell,  $n_x$  and  $n_y$ , the equations (4) and (5) can be rewritten as:

$$n_x^2 \frac{\partial w}{\partial x} - n_y^2 \frac{\partial u}{\partial y} - n_x n_y \left( \frac{\partial u}{\partial x} - \frac{\partial w}{\partial y} \right) = 0 \tag{6}$$

$$n_x u + n_y v = 0 \tag{7}$$

The velocity component shown in Figure 6 can be used to find a first order accurate approximation of the derivatives in the free slip condition at the collocation point indicated by the small circle in Figure 6. At his same position the impermeability of the slope can be approximated second order accurately by using linear interpolation. In this way two linear equations are found from which the virtual velocities can be determined. For each cell category the two virtual velocities involved are chosen such that all velocities needed for the discretization of the Navier-Stokes equation are available. Furthermore, the virtual velocities determined for one cell do not coincide with the virtual velocities of another cell.

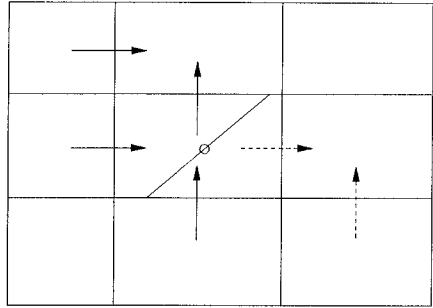


Figure 6 Virtual velocity components for a cell of category 4

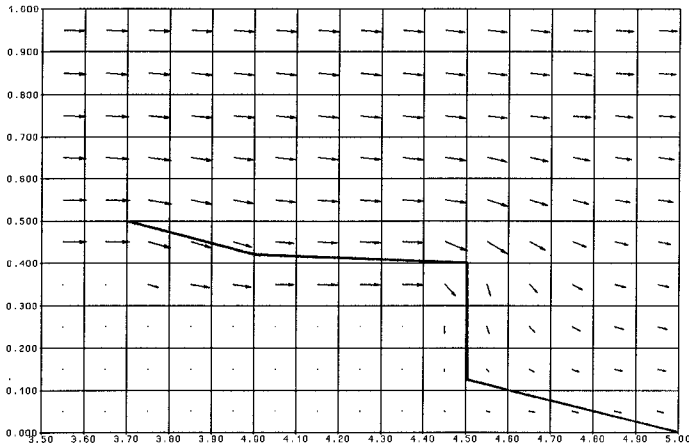


Figure 7 Test for impermeable free-slip boundaries

In Figure 7 we show the result of a computation with a falling slope. The components of the velocity vectors shown here were determined as the averaged values of the velocity components at the boundaries of each cell. The velocities beneath the impermeable boundary are partially determined by the virtual velocities. As can be seen in this figure, the resulting flow near the structure is well aligned with the surface of the structure.

## OVERTOPPING BOUNDARY CONDITIONS

Computations with the VOF method are very costly. Especially if the cell sizes are small the explicit time solver will need very small time steps to keep the computations stable. In each time step a Poisson pressure equation needs to be solved to ensure the incompressibility of the fluid. This leads to a set of equations to be solved for the pressure in each cell. The computational effort to solve the pressure equations is roughly proportional to  $(N*M)^{2.5}$  where  $N$  is the number of cells in horizontal direction and  $M$  the number in vertical direction. In cases where a low-crested structure is to be modelled the computation can be carried out applying two separate computational domains, provided that the flow at the top of the crest has supercritical velocity.

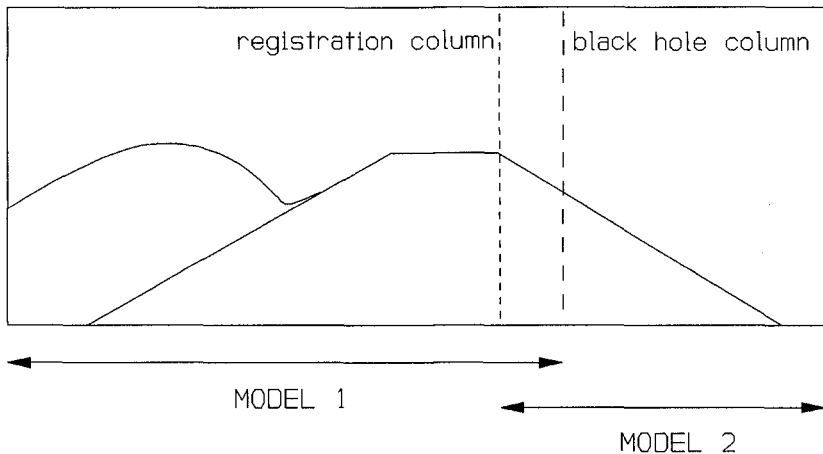


Figure 8 Registration and black hole column at different locations used in the two model approach

The first part of the computation takes place in model 1 as indicated in Figure 8. At the right boundary indicated by 'black hole column' we use the boundary conditions  $u_x = 0$  and  $w_x = 0$ . Furthermore, we set the  $F$  value equal to zero in this column each time step. The  $F$  values and velocity components are registered during the

computation in the 'registration column' each time step. The registered quantities are used during the second computation which involves the flow in model 2 as indicated in Figure 9.

In a strict sense the incompressibility condition can only be satisfied in a simply connected domain by solving the pressure Poisson equation. We expect, however, that in the case where free slip boundary conditions are used and the layer of water at the crest of the structure flows with a supercritical velocity, the errors introduced by using this method will be small.

### VALIDATION OF WAVES ON A 1:20 BAR

In order to gain insight in the performance of the numerical model, physical model tests were performed with waves on a submerged bar with a front slope of 1:20. Here we did not use the two-model approach as the velocities at the top of the structure would not be supercritical. Incident regular waves broke on this bar as weakly plunging breakers. Figure 9 shows the experimental set-up used. The numerical set-up used in the verification runs was simpler because at the time the verification took place the falling slope option had not been implemented. Figure 10 shows the left part of the slope used in the experiment.

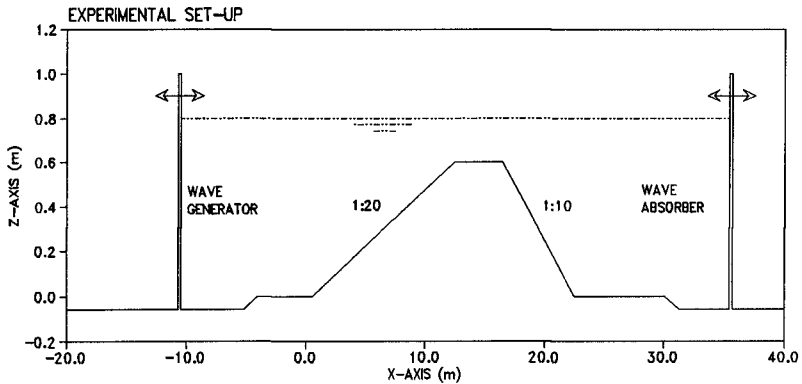


Figure 9 Bottom topography used in wave flume

Velocity profiles at a large number of locations were measured with Laser-Doppler Velocity meters. Those positions are indicated by the blocks in Figure 10. The wave profile was recorded using a video camera. The position of the free surface was determined electronically from the video registration, which resulted in two or more lines in regions with much air entrainment. As the position of the free surface is not a variable in the VOF method the free surface had to be defined using the

F-function. This quantity is the volume fraction of the cell which is filled with fluid (which explains the name Volume Of Fluid). We chose the value  $F = 1/2$  to define the location of the free surface. To send in waves into the numerical model we used solutions obtained by the R&F (1981) method. The parameters used to get this solution were obtained by comparing the free surface as prescribed by R&F with the measured free surface of the incoming waves assuming the reflected waves to be negligibly small.

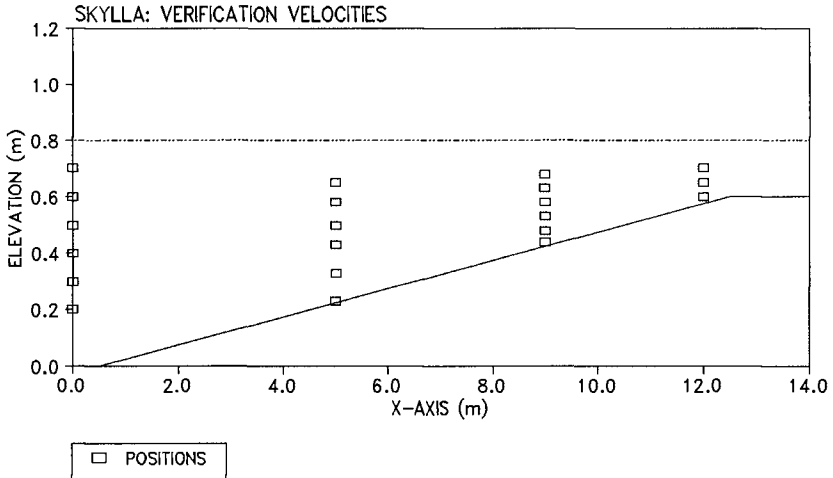


Figure 10 Schematized bottom used in numerical simulation

The following wave parameters were found:

Wave height : 0.29 m  
 Wave period : 1.80 s  
 Still water level : 0.80 m

For the R&F solution we used 16 Fourier components. The mean Eulerian velocity was set to zero m/s. The resulting wave length of the incoming waves was 4.41 m. Comparison of the velocity profiles of the R&F solutions and the measured velocities showed that the crest velocities were somewhat too large whereas the trough velocities were underestimated in an absolute sense. We expect this to be caused by the fact that the undertow is assumed to be uniformly distributed over the vertical in the potential model solved by R&F. In practice, however, smaller velocities occur near the bottom and higher velocities more upward in the vertical.

For the computation 480 cells were used in horizontal direction and 50 in the vertical. The kinematic viscosity was set to  $0.001 \text{ m}^2/\text{s}$ .

After the numerical solutions had become periodic we started the comparison. Figure 11 shows the first of the comparisons. Here we see that once the waves start climbing the slope the wave length of the numerical waves become smaller than the measured value.

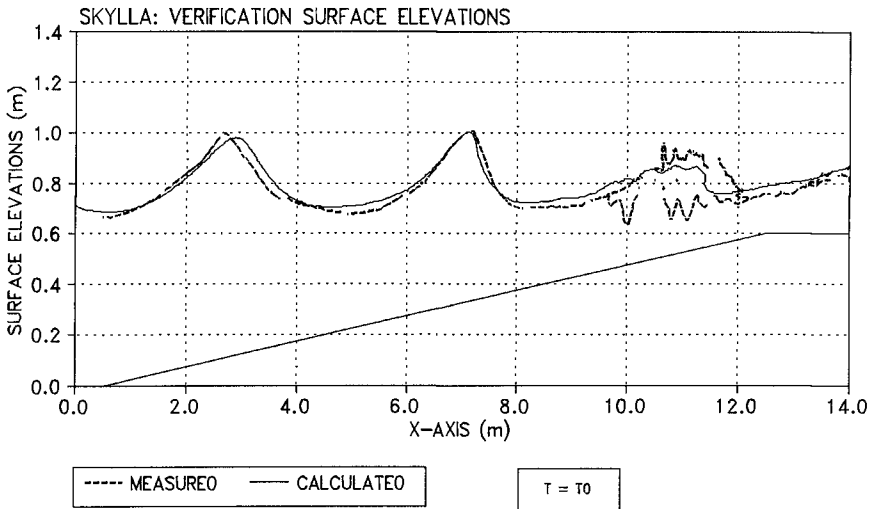


Figure 11

Here we can also see that, the breaking process in the numerical model takes place at the right position. Figures 12 and 13 show the comparison at time intervals of 0.48 s.

The effect of shoaling which is clearly visible in Figure 12 for the measured spilling wave at 8.5 m is not represented well in the numerical simulation. Furthermore, it can be seen in Figure 13 that the breaking process itself develops faster in the numerical model as the decrease in wave height is faster. The transmitted waves at the right boundary, however, were found to be rather accurate.

In Figure 14 we show the measured and computed horizontal and vertical velocities at the left boundary of the model. The problems which arise when in using R&F solutions regarding undertow which were mentioned earlier, reduce the absolute velocity at the trough of the waves. In Figures 15 and 16 we show the comparison of these velocities at 5 and 9 m from the left boundary of the computational domain. All velocities shown here were measured at about 0.5 m from the zero level of the wave flume.

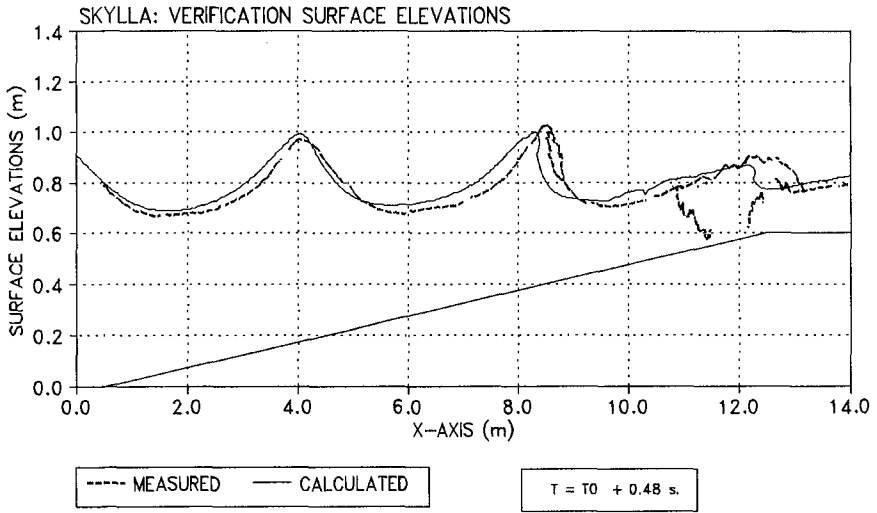


Figure 12

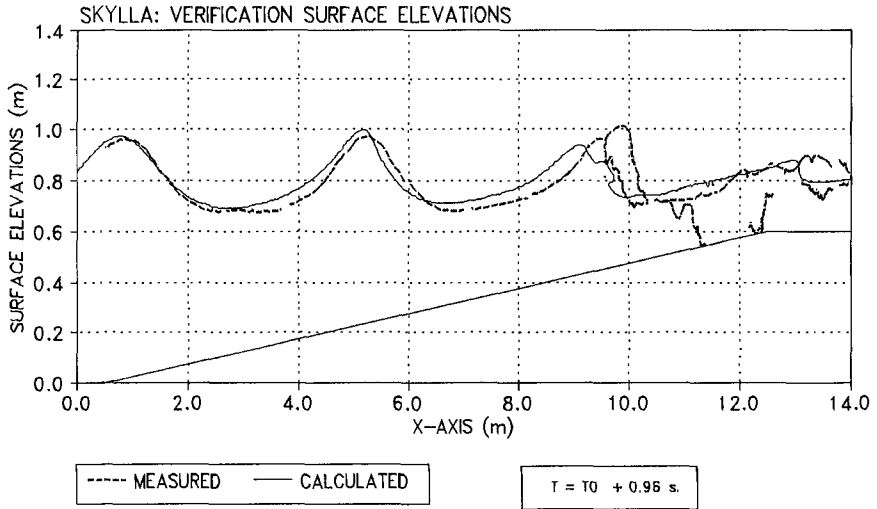


Figure 13

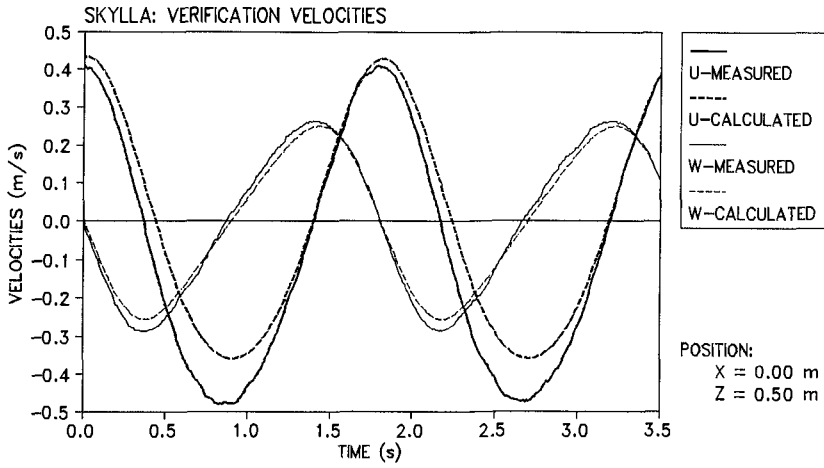


Figure 14 Comparison of measured and calculated velocities; u denotes horizontal velocities, w denotes vertical velocities

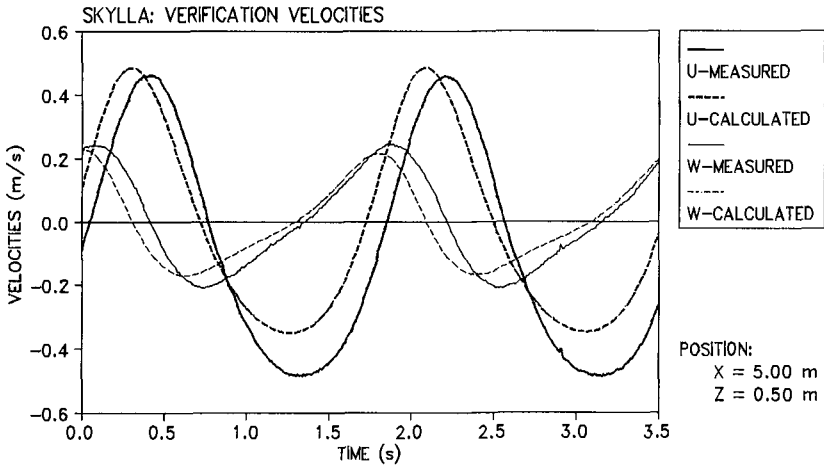


Figure 15 Comparison of measured and calculated velocities; u denotes horizontal velocities, w denotes vertical velocities

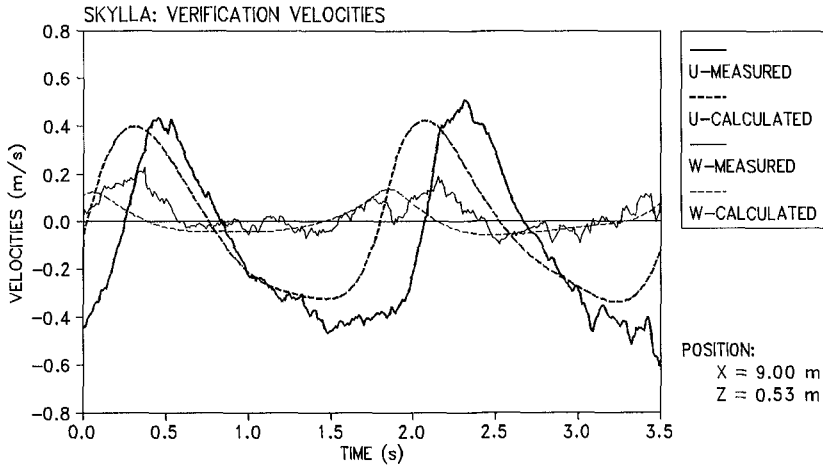


Figure 16 Comparison of measured and calculated velocities;  $u$  denotes horizontal velocities,  $w$  denotes vertical velocities.

## CONCLUSIONS

The VOF method has been made applicable for the computation of breaking waves on coastal structures. Verification with measurements has shown that the program can fairly well simulate waves on a structure. The differences with measurements found in the comparison can partly be explained by the way the boundary conditions were used to define the incoming waves.

## ACKNOWLEDGEMENT

This work was funded by the Ministry of Public Works of the Netherlands, Rijkswaterstaat, Road and Hydraulic Engineering Division.

## REFERENCES

- Ashgriz, N. and J.Y. Poo (1991). "FLAIR: Flux Line-Segment Model for Advection and Interface Reconstruction", *J. of Comp. Physics* 93.
- Broeze, J. (1993). "Numerical Modelling of Nonlinear Free Surface Waves with a 3D Panel Method", Ph.D. Thesis, Twente University, Enschede.



- Hirt, C.W. and Nichols, B.D. (1981). "Volume Of Fluid method for the dynamics of free boundaries". *J. of Comp. Physics* 39.
- Klopman, G. (1987). "Numerical simulation of breaking waves on steep slopes", *Coastal Hydrodynamics*, ed. R.A. Dalrymple.
- Kobayashi, N., Otta A.K. and Roy I. (1987). Wave reflection and run-up on rough slopes, *J. of Water ways, Ports, Coastal and Ocean Engrg.*, ASCE, Vol. 113, no. 3.
- Petit, H.A.H. and Van den Bosch, P. (1992). SKYLLA: Wave motion in and on coastal structures. Numerical analysis of program modifications. Delft Hydraulics Report H1351.
- Petit, H.A.H, Van den Bosch, P and Van Gent, M.R.A. (1994). SKYLLA: Wave motion in and on coastal structures, Implementation of impermeable slopes and overtopping-boundary conditions. Delft Hydraulics, report no H1780.11.
- Rienecker, M.M. and Fenton, J.D. (1981). "A Fourier Method for Steady Water Waves", *J. of Fluid Dynamics*, Vol. 104.
- Van Gent, M.R.A., De Waal, J.P., Petit, H.A.H. and Van den Bosch, P. (1994). SKYLLA: Wave motion in and on coastal structures, Verification of kinematics of breaking waves on an offshore bar. Delft Hydraulics, report no H1780.03.
- Van Gent, M.R.A. (1994). "The modelling of wave action on and in coastal structures", *Coastal Engineering*, Elsevier, Amsterdam. Vol. 22.
- Van Gent, M.R.A., Petit, H.A.H., Van den Bosch, P. (1993). SKYLLA: Wave motion in and on coastal structures, Implementation and verification of flow on and in permeable structures. Delft Hydraulics, report no H1780.
- Van der Meer, J.W., Petit, H.A.H., Van den Bosch, P., Klopman, G. and Broekens, R.D. (1992). "Numerical Simulation of Wave Motion on and in Coastal Structures". ASCE, Proc. 22nd ICCE, Venice, Italy.

## CHAPTER 39

### Wave Velocity Field Measurements over a Submerged Breakwater.

Marco Petti,<sup>1</sup> Paul A. Quinn,<sup>2</sup> Gianfranco Liberatore<sup>3</sup> & William J. Easson<sup>4</sup>

#### Abstract

The main focus of the experiment was to observe and measure large-scale vortices generated by breaking waves over a submerged breakwater. These flow structures are important in sediment transport due to their ability to trap sediment particles negating their normal settling velocity. The technique of Particle Image Velocimetry (PIV) was used to measure the spatial distribution of velocities at an instant; an approach which is essential for measuring coherent structures in the flow. Experiments were conducted in the 50m flume at The University of Florence which was fitted with a 1:100 beach, wave elevations, as well as velocity fields, were measured.

The paper deals with the experimental details and a display of the velocity and vorticity maps obtained using PIV.

#### Introduction

There is considerable interest in the use of submerged breakwaters for coastal protection purposes, but there is little information on the efficiency of such structures due to the poor knowledge of the local hydrodynamics. Consequently there are no analytical or numerical models (Kobayashi & Wurjanto, 89) which can fully describe the processes involved, and so experimental data is still valuable (Arhens, 89, Van der Meer, 90, Petti & Ruol, 91, 92). This study attempts to examine the velocity fields of waves breaking over submerged breakwaters, paying particular attention to the formation of large scale vortices formed by the breaking waves. These play a major part in sediment transport because sediment

---

<sup>1</sup>Lecturer, Department of Civil Engineering, The University of Florence, Via di S. Marta, 3, I-50139 Florence, Italy.

<sup>2</sup>Research Associate, Fluid Dynamics Unit, Dept. of Physics & Astronomy, The University of Edinburgh, Edinburgh, EH9 3JZ, UK.

<sup>3</sup>Professor, University of Udine, Via Cotonificio, 114, 33100 Udine, Italy.

<sup>4</sup>Senior Lecturer, Department of Mechanical Engineering, The University of Edinburgh, Edinburgh, EH9 3JL, U.K.

particles can become trapped in vortices thereby losing their normal settling rates (Nielsen, 92, 94). Consequently how far these vortices travel and the time they take to decay is of significant interest. A further aspect to consider is the effect localised scour, due to large scale vortices, has on the stability of the structure. This paper concentrates on the experiments carried out and the initial results found, which are presented in the form of velocity and vorticity maps.

It is the technique of Particle Image Velocimetry (PIV) which is possibly the most novel aspect of this work; as it provides a spatial distribution of velocities at an instant it is ideal for measuring coherent structures. Previous experiments have used point measuring systems such as directional micro-propellers (Petti & Ruol, 1992) or electromagnetic velocimeters (Mizutani et al, 1992). This approach has the drawback that as only a time history of the wave velocity is obtained at a single point, coherent structures in the flow, such as large scale vortices, tend to get averaged out.

### Particle Image Velocimetry (PIV)

A review of PIV is given by Adrian (1991) and an introduction to the process in a coastal engineering context is given by Greated et al (1992). Further references to work using PIV in this publication include Quinn et al (1994) and Earnshaw et al (1994). In order to avoid duplication I refer you to those papers for a brief overview of the processes involved.

The only additional point relating to these experiments was that the technique of image shifting was used (Bruce et al, 1992, Earnshaw et al, 1994). Without going into detail this allows us to measure zero and near-zero velocities and resolves the 180° directional ambiguity inherent with the autocorrelation method of PIV analysis; it is analogous to frequency shifting in Laser Doppler Anemometry (LDA).

### Experiments

Experiments were carried out in the 50m flume at The University of Florence, which was fitted with a 1:100 sloping beach. For this study a submerged breakwater was installed about 26m from the wave maker and 22m from the foot of the beach. The breakwater was constructed of perspex with an Aluminium support structure and was 13.6cm high and 26 cm wide at the top, with an offshore facing slope of 1:3.5 and a shoreward facing slope of 1:1.5. The wave flume is shown in Figure 1 and the positions of the breakwater, PIV measurement section and wave gauges are indicated.

PIV was used to measure the velocity fields and a set of 16 parallel-wire resistance-type wave gauges were used to measure the surface elevations of the waves. The 15W Argon ion laser, PIV illumination system and photographic equipment were brought over from The University of Edinburgh for this collaborative study. The laser light sheet required for PIV has to be introduced into the

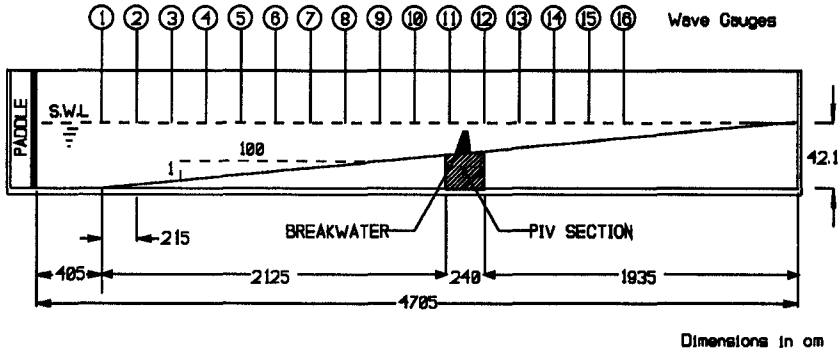


Figure 1: The Wave Flume at The University of Florence.

Test No.	Period, $T_0$ (s)	Wave Height, $H_0$ (m)	Ursell No.
1	2	0.10	19.2
2	3	0.10	47.0
3	4	0.14	89.3

Table 1: Wave Parameters

water from below the beach surface. As the bottom of the flume is not made of glass, a special section of the beach had to be built. This allowed the laser sheet in through the side of the flume, below the level of the beach and reflected it off an underwater mirror vertically up through a transparent strip in the beach into the flow. This is shown in Figure 2.

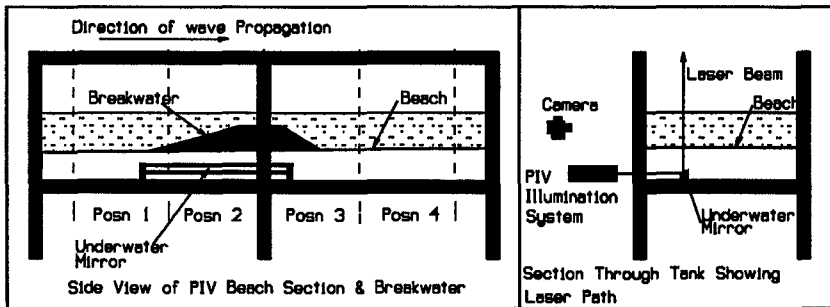


Figure 2: The PIV Beach Section

Three regular waves were used whose parameters are shown in Table 1. These

were chosen to break before, over and behind the structure. The waves were generated by a absorbing piston-type wave maker, in a water depth of 0.42m. PIV measurements were made at four positions around the breakwater and four phases of each wave, were recorded at each position, the phases being separated by  $90^\circ$ .

### Wave Gauge Results

Figure 3 shows typical surface elevation records from gauges 1, 3, 5 & 7 for the 3s wave; Figure 4 shows the same for gauges 9, 11, 13 & 15. There are a couple of points worth noting here, firstly that gauge No. 1 is in constant depth water ( $h_0 = 0.42\text{m}$ ) and secondly that gauge No. 11 is just in front of the breakwater.

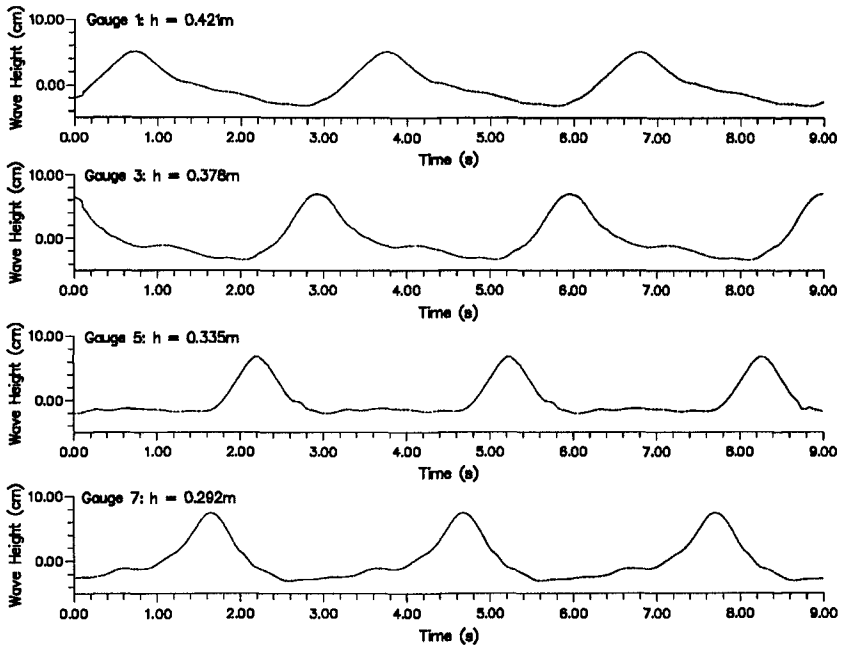
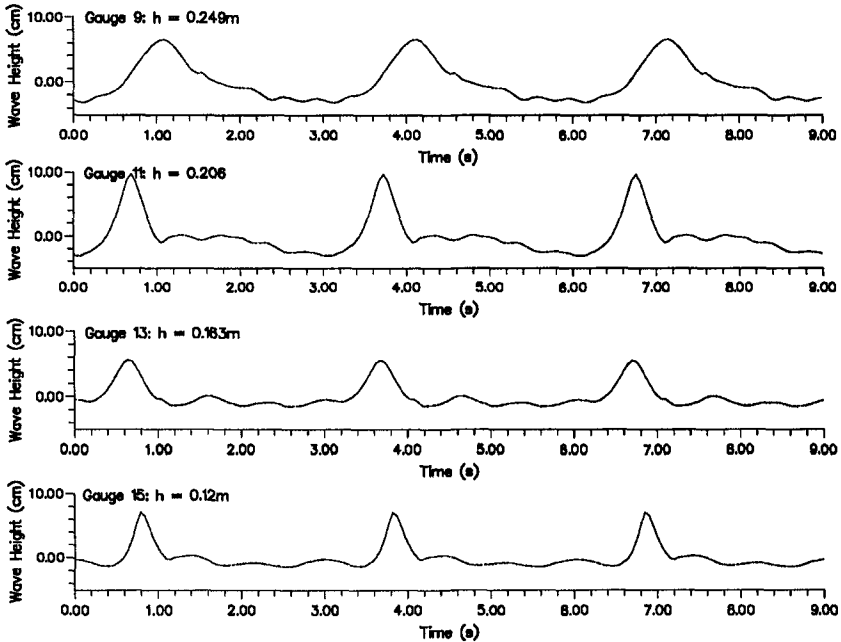


Figure 3: Wave Heights ( $T = 3\text{s}$ )

The first thing to notice from gauge 1 is that solely monochromatic waves are not being produced. There is definite evidence of a second wave being generated, and judging from the subsequent gauges this is a free wave, although it is at least of a much smaller amplitude than that of the main one. One can ascribe this generation of a free wave to the relatively high non-linearity of these waves. The Ursell numbers, calculated from Equation 1 are shown in Table 1; the values for the 3s & 4s waves being particularly high. It is perhaps not too surprising to see

Figure 4: Wave Heights ( $T = 3s$ )

this kind of instability from a wave maker trying to generate sinusoidal waves, Osborne & Petti (1994) give a more detailed description of this phenomenon.

$$U_0 = (H_0 L_0^2) / h_0^3 \quad (1)$$

Gauges 9 and 11 show significant reflected high-frequency waves, particularly in the troughs, with gauge 11 also showing the maximum wave elevation, of about 0.1m, due to its position just in front of the breakwater. In addition to this, one can also see (from Figures 3 & 4) how the phase celerity decreases as the waves approach the breakwater. Gauges 13 & 15 show diminished wave height and increased high frequency components following breaking, with evidence from gauge 15 of some frequency recombination as the wave crests have increased in height and sharpened in profile.

With the generation of a free wave and a measured reflection coefficient value of about 10%, there was a noticeable variation of wave heights at all the wave gauge positions. A zero-up-crossing significant wave height analysis from all 16 wave gauges was carried out and this gives a good indication of the scatter in wave heights. This zero-crossing analysis is given for all three waves in Figure 5

Although there is some significant scatter of the wave heights one can see the general trend of increasing wave height towards the breakwater, located just

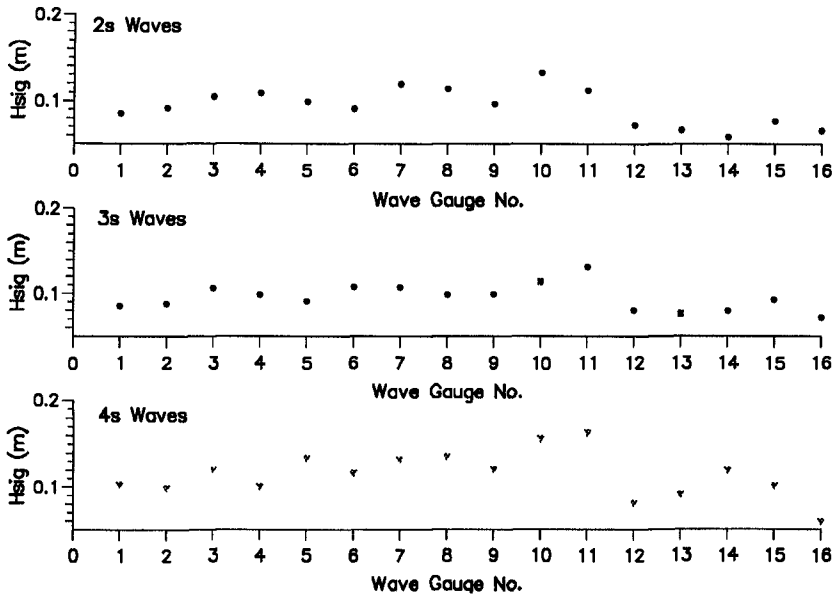


Figure 5: Zero up-crossing significant wave height distribution.

after gauge 11, and a decrease following breaking. The maximum waveheight was recorded at gauge number 10 for the 2s wave, this is due to the fact that the wave has already started to break by the time it reaches gauge 11. There is further evidence of post-breaking recombination of frequency components with the increase in significant wave height after the initial decrease due to breaking. This is particularly so for the 4s waves.

#### PIV Results

Due to the large number of measurements taken only a small set of the 48 velocity vector maps can be shown here. As the focus of the paper is the measurement of vortices generated by the breaking waves, only one example of a wave breaking on the front face of the breakwater is shown. The other results are presented, by means of velocity and vorticity maps, for the positions behind the breakwater. The convention of positive vorticity indicating an anti-clockwise rotation has been adopted throughout.

Figure 6 shows a 2s wave breaking on the front face of the breakwater. It is interesting to notice that the wave is breaking where the wave meets the fast flowing backwash, returning over the breakwater, and not at the top of the wave as one might expect. This formation of a localised bore on the structure gives

rise to small waves which travel in the offshore direction.

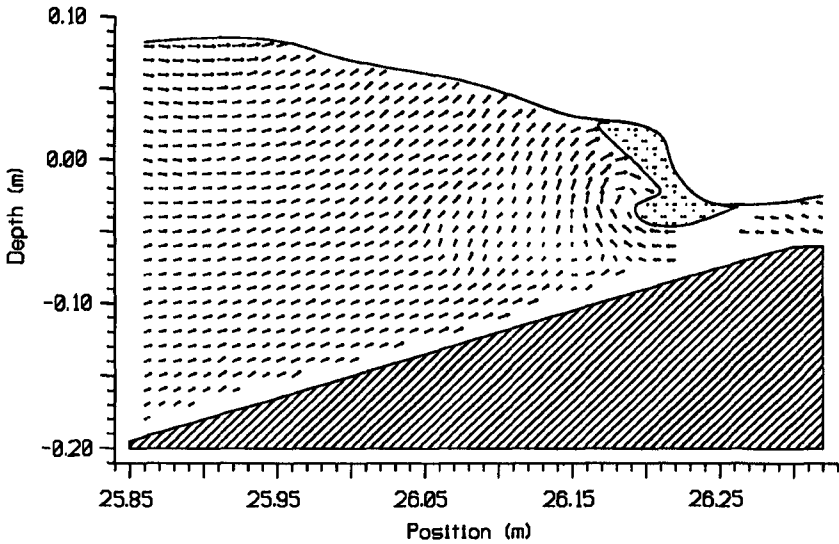


Figure 6: Vector map: 2s wave: Phase 4: Position 2.

Considering now the 3s wave, Figures 7, 9 & 11 show velocity maps for the first three phases at position three, with Figures 8, 10 & 12 showing the corresponding vorticity maps.

Phase 1 shows a positive vortex down near the bottom of the breakwater in an area particularly sensitive to scour, (Liberatore, 92) . Phase 2 shows a large region of negative vorticity near the surface to the right caused by the overturning of the wave that has just broken, sweeping upwards the positive vortex that was located near the foot of the structure in the previous phase. A small negative vortex is also being shed by the top corner of the breakwater. The third phase shows that the main negative vortex of the previous phase has reduced to a ring of smaller vortices and the positive vortex has now either dissipated or been carried back over the structure.

If we now look at position 4 (shorewards of position 3) for the 3s wave we can see from Figures 13 & 14 that at phase 4 there is still a significant negative vortex. This is most likely to have been generated by the previous wave and has, therefore, persisted for about 5s and moved about 0.55m from the rear of the breakwater.

Turning our attention now to the 4s waves, Figures 15 & 17 show velocity maps for phases 2 & 3 at position 3, with Figures 16 & 18 showing their corresponding vorticity maps.



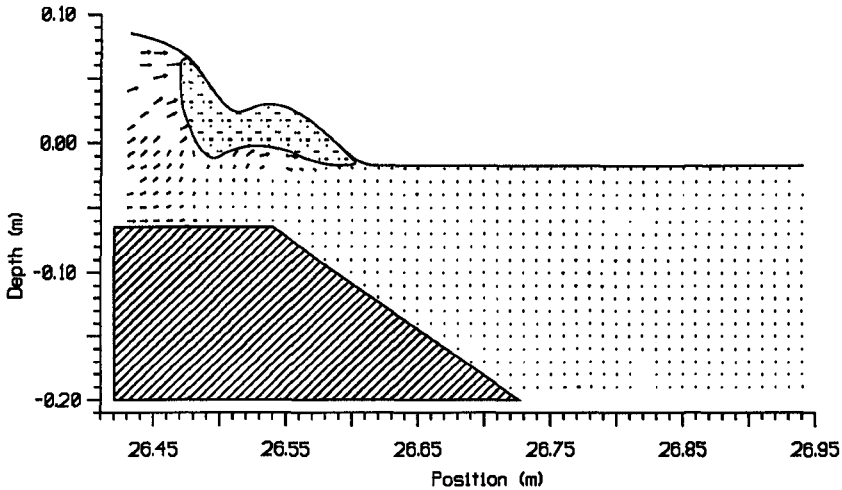


Figure 7: Vector map: 3s wave: Phase 1: Position 3.

Phase 2 shows negative vortices near the top right and on the top corner of the breakwater, the former being generated by the overturning breaker. There is a positive vortex above the rear toe of the structure in a similar position to the positive vortex shown at the same phase and position for the 3s wave. In phase 3, however, we can see that the large negative vortex has been swept into the next position and all that remains are two positive vortices near the bed and surface and a positive vortex being generated at the top corner of the structure as the flow returns back over the breakwater.

Moving on to the final position, Figure 19 shows the velocity maps for phase 2 again and Figure 21 shows the same for phase 4. Figures 20 & 22 show their vorticity maps, respectively. Phase 2 occurs just after the wave has broken and there is still some aeration of the flow near the surface, particularly near the centre of the figure. It has the greatest magnitude of vorticity values of any of the waves, with large negative vortices near the surface on the right of Figure 20 and near the bed on the left. Two phases later we can see that both negative vortices have persisted with the main one, centred about 27.09m in Figure 22 and the second one located on the left hand side of the flow.

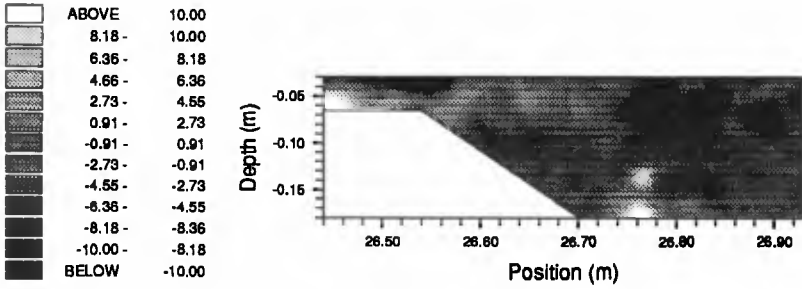


Figure 8: Vorticity map: 3s wave: Phase 1: Position 3.

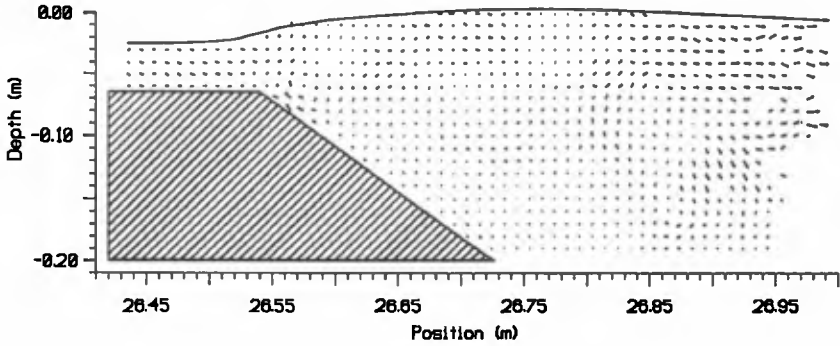


Figure 9: Vector map: 3s wave: Phase 2: Position 3.

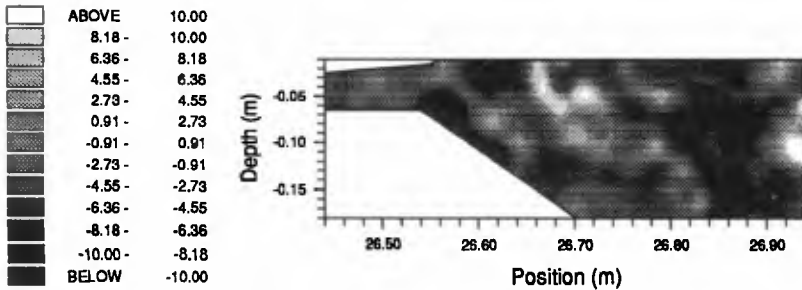


Figure 10: Vorticity map: 3s wave: Phase 2: Position 3.

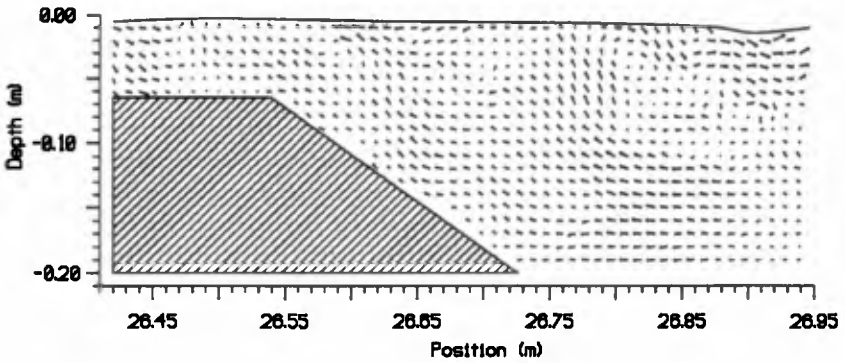


Figure 11: Vector map: 3s wave: Phase 3: Position 3.

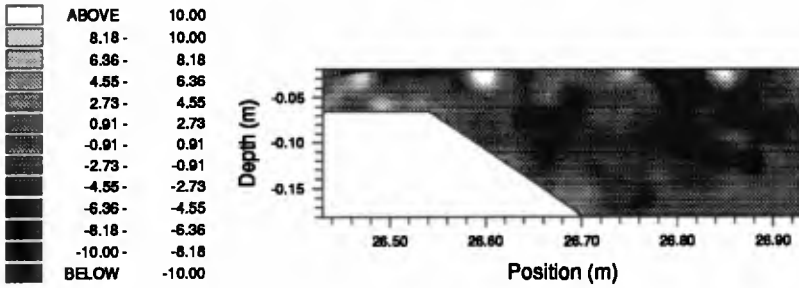


Figure 12: Vorticity map: 3s wave: Phase 3: Position 3.

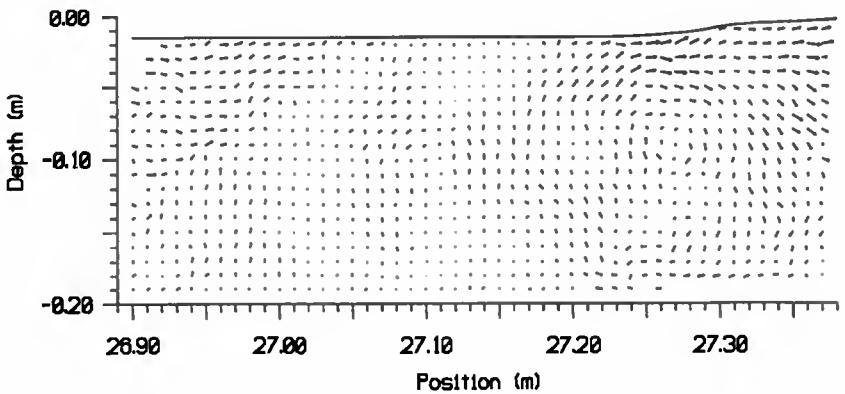


Figure 13: Vector map: 3s wave: Phase 4: Position 4.

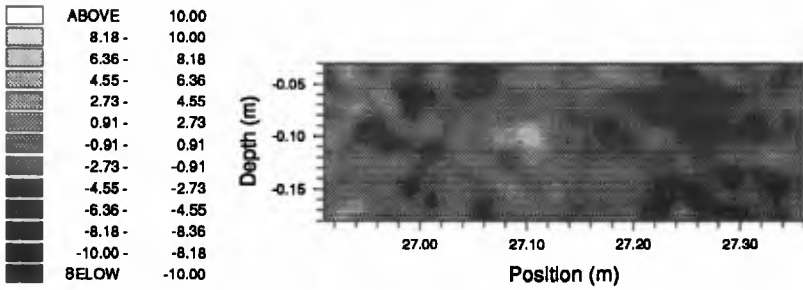


Figure 14: Vorticity map: 3s wave: Phase 4: Position 4.

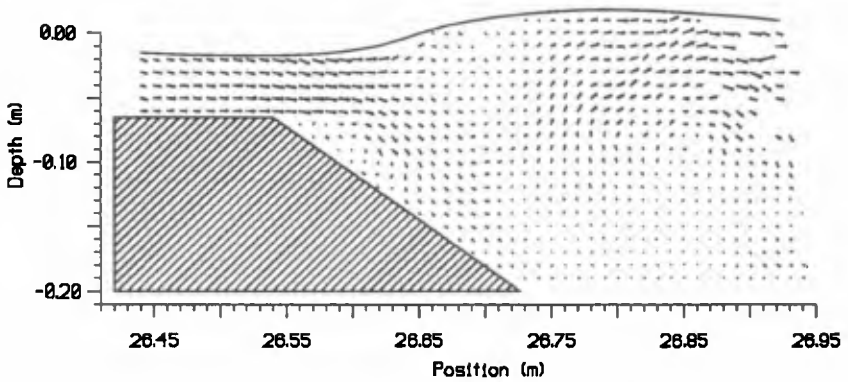


Figure 15: Vector map: 4s wave: Phase 2: Position 3.

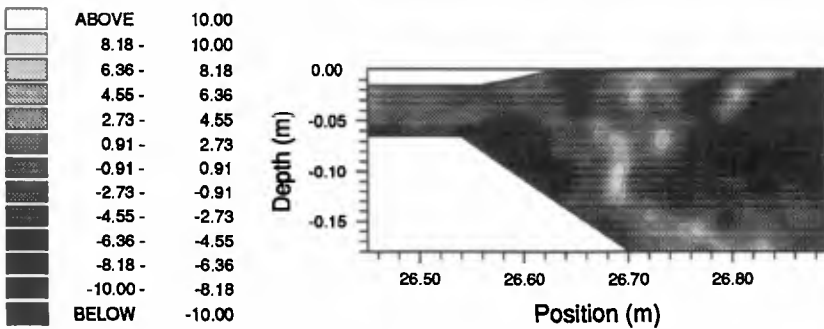


Figure 16: Vorticity map: 4s wave: Phase 2: Position 3.

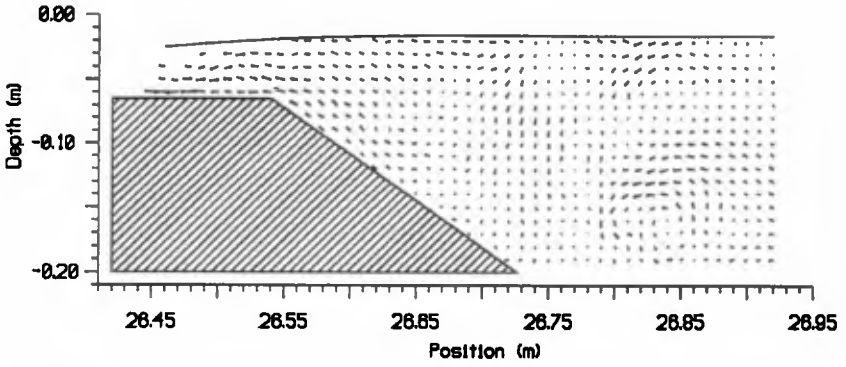


Figure 17: Vector map: 4s wave: Phase 3: Position 3.

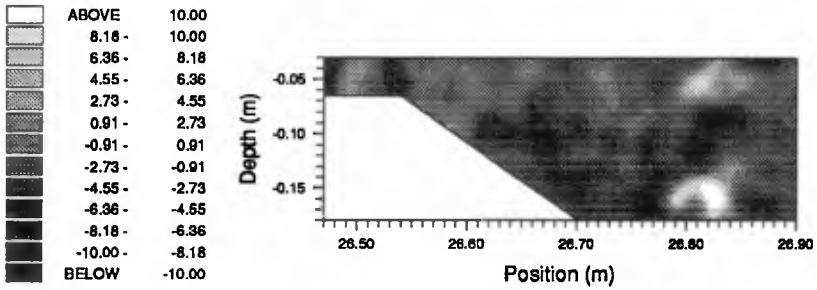


Figure 18: Vorticity map: 4s wave: Phase 3: Position 3.

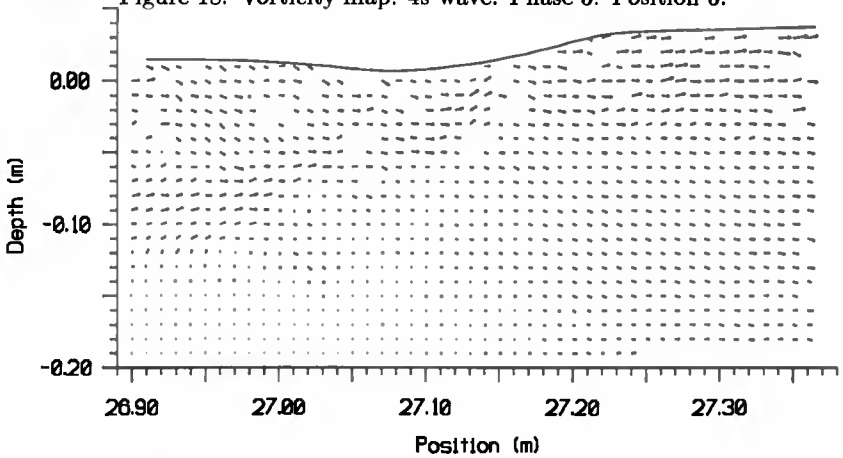


Figure 19: Vector map: 4s wave: Phase 2: Position 4.

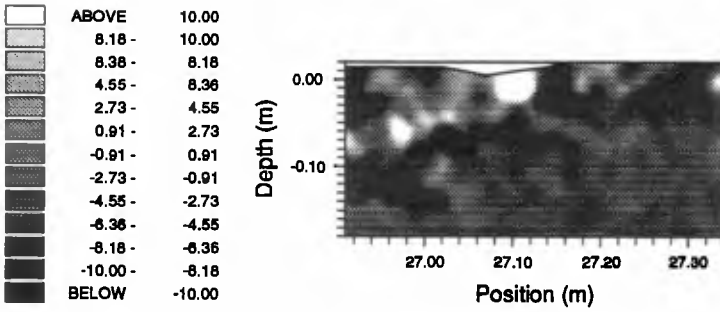


Figure 20: Vorticity map: 4s wave: Phase 2: Position 4.

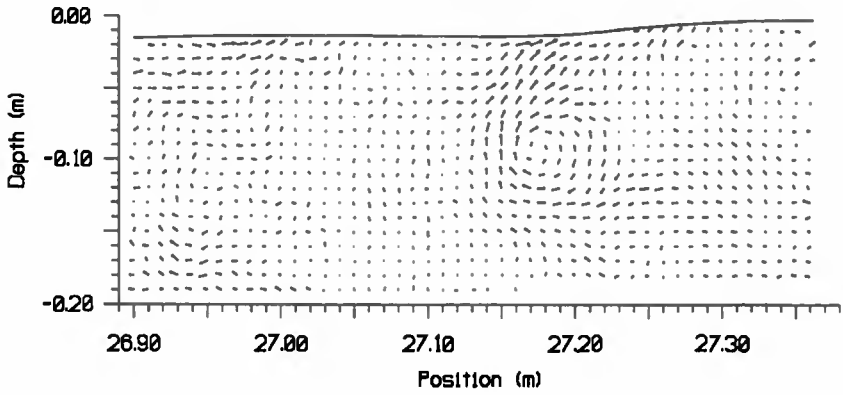


Figure 21: Vector map: 4s wave: Phase 4: Position 4.

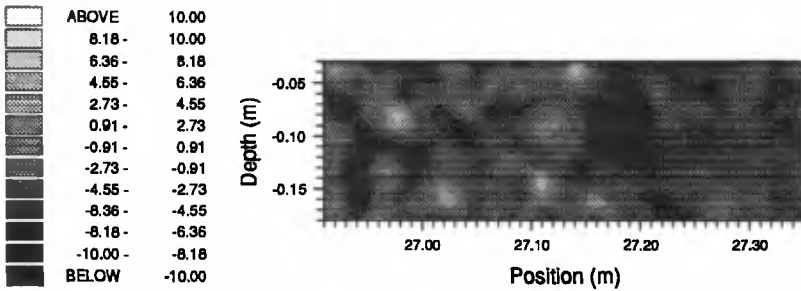


Figure 22: Vorticity map: 4s wave: Phase 4: Position 4.

### Conclusions

The main focus of this study is to demonstrate the scale and significance of large scale vortices generated by waves breaking over a submerged breakwater. The ability to do this lies in the use of PIV as the measurement system, due to the fact that these flow structures are only measurable with a technique which records the spatial distribution of velocities at an instant. The detail of these measurements is apparent and a thorough analysis of the data is now called for. However, one can get an initial impression, from the results presented (eg. Figures 7-10 showing phases 1 & 2 of the 3s waves at position 3), of the importance of including vortex generation and interaction in the formulation of sediment transport numerical models. One such model is the Discrete Vortex Model described in Pedersen et al, 1992.

### Acknowledgements

This work was undertaken as part of the MAST G8-M Coastal Morphodynamics research programme. It was funded by the Commission of the European Communities Directorate General for Science, Research and Development under contract N°. EC MAST-II OCT 92 0027; their support is greatly appreciated.

The authors also wish to extend their gratitude to the technicians, Mauro Gioli, Muzio Mascherini and Frank Morris, who played an essential role in conducting the experiments in Italy with such a tight time limit.

### References

- Adrian, R.J. (1991) *Particle Imaging Techniques for Experimental Fluid Dynamics*. Ann. Rev. Fluid Mechanics, 23:261-304.
- Arhens, R.J. (1991) *Stability of Reef Breakwaters*. J. Waterway, Port, Coastal and Ocean Engineering, ASCE, 1729-1738.
- Bruce, T. & Easson, W.J., (1992) *The Kinematics of Wave Induced Flows Around Near-bed Pipelines*. Proc. 23rd Int. Conf. Coastal Eng. 229:2990-2998.
- Earnshaw, H.C., Bruce, T., Greated, C.A. & Easson, W.J. (1994) *PIV Measurements of Oscillatory Flow over a Rippled Bed*. Proc. 24th Int. Conf. Coastal Eng., Kobe, Japan.
- Greated, C.A., Skyner, D.J. and Bruce, T., (1992) *Particle Image Velocimetry (PIV) in the Coastal Engineering Laboratory*. Proc. 23rd Int. Conf. Coastal Eng. 15:212-225.
- Kobayashi, N. & Wurjanto, K. (1989) *Wave Transmission over Submerged Break-*

- waters. J. Waterway, Port, Coastal and Ocean Eng., ASCE, (115) 5, 662-680.
- Liberatore, G. (1992) *Detached Breakwaters and their use in Italy*. Proc. Short Course on Design and Reliability of Coastal Structures, 23rd Int. Conf. Coastal Eng.
- Mizutani, N., Iwata, K., Rufin, T.M. and Kurata, K. (1992) *Laboratory Investigation on the Stability of a Spherical Armour Unit as a Submerged Breakwater*. Proc. 23rd Int. Conf. Coastal Eng. pp 1400-1413.
- Nielsen, P. (1992) *Coastal Bottom Boundary Layers and Sediment Transport*. World Scientific, Singapore.
- Nielsen, P. (1994) *Suspended Particle Motion in Coastal Flows*. Proc. 24th Int. Conf. Coastal Eng., Kobe, Japan.
- Osborne, A.R. & Petti, M. (1994) *Laboratory Generated Shallow-Water Surface Waves: Analyses using the Periodic, Inverse Scattering Transform*. Physics of Fluids, Vol. 6, No. 5, 1727-1744.
- Pedersen, C., Deigaard, R., Fredsøe, J. & Hansen, E.A. (1992) *Numerical Simulation of Sand in Plunging Breakers*. Proc. 23rd Int. Conf. Coastal Eng. pp 2344-2357.
- Petti, M. and Ruol, P. (1991). *Experimental Studies on the Behaviour of Submerged Breakwaters*. Proc. 3rd Int. Conf. Coastal and Port Eng. in Developing Countries, 167-178.
- Petti, M. and Ruol, P. (1992). *Laboratory Tests on the Interaction between Non-linear Long-waves and Submerged Breakwaters*. Proc. 23rd Int. Conf. Coastal Eng. pp 792-803.
- Quinn, P.A., Petti, M., Drago, M. & Greated, C.A. (1994) *Velocity Field Measurements and Theoretical Comparisons for Non-Linear Waves on Mild Slopes*. Proc. 24th Int. Conf. Coastal Eng., Kobe, Japan.
- Van der Meer, J.W. & Pilaczyk, K.W. (1990) *Stability of Low-Crested and Reef Breakwaters*. Proc. 22nd Int. Conf. Coastal Eng., ASCE, 1375-1388.



## CHAPTER 40

### Velocity Field Measurements and Theoretical Comparisons For Non-Linear Waves on Mild Slopes.

Paul A. Quinn,<sup>1</sup> Marco Petti,<sup>2</sup> Michele Drago<sup>3</sup> & Clive A. Greated<sup>4</sup>

#### Abstract

The way in which the Boussinesq and Serre models deal with the internal kinematics of waves on mildly sloping beaches is examined. The equation normally used on the depth-averaged horizontal velocity to impose a parabolic profile vertically up through the wave is studied using experimentally and theoretically obtained values. In general, it is found that for near-bed regions the equation provides satisfactory comparisons, however, as one approaches the surface the theoretical values can substantially exceed the experimental ones, particularly in the crest of the wave.

#### Introduction

A great deal of emphasis has been placed recently on the use of the Boussinesq and Serre models in determining near-shore wave motion (Dingemans, 94a, 94b), mainly due to its recently improved frequency dispersion capabilities. It has some shortcomings, however, in its treatment of the internal wave kinematics based mainly on the fact that it only predicts explicitly the depth-averaged horizontal velocity and relies on an equation to provide a vertical profile of velocity up through the wave, and the divergence of that equation to provide a distribution of the vertical component of velocity.

A description of the Boussinesq and Serre models used in this comparison can be found in Brocchini et al, (1992). They also give the equation for the parabolic profile of velocity as:

---

<sup>1</sup>Research Associate, Fluid Dynamics Unit, Department of Physics & Astronomy, The University of Edinburgh, Edinburgh, EH9 3JZ, U.K.

<sup>2</sup>Lecturer, Department of Civil Engineering, The University of Florence, Via di S. Marta, 3, I-50139 Florence, Italy.

<sup>3</sup>ENVI, Snamprogetti SpA., Fano, Italy.

<sup>4</sup>Professor of Fluid Dynamics, Department of Physics & Astronomy, The University of Edinburgh, Edinburgh, EH9 3JZ, U.K.

$$u(z) = \bar{u} - (h/2)(h\bar{u})_{xx} + (h^2/6)\bar{u}_{xx} - z(h\bar{u})_{xx} - (z^2/2)\bar{u}_{xx} \quad (1)$$

Where  $u$  is the horizontal velocity component,  $\bar{u}$  is its depth-average,  $\bar{u}_{xx}$  is its second derivative with respect to  $x$  and  $h$  is the local depth from the still water level (SWL). If the bottom topography is known then all that is required to calculate  $u(z)$  is a spatial distribution of  $\bar{u}$ . As Particle Image Velocimetry provides a 2-D spatial distribution of the velocity field it is ideally suited for use in Equation 1.

The first part of this paper uses the values for  $\bar{u}$  and  $\bar{u}_{xx}$  from PIV results in Equation 1 to calculate the vertical profile of velocity,  $u(z)$ , and then compares this to the actual profile measured in the experiments. This is based upon the supposition that the best fit to the actual velocity profile will be obtained using the experimental values of  $\bar{u}$  and  $\bar{u}_{xx}$  in Equation 1. Alternatively, if the model predicted the depth-averaged velocity distribution perfectly will it then provide the correct vertical profile of velocity?

The second part of the paper is then to compare the distribution of the depth-averaged horizontal velocity predicted by the Boussinesq and Serre models with the experiments and then calculate their vertical profiles of velocity.

### Particle Image Velocimetry (PIV)

Although there are a number of institutions around the world who now use PIV as a matter of course, it is still relatively new in the field of coastal engineering when compared to techniques like Laser Doppler Anemometry (LDA), and as such warrants a brief description. A comprehensive review of PIV is given by Adrian (1991) and an introduction to the process in a coastal engineering context is given by Greated et al (1992). Quinn et al (1993) gives an account of the errors inherent in the technique and uses as an example the measurement of waves breaking on a 1:30 plane sloping beach. Powell et al (1992) gives an account of the specific application to waves breaking on non-uniform beach slopes.

The first stage of PIV is to photograph the flow, which is seeded with tiny particles and illuminated with a pulsing laser light sheet. The idea is that the camera shutter is held open for several, say four, pulses of the light sheet so that on the photographic negative there will appear four multiple images of each of the seeding particles in the flow. Measuring the separation of the multiple images at any point will yield the velocity at that point, when coupled with the time separation of the light pulses. The seeding particles used in these experiments was Conifer Pollen which has a diameter of 50-70  $\mu\text{m}$  and is almost exactly neutrally buoyant in water. Typical illumination pulse intervals are about 5ms, and the shutter speed of the camera is usually set at 1/60s for this type of flow.

The second stage of the technique is to analyse the developed negative. The analysis is carried out on an automated rig described in some detail in Greated et al (1992) and Quinn et al (1993). The process involves probing the negative on

a regular grid (normally 1mm x 1mm) with the beam from a low power Helium-Neon laser. The multiple images of the seeding particles illuminated in the 1mm diameter laser beam cause an interference fringe pattern which is captured by a CCD camera and passed to a Personal Computer (PC). The separation and orientation of the fringes is calculated which gives the average displacement of the multiple images in the small interrogation area of the negative and hence the velocity vector at that point. This process is carried out for every point in the flow field and results in a 2-D velocity array.

### Experiments

Beach slopes of 1:30 and 1:100 were used in this study. The experiments were carried out in the Universities of Edinburgh and Florence respectively.

Considering the 1:30 slope first, the experiments were conducted in a 10m wave flume with a SWL of 0.75 m. The wave maker is a hinged, absorbing paddle (Salter, 1982). Due to the restricted length of the flume a 1:30 beach does not reach the bottom of the tank. As we have a hinged paddle rather than a piston-type wave maker, the water depth cannot be altered significantly, so a ramp was installed from the bottom of the wave maker to the foot of the beach, 3m away. The water depth at the foot of the beach was 0.19m and as the waves were so small, ( $T = 1s$ ,  $H = 0.032m$ ) the set-up was deemed, if not ideal, then at least satisfactory. A section of the tank showing the beach and the PIV illumination system is shown in Figure 1.

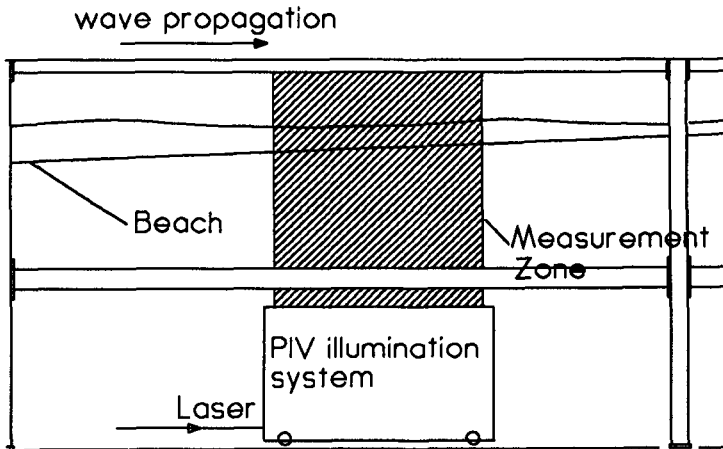


Figure 1: The Flume and PIV Illumination Section.

Regular waves with a period of 1s and a wave height of 0.032m were used. PIV measurements were made at five adjoining positions along the beach, each

position being 0.6m in length. Four phases of the wave were recorded at each position.

As the 1:100 beach slope was too mild for the wave flume in Edinburgh the experiments on this slope were carried out in the 50m flume at The University of Florence, Italy. The laser and PIV illumination system were taken over to Florence, from Edinburgh, for these collaborative experiments. As the flume in Florence does not have a glass bottom a special section of the beach had to be built which allowed the PIV laser light sheet in through the side of the tank, below the level of the beach, and reflected it off an underwater mirror up through the beach and into the flow. This is shown in Figure 2.

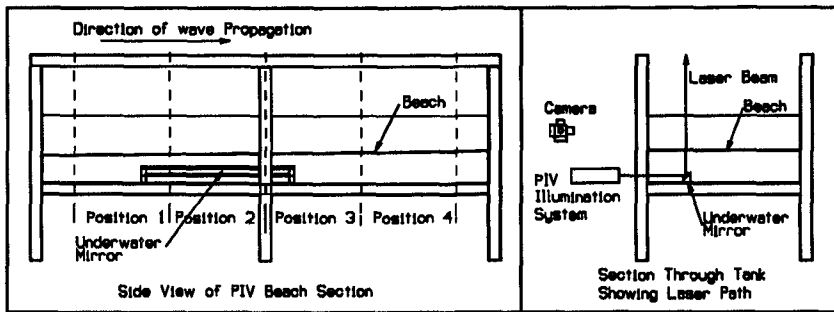


Figure 2: The PIV Beach Section in Florence.

Once again regular waves were used, this time with a period of 3s and a height of 0.1m. The waves were generated in a water depth of 0.42m and propagated about 25m up the beach before they broke. Eight positions were measured around the breaking zone and four phases of the wave were measured at each position.

The wave flume in Florence is fitted with a piston-type wave maker which does have an absorbing system, however, for this experimental set-up with an extremely mild beach slope and no structure to provide a significant reflection, the wave repeatability, as measured by wave-gauge analysis, was worse with the absorbing system activated. For this reason the absorbing system was switched off for these experiments. In order to minimise the effect of the unrepeatability of the waves the first PIV measurement was taken 40s after the start of the wave maker and the subsequent phases were taken from successive waves. The tank was allowed to settle for about 5 to 10 minutes between runs.

### Velocity Profile Analysis

Returning to the main aim of the paper, to examine the equation providing a vertical profile of velocity from the depth-averaged velocity component given by the Boussinesq and Serre models. All that is required to calculate the vertical

profile of the horizontal velocity component,  $u(z)$ , from Equation 1, is a spatial distribution of the depth-averaged horizontal velocity. This can easily be calculated from PIV measurements. If one considers Figure 3, which shows the velocity field of the crest phase of a 1s wave on a 1:30 slope, the depth-averaged velocity can be calculated for each column of vectors. Figure 4 shows the resulting spatial distribution of the depth-averaged velocity.

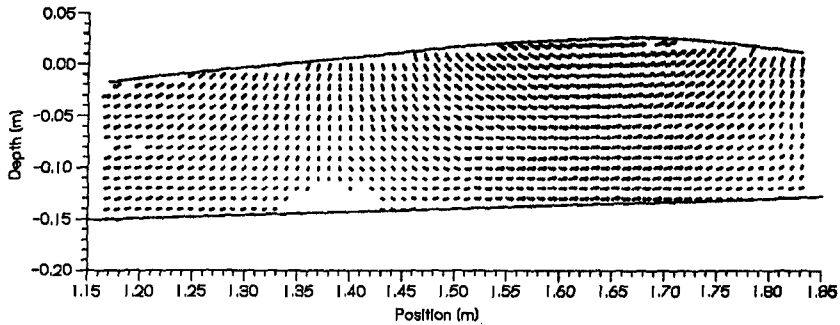


Figure 3: Velocity Vector map for a 1s wave on a 1:30 slope.

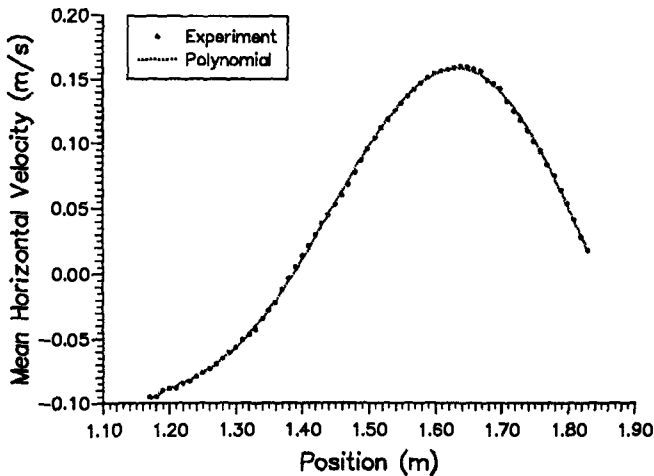


Figure 4: Depth-averaged velocity distribution for a 1s wave on a 1:30 slope.

In Figure 4 the points are the depth-average horizontal velocity components calculated from the vector map (Figure 3). The curve is a least squares poly-

nomial and has been used to calculate  $\bar{u}_{xx}$  and  $(h\bar{u})_{xx}$ . It was not possible to calculate these derivatives from the actual values of  $\bar{u}$  because the standard deviation in calculating the means was of the same order of magnitude as the difference between the mean values at adjacent positions. This resulted in the second derivatives being wildly inaccurate. The curve has been used to smooth out this essentially statistical variation, and as the fit is so good it is not thought to introduce any significant errors.

One can now look at the parabolic velocity profiles calculated from the experimentally obtained values of  $\bar{u}$ ,  $\bar{u}_{xx}$  and  $(h\bar{u})_{xx}$  together with the actual measured profiles. Figure 8 shows this at 5cm steps along the wave.

There are several things to notice from Figure 8: firstly the agreement in general is quite good and particularly so near the bed. For  $x = 1.20\text{cm}$  the poor agreement is due to an error introduced by trying to fit the polynomial approximation, used to calculate  $\bar{u}_{xx}$ , near the edges of the data. There is a tendency for the parabolic profile to exceed the measured values in the near-surface region of the crest. This effect is even more noticeable further up the beach where the wave is more non-linear. This is shown in Figure 9 for a 3s wave approaching breaking on a 1:100 slope, the vectorplot of which is shown in Figure 5. The same effect also occurs on the 1:30 slope.

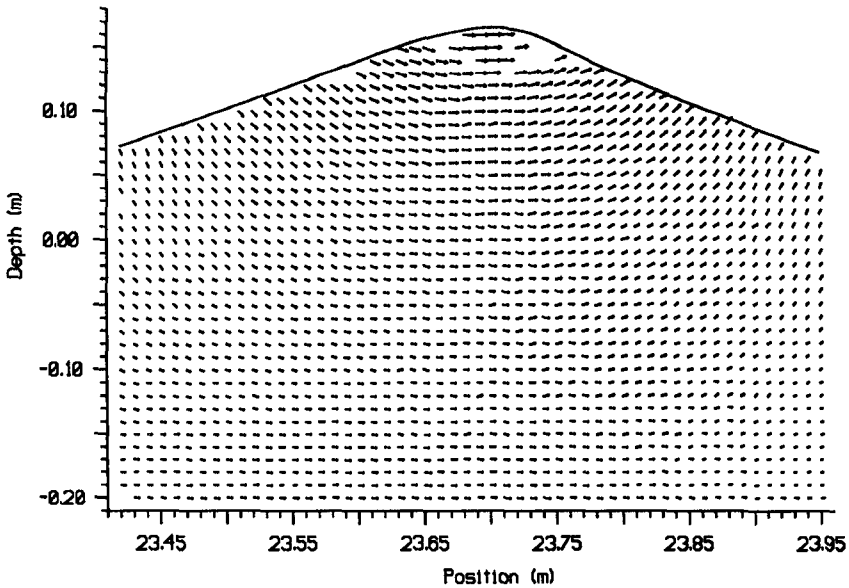


Figure 5: Vector map for a 3s wave on a 1:100 beach

The next step is to see how well the Boussinesq and Serre models can predict

the depth-averaged horizontal velocities. The models were given the same wave input parameters, the bottom slope and initial depth for the 1:30 beach. Figure 6 shows the comparison of the distribution of the depth-averaged horizontal velocity given by the Boussinesq and Serre models with the measured values from the vector map in Figure 3.

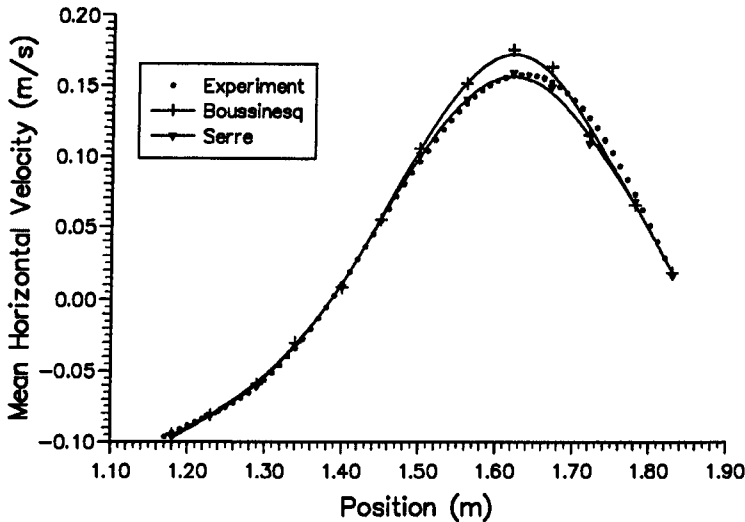


Figure 6: Comparison with the Boussinesq and Serre Models on a 1:30 Beach

In order to calculate the velocity profiles from the models' predictions a least squares polynomial was used, once again. This is also shown in Figure 6. The velocity profiles, calculated in the same way as before are now shown in Figure 10.

Doing the same for a position further up the beach we get the comparison shown in Figure 7 and the velocity profiles shown in Figure 11.

### Conclusions

PIV results have been used to test the equation used by the Boussinesq and Serre models to provide a profile of velocity up through the wave.

In general the comparison of a parabolic profile calculated from experimental values agreed fairly well with the measured profiles. The agreement was particularly good near the bed.

There was a consistent overestimate of the measured velocity by the parabolic profile in the near-surface region of the crest of the wave, which appears to get worse as the wave steepens. The degree to which this discrepancy increases with non-linearity has yet to be quantified. One can briefly envisage one of the problems; Equation 1 is derived assuming the same range of validity as the

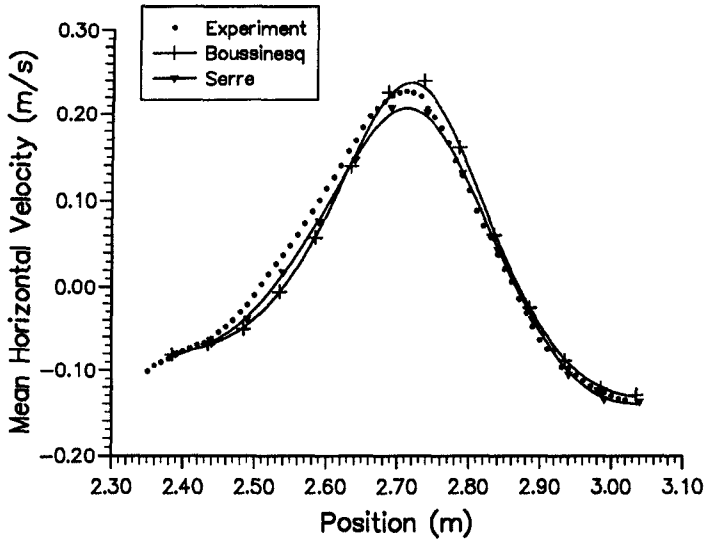


Figure 7: Comparison with the Boussinesq and Serre Models on a 1:30 Beach

Boussinesq and Serre models i.e., they include terms of order  $(kh)^2$ , but they ignore those of order  $(a/h)(kh)^2$ , where  $a$  is the wave amplitude; however, as one approaches breaking  $a/h = O(1)$  and so the neglected terms are of the same order of magnitude as the included ones.

The comparison of the Boussinesq and Serre model predictions of the depth-averaged horizontal velocity with the measured values shows an overestimate of the peak velocity by the Boussinesq model and a very close estimate for the Serre model at the first position shown. In the second position, further up the beach, the Boussinesq still overestimates the peak value but the Serre now underestimates it. In both positions the models provided a slightly sharper mean velocity distribution than that given by the measurements.

The velocity profiles calculated from the Boussinesq and Serre model predictions did not show particularly good agreement. This is due to the difference between the predicted and measured spatial distributions of the depth-averaged horizontal velocity, and manifests itself by a shift along the  $x$ -axis of the models' profiles with respect to the experiment's. The shape of the curves predicted by the models is similar to that of the experimental profiles, but it still tends to overestimate the curvature of the parabola leading to an overestimate of the near-surface velocity in the crest region. This indicates the sensitivity of the variable  $\bar{u}_{xx}$  because small differences in the predicted and measured distributions of  $\bar{u}$  can lead to large differences in the parabolic profile. Only the near-bed velocities were adequately modelled on a consistent basis.



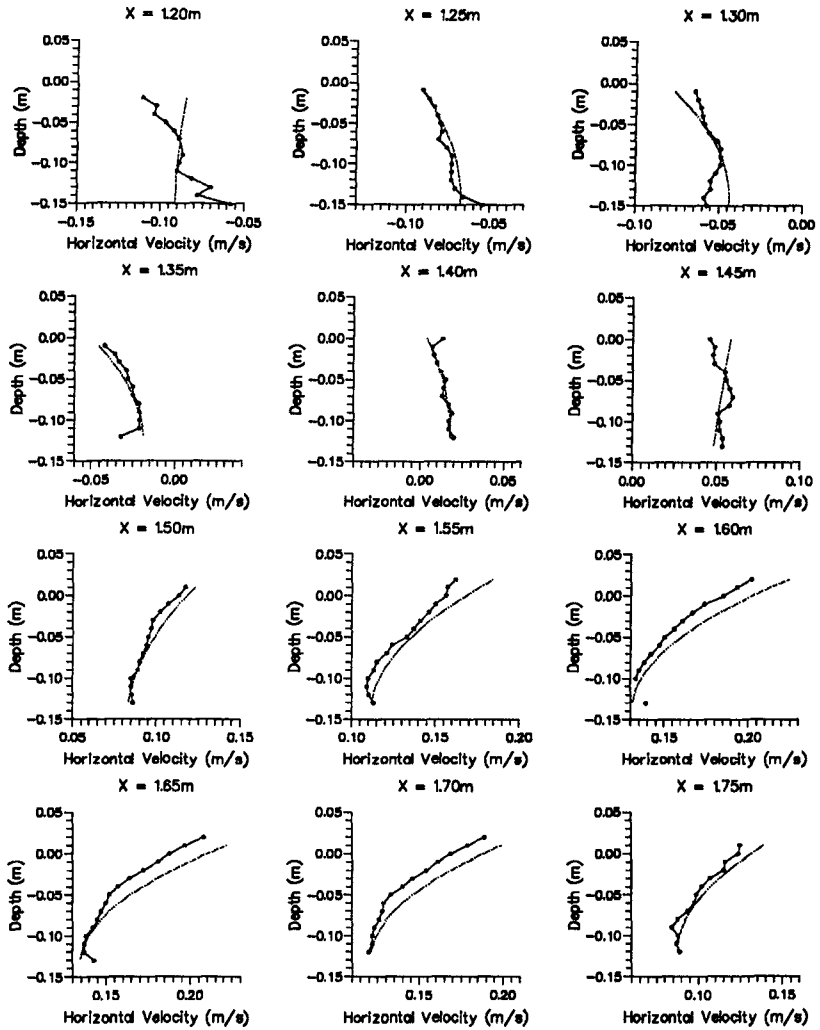


Figure 8: Calculated and Measured Velocity Profiles at Different Horizontal Positions ( $x$ ) in the 1s wave on a 1:30 Beach.

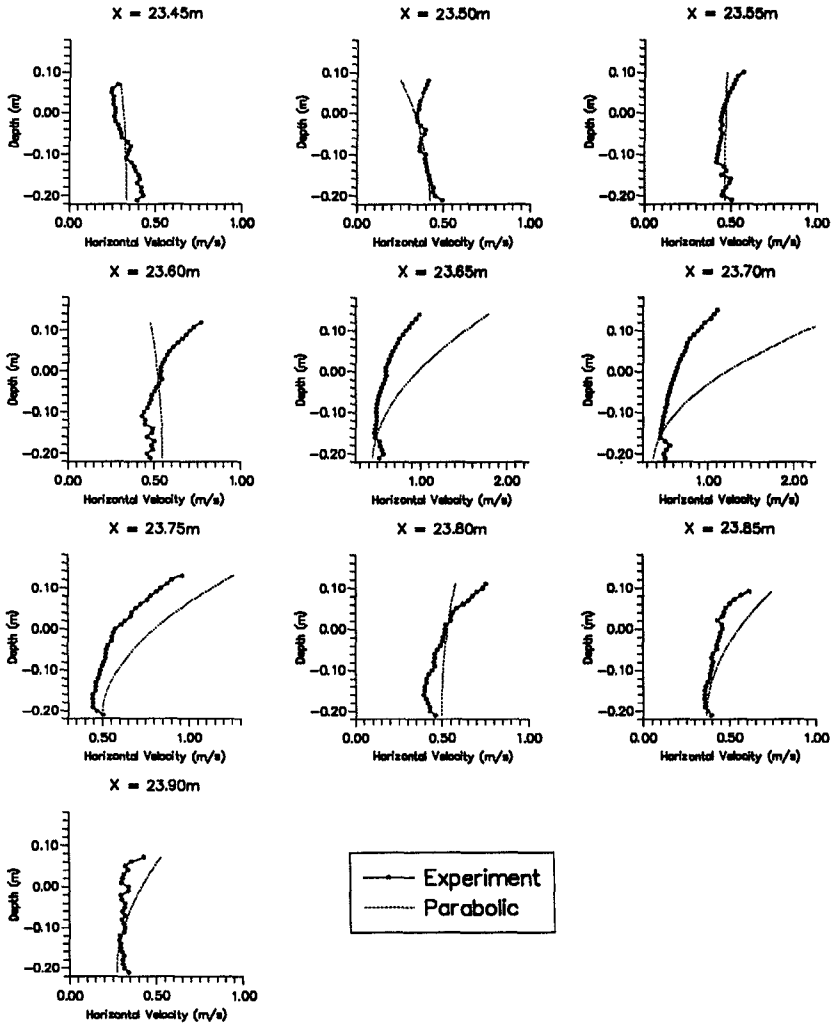


Figure 9: Calculated and Measured Velocity Profiles at Different Horizontal Positions ( $x$ ) in the 3s wave on a 1:100 Beach.

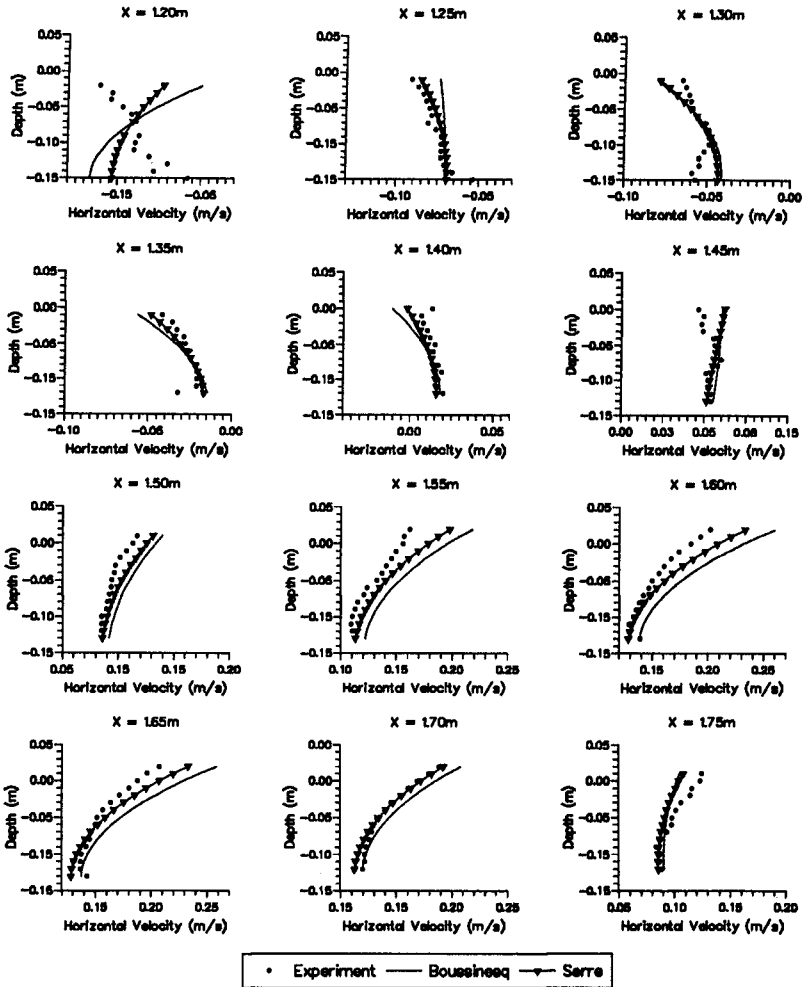


Figure 10: Modelled and Measured Velocity Profiles at Different Horizontal Positions ( $x$ ) in the 1s wave on a 1:30 Beach.

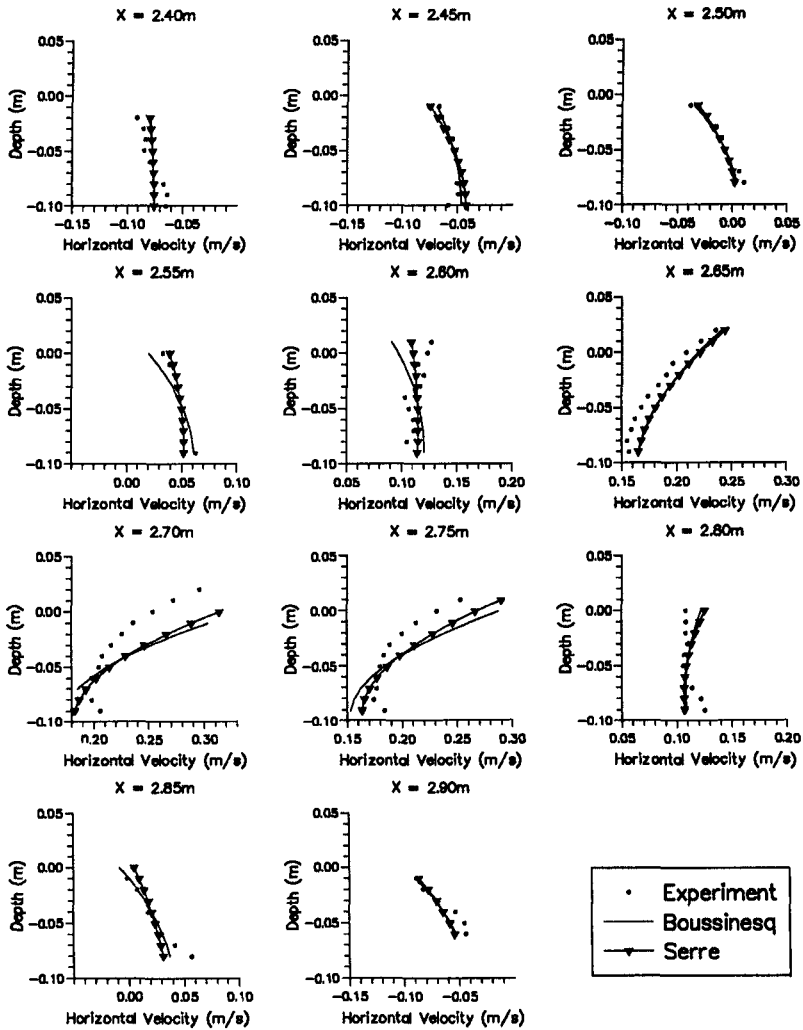


Figure 11: Modelled and Measured Velocity Profiles at Different Horizontal Positions ( $x$ ) in the 1s wave on a 1:30 Beach.

### Acknowledgements

This work was undertaken as part of the MAST G8-M Coastal Morphodynamics research programme. It was funded by the Commission of the European Communities Directorate General for Science, Research and Development under contract N°. EC MAST-II OCT 92 0027; their support is greatly appreciated.

The authors also wish to extend their gratitude to the technicians, Frank Morris, Mauro Gioli and Muzio Mascherini, who played an essential role in conducting the experiments in Italy with such a tight time limit.

### References

- Adrian, R.J. (1991) *Particle Imaging Techniques for Experimental Fluid Dynamics*. Ann. Rev. Fluid Mechanics, 23:261-304.
- Brocchini, M., Drago, M. & Iovenitti, L., (1992) *The modelling of short waves in Shallow Waters. Comparison of numerical models based on Boussinesq and Serre equations*. Proc. 23rd Int. Conf. Coastal Eng. 4:76-88.
- Dingemans, M.W. (1994a) *Boussinesq Approximations* Proc. EC MAST G8-M Workshop, Gregynog, Wales. (Abstract in Depth)
- Dingemans, M.W. (1994b) *Water Wave Propagation over Uneven Bottoms*. World Scientific, Singapore. (To be published)
- Greated, C.A., Skyner, D.J. and Bruce, T., (1992) *Particle Image Velocimetry (PIV) in the Coastal Engineering Laboratory*. Proc. 23rd Int. Conf. Coastal Eng. 15:212-225.
- Powell, K.A., Quinn, P.A. and Greated, C.A., (1992) *Shingle Beach Profiles and Wave Kinematics*. Proc. 23rd Int. Conf. Coastal Eng. 181:2358-2369.
- Quinn, P.A., Skyner, D.J., Gray, C., Greated, C.A. and Easson, W.J., (1993) *A Critical Analysis of the Particle Image Velocimetry Technique as applied to Water Waves*. In *Flow Visualization and Image Analysis*, Ed. F.T.M. Nieuwstadt. Kluwer Academic Publishers, Dordrecht, The Netherlands.
- Salter, S.H., (1982) *Absorbing Wave Makers and Wide Tanks*. Proc. Conf. Directional Wave Spectra Applications, ASCE, 185-200.

## CHAPTER 41

# The Concept of Residence Time for the Description of Wave Run-Up, Wave Set-up and Wave Run-Down

Holger Schüttrumpf<sup>1</sup>, Hendrik Bergmann<sup>1</sup>, Hans-Henning Dette<sup>2</sup>

### Abstract

Wave run-up, wave set-up and wave run-down are determined by using the residence time in the form of a duration curve. This method introduced by FÜHRBÖTER and WITTE (1991) considers the totality of a run-up series without considering individual run-up events separately. By using the residence time concept, wave run-up is not any more a timeless event but can be described as a time dependent variable. The results obtained by using this concept are in good agreement with previous studies based on other methods for defining wave run-up, wave set-up and wave run-down. The residence time concept has been used for regular and random waves. This concept is particularly useful for random waves, because there is no need to count the number of waves loading a dike.

### 1. Introduction

In the past different methods were used to define wave run-up, wave set-up and wave run-down in the swash zone. Furthermore these methods didn't consider the time the slope is covered by water during an individual run-up event. This led to the concept of the residence time developed by FÜHRBÖTER and WITTE (1991) which allows to define wave run-up, wave set-up and wave run-down. FÜHRBÖTER and WITTE verified this concept for a 1:6 slope and for wave run-up. But the concept of the residence time also allows to obtain results for wave

---

<sup>1</sup> Assistant Scientist Dipl.-Ing., Department of Hydrodynamics and Coastal Engineering, Leichtweiss-Institute for Hydraulics, Technical University of Braunschweig, Germany

<sup>2</sup> Academ. Director Dr.-Ing.

set-up and wave run-down. Therefore, the concept of the residence time has been verified with a more extensive amount of data obtained from tests in the Large Wave Flume of Hannover for different slope steepnesses as well as for composite slopes. First results are presented in this paper.

Results for shock pressures obtained by the same tests are reported by GRÜNE and BERGMANN (1994).

## 2. Experimental Set-Up and Test Conditions

Results of wave run-up tests in the Large Wave Flume (GWK) in Hannover, Germany, for dikes and similar structures are presented. These tests were carried out for uniform slopes with steepnesses of 1:6 and 1:12 as well as for composite slopes with a steepness of 1:3 for the lower slope and with a steepness of 1:6 for the upper slope (Fig. 1). A slope steepness of 1:6 was selected because it corresponds to the steepest slope recommended for seadikes in Germany (EAK, 1993). The composite slopes can be characterized by the elevation of the front edge  $d_k$  and the water depth  $d$ :

- 1.) position of the front edge  $d_k=3.3\text{m}$ , water depth  $d=4.0\text{m}$
- 2.) position of the front edge  $d_k=3.3\text{m}$ , water depth  $d=5.0\text{m}$
- 3.) position of the front edge  $d_k=4.5\text{m}$ , water depth  $d=4.0\text{m}$
- 4.) position of the front edge  $d_k=4.5\text{m}$ , water depth  $d=5.0\text{m}$

This yields ratios of  $d_k/d=0.825$ ,  $0.660$ ,  $1.125$  and  $0.900$  for the composite slopes. For the two uniform slopes the water depth was  $d=5.0\text{m}$ . The slopes in the wave flume were composed of an asphalt concrete layer covering a sand core. For these experiments a wave run-up gauge was used (GRÜNE, 1982). All the tests were carried out using PIERSON-MOSKOWITZ and JONSWAP wave spectra covering a range between  $H_S/L_0=0.001$  and  $H_S/L_0=0.031$  ( $H_S$  = significant wave height,  $L_0$  = deep water wave length).

## 3. The Concept of the Residence Time

Wave run-up and wave run-down occur in the swash zone (Fig. 2). The highest point represents the maximum wave run-up and the deepest point the maximum wave run-down. The elevation of the mean water level (MWL) over still water level (SWL) at the dike is defined as the maximum landward wave set-up. These three processes are described below using the residence time concept.

The wave run-up on a slope can be given as a function of time. The run-up height can be found by the difference between the highest run-up level on the slope and the mean water level (MWL) using common methods like a crest to crest, a trough

to trough or an upcrossing method. The wave run-up is treated as a time dependent event. The time during which a step on the slope is covered by water provides the loading time and the time of overtopping can be derived.

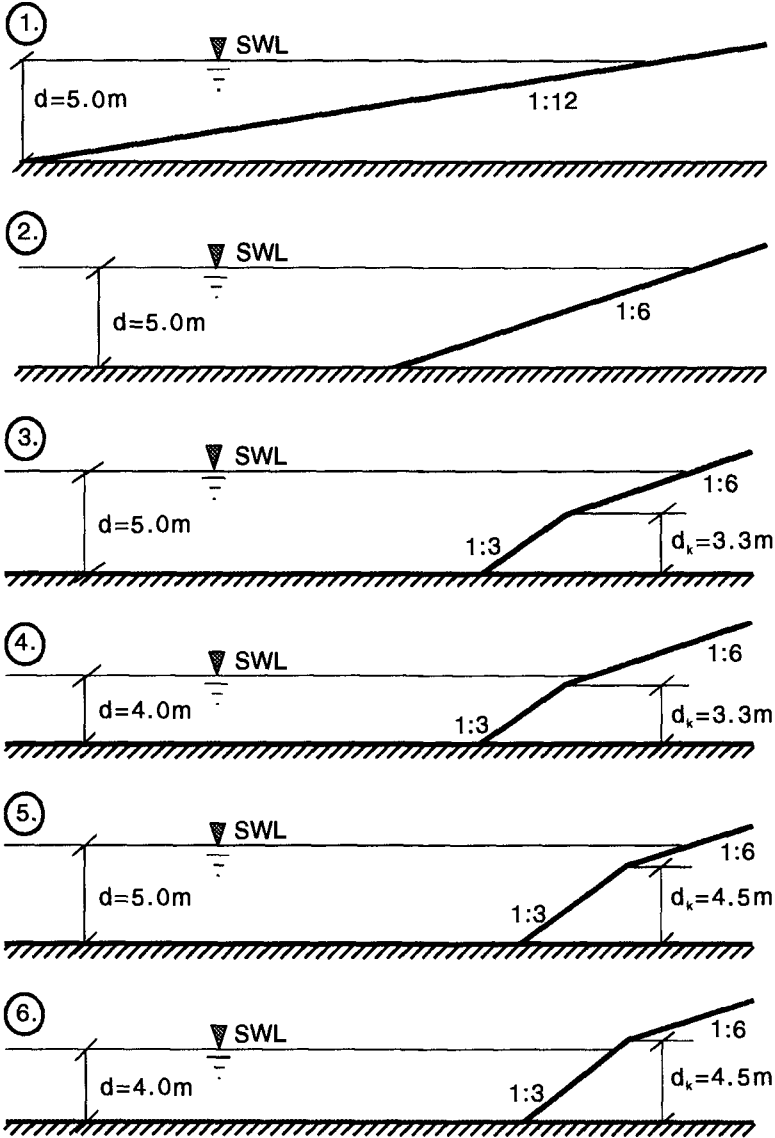
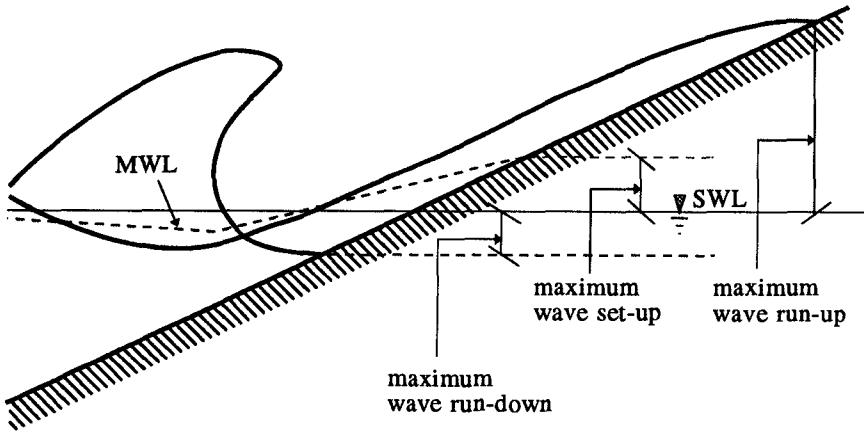


Fig. 1: Slope Configuration of the Model Dikes





**Fig. 2:** Swash Zone - Definition Sketch -

The concept of residence time is illustrated by Fig. 3. In the left part the wave run-up is plotted versus time. The maximal wave run-up and the maximal wave run-down can easily be found. The time  $\Delta t(r)_i$  during which a fixed step on the slope is covered by water can be calculated for each wave run-up  $i$ . The sum of the individual times  $\Delta t(r)_i$  leads to the percental residence time  $D_r$  for each step  $r$  on the slope. The right part of Fig. 3 shows wave run-up as a function of the residence time  $D_r$  obtained by the residence time concept.

The residence time  $D_r$  can be calculated by the following equation:

$$D_r = \frac{1}{t} \left( \sum_{i=1}^{i=n} \Delta t(r)_i \right) \cdot 100 \quad [\%] \quad (1)$$

$t$  = total duration of the record

The residence time is limited by the extreme values  $D=0\%$  and  $D=100\%$ .

$D=0\%$  corresponds to the highest run-up level  $r(D=0\%)$  and  $D=100\%$  to the deepest run-down level  $r(D=100\%)$ . The points  $r(D=0\%)$  and  $r(D=100\%)$  are shown on Fig. 3.

In analogy to the 2% run-up exceedance level  $R_{u2\%}$  (2% of the run-up events exceed this run-up height by an upcrossing method) mainly used by other authors (WASSING, 1942, FÜHRBÖTER and WITTE, 1989, VAN DER MEER and JANSSEN, 1994) a  $r(D=2\%)$  run-up height is defined. The run-up height is exceeded within 2% of the total duration  $t$ . The wave run-down height is indicated by  $r(D=98\%)$ , exceeded within 98% of the total duration. Between these two extreme values wave set-up is defined as the wave-induced vertical elevation of the mean water level (MWL) above still water level (SWL) (GOURLAY, 1992). The value  $r(D=50\%)$  fits well with this definition because the method of the residence time is highly time dependent.

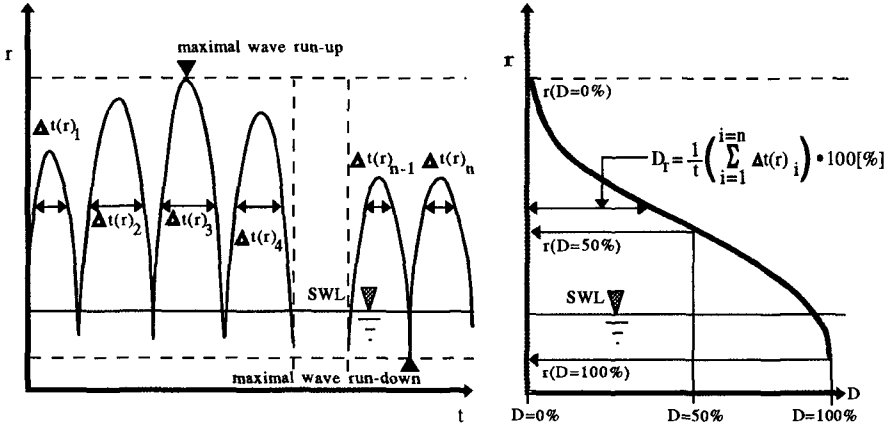


**Fig. 3:** Definition of the Residence Time

The difference between  $r(D=2\%)$  and  $r(D=98\%)$  yields the loaded area on the slope:

$$r_{AB} = r(D=2\%) - r(D=98\%) \quad (2)$$

An example for a duration curve is shown in Fig. 4 for a composite slope with a front edge at  $d_K=3.3\text{m}$ , a water depth  $d=4.0\text{m}$ , a wave height  $H_S=0.75\text{m}$  and a wave period  $T_P=8.0\text{s}$ . Wave run-up  $r(D=2\%)$ , wave run-down  $r(D=98\%)$  and wave set-up  $r(D=50\%)$  are also indicated.

#### 4. Wave Run-Up, Wave Run-Down and Wave Set-Up Described by the Residence Time Concept

Wave run-up, wave run-down and wave set-up are dependent on the wave parameters (wave height  $H_S$  and wave period  $T_P$ ) and the slope angle  $\alpha$ . Using the

wave steepness  $H_S/L_0$  ( $H_S$  = significant wave height in front of the structure,  $L_0$  = deep water wave period corresponding to  $T_p$ ) and the slope angle  $\alpha$ , the breaking wave can be described by the surf similarity parameter  $\xi_0$  (BATTJES, 1974):

$$\xi_0 = \frac{\tan \alpha}{\sqrt{H_S / L_0}} \tag{3}$$

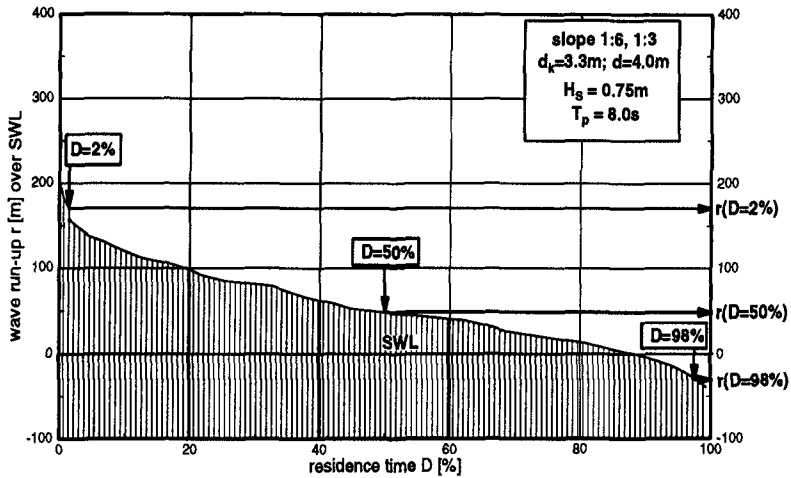


**Fig. 4:** The Residence Time as a Duration Curve for a Test on a Composite Slope ( $H_S=0.75m$ ,  $T_p=8.0s$ )

The equivalent slope angle  $\alpha'$  for the composite slopes is calculated using SAVILLE's method (SAVILLE, 1958) which has been verified by several authors (e.g. MAYER and KRIEBEL, 1994). This leads to an equivalent surf similarity parameter  $\xi_{eq}$  for composite slopes.

$$\xi_{eq} = \frac{\tan \alpha'}{\sqrt{H_S / L_0}} \tag{4}$$

Relative wave run-up  $r(D=2\%)/H_S$ , relative wave run-down  $r(D=98\%)/H_S$  and relative wave set-up  $r(D=50\%)/H_S$  can be related to the surf similarity parameter  $\xi_{eq}$  by using the following expression:

$$\frac{r(D)}{H_S} = A + C \cdot \xi_{eq}^E \quad (5)$$

A, C, E = coefficients

Fig. 5 shows a synopsis of the results for relative wave run-up, relative wave run-down and relative wave set-up versus surf similarity parameter  $\xi_{eq}$ .

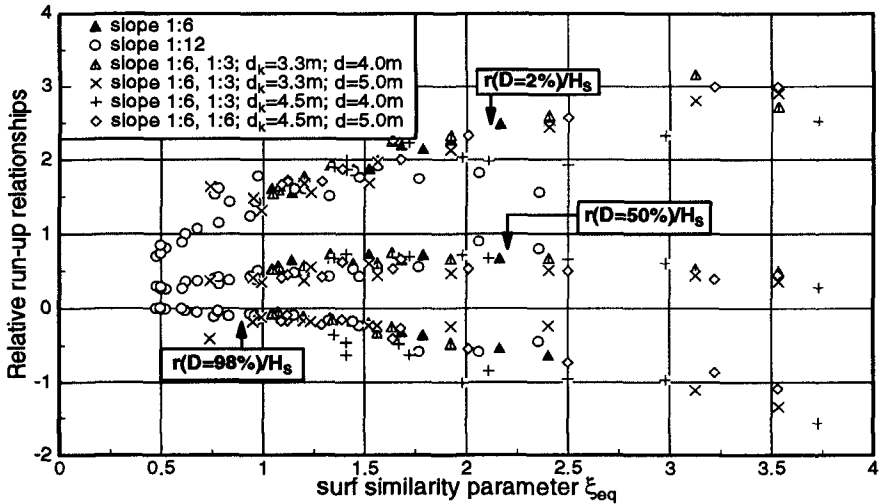


**Fig. 5:** Wave Run-up, Wave Set-up and Wave Run-down for Smooth Uniform and Composite Slopes

### Wave Run-up

A large number of contributions to wave run-up have been published in the past. In most of them the recommended design formulas are extensions of the wave run-up formula proposed by HUNT (1959). Extensive studies were carried out in the Netherlands by VAN DER MEER and JANSSEN (1994) for uniform and composite slopes who suggested the following formula:

$$\frac{R_{u2\%}}{H_S} = 1.5 \xi_{eq} \quad (6)$$

with a maximum relative run-up height of 3.0.

By using the concept of residence time wave run-up becomes smaller due to the slightly different definition of wave run-up. Wave run-up can be calculated by

$$\frac{r(D=2\%)}{H_S} = 1.44 \xi_{eq} \tag{7}$$

for small surf similarity parameters  $\xi_{eq} < 1.0$  (Fig. 6).

For  $\xi_{eq} > 1.0$  relative wave run-up can be expressed by the following formula:

$$\frac{r(D=2\%)}{H_S} = 1.44 + 0.75 (\xi_{eq} - 1.0) \tag{8}$$

It can be seen that equations (7) and (8) lead to smaller wave run-up heights than equation (6) by VAN DER MEER and JANSSEN (1994). Therefore the ratio  $r(D=2\%)/R_{u2\%}$  is plotted against surf similarity parameter  $\xi_{eq}$  in Fig. 7. The average deviation is about 15% with an increasing difference for higher surf similarity parameters ( $\xi_{eq} > 1.0$ ) and a smaller difference for smaller surf similarity parameters ( $\xi_{eq} < 1.0$ ).

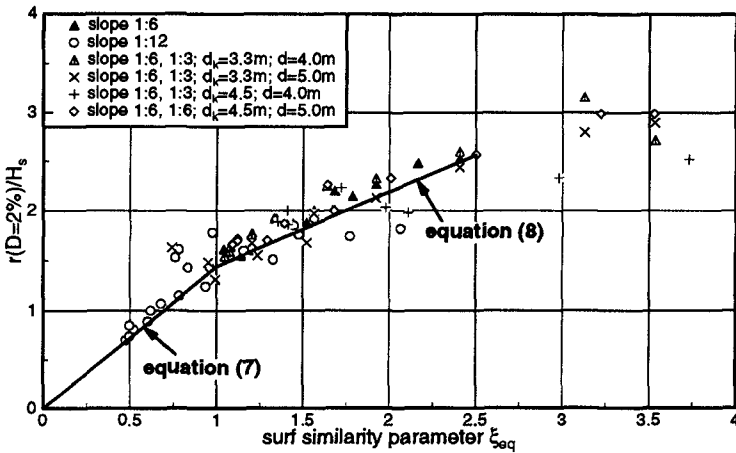


Fig. 6: Wave Run-up on Smooth Slopes

### Wave Set-up

For wave set-up in the swash zone most of the known studies were performed for very smooth slopes (in GOURLAY, 1992) between  $\tan\alpha=0.022$  and  $\tan\alpha=0.100$ .

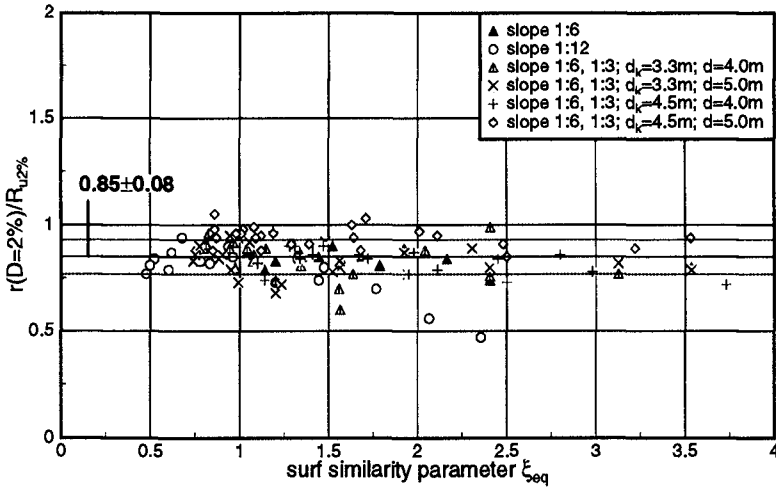


Fig. 7: Ratio  $r(D=2\%)/R_{u2\%}$  versus surf similarity parameter  $\xi_{eq}$

GOURLAY (1992) presented the following formulas for maximum set-up  $\eta_m$  based on field data:

$$(\eta_m - \eta_b)/H_b = 0.31 \pm 0.05 \quad \text{for } 0.083 < \tan \alpha < 0.1 \quad (9)$$

and

$$(\eta_m - \eta_b)/H_b = 0.14 \pm 0.03 \quad \text{for } 0.022 < \tan \alpha < 0.04 \quad (10)$$

$\eta_b$  = Wave set-down at the breaking point

Previous studies based on field measurements by YANAGISHIMA and KATOH (1990) for a beach slope of 1:60 yield the following relationship between maximum wave set-up  $\eta_m$ , significant deep water wave height  $H_{0S}$  and surf similarity parameter  $\xi_0$ :

$$\frac{\eta_m}{H_S} = 0.267 \xi_0^{0.4} \quad (11)$$

In the present paper data for relatively steep slopes between  $\tan \alpha = 0.083$  (1:12) and  $\tan \alpha = 0.333$  (1:3) are presented. Fig. 8 shows a relation between the relative wave set-up  $r(D=50\%)/H_S$  and the surf similarity parameter  $\xi_{eq}$ .

For  $0.5 < \xi_{eq} < 2.5$  the relative wave set-up can be expressed by the following formula:

$$\frac{r(D=50\%)}{H_S} = 0.45 \xi_{eq}^{0.56} \tag{12}$$

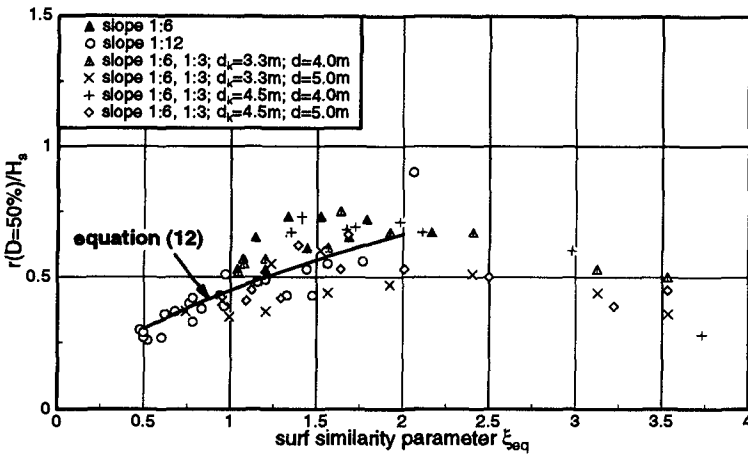


**Fig. 8:** Wave Set-up on Smooth Slopes

**Wave Run-down**

Only very few investigations on wave run-down have yet been performed. VAN DER MEER and BRETELER (1990) presented large-scale model results for wave run-down  $r_d$  on a 1:3 smooth slope and found the following relationship for similarity parameters  $\xi_0$  in the range between 2.0 and 4.3:

$$\frac{r_d}{H} = 0.1 \xi_0^2 - \xi_0 + 0.5 \tag{13}$$

The concept of residence time can also be used for wave run-down. The relationship between  $r(D=98\%)/H_S$  and  $\xi_{eq}$  is shown in Fig. 9.

For  $0.5 < \xi_{eq} < 2.5$  the following formula can be established:

$$\frac{r(D=98\%)}{H_S} = -0.1 \xi_{eq}^{2.21} \tag{14}$$

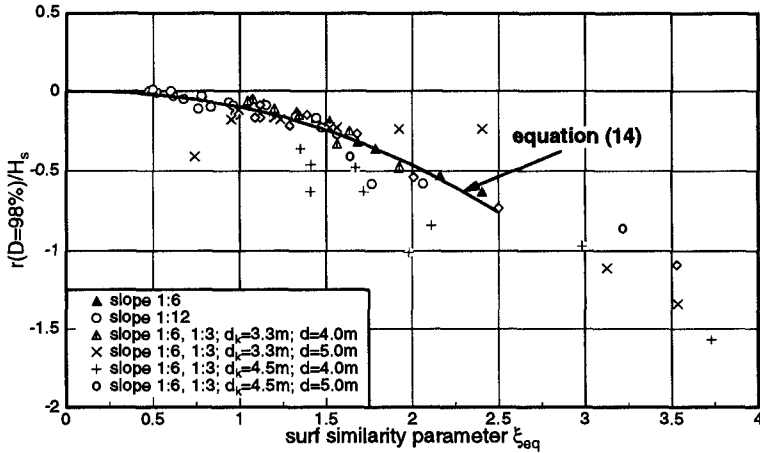


Fig. 9: Wave Run-down on Smooth Slopes

Due to a different definition of wave run-down by using the concept of residence time the obtained results are likewise smaller than the results by VAN DER MEER and BRETELER (1990).

## 5. Concluding Remarks

Wave run-up, wave run-down and wave set-up have been determined by using the concept of residence time in form of a duration curve. This method is highly time dependent. First results obtained by the concept of residence time have been compared to standard formulas, showing that this concept leads to:

- smaller wave run-up heights
- heigher wave set-up heights
- smaller wave run-down heights

## Acknowledgements

This study is a part of the basic research Project A1 on sea dikes initiated by Prof. Führböter within the Coastal Engineering Research Unit "SFB 205". The support by the "Deutsche Forschungsgemeinschaft" (DFG), Bonn, is gratefully acknowledged.



## 6. References

- BATTJES, J.A. (1974). Surf Similarity. Proc. 14th Coastal Eng. Conf.. Copenhagen
- EAK (1993). Empfehlungen Arbeitsausschuß Küsteningenieurwesen. Die Küste, No. 45
- FÜHRBÖTER, A., SPARBOOM, U. and WITTE, H.-H. (1989). Großer Wellenkanal Hannover: Versuchsergebnisse über den Wellenauflauf auf glatten und rauhen Deichböschungen mit der Neigung 1:6. Die Küste. No. 50.
- FÜHRBÖTER, A. and WITTE, H.-H. (1991). Die dynamische Verweilzeit und ihre Beziehungen zum Wellenauflauf und -ablauf an einer Deichböschung 1:n=1:6. Die Küste. No. 52.
- GOURLAY, M.R. (1992). Wave set-up, wave run-up and beach water table: Interaction between surf zone hydraulics and groundwater hydraulics. Coastal Engineering, No. 17.
- GRÜNE, J. (1982). Wave Run-up caused by Natural Storm Surge Waves. Proc. 18th Coastal Eng. Conf., Kapstadt
- GRÜNE, J. and BERGMANN, H. (1994). Wave loads on seadykes with composite slopes and berms. Proc. 24th Coastal Eng. Conf., Kobe
- HUNT, I.A. (1959). Design for Seawalls and Breakwaters. Proc. ASCE, Vol. 85, No. WW3
- MAYER, R.H. and KRIEBEL, D.L. (1994). Wave run-up on composite-slope and concave beaches. Proc. 24th International Conference on Coastal Engineering. Kobe, Japan
- SAVILLE, T. (1958). Wave run-up on composite slopes. Proc. 6th Conf. on Coastal Eng., Gainesville
- VAN DER MEER, J.W. and BRETELER, M.K. (1990). Measurements and computation of wave induced velocities on a smooth slope. Proc. 22nd Conf. on Coastal Eng.. Delft
- VAN DER MEER, J.W. and STAM, C.-J. M. (1992). Wave runup on smooth and rock slopes of Coastal Structures. Journal of Waterway, Port, Coastal and Ocean Engineering, Vol. 118, No. 5
- VAN DER MEER, J.W. and JANSSEN, J.P.F.M. (1994). Wave run-up and wave overtopping at dikes and revetments. Publications Delft Hydraulics. No. 485
- WASSING, F. (1957). Model investigations of wave run-up on dikes carried out in the Netherlands during the last twenty years. Proc. 6th ICCE. Gainesville, Florida
- YANAGISHIMA, S. and KATOH, K. (1990). Field observation on wave set-up near the shoreline. Proc. 22nd Conf. on Coastal Eng.. Delft

## CHAPTER 42

### Bottom Shear Stresses under Random Waves with a Current superimposed.

Richard R.Simons<sup>1</sup>  
Tony J.Grass<sup>2</sup>  
Wameidh M.Saleh<sup>3</sup>  
Mehrdad M.Tehrani<sup>3</sup>

#### Abstract

This paper describes experiments performed with the UCL shear plate device to make direct measurements of the bottom shear stress vector under the action of combined waves and currents. The three corresponding velocity components have also been recorded simultaneously, enabling the results to be expressed in terms of a friction factor. The scope of the work extends that of earlier tests on regular waves, and includes three sequences of random waves propagating above a fixed rough bed in still water and over two orthogonal currents.

The results show that, for the range of conditions considered, the addition of an orthogonal current has no discernable effect on the amplitude of the shear stress time series or on the friction factors used to characterize the complete sequence. If a single friction factor is used to describe the shear stress throughout a sequence of random waves, and if that factor is calculated from the RMS of the shear stress during the sequence scaled on an equivalent regular wave with a bottom orbital velocity amplitude of  $u_{rms}\sqrt{2}$ , then the results agree well with earlier observations from tests on regular waves, and  $f_w$  can be predicted from standard formulae.

---

<sup>1</sup>Senior Lecturer, Civil & Environmental Engineering Dept, UCL

<sup>2</sup>Professor, Civil & Environmental Engineering Dept, UCL.

<sup>3</sup>Research Fellow, Civil & Environmental Engineering Dept,  
University College London, Gower Street, London WC1E 6BT.

## Introduction

The prediction of shear stresses at the sea bed is an important requirement for coastal engineers wishing to estimate wave energy loss, current strength, and sediment transport around our coastline. These stresses are applied both by wave action and by currents, so any non-linear interaction between the two scales of motion in a combined wave-current flow makes the prediction of bottom shear stress a non-trivial task.

There are over thirty different theories that have been developed taking into account non-linear interaction when predicting bed shear stresses under combined wave-current conditions. Many of these have been reviewed by Soulsby et al. (1993) in a paper that also brought together existing data sets against which the behaviour of the theories could be tested. But whereas this paper concentrated on monochromatic wave conditions, other researchers have tried to address the problem of currents interacting with a **random** wave sequence. For instance, Lee (1987) proposed a linearization technique for bed shear stress in order to predict bottom frictional dissipation under irregular waves; and, in the light of a recent field study under random wave conditions, Black and Gorman (1994) suggested a modified form of the Christoffersen and Jonsson model. Zhao and Anastasiou (1993) have presented a more rigorous approach to the problem, deriving a theory based on the regular wave model of O'Connor and Yoo (1988) - itself built on the work of Bijker (1966). Equations were derived separately for wave-dominated and current-dominated conditions as well as for the general case, and comparisons were made with published data. Ockenden and Soulsby (1994) have considered the same problem but with the specific requirement of estimating sediment transport rates under irregular waves and currents. They put forward a simple solution based on an equivalent regular wave ( $u_b = \sqrt{2} \cdot u_{rms}$ ,  $T_p =$  peak spectral period), and accounted for non-linear effects by adopting a parameterised version of the desired wave-current model as presented in Soulsby et al. (1993). And, finally, Madsen (1994) has developed a modified version of the Grant and Madsen (1979) model to be applied when irregular waves propagate over a current.

While there is increasing attention being paid to the theoretical prediction of bed friction under irregular waves on a current, experimental results from tests under combined wave-current conditions in general relate to monochromatic waves only, and relatively little work has been done under the practical case of random waves on a turbulent current. One of the reasons for this is the difficulty of making direct measurements of bed friction generated by unsteady flows, and shear stresses have often had to be deduced from modified velocity profiles or energy principles. However, Simons et al. (1992) have reported direct measurements of bottom shear stress using a novel shear plate device deployed in a large wave basin when regular waves are propagated orthogonally across a turbulent current, and the present paper extends that work to include sequences of random long-crested waves propagating across the same currents.

### Wave Basin

The tests were performed in a wave basin measuring 20m by 18m, designed for a water depth of 1.5 m but with a raised central test area, 9 m by 6 m, over which the still water depth was reduced to 700 mm. This plateau area was coated with a fixed layer of sand (nominal diameter of 2 mm) to produce a uniform rough boundary with a Nikuradse roughness,  $k$ , of 1.5 mm - see Simons et al. (1992).

Ten ram-type wave generators were mounted along one wall of the basin. Each ram could be operated under independent control to produce waves with periods between 1 s and 3 s, and with heights up to 300 mm. The other three walls supported permeable beach units 2.5 m long round the perimeter of the basin. This beach system was constructed of synthetic "hairlock" sheets on a rigid frame, with a slope of  $15^\circ$  down to half-depth but with a vertical permeable face below that level. To avoid reflections of the relatively shallow water waves from this area, the  $15^\circ$  slope on the wall facing the wave generators was continued down with shingle "fill" to meet the raised bed in the centre of the basin.

Currents were introduced through a set of gate valves under the beaches in one of the side walls, flow being removed through a corresponding set of openings in the other side. The current strength was controlled by adjusting the speed of a pump which circulated water through a 2-compartment channel round the perimeter of the basin.

### Instrumentation

For successful completion of the work, it was important that direct observations could be made of the shear stresses exerted on the bed of the basin by both currents and waves. A shear plate device had been developed in a preceding project exactly for this purpose, employing a circular "active" element supported on 4 thin columns and operating in sway mode in response to the instantaneous force vector. The system was described by Simons et al. (1992), and the same instrument was used in the present tests.

To determine the velocity field in the three-dimensional flow created by intersecting waves and currents, measurements were made using an ultrasonic current meter (UCM) capable of yielding three velocity components simultaneously. The transmitters on this instrument "pinged" at 100Hz, giving a response time of 1/30s and a resolution of 1mm/s in a range up to 1 m/s. The UCM was used to record the flow field immediately above the wave boundary layer (to correlate with the shear plate measurements), and up to the water surface. However, its size (with a measuring volume 15 mm in diameter) meant that it was unable to provide detailed information within the relatively thin wave boundary layer.

**Table 1: Observed waves and current test conditions**

Run Code:	Tz (s.)	Hsig (cm)	U <sub>50m</sub> curr. cm/s	U <sub>rms</sub> wave cm/s	$\tau_m$ curr. N/m <sup>2</sup>	$\tau_{rms}$ wave N/m <sup>2</sup>	a/k	f <sub>w</sub>
CU2			11.3	1.7	0.04	0.01		
CU1			20.1	2.7	0.08	0.02		
WR1P	1.28	14.5	-0.4	7.2	0.00	0.30	13.8	0.058
WR1CC	1.28	14.4	10.5	7.4	0.03	0.32	14.2	0.058
WR1C	1.29	14.5	19.5	7.8	0.08	0.35	15.1	0.058
WR2P	1.49	14.2	0.7	8.9	0.00	0.36	19.9	0.045
WR2CC	1.48	14.4	10.8	9.2	0.03	0.36	20.4	0.043
WR2C	1.50	14.7	19.7	9.6	0.08	0.38	21.6	0.041
WR3P	1.29	17.2	-0.8	8.9	0.00	0.37	17.2	0.047
WR3CC	1.29	17.2	10.6	9.3	0.04	0.37	18.0	0.043
WR3C	1.31	17.5	18.9	9.5	0.09	0.42	18.7	0.047

The water surface elevation was monitored over a 2m by 2m area centred above the shear plate using a square array of 16 resistance-type wave monitors. Data were sampled at approximately 100Hz on 22 channels for test runs lasting approximately 6 minutes.

### Test Conditions

Three different "random" wave sequences were used (coded WR1, WR2 and WR3), all generated from a Jonswap target spectrum with peak periods of 1.3s and 1.5s - **fig.1**. Spectra observed at the four wave probes immediately surrounding the shear plate (**fig.2**) show that there were significant reflections in the basin at discrete frequencies, but these did not hinder the main objective of the research which was to correlate observed bottom shear stresses to the velocities immediately above the bed.

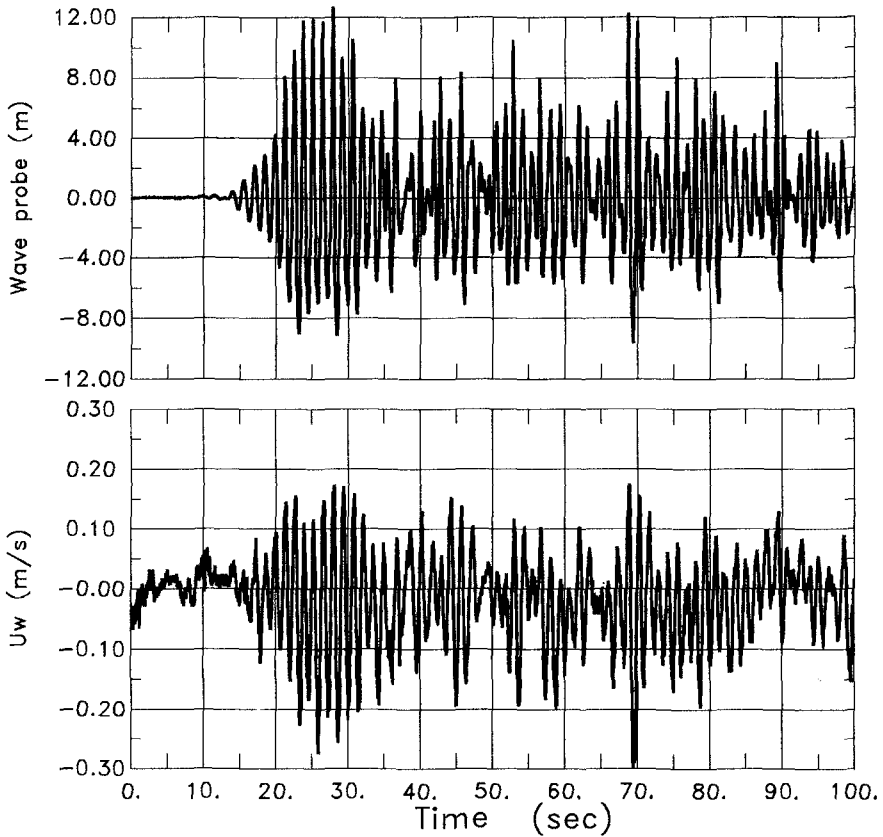


*Figure 1* Sample of random wave sequence WRI with strong current added.

Each wave spectral sequence was tested under three flow conditions: firstly through initially still water, secondly over a current with a mean velocity of 0.1 m/s, and finally over a current with a mean velocity of 0.2 m/s. The two currents were also tested without waves. Test conditions are listed in **Table 1**.

The wave sequences were reproducible, so that each test could be repeated with the UCM positioned at different heights above the bed. In this way velocity data were obtained at 18 positions through the flow depth for each test condition, while at the same time recording bottom stresses and wave surface elevations as a check on repeatability. The wave signal generator was not directly synchronised with the data recording system, so comparison between time-series from different tests required a small manual time-shift.

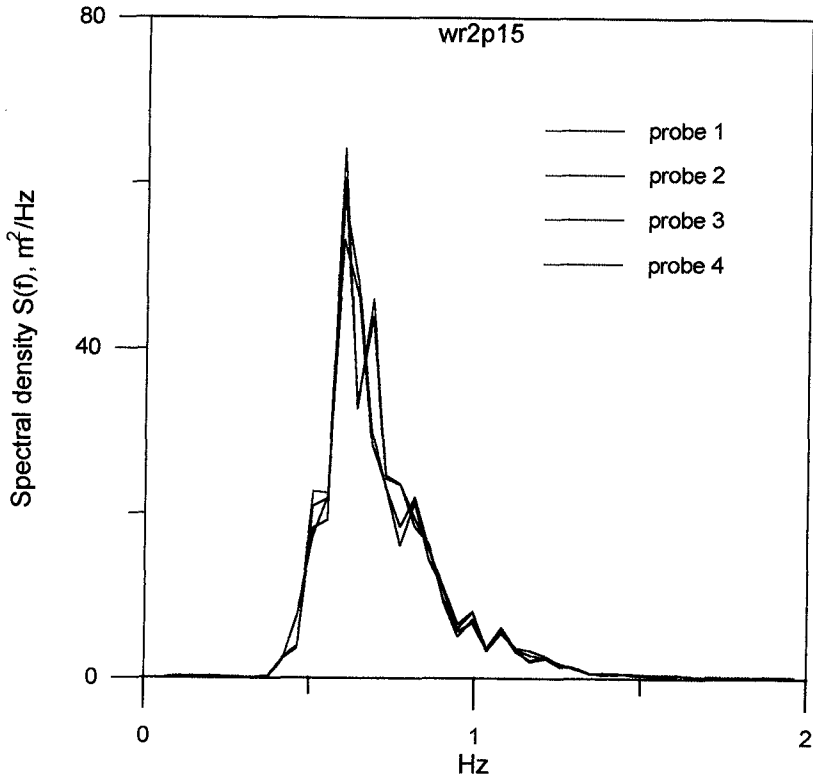


**Figure 2** Spectra measured at 4 wave probes close to the shear plate.

The repeatability of the wave sequences was confirmed by the ease with which it was possible to overlay the time-series from tests with waves alone and those with orthogonal currents superimposed - as in **fig.3**.

#### Analysis

Because of the characteristics of the shear plate, it was necessary in the initial analysis of observed "shear stresses" to correct for the wave-induced pressure on the edge of the active plate. Under regular wave conditions it is possible (assuming an appropriate wave theory) to infer the pressure field across the bed of the basin from the fluid acceleration at a single point just outside the wave boundary layer above the centre of the plate. This procedure becomes more questionable under

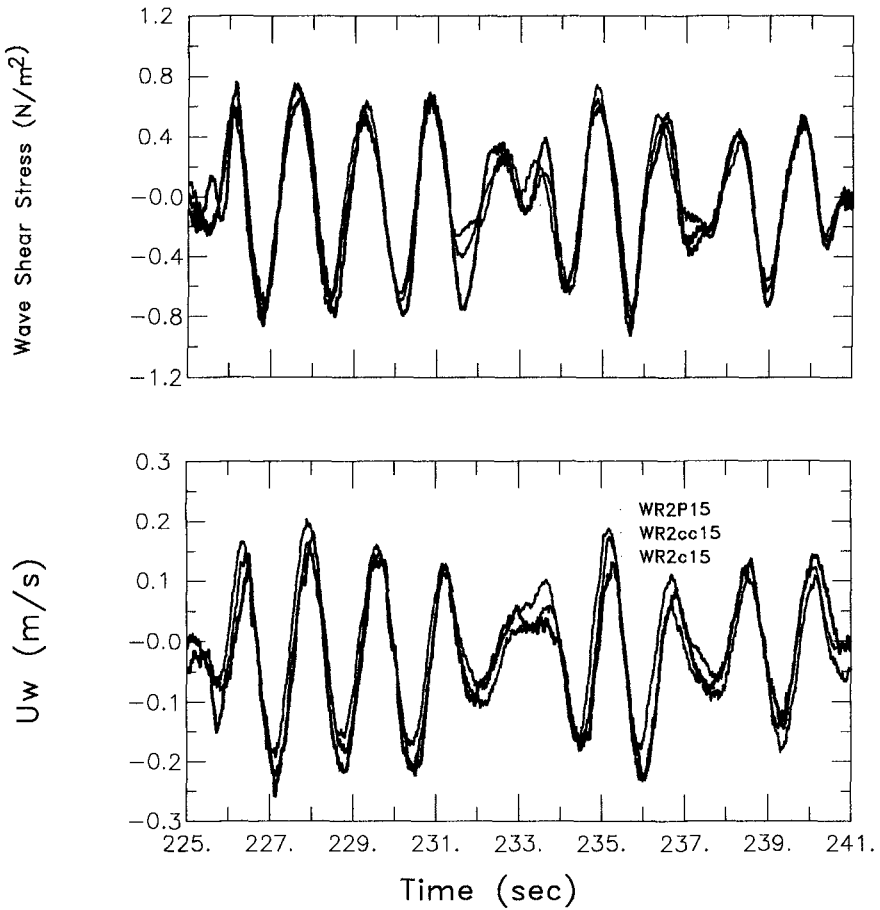


**Figure 3** Wave-induced velocities and shear stresses for random waves:  
*a) in still water, b) with weak current, c) with stronger current.*

irregular wave conditions, and in the present tests the calculation was simplified by taking the pressure gradient to be constant across the whole plate area.

It was also possible to apply a further correction to account for the pressure/inertia force being applied to the sand grain roughness attached to the plate. Although this force is a real effect, acting to generate sediment transport and dissipate wave energy, its consequences are far greater in laboratory scale experiments (with the ratio of wave length to grain diameter approximately  $10^3$ ) than in the field (ratio



greater than  $10^5$ ), and might distort the interpretation of bottom forces. However, it was largely this force component that gave the "shear stress" a significant phase lead over the near-bed velocity.

Analysis of the random wave tests was performed both wave-by-wave, comparing maximum and minimum shear stresses and velocities during each wave crest and wave trough, and also in terms of the RMS of these quantities for the complete wave sequence (neglecting the first 20s start-up period), measured under the three different current conditions.

## Results

**Table 1** summarises results from the 11 test runs considered in the present paper, recording the changes in wave characteristics induced by the addition of currents, and vice versa. The effect of adding random waves to the mean flow was less significant than in the earlier tests using regular waves, but from the mean velocity profiles (**fig.4**) it was still possible to discern a reduction in velocity in the outer flow, with a corresponding increase closer to the bed. Experimental procedures meant that measurements at different heights above the bed for the same current flow were carried out on different days, so the scatter in mean velocity data can probably be attributed to the difficulty in resetting the current. The scale of the alteration in mean velocity profile can be judged from the negligible change in mean bed shear stress in the current direction sensed by the shear plate when the waves were superimposed.

The friction factor  $f_w$  and  $a/k$  ratio were both calculated from the root mean square properties of the full random wave sequences. The equivalent regular wave used in the normalisation procedure was chosen to have the period of the spectral peak  $T_p$  and an amplitude yielding the same RMS variation as that recorded in the random wave sequences:

$$f_w = \frac{\tau_{rms}}{\frac{1}{2}\rho(u_{rms}\sqrt{2})^2} ; \quad \frac{a}{k} = \frac{u_{rms}\sqrt{2} \cdot T_p}{2\pi k}$$

**Fig.5** shows these values of friction factor in comparison with previous data and theories for predicting wave-induced friction. The agreement is very good, and suggests that the use of  $u_{rms}\sqrt{2}$  as the scaling velocity is an appropriate choice. It is also apparent that the data from all 9 tests lie very closely clustered and thus the addition of the two currents has made no significant difference to the wave-induced shear stress. Such a lack of enhancement is in agreement with the earlier results using regular waves (Simons et al. 1992) and with the work of Arnskov et al. (1993).

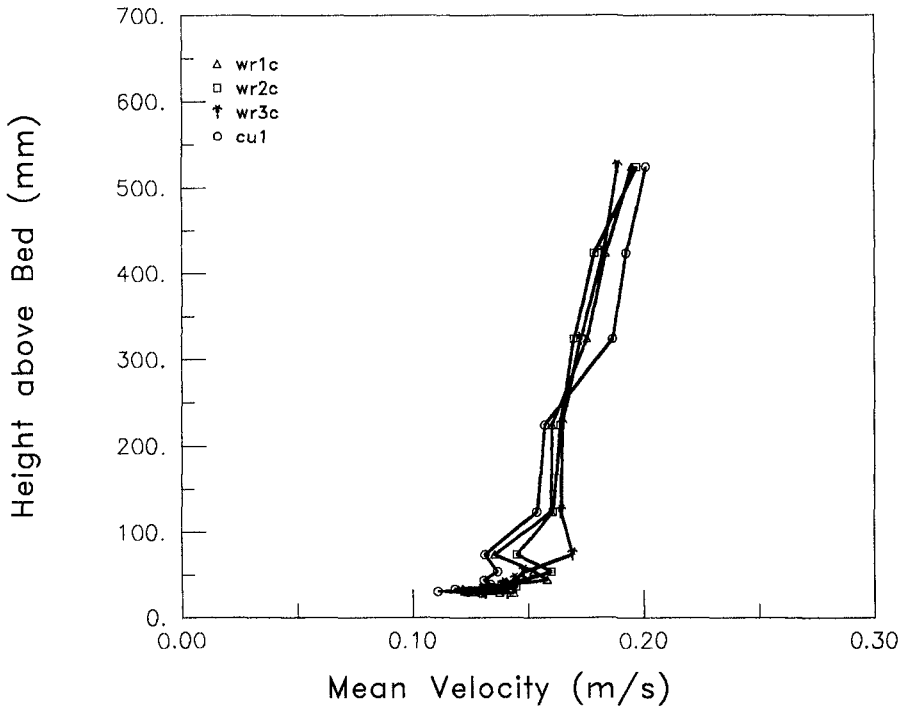


**Figure 4** Mean velocity profiles for current alone and with random waves added.

While it is sometimes helpful to be able to characterise a random sea in terms of regular wave parameters, it is more important in assessing sediment transport to be able to predict particular "events" when the wave-induced shear stress exceeds that needed to initiate movement of the seabed material. To give an insight into the wave-by-wave behaviour of random waves, each of the present sequences of velocities and shear stresses was considered as independent half-cycles (between velocity zero-crossings). Friction factors were calculated from the half-cycle amplitude of shear stress (between consecutive maxima and minima) and the corresponding amplitude of wave-induced velocity, and a typical data sample is shown in **fig.6**. This method avoided the anomalous results caused by long waves if absolute maximum and minimum values were used in the calculations, when significant shear stresses could apparently be induced by infinitesimally small velocity fluctuations. It was also decided to ignore all values for waves with an amplitude less than 1.5 mm, as this was not felt to be within the measuring accuracy of the UCM.

**Fig.7** shows the friction factors produced from one of the random wave sequences,

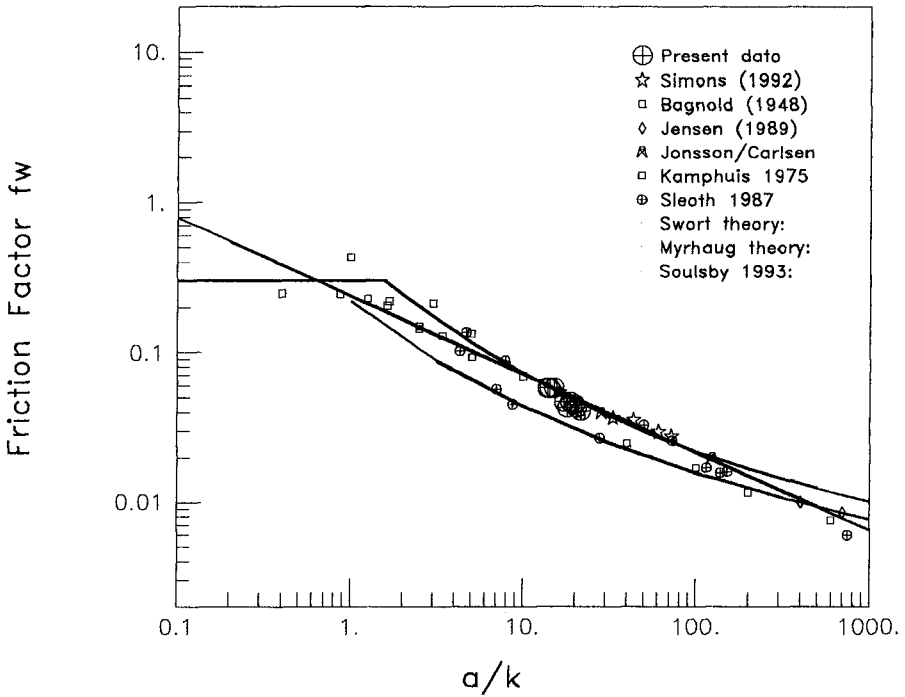


**Figure 5** Variation of friction factor with relative bed excursion for random waves with/without current superimposed: (uses equivalent wave velocity  $u_{rms}\sqrt{2}$ )

firstly propagating through still water, then with the weaker current superimposed, and finally with the stronger current flowing. The first thing to note is that for low  $a/k$ , the friction factors are greater than predicted by theories for fully rough turbulent flow, but that as  $a/k$  increases, so the friction factor falls back in line with those formulae - Soulsby et al. (1993) for instance. While the underprediction of  $f_w$  at low  $a/k$  is at first sight worrying, it can almost certainly be attributed to the relatively low oscillatory Reynolds numbers  $[ua/\nu]$  associated with these waves, when viscous effects are to be expected. In fact, the trend line formed by the scattered data lies parallel to (and almost exactly a factor of 2 above) the prediction for completely laminar flow over a smooth bed when the friction factor is given as:

$$f_w = \frac{2}{\sqrt{(Re)}} = \frac{2}{\sqrt{(ua/\nu)}}$$

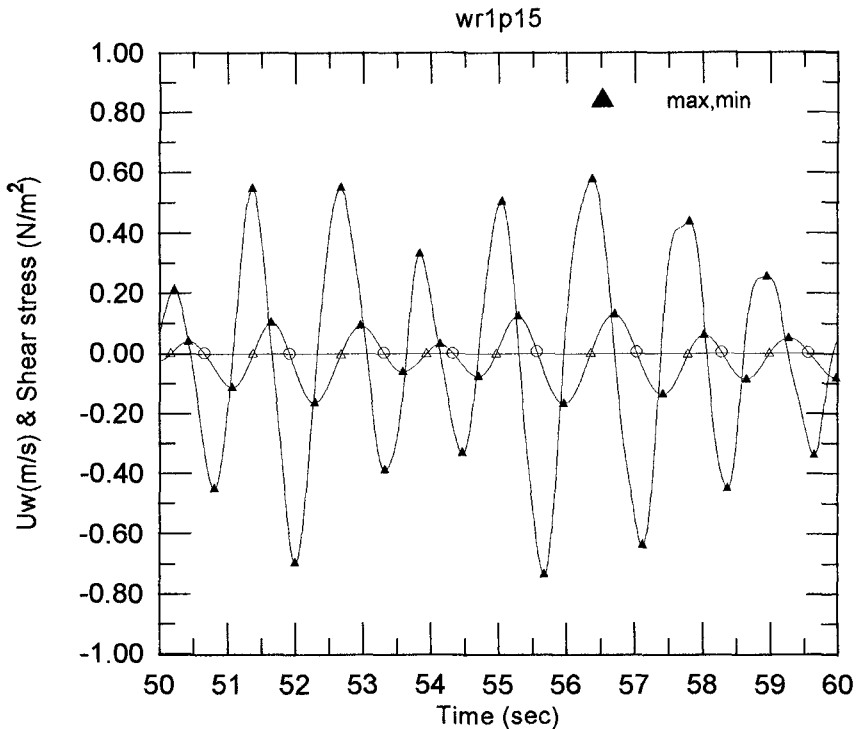


**Figure 6** Sample of shear stress and velocity data used to identify friction factors.

Much of the data lies in the rough transitional flow regime, and these values are not out of line with the observations of Kamphuis (1975) for similar conditions.

The main aim of the project was to identify what effect the addition of an orthogonal current would have on the bottom friction, and it is clear from fig.7 that all three sets of data have very similar distributions, implying that the current has caused no obvious change. The same lack of sensitivity to the addition of an orthogonal current was also found for the other two random wave sequences, and confirms the results discussed above for the friction factors based on an equivalent regular wave representative of the complete test run, namely, that the current has little effect.

Although these results indicate that the presence of longshore currents can be ignored when considering wave energy dissipation in the onshore direction, it

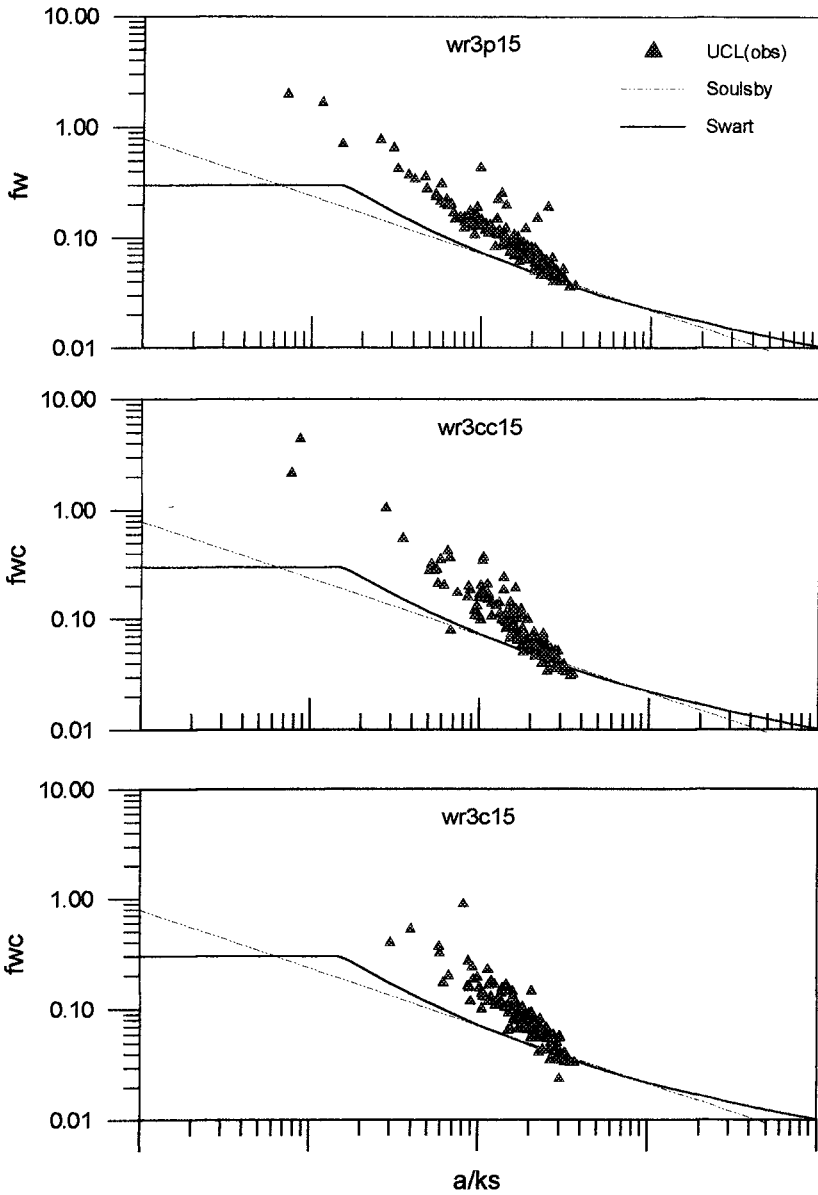


**Figure 7** Friction factors for each half-cycle during random wave sequences: a) in still water, b) with weak current, c) with stronger current added.

should be noted that Lodahl et al. (1994) have recently reported results from tests over a smooth boundary. These suggest no increase in oscillatory shear stress when weak currents are added, but that friction factors do increase with the addition of currents at Reynolds numbers very much greater than those reported here. It is not unreasonable to expect that the interaction between a fully turbulent wave boundary layer and a turbulent steady current boundary layer is likely to be qualitatively different from the corresponding interaction at the low Reynolds numbers prevailing in the present tests.

### Summary

Tests have been performed with 3 different sequences of Jonswap spectrum random waves, and direct measurements have been made of the bottom shear stresses with the UCL shear plate.

Friction factors have been calculated to represent the complete test sequence, using the RMS of the shear stress. When scaled on an equivalent regular wave with bed orbital velocity  $u = u_{rms} \sqrt{2}$  and period  $= T_p$ , the results correspond to standard predictions for fully rough turbulent wave-induced motion.

Friction factors have also been calculated for each half-cycle during the tests. These reflect the transitional regime in which the data lie, at low  $a/k$  indicating higher values than predicted for fully rough turbulent oscillatory flow, but giving good agreement at higher  $a/k$ , where the flow approaches the fully turbulent regime.

For the three random wave spectra tested, the addition of a current was found to have little effect either on the wave-induced velocities near the bed or on the oscillatory shear stresses and friction factors.

### Acknowledgements

This work was undertaken as part of the G8 Coastal Morphodynamics research programme. It was funded jointly by the Science and Engineering Research Council, and by the Commission of the European Communities Directorate General for Science, Research and Development under contract no. MAS2-CT-92-0027. The authors also acknowledge their gratitude to H.R. Wallingford for the use of their facilities.

### References

Arnskov, M.M., Fredsoe, J. and Sumer, B.M. (1993) Bed shear stress measurements over a smooth bed in three-dimensional wave-current motion. Coastal Engineering, 20, pp.277-316.

Bijker, E.W. (1966) The increase of bed shear in a current due to wave motion. Proc. 10th Int. Conf. on Coastal Engng., Vol.1, pp.746-765.

Black, K.P. and Gorman, R.M. (1994) Observation of wave dynamics influenced by wave-current enhanced bed friction on an exposed coast. Victorian Institute of Marine Sciences, St Andrews Place, Melbourne, Australia.

Grant, W.D. and Madsen, O.S. (1979) Combined wave and current interaction with a rough bottom. J.Geophys. Res., 84 (C4), pp.1797-1808.

Kamphuis, J.W. 1975 Friction factors under oscillatory waves. J. Waterway Harbours Coastal Engng. Div., ASCE, 101, pp.135-144.

Lee, D-Y. (1987 ) Bottom frictional dissipation if irregular waves. Ocean Engng. 9, (1,2), pp.39-44.

Lodahl, C., Sumer, B.M. and Fredsoe J. 1994 Experiments on co-directional waves and currents at large Reynolds numbers. Proc. 24th Int. Conf. on Coastal Engng., Kobe, Japan, Oct.1994. ASCE, paper 82.

Madsen, O.S. (1994) Spectral wave-current bottom boundary layer flow. Proc. 24th Int. Conf. on Coastal Engng., Kobe, Japan, Oct.1994. ASCE, paper 83.

O'Connor, B.A. and Yoo, D. (1988) Mean bed friction calculation of combined wave-current flow. Coastal Engineering, 12, pp. 1-21.

Ockenden, M.C. and Soulsby, R.L. 1994 Sediment transport by currents plus irregular waves. HR Wallingford Report SR 376, February 1994.

Simons, R.R., Grass, A.J. and Mansour-Tehrani, M. (1992) Bottom shear stresses in the boundary layer under waves and currents at right angles. Proc. 23rd Int. Conf. on Coastal Engng. Venice, Italy, Ch.45, pp.604-617

Soulsby, R.L., Hamm, L., Klopman, G., Myrhaug, D., Simons, R.R., and Thomas, G.P. (1993) Wave-Current Interaction within and outside the bottom boundary layer. Coastal Engineering, 21, pp.41-69.

Zhao, Y and Anastasiou, K. (1993) Bottom friction effects in the combined flow field of random waves and currents. Coastal Engineering, 19, pp.223-243.

## CHAPTER 43

### EFFECTS FROM DIRECTIONALITY AND SPECTRAL BANDWIDTH ON NON-LINEAR SPATIAL MODULATIONS OF DEEP-WATER SURFACE GRAVITY WAVE TRAINS

Carl Trygve Stansberg <sup>1</sup>

#### Abstract

The non-linear nature of the largest waves in random wave trains is studied. Experimental wave elevation records from measurements in a large wave basin are analysed. Longcrested as well as shortcrested wave conditions, with various spectral shapes, are included. The spatial development of spectral and statistical properties of the wave trains are analysed. The results indicate that closer than 10-15 wavelengths, observed deviations from linear theory may be explained by 2nd order effects. Further away, higher-order modulational instabilities may lead to a stronger increase of extreme waves. This is especially observed in narrow-banded long-crested waves, while observations in short-crested sea show very little content of these space-dependent modulational effects.

#### 1. Introduction.

Extreme waves observed in random wave trains on deep water have in many cases exceeded predicted levels based on linear wave theory and Rayleigh statistics. Examples on this may be found in laboratory experiments (Stansberg 1991, 1992) as well as in full scale records (Sand et. al. 1990, Kjeldsen 1990, Jonathan et. al. 1994, and others). Second-order random wave theory (Longuet-Higgins 1963) explains a significant part of the deviations from linear theory (Marthinsen and Winterstein 1991, Stansberg 1993, 1994, Vinje and Haver 1994). Some of the observed effects, however, need other explanations. Such results have been published in e.g. Stansberg (1992), where experiments with long-crested waves in a large wave basin were reported. Those experiments seemed to indicate that laboratory generated random wave trains travelling more than 10 - 15 wavelengths

---

<sup>1</sup> Senior Principal Research Engineer, Norwegian Marine Technology Research Institute (MARINTEK), P.O.Box 4125 Valentinlyst, N-7002 Trondheim, Norway.



from the wavemaker are modulated due to higher-order non-linear wave-wave couplings. These may then lead to extreme waves clearly higher than estimates from linear as well as from second-order theory. A possible connection between these observations and the well-known "Benjamin-Feir-modulations" in regular waves (Benjamin and Feir 1967, Lake et. al. 1977, Lo and Mei 1985, and others) was discussed on basis of the experiments. Numerical simulations on related problems have shown a similar connection (Wang et. al. 1992, Yasuda et. al. 1992, Yasuda and Mori 1994).

The significance of such higher-order modulational instabilities in random waves is, however, still not quite clear. Although their existence have been more or less documented, it is a question how stable they are in time and space, and how they depend on various parameters such as the spectral shape and the wave directionality. Previous works (see e.g. the experiments by Su et. al. 1982) have indicated, however, that there is a connection between non-linear modulations and wave directionality, and the simulations by Yasuda and Mori (1994) show some dependence on spectral bandwidth. On this background, new systematic and controlled experiments have been carried out with random waves in MARINTEKs Ocean Basin. Long-crested (unidirectional) as well as short-crested (directional) waves were run, with various spectral bandwidths. The present paper describes a preliminary, empirical analysis study based on the measurements. Thus some main results are shown and interpreted in light of the relationships discussed above. The presentation starts with some simple, but illustrating examples in bichromatic waves, and this is then followed by the main part dealing with random waves.

## **2. Tests with bi-chromatic waves**

### 2.1. Test facility with set-up.

The tests were carried out in MARINTEKs 50mx80m Ocean Basin, which is equipped with a longcrested wavemaker along one full short side, and with a multiflap directional wavemaker along 63m of one long side. Rigid sloped beaches are installed at the opposite sides of the basin. The depth of the adjustable bottom was set to 4m, which corresponds to deep water for the actual waves considered. Wave elevation was measured with wave staffs at a number of locations at different distances from the wavemakers. In the present study, records taken at 10m meters intervals in the actual wave directions are reported.

### 2.2. Directional effects in bichromatic waves.

As shown in previous experiments (e.g. Stansberg 1992), non-linear wave modulations are rather rapidly developing in long-crested bichromatic wave trains with the 2 frequencies quite close to each other. These modulations, also identified through spatially developing side-bands in the frequency domain, give rise to asymmetry in the wave groups. This develops into groups with extreme individual

waves that may become significantly higher than in the initial wave trains. In the new experiments, similar tests were run with longcrested as well as with shortcrested (bi-directional) waves. Examples from the results are shown in fig. 1, including time series samples taken at 3 different distances from the wavemakers. As seen from this, the strong modulations in the longcrested case (which confirms the previous results referred to above) almost disappear completely in the shortcrested case. This is a strong support of the idea that the directionality is an important parameter in the study of non-linear wave modulations.

As a check on the influence from the basin geometry, additional long-crested wave tests were run from the multiflap wavemaker, as well as from the longcrested wavemaker. The characteristic nature of the modulations in fig. 1a was observed in both cases.

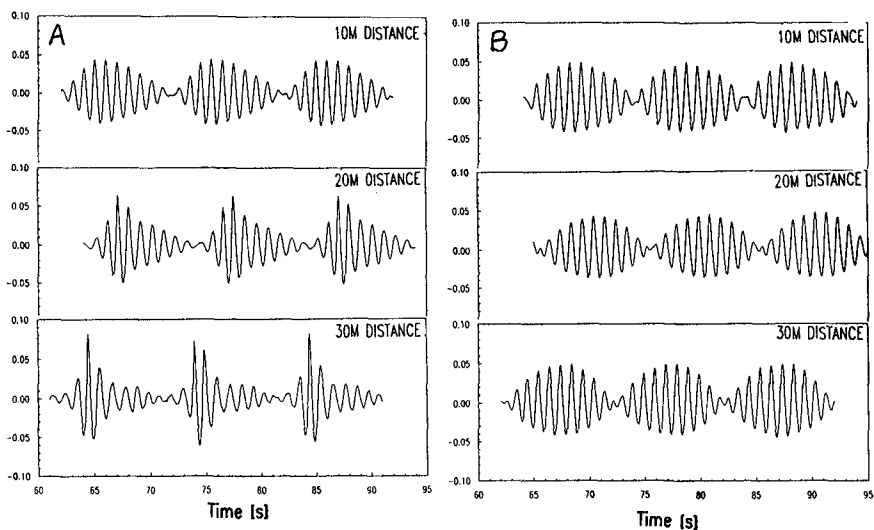


*Fig. 1. Wave elevation from bichromatic test records.  
A = long-crested. B = short-crested (bi-directional).*

### 3. Tests with random waves.

All wave records presented below are from measurements in the MARINTEK Ocean Basin. For a brief description of the facility and the set-up, see section 2.1 above.

### 3.1. An example.

The random wave elevation sample records in fig. 2a illustrate how a long-crested wave group develops throughout space, finally resulting in a very large wave event. Similarly, fig. 2b shows how a group propagates in a directional sea. A basic difference is observed between the 2 cases: The long-crested group continues over a long distance, while the short-crested one exists only over a limited area. It seems reasonable to state that the spatial development of non-linear modulations in such wave groups must be different in the 2 cases. Intuitively, one would expect stronger modulational effects in the longcrested case, where these non-linear effects may grow over many wavelengths, than in the shortcrested case, where the wave groups disappear more quickly. (This can be seen in relation to a comment in Taylor and Haagsma (1994), where a simple argument indicates that these wave-wave interactions are less significant in spread sea than in unidirectional sea). Thus the study of non-linear extreme waves is closely connected to the study of non-linear wave group evolution, as indicated in Wang et. al. (1994).

### 3.2. Brief description of the tests and procedures.

A systematic test program with a large number of different longcrested and shortcrested wave conditions was run. Shortcrested waves were run from the multiflap wavemaker, while longcrested waves were basically run from the other, longcrested wavemaker. Since they generate waves in different directions in thebasin, some longcrested waves were also run from the multiflap wavemaker, as a check on possible noise effects from the basin geometry etc. Here we report mainly on tests with initial spectral peak periods  $T_p$  at 1.0 seconds, which corresponds to relatively short waves in this large basin. This is chosen in order to let the waves propagate a large number of wavelengths across the measuring area, for the study of spatially developing non-linear modulations.

The wave elevation was simultaneously recorded at a number of locations in the basin, as described in 2.1 above. Each random wave record includes about 1500 zero-crossing waves, in non-repeating wave trains. This is considered sufficient for the study of non-linear wave statistics. The following presentation focuses on the spatial development of spectral, grouping and statistical properties of the wave records. The dependence on the travelled distance (in number of wavelengths), directionality, spectral bandwidth and wave steepness is emphasized. Wave groups are analysed by the Hilbert envelope technique, where the square wave envelope represents the continous "group signal" (Stansberg 1983).

### 3.3. Presentation of results.

Figs. 3 & 4 show examples on the spatial development of the elevation power spectra. 3 different long-crested wave conditions are presented in fig. 3, while 2 short-crested conditions are presented in fig. 4. The short-crested conditions are

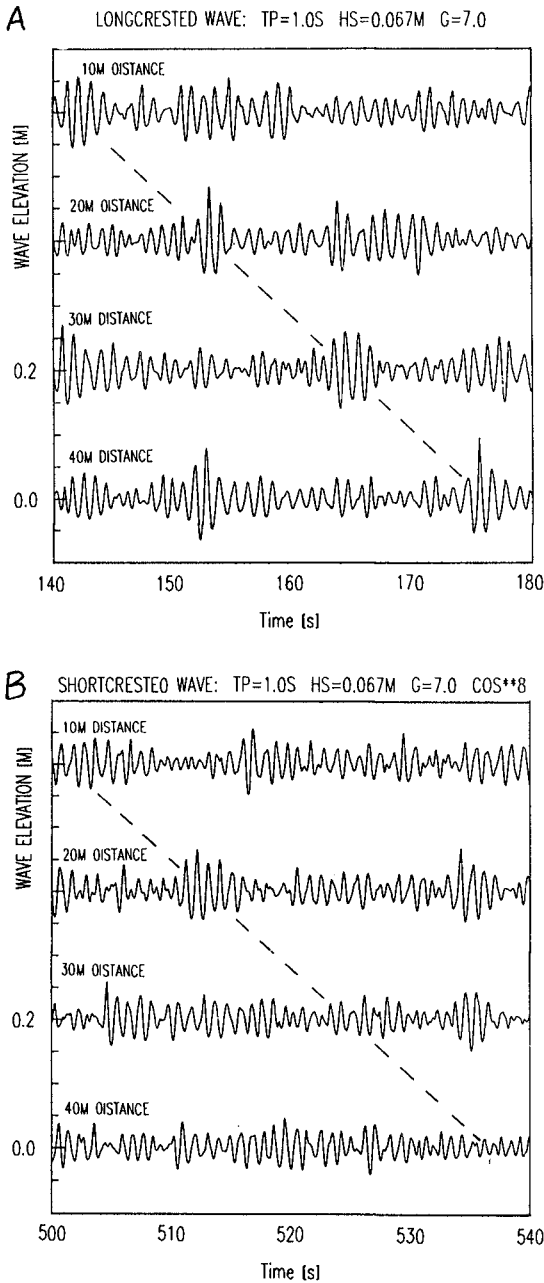


Fig. 2. Sample records illustrating wave group development.

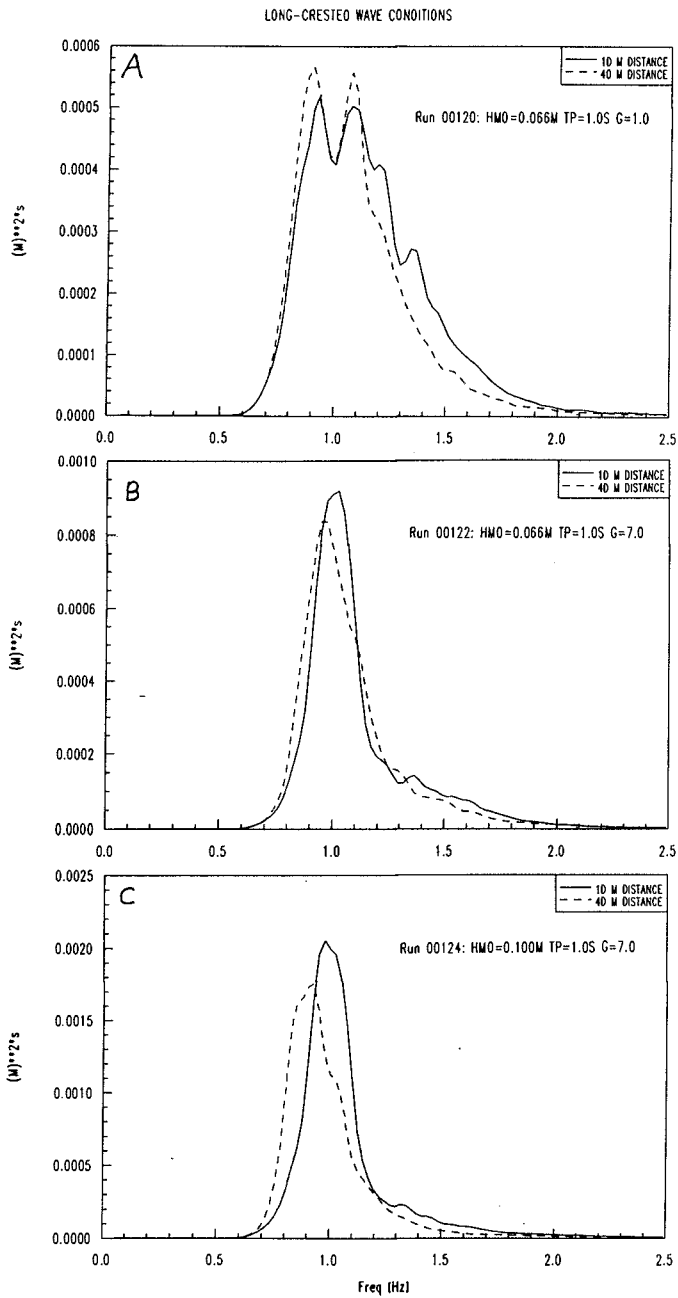


Fig. 3. Power spectra, 3 longcrested wave conditions, each at 2 locations (10 m and 40 m).

comparable, in scalar spectral parameters, to the 2 narrow-banded long-crested spectra. Each plot includes spectra measured both at 6 and 25 wavelengths distances (corresponding to 10 and 40 meters).

With location 10 m, nearest to the wavemaker, defined as the reference signal, amplitude amplification factors at location (40 m) are calculated for the same 5 sea states as in figs. 3 & 4. The results are presented in fig. 5, with 1 plot for longcrested, and 1 plot for short-crested waves. This factor is simply estimated as the square root of the ration between the corresponding spectra.

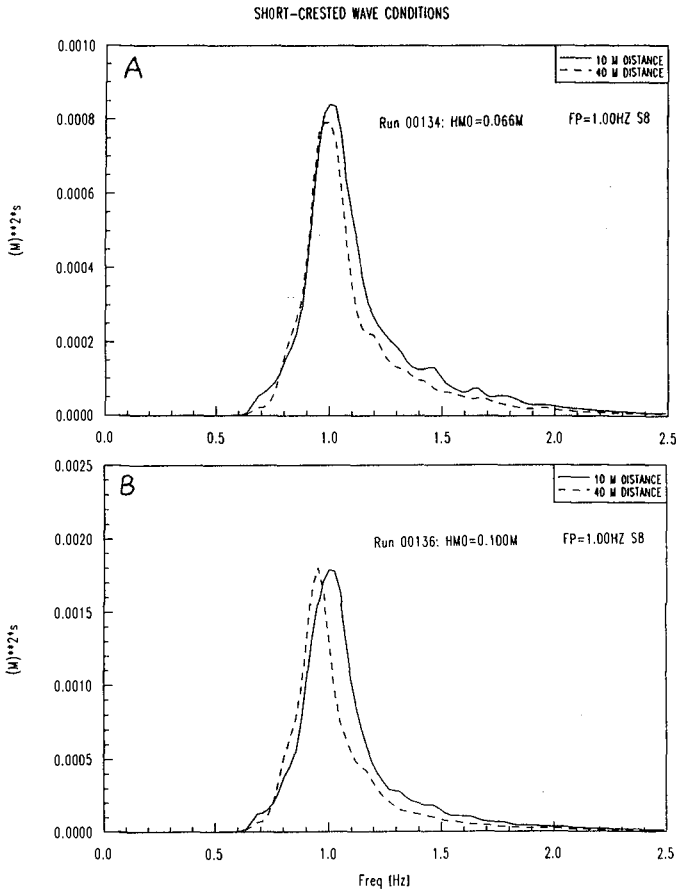


Fig. 4. As fig. 3, but for 2 shortcrested conditions. ( $\cos^8$  - distributions).

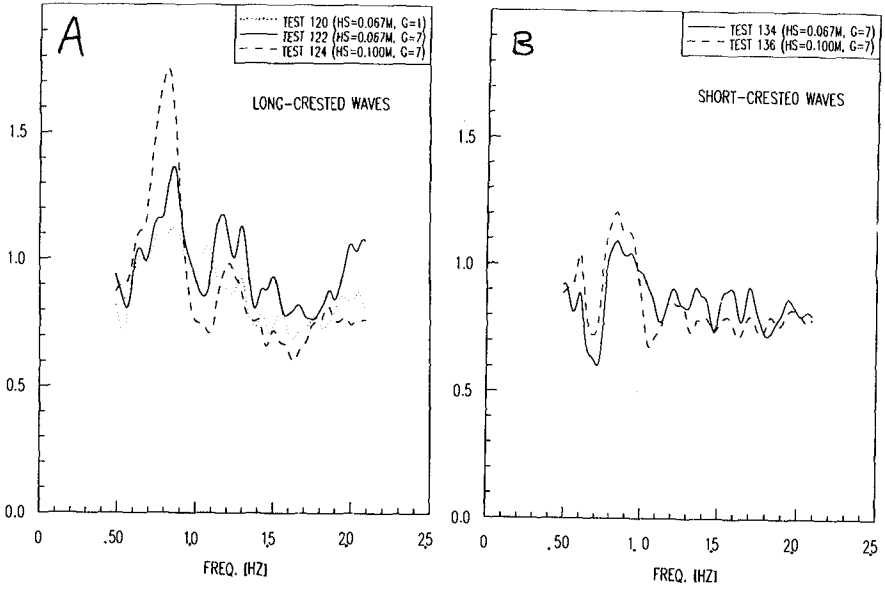


Fig. 5. Amplitude amplification from 10 m to 40 m distance.

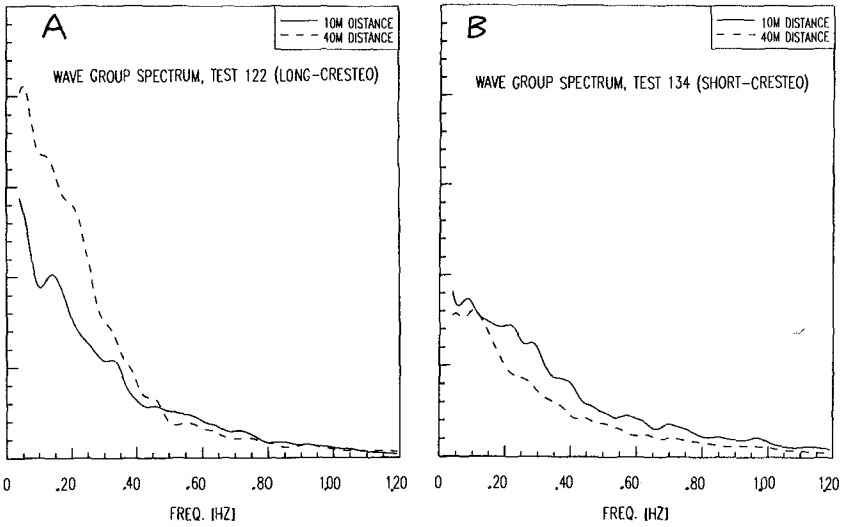


Fig. 6. Wave group spectra, for conditions in figs. 3B (long-crested) and 4A (short-crested).

The most pronounced modulations and non-Gaussian statistics are observed in the narrow-banded long-crested test case 122 (figure 3 B). For this case, wave group spectra and crest and waveheight distributions are presented in figs. 6A and 7, respectively. For comparison, the same type of results for the corresponding short-crested case are plotted in figs. 6B and 8.

For a concentrated illustration of the basic non-linear statistical properties of the recorded data, and their relations to other relevant parameters, the statistical skewness and kurtosis of some of the records are shown in fig. 9. The skewness is based on 3rd order statistical moment of the time series, and is calculated as:

$$\gamma_1 = \frac{1}{N\sigma^3} \sum_{i=1}^N (x_i - \bar{x})^3 \quad (1)$$

where

- $x_i$  = sample value of time history
- $\bar{x}$  = mean value of  $x_i$
- $\sigma$  = standard deviation of  $x_i$
- $N$  = number of time history samples.

The kurtosis is based on the 4th order statistical moment, and is calculated as:

$$\gamma_2 = \frac{1}{N\sigma^4} \sum_{i=1}^N (x_i - \bar{x})^4 - 3 \quad (2)$$

(with this definition also called "the excess of kurtosis")

Both these parameters are expected to be zero for Gaussian records (linear waves), but they are always subject to some statistical scatter. With the long records available here, the scatter is believed not to be a problem. The skewness is an indicator of 2nd order contents in the wave signal (Vinje and Haver 1994), while the kurtosis indicates the presence of 3rd and higher order contents. Thus the skewness gives information on crest heights, while the kurtosis indicates possible non-linear wave height statistics. The skewness values are plotted for all records of the total experiment, as a function of the typical steepness of the record. ( $S = H_s / L_p$ , with  $L_p = (g / 2 \pi) \cdot T_p^2$ ,  $T_p$  = spectral peak period). The kurtosis values, however, are here plotted only for one set of  $H_s$  and  $T_p$  ( $H_s=0.067\text{m}$ ,  $T_p=1.0\text{s}$ ), as a function of the normalized travelled distance  $D_r$  (number of propagated wavelengths). ( $D_r = D / L_p$ ). This is done in order to highlight observed relationships.



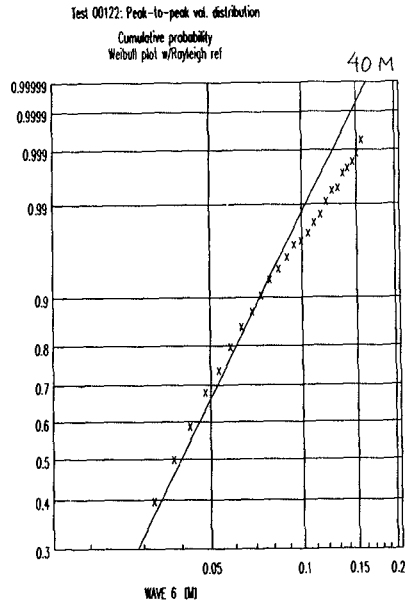
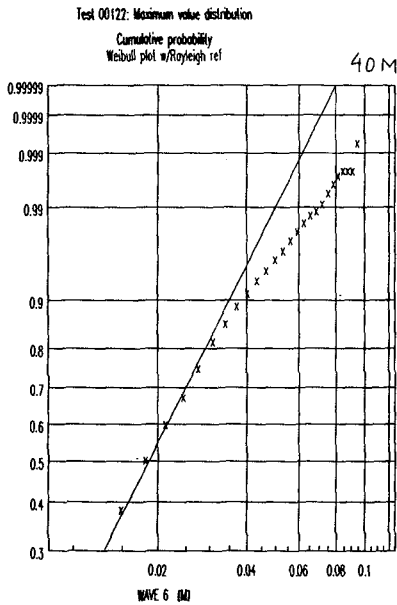
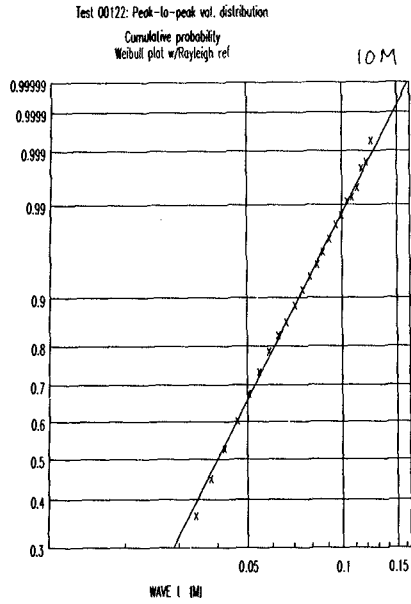
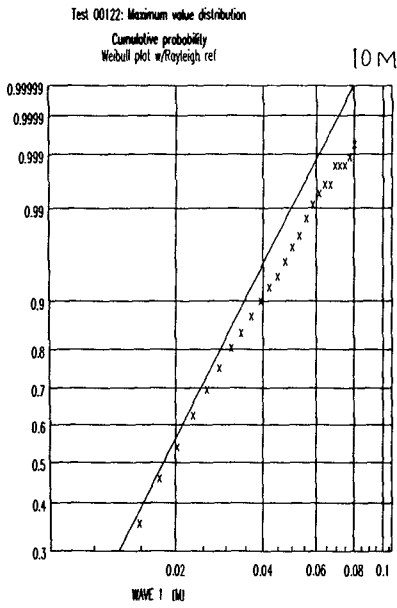


Fig. 7. Crest and wave height distributions, same conditions as in fig. 6A (long-crested).

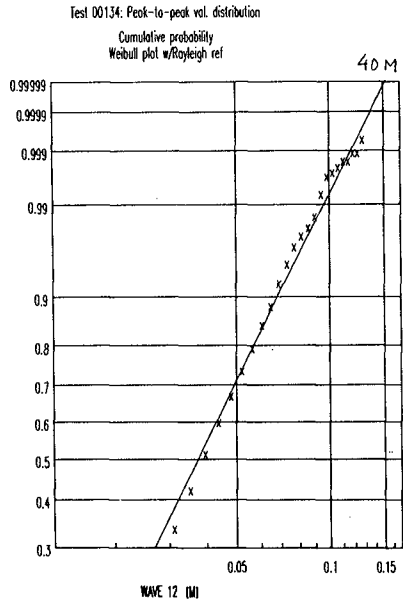
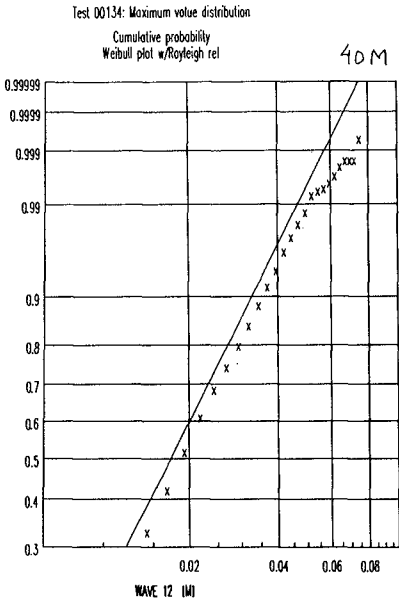
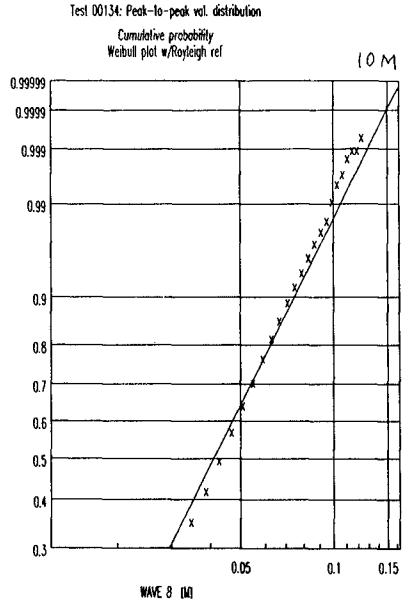
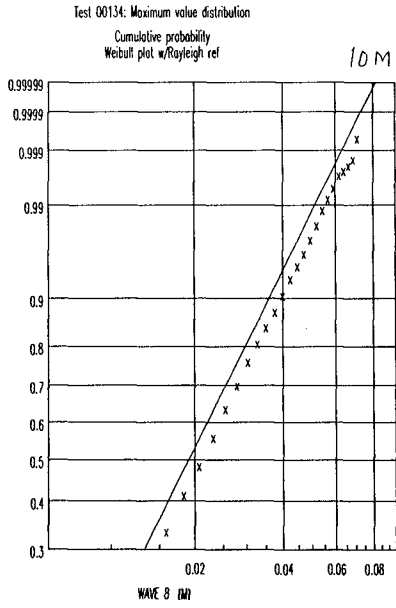


Fig. 8. As fig. 7, but same conditions as in fig. 6B (short-crested).

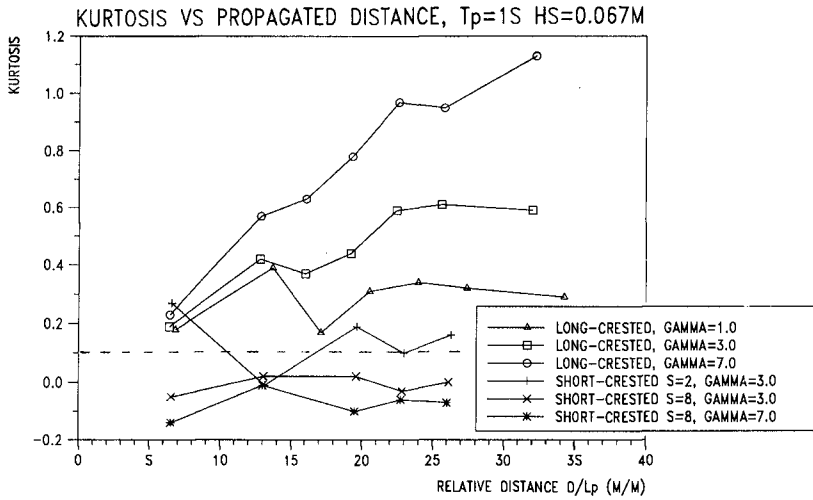
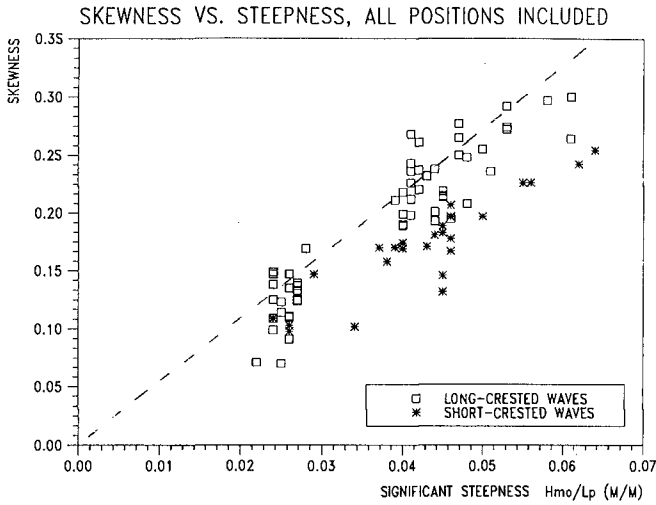


Fig. 9. Skewness vs. steepness, and excess of kurtosis vs. normalized travelling distance. Dotted line: estimated from 2nd order theory (Vinje & Haver 1994).

#### 4. Discussion of results.

The power spectrum plots in figs. 3 & 4 show some changes in the spectra with increasing travelling distance. This is especially seen when the wave steepness is very high. In general, the energy in the high-frequency part of the spectrum is somewhat reduced due to dissipation. (At very high frequencies, however, the energy content seems to be more stable, probably due to bound harmonics). Energy shift is also observed from the peak frequency region to the surrounding upper and lower frequencies, particularly in longcrested waves. This is especially pronounced in the very steep sea condition in which case a net transfer to lower frequencies is also taking place together with some loss of energy (to some extent connected with dissipation due to breaking).

The energy transfer is further illustrated by the amplification plots in fig. 5. Of particular interest here is the apparent growth of side bands around the initial peak frequency, mainly observed in narrow-banded longcrested waves. This observation indicates a similarity with the side bands due to non-linear modulational effects in monochromatic and bichromatic waves discussed earlier. Therefore it fits well together with the observed increase in the far-distance wave group spectrum in fig. 6, and also with the crest height statistics deviating systematically from the Rayleigh model (fig. 7). While the distribution in fig. 7, at 10 m, (with extreme crests exceeding the Rayleigh estimate by 15-20 %) can be explained by 2nd order effects, the distributions at 40 m must be explained by higher-order effects. Crest levels up to 40% higher than the Rayleigh prediction are observed in the latter case.

The non-Gaussian statistics observed in the amplitude distribution plots are also recognized in the skewness and kurtosis plots. The plot of skewness shows that it depends more or less only on the steepness of the sea state, and less on other parameters such as directionality, propagation etc. The theoretical curve from Vinje and Haver (1994), based on 2nd order theory, fits reasonably well. (A slight skewness reduction is observed in directional sea). We interpret the result in the way that the 2nd order contribution is quite stable, regardless of other circumstances. The kurtosis, however, varies significantly with travelling distance, wave directionality and with the spectral width.

A clear increase in non-linear modulation effects with narrower spectral width is observed from the measurements. We interpret this, qualitatively, as a consequence of modulation periods possibly around 4 - 6 times the wave periods. It is reasonable to assume that this will affect long wave groups (narrow spectra) stronger than it will affect short wave groups (broader spectra). (Side-band instabilities may more easily become "smeared out" by disturbing neighbouring frequencies).

As already commented, the above non-linear effects are only to a limited extent

observed in short-crested waves in the present measurements. This is an important observation, which confirms the conclusion from the bichromatic test examples in fig. 1. Thus it seems reasonable to conclude from this that extreme wave events due to non-linear modulations are most pronounced in longcrested waves. It appears to be a possible connection between these effects and the direction of the local phase gradient relative to that of the energy gradient. For more firm conclusions to be drawn on this, more analysis work is to be made, possibly including comparisons to theoretical/numerical models.

## 5. Acknowledgement

This work has been financially supported by the Royal Norwegian Research Council.

## 6. References.

- Benjamin, T.B. & Feir, J., (1967), "The Disintegration of Wave Trains on Deep Water", *J. Fluid Mech.*, Vol. 27, pp. 417-430.
- Jonathan, P., Taylor, P.H. & Tromans, P. S., (1994), "Storm Waves in the Northern North Sea", *Proceedings*, Vol. 2, the 7th BOSS Conference, MIT Cambridge, USA (Published by Pergamon / Elsevier, Oxford, UK), pp. 481-494.
- Kjeldsen, S.P. (1990), "Breaking Waves", in *Water Wave Kinematics*, ed. A. Tørum & O.T. Gudmestad, Kluwer Academic, Dordrecht, the Netherlands, pp. 453-473.
- Lake, B.M., Yuen, H.C., Rungaldier, H. & Ferguson, W.E., (1977), "Non-linear Deep-water Waves: Theory and Experiment. Part 2: Evolution of a Continuous Wave Train", *J. Fluid Mech.*, Vol. 83, pp. 49-74.
- Lo, E. & Mei, C.C., (1985), "A Numerical Study of Water-wave Modulation Based on a Higher-order Nonlinear Schrödinger Equation", *J. Fluid Mech.*, Vol. 150, pp. 395-416.
- Longuet-Higgins, M.S. (1963), "The Effect of Non-Linearities on Statistical Distributions in the Theory of Sea Waves", *J. Fluid Mech.* Vol. 17, pp. 459-480.
- Marthinsen, T. and Winterstein, S. (1992), "On the Skewness of Random Surface Waves", *Proceedings*, Vol. III, the 2nd ISOPE Conference, San Francisco, USA, pp. 472-478.
- Sand, S.E. et al. (1990), "Freak Wave Kinematics", in *Water Wave Kinematics*, ed. A. Tørum & O.T. Gudmestad, Kluwer Academic, Dordrecht, the Netherlands, pp. 535-549.

Stansberg, C.T. (1983), "Statistical Analysis of Slow Drift Responses", *Journal of Energy Resources Technology*, Vol. 105, pp. 310-317.

Stansberg, C.T. (1991), "Extreme Wave Asymmetry in Full Scale and Model Scale Experimental Wave Trains", *Proceedings, the 10th OMAE Conference, Stavanger, Norway*, pp. 215-222.

Stansberg, C.T., (1992), "On Spectral Instabilities and Development of Non-linearities in Deep-water Propagating Wave Trains", *Proceedings, Vol. 1, 23rd International Conference on Coastal Engineering, Venice, Italy*, pp. 658-671.

Stansberg, C.T., (1993), "Second-Order Numerical Reconstruction of Laboratory Generated Random Waves", *Proceedings, Vol. II, the 12th OMAE Conference, Glasgow, Scotland*, pp. 143-151.

Stansberg, C.T., (1994), "Second-Order Effects in Random Wave Modelling", *Proceedings, Vol. II, the International Symposium, "Wave-Physical and Numerical Modelling", the University of British Columbia, Vancouver, Canada*, pp. 793-802.

Su, M.-Y., Bergin, M., Marler, P. & Myrick, R., (1982), "Experiments on nonlinear instabilities and evolution of steep gravity-wave trains", *J. Fluid Mech.*, Vol. 124, pp. 45-72.

Taylor, P.H. & Haagsma, I.J., (1994), "Focusing of Steep Wave Group on Deep Water", *Proceedings Vol. II, International Symposium on "Waves-Physical and Numerical Modelling", University of British Columbia, Vancouver, Canada*, pp. 862-870.

Vinje, T. & Haver, S. (1994), "On the Non-Gaussian Structure of Ocean-Waves", *Proceedings, Vol. 2, the 7th BOSS Conference, MIT Cambridge USA, (Published by Pergamon / Elsevier, Oxford, UK)*, pp. 453-480.

Wang, P., Yao, Y. and Tulin, M.P., (1993), "Wave Group Evolution, Wave Deformation, and Breaking: Simulations Using LONGTANK, a Numerical Wave Tank", *Proceedings, Vol. III, the 3rd ISOPE Conference, Singapore*.

Yasuda, T., Mori, N. & Ito, K., (1992), "Freak Waves in Unidirectional Wave Trains and their Properties", *Proceedings, Vol. 1, 23rd International Conference on Coastal Engineering, Venice, Italy*, pp. 751-764.

Yasuda, T. & Mori, N. (1994), "High Order Nonlinear Effects on Deep-Water Random Wave Trains", *Proceedings, Vol. II, International Symposium on "Waves-Physical and Numerical Modelling", University of British Columbia, Vancouver, Canada*, pp. 823-832.

## CHAPTER 44

### SHEAR STRESSES AND MEAN FLOW IN SHOALING AND BREAKING WAVES

Marcel J.F. Stive<sup>1)</sup> and Huib J. De Vriend<sup>2)</sup>

#### ABSTRACT

We investigate the vertical, wave averaged distributions of shear stresses and Eulerian flow in normally incident, shoaling and breaking waves. It is found that shear stresses are solely due to wave amplitude variations, which can be caused by shoaling, boundary layer dissipation and/or breaking wave dissipation. The resulting shear stress and mean flow distributions for these cases are derived, and compared with earlier work.

The attractive, now frequently used modelling choice of specifying a shear stress at the mean surface level is discussed in the context of the constituent equations and related boundary conditions and constraints. A derivation of the shear stress at the mean surface level is given both by using the momentum balance and energy balance equations, which is shown to lead to the same result, if the effects of a changing roller are incorporated correctly<sup>3)</sup>.

Finally, matching solutions for the shoaling and breaking wave cases between the boundary layer and the middle layer for the shear stresses and the wave averaged flow are derived.

#### INTRODUCTION

The intentions of the present paper are to present a conceptual view on the constituent equations and related boundary conditions and constraints for the vertical distributions of wave averaged shear stresses and Eulerian flow for the cases of

- 
- 1) Netherlands Centre for Coastal Research, Delft University of Technology, Faculty of Civil Engineering, PO Box 5048, 2600 GA Delft, The Netherlands; and Delft Hydraulics, PO Box 152, 8300 AD Emmeloord, The Netherlands (Internet: marcel.stive@wldelft.nl)
  - 2) University of Twente, Section Civil Engineering and Management, PO Box 217, 7500 AE Enschede, The Netherlands (Internet: h.j.devriend@sms.utwente.nl)
  - 3) See Appendix to this paper: "Mean surface shear stress due to a changing roller" by Rolf Deigaard

shoaling and breaking waves, including boundary layer dissipation effects. While the relevant physical phenomena are indicated, it is not intended to suggest optimal closure hypotheses for all the phenomena, but rather to indicate their physical consequences in a transparent way. Examples are the eddy viscosity assumptions and the roller effects, for which simplified choices are made, which are, to a certain degree, not essential but only made for simplicity and transparency of the concept.

It is found that the sloping bottom does not introduce additional terms in the shear stress distributions found by Deigaard and Fredsoe (1989). The separate cases of no-breaking and breaking are discussed.

Furthermore, it is shown how a general expression for the mean Eulerian flow may be derived, which incorporates the effects of sloping bottom and wave amplitude variations, either due to boundary layer dissipation, shoaling or breaking. In the special cases of horizontal bottom and no-breaking and of sloping bottom and no-breaking, the expression reduces to Longuet-Higgins' conduction solution (1953) and to Bijker et al's shoaling solution (1974), respectively.

## CONSTITUENT EQUATIONS AND CONDITIONS

If we neglect the effects of advective acceleration for the time-mean flow and assume a wave-averaged eddy viscosity approximation for the Reynolds' stresses, the local momentum equation most commonly used to solve the wave averaged Eulerian flow reads:

$$\frac{\partial}{\partial z} \nu_t \frac{\partial U}{\partial z} = g\overline{\eta}_x + (\overline{u^2})_x - (\overline{w^2})_x + (\overline{uw})_z \quad (1)$$

where:

- $U$  is the wave averaged Eulerian flow,
- $\nu_t$  is the eddy viscosity,
- $\eta_x$  is the mean water level set-up, and
- $u, w$  are the horizontal and vertical wave-orbital velocities.

This equation is assumed to be valid in the full vertical domain, except for the region near the free surface. Somewhat heuristically, we assume the equation to be valid unto mean water level, since a wave averaged situation is considered, and we let the effects of the near surface layer (such as the roller) be effectuated in a shearstress acting at the mean water level.

Let us introduce the common assumption that the wave terms (orbital velocity moments) can be derived independently from the mean flow, i.e. we assume that there exists a sufficiently accurate wave theory to describe the wave terms which neglects the wave-current interaction. This is of course a simplification, and we may state that a true break-through here would be achieved if we could tackle the problem with a Lagrangian approach in which waves and currents would be considered



simultaneously, which at the same time would allow us to deal consistently with the near surface layer (NSL). However, until such an approach is developed we rely on the experience that the suggested approach is shown to yield sufficiently accurate results for the moment.

Let us further assume that the turbulence viscosity is constant over depth. Note that this is only for the clarity of the argumentation. The rationale which follows would also allow for a depth-varying viscosity, as long as it is time invariant and does not depend on the undertow solution itself.

The above implies that we have one equation to solve for the undertow and the mean water level set-up. Integrating the equation twice yields:

$$v_t U = \frac{1}{2} g \overline{\eta} z'^2 + \int_0^{z'} \int_0^{z'} (\overline{u^2})_x dz dz - \int_0^{z'} \int_0^{z'} (\overline{w^2})_x dz dz + \int_0^{z'} (\overline{uw}) dz + C_1 z' + C_2 \quad (2)$$

This expression contains three unknowns, viz. the two constants of integration,  $C_1$  and  $C_2$  remaining in this expression, and the set-up gradient. We therefore need, in addition to this equation, three boundary conditions and/or constraints:

- (1) no-slip condition at the bottom ( $U = 0$ ), from which we can find  $C_2$ ;
- (2) shear stress condition at the transition from the middle layer (ML) to the NSL ( $\tau_t$  given), from which we can find  $C_1$ ;
- (3) mass balance constraint (total mass flux in the lower layers balances that in the NSL), from which we can derive the set-up gradient.

The essential information which we need here is related to the NSL. In fact, condition (2) is based on the assumption that we know the shear stress at the lower end of the NSL from the momentum balance for this layer. Similarly, when formulating the constraint (3), we assume the total mass flux in the NSL to be known.

This route is suggested by Stive and De Vriend (1987) and also followed by Deigaard et al. (1991). The former derive a formal expression through a third depth integration, while the latter use an iteration procedure which sees to it that a set-up gradient is created such that the correct depth-average mass flux is created. The result should be the same.

Alternatively, one could use the depth-averaged horizontal mass and momentum equations, with the wave-induced radiation stresses and mass fluxes properly modelled, instead of giving  $\tau_t$  and imposing constraint (3). Note also that imposing constraint (3) is not correct in 3-D situations, where the mass flux in the NSL is not necessarily compensated in the lower parts of the same water column (cf. De Vriend and Kitou, 1990). In fact, later we shall use the depth-averaged momentum equation, with the usual expressions for the radiation stresses, to derive an expression for  $\tau_t$ . Note that in either case we face the problem of describing the NSL, via  $\tau_t$  and the mass flux, or via the wave-related terms in the depth-averaged mass and momentum equations.

## DISTRIBUTION OF ORBITAL VELOCITY MOMENTS AND SHEAR STRESSES ON A SLOPING BOTTOM IN THE MIDDLE LAYER

In order to derive the shear stress distribution the orbital velocities outside and a little away from the bottom boundary layer need to be known. The idea is to use these results to look at the shear stress distribution in the middle layer for the cases of sloping bottom and boundary layer dissipation and of sloping bottom and breaking wave dissipation. Furtheron, we will look at these cases with boundary layer effects on the shear stress distribution included.

Since we are interested in the case of spatially varying waves on a sloping bottom, we must at least rely on a non-uniform depth approximation. This has been done by De Vriend and Kitou (1990) and recently also by Rivero and Arcilla (1994) for the shallow water approximation to shoaling waves. The result as obtained for the orbital velocity moments reads:

$$\begin{aligned}\overline{u^2} &= \frac{1}{2} A^2 + O\left(A^2 \frac{\lambda^2}{L^2}\right) \\ \overline{w^2} &= O\left(A^2 \frac{h^2}{L^2}\right)\end{aligned}\quad (3)$$

$$\overline{uw} = \frac{1}{2} A^2 h_x - \frac{1}{4} (A^2)_x z'$$

where

$\lambda$  = wave length,  
 $L$  = scale of horizontal variations, and  
 $A = (a\omega)/(kh)$ .

Based on these results we can investigate our two cases.

### (1) The case of a sloping bottom and boundary layer dissipation

Using the above results the shear stress becomes

$$\tau(z')/\rho = v_t U_z = \overline{g\eta_x} z' + \frac{1}{4} (A^2)_x z' + \frac{1}{2} A^2 h_x + C_1 \quad (4)$$

Because of the absence of dissipation in the NSL there is no shear stress at the mean water level, sothat

$$\tau(z')/\rho = \overline{g\eta_x} (z' - d_m) + \frac{1}{4} (A^2)_x (z' - d_m) \quad (5)$$

In fact, no shear stresses will exist in the whole of the middle layer for (Deigaard and Fredsoe, 1989):

$$\rho g \overline{\eta_x} d_m = -\frac{1}{4} \rho (A^2)_x d_m = -\frac{1}{2} E_x \quad (6)$$

which complies with the fact that no shear stresses can be maintained in the middle layer due to the existence of irrotational flow. However, we will show later that due to the constraint of depth averaged zero mean flow, the existence of an additional mean water level gradient is required.

## (2) The case of a sloping bottom and wave breaking dissipation

Again using the above results the shear stress in this case becomes:

$$\tau(z')/\rho = g \overline{\eta_x} (z' - d_m) + \frac{1}{4} (A^2)_x (z' - d_m) + \tau_t \quad (7)$$

Now a shear stress at mean water level exists due to the presence of the roller. The mean water level gradient again follows from the mean flow constraint.

## DERIVATION OF THE SHEAR STRESS AT MEAN WATER LEVEL

Here derivations of the shear stress at mean water level are presented, and we show that the result is consistent between using either momentum flux or energy flux considerations.

From the above Equation (7) we find for the bottom shear stress:

$$\tau_b = -\rho g d_m \overline{\eta_x} + \tau_t - \frac{1}{4} \rho (A^2)_x d_m \quad (8)$$

Since we consider wave breaking dissipation only, the mean bottom shear stress  $\tau_b$  should be zero.

The shear stress  $\tau_t$  may be resolved between the  $\tau_b$  equation and the depth mean horizontal momentum balance equation. In order to do this we need to introduce an expression for the radiation stress which at least needs to be extended with the roller effect. Following Svendsen (1984), Deigaard and Fredsoe (1989) suggest the shallow water approximation

$$S_{xx} = S_{xx,p} + S_{xx,u} = \frac{1}{2} E + \left[ E + \rho \frac{Rc}{T} \right] \quad (9)$$

where R is the roller area.

The above implies that the set of equations available to resolve the shear stress  $\tau_t$  reads:

$$\frac{dS_{xx}}{dx} + \rho g d_m \overline{\eta}_x = 0 \quad (10)$$

$$\frac{dS_{xx}}{dx} = \frac{3}{2} E_x + \frac{\rho}{T} (Rc)_x \quad (11)$$

$$\tau_b = -\rho g \overline{\eta}_x d_m + \tau_t - \frac{1}{4} \rho (A^2)_x d_m = -\rho g \overline{\eta}_x d_m + \tau_t - \frac{1}{2} E_x = 0 \quad (12)$$

which yields:

$$\tau_t = -E_x - \frac{\rho}{T} (Rc)_x \quad (13)$$

and

$$\tau(z') = -E_x \left( 1 + \frac{d_m - z'}{2d_m} \right) - \rho g \overline{\eta}_x (d_m - z') - \frac{\rho}{T} (Rc)_x \quad (14)$$

These equations are equivalent to equations (56) and (58) of Deigaard and Fredsøe (1989), when introducing the relation

$$E_x = \frac{1}{c} (E_f)_x = -\frac{D}{c} \quad (15)$$

where  $E_f$  is the energy flux and  $D$  is the dissipation due to wave breaking.

In slightly different notation Equation (13) reads:

$$\tau_t = -\frac{1}{c} (E_f)_x - (2E_r)_x \quad (16)$$

where  $E_f$  is the energy flux, now using the expression of kinetic roller energy  $E_r$  (introduced by Svendsen, 1984, and used by Nairn et al., 1990):

$$2E_r = S_{xx,roller} = \rho Rc^2/L = \rho Rc/T \quad (17)$$

The presence of the roller leads to the additional term, which is due to the nonnegligible velocity contribution to the momentum flux, since the velocities are of magnitude  $c$ . The contribution due to the roller enhanced pressure is probably not

only small, but may also be already included in  $(E_f)_x$  since this property is quantified using the surface elevation variance.

One may, however, observe that the shear stress at NSL also appears in the energy balance equation, which according to Nairn et al. (1990) reads:

$$(E_f)_x + (E_r c)_x + \tau_t c = 0 \quad (18)$$

where they have introduced Svendsen's (1984) suggestion for the energy flux due to the roller and the result given in Deigaard and Fredsoe (1989) that the dissipation  $D$  is due to the work done by the shear stress due to the roller acting on the fluid right below it. Again, the roller related contribution is due to the mean transfer of kinetic energy (proportional to  $c^2$ ) with the roller velocity (equal to  $c$ ).

Rearranging the last equation for  $\tau_t$  yields

$$\tau_t = -\frac{1}{c} (E_f)_x - \frac{1}{c} (E_r c)_x \quad (19)$$

which indicates that when we accept that the spatial variations in  $c$  are small relative to those in  $E_r$  we are faced with a factor 2 difference. Note that here also we have assumed that the horizontal component of the shear stress is negligibly different from the shear stress along the roller-wave interface.

It appears that the apparent inconsistency is caused by the complicated situation that occurs when the volume of the roller is changing in the wave propagation direction (see Appendix). Beside the shear layer between the roller and the wave there is a net transfer of water from the wave to the roller. If the roller is losing water ( $dR/dx < 0$ ) the horizontal momentum transfer from the roller to the wave is not only that due to the shear layer, but also the momentum of the water leaving the roller. If the roller gains water ( $dR/dx > 0$ ), the water leaving the wave has negligible horizontal velocity and does not change the momentum of the water remaining in the wave. In both cases, however, there is an additional energy dissipation of

$$\rho \frac{1}{2} c^2 \left| \frac{dR}{dt} \right| \quad (20)$$

The corrections that these considerations give to the NSL shear stress and to the energy dissipation rate were derived in Deigaard (1993), and it appears that the energy balance equations in both cases yield:

$$(E_f)_x + (2E_r c)_x + \tau_t c = 0 \quad (21)$$

which removes the discrepancy and implies a correction to Nairn et al. (1990) and Stive and De Vriend (1994).

## MATCHING SOLUTION BETWEEN BOUNDARY LAYER AND MIDDLE LAYER

Where in the foregoing we have neglected the bottom boundary layer effects on the time- and depth-averaged momentum equation since it is a second-order effect in the overall momentum balance, we present in this section a matching solution to derive the mean Eulerian flow over the vertical, with accuracy near the bottom. Due to the existence of the bottom boundary layer the near-bottom horizontal orbital velocity may be shown to include a phase difference compared to the orbital velocity in the middle layer (cf. Longuet-Higgins, 1953). Because of the sloping bottom and/or due to wave breaking a variation of the wave amplitudes results which may be shown to yield the following matched result for the horizontal orbital velocity (cf. Bijker et al., 1974):

$$u = A(x)[\cos\chi - e^{-\phi}(\chi - \phi)] \quad (22)$$

where

$$\begin{aligned} \phi &= z/\delta \\ \delta^2 &= 2\nu_r/\omega \\ \chi &= \omega t - \psi \\ k &= d\psi/dx. \end{aligned}$$

By using continuity

$$w_z = -u_x \quad (23)$$

and depth integration

$$w = -\int_0^{z'} u_x dz' \quad (24)$$

we may derive the following expressions for the time-averaged values of the wave terms needed in Equation (1):

$$\overline{u^2} = \frac{1}{2} A^2 [1 + e^{-2\phi} - 2e^{-\phi} \cos\phi] \quad (25)$$

$$\begin{aligned} \overline{uw} &= A^2 k \delta \left[ -\frac{1}{4} + \frac{\phi}{2} e^{-\phi} \sin\phi - \frac{e^{-\phi}}{4} + \frac{e^{-\phi}}{2} \cos\phi \right] - \\ &- \left( \frac{A^2}{2} \right)_x \frac{\delta}{2} \left[ -\frac{1}{2} + \phi + e^{-\phi} \cos\phi - \phi e^{-\phi} \cos\phi - \frac{e^{-2\phi}}{2} \right] \end{aligned} \quad (26)$$

These equations were derived by Bijker et al. (1974) for the shoaling wave case, but they are equally valid for the case of wave breaking, since in the shoaling case it is the amplitude variation only that impacts on these terms. The difference being solely that during shoaling the amplitudes increase, while due to breaking they decrease.

Using the above expressions for the wave-averaged orbital terms we may resolve Equation (2) and the set of three boundary conditions and constraints to yield:

$$\begin{aligned} v_t U = & \left( \overline{g\eta_x} + \frac{1}{4} (A^2)_x \right) \left[ \frac{1}{2} z^2 - z'd_m \right] + \frac{\tau_t}{\rho} [z'] + \\ & + (A^2)_x \frac{\delta^2}{4} \left[ 2e^{-\phi} \sin\phi + \frac{1}{2} e^{-\phi} \cos\phi + \frac{1}{2} \phi e^{-\phi} (\sin\phi - \cos\phi) + \frac{1}{4} e^{-2\phi} - \frac{3}{4} \right] + \quad (27) \\ & + A^2 k \frac{\delta^2}{2} \left[ -\frac{1}{2} e^{-\phi} \phi (\sin\phi + \cos\phi) - e^{-\phi} \cos\phi + \frac{1}{2} e^{-\phi} \sin\phi + \frac{1}{4} e^{-2\phi} + \frac{3}{4} \right] \end{aligned}$$

Note that for transparency we have assumed an eddy viscosity invariant over depth, which is not necessary: it only yields an attractive, analytical expression over the total depth, which allows us to point out the respective approximations for the cases derived before. Longuet-Higgins' solution (1953) contains the fourth term of Equation (19) only. In the shoaling case of Bijker et al. (1974) we have

$$\begin{aligned} \overline{g\eta_x} &= -\frac{1}{4} (A^2)_x \quad \text{and} \quad (28) \\ \tau_t &= 0 \end{aligned}$$

so that only the last two terms of Equation (27) result. For breaking waves on a sloping bottom we need all four terms. Note that in all cases a small mean water level gradient may be necessary to comply with a depth-averaged zero Eulerian flow.

Here, we refrain from a deeper analysis of the surfzone situation with strong, breaking induced wave amplitude variations. Clearly, the mean water level gradient and the NSL shear stress (as represented by the first two terms in Equation (27)) will exert a major influence on the mean Eulerian flow distribution. However, we may expect that especially near the bottom the boundary layer term and the amplitude variation term will show their significance. An insight into their qualitative influence is given below.

For the shoaling wave case the mean Eulerian flow distribution reads:

$$U = \frac{A^2 k}{\omega} f'(\phi) + \frac{A}{\omega} \frac{dA}{dx} g'(\phi) \quad (29)$$

where the vertical form functions are given by

$$f'(\phi) = \left[ -\frac{1}{2} e^{-\phi} \phi (\sin\phi + \cos\phi) - e^{-\phi} \cos\phi + \frac{1}{2} e^{-\phi} \sin\phi + \frac{1}{4} e^{-2\phi} + \frac{3}{4} \right] \quad (30)$$

$$g'(\phi) = \left[ 2e^{-\phi} \sin\phi + \frac{1}{2} e^{-\phi} \cos\phi + \frac{1}{2} \phi e^{-\phi} (\sin\phi - \cos\phi) + \frac{1}{4} e^{-2\phi} - \frac{3}{4} \right] \quad (31)$$

Their behaviour is graphically illustrated in Figure 1, which teaches us that close to the bottom the amplitude variation effect strengthens the streaming effect in the shoaling zone, but weakens it in the breaker zone. Whether this actually occurs is depending on the relative magnitude of these terms, which may be estimated as follows. At the edge of the boundary layer we find:

$$U_{\infty} = \frac{3}{4} \frac{A^2 k}{\omega} - \frac{3}{4} \frac{A}{\omega} \frac{dA}{dx} \quad (32)$$

$$= \frac{3}{4} \frac{A^2 k}{\omega} \left[ 1 - \frac{1}{Ak} \frac{dA}{dh} \frac{dh}{dx} \right]$$

Using linear shoaling it may be shown (Bijker et al., 1974) that  $1/(Ak) dA/dh = O(1)$  for  $kh \geq 1$ , so that only in the breaker zone and with relative steep slopes the amplitude variation effect becomes important.

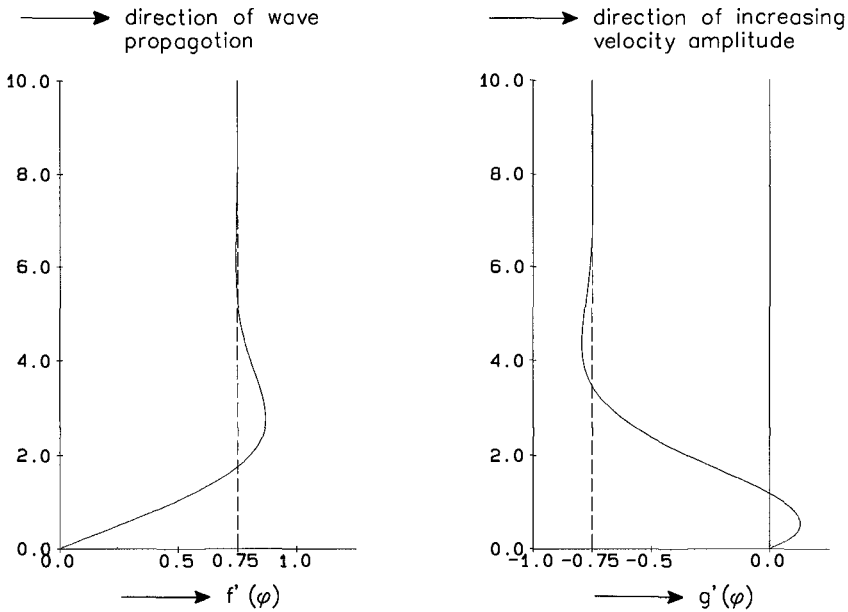


Figure 1 Form functions of streaming effect ( $f'(\phi)$ ) and amplitude variation effect ( $g'(\phi)$ )



## CONCLUSIONS AND DISCUSSION

A conceptual view is presented on the constituent equations and related boundary conditions and constraints for the vertical distributions of wave averaged shear stresses and Eulerian flow for the cases of shoaling and breaking waves, including boundary layer dissipation effects. We have refrained from suggesting optimal closure hypotheses for the relevant processes, but we have tried to indicate their physical consequences in a transparent way. It is found that shear stresses are solely due to wave amplitude variations, which can be caused by shoaling, boundary layer dissipation and/or breaking wave dissipation. The resulting shear stress and mean flow distributions for these cases are derived, and compared with earlier work.

The specification of the shear stress at the mean surface level is discussed in the context of the constituent equations and related boundary conditions and constraints. A derivation of the shear stress at the mean surface level is given both by using the momentum balance and energy balance equations, which is shown to lead to the same result, if the effects of a changing roller are incorporated correctly (see Appendix). Finally, matching solutions for the shoaling and breaking wave cases between the boundary layer and the middle layer for the shear stresses and the wave averaged flow are derived.

We conclude by noting that the foregoing considerations concern the 2-D wave-induced water motion in a vertical plane parallel to the direction of wave propagation. The currents are weak and boundary-layer processes are primarily wave-induced. The wave orbital motion and the mean current higher up in the vertical can be treated separately, the former as inviscid, the latter as viscous flow. Advection plays no significant role in the mean current field.

Although this situation must occur now and then in nature, it rather concerns a wave flume. The common situation on a natural beach is more complicated, because

- the wave field is directionally spread, so whatever definition is chosen for "the" direction of wave propagation, there are always wave components in other directions;
- the waves are not monochromatic, there is always energy in the low-frequency bands (edge waves, surfbeat, shear waves, etc.);
- there can be strong currents, tidal, wave-driven or otherwise, and not necessarily in the alongshore direction; in general, these currents make a non-zero angle with the direction of wave propagation;
- strong spatial gradients of the bed topography and wave or current parameters can occur in any direction.

As a consequence, one would have to abandon a number of simplifying assumptions which underlie the present 2-D vertical (2-DV) model. One of these for instance is that in 3-D situations the mass flux in the NSL is not necessarily compensated in the lower parts of the same water column (cf. De Vriend and Kitou, 1990).

## ACKNOWLEDGEMENT

A large part of this paper is based on work in the "G8 Coastal Morphodynamics" research programme, which is funded partly by the Commission of the European Communities in the framework of the Marine Science and Technology Programme (MAST), under contract no. MAS2-CT92-0027. The work is co-sponsored by Delft Hydraulics, in the framework of the Netherlands Centre for Coastal Research.

## REFERENCES

- Bijker, E.W., Kalkwijk, J.P.Th. and Pieters, T. (1974). Mass transport in gravity waves on a sloping bottom. Proc. 14th Conf on Coastal Eng, ASCE, pp 447-465
- Deigaard, R. (1993). A note on the three-dimensional shear stress distribution in a surf zone. Coastal Engineering, 20, 157-171.
- Deigaard, R. (1994). Mean surface shear stress due to a changing roller. Appendix to this paper.
- Deigaard, R. and Fredsøe, J. (1989). Shear Stress Distribution in Dissipative Water Waves. Coastal Engineering, 13, 357-378.
- Deigaard, R., Justesen, P. and Fredsøe, J. (1991). Modelling of undertow by a one-equation turbulence model. Coastal Engineering, 15, 431-458.
- De Vriend H.J. and Kitou, N. (1990). Incorporation of wave effects in a 3D hydrostatic mean current model. Proc. 22nd Coastal Eng. Conf., ASCE, 1005-1018.
- De Vriend, H.J. and Stive, M.J.F. (1987). Quasi-3D Modelling of Nearshore Currents. Coastal Engineering, 11, 565-601.
- Longuet-Higgins, M.S. (1953). Mass transport in water waves. Philos. Trans. R. Soc., Ser. A, 245, 535-581.
- Nairn, R.B., Roelvink, J.A. and Southgate, H.N. (1990). Transition zone width and implications for modelling surfzone hydrodynamics. Proc. 22nd Conf on Coastal Eng, ASCE, pp 68-81.
- Rivero, F.J. and S.-Arcilla, A. (1994). On the vertical distribution of  $\langle uw \rangle$ . Abstract MAST Overall Workshop, Gregynog, Wales.
- Stive, M.J.F. and De Vriend, H.J. (1987). Quasi-3D nearshore current modelling: wave-induced secondary currents. Proc. Special Conf. on Coastal Hydrodynamics, ASCE, 356-370.
- Stive, M.J.F. and De Vriend, H.J. (1994). Verification of the shear stress boundary conditions in the undertow problem. Proceedings Coastal Dynamics '94 (in press).
- Svendsen, I.A. (1984). Wave Heights and Set-up in a Surf Zone. Coastal Engineering, 8, 303-330.

## APPENDIX

## MEAN SURFACE SHEAR STRESS DUE TO A CHANGING ROLLER

Rolf Deigaard

Institute of Hydrodynamics and Hydraulic Engineering, Technical University of Denmark, Building 115, DK-2800 Lyngby, Denmark

The apparent inconsistency, mentioned in Section 4 of the above paper, is caused by the complicated situation that arises when the volume of the roller is changing in the propagation direction. In this case the formulation of the energy dissipation and of the surface shear stress will have to be modified. In the following, the notation of the paper is used.

Due to the existence of a shear layer between the roller and the wave a shear stress (averaged over a wave length)  $\tau_t$  exists which is assumed to apply at the mean water level. In addition there is a net transfer of water from the wave to the roller of:

$$\frac{1}{L} \frac{dR}{dt} = \frac{c}{L} \frac{dR}{dx} = \frac{1}{T} \frac{dR}{dx} \quad (\text{A.1})$$

We are interested in the horizontal momentum transferred from the roller to the wave. If the roller is losing water ( $dR/dx < 0$ ) this momentum is not just  $\tau_t$ , but also the momentum of the water leaving the roller, which has a horizontal velocity of  $c$ . If the roller gains water ( $dR/dx > 0$ ), the water leaving the wave has a negligible horizontal velocity, and it does not change the momentum of the water remaining in the wave.

If there is a net transfer of water to or from the roller this water will be mixed with the water in the roller ( $dR/dx > 0$ ) or in the wave ( $dR/dx < 0$ ). In both situations there is an additional energy dissipation, just as energy is lost when a rain drop hits the wind screen of a fast car, or if the car loses a drop of water on the road. The additional energy dissipation is:

$$\rho \frac{1}{2} c^2 \left| \frac{dR}{dt} \right| \quad (\text{A.2})$$

The force between the roller and wave is split into a (symmetric) shear stress and a contribution from the net transfer of water makes the analysis complex. In Deigaard (1993) the shear stress in the shear layer was modelled as a Reynolds' stress with an exchange of water between the roller and the wave. A variation in the roller volume is then represented by a difference between the rate of fluid moving up and down.

With the modified energy dissipation and momentum transfer to the wave the analysis can proceed for the two cases, a decreasing roller and a growing roller:

Case 1:  $\frac{dR}{dx} < 0$

Dissipation rate:

$$D = \tau_t c - \rho \frac{1}{2} \frac{c^2}{L} \frac{dR}{dt} = \tau_t c - \rho \frac{1}{2} c^2 \frac{c}{L} \frac{dR}{dx} = \tau_t c - \frac{\rho}{T} \frac{c^2}{2} \frac{dR}{dx} \quad (\text{A.3})$$

Energy dissipation expressed as a gradient in the energy flux:

$$D = - \frac{dE_f}{dx} - \frac{\rho}{T} \frac{d(\frac{1}{2}Rc^2)}{(dx)} \quad (\text{A.4})$$

Horizontal momentum transferred to the wave surface (averaged over a wave length):

$$\begin{aligned} \tau_s &= \tau_t - \rho \frac{c}{L} \frac{dR}{dt} = \tau_t - \rho \frac{c}{L} c \frac{dR}{dx} = \tau_t - \rho \frac{c^2}{L} \frac{dR}{dx} \\ \tau_t - \rho \frac{c}{T} \frac{dR}{dx} &= \left( \frac{D}{c} + \frac{\rho}{T} \frac{c}{2} \frac{dR}{dx} \right) - \rho \frac{c}{T} \frac{dR}{dx} = \\ &= - \frac{1}{c} \frac{dE_f}{dx} - \frac{\rho}{2Tc} \frac{d(Rc^2)}{dx} - \frac{\rho}{2T} \frac{cdR}{dx} = \\ &= - \frac{1}{c} \frac{dE_f}{dx} - \frac{\rho}{2T} \frac{dRc}{dx} - \frac{\rho}{2T} \frac{Rdc}{dx} - \frac{\rho}{2T} \frac{cdR}{dx} = \\ &= - \frac{1}{c} \frac{dE_f}{dx} - \frac{\rho}{T} \frac{dRc}{dx} = - \frac{1}{c} \frac{dE_f}{dx} - \frac{d(2E_r)}{dx} \end{aligned} \quad (\text{A.5})$$

Case 2:  $\frac{dR}{dx} > 0$

Dissipation rate:

$$D = \tau_t c + \rho \frac{1}{2} \frac{c^2}{L} \frac{dR}{dt} = \tau_t c + \frac{\rho}{T} \frac{c^2}{2} \frac{dR}{dx} \quad (\text{A.6})$$

Horizontal momentum transferred to the wave surface:

$$\begin{aligned} \tau_s = \tau_t &= \frac{1}{c} D - \frac{\rho}{T} \frac{c}{2} \frac{dR}{dx} = \\ &= -\frac{1}{c} \frac{dE_f}{dx} - \frac{\rho}{2Tc} \frac{d(Rc^2)}{dx} - \frac{\rho}{2T} \frac{cdR}{dx} = \\ &= -\frac{1}{c} \frac{dE_f}{dx} - \frac{\rho}{T} \frac{dRc}{dx} = -\frac{1}{c} \frac{dE_f}{dx} - \frac{d(2E_r)}{dx} \end{aligned} \quad (A.7)$$

As appears from the above derivations, an additional energy dissipation occurs due to a growing as well as a decreasing roller volume which causes additional work done, and consequently increases the shear stress, expressed by  $\tau_s$ , which we have to apply at the mean water level. This removes the apparent inconsistency as noted in Section 4.

## CHAPTER 45

# Prediction of the maximum wave on the coral flat

Dede. M. Sulaiman<sup>1</sup>, Shigeaki Tsutsui<sup>2</sup>, Hiroshi Yoshioka<sup>3</sup>, Takao Yamashita<sup>3</sup>,  
Shinichi Oshiro<sup>4</sup>, and Yoshito Tsuchiya<sup>5</sup>, M. ASCE

### Abstract

Beach erosion has become a major problem at coral-sand beaches in Bali, Indonesia, due to the rapid changes in natural environment and utilization of coastal areas. An observation of waves was carried out at Sanur beach in Bali to know what waves are effective for beach processes. The representative waves are predicted by use of the mild-slope and KdV equations with evaluation of the coefficient of bottom friction. Empirical formulae of wave energy dissipation are proposed for taking into account of wave height damping due to breaking on the coral flat. The maximum wave on the coral flat, occurring in the reforming region of waves after breaking near the reef edge, can be decided by the theoretical results of the highest wave of permanent-type on water of uniform depth. Sanur beach has observed swells with a period longer than 15 sec, being incident onto the coral flat without breaking. This maximum wave of non-breaking progressive-type is, therefore, evaluated by the experimental wave height criteria.

### INTRODUCTION

Indonesia, one of the largest archipelagos, is located in the tropics and is consisted of about 13,7000 islands. Among them the total area of islands surrounded with the coral reef, such as Bali, is about 1,900,000 km<sup>2</sup>. Many rivers in the south parts of Bali island, as shown in Figure 1, supply sand sediment sources into the beach. The length of coastline of Bali is about 430 km, and main coastal engineering problems are beach erosion, river mouth closing, and tidal flood (Syamsudin, 1993). Especially in Sanur, Kuta, and Nusa Dua

<sup>1</sup> Researcher, Research Institute for Water Resources Development, Ministry of Public Works, Bandung, 40135, Indonesia.

<sup>2</sup> Professor, Dept. of Civil Engineering and Architecture, Faculty of Engineering, Univ. of the Ryukyus, Okinawa, 903-01, Japan.

<sup>3</sup> Instructor, Disaster Prevention Research Institute, Kyoto Univ., Uji, 611, Japan.

<sup>4</sup> Graduate Student, Civil Engineering and Architecture, Faculty of Engineering, Univ. of the Ryukyus, Okinawa, 903-01, Japan.

<sup>5</sup> Professor Emeritus, Kyoto Univ., and Professor, Meijo Univ., Nagoya, 468, Japan.

coral-sand beaches, located nearby the southern peninsular of coral limestone forming beautiful steep sea cliffs, beach erosion has become a major problem for which effective countermeasures are needed. There should be interrelation between coastal processes concerned with beach erosion in these beaches and changes in natural environment due to utilization of coastal areas. Clarification of the relation is very useful for other coral-sand beaches to predict what beach processes will occur in the future.

The successful control of coral-sand beach processes requires the knowledge of prediction of the maximum wave on the coral flat, i.e., what waves are the most effective for beach change. As the first step, therefore, an observation of waves, as joint investigation between the Research Institute for Water Resources Development and the Disaster Prevention Research Institute, Kyoto University, has been carried out at Sanur beach. This paper examines changes in wave heights and periods by using wave data, and predicts wave transformation in the coral reef beach, both by the mild-slope and KdV equations, and the maximum wave on the coral flat, where the effects of wave breaking and bottom friction are introduced.

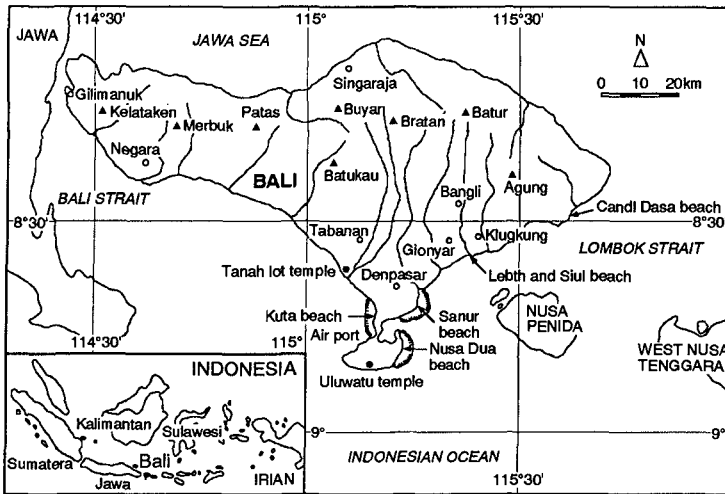


Figure 1. Bali island and coral-sand beaches.

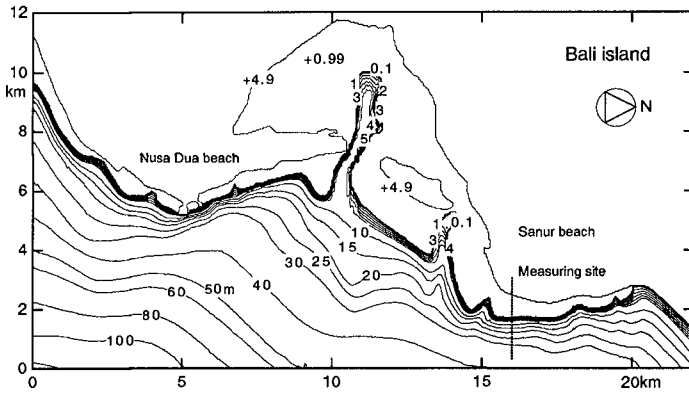
## COASTAL ENVIRONMENTS

### Field measurements

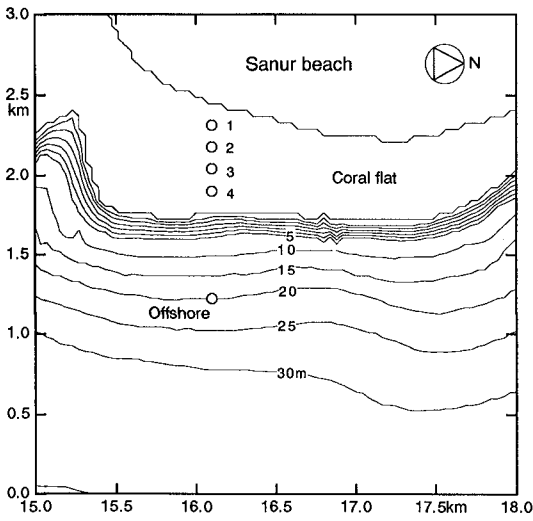
#### (1) Bathymetry near Sanur coral reef beach and wave measuring stations

As seen in Figure 2(1), Sanur beach is about 7 km long having coral flats, 500 - 800 m wide. The coral reef beach profile is of slope-type, as seen in Figure 2(3), where the water depth increases gently in the outer reef with the bottom slopes of  $1/20 - 1/50$ . This geometric feature is different from that in the Okinawa islands, Japan, where the step and barrier-type coral reefs are formed.

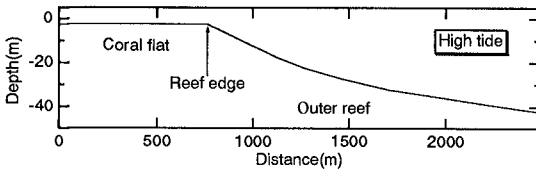
The linear array of five wave gauges was set up perpendicular to the reef edge, as shown in Figure 2(2) by the circles. The offshore station was set up at the location of 20 m water depth for measuring incident waves, and the others (St. 1, 2, 3, and 4) were installed on the coral flat at intervals of 100 m from the reef edge. The offshore wave gauge is supersonic-type and those on the coral flat are of capacitance-type.



(1) Bathymetry near Sanur and Nusa Dua beaches.



(2) Wave array installed at Sanur beach, shown by circles.



(3) Beach profile along the course of wave array.

Figure 2. Bathymetry around Sanur beach in Bali and the wave probe linear array.



(2) The period of observation

The seasonal variations of incident wave characteristics at Sanur coral reef beach, shown in Figure 3, indicate significance of the waves in the dry season for the beach process. The wave direction is almost unchanged throughout the year and the maximum wave heights and the corresponding wave periods ( $H_{max}$ ,  $T_{max}$ ) in the dry season (June - August) are greater than those in the wet season (December - February). The observation was therefore carried out in the period of July 16 - 19, 1992 under the usual sea conditions. After preliminary measurements on July 16, three runs of measurements were put into operation from 11:00 to 24:00 on July 17, from 9:00 on July 18 to 1:00 on July 19, and from 9:00 to 17:00 on July 19. The sample size of the data used is 20 minutes for all measuring stations, and the data were obtained at intervals of two hours for the offshore station and one hour for the other stations on the coral flat. At the offshore station, in addition, two-directional (NS and EW) water particle velocities were measured for a period of 20 minutes in every two hours, by using the sonic-type current meter.

(3) Wave direction

Figure 4 shows velocity vectors at the offshore measuring station, which were estimated from the two-directional (NS and EW) components of water particle velocities at high (12:00, 24:00) and low (18:00) tides. In the expression, the velocity components are normalized by each maximum value. The predominant directions of currents are ESE and WNW, indicating that offshore waves are incident from the direction of ESE. According to the results of numerical calculation of wave rays (Syamsudin, 1993), waves propagating in the Indonesian Ocean from the direction of SE are coming onto the beach, nearly perpendicular to the reef edge. Judging from the bathymetry of the beach in Figure 2(2) and the velocity vectors in Figure 4, offshore waves can be assumed to be incident normally to the reef edge in the period of the present observation.

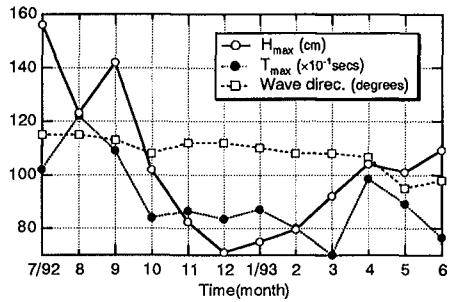


Figure 3. Seasonal variations of incident wave characteristics at Sanur beach.

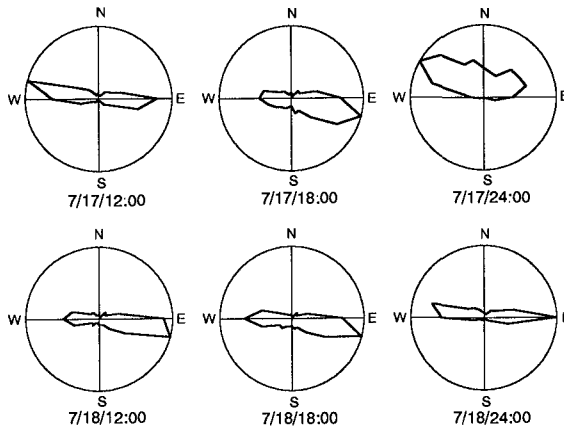


Figure 4. Velocity vectors at the offshore measuring station.

**Wave characteristics**

(1) Power spectra and wave energy dissipation

According to the tidal record measured at Benoa harbor nearby Sanur beach, the highest tidal level of water rises up to +2.3 m and +2.5 m in the period of July 17 - 18, as shown in Figure 5 by thin solid lines. The water depth at low tide is extremely shallow so that there appear some places dried up. The significant wave heights and periods ( $H_{1/3}, T_{1/3}$ ) measured in the reef vary in phase with the tide level, as shown in Figure 5. Waves can enter onto the coral reef at high tidal phase of several hours, but the wave heights decrease gradually due to bottom friction with wave propagation toward the shore. Waves in the reef are, therefore, subjected to the water depth on the coral flat and incident waves at high tide are effective for coral-sand beach processes.

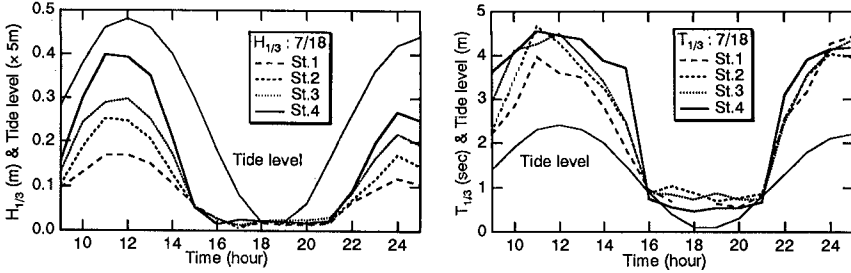
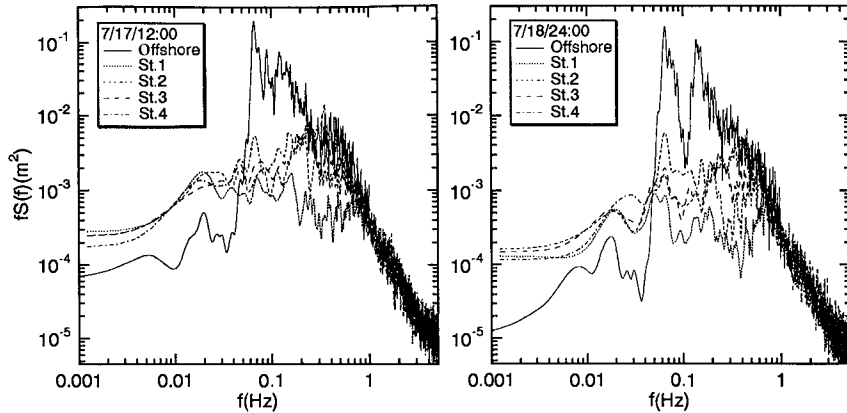


Figure 5. Significant wave heights (left) and periods (right), varying with the tide level on the coral flat (July 18).



(1) July 17 at 12:00

(2) July 18 at 24:00

Figure 6. Frequency spectra for waves in and outside the reef at high tide.

Figure 6 shows typical examples of frequency spectra at high tide on July 17 - 18. In the ordinates, power spectra  $S(f)$  are multiplied by the frequency  $f$  to obtain dominant peak frequencies clearly (Kai, 1985). The sampling time is 0.5 sec for offshore data and 0.1 sec for data on the coral flat.

Power spectra of offshore waves (solid lines) have several dominant peaks, showing that the waves include swells with a period of about 15 sec and wind waves with periods less

than 8 sec. As can be seen in spectra at the stations 1 to 4 on the coral flat, high energy components with periods of 3 - 20 sec in offshore waves decrease suddenly by breaking near the reef edge. Long waves less than 0.05 Hz are then generated clearly on the reef. These long waves might be consisted of two components; incident swells onto the coral flat without breaking near the reef edge and waves generated by nonlinear interaction of incident and reflected waves on the reef, resulting in wave setup (Goda, 1975; Hino et al., 1989). The former can be confirmed in the following discussion on Figure 7. The power spectral shape on the coral flat becomes flat and the spectral width seems to be wider than that of offshore ones. Note, however, that the energy of swells with a period of about 15 sec, though decrease by breaking, is still predominant in the reef, as clearly shown in Figure 6(2). At the lowest tidal phase, on the other hand, the water depth becomes very shallow, and there exist strong offshore-wards currents from the reef edge, as shown in Figure 4. A few waves thus coming into the reef flat, most waves measured on the coral flat are, as shown in Figure 5, wind waves with periods less than 1 sec, of which the energies are very small.

If the frequency region of power spectra at high tide is divided into three regions; long waves ( $f < 0.04$ ), swells ( $0.04 < f < 0.1$ ), and wind waves ( $f > 0.1$ ), respectively, each wave energy component  $E_i$  changes in and outside the reef due to wave breaking and bottom friction, as shown in Figure 7. The abscissa indicates the measuring stations and the ordinate does the energies relative to the total energy of incident waves,  $E_T$ . It is noted that the energy of long waves with periods greater than 25 sec, having small partition rate of the wave energy, are unchanged both in and outside the reef. The result shows that the coral reef in the beach is not effective for dissipating long period waves.

(2) Significant waves

At high tidal phase the significant wave heights and periods ( $H_{1/3}, T_{1/3}$ ) change in and outside the reef, i.e., in the wave propagation direction, as shown in Figure 8. The abscissa shows the measuring stations and the subscript 0 denotes quantities of

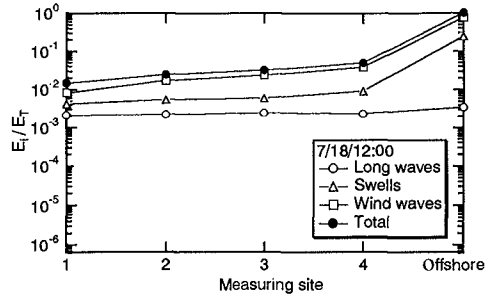


Figure 7. Wave energy dissipation on Sanur coral flat due to wave breaking and bottom friction at high tide (July 17 at 12:00).

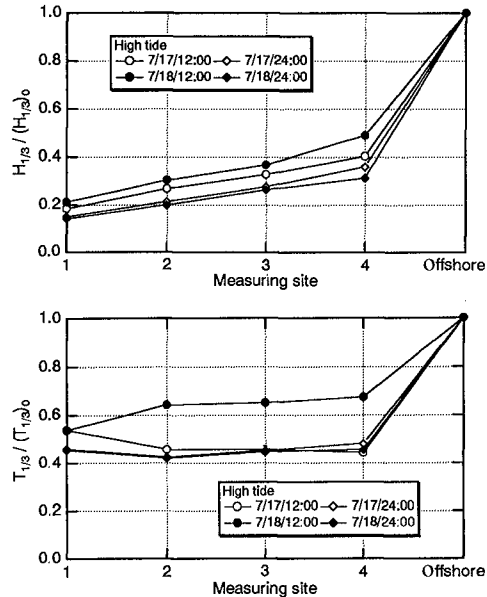


Figure 8. Changes in the significant wave heights (upper) and periods (lower) at high tide.

the offshore incident waves. After entering onto the coral flat, the significant wave heights decrease suddenly by breaking nearby the reef edge, and furthermore decrease gradually due to bottom friction on the coral flat. Similarly, the significant wave periods change suddenly near the reef edge, but they remain nearly constant on the coral flat. The main reasons of decrease in wave period are due to short-period waves generated in the course of wave breaking, and, probably, fission of long-period waves into solitons taking places on the coral flat. The prediction of wave properties should become taking into account of the change in wave period caused both by wave breaking and fission.

**PREDICTION OF REPRESENTATIVE WAVE HEIGHTS**

**Model equations**

The mild-slope (MS) and KdV equations are applied herein to predict representative wave heights for irregular waves on the coral flat. The MS equation is useful for estimation of transformation of waves propagating on the step-type reef with bathymetric discontinuity (Tsutsui & Zamami, 1993), as shown schematically on the left in Figure 9. Coral reefs of step-type are formed in the Okinawa islands, but those of slope-type are formed in Sanur beach, as shown schematically in the figure. As the offshore-side bottom slope changes gradually from 1/20 to 1/50, the KdV equation can be applied, but not for the step-type reef. Notice that all the physical quantities in this section are written in dimensionless form by using the representative quantities, the length being the nominal water depth  $h_0$ , the time  $\sqrt{h_0/g}$ , the velocity  $\sqrt{gh_0}$ , and the acceleration of gravity  $g$ .

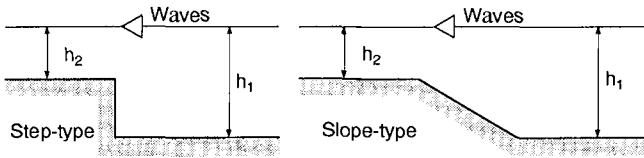


Figure 9. Step and slope-type reefs.

(1) The MS equation

The MS equation with the effects of wave energy dissipation due to wave breaking and bottom friction is given in the form (Dalrymple et al., 1984)

$$\nabla(c c_g \nabla \eta) + [(c_g/c) \sigma^2 - i \sigma f_d] \eta = 0 \tag{1}$$

where  $\nabla = (\partial/\partial x, \partial/\partial y)$  is the horizontal differential operator,  $(x, y)$  are the horizontal coordinates,  $c$  is the wave velocity,  $c_g$  the group velocity,  $\eta$  the water surface displacement,  $\sigma = 2\pi/T$  the frequency,  $T$  the wave period, and  $f_d$  the dimensionless coefficient of wave energy dissipation due to breaking and bottom friction. In the present study, after transformation into the two-dimensional form (Tsutsui, 1991), the MS equation (1) is calculated numerically by the finite element method.

(2) The KdV equation

The KdV equation with the effects of wave energy dissipation due to wave breaking and bottom friction is given in the form (Tsutsui, 1986; Yasuda & Nishio, 1990)

$$\eta_x + \frac{3}{2} h^{-3/2} \eta \eta_\xi + \frac{1}{6} h^{1/2} \eta_{\xi\xi\xi} + \frac{1}{4} h^{-1} h_x \eta = \frac{1}{2} \kappa h^{-3/2} \eta_{\xi\xi} - \frac{1}{2} s h^{-2} \eta |\eta| \tag{2}$$

with  $\xi = \int h^{-1/2} dx - t$  (3)

where  $h$  is the local still water depth,  $\kappa$  the dimensionless coefficient of wave energy dissipation,  $s$  the coefficient of bottom friction, and the subscripts denote partial derivatives. Note that the wave energy dissipation is estimated by two terms on the right-hand side of Eq.(2). The term of diffusion, the first term, plays an important role in evaluating the effect of wave height damping due to breaking, and the second term does due to bottom friction. The equation (2) can be calculated numerically by the finite difference method (Tsutsui, 1986).

The sudden decrease in wave periods due to fission of long-period waves into solitons just after wave incidence upon the reef can be confirmed numerically, by making use of the KdV equation without wave breaking and bottom friction. Figure 10 shows an example for a gradually varying reef shown in the bottom of the figure, where  $U_r$  is the Ursell number,  $\varepsilon = h_2/h_1$  the ratio of the shallower water depth  $h_2$  on the reef to the offshore water depth  $h_1$ ,  $H$  is the wave height, and the subscript  $i$  stands for quantities of an incident wave. The wave height and period vary periodically with respect to wave propagation because of nonlinear interaction of solitons. Just after the fission, its period decreases suddenly to a value less than half of the incident wave period. As shown in Figure 8, the value nearly equals those obtained from observation. In the course of wave propagation the wave period becomes longest in the phase of reformation of waves, at which the wave height decreases a little.

#### Coefficient of energy dissipation

In order to use Eqs.(1) and (2) for calculating wave properties on the coral reef, the coefficient of wave energy dissipation due to breaking and bottom friction must be evaluated. The equation of wave energy conservation is given by

$$\frac{d}{d\xi}(Ec_g) = -f_d E \quad (4)$$

where  $E$  is the total wave energy and  $\xi$  is the horizontal coordinate in the direction of wave propagation. We use the expression for the coefficient of wave energy dissipation,  $f_d$ , introduced by Izumiya & Horikawa (1984), considering bottom friction, under the assumption of homogeneity of turbulence in the breaker zone. As the total water depth including wave setup is used in the expression, using linear wave theory, it can be modified (Yamashita et al., 1990; Tsutsui & Zamami, 1993) as

$$f_d = \left[ \frac{1}{2} C_f^* + \frac{\beta_0}{8} \sqrt{\left(\frac{H}{h}\right)^2 - \left(\frac{H}{h}\right)_s^2} \right] \frac{H}{h} \frac{c_g}{h} \quad (5)$$

in their notations, where  $(H/h)_s$  is the minimum wave height relative to the water depth in the wave damping region,  $C_f^*$  the coefficient of bottom friction, and  $\beta_0$  the dimensionless coefficient related with wave energy dissipation due to breaking.

Based on the experimental estimation of the coefficient  $\beta_0$  for the step-type reef, the wave height distribution in the breaker zone can be estimated correctly (Tsutsui & Zamami,

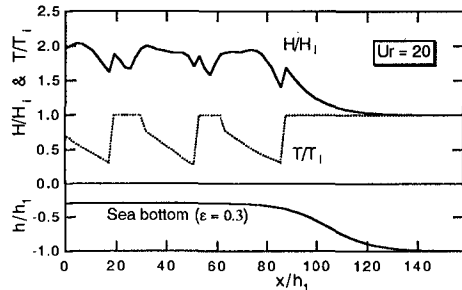


Figure 10. Changes in the wave height and period on the reef due to fission of a wave into solitons.

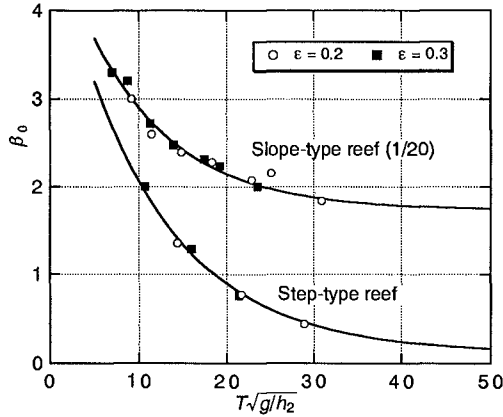


Figure 11. Coefficients  $\beta_0$  for the slope and step-type reefs.

1993). Similarly, we can determine the coefficient  $\beta_0$  on the slope-type reef, as shown in Figure 11, where the offshore slope is 1/20 and the abscissa indicates the dimensionless wave period  $T\sqrt{g/h_2}$  on the coral flat. In the limiting state of  $T\sqrt{g/h_2} \rightarrow \infty$ , the value of  $\beta_0$  on the slope-type reef can be approximated as  $\beta_0 \approx \sqrt{3}$  (Appendix), by referring to the breaking model for the solitary wave (Le Méhauté, 1963). The empirical formulae of the coefficient  $\beta_0$  are, for the slope-type reef,

$$\beta_0 = 3.27 \exp[-0.1027T\sqrt{g/h_2}] + 1.73, \quad T\sqrt{g/h_2} > 5 \tag{6}$$

and for the step-type reef,

$$\beta_0 = 4.48 \exp[-0.0921T\sqrt{g/h_2}] + 0.12, \quad T\sqrt{g/h_2} > 5 \tag{7}$$

Figure 12 shows typical examples of experimental wave height distributions for periodic waves on the slope-type reef, comparing with numerical results by the MS and KdV equations without bottom friction. The abscissa is taken as the distance from the reef edge and the ordinate denotes the dimensionless wave height. In the MS equation the coefficient of wave energy dissipation  $f_d$  with  $\beta_0$  given by Eq.(6) is used in estimation of wave damping, whereas the coefficient of energy dissipation in the KdV equation is evaluated by

$$\kappa = f_d/4 \tag{8}$$

to express the effect of wave breaking by the term of diffusion. Generally, for shorter period waves the wave height distributions by the MS equation agree well with experimental ones, whereas

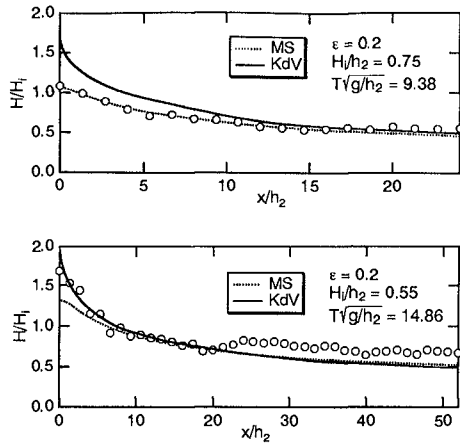


Figure 12. Wave height distributions on the slope-type reef.

the KdV equation gives good estimation of the wave height distributions for longer period waves. This reason is that, for longer period waves, the breaking wave heights at the reef edge estimated by KdV equation are agree fairly with experimental ones, but the MS equation shows to underestimate them. Therefore, the discrepancy between the calculated and experimental values of relative wave height near breaking point becomes remarkably. However, in a region far from the reef edge, both the MS and KdV equations are applicable for wave height estimation after wave breaking.

**Wave height prediction on Sanur coral flat**

As mentioned previously, wave setup takes place on the coral flat due to wave breaking. Hereafter, the amount of wave setup  $\Delta h$  is assumed to be 30 cm according to the results of

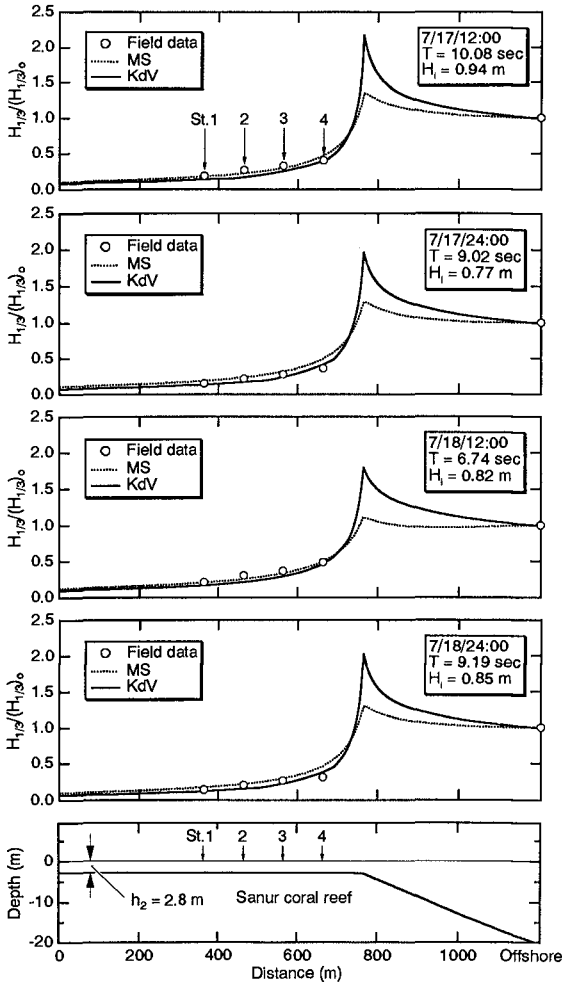


Figure 13. Wave height prediction on Sanur coral flat with the MS and KdV equations.

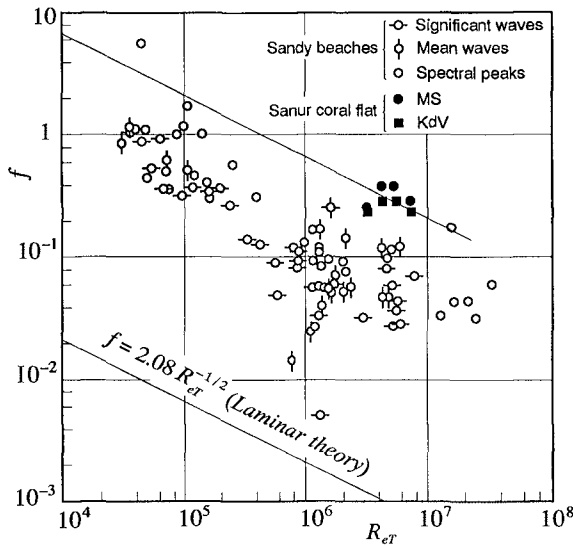


Figure 14. Coefficient of bottom friction on Sanur coral flat.

Goda (1975) and Hino et al. (1989).

When the significant waves on the coral flat at high tide were estimated by the MS and KdV equations, taking into account only of wave damping due to breaking, the values of wave heights were greater than those of observation. The result indicates the significant role of bottom friction to the wave energy dissipation on the coral flat. However, the value of the coefficient of bottom friction in the coral flat is unknown. Therefore, the coefficient of bottom friction was evaluated such that wave heights estimated coincide with the observed data. Figure 13 shows the results of prediction of significant wave heights on the coral flat at the highest tidal level of water, where the distance is taken offshore-ward from the shoreline. Discrepancy in numerical estimations by the MS and KdV equations (solid and dotted lines) becomes remarkably near the breaking point, i.e., the reef edge. The relative distances between the measuring station 4 and the reef edge are within  $35 < x/h_2 < 40$ , showing that all the measuring stations are located in the region where the damping of wave heights due to breaking is not effective, as shown in Figure 12. The MS and KdV equations, therefore, predict well the wave height distributions observed.

On the bottom friction, as seen in the data for sandy beaches shown by open symbols in Figure 14 (e.g., Iwagaki & Kakimuna, 1962), there exists a linear relation between the coefficient of bottom friction  $f$  and the wave Reynolds number  $Re_T = u_{h_{max}}^2 T / \nu$ , where  $u_{h_{max}} = \sigma H / 2 \sinh kh$ ,  $k$  is the wave number, and  $\nu$  is the kinematic viscosity. The values of bottom friction on Sanur coral flat are plotted by the solid symbols (●, ■). The coral flat composed of unevenness is covered by sea glasses so densely that the bottom friction is evaluated greater than those on sandy beaches. The values of bottom friction on the coral flat are not enough to design the relation, but may follow the linear relation shown in the figure by the solid line.

**THE MAXIMUM WAVE ON THE CORAL FLAT**

We consider two kinds of the maximum waves on the coral flat in relation to the rate of



wave breaking near the reef edge. Waves of small wave heights can propagate on the coral flat without breaking but the waves may break after propagation of some distances when they become large. The first kind of the maximum wave is then for progressive waves propagating onto the coral flat without breaking. Figure 7 has already indicated the incident possibility of long-period waves into Sanur beach. Due to the low breaking rate of irregular waves at the reef edge, the maximum wave arriving at the shore is therefore subjected to this breaking criterion for progressive waves on the reef. As the results of experiments for periodic waves on the step-type reef (Tsutsui & Zamami, 1993), this breaking criterion is given by

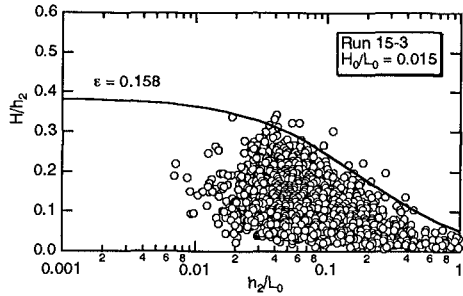
$$\frac{H_b}{h_2} = \frac{c_0}{1 + c_1 \zeta + c_2 \zeta^2}, \quad \zeta = \frac{2\pi h_2}{L_0} \tag{9}$$

with

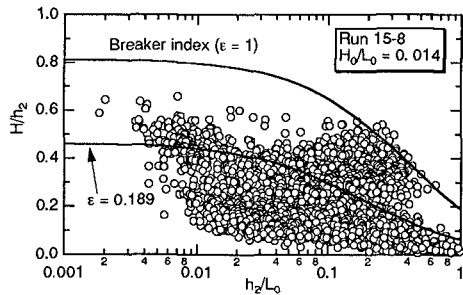
$$\left. \begin{aligned} c_0 &= 2.45 \epsilon, \quad \text{for } \epsilon < 0.2 \\ c_0 &= 0.4 \frac{1 + 1.34\sqrt{\epsilon - 0.17}}{1 + 0.1\sqrt{\epsilon - 0.17}}, \quad \text{for } \epsilon \geq 0.2 \\ c_1 &= 1 - 0.6 \epsilon, \quad c_2 = 0.02 \end{aligned} \right\} \tag{10}$$

On the other hand, when incident waves are relatively large to the water depth, they break very close to the reef edge on the step-type reef, forming partial standing waves in the offshore deeper region of the reef, but they break near the reef edge on the slope-type reef. In this case of high wave breaking rates of irregular waves, the second kind of the maximum wave arriving at the shore is subjected to the waves that are reformed after strong wave breaking.

As the results of experiments for irregular waves on the step-type reef, Figure 15 shows examples of the relationship between the wave height relative to the water depth on the coral flat,  $H/h_2$ , and the shallowness  $h_2/L_0$ , where all the individual waves measured in the reforming region after wave damping due to breaking are plotted by the open circle. In the parameters,  $L_0$  is the wave length in deep water for the individual wave and  $H_0/L_0$  is the wave steepness in deep water for the significant waves. In the upper figure (1), the significant wave height is smaller than the critical wave height shown by the solid line, Eqs.(9) and (10), and it seems that the rate of wave breaking is low. This solid line indicates the maximum wave, which shows the envelope of the data.



(1) Low rate of wave breaking.



(2) High rate of wave breaking.

Figure 15. Maximum waves on the step-type reef according to the rate of wave breaking.

The result in the case of high wave breaking rate is shown in the lower figure (2), where the significant wave height is larger than the critical wave height shown by the lower solid line, and most waves break at the reef edge. The upper solid line with  $\epsilon = 1$  indicates the breaker index for the flat sea bottom (Goda, 1970), an approximation of the highest wave of permanent-type on water of uniform depth (Yamada and Shiotani, 1968), and it becomes the envelope of all the experimental data. Therefore, the maximum wave after strong wave breaking near the reef edge is determined by the breaker index for the flat sea bottom.

Similarly, the relation of the relative wave height  $H/h_2$  on Sanur coral flat and the shallowness  $h_2/L_0$  is shown in Figure 16, where all the individual waves measured at the station 4 near the highest tidal phase are plotted by the open circle. The breaker type near the reef edge is for progressive waves because Sanur beach is of slope-type reef with the offshore slopes of 1/20 - 1/50. Therefore, we can use Eqs.(9) and (10) as the breaking criterion, when the water depth ratio  $\epsilon = h_2/h_1$  is given as the ratio of the water depth  $h_2$  on the coral flat to the offshore water depth  $h_1$ , where the shoaling coefficient given by the small amplitude wave theory takes unity, i.e.,  $h_1/L_0 = 0.057$ . The solid lines in Figure 16 show the results. As  $h_2/L_0 = 0.017 - 0.038$  and  $H/h_2 = 0.303 - 0.346$  for the significant waves, the wave breaking rate is low. Therefore, the curves in Figure 15 indicate the empirical maximum wave on Sanur coral flat with envelopes for the field data. Furthermore, it has been confirmed by laboratory tests that the maximum wave on Sanur coral flat at the high wave breaking rate is also evaluated by the breaker index for the flat sea bottom, as well as for the step-type reef.

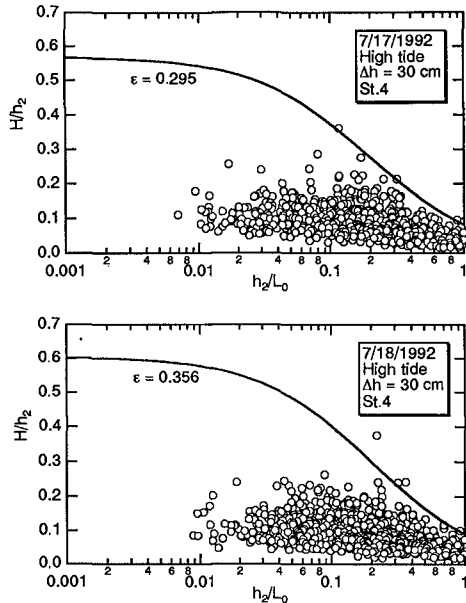


Figure 16. The maximum wave on Sanur coral flat.

**CONCLUSIONS**

Main conclusions of the present analysis of wave properties and the maximum wave based on the experimental and field data at Sanur coral beach are summarized as:

- (1) In Sanur beach, waves in the dry season (June - August) are predominant for the beach process, and they are incident perpendicular to the reef edge. Swells with a period of about 15 sec are most effective for beach change.
- (2) The MS and KdV equations with the effects of wave energy dissipation can predict the wave height distribution on the coral flat, when the coefficients of wave breaking and bottom friction are evaluated.
- (3) In the case of the low wave breaking rate, the experimental wave height criteria for progressive waves, Eq.(9) and (10), give the maximum wave arriving at the shore without breaking. Contrarily, after full breaking of incident waves near the reef edge, the maximum wave on coral flats can be determined by the breaker index for flat sea bottom.

### Acknowledgments

The present research, part of international joint investigation between the Research Institute for Water Resources Development and Disaster Prevention Research Institute, Kyoto University, associated with IDNDR, was supported by the Ministry of Education, Science and Culture of Japan. We wish to thank many individuals who have joined the investigation, in particular, Dr. Badruddin Machbub, Director, Dr. Abdul R. Syamsudin, Chief, Water Resources division, Research Institute for Water Resources Development, Mr. T. Onuki, Nippon-Koei Co. Ltd., and Mr. K. Sakai, Toa Corporation, who kindly provided their supports and cooperation in carrying out this investigation.

**Appendix:** The coefficient  $\beta_0$  for the slope-type reef as  $T\sqrt{g/h_2} \rightarrow \infty$

If the small amplitude wave theory is applied in Eqs.(4) and (5), we have

$$\frac{d}{d\xi} (H^2 c_g) = -\frac{\beta_0}{8} \left[ \left( \frac{H}{h} \right)^2 - \left( \frac{H}{h} \right)_s \right] \frac{H^3}{h^2} c_g \quad (\text{A.1})$$

where the effect of bottom friction is neglected. Dividing by  $H^2 c_g$  and integrating with respect to  $\xi$  within a small increment  $\Delta\xi = \xi_2 - \xi_1$  give

$$\frac{H_2}{H_1} = \left( \frac{c_{g1}}{c_{g2}} \right)^{1/2} \exp \left[ -\frac{\beta_0}{16} \sqrt{1 - (H_s/H_b)^2} \left( \frac{H_1}{h} \right)^2 \frac{\Delta\xi}{h} \right] \quad (\text{A.2})$$

where the subscripts 1 and 2 denote quantities at the locations  $\xi_1$  and  $\xi_2$ , respectively, and  $\bar{h}$  is the mean water depth within the increment  $\Delta\xi$ .

By introducing the bore model, Le Méhauté (1963) evaluated the energy dissipation rate of solitary wave as a spilling breaker as;

$$\frac{H_2}{H_1} = \frac{h_1}{h_2} \left( \frac{c_1}{c_2} \right)^{2/3} \exp \left[ -\frac{\sqrt{3}}{16} \left( \frac{H_1}{h} \right)^{5/2} B \frac{\Delta\xi}{h} \right] \quad (\text{A.3})$$

$$\text{with } B = \frac{[(1 + H/h) - \beta(1 + \beta H/h)]}{(1 + H/h)(1 + \beta H/h)} (1 - \beta)^3 \quad (\text{A.4})$$

where  $\beta$  is the dimensionless parameter that defines the range of surface disturbance due to wave breaking and then  $0 \leq \beta \leq 1$ . The condition that  $\beta = 1$  corresponds to non-breaking ( $B = 0$ ), and  $\beta = 0$  to full breaking ( $B = 1$ ). The coefficient  $B$  is then call the breaking coefficient. In case of non-breaking, Eq.(A.2) gives the so-called Green's law for long period waves as :  $H_2/H_1 \approx (h_1/h_2)^{1/4}$ , and Eq.(A.3) gives  $H_2/H_1 \approx (h_1/h_2)^{4/3}$ . This difference is due to the validity of using the solitary wave theory in analyzing wave motion on a slope. However, Eq.(A.3) is applicable for waves on the coral flat because the coefficients of the exponential terms in Eqs.(A.2) and (A.3) can be approximated as unity. Equation (A.2) must be asymptotic to Eq.(A.3) as  $T\sqrt{g/h_2} \rightarrow \infty$ . Comparing the coefficients in the exponential damping terms gives

$$\beta_0 = \sqrt{3} \sqrt{H_1/h} D, \quad D = B / \sqrt{1 - (H_s/H_b)^2} \quad (\text{A.5})$$

It is easy to show that the effect of sea bottom slope on the parameter  $D$  in Eq.(A.5) through the wave height is very small, by using the breaker index (Goda, 1970) and assuming the breaking point to be the reef edge. Furthermore, waves on slopes steeper than 1/50 break completely (Le Méhauté, 1963). We can thus approximate as  $\beta \approx 0$  and  $D \approx 1$ . Consequently, the coefficient  $\beta_0$  for longer period waves depends only on the breaking wave height  $(H/h)_b$ , i.e.,

$$\beta_0 = \sqrt{3} \sqrt{(H/h)_b} \quad (\text{A.6})$$

Since  $\sqrt{(H/h)_b} = 1.01$  for solitary wave propagating on the gentle slope of 1/20, the coefficient  $\beta_0$  can be approximated by  $\beta_0 \approx \sqrt{3}$  when  $T\sqrt{g/h_2} \rightarrow \infty$ . Note that the breaking wave height takes values within  $0.91 < \sqrt{(H/h)_b} < 1.17$  for the sea bottom conditions varying from the uniform water depth to the slope of 1/10.

## References

- Dalrymple, R. A., J. T. Kirby and P. A. Hwang (1984): Wave diffraction due to areas of energy dissipation, *Jour. Waterway, Port, Coastal, and Ocean Eng.*, ASCE, Vol.110, pp.67-79.
- Goda, Y. (1970): A synthesis of breaker indices, *Proc. JSCE*, Vol.180, pp.39-49 (in Japanese).
- Goda, Y. (1975): Irregular wave deformation in the surf zone, *Coastal Eng. in Japan*, JSCE, Vol.18, pp.13-26.
- Hino, M., E. Nakaza, and S. Yogi (1989): Bore-like surf beat in reef coasts, *Proc. Coastal Eng.*, JSCE, Vol.36, pp.75-79 (in Japanese).
- Iwagaki, Y., T. Kakinuma (1962): On the coefficient of bottom friction at Akita coast, *Proc. 9th Japanese Conf. on Coastal Eng.*, JSCE, pp.81-84 (in Japanese).
- Izumiyama, T. and K. Horikawa (1984): Wave energy equation applicable in and outside the surf zone, *Coastal Eng. in Japan*, Vol.27, pp.119-137.
- Kai, K. (1985): Spectrum climatology of the surface winds in Japan, Part I: The 40-60 day fluctuations, *Jour. Meteorological Soc. Japan*, Vol.63, pp.873-882.
- Le Méhauté, D. Sc. (1963): On non-saturated breakers and the wave run-up, *Proc. 8th Conf. on Coastal Eng.*, ASCE, pp.77-92.
- Syamsudin, A. R. (1993): Beach Erosion in Coral Reef Beaches and its Control, Doctoral Dissertation at Kyoto University, 221p.
- Tsutsui, S (1986): Wind effects on the evolution of solitons, *Proc. 33rd Japanese Conf. on Coastal Eng.*, JSCE, pp.61-65 (in Japanese).
- Tsutsui, S. (1991): A wave prediction model in reef coasts, *Bull. Fac. of Eng., Univ. of the Ryukyus*, No.42, pp.35-43 (in Japanese).
- Tsutsui, S. and K. Zamami (1993): Jump condition of energy flux at the line of bathymetric discontinuity and wave breaking on the reef flat, *Coastal Eng. in Japan*, JSCE, Vol.36, pp.155-175.
- Yamada, H. and T. Shiotani (1968): On the highest water waves of permanent type, *Bull. Disaster Prevention Research Inst., Kyoto Univ.*, Vol.18, Pt.2, pp.1-22.
- Yamashita, T., Y. Tsuchiya, M. Matsuyama and T. Suzuki (1990): Numerical calculation of linear wave propagation in the coastal zone, *Bull. Disaster Prevention Research Inst., Kyoto Univ.*, Vol.40, pp.15-40.
- Yasuda, T. and Y. Nishio (1990): Model for random waves propagating in surf zones, *Proc. Coastal Eng.*, JSCE, Vol.37, pp.66-70 (in Japanese).

## CHAPTER 46

### Development of a Submerged Doppler-Type Directional Wave Meter

Tomotsuka Takayama<sup>1</sup>, Noriaki Hashimoto<sup>2</sup>, Toshihiko Nagai<sup>3</sup>  
Tomoharu Takahashi<sup>4</sup>, Hiroshi Sasaki<sup>5</sup>, and Yoshiki Ito<sup>6</sup>

#### Abstract

This paper presents a newly developed type of submerged directional wave meter having the capability to measure water surface elevation and multiple current velocity components. These components are determined from Doppler frequency shifts using the complex covariance method. The developed system was demonstrated to be capable of successfully obtaining directional wave data, as well as adequately estimating directional wave spectra.

#### 1. Introduction

Many types of wave observation devices have been developed over the years for various scientific and engineering applications. Most, however, were designed to measure only wave height and period, and consequently, a practical instrument incorporating features for satisfactorily measuring directional seas has not yet been obtained.

The most commonly used wave meter in Japan is a submerged ultrasonic-type wave gage that can be installed at a water depth of up to about 50 m. A submerged ultrasonic-type current meter developed for measuring directional seas, however, is limited to 30-m-deep water due to a decay of water particle velocity caused by waves. Obviously then, there is a need to develop a combined measuring system that can operate at 50 m.

---

<sup>1</sup> Director, Hydraulic Engineering Div., Port and Harbour Research Institute (PHRI),  
1-1 Nagase 3-chome, Yokosuka 239, Japan

<sup>2</sup> Chief, Ocean Energy Utilization Lab., Hydraulic Engineering Div., PHRI.

<sup>3</sup> Chief, Marine Observation Lab., Marine Hydrodynamics Div., PHRI.

<sup>4</sup> Managing Director, Japan Marine Surveyors Association,

14-12 Kodenma-cho, Nihonbashi, Chuo-ku, Tokyo 103, Japan

<sup>5</sup> Former manager, Measuring and Control System Div., Kaijyo Corporation,  
3-1-5 Sakae-cho, Hamura-shi, Tokyo 205, Japan

<sup>6</sup> Manager, Research and Development Div., Kaijyo Corporation.

This led to the present paper which describes a new device, named the submerged Doppler-type directional wave meter, that utilizes the Doppler effect of ultrasonic waves in water for measuring directional seas in coastal areas having a water depth of about 50 m.

## 2. Submerged Doppler-type directional wave meter

### 2.1 System description

**Figure 1** shows a circuit block diagram of the measurement system of the submerged Doppler-type directional wave meter. This system is comprised of a submerged transducer, measurement section, and computation unit. The measurement section consists of transceiver and signal processing circuits. The former circuit connects the transducer to the latter one which converts the signals to water surface elevation and current velocities after digitizing received analog quantities. The computation unit statistically analyzes wave data and computes the resultant directional wave spectra.

To measure the water surface elevation, the transducer radiates vertically-upward-directed ultrasonic waves ( $Z$ -axis, **Fig. 1**) and then receives the waves reflected off the water surface. The water surface elevation is estimated using the wave propagation time. By also radiating ultrasonic waves upward in four directions separated by an inclination angle  $\alpha$ , multiple current velocities are measured by receiving the waves scattered back from selected layers of water. The water particle velocity of each layer is estimated from the frequency shift caused by the Doppler

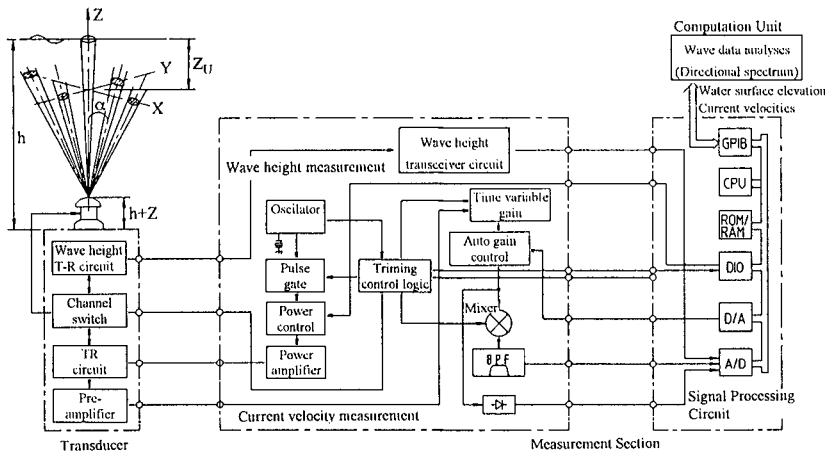


**Fig. 1** Diagram of the measurement system of the submerged Doppler-type directional wave meter.

**Table 1** Specifications of the Doppler-type directional wave meter.

Specification	Current Velocity	Wave Height
Measurement system	Ultrasonic Doppler method	Ultrasonic wave propagation time
Operating frequency	500 kHz	200 kHz
Beam width	1	30
Measurement channel	Orthogonal 4 channels	Vertical 1 channel
Beam tilt	300	—
Maximum output power	300 W	--
Measurement range	0 to $\pm 5$ m/s	0 ~ 30 m
Range resolution	2.3 m	—
Transmission interval	165 ms	165 ms
Measurement period	900 ms	495 ms

effect between the radiated and scattered waves. Use of a time sharing system enables all these measurements to be successively carried out at very short time intervals. Specifications of the new wave meter are summarized in **Table 1**.

## 2.2 Doppler frequency estimation methods

Two different techniques exist for conducting Doppler frequency analysis: (1) use of analog signals, such as the phase lock loop (PLL) or analog filter bank methods; and (2) use of digital signals, such as the fast Fourier transformation (FFT) and complex covariance (CC) methods. Of these, real-time processing is normally performed with the FFT or CC method due to rapid developments in microcomputers and peripheral equipment.

The FFT method has an advantage in that even at a low S/N ratio it can analyze the scattered wave signal to estimate the spectral density over the entire frequency band. At a higher S/N ratio, however, the CC method is more advantageous because computing the spectral moment is easier and the frequency resolution is better.

**Figure 2** shows a flow chart of the CC method's computational procedure, where the the input frequency signals  $\cos(\omega_{in}t + \epsilon)$  are first damped by the local oscillation frequency signals ( $\cos\omega_0t$  and  $\sin\omega_0t$ ) having a phase difference of  $90^\circ$ . Next, the first order moment  $\mu_1$  (average frequency) of the input signal is computed from the complex covariance function  $R(\tau)$  obtained from the outputs  $X_r(t_n)$  and  $X_i(t_n)$ . More specifically, the frequency components of  $\omega_{in} + \omega_0$  and  $\omega_{in} - \omega_0$  are obtained by mixing the input signals  $\cos(\omega_{in}t + \epsilon)$  with the cos and sin components of the local oscillation signals having frequency  $\omega_0$ . The difference component  $\omega_{in} - \omega_0$

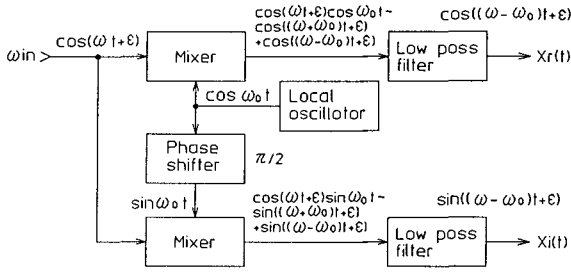


Fig. 2 Analog method for generating complex signals.

is then sent to a low pass filter (LPF) and A/D converter where it digitized. From  $X_r(t_n)$  and  $X_i(t_n)$ , the complex values  $Z(t_n)$  are obtained by  $Z(t_n) = X_r(t_n) + iX_i(t_n)$ , followed by computing  $\mu_1$  using

$$R(\tau) = \frac{1}{N} \sum_{n=1}^{N-1} Z(t_n)Z^*(t_n + \tau) \tag{1}$$

$$\mu_1 = \frac{1}{2\pi\tau} \tan^{-1} \frac{\text{Im}[R(\tau)]}{\text{Re}[R(\tau)]}, \tag{2}$$

where  $Z^*(t_n)$  is the complex conjugate of  $Z(t_n)$ .

This procedure can also be performed by the simple homodyne complex covariance (SHCC) method which simplifies the computation (Ito et al., 1989). Figure 3 shows a flow chart of this method's data processing procedure. Since the received signal is digitized, the sampling frequency  $f_s$  is easily synchronized with the transmitting wave which is four times larger than the transmitting frequency  $f_0$ . The reference signals for the homodyne detection can then be simulated as

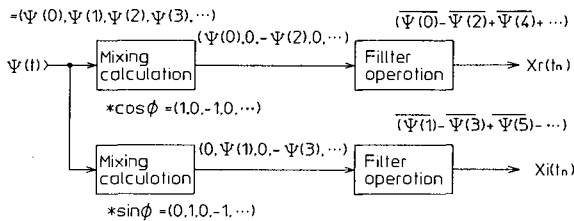


Fig. 3 Data processing for the SHCC method.



$$\begin{aligned}\cos \phi &= (1, 0, -1, 0, 1, 0, -1, \dots) \\ \sin \phi &= (0, 1, 0, -1, 0, 1, 0, \dots)\end{aligned}\quad (3)$$

Therefore, the outputs of homodyne circuit can be approximated by

$$\begin{aligned}\psi(t) \cos \phi &= \psi(0), 0, -\psi(2), 0, \psi(4), 0, \dots \\ \psi(t) \sin \phi &= 0, \psi(1), 0, -\psi(3), 0, \psi(5), \dots\end{aligned}\quad (4)$$

where  $\psi(t)$  is the received signal. If we utilize a LPF, by making block averages (16 points) of these series, the complex beat signal series,  $X_r(t)$  and  $X_i(t)$ , can be obtained. Then  $R(\tau)$  is subsequently determined by Eq. (1) and the Doppler or beat frequency  $\mu_1$  can be estimated as per the CC method (Eq. (2)).

When background noise is approximately stationary during a pulse repetition period, noise compensation can be accomplished using

$$\mu_1 = \frac{1}{2\pi\tau} \tan^{-1} \frac{\text{Im}[R(\tau)] - \text{Im}[R_n(\tau)]}{\text{Re}[R(\tau)] - \text{Re}[R_n(\tau)]}, \quad (5)$$

where  $R_n(\tau)$  indicates the complex covariance of the noise process.

Field experimental data shows this method estimates the current velocity at a S/N ratio corresponding to actual sea conditions with a mean error of about 2 to 6 cm/s and standard deviation of about 1 to 2 cm/s.

### 2.3 Analysis of directional spectrum

The extended maximum likelihood method (EMLM) developed by Isobe et al. (1984) was employed to estimate the directional spectrum because of its high versatility and relatively high accuracy.

Using polar coordinates (**Fig. 4**), the water particle velocity  $U$  in the direction  $r$  with coordinates  $(\alpha, \beta, r)$  is obtained by

$$U(\alpha, \beta, r, h, z_0; \omega, \theta) = H(\alpha, \beta, r, h, z_0; \omega, \theta) \eta(\alpha, \beta, r; \omega, \theta), \quad (6)$$

where  $\eta$  is the water surface elevation and  $H$  the transfer function between  $U$  and  $\eta$ .  $H$  can be expressed using linear wave theory as follows:

$$H(\alpha, \beta, r, h, z_0; \omega, \theta)$$

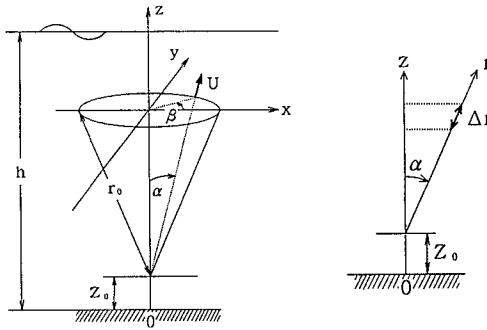


Fig. 4 Definition of polar coordinates.

$$\begin{aligned}
 &= \frac{\omega}{\sinh kh} \left[ \cosh\{k(r \cos \alpha + z_0)\} \right. \\
 &\quad \times \sin \alpha \cos(\theta - \beta) \\
 &\quad \left. - i \sinh\{k(r \cos \alpha + z_0)\} \cos \alpha \right], \tag{7}
 \end{aligned}$$

where  $h$ ,  $k$ ,  $\omega$ ,  $\theta$ , and  $z_0$  respectively represent the water depth, wave number, angular frequency, wave propagation direction, and height at which the meter is installed above the seabed.

When the water surface elevation  $\eta_0$  above the origin  $(0,0,0)$  is used as a basis, the transfer function between  $U$  and  $\eta_0$  is obtained by multiplying Eq. (7) by  $\exp[i\{kr \sin \alpha \cos(\theta - \beta) - \omega \Delta t\}]$ , i.e.,

$$\begin{aligned}
 &H_0(\alpha, \beta, r, h, z_0; \omega, \theta) \\
 &= \frac{\omega \exp(-i\omega \Delta t)}{\sinh kh} \left[ \cosh\{k(r \cos \alpha + z_0)\} \right. \\
 &\quad \times \sin \alpha \cos(\theta - \beta) - i \sinh\{k(r \cos \alpha + z_0)\} \\
 &\quad \left. \times \cos \alpha \right] \exp\{ikr \sin \alpha \cos(\theta - \beta)\}, \tag{8}
 \end{aligned}$$

where  $\Delta t$  is the time lag between the measurement of each velocity component and that of  $\eta_0$ .

The current velocity component detected by a Doppler-type wave meter is not the water particle velocity at a specified location, but instead an average velocity in a volume of known width  $\Delta r$ . Therefore, by disregarding the width around the  $r$  axis

and integrating Eq. (8) in terms of  $r$ , the transfer function between  $U$  in the direction  $r$  with coordinates  $(\alpha, \beta, r)$  and  $\eta_0$  above the origin  $(0,0,0)$  is represented as:

$$\begin{aligned} \bar{H}(\alpha, \beta, r_0, \Delta r, z_0, \omega, \theta) &= \frac{1}{\Delta r} \int_{r_0 - \Delta r/2}^{r_0 + \Delta r/2} H_0(\alpha, \beta, r, h, z_0, \omega, \theta) dr \\ &= \frac{-i\omega \exp(-i\omega\Delta t)}{\Delta r k \sinh kh} \left[ \cosh\{k(r \cos \alpha + z_0)\} \right. \\ &\quad \left. \times \exp\{ikr \sin \alpha \cos(\theta - \beta)\} \right]_{r_0 - \Delta r/2}^{r_0 + \Delta r/2} \end{aligned} \quad (9)$$

Employing Eq. (9) leads to the estimation equation of the directional spectrum by the EMLM, i.e.,

$$S(f, \theta) = \frac{\kappa}{\mathbf{H}^* \Phi^{-1} \mathbf{H}}, \quad (10)$$

where  $\mathbf{H}$  is the matrix comprised of the transfer functions given by Eq. (9),  $\mathbf{H}^*$  the complex conjugate of the transpose matrix of  $\mathbf{H}$ ,  $\Phi^{-1}$  the inverse matrix of matrix  $\Phi$  consisting of the cross-power spectra between each quantity, and  $\kappa$  is a proportionality constant used to normalize the energy of the directional spectrum.

### 3. Field observations

Field observations were carried out off the entrance of Kamaishi Bay (Fig. 5) after installing the transducer 0.95 m above the seabed at a water depth of 35 m. The

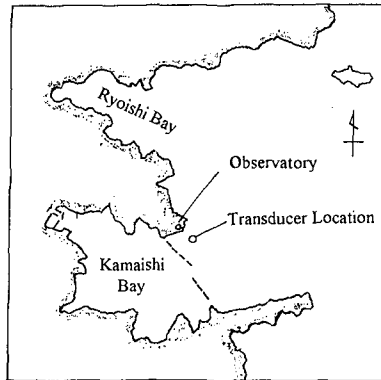


Fig. 5 Field observation location.

**Table 2** Sea conditions during the field observations.

Obs. No.	Date	Runs	Wave height (m)	Wave period (s)	Water depth (m)	Depth of scattered layer $Z_u$ (m)
1	Aug.'90	12	0.69~1.51	9.8~10.6	34.51~35.6	3.56 - 9.90
2	Nov.'90	44	0.32~1.00	6.3~13.3	34.94~36.12	8.99 - 10.17
3	Dec.'90	20	1.16~1.88	9.3~12.7	35.08~36.32	9.13 - 10.37
4	Mar.'91	44	0.76~1.84	5.6~10.6	35.56~36.46	9.01 - 10.51

measured signals were transmitted via a submarine cable to a land-based observatory (Miyako Port Construction Office, 2nd District Port Construction Bureau, Ministry of Transport). The water surface elevation ( $Z$ ) and four current velocity components ( $X^+$ ,  $X^-$ ,  $Y^+$ ,  $Y^-$ ) were recorded on an optical magnetic disk at a 0.99-s sampling interval. **Table 2** summarizes the sea conditions during the field observations.

The current velocities were measured 25 m above the transducer, with the thickness  $\Delta r$  of the scattering layers being about 2.3 m.  $\alpha$  was set at  $30^\circ$  (**Fig. 1**). We assumed a constant sound velocity of 1500 m/s for the computation.

3.1 Validity of the transfer function

The validity of the Eq. (9) transfer function cannot be directly verified using the observed data. However, by linear wave theory, the value  $\{\text{Re}(\bar{H})\}^2 + 2\{\text{Im}(\bar{H})\}^2$  can be approximated by dividing the sum of the power spectrum of water particle

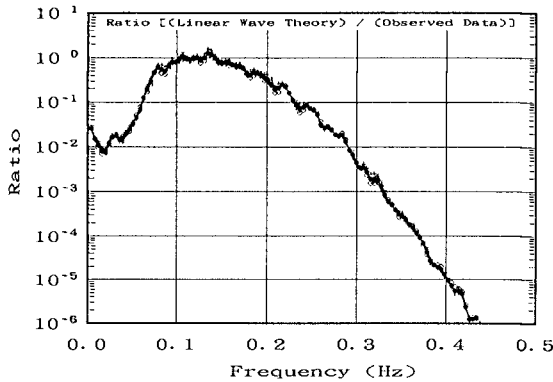


**Fig. 6** Validity of transfer function

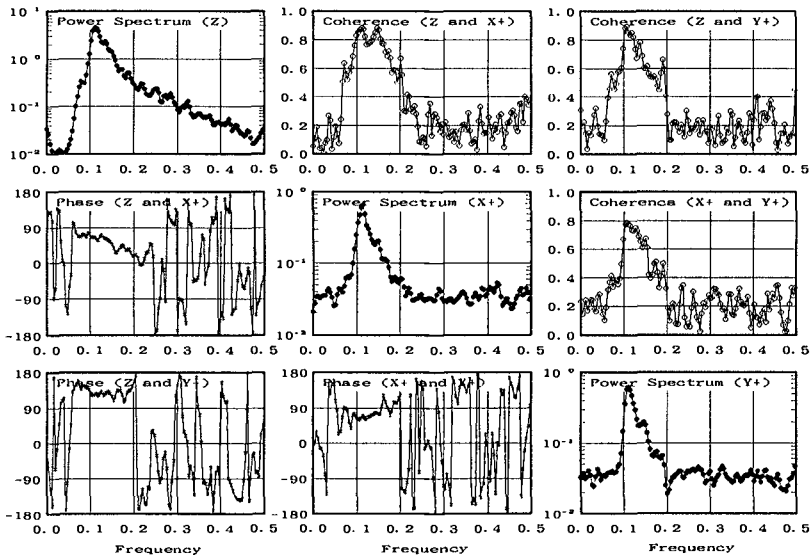


Fig. 7 Typical results of cross-power spectra estimations.

velocities in the X- and Y-directions by the power spectrum of the water surface elevation. **Figure 6** shows this ratio, which is near 1.0 from 0.08 to 0.15 Hz; hence, Eq. (9) can be considered as being valid.

### 3.2 Estimation of directional spectrum

Typical cross-power spectra estimated from the observed data are shown in **Fig. 7**, where the coherence between each wave quantity is high near the peak frequency of the power spectra and the phase angle shows continuous, smooth fluctuations from 0.06 to 0.2 Hz. These results indicate the field observation cross-power spectra are reasonable.

**Figure 8** shows typical directional spectra estimated by the EMLM, where various combinations of quantities are indicated since the EMLM enables using a data set consisting of three or more quantities. The entrance of Kamaishi Bay faces east, and all these results clearly show that waves come from the appropriate direction.

In addition, a reasonable directional spectrum was estimated in 99 out of 122 observations. Of the 23 observations from which adequate results were not estimated, 16 had water surface elevation contaminated by the noise, while the remaining 7 contained erroneous measurements.

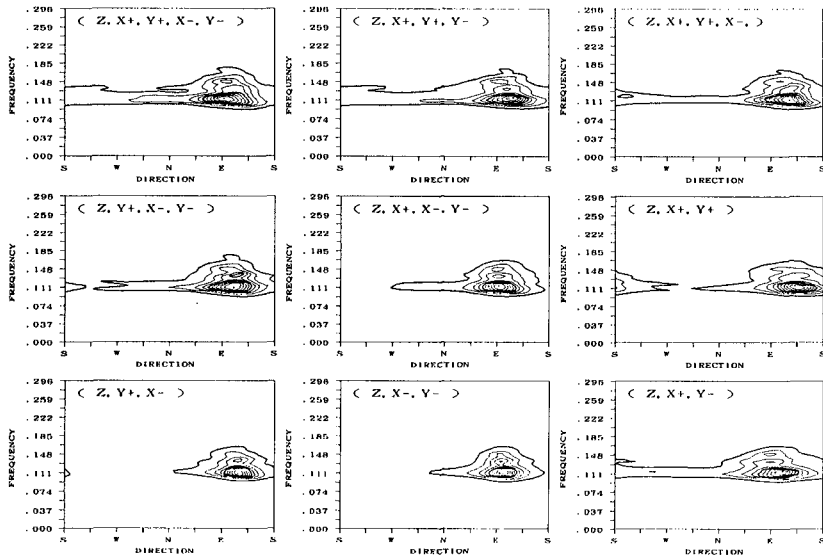


**Fig. 8** Typical directional spectra estimated using various combinations of quantities.

In cases where reasonable results were obtained, for  $z_U$  from 9 to 10 m, a measurement was obtained even when the significant wave height was only 35 cm at a significant wave period of about 10 s. Furthermore, at a significant wave period of about 6 s, waves with a significant wave height of 1 m were measured. It should be realized that the highest significant wave height for these observations was 1.85 m, which is not a severe sea condition. Under more severe sea conditions, however, measurement is believed to be possible by increasing  $z_U$ .

#### 4. Conclusions

Knowledge of directional spectra is essential for clarifying various coastal engineering problems. However, difficulties in measuring directional seas have led to insufficient information being available. Since the submerged Doppler-type directional wave meter can be employed to measure directional seas with only one set of units and provide an accurate estimation of directional spectrum. It is considered to be the best measuring system for investigation and research on directional seas. In fact, in the near future, Japan's Nationwide Ocean Wave information network for Ports and HARbourS (NOWPHAS) (Nagai et al., 1993) will install this instrument at all their coastal wave observation stations.

### Acknowledgments

This research was jointly carried out by the Port and Harbour Research Institute, Ministry of Transport, and Japan Marine Surveyors Association under the direction of the Committee for the Development of a Submerged Doppler-Type Directional Wave Meter (Chairman, Professor Y. Goda, Yokohama National University) organized by the Japan Marine Surveyors Association. The analyzed field wave data were contributed by the Second Port Construction Bureau, Ministry of Transport. Sincere gratitude is extended to all those involved in this study.

### References

- Isobe, M., K. Kondo and K. Horikawa (1984): Extension of MLM for estimating directional wave spectrum, Proc. Symp. on Description and Modeling of Directional Seas, Paper No. A-6, 15 p.
- Ito, Y., Y. Kobori, M. Horiguchi, M. Takehisa and Y. Mituta (1989): Development of Wind Profiling Sodar, J. Atmos. Oceanic Tech., Vol. 6, pp.779-784.
- Nagai, T., K. Sugahara, N. Hashimoto and T. Asai (1993): 20-year statistics of the Nationwide Ocean Wave information network for Ports and HARbourS (NOWPHAS 1970-1989), Tech. Note of Port and Harbour Res. Inst., No. 744, 247 p.
- Nagai, T., K. Sugahara, N. Hashimoto and T. Asai (1993): Annual Report on the Nationwide Ocean Wave information network for Ports and HARbourS (NOWPHAS 1991), Tech. Note of Port and Harbour Res. Inst., No. 745, 304 p.

## CHAPTER 47

# Bragg Scattering of Waves over Porous Rippled Bed

Hajime Mase<sup>1</sup> and Ken Takeba<sup>2</sup>

**ABSTRACT:** A time-dependent and a time-independent wave equations are developed for waves propagating over porous rippled beds taking account of the effects of porous medium. The mean water depth and the thickness of porous layer are assumed to be slowly varying compared to the wavelength of surface gravity waves, and the spatial scale of ripples is assumed to be the same as the wavelength of surface waves. By using the time-independent equation, the Bragg scattering is examined in one-dimensional case. The results show that the reflected and transmitted waves become smaller than those in the case of impermeable rigid rippled bed due to energy dissipation in porous medium.

### Introduction

Davies and Heathershaw (1984) studied the reflection from sinusoidal undulation over a horizontal bottom and derived a solution of reflection coefficient. Their experimental results showed a resonant Bragg reflection at the condition where the wavelength of the bottom undulation is one half the wavelength of the surface wave as predicted by their theory. Mei (1985) and Naciri and Mei (1988) developed theories of wave evolution at and close to the resonant condition by shore-parallel sinusoidal bars and two-dimensional doubly sinusoidal undulations over a slowly varying topography. For more realistic natural topography, Kirby (1986) derived a general wave equation which extends the mild slope equation of Berkhoff (1972). These existing theories don't take account of the effects of seabed permeability.

---

<sup>1</sup> Assoc. Prof., Dept. of Civil Eng., Kyoto Univ., Kyoto, 606, Japan.

<sup>2</sup> Grad. Student, Dept. of Civil Eng., Kyoto Univ., Kyoto, 606, Japan.



The strong reflection of incident waves due to the Bragg reflection results in rough offshore sea. Since it is desirable to reduce the transmitted and reflected waves, artificial porous ripples or bars would be more convenient.

In this study, a time-dependent wave equation is developed, by extending the theory of Kirby (1986), for waves propagating over permeable rippled beds in order to take into account the effects of porous medium. Some numerical calculations are carried out to show the effects of seabed permeability on wave transformations or on the Bragg scattering by ripples in one-dimensional case.

### Derivation of Wave Equation over Porous Rippled Bed

The coordinate system and main quantities are shown in Fig.1. The actual depth,  $h'(\mathbf{x})$ , is divided into the rapidly varying small amplitude undulation,  $\delta(\mathbf{x})$ , and the slowly varying mean water depth,  $h(\mathbf{x})$ :

$$h'(\mathbf{x}) = h(\mathbf{x}) - \delta(\mathbf{x}) \quad (1)$$

where  $\mathbf{x} = (x, y)$ . Thickness of the porous layer,  $h'_s(\mathbf{x})$ , is expressed as

$$h'_s(\mathbf{x}) = h_s(\mathbf{x}) + \delta(\mathbf{x}) \quad (2)$$

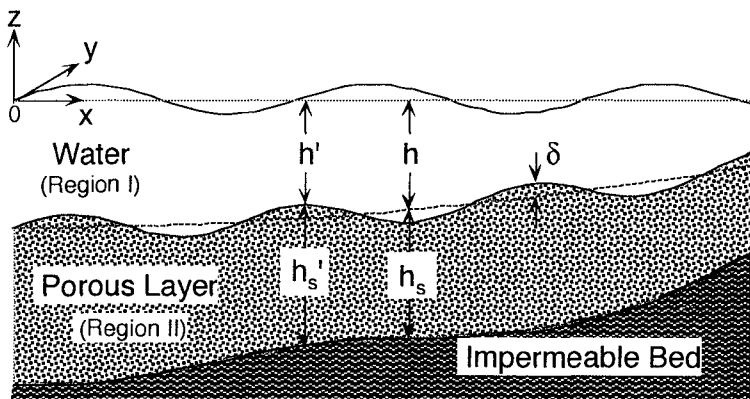


Fig.1 Definition of variables

where  $h_s(x)$  is the slowly varying mean thickness. The bottom beneath the porous layer is assumed to be impermeable and rigid.

The horizontal scales of changes of  $h(x)$ ,  $h_s(x)$  and  $\delta(x)$  are

$$O\left(\frac{\nabla_h h}{kh}\right) \approx O(k\delta) \ll 1 \quad (3)$$

$$O\left(\frac{\nabla_h (h + h_s)}{kh}\right) \approx O(k\delta) \ll 1 \quad (4)$$

and

$$O\left(\frac{\nabla_h \delta}{k\delta}\right) \approx O(1) \quad (5)$$

where  $\nabla_h$  is the gradient operator as  $(\partial/\partial x, \partial/\partial y)$ , and  $k$  is the wave-number.

The analytical domain is divided into two regions: the region (I) is the fluid domain above the porous layer; the region (II) is the porous layer, as shown in Fig. 1.

In the region (I), the irrotational motion of incompressible and inviscid fluid is described by a velocity potential,  $\phi$ , as follows:

$$\nabla_h^2 \phi + \phi_{zz} = 0 ; \quad -h \leq z \leq 0 \quad (6)$$

$$\phi_{tt} + g\phi_z = 0 ; \quad z = 0 \quad (7)$$

$$\phi_z = -\nabla_h h \cdot \nabla_h \phi + \nabla_h \cdot (\delta \nabla_h \phi) + w^{(1)} ; \quad z = -h \quad (8)$$

Eq.(6) is the Laplace equation, Eq.(7) is the free surface boundary condition combined dynamic and kinematic boundary conditions, and Eq.(8) is the bottom boundary condition expanded about  $z = -h$  to the order of  $O(k\delta)$ , where  $t$  is the time,  $g$  is the acceleration of the gravity, and  $w^{(1)}$  is the discharge velocity at the interface between the region (I) and (II). The pressure,  $p^{(1)}$ , is given by

$$p^{(1)} = -\rho(\phi_t + gz) ; \quad -h \leq z \leq 0 \quad (9)$$

where  $\rho$  is the density of the fluid.

In the region (II), after Sollit and Cross (1972) and Madsen (1974), the unsteady motion of the fluid in the porous medium is described by a continuity equation

$$\nabla \cdot \mathbf{u} = 0 \quad (10)$$

and by a momentum equation

$$\frac{\tau}{n} \frac{\partial \mathbf{u}}{\partial t} = -\frac{1}{\rho} \nabla (p^{(II)} + \rho g z) - f \frac{\omega}{n} \mathbf{u} \quad (11)$$

where  $\mathbf{u}$  is the discharge velocity vector,  $\nabla$  is the gradient operator vector as  $(\partial/\partial x, \partial/\partial y, \partial/\partial z)$ ,  $n$  is the porosity,  $\tau$  is the inertia coefficient,  $f$  is the linearized friction factor,  $p^{(II)}$  is the pressure,  $\omega$  is the angular frequency. Assuming the irrotational motion of the fluid and introducing a discharge velocity potential,  $\varphi$ , we can rewrite Eqs.(10) and (11) as

$$\nabla_h^2 \varphi + \varphi_{zz} = 0 \quad ; \quad -(h+h_s) \leq z \leq -h \quad (12)$$

$$p^{(II)} = -\rho \left( \frac{\tau}{n} \varphi_t + g z + f \frac{\omega}{n} \varphi \right) \quad ; \quad -(h+h_s) \leq z \leq -h \quad (13)$$

The boundary condition at the upper face of the porous layer is

$$\varphi_z = -\nabla_h h \cdot \nabla_h \varphi + \nabla_h \cdot (\delta \nabla_h \varphi) + w^{(II)} \quad ; \quad z = -h \quad (14)$$

and the boundary condition at the bottom of the porous layer is

$$\varphi_z = -\nabla_h (h+h_s) \cdot \nabla_h \varphi \quad ; \quad z = -(h+h_s) \quad (15)$$

where  $w^{(II)}$  is the vertical discharge velocity at the interface between the region (I) and (II).

At the interface, the pressure and the vertical discharge velocity should be continuous:

$$p^{(I)} = p^{(II)} \quad ; \quad z = -h \quad (16)$$

$$w^{(I)} = w^{(II)} \quad ; \quad z = -h \quad (17)$$

The solutions of velocity potentials,  $\phi$  and  $\varphi$ , may be expressed as

$$\phi(\mathbf{x}, z, t) = f^{(I)}(\mathbf{x}, z) \tilde{\phi}(\mathbf{x}, t) + (\text{non-propagating modes}) \quad (18)$$

$$\varphi(\mathbf{x}, z, t) = f^{(II)}(\mathbf{x}, z) \tilde{\varphi}(\mathbf{x}, t) + (\text{non-propagating modes}) \quad (19)$$

Under the condition of horizontal bottom ( $\nabla_h h = \nabla_h h_s = 0$ ), we can obtain the vertical distribution functions of  $f^{(I)}$  and  $f^{(II)}$  as follows:

$$f^{(I)} = \frac{1}{D} \{ \cosh kh_s \cosh k(h+z) + \gamma \sinh kh_s \sinh k(h+z) \} \quad (20)$$

$$f^{(II)} = \frac{1}{D} \gamma \cosh k(h+h_s+z) \quad (21)$$

where

$$D = \cosh kh_s \cosh kh (1 + \gamma \tanh kh_s \tanh kh) \quad (22)$$

$$\gamma = n/(\tau + if) \quad (23)$$

The dispersion relation is given by

$$\omega^2 = gk \frac{\tanh kh + \gamma \tanh kh_s}{1 + \gamma \tanh kh \tanh kh_s} \quad (24)$$

For the case of mild slope bottom, the velocity potentials could be described by Eqs.(18) and (19) with Eqs.(20) and (21). Substituting Eqs.(18) and (19) into the matching condition of pressure yields

$$\tilde{\phi} = \tilde{\varphi} \quad (25)$$

Following Smith and Sprinks (1975) and Kirby (1986), we employ Green's second identity to the propagating component of  $\phi$  and  $f^{(I)}$ :

$$\int_{-h}^0 f^{(I)} \phi_{zz} dz - \int_{-h}^0 \phi f_{zz}^{(I)} dz = \left[ f^{(I)} \phi_z - \phi f_z^{(I)} \right]_{-h}^0 \quad (26)$$

Integrating the above equation yields

$$\begin{aligned} & -\nabla_h \cdot \int_{-h}^0 \nabla_h \tilde{\phi} f^{(I)2} dz - \int_{-h}^0 k^2 \tilde{\phi} f^{(I)2} dz \\ & = -\frac{1}{g} \left( \tilde{\phi}_{tt} f^{(I)2} \right) \Big|_0 - \frac{\omega^2}{g} \left( \tilde{\phi} f^{(I)2} \right) \Big|_0 - \nabla_h \cdot \left( \delta \nabla_h \tilde{\phi} \right) f^{(I)2} \Big|_{-h} \\ & \quad - w^{(I)} f^{(I)} \Big|_{-h} + \tilde{\phi} f^{(I)} f_z^{(I)} \Big|_{-h} + \text{high order terms} \end{aligned} \quad (27)$$

Green's second identity to the propagating component of  $\varphi$  and  $f^{(II)}$  is described by

$$\int_{-(h+h_s)}^{-h} f^{(\text{II})} \varphi_{zz} dz - \int_{-(h+h_s)}^{-h} \varphi f_{zz}^{(\text{II})} dz = \left[ f^{(\text{II})} \varphi_z - \varphi f_z^{(\text{II})} \right]_{-(h+h_s)}^{-h} \quad (28)$$

and the integration yields

$$\begin{aligned} & -\nabla_h \cdot \int_{-(h+h_s)}^{-h} \nabla_h \tilde{\phi} f^{(\text{II})2} dz - \int_{-(h+h_s)}^{-h} k^2 \tilde{\phi} f^{(\text{II})2} dz \\ & = \nabla_h \cdot \left( \delta \nabla_h \tilde{\phi} \right) f^{(\text{II})2} \Big|_{-h} + w^{(\text{II})} f^{(\text{II})} \Big|_{-h} \\ & \quad - \tilde{\phi} f^{(\text{II})} f_z^{(\text{II})} \Big|_{-h} + \text{high order terms} \end{aligned} \quad (29)$$

Eliminating  $w^{(\text{I})}$  and  $w^{(\text{II})}$  (actually  $w^{(\text{I})} = w^{(\text{II})}$ ) from Eqs.(27) and (29) and using  $\phi = \tilde{\phi}$ , we obtain

$$\frac{1}{g} (\tilde{\phi}_{tt} + \omega^2 \tilde{\phi}) - \nabla_h \cdot (\alpha \nabla_h \tilde{\phi}) - k^2 \alpha \tilde{\phi} + \frac{\cosh^2 kh_s}{D^2} (1 - \gamma) \nabla_h (\delta \nabla_h \tilde{\phi}) = 0 \quad (30)$$

where

$$\alpha = p + q / \gamma \quad (31)$$

$$\begin{aligned} p = \int_{-h}^0 f^{(\text{I})2} dz &= \frac{1}{4kD^2} \left\{ \cosh^2 kh_s \sinh 2kh (1 + 2kh / \sinh 2kh) \right. \\ & \quad \left. + \gamma \sinh 2kh_s (\cosh 2kh - 1) + \gamma^2 \sinh^2 kh_s \sinh 2kh \right. \\ & \quad \left. \times (1 - 2kh / \sinh 2kh) \right\} \end{aligned} \quad (32)$$

$$q = \int_{-(h+h_s)}^{-h} f^{(\text{II})2} dz = \frac{1}{4kD^2} \left\{ \gamma^2 \sinh 2kh_s \sinh 2kh (1 + 2kh_s / \sinh 2kh_s) \right\} \quad (33)$$

Eq.(30) is the time-dependent wave equation. Factoring the time out of  $\tilde{\phi}$  as

$$\tilde{\phi} = \hat{\phi} e^{-i\omega t} \quad (34)$$

we can transform Eq.(30) into

$$\nabla_h \cdot (\alpha \nabla_h \hat{\phi}) + \alpha k^2 \hat{\phi} - \frac{\cosh^2 kh_s}{D^2} (1 - \gamma) \nabla_h \cdot (\delta \nabla_h \hat{\phi}) = 0 \quad (35)$$

The effects of the porous medium are taken into account through the complex wavenumber  $k$  given by Eq.(24) and the complex coefficients of  $\alpha$  and  $\gamma$ .

### **Relation to Existing Theories**

#### ***Case of $h_s = 0$ and $\delta = 0$***

In the case that there are not porous layer and rapid undulation, Eq.(35) reduces to the mild slope equations derived by Berkhoff (1972):

$$\nabla_h \cdot (CC_g \nabla_h \hat{\phi}) + k^2 CC_g \hat{\phi} = 0 \quad (36)$$

#### ***Case of $h_s = 0$ and $\delta \neq 0$***

In the case that there is not porous layer and there exists rapid undulation, Eq.(35) reduces to the general wave equation over rippled bed derived by Kirby (1986):

$$\nabla_h \cdot (CC_g \nabla_h \hat{\phi}) + k^2 CC_g \hat{\phi} - \frac{g}{\cosh^2 kh} \nabla_h \cdot (\delta \nabla_h \hat{\phi}) = 0 \quad (37)$$

#### ***Case of very small permeability of porous layer***

The case of very small permeability is treated as a mathematical limit of very small porosity ( $n \rightarrow 0$ ) and very large friction factor ( $f \rightarrow \infty$ ). In this condition, Eq.(35) reduces to the general wave equation expressed as Eq.(37).

#### ***Case of very large permeability of porous layer***

Since  $n \rightarrow 1$  and  $f \rightarrow 0$ , so  $\gamma \rightarrow 1$ . The resultant wave equation becomes the same as the mild slope equation expressed as Eq.(36) where the phase velocity  $C$  and the group velocity  $C_g$  are defined by using the water depth of  $h+h_s$ .

## Numerical Calculations of Bragg Scattering

### *Boundary condition*

At the seaward boundary condition, the following condition has to be satisfied:

$$\hat{\phi}_x = -ik(\hat{\phi} - 2\hat{\phi}_I) \quad (38)$$

where  $\hat{\phi}_I$  is the incident wave potential amplitude. At the downstream boundary condition, the following transmitted condition was needed:

$$\hat{\phi}_x = ik\hat{\phi} \quad (39)$$

### *Numerical conditions*

Numerical conditions followed the experimental ones of Davies and Heathershaw (1984). The water depth  $h$  and the thickness of porous layer  $h_s$  were constant, and the undulation  $\delta$  was given by

$$\delta = D \sin(\lambda x) ; \quad 0 \leq x \leq ml \quad (40)$$

where  $m$ ,  $\lambda$ ,  $l$ , and  $D$  are the number, the wavenumber, the wavelength and the amplitude of the ripples, respectively. Two cases of Case 1 ( $m = 10$  and  $D/h = 0.16$ ) and Case 2 ( $m = 4$  and  $D/h = 0.32$ ) were employed. Actual values of  $D$ ,  $l$  and  $h_s$  in the experiments of Davies and Heathershaw (1984) were 5 cm, 1.0 m and 0 m, respectively. Here we changed  $h_s$  from 0 m to 0.2 m to examine the effects of permeability on the Bragg scattering.

### *Calculated results and discussion*

Figure 2 shows the spatial distributions of wave amplitudes of wave period 1.0 s and 1.3 s, where the solid line corresponds to the case of impermeable rigid bottom, the dotted and the dash-dotted lines correspond to the case of porous bottom of  $f = 1$  and  $f = 10$ , respectively, with  $\tau = 1.0$ ,  $n = 0.4$  and  $h_s = 0.2$  m of Case 1. In Fig.2 (a), the reflection coefficient is less than 0.1; and, in Fig.2(b), the Bragg reflection condition is nearly satisfied, and the variations of the amplitudes are remarkable. It is seen from Fig.2 that when the bottom is permeable, the amplitudes and their variations become small.

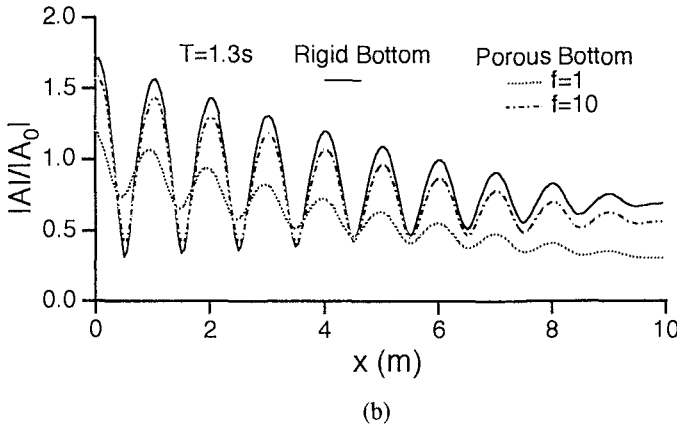
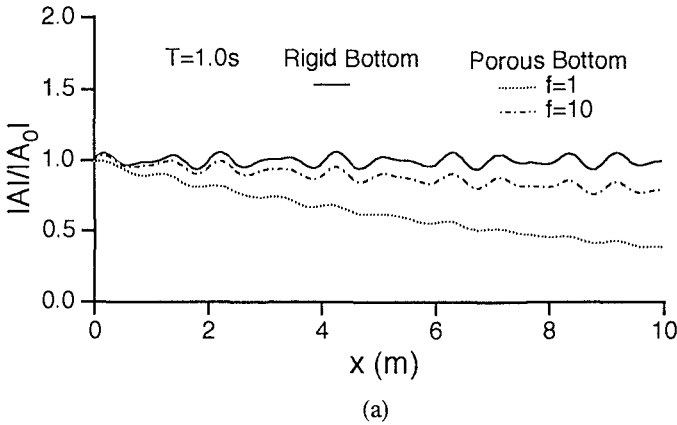
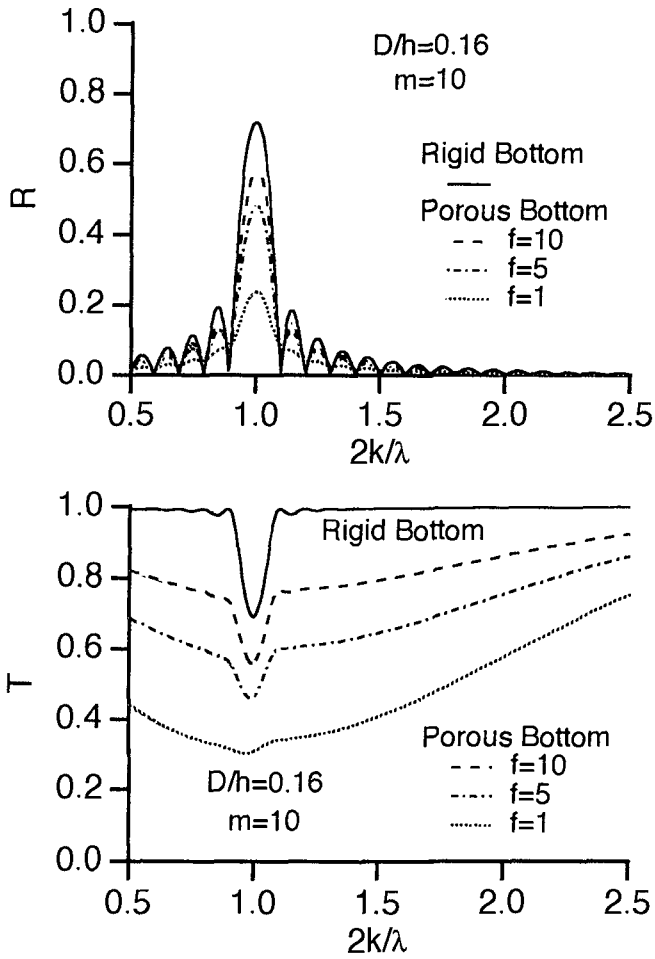


**Fig.2 Spatial distributions of wave amplitudes:**  
**(a) non-resonant condition; (b) resonant condition**

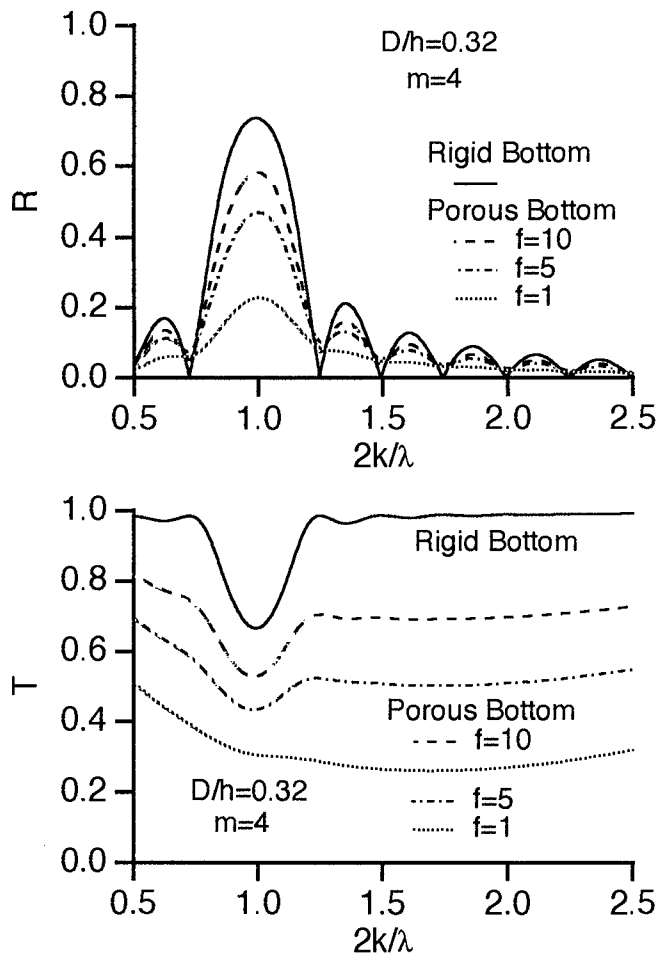
Figure 3 shows the reflection coefficient,  $R$ , and the transmission coefficient,  $T$ , against the ratio of wavenumbers,  $2k/\lambda$ , where the  $k$  is taken as the real part for the case of permeable ripples. In the figures, the linearized friction factor was changed by 10, 5, and 1, keeping  $\tau = 1.0$ ,  $n = 0.4$  and  $h_S = 0.2$  m. The calculated results for impermeable rigid bottom, shown by the solid lines, were obtained by setting  $n = 0$ . In the range of  $1 \leq f \leq 10$ , the reflection and transmission





(a)

**Fig.3 Reflection and transmission coefficients: (a) Case 1; (b) Case 2**



(b)

Fig.3 (Continued)

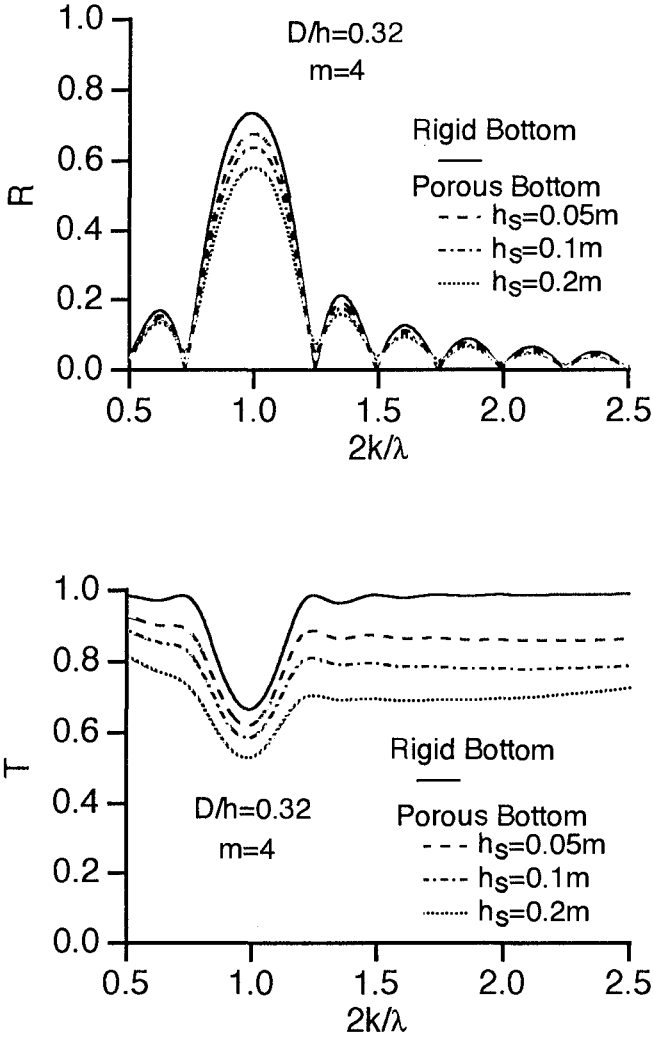


**Fig.4 Effect of thickness of porous layer on reflection and transmission**

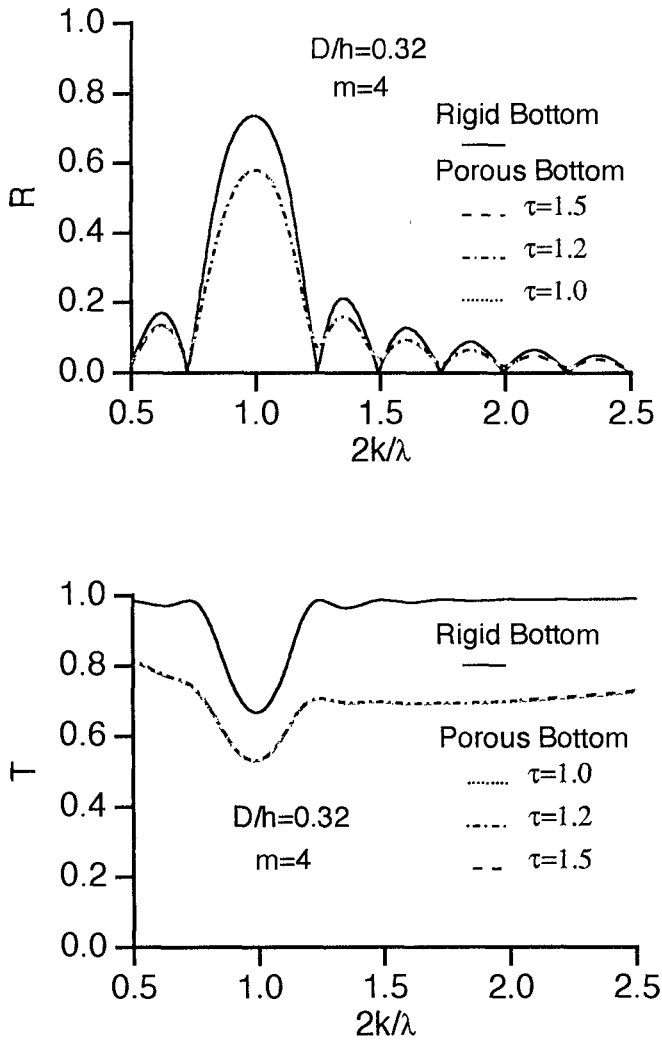


**Fig.5 Effect of inertia coefficient of porous layer on reflection and transmission**

coefficients become small with decrease in the linearized friction factor.

The effect of thickness of the porous layer on the Bragg scattering is shown in Fig.4, by changing  $h_s$ , with  $\tau = 1.0$ ,  $n = 0.4$  and  $f = 10$ . The reflection and transmission coefficients become small with increase in the porous layer thickness, as easily expected.

Figure 5 shows the effect of the inertia coefficient by changing  $\tau$ , with  $f = 10$ ,  $n = 0.4$  and  $h_s = 0.2$  m. It is seen from this figure that there is little effect of  $\tau$ .

It should be noted that though the parameters of  $n$ ,  $f$ , and  $\tau$  were changed independently for the convenience in the calculations so far, these parameters are dependent each other. The determination of the parameters is difficult for arbitrary porous medium.

## Conclusions

In order to deal with wave transformations over a permeable seabed with rapidly varying undulations, we developed the time-dependent and time-independent wave equations taking account of the effects of porous medium.

In the case that there are not porous layer and rapid undulation, the time-independent equation reduces to the mild slope equation derived by Berkhoff (1972). In the case that there is not porous layer and there exists rapid undulation, the time-independent equation reduces to the wave equation over rippled bed derived by Kirby (1986). When the permeability is very small, the time-independent equation reduces to the Kirby's equation. On the other hand, when the permeability is very large, the time-independent equation reduces to the Berkhoff's equation where the water depth is defined by a sum of the water depth and the thickness of porous layer.

Numerical examples of the Bragg scattering were shown in one-dimensional case. The reflected and transmitted waves became small due to the permeability of seabed bottom. The reflection and transmission coefficients were influenced by the friction factor, the thickness of porous layer, and the porosity; however, there was little effect of inertia coefficient.

## Acknowledgments

This study was supported financially by the Maeda Memorial Engineering Foundation. The authors greatly appreciate Dr. Takashi Izumiya (assoc. Prof., Dept. Civil Eng., Niigata Univ., Japan) for showing the computer program to solve the dispersion relation.

## References

- Berkhoff, J.C.W. (1972). Computation of combined refraction-diffraction, Proc. 13rd Int. Conf. Coastal Eng., ASCE, pp.471-490.
- Davies, A.G. and Heathershaw, A.D. (1984). Surface-wave propagation over sinusoidally varying topography, Jour. Fluid Mech., Vol.144, pp.419-443.
- Kirby, J.T. (1986). A general wave equation for waves over rippled beds, Jour. Fluid Mech., Vol.162, pp.171-186.
- Madsen, O.S. (1974). Wave transmission through porous structures, Proc. ASCE, Vol.100, No.WW3, pp.169-188.
- Mei, C.C. (1985). Resonant reflection of surface waves by periodic sand-bars, Jour. Fluid Mech., Vol.152, pp.315-335.
- Naciri, M. and Mei, C.C. (1988). Bragg scattering of water waves by a doubly periodic seabed, Jour. Fluid Mech., Vol.192, pp.51-74.
- Smith, R. and Sprinks, T. (1975). Scattering of surface waves by a conical island, Jour. Fluid Mech., Vol.72, pp.373-384.
- Sollit, C.K. and Cross, R.H. (1972). Wave transmission through permeable breakwaters, Proc. 13rd Int. Conf. Coastal Eng., ASCE, pp.1827-1846.

## CHAPTER 48

### Non-Reflective Multi-Directional Wave Generation by Source Method

Masahiro Tanaka<sup>1</sup>, Takumi Ohyama<sup>1</sup>, Tetsushi Kiyokawa<sup>1</sup>,  
and Kazuo Nadaoka<sup>2</sup>

#### **Abstract**

A new wave-generation system, composed of a source and an absorber, is proposed to realize a non-reflective wave field in a laboratory basin as an advanced alternative to conventional methods. Theoretical studies based on the linear potential theory were carried out to investigate the characteristics of wave fields generated by the proposed method. Performance of the new system was compared to that of conventional *serpent-type* wave-makers. The proposed system was founded to provide a significantly larger effective area for multi-directional waves than does the *serpent-type* wave makers.

Experimental studies using a two-dimensional wave tank were also conducted to verify the performance and practicality of the new system. The results showed that the new devised equipment can produce a nearly non-reflective wave field and can generate waves efficiently even in deep water.

#### **1. Introduction**

Serpent-type wave-maker has been developed to generate multi-directional irregular waves, and has been introduced in many laboratories (Biesel, 1954; Gillbert, 1976; Takayama, 1982). However, this wave-generation system has not yet solved two serious problems. First, re-reflected waves from wave-generating paddles and side walls of a tank disturb the wave field around a model after certain time passed.

1 Institute of Technology, Shimizu Co., 3-4-17, Etchujima, Koto-ku, Tokyo 135, Japan

2 Tokyo Institute of Technology University, 2-12-1, Ohokayama, Meguro-ku, Tokyo 152, Japan

The second problem is that the effective wave area decreases according to increase of the incidence angle of waves.

Funk-Miles (1987), Isaacson (1989) and Dalrymple (1989) have proposed a directional wave-making method considering side-wall reflection to expand an effective wave field. Although this method can slightly widen the effective wave field by controlling reflection waves at side wall, proportion of ineffective wave area in the tank is still large.

On the other hand, Hirakuchi et al. (1991) and Ikeya et al. (1992) have proposed an active directional wave absorption method. In this method, the reflection waves are absorbed by controlling the amplitudes and phases of each paddle corresponding to the heights, phases and directions of the reflection waves. Since this method requires measurement and analysis of a significant amount of waves to control the wave-generating system in an instant time, it is quite difficult to apply to an actual system.

We have devised a non-reflective multi-directional wave-generating system that consists of a distributed wave making source and a wave absorber without using wave-generating paddles.

## **2. Concept of the New System**

The wave-generation system consists of a circular wave-making source and an external wave absorber arranged in a circular tank as shown in Fig. 1. The idea of the proposed method is founded on the principle of two-dimensional numerical wave-generating model (Brorsen-Larsen, 1987; Ohyama et al., 1991). The two-dimensional numerical model employs an effective non-reflective open boundary treatment so that it can be applied to arbitrary wave fields including nonlinear random waves.

The proposed system generates waves by pumping water in and out without using paddles, and the heights and direction of waves are controlled by the intensity and phase of the source. Since this source method does not involve wave paddles unlike conventional wave-makers, it is expected that the reflected waves from model objects permeate through the source without re-reflection, and are absorbed by the external absorber. In addition, since the wave-making source is arranged in a circular shape, an effective wave field is independent of wave directions, whereas the performance of the conventional *serpent-type* wave-makers is significantly direction-dependent.

For practical application, the wave-making source can be composed of a series of



small units mounted in a concentric semicircle. It would require careful provision to minimize the reflection from the source. A practical equipment and its performance of wave generation are shown in Section 4.

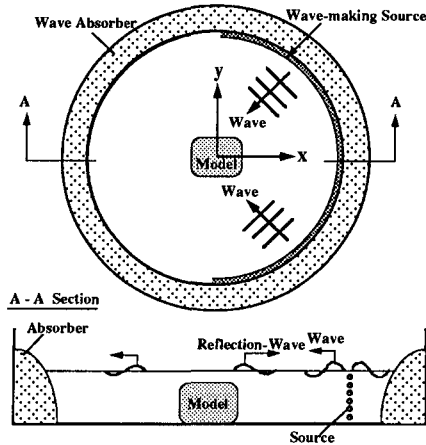


Fig. 1 Concept of non-reflective multi-directional wave generation by source method

### 3. Theoretical Analysis

#### 3.1 Theoretical Formulation

Multi-directional irregular waves are composed of waves with various periods, heights and directions. Since the performance of waves generated by the source method is independent of wave direction, it can be evaluated by using single-directional regular waves.

The coordinate system and definition sketch used in this study are shown in Fig. 2. With the assumption of incompressible, inviscid fluid, and irrotational flow, the fluid motion can be described with a velocity potential,  $\phi(r, \theta, z)e^{-i\omega t}$ . The potential satisfies the following Poisson's equation within the fluid domain and which is subject to boundary conditions at the free surface and the tank bottom.

$$\nabla^2 \phi = U^*(\theta, z)\delta(r - A) \quad (1)$$

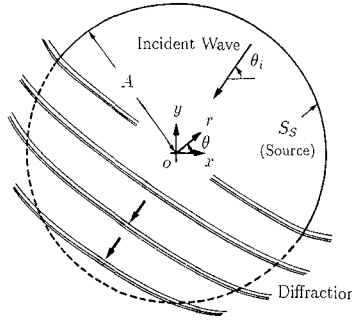


Fig. 2 Definition sketch of theoretical model

Where,  $U^*$  is the source intensity of formulated by Brorsen et al. (1987),  $\delta$ : Dirac's Delta function, and  $A$ : distance (radius) between the center of a tank and a wave making source. Applying the Green's function method to Eq. 1, the velocity potential,  $\phi(P)$ , at an arbitrary point in a basin,  $P(r_p, \theta_p, z_p)$ , is expressed as

$$\phi(P) = -\frac{1}{4} \int_{S_S} U^* G ds \tag{2}$$

in which,  $S_S$  denotes the surface of wave-making source, and  $G$ : the Green's function derived by John (1950) as shown in Eq. 3 and 4.

$$G = \frac{2\pi i(\kappa^2 - v^2)}{h(\kappa^2 - v^2) + v} \cosh k(h+z_p) \cdot \cosh k(h+z) H_0^{(1)}(\kappa R_p) + \sum_{n=1}^{\infty} \frac{4(\kappa_n^2 + v^2)}{h(\kappa_n^2 + v^2) - v} \cdot \cos \kappa_n(h+z_p) \cos \kappa_n(h+z) K_0(\kappa_n R_p) \tag{3}$$

$$R_p = \sqrt{(r_p \cos \theta_p - r \cos \theta)^2 + (r_p \sin \theta_p - r \sin \theta)^2} \tag{4}$$

Where,  $k$ : wave number,  $k_n$ : eigenvalue,  $H_0^{(1)}$ : Hankel function,  $K_0$ : Bessel function,  $v = \omega^2/g$ ,  $g$ : gravity acceleration.

Since waves generated by a source progress to both sides of the source, the intensity of the source can be given as the following equation (Brorsen-Larsen, 1987).

$$U^*(\theta, z) = 2 \left. \frac{\partial \phi_i}{\partial r} \right|_{r=A} \quad \left( \theta_i - \frac{\pi}{2} \leq \theta \leq \theta_i + \frac{\pi}{2} \right) \quad (5)$$

Substituting the potential  $\phi_i$  to Eq. 5, the intensity  $U^*$  can be expressed as shown in Eq. 6.

$$U^*(\theta, z) = -ik \cos(\theta - \theta_i) \frac{gH_i}{\omega} \frac{\cosh k(h+z)}{\cosh kh} e^{-ikA \cos(\theta - \theta_i)} \quad \left( \theta_i - \frac{\pi}{2} \leq \theta \leq \theta_i + \frac{\pi}{2} \right) \quad (6)$$

Substituting Eq. 3 and 6 into Eq. 2, analytical form of the potential  $\phi(P)$  at an arbitrary point P in a tank can be obtained as follows:

$$\phi(P) = \frac{gH_i}{2\omega} \varphi(r_p, \theta_p) \frac{\cosh k(h+z_p)}{\cosh kh} \quad (7)$$

$$\varphi = -\frac{kA}{2} \int_{\theta_i - \frac{\pi}{2}}^{\theta_i + \frac{\pi}{2}} \cos(\theta - \theta_i) e^{-ikA \cos(\theta - \theta_i)} H_0^{(1)}(k\hat{R}_p) d\theta \quad (8)$$

$$\hat{R}_p = \sqrt{(r_p \cos \theta_p - A \cos \theta)^2 + (r_p \sin \theta_p - A \sin \theta)^2} \quad (9)$$

### 3.2 Definition of Performance of Wave-generation

Performance of a wave generating system is generally evaluated with areal extent of effective wave-field. The effective area is defined as an area, in which errors of wave heights and directions from an intended wave are smaller than allowable tolerances, as shown in Fig. 3. The wave height and direction errors,  $\Delta H$  and  $\Delta \theta_w$ , are described as shown in Eq. 10 and 11.

$$|\Delta H| / H_i = |H - H_i| / H_i \quad (10)$$

$$|\Delta \theta_w| = |\theta_w - \theta_i| \quad (11)$$

By defining the extent of the effective wave-field as a ratio of the effective zone's radius to that of basin,  $a/A$ , its dependence on incident wave-direction can be eliminated.

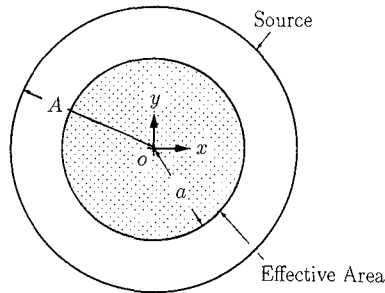


Fig. 3 Definition of effective wave area

### 3.3 Performance of wave-generation by the source method

Characteristics of wave field generated by the source method were examined using a theoretical model (see Fig. 1). In this calculation, non-reflection waves from the wave-making source and the absorber behind the source were assumed.

Wave-heights distributions normalized with an incident wave height is shown in Fig. 4 (a). Where, a tank radius is 3 times of the wave-length ( $A/L = 3.0$ ). Fig. 4 (b) and (c) describe vectors of energy flux and distributions of wave-direction errors at  $A/L = 3.0$ , respectively. It can be seen in Fig. 4 (a) that the relative wave-height errors,  $|(H - H_i)/H_i|$ , are less than 0.05 in the wide area of the tank. The wave-direction errors are less than 5 degrees in the almost all the area as shown in Fig.4 (c). These results indicate that the proposed source method can provide the effective wave field in the wide area of the tank.

Distributions of normalized wave-height and wave-direction errors at  $A/L = 1.0$  are shown in Fig. 5 (a) and (b), respectively. The magnitudes of both errors for this case are much bigger than those for the case of  $A/L = 3.0$ . This difference indicates that  $A/L$  is a significant parameter in the design of the proposed system.

Fig. 6 (a) shows the dependence of the  $a/A$  on the parameter  $A/L$ , when the error tolerance  $(\Delta H/H_i)_{\max}$  is varied from 0.05 to 0.2 with  $|\Delta\theta_w|_{\max}$  fixed at 4 degrees. Fig. 6 (b) also shows characteristic of  $a/A$  versus  $A/L$  corresponding to variation of wave-direction error,  $|\Delta\theta_w|_{\max}$ , when  $(\Delta H/H_i)_{\max}$  is fixed at 0.1. It is seen that the effective area generally increases with  $A/L$ . The effective wave area can be evaluated using the results shown in Fig. 6 (a) and (b). For example, assuming allowable tolerance to be  $(\Delta H/H_i)_{\max} = 0.1$  and  $\Delta\theta_w = 4$  degrees, when the tank radius is set at 2.4 times of incident wave-length, an area of about 80% radius in the tank is provided as the effective wave field.

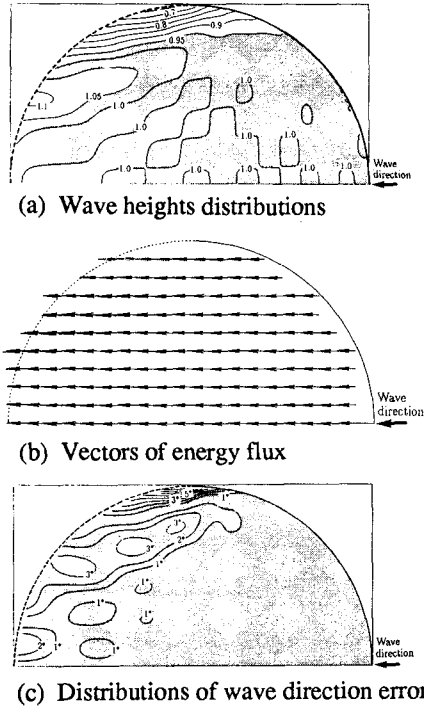


Fig. 4 Wave field generated by the source method ( $A/L = 3.0$ )

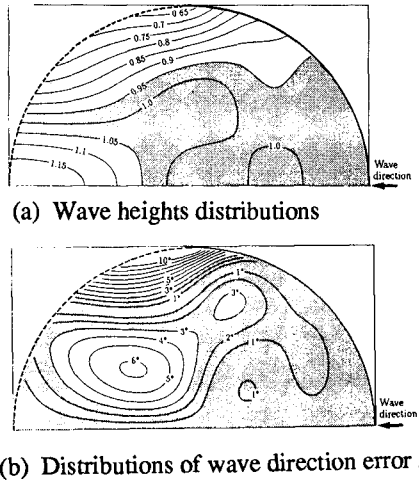
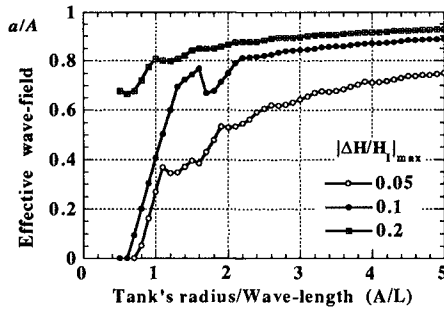
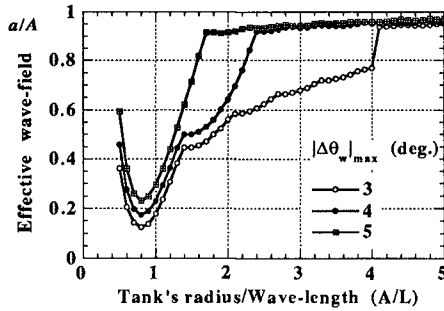


Fig. 5 Wave field generated by the source method ( $A/L = 1.0$ )



(a) Effective wave field with  $|\Delta H/H_1|_{\max}$



(b) Effective wave field with  $|\Delta\theta_w|_{\max}$

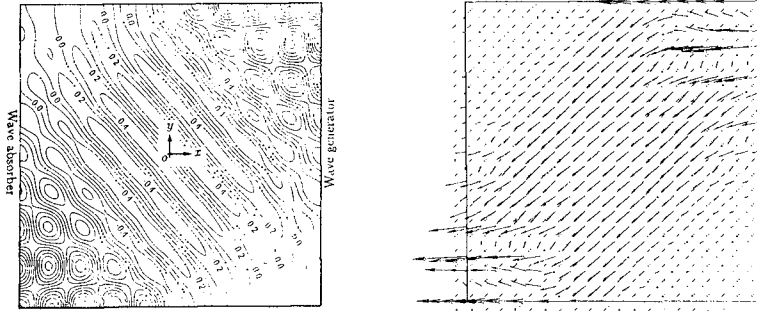
Fig. 6 Effective wave field by the source method

### 3.4 Comparison with serpent-type generator

Wave fields generated by a serpent-type wave-maker was simulated using a theoretical model (Dalrymple, 1989) to compare with performance of the proposed source method. In this calculation, the serpent-type generator was controlled so as to widen the effective wave field by using the side-wall-reflection of the tank.

Fig. 7 (a) and (b) show computed results of water-elevation distribution and vectors of energy flux of waves generated by a serpent-type. Where, the ratio of the tank width to wave length,  $B/L$ , and the incidence angle of wave,  $\theta_i$ , are fixed at 6.0 and 40 degrees, respectively. In this case, the serpent-type wave generator was controlled so as to provide the best performance at  $x=0$ .

Although the serpent-type generator produces uniform wave field in the central area of the tank, it causes standing wave and diffraction waves at the corners and their



(a) Water elevation distributions

(b) Vectors of energy flux

Fig. 7 Wave field generated by a serpent-type ( $B/L = 6.0$ )

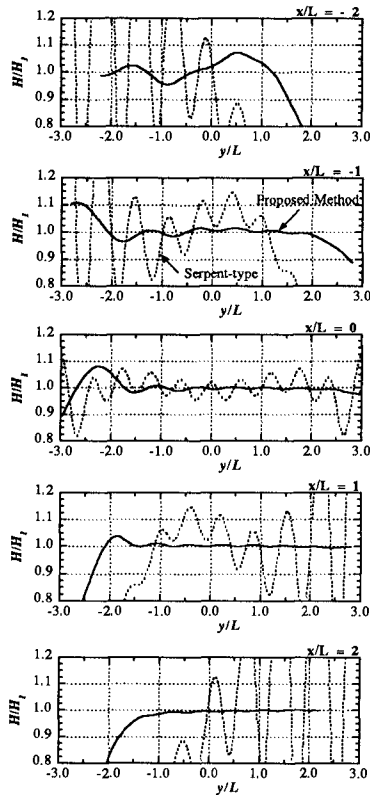


Fig. 8 Comparison of wave height distributions between for the source method and a serpent-type

perimeters. It can be seen in these areas that the magnitudes and directions of energy flux are different from those of the intended waves. As the results, the serpent-type generator provides large ineffective wave field in the tank. The effective wave-field of the serpent-type depends on incident wave directions, decreasing with increase of the incidence angle of waves.

In Fig. 8, normalized wave-height distributions at cross-sections of  $x/L = -2, -1, 0, 1$  and  $2$  generated by a *serpent-type* are compared with those generated by the source method using the results shown in Fig. 4 (a) and 7 (a). The results show that the source method generates waves much more uniformly than does the *serpent-type* not only at  $x/L = 0.0$ , where the serpent-type gives the best performance, but also at  $x/L = \pm 1.0$  and  $\pm 2.0$ . It is expected, therefore, that the proposed source method can provide significantly larger effective fields for multi-directional waves compared to those provided by *serpent-type* wave makers.

#### 4. Application of the source method

##### 4.1 A devised equipment

We have carried out preliminary examinations of various devices to evaluate practicability of a wave-making source. As a result, a device, which supplies and discharges water at tank bottom, has proved to be the most practical source. The principle behind wave-generation by this device is similar to that by a non-reflective wave-making system devised by Goda (1965): it generates a vertically oscillating flow at channel bottom by using a paddle as shown in Fig. 9. The Goda's method was not of practical use because of inefficiency for deep water wave-generating. In addition, the method requires elaborate work to keep nearly water-tightness in an interstice between the pit's walls and the wave paddle.

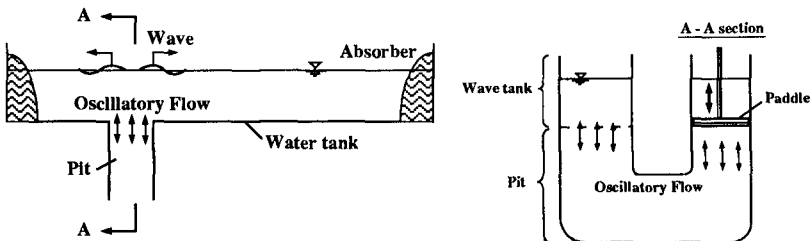


Fig. 9 Non-reflective wave generator with vertical oscillatory flow



To solve these problems, authors have made over this method into a practical equipment, which consists of pumps, valves, and an adjustable pit, as shown in Fig. 10. Vertical oscillating flow by using the pumps, valves and adjustable pit instead of using a wave-paddle: the pump  $P_I$  supplies water into the pit, and the pump  $P_O$  discharges water from the pit. Wave heights and periods are controlled by using two valves,  $V_I$  and  $V_O$ . The pit's height and width,  $d$  and  $B$ , can be adjusted to improve the efficiency of wave generation in deep water (see Fig. 10).

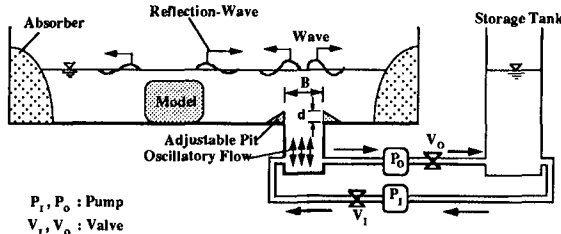


Fig. 10 A practical equipment of the source method

#### 4.2 Performance of wave-generation by the equipment

It is important for the equipment to produce wave field with negligible reflection from the pit and to improve efficiency of wave generation in deep water. To evaluate the effects of the pit's width and height on characteristics of the reflection waves and the efficiency, experiments were carried out using a two-dimensional wave tank. The coefficient of reflection waves caused by the pit is calculated using Eq. 12 (Goda et al., 1964).

$$K_R = \frac{H_{max} - H_{min}}{H_{max} + H_{min}} \tag{12}$$

Where,  $H_{max}$  and  $H_{min}$  are heights of standing wave in front of a vertical wall apart from the pit by  $N$  and  $(N+1/2)$  times of a half wave length, respectively ( $N$ : an integer). On the other hand, the wave generation efficiency is evaluated using a ratio of a wave height to oscillatory flow amplitude in the pit. Calculations were also conducted to estimate the performance of the wave-generating pit by Green function method. As theoretical formulation about the wave generation pit has been described by Tanaka et al. (1993), only a definition sketch of the theoretical model is shown in Fig. 11.

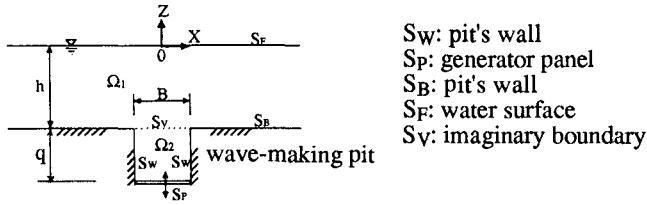


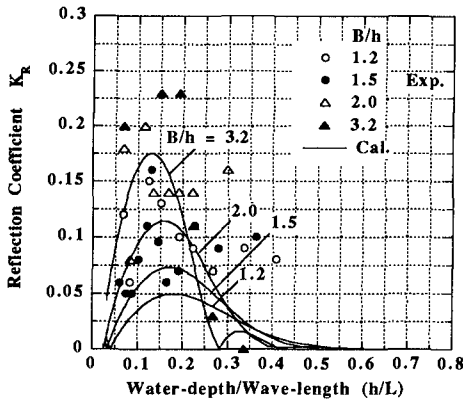
Fig. 11 Definition sketch of a theoretical model of the wave making pit

Fig. 12 (a) shows response of reflection coefficients,  $K_R$ , to parameter,  $h/L$ , as  $B/h$  was varied from 1.2 to 3.2. In this case, the top of the pit is set at the same level of the tank bottom. Fig. 12 (b) also shows the dependence of wave generation efficiency,  $H/2e$ , on  $h/L$  upon the same conditions with Fig. 12 (a). Where,  $h$  is the water depth of the tank,  $L$ : the wave length,  $B$ : the width of the wave-making pit, and  $2e$ : an amplitude of the oscillatory flow in the pit. In the figures, solid lines denote the computed results. Although the experimental and the numerical results agree on the characteristics of  $H/2e$ , both results show large discrepancies in the characteristics of  $K_R$ . Since the detailed reason for the discrepancies has not been made clear, the characteristics of  $K_R$  for the new equipment are evaluated using the experimental results in this paper.

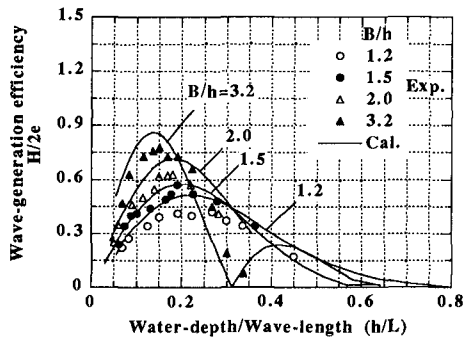
Although the increase in  $B/h$  improves the wave-generating efficiency of the equipment, it enlarges the reflection waves from the pit. Therefore,  $B/h$  should be set so that the equipment can achieve low reflection wave over a wide range of wave periods:  $K_R$  is 0.15 or less for  $B/h = 1.5$ , and further decreases to around 0.1 for  $B/h = 1.2$ .

In Fig. 13 (a), the effect of the pit height on the efficiency of wave generation is shown when  $d/h$  was varied 0, 0.305 and 0.432. Where,  $B/h' = 1.2$ ,  $B = 30$  cm,  $d$ : the pit height,  $h'$ : depth between water surface and the top of the pit ( $h = d+h'$ ). The wave-generation efficiency with  $d/h = 0.305, 0.432$  is significantly improved in the range of  $h/L > 0.3$  compared with that with  $d/h = 0$ . These results indicate that the adjustment of the pit height is effective for the improvement of the wave generation efficiency. In addition, the former maximum efficiencies are greater than the latter one.

Fig. 13 (b) shows characteristics of the reflection waves caused by the pit. The experimental conditions are the same with those of Fig. 13 (a). This equipment can achieve low reflection over a wide range of wave periods even when  $d/h$  is set at



(a) Coefficients of reflection waves from the pit



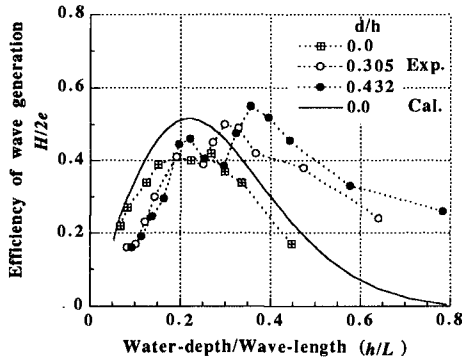
(b) Efficiency of wave generation

Fig. 12 The effects of pit width, B, on performance of wave generation ( $d/h = 0.0$ )

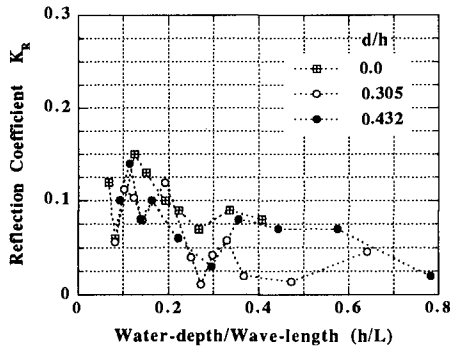
0.305 or 0.432. The results of Fig. 13 shows that the adjustable pit can improve the efficiency of the wave generation without increasing reflection waves.

From the experimental results, the proposed equipment can generate wave with negligible re-reflection from the wave-generating pit, and can efficiently make deep water waves.

It is expected that the equipment would provide nearly non-reflective wave field for multi-directional wave-generation by arranging a series of the units in a concentric semicircle in circle tank.



(a) Efficiency of wave generation



(b) Coefficients of reflection waves from the pit

Fig. 13 The effects of pit height,  $d$ , on performance of wave generation ( $B/h' = 1.2$ )

### 5. Conclusions

Wave-generation by source method, which does not depend on wave-making paddles, has been proposed to produce non-reflective multi-directional waves in a laboratory basin. The characteristics of wave fields generated by the source method were evaluated using a theoretical model. A practical equipment with a wave-making pit at channel bottom was devised to realize the source method, and the performance of the wave-generation was also examined. Major findings of the present study are summarized as follows:

- 1) The wave generation by the source method provides significantly larger effective area for multi-directional waves than does the *serpent-type* wave makers.

- 2) The equipment with a wave-making pit at a channel bottom can produce wave field with negligible reflection by adjusting the width and position of the pit, and can also efficiently generate waves in deep water.

## **References**

- Biesel, F. (1954): Wave machines, Proc. 1st Conf. on Ships and Waves, pp.121-125.
- Brorsen, M. and J. Larsen (1987): Source generation of nonlinear gravity waves with the boundary integral equation method, Coastal Eng., Vol. 11, pp. 93 - 113.
- Dalrymple, R. A. (1989): Directional wavemaker theory with side wall reflection, Jour. Hydraulic Research, Vol. 27, No. 1, pp 23-34.
- Funke, E. R. and M. D. Miles (1987): Multi-directional wave generation with corner reflectors, National Research Council Canada, Hydraulic Laboratory, Tech. Rept., No. TR-HY-021.
- Gilbert, G. (1976): Generation oblique waves, Hydraulics Research Station, Wallingford, England, Notes 18, pp. 3-4.
- Goda, Y. and T. Kikura (1964): The generation of water waves with a vertically oscillating flow at a channel bottom, Report of Port and Harbor Tech. Res. Inst., No.9, pp. 1-24.
- Hirakuchi, H., Y. Kajima, H. Tanaka and T. Ishii (1991): Characteristics of absorbing directional wavemaker, Proc. 38th Japanese Conf. on Coastal Eng., pp. 121-125 (in Japanese).
- Ikeya, T., Y. Akiyama and K. Imai (1992): Active Directional Wave Absorption Theory, Proc. 39th Japanese Conf. on Coastal Eng., pp. 81-85 (in Japanese).
- Isaacson, M. (1989): Prediction of directional waves due to a segmented wave generator, Proc. of 23rd Congress of the Int. Asso. Hydraulic Res. Vol. C, pp. 435-442.
- John, F. (1950): On the motion of floating bodies II, Comm. Pure and Appl. Math., Vol. 3, pp. 45 - 101.
- Ohyama, T. and K. Nadaoka (1991): Development of "Numerical Wave Tank" in nonlinear and irregular wave field with non-reflecting boundaries, Jour. of Hydraulic, Coastal and Environmental Eng., JSCE, Vol.429 II-15, pp. 77-86.
- Takayama, T. (1982): Theoretical properties of oblique waves generated by serpent-type wave-maker, Report of Port and Harbour Research Inst., Vol. 21, No.2, pp. 3-48.
- Tanaka, M., T. Ohyama and T. Kiyokawa (1993): Performance of non-reflective wave generator, Proc. 40th Japanese Conf. on Coastal Eng., pp. 41-45 (in Japanese).

# The Growth of Wind Waves in Shallow Water

L.A. Verhagen and I.R. Young

Dep. of. Civil Engineering, University College, University of New South Wales,  
Canberra, Australia

**Abstract**

The field experiment at Lake George has brought valuable data that was not yet available. The analyses done to the data has shown new insights into shallow water waves. Already from the first analyses we can derive some interesting things. The one-dimensional shallow water spectra seem to have a clear peak enhancement and tail that is proportional to  $f^{-4.5}$ . The directional spread with two-dimensional spectra shows at the higher frequencies (twice the peak frequency) the waves move symmetrically at an angle with the wind. More analysis needs to be done to fit different kind of spectra and to find a function for the directional spread.

**Introduction**

Although most coastal engineering activity is in regions of shallow water, there is little know about the growth of shallow water waves. Many numerical models attempt to incorporate the growth with relationships which are mostly derived from deep water data. The lack of reliable field data in shallow water is a major problem. To overcome this lack of data, a large field experiment is being conducted to study the growth of shallow water waves. The experiment has been set in Lake George (25 km x 12 km) (fig 1) just north of Canberra (Australia). The lake has a flat bed with an approximate depth of 2 meters. There are no high obstacles around the lake to influence the wind significantly.

**Experiment**

Eight wave measuring stations have been established along the north-south axis of the lake (fig 1). Data from these stations are sent by telemetry to a station on the shore where they are logged. The data, after analysis, yield one-dimensional spectra. At station 6, located in the centre of the lake, there is also a cluster of 7 wave measuring gauges to determine the

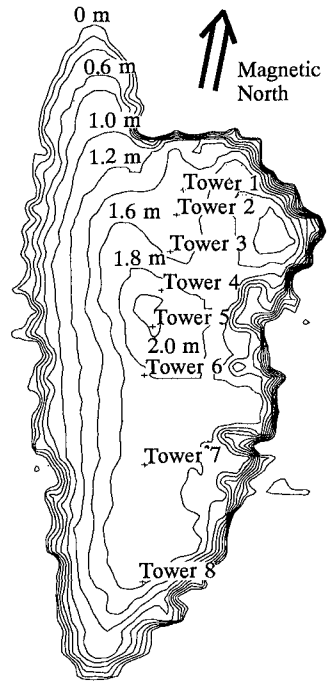


**Figure 1**  
The bathymetry of lake George and the position of the wave measuring towers. Note the platform is at tower 6.

directional spread. The wind speed and direction are measured at 5 locations along the lake. At various sites other meteorological data such as air and water temperature, air humidity, and solar radiation are also measured.

Seven wave measuring stations are nearly identical. They are space-frame towers, with a wave measuring device mounted on the side (fig 2). The towers are moored to the lake bed by 4 guy wires which were anchored into the bed. The wave measuring devices are Zwarts poles (Zwarts 1974). The Zwarts poles consist of an aluminium outer (55 mm)

and inner pole (20 mm) which determine the electrical properties. These wave measuring devices have the advantage that they do not require much maintenance. Other wave measuring devices like resistance gauges, capacitance gauges or waverider buoys needed too high level of maintenance or are outside the frequency range of the waves on Lake George. The poles were calibrated both dynamically and statically in the lab. The data were sent to a base station on the shore via a telemetry link. The radio was powered by two solar cells on the top of the tower (fig 2). At five of the towers, there were 10 meter high masts with an anemometer on top (fig 3).

At two towers the air humidity and temperature (fig 2) were measured together with the water temperature at three levels (0.5, 1, 1.5 meters for the lake bed).

### Wind Analysis

The wind was measured at 5 stations (stations 2,4,6,7,8) on the lake. However there was only a very short time period that all 5 anemometers were working. The anemometer on the platform (station 6) worked most of the time. All anemometers



**Figure 2** Details of the tower. From left to right; the aerial to send back the data by telemetry. The box with batteries the radio and the electronics box for the ZWARTS pole, just in front the anemometer mast and the hydrometer, on top the solar cell, and on the back side the ZWARTS pole.



**Figure 3** A complete view of one of the towers with a 10 meter anemometer mast.

were mounted on 10 meter high mast above the water surface. The anemometer on the platform (station 6) was a "Young" anemometer and the anemometers on the towers were "VDO" anemometers.

A major problem is knowing the exact wind speed along the fetch. This is a serious problem when there is a change of roughness length of the surface (e.g. from land to water). Taylor (1984) gives some guidelines. The basic principle is that the boundary layer adjusts it self after a certain length. The flow will have an internal boundary layer with a depth of  $\delta_i$ . Outside this internal boundary layer the wind velocity is the as equation 1.

$$U_z = \frac{U_*}{\kappa} \ln \left( \frac{z}{z_o} \right) \quad (1)$$

In which  $Z$  is the elevation at which  $U_z$  is measured.  $\kappa$  is the von Karman's constant ( $\kappa = 0.4$ ),  $Z_o$  is the roughness length of the surface and  $U_*$  is the friction velocity. The internal boundary layer grows according to

$$\delta_i = 0.75 Z_o \left( \frac{x}{Z_o} \right)^{0.8} \quad (2)$$

Where  $x$  is the distance along the fetch and  $Z_o$  is the roughness length at  $x$ . Inside the boundary  $\delta_i$  layer the wind speed at elevation  $Z$  is

$$U_z = \frac{\ln \left( \frac{Z}{Z_o} \right) \ln \left( \frac{\delta_i}{Z_{ou}} \right)}{\ln \left( \frac{\delta_i}{Z_o} \right) \ln \left( \frac{Z}{Z_{ou}} \right)} U_{ou} \quad (3)$$

With  $Z_{ou}$  being the roughness length of the upwind boundary,  $U_{ou}$  the upwind wind velocity and  $U_z$  the wind speed at elevation  $Z$ . The wind is usually only measured at a point or a few points along the fetch. As indicated in equations 2 & 3 the wind speed varies after a change of roughness length. Since the wave growth is dependent on the wind speed it is wise to calculate an average wind speed for the fetch. One could also argue that even a mean of the wind speed along the fetch is not good enough and a more sophisticated average should be taken.

We tested the Taylors (1984) method with the data set when all five anemometers were working. The results from the theory and the measured wind speeds were nearly the same. Therefore the anemometer at station 6 (the platform) was used to calculated the wind speed along the north south fetch for each event.



There is a large debate about which wind speed to use, in the making the wave height, wave frequency, fetch and water depth dimensionless. In general the wind speed is measured at 10 meters above the surface level. If the wind speed is measured at a different level it can be converted to  $U_{10}$  using the logarithmic form of the boundary layer (see equation 1). There are several other wind speeds to make the wave height, wave frequency, fetch and water depth dimensionless. They are usually based on either the friction velocity like Wu (1980) describes, the inverse wave age ( $U/c_p$ ) like Donelan (1985) argues, or a combination of both like HEXOS (Smith et al. 1992). The wind speed used here was the wind speed measured at 10 meters above the surface, because the other did not give a clear advantage and they were not measured directly.

**Growth Curves**

The fetch limited growth curves for shallow water have two limits. One limit is the JONSWAP (Hasselmann et al. 1973) deep water growth, and the other is the maximum wave height by a finite depth and wind speed. Vincent in his first paper (1985) suggested that the relation between dimensionless water depth and dimensionless wave height,

$$\frac{H_s g}{u^2} = \left( \frac{d g}{u^2} \right)^{0.5} \quad (4)$$

Where  $H_s$  is the significant waveheight,  $d$  the waterdepth,  $g$  the gravitational constant and  $u$  the wind speed at 10

meters above the surface. Later Vincent and Hughes (1985) had taken measurements from Lake Okeechobee (Florida, USA) to determine the maximum dimensionless wave height. From these data and from an analytic procedure, they suggested that the relation between dimensionless water depth and dimensionless wave height was

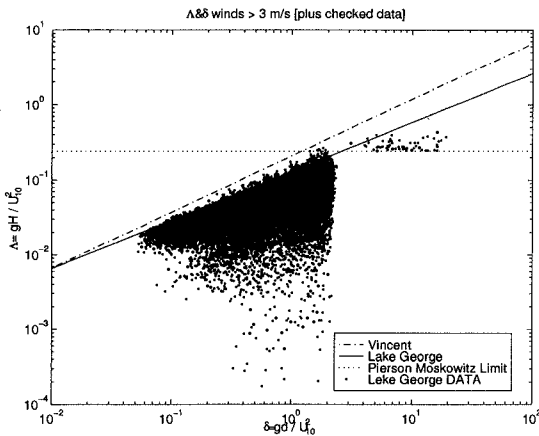


**Figure 4** Lake George Data. Dimensionless waterdepth is set out against dimensionless waveheight. Note the spreading in the wave data with wind speeds greater than 3 m/s is caused by the fact that not all the wave are fully developed.

$$\frac{H_s g}{u^2} = \left( \frac{d g}{u^2} \right)^{0.75} \quad (5)$$

Data from Lake George was used to test this. All the data from Lake George with wind speeds greater than 3 m/s were used together with selected data where the wind speed was smaller than 3 m/s. These last data were selected if the wind speed and direction were constant 8 hours before and 3 hours after the event. The Lake George data tend to indicate a less steep slope than what Vincent and Hughes suggested (fig 4). If one projects the Lake Okeechobee data on a graph similar to the Lake George data (fig 5) one can see that the Lake Okeechobee has the same tendency. Purely on empirical grounds the following seems to be more appropriate.

$$\frac{H_s g}{u^2} = \left( \frac{d g}{u^2} \right)^{0.65} \quad (6)$$

The upper limit for the growth in deep water is the Pierson Moskowitz limit (1964). Pierson Moskowitz (1964) proposed, integrating the spectrum resulting in a limit

$$\frac{H_s g}{u^2} = 0.2433 \quad (7)$$

Vincent and Hughes (1985) do not have a limit because they had not found evidence for this. Data for this limit is indeed very hard to find because of the long fetch and time necessary for the full development of the waves. This only happens during very low wind speeds. Because of swell and other wind waves generated elsewhere it is very hard to measure the growth of smaller waves in ocean environments. However in a lake this possible. During the Lake George experiment there were a number of these events. These events were specially selected because of the tendency of the wind varying in both speed and direction at low wind speeds. The events selected with wind speeds lower than 3 m/s had to have a constant wind speed and wind direction, during a period of 8 hours before and 3 hours after. In figure 4 the Pierson Moskowitz limit with the selected data is shown.

It is believed that the lake sides have a small influence on the observed growth rates. Attempts to measure this effect using three different numerical models have been unsuccessful. The models [WAM (WAMDI 1988), HISWA (Holthuijsen et al. 1988), ADFA1 (Young 1988)] produced conflicting results and all significantly deviate from the observed data. Therefore no correction factors have been applied to the data to compensate for the sides of the lake.

In general the data are consistent with the commonly used CERC (SPM 1984) growth curves, but at small values of dimensionless fetch tend to yield lower dimensionless energy. This could be due to the effects of the change in surface roughness length between land and water. Because of this and because of uncertainty in determining the exact location of the upwind boundary, the fetch of the first station is set equal to the corresponding

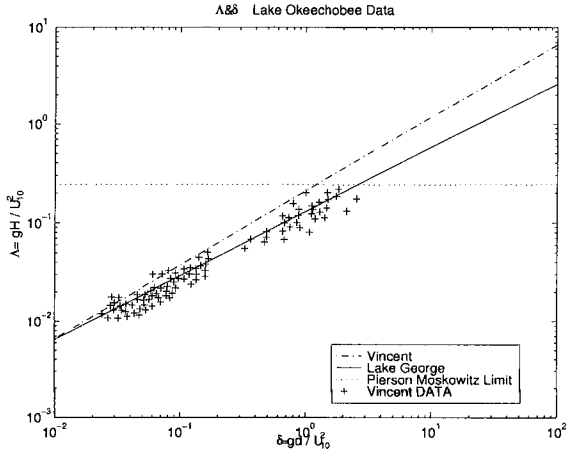


**Figure 5**

The same graph as with the Lake George data, except with the Lake Okeechobee data. The Lake George line looks like a better estimate. From the data new curves were calculated (fig 6 and fig 6).

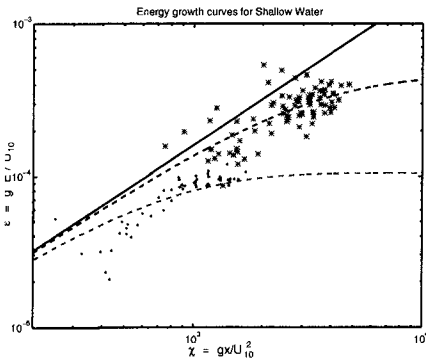


**Figure 6**

Two growth curves for dimensionless Energy set out against dimensionless fetch. The curves are calculated from the points with the same dimensionless depth. The most upwind point is set on the deep water growth (JONSWAP, Hasselmann et al. 1973)

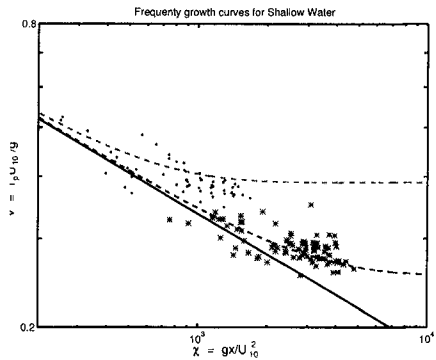


**Figure 7**

Two growth curves for dimensionless frequency set out against dimensionless fetch. The curves are calculated from the points with the same dimensionless depth. The most upwind point is set on the deep water growth (JONSWAP, Hasselmann et al. 1973)

### One-Dimensional Spectra

The one-dimensional spectrum has some of the characteristics of deep water spectra. The data used in the analyses of the spectra along the lake is only during north and south wind events with wind speeds greater than 3 m/s. In figure 8 the spectral peak moves toward lower frequencies as the fetch increases. In figure 8 one can see a small but very distinct peak enhancement. The spectra decay with  $f^{-4.5}$  from the peak frequency ( $f_p$ ) until approximately  $3 f_p$ , and at  $f^{-5}$  at higher frequencies (fig 9). The decay of  $f^{-5}$  however could be caused by a doppler shifting of the high frequency waves "riding" on the back off lower frequency waves. More analyses of these one-dimensional spectra are under way, including the differential growth between the wave measuring stations.

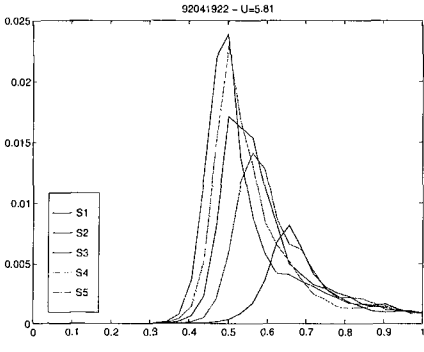


**Figure 8**  
Different stages of the spectra during growth. The spectral peak moves toward the lower frequencies as the fetch (or growth) increases. The peak enhancement can easily be seen. The frequency is set out against the Energy

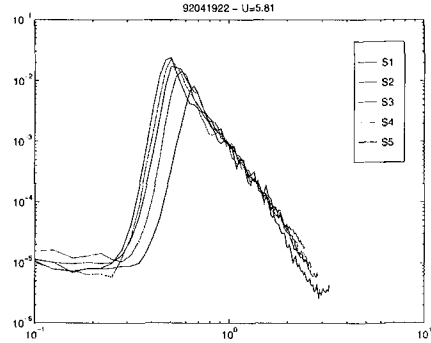


**Figure 9**  
This is a loglog plot of the different stages of the spectral growth. The Energy decays in the tail of the spectrum is related to  $f^{-4.5}$ . At higher frequencies the Energy decay is related to  $f^{-5}$ . The frequency is set out against the Energy

### Two-Dimensional Spectra

At the platform (station 6) the directional spectra were measured by an array of 7 Zwarts poles. The array could be operated by modem via the base station from the University College. The array was formed like a Mercedes star (Young 1995). For the analyses the Maximum Likelihood Method (MLM) was used. This method has the advantage over the Maximum Entropy Method (MEM) that it does not produce false peaks. The disadvantage is that the MLM produces a broader spectrum and has trouble analysing bi-modal seas. Lake George however, does not have any bi-model seas.

Due to the large number of wave measuring gauges in the array, the directional resolution is much higher than pitch-roll buoys or p, u, v meters. In figure 10 the normalised directional spreading function at  $\frac{1}{2}f_p$ ,  $f_p$ ,  $2f_p$  and  $3f_p$  is shown. The spectrum at  $f_p$  is quite narrow and aligned with the wind direction. However at  $2f_p$

and  $3f_p$  the spectrum is quite broad and develops a bidirectional mode, with more energy propagating at an angle to the wind than in the wind direction.

### Conclusions

The first analyses look promising. However more work needs to be done in analysing all the data. We are trying to fit different types of spectra like the JONSWAP and TMA spectra to see which fit better and with which parameters. With the Two-Dimensional Spectra we are trying to fit a spreading function that is dimensionless frequency depended.

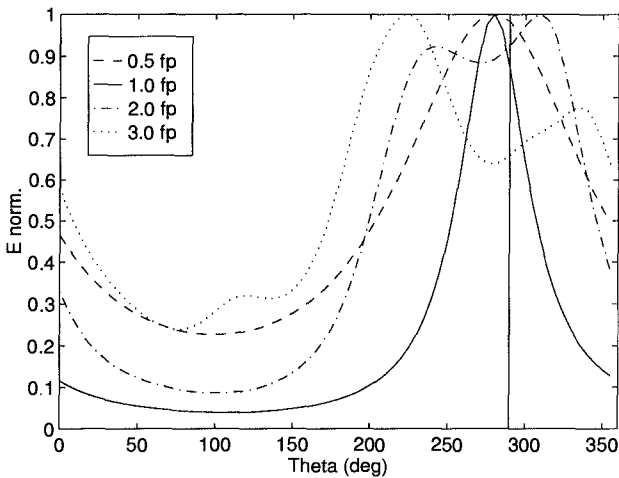


**Figure 10**

Cuts of the directional spectra at  $\frac{1}{2}f_p$ ,  $f_p$ ,  $2f_p$  and  $3f_p$ . The spectrum has one peak at frequency smaller than  $2f_p$ . The waves are travelling in the direction of the wind (thick line). However at frequencies greater than  $2f_p$  there is splitting of the directional spread. This means that the waves are travelling at an angle with the wind.

### References

- Donelan M.A., Hamilton J. and Hui W.H. 1985. Directional Spectra of Wind-Generated Waves. *Phi. Trans. R. Soc. Lond. A* 315, pp. 509-563
- Hasselmann K., Barnett T.P., Bouws E., Carlson H., Cartwright D.E., Enke K., Ewing J.A., Gienapp H., Hasselmann D.E., Kruseman P., Meerburg A., Müller P., Olbers D.J., Richter K., Sell W., Walden H. 1973. Measurements of Wind-Wave Growth and Swell Decay during the Joint North Sea Wave Project (JONSWAP), Deutsches Hydrographisches Institut, Hamburg

- Holthuijsen L.H., Booij N. and Hebers T.H.C. 1988 "A prediction model for stationary short-crested waves in shallow water with ambient currents", *Coastal Engineering*, 13, 23-54
- Pierson W.J. and Moskowitz L. 1964. A proposed Spectral Form for Fully Developed Windseas Based on Similarity Theory of S.A. Kitaigorodskii, *Journal of Geophysical Research*, Vol. 69, pp. 5181-5190
- Shore Protection Manual 1984. US Army Engineer Waterway Experiment Station, Coastal Engineering Research Center (CERC), US Government Printing Office, Washington, D.C. , 4th edition, 2 Volumes
- Smith D.S., Anderson J.R., Oost W.A., Kraan C., Maat N., DeCosmo J., Katsaros K.B., Davidson K.L., Bumke K., Hasse L., Chadwick H.M. 1992. Sea Surface Wind Stress and Drag Coefficients, The HEXOS Results, *Boundary-Layer Meteorology*, Vol. 60, pp. 109-142
- Taylor P.A. and Lee R.J. 1984. Simple Guidelines for Estimating Wind Speed Variations due to Small Scale Topographic Features, *Climatological Bulletin*, Vol. 18, No. 2, pp. 3-32
- Vincent C.L., Hughes S.T. 1985. Wind Wave Growth in Shallow Water, *Journal of Waterway, Port, Coastal and Ocean Engineering*, Vol. 111, No. 4, pp. 765-770
- Wamdi Group 1988. The WAM Model- A Third Generation Ocean Wave Prediction Model, *Journal of Physical Oceanography*, Vol. 18, pp. 1775-1810
- Wu J. 1980. Wind-Stress Coefficients over Sea Surface near Neutral Conditions-A Revisit, *Journal of Physical Oceanography*, Vol. 10 Part 1, pp 727-740
- Young I.R., 1988, A shallow water spectral wave model, *Journal of Geophysical Research*, Vol. 93,C5, pp. 5113-5129
- Young I.R., 1995, On the Measurement of Directional Wave Spectra, In press, *Applied Ocean Research*
- Zwarts C.M.G. 1974. Transmission Line Wave Height Transducer, *Proceedings International Symposium on Ocean Wave Measurement and Analysis*, New Orleans, ASCE, Vol. 1, pp. 605-620

## CHAPTER 50

### Estimation of Typhoon-Generated Maximum Wave Height along the Pacific Coast of Japan Based on Wave Hindcasting

Masataka Yamaguchi<sup>1</sup> and Yoshio Hatada<sup>2</sup>

#### Abstract

Wave hindcastings in the West Pacific Ocean and at selected locations along the Pacific coast of Japan by the use of two wave prediction models are conducted for 118 typhoons which occurred from 1940 to 1991 to estimate maximum wave height at each point during a typhoon. Combination with maximum wave height data in the concerned area for 125 typhoons from 1934 to 1983 obtained by Yamaguchi et al. (1987a, 1987c) results in data sets of maximum wave heights caused by 243 typhoons from 1934 to 1991. Spatial distribution of the most extreme wave height and wave height for return period of 100 years, and their variation along the Pacific coast of Japan are re-examined on the basis of statistical analysis of the data and compared with the Yamaguchi et al. results (1987a, 1987c), in which case there is little change in the distribution except for the Western Kyushu coast. In addition, maximum wave height along the coast of the Japan Sea is evaluated in a similar manner.

#### 1. Introduction

As the coastal areas of Japan facing the Pacific Ocean and the East China Sea have been heavily damaged by attacks of huge waves generated by powerful typhoons, the reasonable estimation of the typhoon-generated extreme waves around the Japanese coast is essential to planning and design of coastal protection systems for mitigation

- 
- 1 Prof., Dept. of Civil and Ocean Eng., Ehime Univ., Bunkyocho 3, Matsuyama 790, Ehime Pref., Japan
  - 2 Research Assistant, Dept. of Civil and Ocean Eng., Ehime Univ., Bunkyocho 3, Matsuyama 790, Ehime Pref., Japan

of wave-induced coastal hazards. The extreme waves expected in 50 or 100 years in the concerned sea area or location are usually evaluated based on statistical analysis of wave data hindcasted for many severe storms over a long term period of more than 30 years rather than measured wave data, because acquirement of measured data which is acceptable in quality and quantity is difficult.

Yamaguchi et al.(1987a, 1987c) estimated the spatial distribution of maximum significant wave height generated by typhoons in the West Pacific Ocean and around the Pacific coast of Japan, based on wave hindcasting for 125 typhoons in the past 50 years using two kinds of spectral wave prediction models. But re-estimation of probable extreme waves around the Pacific coast of Japan is required, because in recent years abnormally high waves and the consequent severe coastal hazards have been brought about by successive attacks of powerful typhoons such as Typhoons 8712 and 9119.

In this paper, wave hindcastings in the West Pacific Ocean and at selected locations along the Pacific coast of Japan by the use of two wave prediction models are conducted for 118 typhoons which occurred from 1940 to 1991 to estimate maximum wave height at each point during a typhoon. Combination with maximum wave height data in the concerned area for 125 typhoons from 1934 to 1983 obtained by Yamaguchi et al.(1987a, 1987c) results in data sets of maximum wave heights caused by 243 typhoons from 1934 to 1991. Spatial distribution of the most extreme wave height and wave height for return period of 100 years, and their variation along the Pacific coast of Japan are re-examined on the basis of statistical analysis of the data. In addition the most extreme wave height along the coast of the Japan Sea is also evaluated based on wave hindcastings for intense storms with use of the wave prediction models and their statistical analysis.

## 2. Outline of Wave Hindcast System

### (1) Wind hindcast model

A parametric typhoon model is used for the estimation of typhoon-generated winds. The model computes the spatial distribution of wind speed and wind direction in a typhoon by composing axisymmetrical gradient wind components and wind components related to the movement of a typhoon. The exponential function is assumed for the pressure distribution in a typhoon. The model parameters such as central pressure, position of typhoon center, radius to maximum winds and wind inflow angle are given every 6 hours, and wind field every 1 hour is estimated



through a linear interpolation of the typhoon parameters. Correction factor to wind speed at the height of 10 m is 0.60.

(2) Wave hindcast model

The wave prediction models developed by the authors are used in the wave hindcasting. The first model referred to as the grid model (Yamaguchi et al., 1987a) is a coupled discrete model belonging to the second generation model which solves the energy balance equation on a regular grid. The grid with a spacing of 80 km is used for the estimation of spatial distribution of deep water extreme waves in the West Pacific Ocean shown in Fig. 1.

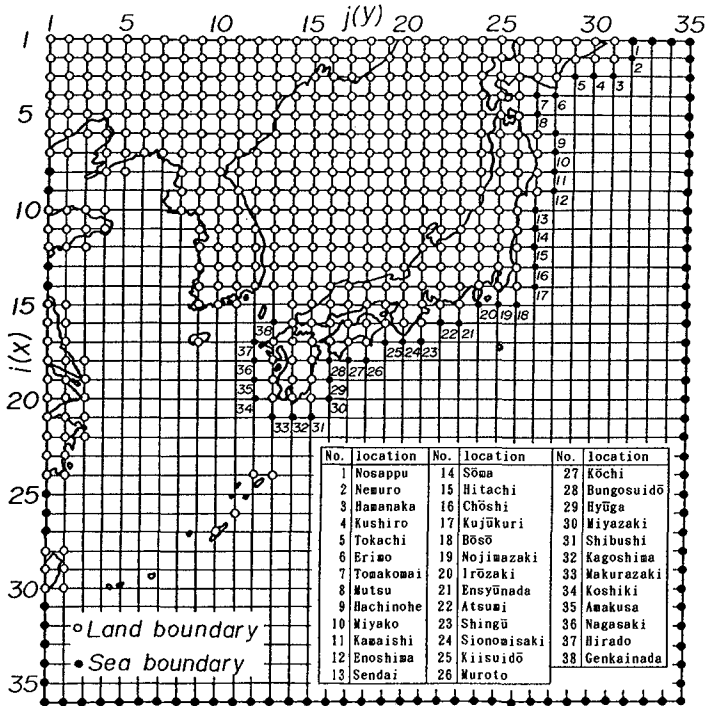


Fig. 1 Coarse grid used in wave hindcasting with grid model.

The second model referred to as the point model (Yamaguchi et al., 1987b) is a decoupled propagation model classified into a category of the first generation model in which the evolution of directional spectrum is traced along a wave ray for individual spectral component

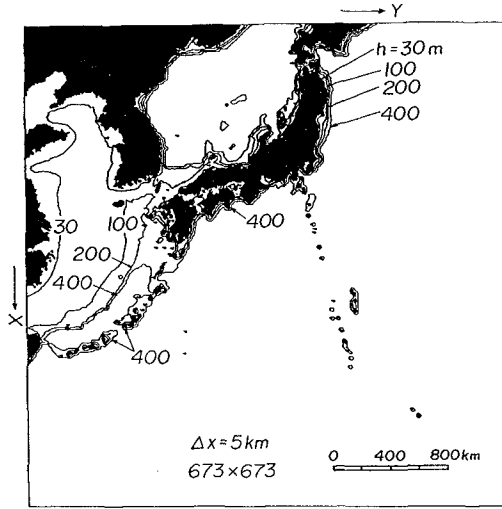


Fig. 2 Computation area used in wave hindcasting with point model and contour plot of water depth.

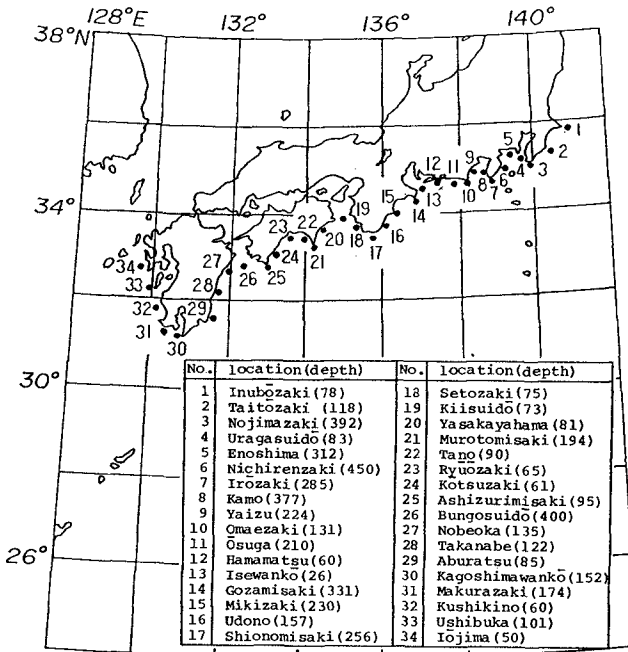


Fig. 3 Locations selected for wave hindcasting with point model.

focusing on a single position. The high topographical resolution grid with a spacing of 5 km is used in the point model to estimate the effect of shallow water on extreme waves in the nearshore region, as indicated in Fig. 2. Fig. 3 shows location of 34 selected points where wave hindcastings are conducted along the coastal region of Western Japan.

In hindcasting, 20 frequency components from 0.045 to 1.0 Hz and 19 directional components from 0 to 360 degrees are used in the grid model and 23 frequency components from 0.035 to 0.5 Hz and 37 directional components from 0 to 360 degrees are used in the point model. At the land boundary the directional spectrum is set at zero, and at the open boundary the directional spectrum computed from the product of frequency spectrum based on the Ross model (Ross, 1976) and an angular distribution is given in both models.

### 3. Typhoons Selected for Wave Hindcasting

In this study, 118 intense typhoons are newly selected for wave hindcasting by surveying the published reports. They include annual reports of wave data with ocean buoys deployed around Japan by the Japan Meteorological Agency, annual reports of wave data acquired with sonic-type wave gauge around the coastal area of Japan by the Harbor Construction Bureau, Ministry of Transport, a report of Typhoon Summary of Japan 1940-1970 edited by the Japan Meteorological Association and a report of Tropical Cyclone Tracks in the Western North Pacific 1951-1990 edited by the Japan Meteorological Agency. Extremes of typhoon-generated wave height are estimated based on the results of wave hindcasting for the 243 typhoons from 1934 to 1991, in which case wave hindcastings for the 125 typhoons from 1934 to 1983 have already been carried out by Yamaguchi et al. (1987a, 1987c).

Fig. 4 shows tracks of the 243 typhoons with those of the 125 typhoons used in wave hindcasting by Yamaguchi et al. (1987a, 1987c). Tracks of the 243 typhoons cover a wide area of the West Pacific Ocean far more densely than tracks of the 125 typhoons. Yearly consecutive typhoon data is available only for the period of 42 years from 1950 to 1991, because the typhoon data preceding the period are limited to huge typhoons which caused severe damages. Data of annual maximum wave height used in extreme wave statistics are those estimated for the 221 typhoons which occurred over the period of 42 years.

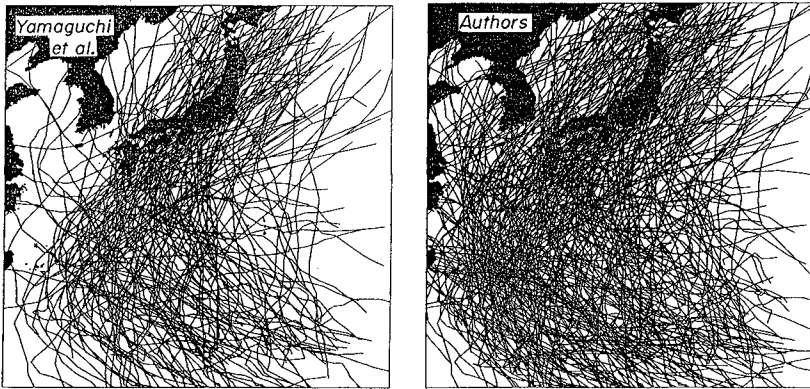


Fig. 4 Tracks of typhoons used in wave hindcasting.

4. Estimation of Maximum Wave Height

(1) Spatial distribution of maximum wave height

Superimposing maximum wave height obtained from hindcasted wave heights every 1 hour for the 243 typhoons at a point produces the most extreme wave height from 1934 to 1991 at the point. Fig. 5 shows spatial distribution of the most extreme wave height estimated by the wave hindcasting using the grid model of Yamaguchi et al. (1987a) and the authors' revised results. As the typhoon-generated extreme wave height at a point is strongly dependent on tracks of powerful typhoons which passed over near the point, it varies remarkably from place to

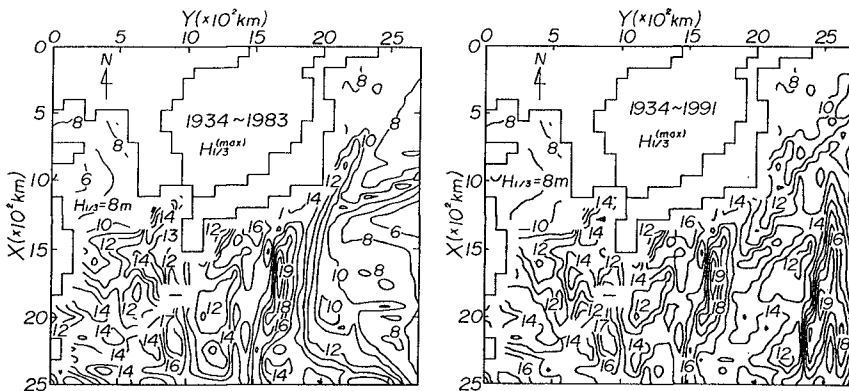


Fig. 5 Spatial distribution of the most extreme wave height.

place. Differences between both the results are seen at the southeast and southwest parts of the computation area and the western part of Kyushu Island. Especially, maximum wave height along the western part of Kyushu Island is replaced from 12-13m to 14 m associated with Typhoons 8712 and 9119.

(2) Alongshore distribution of the most extreme waves

Fig. 6 illustrates alongshore distributions of the most extreme wave height and frequency of occurrence of waves more than 10 m high estimated from wave data hindcasted with the grid model and observed data. Name and number of the location indicated along the horizontal axis in the figure are given in Fig. 1. In a qualitative sense, alongshore distribution of extreme wave height looks similar, but in a quantitative sense, hindcasted results give much higher estimation than observed results except for the northern part of the Japanese coast such as Sendai or Tomakomai where the most extreme waves are frequently generated by strong monsoon winds in winter. The reasons are that the wave model does not take into account the shallow water effects, that the grid system of poor topographical resolution is used in the wave hindcasting and that the period of wave observation is too short compared to the period of wave hindcasting. The most extreme wave height estimated by Yamaguchi et al.(1987a) is updated 2 m near Nagasaki by Typhoons 8712 and 9119, and updated 1 m near Chōshi by Typhoon 8913. Maximum of the most extreme wave height exceeding 15 m is observed at the sea area near Shionomisaki.

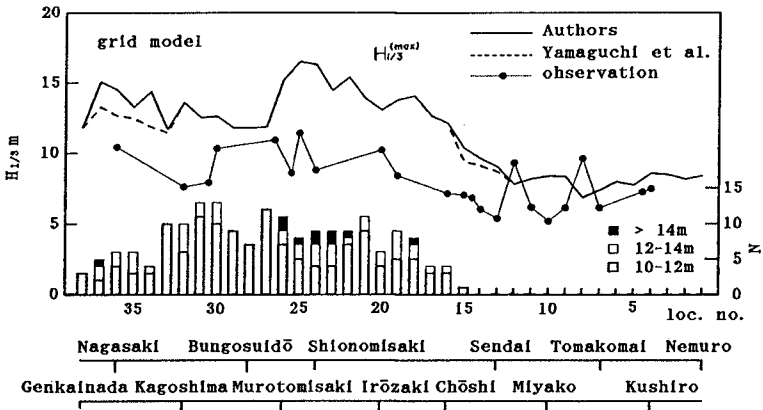


Fig. 6 Variation around the Pacific coast of Japan of the most extreme wave height and frequency of occurrence of waves more than 10 m high estimated from wave data hindcasted with grid model and observed wave data.

In addition, Fig. 7 shows alongshore distributions of the most extreme wave height estimated from wave hindcasting with the point model. Name of location corresponding to the figure along the abscissa is summarized in Fig. 3. The most extreme wave height and occurrence rate of high waves estimated with the point model are relatively lower than that with the grid model and varies significantly from location to location, because the point model can take into account the topographical effect in much more detail than the grid model.

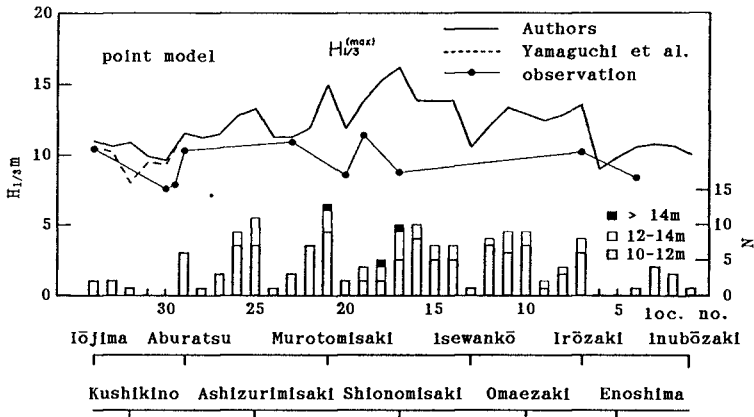


Fig. 7 Variation around the Pacific coast of Western Japan of the most extreme wave height and frequency of occurrence of waves more than 10 m high estimated from wave data hindcasted with point model and observed wave data.

Alongshore distributions of the most extreme wave height estimated by both the grid model and the point model and observed wave data are compared in Fig. 8. Notation of the abscissa is the same as Fig. 6. Extreme wave height estimated by the point model gives a consistently smaller value than that of the grid model and varies remarkably from location to location, as the point model can take into account the effect of water depth variation and topography by usage of fine computation grid. The most extreme wave height estimated with the point model shows a closer value to the observed extreme wave height than the result with the grid model. As mentioned before, the most extreme wave height observed near Sendai and Tomakomai exceeds the estimate with the grid model. This suggests that the most extreme wave height in northern Japan is caused by not only typhoons but also by monsoons.

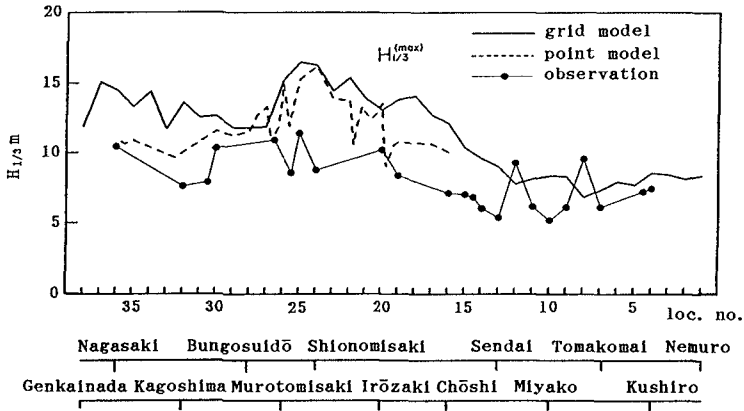


Fig. 8 Variation around the Pacific coast of Japan of the most extreme wave height estimated from wave data hindcasted with both grid model and point model and observed wave data.

(3) Wave height for return period of 100 years

Yearly variations of the annual maximum wave heights at Irōzaki estimated with the grid model and point model and the corresponding observed data are shown in Fig. 9. Both hindcasted results agree relatively well with the observed data, because Irōzaki is exposed directly to open sea and water depth of the installed wave gauge of 50 m is enough to measure deep water waves. Maximum wave height varies remarkably from year to year due to strong annual change of powerful typhoons attacking the Pacific coast of Japan, in which cases the severest sea state occurred in the nineteen-fifties and the nineteen-sixties.

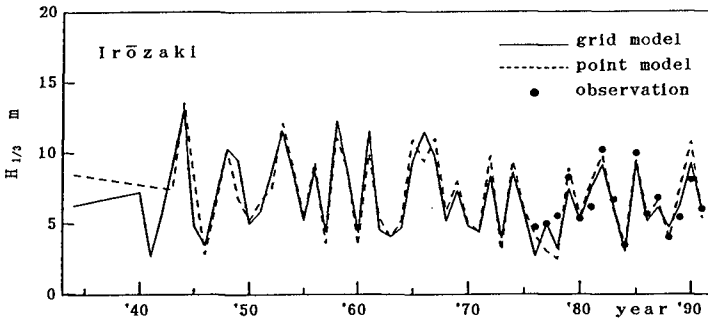


Fig. 9 Yearly variation of annual maximum wave height at Irōzaki.

The log-normal distribution with three parameters is fitted to the data of annual maximum wave height for the period of 42 years from 1950 to 1991, in which the estimation of parameters is due to the moment method. Fig. 10 shows an example of the fitting. At Irōzaki, wave heights with a return period of 100 years are 13.8 m and 13.5 m for the data hindcasted with the grid model and point model, and 11.9 m for the observed data. Observed data give a smaller estimation of extreme wave height, because the observation period is short compared to the wave hindcast period and the observed waves are affected by bottom topography in rough sea condition even if the wave gauge is installed at the point of 50 m deep.

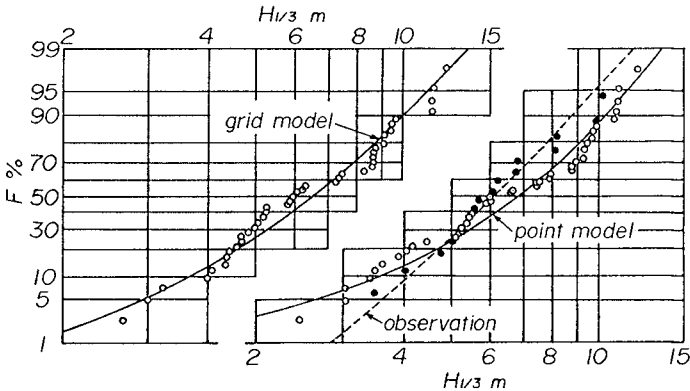


Fig. 10 Fitting of log-normal distribution to annual maximum wave height data at Irōzaki.

Fig. 11 describes the spatial distribution of wave height for a return period of 100 years over the West Pacific Ocean and the East China Sea. The spatial distribution is estimated by the fitting of log-normal distribution with three parameters to the annual maximum wave height data obtained from wave hindcastings by use of the grid model for the period from 1950 to 1991. Being similar to the spatial distribution of the most extreme wave height in this area, return wave height over 19 m is observed in the offshore sea area and return wave height becomes smaller around the Japanese coast, especially in the northern part because of the decay in typhoon intensity.

Fig. 12 illustrates alongshore distributions of wave height for a return period of 100 years estimated from wave data hindcasted with the grid model and observed wave data. Name of the location corresponding to the number along abscissa in the figure is given in Fig. 1. Except near Nagasaki, the present results are similar to



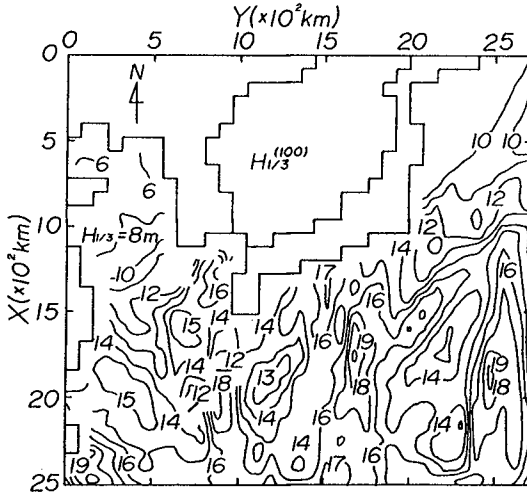


Fig. 11 Spatial distribution of wave height for return period of 100 years.

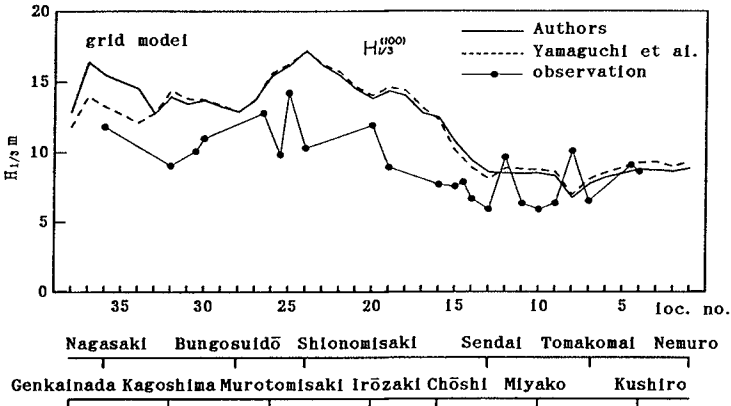


Fig. 12 Variation around the Pacific coast of Japan of wave height for return period of 100 years estimated from wave data hindcasted with grid model and observed data.

the results of Yamaguchi et al.(1987a), despite the fact that the number of annual maximum wave height data and cases of typhoon for wave hindcasting increased from 34 to 42 and from 107 to 221 respectively.

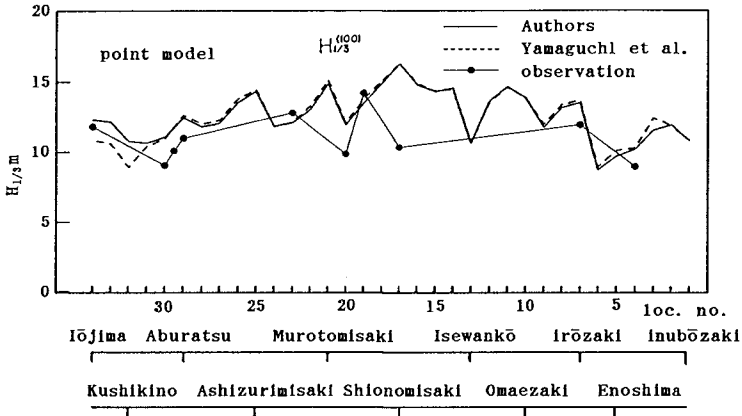


Fig. 13 Variation around the Pacific coast of Western Japan of wave height for return period of 100 years estimated from wave data hindcasted with point model and observed wave data.

Fig. 13 shows alongshore distributions of wave height for a return period of 100 years estimated with the point model by the authors and Yamaguchi et al. (1987c), which includes the corresponding results based on observed data. Name of numbered location is indicated in Fig. 3. Hindcasted results produce smaller estimates at Ryūōzaki and Kiisuido than observed results. But, the reliability of the observed results is relatively low, because the number of annual maximum wave height data used in extreme analysis is less than 10 at these points.

Alongshore distributions of wave height for a return period of 100 years evaluated with three kinds of wave data are given in Fig. 14. Return wave height estimated from the results hindcasted with the grid model varies from 9 m to 17 m and is greater than the other results because of poor topographical resolution of the grid system used in wave hindcasting. But at the open coastal locations, both models produce comparative results. Return wave height based on the point model using the grid system with high topographical resolution varies greatly from location to location, which is in closer agreement with that estimated with observed data. It should be noted that at most locations, the return wave height evaluated with observed data takes a lower value than that with hindcasted data, because the observation period is far shorter compared to the hindcast period.

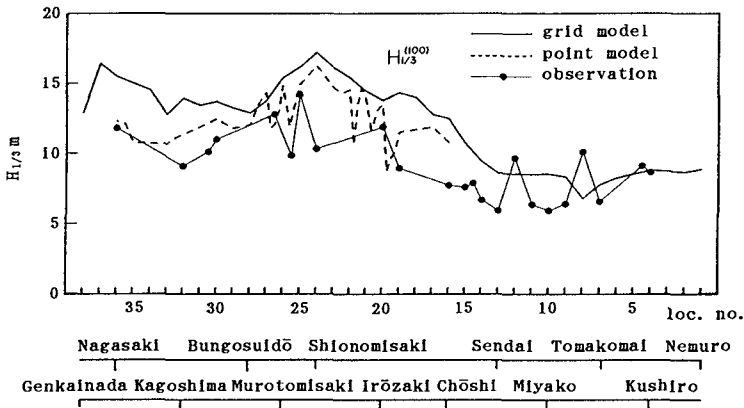


Fig. 14 Variation around the Pacific coast of Japan of wave height for return period of 100 years estimated with both grid model and point model and observed wave data.

#### 5. Estimation of Maximum Wave Height along the Coast of the Japan Sea

Finally, maximum wave height along the coast of the Japan Sea is briefly discussed to contrast the characteristics of the maximum wave height along the Pacific coast. To evaluate maximum wave height along the coast of the Japan Sea, wave hindcasting for 143 storms which occurred from 1962 to 1991 is carried out with the same spectral wave prediction models as mentioned before. Wind distributions are estimated by weather map analysis, as high waves in the Japan Sea are predominantly generated by winter monsoons. The weather map analysis consists of a spline interpolation onto regular grid of irregularly-distributed atmospheric pressure data and an application of the Bijvoet wind model(1957).

Fig. 15 shows alongshore distribution of the most extreme wave height estimated from the wave data hind-casted for intense meteorological disturbances over 30 years from 1962 to 1991 with both the grid model and the point model and the observed wave data of shorter period. Usually, annual maximum wave height along the Japan Sea coast does not change so greatly as that along the Pacific coast, because in most cases it is generated by winter monsoons with weak yearly variation and the Japan Sea is

a semi-closed and limited basin. The most extreme wave height along the coast of the Japan Sea ranges from 6 m to 10 m and is about 5 m lower than that along the southern Pacific coast shown in Fig. 8 due to the limited sea area.

Sheltering effect of waves by Sado Island can be observed from Naoetsu to Sakata by comparing the estimates with the grid model and point model. Grid system with a grid distance of 40 km used in the grid model is too coarse to resolve the presence of Sado Island and consequently the grid model overestimates the wave conditions in the coastal sea area of Hokuriku district behind Sado Island.

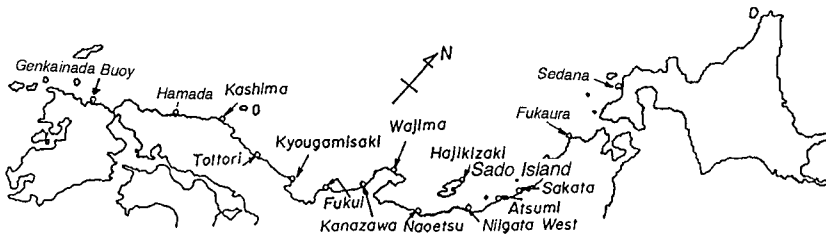
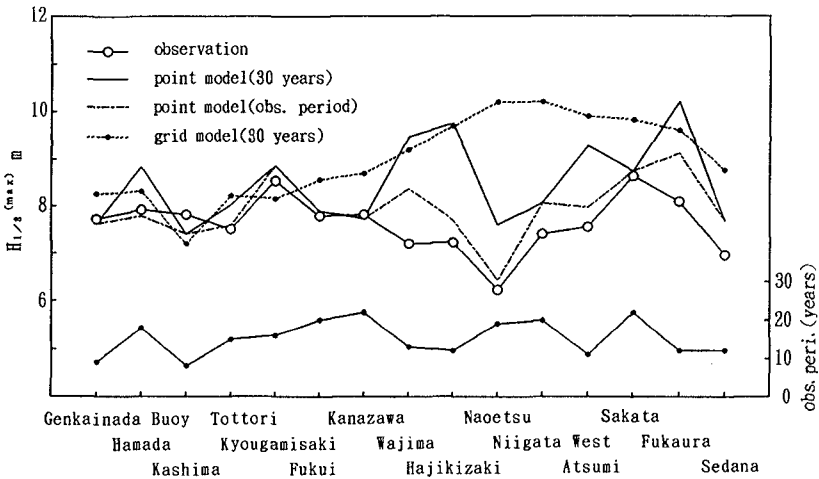


Fig. 15 Variation around coast of the Japan Sea of the most extreme wave height estimated from wave data hindcasted with both grid model and point model and observed wave data.

## 6. Conclusions

The most extreme waves expected in 100 years in the West Pacific Ocean and around the Japanese coast were evaluated based on statistical analysis of the wave data hindcasted with the use of two kinds of wave prediction models for the 243 typhoons which occurred from 1934 to 1991. It is deduced that maximum wave height around the Japanese coast exceeds 15 m. The most extreme wave heights along the Japan Sea coast were also estimated in similar manner. The result is that the wave height ranges from 6 m to 10 m which is about 5 m lower than that along the Pacific coast for the reasons of a limited sea area with restricted fetch and monsoon-dominated wind conditions in the sea area.

## 7. Acknowledgements

A part of this study was accomplished with the support of the Science Research Fund (No. 06680431) of the Ministry of Education, for which the authors express their appreciation. Thanks are also due to Mr. M. Ofuku, Technical Officer of Civil and Ocean Engineering, Ehime University and Mr. H. Satoh, former graduate student of Civil and Ocean Engineering, Ehime University for their sincere assistance during the study.

## References

- Bijvoet, H.C.(1957): A new overlay for the determination of the surface wind over sea from surface weather charts, KNMI, Mededelingen en Verhandelingen, Vol. 71, pp. 1-35.
- Ross, D.B.(1976): A simplified model for forecasting hurricane generated waves, Bull. American Meteorol. Soc., 113.
- Yamaguchi, M. et al.(1987a): Estimation of alongshore distribution of typhoon-generated maximum wave height around the Japanese coast based on wave hindcasting, Proc. JSCE, No. 381/II-7, pp. 131-140 (in Japanese).
- Yamaguchi, M. et al.(1987b): A shallow water prediction model at a single location and its applicability, Proc. JSCE, No. 381/II-7, pp. 151-160 (in Japanese).
- Yamaguchi, M. et al.(1987c): Alongshore distribution of extremes of typhoon-generated waves around the Pacific coast of Western Japan on the basis of wave hindcasting, Proc. JSCE, No. 387/II-8, pp.281-290 (in Japanese).

## CHAPTER 51

### RUN-UP OF IRREGULAR WAVES ON GENTLY SLOPING BEACH

YOSHIMICHI YAMAMOTO<sup>1</sup>, KATSUTOSHI TANIMOTO<sup>2</sup>, KARUNARATHNA G. HARSHINLE<sup>3</sup>

#### ABSTRACT

Irregular wave run-up on beaches has been studied on the basis of laboratory and field data, which confirmed that long-term wave run-up corresponding to surf beat (or infragravity waves) appears in case of a sea bottom slope gentler than about 1/20. Moreover analytical and numerical models to calculate surf beat caused by wave groups are investigated, and empirical and numerical models to predict the long period wave run-up are proposed.

#### 1. INTRODUCTION

Various patterns of wave run-up on beaches due to irregular incident waves with surf beat are observed in laboratories and fields. Figure 1 shows schematic patterns of time profiles of run-up height for incident wave groups.

- 1) Pattern-(a): When a sea bottom slope is steep, the state that individual run-up heights almost correspond to individual incident waves is dominant. This pattern is called "predominant incident wave type".
- 2) Pattern-(b): When the bottom slope is gentler than that of pattern-(a), because the width of the surf zone with swash zone is wider than that of pattern-(a), the disappearance of small waves by run-down, and the capturing and overtaking of waves predominates in the swash zone. This pattern is called "intermediate type".
- 3) Pattern-(c): When the bottom slope is sufficiently gentle, because the width of the surf zone is wide enough, short period waves are almost eliminated by wave breaking, and the reflection coefficient of short period waves becomes very small. Thus the run-up of long period waves (surf beat or infragravity waves) is dominant. This

---

<sup>1</sup> Dr.-Eng., Coastal Engineer, INA Corporation, 1-44-10 Sekiguchi, Bunkyo-ku, Tokyo, 112, Japan.

<sup>2</sup> Dr.-Eng., Professor, Department of Civil & Environmental Engineering, The University of Saitama, Urawa, Japan.

<sup>3</sup> Graduate Student, Doctoral Course, Ditto.

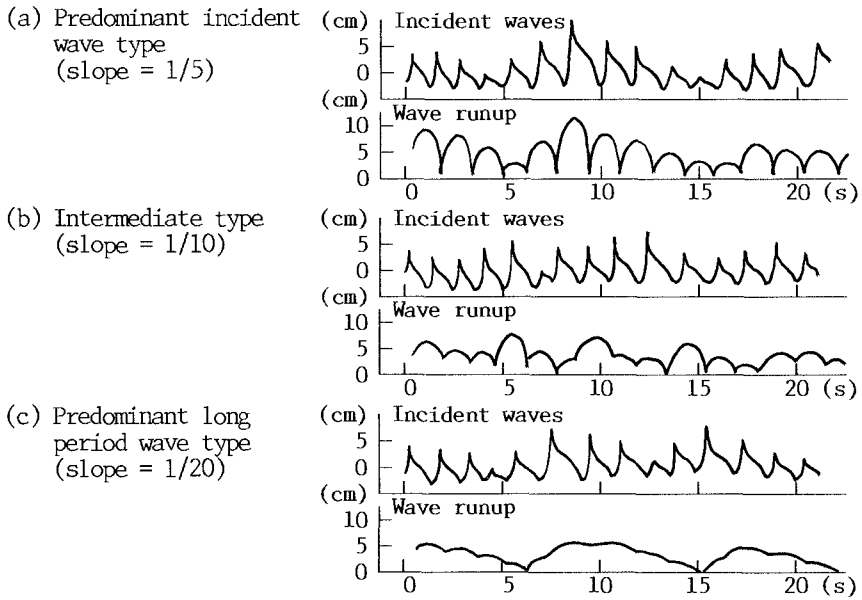


Fig.1 Type of wave run-up profiles.

pattern is called "predominant long period wave type" and the periods of these correspond to those of wave groups.

Mase and Iwagaki (1984) showed that the number of run-up waves becomes smaller as the surf similarity parameter,  $\xi$  [= the bottom slope / (the wave steepness)<sup>1/2</sup>], becomes smaller. Since the distribution width of bottom slopes is wider than that of the square root of wave steepness, and the groupiness of incident waves can be expressed by the total run length, it is possible to arrange available data by using the mean bottom slope in the surf zone  $\bar{i}$  and the mean total run length  $\bar{j}_{2m}$ . Figure 2 shows the relation between  $\bar{i}$  and  $\bar{j}_{2m}$  for different types of run-up (Yamamoto and Tanimoto, 1994 : by experimental and

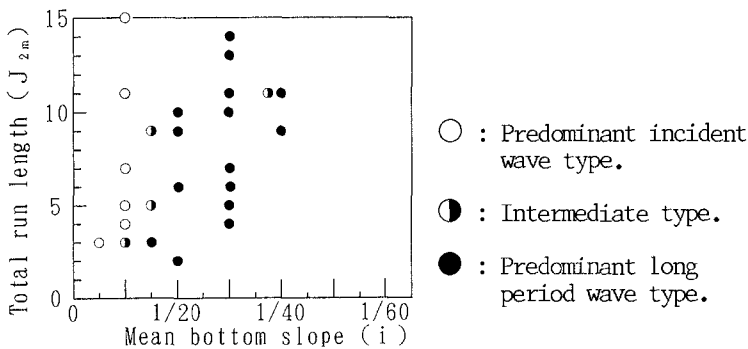


Fig.2 Relation between  $\bar{i}$  and  $\bar{j}_{2m}$  for different run-up types.

field data). As shown in Fig.2, it can be stated that the predominant incident wave type appears mostly when  $i$  is steeper than about 1/10, while the predominant long period wave type appears when  $i$  is gentler than 1/20. As reasons why data at the slope  $i=1/37$  is peculiar, unsuitable estimation of the slope  $i$  and disregard of wave steepness are considered.

In this paper, the predominant long period wave run-up type is investigated. First, the generation mechanism of two-dimensional surf beat is discussed using analytical and numerical models. Then, empirical and numerical models to predict the run-up height are proposed.

## 2. GENERATION MECHANISM OF SURF BEAT

### 2.1 Synopsis of Generation Theories

Various theories have been presented concerning the mechanism of generation of surf beat. Since there is a strong correlation between surf beat and run length of offshore waves, the contribution of the long period waves due to wave groupiness under two-dimensional conditions is considered to be very significant.

Two theories have been presented on the generation of long period waves due to wave groupiness.

#### a) Bound Long Wave (BLW) Theory

The BLW theory was presented by Longuet-Higgins and Stewart(1962). According to this theory, long period waves, whose velocity is constrained by the group velocity, are generated by the periodic variation of the mean water level due to wave groupiness outside the breaker zone. Since the velocity of these waves becomes equal to the velocity of long waves near the breaking point, it is possible to consider that the long period waves propagate landwards as free long waves after breaking of incident waves.

#### b) Breakpoint-Forced Long Wave (BFLW) Theory

The BFLW theory was presented by Symonds et al.(1982). According to this theory, long period waves are generated by the periodic variation of the mean water level in the breaker zone, caused by the periodic movement of the breakpoint due to wave groupiness. Because the discrepancy between calculated values by their model and measured values was not negligible, Nakamura and Katoh (1992) was later modified model of Symonds et al.

A numerical model embracing both these theories has recently been developed by Goda (1990) and List (1992a,b). The numerical results given by List indicate that, in the case of a uniformly sloping sea bottom, BLW will predominate when the period ratio of the long period waves to incident waves falls below around 10, while BFLW will predominate when the above ratio is greater than 10.

The characteristic of surf beat in surf zone is investigated in the following.

### 2.2 Treatment of Irregular Waves with Wave Groupiness

In an attempt to simplify the treatment of irregular waves, the wave height  $H_{0.11}$  at the offshore boundary is expressed as follows :



$$H_{orff} = H_{orffm} - a_H \times \sin(2\pi t / T_{Lm}) \tag{1}$$

where,  $H_{orffm}$  is the mean wave height,  $a_H$  is the amplitude of the wave height fluctuation,  $T_{Lm}$  is the mean period of surf beat.

By Substituting Eq.(1) into the theoretical equation for BLW given by Longuet-Higgins and Stewart, the wave height of BLW can be expressed as follows :

$$\frac{H_L}{H_{orffm}} \approx \frac{1}{2} \left[ \frac{(2c_g/c) - 1/2}{1 - (c_g^2/gh)} \right] \frac{a_H}{h} \tag{2}$$

where,  $c_g$  is the group velocity,  $c$  is the wave velocity,  $g$  is the acceleration due to gravity, and  $h$  is the water depth.

By assuming that the period distribution of irregular waves is narrow, the distribution of  $H_L$  corresponds to the distribution of  $a_H$ . Thus the incident wave height corresponding to the statistical value of the wave height of surf beat is given by Eq.(1) with specified  $a_H$ .

The amplitude  $a_H$  corresponding to the significant wave height of surf beat can be expressed (Nakamura and Katoh, 1992) as follows :

$$a_H \approx 0.4714 H_{orff1/3} \tag{3}$$

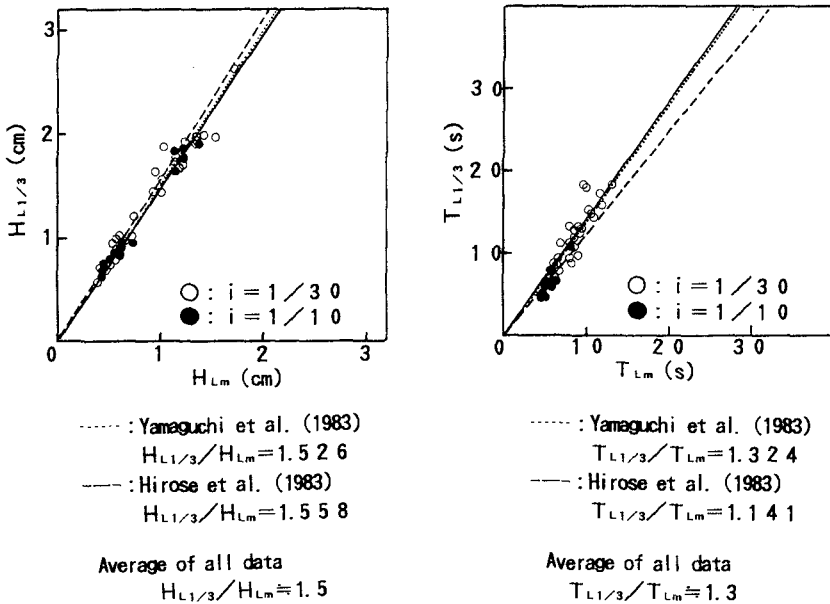


Fig.3 Relation between mean and significant wave heights, and that of wave periods on surf beat respectively (Yamamoto and Tanimoto, 1994).

where,  $H_{o.f1/3}$  is the significant wave height.

Moreover, by experimental and field data as shown in Fig.3, the relationship between the mean wave height and the significant wave height of surf beat ( $H_{Lm}$ ,  $H_{L1/3}$ ) is expressed as follows :

$$H_{Lm} \approx H_{L1/3} / 1.5 \tag{4}$$

Thus the amplitude  $a_H$  corresponding to the mean wave height of surf beat can be expressed as follows :

$$a_H \approx 0.4714 H_{o.f1/3} / 1.5 \approx 0.50 H_{o.f1/3} \tag{5}$$

### 2.3 Investigation by Analytical Model

Nakamura and Katoh have shown that it is possible to provide a fairly accurate representation of the surf beat in the breaker zone by considering the time lag of breaking accompanying the propagation of waves according to theory of Symonds et al.

The on-offshore distribution of wave heights of surf beat obtained by their model is indicated by the broken lines in Fig.4. In the top three graphs, the calculated values are compared with field data taken at Hazaki Beach (Ibaraki Prefecture in Japan) by Katoh et al. (1991). The bottom two graphs show a comparison between experimental data (at the University of Saitama) and calculated results. In all cases, the surf beat to incident wave period ratio is around 10:1.

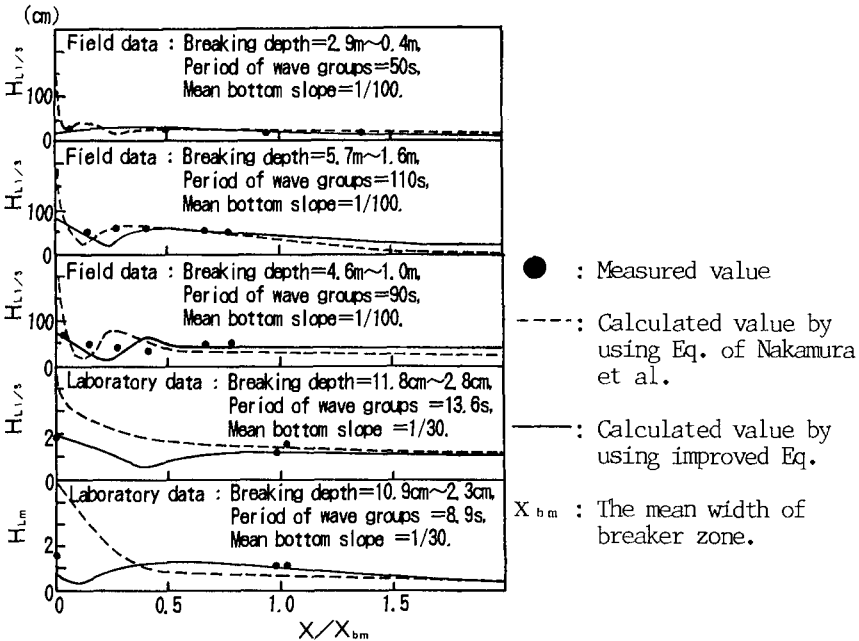


Fig.4 Comparison between observed data and predicted curve.

As can be understood from Fig.4, however, the results obtained by method of Nakamura et al. are abnormally large values near the shoreline. The following improvements were made here, as this study is also concerned also with wave heights at the shoreline.

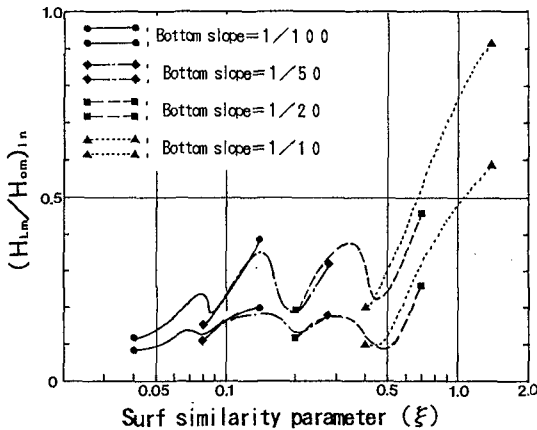
One of the reasons for the abnormally large values near the shoreline could be the absence of considerations for the water level rise in the values used for the water depth in the basic equation proposed by Katoh et al. An improvement can be made for this by solving the following basic equation :

$$\left. \begin{aligned} \frac{\partial U}{\partial t} + g \frac{\partial \zeta}{\partial x} &= - \frac{1}{\rho D} \frac{\partial S_{xx}}{\partial x} \\ \frac{\partial \zeta}{\partial t} + \frac{\partial (DU)}{\partial x} &= 0, \quad D = h + \zeta_0 \end{aligned} \right\} \quad (6)$$

where,  $U$  and  $\zeta$  are the horizontal velocity and the water level of long period waves respectively,  $t$  is the time,  $x$  is the horizontal coordinate whose origin is the point of intersection between the bottom slope and the still water level,  $\rho$  is seawater density,  $D$  is the water depth including mean water level rise ( $\zeta_0$ ), and  $S_{xx}$  is radiation stress.

The details of the solution are described in the appendix.

The variables relating to BFLW in the breaker zone include the minimum and the maximum widths of the breaker zone ( $X_{b1}$  and  $X_{b2}$ ), the period of the surf beat ( $T_L$ ), sea bottom slope in the surf zone ( $i$ ), and the wave height - water depth ratio ( $2\gamma$ ) in Eqs.(A.2), (A.5) and (A.6) in the appendix.  $\gamma$  can be ignored as it shows little variation on a gently sloping sea bottom.  $T_L$  can be related to the period of short waves ( $T$ ) using the expression  $T_{L1/3} \propto T_{1/3}$  given by Nakamura and Katoh (1992). Furthermore,  $L_o = (g/2\pi) T^2$ ; hence  $T_L^2 \propto L_o$ . There is a proportionality between  $X_b$  and  $H_o$ . Thus  $H_o/L_o$  and  $i$  can be used as approximate indices for the



The subscript "in" stands for mean values inside the breaker zone.

Fig.5 Relation between  $\xi [= i/(H_o/L_o)^{1/2}]$  and  $H_{Lm}/H_{om}$ .

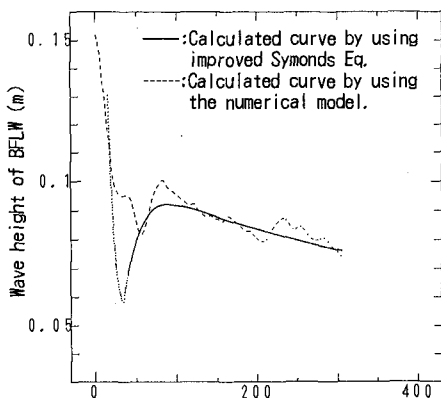
determination of BFLW in the breaker zone.

In Fig.5, the mean wave heights of surf beat ( $H_{L,m}$ ) are rendered dimensionless and averaged out within the breaker zone, and then arranged by the surf similarity parameter  $\xi$ . The values for the cases falling within the range  $0.01 < \text{wave steepness} < 0.06$  have been selected, and ranges in which these values fall are shown by double curves.

### 2.4 Investigation by Numerical Model

Since real surf beat composed of BFLW and BLW, List's numerical model is improved by taking the change of depth due to the long period waves into account [ $D = h + \zeta$  is used instead of  $D = h + \zeta_0$  of Eq. (6)]. In this model, incident waves propagate with group velocity. Radiation stress is calculated by the small amplitude wave theory. Breaking points are determined by using Goda's breaker index (1975). BFLW is calculated by giving the radiation stress only in the breaking zone.

The example of calculated wave heights given in Fig.6 are for the BFLW on a beach with a bottom slope of 1/40, caused by wave groups with a mean wave height of 0.8m at a water depth of about 8m, a period of 8.0s and a long wave period of 61.6s. The solid lines in the figure indicate the results obtained using the modified version of the model of Symonds et al., while the dotted lines in the figure indicate the results obtained with the numerical model. This example indicates that the numerical model will give values for BFLW which are more or less the same as those obtained by the theory of Symonds et al. Since the numerical model does not allow the water level to fall below the ground level, the discrepancy between calculated values of both models becomes great near the shoreline.



The same conditions as List's experiment are used.

$$H_{off} = 0.8 - 0.4 \times \sin(2\pi t / 61.6),$$

$T = 8.0, T_L = 61.6,$   
(units in m and s).

Fig.6 Wave height of BFLW ( $i=1/40$ ).

Given in Fig.7 are the calculated results for the waves generated on a beach with a relatively steep slope at points shallower than 0.8m

and a gentle slope of around 1/70 at points further offshore. Incident wave groups are taken to have mean offshore wave height 0.36m, period 10.9s and long wave period 70s. Since the shallow area where the group velocity is close to the phase velocity of long waves extends widely outside the surf zone, BLW can develop sufficiently.

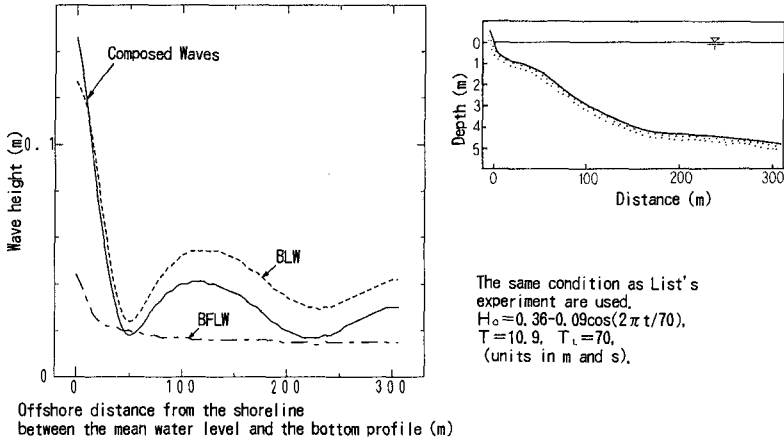


Fig.7 Wave height of surf beat (a concave type coast).

If this assumption is correct, one can expect BFLW to predominate on a beach with opposite slope characteristics. Given in Fig.8 are the calculated results for the waves generated on a beach with a horizontal reef with a water depth of about 2m extending for approximately 500m from the shoreline. Offshore incident waves in this case are considered to have a mean wave height of 2.88m, period of 13.8s, and

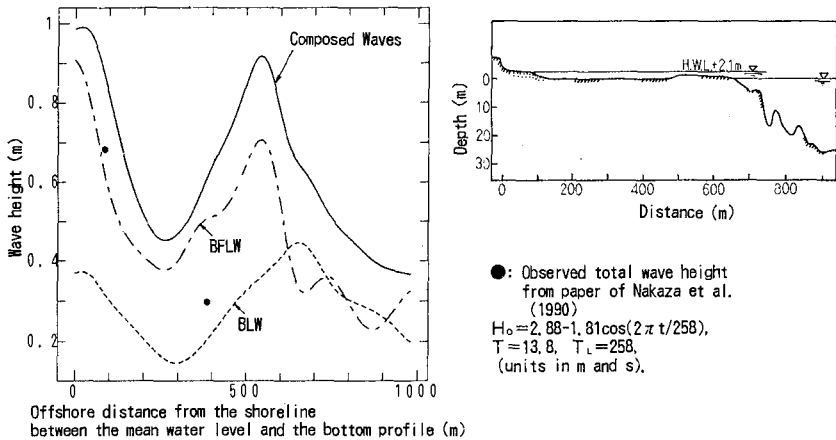


Fig.8 Wave height of surf beat (a convex type coast).

long wave period of 258s. After comparison of calculated results with actual field data, it can be stated that the numerical model has sufficient accuracy.

### 3. EMPIRICAL AND NUMERICAL MODELS OF WAVE RUNUP

#### 3.1 Empirical Method

By improving Goda's equation (1975) with field and experimental data, the significant wave height of surf beat can be expressed by the following relation (Yamamoto and Tanimoto, 1994) :

$$\left. \begin{aligned} \frac{H_{L1/3}}{H_{O1/3}} &\approx \frac{0.066 \hat{i}^{1/6}}{[(H_{O1/3}/L_{O1/3}) \times (1+h/H_{O1/3})]^{1/2}} \\ \frac{H_{Lm}}{H_{Om}} &\approx \frac{0.067 \hat{i}^{1/6}}{[(H_{Om}/L_{Om}) \times (1+h/H_{Om})]^{1/2}} \end{aligned} \right\} (7)$$

(1/10 ≥  $\hat{i}$  ≥ 1/70)

where,  $L_{O1/3}$  and  $L_{Om}$  is significant, mean wavelengths in deep-water respectively,  $\hat{i}$  is the mean bottom slope in the surf zone, and  $h$  is the water depth below the still water level.

Assuming the run-up oscillation of surf beat is a parabolic motion, the wave run-up length along the slope can be expressed as follows :

$$y_r \approx C_1 U_s t - C_2 g \hat{i} t^2 / 2 \quad (8)$$

where,  $U_s$  is a maximum velocity at shore line [  $\approx C_3 (g H_{Ls})^{1/2}$  ],  $C_1$ ,  $C_2$  and  $C_3$  are empirical coefficients, and  $H_{Ls}$  is the wave height of surf beat at the shoreline.

Substitution of Eq.(7) into Eq.(8), and the determination of coefficients  $C_1$ ,  $C_2$  and  $C_3$  by using field and laboratory data, the period and the run-up height of the surf beat can be expressed by the following equations (Yamamoto and Tanimoto, 1994) :

$$\left. \begin{aligned} (T_{Lm})_{in}^2 &\approx 288.0^2 (H_{Lm}/g)_{in} \\ (T_{L1/3})_{in}^2 &\approx 305.7^2 (H_{L1/3}/g)_{in} \end{aligned} \right\} (9)$$

(1/20 >  $\hat{i}$  ≥ 1/60 and  $H_{Om}/L_{Om}$  ≥ 0.015)

$$\left. \begin{aligned} R_{Lm}/H_{Om} &\approx 1.52 \hat{i} / (H_{Om}/L_{Om})^{1/2} \\ R_{L1/3}/H_{O1/3} &\approx 1.50 \hat{i} / (H_{O1/3}/L_{O1/3})^{1/2} \end{aligned} \right\} (10)$$

(1/20 ≥  $\hat{i}$  ≥ 1/60)

where,  $T_{Lm}$ ,  $T_{L1/3}$  are the mean, significant periods of the surf beat respectively,  $R_{Lm}$  and  $R_{L1/3}$  are the mean, significant, run-up heights of the surf beat respectively, and the subscript "in" stands for the mean value inside the surf zone.

Substitution of Eq.(7) and  $T_{1/3} \approx 3.86(H_{1/3})^{1/2}$  (units in s and m, Bretshneider, 1954) into Eq.(9), and by assuming  $H_{O1/3}/h \sim 1$  in the surf zone, the same relationship that Nakamura and Katoh (1992) obtained by analysis of field data can be derived ( $T_{L1/3} \propto T_{1/3}$ ).

The agreement between  $R_{Lm}$  calculated by Eq.(10) and experimental

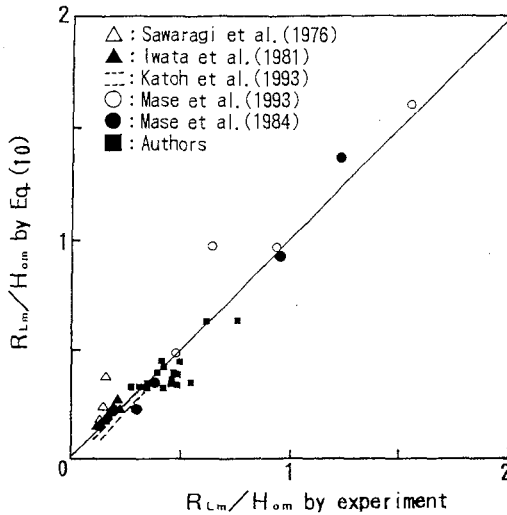


Fig.9 Comparison of  $R_{Lm}$  calculated by Eq.(10) with measured data. and field data are good as shown in Fig.9.

**3.2 Numerical Model**

Considering the convection and friction terms, the basic equations averaged over the wave period are expressed as follows :

$$\left. \begin{aligned}
 &\frac{\partial \zeta}{\partial t} + \frac{\partial (DU)}{\partial x} = 0 \\
 &\frac{\partial (DU)}{\partial t} + \frac{\partial}{\partial x} \left( \frac{(DU)^2}{D} \right) + gD \frac{\partial \zeta}{\partial x} \\
 &= - \frac{1}{\rho} \frac{\partial S_{60}}{\partial x} - \frac{f}{D^2} (DU) |DU| \\
 &D = h + \zeta
 \end{aligned} \right\} \quad (11)$$

where,  $S_{60}$  is the 60% value of the radiation stress [Mase et al. (1986) states that the equation by the small amplitude wave theory gives excessively large values for the radiation stress and recommends the use of values corresponding to 60% of the obtained value.], and  $f$  is the mean bottom friction coefficient, which is obtained by using the following equation based on Freeman and LeMehaute's wave run-up height equation (1964) :

$$f \approx \left[ \frac{(1 + C_v)(1 + 2C_v)}{C_L} - 1 \right] i C_v^2 \quad (12)$$

where,  $C_v$  is the wave velocity - particle velocity ratio, and  $C_L$  is the loss between potential energy of wave run-up and kinetic energy of waves on a shoreline. According to Yamamoto et al.(1994), these param-

eters for sand beach are expressed as follows :

$$\left. \begin{aligned} C_v &\approx 24.2 \dot{i}^{1.9/3.0} (H_{om}/L_{om})^{1/4} \\ C_L &\approx 2221 \dot{i}^{2.2/1.5} (H_{om}/L_{om})^{1/4} \\ &\quad (\dot{i} \leq 1/30) \end{aligned} \right\} \quad (13)$$

Some calculations on the run-up of the surf beat have been conducted by using the numerical model based on Eq.(11). An example [the incident wave height is  $0.8-0.4 \times \sin(2\pi t/61.6)$  (units in m and s), the wave period is 8.0s, the bottom slope is 1/40] is shown in Fig.10. A relatively close agreement is found between the result obtained by the numerical model and that by the empirical Eq.(10).

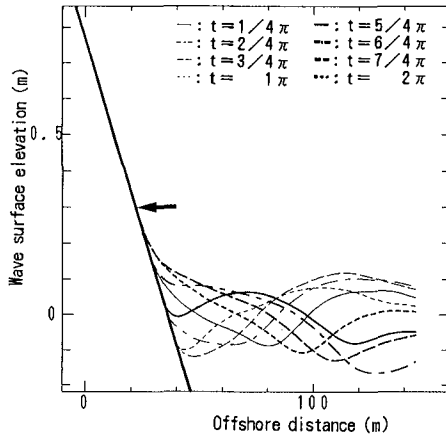


Fig.10 An example of long period wave runup. (The arrow shows  $R_{Lm}$  calculated by Eq.(10))

A comparison between wave run-up heights computed by the numerical model for beaches with bottom slopes ranging from 1/30 to 1/60 and those obtained by empirical Eq.(10) is shown in Fig.11. Relatively close agreement is found between the model and Eq.(10).

#### 4. CONCLUSIONS

- 1) Patterns of irregular wave run-up can be classified into three types : predominant incident wave type, intermediate type and predominant long period wave type. The predominant long period wave type appears when the mean bottom slope in the surf zone is gentler than 1/20.
- 2) Model of Symonds et al. and List's model were modified to allow more accurate calculation of surf beat near the shoreline. The tests conducted with the numerical model show that BLW can develop when the shallow area having a group velocity close to the phase velocity of long waves extends widely outside the surf zone, on the other hand, BFLW can develop when a wide shallow area exists within



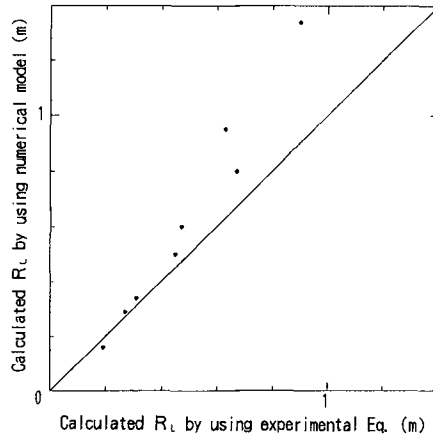


Fig.11 Relation between wave runup height using the numerical model and those using the empirical Eq.(10).

the surf zone such as a reef.

- 3) Run-up height of long period waves caused by wave groupiness in incident irregular waves can be predicted by both empirical and numerical models.

#### ACKNOWLEDGEMENT

The authors are grateful to Dr. Kiyoshi Horikawa and Mr. Hiroaki Nakamura of the University of Saitama for making useful suggestions.

#### REFERENCES

- (1) Bretschneider, C. L.(1954). Generation of wind waves over a shallow bottom. U.S. Army Corps of Engrs., Beach Erosion Board Tech. Memo., No.51, 24pp.
- (2) Freeman, J. C. and B. LeMehaute(1964). Wave breakers on a beach and surges on a dry bed. Proc. ASCE, Vol.90, No. HY2, pp.187~216.
- (3) Goda, Y.(1975). Deformation of irregular waves due to depth-controlled wave breaking. Report of the Port and Harbour Research Institute, Vol.14, No.3, pp.59~106 (in Japanese).
- (4) Goda, Y., T. Isayama and S. Satoh(1990). Field observation and experiment on development mechanism of long period waves inside surf zone. Proc. 37th Japanese Conf. Coastal Eng., pp.96~100 (in Japanese).
- (5) Iwata, K., T. Sawaragi and W. Nobuta(1981). wave run-up height and period of irregular waves on a gently sloping beach. Proc. 28th Japanese Conf. Coastal Eng., pp.330~334 (in Japanese).
- (6) Katoh, K., S. Nakamura and N. Ikeda(1991). Estimation of infra-gravity waves in consideration of wave groups. Report of the Port and Harbour Research Institute, Vol.30, No.1, pp.137~163 (in Japanese).

- (7) Katoh, K. and S. Yanagishima(1993). Beach erosion in a storm due to infragravity waves. Report of the Port and Harbour Research Institute, Vol.31, No.5, pp.73~102.
- (8) List, J. H.(1992a). A model for two-dimensional surf beat. J.G.R., Vol.97, No.C4, pp.5623~5635.
- (9) List, J. H.(1992b). Breakpoint-forced and bound long waves in the nearshore. Proc. 23rd Coastal Eng. Conf., ASCE, pp.860~873.
- (10) Longuet-Higgins, M. S. and R. W. Stewart(1962). Radiation stress and mass transport in gravity waves, with application to "Surf Beat". J.F.M., Vol.13, pp.481~504.
- (11) Mase, H. and Y. Iwagaki(1984). Run-up of random waves on gentle slopes. Proc. 19th Coastal Eng. Conf., ASCE, pp.593~609.
- (12) Mase, H., A. Matsumoto and Y. Iwagaki(1986). Calculation model of random wave transformation in shallow water. Proc. JSCE, No.375, II-6, pp.221~230 (in Japanese).
- (13) Mase, H. and N. Kobayashi(1993). Low-frequency swash oscillation. Proc. JSCE, No.461, II-22, pp.49~57 (in Japanese).
- (14) Nakamura, S. and K. Katoh(1992). Generation of infragravity waves in breaking process of wave groups. Proc. 23rd Coastal Eng. Conf., ASCE, pp.990~1003.
- (15) Nakaza, E., S. Tsukayama and M. Hino(1990). Bore-like surf beat on reef coasts. Proc. 22nd Coastal Eng. Conf., ASCE, pp.743~756.
- (16) Sawaragi, T., K. Iwata and A. Morino(1976). wave run-up characteristic on a gently sloping beach. Proc. 23rd Japanese Conf. Coastal Eng., pp.164~169 (in Japanese).
- (17) Symonds, G., D. A. Huntley and A. J. Bowen (1982). Two-dimensional surf beat : long wave generation by a time-varying breakpoint. J.G. R. Vol.87, No.C1, pp.492~498.
- (18) Yamamoto, Y and K. Tanimoto(1994). A study on long period run-up waves caused by irregular incident waves. Proc. JSCE, No.503, II-29, pp.109~118 (in Japanese).
- (19) Yamamoto, Y., K. Tanimoto and H. Nakamura(1994). Run-up of long period waves caused by wave groups. Proc. 49th Annu. Conf. JSCE, II, pp.644~645 (in Japanese).

APPENDIX : SOLUTION WITH CONSIDERATIONS FOR MEAN WATER LEVEL RISE

The radiation stress in Eq.(6) may be expressed as follows in terms of its relationship to the amplitude [  $A_{mp} = \gamma (X_i + \zeta_0)$  ] of the incident waves :

$$S_{xx} = (3/4)\rho g (A_{mp})^2 \tag{A.1}$$

Eq.(6) is then made dimensionless by using the following dimensionless parameters :

$$\left. \begin{aligned} A &= \frac{a}{X_{bm}}, \quad X = \frac{X}{X_{bm}}, \quad \tau = t \frac{2\pi}{T_L}, \quad X_{b1} = \frac{X_{b1}}{X_{bm}}, \quad X_{b2} = \frac{X_{b2}}{X_{bm}} \\ U(X, \tau) &= \frac{3}{2} \gamma^2 \frac{2\pi}{T_L} X u, \quad Z(X, \tau) = \frac{\zeta(X, t)}{1.5\gamma^2 X_{bm} i} \end{aligned} \right\} \tag{A.2}$$

where,  $a$  is  $(X_{b1} - X_{b2}) / 2$ ,  $X_{bm}$  is  $(X_{b1} + X_{b2}) / 2$ ,  $\gamma$  is (wave height - water depth ratio at breaking limit) / 2, and  $i$  is bottom slope.

The dimensionless horizontal flow velocity  $U$  is then eliminated from the dimensionless form of the basic equation, and the differential equation for the dimensionless water level  $Z$  is obtained. If the term for the radiation stress in this differential equation is expressed by Fourier series, the following equation will be given :

$$\begin{aligned}
 X' \frac{\partial^2 Z}{\partial \tau^2} - \frac{dX''}{dX} \frac{\partial Z}{\partial X} - X'' \frac{\partial^2 Z}{\partial X^2} \\
 = \frac{d}{dX} \left\{ X'' \frac{dX''}{dX} \left( a_0 + 2 \sum_{n=1}^{\infty} a_n \cos(n\tau) + 2 \sum_{n=1}^{\infty} b_n \sin(n\tau) \right) \right\}
 \end{aligned}
 \tag{A.3}$$

where,  $X' = \left( \frac{2\pi}{T_L} \right)^2 \frac{X}{g i}$ ,  $X'' = X + \frac{3}{2} \gamma^2 Z_0(X)$ ,

$Z_0$  is dimensionless mean water level rise, and  $a_0, a_n, b_n$  is Fourier coefficients ( $n$  : term number) - The methods for calculation of these coefficients are given in Nakamura and Katoh (1992).

The solution to Eq.(A.3) may be expressed as follows.

$$Z(X, \tau) = Z_0(X) + \sum_{n=1}^{\infty} Z_n(X, \tau)
 \tag{A.4}$$

$Z_0$  can easily be obtained from the dimensionless equation of motion, as shown in the first expression in Eq.(A.5) below. For areas further offshore than  $X_{b1}$ , however, the values given by Symonds et al. for  $Z_0$  are used without alteration, assuming that the effects of the mean water level rise on the water depth here are negligibly small.

$Z_n$  can be obtained in a similar manner to Symonds et al. by means of approximated expression,  $dX''/dX \approx 1$  (found to be a valid approximation in investigations conducted by substituting actual physical values) during the calculation of the particular solutions between  $X_{b1}$  and  $X_{b2}$ .

a) From shore-edge to  $X_{b1}$

$$\left. \begin{aligned}
 Z_0(X) &= (1 - X + 1.5\gamma^2 A) / (1 + 1.5\gamma^2) \\
 Z_n(X, \tau) &= - (I_{bn} + I_{an}) J_0(z) \cos(n\tau) \\
 &\quad - I_{bn} J_0(z) \sin(n\tau) \\
 z &= 2n(2\pi/T_L) [X_{bm} / (g i)]^{1/2} \\
 &\quad \times (1 + 1.5\gamma^2) (X + 1.5\gamma^2 Z_0)^{1/2}
 \end{aligned} \right\}
 \tag{A.5}$$

Here,  $J_0(z)$  is zero-degree Bessel function.

b) From  $X_{b1}$  to  $X_{b2}$

$$\left. \begin{aligned}
 Z_0(X) &\approx \left\{ (1 - X) \cos^{-1} [(X - 1) / A] \right. \\
 &\quad \left. - [A^2 - (X - 1)^2]^{1/2} \right\} / \pi \\
 Z_n(X, \tau) &= \left[ - (I_{bn} + I_{an}) J_0(z) \right. \\
 &\quad \left. + C_n N_0(z) + \eta_{na} \right] \cos(n\tau)
 \end{aligned} \right\}$$

$$\left. \begin{aligned}
 z &= 2n(2\pi/T_L)[X_{bm}/(g \dot{i})]^{1/2} \left\{ \begin{aligned}
 &+ [-I_{bN} J_0(z) + \eta_{pb}] \sin(n\tau) \\
 &\times \{1 + 1.5\gamma^2 \cos^{-1}((X-1)/A)/\pi\} \\
 &\times (X + 1.5\gamma^2 Z_0)^{1/2}
 \end{aligned} \right\} \\
 \eta_{pa} &\doteq 2\pi \left[ \int_{x_{a1}}^{x_{a2}} X_{an} N_0(z) dX J_0(z) \right. \\
 &\quad \left. - \int_{x_{a1}}^{x_{a2}} X_{an} J_0(z) dX N_0(z) \right] \\
 \eta_{pb} &\doteq 2\pi \left[ \int_{x_{b1}}^{x_{b2}} X_{bn} N_0(z) dX J_0(z) \right. \\
 &\quad \left. - \int_{x_{b1}}^{x_{b2}} X_{bn} J_0(z) dX N_0(z) \right] \\
 X_{an} &= d[(X + 1.5\gamma^2 Z_0) a_n] / dX \\
 X_{bn} &= d[(X + 1.5\gamma^2 Z_0) b_n] / dX
 \end{aligned} \right\} \tag{A.6}$$

Here,  $C_n = 0$  (onshore),  $C_n = I_{aJ}$  (offshore), and  $N_0(z)$  is zero-degree Neumann function.

c) Offshore from  $X_{b2}$

$$\left. \begin{aligned}
 Z_0(X) &= 0 \\
 Z_n(X, \tau) &= -I_{bJ} J_0(z) \cos(n\tau) \\
 &\quad - I_{bJ} N_0(z) \sin(n\tau) \\
 z &= 2n(2\pi/T_L)[X_{bm}/(g \dot{i})]^{1/2} X^{1/2}
 \end{aligned} \right\} \tag{A.7}$$

$I_{aJ}$ ,  $I_{aN}$ ,  $I_{bJ}$ , and  $I_{bN}$  in Eqs.(A.5) to (A.7) can be obtained as follows using  $z$ ,  $X_{an}$ , and  $X_{bn}$  in Eq.(A.6) :

$$\left. \begin{aligned}
 I_{aJ} &\doteq 2\pi \int_{x_{a1}}^{x_{a2}} X_{an} J_0(z) dX \\
 I_{aN} &\doteq 2\pi \int_{x_{a1}}^{x_{a2}} X_{an} N_0(z) dX \\
 I_{bJ} &\doteq 2\pi \int_{x_{b1}}^{x_{b2}} X_{bn} J_0(z) dX \\
 I_{bN} &\doteq 2\pi \int_{x_{b1}}^{x_{b2}} X_{bn} N_0(z) dX
 \end{aligned} \right\} \tag{A.8}$$

It should be noted here that partial integration was used for the integration of the above equations.

## CHAPTER 52

# Soliton-Mode Wavemaker Theory and System for Coastal Waves

Takashi Yasuda<sup>1</sup>, Seirou Shinoda<sup>2</sup>, and Takeshi Hattori<sup>3</sup>

### Abstract

A theory of wavemaker system for coastal waves (nonlinear random waves in very shallow water) having the desired statistics is developed under the assumption that they are treated as random trains of the KdV solitons and further its applicability is examined experimentally. This wavemaker system is shown usefull to generate accurately nonlinear waves having the desired water surface profiles of which nonlinearity is specified by the Ursell number  $U_r \geq 15$  for regular waves (cnoidal waves) and  $U_r \geq 8$  for random ones (coastal waves).

### Introduction

Waves in shallow water come to behave like trains of independent individual waves with the shoaling water. In shallow to very shallow water, particle-like property of each individual wave is more strengthened because of the pronounced nonlinear effect, so that its time sequence becomes increasingly important to coastal engineering problems, such as dynamic response of coastal

---

<sup>1</sup>M. ASCE, Prof., Dept. of Civil Eng., Gifu Univ., 1-1 Yanagido, Gifu 501-11, Japan

<sup>2</sup>Assoc. Prof. of Institute for River Basin Environmental Studies, Gifu Univ., 1-1 Yanagido, Gifu 501-11, Japan

<sup>3</sup>Civil Engineer, Penta-Ocean Construction Co. LTD., 2-2-8 Koraku, Bunkyo-ku, Tokyo 112, Japan

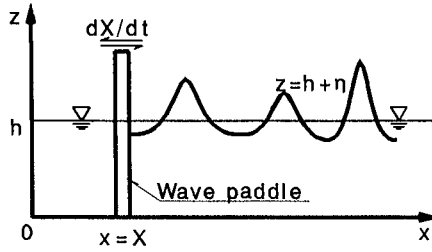


Figure 1. Definition of coordinate system and symbols

structures, nearshore current system and so on. It hence is required in experimental works to generate the wave train having the desired sequence of wave crest. However, usual methods based on the Biesel-Suquet wavemaker theory and the envelope theory assuming a narrow-banded Gaussian process cannot be used to generate strongly nonlinear random waves in very shallow water (called here as coastal waves).

Authors(Yasuda et. al., 1987) already showed that coastal waves can be treated as a random train of solitons and their kinematics can be described using the asymptotic multi-soliton solution of the KdV equation. Hence, treating individual waves defined by the zero-crossing method as solitons and using a stochastic model (Shinoda et al., 1992) of solitons, we can generate straightforwardly coastal waves having the desired sequence of individual waves as a train of solitons.

In this study, we suggest a nonlinear wavemaker theory for the coastal waves and then develop a soliton-mode wavemaker system to generate them in a wave tank. Further, the performance of the system is examined by generating cnoidal waves (treated as uniform trains of solitons) and coastal waves (as random trains of solitons) having the desired sequence.

### Wavemaker Theory

The boundary value problem for the wavemaker in a wave tank follows directly from that for two-dimensional waves propagating in an incompressible and irrotational fluid. For the coordinate depicted in **Figure 1**, it is required to solve the following equations,

$$\phi_{xx} + \phi_{zz} = 0, \tag{1}$$

$$\eta_t + \eta_x \phi_x - \phi_z = 0|_{z=h+\eta}, \tag{2}$$

$$\phi_t + (\phi_x^2 + \phi_z^2)/2 + g\eta = 0|_{z=h+\eta}, \tag{3}$$

$$\phi_z = 0|_{z=0}, \quad (4)$$

$$dX/dt = \phi_x|_{x=X}, \quad (5)$$

where  $\phi$  denotes the velocity potential,  $\eta$  the water surface elevation,  $g$  the acceleration of gravity,  $h$  the mean water depth, and  $X$  the displacement of a piston type paddle.

Integrating eq.(1) from  $z = 0$  to  $z = h + \eta$  and substituting eqs.(2) and (4) into the resultant equation, we can obtain the following equation,

$$\int_0^{h+\eta} \phi_x dz = - \int \eta_t dx + \text{const.} \quad (6)$$

Since eq.(5) can not be satisfied for the arbitrary  $z$ -coordinate as long as piston-type wave paddle is used, the vertically integrated equation instead of eq.(5) is employed as the boundary condition with regard to the depth-averaged velocity by following Goring and Raichlen's approach(1980). Integration of eq.(5) from  $z = 0$  to  $z = h + \eta$  yields to

$$\int_0^{h+\eta} \frac{dX}{dt} dz = \int_0^{h+\eta} \phi_x dz \Big|_{x=X}. \quad (7)$$

Substituting eq.(6) into eq.(7), we obtain the following relation satisfying eqs.(1), (2), (4) and (5).

$$\int_0^{h+\eta} \frac{dX}{dt} dz = - \int \eta_t dx + \text{const.} \Big|_{x=X}. \quad (8)$$

Since the value of  $\eta_t$  becomes zero in the still water and the wave paddle is also at rest, the integral constant in eq.(8) is regarded as zero. Further, since  $dX/dt$  is independent of  $z$  in the present piston-type wavemaker system, we can derive the following equation for the paddle motion to generate the wave profile  $\eta$  from eq.(8).

$$\frac{dX}{dt} = \frac{-1}{h + \eta} \int \eta_t dx \Big|_{x=X}. \quad (9)$$

Here, the following dimensionless variables with asterisk are defined for convenience of numerical computations.

$$\phi^* = \phi/\sqrt{gh^3}, \quad \eta^* = \eta/h, \quad X^* = X/h, \quad x^* = x/h, \quad z^* = z/h, \quad t^* = t\sqrt{g/h} \quad (10)$$

However, the asterisks are omitted for simplicity hereinafter, so that eq.(9) is rewritten as

$$\frac{dX}{dt} = \frac{-1}{1 + \eta} \int \eta_t dx \Big|_{x=X}. \quad (11)$$

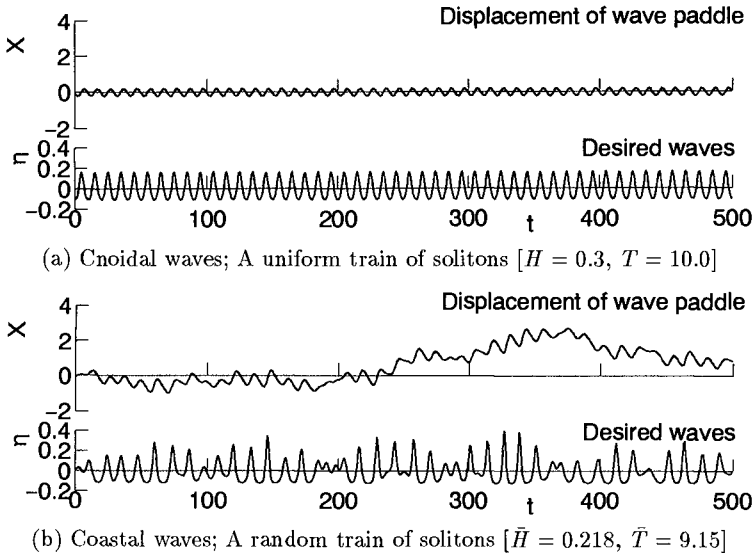


**Figure 2.** Wave profiles of a soliton train having the desired sequence and the displacement of wave paddle to generate it;  $H$  is the dimensionless wave height corresponding to the amplitude of solitons,  $T$  the dimensionless wave period corresponding to the distance of adjoining solitons,  $\bar{H}$  the dimensionless mean wave height, and  $\bar{T}$  the dimensionless mean wave period

If waves to be generated are trains of solitons and satisfy eqs.(1)~(4) in the order of the KdV equation,  $\eta$  can be represented as

$$\eta(x, t) = \sum_{j=1}^N \eta_j(x, t) \tag{12}$$

$$\left. \begin{aligned} \eta_j(x, t) &= A_j \operatorname{sech}^2 \frac{\sqrt{3A_j}}{2} \{x - c_j(t - \delta_j)\} - \frac{\eta_0}{N}, \\ c_j &= 1 + \frac{A_j}{2} - \frac{3}{2}\eta_0, \quad \eta_0 = 4\sqrt{\frac{A_j}{3}} \frac{c_j T_0}{h} \end{aligned} \right\} \tag{13}$$

where  $A_j$  is the amplitude of the  $j$ -th soliton non-dimensionalized with  $h$ ,  $N$  the number of solitons,  $T_0$  the observation period and  $\delta_j$  the phase constant of the  $j$ -th soliton.

As a result, the problem to solve eqs.(1)~(5) can be finally reduced to that to solve the following nonlinear ordinary differential equation with regard to the



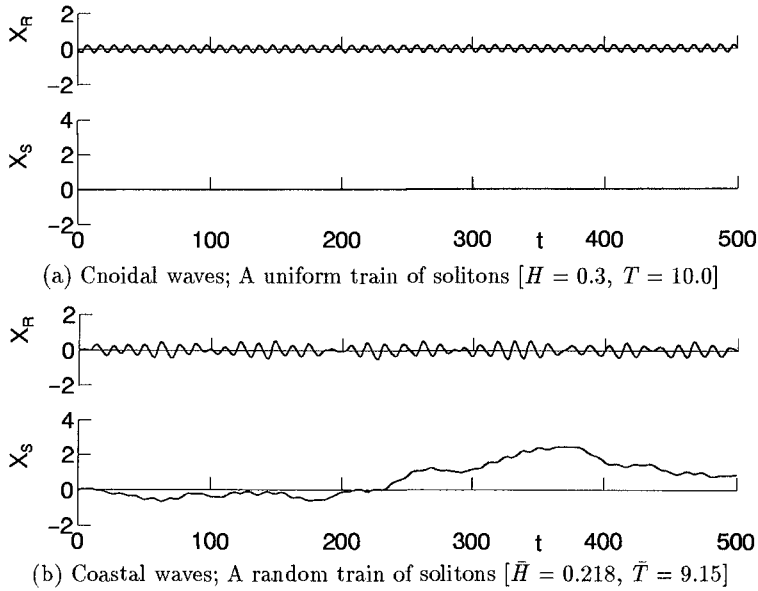


**Figure 3.** Decomposed displacement of the wave paddle; time history of  $X_R$  and  $X_S$

displacement  $X$ , by combining eqs.(11) and (12),

$$dX/dt = \sum_{j=1}^N c_j \eta_j(X, t) / \left\{ 1 + \sum_{j=1}^N \eta_j(X, t) \right\}. \quad (14)$$

Thus, eq.(14) is solved numerically for given values of  $\eta_j$  and  $c_j$  ( $j = 1, \dots, N$ ), so that the displacement  $X$  of the wave paddle required to generate the desired waves is uniquely determined. Hence, if the waves to be generated are represented as a train of solitons described by eq.(12) and the ensembles of the soliton parameters  $A_j$  and  $\delta_j$  governing them are substituted into eq.(14) through eqs.(12) and (13), the displacement  $X$  required to regenerate the waves in a wave tank can be easily known by solving eq.(14).

## Wavemaker System

Wavemaker system to be used here is required to enable the wave paddle to follow accurately the displacement  $X$  given by eq.(14). Hence, in order to investigate the displacement  $X$  required to generate cnoidal waves (uniform trains of solitons) with  $H = 0.3$  and  $T = 10.0$  and coastal waves (random



**Photo 1.** A rotary actuator and cylinder actuator attached to the wavemaker

trains of solitons) with  $\bar{H} = 0.218$  and  $\bar{T} = 9.15$ , time histories of  $X$  are shown in **Figure 2** together with their surface profiles. Here,  $H$  and  $T$  denote the dimensionless wave height and period, respectively, and the over-bar means their mean values. While the displacement for cnoidal waves is periodic and stays within a stroke less than the mean water depth, that for coastal waves is aperiodic and accompanies a slow drift oscillation with a large amplitude exceeding two times of the water depth. Thus, a wavemaker system having a long stroke wave paddle is required to generate coastal waves. However, the motion of wave paddle seems to be a rapid movement with short stroke riding on a slow drift with long stroke, although the stroke of the paddle exceeds two or more times distance of water depth. By aiming at this point, the displacement  $X(t)$  was decomposed into a rapid but short displacement  $X_R(t)$  and a slow but long one  $X_S(t)$  as shown in **Figure 3**, and thus a double mode wavemaker having a high-speed driving part with short stroke and a low-speed driving part with long stroke was newly developed.

The double-mode wavemaker has two types of movement corresponding to  $X_R$  and  $X_S$ . **Photo 1** shows the high-speed driving part with a rotary

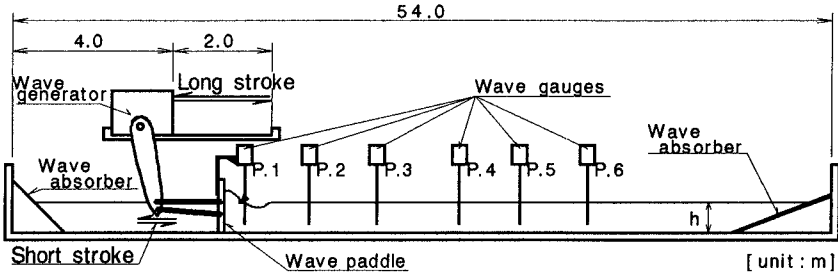


Figure 4. Sketch of the wave tank used here and location of wave gauges installed

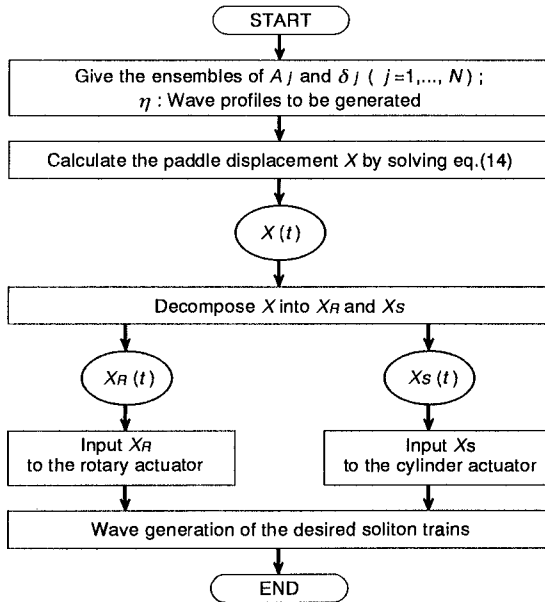
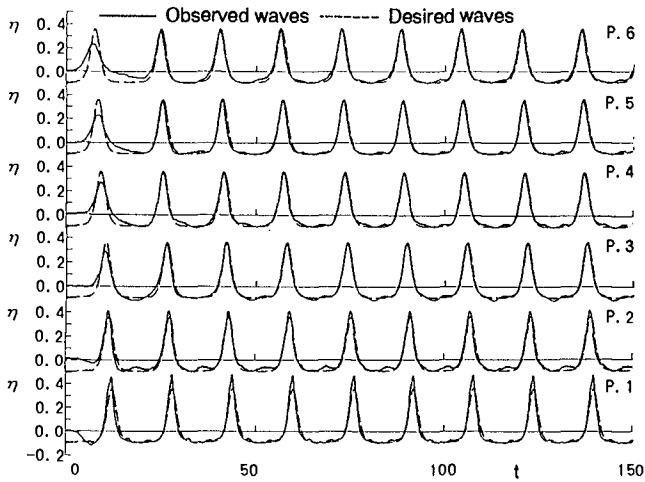


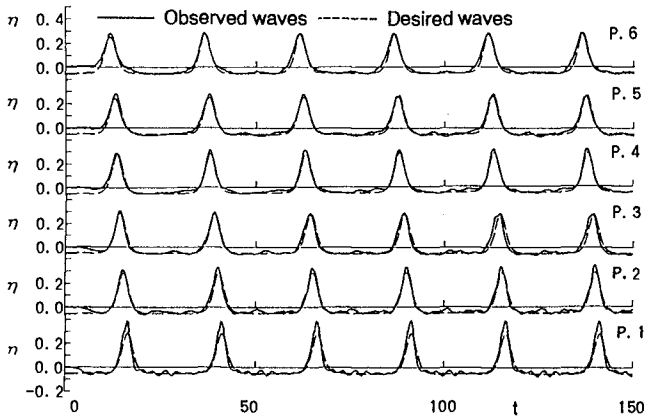
Figure 5. Flow chart of the procedure to generate the soliton trains as desired

actuator and the low-speed driving part with a cylinder actuator attached to the wavemaker, and **Figure 4** illustrates its schematic sketch. The rotary actuator enables short stroke but high speed motion corresponding to  $X_R$  and has a performance of the maximum speed of 60cm/s and stroke of 30cm. The cylinder actuator enables slow but long stroke motion corresponding to  $X_S$  and has a performance of the maximum speed of 7.3cm/s and stroke of 2m.

As a result, the procedure using the double-mode wavemaker to generate the desired waves is summarized as follows: The ensemble of  $A_j$  and  $\delta_j$  for the



(a)  $H = 0.452, T = 16.0$



(b)  $H = 0.334, T = 25.0$

**Figure 6.** Comparisons for a train of uniform solitons between the desired wave profiles and the observed ones

soliton trains to be generated are given to eq.(14) and then the displacement  $X$  required to generate them is determined by solving eq.(14). Further, the displacement  $X$  is decomposed into  $X_R$  and  $X_S$  and the values of  $X_R$  and  $X_S$  at each time step are given to the rotary actuator and cylinder one, respectively, as input signal. Thus, the wave paddle follows the composed motion of  $X_R$  and

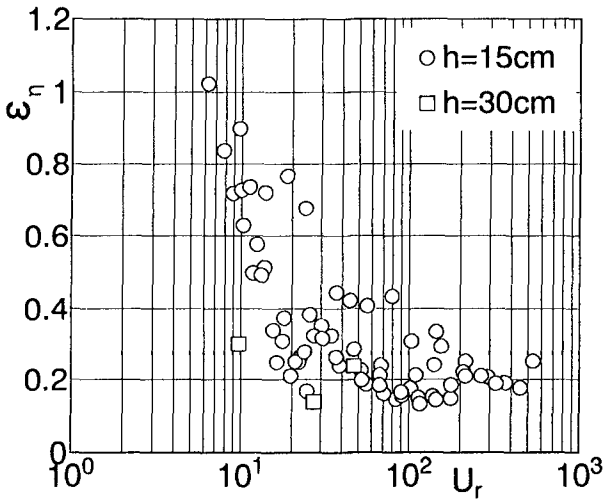


**Figure 7.** Relationships for cnoidal waves between the Ursell number  $U_r$  and the error index  $\epsilon_\eta$

$X_S$  and produce the soliton trains as desired. Flow chart of the procedure explained above is illustrated in **Figure 5**.

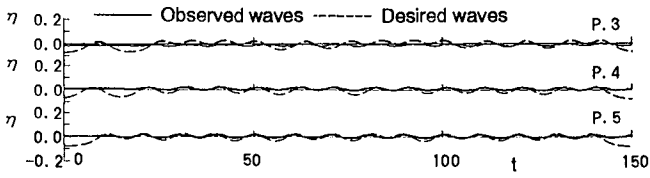
**Performance Test**

Experiments using the wave tank and gauges shown in **Figure 4** were undertaken to examine the performance of the double-mode wavemaker system. Six wave gauges were installed at six locations from P.1 to P.6 in the tank. Distance between each wave gauges is evenly about 2.5m.

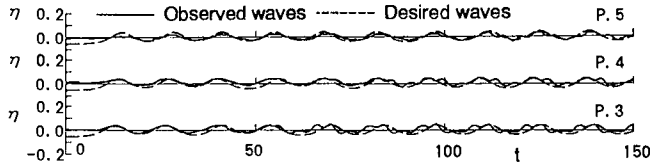
**Cnoidal waves (Uniform trains of solitons)**

Since cnoidal waves can be represented as a uniform train of solitons having constant amplitude and period, they can be generated in a wave tank by producing a uniform soliton train having a given constant amplitude and period in order. Water surface elevations of generated trains of solitons can be regarded as cnoidal waves as shown in **Figure 6**, where the comparisons between the measured temporal water surface elevations of the waves generated as a train of solitons and theoretical ones of the cnoidal waves to be generated are made. This result further demonstrates that the soliton is the elementary excitation of waves in very shallow water and therefore the desired cnoidal waves can be generated as train of solitons.

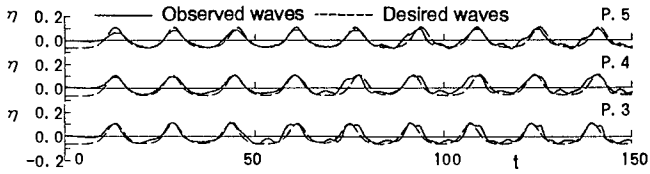
However, the soliton can not exist in shallow to deep water and becomes



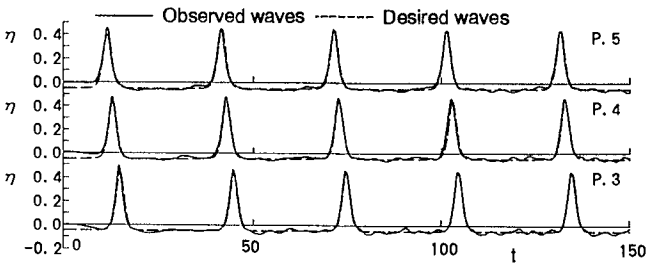
(a)  $H = 0.097, T = 10.0, \epsilon_\eta = 0.897$



(b)  $H = 0.097, T = 14.0, \epsilon_\eta = 0.765$



(c)  $H = 0.174, T = 16.0, \epsilon_\eta = 0.422$



(d)  $H = 0.502, T = 30.0, \epsilon_\eta = 0.177$

**Figure 8.** Comparisons for a train of uniform solitons between the desired wave profiles and the observed ones having a typical value of  $\epsilon_\eta$

physically meaningless wave there. The present soliton-mode wavemaker can not generate waves in shallow to deep water and therefore its applicable region should be made clear since there is the applicable limit to the wavemaker. In

**Table 1.** Experimental code numbers and conditions for coastal waves

Code No.	$\bar{H}$	$\bar{T}$	$U_r$	Skewness
R01	0.218	9.15	23.95	1.136
R02	0.321	10.25	40.44	0.760
R03	0.102	10.12	13.06	1.308
R04	0.207	12.21	38.21	1.305
R05	0.297	11.80	55.16	1.612

order to clarify quantitatively the applicable limit, an error index  $\varepsilon_\eta$  is defined as

$$\varepsilon_\eta = \sqrt{\int_0^{T_o} (\eta_{obs} - \eta_{des})^2 dt} / \sqrt{\int_0^{T_o} (\eta_{des})^2 dt}, \quad (15)$$

where  $\eta_{obs}$  denotes the water surface elevation of the observed waves in the wave tank and  $\eta_{des}$  that of the desired waves given to eq.(12) as input data. Relationships between the Ursell number  $U_r$  of generated waves and the error index  $\varepsilon_\eta$  are shown in **Figure 7**. The values of  $\varepsilon_\eta$  increase with the decreasing of the value of  $U_r$  and particularly is amplified rapidly from the region where the value of  $U_r$  begins to be less than about 15. Moreover, the difference of surface profile between  $\eta_{obs}$  and  $\eta_{des}$  can be approximately ignored as shown in **Figure 8** if the value of  $\varepsilon_\eta$  is less than 0.8. It hence could be stated that the present wavemaker system can generate cnoidal waves with  $U_r \geq 15$  as desired.

### Coastal waves (Random trains of solitons)

Intensive experiments generating various trains of solitons were undertaken to examine how to present wavemaker can accurately regenerate coastal waves having various statistics as desired. Representative cases of them are shown in **Table 1**, in which their code numbers and wave statistics are indicated. R01 and R02 denote the coastal waves observed on Ogata coast facing the Japan sea, and R03, R04 and R05 indicate the coastal waves simulated as random trains of solitons by using a digital simulation method (Shinoda et al., 1992).  $\bar{H}$  and  $\bar{T}$  are their mean wave heights and periods respectively. The values of  $U_r$  and Skewness show that all the waves to be regenerated have pronounced nonlinearity and can not be generated with usual methods based on the Biesel-Suquet wavemaker theory.

**Figure 9** shows the comparisons of wave profiles of R01 and R02 between the observed waves in field and the regenerated waves in the wave tank. Both the wave profiles are in almost complete agreement and demonstrate that the

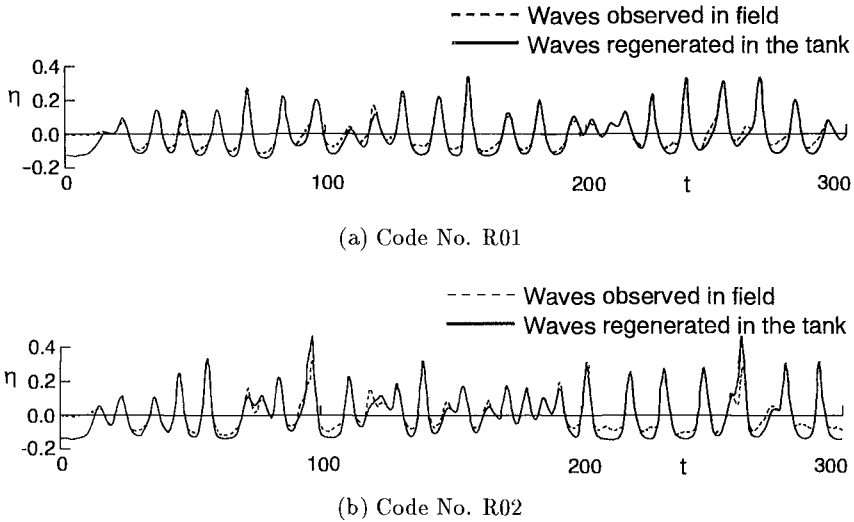


**Figure 9.** Comparison of wave profiles between waves observed in field and regenerated ones in the wave tank

present wavemaker can regenerate coastal waves having the given statistics including time sequence of wave crest as desired. It should be particularly noted that coastal waves in field can be almost completely regenerated in the tank even if they partially break.

Further, **Figure 10** shows the comparisons of wave profiles of R03, R04 and R05 between the digitally simulated waves using a stochastic mode of solitons and the regenerated waves in the tank. Although the surface profiles of the regenerated waves get to deviate slightly from those of the simulated waves as the waves propagate from P.2 toward P.3 and further P.6, both the profiles keep a good agreement and shows that the present wavemaker can generate the coastal waves having arbitrary wave statistics by making random trains of solitons in order only if the value of the statistics are given.

In order to make clear the applicable limit of the present wavemaker system to coastal waves, the relations between the Ursell number  $U_r$  of coastal waves to be generated and the error index  $\varepsilon_\eta$  for the regenerated waves in the tank are examined and shown in **Figure 11**. The value of  $\varepsilon_\eta$  is less than 0.8 almost independently of the Ursell number. Since the values of  $\varepsilon_\eta$  in all the cases shown in **Figures 9** and **10** are at most 0.644, the generated waves in the tank could



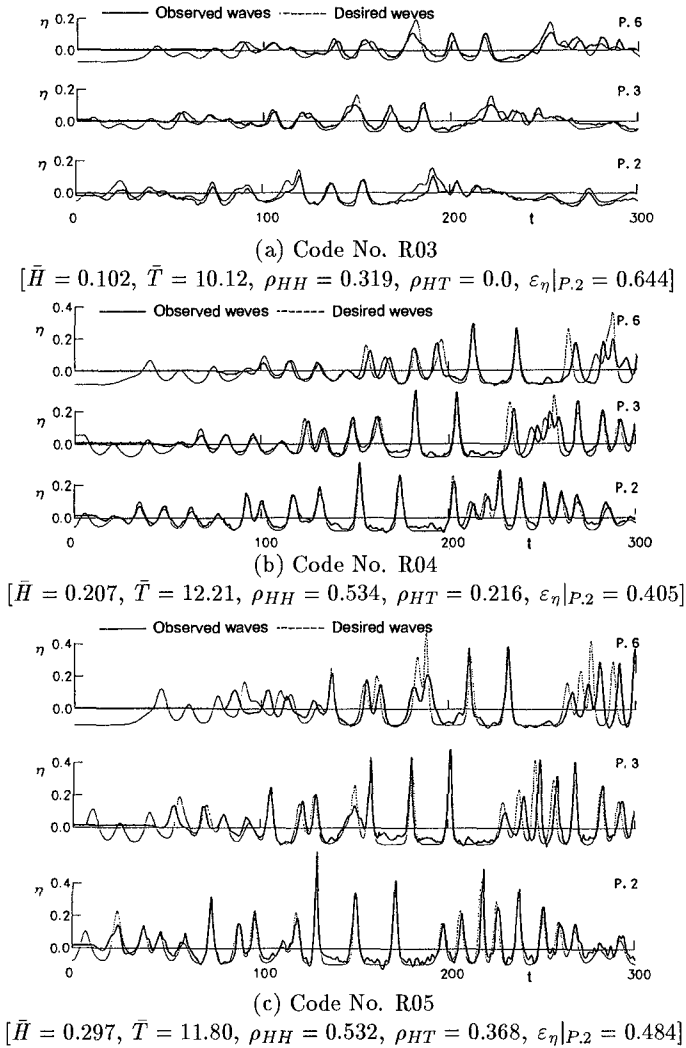


**Figure 10.** Comparisons between the desired wave profiles for a random train of solitons and those measured in the wave tank

be regarded as almost desired if the value of  $\varepsilon_{\eta}$  is less than 0.8, that is, the value of  $U_r$  is almost more than 8. It hence could be stated that the present wavemaker can generate the coastal waves having given statistics as desired if their Ursell numbers are more than 8.

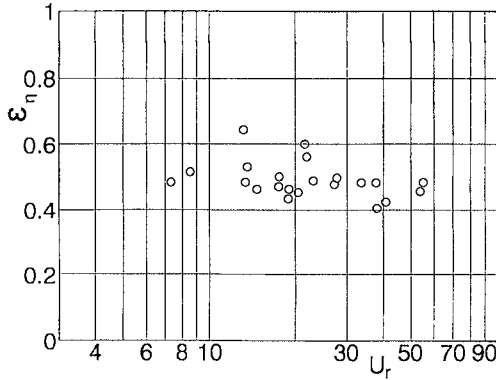


**Figure 11.** Relationships for coastal waves between the Ursell number  $U_r$  and the error index  $\epsilon_\eta$  at the measurement point P.2

### Conclusions

A wavemaker theory to generate nonlinear waves in very shallow water as trains of solitons was developed by solving mathematically wavemaker problem in the order of the KdV equation. The paddle motion given by the theory showed that the displacement required to generate them as desired exceeds two times or more of the water depth and a wavemaker having long stroke paddle is necessary. Hence, a new type wavemaker was thought out and developed under the cooperation of ISEYA Manufacturing Co. in order to solve this problem, by noticing that the displacement can be separated into two parts; the one is rapid but short stroke part and the other is slow but long stroke part. This wavemaker can generate the desired soliton trains in order by equipping a double-mode movement having a rotary actuator enabling short but rapid motion and a cylinder actuator enabling slow but long stroke motion was thought out and newly developed. Experimental examination verifies that the system is useful to generate strongly nonlinear waves having the desired water surface profiles of which nonlinearity is specified by the Ursell number  $U_r \geq 15$  for cnoidal waves and  $U_r \geq 8$  for coastal waves. Thus, the double-mode movement is essential to the soliton-mode wavemaker to generate the desired coastal waves.

Hence, it could be stated that the present wavemaker system can almost completely generate both the cnoidal and coastal waves having not only the desired statistics including sequence of wave crest but also the desired wave profiles, if the input signal to the wave paddle is given by the present wavemaker theory and given to the soliton-mode wavemaker as input signal and further the waves to be generated are within the aforementioned applicable region of this

system.

The authors wish to thank Iseya Manufacturing Co. for their developing and manufacturing the present double-mode wavemaker. Further, the authors are grateful for the supports by the Kajima Foundation's Research Grant and the Grant-in-Aid for Scientific Research (No. 06750542), The Ministry of Education, Science and Culture.

## References

Goring, D. and F. Raichlen (1980). The generation of long waves in the laboratory. *Proc. 17th Conf. on Coast. Eng., Sydney, A.S.C.E.*, pp. 763-783.

Shinoda, S., T. Yasuda, T. Hattori, and Y. Tsuchiya (1992). A stochastic model of random waves in shallow water. *Proc. of 6th IAHR Int. Symp. on Stochastic Hydraulics*, pp. 329-336.

Yasuda, T., S. Shinoda, and R. A. Dalrymple (1987). Soliton mode representation for kinematics of shallow water swell. *Coastal Hydrodynamics, ASCE, R. A. Dalrymple ed.*, pp. 751-764.

## CHAPTER 53

# On a Method for Estimating Reflection Coefficient in Short-Crested Random Seas

Hikomune Yokoki\*  
Masahiko Isobe†  
Akira Watanabe†

### Abstract

A method for estimating the directional spectrum as well as the reflection coefficient in a incident and reflected wave field is developed for practical uses. In the method, the directional spectrum is assumed to be expressed by a circular normal distribution which includes several parameters, Then the parameters are estimated by the maximum likelihood method. The validity of the method is verified by numerical simulation.

## 1 Introduction

The randomness of sea waves has recently become accounted for in the design of coastal and ocean structures. Directional spectra have often been used to describe multi-directional random sea waves. However, to evaluate the reflection coefficient of structures, a theory for uni-directional random waves has usually been applied with a slight modification. This is because a theory for multi-directional random waves has not yet been established for practical uses.

The purpose of this paper is to derive a method to estimate the directional spectrum as well as the reflection coefficient of structures for multi-directional random waves and to examine its validity by applying it to simulated data.

In various methods to estimate the directional spectrum, the maximum likelihood method (MLM) has a high resolution (Capon, 1969). Isobe and Kondo

---

\*Research Associate, Dept. of Civil Eng., Univ. of Tokyo, Bunkyo-ku, Tokyo, 113 Japan

†Professor, ditto

(1984) proposed the modified maximum likelihood method (MMLM) to estimate the directional spectrum in a combined incident and reflected wave field, taking into account the fact that there is no phase difference between the incident and reflected waves at the reflective wall.

Recently for practical purposes, Isobe (1990) proposed a method to estimate the directional spectrum of a standard form in which the spectrum is expressed in terms of a few parameters. Yokoki *et al.* (1992) extended this method in order to estimate the directional spectrum in an incident and reflected wave field.

In this study, we modify the method to improve the numerical efficiency by assuming a circular normal distribution for the directional function.

## 2 Theory

### 2.1 Formulation of cross power spectrum

#### 2.1.1 Definition of cross power spectrum

In a monochromatic wave field which consists of incident and reflected waves, the water surface fluctuation,  $\eta(\mathbf{x}, t)$ , at the position,  $\mathbf{x}$ , are represented by Eq. (1):

$$\eta(\mathbf{x}, t) = A(\mathbf{k}, \sigma) \{ \cos(\mathbf{k}\mathbf{x} - \sigma t + \epsilon) + r \cos(\mathbf{k}_r\mathbf{x} - \sigma t + \epsilon) \} \quad (1)$$

The definitions of the variables in the above equation are given in Table 1. We integrate Eq. (1) with respect to  $\mathbf{k}$  and  $\sigma$ , and get the expression of  $\eta(\mathbf{x}, t)$  for multi-directional random waves as Eq. (2):

$$\eta(\mathbf{x}, t) = \int_{-\infty}^{\infty} \int_{\mathbf{k}} A(d\mathbf{k}, d\sigma) \times \{ \exp [i(\mathbf{k}\mathbf{x} - \sigma t + \epsilon)] + r \exp [i(\mathbf{k}_r\mathbf{x} - \sigma t + \epsilon)] \} \quad (2)$$

where complex variables are introduced to represent the amplitude and phase. From Eq. (2), the directional spectrum (wavenumber-frequency spectrum),  $S(\mathbf{k}, \sigma)$ , is defined as Eq. (3):

$$S(\mathbf{k}, \sigma) d\mathbf{k} d\sigma = \langle A^*(d\mathbf{k}, d\sigma) A(d\mathbf{k}, d\sigma) \rangle \quad (3)$$

Table 1: Definitions of variables in Eq. 1

$A(\mathbf{k}, \sigma)$	Amplitude (Eq. (1)),
$A(d\mathbf{k}, d\sigma)$	Complex amplitude (Eq. (2))
$\mathbf{k}$	Wave number vector of incident waves
$\mathbf{k}_r$	Wave number vector of reflected waves
$\sigma$	Angular frequency
$\epsilon$	Phase

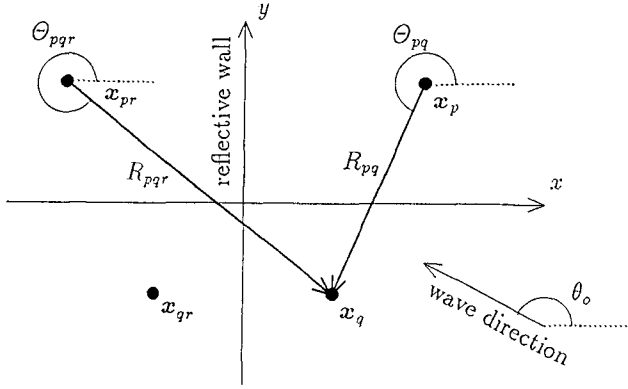


Figure 1: Definitions of variables

where  $\langle \rangle$  represents the ensemble average and  $A^*$  the complex conjugate of  $A$ . Then, the cross power spectrum,  $\Phi_{pq}(\sigma)$ , can be defined by Eq. (4) (Horikawa, 1988, Isobe and Kondo, 1984):

$$\Phi_{pq}(\sigma) = \int_{\mathbf{k}} S(\mathbf{k}, \sigma) \times \{ \exp(i\mathbf{k}\mathbf{x}_p) + r \exp(i\mathbf{k}\mathbf{x}_{pr}) \} \{ \exp(-i\mathbf{k}\mathbf{x}_q) + r \exp(-i\mathbf{k}\mathbf{x}_{qr}) \} d\mathbf{k} \quad (4)$$

in which the variables are defined in Fig. 1.

We rewrite Eq. (4) by using the transformation of variables as follows. The definitions of variables are also indicated in Fig. 1.

$$\left. \begin{aligned} \mathbf{k} &= (k \cos \theta, k \sin \theta) \\ \mathbf{x}_p - \mathbf{x}_q &= (R_{pq} \cos \Theta_{pq}, R_{pq} \sin \Theta_{pq}) \\ \mathbf{x}_{pr} - \mathbf{x}_{qr} &= (R_{pq} \cos(\pi - \Theta_{pq}), R_{pq} \sin(\pi - \Theta_{pq})) \\ \mathbf{x}_{pr} - \mathbf{x}_q &= (R_{pqr} \cos \Theta_{pqr}, R_{pqr} \sin \Theta_{pqr}) \\ \mathbf{x}_p - \mathbf{x}_{qr} &= (R_{pqr} \cos(\pi - \Theta_{pqr}), R_{pqr} \sin(\pi - \Theta_{pqr})) \end{aligned} \right\} \quad (5)$$

Then we get the expression of the cross power spectrum,  $\Phi_{pq}(f)$ :

$$\Phi_{pq}(f) = \int_0^{2\pi} S(f, \theta) \times [ \exp\{ikR_{pq} \cos(\theta - \Theta_{pq})\} + r^2 \exp\{ikR_{pq} \cos(\theta - \pi + \Theta_{pq})\} + r \exp\{ikR_{pqr} \cos(\theta - \Theta_{pqr})\} + r \exp\{ikR_{pqr} \cos(\theta - \pi + \Theta_{pqr})\} ] d\theta \quad (6)$$

where  $f$  represents the frequency connected with the wave number vector,  $\mathbf{k}$ , by the dispersion relation, and  $r$  the reflection coefficient of the reflective wall (shown in Fig. 1).

### 2.1.2 Directional spectrum function

Three standard functions have been proposed to express the directional spectrum except the Fourier series.

The first one is the function proposed by Mitsuyasu *et al.* (1975) shown as:

$$G(\theta|f) \equiv \frac{S(f, \theta)}{P(f)} \propto \cos^{2s} \left( \frac{\theta - \theta_o}{2} \right) \quad (7)$$

where  $P(f)$  indicates the frequency spectrum,  $s$  the degree of directional concentration, and  $\theta_o$  the peak wave direction. Yokoki *et al.* (1992) used this standard directional function. However, it took fairly much time to calculate the cross power spectrum,  $\Phi_{pq}$ .

The second one is the square of the hyperbolic secant function, which is proposed by Donelan *et al.* (1985):

$$G(\theta|f) \propto \text{sech}^2 \beta (\theta - \theta_o) \quad (8)$$

where  $\beta$  indicates the degree of directional concentration.

The last one is the circular normal distribution function proposed by Borgman (1969):

$$G(\theta|f) \propto \exp \{ a \cos(\theta - \theta_o) \} \quad (9)$$

where  $a$  indicates the degree of directional concentration.

In the present study, we assume the directional spectrum,  $S(f, \theta)$ , to be expressed by using the circular normal distribution function, because we can obtain the cross power spectrum analytically to some extent and the numerical calculation becomes faster. Therefore, the directional spectrum,  $S(f, \theta)$ , is expressed by Eq. (10):

$$S(f, \theta) = P(f) \frac{1}{2\pi I_o(a)} \exp \{ a \cos(\theta - \theta_o) \} \quad (10)$$

where  $I_o$  is the modified Bessel function.

### 2.1.3 Formulation of cross power spectrum

To rewrite Eq. (6) in a simpler form, we define a new function  $\varphi$  as follows:

$$\begin{aligned} \varphi(a, \theta_o, R, \Theta|f) \\ = \frac{1}{2\pi I_o(a)} \int_0^{2\pi} \exp \{ -ikR \cos(\theta - \Theta) \} \exp \{ a \cos(\theta - \theta_o) \} d\theta \end{aligned} \quad (11)$$

By using the above definition, Eq. (6) can be written as Eq. (12):

$$\Phi_{pq}(f) = \left\{ \begin{array}{l} \varphi(a, \theta_o, R_{pq}, \Theta_{pq} | f) \\ + r^2 \varphi(a, \theta_o, R_{pq}, \pi - \Theta_{pq} | f) \\ + r \varphi(a, \theta_o, R_{pqr}, \Theta_{pqr} | f) \\ + r \varphi(a, \theta_o, R_{pqr}, \pi - \Theta_{pqr} | f) \end{array} \right\} \times (1 + \delta_{pq} \varepsilon_p) P(f) \quad (12)$$

**Table 2:** Directional spectrum parameters

$a$	Degree of directional concentration
$\theta_0$	Peak wave direction
$r$	Reflection coefficient
$P(f)$	Frequency or power spectrum
$\varepsilon_p$	Ratio of the noise component to the power ( at the $p$ -th point; $p = 1 \sim 3$ )

where  $\varepsilon_p$  indicates the ratio of the noise component to the power,  $\Phi_{pp}(f)$ . We finally get the expression of the cross power spectrum in terms of the seven parameters which are summarized in **Table 2** and called the directional spectrum parameters in this paper.

The integral on the right-hand side of Eq. (11) can be expressed by using the integral expression of the Bessel function and the modified Bessel function (*e.g.* Abramowitz and Stegun, 1972):

$$\begin{aligned} \varphi(a, \theta_0, R, \Theta | f) &= J_0(kR) \\ &+ 2 \sum_{m=1}^{\infty} (-1)^m \cos(2m\beta) J_{2m}(kR) \frac{I_{2m}(a)}{I_0(a)} \\ &+ 2i \sum_{m=0}^{\infty} (-1)^m \cos[(2m+1)\beta] J_{2m+1}(kR) \frac{I_{2m+1}(a)}{I_0(a)} \end{aligned} \quad (13)$$

In the present study, we use Eqs. (12) and (13) to calculate the cross power spectrum.

## 2.2 Maximum likelihood method

### 2.2.1 Definition of likelihood

The maximum likelihood method is used to get the most probable values of the directional spectrum parameters. The likelihood,  $L$ , is defined by Isobe (1990):

$$\begin{aligned} L(A^{[j]}; \Phi) &= \left\{ p(A^{[1]}) \times p(A^{[2]}) \times \dots \times p(A^{[j]}) \times \dots \times p(A^{[J]}) \right\}^{1/J} \\ &= \frac{1}{(2\pi \Delta f)^M |\Phi|} \exp \left( - \sum_{p=1}^M \sum_{q=1}^M \Phi_{pq}^{-1} \hat{\Phi}_{qp} \right) \end{aligned} \quad (14)$$

where  $p(A^{[j]})$  is a joint probability density function of the Fourier coefficients,  $A^{[j]}$ , of the time series data,  $\Delta f$  the frequency interval, and  $|\Phi|$  the determinant of the matrix,  $\Phi_{pq}$ . The quantity  $\hat{\Phi}_{qp}$  which is represented by Eq. (15) corresponds to the power spectrum ( $q = p$ ) or the cross spectrum ( $q \neq p$ ) with a use of rectangular filter.



$$\hat{\Phi}_{qp} = \frac{1}{2J\Delta f} \sum_{j=1}^J \bar{A}_q^{[j]} A_p^{[j]} \quad (15)$$

where  $\bar{A}$  denotes the complex conjugate of  $A$ .

### 2.2.2 The most probable values of the parameters

In this Section, we show the procedure to estimate the directional spectrum parameters including the reflection coefficient by using the likelihood defined above.

The maximum likelihood method implies that the most probable values of  $\lambda_i$  are the solutions of the algebraic equation:

$$\frac{\partial L}{\partial \lambda_i} = \sum_{j=1}^M \sum_{l=1}^M \frac{\partial L}{\partial \Phi_{jl}} \frac{\partial \Phi_{jl}}{\partial \lambda_i} = 0 \quad (16)$$

From Eq. (14), Eq. (17) is obtained.

$$\begin{aligned} \frac{\partial L}{\partial \Phi_{jl}} &= \frac{\partial}{\partial \Phi_{jl}} \left[ \frac{1}{(2\pi\Delta f)^M |\Phi|} \exp \left( - \sum_{p=1}^M \sum_{q=1}^M \Phi_{pq}^{-1} \hat{\Phi}_{qp} \right) \right] \\ &= - \frac{1}{(2\pi\Delta f)^M |\Phi|^2} \exp \left( - \sum_{p=1}^M \sum_{q=1}^M \Phi_{pq}^{-1} \hat{\Phi}_{qp} \right) \frac{\partial |\Phi|}{\partial \Phi_{jl}} \\ &\quad + \frac{1}{(2\pi\Delta f)^M |\Phi|} \exp \left( - \sum_{p=1}^M \sum_{q=1}^M \Phi_{pq}^{-1} \hat{\Phi}_{qp} \right) \\ &\quad \times \left( - \sum_{p=1}^M \sum_{q=1}^M \frac{\partial \Phi_{pq}^{-1}}{\partial \Phi_{jl}} \hat{\Phi}_{qp} \right) \\ &= -L \times \left( \frac{1}{|\Phi|} \frac{\partial |\Phi|}{\partial \Phi_{jl}} \right) + L \times \left( - \sum_{p=1}^M \sum_{q=1}^M \frac{\partial \Phi_{pq}^{-1}}{\partial \Phi_{jl}} \hat{\Phi}_{qp} \right) \end{aligned} \quad (17)$$

Also, the following relations are obtained from the theorem of the matrices.

$$\frac{\partial |\Phi|}{\partial \Phi_{jl}} = |\Phi| \Phi_{lj}^{-1} \quad (18)$$

$$\frac{\partial \Phi_{pq}^{-1}}{\partial \Phi_{jl}} = -\Phi_{lq}^{-1} \Phi_{pj}^{-1} \quad (19)$$

By using Eqs. (18) and (19), Eq. (17) is rewritten as follows:

$$\frac{\partial L}{\partial \Phi_{jl}} = L \times \left\{ -\Phi_{lj}^{-1} + \sum_{p=1}^M \sum_{q=1}^M \Phi_{lq}^{-1} \hat{\Phi}_{qp} \Phi_{pj}^{-1} \right\} \quad (20)$$

Substituting Eq. (20) into Eq. (16) and considering that  $L \neq 0$ , we obtain

$$\sum_{j=1}^M \sum_{l=1}^M \left\{ -\Phi_{lj}^{-1} + \sum_{p=1}^M \sum_{q=1}^M \Phi_{lq}^{-1} \hat{\Phi}_{qp} \Phi_{pj}^{-1} \right\} \frac{\partial \Phi_{jl}}{\partial \lambda_i} = 0 \quad (21)$$

The directional spectrum parameters,  $\lambda_i$ , which satisfy Eq. (21) for all  $i$  ( $i = 1 \sim 7$ ) are the most probable values. Then the directional spectrum parameters, including the reflection coefficient, are estimated.

The solutions,  $\lambda_i$ , of Eq. (21) are obtained numerically by using the Newton-Raphson method. The left-hand side of Eq. (21) is first defined as a function of the directional spectrum parameters:

$$f_i(\lambda_{i'}) = \sum_{j=1}^M \sum_{l=1}^M \left\{ -\Phi_{lj}^{-1} + \sum_{p=1}^M \sum_{q=1}^M \Phi_{lq}^{-1} \hat{\Phi}_{qp} \Phi_{pj}^{-1} \right\} \frac{\partial \Phi_{jl}}{\partial \lambda_i} \quad (22)$$

In the Newton-Raphson method, the values of  $\lambda_i^{(j+1)}$  at the  $(j+1)$ -th iteration of the calculation is expressed in terms of the previous values,  $\lambda_i^{(j)}$ , as follows.

$$\lambda_i^{(j+1)} = \lambda_i^{(j)} - \left[ \sum_{i'=1}^I \left[ \frac{\partial f_i}{\partial \lambda_{i'}} \right]^{-1} f_{i'} \right]_{\lambda_i = \lambda_i^{(j)}} \quad (23)$$

where  $\partial f_i / \partial \lambda_{i'}$  is expressed by Eq. (24):

$$\begin{aligned} \frac{\partial f_i}{\partial \lambda_{i'}} &= \sum_{j=1}^M \sum_{l=1}^M \left\{ -\Phi_{lj}^{-1} + \sum_{p=1}^M \sum_{q=1}^M \Phi_{lq}^{-1} \hat{\Phi}_{qp} \Phi_{pj}^{-1} \right\} \frac{\partial^2 \Phi_{jl}}{\partial \lambda_{i'} \partial \lambda_i} \\ &\quad - \sum_{j'=1}^M \sum_{l'=1}^M \sum_{j=1}^M \sum_{l=1}^M \frac{\partial \Phi_{j'l'}}{\partial \lambda_{i'}} \frac{\partial \Phi_{jl}}{\partial \lambda_i} \\ &\quad \times \left[ -\Phi_{l'j}^{-1} \Phi_{lj'}^{-1} + \left\{ \begin{array}{l} \Phi_{lj'}^{-1} \sum_{p=1}^M \sum_{q=1}^M \Phi_{l'q}^{-1} \hat{\Phi}_{qp} \Phi_{pj}^{-1} \\ + \Phi_{l'j}^{-1} \sum_{p=1}^M \sum_{q=1}^M \Phi_{lq}^{-1} \hat{\Phi}_{qp} \Phi_{pj'}^{-1} \end{array} \right\} \right] \quad (24) \end{aligned}$$

In calculations of the present method, it sometimes happened that we obtained the parameters,  $\lambda_i^{(j+1)}$ , which made the value of the likelihood,  $L$ , smaller than the preceding parameters,  $\lambda_i^{(j)}$ . This was because the present procedure sometimes finds the minimum likelihood in stead of the maximum likelihood. Therefore, we put the additional procedure that we replace  $\Delta \lambda_i$  ( $= \lambda_i^{(j+1)} - \lambda_i^{(j)}$ ) with  $-\Delta \lambda_i$  if  $(\partial L / \partial \lambda_i) \Delta \lambda_i < 0$ . With this procedure, we can obtain converged solutions of the parameters of Eq. (21) from various initial values of the parameters.

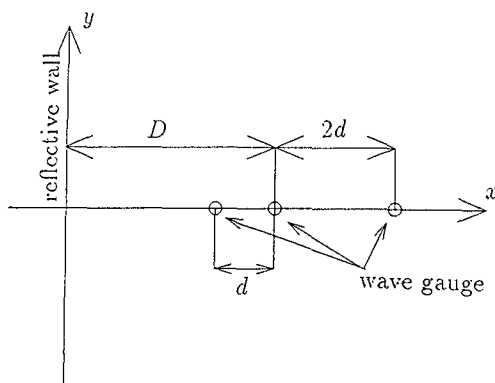
### 3 Numerical calculation

#### 3.1 Simulated cross power spectrum

To verify the validity of the present method, we applied it to simulated data.

**Table 3:** Values of the directional parameters

Case No.	$f$ (Hz)	$s$	$\theta_o$ ( $^\circ$ )	$P(f)$ ( $m^2s$ )	$r$	$\varepsilon_1$	$\varepsilon_2$	$\varepsilon_3$
PA01	0.1	5.0	120	1.0	0.1	0.1	0.1	0.1
PA02	0.1	10.0	120	1.0	0.1	0.1	0.1	0.1
PA03	0.1	5.0	120	1.0	0.5	0.1	0.1	0.1
PA04	0.1	5.0	120	1.0	0.1	0.3	0.3	0.3
PA05	0.1	5.0	120	1.0	0.1	0.1	0.2	0.3
PA06	0.2	5.0	120	1.0	0.1	0.1	0.1	0.1

**Figure 2:** Arrangement of wave gauges

First, we created sets of  $\hat{\Phi}_{pq}$  by using of the directional spectrum proposed by Mitsuyasu *et al.* (1975) for each set of directional spectrum parameters given in **Table 3**.

The arrangement of wave gauges used to calculate  $\hat{\Phi}_{pq}$  is shown in **Fig. 2**. In the figure, we vary the distance between the reflective wall and the wave gauges,  $D$ , and that between the wave gauges,  $d$ , as shown in **Table 4**. We finally calculated  $\hat{\Phi}_{pq}$  for each combination of the arrangement of wave gauges and the set of the directional spectrum parameters. Then we applied the present method to each set of the cross power spectra,  $\hat{\Phi}_{pq}$ .

### 3.2 Results of estimation

**Figure 3** shows contour maps of likelihood in terms of the directional spectrum parameters,  $a$ ,  $\varepsilon_p$ ,  $r$  and  $\theta_o$ . In these figures, the directional spectrum is calculated

**Table 4:** Arrangement of wave gauges

Case No.	$D(m)$	$d(m)$
WG01	20	5
WG03	40	5
WG05	40	15
WG07	60	5
WG09	60	15

from the set of the parameters, PA01, shown in **Table 3**. WG01, WG03 and WG05 indicates the arrangement of wave gauges as shown in **Table 4**.

From these figures, we can see that the likelihood becomes maximum at the points which correspond to the given values of the directional spectrum parameters.

**Table 5** shows the results of estimations for all combinations of the directional spectrum parameters and the arrangements of wave gauges. For these directional spectrum parameters, estimated parameters agree quite well with the true values, as shown in **Table 3**.

However, for the directional spectrum parameters, PA06, the agreement is not good. This is because the distance between the wave gauges are too long compared to the wavelength.

## 4 Conclusion

By using a circular normal distribution as the directional function, a parametric method for estimating the directional spectrum as well as the reflection coefficient in an incident and reflected wave field is proposed. From the results of numerical simulations, the method is proved to be valid as long as the arrangement of wave gauges is appropriately designed.

## References

- [1] Abramowitz, M. and I. A. Stegun, (ed.) (1972): Handbook of Mathematical Functions with Formulas, Graphs, and Mathematical Tables, Dover Pub. Inc., pp. 355-433.
- [2] Borgman, L. E. (1969): Directional spectra models for design use for surface waves, Tech. Rep. HEL 1-12, Univ. of Calif. 56p.
- [3] Capon, J. (1969): High-resolution frequency-wavenumber spectrum analysis, Proc. IEEE, Vol. 57, No. 8, pp. 1408-1418.

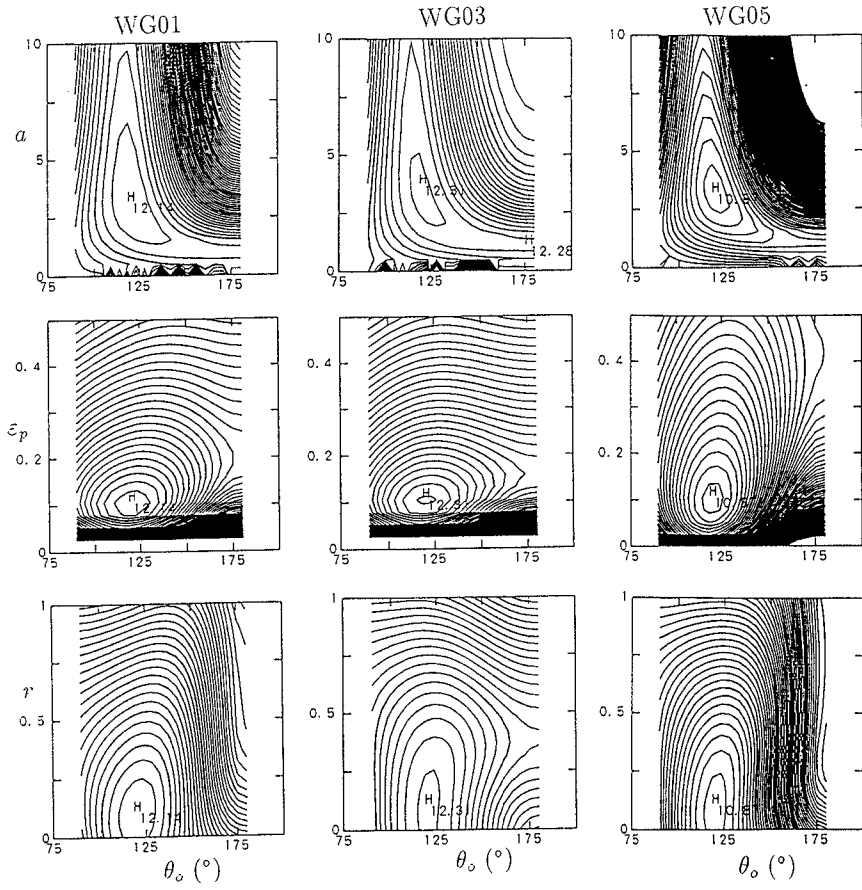


Figure 3: Contour map of the likelihood

Table 5: Results of estimation

Case No.	Case No.	$f(\text{Hz})$	$a$	$\theta_o(^{\circ})$	$P(f)$ ( $\text{m}^2\text{s}$ )	$r$	$\varepsilon_1$	$\varepsilon_2$	$\varepsilon_3$
PA01	WG01	0.1	3.22	120	1.00	0.098	0.10	0.099	0.10
	WG03	0.1	3.22	120	1.00	0.10	0.099	0.10	0.099
	WG05	0.1	3.01	121	1.01	0.11	0.096	0.088	0.096
	WG07	0.1	3.55	121	0.99	0.13	0.10	0.098	0.10
	WG09	0.1	3.08	120	1.01	0.081	0.095	0.091	0.10
PA02	WG01	0.1	5.65	120	1.00	0.098	0.10	0.10	0.099
	WG03	0.1	5.74	120	1.00	0.10	0.098	0.10	0.097
	WG05	0.1	5.58	120	1.00	0.092	0.10	0.096	0.096
	WG07	0.1	5.97	121	0.99	0.12	0.10	0.099	0.099
	WG09	0.1	5.62	120	1.00	0.094	0.099	0.098	0.098
PA03	WG01	0.1	3.04	120	1.01	0.48	0.10	0.099	0.10
	WG03	0.1	2.81	120	1.02	0.46	0.099	0.10	0.097
	WG05	0.1	2.82	119	1.03	0.45	0.11	0.097	0.093
	WG07	0.1	3.64	121	0.99	0.50	0.10	0.099	0.099
	WG09	0.1	2.75	118	1.04	0.44	0.095	0.098	0.10
PA04	WG01	0.1	3.13	121	1.00	0.095	0.30	0.30	0.30
	WG03	0.1	3.72	120	1.00	0.12	0.29	0.30	0.29
	WG05	0.1	3.07	120	1.01	0.10	0.29	0.28	0.29
	WG07	0.1	3.35	121	0.99	0.11	0.30	0.30	0.30
	WG09	0.1	3.05	120	1.01	0.085	0.30	0.29	0.30
PA05	WG01	0.1	3.07	120	1.01	0.096	0.099	0.20	0.30
	WG03	0.1	3.74	120	1.01	0.12	0.097	0.20	0.29
	WG05	0.1	3.08	120	1.01	0.11	0.096	0.19	0.29
	WG07	0.1	3.37	121	0.99	0.11	0.10	0.20	0.30
	WG09	0.1	3.07	120	1.01	0.081	0.096	0.19	0.30
PA06	WG01	0.2	3.17	122	0.98	0.19	0.13	0.063	0.11
	WG03	0.2	3.17	121	1.00	0.12	0.10	0.091	0.10
	WG05	0.2	2.89	120	1.02	0.10	0.071	0.068	0.077
	WG07	0.2	3.12	120	1.01	0.082	0.10	0.095	0.10
	WG09	0.2	2.81	120	1.04	0.12	0.056	0.048	0.060

- [4] Donelan, M. A., J. Hamilton and W. H. Hui (1985): Directional spectra of wind-generated waves, *Phil. Trans. Roy. Soc. Lond., Ser. A*, vol. 315, pp. 509-562.
- [5] Horikawa, K. (ed.) (1988): *Nearshore Dynamics and Coastal Processes*, Univ. Tokyo Press, Part. V, pp. 407-411.
- [6] Isobe, M. and K. Kondo (1984): Method for estimating directional wave spectrum in incident and reflected wave field, *Proc. 19th Int. Conf. on Coastal Eng.*, pp. 467-483.
- [7] Isobe, M. (1990): Estimation of directional spectrum expressed in standard form, *Proc. 22nd Int. Conf. on Coastal Eng.*, pp. 647-660.
- [8] Mitsuyasu, H., F. Tasai, T. Suhara, S. Mizuno, M. Ohkusu, T. Honda and K. Rikiishi (1975): Observations of directional spectrum of ocean waves using a cloverleaf buoy, *Jour. of Physical Oceanography*, Vol. 5, pp. 750-760.
- [9] Yokoki, H., M. Isobe and A. Watanabe (1992): A method for estimating reflection coefficient in short-crested random seas, *Proc. 23rd Int. Conf. on Coastal Eng.*, pp. 765-776.

## CHAPTER 54

### The Directional Wave Spectrum in the Bohai Sea\*

Yuxiu Yu<sup>1</sup> and Shuxue Liu<sup>2</sup>

#### Abstract

The directional spectrum is one of the basic characteristics of sea waves. The observations of directional spectrum of sea waves are successfully conducted at platform Bohai 8 during 1991 and 1992 using a wave gage array and it is the first time in China. Based on the field data, the directional spectrum which depends on the wave growth is given in this paper. Before observations, the effects of the figure of gage array, the distance between the gages and the platform itself on the measured results and the precision of some methods for estimating the directional spectrum were investigated and compared with the methods of numerical simulations and model tests of multi-directional irregular waves. This ensures the quality of the observations and estimations of the directional spectrum.

#### Introduction

One of the main practical problem for research of the sea wave theory and its application is to seek the directional spectrum because it is the key for studying the generating mechanism of the wind waves and the wave deformation as it propagate into shallow water. It is also the important reference for the design of maritime structures. But there is less research work on the directional spectrum due to the complex of the sea wave phenomena and the difficulty of the observation and the analysis of directional spectrum.

At present, the main method for obtaining directional spectrum is observations in field. The commonly used direct measurement methods may be of three types. Early in 1954, Barber(1954) had used wave gage array to measure the directional

---

\* The project is supported by National Natural Science Foundation of China.

1. Professor, State Key Laboratory of Coastal and Offshore Engineering, Dalian University of Technology, Dalian 116024, China.

2. Assistant Researcher, State Key Laboratory of Coastal and Offshore Engineering, Dalian University of Technology, Dalian 116024, China.



spectrum and gave proposals concerning the wave gage number and the distance between gages for a linear array. After that, some researchers studied several types of gage array with numerical and physical simulation. Longuet-Higgins et al.(1963) used pitch-and-roll buoy to measure the water surface elevation and the orthogonal components of wave surface slopes, and estimated the directional spectrum with Fourier series method. Mitsuyasu et al.(1975) designed a cloverleaf buoy which can measure three components of surface curvature besides the water surface elevation and two components of wave slopes. Therefore, the directional resolution of buoy measurement was enhanced. Also, he gave a formula of directional spectrum which was called Mitsuyasu type spectrum according to the measurement results in the sea of Japan. The another commonly used method is to measure the two horizontal components of orbital velocities by a two-axis current meter and the wave surface which was first proposed by Nagata(1964). This method is simpler and has a higher directional resolution. Besides, the remote sensing such as the stereo wave observation and the microwave technique is also used to measure directional spectrum.

The observations of directional spectrum in China were carried out later. After the ENDECO 956 buoy was introduced from U.S.A. in 1982, it is used to measure the waves for general engineering design. Because there are some disputes about their measured directional spectrum, so less systematic study has been done on it. The Ocean University of Qingdao tried observing directional spectrum with stereophotogrametry several years ago. In this paper, the observation and estimation methods of directional spectrum is mainly studied. Based on the analysis of existing observations of the directional spectrum, and the existing facilities(equipments) and the condition of experiment, wave gage array method is used to measure the directional spectrum for two times. The advance research works were conducted in laboratory and then the available methods of measurement and analysis were set up. Based on the observation results, the directional spectrum of the wind-waves is given in the paper.

## **Measurement Program**

### *Observation method*

At present, there are several measurement and analysis methods of directional spectrum. But their results have a big difference each other. So the measurement and estimation of directional spectrum themselves are an important research problem and they are studied with the numerical simulation and the laboratory experiments(Yu and Liu, 1992, 1993). Considering the present conditions of the equipments and laboratory in China, the wave gage array method which is more reliable and easily carried out on platform is selected to measure the directional waves.

### *Type and dimension of array*

Platform Bohai-8 is almost situated in the center area of the Bohai Sea (39°09'N, 119°42'E). The water depth  $d$  is 27.0 m. It consists of a life platform and a working platform and they are linked with a bridge of 50m long. The orientation of the bridge is west-east. The number of wave gages must be greater than 3. 5 wave gages of BCS vertical line type (made by the Institute of Oceanology, Academia Sinica) are used in the observation and they can be arranged in many types. The effects of the array type including linear array, T-type array and pentagon array and the spacing of wave gages on the directional resolution are investigated through numerical simulation and model tests in 3-dimensional basin respectively (Yu and Liu, 1992). The results show that the linear array is only suitable for the waves which have a narrow directional spreading and whose main direction has a large angle with the axis of the array and the gage number must be greater than 5. Both T-type and pentagon array have higher resolutions and the imposing restrictions on gage spacing are not so strict. Considering the situation of the Platform Bohai 8, T-type array is selected.

The wave gage spacing in an array has a big effect on the directional resolution. The results of the numerical and physical simulation show that the minimum spacing should be less than the half of the measured wave length. Considering the irregularity of the sea waves, the ratio between the minimum spacing and the wave length corresponding to the peak frequency of the spectrum can be about equal to 0.3. The vector distance of each pair of gage should be distributed as uniformly as possible in a range as wide as possible and no pair of wave gages should have the same vector distance. According to above guidelines and the real situation of the platform, the T-type array is arranged as Fig.1, in which the minimum distance between wave gages is 4.9m and the maximum value is 21.2m. It can be available for the waves with the period larger than 2.5s.

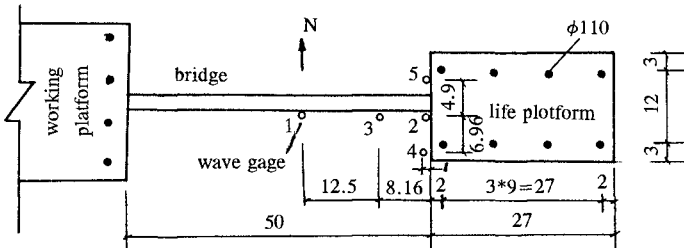


Fig.1 The arrangement of the wave gage array

#### *Effect of the platform on the results*

The life platform is supported by 8 steel cylinders and there are some horizontal and inclined cylinders between them. To check the effect of the platform on the waves from all directions, the model tests with the multi-directional irregular waves are carried out in the basin of the State Key Laboratory of Coastal and

Offshore Engineering in Dalian University of Technology, the model scale is 1:40. The test results show that the effects of the platform structure on the directional spreading are small.

### **The Observations and Data Analysis**

#### *Situation of the measurement*

The T-type array consisted of 5 gages is arranged as Fig.1. The wave data are acquired simultaneously and automatically with computer for 1200 seconds every hour. The time interval is 0.25s. At the circumstance of strong wind, the continuous wave data are acquired by artificial control. The velocity and direction of wind are recorded simultaneously by wind-velocity-direction meter. At the same time, according to the request of the Specification of Ocean Inspection, the sea state, the wave pattern and the wave direction are observed visually in the daytime. During October 20 to November 4, 1992, 271 runs of 4 wind histories are recorded. There are 144 runs whose significant wave height are larger than 0.5m. The measured maximum wind velocity is 21m/s and the maximum significant wave height is 2.58m.

#### *The Selection of the data*

The Bohai sea is basically a closed inner sea and can not be affected by the ocean swell. The directional spectrum formed by a single wind is emphatically investigated in this paper and the wave data are selected according to following principles: (1) The frequency spectra have only one peak, (2) the frequency spectra measured by the 5 gages are almost identical each other and (3) the directional spreading function also basically has one peak and the directional range of the wave energy is narrower. So the 51 runs of data (Table 1) are analyzed. In the table,  $U$  is the wind velocity at 10m elevation above the sea level.  $C_p$  is the wave velocity corresponding to the peak frequency.  $H_{1/3}$ ,  $T_{H1/3}$  and  $L_s$  are the significant wave height, period and length respectively. Because  $U$  is used in most of the present formula of the directional spectrum, 32 runs of wave data with the angle between the wind direction and the main wave direction being less than  $45^\circ$  are used as the observation results being compared with the formulas.

#### *Analysis method of directional spectrum*

There are several methods for analyzing directional spectrum. For selecting the optimum method, the single direction per frequency method (Yu and Liu 1991) is used to simulate the multi-directional waves on computer and in 3-dimensional basin and then the waves are measured by a T-type array including 5 wave gages. Afterwards, the directional spreading is analyzed by the parameterized method, the direct Fourier transform method, the extension maximum likelihood method and the Bayesian approach and their results are compared with the input one. It is

Table.1 The main parameter of the selected data

Date	Runs	Time	U/C <sub>p</sub>	H <sub>1/3</sub> /L <sub>s</sub>	H <sub>1/3</sub>	T <sub>H1/3</sub>
Oct. 22	8	11:00~19:00	0.76~1.17	0.0282~0 .0374	0.90~ 1.45	4.50~5.07
Oct. 23	8	3:00~17:00	1.01~1.32	0.0296~0 .0366	0.93~ 1.23	4.06~4.92
Oct. 24	2	9:00~10:00	1.20~1.44	0.0286~0 .0302	0.63~ 0.72	3.64~4.02
Oct. 25	2	7:00~10:00	0.38~0.49	0.0159~0 .0202	0.50~ 0.66	4.49~4.58
Oct. 26	1	13:00	0.55	0.0157	0.55	4.74
Oct. 28	7	7:00~22:00	0.76~1.31	0.0235~ 0.0335	0.60~ 1.36	3.92~5.26
Oct. 29	3	5:00~13:00	0.50~0.84	0.0264~ 0.0298	1.01~ 1.07	4.66~5.10
Oct. 30	2	19:00~20:00	1.03~1.35	0.0390~ 0.0397	0.86~ 0.87	3.75~3.76
Oct. 31	12	4:00~23:00	0.96~2.52	0.0247~ 0.0447	0.63~ 2.58	3.83~6.53
Nov. 1	6	0:00~5:00	0.68~1.14	0.0249~ 0.0346	1.48~ 2.12	5.98~6.27
Sum	51		0.38~2.52	0.0157~ 0.0447	0.50~ 2.58	3.66~6.40

shown(Yu and Liu 1993) that the Bayesian approach(Hashimoto, et. al., 1987) has the highest directional resolution and small effect by the wave gage number(greater than 4 only), the distance between wave gages and the width of the directional spreading. So the Bayesian approach is used.

### The Frequency Spectrum of the Measured Waves

There are many types of frequency spectrum. The commonly used one is JONSWAP spectrum. In the Technical Specification for Port Engineering of China, the wind-wave frequency spectrum proposed by Wen et al(1989) is adopted. To the equilibrium ranges at high frequency of wave spectra, the slope,  $p$  of  $-5$  is adopted by the former spectrum and the latter one use  $p = -(2 - 0.626H_s/d)$  (where  $d$  is the water depth) i.e.,  $|p| < 4$ . Figure.2 show the measured results of the slopes and the mean value can be taken as  $p = -4.125$ .

For comparing each other, the frequency spectra are nondimensionalized. Comparing the above two spectra with the measured average spectrum shows that the shape of the JONSWAP spectrum is wider and that of the Wen's spectrum is

narrower. The spectrum shape proposed by Hong and Yong(1980) is consisted of two parts and can fit the measured one easily(Fig.3), i.e.

$$s(f) = 0.117 H_s^2 T_p (ff_p)^{-4.125} \exp[-1.171(ff_p)^{-11}] [1 + 3.893(ff_p)^{-11}] \tag{1}$$

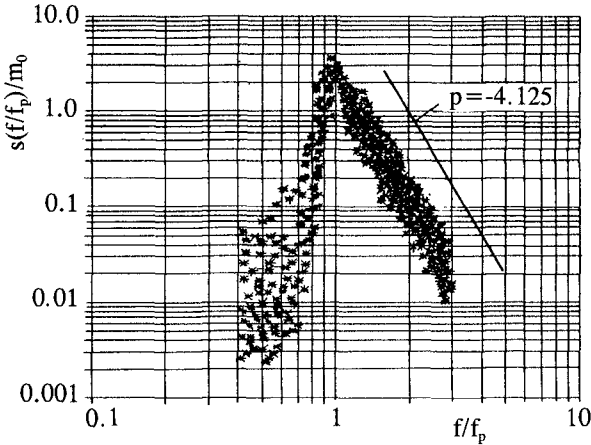


Fig.2 The slope of the equilibrium ranges of the frequency spectrum

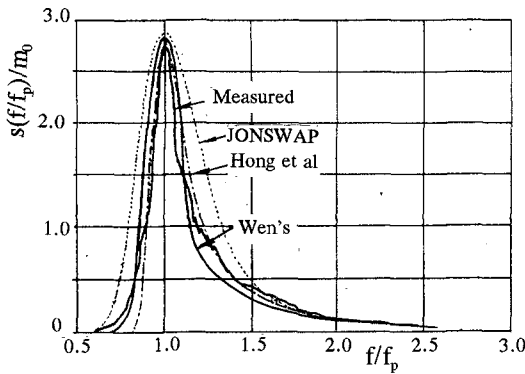


Fig.3 Comparison of the measured frequency spectrum with the fitted one

**The Directional Spectrum of Sea Waves**

The main aim of the observations is to obtain the directional spectrum of sea waves. The directional spectrum is generally expressed as the product of the frequency spectrum and the directional spreading function  $G(f, \theta)$ , i.e.,

$$\left. \begin{aligned} S(f, \theta) &= S(f) \cdot G(f, \theta) \\ \int_{-\pi}^{\pi} G(f, \theta) d\theta &= 1 \end{aligned} \right\} \quad (2)$$

The measured directional spreading functions of the 51 runs data are obtained by the Bayesian approach and compared with 5 existing typical models.

*The present used directional spectrum model*

Equation (2) is used in most models, but the spreading function in each model is different.

1. Simple empirical formula. Assuming the directional spreading is independent of wave frequency.

$$G(f, \theta) = G(\theta) = C(n) \cos^{2n} \theta \quad (3)$$

The coefficient C(n) can be determined by Eq.(2). When n=1, C(n)=1/π; n=2, C(n)=8/3π.

2. Mitsuyasu-type spreading. Longuet-Higgins et al(1963) expressed the directional spreading function as

$$\left. \begin{aligned} G(f, \theta) &= G_0(s) \cos^{2s} \frac{\theta - \theta_0}{2} \\ G_0(s) &= \frac{1}{\pi} 2^{2s-1} \frac{\Gamma^2(s+1)}{\Gamma(2s+1)} \end{aligned} \right\} \quad (4)$$

where θ<sub>0</sub> is the main direction of waves, s is the spreading parameter. According to the data measured by a cloverleaf buoy, Mitsuyasu et al(1975) gave the relationship between s and frequency and wind velocity as following

$$\left. \begin{aligned} s &= s_{\max} (f/f_p)^5 & f &\leq f_p \\ s &= s_{\max} (f/f_p)^{-2.5} & f &> f_p \\ s_{\max} &= 11.5(2\pi f_p U/g)^{-2.5} = 11.5(C_p/U)^{2.5} \end{aligned} \right\} \quad (5)$$

where f<sub>p</sub> is the peak frequency of the spectrum and Goda(1985) proposed that f<sub>p</sub> can be estimated by f<sub>p</sub> = 1/(1.05T<sub>H1/3</sub>). When f=f<sub>p</sub>, s=s<sub>max</sub>, it means that the spreading at the peak frequency is the narrowest. In Eq.(5), Cp/U is the wave age and the less is Cp/U, the younger is the waves. The mean value of Cp/U is around 1.0 for Mitsuyasu's data and it corresponds to fully developed sea waves.

3. Hasselmann directional spreading. Hasselmann et al(1980) used Eq.(4) for

spreading function but gave the following parameters according to the data of JONSWAP:

$$s = s_{\max}(ff_p)^\mu \tag{6}$$

$$\text{When } ff_p \geq 1.0 \quad \left\{ \begin{array}{l} s_{\max} = 9.77 \pm 0.43 \\ \mu = -(2.33 \pm 0.06) - (1.4 \pm 0.45) \left( \frac{U}{C_p} - 1.17 \right) \end{array} \right. \tag{7}$$

$$\text{When } ff_p < 1.0 \quad \left\{ \begin{array}{l} s_{\max} = 6.97 \pm 0.83 \\ \mu = 4.06 \pm 0.22 \end{array} \right. \tag{8}$$

This model is similar to the Mitsuyasu-type spreading, but  $s_{\max}$  and the power are different and only at the high frequency side, the spreading function is dependent on the wind velocity. In Eq. (7),  $U/C_p$  should be greater than 1.0 because of their measured wave data  $U/C_p = 1.0 \sim 1.8$ .

4. Donelan's spreading function. Donelan et al(1985) measured the directional spectrum systematically using an array consisted of 14 wave gages at the Lake Ontario in Canada.  $U/C_p$  of the data is 0.83 ~ 4.6. The directional spreading function was given as

$$G(f, \theta) = \frac{1}{2} \beta \text{sech}^2 \beta \theta \tag{9}$$

$$\left. \begin{array}{l} \beta = 2.61(ff_p)^{1.3}; \quad 0.56 \leq ff_p < 0.95 \\ \beta = 2.28(ff_p)^{-1.3}; \quad 0.95 < ff_p < 1.6 \\ \beta = 1.24 \quad \quad \quad \text{others } ff_p \end{array} \right\} \tag{10}$$

This model does not include the parameter which expresses the wave growing. When  $f/f_p = 0.95$ ,  $\beta_{\max} = 2.44$  and the spreading is the narrowest. When  $f/f_p < 0.56$  and  $f/f_p \geq 1.6$ , the spreading is a constant.

5. Wen's directional spectrum. Wen et al obtained the directional spectrum as follows from the frequency spectrum of each wave propagating direction  $\theta$  which is derived analytically.

$$\left. \begin{array}{l} \tilde{F}(\tilde{\omega}, \theta) = \frac{k_1 k_3}{k_2} P \cos^{\mu} \theta \tilde{\omega}_0^{-p_0} \exp \left[ -\frac{P_0}{q_0} (\tilde{\omega}_0^{-q_0} - 1) \right]; \quad \tilde{\omega} \leq \tilde{\omega}_L \\ \tilde{F}(\tilde{\omega}, \theta) = \frac{\tilde{F}(\omega_L, \theta)}{\tilde{\omega}^4} \tilde{\omega}_L^4; \quad \tilde{\omega} > \tilde{\omega}_L \end{array} \right\} \tag{11}$$

where  $\tilde{F}(\tilde{\omega}, \theta) = \frac{\omega_p F(\omega, \theta)}{m_0}$ ;  $\tilde{\omega}_0 = \frac{1}{k_2 \cos^{\mu} \theta} \tilde{\omega}$ ,  $\tilde{\omega} = \omega / \omega_p$ ,  $\tilde{\omega}_L = \frac{\omega_L}{\omega_p}$ ,  $\omega_L = 2.38 P^{-0.406}$

$$P = 1.69 \frac{U}{C_p} = 1.69 \frac{\omega_p U}{g} \tag{12}$$

P express the peakedness of the frequency spectrum and also the wave growing. Other parameters are related to P.

*The selection of the spreading model*

Figure 4 is an example of the measured directional spectrum and directional spreading function. It is shown that the main directions of the component waves corresponding to different frequency are close to each other. The wave energy are distributed in a narrow direction range and most directional spreading functions are symmetric approximately. The spreading is the narrowest near the peak frequency. These are basically the same as all above models.

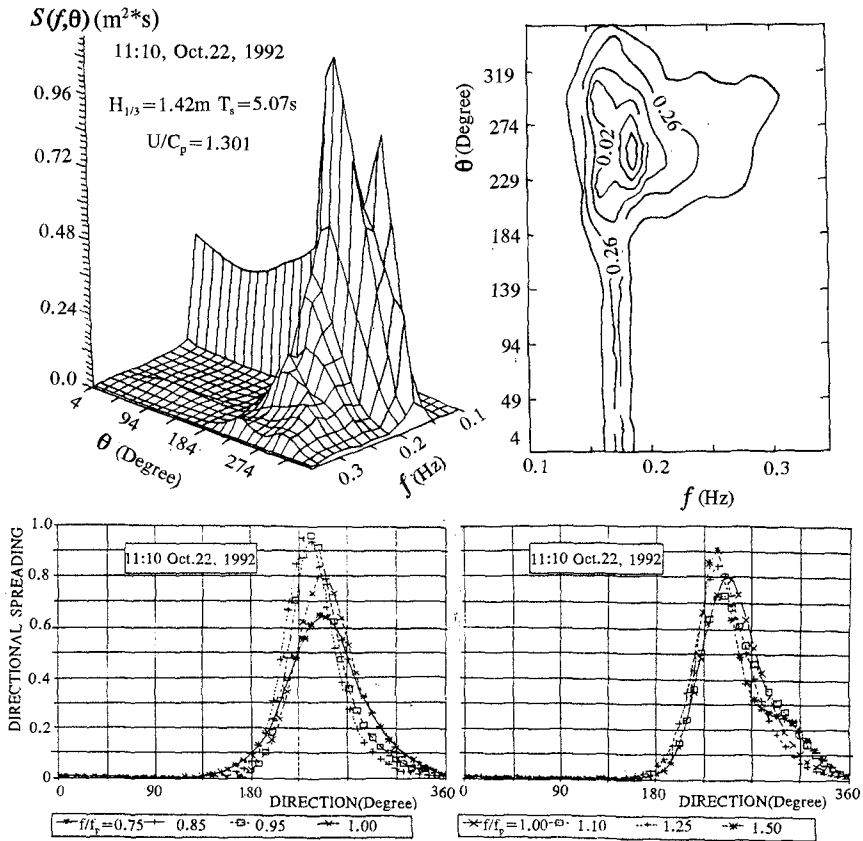


Fig.4 Example of the measured directional spectrum



To check the adaptability of 5 models to the measured results, these results are divided into 2 groups according to that  $U/C_p \geq 1.0$  or  $U/C_p < 1.0$ . The measured results are compared with above 5 models according to the directional spreading curves, the directional cumulative spreading curves (refer to Eqs(13)~(15)), the maximum of the directional spreading function and the standard deviation of the spreading respectively. The results show that the Donelan's model conforms to the measured spreading best and the Wen's model takes the second place, but Donelan's model can not consider the effect of the wave growing and Wen's model is too complex. On the other hand, in Mitsuyasu model, the spreading parameter  $s$  is dependent on the condition of wave growing and this model has been commonly used in the recent years. So the Mitsuyasu model is used to fit the measured spreading and the Donelan's model will be modified in this paper.

#### *Fitting the measured spreading with Mitsuyasu's Model*

Let the cumulative curve of the directional spreading,  $G(f, \theta)$  be

$$F(f, \theta) = \int_{-\pi}^{\theta} G(f, \theta) d\theta \quad (13)$$

then the deviations of two directional spreading functions  $G_x$  and  $G_y$ , and their cumulative curves are as followings respectively

$$\Delta G_{xy}(f) = \left\{ \int_{-\pi}^{\pi} [G_x(f, \theta) - G_y(f, \theta)]^2 d\theta \right\}^{1/2} \quad (14)$$

$$\Delta F_{xy}(f) = \left\{ \int_{-\pi}^{\pi} [F_x(f, \theta) - F_y(f, \theta)]^2 d\theta \right\}^{1/2} \quad (15)$$

When the Mitsuyasu's model X is used to fit the measured spreading, Y, let  $\Delta G_{xy}(f)$  and  $\Delta F_{xy}(f)$  take the minimum, the parameter  $s$  for a given frequency can be calculated and the values of  $s$  are varied with  $f/f_p$  as shown in Fig.5. In this figure, the Mitsuyasu's spreading of  $U/C_p = 0.7, 1.0$  and  $1.3$  are also given. Figure 5 shows that when  $f/f_p > 1.0$ , the power  $-2.5$  basically conforms to the average measured condition, but when  $f/f_p \leq 1.0$  the power  $s$  is obviously too large and  $2.5$  may be suitable.  $s$  takes the maximum value at  $f/f_p = 1.0$ . So the parameter  $s$  can be determined by

$$\left. \begin{aligned} s &= s_{\max} (ff_p)^{2.5}, & f \leq f_p \\ s &= s_{\max} (ff_p)^{-2.5}, & f > f_p \end{aligned} \right\} \quad (16)$$

Concerning  $s_{\max}$ , the measured results show that  $s_{\max}$  is tending to decrease with  $U/C_p$  increasing, but their relationship is not apparent. The growing state of the stable wind-generated waves can be described by  $U/C_p$ , but in fact the wind velocity and wind direction are usually changeable and the wave growth much lags

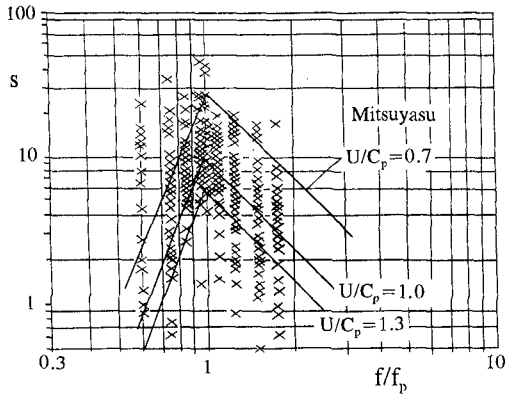


Fig.5 Relation between  $s$  and  $f/f_p$

behind the wind changing. Furthermore, it is very difficult to determine the wind velocity corresponding to the design waves for engineering design. So Goda(1985) proposed that  $s_{max} = 10, 25$  and  $75$  for wind-waves, swell with short decay and swell with long decay distance respectively, but no observation data yet certify it. In another respect, Sverdrup and Munk had obtained the famous relationship between wave steepness ( $H/L$ ) and wave age ( $C/U$ ). When  $C/U > 0.4$ , wave steepness decreases with wave age increasing. The similar results are obtained by this measurement(Fig.6). So the wave steepness is used to express the growing state of the waves, it is convenient for engineering application, and  $s_{max}$  can be determined as follows(Fig.7).

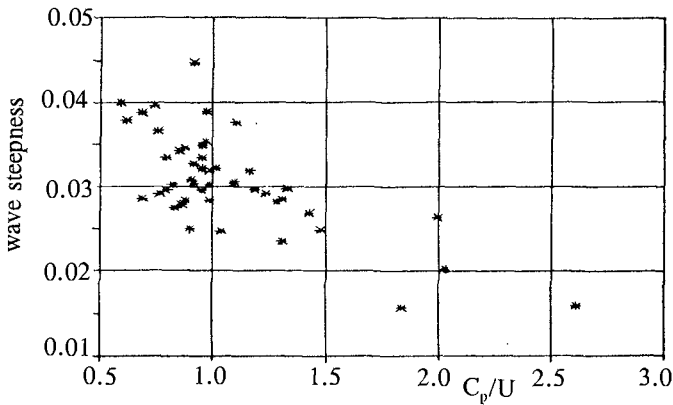


Fig.6 Relation between the significant wave steepness and  $C_p/U$

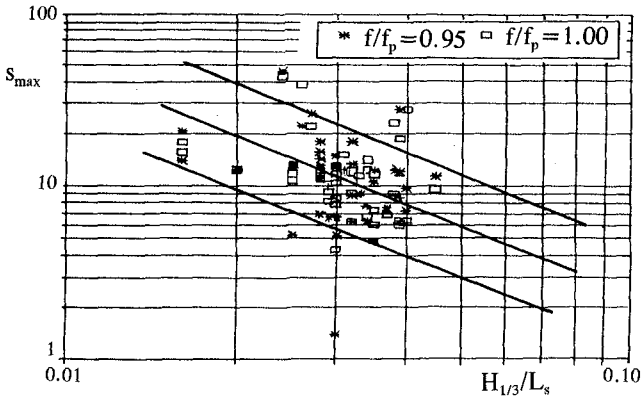


Fig.7 Relation between  $s_{max}$  and  $H_{1/3}/L_s$

$$\left. \begin{aligned}
 s_{max} &= 0.13(H_{1/3}/L_s)^{-1.28} && (Mean) \\
 s_{max} &= 0.26(H_{1/3}/L_s)^{-1.28} && (Upper) \\
 s_{max} &= 0.065(H_{1/3}/L_s)^{-1.28} && (Lower)
 \end{aligned} \right\} \quad (17)$$

The spreading functions with  $s$  calculated by Eqs(16) and (17) are compared with the measured. It is shown that they are close each other.

Wang(1992) obtained similar results from the wave data in severe seas during storms that occurred offshore California.

$$\left. \begin{aligned}
 s_{max} &= 0.11(H_s/L_p)^{-1.28} && (Mean) \\
 s_{max} &= 0.20(H_s/L_p)^{-1.28} && (Upper) \\
 H_s &= 4.0\sqrt{m_0}
 \end{aligned} \right\} \quad (18)$$

*Fitting with Donelan model*

Similar to the above, let deviations  $\Delta G_{xy}(f)$  and  $\Delta F_{xy}(f)$  between measured spreading,  $X$  and that of Donelan's model,  $Y$  take the minimum, the variation of  $\beta$  with  $f/f_p$  is shown in Fig.8. Also the relationship between  $\beta$  in Eq.(9) and  $s$  in Eq.(4) is shown in Fig.9 Figure 8 shows that Donelan model is basically identical to the measured. But the value of  $\beta$  in Eq.(9) is in the large side. Moreover, for considering the effect of wave growing,  $\beta$  can be determined by Eq.(17) and Fig.9.

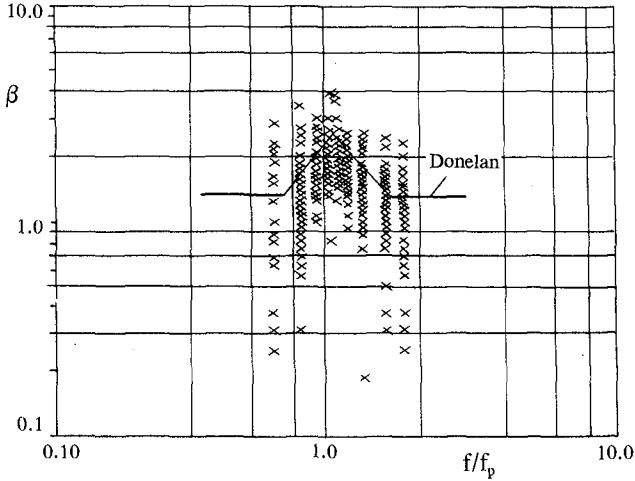


Fig.8 Relation between  $\beta$  and  $f/f_p$

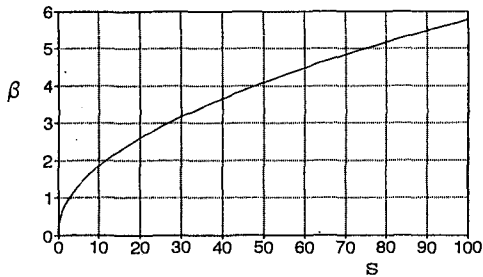


Fig.9 Relation between  $\beta$  and  $s$

**Conclusion**

1. The observation and estimation methods of directional spectrum are investigated in this paper by combining the numerical simulation and the laboratory experiments with the field observations. The results show that a reliable directional spreading can be obtained using a 5-gage array to measure the waves and the Bayesian approach for the directional spectrum analysis. This method is more suitable for measuring waves in laboratory or on a field platform.

2. The results of the spectral analysis show that the power of the equilibrium range of frequency spectra can be selected as  $p=-4.125$ . The frequency spectrum can be expressed as Eq.(1).

3. The wave steepness is used to describe the growing state of wind-waves and the relationship between the directional spreading parameter  $s_{\max}$  and the wave steepness is given in this paper. It is convenient for engineering applications.

4. Using Mitsuyasu model to fit the measured results, the directional spreading function in the Bohai Sea is obtained preliminarily as Eqs(4), (16) and (17). The variation of  $\beta$  in Donelan model with wave steepness is also given in this paper.

5. The process of sea wave growing is very complex and the measured wave data are affected by many factors. In this paper, even if only 51 runs of wave data which generated by a single wind in the center part of the Bohai Sea are used, the datum points obtained from analysis are rather scattered. For obtaining the directional spectrum at coastal and offshore area of China, much more observations with gage array or other methods whose directional resolution is high are needed.

**Acknowledgments**---The work described herein is a part of the project supported by both National Natural Science Foundation of China and the Ministry of Communications. The observations of sea waves were carried out by Mr. X. Yu, J. Xie and B. Fan, First Institute of Oceanography. The authors sincerely wish to express their appreciation to Mrs. X. Wu, Mr. N. Chu, G. Lu, G. Li and the people worked on the platform Bohai 8 for their great helps to this study.

## References

- Barber, N.F., 1954, Finding the direction of travel of sea waves, *Nature*, Vol.174, 1048~1050.
- Donelan M. A., et al, 1985, Directional spectra of wind-generated waves, *Phil. Trans. R. Soc. Lond*, A315, 509~562.
- Goda Y., 1985, *Random seas and design of maritime structures*, University of Tokyo Press.
- Hashimoto N. et al., 1987, Estimation of directional spectrum using the Bayesian approach and its application to field data analysis, *Report of the Port and Harbour Research Institute, Japan*, Vol.12, 58~100.
- Hasselmann K et al, 1980, Directional wave spectra observed during JONSWAP 1973, *J. Phys. Oceanogr.*, 10(8), 1264~1280.
- Hong Guangwen and Yang Zhengyi, 1980, The wind-wave frequency spectrum and its statistical properties in shallow water, *J. of Nanjing Hydraulics Research Institute(in Chinese)*, No.2, 68~86.
- Longuet-Higgins, M.S., D.E. Cartwright and N. D. Smith, 1963, Observation of directional spectrum of sea waves using the motion of floating buoy, *Proc. Conf. Ocean Wave Spectra*, Prentice-Hall Inc., 111~132.
- Mitsuyasu, H. et al, 1975, Observations of directional spectrum of ocean wave using a cloverleaf buoy, *J. Phys. Oceanogr.*, 5(4), 750~760.
- Nagata, Y., 1964, The statistical properties of orbital wave motions and their

- application for the measurement of directional wave spectra, *J. of the Oceanographic Society on Japan*, 19(4), 169~191.
- Wang David Wei-Chi, 1992, Estimation of wave directional spreading in severe seas, *Proc. Second Int. Offshore and Polar Engineering Conf.*, Vol.3, 146~153.
- Wen, Shengcheng et al., 1989, Improved form of wind-wave frequency spectrum, *Acta Oceanologica Sinica*, 8, 467~483.
- Yu Yuxiu, S. X. Liu and L. Li, 1991, Numerical simulation of multi-directional random waves, *Proc. 1st Int. Offshore and Polar Engineering Conf.*, Edinburgh, United Kingdom, 26~32.
- Yu Yuxiu and S. X. Liu, 1992, Study on measurement methods of multi-directional waves by wave gage array, *Proc. 2nd Int. Offshore and Polar Engineering Conf.*, San Francisco, U.S.A, 179~185.
- Yu Yuxiu and S. X. Liu, 1993, The Analyzing methods of directional spectrum, *Proc. 7th China Coastal Engineering Conf.*(in Chinese).

## CHAPTER 55

# IRREGULAR WAVES OVER AN ELLIPTIC SHOAL

Xiping Yu<sup>1</sup> and Hiroyoshi Togashi<sup>2</sup>

### ABSTRACT

A numerical model for the transformation of narrow-banded irregular waves over gradually varying bottom topography is presented. The model is based on the mild slope wave equation for component waves. Perturbation of the mild slope wave equation with respect to the deviation of the angular frequency of any component wave from that of a principal wave, which is a small quantity for waves of narrow-banded spectra, is carried out. The mild slope wave equation, which depends on the frequency of the component wave, can thus be replaced by the perturbation equations in terms of the principal wave parameters. The finite element method is considered for numerical solutions of the perturbation equations. Since the matrix of the linear algebraic finite element equations depends on neither the component wave properties nor the order of the perturbation, numerical solution of an irregular wave field can be efficiently obtained. The model is applied to the computation of the wave motion over an elliptic shoal. The computed wave height distribution shows satisfactory agreement with the available experimental data.

### INTRODUCTION

The mild slope wave equation (Berkhoff, 1972) has been established as an effective model for describing the combined refraction and diffraction of small amplitude waves in nearshore zone. In spite of its widely recognized validity,

---

<sup>1</sup>Assoc. Prof., Dept. Civ. Eng., Nagasaki Univ., Bunkyo-Machi 1-14, Nagasaki City, Nagasaki 852, Japan

<sup>2</sup>Prof., ditto

application of this model in practice has, however, not always been easy. One of the reasons is the considerable computational efforts necessitated to solve the elliptic partial differential equation if the domain of interest has a dimension of over several wavelengths. The situation becomes even more critical if the wave irregularity is assumed to be of primary importance and, therefore, a large number of component waves must be dealt with independently. The research efforts on developing effective numerical methods so that the mild slope wave equation can be applied to the problems with large domain have led to many distinguishable achievements in the past decade. On improving the approach to the wave irregularity, however, less progress has been made.

Real sea waves are always irregular. However, most engineering analyses of the nearshore wave motion had long been based on representation of the real sea by monochromatic waves, usually the significant waves. The inaccuracy of such representation has been pointed out by many researchers who compared the results by the representative wave method with those by other more accurate methods (see, *e.g.*, Goda, 1985). Since the wave transformation processes are always frequency dependent, it can not be expected that the significant wave parameters of an irregular wave field are even close to the wave parameters following the transformation of the significant wave. This is particularly true in a region where waves undergo significant refraction and diffraction.

The most direct approach to the wave irregularity may be the superposition method. This classical method is based on decomposing irregular waves into monochromatic components with different frequencies. By applying a regular wave theory to each of these component waves and reassembling the solutions, the irregular wave field can be computed. As long as the wave is of small amplitude, or, is linear, the superposition method is authoritative. However, a large number of component waves must be considered to ensure the accuracy of results. Since the component waves are numerically independent, considerable computational efforts are necessary.

A rather different approach to the superposition is the energy method originally proposed by Karlsson (1969). This method is based on a governing equation in terms of the energy spectrum, which is generally expressed by the product of a wave height related parameter with a distribution function describing the spread of the wave energy with respect to the frequency and the directional angle. Once the distribution function is assumed to be invariant or to be in a known form in the domain of interest, the wave height can be accordingly solved from the governing energy equation. This method is direct but can not be widely applied because the spectrum is in fact part of the solution of an irregular wave field



and it is not always appropriate to assume its invariance or foreseeability. In particular, if there is a permeable breakwater in the domain of interest, because of the frequency selectivity of the breakwater to reflection and transmission, the wave spectrum, at least, in the vicinity of the breakwater may undergo significant transformation. Any presumption on its form under this circumstance may lead to mistakes.

The present study is to provide a rather different approach to the irregular wave motion in nearshore zone. The method is essentially superposition but the computational effort involved is equivalent to that required by the representative wave method. In the following sections, we first describe the governing equation for the component wave and perturb the equation with respect to the deviation of the angular frequency of the component wave to that of the principal wave. Then, we illustrate the finite element method for solutions of the perturbation equations. Finally, we apply our numerical model to the wave motion over an elliptic shoal and compare the computational results with experimental data.

## THEORY

### The Basic Equation

For the component wave, with a small amplitude and an arbitrary angular frequency, over a gradually varying bottom topography, we employ the mild slope wave equation to describe its motion. Denote the water surface elevation caused by the wave motion by  $\tilde{\eta} = \eta(x, y)e^{-i\sigma t}$ , where  $\sigma$  is the angular frequency and  $\eta(x, y)$  is called the complex amplitude of the component wave (the modulus of  $\eta$  denotes the usual wave amplitude and the argument of  $\eta$  represents the relative phase of the water surface elevation). The governing equation for  $\eta$  can then be written as (Berkhoff, 1972)

$$\nabla \cdot (CC_g \nabla \eta) + k^2 CC_g \eta = 0 \quad (1)$$

where  $\nabla$  is the horizontal gradient operator,  $k$  the wavenumber,  $C$  the wave celerity and  $C_g$  the group velocity. Eq. (1) is for waves without any dissipation. If the dissipation effect is not negligible, we may have to introduce a factor  $\mu = 1 + i\xi$  in the equation so that

$$\nabla \cdot (CC_g \nabla \eta) + \mu^2 k^2 CC_g \eta = 0 \quad (2)$$

Eq. (2) is slightly different from a previous equation proposed by Dalrymple et al. (1984). It is expected that the parameter  $\xi$ , that is, the imaginary part of the factor  $\mu$ , can be more closely related to the conventional energy decaying factor

$\Phi_D$  (see, *e.g.*, Horikawa, 1989) so that the dissipation effect can be readily evaluated. The relation between  $\xi$  and  $\Phi_D$  is clear if we consider a progressive wave in the positive  $x$  direction over a constant water depth. Under this circumstance, the energy decaying factor  $\Phi_D$  is

$$\Phi_D = -\frac{1}{EC_g} \frac{d(EC_g)}{dx} = -\frac{1}{E} \frac{dE}{dx} \quad (3)$$

since  $C_g$ , which depends on the wave frequency and the water depth, is constant.  $E$  in (3) is the average wave energy, which can be expressed by

$$E = \frac{1}{8} \rho g H^2 \quad (4)$$

for small amplitude waves, where  $H$  is the wave height,  $\rho$  the fluid density and  $g$  the gravitational acceleration. Inserting (4) into (3) gives

$$\Phi_D = -\frac{2}{H} \frac{dH}{dx} \quad (5)$$

On the other hand, for a unidirectional wave, Eq. (2) reduces to

$$\frac{d^2 \eta}{dx^2} + \mu^2 k^2 \eta = 0 \quad (6)$$

Eq. (6) has two independent solutions, representing the progressive decaying waves in the positive and negative  $x$  directions, respectively. The wave in the positive  $x$  direction can be expressed by

$$\eta = \eta|_{x_0} e^{-\xi k(x-x_0)} e^{ik(x-x_0)} \quad (7)$$

where  $x_0$  denotes a reference point. Eq. (7) gives the variation of the wave height  $H$  as follows:

$$H = H|_{x_0} e^{-\xi k(x-x_0)} \quad (8)$$

Inserting (8) into (5), we readily obtain

$$\xi = \frac{1}{2k} \Phi_D \quad (9)$$

### Perturbation of the Basic Equation

We introduce a principal angular frequency and denote it by  $\bar{\sigma}$ .  $\bar{\sigma}$  may, but not necessarily, be defined as the peak angular frequency of the incident wave spectrum. With the principal angular frequency, the angular frequency  $\sigma$  of any component wave can be expressed as

$$\sigma = \bar{\sigma}(1 + \epsilon) \quad (10)$$

where  $\epsilon = (\sigma - \bar{\sigma})/\bar{\sigma}$ . As long as we consider only narrow-banded waves,  $\epsilon$  is a small quantity and all the frequency dependent variables may then be expanded into power series of  $\epsilon$  at their principal values. In particular, for the surface elevation  $\eta$ , the wavenumber  $k$  and the product of the wave celerity  $C$  with the group velocity  $C_g$ , we have the following perturbation expressions:

$$\eta = \eta^{(0)} + \epsilon\eta^{(1)} + \epsilon^2\eta^{(2)} + \dots \quad (11)$$

$$k = \bar{k}(1 + \epsilon\alpha^{(1)} + \epsilon^2\alpha^{(2)} + \dots) \quad (12)$$

$$CC_g = \bar{C}\bar{C}_g(1 + \epsilon\beta^{(1)} + \epsilon^2\beta^{(2)} + \dots) \quad (13)$$

where

$$\alpha^{(1)} = \frac{\bar{\sigma}}{\bar{k}} \frac{d\bar{k}}{d\bar{\sigma}} = \frac{1}{\bar{n}} \quad (14)$$

$$\alpha^{(2)} = \frac{1}{2} \frac{\bar{\sigma}^2}{\bar{k}} \frac{d^2\bar{k}}{d\bar{\sigma}^2} = -\frac{1}{2\bar{n}^3} [(2\bar{n} - 1)\bar{m} - \bar{n}^2] \quad (15)$$

$$\beta^{(1)} = \frac{\bar{\sigma}}{C\bar{C}_g} \frac{d(C\bar{C}_g)}{d\bar{\sigma}} = \frac{1}{\bar{n}^2} [(2\bar{n} - 1)\bar{m} - \bar{n}] \quad (16)$$

$$\begin{aligned} \beta^{(2)} &= \frac{1}{2} \frac{\bar{\sigma}^2}{C\bar{C}_g} \frac{d^2(C\bar{C}_g)}{d\bar{\sigma}^2} \\ &= \frac{1}{2\bar{n}^4} [(2\bar{n} - 1)\bar{m}^2 + 3\bar{n}(\bar{n} - 1)(2\bar{n} - 1)\bar{m} - \bar{n}^2(5\bar{n} - 4)] \end{aligned} \quad (17)$$

and

$$\bar{n} = \frac{1}{2} \left( 1 + \frac{2\bar{k}h}{\sinh 2\bar{k}h} \right) \quad (18)$$

$$\bar{m} = \bar{n} + \frac{1}{2} \left( 1 - \frac{2\bar{k}h}{\tanh 2\bar{k}h} \right) \quad (19)$$

The bars are used to denote principal values. It is obvious that  $\alpha^{(1)}$ ,  $\alpha^{(2)}$ ,  $\beta^{(1)}$  and  $\beta^{(2)}$  are all single functions of  $\bar{k}h$  and, consequently, the principal wave effect parameter  $\bar{\sigma}^2 h/g$  if the following dispersion relation for the principal wave is taken into consideration:

$$\frac{\bar{\sigma}^2 h}{g} = \bar{k}h \tanh \bar{k}h \quad (20)$$

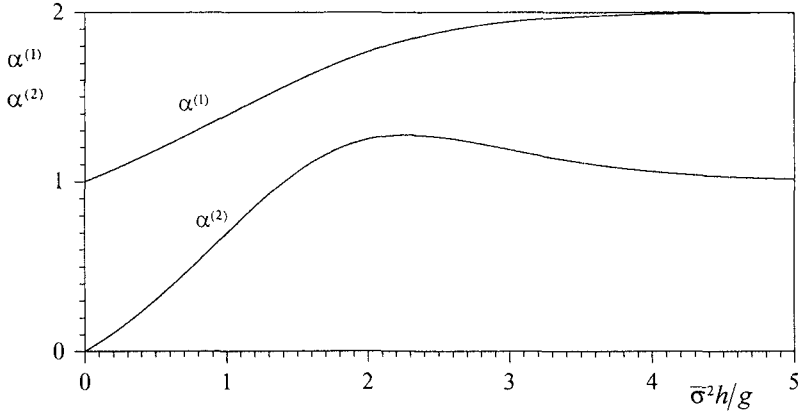


Fig. 1: Variation of  $\alpha^{(1)}$  and  $\alpha^{(2)}$  versus  $\bar{\sigma}^2 h/g$

In Figs. 1 and 2 we show these functional relations for  $0 \leq \bar{\sigma}^2 h/g \leq 5$ . It can be noted that when the principal wave tends to be a long wave, that is,  $\bar{\sigma}^2 h/g$  tends to zero,  $\alpha^{(1)}$  tends to 1 while  $\alpha^{(2)}$ ,  $\beta^{(1)}$  and  $\beta^{(2)}$  all tend to zero. On the other hand, when the principal wave becomes a deep water wave, or, when  $\bar{\sigma}^2 h/g$  tends to infinity,  $\alpha^{(1)}$  tends to 2,  $\alpha^{(2)}$  tends to 1,  $\beta^{(1)}$  tends to -2 and  $\beta^{(2)}$  tends to 3.

Substituting (11), (12) and (13) into the mild slope wave equation (2) and collecting all the terms for each order of  $\epsilon$ , we obtain

$$\nabla \cdot (\bar{C}\bar{C}_g \nabla \eta^{(0)}) + \mu^2 \bar{k}^2 \bar{C}\bar{C}_g \eta^{(0)} = 0 \tag{21}$$

$$\nabla \cdot [\bar{C}\bar{C}_g \nabla \eta^{(1)} + \beta^{(1)} \bar{C}\bar{C}_g \nabla \eta^{(0)}] + \mu^2 \bar{k}^2 \bar{C}\bar{C}_g [\eta^{(1)} + \beta^{(1)} \eta^{(0)} + 2\alpha^{(1)} \eta^{(0)}] = 0 \tag{22}$$

$$\begin{aligned} \nabla \cdot [\bar{C}\bar{C}_g \nabla \eta^{(2)} + \beta^{(1)} \bar{C}\bar{C}_g \nabla \eta^{(1)} + \beta^{(2)} \bar{C}\bar{C}_g \nabla \eta^{(0)}] + \mu^2 \bar{k}^2 \bar{C}\bar{C}_g [\eta^{(2)} + \beta^{(1)} \eta^{(1)} \\ + 2\alpha^{(1)} \eta^{(1)} + \beta^{(2)} \eta^{(0)} + 2\beta^{(1)} \alpha^{(1)} \eta^{(0)} + \alpha^{(1)2} \eta^{(0)} + 2\alpha^{(2)} \eta^{(0)}] = 0 \end{aligned} \tag{23}$$

.....

where  $\mu$  is treated as frequency independent. By considering (21) in (22) and, (21) and (22) in (23), Eqs. (22) and (23) may be simplified to give

$$\nabla \cdot (\bar{C}\bar{C}_g \nabla \eta^{(1)}) + \mu^2 \bar{k}^2 \bar{C}\bar{C}_g \eta^{(1)} + \bar{C}\bar{C}_g \nabla \beta^{(1)} \cdot \nabla \eta^{(0)} + 2\mu^2 \bar{k}^2 \bar{C}\bar{C}_g \alpha^{(1)} \eta^{(0)} = 0 \tag{24}$$

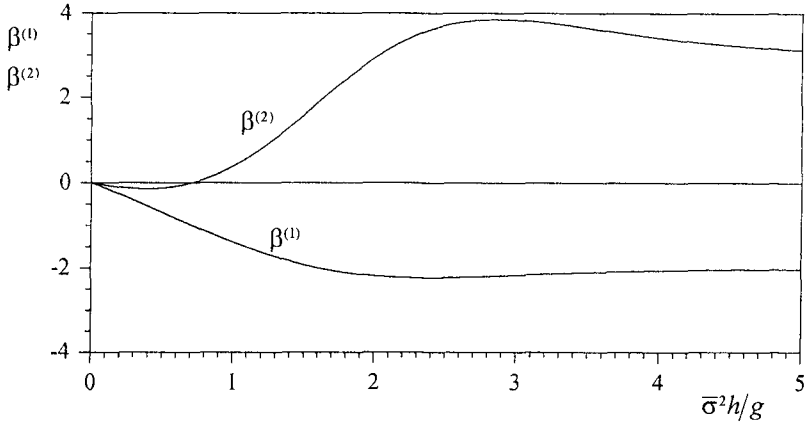


Fig. 2: Variation of  $\beta^{(1)}$  and  $\beta^{(2)}$  versus  $\bar{\sigma}^2 h/g$

$$\nabla \cdot (\bar{C}\bar{C}_g \nabla \eta^{(2)}) + \mu^2 \bar{k}^2 \bar{C}\bar{C}_g \eta^{(2)} + \bar{C}\bar{C}_g [\nabla \beta^{(1)} \cdot \nabla \eta^{(1)} - \beta^{(1)} \nabla \beta^{(1)} \cdot \nabla \eta^{(0)} + \nabla \beta^{(2)} \cdot \nabla \eta^{(0)}] + 2\mu^2 \bar{k}^2 \bar{C}\bar{C}_g [2\alpha^{(1)} \eta^{(1)} + \alpha^{(1)} \alpha^{(1)} \eta^{(0)} + 2\alpha^{(2)} \eta^{(0)}] = 0 \tag{25}$$

Eqs. (21), (24) and (25) may be used to solve  $\eta^{(0)}$ ,  $\eta^{(1)}$ ,  $\eta^{(2)}$  and, therefore,  $\eta$  approximately. It is obvious that the zeroth order equation (21) describes the motion of the principal wave. This implies that the representative wave method is the leading order approximation of the present approach. Eqs. (24) and (25) govern the higher order modifications. The higher order equations all include a source term which depends on the lower order solutions. We also note that the equations for all orders can be expressed in a unified form as follows:

$$\nabla \cdot (\bar{C}\bar{C}_g \nabla \eta^{(m)}) + \mu^2 \bar{k}^2 \bar{C}\bar{C}_g \eta^{(m)} + q^{(m)} = 0 \quad (m = 0, 1, 2, \dots) \tag{26}$$

where

$$q^{(0)} = 0 \tag{27}$$

$$q^{(1)} = \bar{C}\bar{C}_g \nabla \beta^{(1)} \cdot \nabla \eta^{(0)} + 2\mu^2 \bar{k}^2 \bar{C}\bar{C}_g \alpha^{(1)} \eta^{(0)} \tag{28}$$

$$q^{(2)} = \bar{C}\bar{C}_g [\nabla \beta^{(1)} \cdot \nabla \eta^{(1)} - \beta^{(1)} \nabla \beta^{(1)} \cdot \nabla \eta^{(0)} + \nabla \beta^{(2)} \cdot \nabla \eta^{(0)}] + 2\mu^2 \bar{k}^2 \bar{C}\bar{C}_g [2\alpha^{(1)} \eta^{(1)} + \alpha^{(1)} \alpha^{(1)} \eta^{(0)} + 2\alpha^{(2)} \eta^{(0)}] \tag{29}$$

.....

**Boundary Conditions**

We consider two kinds of boundaries. The first kind is where the free surface oscillation is given by

$$\eta = ae^{i\theta} \tag{30}$$

where  $a$  is the amplitude and  $\theta$  the phase. For each order, we require

$$\eta^{(0)} = ae^{i\theta} \tag{31}$$

$$\eta^{(m)} = 0 \quad (m \geq 1) \tag{32}$$

The second kind of boundary condition is assumed to be expressed in the following form:

$$\frac{\partial \eta}{\partial n} - i\lambda k\eta + i\nu k = 0 \tag{33}$$

where  $\lambda$  and  $\nu$  are constants related to the physical situation (Yu et al., 1992). In particular, an impermeable boundary is represented by  $\lambda = 0$  and  $\nu = 0$ .

Substituting (11) and (12) into (33) and collecting all the terms for each order of  $\epsilon$ , we obtain

$$\frac{\partial \eta^{(0)}}{\partial n} - i\lambda \bar{k} \eta^{(0)} + i\nu \bar{k} = 0 \tag{34}$$

$$\frac{\partial \eta^{(1)}}{\partial n} - i\lambda \bar{k} \eta^{(1)} - i\lambda \alpha^{(1)} \bar{k} \eta^{(0)} + i\nu \alpha^{(1)} \bar{k} = 0 \tag{35}$$

$$\frac{\partial \eta^{(2)}}{\partial n} - i\lambda \bar{k} \eta^{(2)} - i\lambda \bar{k} (\alpha^{(1)} \eta^{(1)} + \alpha^{(2)} \eta^{(0)}) + i\nu \alpha^{(2)} \bar{k} = 0 \tag{36}$$

.....

The above equations have the following unified form:

$$\frac{\partial \eta^{(m)}}{\partial n} - i\lambda \bar{k} \eta^{(m)} + p^{(m)} = 0 \quad (m = 0, 1, 2, \dots) \tag{37}$$

where

$$p^{(0)} = i\nu \bar{k} \tag{38}$$

$$p^{(1)} = -i\lambda \alpha^{(1)} \bar{k} \eta^{(0)} + i\nu \alpha^{(1)} \bar{k} \tag{39}$$

$$p^{(2)} = -i\lambda \bar{k} (\alpha^{(1)} \eta^{(1)} + \alpha^{(2)} \eta^{(0)}) + i\nu \alpha^{(2)} \bar{k} = 0 \tag{40}$$

$$\dots \tag{41}$$

**FINITE ELEMENT METHOD**

It is known that the solution of the elliptic equation (26) when subjected to the boundary condition (37) stagnates the following functional in terms of  $\eta^{(m)}$ :

$$\begin{aligned} \Pi = \int_{\Omega} \left[ \frac{1}{2} \bar{C} \bar{C}_g \nabla \eta^{(m)} \cdot \nabla \eta^{(m)} - \frac{1}{2} \mu^2 \bar{k}^2 \bar{C} \bar{C}_g \eta^{(m)} \eta^{(m)} - q^{(m)} \eta^{(m)} \right] d\Omega \\ + \int_{\Gamma_2} \left[ -\frac{1}{2} i \lambda \bar{k} \bar{C} \bar{C}_g \eta^{(m)} \eta^{(m)} + p^{(m)} \eta^{(m)} \right] d\Gamma \end{aligned} \tag{42}$$

where  $\Omega$  is the domain of interest and  $\Gamma_2$  the part of the boundary of  $\Omega$  where (37) must be satisfied. For a finite element solution of  $\eta^{(m)}$  which stagnates  $\Pi$  in some approximate sense, we discretize the domain  $\Omega$  into elements and let all the elements be related to each other through the nodes located on the common boundaries of the elements. Denote

$$\begin{aligned} \Pi^e = \int_{\Omega^e} \left[ \frac{1}{2} \bar{C} \bar{C}_g \nabla \eta^{(m)} \cdot \nabla \eta^{(m)} - \frac{1}{2} \mu^2 \bar{k}^2 \bar{C} \bar{C}_g \eta^{(m)} \eta^{(m)} - q^{(m)} \eta^{(m)} \right] d\Omega \\ + \int_{\Gamma^e} \left[ -\frac{1}{2} i \lambda \bar{k} \bar{C} \bar{C}_g \eta^{(m)} \eta^{(m)} + p^{(m)} \eta^{(m)} \right] d\Gamma \end{aligned} \tag{43}$$

where  $\Omega^e$  is an element and  $\Gamma^e$  its boundary,  $\lambda = 0$  and  $\nu = 0$  if  $\Gamma^e \notin \Gamma_2$ . Eq. (42) can then be written as

$$\Pi = \sum_e \Pi^e \tag{44}$$

We introduce the primed indices  $1', 2', \dots, N'$  in the anti-clockwise fashion in each element for locally numbering the nodes related to the element and assume the global nodal numbers of  $1', 2', \dots, N'$  to be  $n_{1'}, n_{2'}, \dots, n_{N'}$ , respectively. As interpolation functions  $L_{i'}^e(x, y)$  ( $i' = 1', 2', \dots, N'$ ) are defined in each element, any function  $F(x, y)$  in  $\Omega^e$  can be approximated in terms of its nodal values  $F_{1'}, F_{2'}, \dots, F_{N'}$  as

$$F(x, y) = L_{i'}^e F_{i'} \tag{45}$$

where the summation convention is implicit. Therefore,  $\Pi^e$  can be partially evaluated so as to give

$$\Pi^e = \frac{1}{2} K_{i'j'}^e \eta_{i'}^{(m)} \eta_{j'}^{(m)} + f_{j'}^{(m)e} \eta_{j'}^{(m)} \tag{46}$$

where  $K_{i'j'}^e$  is a  $N' \times N'$  matrix depending on the interpolation functions as well as the local features of the principal wave. With the following matrix

$$T_{i'i}^e = \begin{cases} 1 & \text{when } n_{i'} = i \\ 0 & \text{when } n_{i'} \neq i \end{cases} \quad (i' = 1', 2', \dots, N' \text{ and } i = 1, 2, \dots, N) \tag{47}$$

where  $N$  is the total number of nodes, we have

$$\eta_{i'}^{(m)} = T_{i'i}^e \eta_i^{(m)} \tag{48}$$

Eq. (46) can then be expressed by

$$\Pi^e = \frac{1}{2} \left( K_{i'j'}^e T_{i'i}^e T_{j'j}^e \right) \eta_i^{(m)} \eta_j^{(m)} + \left( f_{j'}^{(m)e} T_{j'j}^e \right) \eta_j^{(m)} \tag{49}$$

Therefore,

$$\Pi = \frac{1}{2} \left( \sum_e K_{i'j'}^e T_{i'i}^e T_{j'j}^e \right) \eta_i^{(m)} \eta_j^{(m)} + \left( \sum_e f_{j'}^{(m)e} T_{j'j}^e \right) \eta_j^{(m)} \tag{50}$$

$$= \frac{1}{2} K_{ij} \eta_i^{(m)} \eta_j^{(m)} + F_j^{(m)} \eta_j^{(m)} \tag{51}$$

where

$$K_{ij} = \sum_e K_{i'j'}^e T_{i'i}^e T_{j'j}^e \quad \text{and} \quad F_j^{(m)} = \sum_e f_{j'}^{(m)e} T_{j'j}^e \tag{52}$$

From the necessary condition for  $\Pi$  to be stagnated:

$$\frac{\delta \Pi}{\delta \eta_j^{(m)}} = 0 \tag{53}$$

we obtain the following linear algebraic equations:

$$K_{ij} \eta_i^{(m)} + F_j^{(m)} = 0 \tag{54}$$

since the matrix  $K_{ij}$  is symmetric. When modified so that the forced boundary condition is satisfied, Eq. (54) gives the nodal values of  $\eta^{(m)}$ . It may be noted that the matrix  $K_{ij}$  is independent of the order of perturbation. This implies that, if the LU decomposition method is utilized to solve the finite element equations, we need to carry out the decomposition only once for solving all the perturbation equations. The computational efforts involved in our numerical model are, therefore, equivalent to those required by the representative wave method.

### WAVE MOTION OVER AN ELLIPTIC SHOAL

We apply our numerical model to the study of the unidirectional and narrow-banded irregular wave transformation over an elliptic shoal, a problem which has been investigated by Vincent and Briggs (1989) and by Panchang et al. (1990) with different methods. The topography and the incident wave conditions in our study are made identical to the U4 case of Vincent and Briggs (1989) and Panchang et al. (1990) so that our numerical results may be verified. The computational domain is sketched in **Fig. 3**, where the shoal is centered at  $x = 0$  and  $y = 0$  and the perimeter of the shoal is described by



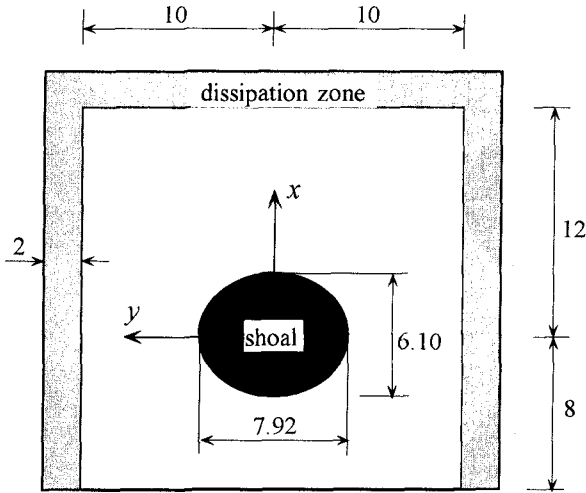


Fig. 3: The computational domain (all numbers are measured in meters)

$$\left(\frac{x}{3.05}\right)^2 + \left(\frac{y}{3.96}\right)^2 = 1 \tag{55}$$

The water depth is

$$h(x, y) = 0.9144 - 0.7620 \left\{ 1 - \left(\frac{x}{3.81}\right)^2 - \left(\frac{y}{4.95}\right)^2 \right\}^{\frac{1}{2}} \quad (\text{m}) \tag{56}$$

over the shoal and is 0.4572m in the rest of the domain.

The incident wave is assumed to have the following  $\sigma$ -spectrum:

$$S(\sigma) = \phi \psi g^2 \sigma \exp \left\{ -1.25 \left(\frac{\bar{\sigma}}{\sigma}\right)^4 + \ln \gamma \exp \left[ -\frac{(\sigma - \bar{\sigma})^2}{2\chi \bar{\sigma}^2} \right] \right\} \tag{57}$$

where  $S$  is so defined that the energy associated with the component waves of the angular frequency between  $\sigma$  and  $\sigma + \Delta\sigma$  is  $E = \rho g S(\sigma) \Delta\sigma$ ; the depth-effect parameter  $\phi$  is evaluated through

$$\phi = \begin{cases} 0.5\nu^2 & \text{for } \nu < 1 \\ 1 - 0.5(2 - \nu)^2 & \text{for } 1 \leq \nu \leq 2 \\ 1 & \text{for } \nu > 2 \end{cases} \tag{58}$$

where  $\nu = \sigma(h/g)^{1/2}$ ; the shape factor  $\chi$  is

$$\chi = \begin{cases} 0.07 & \text{for } \sigma < \bar{\sigma} \\ 0.09 & \text{for } \sigma \geq \bar{\sigma} \end{cases} \tag{59}$$

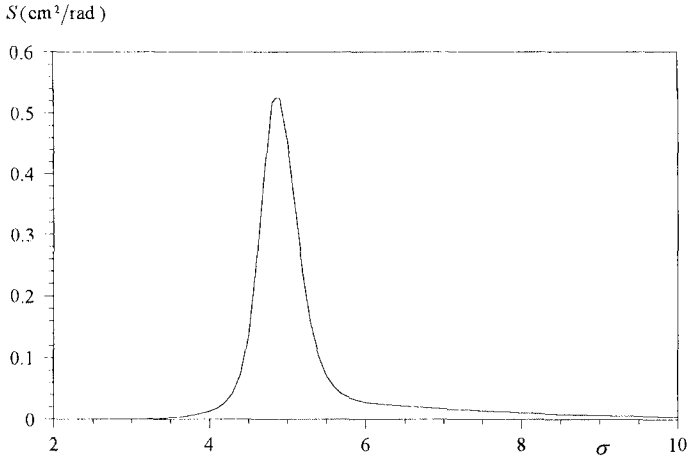


**Fig. 4:** The incident wave spectrum

$\gamma$  is the peak enhancement factor and  $\psi$  the Phillips constant. For the present case where  $\gamma = 20$ ,  $\psi = 0.00047$  and the peak angular frequency  $\bar{\sigma} = 4.833$ , the spectrum is demonstrated in **Fig. 4**. As it can be noted, most of the incident wave energy is banded between  $\sigma = 4$  and 6. It is then reasonable to represent the spectral incident wave by the superposition of the component waves with the following discrete angular frequencies:

$$\sigma_n = 4.0 + n\Delta\sigma \quad (n = 0, 1, \dots, 50) \tag{60}$$

where  $\Delta\sigma = 0.04$ . Following Longuet-Higgins (1957) we have

$$\tilde{\eta} = \sum_{n=0}^{50} a_n e^{i\theta_n} e^{i\sigma_n t} \tag{61}$$

where  $a_n = \sqrt{2S(\sigma_n)\Delta\sigma}$  is the amplitude of the  $n$ th component wave and  $\theta_n$  are random values with a uniform distribution between 0 and  $2\pi$ . The forced boundary condition for the  $n$ th component wave in our problem can then be specified as

$$\eta = a_n e^{i\theta_n} \tag{62}$$

The lateral and downwave boundaries in our problem should be totally transmissive, that is, the boundary conditions should be specified so that the outgoing waves are totally absorbed by the boundaries. This requirement can be approximately met through the following numerical installation. We place a two-meter

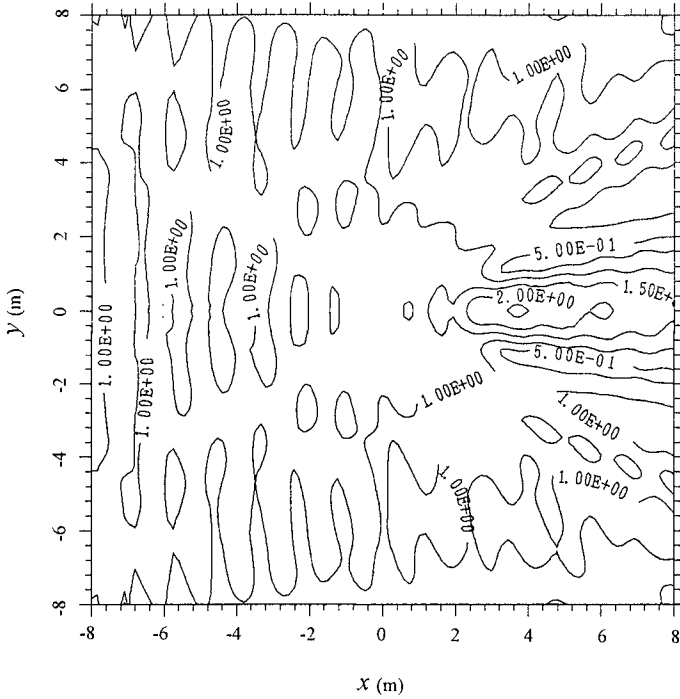


**Fig. 5:** Computed wave height distribution

dissipative layer with  $\mu = 1 + 0.5i$  along the transmissive boundaries. The function of the dissipative layer is as same as the wave absorber in a physical model. The artificial boundaries at  $y = \pm 12\text{m}$  are assumed to be impermeable and, therefore, the boundary conditions there are expressed by (33) with  $\lambda = 0$  and  $\nu = 0$ . The boundary at  $x = 14\text{m}$  is required to be non-reflective to the principal wave. The boundary condition can then be expressed by (33) with  $\lambda = 1$  and  $\nu = 0$ .

In the computation, the domain is discretized into triangular elements with a dimension equivalent to one-fifteenth of the principal wavelength over the flat bottom. Linear interpolation functions are employed. **Fig. 5** shows the resulted distribution of the significant wave height (normalized by the significant incident wave height  $H_0$ ). In **Fig. 6** we compare the computed wave height, at  $x = 2.28\text{m}$ , with the experimental data obtained by Vincent and Briggs (1989) and by Panchang et al. (1990). The agreement between the numerical solution

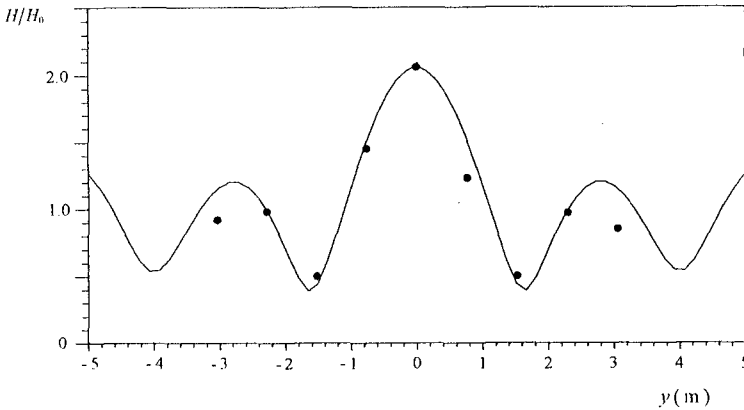


**Fig. 6:** Comparison of the computed wave height with experimental data

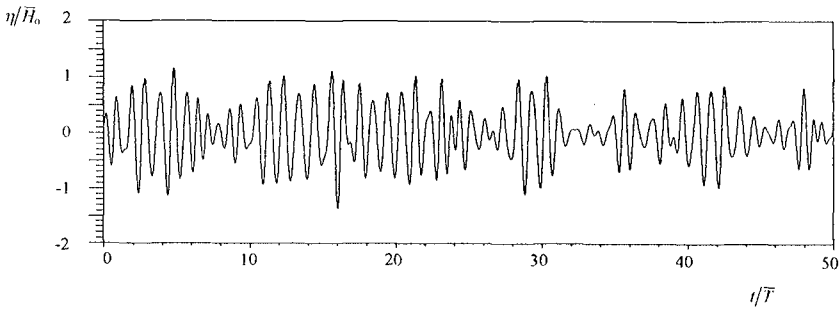


**Fig. 7:** Water surface elevation over the top of the shoal

and laboratory measurement is shown fairly satisfactory. In **Fig. 7** we plot the assembled irregular wave profile (normalized by the mean incident wave height  $\bar{H}_0$ ) over the top of the shoal.

## CONCLUSIONS

We presented a numerical model for the analysis of narrow-banded irregular wave transformation over gradually varying bottom topography. The model is based on the mild slope wave equation for component waves. By regular perturbation, the mild slope wave equation, which depends on the frequency of the component wave, leads to the perturbation equations in terms of the principal wave parameters. The finite element method has been suggested for numerical

solutions of the perturbation equations. Since the matrix of the linear algebraic finite element equations depends on neither the component wave properties nor the order of the perturbation, the computational efforts involved in the present model is equivalent to those required by the representative wave method. The model has been applied to the computation of the wave motion over an elliptic shoal. Satisfactory agreement between the numerical solution and experimental data has been obtained.

## REFERENCES

- Berkhoff, J. W. C. (1972). Computation of combined refraction-diffraction. *Proc. 13th Conf. on Coast. Engrg.*, 471-490.
- Dalrymple, R. A., Kirby, J. T. and Hwang, P. A. (1984). Wave diffraction due to areas of energy dissipation, *J. Wtrwy., Port, Coast. and Oc. Engrg.*, ASCE, 110(1), 67-79.
- Goda, Y. (1985). *Random Seas and Design of Maritime Structures*. University of Tokyo Press, 323p.
- Horikawa, K. (1989). *Nearshore Dynamics and Coastal Processes—Theory, Measurement and Predictive Model*, University of Tokyo Press, 522p.
- Karlsson, T. (1969). Refraction of continuous ocean wave spectra, *Proc. Amer. Soc. Civ. Engrs.*, 95(WW4), 437-448.
- Longuet-Higgins, M. S. (1957). The statistical analysis of a random, moving surface, *Phil. Trans. Roy. Soc. London*, 249(A), 321-387.
- Panchang V. G., Wei, G., Pearce, B. R. and Briggs, M. J. (1990). Numerical simulation of irregular waves propagation over shoal, *J. Wtrwy., Port, Coast. and Oc. Engrg.*, ASCE, 116(3), 324-340.
- Vincent, C. L. and Briggs, M. J. (1989). Refraction and diffraction of irregular waves over a mound. *J. Wtrwy., Port, Coast. and Oc. Engrg.*, ASCE, 115(2), 269-284.
- Yu, X., Isobe, M. and Watanabe, A. (1992). Finite element solution of wave field around structures in nearshore zone, *Cost. Engrg. in Japan*, JSCE, 35(1), 21-33.

## CHAPTER 56

# PERFORMANCE OF A SPECTRAL WIND-WAVE MODEL IN SHALLOW WATER

Gerbrant Ph. van Vledder <sup>1</sup>, John G. de Ronde <sup>2</sup> and Marcel J.F. Stive <sup>1,3</sup>

### Abstract

A full spectral third-generation wave prediction model has been extended with formulations for surf breaking and nonlinear triad interactions and a first assessment of its performance against shallow water wave data has been examined. The formulation for wave energy loss by surf-breaking in shallow water is based on the expression of Battjes and Janssen (1978), which has heuristically been modified to predict the energy loss per spectral component. The source term for nonlinear triad interactions was taken from Abreu et al. (1992). Results of the extended model have been compared against laboratory and field data. The results of the model computations indicate that surf breaking and triad interactions are important processes in the coastal zone. Surf breaking is mainly responsible for the decay of wave energy, whereas triad interactions are mainly responsible for changes in the mean wave period. The applicability of the Abreu formulation is limited and needs further attention.

### Introduction

The modelling of wind waves in shallow water is important for many coastal engineering applications in the nearshore zone. Especially the prediction of both the significant wave height and the mean wave period is still difficult with the presently available wave process formulations. A major problem is that most of the interactions between waves, bottom and currents are nonlinear and poorly understood. This is particularly true for directionally spread random waves in areas with a varying bottom topography.

---

1 Delft Hydraulics, PO Box 152, 8300 AD Emmeloord, The Netherlands.

2 National Institute for Coastal and Marine Management, PO Box 20907, 2500 EX, The Hague, The Netherlands.

3 Netherlands Centre for Coastal Research, Delft University of Technology, Faculty of Civil Engineering, PO Box 5048, 2600 GA, Delft, The Netherlands.

A number of model classes exists to compute wave conditions in the coastal zone (cf. Hamm et al., 1993). Commonly used models are the spectral and probabilistic models because they are relatively efficient to use, partly because they neglect diffraction effects. Such a model is also the topic of this paper. More advanced models solve Boussinesq type equations in the time domain. An advantage of such models is that they are able to model processes in a more attractive, more physical way, and also the interactions between the different processes. A disadvantage, however, is that they are rather time-consuming in comparison with spectral models.

Depending on the dimensionless water depth  $kd$ , different physical effects are important. In deep water ( $kd > 1$ ) the waves are mainly influenced by three physical processes: wave growth by wind, dissipation of energy by white-capping and nonlinear quadruplet wave-wave interactions. In water of intermediate depth ( $kd \approx 1$ ) additional effects become important such as bottom friction and depth- and current refraction. In shallow water ( $kd < 1$ ) also the effects of surf breaking, triad interactions and the effect of waves on currents become noticeable.

The concept of modelling the wave field in terms of the wave spectrum was introduced by Gelci et al. (1957). Since then, many spectral wave models have been developed which are usually classified in terms of their generation, which has mainly do to with the treatment of the nonlinear quadruplet wave-wave interactions and the degrees of freedom of the spectral representation of the wave field.

The first generation of spectral wave models described the evolution of the wave field in terms of parameterized spectra using simple rules, with that implicitly incorporating the effects of nonlinear wave-wave interactions. Spectral models of the second generation incorporated some effects of nonlinear interactions, but they still put limitations to the spectral shape. Only by the development of the discrete interaction approximation for nonlinear quadruplet interactions (Hasselmann et al., 1985) it became possible to develop models of the third generation. Such models explicitly compute all physical effects and they do not impose limitations to the spectral shape. The first full spectral wave model has been developed by the WAM group (WAMDI, 1988). The concept of the WAM model has been extended by Tolman (1991) to account for the effect of instationary current and water level fields. The WAM model can be applied in areas with deep or intermediate water depths, but not in shallow water because it lacks descriptions for typical shallow water processes such as surf breaking and nonlinear triad interactions.

A second generation model for shallow water was described by Holthuijsen et al. (1989). This model, which is parametric in frequency and discrete in direction, includes a formulation for surf breaking but not one for triad interactions. The formulation for wave breaking has been verified against laboratory experiments by Dingemans et al. (1986). Since this model uses one characteristic frequency per direction sector it is not always able to predict the change of the mean wave period in areas with a varying bottom topography. The only way to properly predict the

change of the mean wave period with spectral models is by using a full spectral third-generation wave model which includes all physical processes affecting the waves in shallow water.

The above physical processes have various effects on the mean wave period in shallow water. The main effect of bottom friction is that it reduces wave energy in the lower frequencies and they will decrease the mean wave period, whereas quadruplet wave-wave interactions increase the mean wave period (cf. Young and van Vledder, 1993). Little is known about the spectral modelling of source terms for energy dissipation in shallow water due to breaking waves. The well-known Battjes-Janssen (1978) model predicts the rate of change of the total amount of wave energy, but no information is given about its spectral distribution. Recent experiments by Beji and Battjes (1993), however, indicate that the wave breaking process does not change the shape of the spectrum. Instead, nonlinear triad wave-wave interactions change the spectral shape by the generation of both lower and higher harmonic components. Recently a model was presented by Abreu et al. (1992) which models these triad wave-wave interactions in the spectral domain. Although this model is based on inconsistent assumptions, it is nonetheless considered as a first step in the development of a spectral source term for triad wave-wave interactions.

The purpose of this paper is to further extend the concept of spectral wave modelling in shallow water by introducing the newly available modelling techniques for energy dissipation by breaking waves and nonlinear triad wave-wave interactions, and to give a first assessment of these processes against laboratory and field measurements. In addition, the relative importance of various physical processes in shallow water is assessed.

The present study has been carried out within the framework of the HYDRA project, which is aimed at the determination of hydraulic boundary conditions along the Dutch coast. For the present study DELFT HYDRAULICS's third-generation wave prediction model PHIDIAS has been used.

## 2 The PHIDIAS wave model

The third-generation wave model PHIDIAS has been developed by DELFT HYDRAULICS for application on oceanic, shelf-sea and coastal zone scales, and for application in deep, intermediate depth and shallow water. In addition, it has successfully been implemented in a real-time data assimilation system. The PHIDIAS model can be applied in areas with a spatially-varying bottom topography and time-dependent current fields.

The PHIDIAS model is based on a spectral description of the sea surface in terms of wave action density, which is a convenient description of the wave field in the presence of currents. Wave action density is considered in the PHIDIAS model as a



function of the location  $x$  and  $y$ , wave number  $k$  and direction  $\theta$ . The PHIDIAS model solves the time-dependent action balance equation (cf. Hasselmann et al., 1973):

$$\frac{\partial N}{\partial t} + \frac{\partial}{\partial x}(\dot{x}N) + \frac{\partial}{\partial y}(\dot{y}N) + \frac{\partial}{\partial k}(\dot{k}N) + \frac{\partial}{\partial \theta}(\dot{\theta}N) = S \quad (1)$$

in which  $N = N(x, y, k, \theta; t)$  is the action density defined as the energy density divided by the relative frequency  $\sigma$ . The dot-terms in Eq. (1) are the spectral velocities which follow from linear wave theory (cf. Mei, 1983):

$$\dot{x} = c_{g,x} + U_x \quad (2)$$

$$\dot{y} = c_{g,y} + U_y \quad (3)$$

$$\dot{k} = - \left[ \frac{\partial \sigma}{\partial d} \frac{\partial d}{\partial s} + \vec{k} \cdot \frac{\partial \vec{U}}{\partial s} \right] \quad (4)$$

$$\dot{\theta} = - \frac{1}{k} \left[ \frac{\partial \sigma}{\partial d} \frac{\partial d}{\partial n} + \vec{k} \cdot \frac{\partial \vec{U}}{\partial n} \right] \quad (5)$$

where  $d$  is the local water depth,  $c_{g,x}$  and  $c_{g,y}$  the  $x$ - and  $y$ -components of the group velocity,  $U_x$  and  $U_y$  the velocity components of the ambient flow field, and  $\vec{s}$  and  $\vec{n}$  the components of unit vectors in the direction of and the direction perpendicular to the direction  $\theta$  of a wave component.

The source term  $S$  on the right-hand side of equation (1) contains expressions of all physical processes that affect the action density of a spectral wave component. For deep water applications the source term  $S$  contains state-of-the art expressions for wave growth by the action of the wind (Snyder et al., 1981), dissipation by white-capping (Komen et al., 1984) and nonlinear quadruplet interactions computed with the discrete interaction approximation of Hasselmann et al. (1985). In intermediate water depth applications, the above deep water source terms are scaled as described in WAMDI (1988) and supplemented with state-of-the art formulations for bottom friction (Hasselmann et al, 1973; Madsen et al., 1988). For shallow water, the PHIDIAS model also uses source terms for surf breaking and triad wave-wave interactions. The expressions for surf breaking and triad interactions in a full spectral wave model are recently developed and need some explanation.

A method incorporating the dissipation of wave energy by breaking waves was given by Young (1988). In this method a limit is imposed on the total wave energy and the excess of wave energy is removed from the lowest energy containing waves. This is a rather coarse method because it only removes energy from the lowest

frequencies and because it is not formulated in terms of a source term, i.e. a dissipation rate.

A successful model for computing the energy dissipation in random waves by wave breaking in shallow water was given by Battjes and Janssen (1978). This dissipation model is formulated in terms of the rate of change of the total wave energy  $E_{tot}$ :

$$\frac{\partial E_{tot}}{\partial t} \approx -\frac{1}{4} \alpha f_p Q_b H_{max}^2 \quad (6)$$

where  $\alpha$  is a factor of about 1,  $f_p$  the peak frequency,  $Q_b$  a measure for the fraction of breaking waves and  $H_{max}$  a maximum wave height. The parameter  $Q_b$  is computed from :

$$\frac{1 - Q_b}{\ln(Q_b)} = \left\{ \frac{H_{rms}}{H_{max}} \right\}^2 \quad (7)$$

in which  $H_{rms}$  is the root mean square wave height, which can be computed from the total wave variance  $\sigma^2$  according to:

$$H_{rms} = \sqrt{8} \sigma \quad (8)$$

In the Battjes-Janssen model the maximum wave height is computed according to a combined steepness and depth-limited breaking criterion (Battjes and Stive, 1985):

$$H_{max} = \frac{\gamma_1}{k_p} \tanh \left( \frac{\gamma_2}{\gamma_1} k_p h \right) \quad (9)$$

in which  $\gamma_1$  and  $\gamma_2$  are coefficients and where  $k_p$  is the peak wave number. In this expression the coefficient  $\gamma_1$  controls the breaking on wave steepness and  $\gamma_2$  the depth-limited wave breaking. For application in a full spectral wave model three adaptations are needed of the original Battjes-Janssen model. Firstly, an assumption has to be made about the spectral distribution of wave energy by breaking waves and secondly, the criterion for computing  $H_{max}$  should be adapted to avoid the double counting of breaking on wave steepness in the presence of a white-capping dissipation source term, and thirdly to replace the peak frequency  $f_p$  with a more stable measure of a representative frequency, for instance by the mean frequency  $f_{m01}$ .

The most simple method of distributing the energy dissipation by breaking waves over the spectrum is to assume that this dissipation rate is in proportion to the energy density of each spectral component:

$$S_{brk} = -\frac{1}{4} \alpha f_{m01} Q_b H_{max}^2 \frac{E(k, \theta)}{E_{tot}} \quad (10)$$

This method seems to be supported by laboratory experiments of Beji and Battjes (1993). The criterion for computing the maximum wave height is simplified to:

$$H_{\max} = \gamma_2 h \quad (11)$$

An advantage of expression (11) is that it becomes negligible for deep water. The above formulation has also been included in a recently developed spectral wave model for the coastal zone, developed by Delft University of Technology (Holthuijsen et al., 1993).

The triad interactions are computed by the method proposed by Abreu et al. (1992) on the basis of their equation (34). Their model contains the parameter  $kd_{\text{lim}}$  which limits the range in which interactions between triads can take place. Based on theoretical arguments they set this limit at  $kd_{\text{lim}} = \pi/10$ , but on the basis of a comparison against field measurements they suggest that this limit should be close to 1. Triad interactions conserve energy and they do not directly affect the significant wave height.

### Performance studies

A number of studies has been performed to compare the extended PHIDIAS wave model in shallow water conditions against two sets of laboratory and one set of field data. The laboratory data were collected in wave flumes, using mechanically-generated uni-directional random waves. Field data were obtained from the Egmond site along the coast of the Netherlands for the case of a double bar system. The primary objective of these studies was to investigate the performance of the wave model with respect to the prediction of both the significant wave height and mean wave period. For the field experiment also the relative importance of the modelled physical processes was examined.

The first set of laboratory data were collected by Battjes and Janssen (1978). For the present study results of their experiment numbers 13 and 15 were used, corresponding to wave propagation over an underwater bar. The incident wave conditions and parameter settings are summarized in Table 1. In the Battjes-Janssen experiments no attention was paid to changes in wave periods, and related results will not be shown here.

Experiment number	$H_{rms0}$ (m)	bar-depth (m)	$\gamma_1$	$\gamma_2$	$f_p$ (Hz)
13	0.113	0.267	0.88	0.75	0.497
15	0.154	0.120	0.88	0.75	0.530

The results obtained with the PHIDIAS model are shown in Fig. 1. The computed data for the significant wave height show good agreement with the measured data.

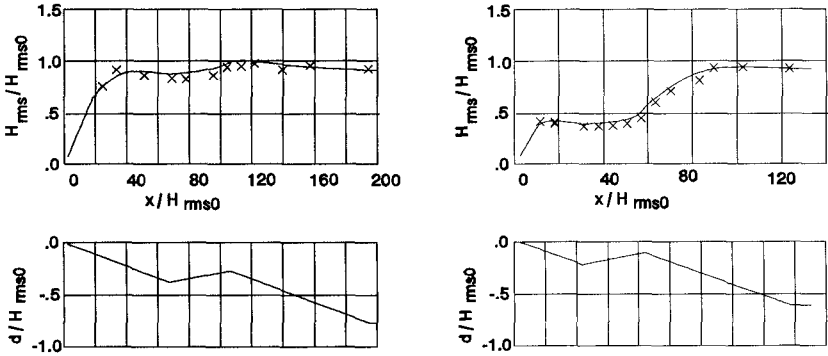
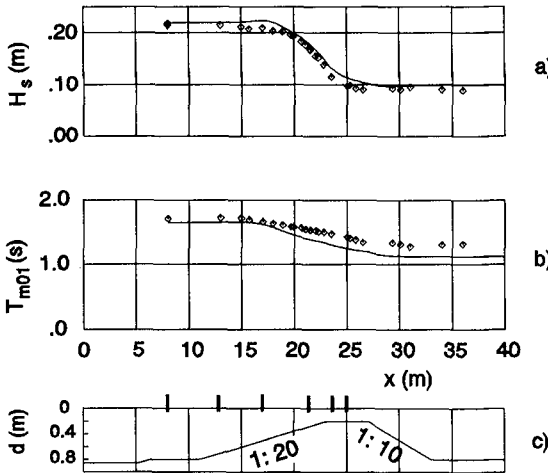


Figure 1: Observed (crosses) and computed (solid line) variation of the root mean square wave height  $H_{rms}$  and water depth  $d$ , normalized with the deep water rms wave height  $H_{rms0}$ , for the cases 13 (left panel) and 15 (right panel) of Battjes and Janssen (1978).

The second set of laboratory wave data were collected in the Schelde flume of DELFT HYDRAULICS in the framework of the MAST program of the European Community. One of these experiments consisted of random wave propagation over an underwater bar. Detailed spectral measurements were performed at 26 locations along the wave flume.



a) Figure 2: Observed (diamonds) and computed (solid line) variation of significant wave height ( $H_s$ ) and mean wave period ( $T_{m01}$ ) in Schelde flume experiment. The tick marks in panel c) refer to the locations for which frequency spectra are shown in Fig. 3.

The input wave conditions comprised a JONSWAP spectrum with a peak period  $T_p = 1.77$  s, a significant wave height  $H_s = 0.22$  m and a peak enhancement factor  $\gamma = 3.3$ . After a number of trial runs with different parameter settings for surf breaking and the triad interactions, good agreement was found for the settings  $kd_{lim} = 0.75$  and  $\gamma_2 = 0.75$ . The cross-section of this flume and the results for the change in significant wave height and the mean wave period ( $T_{m01}$ ) are shown in Fig. 2. The observed and computed frequency spectra for six locations are shown in Fig. 3.

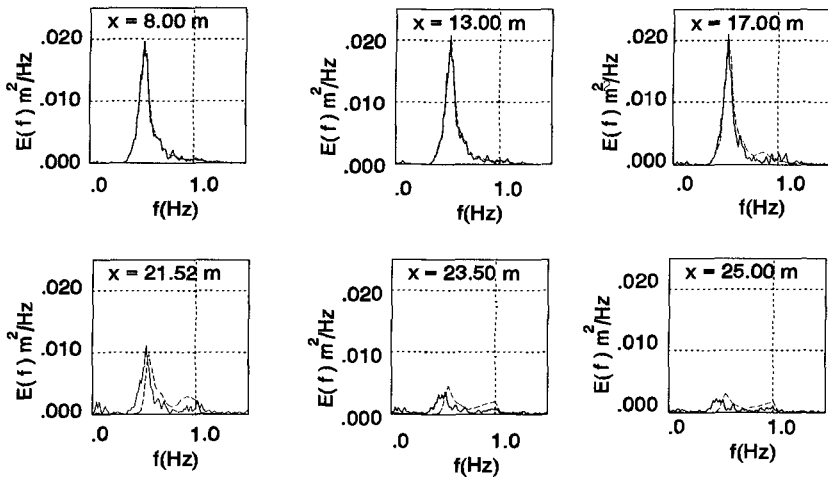


Figure 3: Observed (solid line) and computed (dashed line) frequency spectra in Schelde flume experiment at 6 locations.

The results of the computations show good agreement, not only for the significant wave height but also for the change in the mean wave period. As can be seen in Fig. 3, the change in the mean wave period is due to the generation of a second spectral peak in the vicinity of twice the peak frequency. The generation of this second peak is basically due to the effect of triad interactions. This was demonstrated by performing a computation in which the effect of triad interactions was omitted. Results of other computations (not shown here) with different parameters setting for the triad interactions indicate that the generation of the second spectral peak is controlled by the choice of the upper limit  $kd_{lim}$ . In the case of a high value, the second spectral peak showed excessive growth, such that this peak became larger than the first spectral peak.

Field data were collected for a site along the coast of the Netherlands near the town of Egmond. The bottom profile consists of almost parallel bottom contours with a double bar system. Wave data were collected at four locations along a ray protruding into the sea. The bottom profile of this ray and the locations of wave measurement

instruments are shown in Fig. 4. The outer measurement system consisted of a WAVEC, a directional wave buoy. Closer to the coast three wave poles were used which collected time series of the surface elevation. Directional information was not obtained with the wave poles. Unfortunately, no reliable wave data were obtained with wave pole 2.

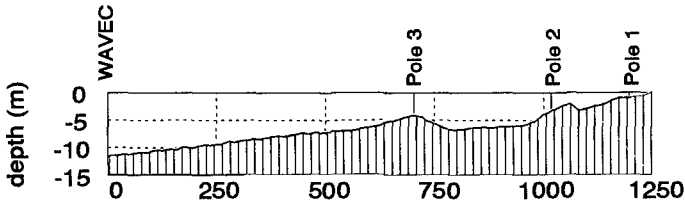


Figure 4: Bottom profile and location of measuring instruments along the Egmond ray.

The wave characteristics observed with the WAVEC buoy were transformed into two-dimensional wave spectra that were used as the boundary conditions for wave computations with the PHIDIAS model. Per frequency a directional distribution was reconstructed on the basis of the mean wave direction and directional spreading according to the  $\cos^{2s}(\theta/2)$ -model. Wind and water level information was obtained from nearby coastal stations.

For a number of situations wave model computations have been performed with the PHIDIAS model with the objectives of predicting the changes in the spectral shape and of studying the relative importance of the various physical processes in the coastal zone.

Results are presented of one computation for the situation on October 16, 1992, 3 hours, the wind speed was 5 m/s, blowing to the shore. The variation of the significant wave height, mean wave period, incident wave direction and directional spreading are shown in Fig. 5. This figure clearly shows the effect of the underwater bars on the above-mentioned wave parameters. As expected, energy dissipation takes place on the bars and in the area closer to the coast. The spatial variation of the incident wave direction and directional spreading resemble the bottom profile. The waves turn towards the coast and the directional spreading becomes smaller as the water becomes shallower, two effects which are both in agreement with the theoretical expectation.

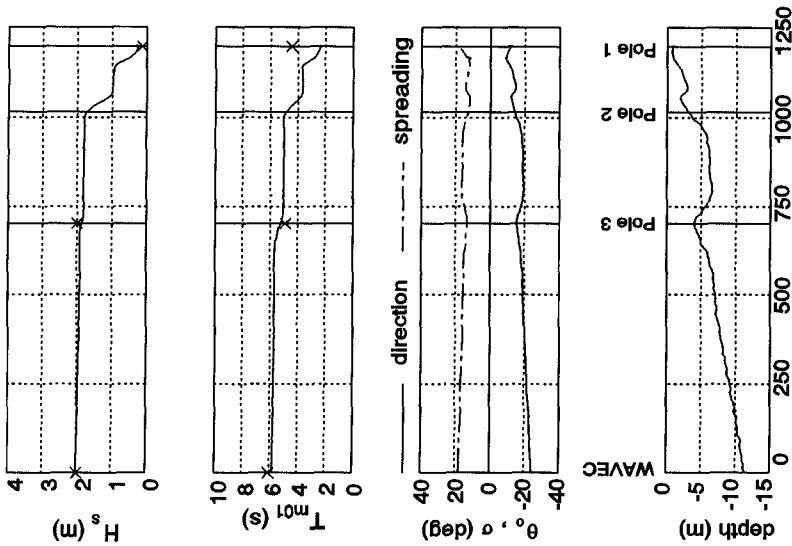


Figure 5: Observed (crosses) and computed (lines) variation of significant wave height ( $H_s$ ), mean wave period ( $T_{m01}$ ), mean wave direction ( $\theta_0$ ) and directional spreading ( $\sigma$ ) along the Egmond ray on October 16, 1992, 3 hours.

A comparison between the computational results with the measurements shows good agreement for the significant wave height, but not for the mean wave period. As can be seen in Fig. 6, the change of the mean wave period is due to the growth of a strong second spectral peak which reduces the mean wave period. Different parameter settings for the triad interactions were tried to obtain better agreement with the observations. However, this was not possible. The origin of the observed second spectral peak at wave pole 3 could not be predicted with the present implementation of the triad interactions. A closer look at the computational results revealed that this second peak could not be generated by the effect of wind. Clearly, the Abreu model is not capable of handling this situation.

The results of the computations for the Egmond site were also analyzed with respect to the strength of the various source terms, representing the various physical processes. The strength of a source term is defined as the integral over all spectral bins. For the nonlinear interaction source terms (quadruplets and triads) the integral over the absolute values was taken because these processes conserve energy. For the same case as above, the spatial variation of the strength of each source term is shown in Fig. 7. For the present case, the source terms for surf breaking and triads interactions are dominant over all other source terms. It can be seen that the strength

of all source terms is influenced by the local water depth. The wind input source function increases in strength because the waves are slowed down on the bar systems such that the relative wind speed increases. All dissipation source terms become stronger (more negative) over the bars, which is an effect that can also be seen in the strength of the nonlinear interaction source terms.

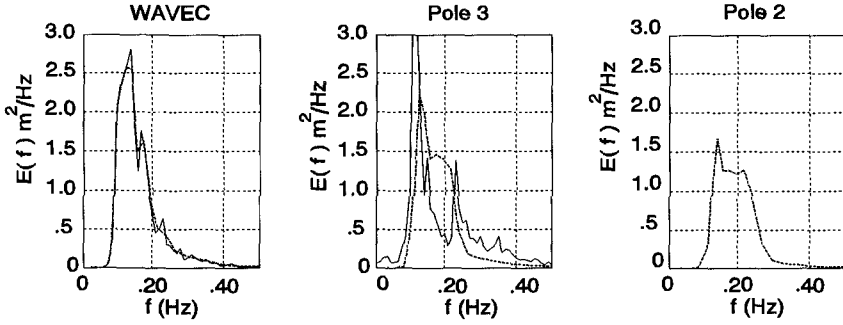


Figure 6: Observed (solid line) and computed (dashed line) frequency spectra along Egmond ray on October 16, 1992, 3 hours.

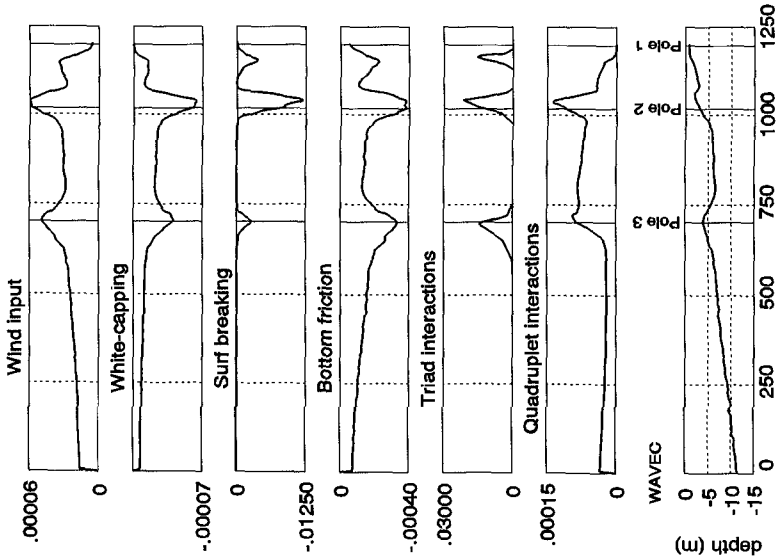


Figure 7: Computed spatial variation of the magnitude of the various physical processes for the Egmond computation of October 16, 1992, 3 hours.



## Discussion

The computational results obtained with the extended PHIDIAS wave model show good agreement with measurements regarding the prediction of the significant wave height in situations where surf breaking plays a dominant role. This is not surprising since the source term for surf breaking is based on a well-tested dissipation model (Battjes and Janssen, 1978; Battjes and Stive, 1985). The spectral distribution of dissipation by surf breaking in proportion to the existing energy density was straightforward and seems to be supported by measurements, although a theoretical basis is still missing.

In the coastal zone the change in the mean wave period is mainly due to the effect of triad interactions, especially if waves propagate over an underwater bar. In such a case relatively large changes occur over short distances. The results of the computations for the Schelde flume indicate that the inclusion of a source term for triad interactions is essential for computing a change in the mean wave period. The results for the Egmond site show that it was not possible to find a proper parameter setting for the triad interactions such that the change of the mean wave period would be predicted correctly. This implies that the spectral method of Abreu et al. (1992) for computing the triad interactions is incomplete.

The problem with the Abreu method is that it is based on inconsistent assumptions (Elgar et al., 1993). It is based on the non-dispersive, shallow water equations and a natural asymptotic closure for directionally spread, non-dispersive waves. A consequence is that only exact resonance is taken into account. Moreover, since the waves are assumed to be frequency non-dispersive, only triads containing waves travelling in the same direction are considered resonant. One of the results is that too much wave energy is transferred to higher frequencies resulting in an excessive growth of secondary spectral peaks. This was found to occur on a sloping beach. In the Schelde flume, however, just enough high frequency energy was produced on the bar to obtain a good prediction of the mean wave period. In the deeper water behind the bar the effect of the triad interactions became negligible.

The nonlinear interactions between quadruplets and triads conserve energy. They do not affect the total amount of wave energy, but only the spectral shape. In shallow water triad interactions are much stronger than quadruplet interactions, whereas in deep water the latter process is more dominant.

The present results provide quantitative information about the relative importance of the various physical processes in the nearshore zone, see also Battjes (1994). Such knowledge can be useful in the preparation of a computational run, e.g. by omitting the relative costly computation of the nonlinear quadruplet interactions.

## Conclusions and future work

The present study was aimed at obtaining a better understanding of modelling waves in shallow water. To that end a full spectral third-generation wave model was extended with formulations for surf breaking and triad interactions, and compared against shallow water wave data. The results of this study led to the following conclusions:

- 1 In the coastal zone surf breaking is dominant over the physical effects of wave growth, bottom friction and white-capping dissipation, and triad interactions are dominant over quadruplet interactions.
- 2 The spectral distribution of wave energy dissipation by surf breaking does not affect the spectral shape.
- 3 The inclusion of a source term for triad interactions is necessary for the prediction of changes in the mean wave period, especially if waves propagate over an underwater bar.
- 4 The method of Abreu et al. (1992) for the computation of triad interactions in a wave spectrum is based on inconsistent assumptions. An improved formulation for these interaction is needed, possibly by the inclusion of the proper frequency dispersion characteristics.

## Acknowledgements

The authors thank Yasser Eldeberky of Delft University of Technology and Maarten Dingemans of DELFT HYDRAULICS for discussions on triad interactions.

## References

- Abreu, M., A. Lazzara and E. Thornton, 1992: Nonlinear transformation of directional wave spectra in shallow water, *J. Geophys. Res.*, Vol. 97. No. C10, 15579-15589.
- Battjes, J.A., 1994: Shallow water wave modelling, *Proc. Int. Symp.: Waves - physical and numerical modelling*, Vancouver, 1-23.
- Battjes, J.A., and J.P.F.M. Janssen, 1978: Energy loss and set-up due to breaking of random waves. *Proc. 16th Int. Conf. on Coastal Eng.*, 569-587.
- Battjes, J.A. and M.J.F. Stive, 1985: Calibration and verification of a dissipation model for random breaking waves. *J. Geophys. Res.*, Vol. 90, C5, 9159-9167.
- Beji, S., and J.A. Battjes, 1993: Experimental investigation of wave propagation over a bar, *Coastal Engineering*, Vol. 19, 151-162.
- Dingemans, M.W., M.J.F. Stive, J. Bosma, H.J. de Vriend and J.A. Vogel, 1988: Directional nearshore wave propagation and induced currents. *Proc. 20th Int. Conf. on Coastal Eng.*, 1092-1106.

- Elgar, S., R.T. Guza and M.H. Freilich, 1993: Observations of nonlinear interactions in directionally spread shoaling surface gravity waves. *J. Geophys. Res.*, Vol. 98, No. C11, 20299-20305.
- Gelci, R., H. Cazalé and J. Vassal, 1957: Prévission de la houle. La méthode des densités spectroangulaires. *Bulletin d'information du comité central océanographie et d'étude des côtes*, Vol. 9, 416-435.
- Hamm, L., P.A. Madsen and D.H. Peregrine, 1993: Wave transformation in the nearshore zone: a review, *Coastal Engineering*, Vol. 21, 5-39.
- Hasselmann, K., T.P. Barnett, E. Bouws, H. Karlson, D.E. Cartwright, K. Enke, J.A. Ewing, H. Gienapp, D.E. Hasselmann, P. Kruseman, A. Meerburg, P. Müller, D.J. Olbers, K. Richter, W. Sell and H. Walden, 1973: Measurements of wind-wave growth and swell decay during the Joint North Sea Wave Project (JONSWAP), *Erganzungsheft zur Deutschen Hydrographischen Zeitschrift*, 12.
- Hasselmann, S., K. Hasselmann, J.H. Allender and T.P. Barnett, 1985: Computations and parameterizations of the nonlinear energy transfer in a gravity wave-spectrum. Part II: Parameterizations of the nonlinear transfer integral for application in wave models. *J. Phys. Oceanogr.*, Vol. 15, 1378-1391.
- Holthuijsen, L.H., N. Booij and T.H.C. Herbers, 1989: A prediction model for stationary, short-crested waves in shallow water with ambient currents, *Coastal Engineering*, Vol. 13, 23-54.
- Holthuijsen, L.H., N. Booij and R.C. Ris, 1993: A spectral model for the coastal zone. *Proc. Int. Conf. WAVES'93*, New Orleans, 630-641.
- Komen, G.J., S. Hasselmann and K. Hasselmann, 1984: On the existence of a fully developed wind-sea spectrum. *J. Phys. Oceanogr.*, Vol. 14, No. 8, 1271-1285.
- Madsen, O.S., Y.-K. Poon and H.C. Graber, 1988: Spectral wave attenuation by bottom friction: theory. *Proc. 21st Int. Conf. on Coastal Eng.*, 492-504.
- Mei, C.C., 1983: *The applied dynamics of ocean surface waves*, Wiley, New York.
- Snyder, R.L., F.W. Dobson, J.A. Elliott and R.B. Long, 1981: Array measurements of atmospheric pressure fluctuations above surface gravity waves. *J. of Fluid Mech.*, Vol. 102, 1-59.
- Tolman, H.L., 1991: A third-generation model for wind waves on slowly varying, unsteady, and inhomogeneous depth and currents, *J. Phys. Oceanogr.*, Vol. 21, No. 6, 782-797.
- WAMDI, 1988: The WAM Model - A third generation ocean wave prediction model, *J. Phys. Oceanogr.*, Vol. 18, 1775-1810.
- Young, I.R., 1988: A shallow water spectral model. *J. of Geophys. Res.*, Vol. 93, No. C5, 5113-5129.
- Young, I.R., and G.Ph. van Vledder, 1993: A review of the central role of nonlinear interactions in wind-wave evolution. *Phil. Trans. Roy. Soc. London*, Vol. 342, 505-524.

## **PART II**

### **Long Period Waves, Storm Surges and Wave Groups**



## CHAPTER 57

### THE GENERATION OF LOW-FREQUENCY WAVES BY A SINGLE WAVE GROUP INCIDENT ON A BEACH

G. Watson <sup>1</sup> T.C.D. Barnes <sup>2</sup> and D.H. Peregrine <sup>3</sup>

#### Abstract

The generation of a single low-frequency wave (LFW) pulse by a single group of waves incident on a beach is investigated by means of laboratory experiments and a numerical model. This simplified case allows the LFW to be measured in isolation, after the incident group has passed and before there is any reflection from the wavemaker. A beach consisting of two different slopes (1:100 and 1:20) was used, and runs were made with the water level on each slope. The results were simulated using a composite numerical model, with Boussinesq equations in the deeper water and nonlinear shallow water equations in the surf zone. For some calculations, a friction term was included. For the 1:20 slope, the outgoing LFW is well predicted even without the friction term. With a 1:100 slope, a friction factor of 0.01 gave a good result, in this case reducing the amplitude of the outgoing LFW by a factor of about 2 compared with the frictionless result. The nondimensional equations show that the friction term is insignificant if the beach slope is large compared with the friction factor. Runs of the surf zone part of the model show the outgoing LFW to be correlated with the swash motion. Its amplitude is largest if the duration of the wave group is similar to the swash period of the largest wave in the group. The model also showed a slightly stronger than linear dependence of LFW amplitude on incident wave amplitude.

---

<sup>1</sup>Research Associate, University of Bristol, Mathematics Department, University Walk, Bristol BS8 1TW, United Kingdom. *Current address:* Disaster Prevention Research Institute, Kyoto University, Gokasho, Uji, Kyoto 611, Japan. (*gary.watson@bristol.ac.uk*)

<sup>2</sup>Research Assistant, University of Bristol. (*tim.barnes@bristol.ac.uk*)

<sup>3</sup>Professor of Applied Mathematics, University of Bristol. (*d.h.peregrine@bristol.ac.uk*)

## 1. Introduction

Low-frequency waves (LFW) with periods typically 5 to 15 times those of wind-generated waves are formed when wind waves meet beaches. Hamm, Madsen & Peregrine (1993) give a general review of the phenomenon, whilst Herbers et al. (1992) give a good review of recent field measurements. Recent work on the theory of LFW generation has been published by Cox et al. (1992), List (1992a,b), Roelvink et al. (1992), Roelvink (1993) and Schäffer (1993). Low-frequency swash oscillations, with bichromatic waves, have also been investigated by Mase (1994).

In this work, our aim was to throw some light on the question of how such waves are generated, by investigating the simplest possible case of LFW generation in as much detail as possible. Watson & Peregrine (1992) investigated the generation of low-frequency waves in the surf zone using a numerical model based on the nonlinear shallow-water equations. A single group of waves was used to illustrate the process whereby a group forces a variable set-up near the shoreline, which then travels offshore as a single LF pulse. This process has now been investigated more quantitatively, by means of laboratory experiments and a wider range of numerical computations. The range of validity of the model has also been extended by coupling the surf zone model to a Boussinesq model in the deeper water.

The reason for choosing a single group of waves rather than continuous bichromatic waves (such as those used by Kostense, 1984) was that this allows the outgoing LFW to be measured in isolation. By the time it reaches the deeper water, the incident wave group has already passed by. It is also measured before reflecting off the paddle. With continuous waves such reflections will contaminate the results unless they are mechanically removed or taken into account in the data analysis. Both of these are difficult to achieve with any degree of confidence.

Details of the experiments, and discussion of one run showing the generation of an outgoing LF pulse, are given in Section 2. A more detailed account of the experiments will be available in the Ph.D. thesis of T. Barnes. The numerical model is described briefly in Section 3 and its results are compared with the measurements, showing the importance of friction effects on the shallower beach slope. Section 4 discusses the influence of friction in more detail. Section 5 illustrates the correlation between swash motions and the outgoing LFW, using results from various other runs of the surf zone part of the model. The importance of the relative timescales of group period and swash period is pointed out. Discussion and conclusions are given in Section 6.

## 2. Experimental Results

### *Description of Experiments*

Experiments were performed in a 50 m long wave flume at Hydraulics

Research Ltd. in Wallingford, England. The flume is 1 m wide. It is equipped with a piston-type wavemaker with two paddles, controlled by a PC. A concrete beach with two slopes, 1:100 and 1:20, was installed in the flume as shown in Figure 1. Runs were performed using two different water depths of 0.35 m and 0.20 m, so that the undisturbed shoreline would lie on a different slope in each case.

An array of resistance-type wave probes was used, and Figure 1 shows their layout for the deeper water runs. Probe 1 was located near the paddle in order to measure the generated wave signal. Probes 2 and 3 were in the deeper water. Probes 4–11 were on the 1:100 slope and Probe 12 was on the 1:20 slope.

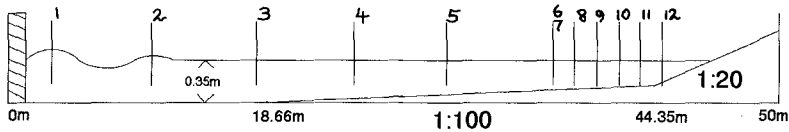


Figure 1: Cross-section of the HR wave flume, showing beach and positions of wave probes (not to scale). A current meter was located at Probe 6.

Since a number of numerical runs were to be performed using just the surf zone model, particular attention was paid to measurements at a point where all but the smallest waves had already broken. In the case illustrated, this was near Probes 6 and 7, (depth 15.5 cm). Two probes were used at this point in order to check for consistency across the tank.

Along-tank velocity data were also collected at this point, using an ultrasonic current meter. The sensor head was placed at about half the water depth, the results having been found not to be very sensitive to the precise placement of the probe. At this location, the incident and outgoing signals are not separated in time, but can be approximately separated by calculating the Riemann invariants. This is done by combining the surface elevation and velocity signals as explained in Section 3.

### *Wavemaker Signal*

Initially, single groups consisting of modulated sine waves were used. However, these waves acquired large second harmonics as they propagated along the tank, with each wave effectively splitting into two. To solve this problem, groups consisting of solitary wave solutions to the Korteweg-deVries equation were used instead. For the shallow water regime of these experiments, this is more appropriate than Stokes theory, which is better in deeper water. Stokes theory requires the Ursell parameter  $U = ka_0/(kh)^3$ , to be small, whereas in these experiments it was of order 1. In the formula for  $U$ ,  $k$  is the wavenumber,  $a_0$  the fundamental amplitude and  $h$  the undisturbed water depth.

The wavemaker signal was designed to produce surface elevation time series of the form

$$\eta = \sum_i \eta_i \operatorname{sech}^2 \sqrt{\frac{3\eta_i}{4h_i^3}} c_i (t - t_i) - (a + a_s) \sin \omega t \quad 0 \leq t \leq \pi/\omega \quad (1)$$

and zero outside that time interval. The wave times,  $t_i$ , were equally spaced. The wave amplitudes,  $\eta_i$ , were sinusoidally modulated by the function  $\eta_i = A \sin \omega t_i$ . The water depth for each wave,  $h_i$ , must be adjusted for the additional sine function:  $h_i = h_0 - (a + a_s) \sin \omega t_i$ . The wave speed  $c_i$  is  $\sqrt{g(h_i + \eta_i)}$ . Velocity was estimated from the shallow-water approximation  $u = \sqrt{g/h_0} \eta$  and then integrated to give the wavemaker displacement signal.

The stroke of the paddle is not great enough to make a succession of solitary waves, each with its own net displacement. For this reason, the sine function was added. This has the same duration as the group and corresponds to a set-down beneath it. This means that there is little net mass flux in the incident wave groups.

### Results

Surface elevations from a typical run in the deeper water (1:20 slope) are shown as the thick lines in Figure 2. All of the runs yielded results which were qualitatively similar. Numerical predictions from the model described below are included for comparison. The shape of the initial wave group, consisting of five waves, is seen in the trace from Probe 1. The form of the solitary waves is preserved quite well along the constant depth section, except for the development of a small dispersive tail (1-3). As the wave group travels into shallower water, the waves steepen and at Probe 6/7 all except the first are breaking. Near the shoreline (11 & 12) a LFW is seen to develop consisting of a peak, apparently like wave set-up, followed by a trough. At the same time the short waves dissipate their energy and get smaller, so that the LFW is more prominent. This wave then propagates offshore, decreasing in amplitude as it does so. At Probe 5 it is separated in time from the incident group. Further offshore it can be identified quite clearly. The moving peak and trough are marked with arrows. It then reflects off the wavemaker (also marked). At Probe 1, the amplitude appears to be twice as big, due to the superposition of the reflection.

The shape and amplitude of the outgoing LFW can be seen more clearly if the vertical scale of the plots is expanded. This is shown for Probes 2-5 in Figure 3.

### 3. Composite Numerical Model

A coupled numerical model, based on the nonlinear shallow-water equations (NLSWE) in the surf zone (Watson and Peregrine, 1992) and the Boussi-



nesq equations in deeper water, is able to simulate the phenomenon.

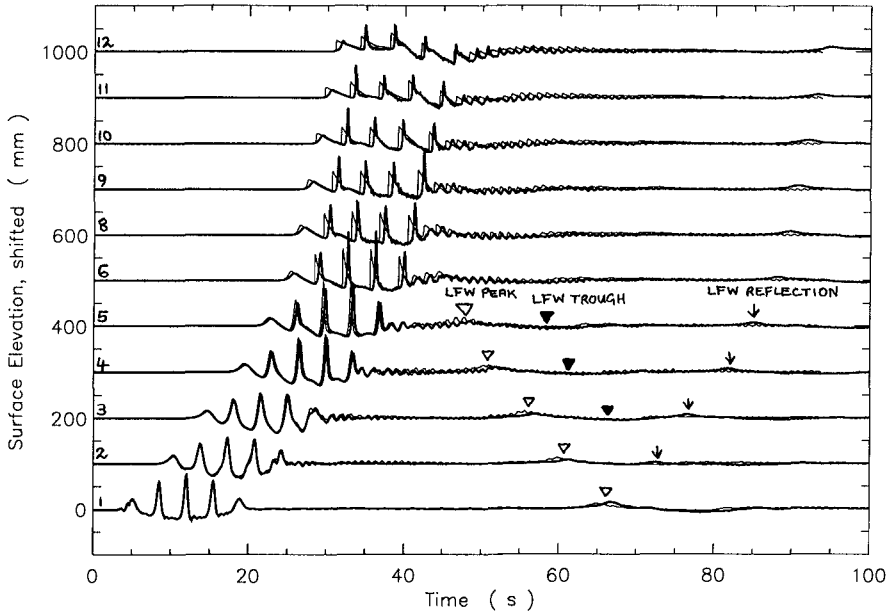


Figure 2: *Thick line:* Surface elevation time series at each probe (except 7) for a group of five solitary waves. *Thin line:* Numerical prediction.

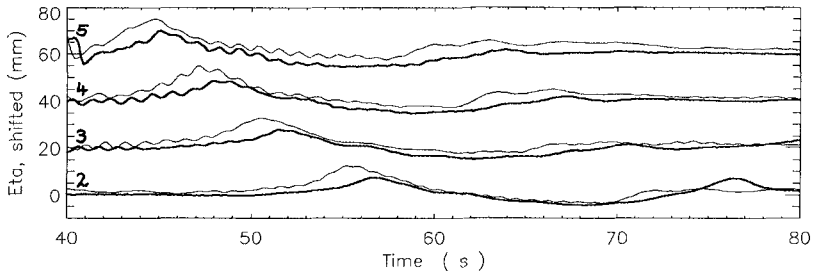


Figure 3: Expanded view of the outgoing LFW in Figure 2, for Probes 2-5. *Thick line:* Measurements. *Thin line:* Numerical prediction.

Our primary interest here is in the mechanisms by which LFW are generated. LFW have their greatest amplitudes in the surf zone, and the most important components of the generation process occur there. It is therefore

important to use a model that includes all the important physics in the surf zone. The nonlinear shallow-water equations for the conservation of mass and momentum, with a friction term, were used:

$$d_t + (ud)_x = 0 \quad (2)$$

$$u_t + uu_x + g\eta_x + \frac{1}{2} f \frac{u |u|}{d} = 0 \quad (3)$$

where  $\eta = d - h$  is the surface elevation,  $d$  is the total water depth,  $h$  the undisturbed water depth,  $u$  the flow velocity,  $g$  gravity and  $f$  an empirical friction coefficient.

These equations are able to represent spilling breakers as travelling hydraulic jumps or bores, which manifest themselves as discontinuities in the solution. Some information on these equations without the friction term, and the numerical method used to solve them has been given previously (Watson & Peregrine, 1992; Watson, Peregrine & Toro, 1992). Treatment of the moving shoreline boundary condition is discussed in the latter paper.

The friction term in the above equations is the simplest that is conventionally used to represent friction. Typical values for  $f$  are of order  $10^{-2}$ . For the present study it was necessary to modify the numerical procedure slightly to allow for this term. This was done by first solving the frictionless equations at timestep  $n$  as before, a procedure which is second-order accurate. After this a simple first-order forward difference step was applied at each grid point, altering the velocity  $u_n$  by an amount

$$-\frac{1}{2} f \frac{u_n |u_n|}{d_n} \Delta t \quad (4)$$

$\Delta t$  must be small enough for this to be reasonably accurate. The inclusion of friction in this manner destroys the second-order accuracy of the scheme. However, since the empirical friction term is rather approximate in any case, the degradation of numerical accuracy here is not important.

In deeper water, the Boussinesq equations are appropriate because they include dispersive terms. The Boussinesq equations in the form due to Peregrine (1967) were used:

$$d_t + (ud)_x = 0 \quad (5)$$

$$u_t + uu_x + g\eta_x = \frac{1}{2} h(hu_t)_{xx} - \frac{1}{6} h^2 u_{xxt} \quad (6)$$

Recently, Dingemans has shown that in some circumstances, particularly on a barred beach, it is important to include further dispersive terms. See Dingemans (1995) for a full discussion. However, in our case it will be seen that the above equations give sufficiently good results. The friction term was not included in these equations, since it becomes small in the deeper water.

The equations were solved numerically using a finite difference scheme due to Peregrine (1967).

#### *Matching the two models together*

The models were matched at the join using a characteristics boundary condition. In the frictionless shallow-water equations, the wave signals propagating in each direction are given by the Riemann invariants  $R^+ = 2c + u$  and  $R^- = 2c - u$ , where  $c = \sqrt{gd}$  and  $d$  is the total water depth. This is also approximately true for the Boussinesq equations, which for waves of sufficiently gentle slope approximate to the shallow-water equations. Thus, an almost non-reflecting join can be made by taking  $R^+$  from the last point of the Boussinesq section and feeding it into the first point of the NLSWE section, and taking  $R^-$  from the first point of the NLSWE section and feeding it into the last point of the Boussinesq section.

This being done, a number of runs were made in order to test the sensitivity of results to the position of the join. It was found that the join could be moved a significant distance without much change in the output, as long as it was somewhere in the vicinity of the break point. The run reported here was done with the join at the location of Probe 6 in Figure 1.

#### *The Seaward Boundary Condition*

At the offshore end of the computational domain, a boundary condition similar to that at the matching point was applied. This used the characteristic equations to allow outgoing waves to pass out with no reflection. The outgoing  $R^-$  was found from data immediately inside the domain, and the surface elevation was forced to be equal to that measured by Probe 1. This was sufficient information to define the incident  $R^+$ . Although the reflections from the paddle that were present in the wave flume were not reproduced, these are not of any interest.

#### *Comparison of Numerical and Experimental Results*

The numerical results for the data in Figures 2 and 3 are shown as thin lines in those figures. The main feature of interest, i.e. the amplitude, shape and propagation of the outgoing LF pulse, is reasonably well predicted — although the amplitude is a little too large and the timing is not precise. Some properties of the short waves are not reproduced very well as the group travels shoreward. Their amplitude is underpredicted, the sharp wave crest is flattened out, and there are small timing errors. Note however that these details do not appear to have a significant effect on the LFW generation process.

The success of this model in predicting the measured LFW shapes and amplitudes is illustrated in more detail using data from Probe 6. Results from two runs are shown. One has the water level set so that the shoreline is on the 1:20 slope, the other with the shoreline on the 1:100 slope.

In both cases the model was run using the measured water depth and velocity at Probe 6, to construct a time series of the Riemann invariant  $R^+ = 2\sqrt{gd} + u$ . The outgoing LFW was then examined by computing the other invariant  $R^- = 2\sqrt{gd} - u$ . This is plotted using dashed lines in Figures 4 and 5 for the two runs, together with the numerical result. Both cases show the LFW quite clearly. There are spikes in the data every time an incident wave passes the probe. This effect is due to the fact that the shallow-water equations on which the Riemann invariant analysis is based do not accurately describe the details of the crests of steep waves, breakers, or bores.

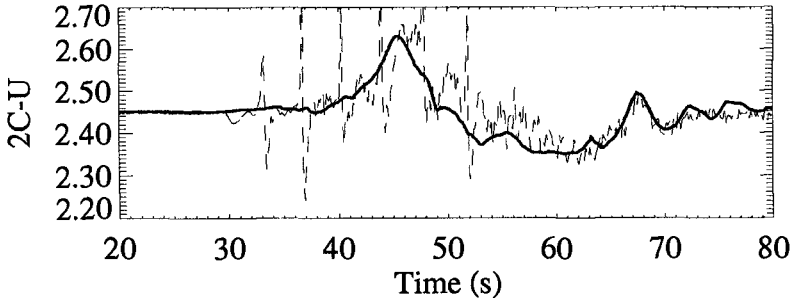


Figure 4: Outgoing signal at seaward boundary in deep water case (composite slope with shoreline on the 1:20 slope). Data (broken), frictionless model (solid).

In the deeper water case (1:20, Figure 4), the agreement between model and data is quite good, except for precise details of the wave shape. In this case, the model gave almost the same result with or without friction. The frictional result is not plotted.

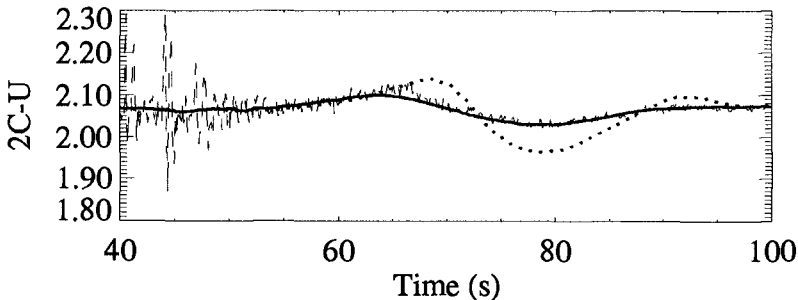


Figure 5: Outgoing signal at seaward boundary in shallow water case (1:100 slope). Data (broken), frictionless model (dotted), frictional model (solid).

In the shallower case (1:100, Figure 5), agreement in the frictionless case is not so good (dotted). The LFW is overpredicted by a factor of about 2. The shape of the pulse is also different, in that the peak occurs about 5 s

late. However when the friction term is included, with the value  $f = 0.01$ , the result is much better — as shown by the solid curve. The effect of friction is discussed in more detail in the following section.

#### 4. The Effect of Friction

The frictional drag force acting between the bottom and the water has an increasingly strong effect as the depth decreases. This is simply because the friction force is primarily determined by the near-bottom velocity of the water, and in the shallow-water approximation it acts on a mass of water that is proportional to the depth. It will thus have its strongest effect in the swash zone, where the water is shallowest. Since this is where LFW processes are particularly important, it is to be expected that friction may have some effect on LFW generation.

For a plane beach of slope  $\alpha$  extending from the shoreline to the offshore boundary, the relative importance of friction effects may be seen from the following scaling argument. Eqs. 2 & 3 may be written using the following non-dimensional variables:

$$x' = x/x_1, \quad d' = d/h_1, \quad \eta' = \eta/h_1, \quad u' = u/u_1, \quad t' = t/t_1$$

where the scaling variables are  $x_1$  (the distance between the offshore boundary and the undisturbed shoreline),  $h_1$  (the undisturbed water depth at the offshore boundary),  $u_1 = \sqrt{gh_1}$  and  $t_1 = x_1/u_1$ . Dropping primes, the equations become:

$$d_t + (ud)_x = 0 \quad (7)$$

$$u_t + uu_x + \eta_x + \frac{1}{2} \frac{f}{\alpha} \frac{u|u|}{d} = 0 \quad (8)$$

where  $\alpha$  is the slope  $h_1/x_1$ .

For breaking waves,  $u^2/d$  is of order 1, so the friction term is of order  $f/\alpha$ . Thus friction can be expected to have a negligible effect if  $f \ll \alpha$ , a noticeable effect if  $f \sim \alpha$  and to dominate everywhere if  $f \gg \alpha$ . In the two cases under consideration, with  $f = 0.01$ ,  $f/\alpha$  takes the values 0.2 and 1.0. In the former case friction had little effect, whereas in the latter the outgoing LFW amplitude was reduced by a factor of about 2.

These conclusions were further confirmed by model runs made using a range of values of  $f$ . The same incident wave group as in Watson & Peregrine (1992) was used, and the height of the outgoing LF pulse was determined by taking the difference between maximum and minimum in  $R^-$  at the offshore boundary. Six runs with values of  $f/\alpha$  ranging from 0.0 to 2.0 were performed. The results are plotted in Figure 6.

The figure shows a strong dependence of outgoing LFW amplitude on the scaled friction factor  $f/\alpha$ . With no friction ( $f/\alpha = 0$ ), the amplitude has its maximum value, but this is reduced quite rapidly as  $f/\alpha$  is increased, so

that for  $f/\alpha = 0.2$  the LFW amplitude is 78% of its maximum value. As  $f/\alpha$  is increased, the amplitude continues to decrease, although more slowly. For  $f/\alpha = 1.0$ , it is 47% of its maximum value. This is roughly consistent with the results in Figures 4 and 5.

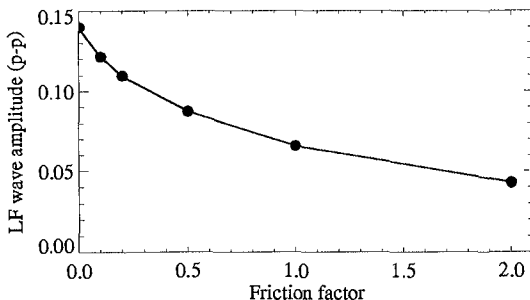


Figure 6: The dependence of outgoing LFW amplitude on scaled friction factor,  $f/\alpha$ .

This means that the agreement which was obtained in the 1:100 case with  $f = 0.01$  is open to the suggestion that it may have been merely coincidental. However, this value was chosen from experience as being one that is typically used.

### 5. The Importance of Swash Motions

During the time that the wave group is in the swash zone, there is a complex interaction between the waves in the group and the swash motion from previous waves. This affects the amplitude and shape of the LFW that finally emerges. The nature of the swash, and the properties of the LFW, depend on the relative values of the various timescales in the problem. Rather than attempt to understand the swash motion in detail, this effect was investigated in a more empirical manner by performing a number of runs of the model with different timescales and hence different swash regimes.

The timing of the incident group is determined by two parameters: the wave period,  $\tau$ , and the number of waves in the group,  $N$ . The total duration of the group is then  $T = N\tau$ . There is a third timescale in the problem, namely the natural period of swash on the beach. Let us call this  $t_s$ . This depends on the amplitude of the incident waves. In the frictionless case (considered here), the swash motion approximates fairly closely to free motion under gravity on the sloping beach. Thus, the larger the incident waves, the greater the initial velocity of the uprush and the longer the swash period  $t_s$ .

A number of runs of the model were performed with different wave periods, different numbers of waves and different swash periods. These were based on variations about a control case, summarized in Figure 7.

The top panel of this figure shows a perspective view of the space-time plot of surface elevation. The input is an idealized group of five sinusoidally modulated sawtooth-shaped waves, which are intended to represent waves that are already breaking. The peak and trough values have been set so that there is no net mass flux in each wave. The curved wave trajectories show how each wave slows down as it approaches the shore, and the wave heights can be seen to diminish in the process. The wave group can be seen to force a mass of water up the beach face on the timescale of the wave group. The seaward-propagating LFW pulse that this forcing generates is just about visible to the right of the wave group in the plot.

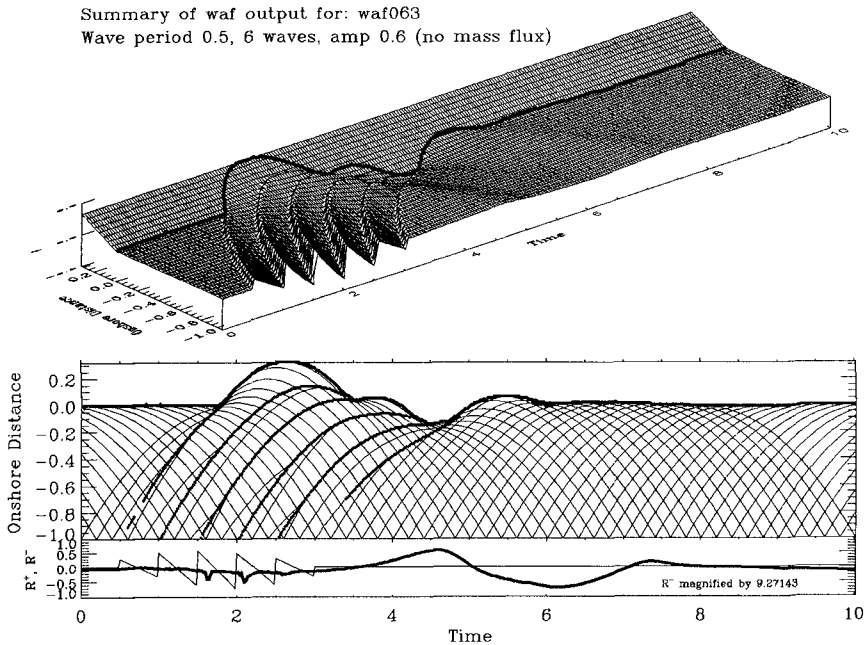


Figure 7: Result from the control case (see text).

The next panel shows shallow-water equation characteristics and bore trajectories (indicated by black dots). The shoreline motion is also shown in plan view. Beneath this, the incident and outgoing signals at the seaward boundary of the model are plotted. These are computed from the Riemann invariants  $R^+$  and  $R^-$  as explained in Section 3. Note that the outgoing signal, which shows the shape of the LFW pulse, has been magnified by the indicated factor in order to make it more clearly visible. In this case it is about 10 times

smaller than the incident signal. The main thing to notice from this plot is that the shape of the LFW pulse is very similar to the shape of the runup, especially after the runup has been averaged over the short-wave oscillations.

The generality of this observation was tested by performing a variety of model runs with different timescales. These were then used to investigate the effect of wave group timing on the LFW amplitude. Runs were performed with a range of values of  $\tau$  and then with a range of values of  $N$ , varying the wave group duration  $T$  in two different ways. Both sets span approximately the same range of  $T$ -values for each wave amplitude, with  $t_s$  roughly central in each case. The runs were repeated with two different amplitudes for the largest wave in each group: 0.1 and 0.6 in dimensionless units. This provided two different values of the swash period. Separate runs using just one incident bore showed that for a wave of height 0.1 above still water level, the swash period was  $t_s = 1.4$ ; whereas for a height of 0.6 it was  $t_s = 2.9$ .

The results of these runs are summarised in Figure 8, with runup plotted next to the LFW signal (at the offshore boundary) for each run. These curves have been smoothed a little to remove discretization effects in the runup, and spikes (due to incident bores) in the LFW signals. Note the clear correlation between the shapes of each pair of signals, with the LFW signal occurring somewhat later than the runup signal. It is significant that this is true despite the runup signals being quite varied in nature.

The runup is plotted so that whatever the range, the vertical extent of the plot is the same. The LFW plots all have the same relative scaling. Ratios of LFW elevation amplitude to incident wave amplitude were in the range 0.015–0.07 (a factor of 4.7). However, ratios of LFW elevation amplitude to runup amplitude were in the narrower range 0.035–0.125 (a factor of 3.6).

These two observations indicate the reflected LFW is better correlated with runup than with the incident wave envelope. This is consistent with the idea that the time-varying set-up within the wave group is manifested as swash when it is near the shore, and then propagates offshore as the outgoing LFW.

The amplitude of the outgoing LFW was found to depend in a consistent way on the relative values of wave group duration  $T$  and swash period  $t_s$ . This is shown in Figure 9. Here the LFW height, defined as the difference between the maximum and minimum in the LFW pulse, is plotted against  $T$  for each run. Four sets of results are presented. Figure 9(a) contains the results for amplitude 0.1, and Figure 9(b) for amplitude 0.6. The thick lines are runs with variable  $N$ , and the thin lines for runs with variable  $\tau$ .

The main feature to note is that each of these curves has a maximum close to the swash period for a single wave of the respective amplitude. This period,  $t_s$ , is marked with an arrow on each plot. There are notable differences between the variable- $N$  and variable- $\tau$  series, and at present the explanation for this is not clear. However, it is suggested that the presence of a peak in each curve can be explained as a quasi-resonance between the wave group forcing



and the natural swash motion of the water on the beach face. If the wave group period is similar to the swash period ( $T \approx t_s$ ), then a sequence of waves can carry water up the beach following, reinforcing and being carried by the initial swash motion. Thus, a large (wave-averaged) swash motion develops.

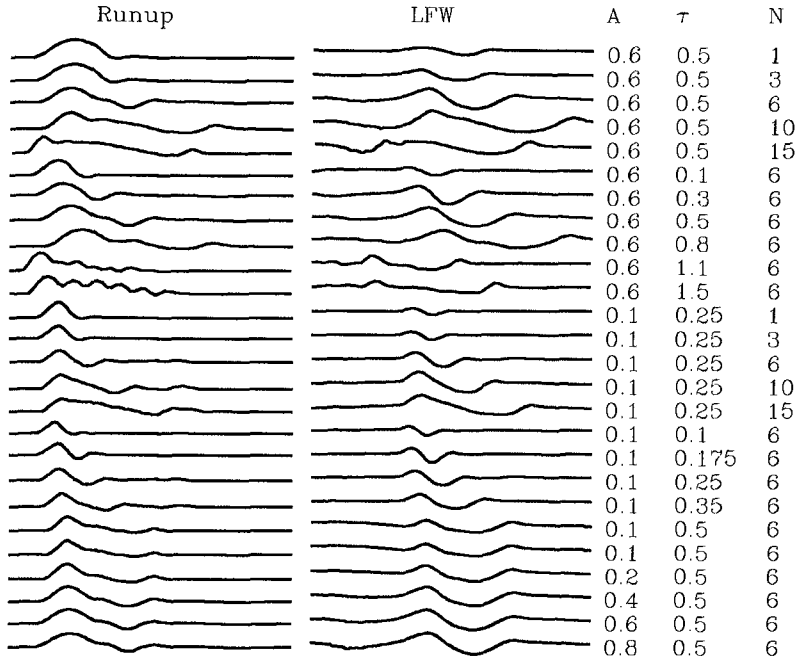


Figure 8: Swash motion and LFW signal for various runs of the model.

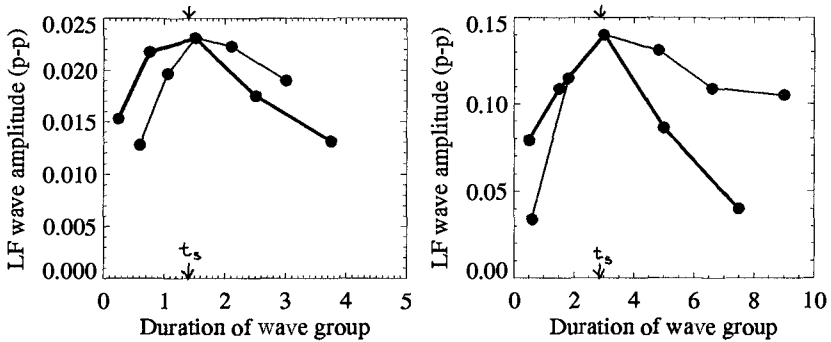


Figure 9: Dependence of LFW amplitude on wave group period  $T$ . (a) Amplitude 0.1. (b) Amplitude 0.6.

If the wave group period is longer than this swash period ( $T \gg t_s$ ), then succeeding waves tend to meet swash already coming down the beach, and this opposing effect restricts the development of a large swash. In the extreme case of uniform waves, the swash zone becomes very narrow. For  $T \ll t_s$ , there is a strong fall-off of LFW amplitude as  $T$  decreases. Figure 8 shows that in these cases, the period of the LF motion does not decrease beyond  $t_s$ . These shorter groups have less momentum and energy, so can drive less and less fluid up the beach as  $T$  decreases.

With continuously modulated waves, rather than a single group, the number of wave groups or fraction of a wave group that is within the surf zone at any one time is expected to be relevant. This may be represented by a group-based surf-similarity parameter,  $G = T/t_b$ , where  $T$  is the duration of the group and  $t_b$  is the time it takes the largest wave to reach the shore after breaking.  $G$  is small for a wide surf zone and large for a narrow one. If  $G$  is small, several groups may simultaneously be generating LFW. There will then be substantial interference, which is likely to be destructive. If it is large, there will only be one or two waves in the surf zone at once: little interaction can occur and LFW generation is expected to be minimal. The strongest LFW generation is expected to occur when  $G$  is of order one. This idea remains to be investigated more thoroughly.

## 6. Discussion and Conclusions

The experiments clearly show the generation of LFW, and the numerical modelling successfully predicts their form and amplitude, even though the finer details of wave breaking are not included. It is clear that friction is important on the gentler slopes, on a laboratory scale, and reduces LFW amplitudes.

In interpreting the numerical and laboratory experiments it appears that the swash zone, and in particular the period of swash from the largest wave of a group, is an important feature. It is not entirely clear however, whether this is an indication of set-up generated in the approach to the shore line or a process centred close to and in the swash zone. In addition, for the practical case where there may be continuous wave modulation we suggest a group surf-similarity parameter based on the size of the surf zone relative to individual groups should be important.

The numerical experiments also indicate a slightly stronger than linear dependence of LFW amplitude on incident wave amplitude, in accord with field observations (Herbers et al., 1992). However, the question as to what LFW are incident on the surf zone, has yet to be resolved. The behaviour of wave groups with differing set-down has been investigated, but is not reported here. The development and decoupling of incident bound waves, as they enter shallow water where the Stokes theory becomes invalid and wave crests behave more like individual solitary waves needs to be determined. This is currently under investigation using a fully nonlinear potential flow solver.

### Acknowledgements

This work was funded by the Commission of the European Communities, DG XII, under Contract No. MAS2-CT92-0027 (MAST-II G8-M Coastal Morphodynamics). The authors are grateful to the staff of HR Wallingford for providing facilities and support for the experiments. T. Barnes was funded by an EPSRC CASE research studentship with HR Wallingford. Dr. E.F. Toro of Cranfield Institute of Technology provided the core of the numerical algorithm used for solving the nonlinear shallow water equations.

### References

- Cox, D.T., N. Kobayashi and A. Wurjanto (1992). Irregular wave transformation processes in surf and swash zones. *Proc. 23rd Int. Conf. Coastal Eng.*, 156–169.
- Dingemans, M.W. (1995). *Water wave propagation over uneven bottoms*. World Scientific, in press.
- Hamm, L., P.A. Madsen and D.H. Peregrine (1993). Wave transformation in the nearshore zone: a review. *Coastal Eng.*, **21**, 5–39.
- Herbers, T.H.C., S. Elgar, R.T. Guza & W.C. O'Reilly (1992). Infragravity-frequency (0.005–0.05 Hz) motions on the shelf. *Proc. 23rd Int. Conf. Coastal Eng.*, 846–859.
- Kostense, J.K. (1984). Measurements of surf beat and set-down beneath wave groups. *Proc. 19th Int. Conf. Coastal Eng.*, 724–740.
- List, J.H. (1992a). Breakpoint-forced and bound long waves in the nearshore: a model comparison. *Proc. 23rd Int. Conf. Coastal Eng.*, 860–873.
- List, J.H. (1992b). A model for two-dimensional surf beat. *J. Geophys. Res.*, **97**, 5623–5635.
- Mase, H. (1994). Uprush-backrush interaction dominated and long wave dominated swash oscillations. *Proc. Int. Symp.: Waves — Physical and Numerical Modelling*, UBC Vancouver, August 21–24 1994, eds. M. Isaacson and M. Quirk, 316–325.
- Peregrine, D.H. (1967). Long waves on a beach. *J. Fluid Mech.* **27**, 815–827.
- Roelvink, J.A., H.A.H. Petit and J.K. Kostense (1992). Verification of a one-dimensional surf-beat model against laboratory data. *Proc. 23rd Int. Conf. Coastal Eng.*, 960–973.
- Roelvink, J.A. (1993). Surf beat and its effect on cross-shore profiles. *Ph.D. Thesis*, Technical University of Delft, 116 pp.
- Schäffer, H.A. (1993). Infragravity waves induced by short-wave groups. *J. Fluid Mech.* **247**, 551–588.
- Watson, G. and Peregrine, D.H. (1992). Low frequency waves in the surf zone, *Proc. 23rd Int. Conf. Coastal Eng.*, 818–831.
- Watson, G., Peregrine, D.H. and Toro, E.F. (1992). Numerical solution of the shallow-water equations on a beach using the weighted average flux method. In *Computational Fluid Dynamics '92*, Volume 1, C. Hirsch et al. (Eds.), 495–502.

## CHAPTER 58

### Influence of Long Waves on Ship Motions in a Lagoon Harbour

Volker Barthel<sup>1</sup> and Etienne Mansard<sup>2</sup>

#### ABSTRACT

A physical model study of a vessel moored inside a lagoon harbour was undertaken in order to optimize a breakwater layout that best reduces the penetration of long wave energy inside the lagoon. The longer the breakwater at the entrance: the smaller the surge motion inside the lagoon. A combination of a short breakwater at the entrance channel and a pair of groynes in front and in the rear of the vessel also led to an efficient reduction of the surge motion. However, cost estimates and evaluation of vessel manoeuvrability are required to make an optimal choice of the breakwater layout. The use of a deterministic approach in wave generation led to a quicker testing procedure.

#### INTRODUCTION

In the design process of a harbour, its location, size and infrastructure are usually determined by economic factors such as the magnitude and structure of the expected marine traffic, the hinterland, the amount of throughput cargo and many other parameters. A preliminary lay-out of basins, berths, access channels, jetties, breakwaters and other coastal structures is then optimized with the help of numerical and/or physical models of tidal motions, currents, waves and sediment transport. However, the fine-tuning of the design such as the length and orientation of breakwaters can be carried out only with the help of a ship mooring study. This is generally done in a physical model, although various promising numerical approaches have been presented in literature (see for instance Sand and Jensen, 1990).

---

<sup>1</sup>Federal Admin. of Waterways and Navigation, Directorate North Kiel, Germany.

<sup>2</sup>Institute for Marine Dynamics, National Research Council of Canada, Ottawa, Canada.

This paper describes a physical model study of a 35,000 tdw bulk carrier moored in a lagoon harbour. The objective of the study was to evaluate the magnitude of vessel response induced by irregular waves. It was therefore, focussed on the propagation of irregular waves through an access channel, past a breakwater, into a lagoon harbour. The modification of the irregular wave train and its group-bound long wave components, during the shoaling process and the effect of various breakwater layouts on their penetration into the lagoon harbour were evaluated by measuring the motions of the moored vessel with highly sensitive instrumentation.

### EXPERIMENTAL SET-UP

Figure 1a is a sketch of the lay-out of the lagoon harbour used in this study. It consisted of an offshore section of 25m depth, a 1:100 sloped bathymetry and a channel at the 15m contour cutting into this slope. At the end of the 1250m access channel, a circular lagoon with a radius of 280m accommodated a trestle structure berth and a ship moored to it. Permeable gravel beaches were installed on either side of the entrance channel to absorb incident wave energy. Slopes of the harbour basin were at 1:10. Since a model bulkcarrier of 35,000 tdw was readily available at a scale of 1:70, the same scale was chosen for the entire investigation. The hydrodynamic similarity of the vessel had been established in previous tests, including the definition of CG, GM, roll period and pitch gyradius. The model ship was ballasted for a 100% load condition.

In order to obtain the highest possible accuracy in vessel response, mooring lines and fenders of the model were designed to reproduce non-linear characteristics of the desired prototype lines and fenders including hysteresis. Forces were measured by high-resolution load cells, while the six-degrees-of-freedom motions of the model were monitored using an optical tracking system. Details of the instrumentation and mooring line simulators can be found in (Barthel, et al., 1989; Laurich, 1989). The model was moored with 12 polypropylene mooring lines arranged in a pattern which had been previously optimized (Kubo and Barthel, 1992, Barthel et al, 1994). Figure 1b shows a photograph of the model set-up.

Water surface elevations were measured in the model basin using capacitance type wave gauges. Their locations are shown in Fig. 1a. The array of gauge 1 - 5 was used to determine reflections coming from the model layout. Simulation of waves in the model basin was carried out using the wave generation package developed at the Hydraulics laboratory of the National Research Council Canada. This package contains several algorithms for simulation of uni and multidirectional waves.

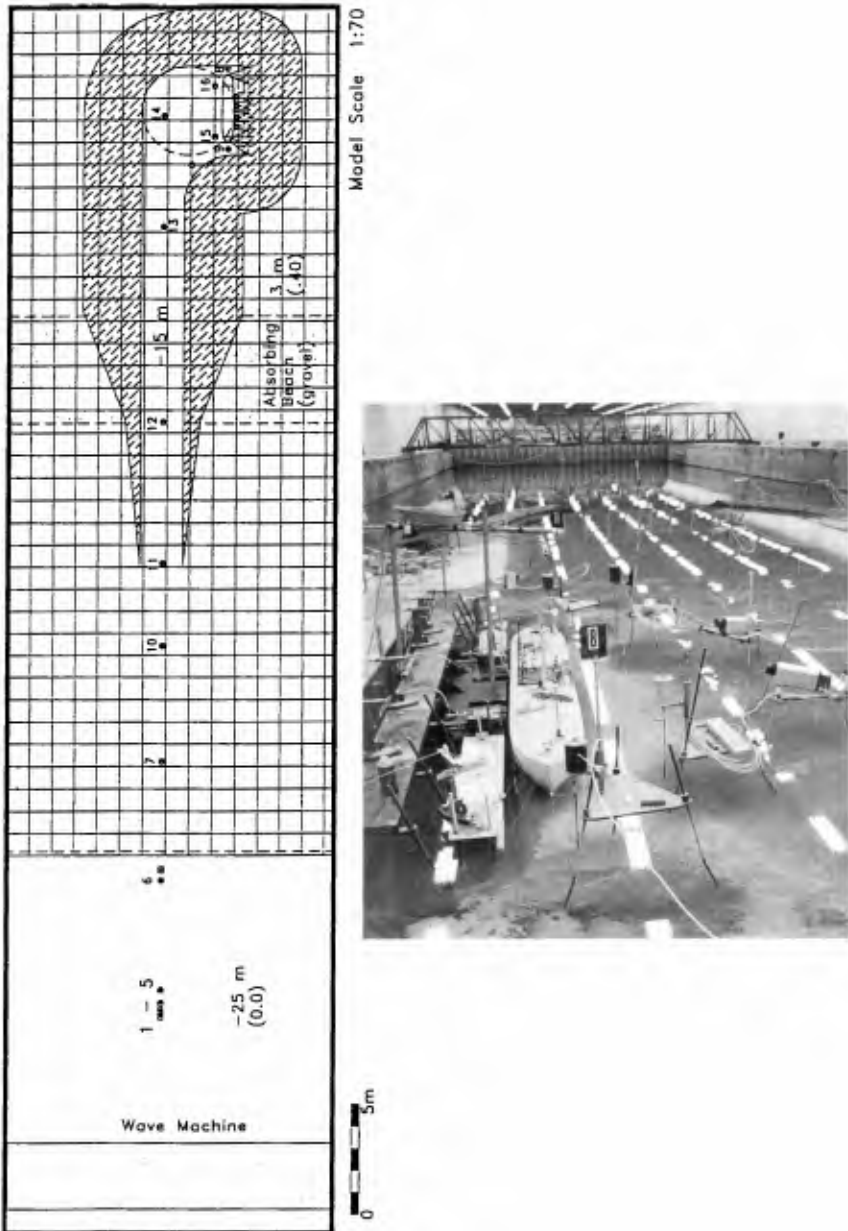


Figure 1 . Layout of the Experimental Set-up : a) Sketch indicating the position of gauges; b) Photograph showing the vessel in place.

## PROPAGATION OF LONG WAVES INTO THE LAGOON

The understanding of the physical processes involved in the propagation of waves on a complex bathymetry and layout such as the one used in this study is limited. However, it can be expected that, as the waves propagate the shoaling of wave groups and their associated group-bound long waves will induce the breaking of the first order (short) waves and cause their energy dissipation. The long waves can then be expected to detach themselves from the group and continue to travel at free wave velocity to be either reflected off the beach or to propagate along the beach at an angle (set-up / edge waves). An experimental description of this process was attempted by (Mansard and Barthel, 1984). The present situation is however more complicated. From what could be observed during tests, the following happens:

During the propagation of waves from deep to shallow water, the shoaling process induces breaking of the first order waves and releases the energy of the group bound long waves that continue then to propagate into the lagoon. These long waves, although hardly visible to the observer because of their small amplitudes, can move the vessel to its maximum limit. In this particular set-up, the surge motion and the loads on the mooring lines which restrained the surge motion, were most sensitive to long waves.

The main objective of this study was therefore to optimize a breakwater lay-out that will reduce the penetration of the long wave energy and the resulting ship motions.

## SHIP MOORING TESTS

### Experimental Procedure

Many laboratories in the world use the stochastic approach in ship mooring tests by subjecting the model to a very long time series of water surface elevation, in order to ensure the inclusion of worst combination of waves that will cause the maximum motions of the vessels, as well as maximum loads on the mooring lines. In this particular study, a deterministic approach was adopted by simulating short time series of pre-defined surface elevation, in order to save testing time and cost of model investigations. This use of short time series was also expected to minimize any potential build-up of long wave energy in the model set-up.

The time series used in this study were 2.4 minutes long in model scale and it corresponded to 20 minutes in prototype duration. This length was also equivalent to 12 periods of 100s long waves that were found to

excite the ship substantially in an earlier study (see Barthel et al, 1994). In order to select time series that would be appropriate for this deterministic approach, the methodology described below was used.

### Synthesis and selection of time series

From a JONSWAP spectrum, time series of water surface elevation were first synthesized by the commonly used random phase spectrum method. This method pairs a given amplitude spectrum with a phase spectrum generated by random numbers. By varying the random numbers, different realizations of wave records, with varying time domain characteristics can easily be simulated.

Since it is believed that narrower spectra result in higher degree of wave grouping, JONSWAP spectra with two different values of  $\gamma$  (i.e.  $\gamma=1$  and  $\gamma=7$ ) were used in this synthesis. (According to Sand (1982), higher degree of grouping results in larger amplitude of group-bound long waves that are responsible for the excitation of the horizontal motions of the vessel). From each target spectrum, ten realizations of time series were synthesized and reproduced in the model. The response of the vessel was then measured for all the twenty realizations of the time series described above. Figure 2 presents the results obtained by this procedure.

The RMS values (i.e. standard deviation) of the long waves measured in the lagoon, in the proximity of the vessel are shown in Figure 2a for the various realizations of time series. These long waves were derived by low-pass filtering the water surface elevation with a frequency cut-off of 0.03 Hz (full scale). Figure 2b illustrates the RMS values of the corresponding surge motions.

The results show that narrower spectra ( $\gamma=7$ ) results in higher long wave content and consequently larger surge motions. Amongst the ten realizations of the time series under each  $\gamma$  value, the 8<sup>th</sup> time series generally leads to the largest response of the vessel. This time series will be denoted in this paper as TRN8. It is also noticeable that the 4<sup>th</sup> realization (TRN4) generally provides the smallest response. The above findings were also confirmed by analyzing the sway motion and the loads on the mooring lines.

Figure 3 shows the time series of water surface elevations corresponding to TRN4 and TRN8 under the two  $\gamma$  values of JONSWAP. The corresponding SIWEH functions which illustrate their grouping pattern are also illustrated along with the appropriate values of Groupiness Factors (see Funke and Mansard, 1979 for the definitions of SIWEH and Groupiness Factor).



Since the length of each of these time series was only 2.4 minutes in model scale, it was decided to use all the four time series (i.e. TRN4 of  $\gamma=1$  and  $\gamma=7$  and TRN8 of  $\gamma=1$  and  $\gamma=7$ ) for the optimization of the breakwater layout, in order to validate the resulting solutions under four different sea states.

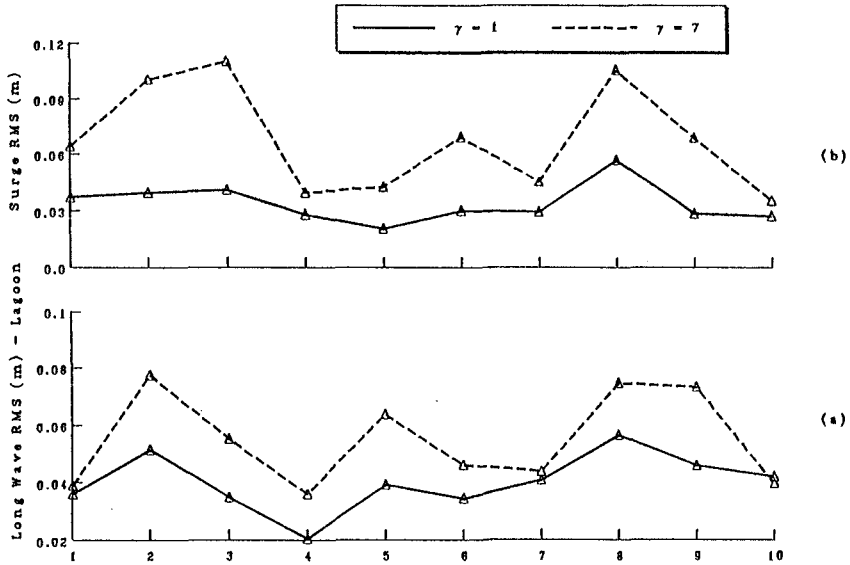


Figure 2. RMS values of long waves and surge motion inside the lagoon harbour for the ten realizations of time series.

### LAYOUT OF BREAKWATERS

Several breakwater configurations were evaluated in this study during the optimization procedure. They are, as can be seen in Figure 4: a long version of the breakwater (BWL), a medium length structure (BWM) and a short breakwater with (BWD) and without (BWS) a second barrier. In addition several versions of groynes (BWSG1, BWSG2 and BWSGD) upstream and downstream of the moored vessel were also tested in conjunction with the short breakwater BWS.

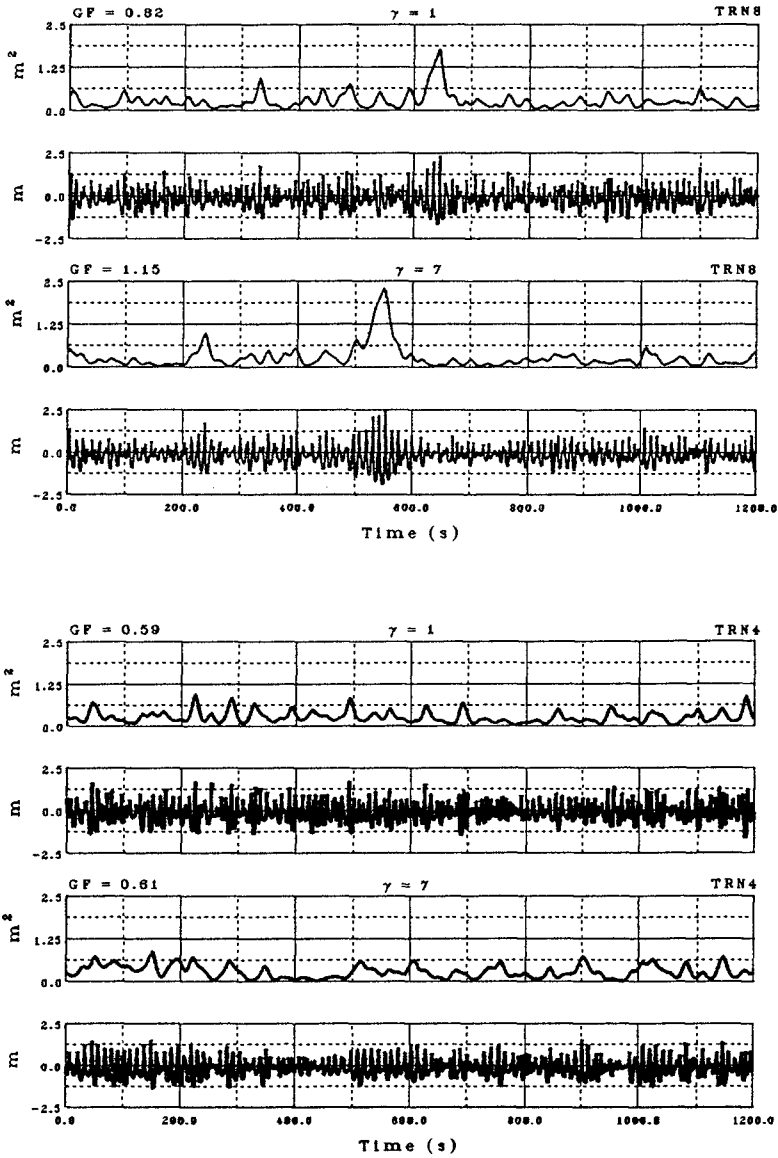


Figure 3. Time Series and SIWEH of the Selected Time Series

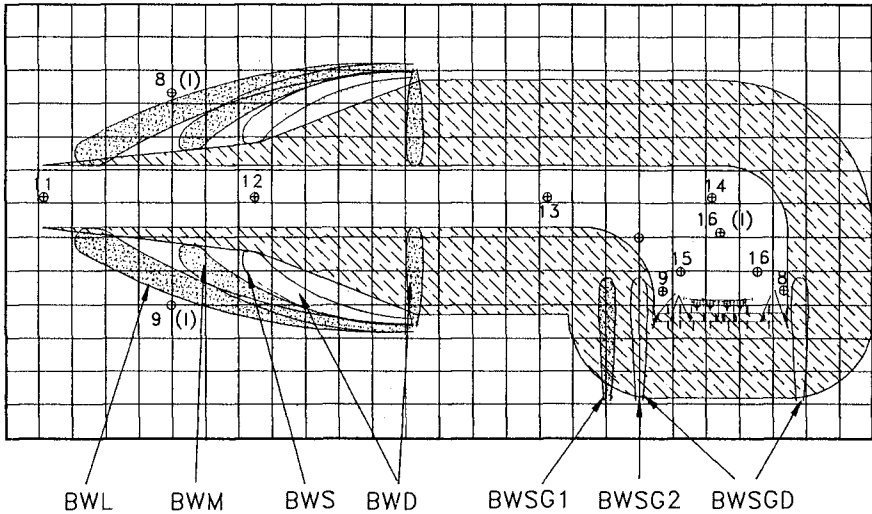


Figure 4: Sketch of the various breakwater options tested

The obvious questions that were expected to be answered by installing these breakwater configurations were the following:

Can a breakwater help reduce the penetration of long wave energy?

Is there an optimal layout which ensures an efficient reduction of energy with smaller capital costs?

## PERFORMANCE OF BREAKWATER LAYOUTS

### Influence of Short Breakwater (BWS)

In terms of engineering practice and as an obvious economical measure for reducing the wave excitation inside the harbour, the short breakwater seemed to be a reasonable solution. This breakwater extended from the high water line at the beach to the edge of the sloped channel. Its performance is illustrated in Figure 5 by comparing it with results obtained without any breakwater (i.e. NBW). In Figure 5a, a comparison of the spectra and the time series measured at the offshore region during the No and Short breakwater tests, are presented to illustrate the similarity in the inputs. Also shown in this Figure is the standard deviation of the long wave energy measured at different locations of the experimental set up (see Figure 1 for the locations).

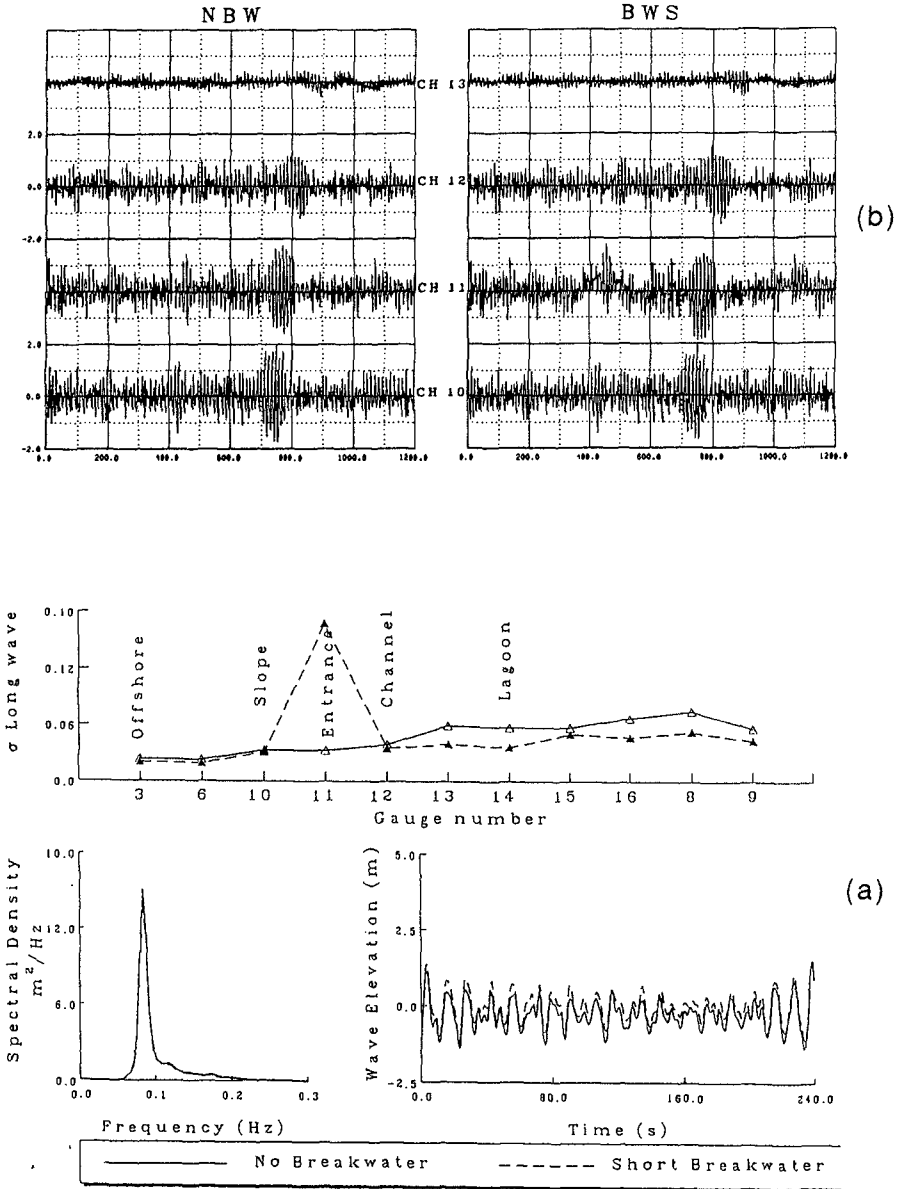


Figure 5. Comparison of results with and without short breakwater

It is interesting to note in Figure 5a that the long wave energy prevailing in the lagoon is substantially reduced by the presence of the short breakwater while at the entrance of the channel, the presence of short breakwater induces a sharp rise in the energy of the long waves. On examining the time series presented in Figure 5b, it appears that this sharp rise may be due to the reflective nature of the breakwater. In spite of this, the net long wave energy that penetrates the channel is shown to be smaller, as the value at gauge 12 illustrates. This reduction leads subsequently to small amplitudes of long waves inside the lagoon. A similar physical process was found when testing with other sea states.

Figure 6 provides an overall view of the results for the four pre-selected sea states, by presenting the spectral densities of long waves measured in the proximity of the vessel by the gauge 8 and the resulting surge spectra. The legends presented in this Figure correspond to the following situations:

GAM7\_TRN8 correspond to  $\gamma=7$  and TRN8; NBW and BWS correspond to No and Short Breakwater situations.

As can be seen in Figure 6a, the shape of the long wave spectra encountered near the vessel remains nearly the same under the two situations of breakwater. The sea state with the largest degree of grouping exhibits the most dramatic influence of the breakwater, possibly due to severe breaking induced by the largest wave group.

### Tests using Bichromatic waves

In order to confirm the good performance of the short breakwater a test series was also undertaken using bichromatic waves. Bichromatic waves are waves composed of two primary frequency components  $f_1$  and  $f_2$ , and a long wave component with a frequency  $(f_1-f_2)$ . In an earlier study of this lagoon harbour, Barthel et al (1994), determined the critical frequency at which the ship responded significantly, by running several combinations of  $(f_1-f_2)$ . The particular bichromatic wave which created this critical frequency (i.e. 100s prototype) was also used in this study to assess the performance of the short breakwater. Figure 7 illustrates the results obtained for three different amplitudes of the long waves characterized by the gain factor. The influence of the short breakwater causing an effective reduction in the long wave amplitude and in the surge motion can easily be appreciated.

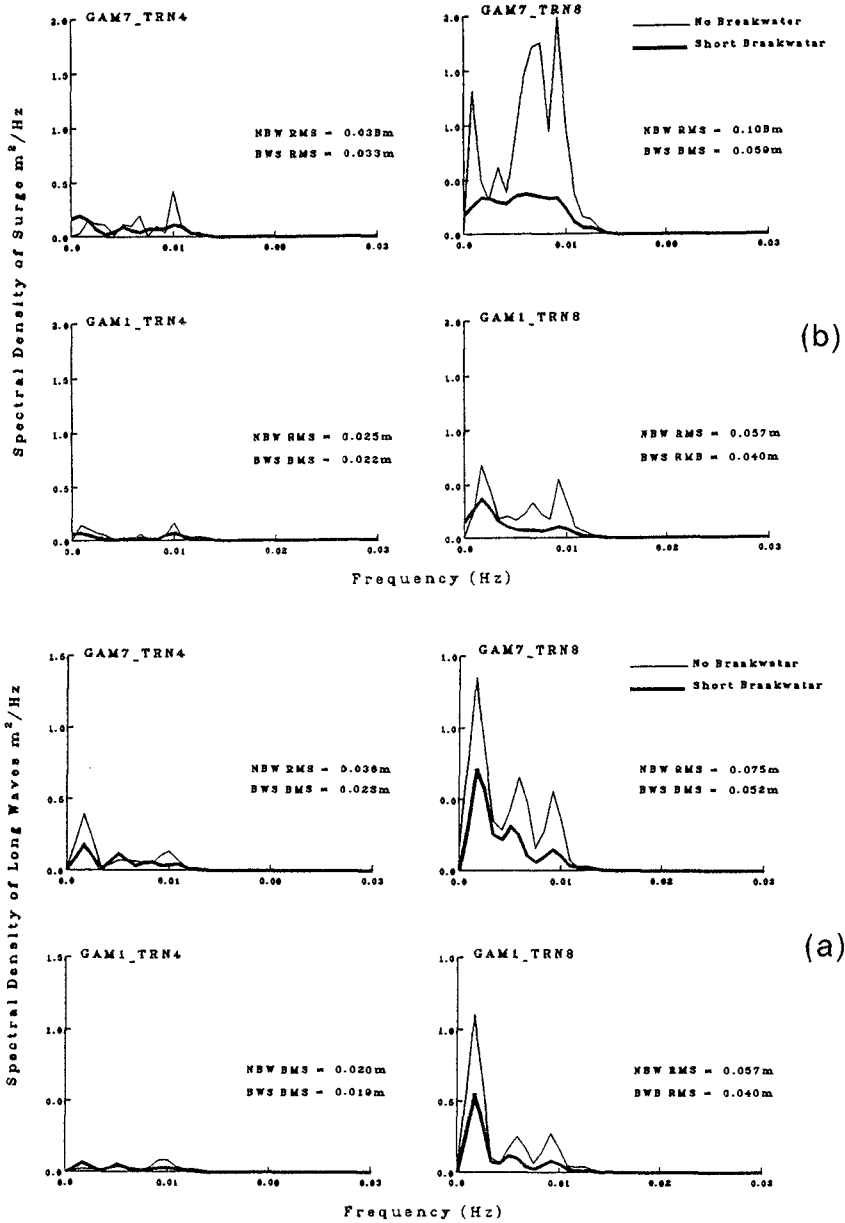


Figure 6 : Spectra of long waves and surge motions under No and Short breakwater situations.

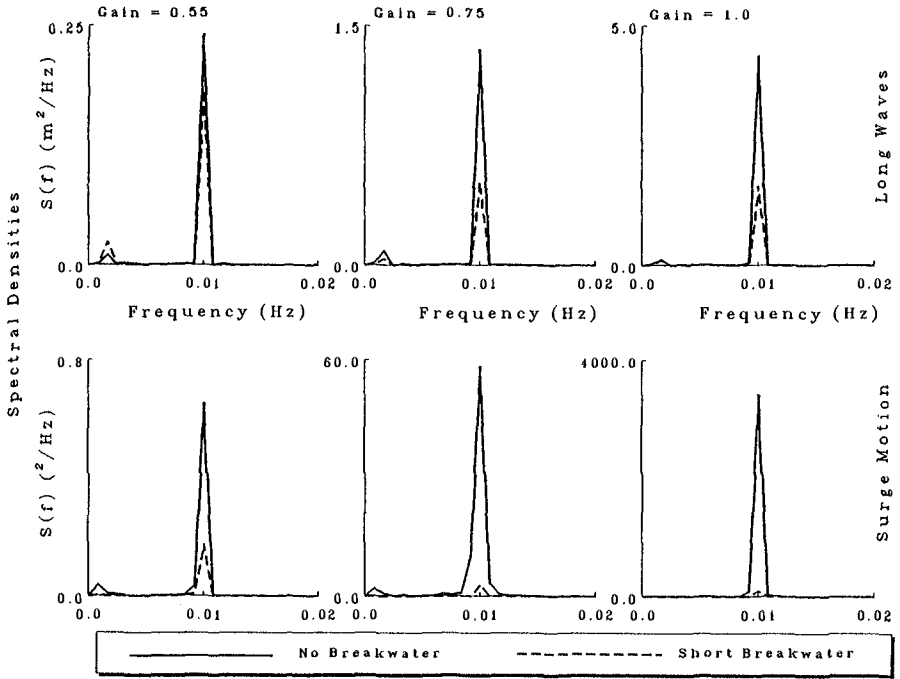


Figure 7. Test results under bichromatic waves

Performance of Other Breakwater Options

A limited series of tests with longer breakwaters (BWM AND BWL) and with the entrance barrier (BWD) showed that they can reduce the ship motions further. However, their results have to be analysed in conjunction with the cost of the structures and with the ship manoeuvrability studies for vessel approach.

Influence of Groynes.

It was speculated that although the short breakwater is effective in reducing the penetration of the long wave energy inside the lagoon, the groynes close to the structure can effectively cut-off the influence of orbital current associated with the long waves and thereby reduce the motions of

the vessel and the loads on the mooring lines. Although the installation of groynes will restrict the manoeuvrability of the vessel, it is believed that tug assistance will be needed in a closed environment such as this lagoon. Hence the trade-off between a longer berthing procedure and a safer mooring system had to be explored. Tests were therefore initiated with one groyne in front of the moored vessel (BWSG1 and BWSG2) and pursued with a combination of one in front and another in the rear (BWSGD). Note that these groynes were evaluated with the short breakwater in place.

As expected, the combination of groynes in front and in the rear generally provided the best protection.

### Test Series with Grouped wave trains

In order to validate this optimization process under different severities of sea states, a grouped wave train, synthesized using the SIWEH concept was used. A JONSWAP spectrum with  $\gamma \approx 3.3$  and a peak period  $T_p = 12$  s was chosen for this simulation. The SIWEH function adopted for this purpose had a Groupiness Factor of 0.9 and a peak period of 120s (see Funke and Mansard 1979 for details on this synthesis process). Six different values of  $H_{m0}$  were used in this test series. The results were then used to assess the relationship that may exist between long wave energy and vessel response. Figure 8 presents the RMS values of the surge measured under different breakwater configurations as a function of the long wave energy measured at gauge 10, just before the entrance of the channel. Although the model was subjected to its maximum response, these results clearly illustrate the the good performance of the BWSGD option (short breakwater with two groynes). Note that for this particular test series, other options such as BWL, BWD and BWSGD1 were not unfortunately explored.

### CONCLUSIONS

A physical model of a ship moored inside a lagoon harbour under the attack of irregular waves with different grouping properties permitted to make the following observations:

- Sophisticated simulation and wave generation techniques including non-linear properties of mooring lines and fenders are required to achieve the necessary accuracy for ship mooring studies;
- Instead of reproducing long time series of water surface elevation, a deterministic approach of using short realizations of pre-selected time



series was adopted successfully in the optimization of the breakwater layout; This approach helped reduce the testing time;

- While inside the lagoon first-order waves were hardly visible, long waves of low amplitudes induced significant motions of the vessel;
- The arrangement of breakwaters at the entrance channel enhanced the dissipation of the long wave energy and reduced the ship motions; The longer the breakwater: the greater the reduction in surge motion.
- Substantial reduction of the surge motion achieved by the short breakwater option was well illustrated by the test series;
- The construction of groynes interrupting the orbital currents associated with long waves is another option to reduce the surge motion further;
- Although efficient breakwater lay-outs have been established in terms of vessel motions inside the lagoon during this experimental program, manoeuvrability of the vessel in the presence of reflections in front of the main breakwater and in the presence of groynes inside the lagoon was not part of this study and therefore has to be explored.

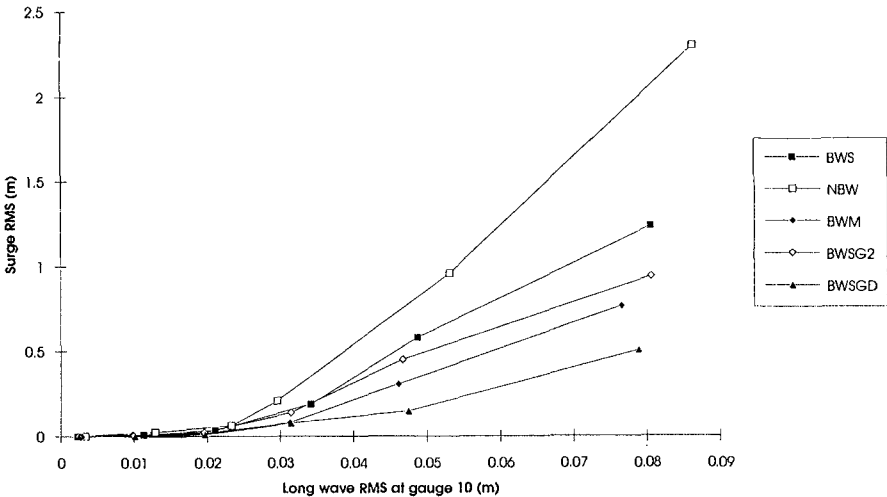


Figure 8 : RMS values of the surge motions as a function of the long wave RMS measured at gauge 10, under different breakwater options.

## ACKNOWLEDGEMENTS

The authors acknowledge their sincere thanks to D.D. Macdonald for his technical assistance. The large number of tests, their analysis and presentation would not have been possible without his help and patience.

## REFERENCES

Barthel, V., Mansard, E.P.D. and Macdonald, D.D., 1994, "Penetration of Long waves into a Lagoon Harbour and Resulting Ship Motions", Proc. HYDRO-PORT'94, Port and Harbour Research Institute, Yokosuka, Japan.

Barthel, V., Funke, E.R. and Laurich P.H., 1989, "Simulation of a Moored Ship in Waves", Instrumentation Workshop of the IAHR. Burlington, Canada.

Funke, E.R. and Mansard, E.P.D., 1979, "On the Synthesis of Realistic Sea States in a Laboratory Flume", Technical Report, National Research Council of Canada, LTR-HY-66.

Kubo, M. and Barthel, V., 1992, "Some Considerations How to Reduce the Motions of Ships Moored at an Open Berth", The Journal of Japan Institute of Navigation, Vol. 87, 91/92.

Laurich, P.H., 1989, "Instrumentation Used at the Hydraulics Laboratory of the National Research Council Canada", Proc. IAHR Workshop on Instrumentation, Burlington, Ontario, Canada.

Mansard, E.P.D. and Barthel, V., 1984, "Shoaling Properties of Bounded Long Waves", Proc 19<sup>th</sup> International Conference on Coastal Eng. Houston, TX, USA: 798-814.

Sand, S.E., 1982, "Wave Grouping Described by Bounded Long Waves", Journal of Ocean Engg., Vol. 9, No. 6.

Sand, S.E. and Jensen, O.J., 1990, "Integration of Marine Simulation in Harbour Design", Proc. 22<sup>nd</sup> ICCE, Delft, The Netherlands.

## CHAPTER 59

### Resonant Forcing of Harbors by Infragravity Waves

Gordon S. Harkins, A. M. ASCE and Michael J. Briggs<sup>1</sup> M. ASCE

#### Abstract

An extensive study of Barbers Point Harbor, including field wave gaging and numerical and physical modeling, was conducted to analyze the harbors response to infragravity wave energy. Infragravity waves have been defined as waves whose periods are greater than 25 sec. Field data collected over a 4-year period were used to calibrate the numerical model while eight extreme events were simulated in the physical model. Agreement between the numerical model, physical model, and the prototype data is good. The importance of spectral shape in the frequency domain also was analyzed by comparing the results from broad and narrow spectra.

#### Introduction

Frequency spectra of ocean waves consist of wind waves whose periods are less than 25 sec and longer period infragravity waves whose periods are greater than 25 sec. Although infragravity waves are rarely seen by the casual beach goer, they are important for coastal processes, including harbor seiching. Harbors with sides on the order of 500 m in length and depths on the order of 10 m are subject to harbor oscillation on the order of 1 minute and longer. Barbers Point Harbor on the Island of Oahu, Hawaii, is a prime example of a harbor that is subject to infragravity harbor resonance.

Sea and swell wave periods contribute the majority of energy in the frequency spectra. Sea waves are locally generated wind waves whose peak period is usually less than 10 sec. Sea waves also are characterized by a broad

---

<sup>1</sup> Research Hydraulic Engineer, USAE Waterways Experiment Station, Coastal Engineering Research Center, 3909 Halls Ferry Rd., Vicksburg, MS 39180.

spectrum both in direction and frequency. Swell waves, on the other hand, are generated far from the area of interest and have peak periods usually greater than 10 sec. These waves, unlike sea waves, tend to exhibit wave groupiness and have both narrow directional and frequency spectra.

Infragravity waves contribute the remaining energy in the frequency spectrum. Infragravity energy can be divided into bound and free wave energy. Bound or forced infragravity waves are nonlinearly coupled to wave groups, traveling at the group velocity of wind waves, and phase locked to sea and swell waves (Longuet-Higgins 1962). Free infragravity waves are further subdivided into leaky and edge waves.

The importance of frequency spread in the generation of infragravity energy has been widely reported from field data and theoretical analysis. Sands (1982) showed theoretically that when peakedness of the frequency spectrum increased, so did the amplitude of long-period waves generated.

This study is unique in that field wave gaging occurred prior to physical and numerical model studies. Numerical and physical models of Barbers Point Harbor were constructed to evaluate the resonant response of six different harbor expansion configurations; however, only results for the existing harbor layout will be discussed in this paper. Eight field wave cases were simulated in the physical model and compared to numerical and prototype results. To evaluate the importance of frequency spread on the generation of long-period waves, 18 empirical seas were analyzed in which the width of the frequency spectra was varied.

### Description of Harbor

Barbers Point Harbor is located on the southwest coastline of Oahu, Hawaii (Figure 1). The harbor complex presently consists of an entrance channel, deep-draft harbor, barge basin, and a resort marina (often referred to as West Beach Marina). The parallel entrance channel is 140 m wide, 945 m long, and 13 m deep (MLLW). The deep-draft harbor basin is 11.6 m deep, 670 m wide, and 610 m long, covering an area of 0.37 sq km. Rubble-mound wave absorbers line approximately 1,400 linear meters of the inner shoreline of the harbor basin. The barge basin, located just seaward of the harbor on the south side of the entrance channel, is poorly sheltered from incident wave energy. It is 67 m by 400 m and is 7 m deep. The private West Beach Marina was built to the west of the deep-draft harbor. It shares the same entrance channel, is 4.6 m deep, and covers approximately 0.08 sq km. The marina was designed to accommodate 350 to 500 pleasure boats.

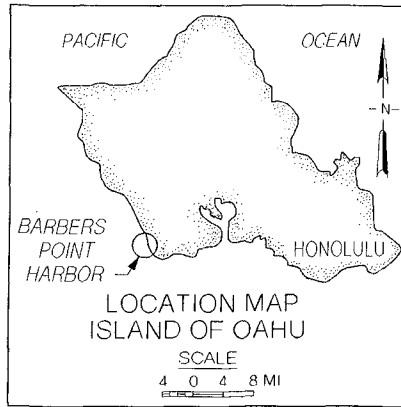


Figure 1. Project location

### Prototype Measurements of Waves

Prototype measurements of waves were made in Barbers Point Harbor between July 1986 and March 1990 as part of the Monitoring Completed Coastal Projects (MCCP) Program and the Coastal Data Information Program (CDIP). These programs provide a network of real-time wave gages and are jointly sponsored by the Corps of Engineers, California Department of Boating and Waterways, and Scripps Institution of Oceanography (SIO). Figure 2 shows selected sites in the main harbor, entrance channel, and nearshore region. Bottom-mounted pressure gages were used to minimize interference with navigation (Briggs et al. 1994).

A four-gage  $S_{xy}$  array was used offshore to measure incident directional spectra conditions in 8.4 m of water. Individual gages were used elsewhere to measure frequency spectra. Other gages included the offshore (Of) and onshore (On) gages, both located shoreward of the  $S_{xy}$  gage. Channel entrance (Ce) and channel mid-point (Cm) gages were located in the entrance channel, where navigation conditions were a consideration. Finally, a gage was located in the south (Sc) corner of the harbor to measure anticipated maximum amplification factors.

A sampling scheme that collected both wind waves (energy) and long period waves (surge) was designed. Initially, energy and surge were obtained from separate records collected by each sensor: 1,024 samples at 1.0 Hz for the energy, and 2,048 samples at 0.125 Hz for the surge. After January 1989, a system upgrade permitted a single record of 4.6 hr at 0.5 Hz (8,192 samples) inside the

harbor, or 1.0 Hz (16,384 samples) outside the harbor, to be collected by each sensor.

Sampling interval was controlled by varying the call-up schedule in the software. The standard interval was every 6 hr in summer and every 3 hr in winter. A threshold routine was built into the system that automatically switched the interval back to 3 hr if significant wave height exceeded 1 m offshore, or 30 cm in the harbor. On the 3 hr schedule, an enhanced sampling scheme provided a continuous record.

The  $S_{xy}$ ,  $C_e$ ,  $C_m$ , and  $S_c$  gages were installed in July 1986. The  $S_{xy}$  gage experienced two major data gaps from cable failures when vessels pulling barges snagged the cable with their tow bridles. This problem was eliminated by moving the shore station to the navigation aid and re-routing the cable away from the entrance channel. Data from the second position of the  $S_{xy}$  ( $S_{xy2}$  in Figure 2) were believed to be more reliable because this gage was further from the edges of the

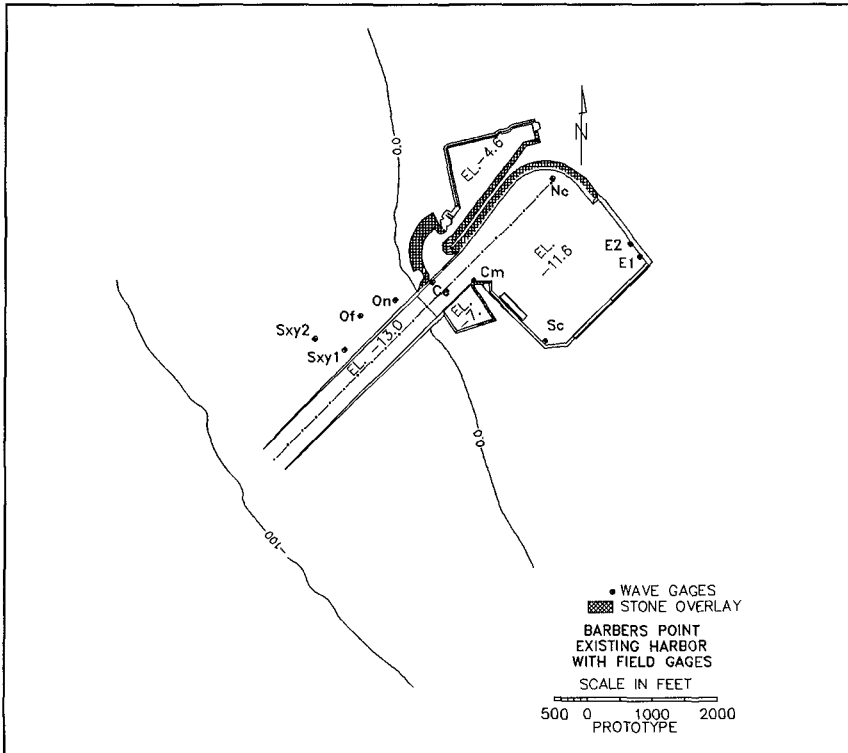


Figure 2. Prototype gage locations

entrance channel and any refractive effects which might have influenced the first position of the array. Construction in the harbor caused longer gaps in the Sc gage. In January 1989, additional sensors were installed in the north (Nc) and east corners to improve spatial resolution. The east corner gages are labeled  $E_1$  and  $E_2$  to differentiate the two different locations. At this time, the entire system was upgraded to the longer sampling scheme.

### Numerical Model Description

The numerical harbor wave-response model, HARBD, was used to estimate wave oscillations in Barbers Point Harbor. HARBD is a steady-state finite element model which calculates linear wave oscillations in harbors of arbitrary configuration and variable bathymetry. The effects of bottom friction and boundary absorption (reflection) are included. Bottom friction is assumed to be proportional to flow velocity with a phase difference. Boundary reflection is based on a formulation similar to the impedance condition in acoustics and is expressed in terms of the wave number (i.e wavelength) and reflection coefficient of the boundary. The model uses a hybrid element solution method which involves the combination of analytical and finite element numerical solutions to determine the response of a harbor to an arbitrary forcing function.

### Numerical Model Formulation

In model formulation for arbitrary depth water waves (i.e., shallow, intermediate, and deepwater waves), the water domain is divided into near and semi-infinite far regions. The near region includes the harbor and all marine structures and bathymetry of interest and is bounded by an artificial 180 deg semicircular boundary offshore of the harbor entrance. The far region is an infinite semicircular ring shape bounded by the 180 deg semicircular boundary of the near region and the coastline. The semi-infinite far region extends to infinity in all directions and is assumed to have a constant water depth and no bottom friction (Chen and Houston 1987). The finite near region, which contains the area of interest, is subdivided into a mesh of nonoverlapping triangular shaped elements. The length of side of each element is determined from the desired grid resolution and design wave parameters. The water depth and bottom friction coefficient are specified at the centroid of each element, and a reflection coefficient is assigned to each element along the solid, near region boundaries. The model requires wave period and direction as input. The solution consists of an amplification factor (i.e., the ratio of local wave height to incident wave height) and a corresponding phase angle for each grid point in the near region. Phase angle represents the difference in phase between the grid point and the incident wave. Contour plots of the amplification factors and corresponding phase angles are used to determine oscillation patterns occurring throughout the harbor.

The governing partial differential equation is derived through application

of linear wave theory to the continuity and momentum equations. All dependent variables are assumed to be periodic in time with angular frequency,  $\omega$ . These steps yield the generalized Helmholtz equation (Chen 1986).

The HARBD model is intended to simulate waves which can be adequately described by the governing generalized Helmholtz equation. Therefore, HARBD does not simulate nonlinear processes such as wave breaking, wave transmission and overtopping of structures, entrance losses, steep bathymetric gradients, and wave-wave and wave-current interaction. Fortunately, these limitations are not dominant for many harbors and HARBD can be applied with some degree of confidence. Since nonlinear processes naturally occur in the prototype, consideration of these effects must be taken in interpretation of results.

A hybrid element method is used to solve the boundary value problem. In this solution, a conventional finite element approximation is used in the finite near region, while an analytical solution with unknown coefficients is used to describe the semi-infinite far region. Conditions in the near and far regions must be matched along the artificial semicircular boundary. This requirement is met by HARBD routines which automatically match the solutions, using the stationarity of a functional, to a series of Hankel Functions which give the solution for the semi-infinite far region (Farrar and Chen 1987). The hybrid element numerical techniques used in the formulation are discussed in greater detail in Chen and Mei (1974).

#### Numerical Model Calibration

The numerical model grid was designed with a grid resolution, the length of each element, equal to approximately one-sixth of the local wavelength, based on linear wave theory using a wave period of 10 sec and the localized water depth. After the grid was generated, individual monochromatic waves with periods from 45 to 24,576 sec were run at increments of 0.00004069 Hz (1/24,576 sec) and the results were compared to the prototype data.

The HARBD numerical model has two free parameters which can be adjusted to match prototype data: bottom friction and reflection coefficients. Other nonlinear processes such as dissipation at the sidewalls and entrance are not included in this model. The boundaries for these long-period waves were felt to be nearly perfectly reflecting. The bottom friction coefficients, however, should be a function of the type of bottom material as a function of the wave period and corresponding wavelength. Therefore, the bottom friction coefficients were varied to calibrate the model predictions to the measured prototype values at each frequency peak or mode.

The HARBD model computes a standing wave for a given frequency. For a low frequency, or very long wavelength, the entire harbor responds as if it were



a reflecting wall. A standing wave against a reflecting wall has a height of twice the incident wave. Therefore, the low-frequency wave height amplitudes predicted by HARBD for input frequencies between 0.000122 (8,196 sec) and 0.001343 (745 sec) were divided by two. Only the Helmholtz mode (or pumping mode of the harbor) was affected by this criteria because the wavelength of this wave encompasses the entire domain of the harbor and outer region to the  $S_{xy}$  gage.

The model was then tested at 0.00004069 Hz frequency increments with varying bottom friction coefficients. Resulting wave height amplifications from each test were compared with prototype measurements to investigate the reduction of wave energy due to the increase of bottom friction. This procedure was repeated until an accurate match of wave height amplification between the model predictions and prototype measurements was possible.

### Physical Model Design

An undistorted, three-dimensional model of Barbers Point Harbor was constructed at a model-to-prototype scale  $L_r = 1:75$ , in accordance with Froude scaling laws. The nearshore area extends to the 30.5 m MLLW contour and includes approximately 1,065 m on either side of the entrance channel. Total area of the model was over 1,000 m<sup>2</sup>.

Waves were generated with the directional spectral wave generator (DSWG) which can produce directional seas at multiple periods. The (DSWG) is an electronically controlled, electromechanical system, designed and built by MTS Systems Corporation, Minneapolis, MN. It is 90 ft long and consists of 60 paddles, each 1.5 ft wide and 2.5 ft high. Each wave paddle is independently driven at its joint by an electric motor operating in piston mode. This configuration, along with flexible plastic plate seals between the paddles, produces a smoother, cleaner wave form (Outlaw and Briggs 1986, Harkins 1991).

### Physical Model Wave Conditions

Eight field events and eighteen empirical unidirectional spectral wave climates were generated. The eight field events were chosen from prototype wave data to obtain the largest wave height and a representative range of wave periods and direction within model constraints. All eight wave conditions represent rare events because of their large wave heights.

Directional spectra were recorded at the  $S_{xy}$  gage for the eight field events chosen. A control signal file for the 60-paddle DSWG was generated by reproducing 30 frequency bins from 0.01 - 0.3 Hz (prototype units) at 2.5° directional bins. Random phase was applied to the control signal generation and thus the long-period waves were not bound to the shorter period waves at the wavemaker. An iterative process was used until a suitable control signal spectrum

was obtained (Briggs et al. 1994).

The entrance channel is aligned approximately S45°W with the principal wave direction of the eight cases distributed around this direction. Table 1 shows the wave parameters for the simulated field wave cases.

**Table 1**  
**Simulated Target Wave Conditions**

No.	Peak Period sec	Significant Wave Ht ft	Average Direction deg	Spread deg
1	12.6	7.1	80	15
2	7.7	9.8	38	17
3	8.3	7.1	45	19
4	10.0	7.4	63	16
5	9.1	10.2	58	7
6	16.7	6.5	43	14
7	16.7	8.2	43	9
8	14.2	7.1	45	9

The eighteen empirical cases consisted of three prototype wave periods (7.69, 11.11, and 16.67 sec), three principal directions (perpendicular to the shoreline and 25 and 30 deg on either side of the orthogonal) and two spectral peakedness parameters ( $\gamma=3.3$  a broad spectrum, and  $\gamma=7.0$  a narrow spectrum).

Long-Wave Harbor Response

Okihiro (1993) postulates that both bound and free infragravity waves are the forcing function for harbor resonance at Barbers Point Harbor. Infragravity waves are long-period waves in the range of 25 to 200 sec on the Pacific coast. Infragravity wave heights are much smaller than wind-wave heights, typically only 10 percent as large. Bound infragravity waves are non-linearly forced by and coupled to wave groups. Bound long waves appear to be the controlling mechanism when swell energy outside the harbor is large (Bowers 1977, Mei and Agnon 1989, Wu and Liu 1990). For this condition, it may be possible to predict harbor resonance given the wind-wave spectrum outside the harbor. Also, they found that wind-wave energy present at swell frequencies produces more bound wave energy than the equivalent amount of energy in sea frequencies.

Recent research (Okihiro and Seymour 1992, Elgar et al. 1992, Herbers et al. 1992, Bowers 1993) indicates that free long waves, in the form of leaky or edge waves, are important and may contribute the bulk of infragravity energy in depths corresponding to the  $S_{xy}$  location. Leaky waves are generated in shallow water and reflected or radiated seaward to the open ocean. Edge waves are generated and radiated seaward like leaky waves but become trapped on the continental shelf due to reflection and refraction and propagate in the longshore direction. Bound waves may even be a source of free infragravity waves in shallow water. The discontinuity of bound infragravity waves across the harbor mouth

may nonlinearly generate free infragravity waves. These free waves would then have energy comparable to bound long waves from outside the harbor.

Outside Barbers Point Harbor, Okihiro and Seymour (1992) found a near-shore coupling between infragravity and wind-wave energy, with a larger infragravity wave height for swell conditions than for higher frequency sea waves. Inside the harbor, they found that infragravity wave heights were highly correlated with infragravity wave heights measured outside the harbor. Furthermore, infragravity wave heights increased as swell energy increased outside the harbor.

### Prototype Analysis Methods

The amplification factor  $A(f)$ , which is a function of frequency, was used to compare the long-period wave height outside the harbor with the long-period wave energy inside the harbor.  $A(f)$  is defined as

$$A(f) = \frac{G_{yy}(f)}{G_{xx}(f)} \quad (1)$$

where  $G_{xx}$  and  $G_{yy}$  are the input and output auto-spectral density functions. The  $S_{xy}$  gage value is used as the input and the harbor gages values are used as the output. Estimates of the auto-spectral density functions  $\hat{G}_{xx}(f)$  and  $\hat{G}_{yy}(f)$  were obtained for each data record by breaking the 4.6-hr-long time series into 2.3-hr records and ensemble averaging the two raw spectral density functions. Estimates of the amplification factor  $\hat{A}(f)$  were calculated from a linear regression on  $\hat{G}_{xx}(f)$  and  $\hat{G}_{yy}(f)$  from all the records as shown in Figure 3 (Lillycrop et al. 1993).

### Physical Model Analysis Methods

In the physical model, a slightly different analysis method called transfer function estimates was utilized. The transfer function is defined as

$$|\hat{H}(f)| = \frac{|\hat{G}_{xy}(f)|}{\hat{G}_{xx}(f)} \quad (2)$$

where  $\hat{G}_{xy}(f)$  is the cross-spectral estimate between input  $x$  and output  $y$  channels and  $\hat{G}_{xx}(f)$  is the auto-spectral estimate for the input  $x$  channel. The auto-spectral estimate is just the frequency spectrum for the  $S_{xy2}$  gage for each wave case. Cross-spectral estimates are similar to auto-spectral estimates except that both input  $S_{xy2}$  and output harbor gages are used in the calculation. One advantage of the cross-spectral analysis over the auto-spectral analysis is that the estimate is not as easily biased by noise in the input or output signal (Briggs 1981). For the transfer function for the south gage ( $S_c$ ), the cross-spectral estimate contains information from both the  $S_{xy2}$  and  $S_c$  gage. A single line was plotted on Figure 3

by averaging the transfer function for the eight wave cases. This increased the statistical confidence of the results.

### Numerical Model Analysis Methods

To analyze long period harbor response in the numerical model, individual monochromatic waves with an amplitude of one were input with direction perpendicular to the bottom contours. The increment between wave frequency was 0.000041 Hz (1/24,576 sec) for wave periods between 45 and 24,576.1 sec. Since the numerical model was tested at three times the frequency of the analyzed prototype measurements, the results were averaged over wave periods one increment above and one increment below the prototype frequencies, analogous to band averaging. This was done so that the numerical frequencies matched those of the prototype. The single line shown in Figure 3 is thus made up of numerous runs. Since the input wave has unit amplitude, the amplification factor is simply the value of the wave amplitude at a particular location.

### Model Comparison

Frequency response of prototype and physical and numerical models is shown in Figure 3. As can be seen, there is good agreement between the three. Values greater than one represent harbor resonance, since there is more energy at that particular frequency inside the harbor than outside. One might note that the physical model does not replicate the longest period resonant mode. This is because limited duration experimental runs were conducted and these long-period modes were not extractable from the data record.

Since the numerical model was tuned to existing conditions of the prototype, one would expect the results to be very similar. The reason for calibrating the numerical model was to investigate alternative harbor layouts.

The prototype results inherently show the effects of both free and bound infragravity wave energy, since both components are present in nature. The physical model was run under extreme wave events and in nature bound waves would be the principal component in the infragravity spectra for these wave conditions. To avoid reflections of wind waves off the sidewalls, wave absorbers were placed along the perimeter of the model. This also dampened the leaky wave energy released at the breaker zone which then would have to reflect off the side walls before propagating into the area of interest. Infragravity energy found in the physical model was generated from nonlinear interactions of the wind wave spectra.

Waves generated in the numerical model are analogous to free leaky waves. The numerical model is linear and is not capable of modelling nonlinear

mechanisms important for the generation of infragravity wave energy.

Independent of the forcing mechanism of infragravity waves, the harbor response is a function of harbor geometry. The numerical and physical model

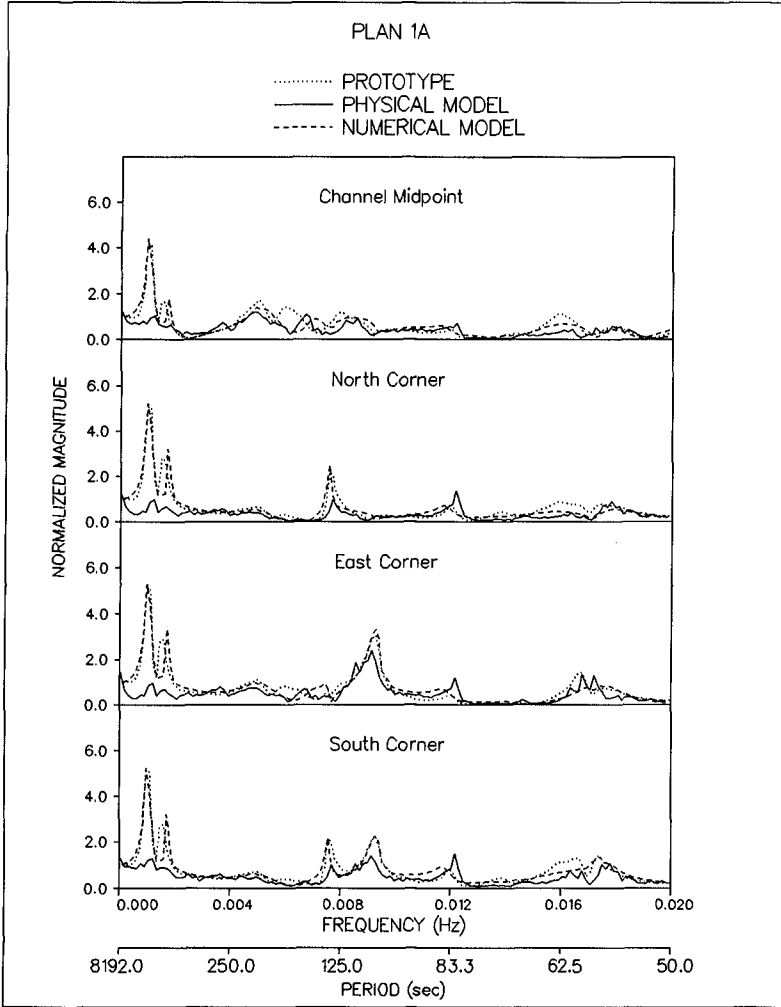


Figure 3. Transfer functions for existing harbor

accurately predict the harbor response.

### Importance of Frequency Spread

The transfer functions shown in Figure 3 for the four corners show amplification or reduction of long-period waves between the  $S_{xy2}$  gage and the four corner gages. To calculate the amplitude of the long-period wave at a particular period inside the harbor, the amplitude of that wave outside the harbor must be known. In nature, there are always some low-amplitude long-period waves present, and in most cases these low levels do not interfere with ship mooring or navigation. One aspect that does appear to be important in the growth of infragravity wave energy is the peakedness of the spectra in the frequency domain.

The JONSWAP spectrum proposed by Hasselman (1973) is characterized by a parameter called the peak enhancement factor,  $\gamma$ , which controls the peakedness of the frequency spectra (Goda 1985). A peakedness parameter  $\gamma=3.3$  (broad spectrum) was found to be the average for the results of the joint wave observation program and is characteristic of sea waves. Waves that have travelled long distances (on the order of 9,000 km) exhibited narrow banded spectrum on the order of  $\gamma=8-9$  (Goda 1983).

To ascertain the importance of the peakedness parameter on generation of infragravity energy, seven gages were located along the 30-m depth contour (offshore gage array) and seven gages were located along the 8.5-m contour (nearshore gage array). The eighteen empirical wave cases then were run with two peakedness parameters. The zeroth moment  $m_0$  or sum of the energy spectra between 25 and 660 sec was used to evaluate the growth of infragravity wave energy. By averaging results between the nine broad-band spectra for the fourteen different wave gages, there was a 183 percent increase in the infragravity wave energy between 30m and 8.5m. The nine narrow band spectra showed a growth of 224 percent between the offshore and nearshore gage arrays.

A comparison between the spectral response of two wave cases with identical parameters, except the peakedness parameter, is shown in Figure 4. The general trend shows an increase in the infragravity wave energy for the narrow band spectra.

### Summary

Results from the physical and numerical models were compared against prototype data. Harbor response of the physical and numerical models showed good agreement with field data. Slightly different analysis techniques were used by each but the final results produced by each technique are comparable.

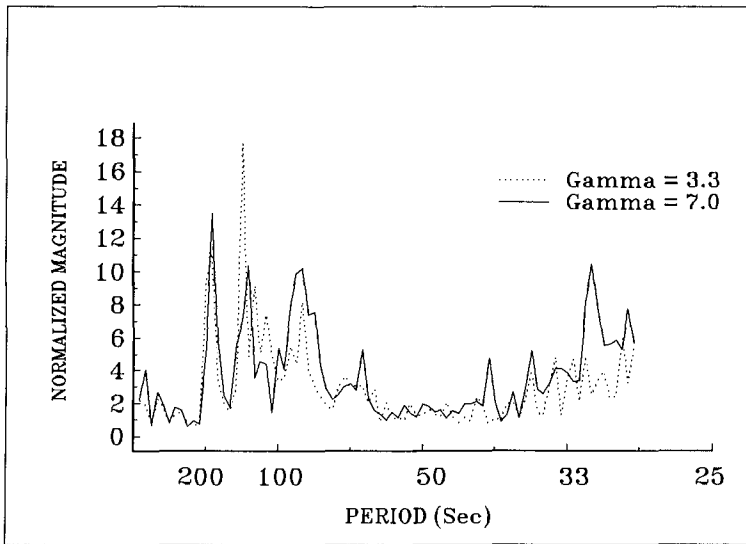


Figure 4. Comparison of infragravity growth between broad  $\gamma=3.3$ , and narrow  $\gamma=7.0$  spectra.

Comparisons between the physical model, numerical model and field data show the resonant response of the harbor. The amplitude of long period waves in the harbor is a function of wave amplitude outside the harbor. One aspect that is important for the evolution of infragravity wave energy outside the harbor is the spectral shape of the wind wave energy in the frequency domain. The growth of infragravity wave energy was evaluated between 30m and 8.5m water depth. Empirical wave spectra with two peakedness parameters were analyzed. The physical model showed that more infragravity wave energy evolved from the narrow banded spectra then evolved from the broad banded spectra.

#### Acknowledgements

The authors wish to acknowledge Headquarters, U.S. Army Corps of Engineers, U.S. Army Engineer Division, Pacific Ocean (POD), and Harbors Division, Department of Transportation (HDOT), State of Hawaii for authorizing publication of this paper. It was prepared as part of a joint effort among the Civil Works Research and Development Program, Monitoring Completed Coastal Projects Program, POD, and DOT. The author would also like to thank the following individuals for their assistance and participation in this project: Messrs. Stan Boc, Dennis Markle, Edward Thompson, Ernie Smith, Frank Sargent, David Daily, Hugh Acuff, Larry Barnes and Mses. Debra R. Green and Linda Lillycrop.

Bibliography

Bowers, E.C. (1977). "Harbor Resonance Due to Set-Down Beneath Wave Groups," J. Fluid Mech., 79, pp 71-92.

Bowers, E.C. (1993). "Low Frequency Waves in Intermediate Depth," Proceedings of 23<sup>rd</sup> International Conference on Coastal Engineering (ICCE).

Briggs, M. J. (1981). "Multichannel Maximum Entropy Method of Spectral Analysis Applied to Offshore Structures," M.S. thesis, Massachusetts Institute of Technology.

Briggs, M. J., Lillycrop, L. S., Harkins, G. S., Thompson, E. F., and Green, D. R. (1994). "Physical and Numerical Model Studies of Barbers Point Harbor, Oahu, Hawaii," Technical Report CERC-94-14, U.S. Army Engineer Waterways Experiment Station, Vicksburg, MS.

Chen, H. S. (1986). "Effects of Bottom Friction and Boundary Absorption on Water Wave Scattering," Applied Ocean Research, Vol 8, No. 2, pp 99-104.

Chen, H. S. and Houston, J. R. (1987). "Calculation of Water Oscillation in Coastal Harbors: HARBS and HARBD User's Manual," Instruction Report CERC-87-2, U.S. Army Engineer Waterways Experiment Station, Vicksburg, MS.

Chen, H. S., and Mei, C. C. (1974). "Oscillations and Wave Forces in an Offshore Harbor," Report No. 190, Department of Civil Engineering, Massachusetts Institute of Technology, Cambridge, MA.

Elgar, S., Herbers, T. C., Okihiro, M., Oltman-Shay, J., and Guza, R. T., (1992). "Observations of Infragravity Waves," Journal of Geophysical Research, Vol 97, No. C10, 15573-15577.

Farrar, P. D., and Chen, H. S. (1987). "Wave Response of the Proposed Harbor at Agat, Guam: Numerical Model Investigation," Technical Report CERC-97-4, US Army Engineer Waterways Experiment Station, Vicksburg, Miss.

Goda, Y. (1985) *Random Seas and Design of Maritime Structures*. University of Tokyo Press, Toyko, Japan.

Goda, Y. "Analysis of Wave Grouping and Spectra of Long-Travelled Swell", Rept. Port and Harbour Res. Inst., Vol 299, 1983, pp. 3-41.

Harkins, G. S. (1991). "Sensitivity Analysis For Multi-Element Wavemakers," Thesis presented to the University of Delaware in partial fulfillment of the requirements of the Degree of Masters of Applied Science.



Hasselmann, K. et al. Measurement of Wind Wave-Growth and Swell Decay During the Joint North Sea Wave Project (JONSWAP), Deutsche Hydr. Zeit, Reihe A (8°), No. 12, 1973.

Herbers, T. C., Elgar, S., Guza, R. T., and O'Reilly, W. C. (1992). "Infragravity-frequency (0.005-0.05 Hz) Motions on the Shelf," Proceedings of 23<sup>rd</sup> International Conference on Coastal Engineering (ICCE).

Lillycrop, L. S., Briggs, M. J., Harkins, G. S., Boc, S. J., and Okihiro, M. S. (1993b). "Barbers Point Harbor, Oahu, Hawaii monitoring study," Technical Report CERC-93-18, U.S. Army Engineer Waterways Experiment Station, Vicksburg, MS.

Longuet-Higgins, M. S. (1962). Resonant Interaction Between Two Trains of Gravity Waves, *J. Fluid Mech.*, Vol 12, pp 321-332.

Mei, C.C., and Agnon, Y. (1989). "Long-Period Oscillations in a Harbor Induced by Incident Short Waves," *J. Fluid Mech.*, Vol 208, pp 595-608.

Okihiro, M., (1993). "Seiche in a Small Harbor," Dissertation presented to the Scripps Institution of Oceanography, University of California, San Diego, in partial fulfillment of the requirements of the Degree of Doctor of Philosophy in Oceanography.

Okihiro, M., and Seymour, R. J. (1992). "Barbers Point Harbor Resonance Study," Scripps Institute of Oceanography, (unpublished manuscript), pp 1-26.

Outlaw, D. G., and Briggs, M. J. (1986). "Directional Irregular Wave Generator Design for Shallow Wave Basins," 21<sup>st</sup> American Towing Tank Conference, August 7, Washington, D.C., pp 1-6.

Sands, S. E., (1982) Long Waves in Directional Seas, *Coastal Engineering*, 6, 195-208.

Wu, J.-K., and Liu, P.L.-F. (1990). "Harbor Excitations by Incident Wave Groups," *J. Fluid Mech.*, Vol 217, pp 595-613.

## CHAPTER 60

### Numerical Simulation of the 1992 Flores Tsunami in Indonesia : Discussion on large runup heights in the northeastern Flores Island

Fumihiko Imamura<sup>1</sup>, Tomoyuki Takahashi<sup>2</sup> and Nobuo Shuto<sup>3</sup>

**ABSTRACT** - Tsunami source model is discussed by numerical analysis for the 1992 Flores Island, Indonesia. Computed results with the composite fault model with two different slip values show good agreements with the measured run-up heights in the northeastern part of Flores Island, except for those in the southern shore of Hading Bay and at Riangkroko. The landslides in the southern part of Hading Bay could generate local tsunamis of more than 10 m, which could be the reason of discrepancy between the measured and computed one. The circular-arc slip model proposed in this study for wave generations due to landslides shows better results than the subsidence model. It is, however, difficult to reproduce the tsunami run-up height of 26.2 m at Riangkroko, which was extraordinarily high compared to other places. Two villages located on the southern coast of Babi Island, back side of the tsunami source region, received severe damages. The simulation model shows that the reflected wave along the northeastern shore of Flores Island, accompanying a high hydraulic pressure, could be the main cause of huge damages in the southern coast of Babi Island.

#### INTRODUCTION

On 12 December 1992, a earthquake of 7.5 Ms and accompanying destructive tsunami struck the northeastern coast of Flores Island (Figure 1). 1,713 casualties and 2,126 injured, half of which were due to tsunami, were reported [Tsuji *et al.*, 1993]. An extremely large tsunami run-up height of 26.2 m was measured at Riangkroko in the northeastern peninsula of Flores Island. There are only two examples in this century --- the 1933 Sanriku earthquake tsunami and the 1993 Hokkaido nansei-oki earthquake tsunami --- in which more than a 20 m tsunami run-up height has been observed.

An International Tsunami Survey Team (ITST) consisting of engineers and scientists from Indonesia, Japan, U.K., Korea and U.S. conducted a field survey

.....  
<sup>1</sup> Assoc.Prof., School of Civil Eng., Asian Inst. of Tech., G.P.O.Box 2754, Bangkok 10501, Thailand.

<sup>2</sup> Res. Assoc., Disaster Control Research Center, Tohoku Univ., Aoba, Sendai 980, Japan.

<sup>3</sup> Prof., Disaster Control Research Center, Tohoku Univ., Aoba, Sendai 980, Japan.

along the northeastern coast of Flores Island and smaller offshore islands, and measured tsunami run-up heights as shown in Figure 2.

In this paper, two of problems ITST pointed out are selected because of their important role in preventing tsunami disasters in the future. First is that run-up heights at Riengkroko and at Uepadung and Waibalan in Hading bay of 17.3 - 26.2 m and more than 10 m, respectively, are surprisingly larger than those on the western part of Flores Island[Gonzalez et al., 1993] (Figure 2). Second is the damage at two villages in Bali Island, which are located on the back side of tsunami source where usually damage due to tsunami is not large.

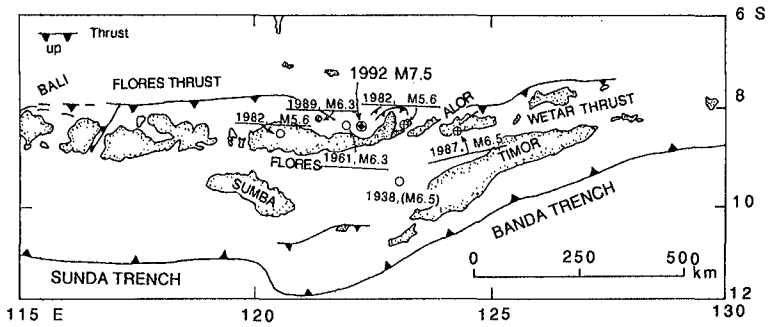


Figure 1 Map of tectonic and epicenter of earthquake in Flores Island which is located in the back arc of eastern Sunda and western Banda thrusts.

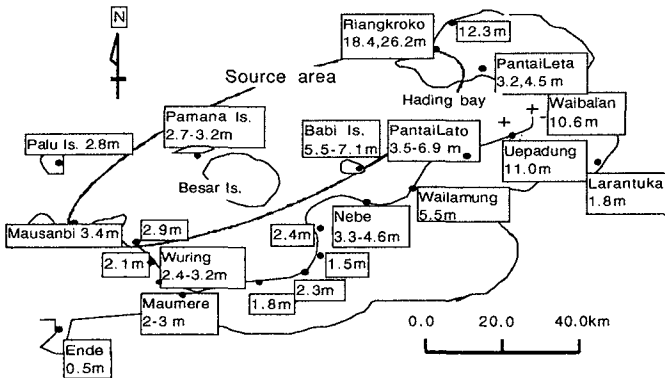


Figure 2 Measured tsunami run-up heights in meter in the eastern Flores Island and the tsunami source [Tsuji et al., 1993]. A general trend of increasing run-up height from west to east in this region is significant. The symbols of cross indicate the location of landslide in the Hading Bay.

## TSUNAMI SOURCE MODEL

Our initial tsunami model uses one fault model, Model-A in Table 1: the quick Harvard CMT solution [ event file M121292Y]. Taking into account the tectonics in this region, that is thrust in the back arc [*Hamilton, 1988*], a shallow dip thrust fault as the source with (strike,dip, slip) =  $(61^\circ, 32^\circ, 64^\circ)$  is selected. According to the distribution of the aftershocks determined by the United State Geological Survey (USGS), the fault plane is estimated to be 100km long and 50km wide. Thus an average dislocation of 3.2 m can be determined by using a rigidity of  $4.0 \times 10^{11}$  dyne/cm<sup>2</sup>.

Table 1 Fault parameter of the 1992 Flores earthquake

	Mo ( $\times 10^{27}$ dyn-cm)	Depth (km)	Strike (deg)	Dip (deg)	Slip (deg)	Length (km)	Width (km)	Dislocation (m)
Model-A	6.4	15	61	32	64	100	50	3.2
Model-B (East)	1.6	15	61	32	64	50	25	9.6
(West)	4.8	15	61	32	64	50	25	3.2
Model-C (East)	1.6	3	61	32	64	50	25	9.6
(West)	4.8	3	61	32	64	50	25	3.2

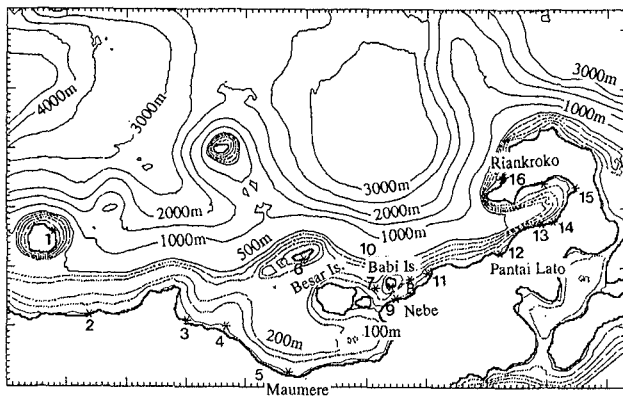


Figure 3 Computational region and geometry, contour of water depth, in the northeastern Flores Island. Spatial grid size of 300 m is used.

A numerical simulation of tsunami generation and propagation, the TUNAMI - N1 code [Shuto *et al.*, 1990 and Imamura *et al.*, 1992], was carried out using this fault model. The area for computation is shown in Figure 3. The lack of detailed topographical data in shallow region and on the land makes it difficult to carry out run-up simulation. Therefore the computed maximum levels along the coastline are directly compared with the measured run-up heights. The computational condition is summarized in Table 2.

Table 2 Computational condition

Governing Equation	Shallow water theory (nonlinear theory)
Spatial grid size	300 m
Time step	1 sec
B.C. of coastal line	Perfect reflection condition (vertical wall)
Reproduction time	1 hour

The computed results with Model-A are smaller than the measured run-up heights in the eastern part, suggesting that the slip value on the eastern side of the fault might have been larger than that on the western side. After several trials, a composite fault model with different slip values : 3.2 and 9.6 m was, therefore, proposed [Imamura & Kikuchi, 1994]. In this model, the seismic moment of  $6.4 \times 10^{27}$  dyne-cm is kept and both segments have the same fault area of 50 km long and 25 km wide (Figure 4). The crustal movements estimated by the composite fault model with a depth of 3 km coincides with the crustal deformation measured by Tsuji *et al.* (1993). Computed results using composite model, Model-B and C, are compared to the measured run-up heights in Figure 5, which shows that the numerical model with the composite fault model reproduces well the distribution of the measured tsunami heights along the northeastern coastline of Flores Island, except for the southern shore of Hading Bay and Riangkroko.

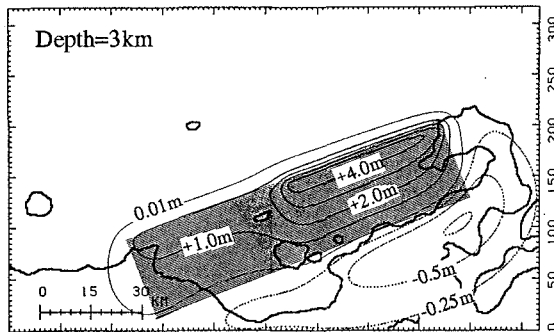


Figure 4 Composite fault model [Imamura & Kikuchi, 1994] and its vertical displacement of ground. Moment release in the eastern part is larger than that in the

western part.

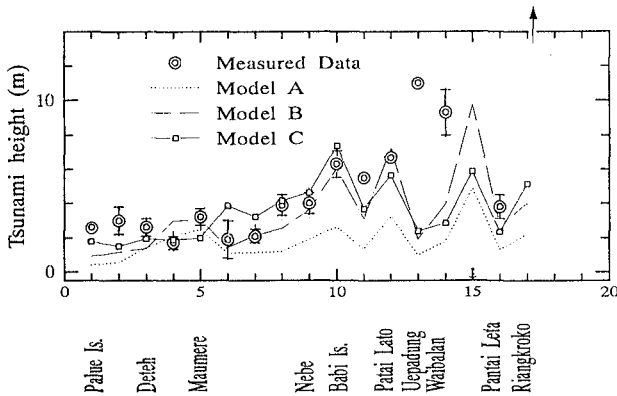


Figure 5 Comparison between the measured run-up heights and the computed maximum water level along the northeastern coast of Flores Island. Computed result show a good agreement with the measured one except for Uepadung, Waibalan and Riangkroko.

## TSUNAMI IN HADING BAY AND RIANGKROKO

### *Landslide in Hading Bay*

As shown in Figure 5, the measured run-up heights of 10.6 m at Waibalan and 7.6 - 11.0 m at Uepadung in the southern shore of Hading Bay are much higher than those at other places in this bay such as Pantai Lato and Pantai Leta, and the computed results with composite fault model. It is possible that abnormal run-up heights were generated by not only earthquake but another geological agents. ITST noticed large landslides along the southern shore of Hading Bay [Yeh *et al.*, 1993] and reported that the landslide shear planes are almost vertical, forming a steep and vertical cliff along the present shoreline and its area is approximately 150 m wide and 2 km long. The large run-up heights observed are limited to the area of subaqueous slumps, suggesting a possibility that they were caused by landslide-generated waves rather than tectonic tsunami waves.

### *Wave Generation Model due to Landslide*

Until now several models for wave generation due to landslides, ranging from the inflow volume method and unit-width discharge method [Ming & Wang, 1993] to two-dimensional boxes dropped vertically at the end of a semi infinite channel [Noda, 1970] have been proposed. Yet, all these methods cannot be applied directly to the present case, because higher tsunami heights were observed not on the opposite side the landslide area but along the landslide and its surrounding area. In addition, the

observed run-up were higher than the level of the top of the landslide. In the present study two models, subsidence and circular-arc slip model (Figure 6), are proposed [Gica, 1994], because the cavity formed by a sudden collapse could generate a wave propagating toward the coast. In the discussion for wave generation due to landslides, the run-up modeling is used. Numerical condition that the averaged depth, 20 m, and height of land, 8 m, is estimated from the field survey, but the radius of circular-arc slip, 30 m, and property of soil are assumed here because there are no data about them. Assuming the same maximum vertical displacement in both models, the computed results showed that the wave run-up height, 3.9 m, of the subsidence model is half that of the circular-arc slip model, 8.2 m. The reason is that the toe of the landslide mass in the circular-arc slip model increases the sea bottom, which causes the disturbances of water surface propagating toward the coastal line. The maximum run-up heights of the circular-arc slip model is 8.2 m and almost same as that of the ground level. The above result suggests that the circular-arc slip model is more suitable to reproduce the tsunami of more than 10 m in height. Unfortunately the lack of field data such as landslide scale under the sea, and soil properties, does not allow us to compare the computed values with the measured in Hading Bay.

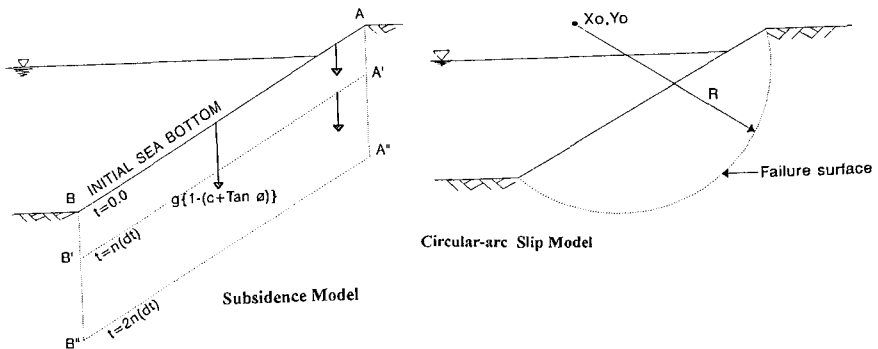


Figure 6 Subsidence (left) and circular-arc slip (right) models for the wave generation due to landslides. The deformation sea bottom is calculated every steps based upon two models.  $c$ ; soil cohesion,  $\phi$ ; soil friction angle,  $g$ : gravitaional acceleration.

### Riangkroko

An extremely large tsunami run-up was measured at the small village of Riangkroko (Figure 7), where 137 people lost their lives (population 406 prior to the event). The village is located at the mouth of a small river, the Nipar River, with its northwestern side facing the Flores Sea. Offshore from the village there is a remarkable steep slope of sea bottom, which is similar to the case of Okushiri Island in the 1994 Hokkaido Nansei Oki earthquake tsunami. The maximum run-up height

measured at Riangkroko was 26 m and the average of heights based on four different tsunami marks was 19.6 m, indicating that the magnitude of the tsunami run-up is probably not an isolated local phenomenon like wave splash-up. Figure 5 shows that the computed results are much smaller than the measured at Riangkroko. The ratio of the measured to the computed values is more than 5, which is considerably large. The reason of such a large run-up height and discrepancy to the computed results should be explained, however no significant geological phenomema such sa landslide at Hading bay was observed on the land. A propagation process on the steep slope of sea bottom could cause the significant amplification of wave, or another geophysical phenomena such as submarine landslide could generate wave. For further discussions, a field investigation on this area and a numerical analysis with the more detailed topography at the offshore and on the land are required.

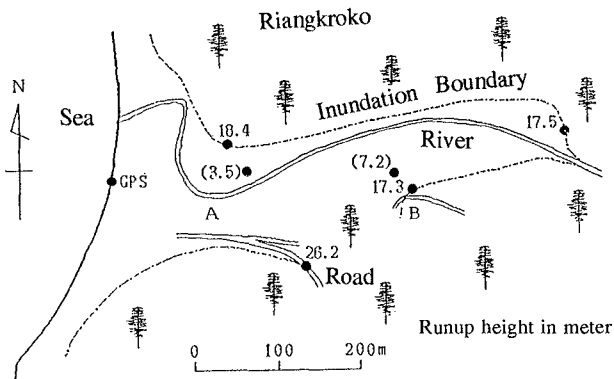


Figure 7 Inundation area and tsunami run-up at Riangkroko. All houses were completely washed away by tsunami. Numerals in pareuthese are the inundated tsunami heights.

H UGE DAMAGE IN BABI ISLAND

*Babi Island*

Babi Island (Figure 8) received significant damage with 263 casualties for 1,100 residences, and a complete loss of all houses. Measured tsunami run-up heights are 5.6 m in the Christian village and 3.6 m in the Moslem village. A maximum of 7.2 m was measured on the cliff in the western side of the island. Although the run-up heights are not as high as those at other damaged places, the damage due to tsunamis was quite severe.

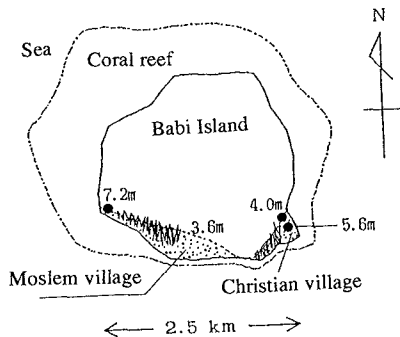


Figure 8 Map of Babi Island.



Babi Island is about 5 km offshore from Flores. It has a conical shape with a 351 m summit elevation and approximately 2 km in diameter. The northern shore faces the Flores Sea and has a wide coral reef, while the southern shore where the two villages were located has a much narrower reef. Even when strong wind waves and swells of the Flores Sea attack from the north, wave conditions on the southern side are usually calm, because most incoming wave energy is dissipated on the wide coral reef on the northern side [Yeh *et al.*, 1993]. However, southern part of the island severely received damages due to tsunami current rather than large wave.

#### *Reflected Waves and Hydraulic Pressure*

In order to explain why the southern coast of Babi Island suffered huge damages due to the tsunami, a numerical simulation with the same condition shown in Table 2 was carried out specifically focusing on Babi Island. Figure 9 shows the water elevation contours and the current vector distributions around this island from 4 minutes to 10 minutes after tsunami generation. Figure 10 shows the time histories of water level, velocity, and hydraulic pressure in front of the Moslem village. The hydraulic pressure is defined as follows [Aida, 1977];

$$[\text{Hydraulic Pressure (m}^3/\text{s}^2)] = [\text{Tsunami Inundated Height (m)}] \times [\text{Current Velocity (m/s)}]^2 \quad (1)$$

It is noticed that current velocity makes effect on hydraulics pressure more than tsunami height.

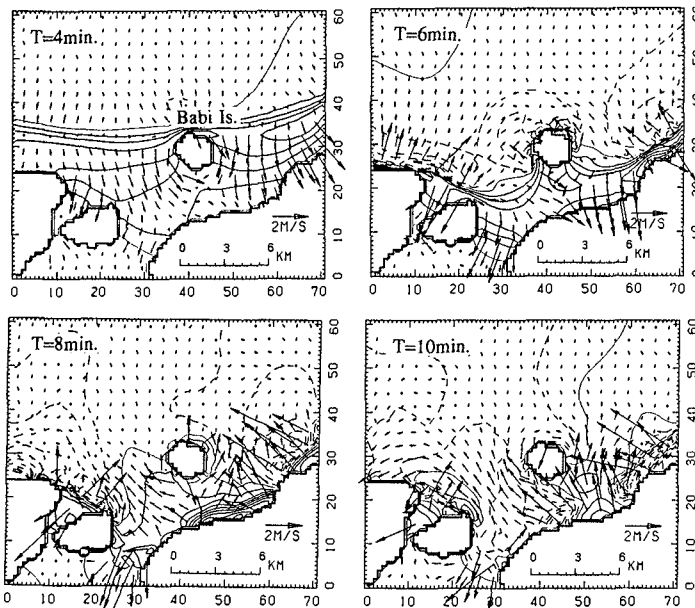


Figure 9 Water elevation contours with intervals of 1 m and current vectors around Babi Island. The first wave was reflected along the northern shore of Flores Island at 8 minutes after earthquake and attacked the southern coast of Babi Island.

Hatori's(1984) empirical result of the relationship between damage on houses and hydraulic properties showed that the hydraulic pressure is the most suitable parameter to estimate the degree of house damages. Figures 9 and 10 show that the first wave attacked the island from the north direction with not a high hydraulic pressure, but the same wave was reflected off the coast of Flores Island and again attacked Babi Island on the southern part accompanied by a high hydraulic pressure. This result is consistent with the eyewitnesses at this island. In addition, the island is located at the nodal point of the standing wave generated along the coast of Flores Island, suggesting that the wave height is small whereas the current is large.

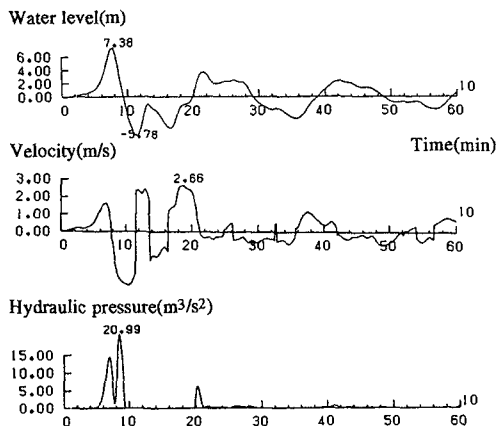


Figure 10 Time histories of water level, velocity and hydraulic pressure. The positive values of velocity component indicate that tsunami propagate from the northern side to the southern one.

#### Measured and Computed Hydraulic Pressure

We could estimate hydraulic pressure and velocity at Wuring near Maumere by measuring the tsunami traces on the wall of the Mosque [Matsutomi, 1993; Imamura *et al.*, 1993] (see Figure 11). Here almost all of the wooden houses were destroyed due to the tsunami. Applying the Bernoulli theorem by assuming energy conservation between the front and back of the Mosque, we calculated the velocity to be 2.7 - 3.6 m/s and the hydraulic pressure to be 6.2 - 15.2  $\text{m}^3/\text{s}^2$ . This estimation coincides with Hatori's(1984) criterion that the hydraulic pressure over 5-9  $\text{m}^3/\text{s}^2$  corresponds to damage of over 50%. The result of the present simulation, a velocity of 2.38 m/s and a hydraulic pressure of 7.70  $\text{m}^3/\text{s}^2$ , agreed with the estimated data well, which supports the accuracy and reliability of this simulation model. In terms of numerical results, the places recorded the hydraulic pressure over 10  $\text{m}^3/\text{s}^2$  are Babi Island, Waibalan, Pantai Lato and Riangkroko. Surprisingly the hydraulic pressure at Riangkroko is over 30

$m^3/s^2$ .

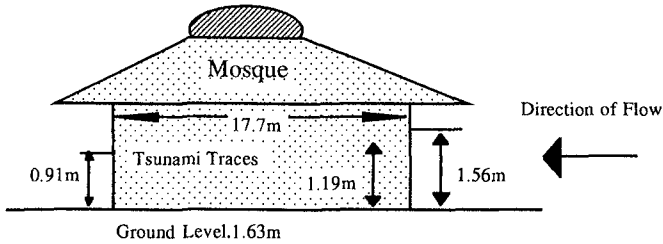


Figure 11 Tsunami traces on the mosque at Wuring, which are used to estimated the current velocity and the hydraulic pressure.

## CONCLUSIONS

The landslide found in the southern shore of Hading bay could generate local waves which are much higher than those obtained by the tsunami simulation with only crustal movement. A new model for wave generation due to landslide, circular-arc slip model, is proposed. This model might reproduce higher run-up heights along the coastline than the subsidence model. The tsunami run-up height at Riangkroko was extraordinarily high compared to other places. The wave propagation process on a steep slope of sea bottom as well as the geological agents such as submarine landslide could be related to this data. Numerical model shows that the reflected wave along the northeastern shore of Flores Island is the main cause of huge damages in southern Babi Island. The computed hydraulic pressure and velocity at Wuring is well corresponding to the measured one.

## ACKNOWLEDGEMENTS

The study was partially supported by a Grant-in-Aid No.04306024 for Cooperative Research (A) and No.06044015 for International Scientific Research Program from the Ministry of Education, Science and Culture, Japan.

## REFERENCES

- Aida, I. (1977), *Numerical experiment for the tsunami inundation - in the case of Suzaki and Usa in Kochi prefecture*, Bull. Earthq. Res. Inst. Univ. Tokyo, 52, 441-460 (in Japanese).
- Gica, E. (1994), *A study on the 1992 Flores Indonesia earthquake tsunami ; Numerical model on the wave generation due to landslide*, Master thesis in Asian

- Institute of Technology, 67p..
- Gonzalez,F., Sutisna,S., Hadi,P.,Bernard,E., and Winnarso,P.(1993), *Some observations related to the Flores Island earthquake and tsunami*, Proc. Int. Tsunami Symp. in Wakayama, 789-801.
- Hamilton,W.B.(1988), *Plate tectonics and Island arcs*, Geological Soc.Am.Bull., 100,1503-1527 .
- Hatori,T.(1984), *On the damage to house due to Tsunamis*, Bull. Earthq. Res. Inst. Univ. Tokyo, 59, 422-439.
- Imamura,F., Shuto,N., Ide,S.,Yoshida,Y. and Abe,Ka(1992),*Estimate of the tsunami source of the 1992 Nicaraguan earthquake from tsunami data*, Geophys. Res.Let., 20 , 1515-1518.
- Imamura,F., Matsutomi,H., Tsuji,Y., Matsuyama,M., Kawata,Y. and Takahashi,T. (1993), *Field survey of the 1992 Indonesia Flores Tsunami and its analysis*, Proc. of Coastal Engng in Japan, 40, 181-185 (in japanese).
- Imamura,F. and Kikuchi,M (1994),*Moment release of the 1992 Flores Island earthquake inferred from tsunami and teleseismic data*, Sci. Tsunami Hazards, Accepted.
- Matsutomi,H.(1993),*Tsunami and damage in the northeast part of Flores Island*, Monthly Ocean, 25 , 756-761. (in Japanese) .
- Ming,D. and Wang,D.(1993), *Studies on waves generated by landslide*, Proc.XXV congress of IAHR, Tech.Session c, 1-8.
- Noda,E.K.,(1970), *Water waves generated by landslide*, J.Waterways, Harbors and Coastal Eng Div., ASCE, 96, 835-855.
- Shuto,N, Goto,C. and Imamura,F.(1990), *Numerical simulation as a means of warning for near-field tsunami*, Coastal Engng in Japan, 33, 2, pp.173-193.
- Tsuji.Y., Imamura,F., Kawata,Y., Matsutomi,H., Takeo,M.,Hakuno,M.,J.Shibuya, Matsuyama,M. and Takahashi,T.(1993), *The 1992 Indonesia Flores earthquake tsunami*, Monthly Ocean, 25 , 735-744,(in Japanese) .
- Yeh,H, Imamura,F.,Synolakis,C., Tsuji,Y., Liu,P. and Shi,S. (1993), *The Flores Island tsunamis*, EOS, Trans. Am. Geophys. Union, 74, 33, 371-373.

## CHAPTER 61

### A Comparative Evaluation of Wave Grouping Measures

E.P.D. Mansard<sup>1</sup> and S.E. Sand<sup>2</sup>

#### ABSTRACT

This paper describes the limitations associated with some of the wave grouping measures that are currently available in the literature. A brief review of the new concepts that have been proposed recently to overcome these limitations is also included in it.

Extensive analysis of prototype waves is carried out worldwide to establish a relationship between the degree of grouping in waves and their variance spectral density. But some of these analyses have been unable to identify any relationship because of the statistical variability inherent to records of finite length. A brief discussion of this variability is included in this paper.

#### INTRODUCTION

The occurrence of wave groups and their importance are well recognized by the engineering community. During the last fifteen years, many studies have illustrated the relevance of wave groups to the design of maritime structures. Much research is therefore being carried out in this field and their main objectives can be summarized as follows:

- (i) to develop an adequate measure of the degree of grouping;
- (ii) to establish a statistical model for the wave groups; and
- (iii) to achieve a better understanding of the effect of wave groups on structural response.

Several measures have been proposed to quantify the degree of grouping in a sea state, but none of them seems fully adequate for practical use. Some of the limitations of these measures are reviewed in this paper, using numerical simulation.

---

<sup>1</sup>Senior Research Officer, Coastal Engineering Program, IMD, NRC.

<sup>2</sup>Manager, Marine Simulation Department, Danish Maritime Institute, Lyngby, Denmark.

In order to establish statistical models for wave groups, many researchers have advanced the concept that all information about wave groups is contained within the primary spectrum. This implies that, once the shape of the primary spectrum is known, the information about wave groups can easily be deduced. A brief evaluation of this hypothesis is carried out in the later sections.

Attempts are made to achieve a better understanding of the complex physics involved in the interaction of wave groups with coastal structures in order to relate the degree of wave grouping to group-induced response of structures. Some of the techniques used for this purpose are also discussed in this paper.

### BRIEF REVIEW OF THE WAVE GROUPING MEASURES

Amongst the large number of concepts that have been proposed to describe wave grouping, the following are some which have been explored in detail.

- i) Statistics of Run Lengths;
- ii) Wave Grouping from the Square of the Water Surface Elevation;
- iii) Correlogram;
- iv) Phase Spectrum; and
- v) Concepts Based on Hydrodynamics of Wave Motion.

Amongst these concepts, only the first two are used extensively. This paper will focus on them, nevertheless indicating relevant bibliography for the remaining three.

#### Statistics of Run Lengths

The Run Length is defined as the number of successive waves with wave heights exceeding a specified threshold; the threshold can be the average, the median or the significant wave height of a sea state. The average run length ( $\bar{j}_1$ ) within a wave record is then used as the measure of the degree of grouping. The total run is analogous to a wave group period, and is defined as the number of waves contained in the interval which commences with the first threshold exceedance of one run and ends with the first exceedance of the next run. The average value of the total run within a wave record is usually denoted as  $\bar{j}_3$ .

Kimura (1980) provides the necessary expressions for predicting the mean and the standard deviation of the run lengths and of the total runs, as a function of a correlation parameter  $\kappa$  derived from wave records. This parameter is related to the correlation coefficient between two successive heights,  $\rho_{HH}$ , and can be calculated from the zero crossing-analysis of waves. But if the time series has to be used anyway for determining this correlation coefficient, the run length statistics can be easily inferred at the same time. It appears therefore that there is no distinct advantage in using Kimura's theory except to compare his predictions with observed values in field data. Hence researchers such as Battjes and van Vledder (1984) promote the use of the correlation parameter  $\kappa$  derived from the spectral density of the sea state as follows:

$$\kappa_f^2 = \frac{1}{m_0^2} \left\{ \left[ \int_0^\infty S(f) \cos(2\pi f \tau) df \right]^2 + \left[ \int_0^\infty S(f) \sin(2\pi f \tau) df \right]^2 \right\}, \quad (1)$$

where:  $m_0$  is the zeroth moment of the spectral density function  $S(f)$  and  $\tau$  is the mean wave period.

If the run length statistics can be satisfactorily predicted from this spectrum-derived correlation parameter  $\kappa_f$ , it can be concluded that most information regarding wave groups is contained in the spectrum itself.

#### Wave Grouping From the Square of the Water Surface Elevation

Several measures have been proposed to quantify the degree of grouping present in a sea state based on the concept of the square of the water surface elevation. A brief description of some of these measures is given below.

#### Smoothed instantaneous wave energy history (SIWEH)

One of the well known measures for characterizing the degree of grouping in a sea state is the Groupiness Factor based on the SIWEH (Funke and Mansard, 1979). The SIWEH is a time series of the low frequency part of the square of the elevation,  $\eta_i^2(t)$ . It is computed by squaring the instantaneous water surface elevation and then smoothing it by a Bartlett low-pass filter of size  $2 \times T_p$  (where  $T_p$  is the peak period of the spectrum). The Groupiness Factor, GF, which is a measure of the degree of grouping, is defined as the standard deviation of SIWEH normalized with respect to its mean value.

#### Hilbert transform of wave record

A technique which involves no low-pass filtering to compute the low frequency part of the square of the water surface elevation is the Hilbert transform technique, proposed by Bitner-Gregersen and Gran (1983) and extensively used by Medina & Hudspeth (1988, 1990).

If the water surface elevation and its conjugate are expressed as  $\eta(t)$  and  $\hat{\eta}(t)$  respectively, it can be shown that they are the Hilbert transform of each other. From these two functions, the envelope of the water surface elevation,  $A(t)$ , the wave height function,  $H(t)$ , and the low frequency part of the square of the water surface elevation,  $\eta_i^2(t)$ , can be computed easily (see Medina et al., 1990 and Medina & Hudspeth, 1990).

A concept similar to the SIWEH Groupiness Factor can also be used in this case to define the degree of grouping. Medina et al. (1990) propose the use of GF defined as the standard deviation of the square of the wave height function normalized by  $8m_0$  ( $m_0$  is the zeroth moment of the sea state spectrum). This approach of computing GF is obviously superior to SIWEH analysis since it involves no low-pass filtering. However, it has some limitations which will be discussed later in this paper.

### Expected wave grouping spectrum

For a given sea state, the expected spectrum of the low frequency part of the square of the water surface elevation (known also as spectrum of wave groups) can be computed easily from the auto-correlation of the primary spectrum, without having to deal with the time series of water surface elevation and its Hilbert transform (see Pinkster, 1984). Figure 1 shows three JONSWAP spectra with different peak enhancement factors,  $\gamma$ , and their corresponding wave grouping spectra. The cut-off frequency used in the low pass filtering of SIWEH is also indicated in Figure 1b for easy reference.

It should be pointed out that individual realization of finite length wave records, simulated from these JONSWAP spectra, can result in grouping spectra that differ from the expected functions illustrated in Figure 1.

### Correlogram

The concept of using the correlogram (i.e. auto-correlation function) to describe wave grouping was attempted by Rye and Lervik (1981) and Sobey & Read (1984) without much success. More recently, Medina and Hudspeth (1990) showed that the correlation parameter  $\kappa$  used in the prediction of run lengths can be derived from the auto-correlation function of the square of the wave height function.

### Phase Spectrum

Funke and Mansard (1981) and Sobey and Read (1984) speculate that phase spectra of sea state may contain some information on the degree of grouping. In fact, Funke and Mansard (1979) showed that, by just changing the phase spectrum, wave trains with different degrees of grouping can be simulated from a given variance spectral density, without however establishing any specific relationship between the degree of grouping and the phase spectrum. Goda (1983) analyzed some swell records for the probability distribution of phases, and concluded that the phases were indeed uniformly distributed between  $-\pi$  and  $\pi$  but not completely random. Nevertheless, the deviation from randomness was only slight.

### Concepts Based on Hydrodynamics of Wave Motions

All the wave grouping concepts presented so far are based only on statistical wave properties such as wave energy spectrum or wave energy envelope. But other approaches, based on the hydrodynamics of wave motions, have also been explored in the literature.

Mase and Iwagaki (1986a and b) carried out investigations using modulational instability theory to describe the wave grouping process. They suggest that a wind wave field could be considered as a modulated non-linear wave train with a single carrier wave. The other approach used to describe wave grouping is the envelope soliton model. Yasuda et al. (1986) postulate that all wave groups observed in waves behave as envelope solitons and can be defined by the multi-envelope soliton solutions of the plural non-linear Schrödinger equations. More research is required in this field for practical applications.



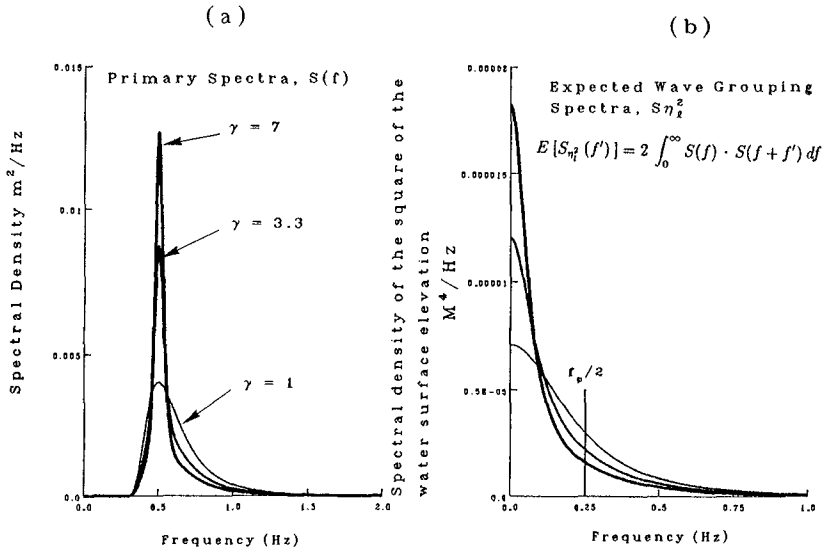


Figure 1. Expected spectra of wave groups for JONSWAP sea states

ANALYSIS OF WAVE GROUPING AND THEIR STATISTICAL VARIABILITY

As indicated above, only the run length statistics and Groupiness Factor are extensively used for quantifying the degree of grouping in a sea state. Hence the detailed evaluation presented below discusses only these two measures.

Many prototype waves have been analyzed in different parts of the world, in order to relate the degree of grouping to the spectral width of the sea state, or to the correlation parameter  $\kappa$ , using the measures of run length and Groupiness Factor. However, some of these analyses have not been too successful because of the various limitations associated with the two wave grouping measures. In order to get a better understanding of these limitations, some investigations were undertaken in this study, using numerical simulation.

Statistical Variability of Wave Grouping Measures

It can be shown that, for records of finite length, it is not easy to establish relationship between the measures of grouping such as GF and  $j_1$  and spectral width parameters such as 'Q<sub>p</sub>' or correlation parameter  $\kappa$ . The statistical variability associated with sea states of finite record length obscures any relationship that might exist between these parameters. To illustrate this point, the following investigations were undertaken.

JONSWAP spectra with three different peak enhancement factors  $\gamma = 1, 3.3$  and  $7$  were first formulated. From each one of these three spectra, 200 different realizations of wave trains ( $N_R = 200$ ) were simulated numerically using the random phase spectrum method. This random phase spectrum method is a technique that pairs a given spectral density with a randomly selected phase spectrum. By varying the random numbers used in this phase spectrum, wave records with different time domain characteristics, and therefore with different Groupiness Factors and run lengths can be generated (Funke et al, 1988). The record length of each of these wave trains,  $T_{R_i}$ , was chosen arbitrarily to be 200s (model scale). At a scale of 1:36, this would represent a 20 minute record in prototype. The peak frequency of the spectrum was made equal to 0.55 Hz, and thus the total number of waves contained in each of these time series was about 120 to 150 waves.

The synthesized time series were subjected to wave grouping analysis, and the 200 values of Groupiness Factor obtained from each one of these spectra, were then subjected to statistical analysis. For all three JONSWAP spectra, the estimated Groupiness Factors exhibited a large variability. It was therefore considered relevant to determine if there is an optimum record length that would ensure a distinct relationship between GF and  $\gamma$ . For this purpose, the numerical simulation described earlier was extended to include several other record lengths during the synthesis process. For instance, instead of simulating 200 time series each 200 s long, 100 time series each 400 s long were simulated and then subjected to wave grouping analysis. In a similar fashion, the record lengths were increased to 800 s, 1600 s, 3333 s, 5000 s and 6667 s respectively. The corresponding number of time series used in the analysis were therefore equal to 50, 25, 12, 8 and 6 respectively. The results of all these analyses are summarized in Figure 2a for the three types of spectra under consideration. This figure shows the mean values of the Groupiness Factors, their maxima and minima and the mean values  $\mp$  one standard deviation obtained from the statistical analysis. Figure 2b illustrates the run length statistics obtained from similar numerical simulations. These statistics correspond to the average run length,  $\bar{j}_i$ , exceeding the significant wave height. Two conclusions are evident from these figures 2a and 2b:

Mean values of GF (i.e.  $\overline{GF}$ ) and  $\bar{j}_i$  (average of  $\bar{j}_i$ ) exhibit an increase with narrower spectra. The statistical variability of GF and  $\bar{j}_i$  decrease as the record length increases. However, even with a record length of 111.12 minutes, there is a small variability in the values of GF and  $\bar{j}_i$ . For instance, the standard deviation of GF which is estimated to be 2 to 3% of the mean value, for record length  $T_R = 55.56$  minutes, does not seem to decrease with more increase in the record length. If the scale factor of 1:36, used earlier to represent 200 s of model time to full scale 20 minutes, is adopted here, the record length of 55.56 minute would correspond to 5.56 hours prototype.

Since natural wave records are often of short duration, it is believed that this figure would be useful for a judicious interpretation of wave group statistics.

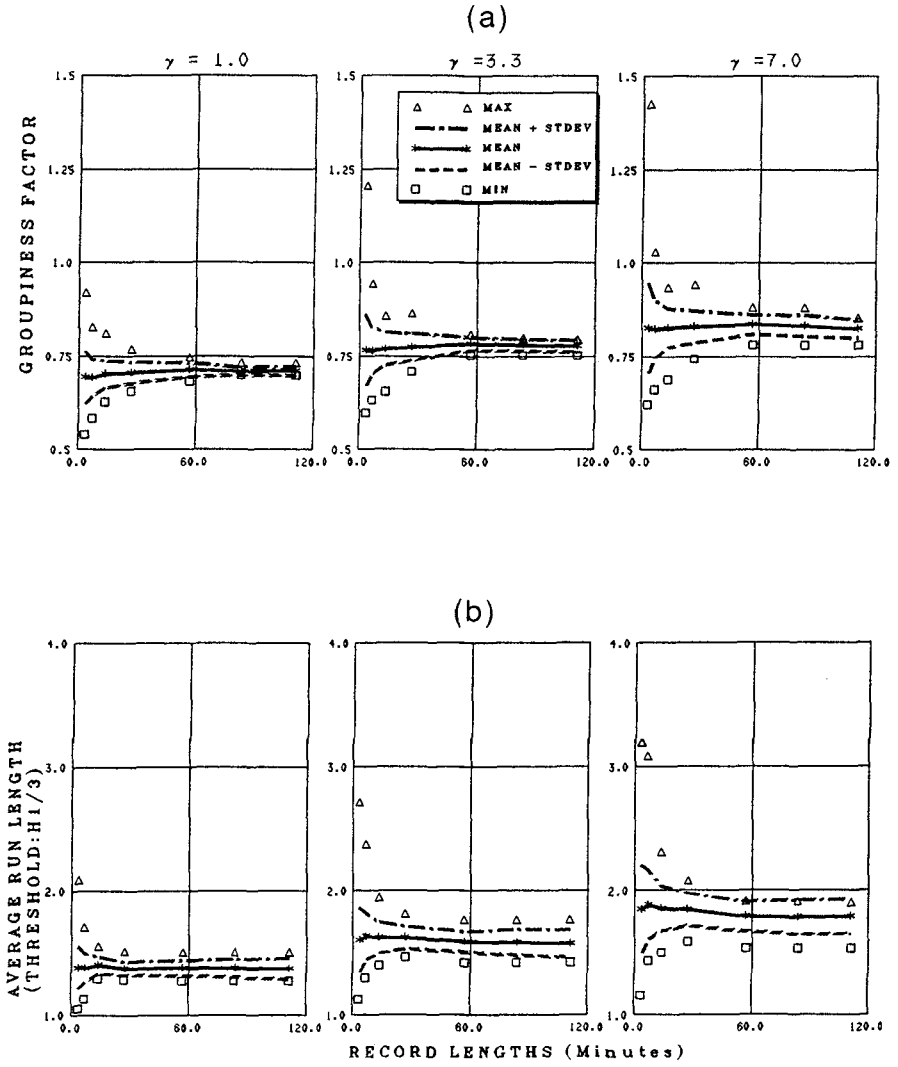


Figure 2. Statistical variability in Groupiness Factors and Run Length statistics.

### COMPARISON BETWEEN VARIOUS WAVE GROUPING MEASURES

In spite of the statistical variabilities described above, GF and run length statistics are being commonly used to provide prototype information on wave groups, for purposes of model testing in laboratory basins. But these two measures do not characterize the degree of grouping in the same fashion, i.e. a large Groupiness Factor does not necessarily mean a long run length.

A discussion on the lack of relationship that exists between these two measures and on the advantages of the Hilbert Transform are given below.

#### Comparison Between Run Length Statistics and Groupiness Factors Derived from SIWEH

The measures of GF and average run length  $\bar{j}_r$  are based on two different approaches: The Groupiness Factor is based on the square of the water surface elevation while the run length is based on the count of successive waves which exceed a certain threshold. A large GF implies the existence of many distinct energy packets of large waves but a long run length does not say much about the wave heights contained in the group except that they exceed the given threshold. It is therefore possible for a wave train with a small GF to have long run lengths and vice versa. A relationship can however be found between the average period of SIWEH and the total run (see Goda, 1983).

Between these two measures, GF is perhaps the parameter which is more commonly used in numerical and physical model studies, since simulation techniques exist to control the value of GF without having to change the spectral characteristics of the sea state. A similar technique is not available for a control of run lengths. Furthermore, the GF provides a measure of the low frequency energy contained in a sea state and therefore could be related to structural response, such as the slow drift oscillations of floating structures, seiches in harbours etc. The run length statistics do not readily provide any indication on the low frequency energy but they may be more appealing for the study of fixed structures.

#### Comparison Between the Concepts of SIWEH and Hilbert Transform

The main criticism that the SIWEH based Groupiness Factor is subjected to is the necessity to perform filtering operations and the arbitrary choice of the filter width. Because of this, researchers such as Medina and Hudspeth (1988, 1990) have been promoting the concept of Hilbert transform to compute  $\hat{\eta}_t$  without any low pass filtering. Figure 3 illustrates the difference between SIWEH and Hilbert Transform approaches. The computation used for obtaining these results was carried out as follows: first a 200s long time series of water surface elevation was synthesized from the JONSWAP spectrum, shown in Figure 3a as the primary spectrum. This time series was then subjected to wave grouping analysis using the SIWEH and Hilbert transform analysis. The time series of the low frequency part of the square of the water surface elevations,  $\eta_t^2$ , derived from these two analyses were then subjected to spectral analysis. It can be seen from Figure 3a that the spectrum of wave groups derived from SIWEH goes nearly to zero at  $f_p/2$  (i.e.

0.25 Hz), while the spectrum from the Hilbert Transform analysis overlaps the primary spectrum. Since the Groupiness Factor is a global measure of the variance contained in the entire low frequency part of the square of the water surface elevation, its value derived from the results of Hilbert transform is larger than the one provided by SIWEH analysis (see Figure 3b). However, neither of these values is directly applicable to predict the structural response of floating structures for the reason indicated below.

The response of a floating structure depends only on the variance contained within the range of its frequency response. Hence the Groupiness Factor which characterizes the total variance of  $\eta_i^2$  is not suitable for the prediction of structural response. To overcome this problem, Mansard and Sand (1992) suggest the use of some alternative concepts.

Care must also be exercised in using the concept of Groupiness Factors for evaluating the sensitivity of fixed structures to the degree of grouping. By using the SIWEH concept, Vidal et al. (1995) and Mansard et al (1994) show that there is a correlation between the degree of grouping defined by the Groupiness Factor and the statistics of large wave heights. (This correlation can be expected, to a certain extent, since the Groupiness Factors are defined by the standard deviation of instantaneous wave energy history in the time domain). Unlike floating structures whose frequency response of horizontal oscillations are in the range of wave group frequency, stability of fixed structures such as breakwaters is highly sensitive to the statistics of large wave heights. Hence higher damage in breakwaters with larger values of GF does not necessarily mean that the degree of grouping is the main cause of damage: it could be induced by the large wave heights associated with high GF. Hence, when evaluating sensitivity of fixed structures to wave grouping, the time series that are selected for testing purposes should exhibit comparable wave height statistics, but different values of GF (see Mansard et al., 1994). Researchers such as Johnson et al. (1978) and Galand and Manoha (1991), who illustrated the influence of wave grouping on breakwater stability, did not specifically evoke the aspects related to wave height statistics, possibly because their intent was to illustrate the unsuitability of qualifying a sea state solely by its frequency domain characteristics. Medina et al. (1990) have recently proposed a new concept which can overcome the difficulty described above. This concept is included below in the discussion on new concepts.

## NEW CONCEPTS OF WAVE GROUPING MEASURES

### Improved Predictor of Run Length Statistics

In recent years, the prediction of run length statistics from the spectrum-derived correlation parameter,  $\kappa_r$ , has undergone substantial advances. Earlier investigations using the spectrum-derived correlation parameter (see Equation 1) resulted in the underprediction of run lengths since the correlation coefficient between successive wave heights computed by zero-crossing analysis was larger than the value derived using  $\kappa_r$ . The main reason for this discrepancy is in the implicit assumption of the narrow-banded process used in defining  $\kappa_r$ . Recently van Vledder using the investigations of Tayfun (1990) on broad-banded spectrum, proposed a modified expression for the spectrum-derived correlation coefficient between successive wave heights  $\rho_{H+T}$  that correlates well with the

estimation made in the time domain,  $\rho_{HH,t}$ . The modified expression is:

$$\rho_{HH,t,new} = \frac{\rho_{HH,t}\left(\frac{1}{2}\hat{T}\right) + 2\rho_{HH,t}(\hat{T}) + \rho_{HH,t}\left(\frac{3}{2}\hat{T}\right)}{2 + 2\rho_{HH,t}\left(\frac{1}{2}\hat{T}\right)} \quad (2)$$

where :

$$\hat{T} = T_{m02} \left(1 - \frac{1}{2}v^2\right) \quad (3)$$

$T_{m02}$  is the average period based on the second spectral moment and  $v$  is the spectral width parameter proposed by Longuet-Higgins (1975). The relationship between  $\rho_{HH,t}$  and the  $\kappa_f$  parameter given in Equation 1 can be found in van Vledder (1992).

#### Motion Equivalent Groupiness Factor

Mansard and Sand (1992) claim that a large Groupiness Factor, derived either from SIWEH or from the Hilbert transform, does not necessarily lead to higher structural response for all test structures. It is possible that the large variance of  $\eta_t^2$  which results in high value of GF, may be outside the range of frequency response of the structures. Mansard and Sand (1992) suggest therefore a new concept of Motion Equivalent Groupiness Factor, which provides an integral measure of the degree of grouping in waves and the frequency response of test structures. As an example of this concept, a new expression was developed relating the surge motion of a simple floating structure to the degree of grouping in waves.

#### Groupiness Factor Distribution Function

Often, the frequency response of structures may be difficult to formulate and will vary from one structure to another. To account for this, Mansard and Sand (1992) suggest the use of a Groupiness Factor Distribution Function, defined by the following equation:

$$GFDF(f_c) = \frac{1}{m_0} * \sqrt{\int_0^{f_c} s_{\eta_t^2}(f) \cdot df} \quad \text{for } 0 < f_c < \infty \quad (4)$$

Instead of using a single value of GF based on the total variance of the low frequency part of the square of the water surface elevation, it is proposed here to take into account the distribution of this variance over different frequency ranges. (Hilbert transform technique is recommended for this application). Although this concept does not provide a unique parameter to characterize the degree of grouping, it is believed that it would find wider application because of its suitability to any arbitrary frequency response.

Envelope Exceedance Coefficient

Recently, Medina et al (1990) advanced a new groupiness measure called Envelope Exceedance Coefficient. It is based on the concept of the wave height function computed using the Hilbert transform technique and can be expressed as follows :

$$\alpha = \frac{\alpha'}{E(\alpha')}, \quad \alpha' = \frac{1}{N} \sum_{n=1}^N \left[ \frac{H(n\Delta t) - H_{1/10}}{H_{1/10}} \right]^2 \cdot \delta(n) \quad (5)$$

$$\delta(n) = 1 \quad \text{if } H(n\Delta t) > H_{1/10}, \quad \delta(n) = 0 \quad \text{if } H(n\Delta t) < H_{1/10}$$

where:

$H_{1/10} = 1.27 H_{m_0}$  ( $H_{m_0}$  is the estimate of significant wave height derived from the spectrum); and  $N$  is the number of data points in the wave height function sampled at  $\Delta t$  intervals.

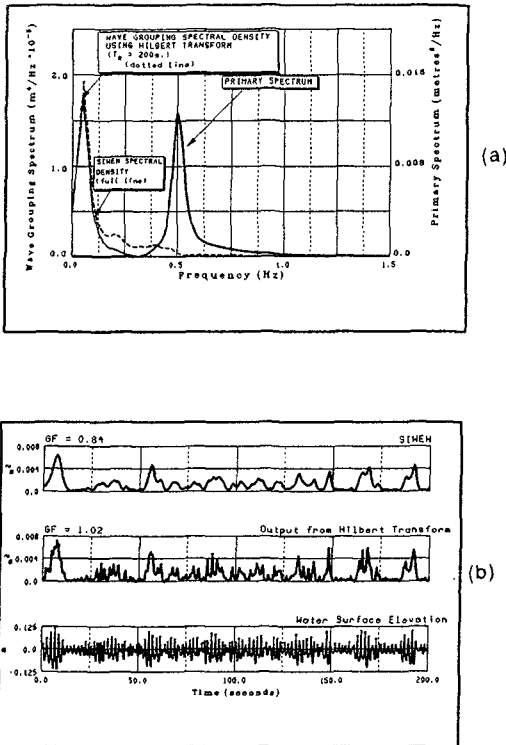


Figure 3. Comparison between SIWEH and Hilbert Transform concepts.

The main assumption used in this concept is that  $H_{1/10}$  is the relevant parameter for breakwater stability as suggested in the Shore Protection Manual of 1984. However, this concept can easily be adapted to account for other wave height parameters that may be considered more relevant to structural response. Its main limitation is that it does not lend itself easily to the control of wave group frequency for evaluating the response of floating structures. The SIWEH concept may still be the most useful technique for this particular application, because it gives the user the flexibility of varying the peak frequency and the spectral width of wave grouping spectrum.

As the envelope exceedance coefficient promises to be a useful tool for testing of fixed structures, it was considered relevant to provide a comparative evaluation of this concept with other well known measures through numerical simulation described below.

#### Comparison of Envelope Exceedance Coefficient with Groupiness Factor and Run Lengths by Numerical Simulation

From a JONSWAP spectrum characterized by its  $\gamma$  value, 100 different realizations of time records were synthesized, using the well known random phase spectrum method. Each wave record, having approximately 650 waves, was then analyzed to provide the values of Envelope Exceedance Coefficient, Groupiness Factors and Run Lengths. For the value of  $H_{1/10}$ , it was decided to use, as Medina et al. (1990) did, the relationship  $H_{1/10} = 1.27 H m_0$ . In the run length analysis, the threshold was chosen to be  $H_{1/10}$ . Two Groupiness Factors, one based on SIWEH and another on the expression  $\sigma[H^2(t)]/8m_0$  proposed by Medina et al. (1990) were computed.

The above simulation and analysis were carried out for three different values of peak enhancement factor  $\gamma = 1, 3.3$  and  $7$ . In order to establish the correlation that exists between the exceedance coefficient  $\alpha$  and other measures,  $\alpha$  values were sorted in the ascending order making sure that their corresponding values of Groupiness Factors and run lengths were also properly re-arranged. A linear polynomial fit was then applied to the various combinations of data sets.

The complete results of these simulations are presented in Figure 4 and they lead to the following conclusions:

The Groupiness Factors, GF, derived from SIWEH increase with  $\gamma$  values. The reasons for this increase can be easily inferred from Figure 1. The goodness of fit between  $\alpha$  and GF in the order of 70%.

The GF values from the wave height function are not sensitive to the spectral width. When  $\alpha=1$ , the GF value is equal to 1. There is a distinct relationship between these two parameters with a goodness of fit in the order of 78%. However, they are not interchangeable.

There is no correlation between  $\alpha$  and run length (goodness of fit less than 10%). The average run length increases with narrower spectral width.



## CONCLUSIONS

All the concepts of wave grouping measures proposed in the literature have some limitations in terms of their practical applications.

Statistical variability of groupiness measures increases as the record length decreases. This statistical variability does not permit an easy evaluation of the relationship that exists between wave grouping and spectral width of prototype sea states.

Expected values of wave grouping measures can be deduced from the spectral information of the primary sea state.

The two commonly used wave measures, Groupiness Factor and run length, do not characterize a given sea state in the same fashion.

The Hilbert transform technique of computing the square of the water surface elevation, eliminates the necessity of smoothing it with a Bartlett filter, but needs some improvements in terms of its application to predict structural response of floating structures.

The three new concepts, Envelope Exceedance Coefficient, Motion Equivalent Groupiness Factor, Groupiness Factor Distribution Function, proposed in the literature, provide promising improvements to the existing concepts and deserve further research in terms of their broader applicability.

## REFERENCES

- Battjes, J.A. and van Vledder, G.Ph. 1984. Verification of Kimura's Theory for Wave Group Statistics. Proc. 19th Int. Conf. on Coast. Engg., Houston, USA.
- Bitner-Gregersen, E.M. and Gran, S. 1983. Local Properties of Sea Waves Derived from a Wave Record. Applied Ocean Research, Vol. 5, No. 4.
- Funke, E.R. and Mansard, E.P.D. 1979. On the Synthesis of Realistic Sea States in a Laboratory Flume. Tech. Report, Hydraulics Laboratory, National Research Council of Canada LTR-HY-66.
- Funke, E.R. and Mansard E.P.D. 1981. On the Meaning of Phase Spectra in the Fourier Transform of Random Waves. Proc. Int. Conf. Hydrodynamics in Ocean Eng., Trondheim, Norway.
- Funke, E.R., Mansard, E.P.D. and Dai, G. 1988. Realizable Wave Parameters in a Laboratory Flume. Proc. 21st Int. Conf. on Coast. Engg., Malaga, Spain.
- Galand, J.C. and Manoha, B. 1991. Influence of Wave Grouping on the Stability of Rubblemound Breakwaters, Proc. XXIV IAHR Congress, Vol. B, Madrid, Spain.
- Goda, Y. 1983. Analysis of Wave Grouping and Spectra of Long Travelled Swell. Rept of the Port and Harbour Res. Inst. Japan, Vol. 22, No. 1.

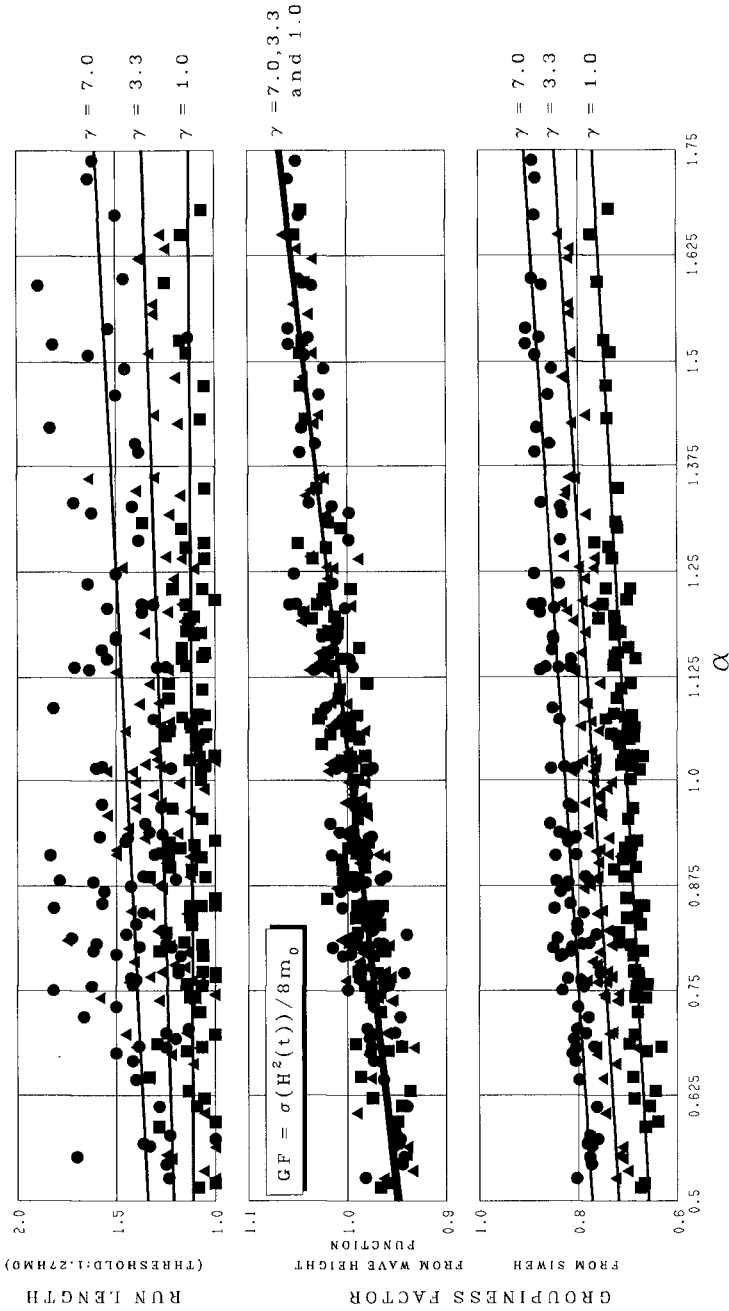


Figure 4. Comparison of four different wave grouping measures

- Johnson, R.R., Mansard, E.P.D. and Ploeg, J. 1978. Effects of Wave Grouping on Breakwater Stability. Proc. 16th Int. Conf. on Coast. Engg., Hamburg, Germany.
- Kimura, A. 1980. Statistical Properties of Random Wave Groups. Proc. 17th Int. Conf. Coast. Eng., Sydney, Australia.
- Longuet-Higgins, M.S. 1975. On the Distribution of Wave Periods and Amplitudes of Sea Waves. J. of Geophysical Research, Vol. 86 (5).
- Mansard, E.P.D., and Sand, S.E. 1992. Towards Improved Concepts for the Description of Wave Grouping. Proc. OMAE'92 Conference Calgary, Canada.
- Mansard, E.P.D., Miles, M.D. and Nwogu, O.G. (1994). Laboratory Simulation of Waves: An Outline of Wave Generation and Analysis Procedures, Proc. Int. Symp. on Waves-Physical and Numerical Modelling, Vancouver, Canada.
- Mase, H. and Iwagaki, Y. 1986a. Wave Group Analysis of Natural Wind Waves Based on Modulational Instability Theory. Coastal Eng., Vol. 10, pp. 341-354.
- Mase, H. and Iwagaki, Y. 1986b. Wave Group Property of Wind Waves from Modulational Instability. Coastal Engineering in Japan, pp. 565-577.
- Medina, J.R., Fassardi, C. and Hudspeth, R.T. 1990. Effects of Wave Groups on the Stability of Rubble-Mound Breakwaters. Proc. 22<sup>nd</sup> Int. Conf. on Coastal Engineering, Delft, The Netherlands.
- Medina, J.R. and Hudspeth, R.T. 1988. Analysis of Wave Groups in Random Fields, Proc., Ocean Structural Dynamics Symposium '88, Corvallis, Oregon
- Medina, J.R. and Hudspeth, R.T. 1990. A Review of the Analyses of Wave Groups. Coastal Engineering, Vol. 14, pp. 515-542.
- Pinkster, J.A. 1984. Numerical Modelling of Directional Seas. Symp. on Description and Modelling of Directional Seas. Copenhagen, Denmark.
- Rye, H. and Lervik, E. 1981. Wave Grouping Studies by Means of Correlation Techniques. Int. Symp. on Hydrodynamic in Ocean Eng., Trondheim, Norway.
- Sobey, R.J. and Read W.W. 1984. Wave Groups in the Frequency and Time Domains. Proc. 19th Int. Conf. in Coast. Eng. Houston, USA.
- Tayfun, M.A. 1990. Distribution of Large Wave Heights, ASCE J. Waterway, Port, Coastal and Ocean Engineering, Vol 116, No.6.
- Vidal, C., Losada, M., and E.P.D. Mansard, 1995. A Suitable Wave Height Parameter for Stability Formulae of Rubble-Mound Breakwaters, to be published in the Mar/Apr issue of ASCE J. on Waterway, Port, Harbour and Coast. Engg.
- Van Vledder, G.P. 1992. Statistics of Wave Group Parameters, Proc. 23rd Int. Conf. on Coastal Engineering, Venice, Italy.
- Yasuda, T., Nakashima, N.K. and Tsuchiya, Y. 1986. Grouping of Waves and Their Expression on Asymptotic Envelope Solution Modes. Coast. Engg in Japan, pp. 864-876.

## CHAPTER 62

### Relationship of a moored vessel in a harbour and a long wave caused by wave groups

Toshihiko Nagai<sup>1</sup> Noriaki Hashimoto<sup>1</sup> Tadashi Asai<sup>1</sup> Isao Tobiki<sup>2</sup>  
Kazunori Ito<sup>3</sup> Takao Toue<sup>3</sup> Akio Kobayashi<sup>3</sup> Takao Shibata<sup>4</sup>

#### Abstract

Loading operations failed at a berth in Sendai New Harbour in 1992. The vessels continuously moved along the berth, in spite of small wave heights and weak winds, which were much less than the criteria for loading operation at the berth. To clarify the cause of the failures, the authors analyzed the observed wave data. The phenomenon related to the time characteristics of wave groupiness. The vessels' motions were caused by the long waves that were bounded by wave groups. Mean Wave Group Period ( $\bar{T}_g$ ) proposed here, can explain the phenomenon.

#### 1. Introduction

The harbour tranquility should be evaluated not only by the wave height at a berth but by the wave period, wind condition, the scale of vessels and so on.

An experienced berth master decides when the loading operation should start considering wave heights, wave periods and wind conditions. But it is frequently reported that due to the continuous motion of a moored vessel, the vessel has to be released, or at worst the mooring devices get damaged, even when the wave heights are small and the winds are weak. Since these failures of the loading operations reduce the rate of effective working days and the safety of working, it is very important to reveal the cause of the failure.

With the observed wave data from the *NOWPHAS* (Nationwide Ocean Wave information network for Ports and HARbourS, Nagai et al, 1994) and the situation

- 
- <sup>1</sup> Port and Harbour Research Institute, Ministry of Transport, 1-1, Nagase 3-chome, Yokosuka, Kanagawa, 239, Japan
  - <sup>2</sup> Second District Port Construction Bureau, Ministry of Transport, 5-57, Kitanaka-dori, Nakaku, Yokohama, 231, Japan
  - <sup>3</sup> Taisei Corporation, Technology Research Center, 344-1, Nasemachi, Totsuka-ku, Yokohama, 245, Japan
  - <sup>4</sup> Tohoku Oil Corporation, LTD, 1-1, Minato 5-chome, Miyagino-ku, Sendai, 985, Japan

of the failure, we investigated the wave characteristics and the situation, and clarified the cause of the operation failure and proposed a new parameter for the harbour tranquility in this report.

## 2. Location and condition of the field study

Sendai New Harbour is located in Miyagi prefecture in Japan as shown in Figure 1. The harbour faces the Pacific Ocean, and it is sheltered by the outer breakwaters and an offshore breakwater that is under extension work. The yearly averaged wave direction is in between SE and SSE. The berth studied here is No. 1 berth owned by Tohoku Oil Company.

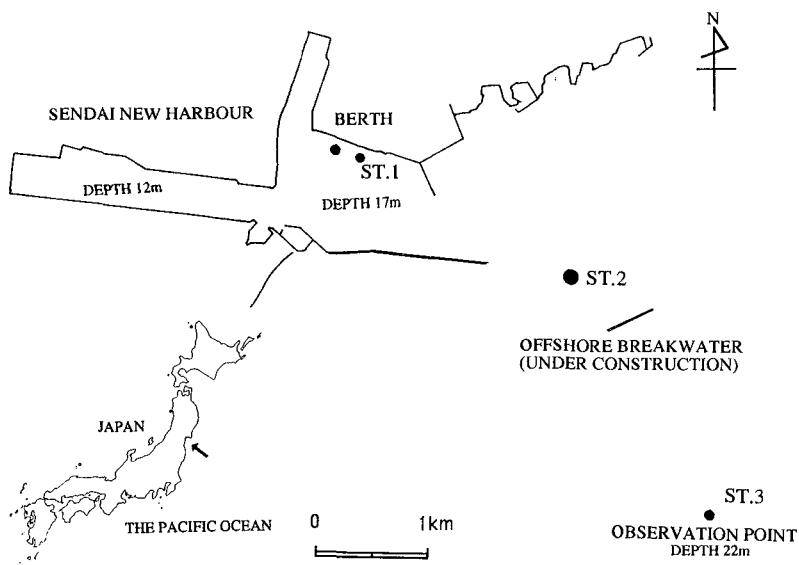


Figure 1 Location of Sendai New Harbour

Wave conditions are measured at three points. One(ST.1) is located at the east side of the berth where the water depth is 17 m, operated by the Tohoku Oil Company. The second(ST.2) is located behind the breakwater, where the water depth is 18 m. The third(ST.3) is located at 2.4 km offshore from the harbour mouth where the water depth is 22 m, one of the *NOWPHAS* offshore observation stations operated by the Second District Port Construction Bureau of the Ministry of Transport. Wave heights are measured by a ultrasonic-type wave gage (USW), and the horizontal currents are measured by an ultrasonic-type current meter (CWD). The sampling interval is 0.5 s, and the data are recorded for 20 minute in every two hours due to *NOWPHAS* standard. The winds are measured at the height of 20 m above the land of the berth.

The conditions of the loading operations are recorded for every operations. The

duration time in which a vessel is moored at the berth and waiting time at offshore is also recorded. The beginning time of the loading operation is equal to the time that the berth master judges if the loading operation is possible. At first, the data of ST.1 and ST.3 are analyzed from June to October in 1990 and 1991 and the two cases in which the operation failed in 1992 are also analysed. Furthermore the data of ST.1, ST.2 and ST.3 are analyzed from January to February in 1994.

### 3. Criteria for loading operation

Start time of loading operation entirely depends on the judgment of the berth master. The berth master generally decides the time considering the wave condition, weather, vessel scale, conditions of the mooring devices, duration time for the loading and so on. It is, however, true that the judgment is quite experiential.

Table1 Wave heights and periods at the berth

YEAR	MONTH	DAY	TIME	OFFSHORE WAVES			VESSEL × 10,000 DWT	WAVES AT THE BERTH	
				H1/3 m	T1/3 s	$\theta$ SE		H1/3 m	T1/3 s
90	6	30	12	0.76	5.98	SE	—	—	—
90	7	7	10	0.7	7.51	SE	—	0.26	4.39
90	7	8	14	0.61	6.19	SEE	—	0.15	4.28
90	7	15	10	0.74	7.57	SE	8.1	0.24	5.5
90	7	17	12	0.76	6.90	SSE	—	0.67	4.46
90	7	18	18	0.79	7.27	SSE	—	0.2	4.04
90	8	8	16	1.06	7.46	SEE	5.4	0.16	6.93
90	8	14	12	0.48	8.36	SE	—	0.09	5.08
90	8	15	18	1.2	5.75	SSE	18.6	0.13	5.55
90	8	24	10	0.94	8.27	SSE	6.5	0.11	6.57
90	8	25	14	0.45	6.74	SSE	—	0.09	4.08
90	8	26	14	0.41	7.20	SSE	—	0.09	4.71
90	9	2	10	0.65	6.59	SE	5.7	0.18	4.33
91	6	7	12	0.73	8.97	SE	6.1	—	—
91	6	17	16	0.89	7.66	SE	—	0.26	5.65
91	6	19	10	0.93	7.11	SSE	—	0.29	5.57
91	6	20	16	0.82	7.55	SE	—	0.22	5.34
91	6	25	10	0.97	7.43	SEE	—	0.23	4.78
91	7	14	12	0.51	6.34	SEE	—	0.41	5.67
91	7	16	10	0.5	7.22	SE	—	0.44	4.23
91	8	3	10	0.5	7.61	SE	7.3	0.19	3.85
91	8	4	14	0.64	4.83	SE	6.2	0.23	3.45
91	8	10	12	0.59	7.77	SEE	—	0.15	3.46
91	8	24	10	1.19	8.07	SE	—	0.34	4.61
91	8	25	18	0.98	9.29	SE	6.1	0.2	5.96
91	8	27	12	0.54	8.42	SE	—	0.15	3.84
91	8	29	14	0.68	6.01	SSE	6.1	0.18	4.24
91	9	4	10	0.55	8.92	SE	21.2	0.14	4.61
91	9	6	12	0.47	8.48	SEE	6.2	0.16	3.43
91	9	18	10	0.78	8.06	SEE	—	0.22	4.75
91	10	3	12	0.6	7.63	S	9.6	—	—
91	10	6	12	0.47	7.48	SE	6.1	—	—
92	10	22	10	2.54	12.3	SEE	22	0.26	5.78
92	11	24	12	1.56	12.67	SE	22	0.22	5.05

$\theta$  : WAVE DIRECTION  
 ---: MISSING OF DATA

The wave heights and periods both at the berth and at the offshore in the beginning of the loading operation are listed in Table 1. In the table, a solid line (—) denotes the missing of data. Two rows from the bottom of the table show the data for failed operations. Wave heights and periods at the berth are smaller than those of offshore as expected. The criteria of the loading operation can be estimated from the table.

The maximum wave height is about  $0.5m$ , and the maximum wave period is about  $6s$  for the judgment of the berth master. The table also shows that the judgment of the berth master is generally quite reasonable. It should be noted that the wave heights are small, and periods are shorts in the failed operation.

#### 4. Investigation of Fail-Operation

##### 4.1 Condition of Fail-Operation

Fail-Operation is defined here as a phenomenon that the loading is not well operated or failed in spite of small wave heights and winds. As the antonym, Normal-Operation is also used. The examples of the Fail-Operation were found on Oct. the 22nd and Nov. the 10th in 1992. The former is defined as case 1 and the later is case 2. The offshore wave heights in Fail-Operations are larger than those of Normal-Operation in 1990 and 1991. But the wave heights at the berth are much less than the criteria for the loading operation as mentioned before due to the extension of the offshore breakwater in 1992.

According to the berth master, the situations in Fail-Operations are as follows;

##### case 1

When 220,000 DWT oil tanker was moored at the berth, the tanker began to move along the berth with a surging motion. The amplitude of motion was about  $1.5m$ . When the amplitude become  $1.0m$  after 4.5 hours, the loading finally could be started.

##### case2

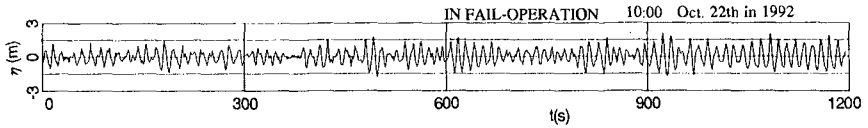
Immediately after being moored at the berth, the vessel continuously moved along the berth also with a surging motion for 24 hours. The vessel was finally had to be released without loading operation.

In both cases, the vessel was moored at the berth with mooring ropes. When the tensile force of mooring ropes achieved the breaking force of the winch, the mooring rope was released automatically, and it was rewinded adequately.

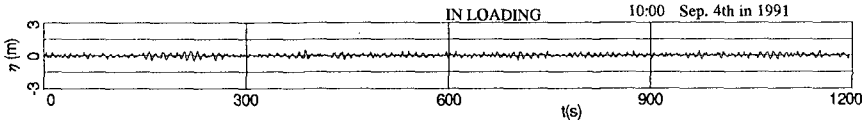
##### 4.2 Offshore wave condition in Fail-Operations

Figure 2 shows that the time series of wave profiles of case1 and case 3, where case 3 is of Normal-Operation on Sep. 4th in 1991. The type of the vessels for each cases are all the same. The wave heights of case 1 are bigger than that of case 3. But the wave height of case 1 at the berth was  $0.26m$ , which is small enough for the loading operation.

The wave direction of case 1 was *SEE* and that of case 3 was *SE*. The offshore breakwater is quite effective to these wave directions. Figure 3 indicates a typical wave directional spectra of case 1. The wave directional spectrum was calculated by the maximum entropy method (*MEP*) developed by Hashimoto et al (1985). The



(a) case 1 Fail-Operation



(b) case 3 Normal-Operation

Figure 2 Wave profiles of offshore wave

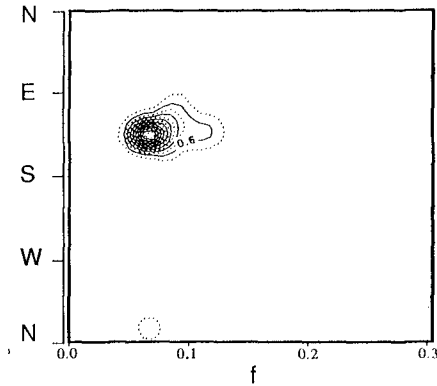


Figure.3 Directional spectrum of observed data

directional spectrum was narrow, and it had one peak. The directional spectra of case 1, case 2 and case 3 were of the same forms.

The wave trains of case 1 and case 2 are characterized by remarkable wave groups. On the contrary, the clear wave group can not be seen in the wave trains of case 3. The characteristics of the wave group are discussed in the next chapter.

### 5. Characteristics of Wave group

#### (1) Evaluation of Wave Groupiness

The characteristics of the wave groups are usually evaluated by Groupiness factor( $GF$  ; Funke and Mansard(1980)), mean run length( $\bar{j}l$ ), and envelop correlation parameter( $\kappa$  ; Battjes and Vledder(1984)). Figure 4 shows the time history of  $GF$  and  $\bar{j}l$  during the Fail-Operations.  $GF$  and  $\bar{j}l$  of case 3 are also



shown for comparison. In Figure 4, the horizontal axis is a elapsed time (hour) from the start of the operation, and the vertical axis is the value of  $GF$  and  $\bar{j}l$ .  $GF$  and  $\bar{j}l$  do not have any difference between the Fail-Operation and the Normal-Operation. As shown in Figure 2, the wave trains of case 1 and 2 have much stronger wave groupiness than case 3. Strong wave groupiness means that the amplitude of the envelop wave is large, and the modulation of high waves is gradual / smooth.

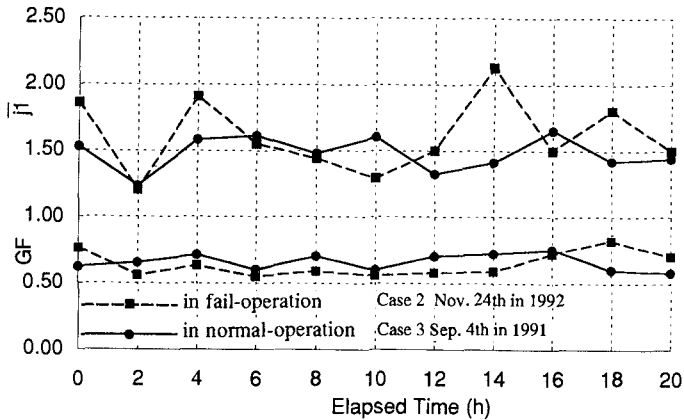


Figure 4 Time series of  $GF$  and  $\bar{j}l$

$GF$  is defined by covariance of  $SIWEH$  (Smoothed Instantaneous of Wave Energy History).  $SIWEH$  expresses the energy distribution of wave train, and is similar to the envelop. It is clear that  $GF$  can not express the sequence of heigh waves and magnitude of wave height because of the difinition. Therefore, if the sequences of two wave trains are same in the shape but different in the amplitude,  $GF$  gives a same value for both wave trains. Therefore,  $GF$  may have large value for the wave train without remarkable wave groups, if the sequence of high waves do not change gradually and the wave train has isolated high waves.

On the other hand, since  $\bar{j}l$  is defined as the number of high waves that exceed the threshold value,  $\bar{j}l$  expresses the time characteristics of wave groupiness. But, since the unit of  $\bar{j}l$  is number, if the sequences of two wave trains are the same in the shape but different in the period,  $\bar{j}l$  gives the same value for both wave trains. And also, the similar discussion of  $GF$  can be made for  $\bar{j}l$ . In the calculation of  $\bar{j}l$ , the threshold value must be known to define the run length. Since the threshold value is usually taken as a statistic value of wave train such as the significant wave height,  $\bar{j}l$  can not express the difference of the magnitude of wave heights between Fail and Normal-Operation.

Figure 5 shows the time history of  $\kappa$ . In the figure, a white circle denotes when

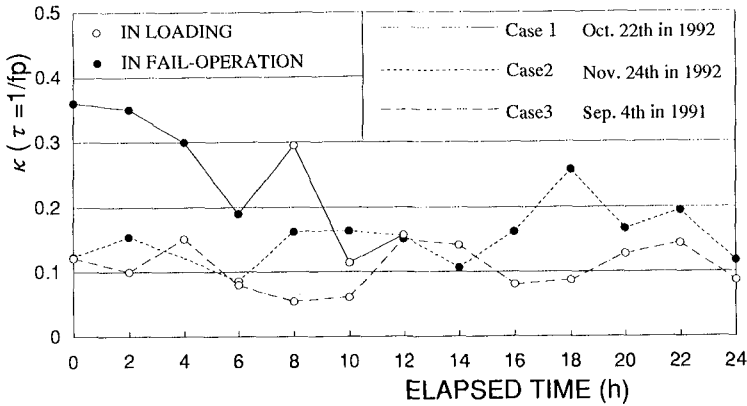


Figure 5 The comparison of  $\kappa$

the loading was possible, and a black circle denotes when indicates the loading was not possible.  $\kappa$  in Fail-Operation, illustrated by a solid line, indicates that  $\kappa$  decreases with the elapsed time. When the moored ship was continuously moving,  $\kappa$  was about 0.35, but when the loading was possible,  $\kappa$  was about 0.15. The  $\kappa$  values can express the difference between Normal and Fail Operation, in contract with the  $GF$  and  $\bar{j}\bar{l}$  values. Because  $\kappa$  is actually auto-correlation of the amplitudes of the wave envelop with a time lag,  $\tau$ . i.e.,  $\kappa$  includes a time characteristics of wave groups. But the difference between Fail-Operation of case 2 and Normal-Operation is not clear.  $\kappa$  is directly calculated by a frequency spectra form based on the narrow band linear theory. If frequency spectrum form is not narrow enough,  $\kappa$  has some error in the calculation.

As shown above, Fail-Operation has a relationship to wave groups. Especially, the time characteristic of the wave groups is important. Since the common parameters such as  $GF$ ,  $\bar{j}\bar{l}$  and  $\kappa$  can not express the difference of two Operations, a new parameter must be introduced to explain the differences.

(2) A new parameter for wave groupiness

Time characteristics of wave groups are an important factor to explain the Fail-Operation. One of the time characteristics of wave groups is a time interval of wave groups. Mean wave Group Period,  $\bar{T}_g$ , is defined as the mean interval of each wave groups.  $T_g$  is equivalent to the total run.  $T_g$ , however, has a dimension of time.  $T_g$  is calculated by eq.(1) and also illustrated in Figure 6. (Of course, we could apply SIWEH to the method that define the wave group periods.)

$$T_g = \sum_{i=1}^N T_i \tag{1}$$

where,  $T_i$  is the zero-crossing wave period,  $N$  is the number of  $T_i$ , where  $N$  is equal to a total run( $j^2$ ).

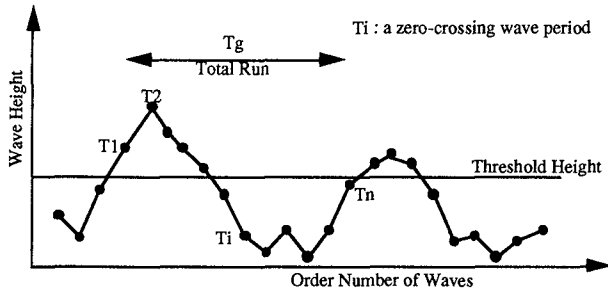


Figure 6 Definisition sketch of  $T_g$

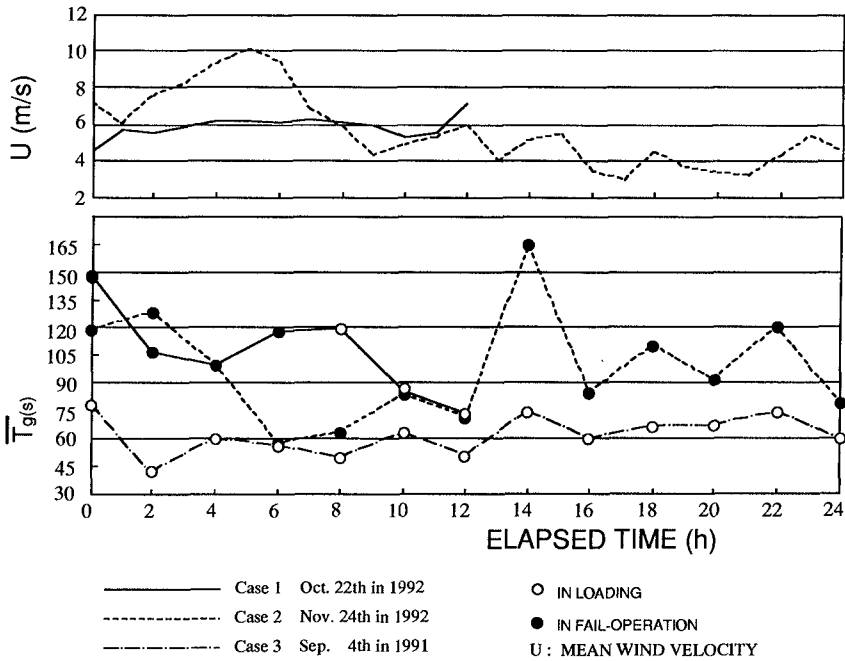


Figure 7 Time series of  $\bar{T}_g$

Figure 7 shows  $\bar{T}_g$  for case 1, case 2 and case 3 with the wind velocity data. In case 1,  $\bar{T}_g$  ranges from 105s to 150s, when the loading was not possible. But, when the loading was possible,  $\bar{T}_g$  was around 75s.  $\bar{T}_g$  in case 2 was also long when the loading was not possible. On the contrary,  $\bar{T}_g$  in case 3 was always

around 60s.

In case 2, there is the time when the loading is not possible in spite of the relatively short  $\bar{T}_g$  ( from 6 to 12 of the elapsed time in the figure). This is because of the strong wind. The shorter  $\bar{T}_g$  is caused by the growth of the wind waves. But, since the moored vessel at the berth was moved due to the wind, the loading was not possible.

It is clear that when the loading was not possible,  $\bar{T}_g$  was long, on the other hand, when the loading was possible,  $\bar{T}_g$  was short. Therefore,  $\bar{T}_g$  is an useful parameter for the harbour tranquility when we consider the loading operation.

5.2 Physical meanings of  $\bar{T}_g$

It is well known that the wave set-down occurs when wave groups propagate. Assuming that temporal wave trains are homogeneous in space and wave trains propagate unidirectional, the wave set-down can be calculated after Longuet-Higgins (1962) by eq.(2) and eq.(3).

$$\zeta = -S_x / \rho (gh - c_g^2) \tag{2}$$

$$S_x = 0.5 \rho g a^2 c_g (2c_g / c - 0.5) \tag{3}$$

where,  $h$  is the water depth,  $\rho$  is the specific gravity of water,  $g$  is the gravity acceleration,  $a$  is a half of zero-crossing wave height,  $c$  is the phase velocity,  $c_g$  is the group velocity, and  $S_x$  is the radiation stress. The radiation stress  $S_x$  is defined by each zero-crossing wave heights and periods, and  $c$  and  $c_g$  are defined by zero-crossing wave periods.

Figure 8 shows the wave set-down calculated from the time series of wave heights in case1. The amplitude of the wave set-down corresponds to the strength of the wave groups.

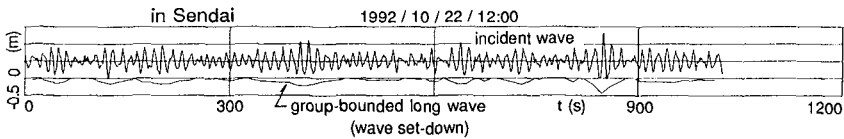


Figure 8 Group-bounded long wave (wave set-down)

Figure 9 indicates the frequency spectrum of the incident wave and the calculated wave set-down. The figure shows the variation of spectrum from Fail-Operations to Normal-Operations. The variation of the power in the low frequency correspond to the events of Fail or Normal-Operation. When the power in the low frequency is large, the loading is not possible. On the contrary, when the power is not large, the loading is possible. Thus, the power in the low frequency is a dominant factor to control the loading operation.

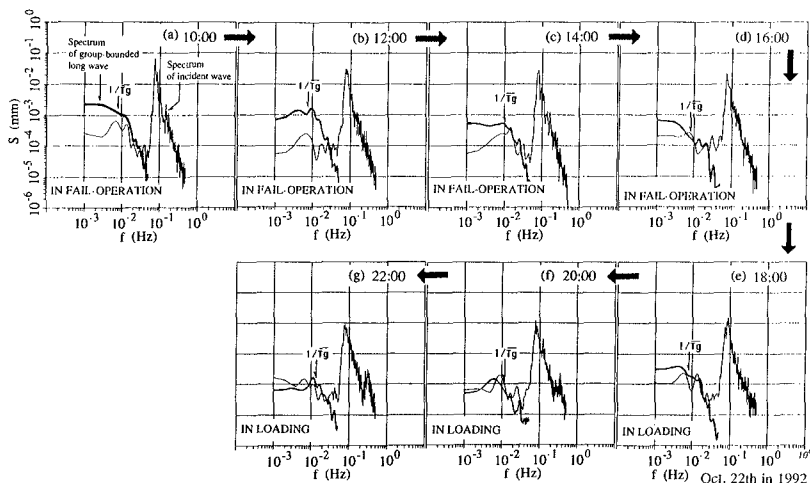


Figure.9 The frequency spectra of incident waves and group-bounded long wave

When the peak frequency in the low frequency of the incident waves is clear, e.g. (b), (c) and (g) in the Figure 9, the peak frequency of the wave set-down and  $1/Tg$  are nearly equal to the peak frequency of the incident waves. Therefore, it may be concluded that  $1/Tg$  is the peak frequency of the long waves in the incident waves and the peak frequency of the wave-set down.

In Fail-Operation from (a) to (c), we can recognize the difference between the spectrum of wave set-down and one of the incident waves. This is because in the low frequency region, the incident waves consist of the group bounded long waves and the progressive long waves, and since the observation time of wave data is only 20 min., it is not long enough to calculate the group-bounded waves.

### 6. Propagation of bounded long wave

It is clear now that the incident waves in Fail-Operation has strong wave groupiness, and the long waves bounded by the wave group are important to explain the difference of the wave groupiness between in Fail and Normal Operation. The discussion above, however, are limited in the offshore waves.

The berth was sheltered by the offshore breakwater, thus, the wave height was small enough for the loading operation. We can guess that the groupiness of the incident waves would disappear by the existence of the offshore breakwater, but, the group-bounded long waves can be free waves and can propagate into the harbour.

As shown in Figure 1, a new field observation point(ST.2) was set in 1994, we observed wave condition at three points. Figure10 indicates the variations of spectra from ST.1 to ST.3.

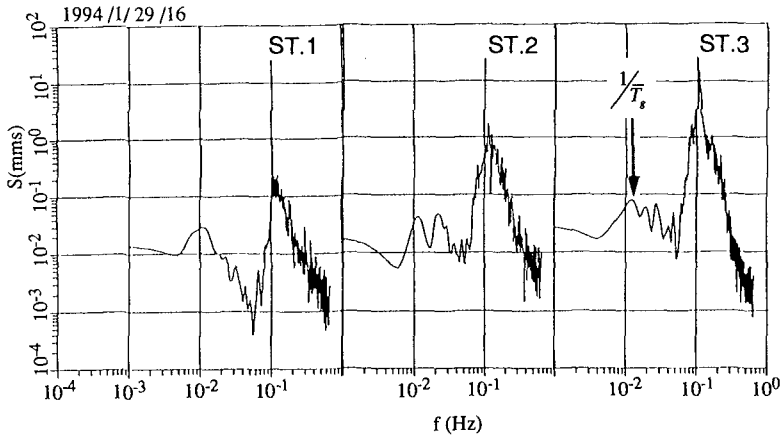


Figure 10 Variation of spectrum as propagation

The power of high frequency region which has the peak frequency around 0.1 Hz decrease as their propagation. On the other hand, the power of low frequency region does not denote remarkable dissipation between ST.1, ST.2 and ST.3. And, the peak frequency of low frequency region is correspond to  $1/\bar{T}_g$  between ST.1, ST.2 and ST.3. Figure 11 shows comparison of statistical values between ST.2 (behind offshore breakwater) and ST.3 (at offshore).  $\tilde{\eta}_{rms}$  is the root mean square value of low frequency components that are less than 0.05 Hz. The significant wave heights at ST.2 are much smaller than those of ST.3 because of the offshore breakwater.  $GF$  and  $\bar{T}_g$  at ST.2 are also smaller than those of ST.3.  $\tilde{\eta}_{rms}$  at ST.2 does not dissipate so much in spite that the waves pass the offshore breakwater. Thus, from figures 10 and 11, we may conclude that the group bounded long wave at offshore exchanges to the progressive long wave behind the offshore breakwater, and, the progressive long wave propagate into the harbour.

## 7. Relationship between harbour oscillation and motion of vessel

It is well known that the slow drift oscillation of vessels are caused by the low frequency modes of waves (Pinkstar(1974)). The motion of the vessel in Fail-Operation might be the slow drift oscillation. Unfortunately, the time series of wave data at the berth in Fail-Operation was not obtained. Thus, the relationship of the waves at the berth and the motion of the moored vessel can not be directly investigated. But, we can guess two causes of a moored vessel's continuous motion (slow drift oscillation). One is that a free long wave directly attacked the moored vessel. The other is that a free long wave excites harbour oscillation.

We simulated the harbour oscillation by J.J.Lee's method(1971). Figure 12 shows

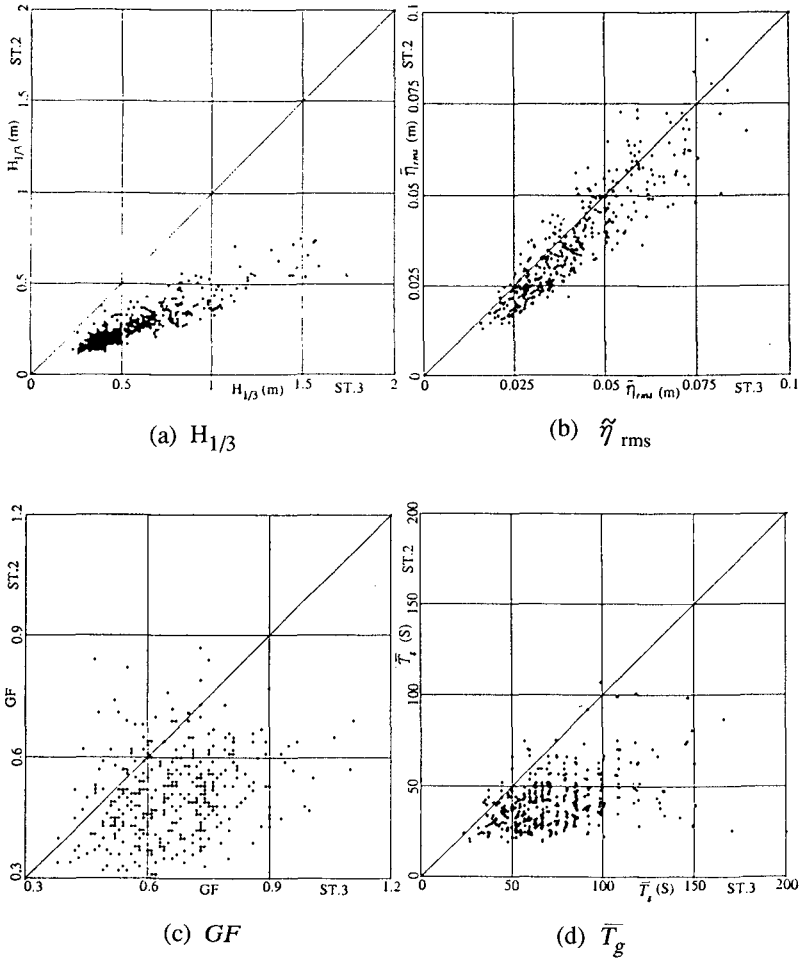


Figure 11 Comparison of statistic values between ST.2 and ST.3

the amplification factor distribution in the harbour. The period of incident wave is equal to  $\bar{T}_g$  (100s ). The position of the berth is near the node point, and the direction of the motion is surging direction. Therefore, the result of simulation implies that the cause of the slow drift oscillation is the harbour oscillation.

If the periods of the long waves were very close to the natural frequency of surging motion of the vessels, the slow drift oscillation would be excited.

A natural frequency of the surging motion of the vessel (220,000DWT) in Fail-

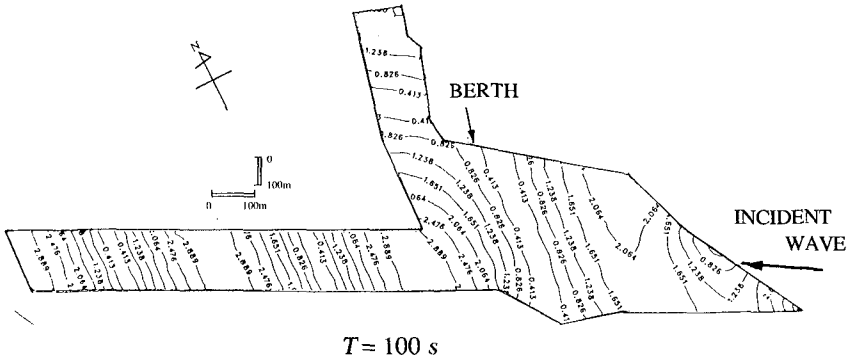


Figure 12 Amplification factor of numerical result

NO.	MOORING LINE	NUMBER
1	NYLON $\phi$ 75	4
2	WIRE $\phi$ 42	3
3	WIRE $\phi$ 42	2
4	WIRE $\phi$ 42	2
5	WIRE $\phi$ 42	2
6	NYLON $\phi$ 75	4

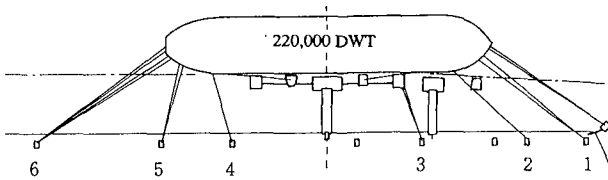


Figure 13 Mooring condition of numerical model

Operation are estimated to 82 s for the mooring system shown in Figure 13. In the estimation, it is assumed that the tensile force of each mooring rope is  $3tf$ , that is constant through the operation. The restoring force in the direction of the berth is also assumed to be the same as the value obtained from the steady analysis. Furthermore the added mass is not considered. As shown in 4.1, the actual operation of mooring is not steady, and the real tensile force of each mooring rope might be weaker than  $3tf$ . Therefore the true natural frequency must be longer than 82 s, i.e., the natural period could be close to the period of the group bounded long wave or  $T_g$ .



## 8. Conclusion

In spite of small waves and weak winds, there was an event that the loading operation failed (Fail-Operation). By analyzing the cause of Fail-Operation, it is found that the group bounded long waves cause Fail-Operation. This means that the information related to the wave group is required for the loading operation in harbors. Wave group period,  $\bar{T}_g$ , proposed here can be a useful information for the harbour tranquility in controlling the loading operation.  $\bar{T}_g$  represents a period of long wave that is bounded by wave groups. A long wave bounded by wave groups at offshore changes to a free long wave behind offshore breakwater, and a free long wave which propagates into a harbour excites a harbour oscillation. When the period of this long wave is close to natural frequency of vessels, and energy of the long wave is large in the harbour, fail-operation would occur.

## ACKNOWLEDGEMENTS

The NOWPHAS is operated by Ports and Harbours Bureau and its associated agencies including District Port Construction Bureaus and PHRI (Port and Harbour Research Institute) of the Ministry of Transport. Authors must express sincere gratitude to all the persons working for the NOWPHAS operations, especially to the engineers responsible for the offshore wave observation of the Shiogama Port Construction Office of the Second District Port Construction Bureau. The authors are also express gratitude to engineers, Oil Receiving and Shipping Sect., Tohoku Oil Co. for their cooperation.

## REFERENCES

- Battjes, J. A. and Van G. Ph. Vledder (1984) : Verification of Kimura's theory for wave group statistics, Proc. 19th Conf., ASCE, pp. 642~648
- Funke, E. R. and E. P. D. Mansard (1980) : On the synthesis of realistic sea states, Proc. 17th Coastal Eng. Conf., ASCE, pp. 2974~2991
- Hashimoto, N. and K. Kobune (1985) : Estimation of directional spectra from the maximum entropy principle, Rept. of P. H. R. I, vol. 26, No. 5, pp. 57~100. (in Japanese), or Kobune, K. and N. Hashimoto (1986) : Estimation of directional spectra from the maximum entropy principle, Proc. 5th Inter. OMAE, symp., Tokyo, pp. 80~85
- Lee, J. J. (1971) : Wave-induced oscillations in harbours arbitrary geometry, J. Fluid Mech., Vol. 45, No. 2, pp. 375~394
- Longuet-Higgins, M. S. and Stewart, R. W. (1962) : Radiation stress and mass transport in gravity waves, with application to 'surf beats', J. Fluid Mech., Vol. 13, pp. 481~504
- Nagai, T., K. Sugahara, N. Hashimoto, T. Asai, S. Higashiyama and K. Toda (1994) : Introduction of Japanese NOWPHAS System and its Recent Topics, Proce. of Hydro-Port'94, pp. 83~92
- Pinkstar, J. A. (1974) : Low frequency phenomena associated with vessels moored at sea, Soc. of Petroleum Engineers of AIME, SEP Paper No. 4837

## CHAPTER 63

### Coherent Structure of Tidal Turbulence in a Rotating System of Osaka-Bay

Tsukasa Nishimura<sup>1</sup>, Tomonao Kobayashi<sup>1</sup>, Goichi Furuta<sup>1</sup>

#### Abstract

Coherent structures dominating in the tidal turbulence field inside the Osaka-Bay were detected by flow visualization through satellite image sensors. To obtain the hydrodynamical characteristics, scale down model experiments were done with the Froude/Rossby similarity law. The tidal residual circulations were reproduced on the ensemble mean turbulence field, which is made very similar to each instantaneous turbulence owing to the robustness of the coherent structure interlocked inside a closed vessel. The earth rotation effects were verified to dominate the turbulence processes in this closed vessel, and a hysteresis due to the moon aging was revealed.

#### Introduction

Hydrodynamical characteristics of turbulence structures interlocked inside the tidal flow field in Osaka-Bay was investigated by employing the coherent structure concept, satellite-based flow visualization and scale down model experiments performed in a rotating system. Figure 1(a) shows an example of the visualized flow pattern, in which the high gain visible data obtained with Mos-1/MESSR is enhanced to snapshot an instantaneous turbulence field at 1028, 23 December 1987.

The Osaka-Bay is an inland sea basin located in the middle part of Japan-Islands, which is enclosed by some populous and industrialized areas (Figure 1(b)). It is about 50km in size and about 50m in average depth, and is therefore 1,000 in the ratio of horizontal and vertical scales. The water quality of this bay, however, is not so seriously polluted owing to the tidal exchange through the two narrow channels connecting to adjoining sea areas; Akashi-Strait to the Harima-Sea and Tomogashima-Strait to the Pacific-Ocean. Further, tidal jets injected through these straits accelerate the transport process inside the bay feeding with its turbulence components.

---

<sup>1</sup>Dept. of Civil Engineering, Science University of Tokyo, Noda-City, 278, Japan

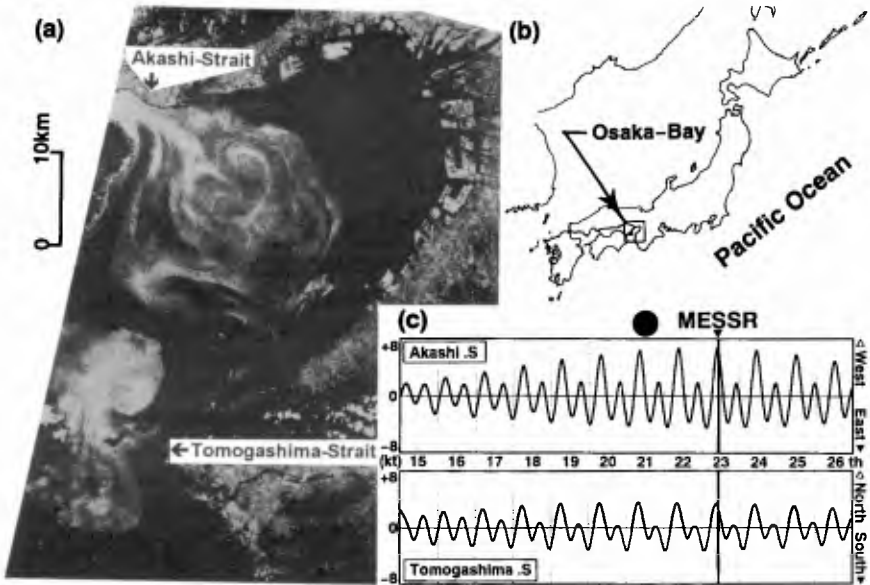


Figure 1. Tidal turbulence in the Osaka-Bay. (a) Flow visualization with Mos-1/MESSR high gain visible data at 1028, 23 December 1987. (b) Location of the site. (c) Tidal change showing with the running speed at Akashi and Tomogashima-Straits in 15-26 December 1987 (Source: forecasted value by the Maritime Safety Agency of Japan).

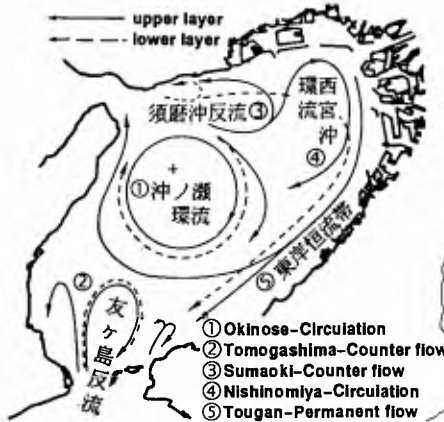


Figure 2. Schema of tidal residual circulations in the Osaka-Bay. (by Fujiwara, 1989)

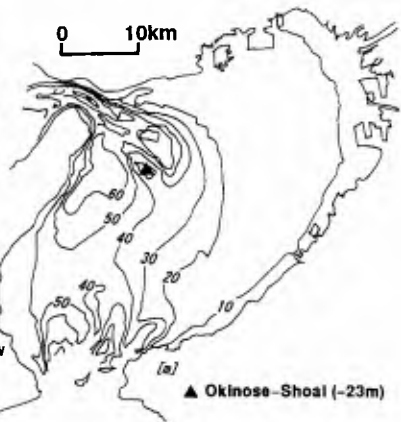


Figure 3. Topography of the rotating closed vessel of the Osaka-Bay.

### **Flow visualization of coherent structure**

On the MESSR image, we detect a coherent structure in the tidal turbulence, which is fed by the tidal jet and is interlocked inside this closed sea basin. Figure 1(c) shows the tidal change indicated with running speed at the two straits. When the MESSR data were received, north tide of about 3 knots in speed is flowing into the bay through the Tomogashima-Strait. On the satellite image, we identify a dipole of a cyclone and an anticyclone is now growing through the inverse cascade of turbulent eddies, which are injected riding on the northward tidal jet. Near the Akashi-Strait, we find another dipole. Through the strait, however, the west tide is discharging out of the bay with about 6 knots in speed. Here, we identify the dipole with that formed by the east tides in the past, which transported the turbulent eddies into the bay. The most impressive is that the dipoles are not independent, but interconnect to organize a coherent structure interlocked in the whole basin. The cyclones and anticyclones are rotating so smoothly just like the gears interlocked in a machine gear box.

### **Morphology and scales of coherent structure**

Tide curves forecasted at the two straits are the time series index of the input of turbulence energy into the Osaka-Bay. The dominant frequency components are those of semidiurnal, diurnal and of half a month due to the moon aging. The coherent structure is equipped with three stages of morphology. The first one is the 3-dimensional turbulent eddies, which are injected into the bay riding on the tidal jets. The time and space scales are minutes and 10 meters, respectively. The second stage relates to the 2-dimensional dipoles near the straits, which is formed through the inverse cascade of injected turbulence. The scales are hours and kilometers. The third stage is the 2-dimensional coherent structure filling the whole bay, which is formed through the inverse cascade of 2-dimensional dipoles. The scales are days and 50km.

### **Tidal residual circulation**

The coherent structure hadn't been so explicitly recognized until the satellite based flow visualization was realized. From surface surveys performed in the past, however, we can extract some onsite information implicitly indicating the physics of turbulence. Figure 2 shows the schema of tidal residual circulations compiled by Fujiwara (1989). The most dominant one is the anticyclonic circulation near the Akashi-Strait, the Okinose-Circulation named after a shallow shoal locating there.

Comparing it with the MESSR image, we find a geometrical similarity. The key of this similarity is in the topographical boundary of this closed vessel (Figure 3). If the vessel interlocked tight the coherent structure, then we would gain ensemble mean turbulence quite similar to each sample of instantaneous turbulence. Here, we identify the tidal residual circulations with the ensemble mean of coherent structure dominating in this rotating closed vessel. To observe the turbulence processes, however, the satellite survey has some disadvantage; such a large period of repetitive observation and so frequent cloud covering against the sequential observation.

### Hydrodynamical experiments in a rotating system

Some laboratory experiments were performed by employing the scale down model of prototype turbulence. Figure 4 outlines the experimental arrangements and methods. The 3-dimensional model of Osaka-Bay was set on a turntable of 2 meter in diameter. Horizontal scaling ratio is 1/50,000, which is determined by the diameter of table. Vertical scaling ratio is set as 1/1,000 to make the surface tension effects negligible. With the Froude's similarity law, the scaling ratio for the time is calculated at 1/1,581. Employing the Rossby's similarity law, the rotation period of the turntable is set as 98 seconds. Under these conditions, topographical  $\beta$ -effect is satisfied.

The tide was generated by two plunger-type tide generators installed outside of the two straits, which are computer-controlled to reproduce the forecasted tide curves at the two straits. The flow field is visualized with floating fine particles of aluminum powder, and the movement was recorded sequentially by a VTR camera.

### Daily-mean velocity and vorticity fields

The sea surface velocity vector distribution was estimated in every hour by applying the pattern matching method to sequential VTR image frames sampled with a certain time interval. Through the time averaging, daily-mean velocity fields were obtained. Taking a spatial differential, the daily-mean vorticity fields were calculated.

Figure 5 shows the daily-mean velocity and vorticity fields in the model basin corresponding to the MESSR image obtained on 23 December 1987. On the velocity field, we detect the tidal residual circulations quite similar to the prototype ones shown in Figure 2 compiled by Fujiwara (1989). The vorticity field looks much like the prototype eddy patterns interpreted on the MESSR image shown in Figure 1.

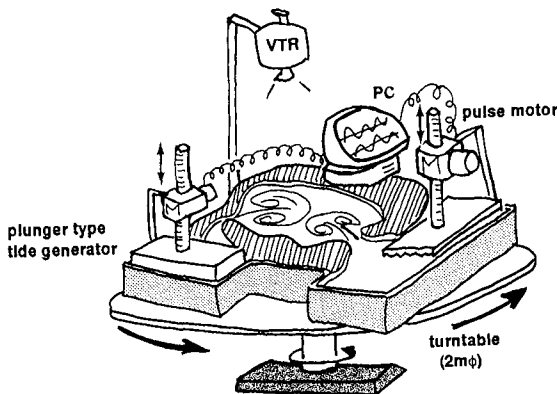


**Figure 4.** Experimental apparatus and methods for the hydrodynamical experiments on the tidal turbulence of Osaka-Bay. The diameter of turntable is 2 meter.

### Earth rotation effects on turbulence

The present model is characterized by the Rossby's similarity law. For the experimental limitation, the model is one order smaller in size, and one order larger in the distortion ratio than the existing models. Table 1 indicates the comparison of some parameters for the present model to those for existing two model basins, which had been also driven for the physical simulation of the tidal flow field in Osaka-Bay. These two models are those designed with the Froude's similarity law alone. The sizes were set one order larger than the present model in order to simulate the bottom friction, but the earth rotation effects on the turbulence were assumed negligible.

For the comparison, the earth rotation effects on the tidal turbulence inside Osaka-Bay was estimated here using the present model. Figure 6 shows one of the experimental results, which were obtained on the stationary table. We see that this Froude model fails to simulate the prototype coherent structure. The vorticity fed through the Akashi-Strait diffuse into the whole basin, and the bay is dominated by a basin scale anticyclonic tidal residual circulation. In the traditional design of physical models, the earth rotation effects were usually neglected for the sea basin of less than 100km in size. There, the bottom friction was estimated as the dominant parameter, and the Reynolds number was made as close as possible to the prototype to take the similarity in the turbulence mixing. Referring to the experiments on geophysical coherent structure, however, the turbulent eddies is made of higher coherence when it is in a rotating system (Nihoul, 1989). Comparing the turbulent fields in Figures 5 and 6, it is shown that the earth rotation effects should be put the first priority in the physical modelling of tidal turbulence in Osaka-Bay of 50km in size.

**Table 1** Scale down model experiments and parameters.

	horizontal scale	vertical scale	distortion ratio	Reynolds number	Froude's similarity	Rosby's similarity
Ishikawa(1979)	1/2,000	1/159	12.5	$1 \times 10^5$	+	
Imamoto(1988)	1/5,000	1/500	10.0	$3 \times 10^4$	+	
Present model	1/50,000	1/1,000	50.0	$1 \times 10^4$	+	+

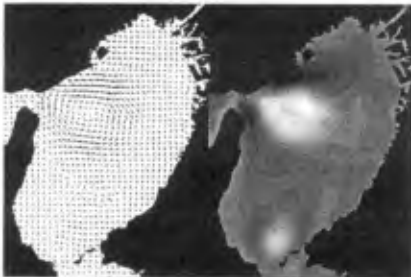


**Figure 5.** Daily-mean velocity and vorticity fields in the Froude/Rosby model.

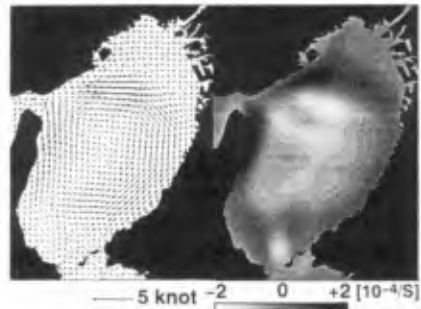


**Figure 6.** Daily-mean velocity and vorticity fields in the Froude model.

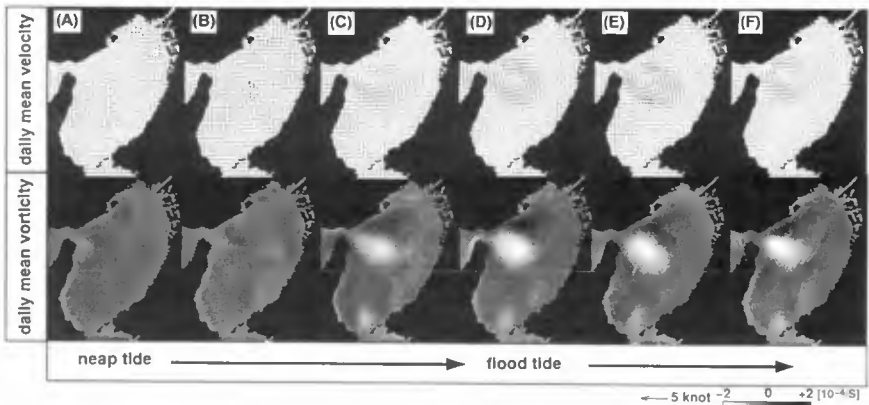
**Hysteresis with moon aging**

An impressive phenomenon in this Froude/Rossby model is the hysteresis detected in the process of coherent structures. Figure 7(a) shows the daily-mean turbulence fields, which were gained at some representative phases of moon aging; neap tide, flood tide and transient phases. Figure 7(b) shows the modelled tide curve at the Akashi-Strait, which corresponds to the prototype in the December 1987, when the MESSR image shown in Figure 1(a) was obtained.

In the case (A) of the neap tide, little trace of the coherent structure is found. In the cases (C)–(E) at the flood tide, the coherent structure is formed, which is similar to the MESSR image and to the schema of tidal residual circulation. By the detailed inspection, we see that the coherence of eddy structure and the similarity to the prototype are both made higher as the moon ages.

The remarkable difference is observed in the transient phases of the moon aging. Comparison between the daily-mean turbulence fields in the cases (B) and (F) denotes a hysteresis in the turbulence processes due to the aging of moon. In the transient phase (B) from neap tide to flood tide, we scarcely find any coherent structures. In the transient phase (F) from flood tide to neap tide, we find a coherent structure, which was established by the preceding flood tides. Although the strength of tide is same, the coherent structure in the bay is much more robust in the decreasing phase of the tide than in the increasing phase. The time scale of this hysteresis phenomenon is estimated at days, which is comparable to the earth rotation.

(a)



(b)

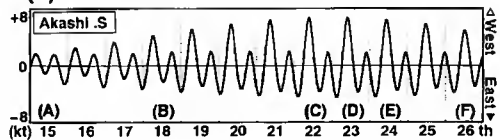


**Figure 7.** Hysteresis in the process of coherent structure in the Froude/Rossby model of Osaka-Bay.

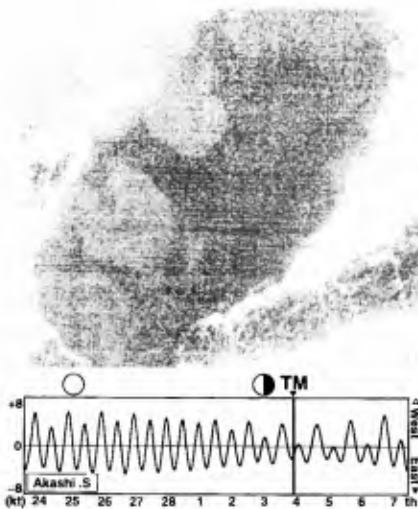
- (a) Daily-mean turbulence fields.
- (b) Tide curve at Akashi-Strait.

**Satellite based verification of the hysteresis**

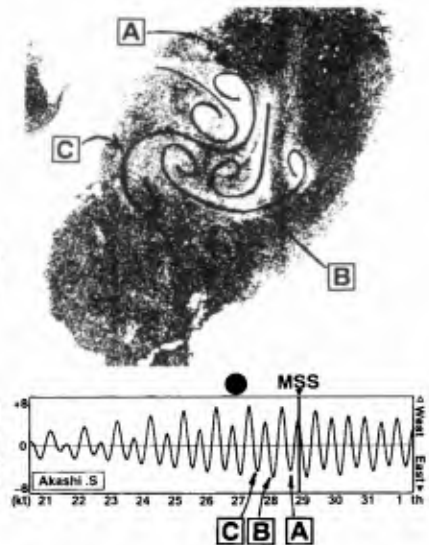
For the physical reasoning of the hysteresis phenomenon, we should remark the three stages of the coherent structure and two stages of inverse cascade processes. Figure 8 shows a Landsat/TM image of the neap tide flow field inside the Osaka-Bay. Although the dipoles are formed near the two straits, the coherent structure in the third stage is not yet organized. In this case, the second stage of inverse cascade fails to proceed, and we can scarcely expect the tidal residual circulations.

Figure 9 shows a Landsat/MSS image in the final phase of flood tide. On the image, we can interpret three dipoles, which were produced through the inverse cascade from the 3-dimensional turbulence injected by the eastward tidal jets of preceding flood tides. They are labelled as A, B and C respectively on the Landsat/MSS image and on the tide curve at the Akashi-Strait. These dipoles are riding on the anticyclonic Okinose-Circulation formed by the preceding flood tides.

Here, we notice that the central part of the set of dipoles is composed of three anticyclones, which would strengthen the Okinose-Circulation feeding it with the anticyclonic vorticity. In the decreasing phase from flood tide to neap tide, such an inverse cascade proceeds effectively, and the tidal residual circulation is maintained to gain the robustness. In the increasing phase, on the other hand, this process is scarcely expected because of the absence of existing Okinose-Circulation. This difference in the second stage inverse cascade cause the hysteresis in the coherent structure with moon aging.



**Figure 8.** Landsat/TM image of the neap tide flow field on 4 March 1986.



**Figure 9.** Landsat/MSS image of the flood tide flow field on 29 August 1984.



**Inverse cascade of 3-dimensional tidal jets**

Based on past research, it is well known that a pulse-like 3 dimensional jet injected into a vessel forms a compact dipole when it is in a rotating system (Nihoul, 1987). Figure 10 shows an experimental verification of the earth rotation effects on the inverse cascade of 3-dimensional tidal jet. To abstract the process, the topography of Osaka-Bay is simplified to a rectangular basin with a single strait and a flat bottom as shown in Figure 10(b). This 2-dimensional model is intended to compare with the Froude model of tidal residual circulation by Yanagi (1976) with 5 times larger size. The tide generator was driven to generate a sinusoidal tide curve at the strait.

Figure 10(a) shows the daily-mean velocity and vorticity fields. In the Froude model (A), the flow field similar to Yanagi(1976) was gained, in which the Okinose-Circulation was formed inside the whole bay similar to the 3-dimensional model shown in Figure 6. In the Froude/Rossby model (B), it was made compact near the strait like the 3-dimensional model shown in Figure 5. For the physical model of the first stage inverse cascade, however, this model is oversimplified. As the topography was made 2-dimensional from the first, the turbulence injected into the bay is composed of 2-dimensional line vortices, which is well known to inverse cascade easily in nature. In order to simulate the inverse cascade from 3-dimensional tidal jets,

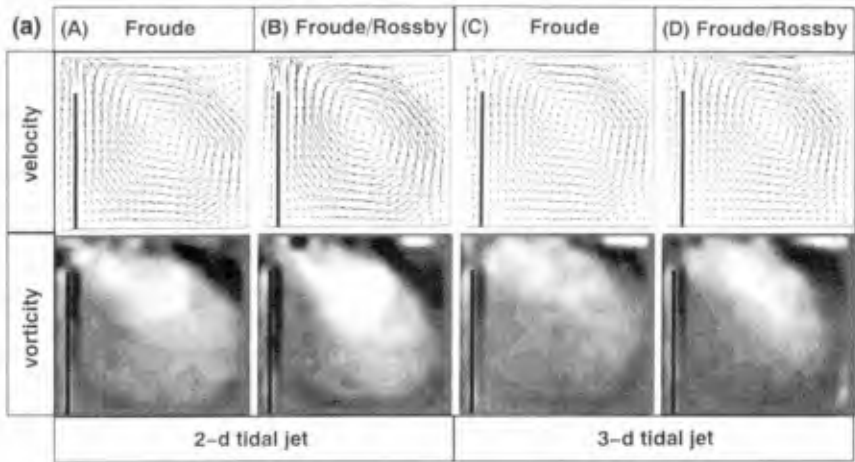
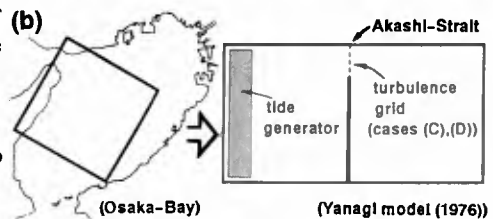


**Figure 10.** Experimental verification of earth rotation effects on the inverse cascade of 3-dimensional tidal jets. (a) Time-mean turbulence field in a simplified model. (b) Simplified modelling of Osaka-Bay referring to the Froude model of tidal residual circulation by Yanagi (1976).



the last two experiments were done installing a turbulence grid at the Akashi-Strait. In the Froude model (C), the inverse cascade didn't proceed so efficiently as in the case of 2-dimensional tidal jets. In the Froude/Rossby model (D), a more compact Okinose-circulation is formed near the strait.

### Earth rotation, roughness and 2-dimensionality of turbulence

In the numerical modelling of tidal flow fields, the earth rotation effects are usually formulated with the Coriolis term. On the simplified physical model, however, the eddy viscosity is also influenced in the rotating system significantly. Then, some turbulence characteristics are expected only from the physical model, however, it is under an experimental limitation from the size of available turntable. As shown in Table 1, the distortion ratio of Froude/Rossby model is 5 times higher than the representative Froude model used by Ishikawa(1979), which has been practically applied to the assessments of physical influence due to reclamations. The higher the distortion rate is set up, it enhances more the 3-dimensionality of the turbulence in the model, and the first stage inverse cascade is relatively underestimated. Figure 11 shows the experimental estimation of the balance of hydrodynamical effects of earth rotation and 2-dimensionality of turbulence, in which the daily-mean turbulence on 23 December 1987 are compared. Case (A) shows the model of 50 in the distortion ratio, which has been examined here in detail. In the Froude/Rossby model, the prototype coherent structure was well simulated excepting some deviations found in the location

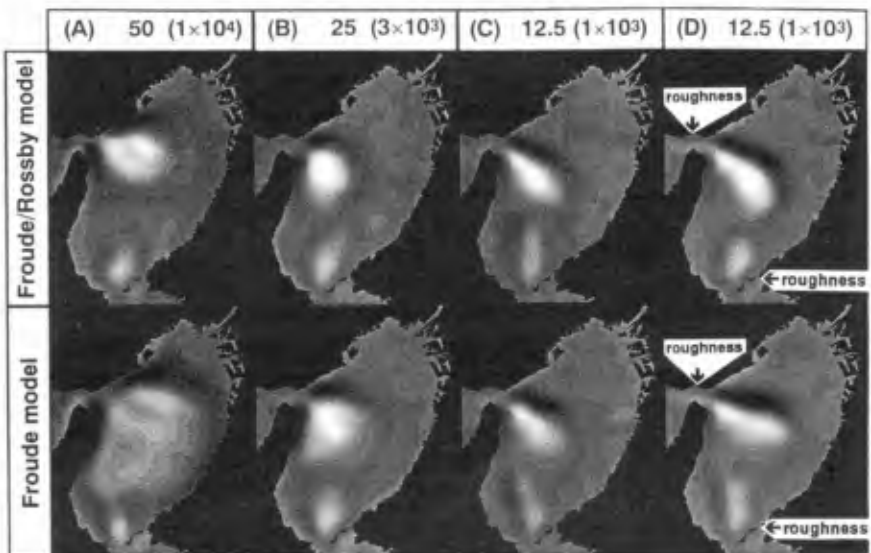


**Figure 11.** Experimental estimation of the balance of hydrodynamical effects of earth rotation and 2-dimensionality of turbulence. The parameters are distortion ratio (Reynolds number) of the 3-dimensional model. The representative length and speed are the mean depth and maximum speed at the Akashi-Strait.

of the Okinose-Circulation. Case (B) shows the results in a model basin of 25 in distortion ratio. Owing to the improvement in the 2-dimensionality of tidal jet, the similarity of Froude/Rossby model is made higher. Here, we also notice that the difference due to the earth rotation is made smaller. In the case (C), the distortion ratio was set at 12.5, same to the representative Froude model for the practical use. As the 2-dimensionality of tidal jet is improved further, the Okinose-Circulation is made positioned nearer to the Okinose-Shoal in the Froude/Rossby model. In the same time, the difference caused by the earth rotation effects are made much smaller.

Here, we should mention that the Reynolds number of the third model is two order less than that of the representative Froude model, and four order less than in the prototype Osaka-Bay. The turbulence energy injected into the model basin is underestimated in this model. To simulate the first stage inverse cascade of tidal jet in the last Case (D), some artificial roughness were attached at the narrowest part of the straits of Akashi and Tomogashima. On the Froude/Rossby model, the Okinose-Circulation is made positioned exactly overhead the Okinose-Shoal. On the Froude model, however, the reproducibility is made less than in the case without roughness, as the first stage inverse cascade of 3-dimensional turbulence scarcely proceeds.

### **Concluding remarks**

From the viewpoint of a turbulence interlocked inside a rotating closed vessel, the physics of the tidal flow field in Osaka-Bay was examined. Through the flow visualization by Mos-1/MESSR, a coherent structure very similar to the tidal residual circulation was detected, which is interlocked tight inside the bay. The morphology and scales of the coherent structure are revealed. To discuss the turbulence processes, laboratory experiments were done using a hydrodynamical model of 1/50,000 in scaling ratio with the Froude/Rossby similarity law. A hysteresis in the turbulence processes was detected, and was verified through the hydrodynamical interpretation of Landsat images. Based on a simplified model experiments, it was shown that the earth rotation accelerates the inverse cascade of 3-dimensional tidal jet. Using four types of scale down models with some difference in distortion ratio and surface roughness, the hydrodynamical balance of earth rotation, bottom friction and 2-dimensionality of turbulence were estimated experimentally.

### **References**

- Fujiwara, T., Higo, T., Takahashi, Y.: On the residual circulations, tidal flows and eddies, Proc. of Coastal engineering, JSCE, Vol.36, pp.209-213, 1989(in Japanese)
- Imamoto, H., Otoshi, K.: Hydrodynamical model experiments on the tidal flow in Osaka-Bay. Proc. of 43th meeting JSCE, pp.778-779, 1988(in Japanese)
- Ishikawa, M., Kumagai, M., Nishimura, H., Fujiwara, T., Hayakawa, N.: Hydrodynamical model experiments on the tidal residual circulation under the stratified condition. Proc. of Oceanogr. Soc. Japan, pp.41-42, 1979(in Japanese)
- Nihoule, C.J., Jamart, M.(Editor): Mesoscale/Synoptic coherent structures in geophysical turbulence. ELSEVIER OCEANOGRAPHY SERIES 50, 1989
- Yanagi, T.: Fundamental study on the tidal residual circulation-I, J. Oceanogr. Soc. Japan, Vol.32, pp.199-208, 1976

## CHAPTER 64

# Development of a Partially Three-Dimensional Model for Ship Motion in a Harbor with Arbitrary Bathymetry

Takumi Ohyama <sup>1</sup> and Mitsuru Tsuchida <sup>2</sup>

### Abstract

A numerical method has been developed for the analysis of ship motions in a harbor with arbitrary bathymetry. A BEM-based 3-D model, applied partially to a near-field surrounding a ship, is combined with a FEM-based 2-D model, utilized in the remainder of harbor domain. This combination may achieve an efficient computation of the ship motions with taking into account of wave deformation in a harbor. Preliminary examinations have been performed to investigate appropriate location of a matching boundary where these two models are coupled. It is found that, for reliable prediction,  $(2 \sim 3)h$  ( $h$ : water depth) is required for the distance between the matching boundary and a body. The numerical results of added mass and damping coefficients for a rectangular floating body in a rectangular basin are then compared with those obtained from a conventional numerical model. Favorable agreement between the results verifies the present numerical method. Ship motions in a harbor with slowly varying depth are also demonstrated.

---

<sup>1</sup>Centre for Water Research, The University of Western Australia, Nedlands, WA6009, AUSTRALIA (on leave from Institute of Technology, Shimizu Corporation, Etchujima 3-4-17, Koto-ku, Tokyo 135, JAPAN)

<sup>2</sup>Institute of Technology, Shimizu Corporation, Etchujima 3-4-17, Koto-ku, Tokyo 135, JAPAN

## **1. Introduction**

Precise prediction of ship motions in a harbor is essential to reliable harbor design. Coastal structures such as breakwaters and bottom topography in a harbor cause incoming waves to be diffracted and refracted before their reaching a floating body. In addition to such deformation of incoming waves, diffracted and radiated waves propagating from the body may be re-reflected by breakwaters and come back to the body again. Therefore, in general, hydrodynamic forces acting on a floating body in a harbor significantly differ from those in the case of open sea.

Under such circumstances, it may be necessary that the wave-ship interaction problem is solved simultaneously with the wave deformation in a harbor. In spite of this, corresponding numerical models, taking into account of coastal structures and bottom topography, have rarely been provided for predicting ship motions in a harbor. Oortmerssen (1976) developed a numerical method to calculate wave-induced motions of a ship moored at a straight quay, whereas Sawaragi and Kubo (1982) applied a two-dimensional boundary element method (2-D BEM) to the case of a rectangular floating body in a rectangular harbor. These basic studies may indicate essential influences of harbor boundaries on the ship motions. However, since these approaches have utilized the principle of mirror image, their applications are limited to harbors with straight boundaries.

In the light of this, Sawaragi et al. (1989) proposed a numerical method applicable to harbors of an arbitrary horizontal configuration. In their approach, a 3-D BEM model using a Green's function derived by John (1950) is applied only to the near-field around a floating body, and is combined with a 2-D BEM model utilized in the remainder of harbor domain. Although the basic idea of this "partially three-dimensional model" may address more practical situations as compared to the aforementioned methods, its application is still restricted to the case of constant depth in a harbor.

In this connection, the present study attempts to develop an alternative "partially three-dimensional model" for more general situations with a slowly varying bottom. A finite element method (FEM) based on the mild-slope equation (Berkhoff, 1972) is employed as a 2-D model in a harbor domain excluding the near-field around a floating body. Taking into account of continuities of fluid mass and momentum, this 2-D FEM model is coupled with a 3-D BEM model in the vicinity of the body.

The basic theory and the numerical formulation are described in Section 2, where the 3-D BEM and 2-D FEM models are solved simultaneously with continuity conditions imposed on a matching boundary. Since the 2-D model is

based on the mild-slope equation, this model is applicable only to the domain where evanescent modes are negligible. In this connection, Section 3 investigates an appropriate location of the matching boundary in a vertical two-dimensional plane. In Section 4, in order to verify the present numerical model, comparisons are made with a conventional model (Sawaragi and Kubo, 1982) for radiation-force coefficients of a rectangular floating body in a rectangular basin. Lastly, a numerical example is given in Section 5 for ship motions in a harbor with an inclined bottom.

## 2. Partially Three-dimensional Numerical Model

### Governing equation and boundary conditions

Let us consider wave diffraction and radiation by a floating body in a harbor with arbitrary bathymetry. Assuming an irrotational small-amplitude motion of an incompressible and inviscid fluid, the fluid motion can be expressed by using the linear potential theory. The velocity potential for the wave-body interaction may be separated into the *propagation mode* and the *evanescent modes*, where the latter diminishes exponentially with distance away from the body. Therefore, in the present model, the harbor domain considered is subdivided into two regions,  $\Omega_1$  and  $\Omega_2$ , as shown in **Fig. 1**. The former region  $\Omega_1$  denotes a small near-field around the floating body where the evanescent modes are significant, whereas the latter  $\Omega_2$  represents a whole domain in a harbor excluding  $\Omega_1$ . It is assumed that the matching boundary,  $S_C$ , between  $\Omega_1$  and  $\Omega_2$  is located sufficiently apart from the body and, hence, only the propagation mode is predominant in  $\Omega_2$ .

The velocity potential,  $\Phi(x, y, z, t)$  can be expressed by the combination of incident, diffraction and radiation potentials:

$$\Phi(x, y, z, t) = \phi_7(x, y, z)e^{-i\sigma t} + \sum_{l=1}^6 \frac{d}{dt}(D_l e^{-i\sigma t})\phi_l(x, y, z), \quad (1)$$

where  $(x, y, z)$  represents Cartesian coordinates (see **Fig. 1**),  $t$  is the time,  $\sigma$  is the angular frequency of incident waves,  $l = 1, 2, \dots, 6$  correspond to the surge, sway, heave, roll, pitch and yaw body motions, respectively,  $\phi_7$  is the sum of incident and diffraction potentials, and  $\phi_l$  and  $D_l$  ( $l = 1 \sim 6$ ) are the radiation potential and the complex amplitude of the  $l$ -th directional body motion.

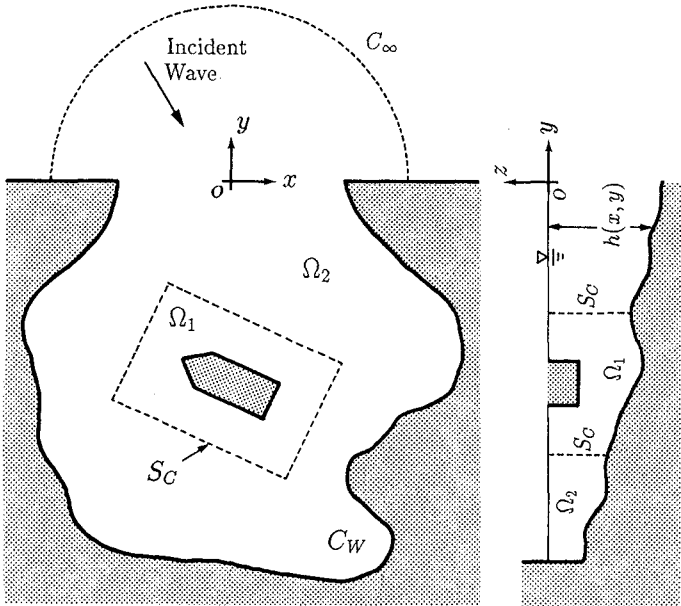


Fig. 1 Schematic diagram of partially three-dimensional model.

The governing equation and the boundary conditions for  $\phi_l$  ( $l = 1 \sim 7$ ) are

$$\frac{\partial^2 \phi_l^{(i)}}{\partial x^2} + \frac{\partial^2 \phi_l^{(i)}}{\partial y^2} + \frac{\partial^2 \phi_l^{(i)}}{\partial z^2} = 0, \quad (l = 1 \sim 7; \text{ in } \Omega_1 [i = 1] \text{ and } \Omega_2 [i = 2]), \quad (2)$$

$$\frac{\partial \phi_l^{(i)}}{\partial z} - \frac{\sigma^2}{g} \phi_l^{(i)} = 0, \quad (l = 1 \sim 7, i = 1, 2; \text{ on } S_F), \quad (3)$$

$$\frac{\partial \phi_l^{(i)}}{\partial n} = 0, \quad (l = 1 \sim 7, i = 1, 2; \text{ on } S_B), \quad (4)$$

$$\frac{\partial \phi_l^{(1)}}{\partial n} = v_l, \quad (l = 1 \sim 7, \text{ on } S_V), \quad (5)$$

$$\left. \begin{aligned} v_1 &= n_x, v_2 = n_y, v_3 = n_z, \\ v_4 &= (y - y_G)n_z - (z - z_G)n_y, \\ v_5 &= (z - z_G)n_x - (x - x_G)n_z, \\ v_6 &= (x - x_G)n_y - (y - y_G)n_x, \\ v_7 &= 0, \end{aligned} \right\} \quad (6)$$

where  $\phi_i^{(1)}$  and  $\phi_i^{(2)}$  denote the velocity potentials in  $\Omega_1$  and  $\Omega_2$ , respectively,  $S_F$  is the free surface,  $S_B$  is the seabed,  $S_V$  is the submerged body surface,  $n$  is the outward normal on each surface,  $(n_x, n_y, n_z)$  are the  $x$ -,  $y$ - and  $z$ -components of the outward unit normal on  $S_V$ , and  $(x_G, y_G, z_G)$  is the gravitational center of the body.

On the other hand, partial wave reflection is considered along the harbor boundary  $C_W$ . Although Isaacson and Qu (1990) proposed a corresponding boundary condition including the effects of wave direction and phase shift, the present study utilizes the following simple condition:

$$\frac{\partial \phi_i^{(2)}}{\partial n} = \frac{i\sigma}{C} \frac{1 - K_{RW}}{1 + K_{RW}} \phi_i^{(2)}, \quad (l = 1 \sim 7, \text{ on } C_W), \quad (7)$$

where  $C$  is the wave celerity and  $K_{RW}$  represents the reflection coefficient imposed.

### 3-D BEM model in $\Omega_1$

Applying Green's theorem to the fluid domain  $\Omega_1$ , the Laplace's equation Eq. (2) is transformed into the following integral equation:

$$\alpha(P)\phi_i^{(1)}(P) + \int_S \left\{ \phi_i^{(1)} \frac{\partial G}{\partial n} - \frac{\partial \phi_i^{(1)}}{\partial n} G \right\} ds = 0, \quad (l = 1 \sim 7), \quad (8)$$

where  $S$  represents the closed boundary surface containing  $\Omega_1$ ,  $P$  denotes an arbitrary position in  $\Omega_1$ , and  $G$  is a Green's function. The coefficient  $\alpha(P)$  is  $2\pi$  if  $P$  is on  $S$ , and is  $4\pi$  in other cases.

Using a Green's function derived by John (1950) and substituting the boundary conditions, Eqs. (3), (4) and (5), into Eq. (8), the following boundary integral equations can be obtained:

$$\alpha(P)\phi_i^{(1)}(P) + \int_{S_C} \left\{ \phi_i^{(1)} \frac{\partial G}{\partial n} - \frac{\partial \phi_i^{(1)}}{\partial n} G \right\} ds + \int_{S_V \cup S_B} \phi_i^{(1)} \frac{\partial G}{\partial n} ds = \int_{S_V} v_l G ds, \quad (l = 1 \sim 7). \quad (9)$$

If the water depth is constant in  $\Omega_1$ , the integral on  $S_B$  involved in Eq. (9) can be eliminated since  $\partial G / \partial n = 0$  (on  $S_B$ ).



**2-D FEM model in  $\Omega_2$**

In  $\Omega_2$ , sufficiently far from the body, we may consider only the propagation mode in the fluid motion over a slowly varying seabed. This allows us to utilize the mild-slope equation (Berkhoff, 1972; Smith and Sprinks, 1975; Lozano and Meyer, 1976).

Thus, the velocity potential  $\phi_l$  in  $\Omega_2$  is approximated by the form

$$\phi_l^{(2)}(x, y, z) = \varphi_l^{(2)}(x, y) \frac{\cosh k(h+z)}{\cosh kh}, \quad (l = 1 \sim 7), \tag{10}$$

where  $k(x, y)$  and  $h(x, y)$  are the wave number and the water depth, respectively. The corresponding mild-slope equation, derived from Eq. (2), is given as

$$\nabla \cdot (CC_G \nabla \varphi_l^{(2)}) + k^2 CC_G \varphi_l^{(2)} = 0, \quad (l = 1 \sim 7, \text{ in } \Omega_2), \tag{11}$$

where  $\nabla \equiv (\partial/\partial x, \partial/\partial y)$  and  $C_G$  is the group velocity.

According to Chen and Mei (1975), a variational approach is employed in a FEM-based formulation to solve Eq. (11). Along the open boundary, denoted by  $C_\infty$  in Fig. 1, the finite elements are coupled to the *superelement* which satisfies the radiation condition analytically. The exterior region outside  $C_\infty$  is assumed to have a constant water depth.

The variational function for the governing equation [Eq. (11)], the boundary condition on  $C_W$  [Eq. (7)] and the radiation condition is given as

$$J_l = (J_1)_l + (J_2)_l + (J_3)_l + (J_4)_l, \quad (l = 1 \sim 7), \tag{12}$$

$$\left. \begin{aligned} (J_1)_l &= \int_{\Omega_2} \frac{1}{2} \left\{ CC_G (\nabla \varphi_l^{(2)})^2 - \frac{C_G}{C} \sigma^2 (\varphi_l^{(2)})^2 \right\} d\Omega, \\ (J_2)_l &= \int_{C_\infty} CC_G \left\{ \left( \frac{1}{2} \bar{\varphi}_l - \varphi_l^{(2)} + \frac{1}{2} \delta_{l7} \varphi_0 \right) \frac{\partial \bar{\varphi}_l}{\partial n} - \frac{1}{2} \delta_{l7} (\bar{\varphi}_l - \varphi_0) \frac{\partial \varphi_0}{\partial n} \right\} dc, \\ (J_3)_l &= - \int_{C_W} \frac{1}{2} i \sigma C_G \frac{1 - K_{RW}}{1 + K_{RW}} (\varphi_l^{(2)})^2 dc, \\ (J_4)_l &= - \int_{C_C} CC_G \frac{\partial \varphi_l^{(2)}}{\partial n} \varphi_l^{(2)} dc, \end{aligned} \right\} \tag{13}$$

where  $\delta_{ij}$  is the Kronecker's delta,  $\varphi_0$  is the velocity potential of incident waves,  $C_C$  is the intersection of the free surface and the matching boundary  $S_C$ , and  $\bar{\varphi}_l$  denotes the exterior analytical solution (Chen and Mei, 1975).

Discretizing Eq. (12) by using linear triangular elements and applying the variational principle, we finally obtain a set of simultaneous equations for  $\varphi_l^{(2)}$  in  $\Omega_2$  including  $C_C$  and  $\partial \varphi_l^{(2)} / \partial n$  on  $C_C$ .

Continuity conditions on the matching boundary

The velocity potential,  $\phi_l$ , and its normal derivative,  $\partial\phi_l/\partial n$ , must be continuous across the matching boundary  $S_C$ :

$$\phi_l^{(1)} = \phi_l^{(2)}, \quad \frac{\partial\phi_l^{(1)}}{\partial n} = \frac{\partial\phi_l^{(2)}}{\partial n}, \quad (l = 1 \sim 7, \text{ on } S_C). \quad (14)$$

Since the magnitude of evanescent modes is assumed negligible on  $S_C$ , these equations are rewritten by

$$\left. \begin{aligned} \phi_l^{(1)} &= \varphi_l^{(2)} \frac{\cosh k(h+z)}{\cosh kh}, \\ \frac{\partial\phi_l^{(1)}}{\partial n} &= \frac{\partial\varphi_l^{(2)}}{\partial n} \frac{\cosh k(h+z)}{\cosh kh} + \varphi_l^{(2)} \frac{\partial}{\partial n} \left( \frac{\cosh k(h+z)}{\cosh kh} \right), \end{aligned} \right\} (l = 1 \sim 7, \text{ on } S_C). \quad (15)$$

Substituting Eq. (15) into Eq. (9), we obtain

$$\begin{aligned} \alpha(P)\phi_l^{(1)}(P) + \int_{C_C} \left\{ \varphi_l^{(2)}(I_A - I_B) - \frac{\partial\varphi_l^{(2)}}{\partial n} I_C \right\} dc + \int_{S_V \cup S_B} \phi_l^{(1)} \frac{\partial G}{\partial n} ds, \\ = \int_{S_V} v_l G ds \quad (l = 1 \sim 7), \end{aligned} \quad (16)$$

where

$$\left. \begin{aligned} I_A &= \int_{-h}^0 \frac{\cosh k(h+z)}{\cosh kh} \frac{\partial G}{\partial n} dz, \\ I_B &= \int_{-h}^0 \frac{\partial}{\partial n} \left\{ \frac{\cosh k(h+z)}{\cosh kh} \right\} G dz, \\ I_C &= \int_{-h}^0 \frac{\cosh k(h+z)}{\cosh kh} G dz. \end{aligned} \right\} \quad (17)$$

Equation (16) is discretized into a finite number of facets on  $S_V$  and  $S_B$ , and of line elements on  $C_C$ . In the resultant discretized equation, the position of the control point  $P$  is set at the center of each element on  $S_V$ ,  $S_B$  and  $C_C$ . This leads to  $(N_V + N_B + N_C)$  linear algebraic equations involving  $\phi_l^{(1)}$  (on  $S_V$ ,  $S_B$ ),  $\varphi_l^{(2)}$  (on  $C_C$ ) and  $\partial\varphi_l^{(2)}/\partial n$  (on  $C_C$ ) as unknown variables, where  $N_V$ ,  $N_B$  and  $N_C$  are the number of elements on  $S_V$ ,  $S_B$  and  $C_C$ , respectively. These equations are solved simultaneously with those obtained from the 2-D FEM model so as to determine the velocity potential in the both domains.

### 3. Location of the matching boundary

Prior to computing ship motions in a harbor, preliminary examinations are conducted to investigate the effect of the location of the matching boundary. As described in the previous section, the matching boundary must be set far enough away from the body so as to satisfy the assumption of negligible magnitude of evanescent modes.

For this examination, we consider a wave-diffraction problem in a vertical plane. In general, the horizontal variation of the magnitude of evanescent modes may be represented by

$$A_m e^{-k_m X}, (m = 1, 2, \dots),$$

where  $X$  denotes the horizontal distance from the origin of wave scattering,  $k_m$  is the  $m$ -th eigen value ( $k_m \tan k_m h = -\sigma^2/g$ ), and  $A_m$  is a constant corresponding to the magnitude of the  $m$ -th mode at  $X = 0$ . Since  $e^{-k_1 X} \geq e^{-k_2 X} \geq \dots$  ( $k_1 < k_2 < \dots$ ), we may examine only the first mode,  $A_1 e^{-k_1 X}$ . The magnitude ratio of the first mode, normalized by  $A_1$ , is then defined as

$$p(X) \equiv e^{-k_1 X}. \quad (18)$$

As an example, **Fig. 2** shows the computed reflection coefficient of a submerged rectangular shelf,  $K_R$ , for different values of  $p$ . In the figure, the abscissa denotes the normalized wave frequency, the solid line is the corresponding analytical solution obtained from an eigen-function expansion method, and  $S_R$  and  $S_T$  are the matching boundaries. The combination of a 1-D FEM model with a 2-D BEM model was employed for these computations.

As seen in the result for  $p = 0.1$ , a large value of  $p$  (small  $X$ ) causes an apparent deviation from the analytical solution. In this case, the magnitude of evanescent modes may be still significant at the matching boundaries. While a slight discrepancy is observed for  $p = 0.05$ , the numerical results for  $p = 0.01$  and  $0.005$  agree well with the linear theory in the entire frequency range examined, indicating that the assumption of negligible evanescent modes becomes appropriate.

In **Fig. 3**, the normalized distance,  $X/h_0$  ( $h_0$ : the water depth), is plotted for different values of  $p$ . It is found that  $X/h_0$  corresponding to a constant  $p$  is insensitive to the wave frequency. The results shown in **Figs. 2** and **3** may conclude that the distance  $X$ , required for reliable prediction, is  $2 \sim 3$  times as long as the water depth.

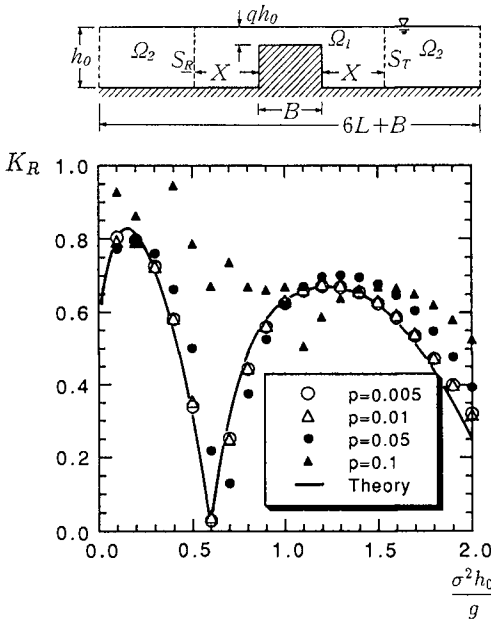


Fig. 2 Variation in computed reflection coefficients of a submerged rectangular shelf, with the location of matching boundaries.

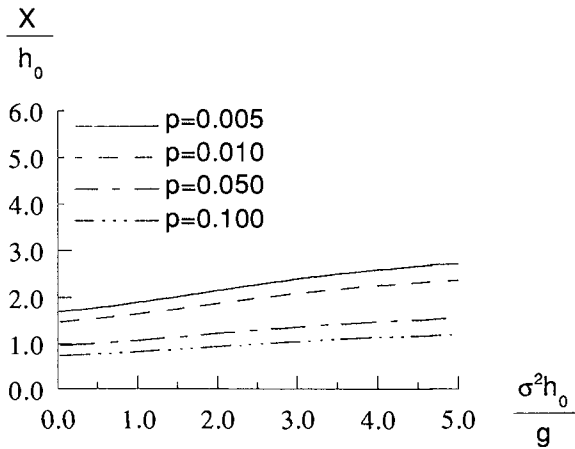


Fig. 3 Relation between the normalized distance  $X/h_0$  and the parameter  $p$ .

For 3-D cases, the distribution of evanescent modes in a horizontal plane may be expressed as

$$B_{nm}K_n(k_m R) \cos n\theta, \quad (n = 0, 1, \dots, m = 1, 2, \dots),$$

where  $(R, \theta)$  is local polar coordinates,  $B_{nm}$  is a constant and  $K_n$  is the modified Bessel function of the  $n$ -th order. Although the examinations were performed only in a vertical 2-D domain, the results obtained here may also be valid for 3-D cases since  $K_n(k_m R)$  can be represented by using an exponential function  $e^{-k_m R}$  for large  $R$ .

#### 4. Comparison with a conventional numerical model

Sawaragi and Kubo (1982) computed hydrodynamic forces on a rectangular floating body in a rectangular basin by using a 2-D BEM model. Although the application of their model is limited to a rectangular harbor with a constant depth, the comparison with their results may confirm the validity of the present numerical model.

The numerical results for added mass and damping coefficients in the sway motion,  $M_{22}$  and  $N_{22}$ , are given in **Fig. 4**, where  $\Delta$  and  $L_s$  are the weight and the length of the floating body. In the figure, the configurations of the basin and the floating body are also illustrated in a horizontal plane. The body's submergence and the water depth are  $0.2m$  and  $0.5m$ , respectively, and the harbor boundaries are fully reflective ( $K_{RW} = 1$ ).

As shown in this figure, predominant peaks of the hydrodynamic forces emerge at certain frequencies corresponding to harbor resonance. This peak phenomenon may suggest an importance of surrounding-boundary effects in predicting ship motions in a harbor. A favorable agreement between the results obtained from the present model and those from the 2-D BEM model (Sawaragi and Kubo, 1982) indicates the reliability of the present numerical model.

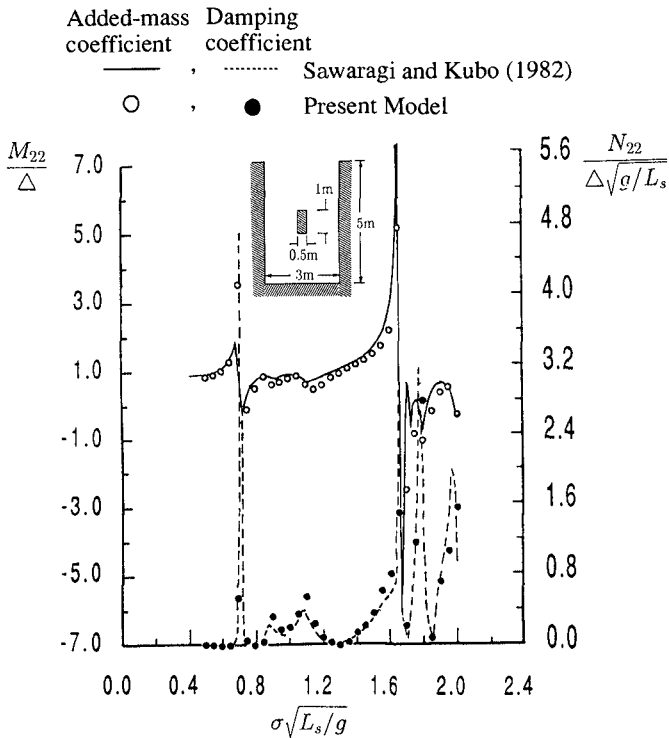
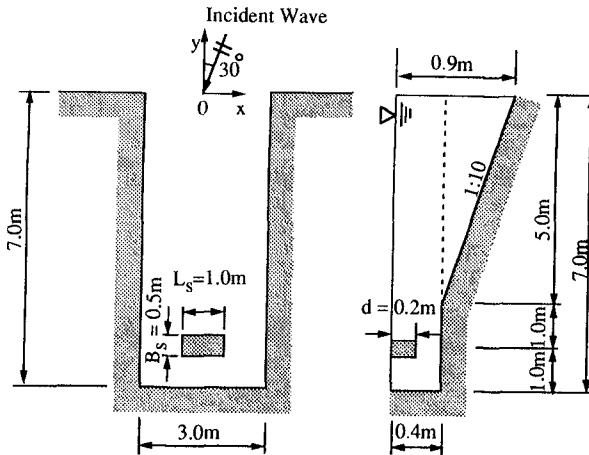


Fig. 4 Added-mass and damping coefficients in sway motion of a rectangular floating body in a rectangular basin.

## 5. Numerical Example

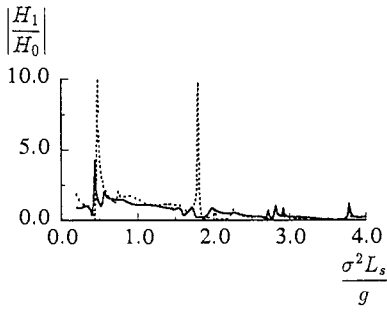
In addition to the influence of harbor boundaries, seabed topography may be one of the important factors for precise prediction of ship motions in a harbor. However, as mentioned in Introduction, most conventional approaches applied to this problem have assumed a constant water depth in a harbor. In this section, therefore, a numerical example is given for the case of a harbor with an inclined bottom.

The configurations of a floating body and a harbor examined are illustrated in **Fig. 5**. For reference, computations were also conducted for a flat-bottom case, for which the water depth is denoted by a broken line in this figure. The propagation direction of the incident waves is 30 degrees oblique to the harbor mouth.

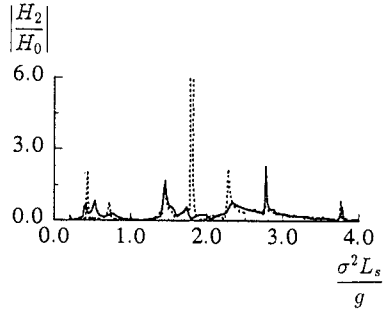


**Fig. 5** Configurations of a floating body and a harbor examined.

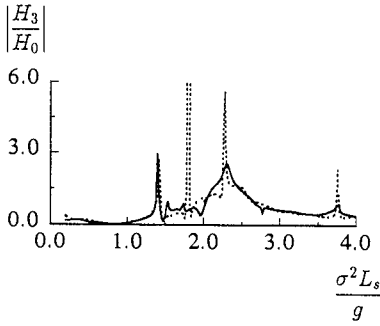
The resultant frequency responses of ship motions are shown in **Fig. 6**, where the solid and dotted lines represent the numerical results for the flat bottom and the inclined bottom, respectively, and  $H_0$  is the incident wave height. Although resonant peaks emerge in the both numerical results, the corresponding peak frequencies are different between the cases. In particular, the computed responses for the inclined-bottom case shows distinctive peaks at  $\sigma^2 L_s / g = 1.8$ , which are not observed in the result for the flat-bottom case. This difference is attributed primarily to the variation in natural frequencies of the harbor. The results given in **Fig. 6**, therefore, may indicate an importance of a depth-variation effect on the ship motions in a harbor.



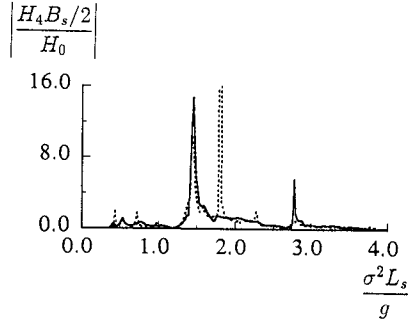
(a) Surge



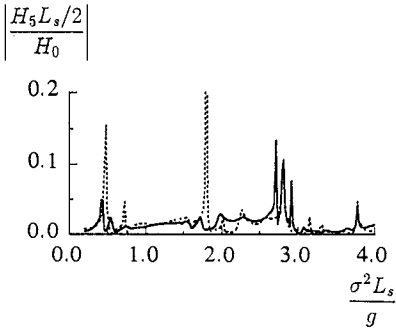
(b) Sway



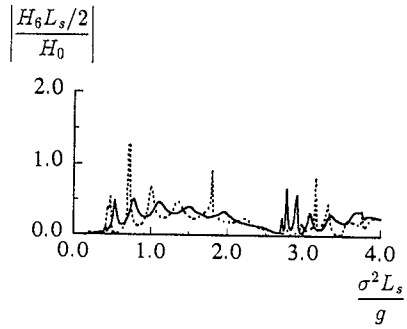
(c) Heave



(d) Roll



(e) Pitch



(f) Yaw

Fig. 6 Frequency responses of the ship motions for the flat-bottom case ( ——— ) and the inclined-bottom case ( ······ ).



## **6. Conclusions**

A numerical method, composed of a BEM-based 3-D model and a FEM-based 2-D model, has been developed for the analysis of ship motions in a harbor with arbitrary bathymetry. This combination of the two different models may achieve efficient computation with taking into account of wave deformation in a harbor. Since the mild-slope equation is employed in a horizontal 2-D domain in a harbor, the present method can be applied to more general cases with varying water depth as compared to a conventional "partially 3-D model" (Sawaragi et al., 1989).

Basic examinations have been performed to investigate appropriate location of a matching boundary where the two models are coupled. The results show that, for reliable prediction, the distance between the matching boundary and a body is required to be  $2 \sim 3$  times as long as the water depth. This practically satisfies a basic assumption that the magnitude of evanescent modes is negligible at the matching boundary.

The numerical results of radiation-force coefficients for a rectangular floating body in a rectangular basin are then compared with those obtained from a conventional method (Sawaragi and Kubo, 1982). Favorable agreement between the results verifies the present numerical method.

Lastly, ship motions in a harbor with an inclined bottom are demonstrated. The comparison between the numerical results for the flat-bottom and inclined-bottom cases indicates that the bottom topography may cause a variation in natural frequencies of harbor, which significantly influence the resultant ship motions.

## **References**

- Berkhoff, J. C. W. (1972). "Computation of combined refraction-diffraction," *Proc. 13th Coastal Eng. Conf., ASCE*, 471-490.
- Chen, H. S. and C. C. Mei (1975). "Hybrid-element method for water waves," *Proc. the Modelling Techniques Conf.*, 1, 63-81.
- Isaacson, M. and S. Qu (1990). "Waves in a harbour with partially reflecting boundaries," *Coastal Eng.*, 14, 193-214.
- John, F. (1950). "On the motion of floating bodies II," *Comm. Pure and Appl. Math.*, 3, 45-101.

- Lozano, C. J. and R. E. Meyer (1976). "Leakage and response of waves trapped round islands," *Phys. Fluids*, **19**, 1075-1088.
- Oortmerssen, G. V. (1976). "The motions of a moored ship in waves," N.S.M.B. publication No.510, 1-138.
- Sawaragi, T. and M. Kubo (1982). "The motion of a ship in a harbor basin," *Proc. 18th Int. Conf. Coastal Eng., ASCE*, 2743-2762.
- Sawaragi, T., S. Aoki and S. Hamamoto (1989). "Analysis of hydrodynamic forces due to waves acting on a ship in a harbor of arbitrary geometry," *Proc. 8th Int. Conf. Offshore Mech. and Arctic Eng., ASME*, **2**, 117-123.
- Smith, J. D. and T. Sprinks (1975). "Scattering of surface waves by a conical island," *J. Fluid Mech.*, **72**, 373-384.

## CHAPTER 65

### THE MEASURED AND COMPUTED HOKKAIDO NANSEI-OKI EARTHQUAKE TSUNAMI OF 1993

Tomoyuki Takahashi<sup>1</sup>, Nobuo Shuto<sup>1</sup>  
Fumihiko Imamura<sup>2</sup> and Hideo Matsutomi<sup>3</sup>

#### Abstract

The linear long-wave theory is used in the first stage to find the tsunami initial profile. The perfect reflection is assumed at the land boundary. On comparing the computed with the measured overall runup distribution, the best fault model is found among 24 models. It consists of three sub-faults dipping westward. It satisfies the measured land subsidence and overall distribution of runup heights in Okushiri Island.

Then, the shallow-water theory with bottom friction is used to simulate runup. The runup condition is used as the land boundary condition. The arrival time and runup heights agree well with the measured.

#### Introduction

At 22:17, July 12th, 1993, an earthquake of  $M_s=7.8$  occurred off the southwestern coast of Hokkaido, in the Japan Sea. A giant tsunami was generated. It hit the island of Okushiri about 5 minutes after the earthquake, and claimed more than 200 lives. A big fire, caused by the tsunami, burned houses which were saved from the direct attack of the tsunami in Aonae, a small town at the southern end of Okushiri Island. The area of concern is shown in Fig.1 (Hokkaido Tsunami Survey Group, 1993).

Since the tsunami hit at night, its details could not be obtained from witnesses. The most reliable data would be the tsunami traces. Many parties were dispatched to

---

<sup>1</sup>Disaster Control Research Center, Tohoku Univ., Sendai 980-77, Japan

<sup>2</sup>School of Civil Eng., Asian Inst. of Tech., G.P.O.Box 2754, Bangkok 10501

<sup>3</sup>Dept. of Civil Eng., Akita Univ., Akita 010, Japan

measure runup heights and collect such data as tide records. The authors also organized a survey team of 19 persons, and sent it to the site two days after the disaster. At the same time, the authors simulated the tsunami with the Harvard CMT solution. On exchanging results by faxes and phone calls between the survey team and the simulation team every morning and night, places and density of measurement points were determined. The authors considered that if there was a difference between the measured and the computed, this difference was really important to distinguish the special feature of the tsunami.

In the second section, tsunami data are shown and the special feature of this tsunami which should be satisfied by the simulation is summarized. In the third section, the method of simulation is briefly given. In the fourth section, initial profiles

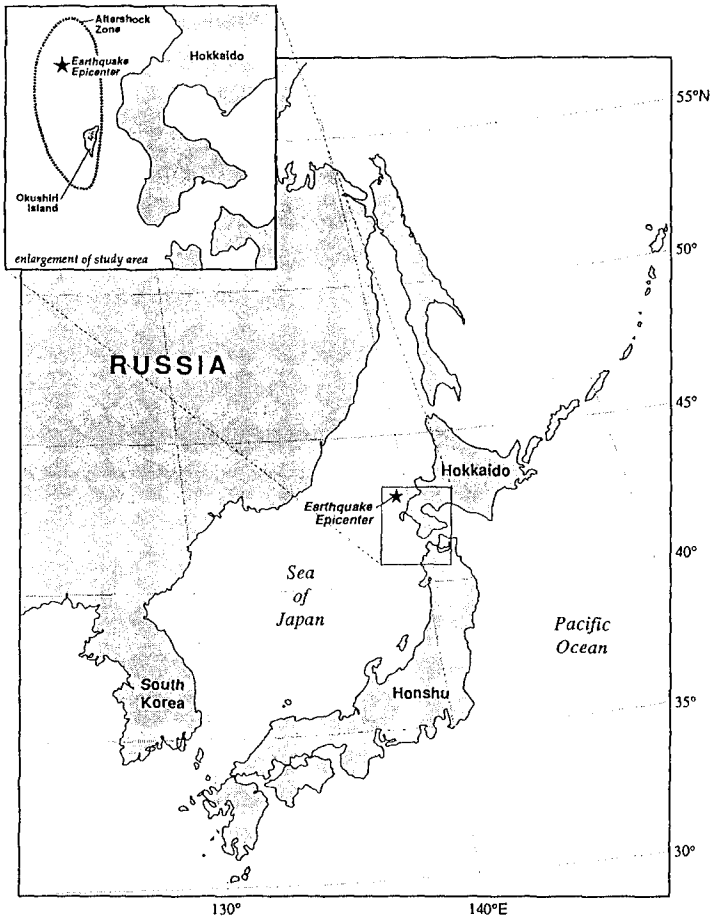


Fig.1 Location of the area studied.

obtained from seismic data are shown and their defect are discussed. In the fifth section, a comparison is made between the measured tsunami runups and the simulated with the Harvard CMT solution. In the sixth section, a model of two sub-faults, DCRC-2, is proposed and examined. In the seventh section, a model of three sub-faults, DCRC-17a, is introduced. Among 24 models examined by the authors, the DCRC-17a model is considered the best at present. In the same section, the problems which requires a further study are also discussed.

### Measured Runup Heights, Tide Records, Arrival Time and Ground Subsidence

Positions of aftershocks are shown in Fig.2 (Hokkaido Univ. et al, 1993). The vertical distribution of aftershocks in each section implies that it is very hard to determine the inclination angle of fault, which is closely related to the location of the crest of the initial tsunami profile. A reverse-slip fault dipping eastward (westward) makes the crest far from (near to) Hokkaido Island and results in a late (early) arrival of the tsunami.

Figure 3(a), (b) shows the measured runup heights in Okushiri Island and the mainland of Hokkaido. The highest runup of 31.7 m was obtained on the western shore of Okushiri Island directly facing the earthquake fault. It was found at the

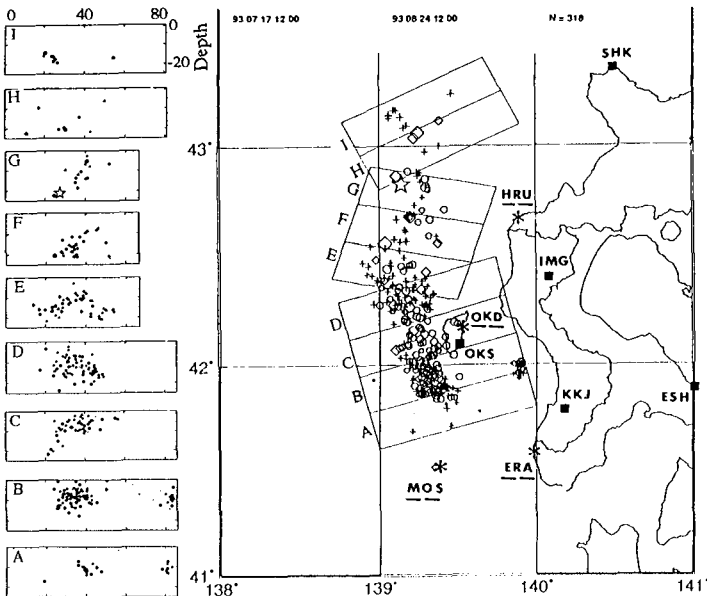


Fig.2 Distribution of aftershocks. Left figures are vertical distributions in the areas given by rectangles in the right figure.

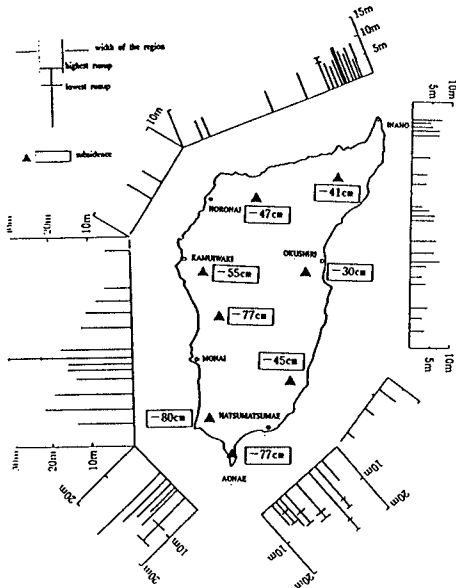


Fig.3(a) Measured runup heights in Okushiri island with the measured subsidence shown in rectangles.

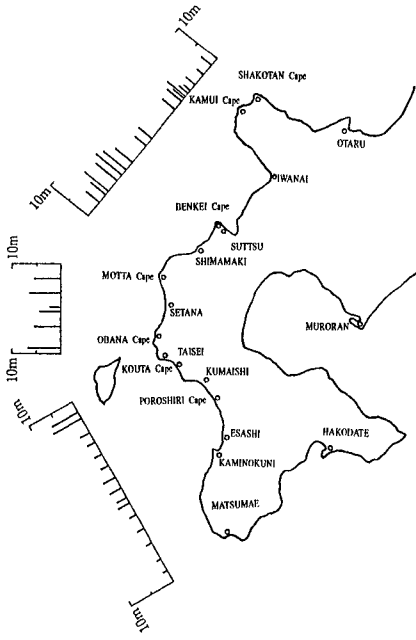


Fig.3(b) Measured runup heights in Hokkaido.

bottom of a tiny valley 50 m wide at its mouth on a pebble pocket beach 250 m long backed by cliffs. At the valley mouth and on the cliffs, runup heights were 22 m to 24 m. In order to simulate this high runup, very fine spatial grids (and, of course, very detailed maps) will be required.

Even on the eastern coast of Okushiri Island, high runup of 20 m was measured at Hamatsumae which is located in the sheltered area of Aonae Point. This may be a result of concentration due to refraction caused by the Okushiri Spur, a very wide shallow extending in the sea south of the point. In order to simulate the refraction effect, not only the detailed sea bottom contours but also the angle of tsunami incidence is important. This is closely related with the strike angle of the fault.

Along the eastern coast of Okushiri Island, runups show a wavy distribution, which implies the interaction of the tsunami entrapped around the island and the tsunami reflected from the mainland of Hokkaido.

Along the Hokkaido coast, tsunami runups are high from Taisei to Shimamaki and not high in the other region.

In the first column of Table 1, the arrival times collected from witnesses or determined from submerged clocks are summarized.

In Fig.3(a), the measured ground subsidence are also shown (Kumaki, Y. et al., 1993). Any fault model should yield the ground displacement coincident with them.

Method of Simulation

Two kinds of equations are used in the following simulation; the linear long-wave theory and the shallow-water theory with the bottom friction term included. The former is reduced to a set of difference equations, TUNAMI-N1, and the latter to TUNAMI-N2, by using the staggered leap-frog scheme. The details are given elsewhere (e.g., Shuto et al., 1986).

The area of simulation is from 138° 30'E to 140° 33'E and from 40° 31'N to 43° 18'N.

The initial tsunami profile is calculated with the Mansinha-Smylie method (1971) from fault parameters.

In simulations for modification and examination of fault models, TUNAMI-N1 is used with the perfect reflection condition at the land boundary. Overall agreements between the measured and computed are compared. The spatial grid is 450 m wide

Table 1 Arraival times

Aonae (west)	Aonae (east)	Esashi	Taisei	Setana	Sukki	Shima-maki	Iwanai
4.5	4.5	11	5	5	3	5	15

(unit:minute)

and the time step interval is 1 second.

TUNAMI-N2 is applied to the DCRC-17a model, selected as the best among 24 models. The spatial grids are varied; 450 m in Domain A, 150 m in Domain B and 50 m in Domain C. The runup condition is used at the land boundary,

### Initial Profiles Proposed

Figure 4 compares tsunami initial profiles by different researchers and institutions. These profiles are obtained, based upon seismic data. Differences are resulted from the frequency range of seismic waves used in the analysis and from the locations of stations where the data were acquired.

With the accumulation of detailed and accurate seismic data, the situation became more and more complicated. No seismologists dare to determine what happened. Different from ordinary interplate earthquakes, no clear evidence was found about which plate is sinking below another. Almost a year later, many seismologists agree to think that the fault may dip westward.

Seismologists are now skeptical about the validity of vertical ground displacements which are calculated with such a method as the Mansinha-Smylie's. On contrary to the homogeneous displacement on the fault plane assumed in these methods, an actual fault motion is heterogeneous, and the resulted ground displacement is more complicated.

There is no other method and no other theory than the use of tsunami simulations, at present, to estimate the vertical displacement of sea bottom. One way is the tsunami inversion method introduced by Satake (1985), by which the initial profile is calculated back from tide records. The present paper uses another method, the trial-and-error repetition. We start the numerical tsunami simulation with an assumed initial profile, compare the simulated results with the measured runup heights to find the difference, modify the assumed initial profile, and repeat the procedure again.

When a tsunami model is determined, the number of faults is important. In the beginning, the authors used the Harvard CMT solution, which assumed a single fault. This model, however, could not simulate the tsunami well. Then, models of plural faults were examined. In this paper, one of two-fault models, DCRC-2, and one of three-fault models, DCRC-17a, are discussed.

### Harvard CMT Solution

Immediately after the earthquake, seismic data seemed to support one of the Harvard CMT solution, the fault plane of which gently dipped eastward. Figure 5



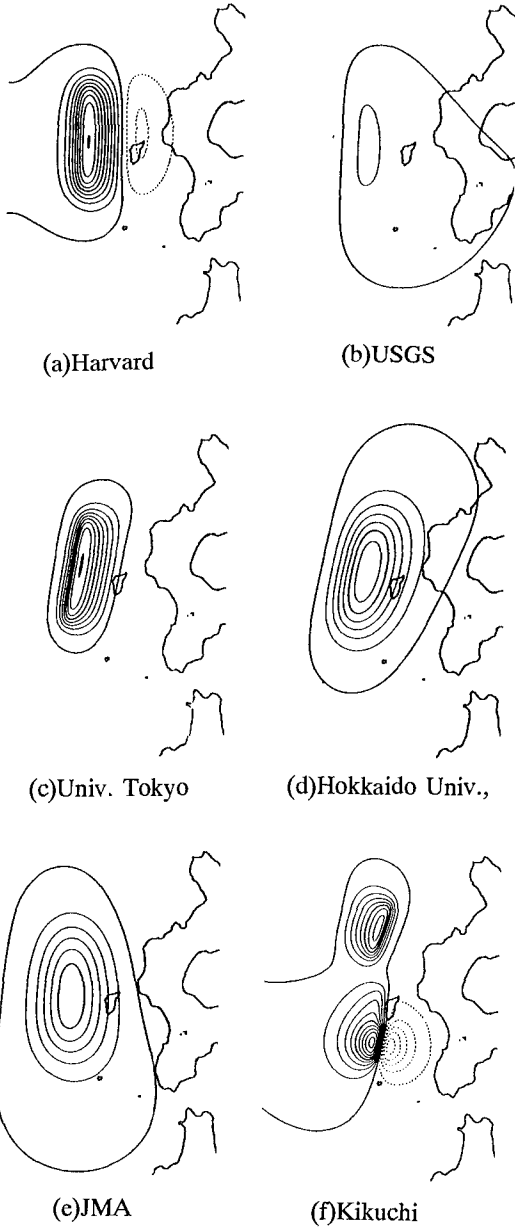


Fig.4 Proposed tsunami initial profiles. Solid lines are for upheaval and dotted lines for subsidence.

shows the vertical ground displacement (= tsunami initial profile) calculated for this solution. The crest is located at the western end of the tsunami source area.

With accumulation of seismic, geographical and tsunami data, differences of this model from the measured became non-negligible. Although this solution and the measured give the subsidence in Okushiri Island (Fig.6), the former gives the larger subsidence at the northern end of the island, while the latter reveals the larger subsidence of about 90 cm at the southern end.

The most important difference is found in the arrival time of tsunami. Every witnesses at Aonae confirm the fast arrival of the tsunami 4 to 5 minutes after the earthquake. The simulation, however, gives the arrival 7.5 minutes after the earthquake, as shown in Fig.7. In order to simulate this early arrival, the crest of tsunami initial profile should be located near the island; i.e., the fault should dip westward.

In Fig.8(a), (b), the computed runups are compared with the measured in Okushiri Island and Hokkaido. At Hamatsumae of Okushiri Island, the computed is too small. The same difference is found at Shimamaki of Hokkaido.

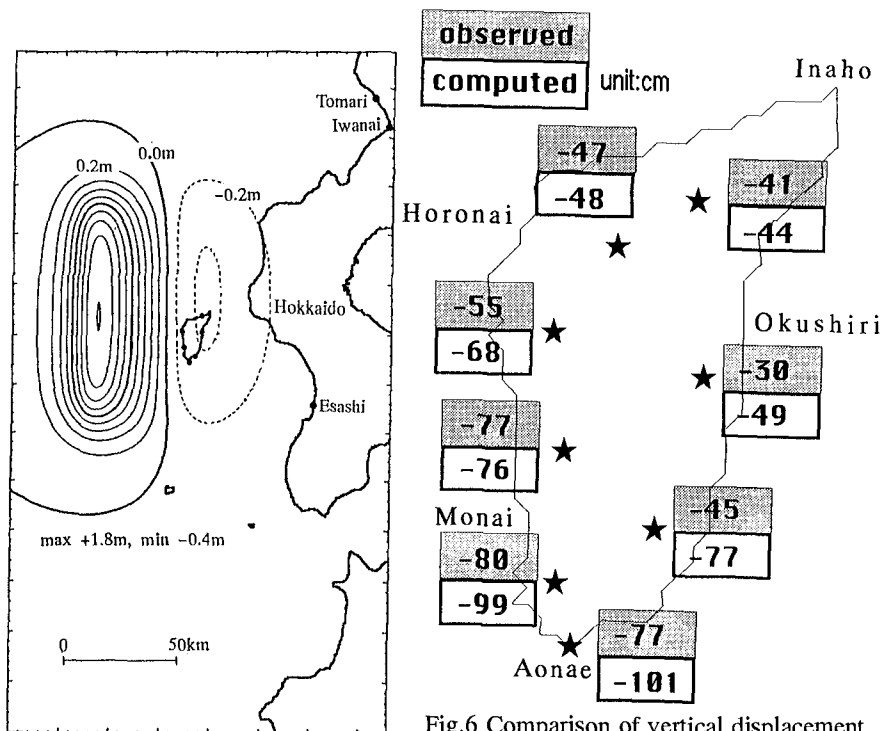


Fig.5 Tsunami initial profile computed for the Harvard CMT solution.

Fig.6 Comparison of vertical displacement in Okushiri Island between the measured and the computed with the Harvard CMT solution.

DCRC-2

Stimulated by the Kikuchi model (Fig.4 (f)), the authors assume plural faults. The first trial is DCRC-2, composed of two fault planes.

At the beginning of the modification, the authors take the following facts into consideration; aftershock distribution, ground subsidence in Okushiri Island and the witnessed arrival time of tsunami. The conclusion is that the faults must be reverse-slip faults inclining westward with a large dip angle.

Then, high runups at Hamatsumae is simulated. According to authors' assumption that these high runups are due to refraction, the strike direction of the south fault is adjusted because it governs the incident direction of the tsunami.

With these consideration, the initial profile for DCRC-2 is obtained as shown in Fig.9. Different from the Harvard CMT solution, there are two wave crests, both of which are located close to Okushiri Island. Contours are of more complicated shape.

The computed runups are compared with the measured in Fig.10. There are differences along the western coast. Along the south shore, the computed is much smaller than the measured, while the former is slightly smaller than the latter.

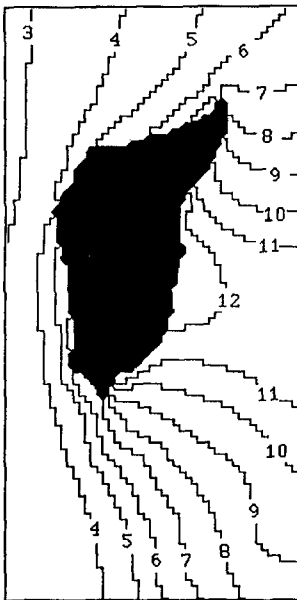


Fig.7 Arrival time computed with the Harvard CMT solution. Numerals are in minutes after the earthquake.

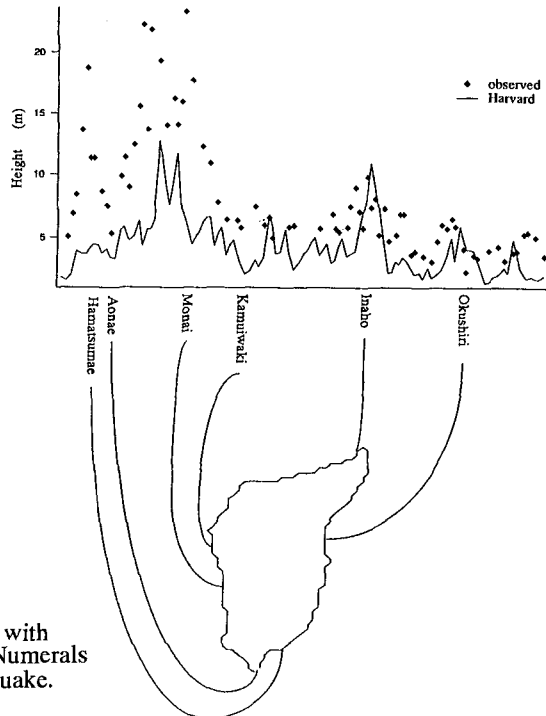


Fig.8(a) Comparison of runup heights between the computed with the Harvard CMT solution (solid line) and the measured (marks) along Okushiri Island.

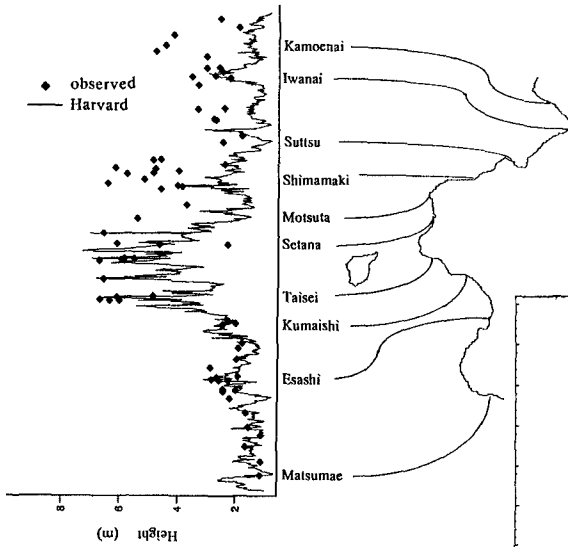


Fig.8(b) Comparison of runup heights between the computed with the Harvard CMT solution (solid line) and the measured (marks) along Hokkaido.

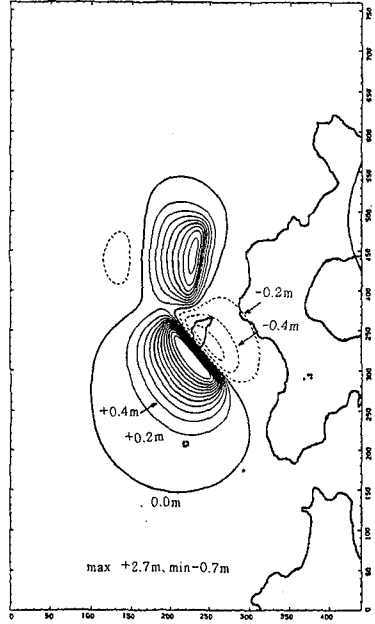


Fig.9 Tsunami initial profile computed for DCRC-2.

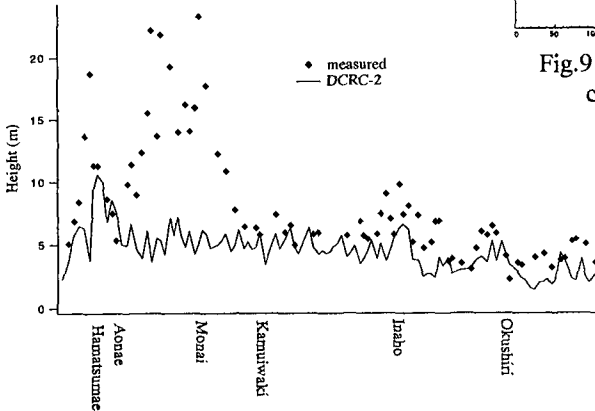


Fig.10 Comparison of runup heights between the computed with DCRC-2 (solid line) and the measured (marks) along Okushiri Island.

DCRC-17a

In order to solve the difference above mentioned, the authors divide the south fault into two faults with almost same strike directions. After several trials, DCRC-17a is found as the best. Its three fault planes are shown in Fig.11. The north fault is made longer than DCRC-2 in order to cover locations of aftershocks. Fault parameters are given in Table 2.

The initial profile of DCRC-17a is shown in Fig.12. The crest corresponding to the south sub-fault is 4.9 m high. Another crest is 2.2 m high, corresponding to the north sub-fault. The central fault does not yield any crest, because its slip is small.

The computed vertical displacement in Okushiri Island is compared with the measured in Fig.13. Compared to the Harvard CMT solution (see Fig.6), the agreement is much better.

Figure 14 shows the computed arrival time. The tsunami arrives at Aonae about five minutes after the earthquake, while it does 7.5 minutes in Fig.7 for the Harvard CMT solution.

Figure 15 compares runup height distributions around Okushiri Island. Overall agreement is fairly well, except for the neighborhood of Monai on the western coast, where the differences between the measured and the computed can only be explained by another simulation with very fine spatial grids as stated in the section of the measured runup heights. In order to evaluate the agreement, Aida's parameters,  $K$  and  $\kappa$ , the geometric mean of the ratio of the measured to the computed runup height and the corresponding variance, are used. For the whole island of Okushiri,  $K=1.048$  and  $\kappa = 1.469$ . Distribution of  $K$  and  $\kappa$  for every coast is shown in Fig.16.

Figure 17 compares runup height distributions along Hokkaido. In the neighborhood of Esashi, the computed is higher than the measured. This indicates the need of a further modification. The initial tsunami height in the southern part of south fault should be made smaller than in the present model. In addition, a slight modification may be necessary to adjust the computed results near Suttsu and its neighborhood.

Table 2 Fault parameters of DCRC-17a.

Fault	$M_0(\times 10^{27})$	depth	Strike( $^\circ$ )	Dip( $^\circ$ )	Slip( $^\circ$ )	Length	Wide	dislocation
North	3.85	10km	188	35	80	90km	25km	5.71m
Central	0.56	5km	175	60	105	30km	25km	2.50m
South	2.21	5km	163	60	105	24.5km	25km	12.00m
Total	6.62							

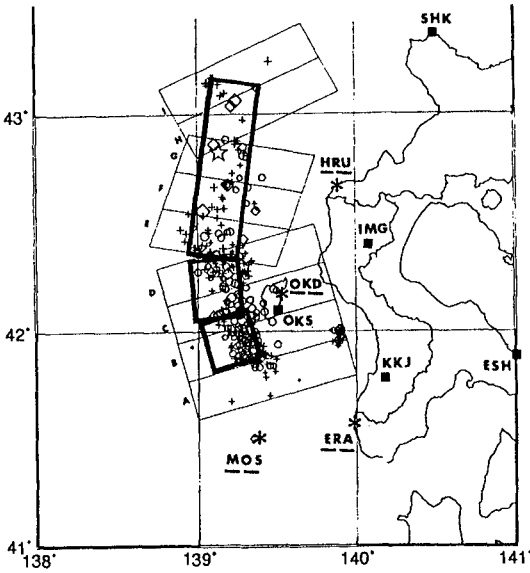


Fig.11 Three fault planes of DCRC-17a.

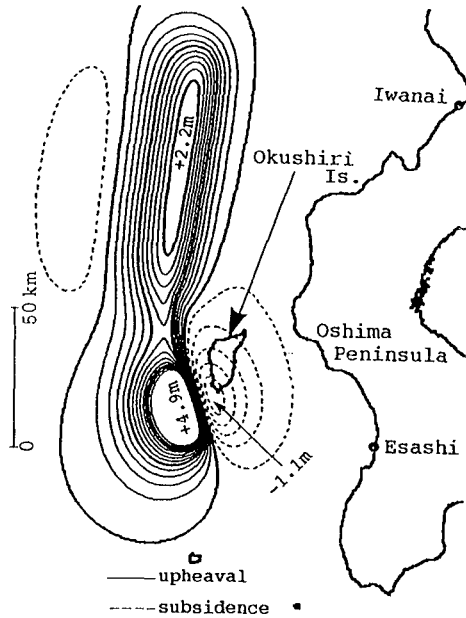


Fig.12 Tsunami initial profile computed for DCRC-17a.

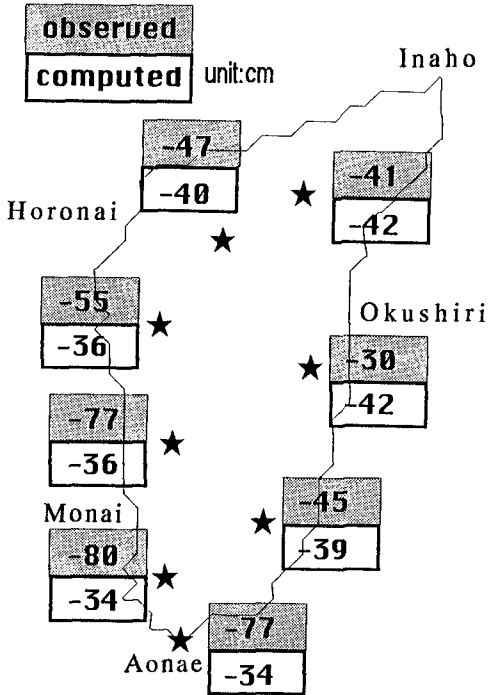


Fig.13 Comparison of vertical displacement between the computed with DCRC-17a and the measured in Okushiri Island.

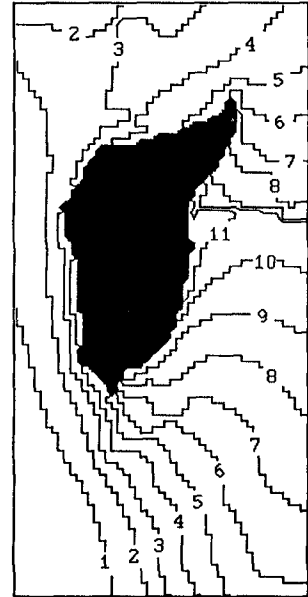


Fig.14 Arrival time computed with DCRC-17a. Numerals are in minutes after the earthquake.

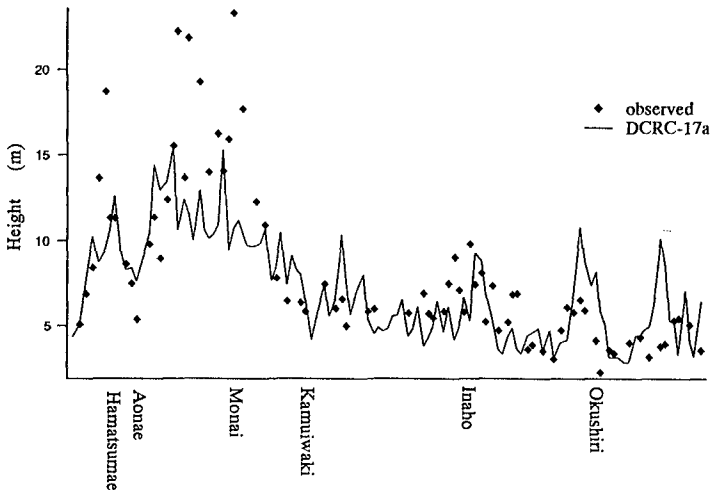


Fig.15 Comparison of runup heights between the computed with DCRC-17a (solid line) and the measured (marks) along Okushiri Island.

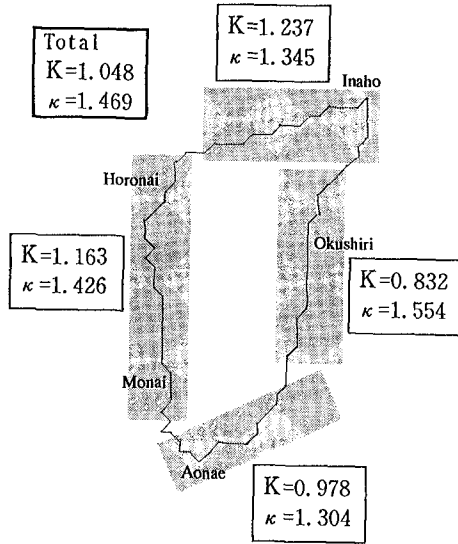


Fig.16 Distribution of K and  $\kappa$  for DCRC-17a along Okushiri Island.

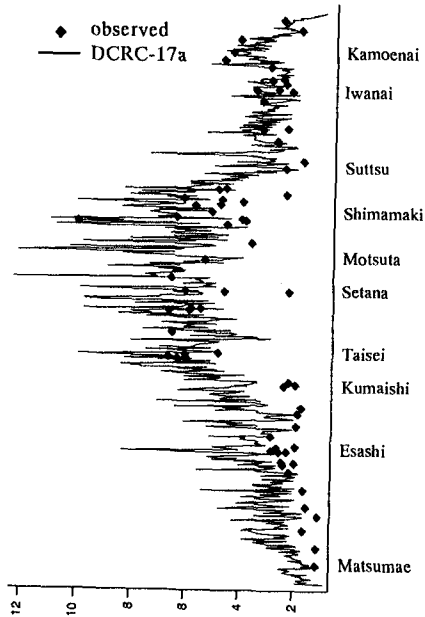


Fig.17 Comparison of runup heights between the computed with DCRC-17a (solid line) and the measured (marks) along Hokkaido.



### Conclusions

In order to simulate the 1993 tsunami around Okushiri Island, the DCRC-17a model composed of three fault planes is obtained, by mostly adjusting the south and central faults. It satisfies the arrival time, runup distribution including high runups at Hamatsumae which is located in the sheltered area, and land subsidence.

In the present simulation, the maximum runup of 31.7 m in the neighborhood of Monai in Okushiri Island is not taken into consideration. A simulation with very fine spatial grids is required to simulate it.

Further adjustments of the south fault is necessary to explain the tsunami in the neighborhood of Esashi, Hokkaido. In addition, another adjustment is necessary for the northern part of the north fault. These adjustments may affect, to some extent, the wavy distribution of runup heights on the eastern coast of Okushiri Island, too.

### References

- Hokkaido Tsunami Survey Group:1993, Tsunami devastates Japanese coastal region, Eos, Transaction, AGU, 74, 417-432.
- Mansinha, L. and Smylie, D.E.:1971, The displacement of the earthquake fault model, Bull. Seismol. Soc. America, 61, 1433-1400.
- Satake, K.:1985, The mechanism of the 1983 Japan Sea earthquake as inferred from long period surface waves and tsunamis, Phys. Earth Planet. Interiors, 37, 249-260.
- Satake, K. et al.:1988, Tide gauge response to tsunamis: Measurements at 40 tide gauge stations in Japan, J. Marine Res., 46, 557-571.
- Shuto, N. et al.:1986, A study of numerical techniques on the tsunami propagation and run up, Science of Tsunami Hazard, 4, 111-124.

## CHAPTER 66

### Quasi-Three-Dimensional Model for Storm Surges and Its Verification

Takao Yamashita<sup>1</sup>, Yoshito Tsuchiya, M.ASCE<sup>2</sup> and Hiroshi Yoshioka<sup>1</sup>

#### Abstract

Three-dimensional model for storm surges was developed, in which momentum equations first were solved in the vertical direction together with mass conservation and turbulence model, then mass conservation in the horizontally two-dimensional coordinates was solved by the finite difference method. Several fundamental tests concerning swing and wind-induced current, were performed to examine the model properties. Finally the hindcasting of the current profile in the Tanabe bay was conducted to test model applicability.

#### Introduction

Storm surge models have been developed as a two-dimensional model, which is called a vertical integrated model or one(single) level model. Because of Japan's recent need for waterfront development, significant environmental problems and coastal disasters will persist during accelerated future developments in the coastal ocean. It is desired to develop a more sophisticated numerical model for storm surges which predicts the profile of current, turbulence, and surge heights. A three dimensional model for tide and storm surges combined with a turbulence and wind-wave prediction model may become popular in coastal ocean assessment in the near future.

Heaps (1973) studied dynamic response of the Irish Sea to a stationary wind stress field by a finite difference model which solves the homogeneous hydrodynamic equations taken in linearized form by transforming them to eliminate the vertical coordinate  $z$ . The system including the coordinates  $x, y, t$ , and  $z$  was solved by an explicit finite difference scheme. This model only considers homogeneous systems, and neglects the convection terms. A series of numerical experiments was also performed with the model to determine the steady state circulation of the Irish Sea system. Sundermann (1974) and Laevastu (1975) extended the method for three dimensional, multi-level, and multi-layer flow systems. Simons (1974 & 1975) studied the circulation in Lake Ontario under strong stresses by

---

<sup>1</sup>Instructor, Disaster Prevention Research Institute, Kyoto University, Uji, Kyoto, 611 Japan

<sup>2</sup>Professor Emeritus of Kyoto University & Professor, Meijyo University, Tenpaku-ku, Nagoya, 467 Japan

using a four layer model. Sundermann (1974) extended Hansen's (1962) basic two dimensional scheme to study three dimensional tidal circulation of the North Sea. This extension involves an assumption of homogeneous density distributions. The basic two-dimensional explicit scheme of Hansen (1962) also has been extended by Laevastu (1975) by using multi-layer modeling.

Another three-dimensional model which is the simple version of  $\sigma$ -coordinates was developed by Koutitas and O'Connor (1980), in which momentum equations together with mass conservation equation and turbulence model first are solved in the vertical direction. Then mass conservation in the horizontally two-dimensional coordinates is solved. This model elaborates on the vertical motion of fluid and reducing the matrix of difference equations.

Numerical prediction in shallow bays or estuaries must be focused to develop an effective three-dimensional model for environment assessment in the coastal ocean, since this is our most probable development space in the coming century. In this paper, a quasi-three-dimensional (Q3-D) model is developed based on Koutitas and O'Connor's (1980) modeling.

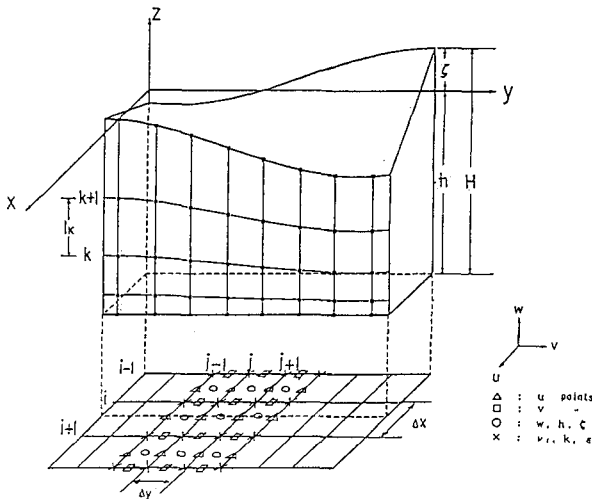


Figure 1 Coordinate system and definition of variables.

Basic Equations and Solution Method

The basic equations for the Q3-D model consist of the momentum equations of mean flow, the equation of continuity and the equations of turbulence model. The following additional relations for the vertical velocity  $w$  and the surface elevation  $\zeta$  are used.

$$w(x, y, z) = -\frac{\partial}{\partial x} \int_{-h}^z u dz - \frac{\partial}{\partial y} \int_{-h}^z v dz \tag{1}$$

$$\frac{\partial \zeta}{\partial t} + \frac{\partial(HU)}{\partial x} + \frac{\partial(HV)}{\partial y} = 0 \tag{2}$$

which is derived from the mass continuity equation by integrating in the vertical direction. This equation satisfies total mass conservation in the horizontally two-dimensional system.

Vertical distribution of turbulence has to be specified to simulate the velocity distribution of wind-induced mean currents. Several turbulence models are now available for the Q3-D modeling: (1) The so-called zero equation model in which the vertical eddy viscosity  $\nu_t$  is assumed. (2) Multi-equation models in which turbulence kinetic energy budget is described by the standard  $k-\epsilon$  model. In order to get an efficient numerical solution to the three-dimensional system of equations, Koutitas and O'Connor (1980) employed a time fractional finite difference method in which advection and propagation are split. The computational domain is covered by a rectangular-grid system in the  $x-y$  plane, and the water depth is divided into a several layer-elements as shown in Figure 1. The finite element Galerkin method is applied to the momentum equations to obtain nodal velocities over the depth. For the depth-averaged continuity equation (2), the finite difference method is applied.

Applying an explicit scheme, the difference equation of the momentum equation in the  $x$ -direction is written as:

$$\begin{aligned} \frac{u^{n+1} - u^n}{\Delta t} = & -u^n \frac{\partial u^n}{\partial x} - v^n \frac{\partial u^n}{\partial y} - w^n \frac{\partial u^n}{\partial z} - g \frac{\partial \zeta^{n+1/2}}{\partial x} \\ & + \frac{\partial}{\partial x} \left( \nu_T \frac{\partial u^n}{\partial x} \right) + \frac{\partial}{\partial y} \left( \nu_T \frac{\partial u^n}{\partial y} \right) + \frac{\partial}{\partial z} \left( \nu_T \frac{\partial u^{n+1}}{\partial z} \right) + f v^n \end{aligned} \quad (3)$$

The  $y$ -momentum equation can be shown by the same manner.

Assuming fractional time step  $t^*$ , the momentum equations can be split up as; for the  $x$ -momentum equation,

$$\frac{u^*}{\Delta t} = \frac{u^n}{\Delta t} - u^n \frac{\partial u^n}{\partial x} - v^n \frac{\partial u^n}{\partial y} - w^n \frac{\partial u^n}{\partial z} - g \frac{\partial \zeta^{n+1/2}}{\partial x} \quad (4)$$

$$\frac{u^{n+1}}{\Delta t} - \frac{\partial}{\partial z} \left( \nu_T \frac{\partial u^{n+1}}{\partial z} \right) = \frac{u^*}{\Delta t} + \frac{\partial}{\partial x} \left( \nu_T \frac{\partial u^n}{\partial x} \right) + \frac{\partial}{\partial y} \left( \nu_T \frac{\partial u^n}{\partial y} \right) + f v^n \quad (5)$$

for the  $y$ -momentum equation,

$$\frac{v^*}{\Delta t} = \frac{v^n}{\Delta t} - u^n \frac{\partial v^n}{\partial x} - v^n \frac{\partial v^n}{\partial y} - w^n \frac{\partial v^n}{\partial z} - g \frac{\partial \zeta^{n+1/2}}{\partial y} \quad (6)$$

$$\frac{v^{n+1}}{\Delta t} - \frac{\partial}{\partial z} \left( \nu_T \frac{\partial v^{n+1}}{\partial z} \right) = \frac{v^*}{\Delta t} + \frac{\partial}{\partial x} \left( \nu_T \frac{\partial v^n}{\partial x} \right) + \frac{\partial}{\partial y} \left( \nu_T \frac{\partial v^n}{\partial y} \right) - f u^n \quad (7)$$

and the vertical velocity  $w$  is calculated by

$$w(x, y, z) = -\frac{\partial}{\partial x} \int_{l_k} u(x, y, z) dz - \frac{\partial}{\partial y} \int_{l_k} v(x, y, z) dz \quad (8)$$

The finite element Galerkin method is applied to Eqs. (4) to (7) to solve the nodal velocities over the depth. Substituting the approximated velocity  $\tilde{u}$  into

the original momentum equation and integrating it between nodal points over a whole area, we get the following residual equation in the  $x$ -direction.

$$\int \tilde{u} \frac{u^*}{\Delta t} dz = \int \tilde{u} \frac{u^n}{\Delta t} dz - \int \tilde{u} u^n \frac{\partial u^n}{\partial x} dz - \int \tilde{v} v^n \frac{\partial u^n}{\partial y} dz - \int \tilde{w} w^n \frac{\partial u^n}{\partial z} dz - \int \tilde{u} \frac{\partial \zeta^{n+1/2}}{\partial x} dz \tag{9}$$

Applying this relation to Eqs. (4) to (7), a set of linear equations can be reduced to

$$\left. \begin{aligned} \mathbf{A} \mathbf{u}^* &= \mathbf{a}^n, & \mathbf{B} \mathbf{u}^{n+1} &= \mathbf{b}^* \\ \mathbf{C} \mathbf{v}^* &= \mathbf{c}^n, & \mathbf{D} \mathbf{v}^{n+1} &= \mathbf{d}^* \end{aligned} \right\} \tag{10}$$

where  $\mathbf{A}$  is the  $2 \times 2$  matrix,  $\mathbf{B}$  the  $2 \times 4$  matrix,  $\mathbf{a}$  and  $\mathbf{c}$  are two component vectors, and  $\mathbf{b}$  and  $\mathbf{d}$  are four component vectors.

The linear interpolation function is used as

$$u = N_k u_k + N_{k+1} u_{k+1} \tag{11}$$

where

$$N_k = \frac{1}{l_k} (z_{k+1} - z), \quad N_{k+1} = \frac{1}{l_k} (z - z_k) \tag{12}$$

where  $l_k$  is the element length defined by  $l_k = z_{k+1} - z_k$ .

The three-dimensional current field is obtained by computing these equations which can be solved by the Gaussian elimination method. When velocities  $u(x, y, z)$  and  $v(x, y, z)$  are calculated in the time step  $n$ , the corresponding vertical velocity  $w(x, y, z)$  is computed by

$$w(x, y, z) = - \int_{l_k} u(x, y, z) dz - \int_{l_k} v(x, y, z) dz \tag{13}$$

The surface elevation  $\zeta$  is calculated by

$$\frac{\zeta^{n+1/2} - \zeta^{n-1/2}}{\Delta t} = - \frac{\partial(HU)^n}{\partial x} - \frac{\partial(HV)^n}{\partial y} \tag{14}$$

In the above-mentioned computation processes, the kinematic eddy viscosity  $\nu_t$  in the time-space domain has to be specified. Three types of turbulence models are incorporated into the numerical model for Q3-D storm surge prediction:

(1) For the zero-equation turbulence model,  $\nu_t$  is assumed as:

$$\nu_t = \text{constant} \quad \text{or} \quad \nu_t = l^2 \left| \frac{\partial u}{\partial z} \right| \tag{15}$$

(2) For the one-equation turbulence model,  $\nu_t$  is calculated as:

$$\nu_t = \sqrt{k} l \tag{16}$$

where  $l$  is the eddy length scale and  $k$  is calculated by the  $k$ -equation.

(3) For the two-equation turbulence model,  $\nu_t$  is calculated as:

$$\nu_t = C_D \frac{k^2}{\varepsilon} \tag{17}$$

where  $k$  and  $\varepsilon$  are obtained by the  $k$ - $\varepsilon$  model. Details of the  $k$ - $\varepsilon$  model are shown below.

The  $k$  equation is discretized by the Crank-Nicholson scheme as:

$$\begin{aligned} & \frac{k^{n+1}}{\Delta t} + \frac{1}{2} \left( w^n \frac{\partial k^{n+1}}{\partial z} \right) - \frac{1}{2} \left( \frac{\partial}{\partial z} \left( \frac{\nu_T}{\sigma_k} \frac{\partial k^{n+1}}{\partial z} \right) \right) \\ &= \frac{k^n}{\Delta t} - \frac{1}{2} \left( w^n \frac{\partial k^n}{\partial z} \right) + \frac{1}{2} \left( \frac{\partial}{\partial z} \left( \frac{\nu_T}{\sigma_k} \frac{\partial k^n}{\partial z} \right) \right) + P^n - \varepsilon^n \end{aligned} \tag{18}$$

The finite element formulation is made by multiplying the weighting function,  $\tilde{k}$ , to this equation and integrating it over the depth as:

$$\begin{aligned} & \int \tilde{k} \frac{k^{n+1}}{\Delta t} dz + \int \tilde{k} \left\{ \frac{1}{2} w^n \frac{\partial k^{n+1}}{\partial z} \right\} dz - \int \tilde{k} \left\{ \frac{1}{2} \frac{\partial}{\partial z} \left( \frac{\nu_T}{\sigma_k} \frac{\partial k^{n+1}}{\partial z} \right) \right\} dz = \int \tilde{k} \frac{k^n}{\Delta t} dz \\ & - \int \tilde{k} \left\{ \frac{1}{2} w^n \frac{\partial k^n}{\partial z} \right\} dz + \int \tilde{k} \left\{ \frac{1}{2} \frac{\partial}{\partial z} \left( \frac{\nu_T}{\sigma_k} \frac{\partial k^n}{\partial z} \right) \right\} dz + \int \tilde{k} P^n dz - \int \tilde{k} \varepsilon^n dz \end{aligned} \tag{19}$$

The linear shape function, Eq. (20), is assumed in the finite element formulation.

$$N_k = \frac{1}{l_k}(z_{k+1} - z), \quad N_{k+1} = \frac{1}{l_k}(z - z_k) \tag{20}$$

where  $k$  is the nodal number,  $l_k$  the element length, and  $z_k$  the position of  $k$  in the  $z$  axis.

The point of  $z$  is interpolated by,

$$z = N_k z_k + N_{k+1} z_{k+1} \tag{21}$$

Applying the Galerkin method, the integrations of each term in the equation are shown respectively as:

Equations for  $\varepsilon$  are derived in the same manner, and are solved numerically together with the  $k$  equations by the Gaussian elimination method.

Fundamental Tests of Q3-D Model

Model parameters in the  $k$ - $\varepsilon$  equations will now be discussed along with several fundamental tests in the rectangular flume (i.e. swing and wind-induced current tests).

**Boundary conditions at the bottom and surface:** For time-averaging turbulence models, such as the  $k$ - $\varepsilon$  and one equation models, the boundary conditions at the bottom and surface have to be carefully discussed because of its strong

shear flow characteristics. Usual modeling method in this area apply the knowledge called the universal law of the wall, which depicts the velocity distribution of shear flow by a logarithmic law given by

$$\frac{u}{u_\tau} = \frac{1}{\kappa} \ln \frac{E u_\tau y}{\nu} \quad (22)$$

where  $u_\tau$  is the friction velocity,  $\kappa$  the Kármán constant,  $E$  the roughness parameter,  $y$  the distance from the wall, and  $\nu$  the kinematic viscosity of the fluid. When we assume a hydraulically smooth wall, the roughness parameter may be evaluated by  $E = 9$  in the range of  $30 < u_\tau y / \nu < 100$ . This concept is useful in the modeling of mean flow field in the boundary layer. Equation (22) is used to develop a quasi-three dimensional model for simulation of storm surges.

On the other hand, the boundary condition of the turbulence model is posed by the assumption of balancing production and dissipation, which results in the following relation

$$\frac{k}{u_\tau^2} = \frac{1}{\sqrt{c_\mu}}, \quad \varepsilon = \frac{u_\tau^3}{\kappa y} \quad (23)$$

for the  $k$ - $\varepsilon$  model.

To compute the mean flow in the interior region, we have to specify the velocity at the interface between the interior region and boundary layer with the relation of shear stresses and eddy viscosity given respectively by

$$\left( \nu_t \frac{\partial u}{\partial z} \right)_{z=\zeta} = \tau_s \quad \text{at the surface} \quad (24)$$

$$\left( \nu_t \frac{\partial u}{\partial z} \right)_{z=-h} = \tau_b \quad \text{at the bottom} \quad (25)$$

where  $\tau_s$  and  $\tau_b$  are the shear stresses at the surface and bottom of the sea respectively.

When we specify the shear stresses ( $\tau_s$  and  $\tau_b$ ), and turbulence properties ( $k$  and  $\varepsilon$ ), it is possible to get the boundary condition for mean flow field by velocity gradient. The following relation is used to evaluate the eddy viscosity,  $\nu_t$ .

$$\nu_t = c_\mu \frac{k^2}{\varepsilon} \quad (26)$$

Dirichlet's problem for the discrete system brings a difficulty in determining the velocity gradient without dependence on grid size. Fine mesh makes the model extremely expensive in the three-dimensional case. To overcome these problems the point where the boundary condition is posed is fixed in this investigation. At the surface layer the point of  $\Delta z_s = 1.35\text{m}$  and  $\Delta z_b = 0.1\text{m}$  at the bottom are set. This means that the distance from the bottom or surface,  $y$ , is fixed by  $\Delta z_s$  or  $\Delta z_b$  in the wall law relation of Eq.(22) or Eq.(23). In the case of the zero-equation turbulence model we do not have any information about turbulence near the boundary, therefore we need some assumptions in evaluating the eddy viscosity  $\nu_t$  or shear stresses  $\tau_b$  and/or  $\tau_s$ . If the two-equation turbulence model is used, we do not need any assumption. We do need much CPU time and information of turbulence at the open boundary. This is usually difficult to get.

For zero-equation modeling, the following text elaborates on the way to determine the bottom shear stresses from the numerical results of swing and wind-induced current tests. For this purpose, both the quasi-three dimensional simulation of  $k-\epsilon$  model version and the horizontally two-dimensional simulation are also conducted under the same computational condition. These results are used as indexes to determine the bottom shear stresses at the fixed point  $\Delta z_b$  by comparison of surface elevations. Moreover, a simulation of flow combined tides and wind-induced currents is performed by the model of zero-equation turbulent version.

**Swing test** Free oscillation of water in the closed flume may be simulated fairly well by the so-called single level model (horizontally two-dimensional model). By comparing the water surface oscillations computed by the single level model and those by the Q3-D model, the bottom shear stress of Q3-D model can be evaluated. As previously stated, this is one of the parameters which has to be determined in the Q3-D model. A closed flume which is used for the swing test has a dimensions of uniform water depth of 20 m deep,  $L=10,000$  m in length and  $B=3,000$  m in width. The horizontal spacing of the grid system is  $\Delta x=1000$  m and the number of the vertical nodes is 35. Time increment is fixed by  $\Delta t=10$  sec. The initial surface profile is given by  $\zeta(x) = 0.0001x - 0.5$ . For the zero-equation version of Q3-D model, the vertical distribution of eddy viscosity is assumed by the following equation which is obtained by fitting the mean velocity distribution with Baines and Knapp's experiment.

$$\nu_t = 0.01 + \kappa C_\mu \left(1 - 3.6 \frac{z}{h}\right) \frac{z}{h} \quad (27)$$

This assumption of eddy viscosity distribution will be further discussed later by comparing zero and two equation models in  $\nu_t(z)$ .

Surface elevation at the right end is shown in Figure 2 together with the results computed by the leap-frog scheme(dotted line). Bottom friction is neglected in the computation by leap-frog scheme. The computed propagation speed of the disturbance on the uniform depth of 20 m is 1428 sec, which is equivalent to the long wave celerity. It can be recognized that almost uniform velocity distribution of the mean current is computed in the case of swing test with no bottom friction.

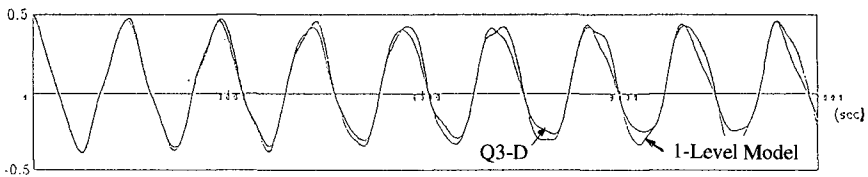


Figure 2 Comparison of water surface oscillation at the flume computed by Q3-D model (solid line) and 1-Level Model (dotted line).

**Wind-induced current test** The three-dimensional model is of course more effective than the horizontally two-dimensional in the computation of wind induced current which is characterized by the strong shear near the surface. In the case of a closed basin, a return flow is observed near the bottom.



A wind-induced flow test in the closed flume is conducted and the vertical distribution of eddy viscosity as well as mean flow is discussed together with surface elevation property. This is calibrated by a comparison with theoretical formulation of wind set-up using Eq. (28).

$$\zeta_{\max} = \frac{3\rho_a C_D L W^2}{4g D \rho_w} \tag{28}$$

where  $\zeta_{\max}$  is the maximum water surface elevation,  $C_D$  the drag coefficient at the surface,  $L$  length of the flume,  $W$  the wind velocity,  $D$  the total depth,  $\rho_a$  the density of air, and  $\rho_w$  the density of sea water.

As mentioned before, shearing stresses both at the surface and bottom are not uniquely determined in the Q3-D model of the zero-equation version of turbulence. They depend on the spacing of nodes just inside the interface because an approximation accuracy of the mean flow gradient depends on node spacing. When the number of vertical node points is fixed, shearing stresses are dependent upon the total depth. Figure 3 depicts this effect, in which four different results in the maximum surface elevation under the same condition are compared. Changing the still water depth in the range of 5 to 40 m, the maximum wind set-up is computed under the condition of uniform wind speed of 20 m/sec in the same flume as swing test. Gradually increasing wind speed from 0 to 20 m/sec for 3000 sec is assumed in the test to reduce time to be steady state which means small tank oscillation is expected. In the figure, Q3-D CONST indicates the results computed by using the uniform distribution of eddy viscosity in the Q3-D model of zero-equation turbulence version, Q3-D QUARD indicates those expressed by the distribution resulting from Eq. (27), 1LEVEL MODEL indicates those developed by the horizontally two dimensional model.

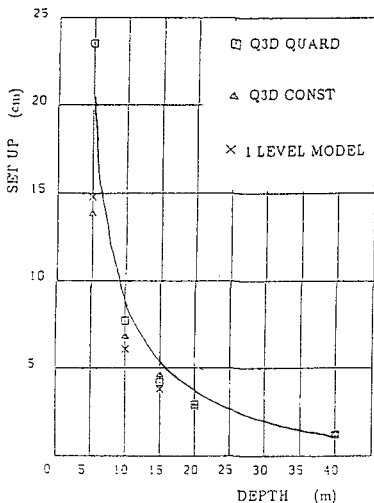


Figure 3 Relation between the water depth and the computed set-up.

It can be recognized that the wind set-up computed by Q3-D QUARD is larger than that computed by other models in the region shallower than 10 to 5 m. This means that it may result in over-estimate of the shearing stress at the surface, and

a lower-estimate at the bottom in the very shallow region, because the their real distribution may become uniform as the depth becomes shallower. The difference between 1LEVEL MODEL and the solid line comes from the difference of out-put points. The out-put point of numerical computation is just inside of the end-wall.

Vertical distributions of the mean flow and eddy viscosity at the center of the flume in steady state is shown in Figure 4 where the column is the depth nondimensionarized by the still water depth, while the abscissas indicates the horizontal velocity normalized by friction velocity. White circles in the figure indicate the experimental values of Baines-Knapp showing the null-velocity point at 0.7 in nondimensional depth.

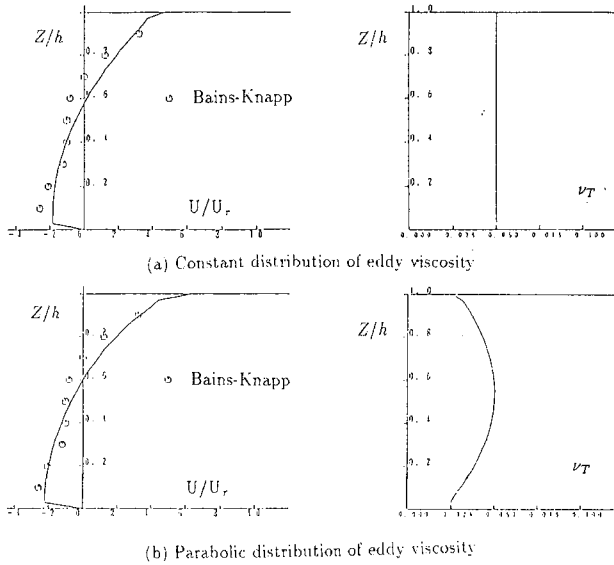


Figure 4 Vertical distribution of the mean flow and eddy viscosity at the center of the flume in steady state by Q3-D model of zero-equation turbulence version.

On the other hand, Figure 5 also shows the vertical distribution of both mean flow velocity and eddy viscosity which were computed in terms of the Q3-D model of  $k-\epsilon$  version whose boundary conditions are given by Eq. (23) for  $k$  and Eq. (29) for  $\epsilon$ .

$$\epsilon_s = \frac{k_s^{\frac{3}{2}}}{\kappa L_s}, \quad \epsilon_b = \frac{k_b^{\frac{3}{2}}}{\kappa L_b} \tag{29}$$

where the length scale parameters are assumed as  $L_s = 100\Delta z_s$  and  $L_b = \Delta z_b$  by comparison of mean flow velocity distribution with Baines and Knapp's experiments.

From these figures it is found that the null-velocity point of the vertical distribution of mean flow is located around the nondimensional depth of 0.6 which is slightly lower than that by experiment. Moreover the vertical distribution of computed eddy viscosity by the  $k-\epsilon$  model is similar to that of a parabola,

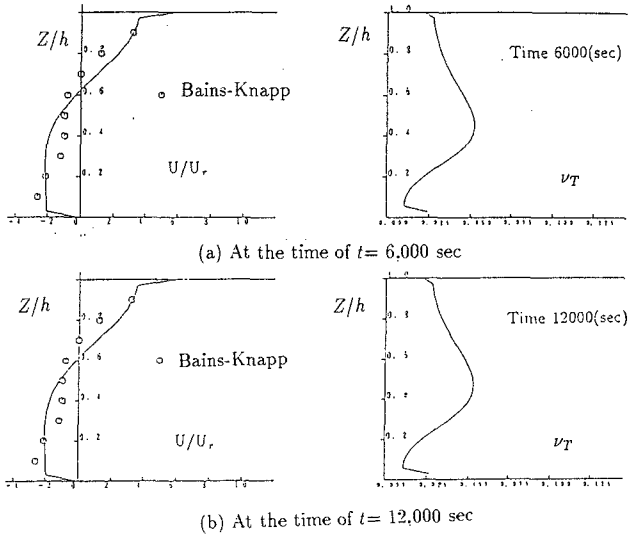


Figure 5 Vertical distributions of the mean flow and eddy viscosity at the center of the flume in steady state by Q3-D model of  $k-\epsilon$  version.

Eq. (27), which is assumed for the model of zero-equation version. The computed eddy viscosity, however, skews downward with its maximum at 0.4 in the nondimensional depth.

Application to wind-induced currents in Tanabe Bay

Observations of vertical velocity distribution in terms of an acoustic Doppler current profiler (ADCP) have been conducted since 1989 in Tanabe Bay by the Shirahama Oceanographic Observatory, Disaster Prevention Research Institute, Kyoto University. Tide and wind vector on the sea surface are also observed at the Oceanographical observation tower whose location is indicated in the map of Tanabe Bay (Figure 6) together with ADCP's location and depth contours.

As this data is very useful for calibration of three-dimensional numerical model, simulation tests of mean flow in Tanabe Bay are carried out to compare with observation in the current profile. Because the model assumes a well-mixed situation in the sea, the observed profile of mean current of horizontal component in winter season is selected for comparison. Figure 7 shows the time changes in wind vector(upper), tide(middle) and current profile(bottom) which are used for model calibration here. Current vector in this figure is defined by NS-WE system in which the northward component is plotted upward and the westward current is leftward. A typical feature of this data is the strong wind-induced currents whose direction is ESE and the return flow to the direction of W.

The sea bottom topography is reproduced from the chart (No. 74) with the grid system of  $\Delta x = 100$  m. Total point number is  $89 \times 110$  and the origin is  $33^\circ 44' 40''$  north latitude and  $135^\circ 17' 00''$  east longitude. For actual computation, 200m horizontal grid size, 19-point vertical nodal points, and 5sec time increment

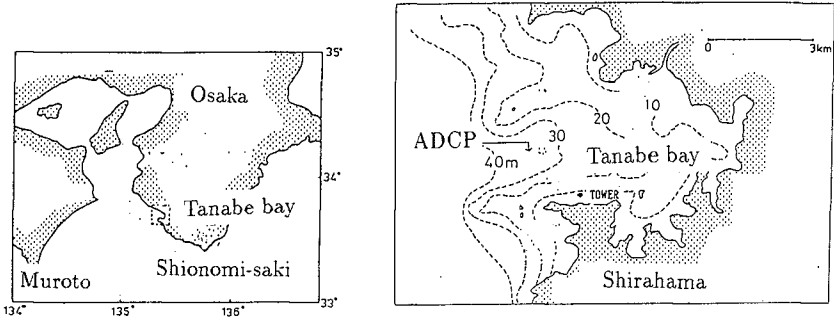


Figure 6 Location of the Tanabe Bay and the oceanographical observation tower together with ADCP's observation point.

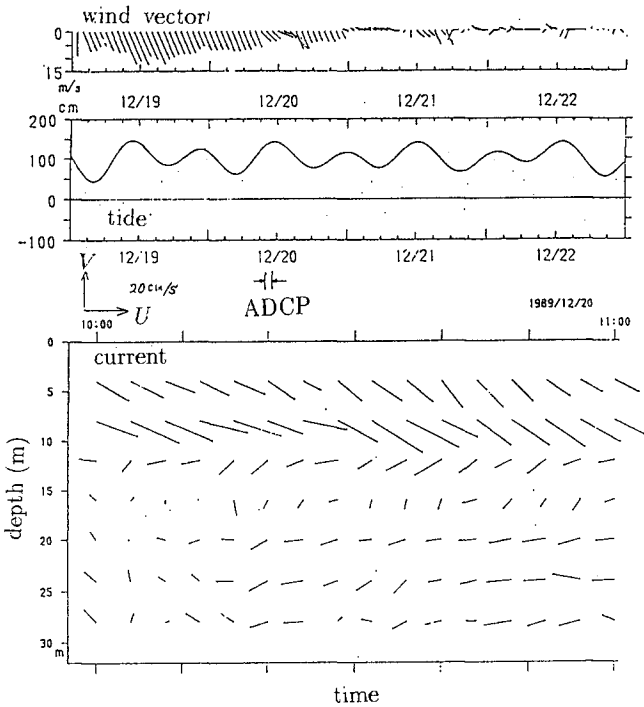


Figure 7 The data of wind vector(upper), tide(middle) and current profile(bottom), observed on December 12, 1989.

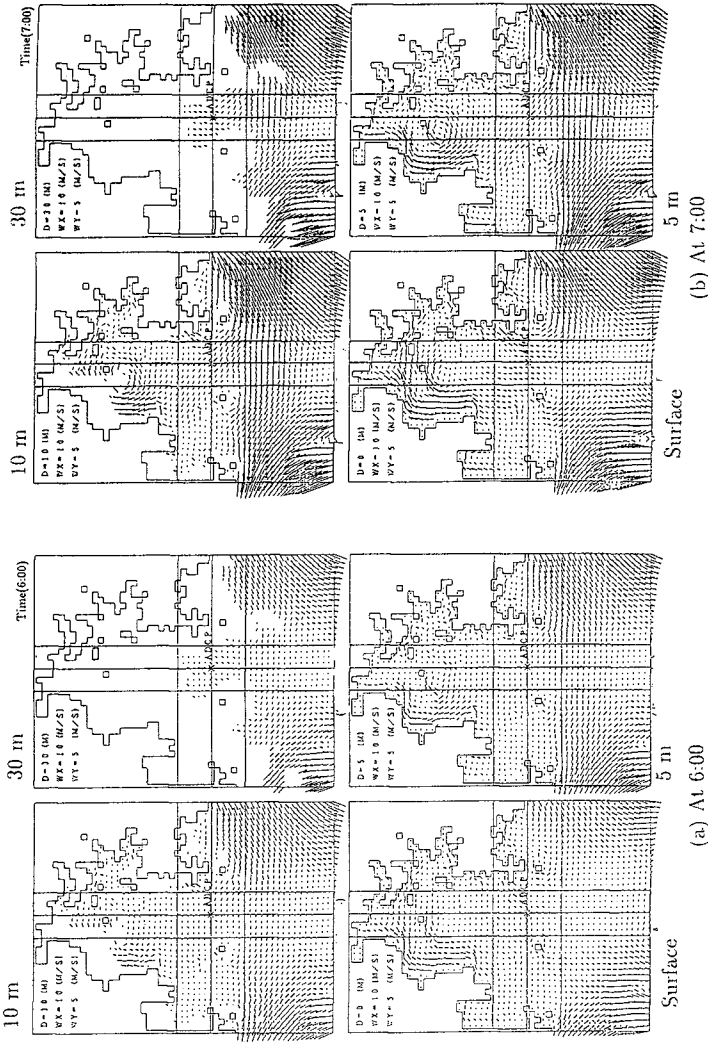


Figure 8 Computed mean flow vectors in Tanabe Bay at the surface level, 5m level, 10m level and 30m level by Q3-D model of zero-equation version.

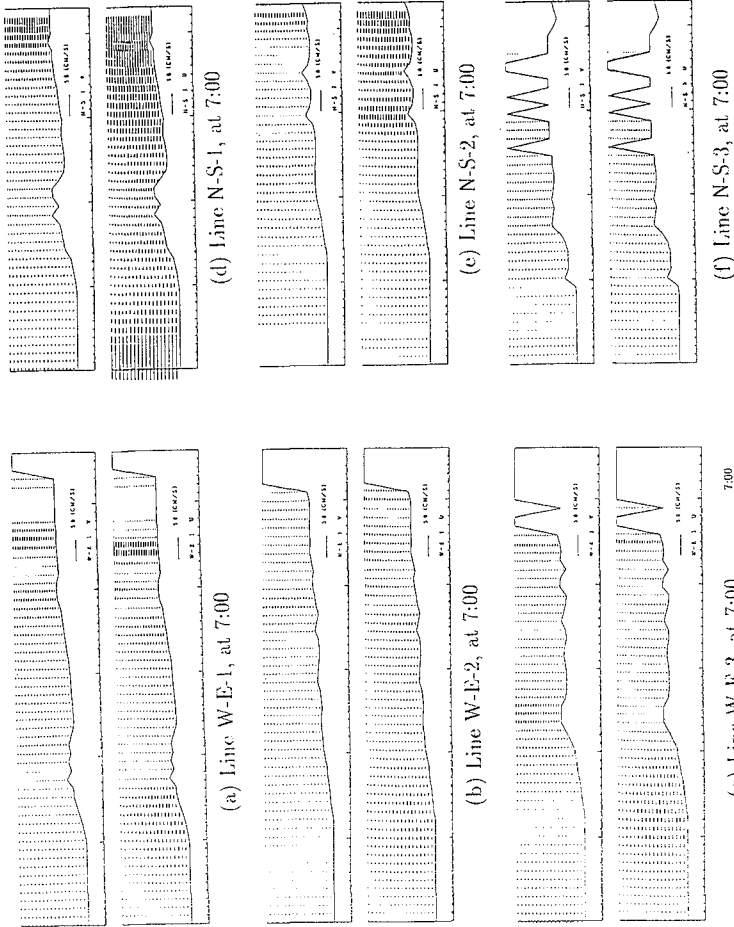
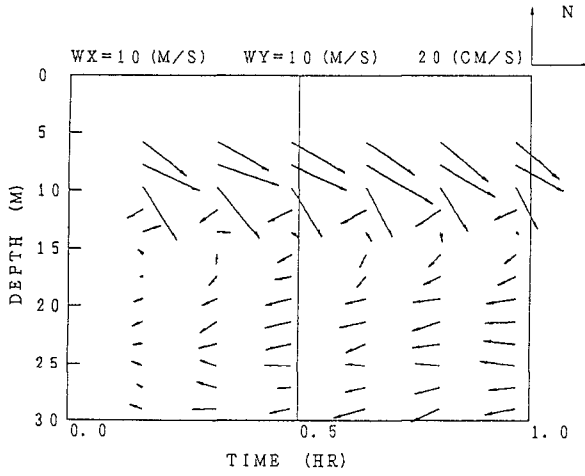
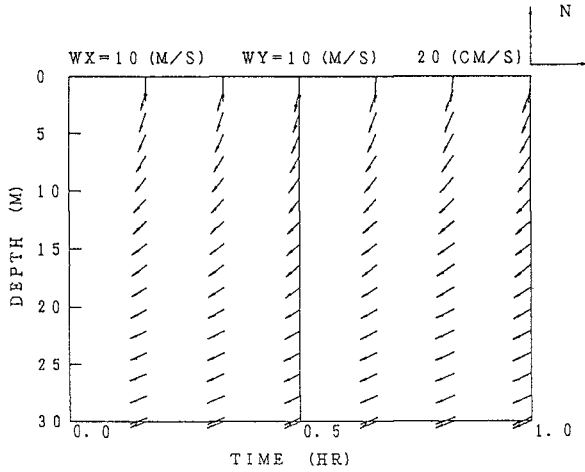


Figure 9 Current profile distribution on the observation lines of N-S-1, N-S-2, N-S-3, W-E-1, W-E-2 and W-E-3.



(a) Observed velocity profile by ADCP



(b) Computed velocity profile by Q-3D model

Figure 10 Comparison between observation and simulation of current profile. Observation of 2 min and 10 min averaging and computation output of 10 min interval.

are employed. Simulation period is 5:00-11:00, 20 December, 1989 which covers ADCP observation, 10:00-11:00. Wind condition is assumed to be constant NW wind whose velocity is 10 m/sec.

A sample of the computed mean flow vectors at the surface level, 5m level, 10m level and 30m level are shown in Figure 8. The vertical velocity distribution on six lines of N-S-1, N-S-2, N-S-3, W-E-1, W-E-2 and W-E-3 are shown in Figure 9. Figure 10 is the comparison between observation and simulation, in which observation of 2 min and 10 min averaging and computation output of 10 min interval are shown. The strong wind-induced flow is not simulated in the numerical model, however, the return flow (probably the tidal current) is well simulated both in its magnitude and direction. One possibility which may cause this discrepancy may be the open boundary condition. The other may be some trouble in the ADCP observation. Further discussion about this will be needed in terms of continuous efforts in executing simulations and ADCP observations.

### Conclusions

A three-dimensional model for storm surges was developed and its fundamental tests were carried out. The obtained main results in this paper are shown below.

(1) From the swing test, propagation speed of the initial disturbance was confirmed to be in good agreement with that of free long waves.

(2) From the wind-induced current test in the two-dimensional flume, it was found by fitting the mean velocity profile with the Baines and Knapp's experiment that the eddy viscosity  $\nu_t$  was around 0.01-0.02 m<sup>2</sup>/s for Q3-D model of zero-equation version. Moreover the profile of eddy viscosity computed by the  $k$ - $\epsilon$  model was similar to that assumed the parabolic profile in the zero-equation version.

(3) The simulation of the flow fields in the Tanabe Bay was performed, in which both tides and wind-induced currents were taken into consideration. The velocity profile observation with ADCP also was conducted in the bay. From the comparison of velocity profile between observations and computations, it was found that the strong surface wind-induced flow was not simulated, however the return flow was well simulated both in its magnitude and direction.

### References

- Hansen, W.(1962), Hydrodynamical methods applied to oceanographic problems, Mitt. Inst. Meereskd., University of Hamburg, Hamburg.
- Heaps, N.S.(1973), Three-dimensional model of the Irish Sea, Geophys. J. R. Astron. Soc., Vol.35, pp.99-120.
- Koutitas, C. and B.A. O'Connor(1980), Modeling three-dimensional wind-induced flow, Proc. ASCE, Jour. Hydraulics Div., Vol.106, HY11, pp.1843-1865.
- Laevastu, T.(1975), Multilayer hydrodynamical-numerical models, Proc. Symp. Modelling Tech., ASCE, p.1010.
- Simons, T.J.(1974), Verification of numerical models of Lake Ontario: Part I. Circulation in spring and early summer, Jour. Phys. Oceanogr., Vol.4, p.507.
- Simons, T.J.(1975), Verification of numerical models of Lake Ontario: Part II. Stratified circulation and temperature changes, Jour. Phys. Oceanogr., Vol.5, pp.98-110.
- Sundermann, J.(1974), A three-dimensional model of a homogeneous estuary, Proc. 14th ICCE, ACSE, pp.2337-2390.





# **PART III**

## **Coastal Structures**



## CHAPTER 67

### Analysis of practical rubble mounds

Allsop N.W.H.<sup>1</sup>, Jones R.J.<sup>2</sup>, Besley P.<sup>2</sup> & Franco C.<sup>3</sup>

#### ABSTRACT

This paper describes results from an unusual research project completed under Topic 3R2 of the European Union's MAST research project G6-S Coastal Structures. In this project, data were collected from the major European hydraulics laboratories on the hydraulic and structural responses of example rubble mound breakwaters and sea walls that each laboratory had previously studied in wave flume or wave basin tests. The main responses considered here are:

- a) Main armour stability, given by measurements of armour movement and/or displacement under wave action.
- b) Wave overtopping, described by the number of waves passing over the structure crest, or by the mean overtopping discharge;

The paper describes some of the analysis of armour stability and hydraulic performance of these structures, and explores the potential to develop general conclusions from ad hoc studies. This paper develops some of the analysis described initially within the G6-S project by Allsop & Franco (1992), but also re-considers and revises some of the early analysis and initial conclusions.

#### 1. OUTLINE OF THE STUDY

Within the MAST I project G6-S Coastal Structures, work under Topic 3R addressed the performance of rubble mound breakwaters. Such structures may be used to protect harbours, cooling water intakes or outfalls, and related areas of coastal development, against wave action. Rubble mound breakwaters are formed by constructing the inner part of the mound, termed the core, from quarried rock. The core is protected against erosion by armour layers, supported by filter or under-layers. The size of the armour is closely related to the height of the design waves. Such structures may include a crown wall, a number of armour and underlayers on the seaward and lee faces. They are usually designed with a number of different levels from foundation and toe layers to crest armouring (Fig 1).

---

<sup>1</sup> Manager Coastal Structures, HR Wallingford, Howbery Park, Wallingford, UK;  
Professor (associate) University of Sheffield

<sup>2</sup> Engineer, Coastal Structures, HR Wallingford, Howbery Park, Wallingford, UK.

<sup>3</sup> Institute of Hydraulic Engineering, University of Rome

Rubble mounds are used to reduce levels of wave activity by limiting wave overtopping or transmission, and/or to protect against erosion. The degree of wave reduction needed, and hence the hydraulic responses required, depend on the requirements of the harbour or coastal development. The structural design of the breakwater must ensure that it can serve its stated purpose over its full design life, and that damage to the structure is therefore kept below accepted limits.

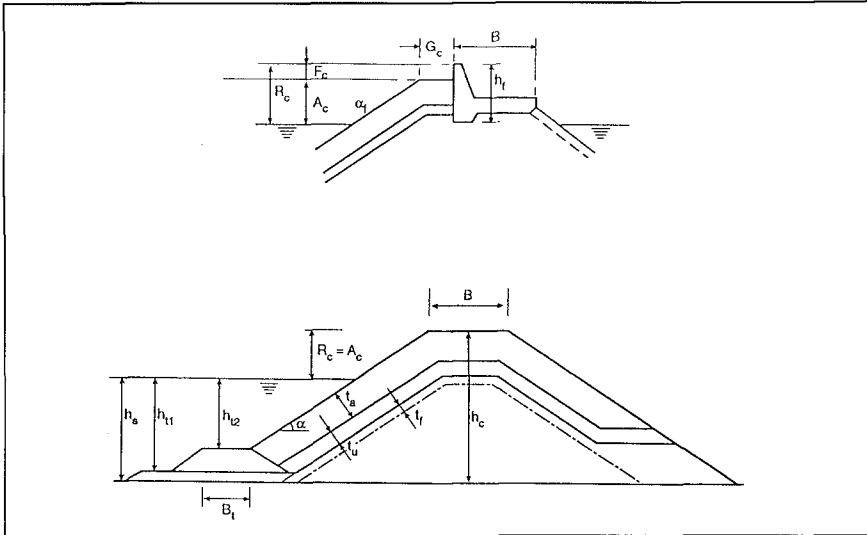


**Figure 1 Rubble mound breakwaters, main geometrical parameters**

The main methods used in the design of rubble mound breakwaters are based on empirical formulae, supported by results from hydraulic model tests. Such methods are therefore derived for simplified structure sections tested under normal wave attack. Very few methods address the stability of structures incorporating complex or "non-standard" details; under oblique wave attack; at and around the outer breakwater end or roundhead; or at junctions with dis-similar construction.

These types of structures are used worldwide wherever quarried rock is available in adequate sizes and quality for construction of coastal structures. Many such structures have however suffered significant damage, with an apparent peak between about 1977 and 1988. In analysing these failures, and difficulties with similar structures, it has become clear that analysis and design methods have been insufficiently reliable. A programme of studies were therefore proposed to the European Union. The programme that was contracted was somewhat restricted, but included key elements of the original proposal.

### 1.1 Work in G6-S Coastal Structures

The MAST I research project "G6-S Coastal Structures" addressed techniques available for the analysis and design of coastal and harbour structures such as sea walls, revetments, and breakwaters. The research covered three technical topic areas:

Topic 1. Wave action on and in coastal structures;

Topic 2.	Wave impact loading on vertical structures;
Topic 3B/R.	Berm and rubble mound breakwaters.

Within this project, studies under Topic 3R addressed the stability and hydraulic performance of rubble mound breakwaters and sea walls using analysis of previous model test data, described here, and by new model tests described by Galland (1994).

The main objective of the desk study described here was to provide information on the stability and performance of rubble mound breakwaters, where possible at singular points. These include: roundheads; junctions; bends; toe and rock berms. The study was based on the collection of data from study reports from the major hydraulic laboratories in Europe. It was agreed that HR Wallingford would design the study approach; that each laboratory would be responsible for the collation of their own test results; data; and that HR collect together and analyse the results. The objectives of the project were to:

- a) Identify whether data on responses from practical studies could be used to draw general design guidance;
- b) Collect data from many different institutes, and retain in consistent form for analysis;
- c) Contrast data from ad hoc studies with predictions made using methods based on idealised structures;
- d) Identify new or modified design methods based on these data;
- e) Identify gaps in present design information or methods;
- f) Provide justification for further research on rubble mound breakwaters.

The approach taken was firstly to identify the main breakwater failure modes and the principal parameters influencing failure, and to develop standardised parameter definitions and notation. These were used to design a database spreadsheet to hold model test data on breakwater structures and responses. Test results were then collected from each partner in the project. In parallel with this work, the prediction methods for the main design parameters were summarised, see Allsop (1993) and these were then used to devise the analysis strategy.

## 2 DATA COLLECTED

The data analysis was based on responses measured previously in site specific studies conducted by the institutes. The data used were therefore confined to those aspects of structure performance of concern to the designers of the particular structures, and were limited to those combinations of wave conditions and water levels for which the tests had been conducted.

The principal responses recorded were:

- a) Toe armour stability, given by measurements of toe armour movement and/or displacement;
- b) Main armour stability, again by movement and/or displacement, often using the damage parameters  $S$  or  $N_{ds}$ ;
- c) Wave overtopping, described by the number of waves passing the crest,  $N_{wo\%}$ , or by the mean overtopping discharge,  $Q$ ;

Each set of results were combined by response types, and then compared with the simple design methods to test their use, and/or to identify whether new prediction methods could be derived. The data collected in this study were too great to handle as a single spreadsheet. During the analysis process, the larger data sets were split into smaller and increasingly more specific sets, mirrored by the sections within this chapter. Typical

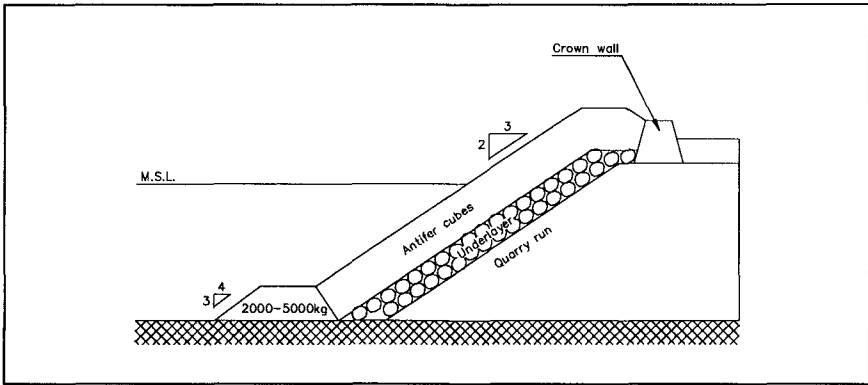


**Figure 2 Rubble mound breakwater armoured by Antifer Cubes**

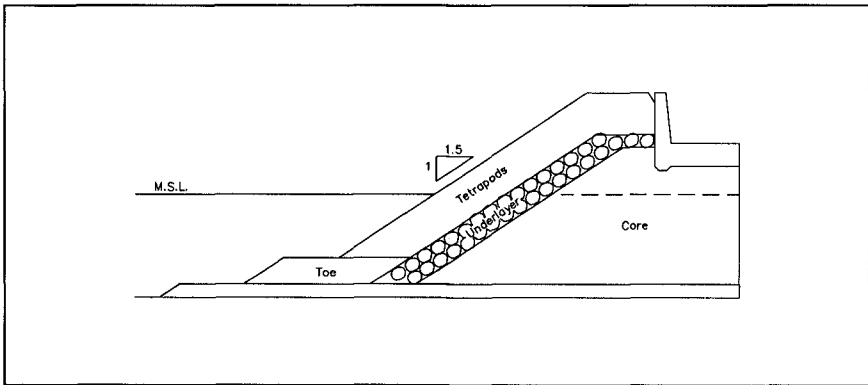


**Figure 3 Rubble mound breakwater armoured by Tetrapods**

cross-sections through the structure are shown in Figures 2-5. The influences on overtopping and armour damage of armour type, cross-section geometry, and plan configuration have been treated separately. This paper describes only the analysis of armour movement and wave overtopping.

**3 ANALYSIS OF ARMOUR MOVEMENTS**

Design methods for rubble mound armour layers focus principally on the calculation of the median armour unit mass,  $M_{50}$ , or the nominal median stone diameter,  $D_{n50}$ , for given levels of armour damage. In most instances damage is defined in terms of erosion area  $A_e$  or number (%) of armour units displaced,  $N_{d\%}$ . Damage may also be described by  $N_{od}$  referring to the number of unit displaced related to a width along the breakwater of  $1.0D_n$ . For a Tetrapod,  $D_n$  is  $0.65 D$  where  $D$  is the height of the Tetrapod; and for Accropode  $D_n$  is  $0.7 D$ . The definition of units displaced  $N_{od}$  may be compared with the damage parameter  $S$ . Generally  $S$  is about  $2 N_{od}$ , but the relationship differs for different armour units laid at different porosities:

For Cubes  $S = 1.8 N_{od} + 0.4$  (1a)

Tetrapods and Accropode  $S = 2 N_{od} + 1$  (1b)

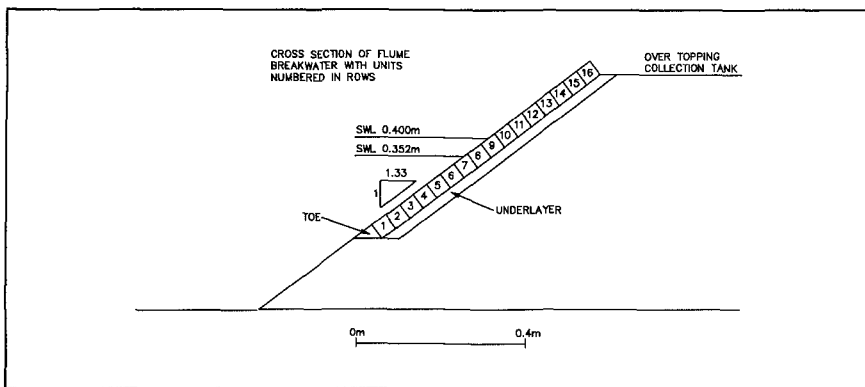


**Figure 4 Rubble mound slope armoured by Hollow Cubes**

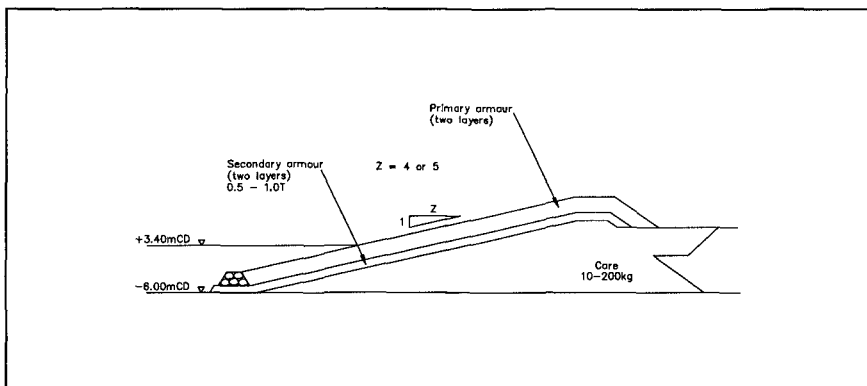


**Figure 5 Rubble mound slope armoured by rock**

The initial analysis of armour response presented by Allsop & Franco (1992) sought to identify the effects of wave obliquity and trunk versus roundhead on armour damage. Data from tests on structures armoured with Rocks, Tetrapods and Cubes formed the main body of the analysis. The data was collected from diverse sources, and much effort was expended to try to harmonise values of the input parameters for this analysis. Damage was presented in the database as displacement in % of units related to a certain area, or as the damage parameter  $S = A_e / D_{n50}^2$  in which  $A_e$  is the area eroded around SWL. When the level of displacement was given, this was often divided into classes in relation to the nominal diameter  $D_{n50}$  of the armour unit:

- $N_{D1}$ : units displaced less than  $0.5D_{n50}$
- $N_{D2}$ : units displaced more than  $0.5D_{n50}$  and less than  $1D_{n50}$
- $N_{D3}$ : units displaced more than  $1D_{n50}$

Sometimes the number of rocking units were also given. Comparisons with other data sets and with predictions methods demanded that damage be presented in a consistent way, and in this analysis, damage was always defined by S. Unfortunately, values of damage have not often been expressed as S in the past, so an alternative approach was

needed. In the initial analysis, a simple method was suggested to relate damage in these various classes to S using:

$$S = 0.8 (0.25N_{D1} + 0.75N_{D2} + 1.0N_{D3}) \tag{2}$$

Some of the data sets contain information on very small movement, perhaps as small as  $0.1D_{n50}$ , but these were not included in this analysis. In many cases the collaborating laboratories themselves combined categories  $N_{D2}$  and  $N_{D3}$ .

A damage formula developed by Van der Meer (1988) from the Hudson formula was used to compare damage data with values of Hudson's stability coefficient,  $K_D$ :

$$H_g/\Delta D_{n50} = a (K_D \cot \alpha)^{1/3} S^b \tag{3}$$

where for rock armour  $a=0.67, b=0.16$   
 and for Tetrapods and Cubes  $a=0.69, b=0.14$

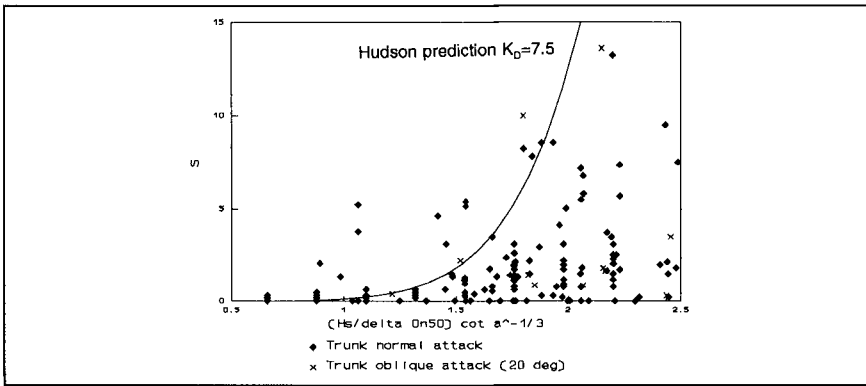


**Figure 6 Stability of cube armour, analysis includes movement in categories  $N_{D2}$  and  $N_{D3}$**

The stability of cube armour is illustrated in Figure 6, which shows the damage S against  $H_g/\Delta D_{n50} \cot \alpha^{-0.333}$ . The plot shows a great deal of scatter with many data points above the prediction line using  $K_D=7.5$ . Analysing measurements in category  $N_{D3}$  only, it was clear that relatively few small movements had been recorded, and the damage values calculated for  $N_{D3}$  only lie in very similar positions.

Designers of breakwaters using concrete armour units have been more rigorous in requiring more information on small movements in recent years, particularly for slender units. The use of these small categories in calculating an equivalent value of S less certain than suggested in eqn (2). It is probable that the use of  $N_{D3}$  alone to calculate S will under-estimate the damage, but the simple method used by Allsop & Franco (1992) to include the influence of small movements appears to lead to significant over-estimates of damage compared to existing prediction methods. This is particularly so where cumulative damage is estimated by summing damage in individual tests. This problem was illustrated when considering damage to Tetrapod armoured slopes.



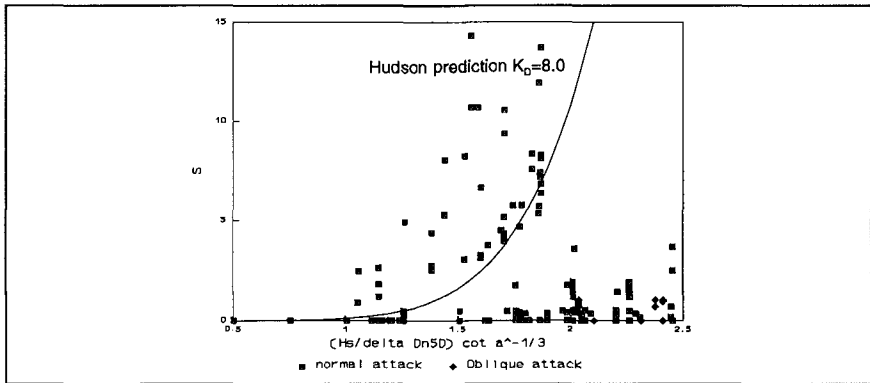


**Figure 7** Stability of Tetrapod armour, analysis includes movement in Categories  $N_{D2}$  and  $N_{D3}$

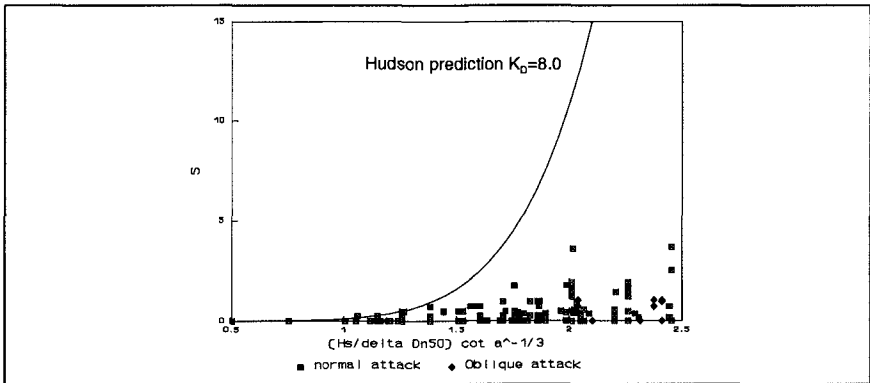


**Figure 8** Stability of Tetrapod armour, analysis only includes movement in category  $N_{D3}$

Damage to Tetrapods was also analysed, with damage categories  $N_{D2}$  and  $N_{D3}$  used to calculate  $S$ , plotted in Figure 7. Again the damage appears to be much greater than predicted by  $K_D=8.0$ . The affect of plotting points in category  $N_{D3}$  only is shown in Figure 8, which shows that the contribution of the smaller movements had a substantial influence on the comparison. Now all the data point lie below the prediction curve.

This exercise leads to a rather disappointing, but not altogether surprising conclusion. Unless the damage definitions used in design formulae precisely reflect those used by design engineers in site specific studies, a correlation of data from these studies with simple formulae may lead to considerable uncertainty, if not confusion. This is however to be expected, as the sophisticated designer and experienced modeller should be expected to use more sophisticated descriptions of structure response than those appropriate for simple design formulae.

## 4 ANALYSIS OF OVERTOPPING

Wave overtopping may be described by the number or percentage of waves passing over the crest expressed as  $N_{wo}$ ; or by the mean overtopping discharge per unit length,  $Q$ . The data returned seldom identified both responses, so analysis had to concentrate on the two sets of data separately. Most recent research has been concentrated on the prediction of the mean overtopping discharge  $Q$ , so most of this section will address this response. Some initial work was however completed on analysing the data returns that only gave the number of waves overtopping, expressed as  $N_{wo}$ .

### 4.1 Number of waves overtopping, $N_{wo}$

The test data examined in this study were limited to structures under normal wave attack. Structures were constructed with crown wall elevations equal to or below the front armour crest level. Four sets of data for which the number of waves overtopping had been recorded were analysed.

Example results for slopes armoured with Cubes and Tetrapods under waves of constant steepness of  $s_m=0.030$  were analysed by plotting  $\ln(N_{wo}/100)$  against  $R^*$  as derived by Owen (1980, 1982). The scatter of the data on  $N_{wo}$  was wide, even when restricted to a single sea steepness. Agreement between measured and predicted values were not good for the Cube structure. A better agreement was found for the Tetrapod armoured structure. The methods used to predict the number of overtopping waves is described by Allsop and Franco (1992). It was concluded that there was little to be gained by extending the analysis. These uncertainties confirmed that the mean overtopping discharge  $Q$  gives a more reliable description of overtopping of such structures.

### 4.2 Mean overtopping discharge, $\bar{Q}$

The main aim of this analysis was to examine the influence on overtopping discharges of singular points such as crown wall element geometries, armour crest levels, and slope configurations. The overtopping performance of structures armoured with rock, Antifer cubes, Tetrapods, and high-porosity Hollow Cubes, were examined.

The mean wave overtopping discharge depends on freeboard  $R_c$ ,  $H_s$  and  $T_m$ . The prediction method developed by Owen (1980) relates dimensionless parameters  $Q^*$  and  $R^*$  by an exponential equation with a roughness coefficient,  $r$ , and coefficients  $A$  and  $B$  for each slope angle:

$$Q^* = A \exp(-B R^* / r) \quad (4)$$

Where  $Q^* = \bar{Q} / (g T_m H_s)$  and  $R^* = R_c / T_m (g H_s)^{0.5}$ , and for smooth slopes,  $r = 1.0$ , and values of  $A$  &  $B$  have been derived for slopes from 1:1.0 to 1:4.0:

Slope	A	B
1:1.0	0.0079	20.1
1:1.5	0.0102	20.1
1:2.0	0.0125	22.1
1:3.0	0.0163	31.9
1:4.0	0.0192	47.0

**Table 1 Values of A and B for smooth slopes,  $r=1$**

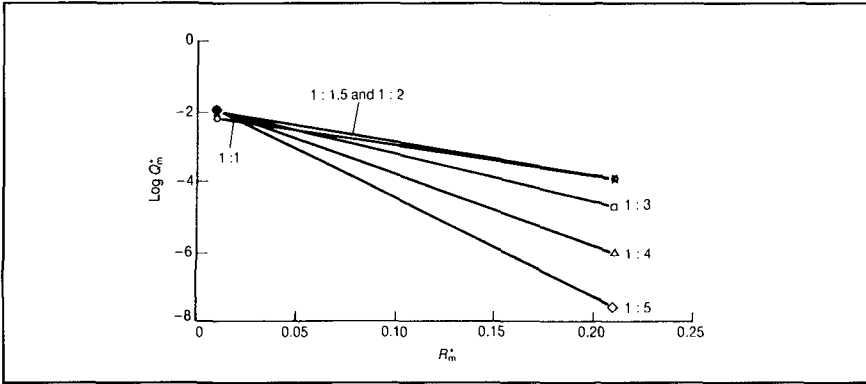


**Figure 9** Overtopping of smooth straight slopes (Owen 1980)

A design graph such as that shown in Figure 9 can be compiled by plotting  $Q^*$  as a function of  $R^*$  and using the constants  $A$  and  $B$  described in Table 1. For structures with small relative freeboards and/or large wave heights, the regression lines come together at one point, indicating that the slope angle, and relative roughness are no longer effective in controlling the overtopping discharge. The discharge characteristics for slopes 1:1, 1:1.15 and 1:2 are very similar, but overtopping reduces significantly for slope angles less than 1:2.

Owen's method was developed initially from results for smooth slopes only, but the use of the roughness factor,  $r$ , allowed its extrapolation to study the overtopping performance of rough, and even armoured slopes. Since 1980, various researchers have explored alternative prediction methods for armoured slopes, see Bradbury & Allsop (1988) and Aminti & Franco (1988), but no new method has proved any more reliable. The advantage of Owen's method is its simplicity, and the ready availability of data to support particular coefficient values. Three alternative approaches have therefore been developed:

- a) Use Owen's method and coefficients  $A$  and  $B$  with  $r$  derived from tests with the correct slope geometry;
- b) Use Owen's general equation, but with new values of  $A$  and  $B$  derived for similar cross section, and  $r = 1.0$ ;
- c) Develop alternative equation, with new coefficients for that section.

The overtopping performance of armoured breakwater structures with and without crown walls have been studied. Owen (1980, 1982) showed that in relatively shallow water berms or beaches in front of a structure will reduce overtopping. The toe design of the structures vary somewhat, but it is likely that these differences will have little bearing on the overtopping discharge during the deep water test analysed here. Although the crest detail of the various structures was not identical, the crown wall level was generally equal or below the armour crest, so it might be expected that the variations of crest detail would have had little affect on the overtopping discharge.

Measurements show that there is a good relationship between  $Q^*$  and  $R^*$  for all the structures studied. Data for Tetrapod and Antifer cube armoured structures are shown in Figures 10 and 11 respectively. The data presented here show that for the rough armour

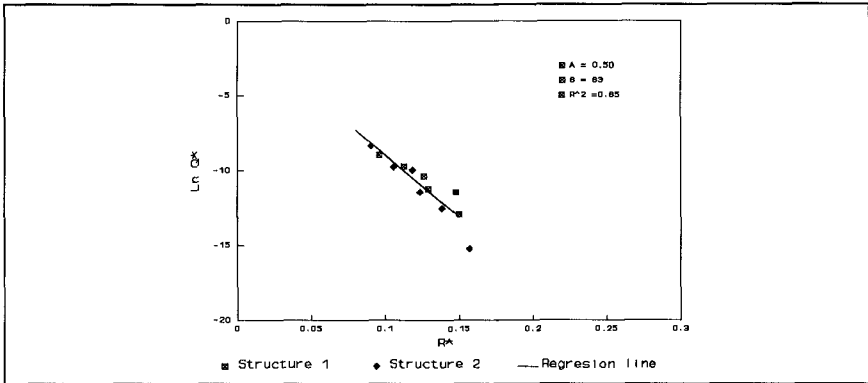


**Figure 10 Overtopping of Antifer Cube armoured structure**

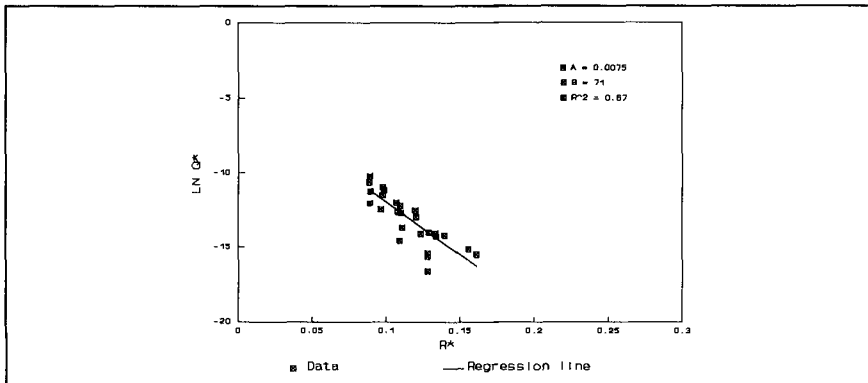


**Figure 11 Overtopping of Tetrapod armoured structure**

structures analysed the overtopping performance is better described by modifying the coefficients A and B. The overtopping data for rough structures shows that regression lines passing through data points have varying steepness. This change in steepness is due to the increased turbulence and friction caused by the 'rough armour'. The regression lines cross the  $R^*$  axis at different points depending on the armour type. This is not taken into account in the earlier theory as the coefficient A remains constant for a constant slope angle. This suggests that the hydraulic responses cannot be represented correctly by the roughness coefficient alone.

For armoured slopes, it is therefore suggested that the original Owen formula equation (4) should be used for overtopping, but that the coefficients A and B should be changed depending on the armour type and structure slope. The original Owen method using values of the roughness coefficient is not as accurate as using regression lines for site specific data. The simple Owen method is however very quick and easy to use where little site specific data is available.

The values of the coefficients A and B for rough slopes analysed during the study are tabulated below. The regression lines of the Tetrapod and Antifer cube structures are shown in Figures 10 and 11.

Structure	Slope	A	B
Cob units	1:1.33	0.00839	46.5
Shed units	1:1.33	0.00268	29.9
Antifer Cubes	1:1.5	0.496	82.7
Efficient units	1:1.5	0.016	60.0
Tetrapod	1:1.5	0.0075	71.0

**Table 2 Values of A and B for armoured structures, r=1**

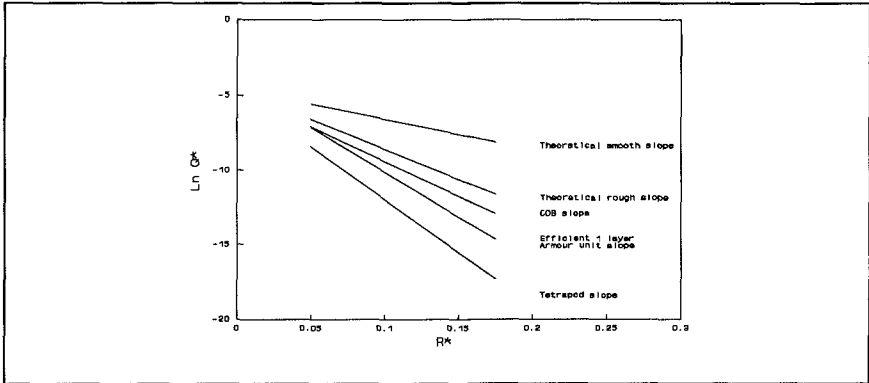


**Figure 12 Variation of overtopping with armour type**

The overtopping performance of 1:1.5 sloping structures armoured with Tetrapod, Antifer cube and efficient single layer armour units are compared in Figure 12. For similar armour units and structure designs it may be expected that for a given  $R^*$  the overtopping discharge would be equal. However, Figure 12 shows that as the porosity of the armour units increases, overtopping discharge decreases. The two layer Tetrapod system performs significantly better than the single layer structures. The armour efficiency increases as the relative freeboard increases.

The effect of armour layout is shown in Figure 13. This figure describes the overtopping performance of a single layer and a double layer hollow cube armour system. The armour units had a porosity of about 60%, and were placed to a tight pattern on a slope of 1:1.3. The overtopping is reduced for the two layer structure, but not as effectively as on the much thicker Tetrapod armour.

So far only simple structures have been considered. A similar method can be used to assess structures with berms or crest detail. Two test series have been carried out on two layer rock structures and the overtopping performance is shown in Figure 14. The data at the crest of the 1:4 slope shows a slightly lower overtopping discharge compared with the Owen theoretical rough slope. The 1:5 slope crest data shows a small increase

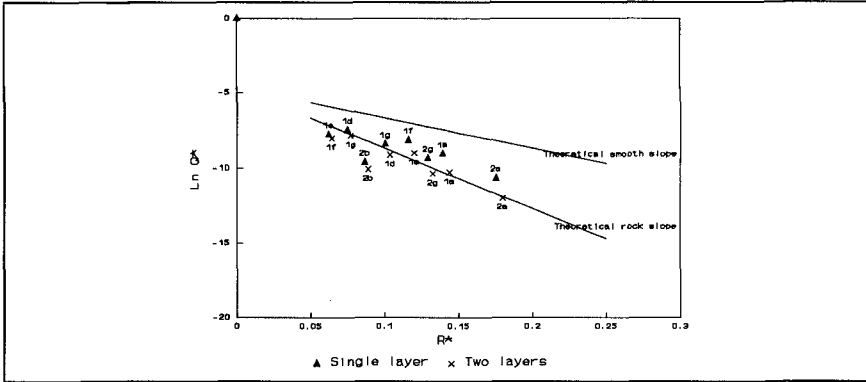


Figure 13 Overtopping of hollow cube armoured structure

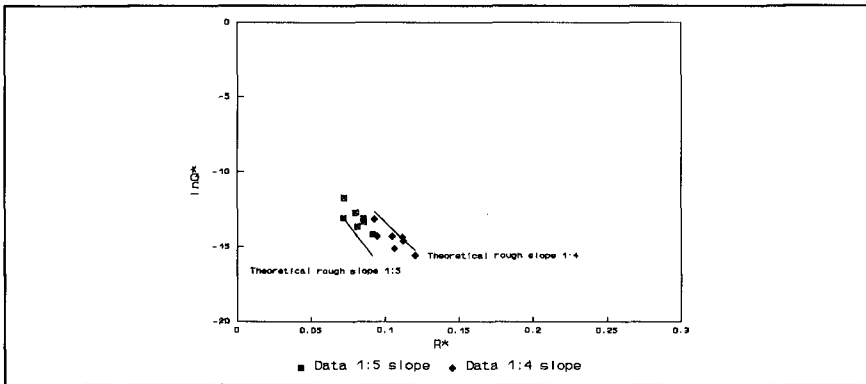
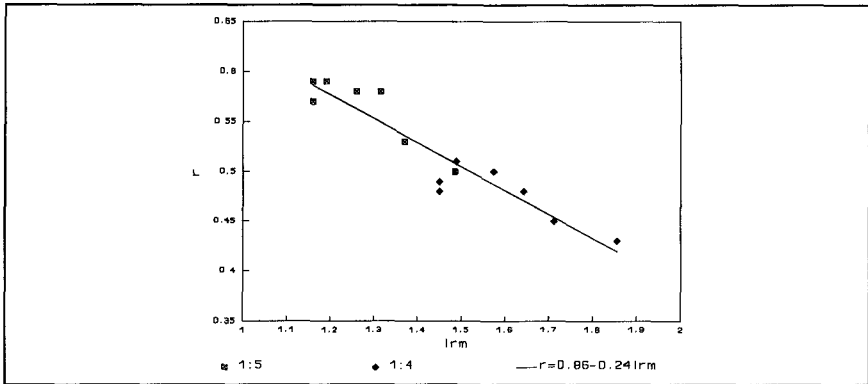


Figure 14 Overtopping of rock armoured structure

in overtopping discharge compared with the Owen theoretical rock slope  $r=0.5$ . Within the accuracy of the measurement, the prediction lines show a relatively good fit for the rock armour slopes with shallow slope angles.

The data shown in Figure 14 suggests that the roughness coefficient may be affected by the slope of the structure and the wave conditions. A value of  $r$  may be calculated for the measured discharges using Owen's value of  $A$  and  $B$  for a given slope angle. When the  $r$  value is plotted against the Iribarren number  $I_m$ , the value of  $r$  decreases as  $I_m$  increases, this relationship is shown in Figure 15. The result is consistent with the conclusions described earlier noting that both  $A$  and  $B$  values need to be modified when investigating the overtopping of permeable seawalls when using the Owen formula for structures armoured with 'rough' material.

For the same wave conditions overtopping discharges 10m behind the crest were about one-tenth of those measured at the crest. The crest detail of the 1:4 slope structure was



**Figure 15** Variation of the roughness coefficient with Iribarren number for rock armoured structures

altered to include a wave return wall. The armour crest freeboard  $A_c = 6.8\text{m}$  and the wave wall freeboard  $R_c = 8.8\text{m}$ . The performance of this structure can be compared with the structure with no wave wall,  $R_c = A_c = 8.8\text{m}$ . Although the inclusion of a wave wall shows a higher overtopping discharge compared with the full length armour slope, the wave wall design does have its advantages. The number of units and the volume of underlayer material required to build the structure is reduced and the structure may therefore be cheaper to build.

Where values of A and B cannot be calculated using site specific data, the analysis has shown that the original Owen formula with values of A and B for various slopes can be used with a roughness coefficient appropriate for the armour concerned. Values of the roughness coefficient for various armour units are given in Table 3.

Armour type	r
Rock	0.5-0.6
Hollow cubes	0.5
Dolos	0.4
Stabits	0.35
Tetrapods	0.3

**Table 3** Recommended values of r for armoured structures using A and B values given in Table 1

**5 CONCLUSIONS**

Overall The spreadsheet database worked adequately, but needed plans and sections to convey important information.

Armour on trunks and roundheads Analysis of damage was complex. Initial comparisons show wide scatter, with many tests showing little damage when prediction methods suggest severe damage. Cumulative damage is not given by design methods.

Overtopping Few studies recorded both  $N_{wo\%}$  and  $Q$ . Selected studies gave data on overtopping allowing new coefficients to be derived. The original Owen formula should be used for rough slopes, but both the coefficients A and B must be changed depending on the armour type and structure slope. The original Owen method is not as accurate as using regression lines for site specific data, but is simple to use where little site specific data is available.

## ACKNOWLEDGEMENTS

This research study was part-supported under the European Union's MAST research programme. Additional support was provided by Delft Hydraulics, Danish Hydraulics Institute, Laboratoire National d'Hydraulique, CEPYC in Madrid, and HR Wallingford. The model test results analysed in this report were supplied by the partner laboratories of G6-S. Their work was not limited to supplying the original data returns, but in supplying supplementary information and advice during the analysis period.

The analysis of test data was conducted by Claudio Franco on research attachment to HR Wallingford from the Hydraulics Department of the University of Rome, assisted the Coastal Structure Section at HR Wallingford. The preparation of this paper was supported by HR Wallingford and the University of Sheffield.

## REFERENCES

- Allsop N.W.H. (1993) "Formulae for rubble mound breakwater failure modes" Final report of PIANC, PTC II, Report of Sub-group A of Working group 12, PIANC, Brussels, April 1993
- Allsop N.W.H. & Franco C (1992) "MAST G6-S Coastal Structures Topic 3R: Performance of rubble mound breakwaters singular points" Paper 3.12 to G6-S Final Overall Workshop, Lisbon, November 1992
- Aminti P.L. & Franco L. (1988) "Wave overtopping on rubble mound breakwaters". Proc 21st ICCE, Malaga, ASCE, June 1988.
- Bradbury A.P. & Allsop N.W.H. (1988) "Hydraulic effects of breakwater crown walls" Proc Conference Breakwaters '88, ICE, Eastbourne, May 1988
- CERC (1984) Coastal Engineering Research Centre. "Shore Protection Manual", Vols I-II, US Gov Printing Off, Washington, 4th edition 1984
- CIRIA (1991) Simm J.D. (Ed) "Manual on the use of rock in coastal and shoreline engineering" CIRIA Special Publication 83 / CUR Report 154, November 1991
- Galland (1994) "Rubble mound breakwaters stability under oblique waves: an experimental study" 24th ICCE, Kobe, ASCE, October 1994
- Owen M.W. (1980) "Design of seawalls allowing for wave overtopping" Report EX 924, HR Wallingford, June 1980.
- Owen M.W. (1982) "Overtopping of sea defences" Proc. Conf. Hydraulic Modelling of Civil Engineering Structures, BHRA, Coventry, September 1982.
- Van der Meer J.W. (1988) "Rock slopes and gravel beaches under wave attack", PhD thesis Delft University of Technology, April 1988.



# Friction and clamping forces in wave loaded placed block revetments

Adam Bezuijen\*

## Abstract

A calculation method is presented to determine the strength of a block revetment against wave loading. The critical loading on such a revetment is present during wave run-down when still relatively high pore pressures exist in the filter layer and the blocks can be pushed out of the revetment. The strength of placed block revetments against this loading is not only composed of the weight of the blocks, but also of the friction and clamping forces. Friction and clamping forces are incorporated in a calculation method, using a simplified model that takes into account the horizontal and vertical forces separately. Example calculations show the forces that can be expected in such a cover layer.

## 1 Introduction

The placed block revetment is a commonly used type of revetment in the Netherlands to protect the dikes around the estuaries against wave attack. A typical cross-section of such a revetment is shown in Figure 1. In a long term research project the failure mechanisms for this type of revetment were investigated, calculation models were developed to simulate the loading on the revetment (Bezuijen et al, 1990; Burger et al, 1990; Bezuijen & Klein Breteler, 1992). Furthermore the strength of the dike itself after damage to the revetment was studied (Rigter, 1994). Results of this research have been used for the design of revetments, see Bezuijen et al. (1988) for an example.

The principal loading on such a revetment is different from the loading on for example a rip-rap revetment. Damage to a placed block revetment is not caused by severe water motion on the revetment, but by the pore pressures present in the filter layer. At wave run-down the water level in the filter layer is considerably higher than on the cover layer. Furthermore flow in the filter layer underneath the next incoming wave causes high pore pressures in the filter layer. The combination of a high water level and high pore pressures in the filter layer leads to an uplift pressure underneath the blocks just in front of

---

\*Delft Geotechnics, P.O. Box 69, 2600 AB Delft, The Netherlands

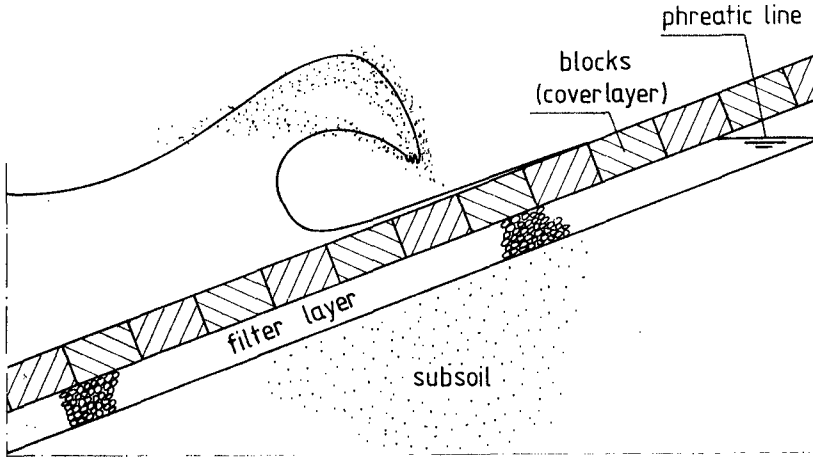


Figure 1: Typical cross-section of a placed block revetment with wave loading.

the next incoming wave, the situation as sketched in Figure 1. The strength of the revetment must be large enough to resist this uplift pressure.

Field measurements and large scale model tests have shown that the weight of a single block in a placed block revetment is often not sufficient to resist the maximum uplift pressure that is recorded underneath the blocks during severe wave attack. The strength of the revetment against lifting of blocks however, is also determined by the clamping and friction forces between the blocks. Only a small area of the revetment is loaded with the maximum uplift pressure and due to the clamping and friction forces the maximum load can be distributed over a larger area of the block revetment. Some calculation models, see for example Burger et al (1990), include the influence of friction between the blocks, and include the influence of block movement and inertia (Townson, 1988 and Bezuijen et al, 1990). However, these models are not capable to explain the high pull out forces, necessary to lift one block out of the revetment, as measured during field tests (Stoutjesdijk et al, 1992). The reason is that the influence of clamping was not considered. If the friction forces between two blocks exceed a certain limit, then one moving block causes rotation of adjacent blocks. Since the possibilities of rotation of blocks are rather limited in a placed block revetment, the result of such a rotation will be a force in the plane of the slope, see Figure 2, leading to higher friction forces and in this way increasing the strength of the revetment considerably.

## 2 Theory, strength of revetment

During wave attack a high load will be present on a part of the block revetment. How this area is calculated will be dealt with in the next section. This area can

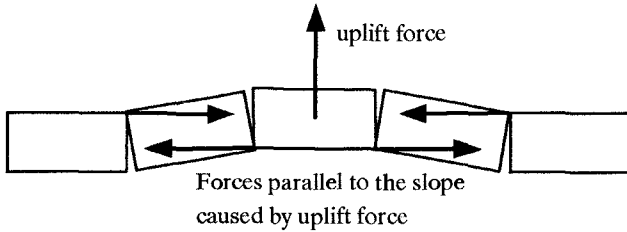


Figure 2: Sketch how forces develop in a row of blocks when one block is lifted out of the revetment.

cover several rows and columns (the blocks on the same level in a horizontal line along the revetment are called a row in this paper and the blocks to be seen in a cross-section are called a column). When uplift force exceeds the weight of the blocks, there will be some, very small, movement causing the development of friction and clamping forces. Whether or not this situation is unstable depends on the friction and clamping forces between the blocks. The influence of the friction forces also depends on the area of blocks that is lifted. If this is a large area, then the influence of the friction forces becomes less, because the friction forces only act on the boundaries of the loaded area.

It appeared from the field tests that the clamping forces can be very high. The question is, what conditions are necessary for clamping forces to develop. There is no need for a detailed calculation of deformations, because it is known that for blocks of  $0.5 \times 0.5 \times 0.25 \text{ m}^3$  with a self weight of 85 kg under water, in case of good clamping a lift force of 900 kg leads to a vertical displacement of less than 25 mm (Stoutjesdijk, 1992). Furthermore such a calculation is only possible with detailed knowledge of the flexibility of the joints, the width of the joints and the exact dimensions of all blocks.

Therefore the calculation model described in this paper only takes into account the forces acting on the blocks. The deformations are disregarded. Another simplification is that either forces in a horizontal row of blocks are calculated, or in a column along the slope from top to the lower end of the revetment. This means that, as another simplification, the situation of blocks shifted half a block on each row is not taken into account.

When blocks in a row are loaded with a lift force higher than the weight of a block, as shown in Figure 2, some movement will occur. This movement is assumed to be very small, but the contact between the block and the subsoil will be lost. Stability is only possible if the total lift force, caused by the excess pore pressure in the filter layer, can be compensated by the total weight of the blocks and the number of blocks without contact with the subsoil will be larger than the number of blocks with a lift force exceeding the weight of the block.

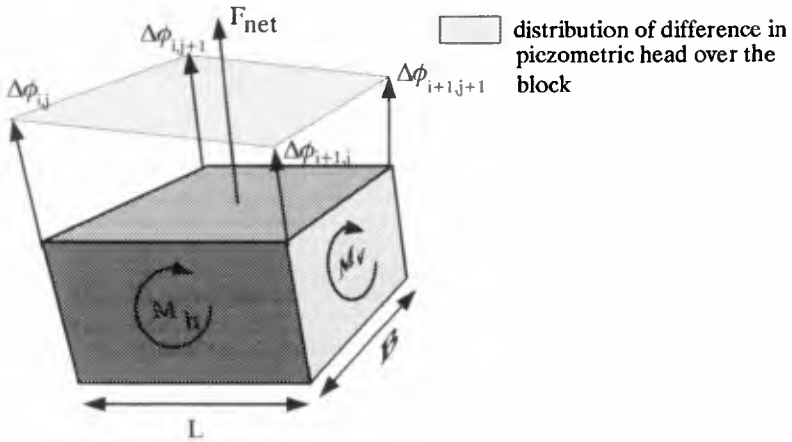


Figure 3: Definition sketch Forces and momentum on a block.

The calculation method assumes that the piezometric head is known on the corners of the block and that there is a linear distribution of the piezometric head over the block, see Figure 3. This leads to the following relation for the force on the block and the horizontal and vertical momentum:

$$F_{net} = \rho_w g B L \frac{\Delta\phi_{i,j} + \Delta\phi_{i+1,j} + \Delta\phi_{i,j+1} + \Delta\phi_{i+1,j+1}}{4} - (\rho_b - \rho_w) g D B L \cos \alpha \quad (1)$$

$$M_v = \frac{1}{12} \rho_w g L B^2 \frac{\Delta\phi_{i,j} + \Delta\phi_{i+1,j} - \Delta\phi_{i,j+1} - \Delta\phi_{i+1,j+1}}{2} \quad (2)$$

$$M_h = \frac{1}{12} \rho_w g B L^2 \frac{\Delta\phi_{i,j} + \Delta\phi_{i,j+1} - \Delta\phi_{i+1,j} - \Delta\phi_{i+1,j+1}}{2} \quad (3)$$

Where  $F_{net}$  is the "net" force on the block. If this force is larger than zero the block will be unstable in a situation without friction or clamping.  $M_v$  and  $M_h$  is the momentum in vertical and horizontal direction respectively, see also Figure 3.  $D$  is the thickness of the block and  $L$  and  $B$  the length and width of the block,  $B$  is in the direction of the slope, see Figure 4.  $\Delta\phi_{i,j}$  is the difference in piezometric head over the block, expressed in metres water. Finally  $\rho_b$  and  $\rho_w$  is the density of the blocks and water respectively. With equation (1) it can be calculated whether or not the uplift pressure is higher than the weight of the block. If it is higher, then stability can only be obtained by friction and clamping forces.

Whether or not clamping will occur depends on the friction coefficient between the blocks and the initially available pre-stress. In a row the pre-stress is most important. In a column the forces along the slope are composed of

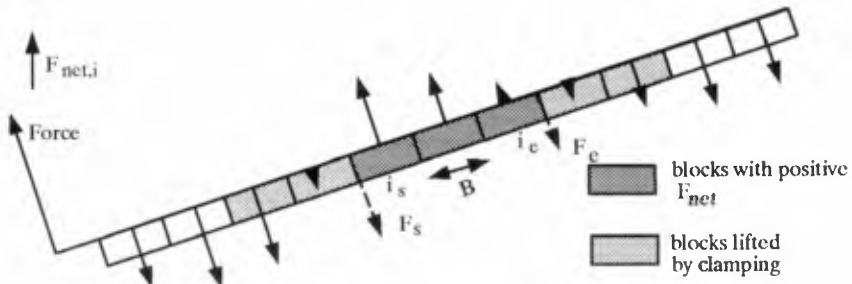


Figure 4: Example of the distribution of forces over a column of blocks for the determination of  $F_s$  and  $F_c$ . Explanation  $F_s$  and  $F_c$  see text.

the weight component along the slope of some blocks above the most loaded row. During storm conditions some blocks above the most loaded row will slide downwards when the friction coefficient with the subsoil is exceeded. With a given friction coefficient and load distribution on the blocks, it can be calculated whether the blocks will slide along each other or that clamping will occur.

As is shown in Figure 2, block movement with clamping leads to forces in the plane of the cover layer. In a horizontal row these forces can become very large. However, in a column these forces are limited by the weight of the blocks above the loaded block and some friction between the blocks and the subsoil. When the calculated force parallel to the slope becomes too large, the blocks will be pushed up along the slope and failure will occur. To calculate the friction forces it is essential to know the horizontal force that develops between the blocks. In the situation of Figure 2 the clamping force is a function of the loading and this situation will be calculated. Looking at a number of blocks in a column, see Figure 4, equation (1) can be used to determine the number of blocks with an uplift pressure higher than the weight of the blocks and the total force that is not compensated by the weight of the blocks that are "lifted". This force has to be compensated by the blocks next to lifted blocks. This means that due to friction there must be two forces next to the "lifted" blocks together as large as the sum of the net uplift forces but with the direction opposite to the uplift forces, see Figure 4. "Lifted" is put between quotes because the blocks are not really lifted but only the contact with the subsoil is lost (grain stress is zero).

Assuming that the force in the plane of the blocks is constant, which is nearly correct because the forces due to the weight are in most cases much smaller than the forces due to clamping, the forces  $F_s$  and  $F_c$  can be calculated using the momentum equation. Using the point of application of the force  $F_s$  as the point from which the momentum is calculated, the momentum equation

reads:

$$(i_e - i_s + 1)BF_e - \sum_{i=i_s}^{i_e} (F_{net,i}(i - i_s + 0.5)B + M_{v,i}) = 0 \quad (4)$$

A comparable equation can be derived for  $F_s$ . According to "action is reaction" the forces  $F_s$  and  $F_e$  at the end of the blocks with an uplift pressure higher than corresponding to the weight of the block will lead to an equal force with opposite sign in the block next to it. With these forces the total number of blocks that start to move can be calculated. A block will loose contact with the subsoil as long as:

$$\sum_{i=i_c}^i F_{net,i} - F_e > 0 \quad (5)$$

for  $i_n > i_e$ . Again a comparable equation can be derived for  $F_s$ .  $F_s$  or  $F_e$  will be the largest vertical force in the revetment near a joint. Let's assume  $F_s$  is the largest, then the clamping force ( $F_{vm}$ ) in the cover layer will be approximately:

$$F_{vm} = \frac{B}{D} F_s \quad (6)$$

In the computer program this is calculated more accurately taking into account the momentum ( $M_v$ ) and net force ( $F_{net}$ ) on each block. This force parallel to the slope can be compared with the maximum possible force in the column, the weight component of the blocks along the slope and the friction of these blocks with the subsoil. If this force is exceeded, then the blocks will be pushed upward and failure will occur.

The same calculation principle can be used to calculate the force in a row. However, no minimum force in the revetment row before clamping starts can be calculated. This depends strongly on the way the blocks are placed. There can be loose blocks in a row without horizontal friction and consequently no clamping. Furthermore it is not possible to determine a maximum clamping force. In principle this force can be very large.

### 3 Loading on revetment

Calculation of the clamping forces is only possible if the load distribution on a placed block revetment is known. This load is the uplift pressure over the blocks. The computer program STEEN3D (Bezuijen, 1992) calculates uplift pressure over an area of the block revetment. This finite difference program takes into account the turbulent flow conditions that will mostly occur in the filter layer and through the cover layer. To perform a calculation, the wave pressure distribution on the revetment at a certain moment, the geometry and the permeabilities of cover layer and filter layer must be known. An example of such a wave distribution, for regular waves measured in a wave basin, is presented in Figure 5. The resulting calculated distribution of the uplift pressure is presented in Figure 6.

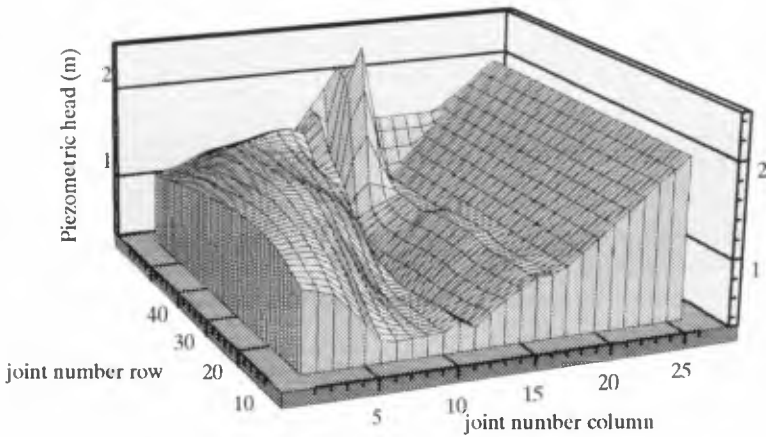


Figure 5: Example of measured distribution of piezometric head on the slope. Oblique wave with an angle of incidence of  $30^\circ$  from the line perpendicular to the slope. Wave height is 1.2 m, wave period 1.4 s.

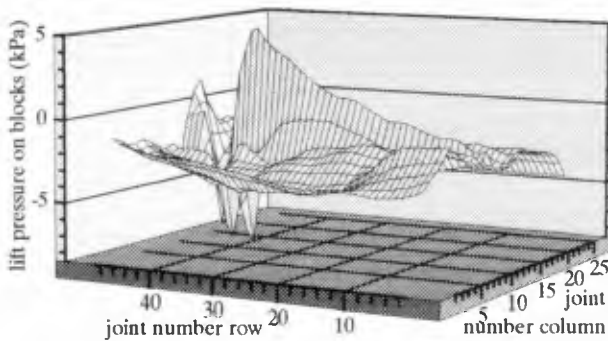


Figure 6: Calculated uplift pressure distribution for a wave loaded block revetment. For positive loading the revetment is potentially unstable.

In this figure the pressure corresponding to the weight of the blocks is subtracted from the calculated pressure, which means that a pressure higher than 0 is a potentially unstable situation. The calculation is performed for blocks of  $0.5 \times 0.5 \times 0.2 \text{ m}^3$ , a wave height of 1.2 m and a leakage length of 1.1 m. The leakage length ( $\Lambda$ ) is defined as  $\Lambda = \sqrt{bDk/k'}$ , where  $b$  is the thickness of the filter layer,  $D$  the thickness of the blocks,  $k$  the permeability of the filter layer and  $k'$  the permeability of the cover layer. Comparing Figure 5 and Figure 6 it appears that the calculated uplift pressures are at maximum before the wave impact.

#### 4 Computer model BLOKKEN

The computer model BLOKKEN, made to evaluate the equations presented in section 2, uses a pressure distribution as shown in Figure 6 to calculate the force on individual blocks. For each row and column the blocks are selected with a lift force higher than the weight of the block and it is checked whether or not the friction forces between the blocks are large enough to cause initial movement of the blocks next to the blocks with the high lift force. The horizontal force in the the revetment is calculated as explained in section 2. From Figure 6 it appeared, that the pressure distribution in horizontal direction differs from the loading in vertical direction. In horizontal direction there is only one row that is really loaded (the 'crest' in the figure). Looking at different columns the loading is comparable. This means that the stability of the maximum loaded row is increased by the friction forces. If on the other hand a column is loaded to failure, then the neighbouring columns will have a comparable loading and the loading can only be resisted by the strength of the column itself. The program takes this into account by assuming a friction force between the different rows but not between the columns. The program is written as a post-processing program on the results of the STEEN3D program. This has the advantage that for a calculated pressure distribution the reaction of the blocks can be calculated for different weights of the blocks or different friction coefficients. Figure 7 is a result of a calculation with the model along a horizontal row. This calculation is performed for the row with the maximum loading from Figure 6. In this case the friction with other rows is assumed to be zero. The figure shows clearly that the blocks with a positive lift force are stabilized by blocks with a negative lift force. For all of these blocks the grain stress with the filter layer will be zero. Note the high clamping force parallel to the cover layer of the revetment necessary to obtain a stable situation, 11.55 kN, approximately 10 times the weight of a single block. The situation shown in this figure can only exist if the initial friction force between the blocks is large enough to make sure that one moving block will cause movement of other blocks in the row. In Figure 7 the loading on a row is presented. However, the result of a calculation presents the situation for the blocks in an area of the revetment, see the Figures 8 and 9 to be explained in the next section.



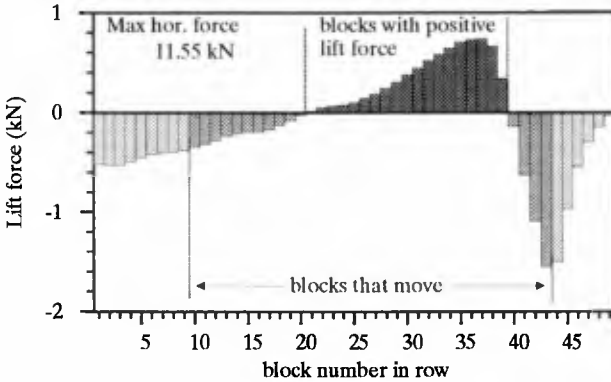


Figure 7: loading on blocks and lifted blocks.

### 5 Example calculations

Calculations will be presented for two situations. The first example is a typical revetment in an estuary. Calculations were run to show the influence of the leakage length on the loading on the revetment. The second example shows the influence of a non permeable transition in a revetment on the loading and strength. These These calculations were performed as a part of a study for a revetment in the southern part of Terschelling, one of the Dutch Wadden islands. Calculations were made to advise on the stability of this revetment. For these calculations it was not possible to simulate the revetment exactly, because wave pressure measurements were not available this location.

For the first example, calculations were performed for a leakage length ( $\Lambda$ ) of 1.1 and 0.84 m. The parameters used in the calculations are shown in Table 1 and the results in the Figures 8 and 9. These figures show the loading on the blocks. They show only a part of the revetment area for which the calculation was run, the part which the highest loading. The area for which the calculation was run had 26 rows and 49 columns. The stability of the columns was investigated. Different grey values show the influence of the loading on the blocks, see Figure 8. It appears that there are three areas with a high loading. Comparing this figure with Figure 6 it appears that the largest area with high loading on the blocks is present during wave run-down, as could be expected from Figure 6, but that there are also two small area's near the wave impact. The black blocks indicate that for those blocks the force parallel to the slope, caused by the weight component of the column of blocks above, is not high enough. This means that the column above these blocks will be pushed upwards and failure will occur. However, this depends on the situation. This calculation was run assuming that the blocks, that are loaded to a degree that

		1st example	Terschelling
slope		1:4	1:4
block length ( $L$ )	(m)	0.5	0.3
block width ( $B$ )	(m)	0.5	0.22
block thickness ( $D$ )	(m)	0.2	0.18
density blocks ( $\rho_b$ )	(kg/m <sup>3</sup> )	2350	2900
friction coeff. block-block ( $wb$ )	(-)	0.4	0.3
friction coeff. block-filter ( $wo$ )	(-)	0.4	0.3
<i>blocks with pos. lift force</i>			
$\Lambda=1.1\text{m}$		65	
$\Lambda=0.84\text{m}$		28	
$\Lambda=0.52\text{m}$ middle of revetment			26
$\Lambda=0.52\text{m}$ near transition			20

Table 1: Parameters used in calculations with BLOKKEN. In the calculations the wave pressure distribution as shown in figure 5 is used.

they slide downwards, have a contribution to the strength. Blocks higher on the revetment do not contribute, because there is a gap between the blocks that have slid downwards and those that have not. This gap prevents friction and clamping. Such gaps will not exist in a well maintained revetment and in that case all blocks above the most loaded block will contribute to the force parallel to the slope. The calculation was also run for a well maintained revetment and in that case the black blocks disappear, which means that the revetment is stable. The calculations also show that the leakage length has a large influence on the loading on the blocks. A reduction in the leakage length from 1.1 to 0.84 m reduces the number of blocks with a force higher than the weight of the block from 65 to 28. The revetment on Terschelling is made with granite blocks of, on average,  $0.3 \times 0.22 \times 0.18 \text{ m}^3$  with a higher density and a lower friction coefficient than concrete, see Table 1. Relatively large joints are present between the blocks, leading to a permeable cover layer and as a consequence to a short leakage length (Bezuijen et al, 1990). An impermeable transition is planned on the top of the revetment. At this height a shoulder is planned in the dike profile and on this shoulder a road will be built. During design conditions this road will be well below the water line and severe wave attack can be expected on the transition. The calculated maximum wave loading on various sections of the dike varied between 0.6 and 1.3 m. Calculations were run for a wave height of 1.2 m, again with an incident wave angle of  $30^\circ$ . When the maximum loading was exerted on the middle of the revetment it appeared that the uplift force exceeds the weight of the block for 20 blocks. These blocks were found on 3 different rows. Friction between the blocks appeared enough to prevent failure. However, when the model was run for the situation with the

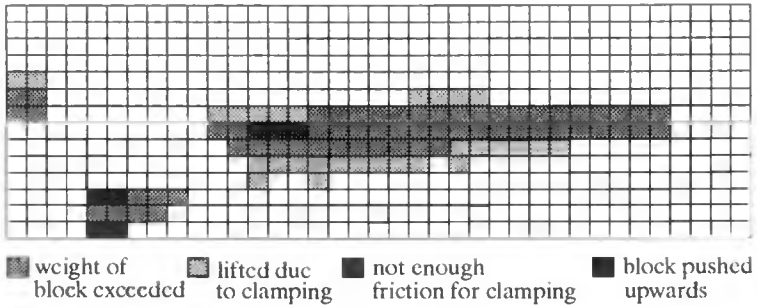


Figure 8: Calculated loading on a revetment. Each square represents a block.  $\Lambda = 1.1$  m, wave loading see Figure 5

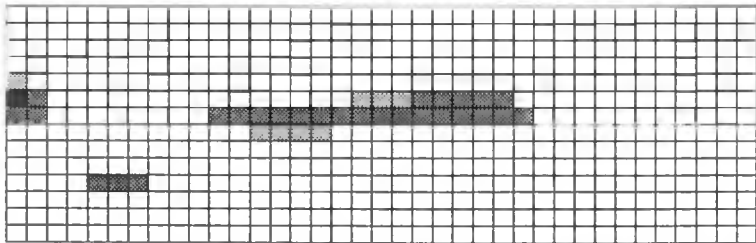


Figure 9: Calculated loading on a revetment. Each square represents a block.  $\Lambda = 0.84$  m, wave loading see Figure 5.

maximum loading near the transition, then the number of blocks with an uplift force higher than its weight increased to 26 and all these blocks were found in the top row of the revetment near the transition. According to the calculation this top row will not be stable for this loading condition. From these results it was concluded that the transition will be a weak point in the revetment. The loading is increased on what can be called the weakest row in the revetment, because there are no overlaying blocks that contribute by their weight to the force parallel to the revetment. It was therefore decided to strengthen the transition by applying bitumen between the blocks and in the filter layer up to 0.6 m below the transition.

## 6 Conclusions

The strength of a placed block revetment is not determined by the weight of the blocks only. The interaction between the blocks is of great importance. Calculations with the computer model BLOKKEN showed that, for a given friction coefficient, a horizontal pre-stress in the revetment can greatly increase the strength. This pre-stress can be obtained by putting gravel over the revetment with a comparable diameter as the joints. This will decrease the permeability and in this way increase the loading during wave attack. However, the increase in strength will more than compensate this and a more stable revetment will be obtained. For this aspect the model presents a theoretical base for a general practice in the Netherlands. The results of this model are qualitatively in agreement with results of large scale model test performed for this type of revetments (Burger, 1985). The applicability of the model as presented in this paper is limited by:

- the still limited quantitative knowledge of the forces parallel to the slope in a row before it is "lifted". Therefore the possible contribution of clamping in a row to the stability cannot be calculated.
- the limited number of wave pressure registrations on a slope area. These registrations are only available for regular waves. Most registrations were made in a wave flume for a wave loading perpendicular to the slope. However, the results show that the obliqueness of the waves has a large influence on the number of blocks that are "lifted" and this will certainly also influence the stability.

The method as presented is already useful to investigate the influence of transitions on the loading and the number of blocks loaded.

The model predicts a decrease in strength for blocks higher on the slope. This means that for a constant wave loading the likelihood of failure increases when the water level increases.

## 7 References

- Bezuijen A., Laustrop C. and Wouters J. (1988), Design of block revetments with physical and numerical models. *Proc. 21th Int. Conf. on Coastal Engineering, Malaga*
- Bezuijen A., Klein Breteler M. and Burger A.M. (1990) Placed block revetments Chapter in 'Coastal Protection' Pilarczyk (ed.) Balkema, Rotterdam ISBN 90 6191 1273
- Bezuijen A. and Klein Breteler M. (1992) Oblique wave attack on block revetments *Proc. 23rd ICCE, Venice*
- Burger A.M. (1985), Strength dams along the Eastern Scheldt under concentrated wave loading (in Dutch), *Delft Hydraulics, Project M2036*
- Burger A.M. et al. (1990) Analytical design method for relatively closed block revetments. *ASCE Journal Waterway Port, Coastal and Ocean engineering, Vol 115, pp 525-544*
- Rigter B.P, Klein Breteler M and Kruse G.A. (1994) Strength of sea dikes is limited (in Dutch). *Land + Water No 5*
- Stoutjesdijk T.P., B.P. Rigter and A. Bezuijen (1992) Field measurements on placed block revetments *Proc. 23rd ICCE, Venice*
- Townson, J.M. (1988) The simulated motion of a loose revetment block *Journal of Hydraulic research, vol. 26, no. 2, pp 225-242.*

## CHAPTER 69

### A FIELD EXPERIMENT ON THE INTERACTIONS WAVES-REFLECTING WALL

Paolo Boccotti

Department of Fluid Mechanics and Offshore Engineering  
University of Reggio Calabria  
Via E. Cuzzocrea, 48 - 89100 Reggio Calabria - Italy  
Fax. +39 965 875220

#### Abstract

A special reflecting wall 12 m long and 2.1 m high was built off the beach at Reggio Calabria, and 30 wave gauges were assembled before the wall and were connected to an electronic station on land. It was possible to observe the reflection of wind waves generated by a very stable wind over a fetch of 10 Km. The experiment aimed to verify the general closed solution for the wave group mechanics (Boccotti, 1988, 1989), for the special case of the wave reflection.

#### 1 Introduction

Starting on 1990, a few small scale field experiments were executed off the beach at Reggio Calabria on the eastern coast of the Straits of Messina. The original aim was to verify the closed solution for the mechanics of the highest 3-D wave groups in the wind generated sea states (Boccotti, 1988, 1989).

The tide excursion in the area is very small and a local wind often remains constant from the North West for several consecutive days. After two days of NW wind, the Southerly swells vanish and the sea states in front of Reggio Calabria consist of pure wind waves with significant height typically within 0.2 and 0.4 m and dominant period within 1.8 and 2.5 s.

Because of the small wave size and of the very small tide excursion, it is possible to operate like in a big wave tank. Moreover, the water is exceptionally clear because of the Strait current which flows for about one half an hour in 12 hours. The clearness of the water enables

underwater works of high precision.

The first experiment (May, 1990) was concerned with the progressive waves on deep water. An array of nine wave gauges and nine pressure transducers supported by vertical iron piles provided space-time information on waves generated over a fetch of approximately 10 Km. It was confirmed that the general 3-D configuration of the extreme wave groups was consistent with the theoretical predictions (Boccotti et al., 1993-a).

Given that the closed solution for the mechanics of the highest wave groups holds (to the Stokes first order) for an arbitrary shape of the solid boundary, it particularly predicts the reflection of a 3-D wave group by a wall. Thus, a second experiment was executed on May, 1991 with the main purpose to verify whether the reflection of the 3-D wave groups was consistent with the theoretical prediction. Here a few results of this verification are shown. Previously, the experiment's data were used by Boccotti et al. (1993.b) to test a few predictions on the variations of wave energy and band-width with distance from the wall.

## 2 The closed solution for the mechanics of the wave groups on the sea surface (Boccotti, 1988, 1989)

Let us consider a random wind-generated sea state assumed Gaussian (Longuet-Higgins, 1963 and Phillips, 1966). The extreme wave events have been shown by the writer to occur in a well defined way that can be specified in terms of the autocovariance function. The theory admits that the random wave field is generally non-homogeneous: it can be homogeneous like in an open sea or non-homogeneous like before a reflecting wall.

Specifically, if the extreme wave crest occurs at  $\underline{x}_0 = (x_0, y_0)$  at time  $t_0$ , with a crest-to-trough height of  $H$ , the mean surface configuration in space and time is given by

$$\eta_c(\underline{x}_0 + \underline{X}, t_0 + T) = \frac{H}{2} \left\{ \frac{\Psi(\underline{X}, T) - \Psi(\underline{X}, T - T^*)}{\Psi(\underline{0}, 0) - \Psi(\underline{0}, T^*)} \right\} \quad (2.1)$$

where  $\Psi$  is the autocovariance function of the surface displacement of the random wave field

$$\Psi(\underline{X}, T) = \langle \eta(\underline{x}_0, t) \eta(\underline{x}_0 + \underline{X}, t + T) \rangle \quad (2.2)$$

and  $T^*$  is the abscissa of the absolute minimum of the autocovariance function  $\Psi(\underline{0}, T)$ , which is assumed to exist and to be the first minimum after  $T=0$ . Superimposed on the deterministic form (2.1) is of course the random noise of the residual wave field, but when  $H/\sigma(\underline{x}_0)$  is large ( $\sigma(\underline{x}_0)$  being the r.m.s. wave elevation at location  $\underline{x}_0$ ), the variations in the actual sea surface configuration surrounding  $\underline{x}_0, t_0$  are small compared with  $\eta_c$  itself.

Associated with the configuration (2.1) is a distribution of velocity

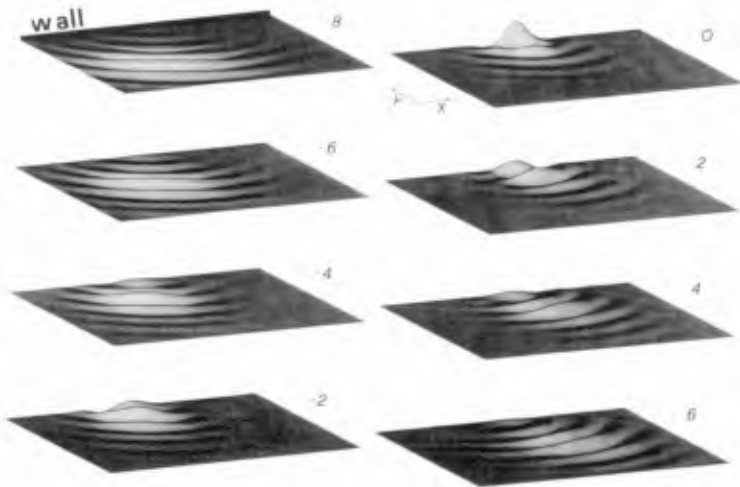


*Fig.1 Occurrence of a wave of given very large height at a reflecting wall. The wall is along the upper x-parallel side of the framed rectangle, and the interval between two consecutive configurations is of  $2 Td$  ( $Td$  being the dominant period of the random sea state). The wave group impacts the wall, at the apex of the development stage (minimum width of the wave front and maximum height of the central wave), it is reflected mirrorwise and goes back seaward.*

potential in the water, which to the lowest order in a Stokes expansion is given by

$$\phi_c(\underline{x}_o + \underline{X}, z, t_o + T) = \frac{H}{2} \left\{ \frac{\Phi(\underline{X}, z, T) - \Phi(\underline{X}, z, T - T')}{\Psi(\underline{0}, 0) - \Psi(\underline{0}, T')} \right\} \quad (2.3)$$

where

$$\Phi(\underline{X}, z, T) = \langle \eta(\underline{x}_o, t) \phi(\underline{x}_o + \underline{X}, z, t + T) \rangle. \quad (2.4)$$

The theory holds for arbitrary solid boundary conditions, and it can be formally proved that deterministic functions  $\eta_c$  and  $\phi_c$  satisfy the Stokes equations to the first order as well as an arbitrary set of solid boundary conditions, if random functions  $\eta$  and  $\phi$  satisfy those equations and boundary conditions. Note that the hypothesis that  $H/\sigma(\underline{x}_o)$  is large is not necessarily inconsistent with the use of the lowest order (linear) terms in a Stokes expansion, provided  $H$  remains small with respect to the wave length and the water depth.

The covariances (2.2) and (2.4) can be readily obtained from the directional frequency spectrum of the random sea state. In the case that the random sea state interacts with some obstacle, e.g. with a



reflecting wall, the covariances can be obtained from the directional frequency spectrum of the wave field that there would be if the obstacle was not there (see Appendices A and B).

From equation (2.1) we find that a wave of given very large height  $H$  at a location  $x_0$  in an open sea occurs because a *well defined wave group* transits that location, when it is at the apex of its development stage. A few 3-D pictures of the wave group can be seen in the papers of Boccotti (1988) and (1989) and of Boccotti et al. (1993-a). The basic phenomena that occur during the course of evolution of the group are not dependent on the detailed shape of the wave spectra, though the shape of the group does vary somewhat. Specifically, the wave group has always a development stage in which the height of its central wave grows to a maximum and the width of the wave front reduces to a minimum. Then a decay stage follows with the opposite features. The individual waves have a propagation speed greater than the envelope so that each wave crest is born at the tail of the group, grows to a maximum when it reaches the central position, and then dies at the head of the group.

From equation (2.1) we find also that a wave of given very large height at a location  $x_0$  of a reflecting wall, occurs because a wave group impacts the wall, when it is at the apex of the development stage -see Figure 1-. Then we find that a very high wave at a location  $x_0$  far from the wall occurs because of the collision of two wave groups -the first one approaching the wall, and the second one going back seaward after having been reflected.

Finally, equation (2.1) shows that a very high wave at a location  $x_0$  behind a wall (we mean "very high with respect to the mean wave height at this location") occurs because a wave group targets on the wall-end, and, after the impact with the wall, one half of the wave front goes on and penetrates into the shadow cone. The relevant 3-D pictures can be seen in the papers of Boccotti (1988).

### 3 The experiment of May 1991 off the beach at Reggio-Calabria

Eq.(2.1) holds not only for the surface waves but also for the pressure head waves at some fixed depth. In this case,  $\eta$  is to be intended as the fluctuating pressure head at the fixed depth. This property is a consequence of the fact that, to the Stokes first order, the fluctuating pressure head at some fixed depth represents a stationary Gaussian process of time like the surface displacement. Therefore, aiming to test eq.(2.1), the decision was taken to deal with the pressure head waves at a fixed depth, given that the fluctuating pressure head can be measured by transducers of high precision and low cost.

A set of pressure transducers was assembled before (seaward) a special upright reflecting wall 12 m long and 2.1 m high with a rubble mound .2 m high. The structure consisted of a steel truss whose stability was ensured by a dead weight of pig iron discs, and the reflecting plane was formed by aluminium panels with a thickness of .05 m.

The transducers were supported by three horizontal beams .6 m below

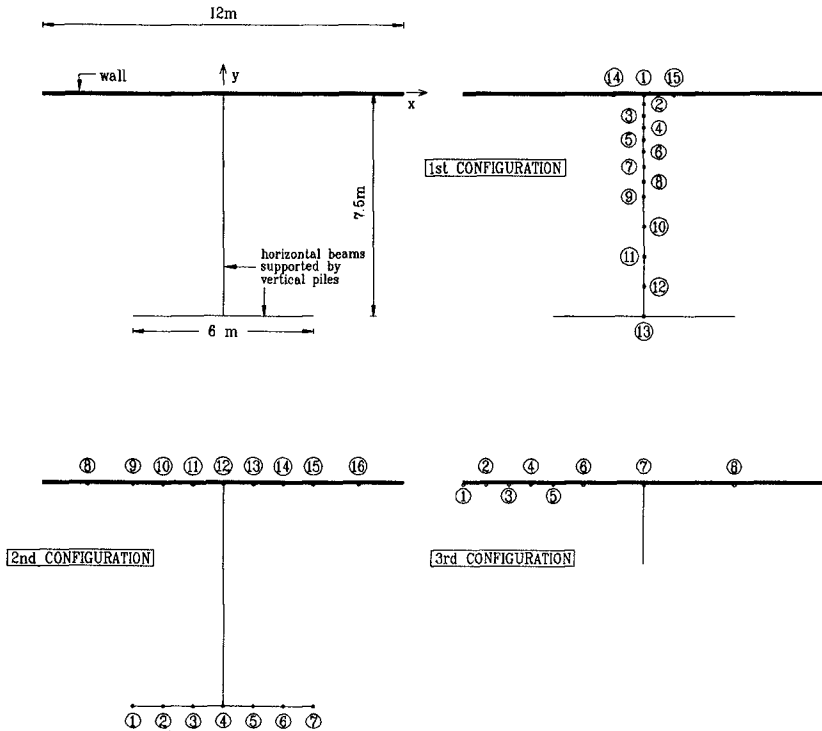


Fig.2 Plan view of the pressure transducers before the wall.

the mean water level -see Figure 2-. The average bottom depth in the area covered by the gauges was of 2.0 m. Both the horizontal beams and the supporting piles were designed to get an high degree of stiffness as well as a small section, and in particular each upright pile of the diameter of .05 m was stiffened by four small steel cables. The pressure transducers were connected by submarine cables to an A/D converter unit in an onshore building and the sampling rate was 10 hz. Besides the pressure transducers, an ultrasonic wave probe far from the wall provided information on the undisturbed waves.

Three different configurations of the gauges were assembled during the experiment -see Figure 2-. A set of 9 records was obtained with the first configuration, and sets of 27 and of 16 records were obtained respectively with the second and with the third configuration. The total number of the records was then of 52, each of 9 minutes and containing 250 to 300 dominant waves. The significant height  $H_s$  ranged within .17 and .42m and the dominant period  $T_d$  within 1.9 and 2.6s.

#### 4 A few results of the experiment

The covariances can be found directly from the measurements by cross-correlation of the time series obtained at the discrete measurement locations and if an extreme wave of the pressure head, with a crest-to-trough height of  $H$ , is encountered at one such location, the time history of the expected pressure head configuration at this and the other locations can be obtained from (2.1).

With  $x_0$  taken as location 1 at the wall-center (first configuration of the gauges), the vectors  $X$  were specified by the relative locations of the other gauges. The time series data of record 17 provided measured auto-covariances as a function of  $T$  for the various gauge locations and these were used *without smoothing* on the right hand side of equation (2.1) to estimate  $\eta_c(t_0+T)$  at these locations in an extreme wave. The results are shown in Figure 3.

The covariances were found also from a theoretical spectrum. The classic JONSWAP frequency spectrum (Hasselmann et al., 1973) and the spreading direction function of Mitsuyasu et al. (1975) were assumed for the two dimensional spectrum of the wave field that there would be if the wall was not there. The spreading direction parameter  $n_0$  of Mitsuyasu et al. was taken equal to 20, that is the suggested value for the conditions of our experiment: fetch 10000 m, wind velocity 7-8 m/s. The dominant wave period and the dominant direction were given the values of record 17. The dominant period was of 1.9 s. The direction was estimated accurately since the front of wave A at the traverse of locations 14-1-15 (at the wall) proves to be nearly straight. The relative phases indicated an angle of incidence of 13°.

The substitution of the theoretical covariances in equation (2.1) leads to Figure 4. Like Figure 3, this shows the expected waves in the time domain, at the various gauge locations, if a wave of given very large height  $H$  occurs at location 1 at the wall-center, with the first configuration of the gauges. The likeness of the two figures is amazing - figure 3 was obtained from the time series data, while figure 4 was obtained from a theoretical spectrum!

In the figures, A represents the wave of given very large height  $H$  at location 1, B, C and D are the waves immediately before this one, and B', C', D' are the waves immediately after A. At the wall, A occupies the envelope center.

The wave height exhibits a local minimum (node) at location 5, because the waves approaching the wall overlap the reflected waves in phase opposition. Then, a local maximum of the wave height (antinode) takes place at location 8, where the waves overlap themselves in phase coherence. The dominant wave length  $L_d$  was of nearly 6 m, so that the node was at  $\frac{1}{4}L_d$  from the wall, and the antinode was at  $\frac{1}{2}L_d$  from the wall. At the antinode, two waves of the same height occupy the envelope center, the first one is the overlap of wave A approaching the wall and of preceding wave B going back after having been reflected; the second one is the overlap of wave A going back seaward and of succeeding wave B' approaching the wall. At greater distances from the wall, nodes and antinodes tend to disappear because the central waves of the group

FROM CROSS-CORRELATION OF THE TIME SERIES DATA

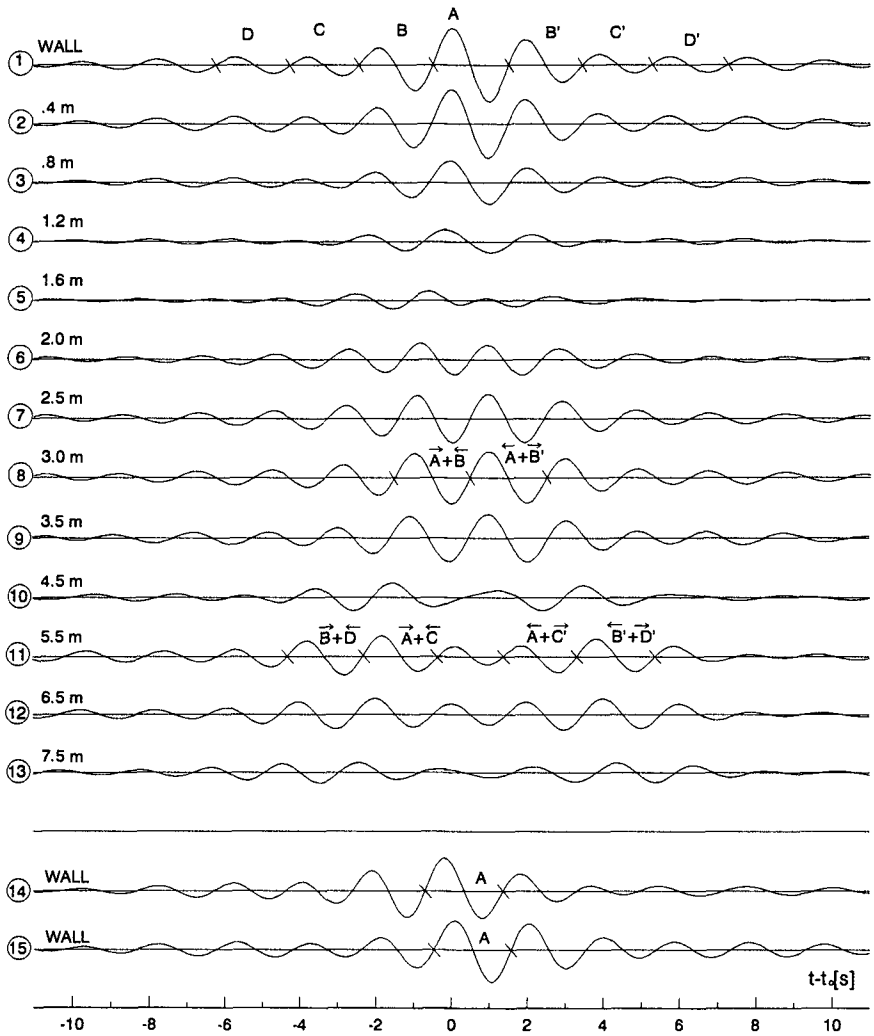


Fig.3 Expected waves at the various gauge locations if a wave of given very large height  $H$  occurs at location 1 (wall-center) with the first configuration of the gauges. Calculation from equation (2.1), directly with the time series data of record 17, without smoothing.

FROM THE JONSWAP SPECTRUM

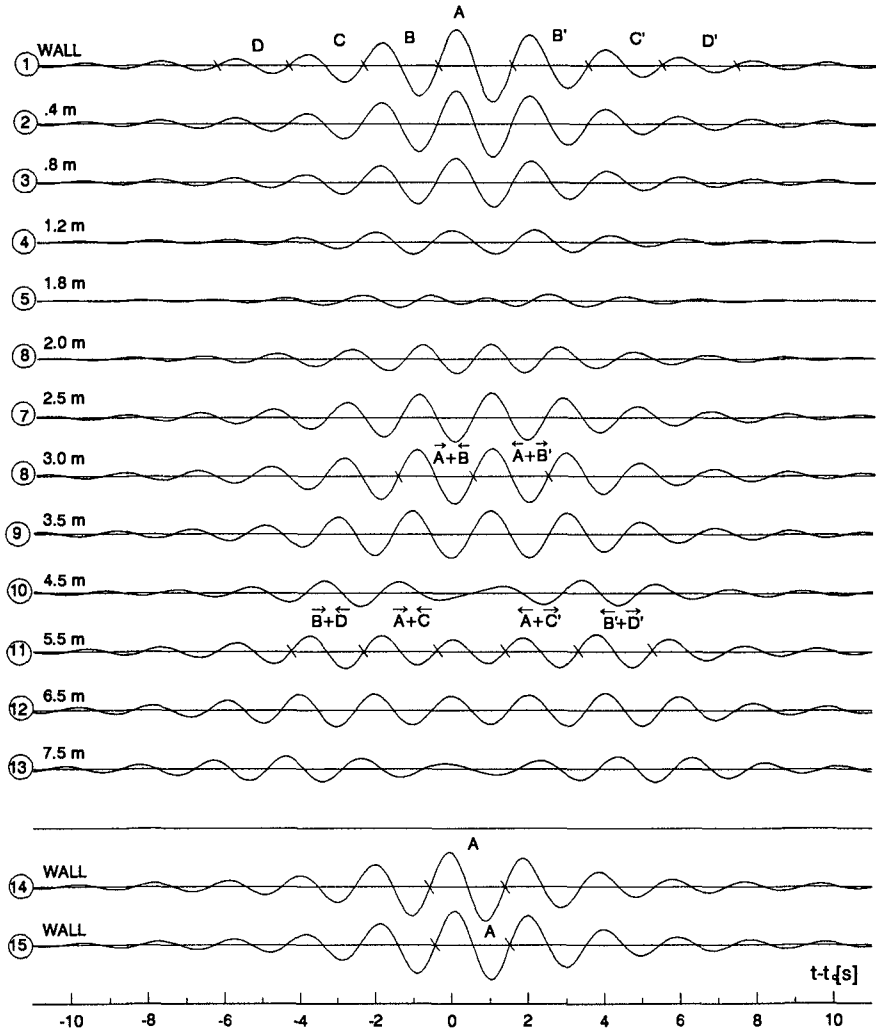
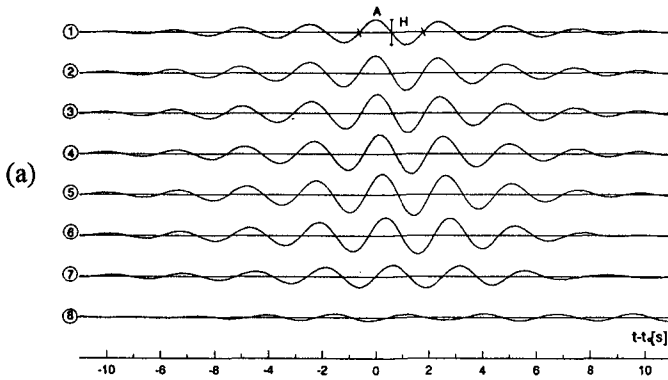


Fig.4 Expected waves at the various gauge locations if a wave of given very large height  $H$  occurs at location 1 (wall-center) with the first configuration of the gauges. Calculation from equation (2.1), with the JONSWAP spectrum and the spreading direction function of Mitsuyasu et al.(1975).

FROM CROSS-CORRELATION OF THE TIME SERIES DATA



FROM THE JONSWAP SPECTRUM

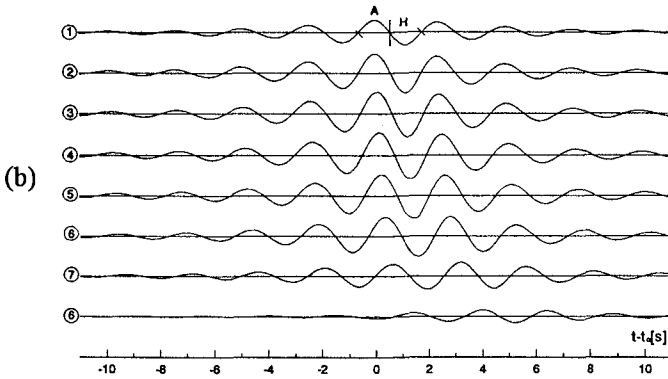


Fig.5 Expected waves at the various gauge locations if a wave of given very large height  $H$  occurs at location 1 (wall-end) with the third configuration of the gauges. Calculation from eq.(2.1). Panel (a): covariances obtained by cross-correlation of the time series data of record 30. Panel (b): covariances obtained with the JONSWAP spectrum and the spreading direction function of Mitsuyasu et al.(1975).

do not overlap themselves, and it is possible to distinguish the wave group approaching the wall from the wave group going back seaward. In particular, at location 13, which is the most remote from the wall, we see the wave group approaching the wall, then a short calm, then the wave group going back.

Fig.5 shows the expected time histories at the locations of the third gauge configuration if a wave of fixed very large height  $H$  occurs at the wall-end ( $H$  is intended to be very large with respect to the

mean wave height at the wall-end). The calculation was made by means of eq.(2.1). The covariances used for Fig.5.a were obtained by cross-correlation of the time series of record 30, while the covariances used for Fig.5.b were obtained from a theoretical spectrum (see Appendix B). The general form of the theoretical spectrum was that used for Fig.4, and the dominant wave period and wave direction were given the values of record 30. The dominant period was 2.5 s and the angle of the dominant wave direction with the wall-orthogonal was 22°.

A very high wave at the wall-end, with a very high probability, occurs because the front center of a wave group targets on the wall-end. For this reason, the wave height along the wall, on the one hand has to decrease starting on the wall-end because of the increasing distance from the front center, and on the other hand it has to increase because of the raising produced by the wall. The result is that a local maximum of the wave height takes place at some distance from the wall-end. This observation should permit to understand the overall configurations of figures 5.a and 5.b. These configurations are strongly similar to each other, and particularly we can see, in both two the figures, that the local maximum of the wave height falls within locations 4 and 5, at nearly  $\frac{1}{3}$  wave length from the wall-end.

Figs.3 and 5.a prove that the wind wave field has something like a "genetic code" showing what essentially happens if a very high wave occurs at any fixed location. Given that  $x_0$  can be anyone of the gauge locations, we drew a number of pictures like Figs.3 and 5.a from each record, and the expected time histories were always smooth and consistent with one another as in the figures shown in this paper. Although the records from single realizations of very high waves were more irregular than the expected profiles, the essential features of these profiles were still evident and provided good support for the theoretical connection. This topic is dealt with in a forthcoming paper giving also a more simple formal proof of the theory.

#### Appendix A. Autocovariance of the wind waves being subject to reflection A.a Surface waves

According to the theory of the sea waves to the Stokes first order (Longuet-Higgins, 1963), the surface displacement of a progressive wave field is

$$\eta(x, y, t) = \sum_{i=1}^N \alpha_i \cos(k_i x \sin \theta_i + k_i y \cos \theta_i - \omega_i t + \epsilon_i), \quad k_i \tanh(k_i d) = \omega_i^2 / g. \quad (A.1)$$

where it is assumed that number N is very large, phases  $\epsilon_i$  are distributed purely at random in  $(0, 2\pi)$ , frequencies  $\omega_i$  are different from one another. Then it is assumed that  $\alpha_i$ ,  $\omega_i$  and  $\theta_i$  (this being the angle of wave direction and y-axis) are such as to form a directional frequency spectrum

$$S(\omega, \theta) \delta\omega \delta\theta = \sum_i \frac{1}{2} \alpha_i^2 \quad \text{for } i \text{ such that } \omega < \omega_i < \omega + \delta\omega \text{ and } \theta < \theta_i < \theta + \delta\theta. \quad (A.2)$$

If a vertical reflecting wall is put along the x-axis (line y=0), random wave field (A.1) takes on the form (Boccotti, 1988)

$$\eta(x, y, t) = 2 \sum_{i=1}^N \alpha_i \cos(k_i x \sin \theta_i - \omega_i t + \epsilon_i) \cos(k_i y \cos \theta_i). \quad (A.3)$$

From this equation of the surface displacement, and definition (2.2) of the autocovariance, we have

$$\Psi(\underline{X}, T) = 4 \sum_{i=1}^N \sum_{j=1}^N \alpha_i \alpha_j \cos(k_i y_o \cos \theta_i) \cos[k_j (y_o + Y) \cos \theta_j] \cdot \langle \cos(k_i x_o \sin \theta_i - \omega_i t + \epsilon_i) \cos(k_j x_o \sin \theta_j - \omega_j t + \epsilon_j + k_j X \sin \theta_j - \omega_j T) \rangle, \quad (A.4)$$

where

$$\underline{x}_o = (x_o, y_o), \quad \underline{X} = (X, Y), \quad (A.5)$$

and the angle brackets denote an average with respect to time t. Eq.(A.4) is reduced to

$$\Psi(\underline{X}, T) = 4 \sum_{i=1}^N \frac{1}{2} \alpha_i^2 \cos(k_i X \sin \theta_i - \omega_i T) \cos(k_i y_o \cos \theta_i) \cos[k_i (y_o + Y) \cos \theta_i], \quad (A.6)$$

and with the definition (A.2) of  $S(\omega, \theta)$

$$\Psi(\underline{X}, T) = 4 \int_0^\infty \int_0^{2\pi} S(\omega, \theta) \cos(k X \sin \theta - \omega T) \cos(k y_o \cos \theta) \cdot \cos[k (y_o + Y) \cos \theta] d\theta d\omega. \quad (A.7)$$

Thus, if we specify function  $S(\omega, \theta)$  and location  $\underline{x}_o$  we can evaluate the autocovariance. Note that eq. (A.7) depends on  $y_o$  but does not depend on  $x_o$ . This is a consequence of the fact that the wall is assumed to be very long, so that the autocovariance generally changes with distance  $|y_o|$  from the wall, but does not change with position  $x_o$  along the wall.

**A.b Pressure head waves**

In this section  $\eta(x, y, t)$  is intended to be the fluctuating pressure head at some fixed depth  $z_o$ . Before a long reflecting wall, this is given by

$$\eta(x, y, t) = 2 \sum_{i=1}^N \alpha_i \frac{\cosh k_i (d + z_o)}{\cosh k_i d} \cos(k_i x \sin \theta_i - \omega_i t + \epsilon_i) \cos(k_i y \cos \theta_i), \quad (A.8)$$

so that the autocovariance (2.2) turns out to be

$$\Psi(\underline{X}, T) = 4 \int_0^\infty \int_0^{2\pi} S(\omega, \theta) \frac{\cosh^2 k (d + z_o)}{\cosh^2 k d} \cos(k X \sin \theta - \omega T) \cos(k y_o \cos \theta) \cdot \cos[k (y_o + Y) \cos \theta] d\theta d\omega. \quad (A.9)$$

This equation was used to obtain Fig.4.

**Appendix B. Autocovariance of the wind waves being subject to diffraction**

Near the wall-end, a more appropriate theory is that of the semi-infinite breakwater. If a semi-infinite breakwater is put along the x-axis, random wave field (A.1) takes on the form

$$\eta(r, \alpha, t) = \sum_{i=1}^N \alpha_i [F(r, \alpha; \omega_i, \theta_i) \cos(\omega_i t + \epsilon_i) + G(r, \alpha; \omega_i, \theta_i) \sin(\omega_i t + \epsilon_i)], \quad (B.1)$$



where  $r, \alpha$  are polar coordinates with origin at the breakwater-end ( $\alpha = 0$  at the protected wall,  $\alpha = 2\pi$  at the wave beaten wall) and  $F(r, \alpha; \omega, \theta)$  and  $G(r, \alpha; \omega, \theta)$  are the functions of Penny and Price (1952) for a wave whose angular frequency is  $\omega$  and whose direction makes an angle  $\theta$  with the wall-orthogonal. If we define

$$\underline{x}_o = (r_o, \alpha_o) \quad , \quad \underline{x}_o + \underline{X} = (r, \alpha), \quad (B.2)$$

from general eq. (2.2) of the autocovariance we have

$$\Psi(\underline{X}, T) = \sum_{i=1}^N \sum_{j=1}^N a_i a_j \langle [F_i(r_o, \alpha_o) \cos(\omega_i t + \epsilon_i) + G_i(r_o, \alpha_o) \sin(\omega_i t + \epsilon_i)] \cdot [F_j(r, \alpha) \cos(\omega_j t + \epsilon_j + \omega_j T) + G_j(r, \alpha) \sin(\omega_j t + \epsilon_j + \omega_j T)] \rangle, \quad (B.3)$$

where, for simplicity, we have used the compact notation

$$F_i(r, \alpha) = F(r, \alpha; \omega_i, \theta_i). \quad (B.4)$$

Eq. (B.3) is reduced to

$$\Psi(\underline{X}, T) = \sum_{i=1}^N \frac{1}{2} a_i^2 \{ [F_i(r_o, \alpha_o) F_i(r, \alpha) + G_i(r_o, \alpha_o) G_i(r, \alpha)] \cos \omega_i T + [F_i(r_o, \alpha_o) G_i(r, \alpha) - G_i(r_o, \alpha_o) F_i(r, \alpha)] \sin \omega_i T \}, \quad (B.5)$$

and from the definition (A.2) of  $S(\omega, \theta)$

$$\Psi(\underline{X}, T) = \int_0^{\infty} \int_0^{2\pi} S(\omega, \theta) \{ [F(r_o, \alpha_o; \omega, \theta) F(r, \alpha; \omega, \theta) + G(r_o, \alpha_o; \omega, \theta) G(r, \alpha; \omega, \theta)] \cos \omega T + [F(r_o, \alpha_o; \omega, \theta) G(r, \alpha; \omega, \theta) - G(r_o, \alpha_o; \omega, \theta) F(r, \alpha; \omega, \theta)] \sin \omega T \} d\theta d\omega. \quad (B.6)$$

This is the autocovariance of the surface waves. Then, autocovariance of the pressure head waves at some fixed depth  $z_o$  has one more factor in the integral. This is

$$\cosh^2 k(d + z_o) / \cosh^2 kd.$$

Eq. (B.6) with this additional factor was used to obtain Fig.5.b.

## References

- Boccotti P., 1988, Refraction, reflection and diffraction of irregular gravity waves, Excerpta of the Italian Contribution to the Field of Hydraulic Engng., vol.3, Libreria Progetto Publ., Padova.
- Boccotti P., 1989, On mechanics of irregular gravity waves, Atti Acc. Naz. Lincei, Memorie (Trans. Nat. Acc. Lincei), VIII, 19.
- Boccotti P. et al., 1993-a, A field experiment on the mechanics of irregular gravity waves, J. Fluid Mech., 252.
- Boccotti P. et al., 1993-b, An experiment at sea on the reflection of the wind waves, Ocean Engng., 20.
- Hasselmann K. et al., 1973, Measurements of wind wave growth and swell decay during the Joint North Sea Wave Project (JONSWAP), Deut. Hydrogr. Zeit., A-8.
- Longuet-Higgins M.S., 1963, The effects of non-linearities on statistical distributions in the theory of sea waves, J. Fluid Mech., 17.
- Mitsuyasu H. et al., 1975, Observation of directional spectrum of ocean

waves using a clover-leaf buoy, *J. Phys. Oceanography*, 5.

Penny W.G. and Price A.T., 1952, The diffraction theory of sea waves by breakwaters, *Phil. Trans. Roy. Soc.*, A-244.

Phillips O.M., 1967, The theory of wind generated waves, *Adv. in Hydroscience*, 4.

## CHAPTER 70

# The application of load-cell technique in the study of armour unit responses to impact loads

Hans F. Burcharth<sup>1</sup> Zhou Liu<sup>2</sup>

### Abstract

The slender, complex types of armour units, such as Tetrapods and Dolosse are widely used for rubble mound breakwaters. Many of the recent failures of such structures were caused by unforeseen early breakage of the units, thus revealing an imbalance between the strength (structural integrity) of the units and the hydraulic stability (resistance to displacements) of the armour layers. Breakage is caused by stresses from static, pulsating and impact loads. Impact load generated stresses are difficult to investigate due to non-linear scaling laws. The paper describes a method by which impact loads on slender armour units can be studied by load-cell technique. Moreover, the paper presents Dolos design diagrams for the prediction of both breakage and hydraulic stability.

### Introduction

The slender complex types of armour units, such as Tetrapods and Dolosse are widely used. Breakage of the armour units has caused many of the recent breakwater failures. Thus there is a need for studying stresses in the units.

Due to the stochastic nature of the wave loads, the complex shape of the armour units and their random placement, the problem cannot be dealt with on a deterministic basis, but must be handled as a probabilistic problem.

Consequently, a very large number of situations must be investigated. This can be performed at reasonable costs only by small scale experiments. Stresses in small scale armour units are studied by the use of load-cells inserted in the units. Burcharth et al.(1992) presented design diagrams for structural integrity based on stress exceedence probability, which, however, do not express the proportion of the units that will break. The present paper presents a new set of diagrams for the prediction of the amount of breakage.

---

<sup>1</sup>Prof. of Marine Civil Engineering, Aalborg University, Denmark.

<sup>2</sup>Research Engineer, Ph.D. Aalborg University, Denmark.

Load-cell technique involves a number of complications. The installation of the load-cell makes the material properties of the unit different from those of the homogeneous prototype units and consequently the impact responses, which depend on the elastic behaviours of the bodies, cannot be directly reproduced in model tests. Besides this, the responses of the instrumented units could involve dynamic amplification effects. Moreover, the ultra short duration of solid body impact loads and the wave slamming necessitates high frequency sampling which results in data storage capacity problem. The frequencies of the impact stresses are in the order of 800-1500 Hz for the applied model units.

The paper first discusses the scale law for the impact stress in the armour units and presents results of impact calibration of the load-cell instrumented Tetrapods and Dolosse. The paper then presents the model test results on impact stresses of Dolosse and finally presents the design diagrams which incorporate both the hydraulic stability and the structural integrity of Dolos armour layers. The diagrams are different from the earlier ones presented by the authors in that they contain information on the proportion of the units that will break, instead of the stress exceedence probability.

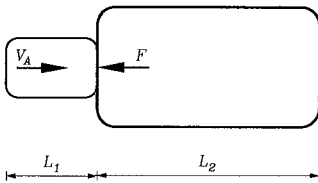
**Duration of impacts**

When two solid bodies collide the impact force and the related stresses will depend on the duration of the impact, i.e. the time of contact,  $\tau$ . Due to the non-linear material properties of concrete and to the complex shape of slender armour units it is not possible to establish a formula by which  $\tau$  can be quantified. However, it is sufficient for the present research to formulate a qualitative expression for  $\tau$ . In the following are discussed two realistic models for estimation of  $\tau$ . It is shown that for geometrically similar systems and constant Poisson's ratio it is reasonable to assume

$$\tau \sim L \sqrt{\frac{\rho_A}{E_A}} \tag{1}$$

where  $\sim$  means proportional to.

*Case 1. Impacting blunt bodies of identical linear elastic material.*



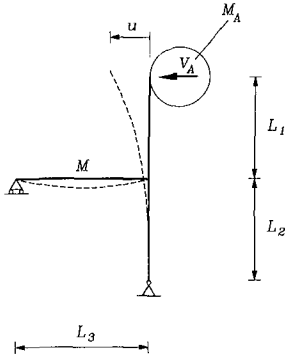
$L_1$  and  $L_2$  are proportional to the characteristic length  $L$  of the system.

It is assumed that the impact generates mainly one-dimensional compression

longitudinal shock waves which travel with the rod wave speed,  $C = \sqrt{E_A/\rho_A}$ , the distances  $L_1$  and  $L_2$  to the free edges, where they are reflected as tension waves. The two bodies will loose contact at the first return of a tension wave to the impact surface. Consequently, because  $L_1 < L_2$

$$\tau = \frac{2 L_1}{C} = \frac{2 L_1}{\sqrt{\frac{E_A}{\rho_A}}} \quad \text{or} \quad \tau \sim L \sqrt{\frac{\rho_A}{E_A}}$$

*Case 2. Slender body impacted by blunt body of identical linear elastic material.*



$$L_1 \sim L_2 \sim L_3 \sim L$$

$$M \sim M_A \sim \rho_A L^3$$

The impacting blunt body of mass  $M_A$  hits the slender structure of mass  $M \sim M_A$  with impact velocity  $V_A$  by which a vibration mainly caused by bending and shear is initiated. It is assumed that the maximum value of  $\tau$  corresponds to contact between the two bodies during approximately one half period  $T$  of the first mode of vibration for the slender body.

If it is assumed that the slender structure has a linear response corresponding to transverse impacts on free and simply supported beams then the system corresponds in principle to a mass-spring system with spring stiffness

$$k \sim \frac{E_A I}{L^3} \tag{2}$$

where  $I \sim L^4$  is the moment of inertia.

The deflection time defined as one half period of the first mode of vibration is

$$\tau \simeq \frac{T}{2} \simeq \sqrt{\frac{M_A + M_o}{k}} \tag{3}$$

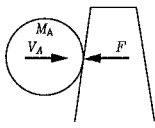
where  $M_o \sim M \sim M_A \sim \rho_A L^3$  is the modal mass of the slender body.

From eqs (2) and (3) is then obtained eq (1). This conclusion was already presented in Burcharth (1984).

**Scaling law for impact stresses of armour units**

*Case 1. Scale law in case of free fall impinging body*

Geometrical similarity and constant coefficient of restitution are assumed



$$\begin{aligned} V_A &\sim \sqrt{2g L} \\ M_A &\sim \rho_A L^3 \end{aligned} \tag{4}$$

The momentum equation reads

$$F \tau = M_A \Delta V_A \sim M_A V_A \tag{5}$$

where  $\tau$  is the duration of the impact and  $\Delta V$  is the velocity difference of the impinging body before and after the collision.  $\Delta V \sim V_A$  is due to the assumed constant coefficient of restitution.

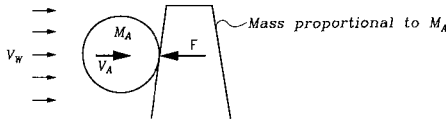
Inserting eqs (1) and (4) in eq (5) yields

$$F \sim \frac{\rho_A L^3 (g L)^{0.5} E_A^{0.5}}{L \rho_A^{0.5}} = \rho_A^{0.5} E_A^{0.5} g^{0.5} L^{2.5}$$

Introducing  $\lambda = \frac{\text{model value}}{\text{prototype value}}$  we obtain

$$\lambda_{\sigma_{Impact}} = (\lambda_{\rho_A} \lambda_{E_A} \lambda_L \lambda_g)^{0.5} \tag{6}$$

*Case 2. Scale law of impinging body affected only by flow forces*



$V_A$  is found from Newton's equation

$$F_W = M_A \frac{dV_A}{dt} \tag{7}$$

$$V_A = \frac{F_W}{M_A} t = \frac{F_W}{\rho_A L^3} t \tag{8}$$

where  $F_w$  is the flow force on the impinging body.

By the use of eqs (1), (5) and (8) is obtained

$$F \sim \frac{\rho_A L^3 F_W t E_A^{0.5}}{\rho_A L^3 L \rho_A^{0.5}} = \rho_A^{-0.5} L^{-1} F_W t E_A^{0.5}$$

$$\lambda_{\sigma_{Impact}} = \lambda_{\rho_A}^{-0.5} \lambda_L^{-3} \lambda_{F_W} \lambda_t \lambda_{E_A}^{0.5} \tag{9}$$

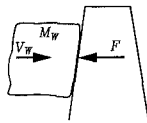
Because in the Froude model,  $\lambda_{F_W} = \lambda_{\rho_W} \lambda_L^3$  and  $\lambda_t = \lambda_L^{0.5}$ , then

$$\lambda_{\sigma_{Impact}} = \lambda_{\rho_A}^{-0.5} \lambda_{\rho_W} \lambda_{E_A}^{0.5} \lambda_L^{0.5} \tag{10}$$

The variation in  $F_w$  due to viscous effects is neglected. This, however, introduces some unknown bias, the size of which depends on the Reynolds number range.

*Case 3. Collision between impinging water (slamming) and a solid body.*

The air-cushioning effect is neglected because it is unlikely that air-pockets will be entrapped due to the limited size and rounded shape of the elements.



$$V_W \sim \sqrt{gL}$$

$$M_W \sim \rho_W L^3 \tag{11}$$

$\tau$  is assumed given by (1) because the solid body stress wave is reflected from a free surface of the armour unit long time before reflection from a free surface of the wave (travel distance  $\simeq H_s >$  dimension of armour unit; shock wave speed is smaller in water than in concrete) and the deflection time will be shorter than the transverse time of the elastic wave in the water.

From the momentum equation

$$F \tau = M_W \Delta V_W \sim M_W V_W \tag{12}$$

and eqs (1) and (8) is obtained

$$F \sim \frac{\rho_W L^3 g^{0.5} L^{0.5} E_A^{0.5}}{L \rho_A^{0.5}} = \rho_A^{-0.5} \rho_W E_A^{0.5} L^{2.5} g^{0.5}$$

and consequently

$$\lambda_{\sigma_{Impact}} = \lambda_{\rho_A}^{-0.5} \lambda_{\rho_W} \lambda_{E_A}^{0.5} \lambda_L^{0.5} \lambda_g^{0.5} \tag{13}$$

The difference between the above three scaling laws eqs (6), (10) and (13) is related to the scales of the densities only, because generally

$$\lambda_{\rho_A} \neq \lambda_{\rho_A}^{-0.5} \lambda_{\rho_W} \tag{14}$$

As long as the model is made of approximately the same concrete as the prototype, eq (6) can be chosen as the scaling law for the impact stresses, as it introduces less than 1% error for  $0.97 \leq \lambda_{\rho_A} \leq 1.00$  and  $0.98 \leq \lambda_{\rho_w} \leq 1.00$ .

**Apparent elasticity of the units with load-cell**

The scaling law for the impact stresses of armour units is related to the elasticity of the material. Unfortunately, the insertion of the load-cell destroys the homogeneity of the material. This means that the impact stresses recorded in the small scale model tests cannot be scaled up to prototypes by the use of eq (6) valid only for homogeneous materials. Fig.1 shows the 200 g Dolos and 280 g Tetrapod with the load-cells.

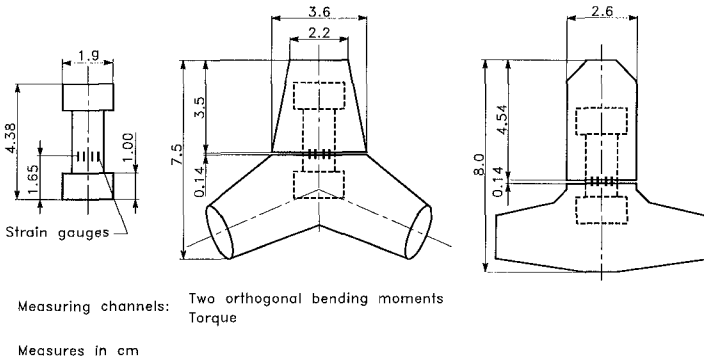


*Fig.1. 200 g Dolos and 280 g Tetrapod with the load-cells.*

However, by comparison of small scale impact test results for Dolosse and Tetrapods with results of the similar large scale impact tests (Burcharth, 1980, Bürger et al. 1990), it is possible to obtain an apparent elasticity for the small scale units. The apparent elasticity is then used for the interpretation of the impact signals recorded in the hydraulic flume tests.

The impact calibration results of the small scale Dolosse with load-cell have been published in Burcharth et al.(1990). The results of impact calibration of the Tetrapods are given in Fig.2. For the applied pendulum test set-up the reference is made to Bürger et al.(1990).

A way of checking the apparent elasticity is to compare the impact duration of the small load-cell mounted units with those of the various large size units, cf. eq (1). Fig.3 shows the ratio of dimensionless stress of various sizes of Dolosse using the apparent elasticity of the 200 g Dolos. Even though there is a big scatter, it can be seen that most ratios are around the value of 1, thus confirming the value of the apparent elasticity.



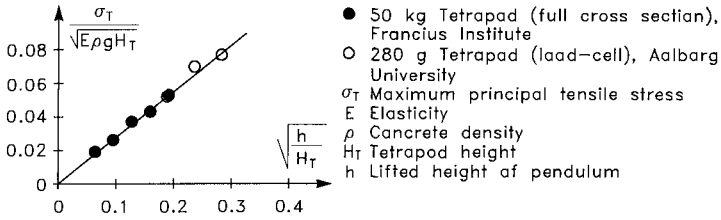


Fig. 2. Comparison of pendulum test results of the large scale Tetrapod with surface mounted strain gauges and the small scale Tetrapod with load-cell. Apparent elasticity  $E = 4799 \text{ MPa}$ .

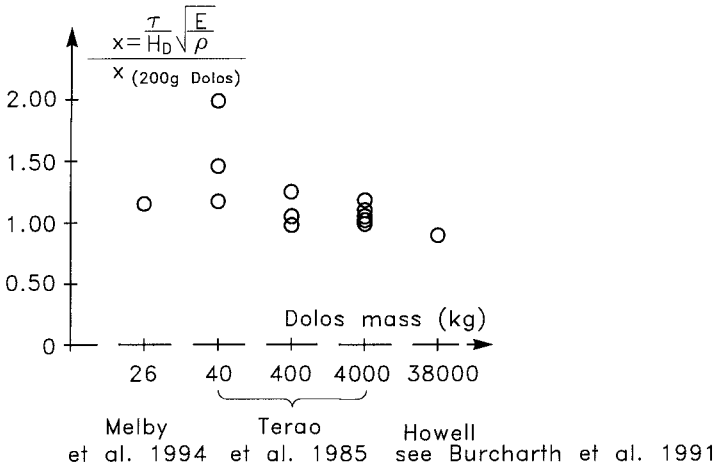
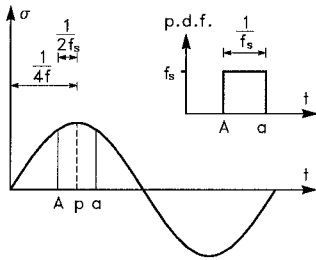


Fig. 3. Ratios of the dimensionless impact duration of large scale Dolosse against 200 g Dolos with load-cell. Apparent elasticity  $E = 3500 \text{ MPa}$ .

**Sampling frequency**

The ultra short duration of solid body impact loads and wave slamming requires a very high sampling frequency. The following analysis gives the underestimation of the stress corresponding to a certain sampling frequency.

Suppose the stress signal is recorded at frequency  $f_s$  and the stress signal is sinusoidal with the maximum stress  $\sigma_p$  and the frequency  $f$ .



$$\sigma = \sigma_p \sin(2\pi f t) \tag{15}$$

Fig. 4. Sinusoidal stress signal.

The most unfavourable case is when the two adjacent sampling points,  $A$  and  $a$ , are symmetrically located around the center of the peak  $p$ . For this case the sampled maximum stress  $\sigma_A$  is

$$\sigma_A = \sigma_p \sin(2\pi f t_A) = \sigma_p \sin\left(2\pi f\left(\frac{1}{4f} - \frac{1}{2f_s}\right)\right) \tag{16}$$

and the maximum relative error is

$$\frac{\sigma_p - \sigma_A}{\sigma_p} = 1 - \sin\left(\pi\left(\frac{1}{2} - \frac{f}{f_s}\right)\right) \tag{17}$$

On the other hand, if the sampling points are uniformly distributed along the length ( $A$ - $a$ ), the average of the sampled maximum stress is

$$\begin{aligned} \bar{\sigma} &= \int_{t_A}^{t_a} \sigma_p \sin(2\pi f t) f_s dt \\ &= \frac{\sigma_p f_s}{2\pi f} \left( \cos\pi\left(\frac{1}{2} - \frac{f}{f_s}\right) - \cos\pi\left(\frac{1}{2} + \frac{f}{f_s}\right) \right) \end{aligned} \tag{18}$$

and the average relative error is

$$\frac{\sigma_p - \bar{\sigma}}{\sigma_p} = 1 - \frac{1}{2\pi} \frac{f_s}{f} \left( \cos\pi\left(\frac{1}{2} - \frac{f}{f_s}\right) - \cos\pi\left(\frac{1}{2} + \frac{f}{f_s}\right) \right) \tag{19}$$

The maximum relative error and the average relative error are depicted in Fig.5. However, the actual impact signals are not sinusoidal, cf. Fig.6. In order to check the influence of the sampling frequency a series of Dolos pendulum tests with different sampling frequencies have been performed. The results are depicted in Fig.6. It can be seen that the sinusoidal results hold also for the actual impact signal when the offset for  $f_s = 10000 \text{ Hz}$  is considered.

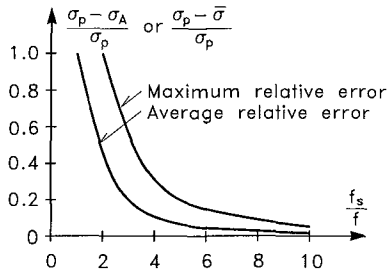


Fig. 5. Maximum relative error and average relative error due to the limited sample frequency.

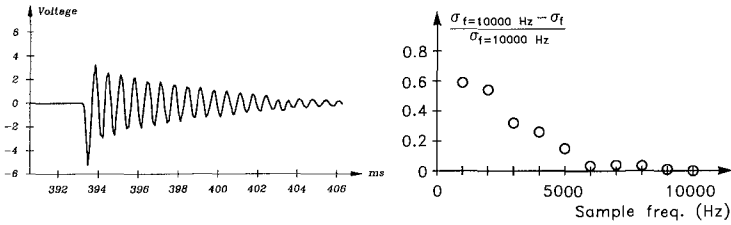


Fig. 6. Example of the impact signals of the 200 g load-cell instrumented concrete Dolosse ( $f = 1500 \text{ Hz}$ ) and the relative error of the Dolos pendulum test results as function of the sampling frequency.

In the Dolos hydraulic model test, the applied sampling frequency is  $f_s = 6000 \text{ Hz}$  and the damped natural frequency of the instrumented Dolosse  $f = 1500 \text{ Hz}$ . On average the sampled maximum impact stress is underestimated by 10% due to the limited sampling frequency. Therefore, in the data processing all sampled maximum impact stresses were increased by 10% .

**Check for the dynamic amplification by wave slamming**

It is well-known that resonance occurs when the frequency of the load is close to the natural frequency of the system. The installation of the load-cell into the model Dolos makes its natural frequency smaller, cf. eq (1). In order to check if the reduced natural frequency of the Dolosse is close to the wave slamming frequency, and hence introduces dynamic amplification, the frequency of the wave slamming on the Dolos armour layer was recorded by a pressure transducer installed in the stem of the Dolos. The pressure transducer did in all tests face the breaking waves. The results are given in Fig.7, showing the highest frequency of the wave slamming on the Dolos armour to be 330 Hz, far away from the

natural frequency of 1500 Hz for the Dolosse with the load-cells. Consequently, no dynamic amplification are present in the model tests.

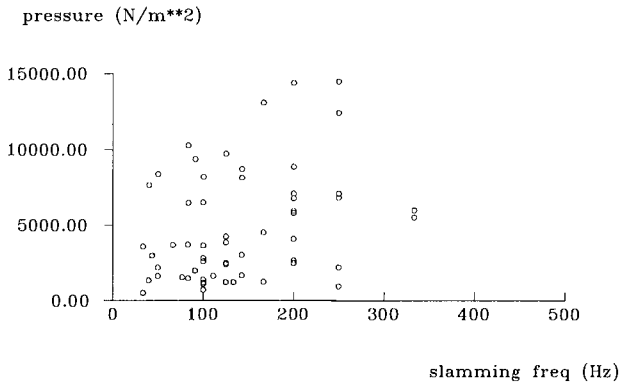


Fig. 7. Recorded frequencies of the wave slamming on the Dolos armour units.

**Description of the experiments**

A 1 : 1.5 slope armoured with 200 g concrete Dolosse of waist ratios 0.325, 0.37 and 0.42 were exposed to irregular waves in a wave flume with a foreshore slope of 1 : 20. Fig. 8 shows the set-up of the model and the cross section of the breakwater. The hydraulic stability formula of Dolos armour layer is given by (Burcharth et al. 1992)

$$\begin{aligned}
 N_s &= \frac{H_s}{\Delta D_n} = (47 - 72 r) \varphi_{n=2} D^{1/3} N_z^{-0.1} \\
 &= (17 - 26 r) \varphi_{n=2}^{2/3} N_{od}^{1/3} N_z^{-0.1}
 \end{aligned}
 \tag{20}$$

- where  $H_s$  significant wave height in front of breakwater
- $\Delta$   $(\rho_{concrete}/\rho_{water}) - 1$ ,  $\rho$  is the mass density
- $D_n$  length of cube with the same volume as Dolosse
- $r$  Dolos waist ratio
- $\varphi_{n=2}$  packing density
- $D$  relative number of units within levels SWL  $\pm 6.5 D_n$  displaced one Dolos height  $h$ , or more (e.g. for 2% displacement insert  $D = 0.02$ )
- $N_{od}$  number of displaced units within a width of one equivalent cubic length  $D_n$ .
- $N_z$  number of waves. For  $N_z \geq 3000$  use  $N_z = 3000$ .

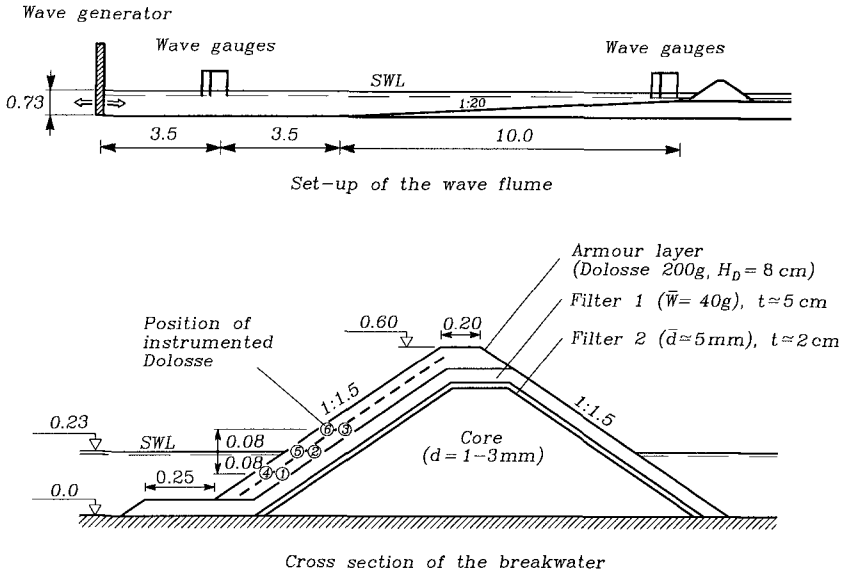


Fig. 8. Set-up of the wave flume and the cross section of the breakwater.

**Distribution of stresses over the slope**

The distribution of  $\sigma_T$  over the slope is of interest in order to identify the potential areas for armour breakage.

Fig. 9 shows typical distributions given by the 2% exceedence values of  $\sigma_T$  for each of the six instrumented Dolos positions for 10t and 50t Dolos of waist ratios 0.325 and 0.42 exposed to wave action levels,  $N_S = \frac{H_{m0}^3}{\Delta D_n} = 0.9, 1.8$  and 2.6.

The following conclusions can be drawn from the analyses of a large number of distributions of maximum  $\sigma_T$  over the slope:

- The contribution of the impact stress to the maximum principal tensile stress  $\sigma_T$  is small for  $N_S \leq 2.0$ .
- The contribution from the impact stress to  $\sigma_T$  is small in the bottom layer.
- The contribution from the impact stress to  $\sigma_T$  is very significant in the top layer.
- Breakage will in most cases start in the top layer in the zone just below SWL. This zone is more vulnerable to breakage than the zone above SWL.

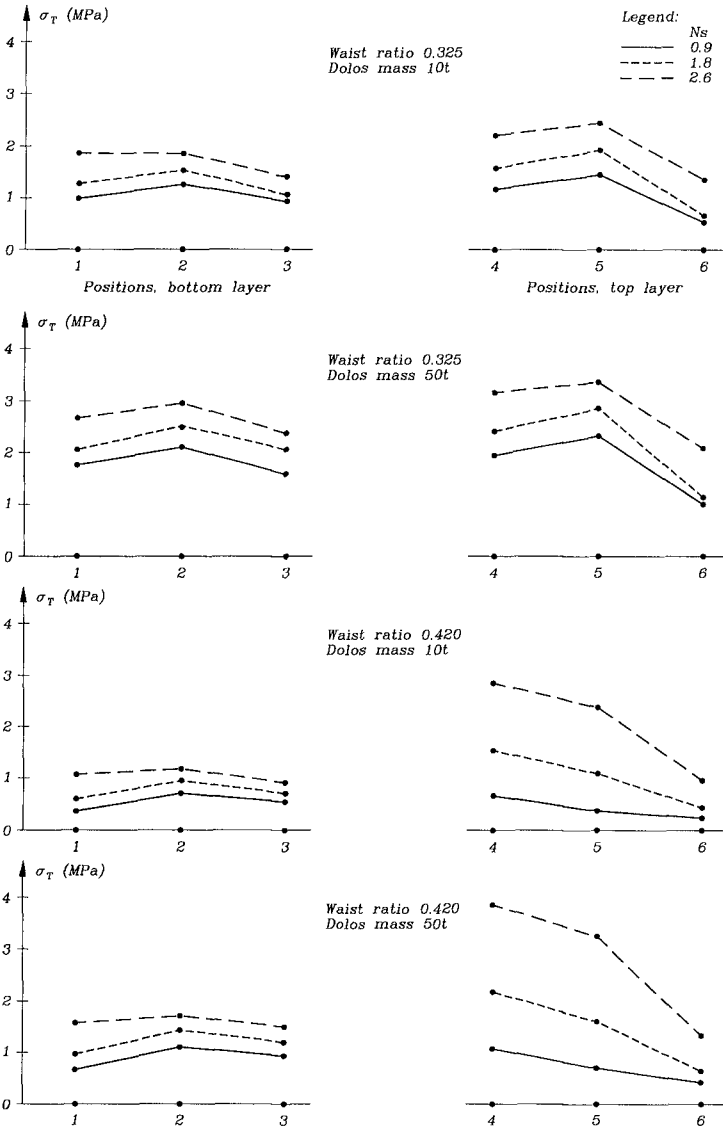


Fig. 9. Distribution of  $\sigma_T$  over the slope, Dolos positions 1 to 6, cf. Fig. 8. 2% stress exceedance probability level.

## Design diagramme

In the analysis of breakage it is only the maximum value of  $\sigma_T$  in each instrumented Dolos within a test run which is of interest. Repeated short test runs of 100-300 waves were used because most movements take place in the beginning of each test.

The authors presented Dolos design diagrammes in ICCE'92 based on stress exceedence probability, which do not give exactly the proportion of the units that will break. A reanalysis was performed in which the maximum stress of each load-cell instrumented Dolos within each test run was compared with the strength of concrete in order to obtain the relative number of units that will break.

The results are given in the design diagrams, one of which is shown in Fig.10. For the complete set of the design diagrams reference is made to Burcharth (1993). The concrete tensile strength in the diagrams is the one corresponding to static load. However, the diagrams take into account the dynamic amplification of the strength when impacts are involved.

The design diagrams have been checked against observed behaviour of prototype Dolos breakwaters and good agreement was found, cf. Table 1.

Table 1. Observed and predicted damage of some Dolos breakwaters

	Crescent City USA	Richards Bay SA	Sines POR
$H_s$ (m)	10.7 <sup>(1)</sup>	5 <sup>(2)</sup>	9 <sup>(3)</sup>
slope	1:4	1:2	1:1.5
Dolos mass (ton)	38	20	42
Waist ratio	0.32	0.33	0.35
Dolos packing density	0.85	1	0.83
Concrete density ( $kg/m^3$ )	2500	2350	2400
Elasticity (MPa) <sup>(4)</sup>	30,000	30,000	30,000
Tensile strength (MPa) <sup>(4)</sup>	3	3	3
Reported displacement	7.3%		
Reported breakage	19.7%		
Reported displacement+breakage	26.8%	4%	collapse
Predicted displacement	3.6%	0.6%	3.6 %
Predicted breakage	> 10%	5%	> 10%

(1) depth limited in front of breakwater

(2) in front of breakwater

(3) offshore  $\approx$  in front of breakwater

(4) estimated values

Legend:

- Hydraulic stability limit ( $N_z=1000, \varphi=0.74, \Delta=1.29$ ) corresponding to relative number of displaced Dolosse D.
- Tensile strength limit corresponding to relative number of broken Dolosse B
- $H_{mo}^t$  Significant wave height in front of breakwater
- r Dolos waist ratio
- S Concrete tensile strength
- B Relative number of broken Dolosse
- O Relative number of displaced Dolosse

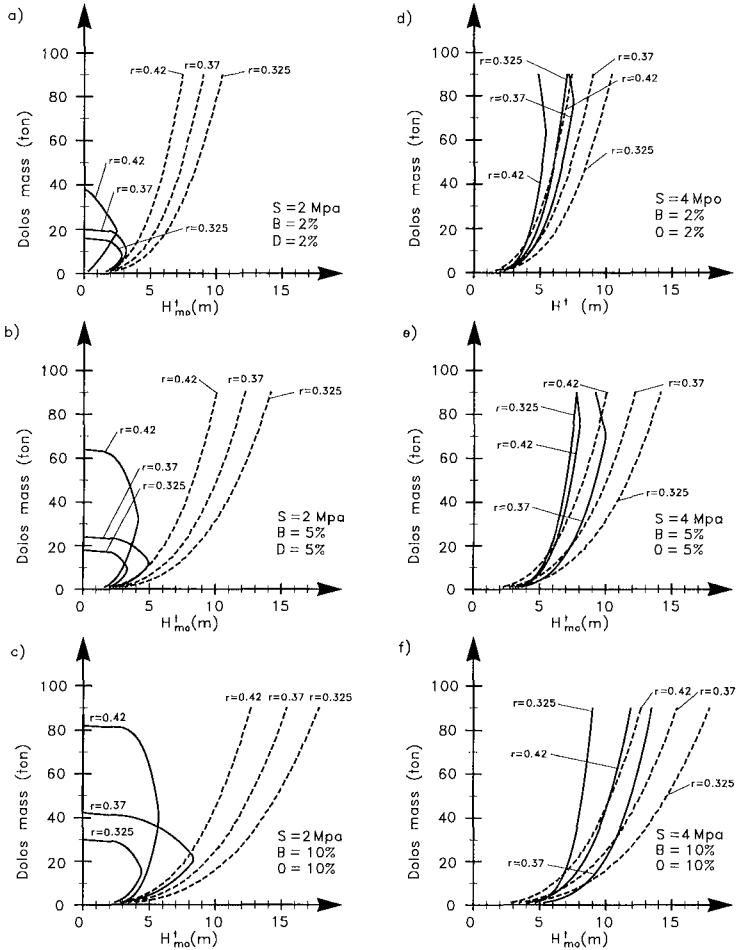


Fig. 10. Design diagrams for structural integrity and hydraulic stability of Dolos armour. Reference area  $SWL \pm 6.5D_n$ .



## Acknowledgements

The load-cells applied in this study were kindly made available by CERC, USA. The project was partly sponsored by the Commission of the European Community under the Marine Science And Technology Research Program (MAST II), and partly sponsored by the Danish Technical Research Council under the MARIN TEKNIK Research Program.

## References

- Burcharth, H.F. (1981). Full-scale dynamic testing of Dolosse to destruction. *Coastal Engineering*, 4 (1981).
- Burcharth, H.F. (1984). Fatigue in breakwater armour units. Proceedings of the 19th International Conference on Coastal Engineering, Houston, Texas, 1984.
- Burcharth, H.F. and Liu, Z.(1990). A general discussion of problems related to the determination of concrete armour unit stresses inclusive specific results related to static and dynamic stresses in Dolosse. Proc. Seminar on Structural Response of Armour Units. CERC, Vicksburg, MISS, USA.
- Burcharth, H.F., Howell, G.L. and Liu, Z.(1991). On the determination of concrete armour unit stresses including specific results related to Dolosse. *Coastal Engineering*, 15 (1991), pp 107-165.
- Burcharth, H.F. and Liu, Z. (1992). Design of Dolos armour units. Proceedings of the 23rd International Conference on Coastal Engineering. Venice. Italy.
- Burcharth, H.F. (1993). Structural integrity and hydraulic stability of Dolos armour layers. Series Paper 9, published by the Department of Civil Engineering, Aalborg University, Denmark, 1993
- Bürger, W.W., Oumeraci, H., Partenscky, H.W. (1990). Impact strain investigations on tetrapods results of dry and hydraulic tests. ASCE Proc. Seminar Stresses in Concrete Armor Units.
- Melby, J.A. and Turk, G.F. (1994). Scale and modeling effects in concrete armor experiments. *Coastal Dynamics'94*, Barcelona, Spain.
- Terao, T., Terauchi, K., Ushida, S., Shiraishi, N., Kobayashi, K. and Gahara, H. (1985). Prototype testing of Dolosse to destruction. Proc. Workshop on Measurement and Analysis of Structural Response in Concrete Armor Units. U.S. Army Corps of Engineers, CERC, WES, Vicksburg, MISS., USA.

## CHAPTER 71

### Steep wave diffraction by a submerged cylinder

J. T. Aquije Chacaltana & A. F. Teles da Silva

#### Abstract

The steep wave diffraction by a fixed circular submerged cylinder is numerically simulated as a completely nonlinear time domain evolution from an initial condition. Attention is focused on two aspects of the problem. The first is a study of the perturbation introduced by the cylinder on the wave field; the second is a study of the hydrodynamic forces on the cylinder due to the waves.

#### Introduction

We study the diffraction of steep waves on a fixed, submerged circular cylinder in deep water; being particularly interested in the hydrodynamic forces induced by the waves on the cylinder and the disturbances produced by the cylinder on the wave field.

The problem of a cylinder held fixed beneath waves field was first studied by Dean (1948) in the context of gentle waves in deep water; Dean finds, to the linear approximation, that incoming waves are not reflected and the only disturbance produced by the cylinder on the waves is an uniform phase delay. Ogilvie (1963) extend the method of Ursell(1950) to study some related problems of wave-body interaction and shows, in the linear approximation for the problem of a restrained circular cylinder, that the hydrodynamic force components oscillate in quadrature with the wave period, have the same amplitude and a phase difference of  $\frac{\pi}{2}$ ; a second order,

---

Inst. de Matemática & Lab. Mec. Fluidos.

Address :

PEM – COPPE / UFRJ, CP 68503, CEP 21945–970, R.J.–BRAZIL

steady vertical force component is calculated from the first order potential, but the steady horizontal force component is found to be zero. Mehlum (1980) gives a first order potential solution for a restrained cylinder under waves which is very easy to compute. Salter et al. (1976) measures forces on a submerged circular cylinder and finds that mean horizontal forces are quite small and come to be negative for steeper waves. Chaplin (1984) makes experiments with a submerged cylinder under waves finding no wave reflection, even for the highest waves; it is also found that the phase lag is smaller than predicted by the linear theory for Keulegan Carpenter,  $K_c$ , numbers smaller than 2. Vada (1987) calculates the second order oscillatory forces on a cylinder of arbitrary cross section; for the case of circular cylinders and  $K_c$  numbers smaller than results agree well with Chaplin's (1984). Palm (1991), working with a high order perturbation scheme, shows that there is no reflection at the order  $m$  and frequency  $m\omega$ , where  $m$  is an integer and  $\omega$  is the frequency, for monochromatic incident waves. Bichromatic waves are shown to have a null second order reflection coefficient; this result is shown to hold for higher order terms. Liu, Dommermuth & Yue (1992) working with a time domain, higher order perturbation scheme calculate, numerically, the wave diffraction by a circular cylinder, giving results for the steady force components on the cylinder, and the transmission coefficients.

### Mathematical Formulation

We assume that the flow is incompressible and irrotational being thus described by a velocity potential  $\phi$ . The free surface is described parametrically by  $\mathbf{R}(\xi, t) = [X(\xi, t), Y(\xi, t)]$  to allow for overturning. The velocity potential satisfy the nonlinear boundary value problem:

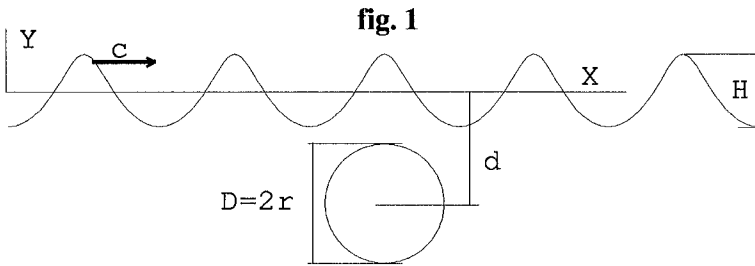
$$\nabla^2 \phi = 0 \quad (1)$$

$$\phi_t + \frac{1}{2}(\nabla \phi)^2 + gY = 0 \quad (2)$$

$$\frac{D\mathbf{R}}{Dt} = \nabla \phi \quad (3)$$

$$\frac{\partial \phi}{\partial n} = 0 \quad (4)$$

(1) is to be valid inside the fluid region, (2) and (3) on the free surface and (4) along the cylinder's surface. At some initial time, e. g.  $t = 0$ , values for  $\mathbf{R}$  and  $\phi|_{\mathbf{R}}$  must be prescribed; we set a steep nonlinear steady wave, impulsively, above a submerged cylinder in deep-water, see figure 1. The steep steady wave, was computed through a numerical code described in Teles da Silva & Peregrine (1988). The nonsteady evolution of the initial condition is computed by a Boundary Integral code which is an extension of the one developed by Dold & Peregrine (1984) to compute the evolution of surface waves on water of uniform finite depth; in the original scheme the free surface is mapped on a closed curve and the horizontal bed into a circle which is surrounded by the mapped free surface; the mapped free surface is then reflected about the bed to ensure impermeability; in the present case the transformed free surface is reflected about the transformed cylinder contour, instead of about the bed, Peregrine (1989).



### Results

Lengths have been scaled by  $\frac{1}{k}$ , where  $k$  is the wave number, accelerations by gravity  $g$ , and time by  $(gk)^{-\frac{1}{2}}$ .

The solutions of the problem depend on three parameters which are: i) wave-height  $H$ , ii) cylinder radius  $R$ , iii) the depth of the cylinder  $d$ . The potential flow modelling, given in the last section, poses strong limitations on the variation of these parameters: first, The Keulegan-Carpenter numbers,  $K_c$ , used as measure of the vortex-shedding, must be kept low, smaller than 1.5 or 2.0 according to the depth of the cylinder, Chaplin (1984); second, wave break-

ing stops the computations; and third, because of the imaging, the cylinder cannot be uncovered.

Most of the computations were made on a Sun Sparc Station 2. The simulation of five wave crests moving over the submerged cylinder, during five wave periods, with twenty numerical points per wave takes 9.9 CPU seconds.

Figure 2 presents the time evolution of an initial wave, for  $r = \frac{4}{3}$ ,  $d = \frac{5}{3}$ , which are the data used by Dean in his 1948 paper; the wave must be small,  $H = 0.1$ , for the cylinder being near the mean level, higher waves would break or uncover it; the centre of the cylinder, is at the start, located below the sixth crest at the position  $x = \pi$ ; the wave length is  $\frac{1}{11}\pi$ ; the numerical simulation is made during a time of 11 wave periods.

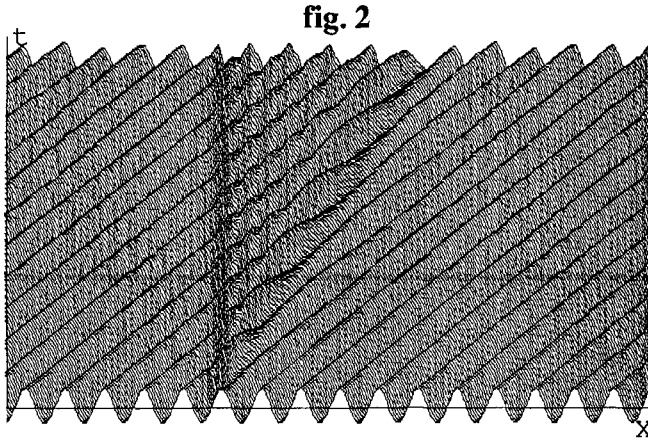
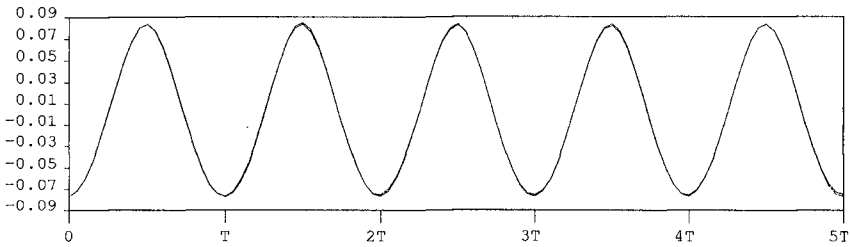


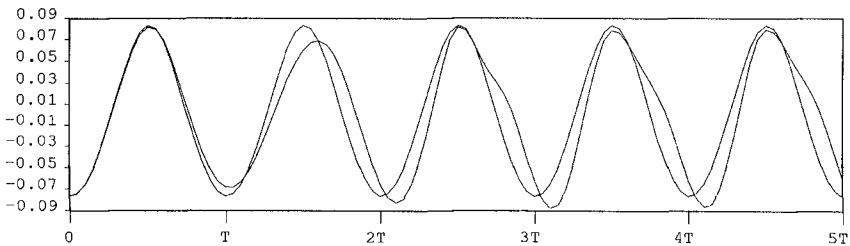
Figure 2 reveals some important aspects of the wave diffraction. With the exception of a faint disturbance starting above the cylinder at time zero, propagating upstream, due to the impulsive start of the numerical experiment, no other disturbances move upstream of the cylinder. This appears to be a nonlinear confirmation of Dean, and Palm's results about the absence of wave reflection in deep water. Following the lines of the crests in the space time diagram, Figure 2, we see that waves lose their steady shape as they pass a region of perturbation shaped like a 'V'; putting a ruler over a crest line we see that as the waves pass the cylinder the crests are over this

line meaning that they are delayed; it is also possible to see for some crests, those that start nearer the cylinder, with the ruler, that after they leave the 'V' region of perturbation they get back to the original line, meaning that once outside the 'V' crests recover the delay. Another feature, in Figure 2, is that the wavelength of the perturbation on the 'V' appears to get longer towards its downstream edge as it would be for a wave group; with a ruler it is possible to estimate the slope of the 'V's edge and hence the velocity of propagation of the perturbations; these estimated velocities agree with the group velocity of small deep water waves with a wave-length which is a half of the wave length of the incident waves. The fact that the perturbed region be defined by a second harmonic of the transmitted wave suggests an analysis of the harmonics of the incident and the perturbed wave.

**Fig. 3a**



**Fig 3b**



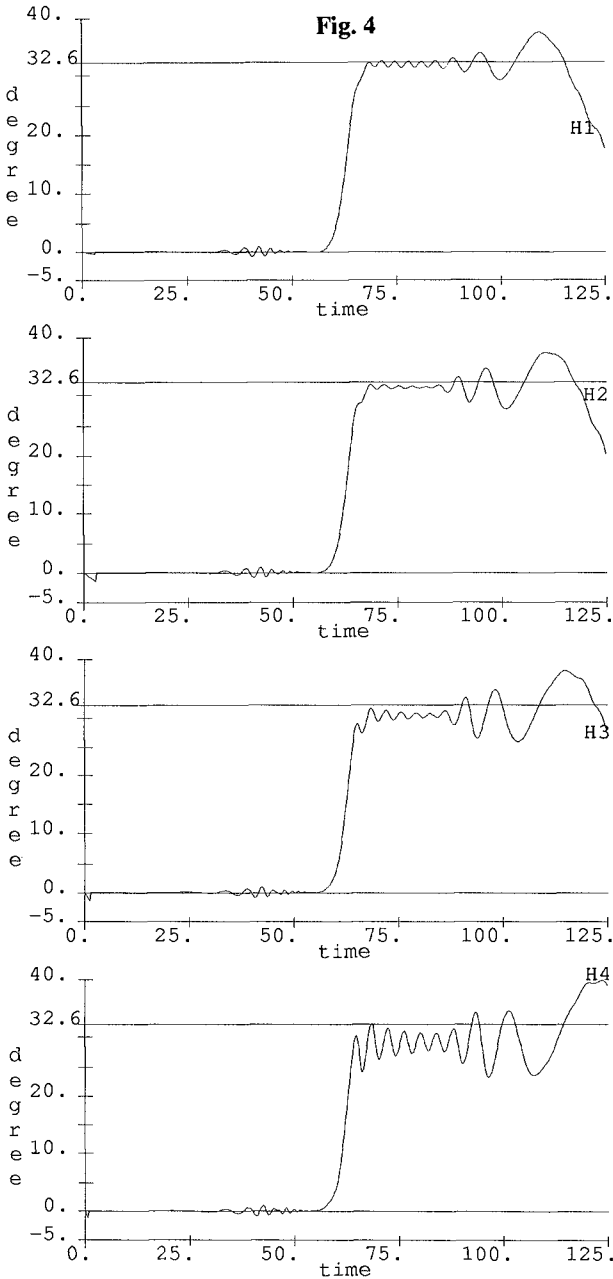
In order to have an idea of the relative magnitude of wave harmonics in simulations, the time history of the elevation of 2 points on the free surface have been recorded for some cases; the points have been placed at a horizontal distance of eight times the radius of the

cylinder, one downstream and the other upstream. A typical case is shown in Figure 3 where, for an incident wave of height  $H = 0.16$  and a cylinder of radius  $r = 0.4$  submerged at the depth of  $d = 0.8$ , the time histories of the upstream, Figure 3a, and downstream, Figure 3b, surface elevation are depicted; in both cases, for comparison, the time history for the original steady wave has been included. In Figure 3a the time history of the upstream free surface elevation is indiscernible from that of the steady wave supporting the conclusion that waves are not reflected; the same does not happen for the upstream elevation where from the third wave period a conspicuous second harmonic appears in the perturbed wave. To see it more clearly we decomposed the time histories in its Fourier modes in the same way as for the forces in equations 5 and 6 below. The results are shown in Table 1 where the most important features, when we compare the upstream elevation with the elevation of the incident steady wave, appear to be the permanence of the first harmonic and the great increase of the higher harmonics; among the higher harmonics the most important is the second which in fact shapes the 'V'.

**Table 1**

Harmonic	Steady Wave	Upstream Wave	Downstream Wave
$a_0$	0.000010	-0.000106	0.000200
$r_1$	0.079812	0.078808	0.078772
$r_2$	0.003213	0.003252	0.016048
$r_3$	0.000213	0.000219	0.003312
$r_4$	0.000029	0.000003	0.001447
$r_5$	0.000022	0.000008	0.000195
$r_6$	0.000004	0.000006	0.000167

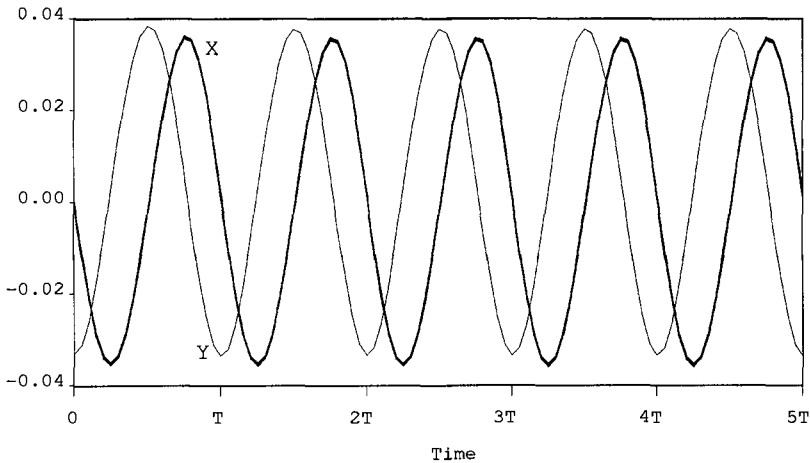
A remarkable fact in Figure 2 is that outside the perturbed 'V' region the waves recover their original shape and steadiness with no traces of the interaction with the cylinder although the interaction is nonlinear; this is the same for the steeper waves provided they do not break. Comparing the position of the crests going past the cylinder with the position they should have in the absence of the





cylinder, we find the phase lag. Figure 4 shows the time evolution for the phase lag, vertical axis in degrees, for four different waves; namely, wave 1:  $H = 0.1$ ,  $T = 6.275$ ,  $c = 1.001$ , wave 2:  $H = 0.2$ ,  $T = 6.252$ ,  $c = 1.005$ , wave 3:  $H = 0.3$ ,  $T = 6.213$ ,  $c = 1.011$ , wave 4:  $H = 0.4$ ,  $T = 6.1588$ ,  $c = 1.0202$ ;  $H$ ,  $T$  and  $c$  are respectively the nondimensional wave-height, period and phase speed. In all this experiments  $r = 2\pi$  and  $\frac{d}{r} = 1.2$ ; for this same radius and submergence Mehlum (1980) calculates a phase lag of 32.6 degrees. Note that this is nearly exact for wave 1, but, the phase lag tend to decay with wave-height. A bigger wave with  $H = 0.5$  would break. In all the above cases, in given time, the phase lag returns to zero as the tails of the first two waves suggest; a permanent phase lag is an asymptotic result

Fig. 5



A typical time history for the  $X$  and  $Y$  force components is shown in figure 5 for a wave of height  $H = 0.5$ ; the figure shows a remarkable periodicity from a few periods after the beginning of the experiment. For small waves the linear theory predicts that the  $X$  and  $Y$ , horizontal and vertical, force components have the same amplitudes, oscillate in quadrature with the wave period and there is a phase difference of  $\frac{1}{2}\pi$  between them. We observed these results to hold for smaller waves; however for the higher waves we find the

phase difference between the  $X$  and  $Y$  force components to become smaller, by as much as 10%, than  $\frac{\pi}{2}$ . The  $X$  and  $Y$  force components have been, both, decomposed in Fourier modes:

$$\frac{a_0}{2} + \sum (a_n \cos \theta_n t + b_n \sin \theta_n t)$$

where  $\theta_n = \frac{2n\pi}{T}$ ,  $T$  being the wave period; or similarly as

$$\frac{a_0}{2} + \sum r_n \cos[\theta_n t - \delta_n] \tag{5}$$

$$r_n = (a_n^2 + b_n^2)^{\frac{1}{2}} \tag{6}$$

where  $\delta_n$  is a phase shift. Results for fixed parameters 'R' and 'd' and a set of four waves with increasing wave height are displayed in table 2. We find for all waves a negative horizontal drift,  $\frac{a_0}{2}$ , which increases with the wave-height.

Despite the fact that the amplitudes of the  $X$  and  $Y$  force components are the same, irrespective of wave-height, the amplitudes of the Fourier modes of the same frequency increasingly differ for the higher waves. The vertical drift,  $\frac{a_0}{2}$ , increases with wave height reaching, for the last wave  $H = 0.7$ , an amplitude greater than any other Fourier mode, except the first.

As should be expected, the force harmonics for the smaller waves behave as in a perturbation expansion in the small parameter  $\epsilon = H$ , which is the dimensional wave height scaled by  $\frac{1}{k}$ ; representing either the vertical or horizontal force components as:

$$f_1 \epsilon + f_2 \epsilon^2 f_3 \epsilon^3 + \dots$$

where the first term in the expansion represents the first harmonic of the vertical or horizontal force component, the second term represents the second harmonic and so on. Observe in Table 2 that: the first harmonic for  $H = 0.3$  is roughly three times the first one for  $H = 0.1$ ; the second harmonic for  $H = 0.3$  is roughly nine times the second one for  $H = 0.1$ ; the steady components for  $H = 0.3$

are roughly nine times the steady components for  $H = 0.1$ . For the waves with  $H = 0.5$  and  $H = 0.7$  these relations hold approximately only for the first harmonic. This provides a measure of the range of validity of the linear and weakly nonlinear results and also a way to estimate the force components of waves from the force components of particular wave. This is not new but it is very interesting to know that it holds for the first harmonics of a wave with  $H = 0.7$  that is over 80% the height of the highest mathematically, not physically, possible wave.

**Table 2**

Wave/cylinder	Harmonic	X-component	Y-component
H=0.1	$a_0$	-0.000002	0.000289
T=6.2753	$r_1$	0.007285	0.007285
c=1.0012	$r_2$	0.000029	0.000029
D=0.5,d=1.	$r_3$	0.000001	0.000001
Kc=0.23	$r_4$	0.000000	0.000001
H=0.3	$a_0$	-0.000021	0.002489
T=6.2129	$r_1$	0.021710	0.021704
c=1.0113	$r_2$	0.000310	0.000313
D=0.5,d=1.	$r_3$	0.000003	0.000004
Kc=0.69	$r_4$	0.000003	0.000003
H=0.5	$a_0$	-0.000111	0.006417
T=6.0899	$r_1$	0.035615	0.035549
c=1.0317	$r_2$	0.001097	0.001102
D=0.5,d=1.	$r_3$	0.000035	0.000028
Kc=1.08	$r_4$	0.000005	0.000008
H=0.7	$a_0$	-0.000200	0.010207
T=5.9107	$r_1$	0.044369	0.044097
c=1.0630	$r_2$	0.002526	0.002534
D=0.5,d=1.	$r_3$	0.000192	0.000183
Kc=1.56	$r_4$	0.000037	0.000019

## Conclusions

A numerical scheme for the time domain simulation for the nonlinear steep wave diffraction by a submerged cylinder has been successfully implemented. Results have been checked, with very good agreement, with analytic, semi-analytic and experimental results given in the literature, namely Ogilvie (1963), Mehlum (1980), Vada (1987) and Chaplin (1984). In these comparisons an important point appears: many of the analytic and semi-analytic results presented in the literature are for waves that actually break; specially these for small cylinder depth where the diffraction effects are enhanced; by one side when waves break the flow ceases to be a potential flow and results should not be valid, but by another side Chaplin finds with experiments that, in his case E experiment, the mean vertical force agrees well with Ogilvie's results and the total force is smaller than that predicted by Ogilvie's results. This may suggest that approximate results frequently provide a good prediction of phenomena and sometimes give an upper bound for quantities.

Despite the limitations inherent to potential theory, and the computational costs in a time domain simulations, which preclude their use for a thorough description of the phenomenon, some important aspects of the problem can be studied and complemented with frequency domain and experimental investigation; since computational costs are comparatively very cheap for frequency domain calculations and potential modelling is not a problem with experiments.

With respect to the disturbances on the waves due to the presence of the cylinder we have two main aspects: the phase-lag on the transmitted wave and the transmission and reflection coefficients. With respect to the phase lag, we find that the linear potential given by Mehlum (1980) gives cheap and accurate results for smaller waves and for the higher ones these results provide an upper bound. With respect to reflection our results support the linear prediction of no reflection; regarding the transmitted wave we find that the presence of the cylinder greatly enhances the higher harmonics; but to this stage there is not yet a satisfactory description of the dependence of

this phenomenon on the parameters; neither have we yet attempted to quantify it with the help of transmission coefficients.

Regarding the forces on the cylinder due to waves an important result is that for the very steep waves the horizontal and vertical steady force components become evident and the vertical steady component come to be at the same order of magnitude as the first harmonic. Also important is the increase of the magnitude of the higher harmonics which is inherent to the very nonlinear character of steep waves; this increase in magnitude of the harmonics is followed by a loss of symmetry between the horizontal and vertical components.

### Acknowledgements

The authors acknowledge support from the Conselho Nacional de Desenvolvimento Científico e Tecnológico, CNPq, for this research.

### Bibliography

- AQUIJE, J. T. 1993 Non-linear diffraction of water waves by a submerged body, M.Sc. degree, Prog. Eng. Mech. COPPE/UFRJ
- CHAPLIN, J. R. 1984 Nonlinear forces on a horizontal cylinder beneath waves, *J. Fluid Mech.* **147**, 449 – 464.
- DEAN, W.R. 1948 On the reflection of surface waves by a submerged cylinder, *Camb. Phil. Soc.* **44**, 483 – 491.
- DOLD, J.W. & PEREGRINE, D.H. 1984 Steep unsteady water waves. An efficient computational scheme, *Proc. 19th ICCE*, Houston, Texas, **1**, 995 – 967.
- LIU, Y., DOMMERMUTH, D. G. & YUE, D. K.P. 1992 A high-order spectral method for nonlinear wave-body interactions, *J. Fluid Mech.* **245**, 115 – 136.
- MEHLUM, E. 1980 A circular cylinder in water waves, *App. Ocean Res.* **2**, 171 – 177.
- OGILVIE, T. F. 1963 Frirstand second order forces on a cylinder submerged under a free surface, *J. Fluid Mech.* **16**, 451 – 472.
- PALM, E. 1991 Non-linear wave reflection from a submerged circular cylinder *J. Fluid Mech.* **233**, 49 – 63.

PEREGRINE, D. H. 1989 private communication

SALTER, S. H., JEFFREY, D.C. & TAYLOR, J.R.M 1976 *The Naval architect*, Jan. 1976, pp.21 - 24.

TELES DA SILVA, A. F. & PEREGRINE, D. H. 1988 Steep, steady finite depth const. vort. water waves, *J. Fluid Mech.* **195**, 281 - 302.

VADA, T. 1987 A numerical solution of the second order wave-diffraction problem for a submerged cylinder of arbitrary shape, *J. Fluid Mech.* **174**, 23 - 37.

URSELL, F. 1950 Surface waves on deep water in the presence of a submerged circular cylinder, I, *Proc. Camb. Phil. Soc.* **46**, 141 - 152.

# Wave Stresses on Rubble-Mound Armour

Andrew Cornett\* and Etienne Mansard\*

## Abstract

In this study, physical experiments are used to investigate the relationship between fluid velocities on the surface of two rubble-mounds and the shear stresses  $\tau$  and normal stresses  $\sigma$  acting on the surface layer of rock armour. Results presented herein indicate that the peak magnitude of slope-parallel hydrodynamic forces on rubble-mound armour located below the still waterline can be reasonably well estimated using wave friction factors originally developed for rough turbulent oscillatory flow over impermeable horizontal beds. Stresses on rubble-mound armour are also compared to the prevailing surf similarity (Iribarren) parameter. The largest stresses are found to result from waves that form collapsing breakers.

## 1 Introduction

Fluid flows on a rubble-mound under wave attack are highly variable in space and time. The spatial and temporal distribution of kinematics depends in a complex manner on the character of the incident waves, the type of wave breaking, and properties of the structure such as slope, roughness and permeability. Not surprisingly, the normal and shear stresses induced by such kinematics are also temporally and spatially variable.

Kobayashi et. al. (1990a, 1990b, 1990c) describe and present results from a numerical model of wave interaction with rough permeable slopes that includes an analysis of the stability of armour stones. In this model, the hydrodynamic forces acting on armour stones in the surface layer are separated into drag, inertia and lift forces that are calculated in terms of the fluid velocity and acceleration parallel to, and above, the surface of the structure. In this formulation, the forces on armour stones are independent of the kinematics normal to the surface of the rubble-mound.

Tørum (1994) measured regular wave loads on a single irregularly shaped armour stone with a mass of 0.152 kg located 10.3 cm below the still waterline on the

---

\*National Research Council of Canada, Institute for Marine Dynamics, Building M32, Ottawa, Ontario, Canada K1A 0R6

surface of a reshaped berm breakwater. Measurements of fluid kinematics close to the stone were used to model the slope-parallel force component as a summation of drag and inertia forces calculated from slope-parallel kinematics. The slope-parallel force was found to be drag dominated, such that the force peaks occurred in phase with the peaks of slope-parallel velocity. The slope-normal force was modelled using a similar drag and inertia formulation, augmented by an additional term to represent lift force. In this case, drag and inertia forces were calculated from slope-normal kinematics, while the lift force was computed from the slope-parallel velocity. The peaks of the slope-normal force led those of the slope-parallel force, and were significantly smaller in magnitude. Tørum concludes that the slope-normal force is not dominated by lift, and could not be adequately modelled by the assumed augmented formulation of the Morison equation.

Shear stresses on an impermeable horizontal bed under oscillatory flow are commonly expressed in terms of a wave friction factor  $f_w$ , defined by

$$f_w = \frac{2\tau_{\max}}{\rho u_{\max}^2} \quad (1)$$

where  $\tau_{\max}$  is the maximum shear stress at the bed, and  $u_{\max}$  is the maximum orbital velocity just outside the boundary layer. Riedel et. al. (1972) and Kamphuis (1975) report results on  $f_w$  obtained with a shear plate in an oscillating water tunnel as functions of the maximum amplitude Reynolds number  $Re = u_{\max}a/\nu$  and the relative roughness  $a/k_s$  where  $\nu$  is the kinematic viscosity,  $a$  is the amplitude of water particle orbits just outside the boundary layer,  $k_s$  is the Nikuradse sand grain roughness, given by  $k_s \simeq 2D_{90} \simeq 2.5D_{n50}$ , where  $D_{n50}$  is the nominal diameter of particles on the bed. Different flow regimes were delineated, corresponding to laminar, smooth turbulent, and rough turbulent flow. For rough turbulent flow, the wave friction factor was found to be independent of  $Re$  and could be well represented by the simple expression

$$f_w = \frac{2}{5} \left( \frac{a}{k_s} \right)^{-3/4} \quad \text{for } \frac{a}{k_s} \leq 100. \quad (2)$$

## 2 Experiments

Experiments to measure the wave stresses on rubble-mound armour were performed in the 'Coastal Wave Basin' of the National Research Council of Canada at Ottawa. Figure 1 shows a sketch of the lay-out for these experiments. Three separate test channels, each 0.65 m wide, were constructed near the centre of a 14 m wide wave flume. The entrances to each channel were calibrated to ensure very similar wave conditions. Two dimensional sections of a rubble-mound breakwater were constructed in two of the three test channels. The third test channel was left open to record incident wave conditions using an array of capacitance wave probes. Stresses on the armour layer due to waves were measured in the central test channel using a pair of instrumented armour panels, described below



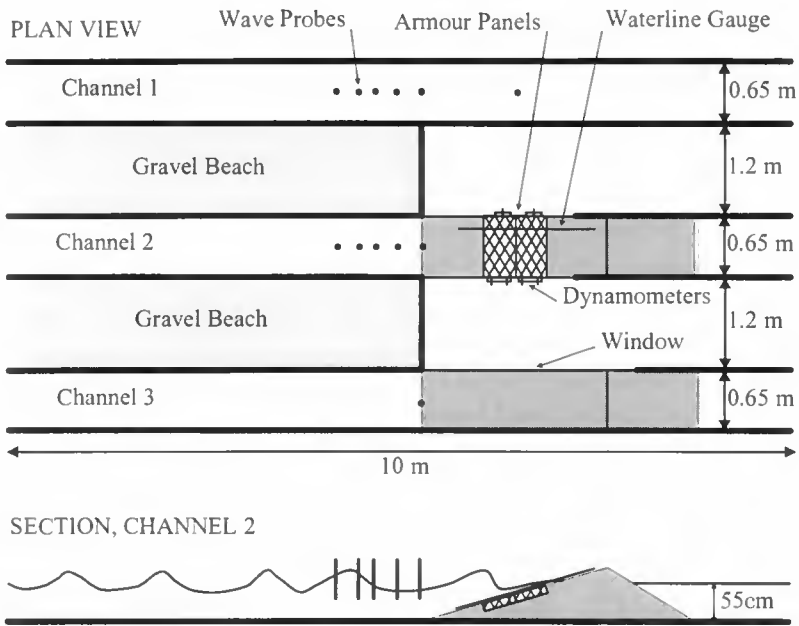


Figure 1: Sketch of the experiment lay-out.

in more detail. The third test channel was used to monitor damage to an identical rubble-mound constructed entirely from loose stones. The end of the wave flume was lined with a porous gravel beach that limited wave reflections to 5% or less. Similar absorbing beaches were installed between the three test channels. This set-up allowed simultaneous measurement of the incident waves, stresses on armour stones, and armour damage, relatively uncontaminated by spurious wave reflections.

Results for two different structures (test series 4 and 5) are reported here. Pertinent characteristics are summarized in Table 1. Cross-sections are sketched in Figures 2 and 3. The armour for both structures consists of finely graded, angular, granite rock with nominal diameter  $D_{n50} = (M_{50}/\rho_a)^{1/3} = 4.2 \text{ cm}$  placed in two layers. The series 4 rubble-mound features a sea-ward slope of  $\cot \alpha = 1.75$ , a permeable core with  $D_{n50} = 2.6 \text{ cm}$ ,  $D_{85}/D_{15} = 1.3$  and no filter layer. The series 5 structure features a milder slope of  $\cot \alpha = 3$ , a thin filter layer with  $D_{n50} = 1.9 \text{ cm}$ ,  $D_{85}/D_{15} = 1.3$  over an impermeable core.

## 2.1 Armour panels

Each instrumented armour panel consists of 50 individual, irregularly shaped, aluminum model rocks, bonded together by spot-welds into a rigid, porous, rect-

	Series 4	Series 5
water depth (cm)	55	55
slope, $\cot(\alpha)$	1.75	3
core	permeable	impermeable
filter thickness (cm)	-	4
filter $D_{n50}$ (cm)	-	1.9
filter $D_{85}/D_{15}$	-	1.3
armour thickness (cm)	8	8
armour $D_{n50}$ (cm)	4.2	4.2
armour $D_{85}/D_{15}$	1.1	1.1
panel 1, centroid elev. (cm)	43.5	41.5
panel 2, centroid elev. (cm)	31.5	33.5

Table 1: Characteristics of the series 4 and 5 rubble-mounds.

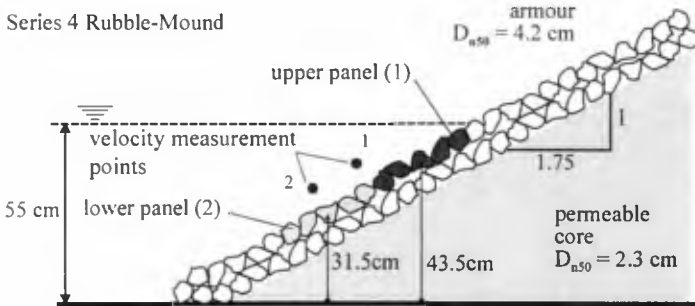


Figure 2: Cross-section sketch of the series 4 rubble-mound.

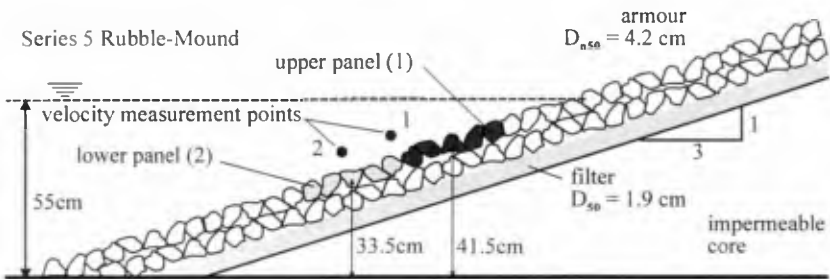


Figure 3: Cross-section sketch of the series 5 rubble-mound.

angular mat of armour stones in a single layer with approximate overall dimensions 64 cm by 23 cm by 5 cm. Each panel represents a 0.15 m<sup>2</sup> rectangular patch of armour stones. The panels were installed on the outer surface of the rubble-mound test sections, just below the still waterline, as sketched in Figures 2 and 3. The upper and lower panels are denoted as panels 1 and 2, respectively. The elevations of the panel centroids are included in Table 1. Each panel was connected at three points to a custom-built, five degree-of-freedom dynamometer located outside the walls of the test channel. Armour stones immediately surrounding the panels were glued in place so that the panels were isolated from adjacent materials by a thin ( $\sim 2$  mm) gap that followed their irregular shape. Away from the armour panels, wire mesh was placed over the surface of the rubble-mound to restrain the motion of loose armour stones. This set-up was adopted as a trade-off between the need to isolate the panels from the surrounding breakwater materials, and the desire to minimize distortions in the modelling of the rubble-mound.

The total fluid force  $\mathbf{F}_f$  acting on an armour panel can be written  $\mathbf{F}_f = \mathbf{F} + \mathbf{F}_b$  where  $\mathbf{F}$  is the hydrodynamic force and  $\mathbf{F}_b$  is the buoyancy force. For a panel that remains fully submerged, the buoyancy force is constant and equals the mass of fluid displaced by the panel and some dynamometer hardware. In this case, isolation of the hydrodynamic force is relatively straightforward. When the submergence of the panel varies with time, the magnitude of the time varying buoyancy force  $F_b(t)$  can be estimated from the instantaneous elevation of the waterline on the surface of the rubble-mound  $\eta_s(t)$  as

$$F_b(t) = |\mathbf{F}_b(t)| = \begin{cases} F_{b,\max} & \text{for } \eta_s(t) > \eta_{s,0} + l \sin \alpha, \\ F_{b,\max} \left( \frac{\eta_s(t) - \eta_{s,0}}{l \sin \alpha} \right) & \text{for } \eta_{s,0} \geq \eta_s(t) \geq \eta_{s,0} + l \sin \alpha, \\ 0 & \text{for } \eta_s(t) < \eta_{s,0}, \end{cases} \quad (3)$$

where  $F_{b,\max}$  is the buoyancy force when fully submerged,  $\eta_{s,0}$  is the largest value of  $\eta_s$  for which the panel remains entirely dry, and  $l \sin \alpha$  is the effective vertical distance between the lowest and highest parts of the panel. Appropriate values of  $l$  and  $\eta_{s,0}$  for each panel were determined by experiment.

Both panels were located entirely below the still waterline. The lower panel remained entirely submerged during all wave conditions, while the upper panel became partially submerged during attack by larger waves. When necessary, (3) was applied to estimate the time-varying buoyancy force in order to isolate of the hydrodynamic force acting on the upper panel.

## 2.2 Waves, waterline motion and kinematics

The rubble-mounds were exposed to a variety of regular and irregular waves; however, results in regular waves alone are reported here. Incident wave characteristics were computed by zero-crossing analysis of the water surface elevation  $\eta(t)$  recorded in the side channel at a location corresponding to the toe of the rubble-mounds. The regular waves ranged in height from 10 cm to 22 cm at peri-

ods of 1.5, 2.0 and 3.0 s. For each wave condition, reported values were averaged over 100 wave cycles.

The vertical motion of the waterline  $\eta_s(t)$  on the surface of the instrumented rubble-mound was recorded using a capacitance wire wave gauge inclined parallel to, and located approximately 1 cm above, the surface of the structure.

Fluid velocities were measured using a pair of bi-directional electromagnetic velocimeters located 4 cm above the upper surface of the instrumented armour panels at the positions shown in Figures 2 and 3. These locations are believed to be outside the boundary layer. Sleath (1992) gives the approximate displacement thickness  $\delta$  of an oscillatory boundary layer as  $\delta \simeq 0.5 f_w a$ . For rough turbulent flow, (2) may be re-arranged to give  $a = 0.295 k_s f_w^{-4/3}$ , whence the displacement thickness can be estimated by

$$\delta \simeq 0.147 k_s f_w^{-1/3} . \tag{4}$$

With  $k_s = 2.5 D_{n50} = 0.105 m$ , and  $f_w = 0.15$ , this equation gives  $\delta \approx 0.029 m$ , which suggests that the positions of velocity measurement are outside the boundary layer. Velocity components parallel and normal to the surface of the rubble-mound are denoted by  $u$  and  $w$ , respectively, where  $u$  is positive up-slope and  $w$  is positive away from the structure.

Water particle orbits are estimated by integration of the Eulerian velocity signal. In particular, the water particle displacement parallel to the face of the structure at time  $t_1$  is given by

$$s(t_1) = \int_0^{t_1} u(t) dt . \tag{5}$$

### 3 Shear and Normal Stresses

The armour panels provided a steady, repeatable measure of the fluid forces exerted on a patch of surface layer stones due to wave attack. The hydrodynamic component of the fluid force was isolated by compensating the measured force for the buoyancy of the armour panel. The hydrodynamic force was separated into orthogonal components  $F_P$  and  $F_N$ , acting parallel and perpendicular to the surface of the rubble-mound.  $F_P$  was defined positive up-slope, while  $F_N$  was defined positive away from the structure. These hydrodynamic force components can be expressed as a shear stress  $\tau$  and a normal stress  $\sigma$ , defined by

$$\tau(t) = \frac{F_P(t)}{A} , \quad \sigma(t) = \frac{F_N(t)}{A} \tag{6}$$

where  $A = 0.15 m^2$  is the surface area occupied by a panel. The surface area can be expressed in terms of the number of armour stones  $N_a$ , and the porosity of the armour  $n$ , as  $A = N_a D_{n50}^2 / (1 - n)$ . The average hydrodynamic force components acting on a single armour stone located within the patch are denoted by  $f_P$  and

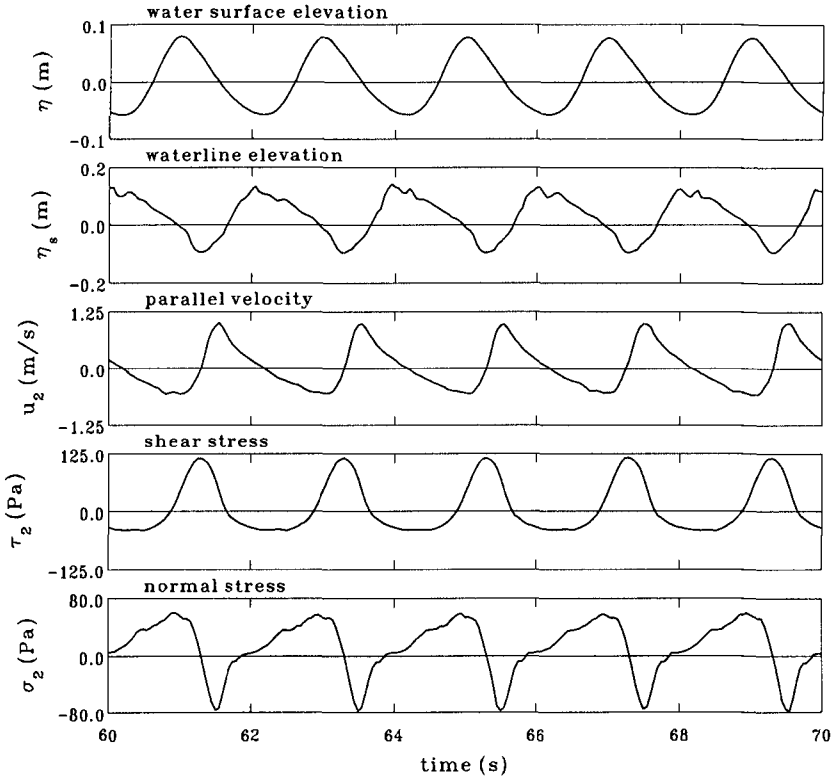


Figure 4:  $\eta(t)$ ,  $\eta_s(t)$ ,  $u_2(t)$ ,  $\tau_2(t)$ ,  $\sigma_2(t)$  on the series 5 rubble-mound ( $H = 14\text{ cm}$ ,  $T = 2\text{ s}$  and  $\xi = 2.2$ ).

$f_N$ , and can be estimated in terms of the shear and normal stresses as

$$f_P(t) = \frac{D^2}{1-n} \cdot \tau(t) \quad , \quad f_N(t) = \frac{D^2}{1-n} \cdot \sigma(t) \quad . \quad (7)$$

The shear and normal stresses defined by (6) include contributions from all hydrodynamic forcing mechanisms, including drag, inertia and lift forces.

Short segments of  $\eta(t)$ ,  $\eta_s(t)$ ,  $u_2(t)$ ,  $\tau_2(t)$  and  $\sigma_2(t)$  from a series 5 regular wave test with  $H = 14\text{ cm}$  and  $T = 2\text{ s}$  are presented in Figure 4. The velocity signal features an asymmetric 'saw-tooth' shape that indicates large positive (up-slope) accelerations immediately prior to the maximum up-slope velocity. Negative (down-slope) accelerations are less intense, but prevail for a longer duration during each flow cycle. The shear stress time series features sharp positive (up-slope) peaks in approximate phase with the large positive accelerations, which

suggests that accelerations are a dominant forcing mechanism. Negative shear stress peaks are significantly smaller and more broad, which parallels the character of the negative fluid accelerations. In these wave conditions, the maxima and minima of the normal stress coincide with the negative and positive velocity peaks, respectively. Significant seepage flows normal to the surface of the rubble-mound, associated with drainage of the permeable outer layers, were observed during the tests, even for structures with an impermeable core. These slope-normal flows are an important factor contributing to the normal stresses on the surface layer of armour.

Individual flow cycles on the rubble-mound were defined to start and finish at the times of maximum runup. During each flow cycle, the maximum and minimum values of velocity, fluid particle displacement, shear stress, and normal stress were obtained and then averaged over 100 regular waves to give representative quantities, which are denoted by the subscripts  $_{\min}$  and  $_{\max}$ ; i.e.  $u_{\min}$ ,  $u_{\max}$ , etc. Peak-to-peak values are denoted by subscript  $_{pp}$ , and are defined as the positive difference between the maximum and minimum value; i.e.  $u_{pp} = u_{\max} - u_{\min}$ .

For a given wave height incident to a given rubble-mound structure, the wave period influences the type of wave breaking that prevails. The effect of wave period on the type of wave breaking, and on the stability of rock armour, is commonly quantified in terms of the surf similarity (or Iribarren) parameter  $\xi = \tan \alpha \sqrt{gT^2 / (2\pi H)}$ . Battjes (1974) observed that the character of wave breaking on a slope depends on  $\xi$ , such that collapsing breakers prevail for  $\xi \sim 3$ , while plunging breakers prevail for  $\xi < 2$ , and surging breakers prevail for  $\xi > 4$ .

Van der Meer (1988) presented separate design formulae for the stability of rubble-mound armour under plunging and surging wave attack. His equations suggest that minimum stability occurs under collapsing breakers and that wave period has a strong influence on stability for plunging waves ( $\xi < 2$ ), but has much less influence on stability for surging waves ( $\xi > 4$ ). Van der Meer's equations also describe a dependence between armour stability and the permeability of a rubble-mound, such that stability is enhanced on more permeable structures.

Figure 5 shows peak-to-peak values of **shear** stress as a function of surf similarity for the upper and lower panels of the series 4 and 5 rubble-mounds. Here,  $\tau_{pp}$  has been made non-dimensional by the factor  $\rho g H$ , which represents the pressure under a static column of water with height  $H$ . Several observations can be made.

- Panel 1 (the upper panel) always experiences greater shear stresses. This result is consistent with the numerical simulations of Kobayashi et. al. (1990c) which suggest that armour damage is most likely to occur at an elevation approximately  $0.75H$  below the still waterline, and that the likelihood of damage decreases below and above this elevation.
- On both panels, the normalized peak-to-peak shear stress is maximized for  $\xi \sim 2.5$ . For a given wave height, the shear stress exerted on a patch of armour stones is greatest for waves with periods such that  $\xi \sim 2.5$ . These

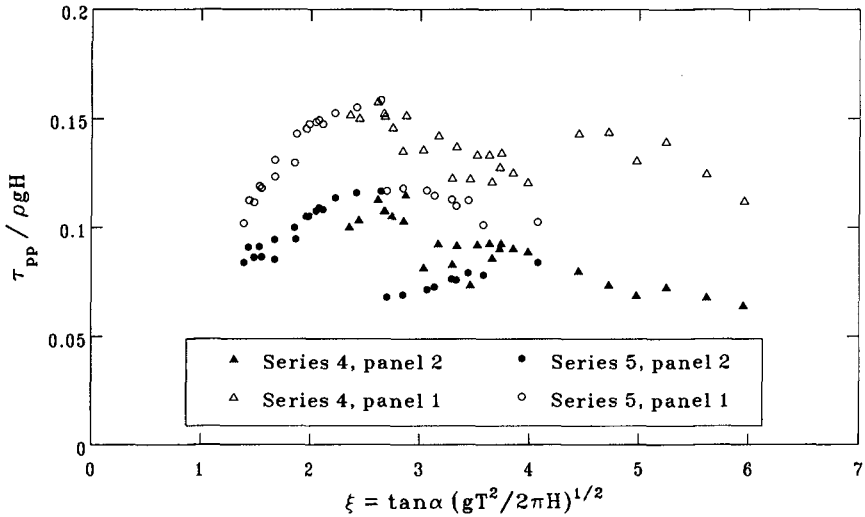


Figure 5: Non-dimensional peak-to-peak shear stress.

conditions are close to those associated with collapsing breakers. This result is consistent with idea that stability is minimized for collapsing breakers, and supports the form of stability design equation proposed by van der Meer (1988).

- Surf similarity has a strong effect on the normalized peak-to-peak shear stress in plunging waves ( $\xi < 2$ ), but has relatively little influence on the shear stress in surging waves ( $\xi > 4$ ). This result is also consistent with the design equations of van der Meer (1988), and suggests that plunging and surging breakers represent distinctly different processes.
- Tørum (1994) computes a shear stress of  $\tau = 216 \text{ Pa}$  for a specific regular wave with  $H = 0.2 \text{ m}$  and  $T = 1.8 \text{ s}$ . In non-dimensional terms, this is equivalent to  $\tau / \rho g H = 216 / (9810 \cdot 0.2) = 0.11$ , which is in general agreement with the shear stresses reported here.

A similar plot of non-dimensional maximum **normal** stress  $\sigma_{\max} / \rho g H$  on the lower and upper panels of the series 4 and 5 rubble-mounds is presented in Figure 6. Positive normal stresses act to lift armour stones out of the surface layer and thus are critical to the stability and initial motion of armour units. In general, the variation in maximum normal stress measured on these two structures in various wave periods are less well described by  $\xi$  alone. In spite of this, the following observations can be made.

- Normal stresses are greater on the upper panel. Again, this supports the result that armour stones just below the still waterline are more susceptible

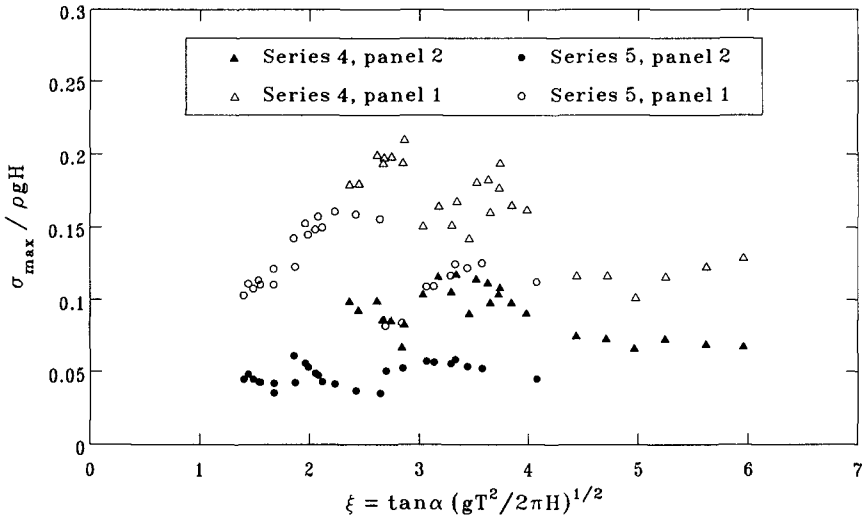


Figure 6: Non-dimensional maximum normal stress.

to damage than those lower down the rubble-mound. The normal stress maxima measured on the upper panel generally exceed the peak-to-peak shear stress in the same wave condition.

- For the same value of  $\xi$ , larger normal stresses are exerted on the armour of the steeper, more permeable series 4 rubble-mound.
- Surf similarity has a significant effect on the normal stress exerted on the upper panel, but has only a small influence on the normal stress acting on the lower panel.

## 4 Friction Factors for Rubble-Mound Armour

Flows on the surface of a rubble-mound under wave attack exhibit similarities and differences compared to wave driven flows on a horizontal seabed. While both flows are fundamentally oscillatory, flows on a rubble-mound tend to exhibit proportionately larger high-frequency content that produces ‘saw-tooth’ velocity fluctuations and larger accelerations. Flows on a rubble-mound also vary greatly with position. Near the toe, flows are similar to those on a horizontal seabed at similar depth, however, approaching the still waterline, velocities and accelerations are significantly amplified. Above the point of minimum rundown, the surface of the rubble-mound is only intermittently submerged. In this zone, the depth of flow can vary greatly throughout a wave cycle. When the water level outside the structure exceeds the level of the internal phreatic surface, water flows into the



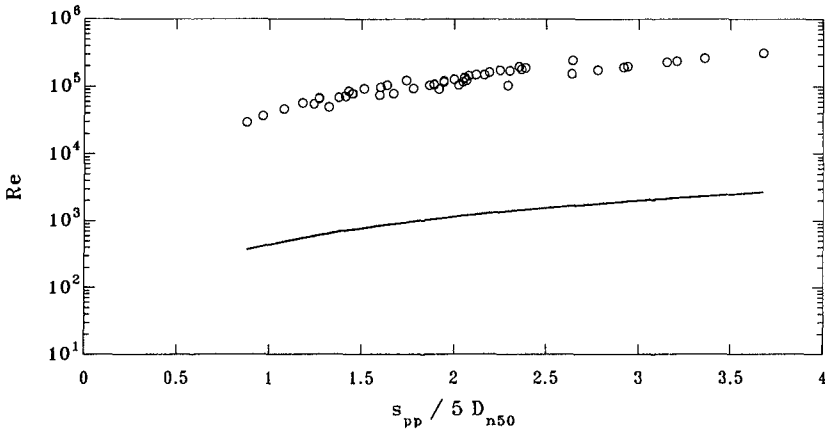


Figure 7: Orbital amplitude Reynolds number at velocimeter 2.

permeable outer layers. As the external water level recedes below the internal phreatic surface, water flows out of the permeable outer layers. Infiltration flow generally occurs above the mean water level during uprush while seepage flow is concentrated below the mean water level during downrush.

Kamphuis (1975) suggests the following criterion for the lower limit of rough turbulent flow:

$$Re = \frac{u_{max}a}{\nu} \geq 200 \frac{a}{k_s} \sqrt{\frac{f_w}{2}} \quad \text{for rough turbulent flow.} \quad (8)$$

Substituting (2) for  $f_w$  yields

$$Re \geq 447 \left( \frac{a}{k_s} \right)^{1.375} \quad \text{for } \frac{a}{k_s} \leq 100. \quad (9)$$

An equivalent orbital amplitude Reynolds number for the surface of a rubble-mound can be written

$$Re_{pp} = \frac{u_{pp} s_{pp}}{\nu} = \frac{u_{pp} s_{pp}}{4\nu}. \quad (10)$$

The relative roughness of the flow on a rubble-mound can be written

$$\frac{s_{pp}/2}{2.5D_{n50}} = \frac{s_{pp}}{5D_{n50}} \quad (11)$$

which is equivalent to the quantity  $a/k_s$ . Figure 7 shows values of  $Re_{pp}$  at velocimeter 2, in which the solid line indicates the threshold criterion for rough turbulent flow given by (9). The data span the range of  $s_{pp}/5D_{n50}$  (relative roughness) from 0.8 to 3.7 and indicate that rough turbulent flow prevails for all test conditions.

Measurements of the shear stress on panel 2 and the kinematics at position 2 have been used to construct friction factors for rubble-mound armour. Separate

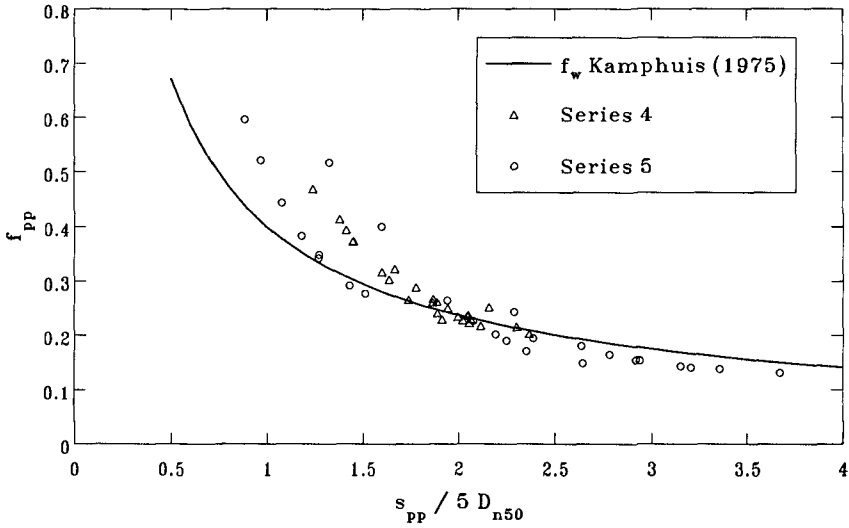


Figure 8: Friction factors on panel 2 for the series 4 and 5 rubble-mounds.

friction factors are computed for the uprush and downrush portions of the flow cycle according to

$$\begin{aligned}
 f_u &= \frac{2\tau_{ppmax}}{\rho u_{max}^2} && \text{for uprush} \\
 f_d &= \frac{-2\tau_{ppmin}}{\rho u_{min}^2} && \text{for downrush.}
 \end{aligned}
 \tag{12}$$

A friction factor for the complete flow cycle is defined in terms of the peak-to-peak velocity  $u_{pp}$  and peak-to-peak shear stress  $\tau_{pp}$  as

$$f_{pp} = \frac{2(\tau_{pp}/2)}{\rho (u_{pp}/2)^2} = \frac{4\tau_{pp}}{\rho u_{pp}^2} \quad \text{for the complete flow cycle.}
 \tag{13}$$

Friction factors for the complete flow cycle  $f_{pp}$  measured on panel 2 during regular wave attack of the series 4 and series 5 rubble-mounds are favorably compared in Figure 8 to estimates of  $f_w$  from (2). Data from the two different rubble-mounds show good agreement, however, there is evidence of a stronger variation with relative roughness than predicted by (2). Overall, these results suggest that the relation between friction factor and relative roughness on a rubble-mound under wave attack is similar to that for a rough, impermeable, horizontal bed under oscillatory flow. Moreover, these results suggest that wave friction factors might be used to estimate the shear stresses acting on rubble-mound armour exposed to wave attack.

Friction factors for the uprush and downrush portions of the flow cycle are presented in Figures 9 and 10. Most of the data for the uprush friction factor suggest that  $f_u < f_w$ , while most of the data for the downrush friction factor

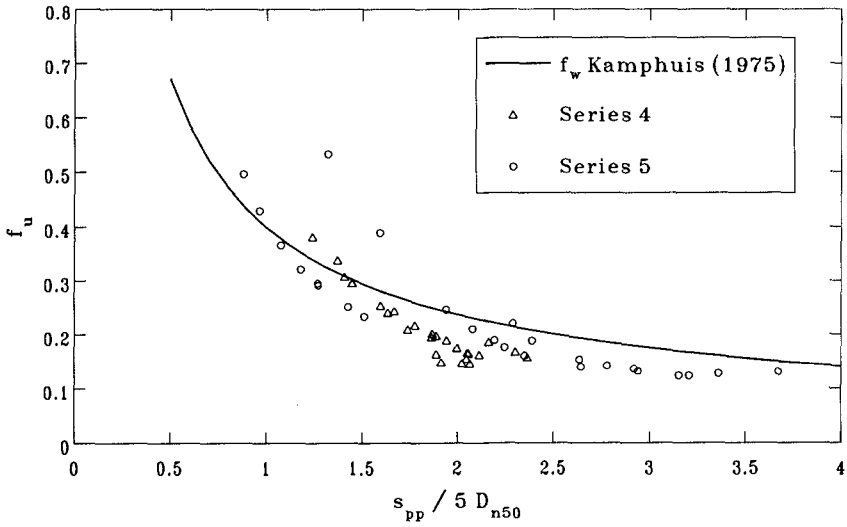


Figure 9: Uprush friction factors on panel 2 for the series 4 and 5 rubble-mounds.

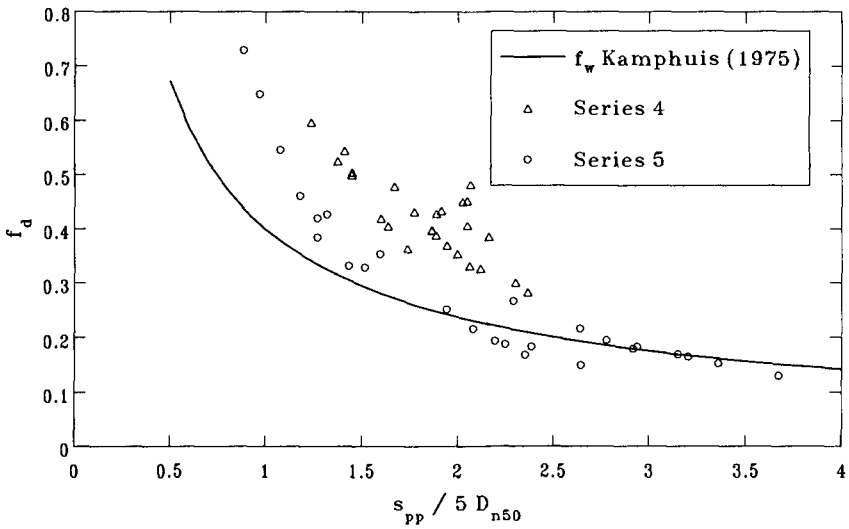


Figure 10: Downrush friction factors on panel 2 for the series 4 and 5 rubble-mounds.

suggest that  $f_d > f_w$ . In other words, the peak shear stress acting down-slope is generally larger than that predicted by (2), while the peak shear stress acting up-slope is generally smaller. The trend is particularly evident for the steeper, more permeable, series 4 rubble-mound. This behavior is not entirely surprising, considering the distorted, asymmetric, quasi-oscillatory flow cycles that prevail on the surface of a rubble-mound (see Figure 4), in contrast to the more symmetric flow cycles that prevail over horizontal beds under waves.

Kobayashi et. al. (1990a, 1990b, 1990c) assumed a constant friction factor of  $f_w = 0.3$  in numerical simulations of regular and irregular waves on conventional rubble-mounds. Tørum and van Gent (1992) used a constant wave friction factor  $f_w = 0.15$  in their numerical simulations of regular wave interaction with a permeable berm breakwater, while Tørum (1994) used  $f_w = 0.3$ . These values are in general agreement with the results reported here. However, the present results confirm that the friction factor for rubble-mound armour is a variable quantity that, for rough turbulent flow, depends on the relative roughness in a manner that is similar to that for oscillatory flow over a rough, impermeable, horizontal bed, and can be reasonably well predicted by (2).

## 5 Conclusions

Measurements of the shear and normal stresses acting on rubble-mound armour under regular wave attack have been presented. The stresses were measured on a pair of rigid porous armour panels, each supported by a five degree-of-freedom force dynamometer, and installed to minimize distortions to internal flows within the test structures. Results from two different structures have been considered.

- Greater shear and normal stresses were measured just below the still waterline than lower down the rubble-mound.
- Shear and normal stresses are maximized in waves for which  $\xi \sim 2.5$ , suggesting that collapsing breakers exert greater forces on armour stones and are therefore most critical to their stability.
- The influence of wave period on shear stress is strong for plunging waves ( $\xi < 2$ ), and relatively weak for surging waves ( $\xi > 4$ ).
- The shear stresses reported here are in general agreement with the force measurements on a single armour stone reported by Tørum (1994).
- In some cases, normal stresses were measured that exceed the shear stresses.
- Greater normal stresses were recorded on the steeper, more permeable, series 4 rubble-mound.
- Friction factors for rubble-mound armour under regular wave attack are in general agreement with the wave friction factors  $f_w$  for rough turbulent flow computed from (2).

- Friction factors for uprush are generally less than  $f_w$ , while friction factors for downrush are generally greater. This behavior is related to the asymmetric, quasi-oscillatory nature of surface flows on a rubble-mound.

## 6 Acknowledgment

The authors gratefully acknowledge the contributions to this work made by Mr. E. Funke, the staff at M32 and the support of the National Research Council.

## References

- [1] Battjes, J.A. 1974. Surf Similarity. *Proc. 14th Int. Conf. Coastal Eng.* Copenhagen, Denmark. Chapter 26.
- [2] Kamphuis, J.W. 1975. Friction Factor under Oscillatory Waves. *J. Waterways, Harbors and Coastal Eng.* ASCE, Vol. 101 (WW2), pp. 135-144.
- [3] Kobayashi, N., Wurjanto, A. and Cox, D. 1990a. Irregular Waves on Rough Permeable Slopes. *J. Coastal Research*. Special Issue No. 7, pp. 167-184.
- [4] Kobayashi, N., Wurjanto, A. and Cox, D. 1990b. Numerical Model for Waves on Rough Permeable Slopes. *J. Coastal Research*. Special Issue No. 7, pp. 149-166.
- [5] Kobayashi, N., Wurjanto, A. and Cox, D. 1990c. Rock Slopes Under Irregular Wave Attack. *Proc. 22nd Int. Conf. Coastal Eng.* pp. 1306-1319.
- [6] Nielsen, P. 1992. *Coastal Bottom Boundary Layers and Sediment Transport*. World Scientific, London.
- [7] Riedel, H.P., Kamphuis, J.W. and Brebner, A. 1972. Measurement of Bed Shear Stress under Waves. *Proc. 13th Int. Conf. Coastal Eng.* Vancouver, Canada. pp. 587-603.
- [8] Sleath, J.F.A. 1984. *Sea Bed Mechanics*. John Wiley & Sons, Toronto.
- [9] Tørum, A. and van Gent, M. 1992. Water Particle Velocities on a Berm Breakwater. *Proc. 23rd Int. Conf. Coastal Eng.* pp. 1651-1665.
- [10] Tørum, A. 1994. Wave-Induced Forces on Armour Unit on Berm Breakwaters. *J. Waterway, Port, Coastal and Ocean Eng.* ASCE, Vol. 120, No. 3, pp. 251-268.
- [11] Van der Meer, J.W. 1988. Rock Slopes and Gravel Beaches under Wave Attack. Doctoral Thesis, Delft Univ. of Tech. Delft, The Netherlands.

## CHAPTER 73

### DAMAGE ANALYSIS FOR RUBBLE-MOUND BREAKWATERS

Michael H. Davies  
Etienne P.D. Mansard, and  
Andrew M. Cornett<sup>1</sup>

#### Abstract

Storm damage to rubble-mound structures can range from the piece-wise removal of individual armour stones to the large-scale sliding of the entire armour layer. This paper presents an overview of qualitative and quantitative descriptions of various types of armour layer damage due to wave action. This work is based on a series of large-scale physical models of revetment stability. The discussion includes methods for measuring the change in profile and the use of the normalized area eroded,  $S$ . A new parameter,  $d_c$  is introduced as a measure of the minimum depth of cover remaining on the structure. An analysis method is presented which predicts the armour layer's factor of safety against sliding.

#### Introduction

Coastal structures are often designed to survive severe storms with no significant damage while undergoing tolerable damage during more extreme events. For such designs it is essential that the damage be both predictable and repairable - the failure mode should be ductile not brittle. Physical hydraulic models are a key tool in the design of structures where damage levels need to be determined. In addition to accurately reproducing the wave loading on the structure and the physical characteristics of the structure it is important to be able to accurately measure and quantify the damage which occurs.

#### Damage analysis

The two common measures for rubble-mound damage due to wave action are visual assessment and profiling. Visual assessment includes the monitoring of the development of holes in the armour, observation of the exposure of under-layers and counting the number of armour units displaced. Profile analysis includes measurement of the eroded profile and calculation of the eroded cross-sectional area,  $A$ .

---

<sup>1</sup> Coastal Engg. M-32, Institute for Marine Dynamics, National Research Council Canada, Montreal Rd, Ottawa, Ontario, K1A 0R6.

At low damage levels the breakwater damage can be readily estimated by visually counting the number of rocks displaced. This becomes difficult however, when more than, say, 50 stones are displaced or when stones which have been moved slightly by one storm condition are subsequently moved further downslope by a subsequent storm sequence. Image processing allows visual techniques to be used at higher damage levels. The size of the damaged area can be measured using photogrammetry and digital image processing. Also, the movement of individual stones can be tracked using image processing software. The limitations on these techniques are that it is often necessary to drain the basin prior to image-capture to allow measurement below the still water line and that image quality can restrict accuracy. Furthermore, most techniques allow an estimation of only the damaged surface area, not the depth of penetration of the damage. This can sometimes be overcome by colour coding the various layers of revetment.

For damage quantification based on stone count, the 1984 Shore Protection Manual (CERC, 1984) defines damage as the percentage of stones removed from within the active zone. The active zone is defined as extending from the middle of the breakwater crest down to one zero-damage wave height below the still water level.

$$\text{Damage (\%)} = \frac{\text{Number of stones removed}}{\text{Number of stones within active zone}} \times 100 \quad (1)$$

This has the limitation that it depends on visual stone counts (which can be unreliable at higher damage levels) and that the number of stones within the active zone is very dependent upon structure geometry.

Several mechanical and electro-mechanical profiling methods exist for the determination of breakwater profile. All have their limitations. The more sophisticated profilers which operate on the principles of electrical resistivity or light or acoustic beams to locate the profile generally require the flume to be either fully drained or fully flooded so that measurements are made in either the dry or in the wet - measurement through the air-water interface is difficult. The need to flood or drain the basin between each test sequence can be very time consuming. Measurement methods which use mechanical contact with the rocks to locate the profile can readily cross the air-water interface but often provide lower resolution and sparser data.

Measurement of the cross-sectional profile is often the fastest and most reliable means of damage assessment and is used in most hydraulics laboratories. Hughes (1993) reviews some of the visual and profiling methods available for damage analysis. Van der Meer (1988) reports on the use of a mechanical profiler for measuring damage to rubble-mound breakwaters. Latham et al. (1988) report on the use of high resolution mechanical profiling methods for breakwater damage analysis. Medina et al. (1994) reports on the use of mechanical profiles for damage analysis.

If profiles of the damaged cross-section are obtained, the damage can be represented by the mean cross-sectional area removed from the profile,  $A$ . In this analysis the eroded quantity,  $A$  is determined by integration of the difference between the damaged and initial profiles. The most widely accepted method for interpreting the damage data from profiling is the damage index,  $S$  as adopted by van der Meer. The damage index,

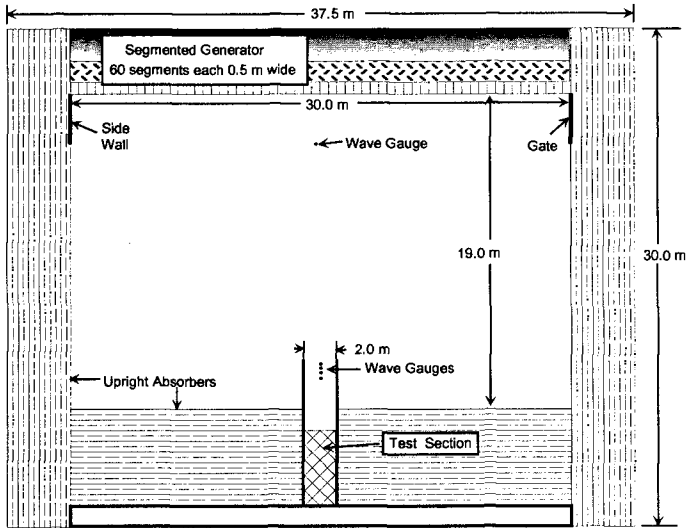


Figure 1 Test configuration for NRC revetment stability study.

S is defined as:

$$S = \frac{A}{D_{n50}^2} \quad \text{where } D_{n50} = \sqrt[3]{\frac{M_{50}}{\rho_s}} \quad (2)$$

S corresponds to the number of cubic stones of size  $D_{n50}$  removed from the average profile line.  $M_{50}$  is the median of the cumulative stone mass distribution and  $\rho_s$  is the density of stone (typically  $2,650 \text{ kg/m}^3$ ).

For comparison between counted stone damage and profile analysis a visual estimate of the damage,  $S_{\text{visual}}$  can be derived as follows:

$$S_{\text{visual}} = \frac{\# \text{ stones removed}}{(\text{Structure width}/D_{n50})(1-n)} \quad (3)$$

Here n is the placement density determined by profiling the armour and underlayers and from knowing the total mass of rock placed.

**NRC Experiments on breakwater damage**

NRC has recently completed a series of large-scale 2-D experiments on revetment stability for the Société d'énergie de la Baie James. This study examined the existing revetment along with proposed repair schemes for some of the earth dams and dykes of the La Grande hydroelectric complex near James Bay in northern Québec. Some details of this model study are reviewed in Mansard et al (1994). This test series was performed in the NRC Multi-directional Wave Basin at scales ranging from 1:10 to 1:15



depending on the structure being tested. Figure 1 shows the experimental setup used for these tests. The wave climates used in the tests were calibrated prior to installation of the structures in the test section to allow determination of the time-domain characteristics of the incident wave climate in the absence of reflections from the structure. The results from some of the testing performed in this study will be used in this paper to illustrate various damage analysis methods.

The NRC breakwater profiler (shown schematically in Figure 2) uses a carriage-mounted mechanical pivoting arm to track the breakwater profile. The arm is connected to a rotational potentiometer which measures the angle of declination,  $\theta$ . The horizontal location of the carriage, R is measured using a potentiometer connected to the cable system which drives the carriage. The contact point between the rotating arm and the armour layer is a wheel of diameter roughly equal to the mean stone size,  $D_{50}$ . Thus each profile is averaged mechanically so that gaps in the armour layer smaller than  $D_{50}$  are ignored. Output from the two potentiometers is sampled at 20Hz using the NRC Gedap data acquisition and analysis system. In processing, the data files,  $R(t)$  and  $\theta(t)$  are reduced to a single file containing  $z(x)$  using the relationships:

$$x=R-L\cos(\theta) \text{ and } z=(\text{Elevation of beam}) - L \sin(\theta) \text{ where } L \text{ is the profile rod length.} \tag{4}$$

Typically nine evenly-spaced profile lines are measured. Analysis can be performed on individual profile lines to obtain details on the spatial distribution of damage or the measured profile lines can first be averaged then integrated. The cross-sectional area of material eroded from the armour layer is determined by integration using Simpson's method,  $A_1(x)$ :

$$A_1(x) = \int_{x_0}^x [z_1(x) - z_0(x)] dx \tag{5}$$

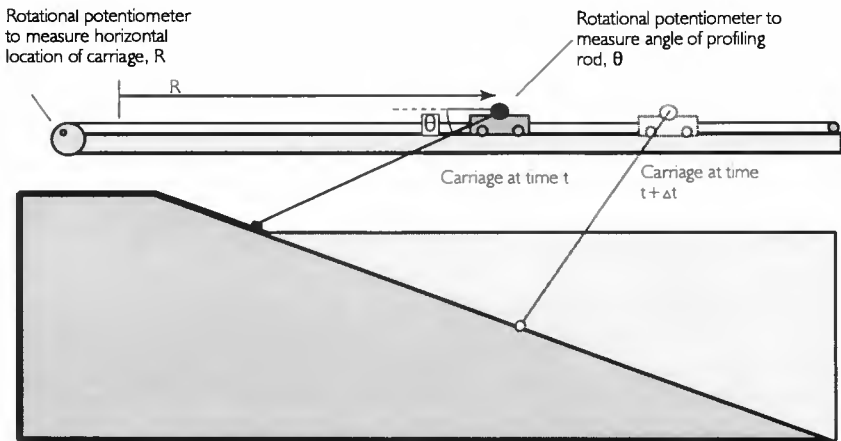


Figure 2 NRC electro-mechanical profiler.

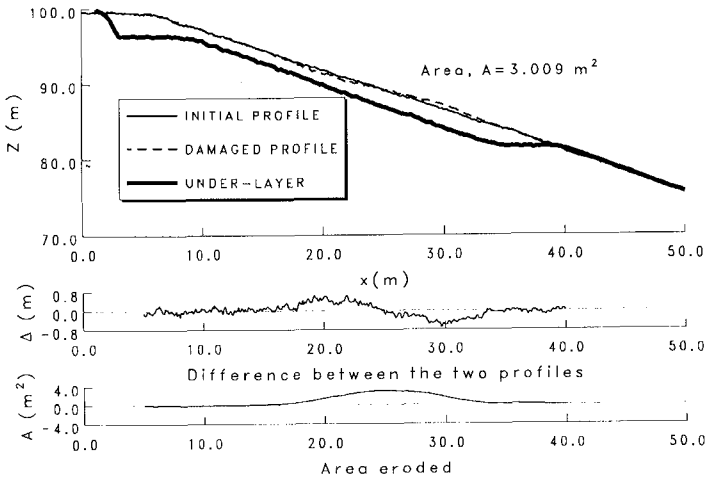


Figure 3 Typical average profile analysis.

where  $A_i(x)$  is the indefinite area integral and  $z_i$  and  $z_o$  are the damaged and original (undamaged) profile lines, respectively,  $x_o$  is the lower limit of integration (typically the top of the slope).  $S$  is determined as the maximum value of  $A_i(x)$  normalized by the square of the nominal diameter.

$$S_i = \frac{\max[A_i(x)]}{D_{n50}^2} \tag{6}$$

Figure 3 shows the results of average profile analysis - the upper plot shows the original and damaged profiles ( $z_o(x)$  and  $z_i(x)$ ), the middle plot shows the vertical difference between the two profiles,  $\Delta(x)$  and the bottom plot shows the indefinite integral,  $A_i(x)$ .

When sparse data is collected (e.g. foot method) curve fitting is often used to define a function describing the eroded area,  $A(x)$  (e.g. Medina et al, 1994 using a sinusoidal smoothing function). Previously integration had been performed only on the measured erosion by first removing the negative portion of the  $\Delta(x)$  curve in an attempt to increase the accuracy of the determination of  $S$  (e.g. Vidal et al, 1992). This method then requires accurate delineation of the range of integration since random noise in the  $\Delta(x)$  signal produces a positive bias in the integration. Recent refinements to NRC's profiling and data analysis methods have made such pre-processing of the data unnecessary.

While  $S$  analysis does give a reasonable measure of the average cross-sectional area of material eroded from the profile, it does not necessarily give sufficient information regarding the severity of damage. As illustrated in Figure 4 a value of  $S=3$  could represent a deep hole in the armour layer near the water line, or equally it could

represent shallow damage spread over a wider area. The significance of  $S$  depends strongly on stone size and armour layer thickness. When the damage index,  $S$  is applied to berm-type revetments the absolute value of  $S$  loses its physical significance although the stabilization of damage (attainment of an equilibrium profile) is characterized by a constant value of  $S$ .

#### Analysis of Conventional Armour Layers

Van der Meer suggests using a value of  $S=2$  for the initiation of damage (zero-damage condition of Shore Protection Manual - 0 to 5% damage). Medina et al. suggest that lower values of  $S$  perhaps better describes the initiation of damage. Based on a series of 40 experiments on revetment stability performed at the National Research Council, it has been seen that  $S=2$  provides a good estimate of the start of damage. Lower damage levels have been seen to exhibit greater experimental variability.

Figure 5 illustrates a repeatability test, two realizations of the exact same test, this figure shows that agreement between the two experiments improves as  $S$  increases above 2. Figure 6 shows a comparison between the values of  $S$  obtained from profile analysis and the estimates of  $S$  based on visual stone counts. The good agreement obtained between these two methods illustrates the accuracy of the profiling method. Once the stone count gets above 60 to 80 stones the reliability of the visual method drops - it becomes difficult to visually monitor the movement of so many stones.

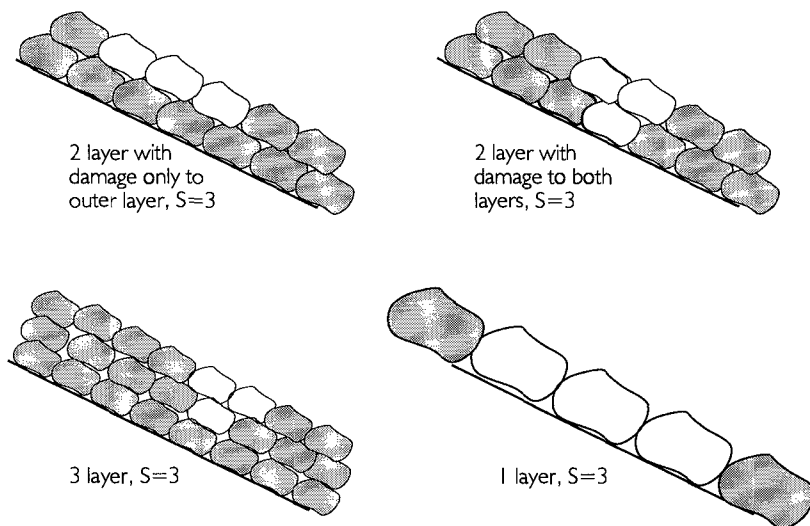


**Figure 4** Various possible damage configurations with same  $S$ .

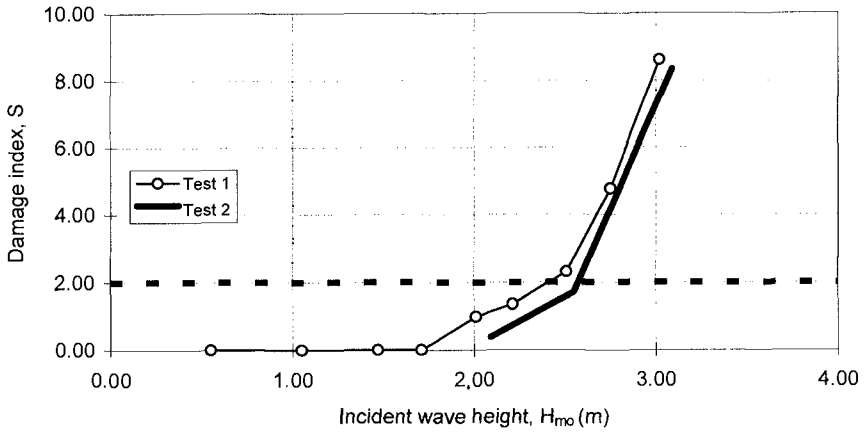


Figure 5 Repeatability test for typical revetment.

For berm breakwaters, the absolute value of  $S$  loses its direct relevance to damage (since many stones can move in the process of re-shaping to a stable profile). However, the shape of the damage evolution curves ( $S$  vs time,  $t$  or  $S$  vs number of waves,  $N$ ) does serve as a useful indication of performance. A stable berm should tend

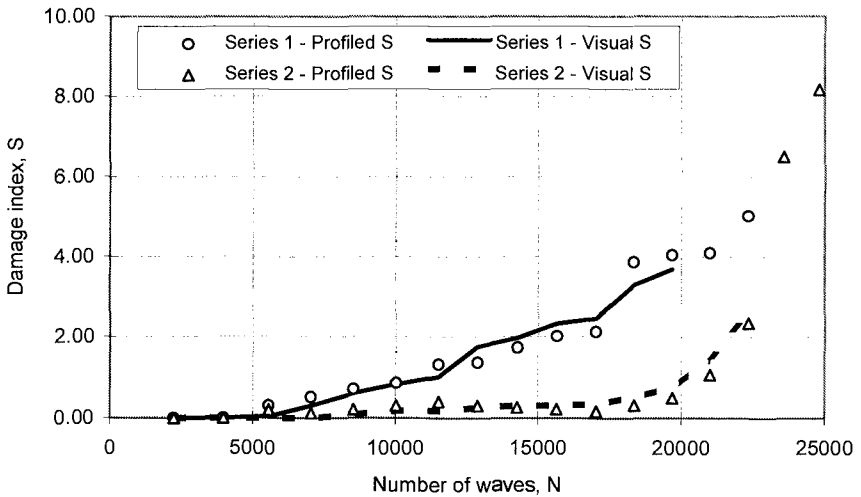
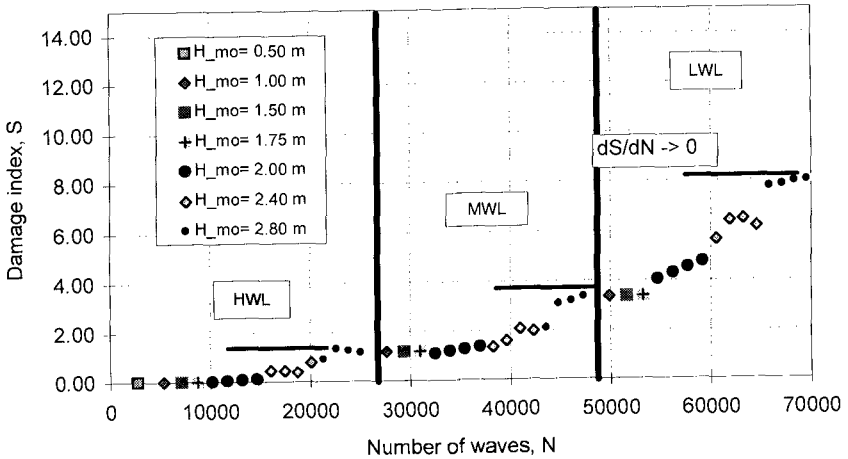


Figure 6 Comparison between  $S$  and  $S_{visual}$  for two typical revetment tests.



**Figure 7** S vs N for a berm tested and found stable ( $dS/dN=0$ ) at three water levels.

towards  $dS/dN=0$  under design conditions. This pattern is illustrated in Figure 7 where, during waves of  $H_{m0}=3.0$  m, the berm stabilizes and  $dS/dN$  approaches zero.

**Depth of cover**

The purpose of the outer revetment on a breakwater is to prevent the wave action from attacking the finer underlayers. Since failure of a breakwater is primarily caused by removal of the armour layer resulting in exposure and subsequent rapid removal of the finer underlayers it is reasonable to quantify the damage in terms of the existence of holes in the armour layer. For such analysis the quantity of material removed is inconsequential, it is the protection remaining which matters. This can be quantified as the depth of cover remaining on the structure,  $d_c$ . By measurement of the profile of the underlayer during construction and taking the difference between measured profiles of the revetment during testing and the reference underlayer profile one can calculate the thickness of the revetment, and the minimum thickness of the revetment,  $d_c$ . For most analyses the average minimum depth of cover is used. For example, in a series of two-dimensional flume experiments, nine profiles were taken over the 2 m width of the test section, the average profile was then subtracted from the average underlayer profile and the minimum cover thickness,  $d_c$  was computed. The resulting measured average minimum depth of cover can be compared to  $D_{n50}$ , such that when  $d_c$  drops below  $D_{n50}$  it can be inferred that there is some exposure of underlayer across the width of the test section. Should  $d_c$  drop to zero, the damage is severe enough that significant damage to the underlayer is likely to have occurred. Figure 8 shows typical depth of cover analysis for a revetment scheme. The left hand plot shows the profile (initial, damaged and under-layer), the armour layer thickness for both the initial and damaged conditions is shown in the right hand plot. The cover thickness is calculated as the slope-normal distance between the armour layer profile and the under-layer. The depth of cover,  $d_c$  is taken as the minimum of the cover thickness over the range of interest. As shown

in the plot,  $d_c$  for the initial conditions occurs at a different location than  $d_c$  for the damaged conditions.

When applied to berm-style revetments, the performance criteria is typically that the depth of cover,  $d_c$  should not drop below a certain level under design storm conditions. Figure 9 shows a  $d_c$  vs  $N$  plot for a berm-style structure (again tested at three water levels).

### Sliding failure

Other than the conventional unravelling of coastal structures due to the removal of individual stones by wave action, revetment failure can also occur by the large-scale sliding of the entire protection layer. This geotechnical failure mode has been discussed by other researchers but without an analytical framework within which to analyze such failures, the literature on this subject remains mostly anecdotal. In several of the revetment stability tests performed at NRC large-scale sliding of the armour layer was observed. Often this occurred with minimal prior damage to the structure. Several such failures were observed for steep sloped (1.6:1 and 1.7:1) structures. None were observed for structures with milder slopes (1.8:1 and 2.2:1). Figure 10 shows the measured profile of a revetment after sliding occurred near the mean water level (MWL). The profile of the slope after a sliding failure looks similar to other wave-eroded profiles - the key difference being the rapid rate of damage. This damage occurred during a single wave group (5 or 6 individual waves) and involved the downslope movement of the armour layer 'en masse'. Profile analysis is of little use in interpreting sliding - the main tools are visual observation and geotechnical analysis of the slope's factor of safety against sliding.

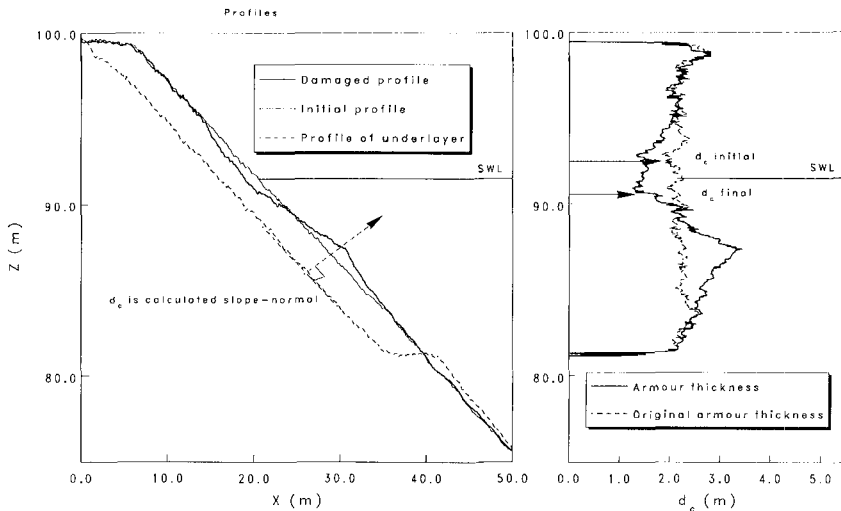
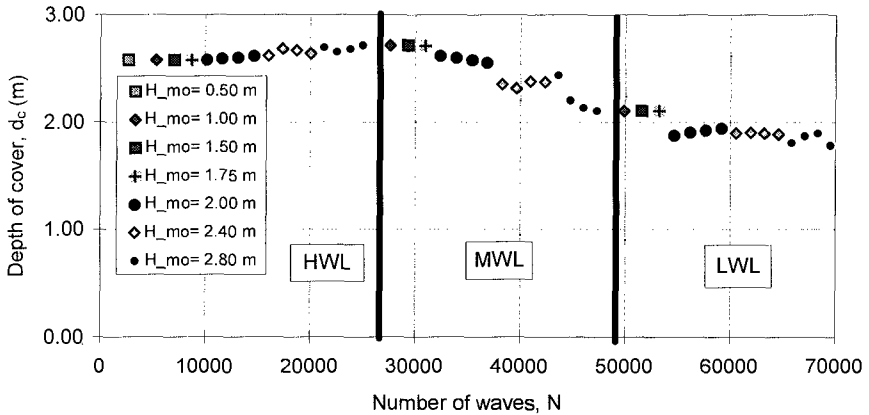


Figure 8 Typical depth of cover analysis.



**Figure 9** Depth of cover,  $d_c$  vs  $N$  for a berm.

A separate series of NRC experiments measuring the force exerted on breakwater revetments by wave action provides us with a reliable tool for estimating the wave loading on the revetment (Cornett and Mansard, 1994). These wave forces are then integrated into a limiting equilibrium translational sliding model. This uses conventional geotechnical stability analysis in conjunction with estimates of wave-induced lift and drag forces to evaluate the factor of safety of the slope against large-scale sliding failure. Comparisons between the sliding model results and breakwater testing have verified the ability of this method to predict the likelihood of sliding (Davies et al., 1994). This failure mode is most predominant for very steep breakwater slopes - 1:1.6 up to 1:1.3. Much of the literature on sliding of armour layers is related to the sliding which can occur once wave attack has created a hole in the armour layer, thereby providing an unsupported protection layer above the hole. This analysis is valid for such problems but is of more interest in the case of steep slopes where large-scale sliding is shown to occur without prior removal of the armour layer.

### Block model for sliding

Under the action of gravity alone, a slope of cohesionless soil will fail through translatory sliding. Under wave action, application of the driving force is limited to the zone around the still water line. In this case, the failure will be a block translational slide.

For the static problem, the planar translational slide predominates, and the factor of safety,  $FS$  (in the absence of external loadings) is simply the ratio of the tangent of the mobilised angle of shear resistance at failure,  $\phi'$  to the tangent of the slope angle,  $\theta$ .

$$FS = \frac{\tan \phi'}{\tan \theta} \tag{7}$$

The factor of safety is reduced when additional forces are exerted by wave action. The downslope shearing force due to wave action,  $F_{shear}$  can be estimated using the wave friction factor of Kamphuis (1975). The applicability of this type of analysis for the steep and very rough slopes of rubble-mound breakwaters has recently been verified at NRC by Cornett. In a series of hydraulic model tests, the wave forces exerted on breakwater armour have been measured and compared to the friction factor,  $f_w$  calculated using wave orbital velocity measurements just above the measuring section (see Cornett's figure 8 these proceedings, 1995). It is assumed that the wave-induced shear stress is applied uniformly over the region from the still water level down to  $H$  (measured vertically). This corresponds approximately to the range over which force measurements were made by Cornett.

Applying solitary wave theory to the breakwater slope, we can estimate the peak orbital velocity,  $u_b$  and the corresponding orbital amplitude,  $a_b$  as follows:

$$u_b = 0.61 \sqrt{gd_b} \quad \text{and} \quad a_b = \frac{u_b T}{2\pi} \tag{8}$$

here  $u_b$  is determined at an elevation equal to 1/2 the breaking depth of the wave (i.e. at  $z=d_b/2$ , where  $d_b=1.28 H$ ).

Applying the friction factor relationship of Kamphuis:

$$f_w = 0.4 \left( \frac{k_s}{a_b} \right)^{0.75} \quad \text{where} \quad k_s = 2D_{90} \tag{9}$$

This allows estimation of the shear stress acting on the surface,  $\tau$ :

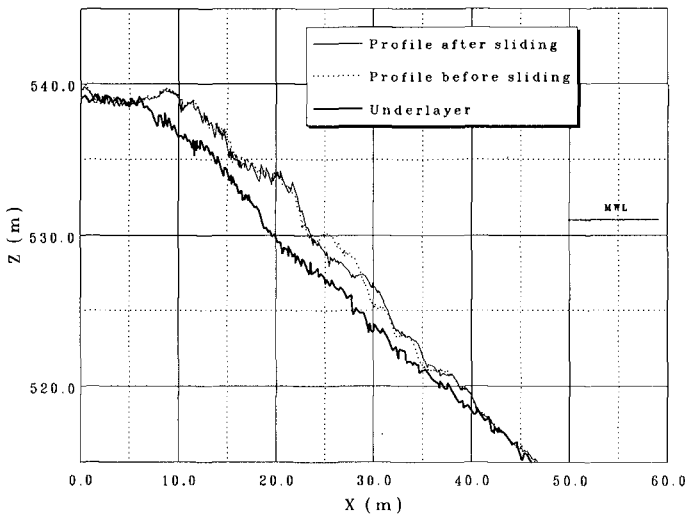
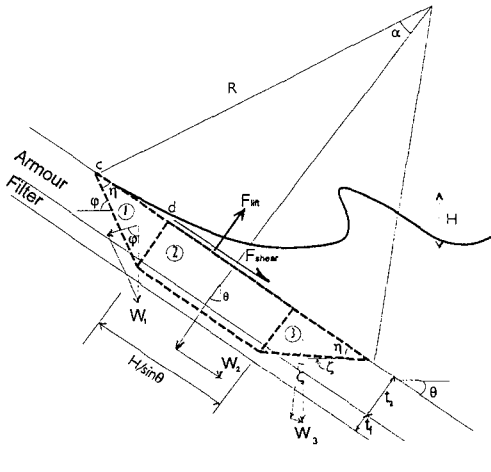


Figure 10 Profile after sliding near MWL.





$$R = \left[ \left( \frac{H/\sin\theta}{2} \right)^2 + \left( \frac{t_f}{2} \right)^2 \right] / t_f$$

$$\alpha = \cos^{-1} \left[ \frac{R - t_f/2 - t_a}{R} \right]$$

$$\eta = \tan^{-1} \left[ \frac{t_a + t_f/2}{R \sin\alpha - \frac{H/\sin\theta}{2}} \right]$$

$$\varphi = \theta + \eta$$

$$\zeta = \theta - \eta$$

$$cd = R \sin\alpha - \frac{H/\sin\theta}{2}$$

Figure 11 Block model for sliding failure.

$$\tau = \frac{f_w \rho u_b^2}{2} \tag{10}$$

Assuming that this shear stress acts over a vertical range of H, the total shear force (per unit width of structure),  $F_{shear}$  becomes:

$$F_{shear} = \tau \frac{H}{\sin\theta} \tag{11}$$

The measurements by Cornett integrate the effects of internal fluid velocities within the filter and armour layers, internal pore pressures and lift forces on the armour layer due to velocity gradients through the measurement of the lift force on the armour panel, measured perpendicular to the slope. Generally, these measurements indicate that  $F_{int} \approx F_{shear}$ . From observations of the tests at NRC, we have observed that sliding failures occurring near the still water level have a failure plane passing through the filter layer over a distance approximately equal to the wave height, H. In the present analysis, we divide the failure zone into three blocks as shown in Figure 11. As described in Davies et al. a failure zone is assumed which passes through the filter zone over an along-slope distance of  $H/\sin\theta$  and passes through the armour zone at angle  $\eta$ . This geometry is defined by assuming the failure zone follows a 'slip-circle' which passes through the filter zone over an along-slope distance of  $H/\sin\theta$ .

Using this assumed failure model, we can analyze the resisting and driving forces along the three failure planes (at the bases of blocks 1, 2 and 3).

Forces acting on Block 1:

$$\begin{aligned}
 \text{Weight: } W_1 &= 1/2 \text{ base} \times \text{height} \times \gamma' \\
 &= \gamma'/2 \ cd \ (t_a + t_f/2) \\
 \text{Driving force along failure plane: } F_{D1} &= W_1 \sin \phi \\
 \text{Resisting force: } F_{R1} &= W_1 \cos \phi_1 \tan \phi'
 \end{aligned} \tag{12}$$

Forces acting on Block 2:

$$\begin{aligned}
 \text{Weight: } W_2 &= \frac{H \sin \theta}{2} (t_a + t_f/2) \ \gamma' \\
 \text{Driving force along failure plane: } F_{D2} &= W_2 \sin \theta + F_{\text{shear}} \\
 \text{where } F_{\text{shear}} &= \tau_{\text{waves}} \frac{H \sin \theta}{2} \\
 \text{Resisting force: } F_{R2} &= (W_2 \cos \theta - F_{\text{lift}}) \tan \phi'
 \end{aligned} \tag{13}$$

Forces acting on Block 3:

$$\begin{aligned}
 \text{Weight: } W_3 &= \gamma'/2 \ c d \ (t_a + t_f/2) \\
 \text{Driving force along failure plane: } F_{D3} &= W_3 \sin \zeta \\
 \text{Resisting force: } F_{R3} &= W_3 \cos \zeta \tan \phi'
 \end{aligned} \tag{14}$$

The overall stability of the failure zone is calculated as the ratio of the sum of all resisting forces to the sum of all driving forces:

$$\begin{aligned}
 \text{Factor of safety, FS} &= \frac{\sum F_{\text{Resisting}}}{\sum F_{\text{Driving}}} \\
 \text{FS} &= \frac{F_{R1} + F_{R2} + F_{R3}}{F_{D1} + F_{D2} + F_{D3}}
 \end{aligned} \tag{15}$$

Using the above translational block sliding analysis, we can estimate the factor of safety of the revetment against failure.

Calculations have been made of the factor of safety against sliding for a slope of 1:1.7, an armour thickness of  $t_a=1.3\text{m}$ , a filter layer thickness of  $t_f=0.6\text{m}$  and a placement density of  $\gamma=1850\text{kg/m}^3$ . In this analysis, the shear strength of the rockfill is taken to be  $\phi'=42.8$ . This is based on the average of a series of tilting tests, where a cross-section of the dyke core, filter and armour layers were prepared in a rigid box, the box was then slowly lifted and the angle at which the slope failed was measured. This value corresponds well with reported natural angles of repose from field observations.

The translational block sliding analysis has been used to estimate the factor of safety against sliding for a given wave height for various layer geometries. In this analysis we have used  $H_{1/100}$  (roughly equal to  $1.8H_s$ ) as being representative of the larger waves in

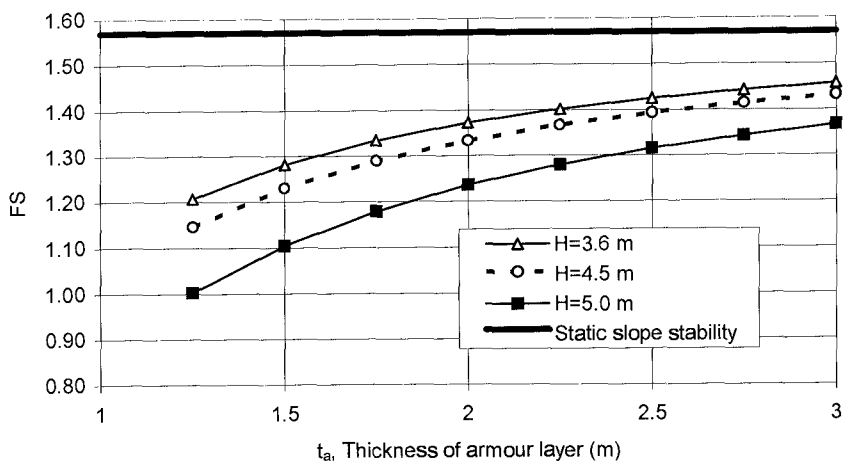


**Figure 12** Effect of armour layer thickness on factor of safety against sliding.

the time series. Figure 12 shows how the factor of safety varies with slope geometry. This analysis suggests that layer thickness has a strong influence on sliding stability (assuming that the preferred failure plane is through the filter layer).

This analysis suggests that single layer revetment is particularly prone to sliding failures and that the thickness of the armour layer is a significant factor in the sliding process. Thicker armour layers have a greater resistance to sliding failures which pass through the filter layer. Preliminary application of this translational block sliding analysis to observed sliding failures agrees well with observations, indicating that layer thickness and slope are the key factors affecting sliding potential. Detailed analysis of individual failures requires a less simplified model of the block sliding process. Recent work by Altae (1994) shows that a non-linear, stress and consolidation finite element model can be applied to this revetment stability problem. This work further supports the existence of a potential sliding failure zone in the filter layer just below the still water level. Work on these analysis methods is continuing.

## Conclusions

For profile analysis, reliable and efficient techniques have been developed using electro-mechanical profiling resulting in excellent agreement between  $S$  measured by profiling and  $S_{\text{visual}}$  measured from stone counting. There are inherent limitations in  $S$  as an analysis tool for breakwater damage due to the variability in the significance of  $S$  with structure type. Depth of cover,  $d_c$  has been shown to be a useful quantification of the damage related directly to the main failure criterion - the exposure of under-layers. This type of analysis is valid regardless of structure type.

Sliding has been seen to be a second failure mechanism for steep sloped structures. Visual observation, coupled with evaluation of the slope's factor of safety against sliding

in the presence of wave action is the best tool for damage analysis when sliding occurs. Block sliding analysis illustrates the importance of layer thickness in providing resistance to sliding. The translational block sliding model provides an analytic framework for interpreting the sliding potential of armour layers.

### Acknowledgements

The authors would like to thank Herman Claes, David Watson and Rod Girard without whose assistance and attention to detail this work would not have been possible. The input and advice of many of the staff of the Hydraulics and Geology and Soil Mechanics Departments of SEBJ are also gratefully acknowledged.

### References

- Altae, A. (1994). Feasibility study for numerical analysis of revetment stability under wave loading. Internal report by Anna Geodynamics Inc. to NRC (Ref. 93-1466/6297).
- Cornett, A.M. and Mansard, E.P.D. (1994) Wave stresses on rubble-mound armour. Proc. 24th Int. Coastal Engg. Conf. ASCE, New York, NY.
- Davies, M.H., Mansard, E.P.D. and Parkinson, F.E. (1994) Études sur modèles de la stabilité des ouvrages TA13 et KA3. NRC Controlled Technical Report IECE-CEP-CTR-001. Report prepared for Société d'énergie de la Baie James (in french).
- Hughes, S.A. (1993) Physical models and laboratory techniques in coastal engineering. Advanced Series on Ocean Engg. - Vol. 7. World Scientific Publishing, Singapore, 568 pp.
- Kamphuis, J.W. (1975) Friction factor under oscillatory waves. J. Waterways, Harbours and Coastal Engg. ASCE Vol. 101 (WW2). pp. 135-144.
- Latham, J.P., Poole, A.B., and Mannion, M.B. (1988) Developments in the analysis of armour layer profile data. Design of Breakwaters - Proc. of the Conference Breakwaters '88, ICE, Thomas Telford Ltd., London, UK, pp. 343-361.
- Medina, J.R., Hudspeth, R.T., and Fassardi, C. (1994) Breakwater armour damage due to wave groups. J. of Waterway, Port, Coastal and Ocean Engg., Vol. 120, No. 2, March/April 1994. pp. 179-198.
- Coastal Engineering Research Centre (1984) Shore Protection Manual. Coastal Engineering Research Center, U.S. Army Waterways Experiment Station, U.S. Govt. Printing Office, Washington, DC, 1984.
- van der Meer, J. (1988). Rock slopes and gravel beaches under wave attack. Ph.D. thesis, Delft Technical University, April. 152 pp.
- Vidal, C., Losada, M.A., Medina, R., Mansard, E.P.D. and Gomez-Pina, G. (1992). A universal analysis for the stability of both low-crested and submerged breakwaters. Proc. 23rd Int. Coastal Engg. Conf. ASCE, New York, NY.

## CHAPTER 74

### NUMERICALLY MODELING PERSONNEL DANGER ON A PROMENADE BREAKWATER DUE TO OVERTOPPING WAVES

Kimihiko Endoh<sup>1</sup> and Shigeo Takahashi<sup>2</sup>

#### ABSTRACT

Prototype experiments were carried out to quantify when personnel on top of a promenade breakwater will lose their balance due to overtopping waves. The danger of being carried out into the sea was also investigated using model experiments. Based on our results, we developed an empirical formula for calculating the wave height at which personnel danger occurs.

#### 1. INTRODUCTION

Public access to breakwater areas is usually prohibited in Japan due to safety reasons, yet many people nevertheless enter these areas to enjoy the comfortable sea environment. The Japanese Ministry of Transport (MOT) has recently developed a new type of breakwater, named the "Promenade Breakwater," which serves a dual purpose of protecting a harbor from storm waves while also providing the public with amenity areas. **Figure 1** shows a photograph of a promenade breakwater constructed in Wakayama Port.

Because Japanese breakwaters are typically the low-crown type, wave overtopping sometimes occurs, and therefore, it is essential for the design of a promenade breakwater to consider maintaining personnel safety. Based on this important concern, the Port and Harbour Research Institute (PHRI) initiated research to investigate the types of danger a person may be subjected to while on a top of a breakwater.<sup>1)2)</sup>

---

1 Port and Harbor Engineering Section, Civil Engineering Research Institute, Hokkaido Development Agency, 1-3 Hiragishi, Sapporo 062, Japan

Tel:+81-11-841-1111(283) Fax:+81-11-842-9169

2 Chief of Maritime Structures Lab., Hydraulic Div., Port and Harbour Research Institute, Ministry of Transport, 3-1-1 Nagase, Yokosuka 239, Japan

Tel:+81-468-44-5011 Fax:+81-468-42-7846



**Figure 1** Promenade breakwater constructed in Wakayama port

## 2. PERSONNEL DANGER WHILE ON A BREAKWATER

Personnel danger on a breakwater is closely related to the wave conditions around it. **Figure 2** shows four successive stages of danger that a person can be subjected to while on a breakwater. Here, we classify personnel danger into the following four stages:

- 1st stage: A splash occurs over the breakwater.
- 2nd stage: An overtopping wave occurs.
- 3rd stage: A person is knocked over by the overtopping wave.
- Final stage: A person is carried into the sea by overtopping flow.

When a wave splashes over a breakwater (1st stage), a person may feel scared although no substantial danger exists. The danger, however, is substantial at the 2nd stage, with the 3rd and final stages being extremely dangerous since a serious accident may inevitably happen.

Using experimental results, empirical models were developed to quantify the four stages of personnel danger. **Figure 3** shows a basic flow chart of how the models were employed in the calculations. Wave conditions in the 1st and 2nd stages can be calculated by the overtopping wave model (OWM), which is explained in detail in **Ref. 3**. The "loss of balance model" and "carry model" were developed to quantify the 3rd and final stages, respectively. The present study discusses the danger of each stage, being focused on the 3rd and final stages, and quantitatively describes these conditions using the wave height and wave crest height included in the models.

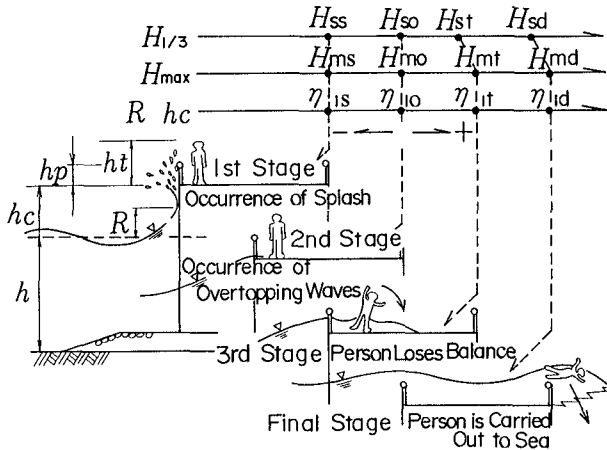


Figure 2 Four successive stages of personnel danger while on a breakwater

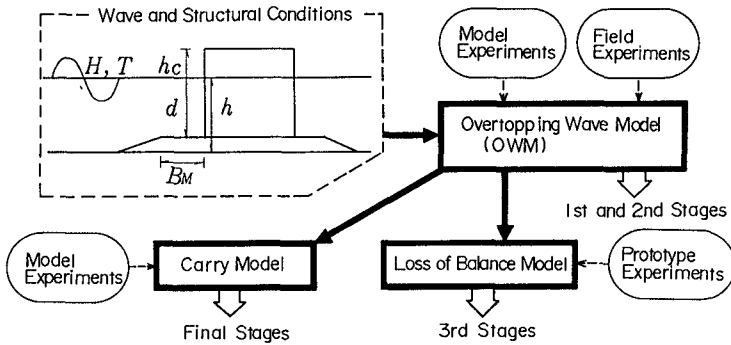


Figure 3 Numerical models of personnel danger while on a breakwater

### 3. PERSONNEL LOSS OF BALANCE IN OVERTOPPING FLOW

#### 3.1 Prototype Experiments

A series of prototype experiments were conducted in a large current basin (50-m-long, 20-m-wide) to investigate the stability of a person under various flow conditions, i.e., we measured the current force on a person and observed personnel loss of balance.

Component load cells were used to measure the forces acting on three human bodies subjected to steady flow. **Table 1** summarizes the physique of each person (sample A-C). The angle of the person's body against the current,  $\theta$ , was varied (0, 45 and

Table 1 Physiques of personnel participating in the experiment

	Sample A	Sample B	Sample C
Height (cm)	183	164	174
Weight (kg)	73	65	64
Deviation from standard weight (%)	-2.3	12.8	-3.9
Length of inside leg (cm)	88	73	80
Waist (cm)	78	80	76

90°), as was the width between feet,  $L_f$  (0, 25 and 50 cm). Three different types of clothes were used.

Loss of the balance under various flows was observed with a high-speed video camera (200 frames/s). Two pairs of shoes with different type soles were used, having a coefficient of friction  $\mu_s$  of 0.71 and 0.37.  $L_f$  was 25 cm and  $\theta$  was 0, 90, and 180°.

**Figure 4** shows the current force acting on a person's body in steady flow, where the x-axis indicates the current velocity and the y-axis indicates the force of current acting on the body. This force is proportional to the flow velocity squared, and can be expressed as a drag force:

$$F = \frac{w_0}{2g} C_D \cdot A \cdot U^2 \quad (1)$$

The coefficient of the drag force,  $C_D$ , is dependent on several parameters, i.e.,  $\theta$ ,  $L_f$ , and water depth, and can be expressed as

$$C_D = 1.1(1 - L_f/ht) \quad : \theta = 0^\circ$$

$$1.1(1 + L_f/ht) \quad : \theta = 45^\circ, 90^\circ, \quad (2)$$

where  $A$  is the projected area of the body against overtopping flow,  $U$  the current velocity during wave overtopping,  $w_0$  the specific weight of sea water, and  $g$  the gravitational acceleration. Note that when  $L_f \neq 0$ ,  $C_D = 1.1$ .

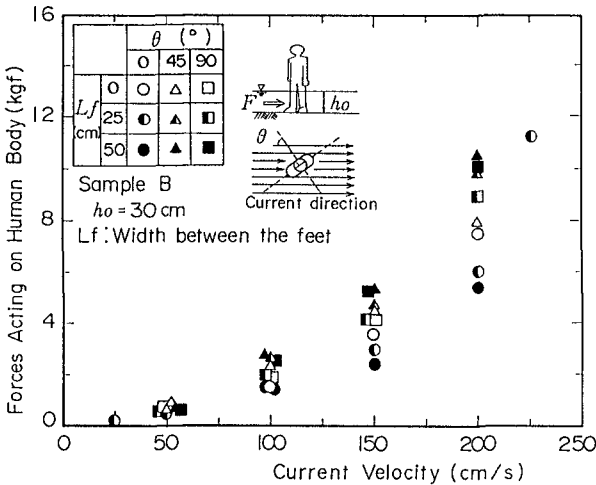


**Figure 4** Current forces acting on a person's body

### 3.2 Loss of Balance Model

**Figure 5** represents the loss of balance model which considers the two main types: "tumbling" and "slipping". In the tumbling type, a person is knocked over by the overtopping flow in the downstream direction. This type occurs when the moment produced by the current forces around the feet is greater than the moment produced by the person's weight, being expressed by



$$F \cdot h_G \geq W_0 \cdot l_G, \tag{3}$$

where  $h_G$  is the vertical distance from the floor to the point where the resultant force acts,  $W_0$  is the weight of a human body in overtopping flow, and  $l_G$  is the horizontal distance between the center of the gravity and the fulcrum of the moment.

In the slipping type, a person is knocked over in the upstream direction, which occurs when the current force is greater than the friction force between the shoes and ground. This type of loss of balance is represented using

$$F \geq \mu_s \cdot W_0, \tag{4}$$

where  $\mu_s$  is the coefficient of friction between the shoes and the ground.

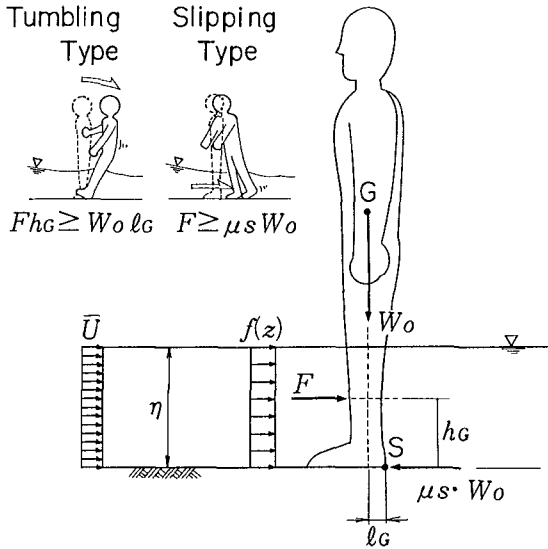


Figure 5 Effect of overtopping flow on the static balance of a person

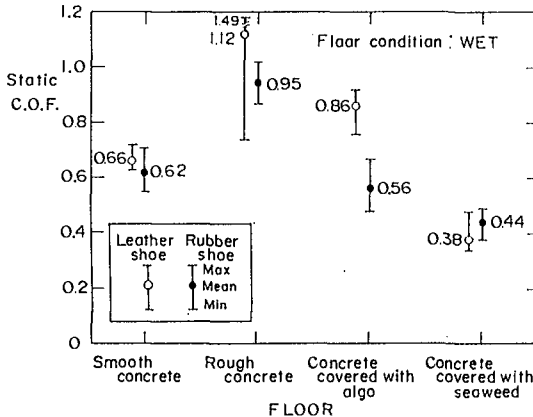
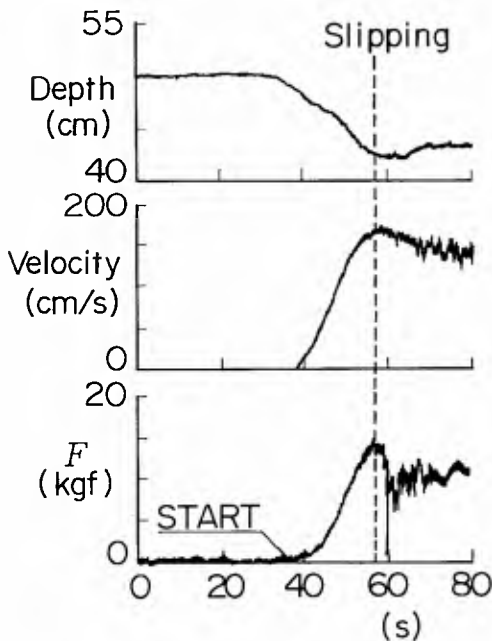


Figure 6 Coefficient of friction between shoe and wet concrete

**Figure 6** shows measured field values of  $\mu_s$  between the shoes (leather and rubber soles) and various types of wet concrete (smooth concrete, rough concrete, concrete covered with alga, and concrete covered with seaweed), where  $\mu_s$  for the rough concrete is larger than that for smooth concrete. If the floor is covered with alga or seaweed,  $\mu_s$  naturally decreases. In the loss of balance model, we used a  $\mu_s$  value of 0.4 for covered concrete and 0.6 otherwise.

### 3.3 Loss of Balance Observation

**Figure 7** shows analogue data of water depth, current velocity, and force acting on the human body, where the current velocity increases after the current generator starts. When the current velocity is 165 cm/s and the force acting on the human body is 14 kgf, a person is knocked over (slipping type loss of balance) as shown in **Fig. 8** (the flow direction is from left to right and the person faces upstream).  $\mu_s$  between the shoes and ground was about 0.3.



**Figure 7** Measured analogue data during loss of balance experiment



**Figure 8** Loss of balance by slipping

**Figure 9** shows experimental results of a person's stability under various flow conditions. The x-axis is the water depth where the person is standing, while the y-axis is the current velocity there. The solid line indicates the calculated stable limit as determined by the slipping type loss of balance model. The good agreement between the calculated and experimental results is clearly apparent.

**Figure 10** shows the critical water depth on a caisson at the seaward edge,  $\eta_{1t}$ , when a person is knocked over.  $\eta_{1t}$  is calculated by the loss of balance model in which we assumed that  $\mu_s = 0.4$ , the person is standing at the most dangerous location facing the seaward side ( $\theta = 0^\circ$ ), and the person's legs are spread to 22% of their height. Note that  $\eta_{1t}$  tends to increase as the person's height increases or as the body shape becomes more slender. If a person is 152 cm in height and has a standard body shape,  $\eta_{1t} = 50$  cm. In this condition, the tumbling type loss of balance occurs at the seaward edge of a caisson where the maximum current velocity is 0.9 m/s.

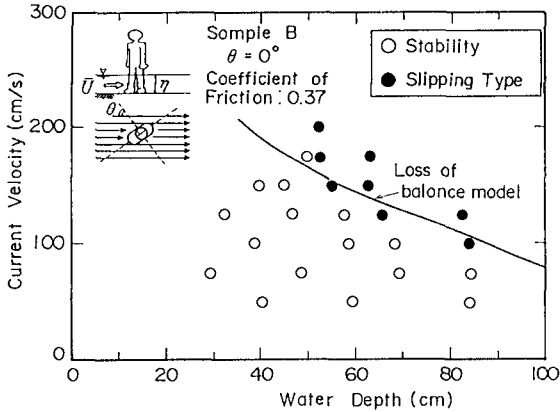


**Figure 9** Verification of the loss of balance model

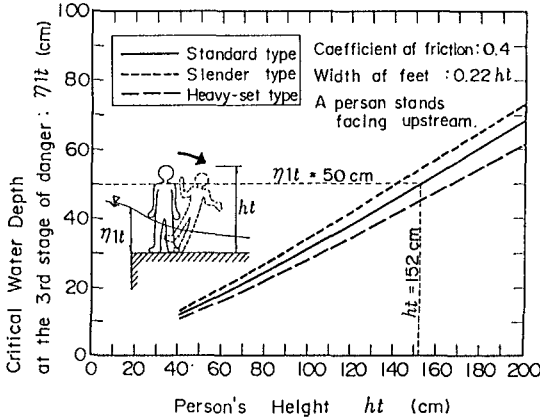


**Figure 10** The relation between a person's height and wave crest elevation when loss of balance occurs

4. CARRIED INTO THE SEA BY OVERTOPPING WAVES

4.1 Outline of Model Experiments

A series of model experiments were conducted in a wave channel to investigate the danger of a person being carried into the sea by overtopping waves. Experiments involve measuring overtopping flow with handrails present and observation of human body movement.

We measured the motion of overtopping waves using a wave gauge, current meter, and high-speed video camera. Handrails were installed at the seaward and landward edge of a caisson.

Figure 11 shows model handrails having four opening ratios  $\epsilon = 0, 0.24, 0.44, \text{ or } 0.61$ .

The motion of a human body model in overtopping flow was also observed by a high-speed video camera under various wave conditions with different shaped handrails. The human body model has a cylindrical shape with a diameter of 2 cm and height of 7.6 cm. At a model scale of 1/20, the corresponding height is 152 cm. It is made from wood whose specific gravity is 0.8.

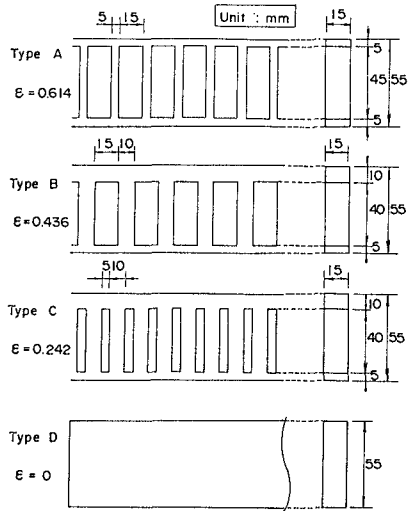


Figure 11 Diagram of model handrails

4.2 Handrail Effects on Overtopping Flow Motion

Figure 12 shows the seaward handrail's effect on water depth on a caisson during wave overtopping. The x-axis is the maximum water depth on a caisson at the seaward edge,  $\eta_1$ , and the y-axis is that 40 cm from the seaward edge,  $\eta(x = 40)$ . When no handrail is installed,  $\eta(x = 40)$  is about 40% of  $\eta_1$ . If a handrail is installed at the seaward edge, the water depth behind it decreases in comparison to that if no handrail is present. Note that the water depth decreases as the opening ratio of the handrail decreases. The effect of a handrail can be quantitatively estimated as

$$\eta(x) = 0.4 \{ \eta_1 - hp(1 - \epsilon_1)^2 \}, \tag{4}$$

where  $hp$  is the height of the handrail and  $\epsilon_1$  is the opening ratio of the seaward handrail.

Figure 13 shows the distribution of the maximum flow velocity on a caisson near the landward handrail with an opening ratio of 0.61. The length of a vector indicates the flow velocity value, while the solid line indicates the maximum water depth on the caisson. Since this handrail has a high  $\epsilon_2$  value, the flow near it is not even disturbed. However, if the handrail's  $\epsilon_2$  is small, the water depth near it will significantly increase. This effect can be formulated as

$$\eta_2 = \min \{ \eta_1, 0.4\eta_1 + (1 - \epsilon_2)hp \}, \tag{5}$$

where  $\epsilon_2$  is the opening ratio of the landward handrail and  $\eta_2$  is the maximum water depth at the landward edge.

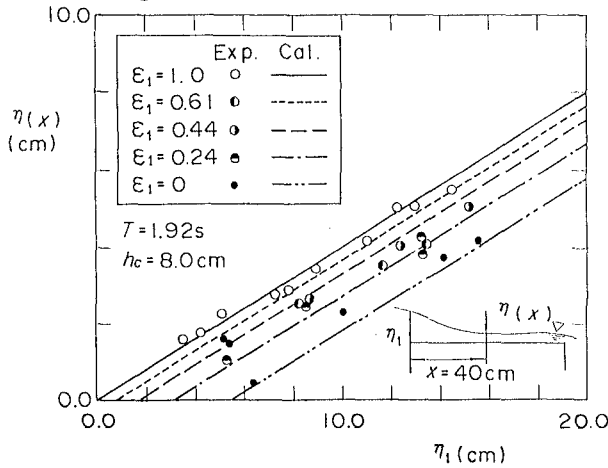


Figure 12 Maximum water depth behind the seaward handrail

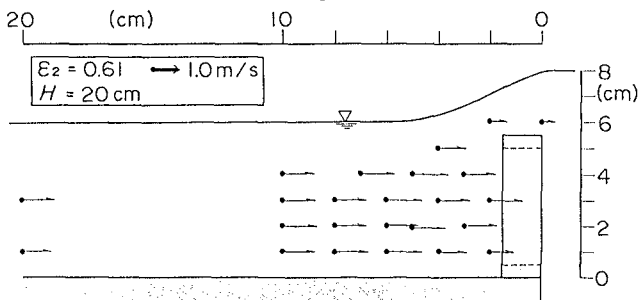


Figure 13 Distribution of current velocity near the landward handrail

### 4.3 Body Motion in Overtopping Flow

Figure 14 shows wave-induced movement of the human body model when it is placed near the landward handrail. Each diagram depicts the effect of  $\epsilon_2$  on model movement. When  $\epsilon = 0$ , the higher handrail is considered to be an impermeable wall. Note that as  $\epsilon_2$  decreases, the model is lifted up; thereby indicating a strong relation exists between movement and the water depth near the handrail, i.e., the maximum water depth at the landward handrail strongly influences whether or not a person will be carried into the sea. The critical water depth at which the model was carried over the handrail into the sea was found to be about 17% of its height. An expression representing this danger is

$$\eta_{2cr} = 0.17ht + hp, \tag{6}$$

where  $\eta_{2cr}$  is the critical water depth at the caisson's landward edge which will carry a person into the sea, and  $ht$  is a person's height.

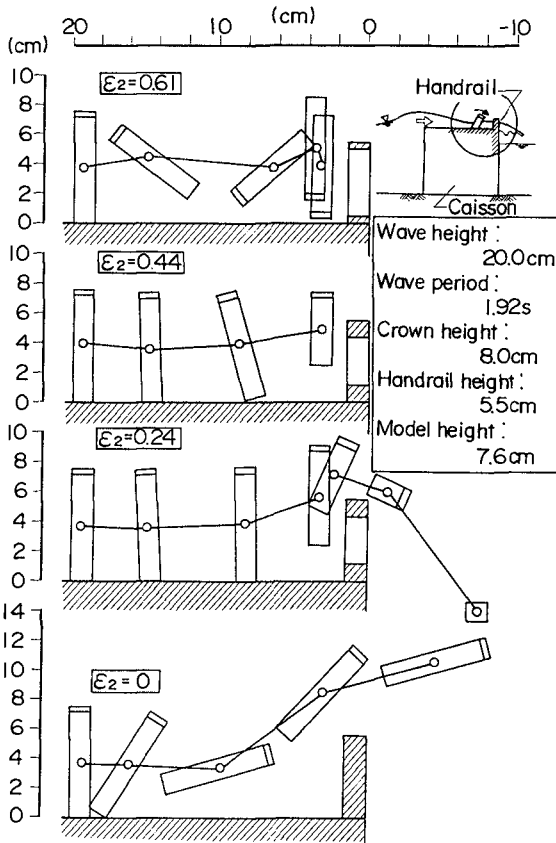


**Figure 14** Diagram of human body movements in overtopping flow at various  $\epsilon_2$  values

**4.4 Carry Model**

The carry model can estimate the effect of the seaward and landward handrails on the maximum water depth using Eqs. (4) and (5), respectively, whereas Eq. (6) enables calculating the maximum water depth at the caisson's seaward edge which will carry a person into the sea.

**Figure 15** shows the critical water depth (contour lines) at the caisson's seaward edge as determined by the carry model. The x- and y-axis respectively indicate the opening ratio of the seaward and landward handrail. It is assumed that a person is 152-cm tall and the height of the handrails is 110 cm. As shown, if no handrails are installed, the critical water level is only 0.7 m. However, if both handrails have an opening ratio of 0.7, this increases the critical water depth to 2.1 m. These results verify that handrails effectively prevent a person from being carried into the sea.

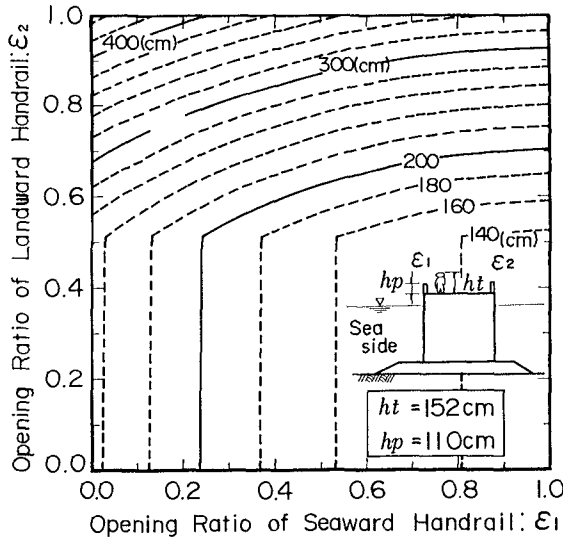


Figure 15 The critical water depth on the caissons seaward edge which carries into the sea

5. WAVE HEIGHT DURING EACH DANGER STAGE

5.1 Dangerous Wave Height Formula

As shown next, the wave height at each successive stage of danger can be formulated by the OWM.

5.1.1 Critical wave height of splash:  $H_{ms}$

$$H_{ms} = \frac{-1 + \sqrt{1 + 2.8\alpha_1 hc/hm}}{2\alpha_1} \times hm \tag{7}$$

$$\begin{aligned} hm &= d && : B_M/L \geq 0.16 \\ d + (h - d) \frac{0.16 - B_M/L}{0.05} &&& : 0.11 < B_M/L \leq 0.16 \\ h &&& : 0.11 < B_M/L \end{aligned} \tag{8}$$

where  $hc$  is the breakwater's crown height, and  $\alpha_1$  is a coefficient representing the breakwater superstructure, being 1.0 for a vertical breakwater and 0.5 for a slit-caisson breakwater or a composite breakwater with wave-dissipating blocks. Also,  $d$  is the water depth above the mound foundation,  $h$  the water depth above the sea bottom,  $B_M$  the width of the mound shoulder, and  $L$  the wave length at the depth of the breakwater.

5.1.2 Critical wave height at overtopping:  $H_{mo}$

$$H_{mo} = \frac{-1 + \sqrt{1 + 4\alpha_1 (hc + hp^*)/hm}}{2\alpha_1} \times hm \tag{9}$$

$$\begin{aligned} hp^* &= 0 && : \varepsilon_1 \neq 0 \\ hp &&& : \varepsilon_1 = 0 \end{aligned} \tag{10}$$

where  $hp$  is the handrail height and  $\varepsilon_1$  is the opening ratio of the seaward handrail

**5.1.3 Critical wave height for being knocked over:  $Hmt$**

$$Hmt = \frac{2(hc^* + \eta_{1t})}{1 + \sqrt{1 + 4\alpha_1 hc^*/hm}} \tag{11}$$

$$\begin{aligned} hc^* &= hc && : \varepsilon_1 \geq 0.4 \\ &hc + hp && : \varepsilon_1 < 0.4 \end{aligned} \tag{12}$$

where  $\eta_{1t}$  is the maximum water depth at the caisson's seaward edge when a person is knocked over. In Eq. (11),  $\eta_{1t}$  is assumed as 0.5 (m), which is the critical value for a 152 cm tall person (average 12 years old person in Japan).

**5.1.4 Critical wave height for being carried into the sea:  $Hmd$**

$$Hmd = \frac{2(hc + \eta_{1d})}{1 + \sqrt{1 + 4\alpha_1 hc^*/hm}} \tag{13}$$

where  $\eta_{1d}$  is the maximum water depth at the caisson's seaward edge when a person is carried into the sea (Table 2, Figure 16).

**Table 2**  $\eta_{1d}$  against the types of handrail ( $hp = 1.1$  m) for 152 cm tall person (unit : m)

Seaward handrail	Fence type	Wall type	Chain type or nothing
Landward handrail			
Fence type	2.1	3.1	2
Wall type	1.5	2.5	1.4
Chain type or nothing	0.8	1.3	0.7

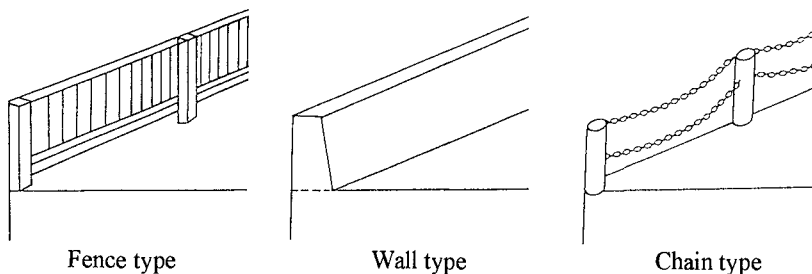


**Figure 16** Handrail types



**5.2 Example Calculation**

Using the following conditions, an example will be shown calculation that determines the critical wave for causing danger at each danger stage;

$$hc = 2 \text{ m}, hp = 1.1 \text{ m}, d = 8 \text{ m}, h = 10 \text{ m}, B_M = 5 \text{ m}, \epsilon_1 = \epsilon_2 = 0.7, T = 6 \text{ s}.$$

Under these conditions, a splash occurs over the breakwater at a maximum wave height  $H_{max} \geq 1.2 \text{ m}$  (*Hms*), while overtopping wave occur at  $H_{max} = 1.7 \text{ m}$  (*Hmo*). A person on the breakwater is knocked over at  $H_{max} \geq 2.1 \text{ m}$  (*Hmt*), and is carried over the handrail into the sea at  $H_{max} \geq 3.5 \text{ m}$  (*Hmd*). If no handrails are installed, however, the final stage requires an  $H_{max}$  value of only 2.3 m.

A significant wave height for occurring dangers without breaking condition are assumed to be the  $H_{max}$  value divided by 1.8 for splash and overtopping danger (*Hss* and *Hso*), while the  $H_{max}$  value divided by 2.0 for 3rd and final stages of danger (*Hst* and *Hsd*), i.e.,  $Hss = 0.7 \text{ m}$ ,  $Hso = 0.9 \text{ m}$ ,  $Hst = 1.1 \text{ m}$ , and  $Hsd = 1.8 \text{ m}$  under the same condition.

**6. EFFECTS OF OVERTOPPING FLOW RATE ON PERSONNEL DANGER**

Figure 17 shows the relationship between the significant wave height and the overtopping flow rate under the same conditions used in the example calculation. The overtopping flow rate is calculated using the OWM<sup>(3)</sup>, which can evaluate this flow rate and the maximum overtopping flow rate for a regular wave. The overtopping flow rate for irregular waves is calculated based on the assumption that the Rayleigh distribution of wave heights holds. We assume the wave number is 1700, in which the maximum wave height is just two times the significant wave height.

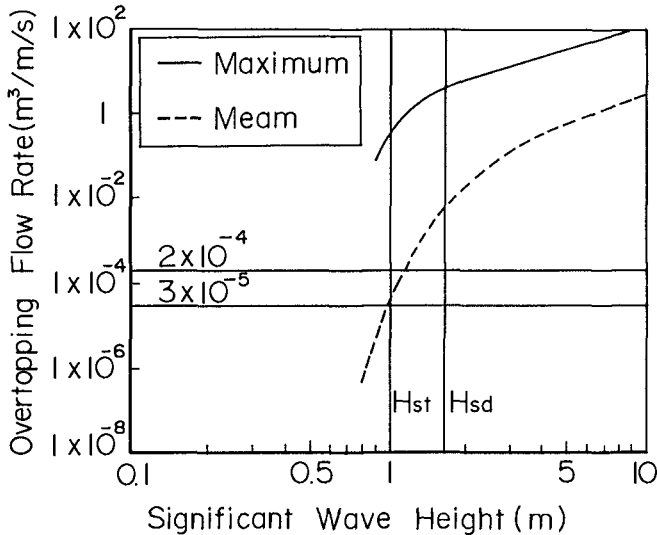


Figure 17 Overtopping flow rate when a person faces the several danger

Under these conditions and those used in the example calculations, the mean overtopping flow rate that knocks over a person is  $4 \times 10^{-5} \text{ m}^3/\text{m/s}$ , while at  $6 \times 10^{-3} \text{ m}^3/\text{m/s}$  the person is carried into the sea.

Fukuda et al. (1974) found that the wave overtopping flow rate to provide a probability of 50 and 90% personnel safety on a seawall is  $2 \times 10^{-4}$  and  $3 \times 10^{-5} \text{ m}^3/\text{m/s}$ , respectively. Note that our overtopping flow rate for being knocked over falls within these probabilities of safety.

## 7. CONCLUDING REMARKS

The types of overtopping wave-induced personnel dangers that can occur while standing on a breakwater were experimentally investigated. Our main conclusions are:

- 1) Based on prototype experiments, we developed a loss of balance model to calculate the critical water depth at a breakwater's seaward edge. If a person is 152-cm-tall and has standard body physique, the critical water depth is 0.5 m which causes a person to their balance.
- 2) The proposed carry model can calculate the critical water depth at the breakwater's seaward edge which will carry a person into the sea. This depth is dependent on the opening ratios of handrails installed at the breakwater's seaward and landward edge. If fence-type handrails having a 0.7 opening ratio are installed at the both edges, the critical water depth is 2.1 m for a 152-cm-tall person.
- 3) When no handrails are present, the calculated critical water depth which carries a person into the sea is only 0.7 m for a 152-cm-tall person, thus handrails are demonstrated to be a very effective measure for preventing a person from being carried into the sea by overtopping waves.
- 4) The proposed breakwater formula for evaluating the wave height at which personnel dangers will occur during successive stages of wave overtopping should be employed in the design of promenade breakwaters.

## REFERENCES

- 1) S. Takahashi, K. Endoh and Z. Muro: Experimental study on people's safety against overtopping waves on breakwaters, Rept. of Port and Harbour Res. Inst., Vol. 31, No. 4, 1992, pp. 3 - 29. ( in Japanese )
- 2) S. Takahashi et. al. : Experimental study on people's carriage into the sea caused by overtopping waves on breakwaters, Rept. of Port and Harbour Res. Inst., Vol. 33, No. 1, 1994, pp. 3 - 29. ( in Japanese )
- 3) A. Hujii, S. Takahashi and K. Endoh: An investigation of the wave forces acting on breakwater handrails, 24th ICCE, 1994
- 4) S. Takahashi, K. Endoh and Z. Muro: Wave height and overtopping rate in relation to the risk of falling on promenade breakwater, Proceeding of Civil Engineering in the Ocean, Vol. 9, 1993, pp.295-300. (in Japanese)
- 5) Fukuda, N., T. Uno and I. Irie : Field observations of wave overtopping of wave absorbing revetment, Coastal Engineering in Japan, No.17.

## CHAPTER 75

### WAVE OVERTOPPING ON VERTICAL AND COMPOSITE BREAKWATERS

L. Franco<sup>1</sup>, M. de Gerloni<sup>2</sup>, J.W. van der Meer<sup>3</sup>

#### Abstract

After an extensive series of 2-D model tests on the overtopping response of various caisson breakwaters, general conceptual design formulae and graphs have been derived which relate the mean discharge with the relative freeboard. The influence of geometrical changes is described by reduction factors with reference to the pure vertical structure. A simple correlation has been made with the overtopping performance of sloping structures. Overtopping volumes per wave were also measured and fitted with a universal probability function; their effects on model persons and cars behind the crownwall were statistically evaluated, thus allowing an upgrading of the existing criteria for the admissible overtopping on breakwaters.

#### Introduction

Wave overtopping is one of the most important hydraulic responses of a breakwater, since it significantly affects its functional efficiency and to a minor extent even its structural safety (though the latter effect is often negligible for monolithic breakwaters). The overtopping discharge is in fact the main parameter for the design of shape and height of the breakwater crest.

However, little research work had been addressed to this subject in the past, since most attention had been paid to wave forces and breakwater stability. It may be

---

<sup>1</sup> Prof. Coastal Eng., DIIAR Politecnico di Milano, piazza Leonardo da Vinci 32, 20133 Milano, Italy.

<sup>2</sup> Manager Modelling Unity, ENEL SpA - CRIS, via Ornato 90/14, 20162 Milano, Italy.

<sup>3</sup> Dr., Delft Hydraulics, P.O.Box 152, 8300 AD Emmeloord, The Netherlands.

noted that these aspects are interrelated since the wall crest elevation influences the amount of wave force. Few overtopping studies are available for seawalls (Owen, 1980; Goda, 1985;) and more recently for rubble mound breakwaters (Jensen and Juhl, 1987; Aminti and Franco, 1988; Bradbury and Allsop, 1988; de Waal and van der Meer, 1992). Goda (1985) remains the main reference for the design of vertical and composite structures.

An extensive laboratory investigation on the overtopping performance of modern vertical-face breakwaters has been started in Milano since 1989, with random wave flume model testing. Preliminary results were presented by de Gerloni et al. (1989, 1991).

Additional model tests and a more detailed analysis of the test results have been carried out in 1993 with the support of the UE-MAST 2-MCS (Monolithic Coastal Structures) project funding. Moreover the results obtained by other European hydraulic laboratories from specific studies on similar structures have been incorporated in the analysis to enlarge the data set and improve validation. The first main results have been reported by Franco (1993, 1994) at the MAST workshops.

#### **Experimental setup, test conditions and procedures**

Model tests were carried out in the 43 m long, 1.5 m deep random wave flume of ENEL SpA - Center for Hydraulic and Structural Research (CRIS) laboratory in Milano. A special device was used for measuring the overtopping volumes: a tray suspended through a load cell to a supporting beam. The load cell signal reading after each overtopping wave allows the measurement of its individual volume; the number of overtopping waves, the total volume and hence the mean discharge in each test can then be easily computed.

The effects of each overtopping wave were analyzed by placing a few model cars and model persons along the center of the crown slab behind the wall, and by accurately observing the number of displacements and relative distance from the former position after each overtopping event (then repositioning the "targets").

The proper model scaling of the human behaviour (to 1:20) was assessed with a simplified full-scale test procedure: a large bucket and a plastic pipe were used to direct known amounts of water, from an elevation of 4.5 m and without notice, against both a volunteer (the first author of this paper) and a human-size plastic dummy. It was found that the dummy had to be ballasted up to 1500 N (twice the man weight) to have the same falling response of the man.

To improve the statistical validity rather long test durations were used with no less than 1000 waves. Peak periods ( $T_p$ ) of JONSWAP spectra (bimodal spectra were also generated) varied between 7 and 13 s, significant wave heights ( $H_s$ ) between 2.5 and 6 m with water depths/wave heights ratios ( $h/H_{so}$ ) ranging between 3 to 5 (all figures are expressed in prototype terms for easier engineering interpretation). A total of about 250 tests with non-breaking wave conditions were performed.

Model breakwater configurations are shown in Fig. 1. They include traditional vertical-face caissons, perforated ones (14%, 25%, 40% porosity), shifted sloping parapets and a caisson with rubble mound protection (horizontally composite) with variable elevation and width of the homogeneous porous rock berm (S1 to S6 in Fig.1). All structures were designed for low overtopping conditions (i.e. high freeboard).

Additional results from model studies on similar structures designed in Italy and carried out by other European laboratories were included in the analysis, to enlarge the data set by covering a wider range of geometric and hydraulic conditions ( $H_s=2+8m$   $T_p=6+15s$   $h=9+18 m$ ). They were performed at Delft Hydraulics (DH) on vertical and shifted caissons and at Danish Hydraulic Institute (DHI) on perforated shifted-wall caissons. Further model test results from a research study on a simple vertical wall were supplied by CEPYC laboratory in Madrid. All these additional model test data typically only refer to the mean overtopping rate.

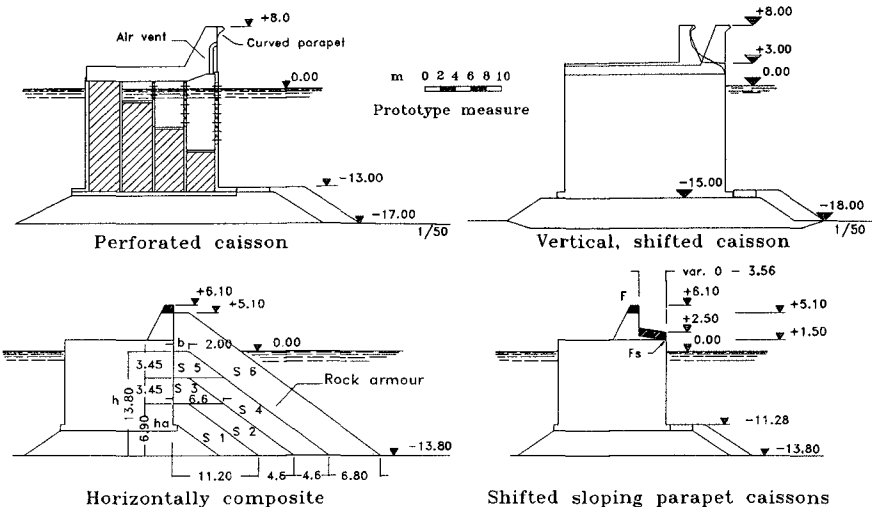


Fig 1 Model test sections of caisson breakwaters.

The influence of onshore winds on the overtopping effects was considered negligible particularly for large water flows above vertical walls. This assumption has been confirmed by a recent laboratory study (de Waal, 1994) which shows that the additional spray transport due to wind never exceeds 3 times the mean rate and is less than 1.4 times in typical deep water conditions similar to the tested ones. This increase is small compared to the much larger variability of overtopping with the wave height.

### Admissible overtopping rates

The definition of tolerable limits for overtopping is still an open question, given the high irregularity of the phenomenon and the difficulty of measuring it and its consequences. Many factors, not only technical ones, should be taken into account to define the safety of the increasing number of breakwater users such as the psychology, age and clothing of a person surprised by an overtopping wave.

Still the current admissible rates (expressed in  $\text{m}^3/\text{s}$  per m length) are those proposed by the Japanese guidelines, based on impressions of experts observing prototype overtoppings (Fukuda et al. 1974; Goda, 1985). They are included in CIRIA/CUR-manual (1991), and in British Standards (1991) (Fig. 2). The lower limits of inconvenience to pedestrians may correspond to safe working conditions on the breakwater, while the upper limits of danger to personnel may correspond to safe ship stay at berth.

Obviously the overtopping criteria for design depend upon the function and degree of protection required, and upon the associated risk considerations, taking into account the joint probability of wave heights and water levels. In fact relatively large overtopping might be allowed during extreme storms (structural design conditions) if transit on the breakwater is then prohibited (functional limit).

The structural safety of the breakwater typically demands less restrictive limits than the safety of its utilization (functional safety). The maximum admissible overtopping discharge for the structural safety of dikes and revetments are shown by Goda (1985). If the features of cast-in-situ concrete superstructures of modern caisson breakwaters are considered, the higher limit given for paved revetments ( $0.2 \text{ m}^3/\text{s}/\text{m}$ ) can be assumed.

As far as the functional safety is concerned (e.g. drainage behind seawalls), the figure of  $0.01 \text{ m}^3/\text{s}/\text{m}$  is considered as the tolerable discharge for direct

protection of densely populated coastal areas (Goda, 1985). Much lower discharges ( $0.0001 \text{ m}^3/\text{s}/\text{m}$ ) are given for the safe transit of vehicles, such as along a coastal highway. Few data are available on the critical overtopping discharges for the safety of various harbour operations and ship mooring on the breakwater rear side. A value of  $0.00042 \text{ m}^3/\text{s}/\text{m}$  in the 50 year design storm is proposed by Sigurdarson and Viggosson (1994) as criterion for damage to equipment and cargo on quay.

One of the aims of this model study was to assess better criteria in the case of caisson breakwaters. It was then believed that the overtopping volume per wave ( $V$ ), being actually responsible for the damage on the breakwater crown, was a far better hydraulic parameter than the mean discharge for this analysis, when there is no need of land reclamation drainage.

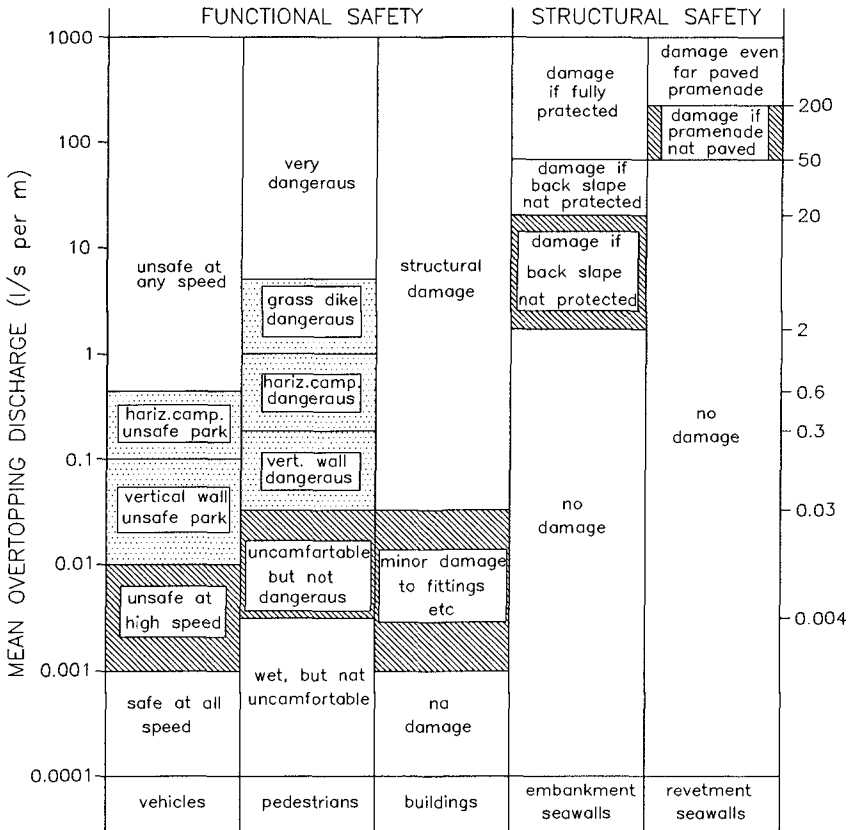


Fig. 2 Critical overtopping discharges of existing guidelines integrated with new safety bands (dotted) for transit on breakwaters.

For each breakwater configuration the individual overtopping volumes recorded in any tests were divided in classes of  $0.1 \text{ m}^3/\text{m}$  and the corresponding effects on model cars and pedestrians were statistically evaluated for each class. Some results obtained for pedestrians are shown in Fig. 3. It is interesting to observe that the effect is dependent on the structure geometry itself. The same overtopping volume is likely to be more dangerous if the breakwater is purely vertical than in the case of perforated or shifted-parapet caissons or horizontally composite ones. This is probably due to the different overflow mechanism which produces a more concentrated and fast water jet falling down from the crest of a vertical wall in comparison with a slower, more aerated, horizontal flow over a sloping structure. It was also observed that pedestrians are slightly more "stable" than vehicles under the same overtopping wave.

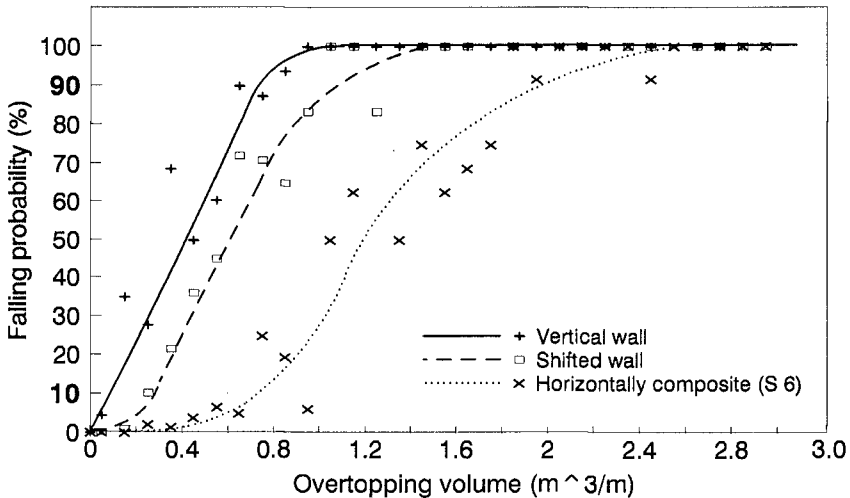


Fig. 3 Risk curves for pedestrians on caisson breakwaters from model tests.

From Fig. 3 it can be seen that the "critical bands" of overtopping volume (being dangerous above the upper limit and safe below the lower one) lie between  $0.2$  and  $2.0 \text{ m}^3/\text{m}$  (but a concentrated jet of  $0.05 \text{ m}^3/\text{m}$  on the upper body can be enough to make a person fall down as shown by the full scale calibration tests)

These results may be translated in terms of traditional mean rates for easier comparison with the previous criteria, by using the graph of Fig. 4, where the correlation between the mean discharge and the maximum (one in 1000 waves) volume is shown for some structural configurations. The critical band volumes



within the range of 10% to 90% falling probability in Fig. 3 are assumed as  $V_{\max} = V_{0.1\%}$  in a conservative approach to enter in Fig. 4.

The new proposed critical discharges, which are at least 10 times higher than the previous ones, are illustrated in Fig. 2, which also includes the results of recent large scale tests (Smith et al., 1994) showing that the dangerous discharge for a man standing on a dike is in the range  $(1 \div 10) \cdot 10^{-3} \text{ m}^3/\text{s}/\text{m}$ . From Fig. 4 it can be observed that this discharge actually corresponds to maximum volumes of  $0.5 \div 2 \text{ m}^3/\text{m}$  while in the same range of  $V_{\max}$  the average discharge over a vertical wall is  $(0.1 \div 0.5) \cdot 10^{-3} \text{ m}^3/\text{s}/\text{m}$ . The ratio  $V_{\max}/q$  can in fact vary between 100, for large mean discharges and percentage of overtopping waves, and 10,000, for small mean discharges and for vertical structures.

Thus it is confirmed that the significant parameter for the breakwater functional safety is the overtopping volume rather than the mean discharge. A relationship exists between the two parameters but it varies with the structure geometry and wave conditions.

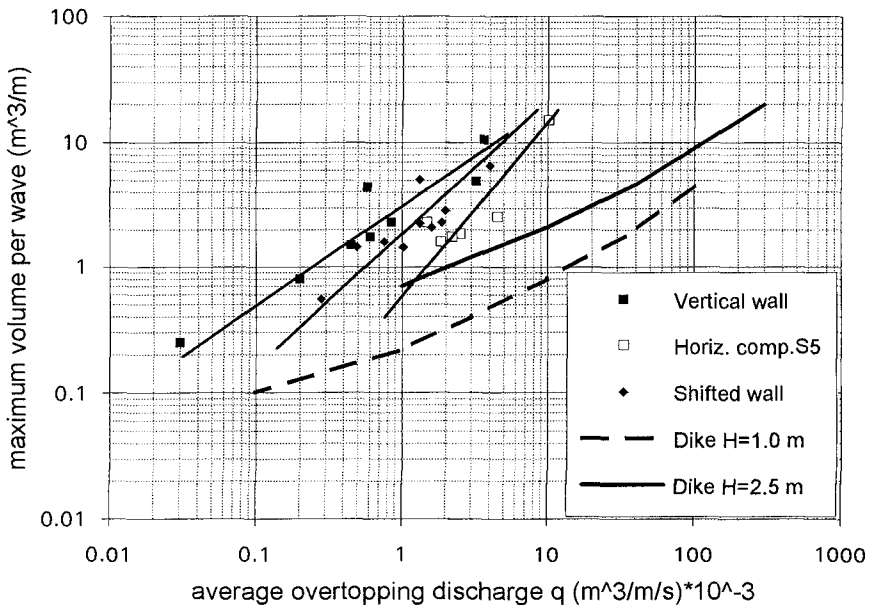


Fig. 4 Relation between mean discharge and maximum overtopping volume.

**Probability distribution of individual overtopping waves**

Overtopping events occur unevenly both in time and amount, often just a few waves overtopping among the thousands. The measurement of the individual overtopping volumes carried out during the model tests allowed the definition of their probability distribution. Considering the tests with a number of overtopping waves  $N_{ow} > 30$  (for obvious reasons of statistical significance) the exceedance probability of each overtopping volume  $P_v$  was calculated and a 3-parameter Weibull distribution function gave best fit to the data as shown in the example of Fig. 5:

$$P_v = 1 - \frac{i}{N_w + 1} = C \cdot \exp\left(-\frac{V}{A}\right)^B = \exp\left(-\frac{V-C}{A}\right)^B \quad (1)$$

where  $N_w$  is the number of waves in the test,  $V$  is a volume in the  $i^{th}$  rank and  $A, B, C$  are fitting constants.

It would also be possible to use in Fig. 5 on the horizontal axis the probability related to the number of overtopping waves ( $N_{ow}$ ) instead of the incident waves ( $N_w$ ). In that case the graph would start at 100% and  $C$  in eq. 1 would become 1.0.

It can be demonstrated with some mathematics that the scale parameter  $A$  can be defined by the equation:

$$A = 0.84 \cdot \bar{V} = \frac{0.84 \cdot T_m \cdot q}{\frac{N_{ow}}{N_w}} \quad (2)$$

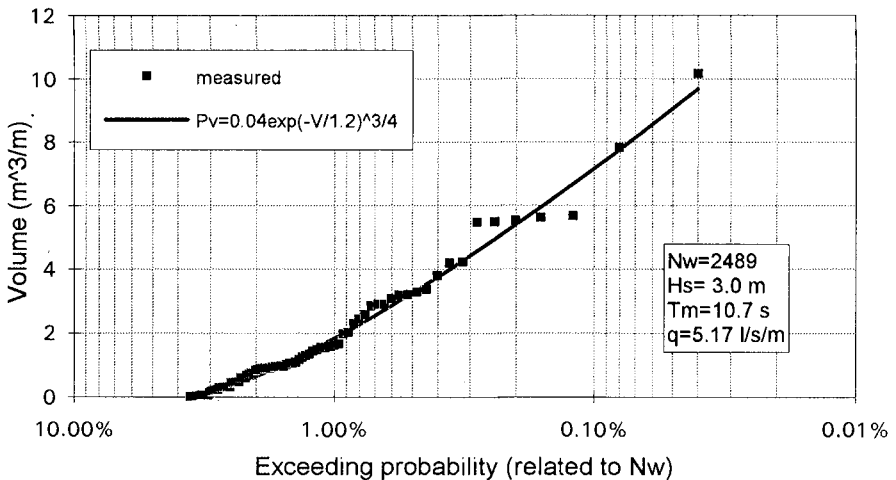


**Fig. 5 Example of probability distribution of overtopping volume per wave: vertical wall caisson, test 21.**

where  $T_m$  is the mean wave period,  $q$  is the average overtopping discharge and  $\bar{V}$  is the average overtopping volume per wave. Hence the exceedance probability of a given volume is related to the mean discharge and to the overtopping probability. Even  $V_{max}$  can be related to the other two overtopping parameters from eq. 1 as:

$$V_{max} = A \cdot \ln(N_{ow})^{4/3} \quad (3)$$

The shape parameter  $B$  was found to have a little variability around a mean value of 0.75, which is the same found by Van der Meer and Janssen (1994) for dikes. Then  $B=0.75$  is assumed to be constant.

The "set-off" coefficient  $C$ , being the intercept with the  $x$  axis (Fig. 5), represents the percentage (probability) of overtopping waves ( $N_{ow}/N_w$ ), which is assumed to be Rayleigh distributed, and can be expressed by the following equation (Fig. 6):

$$C = \frac{N_{ow}}{N_w} = \exp\left(-\frac{1}{k} \frac{R_c}{H_s}\right)^2 \quad (4)$$

where best fitting gives  $k=0.91$  for caisson breakwaters and  $R_c/H_s=R$  is the relative freeboard,  $R_c$  being the wall crest height above the sea level.

The assumption that  $C$  represents the overtopping probability was confirmed experimentally as shown in Fig. 7, which presents the comparison between measured ratios  $C=N_{ow}/N_w$  and the corresponding values calculated from data fitting in eq. 1; the experimental verification of eq. 2 for coefficient  $A$  is also shown.

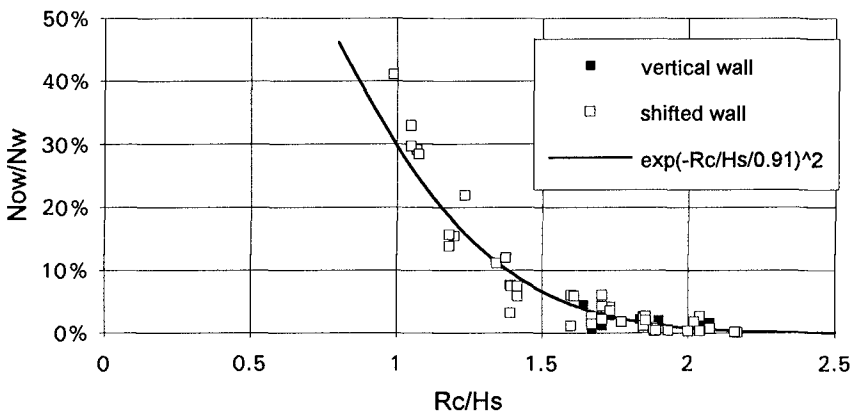


Fig. 6 Correlation between the percentage of overtopping waves and the relative freeboard.

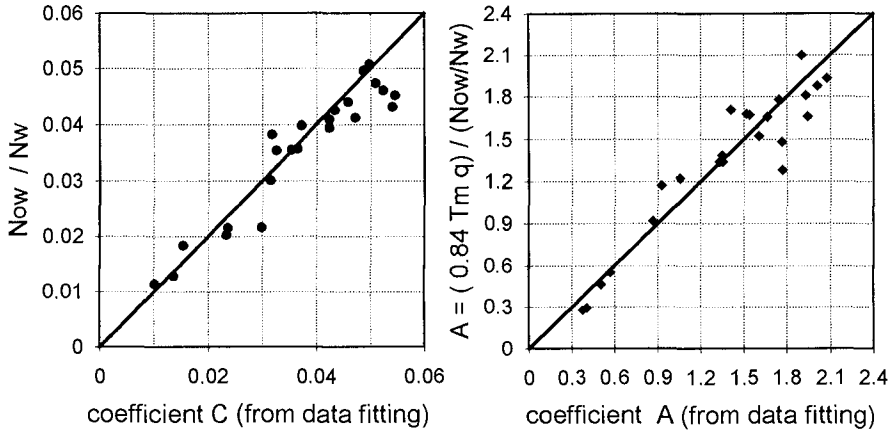


Fig. 7 Verification of functional relationship of coefficients C and A.

### Conceptual design formulae

The method of analysis proposed by van der Meer and de Waal (1992) to derive a general design formula was applied to the tests results (restricted to a wave steepness range of 0.018-0.038) in terms of mean overtopping discharge allowing a direct comparison with the above admissible limits and an easy evaluation of the overtopping volumes per wave with eq. 1 and 2.

Consistent curves have been fitted with the least square method to the experimental data representing the dimensionless mean overtopping discharge  $Q = q / \sqrt{g \cdot H_s^3}$  against the relative freeboard  $R_c / H_s$ , which is the most important parameter. Since an exponential relationship is assumed according to Owen (1980), the data should give a straight line on a log-linear plot:

$$Q = a \cdot \exp\left(-\frac{bR_c}{H_s}\right) \quad (5)$$

It was found (Fig. 8) that for vertical-face breakwaters  $b=4.3$  and  $a=0.192$ , which is close to the one found by van der Meer and Janssen (1994) for sloping structures ( $a=0.2$ ); the value  $a=0.2$  was then kept constant for the successive regressions with different geometries which generally showed a high correlation coefficient (Fig. 9). The physical interpretation of "a" is the dimensionless mean discharge when the freeboard is set at the mean water level. It may be observed in Fig. 9 that the overtopping rates predicted by eq. 5 are

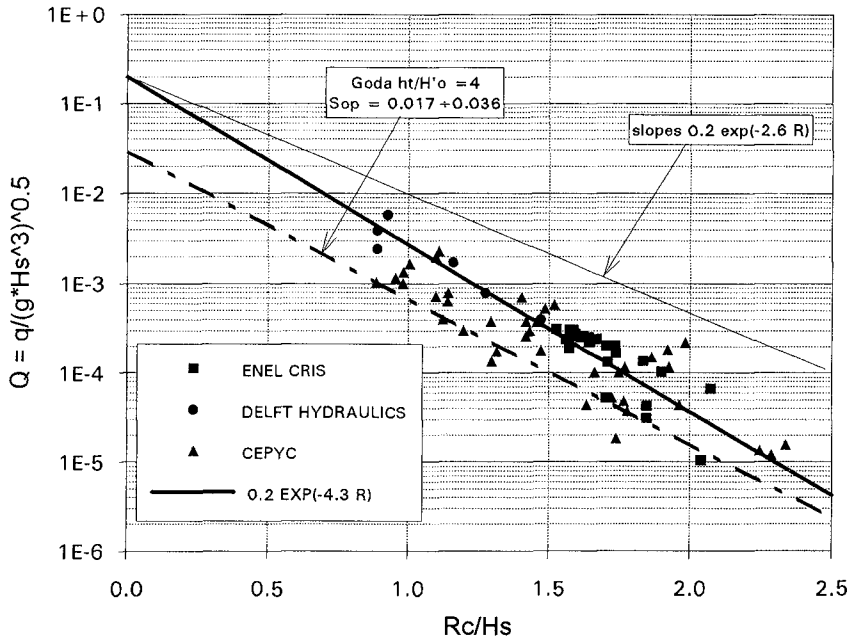


Fig. 8 Regression of wave overtopping data for vertical wall breakwaters.

slightly larger than those predicted by Goda (1985) for deep water vertical walls and with similar wave steepness range, besides the small differences in seabed slope and toe geometry. A similar underprediction of Goda's curves was also found by De Waal (1994).

Then the influence of structural modifications with reference to the vertical-face breakwater can be described by suitable freeboard reduction factors ( $\gamma$ ), which are the ratios between the reference value  $b=4.3$  and the various  $b$  coefficients fitted by eq. 5 as given in Fig. 9. Even the sloping structures (under non-breaking conditions) can be easily compared with the vertical ones considering the ratio  $\gamma_s=4.3/2.6=1.66$ , 2.6 being the fitting coefficient obtained by van der Meer and Janssen (1994) as also shown in Fig. 8. All the data can be plotted together (Fig. 10) after correction of the  $R_c/H_s$  values for each geometry with the corresponding  $\gamma$ , the general equation thus becoming:

$$Q = 0.2 \cdot \exp\left(-\frac{4.3 R_c}{\gamma H_s}\right) \tag{6}$$

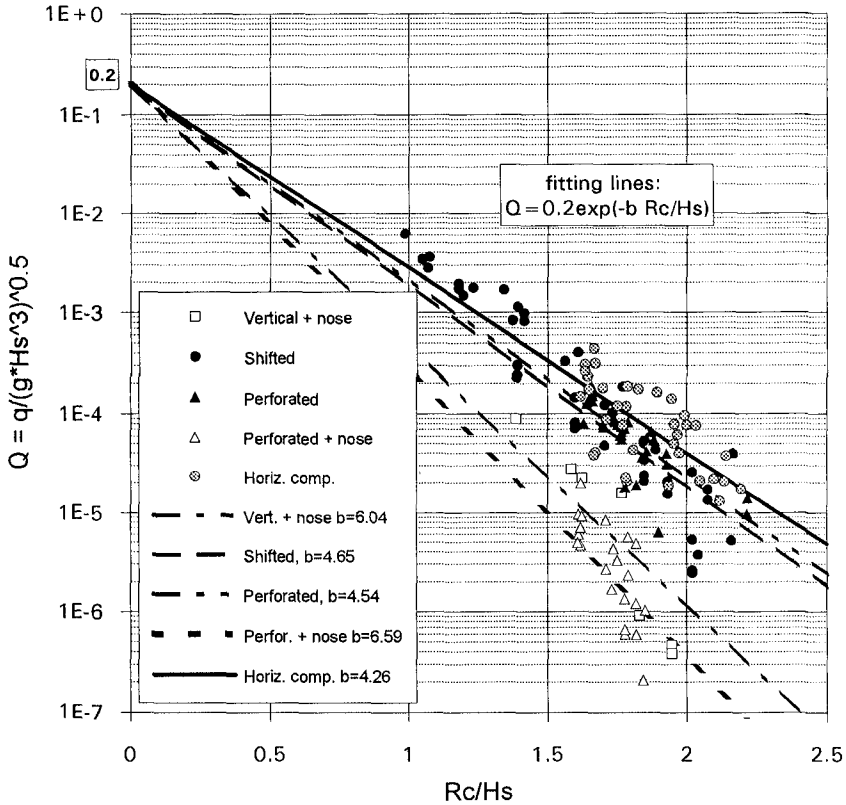


Fig. 9 Wave overtopping data for various types of caisson breakwaters.

which can be effectively used for the preliminary design of vertical breakwaters. The reliability of the formula 6 can be given by taking the coefficient 4.3 as a normally distributed stochastic variable with a standard deviation  $\sigma=0.3$ .

From the influence factors of the various caisson geometries, as compared to the plain vertical wall some useful engineering conclusions can be distilled:

- the greatest overtopping reduction can be achieved by introducing a recurved parapet (nose) at the crest of a vertical front wall: the corresponding  $\gamma_n=0.7$  means a 30% crest elevation reduction to get the same overtopping rate; this may however be limited to relatively small discharges;
- for simply perforated or shifted caissons the freeboard saving is only 5÷10%;

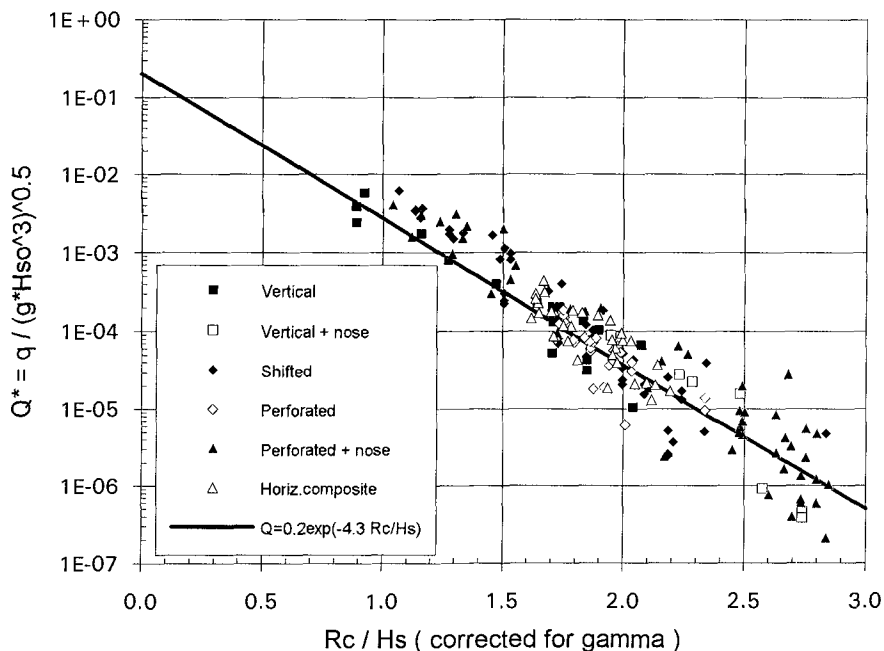


Fig. 10 Wave overtopping on vertical and composite breakwaters: conceptual design graph.

- if a nose is adopted at the crest of a perforated caisson, then the combined reduction factor can achieve 0.65, while its effect on a shifted parapet is negligible;
- the overtopping of horizontally composite breakwaters is influenced by porosity, slope, width and elevation of the mound. Overtopping increases if the armour crest is below or at mean sea level ( $\max \gamma_{SS}=1.15$ ).

#### Conclusions and further work

The results of an extensive 2D model test investigation on the overtopping performance of caisson breakwaters have been analysed to produce updated criteria for their functional safety and a new comprehensive conceptual design method.

The following remarks, valid for structures designed for relatively small overtopping, may be outlined:

- the proposed admissible overtopping discharges ( $q$ ) for the safety of people and vehicles on breakwaters are

larger than those presently recommended in the manuals and are dependent on the structure geometry;

- the overtopping volume ( $V$ ) is however a better parameter for allowable criteria;
- overtopping discharges on deepwater vertical walls are slightly larger than those predicted by Goda (1985) and quite smaller than those for an equivalent sloping structure (dike);
- the same exponential relationship between  $Q$  and  $Rc/Hs$  applies for both structure types (the reduction factor for vertical walls being 0.6), whereas very different and large ratios  $V_{max}/q$  can be observed;
- the combination of a perforated wall with a recurved crest (nose) on the front wall produces the largest overtopping reduction, whereas a rock protection in front of the caisson up to the sea level can increase overtopping;
- the probability distribution of overtopping volumes per wave is well defined by a Weibull distribution with a shape factor of 0.75 and a scale factor dependent on  $q$  and on the percentage of overtopping waves.

Further work is necessary to take into account the effects of wave obliquity and directional spreading. Actually a 3D caisson model study has just been carried out at Delft Hydraulics within the same European MAST-MCS project and results will be published soon. Additional analysis should also be performed to verify the influence of other less important structural and hydraulic parameters. The critical overtopping for the structural integrity of the caisson foundation system as well as for other facilities on and behind the breakwater should be also evaluated.

Finally, large scale model studies and prototype measurements of wave overtopping on real breakwaters are recommended to verify the present guidelines.

### Acknowledgements

The experimental research study has been carried out with the financial support of ENEL-CRIS, MURST (Italian Ministry of University and Research) and the European Union within the MAST-MCS project contract 0047. The contribution of J.Juhl (DHI) and B.G. Madrigal (CEPYC) for supplying their flume data is also gratefully acknowledged.



**References**

- Aminti P., Franco L. (1988), "Wave overtopping on rubble mound breakwaters." Proc. XXI ICCE, Malaga, ASCE, N.Y.
- Bradbury A.P., Allsop N.W.H. (1988), "Hydraulic effects of breakwater crownwalls." Proc. ICE Conference BREAKWATERS'88, Eastbourne, T. Telford, London.
- British Standard BS 6349: part 7 (1991), "Maritime Structures: Guide to the design and construction of breakwaters." London.
- CIRIA/CUR (1991), "Manual on the use of rock in coastal and shoreline engineering." CIRIA S.P.83-CUR Rep. 154.
- de Gerloni M., Franco L., Noli A, Rossi U. (1989), "Porto Torres industrial Port. Model tests on the new west breakwater." 2nd AIOM Congress, Napoli (in Italian).
- de Gerloni M., Franco L., Passoni G. (1991), "The safety of breakwaters against wave overtopping." Proc. ICE Conf. on Breakwaters and Coastal Structures, T. Telford, London.
- de Waal J.P. (1994), "Wave overtopping of vertical coastal structures. Influence of wave breaking and wind." Delft Hydraulics report H1635.
- De Waal J.P. and van der Meer J.W. (1992), "Wave runup and overtopping on coastal structures." Proc. XXIII ICCE, Venice, ASCE, N.Y., Vol. 2, pp. 1758-1771.
- Franco L. (1993), "Overtopping of vertical breakwaters: results of model tests and admissible overtopping rates." MAST2-MCS, 1<sup>st</sup> workshop, Madrid.
- Franco L. (1994), "Further results of hydraulic model tests on wave overtopping." MAST2-MCS, 2<sup>nd</sup> workshop, Milano.
- Fukuda N., Uno T. and Irie I. (1974), "Field observations of wave overtopping of wave absorbing revetment." Coastal Eng. in Japan, 17.
- Goda Y. (1985), "Random seas and design of maritime structures." University of Tokyo Press.
- Jensen O.J. and Juhl J. (1987), "Wave overtopping on breakwaters and sea dikes." Proc. II COPEDEC Conf., Beijing.
- Owen M.W. (1980), "Design of seawalls allowing for wave overtopping." Rep. EX924, Hydraulics Research Wallingford.
- Smith G.M., Klein Breteler M, Seijffert J.W.W., van der Meer J.W. (1994), "Erosion and overtopping of a grass dyke: 1:1 scale model tests." Proc. ICCE 94, Kobe.
- Sigurdarson S, Viggosson G. (1994), "Berm breakwaters in Iceland, practical experiences", Proc. Hydro-port '94, PHRI, Yokosuka.
- Van der Meer J.W., Janssen P.F.M. (1994). "Wave forces on inclined and vertical wall structures" to be published on ASCE, ed. Z.Demirbilek.



**Photo 1** Assessing first author's stability under water jets; a ballasted manikin (on the left) is waiting for its turn.



**Photo 1** Effects of wave overtopping on model cars and model persons on a caisson breakwater.

## CHAPTER 76

### AN INVESTIGATION OF THE WAVE FORCES ACTING ON BREAKWATER HANDRAILS

Atsushi HUIJI<sup>1</sup>, Shigeo TAKAHASHI<sup>2</sup> and Kimihiko ENDOH<sup>3</sup>

#### ABSTRACT

We carried out model experiments to quantitatively elucidate the motion of overtopping waves on a caisson breakwater, with results leading to the development of an empirical model that can evaluate the maximum current velocity and depth of such waves on a breakwater. In addition, we developed a formula for calculating the wave forces acting on breakwater handrails, then confirmed its validity using field experiments.

#### 1. INTRODUCTION

Seawalls and breakwaters are ideal locations from which people can comfortably enjoy a seafront environment. In Japan, such structures allowing public access are called promenade seawalls or breakwaters. Because such facilities are a dangerous place for personnel, thorough safety measures must be in place before opening them to the public. Handrails installed on seawalls and breakwaters are a basic safety feature, being present on almost all of Japan's promenade facilities.

Many facilities, however, have been damaged by high overtopping waves; thereby creating serious problems for facility safety management. **Figure 1** shows a photograph of damaged promenade breakwater handrails. Obviously then, overtopping wave forces are a major consideration in handrail design, yet only a limited amount of associated quantitative information is available. In addition to determining the wave forces acting on handrails, the motion of overtopping waves must also be clarified.



**Figure 1** Photograph of damaged breakwater handrails

---

1 Niigata Investigation and Design Office, the First District Port Construction Bureau, MOT, 1-332 Hakusan-ura, Niigata 951, Japan

2 Maritime Structures Laboratory, Port and Harbour Research Institute, MOT

3 Port and Harbor Engineering Section, Civil Engineering Research Institute, HDA

This led to the present study which uses laboratory model experiments to (i) examine the characteristics of overtopping waves above a breakwater and (ii) develop a formula for obtaining wave forces acting against a handrail. We also examine the characteristics of wave forces on handrails, then verify the proposed formula using field experiments.

## 2. MOTION OF OVERTOPPING WAVES ON A CAISSON

### 2.1 Experiment Outline

To examine the basic characteristics of overtopping wave motion on a composite breakwater, and to develop a model of the motion, we conducted a laboratory model experiment using relatively low wave heights. During this experiment (Experiment A), a 163-m-long, 1-m-wide, and 1.5-m-deep wave flume was employed to measure water depths and current velocities above a model caisson.<sup>1)</sup>

We also conducted another laboratory experiment using relatively high wave heights over other types of model breakwaters; hence enabling the development of an empirical formula. During this experiment (Experiment B), a 38-m-long, 1-m-wide, and 1.5-m-deep wave flume was employed to measure water depths and current velocities above composite breakwaters, breakwaters covered with wave-dissipating blocks, and slit-caisson breakwaters. Wave forces acting on model handrails were also measured.<sup>2)</sup>

This paper primarily reports on the fundamental motion characteristics of overtopping waves (Experiment A).

### 2.2 Overtopping Wave Motion

Figure 2 shows overtopping wave motion above a caisson at  $hc/H = 0.293$ ,  $H/L = 0.051$ , and  $\Delta t = 0.05$ , being obtained using a high-speed video camera that records 200 frames/s. Note that after the water level in front of the breakwater rises and the wave grows higher than the crown, its shape gradually shifts toward the crown's landward edge. The overtopping wave then crashes on the breakwater, being transformed into one-directional landward flow. We classify these phenomena into the following two stages:

- 1) "Green wave stage": the phenomena occurring from the wave's run-up above the crown to its crash onto it.
- 2) "Overtopping flow stage": the phenomena occurring when the crashed overtopping wave is transformed into fast, landward-directed flow.

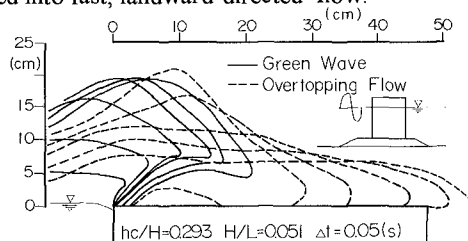


Figure 2 Overtopping wave motion above a caisson

### 3. OVERTOPPING WAVE MODEL

Figure 3 shows a diagram representing the "overtopping wave model (OWM)," which we apply to empirically evaluate the maximum water depth and current velocity which occurs above a caisson during overtopping. Input data consists of wave and breakwater structural conditions, as well as water depth in front of the caisson.

The green wave stage is characterized by the overtopping wave front having a parabolic trajectory. The distance between the caisson's seaward edge and the crash point of the wave front is called the "green wave range," and is represented by  $l_3$ . The value of  $l_3$  is determined by the velocity of the rising wave crest (wave crest rise velocity) above the caisson's seaward edge and the wave velocity. The maximum water depth and current velocity are considered to be constant within the green wave range.

In the overtopping flow stage, the maximum water depth above the crown changes over time, i.e., it decreases within a certain distance from the seaward edge, called the "accelerated flow range," then tends to be almost constant, called the "constant flow range." The maximum current velocity in the former range increases as the wave approaches the landward side, becoming nearly uniform in the latter range. In the model,  $\eta_1$  represents the maximum water depth at the top of the caisson's seaward edge, while  $l_1$  represents the horizontal distance over which the water depth changes.

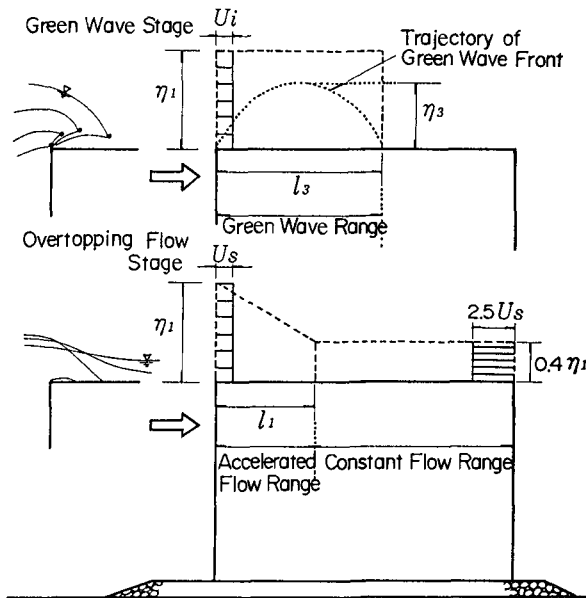


Figure 3 Overtopping wave model

3. 1 Green Wave

3.1.1 Wave Crest Rise Velocity

The rise velocity of the overtopping wave crest at the moment it runs up above the crown,  $V_{sf}$ , is equal to the vertical velocity of the wave's surface profile.  $V_{sf}$  can be evaluated using a second-order approximation formula for finite amplitude standing waves. If the breakwater superstructure is the composite type, the effects of its rubble mound must be considered because they differ depending on wave length  $L$  and mound shape. It is reasonable to consider that the mound has a significant effect on waves when the mound shoulder width,  $B_M$ , is relatively large in comparison with  $L$ , and also that the mound has only a slight effect when  $B_M$  is relatively small. Thus, use of the ratio  $B_M/L$  enabled us to develop a functional formula for obtaining the representative water depth  $hm$ , which subsequently determines overtopping wave motion, i.e.,

$$\begin{aligned}
 hm = d & & : B_M/L \geq 0.16 \\
 d + (h - d) \frac{0.16 - B_M/L}{0.05} & & : 0.11 < B_M/L \leq 0.16 \\
 h & & : B_M/L < 0.11
 \end{aligned}
 \tag{1}$$

where  $h$  is the natural water depth in front of the breakwater and  $d$  is the water depth above the rubble mound.

Figure 4 shows the relationship between  $B_M/L$  and  $V_{sf}$  using Eq. (1), where the experimental and calculated values clearly indicate good agreement.

Overtopping waves move landward as soon as they run up over the crown, and at this moment, the wave crest horizontal velocity at  $hm$  has a proportional relation with wave velocity  $C_m$ , i.e., it is about 30% smaller than  $C_m$  regardless of crown height. Thus, if we consider the motion of the front to be in free-fall, having come over the caisson's seaward edge at  $V_{sf}$  with a horizontal velocity of  $0.3C_m$ , then a functional formula can be developed to determine the trajectory of the green wave front, with  $l_3$  being subsequently expressed as

$$l_3 = 0.6C_m \cdot V_{sf}/g,
 \tag{2}$$

where  $g$  is gravitational acceleration.

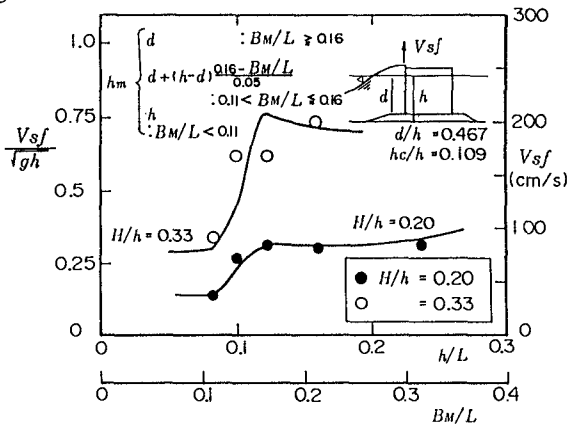


Figure 4 Relation between  $B_M/L$  and  $V_{sf}$

### 3.1.2 Maximum Water Depth and Current Velocity

The distribution of the maximum water depth in the green wave stage is considered to be constant within the green wave range, being equal to the overtopping flow stage's maximum water level  $\eta_1$  at the caisson's seaward edge. Experiment results enable the corresponding maximum current velocity,  $U_i$ , to be expressed as a function of  $Cm$  and wave height  $H$ , i.e.,

$$U_i = 0.8Cm(1.67H/hm - 0.67)^{1/3} \quad : H/hm \geq 0.4 \quad (3)$$

$$0 \quad : H/hm < 0.4$$

## 3.2 Overtopping Flow

### 3.2.1 Maximum Crest Height over The Caisson's Seaward Edge

Goda et al.<sup>3)</sup> developed the following formula for determining the wave crest height ratio  $K$  for standing waves, being the ratio of the run-up height above the still water level in front of a caisson,  $R$ , to the wave height,  $H$ :

$$K = \min \left\{ \left[ 1.0 + a(H/h) + b(H/h)^2/Ksb \right], c \right\}, \quad (4)$$

where  $Ksb$  is the coefficient expressing nonlinear shoaling effects and breaker decay, while  $(a, b, c) = (1.0, 0.8, 10.0)$  for vertical walls.  $K$  is 1.0 for small amplitude standing waves and exceeds 1.0 as their finite amplitude increases. The second term in the brackets of Eq. (4) represents the effect in which  $K$  increases in proportion to  $H/h$  under the condition that no breakers exist, while the third term represents a green wave generated in front of the caisson by breakers. When breaking waves hit the caisson, overtopping waves run up high above it and produce splashing. The quantity of splashed water, however, is relatively small; thus we neglected the third term.

In general, breakwaters can handle large quantities of water from overtopping waves, and because wave overtopping reduces the value of the reflection coefficient,  $K$  tends to become constant and is not proportional to  $H$  per Eq. (4). We therefore included the effect of overtopping waves using the following formula:

$$K = 1 + \alpha_1 H/hm \quad : H/hm < \frac{-1 + \sqrt{1 + 4\alpha_1 hc/hm}}{2\alpha_1}$$

$$\frac{1 + \sqrt{1 + 4\alpha_1 hc^*/hm}}{2} \quad : H/hm \geq \frac{-1 + \sqrt{1 + 4\alpha_1 hc/hm}}{2\alpha_1} \quad (5)$$

$$hc^* = hc \frac{H/hm}{2H/hm - \frac{-1 + \sqrt{1 + 4\alpha_1 hc/hm}}{2\alpha_1}} \quad (6)$$

The resultant  $K$  values enable calculating the maximum wave crest run-up height at the caisson's seaward edge, i.e.,

$$\eta_1 = K \cdot H - hc, \quad (7)$$

where  $hc$  is the breakwater crown height and  $\alpha_1$  is a correction factor dependent on the breakwater structure. For a composite breakwater,  $\alpha_1 = 1.0$ ; whereas  $\alpha_1 = 0.5$  for a breakwater covered with wave-dissipating blocks or a slit-caisson breakwater.

**Figure 5** shows the experimental (when overtopping occurred) and calculated (Eq. (5))  $K$  values for Experiment A, where the experimental values ranged from 0.9 to 1.1 when  $hc/h = 0.109$ , and from 1.0 to 1.2 when  $hc/h = 0.207$ : results that confirm a higher crown height will increase  $K$ . In addition, when overtopping waves

occurred, the values calculated using Eq. (5) tended to be constant and independent of changes in wave height, being in good agreement with the experimental values.

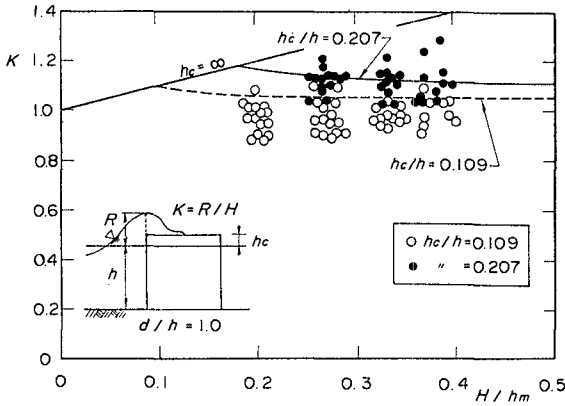


Figure 5 Wave crest height ratio

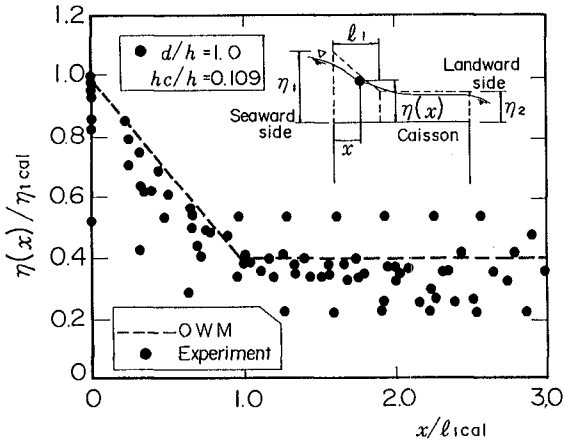


Figure 6 Distribution of maximum water depth above a caisson

### 3.2.2 Maximum Water Depth

The accelerated flow range  $l_1$  can be expressed as a function of  $hc$ , maximum water depth  $\eta_1$ , and wave velocity  $Cm$ . The maximum water depth in the constant flow range is known to be about 0.4 times smaller than  $\eta_1$  at the caisson's seaward edge, and therefore, the maximum water level at an arbitrary crown point  $\eta(x)$  can be calculated using the values of  $\eta_1$  and  $l_1$  occurring during overtopping flow stage, i.e.,

$$\eta(x) = \begin{cases} \frac{l_1 - 0.6x}{l_1} \eta_1 & : x < l_1 \\ 0.4\eta_1 & : x \geq l_1 \end{cases} \quad (8)$$



Figure 6 shows the distribution of experimental and calculated maximum water levels above the crown of a vertical breakwater with  $hc = 8.2$  cm ( $hc/h = 0.109$ ), in which the water depth and distances from the caisson's seaward edge are respectively non-dimensionalized by  $\eta_1$  and  $l_1$ . Note that the experimental values are scattered, and also that when  $x/l_1 = 0$ ,  $\eta/\eta_1$  ranges from 0.8 to 1.0, becoming 0.25 to 0.55 in the constant flow range. Since the experimental values are roughly dispersed around the calculated ones, this indicates good agreement.

**3.2.3 Maximum Current Velocity**

Since our Experiments A clarified that the current velocity in the overtopping flow stage has a relationship with water depth, and also that their maximum values have only a slight phase difference, this indicates the maximum current velocity  $U_s(x)$  can be determined by dividing the maximum overtopping wave quantity  $q_{max}$  by  $\eta(x)$  (Eq.(8)). Based on a formula modeling steady flow in a dam, we used tests to examine the flow coefficient  $C_1$ , which enables calculation of the overtopping wave quantities. Consequently, a functional formula was developed to obtain  $q_{max}$ , i.e.,

$$q_{max} = (0.68 + 1.10 \cdot H/hm)C_1\eta_1^{3/2} \quad : H/hm < 0.4$$

$$\left(0.8 + \frac{0.32}{(10H/hm - 4)^2 + 1}\right)C_1\eta_1^{3/2} \quad : H/hm \geq 0.4 \quad (9)$$

where  $C_1 = 1.61$  ( $m^{0.5}/s$ ).

Figure 7 shows the distribution of the maximum current velocity above the caisson for  $d/h = 1.0$  and  $hc/h = 0.109$ . The x-axis is the distance from crown's seaward edge,  $x$ , divided by  $l_1$ , while the y-axis is the maximum current velocity at each point,  $U_s(x)$ , divided by the maximum current velocity in the constant flow range,  $U_{scal}(\infty)$ . When  $x/l_1$  is less than 1.0, i.e., within the accelerated flow range, the experimental current velocity increases as  $x$  increases. It is clear that in the constant flow range, the value of  $U_s(x)/U_{scal}(\infty)$  tends to be constant, ranging from 0.9 to 1.15. Note the rough agreement between experimental and calculated values.

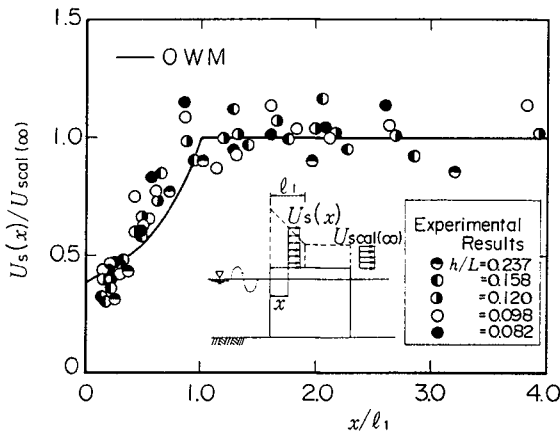


Figure 7 Distribution of maximum current velocity above a caisson

4. FORMULA FOR WAVE FORCE ACTING ON HANDRAILS

Overtopping wave forces acting on column-shaped handrail members may include: (i) an impulsive wave force that occurs when an overtopping wave hits, and (ii) a drag force that is dependent on the current velocity of overtopping waves. Because these members have relatively small diameters, the impulsive component was assumed to be negligible, and therefore, only the drag force was considered. Neglecting the effect of impulsive pressure was confirmed to be appropriate using field experiments. The drag force can be expressed as

$$F = \frac{w_0}{2g} C_D \cdot A \cdot U_{max}^2 \tag{10}$$

where  $A$  is the horizontally projected area of a submerged handrail at the maximum water depth,  $C_D$  is the drag coefficient, and  $U_{max}$  is the maximum current velocity estimated to occur at the handrail installation point. We used the largest values of  $U_{max}$  observed in the green wave and overtopping flow stages.

Figure 8 shows the ratio of experimental to calculated wave forces,  $F_{exp}/F_{cal}$ , acting on a handrail. Wave forces acting on handrail members installed on the caisson's seaward and landward edge are indicated. Since the handrail was made of cylindrical column-shaped members, we assumed  $C_D = 1.0$ . At the seaward edge, the maximum current velocity in the green wave stage is larger than that in the overtopping flow stage, and consequently, the wave forces at this edge were calculated using the maximum velocity  $U_i$  in the green wave stage. Since the landward edge is in the constant flow range outside the green wave range, we used the maximum current velocity  $U_s$ . At the seaward edge handrail,  $F_{exp}/F_{cal}$  ranged from 0.7 to 1.2, with good agreement being present between experimental and calculated values. At the landward edge handrails,  $F_{exp}/F_{cal}$  was slightly less (0.4 to 0.7), which indicates that calculated values are comparatively slightly larger. These experimental results confirm that Eq.(10) is suitable if  $C_D = 1.0$  for cylindrical column-shaped members.

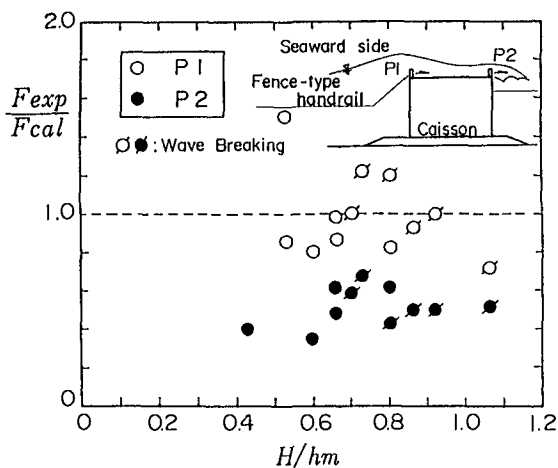


Figure 8 Wave forces acting on a model handrail

At a high Reynolds number,  $Re$ , however, the  $C_D$  value is lower for this type of handrail. Consequently, since  $Re$  values are higher in the field than in experiments, a possibility exists that  $C_D$  is actually less than assumed. It should be realized that the characteristics of impulsive wave forces could not be determined because the experimental response characteristics of handrail members did not agree with field results, possibly being due to measuring the wave forces with strain gages. This problem led to using field experiments to examine the characteristics of wave forces and impulsive wave forces (Section 5).

### 5. FIELD EXPERIMENTS

#### 5.1 Background

##### 5.1.1 Location of Field Experiments

Field experiments were conducted from November 1991 to March 1992 above the Second North Breakwater of Sakata Port in northeastern Japan. **Figure 9** shows plane and cross-section views of the field site. Although this front-line breakwater is installed in deep water ( $\approx 16$  m), its crown height is relatively low (4.5 m) because it was under construction during the tests. The upper seaward edge of the caisson has a  $45^\circ$  slope. An observation house was built about 2 km away from the test breakwater to record measured data transmitted through optical fiber cables.

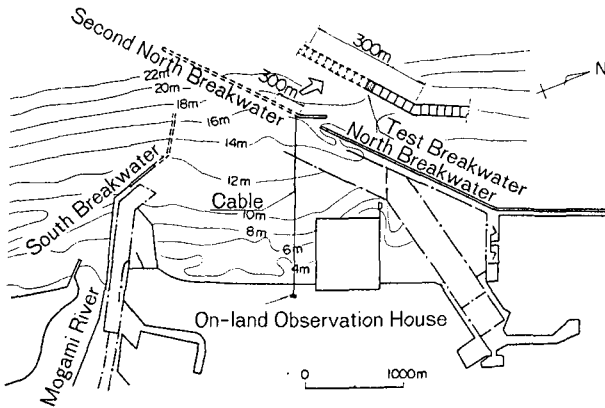


Figure 9 (a) Plane view of Sakata Port

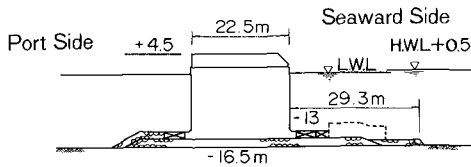
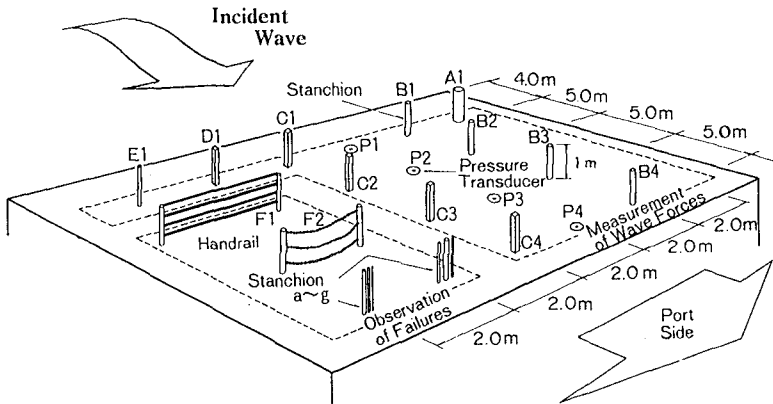


Figure 9 (b) Cross-section view of test breakwater

**Table 1** Stanchion shapes

Name	Shape	Diameter (mm)	Thickness (mm)	Allowable wave height (m)
A1	Round steel pipe	216.3	8.2	-----
B1-4	Round steel pipe	101.6	4.2	-----
C1-4	Round steel pipe	48.6	3.2	10
D1	Square steel pipe	100	4.5	-----
E1	Square steel pipe	75	4.5	-----
a	Round steel pipe	27.7	2.3	4.6
b	Round steel pipe	76.3	3.2	14.8
c	Round steel pipe	139.8	4.5	-----
d	Round steel bar	13	---	4
e	Round steel bar	25	---	7.7
f	Round steel bar	38	---	12.3
g	Round steel bar	48	---	-----
F1	Fence-type	60.5	3.2	4
F2	Chain-type	114.3	6	-----



**Figure 10** Field experiment setup

**5.1.2 Experiment Outline**

A wave force measurement test and failure test were carried out in the field. For the wave force test, five kinds of test stanchions (1-m-tall, round or square steel pipes) were installed on the breakwater crown (Table 1), and we measured the strain generated at their bottoms. Figure 10 shows the employed stanchion setup. Stanchions of each type (A1-E1) were installed 4 m away from the seaward edge. Stanchions B and C were also installed 9, 14, and 19 m away from the seaward edge.

For the failure test, we installed conventionally used fence- and chain-type handrails (F1 and F2), round steel pipes (a-c), and round steel bars (d-g) in order to observe tilt angles and other failure conditions that can occur after a major storm (Table 1, Fig. 10). Wave pressure, current velocity, and wave height were obtained corresponding to when the bottom of a stanchion reaches allowable stress. The fence-type handrail (F1) had an allowable wave height of only 4.0 m, which indicates that it will fail at comparatively low wave heights.

To examine the motion characteristics of overtopping waves above the crown, we installed four pressure transducers (*P1-4*) at various locations on the crown. Water depth during an overtopping wave was determined by removing the impulsive component from vertical pressure, i.e., only the static pressure component was used to obtain water depth. We calculated the current velocities during overtopping waves using phase differences in the pressure profiles.

**5.1.3 Analysis Method**

By assuming the wave pressure acting on the test stanchions is equally distributed, we could calculate strain-produced pressure. Peak pressures were then compared with observed maximum wave heights. These heights were measured about 250 m away from the breakwater along its normal line; hence some errors may arise when evaluating the wave pressure characteristics. Wave direction data was obtained about 7 km directly seaward of the breakwater, being a location where good correlation is present.

**5.2 Wave Forces Acting on Handrails**

**5.2.1 Typical Strain and Water Pressure Profiles**

Figure 11 shows typical profiles of the strain which occurred at the bottom of the test stanchions and those of water pressure in response to a maximum wave height of 7.4 m ( $hc/H_{max} = 0.50$ ) (January 24, 1992, 8:14-8:34a.m.). Strain profiles for stanchions *A1*, *B1-4*, *C1-2*, and *D1* are shown with water pressure profiles from *P1-4*. The maximum water depth calculated from the water pressure profiles is 3.2 m at *P1*, the most seaward point, and 1.2 m at *P4*, the most landward point, which indicates that the water depth exceeded the height of the stanchions over the entire the crown area. The average current velocity determined from the phase difference of these maximum water levels is 9.1 m/s between *P1* and *P2*, 11.1 m/s between *P2* and *P3*, and 12.5 m/s between *P3* and *P4*, showing a slight increase toward the landward edge.

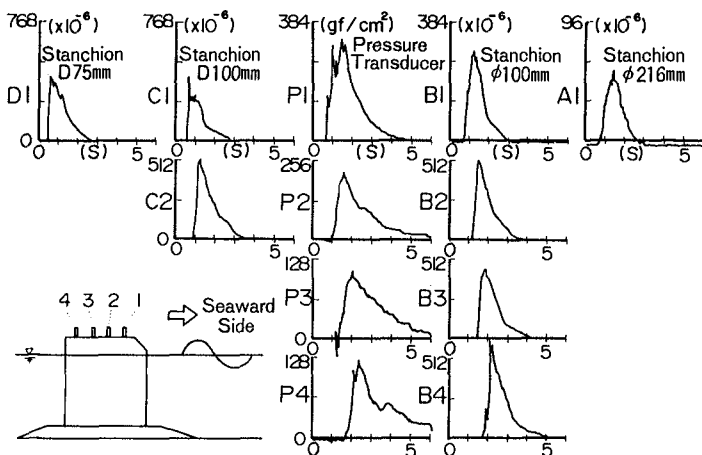


**Figure 11** Strain and pressure profiles

As can be seen in *C1*'s profile, strain in the stanchion includes both impulsive and drag force components. The impulsive component seems to occur when a portion of an overtopping wave smashes into the stanchions. Its pressure profile is a strong, sharp peak acting over a relatively short time. In comparison, the drag force component is dependent on current velocity, displaying a relatively mild peak acting over a long time. With the exception of *C1*, the profiles of *C2*, *A1*, and *B4* indicate the presence of an impulsive component, although it is much smaller than the drag force.

Regarding the drag force component of strain, similar to current velocity, strain increased toward the landward edge, e.g., the non-dimensional wave pressure,  $p/w_oH$ , at *B1-4* was respectively 0.28, 0.47, 0.46, and 0.57.

The stanchion shape also affected the wave force acting against it. If we compare the drag force component of  $p/w_oH$  at the most seaward stanchions, the cylindrical column-shaped ones (*A1* and *B1*) had values of 0.2 and 0.28, whereas those of the square-column ones (*C1* and *D1*) were twice as large at 0.42 and 0.45. This result suggests a difference occurs in the drag coefficient.

**5.2.2 Wave Pressure Acting on Stanchions**

**Figure 12** shows the wave pressure acting on stanchion *B1* in the form of the non-dimensional wave pressure  $p/w_oH$ , where peak values of the drag force component and of any impulsive component are indicated. Although the data is scattered due to the effects of different tide levels and wave directions, at a maximum wave height of 6 m or greater,  $p/w_oH$  ranges from 0.25 to 0.4 for the drag force component and from 0.3 to 0.5 for the impulsive component. Similarly, the drag force component of the pressure ranges from 0.2 to 0.6 for the cylindrical column stanchions and from 0.3 to 1.0 for the square column stanchions, though the degree of scattering varies with position.

Since impulsive wave pressures vary with position depending on the overtopping wave conditions, as well as showing great variations in scale, peak impulsive pressures were compared with peak drag pressures as shown in **Fig. 13**. The x-axis indicates drag pressures  $P_s$ , while the y-axis indicates  $P_n$ , the peak values

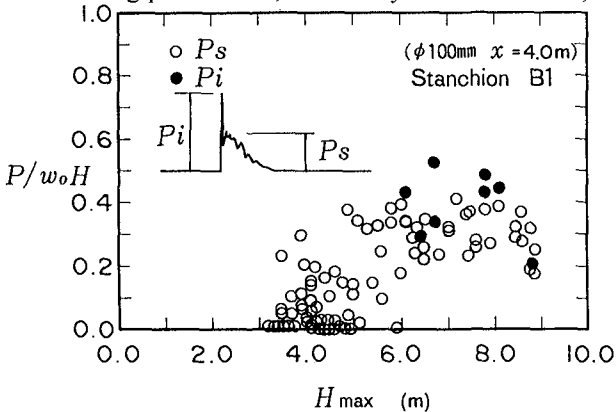


**Figure 12** Non-dimensional wave pressure acting on stanchion B1

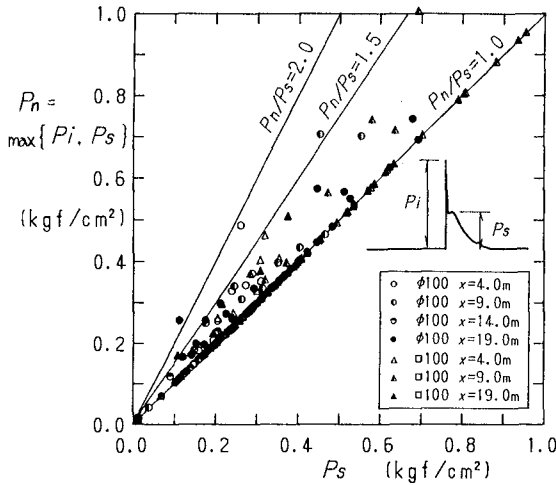


Figure 13 Impulsive pressure

of  $P_s$  and impulsive pressure  $P_i$ . When  $P_n/P_s$  equal to 1.0, the peak pressures are caused by the drag force component, whereas when greater than 1.0, they are caused by the impulsive component. Although the maximum  $P_n/P_s$  value is around 2.0, it generally is less than 1.5; hence, impulsive pressures do not generally exceed the drag pressures by much. In addition, the impulsive pressures measured at the stanchions were less frequent and smaller than those measured by pressure transducers located the same distance away from the seaward edge. The relatively small impulsive pressures observed on stanchions may be due to their thin columnar shape or a dynamic response at their natural frequencies (1.5-7 Hz). Measured impulsive wave pressures are expected to be conservative in comparison to those on actual handrails, because actual handrails have the same quality and are fabricated from same material as the test stanchions, and also their natural frequencies are slightly less due to no transverse members being present. Therefore, neglecting impulsive wave pressures during handrail design, as is done in the conventional breakwater design method, is considered acceptable.

5. 3 Comparison with Wave Force Formula

5.3.1 Comparison Between Measured and Calculated Wave Forces

Figure 14 compares measured and calculated wave forces, where the x-axis indicates the non-dimensional value of  $l_1$  divided by the distance  $x$  away from the caisson's seaward edge, and the y-axis indicates the ratio of the measured wave force  $F_m$  to the calculated one  $F_c$ . For the measured wave force, only the drag force component was included, and for the calculated force, a  $C_D$  value of 1.0 and 2.0 was used for the cylindrical and square stanchions, respectively. As shown, in a relatively seaward area where  $x/l_1$  is less than 1.0, the measured forces for the cylindrical and square columnar stanchions are only 40-90% of their calculated forces (ave.≈60%). On the other hand, in a relatively landward area where  $x/l_1$  is greater than 1.0, the

$F_m/F_c$  values are close to 1.0 on the average, though they are widely scattered from 0.3 to 1.5. These results confirm the calculated values are roughly suitable.

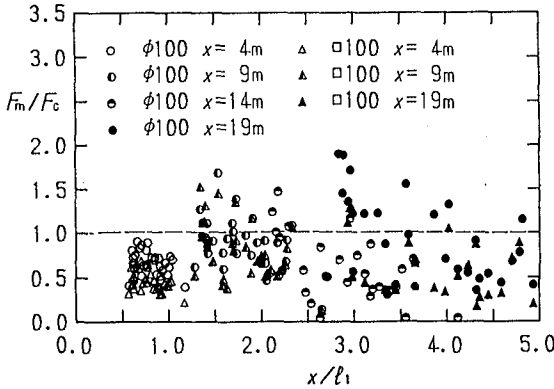


Figure 14 Comparison of measured and calculated forces acting on stanchions

5.3.2 Reproducing Failure Conditions Using Calculated Stress

Structures that tilted or completely fell over during the experiment are: stanchion *E* used in the wave force measurement; and stanchions *a*, *d*, *e*, and handrail *FI* used in the failure test. Since the allowable wave heights for all these damaged members is 10 m or less (Table 1), these failures could easily be predicted by wave observation results. The strongest storm during the experiment produced a maximum wave height of 10.5 m (Dec. 28-30, 1991), and stanchion *e* was tilted. Stanchions *a*, and *d* and handrail *FI* failed in a storm on Nov. 19-21, 1991.

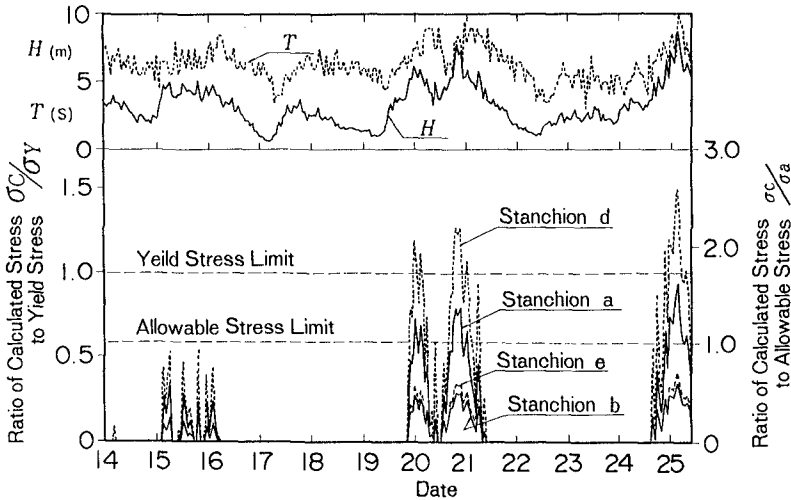


Figure 15 Comparison of calculated and allowable stresses at the bottom of stanchions



**Figure 15** shows wave conditions and calculated stresses at the bottom of several stanchions from Nov. 14-25, 1991. We examined damaged stanchions *a* and *d* and undamaged stanchions *b* and *e*. The wave condition data was used to determine calculated stress  $\sigma_c$ , which was non-dimensionalized by dividing with either allowable stress  $\sigma_a$  or yield stress  $\sigma_y$ .

When wave forces act on a stanchion, the stresses generated in it are generally the greatest at the bottom. When the stresses there exceed allowable stresses, i.e.,  $\sigma_c/\sigma_a > 1.0$ , a greater possibilities exists for tilting or other failures to occur. From Nov. 14-25, two major storms produced maximum wave heights of 5.0 m greater, with one wave having a maximum height of 8.8 m. During storms before Nov. 19, stanchions *a* and *d* both had  $\sigma_c/\sigma_a < 1.0$ , and no failure took place. However, when their maximum  $\sigma_c/\sigma_a$  ratios increased to 1.4 and 2.1 during the Nov. 19-22 storms, both suffered failure. In addition, their maximum value of  $\sigma_c/\sigma_y$  increased to 1.5 and 0.75. In contrast, both these ratios for stanchions *b* and *e* were less than 1.0, and they were not damaged. For the fence-type handrail *F1*, which failed during same period,  $\sigma_c/\sigma_y > 1.5$ . These results indicate that the stress calculated using Eq. (10) is accurate enough to be used to the practical design.

## 6. CONCLUDING REMARKS

We have shown that the motion of an overtopping wave above a caisson can be classified two distinct stages: the "green wave" and "overtopping flow" stages. The fundamental characteristics of each stage were also classified, which enabled developing a model of the motion. Our resultant model can effectively determine maximum water depth and the maximum current velocity above a caisson.

Through the field experiments using handrails, it was possible to understand the effects of impulsive wave forces and the practical wave force characteristics in the region of high Reynolds numbers. It also was possible to estimate the wave force acting on a breakwater handrail as a drag force and to verify the appropriateness of the estimation through wave force measurement and failure tests.

## ACKNOWLEDGMENTS

Sincere gratitude is extended to Dr. Tomotsuka Takayama, Director of the Port and Harbour Research Institute for his valuable advice and encouragement.

## REFERENCES

- 1) Takahashi, S., Endoh, K., and Muro, Z. : Experimental study on motions and forces of overtopping waves, Rept. of Port and Harbour Res. Inst. Vol.31, No.1, 1992, pp.3-50. (in Japanese)
- 2) Sugawara, K., et. al. : Experimental study of wave forces acting on handrails on breakwaters, 39, pp.716-720. (in Japanese)
- 3) Goda, Y., et. al. : Laboratory investigation on the overtopping rate of seawalls by irregular waves, Rept. of Port and Harbour Res. Inst. Vol.14, No.4, 1975, pp.3-45. (in Japanese)

## CHAPTER 77

### **Rubble Mound Breakwater Stability Under Oblique Waves : An Experimental Study**

J.-C. Galland<sup>1</sup>

#### **Abstract**

A series of model tests was carried out in a wave basin at LNH to quantify the effect of long-crested, oblique waves on rubble mound breakwaters. Four types of armouring units (quarry stone, Antifer cube, tetrapod and ACCROPODE®) were tested, under six angles of wave attack (0°, 15°, 30°, 45°, 60°, and 75°). Overtopping, toe berm and main armour stability were studied as functions of wave obliquity. A method is proposed to reduced the results obtained under oblique waves to those obtained under normal waves, allowing thus for the use of formulae derived under normal waves for the design of a breakwater under oblique wave attack.

#### **Introduction**

Scale model tests aimed to define guidance for the design of breakwaters are mainly conducted in wave flumes, because this is the easiest (and then the cheapest) way to vary the numerous structural parameters involved. Therefore, the effect of wave obliquity on the stability of such structures has been hardly investigated so far, and the estimation of the possible influence of that parameter is often based upon conjectures or derived from tests not directly related to breakwater stability (run-up measurements on smooth mild slopes mainly).

A few tests, or re-analysis of tests, have been found in the literature, which give some trends for the stability of rubble mound breakwaters under oblique waves.

Whillock (1977) made tests on a 1:2 slope armoured with dolosse under regular wave attack at a fixed period. Results of his tests showed a slight decrease in stability up to an angle of wave attack  $\beta$  of 60° and then, at  $\beta = 75^\circ$ , quite a large increase in stability.

This trend for dolosse was also mentioned by Gravesen and Sorensen (1977) who, reviewing tests data with random waves, stated a slight decrease in stability when increasing  $\beta$  (with a minimum at  $\beta = 45^\circ$ ), although they did not noticed such a large increase for angles higher than 60°. For quarry stone, the same authors found

---

<sup>1</sup> EDF - Laboratoire National d'Hydraulique, 6 Quai Watier, 78400 Chatou, France.

that stability was not much affected for  $\beta$  ranging from  $0^\circ$  to  $45^\circ$ , but was then increased a lot at higher angles.

Van de Keeke (1969) performed tests with regular waves (at a fixed period) on rocks for 3 different slope angles (1:1.5, 1:2 and 1:3) and for  $\beta = 0^\circ, 30^\circ, 45^\circ, 60^\circ$  and  $90^\circ$ . He found exactly the same trends as the above mentioned ones.

Gamot (1969) reported tests on a breakwater armoured with tetrapod and stated that the armour stability was increased with increasing angle of incidence, this effect being noticeable as soon as  $\beta > 40^\circ$ . He also mentioned that, once they are initiated, damage increase faster under oblique waves than under normal waves.

Finally, Markle (1989) conducted tests in which toe berm stability was investigated, some of these tests being performed at  $\beta = 45^\circ$ . What he concluded, despite very few tests were conducted, is that there was no great difference in stability associated with different angles of wave attack. Some general trend of higher stability under oblique wave could however be seen, although not well defined.

As only very few papers exist in the literature, a series of model tests was carried out at LNH to quantify the effect of long-crested, oblique waves on the stability of rubble mound breakwaters. Advantage was taken from these tests to study also the influence of oblique waves on overtopping and toe stability. Four types of armouring units - quarry stone, Antifer cube, tetrapod (two layers units) and ACCROPODE® (one layer unit)- were tested, under six angles of wave attack  $\beta - 0^\circ$  to  $75^\circ$ , each  $15^\circ$ . A comprehensive description of these tests is given in Galland (1993).

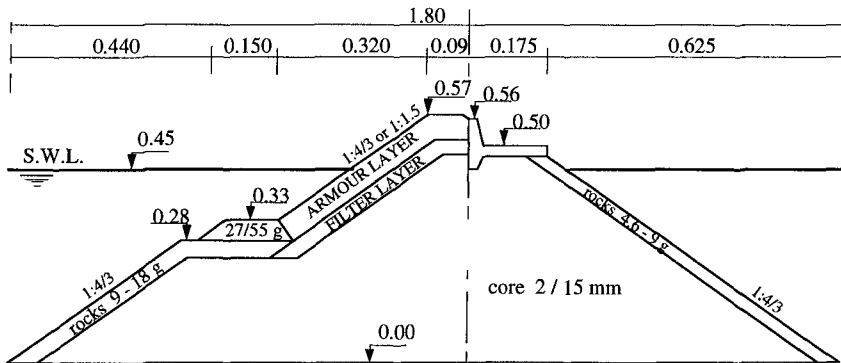


Fig. 1 Breakwater cross-section (measures in m).

**Model design and layout**

Although these tests do not refer to any field study, the cross-section of the breakwater was defined in such a way that it could represent an actual one. With reference to the maximum significant wave height to be tested ( $H_s = 0.135$  m), the depth of the toe berm below the water level ( $h_t = 0.12$  m) was chosen so that the toe was under strong influence of hydrodynamic forces and the crest elevation ( $h_c = 0.12$  m) so that overtopping was allowed at the same time as damage should start (under normal waves). Doing this way also ensures that the armour layer (which is the main element under study) has a realistic number of units rows, and then a behaviour similar to the one that could occur in the field.

The breakwater consisted in four trunks, each one being 3 m long and armoured with one of the studied units. The total length of the breakwater, including two roundheads, was about 16 m. The rear slope and the crown wall blocks were artificially stabilised, in order to prevent destruction of the breakwater by rear slope degradation and/or crown wall tilting.

### **Breakwater cross-section**

The cross-sections for concrete units were identical and a 1:4/3 slope was chosen (fig. 1). For quarry stones however, the slope was changed into 1:1.5, which is a more realistic value for that armouring unit.

The crown wall blocks, the core, the toe berm, the rear armour layer and the lower part of the front cover layer were identical for all armour units.

### **Characteristics of the units**

Characteristics of the armouring units and toe rocks are given in table 1. The weights and mass density are mean values over at least 30 dry units. In the following,  $\Delta$  is the relative mass density and  $D_n$  the nominal diameter of the unit considered.

Block	$\rho_r$ (kg/m <sup>3</sup> )	W (10 <sup>-3</sup> kg)	$\Delta D_n$ (10 <sup>-2</sup> m)
ACCROPODE®	2310	44.7	3.51
Antifer block	2400	48.6	3.82
Tetrapod	2540	61.6	4.48
Armour rock	2850	(W <sub>50</sub> ) 90.0	5.85
Toe rock	2500	(W <sub>50</sub> ) 38.0	3.75

*Table 1. Characteristics of units.*

Grading characteristics of the rocks used for that study are presented in table 2, together with their mass density.

Rock	W <sub>min</sub> (10 <sup>-3</sup> kg)	W <sub>max</sub> (10 <sup>-3</sup> kg)	W <sub>50</sub> (10 <sup>-3</sup> kg)	W <sub>85</sub> /W <sub>15</sub>	$\rho_r$ (kg/m <sup>3</sup> )
Armour layer (main)	55.0	145.0	90.0	2.05	2850
Underlayer	1.8	9.3	5.0	1.83	2650
Toe berm	27.0	55.0	38.0	1.34	2500
Rear slope	2.8	10.0	6.6	1.57	2660
Cover-layer (lower part)	5.0	17.0	10.0	1.93	2630

*Table 2. Characteristics of rocks.*

Placement of armouring units was realised according to the procedure relative to each unit : for concrete units, this means that the prescribed mesh was respected and, for quarry stones, that they were tipped on the slope. A cover layer armoured with a given armouring unit was always built by the same person, to ensure a good reproducibility in the way of placing the units.

### **Test conditions**

The programme included 6 series of tests, each one being defined by its angle of wave incidence (0°, 15°, 30°, 45°, 60° and 75°). The normal wave test was aimed to

be the reference when analysing the results. To limit the number of investigated stability parameters, the breakwater was placed on a flat bottom (water depth  $h = 0.45$  m) and, as one test consisted in 8 steps with increasing wave height, the peak wave period was tuned at each step so that the wave steepness remains a constant ( $s_{0p} \cong 4\%$ ). The steps duration was adapted so that the total number of waves in each one was 2000. It was large enough a number to ensure both a suitable statistical distribution of waves and a stabilised damage evolution at the end of each step. Targeted wave characteristics are presented in table 3.

Step	1	2	3	4	5	6	7	8
$H_s$ (m)	0.030	0.045	0.060	0.075	0.090	0.105	0.120	0.135
$T_p$ (s)	0.71	0.87	1.00	1.12	1.22	1.32	1.41	1.50
$L_{Op}$ (m)	0.78	1.18	1.56	1.96	2.32	2.72	3.10	3.51
Duration (')	22	26	30	34	37	40	42	45

Table 3. Targeted wave characteristics.

### Test facilities

The tests were performed in a wave basin (fig. 2) which overall dimensions are 33 m x 28 m x 1 m, the maximum water depth being 0.45 m. This basin is fitted out with a hydraulic flap-type wave maker, which paddle is 17 m long, 0.85 m high and can move round the basin, allowing this way for a 180° rotation. The four walls of the basin were equipped with wave absorbers in order to avoid re-reflection.

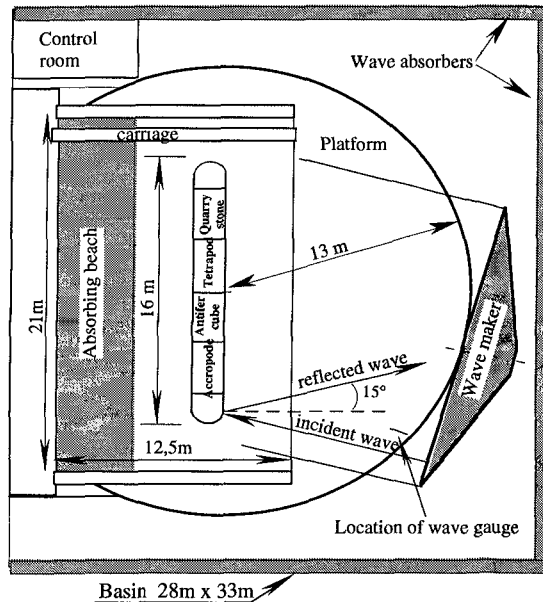


Fig. 2. Test set-up and location of surface elevation measurement for oblique wave attack (example,  $\beta = 15^\circ$ ).

## **Test procedures**

### **Generation and measurement of waves**

Random waves were generated according to a JONSWAP type spectrum, with  $\gamma = 3.3$ . The wave signals were calculated following the "Deterministic Spectral Amplitude" method, by adding 100 sinusoidal components. They covered the whole steps duration and were computed prior to the tests, which ensured a good reproducibility in the succession of waves during a given step for all tests.

Evaluation of the wave heights is of prime importance for such a study. Under normal waves, water surface elevation was measured with three gauges, which enables to separate incoming and reflected waves by mean of a spectral analysis. Incoming waves characteristics (peak period  $T_p$  and significant wave height  $H_s$ ) were determined this way.

Under oblique waves however, it was not possible to separate incoming and reflected waves. It has then been decided to measure only a "global wave height" (incoming+reflected) at a location in the wave basin that was not optically under direct influence of reflection (cf. fig. 2).

Surface elevations were also measured in front of each test section to ensure that the wave field was homogenous. Wave measurements and their analysis were performed over the whole duration of each step, i.e. over 2000 waves.

### **Damage evaluation**

Damage level to the armour layer  $D_a$  was determined by counting, at the end of each step, both blocks that were removed out of the cover-layer and blocks that were distinctly displaced. Armouring units were coloured and the armour layer consisted in a succession of horizontal coloured stripes, the width of which was two blocks (two median diameters for rock), so that displaced blocks were those displaced out of their coloured band, while still standing in the cover layer. All displaced or removed blocks were counted at the end of each step, so that *cumulated* damage was evaluated.

Cumulated damage to the toe berm  $D_t$  was determined in the same way, but by counting the number of removed blocks only (reshaping not considered).

Damage measurements were made on a 1 m wide section in the centre part of each trunk, called the test section in the following, in order to avoid side effects at the junction of two trunks when oblique waves are performed. Before counting, the water level was lowered to the toe mound. Damage levels are expressed as the percentage of displaced and removed units in the test section.

### **Overtopping measurement**

The number of overtopping waves was recorded on a paper-recorder, over the whole duration of each step, at the centre of each trunk by use of a wave gauge placed on top of the structure. Calibration enabled to discriminate between green water and broken spray. Overtopping was expressed as the percentage of overtopping waves  $N_{ov}$ .

## **Experimental results**

### **Wave field**

The main problem here is the impossibility to separate incoming and reflected waves for the tests under oblique waves, which makes questionable the comparison

between the results of these tests, and even more with those under normal waves. To clear up that point, all steps 7 were re-run with normal waves after all tests had been performed, ensuring very carefully that waves were measured in strictly identical conditions : same wave signal, same location of the wave gauges, same position for the wave guides as during the tests. The global wave height measured under oblique wave was then compared to the incident normal wave height. As their relative difference is expected to grow up with increasing wave height (the reflected wave becoming higher), the comparison between these two values for step 7 is a good evaluation of the accuracy of the global wave height as an estimate for the incident wave height under oblique waves. As this relative difference was lower than 6% for all tests, the global wave height as measured under oblique waves was thus considered as a reasonable approximation of the actual incident one.

### Armour stability

The curves shown hereafter present the percentage of moved armour blocks  $D_a$  as a function of the non-dimensional significant wave height  $H_s/\Delta D_n$ , and are limited to  $D_a < 20\%$ , which is their most significant part.

Table 4 below gives the relative variation in wave height with respect to normal wave when increasing obliquity, corresponding to several given damage levels (start of damage,  $D_a = 5\%$  and  $D_a = 10\%$ ).

$\beta$ (°)	15	30	45	60	75
Antifer Cube					
$D_a < 0.1\%$	+ 56 %	+ 52 %	+ 54 %	+ 130 %	+ 140 %
$D_a = 5\%$	+17 %	+ 31 %	+ 31 %	-	-
$D_a = 10\%$	+ 4 %	+ 13 %	+ 18 %	-	-
Tetrapod					
$D_a < 0.1\%$	+ 52 %	+ 50 %	+ 44 %	+ 48 %	+ 140 %
$D_a = 5\%$	+ 8 %	+ 4%	+ 5 %	+ 22 %	-
$D_a = 10\%$	- 3 %	- 4 %	+ 2 %	+ 16 %	-
Rock					
$D_a < 0.1\%$	- 17 %	+ 65 %	+ 35 %	+ 49 %	+ 98 %
$D_a = 5\%$	0 %	+ 10 %	+ 6 %	+ 6 %	-
$D_a = 10\%$	- 4 %	+ 6 %	+ 15 %	+ 18 %	-
ACCROPODE <sup>®</sup>					
$D_a < 0.1\%$	- 23 %	+ 23 %	+ 38 %	+ 21 %	-
$D_a = 1\%$	+ 12 %	+ 19 %	+ 26 %	-	-

Table 4. Relative variation of  $H_s/\Delta D_n$  with  $\beta$ , with respect to normal waves, for start of damage ( $D_a < 0.1\%$ ),  $D_a = 5\%$  and  $D_a = 10\%$ , or  $D_a = 1\%$ . (- indicate that the corresponding damage level was not reached).

Some trends can be seen in table 4 which indicate an increase in stability with increasing angle of wave incidence. Results are detailed below for each unit.

#### Antifer cube

Four trends can be observed from table 4 and fig. 3 :

- stability increases with increasing wave obliquity,
- start of damage is delayed under oblique waves : it corresponds to a wave height 50 % higher for  $\beta = 15^\circ$ ,  $30^\circ$  and  $45^\circ$  than under normal waves,

- damage, once initiated, increases faster under oblique waves than under normal waves : about two times faster for  $\beta = 15^\circ, 30^\circ$  and  $45^\circ$ ,
- For  $\beta > 45^\circ$ , the increase in stability is so high that nearly no damage occurs.

Tetrapod

Exactly the same trends (cf. table 4 and fig. 4) as for Antifer cube can be noted, although they are somewhat less pronounced and valid mainly for  $D_a < 10\%$

These results (increasing stability with increasing obliquity, faster damage increase under oblique waves) are consistent with those reported by Gamot (1969).

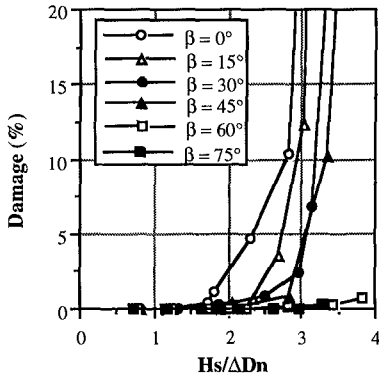


Fig. 3. Armour stability - Antifer cube

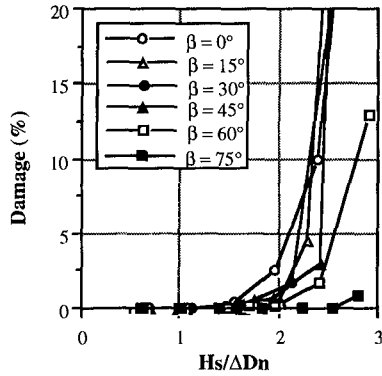


Fig. 4. Armour stability - Tetrapod

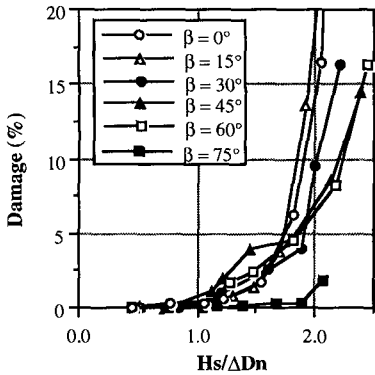


Fig. 5. Armour stability - Quarry stone

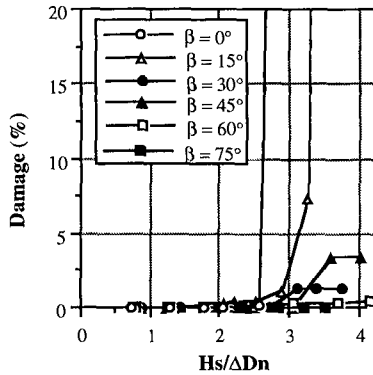


Fig. 6. Armour stability - ACCROPODE®

Quarry stone

From fig. 5 and table 4, start of damage seems to be slightly delayed under oblique waves, but quarry stone is seen to be not very sensitive to wave obliquity, at least at low damage levels ( $D < 5\%$ ). For higher damage levels and  $\beta \geq 30^\circ$ , some trend is noticeable that could indicate an increasing stability for increasing angle of incidence. However, stability strongly increases at  $\beta = 75^\circ$  only.



These points are in accordance with the results of previous works (Gravesen and Sorensen (1977), Van de Keeke (1969)), although the increase in stability was noticed as soon as  $\beta \geq 60^\circ$ .

### ACCROPODE®

Evolution of ACCROPODE® stability with increasing wave obliquity (fig. 6) is quite different from those observed till now. At  $\beta = 15^\circ$ , the armour layer behaves similarly as under normal wave attack, with a very sudden failure (characteristic of a one layer unit) which has led to retain a zero-damage criteria for the design of breakwaters armoured with this unit. At higher angles, its behaviour however significantly differs : after some damage, units rearrange so that the armour is stable again and no more damage occur. This could be explained by the high interlocking of this one layer unit.

### **Toe berm stability**

The curves shown below present the percentage of removed toe blocks  $D_t$  as a function of the non-dimensional significant wave height  $H_s/\Delta D_n$ .

A distinction can be made here between the results for Antifer cube and tetrapod on one hand, and quarry stone and ACCROPODE® on the other hand.

#### Toe berm at Antifer cube and Tetrapod armour layer

The same trends as for the corresponding armour unit can be made (fig. 7 and 8) :

- stability increases with increasing wave obliquity,
- start of damage is delayed under oblique waves : it corresponds to a wave height 45 % higher for  $\beta = 15^\circ, 30^\circ$  and  $45^\circ$  than under normal waves,
- damage, once initiated, increase faster under oblique waves than under normal waves : about 1.6 time faster for  $\beta = 15^\circ, 30^\circ$  and  $45^\circ$ ,
- For  $\beta = 75^\circ$ , the increase in stability is so high that nearly no damage occurs.

What could be add is that, provided that high damage levels to the toe are accepted, a  $15^\circ$  wave incidence could be more dangerous than normal wave.

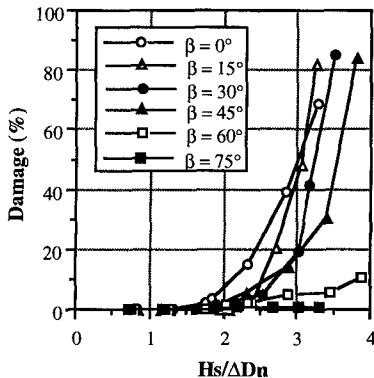


Fig. 7. Toe stability - Antifer cube

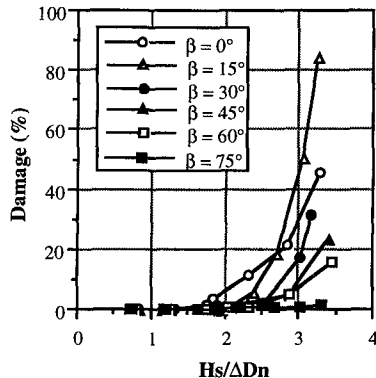


Fig. 8. Toe stability - Tetrapod

#### Toe berm at quarry stone and ACCROPODE armour layer

The behaviour of toe berm at quarry stone and ACCROPODE® armour layer (fig. 9 and 10) is rather atypical. Initiation of damage is not so much delayed under oblique

waves, and the only marked trend is an increase in stability with increasing wave incidence for  $\beta \geq 30^\circ$ . However for ACCROPODE®, the same trend as for Antifer cube and tetrapod can be noticed, that is that damage could possibly be higher at  $15^\circ$  than under normal waves.

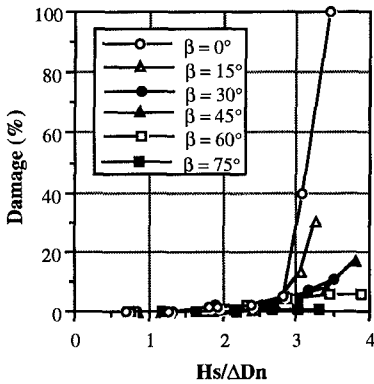


Fig. 9. Toe stability - Quarry stone

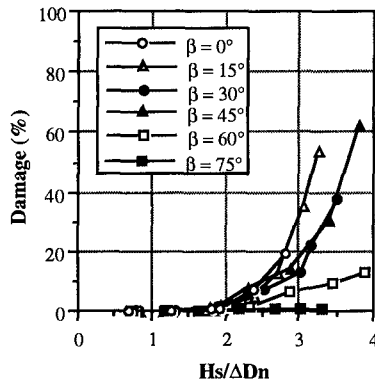


Fig. 10. Toe stability - ACCROPODE®

Out of the scope of this study but important to notice, is that very high damage levels to the toe berm were reached without endangering the stability of the armour layer.

**Overtopping**

The curves shown hereafter present the percentage of overtopping waves  $N_{ov}$  as a function of the significant wave height  $H_s$ .

For all the units studied here, the percentage of overtopping wave  $N_{ov}$  is seen to present the same features (fig. 11 to fig. 14):

- overtopping is equivalent under normal waves and a  $15^\circ$  incidence,
- overtopping then decreases with increasing wave obliquity,
- at  $\beta \geq 60^\circ$ , overtopping is reduced to nearly zero, except for quarry stone.

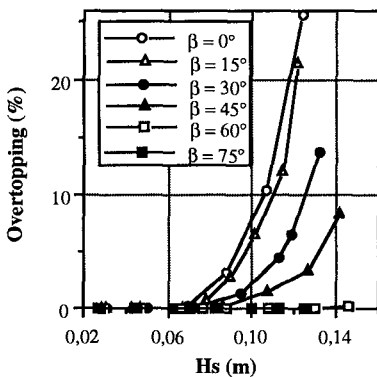


Fig. 11. Overtopping - Antifer cube

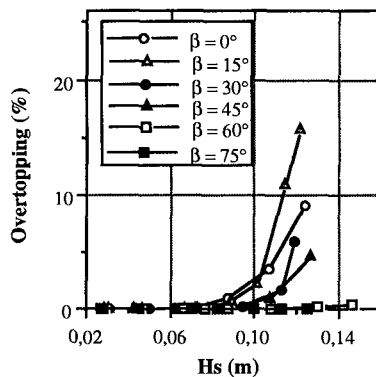


Fig. 12. Overtopping - Tetrapod

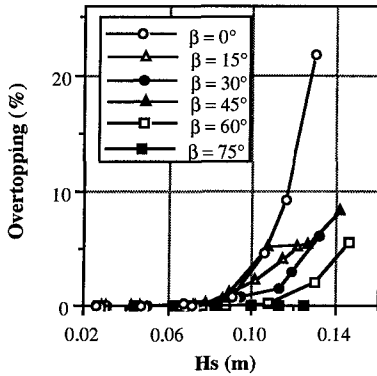


Fig. 13. Overtopping - Quarry stone

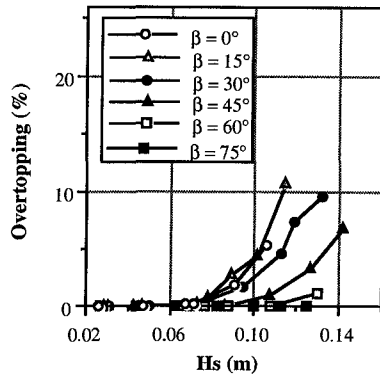


Fig. 14. Overtopping - ACCROPODE®

**Discussion**

The aim of this study was not to derive new formulae for the design of rubble mound breakwaters armour layer and toe berm or for the evaluation of overtopping rates, but to provide a better idea of the influence of wave obliquity and also to propose a way for taking into account that influence in existing formulae.

In this idea, and as the apparent slope of the breakwater turns from  $\text{tg}\alpha$  under normal waves into  $\text{tg}\alpha \cdot \cos\beta$  under a  $\beta$  angle of wave attack, it is of interest to study all the above mentioned phenomena as functions of  $H_s \cdot \cos\beta^x$  instead of functions of  $H_s$  only,  $H_s \cdot \cos\beta^x$  being then an *equivalent normal wave height*.

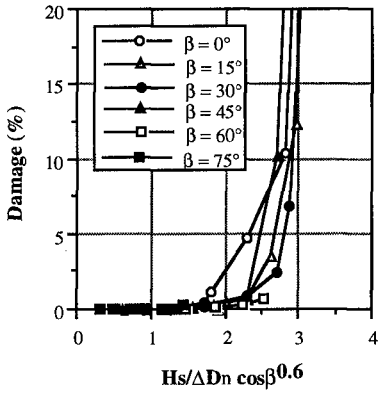
The remaining problem is of course to determine the coefficient  $x$  : results are not numerous enough to allow for the use, from a scientific point of view, of a numerical "best fit" method and the evaluation of  $x$  has then to be derived by visual adjustment, being thus subject to some interpretation.

All the curves for armour, toe berm stability, and overtopping have been re-plotted against  $H_s \cdot \cos\beta^x$ , with the best estimates for  $x$  (fig. 15 and fig. 16). A summary of the values obtained for  $x$  is given in table 5 below.

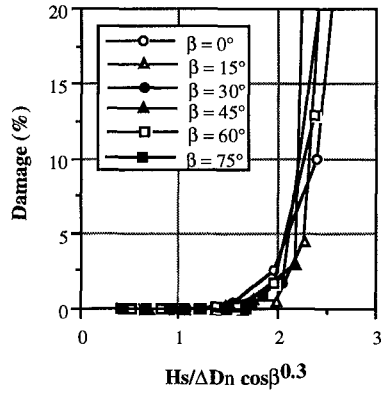
Such an approach is not fully satisfactory : first because, in some cases, the adjustment is not very good and second because it can not represent the change in the slope of some of the curves that occurs under oblique wave. Nevertheless it could be very useful for the preliminary design of breakwaters.

	Antifer cube	Tetrapod	Quarry stone	ACCROPODE®
Armour stability	0.6	0.3	0.25	1
Toe stability	0.6	0.4	0.6	0.4
Overtopping	1	0.6	1/3	0.75

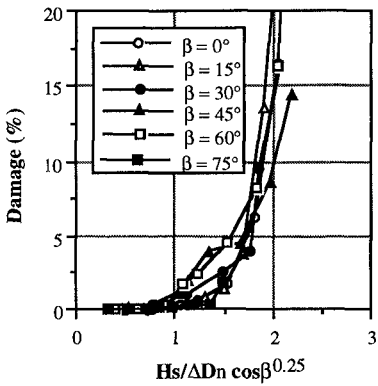
Table 5. Coefficient  $x$  for the equivalent normal wave height  $H_s \cdot \cos\beta^x$ .



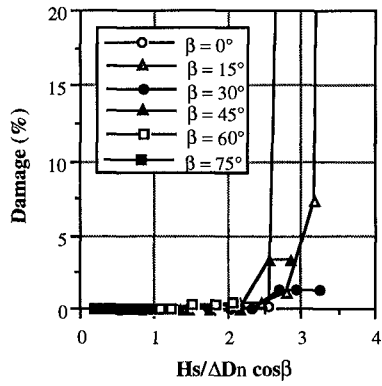
a. Stability - Antifer cube



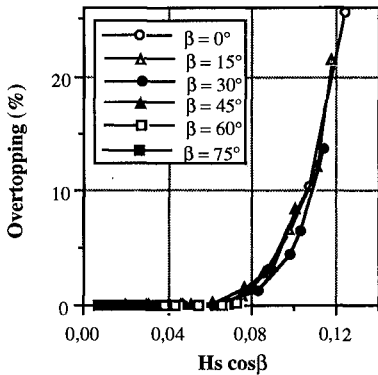
b. Stability - Tetrapod



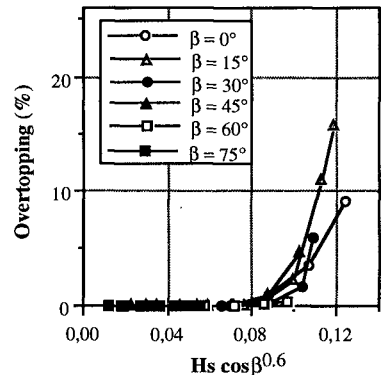
c. Stability - Quarry stone



d. Stability - ACCROPODE®

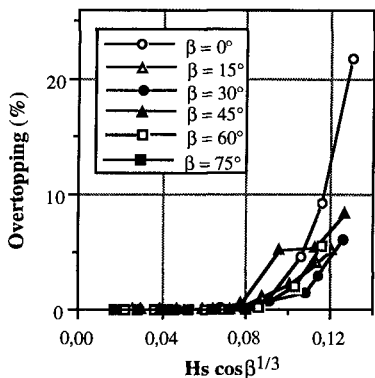


e. Overtopping - Antifer cube

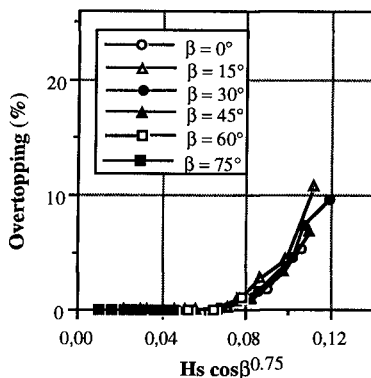


f. Overtopping - Tetrapod

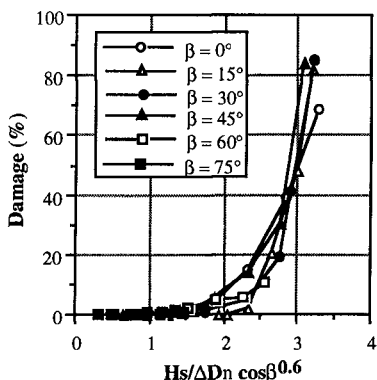
Fig. 15. Re-plot of the results against the equivalent normal wave height



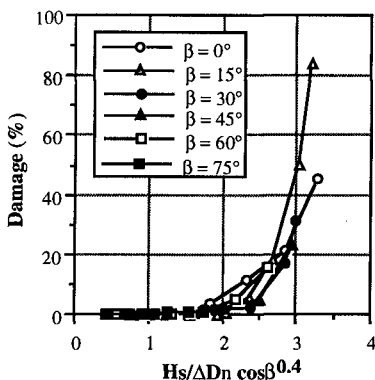
a. Overtopping - Quarry stone



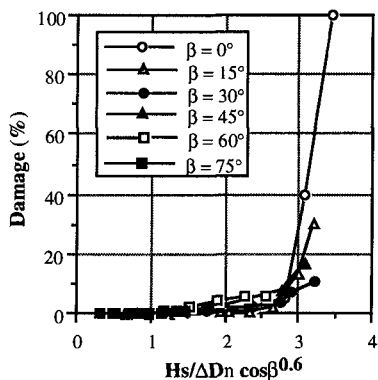
b. Overtopping - ACCROPODE®



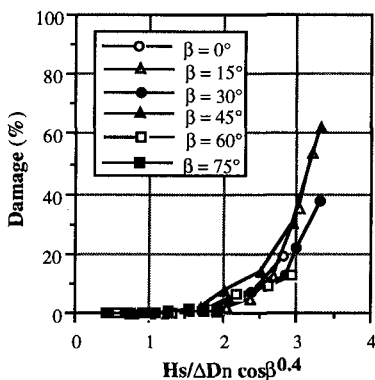
c. Toe stability - Antifer cube



d. Toe stability - Tetrapod



e. Toe stability - Quarry stone



f. Toe stability - ACCROPODE®

Fig. 16. Re-plot of the results against the equivalent normal wave height

As a general remark, it should be noted that the results obtained within this study do not support the vague belief in a lower stability at small angles of wave incidence (say  $\beta = 10^\circ$ - $30^\circ$ ). Such a belief is mainly based on run-up measurements, which have been shown to be maximum at  $\beta = 10^\circ$ - $30^\circ$  on smooth, mild slopes (Tautenhain et al. (1982), CUR/CIRIA (1991)).

The numerical values derived within this study are to be taken with great care, as they result from a single test at each wave angle. Many authors (Jensen (1984), Burcharth et al. (1986), Galland and Manoha (1991) for instance) have indeed stated a large scatter in results of such tests, so that a well-defined characterisation of the influence of wave obliquity should be derived from series of identical tests.

But what is important here, is that the results are not drowned into the scatter but *do really define* the trends reported above ; only the actual values of the gains obtained under oblique waves are not known exactly.

## Conclusions

Under the conditions tested :

- flat bottom (no shoaling effect),
- JONSWAP spectrum,  $\gamma = 3.3$  (no influence of spectrum width or wave groupiness),
- constant wave steepness,  $s_{op} \cong 4\%$  (constant surf similarity parameter  $\xi_{op}$ ),
- 2000 waves per step (no influence of storm duration),
- one series of tests per angle of wave incidence (scatter not considered),

the following conclusions can be drawn :

### Armour stability

#### *Concrete units*

- armour stability increases with increasing angle of incidence,
- initiation of damage is delayed under oblique waves,
- once initiated, damage increases faster under oblique waves (Antifer cube, tetrapod).

#### *Quarry stone*

- armour stability is not much influenced by wave obliquity at damage levels lower than 5%,
- at higher damage levels and at incidence higher than  $15^\circ$ , armour stability slightly increases with increasing wave obliquity.

### Overtopping

#### *All units*

- overtopping is equivalent under normal waves and at a  $15^\circ$  angle of wave incidence,
- then, it continuously decreases with increasing incidence.

### Toe berm stability

#### *Concrete units*

- toe berm stability is equivalent, and can even be lower, at a  $15^\circ$  angle of wave attack and under normal waves,
- then it increases with wave obliquity.

#### *Quarry stone*

toe berm stability continuously increases with increasing obliquity.

### Equivalent normal wave height

Results obtained at an angle of wave attack  $\beta$  and a wave height  $H_s$  are equivalent to those obtained under a normal wave height  $H_s \cdot \cos\beta^x$ ,  $x$  being a coefficient which depends on the phenomenon and the unit under consideration. This way, it is possible to use formulae derived under normal wave attack to take into account wave obliquity, for preliminary design of breakwaters.

However it is important to keep in mind that these conclusions result from a single series of tests at each wave incidence, and therefore do not take into account the scatter often reported. Trends presented in this paper are assessed because of the continuity in the evolution of the phenomena they represent, but numerical values should be taken just as estimates. Further testing is still required in order to derive reliable laws taking into account the influence of wave obliquity on the stability of rubble mound breakwaters.

### Acknowledgement

This work was funded partly by the EC under contract n° MAST - 0032 - M (JR) and partly by the French Sea State Secretary (STCPMVN).

### References

- Burcharth, H. F. and Brejnegaard-Nielsen, T., 1986. The influence of waist thickness of dolosse on the stability of dolosse armour. I.C.C.E. Taiwan, vol. 2, chp. 130, pp. 1783-1796.
- CUR / CIRIA, 1991. Manual on the use of rock in coastal and shoreline engineering. Published by CIRIA, London, UK and CUR, Gouda, The Netherlands.
- Galland, J.-C. and Manoha, B., 1991. Influence of wave grouping on the stability of rubble mound breakwaters. Proc. XXIV IAHR Conf., Madrid.
- Galland, J.-C., 1993. Rubble mound breakwaters stability under oblique waves. LNH Report HE-42/93-18, prepared for MAST G6-S Coastal Structures.
- Gamot, J.-P., 1969. Stabilité des carapaces en tétrapodes de brise lame à talus. La Houille Blanche n° 2 (in French).
- Gravesen, H. and Sorensen, T., 1977. Stability of rubble mound breakwaters. PIANC, 24<sup>th</sup> Int. Navigation Congress, Leningrad.
- Jensen O. J., 1984. A monograph on rubble breakwaters. DHI, 209 p.
- Markle, D. G., 1989. Stability of toe berm armour and toe buttressing stone on rubble mound breakwaters and jetties; Physical model investigation. CERC, Vicksburg, Technical Report REMR-CO-12.
- Tautenhain, E., Kohlhase, S., Partensky, H.W., 1982. Wave run-up at sea dikes under oblique wave approach. I.C.C.E. Cape Town, vol. 1, chp. 50, pp. 804-810.
- Van de Kreeke, J., 1969. Damage function of rubble mound breakwaters. J. Waterways and Harbours Division, Proc. ASCE, Vol. 95, n° WW3.
- Whillock, A. F., 1977. Stability of dolos blocks under oblique wave attack. Hydraulics Research Station, Wallingford, report n° IT 159.

## CHAPTER 78

### WAVE LOADS ON SEADYKES WITH COMPOSITE SLOPES AND BERMS

by  
Joachim Grüne<sup>1</sup> and Hendrik Bergmann<sup>2</sup>

#### Abstract

This paper deals with investigations on loads from wave-induced shock pressures on seadykes with composite slopes and berms. The investigations have been done with large scale laboratory tests, using different wave climate characteristics ( regular waves, PM - spectra and field spectra ). Two different types of dyke cross-sections have been investigated: one with an upper slope 1:6 and a berm in front, and the other one with composite slopes 1:3 in the lower part and 1:6 in the upper part. The presented results were discussed with respect to the influences of wave climate, of absolute waveheights and of geometrical conditions.

#### Introduction

Due to the increasing of storm surges and the supposed long-term rising of water levels at the coastlines of the North Sea, wave loads on seadykes have become again more important for savety analysis of existing dykes. Air entrainment and wave climate characteristics under real sea state conditions play an important role both on shock pressure occurrence and on wave run-up process. Thus boundary effects and scale effects have to be minimized by using field data or large scale laboratory test data. The results presented in this paper were obtained from large scale laboratory tests in the "Large Wave Channel" ( GWK ) at Hannover, Germany, within an extensive research program on stability on sloping seadykes and revetments ( supervision Prof. Führböter + ), which had been supporting partly by the German Research Foundation ( DFG ) for more than 10 years. Previous results from this research program on wave loads on **uniform slopes** have been reported recently for example by Grüne ( 1992 ) for shock pressures and by Sparboom, Grüne, Haidekker & Grosche ( 1990 ) for wave run-ups.

<sup>1</sup> Dipl.-Ing., Senior researcher, Deputy Operation Manager of Joint Institution Large Wave Channel ( GWK ) of the University of Hannover and the Technical University of Braunschweig, Merkurstrasse 11, 30419 Hannover, Germany.

<sup>2</sup> Dipl.-Ing., Researcher, Hydrodynamic and Coastal Engineering Dept. of Leichtweiß Institute of the Technical University of Braunschweig.



First results from the recent investigations with **composite slopes and berms** on loads from shock pressure occurrence will be presented in this paper. First results on loads from the wave-run-ups measured synchronously within the same testseries are reported by Schüttrumpf, Bergmann & Dette ( 1994 ).

### Test equipment and data recording

The investigations have been conducted in the Large Wave Channel ( GWK ) at Hannover ( Grüne, Führböter, 1976 ), which is a joint institution both of the University of Hannover and the Technical University of Braunschweig.

Two different types of dyke cross-sections were installed, which are shown in figure 1. A uniform slope of 1:6, which had been used for previous investigations, in its lower part, firstly was replaced by a berm up to 3.3 m above bottom ( upper cross-section in Fig.1 ), then secondly replaced by lower slopes of 1:3 ( middle and lower cross-section in Fig.1 ). To get a wide range for the vertical distance  $D_c$  between stillwaterlevel *SWL* and slope junction, the replacing by lower slopes of the composite slope cross-sections has been done in two steps. In the first step the lower slope was built up to the same level as the berm ( 3.3 m above bottom ), in the second step up to 4.5 m above bottom.

Waves were measured with wire gauges in front of the wave generator and in front of the dyke cross-sections. The wave induced shock pressures were measured with pressure cells on the slope surfaces in vertical distances of roughly 10 cm. The areas on the dyke surface with installed pressure cells are indicated in figure 1. For the testseries with the berm and the composed slopes with a lower slope up to 3.3 m above bottom pressure cells only were installed on the upper slope 1:6. Furthermore wave run-up was recorded with a step run-up gauge.

The testseries for each of the three dyke cross-sections in figure 1 were conducted with two water levels ( 4.0 m and 5.0 m above bottom ). For each testseries with one of these both waterlevels three different types of wave characteristics were generated: Regular waves, PM - spectra ( narrow banded ) and field spectra ( wide banded ); roughly 15 single tests with each of these three wave climate types. The generated field spectra had been measured in front of similar dyke cross-sections at the german coast during high storm surges.

For data collecting two different modes have been used: With the first one all analog signals from pressures cells, waves gauges and wave-run-up gauges were continuously digitized with 100 Hz and then stored by the main processing computer. With the second mode only higher individual shock pressure events were stored additionally by a personal computer, using 200 ms long time intervals of the pressure signals as uncontinuous windows with a digitation rate of 1 kHz. The advantage of this sample method is the high digitation rate, but due to that the disadvantage is, that the sample is time-restricted, which leads to lossings of total

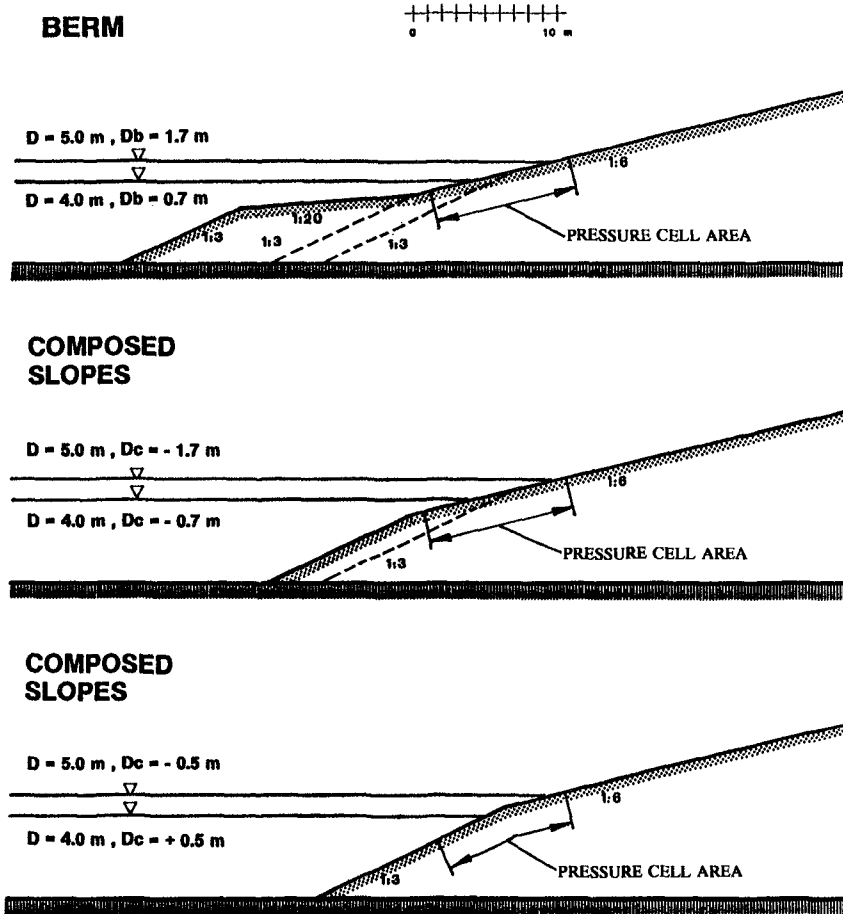


Fig. 1 Dyke cross-sections with berm and composed slopes, investigated in the LARGE WAVE CHANNEL (GWK)

events, especially if the threshold level is accomplished by high quasi-static pressures or by spikes from noises. Therefore a complete data analyzing of all testseries with all pressure cells was done from the 100 Hz digitized datafiles. It must be mentioned, that there were some reduced peak pressure values for higher shock pressure events compared with the 1 kHz-digitation-mode, depending on the peak pressure rising time. The reductions mostly were small, but some rare events were reduced up to approximately 30%. With respect to the stochastic behaviour the influence of partly reduced maximum peak pressure values on the general characteristics of shock pressure occurrence seems to be small.

### Analyzing of shock pressures, definitions

Shock pressures occurring on sloping dyke surfaces are damped more frequently compared to those on vertical walls. Furthermore, especially under real sea state conditions, partly they are mixed with pressure components from waves and wave run-ups. Thus it is often very difficult to distinguish the real shock pressures from the steep wavefronts or the wave run-up fronts, especially if one use normal speed records. In previous reports the author has described an detailed method of analyzing pressure-time histories from high-speed records, which allows a summerizing of the numberless different occurring shapes of pressure-time histories by anatomy parameters ( Grüne 1988a, 1988b, 1992 ).

Using this parameterizing mode, it was possible to evaluate a generalized model of shock pressure occurrence with respect to deterministic and stochastic characteristics. The deterministic parts of the model are represented by local distributions of the anatomy parameters on dyke surface. The local distributions may be divided into different local ranges, which each of it represents a certain state during the breaking process.

For the stochastic part of the generalized model stands the superposition with the stochastic fluctuations of the anatomy parameters. Most data of the different anatomy parameters spread like stars at the sky. But nevertheless there are some clear tendencies and some envelope conditions. There are many possibilities of relating the parameters one with another, reasonable trends were found in dependence on the peak pressure values  $P_{max}$ . In all cases the quality of correlation increase with increasing  $P_{max}$ . Thus the higher peak pressures may be seen as indicators both for general shock pressure occurrence and for details of anatomy parameters.

The following definitions and notations have to be given with respect to the presentation of the results in this paper:

- The maximum pressure value ( peak pressure ) of an individual shock pressure event usually is defined as  $P_{max}$  [  $10^4$  Pa , ( m waterhead ) ].
- The maximum value of all peak pressures  $P_{max}$ , recorded during one single test is defined as  $Max P_{max}$  and is either analyzed from the data of each pressure cell separately, when the results are presented as local distributions or analyzed from all pressure cells, when presented in dependence of the breakerindex  $\xi$ . All pressure data are related to waveheights  $H$  and are therefore dimensionless, using [ m waterhead ] for pressures and [ m ] for waveheights.
- The waves were generated with a closed loop system, to prevent rereflexion at the wave generator. Thus the generated waveheights have been used. A comparison with the waves, measured in front of the dyke shows sufficient agreements, especially for irregular waves. All waveheights  $H$  are defined as mean waveheights for regular waves and as significant waveheights  $H 1/3$  for irregular waves.

- The unit for the local distribution on the slope surface is defined as waveheight related vertical distance  $\Delta D/H$  between pressure cell and stillwaterlevel SWL as shown in figure 2. The vertical distance between the slope junction and SWL is defined as  $D_c$ , as shown in figure 3. The waterdepth on the slope as  $D$  and the waterdepth on the berm as  $D_b$ .
- The pressure data are either presented in dependence of the breakerindex

$$\xi = H * \tan \alpha / \sqrt{H/L_0}$$

with  $H = H_m$ ,  $T = T_m$  for regular waves and  $H = H/3$ ,  $T = T_p$  for irregular waves or as local distributions. An example for a local distribution of the waveheight related maximum peak pressures  $Max P_{max}/H$  is shown in figure 4. The lefthand plot shows for one single test the local distribution of  $Max P_{max}/H$  for each pressure cell. In the righthand plot such local distributions from all tests within a testseries with constant boundary conditions ( for this example:  $D = 5.0$  m,  $D_c = - 0.5$  m, PM - spectra,  $H = 1.10$  m ) have been summarized by an envelope curve.

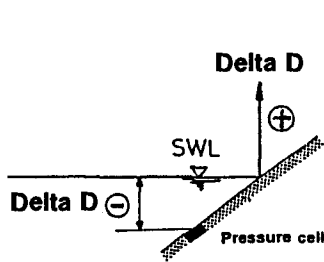


Fig. 2 Definition of  $\Delta D$

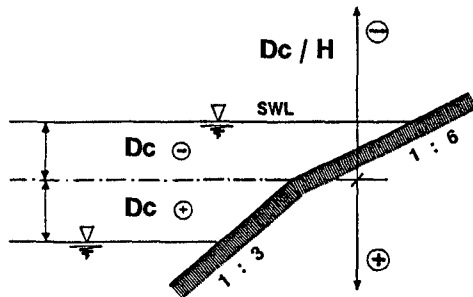


Fig. 3 Definition of  $D_c$

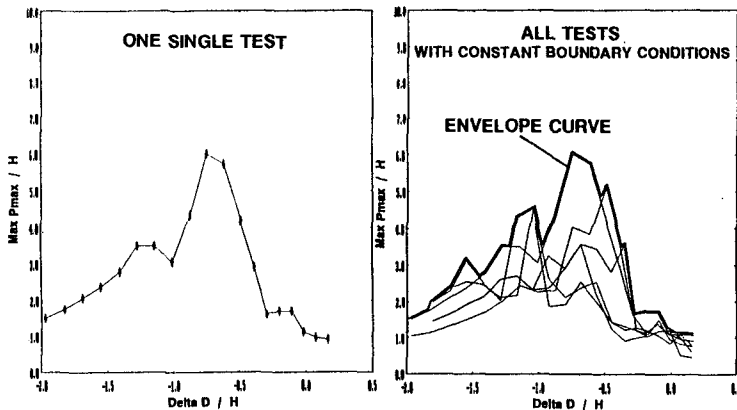


Fig. 4 Example for a local distribution of pressure data  $Max P_{max}/H$

### Results for the dyke with a berm

Figure 5 shows the local distributions of the envelope curves for the testseries with regular waves. It is obvious, that for the testseries with a waterdepth of 5.0 m ( left hand plot ) there is a clear trend of higher waveheight related pressures  $Max P_{max}/H$  with decreasing absolute waveheight  $H$ , which may easily be explained by stronger breaking of higher waves on or in front of the berm due to restricted waterdepths  $Db$  on the berm. There is also a trend of shifting of the local maximum value area to smaller related waterdepths  $Delta D/H$  with increasing absolute waveheight  $H$ , which is also caused by the restricted waterdepth on the berm. A comparison with the corresponding results for the 4.0 m waterdepth in the left hand plot shows, that the trend to higher pressure values is only dominant for waveheights  $H \leq 0.5$  m. With the waterdepth  $Db$  of 0.7 m all higher waves must be broken at least partly.

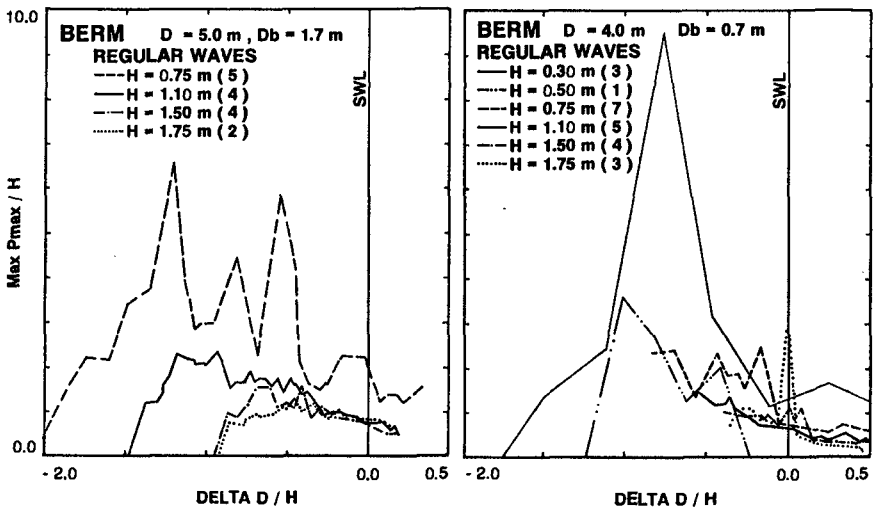


Fig. 5 Local distributions of  $Max P_{max}/H$  for testseries with regular waves

The same trends were found for the results of the testseries with PM - spectra in figure 6, but the differences between the values  $Max P_{max}/H$  of the different waveheights  $H1/3$  are smaller. That is caused by the fact, that not all waves in the irregular wave train were broken compared to a regular wave train with same waveheight  $H$  as  $H1/3$  in the irregular wave train. The same trend also is obvious in figure 7, where the data  $Max P_{max}/H$  of all single tests with regular and irregular waves are plotted versus the breakerindex  $\xi$ .

The envelope curves of the local distribution for all tests with an absolute waveheight  $H$  ( $H1/3$ ) of 1.10 m are plotted for the different wave characteristics

in figure 8. The results indicate for all tests with regular waves smaller pressure values  $Max Pmax/H$  than for irregular waves. Similar results were found for other waveheights. The influence of wave characteristic also comes out in figure 9, where all test results are plotted versus the breakerindex  $\xi$ . Both the influence of wave characteristics and of restricted waterdepth can be seen distinctly.

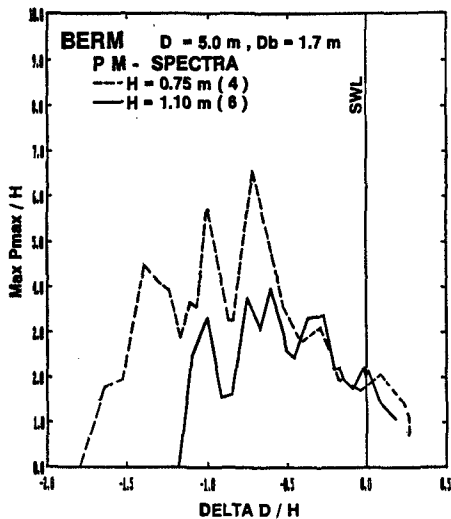


Fig. 6 Local distribution of  $Max Pmax/H$  for testseries with PM - spectra

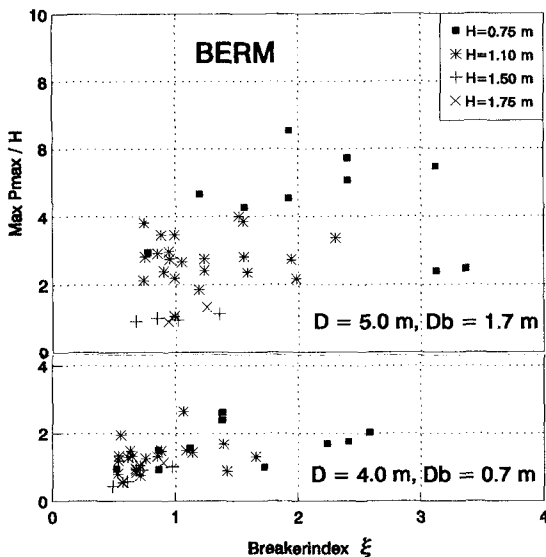


Fig. 7  $Max Pmax/H$  versus breakerindex  $\xi$  for of regular and irregular waves

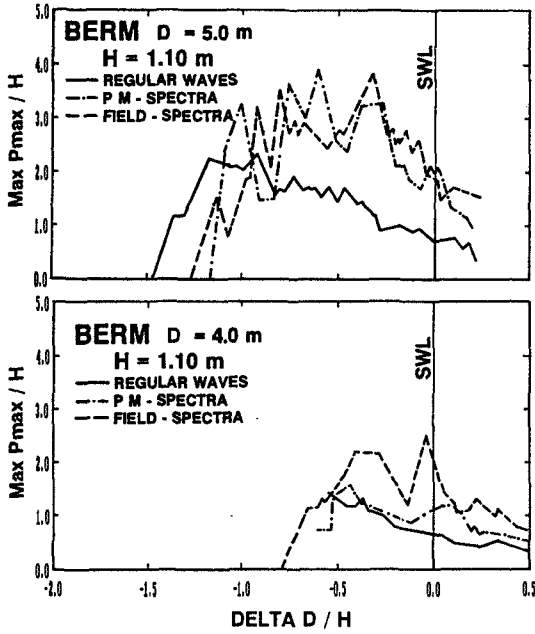


Fig. 8 Local distribution of  $Max P_{max}/H$  for different wave characteristics

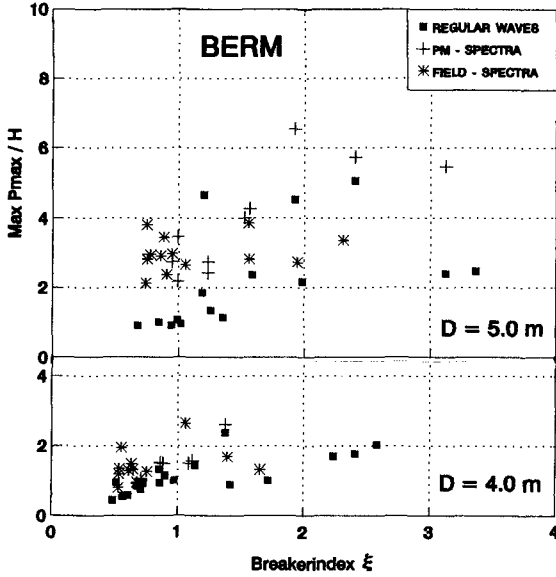


Fig. 9  $Max P_{max}/H$  versus breakerindex  $\xi$  for different wave characteristics

The mentioned trends lead to summarizing all test results as shown in figure 10, where the maximum peak pressures  $Max P_{max}/H$  are plotted versus the waveheight related waterdepth  $Db/H$  on the berm. Both for regular and for irregular waves the same tendency comes out clearly, but with a different mean or upper value gradient. The corresponding maximum value  $Max P_{max}/H$  for an uniform slope 1:6 is plotted in figure 10 as a dotted line. This value is a constant one due to much higher waterdepth and was estimated from previous field and large scale laboratory investigations.

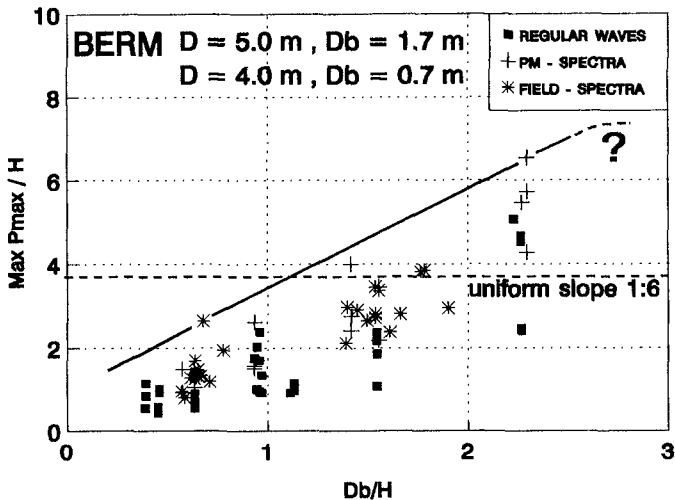


Fig. 10  $Max P_{max}/H$  versus waveheight related waterdepth  $Db/H$  on the berm

It is obvious, that compared to the uniform slope value for the berm, there are as well lower as higher pressure values, depending on the waveheight related waterdepth  $Db/H$  on the berm. Both effects may be explained either by the wave breaking effect in front of the berm ( slope 1:3 ) for lower  $Db/H$  or by the wave shoaling effect on the 1:20 slope of the berm for higher  $Db/H$ . Further it can be expected, that the increasing effect due to shoaling is limited by higher related waterdepths and that the upper value curve goes finally back to the uniform slope 1:6 value. Finally it must be remarked, that decreasing pressure values on upper slope 1:6 due to wave breaking automatically cause higher pressure values on the berm slopes 1:20 and 1:3, which could be recognized during the tests visually and acoustically.

#### Results for the dyke with composed slopes

The trends with respect to absolute waveheight and to wave characteristics differ for the results of the testseries with composite slopes between the testseries in dependence on the level of slope junction and stillwaterlevel. In contrast to the



results for the berm the trend of higher peak pressures  $Max P_{max}/H$  in dependence on the absolute waveheights  $H$  for the testseries, which is most influenced by the upper slope 1:6 ( $D = 5.0$  m,  $D_c = -1.7$  m), is negligible for regular waves and only small for irregular waves, respectively, as shown in figure 11.

If one compare the influences of the different wave characteristics on the results in figure 12, there is the same trend to lower pressure values  $Max P_{max}/H$  for regular waves, which was found for the berm, but with a smaller magnitude.

The maximum values of all single tests of this testseries are plotted in dependence on the breakerindex  $\xi$  in figure 14a. There is a certain influence of the wave characteristics, but the influence of the absolute waveheights was found to be more or less negligible.

A different trend was found for the testseries, which is mostly influenced by the lower slope 1:3, as the junction of the slope is 0.5 m above SWL ( $D = 4.0$  m,  $D_c = +0.5$  m). The tendency on the influence of absolute waveheights in figure 13 changes to higher values  $Max P_{max}/H$  with higher absolute waveheights, less clear for regular waves, but very clear for the PM - spectra.

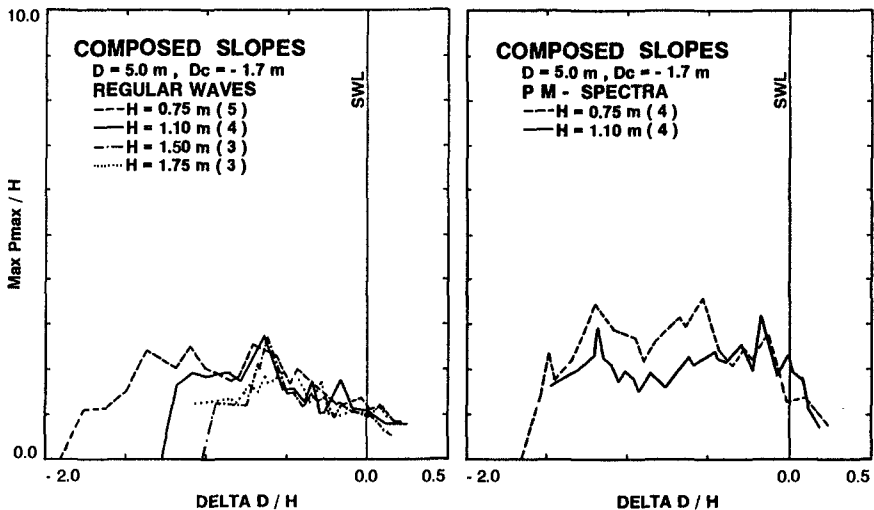


Fig. 11 Local distribution of  $Max P_{max}/H$  for testseries with regular waves.

For the different wave characteristics in figure 15 still a trend was found to higher pressure values with irregular wave trains, which also comes out clearly with the plot of all results versus the breakerindex  $\xi$  in figure 14d.

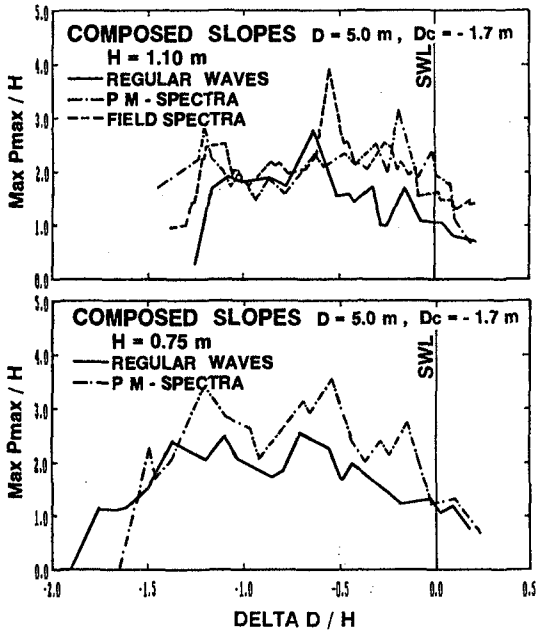


Fig. 12 Local distribution of  $Max P_{max}/H$  for different wave characteristics

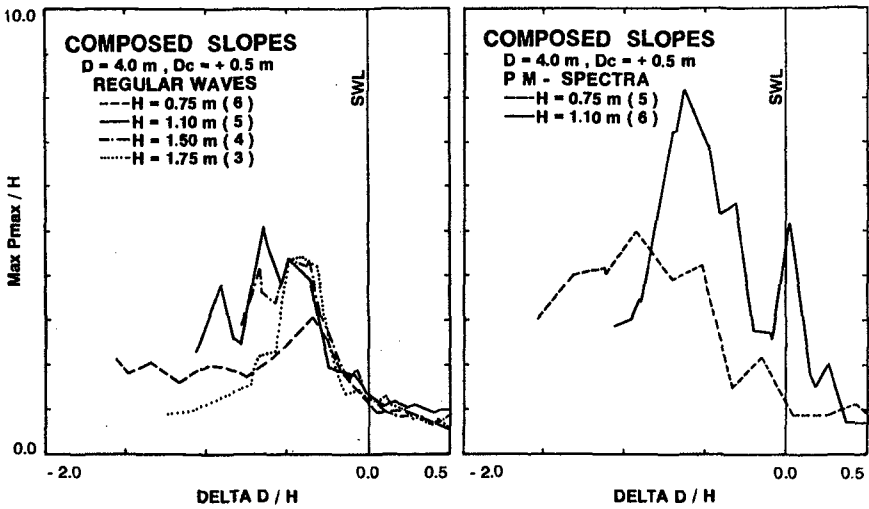


Fig. 13 Local distribution of  $Max P_{max}/H$  for regular waves and PM - spectra

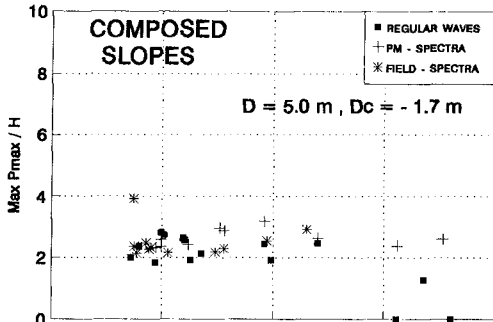


Fig. 14 a

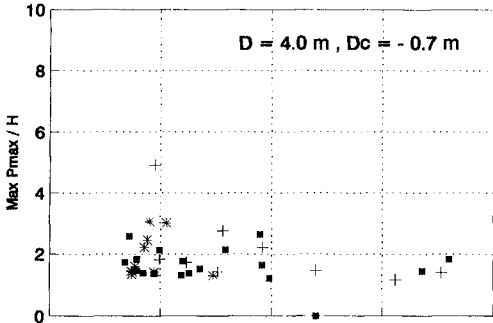


Fig. 14 b

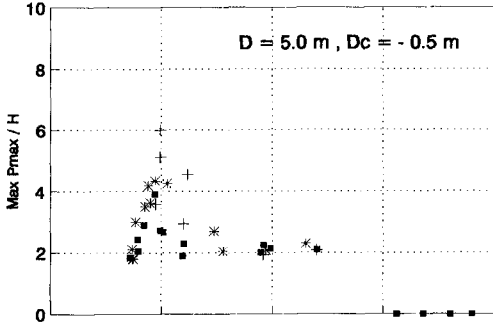


Fig. 14 c

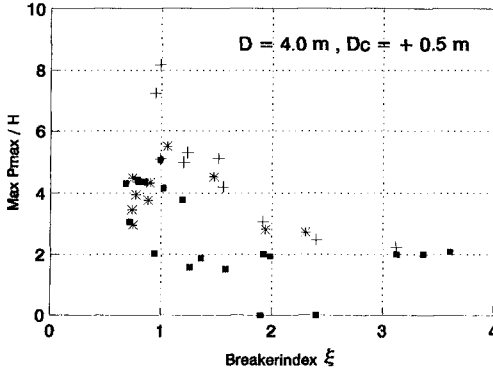


Fig. 14 d

Fig. 14 *Max Pmax/H* versus breakerindex  $\xi$  for all testseries with composed slopes

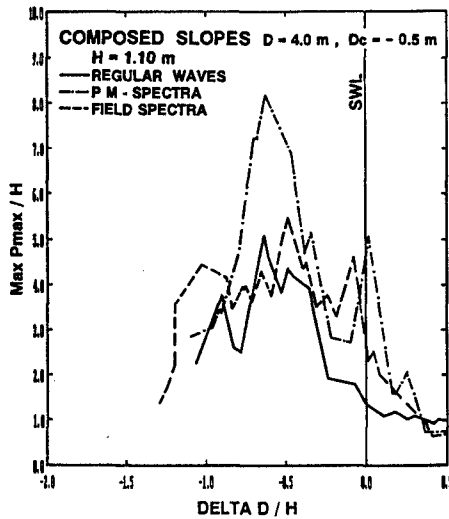


Fig. 15 Local distribution of  $Max P_{max}/H$  for different wave characteristics

Similar results were found with the other both testseries ( $D = 4.0$  m,  $D_c = -0.7$  m;  $D = 5.0$  m,  $D_c = -0.5$  m): Firstly, no distinct trend for the dependence on absolute waveheight  $H$  for regular waves, but a small one for irregular waves. Secondly, the influence of the wave characteristics is evident as shown in figure 14b and 14c, where all test results are plotted versus the breakerindex  $\xi$ . Smaller pressure values  $Max P_{max}/H$  were found for regular waves, as well as in all other testseries.

To summarize the pressure results from all 4 testseries with composed slopes, the pressure values  $Max P_{max}/H$  of all single tests have been plotted versus the waveheight related vertical distance  $D_c/H$  between slope junction and stillwaterlevel  $SWL$  as shown in figure 16 for regular waves (upper part) and irregular waves (lower part). If the slope junction lies below  $SWL$ , the slope 1:6 seems to be dominant. If the slope junction lies above  $SWL$ , the lower slope 1:3 with higher pressure values is dominant. The transition range has a high gradient, if the slope junction is around till roughly half a waveheight below  $SWL$ . The eye-fitted upper value distributions are plotted as dotted lines in figure 16. A qualitative generalisation is given in figure 17. The asymmetry of the influences from both slopes with respect to the distance  $D_c/H$  between slope junction and  $SWL$  is distinct.

Also peak pressure values smaller than for any of both slopes occur at  $D_c/H$  roughly half a waveheight below  $SWL$  from the testseries with  $D = 4.0$  m,  $D_c = -0.7$  m. From the local distributions of the results it was found, that these results may be partly effected by the restricted pressure cell area below  $SWL$ , because for this testseries pressures only have been measured on the upper slope 1:6.

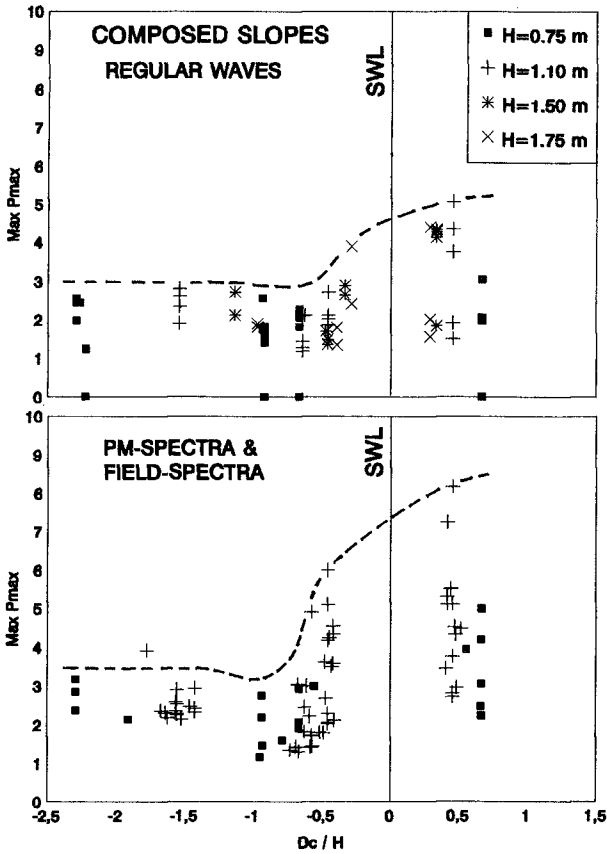


Fig. 16  $Max Pmax/H$  versus  $Dc/H$  for all tests with composed slopes

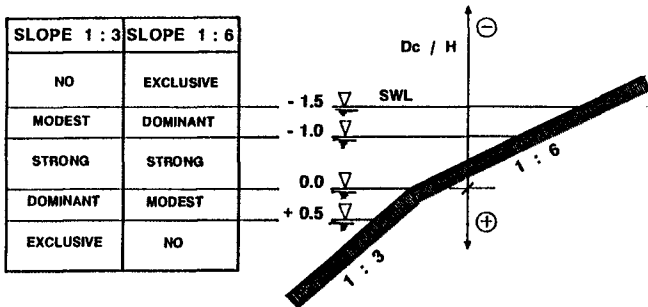


Fig. 17 Scheme of influence of slopes on shock pressure occurrence

### Conclusion

From the results the following statements on the maximum peak pressure occurrence may be concluded:

- There are trends in dependence of the absolute waveheight, but in different ways:
  - a.) Where wave trains are broken at least partly, before they reach the slope ( for instance at the berm ), the waveheight related maximum pressure values  $Max P_{max}/H$  increase with decreasing absolute waveheights  $H$ .
  - b.) Where waves trains are broken completely by the slope ( for instance at composed slopes ), the pressure values  $Max P_{max}/H$  may increase with increasing absolute waveheights  $H$ .
  
- There are strong influences of the wave characteristics:
 

Regular waves always lead to smaller related pressure values  $Max P_{max}/H$ , if regular waveheights  $H$  are compare with irregular waveheights  $H1/3$ . This confirmed previous results for the uniform slopes, that for comparison one should use mean waveheights both for regular and irregular waves. Nevertheless one should not use regular wave results for design of coastal protection works generally.
  
- Some special effects of geometrical conditions can be stated:
  - a.) For a slope with a berm in front, the peak pressures  $Max P_{max}/H$  may decrease due to breaking effect or increase due to shoaling effect depending on waterdepth on the berm.
  - b.) For composed slopes there is a transition range, which is asymmetric with respect to the distance  $D_c$  between slope junction level and stillwaterlevel  $SWL$ .

### References :

- GRÜNE, J., FÜHRBÖTER, A. ( 1976 ). Large Wave Channel for "full-scale modelling" of wave dynamics in surf zones. Proc of Symp. on Modelling Techniques, San Francisco, pp. 82-100.
- GRÜNE, J. ( 1988a ). Anatomy of shock pressure ( surface and sand core ) induced by real sea state breaking waves. Proc. of the Intern. Symp. on Modelling Soil-Water-Structure Interactions ( SOWAS 88 ), Delft, pp. 261-270.
- GRÜNE, J. ( 1988b ). Wave-induced shock pressures under real sea state conditions. Proc. of the 21st International Conference on Coastal Engineering ( ICCE'88 ), Malaga, pp. 2340-2354.
- GRÜNE, J. ( 1992 ). Loads on sloping seadykes and revetments from wave-induced shock pressures. Proc. of the 23rd International Conference on Coastel Engineering ( ICCE '92 ), Venice, pp. 1175-1188.
- SCHÜTTRUMPF, H., BERGMANN, H., DETTE, H.-H. ( 1994 ). The concept of residence time for the description of wave run-up, wave set-up and wave run-down. Proc. of the 24st International Conference on Coastel Engineering ( ICCE'94 ), Kobe.

## CHAPTER 79

### COMPUTERISED METHODOLOGY TO MEASURE RUBBLE MOUND BREAKWATER DAMAGE

Bruno CHILO<sup>1</sup> , Franco GUIDUCCI<sup>1</sup>

#### Abstract

The damage of rubble mound breakwater is a basic interest in the field of design and realisation of coastal works. The individuation of formulations to associate this element with the geometrical characteristics of structures and wave climate conditions is carried out using physical model tests. It is therefore necessary to implement an objective damage valuation method able to point out armour units movements on the layer from the settlement phase to the collapse.

A methodology able to permit an exact measurement of the external layer armour units movements and its damage has been carried out by ESTRAMED S.p.A.; it consists on a computerised analysis of armour units movements in order to give an objective valuation of the damage.

Such methodology is based on photographic images analysis of the armour taken from a fixed point. The procedure permits to determine the position of each armour unit on the images relative to the subsequential damage stages and the movement of each armour unit.

#### Introduction

The experiences relevant to the Port of Sines Main Breakwater, the improvement of computers capabilities, the wider use and the development of the physical modelling and the studies carried out in the last years improved the analysis of the rubble mound breakwater damage. Relations between rubble mound breakwater stability and incident waves and section characteristics were deduced.

---

<sup>1</sup> ESTRAMED S.p.A. - Via Campobello n°6 - 00040 POMEZIA - ROMA - ITALY.

The breakwater stability is usually referred to the eroded volume or to the percentage of units moved more than a fixed threshold.(A.I.P.C.N. 1992, British Standard, 1991).

The measurements of these parameters are extremely important to carry out investigations on the rubble mound breakwater damages and to grow research in this field.

The use of objective methodology to describe the phenomenon from the first movement up to the collapse is essentially.

### Methodology purposes

At ESTRAMED S.p.A. a methodology that allows to measure the external layer armour units movements by a computerised procedure, was developed.

Aims of the methodology were the following:

- to get information on the small armour units movements;
- to obtain objective measurements of the layer damages;
- to analyse armour units movements in a time comparable with the stability test duration.

It is necessary to obtain information on the small armour units movements as the experience on the physical models to test the rubble mound breakwater stability indicates. Small armour units movements are very important because they allow the description of layer damages under the action of ordinary wave motions and to evaluate the entity of the first settlement of the breakwater and therefore, on experiments in which comparative or repetitive tests are required, to make a correct comparison of breakwaters behaviour under the action of extreme waves.

A precise knowledge of small and large movements of the units make possible to draw graphs of the damage on the basis of the incident waves characteristics. These graphs are useful tools for the designer in order to choose the best solution considering the entire structure behaviour, not only in severe damage conditions. Small armour units movements analysis is of interest for the comparison of different solutions even when no severe damage level is reachable, for example, during tests on structures where the wave attack is limited by bottom effects.



The use of a standard laboratory method to measure rubble mound breakwater damage guarantees the repetitiveness of test results and permits to compare results obtained from a large number of experiences carried out by different laboratories, increasing in this way the base of available experimental data for further formulations.

To obtain analysis results of armour units movements in a time comparable with the tests duration allows to make strategy choices on the next tests to be carried out. This permits the optimization of the tests programme and therefore, a large number of damages stages can be easily examined obtaining more information compared to the methodologies often used to measure rubble mound breakwater stability.

### Methodology description

The methodology consists of five subsequent activities:

- set up of rubble mound breakwater armour units;
- acquisition of breakwater images in the subsequent conditions of damage and their importation into the computer;
- images processing;
- check and eventual corrections of images processed;
- print out of the analysis results.

Armour units in nine different colours are employed to build the external layer of the armour so that two units of different colours are located between two units of the same colour and the individuation of the position of each armour unit on each images is facilitated.

The colour selection for armour units painting is very important in this methodology. Each colour must be detected as different from the others by the computer analysis. The achievement of this objective depends on armour units colouring, lighting sources, breakwater contour characteristics, photographic equipment and images filtration; a useful set of colours was selected by Estramed carrying out several tests.

Once placed the units, it is necessary to draw a white point on the sight view of each of them as shown in figure 1 where in the white window are highlighted the units with the same colour. The movement of this point on the sequential images will show the armour unit movement.

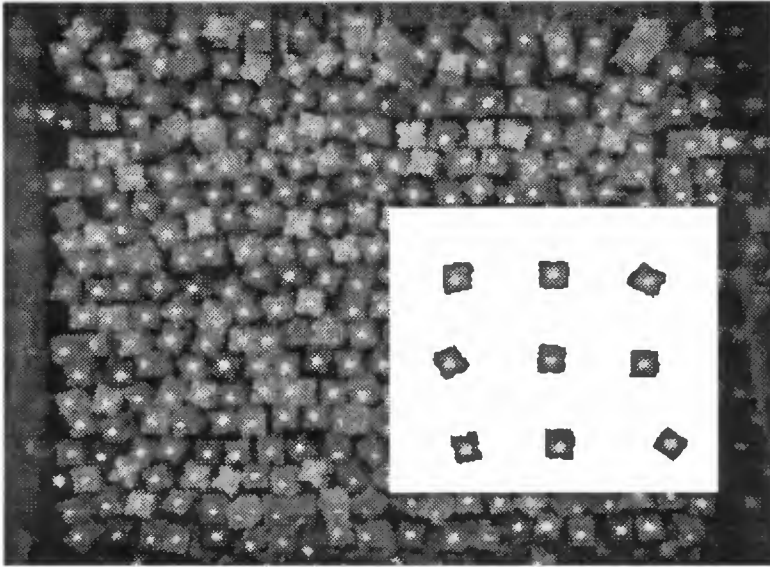


Figure 1 - Set up of rubble mound breakwater armour units

In order to permit the comparison of the different images, at the beginning of the experiments it is necessary to put three marks in the model so that the software can be able to compensate eventual shot point movements and to adopt one single coordinates system to locate each armour unit on each image.

The methodology permits to acquire rubble mound breakwater images in different damage stages and to import them into the computer. The camera station must be fixed and located in such a way that the shooting plane is parallel to the breakwater armour. Images have to be acquired without water in order to avoid reflection and refraction phenomena. The procedure uses a still video camera and a digitiser card with a resolution of 768x576 pixel to acquire and to import the images into a personal computer. Images must be taken at the end of the section construction and after each wave attack.

Once imported into the computer the images are analysed by a software that was set-up by Estramed. Such analysis individuates for each armour unit its colour and the coordinates of the white point located on it as pointed out in figure 2.

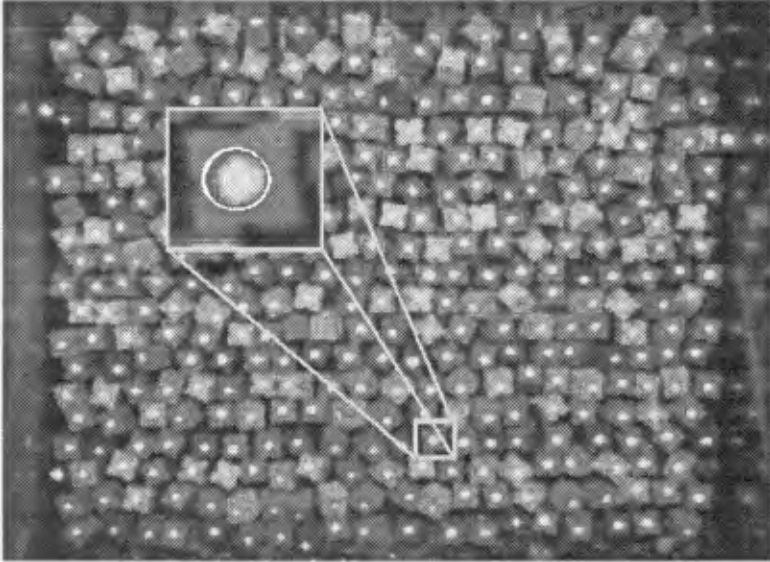


Figure 2 - Example of the analysis result

At the end of this phase, a further analysis is carried out on the files containing, for each image, the coordinates and the colours of the units in order to verify the number of armour units of each colour among all the images. If any inconsistencies arises (for example the number of armour units can be lower compared to the previous one in the case where one or more units rotate on themselves without originate unit barycentric movements, hiding the white evidence point) the operator, who disposes of an edit menu, points out and solves them.

Scope of the second analysis phase is to individuate the position of the same armour unit among all the different images. The procedure performs an analysis examining two files relevant to subsequent images: the file relevant to the less damaged condition is considered as reference for the computation of the units movements. The analysis is carried out taking into account separately armour units of the same colour. As first step, each armour unit of the first image is coupled with the nearest unit of the second image having the same colour in a range less than 0.5 times the characteristic length of the unit. Successively, the analysis is carried out on the not yet associated units increasing the range up to two and half times the characteristic length of the unit as shown in figure 3.

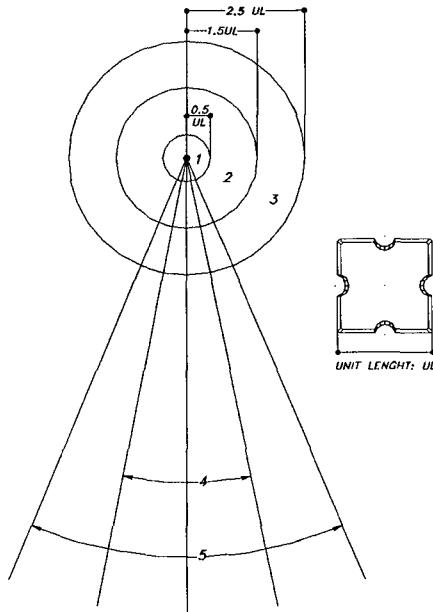


Figure 3 - Scheme of criteria to identify same unit in two successive images

The successive step on the not yet associated units is the coupling of the units present inside circular sectors (see figure 3) which centres are located on the units of the first image, which axis of symmetry is a vertical line and which angle is initially equal to  $10^\circ$  and is successively increased by step of  $10^\circ$  up to  $180^\circ$ . If two possible associations are individuated in the sector, the procedure chooses the one with the minimum angular value compared to the vertical.

Once the coupling of the units has been carried out, the results of the analysis are submitted to the operator for check and for eventual corrections.

The software shows a screen with four windows as shown in figure 4. An image is shown in the upper left window while the successive one appears in the upper right one. The lower right window shows the armour units movements and the lower left one displays an edit menu and the following information:

- number of units for each colour individuated in the two images;
- total number of units individuated in each image;

- number of reference marks individuated in each image.

If any inconsistencies arise the operator can correct the results using the edit menu in a proper way.

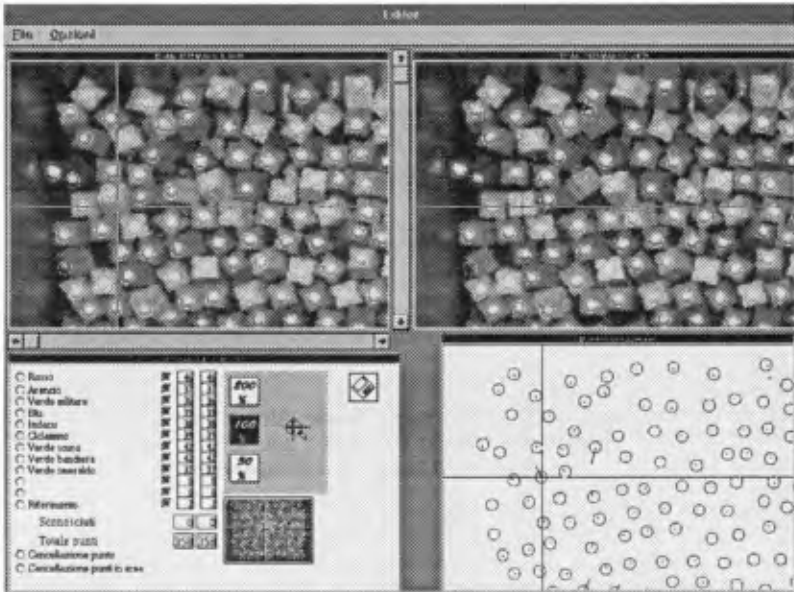


Figure 4 - An example of the results of the units movements analysis

A sequence of the results of the units movement analysis relevant to a test series with increasing waves is shown in figure 5.

The first image (upper left) of figure 5 was taken after the construction of the model and before the start of the tests. The second image (upper right) shows the units movements measured after a test with a very low significant wave height while the last image (lower right) shows the damage of the breakwater after a test characterised by a significant wave height higher than the design one.

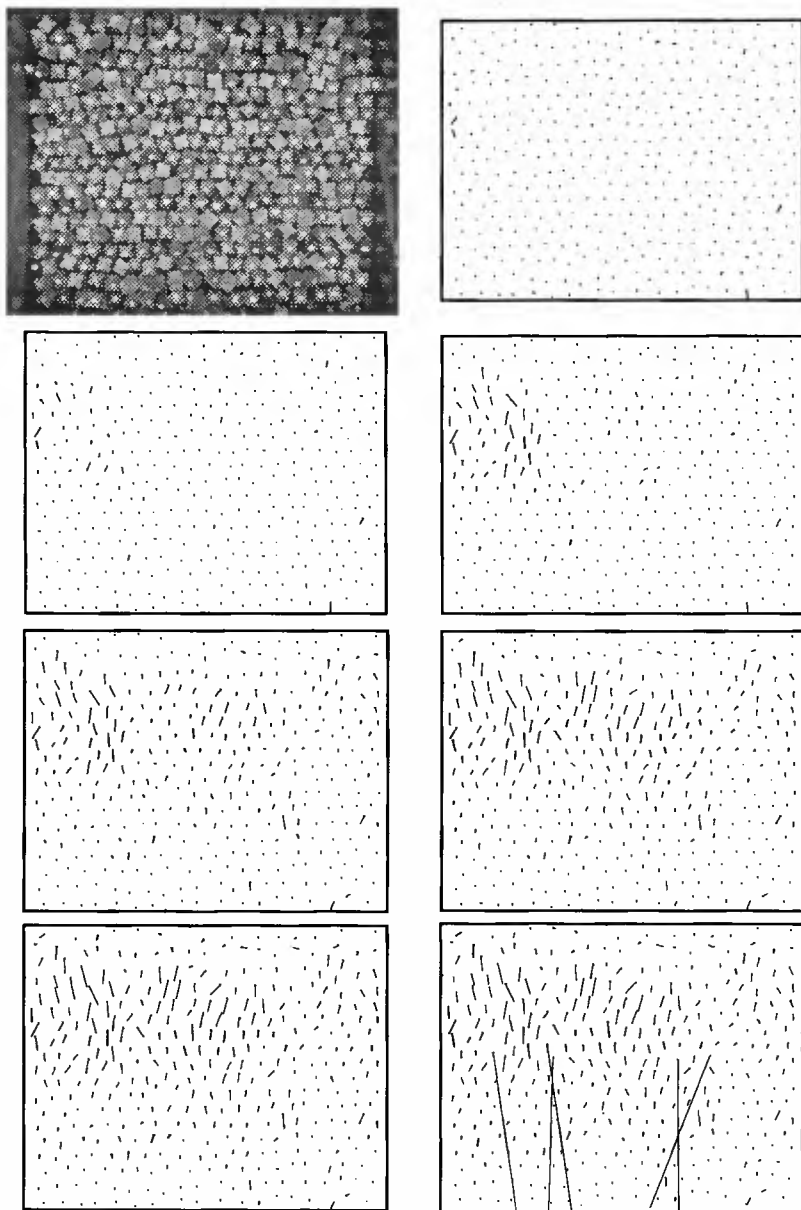


Figure 5 - A sequence of the results of the units movements analysis

The methodology allows to obtain a wide range of information about the units movements. Many information on the small movements of the units can be obtained, too.

A standard plot of the results of the analysis indicates for each test or wave height the percentage of armour units which movements were less than fixed values that are generally part of the characteristic unit length (B). In figure 6 a plot of the results relevant to the analysis of figure 5 is shown.

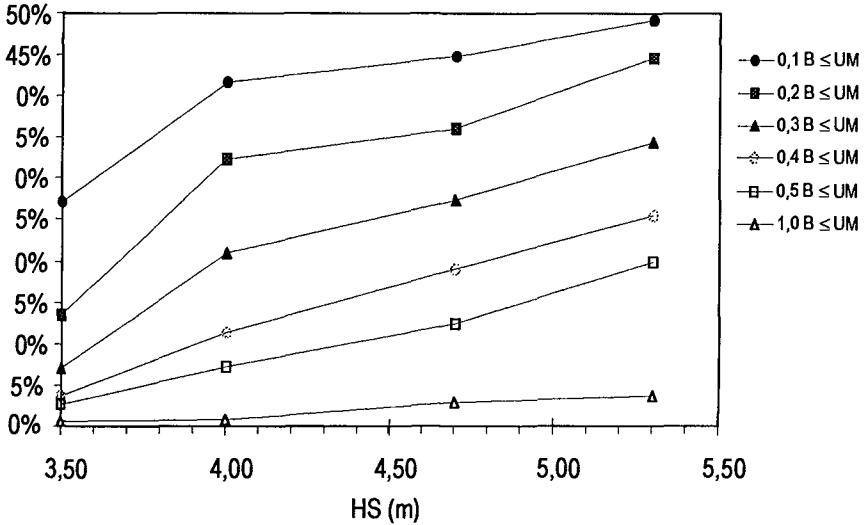


Figure 6 - Units movements versus significant wave height

The methodology has been tested comparing its results with those obtained using a traditional approach. The agreement was very good, at any rate, it must be noted that both methods find difficulties when an unexpected collapse of the whole breakwater happens (with more than 30% of armour units dislocated). This is not a real limit to the method application because, in such conditions the single armour unit movements doesn't give any essential indication on breakwater stability.

Fields of application of the methodology

The methodology has several fields of application in laboratory testing.

A first field is relevant to the two dimensional physical modelling. The methodology allows to carry out objective measurements which are essential for repetitive or comparative tests; to describe accurately the damage behaviour of the breakwater armour and to obtain results in a very short time. In the Estramed S.p.A. Laboratory the methodology has been employed in two dimensional tests to individuate also the movements of toe protection blocks and submerged crest blocks.

A second field is relevant to the three-dimensional physical modelling. Treating these models as plane images, the methodology cannot describe the armour units absolute movements but the parameters to asses a roundhead stability are various and not limited to the armour units movement. Therefore the computerised analysis gives a useful contribute that can be surpassed only using a very sophisticated three dimensional survey system.

Two-dimensional and three-dimensional applications of the methodology are currently used at Estramed S.p.A. Laboratory.

### Conclusion

The computerised methodology allows a reliable and objective measurement of rubble mound breakwaters damage.

The analysis of a stability test is obtained at the end of each run in a shorter time than the test duration.

The use of this methodology permits the standardisation of test modalities and damage levels measurements.

The application in reality of this methodology, with some modifications could bring a remarkable increasing to rubble mound breakwaters know-how.

### Acknowledgements

A special thank goes to Mr. Spartaco Coletta, to Mr. Pompeo Forte and to Mr. Danilo Marinucci for their contribution and cooperation.



Bibliography

- Abecasis,F. - Pita,C.: Monitoring mound breakwater : the case of Sines - Coastal Engineering - 1992.
- British Standards: "Maritime Structures" Part. 7 - Guide to the Design and Construction of Breakwaters, 1991
- Burcharth, H.F.: Design innovations, including recent research contributions - Coastal structures and breakwaters - Institutions of Civil Engineers - London -November 1991.
- PIANC : Analysis of rubble mound breakwaters - Report of Working Group n°12 - Supplement to PIANC Bulletin n° 78/79 - 1992.
- Van der Meer,J.W. : Rock slopes and gravel beaches under wave attack - PhD Thesis - Delft University of Technology - Delft - 1988-

## CHAPTER 80

# WAVE BREAKING OVER PERMEABLE SUBMERGED BREAKWATERS

Masataro Hattori<sup>1</sup> and Hiroyuki Sakai<sup>2</sup>

### Abstract

A laboratory experiment was carried out in a wave tank to examine significant features of wave breaking over permeable submerged breakwaters and to determine the breaker height and depth indices. Submerged trapezoidal-shaped breakwaters were placed on a 1/20 steel slope, and permeability of the breakwaters was varied.

The experiment showed that the breaker height and depth change with the breakwater permeability governing the strength of return flow over the breakwater. Breaker height index was developed in terms of the integrated parameter  $\xi_s$  proposed by Hara et al. (1992), which consists of the geometrical and structure properties of the breakwater as well as properties of incident waves. To determine the breaking position or depth, additional indices were also proposed. Validity of the computation scheme of the breaker height and position were confirmed by comparisons with the experiments.

### INTRODUCTION

As is commonly known, permeable and submerged, low-crested rubble-mound, breakwaters force to break incoming steep waves and dissipate effectively the wave energy. Therefore, many breakwaters of this type have been built or planned at various locations to stabilize an eroded beach and to reduce damages of coastal and harbor structures due to severe wave actions.

---

<sup>1</sup> Professor, Department of Civil Engineering, Chuo University, Kasuga 1-13-27, Bunkyo-ku, Tokyo 112.

<sup>2</sup> Engineer, Urban Development Bureau, Yokohama City, Minato-cho 1-1, Naka-ku, Yokohama City 231, Kanagawa Prefecture.

To meet requirements of the design and construction of the structures, many theoretical and experimental studies are extensively making to deepen understanding of the physics of wave breaking due to the submerged breakwater. The wave breaking may be sufficient to provide the principal control over the wave motion and resulting phenomena around the submerged breakwater, especially behind the breakwater, such as wave transmission, wave set-up, and so on. It seems likely that lack of a sound understanding of wave breaking over the submerged breakwater acts as a bottleneck of the physical and numerical examinations on the hydraulic function of the submerged breakwater.

A series of laboratory experiments was conducted to examine breaking wave properties over permeable submerged breakwaters and to determine the empirical relationships or breaker indices developed from measurements.

The results from the study will be useful for modeling the nearshore wave field around the breakwater and for predicting the evolution of the protected beach profile.

## EXPERIMENTAL EQUIPMENT AND MEASUREMENTS

### Experimental

Figure 1 shows the general arrangement of equipment. Experiments were carried out in a 20-m-long, 0.30-m-wide, and 0.55-m-high glass-walled wave tank, containing a steel beach of 1 on 20 slope. Monochromatic waves were produced by a reflection-absorbed wave maker of flap-type, installed at one end of the tank.

Six model breakwaters of same geometry, as shown in Fig. 2 and composed of the gravel materials or armor concrete blocks, were placed on the slope.

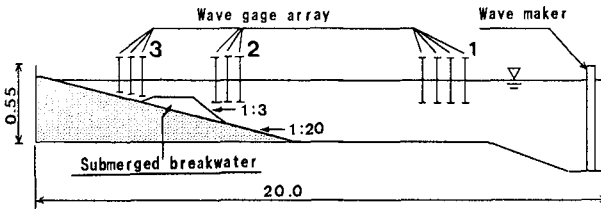


Fig. 1 General arrangement of equipment (units: m).

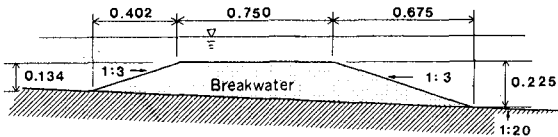


Fig. 2 Dimension of model breakwaters (units: m).

placing condition of the breakwater were determined based on actual breakwaters in Japan. The breakwaters had an upslope and downslope ( $\tan\theta$ ) of 1:3, a 0.75m crest width ( $B$ ), and a 0.225m height ( $d_s$ ). The porosity ( $\epsilon$ ) were varied between 0.17 and 0.52 by changing the material size. In situ porosities were determined from the weight, volume and specific gravity of the materials used. Physical properties of the materials are listed in Table 1.

Table 1 Physical properties of materials used.

Porosity $\epsilon$	Material Used	Material Size (cm)
0	Concrete	---
0.17	Gravel	1.7
0.25	Gravel	2.8
0.38	Gravel	4.0
0.50	Armor Block	7.5
0.52	Gravel	5.0

### Measurements

As see in Fig. 1, water surface elevations were recorded at three wave gage arrays, which consist of either three or four capacitance-type gages. Wave array 1 was located at an uniform water depth section to resolve the incident and reflected wave heights using the method of Mizuguchi (1990). Wave array 2 was placed at the section of the seaward toe of structure slope to measure the incident wave height. Array 3 was set behind the breakwater to measure the transmitted wave height.

Wave data were collected for 2 minutes at 100 Hz, but only 10 successive waves were analyzed to obtain the wave height, mean surface elevation  $\bar{\eta}$  and its variance  $\eta_{rms}$ . Wave profiles on and around the breakwater were recorded by a high-speed video of 200 frames per second. The wave properties were read from the still pictures, with aids of 1.0 cm square grid system attached on the sidewall glass. Incident wave parameters are listed as follows;

- Incident Wave Height :  $H_1 = 2.0 \text{ cm} - 10.0 \text{ cm}$   
 Incident Wave Period :  $T = 0.8 \text{ s} - 1.5 \text{ s}$   
 Water Depth  
   on Horizontal Bottom :  $h_1 = 31.2 \text{ cm}$  and  $35.0 \text{ cm}$   
   above Breakwater Crest :  $R = 3.75 \text{ cm}$  and  $7.50 \text{ cm}$

## INCIPIENT BREAKING

A schematic of a wave profile at breaking on the structure seaward slope of breakwater is depicted in Fig. 3.  $H_B$  and  $h_B$  are the wave height and the water depth at breaking.

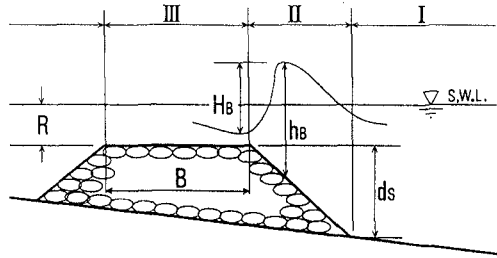


Fig. 3 Definition sketch of breaking wave and demarcation of breaker zone.

There are several ways of defining the break point. After careful inspection of the video pictures of breaking waves profile,

we defined the breaking point as the point where the wave height is maximum. This definition ensured us stable judgement of the breaking point from video pictures. Breaker types observed over the submerged breakwater were basically the same to these over a plane sloping beach, spilling, plunging, and collapsing.

Breaking range of waves passing across the breakwater is demarcated into the three following zones, as shown in Fig. 3;

- Zone I : on the offshore sloping beach in front of the breakwater,
- Zone II : on the structure seaward slope, and
- Zone III : on the breakwater crest.

Thus we will examine characteristics of the wave breaking for each zone.

High-speed videos of the wave profile over the breakwater revealed that return flow over the crest and offshore slope of the breakwater influences the wave height and position at incipient breaking. In particular, a strong return flow over a impermeable submerged breakwater produces a variety of collapsing breaker, which the wave crest remains unbroken and the lower part of the front face breaks just like a hydraulic jump due to rapid flows (Smith and Kraus, 1990; Katano et al., 1992). The effects of the return flow on the breaker characteristics are weakened rapidly with decrease of the return flow strength, in other words, with increase of the breakwater permeability.

## BREAKER HEIGHT INDEX ON OFFSHORE SLOPING BEACH, ZONE I.

Due to the permeability and low crest of the submerged breakwater, wave reflection from the breakwater is low, but slightly higher than the plane sloping beach (Katano et al., 1992). As the result, experiments confirmed that the incipient breaker height in Zone I is predicted reasonably well by Goda's breaker index (1978), as given by Eq. (1), with a slight change of the value of empirical constant  $A$  from 0.17 to 0.15.

$$\frac{H_B}{L_0} = A \left[ 1 - \exp\left(-1.5 \frac{\pi h_B}{L_0} (1 + 15 \tan^4 \beta)\right) \right] \quad (1)$$

,in which  $H_B$  and  $h_B$  are the wave height and water depth at breaking,  $L_0$  the wave length in deep water, and  $\tan \beta$  the offshore beach slope. It is, therefore, considered that a steep wave approaching the breakwater is transformed principally by the shoaling effect caused by the plane slope of offshore beach.

## BREAKER HEIGHT INDEX ON THE BREAKWATER, ZONES II AND III.

### Integrated Parameter for Breaker Height.

Previous studies have been made on the wave breaking forced by low crested mound-type breakwaters as well as by barred and reef beaches. However, those have still failed to determine an appropriate breaker index as a function of the breakwater properties and the incoming wave parameters.

Hara et al. (1992) conducted extensive numerical experiments on the transformation of a solitary wave passing across an impermeable submerged breakwater of trapezoidal type, located on horizontal sea bottom. Based on regression analyses of the numerical computations, they propose a parameter for the breaker height index,  $\xi_s''$ , given by Eq. (2). It refers to a modified surf similarity parameter.

$$\xi_s'' = \left[ \frac{B}{h_s} + \frac{(d_j/h_s)}{(3.5 \tan \theta)^{0.2}} \right] \frac{(d_j/h_s)}{(H_j/h_s)^{0.4}} \quad (2)$$

,where  $H$  is the wave height, and subscript S denotes the quantity at the offshore toe of breakwater. The parameter comprises the physical properties and placing condition of the breakwater as well as incident wave properties. From this context, the parameter  $\xi_s''$  is named the integrated parameter of breaker height.

Prior to employment of the integrated parameter, we will discuss briefly influences induced by differences in the experimental conditions of the present and Hara's studies, such as the character of incident wave, bottom profile, and permeability of the breakwater.

The experiments indicated that an incident periodic wave passing across the breakwater behaves almost like solitary wave. In addition, it was found that wave and current field in the vicinity of the breakwater display a very similar one produced in the numerical simulation, owing to the low wave reflection of the breakwater. As for the bottom slope, the wave shoaling on a plane slope was taken account by replacing the wave height in  $\xi_s''$  with that at offshore toe of the breakwater.

**Breaker Height Index as a Function of Integrated Parameter.**

Complete analyses of the wave data on incipient breaking waves yield an empirical relation for the breaker height in terms of the integrate parameter  $\xi_s''$ , as given by Eq. (3).

$$\frac{H_B}{L_0} = A_B \left(\epsilon, \frac{R}{h_s}\right) \left(\frac{2B}{5d_s}\right)^3 \left(\frac{h_s}{L_0}\right) \xi_s'' \tag{3}$$

,where  $R$  is the water depth above the crest, and  $A_B$  is the empirical function and is written as

$$A_B \left(\epsilon, \frac{R}{h_s}\right) = [1.0 - 0.12\left(\frac{R}{h_s}\right) - 0.6\epsilon] \exp \epsilon \tag{4}$$

, representing the permeability effect of total breakwater system. However, the value of  $A_B$  varies very slightly between 1.0 and 1.2 within limits of the experiments.

Figures 4 and 5 show plots of the breaking wave steepness,  $H_B/L_0$  versus the relative wave height at seaward toe of the breakwater,  $H_s/h_s$ , to illustrate the ability of Eq. (3). It is noticed that the breaker height index, Eq. (3), describes surprisingly well the measurements.

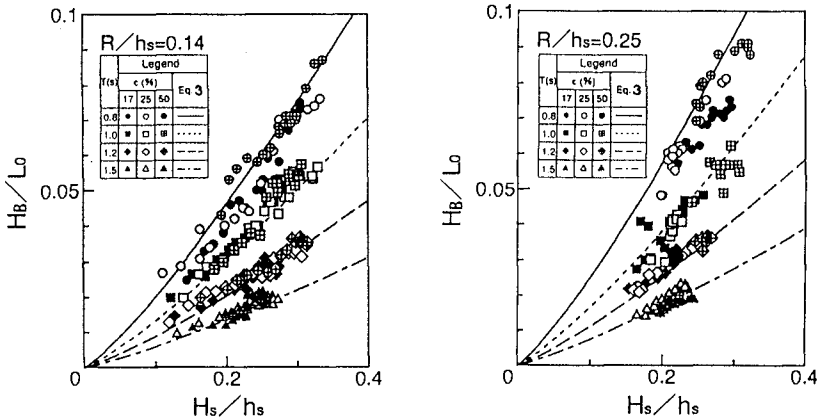


Fig. 4 Relation between  $H_B/L_0$  and  $H_s/h_s$ . Fig. 5 Relation between  $H_B/L_0$  and  $H_s/h_s$ .

Calibration of Eq. (3) is also made by using wave data of Izumiya et al. (1989). They carried out experiments of the wave transformation due to a two-layered submerged breakwater having rather complicated structure, as shown in Fig. 6. Porosity of the main breakwater body is 0.20. Figure 6 is an example of the

comparison of Eq. (3) with their measurements. Although there is some scatter to the measurements, Fig. 7 shows reasonable agreements between the measured and computed breaker heights for their whole data.

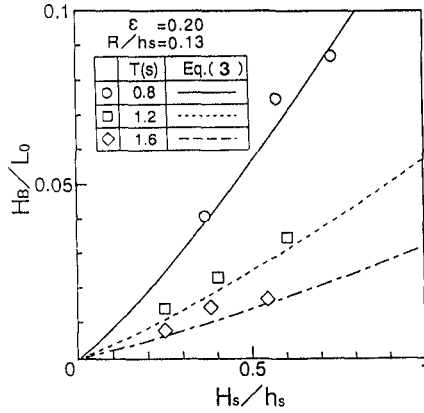
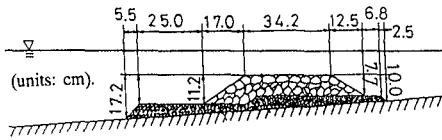


Fig. 6 Comparison of Eq. (3) with data of Izumiya et al. (1989).

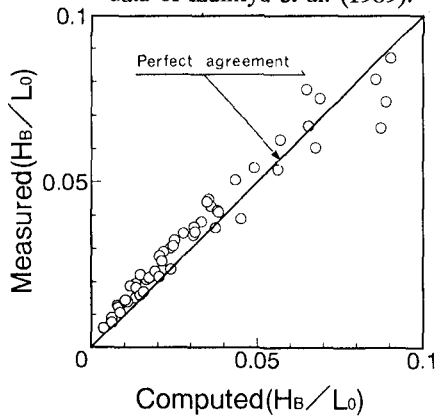


Fig. 7 Agreement of Eq. (3) with the whole data of Izumiya et al. (1989).



The agreements in Figs. (4) through (7) substantiate the validity and applicability of the proposed breaker height index Eq. (3). In addition to this, the integrated parameter  $\xi_s$  is likely to be very promising to other problems, such as wave breaking on barred and reef beaches. Using data of wave breaking over a triangle-shaped bar of Smith and Kraus (1990), breaker steepness  $H_B/L_0$  is shown, in Fig. 8, as a function of the relative wave height at offshore toe of the bar. Equation (5), represented by lines in Fig. 8, agrees the data and follows their trend well.

$$\frac{H_B}{L_0} = 0.35 \left( \frac{h_s}{L_0} \right) \xi_s^{-3} \quad (5)$$

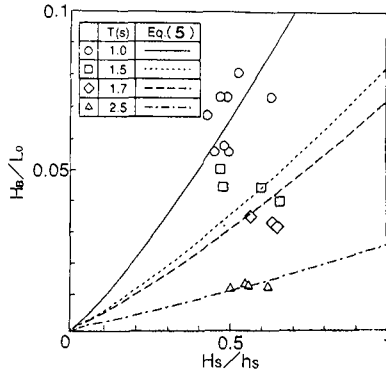
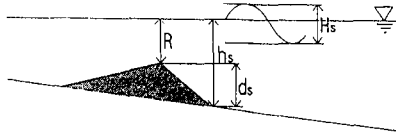


Fig. 8 Relation of  $H_B/L_0$  to  $H_s/h_s$ , illustrating the ability of  $\xi_s$ . Wave breaking over triangle-shaped bar. (Smith and Kraus, 1992)

**Breaking Position or Depth on the Breakwater**

Breaker depth  $h_B$  can not be calculated directly from the breaker height index, because Eq. (3) does not include explicitly the breaker depth. It is, therefore, required an additional index completely to determine the breaking condition on the breakwater. To do this, at first, we will examine the wave breaking on the breakwater crest, in Zone III, where the still water depth is very shallow and constant.

Following Goda (1964), the relative wave height  $H_B/R$  is plotted, in Fig. 9, as

a function of the relative wave crest height  $h_c/R$  to determine the breaking position on breakwater crest.  $h_c$  and  $R$  are the wave crest height and the still water depth above breakwater crest. Plus and cross marks represent measurements for nonbreaking wave, and various solid and open marks for breaking waves.  $\eta_c$  is the wave crest height from still water level. The lines of  $\eta_c = 0.5H$  and  $H$  refer to relations for small amplitude wave and solitary wave, respectively. Broken line in Fig. 9 represents the bounds that incident waves pass across the breakwater without breaking.

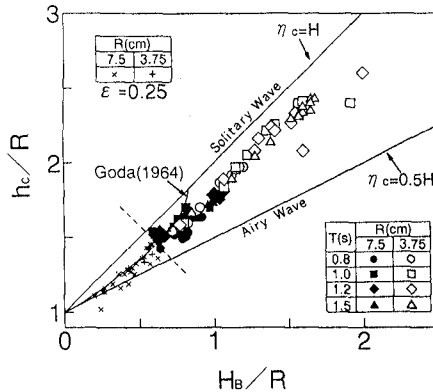


Fig. 9  $h_c/R$  as a function of  $H_B/R$  for the incipient breaking on breakwater crest.

As noticed from Fig. 9, the breaker crest height approaches that of a solitary wave, as increasing the breaker height,  $\eta_c \approx 0.75H_B$ . This indicates that the wave breaking on breakwater crest depends clearly on the trough depth of preceding wave and not on the still water depth above the crest,  $R$ . As a result, wave breaking on the crest is of a depth-limited wave, mainly controlled by the vertical asymmetry of incoming wave profile. Based on the results, the conditions under which waves break on the breakwater crest are examined by relationships between  $H_B/R$  and  $\epsilon$ . In Fig. 10, solid circle and triangle marks represent the lowest wave height when breaking occurs on the crest. And open

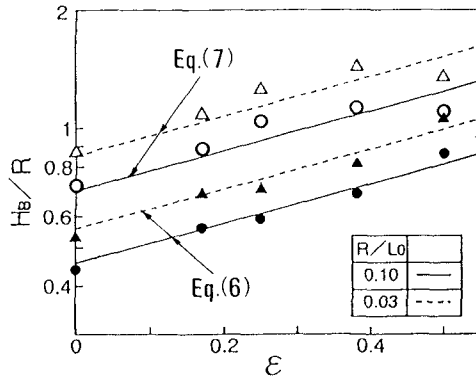


Fig. 10 Relation between  $H_B/L_0$  and  $\epsilon$  for determining the bounds of wave breaking on breaker crest.

marks represent the lowest wave height when breaking occurs on the crest. And open

ones show the breaker height at top of the structure slope. Two conditions of wave breaking on the breakwater crest can be determined as follows; (1) the lowest breaker height at the shoreward limit of wave breaking is given by,

$$\frac{H_B}{L_0} = \left(\frac{R}{L_0}\right)^{\frac{6}{7}} \exp(2.7\epsilon - 1.8) \quad (6)$$

Therefore, Eq. (6) refers to the condition that if breaker height computed from Eq. (3) is lower than that from Eq. (6), the wave passes across the breakwater without breaking. And (2) the breaker height at top of the seaward structure slope is

$$\frac{H_B}{L_0} = \left(\frac{R}{L_0}\right)^{\frac{6}{7}} \exp(1.2\epsilon - 0.8) \quad (7)$$

Visual analyses of the wave profile videos reveal that the breaker height changes exponentially with distance from top of the seaward breakwater crest, and that the shoreward limit of breaking position on the crest depends mostly on the breakwater porosity  $\epsilon$ . Equation (8) is derived from the results with respect to the shoreward distance,  $x_{NB}$ , from top of the structure slope to the bound beyond which wave breaking does not occur.

$$\frac{x_{NB}}{B} = 0.5 - 0.75\epsilon \quad (8)$$

Equation (8) indicates that the breaking position displaces toward the top of structural slope with increasing the breakwater porosity, this results in reduction of the return flow strength over the crest. The wave breaking on breakwater crest depends basically on the permeability rather than roughness of the crest surface.

By taking account of Eqs. (6) and (7), an empirical equation (9) for estimating the position of wave breaking on the crest is determined:

$$\frac{x}{B} = \frac{1}{2} \left[ \ln \left\{ \left(\frac{H_B}{L_0}\right) \left(\frac{R}{L_0}\right)^{-\frac{6}{7}} \right\} - 1.2\epsilon + 0.8 \right] \quad (9)$$

This relation refers to as the breaking position index.

### Breaking Position or Depth in Zone II

As pointed out by the previous experimental and numerical studies (Rojanakamthorn et al.,1990), we also found experimentally that wave breaking on the seaward structural slope of the breakwater can be described reasonably well by

a criterion, similar to Miche (1951) and Hamada (1951). Their criterion can be rewritten by using the dispersion relation of linear waves, as Eq. (10).

$$\frac{H_B}{L_0} = A'_m \tanh^2(k_B h_B) \tag{10}$$

, in which  $k_B$  and  $h_B$  are the wave number and water depth at breaking.  $A'_m$  is the coefficient determined from the continuity condition of breaker height at top of the seaward structure slope ( the boundary between Zones II and III). Using Eq. (7),  $A'_m$  is written as·

$$A'_m = \left[ \left( \frac{R}{L_0} \right)^6 \exp(1.2\varepsilon - 0.8) \right] / \tanh^2(k_R R) \tag{11}$$

, in which  $k_R$  is the wave number for the water depth above the crest. Figure 11 displays the range of the minimum and maximum values of  $A'_m$  as a function of the porosity  $\varepsilon$ , within the limits of the experiments. It is noticed from this figure that the value of  $A'_m$  in case of  $\varepsilon = 0$  is almost the same to Miche's coefficient of  $A'_m = 0.142$  for a plane sloping beach.

To confirm applicability of the breaker height index Eq. (10), Fig. 12 shows predicted and measured values of  $H_B/L_0$  as a function of  $k_B h_B$ . Equation (10) agrees with the measured breaker height on the seaward structure slope.

**Comparisons Between Measured and Calculated Breaker Height over the Breakwater**

In the two previous sections, the two additional breaker indices, Eqs. (9) and

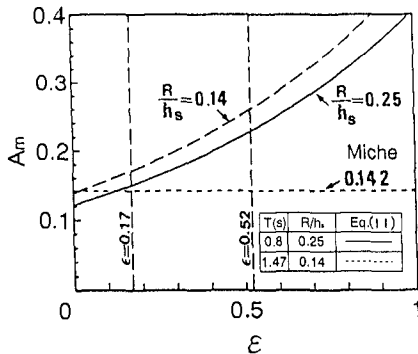


Fig. 11 Relation between  $A'_m$  and  $\varepsilon$ .

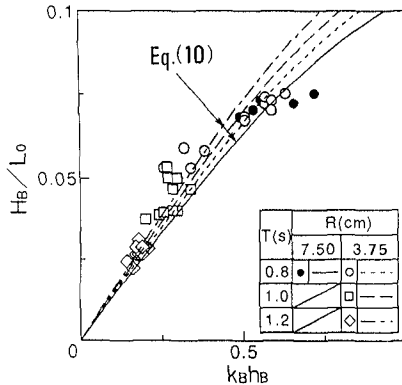


Fig. 12  $H_B/L_0$  as a function of  $k_B h_B$ , illustrating the validity of Eq. (10).

(10), have been developed for the breaking zones II and III in order to determine the breaking position. Consequently, substitution of Eq. (3) into Eqs. (9) and (10) yields the distance of breaking position for Zone III and the breaking depth for Zone II, respectively.

Figures 13 and 14 are prepared to confirm this approach. Wave steepness  $H_B/L_0$  at incipient wave breaking over permeable submerged breakwater is shown as a function of the relative distance  $x/B$ , from top of the structure slope. It is noticed that synthetic trends generated by Eqs. (9) and (10) follow observed data trends very well. Discrepancies between predicted and observed values appear to result from variability inhering in the wave breaking.

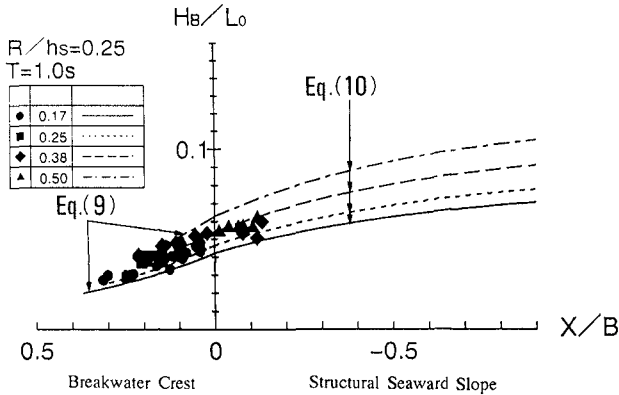


Fig. 13 Variation of  $H_B/L_0$  as a function of  $x/B$ .

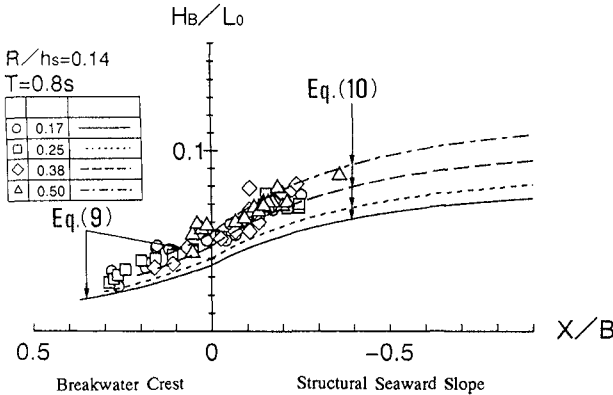


Fig. 14 Variation of  $H_B/L_0$  as a function of  $x/B$ .

## CONCLUDING REMARKS

A laboratory experiment was conducted to discuss and determine the conditions of incipient breaking over permeable submerged breakwaters. In this study, Breaking range of waves passing across the breakwater was divided into the three following zones; Zone I: on the offshore sloping beach, Zone II: on the seaward structure slope of the breakwater, and Zone III: on the breakwater crest. Height and position of the breaking wave were examined for each zone, and the breaker height and position indices were developed from measurements.

Main findings are summarized as follows;

- (1) Permeability of the submerged breakwater plays an important role in reduction of the strength of return flow over the breakwater. The return flow changes the breaker height and breaking position as well as the breaker type.
- (2) The integrated parameter  $\xi_s$  of Hara et al. (1992) expresses remarkably well synthetic trends of observed data of the wave breaking over the breakwater. The parameter is versatile; it can be applied to cases of wave breaking over barred and reef beaches.
- (3) Breaker height and depth for Zone I are calculated from Goda's breaker index, Eq. (1), by changing value of the empirical constant to  $A=0.15$ . Breaker height index, Eq. (3), for Zones II and III is determined as a function of  $\xi_s$ .
- (4) Additional indices, Eqs. (9) and (10), are developed to estimate the breaking position in Zone III and breaker depth in Zone II, respectively.

In conclusion, the computation scheme of the breaker height and depth (position) on and around permeable submerged breakwaters is shown as follows;

Zone I: On the offshore sloping beach,  
 $H_B$  and  $h_B$ , calculated from Eq. (1).

Zone II: On the seaward structure slope of the breakwater,

$$Eq.(1)|_{h_B=h_s} > \frac{H_B}{L_0}|_{Eq.(3)} \geq Eq.(7)$$

$H_B$  and  $h_B$ , calculated from Eqs. (3) and (10).

Zone III: On the breakwater crest,

$$Eq.(7) > \frac{H_B}{L_o} \Big|_{Eq.(3)} \geq Eq.(6)$$

$H_B$  and  $x_B$ , calculated from Eqs. (3) and (9).

If wave height calculated from Eq. (3) is smaller than that given by Eq. (6), the wave will pass across the submerged breakwater without breaking.

## ACKNOWLEDGEMENTS

We are grateful to Mr. K. Tachikawa, student of the Graduate School of Science and Engineering of Chuo University, for his help in the experiments and data analyses.

## REFERENCES

- Goda, Y. (1964): Wave forces on a vertical circular cylinder, Experiments and a proposed method of a wave force computation, Rept. of Port and Harbour Res. Inst., No. 8.
- Goda, Y. (1970): A synthesis of breaker indices, Proc. Japan Soc. Civil Engrs., No. 180, pp. 39-49 (in Japanese).
- Hamada, T. (1951): Breakers and beach erosion, Rept. Transportation Tech. Res. Inst., Ministry of Transportation, No. 1, 165 pp.
- Hara, M., T. Yasuda, and Y. Sakakibara (1992): Characteristics of a solitary wave breaking caused by a submerged obstacle, Proc. 23rd ICCE, pp. 253-266.
- Izumiya, T., H. Komata, and J. Mizukami (1990): Evaluation of friction factor and local reflection coefficient for a permeable structure, Proc. of Coast Eng., JSCE, Vol. 36, pp. (in Japanese).
- Katano, A., M. Hattori, and S. Murakami (1992): Proc. of Coastal Eng., JSCE, Vol. 39, pp. 646-650 (in Japanese).
- Miche, R. (1951): Le pouvoir réfléchissant des ouvrages maritimes exposés à l'action de la houle, Annales Pont et Chaussées., 121<sup>e</sup> Année, pp. 285-319.
- Mizuguchi, M. (1990): Reflection from swash zone on natural beaches, Proc. 22nd ICCE, pp. 570-583.
- Rojanakamthorn, S., M. Isobe, and A. Watanabe (1990): Modeling of wave transformation on submerged breakwater, Proc. 22nd ICCE, pp. 1060-1073.
- Smith, E.R. and N.C. Kraus (1990): Laboratory study on Macro-features of wave breaking over bars and artificial reefs, Tech. Ret. 90-12, CERC, 155 p.

## CHAPTER 81

### WAVE FORCES ACTING ON A VORTEX EXCITED VIBRATING CYLINDER IN WAVES

Kenjiro Hayashi<sup>1</sup>, Futoshi Higaki<sup>2</sup>, Koji Fujima<sup>3</sup>  
Toshiyuki Sigemura<sup>4</sup>, M.ASCE and John R. Chaplin<sup>5</sup>, M.ASCE

#### ABSTRACT

An experimental investigations into the wave forces acting on the vortex-excited vibrating vertical circular cylinder in regular waves have been performed with emphasis being placed on the amplification of the wave forces caused by the fluid-structure interaction. The cylinder is vibrating only in the transverse, cross-flow, direction by means of the restriction of the vibration of the in-line direction. The results indicate that the existence of amplification of the lift forces acting on the vortex-excited vibrating cylinder in comparison with the stationary cylinder is a function of the ratio of wave frequency  $f_w$  to the natural frequency of the cylinder in water  $f_{nw}$  and Keulegan-Carpenter number at still water level  $CKC$ . The in-line forces are also amplified in the range of  $CKC$  where large amplitude of oscillation in the transverse direction occurs.

#### INTRODUCTION

The wave forces acting on a small diameter offshore structure are usually resolved into two components. One, the inline force, acts in the direction of wave propagation and the other, the lift force or transverse force, acts in the transverse direction of it. The predominant frequency of lift force caused by vortex shedding is a multiple of that of the inline force. Therefore, the

-----  
<sup>1</sup>Assoc. Prof., Civ. Engrg. Dept., The National Defense Academy, 1-10-20 Hashirimizu Yokosuka, 239, Japan.

<sup>2</sup>Post graduate student, Civ. Engrg. Dept., N.D.A.

<sup>3</sup>Lecturer, Civ. Engrg. Dept., N.D.A.

<sup>4</sup>Professor, Civ. Engrg. Dept., N.D.A.

<sup>5</sup>Professor, Civ. Engrg. Dept., The City University, Northampton Square London, EC1V 0HB, England.



structure's dynamic response to the lift forces "Vortex-excited vibration" must be considered more significantly.

A great number of studies for the vortex-excited vibration of a circular cylinder in steady flow have been made. An important phenomenon of this vibration is that of "lock-in" between the frequency of the vortex shedding and the frequency of the vibrating cylinder. Under "lock-in" condition, large resonant vibration occurs and the lift forces acting on this vibrating cylinder are amplified by the fluid-structure interaction, Blevins (1977).

A similar phenomenon may occur under certain conditions if a flexible cylinder is placed in planar oscillatory flow or in waves. However, this has not been sufficiently understood and relatively little work has been carried out into this interesting problem in harmonic flow and in waves.

The results for the amplification of the forces acting on a vortex-excited vibrating cylinder in harmonic flows have been reported by Sarpkaya and Rajabi (1979), Hayashi et al. (1990) and Sumer et al. (1994). Sarpkaya and Rajabi (1979) show that at perfect resonance, the lift forces acting on a vortex-excited vibrating cylinder in planar oscillating flow are amplified nearly two times compared to that of rigidly mounted cylinder. Hayashi et al. (1990) show that the lift and in-line forces acting on a vortex-excited cylinder vibrating only in cross flow direction being resonant with the second harmonic component of the lift are amplified in the ranges of Keulegan-Carpenter number  $4 < KC < 8$  and  $6 < KC < 16$  respectively. The maximum increase in the lift force is about 200% at around  $KC=6$  and that in the in-line force is about 100% at around  $KC=8$ . Sumer et al. (1994) have studied the influence of  $KC$ , reduced velocity  $V_r$ , amplitude of cylinder vibration and wall-proximity effect to the forces acting on a cylinder vibrating only in cross-flow direction. Their results show that the increase in the drag coefficient is about 50-200% for around  $KC=10$  and nearly negligible for the range  $60 < KC$  and the increase in lift force is up to 200%.

The results for the amplification of the forces acting on a vortex-excited vibrating vertical cylinder in waves have been reported by Isaacson and Maull (1981), Zedan and Rajabi (1981), Angrilli and Cossalter (1982). They show that the increases of lift forces acting on a vortex-excited vertical cylinder are 70-290% for  $f_w/f_{nw}=1/2$ ,  $CKC=10-12$  and  $kd=1-3.9$ , 60% for  $f_w/f_{nw}=1/3$ ,  $CKC=17.8$ , and  $kd=0.88$ , and 90% for  $f_w/f_{nw}=1/4$ ,  $CKC=35.9$ , and  $kd=0.62$ , where  $f_w$  and  $f_{nw}$  are the incident wave frequency and the natural frequency of cylinder in water,  $k$  is the wave number, and  $d$  is the mean water depth.

Hayashi (1984) shows that the lift forces acting on

a vortex-excited vibrating vertical cylinder in waves are amplified in the range of  $5 < CKC < 15$  for  $f_w/f_{nw}=1/2$  and  $kd=1.83$  and in the range of  $18 < CKC < 30$  for  $f_w/f_{nw}=1/3$  and  $kd=1.01$ . Maull and Kaye(1988) shows similarly that when  $f_w/f_{nw}$  is fixed at  $1/2$ , the lift forces are amplified in the range of  $5 < CKC < 12$  for  $kd=1.32$  and  $1.73$ .

The forces acting on a partial parts of a flexibly mounted vertical cylinder in waves have been measured by Bearman(1988) and Borthwick and Herbert(1988). Force coefficients of in-line and lift forces from the flexibly mounted cylinder are found to be larger than those for the same cylinder but with a rigid mounting.

In the present paper, experimental investigations into the wave forces acting on the vortex-excited vibrating vertical cylinder in regular waves have been described with emphasis being placed on the amplification of the forces acting on the cylinder caused by the fluid-structure interaction.

EXPERIMENTS

Laboratory experiments were carried out in a wave flume 40m long, 0.8m wide, and 1m deep. The general arrangement of the test cylinder is shown in Figure 1. In order to give a high degree of rigidity to the test cylinder, both ends of it are connected to the core cylinder. The flange weights are attached to the core cylinder above the test cylinder to adjust the equivalent mass  $m_e$  of the test cylinder.

The support plate is attached to the holder flag at the bottom end of the test cylinder. Both end in the inline direction of the support plate are pivoted on the floor of the flume to prevent vibration in the inline direction. The upper end of the core cylinder, above the water level, is mounted with springs only in the transverse direction. Each spring is connected to a strain-gauged steel canti-

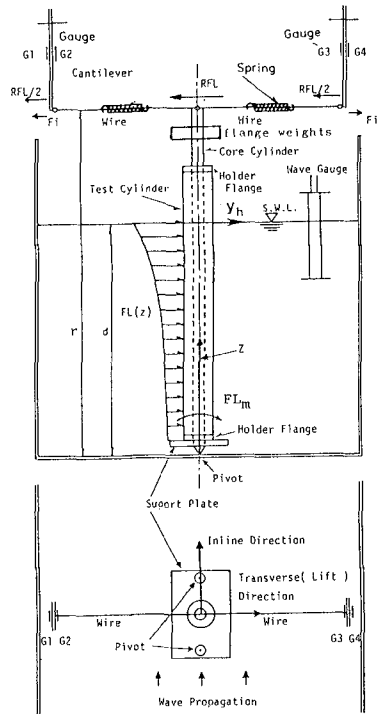


Fig. 1 General Arrangement of Test Cylinder

lever by wire. Two strain gauges were fixed on each cantilever to measure its bending moment produced by the force acting on the end of it through the springs and wires. Strain gauges were connected into a wheatstone bridge circuit in the bridge conditioner to produce the output signal corresponding to the displacement of the top end of the core cylinder in the transverse direction.

In order to obtain the relationship between the output voltage signals from the bridge circuit and the top end displacements of the core cylinder, known loads are applied horizontally to the top end of the core cylinder by weights hung over a pulley.

Free vibration tests are performed in air and in still water. The damping factor, obtained from the logarithmic decrement, and the natural frequency of the test cylinder are measured by releasing its top end from an initial displacement and recording amplitude decay of the transient oscillation of the cylinder. The equivalent mass per unit length of the test cylinder in water,  $m_e$ , is calculated from the measurements of natural frequency and stiffness of test cylinder in still water, Hayashi(1984). Thus the value of  $m_e$  includes the mass of structure and the entrained fluid.

Two kinds of experiments, Tests-A and Tests-B, are carried out. The experimental conditions in Tests-A are shown in Table 1. Where  $k(=2\pi/L, L=\text{wave length})$  is the wave number,  $f_{na}$  and  $f_{nw}$  are the natural frequencies of the test cylinder in air and in water,  $h_{ta}$  and  $h_{tw}$  are damping factor of the cylinder in air and in water,  $\rho$  is the density of water, and  $\beta(=D^2 f_w / \nu, \nu = \text{kinematic viscosity of water})$  is the viscous-frequency parameter.

The still water depth  $d$  is 40cm. The test cylinder, of outside diameter  $D=1.9\text{cm}$  and  $73.7\text{cm}$  length, is at-

Table 1 Experimental Conditions in Tests-A

Case	D (cm)	d (cm)	$f_w$ (Hz)	$f_w/f_{nw}$	$kd$ ( $2\pi \cdot d/L$ )	CKC	$\beta$
V1	1.9	40	1.07	1/2	1.92	5.2-26.4	386
V2	1.9	40	0.7	1/3	1.03	5.6-38.0	253
V3	1.9	40	0.53	1/4	0.73	4.5-35.1	191
$f_{na}=2.17\text{Hz}, f_{nw}=2.12\text{Hz}$ $h_{ta}=0.002, h_{tw}=0.005$ Mass ratio : $m_e/(\rho_w D^2)=14.9$ Reduced damping : $K_s=2m_e(2\pi h_{ta}/(\rho_w D^2))=0.37$							
S1	1.9	40	1.07		1.92	5.5-25.5	386
S2	1.9	40	0.70		1.03	2.8-39.9	253
S3	1.9	40	0.53		0.73	2.1-36.4	191

tached to the support plate(25x10x0.2cm) with the core cylinder of 0.9cm diameter and 78.5cm length.

In Case V1-V3, the relationship between the vortex-excited vibration of the test cylinder and the Keulegan-Carpenter number at still water level  $CKC=U_{ms}.T/D$ , is measured. Where  $U_{ms}$  is the maximum horizontal water particle velocity at still water level and  $T$  is the wave period. In each of these Cases, the frequency ratio,  $f_w/f_{nw}$ , is fixed at around one value of the values of the resonance frequency ratios,  $f_w/f_{nw}=1/2, 1/3$ , and  $1/4$ .

In Case S1, S2, and S3, the base bending moment  $FL_m$ (=the moments about the bottom of the test cylinder) due to the lift forces acting on the test cylinder rigidly mounted with strings replacing the springs in the transverse direction are measured in the similar waves used in the Case V1, Case V2 and Case V3.

In Tests-B, in-line and transverse forces acting on a partial part of the test cylinder are measured by using a force sleeve supported by two components small load cell installed in the test cylinder as shown in Figure 2. The force sleeve of outside diameter  $D=3\text{cm}$  and 3cm length is positioned 15.9 cm below still water level with water depth  $d=80\text{cm}$ . The test cylinder of outside diameter  $D=3\text{cm}$  and 98.5cm length is attached to the support plate(20x5x0.6cm) with the core cylinder of 1cm diameter and 104.6cm length. The conditions are shown in Table 2. The measurements are made for both cases of vortex-excited cylinder being resonant with the second to sixth harmonic components of lift forces( $f_w/f_{nw}=1/2-1/6$ ) and rigidly mounted cylinder for comparison.

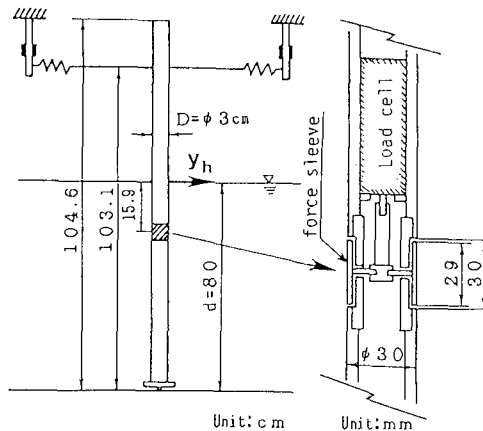


Fig. 2 Experimental Set-up (Force Sleeve and Load Cell)

Table 2 Experimental Conditions in Tests-B

Case	D (cm)	d (cm)	$f_w$ (Hz)	$f_w/f_{nw}$	kd ( $2\pi \cdot d/L$ )	CKC	$\beta$
LV2	3.0	80	0.85	1/2	2.41	6.0-20.6	655
LV3	3.0	80	0.56	1/3	1.20	6.9-30.5	426
LV4	3.0	80	0.42	1/4	0.90	4.4-29.7	342
LV5	3.0	80	0.34	1/5	0.69	9.3-29.4	274
LV6	3.0	80	0.28	1/6	0.56	5.2-40.7	228
$f_{na}=1.79\text{Hz}, f_{nw}=1.69\text{Hz}$ $h_{ta}=0.0035, h_{tw}=0.014$ Mass ratio, : $m_e/(\rho_w D^2)=8.34$ Reduced damping : $K_S=2m_e(2\pi h_{ta}/(\rho_w D^2))=0.37$							

MODEL FOR VIBRATION

The definition sketch of the test cylinder, which illustrates the transverse response of the cylinder which is rod pivoted on the bottom of flume and supported by spring in the transverse direction, is shown in Figure 3. The dynamic response of the cylinder to the lift forces may be described by using the equation of motion as

$$M_{mt} \cdot \ddot{y}_h + C_{mt} \cdot \dot{y}_h + K_{mt} \cdot y_h = FL_m, \quad \text{--- (1)}$$

where  $\ddot{y}_h$ ,  $\dot{y}_h$  and  $y_h$  are the transverse displacement, velocity and acceleration of the cylinder at still water level,  $M_{mt}$ ,  $C_{mt}$  and  $K_{mt}$  are the effective mass, damping and stiffness of system.  $M_{mt}$  includes the mass of cylinder and added mass in water.  $C_{mt}$  includes the structural damping and fluid damping.  $K_{mt}$  includes the stiffness due to the spring force, and the buoyancy and distributed weight when the cylinder is in a deflected position from the vertical.  $FL_m$  is the bending moments around the pivot which is produced by the lift force acting on the cylinder.

$M_{mt} \cdot \ddot{y}_h$ ,  $C_{mt} \cdot \dot{y}_h$  and  $K_{mt} \cdot y_h$  show the moments

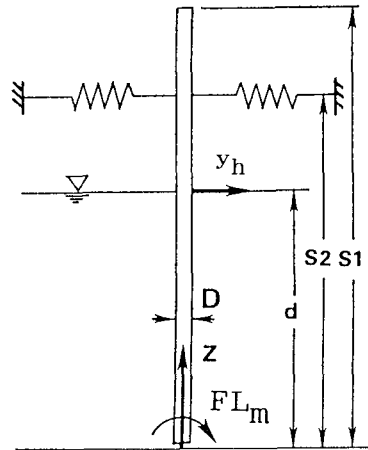


Fig. 3 Coordinate System

produced by the inertia forces, the damping forces and the stiffness of the structure respectively. Thus, Eq.(1) shows the equivalence of the moments taken about the pivot of the base, Hayashi(1984).  $FL_m$  may be expressed in a series form as

$$FL_m = FL_m(n) \cdot \sin[2\pi \cdot n \cdot f_w \cdot t + \phi(n)], \quad \text{---(2)}$$

where  $FL_m(n)$ ,  $n=1,2,3---$ , is the  $n$ th frequency component of  $FL_m$  and  $\phi(n)$  is the phase lag. The amplitude  $Y_h(n)$  of response vibration  $y_h$  to  $FL_m(n)$  may be given as the solution of Eq.(1) as

$$Y_h(n) = FL_m(n) / K_{mt} \cdot [ \{ 1 - (n \cdot f_w / f_{nw})^2 \}^2 + (2h_{tw} \cdot n \cdot f_w / f_{nw})^2 ]^{-1/2} \quad \text{---(3)}$$

, where  $h_{tw}$  is the total damping factor of the cylinder in water and may be expressed as the sum of the structural damping factor  $h_s$  and fluid damping factor  $h_f$ , Hayashi and Chaplin (1991).

RESULTS AND DISCUSSION FOR TESTS-A

Figure 4 shows the decay of free oscillations  $y_h$  of the test cylinder in air and in water, which is used in the experiments of Tests-A. Figure 5 shows the variation of the damping factor  $h_{tai}$  in air and  $h_{twi}$  in still water,  $d=40$ cm, with the non dimensional amplitude  $Y_{hi}/D$ . Where  $Y_{hi}$  is the amplitude of  $i$ -th oscillation of the cylinder  $y_h$  at still water level. The values of  $h_{tai}$  and  $h_{twi}$  for each amplitude of  $Y_{hi}/D$  are defined as

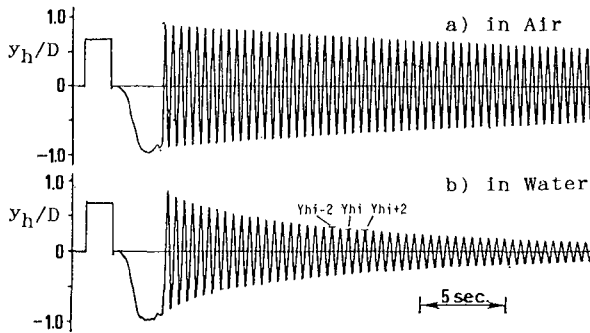


Fig. 4 Decay of Free Oscillation

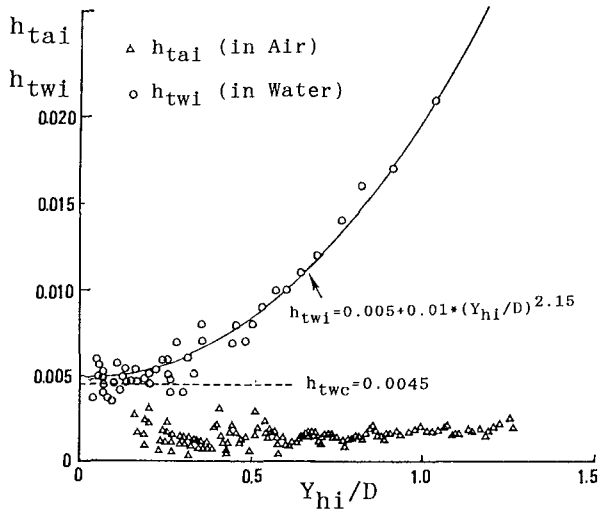


Fig. 5 Variation of Damping Factor with  $Y_{hi}/D$

$$h_{tai} \text{ or } h_{twi} = 1/(2\pi) * \{\ln(Y_{hi-2}/Y_{hi+2})\}/4, \quad \text{---(4)}$$

where  $Y_{hi-2}$  and  $Y_{hi+2}$  are the amplitudes of the  $(i-2)$ th and  $(i+2)$ th periods respectively (see Figure 4).

The value of  $h_{tai}$ , which shows the structural damping factor, is nearly independent of the value of  $Y_{hi}/D$ . The constant value of  $h_{ta} = 0.002$  is written in Table 1. On the other hand, the value of  $h_{twi}$ , which is composed of structural damping and fluid damping, is independent of amplitude effect only for low values of  $Y_{hi}/D$  and it becomes amplitude dependent at higher value of  $Y_{hi}/D$  owing to the characteristics of the fluid damping. The constant value of  $h_{twi}$ ,  $Y_{hi}/D < 0.3$ , is nearly corresponding to the theoretical value of  $h_{twc} = 0.0045$  which is derived from the Stokes's theory, Stokes (1851), for the forces on a cylindrical pendulum bobs oscillating at low KC number, Hayashi and Chaplin (1991). The increase of  $h_{twi}$  in  $Y_{hi}/D > 0.3$  may be due to the appearance of vortex-sheddings. The variation of the  $h_{twi}$  with  $Y_{hi}/D$  is approximated by the regression equation as

$$h_{twi} = 0.005 + 0.01 * (Y_{hi}/D)^{2.15}. \quad \text{---(5)}$$

The variation of  $Y_{hm}(n)/D$  and  $Y_{hc}(n)/D$ ,  $n=2,3,4$  are shown in Figure 6 (a),(b),(c) where  $Y_{hm}(n)$  is the Fourier amplitude of measured displacement  $y_h$  and  $Y_{hc}(n)$  is a calculated value obtained by substituting the measured

moments  $FL_m(n)$  acting on the rigidly mounted cylinder into Eq.(3). Here  $FL_m(n)$ ,  $n=1-4$ , is the first four harmonics of  $FL_m$ , which are measured for the three values of  $kd=1.92$ , 1.03 and 0.73 in Case S1, S2 and S3. In calculation, Eq.(3) is coupled to Eq.(5) by means of  $Y_h(n)=Y_h=Y_{hi}$ .

The measured response  $Y_{hm}(n)$ ,  $n=1, 2, 3$ , is above the predicted response  $Y_{hc}(n)$  in the range of  $8 < CKC < 15$  for the case of  $f_w/f_{nw}=1/2$ , in the range of  $12 < CKC < 23$  for the case of  $f_w/f_{nw}=1/3$ , and  $25 < CKC$  for the case of  $f_w/f_{nw}=1/4$  respectively. These phenomena may be due to the amplification of the lift acting on the vortex-excited vibrating cylinder caused by the fluid-structure interaction. Similar phenomena are obtained by Maull and Kaye (1988) for the case of  $kd=1.73$  and 1.32.

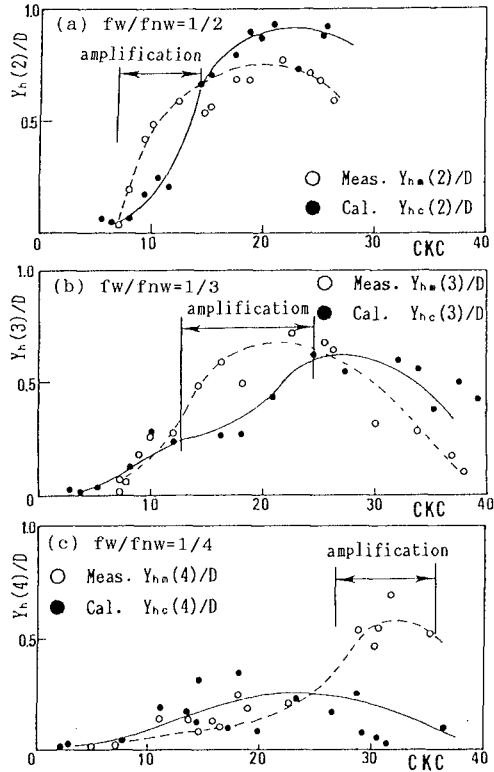


Fig. 6  $Y_{hm}(n)$  and  $Y_{hc}(n)$

RESULTS AND DISCUSSION FOR TESTS-B

The traces for free decay of oscillations  $y_h$  and of the forces  $dF_Y$  in air and in water are shown in Figure 7 (a) and (b), where  $dF_Y$  is the transverse, Y-direction, forces acting on the unit length of the force sleeve, which is measured by the load cell in the test cylinder used in Tests-B. The relationship between these  $dF_Y$  and  $y_h/D$  are shown in Figure 7 (c). From this figure,  $dF_Y$  in air and in water may be expressed as

$$dF_Y, (\text{in air}) = dF_{Y1a} = m_{sa} * d^2y_h/dt^2 = 2.37 * y_h/D, \quad \text{--- (6)}$$

$$dF_Y, (\text{in water}) = dF_{Y1w} = m_{sw} * d^2y_h/dt^2 = 5.17 * y_h/D, \quad \text{--- (7)}$$



where  $dF_{Y1a}$  and  $dF_{Y1w}$  are inertia forces acting on the unit length of force sleeve in air and in water, and  $m_{sa}$  and  $m_{sw}$  are reduced mass per unit length of the force sleeve in air and in water.

The variations of  $\eta$ ,  $y_h/D$ ,  $dF_Y$ ,  $dF_{Ya}$ ,  $dF_{Yw}$ ,  $dF_X$  with time for both cases of vortex-excited cylinder and rigidly mounted cylinder for comparison for the case of  $f_w/f_{nw}=1/2$ ,  $CKC=12$ ,  $kd=2.41$  are shown in Figure 8 (a),(b) and (c). Here  $\eta$  is the water surface elevation. The Keulegan-Carpenter number at the level of force sleeve, 16cm below the still water level is  $LKC=7.5$ .  $dF_X$  and  $dF_Y$  are in-line and lift force acting on the unit length of force

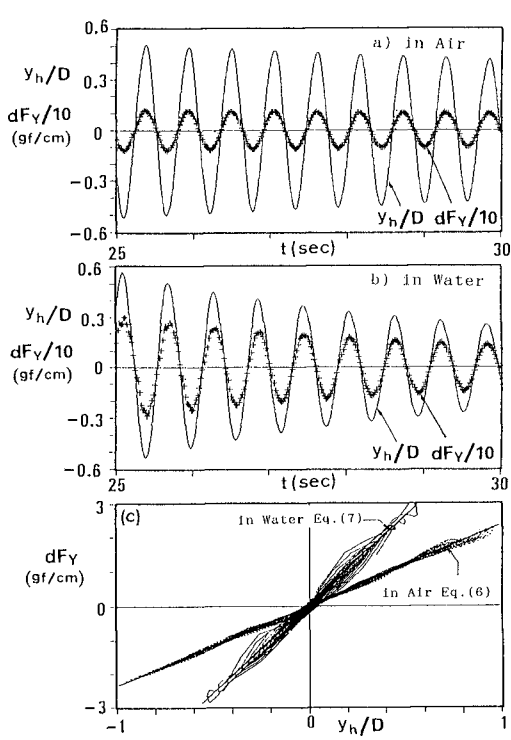
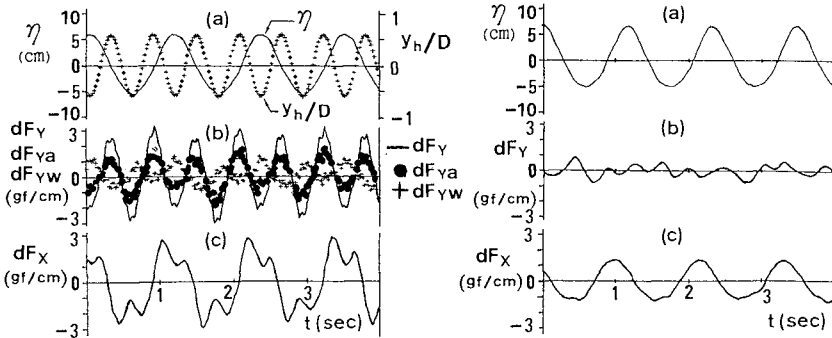


Fig. 7 Decay of Free oscillation



(A) Vibrating Cylinder

(B) Rigid Cylinder

Fig. 8  $\eta$ ,  $y_h/D$ ,  $dF_Y$ ,  $dF_{Ya}$ ,  $dF_{Yw}$ ,  $dF_X$  versus time

sleeve, which are measured by the two components small load cell.  $dF_{Ya}$  and  $dF_{Yw}$  are defined as

$$dF_{Ya} = dF_Y - dF_{YIa} = dF_Y - 2.37 \cdot y_h/D, \quad \text{---(8)}$$

$$dF_{Yw} = dF_Y - dF_{YIw} = dF_Y - 5.17 \cdot y_h/D. \quad \text{---(9)}$$

$dF_{Ya}$  shows the transverse fluid force acting on the unit length of the force sleeve.  $dF_{Ya}$  may be composed of the inertia force due to the added mass of water, the fluid damping force and the loading force per unit length of force sleeve. Thus  $dF_{Yw}$  shows the transverse force which is composed of the damping and the loading force per unit length of force sleeve in water. When the test cylinder is vibrating in resonance condition,  $f_w/f_{nw} = 1/2, 1/3, 1/4, 1/5, 1/6$ ,  $dF_{YIa}$  and  $dF_{YIw}$  may be estimated by using Eq.(6) and Eq.(7).

$dF_X$  shows the in-line fluid force acting on a unit length of force sleeve in water because the vibration of the in-line direction is restricted.

We can recognize that the forces  $dF_X$ ,  $dF_{Ya}$  and  $dF_{Yw}$  acting on the

- Isaacson and Mall [fw/fnw=1/2 Ks=3.54]
- ▼ Zedan and Rajabi [fw/fnw=1/2 Ks=0.83]
- Anglilli and Cossalter [fw/fnw=1/2 Ks=0.98]
- [fw/fnw=1/3 Ks=0.98]

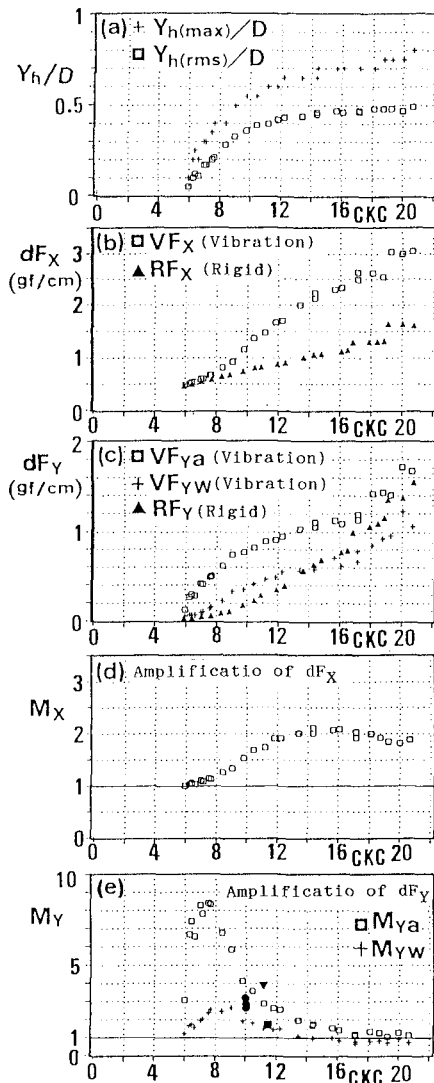


Fig. 9 Amplification versus CKC for fw/fnw=1/2

vibrating cylinder are large compare to the forces  $dF_X$  and  $dF_Y$  acting on the rigidly mounted cylinder.

Fig. 9 (a)-(e) show the variation of the non-dimensional cylinder vibration ( $Y_h/D$ ), wave forces ( $dF_X$ ,  $dF_Y$ ), and amplification factor ( $M_X$ ,  $M_Y$ ) with CKC for the case of  $f_w/f_{nw}=1/2$ . Here  $Y_h(\max)$  and  $Y_h(\text{rms})$  are the maximum half-amplitude and the root mean square value of the cylinder displacement  $y_h$  at still water level.  $VF_X$ ,  $VF_{Ya}$  and  $VF_{Yw}$  are the root mean square values of in-line and transverse forces,  $dF_X$ ,  $dF_{Ya}$  and  $dF_{Yw}$ , acting on the force sleeve of vibrating cylinder.  $RF_X$ ,  $RF_{Ya}$  and  $RF_{Yw}$  are the root mean square values of those of the rigidly mounted cylinder. The amplification factors  $M_X$ ,  $M_{Ya}$  and  $M_{Yw}$  are defined as

$$M_X = VF_X / RF_X, \quad \text{---(10)}$$

$$M_{Ya} = VF_{Ya} / RF_Y, \quad \text{---(11)}$$

$$M_{Yw} = VF_{Yw} / RF_Y. \quad \text{---(12)}$$

Figure 9 (d) and (e) shows that  $M_X$  increases with increasing  $Y_h/D$  and  $M_{Ya}$  is little affected with increasing  $Y_h/D$ .  $M_{Ya}$  is large in the range of  $6 < \text{CKC} < 13$  where  $Y_h/D$  increases rapidly with increasing CKC. This range of CKC, where the amplification of lift force is large, is nearly consistent with the results obtained for  $f_w/f_{nw}=1/2$  in Tests-A, see Figure 6 (a). The amplification factor  $M_Y$  obtained by Isaacson and Maull(1981), Zedan and Rajabi(1981), and Anglilli and Cossalter(1982) for the case of  $f_w/f_{nw}=1/2$  are plotted in Figure 9 (e) only for reference. It should be noted that their results are obtained for the total lift forces acting on the vertical cylinder in waves.

The variations of the cylinder vibration  $Y_h/D$  and the amplification factors with CKC for  $f_w/f_{nw}=1/3$ ,  $1/4$ , and  $1/6$  are shown in Figure 10 (A),(B) and (C) respectively. We can also recognize that  $M_X$  increases with increasing  $Y_h/D$ , which is nearly consistent with the results obtained in the case of steady flow, Griffin et al.(1975) and Sumer et al. (1994), and  $M_{Ya}$  is a little affected with increasing  $Y_h/D$ .  $M_{Ya}$  is a function of  $f_w/f_{nw}$  and CKC. The amplification factor  $M_Y$  obtained for the total lift acting on the vertical cylinder by Anglilli and Cossalter (1982) for the case of  $f_w/f_{nw}=1/3$  is also plotted in Figure 11.

The value of  $M_{Yw}$  is bigger than 1 in the range of  $6 < \text{CKC} < 13$  for  $f_w/f_{nw}=1/2$ . On the other hand, it is less than 1 for  $f_w/f_{nw}=1/3$ ,  $1/4$  and  $1/6$ . We need more consideration to the characteristics of  $M_{Yw}$ .

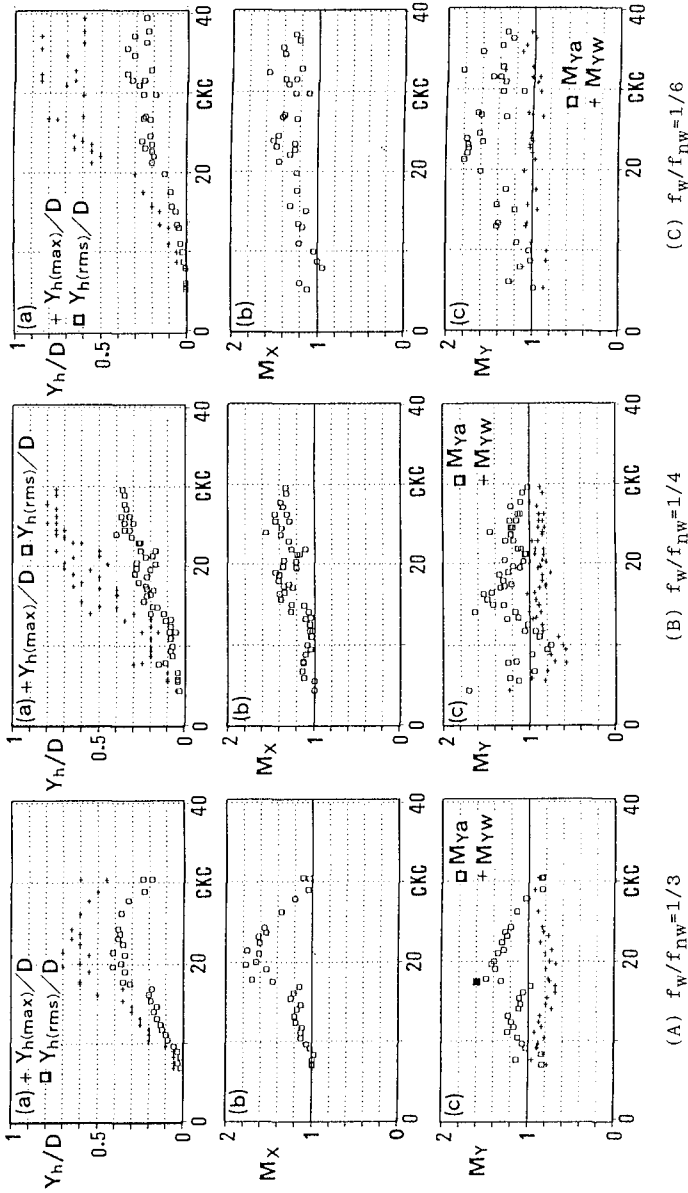


Fig. 10 Cylinder Vibration and Amplification Factor

## CONCLUSIONS

The main conclusions obtained in this study are summarized as follows:

- 1). The existence of the amplification of lift force acting on the vortex-excited vibrating cylinder in comparison with the rigidly mounted cylinder is a function of the ratio of wave frequency  $f_w$  to the natural frequency  $f_{nw}$  of the cylinder in water and Keulegan-Carpenter number at still water level. When  $f_w/f_{nw}$  is fixed at about 2, large amplitude of transverse, cross-flow, vibration  $Y_h/D$  of cylinder occurs in the wide range of CKC, but the amplification of lift occurs only in the range of  $6 < CKC < 13$ .
- 2). The in-line force acting on the partial part of the vortex-excited vibrating cylinder is amplified with increase of cross-flow vibration  $Y_h/D$ .

## REFERENCES

- Angrilli, F., and Cossalter, V. (1982). "Transverse oscillations of a vertical pile in waves." *Journal of Fluids Engineering*, Vol.104, pp.46-53.
- Bearman, P. W. (1988). "Wave loading experiments on circular cylinders at large scale." *Proc., Int. Conf. on Behavior of Offshore Structures BOSS 88*, Trondheim, Norway, June, 2, pp.471-487.
- Blevins, D. B. (1977). "Flow-induced vibration." *Van Nostrand Reinhold*, New York, N.Y.
- Borthwick, A.G.L, and Herbert, D.M. (1988). "Loading and response of a small diameter flexibly mounted cylinder in waves." *Journal of Fluids and Structures*, Vol.2, pp.479-501.
- Hayashi, K. (1984). "The non-linear vortex-excited vibration of the vertical cylinder in waves." Ph.D. Thesis, University of Liverpool.
- Hayashi, K., Ogihara, Y., Fujima, K., and Shigemura, T. (1990). "Forces acting on a vortex-excited vibrating cylinder in planar oscillatory flow." *Hydraulic Engineering Proceedings 1990 National Conference*, HY. Div /ASCE, San Diego, Vol.3, pp.91-96.
- Hayashi, K and Chaplin, J.R. (1991). "Damping of a vertical cylinder oscillating in still water." *Proceedings of 1st International Offshore and Polar Engineering Conference*, Edinburgh, UK., pp.346-353.
- Isaacson M.Q. and Maull D.J. (1981). "Dynamic response of vertical piles." *International Symposium on Hydrodynamics in Ocean Engineering*, The Norwegian Institute of Technology, pp.887-904.

- Mauil, D.J. and Kaye, D. (1988). "Oscillations of a flexible cylinder in waves." Proceedings of International Conference on Behavior of Offshore Structures BOSS'88 , Trondheim, pp.535-549.
- Sarpkaya, T. and Rajabi F. (1979). "Dynamic response of piles to vortex shedding in oscillating flows." Off-shore Technology Conference in Houston, pp.2523-2528.
- Stokes, G.G. (1851). "On the effect of the internal friction of fluids on the motion of pendulums." Trans. Camb. Phil. Soc. 9, pp.8-106.
- Sumer, B.M., Fredsoe, J., Jensen, B.L., and Christiansen, N.(1994). "Forces on vibrating cylinder near wall in current and waves." Journal of Waterway, Port, Coastal and Ocean Engineering, Vol.120, No.3, pp.233-248.
- Zedan, M.F. and Rajabi, F. (1981). "Lift forces on cylinders undergoing hydroelastic oscillations in waves and two dimensional harmonic flow." International Symposium on Hydrodynamics in Ocean Engineering, The Norwegian Institute of Technology, pp.239-262.

## CHAPTER 82

# Overtopping of sea walls under random waves

D M HERBERT<sup>1</sup>, N W H ALLSOP<sup>1</sup> and M W OWEN<sup>2</sup>

### Abstract

Over the last fifteen years a long running research programme has been undertaken at HR Wallingford to investigate the overtopping discharge performance of a wide range of sea walls. The research, which is funded by the Ministry of Agriculture, Fisheries and Food, is principally aimed at deriving methods to enable design engineers to determine the overtopping performance of a particular sea wall cross-section under a range of wave and water level conditions. The studies have generally used random wave physical model tests in order to collect data which can then be employed to derive empirical equations that describe the level of overtopping discharge.

### 1 Introduction

This paper describes recent research work at HR Wallingford, based on the results of physical model tests, aimed at quantifying the overtopping performance of recurved and vertical sea walls. The work is a continuation of a large research programme which has resulted in the derivation of empirical methods for assessing overtopping discharges on embankment sea walls.

### 2 Summary of previous work

Considerable stretches of the United Kingdom (UK) coastline are protected by a simple earth embankment, consisting of a sloping seaward face, a horizontal crest just a few metres wide and possibly a rear slope. These embankments are

---

<sup>1</sup> Coastal Group, HR Wallingford, Wallingford, OX10 8BA, UK

<sup>2</sup> Llanfair Caereinion, Welshpool, Powys, SY21 0DS, UK

particularly frequent in rural areas, where the seaward face is often protected either by grass or pitched stone. In the late 1970's the then Hydraulics Research Station carried out an extensive research programme to determine the overtopping discharge behaviour of embankment type sea walls, culminating in the production of design guidelines (Owen, 1984).

The design method established for embankment sea walls is based on a dimensionless discharge parameter,  $Q_*$ , and a dimensionless freeboard,  $R_*$ . These two parameters are defined below:-

$$Q_* = Q / (T_m g H_s) \quad (1)$$

$$R_* = R_c / (T_m \sqrt{gH_s}) \quad (2)$$

where  $Q$  is the mean discharge overtopping the crest of the sea wall,  
 $T_m$  is the mean wave period,  
 $H_s$  is the significant wave height,  
 $g$  is acceleration due to gravity  
and  $R_c$  is the sea wall freeboard (the height of the sea wall crest above still water level).

The dimensionless parameters are connected by the following exponential equation:-

$$Q_* = A \exp (-BR_*/r) \quad (3)$$

where  $r$  is a roughness coefficient  
and  $A$  and  $B$  are empirically derived coefficients dependent upon the structure slope.

Typical values of these empirical coefficients vary from  $A=0.00794$  and  $B=20.12$  for a 1:1 slope to  $A=0.025$  and  $B=65.2$  for a 1:5 slope. Recommended values of the roughness coefficient vary from  $r = 1.0$  for smooth impermeable slopes,  $r = 0.85-0.9$  for turf,  $r = 0.8$  for one layer of stone rubble on an impermeable base and  $r = 0.5-0.6$  for two or more layers of rubble.

Further work on bermed sea walls (Owen, 1984) showed that equations (1) - (3) could also be applied to these type of structures by modifying the empirical coefficients  $A$  and  $B$ . This work illustrated that, in general, the most effective berm for reducing overtopping is located at or close to still water level.

Wave basin tests using long crested waves (Owen, 1984) indicated that overtopping can increase for angles of approach up to  $30^\circ$  off normal with the



worst overtopping occurring at about 15° off normal. Under short crested seas (CIRIA, 1991) the overtopping discharge remains roughly constant for wave directions between 0° and 30° off normal before tailing off at larger angles.

Allsop and Bradbury (1988) completed model tests in which measurements were made of the overtopping discharge for vertically faced crown walls mounted on top of rock revetments or breakwaters. A change to the relationship given by Owen (1984) was suggested with the introduction of a new dimensionless freeboard parameter,  $F_*$ , defined as follows:-

$$F_* = R_c^2 / (H_s^2 g T_m) \quad (4)$$

The equation connecting the dimensionless discharge and freeboard was also modified:-

$$Q_* = A F_*^B \quad (5)$$

where A and B are coefficients dependent upon the geometry of the structure cross-section.

### 3 Recurved Walls

In many urban areas the traditional embankment type sea wall frequently incorporates a wave return wall at its crest. This wall can be located either at the top of the seaward slope, or else it can be sited a few metres back allowing the crest berm to be used as a promenade. A series of physical model tests were subsequently undertaken to measure the overtopping discharges of a range of recurved wave return walls for different sea wall slopes, water levels and wave conditions (Owen and Steele, 1991).

The model tests were carried out in a wave flume at a nominal geometric scale of 1:15. Smooth impermeable sea wall slopes of 1:2 and 1:4 were tested under a range of wave and water level conditions but always with a constant sea steepness (based on the mean deep water wave length) of  $s=0.045$ . Although wave return walls with a very wide range of profiles have been constructed at different locations around the UK coastline, only the basic profile originally suggested by Berkeley - Thorne and Roberts (1981) was used in this study. However, the distance between the top of the seaward slope and the foot of the wave recurve was varied throughout testing. Figure 1 illustrates the general configuration of the model tests.

Two options were investigated as a means of defining the effectiveness of wave return walls. The two alternative definitions were:

- the ratio of the measured overtopping discharge to the discharge which

would have occurred if the return wall had been removed, and the seaward slope had been extended up to the same elevation as the top of the return wall.

- the ratio of the measured overtopping discharge to the discharge which would have occurred if the return wall had been absent.

The second definition was the most appropriate as it appeared to be a much more direct indicator of the performance of the return wall. During the course of the analysis it became clear that one factor governing the effectiveness of the return wall was the height of the wall relative to its position above the still water line. Accordingly the dimensionless height of the wave return wall was defined as:-

$$W_* = W_h/R_c \quad (6)$$

where  $W_h$  is the height of the wave return wall from its base to its top and  $R_c$  is the freeboard between the top of the seaward slope (which is at an identical elevation to the base of the return wall) and the still water line.

Using the above definition of the effectiveness of the wave return wall, it is necessary to know the overtopping discharge which would have resulted during the tests if the wave return wall had been absent, for identical wave conditions, water levels and sea wall geometry. Measurements of these discharges were not made specifically for this study but used the results of the earlier research programme (Owen, 1984).

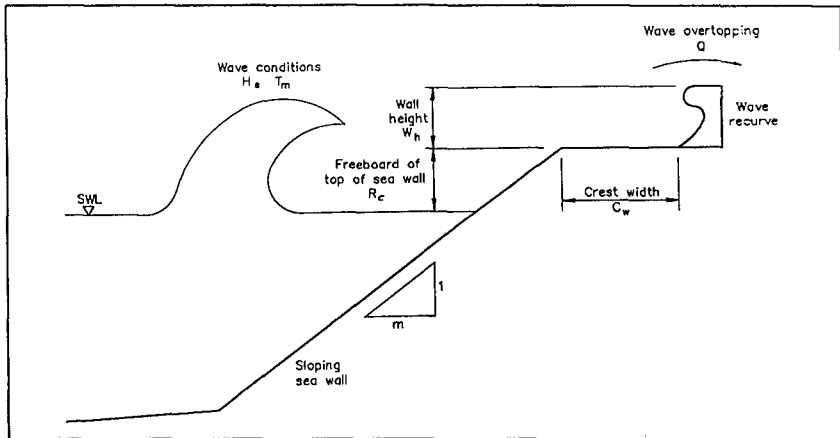


Figure 1 Definition of parameters, recurve wall

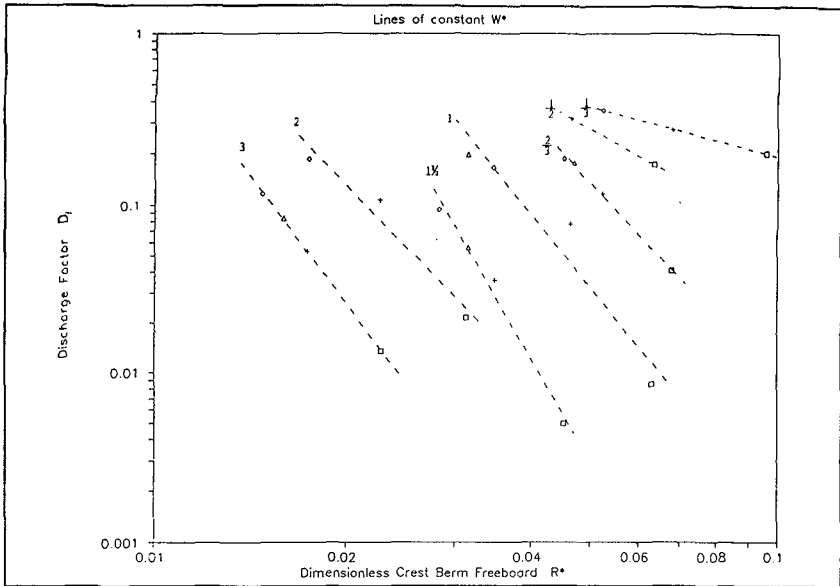


Figure 2 Recurve wall results, 1:2 slope, 0m crest width

For each test in the present study, the overtopping discharge to be expected without the wave return wall was calculated using equations (1) - (3). The measured discharge overtopping the wave return wall, expressed in dimensionless terms as  $Q_{*w}$ , could then be compared with the dimensionless discharge at the crest of the sea wall,  $Q_*$ , (ie the recurve has been removed) to give the discharge factor,  $D_f$ . Thus:-

$$Q_{*w} = Q_w / (T_m g H_s) \tag{7}$$

$$D_f \approx Q_{*w} / Q_* \tag{8}$$

where  $Q_w$  is the mean discharge overtopping the wave recurve.

In selecting a method of presenting the data, consideration was given to the way in which a designer could use the information. Figure 2 shows the form of presentation which was finally selected, in this case for a sea wall with a 1:2 slope and with the wave return wall placed directly at the top of the slope (ie the crest width,  $C_w = 0$ ). In this graph the abscissa is the dimensionless crest berm freeboard,  $R_*$ , as defined in equation (2), which can be calculated from the actual freeboard and the wave height and period. Each line on the graph represents a constant value of the dimensionless wave return wall height,  $W_*$ , which can be

determined from the wall height and the actual freeboard. Knowing the values of  $R_*$  and  $W_*$  allows a discharge factor  $D_f$ , to be established from Figure 2. Use of equation (3) to calculate the dimensionless discharge at the crest of the sea wall,  $Q_*$ , then enables  $Q_{*w}$  to be determined from equation (8). The mean discharge overtopping the wave recurve,  $Q_w$ , may be determined from equation (7).

The method outlined above allows the overtopping discharge of a sea wall with a recurve wall to be estimated provided that the crest width and sea wall slope are equal to one of those combinations tested. However, a single design graph would be preferable, together with some means of estimating the overtopping discharge for conditions not specifically tested. Given the scatter of results in Figure 2, and the fact that fewer than the ideal number of tests were completed for each structure cross-section, it was decided to investigate whether a standard slope could be fitted to all lines having the same dimensionless wall height.

All of the individual graphs were overlain and, using the 1:2 slope with a zero crest width as the baseline, the data sets displaced in the horizontal direction. With the appropriate displacements the individual  $W_*$  data sets tended to collapse on to a straight line. An iterative procedure was used to find the displacements which, using the method of least squares to find the line of best fit, gave the highest overall coefficient of correlation for all the data sets. This overall coefficient of correlation was taken as the average of all the coefficients of correlation of all the data sets for different dimensionless wall heights.

The result of the analysis described above was a single design graph which is illustrated in Figure 3. In this figure the abscissa is the dimensionless adjusted crest berm freeboard,  $X_*$ , which is defined as follows:-

$$X_* = R_* A_f \quad (9)$$

where  $A_f$  is an adjustment factor dependent on the structure cross-section.

Hence  $R_*$  may be calculated from equation (2), whilst typical adjustment factors are given in Table 1. Thus a discharge factor can be obtained from Figure 3 and the overtopping discharge calculated as before (see equations (1), (7), and (8)).

The results of the model tests showed that recurved wave return walls can have a very dramatic effect on the overtopping discharges of sea walls. For some test conditions the discharge was reduced by almost three orders of magnitude compared to the expected situation without the return wall. Although some reduction would be obtained by simply raising the basic sea wall by the same amount as the height of the return wall, calculations indicated that only one order of magnitude reduction in overtopping could be expected. This point is well illustrated in Figure 4. For either a 1:2 or a 1:4 sea wall, the figure shows a plot of the overtopping discharge against the total height of the sea wall, for a

Sea wall slope	Crest width, $C_w$	$W_B/R_c \geq 2/3$	$W_B/R_c \leq 1/2$
		Adjustment factor, $A_f$	Adjustment factor, $A_f$
1:2	0	1.00	1.00
1:2	4	1.07	1.34
1:2	8	1.10	1.38
1:4	0	1.27	1.27
1:4	4	1.22	1.53
1:4	8	1.33	1.67

Table 1 Adjustment factors

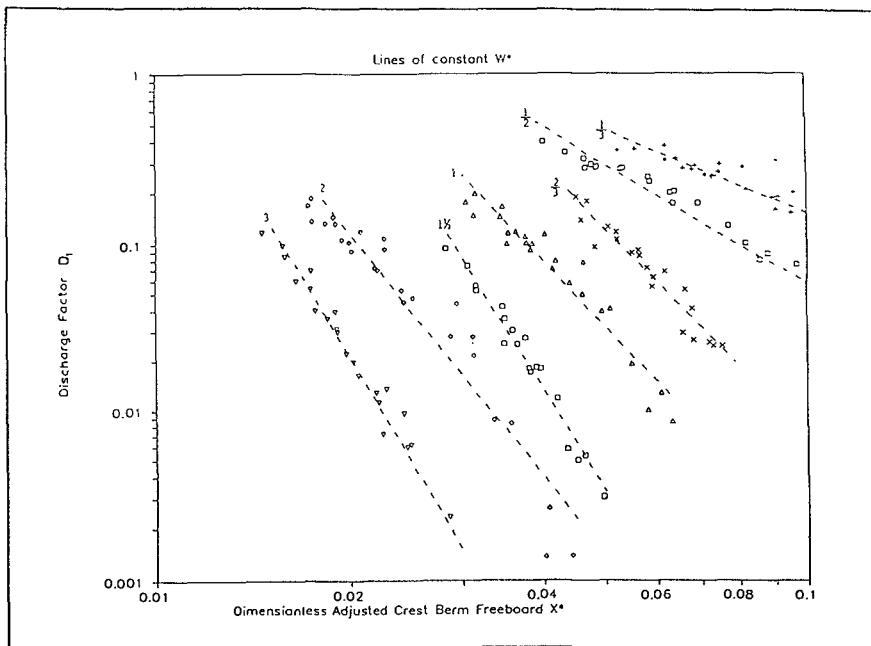


Figure 3 Design graph, recurve wall

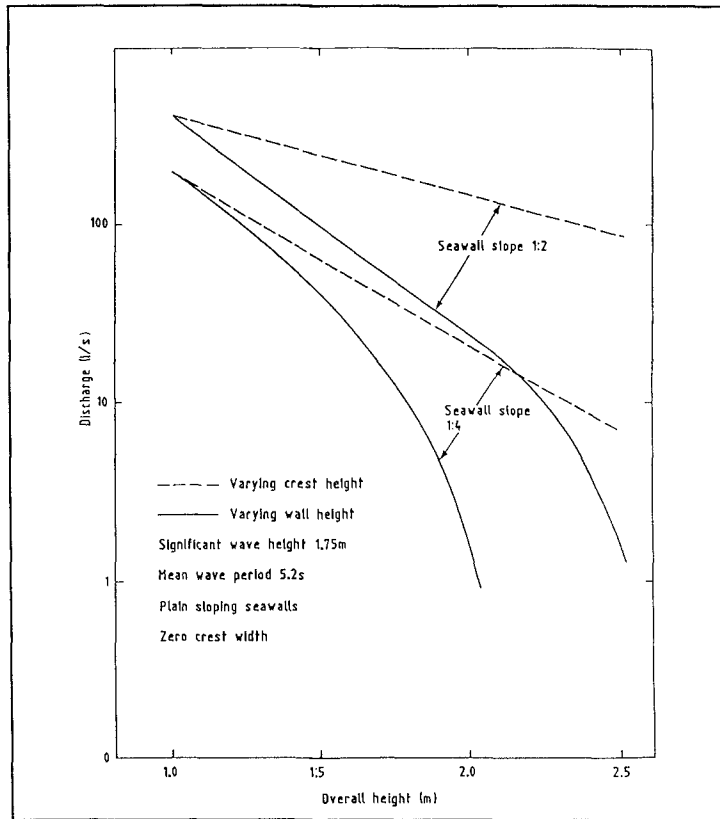


Figure 4 Effect of raising the crest

particular wave condition and water level. Starting from a crest elevation of 1.0m with no wave return wall, the solid lines show the reduction in discharge which is obtained by adding a return wall of gradually increasing height. The broken line shows the reduction obtained by raising the crest height, without any wave return. For a given total height of sea wall, the incorporation of a wave return wall greatly reduces the overtopping discharge compared to simply raising the crest.

The analysis outlined above was also applied to the data obtained by Allsop and Bradbury (1988) who measured the discharges overtopping a rock armoured slope topped with a crown wall. In all cases these tests were carried out for a seaward slope of 1:2 and a crest width equivalent to two rock diameters. The crown wall had a significantly less efficient profile than that proposed by Berkeley-Thorn and Roberts (1981) as used in the other recurved wall tests.

The results, which are illustrated in Figure 5, showed considerably more scatter than for the smooth impermeable slopes. This was thought to be due to the different degrees of energy absorption on the slope and of drainage into the crest for different wave and water level conditions. Also shown in Figure 5 are the discharge factors for the equivalent smooth impermeable slope with a crest width of  $C_w = 4.0$  metres. The discharge factors for a return wall mounted on top of a rock slope are very much better (lower) than for a smooth slope despite the less effective recurve. The reduction in discharge factor must therefore be due to the effects of the rock slope.

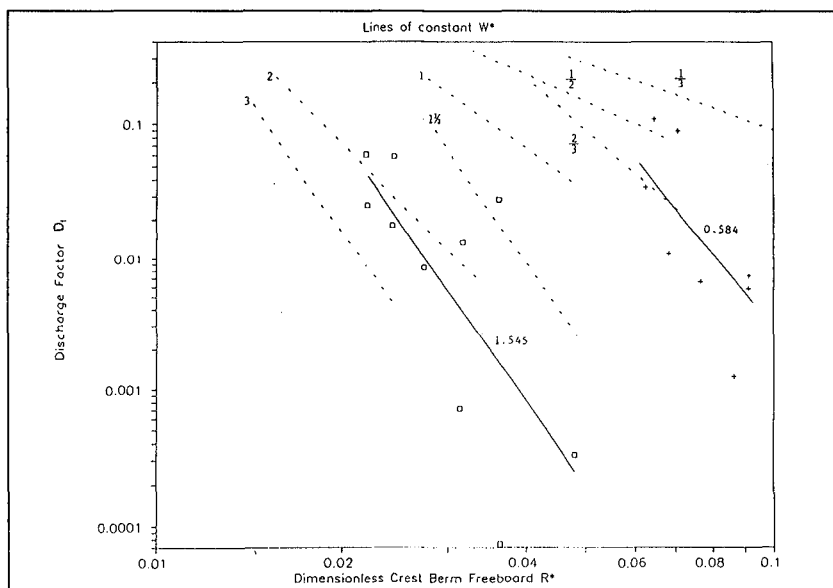


Figure 5 Rock slope compared with 1:2 slope with recurve, 4m crest width

The probable explanation for the lower discharge factors on the rock slope is as follows. As the wave runs up the slope and on to the crest, its forward progress is arrested by the return wall, increasing the depth of water on the crest. For an impermeable slope the remainder of the wave run-up to some extent rides over this cushion of water and a fraction overtops the wave return wall. On a permeable slope water reaching the return wall is able to drain away through the armour layer thereby limiting the depth of water at the crest. Hence wave run-up finds it more difficult to overtop a wave return wall on permeable than an impermeable slope.

Recent work has concentrated on assessing the efficiency of recurve walls under

oblique wave attack. Physical model tests have been completed, at a scale of 1:25, using both short and long crested random waves with angles of wave attack ranging from 15° to 45° off normal. The preliminary analysis of the oblique data appears to indicate that discharge factors are larger, and hence the recurve is not as efficient, when compared to normal wave attack.

#### 4 Vertical walls

Vertical or near vertical sea walls are common in urban areas and are often sited behind shingle or sandy beaches. Work detailing the overtopping performance of vertical walls had previously been completed by Goda (1975). Goda investigated approach slopes of 1:10 and 1:30 and offshore sea steepness of  $s_{om} = 0.012, 0.017$  and 0.036. These conditions were considered to be unrepresentative of conditions around the UK coastline where the steepness of storm waves is greater and the bathymetry of approach is generally shallower.

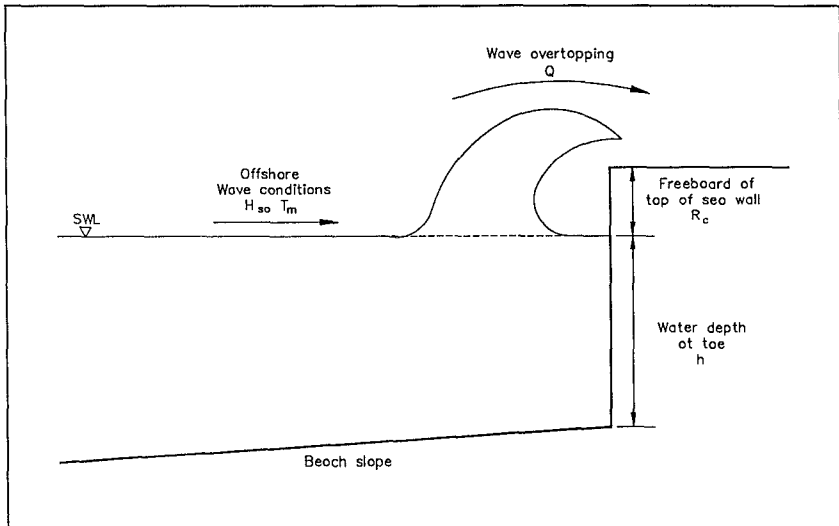


Figure 6 Definition of parameters, vertical wall

A series of physical model tests was therefore undertaken with the aim of confirming and extending the work of Goda so that it was more applicable to UK coasts (Herbert, 1993). Consequently three approach bathymetries of 1:10, 1:30 and 1:100 were used in the model with offshore sea steepness ranging from 0.017 - 0.060. Other parameters that were varied included the offshore wave height, the water depth at the toe of the sea wall and the freeboard of the wall. These parameters, which are illustrated in Figure 6, were varied to ensure that the model tests were completed in the zone of interest identified by Goda.



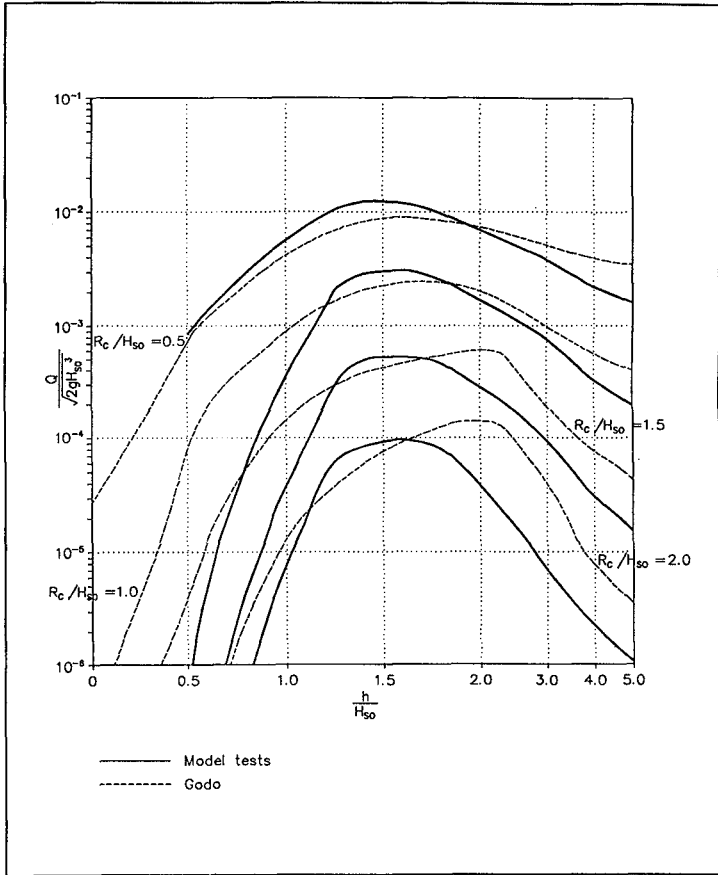


Figure 7 Vertical wall discharges, 1:30 slope,  $s_{om} = 0.036$

The model data gave good agreement with the work of Goda. This is illustrated in Figure 7 where a dimensionless discharge,  $Q^\#$ , is plotted against a dimensionless water depth,  $h/H_{so}$ , where:-

$$Q^\# = Q / (2gH_{so}^3)^{1/2} \tag{10}$$

$H_{so}$  is the offshore significant wave height and  $h$  is the water depth at the toe of the structure.

Lines of constant values of the dimensionless freeboard,  $R_c/H_{so}$ , are illustrated on the graph where  $R_c$  is the height of the crest above still water level.

For a given dimensionless freeboard, maximum overtopping discharges occurred when  $1.4 < h/H_{s0} < 2.0$ . These conditions correspond to waves breaking immediately seaward of the structure toe. The breaking waves often pass directly over the crest of the seawall. For  $h/H_{s0} < 1.4$  waves break before they reach the vertical wall. A considerable amount of energy is dissipated during breaking and hence overtopping is reduced. If  $h/H_{s0} \ll 1.4$  the waves break farther offshore and overtopping is further reduced. Conversely, for  $h/H_{s0} > 2.0$ , waves are unbroken when they reach the structure and this also leads to a reduction in peak overtopping discharge. As waves travel into shallower water they steepen before breaking. When the water depth at the structure is large relative to  $H_{s0}$  little or no shoaling occurs and overtopping is commensurately lower. For unbroken waves, as the  $h/H_{s0}$  ratio increases the level of shoaling, and hence overtopping, is reduced. Eventually the effect of water depth at the structure and bed slope will become insignificant and overtopping will be a function of wave height and freeboard only. Therefore, for large values of  $h/H_{s0}$ , overtopping discharges will approach a constant value for a given dimensionless freeboard,  $R_c/H_{s0}$ .

## 5 Further work

A fieldwork deployment, designed to measure overtopping discharges at prototype sites, has been completed on the North Wales coast. This work is being analysed and compared with results from physical model tests. Furthermore measured discharges are being compared with present guidance on allowable overtopping with particular reference to vehicular and pedestrian safety.

Work is presently being undertaken to assess the performance of a wide range of sea wall cross-sections under oblique wave attack. The structure cross-sections, which are being physical model tested using both long and short crested waves, include simply sloping sea walls with and without recurved walls, bermed sea walls and vertical walls.

A design manual is being planned which will describe and detail the overtopping performance of sea walls and the standards to which they should be designed. It is anticipated that draft copies of this manual will be available in the latter part of 1995.

## 6 Acknowledgements

The authors would like to thank the Ministry of Agriculture, Fisheries and Food for their continued support for the work described in this paper. The work of Mr A A J Steele, who performed the majority of the experimental work, is also gratefully acknowledged.

## 7 References

Allsop N W H and Bradbury A P. 'Hydraulic performance of breakwater crown walls'. HR Wallingford, Report No. SR146, March 1988.

Berkeley - Thorn, R and Roberts A C. 'Sea defence and coast protection works'. Published by Thomas Telford Ltd, 1981.

CIRIA. 'Manual of the use of rock in coastal and shoreline development'. CIRIA Special Publication 83/CUR Report No. 154, 1991.

Goda, Y, Kishira, Y, and Kamiyama, Y. 'Laboratory investigation on the overtopping rates of seawalls by irregular waves'. Ports and Harbour Research Institute, Vol 14, No. 4, pp 3-44, 1975.

Herbert D M. 'Wave overtopping of vertical walls'. HR Wallingford, Report No. SR316, February 1993.

Owen M W. 'Design of sea walls allowing for wave overtopping'. Hydraulics Research Station, Report No. EX924, June 1984.

Owen M W and Steele A A J. 'Effectiveness of recurved wave return walls'. HR Wallingford, Report No. SR261, February 1991.

## CHAPTER 83

### Stability of High-specific Gravity Armor Blocks

Masahiro Ito<sup>1</sup>, Yuichi Iwagaki<sup>1</sup>, Hiroshi Murakami<sup>2</sup>  
Kenji Nemoto<sup>3</sup>, Masato Yamamoto<sup>3</sup> and Minoru Hanzawa<sup>3</sup>

#### Abstract

The stability coefficient of the well-known the Hudson formula,  $K_D$ , has been established by many laboratory tests for various types of armor blocks with a range of specific gravity 2.16~2.47 representative of normal concrete. Design manuals for coastal structures do not describe the adoption of high-specific gravity armor blocks for use in field construction. To examine the effect of specific gravity on stability of Tetrapods, then a laboratory test was conducted by using Tetrapod models of different weights which are composed of five values of specific gravities. Temporal changes of damage ratio arranged test conditions that satisfy the Hudson formula do not coincide among each other, depending on wave period and specific gravity. The effect of the specific gravity on their stability is discussed. As a result, it is found that the relationship between the stability and the specific gravity is considerably affected by the surf similarity parameter and Reynolds number.

#### Introduction

The stable weight of armor units which are used in the cover layer of groins, breakwaters and wave absorbing works is evaluated by the Hudson formula (1959). The Hudson's stability coefficient of armor blocks made from a normal concrete with specific gravity of about 2.30, such as Tetrapod and Dolos, have been determined on the basis of laboratory tests. These tests have been performed using a wide range of experimental conditions for wave height, wave period, and structure slope, using regular waves. As for the use of the armor blocks on beaches and coast lines, there are the following problems and needs:

---

<sup>1</sup> Professor, Department of Civil Engineering, Meijo University, Shiogamaguchi 1-501, Tempaku-ku, Nagoya 468, JAPAN.

<sup>2</sup> Doctor Course, Department of Civil Engineering, Meijo University.

<sup>3</sup> Nippon Tetrapod Co. Ltd.

armor blocks, that is to say, the maximum weight of Tetrapod as a armor block is 784 kN (80 tf) at the present time, but this weight becomes unstable for wave heights over 9 m for seaward slopes of 1 on 4/3 of typical breakwaters.

- (2) When large scale construction equipment such as floating cranes or derrick barges are difficult to move the place such a far detached-island, then small size and more stable armor blocks have to be used.
- (3) Construction site with limited storage space for armor blocks.
- (4) Armor blocks in a corner or head of breakwaters, groins or wave absorbing works receive the complex wave action due to the combined wave-flow induced due to waves. Then, thus parts a weak point in armor blocks and are easily broken.
- (5) To hold the natural beauty of beaches, coastlines, and harbors, smaller and stable armor blocks are required.

For these problems and needs, high-specific gravity armor blocks are considered more suitable. These armor blocks are smaller than the same weight units made from normal concrete. They are more stable against waves. Also it is possible to reduce structure size by using these armor blocks.

A manufacturing method for producing high specific gravity armor blocks is made possible by mixing a heavy stone, or crushed or grained iron ore such as pyrite into the concrete. The "heavy stone" concrete reaches specific gravity of about 2.7~2.8. In the iron ore concrete mixture, the specific gravity becomes greater than 3.0. Such high-specific gravity armor blocks have been already put to a practical use in Japan.

Previous investigation of the high-specific gravity armor blocks, Zwamborn (1978) discussed the effect of specific gravity as the ratio of armor unit volume to wave height based on the past laboratory data that had been performed using rubble-stones of different specific gravity by Kydland and Sodefjed, and dolosse of different specific gravity by Gravesen and Sørensen. Zwamborn reported that by rearranging some test data with dolosse of different specific gravities (2.4, 2.75 and 3.05), the dimensionless wave height,  $(V/H^3)\cot\theta$ , based on block volume,  $V$ , wave height,  $H$ , and slope angle of armor layer,  $\theta$ , is proportional to the specific gravity in water to  $-3.0$ ,  $-3.0$  and  $-4.0$  power for 1, 2, and 5 per cent damage, respectively. But in the Hudson formula, its exponent value is constant ( $-3$ rd power) and well accepted. The authors (1992a, 1992b, 1994) have been carrying out the laboratory study using Tetrapod models of various sizes and specific gravities in order to investigate the effect of specific gravity on the stability for waves. On the basis of the tests results, this paper discusses the effect of specific gravity, surf similarity parameter, and Reynolds number as a function of the block-size and wave characteristic. Recently, Takeda et al. (1993) discussed the relationship between stability and specific gravity, based on the laboratory tests using high-specific gravity armor blocks. He pointed out that the wave period considerably affects the stability-specific gravity relationship.

Thus, investigations on the stability of high-specific gravity armor blocks have been not insufficient up until the present time. Design manuals for coastal structures do not describe the adoption of high-specific gravity armor blocks for use in field construction. The effect of the specific gravity on armor unit stability, therefore, must be further investigated.

**Advantages of high-specific gravity armor blocks**

The effect of the specific gravity on the resistance against wave action is possible to be calculated using the Hudson formula. Assuming that the Hudson's stability coefficient  $K_D$  is a constant for Tetrapod (8.3), the slope angle of armored structure is a constant, the unit weight of normal concrete  $w_c$  is  $22.54 \text{ kN/m}^3$  ( $2.3 \text{ tf/m}^3$ ), and the unit weight of water  $w_w$  is  $9.8 \text{ kN/m}^3$  ( $1 \text{ tf/m}^3$ ), then, we can obtain the ratio of the design wave height for high-specific gravity armor block,  $H/H_c$  to the change of the relative specific gravity against the normal concrete,  $S_r (=w_r/w_w)$ , from the Hudson formula assuming that both blocks are the same size ( $l_B = \text{const.}$ ). Where  $w_r$ ,  $w_c$  and  $w_w$  are the unit weight of any specific gravity armor units, normal concrete, and water, respectively. The effect of  $S_r$  on  $H/H_c$ , the resistance against wave action is shown with a solid curve in Fig. 1. The results show the relative block weight  $W/W_c$  of high-specific gravity to normal concrete, which is also shown with a broken line curve in Fig. 1. Here  $H$  and  $H_c$  are the design wave height of any specific gravity and normal concrete, respectively. It can be seen from this figure that  $H$  in the armor blocks of specific gravity  $S_r = 3.0$  is possible to resist about 1.5 times wave height,  $H_c$ , for the normal concrete of the same size. However, this finding holds only when  $K_D$ -values are the constant though the specific gravity ranges.

**Laboratory test**

To examine the effect of specific gravity on stability of Tetrapod, models of different weight were used, composed of five different values of specific gravities (1.82, 2.30, 2.77, 3.40, 4.27). A total of 21 different Tetrapod models were used. The range of Tetrapod models used varied between a vertical height of  $l_B = 3.29 \sim 16.6 \text{ cm}$  and a weight of  $W = 0.27 \sim 22.85 \text{ N}$  ( $27.7 \sim 2329.6 \text{ gf}$ ). The sizes and weights of Tetrapod models used in the laboratory tests are listed in Table 1. Model weights on each row (A, B, C, D, and E) within this table are obtained for each specific gravity

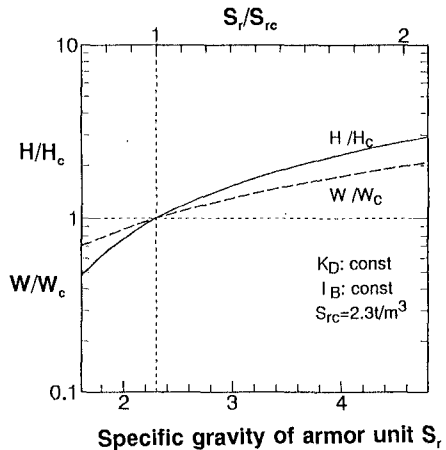


Fig. 1. Effect of specific gravity on stability of armor blocks for waves

Table 1. Specific gravities, sizes and weights of Tetrapod models

Marks of model	Class Nos. of specific gravity	5	4	3	2	1	Design Wave height at 1% damage H(cm)
		$w_r/w_w$					
A	$\phi_s$ (cm)	7.16	4.52	3.29			8.6
	W (gf)	186.4	58.9	27.7			
B	$\phi_s$ (cm)	9.04	5.68	4.14			10.8
	W (gf)	372.7	117.8	55.4			
C	$\phi_s$ (cm)	12.24	7.72	5.68	4.14	3.08	14.7
	W (gf)	931.8	294.4	141.8	68.0	34.2	
D	$\phi_s$ (cm)	16.82	10.48	7.72	5.68	4.14	19.9
	W (gf)	2329.6	736.0	354.6	174.1	85.4	
E	$\phi_s$ (cm)		14.15	10.48	7.72	5.68	26.9
	W (gf)		1811.0	886.4	435.2	218.6	
F	$\phi_s$ (cm)		8.28				15.7
	W (gf)		368.0				

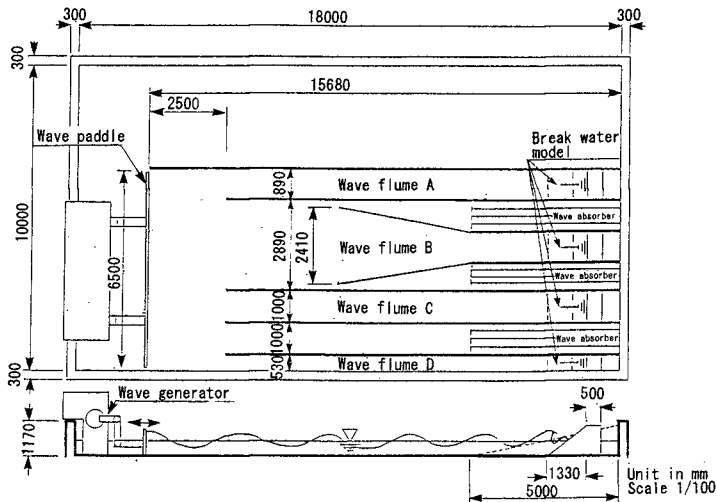


Fig. 2. Wave flumes to minimize the multiple wave reflection

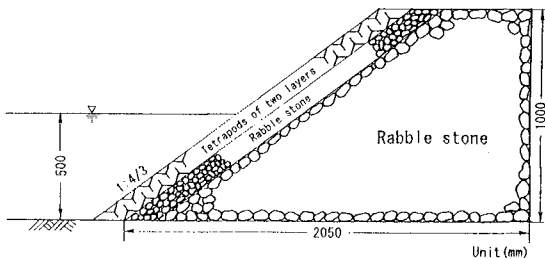


Fig. 3. Breakwater model armored with Tetrapods of two-layer

Table 2. Experimental conditions

Waves	Water depth (cm)	50.60
	Wave height (cm)	5~40
	Period (sec)	1~3
	Wave steepness H <sub>o</sub> /L <sub>o</sub>	~0.14
Tetrapods	Specific gravity $w_r/w_w$	1.82, 2.30, 2.77 3.40, 4.27
	Weight (gf)	34.2~2329.0
	Vertical height (cm)	3.08~16.6.0
Breakwater	Front slope of cover layer	1:4/3
Slope of Sea-floor		horizon
Wave operation time (min) (Wave numbers t/T)		50~70 (80~2000)

by giving  $K_D=8.3$  (in  $0 < \text{Damage ratio} \leq 1\%$ ),  $\cot\theta=4/3$ ,  $w_w=9.8 \text{ kN/m}^3$  ( $1 \text{ tf/m}^3$ ), and given a constant Hudson formula design wave height. The design wave height of the models in each row of Table 1, becomes nearly equal, despite difference in specific gravity.

As shown in Fig. 2 the wave basin was divided into the seven flumes, each having a free water zone of 2.5 m in front of the wave paddle. Model breakwaters used in the stability test were constructed within every other flume. The control flumes had wave absorbing net-mats, which were set on a slope of 1 on 10 used to minimize the multiple wave reflection which takes place between wave paddle and breakwater model in normal flumes. In the laboratory test, regular waves were generated continuously on the Tetrapod model for a total of about 1,500 waves under no-overtopping conditions. The 1,500 waves are equivalent to prototype wave action of about 4 hours for a wave period of 10 sec. Wave flume B was constructed with a geometry to increase wave height. Each Tetrapod model was constructed randomly in two layers, on a slope of 1 on 4/3 as shown in Fig. 3. Laboratory test conditions are summarized in Table 2. The damage progression of Tetrapod models was observed continuously by a 8 mm Vidco-camera. The damage rate, defined as the ratio of the number of blocks that moved to the total number of armor blocks in the two layers, was measured with a display playing back the Video.

## Test results

A temporal damage change of Tetrapod models attributed to the difference of specific gravity based on test data, is shown in Fig. 4. The damage to the Tetrapod models of each different specific gravities should be similar to each other. These Tetrapod models (A-3, A-4, A-5) are listed the same row of Table 1. The design wave height of these armor units is nearly equal. However, these damage curves differ due to specific gravity. As to a reason for the difference,



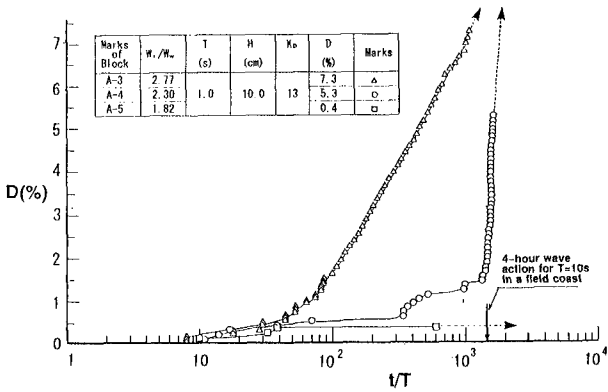


Fig. 4. Temporal damage changes due to the difference of specific gravity

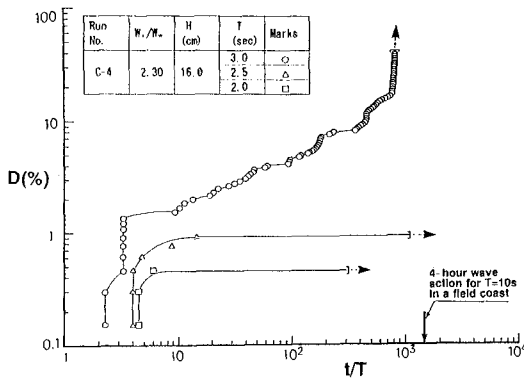


Fig. 5. Temporal damage changes due to the difference of wave period

Table 3. Damages of detached breakwaters, groins, and seawall with Tetrapods due to storm waves in Japan

Locations of port and harbour in Japan	W (tf)	T (s)	Damage ratio (%)	H <sub>1/3</sub> (m)	K <sub>0</sub>	R <sub>0</sub>	ξ	Remarks
Hamana	3	13	50	5.6	64.6	6.7E+06	4.3	Typhoon 7219
Hamada	20	13	50	8.0	23.6	1.6E+07	3.6	Depression, Jan. 1971
Simoda	8	12	30	5.0	14.4	9.3E+06	4.2	Typhoon 7010
Simoda	16	12	30	5.0	7.2	1.2E+07	4.2	Typhoon 7020
Nobeoka	13	14	50	4.0	4.7	9.6E+06	5.4	Typhoon 7123
Miyazaki	8	14	50	4.0	7.4	8.3E+06	5.4	Typhoon 7119
Miyazaki	5	14	50	4.0	11.8	7.1E+06	5.4	Typhoon 7119

considerations must be given to the fact that stability is affected by the specific gravity. Selecting identical wave heights from the test data in the same size Tetrapod model, a temporal damage change is shown for each wave period in Fig. 5. Damage curves, generally, must be similar to each other regardless of the difference in wave periods. Hudson's (1959) stability coefficient is independent of wave period. But from Fig. 5 it is recognized that stability becomes a function of the wave period.

From field data, we can investigate damage ratio, significant wave height, and block weight of Tetrapod. The technical report by Takeyama and Nakayama (1975) reported on damage of failure of coastal structures by large waves in Japan. These field data are listed in Table 3. The field data includes the effects of oblique incident waves, deflection waves, and scour in or around the toe of breakwater slope. The damage ratios shown in this table, then, are considerable large (range from 30% to 50%). Hudson's stability coefficient in this table is obtained by converting wave height to equivalent significant wave height. Regular waves were converted based on the equation,  $H = 1.5H_{1/3}$ . This equation follows the equations proposed by Fan et al. (1983) and Tanimoto (1985) as

$$H = 1.4H_{1/3} \quad (\text{Fan et al.}) \quad (1)$$

$$H = (1.5 \pm 0.37)H_{1/3} \quad (\text{Tanimoto et al.}) \quad (2)$$

The evaluated surf similarity parameter  $\xi$  and Reynolds number  $R_s$  are also listed in Table 3.

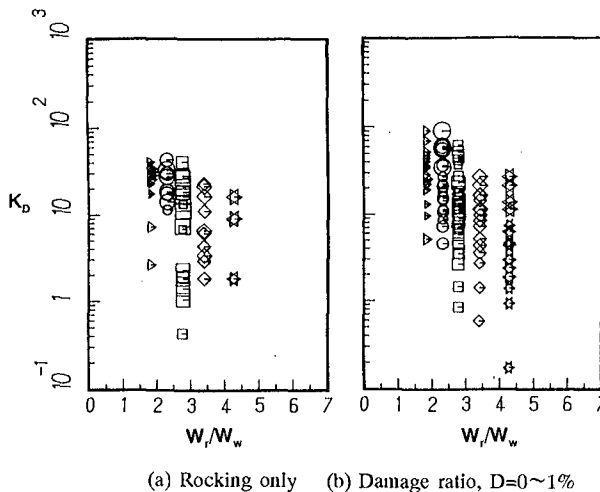


Fig. 6. The relationship between  $K_D$ -values and specific gravity in two types of damages

### Effect of specific gravity on stability

The rocking only (no-damage) and the 0~1 % damage are selected from the laboratory test data. Fig. 6 shows these data which show the relationship between Hudson's stability coefficient,  $K_D$ , and the specific gravity in water,  $S_r-1$ . In this figure, the  $K_D$ -values scatter wildly for the difference in the specific gravity in water. The effect of the specific gravity on stability (rocking only and 0~1% damage) can not be clearly established from this figure. In the Hudson formula, the stability coefficient  $K_D$  should be constant because it should considerably depend on the shape of armor units. Therefore, the stability coefficient must be independent of the change of specific gravity. But  $K_D$ -values scatter wildly for the different  $S_r-1$  values as shown in Fig. 6. Then the Hudson formula may not satisfy the test data.

### Theoretical discussion

As above discussed, the effect of the specific gravity on the stability disagrees with the Hudson formula. As this reason it is considered that many factors affect Hudson's stability coefficient, including effects due to wave steepness, relative depth, Reynolds number, drag coefficient, acceleration of wave motion etc. as described by Hudson (1959).

Reviewing the Hudson formula, the stability coefficient  $K_D$  is expressed by;

$$K_D = \frac{w_r H^3}{W(S_r - 1)^3 \cot \theta} \quad (3)$$

where,  $W$  is the weight of armor unit,  $w_r$  is the unit weight of armor unit,  $H$  is the design wave height,  $S_r (=w_r/w_w)$  is the specific gravity of armor unit,  $w_r$  is the unit weight of armor unit,  $w_w$  is the unit weight of water,  $\theta$  is the angle of structure slope measured from horizontal in degrees, and  $K_D$  is the stability coefficient varying primarily with the shape of the armor units, degree of interlocking, damage rate, etc.

The behaviors of armor units is affected by slope angle, wave breaking, wave runup, and rundown, and is sensitive to the surf similarity parameter  $\xi$ ,

$$\xi = \frac{\tan \theta}{\sqrt{H/L_o}} \quad (4)$$

where  $L_o$  is the wave length in deep water.

Hudson (1959), Dai and Camel (1969), and Sakakiyama and Kajima (1990) have pointed out that the stability of armor units is affected by the Reynolds number related the scale of laboratory tests. The Reynolds number is expressed

using the velocity of wave motion and a characteristics length of the armor block as

$$R_e = \frac{\sqrt{gH}(W/w_r)^{1/3}}{\nu} \tag{5}$$

where  $\nu$  is the kinematic viscosity,  $g$  is the acceleration due to gravity. Rewriting Eq. (3) using Eqs. (4) and (5), the stability coefficient  $K_D$  is expressed as follows:

$$K_D = \frac{R_e^2}{\xi^4(S_r - 1)^3} C_R \tag{6}$$

where

$$C_R = \frac{L_o^2 v^2}{g} \left(\frac{w_r}{W}\right)^3 \tan^5 \theta \tag{7}$$

From Eq. (6), it is shown that the stability coefficient  $K_D$  is proportional to the -3rd power of the specific gravity in water, the -4th power of the surf similarity parameter, and the 2nd power of the Reynolds number.

**Stability and Surf similarity parameter**

Fig. 7 shows the relationship between  $K_D$ -values and the surf similarity parameter for the test data and the field data listed Table 3. In this Figure, the  $K_D$ -

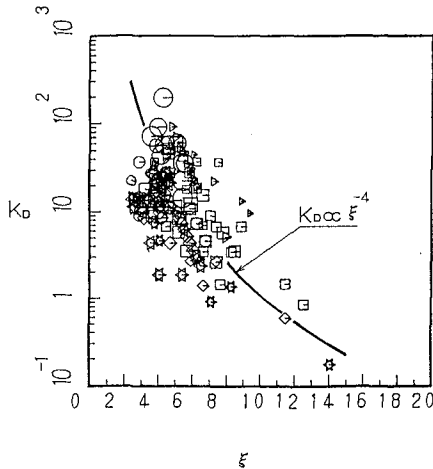
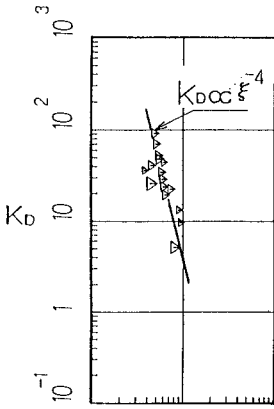
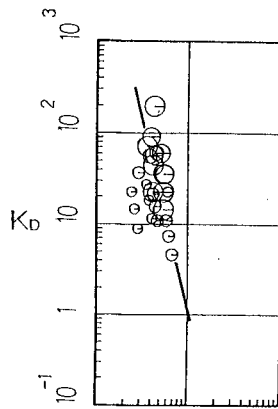


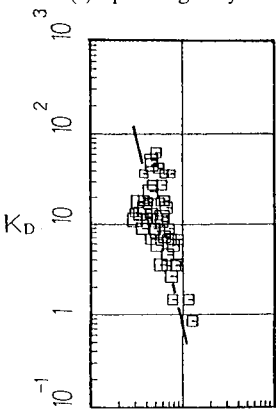
Fig. 7. The relationship between  $K_D$ -values and surf similarity parameter of test data and field data



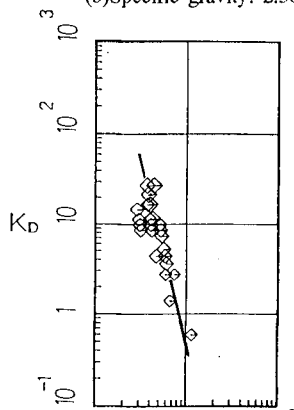
(a) Specific gravity: 1.82



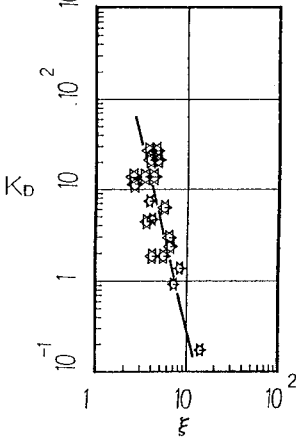
(b) Specific gravity: 2.30



(c) Specific gravity: 2.77



(d) Specific gravity: 3.40



(e) Specific gravity: 4.27

Fig. 8. The relationship between  $K_D$ -values and surf similarity parameter for each specific gravity

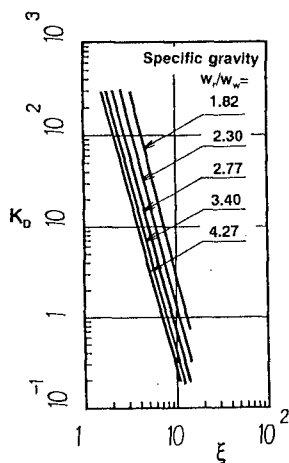


Fig. 9. The relationship between  $K_D$ -values and surf similarity parameter due to the difference of specific gravity

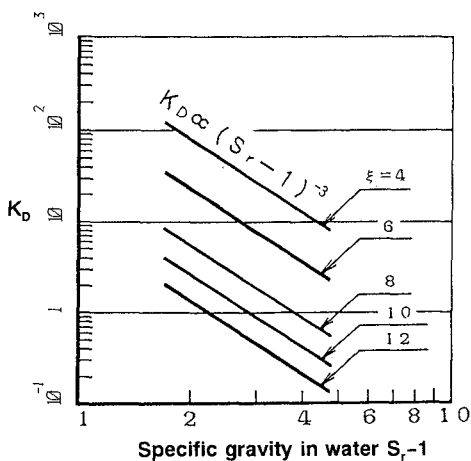


Fig. 10. The relationship between  $K_D$ -values and specific gravity in water due to the difference of surf similarity parameter

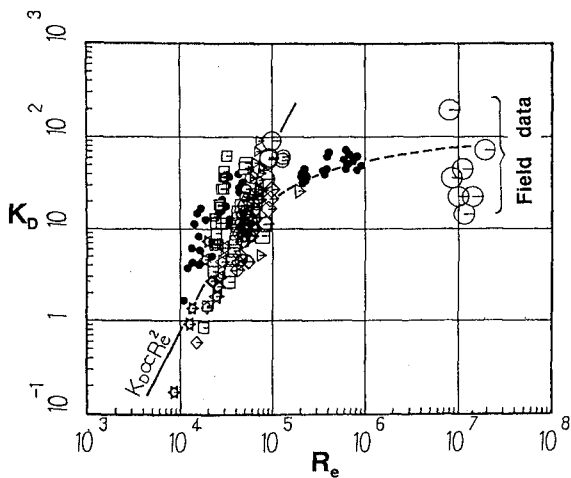


Fig. 11. Effect of Reynolds number on  $K_D$ -values

values agrees well with the solid curve expressing the relationship of  $K_D \propto \xi^{-4}$  in Eq. (6). The relationship between the  $K_D$ -values and the surf similarity parameter for each specific gravity are shown in Fig. 8(a)-(c), respectively. From these figures, the relationship between the  $K_D$ -values and the surf similarity parameter agrees well the solid line indicating the relationship of  $K_D \propto \xi^{-4}$ . Fig. 9 shows the relation

of  $\xi$  to  $K_D$  arranged together from Fig. 8(a) to Fig.8(e) using the specific gravity as a parameter. Fig. 10 shows the relationship between the stability coefficient and specific gravity in water. This figure was obtained by rearranging Fig. 9 taking the surf similarity parameter as a parameter. From Fig. 10, it can be seen that the stability coefficient decreases with increasing specific gravity in water dependent on  $K_D \propto (S_r - 1)^{-3}$ , as indicated in Eq. (6). From Fig. 10, stability is affected by the surf similarity parameter, and increases with decreasing the surf similarity parameter.

Sawaragi et al. (1983) pointed out that Iribarren's number reaches a minimum value around the surf similarity parameter of  $\xi \approx 3$  due to the occurrence of wave-armor unit resonance on the basis of the laboratory tests of rubble mound breakwaters. Losada (1990) discussed the effect of the surf similarity parameter on the stability function,  $\varphi = 1/(K_D \cot \theta)$ , by rearranging laboratory test data for various armor units. Then he pointed out that the stability function increases inversely proportional to decreasing surf similarity parameter. These findings are contrary to authors results as above discussed. The discrepancy between the authors and Losada may cause the reason that the range of the surf similarity parameter used and the size of armor unit model is not in agreement.

### Stability and Reynolds number

It can be considered from Eq. (6) that the stability coefficient  $K_D$  is affected by the Reynolds number. Then, the relationship between the Reynolds number and the  $K_D$ -values of the zero damage test data and the field data listed in Table 3, is plotted in Fig. 11. This figure is also plotted with the dark circle indicating Tetrapods only from the paper by Simada et al. (1986), who investigated the stability of Tetrapods, Dolosse, and Koken-blocks. These armor units are made from normal concrete ( $w_c/w_w = 2.30$ ). The armor blocks had a weight range of  $W = 0.16 - 484$  kN (16 gf - 49.39 kgf), and were tested in the medium and large wave tanks. It is shown from Fig. 11 that the  $K_D$ -values increase rapidly with increasing Reynolds number, up to  $R_e = 10^5$  which corresponds to small and medium test scales in the range of Reynolds number  $R_e = 8 \times 10^3 - 10^5$ . Over this value the  $K_D$ -values gradually reach a constant. The  $K_D$ -values fit well with the solid line indicating the relation of  $K_D \propto R_e^2$ . The  $K_D$ -values beyond  $R_e = 10^5$  deviates from the trend depicted by the solid line. Such changes in  $K_D$ -values may be caused by scale effects. This has been indicated by Dai and Camel (1969) and Shimada et al. (1986). A wider range of scales and numerous test data are needed to further the understanding of the affects of specific gravity and the surf similarity parameter as they related to  $K_D$ -values and the Reynolds number.

### Conclusions

The effect of the specific gravity on the hydraulic stability of Tetrapod is examined on the basis of numerous laboratory test data. These data were obtained using the total of 21 different models composed five values of specific gravity;

1.82, 2.30, 2.77, 3.40, and 4.27. The discussion includes test and field data reported by another researchers. Conclusions drawn from the results obtained in this study are as follows:

- (1) Hudson's formula does not include the effect of wave period. Then Hudson's stability coefficient must be independent of wave period. But this coefficient is considerably influenced by wave period.
- (2) Trends are not seen for the relationship between  $K_D$ -values and specific gravity. But by arranging the relationship as a function of the surf similarity parameter, it is found that the  $K_D$ -values decrease with increasing surf similarity parameter, where  $K_D \propto \xi^{-4}$ .
- (3) The relationship between the  $K_D$ -values and the specific gravity in water is shown by the relation,  $K_D \propto (S_r - 1)^{-3}$ , when the surf similarity parameter is taken into account. The  $K_D$ -values decrease with increasing specific gravity.
- (4)  $K_D$ -values from the test data correspond well to the 2nd power of the Reynolds number within a range of Reynolds number between  $R_e = 8 \times 10^3 - 10^5$ . In  $R_e \geq 10^5$ , the  $K_D$ -values gradually reach a constant as Reynolds number increases. Therefore the stability of high-specific gravity armor blocks, is affected significantly by scale effects.

It should be remarked that the conclusions of (1), (2), and (3) are results that are discussed on the basis of the data of small and medium test scale included the scale effects.

### Acknowledgement

The authors would like to thank Mr. George F. Turk, Research Hydraulic Engineer of U.S. Army Coastal Engineering Research Center for proofreading the draft paper. We also grateful to the undergraduate and graduate students of Department of Civil Engineering at Meijo University for their kind assistance in the laboratory test.

### References

- Bandtzcag, A. (1978). "The effect of unit weights of rock and fluid on the stability of rubble mound breakwaters." *Proc. 16th Int. Conf. on Coast. Engrg, ASCE*, 990-1021.
- Dai, Y.B. and Kamel, A.M. (1969). "Scale effect tests for rubble-mound breakwaters hydraulic model investigation." Research Report H-69-2.
- Fan, Q., Horikawa, K. and Watanabe, A. (1983). "Experimental study on the stability of a concrete block mound breakwater under irregular waves." *Proc. of 30th Coastal Eng. Conf., JSCE*, 352-356, (in Japanese).
- Gravcsen, H. and Sørensen T. (1977). "Stability of rubble mound breakwaters." *Proc. 24th Int. Nav. Congress, PINAC*, Leningrad.
- Hudson, R. Y. (1959). "Laboratory investigation of rubble-mound breakwaters." *J. Wrtway. and Harb. Div., ASCE*, 93-118.
- Ito, M., Iwagaki, Y., Yamada, T., Nemoto, K., Yamamoto, H. and Hanzawa, M. (1992a). "An influence of surf similarity parameter on stability of high-specific



- gravity armor units." *Proc. of Coastal Engineering*, JSCE, Vol.39, 666-670, (in Japanese).
- Ito, M. Iwagaki, Y., Yamada, T., Nemoto, K., Yamamoto, H. and Hanzawa, M. (1992b). "On the effect of specific-gravity change on stability in armor units". *Proc. of Civil Engineering in Ocean*, JSCE, Vol.8, 75-80, (in Japanese).
- Ito, M., Ogawa, K and Murakami, H. (1994). "An experimental study on the vibration of armor unit by wave action". *Proc. of Civil Engineering in Ocean*, JSCE, Vol.10, 171-175, (in Japanese).
- Losada, M. A. (1990). "Recent Development in the Design of Mound Breakwaters". *Handbook of Coastal and Engineering*, Vol.1, Herbich, J.B. Ed., Gulf Publishing Co.
- Sakakiyama, T. and Kajima, R. (1990). "Scale effect of wave force on armor units." *Proc. 22nd Int Conf. on Coast. Engrg.*, ASCE, 1716-1729.
- Sawaragi, T., Iwata, K. and Ryu, C. (1983). "Consideration of the destruction mechanism of rubble mound breakwaters due to resonance phenomenon." *Proc. 8th Int. Harbor Congress*, 3.197-3.208.
- Shimada, M., Fujimoto, T., Saito, S., Sakakiyama, T. and Hiraguchi, H. (1986). "Scale effect on stability of amour units." *Proc. of 33th Coastal Eng. Conf.*, JSCE, 442-445, (in Japanese).
- Takeda, H, Yamamoto, Y., Sasajima, T., Kikuchi, S. and Mizuno, Y. (1993). "Stability of high-specific gravity artificial concrete blocks by irregular-wave test." *Proc. of Civil Engineering in Ocean*, Vol. 9, 313-318, (in Japanese).
- Takeyama, H. and Nakayama, T. (1975). " Disasters of breakwaters by wave action." *Technical Note*, No.200, Port and Harbor Res. Inst. Ministry of Trans., Japan, (in Japanese).
- Tanimoto, K., Haranaka, S. and Yamazaki, K. (1985). "Experimental study on the stability of wave dissipating concrete blocks against irregular waves." *Report of the Port and Harbor Res., Ins.*, Vol.24, No.2, 86-121, (in Japanese).
- Zwamborn, J.A. (1978). "Effect of relative block density." *Proc. 16th Int. Conf. Coast. Engrg.*, ASCE, 2285-2304.

## CHAPTER 84

### Rock armoured beach control structures on steep beaches

Jones R.J.<sup>1</sup> & Allsop N.W.H.<sup>2</sup>

#### ABSTRACT

This paper presents the results of a research study to quantify the stability of rock armoured groynes on steep shingle beaches. The research was needed to identify why significant numbers of rock revetments and groynes have suffered greater damage than would be predicted by conventional design methods. The paper describes the design and execution of tests in a large wave basin, at notional scales of 1:10-20, on four types of typical beach control structures. The test structures were constructed on a model shingle beach of slope 1:7, and were subjected to random waves of steepnesses  $s_m=0.02$  or  $0.04$ .

The tests confirmed that armour damage may be substantially greater than predicted by existing methods, even on simple slopes under normal wave attack. The results of the damage analysis have been used to suggest modified coefficients to van der Meer's plunging wave formulae.

#### 1. INTRODUCTION

The use of shingle beaches in a coastal defences increasingly requires control structures to maintain and retain the beach. A variety of structures are in use (Fig 1), including rock groynes and/or breakwaters, and revetments. The main structure types in use, not necessarily in the UK, may be summarised:

- a) near-shore, detached, breakwaters;
- b) low-crest or reef breakwaters;
- c) submerged breakwaters or sills;
- d) rock groynes, bastion or inclined;
- e) rubble revetments.

Studies at Wallingford on the influence of the control structures on the beach response to wave action, reported by Coates (1994), suggest that rubble groynes are often the most cost-effective of these structures in controlling movements of shingle beaches, and significant research is underway to describe the effect of structure plan configuration and geometry on the plan re-shaping of the beach. As shingle beaches may become depleted without re-nourishment, or may be locally denuded by strong oblique wave attack, back-

---

<sup>1</sup> Engineer Coastal Group, HR Wallingford, Howbery Park, Wallingford, UK

<sup>2</sup> Professor (associate), Department of Civil Engineering, University of Sheffield; Manager Coastal Structures, HR Wallingford, Howbery Park, Wallingford, UK.

beach rubble revetments may also be required to form a stronger rear defence.

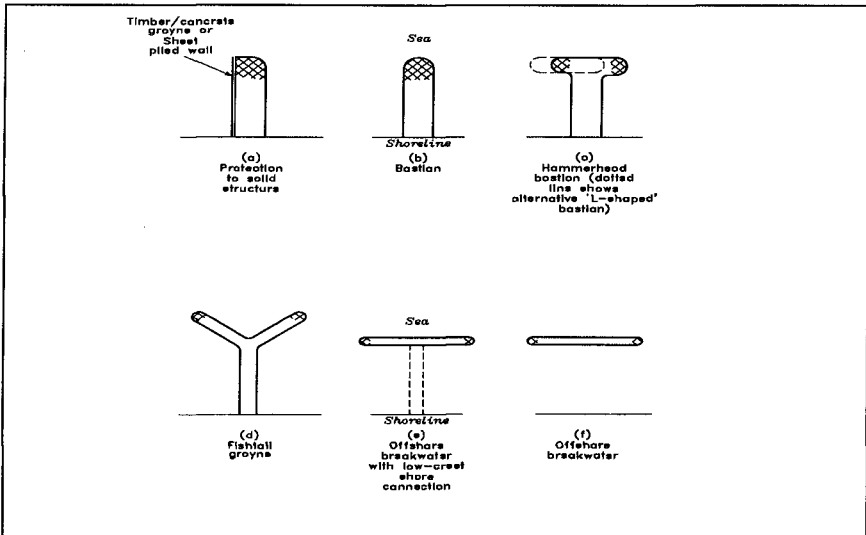


**Figure 1 Beach control structures**

The main parameter set by structural considerations on all armoured control structures is the median armour size. The armour slope angle chosen interacts with the armour size needed for a given stability level, but is also set by consideration of wave reflections and overtopping. Many other dimensions, and aspects of construction practice, relate closely to the unit armour size. If under-sized, rock armour will move excessively, leading to deterioration of the armour, and/or erosion of fill. Structural changes to the groyne will in turn lead to higher wave overtopping, and/or beach erosion. It is important therefore to ensure that any damage to the structure remains below acceptable limits. Various methods may be used to calculate the armour size, but are only fully valid for normal attack on simple cross-sections. Allsop et al (1995) present evidence where some structures have experienced more damage than expected by their designers, and/or deemed acceptable by their owners.

The problem of increased damage armour appears to have been most severe on steep shingle beaches, typically in the UK at slopes between 1:5 to 1:10, with the average near to 1:7. It is likely that such steep slopes have significant influences on the form and strength of wave breaking onto any structure constructed on the beach, thus modifying the waves from the form of deep or intermediate depth waves for which most design methods have been derived. Most of this paper therefore describes hydraulic model studies conducted to measure armour damage on beach control structures on steep beaches, and the analysis then conducted to devise appropriate design methods.

## 2 METHODS TO CALCULATE ARMOUR STABILITY

Design methods for rock armour focus on calculation of the median armour unit mass,  $M_{50}$ , or the nominal median diameter  $D_{n50}$  defined in terms of the median unit mass and rock density  $\rho_r$ :  $D_{n50} = (M_{50}/\rho_r)^{1/3}$ . The most common calculation methods are the Hudson

formula given in the Shore Protection Manual by CERC (1984); or equations by Van der Meer (1988). Hudson developed a simple expression for the minimum armour weight for regular waves which may be written in terms of the median armour unit mass,  $M_{50}$ , and wave height,  $H$ :

$$M_{50} = \rho_r H^3 / (K_D \cot \alpha \Delta^3) \quad (1)$$

where  $\rho_r$  is the density of rock armour ( $\text{Kg/m}^3$ );  $\rho_w$  is the density of (sea) water;  $\Delta$  is the buoyant density of rock,  $= (\rho_r/\rho_w)-1$ ;  $\alpha$  is the slope of angle of the structure face; and  $K_D$  is a stability coefficient to take account of the other variables. Values of  $K_D$  corresponded to the wave height giving least stability in tests with regular waves on permeable cross-sections subject to little overtopping. Slight re-shaping of armour was expected, and values of  $K_D$  correspond to "no damage" where 0-5% of the armour was displaced.

An alternative method was derived by Van de Meer (1988) who included model data by Thompson & Shuttler at Wallingford, extended this by further tests at Delft, and derived new formulae for armour damage which include the effects of random waves, range of core / underlayer permeabilities, and distinguish between plunging and surging wave conditions respectively.

$$H_s/\Delta D_{n50} = 6.2 P^{0.18} (S/\sqrt{N_z})^{0.2} \xi_m^{-0.5} \quad (2a)$$

$$H_s/\Delta D_{n50} = 1.0 P^{0.13} (S/\sqrt{N_z})^{0.2} \sqrt{\cot \alpha} \xi_m^P \quad (2b)$$

where the parameters not previously defined are:

- P notional permeability factor
- S design damage number  $= A_e/D_{n50}^2$ , and  $A_e$  is erosion area
- $N_z$  number of waves
- $\xi_m$  Iribarren number  $= \tan \alpha / s_m^{0.5}$
- $s_m$  wave steepness  $= 2\pi H_s/gT_m^2$ , and  $T_m$  is the mean period;

and the transition from plunging to surging is given by a critical value of  $\xi_m$ :

$$\xi_m = (6.2 P^{0.31} (\tan \alpha)^{0.5})^{1/(P+0.5)} \quad (2c)$$

Damage to armour on a range of core / underlayer configurations were analysed. Values of  $P$  given by Van de Meer vary from 0.1 for armour on underlayer over an impermeable slope, to 0.6 for a homogeneous mound of armour, with intermediate values of 0.4 and 0.5 also described. These formulae were derived for normal wave attack, and do not include corrections for roundheads or junctions.

### 3. DESIGN OF MODEL STUDIES

#### 3.1 Test structures and facility

The objective of the physical model tests was to quantify the stability of rock armour on four typical rock armoured structures on a 1:7 beach slope:

- a) a breakwater or groyne roundhead, Type 2, (Fig 2);
- b) an L-shaped groyne, formed from a) above;
- c) an inclined groyne, Type 1, (Fig 3); and
- d) a simple 1:2 rubble sea wall slope.

The 1:2 sea wall section was tested primarily as a control structure, damage to which could be compared directly with predictions by the existing design formulae.

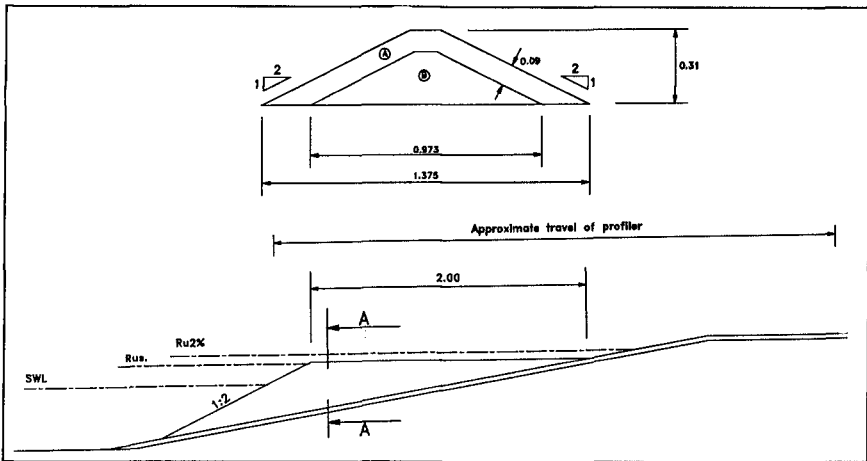


Figure 2 Type 2 roundhead groyne

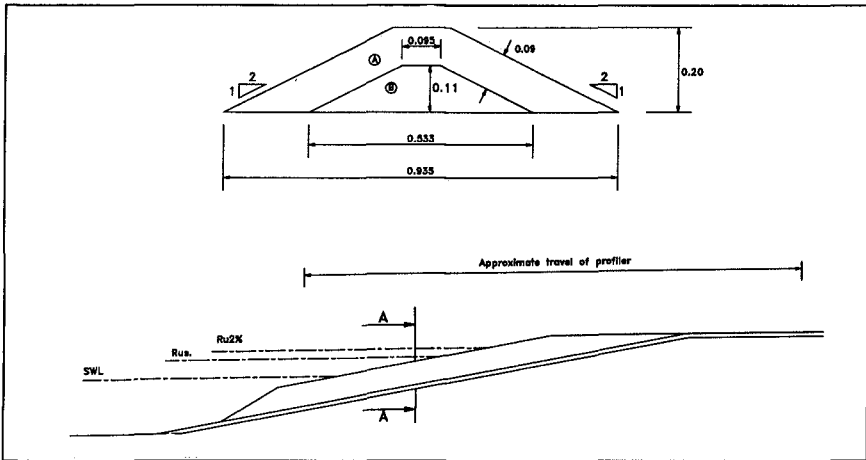
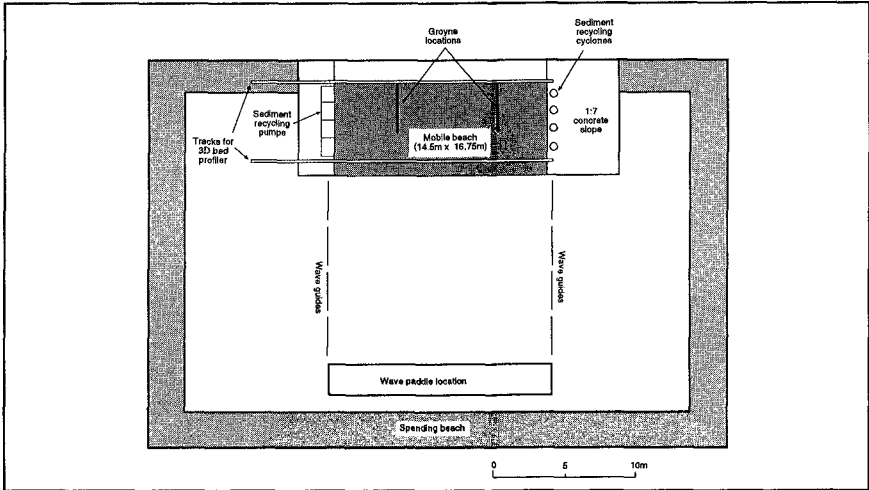


Figure 3 Type 1 groyne

Early in the research, a review of prototype structures suggested that the crest level should allow overtopping, and often fell between significant and 2% run up levels. The 2% run-up level was calculated using empirical prediction methods in CIRIA (1991). The principal test parameters may be summarised:

Water and bed levels	0.0m; -0.7m
Target wave height	$H_s = 0.13\text{m}$ , ( $H_s/\Delta D_{n50} = 1.7$ )
Mean sea steepnesses	$s_m = 0.02$ and $0.04$
Test duration	$N_z = 1000$ and $3000$ waves
Armour and core size	$D_{n50} = 0.045\text{m}$ ; $D_{n50} = 0.024\text{m}$
Side slope angles	$\text{Cot } \alpha = 2.0$
Toe and crest levels	$-0.36\text{m}$ , ( $-8D_{n50}$ ); $+0.22\text{m}$ , ( $+5D_{n50}$ )



**Figure 4 Roundhead Basin test facility**

The structures were constructed and tested in a large wave basin which measured 40m by 27m (Fig 4). The models were not to a particular scale, so analysis of measurements used dimensionless terms, but the structures may be viewed as modelled at ratios of between 1:10 and 1:20. Two structures were tested at one time. Type 1 and 2 groynes were tested in the first series. The Type 1 groyne was then replaced by the sea wall, and the Type 2 groyne was modified to the "L" shape (Fig 5).

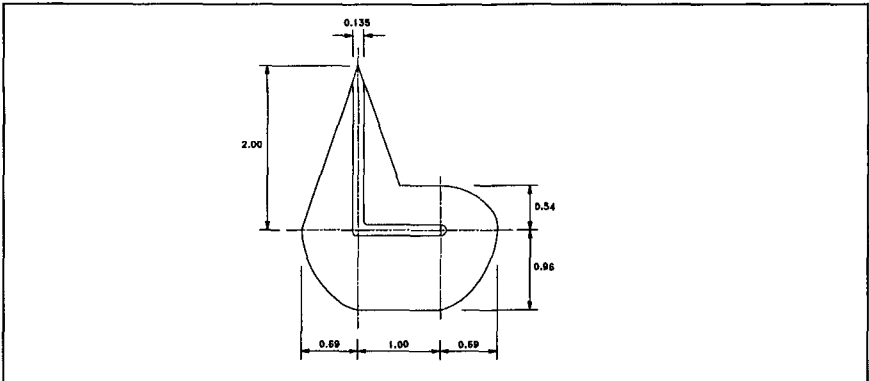


**Figure 5 Plan of L-shaped groyne**

The 1:2 slope sea wall section was 1.0m wide (equivalent to  $22 D_{n50}$ ). The toe was set at the same level as the toe of the "L" shaped and roundhead groynes.

The low level groyne, Type 1, was 4.7m long ( $105 D_{n50}$ ), 0.94m ( $21 D_{n50}$ ) wide at the base, and reached a height of 0.2m ( $4.4 D_{n50}$ ) above the beach. The armour was laid to a thickness  $t_a=2D_{n50}$ , slopes of 1:2, and crest width of  $3D_{n50}$ .

The high level roundhead groyne, Type 2, was shorter and wider than the Type 1 groyne at 2.95m (66  $D_{n50}$ ) long and 1.38m (31  $D_{n50}$ ) wide at the widest part of the roundhead. The crest was 0.31m (6.9  $D_{n50}$ ) above the beach at the seaward end.

The "L" shaped groyne was formed by extending from the roundhead of the Type 2 groyne. The groyne was 2.96m (66  $D_{n50}$ ) long, with a side limb of 2.38m (53  $D_{n50}$ ). A straight section of 1.0m (22  $D_{n50}$ ) formed the "L" shape.

Three 5m random wave paddles produced normal wave attack for these tests. The 1:7 slope beach used by Coates (1994) measured 12.5m by 8m, and this area was covered by an automatic three-axis bed profiler. Profile measurements of the structures were recorded on a personal computer, allowing armour displacements to be quantified by comparing profile lines over selected areas of each model. The measured damage was compared with damage predicted by the Van der Meer method for simple sections.

**3.2 Test conditions**

These tests were designed to give useful data over a wide range of structural and environmental variables. The experiments were intended to give intermediate armour damage at wave heights less than the maximum possible in the basin, equivalent to  $H_s/\Delta D_{n50}=2.6$  for armour of  $D_{n50}=0.045m$ . The "target" wave height was equivalent to  $H_s/\Delta D_{n50}=1.7$ , and this wave height was used in the design of the model structures.

Around European coastlines, storm wave conditions are generally steep and narrow-banded, often described well by the JONSWAP spectra. Storm waves are relatively steep, but armour damage also depends upon sea steepness. These tests used two steepnesses,  $s_m=0.02$  and  $0.04$  to explore the possible effects of longer waves. Each test was planned to be run for  $N=1000$  and  $3000$  waves duration.

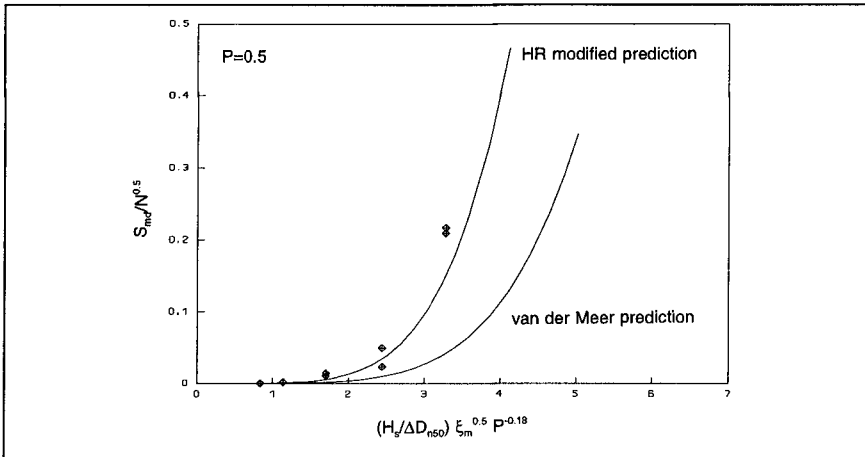


**Figure 6** Sea wall damage,  $s_m=0.04$ ,  $P=0.5$

**3.3 Test procedures**

The first part of each test used 100 waves, during which close observations were made of

the structures. If no movement was seen in these 100 waves, the test was stopped. If any damage (including rocking) was observed, then the test continued to 1000 waves when each profile line was re-surveyed. The test then continued for a further 2000 waves. After each test the structures were re-surveyed and photographed. If they had been damaged such that repair was necessary, the armour was re-built around the zones damaged. Testing was stopped when the structures needed re-building.

Profiling covered set lines over each of the groyne under test. The profiler incorporated a touch-sensitive foot of diameter equivalent to  $0.8D_{n50}$ , and took observations at  $0.5D_{n50}$  intervals along each profile line. The profile results were used to calculate the area of erosion on each profile line,  $A_g$ , and hence the damage parameter  $S$  defined in section 2.

4. TEST RESULTS

4.1 Simple slopes

The test results were initially very surprising, as virtually all of the profiles showed significantly more damage than predicted by conventional formulae (Fig 6). Some local increases in damage had been expected, but not the consistently greater damage found here. Analysis attention was focused first on the 1:2 sea wall slope, and equivalent section on the L-shaped groyne, but even these simple cases showed significantly greater damage than predicted by the Van der Meer equations. During the analysis period, additional data on the performance of armoured groyne on two bed slopes became available from tests at CEPYC in Madrid. Initial analysis of these had been presented by Baonza & Berenguer (1992), and their test data were further analyzed by Allsop & Franco (1992) as part of the EC MAST project G6-S. These data also indicated that the sea bed slope might be significant in increasing armour damage.

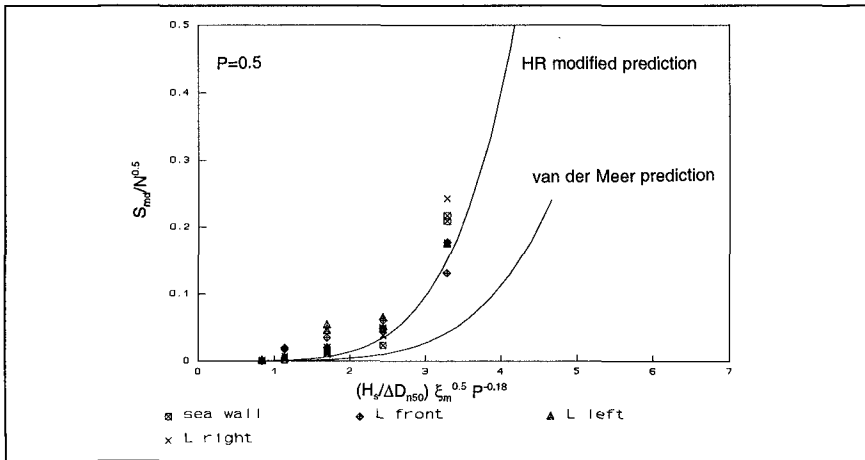


Figure 7 Sea wall and front face of "L" shaped groyne

Damage results for the sea wall section alone are summarised in Figure 6, using axes based on equation (2a) that allow results for each wave steepness and test duration to be presented together. The standard Van der Meer equation for plunging waves is shown, together with a version of the equation with a revised coefficient:



$$H_g/\Delta D_{n50} = 4.8 P^{0.18} (S/\sqrt{N_z})^{0.2} \xi_{cm}^{-0.5} \tag{3a}$$

The fit of the data to this modified equation is good over the area of main interest. Further support for the revised equation is given by the comparison of damage on the front face of the "L" shaped groyne with the sea wall, shown in Figure 7.

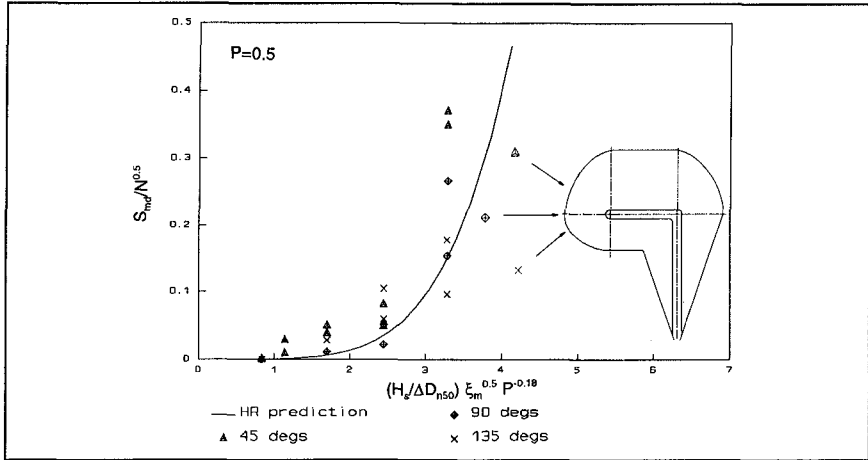


**Figure 8** Damage to curved parts of "L" shaped groyne

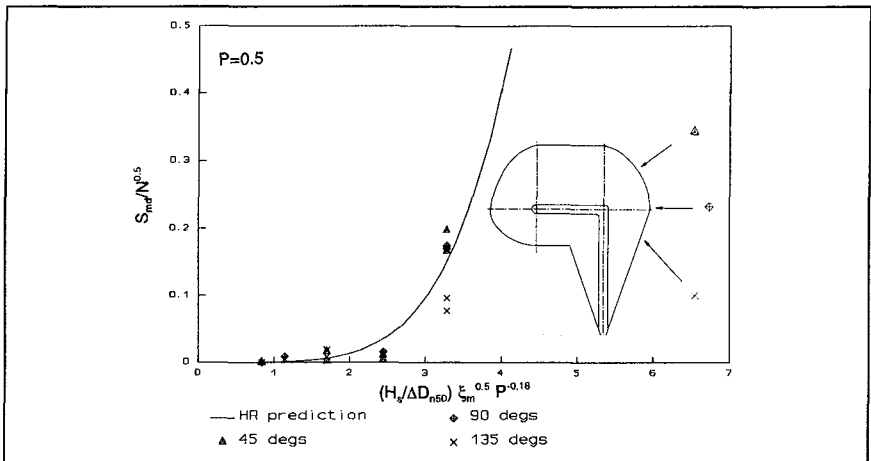


**Figure 9** Damage to curved parts of "L" shaped groyne

The first result from this analysis was therefore the conclusion that damage is significantly increased by steep (local) beach slopes, even for simple slopes subject to normal wave attack. A modification to the Van der Meer equation for plunging waves is given in equation (3a), and a similar increase for surging waves would be given by:

$$H_g/\Delta D_{n50} = 0.77 P^{-0.13} (S/\sqrt{N_z})^{0.2} \sqrt{\cot \alpha} \xi_{cm}^P \tag{3b}$$

**4.2 Roundhead and "L" shaped groynes**

Once the effect of the steep beach slope had been accounted for, the test results suggest that some sections of the more complex 3-dimensional structures experience greater damage than the simple slopes under normal wave attack, but that the spread of damage spatially is somewhat variable. This is shown in Figures 8 and 9 where damage on the opposing sides of the "L" shaped groyne are contrasted with the new equation (3a). For most positions, the modified prediction method in eqn (3a) gives a reasonable estimate of the damage, but for the zones shown in Figure 8, damage at larger wave heights is still greater than would be predicted by the new method. In itself, this is not surprising, as it is well known that breakwater roundheads require larger armour units, and/or shallower slopes for the same stability as trunk sections.

**4.3 Inclined, Type 1, groyne**

Damage to the inclined groyne, Type 1, varied along its length, with the location of greatest damage depending on wave height and period. The mean level of damage taken over the active length of the groyne, and derived by averaging the erosion areas from each profile, fits the general prediction given by eqn (3a), and is summarised in Figure 10.

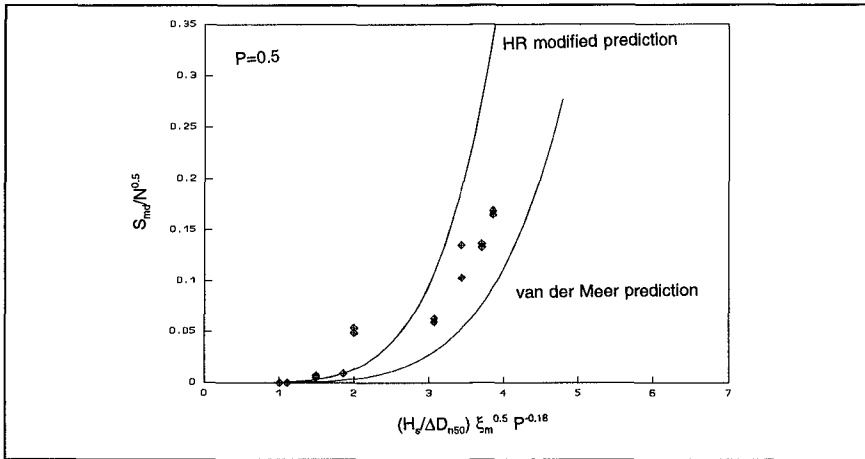


**Figure 10 Summary of Type 1 groyne results**

Peak values of (local) damage along the length of the groyne however often reached twice the mean, often at the wave run-up and run-down limits along the groyne, and this is illustrated in Figures 11-13 which show local levels of damage plotted against position along the groyne from the landward end for increasing relative wave heights. For  $H_s/\Delta D_{n50}$  up to 1.72 (Figures 11-13), damage only exceeds  $S=5$  at 1000 waves over small regions. For  $H_s/\Delta D_{n50}=2.16$  (Fig 14) however, damage over most of the length of the structure has exceeded this criterion.

**8 CONCLUSIONS**

These tests have shown that the stability of armour on beach control structures depends critically on the local sea bed slope. Results from tests using a beach of 1:7 were used to

develop a modified coefficient for use in the Van der Meer equation. The changes to the coefficients are equivalent to increasing the mean armour mass by a factor of 2.2 to maintain armour stability.

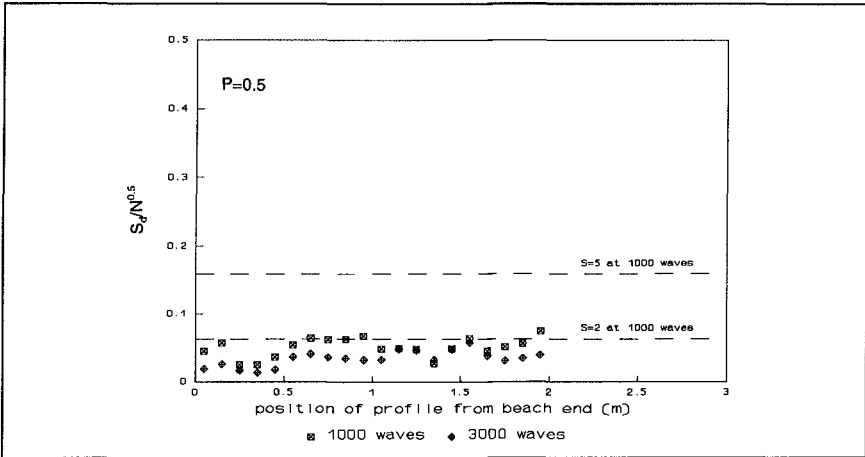


Figure 11 Type 1 groyne,  $s_m=0.04$ ,  $H_s/\Delta D_{n50}=0.83$

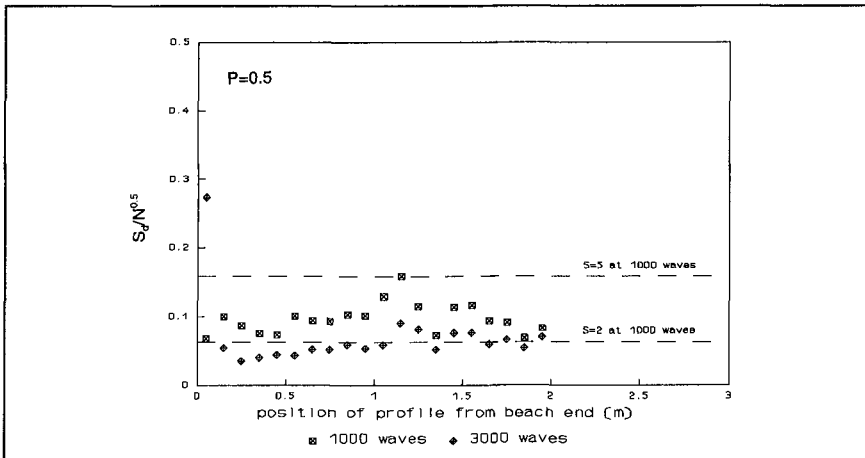
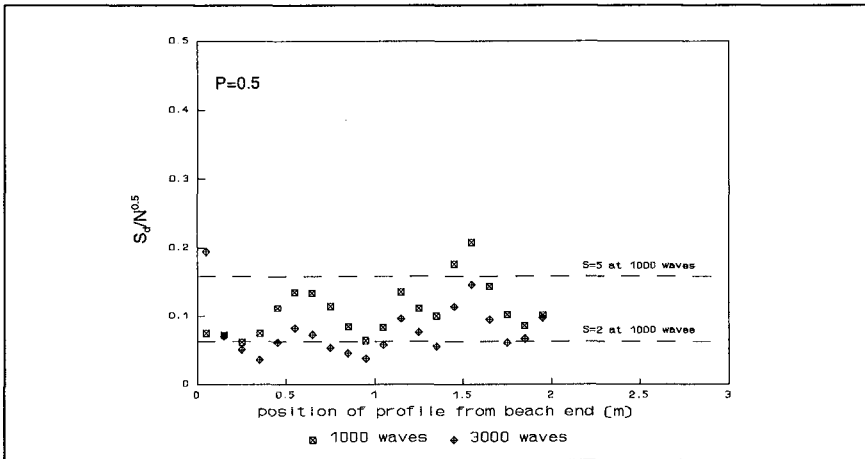
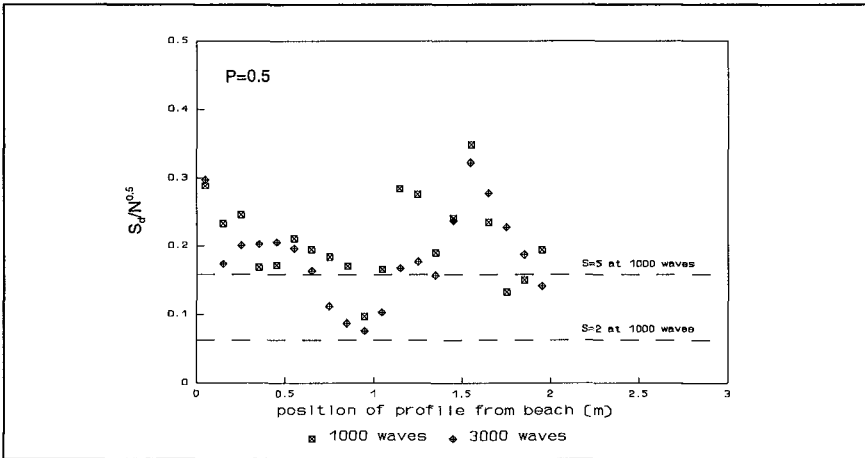


Figure 12 Type 1 groyne,  $s_m=0.04$ ,  $H_s/\Delta D_{n50}=1.12$



**Figure 13** Type 1 groyne,  $s_m=0.04$ ,  $H_s/\Delta D_{n50}=1.72$



**Figure 14** Type 1 groyne,  $s_m=0.04$ ,  $H_s/\Delta D_{n50}=2.16$

This study has identified some unusual effects, and some unexpected conclusions. The tests suggest that steep beach slopes may change the form of wave breaking such that the performance of structures in or behind steep (beach) slopes should be reviewed to identify whether a more general effect may lead to problems.

**ACKNOWLEDGEMENTS**

The laboratory studies covered in this paper were supported by the UK Ministry of Agriculture, Fisheries, and Food under Research Commissions on Flood Defence. Additional support was given by the European Union under MAST I project G6-S, and by HR Wallingford. The hydraulic model tests covered in section 5 were conducted by RJ

Jones assisted by MK Reeves and P Bona in the Coastal Group of HR Wallingford, and supervised by NWH Allsop. The authors are most grateful for the assistance of Andrew Bradbury of the Coast Protection Unit of New Forest District Council for valuable advice in the analysis of the laboratory tests, and for the additional data from Hurst Spit; to CEPYC and to C Franco of University of Rome for assistance in the MAST project G6-S topic 3R2.

Preparation of this paper was supported by the University of Sheffield and HR Wallingford.

## REFERENCES

- Allsop NWH (1994) "Design of rock armoured beach control structures" Paper 2.1 in Proceedings of 29th Conference of River and Coastal Engineers, MAFF, Loughborough, July 1994
- Allsop NWH & Franco C (1992) "MAST G6-S Coastal Structures Topic 3R: Performance of rubble mound breakwaters singular points" Paper 3.12 to G6-S Final Overall Workshop, Lisbon, November 1992
- Allsop NWH, Jones RJ & Bradbury AP (1995) "Design of beach control structures on shingle beaches" Paper to Conference on Coastal Structures and Breakwaters, Institution of Civil Engineers, London, April 1995
- Baonza A & Berenguer JM (1992) "Experimental research on groyne stability under very oblique wave action" Proc. Conf. Civil Engineering in the Oceans V, ASCE, Texas, 1992
- CIRIA (Simm JD, Ed.) (1991) "Manual on the use of rock in coastal and shoreline engineering" CIRIA Special Publication 83, London, November 1991
- Coastal Engineering Research Centre, CERC (1984) "Shore Protection Manual", Vols I-II, US Gov Printing Off, Washington, 4th edition 1984
- Coates TT (1994) "Physical modelling of the response of shingle beaches in the presence of control structures" Proc Conf Coastal Dynamics '94, Universtat Politecnica de Catalunya, Barcelona, February 1994
- Jones RJ & Allsop NWH (1993) "Stability of rock armoured beach control structures" HR report SR 289, HR Wallingford, March 1993
- Van der Meer JW. (1988) "Rock slopes and gravel beaches under wave attack", PhD thesis Delft University of Technology, April 1988. (available as Delft Hydraulics Communication 396)

## CHAPTER 85

### Effect on Roughness to Irregular Wave Run-up

Jea-Tzyy Juang\*

#### ABSTRACT

A study of the irregular wave runup and rundown phenomenon on rough impermeable slope is conducted in order to investigate the effects of various surface roughness to the wave runup-rundown activities based on various kind of dyke and incident wave conditions. The roughness of dyke surface was defined as  $f_r$  which is functions of shape of the slender rectangular obstacles and its displacement distance. Results shows that the correlation between the relative significant runup height ( $R_{us}/H_s$ ) and the incident wave steepness ( $H_s/L$ ) have the same tendency either in regular or in irregular waves. The relative runup height has its maximum value when the dyke slope ( $\cot\theta$ ) near 2. Next, the runup characteristics in regular wave was agree well with the Rayleigh distribution but it is a little bit smaller than that the Rayleigh's in irregular wave. Besides, the strong correlation between the wave runup and the surf similarity parameter  $\xi$  was found. The decrease of the relative run-up height with the increase of the surface roughness was got also. It may be useful to applied into the design work of the seawall.

#### INTRODUCTION

Wave run-up on coastal structures such as seawalls, dykes and so forth, is an important factor in the design of the height of the structures; therefore, many studies on the wave runup phenomenon and its characteristics have been carried out. However, the studies of the effect of roughness on the dyke to the run-up height are still scarce to find. Therefore, a study of the irregular wave run-up and run-down phenomenon on rough impermeable slope was conducted here in order to investigate the effect of various surface roughness to the wave runup-rundown activities based on the different kind of the dyke and the incident wave conditions.

---

\* Deputy Director, Institute of Harbour & Marine Technology  
Wu-Chi, Taichung Hsien, Taiwan, ROC.

ANALYTICAL CONSIDERATION

Based on the concept of control volume, the correlation among the incident wave energy, the reflected wave energy and the energy dissipation during the wave run-up and overtopping (as shown in Fig. 1) can be written as (Cross, 1972)

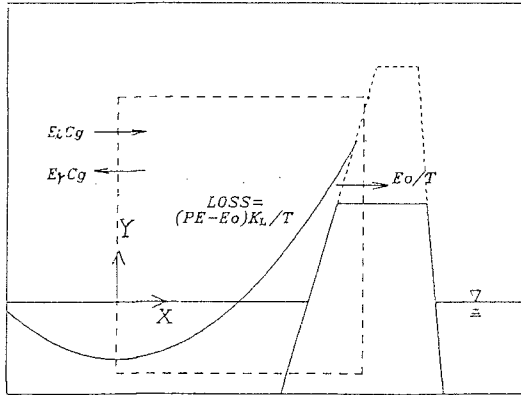


Fig.1 Definition sketch of runup and overtopping

$$E_i \cdot C_g - E_r \cdot C_g - \frac{E_o}{T} = \frac{PE - E_o}{T} \cdot K_1 \tag{1}$$

- where  $E_i$ : Incident wave energy density
- $E_r$ : Reflected wave energy density
- $C_g$ : Group velocity
- $E_o$ : Overtopping energy
- PE: Potential energy of the entire runup wedge above SWL
- $K_1$ : Rundown energy loss coefficient
- T : Wave period

By condition of no overtopping, the above equation can be simplified as

$$E_i \cdot C_g - E_r \cdot C_g = \frac{PE}{T} \cdot K_1 \tag{2}$$

The potential energy PE can be computed (Juang, 1992) by the following equation with all notations was shown in Fig. 2.

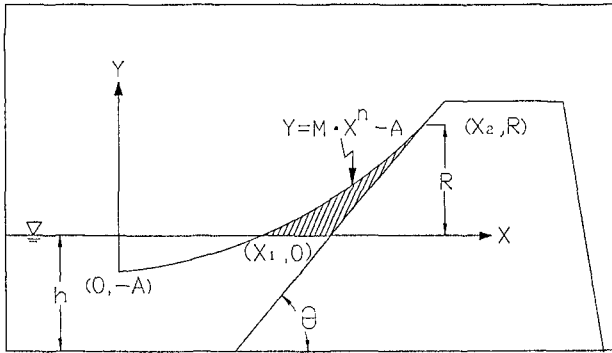


Fig.2 The shape of runup wedge

$$\begin{aligned}
 PE &= \rho g \left\{ \int_{X_1}^{X_2} \frac{Y^2}{2} dx - \frac{R^3}{6\alpha} \right\} \\
 &= \frac{1}{2} \rho g \left\{ \frac{M^2}{2n+1} (X_2^{2n+1} - X_1^{2n+1}) - \frac{2 \cdot MA}{n+1} (X_2^{n+1} - X_1^{n+1}) \right. \\
 &\quad \left. + A^2 (X_2 - X_1) - \frac{R^3}{3\alpha} \right\} \tag{3}
 \end{aligned}$$

in which Y is the water surface elevation above the still water level at maximum runup. Its corresponding equation is

$$Y = M \cdot X^n - A \tag{4}$$

where X is the distance from the trough shoreward; A is the amplitude at the trough and M, n the coefficients that was function of surf parameter  $\xi (= \tan\theta / \sqrt{H/L})$  as shown in Table 1.

By using the linear wave theory, the wave height in front of the inclining dyke becomes

Table 1 Values of M and n

cot $\theta$	0.5	1.0	2.0	3.0
M	$54.228 \xi^{-3.5}$	$5.993 \xi^{-3.68}$	$1.748 \xi^{-4.67}$	$0.437 \xi^{-3.19}$
n	$1.0075 \xi^{0.19}$	$0.608 \xi^{0.59}$	$0.858 \xi^{0.64}$	$0.873 \xi^{0.59}$



$$H = H_i + H_r = H_i(1 + K_r) \quad (5)$$

where  $H_i$ : incident wave height  
 $H_r$ : reflected wave height  
 $K_r$ : reflection coefficient

Due to the wave energy was proportional to the wave height, therefore we can have

$$E_r = K_r^2 \cdot E_i \quad (6)$$

Substitute eq.(6) into eq.(2), the equation becomes

$$E_i(1 - K_r^2) \cdot C_g \cdot T = PE \cdot K_1$$

$$\text{or } PE = \frac{1 - K_r^2}{K_1} \cdot E_i \cdot C_g \cdot T$$

#### DEFINITION OF ROUGHNESS COEFFICIENT

The roughness of the dike surface in this experiment study was made of small rectangle slender obstacles on the dyke as shown in Fig.3. The idea of that frame was come from the stream flow. Because the roughness coefficient at the bottom of the river was proportional to the diameter of the bed particles. Therefore, the roughness coefficient  $f_r$  in this study was defined by the following step.

- (1)  $f_r \propto D$ ; the higher the height of the slender obstacle, the rougher the roughness coefficient.
- (2)  $f_r \propto 1/W$ ; the wider the width of the slender obstacle, the smoother the roughness coefficient.
- (3)  $f_r \propto A_r = BD/D_m(B+W_m)$ ; the bigger the ratio of the effective cross section  $A_r$  to the maximum cross section, the rougher the roughness coefficient.

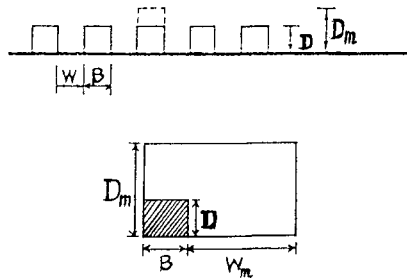


Fig.3 Definition diagram of the roughness coefficient

To view the whole situation that mentioned above, we can defined the roughness coefficient as follow

$$f_r = \frac{BD^2}{WD_m(B + W_m)}$$

Various roughness coefficient (include  $f_r=0$ ) with different ratio of D/B and W/B was shown in Table 2.

Table 2 Contrast table among D/B, W/B and  $f_r$

D/B	0	0.25	0.25	0.25	0.5	1.0	1.0	1.0
W/B	0	4.5	3.0	1.5	1.5	4.5	3.0	1.5
$f_r$	0	0.0025	0.0038	0.0076	0.0303	0.0404	0.0606	0.1212

#### EXPERIMENT STUDY

A series of tests was carried out in a 100m long, 1.5m wide and 2m height wave flume. A random wave generator of servo-controlled electro-hydraulic system that was made by Danish Hydraulic Institute in Denmark is installed at one end. Artificial dyke model of various rough surface (include smooth) with four different kind of dyke slopes ( $\cot \theta = 0.5, 1, 2, 3$ ) were installed at the other end where was 45m from the wave generator. The flume was divided into two sections. One equal 100 cm and the other 40 cm. The later (smaller) channel was used for measure the incident wave which will not to interfere by the reflected wave. All the experimental apparatus is shown in Fig.4.

Several wave gauge (ch.1 to 5) of capacitance type was used for measured the incident waves (Ch.1 to 4) and the run-up (Ch.5). The experiment was complete in conditions on fixed water depth (40cm) and incident wave period (1.2sec). The incident significant wave height are approximate to 3.5, 5.8, 6.8, 7.5, 8.0 and 8.8cm separately. The random waves used for tests were simulated to have Pierson-Moskowitz type spectra. Both of water surface variations of incident wave and run-up height were recorded simultaneously by an analog data recorder. The recorders were digitized by an A-D converter at a sampling interval of 0.025 sec. The measuring duration is about 100 sec.

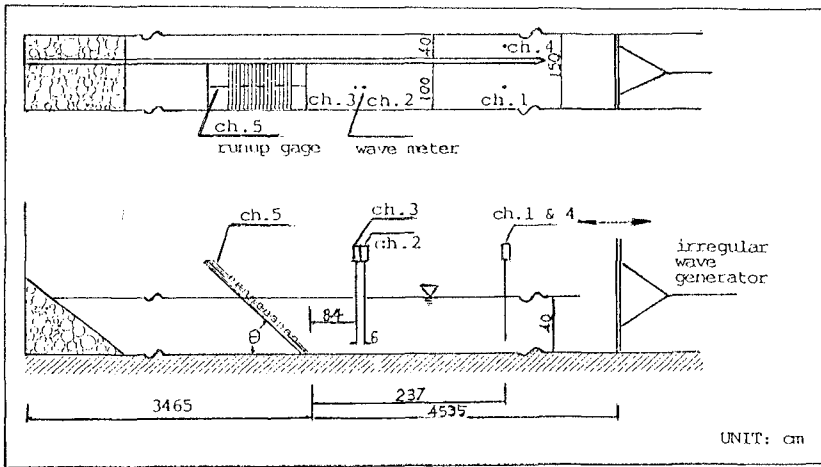


Fig.4 Layout of the test flume

For data analysis, at the beginning, there have two ways to analyze the characteristics of incident and run-up waves. One is the statistics method to count out the significant wave. The other is the spectra analysis method to calculate the spectra energy then the significant wave height. Due to wave height and period are very important factors in wave structure interaction such as wave run-up. Therefore, the dimensionless distribution of relative wave height ( $H/H_m$ ) to wave period ( $T/T_m$ ) of the experimental waves was compared as shown in Fig.5. In the figure, it can be seen that the relative wave period ( $T/T_m$ ) increases with the increase of wave height in the smaller waves ( $H < 1.3H_m$ ), but wave periods are distributed around  $T/T_m=1.3$  in the wave field higher than arbitrary critical value ( $H > 1.3H_m$ ). Meanwhile, from the data shown in the figure, we have

$$\begin{aligned}
 H_{1/10} &= 1.97 H_m \\
 H_{1/3} &= 1.56 H_m \\
 T_{1/3} &= T_{1/10} = T_{max} = 1.3 T_m
 \end{aligned}$$

It is identified from the above results that the joint distribution of wave height and period has a good agreement with the analyzed results of field data by Goda (1985). In other words, it can be stated that the simulated irregular waves used in model tests represent random ocean waves fairly well.

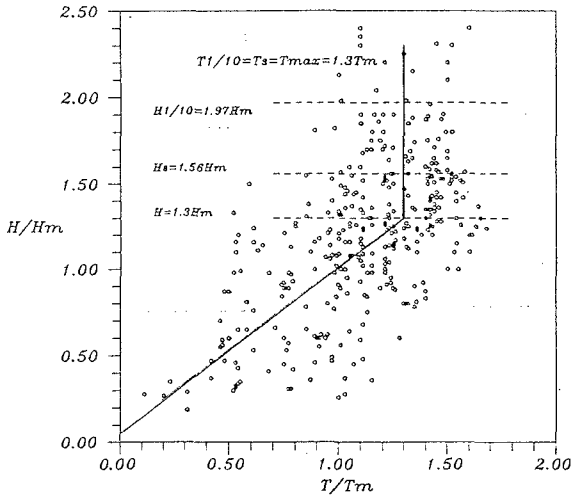


Fig.5 Joint distribution of wave height and wave period

In order to investigate the distribution status of the run-up waves of the irregular wave. The computational method of statistical significant wave height was used for counting the significant runup height ( $R_{us}$ ) also. Part of the results ( $f_r=0$  &  $f_r=0.1212$ ) was shown in Fig.6 and Fig.7 respectively. From those figures, we can find the distribution of irregular wave runup heights ( $R_{us}$  to  $R_{um}$ ) provides a good approximation to the Rayleigh distribution on the smooth surface dyke. But it will be overestimated when the dyke slope milder than 1 to 2 in rough surface ( $f_r=0.1212$ ) test.

Secondly, all the experiment data which shows the relationship between the significant relative run-up and run-down height with the surf parameter was shown in Fig.8. In the figure, the envelope lines (1) and (2) indicate the extreme value of the relative run-up and run-down height respectively. Which was got from the experiment result by  $X_{ue}$  (1991) in condition of smooth dyke slope.

As to the effect of roughness to irregular wave runup, the relation diagram between the significant relative runup height and the surf similarity parameter in different kind of the surface roughness ( $f_r=0\sim 0.1212$ ) was shown in Fig.9. From those figures, we can find that the effect of roughness to the relative runup height was certainly. If we sum up those correlation curves toge-

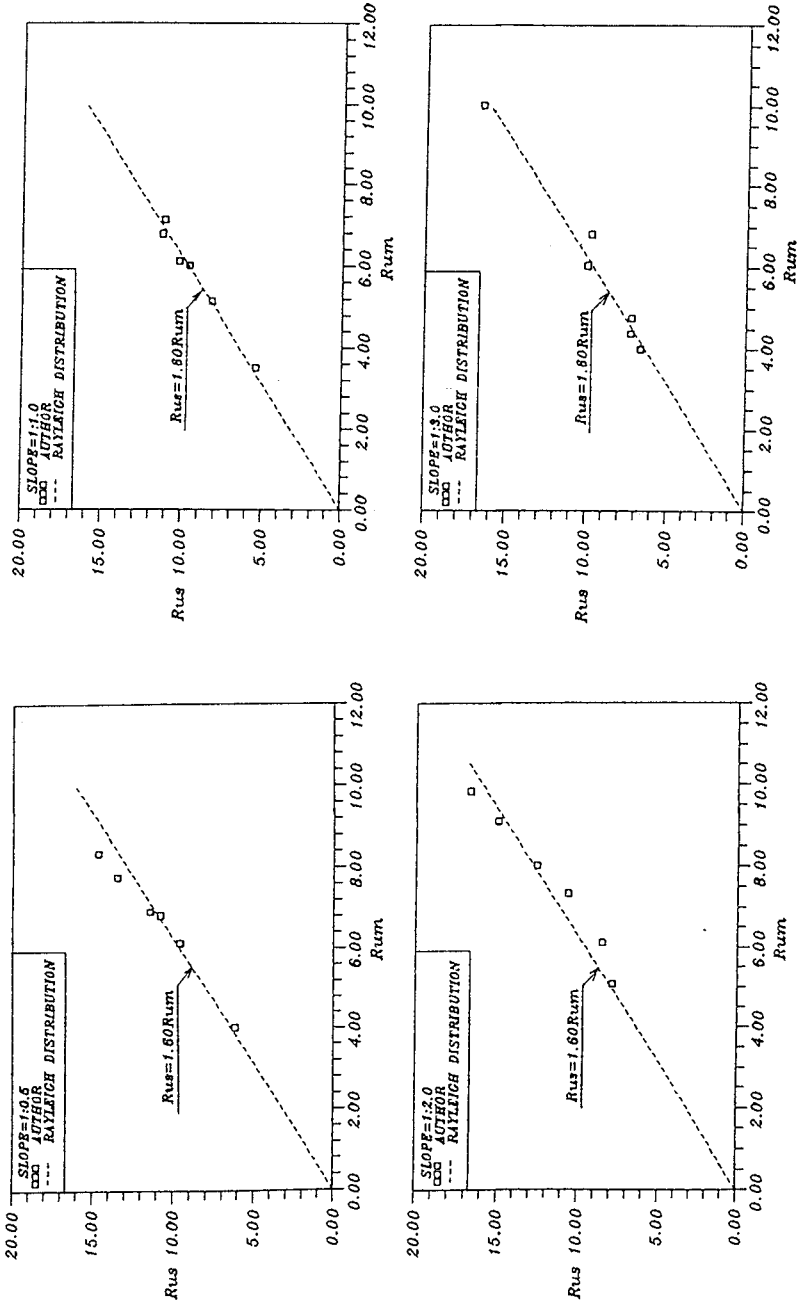


Fig. 6 Relationship between significant runup height and mean runup height in smooth dike

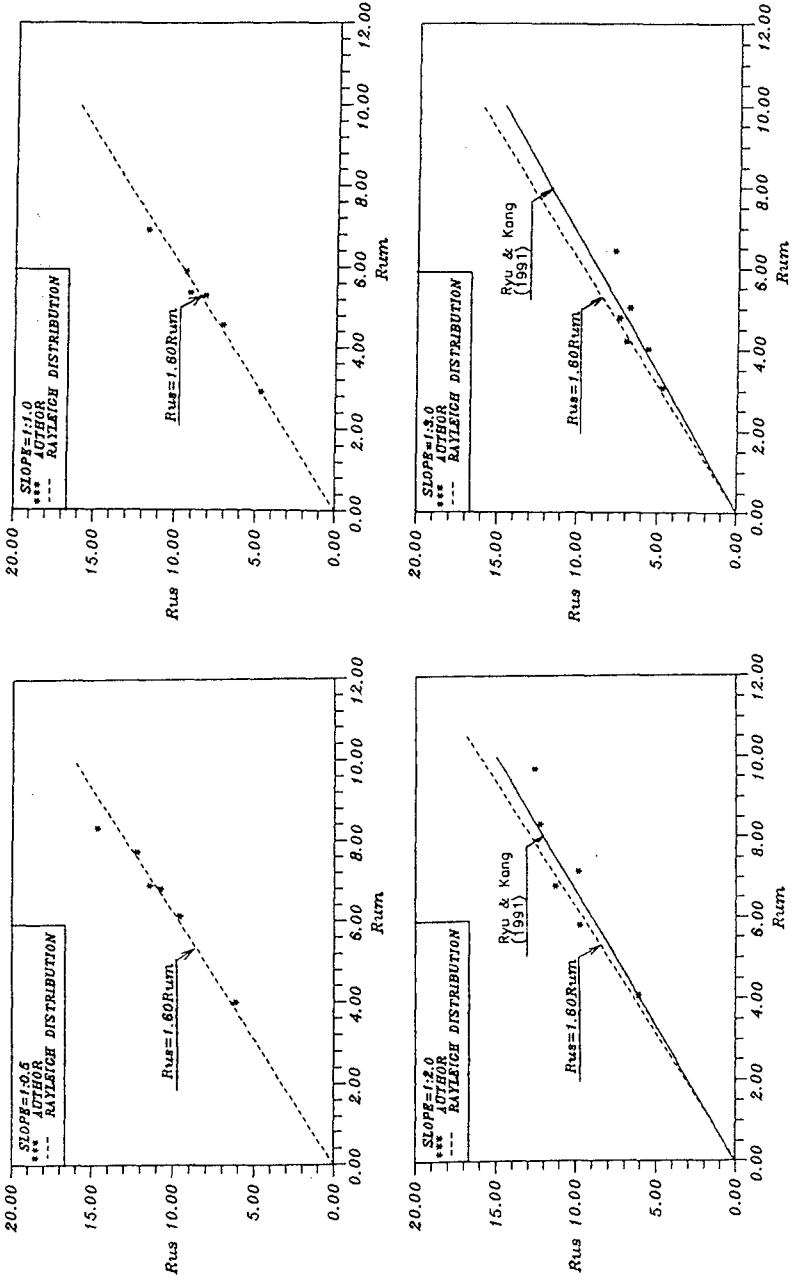


Fig. 7 Relationship between significant runup height and mean runup height in rough dike

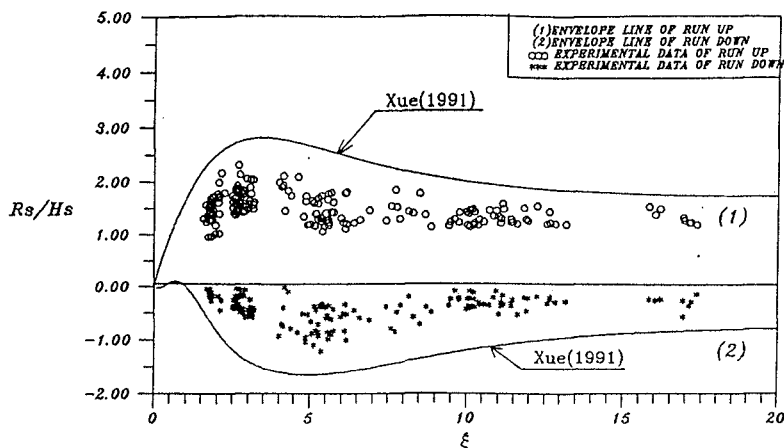


Fig.8 Relationship between run-up-down height and surf parameter

ther, we can find the rougher the surface of the dyke slope, the lower the relative runup height decreased as shown in Fig.10. When the roughness coefficient approach to 0.1212, the corretation curve between the relative runup and the surf parameter was very similar with those results which was presented by Ryu in 1990 in rubble mound experiment.

At last, the normalized relationship between the relative run-up and rundown height and the surf parameter was shown in Fig.11 and 12 respectively. The meaning of normalized stand for the ratio of relative run-up(down) height in rough dyke compared with those in smooth dyke. From the figures, we can see that when the surf parameter becomes bigger, that means the dyke slope approach to vertical, the influence of roughness to wave run-up-down height will vanished.

### CONCLUSIONS

- 1.The distribution of the irregular wave runup heights provides a good approximation to the Rayleigh distribution on the smooth surface dyke. But it will be overestimated when the dyke slope milder than 1 to 2 in rough surface test.
- 2.The effect of roughness to the relative runup height was certainly and the rougher the surface of the dyke slope, the lower the relative runup height will decreased.
- 3.When the roughness coefficient approach to 0.1212, the relation

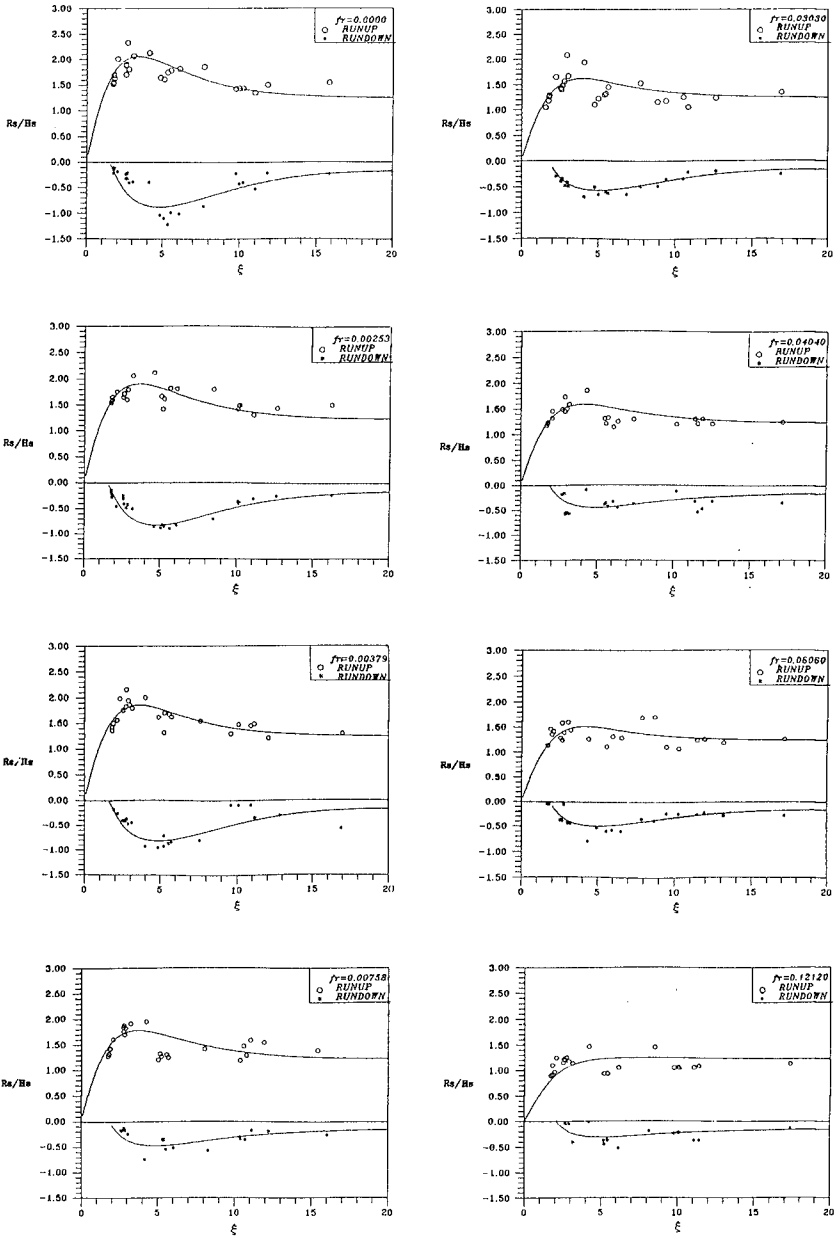


Fig.9 Relationship between significant relative runup height and the surf parameter



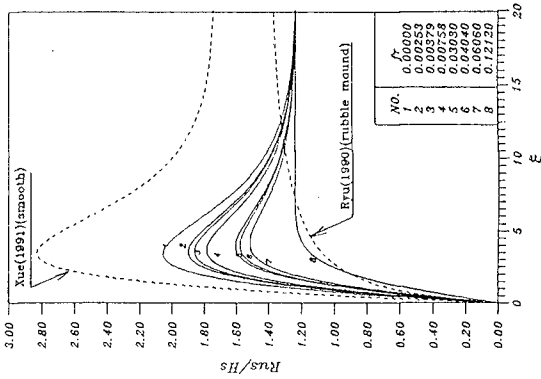


Fig.10 Comparison of relative runup in various rough surface

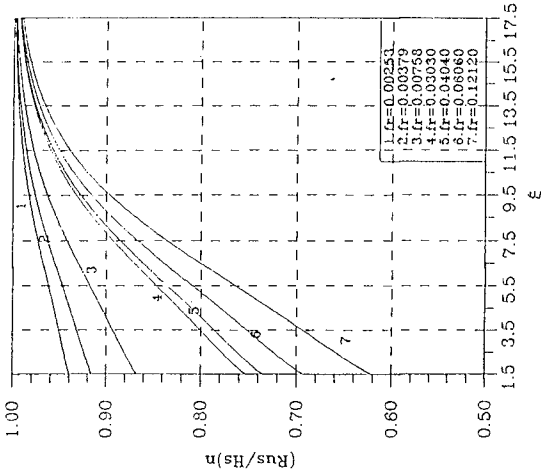


Fig.11 Normalized correlation of runup height to surf parameter

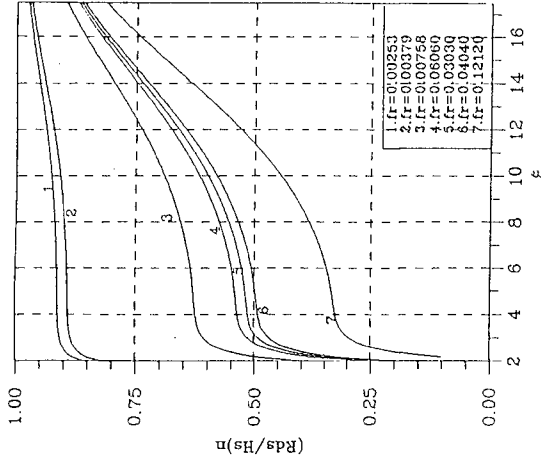


Fig.12 Normalized correlation of rundown height to surf parameter

curve between the relative runup height and the surf parameter was quite similar with those results in rubble mound experiment.

4. When the surf parameter becomes bigger, that's the dyke slope approach to vertical, the influence of roughness to wave run-up-down height will vanished.

#### ACKNOWLEDGEMENTS

This study was sponsored by the National Science Council of ROC under Grant NSC 81-0209-E124-01. The author would like to thank Mr. J. M. Chou, C. C. Chien and Miss E. J. Chien for their assistance in experiment and preparing the manuscript.

#### REFERENCES

- Cross, R.H. and C.K.Sollitt(1972): Wave transmission by overtopping, Journal of Waterway, Port and Coastal Engineering, Vol.98, No. WW3, PP.295-309.
- Goda, Y.(1985): Random seas and design of maritime structures, University of Tokyo Press, PP.1-323.
- Juang, J.T.(1992): Effect on wind speed to wave runup, Coastal Engineering, ASCE, Vol.2, PP.1245-1257.
- Kobayashi, N., D. T. Cox and A. Wurjanto (1990): Irregular wave reflection and runup on rough impermeable slopes, Journal of Waterway, Port, Coastal and Ocean Engineering, Vol.116, No.6, PP.708-726.
- Mase, H.(1989):Random wave runup height on gentle slope, Journal of Waterway, Port, Coastal and Ocean Engineering, Vol.115, No.5, PP. 649-661.
- Meer, J.W. and C.M.Stam(1992): Wave runup on smooth and rock slopes of coastal structures, Journal of Waterway, Port, Coastal and Ocean Engineering, Vol.118, No.5, PP.534-550.
- Ryu, C.R. and H.Y. Kang(1990): A prediction model of irregular wave runup height on coastal structures, Proc. Coastal engineering, ASCE, Vol.1.1, PP.371-383.
- Xue, H.C., D. Guo, S.H. Pan and H.S.Zhong(1991): Wave runup-rundown amplitude on slopes, China Ocean Engineering, Vol.5, No.1, PP.39-49.

## CHAPTER 86

# Wave Overtopping of Breakwaters under Oblique Waves

Jørgen JUHL<sup>1</sup> and Peter SLOTH<sup>1</sup>

### Abstract

A series of hydraulic model tests has been carried out in a wave basin with the aim of studying the effect of oblique waves on the wave overtopping of traditional rubble mound breakwaters without superstructure. The model tests concentrated on measuring the mean overtopping discharge for wave attacks varying from 0° (perpendicular to the structure) up to 50°. Analyses of the overtopping results were made with respect to the significant wave height, wave steepness, crest free board, crest width and angle of wave attack. The paper describes the influence of these parameters on the mean overtopping discharge for a traditional rubble mound breakwaters with an armour layer slope of 1:2.0.

### Introduction

Wave overtopping of coastal structures is influenced by a large number of parameters related to breakwater geometry, construction materials, and hydrographic data. Some of the main parameters are listed below:

*Geometrical parameters:*

free board, crest configuration and width, slope of armour layer (irregular slope), and water depth

*Construction material parameters:*

porosity, stone shape and diameter (artificial blocks)

*Hydrographic parameters:*

wave height, wave period, angle of wave attack, wave steepness, spreading, wave sequences, wind conditions, and water level

---

<sup>1</sup> Danish Hydraulic Institute, Agern Allé 5, DK-2970 Hørsholm, Denmark

Wave overtopping is normally studied under perpendicular wave attack in wave flumes. Jensen and Juhl (1987) have shown overtopping data from model testing of rubble mound breakwaters and sea dikes. The paper mainly concentrates on mean overtopping discharges, but also includes a description of the horizontal distribution of the overtopping behind a breakwater, individual wave overtoppings and the influence of wind on wave overtopping, and a comparison to prototype measurements.

Franco et al (1994) have established a formula for the mean overtopping discharge for vertical breakwaters exposed to perpendicular wave attack. The influence of various geometrical types of breakwaters is taken into account using influence factors in connection with the general formula for a fully vertical breakwater. Further, a prediction formula for the probability distribution of individual overtopping volumes is presented. The effect of overtopping volumes on persons and cars behind a crown wall of a vertical breakwater was assessed by Franco (1993), and a set of critical overtopping discharges were proposed (safety criteria).

Only a little research has been made to study the influence of the angle of wave attack on the amount of overtopping water. De Wall and Van der Meer (1992) have carried out tests on the influence on wave run-up and overtopping on smooth slopes. The angle of wave attack,  $\beta$ , was varied from  $0^\circ$  up to  $80^\circ$ , and tests were performed with both long-crested and short-crested waves. For long-crested waves, a few tests showed larger run-up for angles between  $10^\circ$  and  $30^\circ$  than for perpendicular waves, but on average no increase was found. This also applies to the average measured overtopping discharges. For perpendicular wave attack, no difference in wave overtopping was measured between tests with long-crested and short-crested waves, whereas for oblique waves the influence of the angle of wave attack was less for short-crested waves. A reduction in the mean overtopping discharge of about 40 per cent was found for long-crested waves with an angle of  $50^\circ$  and of about 15 per cent for short-crested waves.

Galland (1994) has measured the number of waves overtopping rubble mound breakwaters exposed to oblique wave attack. The model tests were made with four different types of armour units, ie quarry stones, accropodes, antifer cubes and tetrapodes. In the case with quarry stones, the test results for long-crested waves showed a significant decrease in the percentage of waves overtopping the crest by increasing the angle of wave attack. For a dimensionless free board,  $R_c/H_s$ , higher than 2.0, no overtopping waves were measured, and for  $R_c/H_s = 1.0$  the percentage of overtopping waves was about ten per cent for perpendicular waves which was reduced to no overtopping waves for an angle of  $75^\circ$ .

## Model Set-up and Test Programme

Physical model tests have been carried out in a wave basin at the Danish Hydraulic Institute with the aim of measuring mean overtopping discharges defined as the volumes of wave overtopping per unit length of the breakwater per unit time. The basin was equipped with a movable wave generator in order to study the effect for different angles of wave attack, see Fig 1. The tests were carried out using long-crested irregular waves generated on basis of a Pierson-Moskowitz spectrum.

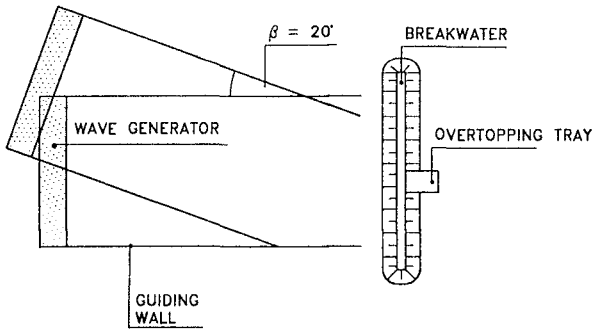


**Fig. 1** Model plan for the basin tests showing the set-up for perpendicular and 20° wave attack.

The modelled structure had a total length of about seven metres and was constructed as a traditional rubble mound breakwater with a core, filter layer and armour layer of quarry stones, see Fig. 2. The size of the armour stones was selected not to allow for significant damage during testing, ie a nominal diameter,  $D_{n,50}$ , of about 0.04 m. The model consisted of a horizontal seabed which together with the use of a fixed breakwater height of 0.45 m means that variations in the crest free board were obtained by changes in the water level.

The wave conditions in the model were measured by seven resistance type wave gauges located in front of the breakwater. For perpendicular wave attack, the incident wave conditions and the reflection coefficients have been calculated using a multi-gauge technique. The significant wave height was calculated as  $4 \times \sqrt{m_0}$ , where  $m_0$  is the zeroth moment of the spectral energy density function.

The overtopping water was collected in a 0.6 m wide tray located immediately behind the breakwater in a level corresponding to the crest elevation of the breakwater. This means that the recorded wave overtopping refer to water passing the rear edge of the breakwater crest. By measuring the total amount

of overtopping water after each test with a duration of 600 to 1800 seconds, the mean overtopping discharge,  $q$ , was calculated.

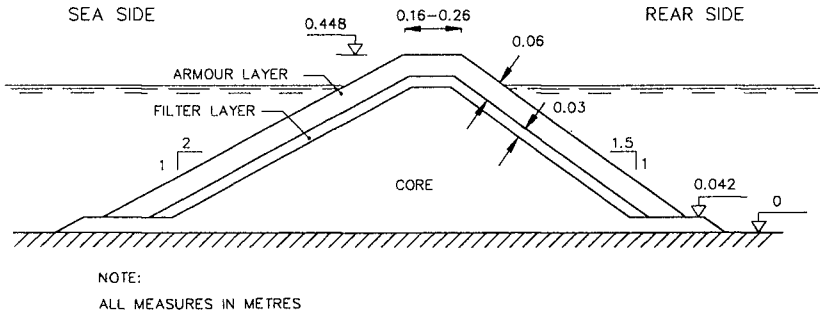


**Fig. 2** Typical cross-section of breakwater used in the overtopping tests.

The following ranges of parameters were tested in the model study (all measures are in model measures):

- Significant wave height,  $H_s$ : 0.05 to 0.11 m
- Peak wave period,  $T_p$ : 0.8 to 2.0 s
- Wave steepness,  $s_{0p}$ : 0,018, 0,025, 0,030 and 0,045
- Crest free board,  $R_c$ : 0.050, 0.075 and 0.100 m
- Width of crest,  $B$ : 0.16 ( $4 \cdot D_{n50}$ ), 0.21 and 0.26 m
- Slope angle,  $\cot \alpha$ : 2.0
- Angle of wave attack,  $\beta$ :  $0^\circ$  to  $50^\circ$  in steps of  $10^\circ$

The wave steepness is given by the ratio between the significant wave height and the deep water wave length calculated on basis of the peak wave period:

$$s_{0p} = H_s/L_{0p} = 2\pi/g \cdot H_s/T_p^2$$

A parameter often used in the research on coastal structures is the surf similarity parameter given as:

$$\xi_{0p} = \tan \alpha / \sqrt{s_{0p}}$$

The model tests were run in test series with fixed wave steepness, ie a fixed ratio between the significant wave height and the deep water wave length. Thus all tests were made with a surf similarity parameter larger than 2 (two), which means that the wave conditions can be characterised as non-breaking waves.

The dimensionless free board, defined as  $R_c/H_s$ , varied between 0.5 and 2.0, which means that the tests covered both low and high crested breakwaters.

## Test Results

This section includes analyses of the influence of the various tested parameters (wave height, wave steepness, crest free board, crest width and angle of wave attack) on the mean overtopping discharge. The influence of each of the parameters is described in the following.

Previous studies and the analysis of the test results showed that it is important to distinguish between situations with a large amount of water passing the breakwater crest, 'green water', and situations with a small amount of water passing the crest, 'spray'. Observations in the model showed that a rule of thumb to distinguish the two types of wave overtoppings is the dimensionless free board,  $R_c/H_s$ . It was found that for  $R_c/H_s$  larger than unity, the major part of the wave overtopping will occur as spray, whereas for  $R_c/H_s$  less than unity green water is dominant.

### Influence of Wave Height

Previous research on wave overtopping has shown that the wave overtopping increases almost exponentially with the wave height, which is confirmed by the present model tests. An example of the influence of the significant wave height on the overtopping volume is shown in Fig. 3 for an angle of wave attack of  $40^\circ$ . It should be noted that also the wave period changes due to the fixed wave steepnesses. It is observed that for perpendicular waves, the wave steepness has some influence on the overtopping. This influence became smaller for oblique waves, and for  $40^\circ$  no influence is found.

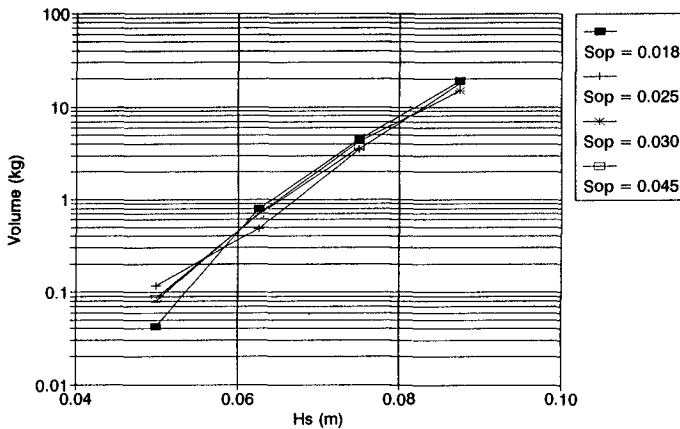


**Fig. 3** Plot of the overtopping volume as function of the significant wave height,  $H_s$ . Crest free board,  $R_c=0.05$  m. Crest width,  $B=0.16$  m. Angle of wave attack,  $\beta=40^\circ$ .

### Influence of Wave Steepness

The influence of the wave steepness is shown in Fig. 4 for two crest free boards, ie a low-crested and a high-crested breakwater. From the results, it is found necessary to distinguish between two different cases, ie  $H_s > R_c$  and  $H_s < R_c$ . There is a tendency for decreasing overtopping volumes by an increase in the wave steepness for the case of  $H_s > R_c$ , whereas there is a tendency for increasing overtopping volumes for the case of  $H_s < R_c$ . The test results show that the influence of the wave steepness is decreasing for oblique waves, and generally no influence is found for an angle of wave attack of  $30^\circ$  as shown in Fig. 7.

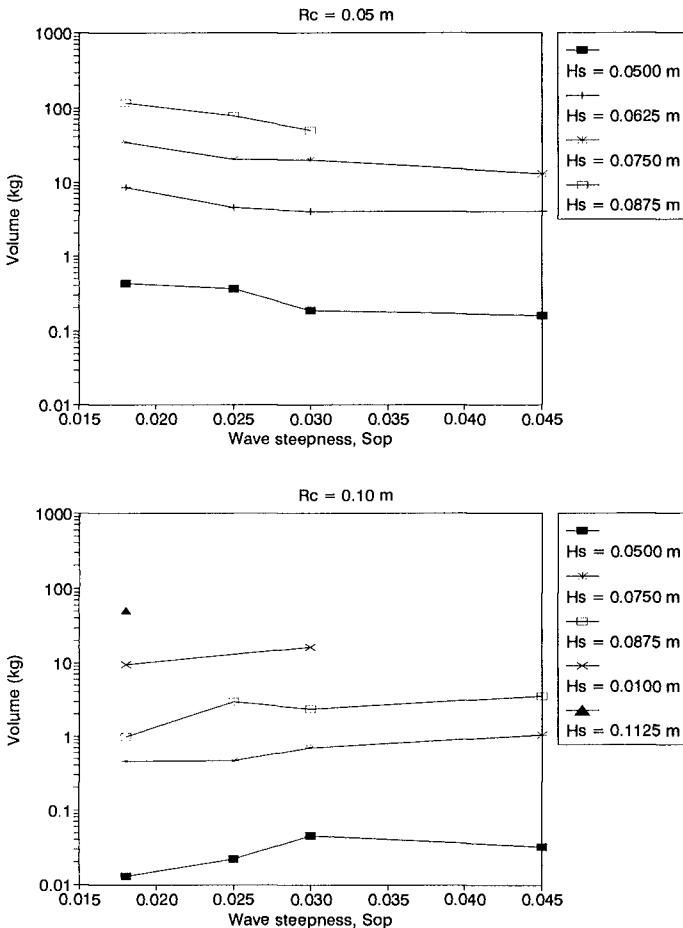
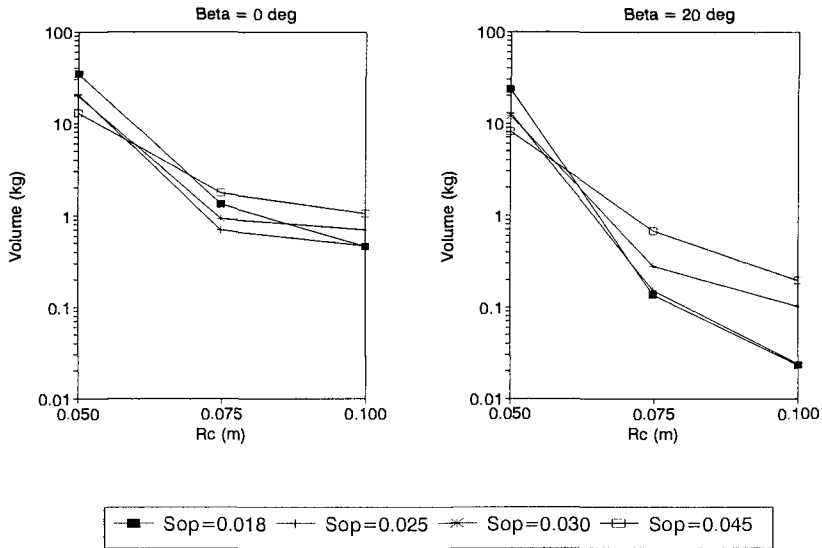


Fig. 4 Plots of the overtopping volume as function of the wave steepness,  $S_{op}$ . Crest width,  $B=0.16$  m. Angle of wave attack,  $\beta=0^\circ$ .



### Influence of Crest Free Board

Tests were made with three different crest free boards, which resulted in a dimensionless freeboard,  $R_c/H_s$ , ranging from 0.5 up to 2.0. The crest freeboard together with the significant wave height are the major parameters governing the amount of water overtopping a breakwater. Examples of the influence of the crest free board are shown in Fig. 5. Comparison of the result for perpendicular wave attack and for an angle of  $20^\circ$  shows that the influence of an increase of the crest free board is larger for the latter case, which is due to an increased distance from the intersection of the still water level with the main armour layer to the rear side of the crest (the location of the measuring tray).



**Fig. 5** Plots of the overtopping volume as function of the crest free board,  $R_c$ .  $H_s=0.075$  m. Crest width,  $B=0.16$  m.

### Influence of Crest Width

Three crest widths were studied for perpendicular wave attack. Generally, it was found that the overtopping volume is decreasing with increasing crest width. However, the influence is smaller than the influence of the significant wave height and the crest free board. An example of the test results is presented in Fig. 6.

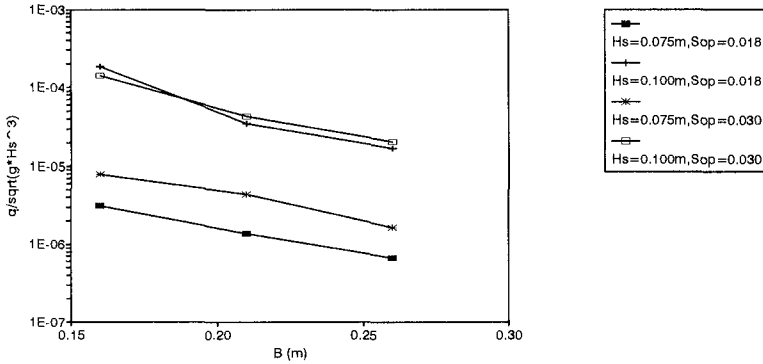


**Fig. 6** Plots of the overtopping volume as function of the crest width,  $B$ . Crest free board,  $R_c=0.10$  m. Angle of wave attack,  $\beta=0^\circ$ .

### Influence of Angle of Wave Attack

Test were carried out with angles of wave attack varying from  $0^\circ$  (perpendicular waves) up to  $50^\circ$  in steps of  $10^\circ$ . Typical examples of the influence of the angle are shown in Fig. 7, which includes the dependency of the wave steepness (it should be noted that the overtopping volumes are plotted in a linear scale). A pronounced characteristic in some of the cases is a maximum in the amount of wave overtopping for an angle of  $10^\circ$ .

In order to study in more details the influence of the angle of wave attack, dimensionless plots of the test data are shown in Fig. 8. These plots present the ratio between the overtopping volume for oblique waves and for perpendicular waves as function of the angle of wave attack for each of the three tested crest free boards. This ratio corresponds to a reduction factor taking into account wave obliquity. The plots show some scatter, but general trends can be recognised.

In the case with the smallest tested free board ( $R_c=0.05$  m), the average of the tests shows a maximum in the mean overtopping discharge for an angle of  $10^\circ$ . A pronounced decrease in the overtopping is found increasing the angle of wave attack to  $20^\circ$  and  $30^\circ$ . For an angle of about  $50^\circ$ , the amount of overtopping water is on average reduced by 90 per cent compared to perpendicular wave attack, ie a reduction factor of 0.1. This reduction in the wave overtopping for an angle of wave attack of  $50^\circ$  is significantly higher than the reduction of about 40 per cent found for smooth slopes in De Wall and Van der Meer (1992).

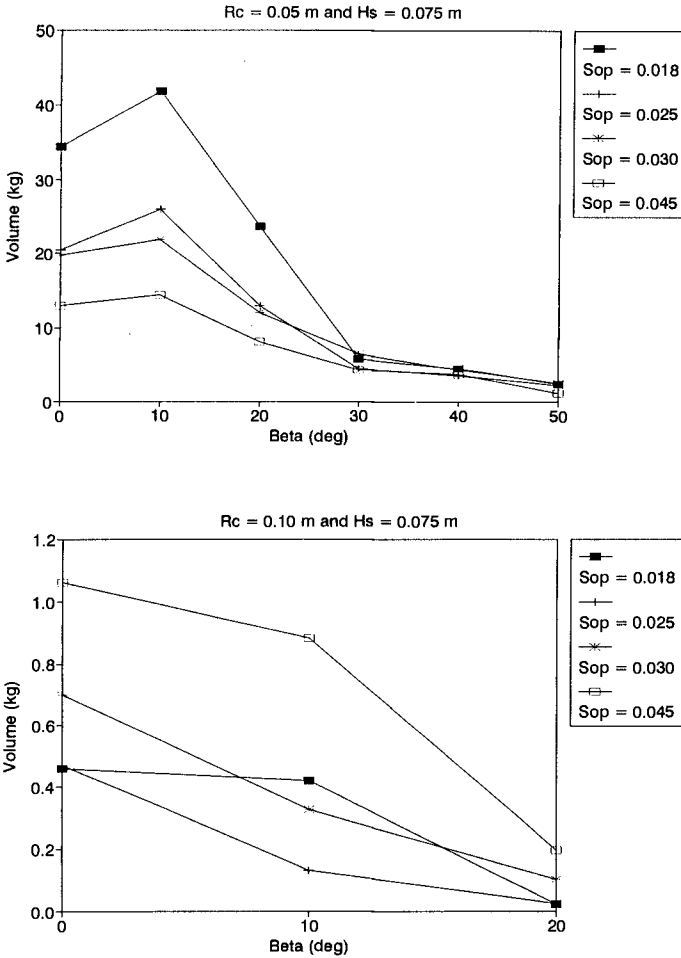


**Fig. 7** Plots of the overtopping volume as function of the angle of wave attack,  $\beta$ . The plots include the influence of the wave steepness,  $s_{op}$ . Crest width,  $B=0.16 \text{ m}$ .

For the cases with higher free boards, only a few tests show a maximum in the overtopping for an angle of  $10^\circ$ , and on average a decrease is found. Comparing the three plots, it is found that the influence of the angle is getting more pronounced for the cases with the higher free boards. For the highest tested free board ( $R_c=0.10 \text{ m}$ ), a reduction factor of about 0.2 is found for an angle of  $20^\circ$ .

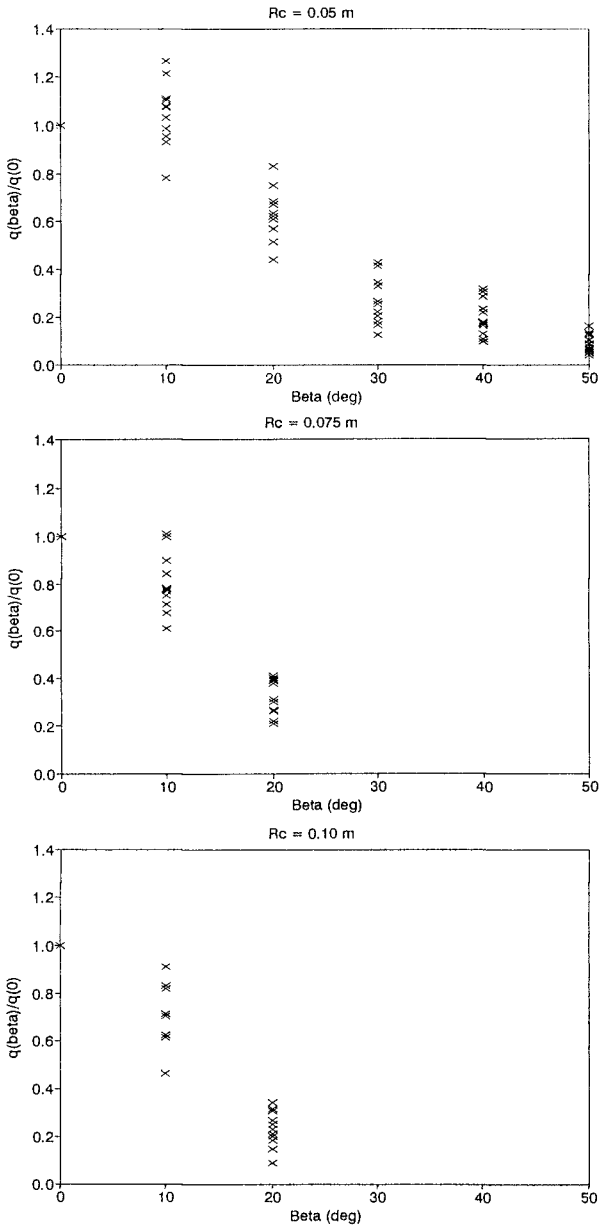


**Fig. 8** Plots of the ratio between the overtopping discharge for oblique waves,  $q_\beta$ , and for perpendicular waves,  $q_0$ , as function of the angle of wave attack.

The overtopping volumes in De Wall and Van der Meer (1992) refer to the amount of water passing the crest of a slope, which is a relevant measure in the case of an impermeable slope. In the case of a permeable rubble mound breakwater, the amount of overtopping water will be dependant on the location of the measurement, ie the volume will be different when measuring at the front side edge or rear side edge of the crest due to the porous crest of the breakwater. The difference in the reference location of the overtopping measurements will have an effect on the influence of the angle of wave attack, as the distance from the front edge to the rear edge of the breakwater will increase with the angle of wave attack. Further, in the case of a rubble mound breakwater, the permeable layers will result in a faster decrease of the overtopping volume than for an impermeable slope.

## Dimensionless Presentations

Through the years, overtopping results have been presented in numerous ways, including dimensionless plots. The most used dimensionless parameters are the dimensionless overtopping discharge,  $Q=q/\sqrt{gH_s^3}$ , and the dimensionless free board,  $R=R_c/H_s$ .

Examples of dimensionless plots of the test results obtained for perpendicular waves and for waves with an angle of  $50^\circ$  are shown in **Fig. 9**. The plots show that the test data for dimensionless free boards less than about 1.5 can be fitted to a straight line, ie  $Q$  can be described by an exponential function of  $R_c/H_s$ .

The model tests carried out with different crest widths showed that this parameter has an influence on the overtopping, and it is found that a combination of the crest free board and width can be used for describing the combined influence of these two parameters. For a fixed wave steepness, the dimensionless mean overtopping discharge can be fitted to an exponential function using  $(2R_c+0.35B)/H_s$  as parameter.

The test results show that the influence of the wave steepness is small compared to the influence of the other tested parameters, and that it is decreasing for oblique waves. A dimensionless plot excluding the influence of the wave steepness is presented in **Fig. 10** for all the tests made with perpendicular waves. The overtopping data are found to fit reasonable to the dimensionless parameter,  $(2R_c+0.35B)/H_s$ , ranging between about 1.5 and 4.0.

Dividing the dimensionless overtopping discharge with average reduction factors for wave obliquity (see the plots presented in **Fig. 8**), all the overtopping data are presented in a dimensionless plot in **Fig. 11**. The figure presents the dimensionless overtopping discharge divided by the influence factor as function of the established dimensionless parameter,  $(2R_c+0.35B)/H_s$ , taking into account both the crest free board and width. It is concluded that the influence of oblique

waves on the wave overtopping discharge can be described by an influence factor for wave obliquity. A slight increase in the scatter is found including the data for oblique waves, see **Figs. 10 and 11**.

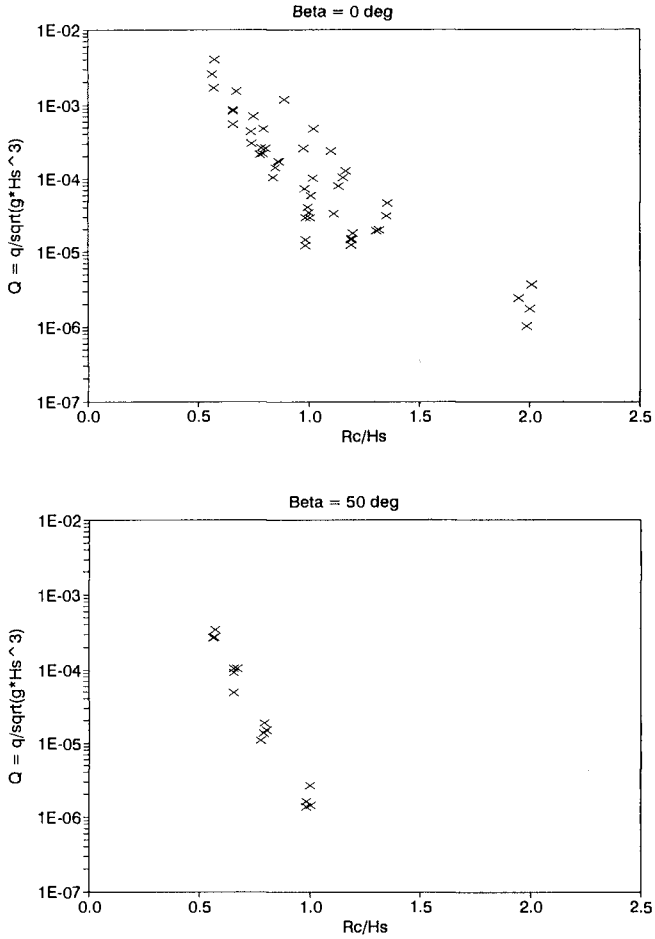


**Fig. 9** Dimensionless overtopping discharge,  $Q$ , as function of dimensionless free board,  $R_c/H_s$ . Crest width,  $B=0.16$  m.

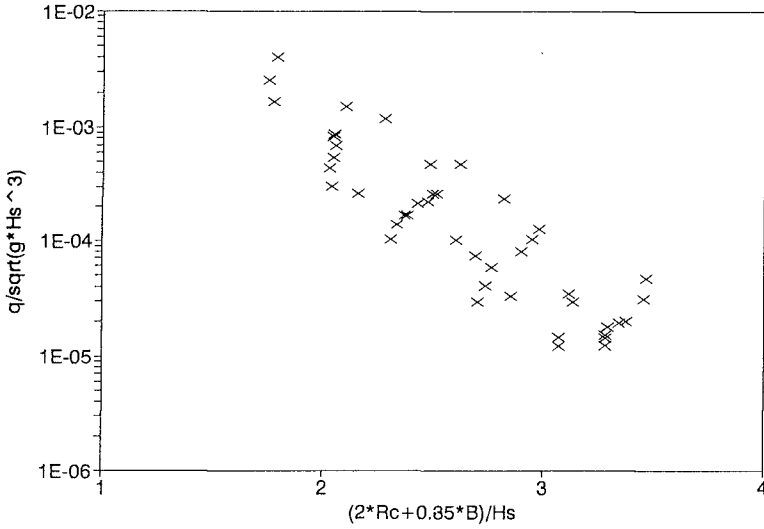


**Fig. 10** Dimensionless overtopping discharge,  $Q$ , as function of the dimensionless parameter,  $(2R_c + 0.35B)/H_s$ . Angle of wave attack,  $\beta = 0^\circ$ .

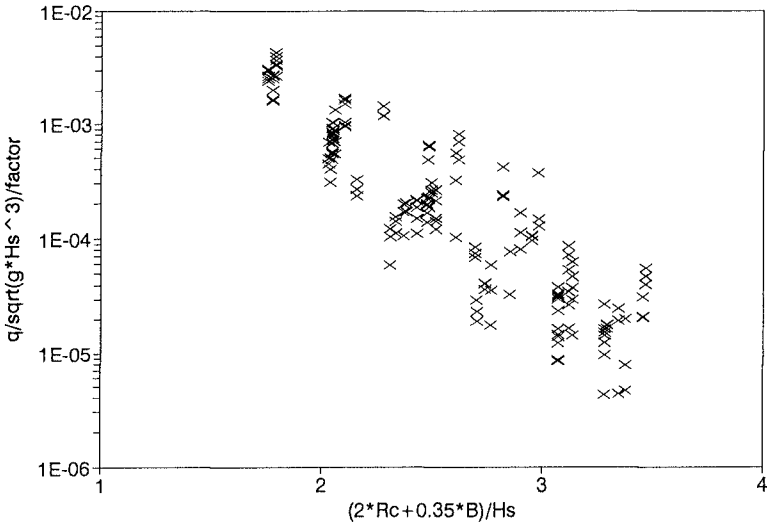


**Fig. 11** Dimensionless overtopping discharge including an influence factor to take into account wave obliquity,  $Q/\text{factor}$ , as function of the dimensionless parameter,  $(2R_c + 0.35B)/H_s$ .

## Conclusions

A wide range of parameters influence wave overtopping of coastal structures. The present research study on overtopping of a traditional rubble mound breakwaters with an armour layer slope of 1:2.0 has concentrated on the angle of wave attack, the crest free board, crest width, and the general wave parameters ( $H_s$ ,  $T_p$ , and  $s_{op}$ ).

Model tests were carried out in a wave basin for measuring the mean overtopping discharge,  $q$  ( $m^3/m/s$ ), and covered angles of wave attack ranging from  $0^\circ$  (perpendicular waves) up to  $50^\circ$  in step of  $10^\circ$ .

The significant wave height and the crest free board are the most important parameters with respect to wave overtopping. The crest width is found to have some smaller influence.

Testing with four wave steepnesses show that this parameter has an influence on the wave overtopping for perpendicular waves, whereas the influence is decreasing for oblique waves. However, the influence is small compared to the influence of the other tested parameters.

From analyses of the test results, it can be concluded that the reduction factor for wave obliquity (described by the ratio between the overtopping for oblique waves and perpendicular waves) is dependent on the crest free board. In case of a low-crested breakwater, the average of the tests show a maximum in the mean overtopping discharge for an angle of  $10^\circ$ . A pronounced decrease is found increasing the angle to  $20^\circ$  and  $30^\circ$ . For an angle of  $50^\circ$ , an average reduction factor of 0.1 is estimated. For breakwaters with a higher crest free board, the influence of the angle is larger, eg for the high-crested breakwater a reduction factor of about 0.2 is found for  $20^\circ$ .

The dimensionless overtopping discharge data for perpendicular waves (including all four wave steepnesses) show to fit well when plotted against a dimensionless parameter combining the influence of the crest free board and width  $(2R_c + 0.35B)/H_s$ . Dividing the dimensionless overtopping discharges with average reduction factors for wave obliquity, it is found that the same dimensionless parameter gives a reasonable fit also for oblique waves. This means that for rubble mound breakwaters with a slope of 1:2.0, the dimensionless overtopping discharge including a reduction factor for wave obliquity can be described by an exponential function of  $(2R_c + 0.35B)/H_s$ .

In order to establish a general overtopping formula for rubble mound breakwaters, it will be required to include the influence of, for instance, alternative breakwater geometries, water depth, artificial armour units, and superstructures.



## Acknowledgement

The research has been funded by the Danish Research Council and the Danish Hydraulic Institute. The authors would like to thank Ms Kirsten Bossen, Mr Christian Paulsen, Mr Andreas Roulund and Mr Micael Aamann for carrying out the model tests and making the preliminary analysis, which were part of their B.Sc. dissertations at the Danish Academy of Engineering.

## References

- De Wall, J.P. and J.W. van der Meer. (1992). *Wave run-up and overtopping on coastal structures*. Proceedings of 23rd International Conference on Coastal Engineering, Venice, Italy.
- Galland, J-C. (1994). *Rubble mound breakwaters stability under oblique waves: an experimental study*. Proceedings of 24th International Conference on Coastal Engineering, Kobe, Japan.
- Jensen, O.J. and J. Juhl. (1987). *Wave overtopping on breakwaters and sea dikes*. Proceedings of Second International Conference on Coastal and Port Engineering in Developing Countries, Beijing, China.
- Franco, L. (1993). *Overtopping of vertical face breakwaters: results of model tests and admissible overtopping rates*. Proceedings MAST2-MCS, 1st project workshop, Madrid, Spain.
- Franco, L.; M. de Gerloni and J.W. van der Meer. (1994). *Wave overtopping at vertical and composite breakwaters*. Proceedings of 24th International Conference on Coastal Engineering, Kobe, Japan.
- Van der Meer, J.W. and C-J.M. Stam. (1992). *Wave run-up on smooth and rock slopes of coastal structures*. Journal of Waterway, Port, Coastal, and Ocean Engineering, Vol 118, No 5, 1992.

## SUBJECT INDEX

Page number refers to first page of paper

- Aeration, 1895  
Aerial photographs, 1998  
Air entrainment, 1496  
Airport runways, 2683  
Aquatic plants, 142  
Armor units, 918, 958, 986, 1001, 1061,  
1090, 1143, 1157, 1227, 1388, 1412,  
1426, 1439, 1511, 1541, 1568, 1625,  
1641, 1713  
Artificial islands, 1568  
Barrier islands, 181, 2222, 2417, 2886,  
3251, 3491  
Bathymetry, 871  
Beach erosion, 315, 609, 1197, 1880,  
1934, 2070, 2252, 2340, 2380, 2434,  
2449, 2571, 2683, 2726, 2943, 3208,  
3393, 3478, 3491  
Beach nourishment, 1359, 1797, 1934,  
2100, 2222, 2395, 2668, 2886, 3016,  
3208, 3491, 3507, 3548, 3564, 3579  
Beaches, 540, 1157, 1782, 1812, 1880,  
2115, 2325, 2395, 2449, 3167, 3378  
Bed load, 3360  
Bed load movement, 2513  
Bed ripples, 635, 1975, 2013, 2043, 2070,  
2140  
Bed roughness, 300  
Bedforms, 2185  
Benefit cost analysis, 3237  
Berms, 1075, 1343, 1625, 2252, 2712,  
3594  
Blocks, 932  
Boundary conditions, 272, 442, 594, 886,  
1770  
Boundary element method, 871, 1241,  
1700  
Boundary layer, 594, 1827  
Boundary layer flow, 384, 2527  
Breaking waves, 219, 330, 399, 412, 511,  
525, 594, 609, 1101, 1255, 1312,  
1496, 1553, 1672, 1739, 1895, 1961,  
2252, 2282, 2365, 2461, 2503, 2557,  
2583, 2813, 2856, 3167  
Breakwaters, 272, 525, 791, 1016, 1030,  
1046, 1101, 1255, 1269, 1298, 1343,  
1359, 1373, 1397, 1412, 1426, 1439,  
1454, 1580, 1595, 1625, 1657, 1700,  
1754, 1880, 2583, 2653, 2668, 2871,  
3167, 3208, 3420, 3564, 3608  
Buoyant jets, 3045  
Buried pipes, 1553, 2571, 3099  
Caissons, 1030, 1046, 1255, 1298, 1373,  
1580  
Calibration, 207  
Case reports, 3491, 3507, 3564, 3579,  
3594  
Channel bends, 128  
Channels, waterways, 128, 3002, 3060,  
3139, 3533  
Circular channels, 1373  
Climatic changes, 3193, 3251, 3462  
Coastal engineering, 1, 1837  
Coastal management, 3579  
Coastal morphology, 142, 1782, 1797,  
1837, 1906, 2100, 2207, 2222, 2252,  
2340, 2417, 2513, 2871, 3126, 3223,  
3251  
Coastal processes, 57, 2380, 2406, 3237,  
3335  
Coastal structures, 511, 2476, 3154, 3167,  
3522, 3564  
Cohesionless sediment, 2043, 2406  
Cohesive sediment, 2004, 2058, 3060  
Collisions, 3030  
Comparative studies, 3208  
Composite structures, 1030  
Computer analysis, 1090  
Computer models, 2311  
Concrete, 1426, 1641  
Concrete blocks, 1269  
Conical bodies, 1595  
Consolidation, soils, 2004, 2902  
Construction, 3594  
Coral reefs, 609  
Cost effectiveness, 1412  
Cross sections, 1130  
Currents, 113, 384, 565, 624, 1484, 2476,  
2503  
Cylinders, 973, 1115, 1212

**Volume 1 1-1196**

**Volume 2 1197-2416**

**Volume 3 2417-3614**

- Dam breaches, 2755
- Damage assessment, 2197
- Damage estimation, 1412
- Damage patterns, 1001, 1090, 1157, 1657
- Deep water, 12, 412, 455, 579, 973, 1343, 3608
- Deltas, 2542
- Design, 1327, 1359
- Digital mapping, 1998
- Dikes, 1075, 1169, 2197, 2639, 2755, 3350
- Dilution, 3045
- Discrete elements, 192
- Dispersion, 3071
- Displacements, 1255, 1625
- Distribution, 3086
- Distribution patterns, 192
- Dolos, 958, 1388, 1426, 1511, 1641
- Drainage systems, 1568, 2571
- Dredge spoil, 2928, 3305, 3507, 3579
- Dredging, 2972, 3002, 3016, 3060, 3139, 3393, 3533
- Dunes, 1934, 2028, 2197, 2434, 2488, 2755, 2770
- Earthquakes, 886
- Eddy viscosity, 384
- Embankments, 1130
- Energy dissipation, 635, 1454, 2557
- Energy losses, 761
- Entrainment, 3071
- Entropy, 232, 340
- Environmental impacts, 3178
- Erosion, 2058, 2170, 2488, 2542, 2639, 3360
- Erosion control, 1880, 1934, 2070, 2155, 2683, 2712, 3193, 3208, 3378, 3491
- Estuaries, 2004, 3060, 3178, 3281, 3408, 3533
- Failure modes, 1388, 1713
- Failures, 1526, 1657, 1754, 3350
- Field investigations, 540, 719, 1946, 2028, 2513, 3522
- Field tests, 665, 689, 945, 1269, 2115, 2610, 2799
- Filters, digital, 168
- Finite element method, 746, 871, 1388
- Fish habitats, 3420
- Fisheries, 1484, 3447, 3478
- Flocculation, 3060
- Flood control, 3126, 3193
- Flooding, 2197, 2755, 3154
- Flow characteristics, 27
- Flow measurement, 1975
- Flow patterns, 1770
- Flow rates, 98, 1975, 2058, 2085
- Flow simulation, 2140
- Flow visualization, 861, 3045
- Fluid flow, 98
- Fluid-structure interaction, 1115
- Flumes, 86, 1641, 1880, 2843, 2913
- Free surfaces, 86
- Frequency analysis, 12
- Frequency response, 207
- Friction, 1983
- Friction factor, 565, 986
- Geomorphology, 1837
- Global warming, 3462
- Grasses, 2639
- Gravel, 1880
- Gravity waves, 86, 579, 635, 1919, 3071
- Greens function, 442
- Groins, structures, 1157, 1327, 1782, 2668, 3564
- Harbor engineering, 791, 806
- Harbor structures, 3507
- Harbors, 871, 2987
- Hydraulic models, 1001, 1182, 1197, 1269, 2987, 3447
- Hydraulic performance, 918, 1373
- Hydraulic properties, 1454
- Hydraulic roughness, 2871
- Hydraulics, 2902
- Hydrodynamic pressure, 973, 1484
- Hydrodynamics, 861, 1849, 1919, 2282, 2340, 2741, 3099, 3432
- Hydrologic aspects, 3251
- Impact loads, 958, 3522
- Impulsive loads, 1580
- Indonesia, 609, 821
- Inlets, waterways, 2943, 3432
- Instrumentation, 42
- Japan, 1, 247, 674, 886, 1016, 1046
- Jetties, 2799

- Kinematics, 540
- Laboratory tests, 42, 98, 128, 168, 650,  
689, 776, 1075, 1101, 1143, 1157,  
1212, 1241, 1284, 1610, 1641, 1782,  
1946, 2115, 2325, 2449, 2461, 2476,  
2488, 2843, 2856, 3295
- Lagoons, 2928, 3223
- Lagrangian functions, 2828
- Lakes, 2380, 3281
- Land reclamation, 2972, 3178, 3305
- Landslides, 821
- Layered soils, 3360
- Lift, 1115, 3099
- Linear analysis, 285
- Liquefaction, 2698, 3350
- Littoral currents, 27, 1895, 1919, 1983,  
2237, 2267, 2282, 2297, 2503, 2741
- Littoral deposits, 1327
- Littoral drift, 2513, 2595, 2625, 2726,  
2799, 2943, 2972, 3478, 3507
- Long waves, 455, 791, 847, 886, 1961
- Marshes, 3548
- Mass transport, 86, 2828, 2913
- Mathematical models, 1241, 1727, 2125,  
2197, 2350, 2755, 2928, 3223
- Measuring instruments, 42, 207
- Meteorological data, 79
- Mining, 3335, 3393
- Mixing, 3071, 3281
- Model accuracy, 57, 2595
- Model analysis, 57
- Model studies, 1880, 2770
- Model tests, 1030, 1061, 1182, 1197, 1298
- Model verification, 901, 1961, 2595, 2610,  
2785, 3223
- Monitoring, 1511, 1812, 2100, 2222,  
2799, 2886, 3522, 3579
- Monsoons, 3378
- Mooring, 791, 847
- Movable bed models, 300, 1782, 1906,  
2972
- Mud, 2004, 2913, 3266, 3360, 3408
- Navier-Stokes equations, 511, 1739, 2297
- Navigation, 3139, 3533
- Nearshore circulation, 68, 207, 272, 330,  
1895, 2237, 2267, 2340, 2365, 2461,  
2583, 2610, 2741, 3420
- Netherlands, 2886, 3193, 3208, 3350
- Nonlinear analysis, 157, 285, 427, 467,  
1961
- Normal stress, 986
- North Sea, 261, 1359, 1797
- Numerical calculations, 427
- Numerical models, 27, 79, 113, 157, 192,  
272, 442, 467, 511, 689, 746, 776,  
806, 821, 871, 886, 1016, 1672, 1700,  
1739, 1880, 1919, 1946, 1983, 2043,  
2070, 2140, 2155, 2237, 2311, 2434,  
2503, 2542, 2557, 2610, 2653, 2741,  
2785, 2843, 2871, 3086, 3295, 3305,  
3420
- Ocean mining, 3393
- Ocean waves, 232, 340, 806, 1526
- Offshore engineering, 2928
- Offshore structures, 1115
- Oscillations, 847, 1255, 2987
- Oscillatory flow, 1541, 1553, 1975, 1983,  
3408
- Outfall sewers, 1553, 3045, 3071, 3564
- Overtopping, 511, 918, 1016, 1030, 1046,  
1130, 1182, 1373, 1568, 1687, 1700,  
2028, 2639, 3154
- Oxygen content, 3447
- Oxygenation, 3167
- Particle motion, 2406
- Permeability, 1101
- Perturbation, 746, 973, 1469
- Photogrammetry, 1998
- Photographic analysis, 1511
- Plates, 1312, 1454
- Plunging flow, 1739
- Polders, 2197
- Pollution, 3071
- Pore pressure, 932, 1727, 2698, 3111
- Pore water pressure, 3030, 3369
- Porous media, 635, 1770
- Porous media flow, 1739
- Ports, 1197, 3608
- Portugal, 3608
- Pressure distribution, 1770
- Probabilistic methods, 1754, 3154
- Probability density functions, 482
- Probability distribution, 247, 356, 482,  
497
- Progressive waves, 86

- Prototypes, 1016  
 Public safety, 1016, 1046  
 Random waves, 192, 272, 285, 300, 370,  
     412, 427, 482, 553, 565, 579, 704,  
     719, 1130, 1157, 1610, 2125, 2252,  
     2843  
 Recreation, 2395  
 Recreational facilities, 2668  
 Reefs, 1484  
 Regression models, 247  
 Rehabilitation, 3594, 3608  
 Research, 1  
 Residence time, 553  
 Residual strength, 2639  
 Return flow, 1101  
 Revetments, 932, 1001, 1269, 1687  
 Rip currents, 2583  
 Riprap, 3320  
 Risk analysis, 3154  
 Rivers, 3002, 3126, 3295  
 Rotational flow, 861  
 Rubble-mound breakwaters, 918, 958,  
     986, 1001, 1061, 1090, 1182, 1227,  
     1397, 1511, 1526, 1610, 1713, 1727,  
     3594  
 Salinity, 2928, 3533  
 Sand, 3360  
 Sand transport, 2557  
 Sandbars, 157, 1837, 1865, 2222, 2311,  
     2325, 2571, 2712, 2770, 2856, 3126,  
     3548  
 Scale effect, 1143, 2668, 2770  
 Scour, 1284, 1595, 3320  
 Scouring, 1212  
 Sea cliffs, 2170  
 Sea floor, 3111, 3139, 3320, 3369  
 Sea level, 2115, 2311, 2340, 3193, 3462  
 Sea state, 247  
 Sea walls, 1046, 1130, 1169, 1496, 1568,  
     1672, 1812, 3154, 3335  
 Sediment concentration, 1827, 2085, 2125,  
     2476, 2813  
 Sediment deposits, 2185, 3305  
 Sediment transport, 27, 98, 142, 300, 370,  
     525, 1212, 1327, 1770, 1827, 1837,  
     1849, 1865, 1906, 1919, 1946, 1975,  
     2028, 2043, 2070, 2125, 2140, 2185,  
     2282, 2406, 2503, 2513, 2527, 2595,  
     2625, 2770, 2785, 2799, 2843, 2871,  
     2902, 2928, 2928, 2972, 3295, 3360,  
     3478  
 Sedimentation, 2004, 3002, 3139  
 Sensors, 2185, 2799  
 Settling velocity, 3408  
 Shallow water, 261, 330, 370, 455, 467,  
     482, 665, 704, 731, 761, 1212, 1343,  
     1849, 2350, 2928, 3281  
 Shape, 1343, 1388, 1439, 1625  
 Shear stress, 98, 565, 594, 986, 1595,  
     2058  
 Shear waves, 1919  
 Shellfish, 3086, 3420  
 Ship motion, 791, 847, 871  
 Ships, 3030  
 Shoaling, 12, 467, 594, 2365  
 Shock, 1075  
 Shore protection, 142, 3237, 3335  
 Shoreline changes, 1327, 1782, 1812,  
     1837, 1906, 1946, 1998, 2380, 2610,  
     2625, 2653, 2683, 2726, 2755, 2785,  
     2813, 2943, 3178, 3295, 3335, 3378,  
     3393, 3462, 3478  
 Silts, 2902, 3060  
 Simulation models, 821, 3266  
 Sliding, 1580  
 Slope stability, 1553  
 Slopes, 315, 746, 1075, 1568, 1865, 2325,  
     2350, 3167  
 Soil mechanics, 2902, 3030  
 Soil permeability, 2902, 3111  
 South Africa, 1511  
 Spatial distribution, 579, 674  
 Spectral analysis, 12, 68, 384, 731  
 Spits, coastal, 2380, 2726, 3478  
 Stability, 918, 932, 1061, 1143, 1227,  
     1397, 1426, 1439  
 Stability analysis, 1865  
 Standing waves, 3369  
 State-of-the-art reviews, 1, 832  
 Statistical analysis, 674  
 Statistical data, 832  
 Statistics, 79  
 Stones, 1553, 1625  
 Storm surges, 901, 2170, 2434  
 Storms, 79, 261, 1526, 1849, 1934, 2843,  
     3491, 3608  
 Stratification, 3360  
 Stratified flow, 3447

- Strength, 1388  
 Stress distribution, 1713  
 Structural response, 832, 1412, 1641  
 Structural strength, 958  
 Submerged discharge, 3320  
 Subsidence, 1541  
 Surf beat, 399, 689, 1961  
 Surf zone, 98, 315, 399, 553, 1895, 1934,  
     2085, 2155, 2237, 2267, 2282, 2350,  
     2503, 2513, 2542, 2712, 2813, 2856  
 Surface roughness, 1169  
 Surface waves, 467, 635, 3111  
 Suspended load, 3360  
 Suspended sediments, 1827, 1849, 1865,  
     2013, 2043, 2085, 2125, 2406, 2476,  
     2527, 2770, 2813, 3002, 3016, 3281  
 Suspended solids, 3408  
  
 Tensile stress, 1713  
 Three-dimensional flow, 370  
 Three-dimensional models, 871, 901,  
     1227, 2267, 2297, 2340, 2461, 2741,  
     3432  
 Tidal currents, 2282, 3281  
 Tidal hydraulics, 861  
 Tidal marshes, 3251  
 Tidal waters, 181, 2417, 3533  
 Tides, 3462  
 Time dependence, 272, 285, 553, 635  
 Tin, 3393  
 Tombolo, 1197, 2653  
 Topography, 272, 746, 1212, 1865, 1946,  
     2325, 2557, 2610, 3126  
 Transport rate, 2785, 2828, 2913, 2972  
 Tsunamis, 821, 886  
 Turbidity, 3016  
 Turbulence, 98, 861, 901, 2712, 3281  
 Turbulent boundary layers, 300, 384  
 Turtles, 3491  
 Two-dimensional analysis, 3447  
 Two-dimensional flow, 27  
 Two-dimensional models, 1030, 2155  
 Typhoons, 1, 219, 674, 2434  
  
 Ultrasonic testing, 624  
 Undertow, 330, 399, 2125, 2610, 2712,  
     2785  
 Uplift pressure, 932, 1298  
  
 Velocity profile, 86  
  
 Vertical cylinders, 1284, 1469, 1595  
 Vibration, 1115  
 Vibration analysis, 455  
 Viscoelasticity, 2913  
 Viscoplasticity, 2913  
 Viscosity, 3408  
 Vortices, 113, 525, 1115, 1975, 2140,  
     2856  
  
 Water content, 3266  
 Water depth, 261, 1343  
 Water flow, 1373  
 Water level fluctuations, 2170  
 Water levels, 2365, 3533  
 Water pollution, 3178  
 Water pressure, 1541  
 Water quality, 2395  
 Water surface profiles, 455, 624, 704,  
     1469  
 Water table, 2115, 2449, 2571  
 Water waves, 455  
 Waterfront facilities, 901  
 Wave action, 315, 918, 1001, 1061, 1212,  
     1227, 1269, 1739, 1934, 2013, 2058,  
     2639, 2698, 2712, 3016, 3045, 3099,  
     3266, 3522  
 Wave attenuation, 1312, 2913  
 Wave climatology, 181, 247, 1526, 2311  
 Wave crest, 356, 497, 540  
 Wave damping, 142, 609  
 Wave diffraction, 128, 285, 442, 973  
 Wave energy, 609, 761, 791, 806, 1454,  
     2698  
 Wave forces, 330, 1046, 1075, 1115, 1298,  
     1312, 1439, 1469, 1484, 1496, 1580,  
     1754  
 Wave generation, 68, 168, 650, 704, 776  
 Wave groups, 689, 776, 832, 847, 945,  
     1526, 1568, 1827, 1961, 2828  
 Wave height, 79, 181, 192, 247, 261, 356,  
     370, 399, 412, 497, 579, 609, 674,  
     746, 1016, 1101, 1182, 1241, 1397,  
     1657, 1754, 2155, 2207, 2311, 2350,  
     2365, 2488, 2698, 2828, 2987, 3266,  
     3608  
 Wave measurement, 42, 57, 207, 232, 624,  
     731, 776, 806, 832, 1610, 1906, 2207  
 Wave pressure, 1312, 1541  
 Wave propagation, 157, 168, 181, 232,  
     665, 1241

- Wave reflection, 128, 168, 442, 719, 945, 1241, 1610, 2434
- Wave refraction, 68, 285, 442
- Wave runup, 27, 315, 399, 553, 689, 761, 776, 821, 886, 1169, 1687, 1727, 2115, 2155, 2170, 2207, 2325, 2488, 2557, 2571, 2583
- Wave spectra, 12, 42, 68, 232, 340, 370, 384, 467, 482, 497, 624, 665, 719, 731, 806, 2843
- Wave tanks, 128, 650, 1469, 1880, 1906, 2207, 2449
- Wave velocity, 427, 525, 540, 565, 986, 1046, 1454, 2527
- Waves, 113, 2476
- Wind, 57
- Wind direction, 79, 3447
- Wind speed, 79, 261, 330, 1687
- Wind waves, 12, 68, 181, 232, 330, 665, 731, 761, 901, 945, 2350

## AUTHOR INDEX

Page number refers to first page of paper

- Ahn, K., 482  
Akeda, S., 3420  
Alexis, A., 2902  
Alexis, Alain, 2004  
Allsop, N. W. H., 918, 1130, 1157, 3154  
Alvarez, J., 3579  
An, Nguyen Ngoc, 2913  
Andrassy, Christopher J., 2100  
Anglin, C. D., 2380  
Aono, Toshio, 12  
Asai, Tadashi, 232, 847  
Asano, Toshiyuki, 27  
Aydin, Ismail, 1770
- Badiei, Peyman, 1782  
Baird, W. F., 3608  
Bakker, Willem T., 1797  
Bakker, Wim T., 2197  
Balzano, Andrea, 2928  
Barnes, T. C. D., 776  
Barthel, Volker, 791  
Basco, David R., 1812  
Battjes, J. A., 157  
Bedford, K., 1827  
Beji, Serdar, 427  
Bellomo, Doug, 1812  
Benoit, Michel, 42, 1610  
Bergmann, Hendrik, 553, 1075  
Bertotti, Luciana, 57, 79  
Besley, P., 918  
Bezuijen, Adam, 932  
Blomgren, Sten H., 1327  
Boccotti, Paolo, 945  
Bodge, Kevin R., 2943  
Booij, N., 68, 261  
Bouws, E., 261  
Brandt, Günther, 181  
Briggs, Michael J., 806  
Brøker, I., 2871  
Brøker, Ida, 2958  
Bruce, T., 1975  
Burcharth, Hans F., 958
- Caballería, Miquel, 1983  
Carnero, Ovidio Varela, 1657  
Cavaleri, Luigi, 57, 79  
Chacaltana, J. T. Aquije, 973  
Chang, C., 1700  
Chang, Chen-Yue, 3045  
Chang, Hsien-Kuo, 2972  
Chaplin, John R., 1115  
Chen, Xinjian, 3281  
Chen, Yih-Far, 3045  
Chen, Z., 3223  
Chilo, Bruno, 1090  
Chin, Ikuo, 3478  
Chisholm, T. A., 1849  
Chou, C. R., 2987  
Christensen, E. Damgaard, 1865  
Christensen, Erik Damgaard, 1919  
Christensen, Morten, 168  
Christiansen, N., 1595  
Chyan, Jih-Ming, 3045  
Cieślakiewicz, Witold, 86  
Coates, T. T., 1880  
Collado, F. R., 2542  
Cornett, Andrew, 986  
Cornett, Andrew M., 1001  
Coussirat, M. G., 2542  
Covarsi, Manuel F., 3564  
Cox, Daniel T., 98  
Cummins, I., 113
- da Silva, A. F. Teles, 973  
Daemrich, Karl-Friedrich, 2828  
Dally, William R., 1895  
Dalrymple, Robert A., 128  
Damgaard, Jesper Svarrer, 1919  
d'Angremond, K., 1713, 1754  
Daniil, E. I., 3167  
Davidson, D. D., 3608  
Davies, Michael H., 1001  
de Gerloni, M., 1030  
De Groot, M. B., 1727  
de Groot, Maarten B., 3350  
de Quirós, Fernando Bernaldo, 3237  
de Ronde, J. G., 261  
de Ronde, John G., 761  
de Ruig, J. H. W., 3208  
de Vriend, Huib J., 594  
Dean, Robert G., 1906, 2449, 3491  
Deguchi, Ichiro, 370, 2476, 3002  
Deigaard, R., 1865, 2043  
Deigaard, Rolf, 1919, 2583  
Dette, Hans H., 1934  
Dette, Hans-H., 2843  
Dette, Hans-Henning, 553  
Dibajnia, Mohammad, 1946



- Dijkman, Michiel, 3522  
 Dodd, N., 1880  
 Dodd, Nicholas, 1961  
 Dowd, Millard, 3491  
 Drago, Michele, 540  
 Dubi, Alfonse, 142
- Earnshaw, H. C., 1975  
 Easson, W. J., 1975  
 Easson, William J., 525  
 Edge, B. L., 3608  
 Edge, Billy, 1687  
 Edge, Billy L., 3491  
 Eldeberky, Y., 157, 261  
 Endo, Taiji, 2395  
 Endoh, Kimihiko, 1016, 1046
- Falqués, Albert, 1983  
 Ferier, P. G. P., 261  
 Fernandez, Joaquin, 3594  
 Fisher, John S., 1998, 2488  
 Foda, Mostafa A., 3099  
 Fontijn, Henri L., 1553  
 Franco, C., 918  
 Franco, L., 1030  
 Fredsøe, J., 1595, 1865, 2043  
 Fredsøe, Jørgen, 1919  
 Frigaard, Peter, 168  
 Fujima, Koji, 1115  
 Fukushima, Masahiro, 2571  
 Furuta, Goichi, 861
- Gal, J. Andorka, 261  
 Galland, J.-C., 1061  
 Gallois, Stéphane, 2004  
 Gärtner, Joachim, 181  
 Giménez, Marcos H., 192  
 Glaser, Detlef, 181  
 Goda, Yoshimi, 1241  
 Goldenbogen, Roland, 3251  
 Gomez, Daniel, 3594  
 Gomez-Pina, G., 3579  
 Gómez-Pina, Gregorio, 3507  
 Goto, Chiaki, 12  
 Gotoh, H., 1541  
 Gotoh, Hitoshi, 2013  
 Gracia, V., 2542  
 Grass, Tony J., 565  
 Greated, C. A., 1975  
 Greated, Clive A., 540
- Grote, Wout V., 1553  
 Grüne, Joachim, 181, 1075  
 Gudmestad, Ove T., 86  
 Guiducci, F., 1343, 1625  
 Guiducci, Franco, 1090
- Hamilton, David G., 1782  
 Han, W. Y., 2987  
 Hancock, Mark W., 2028  
 Hanes, Daniel M., 3016  
 Hansen, E. A., 2043  
 Hansen, N.-E. Ottesen, 3030  
 Hansen, S. B., 1595  
 Hanslow, David J., 207, 2115  
 Hanson, Hans, 1327  
 Hanzawa, Minoru, 1143  
 Hara, Koji, 2461  
 Hardaway, C. Scott, 2653  
 Harkins, Gordon S., 806  
 Harris, J. M., 300  
 Harshinie, Karunarathna G., 689  
 Hashida, Misao, 219  
 Hashimoto, Noriaki, 232, 624, 847  
 Hashimoto, O., 1197  
 Hashimoto, Seiya, 2070  
 Hata, Sadakatsu, 2571  
 Hatada, Yoshio, 247, 674  
 Hattori, Masataro, 1101  
 Hattori, Takeshi, 704  
 Hayashi, Kenjiro, 1115  
 Hazelton, John M., 1812  
 Herbert, D. M., 1130  
 Hibbert, Kevin, 207  
 Higaki, Futoshi, 1115  
 Higano, Junya, 3086  
 Hoekstra, Piet, 2222  
 Holthuijsen, L. H., 68, 261  
 Holtzhausen, A., 1511  
 Holtzhausen, A. H., 1388  
 Hosoi, Yoshihiko, 1454  
 Houwing, Erik-Jan, 2058  
 Houwman, Klaas, 2222  
 Hsu, Tai-Wen, 2972  
 Hujii, Atsushi, 1046  
 Hwang, Kyu-Nam, 2488  
 Hwung-Hweng, Hwung, 3045
- Ikeno, Masaaki, 3320  
 Imamura, Fumihiko, 821, 886  
 Iranzo, Vicente, 1983

- Irie, Isao, 2070  
 Ishii, Toshimasa, 272  
 Isobe, Masahiho, 719  
 Isobe, Masahiko, 272, 285, 2785, 3266  
 Ito, Kazunori, 847  
 Ito, Masahiro, 1143  
 Ito, Yoshiki, 624  
 Itoh, Sadahiko, 1454  
 Iwagaki, Yuichi, 1, 1143  
 Iwata, Koichiro, 1212, 1439  
 Izumi, Tatsuhisa, 3378  
  
 Jaffe, Bruce E., 2085  
 Janssen, Hans, 3522  
 Jensen, Anders, 2958  
 Jensen, Frerk, 181  
 Johnsen, John, 2958  
 Johnson, Hakeem, 2871  
 Johnson, Patrick, 3491  
 Jones, R. J., 918, 1157  
 Juang, Jea-Tzyy, 1169  
 Juhl, J., 1754  
 Juhl, Jørgen, 1182  
  
 Kabling, Michael B., 2557  
 Kaczmarek, L. M., 300  
 Kaihatsu, Sumio, 1269  
 Kaiser, Ralf, 181  
 Kamata, A., 1197  
 Kamphuis, J. William, 1782  
 Kana, Timothy W., 2100  
 Kang, Hong-Yoon, 2115  
 Karjadi, Entin A., 2155  
 Katoh, Kazumasa, 315  
 Katopodi, Irene, 2125, 2527  
 Kawaguchi, T., 1197  
 Kawata, Yoshiaki, 330  
 Kersting, Nico F., 1797  
 Kheyruri, Z., 1727  
 Kim, Chang-Je, 1212  
 Kim, Hyeon-Ju, 1526  
 Kim, Hyoseob, 2140  
 Kim, Kyu Han, 2476  
 Kim, Taerim, 340  
 Kimura, A., 497  
 Kimura, Akira, 356  
 Kimura, Katsutoshi, 1227  
 Kirby, James T., 128  
 Kitou, Nikos, 2125  
 Kittitanasuan, Wudhipong, 1241  
 Kiyokawa, Tetsushi, 650  
 Klammer, P., 1255  
 Klammer, Peter, 1298  
 Klatter, Leo, 3522  
 Kobayashi, Akio, 847  
 Kobayashi, Masonori, 1269  
 Kobayashi, Nobuhisa, 98, 1373, 2028, 2155  
 Kobayashi, Tomonao, 861, 1284  
 Koelewijn, Ria, 2527  
 Kohlhase, Søren, 1298  
 Kojima, Haruyuki, 1312  
 Komar, P. D., 2170  
 Koole, R., 3071  
 Koontanakulvong, Sucharit, 3002  
 Kortenhaus, Andreas, 1298  
 Kos'Yan, R. D., 2185  
 Kraak, A. W., 3208  
 Kraak, Arie, W., 2197  
 Kraus, Nicholas C., 1327  
 Kriebel, D. L., 2325  
 Kriebel, David L., 2207  
 Kroon, Aart, 2222  
 Kung, Chen-Shan, 1837  
 Kunisu, Hiroshi, 1568  
 Kunz, H., 3533  
 Kunz, Hans, 3251  
 Kuriyama, Yoshiaki, 2237  
 Kusuda, Tetsuya, 3408  
 Kuwabara, S., 3420  
 Kuwahara, Hisami, 3086  
 Kwon, J. G., 370  
  
 Lamberti, A., 1343, 1625  
 Larson, Magnus, 2252  
 Larssonneur, Claude, 2282  
 Lastrup, Christian, 1359  
 Law, Adrian W. K., 3099  
 Lee, Dal Soo, 1373  
 Lee, J., 1827  
 Lee, J. J., 1700  
 Lee, Jung Lyul, 2267  
 Lee, Tsong-Lin, 3369  
 Levoy, Franck, 2282  
 Li, Bin, 2297, 3548  
 Liberatore, Gianfranco, 525  
 Lin, Li-Hwa, 340, 2770  
 Lindenbergh, Jaap, 3350  
 Lindo, Mark H., 3594  
 Lintrup, Morten, 2928

- Liu, Shuxue, 731  
Liu, Zhou, 958  
Longo, Sandro, 2527  
Luger, S., 1511  
Luger, S. A., 1388
- MacDonald, N. J., 2311  
Maddrell, Roger, 3548  
Maddrell, Roger J., 2297  
Madsen, Holger Toxvig, 1359  
Madsen, O. S., 1849  
Madsen, Ole Secher, 384  
Madsen, P. A., 399  
Madsen, Per A., 2583  
Magda, Waldemar, 3111  
Magoon, O. T., 3608  
Mano, A., 3126  
Mansard, E., 3608  
Mansard, E. P. D., 832, 1397  
Mansard, Etienne, 791, 986  
Mansard, Etienne P. D., 1001  
Manzenrieder, Helmut, 3139  
Mase, Hajime, 635  
Matsumi, Y., 1397  
Matsumoto, Akira, 442  
Matsunaga, Nobuhiro, 219  
Matsuoka, Michio, 442  
Matsutomi, Hideo, 886  
Mayer, R. H., 2325  
Mayerle, Roberto, 2340  
McDougal, W. G., 2170  
Meadowcroft, I. C., 3154  
Medina, Josep R., 192, 1412  
Melby, Jeffrey A., 1426, 1641  
Memos, Constantine D., 2350  
Miura, H., 2698  
Miyaake, Yoshihito, 1212  
Miyamoto, Y., 3420  
Mizui, Hiroyuki, 219  
Mizumoto, T., 1197  
Mizutani, Norimi, 1439  
Mocke, G. P., 2365, 3335  
Møller, Jacob Steen, 2958  
Monfort, Olivier, 2282  
Mori, Nobuhito, 412  
Moutzouris, C. I., 3167  
Mulder, J. P. M., 2886  
Murakami, Hiroshi, 1143  
Murakami, Hitoshi, 1454  
Murakami, Keisuke, 1469, 2070
- Muraoka, Kohji, 3178  
Muraoka, Kouji, 3447
- Nadaoka, Kazuo, 427, 650  
Nagai, Toshihiko, 232, 624, 847  
Nagao, M., 3126  
Nairn, R. B., 2380  
Nakagawa, Hiroji, 2013  
Nakagawa, Yasuyuki, 427  
Nakamura, Satoshi, 2070  
Nakamura, Tetuya, 1312  
Nakatsuji, Keiji, 3178, 3447  
Nemoto, Kenji, 1143  
Nielsen, Peter, 207, 2115, 2406  
Niemeyer, Hanz D., 181, 1797, 2417  
Nishi, Ryuichiro, 2434  
Nishida, H., 1484  
Nishihira, F., 1484  
Nishimura, Hitoshi, 442  
Nishimura, Tsukasa, 861  
Nochino, Masao, 455  
Nwogu, Okey, 467
- Ochi, M. K., 482  
O'Connor, B. A., 300, 2311  
O'Connor, Brian A., 2140  
Oda, Kazuki, 3305  
Oda, Kenji, 1284  
Oh, Tae-Myoung, 1906, 2449  
Ohhama, Hoiku, 2395  
Ohta, T., 497  
Ohta, Takao, 356  
Ohyama, Takumi, 650, 871  
Okayasu, Akio, 98, 2461  
O'Neil, S., 1827  
Ono, Masanobu, 2476, 3002  
Ono, Nobuyuki, 2070  
Oshiro, Shinichi, 609  
Osiecki, Daniel A., 1895  
Osmond, Bill, 3548  
Oumeraci, H., 1255, 1672  
Oumeraci, Hocine, 1298  
Overton, Margery F., 1998, 2488  
Owen, M. W., 1130
- Park, Woo Sun, 1373  
Partenscky, H.-W., 1255, 1672  
Péchon, Philippe, 2503  
Peerbolte, E. Bart, 3193  
Peña, Carlos, 3564

- Peña-Santana, Patricia G., 2395  
Peregrine, D. H., 776, 1496  
Perrier, G., 2043  
Petit, H. A. H., 511, 1739  
Petti, Marco, 525, 540  
Phelp, D., 1511  
Phelp, D. T., 1388  
Pluijm, M., 3208  
Podymov, I. S., 2185  
Presti, A. Lo, 2625  
Prieto, J., 2542  
Pruszek, Zbigniew, 2513  
Putrevu, U., 2741  
  
Quinn, Paul A., 525, 540  
  
Ramadan, Khaled A. H., 2527  
Ramírez, Jose L., 3507  
Raudkivi, Arved J., 1934  
Reeve, D. E., 3154  
Ribberink, Jan S., 2527  
Ris, R. C., 68  
Rodriguez, A., 2542  
Roelvink, J. A., 3223  
Rousset, Hélène, 2282  
Rubin, David M., 2085  
Ruessink, Gerben, 2222  
Rufin, Teofilo Monge, Jr., 1439  
Ruggiero, P., 2170  
Ruiz, Luis Felipe Vila, 3237  
Rutledge, J., 1397  
Ryu, Cheong-Ro, 1526  
  
Sakai, Hiroyuki, 1101  
Sakai, T., 1541  
Saleh, Wameidh M., 565  
Sallenger, Asbury, Jr., 2085  
Sánchez-Arcilla, A., 2542, 2625  
Sánchez-Carratalá, Carlos R., 192  
Sancho, F. E., 2741  
Sand, S. E., 832  
Sasaki, Hiroshi, 624  
Sato, Michio, 2434, 2571  
Sato, Shinji, 2557  
Sawamoto, M., 3126  
Sawamura, Yoshiyuki, 1454  
Sawaragi, Toru, 2476, 3002  
Schäffer, H. A., 399  
Schäffer, Hemming A., 2583  
Schiereck, Gerrit J., 1553  
Schmeltz, Edward J., 3594  
Schoonees, J. S., 2595, 2668  
Schroeder, Ernst, 3251  
Schröter, Andreas, 2340  
Schüttrumpf, Holger, 553  
Scott, R. D., 2380  
Seijffert, J. W. W., 2639  
Sekimoto, Tsunehiro, 1568  
Shen, Daoxian, 3266  
Sheng, Y. P., 3432  
Sheng, Y. Peter, 3281  
Shiba, Kazuhiko, 2785  
Shibata, Takao, 847  
Shibayama, Tomoya, 2461, 2813, 2913, 3295  
Shigematsu, Takaaki, 3305  
Shih, S.-M., 2170  
Shim, Youngbo, 2140  
Shimizu, Takao, 3320  
Shimizu, Takuzo, 1946, 2610  
Shimosako, Kenichiro, 1580  
Shinoda, Seirou, 704  
Shiraishi, Naofumi, 2395  
Shuto, Nobuo, 821, 886  
Sierra, J. P., 2625  
Sigemura, Toshiyuki, 1115  
Simons, Richard R., 565  
Simonsen, B. C., 3030  
Sistermans, Paul G. J., 1553  
Sloth, Peter, 1182  
Smit, F., 2365  
Smith, G. G., 3335  
Smith, G. M., 2639  
Sørensen, O. R., 399  
Sørensen, Ole R., 2583  
Stansberg, Carl Trygve, 579  
Steetzel, Henk J., 2197  
Sterndorff, M. J., 3030  
Stive, Marcel J. F., 594, 761  
Stive, Marcer, 1837  
Stoutjesdijk, Theo P., 3350  
Sueyoshi, Toshiaki, 3178  
Sugihara, Yuji, 219  
Suh, Kyung Duck, 2653  
Sulaiman, Dede M., 609  
Sumer, B. M., 1595  
Sunamura, Tsuguo, 2856  
Svendsen, I. A., 2741  
Swan, C., 113, 3071  
Swart, D. H., 2668, 3335

- Syamsudin, Abdul R., 2683  
 Tada, A., 1484  
 Takahashi, S., 2698  
 Takahashi, Shigeo, 1016, 1046, 1227, 1580  
 Takahashi, Tomoharu, 624  
 Takahashi, Tomoyuki, 821, 886  
 Takayama, Tomotsuka, 624  
 Takeba, Ken, 635  
 Tamashita, Takao, 901  
 Tanaka, Masahiro, 650  
 Tanimoto, Katsutoshi, 689, 1227, 1580  
 Tehrani, Mehrdad M., 565  
 Teisson, Charles, 42, 1610, 2503  
 Theron, A. K., 2595  
 Thomas, P., 2902  
 Thomas, Pierre, 2004  
 Tillotson, K. J., 2170  
 Ting, Francis C. K., 2712  
 Toba, E., 3579  
 Tobikik, Isao, 847  
 Togashi, Hiroyoshi, 746  
 Tolman, H. L., 261  
 Tomasicchio, G. R., 1343, 1625  
 Toms, Geffery, 1837  
 Tonder, A. van, 1388, 1511  
 Tønjes, P., 511, 1739  
 Tøorum, Alf, 142  
 Topliss, M. E., 1496  
 Torfs, Hilde, 3360  
 Toue, Takao, 847  
 Tsai, Ching-Piao, 3369  
 Tsuchida, Mitsuru, 871  
 Tsuchiya, Toshito, 609  
 Tsuchiya, Yoshito, 2683, 3378, 3478  
 Tsujimoto, Tetsuro, 2013  
 Tsuru, Masahito, 2610  
 Tsutsui, Shigeaki, 609  
 Turk, George F., 1426, 1641  
 Uda, Takaaki, 2726  
 Ujiie, Hisayoshi, 3320  
 Valdecantos, Vicente Negro, 1657  
 van de Graaff, Jan, 2197  
 van de Kreeke, J., 2886  
 van den Bosch, P., 511, 1739  
 van der Lem, J. C., 3208  
 van der Meer, J. W., 1030, 1713, 1754, 2639  
 Van Dongeren, A. R., 2741  
 Van Evra, R., 1827  
 van Gent, M. R. A., 511, 1727, 1739  
 van Nes, C. P., 1713  
 van Rijn, Leo C., 2058  
 van Vessem, P., 2886  
 van Vledder, Gerbrant Ph., 761  
 Verhagen, L. A., 665  
 Villaret, C., 2043  
 Visser, Paul J., 2197, 2755  
 von Lany, P. H., 3154  
 Vongvisessomjai, Suphat, 3393  
 Walstra, D. J. R., 3223  
 Wang, Hsiang, 340, 2267, 2434, 2770, 2843  
 Wang, Xu, 2770  
 Ward, Donald L., 1687  
 Watanabe, Akira, 272, 719, 1946, 2610, 2785, 3266  
 Watson, G., 776  
 Weggel, J. R., 3608  
 Whalin, R. W., 3608  
 White, Thomas E., 2799  
 Wibner, Christopher G., 1687  
 Williams, Greg, 1812  
 Wind, Herman G., 3193  
 Winyu, Rattanapitikon, 2813  
 Woltering, Stefan, 2828  
 Wright, L. D., 1849  
 Wu, N. T., 1672  
 Wu, Yongjun, 2843  
 Yamada, Akiko, 3295  
 Yamada, Minoru, 3478  
 Yamaguchi, Masataka, 247, 674  
 Yamamoto, Koji, 2726  
 Yamamoto, Masato, 1143  
 Yamamoto, S., 2698  
 Yamamoto, T., 1541  
 Yamamoto, Yoshimichi, 689  
 Yamanishi, Hiroyuki, 3408  
 Yamashita, Takao, 609, 2683, 3378  
 Yamauchi, Kazuaki, 3320  
 Yamazaki, H., 1727  
 Yamazaki, Tsuyoshi, 1568  
 Yan, Yixin, 3060  
 Yang, David W., 3594  
 Yano, K., 3420

- Yassuda, E. A., 3432  
Yassuda, Eduardo A., 3281  
Yasuda, Takashi, 412, 704  
Yen, Kai, 3060  
Yokoki, Hiromune, 719  
Yoon, Jong Seong, 3447  
Yoshida, Akinori, 1312, 1469  
Yoshioka, Hiroshi, 609, 901  
Young, I. R., 665  
Ysuchiya, Yoshito, 901  
Yu, Hong-Sun, 1212  
Yu, Xiping, 746  
Yu, Yuxiu, 731  
Zeidler, Ryszard B., 2513, 3462  
Zeng, Xiaochuan, 3060  
Zhang, Da Ping, 2856  
Zhang, Jun, 1687  
Zhuang, F., 1700  
Zielke, Werner, 2340  
Zou, Zhili, 1961  
Zuzek, P. J., 2380  
Zyserman, J. A., 2871

VOLUME 2

RAW

# Coastal Engineering 1994

Proceedings of the  
twenty-fourth international conference

October 23-28; 1994  
Kobe, Japan

Conference held under the auspices of the  
Coastal Engineering Research Council of the  
American Society of Civil Engineers

Organized by the Japan Society of Civil Engineers

Edited by Billy L. Edge



Published by the  
American Society of Civil Engineers  
345 East 47th Street  
New York, New York 10017-2398

## ABSTRACT

This proceedings contains over 200 papers presented at the 24th International Conference on Coastal Engineering which was held in Kobe, Japan, October 23-28, 1994. The book is divided into six parts: 1) Characteristics of coastal waves and currents; 2) long waves and storm surges; 3) coastal structures; 4) coastal processes and sediment transport; 5) coastal, estuarine and environmental problems; and 6) case studies. The individual papers include such topics as the effects of wind, waves, storms and currents as well as the study of sedimentation and beach nourishment. Special emphasis is given to case studies of completed engineering projects. With the inclusion of both theoretical and practical information, these papers provide the civil engineer and related fields with a broad range of information on coastal engineering.

Coastal engineering 1994: proceedings of the twenty-fourth international conference, October 23-28, 1994, Kobe, Japan  
edited by Billy L. Edge.

p. cm.

"Conference held under the auspices of the Coastal Engineering Research Council of the American Society of Civil Engineers; organized by the Japan Society of Civil Engineers (JSCE)." Papers presented at the 24th International Conference on Coastal Engineering.

Includes index.

ISBN 0-7844-0089-X

1. Coastal engineering—Congresses. 2. Ocean waves—Congresses. 3. Shore protection—Congresses. I. Edge, Billy L. II. Coastal Engineering Research Council (U.S.) III. Doboku Gakkai. IV. International Conference on Coastal Engineering (24th: 1994: Kobe, Japan)

TC203.5.C6184 1995  
627'.58—dc20

95-18653  
CIP

The Society is not responsible for any statements made or opinions expressed in its publications.

Photocopies. Authorization to photocopy material for internal or personal use under circumstances not falling within the fair use provisions of the Copyright Act is granted by ASCE to libraries and other users registered with the Copyright Clearance Center (CCC) Transactional Reporting Service, provided that the base fee of \$2.00 per article plus \$.25 per page copied is paid directly to CCC, 222 Rosewood, Drive, Danvers, MA 01923. The identification for ASCE Books is 0-7844-0089-X/95 \$2.00 + \$.25. Requests for special permission or bulk copying should be addressed to Permissions & Copyright Dept., ASCE.

Copyright © 1995 by the American Society of Civil Engineers,  
All Rights Reserved.  
Library of Congress Catalog Card No: 95-18653  
ISBN 0-7844-0089-X  
Manufactured in the United States of America.



# CONTENTS

## PART I

Plenary Session THE PRESENT AND FUTURE OF COASTAL ENGINEERING IN JAPAN.....	1
<i>Yuichi Iwagaki</i>	
Chapter 1 ON THE CHARACTERISTICS OF ONE-DIMENSIONAL SPECTRA AND NON-DIMENSIONAL PARAMETERS OF WIND WAVES.....	12
<i>Toshio Aono, Chiaki Goto</i>	
Chapter 2 SWASH MOTION DUE TO OBLIQUELY INCIDENT WAVES.....	27
<i>Toshiyuki Asano</i>	
Chapter 3 LABORATORY COMPARISON OF DIRECTIONAL WAVE MEASUREMENT SYSTEMS AND ANALYSIS TECHNIQUES .....	42
<i>Michel Benoit, Charles Teisson</i>	
Chapter 4 ACCURACY OF WIND AND WAVE EVALUATION IN COASTAL REGIONS.....	57
<i>Luciana Bertotti, Luigi Cavaleri</i>	
Chapter 5 A SPECTRAL MODEL FOR WAVES IN THE NEAR SHORE ZONE.....	68
<i>R.C. Ris, L.H. Holthuijsen, N. Booij</i>	
Chapter 6 WIND VARIABILITY AND EXTREMES STATISTICS.....	79
<i>Luigi Cavaleri, Luciana Bertotti</i>	
Chapter 7 MEAN FLUX IN THE FREE SURFACE ZONE OF WATER WAVES IN A CLOSED WAVE FLUME.....	86
<i>Witold Cieslikiewicz, Ove T. Gudmestad</i>	
Chapter 8 VERTICAL VARIATIONS OF FLUID VELOCITIES AND SHEAR STRESS IN SURF ZONES .....	98
<i>Daniel T. Cox, Nobuhisa Kobayashi, Akio Okayasu</i>	

Chapter 9	
VORTICITY EFFECTS IN COMBINED WAVES AND CURRENTS .....	113
<i>I. Cummins, C. Swan</i>	
Chapter 10	
WAVES IN AN ANNULAR ENTRANCE CHANNEL .....	128
<i>Robert A. Dalrymple, J.T. Kirby</i>	
Chapter 11	
WAVE DAMPING BY KELP VEGETATION .....	142
<i>Alfonse Dubi, Alf Tørum</i>	
Chapter 12	
NONLINEAR COUPLING IN WAVES PROPAGATING OVER A BAR .....	157
<i>Y. Eldeberky, J.A. Battjes</i>	
Chapter 13	
AN ABSORBING WAVE-MAKER BASED ON DIGITAL FILTERS .....	168
<i>Peter Frigaard, Morten Christensen</i>	
Chapter 14	
WAVE CLIMATE STUDY IN WADDEN SEA AREAS .....	181
<i>Ralf Kaiser, Günther Brandt, Joachim Gärtner, Detlef Glaser, Frerk Jensen, H.D. Niemeyer, Joachim Grüne</i>	
Chapter 15	
FALSE WAVES IN WAVE RECORDS AND NUMERICAL SIMULATIONS .....	192
<i>Marcos H. Giménez, C.R. Sánchez-Carratalá, J.R. Medina</i>	
Chapter 16	
MEASURING WAVES WITH MANOMETER TUBES .....	207
<i>David J. Hanslow, P. Nielsen, K. Hibbert</i>	
Chapter 17	
QUANTITY OF SPRAY TRANSPORTED BY THE STRONG WIND OVER BREAKING WAVES .....	219
<i>Nobuhiro Matsunaga, Misao Hashida, Hiroyuki Mizui, Yuji Sugihara</i>	
Chapter 18	
EXTENSION OF THE MAXIMUM ENTROPY PRINCIPLE METHOD FOR DIRECTIONAL WAVE SPECTRUM ESTIMATION .....	232
<i>Noriaki Hashimoto, Toshihiko Nagai, Tadashi Asai</i>	

Chapter 19	
A REGRESSION MODEL FOR ESTIMATING SEA STATE PERSISTENCE .....	247
<i>Yoshio Hatada, Masataka Yamaguchi</i>	
Chapter 20	
THE MAXIMUM SIGNIFICANT WAVE HEIGHT IN THE SOUTHERN NORTH SEA .....	261
<i>L.H. Holthuijsen, J.G. de Ronde, Y. Eldeberky, H.L. Tolman, N. Booij, E. Bouws, P.G.P. Ferier, J. Andorka Gal</i>	
Chapter 21	
IMPROVED BOUNDARY CONDITIONS TO A TIME-DEPENDENT MILD-SLOPE EQUATION FOR RANDOM WAVES .....	272
<i>Toshimasa Ishii, Masahiko Isobe, Akira Watanabe</i>	
Chapter 22	
TIME-DEPENDENT MILD SLOPE EQUATIONS FOR RANDOM WAVES .....	285
<i>Masahiko Isobe</i>	
Chapter 23	
MODELLING MOVEABLE BED ROUGHNESS AND FRICTION FOR SPECTRAL WAVES .....	300
<i>L.M. Kaczmarek, J.M. Harris, B.A. O'Connor</i>	
Chapter 24	
DIFFERENCE BETWEEN WAVES ACTING ON STEEP AND GENTLE BEACHES .....	315
<i>Kazumasa Katoh</i>	
Chapter 25	
WAVE BREAKING UNDER STORM CONDITION .....	330
<i>Yoshiaki Kawata</i>	
Chapter 26	
APPLICATION OF MAXIMUM ENTROPY METHOD TO THE REAL SEA DATA .....	340
<i>Taerim Kim, Li-Hwa Lin, Hsiang Wang</i>	
Chapter 27	
PROBABILITY OF THE FREAK WAVE APPEARANCE IN A 3-DIMENSIONAL SEA CONDITION .....	356
<i>Akira Kimura, Takao Ohta</i>	

Chapter 28	
ON THE JOINT DISTRIBUTION OF WAVE HEIGHT, PERIOD & DIRECTION OF INDIVIDUAL WAVES IN A 3-DIMENSIONAL RANDOM SEAS.....	370
<i>J.G. Kwon, Ichiro Deguchi</i>	
Chapter 29	
SPECTRAL WAVE-CURRENT BOTTOM BOUNDARY LAYER FLOWS.....	384
<i>Ole Secher Madsen</i>	
Chapter 30	
TIME DOMAIN MODELLING OF WAVE BREAKING, RUNUP AND SURF BEATS .....	399
<i>Per A. Madsen, O.R. Sørensen, H.A. Schäffer</i>	
Chapter 31	
ORTHONORMAL WAVELET ANALYSIS FOR DEEP-WATER BREAKING WAVES .....	412
<i>Nobuhito Mori, Takashi Yasuda</i>	
Chapter 32	
A FULLY DISPERSIVE-NONLINEAR WAVE MODEL AND ITS NUMERICAL SOLUTIONS .....	427
<i>Kazuo Nadaoka, Serdar Beji, Yasuyuki Nakagawa</i>	
Chapter 33	
A GENERALIZED GREEN-FUNCTION METHOD FOR WAVE FIELD ANALYSIS .....	442
<i>Hitoshi Nishimura, Michio Matsuoka, Akira Matsumoto</i>	
Chapter 34	
COUPLED VIBRATION EQUATIONS FOR IRREGULAR WATER WAVES.....	455
<i>Masao Nochino</i>	
Chapter 35	
NONLINEAR EVOLUTION OF DIRECTIONAL WAVE SPECTRA IN SHALLOW WATER .....	467
<i>Okey Nwogu</i>	
Chapter 36	
NON-GAUSSIAN PROBABILITY DISTRIBUTION OF COASTAL WAVES .....	482
<i>M.K. Ochi, K. Ahn</i>	

Chapter 37		
PROBABILITY CHARACTERISTICS OF ZERO-CROSSING WAVE HEIGHT .....		497
	<i>Takao Ohta, Akira Kimura</i>	
Chapter 38		
NUMERICAL SIMULATION AND VALIDATION OF PLUNGING BREAKERS USING A 2D NAVIER-STOKES MODEL.....		511
	<i>H.A.H. Petit, P.Tönjes, M.R.A. Van Gent, P. Van Den Bosch</i>	
Chapter 39		
WAVE VELOCITY FIELD MEASUREMENTS OVER A SUBMERGED BREAKWATER .....		525
	<i>Marco Petti, Paul A. Quinn, Gianfranco Liberatore, William J. Easson</i>	
Chapter 40		
VELOCITY FIELD MEASUREMENTS AND THEORETICAL COMPARISONS FOR NON-LINEAR WAVES ON MILD SLOPES .....		540
	<i>Paul A. Quinn, Marco Petti, Michele Drago, Clive A. Greated</i>	
Chapter 41		
THE CONCEPT OF RESIDENCE TIME FOR THE DESCRIPTION OF WAVE RUN-UP, WAVE SET-UP AND WAVE RUN-DOWN .....		553
	<i>Holger Schüttrumpf, Hendrik Bergmann, Hans-Henning Dette</i>	
Chapter 42		
BOTTOM SHEAR STRESSES UNDER RANDOM WAVES WITH A CURRENT SUPERIMPOSED.....		565
	<i>Richard R. Simons, Tony J. Grass, Wameidh M. Saleh, Mehrdad M. Tehrani</i>	
Chapter 43		
EFFECTS FROM DIRECTIONALITY & SPECTRAL BANDWIDTH ON NON-LINEAR SPATIAL MODULATIONS OF DEEP-WATER SURFACE GRAVITY WAVE TRAINS .....		579
	<i>Carl Trygve Stansberg</i>	
Chapter 44		
SHEAR STRESSES AND MEAN FLOW IN SHOALING AND BREAKING WAVES .....		594
	<i>Marcel J.F. Stive, Huib J. De Vriend</i>	

Chapter 45	
PREDICTION OF THE MAXIMUM WAVE ON THE CORAL FLAT .....	609
<i>Dede M. Sulaiman, Shigeaki Tsutsui, Hiroshi Toshioka,</i>	
<i>T. Yamashita, S. Oshiro, Y. Tsuchiya</i>	
Chapter 46	
DEVELOPMENT OF A SUBMERGED DOPPLER-TYPE DIRECTIONAL	
WAVE METER .....	624
<i>Tomotsuka Takayama, Noriaki Hashimoto, Toshihiko Nagai,</i>	
<i>Tomoharu Takahashi, Hiroshi Sasaki, Yoshiki Ito</i>	
Chapter 47	
BRAGG SCATTERING OF WAVES OVER POROUS RIPPLED BED .....	635
<i>Hijime Mase, Ken Takeba</i>	
Chapter 48	
NON-REFLECTIVE MULTI-DIRECTIONAL WAVE GENERATION	
BY SOURCE METHOD .....	650
<i>Masahiro Tanaka, Takumi Ohyama, Tetsushi Kiyokawa, Kazuo Nadaoka</i>	
Chapter 49	
THE GROWTH OF WIND WAVES IN SHALLOW WATER .....	665
<i>L.A. Verhagen, I.R. Young</i>	
Chapter 50	
ESTIMATION OF TYPHOON-GENERATED MAXIMUM WAVE	
HEIGHT ALONG THE PACIFIC COAST OF JAPAN BASED ON	
WAVE HINDCASTING .....	674
<i>Masataka Yamaguchi, Yoshio Hatada</i>	
Chapter 51	
RUN-UP OF IRREGULAR WAVES ON A GENTLY SLOPING BEACH .....	689
<i>Yoshimichi Yamamoto, Katsutoshi Tanimoto, Karunarathna Harshinie</i>	
Chapter 52	
SOLITON-MODE WAVEMAKER THEORY AND SYSTEM FOR	
COASTAL WAVES .....	704
<i>Takashi Yasuda, Takeshi Hattori, Seirou Shinoda</i>	
Chapter 53	
ON A METHOD FOR ESTIMATING REFLECTION COEFFICIENT	
IN SHORT-CRESTED RANDOM SEAS .....	719
<i>Hirumune Yokoki, Masahiko Isobe, Akira Watanabe</i>	

Chapter 54	
THE DIRECTIONAL WAVE SPECTRUM IN THE BOHAI SEA.....	731
<i>Yuxiu Yu, Shuxue Liu</i>	

Chapter 55	
IRREGULAR WAVES OVER AN ELLIPTIC SHOAL.....	746
<i>Xiping Yu, Hiroyoshi Togashi</i>	

Chapter 56	
PERFORMANCE OF A SPECTRAL WIND-WAVE MODEL IN SHALLOW WATER.....	761
<i>Gerbrant Ph. van Vledder, John G. de Ronde, Marcel J.F. Stive</i>	

## PART II

Chapter 57	
THE GENERATION OF LOW-FREQUENCY WAVES BY A SINGLE WAVE GROUP INCIDENT ON A BEACH.....	776
<i>Gary Watson, Timothy C.D. Barnes, D. Howell Peregrine</i>	

Chapter 58	
INFLUENCE OF LONG WAVES ON SHIP MOTIONS IN A LAGOON HARBOUR.....	791
<i>Volker Barthel, Etienne Mansard</i>	

Chapter 59	
RESONANT FORCING OF HARBORS BY INFRAGRAVITY WAVES.....	806
<i>Gordon S. Harkins, Michael J. Briggs</i>	

Chapter 60	
NUMERICAL SIMULATION OF THE 1992 FLORES TSUNAMI IN INDONESIA: DISCUSSION ON LARGE RUNUP HEIGHTS IN THE NORTHEASTERN FLORES ISLAND.....	821
<i>Fumihiko Imamura, Tomoyuki Takahashi, Nobuo Shuto</i>	

Chapter 61	
A COMPARATIVE EVALUATION OF WAVE GROUPING MEASURES.....	832
<i>E.P.D. Mansard, S.E. Sand</i>	

Chapter 62	
RELATIONSHIP OF A MOORED VESSEL IN A HARBOUR AND LONG WAVE CAUSED BY WAVE GROUPS.....	847
<i>Toshihiko Nagai, N. Hashimoto, T. Asai, I. Tobiki, K. Ito, T. Toue, A. Kobayashi, T. Shibata</i>	

Chapter 63	
COHERENT STRUCTURE OF TIDAL TURBULENCE IN A ROTATING SYSTEM OF OSAKA-BAY .....	861
<i>Tsukasa Nishimura, Tomonao Kobayashi, Goichi Furuta</i>	

Chapter 64	
DEVELOPMENT OF A PARTIALLY THREE-DIMENSIONAL MODEL FOR SHIP MOTION IN A HARBOR WITH ARBITRARY BATHYMETRY .....	871
<i>Takumi Ohyama, M. Tsuchida</i>	

Chapter 65	
THE MEASURED AND COMPUTED HOKKAIDO NANSEI-OKI EARTHQUAKE TSUNAMI OF 1993 .....	886
<i>Tomoyuki Takahashi, Nobuo Shuto, Fumihiko Imamura, Hideo Matsutomi</i>	

Chapter 66	
QUASI-THREE-DIMENSIONAL MODEL FOR STORM SURGES AND ITS VERIFICATION .....	901
<i>Takao Yamashita, Yoshito Tsuchiya, Hiroshi Yoshioka</i>	

### PART III

Chapter 67	
ANALYSIS OF PRACTICAL RUBBLE MOUNDS .....	918
<i>N.W.H. Allsop, R.J. Jones, P. Besley, C. Franco</i>	

Chapter 68	
FRICTION AND CLAMPING FORCES IN WAVE LOADED PLACED BLOCK REVETMENTS .....	932
<i>Adam Bezuijen</i>	

Chapter 69	
A FIELD EXPERIMENT ON THE INTERACTION WAVES-REFLECTING WALL .....	945
<i>Paolo Boccotti</i>	

Chapter 70	
THE APPLICATION OF LOAD-CELL TECHNIQUE IN THE STUDY OF ARMOUR UNIT RESPONSES TO IMPACT LOADS .....	958
<i>Hans F. Burcharth, Zhou Liu</i>	



Chapter 71	
STEEP WAVE DIFFRACTION BY A SUBMERGED CYLINDER.....	973
<i>J.T. Aquije Chacaltana, A.F.T. da Silva</i>	
Chapter 72	
WAVE STRESSES ON RUBBLE-MOUND ARMOUR .....	986
<i>Andrew M. Cornett, Etienne Mansard</i>	
Chapter 73	
DAMAGE ANALYSIS FOR RUBBLE-MOUND BREAKWATERS .....	1001
<i>Michael H. Davies, Etienne P.D. Mansard, Andrew M. Cornett</i>	
Chapter 74	
NUMERICALLY MODELING PERSONNEL DANGER ON A PROMENADE BREAKWATER DUE TO OVERTOPPING WAVES .....	1016
<i>Kimihiko Endoh, Shigeo Takahashi</i>	
Chapter 75	
WAVE OVERTOPPING ON VERTICAL AND COMPOSITE BREAKWATERS.....	1030
<i>L. Franco, M. de Gerloni, J.W. van der Meer</i>	
Chapter 76	
AN INVESTIGATION OF THE WAVE FORCES ACTING ON BREAKWATER HANDRAILS .....	1046
<i>Atsushi Hujii, Shigeo Takahashi, Kimihiko Endoh</i>	
Chapter 77	
RUBBLE MOUND BREAKWATER STABILITY UNDER OBLIQUE WAVES: AN EXPERIMENTAL STUDY .....	1061
<i>J.-C. Galland</i>	
Chapter 78	
WAVE LOADS ON SEADYKES WITH COMPOSITE SLOPES & BERMS .....	1075
<i>Joachim Grune, Hendrik Bergmann</i>	
Chapter 79	
COMPUTERISED METHODOLOGY TO MEASURE RUBBLE MOUND BREAKWATER DAMAGE .....	1090
<i>Bruno Chilo, Franco Guiducci</i>	

Chapter 80	
WAVE BREAKING OVER PERMEABLE SUBMERGED BREAKWATERS .....	1101
<i>Masataro Hattori, Hiroyoki Sakai</i>	
Chapter 81	
WAVE FORCES ACTING ON A VORTEX EXCITED VIBRATING	
VERTICAL CYLINDER IN WAVES .....	1115
<i>Kenjirou Hayashi, Futoshi Higaki, Koji Fujima,</i>	
<i>Toshiyuki Sigemura, John R. Chaplin</i>	
Chapter 82	
OVERTOPPING OF SEA WALLS UNDER RANDOM WAVES .....	1130
<i>D.M. Herbert, N.W.H. Allsop, M.W. Owen</i>	
Chapter 83	
STABILITY OF HIGH-SPECIFIC GRAVITY ARMOR BLOCKS .....	1143
<i>Masahiro Ito, Y. Iwagaki, H. Murakami, K. Nemoto, M. Yamamoto,</i>	
<i>M. Hanzawa</i>	
Chapter 84	
ROCK ARMoured BEACH CONTROL STRUCTURES ON	
STEEP BEACHES .....	1157
<i>R.J. Jones, N.W.H. Allsop</i>	
Chapter 85	
EFFECT ON ROUGHNESS TO IRREGULAR WAVE RUN-UP.....	1169
<i>Jea-Tzyy Juang</i>	
Chapter 86	
WAVE OVERTOPPING OF BREAKWATERS UNDER OBLIQUE WAVES.....	1182
<i>Jørgen Juhl, Peter Sloth</i>	
Chapter 87	
CONSTRUCTION OF OFFSHORE FISHING PORT FOR PREVENTION	
OF COASTAL EROSION .....	1197
<i>Takeshi Kawaguchi, O. Hashimoto, T. Mizumoto, A. Kamata</i>	
Chapter 88	
TOPOGRAPHICAL CHANGE AROUND MULTIPLE LARGE	
CYLINDRICAL STRUCTURES UNDER WAVE ACTIONS.....	1212
<i>Chang-Je Kim, Koichiro Iwata, Yoshihito Miyaike, Hong-Sun Yu</i>	

Chapter 89	
STABILITY OF RUBBLE MOUND FOUNDATIONS OF COMPOSITE BREAKWATERS UNDER OBLIQUE WAVE ATTACK .....	1227
<i>Katsutoshi Kimura, Shigeo Takahashi, Katsutoshi Tanimoto</i>	
Chapter 90	
ANALYSIS OF NONLINEAR COEFFICIENTS OF REFLECTION AND TRANSMISSION OF WAVES PROPAGATING OVER A RECTANGULAR STEP .....	1241
<i>Wudhipong Kittitanasuan, Yoshimi Goda</i>	
Chapter 91	
OSCILLATORY MOTIONS AND PERMANENT DISPLACEMENTS OF CAISSON BREAKWATERS SUBJECT TO IMPULSIVE BREAKING WAVE LOADS.....	1255
<i>P. Klammer, H. Oumeraci, H.-W. Partenscky</i>	
Chapter 92	
HYDRAULIC CHARACTERISTICS AND FIELD EXPERIENCE OF NEW WAVE DISSIPATING CONCRETE BLOCKS (ACCROPODE) .....	1269
<i>Masanori Kobayashi, Sumio Kaihatsu</i>	
Chapter 93	
EXPERIMENTAL STUDY ON DEVELOPING PROCESS OF LOCAL SCOUR AROUND A VERTICAL CYLINDER.....	1284
<i>Tomonao Kobayashi, Kenji Oda</i>	
Chapter 94	
WAVE-INDUCED UPLIFT LOADING OF CAISSON BREAKWATERS .....	1298
<i>Andreas Kortenhaus, Hocine Oumeraci, Søren Kohlhase, Peter Klammer</i>	
Chapter 95	
LINEAR AND NONLINEAR WAVE FORCES EXERTED ON A SUBMERGED HORIZONTAL PLATE.....	1312
<i>Haruyuki Kojima, A. Yoshida, T. Nakamura</i>	
Chapter 96	
MODERN FUNCTIONAL DESIGN OF GROIN SYSTEMS.....	1327
<i>Nicholas C. Kraus, Hans Hanson, Sten H. Blomgren</i>	
Chapter 97	
RESHAPING BREAKWATERS IN DEEP AND SHALLOW WATER CONDITIONS.....	1343
<i>A. Lamberti, G.R. Tomasicchio, F. Guiducci</i>	

Chapter 98	
DESIGN OF BREAKWATERS AND BEACH NOURISHMENT .....	1359
<i>Christian Laustrup, Holger Toxvig Madsen</i>	
Chapter 99	
CIRCULAR CHANNEL BREAKWATER TO REDUCE WAVE OVERTOPPING AND ALLOW WATER EXCHANGE .....	1373
<i>Dal Soo Lee, Woo Sun Park, Nobuhisa Kobayashi</i>	
Chapter 100	
INCREASED DOLOS STRENGTH BY SHAPE MODIFICATION .....	1388
<i>S.A. Luger, D.T. Phelp, A. Van Tonder, A.H. Holtzhausen</i>	
Chapter 101	
INFLUENCE OF WAVE DIRECTIONALITY ON STABILITY OF BREAKWATER HEADS.....	1397
<i>Y. Matsumi, E.P.D. Mansard, J. Rutledge</i>	
Chapter 102	
COST-EFFECTIVENESS OF D-ARMOR BREAKWATER.....	1412
<i>Josep R. Medina</i>	
Chapter 103	
THE CORE-LOC: OPTIMIZED CONCRETE ARMOR.....	1426
<i>Jeffrey A. Melby, George F. Turk</i>	
Chapter 104	
STABILITY OF ARMOR STONES OF A SUBMERGED WIDE-CROWN BREAKWATER .....	1439
<i>Norimi Mizutani, Teofilo Monge Rufin, Jr., Koichiro Iwata</i>	
Chapter 105	
WAVE INDUCED FLOW AROUND SUBMERGED SLOPING PLATES .....	1454
<i>Hitoshi Murakami, Sadahiko Itoh, Yoshihiko Hosoi, Yoshiyuki Sawamura</i>	
Chapter 106	
SECOND-ORDER WAVE INTERACTION WITH ARRAYS OF VERTICAL CYLINDERS OF ARBITRARY CROSS SECTION .....	1469
<i>Keisuke Murakami, Akinori Yoshida</i>	
Chapter 107	
HYDRODYNAMIC FORCES ON BOTTOM-SEATED HEMISPHERE IN WAVES AND CURRENTS.....	1484
<i>Hidenori Nishida, A. Tada, F. Nishihira</i>	

Chapter 108	
THE PRESSURE FIELD DUE TO STEEP WATER WAVES INCIDENT ON A VERTICAL WALL .....	1496
<i>D.H. Peregrine, M.E. Topliss</i>	
Chapter 109	
RESULTS OF EXTENSIVE FIELD MONITORING OF DOLOS BREAKWATERS.....	1511
<i>D. Phelps, S. Luger, A. Van Tonder, A. Holtzhausen</i>	
Chapter 110	
FAILURE OF RUBBLE MOUND STRUCTURES DUE TO THE STORM DURATION AND THE IRREGULARITY OF OCEAN WAVES .....	1526
<i>Cheong-Ro Ryu, Hyeon-Ju Kim</i>	
Chapter 111	
BLOCK SUBSIDENCE UNDER PRESSURE AND FLOW .....	1541
<i>T. Sakai, H. Gotoh, T. Yamamoto</i>	
Chapter 112	
STABILITY OF ROCK ON BEACHES.....	1553
<i>Gerrit J. Schiereck, Henri L. Fontijn, Wout V. Grote, Paul G.J. Sijstermans</i>	
Chapter 113	
SHORT TERM WAVE OVERTOPPING RATE OF BLOCK ARMORED SEAWALL .....	1568
<i>Tsunehiro Sekimoto, Hiroshi Kunisu, Tsuyoshi Yamazaki</i>	
Chapter 114	
ESTIMATING THE SLIDING DISTANCE OF COMPOSITE BREAKWATERS DUE TO WAVE FORCES INCLUSIVE OF IMPULSIVE FORCES .....	1580
<i>Kenichiro Shimosako, S. Takahashi, K. Tanimoto</i>	
Chapter 115	
BED SHEAR STRESS AND SCOUR AROUND COASTAL STRUCTURES .....	1595
<i>B.M. Sumer, J. Fredsøe, N. Christiansen, S.B. Hansen</i>	
Chapter 116	
LABORATORY MEASUREMENT OF OBLIQUE IRREGULAR WAVE REFLECTION ON RUBBLE-MOUND BREAKWATERS.....	1610
<i>Charles Teisson, Michel Benoit</i>	

Chapter 117	
STONE MOVEMENT ON A RESHAPED PROFILE .....	1625
<i>G. Roberto Tomasicchio, A. Lamberti, F. Guiducci</i>	
Chapter 118	
THE LARGE SCALE DOLOS FLUME STUDY.....	1641
<i>George F. Turk, Jeffrey A. Melby</i>	
Chapter 119	
H <sub>0</sub> PARAMETER FOR PRELIMINARY DESIGN OF CONVENTIONAL BREAKWATER STRUCTURAL HEAD: DATA ANALYSIS OF SPANISH NORTH COAST HARBOURS .....	1657
<i>Vincente Negro Valdecantos, Ovidio Varela Carnero</i>	
Chapter 120	
NUMERICAL MODELLING OF BREAKING WAVE IMPACTS ON A VERTICAL WALL .....	1672
<i>N.T. Wu, H. Oumeraci, H.-W. Partenscky</i>	
Chapter 121	
WIND EFFECTS ON RUNUP AND OVERTOPPING.....	1687
<i>Donald L. Ward, Christopher G. Wibner, Jun Zhang, Billy L. Edge</i>	
Chapter 122	
MODELLING OF WAVE OVERTOPPING OVER BREAKWATER.....	1700
<i>F. Zhuang, C. Chang, J.J. Lee</i>	
Chapter 123	
STRESSES IN TETRAPOD ARMOR UNITS INDUCED BY WAVE ACTION....	1713
<i>Kees d'Angremond, J.W. van der Meer, C.P. van Nes</i>	
Chapter 124	
PORE PRESSURES IN RUBBLE MOUND BREAKWATERS.....	1727
<i>M.B. de Groot, H. Yamazaki, M.R.A. van Gent, Z. Kheyruri</i>	
Chapter 125	
WAVE ACTION ON AND IN PERMEABLE STRUCTURES.....	1739
<i>M.R.A. van Gent, P. Tönjes, H.A.H. Petit, P. Van Den Bosch</i>	
Chapter 126	
PROBABILISTIC CALCULATIONS OF WAVE FORCES ON VERTICAL STRUCTURES.....	1754
<i>J.W. van der Meer, K. d'Angremond, J. Juhl</i>	

## PART IV

Chapter 127	
VELOCITY AND PRESSURE BOUNDARY CONDITIONS FOR FLOW OVER THE PERMEABLE BOUNDARY OF A POROUS MEDIUM.....	1770
<i>Ismail Aydin</i>	
Chapter 128	
PHYSICAL EXPERIMENTS ON THE EFFECTS OF GROINS ON SHORE MORPHOLOGY.....	1782
<i>Peyman Badiei, J. William Kamphuis, David G. Hamilton</i>	
Chapter 129	
LINE-MODELING OF SHOREFACE NOURISHMENT .....	1797
<i>Willem T. Bakker, Nico F. Kersting, Hanz D. Niemeyer</i>	
Chapter 130	
STATISTICAL VARIATIONS IN BEACH PARAMETER CHANGE RATES FOR WALLED & NON-WALLED PROFILES AT SANDBRIDGE, VA.....	1812
<i>John M. Hazelton, David R. Basco, D. Bellomo, G. Williams</i>	
Chapter 131	
A BOTTOM BOUNDARY LAYER SEDIMENT RESPONSE TO WAVE GROUPS .....	1827
<i>J. Lee, S. O'Neil, K. Bedford, R. Van Evra</i>	
Chapter 132	
GEOMORPHOLOGICAL ANALYSIS OF A BEACH AND SANDBAR SYSTEM.....	1837
<i>Chen-Shan Kung, Marcer Stive, Geffery Toms</i>	
Chapter 133	
SUSPENDED SEDIMENT TRANSPORT IN INNER SHELF WATERS DURING EXTREME STORMS.....	1849
<i>O.S. Madsen, T.A. Chisholm, L.D. Wright</i>	
Chapter 134	
SEA BED STABILITY ON A LONG STRAIGHT COAST.....	1865
<i>E. Christensen, R. Deigaard, J. Fredsoe</i>	
Chapter 135	
THE RESPONSE OF GRAVEL BEACHES IN THE PRESENCE OF CONTROL STRUCTURES .....	1880
<i>T.T. Coates, N. Dodd</i>	

Chapter 136	
THE ROLE OF ROLLERS IN SURF ZONE CURRENTS.....	1895
<i>William R. Dally, Daniel A. Osiecki</i>	
Chapter 137	
THREE DIMENSIONAL MORPHOLOGY IN A NARROW WAVE TANK: MEASUREMENTS AND THEORY .....	1906
<i>Robert G. Dean, Tae-Myoung Oh</i>	
Chapter 138	
NUMERICAL SIMULATION OF FINITE AMPLITUDE SHEAR WAVES & SEDIMENT TRANSPORT .....	1919
<i>Rolf Deigaard, Erik Damgaard Christensen, Jesper Svarrer Damgaard, Jørgen Fredsøe</i>	
Chapter 139	
BEACH NOURISHMENT AND DUNE PROTECTION.....	1934
<i>Hans H. Dette, Arved J. Raudkivi</i>	
Chapter 140	
PROFILE CHANGE OF A SHEET FLOW DOMINATED BEACH.....	1946
<i>Mohammad Dibajnia, Takuzo Shimizu, Akira Watanabe</i>	
Chapter 141	
A NONLINEAR SURF BEAT MODEL.....	1961
<i>Zhili Zou, Nicholas Dodd</i>	
Chapter 142	
PIV MEASUREMENTS OF OSCILLATORY FLOW OVER A RIPPLED BED....	1975
<i>H.C. Earnshaw, T. Bruce, C.A. Greated, W.J. Easson</i>	
Chapter 143	
SHEAR INSTABILITY OF LONGSHORE CURRENTS: EFFECTS OF DISSIPATION AND NON-LINEARITY .....	1983
<i>Albert Falqués, Vicente Iranzo, Miquel Caballería</i>	
Chapter 144	
INTERPRETATION OF SHORELINE POSITION FROM AERIAL PHOTOGRAPHS .....	1998
<i>John S. Fisher, Margery F. Overton</i>	



Chapter 145	
SETTLING COLUMNS PARAMETRIC TESTS APPLIED TO COASTAL SEDIMENT CONSOLIDATION.....	2004
<i>Stephane Gallois, Alain Alexis, Pierre Thomas</i>	
Chapter 146	
SEDIMENT-CLOUD BASED MODEL OF SUSPENSION OVER RIPPLE BED DUE TO WAVE ACTION .....	2013
<i>Hitoshi Gotoh, Tetsuro Tsujimoto, Hiroji Nakagawa</i>	
Chapter 147	
WAVE OVERTOPPING AND SEDIMENT TRANSPORT OVER DUNES.....	2028
<i>Mark W. Hancock, Nobuhisa Kobayashi</i>	
Chapter 148	
SEDIMENT TRANSPORT OVER RIPPLES IN WAVES AND CURRENT .....	2043
<i>Gilles Perrier, Erik Asp Hansen, C. Villaret, Rolf Deigaard, Jorgen Fredsøe</i>	
Chapter 149	
IN-SITU DETERMINATION OF THE CRITICAL BED-SHEAR STRESS FOR EROSION OF COHESIVE SEDIMENTS.....	2058
<i>Erik-Jan Houwing, Leo C. van Rijn</i>	
Chapter 150	
CONTROL OF CROSS-SHORE SEDIMENT TRANSPORT BY A DISTORTED RIPPLE MAT.....	2070
<i>Isao Irie, N. Ono, S. Hashimoto, S. Nakamura, K. Murakami</i>	
Chapter 151	
HOW MUCH VELOCITY INFORMATION IS NECESSARY TO PREDICT SEDIMENT SUSPENSION IN THE SURF ZONE? .....	2085
<i>Bruce E. Jaffe, David M. Rubin, Asbury Sallenger, Jr.</i>	
Chapter 152	
BEACH PROFILE SPACING: PRACTICAL GUIDANCE FOR MONITORING NOURISHMENT PROJECTS.....	2100
<i>Timothy W. Kana, Christopher J. Andrassy</i>	
Chapter 153	
WATERTABLE OVERHEIGHT DUE TO WAVE RUNUP ON A SANDY BEACH.....	2115
<i>Hong-Yoon Kang, P. Nielsen, D.J. Hanslow</i>	

Chapter 154	
A MODEL FOR CROSS SHORE SEDIMENT TRANSPORT .....	2125
<i>Irene Katopodi, Nikos Kitou</i>	
Chapter 155	
NUMERICAL MODELLING OF FLOW OVER RIPPLES USING SOLA METHOD.....	2140
<i>Hyoseob Kim, Brian A. O'Connor, Youngbo Shim</i>	
Chapter 156	
SWASH DYNAMICS UNDER OBLIQUELY INCIDENT WAVES .....	2155
<i>Nobuhisa Kobayashi, Entin A. Karjadi</i>	
Chapter 157	
WAVE RUN-UP AND SEA CLIFF EROSION .....	2170
<i>S.-M. Shih, P. Komar, K.J. Tillotson, W.G. McDougal, P. Ruggiero</i>	
Chapter 158	
MEASUREMENT OF PARAMETERS, DIRECTION AND RATE OF BEDFORM MIGRATION .....	2185
<i>Ruben D. Kos'yan, I.S. Podymov</i>	
Chapter 159	
BREACH-GROWTH RESEARCH PROGRAMME AND ITS PLACE IN DAMAGE ASSESSMENT FOR A POLDER.....	2197
<i>Arie W. Kraak, W.T. Bakker, J. van de Graaff, H.J. Steetzel, P.J. Visser</i>	
Chapter 160	
SWASH ZONE WAVE CHARACTERISTICS FROM SUPERTANK .....	2207
<i>David L. Kriebel</i>	
Chapter 161	
MORPHOLOGICAL MONITORING OF A SHOREFACE NOURISHMENT NOURTEC EXPERIMENT AT TERSCHELLING, THE NETHERLANDS.....	2222
<i>Aart Kroon, Piet Hoekstra, Klass Houwman, Gerben Ruessink</i>	
Chapter 162	
NUMERICAL MODEL FOR LONGSHORE CURRENT DISTRIBUTION ON A BAR-TROUGH BEACH .....	2237
<i>Yoshiaki Kuriyama</i>	

Chapter 163	
PREDICTION OF BEACH PROFILE CHANGE AT MESOSCALE UNDER RANDOM WAVES .....	2252
<i>Magnus Larson</i>	
Chapter 164	
A QUASI-3D SURF ZONE MODEL .....	2267
<i>Jung Lyul Lee, Hsiang Wang</i>	
Chapter 165	
QUANTIFICATION OF LONGSHORE TRANSPORT IN THE SURF ZONE ON MACROTIDAL BEACHES .....	2282
<i>Franck Levoy, Olivier Monfort, Helene Rousset, Claude Larssonneur</i>	
Chapter 166	
A THREE DIMENSIONAL MODEL FOR WAVE INDUCED CURRENTS .....	2297
<i>Bin Li, Roger J. Maddrell</i>	
Chapter 167	
INFLUENCE OF OFFSHORE BANKS ON THE ADJACENT COAST .....	2311
<i>N.J. MacDonald, B.A. O'Connor</i>	
Chapter 168	
WAVE RUNUP ON COMPOSITE-SLOPE AND CONCAVE BEACHES .....	2325
<i>Robert H. Mayer, D.L. Kriebel</i>	
Chapter 169	
SIMULATION OF NEARSHORE WAVE CURRENT INTERACTION BY COUPLING A BOUSSINESQ WAVE MODEL WITH A 3D HYDRODYNAMIC MODEL .....	2340
<i>Roberto Mayerle, Andreas Schröter, Werner Zielke</i>	
Chapter 170	
EXPERIMENTAL RESULTS OF WAVE TRANSFORMATION ACROSS A SLOPING BEACH.....	2350
<i>Constantine D. Memos</i>	
Chapter 171	
A RELATIVE INTERCOMPARISON BETWEEN VARIABLE WAVE SHOALING, BREAKING AND TRANSITION ZONE FORMULATIONS .....	2365
<i>G.P. Mocke, F. Smit</i>	

Chapter 172	
ANALYSIS OF COASTAL PROCESSES AT TORONTO ISLANDS.....	2380
<i>R.B. Nairn, R.D. Scott, C.D. Anglin, P.J. Zuzek</i>	
Chapter 173	
STABILITY AND MANAGEMENT OF AN ARTIFICIAL BEACH.....	2395
<i>Naofumi Shiraishi, Hoiku Ohhama, Taiji Endo,</i> <i>Patricia G. Pena-Santana</i>	
Chapter 174	
SUSPENDED SEDIMENT PARTICLE MOTION IN COASTAL FLOWS.....	2406
<i>Peter Nielsen</i>	
Chapter 175	
LONG-TERM MORPHODYNAMICAL DEVELOPMENT OF THE EAST FRISIAN ISLANDS AND COAST .....	2417
<i>Hanz D. Niemeyer</i>	
Chapter 176	
FIELD OBSERVATION AND NUMERICAL SIMULATION OF BEACH AND DUNE SCARPS.....	2434
<i>Ryuichiro Nishi, Michio Sato, Hsiang Wang</i>	
Chapter 177	
EFFECTS OF CONTROLLED WATER TABLE ON BEACH PROFILE DYNAMICS .....	2449
<i>Tae-Myoung Oh, R.G. Dean</i>	
Chapter 178	
LABORATORY EXPERIMENTS ON 3-D NEARSHORE CURRENTS AND A MODEL WITH MOMENTUM FLUX BY BREAKING WAVES.....	2461
<i>Akio Okayasu, Koji Hara, Tomoya Shibayama</i>	
Chapter 179	
SUSPENDED SEDIMENT CAUSED BY WAVES AND CURRENTS .....	2476
<i>Masanobu Ono, Kyu Han Kim, Toru Sawaragi, Ichiro Deguchi</i>	
Chapter 180	
DEVELOPMENT OF A DUNE EROSION MODEL USING SUPER TANK DATA.....	2488
<i>Margery F. Overton, John S. Fisher, Kyu-Nam Hwang</i>	

Chapter 181	
NUMERICAL MODELLING OF THREE-DIMENSIONAL WAVE-DRIVEN CURRENTS IN THE SURF-ZONE.....	2503
<i>Philippe Péchon, Charles Teisson</i>	
Chapter 182	
SEDIMENT TRANSPORT IN VARIOUS TIME SCALES .....	2513
<i>Zbigniew Pruszek, Ryszard B. Zeidler</i>	
Chapter 183	
SEDIMENT TRANSPORT UNDER (NON)-LINEAR WAVES AND CURRENTS .....	2527
<i>Jan S. Ribberink, Irene Katopodi, Khaled A.H. Ramadan, Ria Koelewijn, Sandro Longo</i>	
Chapter 184	
WAVES AND CURRENTS AT THE EBRO DELTA SURF ZONE: MEASUREMENTS AND MODELLING .....	2542
<i>A. Rodriguez, A. Sánchez-Arcilla, F.R. Collado, V. Gracia, M.G. Coussirat, J. Prieto</i>	
Chapter 185	
A NUMERICAL SIMULATION OF BEACH EVOLUTION BASED ON A NONLINEAR DISPERSIVE WAVE-CURRENT MODEL .....	2557
<i>Shinji Sato, Michael B. Kabiling</i>	
Chapter 186	
AN EXPERIMENTAL STUDY ON BEACH TRANSFORMATION DUE TO WAVES UNDER THE OPERATION OF COASTAL DRAIN SYSTEM.....	2571
<i>Michio Sato, Sadakatsu Hata, Masahiro Fukushima</i>	
Chapter 187	
WAVE BREAKING AND INDUCED NEARSHORE CIRCULATIONS .....	2583
<i>Ole R. Sørensen, Hemming A. Schäffer, Per A Madsen, Rolf Deigaard</i>	
Chapter 188	
ACCURACY AND APPLICABILITY OF THE SPM LONGSHORE TRANSPORT FORMULA.....	2595
<i>J.S. Schoones, A.K. Theron</i>	

Chapter 189	
FIELD VERIFICATION OF A NUMERICAL MODEL OF BEACH TOPOGRAPHY CHANGE DUE TO NEARSHORE CURRENTS, UNDERTOW AND WAVES .....	2610
<i>Takuzo Shimizu, Masahito Tsuru, Akira Watanabe</i>	
Chapter 190	
AN ATTEMPT TO MODEL LONGSHORE SEDIMENT TRANSPORT ON THE CATALONIAN COAST .....	2625
<i>J.P. Sierra, A.I. Presti, A. Sánchez-Arcilla</i>	
Chapter 191	
EROSION AND OVERTOPPING OF A GRASS DIKE LARGE SCALE MODEL TESTS .....	2639
<i>G.M. Smith, J.W.W. Seiffert, J.W. van der Meer</i>	
Chapter 192	
CALCULATION OF TOMBOLO IN SHORELINE NUMERICAL MODEL.....	2653
<i>Kyung Duck Suh, C. Scott Hardaway, Jr.</i>	
Chapter 193	
BEACH IMPROVEMENT SCHEMES IN FALSE BAY .....	2668
<i>D.H. Swart, J.S. Schoonees</i>	
Chapter 194	
BEACH EROSION IN KUTA BEACH, BALI & ITS STABILIZATION .....	2683
<i>Abdul R. Syamsudin, Yoshito Tsuchiya, Takao Yamashita</i>	
Chapter 195	
FUNDAMENTAL CHARACTERISTICS OF A NEW WAVE ABSORBING SYSTEM UTILIZING SAND LIQUEFACTION .....	2698
<i>Shigeo Takahashi, S. Yamamoto, H. Miura</i>	
Chapter 196	
LABORATORY STUDY OF SURF-ZONE TURBULENCE ON A BARRED BEACH .....	2712
<i>Francis C.K. Ting</i>	
Chapter 197	
BEACH EROSION AROUND A SAND SPIT—AN EXAMPLE OF MIHONO-MATSUBARA SAND SPIT .....	2726
<i>Takaaki Uda, Koji Yamamoto</i>	

Chapter 198	
SHORECIRC: A QUASI 3-D NEARSHORE MODEL .....	2741
<i>A.R. Van Dongeren, F.E. Sancho, I.A. Svendsen, U. Putrevu</i>	
Chapter 199	
A MODEL FOR BREACH GROWTH IN SAND-DIKES .....	2755
<i>Paul J. Visser</i>	
Chapter 200	
SCALING EFFECTS ON BEACH RESPONSE PHYSICAL MODEL .....	2770
<i>Xu Wang, Li-Hwa Lin, Hsiang Wang</i>	
Chapter 201	
A NUMERICAL MODEL OF BEACH CHANGE DUE TO SHEET-FLOW .....	2785
<i>Akira Watanabe, Kazuhiko Shiba, Masahiko Isobe</i>	
Chapter 202	
FIELD TESTS OF RADIATION-STRESS ESTIMATORS OF LONGSHORE SEDIMENT-TRANSPORT .....	2799
<i>Thomas E. White</i>	
Chapter 203	
SUSPENDED SEDIMENT CONCENTRATION PROFILES UNDER NON-BREAKING AND BREAKING WAVES .....	2813
<i>Rattanapitikon Winyu, Tomoya Shibayama</i>	
Chapter 204	
MASS TRANSPORT AND ORBITAL VELOCITIES WITH LAGRANGEIAN FRAME OF REFERENCE .....	2828
<i>Stefan Woltering, Karl-Friedrich Daemrich</i>	
Chapter 205	
CROSS-SHORE PROFILE MODELLING UNDER RANDOM WAVES .....	2843
<i>Yongjun Wu, H-H Dette, H. Wang</i>	
Chapter 206	
MULTIPLE BAR FORMATION BY BREAKER-INDUCED VORTICES: A LABORATORY APPROACH .....	2856
<i>Da Ping Zhang, Tsuguo Sunamura</i>	
Chapter 207	
IDENTIFICATION OF SOME RELEVANT PROCESSES IN COASTAL MORPHOLOGICAL MODELLING .....	2871
<i>Hakeem Johnson, Ida Brøker, Julio A. Zyserman</i>	

Chapter 208	
EXPERIMENTAL SHOREFACE NOURISHMENT, TERSCHELLING, (NL) .....	2886
<i>J.P.M. Mulder, J. van de Kreeke, P. van Vessem</i>	

## PART V

Chapter 209	
IMPORTANCE OF PERMEABILITY IN THE SEDIMENTATION CONSOLIDATION PROCESS.....	2902
<i>Alain Alexis, P. Thomas</i>	
Chapter 210	
WAVE-CURRENT INTERACTION WITH MUD BED .....	2913
<i>Nguyen Ngoc An, T. Shibayama</i>	
Chapter 211	
ON RESIDUAL TRANSPORT IN SHALLOW TIDAL BASINS .....	2928
<i>Andrea Balzano</i>	
Chapter 212	
THE EXTENT OF INLET IMPACTS UPON ADJACENT SHORELINES .....	2943
<i>Kevin R. Bodge</i>	
Chapter 213	
THE SPREADING OF DREDGING SPOILS DURING CONSTRUCTION OF THE DENMARK-SWEDEN LINK.....	2958
<i>Ida Brøker, John Johnsen, Morten Lintrup, Anders Jensen, Jacob Steen Møller</i>	
Chapter 214	
EXPERIMENTAL STUDIES ON THE EFFECT OF THE DREDGING ON CHANG-HWA RECLAMATION AREA, TAIWAN .....	2972
<i>Tai-Wen Hsu, Hsien-Kuo Chang</i>	
Chapter 215	
OSCILLATIONS INDUCED BY IRREGULAR WAVES IN HARBOURS .....	2987
<i>C.R. Chou, W.Y. Han</i>	
Chapter 216	
MECHANISM AND ESTIMATION OF SEDIMENTATION IN BANGKOK BAR CHANNEL.....	3002
<i>Ichiro Deguchi, Toru Sawaragi, Masanobu Ono, Sucharit Koontanakulvong</i>	



Chapter 217	
TURBIDITY & SUSPENDED SEDIMENT ASSOCIATED WITH BEACH NOURISHMENT DREDGING .....	3016
<i>Daniel M. Hanes</i>	
Chapter 218	
SOIL MECHANICS OF SHIP BEACHING .....	3030
<i>N.-E. Ottesen Hansen, B.C. Simonsen, M.J. Sterndorff</i>	
Chapter 219	
THE DILUTION PROCESSES OF ALTERNATIVE HORIZONTAL BUOYANT JETS IN WAVE MOTION .....	3045
<i>Hwung-Hweng Hwung, Jih-Ming Chyan, Chen-Yue Chang, Yih-Far Chen</i>	
Chapter 220	
STUDY ON THE BEHAVIORS OF THE COHESIVE SEDIMENT IN THE YANGTZE ESTUARY .....	3060
<i>Xiaochuan Zeng, Yixin Yan, Kai Yen</i>	
Chapter 221	
DISPERSION OF POLLUTION IN A WAVE ENVIRONMENT .....	3071
<i>R. Koole, C. Swan</i>	
Chapter 222	
MODEL OF BIVALVE ON/OFFSHORE MOVEMENT BY WAVES .....	3086
<i>Hisami Kuwahara, Junya Higano</i>	
Chapter 223	
INITIAL GAP IN BREAKOUT OF HALF-BURIED SUBMARINE PIPE DUE TO WAVE ACTION .....	3099
<i>Adrian W.K. Law, M.A. Foda</i>	
Chapter 224	
ANALYTICAL SOLUTION FOR THE WAVE-INDUCED EXCESS PORE-PRESSURE IN A FINITE-THICKNESS SEABED LAYER.....	3111
<i>Waldemar Magda</i>	
Chapter 225	
RESPONSE CHARACTERISTICS OF RIVER MOUTH TOPOGRAPHY IN WIDE TIME SCALE RANGE.....	3126
<i>A. Mano, M. Sawamoto, M. Nagao</i>	

Chapter 226	
HALF-LIFE PERIOD OF SEDIMENTATION—MODEL TEST ON A SCALE 1:1 .....	3139
<i>Helmut Manzenrieder</i>	
Chapter 227	
RISK ASSESSMENT FOR COASTAL AND TIDAL DEFENCE SCHEMES.....	3154
<i>I.C. Meadowcroft, P.H. von Lany, N.W.H. Allsop, D.E. Reeve</i>	
Chapter 228	
WATER OXYGENATION IN THE VICINITY OF COASTAL STRUCTURES DUE TO WAVE BREAKING .....	3167
<i>C.I. Moutzouris, E.I. Daniil</i>	
Chapter 229	
ENVIRONMENTAL ASSESSMENT OF HYPOTHETICAL LARGE-SCALE RECLAMATION IN OSAKA BAY, JAPAN.....	3178
<i>Keiji Nakatsuji, Toshiaki Sueyoshi, Kohji Muraoka</i>	
Chapter 230	
FLOOD AND EROSION CONTROL IN THE CONTEXT OF SEA-LEVEL RISE.....	3193
<i>E. Bart Peerbolte, Herman G. Wind</i>	
Chapter 231	
OFFSHORE BREAKWATERS VERSUS BEACH NOURISHMENTS— A COMPARISON.....	3208
<i>M. Pluijm, J.C. van der Lem, A.W. Kraak, J.H.W. de Ruig</i>	
Chapter 232	
MORPHOLOGICAL MODELLING OF KETA LAGOON CASE .....	3223
<i>J.A. Roelvink, D.J.R. Walstra, Z. Chen</i>	
Chapter 233	
COST-BENEFIT ANALYSIS OF SHORE PROTECTION INVESTMENTS.....	3237
<i>L. Felipe Vila Ruiz, Fernando Bernaldo de Quirós</i>	
Chapter 234	
PARAMETRIZATION FOR CONCEPTUAL MORPHODYNAMIC MODELS OF WADDEN SEA AREAS .....	3251
<i>Ernst Schroeder, R. Goldenbogen, H. Kunz</i>	

Chapter 235	
MUD TRANSPORT AND MUDDY BOTTOM DEFORMATION BY WAVES .....	3266
<i>Daoxian Shen, Masahiko Isobe, Akira Watanabe</i>	
Chapter 236	
WAVE-INDUCED SEDIMENT RESUSPENSION AND MIXING IN SHALLOW WATERS.....	3281
<i>Y. Peter Sheng, X. Chen, E.A. Yassuda</i>	
Chapter 237	
A NUMERICAL MODEL FOR BEACH DEFORMATION AROUND RIVER MOUTH DUE TO WAVES AND CURRENTS.....	3295
<i>Tomoya Shibayama, Akiko Yamada</i>	
Chapter 238	
DEVELOPMENT OF A NUMERICAL SIMULATION METHOD FOR PREDICTING THE SETTLING BEHAVIOR & DEPOSITION CONFIGURATION OF SOIL DUMPED INTO WATERS .....	3305
<i>Kazuki Oda, Takaaki Shigematsu</i>	
Chapter 239	
PLANE DESIGN OF “SPAC”; COUNTERMEASURE AGAINST SEABED SCOUR DUE TO SUBMERGED DISCHARGE AND LARGE WAVES .....	3320
<i>Takao Shimizu, Masaaki Ikeno, Hisayoshi Ujiie, Kazuaki Yamauchi</i>	
Chapter 240	
MODELLING AND ANALYSIS TECHNIQUES TO AID MINING OPERATIONS ON THE NAMIBIAN COASTLINE .....	3335
<i>G.G. Smith, G.P. Mocke, D.H. Swart</i>	
Chapter 241	
ENGINEERING APPROACH TO COASTAL FLOW SLIDES .....	3350
<i>Theo P. Stoutjesdijk, Maarten B. de Groot, Jaap Lindenberg</i>	
Chapter 242	
EROSION OF LAYERED SAND-MUD BEDS IN UNIFORM FLOW.....	3360
<i>Hilde Torfs</i>	
Chapter 243	
STANDING WAVE INDUCED SOIL RESPONSE IN A POROUS SEABED .....	3369
<i>Ching-Piao Tsai, Tsong-Lin Lee</i>	

Chapter 244	
EROSION CONTROL BY CONSIDERING LARGE SCALE COASTAL BEHAVIOR .....	3378
<i>Yoshito Tsuchiya, Takao Yamashita, Tatsuhisa Izumi</i>	
Chapter 245	
SHORELINE EROSION DUE TO OFFSHORE TIN MINING .....	3393
<i>Suphat Vongvisessomjai</i>	
Chapter 246	
BEHAVIORS OF FLUID MUD UNDER OSCILLATORY FLOW .....	3408
<i>Hiroyuki Yamanishi, Tetsuya Kusuda</i>	
Chapter 247	
FORMATION OF HABITATS FOR BIVALVES BY PORT AND HARBOR STRUCTURES .....	3420
<i>Kenji Yano, S. Akeda, Y. Miyamoto, S. Kuwabara</i>	
Chapter 248	
USE OF THREE-DIMENSIONAL HYDRODYNAMICS MODEL FOR TIDAL INLETS STUDIES .....	3432
<i>E.A. Yassuda, Y.P. Sheng</i>	
Chapter 249	
STUDY OF UPWELLING PHENOMENA OF ANOXIC WATER “A-OSHIO” ....	3447
<i>Jong Seong Yoon, Keiji Nakatsuji, Kouji Muraoka</i>	
Chapter 250	
SEA LEVEL RISE AND COAST EVOLUTION IN POLAND .....	3462
<i>Ryszard B. Zeidler</i>	

## PART VI

Chapter 251	
FORMATION OF DYNAMICALLY STABLE SANDY BEACHES ON AMANOHASHIDATE COAST BY SAND BYPASSING .....	3478
<i>Ikuo Chin, Minoru Yamada, Yoshito Tsuchiya</i>	
Chapter 252	
THE RECONSTRUCTION OF FOLLY BEACH .....	3491
<i>Billy L. Edge, Millard Dowd, Robert G. Dean, Patrick Johnson</i>	

Chapter 253	
THE COMPLEMENTARY INTERACTION BETWEEN BEACH NOURISHMENT AND HARBOUR MANAGEMENT: FOUR CASES IN SPAIN .....	3507
<i>Gregorio Gómez-Pina, Jose L. Ramírez</i>	
Chapter 254	
WAVE IMPACTS ON THE EASTERN SCHELDT BARRIER EVALUATION OF 5 YEARS FIELD MEASUREMENTS .....	3522
<i>Leo Klatter, Hans Janssen, Michiel Dijkman</i>	
Chapter 255	
SALINITY & WATER LEVELS IN THE WESER ESTUARY DURING THE LAST HUNDRED YEARS—ANTHROPOGENIC INFLUENCES ON THE COASTAL ENVIRONMENT .....	3533
<i>Hans Kunz</i>	
Chapter 256	
REVIEW OF SOME 30 YEARS BEACH REPLENISHMENT EXPERIENCE AT DUNGENESS NUCLEAR POWER STATION, UK .....	3548
<i>Roger Maddrell, Bill Osmond, Bin Li</i>	
Chapter 257	
PROJECT, WORKS AND MONITORING AT BARCELONA OLYMPIC BEACHES .....	3564
<i>Carlos Peña, Manuel F. Covarsi</i>	
Chapter 258	
SANTA CRISTINA BEACH NOURISHMENT WORKS AND MONITORING PROGRAM .....	3579
<i>Eduardo Toba, G. Gomez-Pina, J. Alvarez</i>	
Chapter 259	
DESIGN & CONSTRUCTION OF AN EXTENDED BERM BREAKWATER AT PORT OF HAINA, DOMINICAN REPUBLIC .....	3594
<i>David W. Yang, Mark H. Lindo, Edward J. Schmeltz, Joaquin Fernandez, Daniel Gomez</i>	
Chapter 260	
REHABILITATION OF THE WEST BREAKWATER— PORT OF SINES .....	3608
<i>Orville T. Magoon, J.R. Weggel, B.L. Edge, E. Mansard, R.W. Whalin, W.F. Baird</i>	

Subject Index .....3615  
Author Index .....3621

## CHAPTER 87

### Construction of Offshore Fishing Port for Prevention of Coastal Erosion

T. Kawaguchi<sup>1</sup>, O. Hashimoto<sup>1</sup>, T. Mizumoto<sup>2</sup>, A. Kamata<sup>2</sup>

#### Abstract

When constructing a small fishing port along sandy beach, the most important considerations are how to prevent sand deposition at the port entrance and beach erosion along the down-drift side of the port. To solve these problems, an offshore fishing port connected to the shore by a bridge was planned at Kunnui, Hokkaido Prefecture. The port was designed to allow littoral drift to pass between the port and the shore. The appropriate shape and offshore distance of the port to restrict the development of tombolo was determined by hydraulic model tests and numerical simulations of wave-induced current near the port. Bottom sounding was carried out in parallel with the construction work. As a result, development of tombolo was restricted to some extent and no serious beach erosion occurred. This port seems to have generated unexpected strong cell-like circular currents on both sides, and sand deposits deposited by these currents. There are, however, no problems at present concerning the shape, offshore distance and location of the port entrance.

#### Introduction

In planning a small fishing port along sandy beach, the most important points to be taken into consideration are how to prevent shoaling of the port entrance by drift sand and how to eliminate adverse effects of the structures on coastal topography such as down stream erosion and excessive accretion at the updrift beach. Movement of sea bottom materials is very active in the littoral zone, and even a small sized fishing port must be designed to avoid littoral sand deposits at the port entrance. Extended breakwaters, however, act as a dam and intercept the flow of sediments, and accretion occurs at the updrift side. This creates in some cases deficiency in material supply to the down coast, where erosion occurs. Out of about 3,000 fishing ports in Japan, seventy five percent are in the category of type I according to Japanese classification, which is small scale, used only by fishermen from several adjoining fishing communities and serving an average of 100 boats less than 3 Gross Tonnages.

---

<sup>1</sup>Construction Div., Fisheries Agencies, Ministry of Agriculture, Forestry and Fisheries. 1-2-1, Kasumigaseki, Chiyoda-Ku, Tokyo 100, JAPAN.

<sup>2</sup>Fishing Port Div., Fisheries Dept., Hokkaido Prefecture, 7, Kita-Sanjyo-Nishi, Chuo-Ku, Sapporo, Hokkaido 060, JAPAN.

The offshore fishing port discussed here was constructed with its entrance out of the surfzone, and thus free of sediment deposition, and connected by a bridge so as to allow littoral drift to pass behind. In case of such a small port, it is not necessary to locate the port very far from the coast, and construction costs are reasonable. The problem is to determine the offshore distance needed to restrict development of tombolo to the extent to allow the passage of drift sand. From this standpoint, this offshore fishing port was planned at Kunnui, in Uchiura Bay, southern part of Hokkaido in 1985 and completed in 1994. This report represents the characteristics of drift sand in the Bay of Uchiura, several investigations to determine the layout of the port, and changes in the bathymetry of the site during the construction.

## Outline of The Project Site Conditions

### Topography

Kunnui fishing port is located at the head of Uchiura Bay along the eastern side of the Oshima Peninsula. As shown in Fig. 1, the bay is almost a circle, 50 km in diameter and 150 km in length along the coastline. The entrance is open to Pacific Ocean at the southeast side and the width of this entrance is 28 km. The bay is roughly divided into three sections from the viewpoint of the geographical, meteorological and oceanographical conditions such as wind, wave and littoral current.

#### ① Northeast Coast

This section is between Muroran and Shizukari, consisting of coastal cliff made of igneous rock which has strong resistance against erosion and narrow coastline between the cliff and sea. The coastline is generally monotonous and slightly concave or bow-shaped.

#### ② Northwest Coast

This section, between Shizukari and Yakumo, is located in front of the bay entrance. The coast is monotonous, bow-shaped and of sand. The particle diameter of sand at the foreshore is almost uniform. This coast is topographically of emergent, caused by land upheaval. Especially between Shizukari and Kunnui, there is a flat coastal plain. Kunnui fishing port is located at around the middle of this coast.

#### ③ Southwest Coast

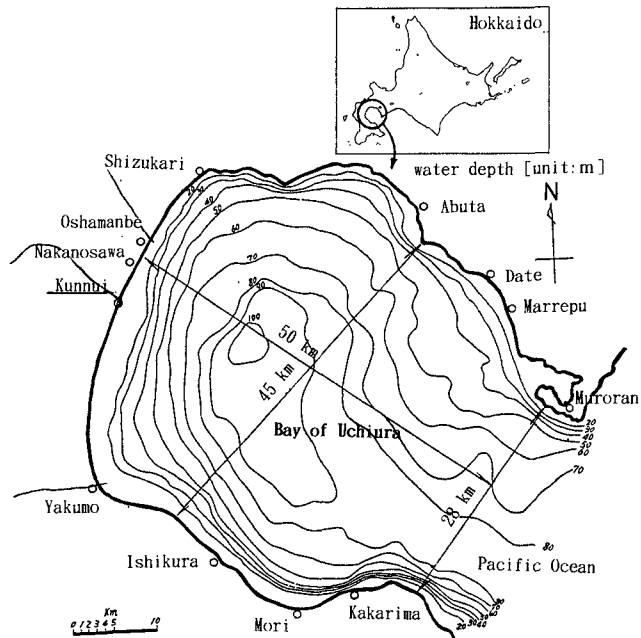


Fig.1 Uchiura Bay



This region, between Yakumo and Mori, has eroding beaches approached by hills. Sandy coast is limited with, one to two kilometers sandy beaches between capes that exist at intervals. Capes are made of sedimentary rock and considerably eroded. Recently, the construction of a coastal seawall is serving to protect and preserve this coast.

**Sea Waves**

In this bay, there is hardly any seasonable change in waves, but there are occasional higher waves caused by typhoons in autumn, and low atmospheric pressures passing through the Sea of Japan in winter.

Along the northwest coast, where Kunnui fishing port is located, principal wave direction is ENE~SE, and mostly at a right angle to the coastline. Wave observation is conducted at Nakanosawa, located 5 kilometers north-north-east of Kunnui. Probability of non-exceedance on wave height and period from 1968 to 1981 are shown in Fig. 2. Waves less than 0.5 m account for 90 percent. Frequency distribution of waves is shown in Fig. 3. This figure indicates predominant wave periods are around 5 sec. and over 9 sec. This shows two types of waves, one generated in the bay and the other from the Pacific Ocean. As shown in Table 1, incident waves range from ENE to SSE, but predominant wave direction is from ESE to SE, and is almost at a right angle to the coastline.

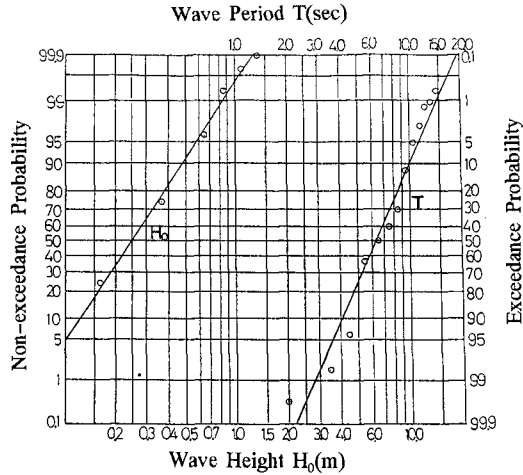


Fig.2 Non-exceedance Probability of Waves (Nakanosawa Observation Point)

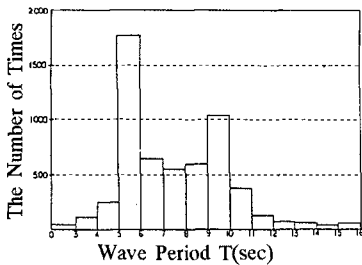


Fig.3 Frequency Distribution of Observed Waves (1968~1981, at Nakanosawa)

Table 1 Wave Height[H] Distribution by Directions (1968~1981, at Nakanosawa)

Wave Height H(m)	Direction					Total
	ENE	E	ESE	SE	SSE	
0.0~0.5	-	39	2157	1889	30	4115
0.5~1.0	-	1	682	736	-	1419
1.0~1.5	70	-	33	11	2	116
1.5~2.0	-	-	3	-	-	3
2.0~2.5	-	-	3	-	-	3
2.5<	-	-	-	-	-	0
Total	70	40	2878	2636	32	5656
%	1.24	0.71	50.88	46.60	0.57	100.00

Average wave height is 0.4 meters, and average wave period is 7.5 sec.

According to the significant design wave investigations for the port conducted by Hokkaido prefecture, maximum yearly wave height is for storm wave coming from the Pacific Ocean, and wave heights with some return periods were obtained by

Table 2 Wave Height with a Return Period of N years

Direction	Return Period of N years		1 year	3 years	5 years	10 years	20 years
E S E	Wave Height	H(m)	2.1	3.7	4.5	5.6	6.8
	Period	T(sec)	6.4	7.8	8.5	9.4	10.4
S E	Wave Height	H(m)	2.9	5.0	5.9	7.0	8.0
	Period	T(sec)	7.1	8.9	9.6	10.6	11.4

Table 3 Equivalent Deepwater Wave

Condition	Direction	Deep Sea Wave		Equivalent Deepwater Wave Height $H_o'$ (m)	Direction	Breaker Depth $h_b$ (m)
		$H_o$ (m)	$T_o$ (sec)			
Ordinal Storm (in 1 year)	E S E	2.1	6.0	1.3	E S E	2.15
	S E	2.9	8.0	1.7	E S E	2.89
Storm (in 20 years)	E S E	6.8	10.0	3.5	E S E	5.67
	S E	8.0	11.0	4.1	E S E	6.64

statistical analysis on 20 waves each for ESE and SE, applying the Weibull Distribution Method. The result is as per Table 2.

Deep sea significant design wave was decided as wave height of 8.0 m and wave period of 11.4 sec with return period of 20 years. The bay entrance is not very wide, so equivalent deepwater wave height is calculated based on angular spreading of wave energy and refraction coefficient. For these effects, equivalent deep sea wave height of design wave 4.1 m and breaker depth is 6.6 m from ESE, as per Table 3.

**Tidal and Littoral Current**

Highest water level on record is +2.00 meters, mean monthly-highest water level is 1.4 meters, mean water level is 0.5 meters and mean monthly-lowest water level is 0.0 meters above datum level. As for littoral and tidal currents, field investigations conducted by Civil Laboratory of Hokkaido Development Bureau, for 2 years 1963 to 1965, were available, as per Fig. 4. Characteristics are as follows:

① Tidal current in the bay becomes a loop current, clockwise in summer and counter clockwise in winter, influenced by ocean currents outside the bay.

② Correlation between direction of littoral current and incident wave direction is high, and the dominant direction of littoral current corresponds to prevailing direction of incident wave.

③ In normal weather, littoral current in the bay depends on season. Along northeast and southwest coasts, direction is towards the head of bay in summer, and from head forward the entrance in winter. But along the northwest coast, direction is opposite on the Shizukari side and Yakumo side, with the neighborhood of Oshamanbe as a border.

④ Velocity of tidal current is about 16 cm/sec.

**Bottom Slope**

Contour lines are almost parallel to coastline. Bottom slope is approx. 1/90 as far as -7.0 meters. Depending on season, a step is formed, in some cases at water depth of 2 to 3 meters.

**Bottom Materials**

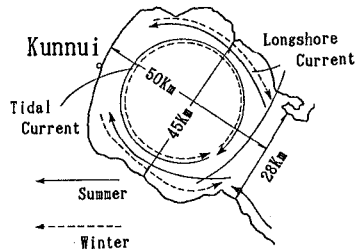


Fig.4 Currents in Uchiura Bay

This coast is emergent, and the existing coastline is assumed to have been deposited at about -20 m sea bottom. Particle diameter of sand is less than 0.22 mm, and well sorted. Median grain size ( $d_0$ ) has a smaller value depending on water depth toward offshore. Median grain size and coefficient of screening by water depth is shown in Table 4.

Table 4 Median Grain Diameter[ $d_{50}$ ] and Sorting Coefficient[ $S_0$ ] by Water Depth

Date	Offshore Distance (m)	- 60	+ 60	+300	+500	+700
	Water Depth (m)	+1.0	-1.0	-4.5	-7.0	-8.5
Nov., 1984	$d_{50}$ (mm)	0.25	0.21	0.17	0.15	0.08
	$S_0=(d_{75}/d_{25})^{1/2}$	1.48	1.43	1.21	1.38	1.42
Jul., 1985	$d_{50}$ (mm)	0.29	0.22	0.16	0.15	0.14
	$S_0=(d_{75}/d_{25})^{1/2}$	1.19	1.23	1.21	1.20	1.33

**Drift Sand**

**Changes of Coastline**

According to field interviews, the shoreline around Kunnui fishing port retreated about 25 m during the 40 years from 1925 to 1965, and yearly average retreat was 0.6 m/year. Further, according to the coastal deformation map based on topographical maps (1/50,000) made by the Geographical Survey Institute from 1896 to 1975 at Oshamanbe, 10 km from the port, shoreline retreat continued up to around 1969

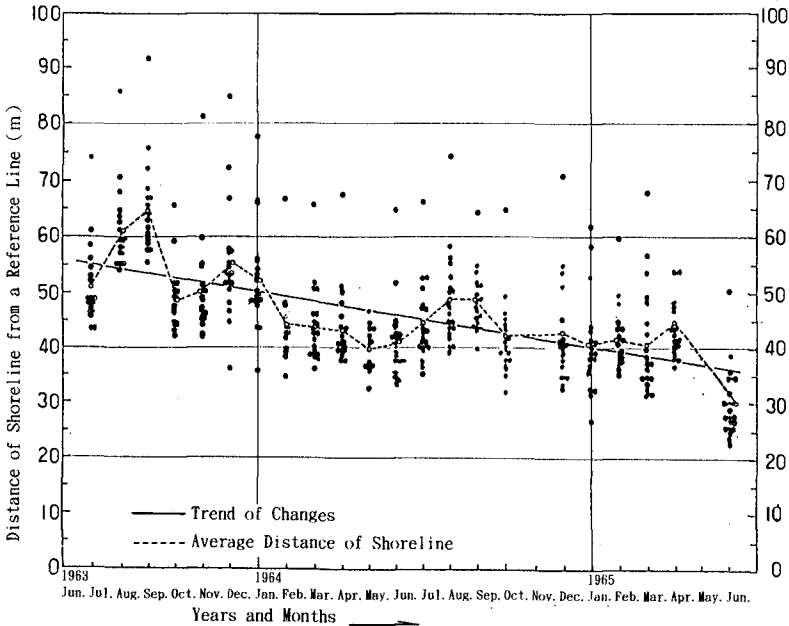


Fig.5 Changes of Shoreline from a Reference Line (at Nakanosawa)

but there was little retreat afterwards. Today, a balanced situation is maintained, but considerable seasonal changes seem to be occurring. Fig. 5 shows the investigation results on change of coastline at Nakanosawa from June 1963, to June 1965. Distances to coastline measured from 21 key piles installed at 50 meters intervals are

plotted monthly. Average distance is shown by a dotted line and the total trend by a solid line. The trend is forwards coastline advance in summer and retreat in winter. For those 2 years, the coastline retreated by about 20 meters on an average but seasonal change was also substantial, from 10 to 15 meters. From this figure the following features are recognized;

- ① Throughout the year, accretion and erosion repeat alternately and a seasonal cycle is observed.
- ② Erosion trend is observed from October to February and deposition from March to September, though there exist some variations depending on the annual wave conditions.
- ③ Retreat of shoreline is, in most cases, sudden rather than gradual. It is assumed that coastal erosion is caused by waves generated by typhoon around autumn and cyclones passing through the Sea of Japan in winter, and that in such cases erosion is not completely recovered even after a long period of calm sea.

• Relation among Wave Energy, Average Length to Coastline and Foreshore Sand Volume

Assuming that  $E_h$  is wave energy transmitted across a plane of unit width perpendicular to the direction of wave advance at water depth  $h$ ; and  $E_b$  is wave energy at breaker position;  $E_b = (b_n/b_b)E_h$ ; and  $E_a$  is energy passing through unit width parallel to coastline per unit time, therefore  $E_a = E_b \cdot \sin \alpha \cdot \cos \alpha$ . In these equations  $b_n/b_b$  is sq. of refraction coefficient and  $\alpha$  is wave crest angle with shoreline at breaker position. Assuming that at water depth  $h$ ,  $H$  is wave height,  $L$  is wave length and  $T$  is wave period, from Small Amplitude Waves Theory,  $E_h = n H L \gamma / 8T$ , and  $\gamma$  is unit weight of sea water and  $n$  is ratio between wave velocity and group velocity. Therefore, incident angle is divided to  $+\alpha$  and  $-\alpha$ , if right angle direction against coastal line is set as 0. Assuming that  $E_L$  is the energy of waves come in from left hand side and  $E_R$  from right hand side. Fig. 6 shows change of length and foreshore sand volume up to coastline from key pile and the relation with  $\sum E_L$  as well as  $\sum E_R$  and also  $(\sum E_L - \sum E_R)$ . For calculation of  $\sum E$ , it was assumed that the measured waves at noon continued until the following noon, and the energies from the both sides are added up separately for each month. Shoreline advance occurred when  $(\sum E_L - \sum E_R)$  is within the range of  $E_R$ , and shoreline retreated when this is within the  $E_L$  range. As a result of this survey, it was concluded that in this area, onshore-offshore sand transport is dominant under usual wave occurrence, and under unusual weather conditions, longshore littoral transport

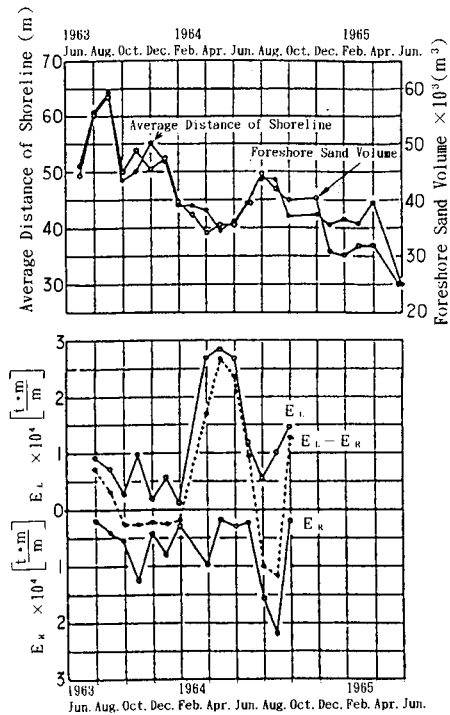


Fig.6 Relationship between Average Shoreline, Sand Volume and Wave Energy(at Nakanosawa)

parallel to the coast is predominant. The coastline thus advances when  $E_R$  surpasses  $E_L$ , and vice-versa. Direction of predominant littoral transport is from right to left.

### Coastal Changes of the Adjoining Fishing Port and Coastal structures

#### Yakumo Fishing Port

Yakumo fishing port is located at 23 km from Kunnui. Construction work began in 1951. Fig. 7 shows the coastal changes of this port. Due to drift sand moving from right to left, sand was deposited along the upstream shore, and it became difficult to maintain water depth at the port entrance. Considering the smallness of particle diameter at this coast, and the changing direction of dominant longshore current depending on season,

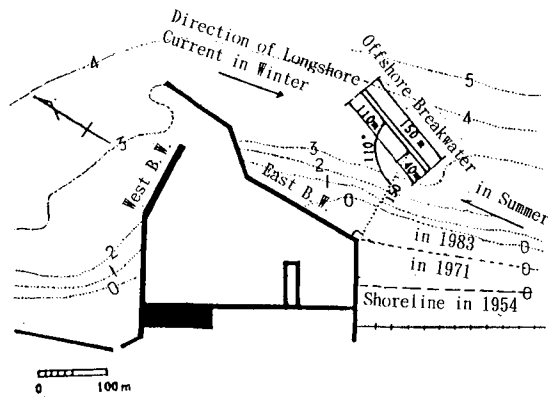


Fig.7 Shoreline Changes at Yakumo Fishing Port

as shown in this figure was installed. Sand accumulates at the back of the offshore breakwater in summer and when wave and flow change direction in winter, flushing of sand by natural forces acts as a counter-measure. Consequently, this counter-measure succeeded in preventing excessive sedimentation at the port entrance.

However, as water depth at the port entrance had already been reduced to 3 meters, and onshore drift sand is flowing in from the port entrance, maintenance dredging is still carried out every year.

#### Offshore Breakwaters for Shellfish Propagation Ground at Yakumo

From 1976 to 1981, three offshore breakwaters had been constructed with the purpose of "sakhalin surf-cram" propagation grounds about 13 km from Kunnui. The specifications of these offshore breakwaters are; 200 m in length, 50 m between successive breakwaters, 200 m of offshore distance and -3.0 m as site depth. As this area is very near and topographically similar to Kunnui, bottom materials and slope are similar to that at Kunnui. Fig. 8 shows coastal changes caused by the construction of these offshore breakwaters. The type of the breakwater is of permeable riprapping tetrapod with crown height of D.L.+3.0 m.

As shown in Fig. 8, as the construction work progressed, extensive tombolo developed behind the breakwaters and the coastline advanced by about 100 m at low water level. The adjoining coast was eroded, and at the left-hand coast even the foundation of the existing seawall was eroded. Accretion was remarkable and three tombolo were connected to each other. Fig. 9 shows bathymetry in August of 1984. As the development of the right-side tombolo is greater and coastal erosion is greater than on the left side, the dominant direction of drift sand is supposed to be from right to left.

#### Plan of the Fishing Port

In the past, before Kunnui fishing port was developed, fishing boats were hauled

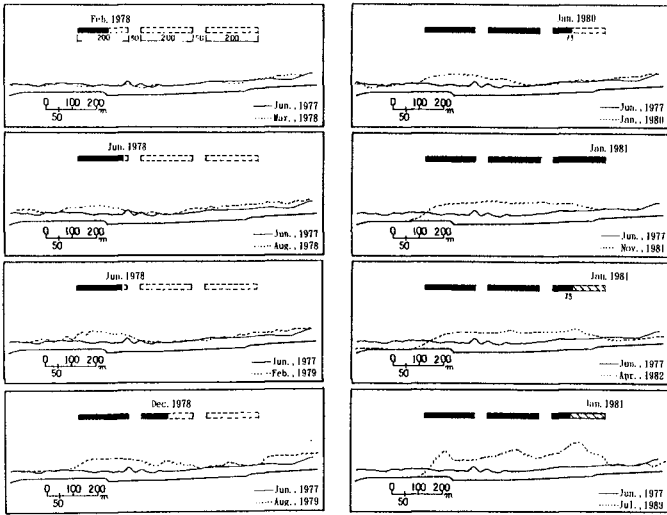


Fig.8 Changes of Shoreline behind Offshore Breakwater at Yakumo

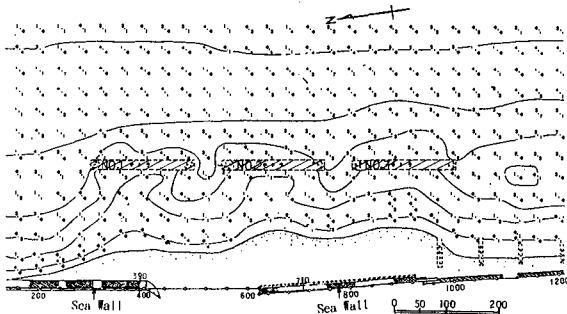


Fig.9 Bathymetry of Yakumo Shell-Fish Propagation Ground (Aug., 1984; Two and Half Years after the Completion of Offshore Breakwater)

up on the foreshore, much man power and time was needed for lifting and launching fishing boats. Major catches are scallop, flatfish, salmon and tuna. The fisheries are managed under stable conditions with gillnet, small setnet and salmon large setnet fisheries, and shallow water aquaculture of scallop. Kunnui fishing port was designed to serve as a vessel mooring area and a base for preparing and managing fishery operation.

**Shape of the Port**

Merits and demerits of detached fishing ports are discussed by Sakai. In case of small-scale ports, a large area for port facilities is not required, but if a plan be conducted only directing our attention to the scale of a plane layout, or the port design is concentrated only on facility layout, ignoring the presence of littoral drift,

and the port entrance is set inside the breaker zone where drift sand movement is heavy, then the function of the port may be impaired. On the other hand, if the port layout is determined from a viewpoint of preventing sedimentation at the port entrance, a rather large-scale port design is indispensable in order to set the port entrance far offshore side beyond the breaker zone. In this respect, however, a port constructed at a properly selected offshore site as a kind of man-made island may not require higher total costs than a conventional port.

Several draft plans were examined, considering the influence on adjoining coast, sedimentation at port entrance, ease of construction and construction cost. Two basic configurations were considered; one was a conventional type extending offshore; and the other was a detached island type. Further, two detached types were considered; one with a curved shape to decrease wave dumping effect by the port, and the other with an angular form. Fig. 10 shows these types;

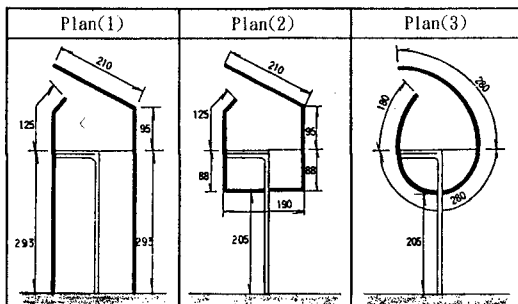


Fig.10 Layout Plan of Kunnui Fishing Port

① Plan 1 : Conventional type of port ② Plan 2 : Island type of port with angular lines ③ Plan 3 : Island type with curved breakwater to produce rough waves behind the sheltered area. Although Kunnui is a small port, if the port was constructed based on the conventional method of installing shore-connected breakwaters, it was assumed that longshore transport would be interrupted and beach accretion up-coast as well as erosion down-coast would occur. Further, if the port entrance was set in the surf zone, there was a risk of sedimentation at the port entrance. In fact, these troubles occurred at Yakumo port, as already mentioned. In order to prevent the influence of drift sand as much as possible, an offshore island type fishing port was adopted.

From a standpoint of coastal structure, an island fishing port is considered to be very similar to an offshore breakwater. In this case, the point was how to balance the need to prevent development of tombolo with construction costs. The longer the offshore distance, the smaller the development of tombolo, but the higher the construction cost. Therefore, the following conditions are key for determination;

① Water depth at the port entrance is deep enough to prevent being blocked by drift sand under adverse wave conditions. ② Port is designed such as to decrease formation of tombolo. ③ Offshore distance has to be great enough to prevent the port from being connected to shore by development of tombolo. ④ Reasonable construction cost based on comparison with costs estimated for conventional port, including relation between offshore distance, maintenance and management cost if longshore drift transport were totally interrupted and beach erosion occurred.

Offshore distance was initially set at around 200 m, and investigations were carried out for several different distances.

#### Scale of the Fishing Port

Port scale was planned according to the forecasted number of fishing boats which would utilize the port, as per Table 5. Pursuant to Fishing Port Planning Criteria, the facilities and scale are as per Table 6.

#### • Entrance Water Depth

If a port is constructed offshore, the risk for sedimentation at the entrance

becomes lower as the entrance water depth gets deeper, but cost increases. For deciding the depth of the port entrance, critical depth for sediment movement is adopted as a yardstick. This critical depth is classified into two types; critical water depth for surface sediment movement and critical water depth for complete sediment movement. The former concerns mass movement of surface sand at the bottom along wave direction; and the latter indicates movement which can cause change of water depth. According to the formula developed by Sato and Tanaka, these depths are expressed as follows;

Table 5 Usage of Kunnui Fishing Port[G.T.: gross tonnage]

The Grade of Fishing Boats	1983 (Results)		after Completion(Forecast)	
	The Number of Fishing Boats	Total G. T.	The Number of Fishing Boats	Total G. T.
< 3 G. T.	32	67	6	67
3~ 5 G. T.	7	24	46	161
5~10 G. T.	0	0	4	28
T o t a l	39	91	56	256

Table 6 Necessary Facilities

	Facilities	Length or Area
Mooring Facilities	Quay Wall -3.0m	100 m
Land for Facilities	Boat Yard[Shipway]	80 m
	Land for Facilities +3.0m	12,100 m <sup>2</sup>

(Surface Sediment Movement)

$$\frac{H_0}{L_0} = 1.35 \left( \frac{d}{L_0} \right)^{\frac{1}{3}} \left( \sinh \frac{2\pi h_i}{L} \right) \left( \frac{H_0}{H} \right)$$

(Complete Sediment Movement)

$$\frac{H_0}{L_0} = 2.4 \left( \frac{d}{L_0} \right)^{\frac{1}{3}} \left( \sinh \frac{2\pi h_c}{L} \right) \left( \frac{H_0}{H} \right)$$

Where,

Affix o : offshore wave

$h_i$  : Critical water depth for surface sediment movement

$h_c$  : Critical water depth for complete sediment movement

As a result of bottom survey, median diameter of bottom sand is  $d_{50} = 0.08-0.26$ . During investigation period,  $H_0 = 2.2$  m and  $T = 12.3$  sec were observed. After storm wave subsided, recognized isobath was up to  $-6.5$  m, with  $d_{50}$  of 0.26 mm. The calculated values were  $h_i = 6.6$  m and  $h_c = 3.1$  m. For wave with return period of one year, equivalent deep water wave height  $H_0$  is 1.7 m, with  $h_i = 7.7$  m-12.5 m and  $h_c = 3.7$  m-5.7 m. According to these results, the entrance depth was determined to be deeper than D.L-5.7 m.

These factors were established based on the analysis of existing materials, site investigations and simulations, and thus may not represent in full the actual site conditions. Consequently, an hydraulic model test was conducted, and the results were compared.

### Layout of the port

#### • Model Test

To compare the angular and curved offshore fishing ports, a hydraulic model test was carried out. As bottom slope is gentle, the distorted model was applied through trial and error. Model Scale was 1/100 in horizontal and 1/70 in vertical. Tests were carried out for the angular type (Plan 2) and the curved type (Plan 3) with waterdepth  $-5.5$  m,  $-6.5$  m,  $-7.0$  m. Offshore distance was initially set at 200 m and tests were conducted for several distances around this figure. Sand used in the tests has a



median grain size of 0.22 mm. The purpose of the tests was qualitative comparison of tombolo development.

Test Waves were for waves with return period of 1 year and 20 years, and wave direction was ESE and SE. As a verification method, sand movement by tracer in the Model was arranged to correspond to the move of fluorescent sand at the site. As it is difficult to reproduce actual site conditions in the model, only qualitative comparisons were conducted.

A total of 24 hydraulic model tests were performed for various wave conditions and offshore distances.

As a qualitative comparison between angular type and circle type, tests showed no tombolo protruding from water surface for the circle type, because of higher wave height and rougher water behind the port compared to the angular type. Two examples of the results of the tests are shown in Fig. 11 and Fig. 12.

In this case of the angular type, conspicuous tombolo was observed, while no tombolo appeared in the circle type even though incident wave was a little higher. A long and slender shoal, however, elevation of which was the same as the water surface, was formed along the center line behind the port, where waves from both sides collided with each other. Another characteristic was local scouring along and at the corners of breakwaters in the angular type, in contrast to that deposition area appeared along breakwaters up to water depth of  $-5.0$  m to  $-6.0$  m in the circle type. This phenomena seemed to be caused by strong return flow along the structures.

#### • Numerical Simulation of Wave Induced Current

For Plan 3, numerical calculation of wave induced offshore current was conducted to confirm the speed of return flow. The result of the computation is shown in Fig. 13.

The wave conditions in this case are; wave direction ESE, equivalent deep water wave height is 2.2 m (at depth of  $-6.0$  m it is about 2.0 m), and wave period 8.0 sec. The range of computation is 1,000 m, along the coast and offshore. Mesh interval is 20 m. In this case, a circular current with velocity 10 to 30 cm/sec developed behind the port. Part of this current flows offshore along outlying facilities as return flow. This flow might result in sediment transport and deposition along port outlying facilities as seen in the model test. If the  $-2$  m isobath reaches the port entrance, the entrance may not be maintained. In the hydraulic model test, this phenomenon occurred until initial water depth of  $-3.5$  m.

These qualitative tests, however, were unable to confirm what would occur at the actual site. Furthermore, although conspicuous tombolo was not formed in the model

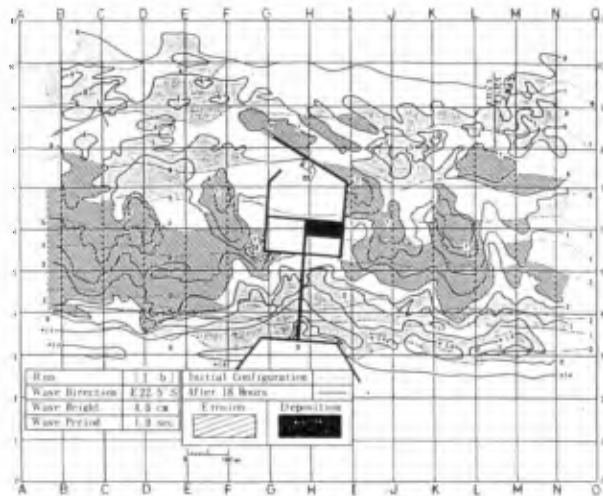


Fig.11 Example of Sea Bottom Change by Hydraulic Model Test[Plan(2)]

test, a considerable size of tombolo was assumed to develop from this calculation. Putting all these various results together, along with last but not least, consideration of total cost, layout shown in Fig. 14 was adopted.

**Topographic Changes During Construction**

The construction work commenced in 1988, and proceeded in the following order:  
 ① Road bridge  
 ② West side seawall  
 ③ Bridge approach

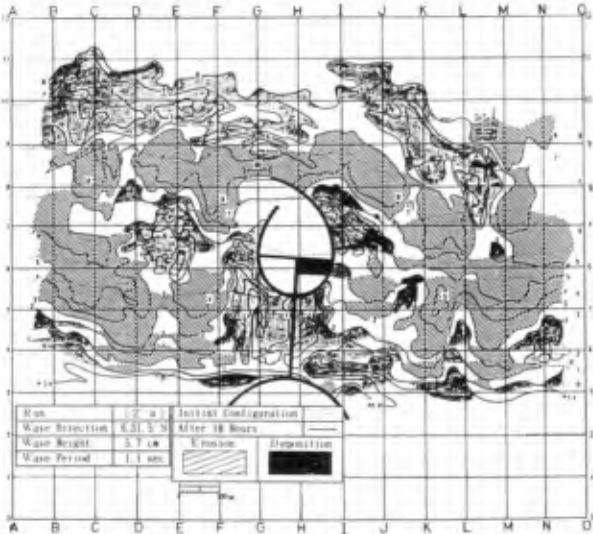


Fig.12 Example of Sea Bottom Change by Hydraulic Model Test[Plan(3)]

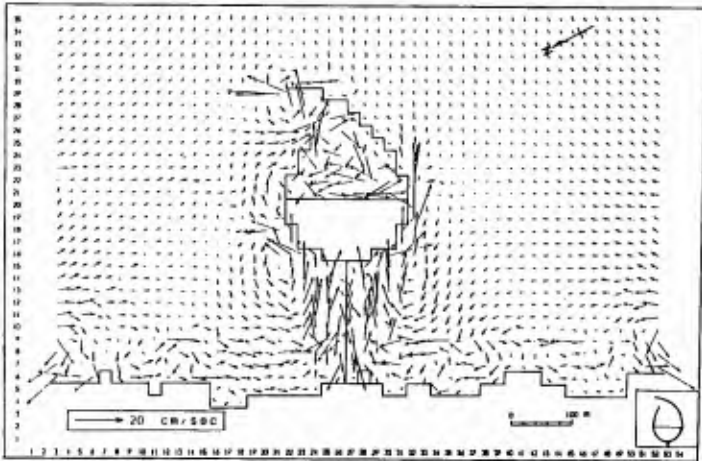


Fig.13 Nearshore Current by Numerical Simulation [H<sub>0</sub>=3.6m, T=8.0sec.: H=2.0m at h=-6.0m]

- ④ Southern seawall ⑤ Southern breakwater ⑥ Eastern breakwater ⑦ Northern seawall
- ⑧ Northern breakwater
- ⑨ Mooring facilities ⑩ Reclamation of land for facilities. During the construction, sounding survey was conducted every year around August and September. The coastal configuration at each stage of work was compared against with the base survey conducted in August, 1985. As was predicted, a tombolo was formed at the rear of the port. Fig. 15 shows changes of coastline (development of tombolo) at

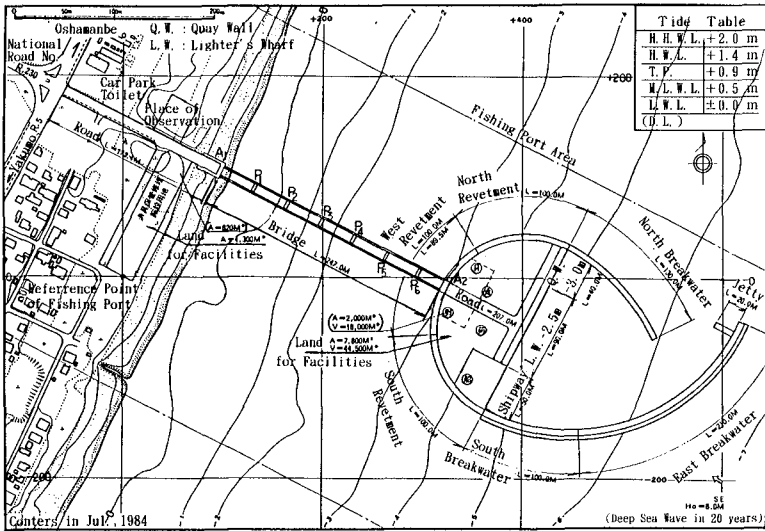


Fig.14 Final Plan of Kunnui Fishing Port

M.W.L. (D.L.+0.5 m). The tip of the tombolo advances seaward with the progress of the construction work. But maximum length of advancement is only about 60 m and the size is not so great. Fig. 16 illustrates the changes of shoreline at L.W.L. (D.L.+0.0 m). The seaward tip of the coastline is long and sharp but changes its shape adapting to imposed wave conditions much like a kind of cusped spit, and almost touches the port in recent years. Fig. 17 shows bathymetric changes. Since this port consists of impermeable breakwater and a coastal structure 300 m long and 200 m wide, bathymetric change is, in general, different from that of a conventional offshore breakwater shown in Fig. 9, which is of permeable type with low crown height. In the case of common offshore breakwaters, local scouring is generally observed at both ends, but in the case of an offshore fishing port, there exists no scouring because of the smooth linear change in the line of the structure. Due to influence of return flow, sand deposition occurs as far as -6 m on the right-side and -5 m on the left-side along the port and shape of the isobath becomes convex near the port.

At the planning stage of this port, we considered only the similarities with an offshore breakwater, but in reality, coastal changes adjoining the port also show similarities with the changes usually caused by a long jetty.

Bathymetric changes since 1992 hint at the existence of large scale and strong cell-like circular currents on both sides of the port. Along this current, scouring of sea bottom occurs in the onshore direction and deposition in the offshore direction. The width of this circular current is approximately 400 m, and this results in the start of tombolo 300 m - 350 m on both sides from the center line of the port. Retreat of the coastline is 30 m at right and 10 m at left and stable. In comparison with yearly shoreline changes by attacking waves before the construction of the port, this retreat is small and stable and thus there are no problems concerning coastal erosion, even though there is no seawall at this beach. Over a distance of 400 m from the center line, no particular change can be seen in the coast except for seasonal changes.

The point is whether we have obtained the desired results or not. At this coast,

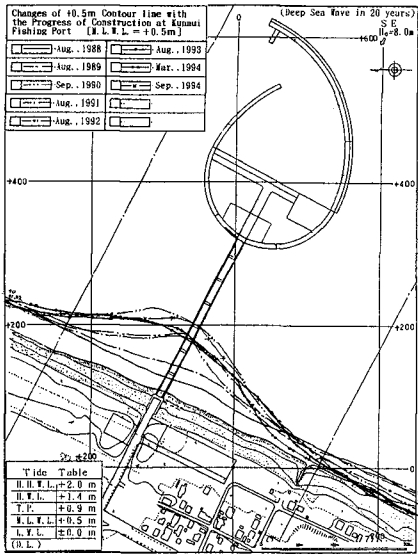


Fig.15 Change of +0.5m Contour line with the Progress of Construction at Kunnuui Fishing Port [M.L.W.L.=+0.5m]

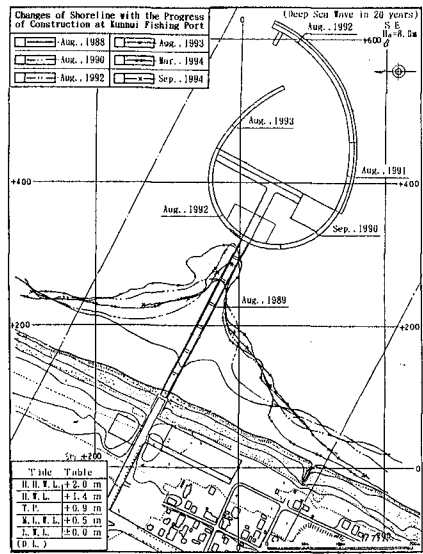


Fig.16 Changes of Shoreline with the Progress of Construction at Kunnuui Fishing Port [at L.W.L.=±0.0m]

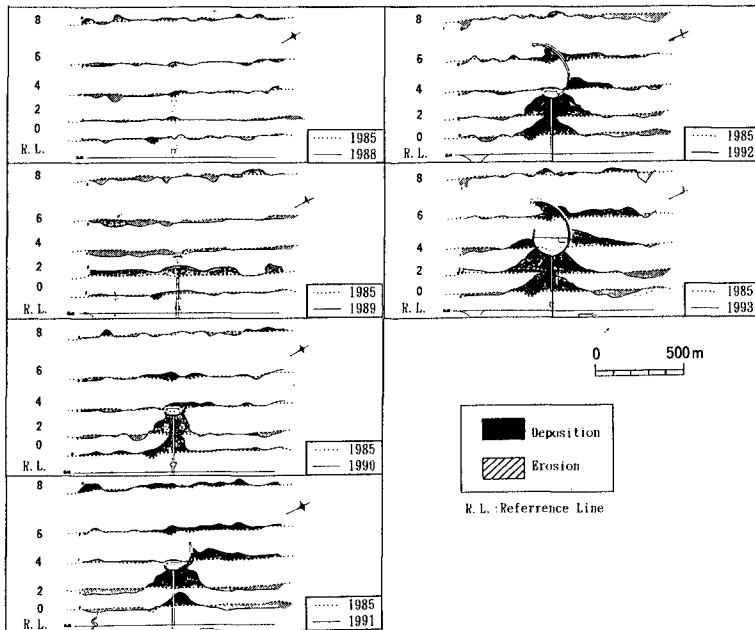


Fig.17 Changes of Contours with the Progress of Construction at Kunnuui Fishing Port

onshore-offshore sand drift dominates under normal conditions and longshore sand drift during high waves, but except for low water, there remains a channel at the rear, and we thus think it stands to reason that littoral current flows behind the port. It is only 3 years, however, since the port took shape, and we are thus going to continue field observations and make a final decision in the future.

### **Conclusion**

Our research focused on how to prevent beach erosion and sand deposition at the port entrance. For the time being, this purpose seems to be satisfied at Kunnui fishing port, but careful examination of bathymetric charts conducted in parallel with the construction work indicated that there occurred large scale cell-like circular currents at both side of the port. This current transports sand onshore and scours the sea-bottom en-route and deposits sand behind and along the port when it is flowing in the offshore direction. In this sense, the location of port entrance at the depth of -6.5 m, and over 400 m offshore from the coastline is supposed to be adequate in this case. We learned that it is important not only to restrict tombolo generation but also to predict the scale and strength of cell-like circular currents in planning this type of fishing port.

### **References**

- Fishing Port Planning Manual. (1980): Committee on Fishing Port and Community Planning, All Japan Fishing Port Association, Tokyo.
- Fishing port Div., Hokkaido Prefecture, (1985): Investigations on Layout of Breakwaters of Kunnui Fishing Port, Fishing Port Div. Fisheries Dept. Hokkaido Prefecture.
- Fishing Port Div., Hokkaido Prefecture, (1986): Report on Hydraulic Model Test of Kunnui Fishing Port, Fishing Port Div. Fisheries Dept. Hokkaido Prefecture.
- Kogami, Y., H.Inami, F.Hoshi, (1970): Characteristics of Beach Erosion along the Pacific Coast of Hokkaido, Coastal Engineering in Japan, JSCE, Vol. 17, pp.283-288.
- Research Committee on Beach Erosion, (1967): Field Investigations on Beach Erosion around the Uchiura Bay in Hokkaido, Report of the Civil Engineering Research Institute, No. 43, Civil Engineering Research Institute Hokkaido Development Bureau, pp 85-91.
- Sakai, I., (1990): A Study on a Fishery Harbor Construction Project along Sandy Beach.
- Sato, S., T.Shoji, N.Tanaka, (1966): Sand Drift along the Coast of Sendai Bay, Coastal Engineering in Japan, JSCE, Vol.13, pp.176-182.
- Standard Design Criteria of Fishing Port Facilities. (1988): Fisheries Agencies of Japanese Government, All Japan Fishing Port Association, Tokyo.

## CHAPTER 88

# Topographical Change around Multiple Large Cylindrical Structures under Wave Actions

Chang-Je KIM<sup>1</sup>, Koichiro IWATA<sup>2</sup>, Yoshihito MIYAIKE<sup>3</sup> and Hong-Sun YU<sup>4</sup>

### Abstract

This paper is aimed to investigate theoretically and experimentally the topographical change and the local scouring around multiple large cylindrical structures under wave actions. It is revealed from laboratory experiments that the bottom configuration, the local scouring area and its depth around the cylindrical structures are changed largely according to the number of cylindrical structures, the structure's diameter, the incident wave angle and the sediment size. The theoretical model which developed newly is shown to predict well the topographical change around the structures.

### 1. Introduction

Cylindrical structures are one type of the widely-used coastal and offshore structures such as large volumed gravity platforms or water intake towers for power plants. Very recently, multiple large cylindrical structures have been constructed in shallow water depth and have been reported to suffer from local scouring around the cylindrical structures under wave actions in Japan. It goes without saying that the prediction of topographical change and the evaluation of local scouring area and depth around structures are indispensable for safety design of the structures. The accumulated knowledge of bottom topographical change around multiple large cylinders is, however, little compared with that of one large cylinder or small cylinders.

<sup>1</sup>Lecturer, Korea Maritime University, Busan, 606-791, KOREA

<sup>2</sup>Professor, Nagoya University, Nagoya 464-01, JAPAN

<sup>3</sup>General Manager, Chubu Electric Power Co. Ltd., Nagoya 461, JAPAN

<sup>4</sup>Professor, Korea Maritime University, Busan, 606-791, KOREA

This paper is to discuss theoretically and experimentally the bottom topographical change and local scouring around the two or three large cylinders under wave actions. First, the theoretical model is newly developed to evaluate the topographical change and to predict the scouring area and depth. Next, elaborate laboratory experiments are conducted to investigate the change of bottom configuration due to changes of the number of the large cylinders, their diameters, the incident wave and angle, and the sediment size. Comparing with laboratory experiments, the theoretical model proposed in this paper is shown to be very useful to evaluate the bottom topographical change and the local scouring around multiple large cylindrical structures.

## 2. Theoretical model

### 2.1 Diffraction theory

The diffraction theory is applied to evaluate the wave kinematics and wave deformation around the circular cylinders, since the ratio of the cylinder's diameter to the wavelength (diffraction parameter),  $D/L$  is more than 0.2. The source distribution function method using a vertical line wave source Green's function (Issacson, 1978) is employed in this paper under the assumptions of inviscid and incompressible fluid, and irrotational wave motion. The water particle velocities can be described with velocity potential  $\Phi (= \Phi_I + \Phi_S$ ;  $\Phi_I$  is the incident velocity potential,  $\Phi_S$  the scattered velocity potential), which satisfies Laplace equation.  $\Phi$ ,  $\Phi_I$ , and  $\Phi_S$  are all functions of  $x$ ,  $y$ ,  $z$ , and  $t$ , and  $(x, y, z)$  are the Cartesian coordinates of a point in the fluid field at which the potentials ( $\Phi$ ,  $\Phi_I$ , and  $\Phi_S$ ) are calculated at time  $t$ . When it is assumed that the wave height is sufficiently small for linear wave theory to apply, the incident wave velocity potential  $\Phi_I$  is a known value, and the scattered wave velocity potential  $\Phi_S$  is obtained from the source distribution function method (see, Kim and Iwata, 1993).

The wave height  $H$  around structures is given as

$$H = 2 \left| \frac{i\sigma}{g} \{ \phi_I(x, y) + \phi_S(x, y) \} \right| \quad (1)$$

where  $i = \sqrt{-1}$ ,  $\sigma$  denotes the wave angular frequency,  $g$  the gravitational acceleration,  $\phi_I$  the complex amplitude of the incident velocity potential  $\Phi_I$ ,  $\phi_S$  the complex amplitude of the scattered velocity potential  $\Phi_S$ , and  $| \quad |$  the absolute value.

The water particle velocities  $U_b(x, y; t)$ ,  $V_b(x, y; t)$  in the  $x$ -,  $y$ - directions near bottom around structures are as follows, respectively.

$$U_b = \text{Real}\left[\frac{\partial\Phi}{\partial x}\Big|_{z=-h}\right] = \text{Real}[U_0(x, y) \exp(-i\sigma t)] \quad (2)$$

$$V_b = \text{Real}\left[\frac{\partial\Phi}{\partial y}\Big|_{z=-h}\right] = \text{Real}[V_0(x, y) \exp(-i\sigma t)] \quad (3)$$

in which Real denotes the real part of the expression following,  $h$  the still water depth,  $U_0$  and  $V_0$  are the complex amplitudes of  $U_b$  and  $V_b$ , respectively.

It has been reported that the wave height and the bottom velocity evaluated with the source distribution function method using a vertical line wave source Green's function, were in good agreement with those by experiments (Kim and Iwata, 1993, Kim et al., 1994).

## 2.2 Mass transport velocity

Taking constant viscosity into account, Lagrangian mass transport velocities  $\overline{u_L}$ ,  $\overline{v_L}$  in the  $x$ -,  $y$ - directions in the bottom boundary layer combined Stokes' mean drift with Eulerian mean drift are given as (Carter et al., 1973)

$$\overline{u_L} = \frac{1}{4\sigma} \text{Real} \left\{ F_5 U_0 \frac{\partial U_0^*}{\partial x} + F_6 V_0 \frac{\partial U_0^*}{\partial y} + F_7 U_0 \frac{\partial V_0^*}{\partial y} \right\} \quad (4)$$

$$\overline{v_L} = \frac{1}{4\sigma} \text{Real} \left\{ F_5 V_0 \frac{\partial V_0^*}{\partial y} + F_6 U_0 \frac{\partial V_0^*}{\partial x} + F_7 V_0 \frac{\partial U_0^*}{\partial x} \right\} \quad (5)$$

where \* means the complex conjugate,  $F_5$ ,  $F_6$  and  $F_7$  are expressed as

$$F_5 = -8i \exp\{-(1-i)\xi\} + 3(1+i) \exp\{-2\xi\} - 3 + 5i \quad (6)$$

$$F_6 = -4i \exp\{-(1-i)\xi\} + (1+2i) \exp\{-2\xi\} - 1 + 2i \quad (7)$$

$$F_7 = F_5 - F_6 \quad (8)$$

where  $\xi = z_1/\delta$ ,  $z_1$  is the distance away from the bottom and points normally into the inviscid region,  $\delta (= \sqrt{2\nu/\sigma})$ ;  $\nu$  is the kinematic viscosity) the thickness of the boundary layer.

With the known expressions of  $U_0$ ,  $V_0$  or  $U_0^*$ ,  $V_0^*$  in Eqs.(2) and (3), Lagrangian mass transport velocities  $\overline{u_L}$ ,  $\overline{v_L}$  in the bottom boundary layer in Eqs.(4)and(5) can be evaluated.



2.3 The sediment transport rate model

From the sediment transport field, the development of the topographical change or the local scouring around structures is calculated by the continuity equation for the sediment given as

$$\frac{\partial h(x, y; t)}{\partial t} = \left\{ \frac{\partial q_x(x, y; t)}{\partial x} + \frac{\partial q_y(x, y; t)}{\partial y} \right\} \tag{9}$$

in which  $h$  is the above-mentioned still water depth,  $q_x$  and  $q_y$  are the sediment transport rates in volume of material per unit time and width in the  $x$ - and  $y$ - directions, respectively.

Consider the sediment transported in the  $s$ - direction by mass transport  $V(= \sqrt{u_L^2 + v_L^2})$ , as shown in Fig. 1. The sediment transport model  $q_s$ , proposed by Watanabe(1981) is widely used in and out the surf zone.

$$q_s = \frac{A_1 w_f}{(1 - \lambda_0) s_0 g \sqrt{s_0 g d_{50}}} (u_*^2 - u_{*c}^2) u_* \tag{10}$$

in which  $A_1$  represents dimensionless parameter,  $w_f$  the sediment settling velocity,  $\lambda_0$  the porosity of the bed material,  $s_0$  the specific weight of the sediment in water,  $d_{50}$  the median diameter of the sediment,  $u_*$  the friction velocity and  $u_{*c}$  the critical shear velocity.

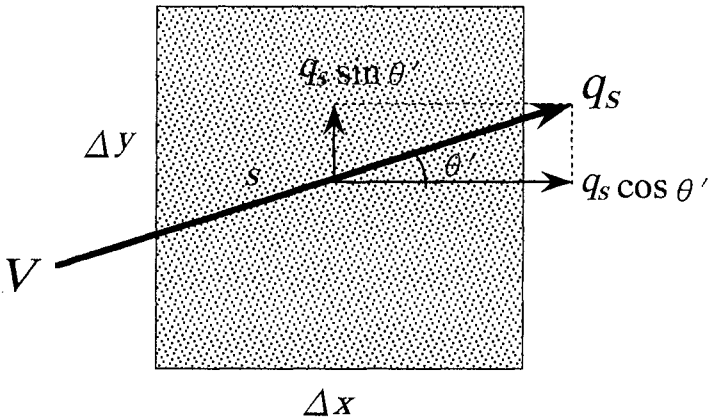


Fig. 1 Simplified model of the sediment transport rate

The sediment transport rate of Eq. (10) is generally based on the sediment transported by breaking wave over the slope bed. Therefore, Eq. (10) is applied to the sediment transport over the plane bed like the present study, the sediment transport rate may be overestimated. Consequently, the new model for the sediment transport applicable to the cases that the spatial change of the wave height is dominant, is proposed on the approximation described in the following.

Equation (10) can be approximated by

$$q_s \sim u_*^3/g \sim V_{bmax}^3/g \sim \frac{H^3}{gT^3 \sinh^3 kh} \quad (11)$$

where  $V_{bmax} = \sqrt{(U_b^2 + V_b^2)}|_{max}$ ,  $T$  is the period of the incident wave,  $k$  the wave number.

Similarly, the mass transport velocity  $V$  can also be approximated as follows.

$$V \sim \frac{1}{\sigma} U_{0s} \frac{\partial U_{0s}}{\partial s} \sim \frac{H^2}{gT^3 \sinh^3 kh} \quad (12)$$

where  $U_{0s}$  indicates the water particle velocity in the  $s$ -direction near the bed.

The following Eq. (13) is obtained by combining Eq. (11) with (12).

$$q_s \sim VH \quad (13)$$

Equation (13) means that the sediment transport rate is proportional to  $VH$ . The wave height  $H$  in the vicinity of large scale structures changes largely in space due to the scattered wave superimposed on the incident wave, and since the wave height  $H$  corresponds to the dynamic pressure, its magnitude represents the extent of the sediments suspension. From this point of view, it seems to be more reasonable that the wave height  $H$  is explicitly included in the sediment transport rate. In the present study, consequently, the sediment transport rate  $q_s$  at an equilibrium state is given as

$$q_s = \frac{A}{1 - \lambda_0} (\Psi_m - \Psi_c) VH \quad (14)$$

where  $A$  indicates the dimensionless parameter,  $\Psi_m (= f_w V_{bmax}^2 / (2s_0 g d_{50})$ ;  $f_w$  is the wave friction factor) the Shields parameter,  $\Psi_c$  the critical Shields parameter.

In calculating Eq. (14), the wave height  $H$  is evaluated with Eq. (1), the water particle velocities  $U_0$  and  $V_0$  are evaluated with Eqs. (2) and (3) using

the source distribution function method, and the mass transport velocities  $\overline{u_L}$  and  $\overline{v_L}$  are also evaluated with the values  $(U_0, V_0, U_0^*$  and  $V_0^*)$  by means of Eqs. (4) and (5).

### 2.4 Topographical change at an equilibrium state

It is assumed that the wave field has little change after the bottom profile change, that is, the sediment transport rates at the equilibrium condition can be evaluated with those  $q_x(x, y; 0)$ ,  $q_y(x, y; 0)$  at  $t=0$ , and the acting time  $T_c$  of wave when the bottom topography reaches an equilibrium state is determined from the experimental results, since the present study aims to establish the simple method that is able to predict the topographical change, the local scouring depth around structures.

From Eq. (9),

$$\begin{aligned} \Delta h_c(x, y) &= \int_0^{t_c} \left\{ \frac{\partial q_x(x, y; t)}{\partial x} + \frac{\partial q_y(x, y; t)}{\partial y} \right\} dt \\ &\cong \left\{ \frac{\partial q_x(x, y; 0)}{\partial x} + \frac{\partial q_y(x, y; 0)}{\partial y} \right\} T_c \\ &= \left\{ \frac{\partial(q_s \cos \theta')}{\partial x} + \frac{\partial(q_s \sin \theta')}{\partial y} \right\}_{t=0} T_c \end{aligned} \tag{15}$$

in which,  $\Delta h_c(x, y)$  represents the change of the still water depth, and  $\Delta h_c > 0$ ,  $\Delta h_c < 0$  and  $\Delta h_c = 0$  correspond to, respectively, the scouring, the deposition and no-change. Eq. (14) is applied to Eq. (15) to evaluate  $\Delta h_c$ . The pattern of the bottom configuration around structures is divided into three parts such as the scouring area ( $\Delta h_c > 0$ ), the deposition area ( $\Delta h_c < 0$ ) and no change area ( $\Delta h_c = 0$ ).

### 2.5 Numerical computation

In Eq. (14), the values of the dimensionless parameter  $A$ , the porosity of the bed material  $\lambda_0$ , the specific weight of the sediment in water  $s_0$ , and the critical Shields parameter  $\Psi_c$ , respectively, were taken as 0.02~0.05, 0.4, 1.65, and 0.08 for the relatively fine sand ( $d_{50}=0.015\text{cm}$ ) and 0.07 for the relatively coarse sand ( $d_{50}=0.038\text{cm}$ ). Then, the mass transport velocity  $V$  at a middle point ( $\xi=1/2$ ) within the boundary layer were used. In the case of the wave friction factor  $f_w$ , Eq. (16) presented by Swart(1974) was applied.

$$f_w = \exp\{-5.977 + 5.213(a_m/k_s)^{-0.194}\} \tag{16}$$

in which  $a_m$  is the amplitude of the orbital motion at the bottom,  $k_s$  the bed roughness and took the median diameter  $d_{50}$  of sand.

In calculating Eq. (15),  $T_c=5200 \times T$  was chosen from the experimental results as will be mentioned later.

### 3 Laboratory experiments

#### 3.1 Dimensional analysis

Taking the structures installed in a line with the same diameters into consideration, the non-dimensional bottom configuration change  $\Delta h_c/H_I$  around the three large cylindrical structures at an equilibrium state is mainly governed by the following 9 parameters.

$$\frac{\Delta h_c}{H_I} = \phi_1 \left\{ \frac{r}{D}, \theta, \frac{D}{L}, \frac{e_1}{D}, \frac{e_2}{D}, \alpha, \frac{H_I}{L}, \frac{h}{L}, \frac{d_{50}}{L} \right\} \quad (17)$$

where  $r$  is the radial distance,  $\theta$  the clockwise angle along the structures measured from the first point of the structures where the incident wave contacts,  $e_1$  the distance between structures I(the right one from the incident wave) and II(the center one),  $e_2$  the distance between structures II and III(the left one) and  $\alpha$  the incident wave angle.  $e_2/D = \infty$  corresponds to the case of two structures and  $e_1/D = e_2/D = \infty$  does to one structure. In the present paper, the effects of the following 6 parameters on the topographical change are mainly discussed.

$$\frac{\Delta h_c}{H_I} = \phi_2 \left\{ \frac{r}{D}, \theta, \frac{D}{L}, \frac{e_1}{D}, \alpha, \frac{d_{50}}{L} \right\} \quad (18)$$

#### 3.2 Experimental equipments and conditions

Laboratory experiments were carried out in a wave basin(28m in length, 11m in width and 0.8m in depth) with a flat bottom. A piston-type wave generator was installed at one end and the wave dissipating sandy beach with the slope of 1/10 was constructed at the other end. And the wave absorbing filters were set up on the both sides of the basin to diminish wave reflection from side walls as small as possible. The surface piercing cylindrical structures with the same diameters, were installed in a line on a sandy bed(400cm in length 500cm in width and 7cm in depth). Test conditions for the movable bed are listed in

Table 1 Test conditions for the topographical change

$D$ (cm)	$d_{50}$ (cm)	$h$ (cm)	$T$ (s)	$H$ (cm)	$\alpha$ (deg.)	$e_1/D$	$e_2/D$	$n$
47.2	0.015	20	1.4	5.7	0	1.0	$\infty$	2
						2.0		
						3.0		
					22.5	1.0		
					45			
					67.5			
	90							
	0				1.0			
					2.0			
					3.0			
0.038	22.5	1.0						
	45							
	67.5							
	90							
90	0.015		0					
			45					
	0.038		0					
			45					
47.2	0.015		1.0					
	45							
	0.038	1.0						
	45							
47.2	0.015	1.0						
	45							
	0.038		1.0					
	45							
47.2	0.015	$\infty$	$\infty$	1				
	0.038							
90	0.015							
	0.038							

Table 1, in which  $n$  means the number of structures. The experimental waves satisfied with the live bed state for all the cases, were continuously generated until the bottom topographical change seemed to close to an equilibrium state. The bottom topographical changes were carefully measured with point gauges at all the 2cm-interval mesh points within the sandy bed. The water particle velocities near the bottom and water surface profiles around the structures were measured with electromagnetic type velocity meters and capacitance-type wave gauges, respectively, for the same conditions as the movable bed ones to examine the validity of the employed theory regarding the wave kinematics and the wave heights.

## 4 Results and discussion

### 4.1 Topographical change around structures

Figure 2 represents the time evolution  $t/T$  of the non-dimensional topographical change  $\Delta h/H_I$  at four locations where the comparatively larger scouring depth occurred. In Fig. 2,  $x'$  is the offshoreward distance measured from the structure surface. As shown in Fig. 2, it can be judged that the number  $t/T$  of waves reached the equilibrium state is approximately more than 5000,

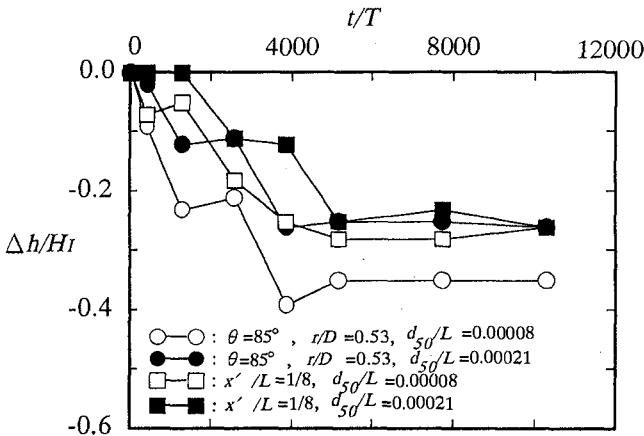


Fig. 2 Time evolution of the topographical change  
 $(D/L = 0.26, e_1/D = 1.0, H_I/L = 0.03, h/L = 0.11, \alpha = 0^\circ)$

regardless of the places and the sediment sizes. This result is almost the same as that of Xie(1981) in front of breakwater, or of Katsui and Toue(1992) around one large cylinder. In the present paper, the topographical change at  $t/T=5200$  is taken to be the equilibrium state, and the experimental results at  $t/T=5200$  are compared with the computed ones(Eq. (15) with  $T_c=5200 \times T$ ).

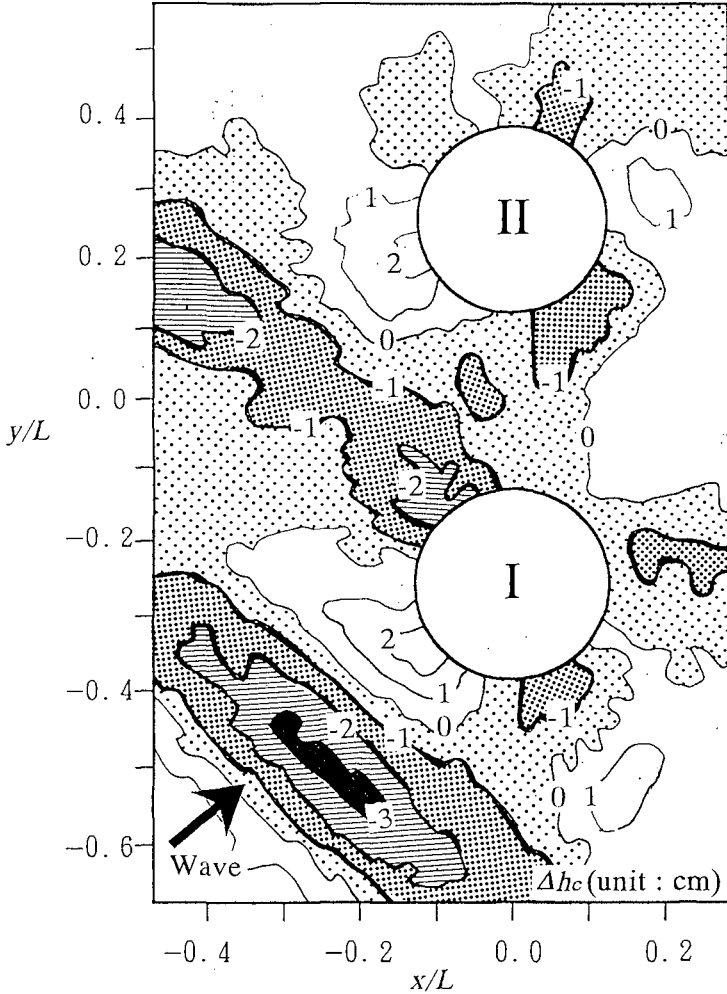


Fig. 3(a) Topographical change around two structures  
 ( $D/L = 0.26, e_1/D = 1.0, H_1/L = 0.03, h/L = 0.11, \alpha = 45^\circ, d_{50}/L = 0.00008$ )

In general, the bottom configuration, the local scouring area and its depth around cylindrical structure are changed according to the number of structures, the structure's diameter, the incident wave angle and the sediment size.

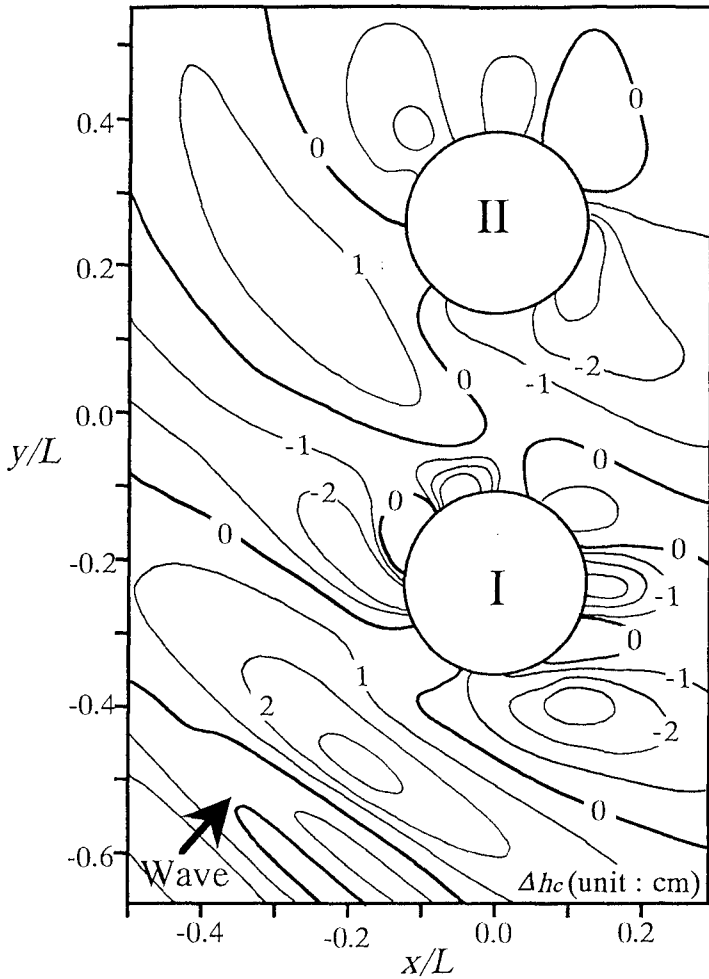


Fig. 3(b) Topographical change around two structures(computed)  
 $(D/L = 0.26, e_1/D = 1.0, H_1/L = 0.03, h/L = 0.11, \alpha = 45^\circ, d_{50}/L = 0.00008)$



Figure 3(a) and (b), respectively, show the experiment result and the computed one of the bottom configuration  $\Delta h_c$  around the two structures in the case of  $\alpha = 45^\circ$ ,  $e_1/D = 1.0$  and  $D/L = 0.26$ . In Fig. 3(a) and (b), the digits indicate the values of the topographical change  $\Delta h_c$ , and the signs of - and +, respectively, indicate the scouring (black area in Fig. 3(a)) and the deposition (white area in Fig. 3(a)). Experiments with the sediment size of  $d_{50} = 0.038\text{cm}$  in place of  $d_{50} = 0.015\text{cm}$  were also conducted and their results were reported by Kim and Iwata (1993). In the case of the relatively fine sediment (this study), the scouring depth and its area are larger and wider than those of the case of the relatively coarse one (Kim and Iwata, 1993). In the cases of obliquely incident waves like  $\alpha = 45^\circ$ , since the onshore structure II is located at the sheltered area of the offshore structure I, a little change or no change is generally found around onshore structure I. Comparing the experimental result with the computed one, it is seen that the bottom configuration around structures can be well estimated with the present theory.

## 4.2 Topographical change along structures

Figure 4 illustrates the non-dimensional topographical change  $\Delta h_c/H_I$  at  $r/D = 0.53$  along the structures with parameter of  $e_1/D$ . In Fig. 4, the solid line represents the experimental result and the dashed line the computed one. The maximum scouring depth takes place at  $\theta = 45^\circ \sim 135^\circ$  (see Fig. 4 and 5) and in Fig. 4, the maximum scouring depth becomes smaller in order of  $e_1/D = 1.0$  (Fig. 4(a)),  $e_1/D = 3.0$  (Fig. 4(b)) and  $e_1/D = \infty$  (Fig. 4(c)). It is inferred that the influence of diffracted wave from one structure on the other one can not be neglected for  $e_1/D = 3.0$ . It is also seen that theoretically estimated values are in good agreement with experiments.

Figure 5 shows the effect of the sediment size on the non-dimensional topographical change  $\Delta h_c/H_I$  for the case of  $D/L = 0.49$ . When the sediment size is smaller (see Fig. 5(a)), the scouring depth and its area are larger and wider, as mentioned above. And the maximum scouring depth for the case of larger diffraction parameter  $D/L = 0.49$  (see Fig. 5(a)) is larger than that of smaller one  $D/L = 0.26$  (see Fig. 4(a)). The reason for this is inferred as follows. When the  $D/L$  becomes large, the spatial difference of the wave height  $H$  also becomes large. As explained before, the sediment is easy to be suspended and to be transported due to mass transport velocity and its large change in space caused by the large difference of the wave height  $H$  in space. Consequently, the scouring depth for the case of larger diffraction parameter becomes larger.

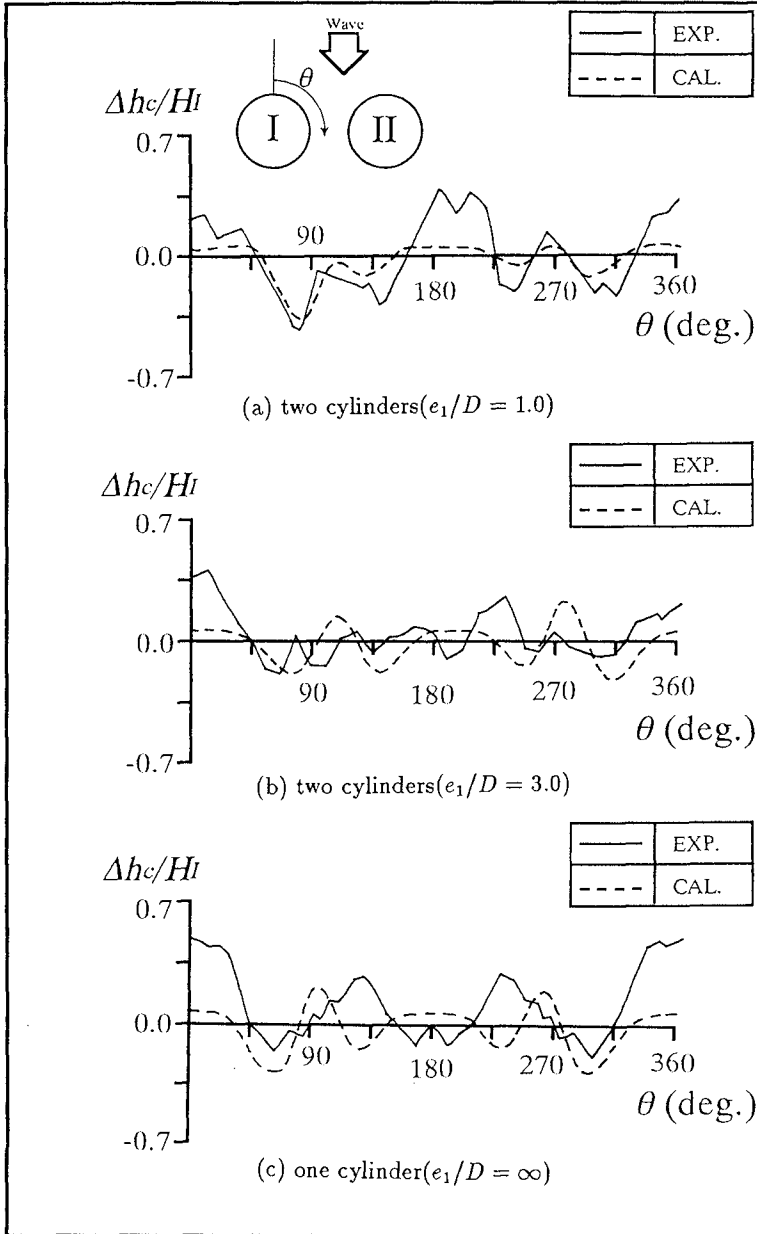


Fig. 4 Topographical change along structures  
 ( $D/L = 0.26, H_1/L = 0.03, h/L = 0.11, \alpha = 0^\circ, d_{50}/L = 0.00008, r/D = 0.53$ )

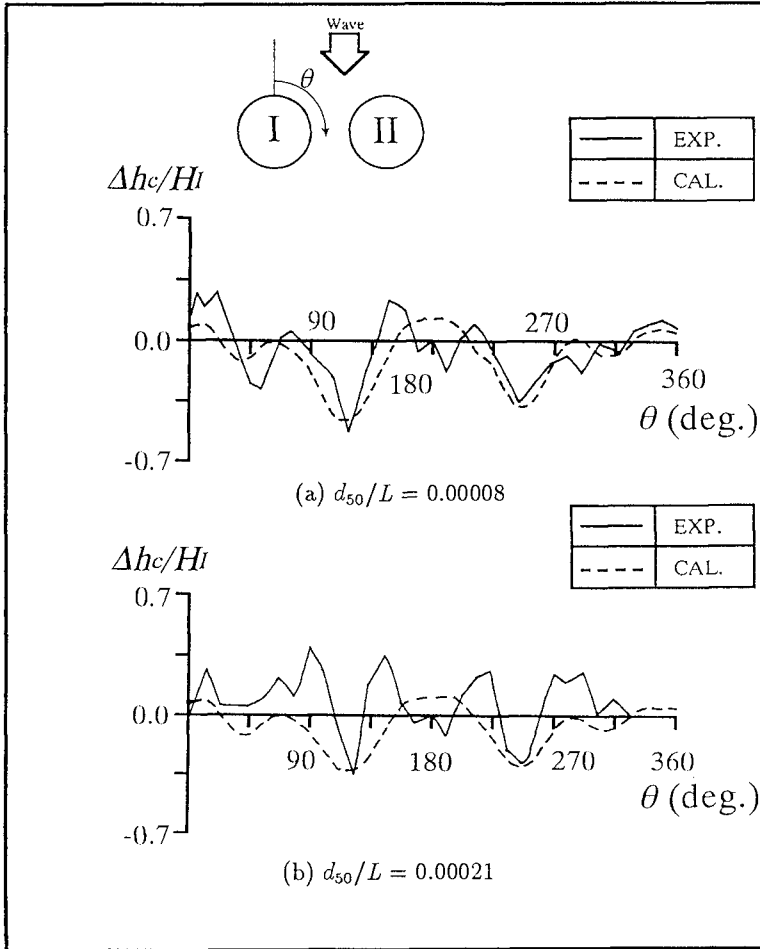


Fig. 5 Topographical change along two structures  
 ( $D/L = 0.49, e_1/D = 1.0, H_1/L = 0.03, h/L = 0.11, \alpha = 0^\circ, r/D = 0.53$ )

### 5 Concluding remarks

The bottom configuration changes around cylindrical structures under wave actions have been discussed. Main conclusions obtained in the present study are summarized as follows.

(1) The bottom configuration, the local scouring area and its depth around cylindrical structure are changed according to the number of structures, the structure's diameter, the incident wave angle and the sediment size.

(2) The bottom topographical change around structures can be well evaluated with the present theory.

(3) Under the obliquely incident wave, the scouring depth along the offshore structure I is larger than that along the onshore structure I.

(4) With increasing of the diffraction parameter  $D/L$ , the scouring depth becomes larger.

## References

Carter, T. G., P. L. F. Liu and C. C. Mei(1973) : Mass transport by waves and offshore sand bedforms, *J. of Waterways, Harbours and Coastal Eng. Div.*, ASCE, Vol. 99, pp. 165–184.

Isaacson, M. Q.(1979) : Wave induced forces in the diffraction regime, in *Mechanics of Wave-Induced Forces on Cylinders*, ed. T. L. Shaw, Pitman, London, pp. 68–89.

Katsui, H. and T. Toue(1992) : Evaluation of the scouring depth around a large scale offshore structure, *Proc. 39th Coastal Engg. Conf.*, pp. 496–500(in Japanese).

Kim, C.-J. and K. Iwata(1993) : Local Scouring around Two Large Circular Cylinders, *Proc. 25th IAHR*, Vol.3, pp. 159–166.

Kim, C.-J., T. Sanada, A. Imai, Y. Miyaike and K. Iwata(1994) : Wave field around multiple large cylindrical structures, *Proc. 41st Coastal Engg. Conf.*, pp. 351–355(in Japanese).

Swart, D. H.(1974) : Offshore transport and equilibrium profiles, *Pub. No. 131*, Delft Hydr. Lab., 244pp.

Watanabe, A(1985) : Nearshore dynamics and coastal processes, edited by K. Horikawa, *Univ. of Tokyo Press*, pp. 272–284.

Xie, X. L.(1981) : Scouring patterns in front of the breakwaters, *Coastal Engg. Group, Dep. of Civil Engg., Delft University of Technology*, 61p.

## CHAPTER 89

### Stability of Rubble Mound Foundations of Composite Breakwaters under Oblique Wave Attack

Katsutoshi KIMURA<sup>1</sup>  
Shigeo TAKAHASHI<sup>2</sup>  
Katsutoshi TANIMOTO<sup>3</sup>

#### ABSTRACT

The armor stability of composite breakwaters has been investigated by large 3-D model experiments using oblique irregular waves. The characteristics of wave-induced flow near the mound, which directly affect the armor stability, are disclosed theoretically and numerically. The stability number of armor units in breakwater trunk, head and tail sections is formulated for oblique wave angles less than 60°. The applicability of the proposed methods is confirmed by prototype failure data, and the analyses of case studies are shown for some practical conditions.

#### INTRODUCTION

Rubble mounds of composite breakwaters are usually covered with armor units heavy enough to withstand severe wave actions. Methods to calculate the minimum weight due to irregular waves have been proposed by Tanimoto et al. (1982) and by Wu et al. (1983). However, these techniques apply only for 2-D conditions, such as armor unit stability in breakwater trunks for normal incident waves.

The scouring of rubble mound foundations caused by neglect of the 3-D effects has been one major reason for composite breakwater failures in Japan. According to the 3-D model test data for irregular waves, Ito et al. (1966) suggested that armor damage increases rapidly under oblique wave attack.

---

<sup>1</sup> Civil Engineering Research Institute, Hokkaido Development Bureau, 1-3 Hiragishi Sapporo, 062 Japan.

<sup>2</sup> Port and Harbor Research Institute, Ministry of Transport, Yokosuka, Japan

<sup>3</sup> Dept. of Civil Eng., Saitama University, Urawa, Japan

Caissons at breakwater heads and tails were sometimes tilted by the scouring of rubble mound foundations. Conventional design procedures recommend that armor units at breakwater heads be 1.5 times heavier than those in breakwater trunks. However, the effect of incident wave angle and the extent of heavy armoring required are not obvious.

In this paper, the minimum weight of armor units required to withstand oblique incident waves is formulated for breakwater trunk, head and tail sections, based on stability tests, considering peak values of wave-induced water particle velocity on the mound.

## ARMOR STABILITY AND WAVE-INDUCED FLOW NEAR MOUND

### Stability Number of Armor Units

Figure 1 shows a standard cross section of a composite breakwater with a vertical wall and a rubble mound foundation. Wave forces acting on the vertical wall can be calculated for the breakwater's trunk, head and tail considering wave directions.

Rubble mound foundations have been however designed on the basis of engineer's experience, according to the following formula:

$$W = \frac{\gamma_d H_{1/3}^3}{N_s^3 (S_r - 1)^3} \quad (1)$$

where  $W$  is the stable weight of armor units (tf);  $\gamma_d$  the unit weight of armor units;  $S_r$  the specific gravity of armor units in sea water;  $H_{1/3}$  the wave height used in design (m); and  $N_s$  the stability number determined by wave factors, mound forms and characteristics of armor units. Equation (1) was developed by Hudson (1959) and has been in general use since Brebner and Donnelly (1962) modified it to estimate the stable weight of rubble mound foundation for vertical walls. Based on experimental results with irregular waves, Tanimoto et al. (1982) proposed the formula below to estimate the stability number of armor

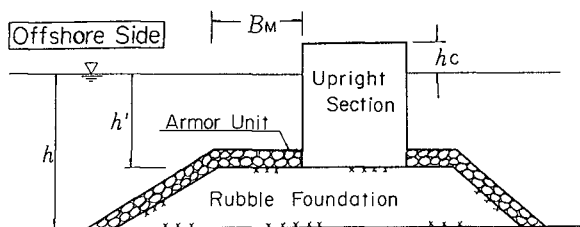


Figure 1 Standard Cross-Section of Composite Breakwater

units (two-layered settlement) against normal incident waves in breakwater trunks:

$$N_s = \max \left\{ 1.8, 1.3 \frac{1-\kappa}{\kappa^{1/3}} \frac{h'}{H_{1/3}} + 1.8 \exp \left[ -1.5 \frac{(1-\kappa)^2}{\kappa^{1/3}} \frac{h'}{H_{1/3}} \right] \right\} \quad (2)$$

where  $\kappa$  is non-dimensional flow speed. Peak horizontal speed of water particle motion  $U$  near the bottom is defined as;

$$U = \sqrt{\frac{gH^2\kappa}{h'}} \quad (3)$$

where,  $H$  is incident wave height,  $h'$  is water depth above the rubble mound foundation and  $g$  is gravitational acceleration. As for wave forces on armor units, it is assumed that drag forces predominate over inertial forces. For the 3-D conditions,  $\kappa$  is formulated considering peak flow of water particle motions as described below.

In breakwater trunk sections for oblique wave attack,  $\kappa$  is defined by the small amplitude wave theory as follows:

$$\kappa = \kappa_1 \cdot (\kappa_2)_B \quad (4)$$

$$\kappa_1 = \frac{2kh'}{\sinh 2kh'} \quad (5)$$

$$(\kappa_2)_B = \max \{ \alpha_s \sin^2 \beta \cos^2(kl/\cos\beta), \cos^2 \beta \sin^2(kl/\cos\beta) \} \quad (6)$$

where  $\beta$  is the incident wave angle defined as the angle between the wave direction and the normal line of the breakwater alignment,  $k$  is wave number ( $= 2\pi/L'$  :  $L'$  is wave length for depth  $h'$ ), and  $l$  is the distance from the vertical wall,  $\kappa_1$  is the parameter of relative depth, and  $(\kappa_2)_B$  expresses the effect of mound shape and wave direction. The first and second terms of  $(\kappa_2)_B$  correspond to the peak flows, components parallel and orthogonal to the alignment, respectively. The slope factor  $\alpha_s$  is determined to be 0.45 from the measured data and is multiplied only by the first term of Eq.(6), as the slope effect does not exist along the breakwater alignment.

Figure 2 shows the relationship between  $(\kappa_2)_B$  and  $l/L'$  for three wave directions;  $\beta=0^\circ$ ,  $45^\circ$  and  $60^\circ$ . For  $\beta = 0^\circ$ ,  $(\kappa_2)_B$  is determined by the second term of Eq.(6), and armor units with wider berm mounds become more unstable.

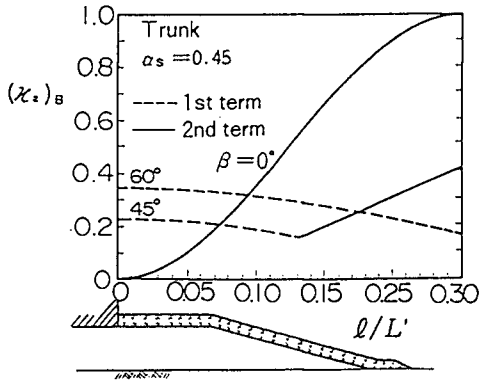


Figure 2 Non-Dimensional Flow Speed in Breakwater Trunk

For oblique incident 60° conditions,  $(\kappa_2)_B$  is determined by the first term of Eq.(6) and slightly decreases away from the vertical wall.

Formulae for Breakwater Head and Tail

For breakwater head and tail sections,  $\kappa$  is formulated from the flow speed at the bottom using the small amplitude wave theory as follows;

$$\kappa = \frac{\kappa_1 \alpha_s \tau^2}{4} \tag{7}$$

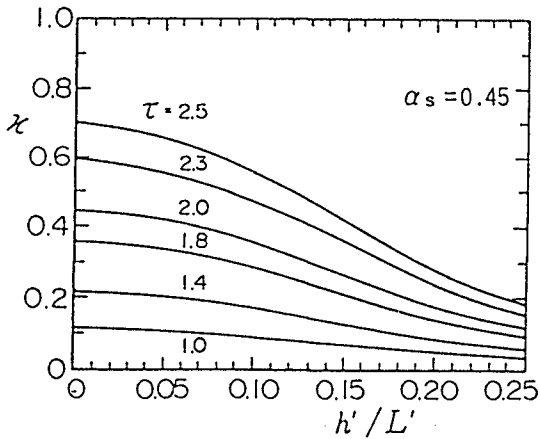


Figure 3 Non-dimensional Flow Speed at Breakwater Head and Tail



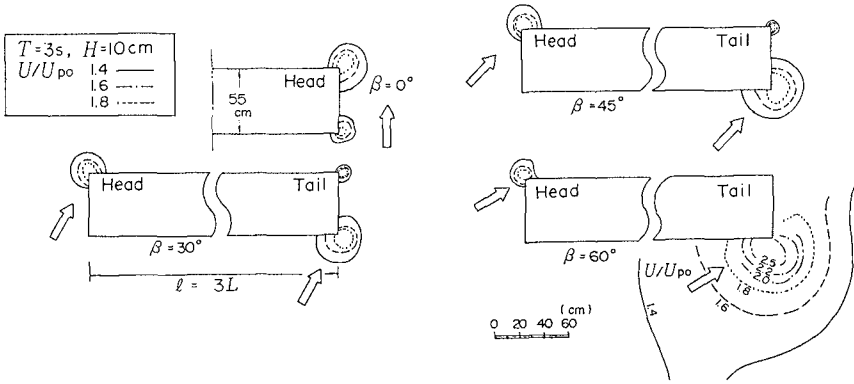


Figure 4 Flow Patterns at Breakwater Head and Tail

where  $\tau$  is the correction factor for local rapid flow around corners. Figure 3 shows the relationship between  $\kappa$  and the relative water depth  $h'/L'$  using  $\tau$  as a parameter. For longer period conditions with smaller relative depth, flow speed becomes larger.

Figure 4 shows numerical results of the mild slope equations. Flow pattern is analyzed for flat bottom conditions with  $h = 30$  cm. The length of breakwater is three times that of incident wave length. The wave condition is  $T = 3.0$  s and  $H = 10$  cm. The peak speed of rapid flow  $U$  is divided by  $U_{p0}$ , the peak water particle velocity at bottom in progressive wave conditions without breakwaters. Rapid flow occurs locally around the offshore- and onshore-corners for normal incident conditions. The oblique  $60^\circ$  incidence leads to remarkable

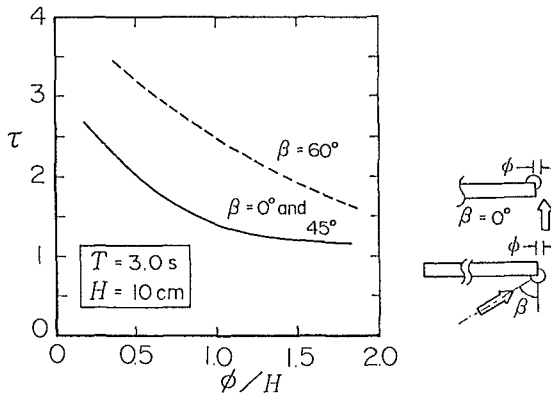


Figure 5 Rapid Flow Area

local flow around corners projecting towards the wave direction at breakwater tails as the standing wave height increases along the breakwater for the wave direction.

Wave-induced flow on the rubble mound is measured by electromagnetic current meters for regular wave conditions. The curved lines in Fig. 5 show the limit of rapid flow areas. Since the stability tests proved that the area to be protected is within the range of  $1.0H$  from the corner,  $\tau=1.4$  can be used for  $\beta=0^\circ$  and  $\beta=45^\circ$  conditions, and  $\tau=2.5$  can be used for  $\beta=60^\circ$  conditions

## STABILITY TESTS

### Experimental Setup

The tests were carried out in a 50m-long, 20m-wide 3-D wave basin. The basin bottom slopes at a gradient of 1/50, as shown in the lower part of Fig.6 (d). The incident wave angles  $\beta$  were  $0^\circ$ ,  $45^\circ$  and  $60^\circ$ , varied by changing the layout of the breakwater model as shown in Fig. 6 (a) ~ (c). The length of the breakwater alignment is more than 2.5 times the wave length for oblique incident conditions.

The standard cross section of the model breakwater was a relatively low mound condition. Water depth  $h$  was 65 cm, mound depth  $h'$  was 45 cm and mound berm width  $B_M$  was 40 cm.

Stability tests of armor units were carried out under irregular wave conditions. The wave range was limited to the non-breaking conditions,  $H_{1/3}/h$  is less than 0.35. Three types of wave period ( $T_{1/3} = 1.64, 2.19$  and  $2.92$  s) were prepared, and the relative depth  $h/L$  was varied from 0.08 to 0.15. The spectrum of the irregular waves was the modified Bretschneider-Mitsuyasu type, and the wave number was about 150 for each experiment.

Standing wave heights in front of vertical wall vary along the breakwater alignment due to diffraction waves. Armor stabilities in the breakwater trunk were examined in front of caissons No. 10 ~ 12 ( Fig. 6(a):  $\beta=0^\circ$ ), No.12~14 ( Fig. 6 (b):  $\beta=45^\circ$ ) and No.9 ( Fig.6 (c):  $\beta=60^\circ$ ), where the standing wave height is approximately twice the incident wave height.

Four types of stones with mean weights of 15, 30, 60 and 100 gf were used as a model of armor units. Physical characteristics of armor stones are shown in Table 1. The wave height was gradually increased without changing the arrangement of armor units.

The inspection area was divided into a 20-cm-square grid, and differently colored armor stones were placed in each square. The number of stones moving out of the grid was counted by visual observation. The damage rate defined as the ratio of moved stones to the total, and maximum damage ratios are used in the following analyses.

### Armor Stability at Breakwater Trunk

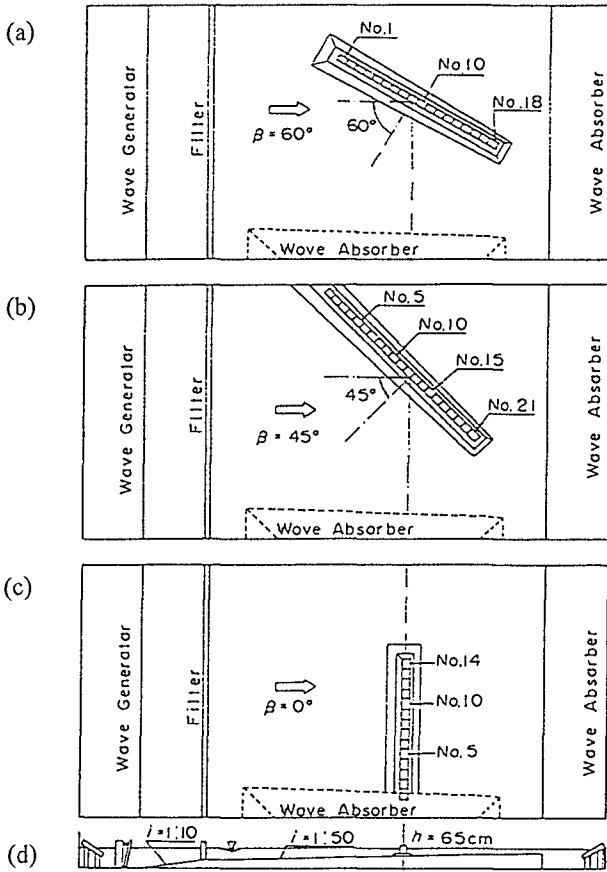


Figure 6 Model Breakwaters in a Three-Dimensional Wave Basin

Table 1 Model Armor Stones

Grade	Weight (gf)		Density ( $\text{gf}/\text{cm}^3$ )
	Average	Standard Div.	
I	15.0	2.05	2.60
II	29.9	3.51	2.59
III	57.3	5.99	2.62
IV	105.5	12.5	2.75

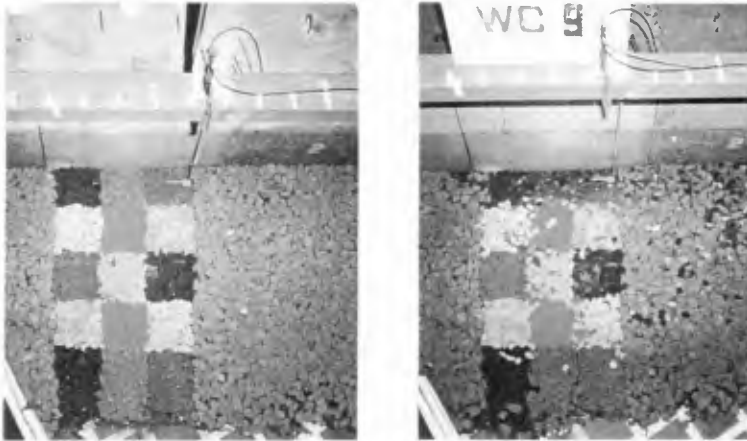


Photo 1 Damage Pattern: Oblique 60° Condition

Photo 1 shows damage patterns for the oblique 60° condition in breakwater trunk. The left part shows the armor conditions before wave action, the right shows them after the wave action of  $T_{1/3} = 2.92$  s and  $H_{1/3} = 23.0$  cm. Armor units of 15 gf were heavily scoured near the vertical wall by the wave-induced rapid flow along the breakwaters.

Figure 7 shows damage ratio, with the incident wave height on the abscissa. The results for normal and 45° oblique waves are very similar, and the damage does not extend with the increase in the wave height. However, when the wave angle  $\beta = 0^\circ$ , the damage starts at small wave heights, and then increases remarkably. This is because the non-dimensional flow speed  $(\kappa_2)_B$  for  $\beta = 60^\circ$  is larger than that for  $\beta = 0^\circ$  and  $\beta = 45^\circ$  when  $l/L' \leq 0.07$  as shown in Fig. 2.

Figure 8 shows the relationship between wave heights and the minimum weights for three wave directions, when  $T_{1/3} = 2.92$  s. The circles show the

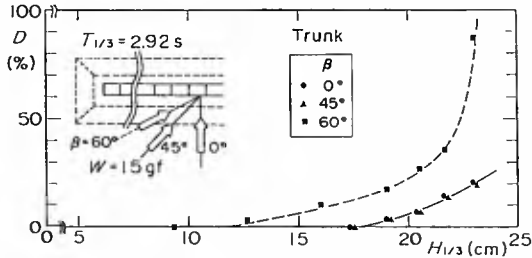


Figure 7 Relationship between Damage and Wave Height

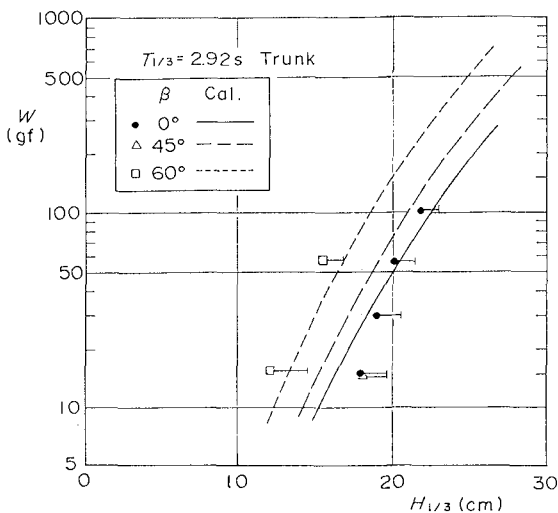


Figure 8 Minimum Armor Weight (Trunk)

limits of damage, with the short, solid horizontal lines indicating the 5% damage range. The curved lines are calculated by the proposed method and agree well with the experimental values. This results confirm the applicability of formulating the wave-induced flow based on the small amplitude wave theory.

Armor Stability at Breakwater Head and Tail

Figure 9 shows scouring patterns at the breakwater head and tail for each of the wave directions with  $T_{1/3} = 2.92$  s. For the normal incident waves, the damage is larger at the shoreward corner of the caisson. For oblique waves, the scouring occurs at projecting corners of the breakwater tail.

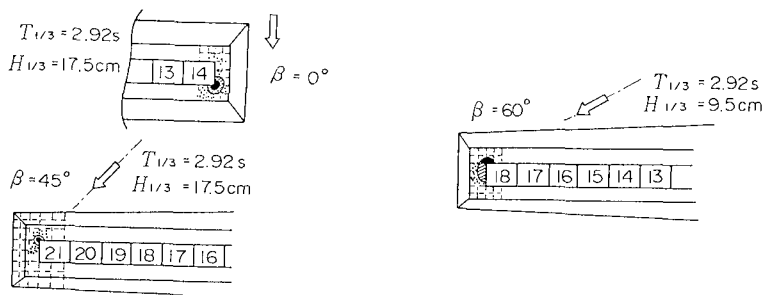


Figure 9 Scouring at Breakwater Head and Tail

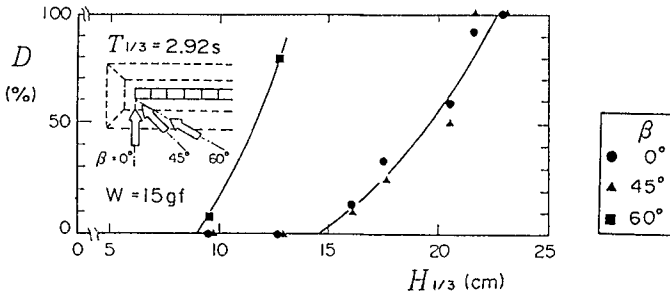


Figure 10 Relationship between Damage and Wave Height

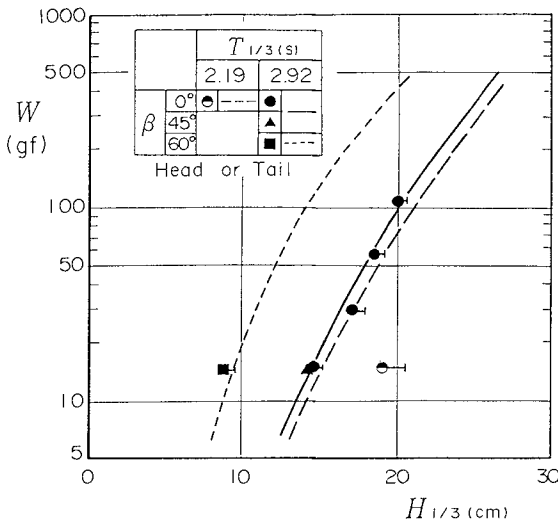


Figure 11 Minimum Armor Weight (Head and Tail)

patterns agree well with the positions where the wave-induced flow speed near the mound is larger as shown in Fig. 4.

Figure 10 shows the damage ratio for breakwater head and tail sections under waves with  $T_{1/3} = 2.92$  s. The results for the normal and 45° oblique waves are very similar. With the 60° oblique waves, the damage begins to occur at small wave heights and then increases remarkably.

Figure 11 shows the relationship between the wave height and the minimum armor weight for each wave direction, when  $T_{1/3}$  is 2.19 s and 2.92 s. No armor damage was recorded for the wave condition of  $T_{1/3} = 1.64$  s. Armor units for

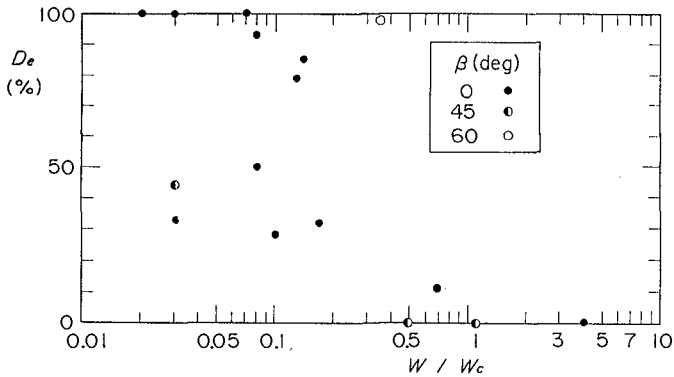


Figure 12 Comparison with Prototype Failures

longer wave periods become more unstable and should be made heavier than those used for shorter wave period.

The curved lines are calculated by the proposed method and agree well with the experimental values. It is shown that the effect of incident wave angles can be expressed by the correction factor  $\tau$  in the calculation of minimum armor weights.

#### Comparison with Prototype Failures

Figure 12 compares the prototype armor failures (1965 ~ 1990) and the proposed methods. The x-axis represents the ratio of the mean weight of armor units  $W$  to the weight calculated by the proposed method  $W_c$ , and the y-axis represents the damage percent of the prototype armor units  $D_e$ .

When  $W/W_c < 1$ , damage is expected, and the applicability of the proposed calculation method is confirmed by the above comparisons.

### EXAMPLE OF ARMOR DESIGN

#### Design Conditions

A composite breakwater, in Fig. 13, is used for the case studies. Design conditions are as follows;

Depth :  $h = 13.0$  m,  $h' = 9.0$  m

Wave Conditions :  $H_{1/3} = 5.0$  m,  $T_{1/3} = 13.0$  s

$B_M = 8.0$  m

$\beta = 0^\circ$  and  $60^\circ$

Armor units : Two layers of stones,  $\gamma_d = 2.65$  tf/m<sup>3</sup>

#### Armor Units for Breakwater Trunk

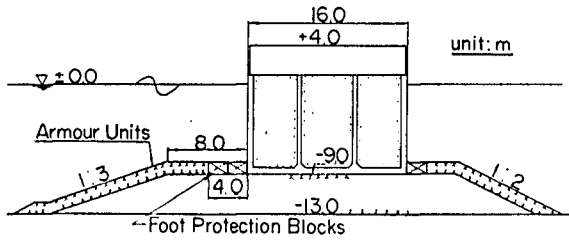


Figure 13 Design Conditions

## (1) Normal incident condition

Substituting  $h'/L' = 0.076$  for Eq.(5),  $\kappa_1$  is calculated as follows;

$$\kappa_1 = \frac{2 \times 2 \times 3.14 \times 0.076}{\sinh(2 \times 2 \times 3.14 \times 0.076)} = 0.863$$

For normal incident conditions, the mound shoulder becomes critical for the stability of armor units.

Substituting  $l = B_M$  for Eq.(6),

$$(\kappa_2)_B = \sin^2 \left( \frac{2 \times 3.14 \times 8.0}{118} \right) = 0.171$$

$$\kappa = \kappa_1 \cdot (\kappa_2)_B = 0.863 \times 0.171 = 0.148$$

Using Eqs.(1) and (2), the stability number and the necessary minimum weight are calculated as follows:

$$N_s = 1.3 \times \frac{1 - 0.148}{0.148^{1/3}} \times \frac{9.0}{5.0} + 1.8 \exp \left[ -1.5 \times \frac{(1 - 0.148)^2}{0.148^{1/3}} \times \frac{9.0}{5.0} \right] = 3.79$$

$$W = \frac{2.65 \times 5.0^3}{3.79^3 \times (2.65/1.03 - 1)^3} = 1.56 \text{ (tf)}$$

## (2) Oblique 60° Condition

Armor stability should be checked; at the outside of foot protection blocks ( $l = 4.0$  m),

$$\begin{aligned} (\kappa_2)_B &= \max \left\{ 0.45 \sin^2 60 \cos \left( \frac{2 \times 3.14 \times 4.0}{118} \right), \cos^2 60 \sin^2 \left( \frac{2 \times 3.14 \times 4.0}{118} \right) \right\} \\ &= \max \{ 0.322, 0.011 \} = 0.322 \end{aligned}$$



$K$ ,  $N_S$  and  $W$  are calculated as follows:

$$\kappa = 0.278, N_S = 2.80, W = 3.88 \text{ (tf)}$$

For the breakwater trunk, the necessary weight of armor units for oblique  $60^\circ$  waves is 2.5 times that for normal incident conditions.

#### Armor Units for Breakwater Head and Tail

##### (1) Normal incident condition

Substituting  $\kappa_1 = 0.863$  and  $\tau = 1.4$  for Eq.(7),  $\tau$  is calculated as follows:

$$\kappa = 0.863 \times \frac{0.45 \times 1.4^2}{4} = 0.190$$

Using Eqs.(1) and (2), the stability number and the necessary minimum weight are calculated as follows:

$$N_S = 3.38, W = 2.20 \text{ (tf)}$$

##### (2) Oblique $60^\circ$ Condition

Substituting  $\tau=2.5$  for Eq.(7),  $K$ ,  $N_S$  and  $W$  are calculated for breakwater tails as follows:

$$K = 0.607, N_S = 2.19, W = 8.11 \text{ (tf)}$$

At the breakwater tail, the necessary weight for oblique  $60^\circ$  waves becomes 3.7 times than that for normal incident waves. Under oblique  $60^\circ$  conditions, the tail section requires armor units two times heavier than the trunk section does.

## CONCLUSIONS

The characteristics of the wave-induced flow near the mound of composite breakwaters, which directly affect the armor stability, were investigated for 3-D conditions. The results of numerical analyses and physical model tests confirmed that armor damages in prototype failures occurred in the rapid flow areas.

The stability number can be calculated by Eq.(2) for oblique wave conditions of non-dimensional flow speed  $\kappa$ . For breakwater trunk sections,  $\kappa$  is formulated by Eqs.(4) through (6). For breakwater head and tail sections,  $\kappa$  is formulated by Eq.(7), and the area to be heavily protected is within the range of  $1.0 H$  from the corner of caissons. The applicability of proposed methods was confirmed by stability model tests and prototype failure analyses.

## REFERENCES

- Brebner, A. and Donnelley, D. (1962): Laboratory study of rubble foundation for vertical breakwater, Proc. of 8th Coastal Engineering Conference, New Mexico City, pp.408-429.
- Wu, G., and Jensen, O. J. (1983): Stability of Rubble Foundation for Composite Breakwaters, Proc. of Conference on Coastal and Port Engineering in Developing Countries, pp.831- 841.
- Hudson, R. Y. (1959): Laboratory investigation of rubble mound breakwaters, Proc. ASCE, Vol.85, No.WW3, pp.93-121.
- Ito, Y., Fujishima, M. and Kitatani T. (1966): On the Stability of Breakwaters, Report of the Port and Harbor Research Institute, Vol.5, No.14, pp.1~134. (in Japanese)
- Tanimoto, K., Yagyu, T. and Goda, Y. (1982): Irregular Wave Tests for Composite Breakwater Foundations, Proc. of 18th Coastal Engineering Conference, pp.2144-2163.

## CHAPTER 90

# ANALYSIS OF NONLINEAR COEFFICIENTS OF REFLECTION AND TRANSMISSION OF WAVES PROPAGATING OVER A RECTANGULAR STEP

Wudhipong Kittitanasuan<sup>1</sup> and Yoshimi Goda<sup>2</sup>

### Abstract

A mathematical model for nonlinear wave propagation over a rectangular step is formulated based on the boundary element method. The wave profile computed by this model gives a more realistic wave profile than that of linear wave theory. The calculation of the height of nonlinear waves is studied, and as a results of the study the reflection and transmission coefficients are computed based on the technique which considered the higher harmonic components in the computation of wave height. The solutions of these coefficients are presented and compared with laboratory experiments.

## 1 Introduction

A land reclamation has been recommended to provide an artificial shallow ledge around its periphery in order to mitigate adverse effects on the environment. This shallow ledge can be considered as a rectangular step placed in finite depth water. A breakthrough of knowledge of the transformations of waves on this marine structure is necessary so that we can design and construct all related structures properly. Transformations of waves on a rectangular step were originally studied by Lamb (1932), who solved this kind of problem by applying basic continuity requirements at the point of discontinuity. Up to now, Bartolomeusz (1958), Newman (1965), Mei and Black (1969), Ijima (1971), *etc.*, have proposed various solutions for the prediction of wave reflection and transmission coefficients. Most of these solutions were derived based on linear wave theory. In

---

<sup>1</sup> D. Eng., Lecturer, Department of Water Resources Engineering, Chulalongkorn University, Phayathai Rd., Bangkok 10330, Thailand

<sup>2</sup> D. Eng., Professor, Department of Civil Engineering, Yokohama National University, Hodogaya-ku, Yokohama 240, Japan

many applications, however, it is the waves of large amplitude which are of primary importance. It is because the large amplitude waves exercise vast influence on the aquatic environment, owing to their strong movements of water particle.

As illustrated by Ohyama and Nadaoka (1991) and Kittitanasuan *et al.* (1993) waves on the step exhibit highly nonlinear behavior exemplified by the enhancement of the higher harmonic components, and therefore, the effect of these nonlinear components should be considered in the computation of the coefficients of wave reflection and transmission of rectangular step. In this study, an attempt is made to provide the solutions of wave reflection and transmission coefficients based on the nonlinear computation.

## 2 Mathematical Formulation

### 2.1 Governing Equation

The nonlinear boundary value problem based on the velocity potential theory is formulated by assuming that the fluid is inviscid and incompressible, and the fluid motion is irrotational. The two-dimensional continuity equation in the fluid domain  $\Omega$  can be written as follows :

$$\frac{\partial^2 \phi}{\partial x^2} + \frac{\partial^2 \phi}{\partial z^2} = 0 \quad (\text{in } \Omega) \quad (1)$$

where  $\phi$  is the velocity potential,  $x$  is the horizontal axis, and  $z$  is the vertical axis taken upward the mean water level.

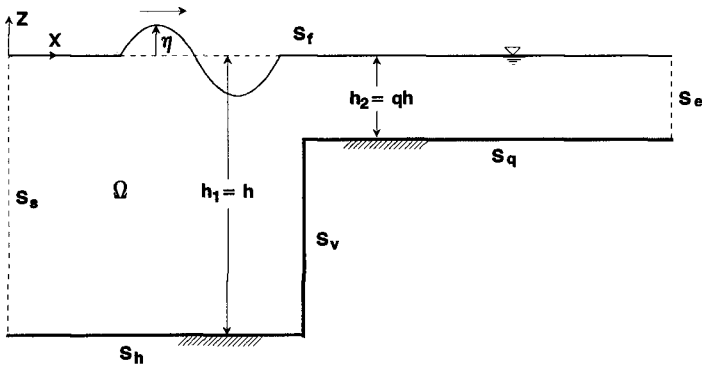


Figure 1: Definition sketch

### 2.2 Boundary Conditions

Along the solid boundaries,  $S_h$ ,  $S_q$ , and  $S_v$  sketched in Fig. 1, the boundary conditions are formulated as shown below.

$$\frac{\partial \phi}{\partial z} = 0 \quad (\text{on } S_h) \quad (2)$$

$$\frac{\partial \phi}{\partial z} = 0 \quad (\text{on } S_q) \quad (3)$$

$$\frac{\partial \phi}{\partial x} = 0 \quad (\text{on } S_v) \quad (4)$$

For the incident boundary,  $S_s$ , at the left-hand side of Fig. 1, the velocity normal to this boundary is equal to the moving velocity of a wave paddle.

$$-\frac{\partial \phi}{\partial n} = \frac{\partial \phi}{\partial x} = U \quad (\text{on } S_s) \quad (5)$$

where  $U$  is the moving velocity of a wave paddle, which is calculated according to the wave maker theory for a given wave height and period. It should be noted that the depth-dependent velocity computed from the orbital velocity of water particle can also be utilized as the velocity  $U$ .

Two free-surface boundary conditions must be satisfied; the first condition is the kinematic boundary condition Eq. (6), and the second condition is the Bernoulli equation Eq. (7) with the assumption of constant pressure everywhere on the free surface.

$$\frac{\partial \phi}{\partial n} = \dot{\eta} \cos \beta \quad (\text{on } S_f) \quad (6)$$

$$\dot{\phi} + \frac{1}{2} \left\{ \left( \frac{\partial \phi}{\partial n} \right)^2 + \left( \frac{\partial \phi}{\partial s} \right)^2 \right\} + g\eta = 0 \quad (\text{on } S_f) \quad (7)$$

where  $\dot{\eta} = \partial \eta / \partial t$ ,  $\dot{\phi} = \partial \phi / \partial t$ ,  $g$  is the acceleration of gravity,  $n$  and  $s$  show the directions of normal and tangent vectors respectively, and  $\beta$  is the angle between the normal vector and the vertical axis.

Both of the free surface boundary conditions are nonlinear and are applied on the free surface, the elevation of which is not known *a priori*.

In order to simulate wave motions for a long duration, an appropriate boundary condition has to be introduced at the vertical boundary  $S_e$ , at the right-hand side of Fig. 1 so that the waves can pass through the boundary without undergoing significant distortion and without influencing the interior solution. A variety of methods have been developed to achieve the non-reflectivity at the boundary for wave propagation problems. Among various methods proposed, use of the Sommerfeld boundary condition appears most appropriate. In this study, we shall utilize the Sommerfeld boundary condition at the boundary  $S_e$ ; therefore, the boundary condition at  $S_e$  can be defined as:

$$\frac{\partial \phi}{\partial x} = -\frac{1}{C} \frac{\partial \phi}{\partial t} \quad (\text{on } S_e) \quad (8)$$

where  $C$  is the phase speed of the wave, and is approximated with that derived by the linear wave theory.

## 3 Numerical Results

### 3.1 Propagating Wave Profile

A study of wave deformation on the step was made through the numerical analysis by the present model and experiment. A numerical flume composed of 105 elements on the free surface and 63 elements on the bottom and lateral boundaries was created. The water depth was set at 0.376 m in front of the step and 0.113 m on the step, the step height of 26.3 cm was utilized. A wave period of 1.74 s was utilized in the computation. On the free surface, the element size of 20 cm was used in the deep water region and 10 cm was used in the shallow water region; these element sizes were equal to  $L/15.3$  and  $L/17.9$ , respectively. A time step of  $T/16$  were utilized in the computation. The spatial profile of wave propagation is computed by the present model and is plotted in Fig. 2. We can see from this figure that when waves enter into the shallow zone, the wave height increases, and the wave crest becomes much sharper than the wave trough, and the secondary crest is developed. The location of this secondary crest on the wave profile changes gradually as the wave propagates into the shallow water zone.

### 3.2 Comparison of Numerical and Experimental Results

In order to verify the results of the present model, a laboratory experiment was conducted in a 17 m long wave flume, equipped with a computer controlled piston-type wave generator. A rectangular step of the same height 26.3 cm as used in the numerical computation was installed in this flume. At the end of the flume, a flat plate of 2.0 m long was installed with a slope of 1/10. On the top of this plate, a wave absorber was placed to reduce wave reflection at the end of the flume. A wave period of 1.74 s was utilized for this experiment. A single wave gage was used to measure time-history wave profiles at 4 measuring points, at the distances of 1.0 m offshoreward from the tip of the step, and 1.0 m, 2.0 m, and 3.0 m inshoreward from the tip of the step.

The wave profiles computed by the present model are compared with the experimental results for four different locations as mentioned above. The comparisons are shown in Figs. 3. In the comparisons of wave profiles about 20 wave cycles were employed in order to have stable wave profiles. The profile of waves computed by the present model illustrates similar wave profiles in the both regions, in front of the step and on the step. The secondary wave crest is also well simulated having a similar shape compared with the experiments. Therefore, it is clear that the present model can accurately predict the wave profile of wave propagation over the rectangular step.

Both results have indicated that the wave profile on the rectangular step is different from that of sinusoidal waves; *i.e.*, the wave crest is much sharper than the wave trough, and a secondary crest is developed.

### 3.3 Higher Harmonic Components

The effect of finite amplitude on the amount of energy transferred to higher harmonic components of waves on the step was numerically and experimentally investigated. For this analysis, the water depth was set at 0.376 m in front of the step and 0.113 m on the step. The wave height was varied at three levels,

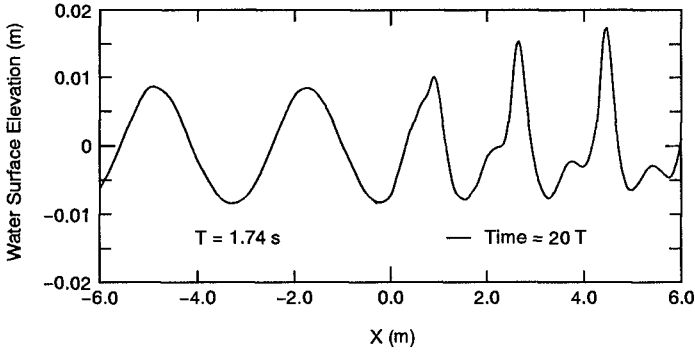


Figure 2: Wave propagating profile

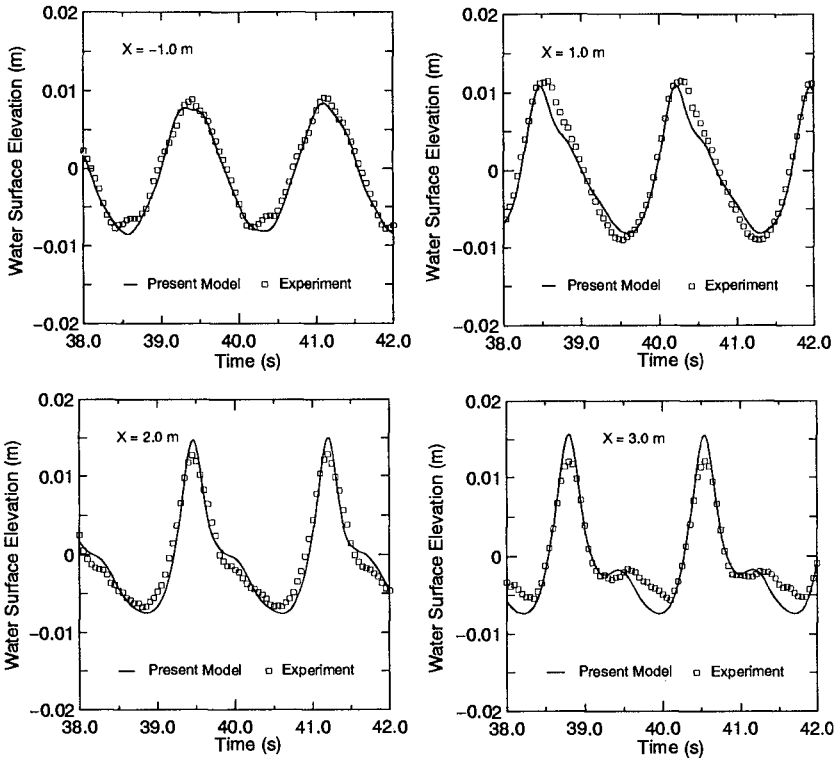


Figure 3: Comparison of wave profiles

while the wave period was fixed at 1.74 s. From the results of wave profiles by numerical model and experiment, the FFT analysis are made to computed the amplitudes of all frequency components. In order to separate the transmitted waves from the reflected waves at the end of the flume, the resolution technique introduced by Goda and Suzuki (1976) is employed. Then, the potential energy of the first, second and third harmonics are computed. In Fig. 4, the ratios of maximum energy of the second and third harmonics to that of the first harmonic are plotted against the relative wave height, the ratio of the height of incident waves  $H_{in}$  to the water depth on the step  $h_2$ . The relative energy is found to be 0.2~0.4 for the second harmonic and 0.01~0.09 for the third harmonic. Therefore, the energy transferred to higher harmonic components is very significant compared with that of the first harmonic.

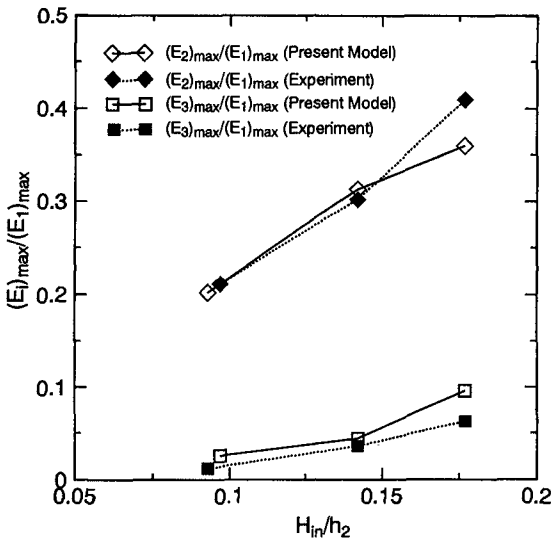


Figure 4: Relative energy of higher harmonic components

## 4 Analysis of the Height of Nonlinear Waves

### 4.1 Conventional Methods

The reflection of water waves is known to associate with every problem of wave and structure interaction. In order to estimate wave heights of incident and reflected waves, we need to have an information of reflection coefficient, or the ratio of reflected to incident wave heights. Up to now, many techniques have been proposed by various researchers, Healy (1953), Thornton and Calhoun (1972), Goda and Suzuki (1976), Morden *et al.* (1976), Mansard and Funke (1980), and others for the estimation of wave reflection. The method introduced by Healy is based on a measurement of wave profile with a single wave gage which is traversed over a distance of more than a half wave length. The methods of Thornton and Calhoun,



Goda and Suzuki, and Morden *et al.* are based on a simultaneous measurement of wave profile at two positions on a line parallel to the direction of wave propagation. Meanwhile, the method by Mansard and Funke employs three-points measurements of the wave profile.

The first method to be described herein is based on the assumption that the total energy is equal to the summation of the energies of incident and reflected waves. The method is later referred as the method (a) in the calculation of wave height of experiments. The formulation of this method can be summarized as follow :

$$E = E_{in} + E_{rf} = \frac{1}{8} \rho g (H_{in}^2 + H_{rf}^2) = (1 + K_{rf}^2) \frac{1}{8} \rho g H_{in}^2 \quad (9)$$

where the subscripts "in" and "rf" refer to the incident and reflected waves respectively, and  $K_{rf}$  is the reflection coefficient. This reflection coefficient is estimated as the ratio of the amplitude of the fundamental component of reflected waves to that of incident waves which are computed by utilizing the resolution technique of Goda and Suzuki (1976).

From Eq. (9), the incident wave height can be computed as

$$H_{in} = \sqrt{\frac{8E}{\rho g(1 + K_{rf}^2)}} = \sqrt{\frac{4(E_1 + E_2)}{\rho g(1 + K_{rf}^2)}} = \sqrt{\frac{4}{\rho g} [(E_1)_i + (E_2)_i]} \quad (10)$$

where

$$(E_1)_i = \frac{E_1}{1 + K_{rf}^2}, \quad E_1 = \frac{1}{2} \rho g \sum_{i=1}^{n/2} (a_i^2 + b_i^2)_1$$

$$(E_2)_i = \frac{E_2}{1 + K_{rf}^2}, \quad E_2 = \frac{1}{2} \rho g \sum_{i=1}^{n/2} (a_i^2 + b_i^2)_2$$

and  $E_1$  and  $E_2$  are the energy calculated from all fourier components of the first and second wave gages, respectively.  $a_i$  and  $b_i$  are the amplitudes of sine and cosine terms obtained from the Fourier analysis of recorded wave profiles, respectively. The subscripts 1 and 2 represent the first and second wave gages, respectively.

The second method, to be referred as the method (b), is the method introduced by Goda and Suzuki (1976) for the calculation of wave heights of incident and reflected waves of irregular waves. The method is based on two main assumptions. The first one is that the energy of composite waves is represented with the sum of the energies of individual wave trains. The second one is that the proportionality of representative wave heights to the square root of wave energy holds for such composite wave too, regardless of the directions of individual wave trains. In general, the basic concept of the approach is similar to that the first method, except that the energy is estimated from the wave height of zero-crossing method. The wave height of incident waves of this method can be computed as

$$H_{in} = \frac{1}{2\sqrt{1 + K_{rf}^2}}(\bar{H}_1 + \bar{H}_2) \quad (11)$$

where  $\bar{H}_1$  and  $\bar{H}_2$  are the average wave heights computed by the zero-downcrossing method of the first and second wave gages, respectively.

## 4.2 Method by Kittitanasuan et al. (1993)

In the calculation methods of wave heights of incident and reflected waves described above, the reflection of waves is treated as a single value of the reflection of fundamental component, but the harmonic components of incident and reflected waves are not given appropriate consideration. As illustrated by Kittitanasuan *et al.* (1993), the second and third harmonic components play an important role on waves propagating in the shallow water. Therefore, these harmonic components should be considered in the calculation of the height of waves exhibiting nonlinear behavior. In this study, the method proposed by Kittitanasuan *et al.* for the calculation of wave height when waves contain enhanced higher harmonic components will be reviewed. The basic concept of this method is the conservation of energy density over a range of frequencies. The energy is considered to preserve within the range of major frequency components, *i.e.* the first, second and third harmonic components. In this method, the reflection of each harmonic component is treated individually. That means the energy density of incident and reflected waves are computed from the summation of energies of all resolved components of incident and reflected waves, respectively. In the resolution of incident and reflected components, the technique introduced by Goda and Suzuki (1976) is utilized.

According to this method, the wave height is calculated by converting the energy of all resolved incident and reflected components as shown in the following.

$$H_{in}^* = 2\sqrt{\frac{2E_{in}}{\rho g}} \quad ; \quad H_{rf}^* = 2\sqrt{\frac{2E_{rf}}{\rho g}} \quad (12)$$

where

$$E_{in} = \frac{1}{2}\rho g \sum_{i=f_{min}}^{f_{max}} (a_{in})_i^2 \quad ; \quad E_{rf} = \frac{1}{2}\rho g \sum_{i=f_{min}}^{f_{max}} (a_{rf})_i^2 \quad (13)$$

in which  $(a_{in})_i$  is the amplitude of a resolved component of incident waves and  $(a_{rf})_i$  is that of reflected waves.  $f_{min}$  and  $f_{max}$  are the minimum and maximum frequencies corresponding to the resolution technique.

Use of the whole energy is made to minimize the effect of energy spreading around the harmonic frequencies by the FFT analysis. In fact, the energy of frequency components outside the three consecutive frequencies around the harmonics was less than 5% in the present analysis.

By knowing these wave heights, the reflection coefficient can be calculated as follow :

$$K_{rf} = \frac{H_{rf}^*}{H_{in}^*} \quad (14)$$

The transmission coefficient,  $K_{tr}$ , can also be calculated as the ratio of the representative incident wave height on the step to the representative incident wave height in front of the step.

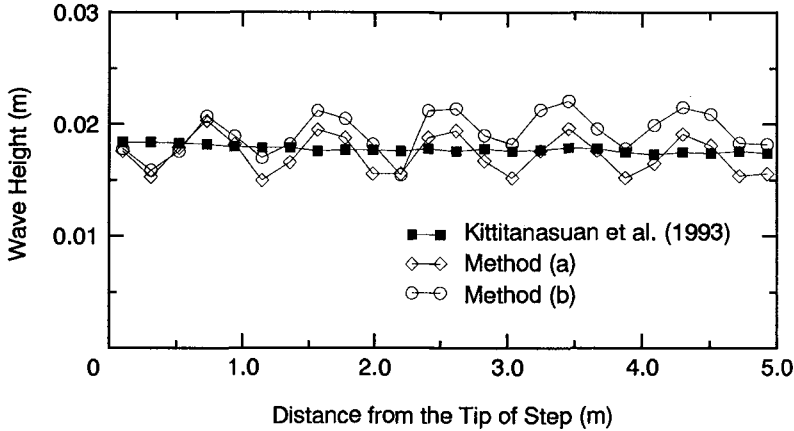


Figure 5: The comparison of computed wave heights

The three methods, methods (a), (b) and method by Kittitanasuan *et al.* (1993), were applied for the experimental data on the step. The water depths were set at 0.376 m in front of the step and 0.113 m on the step. A wave period of 1.74 s are utilized. The comparison of results of these three methods are illustrated in Fig. 5. The wave height computed by the method by Kittitanasuan *et al.* give a slight fluctuation of wave height along the shallow zone, and meanwhile the other two conventional methods give considerable fluctuations of wave heights. Among the three methods, it is evident that the method proposed by Kittitanasuan *et al.* yields the smallest fluctuation of the wave height on the step. Therefore, this method will be utilized for the computation of wave height through out the present study.

If we compare the wave heights computed from the methods (a) and (b) with that of Kittitanasuan *et al.* (1993), the method (a) is seen to under-estimate, and the method (b) tends to over-estimate the wave height. In the partial standing wave system, the maximum and minimum vertical displacements are results of the superposition of the profiles of the incident and reflected waves. When the wave height is measured directly by these maximum and minimum displacements as in the zero-crossing method, there is a possibility of over-estimation of the wave height.

The fluctuation of the wave heights computed by the two conventional methods was investigated. A relatively high reflection of waves from the wave absorber at the end of rectangular step is considered to be the reason of the fluctuation. The maximum wave reflection coefficient computed at all measuring points is found to be 0.26. The variation of wave height shown in Fig. 5 is considered to be corresponding to the wave height envelope in the partial standing wave system. Therefore, the wave length estimated by the wave height envelope was examined to confirm the assumption. The estimated wave length is 1.80 m, and this length corresponds to the wave length computed from the dispersion relationship of linear wave theory which is 1.79 m for this case. Therefore, we can conclude that the fluctuation of wave heights computed by the two conventional methods is caused by the reflection of waves at the end of rectangular step.

## 5 Reflection and Transmission Coefficients

### 5.1 Coefficients of Nonlinear Wave Reflection and Transmission

The numerical model based on the boundary element method described earlier is used to compute the profile of wave propagating over a rectangular step. The free surface boundary was discretized into 104 elements, 36 elements in the deep water side and 68 elements in the shallow water side. Besides the free surface boundary, there were 63 elements on the bottom and lateral boundaries. The element size on the free surface is selected to include the first three major harmonic components in the resolution of reflected waves. This element size is ranged between  $L/18.1$  to  $L/16.1$ . Three levels of water depth ratio  $q$ , the ratio of water depth on the step to the water depth in front of the step, were setup. The computations were conducted for 45 cases, 15 cases for each water depth ratio  $q$ . Three values of the relative wave depth on the step  $h_2/L_0$ , 0.025, 0.05 and 0.1, are utilized in the computations. The incident wave height is varied from 1% of water depth on the step to 26% of water depth on the step for the maximum case. A time step of  $T/16$  is used for all the computations. After obtaining time-history displacement of all nodal points, the wave height of incident, reflected and transmitted waves are computed by using the technique proposed by Kittitanasuan *et al.* (1993). Because of the spatial variation of wave heights on the step, the reflection and transmission coefficients are computed based on their average values.

The reflection coefficients of a rectangular step computed by the present model are illustrated in Fig. 6. The reflection coefficients computed by the analytical solutions derived by using Ijima's technique, are also included in these figures. The reflection coefficients computed by the present model give nearly the same values as those computed from the analytical solutions for  $q = 0.5$  and  $0.3$ . For  $q = 0.1$ , the reflection coefficients computed by the model give smaller values than those computed from the analytical solution for  $h_2/L_0$  less than 0.05. From these figures, it is seen that the incident wave height has a rather small effect on the reflection coefficients.

The transmission coefficients of waves propagating over a rectangular step computed by the present model are exhibited in Fig. 7. The transmission coefficients computed by the present model give nearly the same values as those computed by the analytical solution for the water depth ratio  $q$  of 0.5 and 0.3.

However, the coefficients by the present model yield lower values than those of the analytical solution for  $q=0.1$ . From the results of these transmission coefficients, the coefficients increase as the incident wave height increases for the relative depth  $h_2/L_0$  less than 0.05. However, the effect of this wave height is quite small.

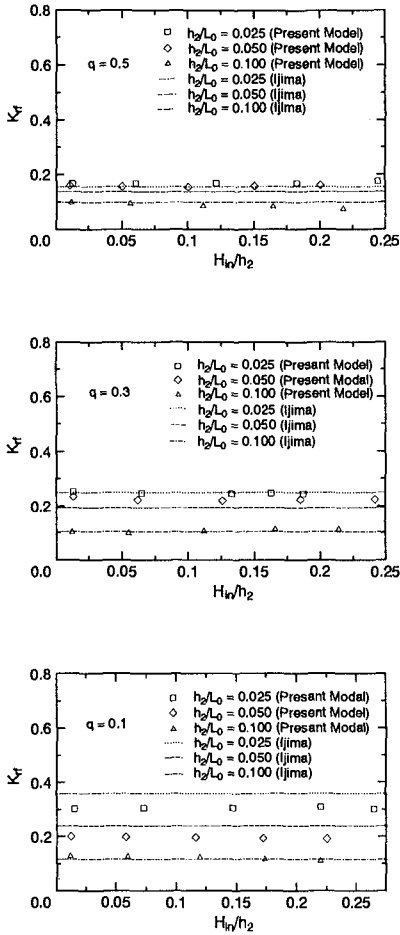


Figure 6: Comparisons of nonlinear and linear reflection coefficients

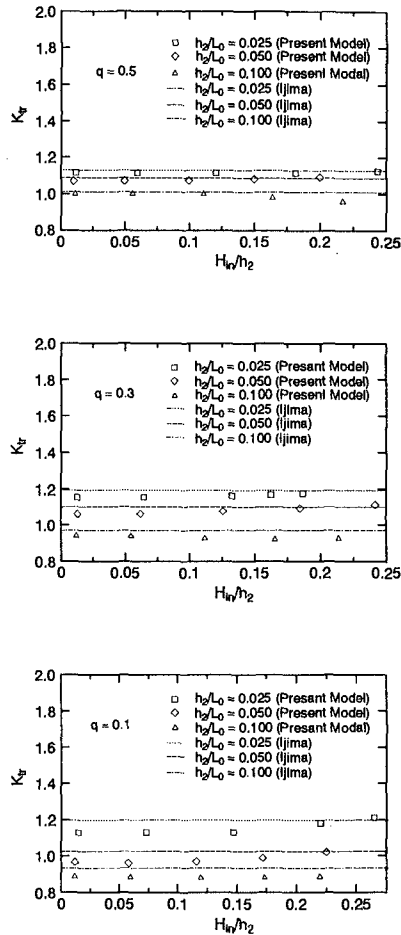


Figure 7: Comparisons of nonlinear and linear transmission coefficients

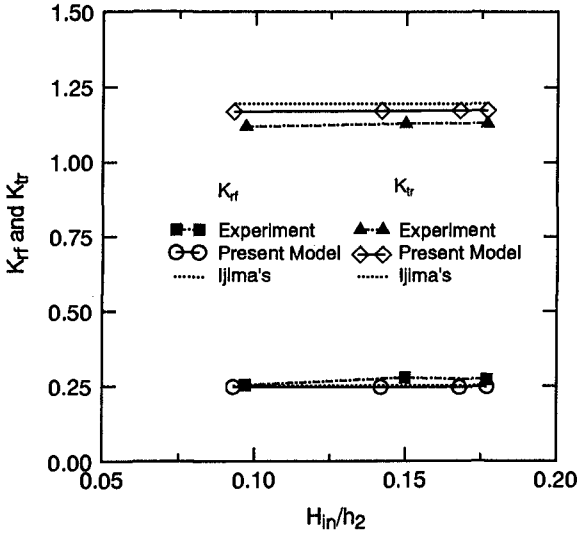


Figure 8: Comparisons of wave reflection and transmission coefficients,  $K_{rf}$  and  $K_{tr}$  ( $h = 0.376$  m,  $qh = 0.113$  m,  $T = 1.74$  s)

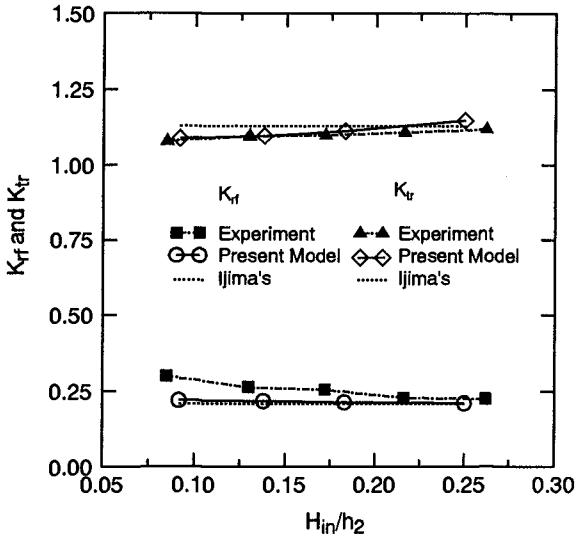


Figure 9: Comparisons of wave reflection and transmission coefficients,  $K_{rf}$  and  $K_{tr}$  ( $h = 0.376$  m,  $qh = 0.113$  m,  $T = 1.30$  s)

## 5.2 Comparison of Reflection and Transmission Coefficients with Experimental Data

Laboratory experiments were conducted to verify the reflection and transmission coefficients computed by the present model. The wave flume installed with a rectangular step of 26.3 cm high was used in these experiments. The water depth was set at 0.376 m in front of the step and 0.113 m on the step, the water depth ratio  $q$  is equal to 0.3. Comparisons between the reflection and transmission coefficients by the present model, Ijima's solution, and the experiments were made for two different cases of wave period. For the first case, a wave period of 1.74 s was utilized. In the comparison of the coefficients shown in Fig. 8, both Ijima's solution and the present numerical model show an identical prediction of the reflection coefficient  $K_{rf}$  which almost agree with the experimental results. For the transmission coefficient  $K_{tr}$ , the result from the present model gives a better agreement with the experimental result than that of Ijima's solution.

For the latter case, the water depths were 0.376 m offshoreward and 0.113 m inshoreward from the tip of the step and the wave period was 1.3 s. In the comparison of the reflection coefficient with Ijima's solution and experiments shown in Fig. 9, the reflection coefficient computed from the present model and Ijima's solution are almost the same. They are in agreement with the experimental data, with the exception of under-prediction for the wave height ratio,  $H_{in}/h_2$ , less than 0.2. In the comparison of transmission coefficient with Ijima's solution and experiment, the result of the present model shows a better agreement with the experiment than that of Ijima's solution.

## 6 Conclusions

Analysis of the coefficients of nonlinear wave reflection and transmission has been made through the present numerical model and experiments, and major conclusions can be described as follows:

1. The numerical model utilizing the boundary element method has been confirmed to accurately predict the profiles of nonlinear waves propagating over a rectangular step, as demonstrated by comparison with experimental data.
2. Waves propagating over a rectangular step are found to exhibit highly nonlinear behavior exemplified by the enhancement of the energy of the second and third harmonic components.
3. A representative wave height based on the assumption of the conservation of energy density is proposed for a situation in which higher harmonic components maintain a significant amount of wave energy. This definition provides a consistent estimate of wave heights on a rectangular step, where the conventional definitions produce a considerable fluctuation of wave heights.
4. The wave reflection and transmission coefficients computed by the model of nonlinear wave propagation over the step are close to the coefficients computed by the solution of Ijima (1971) with the exception of the water depth ratio  $q$  equal to 0.1. For this case of water depth ratio, the coefficients computed by the model yield smaller values than those of the analytical solutions.

5. The effect of finite amplitude on the reflection and transmission coefficients of wave propagation over the step is found small as long as the energies of higher harmonic components are taken into account.

## References

- Bartholomeusz, E. F. (1958): The reflexion of long wave at a step, *Proc. Camb. Phil. Soc.* 54, pp.106-118.
- Goda, Y., Suzuki, Y. (1976): Estimation of incident and reflected waves in random wave experiments, *Proc. 15th Int. Conf. Coastal Eng.*, pp.828-845.
- Healy, J. J. (1953): Wave damping effect of beaches, *Proc. Minnesota International Hydraulics Convention*, pp.213-220.
- Ijima, T. (1971): Solutions of boundary value problems in recent wave theory and their applications, *Summer Seminar on Hydraulic Engineering*, Committee on Hydraulic Engineering, JSCE, Course B, pp.B-1-1-B-1-30 (in Japanese).
- Kittitanasuan, W., Goda, Y. and Shiobara, T. (1993): Deformation of nonlinear waves on a rectangular step, *Coastal Engineering in Japan*, Vol. 36, No.2, pp. 133-153.
- Lamb, H., (1932): *Hydrodynamics*, 6th, Cambridge Univ. Press., pp.250-282
- Mansard, E. P. D. and Funke, E. R. (1980): The measurement of incident and reflected spectra using a least squares method, *Proc. 17th Int. Conf. Coastal Eng.*, pp.154-172.
- Mei, C. C. and Black, J. L. (1969): Scattering of surface waves by the rectangular obstacles in water of finite depth, *Journal of Fluid Mechanics*, Vol. 38, pp.499-511.
- Newman, J. N. (1965b): Propagation of water waves over infinite step, *Journal of Fluid Mechanics*, Vol. 23, pp.399-415.
- Olyama, T. and Nadaoka, K. (1991): Analysis of wave splitting phenomenon with a submerged breakwater using a numerical wave flume, *Proc. Coastal Eng., JSCE*, Vol. 38, pp.16-20 (in Japanese).
- Thornton, E. B. and Calhoun, R. J. (1972): Spectral resolution of breakwater reflected waves, *Journal of Waterway, Port, Coastal and Ocean Engineering*, vol. 98, pp.443-460.



## CHAPTER 91

# Oscillatory Motions and Permanent Displacements of Caisson Breakwaters Subject to Impulsive Breaking Wave Loads

P. Klammer <sup>1)</sup>; H. Oumeraci <sup>2)</sup>; H.-W. Partenscky <sup>3)</sup>

### Abstract

Small-scale model tests were recently conducted in a wave flume at the University of Hannover in order to study in more detail the relationship between impulsive loading induced by waves breaking on a caisson breakwater and subsequent displacements of the latter. These experiments are briefly described and some first results are discussed. Thereby, particular emphasis is put on the relationships between (i) oscillatory motions and permanent displacements, (ii) wave loading and oscillatory motions and (iii) wave loading and permanent displacements.

The findings presented in this paper are intended to improve the understanding of the stability of caisson breakwaters subject to impulsive breaking wave loads and to help developing proper tools for the dynamic analysis of such structures.

### Introduction

When a monolithic breakwater is subject to a sequence of breaking wave loads, both oscillatory and permanent displacements develop. The peak amplitudes of the former may exceed the ultimate resistance of the foundation, thus resulting in relatively smaller but residual deformations. The latter cumulate, leading to large permanent displacements which may cause the structure to collapse.

---

<sup>1)</sup> Dipl.-Ing., Research Engineer, University of Hannover, Franzius-Institut, SFB 205, TP B3, Nienburgerstr. 4, D- 30167 Hannover, Germany

<sup>2)</sup> Prof. Dr.-Ing., Techn. University of Braunschweig, Beethovenstr. 51a, 38106 Braunschweig, Germany

<sup>3)</sup> Prof. Dr.-Ing. Dr. phys., formerly Director of Franzius-Institut, University of Hannover, SFB 205

In this respect, hydraulic model tests on the impulsive loading and dynamic response of caisson breakwaters using improved measuring techniques for the motions of the structure were conducted at the University of Hannover, SFB 205/TP B3. These tests principally aim at establishing relationships as shown in Fig. 1, i.e. (i) between incident wave parameters and impulsive loading (TF1), (ii) between impulsive loading and dynamic response (TF2), and (iii) directly between incident wave parameters and dynamic response (TF3).

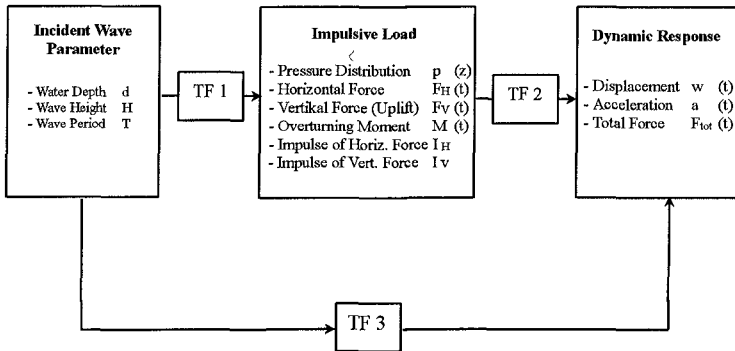


Fig. 1- Definition of Relationships under Study

With the present paper it is intended to discuss some of the results of these investigations, particularly the relationship between the oscillatory motions and the permanent displacements, as well as those between the loading and the response of the structure.

Additional calculations of the safety factor against sliding and overturning and comparison with measurements of the permanent displacements are also presented.

### **Experimental Set-Up, Measuring Techniques, Tests-Conditions and Procedures**

The tests were conducted in a wave flume with 110 m length, 2.2 m width and 2.0 m depth in which both regular and random waves with maximum wave heights up to 40 cm and periods up to 4 s can be generated. The caisson model consists of two distinct parts which can move independently of each other. The first part of the caisson model, for which a cross-section is shown in Fig. 2, is used for the measurement of the impact pressure on the front of the caisson, the uplift pressure on the caisson bottom, as well as the acceleration and displacements of the caisson.

For the pressure measurements piezo-electric pressure transducers of type PDCR 830 from Natec Schultheiss were used which a natural frequency of 28 - 360 kHz and a pressure range from 0.35-5 bar. For the measurement of the acceleration of the caisson three high output accelerometers of type Seitner Model JA-5-M19 with a range of  $\pm 1$  g and  $f_{max} = 200$  Hz are installed at the front top (one vertical) and at the rear top (one vertical and one horizontal) of the caisson.

For the measurement of the caisson motions, a displacement meter of type W2 ATK from Hottinger Baldwin Meßtechnik with the range of  $\pm 2$  mm and a failure of  $\pm 0.2$  %. The displacement transducer is able to record permanent and oscillatory motions of the caisson, while the accelerometers are intended to measure only the latter.

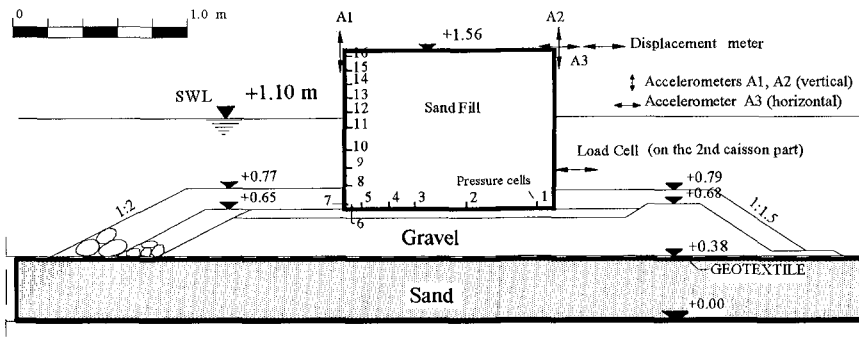


Fig. 2- Instrumented Model Caisson Breakwater

On the second caisson part only total horizontal force measurements behind the structure were performed (shear forces). For this purpose two 20 kN force transducers of type U2 A from Hottinger Baldwin Meßtechnik were used. All these measurements (waves, pressure, total forces, accelerations and displacements), as well as video records were performed simultaneously.

For three different water depths (0.90, 1.00 and 1.10 m) regular and irregular wave tests were conducted with wave heights ranging from 0.10 up to 0.3 m and wave periods from 1.9 - 3.2 s.

**Experimental Results**

**(a) Relationship Between Oscillatory Motion and Permanent Displacements**

A typical time series of the oscillatory motions and permanent displacements of the model caisson breakwater induced by waves ( $H_{max} = 0.30$  m,

$T = 2.4$  s,  $d = 1.00$  m) plunging on the structure front is shown in Fig. 3. The related horizontal force  $F_H$  and uplift force  $F_V$  which induce the permanent displacement  $a_r$  and the oscillatory motion  $x_t$  are shown in Fig. 4.

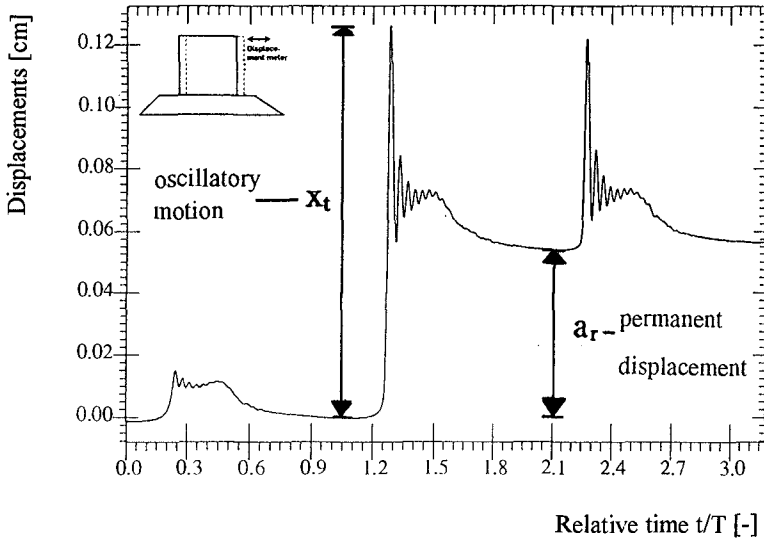


Fig. 3- Oscillatory Motions and Permanent Displacements of the Caisson Breakwater

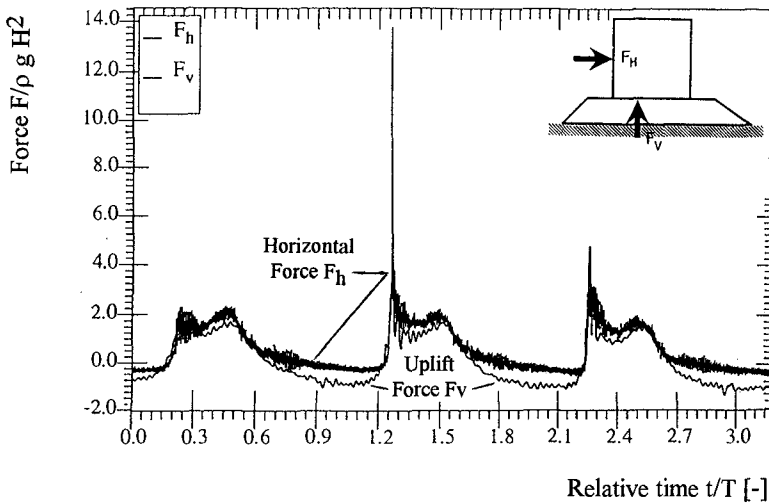


Fig. 4- Horizontal Force  $F_H$  and Uplift Force  $F_V$  Responsible for Caisson Motion in Fig. 3

In order to get an idea about the relations between  $x_t$  and  $a_r$ , the peak values of the oscillatory motions are plotted against the permanent displacements (Fig. 5).

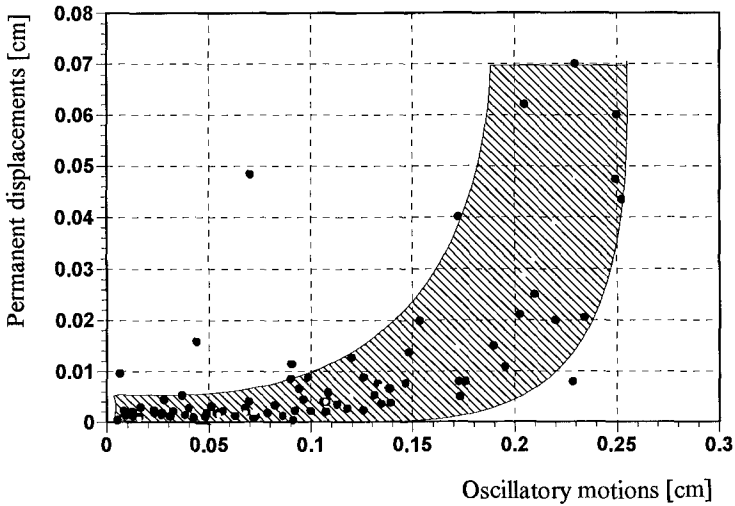


Fig. 5- Peak Values of Oscillatory Motions vs. Permanent Displacements

It is seen from Fig. 5, that:

- for smaller peak amplitudes  $x_t$  of the oscillatory motions (generally  $x_t < 0.1$  mm), almost no permanent displacements  $a_r$  occur;
- for amplitudes  $x_t > 0.1-0.15$  cm, relatively larger permanent displacements  $a_r$  start to occur, suggesting that there is some threshold value of  $x_t$  for which a permanent displacement is initiated;
- despite the scatter of the recorded values, there is a clear tendency of the amplitudes  $a_r$  of the permanent displacements to increase "exponentially" with increasing peak amplitudes  $x_t$ . This relationship strongly depends on the weight of the caisson.

**(b) Relationship Between Wave Loading and Oscillatory Motions of Caisson Breakwater**

A typical result is given by Fig. 6 showing the horizontal impact force, the uplift force, the total overturning moment around the caisson heel and the resulting motions of the caisson in non-dimensional form ( $H = 0.30$  m,  $T = 2.4$  s, water depth  $d = 1.00$  m)

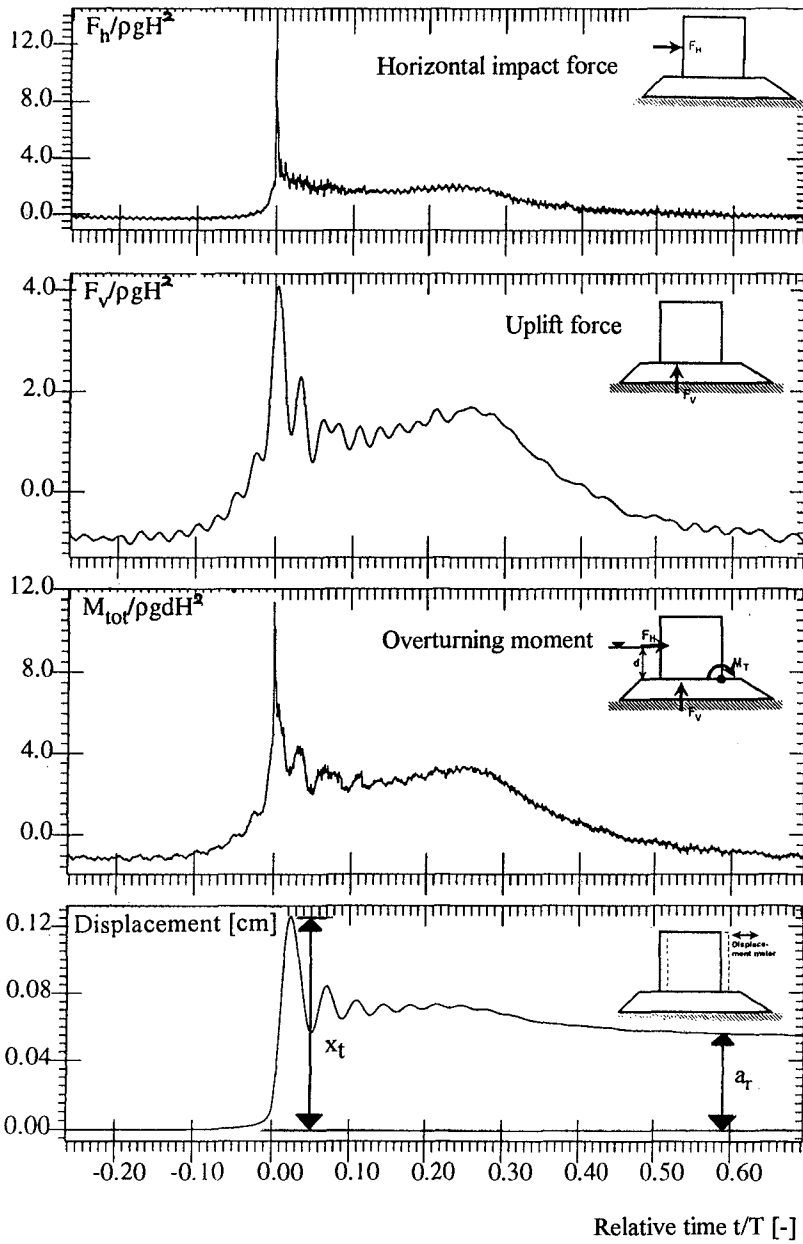


Fig. 6- Simultaneously Recorded Impact Loading and Motions of Caisson Breakwater

For the study of the relation between wave loading and the magnitude of the peak amplitude of the caisson motions  $x_t$ , the horizontal impact force, the uplift force and the total overturning moment around the caisson heel are considered.

Despite the large scatter of the measured values it is seen from Fig. 7 that the peak amplitude  $x_t$  first increase at a higher than at a lower rate with increasing peak of the horizontal force  $F_{hmax}$ .

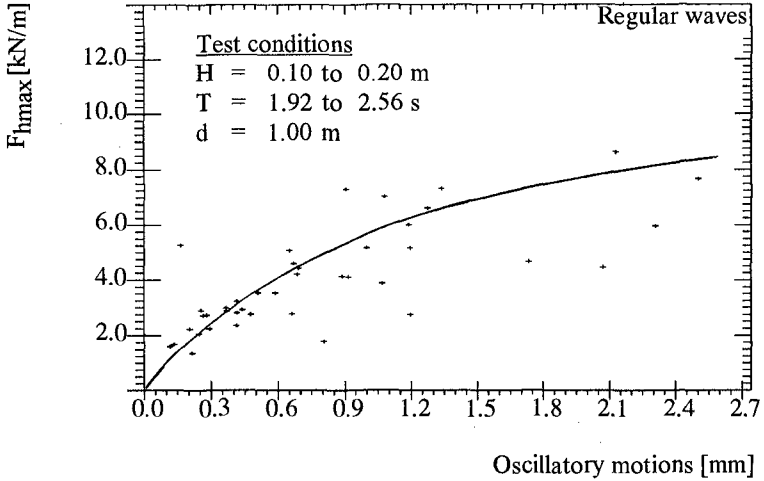


Fig. 7- Peak Amplitude of Oscillatory Motions vs. Horizontal Impact Force

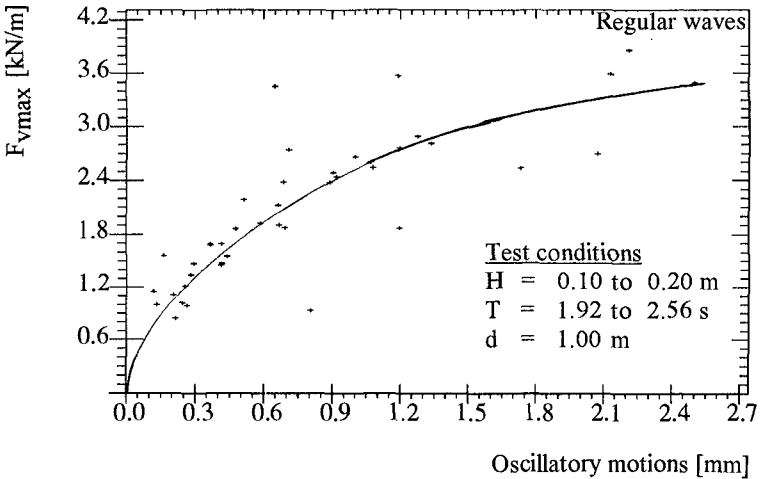


Fig. 8- Peak Amplitude of Oscillatory Motions vs. Uplift Force

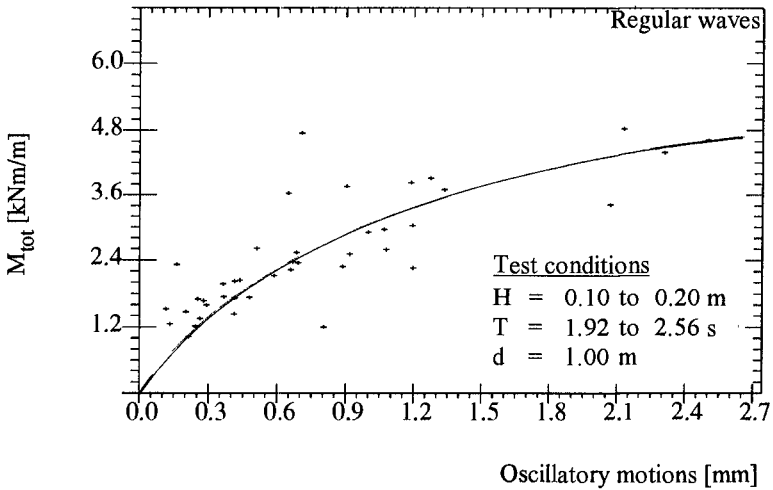


Fig. 9- Peak of Oscillatory Motions vs. Peak of Total Overturning Moment

Almost the same tendency is depicted in Fig. 8 for the relationship between the peak values of the oscillatory motions and the peak values of the uplift forces. The resulting effect of the uplift and the horizontal impact force is shown in Fig. 9 as peak values of the total overturning moment vs. the peak amplitudes of the permanent displacements.

### **(c) Relationship Between Wave Loading and Permanent Displacements**

For the study of the relationship between wave loading and permanent displacements  $a_r$ , the horizontal impact force, the uplift force and the total overturning moment around the caisson heel are considered.

The permanent displacements  $a_r$  are plotted against the peak amplitudes of the horizontal impact force, the uplift force and the total overturning moment in Figs. 10, 11 and 12, respectively.

As compared to Figs. 7, 8, and 9 for the oscillatory motion there is no clear relationship between the wave loading and the permanent displacements. A large scatter is present on the peak values of the critical loading at which a permanent displacement starts to occur, illustrating the fact other characteristics of the loading may also be determinant for the initiation and the magnitude of the permanent displacements.



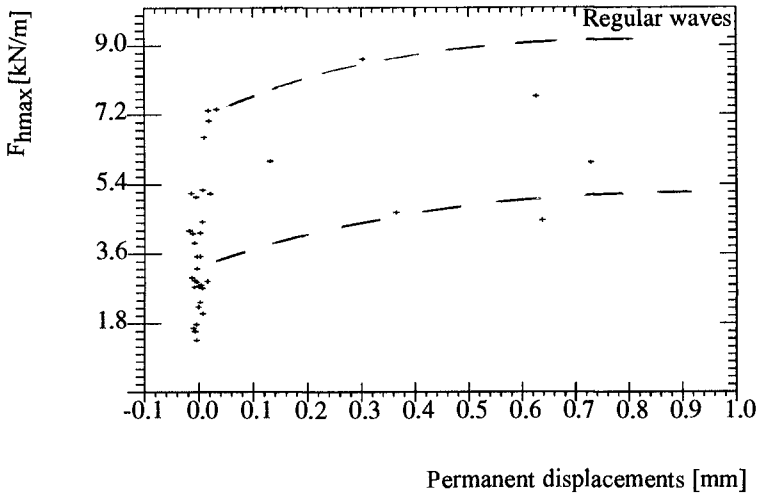


Fig. 10- Permanent Displacements vs. Horizontal Impact Forces

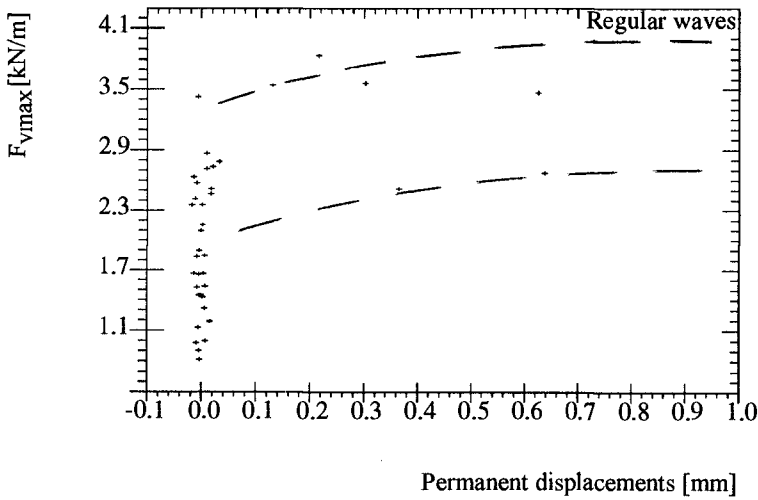


Fig. 11- Permanent Displacements vs. Uplift Forces

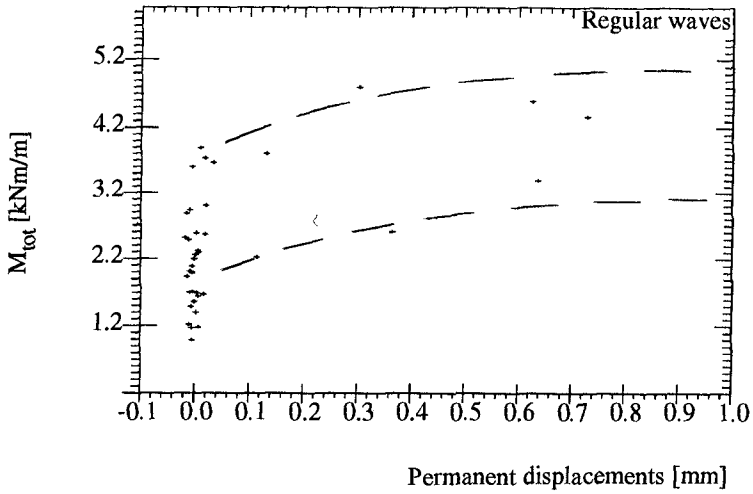


Fig. 12- Permanent Displacements vs. Peak of Total Overturning Moment

#### d) “Safety Factor“ against Sliding

A kind of “safety factor“ against sliding  $\eta_s$  is defined as the ratio of  $F_R/F_{hmax}$  in which the shear resistance or friction force is expressed as

$$F_R = \mu \cdot (W_{cai} - F_V),$$

where  $\mu$  is a “dynamic“ friction coefficient ( $\mu=0.5$ ),  $W_{cai}$  is the weight of the caisson (dry and submerged part) and  $F_V$  is the maximum uplift force (Fig. 13). The horizontal impact force  $F_{hmax}$  is obtained by integrating the pressure recorded on the front face of the caisson.

Plotting the related time history of the measured caisson motions (scaled on the left y-axis) and the calculated safety factor  $\eta_s$  (right y-axis) in Fig. 14 for one event, it can be seen that the displacement of the caisson is initiated for  $\eta_s < 1$ .

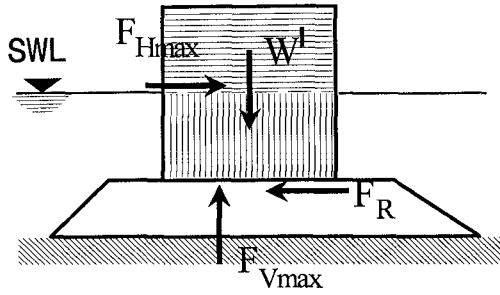


Fig. 13- Definition Sketch

Plotting the related time history of the measured caisson motions (scaled on the left y-axis) and the calculated safety factor  $\eta_s$  (right y-axis) in Fig. 14 for one event, it can be seen that the displacement of the caisson is initiated for  $\eta_s < 1$  (test conditions:  $H= 0.30$  m,  $T= 2.4$  s,  $d= 1.0$  m).

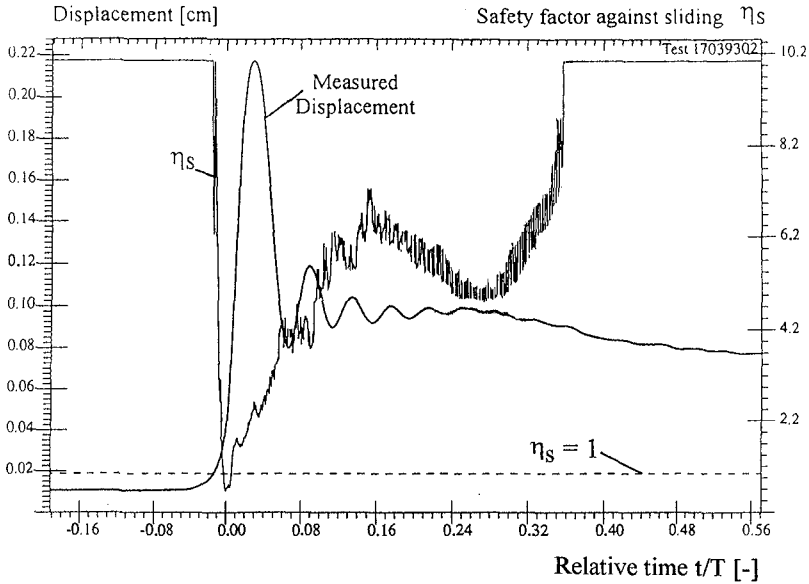


Fig. 14- Related Time History of Measured Displacement and Calculated “Safety Factor“  $\eta_s$

This result is confirmed by a set of more than 40 impacts caused by regular waves where the ratio of  $F_R$  and  $F_{Hmax}$  is plotted against the permanent displacement of the caisson (Fig. 15). It is seen that permanent displacement occurs only for  $\eta_s < 1$ .

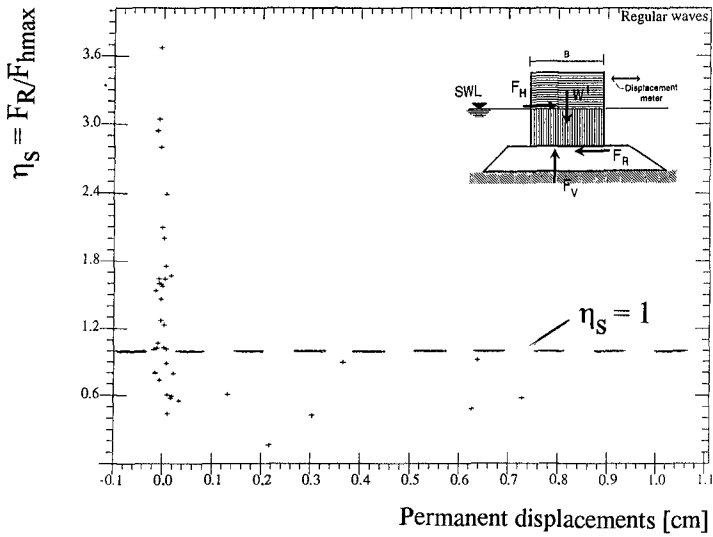


Fig. 15- "Safety Factor" vs. Permanent Displacement

The ratio  $\eta_R = M_R / M_{tot}$  is also considered in analogy to the safety coefficient against overturning, where  $M_R$  is the resistive moment (due to the weight of the caisson) and  $M_{tot}$  the maximum overturning moment around the caisson heel induced by the horizontal peak force  $F_{Hmax}$  and the maximum uplift force  $F_{vmax}$ . It can be seen from Fig. 16 that permanent displacement may occur even for values  $\eta_R > 1$ .

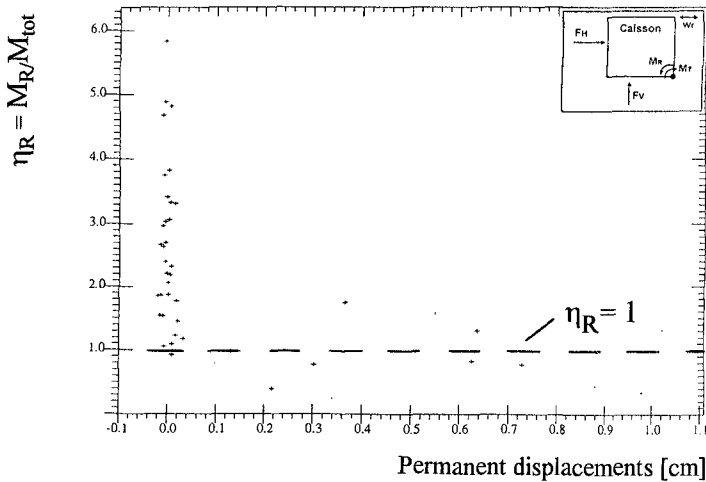


Fig. 16- "Safety Factor"  $\eta_R$  against vs. Permanent Displacements of the Caisson

**e) Cumulative Effect of Permanent Displacements**

As already mentioned above the effect of the impulsive loading induced by waves breaking on the structure is not only limited to small amplitude oscillatory motions of the caisson breakwater. It also consists in incremental small permanent displacements which may cumulate and lead to the collapse of the structure.

Fig. 17 shows the total overturning moments calculated from the horizontal and uplift forces on the caisson induced by a sequence of breaking wave loads and the resulting oscillatory motions and permanent displacements.

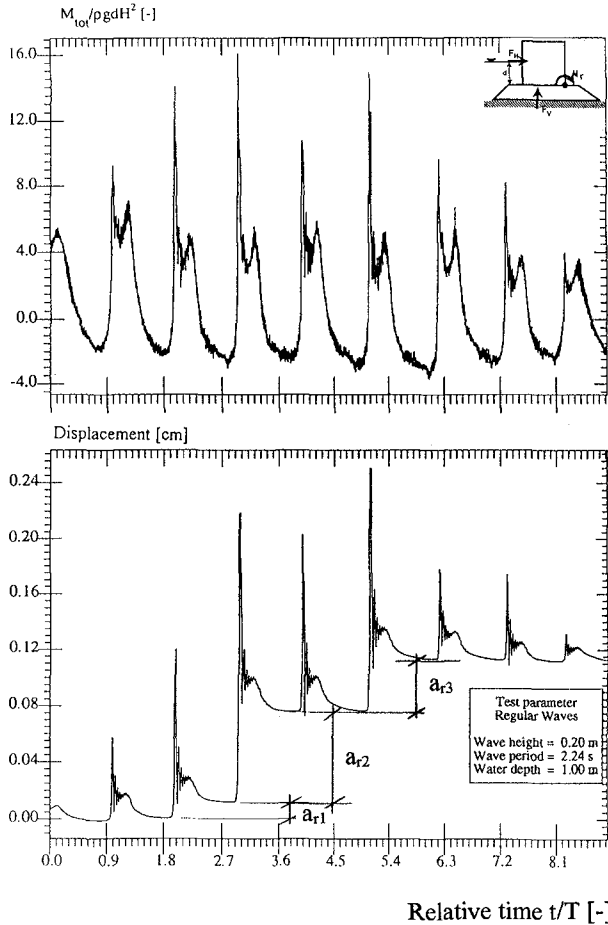


Fig. 17- Cumulative Effect of Permanent Displacements Induced by a Sequence of Breaking Wave Loads (see Fig. 18)

The cumulative effect of permanent displacements may lead to a stepwise failure of the caisson (Fig. 18). This effect is very important and should be taken into account in future design methods, analysis and numerical modelling.

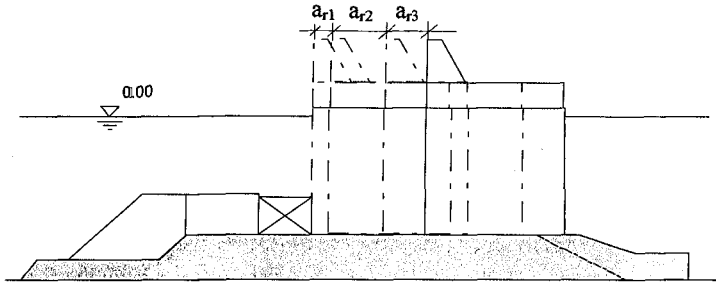


Fig. 18- Stepwise Failure of Caisson Breakwaters Induced by a Sequence of Breaking Wave Loads (see Fig.17)

#### **4. Concluding Remarks**

Although the analysis of the results of the hydraulic model tests is not yet completed they clearly show that the effect of the impulsive loading induced by waves breaking on the structure is not only limited to small amplitude oscillatory motions of the caisson breakwater. It also consists in incremental small permanent displacements which may cumulate and lead to the collapse of the structure.

On the other hand, these first results show that future analysis and numerical models to be developed for the prediction of the stability of caisson breakwaters should also necessarily account for the stepwise failure resulting from the incremental residual displacements (plastic deformations) induced by successive breaking waves on the structure.

#### **5. Acknowledgements**

This study is part of a research programme on breakwaters within the Coastal Engineering Research Unit "SFB 205" at the University of Hannover which is supported by the German Research Council (DFG), Bonn.

Additional support by the European Union within MAST II-Research programme (MAS2-CT92-0047) is also gratefully acknowledged.

## CHAPTER 92

### Hydraulic Characteristics and Field Experience of New Wave Dissipating Concrete Blocks (ACCROPODE)

Masanori Kobayashi<sup>1</sup>, Sumio Kaihatsu<sup>1</sup>

#### ABSTRACT

More than 30,000 pcs. of the ACCROPODE blocks have been applied for the wave dissipator of the breakwaters and the revetments at the Haramachi thermal power station where construction works of the harbor started about four years ago.

Since the ACCROPODE has not been used in Japan beforehand, hydraulic model tests were needed to examine its characteristics and to confirm the feasibility to the project, although extensive tests have been made in the world.

This paper describes the results of tests on the stability, reflection and transmission coefficients of the ACCROPODE blocks and the field experience at the Haramachi power station. Much reduction of the construction costs and good stability against storm waves attacked were obtained which showed its super usage as the wave dissipator.

#### INTRODUCTION

Tohoku Electric Power Company in Japan is now constructing the Haramachi thermal power station. This power station has 2 units of 1,000 MW coal fired thermal power plants, and a port facility capable of mooring a 60,000 DWT class coal carrier ship (Fig.1).

The total length of breakwaters and of revetments are 3.0 kms and 2.5 kms respectively. For the breakwaters two types were employed, one is the rubble-mounded type of 0.7 kms long for the coast shallower than 10 meters and the other is the caisson composite type of 2.3 kms long for the

1. Civil Engineering Dept., Tohoku Electric Power Co., Inc.  
3-7-1 Ichiban-cho Aoba-ku Sendai 980, JAPAN

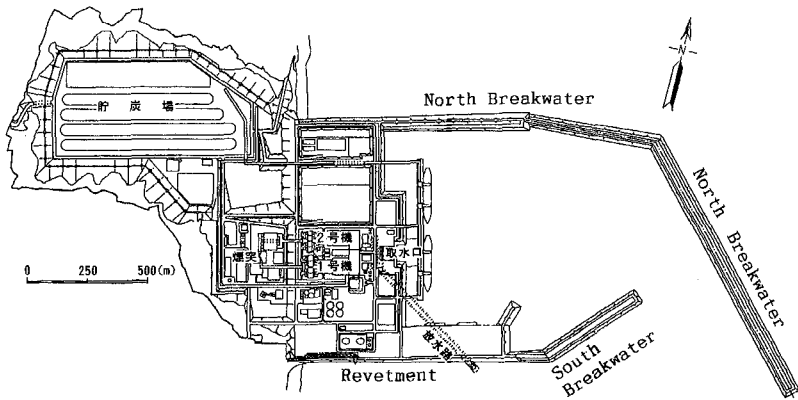


Fig.1 Plan View of The Haramachi Thermal Power Station

deeper zone than 10 meters. Selection was made mainly by the reason of construction costs.

Since 1984 until 1989 the staff members of the civil engineering department of Tohoku Electric Power Company had continued the contact with SOGREAH on the ACCROPODE blocks to be used for the mound of breakwaters and revetments because of the high stability, the financial benefit and the easy construction method. Final decision of employing the ACCROPODE was made through the hydraulic model tests conducted independently by the company itself which confirmed the preceding tests in the world with the detailed data of the reflection and transmission coefficients not supplied beforehand.

This paper describes the results of the tests and the field experience of the Haramachi project exposed to the ocean storm waves up to date without any harm.

## DESCRIPTION OF TESTS

### *Experimental Equipment*

The wave flume in which the model tests were conducted, is shown in Fig.2. It is a two dimensional wave flume, 34 meters long, 5 meters wide, and 1.2 meter deep. The scale was 1:50, following the Froude similarity. The foreshore slope was uniform with 1:100, simulating the sea bottom of the Haramachi field. The tests were carried out by waves generated with the power spectra of the Bretschneider-Mitsuyasu type.



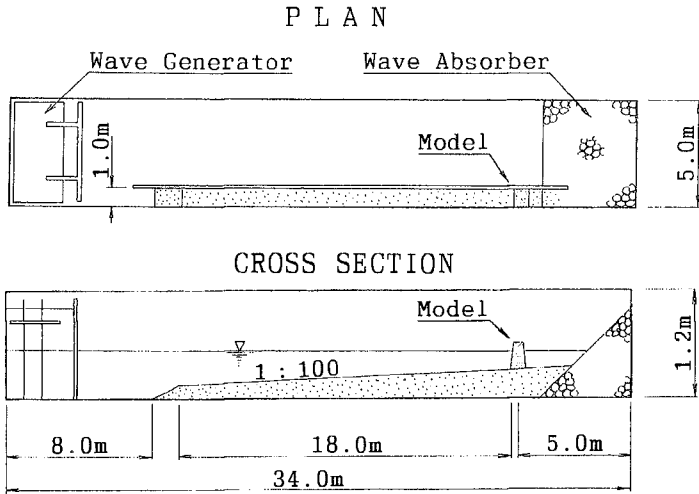


Fig.2 Wave Flume

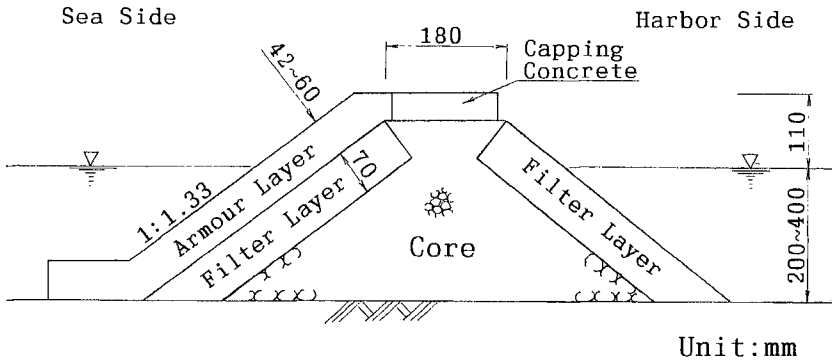


Fig.3 Cross Section of Rubble-mound Breakwater Model

*Test Conditions*

The cross section of the rubble-mound breakwater model is shown in Fig.3. The test conditions are shown in Table 1. More than 20 tests were conducted under various combination of these conditions which are probably expected in the project site.

Table 1 Test Conditions

	Model	Field
Water depth at the structure	20 cm, 30 cm, 40 cm	10 m, 15 m, 20 m
Wave period	1.2 sec, 1.7 sec 2.0 sec, 2.3 sec	8.5 sec, 12.0 sec 14.1 sec, 16.3 sec
Armour layer (ACCROPODE)	74.0 g, 166.3 g	9.3 t, 20.8 t
Filter layer (gravel)	20-30 g	3-4 t
( $\gamma\ell$ block)	32.8 g, 73.6 g	4.1 t, 9.2 t
Core (gravel)	0.5-4 g	50-500 kg

The ACCROPODE blocks were installed in the armour layer, and two types of the ACCROPODE blocks, 74.0 g and 166.3 g, were used.

In the filter layer, gravels and two types of the  $\gamma\ell$  blocks 32.8 g and 73.6 g were used. The  $\gamma\ell$  block is the artificial concrete block, used in lieu of the large rubble stone.

The core was made of gravels which weight was from 0.5 g to 4 g equivalent to 50 kgs to 500 kgs in the field.

The slope of armour face was fixed as 1:1.33 as shown in Fig.3. Owing to the report by CSIR (Holtzhausen and Zwamborn, 1991, Ref.1), the 1:2 slope was more stable than the 1:1.33 slope and the 1:1.5 slope but the rocking displacement before the failure was more remarkable than the latters. On the other hand interlocking by the initial shake down causes units to pack more densely for the 1:1.33 slope while units do not pack much closer during shifting on a flat slope. This was the main reason of this slope which was strongly recommended by SOGREAH.

The tests were carried out with three types of the water depth at the structure, from 20 cm to 40 cm deep, and four types of the significant wave period, from 1.2 sec to 2.3 sec.

In the Haramachi project, design conditions are as follows that the maximum water depth at the breakwater is 10 meters, equivalent to 20 cm in the model, and the design wave period for the significant wave is 16 sec, equivalent to 2.3 sec in the model.

In each cases the crest height of the model above the sea level was 11 cm, equivalent to 5.5 meters in the field.

#### *Arrangement of the ACCROPODE*

The arrangement of the ACCROPODE in the tests is shown in Fig.4. The centers of gravity of each block are plotted in white and black, where H is the height of the block.

The horizontal spacing is 1.24H along horizontal lines, and the distance between each horizontal lines is 0.6H. The thickness of the armour layer is 0.9H.

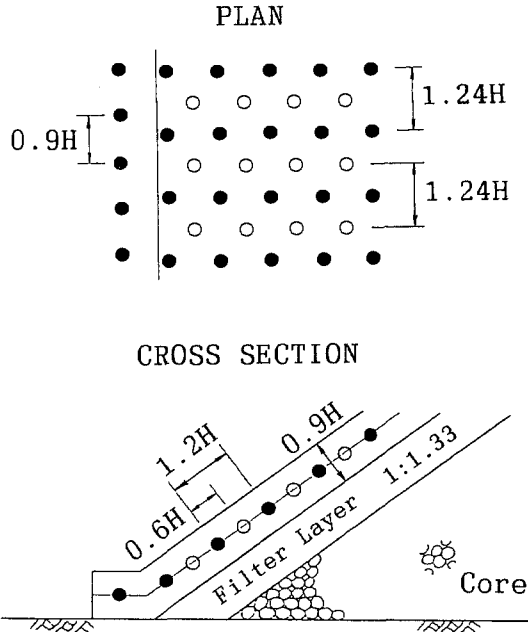


Fig.4 Arrangement of The ACCROPODE

*Definition of damage*

In order to estimate the stability of the ACCROPODE, the damage ratio of the armour layer is defined as follows,

$$D = (n/N) \cdot 100 \tag{1}$$

where,

- D: the damage ratio (%)
- N: the total number of blocks in the test area
- n: the actual number of blocks displaced more than the height of the block

The definition of the test area is shown in Fig.5. The area, from 1.5Hs ( Hs:significant wave height ) below the still-water level to the crest of the model, and 1.0 meter wide, is the test area. In this test area from 200 pcs. to 300 pcs. of the ACCROPODE blocks were included.

According to this definition, 2% of the damage ratio is nearly equivalent to the condition of severe damage.

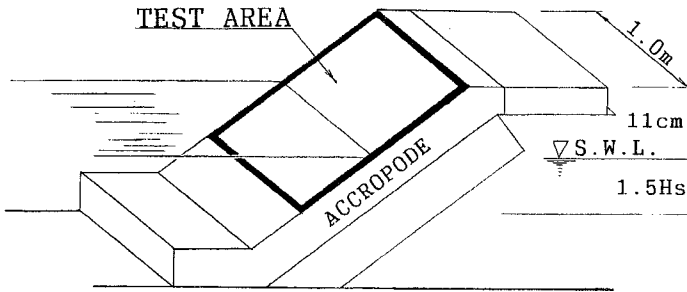


Fig.5 Test Area

## RESULTS OF TESTS

### *KD and Ns values*

The damage ratio  $D$  versus  $KD$  and  $N_s$  values are plotted in Fig.6. The  $KD$  value is the Hudson stability factor. The  $N_s$  value is the stability number given by the following relation with the  $KD$  value.

$$N_s = H_s / \Delta D_n = (KD \cdot \cot \alpha)^{1/3} \quad (2)$$

where,

- $H_s$ : significant wave height in front of the structure
- $\Delta$ : relative mass density of the unit
- $D_n$ : nominal diameter of the unit
- $\alpha$ : slope angle of the structure

In these figures the filter layer is composed of gravels.

At 0% of the damage ratio, the  $KD$  value is estimated in the range of 30 to 50, from 3.5 to 4.0 equivalent in the  $N_s$  value. From these  $KD$  or  $N_s$  value, it can be said the initial stability of the ACCROPODE, in other words the stability against the start of damage is very high compared with the other artificial armour units.

In the region under 2% or 3% of the damage ratio, the  $N_s$  value increases with the rate much higher than that of the damage ratio. But in the region over 2% or 3% of the damage ratio, the  $N_s$  value scarcely increases with the increase of the damage ratio. The  $N_s$  values at the condition of no damage and severe damage (or failure) are very close with each other. This means that the structure fails progressively after damage started.

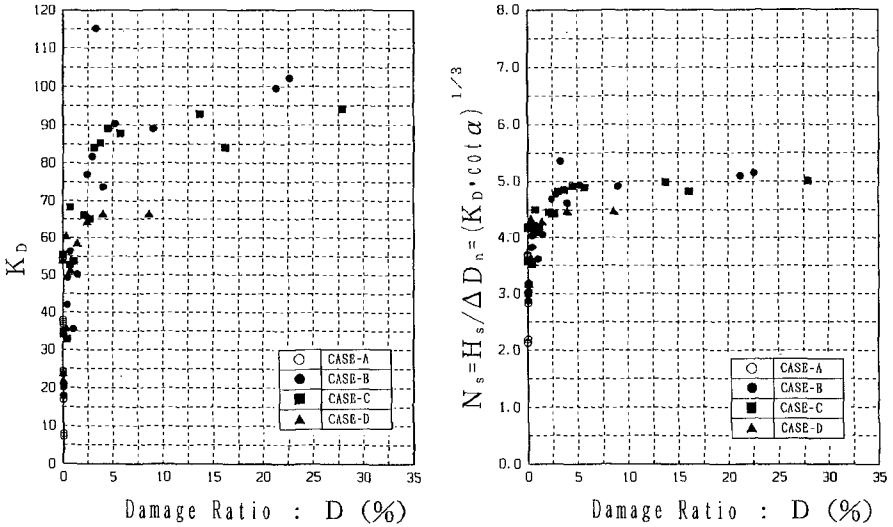


Fig.6 Damage Ratio vs.  $K_D$  &  $N_s$  Values  
(Filter Layer : Gravel)

All the tests carried out under the design condition of water depth at the structure (20 cm in the model) in the Haramachi project, could be found no damage at all.

*Influence of the wave period*

The Iribarren number, or the surf similarity parameter  $\xi z$  is defined as,

$$\xi z = \tan \alpha / (H_s / L_o)^{0.5} \tag{3}$$

where  $L_o$  is the deep water wave length derived by the wave period with zero up-crossing. Fig.7 shows the relation between the  $N_s$  values and the surf similarity parameter  $\xi z$  where the damage ratio is 0% or 2%. The filter layer is composed of gravels. In our tests,  $\xi z$  was in the range of 3 to 5.

In case of 0% of the damage ratio, even though the data is scattered, the  $N_s$  value has a tendency to decrease with the increase of  $\xi z$ . And in case of 2% of the damage ratio, such tendency is not so remarkable in compare to the cases of 0% of the damage ratio. We could find the influence of the wave period in case of the gravel filter.

In case of the  $\gamma \ell$  blocks used for the filter layer, the relation between  $\xi z$  and  $N_s$  is shown in Fig.8. From this figure, the influence of the wave period is not found.

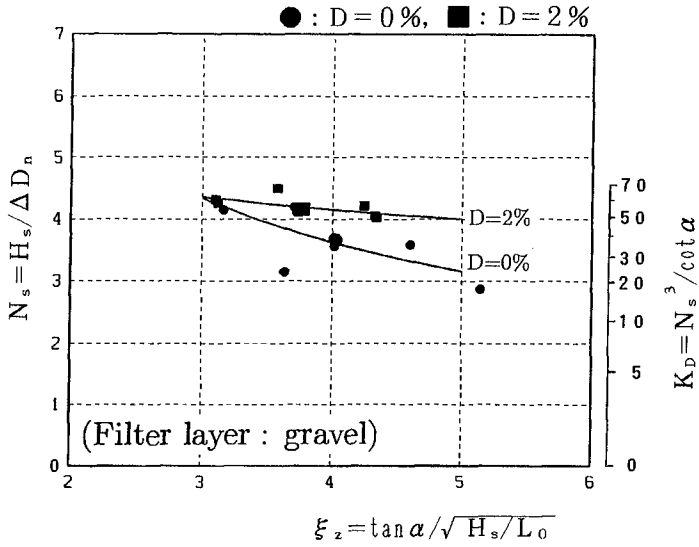
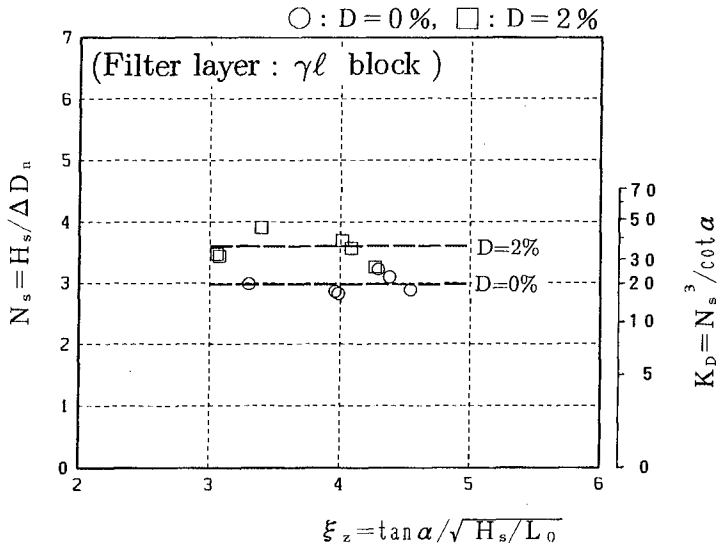


Fig.7 Stability of The ACCROPODE  
(Filter Layer : Gravel)



*Effect of the filter layer's material*

From Fig.7 and Fig.8, it is found that the difference of the filter layer's material, gravels or the  $\gamma\ell$  blocks, has the influence on the stability of the armour layer. At the condition of no damage, the KD value will be estimated in the range of 30 to 50 in case of the gravel filter, showing higher stability than in case of the  $\gamma\ell$  block's filter in which case the KD value will be at only 20.

It could be estimated to choose the most favorable weight (or size) of the  $\gamma\ell$  blocks for the weight of the ACCROPODE units. However such relationship was not recognized since the unevenness of the filter setting seemed to be another origin of data scattering.

*Comparison of results with other investigations*

Fig.9 shows the comparison of results with other investigations, carried out by SOGREAH (Perdreau, 1983, Ref.4) and DELFT hydraulics laboratory (Van der Meer, 1987, Ref.2). Although the influence of wave period was found in case of the gravel filter, our present studies show similar results and tendency of the  $N_s$  value to other investigations.

It should be noted that the difference of the stability number between no damage and severe damage is very much small where  $\xi_z$  was 3 and increases with the increase of  $\xi_z$ . Holtzhausen and Zwamborn (Ref.1) gave caution that the time from start of damage to failure is shorter for steeper slopes.

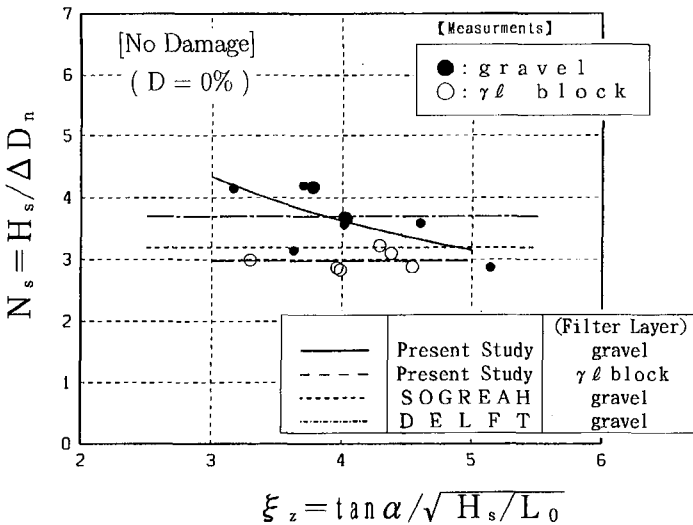


Fig.9-1 Stability of The ACCROPODE by Different Investigations (at No Damage)

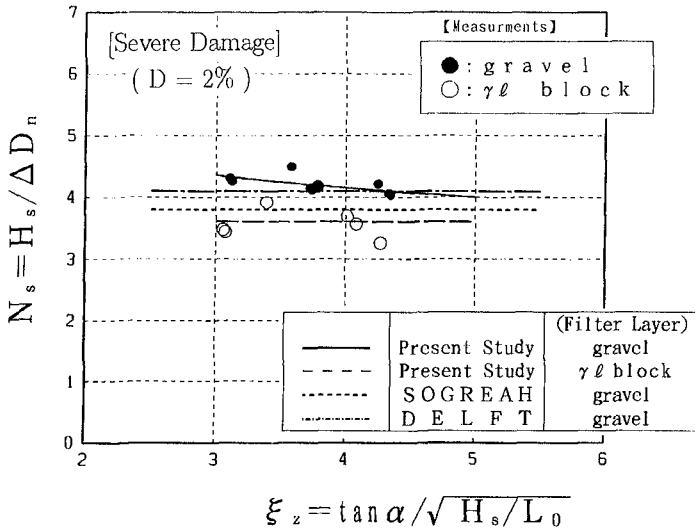


Fig.9-2 Stability of The ACCROPODE by Different Investigations (at Severe Damage)

*Reflection coefficient*

The reflection coefficient KR , as a function of the wave steepness is shown in Fig.10. All the data are distributed in the range of 0.25 to 0.6 of the reflection coefficient. It is found that the reflection coefficient increases with the increase of the water depth and the wave period. This tendency is similar to the characteristics of the other artificial armour blocks.

*Transmission coefficient*

Fig.11 shows the wave height transmission coefficient KT , as a function of the wave steepness in case of 40 cm water depth at the structure. Under the same condition of the wave steepness, the transmission coefficient had a tendency to become larger when the wave period became longer. The transmission coefficient was highly affected by the wave overtopping. Under non-overtopping condition the transmission coefficient was less than 0.2, but when overtopping started it increased up to 0.4.

In Fig.12 the transmission coefficient are plotted as a function of the relative crest height hc/Hs , where hc is the crest height above the sea level. In this figure, the typical curve of the transmission coefficient can be drawn.



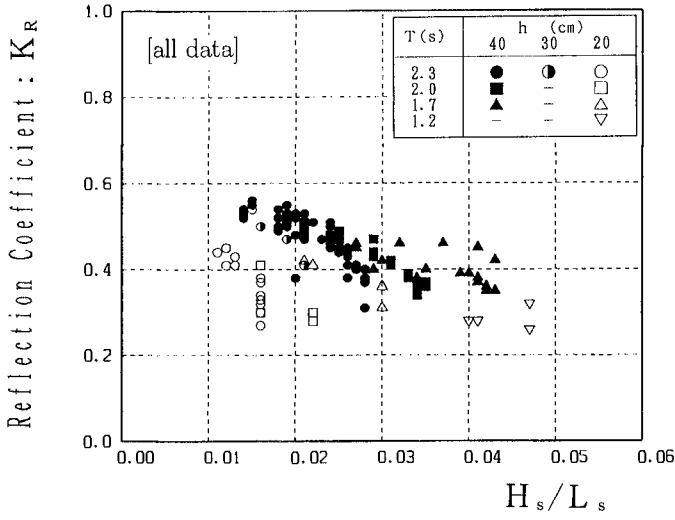


Fig.10 Reflection Coefficient vs. Wave Steepness

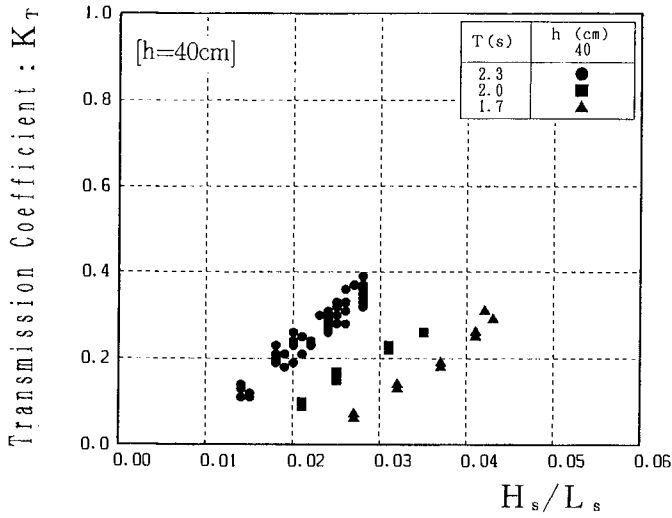


Fig.11 Wave Transmission Coefficient vs. Wave Steepness

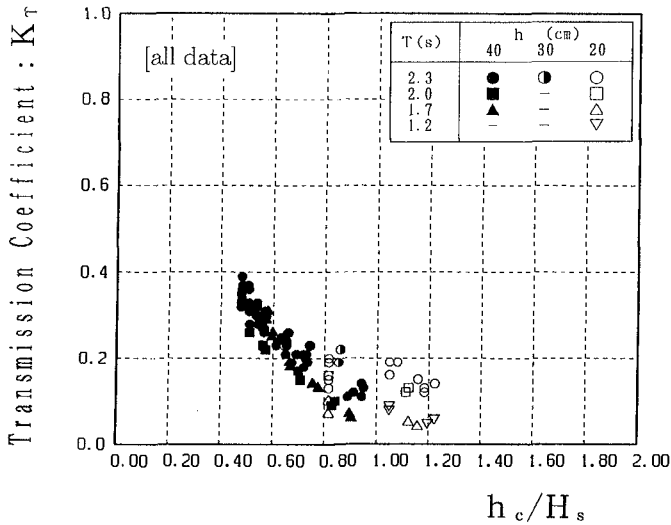


Fig.12 Wave Transmission Coefficient vs. Relative Crest Height ( $h_c/H_s$ )

### *Design conditions*

We decided the weight of the ACCROPODE blocks by the Hudson formula. The design wave height and the weight of the ACCROPODE are shown in table 2.

In the Haramachi project, three types of the ACCROPODE blocks, 14.5 t, 20.7 t, and 27.6 t, are applied to the rubble-mound breakwaters and revetments. As the filter layer, 9 t type of the  $\gamma\ell$  blocks are applied, mainly because of the difficulty of obtaining large stones as many as feeding to the site. The summation of these stones for the filter layer amounted to about 250,000 cubic meters.

The KD value of 10 was applied in our design. In case of the gravel filter, the KD value was estimated from 30 to 50 at no damage condition. But we reduced design KD value, considering the application of the  $\gamma\ell$  blocks in the filter layer, the failure mode, the randomness of installed blocks especially below the sea level, and the unprecedented experience in Japan.

The KD value could be increased even up to 15.

Table 2 Design Conditions

Water depth at the structure	2.0 m	6.0 m	8.0 m
	- 6.0 m	- 8.0 m	- 10.0 m
Slope angle ( $\cot \alpha$ )	1.25	1.33	1.33
Design significant wave height	4.9 m	5.9 m	6.7 m
ACCROPODE's weight (by Hudson's formula)	10.8 t	18.9 t	27.6 t
ACCROPODE's weight (applied)	14.5 t	20.7 t	27.6 t

FIELD EXPERIENCE*Installation of the ACCROPODE*

Total number of blocks which will be installed to the rubble-mound breakwaters and revetments, is about 12,000 pcs. in which about 11,000 pcs. were placed already.

In addition, we have a plan to place the ACCROPODE blocks, 9.2 t and 14.5 t, to the caisson-type composite breakwaters as armour units of the rubble foundation, and 3,000 pcs. have been already installed.

In the Haramachi project more than 30,000 pcs. of the ACCROPODE blocks will be installed in total.

Table 3 The 5 Highest Storm Wave Attacked  
The Construction Site

<u>Maximum Wave</u>			
Date	Wave Height (m)	Wave Period (sec)	Cause
1991. 2.16.	9.41	12.3	Low Pressure
1993.11.14.	8.36	9.5	Low Pressure
1993. 8.27.	7.60	12.5	Typhoon
1993. 3. 8.	7.39	11.0	Low Pressure
1994. 9.19.	7.05	12.5	Typhoon
<u>Significant Wave</u>			
Date	Wave Height (m)	Wave Period (sec)	Cause
1991. 2.17.	5.52	15.8	Low Pressure
1993.11.14.	5.00	10.4	Low Pressure
1993. 3. 8.	4.94	10.8	Low Pressure
1993. 8.27.	4.61	10.9	Typhoon
1992.10.21.	4.11	10.2	Low Pressure

### *Experienced storm wave*

About four years have passed since we began to install the ACCROPODE blocks. Table 3 shows the 5 highest storm wave conditions attacked the construction site after installation. But we have experienced no harm thus far. The stability of the ACCROPODE blocks in the field were very much excellent.

The highest wave was 9.41 meters in the maximum wave height and 5.52 meters in the significant wave height, which occurred on Feb. in 1991.

The design wave conditions at the point of the wave observatory, about 1.8 km offshore, are following : The significant wave height is 7.6 meters, the maximum wave height is 11.9 meters, and the wave period is 16 sec.

As shown in Fig.1, waves attacked obliquely which showed the excellent characteristics even tests were conducted in two dimensional conditions.

### *Results in the field experience*

By applying the ACCROPODE blocks, the followings were recognized in the Haramachi project.

- 1) The area of the fabrication yard was rather small.
- 2) The moulding process was fairly easy, because of the simplicity formed by two symmetrical shells.
- 3) The settlement of blocks in the armour layer was almost completed in the range of 15 cm to 20 cm, after 7 days to 30 days following installation.
- 4) The void ratio of installed blocks was from 45% to 50%.
- 5) The strength of the block element was very high. Few or no blocks were broken.
- 6) The stability of the ACCROPODE in the armour layer against the wave force was good enough.
- 7) In comparison with other artificial blocks, quantity of concrete was saved about 30%, and the total construction costs for armour units, from production to installation to the rubble-mound breakwaters and revetments were reduced about 30%.

### CONCLUSIONS

For the Haramachi project, the hydraulic model tests were carried out on the rubble-mound breakwaters armoured with the ACCROPODE blocks. The followings were observed as conclusions.

- 1) The stability of the ACCROPODE at no damage was very high, but the criteria of no damage and failure were very close.
- 2) The filter layer's material had an influence on the stability of the ACCROPODE in the armour layer. In case of the gravel filter, the KD value was estimated in the range of 30 to 50, but in case of the  $\gamma \ell$  block's filter,

it was 20.

- 3) It was found that the wave period had an influence on the stability of the ACCROPODE in case of the gravel filter.
- 4) The reflection and the wave transmission coefficients were similar to the other artificial armour units.

Field experience showed successful achievement for the expense, the easy construction and the stability of the blocks.

#### ACKNOWLEDGEMENTS

The model of the ACCROPODE blocks were lent by SOGREAH, and their assistance is acknowledged with thanks.

#### REFERENCES

1. A.H.Holtzhausen, J.A.Zwamborn (1991): Stability of Accropode(R) and comparison with dolosse, Coastal Engineering, 15(1991), Elsevier Science Pub. B.V.. Netherlands.
2. Van der Meer, J.W.(1987): Stability of rubble mound breakwaters. Stability formulae for breakwaters armoured with accropode(R), Delft Hydraulics Rep. on basic research, H546. Netherlands.
3. Van der Meer, J.W.(1988): Stability of cubes, tetrapods and accropode, Proc. Conf. Breakwaters '88. England.
4. Perdreau, N.(1983): Le Bloc Accropode. Essais de stabilité en canal en houle non deferlante, Sogreah. France.
5. G.E.Vincent (1988): Stability of a breakwater formed with Accropode(R) blocks under wave attack, Sogreah. France.

## CHAPTER 93

### Experimental Study on Developing Process of Local Scour around a Vertical Cylinder

Tomonao Kobayashi<sup>1</sup> and Kenji Oda<sup>2</sup>

#### ABSTRACT

Time evolution of scoured seabed profiles around a vertical slender cylinder under waves has been investigated by means of laboratory experiments. The characteristics of the scoured bed profiles on the developing process is discussed considering the flow features. The local scoured bed profiles are classified with the location of the maximum scoured point. And the developing scouring process of each classified type is discussed. We found that for each scour type, the scoured bed retains a similar profile during its whole developing process. The ultimate scour depth on the vicinity of the cylinder surface is related to the Keulegan-Carpenter number, and it is independent of the sand bed condition.

#### 1. INTRODUCTION

Local scouring is an important factor to consider when the stability of offshore and onshore structures is analyzed, and different aspects of this have already been investigated by various researchers. Among them, Well and Sorensen (1970) based on laboratory experiments found relations of the ultimate scour depth to the Shields number, Reynolds number, etc. Sumer *et al.* (1992), also based on laboratory tests, proposed the scour depth as a function of the Keulegan-Carpenter (K.C.) number on the live bed, *i.e.* the bottom with continuous sediment motion. Nishizawa and Sawamoto (1988) studied the flow around a vertical slender cylinder under waves using flow visualization techniques, and reported relations between the flow characteristics and the K.C. number. Kobayashi (1993) measured in the laboratory the velocity distributions around a cylinder near the bed on both flat bottom and scoured bed, and discussed about the effect of the scoured seabed configuration on the vortex behavior near the bed around the cylinder.

In most of the available literature about the local scouring phenomenon around a vertical slender cylinder under waves, only the ultimate scoured bed

---

<sup>1</sup>Research Associate, Department of Civil Engineering, Tokyo Rika University, 2641 Yamazaki, Noda city, Chiba 278, Japan.

<sup>2</sup>Tokyu Construction Co., Tokyo, Japan.

TABLE 1. Incident Wave Conditions at The Cylinder

Wave Height	$H$	13~60mm
Wave Period	$T$	1.3~3.0s
Water Depth	$h$	120mm
K.C. number	K.C.	3.95 ~ 30.0

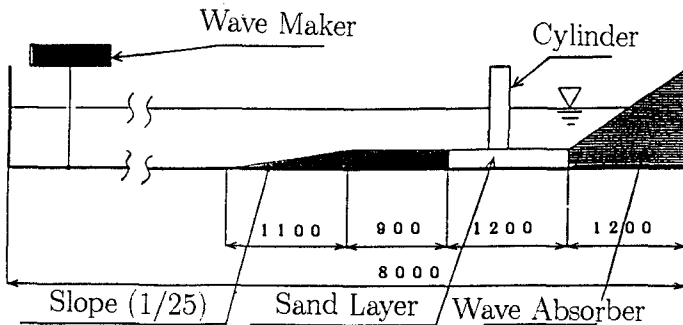
is considered. To recognize this physical phenomenon, however, the developing process of the local scouring should also be studied.

The intent of the present study is therefore to recognize the characteristics of the developing process of the local scour around a cylinder under waves. For this purpose, first, the scoured bed profiles are classified into several typical scour types. Then, for each scour type the characteristics of the time evolution of the scoured bed profiles are discussed by considering the flow features on the bed. Finally, relations of the ultimate scour depth to the typical parameters are also discussed.

2. EXPERIMENTAL APPARATUS

Figure 1 shows a sketch of the wave flume employed. The size of this flume is 8 m in length, 300 mm in width and 150 mm in height. Both flume lateral walls are made of glass to facilitate the observations. Part of the bottom flume was lifted to make a movable bed, and in the transition from the bottom flume to the sand bed a slope was located. The bottom of a cylinder was inserted on the movable bed. To classify the local scoured bed profiles, a cylinder of 30 mm diameter was used for the experiments, and in the case of the time evolution of the local scouring experiments, the cylinder diameter was 22 mm.

The wave conditions at the cylinder are shown in Table 1. The maximum



(Unit : mm)

FIG. 1. Side View of Flume

TABLE 2. Sand Type

Sand type (Collected place)	Diameter $d_{50}$ (mm)	Specific weight $s$
Toyoura	0.17	2.569
Toyouni	0.16	2.556
Makuhari	0.20	2.525
Komesu	0.43	2.695
Oarai	0.17	2.643

velocity at the bottom, that is used to calculate the value of the K.C. number, is evaluated from the wave conditions shown in Table 1 by applying the linear wave theory. During the experiments, the five types of sand shown in Table 2 were employed, and the waves were produced until the scoured bed was considered to be almost stable.

All experiments were done under the clear water condition, because in this way, only the sand near the cylinder moves due to the secondary flow driven by the existence of the cylinder. Hence the characteristics of the flow near the bed around the cylinder are easy to recognize. This is an important matter to understand the local scouring process.

Scoured bed profiles were measured in two dimensions with a sand profile meter.

### 3. CLASSIFICATION OF SCOUR TYPE

The contour maps of the bed profiles around the cylinder in Fig. 2 show typical scour types that were observed during the experiments performance. In this figure, hatched areas indicate scoured regions. The Twin-Horn-Shaped and Cone-Shaped scoured bed profiles in this figure have already been studied by Nishizawa and Sawamoto (1988) among others. In this study, we found the following same results as those reported by them: in the Twin-Horn-Shaped bed the lee side of the cylinder is scoured, and in the case of the Cone-Shaped bed the scouring takes mainly place around the cylinder. When we were performing the experiments, we observed an additional scoured bed type as shown in Fig. 2 (b). Here, both the lee side of the cylinder and the vicinity of the cylinder are scoured. We classified this scour type as Transient-Shaped scoured bed. In this study therefore the scour bed profiles are classified into the categories: Twin-Horn-Shaped, Transient-Shaped and Cone-Shaped bed profiles. An example of each of these bed profiles is shown in Fig. 2. The classification mentioned above, based on the scoured bed profiles, is rather subjective. So, to classify objectively the scour types we introduce the use of the location of maximum scoured point.

Figure 3 shows the distribution of the maximum scoured points of all experimental cases. In this figure, the marks indicate the scour types classified with the scoured bed profile. Here, the Twin-Horn-Shaped bed profiles have two maximum scoured points which are located at both right and left lee sides of the



cylinder. In the case of Cone-Shaped bed profiles the maximum scoured point is located either in front of or beside the cylinder. The location of the maximum scoured point depends on the scour type, and we conclude therefore that this location can be applied to classify objectively the scour type. The maximum scoured point concept is applied for the following discussions.

To investigate the flow pattern near the bed around a cylinder, laboratory experiments were performed for several K.C. numbers. We observed that for low K.C. numbers, flow separation from the cylinder or a pair of symmetric vortices was generated, and this scoured the bed at the lee side of the cylinder. Finally, a Twin-Horn-Shaped scoured bed profile was formed. For large KC numbers, the Cone-Shaped scoured bed profiles were formed and an asymmetric vortex, similar to the Karman vortex appeared. Nishizawa *et al.* (1988) also observed the flow pattern under similar conditions. In general, our observations coincide with theirs. Except that they did not have any horseshoe vortex formation in any cases, even for the Cone-Shaped scored bed profile.

Based on these observations, we conclude that each scour type corresponds to a different flow pattern or vortex structures.

Figure 4 shows the relation of local scour type to the K.C. number. The

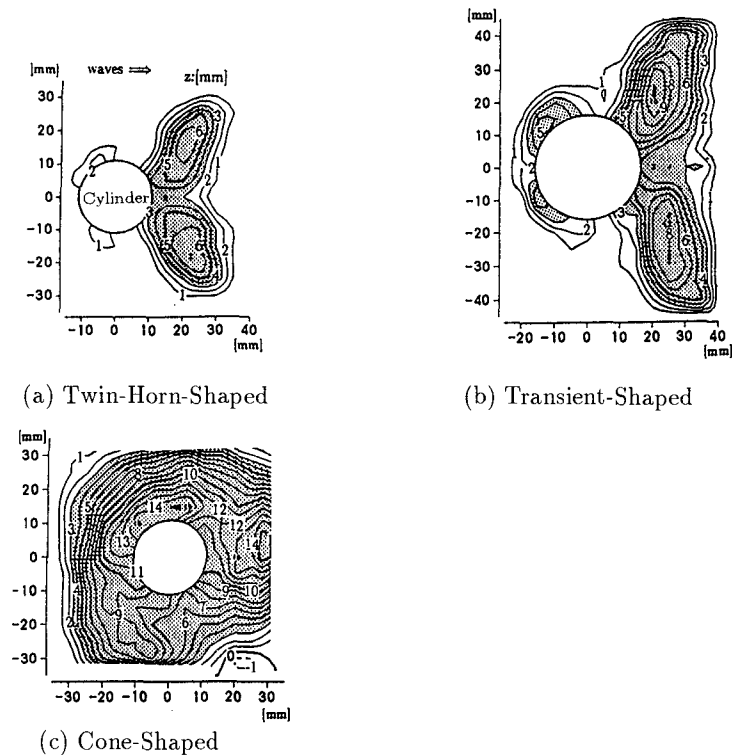


FIG. 2. Typical Scour Bed Profiles

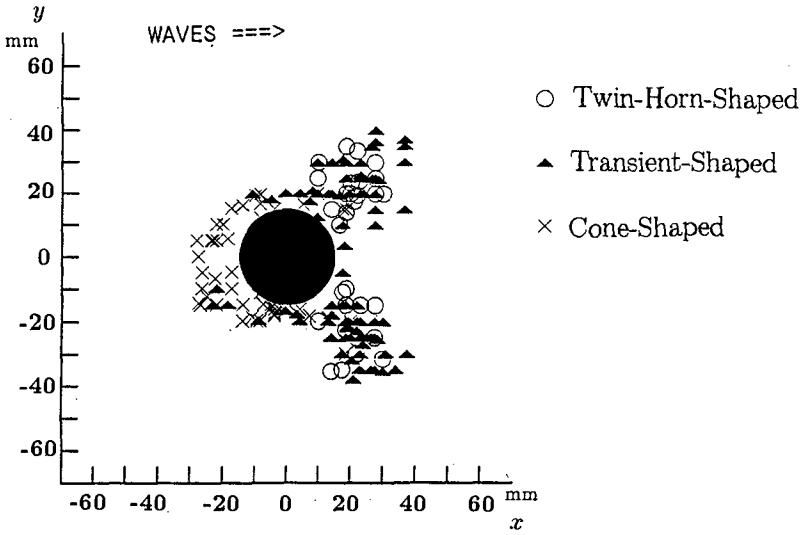


FIG. 3. Distribution of Maximum Scoured Points of All Experimental Cases

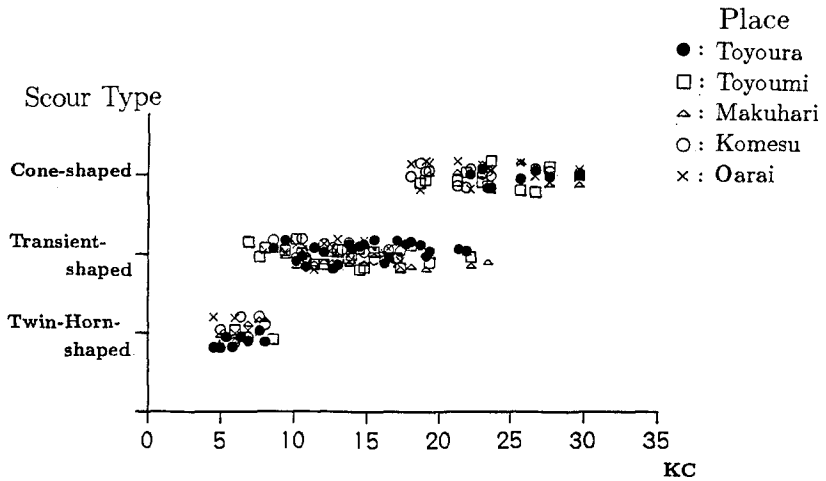


FIG. 4. Relation of Scour Type to The K.C. Number

ordinate in this figure indicates the scour type that is classified with the scoured bed profiles. From this figure it is clear that the flow pattern is well represented by the K.C. number. This relation has already been investigated (c.f. by Nishizawa and Sawamoto; 1988). The results reported by these authors and ours coincide in the following characteristics: the scour type changes from the Twin-Horn-Shaped to the Cone-Shaped as the K.C. number increases. The borders between the bed profiles Twin-Horn-Shaped and Transient-Shaped, as well as Transient-Shaped and Cone-Shaped are about 8.0 and 20.0 in K.C. number, respectively. These borders are independent of the sand diameter.

Figure 4 depicts the relation of scour type to the K.C. number. As the scour type is related to the flow pattern, represented by the K.C. number, and since the location of maximum scoured points are related to the scour types, as we showed previously, we conclude that the flow pattern can be explained in terms of the location of maximum scoured point.

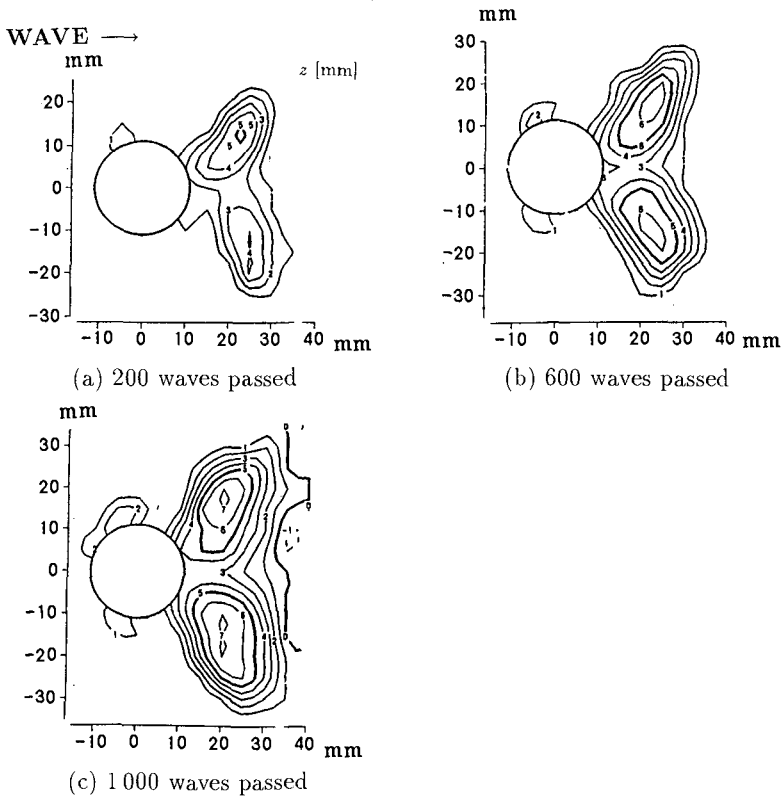


FIG. 5. Bottom Bed Profiles in The Local Scour Developing Process. (K.C. Number: 9.0, Scour Type: Twin-Horn-Shaped)

### 4. SCOUR DEVELOPING PROCESS

The time evolution of the local scour bed profiles around a cylinder was measured in 8 experimental cases. In the experiments, the range of the K.C. number varied from 4.38 to 30.9. The bottom bed profiles around the cylinder were measured every 200 waves passing the cylinder, until we considered that the bottom bed became almost stable. For all experimental cases, the initial bed was flat, and the scoured bed became almost stable after 1000 waves passed the cylinder. The typical developing bed profiles measured are shown in Figs. 5 to 7. Figure 5 shows the Twin-Horn-Shaped scour type. Here, the bed at the lee side of the cylinder was scoured during each developing stage. The bed profiles after 200 and 600 waves passed the cylinder correspond to local scour developing stages. They show similar features to those of the profiles obtained after 1000 waves

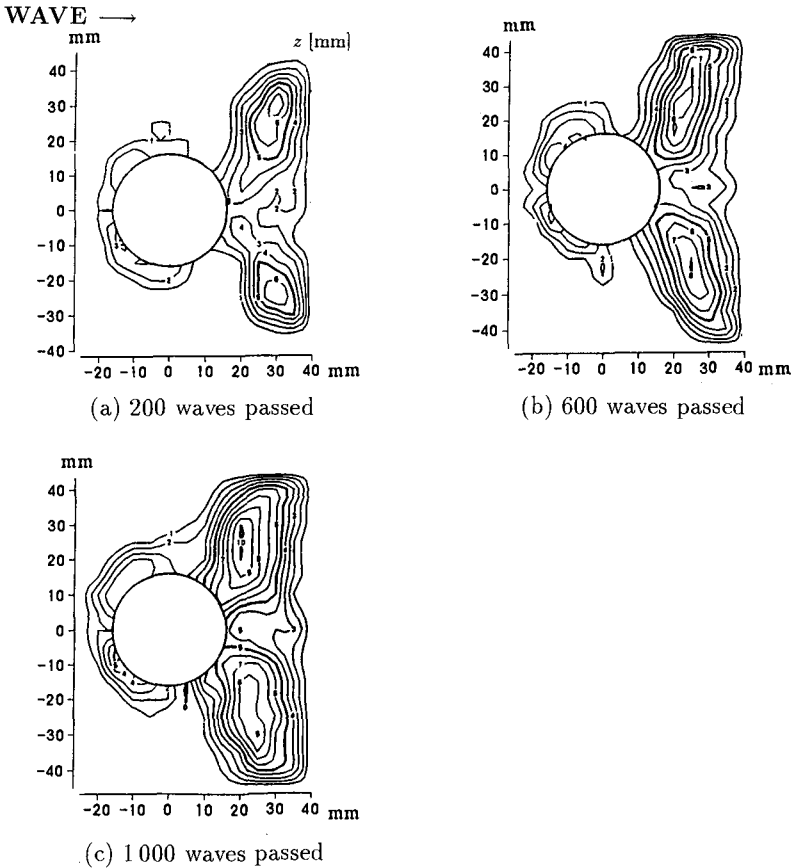


FIG. 6. Bottom Bed Profiles in The Local Scour Developing Process. (K.C. Number: 11.0, Scour Type: Transient-Shaped)

passed, which is considered the equilibrium stage. The maximum scoured point remains located almost in the same place with respect to the cylinder, during every developing stage shown in this figure.

In Fig. 6 the Transient-Shaped scoured bed profile is depicted. This figure shows that the scouring develops at both the lee side of the cylinder and beside this one, during every developing stage. And, as in the case of the Twin-Horn Shaped bed profile, similar shape of bed scouring is retain during the whole developing process.

Figure 7 shows the Cone-Shaped bed profile. Here as in the two previous cases, the scour shape found at the final equilibrium stage is the same that was formed during the earlier stages of the scour developing process. As mentioned in the previous section, the Cone-Shaped bed profile is associated with a horseshoe vortex, and the Twin-Horn-Shaped bed profile is with flow separation from the cylinder or a pair of separated vortices.

No matter however what the flow pattern is, the respective scour bed

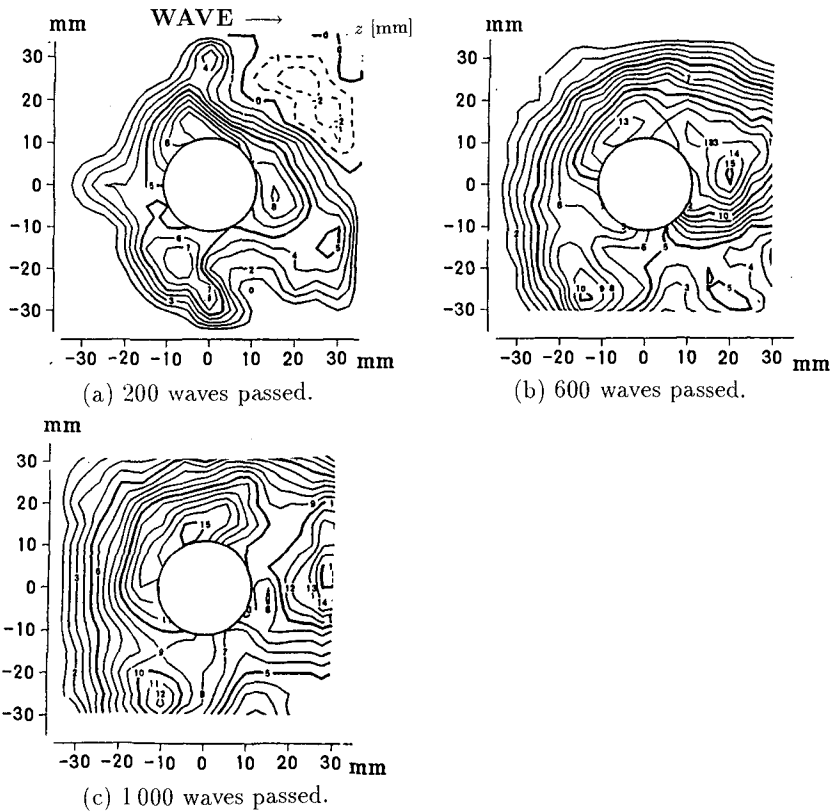
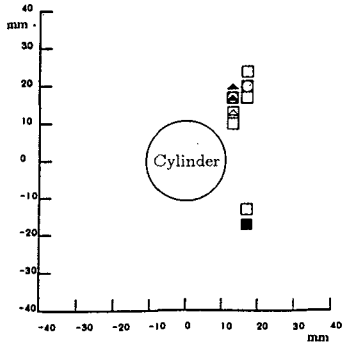
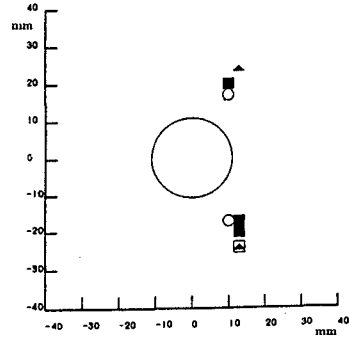


FIG. 7. Bottom Bed Profiles in The Local Scour Developing Process. (K.C. Number: 30.9, Scour Type: Cone-Shaped)

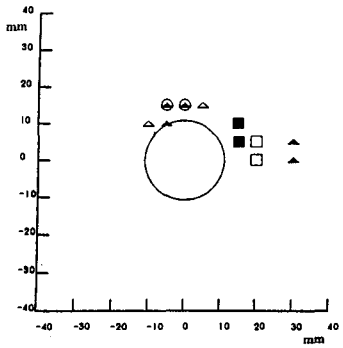
WAVE →



(a) K.C. number : 9.0, Equilibrium Scour Type : Twin-Horn-Shaped.



(b) K.C. number : 11.0, Equilibrium Scour Type : Transient-Shaped.



(c) K.C. number : 30.9, Equilibrium Scour Type : Cone-Shaped.

- : N = 200
- : N = 400
- : N = 600
- △ : N = 800
- ▲ : N = 1000

**FIG. 8. Location of Maximum Scoured Points in Each Developing Stage. *N* Represents the Number of Waves That Passed The Cylinder.**

shapes appearing in the final equilibrium stage of the scour developing process is formed already at the earlier stages. This was confirmed in all experiments performed, and was found to be independent of the scour type.

Next, the developing process of local scour around a cylinder is discussed with the location of maximum scoured point. Figure 8 shows the distribution of maximum scoured points at each developing stage of local scouring for the cases corresponding to Figs. 5 to 7. The maximum scoured points in Figs. 8 (a) and (b) correspond to the cases of Twin-Horn-Shaped and the Transient-Shaped bed profiles, respectively. In both cases, these points are located at the right and left lee side of the cylinder, and they are apart from the cylinder contour. Fig. 8 (c) corresponds to the Cone-Shaped bed profile. Here, the maximum scoured points are located beside the cylinder. During the experiments performance, we observed

that in all cases the location of the maximum scoured points was almost fixed during the whole scouring process. We conclude therefore that the flow pattern near the bed around a cylinder is practically the same during all the local scouring developing process.

Kobayashi (1993) measured velocity distributions around a vertical cylinder on both flat bed and scoured bed, and computed the vorticity distribution shown in Fig. 9. In this figure, the phase  $\theta$  is defined as 0 when a wave crest passes the cylinder axis, these vorticity distribution corresponds then to an instant just after the wave crest passes. Figures 9 (a) and (b) show the vorticity distribution in the initial and equilibrium stage of the developing process of local scouring, respectively. In Fig. 9 (a), the axis of the vortex formed apart from the cylinder contour is almost vertical and parallel to the cylinder axis. And in Fig. 9 (b) the vortex is deformed due to the scoured bed topography, and has an arch shape. From Figures 9 (a) and (b) this author concluded that the scoured bed profile changes the flow pattern near the bed around a cylinder, which contradicts the results obtained in this study. A reason for such contradiction may be attributed to the nonlinearity waves effect. This is because in Kobayashi (1993) study, non-

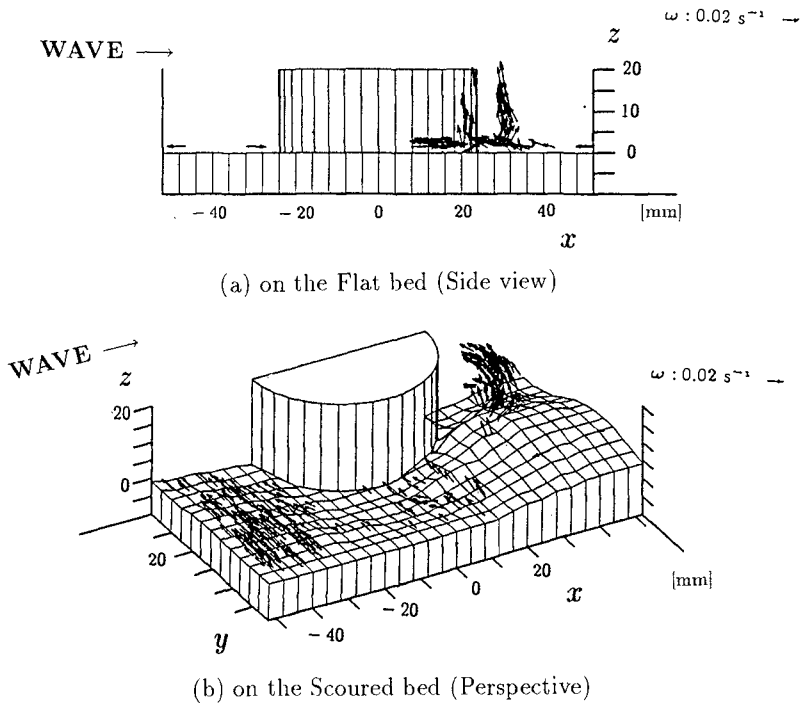


FIG. 9. Vorticity Distribution Near The Bottom Around a Cylinder (Kobayashi, 1993) K.C. Number : 5.2, Phase  $\theta : \pi/4$

linearity of waves could be very important since Ursell number was 83.8. On the other hand, in this study linear waves were reproduced with maximum Ursell number of about 4. This is however just a supposition and studies to clarify the effect of nonlinearity of waves on the local scouring process are required.

**5. ULTIMATE SCOUR DEPTH**

The prediction of the ultimate local scour stage is very important for planning and maintenance of onshore and offshore structures. The predominant parameters in this ultimate stage are the depth and the scoured bed profile. The scoured bed profile has already been examined with the K.C. number: In this section, the local scour depth on the equilibrium stage is discussed.

Figure 10 shows the relation of the ultimate scour depth to the K.C. number. The ordinate in this figure represents the maximum scour depth  $S$  divided by the cylinder diameter  $D$ . Six series of experimental results are shown in this figure. Five of them are results of this study, and one corresponds to experimental results obtained by Sumer *et al.* (1992). The solid line drawn in this figure indicates the relation evaluated empirically by these authors. Their experiments were performed on the live bed condition, and those of this study in clear water condition. In spite of this difference, most experimental results of this study agree well with the solid line. Only the results obtained for K.C. number less than 10 are in relative disagreement with this line; they show deeper maximum scour depths than the solid line does.

The scour bed profile for K.C. number less than 10 is of the Twin-Horn-

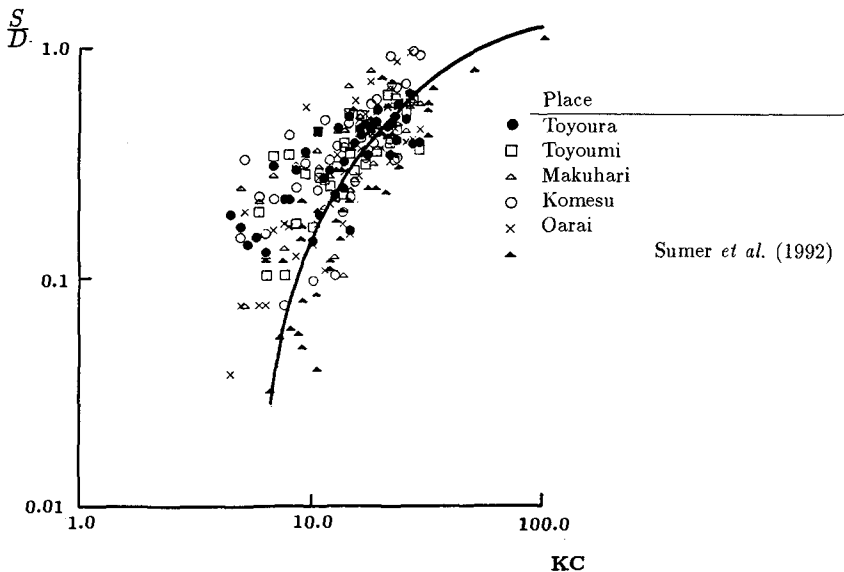


FIG. 10. Relation Between Ultimate Scour Depth and K.C. Number



Shape type, as shown in Fig. 4. For this type of scour profile the maximum scoured points are located apart from the cylinder contour, as observed in Fig. 2(a) or 3. Since for engineering purposes, the local scour just at the vicinity of a cylinder is most serious than that apart from this, the maximum scour depth was reevaluated by considering a reduced area surrounding the cylinder, and excluding the maximum scoured points.

The results obtained after reevaluation are shown in Fig. 11. In this figure, the ordinate represents the ultimate scour depth on the vicinity of the cylinder surface  $S'$  divided by the cylinder diameter  $D$ . In Fig. 11 better agreement of the reevaluated results, for low K.C. numbers, with the solid line estimated by Sumer *et al.* (1992) is observed, comparing with Fig. 2 (a). From this results, we conclude that the maximum scour depth at the vicinity of the cylinder is related with the K.C. number, and is independent of the bed condition, live bed or clear water, as well as the sand diameter.

The reason why in the Twin-Horn-Shaped scoured bed the very near vicinity of the cylinder was not scoured is that, in this case the flow pattern did not show clear formation of the horseshoe vortex. Only flow separation on the lee side of the cylinder or a pair of separated vortices were visible. Sumer *et al.* (1992) reported that horseshoe vortices were absent for K.C. numbers less than 6, and therefore the bed around the cylinder was not scoured under the live bed condition.

Figure 12 shows the relation of the maximum scour depth in the ultimate

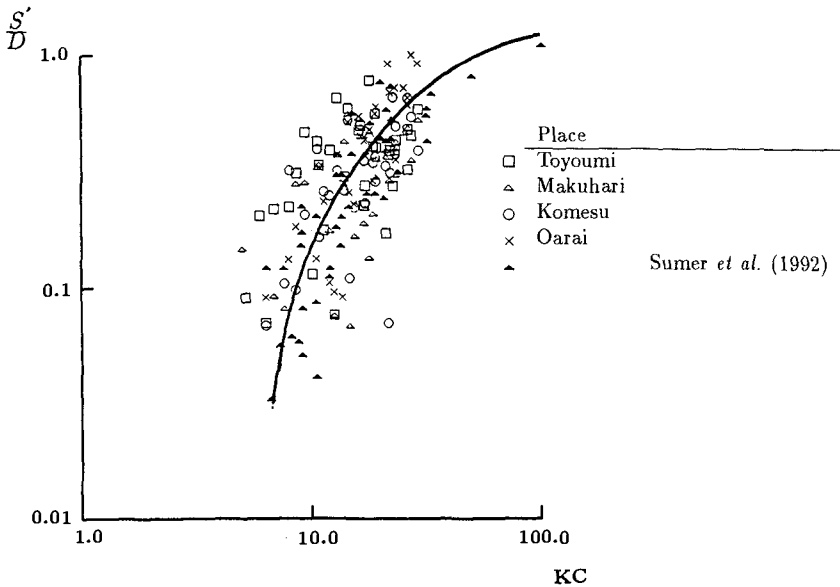
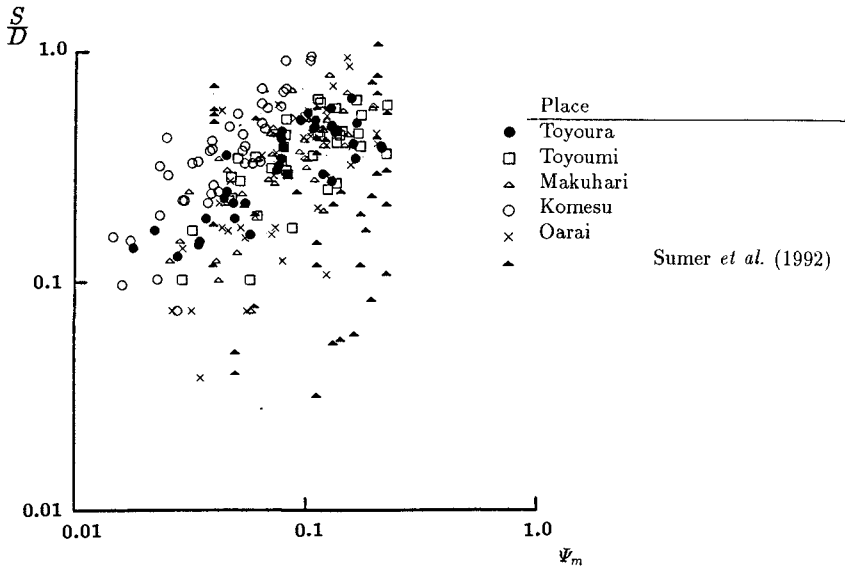


FIG. 11. Relation Between Ultimate Scour Depth on The Vicinity of The Cylinder surface and K.C. number



**FIG. 12. Relation Between Ultimate Scoured Depth to Shields Parameter**

stage to Shields parameter  $\Psi_m$ . The ordinate in this figure indicates the maximum scour depth in the ultimate stage  $S$  divided by the cylinder diameter  $D$ . The Shields parameter  $\Psi_m$  is calculated from the incident wave conditions shown in Table 1, and the sand characteristics listed in Table 2. In Fig. 12 the relation of the maximum scour depth to the Shields parameter is shown. We observe here that the maximum scour depth has a poor relation with the Shields parameter.

## 6. CONCLUSIONS

In this study, local scour around a vertical cylinder and its developing process were investigated experimentally with the flow pattern near the bed. Local scoured bed profiles were classified into the types: Twin-Horn-Shaped, Transient-Shaped and Cone-Shaped. The location of the maximum scoured points was introduced to classify objectively the bed profiles. This location was found to be related to the flow pattern near the bed around the cylinder. In the case of Twin-Horn-Shaped scoured bed profile a pair of maximum scoured points are located at the right and left lee side of the cylinder, and they are apart from the cylinder contour. This type of bed profile is associated with the formation of flow separation or a pair of separated vortices. In the case of the Cone-Shaped scoured bed profile, one maximum scoured point is found, and this is located in front or beside the cylinder. During the whole local scour developing process the bed profiles have a similar shape, and the location of the maximum scoured point or points is almost fixed. These features are independent of the scour type. Finally, we found that

the maximum scour depth has a close relation to the K.C. number, and a very poor relation to the Shields parameter. Also that, this depth is independent of the bottom bed condition, live bed or clear water, and the sand diameter.

#### ACKNOWLEDGEMENTS

We thank Professors A. Watanabe and M. Isobe of the University of Tokyo for their suggestions in this study.

#### REFERENCES

- Kobayashi, T (1993): "3-D analysis of flow around a vertical cylinder on a scoured bed." *Proc. 23rd Int. Conf. on Coastal Engrg.*, ASCE, Vol. 3, pp.3482-3495.
- Nishizawa, M., M. Minami and M. Sawamoto (1988): "Relation of the flow pattern to local scour around a vertical cylinder in wave field." *Proc. of 43rd Conf. of JSCE*, II, pp.758-759 (in Japanese).
- Nishizawa, M. and M. Sawamoto (1988): "Local scour around a vertical cylinder under the wave action." *Proc. of the 6th Congress of APD-IAHR*, pp.121-128.
- Sumer, B. Mutlu, J. Fredsøe, and N. Christiansen (1992): "Scour around vertical pile in waves." *Jour. Waterways, Port, Coastal, and Ocean Engrg.*, ASCE, Vol. 118, No.1, pp.15-31.
- Wells, D. R. and R. M. Sorensen (1970): "Scour around a circular cylinder due to wave motion." *Proc. of the 12th Coastal Eng. Conf.*, pp.1263-1279.

## Wave-induced Uplift Loading of Caisson Breakwaters

Andreas Kortenhaus<sup>1</sup>, Hocine Oumeraci<sup>2</sup>, Søren Kohlhase<sup>3</sup> & Peter Klammer<sup>1</sup>

### ABSTRACT

Wave induced uplift pressures and forces have been investigated by small- and large-scale model tests. Detailed analyses of waves at the structure, forces and structure motions showed that conventional design formulae neglect details of pressure development which contribute to the total uplift force. Direct comparison between quasi-static, dynamic forces and the commonly used formulae show that dynamic effects exhibit a significantly different behaviour in comparison to those observed during quasi-static wave attack. The most relevant of the effects which may be useful for setting up a numerical model for the prediction of uplift pressures are described.

### 1. INTRODUCTION

Wave induced uplift forces for design purposes are commonly calculated by empirical or semi-empirical formulae based on the assumption that the maximum uplift pressure occurs at the seaward bottom edge of the caisson and decreases linearly to zero at the shoreward edge. Generally, it is also implicitly assumed that the maximum horizontal peak force occurs simultaneously with its maximum uplift counterpart and that the caisson structure is fixed and does not exhibit any motion during wave loading. Moreover, the influence of the characteristics of the rubble foundation (permeability, thickness etc.) is totally ignored.

The wave induced flow in the rubble foundation has been studied in a large-scale and a small-scale-model by using a fixed and a movable caisson break-

---

<sup>1</sup> Dipl.-Ing., Franzius-Institut, University of Hannover, Appelstr. 9A, 30167 Hannover, Germany

<sup>2</sup> Prof. Dr.-Ing., University Professor, Techn. University Braunschweig, Beethovenstr. 51a, 38106 Braunschweig, Germany

<sup>3</sup> Prof. Dr.-Ing., Institut für Wasserbau, University of Rostock, Philipp-Müller-Str., 23966 Wismar, Germany

water. The tests principally aim at a better understanding of the generation of uplift pressure under standing, breaking and broken wave conditions and at the establishment of a basis for the development of a conceptual model for the calculation of uplift pressures.

The present paper primarily intends to discussing some of the experimental results. Based on these results an attempt is made to explain the physical processes underneath a vertical caisson structure subject to breaking and nonbreaking wave attack.

## 2. EXPERIMENTAL SET-UP

Small-scale and large-scale model tests have been conducted on a caisson breakwater supported by a rubble foundation (Fig. 1). These investigations were

AM = Acceleration meter; DM = Displacement meter; FT = Force transducer; WO = Wave gauge

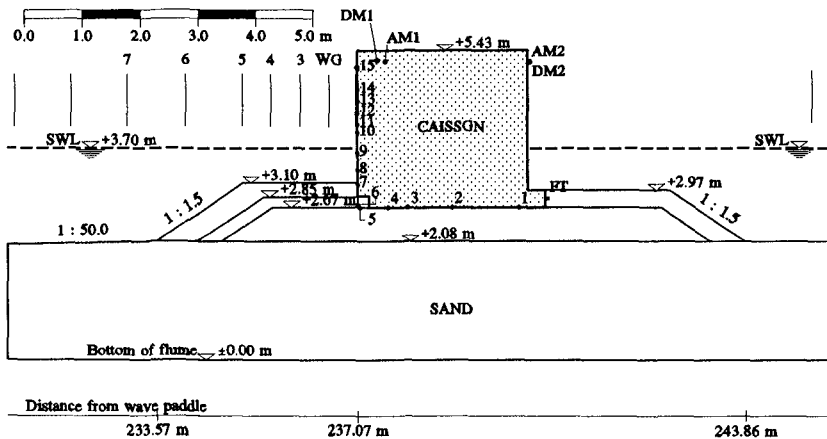


Fig. 1: Large-scale model of caisson breakwater

principally directed towards the examination of the effect of the motions of the caisson on the uplift pressure development. For this purpose, five pressure gauges were installed underneath the structure and two displacement meters were placed at the rear and front top of the caisson, respectively. Further seven pressure gauges were installed along the toe berm in front of the caisson in order to determine the impact pressure gradients along the rubble toe, and hence to better understand the mechanisms associated with the uplift generation. Tests with a fixed and a movable caisson were performed. Further simultaneous measurements of waves, accelerations, total forces and pore pressures in the rubble foundation were conducted.

Since the small-scale model tests are not suitable for the quantitative evaluation of the uplift pressure, flow in the porous rubble foundation is subject to scale effects due to too large viscous forces, large-scale model tests were also performed for different water depths and wave conditions.

Three different wave types were generated throughout the tests: solitary waves, regular waves and random waves (TMA spectra). The wave heights, wave periods and water depths used in the large-scale model tests are summarized in Table 1.

**Table 1: Test programme for large-scale model tests**

<b>SOLITARY WAVES</b>					
<b>Wave heights</b>	<b>steps</b>	<b>Wave periods</b>	<b>steps</b>	<b>Water depth</b>	<b>steps</b>
0.40 - 0.60 m	0.10 m	-	-	3.10 - 3.50 m	0.10 m
0.65 - 1.10 m	0.05 m	-	-	3.50 - 3.90 m	0.20 m
<b>REGULAR WAVES</b>					
<b>Wave heights</b>	<b>steps</b>	<b>Wave periods</b>	<b>steps</b>	<b>Water depth</b>	<b>steps</b>
0.30 - 1.10 m	0.20 m	3.50 - 6.50 s	1.00 s	3.70 - 4.30 m	0.20 m
<b>RANDOM WAVES (TMA spectra)</b>					
<b>Wave heights</b>	<b>steps</b>	<b>Wave periods</b>	<b>steps</b>	<b>Water depth</b>	<b>steps</b>
0.30 - 1.10 m	0.20 m	3.50 - 6.50 s	1.00 s	3.70 - 4.30 m	0.20 m

The small-scale model was about four times smaller than the large-scale model.

### 3. CLASSIFICATION OF BREAKER TYPES

Three major breaker types were identified from the experiments leading to essentially different response of the structure (Fig. 2). All these breaker types could be observed - independently from the type of waves generated. Generally there are more than three different breaker types (*Schmidt et al., 1992*). However, only the three main types shown in Fig. 2 for two time steps  $t_1$  and  $t_2$  are considered below in order to make more clear the physical processes involved.

Four parameters were found suitable to describe the main features of the force histories of both impact and uplift pressures (Fig. 3). These parameters are:

- $t_r$ : rise time of impact force
- $\Delta t$ : time difference between maximum of impact force and maximum of uplift force

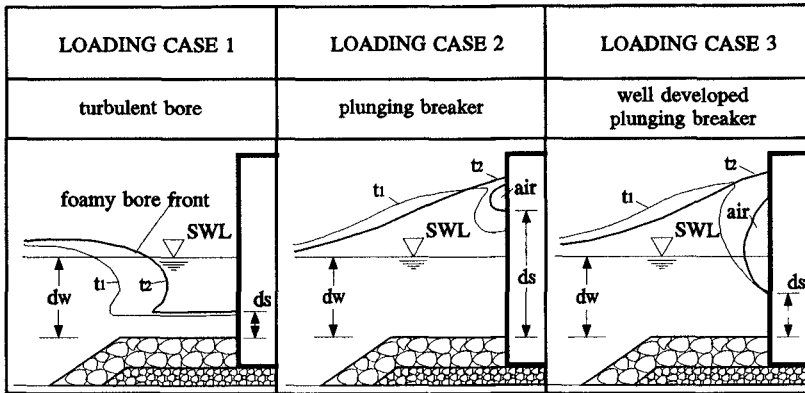


Fig. 2: Main breaker types considered

- $\eta_{F_{m,q}}$ : ratio of quasi-static impact force  $F_{h, qus}$  and maximum impact force  $F_{h, max}$
- $\eta_{F_{h,v}}$ : ratio of maximum uplift force  $F_{v, max}$  and maximum impact force  $F_{h, max}$

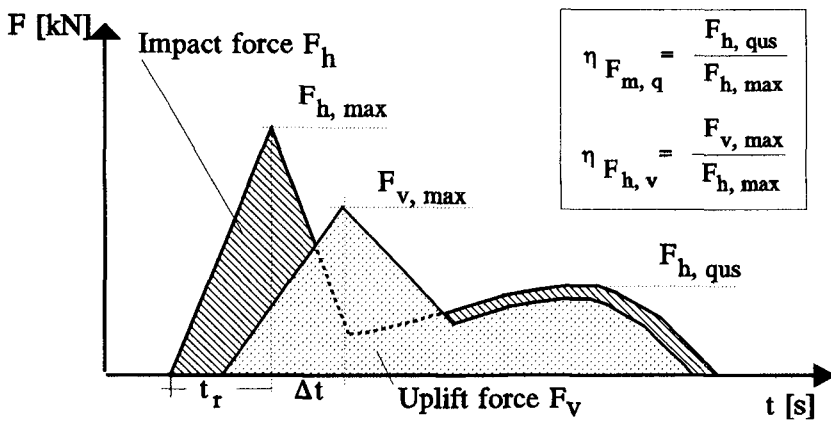


Fig. 3: Parameters for identification of loading cases

## 4. TYPICAL TEST RESULTS

### Force histories

Typical force histories for impact and uplift forces for the three different loading cases can be seen in Figs. 4 to 6 where the aforementioned descriptive parameters are given.

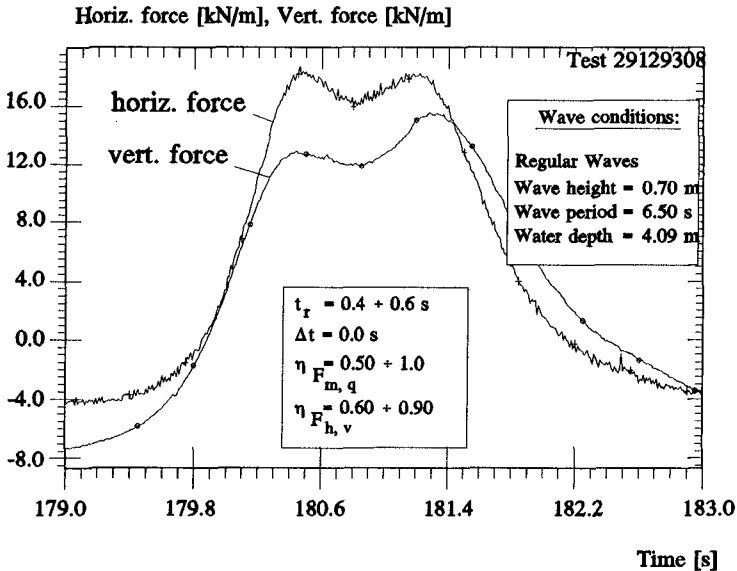


Fig. 4: Typical force histories for loading case 1 (turbulent bore)

The force histories show a high force peak ( $F_{h,max}$ ) caused by the wave hitting the structure and a lower force maximum  $F_{h,qus}$  which occurs when the water of the wave running up the wall falls down again. Between these maxima there is a minimum force (trough) which coincides with the maximum wave run-up.

In loading case 1 (turbulent bore) the wave breaks before reaching the structure, inducing a turbulent air-water mixture. This can be observed from the high frequency oscillations in the time history of the impact forces. There is no time lag between the maxima of impact and uplift force.

The uplift force in loading case 2 shows a double peak for the vertical force which however do not always occurs when a plunging breaker hits the structure. This double peak force is due to the uplift of the structure, which will be discussed in the next chapter.

Loading case 3 shows a very sharp and high peak in the impact force history followed by high frequency oscillations which are due to oscillations of the



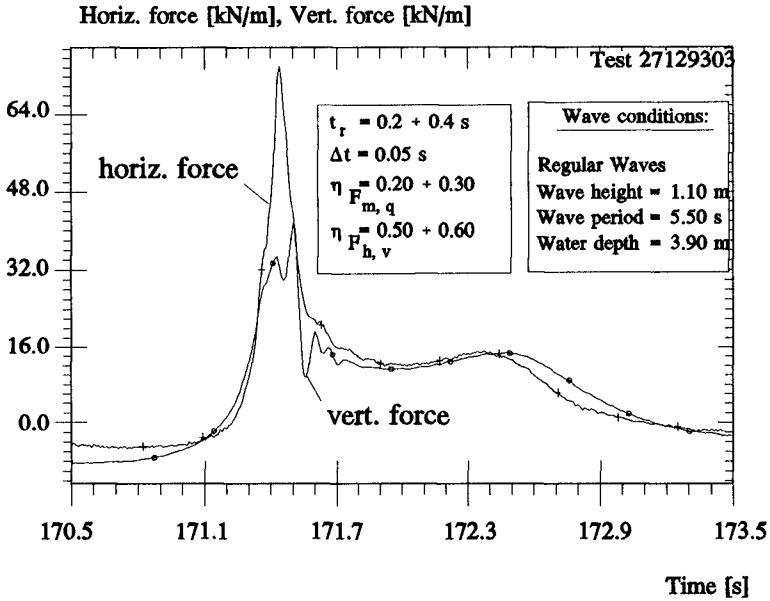


Fig. 5: Typical force histories for loading case 2 (plunging breaker)

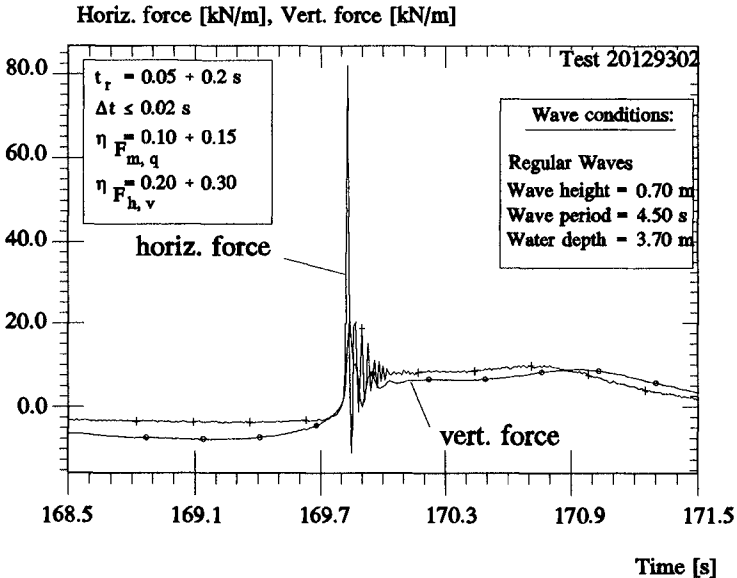


Fig. 6: Typical force histories for loading case 3 (plunging breaker with air entrapment)

entrapped air pocket at the vertical face of the structure. Very often a double peaked force in the impact force history occurs. The first peak is induced by the beaker tongue hitting the structure whereas the second occurs when the rest of the wave front impinges on the structure.

### Pressure distributions

Typical horizontal impact pressure distributions on the front and the bottom of the caisson caused during loading case 2 are given in Fig. 7. In this figure the motion of the structure is amplified by a factor of 200 to make clear:

- whether the structure moves at all,
- the comparison of all loading cases,
- at which time the structure starts to move.

The following typical features of impact and uplift pressures are observed for loading case 1:

- there are almost no temporal changes in the figures (quasi-static behaviour)
- maximum impact pressure is approximately at still water level
- measured impact pressure distribution is very close to the theoretically predicted (SAINFLOU) distribution for a standing wave with little scatter due to reflection coefficients which are actually less than 100%.
- uplift pressures are almost linear but not decreasing to zero pressure at the shoreward edge of the structure
- velocity flow in the rubble foundation has been estimated by an improved Forchheimer equation (*Van Gent, 1993*) to about 5 to 10 cm/s. Therefore, pressures due to velocity head can be neglected

For loading case 2 (Fig. 7), the typical features which are worth to mention are:

- point of application of impact force is in the range of still water level, but the magnitude of the force is much higher
- there are mainly horizontal motions of the structure, but only some slight rotational motions
- compression wave underneath the structure
- lever arm of uplift force is at 2/3 of the width of the structure from its heel

Loading case 3 is an extreme example for plunging breakers with air entrapment inducing a very high short time impact peak followed by high amplitude oscillations. Impact and uplift pressures exhibit the following typical distribution:

- maximum impact is reached within a very short time
- pressure oscillations due to air entrapment occur about 0.2 s after maximum peak
- no motions of structure is induced since peak pressures are too short
- relatively low uplift pressures (showing phenomenon of compression wave)

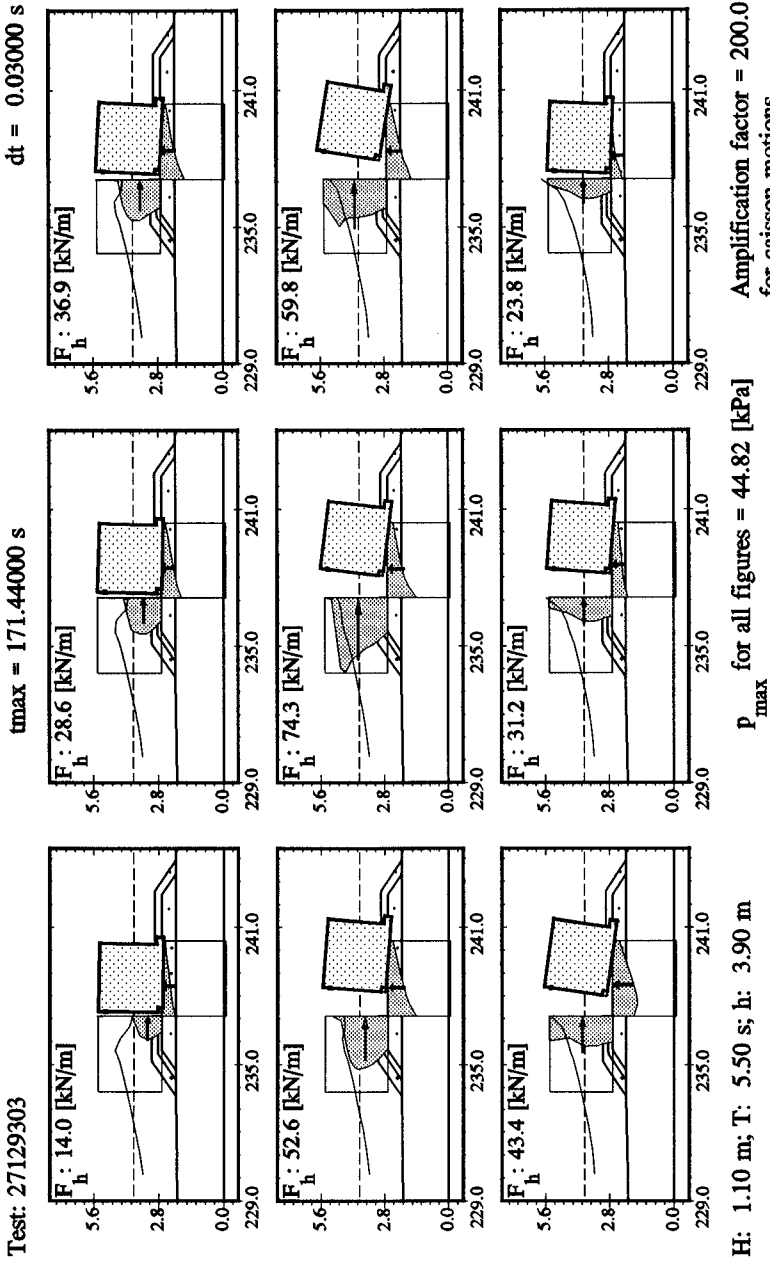
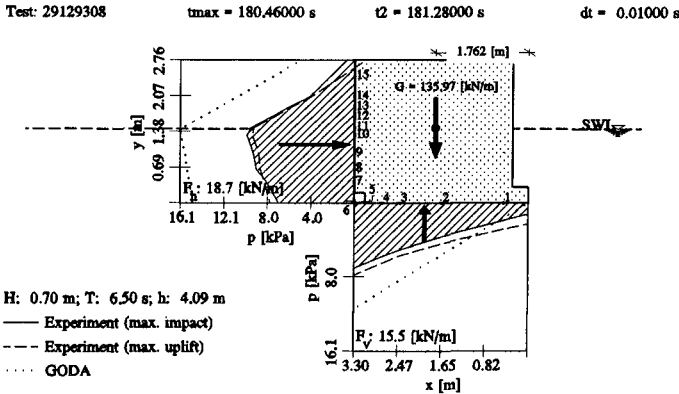


Fig. 7: Typical pressure distribution for loading case 2

**Comparison to Goda formulae**

For the prediction of horizontal wave and uplift forces the Goda formulae are widely used (Goda, 1985). Calculations using these formulae have been performed for the loading cases described in section 3 to show the range of quasi-static and dynamic loads. The results of these calculations are compared to the measurements for each of the loading cases in Figs 8 to 10.



**Fig. 8:** Comparison of loading case 1 with GODA's formulae

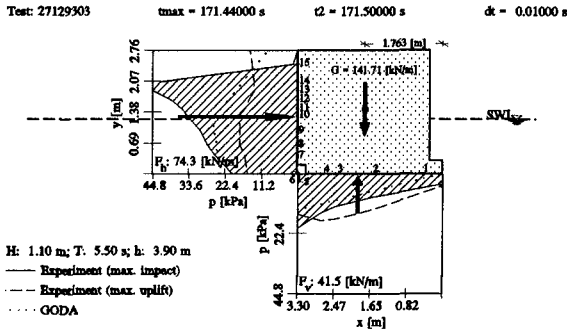


**Fig. 9:** Comparison of loading case 2 with GODA's formulae

For quasi-static loads (loading case 1) the results obtained by Goda formulae are conservative whereas the pressure peaks in the case of highly dynamic loads exceed the calculated pressure by a factor up to 5. Goda's formulae predict approximately correct uplift pressure values at the seaward edge of the breakwater for loading cases 1 and 3, but not for dynamic loading case 2. In this case the maximum uplift force occurs when the compression wave is underneath the structure and has reached 2/3 of the width of the structure from its heel.

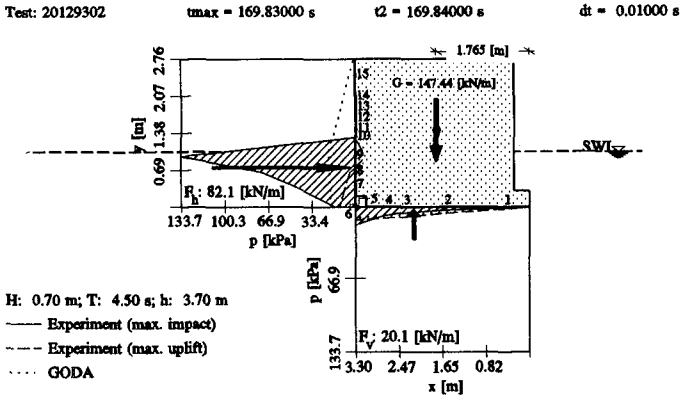


Fig. 10: Comparison of loading case 3 with GODA's formulae

### 5. OBSERVED UPLIFT PHENOMENA

#### Compression wave

For loading cases 2 and 3 a compression wave is induced beneath the structure by the wave impact on the vertical face of the breakwater. To obtain more information about the propagation, velocity of this wave underneath the structure and its effect on the porous rubble foundation the uplift pressure recorded beneath the structure have been plotted for a single wave in Fig. 11. The maxima of the obtained curves were determined and time differences have been plotted versus the

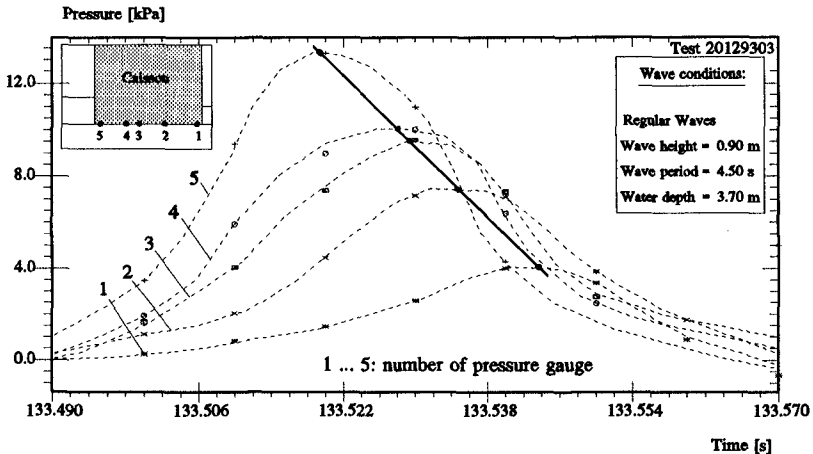


Fig. 11: Analysis of compression wave underneath the structure

spacial difference  $dx_i$  between the respective pressure gauges. This procedure was repeated several times for a test with regular waves (Fig. 12). Similar results have been found for further regular and random waves, showing that the velocity of the compression wave is not affected by the wave parameters.

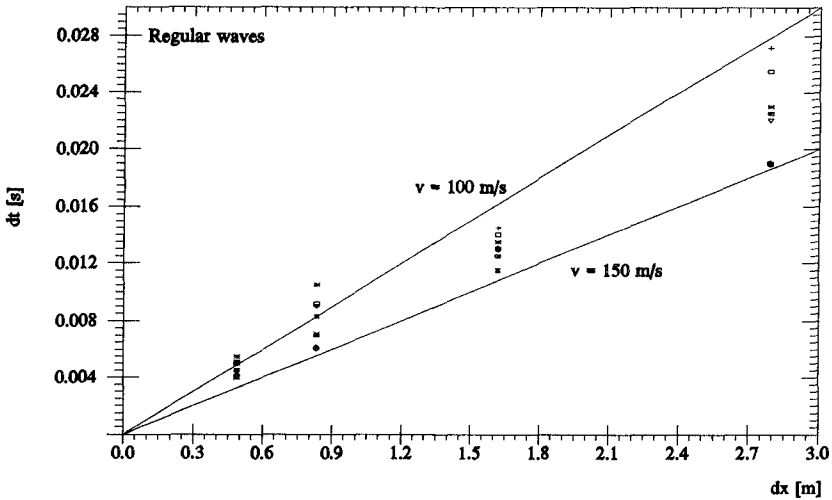
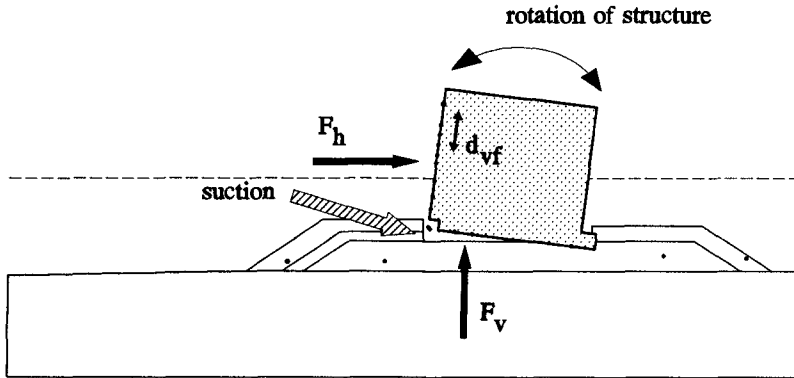


Fig. 12: Velocity of compression wave beneath the structure

**Suction underneath the structure**

Due to the very high impacts inducing a strong horizontal and rotational motion of the structure a gap forms at the front base (Fig. 13). Pressure decreases



$d_{vf}$  = vertical displacement at the front

Fig. 13: Suction beneath a rotating caisson structure

immediately and water flows with relatively high velocities into the gap thus increasing the risk of erosion of the rubble materials (suction). This phenomenon was only observed for high impacts and cannot be considered as typical for normal impact loading. However, it may be a very critical case, due to the aforementioned erosion potential of the high velocity gap flow.

Fig. 14 shows simultaneously recorded uplift forces and displacements at the vertical face front of the structure. It can be seen that the increase of the displacement suddenly leads to a decrease in the uplift force (dashed line in Fig. 14). The uplift force is obtained from the integration of all pressure records at the bottom of the structure. Similar decrease can also be observed in the pore pressure records.

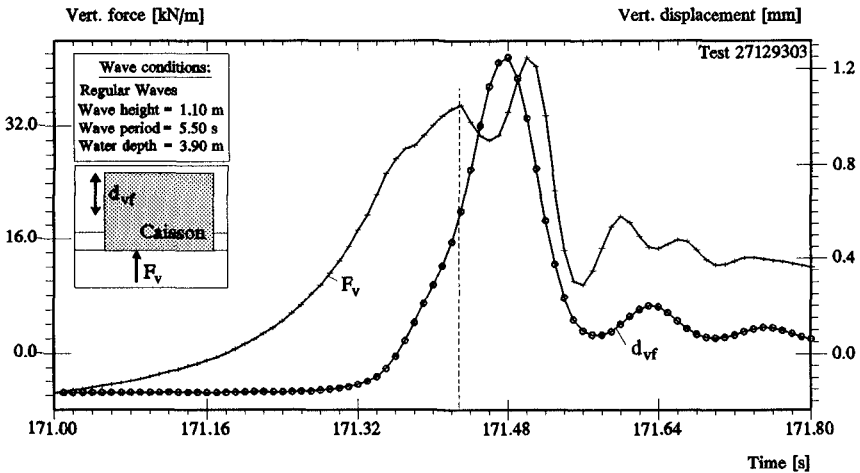


Fig. 14: Time histories of uplift force and vertical displacement at the caisson front

The reduction of uplift force caused by the suction is shown in Fig. 15 where an increase of vertical displacements at the front for small values creates an almost linear increase of uplift forces. Three almost parallel lines were plotted to show this dependency. Furthermore, it can be seen that there is a clear relationship between the water depth and the uplift force where higher water depths at the toe of the rubble mound in front of the structure will result in smaller uplift forces. However, for larger displacement values a sudden bend can be found leading to an increase of uplift forces at a lower rate with increasing displacements. A more detailed analysis in the near future will show whether there are similar relations with respect to different water depths. To obtain quantitative statements more variations in wave parameters have to be considered.

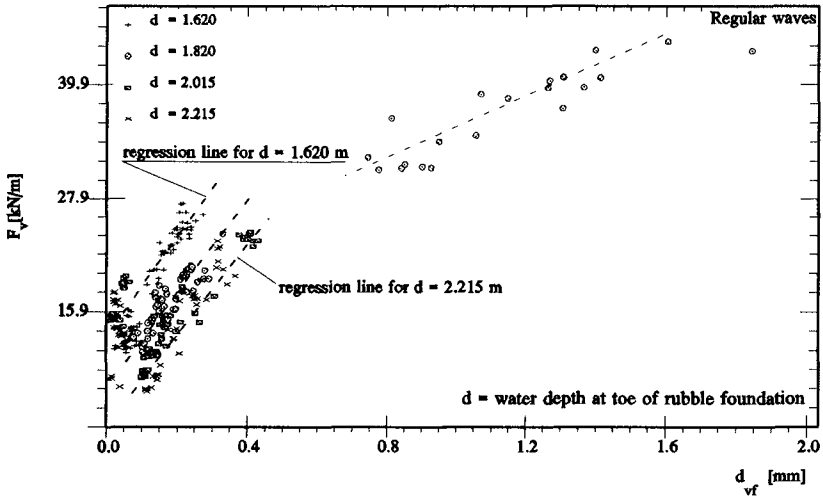


Fig. 15: Reduction of uplift force by suction underneath the structure

**Pressure at shoreward edge**

In all measurements of both breaking and nonbreaking waves the pressure at the shoreward edge of the breakwater was different from zero. This phenomenon was also observed under model and prototype conditions, but could not be explained (Marchi *et al.*, 1975). Several reasons may be considered to explain this phenomenon:

- water level variations behind the breakwater were induced by a flow through the rubble foundation thus leading to hydrostatic pressures at the shoreward edge
- flow induced velocities are responsible for this pressure (velocity head  $v^2/2g$ )
- pressures may be induced by flow resistance in the rubble foundation, since the rubble structure at the rear is higher than the bottom level of the caisson

Since water level variations and flow through the rubble foundation induces pressures which are in the range of 5% of the measured pressures at the rear edge, the latter reason seems to provide the most reasonable explanation. This has to be confirmed by further model tests or numerical modelling.

**6. SUMMARY OF RESULTS AND FUTURE RESEARCH TASKS**

- The widely used assumption of linear pressure distribution underneath the structure is almost valid for quasi-static wave loading. For impulsive loading, however, a non linear distribution occurs. This is due to the effect of com-



pression waves beneath the structure where the maximum uplift pressure no longer occurs at the seaward edge of the structure;

- the assumption of zero pressure at the shoreward edge of the structure seems to be only valid for very low rubble foundation and should be more thoroughly examined for higher rubble substructures;
- for extreme wave conditions suction at the seaward bottom edge of the structure may occur leading to lower uplift pressures and forces at the base of the structure and in the rubble foundation, thus increasing the risk of erosion due to high velocities of the gap flow.

The influencing parameters to be investigated in the future are:

- permeability of the rubble foundation
- geometry of the structure and the rubble foundation (thickness and height)

A numerical model should be developed which accounts for a) the (turbulent) flow and pressures in the rubble mound; b) breaking and nonbreaking wave conditions and c) variations in geometry and permeability of the rubble foundation. This numerical model could be calibrated by the experimental results obtained by this study and might be used for an extensive parameter study. The results of this parameter study will help to develop simple prediction formulae for both uplift pressure distribution and forces as a function of various parameters (water depth, wave parameters, breaker type, properties of rubble material and geometry of structure and rubble foundation).

## ACKNOWLEDGEMENTS

Support by the EEC within the research programme MAST II (MAS2-CT92-0047) is gratefully acknowledged. The support by the German Research Council (DFG) within the SFB 205 at the University of Hannover is also gratefully acknowledged.

## REFERENCES

- GODA, Y. (1985): Random seas and design of maritime structures. Tokyo: University of Tokyo Press, 323 pp.
- MARCHI, E.; E. RAITERI; G. SCARSI and S. STURA (1975): Storm wave pressures on the breakwater of Genoa harbour - measurement station. *Proceedings XVIIth Congress of the International Association for Hydraulic Research (IAHR)*, vol. 1.
- SCHMIDT, R.; H. OUMERACI and H.-W. PARTENSCKY (1992): Impact loads induced by plunging breakers on vertical structures. *Proceedings 23rd International Conference Coastal Engineering (ICCE)*, vol. 2, pp. 1545-1558.
- VAN GENT, M.R.A. (1993): Stationary and oscillatory flow through coarse porous media. *Communications on Hydraulic and Geotechnical Engineering*, Report no. 93-9, Delft University, 62 pp.

## CHAPTER 95

# LINEAR AND NONLINEAR WAVE FORCES EXERTED ON A SUBMERGED HORIZONTAL PLATE

Haruyuki Kojima <sup>1</sup>, Akinori Yoshida <sup>2</sup> and Tetuya Nakamura <sup>3</sup>

## ABSTRACT

Linear and Nonlinear wave forces exerted on a submerged horizontal plate are studied using the method of matched eigenfunction expansions for velocity potential together with the perturbation technique up to second order. Energy damping coefficients are introduced in the formulation to incorporate the effects of vortices and wave breaking. The theoretical results are compared with experimental data to obtain validity and limits of the second-order solution. The theory with proper energy damping coefficients can well simulate the wave forces even when wave breaking occurs over the plate. The second-order oscillatory wave force is relatively small as compared to the first-order one, while time-independent, steady wave force becomes comparable with the first-order one at small relative water depth and its direction is always upward.

## 1 INTRODUCTION

Wave interactions with a submerged horizontal plate have been extensively studied both theoretically and experimentally. Most of the studies, however, deal with linear wave interactions, namely, reflection and transmission characteristics of waves from the submerged plate (e.g., Ijima *et al.*, 1970, and Patarapanich *et al.*, 1989). These studies concluded that the submerged horizontal plate might be one of the promising wave attenuation devices. There is however little information available on the characteristics of wave forces exerted on the plate except for a work by Patarapanich (1984), especially of nonlinear wave forces. Since wave motion over the plate placed at small submergence depth is highly nonlinear, higher harmonic generation usually occurs; the second harmonic wave increases

---

<sup>1</sup>Dept. of Civil Engineering, Kyushu Kyouritu Univ., 1-8 Jiyugaoka, Yahatanishi-ku, Kitakyushu, 807, Japan

<sup>2</sup>Dept. of Civil Engineering Hydraulics, Kyushu Univ., Fukuoka, Japan

<sup>3</sup>Nihonkokudokaihatu Company, Tokyo, Japan

significantly over the plate and at the end of the plate the second harmonic sometimes becomes greater than the first one (Kojima *et al.*, 1990). It is of great interest to study the contribution of the higher harmonic forces to the total wave force. The information on these forces and the overturning moment is essential in designing such a structure.

The main objective of this study is to present a theoretical solution of linear and nonlinear wave forces exerted on a submerged horizontal plate and to understand their characteristics. The solution obtained is valid to second order. Numerical results are compared with experimental data to show the validity and limitation of the second-order solution. The characteristics of wave forces under the extreme condition such as breaking waves are also examined. The study is restricted to the two-dimensional cases of regular waves approaching normal to the thin plate fixed at various submergence below the water surface.

## 2 THEORETICAL FORMULATION

### 2.1 Governing Equations

The nonlinear interaction problem is treated as the water wave boundary value problem for the second-order velocity potential since potential flow assumptions may be valid. Let us consider the second-order Stokes' wave, with its first-order amplitude  $\zeta_0$ , wave number  $k$ , and angular frequency  $\sigma$ , incident upon a submerged horizontal plate from the positive  $x$  direction, as shown in Fig. 1. Since the fluid motion may be assumed to be irrotational, incompressible and inviscid, the governing equations for this problem are as follows:

Laplace equation,

$$\frac{\partial^2 \Phi}{\partial x^2} + \frac{\partial^2 \Phi}{\partial z^2} = 0 \tag{1}$$

the kinematic free surface boundary condition,

$$\frac{\partial \zeta}{\partial t} + \frac{\partial \Phi}{\partial x} \frac{\partial \zeta}{\partial x} - \frac{\partial \Phi}{\partial z} = 0 \quad \text{on } z = \zeta(x, t) \tag{2}$$

the dynamic free surface boundary condition with the Bernoulli constant  $Q$ ,

$$\frac{\partial \Phi}{\partial t} + g\zeta + \frac{1}{2} \left\{ \left( \frac{\partial \Phi}{\partial x} \right)^2 + \left( \frac{\partial \Phi}{\partial z} \right)^2 \right\} = Q \quad \text{on } z = \zeta(x, t) \tag{3}$$

and the kinematic no-flux condition on the plate surface and sea bottom,

$$\frac{\partial \Phi}{\partial z} = 0 \quad \text{on } z = -h_2, -h_d, -h \tag{4}$$

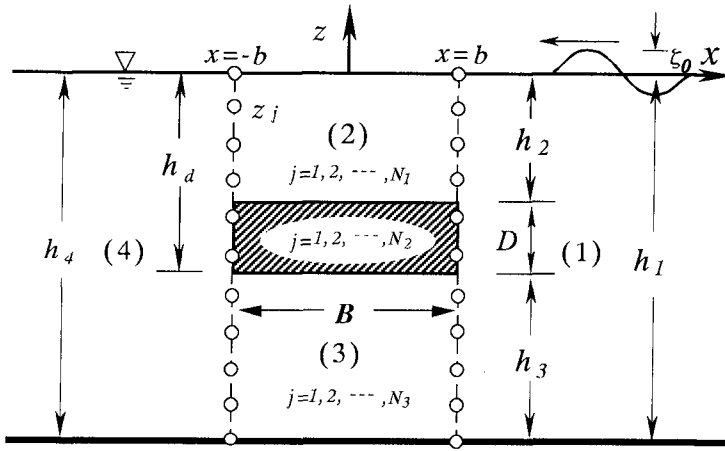


Figure 1 Fluid regions and definition sketch.

### 2.2 Solutions of first and second order

To obtain solutions for the first- and second-order velocity potential, the velocity potential, water elevation and Bernoulli constant are expanded by the perturbation approach in terms of power series in a small parameter  $\epsilon (= k\zeta_0)$  and the combined free surface boundary condition is applied on the still mean water level with help of the Taylor expansion. Then, the velocity potential  $\Phi(x, z, t)$  can be given by

$$\Phi(x, z, t) = \frac{g}{k\sigma} \text{Re} \left[ \epsilon \phi_1^{(1)}(x, z) \exp(i\sigma t) + \epsilon^2 \{ \phi_0^{(2)}(x, z) + \phi_2^{(2)}(x, z) \exp(i2\sigma t) \} + \dots \right] \quad (5)$$

in which  $\phi_1^{(1)}(x, z)$ ,  $\phi_0^{(2)}(x, z)$ ,  $\phi_2^{(2)}(x, z)$  are nondimensional complex functions (hereafter referred to as a potential function) and the subscripts 0, 1 and 2 indicate the degree of harmonic components and the indices (1) and (2) denote the first- and second-order solutions, respectively.

The potential functions  $\phi_1^{(1)}$ ,  $\phi_2^{(2)}$ ,  $\phi_0^{(2)}$  in the regions (1), (2) and (4) with the free water surface can be expressed in terms of a power series as

$$\phi_1^{(1)}(x, z) = \sum_{n=0}^{\infty} \{ C_{in} \exp(k_{in}x) + D_{in} \exp(-k_{in}x) \} Z(k_{in}z) \quad (6)$$

$$\begin{aligned} \phi_2^{(2)}(x, z) = & \sum_{n=0}^{\infty} \{ C_{in}^{(2)} \exp(k_{in}^{(2)}x) + D_{in}^{(2)} \exp(-k_{in}^{(2)}x) \} Z(k_{in}^{(2)}z) \\ & + \sum_{m=0}^{\infty} \sum_{p=0}^{\infty} \Pi_{mp}(x, z) \end{aligned} \quad (7)$$

$$\begin{aligned} \phi_0^{(2)}(x, z) = & \overline{C_0^{(2)}} \frac{x}{b} + \overline{D_0^{(2)}} \\ & + \sum_{n=1}^{\infty} \left\{ \overline{C_n^{(2)}} \exp\left(\frac{n\pi}{h} x\right) + \overline{D_n^{(2)}} \exp\left(-\frac{n\pi}{h} x\right) \right\} \cos \frac{n\pi}{h} z \\ & + \sum_{m=0}^{\infty} \sum_{p=0}^{\infty} \Pi_{mp}^*(x, z) \end{aligned} \tag{8}$$

where  $C_{in}^{(q)}, D_{in}^{(q)}, \overline{C_{in}^{(q)}}, \overline{D_{in}^{(q)}}$  indicate unknown coefficients of  $O(\epsilon^q)$ , the subscript  $i$  denotes the corresponding fluid regions, and the eigenfunction  $Z(k_{in}^{(q)} z)$  is written by

$$Z(k_{in}^{(q)} z) = \frac{\cos k_{in}^{(q)}(z + h_i)}{\cos k_{in}^{(q)} h_i} \tag{9}$$

The eigenvalues  $k_{in}^{(q)}$  can be found from the following dispersion relationship.

$$\frac{(q\sigma)^2 h_i}{g} = -k_{in}^{(q)} h_i \tan k_{in}^{(q)} h_i \quad (i = 1, 2, 4 \quad q = 1, 2) \tag{10}$$

When  $n = 0$ , it becomes an imaginary number ( $k_{i0}^{(q)} = i k_i^{(q)}$ ) and a real number when  $n \neq 0$ .  $\Pi_{mp}(x, z)$  and  $\Pi_{mp}^*(x, z)$  in Eqs. (7) and (8) are given by

$$\left. \begin{aligned} \Pi_{mp}(x, z) &= \frac{\lambda(k_m, k_p)}{\mu_1(k_{mp})} Q_{mp}(x) Z(k_{mp} z) + \frac{\overline{\lambda}(k_m, k_p)}{\mu_1(\overline{k_{mp}})} \overline{Q}_{mp}(x) Z(\overline{k_{mp}} z) \\ \Pi_{mp}^*(x, z) &= \frac{\Upsilon(k_p)}{\mu_2(k_{mp}^*)} Q_{mp}^*(x) Z(k_{mp}^* z) + \frac{\overline{\Upsilon}(k_p)}{\mu_2(\overline{k_{mp}^*})} \overline{Q}_{mp}^*(x) Z(\overline{k_{mp}^*} z) \end{aligned} \right\} \tag{11}$$

where

$$\left. \begin{aligned} Q_{mp}(x) &= C_m C_p \exp(k_{mp} x) + D_m D_p \exp(-k_{mp} x) \\ \overline{Q}_{mp}(x) &= C_m D_p \exp(\overline{k_{mp}} x) + C_p D_m \exp(-\overline{k_{mp}} x) \\ Q_{mp}^*(x) &= C_m C_p^* \exp(k_{mp}^* x) + D_m D_p^* \exp(-k_{mp}^* x) \\ \overline{Q}_{mp}^*(x) &= C_m D_p^* \exp(\overline{k_{mp}^*} x) + C_p^* D_m \exp(-\overline{k_{mp}^*} x) \end{aligned} \right\} \tag{12}$$

$$\left. \begin{aligned} \lambda(k_m, k_p) &= \frac{i}{2k} (3\Gamma^2 + 2k_m k_p + k_p^2), \quad \Upsilon(k_p) = \frac{i}{2k} (\Gamma^2 + k_p^2) \\ \overline{\lambda}(k_m, k_p) &= \frac{i}{2k} (3\Gamma^2 - 2k_m k_p + k_p^2) \end{aligned} \right\} \tag{13}$$

$$\left. \begin{aligned} \mu_1(k_{mp}) &= 4\Gamma + k_{mp} \tan k_{mp} h, \quad \mu_2(k_{mp}^*) = k_{mp}^* \tan(k_{mp}^* h) \\ \mu_1(\overline{k_{mp}}) &= 4\Gamma + \overline{k_{mp}} \tan \overline{k_{mp}} h, \quad \mu_2(\overline{k_{mp}^*}) = \overline{k_{mp}^*} \tan(\overline{k_{mp}^*} h) \end{aligned} \right\} \tag{14}$$

$$\left. \begin{aligned} k_{mp} &= k_m + k_p, \quad \overline{k_{mp}} = k_m - k_p, \quad \Gamma = \sigma^2/g \\ k_{mp}^* &= k_m + k_p^*, \quad \overline{k_{mp}^*} = k_m - k_p^* \end{aligned} \right\} \quad (15)$$

The index \* designates the complex conjugate of the variables. Note that  $\phi_0^{(2)}(x, z)$ , given by Eq.(8) and representing the steady component of the second-order potential function, contributes to neither the second-order water surface displacement nor wave pressure exerted on the plate. The interpretation of the solution for  $\phi_2^{(2)}(x, z)$  is discussed elsewhere (Kojim *et al.*, 1994).

The first- and second-order solutions for the fluid region beneath the plate are assumed to have the following form:

$$\begin{aligned} \phi_3^{(q)}(x, z) &= C_{30}^{(q)} \frac{x}{b} + D_{30}^{(q)} \\ &+ \sum_{n=1}^{\infty} \left\{ C_{3n}^{(q)} \exp(\nu_n x) + D_{3n}^{(q)} \exp(-\nu_n x) \right\} \cos \nu_n(z + d) \end{aligned} \quad (16)$$

in which  $\nu_n = n\pi/h_3$  and  $q = 1, 2$ .

The unknown coefficients in the first- and second-order solutions should be determined by satisfying the no-flux conditions along the vertical faces of the plate as well as flow continuity conditions over the vertical planes separating the fluid regions. Instead of using a conventional technique employing the orthogonality of the eigenfunctions (Ijima, 1971, and Massel, 1983), a "collocation" method of matching is applied in determining unknown coefficients in the expansions. A detailed explanation of the procedure is presented by Kojima *et al.* (1994) and Yoshida *et al.* (1990).

## 2.3 Linear and Nonlinear Wave Forces

### 2.3.1 Expressions for dynamic wave pressures

The dynamic pressure due to wave action against a submerged horizontal plate can be obtained from the unsteady Bernoulli equation. Like the velocity potential  $\Phi(x, z, t)$ , the dynamic pressure  $p(x, z, t)$  may be expanded in terms of power series in  $\epsilon$ , and substituting the determined velocity potential into the Bernoulli equation and collecting terms of each order in  $\epsilon$  yield the non-dimensional dynamic pressure  $p(x, z, t)$  to second order in the following form.

$$\begin{aligned} \frac{p(x, z, t)}{\rho g \zeta_0} &= p^{(1)}(x, z, t) + \epsilon p^{(2)}(x, z, t) \\ &= R\epsilon \left[ p_1^{(1)}(x, z) \exp(i\sigma t) + \epsilon \left\{ p_0^{(2)}(x, z) + p_2^{(2)}(x, z) \exp(i2\sigma t) \right\} \right] \end{aligned} \quad (17)$$

where

$$p_1^{(1)}(x, z) = -i\phi_1^{(1)} \quad (18)$$

$$p_0^{(2)}(x, z) = -\frac{g}{4k\sigma^2} \left\{ \frac{\partial \phi_1^{(1)}}{\partial x} \frac{\partial \phi_1^{(1)*}}{\partial x} + \frac{\partial \phi_1^{(1)}}{\partial z} \frac{\partial \phi_1^{(1)*}}{\partial z} \right\} + Q^{(2)} \quad (19)$$

$$p_2^{(2)}(x, z) = -2i\phi_2^{(2)} - \frac{g}{4k\sigma^2} \left\{ \left( \frac{\partial \phi_1^{(1)}}{\partial x} \right)^2 + \left( \frac{\partial \phi_1^{(1)}}{\partial z} \right)^2 \right\} \tag{20}$$

In the above equations  $p_1^{(1)}(x, z), p_0^{(2)}(x, z), p_2^{(2)}(x, z)$  are non-dimensional dynamic pressure where the superscripts (1) and (2) denote the first- and second-order dynamic pressures, respectively, and  $Q^{(2)}$  is the Bernoulli constant.

### 2.3.2 Vertical wave force

The vertical wave forces exerted on a horizontal plate located at an arbitrary depth  $z$  can be obtained by integrating wave pressures in regions (2) and (3) from  $-b$  to  $b$  in the direction of  $x$

$$F_Z(z, t) = \frac{f_Z(z, t)}{\rho g \zeta_0 B} = \int_{-b}^b \{p_3(x, z, t) - p_2(x, z, t)\} dx \tag{21}$$

By using Eq. (18) through Eq. (20), the normalized wave forces  $f_Z(z, t)/\rho g \zeta_0 B$  can be expressed as

$$F_Z = \frac{f_Z(z, t)}{\rho g \zeta_0 B} = Re \left[ \{F_{Z31}^{(1)}(z) - F_{Z21}^{(1)}(z)\} \exp(i\sigma t) + \epsilon \left\{ \left( F_{Z30}^{(2)}(z) - F_{Z20}^{(2)}(z) \right) + \left( F_{Z32}^{(2)}(z) - F_{Z22}^{(2)}(z) \right) \exp(i2\sigma t) \right\} \right] \tag{22}$$

Since the first-order term is well-known, only the second-order ones are given as follows:

$$F_{Z20}^{(2)}(z) = \int_{-b}^b p_{20}^{(2)}(x, z) dx = \sum_{m=0}^{\bar{n}_2} \sum_{p=0}^{\bar{n}_2} \left[ \alpha(k_m, k_p^*) Z(\overline{k_{2mp}z}) R_{mp}^* + \bar{\alpha}(k_m, k_p^*) Z(k_{2mp}z) \overline{R_{mp}^*} \right] + Q^{(2)} \tag{23}$$

$$F_{Z30}^{(2)}(z) = \int_{-b}^b p_{30}^{(2)}(x, z) dx = -\frac{g}{4k\sigma^2} \left[ \frac{C_{30} C_{30}^*}{b^2} + \frac{C_{30}}{2b^2} \sum_{m=1}^{n_3} \{A(\nu_m)\} \{C_{3m}^* - D_{3m}^*\} Z(\nu_m z) + \frac{C_{30}^*}{2b^2} \sum_{n=1}^{n_3} \{A(\nu_n)\} \{C_{3n} - D_{3n}\} Z(\nu_n z) + \sum_{n=1}^{\bar{n}_3} \sum_{m=1}^{\bar{n}_3} \nu_n \nu_m \left\{ \widehat{R}_{nm}^* Z(\overline{\nu_{nm}z}) - \overline{\widehat{R}_{nm}^*} Z(\nu_{nm}z) \right\} \right] + Q^{(2)} \tag{24}$$

$$F_{Z22}^{(2)}(z) = \int_{-b}^b p_{22}^{(2)}(x, z) dx = -2i \sum_{n=0}^{n_2^{(2)}} \frac{A(k_{2n}^{(2)})}{2k_{2n}^{(2)} b} \{C_{2n}^{(2)} + D_{2n}^{(2)}\} Z(k_{2n}^{(2)} z)$$

$$\begin{aligned}
 & -2i \sum_{m=0}^{\bar{n}_2} \sum_{p=0}^{\bar{n}_2} \left\{ \frac{\lambda(k_m, k_p)}{\mu_1(k_{mp})} R_{mp} Z(k_{2mp}z) + \frac{\bar{\lambda}(k_m, k_p)}{\mu_1(\bar{k}_{mp})} \overline{R}_{mp} Z(\overline{k_{2mp}z}) \right\} \\
 & + \sum_{m=0}^{\bar{n}_2} \sum_{p=0}^{\bar{n}_2} \left\{ \alpha(k_m, k_p) R_{mp} Z(\overline{k_{2mp}z}) + \bar{\alpha}(k_m, k_p) \overline{R}_{mp} Z(k_{2mp}z) \right\} \quad (25)
 \end{aligned}$$

$$\begin{aligned}
 F_{Z_{32}}^{(2)}(z) &= \int_{-b}^b p_{32}^{(2)}(x, z) dx \\
 &= -2i \left[ \{-C_{30}^{(2)} + D_{30}^{(2)}\} + \sum_{n=1}^{n_3} \frac{A(\nu_n)}{2\nu_n b} \{C_{3n}^{(2)} + D_{3n}^{(2)}\} Z(\nu_n z) \right] \\
 &\quad - \frac{g}{4k\sigma^2} \left[ \frac{1}{b^2} C_{30}^2 + \frac{1}{b^2} C_{30} \sum_{n=1}^{n_3} A(\nu_n) \{C_{3n} - D_{3n}\} Z(\nu_n z) \right. \\
 &\quad \left. + \sum_{n=1}^{\bar{n}_3} \sum_{m=1}^{\bar{n}_3} \nu_n \nu_m \left\{ \widehat{R}_{nm} Z(\overline{\nu_{nm}z}) - \overline{\widehat{R}}_{nm} Z(\nu_{nm}z) \right\} \right] \quad (26)
 \end{aligned}$$

where

$$R_{mp}^* = \begin{cases} C_{2m} C_{2p}^* + D_{2m} D_{2p}^* & (m = p = 0) \\ \frac{A(2k_{2mp})}{2k_{2mp}^* b} \{C_{2m} C_{2p}^* + D_{2m} D_{2p}^*\} & \begin{pmatrix} m = p \neq 0 \\ m \neq p \end{pmatrix} \end{cases} \quad (27)$$

$$\overline{R}_{mp}^* = \begin{cases} \exp(-2k_{2m}b) \{C_{2m} D_{2p}^* + C_{2p}^* D_{2m}\} & (m = p \neq 0) \\ \frac{B(k_{2p}, k_{2m})}{2k_{2mp}^* b} \{C_{2m} D_{2p}^* + C_{2p}^* D_{2m}\} & \begin{pmatrix} m = p = 0 \\ m \neq p \end{pmatrix} \end{cases} \quad (28)$$

$$\widehat{R}_{nm}^* = \frac{A(\nu_{nm})}{2\nu_{nm} b} \{C_{3n} C_{3m}^* + D_{3n} D_{3m}^*\} \quad (29)$$

$$\overline{\widehat{R}}_{nm}^* = \begin{cases} \exp(-2\nu_n b) \{C_{3n} D_{3m}^* + C_{3m}^* D_{3n}\} & (n = m) \\ \frac{B(\nu_m, \nu_n)}{2\nu_{nm} b} \{C_{3n} D_{3m}^* + C_{3m}^* D_{3n}\} & (n \neq m) \end{cases} \quad (30)$$

$$R_{mp} = \frac{A(k_{2mp})}{2k_{2mp} b} \{C_{2m} C_{2p} + D_{2m} D_{2p}\} \quad (31)$$

$$\overline{R}_{mp} = \begin{cases} \exp(-2k_m b) \{C_{2m} D_{2p} + C_{2p} D_{2m}\} & (m = p) \\ \frac{B(k_{2p}, k_{2m})}{2k_{2mp} b} \{C_{2m} D_{2p} + C_{2p} D_{2m}\} & (m \neq p) \end{cases} \quad (32)$$

$$\widehat{R}_{nm} = \frac{A(\nu_{nm})}{2\nu_{nm} b} \{C_{3n} C_{3m} + D_{3n} D_{3m}\} \quad (33)$$



$$\overline{\hat{R}}_{nm} = \begin{cases} \exp(-2\nu_n b) \{C_{3n}D_{3m} + C_{3m}D_{3n}\} & (n = m) \\ \frac{B(\nu_m, \nu_n)}{2\nu_{nm}b} \{C_{3n}D_{3m} + C_{3m}D_{3n}\} & (n \neq m) \end{cases} \quad (34)$$

In the above equations,  $A(k_{2mp})$ ,  $B(k_{2p}, k_{2m})$ ,  $Z(k_{2p}^{(2)}z)$ ,  $Z(\nu_n z), \dots$  can be given for each variable in the following forms.

$$\left. \begin{aligned} A(k_{2mp}) &= 1 - \exp(-2k_{2mp}b) \\ B(k_{2p}, k_{2m}) &= \exp(-2k_{2p}b) - \exp(-2k_{2m}b) \\ Z(k_{2p}^{(2)}z) &= \frac{\cos k_{2p}^{(2)}(z + h_2)}{\cos k_{2p}^{(2)}h} \\ Z(\nu_n z) &= \cos \nu_n(z + h_d) \end{aligned} \right\} \quad (35)$$

### 2.3.3 Horizontal wave forces

The horizontal wave forces exerted on the horizontal plate can be obtained by integrating over the plate thickness from  $-h_d$  to  $-h_2$ . The wave force coefficient  $F_x = f_x(z, t)/\rho g \zeta_0 D$  can be expressed as

$$F_X = \frac{f_x(x, t)}{\rho g \zeta_0 D} = Re \left[ \left( F_{X_{i1}}^{(1)}(x) - F_{X_{i1}}^{(1)}(x) \right) \exp(i\sigma t) + \epsilon \left\{ \left( F_{X_{i0}}^{(2)}(x) - F_{X_{i0}}^{(2)}(x) \right) + \left( F_{X_{i2}}^{(2)}(x) - F_{X_{i2}}^{(2)}(x) \right) \exp(i2\sigma t) \right\} \right] \quad (36)$$

$F_{X_{i1}}^{(1)}(x)$ ,  $F_{X_{i0}}^{(2)}(x)$ , and  $F_{X_{i2}}^{(2)}(x)$  can be given by the following equations:

$$F_{X_{i1}}^{(1)}(x) = -2i \sum_{n=0}^{n_i^{(1)}} \left\{ C_{in}^{(1)} \exp(k_{in}^{(1)}x) + D_{in}^{(1)} \exp(-k_{in}^{(1)}x) \right\} Y_n^{(1)} \quad (37)$$

$$F_{X_{i0}}^{(2)}(x) = \sum_{m=0}^{\bar{n}_i} \sum_{p=0}^{\bar{n}_i} \left\{ \alpha(k_m, k_p^*) Q_{imp}^*(x) \overline{Y_{mp}^*} + \bar{\alpha}(k_m, k_p^*) \overline{Q_{imp}^*}(x) Y_{mp}^* \right\} + Q^{(2)} \quad (38)$$

$$\begin{aligned} F_{X_{i2}}^{(2)}(x) &= -2i \sum_{n=0}^{n_i^{(2)}} \left\{ C_{in}^{(2)} \exp(k_{in}^{(2)}x) + D_{in}^{(2)} \exp(-k_{in}^{(2)}x) \right\} Y_n^{(2)} \\ &\quad - 2i \sum_{m=0}^{\bar{n}_i} \sum_{p=0}^{\bar{n}_i} \left\{ \frac{\lambda(k_m, k_p)}{\mu_1(k_{mp})} Q_{imp}(x) Y_{mp} + \frac{\bar{\lambda}(k_m, k_p)}{\mu_1(k_{mp})} \overline{Q_{imp}(x)} \overline{Y_{mp}} \right\} \\ &\quad + \sum_{m=0}^{\bar{n}_i} \sum_{p=0}^{\bar{n}_i} \left\{ \alpha(k_m, k_p) Q_{imp}(x) \overline{Y_{mp}} + \bar{\alpha}(k_m, k_p) \overline{Q_{imp}(x)} Y_{mp} \right\} \end{aligned} \quad (39)$$

where

$$Y_{mp}^* = \begin{cases} 1.0 & (m = p = 0) \\ \frac{2 \cos k_{mp}^* (h_3 + D/2) \sin k_{mp}^* D/2}{k_{mp}^* D \cos k_{mp}^* h} & \begin{pmatrix} m = p \neq 0 \\ m \neq p \end{pmatrix} \end{cases} \quad (40)$$

$$\overline{Y}_{mp}^* = \begin{cases} 1.0 & (m = p \neq 0) \\ \frac{2 \cos \overline{k}_{mp}^* (h_3 + D/2) \sin \overline{k}_{mp}^* D/2}{\overline{k}_{mp}^* D \cos \overline{k}_{mp}^* h} & \begin{pmatrix} m = p = 0 \\ m \neq p \end{pmatrix} \end{cases} \quad (41)$$

$$Y_n^{(2)} = \frac{2 \cos k_n^{(2)} (h_3 + D/2) \sin k_n^{(2)} D/2}{k_n^{(2)} D \cos k_n^{(2)} h} \quad (42)$$

$$Y_{mp} = \frac{2 \cos k_{mp} (h_3 + D/2) \sin k_{mp} D/2}{k_{mp} D \cos k_{mp} h} \quad (43)$$

$$\overline{Y}_{mp} = \begin{cases} 1.0 & (m = p) \\ \frac{2 \cos \overline{k}_{mp} (h_3 + D/2) \sin \overline{k}_{mp} D/2}{\overline{k}_{mp} D \cos \overline{k}_{mp} h} & (m \neq p) \end{cases} \quad (44)$$

The subscript  $i$  is 1 and 4, denoting regions (1) and (4). Since the water depths in regions (1) and (4) are same, the wave numbers  $k_m, k_p$  are equal in these regions.

## 2.4 Incorporation of the effects of energy damping

To incorporate the effects of energy losses due to vortices generated at the plate ends and wave breaking over the plate, the energy losses are assumed to be expressed in terms of flow resistance proportional to square of local flow velocity and to local flow acceleration. The pressure continuity condition along the vertical plane at  $x = b$  may then be written as

$$\frac{1}{\rho}(p_1 - p_2) = -\frac{1}{2}C_D|v_1|v_1 - C_M \frac{\partial v_1}{\partial t} \quad (45)$$

where  $C_D$  and  $C_M$  are energy loss coefficients. By using the Lorentz concept, linearizing a nonlinear term with respect to time and expressing the dynamic wave pressure and velocity in the velocity potential yield the following boundary condition for the potential continuity.

$$\phi_1 - \phi_2 = \beta \left| \frac{\partial \phi_1}{\partial x} \right| \frac{\partial \phi_1}{\partial x} - C_M \frac{\partial \phi_1}{\partial x} \quad (46)$$

where

$$\beta = i \frac{4}{3\pi} \frac{g}{\sigma^2 h} \frac{\zeta_0}{h} C_D \quad (47)$$

### 3 Hydraulic Experiments

Two-dimensional hydraulic experiments are performed to measure the vertical and horizontal wave forces as well as the dynamic pressure along the upper and lower surfaces of the plate using pressure transducers. Fig. 2 illustrates the devices used for these measurements. For horizontal wave forces, as shown on the left-hand side of the figure, two pairs of strain gages were mounted on four steel cylinders attached to the horizontal plate. The horizontal forces may then be obtained through a calibrated strain-force relationship. For vertical wave forces, pressure transducers were mounted on both the top and bottom surfaces of the plate, as shown on the right-hand side of the figure. Integrating pressure distributions along the plate yields vertical wave forces exerted on the plate top and bottom surfaces, and adding these forces gives the resultant vertical wave forces. The height and period of incident waves are varied to investigate the effects of wave breaking over the plate on wave forces.

## 4 RESULTS AND DISCUSSIONS

### 4.1 The first- and second-order wave pressures and forces

The components induced by the nonlinear interactions of the second-order theory include a time-independent, steady component and second-harmonic component which constitute the second-order wave pressure and force. Fig. 3 shows comparison between the computed and measured pressure amplitude distributions along the top surface (upper figure) and the bottom surface (lower figure) of the plate. The lines indicate the computed results and the marks the measured. When energy damping is not taken into consideration, i.e.  $C_D = C_M = 0.0$ , an agreement between the computed and measured pressure distributions is poor, especially for the first harmonic pressure component, as shown in the left-hand side of Fig. 3. This may thus be due to the effects of energy losses caused by the generation of vortices at the two ends of the plate. With proper energy loss coefficients, which are 0.8 for  $C_D$  and 0.0 for  $C_M$  in this case, both 1st- and 2nd-order solutions agree quite well with the experimental results, as seen in the right-hand side of Fig 3. However, the computed 2nd-order steady component somehow deviates from the measured.

The amplitude of the first- and second-order non-dimensional oscillatory wave forces is shown in Fig. 4, where the thin lines indicate the computed results without consideration of energy damping and the thick lines with consideration of energy damping. By comparing the measured wave forces with the computed, an agreement between them is remarkably good when the submergence depth is not so small and the wave height is fairly small. The effects of energy loss indicated by the thick lines affect the normalized vertical force  $F_z$  more than the normalized horizontal one  $F_x$ . The computed second-order oscillatory forces  $F^{(2)}$ , indicated by the broken line, are also consistent with the measured, indicated by

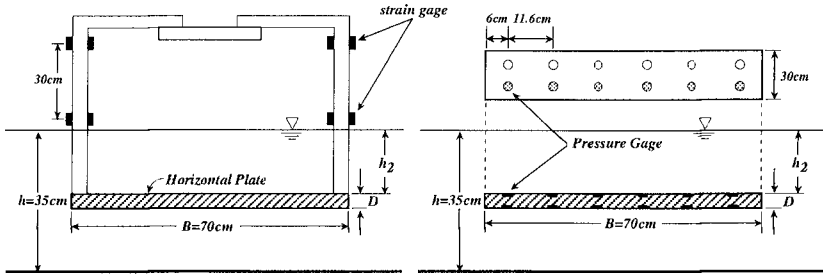


Figure 2 Schematic description of measuring devices for horizontal and vertical wave forces.

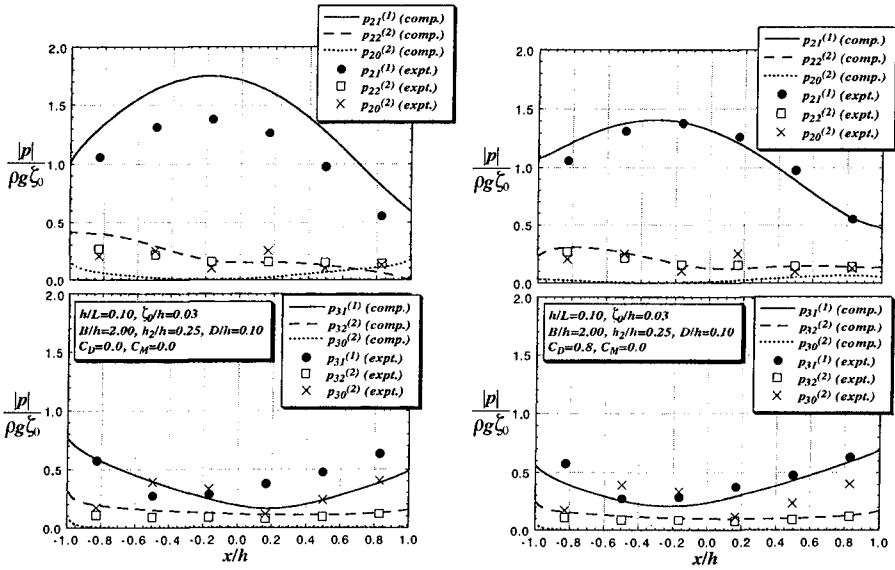


Figure 3 Comparison between computed and experimental wave pressure along the top and bottom surfaces of the plate with and without energy damping consideration.

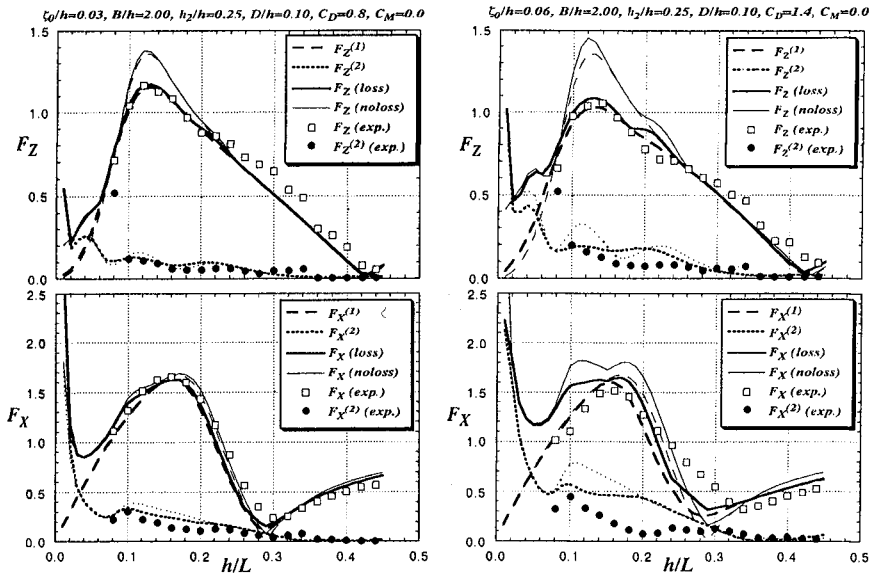


Figure 4 Comparison between computed and measured wave forces exerted on a submerged horizontal plate with  $\zeta_0/h = 0.03$  and  $\zeta_0/h = 0.06$ .

the black circle. Both the vertical and horizontal second-order oscillatory forces are small compared with the first-order ones  $F^{(1)}$  and decrease monochromatically with increase in  $h/L$

The right-hand side of Fig. 4 shows the result of a higher incident wave amplitude ( $\zeta_0/h = 0.06$ ), where wave breaking takes place over the plate when the relative water depth is greater than  $h/L = 0.14$ . The theory with greater  $C_D$  value can simulate the total wave forces fairly well even when wave breaking occurs over the plate. Although the theory overpredicts the 2nd-order oscillatory force, the actual values become quite small. Thus the first-order or linear wave forces dominate the total wave forces.

### 4.2 Variation of wave forces due to the submergence depth

Fig. 5 shows the variations of the normalized 1st-order vertical and horizontal wave forces with relative water depth for three different submergence depths. As the submergence depth  $h_2/h$  decreases, the computed results disagree not only quantitatively but also qualitatively with the measured, as depicted in Fig 5. The theory can fairly well predict the value of the maximum vertical and horizontal wave forces up to  $h_2/h = 0.15$ . At a smaller submergence depth the theoretical values fluctuate with the variation of relative water depth, but the experimental

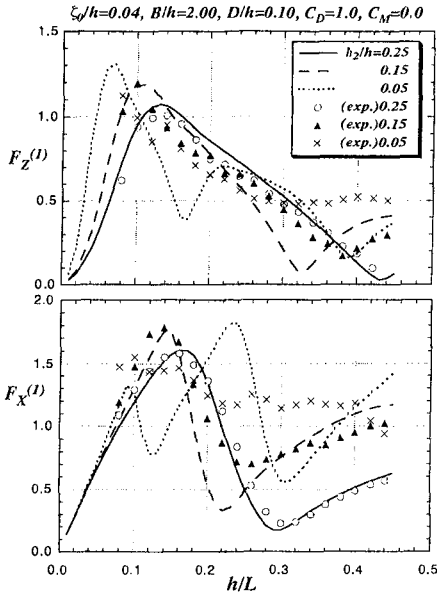


Figure 5 Variations of the first-order wave forces with submergence depth.

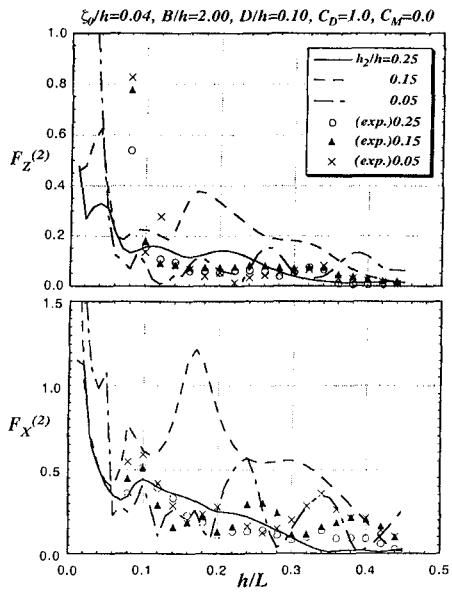


Figure 6 Variations of the second-order wave forces with submergence depth.

ones somewhat flatten over the whole range of relative water depth. The theory also overpredicts the amplitude of the second-harmonic force, as depicted in Fig. 6.

### 4.3 Variation of time-independent, steady wave forces

Another important wave force for design of a submerged horizontal plate is time-independent, steady force. The variations of normalized vertical steady forces for three different incident waves are delineated in Fig. 7, where a rectangular mark indicates the force exerted on the plate's top surface, a triangular mark on the plate's bottom surface, and a black circle the resultant force. When an incident wave height is relatively small, say  $\zeta_0/h = 0.03$ , upward steady forces act on the plate's bottom surface, while downward steady forces act on the plate's top. Since the upward forces are almost always greater than the downward forces, the resultant steady forces become uplift ones. The net steady forces exerted on the plate become comparatively large in magnitude at smaller relative water depth, decreasing almost monochromatically with the increase in relative water depth, and at larger relative water depth the forces come closer to zero. As an incident wave height increases, the normalized steady forces exerted on the both top and bottom surfaces become smaller and the direction of the forces exerted on the top surface changes to the upward at smaller relative water depth.

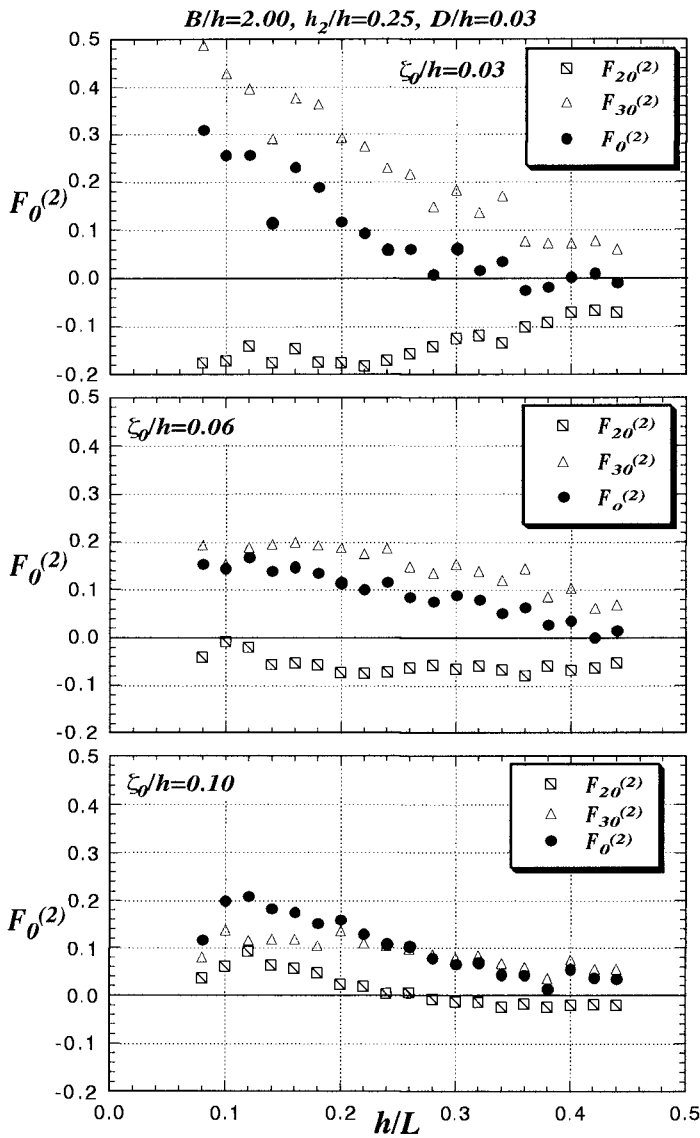


Figure 7 Variations of the steady wave forces with relative water depth for different incident wave heights.

## 5 CONCLUSIONS

The following conclusions are obtained from this study:

1. Linear and nonlinear dynamic wave pressures and forces exerted on a submerged horizontal plate are explained through the non-transient, finite amplitude wave theory that is valid to second order.
2. The theory with proper energy damping coefficients can well simulate the wave forces even when wave breaking occurs over the plate. The second-order wave forces are relatively small as compared to the first-order ones.
3. For the plate placed close to the water surface, the computed wave forces are qualitatively inconsistent with the measured; the computed first-order oscillatory wave forces fluctuate with relative water depth, while the measured vary almost linearly.
4. When wave height is relatively small, an upward steady force acts on the plate bottom surface, while a downward steady force acts on the plate top surface; the direction of the resultant force depends on their magnitude. The steady net uplift force becomes comparatively large in magnitude at smaller relative water depth, decreasing almost monochromatically with increase in relative water depth.

## REFERENCES

- Ijima, T. *et al.* (1970): "Analytical study of breakwater and quay with horizontal plate," *Proc. of the 17th Japanese Conf. on Coastal Eng.*, pp. 97-106 (in Japanese).
- Ijima, T. (1971): "Solutions of boundary value problems in recent wave theory and their application," *Summer Seminar on Hydr. Eng.*, JSCE, Course B, pp.B.1.1-B.1.30 (in Japanese).
- Kojima, H., T. Ijima, and A. Yoshida (1990): "Decomposition and interception of long waves by a submerged horizontal plate," *Proc. 22nd ICCE*, pp.1228-1241.
- Kojima, H., A. Yoshida, and T. Ijima (1994): "Second-order interactions between water waves and a submerged horizontal plate," *Coastal Engineering in Japan*, in press.
- Massel, S.R. (1983): "Harmonic generation by waves propagating over a submerged step," *Coastal Engineering*, Vol. 7, pp.350-380.
- Patarapanich, M. and Hin-Fatt Cheong (1989): "Reflection and transmission characteristics of regular and random waves from a submerged horizontal plate," *Coastal Engineering*, Vol. 13, pp.161-182.
- Patarapanich, M. (1984): "Forces and moment on a horizontal plate due to wave scattering," *Coastal Engineering*, Vol. 8, pp.279-301.
- Yoshida, A., H. Kojima and Y. Tsurumoto (1990): "A collocation method of matched eigenfunction expansions on the boundary-value problem of wave-structure interactions," *Proc. JSCE*, 417/II-13, pp.265-274 (in Japanese).



## CHAPTER 96

### MODERN FUNCTIONAL DESIGN OF GROIN SYSTEMS

Nicholas C. Kraus<sup>1</sup>, Hans Hanson<sup>2</sup>, and Sten H. Blomgren<sup>3</sup>

**ABSTRACT:** Coastal zone management policy in the United States and many other countries discourages use of groins for shore protection, even though properly designed groins can maintain beach width, increase longevity of beach fills, and prevent loss of sand into inlets, navigation channels, and submarine canyons. A lack of a systematic approach to groin functional design and a poor image from incorrect applications are probably responsible for the aversion to groins. In this study, a modern approach to groin functional design is demonstrated by applying the shoreline response model GENESIS to simulate the action of single and multiple groins. Groin bypassing and permeability, evolution of the shoreline in a groin field, and groin tapering are discussed. The balance between net and gross sand longshore transport rates emerges as an important factor controlling groin functioning. A criterion is introduced for judging groin success, and an example design diagram is developed based on this criterion to demonstrate the feasibility of developing a general and rational functional design procedure. Predictions are tested in reproducing shoreline change observed at the 15 groins at Westhampton, Long Island, New York.

#### INTRODUCTION

Coastal zone management policy in the United States and many other countries strongly discourages use of groins for shore protection, despite observations of good performance and their potential for maintaining beach width, increasing longevity of beach fills, and preventing loss of sand into inlets, navigation channels, and submarine canyons. No guidance on groin functional design is available other than rules of thumb, and many examples of poor performance of groins caused by mis-judgments in either design or in planning have turned this structure into a cliché representing automatic beach destruction. The result, however, is that society is losing a valuable shore-protection structure that can function effectively and economically under certain conditions, in particular for increasing the longevity of beach fills (e.g., Truitt et al. 1993) and for stabilizing beaches adjacent to inlets. The purpose of the present work is to demonstrate a framework for groin functional design by use of modern coastal engineering predictive tools and knowledge.

- 
- 1) Director, Conrad Blucher Institute for Surveying and Science, Texas A&M University-Corpus Christi, 6300 Ocean Drive, Corpus Christi, Texas 78412-5503, USA;
  - 2) Assoc. Prof., Department of Water Resources Engineering, Lund Institute of Technology, University of Lund, Box 118, Lund S-221 00, Sweden;
  - 3) Graduate Student, Department of Water Resources Engineering, University of Lund.

This paper concerns the functional design of groins, specifically their interaction with the beach through interruption of longshore sand transport – the "gating" or valve effect of groins (Hanson & Kraus 1989). Sand bypassing, groin permeability, and the balance between net and gross longshore transport will be shown to be key factors entering groin functional design and are central to this study. The functioning of a groin, which at first sight appears to be a simple structure, is governed by a surprising number of parameters, discussed in the next section. We exploit the shoreline change numerical simulation model GENESIS (Hanson & Kraus 1989) to quantify the influence of several of these parameters. For this study, representation of groins in GENESIS was refined based on qualitative observations in the field and laboratory, numerical testing, and data on groin functioning at Westhampton Beach, Long Island, New York (Nersesian et al. 1992). Although the dependence of groin functioning on longshore sand transport is the main focus, cross-shore transport processes are considered qualitatively.

## REVIEW AND SYNTHESIS

Here, groins are defined as shore-perpendicular structures emplaced for the purpose of either (1) maintaining the beach behind them, or (2) controlling the amount of sand moving alongshore. Previous definitions have stated the purpose as "building a beach" or as "trapping littoral drift" (SPM 1984), which implies the removal of sand from the littoral system by entrapment. Because modern coastal engineering practice includes a regional perspective that considers the stability of adjacent beaches (Kraus 1989), groin emplacement may involve beach nourishment so that sand bypasses the system. Therefore, we emphasize *maintaining a beach* for Purpose 1. The second purpose primarily refers to terminal structures built to anchor the beach by limiting removal of sand (Dean 1993), as onto an ebb-tidal shoal or into a navigation channel. Here we focus on the first purpose, maintenance of beaches, i.e., providing a certain minimum beach width.

As a shore-normal structure, groins may not function well (a) if there is a large tidal range, allowing sand to bypass the structures at low tide or to overpass at high tide, or (b) if cross-shore sediment transport is dominant, such as is typical in shallow bays and lagoons, and along portions of the U.S. Great Lakes (Hanson & Kraus 1991a) where strong winds and relatively small fetches make steep (erosive) waves predominate over swell. Undesirable updrift buildup and offshore transport of sediment may be promoted if groins extend too far offshore in relation to the wave average breaker line or if they are not sufficiently permeable, potentially causing sand to be jetted seaward.

Groins are a possible component of shore-protection, beach-saving, and sand-management alternatives in the following situations:

1. Where there is a divergent nodal region in longshore transport, such as in the central area of a crenulate pocket beach, in the border region of a diffraction shadow zone of a harbor breakwater or jetty, or where the curvature of the coast changes greatly.
2. Where there is no source of sand, such as on the down-drift side of a large harbor breakwater or jetty.
3. Where intruding sand is to be managed, such as at the updrift side of an inlet entrance, harbor entrance, or navigation channel (for preventing sand intrusion and for stabilizing or anchoring the beach at the groin, or for stockpiling material for bypassing across the inlet).
4. Where sand movement alongshore is to be controlled or gated, such as to prevent undue loss of beach fill, while providing material to downdrift beaches.

5. Where an entire littoral reach is to be stabilized, such as along a spit, near a submarine canyon, or along a barrier island, for which sand is lost without return in an engineering time frame.
6. Where stabilization of the shoreline is required in the face of extreme sand-transporting conditions, such as on the banks of inlets, where the current alongshore is strong.

### Synthesis of Present Knowledge

Reviews of groin functional design have been given by Bruun (1952, 1972), Balsillie and Berg (1972), Balsillie and Bruno (1972), Nayak (1976), Fleming (1990), and the U.S. Army Corps of Engineers (USACE 1992). These reviews provide some rules of thumb but no method for systematic functional design under a wide range wave, structure, and beach conditions. Although the literature on groins appears to be substantial, most papers describing the functioning of groins tend to restate conclusions from other studies with and without quoting sources. To the unwary reader, the literature may appear to assign validity to certain concepts and conclusions by weight of repetition and not by independent confirmation. Many laboratory tests appear to suffer so severely from scale distortions that the results are questionable or misleading. Some laboratory studies contain interpretations that confuse cross-shore processes with longshore processes. For example, change in wave steepness may change the breaking wave angle and longshore transport while causing either shoreline advance or recession by cross-shore transport. Almost no well-documented field case studies exist that involve shoreline evolution at groins.

The response of the shoreline to groins can be expressed schematically as an unknown functional relation  $Response = F[groin(s); beach; waves, wind, \& tide]$  that involves at least 27 parameters (Table 1), more than the number found for shoreline response to detached breakwaters (Hanson & Kraus 1990). The engineer can control parameters related to the structure(s), such as groin length, spacing, and permeability (elevation, porosity). Grain size may also be controlled somewhat by selection of beach nourishment material.

Major properties that can be attributed to groins and the authors' reasoning behind accepting or questioning the validity of those properties are summarized in Table 2. Laboratory studies and field performance suggest that groins on sandy beaches function best if their spacing is two to four times the groin length (the *SPM* suggests a spacing ratio of two to three). Optimal spacing and groin functioning depend upon: groin length (depth at the groin tip, which controls sand bypassing); groin permeability or porosity (controlling sand throughpassing); groin elevation and tidal range (controlling sand overpassing); predominant wave direction and height; net and gross longshore transport; and sediment grain size (mode of transport as suspended load or bed load).

Field observations reveal that single groins, groin fields, and jetties that function as groins rarely fill to capacity (to their seaward tips). Typically, the updrift shoreline reaches only a modest distance to the tip, indicating that sand bypassing and permeability, as well as variability in wave direction, play an important role in determining transport around the groin and resultant local and regional shoreline change. In a study of a groin field that has been active for almost three decades, Nersesian et al. (1992) found that the 14 groin compartments were still slowly filling in the predominant direction of the littoral drift. Such behavior can be explained by the process of bypassing, whereby each compartment deprives sand to neighboring downdrift compartments until it is filled to the point that bypassing can occur to the adjacent downdrift compartments or beach. If bypassing is not complete, a groin will act as a headland and impound sand far updrift, reducing the supply of sand downdrift along the remaining portion of the littoral cell.

<b>Table 1. Parameters governing beach response to groins.</b>		
<b>Groin(s)</b>	<b>Beach and Sediment</b>	<b>Waves<sup>1</sup>, Wind, &amp; Tide</b>
Length	Depth at Tip of Groin	Wave Height & SD <sup>2</sup>
Spacing (for groin fields)	Beach Morphology (depth contours, berm height, etc.)	Wave Period & SD
Elevation	Depth of Closure <sup>3</sup>	Wave Angle & SD
Porosity	Sediment Availability	Wind Speed & SD
Tapering	Median Grain Size & SD	Wind Direction & SD
Angle to Shoreline	Sediment Density	Wind Duration & SD
Shape (as straight, angled, T-head, spurred, etc.)		Tidal Range
1) Long-term wave statistics or time series, and storms. 2) Standard deviation (representing variability in the given quantity). 3) Can be obtained by beach profile survey or estimated from wave information.		

### Judging Success

How should groins be judged successful in performing their intended function of preserving the position of the (local) shoreline? The criterion imposed here is preservation of shoreline position in a groin compartment or next to a groin such that the shoreline never recedes landward of half the effective groin length. This definition is arbitrary and simply addresses the aim to provide a certain minimum width of beach – others might choose, say, one-fourth the effective length. The effective length of a groin is the distance (on either side) from its seaward tip to the design shoreline, which would normally be formed by beach fill at the time the groins were constructed.

### GROIN BOUNDARY CONDITION

Groins have been represented in GENESIS throughout its development (Hanson 1989, Hanson & Kraus 1989), and shoreline change has been successfully simulated numerically for jetties and groins in the field (e.g., Kraus & Harikai 1983, Hanson & Kraus 1991a) and in physical models (Hanson & Kraus 1991b). However, predicted shoreline response adjacent to groins has been regarded by its developers as needing improvement (Gravens & Kraus 1989), particularly for groins that are permeable as well as diffract waves. The groin boundary condition was revised in this study based upon the following three requirements:

1. Bypassing should be represented such that the shoreline response to a groin, including evolution of the shoreline in time and its equilibrium plan form, depend on groin length (depth at tip of groin), with an increase in length increasing the impact of the structure on the shoreline.
2. Different groin permeabilities should produce different equilibrium plan forms, with increasing permeability decreasing the impact of the structure on the shoreline.
3. A permeability of 100% should result in longshore sand transport and shoreline evolution identical to that with no groin present.

<b>Table 2. Functional properties attributed to groins and critical evaluation.</b>	
<b>Property</b>	<b>Comment</b>
1. Wave angle and wave height are leading parameters (longshore transport).	Accepted. For fixed groin length, these parameters determine bypassing and the net and gross longshore transport rates
2. Groin length is a leading parameter for single groins. (Length controls depth at tip of groin.)	Accepted, with groin length defined relative to surfzone width.
3. Groin length to spacing ratio is a leading parameter for groin fields.	Accepted. See previous item.
4. Groins should be permeable.	Accepted. Permeable groins allow water and sand to move alongshore, and reduce rip current formation and cell circulation.
5. Groins function best on beaches with a predominant longshore transport direction.	Accepted. Groins act as rectifiers of transport. As the ratio of gross to net transport increases, the retention functioning decreases.
6. The updrift shoreline at a groin seldom reaches the seaward end of the groin.  (This observation was not found in the literature review and appears to be original to the present paper.)	Accepted. Because of sand bypassing, groin permeability, and reversals in transport, the updrift shoreline cannot reach the end of a groin by longshore transport processes alone. On-shore transport is required for the shoreline to reach a groin tip, for a groin to be buried, or for a groin compartment to fill naturally.
7. Groin fields should be filled (and/or feeder beaches emplaced on the downdrift side).	Accepted. Filling promotes bypassing and mitigates downdrift erosion.
8. Groin fields should be tapered if located adjacent to an unprotected beach.	Accepted. Tapering decreases the impoundment and acts as a transition from regions of erosion to regions of stability.
9. Groin fields should be built from the downdrift to updrift direction.	Accepted, but with the caution that the construction schedule should be coordinated with expected changes in seasonal drift direction.
10. Groins cause impoundment to the farthest point of the updrift beach and erosion to the farthest point of the downdrift beach.	Accepted. Filling a groin field does not guarantee 100% sand bypassing. Sand will be impounded along the entire updrift reach, causing erosion downdrift of the groin(s).
11. Groins erode the offshore profile.	Questionable and doubtful. No clear physical mechanism has been proposed.
12. Groins erode the beach by rip-current jetting of sand far offshore.	Questionable. Short groins cannot jet material far offshore, and permeable groins reduce the rip-current effect. However, long impermeable jetties might produce large rips and jet material beyond the average surfzone width.
13. For beaches with a large predominant wave direction, groins should be oriented perpendicular to the breaking wave crests.	Tentatively accepted. Oblique orientation may reduce rip current generation.

In GENESIS, the fraction  $F$  of sand that passes a groin by being transported over and through it is represented by a permeability factor  $P$ , and the amount passing around the seaward end is represented by a bypassing factor  $B$  (Hanson & Kraus 1989), such that

$$F = P(1 - B) + B \quad (1)$$

where  $0 \leq P \leq 1$ , and  $0 \leq B \leq 1$ . In the new version of GENESIS, the actual transport rate at the groin  $Q_G^*$ , denoted with an asterisk, is related to the calculated potential rate at the groin  $Q_G$  as

$$Q_G^* = F \cdot Q_G \quad (2)$$

In the original version of GENESIS, the factor  $F$  was applied to the transport rate at the updrift cell, as  $Q_G^* = F Q_{G \pm 1}$ . However, to satisfy Criterion 3, that, in the limit  $P \rightarrow 0$ , the calculation should give the same result as for "no groin present," Eq. 2. is required. The permeability factor is assigned based on groin elevation, groin porosity, and tide range, and the bypassing factor  $B$  is calculated in the model at each time step as (using the present shoreline position to calculate present depth)

$$B = 1 - D_G / D_{LT} \quad (3)$$

where  $D_G$  is the depth at the groin at a particular time step, and  $D_{LT}$  is the depth of active longshore sand transport, taken to be about 1.6 times the significant breaking wave height (Hanson & Kraus 1989). Eq. 3 shows the importance of depth at the groin tip, a parameter related to but more fundamental than groin length, and the form of Eq. 3 suggests that the parameter  $D_G / H_o$  should characterize groin bypassing, where  $H_o$  is the deep-water wave height.

The reasoning behind use of this simple formula, Eq. 3, in development of GENESIS was pragmatic: the cross-shore distribution of longshore transport on a natural beach takes many forms not readily predicted, including peaks in the swash zone and near the breaker line (Kraus et al. 1982), and the presence of a groin in the surf zone will also modify the distribution in some, as yet, unpredictable way. Therefore, a rectangular distribution across shore was originally taken as an easily calculated representative shape. In the new version of GENESIS, the depths in Eq. 3 are calculated from the equilibrium profile with  $y^{2/3}$  shape, where  $y$  is distance offshore.

## Single-Groin Tests

**Time Dependence of Bypassing.** Shoreline change predictions at a single groin were compared for four distributions of transport; rectangular on a plane-sloping profile, triangular with peak at the shore on a plane-sloping profile, and two similar distributions on an equilibrium profile shape. In the test, median grain size was 0.25 mm, used to determine the equilibrium profile shape, the groin was 100 m long on an initially straight shoreline, and waves were constant with deep-water height of 1 m, period of 8 sec, and angle of 20 deg. The model was run for 15 years, and calculated positions of the shoreline directly updrift of the groin divided by the groin length are plotted in Fig. 1. The general trend is for rapid initial buildup followed by a more gradual growth after about two years. The calculated gradual buildup agrees with the qualitative observation that groins seldom fill to capacity, and an influential factor is the increased amount of material bypassing a groin as the shoreline grows. The rectangular distribution based on the equilibrium profile falls between the two extremes and was selected for the new version of GENESIS.

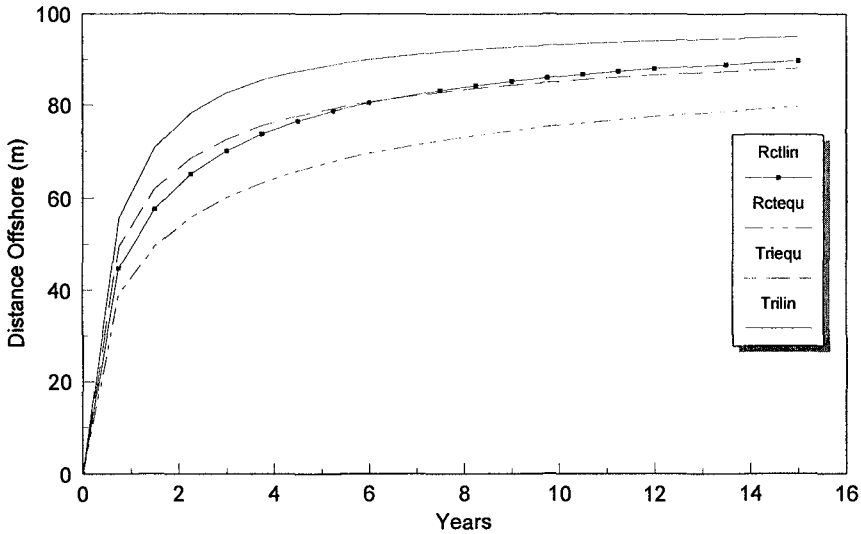


Fig. 1. Shoreline change at groin calculated with different distributions for bypassing.

**Influence of Gross Longshore Transport.** Shoreline change in the vicinity of disturbances that alter transport alongshore is controlled by the gross transport rate as well as the net (Bodge 1992). A single groin was placed on the beach of the previous example, and the directions of hindcast waves from the Westhampton project, discussed below, were modified to change the ratio of the net transport rate  $Q_n$  to the gross  $Q_g$  as  $Q_n/Q_g = 1, 0.5, 0.33,$  and  $0.25$ . The ratio  $Q_n/Q_g$  varies between 0 and 1 for the limiting conditions of perfectly balanced transport (no net) and unidirectional transport, respectively. The ratio  $Q_n/Q_g = 0.5$ , with  $Q_n = 300,000$  cu m is the design condition for Westhampton. The length of the groin  $Y_G$  was also varied in relation to the width of the surfzone (to the breakpoint)  $Y_B$  on the initially straight beach  $Y_G/Y_B = 0.5, 1,$  and  $2$ . Fig. 2 plots calculated shoreline change on the updrift side of the groin for  $Y_G/Y_B = 1$ . Over the 5-year calculation interval, the shoreline approaches the tip of the groin only if the gross and net rates are equal. As the gross rate exceeds the net, the growth decreases, confirming Property 5 in Table 2. Shoreline change with  $Q_n/Q_g = 0.5$  for the three dimensionless groin lengths is plotted in Fig. 3. The updrift shoreline moves seaward more rapidly as the relative groin length increases.

### Multiple-Groin Tests

Shoreline change was calculated for a field of seven groins with  $P = 10\%$  placed on an initially straight beach. The groins were 100 m long with spacing of 400 m. Waves were Raleigh-distributed in height with significant  $H_o = 1$  m, period 8 sec, and deep-water direction 10 deg. Grid spacing was 50 m and time step was 6 hr. Fig. 4 shows calculated shoreline change after 5 and 10 years. The groins slowly filled in the direction of transport, but the shoreline did not reach the tip of the most updrift groin. Updrift groins deprived the downdrift compartments and downdrift (unprotected) beach of sand until substantial bypassing occurred. At 10 years, the most downdrift compartment did not yet benefit from the gradual bypassing, and it lost sand because of groin permeability. Tracking of shoreline position through time (Fig. 5) downdrift of the most updrift groin in the first compartment shows that it first retreated because sand could not enter. Over time, bypassing began to occur and the shoreline advanced.

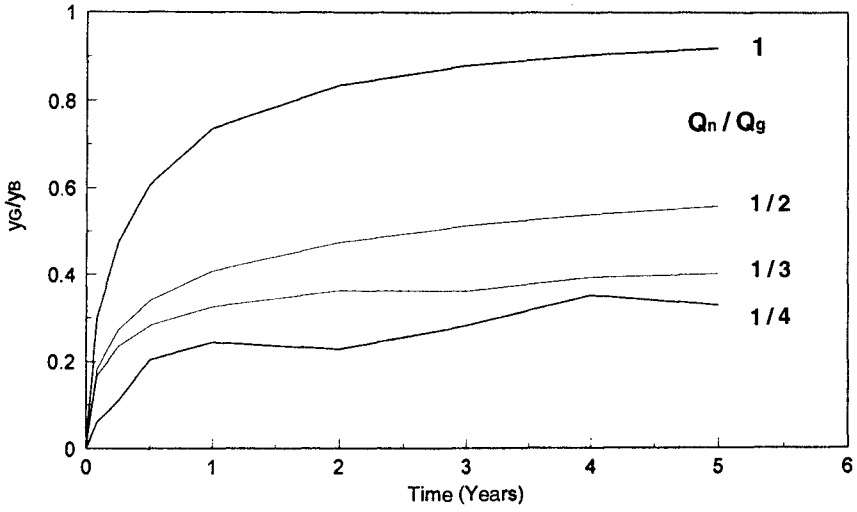


Fig. 2. Shoreline change updrift of groin for different ratios of net to gross transport rate

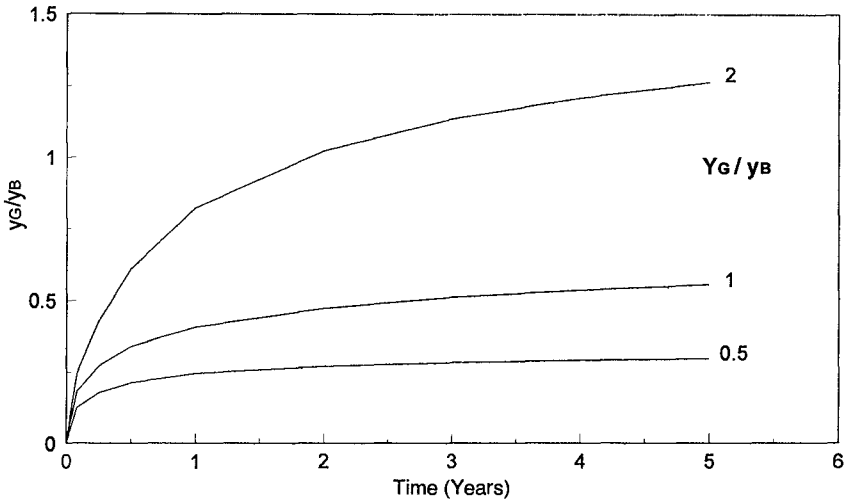


Fig. 3. Shoreline change updrift of groins of different relative length when the net rate equals half the gross rate



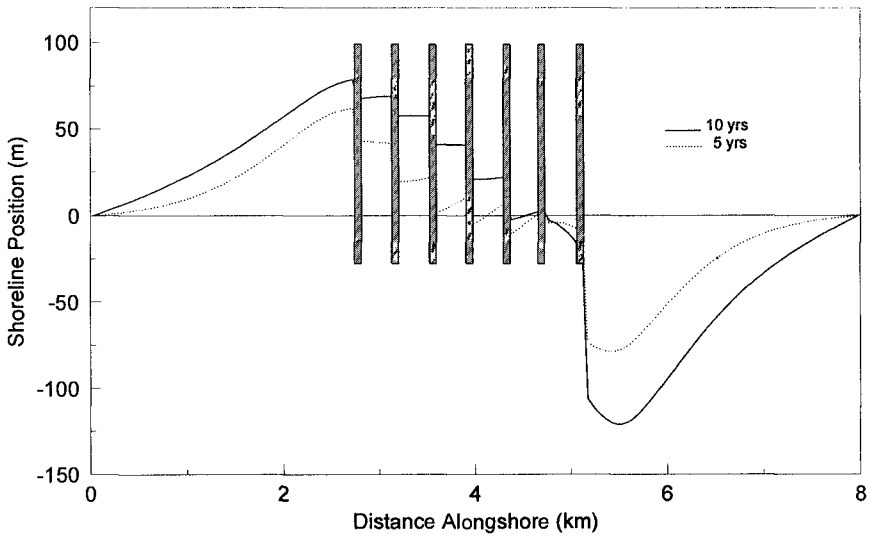


Fig. 4. Shoreline change in a groin field showing gradual filling of compartments in the direction of net drift.

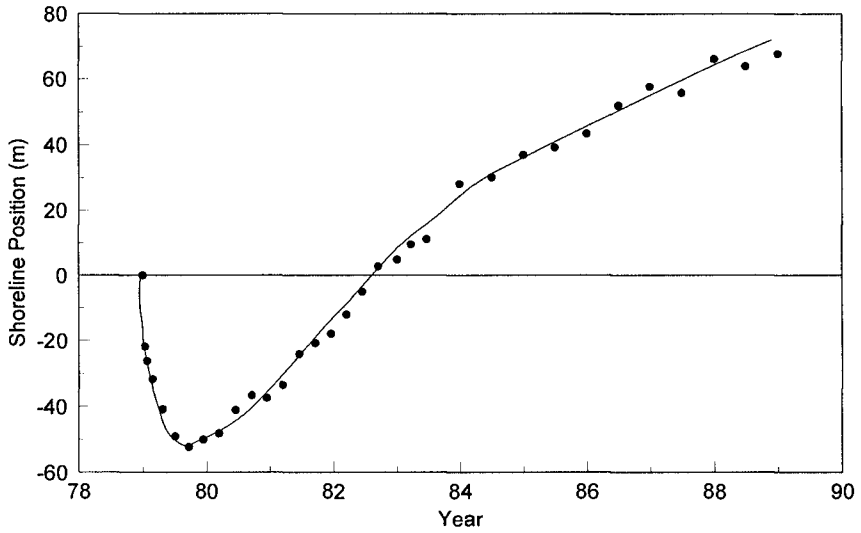


Fig. 5. Evolution of shoreline within most updrift groin compartment.

**Example Design Diagram.** The final example, which demonstrates numerical modeling capability to develop general functional design guidance, concerns a pair of groins placed on a 0.25-mm sand beach. Waves with constant significant deep-water height, period of 8 sec, and deep-water direction of 30 deg were applied for one year. Initial depth at the groin tip was specified for groin lengths of 50, 75, 100, 150, and 200 m, and simulations were also done for  $D_G/H_o = 0.5$  and 1.0 to give groin lengths of 10 and 27 m. The groin spacing  $X_G$  divided by groin length  $Y_G$  was also changed. The resultant shoreline response was classified as either satisfying or not the criterion that the calculated landward-most shoreline position  $Y$  be less than half the effective groin length, where filled circles in Fig. 6 indicate satisfaction of the criterion.

Fig. 6 shows that shorter groins, indicated by smaller  $D_G/H_o$  values, satisfy the criterion with a larger relative groin spacing, suggesting that shorter groins will be more cost effective. For the longest groin tested, the criterion was met for all groin spacings, explained by the fact that for a relative groin spacing exceeding about 8, the two groins no longer interact as a system but function independently. Thus, very long groins satisfy the criterion as a single groin. Care must be used in interpreting a plot such as Fig. 6 which involves non-dimensional parameters. The figure implies, by the imposed success criterion, that a spacing of  $X_G/Y_G = 1/1$  is satisfactory, but only as far as maximum recession is concerned; maximum accretion or filling capacity (by nourishment) for smaller ratios is also much smaller. For example, with longshore spacing of  $X_G = 200$  m, the ratio  $X_G/Y_G = 1/1$  gives a maximum advance of about 14 m, whereas the ratio 1/11 gives a maximum advance of 106 m. Effectiveness in holding a certain width of beach, reduction of down-drift impacts, and initial and maintenance costs must be kept in mind when developing groin functional designs. Shorter relative groin spacing may also increase cost. In using longer groins, relative erosion is limited, whereas absolute erosion increases with groin length.

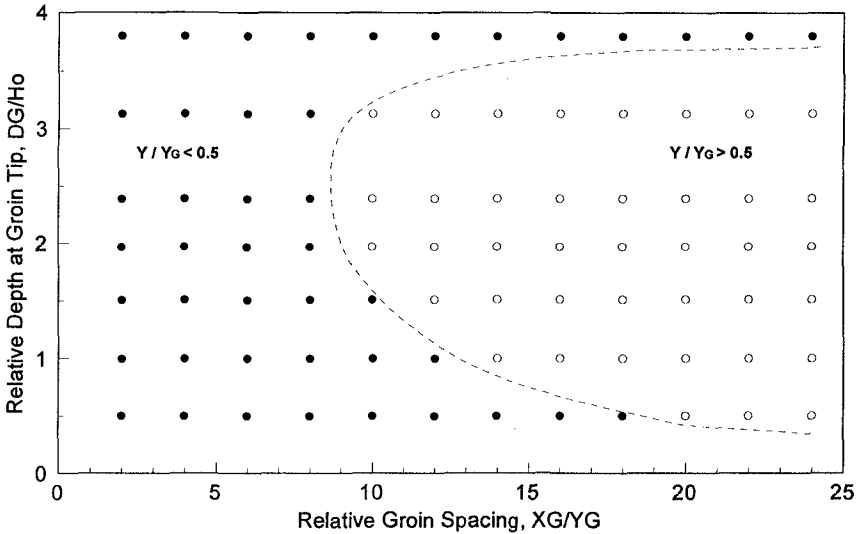


Fig. 6. Example design diagram for a single groin compartment

## SIMULATION FOR WESTHAMPTON BEACH

### Background

Westhampton Beach faces the Atlantic Ocean and is located on a portion of a 24.6-km long barrier island of the southeast shore of Long Island, New York, between Shinnecock Inlet to the east and Moriches Inlet to the west. This coast was devastated by a hurricane in 1938 and further damaged by at least seven other hurricanes and extra-tropical storms that struck the area from 1944 to 1962. As a result, the U.S. Government authorized storm-protection planning for much of the south shore. Groins were constructed initially at Westhampton Beach because it was the section judged to be most vulnerable to breaching and inlet formation to the Great South Bay. Nersesian et al. (1992) describe the regional setting, history of the Westhampton Beach shore-protection project, and the functioning of the groins there. The work described in this section is a continuation of the paper of Nersesian et al. to modeling of shoreline change at Westhampton.

The original plan developed by the U.S. Army Corps of Engineers (USACE 1958) provided for construction of dunes, fronting protective beaches, together with 23 groins if needed. Owing to political and economic considerations (Heikoff 1976) (with law suits against the three levels of Government (Federal, State, County) by private land owners settled in October, 1994), eleven groins were constructed without placement of the dune and beach fill on the eastern 3.8 km of shore extending westerly from a point 10.6 km east of Moriches Inlet. This work was supplemented in 1970 by construction of four groins extending 1.8 km west of the 11 groins, including beach fill in the four new compartments. The groins are made of large quarry stone, and are 146 m long with average spacing of 400 m. The chronology of fills as implemented in the shoreline change simulation is: 1969-1970, 1.49 million cu m placed in last four compartments during and after completion of construction (USACE 1980); 1974, 31,400 cu m (probably dredged beach-quality material from channel maintenance) placed directly downdrift of Groin 15 (assumed to be a rectangular fill 400 m long); and 1977, 44,700 cu m, placed similarly as the 1974 fill.

Westhampton Beach is composed of fine to medium sands, and the net transport rate has been estimated to be on the order of 300,000 cu m/year to the west (Panuzio 1968). Fig. 7 is an oblique aerial view of the Westhampton groin field, looking east, with Groin 15 in the foreground. Over the years, the groin field has very successfully performed its intended *local* function of reinforcing the historically weak section of barrier beach by building a wide beach at the groin field and to the east (updrift) (Nersesian et al. 1992). However, the beach immediately to the west has eroded significantly and was breached on December 18, 1992, during a strong subtropical storm.

### Simulation of Shoreline Change

The shoreline change model was driven with data generated from a recent Corps of Engineers Wave Information Study (WIS) hindcast (Hubertz et al. 1993) that provides wave parameters at 3-hr intervals for the 20-year period 1956-1975. Using representative coefficient values of  $K_1 = 0.54$  and  $K_2 = 0.27$  in the CERC/GENESIS longshore sand transport rate (LSTR) formula (Kraus et al. 1982, Kraus & Harikai 1983), a shoreline orientation of 70 deg from north, and wave shadowing by land masses to achieve a 20-year average annual net of approximately 300,000 cu m (the WIS hindcast gives waves from all directions), GENESIS produced statistics as shown in Table 3, using both the WIS sea and swell components. With the average annual LSTR constrained to approximate the empirically determined rate (Panuzio 1968), the corresponding gross rate was about twice that amount. In the simulations, the grid spacing was 61 m, and the time step was 3 hr. The lateral boundary conditions were a pinned beach located approximately 4 km east of Groin 1 on the east, and a gated boundary defined by the Moriches Inlet jetty about 4 km to the west of Groin 15.



Fig. 7. Aerial view of Westhampton groin field, looking east, Dec. 1992

<b>Table 3. Variability in annual potential longshore sand transport rates (1,000 cu m) calculated from the 20-year WIS wave hindcast (positive net transport to the west).</b>			
<b>Quantity</b>	<b>Net Rate</b>	<b>Gross Rate</b>	<b>Year</b>
Minimum Net	117	471	1967
Maximum Net	685	842	1958
Minimum Gross	189	434	1957
Maximum Gross	685	842	1958
Average	321	610	—
Standard Dev.	130 <sup>1</sup>	114	—
1) Note that ratio of std. dev. over average for the net transport is much greater than for the gross.			

**Variability in Wave Input.** Simulations were performed using four different sequences of ten years of record from the 20-year hindcast wave time series. The series were 1956-1965 and 1966-1975, taken in chronological order by year and in reverse chronological order by year. The resultant calculated shoreline positions showed little difference among each other, which may be explained by the groin system having more control (as through bypassing) than do reasonable variations in wave conditions. The only notable difference produced by the wave sequencing was in position of the shoreline directly west of Groin 15 (downdrift of the groin field), depending on whether the most recent waves arrived more out of the south than out of the north.

**Model Calibration.** Fig. 8 shows measured and calculated shoreline change in December 1989 starting from the February 1966 measured shoreline, which was the pre-construction shoreline. The overall trend in simulated shoreline change follows well that of the actual change. Of particular note is the reproduction in the model of the gradual infilling of the groin compartments from east to west (left to right in the figure). Reproduction of the observed gradual infilling of the groin field in the direction of predominate transport is considered a major success of the model. No attempt was made to adjust the transport coefficient  $K_T$  or otherwise tune the model.

The hump in the measured 1989 shoreline around distance 14 km (east of Groin 1) is anomalous from the perspective of longshore transport processes and may be a result of irregular nearshore bathymetry. The model overpredicts erosion on the west side of Groin 15. Depth soundings made by the first author in reconnaissance of the site in June 1991 indicated that the water adjacent to the west side of Groin 15 was much deeper than at comparable distances offshore of the groin field and the distant unprotected beach. The steeper nearshore profile west of Groin 15 alters wave transformation and sediment transport processes, and it is not accounted for in the shoreline change simulations. Also, occasional strong reversals in direction of longshore transport in the summer, not necessarily accounted for in the hindcast, can create a fillet on the east side of Groin 15. Such fillets are present in autumn/winter 1979 and 1994 aerial photographs. Sand volume in the system increased; we believe the extra volume to be associated with onshore wind-blown sand transport on the wide beach in the groin field, creating lush high dunes and a wide berm.

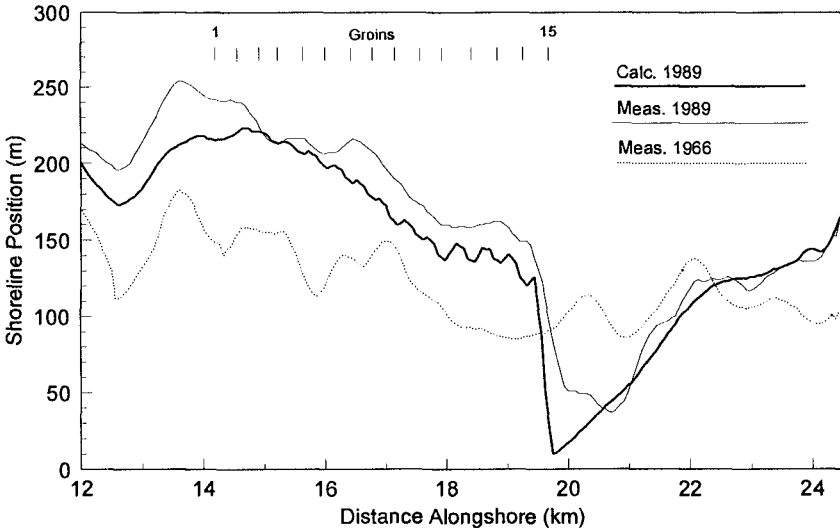


Fig. 8. Calibration of the shoreline change model for Westhampton

**Groin Tapering and Shortening - Alternative Designs.** Tapering and shortening of groins reduce their gating capacity and promote transport of sand out of the groin field in transition of the groins to the unprotected beach. Tapering of the westward-most groins at Westhampton would increase bypassing and movement of sand to the west. Shortening of the groins would release sand to the system, reduce updrift impoundment, and provide stone for constructing additional groins to the west, if needed. Moderate tapering and shortening of the groins would cause a minor decrease in level of protection to the properties in their lee by decreasing berm width.

As a simple example of the use of a shoreline response model in groin functional design, three alternatives were examined to estimate the shoreline plan form at and west of the groin field 20 years into the future. The simulations started from the measured shoreline of March 1989 and finished in July 2009 (Fig. 9). Alternative 1 simulated the existing condition to provide a baseline for comparison. Alternative 2 involved shortening of Groins 14 and 15 to 129.5 and 85.3 m, respectively (groins shortened by 16.8 m and 61.0 m), with addition of a groin between them of 107.4-m length to maintain groin spacing to length ratio, and placement of 2,500,00 cu m in the westernmost eight compartments (including the intermediate groin). Alternative 3 involved shortening all groins by 30.5 m or to the existing shoreline, with addition of 300,000 cu m west of Groin 15 for a distance of 1,600 m. Each year of the WIS wave hindcast was used in the 20-year simulation.

Fig. 9 shows after 20 years, the groin field will be effectively filled, except for the most westward compartment, because it can receive sand from the east, but not from the west (because of the great effective groin length on the west side) during times of reversal from the predominant direction of transport. Tapering plus fill provides maximum benefit to the downdrift beach; clearly, the model could be used to optimize the preferred alternative design to meet planning objectives.

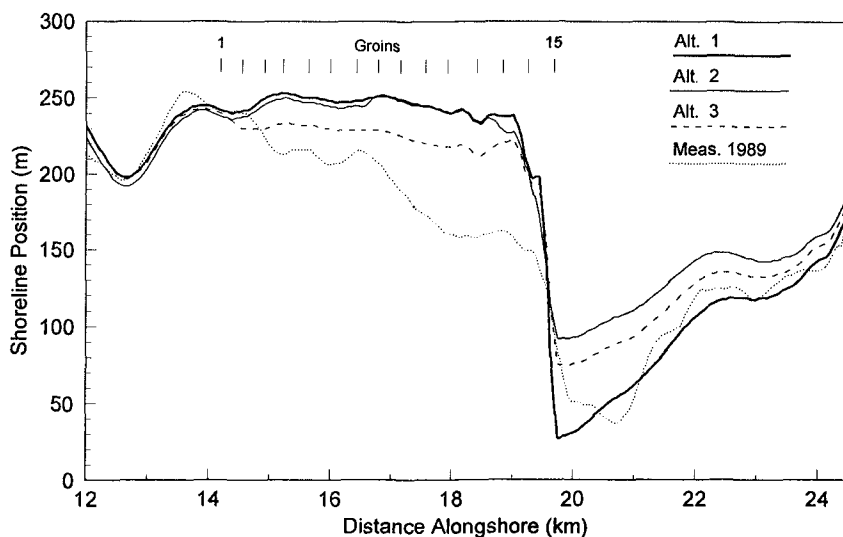


Fig. 9. Comparison of groin shortening and tapering alternatives

## CONCLUSIONS AND RECOMMENDATIONS

1. This paper has demonstrated that modern numerical simulation models can reproduce the main features of shoreline change at single groins and at groin fields, and thus are powerful tools for groin functional design.
2. Bypassing (parameterized by the ratio  $D_G/H_o$ ), structure permeability, and the balance between net and gross longshore transport rates (parameterized by the ratio  $Q_n/Q_g$ ) are three key factors that determine the functioning of groins. These three factors succinctly incorporate many fundamental parameters, such as wave height, direction, period (and their variability), equilibrium beach slope (or grain size), and groin length. Ratio of groin separation distance to groin length is a key controlling factor for groin systems, as found in previous studies.
3. There is great need for comprehensive project-level monitoring of groin behavior, including periodic shoreline surveys (as through aerial photography), and periodic beach profile and sediment surveys together with long-term wave and current monitoring.
4. Field and large-scale laboratory studies are required to quantify groin bypassing, distribution of transport in the presence of a groin, groin permeability, seasonality of waves in inducing both longshore and cross-shore transport, and the offshore jetting effect of groins.
5. Cross-shore sediment transport processes and their intricate and unknown interaction with longshore sediment processes need to be investigated to understand how beach elevation and width can build beyond what can be presently calculated with shoreline change models. It is postulated here that cross-shore transport, such as a strong accretionary event in summer, is a potentially important mechanism for groin filling, because longshore transport alone cannot fill groins to their tips owing to bypassing and variability in direction of transport.

## ACKNOWLEDGEMENTS

This study was supported by the Conrad Blucher Institute for Surveying and Science, Texas A&M University-Corpus Christi, and the Department of Water Resources Engineering, University of Lund. Some concepts developed in this paper were stimulated in coastal engineering studies conducted by the authors for the New York District and the Jacksonville District, U.S. Army Corps of Engineers. The major portion of this work was performed while the second and third authors were in residence as visiting scholars at the Blucher Institute over February to June, 1994. We appreciate discussions with Mr. Gilbert K. Nersesian, Senior Coastal Engineer of the New York District, and Dr. Tsuguo Sunamura, Tsukuba University, Japan. Ms. Rebecca Brooks and Robin Hoban of the Coastal Engineering Research Center provided the wave hindcast data used in this study.

## REFERENCES

- Balsillie, J.H. and Berg, D.W. 1972. State of Groin Design and Effectiveness. *Proc. 13th Coastal Eng. Conf.*, ASCE, 1367-1383.
- Balsillie, J.H. and Bruno, R.O. 1972. Groins: An Annotated Bibliography. Miscell. Paper No. 1-72, Coastal Eng. Res. Center, Vicksburg, Miss.
- Bodge, K.R. 1992. Gross Transport Effects at Inlets. *Proc. 6th Annual National Conf. on Beach Preservation Technology*, Florida Shore & Beach Pres. Assoc., 112-127.
- Bruun, P. 1952. Measures Against Erosion at Groins And Jetties. *Proc., 3rd Coastal Eng. Conf.*, ASCE, 137-164.

- Bruun, P. 1972. The History and Philosophy of Coastal Protection. *Proc. 13th Coastal Eng. Conf.*, ASCE, 33-74.
- Dean, R.G. 1993. Terminal Structures at Ends of Littoral Systems. *J. Coastal Res.*, 18, 195-210.
- Fleming, C.A. 1990. Principles and Effectiveness of Groynes. *Coastal Protection*, Pilarczyk, K.W., (Ed.), Balkema Press, Rotterdam, 121-156.
- Gravens, M.B. and Kraus, N.C. 1989. Representation of Groins in Numerical Models of Shoreline Response. *Proc., 23rd Congress IAHR*, C-515 - C-522.
- Hanson, H. 1989. GENESIS: A Generalized Shoreline Change Numerical Model. *J. Coastal Research*, 5(1), 1-27.
- Hanson, H. and Kraus, N.C. 1989. GENESIS: Generalized Model for Simulating Shoreline Change, Report 1: Technical Reference. TR CERC-89-19, USAE Waterways Expt. Stn., Coastal Eng. Res. Center, Vicksburg, Miss.
- \_\_\_\_\_. 1990. Shoreline Response to a Single Transmissive Detached Breakwater. *Proc. 22nd Coastal Eng. Conf.*, ASCE, 2034-204.
- \_\_\_\_\_. 1991a. Numerical Simulation of Shoreline Change at Lorain, Ohio. *J. Waterway, Port, Coastal and Ocean Eng.*, 117(1): 1-18.
- \_\_\_\_\_. 1991b. Comparison of Shoreline Change Obtained with Physical and Numerical Models. *Proc. Coastal Sediments '91*, ASCE, 1785-1813.
- \_\_\_\_\_. 1993. Optimization of Beach Fill Transitions. in: *Beach Nourishment Engineering and Management Considerations*, Stauble, D.K. and Kraus, N.C. (Vol. Eds.), *Proc. Coastal Zone '93*, ASCE, 103-117.
- Heikoff, J.M. 1976. *Politics of Shore Erosion: Westhampton Beach*. Ann Arbor Science Publishers, Ann Arbor, Mich.
- Hubertz, J.M., Brooks, R.M., Brandon, W.A., and Tracy, B.A. 1993. Hindcast Wave Information for the Atlantic Coast, 1956-1975. USAE Waterways Experiment Station, Coastal Eng. Res. Center, Vicksburg, MS.
- Kraus, N. C. 1989. Beach Change Modeling and the Coastal Planning Process. *Proc. Coastal Zone '89*, ASCE, 553-567.
- Kraus, N.C. and Harikai, S. 1983. Numerical Model of the Shoreline Change at Oarai Beach. *Coastal Eng.*, 7(1): 1-28.
- Kraus, N.C., Isobe, M., Igarashi, H., Sasaki, T., and Horikawa, K. 1982. Field Experiments on Longshore Sand Transport in the Surf Zone. *Proc. 18th Coastal Eng. Conf.*, ASCE, 969-988.
- Nayak, U.B. 1976. On the Functional Design and Effectiveness of Groins in Coastal Protection. Ph.D. Dissertation, U. of Hawaii, 205 pp.
- Nersesian, G.K., Kraus, N.C., and Carson, F.C. 1992. Functioning of Groins at Westhampton Beach, Long Island, New York. *Proc., 23rd Coastal Eng. Conf.*, ASCE, 3357-3370.
- Panuzio, F.L. 1968. "The Atlantic Coast of Long Island," *Proc. 11th Coastal Eng. Conf.*, ASCE, 1222-1241.
- (SPM) *Shore Protection Manual*. 1984. Groins. Coastal Eng. Res. Center, US Army Corps of Engineers, U.S. Govt. Printing Office, Washington, D.C., 5.35-5.56.
- Truitt, C.L., Kraus, N.C., and Hayward, D. 1993. Beach Fill Performance at the Lido Beach, Florida, Groin. In: *Beach Nourishment Eng. and Management Considerations*, Stauble, D.K. and Kraus, N.C. (Vol. Eds.), *Proc. Coastal Zone '93*, ASCE, 31-42.
- U.S. Army Corps of Engineers. 1958. Cooperative Beach Erosion Control and Interim Hurricane Study, Atlantic Coast of Long Island, NY, Fire Island to Montauk Point. USAE District, New York.
- \_\_\_\_\_. July, 1980. Fire Island Inlet to Montauk Point, Long Island, New York, Beach Erosion Control and Hurricane Protection Project. Supplement No. 2 to General Design Memorandum No. 1, Moriches to Shinnecock Reach. USAE District, New York.
- \_\_\_\_\_. 1992. Coastal Groins and Nearshore Breakwaters. Engineer Manual, No. 1110-2-1617, Washington, D.C.



## Reshaping breakwaters in deep and shallow water conditions

A. Lamberti<sup>1</sup>, G.R. Tomasicchio<sup>2</sup>, F. Guiducci<sup>3</sup>

### Abstract

In order to investigate the influence of water depth on the profile of reshaping breakwaters, model tests have been performed in deep, intermediate and shallow water conditions. The results show that the reduction factor for the dimensions of a reshaped profile in intermediate and shallow water conditions does not depend only on the wave height reduction. Other influencing factors are identified as breaking depth, wave steepness and foreshore slope. Moreover, at any water depth condition, the characteristic wave height corresponding to the frequency of stone movements on a reshaped profile is larger than the significant wave height. In the present tests, good results are obtained using the 1/50 wave height. Finally, whereas the offshore evaluated reflection coefficient increases with the water depth at the structure, the same coefficient evaluated in front of the structure shows an opposite trend.

### Introduction

In the last decade researchers have paid great attention to the characteristics of berm breakwaters (Burcharth & Frigaard, 1987; van der Meer, 1988; Juhl & Jensen, 1990; Hall & Kao, 1991). Such structures are also named sacrificial or reshaping breakwaters, as sometimes a berm is present also in the armor layer of a conventional non reshaping breakwater. In a reshaping breakwater, if a sufficient amount of material is provided, a stable S-shape profile is eventually developed. During the reshaping phase, the material is removed from zones where it is unstable and relocated into more stable positions; a sorting process is also active during reshaping since the less stable units in the mound are removed first; at the end of reshaping if a low mobility remains active throughout the phase, a profile with a uniform distribution of mobility is naturally formed. The self armoring response of reshaping breakwaters to wave forces makes them economically attractive because finer rock material can be used than for a conventional breakwater; construction and maintenance can also use less expensive equipments.

---

<sup>1</sup>Alberto Lamberti, Università di Bologna Istituto di Idraulica, v.le del Risorgimento 2, 40136 Bologna, Italy

<sup>2</sup>Giuseppe Roberto Tomasicchio, Università di Perugia Istituto di Idraulica, S. Lucia, 06125 Perugia, Italy

<sup>3</sup>Franco Guiducci, Estramed S.p.A., via Campobello 6, 00040 Pomezia, Italy

Most laboratory investigations aimed to foresee the behavior of the reshaping profiles under deep water conditions. In particular, laboratory investigations have considered 2- and 3-dimensional stability of reshaping breakwaters, referring mainly to the trunk section, but also to the rear side (Andersen & al., 1992) and to the roundhead (Burcharth & Frigaard, 1987). Only few tests have considered reshaping of the seaward profile in shallow water conditions. A large number of breakwaters in the Mediterranean area operate in shallow water conditions and moderate tidal excursion; in these conditions waves, before hitting the structure, undergo a relevant energy decay and an even more pronounced decay of extreme wave height.

This paper investigates the influence of water depth in front of the structure on the seaward profile development of a reshaping breakwater, comparing results of 2-dimensional model tests performed at Danish Hydraulic Institute (DHI) and Estramed laboratories for deep, intermediate and shallow water conditions.

## Description of the model tests

### Flumes

Physical model tests were carried out using the facilities at DHI (Spring 1992) and Estramed (Summer 1993, Summer 1994) laboratories. Tests were performed in glass walled flumes.

In deep water tests (referred to as DHI-92) the flume presented a horizontal foreshore with water depth 0.60 m. Intermediate and shallow water tests were performed using two different flumes. The first flume (referred to as Estramed-93) presented a bottom (fig. 1a) consisting of a foreshore slope 1:20 from 0.60 to 0.36 m water depth, followed by a milder 1:100 slope reaching 0.30 m water depth at structure toe. The second (referred to as Estramed-94) presented a bottom (fig. 1b) with a foreshore slope 1:20 from 0.60 to 0.34 m water depth, followed by a milder 1:100 slope; on this slope the structures were placed at depth 0.30 and 0.14 m. Characteristics of the flume are summarized in table 1.

Table 1. Tests set-up characteristics (measures in m)

No.	Test series	Width	Effective length	Toe depth	Foreshore slope
1	DHI-92	0.60	16.0	0.60	0
2	Estramed-93	1.50	22.6	0.30	1:100
3	Estramed-94	0.75	13.2	0.30	1:100
4	Estramed-94	0.75	33.6	0.14	1:100

### Materials

For present tests, armor materials and wave characteristics were chosen in order to obtain values of the stability number  $H_s/\Delta D_{n50}$ , the index of the armor layer mobility, close to 3. Moreover, water depth was varied in order to obtain values of

the ratio  $h/H_{so}$  as low as 0.85. Values of  $h/H_{so}$  larger than 3.0 provided deep water conditions; values of  $h/H_{so}$  around 2.0 gave intermediate water conditions.

All tested structures were built with crushed stones whose characteristics for the armor and the core are given in table 2. Gradation curves were based on samples of more than 200 stones.

Table 2. Rock material characteristics (measures in cm)

No.	Test series	Armor $D_{n50}$	Armor $D_{n85}/D_{n15}$	Core $D_{50}$	Core $D_{85}/D_{15}$	$\Delta$	Shape
1	DHI-92	3.4	1.42	1.1	2.8	1.68	Angular
2	Estramed-93	2.5	1.50	0.9	2.5	1.65	Angular
3	Estramed-94	2.6	1.66	0.9	2.5	1.65	Angular
4	Estramed-94	1.5	1.66	0.9	2.5	1.65	Angular

**Structure shapes**

Berms were built approximately 0.1 m above mean water level (fig. 2) and a certain amount wider than the foreseen erosion. Seaward slopes of as built structures were in the range 1:1.1 to 1:1.5. The geometrical characteristics of the structures are summarized in table 3.

Table 3. Berm breakwaters sections (measures in cm)

No.	Test series	Toe depth	Berm width	Berm freeboard	Crest width	Crest freeboard
1	DHI-92	60	70	10	30	20
2	Estramed-93	30	55	10	30	20
3	Estramed-94	30	55	10	30	20
4	Estramed-94	14	35	6	20	12

**Wave attacks**

In all the tests irregular waves of the Pierson-Moskowitz spectral shape were generated by hydraulically actuated piston-type wave makers without re-reflection absorption system.

In DHI tests, where depth was constant everywhere offshore the breakwater, 4 wave gauges were installed half way between the wave paddle and the breakwater and some further ones closer to the toe of the structure. The four gauges were used to estimate incident and reflected spectra, while the gauges at the structure toe were used as phase reference for velocity measurements. In Estramed tests, 3 gauges were installed in front of the breakwater and 3 offshore, not far from the wave paddle. In this way both offshore and inshore incident and reflected waves were measured. Waves were recorded continuously throughout all the tests. Wave gauges were statically calibrated (in green water); non linear effects are stronger in shallow water conditions and are not accounted for by the adopted separation method between

incident and reflected spectra (Goda & Suzuki, 1976; Mansard & Funke, 1980). Measures of incident and reflected wave height in shallow water conditions should be regarded as affected by greater experimental uncertainties.

Offshore wave characteristics were measured at 0.60 m water depth and are summarized in table 4.

All tests consisted of a reshaping phase during which design wave conditions were applied lasting 6x1000 waves. Profiles were surveyed by a mechanical sounding, i.e. measuring the depth of the profile relative to a horizontal reference plane. Profile surveys were repeated at least 3 times during reshaping; after 1000, 3000 (or 2000) and 6000 waves. Data were digitized and visually analyzed in order to estimate the characteristic dimensions of the profile according to Vellinga (1986) parameterization scheme. It was observed that the largest portion of berm erosion occurred during the attack of the first few hundreds waves. After this phase, stones moved singularly and rarely.

A small amount of wave overtopping occurred during tests at DHI and no overtopping at all was observed during the other tests.

*Table 4. Offshore wave characteristics (measures in cm, s)*

No.	Test series	Section	$H_{s0}$	$H_{1/50}$	$T_m$	$T_p$	$C_R$
1	DHI-92	1	17.2	26.8	1.96	3.20	0.35
2	DHI-92	1	18.2	28.3	1.79	2.56	0.32
3	DHI-92	1	18.4	28.7	1.91	2.70	0.31
4	Estramed-93	2	18.0	28.1	1.90	2.45	0.33
5	Estramed-94	3	17.4	27.0	2.26	3.65	0.32
6	Estramed-94	3	20.1	32.0	2.06	2.62	0.31
7	Estramed-94	3	26.1	40.1	1.57	1.69	0.29
8	Estramed-94	4	17.5	27.1	2.39	3.25	0.23
9	Estramed-94	4	16.6	24.2	2.09	2.46	0.14
10	Estramed-94	4	16.9	23.3	1.48	1.55	0.13

## Waves on the structures

### Incident waves

Data from present tests have been compared with values computed according to Goda (1985) for a foreshore slope 1:100. Data are presented (fig. 3) as a reduction factor, i.e. as a ratio between characteristic values having the same exceeding frequency in offshore and inshore conditions. Our data present some differences from values foreseen by Goda's formulae; this is probably due to the evaluation procedure and to reflection at present tests. However, mentioned differences do not influence the wave height ratios.

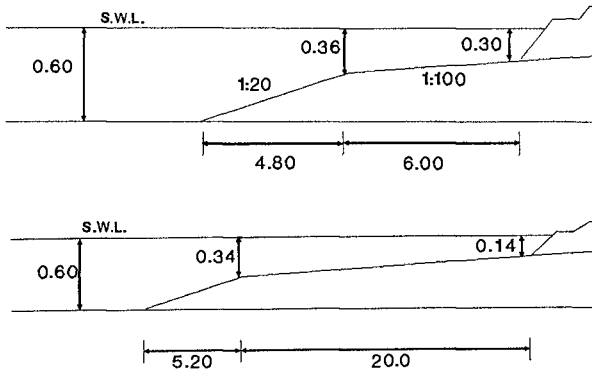


Fig. 1. Bottom conditions at Estramed tests

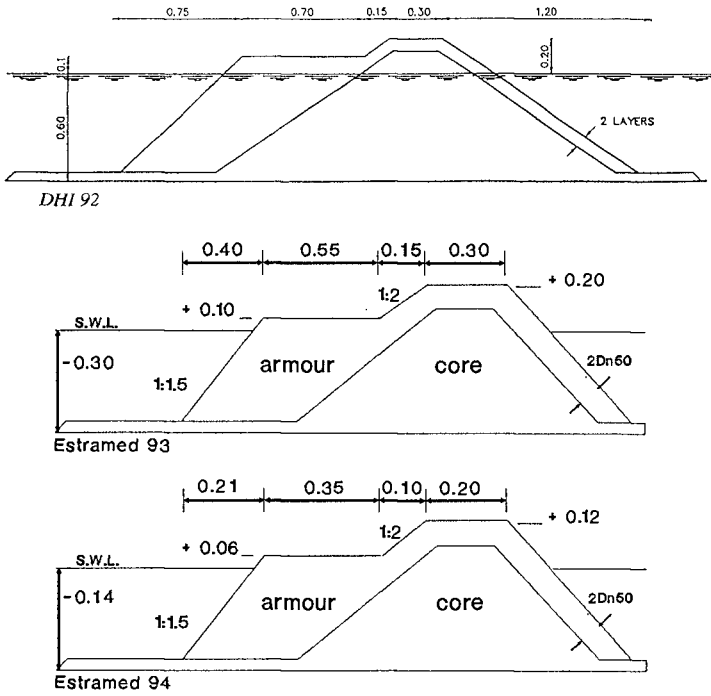


Fig. 2. Cross section of the as built structures (measures in m)

Because inshore wave characteristics were measured at a small but finite distance from the structure, on a water depth larger than at the structure toe, incident wave height on the structure was obtained from measured data applying a small correction which was evaluated according to Goda's formulae. Table 5 gives the observed and calculated inshore wave characteristics.

### Wave height distribution

For deep water conditions, in the case of irregular waves with a narrow spectrum (which is a very frequent case in nature and is almost certainly the case for the highest waves affecting the breakwater in deep water conditions) the wave height distribution is of Rayleigh type, or at least it shows a Rayleigh type upper tail of such an extension that the whole third of highest waves fits the Rayleigh distribution well. As a consequence, the ratio between any characteristic wave height and the significant one is a constant. For instance,  $H_{1/10}/H_{1/3} = 1.27$ ,  $H_{1/50}/H_{1/3} = 1.55$  and  $H_{max}/H_{1/3} = 1.8$ .

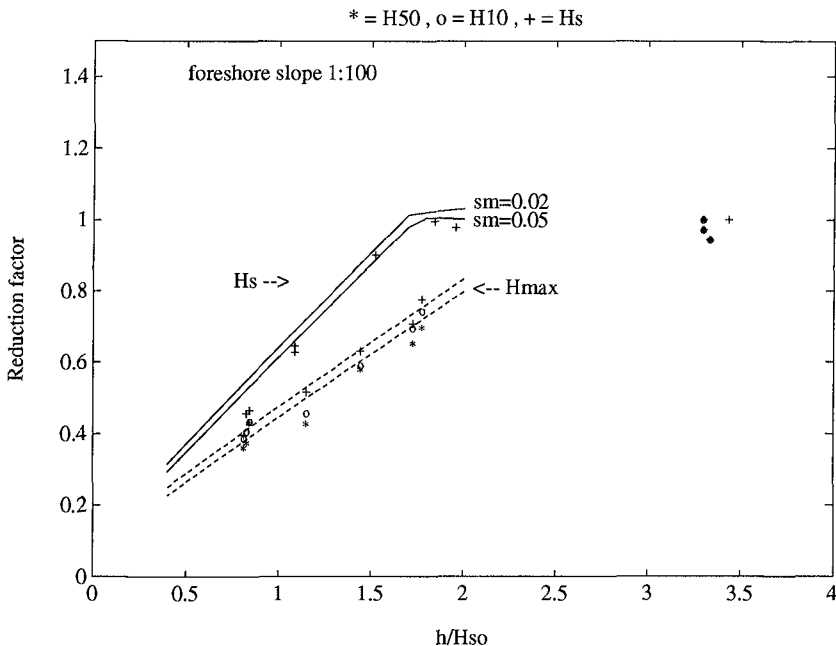


Fig. 3. Wave height reduction factors against relative water depth

In shallow water breaking acts selectively on the highest waves and produces super- and sub-harmonics, broadening the spectrum. For the range of relative water depths of our intermediate and shallow water tests, the ratio between the characteristic wave heights was significantly lower than the mentioned values

derived from Rayleigh distribution. The observed ratios in shallow and intermediate water conditions are:

$$H_{1/10}/H_{1/3} = 1.19 \pm 0.04$$

$$H_{1/50}/H_{1/3} = 1.33 \pm 0.12$$

Table 5. Inshore wave characteristics (measures in m and s)

No.	Test series	$h$ at point of measure	$H_s$	$H_{1/50}$	$T_m$	$C_R$	$h$ at toe	$H_s$	$H_{1/50}$
1	DHI-92	0.60	0.172	0.268	1.96	0.35	0.60	0.170	0.265
2	DHI-92	0.60	0.182	0.283	1.79	0.32	0.60	0.182	0.282
3	DHI-92	0.60	0.184	0.287	1.91	0.31	0.60	0.182	0.284
4	Estramed-93	0.34	0.134	0.181	1.53	0.53	0.30	0.131	0.177
5	Estramed-94	0.32	0.123	0.176	2.09	0.63	0.30	0.123	0.176
6	Estramed-94	0.32	0.136	0.194	2.05	0.52	0.30	0.131	0.186
7	Estramed-94	0.32	0.134	0.173	1.58	0.51	0.30	0.129	0.166
8	Estramed-94	0.16	0.068	0.113	2.40	0.67	0.14	0.078	0.129
9	Estramed-94	0.16	0.077	0.111	1.94	0.66	0.14	0.078	0.112
10	Estramed-94	0.16	0.077	0.097	1.26	0.56	0.14	0.072	0.090

In shallow water the wave height distribution is distorted compared to the Rayleigh one, and a different distribution must be considered (Glukhovskiy, 1966; Klopman & Stive, 1989). In general no 1-parameter distribution will describe the wave height statistics both in shallow water and in deep water conditions. Only for particular purposes a unique characteristic wave height can be used; for instance, aiming to assess the safety of a brittle structure, the maximum wave height may be considered, as in fact it is normally done for vertical wall breakwaters.

### Characteristic wave height

Reshaping of the seaward profile of a berm breakwater is a result of stone movements. During our laboratory investigation, it was observed that their frequency ranged from few single events, when movement starts, to about 50 events in 1000 waves, for the assumed reshaping conditions, producing contemporary movements in more than one place. Therefore we have assumed that a good representative wave height for describing this phenomenon for any water condition is  $H_{1/50}$ .

The frequency of stone movements is described by the *surface damage level* which is defined as:

$$S = N_d \cdot D_{n50}^2/A \tag{1}$$

representing the probability of moving of a generic stone from a one-grain thick layer of the reshaped profile.

The wave height and wave steepness effects on stone movement frequency (Tomasicchio & al., 1994) along a reshaped profile can be described, both in deep and shallow water conditions, by a unique relation if  $H_{1/50}$  is considered (fig. 4). Wave attack intensity is described by the *modified stability number* defined as:

$$N_s^{**} = \frac{H_k}{C_k \Delta D_{n50}} \cdot \left( \frac{s_m}{s_{mk}} \right)^{-1/5} \quad (2)$$

$N_s^{**}$  is a modification of the traditional stability number  $N_s$  accounting for the effect of a non-Rayleighian wave height distribution and of wave steepness. If we assume  $H_{1/50}$  as the wave height  $H_k$ ,  $C_k = 1.55$ . As reference wave steepness we assume  $s_{mk} = 0.03$ . For this wave steepness and for deep water conditions the values of  $N_s$  and  $N_s^{**}$  are equal.

An interpretation of eqn. (2) comes from consideration that, in the case of an orthogonal wave attack, the assumptions that onshore wave energy flux is conserved and that waves break as shallow water waves can be translated as:

$$\frac{1}{8} \rho g H_o^2 c_{go} = \frac{1}{8} \rho g H_b^2 c_{gb} \quad (3)$$

where

$$c_{go} = \frac{1}{2} \sqrt{g/k_o}, \quad c_{gb} = \sqrt{g h_b}$$

and

$$H_b = \gamma \cdot h_b \quad (4)$$

They imply:

$$\frac{H_b}{H_o} = \left( \frac{\gamma}{4k_o H_o} \right)^{1/5} \propto \left( \frac{H_o}{L_o} \right)^{-1/5} \quad (5)$$

According to Komar & Gaughan (1972) the best agreement with reality is obtained assuming  $\gamma = 1.4$  or the proportionality constant in the last relation = 0.56. The comparison of eqn. (2), (3) and (5) shows that the modified stability number  $N_s^{**}$  assumes as relevant wave intensity parameter the onshore energy flux or, if preferred, the breaker height provided the above assumptions hold.

## Scale effects

Reynolds number referred to the mound where waves break on is usually defined combining the characteristic length  $D_{n50}$  with the typical breaking wave velocity  $\sqrt{g H_s}$ :  $Re = D_{n50} \sqrt{g H_s} / \nu$ . With the kinematic viscosity,  $\nu$ , equal to  $10^{-6}$  m<sup>2</sup>/s we obtain in our tests  $2.1 \cdot 10^4 < Re < 4.6 \cdot 10^4$ . Jensen and Klinting (1983) found that in rubble mound breakwater models there is no evident viscosity scale effect if  $Re > 0.6 \cdot 10^4$ .

## Profile dimensions in shallow water

A reshaped or dynamically stable profile for a given wave climate can be described by a small number of geometrical parameters (van Hijum & Pilarczyk, 1982; van der Meer, 1988). Empirically based numerical models to determine such a profile in deep water conditions are available (van der Meer, 1988, 1992 and 1993).

Depth induced breaking cause a reduction in every characteristic wave height and in the dimensions of the developed profile (fig. 4), compared to a breakwater attacked by the same waves in deep water.



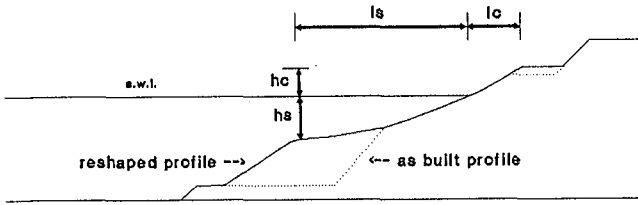


Fig. 4. Parameters for describing the developed profile in shallow water conditions

Accounting for the wave height reduction just in front of the structure is however not sufficient and, as shown first by van der Meer (1988), in order to evaluate the profile parameters, a further reduction factor must be applied.

The relation providing step dimensions suggested by van der Meer (1988) are:

$$h_s = H_{si} \cdot N^{0.07} \cdot 0.22 \cdot s_m^{-0.3} \tag{6}$$

$$l_s = D_{n50} \cdot N^{0.07} \cdot (H_0 T_0 / 3.8)^{1/1.3} \tag{7}$$

Based on very few experimental data, van der Meer proposed the following functional relationship for the reduction factor of the step dimensions,  $r$ , depending on the water depth to incident wave height ratio  $h/H_s$ :

$$r = 1 - 0.75 \left(2.2 - \frac{h}{H_s}\right)^2 \quad \text{if } \frac{h}{H_s} < 2.2 \tag{8.1}$$

$$r = 1 \quad \text{if } \frac{h}{H_s} > 2.2 \tag{8.2}$$

Comparing the two sets of experimental data, the differences between van der Meer's and our test conditions and analysis procedure must be pointed out, see table 6:

Table 6. Differences in laboratory investigations and in the analyses

	van der Meer tests	our tests
Mobility range	$3.5 < N_s < 12$	$2.9 < N_s < 3.4$
Foreshore slope	1:30	$\leq 1:100$
Shape of the built structure	1:3 uniform slope	berm type
Wave measurements	without structure	with the structure in place
Wave analysis	in the time domain	reflection analysis in frequency domain

Figure 5 shows some of the surveyed profiles. After the first few thousands waves if wave conditions are kept constant, the reshaped profile conserves a poor memory of the built profile. The main trace of the original shape observed in our tests refers to the crest: in fact in our tests the crest was usually not clearly above the original berm elevation; therefore the crest position may not depend only on wave intensity but also on the original shape.

The observation of the profiles from our and from other Authors tests suggests the following comments on the qualitative behavior:

- for a breakwater in shallow water, the reshaped profiles can certainly be described by a reduced number of parameters than described by Vellinga (1986): the step height  $h_s$ , the step length  $l_s$ , the crest height  $h_c$  and/or the crest length  $l_c$ ;
- the crest elevation above the original berm was in our tests not evident, not even after a very long reshaping phase; in such case the independent parameters identifying the crest are reduced to only one;
- the step dimensions are reduced in the breaker zone much more than the significant wave height does and therefore a correction factor is necessary;
- the correction cannot be interpreted only as the effect of the reduction of the characteristic wave height ( $H_{1/50}$ ) compared to the significant one, which is not more pronounced than 25%;
- the reduction seems to be due to the change of the kinematic behavior of waves hitting the breakwater: the wave action on the armor stones changes from that of an irrotational green-water breakers plunging on the rubble mound to the action of a white-water roller-shaped bore running up the mound;

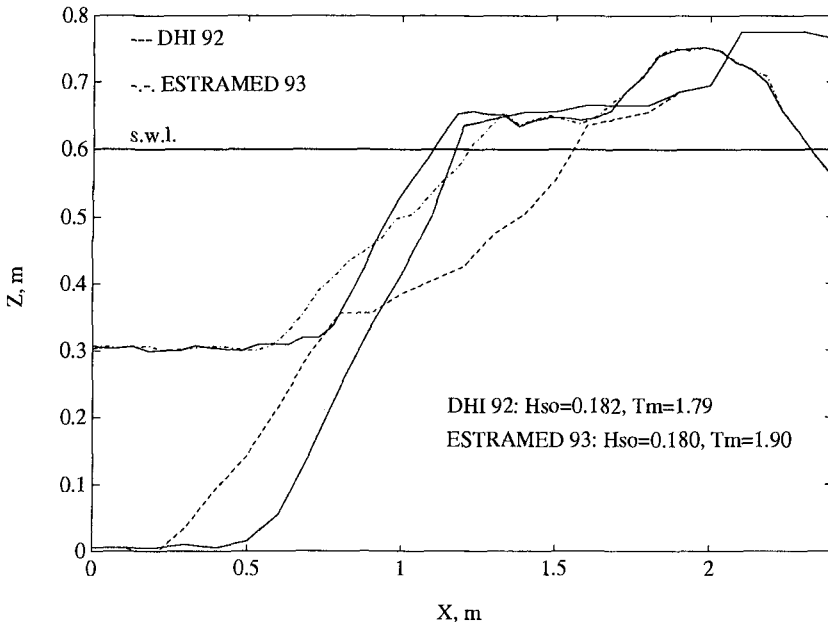


Fig. 5. Surveyed as built and reshaped profiles

- the *corner* separating the step from the lower slope is rather rounded and the mentioned slope is relatively short, therefore sometime the position of the corner is not well defined and the relevance of the slope angle is usually modest;
- the quantification of the dimensions related to stone size is relevant; table 7 gives the observed ratios between typical profile dimensions and the nominal diameter of the armor material.

*Table 7 Relative size of step dimensions*

$h$ at toe, m	$h/H_s$	$h_s/D_{n50}$	$l_s/D_{n50}$
0.30	$2.3 \pm 0.1$	$4 \div 5$	$12 \div 13$
0.14	$1.8 \pm 0.1$	$3 \div 4$	$8 \div 12$

Table 8 presents the dimensions of the profiles surveyed in our tests at the end of each reshaping phase. The following figures present also results relative to surveys performed during the reshaping progress.

*Table 8. Relevant dimensions of the profile at reshaping end*

No.	Test series	Repet.	N	$h_c$	$l_c$	$h_s$	$l_s$
1	DHI-92	1	6000	0.113	0.34	0.310	0.64
2	DHI-92	1	6000	0.128	0.32	0.272	0.66
3	DHI-92	1	6000	0.145	0.34	0.245	0.68
4	Estramed-93	5	5570	0.101 $\pm .006$	0.19 $\pm .02$	0.144 $\pm .009$	0.43 $\pm .04$
5	Estramed-94	1	6000	0.157	0.35	0.103	0.36
6	Estramed-94	1	6000	0.135	0.26	0.107	0.34
7	Estramed-94	1	6000	0.132	0.32	0.100	0.27
8	Estramed-94	1	6000	0.050	0.10	0.050	0.12
9	Estramed-94	1	6000	0.060	0.15	0.063	0.17
10	Estramed-94	1	6000	0.058	0.14	0.053	0.16

In figures 6 data from present tests are reported according to van der Meer's interpretation scheme. Inspection of figs 6 indicates that the data scatter is relatively large and that apparently the relative water depth is not the unique relevant parameter explaining the physical process which results in the reduction of  $l_s$  and  $h_s$ ; other possible parameters influencing the reduction factor are wave period, foreshore slope and breaking depth and probably the mobility conditions.

Figures 7 show the observed values of the reduction factor against the ratio between the depth at structure toe and the depth at breaking point of the characteristic wave (1/50). The figures indicate that the reduction of profile dimensions  $l_s$  and  $h_s$  are highly influenced by breaking of the characteristic waves, which, compared to significant wave breaking, occur at a water depth proportionally greater.

Quantitative results show that:

- our reduction factor are more pronounced than those observed by van der Meer;
- the reduction of the step length is more pronounced than of the step height; average limit values in shallow water conditions are around 0.3 and 0.5, respectively;
- test do not show a perfect repeatability even in the same experimental set-up: compare for instance the results of tests 1 to 3 carried out under very similar wave conditions, or the 5 collectively represented as test no. 4, or test no. 7 which reproduce conditions similar to test no. 4 in a different channel;
- part of the scatter in the reduction coefficient may be interpreted as the effect of the imperfection of the formulae which are actually used below the range of mobility conditions in which they were calibrated; the formulae proposed later by van der Meer (1992) for lower mobility are strongly sensitive to the equivalent slope angle  $\alpha_1$  and  $\alpha_2$ , which are not always well defined (for instance for a very wide berm lower than the significant wave height they become both very small, raising the mobility threshold to unrealistic values), and are no more robust than the original ones; the original ones, (6) and (7), were actually used;

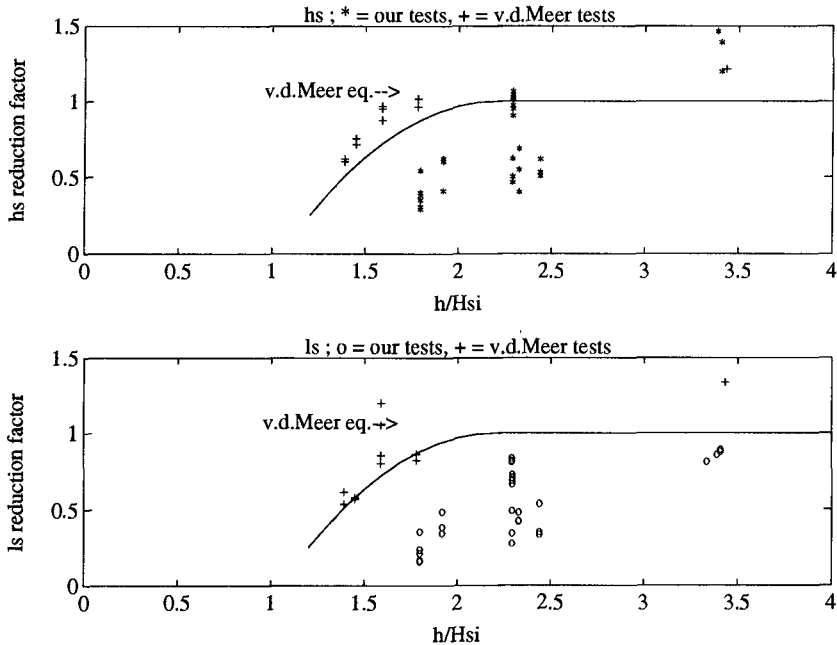


Fig. 6. The reduction factor  $r$  of the step dimensions  $h_s$  and  $l_s$  as function of the water depth to local wave higher ratio  $h/H_s$ .

- the effect of the different evaluation procedure of the significant wave height between our and van der Meer tests has been evaluated in some of our cases where

measurements were performed both in presence and absence of the breakwater; the relation  $H_s = 4.0\sqrt{m_0}$  is experimentally well satisfied at 0.30 and 0.60 m water depth, whereas at 0.14 m depth the coefficient should be reduced to 3.9; the decomposition of incident and reflected waves by the least square method provides a measure of the accuracy of the assumed model: 95-96% of the total variance is represented in intermediate and deep water conditions, whereas the percentage decreases to 87% in shallow water; the resultant wave height is underestimated by few percentage points (from 2% in intermediate and deep water up to 5% in shallow water); the effect should not be disregarded, but it seems however less important than the control of reflection: i.e., when waves are measured in the absence of the structure, waves reflected by the structure should be accurately absorbed in order to obtain a better estimate of the incident wave height than provided by the spectral reflection analysis.

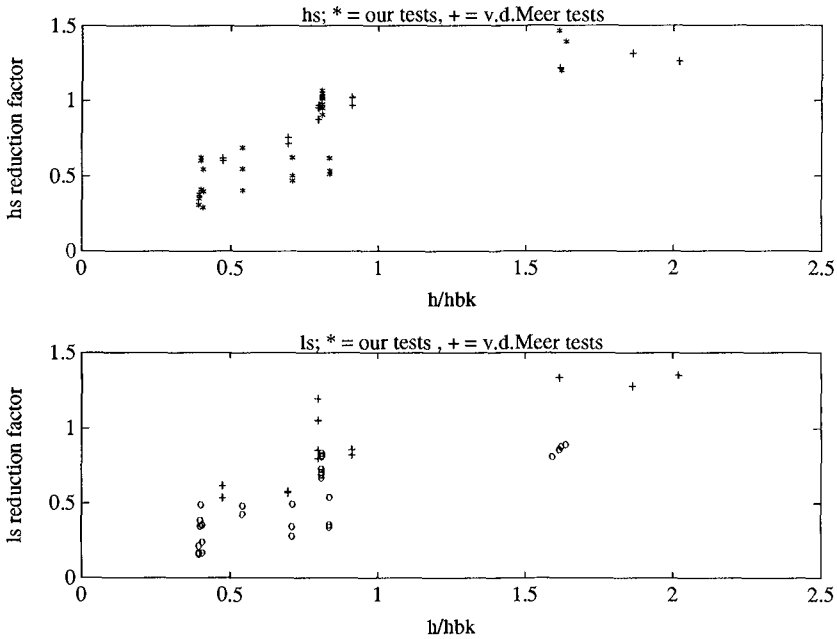


Fig. 7. The reduction factor  $r$  of the step dimensions  $h_s$  and  $l_s$  as function of water depth to breaking depth ratio:  $h/h_b$

### Wave reflection at reshaping breakwaters

Reflection coefficients observed in our tests are summarized in table 9. Wave reflection from berm breakwaters in shallow water conditions is rather heavy

( $\approx 60\%$ ) if measured in front of the structure but it is highly reduced when evaluated offshore the breakers. A comparison of at toe and offshore values indicates that in shallow water conditions reflected waves loose approximately 1/3 of their height through the breaker zone.

*Table 9. Observed reflection coefficient*

Test series	Depth, m	$H_s/H_{s0}$	$C_R$ at toe	$C_R$ offshore
DHI-92	0.60	1.00	$0.32 \pm 0.02$	$0.32 \pm 0.02$
Estramed-93	0.34	0.74	$0.54 \pm 0.04$	$0.31 \pm 0.02$
Estramed-94	0.32	$0.61 \pm 0.09$	$0.62 \pm 0.05$	$0.30 \pm 0.02$
Estramed-94	0.16	$0.42 \pm 0.04$	$0.63 \pm 0.06$	$0.18 \pm 0.05$

## Conclusions

The behavior of reshaping breakwaters in deep and shallow water conditions is qualitatively similar but quantitatively different.

For a reshaping breakwater located in the breaker zone, the profile of the breakwater can be described by a reduced number of parameters.

The step and crest dimensions decrease with  $H_s$ , but  $H_s$  is not the unique influencing factor, since the dimensions of the step are evidently smaller than those expected according to deep water relations and to  $H_s$  incident on the breakwater.

The major cause of the difference between expected and actual dimensions is shown to be the change of kinematics of waves breaking on the structure.

Water depth at the structure toe influences by the breaking process the wave height distribution; its shape changes through the breaker zone. A characteristic wave height, including the effect of limited water depth and representing stone movements in the typical mobility range of breakwaters, is greater than  $H_s$ ; good results were obtained adopting  $H_{1/50}$ .

In particular, consideration of data from present and from van der Meer tests confirms the relevance of the breaking process on the reduction of the profile dimensions, which is well represented by a factor depending on the position of the structure relative to characteristic breakers, quantified as the ratio between the depth at structure toe and the breaking depth of characteristic waves.

Reflection of the breakwater increases with decreasing water depth reaching remarkably high values. Reflected waves are however attenuated through the breaker zone, whereas the encountered incident waves become greater. The offshore apparent reflection coefficient is therefore much lower and decreases with the depth at the structure.

## Acknowledgments

The present study was partially supported by the research and technological development programme in the field of Marine Science and Technology (MAST) financed by the Commission of the European Community, MAST contract 0032.

## List of symbols

$A$	= area of the reshaped profile;
$C_R$	= reflection coefficient;
$c_{go}, c_{gb}$	= offshore and at breaking group velocity;
$D_{\#}$	= sieve diameter of which # % of the material is finer;
$D_{n\#}$	= nominal (volume) diameter of which # % of the material is finer;
$h$	= water depth;
$h_c, h_s$	= crest and step height of the reshaped profile;
$H_k$	= characteristic wave height;
$H_s$	= inshore incident significant wave height;
$H_{so}$	= offshore incident significant wave height;
$H_{1/50}$	= average of the highest 1/50 wave heights;
$k$	= wave number;
$l_c, l_s$	= crest and step length of the reshaped profile;
$N$	= number of waves in a wave attack;
$N_d$	= number of displaced stones after 1000 waves;
$N_s$	= stability number: $H_s/\Delta D_{n50}$ ;
$N_s^{**}$	= modified stability number;
$r$	= reduction factor;
$R_e$	= Reynolds' number;
$s_m$	= fictitious wave steepness, $\frac{2\pi H_s}{gT_m^2}$ ;
$T_m$	= mean wave period;
$S$	= surface damage level;
$\Delta$	= relative mass density of rock;
$\nu$	= kinematic viscosity of water;
$\rho$	= water density.

## References

- Andersen O.H., Juhl J. & Sloth P., (1992).** *Rear side stability of berm breakwaters.* 23<sup>rd</sup> International Conf. on Coastal Eng., Venice
- Burcharth H.F. & Frigaard P., (1987).** *On the stability of berm breakwater roundheads and trunk erosion in oblique waves.* Seminar on Unconventional Rubble Mound Breakwaters, Ottawa, Canada, Sept. 1987
- Dean R.G. & Dalrymple R.A., (1991).** *Water wave mechanics for engineers and scientists.* Advanced Series on Ocean Eng., Vol. 2, World Scientific Publishing Co.

- Glukhovskiy B.Kh., (1966).** *Issledovaniye morskogo vetrovogo volneniya (investigation of sea waves)*. Gidrometeoizdat, Leningrad
- Godá Y. & Suzuki Y., (1976).** *Estimation of incident and reflected waves in random wave experiments*. 15<sup>th</sup> International Conf. on Coastal Eng., Houston
- Godá Y., (1985).** *Random seas and design of maritime structures*. University of Tokyo Press, pp. 68-71
- Jensen O.J. & Juhl J., (1990).** *Practical experience with berm breakwaters*. MAST 1 1st Workshop, 3B Project, Danish Hydraulic Institute
- Jensen O.J. & Klinting P., (1983).** *Evaluation of scale effect in hydraulic models by analysis of laminar and turbulent flows*. Coastal Engineering, vol. 7 no.4, pp. 319-329
- Klopman G. & Stive M., (1989).** *Extreme waves and wave loading in shallow water*. E&P Forum Workshop, October 1989, Paris, France
- Komar P.D. & Gaughan M.K., (1972).** *Airy wave theory and breaker height prediction*. Proc. 13th Int. Conf. Coastal Eng., 405-418.
- Lamberti A. & Tomasicchio G.R., (1991).** *Berm breakwaters physics and research needs*. MAST G6-S 3B, Workshop 9 Dec. 1991, Copenhagen
- Lissev N., (1993).** *Influence of the core configuration on the stability of berm breakwaters*. Report, University of Trondheim, Norway, June 1993
- Mansard E.P.D. & Funke E.R., (1980).** *The measurement of incident and reflected spectra using a least square method*. Proc. 17th Int. Conf Coastal Eng. pp. 154-172.
- Tomasicchio G.R., Lamberti A. & Guiducci F., (1994).** *Stone movement on a reshaped profile*. 24<sup>th</sup> Int. Conf. Coastal Eng., Kobe, Japan
- Tomasicchio G.R., Andersen O.H. & Norton P.A., (1992).** *Measurements of individual stone movements on reshaping breakwaters*. MAST 1 Workshop, Lisbon
- Van der Meer J.W., (1988).** *Rock slopes and gravel beaches under wave attack*. Delft Hydraulics publication no. 396, The Netherlands
- Van der Meer J.W., (1992).** *Stability of the seaward slope of berm breakwaters*. Coastal Engineering, 16 (1992) 205-234.
- Van der Meer J.W., (1993).** *Conceptual design of rubble mound breakwaters*. Delft Hydraulics publ. no. 483, 1993
- Van Hijum E. & Pilarczyk K.W., (1982).** *Equilibrium profile and longshore transport of coarse material under regular and irregular wave attack*. Delft Hydraulics publ. no.274, 1982
- Vellinga P., (1986).** *Beach and dune erosion during storm surges*. Ph.D. thesis, Delft University of Technology



## CHAPTER 98

### DESIGN OF BREAKWATERS AND BEACH NOURISHMENT

Christian Laustrup<sup>1</sup> and Holger Toxvig Madsen<sup>2</sup>

#### Abstract

The subject of this paper is to compare the design forecast and the actual performance of a coastal protection scheme combining segmented near shore breakwaters and beach nourishment.

#### Introduction

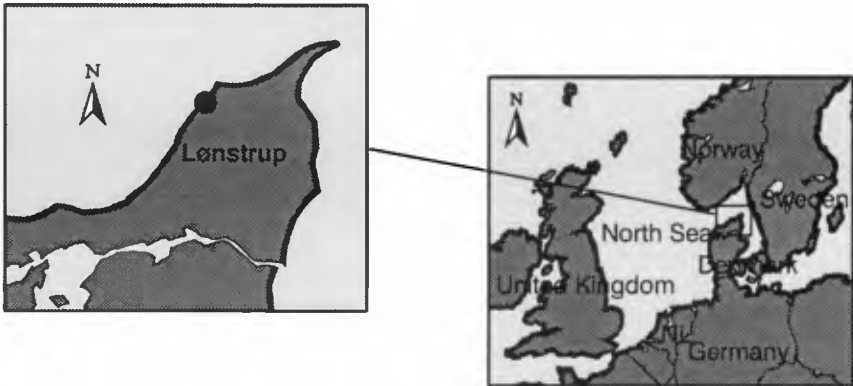


Figure 1. Area Map

The location is a 1100 m coastline at Loenstrup on the Danish North Sea coast. The long term erosion at Loenstrup is 1.4 m per year and the tidal range is 0.3 m.

-----  
1 Deputy Director

2 Head of Department

Danish Coastal Authority, Box 100, DK7620 Lemvig, Denmark.



Figure 2. The Beach and the Cliff

During a storm in 1981, 5–15 m of the cliff was eroded and it was decided to protect the town.

#### Design Method

The design layout was a combination of near shore breakwaters and beach nourishment. The reasons behind this layout were psychological and economical. At that time there was a feeling among the local population that the main component of a coastal protection scheme should be a rigid structure and not "only" beach nourishment. The use of hard structures in this area to stabilize the beach can be justified by the fact that nourishment costs were and are quite high. The cheapest way to get the sand was to transport it by lorries from a harbour 15 km away. The project aims to stop the retreat of the profile and to protect the cliff from further erosion during storm surge. Consequently the scheme should include a revetment. Furthermore it should be taken into

consideration that the beach is used by many tourists in the summer season.

In the design phase a c/b study was carried out with the purpose to determine the combination of breakwater design and beach nourishment volumes with the lowest total costs during the lifetime of the project. The idea of the analyses is that the further off shore and the higher the breakwaters are and the smaller the gaps are, the less nourishment is needed but also the higher the construction costs are.

To do that, the costs and effects of a large number of designs of segmented breakwaters were calculated. The parameters were the breakwater height, the position of the breakwaters relative to the coastline and the gaps between the breakwaters.

For each set of breakwater parameters a wave frequency table for long term wave impact was calculated based on wave recordings and calculations of refraction, shoaling breaking and transmission. The wave decay in the breaker zone was calculated according to Goda (1975).

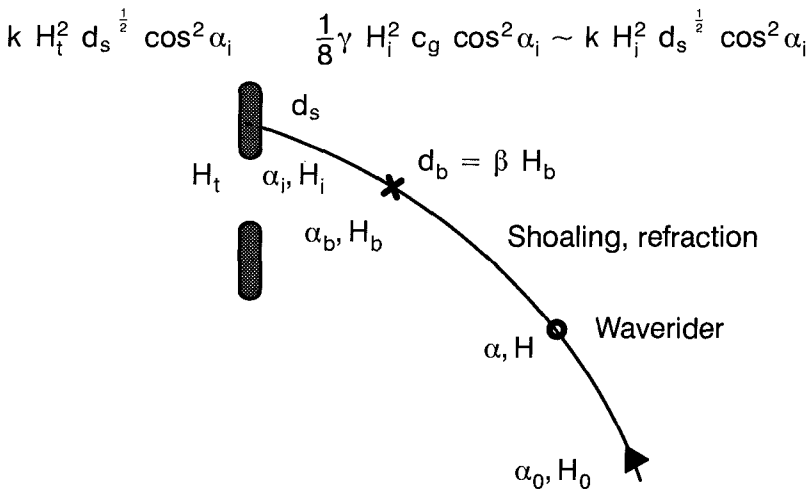


Figure 3. Wave Transformation

For each wave component the wave energy flux per m coast perpendicular to the coast is

$$\frac{1}{8}\gamma H_i^2 c_g \cos^2 \alpha_i f \sim \text{constant} * f * H_i^2 * d_s^{1/2} * \cos^2 \alpha_i$$

$H_i$  = incoming wave height

$c_g$  = group velocity  $\sim (g * d_s)^{1/2}$  at the structure

$\alpha_i$  = incoming wave angle

$f$  = frequency of the wave component

$d_s$  = depth at the structure

To calculate the transmitted wave energy flux,  $H_t$  replaces  $H_i$ . The transmitted wave height over the breakwaters was calculated according to Saville (1963). It was assumed that wave energy would pass the gaps without reduction. By use of the frequency tables, the energy reduction by the breakwaters for average weather conditions could be calculated.

We then assumed that the long term erosion of the profile segment landward of the breakwaters would be reduced with the same percentage as the percentage of energy reduction caused by the breakwaters. The still remaining erosion of the profile out to a certain closing depth should be compensated for by beach nourishment. For different combinations of breakwater parameters the associated building costs and the need for beach nourishment to compensate for erosion were calculated. Only breakwaters that could be built using land based equipment were considered which limited the water depth to be used in the study to apr. 2 m. It was clear from the start that using sea based equipment would be far too expensive.

The present value of the total costs (building + maintenance + nourishment) in the lifetime was calculated for each alternative layout.

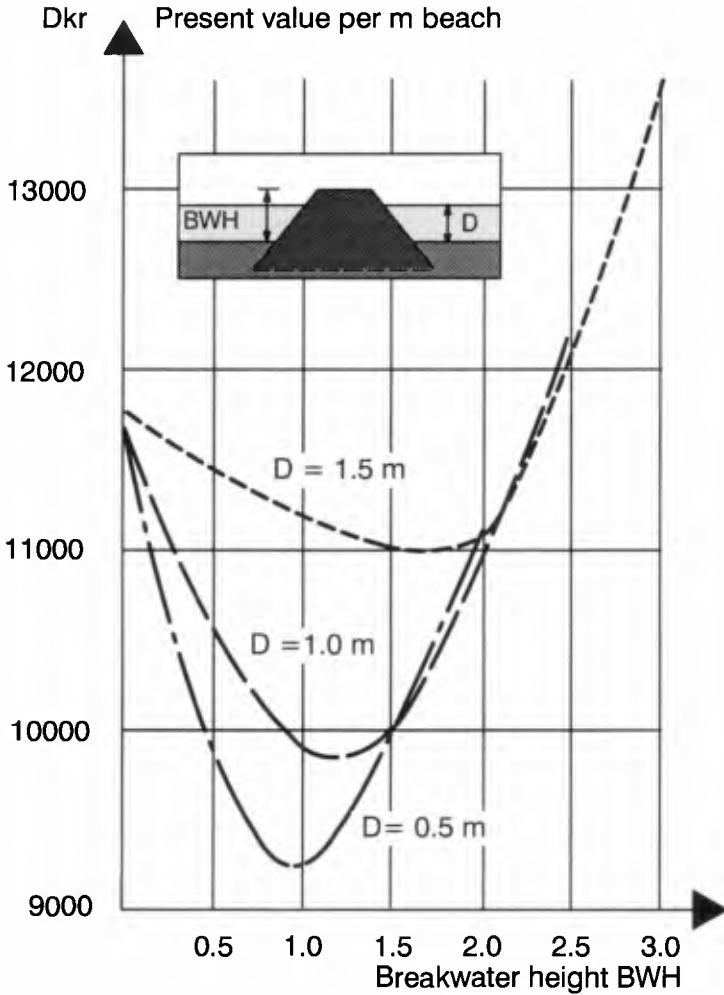


Figure 4. Present Value as a Function of Height and Depth (distance from the beach).

Figure 4 shows examples of design curves where the case of no breakwaters and only nourishment is the intersection with the y - axis. This example represents a case where 50% was breakwaters and 50% was gaps. It shows that down to a water depth of about 1.7 m there is a minimum of costs for certain breakwater heights.

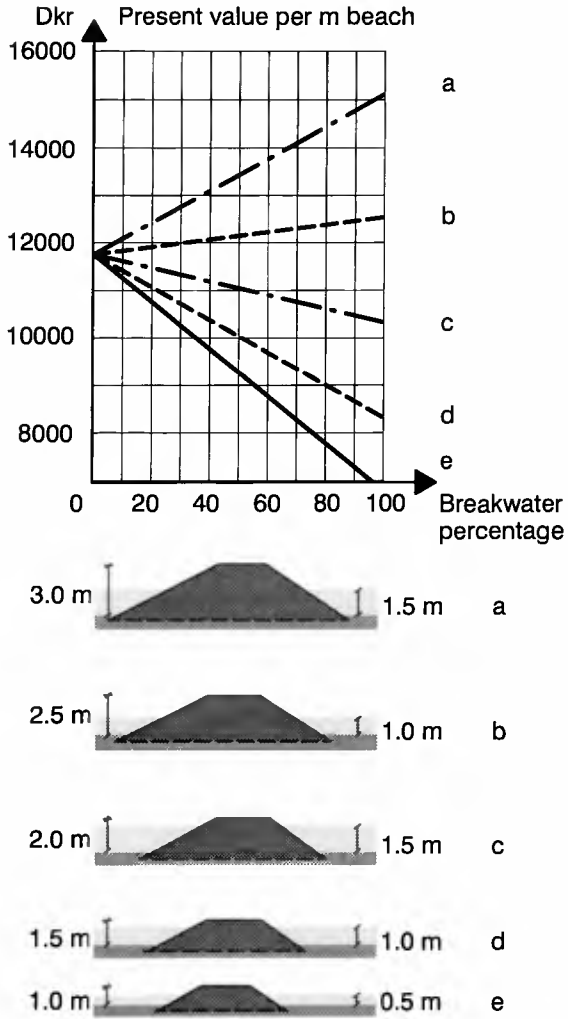


Figure 5. Present Value as a Function of the Percentage of Breakwaters Versus Total Length.

On figure 5 the variation of costs as a function of the percentage of breakwaters is presented and not surprisingly this shows a linear variation. When the total costs are below the costs of only nourishment, the most cost effective solution theoretically is to have 100% breakwaters and no gaps.

Project Layout

When selecting the practical solution we had to consider the need for a certain width of the beach for recreational use. This led to a minimum construction depth of 0.5 m. Furthermore, the gaps should at least be 50% of the total length to allow for swimming. The necessary dimension of the stones in the cover layer resulted in a breakwater height of 1.8 m above sea bed equivalent to a freeboard of 1.3 m relative to normal sea level. The total present value is read from figure 4. It is 10,650 Dkr (1,600 US\$) which is still below the case of no structures.

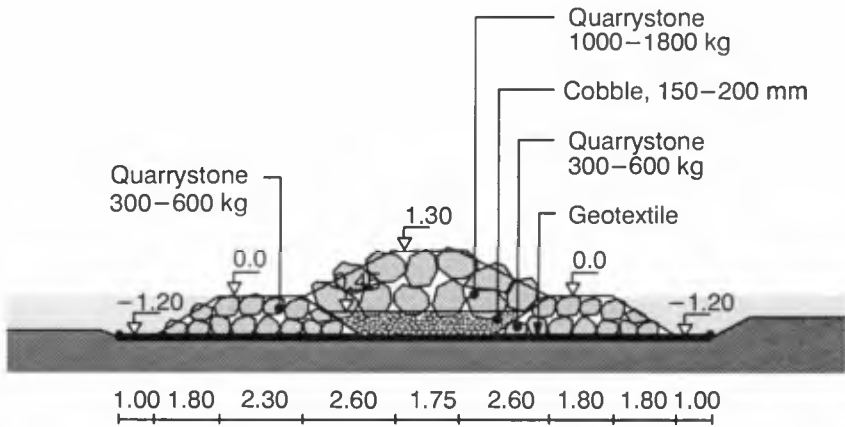


Figure 6. Cross Section.



Figure 7. Aerial Photo of Breakwater Group.





Figure 8. Single Breakwater.

#### Monitoring and Results

The breakwaters were built in 1983 and annual beach nourishment has been carried out since then. The annual nourishment volume has been decided by the need to maintain the beach behind the breakwaters. The profile seaward of the breakwaters was not nourished, so it could be expected that the profile would eventually stabilize in a steeper position.

To find out if the breakwaters have had the expected effect i.e. if they have reduced the erosion behind the breakwaters with the calculated percentage, a monitoring programme was set up. The chosen design should according to our calculations give a reduction of the erosion of about 49.9% in a year with normal weather conditions.

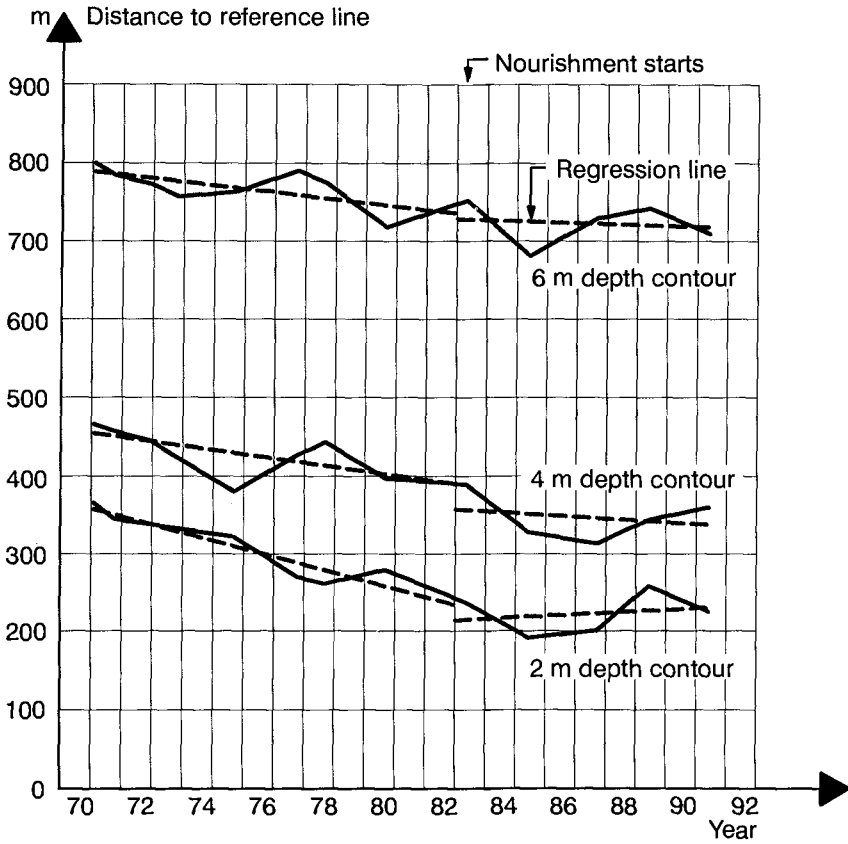


Figure 9. Time Variation of Depth Contours.

Figure 9 shows the time variation of the location of the depth contours. They seem to respond to the new situation a couple of years after the breakwaters were built and the nourishment had started. The 4 and 2 m contours seem to stabilize their position around 1985 resulting in a steeper equilibrium profile.

If the weather had been average since 1983, it would be easy to compare the design forecast of the nourishment volume with the actual annual volumes. The weather has, however deviated significantly from normal since 1983.

Elevation, cm

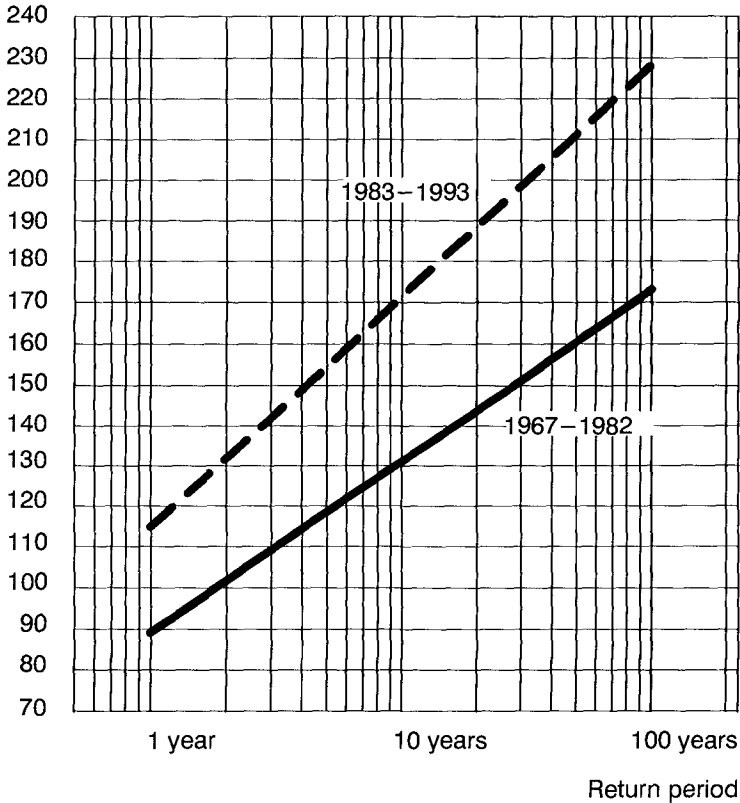


Figure 10. Statistics of Extreme Water Levels

On figure 10, the statistics of extreme water levels are shown. They show a significant difference between the period before and the period after 1983.

The question is if the actual nourishment volumes and the actual weather conditions since 1983 could be expected to result in the measured time variation of volumes in the control box behind the breakwaters when we use the design theory of energy reduction and erosion. To verify this, we have hindcasted this variation of volumes using the actual volumes, the theoretical erosion on the unprotected beach and the theory of energy reduction.

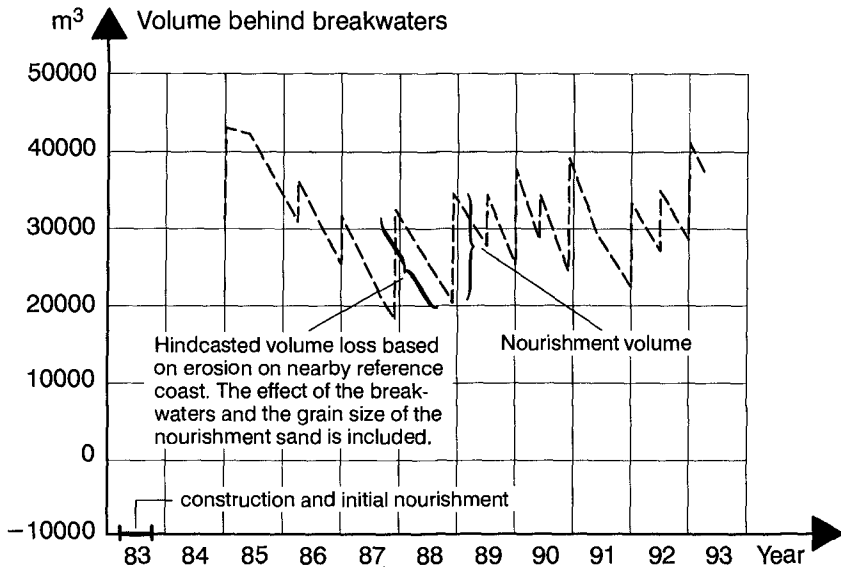


Figure 11. Theoretical Development of Volume Behind Breakwaters

This hindcast of volume development is shown on figure 11. The nearly vertical lines represent the nourishment. The length of the lines represent the actual sand volumes. The sloping lines represent the erosion that would theoretically have occurred in the periods between nourishments if the design theory of the breakwater effect is correct. The slope of the lines is calculated as the rate of erosion that would have occurred if the breakwaters had not been built. Since this rate is unknown the erosion rate of an unprotected reference beach is applied. This erosion rate is then reduced according to the theory of energy reduction caused by the breakwaters developed in the design phase. Since it is the nourishment sand and not the native sand which is eroded, a correction is made using the renourishment factor method (James 1975).

On figure 12, the hindcasted volume curve and the measured volume curve are both shown. It appears, that there is a good agreement between the curves.

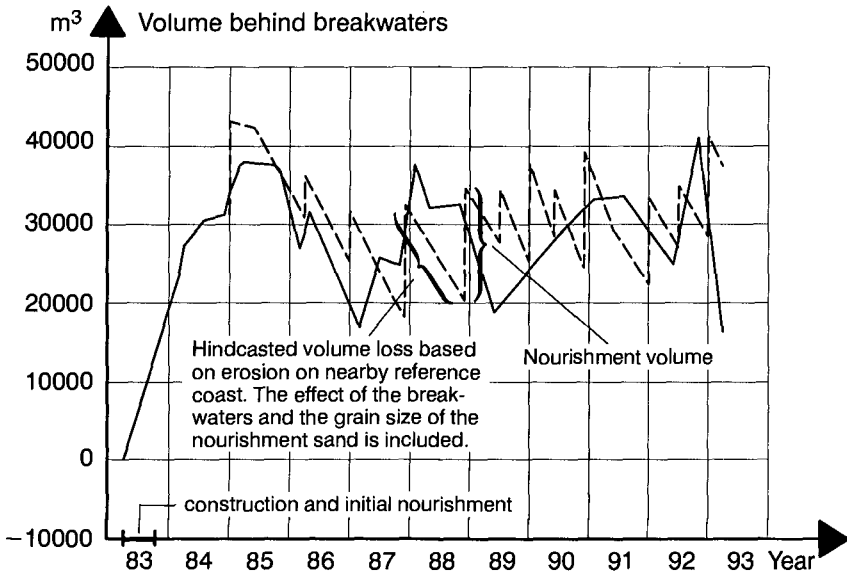


Figure 12. Theoretical(— —)and Measured Volume (——)Development Behind Breakwaters.

### Conclusions

Based on measurements and hindcast calculations it can be concluded, that the effect of the near shore breakwater group in terms of reducing erosion behind the breakwaters is proportional to the ability of the breakwater group to reduce the wave energy flux perpendicular to the coast. However this conclusion should probably be used with caution in cases where the conditions differ significantly from the conditions described in this paper.

### References

Goda, Y. (1975)  
Irregular Wave Deformation in the Surf Zone  
Coastal Engineering in Japan.

James, W. R. (1975)

Techniques in evaluating suitability of borrow material for beach nourishment. Report TM60.

US Army Corps of Engineers, Coastal Engineering Research Center, Vicksburg.

Saville, T. Jr. (1963)

Hydraulic Model Study of Transmission of Wave Energy by Low-Crested Breakwater.

US Army Corps of Engineers, Beach Erosion Board, Washington DC.

## CHAPTER 99

### CIRCULAR CHANNEL BREAKWATER TO REDUCE WAVE OVERTOPPING AND ALLOW WATER EXCHANGE

Dal Soo LEE<sup>1</sup> Associate Member of ASCE,  
Woo Sun PARK<sup>2</sup>, and Nobuhisa KOBAYASHI<sup>3</sup> Member of ASCE

#### Abstract

A new type of breakwater caisson is presented for improving water quality in a harbor. Circular resonance channels connected with flow conduits in the caisson cause clear sea water inflow into a harbor through the conduits. The hydraulic characteristics of this caisson with respect to wave reflection, overtopping and transmission appear excellent compared with those of conventional caissons. The potential of water quality improvement is great due to its high efficiency in normal wave conditions. A simple resonance model is developed to identify an important dimensionless parameter. Experimental results show that the new concept of circular channel breakwater is promising in terms of its hydraulic performance.

#### Introduction

The main function of existing breakwaters is to reduce waves propagating onshore, and for normal wave conditions, the breakwaters are designed for no wave overtopping to secure harbor tranquility. However, it is normally overlooked that the breakwaters usually block sea water exchange at the cost of the harbor

-----  
<sup>1</sup>Principal Res. Engr., Director of Ocean Engrg. Div., Korea Ocean Res. & Dev. Inst., Ansan P.O.Box 29, Seoul 425-600, Korea.

<sup>2</sup>Senior Res. Engr., Ocean Engrg., Div., Korea Ocean Res. & Dev. Inst., Ansan P.O.Box 29, Seoul 425-600, Korea

<sup>3</sup>Professor and Associate Director, Center for Applied Coastal Research, University of Delaware, Newark, Delaware 19716, USA

tranquility. This often causes water pollution problems due to the stagnation of sea water inside the harbors if tidal ranges are not sufficiently large.

Several kinds of breakwaters have already been developed to allow water exchange (Kataoka and Saida, 1986; Tanimoto et. al, 1987; Korea Ocean Research and Development Institute, 1989; Tanimoto et. al, 1989), but most of them are normally effective only in the presence of currents. No breakwater type with water quality improving capability mainly under weak wave action appears to exist at the present. Hence, there is a practical need to develop a breakwater type that causes clear sea water inflow into a harbor through the breakwater using incoming waves as a driving force. In addition, the performance of the breakwater with respect to wave reflection, overtopping and transmission should be improved as much as possible.

The circular channel breakwater(CCB) equipped with flow conduits presented herein has been devised to attain the capability of wave-induced sea water inflow into a harbor as well as low wave reflection and overtopping at the same time. The resonance phenomena of water level in the circular channel is shown to be important in increasing water flow rates for short period waves. A simple resonance model is developed to identify an important dimensionless parameter for the analysis of experimental data. Experimental results show that the concept of CCB is promising.

### Conceptual Description of CCB

Figure 1 shows a conceptual diagram of the Circular Channel Breakwater(CCB). The caisson has circular channels at its front part and flow conduits at its rear part. When incident waves impinge on the CCB, water passes through the channel. Water inflow into a harbor occurs through the conduits due to the pressure difference between the inlet and outlet of these conduits. The inflow induces a small rise of mean water level behind the breakwater, and the pressure driven weak current is subsequently introduced into the harbor but occurs essentially continuously under normal wave conditions. A reverse flow is restricted because the inlets of the conduits are placed near the still water level in the circular channels to create one way flow into the harbor.

The water inflow does not make any significant disturbance of water surface in the harbor under normal wave conditions because



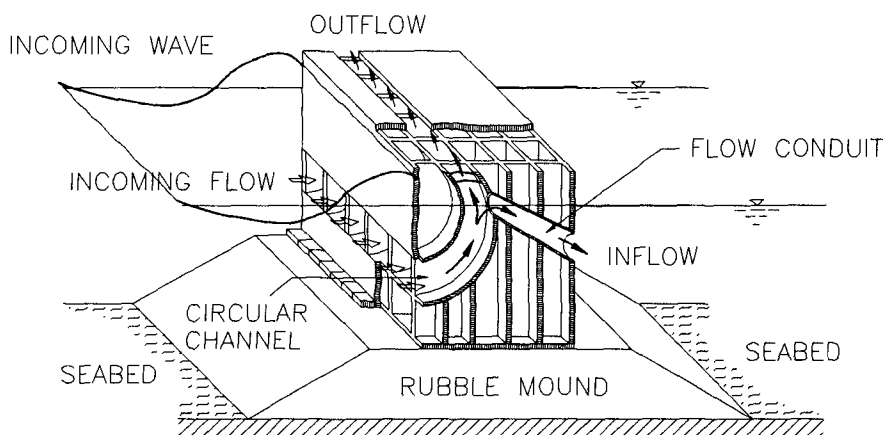


Figure 1. Conceptual diagram of the Circular Channel Breakwater (CCB).

the outlet of the conduits are well submerged. The back face of the caisson may be used as a wharf for small ships under moderate wave conditions when the outlets of the conduits are placed well below the draft of a ship.

Resonant oscillations occur in the circular channel for short period waves and hence enhance the flow rate. On the other hand, when wave overtopping occurs, the outflow issuing from the circular channel collides with the overtopping water flow above the caisson, resulting in increased wave energy dissipation and reduced wave overtopping.

### Simple Resonance Model

A simple resonance model is developed to gain insight into the complicated hydrodynamic process in the circular channel and to identify an important dimensionless parameter for the following experimental data analysis.

Figure 2 shows the geometric parameters and cylindrical coordinate system( $r, \theta$ ) used in the following linear potential flow analysis, where  $R_c$  and  $b$  are the circular channel radius and its width, respectively,  $\eta_c(t)$  is the free surface elevation in the channel,  $\theta_s$  is the value of  $\theta$  at still water level in the channel,

$P_e(t)$  is the pressure at the channel entrance, and  $d$  is the water depth. It is assumed that the circular channel radius  $R_c$  is much larger than its width  $b$ , and that no overflow occurs from the exit of the channel.

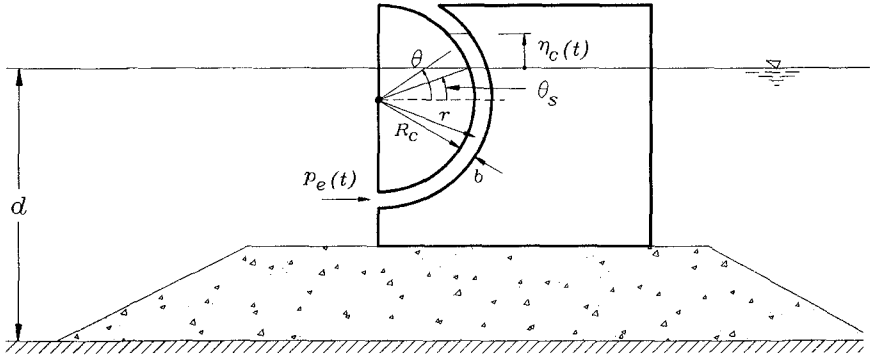


Figure 2. Diagram showing geometric parameters in cylindrical coordinate system.

The Laplace equation for the velocity potential  $\phi$  in the circular channel is expressed as

$$\frac{1}{r} \frac{\partial}{\partial r} \left( r \frac{\partial \phi}{\partial r} \right) + \frac{1}{r^2} \frac{\partial^2 \phi}{\partial \theta^2} = 0 \quad (1)$$

The boundary conditions may be expressed as

$$-\rho \frac{\partial \phi}{\partial t} = P_e(t) \quad \text{at } \theta = -\frac{\pi}{2} \quad (2)$$

$$\frac{\partial \eta_c}{\partial t} = \frac{1}{R_c} \frac{\partial \phi}{\partial \theta} \cos \theta_s \quad \text{at } \theta = \theta_s \quad (3)$$

$$-\frac{\partial \phi}{\partial t} = -g\eta_c \quad \text{at } \theta = \theta_s \quad (4)$$

$$\frac{\partial \phi}{\partial r} = 0 \quad \text{at } r = R_c \quad \text{and} \quad r = (R_c + b) \quad (5)$$

where,  $\phi(r, \theta, t)$  = velocity potential inside the circular channel  
 $P_e(t)$  = dynamic pressure at the entrance of the channel  
 as shown in Figure 2  
 $\rho$  = water density  
 $\eta_c$  = free surface elevation in the channel  
 $\theta_s$  = value of  $\theta$  at the still water level in the channel

Equations (3) and (4) correspond to the linearized kinematic and dynamic free surface boundary conditions.

To satisfy the no flux boundary condition on the curved solid walls given by Equation (5), the solution  $\phi$  of Equation (1) should be independent of  $r$  as

$$\phi(\theta, t) = C_1(t)\theta + C_2(t) \quad (6)$$

Using Equation (3),

$$C_1(t) = \frac{R_c}{\cos \theta_s} \frac{\partial \eta_c}{\partial t} \quad (7)$$

From Equations (2) and (4),

$$\frac{dC_1(t)}{dt} \left(-\frac{\pi}{2}\right) + \frac{dC_2(t)}{dt} = -\frac{1}{\rho} P_e(t) \quad (8)$$

$$\frac{dC_1(t)}{dt} \theta_s + \frac{dC_2(t)}{dt} = -g\eta_c \quad (9)$$

Eliminating  $C_1(t)$  and  $C_2(t)$  from Equations (7), (8) and (9), we get

$$\frac{R_c(\theta_s + \frac{\pi}{2})}{\cos \theta_s} \frac{d^2 \eta_c}{dt^2} + g\eta_c = \frac{1}{\rho} P_e(t) \quad (10)$$

which indicates the free surface oscillation in the channel forced by the dynamic pressure  $P_e(t)$  at the channel entrance.

Assuming simple harmonic motions for  $\eta_c(t)$  and  $P_e(t)$  expressed as

$$\eta_c(t) = R_e[\bar{\eta}_c e^{-i\omega t}] \quad (11)$$

$$P_e(t) = R_e[\bar{P}_e e^{-i\omega t}] \quad (12)$$

where  $R_e$  indicates the real part,  $\bar{\eta}_c$  and  $\bar{P}_e$  are the complex valued amplitudes, and  $\omega$  is the angular frequency. Substituting Equations (11) and (12) into (10) yields :

$$\bar{\eta}_c = \left[ 1 - \frac{R_c(\theta_s + \frac{\pi}{2})\omega^2}{g \cos \theta_s} \right]^{-1} \cdot \frac{1}{\rho g} \bar{P}_e \quad (13)$$

In order to find  $\bar{P}_e$ , the solution in the channel will need to be matched with the solution in front of the caisson. Nevertheless, this simple solution indicates that resonance occurs in the circular channel when,

$$\frac{R_c(\theta_s + \frac{\pi}{2})\omega^2}{g \cos \theta_s} = 1 \text{ for infinite } \eta_c.$$

In reality,  $\eta_c$  will not be infinite due to energy loss especially at the channel entrance.

For the following data analysis the dimensionless parameter  $\omega^*$  is defined as

$$\omega^* \equiv \frac{R_c(\theta_s + \frac{\pi}{2})\omega^2}{g \cos \theta_s} \quad (14)$$

where  $\omega^* = 1$  corresponds to the resonance condition.

### Experiments and Data Analyses

Experiments on the circular channel breakwaters(CCB) were conducted to examine the hydrodynamic characteristics of wave reflection, overtopping, transmission and water discharge through the flow conduits. The experiments were performed with regular waves in a wave flume (53.3 m long, 1.0 m wide, and 1.25 m high)

with a model caisson as shown in Figure 3, where the water depth on the horizontal bottom is  $d=40.5\text{ cm}$ , the caisson crest height above the still water level is  $h_c=8.5\text{ cm}$ , the radius of the front wall of the channel is  $r_{c1}=8.5\text{ cm}$ , the radius of the rear wall of the channel is  $r_{c2}=15\text{ cm}$ , the width of the channel at the entrance is  $b_e=10\text{ cm}$ , and the diameter of the flow conduit is  $D=3.2\text{ cm}$ . The incident wave height  $H_i$  was 3 and 5 cm in these experiments. In this model the channel width was designed to be decreased gradually upward to produce higher runup inside the channel. Additional experiments were also carried out for the solid wall breakwater (SWB, conventional caisson breakwater) for the purpose of comparisons.

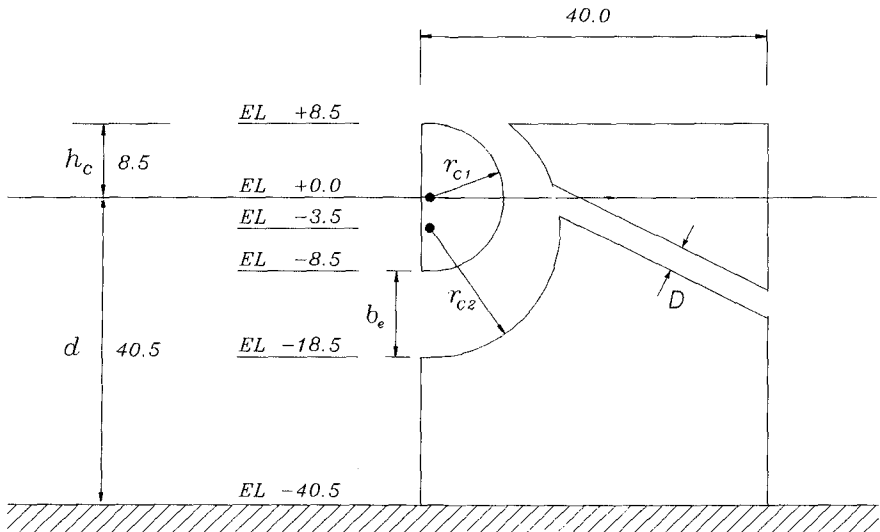


Figure 3. Cross-sectional diagram of model setup without rubble mound foundation(unit : cm).

Figure 4 shows the measured wave runup  $\eta_{c\text{ max}}$  inside the channel normalized by the incident wave height  $H_i$  as a function of  $\omega^*$  defined by (14). Comparing the measured values of  $\eta_{c\text{ max}}/H_i$  with the value of 1.0 in front of a perfectly reflective vertical wall, this runup in the vicinity of  $\omega^*=1$  serves as an amplified potential

for driving inflow into the harbor through the flow conduits.

The occurrence of the peak at the resonance frequency (at the value of  $\omega^*=1$  in Figure 4) means that the resonance plays a major role in the enhancement of runup in the channel. In shelter coastal areas, the waves of short periods and small wave heights prevail, as a result, the energy of normal waves can be effectively used to induce water inflow into a harbor by the use of this type of breakwater.

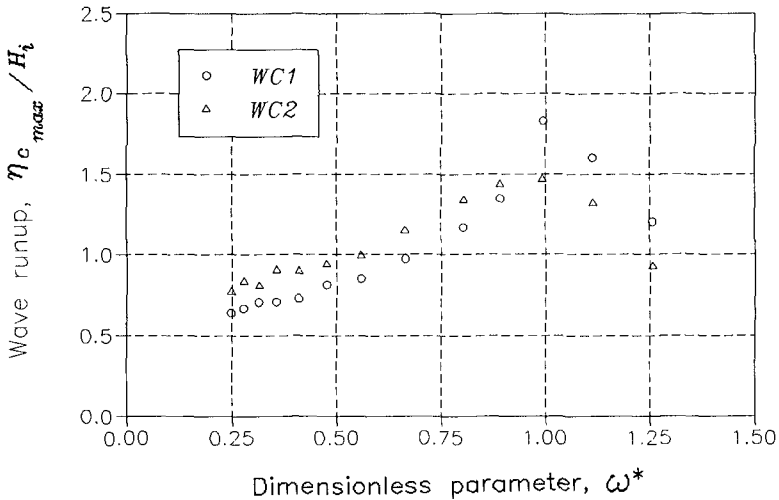


Figure 4. Maximum wave runup inside the circular channel shown in Figure 3 for  $H_i=3cm$  (WC1) and  $H_i=5cm$  (WC2).

Figure 5 shows that the reflection of the CCB is lower than that of the SWB. The occurrence of the lowest reflection near the resonance frequency (near the value of  $\omega^*=1$  in Figure 5) means that the resonance reduces significantly reflection from CCB. The resonance peak in this figure is shifted to slightly higher frequency for the tests with  $H_i=3cm$ .

Figure 6 shows the measured net flow rate  $Q$  normalized by  $\sqrt{2gH_i}A$  with  $g$ =gravitational acceleration and  $A=(\pi/4)D^2$  through one flow conduit of diameter  $D=3.2cm$  for the model caisson shown in Figure 3. The resonant peak in this figure is shifted to slightly lower frequency for the tests with  $H_i=5cm$ .

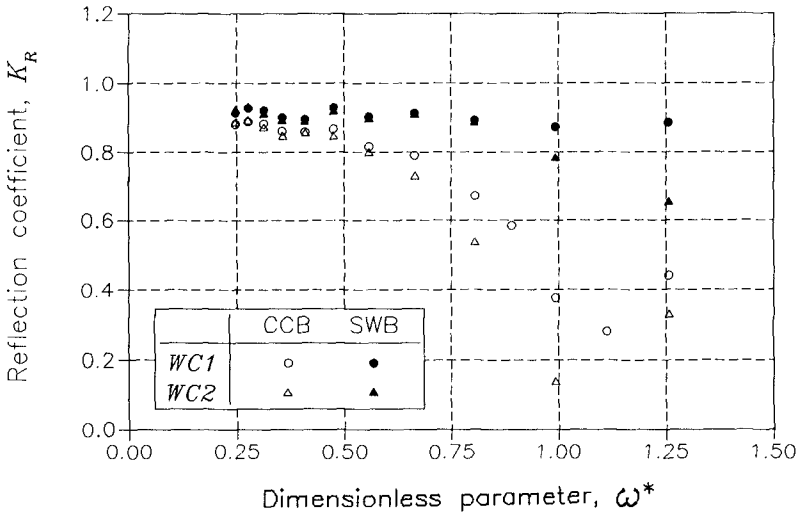


Figure 5. Comparison of reflection coefficients between CCB shown in Figure 3 and SWB for  $H_i=3cm$  (WC1) and  $H_i=5cm$  (WC2).

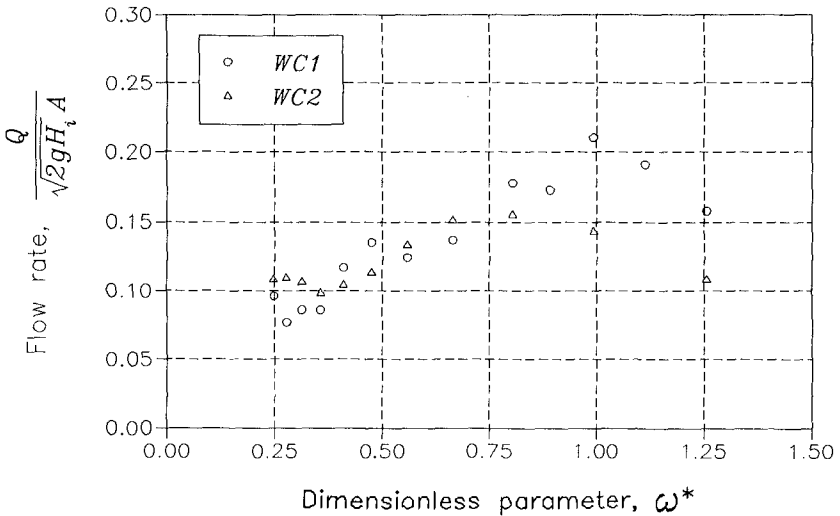


Figure 6. Net inflow rate through one flow conduit with  $D=3.2cm$  for  $H_i=3cm$  (WC1) and  $H_i=5cm$  (WC2).

Figures 7 and 8 show model setup with a rubble mound and the different positions ( $C1$ ,  $C2$  and  $C3$ ) of flow conduit inlets in the circular channel, respectively. The crest elevation  $h_c$  above the still water level was chosen as  $12\text{ cm}$  and  $8\text{ cm}$  by changing the water depth in the tank. In Figures 7 and 8,  $h_c=12\text{ cm}$ , while the water depths on the bottom and above the foundation are  $d=50\text{ cm}$  and  $h=30\text{ cm}$ :

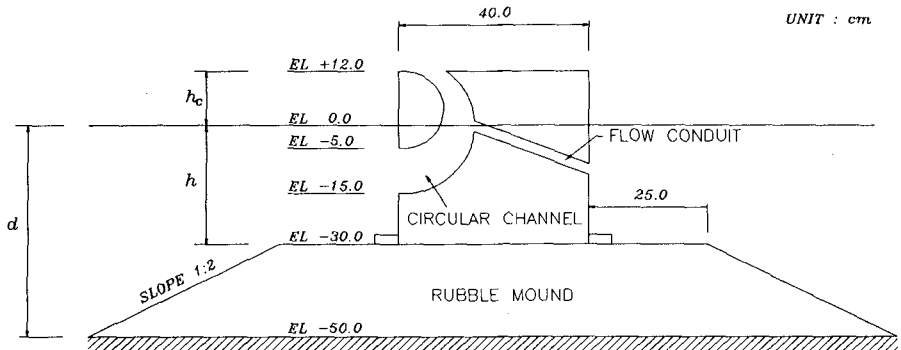


Figure 7. Cross-sectional diagram of model setup with rubble mound foundation.

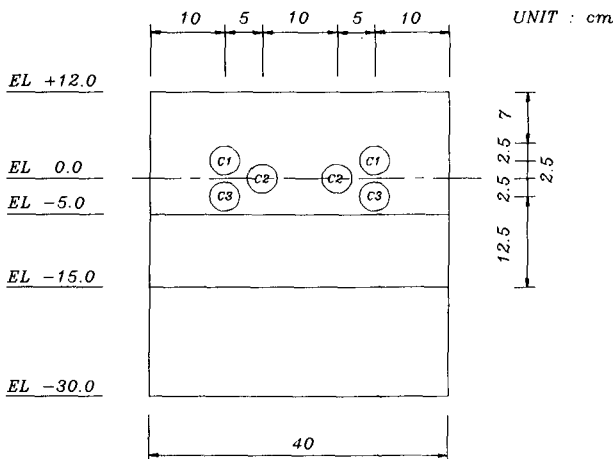


Figure 8. Schematic diagram showing different positions ( $C1$ ,  $C2$  and  $C3$ ) of flow conduit inlets in the circular channel in Figure 7.



Only some of the many geometric parameters involved in the caisson were changed. It should therefore be noted that the experimental results presented hereafter are not general and limited to the adopted model configuration and experimental conditions. For the experimental setup shown in Figure 7 wave overtopping occurred for the incident wave height  $H_i=13\text{ cm}$  and the simple model discussed in the previous section is not applicable.

Figure 9 shows the comparison of the net flow rate  $Q$  through one conduit of diameter  $D=3.2\text{ cm}$  where  $l$  is the length of the flow conduit. At position C3 (below the still water level), the net flow rate is generally low for the longer period waves due to the occurrence of reverse flow in the conduit under the minimum free surface elevation in the channel. At position C1 (above the still water level), the net flow rate is generally low for shorter period waves due to the short duration of the head difference between the inlet and outlet of the flow conduit. At position C2 (at the still water level) the net flow rate remains to be large for any wave period. The variation pattern of the net flow rate with respect to the inlet position may vary if the configuration of the channel is changed.

Figure 10 shows that the reflection from the CCB is lower for all frequencies than that from the SWB. The relative difference increases with the increase of  $\omega^2 d/g$ . This means that CCB retains the merit of low reflection of perforated wall caisson breakwaters.

Figures 11 and 12 show measured values of overtopping rate and transmission coefficient for the water depth condition different from that shown in Figure 7. The caisson crest height above the still water level is  $h_c=8\text{ cm}$ , and the water depths on the bottom and above the foundation are  $d=54\text{ cm}$  and  $h=34\text{ cm}$ , respectively. Figure 11 shows that the overtopping rate  $q$  of CCB per unit width is always lower than that of SWB. This means that the outflow issuing from the exit of the circular channel plays an important role in reducing wave overtopping due to its collision with the landward overtopping water above the caisson. Figure 12 shows the resulting difference in the wave transmission coefficient between CCB and SWB.

The characteristics of low reflection together with low

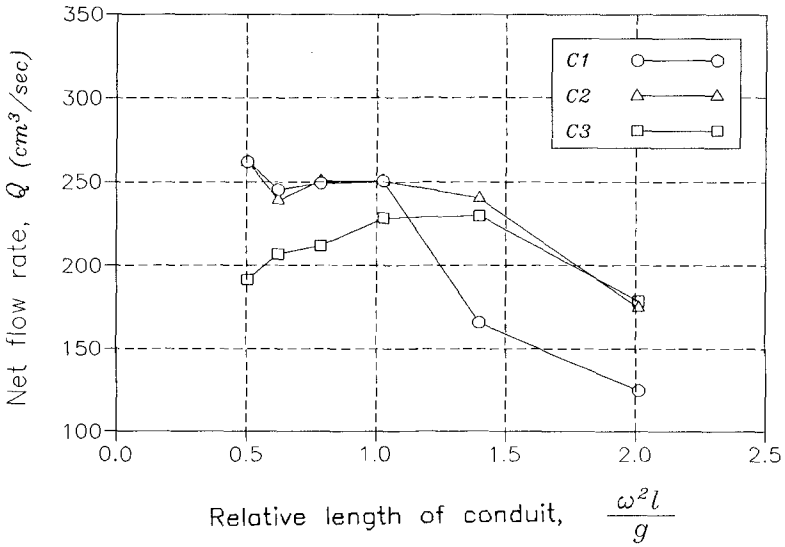


Figure 9. Variations of net inflow rate  $Q$  through one flow conduit in Figure 8 with  $d=50\text{ cm}$ ,  $h=30\text{ cm}$ ,  $h_c=12\text{ cm}$  and  $D=3.2\text{ cm}$  for  $H_i=13\text{ cm}$ .

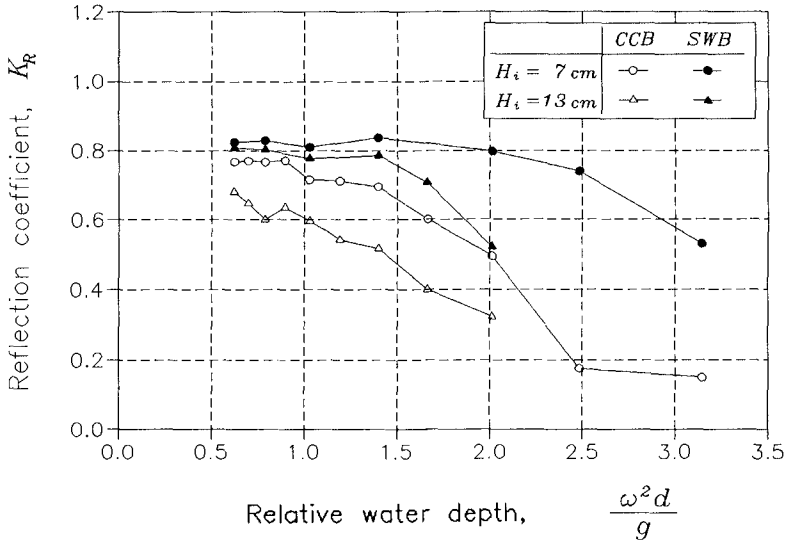


Figure 10. Comparison of reflection coefficients between CCB and SWB with  $d=50\text{ cm}$ ,  $h=30\text{ cm}$ ,  $h_c=12\text{ cm}$  in Figure 7 for  $H_i=7$  and  $13\text{ cm}$ .

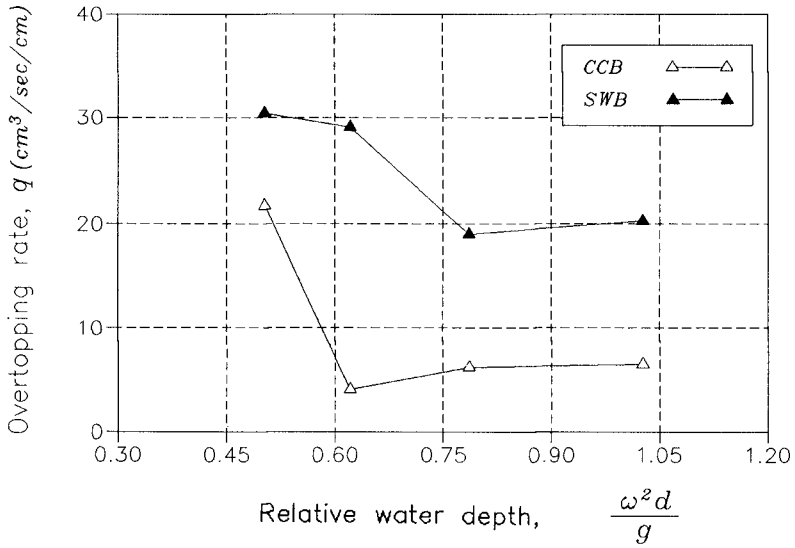


Figure 11. Comparison of overtopping rates between CCB and SWB with  $d=54\text{ cm}$ ,  $h=34\text{ cm}$  and  $h_c=8\text{ cm}$  in Figure 7 for  $H_i=13\text{ cm}$ .

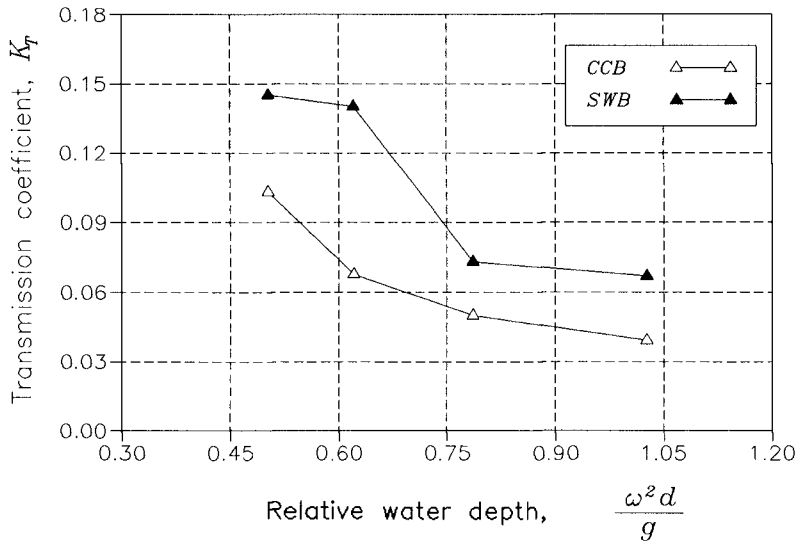


Figure 12. Comparison of transmission coefficients between CCB and SWB with  $d=54\text{ cm}$ ,  $h=34\text{ cm}$  and  $h_c=8\text{ cm}$  in Figure 7 for  $H_i=13\text{ cm}$ .

transmission imply that the hydraulic performance of CCB is superior to that of SWB.

### Conclusions

A circular channel breakwater (CCB) connected with flow conduits was proposed. The performance of CCB in terms of wave reflection, overtopping and transmission is excellent compared with that of conventional solid wall caisson breakwaters.

The capability of inducing clear water inflow through the conduits of CCB into a harbor is enhanced by the resonant oscillations in the circular channel under normal wave conditions. A great potential for improving water quality in harbors is expected under normal wave conditions when water quality problems may become serious. At the same time, CCB maintains the merits of caisson type breakwaters in that the upper and back faces of the caisson can be utilized.

Further studies are needed to reveal the dynamic characteristics related to the pressure distribution and resulting caisson stability.

### Acknowledgements

The present study was financially supported by the Ministry of Science and Technology of Korea through the Project No. BSPN 00232.

### References

- Kataoka, S. and Saida, K. (1986). Compilation of Breakwater Structure, Technical Note of the Port and Harbour Research Institute, Ministry of Transport, Japan, No. 556 (in Japanese).
- Korea Ocean Research and Development Institute, (1989). A Study on the Development of New Coastal Structures for Wave Absorption (I), BSPG 00077-224-2 (in Korean).
- Tanimoto K., Namerikawa, N., Ishimaru, Y. and Sekimoto, T. (1987). Hydraulic Characteristics and Design Wave Forces of Double-cylindrical Caisson - A Study on Development of Deep-water Breakwater, Technical Note of the Port and Harbour Research Institute, Ministry of Transport, Japan, No.

600 (in Japanese).

Tanimoto K., Kataoka, S., Haranaka, S., Suzuki, S., Shimosako, K. and Miyazaki, K. (1989). A Hydraulic Experimental Study on Semi-circular Caisson Breakwaters, Technical Report of the Port and Harbour Research Institute, Ministry of Transport, Japan, Vol. 28, No. 2 (in Japanese).

## CHAPTER 100

### Increased Dolos Strength by Shape Modification

S. A. Luger<sup>1</sup>, D. T. Phelp<sup>1</sup>, A. van Tonder<sup>1</sup> and A. H. Holtzhausen<sup>1</sup>

#### Abstract

A survey of prototype dolos breakages was performed to determine the distribution of failure modes. The results showed that 89% of the failures originate near the fluke-shank intersection. A series of static and dynamic finite element analyses was subsequently performed with the aim of improving the resistance of the dolos against the most commonly observed modes of failure. Of the six dolos shapes analysed, a large fillet extending from the fluke to the centre of the shank was found to be the most effective in reducing the stress in the critical fluke-shank intersection. Compared to a sharp intersection, the large fillet reduces the stress by more than 60%.

#### Introduction

A number of dolos-armoured breakwaters constructed in the 1960's and 1970's in South Africa now require repair work. This repair work generally involves placing additional layers of somewhat heavier dolosse on top of the damaged dolos slope.

A number of methods are available to improve the strength of these repair dolosse. These include an increase in waist ratio, the use of reinforcement (conventional, prestressed, rail or fibre) or a modification to the fluke-shank intersection. Increasing the waist ratio has the disadvantage of reducing the hydraulic stability (Holtzhausen and Zwamborn, 1992), while reinforcing increases the unit cost and there is

---

<sup>1</sup>Ematek, CSIR, P O Box 320, Stellenbosch 7599, South Africa

the potential for corrosion problems. In this paper the method of modifying the fluke-shank intersection is investigated. The initial phase of the study was to perform a survey of prototype dolos breakages. Various modifications to the fluke-shank intersection were then tested using static and dynamic finite element analysis.

### Survey of Prototype Dolos Breakages

The objective of the survey was to identify the main failure modes and determine the relative frequency of each mode. Use was made of close-range photographs taken from a crane on the breakwater crest or from a helicopter. Seven breakwaters were surveyed in this way and each of the 357 observed breakages were classified as one of six failure modes. The dolos masses ranged from 5 to 30 t and the waist ratios from 0,31 to 0,36. The fluke-shank intersections were either sharp or had a small fillet (radius approximately  $0,04H$ , where  $H$  is the dolos height) or a small chamfer (size approximately  $0,057H$ ).

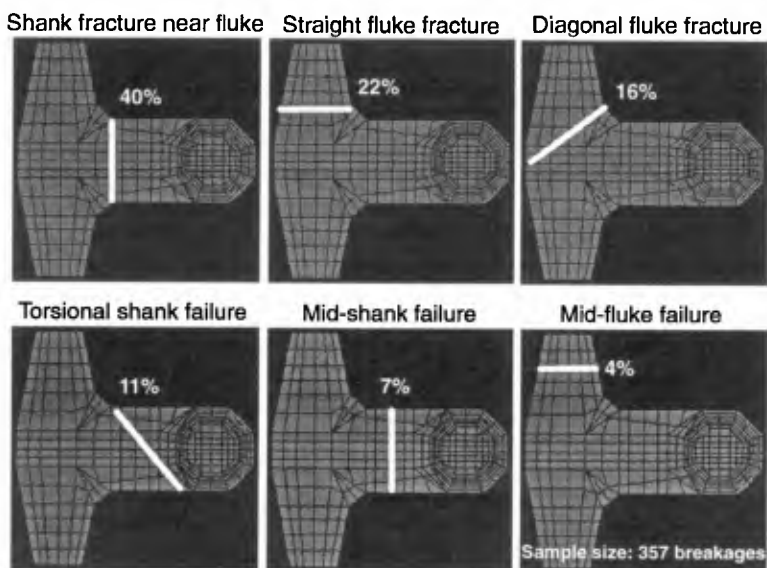


Figure 1. Distribution of prototype dolos failures

The six failure modes and the distribution of the failures are illustrated in Figure 1. The most common failure mode is a failure through the shank adjacent to a fluke. The four failure modes that originate near to the fluke-shank intersection account for 89% of the breakages.

The data set also indicated that dolosse with smaller waist ratios were more susceptible to failures through the shank. The dolosse with waist ratios of 0,31 had 86% shank failures and 14% fluke failures, while the dolosse with waist ratios of 0,34 to 0,36 had only 52% shank failures and 48% fluke failures. The chamfered or filleted units displayed proportionally more torsional failures (16% of all failures) than the dolosse with a sharp fluke-shank intersection (8% of all failures).

**Modifications to the Fluke-Shank Intersection**

The original dolos shape had a sharp fluke-shank intersection (Merrifield and Zwamborn, 1966). Based on photo-elastic stress analysis Lillevang and Nickola (1976) suggested a fillet with a radius of 0,04H, while Tait and Mills (1980) performed fatigue tests on model dolosse including one with a fillet radius of 0,175H. The shape given in the Shore Protection Manual (CERC, 1984) has a chamfer with a dimension of 0,057H. Rosson and Tedesco (1992) performed finite element simulations of the drop test using chamfer sizes of both 0,06H and 0,10H.

Based on the prototype breakages, it is expected that a stronger and more structurally-balanced dolos shape can be developed by further strengthening the fluke-shank intersection. Finite element models were therefore generated for six geometries of fluke-shank intersection. Each model had approximately 1900 quadratic elements and 8500 nodes. The six meshes are illustrated in Figure 2.

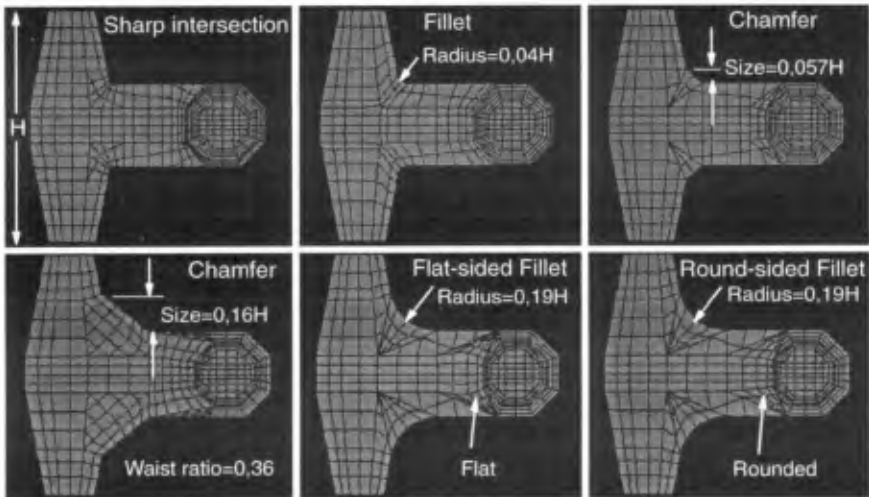


Figure 2. Shapes modelled in F E analyses



The top three shapes in Figure 2 are existing designs representative of the broken prototype dolosse analysed above. The bottom three shapes are new shapes aimed at strengthening the fluke-shank intersection. The dolosse all have a waist ratio of 0,36 while the height (H) was varied to ensure that all shapes had the same mass. The large chamfer extends to the middle of the shank and the angle between the chamfer and the shank is equal to the angle between the chamfer and the fluke. This gives a chamfer size of approximately 0,16H at a waist ratio of 0,36. The large fillet also extends to the middle of the shank which results in a radius of approximately 0,19H at a waist ratio of 0,36. Two different shapes incorporating the large fillet were tested. For the first shape the sides of the fillet consist of flat surfaces while for the second shape the sides of the fillet are rounded to intersect the shank and fluke smoothly.

### Static Finite Element Analyses

A series of static finite element analyses was performed in order to compare the maximum principal tensile stresses for each of the six dolos shapes. Linear elastic material behaviour was assumed and the results are thus only applicable up to the initiation of cracking. The following material properties were used: Density 2400 kg/m<sup>3</sup>, Young's modulus 27 GPa, Poisson's ratio 0,17.

The loading and boundary conditions applying to dolosse on a breakwater are extremely varied and complex and cannot therefore be reproduced in a deterministic finite element analysis. Only three simplified loading conditions (Figure 3) were analysed. The hanging load case was assumed to represent the shank fractures near to a fluke (40% of prototype fractures - refer to Figure 1). The fluke load represents the straight and diagonal fluke fractures (38% of prototype fractures) while the torsional load represents the torsional shank failures (11% of prototype fractures).

The surface stress distributions for the six dolos shapes due to the hanging load case are shown in Figure 4. The stress concentration in the sharp intersection can clearly be seen. The larger 0,16H chamfer does not reduce the stress compared to the 0,057H chamfer, due to the stiffer response of the larger chamfer. The lowest stress occurs for the 0,19H fillet with flat sides, due to the fact that this shape results in a slightly wider fillet than the 0,19H fillet with rounded sides. The torsional plots (Figure 5) show that the 0,16H chamfer again performs poorly. The 0,19H fillet with rounded sides shows the lowest stress. The 0,19H fillet with flat sides has a relatively sharp intersection between the flat sides and the shank which increases the stress in this area.

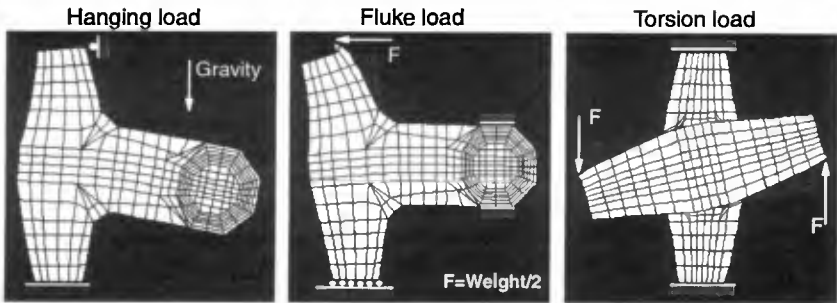


Figure 3. Static load cases

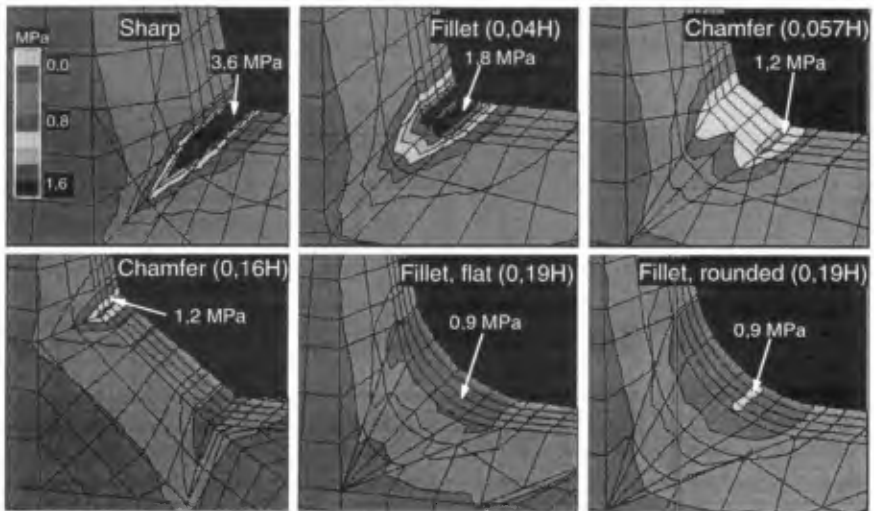


Figure 4. Principal tensile stresses - Hanging load case

Stress reduction factors were determined for each shape relative to the sharp intersection. These reduction factors were then weighted based on the relative frequency of each failure mode. 11% of the prototype failures occurred away from the fluke-shank intersection and this weighting was therefore applied to all the shapes. The results are summarised in Table 1.

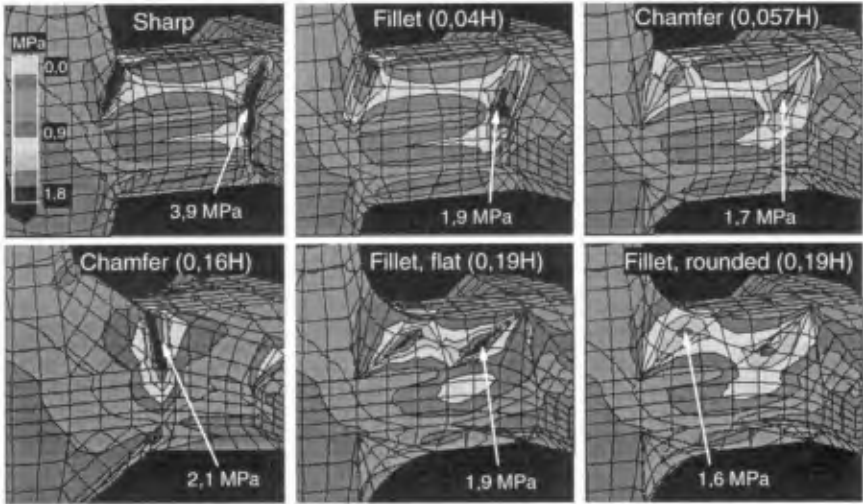


Figure 5. Principal tensile stresses - Torsional load case

	Load case	Geometry of fluke-shenk intersection					
		Sherp	Fillet (0,04H)	Chemfer (0,057H)	Chamfer (0,16H)	Fillet,flat (0,19H)	Fillet,round (0,19H)
Stress reduction factor relative to sherp shape	Shenk	1,00	0,51	0,33	0,34	0,24	0,26
	Fluke	1,00	0,52	0,38	0,47	0,29	0,30
	Torsion	1,00	0,49	0,44	0,52	0,49	0,41
Weighted reduction factor (weighting in brackets)	Shank (0,40)	0,40	0,20	0,13	0,14	0,09	0,10
	Fluke (0,38)	0,38	0,20	0,15	0,18	0,11	0,11
	Torsion (0,11)	0,11	0,05	0,05	0,06	0,05	0,04
	Other (0,11)	0,11	0,11	0,11	0,11	0,11	0,11
Total reduction factor	All	1,00	0,56	0,44	0,48	0,37	0,37

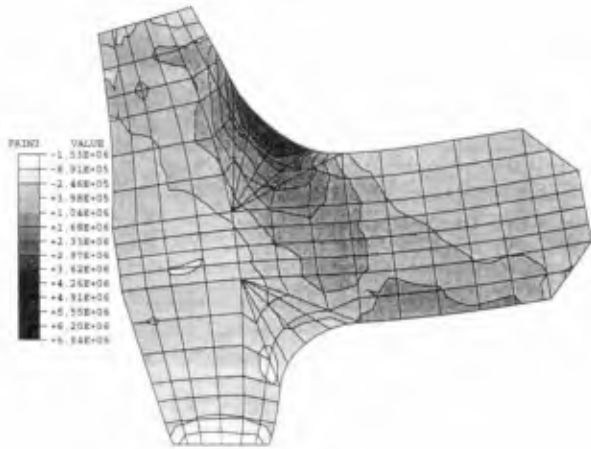
Table 1: Stress reduction factors for static loading

The two 0,19H fillet shapes show total static reduction factors of 0,37 compared to the sharp shape, 0,66 compared to the 0,04H fillet and 0,84 compared to the 0,057H fillet. In general, these modifications to the fluke-shank intersection do not reduce the torsional stresses as significantly as the stresses due to the hanging and fluke loads. This corresponds to the prototype breakages, where fillets or chamfers were found to increase the relative proportion of torsional failures.

**Dynamic Finite Element Analyses**

The response of the six dolos shapes to dynamic impact loading was also compared. The load case selected was the drop test (Burcharth, 1981). The material was modelled as linear elastic and no yield of the impacted surface was allowed. The implicit method of time integration was used with a constant time step of 5  $\mu$ s, which is approximately a quarter of the time required for a stress wave to travel between the integration points in an element.

The maximum principal tensile stresses occurred at the fluke-shank intersection, as illustrated in Figure 6. The computed stress reduction factors relative to the sharp intersection are presented in Table 2. These factors are similar to those computed for the static loads.



1,1 ms after impact, magnification factor = 1000

**Figure 6. Tensile stress distribution during drop test.**

	Geometry of fluke-shank intersection					
	Sharp	Fillet (0,04H)	Chamfer (0,057H)	Chamfer (0,16H)	Fillet,flat (0,19H)	Fillet,round (0,19H)
Drop test reduction factor	1,00	0,54	0,45	0,51	0,32	0,34

**Table 2: Stress reduction factors for dynamic loading**

## Conclusions

89% of prototype dolos breakages were found to occur near to the fluke-shank intersection. The static and dynamic tensile stresses at the fluke-shank intersection can be reduced by more than 60% by incorporating a large fillet extending to mid-shank. Although little difference in performance was found between the flat-sided and the round-sided fillet, the round-sided fillet is preferred due to its superior torsion resistance.

## Applications and Future Developments

The 0,19H fillet with round sides is being used for the repair of a number of breakwaters; the dolos sizes range from 7,5 to 30 t. A series of prototype drop tests has also been performed using 7,5 t dolosse with different fluke-shank intersections.

An aspect that has not been tested is the influence of the 0,19H fillet on the hydraulic stability of the dolos. A comparison between the profile of this shape and the 0,057H chamfer does reveal a large difference - the effect on the interlocking is thus expected to be small. This assumption must, however, still be tested by means of physical model studies.

## References

- Burcharth, H F (1981). Full-scale dynamic testing of dolosse to destruction. *Coastal Engineering Vol 4 No 3*.
- CERC (1984). *Shore Protection Manual*. US Army Coastal Engineering Research Center. US Government Printing Office, Washington DC.
- Holtzhausen, A H and Zwamborn, J A (1992). New stability formula for dolosse. *Proc 23rd ICCE*. Venice, Italy.
- Lillevang, O J and Nickola, W E (1976). Experimental studies of stresses within the breakwater armour piece "Dolos". *Proc 15th ICCE*. Honolulu, Hawaii.
- Merrifield, E M and Zwamborn, J A (1966). The economic value of a new breakwater armour unit "Dolos". *Coastal Engineering Vol 11*.

Rosson, B T and Tedesco, J w (1992). Dynamic response of dolos armour units to drop test impact loads. *Ocean engineering, Vol 19 No 6.*

Tait, R B and Mills, R D (1980). An investigation into the material limitations of breakwater dolosse. *ECOR Newsletter No 12.* Stellenbosch.

## CHAPTER 101

### Influence of Wave Directionality on Stability of Breakwater Heads

Y. Matsumi <sup>1</sup>, E.P.D. Mansard <sup>2</sup> and J. Rutledge <sup>3</sup>

#### Abstract

An experimental investigation was undertaken to investigate the stability of breakwater heads under uni and multidirectional wave attacks. Waves of normal and oblique incidence were used in the investigations and the stability results were assessed along with relevant measurements of wave surface elevation, measured in the proximity of breakwater heads.

#### INTRODUCTION

In spite of the growing number of multidirectional wave facilities around the world, breakwater designs are still evaluated using unidirectional regular or irregular waves, because it is widely believed that testing under unidirectional wave provides conservative results (i.e. overdesigned breakwaters). This may be true for the trunk section of the breakwater where the directional spread associated with the multidirectional seas tends to reduce the wave loads imparted on the structure. For the breakwater heads, this assumption is perhaps not valid. Because of the directional characteristics in multidirectional waves (i.e. 3D waves), some sections of breakwater heads may be exposed to larger wave heights than normally encountered under unidirectional waves (i.e. 2D waves).

---

<sup>1</sup> Associate Professor, Dept. of Social Systems Engineering, Tottori University, Tottori, Japan.

<sup>2</sup> Senior Research Officer, Institute for Marine Dynamics, National Research Council of Canada, Ottawa, Canada.

<sup>3</sup> Port & Marine Dept., Sandwell Inc., Vancouver, Canada.

Generally, under unidirectional waves of normal or oblique incidence, the head sections of breakwaters are more susceptible to damage than their trunk sections owing to the large wave heights and velocities that result from processes such as refraction, diffraction and shoaling on and around the head sections. Because of this, researchers such as Jensen (1984) and Vidal et al. (1991) suggest that the weight of stones for the heads should be about 1.5 to 4 times the weight of armour stones in the trunk section.

Under multidirectional waves, the wave heights that a breakwater head section encounters through the various processes described above, are possibly made even larger due to waves directly attacking the breakwater from other directions. Therefore more wave loads are expected on the heads, resulting thereby in lower stability.

## EXPERIMENTAL SETUP

### Layout of the basin

The physical model tests were carried out, at the National Research Council of Canada, in the multidirectional basin of the Coastal Engineering Laboratory of the Institute for Marine Dynamics.

The basin used for this purpose has a length of nearly 20m and a width of 30m. Figure 1 shows a plan view of the experimental set-up. A sixty-segment wave generator is located along one of the 30m sides of the basin. Perforated expanded sheet absorbers, capable of limiting wave

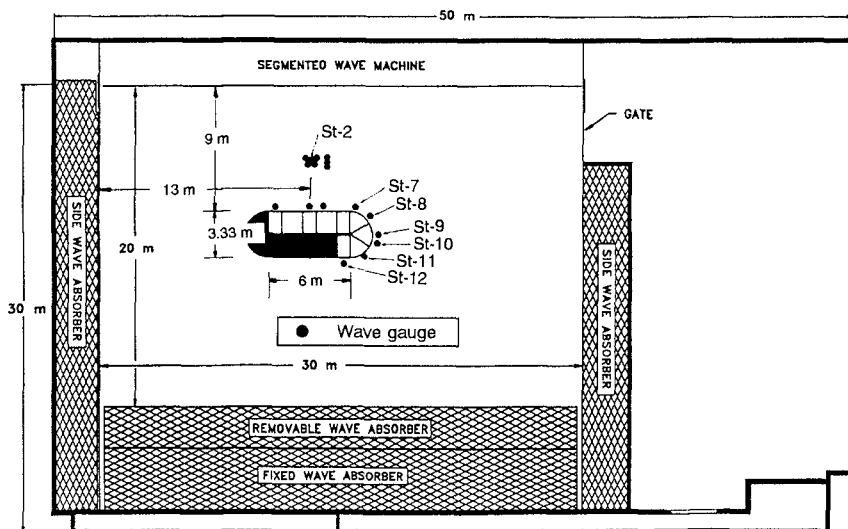


Figure 1. Plan view of the experimental set-up



reflections to 5% for most frequencies of interest, are installed along the remaining three sides of the basin. A 5m long gate and a closure plate of similar length at the two extremities of the wave generator are generally used for techniques that intentionally use corner reflection for increasing the size of the homogeneous area (see Figure 1).

#### Layout of wave gauges

The water surface elevations were measured at 17 different locations indicated by dots in Figure 1. Eight offshore wave gauges were mounted on two frames as a three-gauge and a five-gauge arrays. The three gauge array was set up to analyze the reflection of unidirectional waves of normal incidence by the methodology of Mansard and Funke (1987). The five gauge array was used to analyze the directional characteristics of normal and oblique incidence multidirectional waves with and without the structure in position. The remaining nine wave gauges were placed in the proximity of the model at a distance of 0.5m away from the toe of the structure, at locations shown in Figure 1. (Note that St stands for wave gauge station).

#### Layout of breakwater model

The layout of the breakwater model had to be designed carefully in this study, for the reasons indicated below.

Although sophisticated techniques have been developed to simulate the directional characteristics of the natural sea states inside laboratory environments, the area over which the sea state can be homogeneous in a wave basin is limited because of processes such as diffraction and reflection (see Sand and Mynett, 1987). Therefore careful consideration had to be given in order to ensure similar sea state severities along the entire breakwater section. For this purpose, use was made of the WAGEN model which could predict the water surface elevation and kinematics of the sea states prevailing at different locations in the basin. This model, developed by Isaacson (1992), is based on the boundary integral equation and linear diffraction theory and can account for partial reflection from structures such as breakwaters. A sample output resulting from this program is presented in Figure 2. It illustrates the spatial distribution of wave heights in the basin without the breakwater model, under a multidirectional sea state. The expected wave heights presented in this figure were normalized with respect to target wave heights. Note that their maximum value is only 0.9. This is due to diffraction processes and can be increased by applying an amplification factor. It can be seen from this figure that the useful test area, over which the sea state is homogeneous, is limited by a triangular boundary. According to this figure, the best location for the model would be close to the paddle. However, since this wave basin is not yet equipped with active absorption, an optimum location which would simultaneously ensure an homogeneous sea state

and minimize re-reflections from the paddle had to be chosen.

Since the model breakwater occupied only a portion of the basin width, reflected waves were expected to dissipate through diffraction processes before they are re-reflected by the paddles. Furthermore, since the proposed breakwater geometry had a symmetrical layout, it was considered justifiable to study only one of its head sections. Based on these different criteria, the model was located, as shown in Figure 1, at a distance of 9m from the paddle, and it was also offset by 2m from the center line.

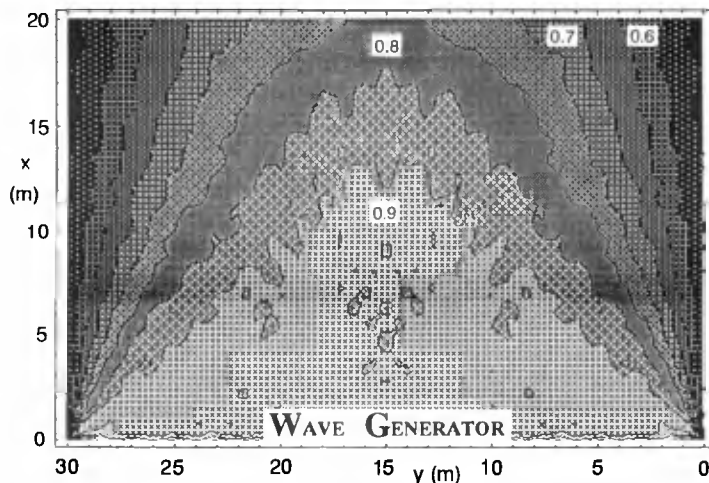


Figure 2. Spatial distribution of wave heights in the basin without the breakwater in place

#### Characteristics of breakwater model

Figure 3 shows both plan and profile views of the breakwater model. In order to achieve a better insight into the individual performance of the various breakwater components, nine sections of interest were separated from the total structure by using a steel frame with different components. Figure 3 shows the six trunk and the three head sections included in the study. The three head sections, called Front Head (FH), Middle Head (MH) and Back Head (BH), cover an area enclosed by an angle of  $60^\circ$  as shown in Figure 3. The remaining parts of the breakwater were covered with a steel mesh having square openings of 1x1cm in size, in order to avoid rebuilding the entire breakwater after every test.

The breakwater was of conventional type, composed of two layers of armour, a filter layer and a relatively porous core. Its height was 80cm and it performed as a non-overtopping structure in a water depth of 50cm. The

front and rear slopes were 1:2. Similar stone weights were used both in the trunk and head sections intentionally, in order to ensure high damage on the head section. One of the main reasons for this is that an accurate assessment of the wave height that causes small degrees of damage is generally difficult because of the experimental variability associated with effects such as interlocking (see Davies et al., 1994).

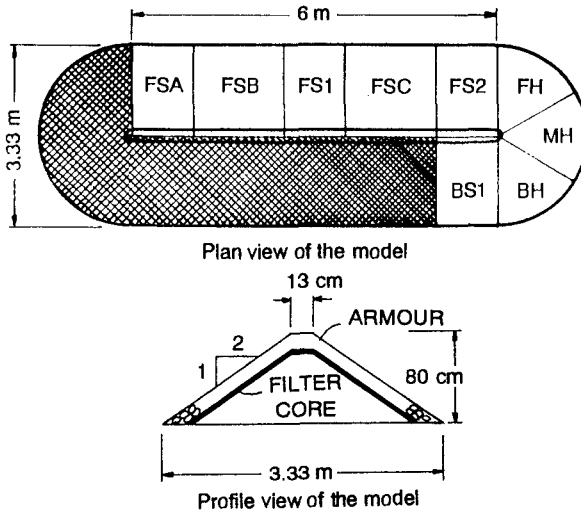


Figure 3. Plan and elevation views of the breakwater model

The characteristics of the core, filter and armour stones used in the experiments are presented in Table 1. The gradations of the armour stone were meticulously checked and the resulting  $D_{n85}/D_{n15}$  ratio for the armour was 1.3. In order to differentiate the various layers, each layer of armour stone and the filter layer were painted with a unique color. With this color scheme, the level of damage in each section could be easily ascertained by visual observation and photographs.

### Measurement techniques

The profiles of the trunk and head sections of the breakwater were measured using the electro-mechanical profiler described in Davies et al. (1994). The profiles taken in the direction normal to the wave paddle, were generally spaced 10cm apart in the trunk and head sections. The head section profiles were then converted into polar coordinates to obtain profiles every  $5^\circ$ . Since the head was subdivided into 3 sections, each covering an

area enclosed by 60°, an average of 11 profiles was used to quantify the damage in these sections.

The eroded area in the head and trunk sections was computed after each test using average profiles of original and final cross-sections. The damage index,  $S$ , was then calculated by normalizing the eroded area with the square of the armour stone's nominal diameter.

Besides establishing damage values by profile data, visual observations were also used to classify the degree of damage according to the four classifications suggested by Vidal et al. (1991): Initial damage, Iribarren's damage, start of destruction and destruction.

To further assist the estimation of damage, color photographs of each individual section were taken after each test. In addition, video pictures were used to record the entire experiment.

Table 1. Summary of the breakwater characteristics

$W_{50}$ weight of armour (g)	118
$W_{50}$ weight of filter (g)	15
$W_{50}$ weight of core (g)	2
$D_{n50}$ nominal diameter of armour (cm)	3.54
porosity	0.45
length of trunk (cm)	600
diameter of head (cm)	333
crest breadth (cm)	13
height of breakwater (cm)	80

$$D_{n50} = (W_{50} / \rho_s)^{1/3}, \rho_s : \text{unit weight of armour unit}$$

## TEST SERIES

Table 2 indicates the characteristics of the waves used in the experiments. The spectra were of the JONSWAP type with two different peak periods ( $T_p = 1.4s$  and  $T_p = 1.7s$ ). The peak enhancement factor  $\gamma$  was chosen to be equal to 3.3. The multidirectional waves were simulated using the well known Single Summation Method in order to eliminate spatial variability of sea states. Since the objective of this study was to assess the sensitivity of damage to spreading of the wave energy, the commonly used  $\cos^{2s}$  model was chosen for directional distribution. Values of  $s=2$  resulting in  $\cos^4$  and  $s=\infty$  were applied to simulate multi and unidirectional waves respectively. In order to assess the influence of obliqueness, two different mean angles of incidence  $\bar{\theta}=0^\circ$  and  $-15^\circ$  were used, ensuring at the same time homogeneity of the sea state at all sections of interest.

In order to minimize statistical variability associated with short lengths of wave records, a recycling period of 20 minutes (in model scale) was used in the synthesis by the Random Phase Method. This length corresponded to about 1000 waves when  $T_p=1.4s$  and 850 for  $T_p=1.7s$ . The ratios of diameter of the head over wave length and length of trunk over wave length are indicated in Table 2.

Eight test series were carried out using different combinations of spreading index and mean angle of incidence. In each series, the spectrum-based significant wave heights  $H_{m0}$  were increased from 5 to 15cm in steps of 2.5cm. Most of these sea states were pre-calibrated in the basin without the structure in position, while keeping all 17 gauges in place.

Tests under each value of  $H_{m0}$  were run until the stabilization of damage. This was achieved in about 2000 to 5000 waves.

Table 2. Characteristics of waves in experiments

Spectrum	$T_p$ (s)	$\gamma$	$\bar{\theta}$ (deg.)	s	$T_R$ (min.)	N	D/L	TL/L
JONSWAP	1.4	3.3	0, -15	$2, \infty$	20	1028	1.3	2.3
JONSWAP	1.7	3.3	0, -15	$2, \infty$	20	847	1.0	1.8

### RE-REFLECTIONS IN THE TEST SET-UP

The reflection characteristics of the breakwater were estimated by the NRC algorithm, under unidirectional waves of normal incidence. Figure 4, which summarizes these results, shows the reflection coefficient,  $C_r$ , to be in the order of 20 to 25%. Although the steepness parameter,  $H_{m0}/L$ , used in the abscissa of the figure, incorporates the relevant wave length of the sea state, longer periods result in higher reflection coefficients.

Table 3 provides a summary of wave heights measured under different experimental combinations for one particular severity of the sea state (i.e.  $H_{m0}=12.5cm$ ).

The description of the various parameters presented in this table is given below.

- $H_{m0}$  is the target significant wave height;
- $H_{m0\_no}$  is the significant wave height measured without the structure at the gauge 2. (This is the middle gauge in the 5 probe array);
- $H_{m0\_with}$  is the significant wave height measured during the experiments by the gauge 2; and
- $H_{m0,i}$  is the incident wave height resolved by reflection analysis.

This table shows that the estimation of the incident wave heights is within an accuracy of 2.5%, while the build-up of wave heights due to re-reflections is in the order of 3.6%. (This small degree of re-reflection was also confirmed by running some regular wave tests and monitoring the build-up). Because the reflection and the re-reflection were small in this set-up, it was considered justifiable to use the wave heights measured by gauge 2 with the structure in position, as the reference wave height in the stability analysis.

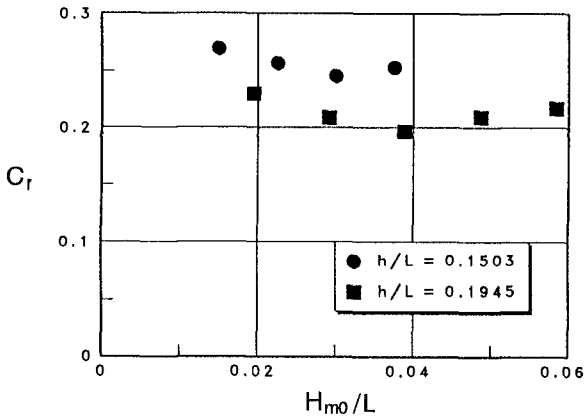


Figure 4. Reflection characteristics of the breakwater

Table 3. Comparison between different estimates of the significant wave heights when the target  $H_{m0}=12.5\text{cm}$

Wave condition	$H_{m0}$ (cm)	$H_{m0\_no}$ (cm)	$H_{m0\_with}$ (cm)	$H_{m0,i}$ (cm)
2D normal waves	12.5	12.83	13.30	12.53
2D oblique waves	12.5	12.83	13.71	-----
3D normal waves	12.5	12.81	12.33	-----
3D oblique waves	12.5	13.04	13.25	-----

RESULTS OF BREAKWATER STABILITY

The analysis of the results from these eight test series, on the stability of the relatively large number of test sections is still proceeding. This paper presents some of the first findings on the stability of head sections. A complete presentation of the results will be given in Matsumi et al. (1995).

### Influence of wave periods

Given the difference in wave lengths under the two peak periods, substantially different patterns of wave diffraction were found in the two cases. In fact, along the trunk section, the non-uniform pattern of damage reported by Vidal et al. (1991) was also found in this study under unidirectional waves. (All results related to trunk sections will be presented in Matsumi et al., 1995). For the head sections, the difference in stability between uni and multidirectional waves was relatively small when  $T_p$  was equal to 1.4s. Numerical simulation of wave heights and kinematics is required to provide a better insight of the influence of wave period. Therefore in the next section, only those results that correspond to 1.7s will be discussed.

### Comparison between the damage under unidirectional waves with normal and oblique incidence

In order to facilitate the interpretation of stability results, the significant wave heights measured at different locations in the proximity of the heads were computed and normalized with respect to the significant wave height measured at gauge 2. (The rationale for using the 2<sup>nd</sup> gauge was discussed earlier).

Figure 5 shows the results of the wave height ratios and the resulting stabilities for unidirectional waves under normal and oblique incidence. Although the difference in the values of significant wave heights realized under normal and oblique wave conditions is small, the stability results show more damage under oblique waves with  $\bar{\theta} = -15^\circ$ .

In order to achieve a better understanding of these results, the numerical model WAGEN, described earlier, was used. Assuming a partial reflection of 30% from the breakwater, the horizontal velocity components in the x and y directions were computed using a regular wave of 1.7s. (Note that x direction is normal to the wave machine, and y direction is parallel to it).

Figures 6a and 6b show the resolutions of the dominant directions of velocity components under normal and oblique wave conditions respectively. It can be seen that these are directed towards the FH section under oblique waves, while under normal waves they wrap around the section. This focussing pattern is believed to be responsible for causing higher damage in FH section when  $\bar{\theta} = -15^\circ$ .

In order to explore the reasons for similar increase in the damage of MH and BH sections, a refraction analysis was carried out using simple cases of regular waves. The intervals between wave rays were found, in this analysis, to be narrower under oblique waves, implying more concentration of energy and thus resulting in lower stability.

The higher damage on the front head under unidirectional waves is however not common for traditional structures. According to Jensen (1984)

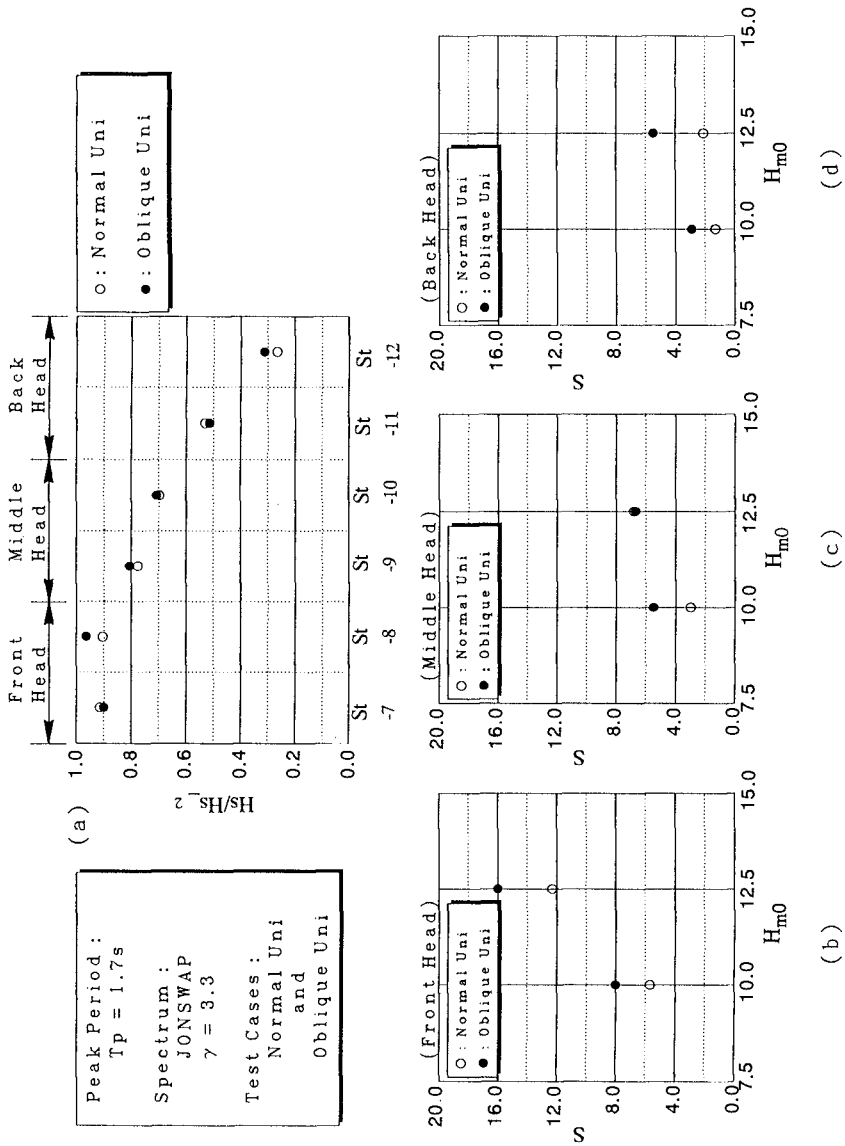


Figure 5. Comparison of significant wave heights around the head, and of damage index, under unidirectional normal and oblique waves



the most susceptible section for damage is at angle of about  $90^\circ$  to  $135^\circ$  relative to the incident wave direction. However for berm breakwaters, which are generally composed of smaller stones than those used in conventional structures, Jensen and Sørensen (1991) report damage to the front head sections. It is therefore possible that the reason for the higher damage in this study is the small gradation of stones used intentionally to cause larger degrees of damage.

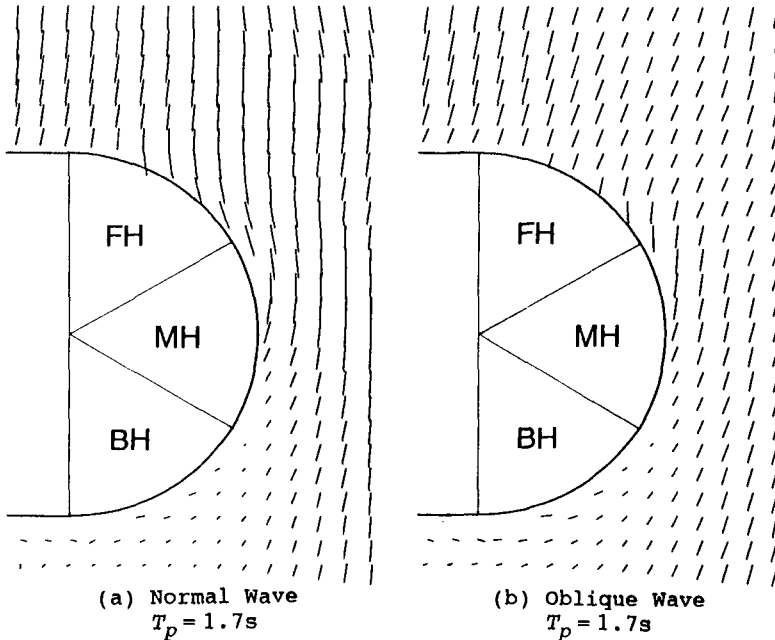


Figure 6. Dominant directions of velocity components under normal and oblique waves (Regular wave  $T=1.7s$ )

#### Comparison between damage under normal uni and multidirectional waves

Figure 7 shows a comparison of the significant wave heights around the head for normal uni and multidirectional waves. It can be seen that the directional spread under multidirectional waves has increased the wave heights on the head sections. This implies higher wave loading under these waves, and the stability results presented in this figure also confirm this fact. However, the difference in damage between uni and multidirectional waves is largest in the MH section when  $H_{m0}$  was equal to 12.5cm. Under

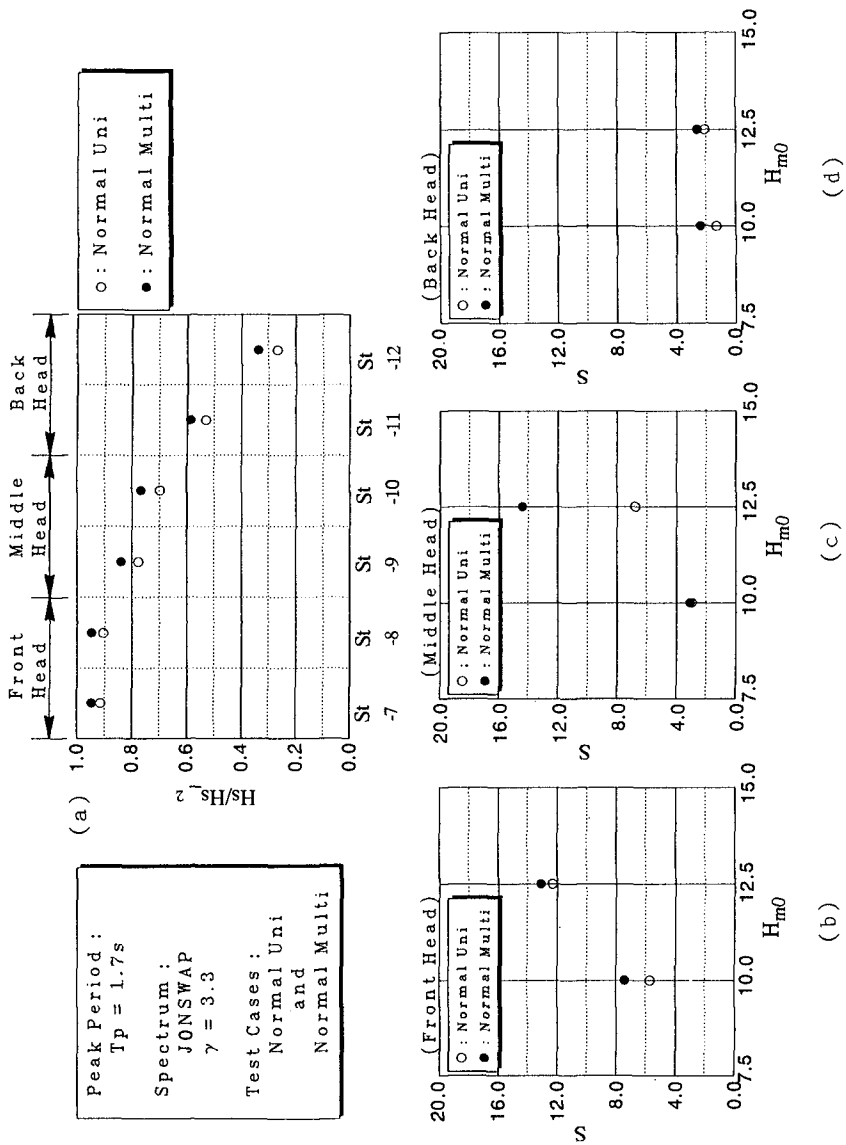


Figure 7. Comparison of significant wave heights around the head, and of damage index, under uni and multidirectional normal waves



Figure 8. Uniform damage pattern in MH section under unidirectional normal waves

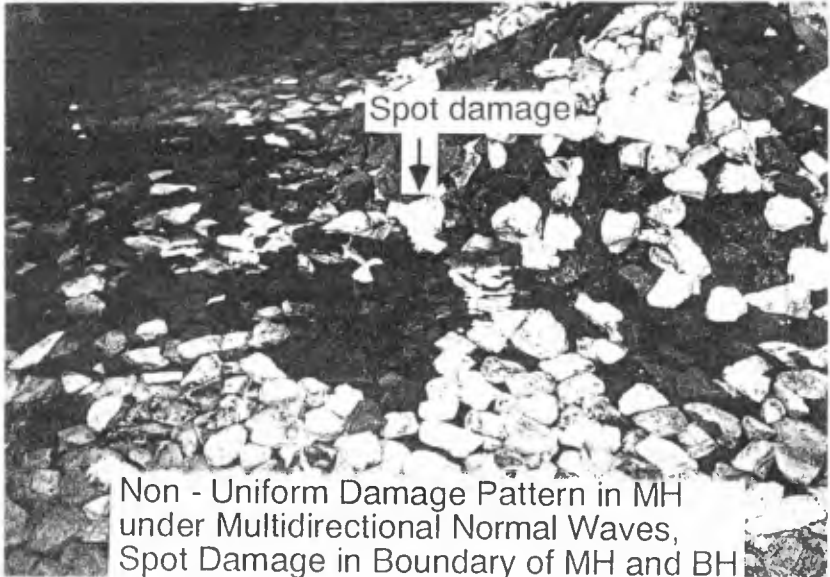


Figure 9. Spot damage pattern in near boundary between MH and BH sections under multidirectional normal waves

unidirectional wave attack, the damage is found to be uniform near the waterline because of the high velocities generated by refraction, shoaling and diffraction processes. In the case of multidirectional waves, the co-existence of the above processes added to the incidence of oblique waves, has resulted in severe spot damage near the boundary between the MH and BH sections (i.e.  $90^\circ$  to  $135^\circ$ ). Figures 8 and 9 present the photographs corresponding to these damages.

For  $H_{m0}=10\text{cm}$ , it is difficult to find any difference between the results of uni and multidirectional waves. The reasons for it are unclear, but are possibly due to experimental variabilities found under low degrees of damage.

To achieve a better insight into the reasons for the increased damage, some velocity measurements were made at St9 and St11, as a continuation of the present study, by the principal author at the Tottori University. The results indicate that the y-component velocities under 3D waves are larger by nearly 1-1/2 to 2 times the values measured under 2D waves. These findings support the stability results presented above.

#### Comparison between damage under oblique uni and multidirectional waves

Under oblique incidence, the multidirectional waves result in large significant wave heights on the middle and back head sections in comparison to the heights obtained under 2D seas. The resulting damages do not display a consistent trend except in the MH section where higher damage was observed under 3D waves when  $H_{m0}$  was equal to 12.5cm. However, the velocity measurements described earlier clearly display larger y-component velocities under 3D waves.

For the FH section, the damages under unidirectional waves are larger than those caused by multidirectional waves (see Matsumi et al. 1995).

#### CONCLUSIONS

In this particular test program, some correspondence was found between the wave heights measured in the proximity of the heads and the resulting damage. A clearer picture emerged when the x and y components of the velocity field were analyzed.

The front head section of the breakwater suffered substantial damage under all combinations of sea states owing to the small gradation of stones used in the tests. For waves of normal incidence, damage on FH section was larger under 3D waves due to directional spreading. However, with  $\bar{\theta}=-15^\circ$ , the trend was opposite (i.e. unidirectional waves induced more damage).

The MH section is more prone to damage under 3D waves because of the co-existence of processes such as refraction, diffraction and shoaling, along with the possibility of direct attack from other directions.

Further analysis of wave kinematics at the Tottori University as a continuation of this test program is expected to provide a better insight into the damage pattern.

### ACKNOWLEDGMENTS

The authors are very grateful to the Institute for Marine Dynamics of the National Research Council of Canada for generously providing the facilities for these experiments.

### REFERENCES

Davies, M.H., Mansard, E.P.D. and Cornett, A.M. (1994), "Damage Analysis for Rubble-Mound Breakwaters", Proc. 26th int. conf. on Coastal Engineering, Kobe, Japan.

Isaacson, M., (1992), "Diffraction Model of Directional Wave Generation in a Basin with Partially Reflecting Boundaries", Report prepared for National Research Council of Canada.

Jensen, O.J., (1984), "A Monograph on Rubble Mound Breakwaters", Danish Hydraulics Institute, Denmark

Jensen, O.J. and Sørensen, T., (1992), "Hydraulic Performance of Berm Breakwater Heads", J. of Hydraulic Research, IAHR, Vol.29, No.6.

Mansard, E.P.D. and Funke, E.R., (1987), "On the Reflection Analysis of Irregular Waves", Hydraulics Laboratory Tech. Report TR-HY-017, National Research Council of Canada.

Matsumi, Y. Mansard, E.P.D. and Rutledge, J. (1995), "Influence of Multidirectional Waves on Breakwater Stability", National Research Council of Canada, Tech. Report (in preparation).

Sand, S.E. and Mynett, A.E. (1987), "Directional Wave Generation and Analysis", Proc. IAHR Seminar on Wave Analysis and Generation in Laboratory Basins, 22nd IAHR Congress, Lausanne, Switzerland.

Vidal, C., Losada, M.A. and Medina, R., (1991), "Stability of Mound Breakwater's Head and Trunk", Journal of Waterway, Port, Coastal and Ocean Engineering, ASCE, Vol.117, No.6, Nov/Dec.

## CHAPTER 102

### COST-EFFECTIVENESS OF D-ARMOR BREAKWATER

Josep R. Medina,<sup>1</sup> Member ASCE

#### ABSTRACT

The cost-effectiveness of conventional and D-armor breakwaters are compared. Initial cost and capitalized anticipated damage during the lifetime of the structure are the basic elements to be considered in the economic optimization problem. A four level structural response function and a linear initial construction cost estimation are used to define the economic function. An exponential approximation to the return period of the design wave storm with an uncertainty factor is used to estimate the economic impact of the wave climate uncertainty. Finally, the adaptative design concept is introduced considering the advantages of designing for repairing and monitoring breakwaters after construction.

#### INTRODUCTION

During the last two decades, a variety of large mound breakwaters have failed in many regions of the world. The Working Group PIANC-PTCII (1985) analyzed more than 160 mound breakwaters all over the world. 28% of the large breakwaters (depth > 10 m., and  $H_s > 6.5$  m.), and 60% of the very large breakwaters (depth > 12 m., and  $H_s > 8.5$  m.) reported, were damaged after or during construction. Most of them were built with special concrete armor units. The position of mound breakwaters worldwide may be worse, because some of the most famous breakwater failures were not analyzed in the report (see Farrow, 1988). Some breakwaters like Sines (Portugal) at 50 m. depth were totally destroyed; other breakwaters like Bilbao (Spain) were partially damaged forcing expensive reparation and reinforcement works. These experiences generated a worldwide lack of confidence in the optimistic extrapolation of the design techniques of the sixties to new deep water conditions. The last decade has been characterized by the critiques

---

<sup>1</sup>Professor, Director of the Lab. of Ports and Coasts, Dep. of Transportation, Univ. Polit cnica de Valencia, Camino de Vera s/n, 46022 Valencia, SPAIN.

and controversy among different designers, constructors, researchers, and laboratories about the collapse of the old design techniques and the necessity of a significantly improved updated methodology to design mound breakwaters. We are now in a transitional phase between a traditional design methodology with a weak scientific and technical support, and a variety of new methodologies with weak real experimental support.

The cost-effective optimization of rubblemound cross sections requires an estimation of a variety of economic factors during the structural life cycle: initial construction cost, maintenance cost, economic losses due to the functional performance, capitalized costs to cover structural damages, and economic losses associated with total failure. Medina(1992a) presented a new design of a rubblemound breakwater cross section named the "D-armor breakwater", which showed similar resistance in the laboratory to the initiation of damage than conventional design but a significant increase of resistance to total failure. The characteristics of the D-armor design appears to be cost-efficient to face high uncertainties of the design wave conditions at the construction site. In this paper, a comparative analysis of the cost-efficiency of conventional and D-armor cross sections is presented. The D-armor breakwater shows a higher cost-effectiveness when uncertainty of design wave conditions and economic losses due to breakwater destruction increase.

A continuous effort has been developed towards a better understanding of the structural and hydrodynamic factors affecting the stability of rubble-mound breakwaters. There are two main goals of the research effort: a) New calculation procedures for a more reliable and accurate estimation of the structural response during the lifetime to optimize the designs; and b) New designs to reduce the construction cost, maintenance and risk of failure in its lifetime.

The design waves of a variety of maritime projects can only be estimated assuming large uncertainties. On the other hand, there are still significant differences in the calculation procedures proposed by different authors to estimate the structural response of conventional breakwaters for given wave conditions (see Medina, 1992a). Additionally, a number of concrete armor unit designs have been proposed and used in conventional cross sections. However, some of the most costly failures involved the use of special concrete armor units (Sines, San Ciprián, Tripoli, Arzew, Giona Tauro, etc.). Finally, some new breakwater cross sections are being proposed to reduce construction cost or to increase armor resistance. However, some failures have been reported recently (St. Paul berm breakwater) with only a few unconventional breakwaters actually built. This paper focuses the attention on the economic evaluation problem associated to breakwater cross sections.

A variety of alternative designs to the conventional rubblemound breakwater cross section have been proposed. The S-shape and berm type breakwaters are the most popular unconventional designs. In spite of the limited number of prototypes

built according to these new designs. There is an increased number of laboratory results which indicate some of their advantages. However, the current practice for the design and construction of mound breakwaters is conservative. The frequent breakwater failures, the unknown risks associated with designs that lack experimental verification, and a general aversion to risk of most decision makers, may explain the general opposition of designers to adopt radical changes in the classic mound breakwater cross section. This paper describes the economic comparative analysis of conventional and the D-armor breakwater concept that could be extended to other breakwater designs. The general goal is to provide an objective evaluation of the economic niche of each design concept. The D-armor breakwater seems to be a robust solution to face large uncertainties associated with long term wave actions at a construction site.

### D-ARMOR: A ROBUST DESIGN

Fig. 1 shows the cross sections corresponding to the Conventional (SPM, 1984), S-Shape (Ergin et al., 1989), and D-armor breakwater (Medina, 1992a). This paper compares the cost-effectiveness of D-armor and conventional mound breakwaters; the D-armor section reshapes to an efficient S-shape armor near the total failure point, and appears to be a reasonable first step towards a convenient evolution from the old conventional breakwater to more efficient designs.

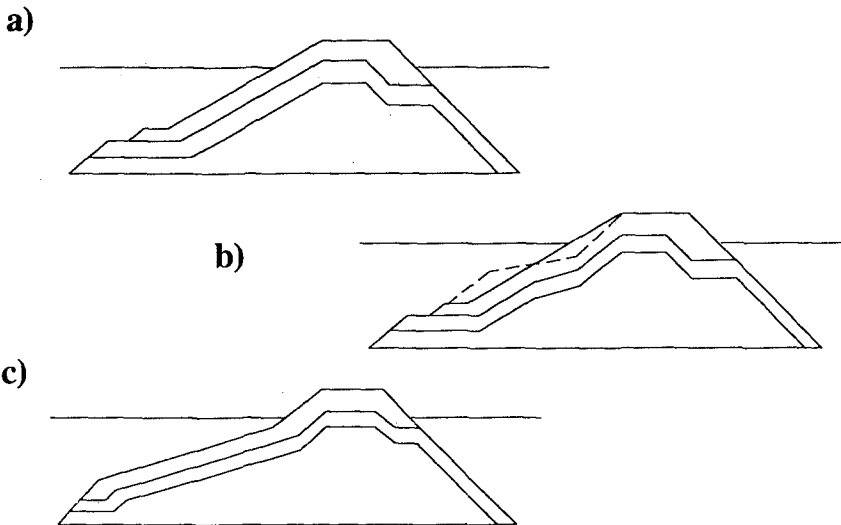


**Figure 1.- Rubble-Mound Breakwater Cross Sections: a)Conventional; b)D-Armor; and c)S-Shape.**



The D-armor model showed a similar initiation of damage, but a significant higher resistant capacity to total failure. Using the definition of armor damage proposed by Medina(1992a), for a structure with as much as 50% more armor erosion capability before total failure, it may be reasonable to consider a "initiation of damage" range as the identifiable damage below the extra active armor area of the D-armor section. Fig. 2 shows the failure functions corresponding to conventional and D-armor breakwater with a 2/3 reduction in the armor weight to equalize the total failure point. On the other hand, the failure function suggested by SPM(1984) for rough quarrrystones fits the line

$$\frac{H_{10}}{H_d} = \left[ \frac{D}{1.6} \right]^{\frac{1}{5}} \tag{1}$$

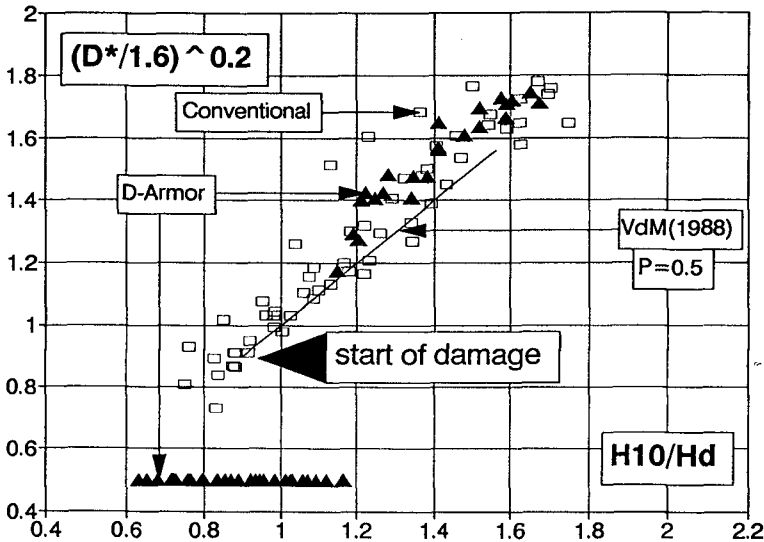


Figure 2.- Equalized Failure Functions of D-Armor and Conventional Breakwaters.

The sensitivity analysis included in the methodologies proposed by Medina(1989, 1992b) for the optimization of rubblemound breakwater cross sectional designs, increases the cost-efficiency of the resistant capacity to total failure, and the flexible structural response to wave attack shown by D-armor. On the contrary, a cost-efficient breakwater design, having brittle structural response, requires a reliable estimation of design wave conditions during its lifetime. From a structural point of view, the D-armor breakwater is similar to a conventional design with a significant increase of the armor thickness in the area where the mean water level crosses the external armor profile of uniform slope. Figs. 1-a and 1-b show the cross sections corresponding to the conventional and D-armor breakwaters.

Before damage, the external profile is the same; however, when armor erosion increases, the D-armor design progressively transforms to an S-shape breakwater (see Fig. 1-c). Because of this characteristic, the structural performance is similar to the conventional breakwater at low levels of armor erosion, but the reshaping process significantly increases the resistance capacity as an S-shape breakwater. Therefore, the D-armor design has the large structural response flexibility required to face the high levels of uncertainty usually associated with the design wave storms. Contrary to the conventional or S-shape breakwaters, the D-armor breakwater is designed to reshape significantly during its lifetime.

From the economic point of view, the structural response of conventional and D-armor breakwaters may be classified in four levels: (I) No armor movement, (II) Identifiable but acceptable armor movement (no repair needed), (III) Partial damages (repair needed but no port disruption), and (IV) Total failure (port disruption and breakwater reconstruction needed). Table 1 shows the  $H_{10}/H_{D=0}$  limits defining the structural response of conventional and D-armor breakwaters.

<b>RESPONSE</b>	<b>Conventional</b>	<b>D-Armor</b>
<b>I - II</b>	<b>0.87</b>	<b>0.87</b>
<b>II - III</b>	<b>1.00</b>	<b>1.25</b>
<b>III - IV</b>	<b>1.65</b>	<b>1.89</b>

**Table 1.-  $H_{10}/H_{D=0}$  Corresponding to the Threshold Levels Between Different Structural Response Stages.**

Most breakwaters are built at a construction site where the long term wave climate or the maximum water depth (MSL to sea bed) can only be estimated with large uncertainties. In those cases, low risk and economically-efficient solutions demand robust designs with a flexible structural response having a wide margin between initiation of damage and total destruction. To face large uncertainties in wave action, economic optimization leads to very conservative and expensive designs for brittle structural responses, and to less expensive and safer designs for flexible structural responses. In those conditions, the D-Armor breakwater seems to be a reasonable first step for a safe migration from the inefficient conventional breakwater to new structural and cost-efficient designs. It appears to have about the same construction cost at prototype scale, with higher stability and structural flexibility, making it appropriate to face high uncertainties in the design wave conditions at the construction site. Therefore, it seems to be a reasonable economically-efficient alternative to the conventional design in both deep and shallow waters.

## BREAKWATER COST-EFFECTIVENESS

Three decades ago, Van der Kreeke and Paape(1964) proposed a methodology to optimize breakwaters, considering initial construction cost and capitalized anticipated damage. The optimum design was dependent on the lifetime, the failure function and the long term wave climate. Mol et al.(1983) analyzed the failure of the breakwater at Port Sines (Portugal) and found the uncertainty of the wave climate to be an important factor to be taken into consideration when designing large breakwaters. A similar conclusion was found by C.E.L.(1983), demonstrating the impact of the uncertainty of long term wave climate on the cost of breakwaters in deep water conditions. Recently, Burchart(1991) reviewed design innovations and research contributions, remarking the importance of the procedures for estimating the uncertainties associated with wave data sets, extrapolation from short data samples and lack of knowledge of the long term distributions.

The uncertainty of the long term wave climate, not taken into account in breakwater design, has been found to be responsible of major breakwater failures in the past decades. The estimation of the wave climate uncertainty and the use of safety coefficients, is a first step towards a better rationalization of the optimum breakwater design problem. More elaborate probabilistic methods, considering estimated uncertainties of the principal wave climate parameters, are the natural evolution of the methods for optimization the breakwater design. During the next decades a significant effort will be made worldwide to reduce the uncertainty of the long term wave climate. Therefore, right now it is necessary to use methods and breakwater designs to face large uncertainties in deep waters.

The cost-effectiveness of alternative breakwater cross sections have to take into account not only estimated initial cost and risk to failure during the lifetime, but also the estimated uncertainty of the principal wave climate variables and the procedures to take advantage of monitoring programs for updating the estimated anticipated capitalized damage during the lifetime. The cost-effectiveness of structures with brittle response in deep waters is critically dependent on the reliability and uncertainty of long term wave climate. On the contrary, the structures with a flexible response are not so critical to a precise description of wave climate. Furthermore, an adequate monitoring program after construction can provide valuable information for a precise evaluation of risk during the lifetime, including additional works of repair and reinforcement.

If it is not possible to minimize the uncertainties of the wave climate which critically affects the risk of failure during the lifetime, it is reasonable to face those uncertainties with robust designs and reinforcement strategies based on adequate monitoring programs. The first years after construction may be the best one to one scale test, since most failures of most breakwaters occurs during this period. An adequate design and monitoring program may be useful to limit the risk of failure and to optimize the breakwater design.

## Initial Construction Cost

The initial construction cost of a breakwater depends critically on the technological and geological conditions. Although the model tests referred to rubblemound breakwaters of quarrystone, it will be assumed that the failure functions are also a reasonable first approximation for large mound breakwaters with robust concrete armor units. Some of the largest mound breakwaters with robust concrete armor units (cubic or parallelipedic blocks) are built on the Spanish coast. Two typical Spanish breakwaters are selected to define a reasonable initial construction cost function: 1)"Dique del Este" in the Mediterranean Port of Valencia, and 2)"Dique de Zierbana" in the Atlantic Port of Bilbao.

Del Moral and Berenguer(1980) published the optimization methodology applied to the "Dique del Este" of the Port of Valencia. The water depth was about 14 m and the  $H_{s100} \approx 8.5$  m. The authors proposed several cross sections following the Iribarren's design criteria for different design wave conditions ( $H_{sd}$ ). Because both monetary and wave climate parameters have different meaning in different countries and years, the costs have been made dimensionless by the cost corresponding to the design for one hundred year return period. The design wave storm have been made dimensionless by that corresponding to one the hundred year return period. In the case of Valencia, the following linear function was fitted:

$$C_0(H_{sd}) \approx C_0(H_{s100}) \left[ 1 + 1.1 \left( \frac{H_{sd} - H_{s100}}{H_{s100}} \right) \right] \quad (2)$$

where  $C_0(H_{sd})$  is the initial construction cost for a design significant wave height of  $H_{sd}$ , and  $H_{s100}$  is the significant wave height for one hundred year return period. In the Cantabric Sea open to the Atlantic Ocean, Uzcanga and González(1992) defined pre-designs for the "Dique de Zierbana" in the Port of Bilbao. The water depth was about 25 m. and the  $H_{s100} \approx 12$  m.. The function that fitted the cost estimation provided by the authors was:

$$C_0(H_{sd}) \approx C_0(H_{s100}) \left[ 1 + 1.5 \left( \frac{H_{sd} - H_{s100}}{H_{s100}} \right) \right] \quad (3)$$

Fig. 3 shows the dimensionless initial construction cost functions for the cases of Valencia and Bilbao. In the following, the initial construction cost of Bilbao will be used for the economic analysis of conventional and D-armor breakwaters. The economic function used to analyze the cost-effectiveness will be based on the initial construction cost function and the long term wave climate function containing an uncertainty factor. With these two basic elements, the economic problem will be reduced to define an economic function with the capitalized anticipated damages due to damages and risk to failure during the lifetime.

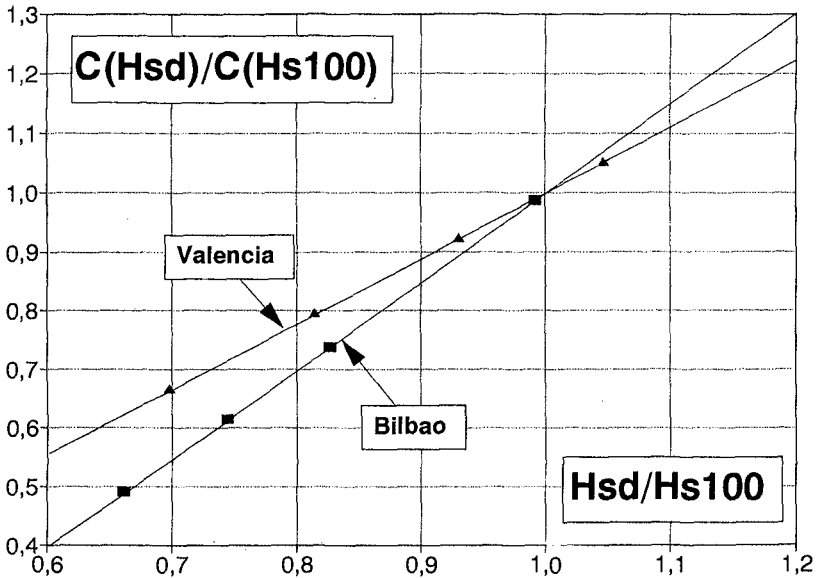


Figure 3.- Dimensionless Initial Construction Cost Functions Corresponding to Mound Breakwaters Built in Valencia and Bilbao.

## Wave Climate

There are a variety of statistical methods for estimating the long term wave climate to be considered in breakwater design. However, both data and methods have an evolution in time changing the "best" estimation to be considered in design. As an example, Copeiro(1978) published a long term wave climate for Bilbao which may be approximated by the following exponential approximation for the return period:  $R \approx \exp(H_s - 7.5)$ . Some years later, the Spanish Ministry of Public Works published a recommended manual for maritime design (ROM 0.3-91) with a long term wave climate for Bilbao which may be approximated by:  $R \approx \exp(H_s - 6.8)$ . In the future, it is reasonable to assume that both methods and data will contribute to modify the recommended long term wave climate for different locations.

In a specific location, in a given year, only an approximation to the real long term wave climate will be available, if that long term wave climate really exists. In addition to the number of sources of risk and uncertainty affecting the long term wave climate of a specific location, some doubts still remain about the interannual stationarity of the wave climate. Therefore, a reasonable way to take into consideration the global uncertainty in the long term wave climate, is to define a model for the return period affected by an uncertainty factor,  $\beta$ . The higher the  $\beta$ , the higher uncertainty on the estimated return period for the given location is

considered: If  $\beta=0$ , no uncertainty is considered for the wave climate.

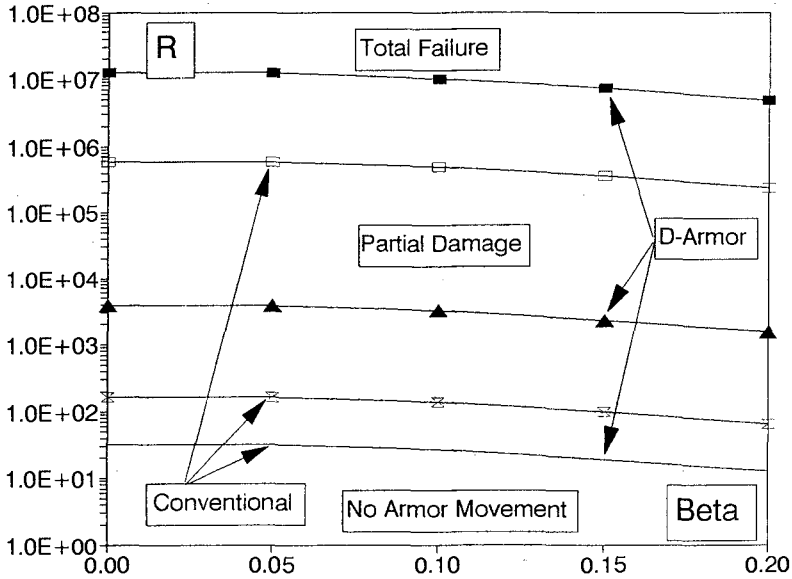


Figure 4.- Return Periods of Conventional and D-Armor Responses.

Taking as a basis an exponential approximation of the return period with a reasonable parameter, say  $R \approx \exp(H_s - 7.5)$ , an ensemble of possible scenarios with different return period functions may be considered. Eq. 4a shows the family of return period functions to be considered and Eq. 4b the return periods to be considered depending on the uncertainty factor.

$$R_i (H_s) \approx \exp(H_s - 7.5 + \beta \omega_i H_{s100}) \tag{4a}$$

$$R(H_s, \beta) = \frac{1}{E \left[ \frac{1}{R_i} \right]} ; E[\omega_i \cdot \omega_{i+k}] = 0, k \neq 0 ; \sigma_\omega^2 = 1 \tag{4b}$$

Eqs. 4a,b defines a one-parameter exponential function for the return period in which the parameter is considered a Gaussian random variable with a mean given by usual wave climate estimations and a standard deviation,  $\sigma(\beta\omega_i) = \beta$ , given by qualitative assessment considering all sources of risk and uncertainty involved in the

designing process. Figure 4 shows the return periods corresponding to the structural response limits shown in Table 1 for conventional and D-armor breakwaters.

## Economic Function

Using the design guidelines of Iribarren, Del Moral and Berenguer(1980) proposed a number of economic ratios that were considered in the economic evaluation of the Valencia breakwater. The most important ratios were: 1)Cost of the conventional armor  $\approx 45\%$  cost of the conventional breakwater, 2)Value of properties defended by the breakwater  $\approx 400\%$  cost of the breakwater, 3)Cost of partial repair  $\approx$  three times the initial construction cost, and 4)Cost of total reconstruction  $\approx$  twice the initial construction cost. In addition, comparing the volume of armor stones used by Medina(1992a) in the conventional and D-armor breakwater, two additional ratios may be used in the economic function: 5)Cost of D-armor  $\approx 50\%$  cost of the conventional breakwater, and 6)Cost of the D-armor breakwater  $\approx 105\%$  cost of the conventional breakwater.

In this paper, the economic function of both conventional and D-armor breakwaters are based on the economic ratios given above, the initial construction cost given by Eq. 3, the structural responses given by Eq. 1 and Table 1, the long term wave climate given by Eqs. 4a,b and the following anticipated capitalized formula to cover risk of failure

$$C_L(H_{sd}) = C_0(H_{sd}) + ac \left[ \frac{(1+i)^L - 1}{i(1+i)^L} \right] \quad (5)$$

in which  $L$  is the lifetime of the structure,  $ac$  is the annual cost to cover the risk of failure,  $C_0$  is the initial construction cost (including maintenance and monitoring in lifetime),  $C_L$  is the total cost (including repair and risk of failure), and  $i$  is the interest rate. The first component of Eq. 5 is an increasing function with the design significant wave height, because a larger and more expensive breakwater is required to resist a stronger design wave storm. On the contrary, the second component of Eq. 5 is a decreasing function, because the risk to failure decreases when the design significant wave height increases. Eq. 5 have a minimum value which corresponds to the optimum economic design point; however, the optimum design point depends on the selection of  $\beta$ ,  $i$ , and  $L$ , which are based on engineering judgement. Fig. 5 shows the economic functions ( $L=100$  and  $i=5\%$ ) of conventional and D-armor breakwater for different values of  $\beta$ . The total cost has been normalized by the initial construction cost of the conventional breakwater for the one hundred year return period significant wave height,  $C_0(H_{s100})$ . The design wave height,  $H_d$ , is related with the design significant wave height by  $H_d = 1.27 H_{sd}$ , which corresponds to the  $H_{10}$  of the design storm.

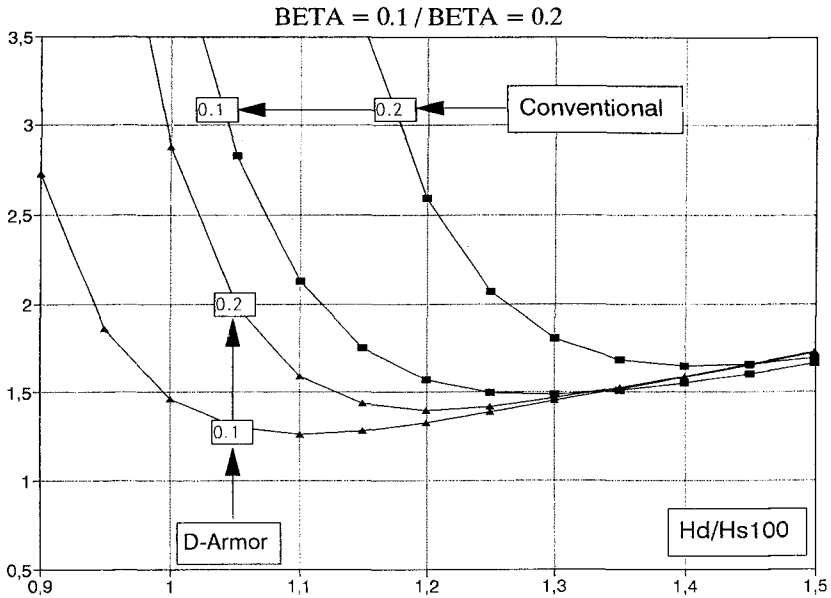


**Figure 5.- Dimensionless Total Cost of Conventional and D-Armor Breakwaters ( $L=100$ ,  $i=5\%$ ).**

The optima points with minima costs shown in Fig. 5 are sensitive to the subjective selection of  $L$ ,  $i$  and  $\beta$ . Therefore, the economic description of the conventional and D-armor alternatives would require not only the economic functions, but also a sensitivity analysis of the factors decided on the basis of judgement, specially  $\beta$ . A preliminary qualitative analysis of the economic functions shown in Fig. 5, shows an increase in the total cost for both the D-armor and conventional breakwaters when  $\beta$  increases. However, D-armor is more efficient because its economic function for  $\beta=0.2$  (high uncertainty) is similar to the economic function of conventional breakwater when  $\beta=0.0$  (no uncertainty).

## UNCERTAINTY AND ADAPTATIVE DESIGNS

According to Medina et al. (1994), most breakwater failures occurred during construction or within a few years after construction. It is obvious that the construction phase and the few years after construction, offers a unique opportunity for a reliable estimation of the risk of failure during the lifetime. An adequate monitoring program may provide a reliable basis for a decision of re-design or structural reinforcement or repair program during the lifetime. Robust designs with



flexible structural responses, like those shown in Table 1, are appropriate to put a limit on the risk to total failure during the monitoring phase. On the basis of robust designs, adaptative designs could be considered in advance to take full advantage of the information obtained during the monitoring phase after construction.

The adaptative design concept may be associated with designing for repairs. In other words, if it seems impossible to design for no damage during the lifetime, the best alternative is to design for having damage during the first years after construction. If the damage actually occurs, a structure designed to be repaired will have to be repaired. In addition, a reliable estimation of risk of failure will have been obtained during the monitoring phase during and after construction until partial damages were reported. If no damage is observed after construction, the reliable estimation of risk of failure during the lifetime obtained from the monitoring phase, will provide the guarantee that a supposed underdesigned breakwater is safe enough for the given lifetime. The economic advantage of the adaptative design concept is so evident than some engineering design strategies applied in practice may be considered in this category.

Two adaptative design alternatives were evaluated on the basis of the D-armor cross section, which was found to be robust enough to be appropriate for testing the new concept. Figs. 6 show the cross sections of the conventional and the two D-armor sections with short and long berm. The sections were very efficient in economic terms with 1.5:1 slope and less armor stone than the conventional breakwater. In order to analyze the structural performance of the two adaptative D-armor designs of Figs. 6, series of 2-D experiments were conducted at the UPV wave flume (30x1.2x1.2 m), divided in two parts to test simultaneously a conventional and a D-armor cross section with berm. A transparent glass divider was used for the verification of the same wave attack on the two cross sections during the experiments. Seven minutes of random wave generation of PM using the DSA-FFT method produced between 200 and 300 waves depending on the  $Ir$  value of the run. An Iribarren's number for random waves defined as  $Ir = [\tan \beta] / [2\pi H_{m0} / g T_{02}^2]^{0.5}$  was constant for all the runs of each test; two different values of  $Ir$  were used for each test ( $Ir = 2.5, 3.0$ ). Starting from the zero-damage design wave height,  $H_{10} = H_d = 12$  cm, the wave height was increased 10% each run ( $H_{10} = H_d [1.1]^k$ ;  $k = 1, 2, \dots, 7$ ). After the seventh run, the sections were re-built to a 2/1 slope, to continue the experiment until total failure of the armor layer.

The berm were found to be reasonably stable, but the behavior of the armors were different than expected in the pre-design phase. The section with short berm showed more resistance to total failure than the section with long berm. After the reinforcement, neither the section with short berm nor the section with long berm show a significant increase of the resistance to total failure shown by the D-armor breakwater with a 2/1 slope (Medina, 1992a). On the contrary, the conventional breakwater increased the resistance to failure after the reinforcement. Additionally, the volume of armor stones required to reinforce the conventional breakwater was significantly lower than the volume required for the sections with berm. Therefore,

the preliminary analysis of results, of the experiments on the two adaptative designs shown in Figs. 6, suggests than both the conventional and the original D-armor breakwater with no berm may be a better adaptative design alternative than those shown in Figs. 6.

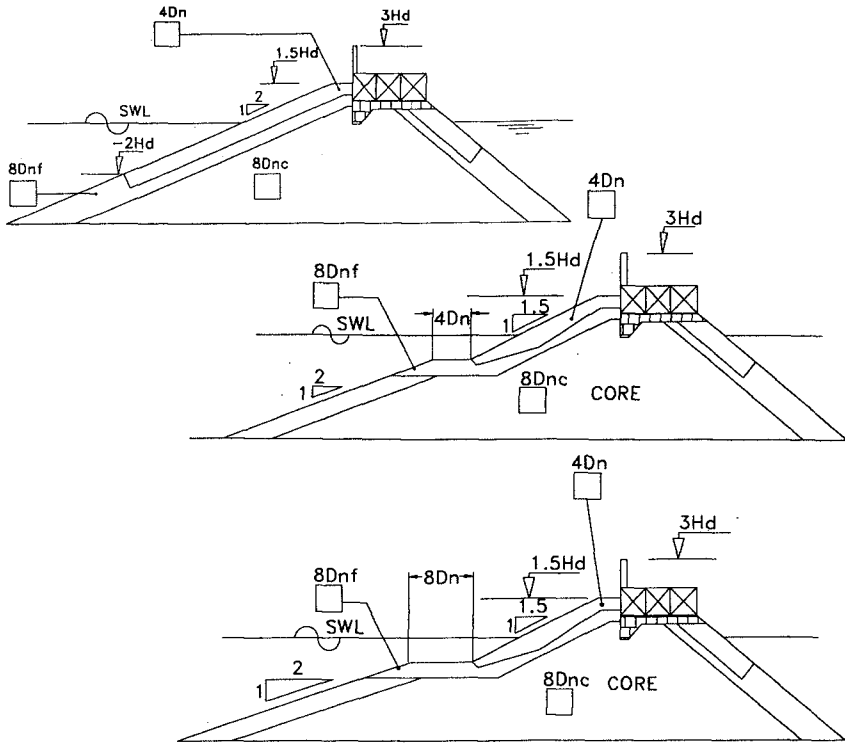


Figure 6.- Breakwater Cross Sections: a)Conventional, b)D-Armor with Short Berm, and c)D-Armor with Long Berm.

## CONCLUSIONS

The cost-effectiveness of conventional and D-armor breakwaters are compared considering different uncertainty levels on the wave climate. In deep water conditions, robust designs with flexible structural responses, monitoring programs and adaptative design strategies after construction, appears to be the rational elements for economic optimization of breakwater design.

## ACKNOWLEDGMENTS

The author gratefully acknowledge the financial support provided by the Dirección General de Investigación Científica y Técnica, under Grant PB92-0411.

## REFERENCES

- Burchart, H.F.(1991)**. Design innovations, including recent research contributions. *Proc. Coast. Struct. and Breakwaters'91*, Institution of Civil Engineers, London, England, 43-81.
- Cubit Engineering Limited(1983)**. Study to Evaluate the Impact of the Accuracy of Wave Statistics on the Cost of Rubble-Mound Structures. *Prepared for the National Ocean Survey, U.S. Department of Commerce*, Feb. 1983.
- Copeiro E.(1978)**. Extremal Prediction of Significant Wave Height. *Proc. 16<sup>th</sup> ICCE*. ASCE. 285-304.
- Del Moral, R., and Berenguer, J.M.(1980)**. *Obras Marítimas*, Servicio de Publicaciones del M.O.P.U., Madrid, 569 p. (in Spanish).
- Ergin, A., Gunbak, A.R., and Yanmaz, A.M.(1989)**. Rubble-Mound Breakwaters with S-Shape Design. *J. of Waterway, Port, Coastal and Ocean Engrg.* 115(5):579-593.
- Farrow, M.C. (1988)**. Construction Line of Business Manager. *Breakwaters'88*, ICE, Eastbourne (U.K.), 167-174.
- Medina, J.R.(1989)**. Cost-Effectiveness of Breakwater Cross Sections,(Discussion). *J. of Waterway, Port, Coastal and Ocean Engrg.*, ASCE, 115(4):572-574.
- Medina, J.R.(1992a)**. A Robust Armor Design to Face Uncertainties. *Proc. 23<sup>rd</sup> ICCE*, ASCE, 1371-1384.
- Medina, J.R.(1992b)**. Deterministic Computer-Aided Optimum Design of Rock Rubble-Mound Breakwater Cross-Sections, (Discussion). *Coastal Engineering*, 17(1992):279-283.
- Medina, J.R., Hudspeth, R.T., and Fassardi, C.(1994)**. Breakwater Armor Damage Due to Wave Groups. *J. Waterway, Port, Coastal and Ocean Engrg.* 120(2):179-198.
- Mol, A., Ligteringen, H. and Paape, A.(1983)**. Risk Analysis in Breakwater Design. *Breakwaters'83*, Institution of Civil Engineers, London, England, 81-87.
- PIANC-PTCII(1985)**. The Stability of Rubble Mound Breakwaters in Deep Water. *Report of a WG of a Permanent Technical Committee II*. Supplement to Bulletin N. 48, 28p.
- Recomendaciones para Obras Marítimas ROM 0.3-91(1984)**. Servicio de Publicaciones del M.O.P.T, Dirección General de Puertos, 76 p., (in Spanish).
- Shore Protection Manual(1984)**. Coastal Eng. Res. Center, Dep. of the Army, Waterways Exp. Stat., Vicksburg, Miss.
- Uzcanga, J., and González, B.(1992)**. Algunas Consideraciones sobre el Diseño de Diques, *Libro de Ponencias de las I Jornadas Españolas de Costas y Puertos*; 86-133, (in Spanish).
- Van de Kreeke, J. and Paape, A.(1964)**. On Optimum Breakwater Design. *Proc. 9<sup>th</sup> Conf. on Coastal Engrg.*, Lisbon, ASCE, 532-552.

## CHAPTER 103

### THE CORE-LOC: OPTIMIZED CONCRETE ARMOR

Jeffrey A. Melby, A.M. ASCE and George F. Turk<sup>1</sup>

**ABSTRACT:** This paper outlines the development and initial testing of a new optimized armor shape, called CORE-LOC, that balances and optimizes engineering performance features such as hydraulic stability, strength, and layer porosity. The new shape has significantly reduced design stresses over many existing shapes, yet has superior interlocking and therefore greater stability. The unit has internal maximum tensile stress levels of approximately half that of dolosse and, therefore, should not need reinforcement. For over 1000 flume tests, the core-loc has demonstrated two-dimensional no-damage stability numbers over 7 and Hudson stability coefficients over 250. In nearly all tests, the core-loc layer could not be damaged up to the wave height-period capacities of the flumes. A site-specific three-dimensional stability test of the proposed Noyo, California, offshore breakwater showed a stable no-damage stability number of 2.7 for  $H_s$  or a Hudson stability coefficient of 13 when the core-loc armor layer was exposed to repeated attack of a very severe design-level storm. The unit has been designed to be used alone or as a repair unit for dolosse. Core-loc-repaired dolos model slopes showed improved stability over the original dolos slopes. Finally, through reduced volumes, the core-loc layer is substantially more economical than all other commonly-used randomly-placed armor.

## INTRODUCTION

The U.S. Army Corps of Engineers (USAE) maintains over 1500 rubble

---

1) Research Hydraulic Engineers, Coastal Engineering Research Center, USAE Waterways Experiment Station, Vicksburg, MS, 39180

structures, 17 of which are protected by concrete armor units. Seven additional concrete armor layer projects are planned or are in the preliminary design phase. The Corps has primarily used dolos and tribar armor units but has also used tetrapods, quadripods, blocks, and tetrahedrons. Interest in concrete armoring has increased in the U.S. recently because stone quarries are becoming inaccessible due to increasing environmental constraints. Also, the existing armor shapes have not performed well, with significant breakage due to instability and structural fragility (Melby and Turk 1994a).

Recently, significant inroads into understanding slender armor unit structural response have been made. Terao et al. (1982), Burcharth (1981), and Melby and Turk (1994b, 1994c) developed and verified armor impact scaling criteria. Zwamborn and Phelp (1990) made measurements of prototype impact response. Timco and Mansard (1982) discussed scaled tensile strength modeling. Howell (1988), Melby and Howell (1989), Howell et al. (1990), and Kendall and Melby (1990, 1992), discussed the first measurements of internal strains in in-situ prototype dolosse as part of the Crescent City Prototype Dolos Study. These measurements led to the calibration for hydrodynamic loading of load cell instrumentation, similar to that developed by Scott et al. (1986), for laboratory measurement of dolos structural response (Markle 1990).

One of the primary conclusions from the Crescent City study was that the maximum wave loading-induced stresses were less than the static mean stress, for large dolosse. So static stresses dominate the structural design of stable non-rocking dolosse. This made accurate measurements of static strains very important; but the prototype data were insufficient to quantify static response because only 17 prototype dolosse were sampled and accurate quantification of the static response statistics requires a tremendous number of permutations of random boundary conditions, slope, and armor unit position on the slope.

Melby and Turk (1994b, 1994c, 1995) made large-scale measurements of 26-kg dolos static, wave loading, and impact strains to fill in the missing pieces in the dolos structural response quantification. Although these data are still being analyzed, they showed that the impact strains are very large and dolos movement should be avoided.

Recently, reasonable design methods for stable dolosse have been proposed based on the prototype and large scale measurements discussed above (Melby 1990, 1993, Melby and Turk 1992). Yet concrete armor breakage surveys of USAE breakwaters and jetties, combined with the existing structural data, have produced conclusive evidence that armor unit structural and hydraulic stability response can be improved significantly through small modifications in armor shape (Melby and Turk 1994a). This is therefore the focus of the research reported herein.

## **DEVELOPING NEW ARMOR SHAPES**

The Corps has an ongoing research effort to develop optimized concrete armor shapes. The optimal armor engineering characteristics are summarized as

follows:

- a.* High hydraulic stability in a single-unit-thickness layer on any slope. Reserve stability for wave conditions exceeding the design event.
- b.* Hydraulically stable with no rocking, even when broken or following reneasting resulting from local instability.
- c.* Efficient combination of porosity and slope roughness to dissipate the maximum amount of wave energy with the minimum armor volume over a critical range of wave periods.
- d.* Hydraulically stable when placed as a repair with other shapes.
- e.* Low internal stresses, so no reinforcement required.
- f.* Constructable casting yard forms and armor layers (need to be able to construct armor layer in low visibility water.)
- g.* Uses minimal casting yard or barge space.
- h.* Utilizes conventional construction materials and techniques.

A new series of concrete armor units, called the CORE-LOC, was recently developed at the USAE Waterways Experiment Station Coastal Engineering Research Center with the above features as prerequisite (Melby and Turk 1993, 1994d). The unit has a balance of the above engineering features such that the armor layer performance is maximized while the armor layer costs are minimized. The core-loc appears to have improved engineering performance due to a balance of the hydraulic stability, structural strength, wave energy dissipation, and constructability. The armor layer costs are reduced through less concrete and fewer and smaller units. The core-loc was designed to be placed in a single-unit-thick layer on steep or shallow slopes. The unit interlocks well on any slope and even interlocks well with dolosse, providing an efficient repair unit for those dolosse slopes in need of repair.

### **CORE-LOC ENGINEERING CHARACTERISTICS**

The core-loc armor unit and its engineering characteristics are shown in Table 1 and Figure 1. Table 1 also gives a comparison with dolos. The design parameters, such as the packing density and volumes, are defined using the traditional Shore Protection Manual (SPM 1984) methodology.

Table 1. Engineering Characteristics of the Core-loc							
Unit	Volume	Number of Layers <sup>1</sup>	Porosity	Layer Coefficient	Packing Density	Typical Slope	Number of Units <sup>2</sup>
	V	n	P as %	k <sub>A</sub>	φ	cotα	N/C <sup>2</sup>
Cora-loc	0.2240C <sup>3</sup>	1	66	1.6	0.54	1.5	1.46
Dolos	0.1561C <sup>3</sup>	2	56	0.94	0.83	2.0	2.86

Footnotas

- The two dolos armor layers are always constructed as a single layer but n = 2 corresponds to k<sub>A</sub> = 0.94 in equations 2 and 3.
- Here the number of units is given per square armor unit dimension.

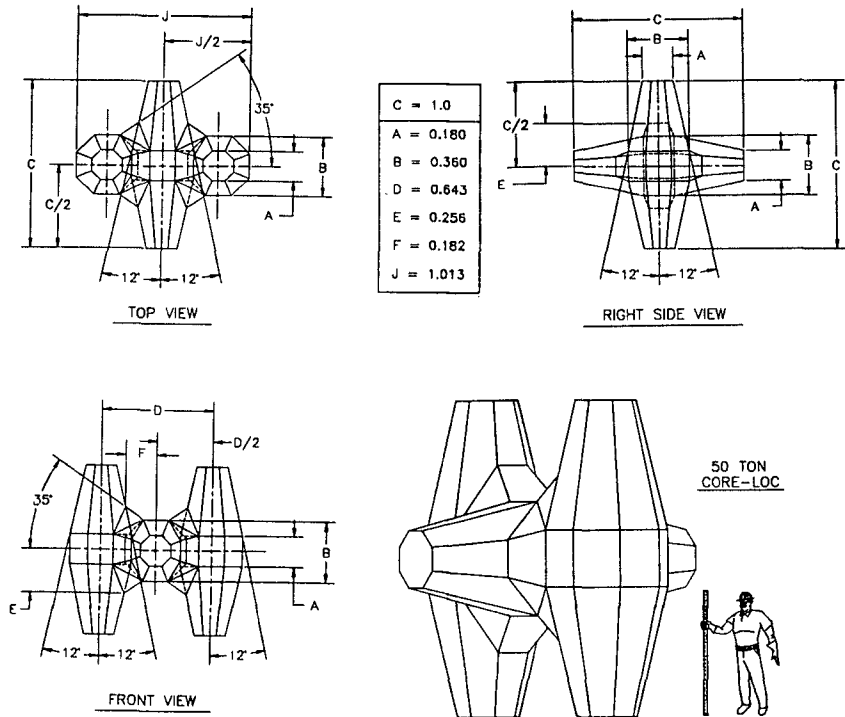


Figure 1. Core-loc Dimensions and Engineering Characteristics

### CORE-LOC STRUCTURAL RESPONSE

Finite element method (FEM) structural analyses have been done to compare the structural response of core-locs to dolos, accropode, and tribar for several loading modes. The model and analysis specifications are shown in Table 2 for the FEM analysis. The FEM grid is shown in Figure 2. An example loading, shown in Figure 2, imposed the worst case flexural condition with one outer member fixed rigidly along the outside surface and the load applied to the end of the opposing member. This condition generated the maximum flexural stresses at the internal intersection on the units. The load was equal to the armor weight, which was 9 tonnes. Another pure flexural loading, a pure torsion loading, and a combined torsion and flexural loading were also analyzed. For the other pure flexure load condition, the load of 9 tonnes was applied transversely at the center of the outer member while the opposing member was held rigid. For the torsion loading, four 4.5-tonne loads were applied to the four outer member tip ends to generate the maximum twisting force on the unit. The unit was pinned at the center for this case. For the combined loading case, two 9-tonne loads imposing torsion and flexure, were applied to one outer member end while the opposing member was held rigid along its entire length. FEM results are shown in Table 3.

Table 2. Finite Element Model Properties	
Model Properties	Fully three-dimensional linear elastic model with about 2000 nodas and 1500 alaments, depending on the unit shepe.
Armor end Material Properties	Armor Weight, $W = 9$ tonnes Modulus of Elasticity, $E = 3.5 \cdot 10^4$ MPe Poisson Ratio, $\nu = 0.21$ Specific Greivity, $S = 2.33$ relative to fresh water

Table 3. FEM Static Stress Comparison				
Load Case	Stress, $\sigma$ , MPe			
	Core-loc	Dolos	Accropoda	Tribar
Torsion	1.12	2.08	1.52	2.98
Flexure - fluke tip load	1.12	2.41	1.52	3.36
Flexure - fluke center load	2.10	3.42	-	-
Combined flexure end torsion	1.91	3.83	-	-



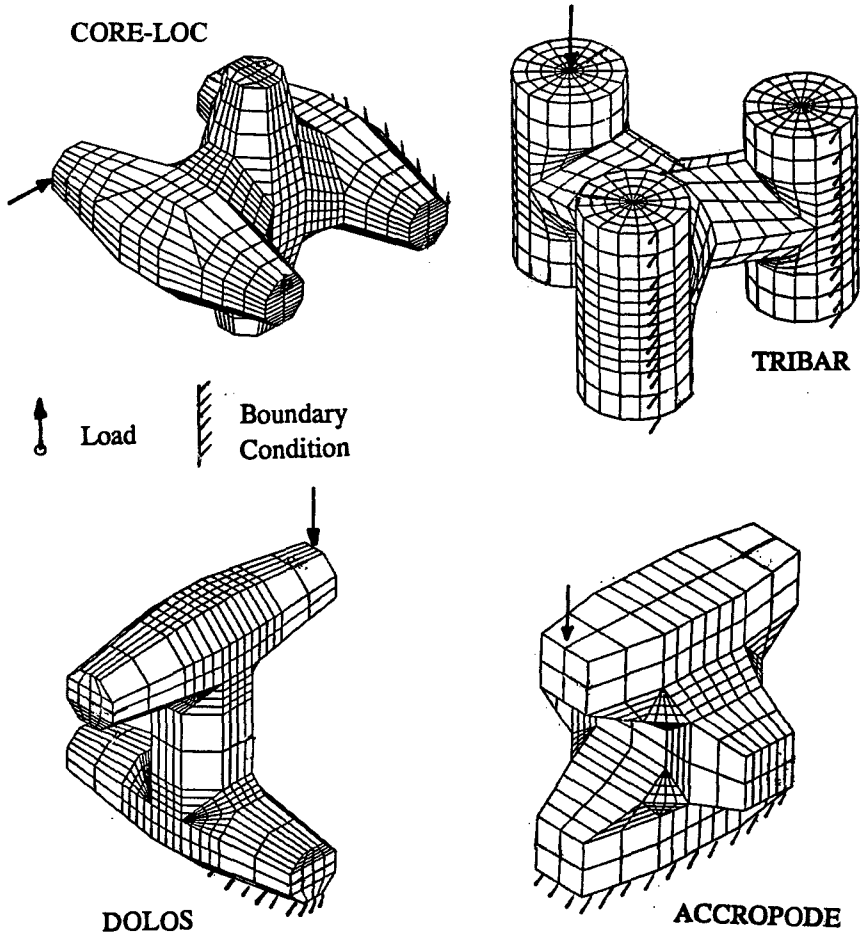


Figure 2. Loading and Boundaries for Flexural Stress Comparison of Core-loc, Tribar, Accropode, and Dolos.

As illustrated in Table 3, for equivalent weight units, the core-loc maximum tensile stress for static loads ranges from 34% to 62% that of dolos. The maximum core-loc tensile stress is 74% for torsion and 74% for flexure that of accropode, and 38% for torsion and 33% for flexure that of tribar.

## CORE-LOC HYDRAULIC STABILITY TEST RESULTS

### *Two-Dimensional Hydraulic Stability*

The first *proof-of-concept* tests of core-loc hydraulic stability were two dimensional and showed the unit to be exceptionally stable, with no damage

measured for Hudson stability coefficients over 300 (stability numbers,  $N_s$ , over 7). The tests were done in a 0.6-m-wide flume with the structure 30 m from the wave generator. A wide range of monochromatic wave conditions were tested. The waves were generated by an electro-hydraulic powered, computer-controlled, bottom-hinged paddle. The approach slope was 1V:20H for 5 m seaward of the structure, 1V:16H for 2.4 m, flat for 6.7 m, and 1V:33.3H to the generator pit. Two three-electrical-capacitance-gage arrays were used to measure water surface elevations near the wave generator and at a position 3 m from the structure toe. The incident and reflected waves were resolved using the method of Goda and Suzuki (1976). The armor layer was composed of 220 g core-locs (Table 4) on a slope of 3V:4H with a stone underlayer mean weight of 41 g and a stone core mean weight of 2 g. The core had a very low permeability and was therefore more critical to armor stability. The maximum wave conditions are summarized in Table 5. The armor could not be damaged up to the limit of the wave generator for nearly all tests. The only instability, the first entry in the table, appeared to be due to low randomness in the armor placement. It was noted during all tests that only a few of the units on the slope were rocking, and then only slightly, even for the most severe wave conditions.

Table 4. Model Core-loc Specifications						
C	B	J	A	Mass	Volume	Specific Gravity
cm				gram	cm <sup>3</sup>	
7.2	2.7	8.0	1.5	220	93.2	2.35
Dimensions are defined in Figure 1. Initial model units not chamfered and had slightly different geometry than shown in Figure 1.						

Table 5. Summary of Initial Stability Test Results for Maximum Wave Conditions						
Depth at Toe (cm)	Wave Period at Gage (sec)	Incident Wave Height (cm)	Reflection Coeff	Movement	Stability Number $N_s$	Stability Coeff $K_o$
46	1.38	36	0.23	1% Displ	6.0	159
46	1.78	32	0.51	nona	5.3	111*
46	1.26	45	0.27	none	7.5	321*
38	1.58	36	0.38	nona	6.0	163*
38	1.96	31	0.51	nona	5.1	102*
38	2.09	18	0.61	nona	3.0	21*
* Wave generation capacity limited, no instability						

Carver and Wright (1994) carried out a much more comprehensive series of two-dimensional hydraulic stability tests of the core-loc and also could not damage the armor layer for significant wave heights corresponding to stability numbers over 7 (Hudson stability coefficients over 250). These tests were done in a 1-m-wide section of an 3.3-m-wide flume 75 m long. The remainder of the flume width was left clear for waves to be dissipated on a rock wave absorber on the rear wall of the flume. A second section of 1 m width was filled with an identical dolos structure for comparative tests partially through this test series. Monochromatic and irregular waves were generated by an electro-hydraulic powered, computer-controlled, horizontal-displacement paddle. For the irregular waves, the spectra were of the TMA type. Incident and reflected waves were resolved from water surface measurements made with two sets of three electrical capacitance wave gages, again using the methods of Goda and Suzuki. The test parameters are summarized in Table 6. The approach slope was at 1V:100H for 6.5 m seaward of the structure, 1V:75H for 34 m, and flat for 15.2 m to the generator pit. The wave gage arrays were positioned near the wave generator and 3.3 m from the structure toe.

<b>Table 6. Flume Stability Test Parameters</b>	
Structure Height	0.9 m
Structure Base Width	2.7 m for 1V:1.33H and 3.0 m for 1V:1.5H
Structure Slopes	1V:1.33H and 1V:1.5H
Mean Armor Mass	219 g
Mean Underlayer Mass	45 g
Mean Core Mass	1 g
Number of Waves per Test	~1000
Water Depths at Structure Toe	36 and 61 cm
Incident Wave Heights, $H_{mo}$	4.6 to 39 cm (61 cm depth)
Peak Period, $T_p$	1.5 to 4.7 sec
Surf Sim. Param, $\xi$	2.13 to 15.9
Relative Depth, $d/L_o$	0.012 to 0.175
Wave Steepness, $H_{mo}/L_o$	0.001 to 0.098

For these tests, several parameters of relative measure were calculated including the surf similarity parameter or Irribarren number,  $\xi = \tan \alpha / (H_{mo}/L_o)^{1/2}$ , the relative depth,  $d/L_o$ , and the wave steepness,  $H_{mo}/L_o$ . Here  $\alpha$  is the structure front slope angle,  $H_{mo}$  is the incident wave height at the shallow gage array,  $L_o = 2\pi/gT_p^2$  is the deep water wave length computed from the peak period at the shallow gage array, and  $d$  is the structure toe depth. The ranges of these

parameters are also summarized in Table 6.

The researchers made note of the fact that the units showed almost no movement on the slope, including in-place rocking. It seems likely that the units would therefore have a very low probability of experiencing impact stresses. Also, in the dolos and core-loc side-by-side tests, the reflection coefficients from the core-loc slope were almost indistinguishable from those of dolosse, indicating that existing dolos reflection and runup design information could be used for preliminary estimation of reflection and runup on core-loc slopes.

These early tests showed that the core-loc armor layer was two-dimensionally stable for wave heights far exceeding those causing damage to most other armor shapes. It was noted that a conservative design would never specify armor weights using very high stability coefficients, such that the non-interlocked armor stability was significantly different from the interlocked stability, because of the risk of catastrophic failure. Therefore these tests show that the core-loc armor, when designed conservatively for two dimensional situations, such as on a revetment, will have considerable reserve stability beyond the design wave or when repeatedly subjected to the design wave.

### *Three-Dimensional Stability*

Although generic three-dimensional stability tests have not been done, several site-specific studies have been completed. Smith et al. (1994) carried out three dimensional stability tests of a core-loc armor layer for a site-specific test of the proposed Noyo, California Harbor offshore breakwater. This site is subjected to depth limited 7 to 9 m breaking waves repeatedly each winter, and therefore provided a very good test of core-loc stability. Also, the breakwater is subjected to very high flow velocities that are due to wave focussing from several surface-piercing pinnacles just off the seaward toe.

Three-dimensional stability tests of the Noyo breakwater were carried out at a geometrically undistorted scale of 1:50 with molded bathymetry. The model offshore breakwater was scaled from prototype dimensions of 122 m length between two round head centers and initial crown widths of 9 m on the large head, 6.1 m on the small head, and 7 m in between. The slope of the breakwater was 1V:1.5H. The initial storm series consisted of 17 tests of 15 minutes model, 106 minutes prototype, each with a succession of 13, 17, and 20 second peak period waves of increasing significant wave heights from 3.4 to 8.4 m (Storm I). The maximum wave height was depth limited. The primary armor tested consisted of approximately 500 28-tonne core-locs on the large head and 500 17-tonne core-locs on the small head.

The core-locs were stable for two successive Storm IA wave series (the 10 highest energy series from storm I) and began to unravel after being subjected to an additional three Storm IB series, each consisting of the 3 highest energy series in Storm I. It appeared that the primary damage was instigated by toe instability, particularly in areas of wave focussing, due to erosion of the toe apron. The stability number corresponding to the larger core-loc was 2.7 for the highest  $H_s$

(Hudson stability coefficient of 13).

The design waves tested above were considered to be quite conservative, so a somewhat more realistic wave condition was also tested. The final storm series consisted of a five-Storm-IB sequence, except that the 20 sec, 8.4 m test was omitted from the middle three series. The apron was mostly stable for this sequence of storms, and only 4 core-loc units, or 0.4%, were displaced. In summary, the core-locs were stable for very high stability coefficients when repeatedly subjected to this very high energy design storm event. The core-loc structure was the only alternative to meet the required economic benefit-to-cost ratio and was accepted as the final design.

### ***Dolos Repair Tests Using Core-loc***

A short series of two-dimensional stability tests was conducted to determine the comparative stability between dolos and a dolos slope repaired with core-locs. The tests were done in shallow water with a 1.5-m-wide fronting reef in the same 0.6-m-wide flume described above. The structure was 17 cm high with a front slope of 1V:1.5H. Monochromatic waves were generated producing a maximum incident wave height of 22 cm and period of 3.75 sec in a depth of 17 cm at the structure. A very high wave height-to-depth ratio occurred at the structure because the fronting reef was narrow relative to the wavelength; therefore, the wave height was not stabilizing before it hit the structure. Approximately 180 waves were generated per run. The number of wave cases and complexity of this experiment were kept to a minimum for this *proof-of-concept* test.

For the dolos stability tests, 97 dolosse were placed at a packing density of 0.83. The armor mass was 125 g. For these tests, 15 units were displaced and most of the dolosse were mobile during the tests. The Hudson stability coefficient for this case was approximately 61, but represented excessive damage.

For the repair tests, the damaged dolos slope was repaired with 15 core-locs. The repair units were 145 g and were placed rather haphazardly along the toe and in two pockets on the slope. The remaining dolosse were not touched. This is not a recommended repair procedure but represents a worst case emergency spot repair. For this test series, 3 core-locs were displaced off the slope and 3 additional dolosse were displaced. It was noted that the core-locs had interlocked and stabilized the original damaged regions on the slope. The displaced units were near the cap and were never interlocked. The additional core-loc weight contributed some to the increased stability of the dolos slope; but the effect was small because the incident wave heights were far greater than those corresponding to the non-interlocked stability threshold. The primary stabilization was from interlocking. For an actual repair, the same weight units would likely be used and the existing armor near the repair region would be removed from the slope so the core-locs could be interlocked with the dolos units as they were placed. It is expected that this more careful repair procedure would have resulted in a much more stable armor layer.

Although very brief, these tests showed that the core-loc-repaired areas

were qualitatively more stable than the original dolos slope, and the higher structural strength of the core-loc further justify its use as a repair unit for dolos slopes. More extensive tests are being done to systematically quantify the stability of a core-loc-repaired dolos slope and to determine the most effective repair methods.

## CONCLUSION

A new armor unit, called the core-loc, was discussed which solves the primary problems of existing randomly-placed units. The core-loc appears to have a unique balance such that the primary engineering performance criteria are maximized while the amount of concrete and number of units are minimized. These primary performance criteria are structural integrity, hydraulic stability, armor porosity, and constructability. A finite element study showed the core-loc maximum tensile stress for combined loading to be approximately 62% that of an equivalent-sized dolos. The study showed the core-loc maximum flexural and torsional tensile stresses to be slightly lower than those in an equivalently sized accropode. Several stability studies are discussed which show two-dimensional flume stability numbers over 7 (Hudson stability coefficients over 300) for long slopes. A three-dimensional site-specific study of the proposed Noyo, California, breakwater showed no-damage stability numbers of 2.7 (Hudson stability coefficients of 13 for  $H_s$ ) for repeated exposure to severe design storms. A simple hydraulic stability test showed that core-locs would be effective at repairing dolos slopes.

Finally, for general design based on  $H_s$ , Hudson stability coefficients of 13 for the head and 16 for the trunk are preliminarily and conservatively recommended for core-locs. Using the stability coefficient of 13, for breaking waves on a head, and the recommended packing density of 0.54, the core-loc armor layer requires 47% less total volume than a dolos armor layer, 57% less than tetrapod, 51% less than tribar, and 24% less than accropode.

## ACKNOWLEDGEMENT

The work described in this paper was conducted as part of both the Coastal Research and Development Program and the Repair, Evaluation, Maintenance, and Rehabilitation Research Program of the US Army Engineer Waterways Experiment Station, US Army Corps of Engineers. Permission to publish this paper was granted by the Chief of Engineers.

## REFERENCES

- Burcharth, H.F. (1981). "Full-scale dynamic testing of dolosse to destruction." *Coastal Engrg.* 4.
- Carver R., Wright, B. (1994). "Stability of CORE-LOC armored, rubble-mound breakwater trunks." Internal Research Report, USAE WES, Vicksburg, MS.

Goda, T. and Suzuki, Y. (1976). "Estimation of incident and reflected waves in random wave experiment." *Proc. 15th Coast. Engrg. Conf. ASCE*, 828-848.

Howell, G.L. (1988). "Measurements of forces on dolos armor units at prototype scale." *Proc. 21st Int. Conf. Coast. Engrg. ASCE*, NY, NY.

Howell, G.L., Rhee, J.P., and Rosati, J. (1990). "Stresses in dolos armor units due to waves." *ASCE/WPCO Sem. on Stres. in Conc. Ar. Un.*, ASCE, 164-179.

Kendall, T.R. and Melby, J.A. (1990). "Continued monitoring of 42-ton dolos movements and static stresses at Crescent City." *ASCE/WPCO Sem. on Stres. in Conc. Ar. Un.*, ASCE, 293-311.

Kendall, T.R. and Melby, J.A. (1992). "Movement and static stress in dolosse: six years of field monitoring at Crescent City." *Proc. 23rd Int. Conf. Coast. Engrg. ASCE*, 1285-1298.

Markle, D.G. (1990). "Crescent City instrumented dolos model study." *ASCE/WPCO Sem. on Stres. in Conc. Ar. Un.* ASCE, 180-200.

Melby, J.A. (1990). "An overview of the Crescent City dolos structural design procedure." *ASCE/WPCO Sem. on Stres. in Conc. Ar. Un.* ASCE, 312-326.

Melby, J.A. (1993). "Dolos design procedure based on crescent city prototype data." *Tech. Rep. CERC-93-10*, USAE WES, Vicksburg, MS.

Melby, J.A. and Howell, G.L. (1989). "Incorporation of prototype dolos static response in a dolos design procedure." *Proc. Int. Assoc. Hyd. Res. XXIII Congress. IAHR*, C391-C398.

Melby, J.A. and Turk, G.F. (1992). "Dolos design using reliability methods." *Proc. 23rd Int. Conf. Coast. Engrg. ASCE*, 1385-1399.

Melby, J.A. and Turk, G.F. (1993). "CORE-LOC - Initial stability results." Internal Research Report, USAE WES, Vicksburg, MS.

Melby, J.A. and Turk, G.F. (1994a). "Concrete armor unit performance in light of recent research results." *ASCE/WPCO Sem. on Case Histories of Design, Constr., and Maint. of Rubble Mound Struc.* ASCE, NY, NY.

Melby, J.A. and Turk, G.F. (1994b). "Scale and modeling effects in concrete armor experiments." *Proc. Coastal Dynamics '94*, ASCE, NY, NY.

Melby, J.A. and Turk, G.F. (1994c). "Large Scale Dolos Flume Study: post-

experiment report." *Tech. Rep. CERC-94-??* in publication, USAE WES, Vicksburg, MS.

Melby, J.A. and Turk, G.F. (1994d). "CORE-LOC concrete armor units." *Tech. Rep. CERC-94-??* in publication, USAE WES, Vicksburg, MS.

Melby, J.A. and Turk, G.F. (1995). "Large Scale Dolos Flume Study." *Proc. 24th Int. Conf. Coast. Engrg.*, ASCE, NY, NY.

Scott, R.D., Turcke, D.J., and Baird, W.F. (1986). "An unique instrumentation scheme for measuring loads in model dolos units." *Proc. 20th Int. Conf. Coast. Engrg.* ASCE, 2212-2223.

Shore Protection Manual (1984). USAE WES, Vicksburg, MS.

Smith, E.R., Cole, J., Bonigut, T., Hennington, L. (1994). "Stability tests of proposed breakwater at Noyo, California." *ASCE/WPCO Sem. on Case Histories of Design, Constr., and Maint. of Rubble Mound Struc.* ASCE, NY, NY.

Terao, T. et al. (1982). "Prototype testing of dolosse to destruction." *Proc. 18th Int. Conf. Coast. Engrg.* ASCE, NY, NY.

Timco, G.W., Mansard, E.P.D. (1982). "Improvements in modeling rubble-mound breakwaters." *Proc. 18th Int. Conf. Coast. Engrg.* ASCE, NY, NY.

Zwamborn, J.A. and Phelp, D. (1990). "Structural tests on dolosse." *ASCE/WPCOE Sem. on Stres. in Conc. Ar. Un.* ASCE, 40-59.



## CHAPTER 104

# STABILITY OF ARMOR STONES OF A SUBMERGED WIDE-CROWN BREAKWATER

Norimi MIZUTANI,<sup>1</sup> Teofilo Monge RUFIN Jr.,<sup>2</sup> and Koichiro IWATA<sup>3</sup>

### Abstract

The stable weight of armor rubbles of a submerged wide-crown breakwater was analyzed in relation to the wave force acting. At first, stability models for armor rubble were derived based on the idealized spherical armor unit; then, the shape effect of armor stones on acting wave forces and stability was investigated experimentally. Based on the results, the proper modification of the stability models for spherical armor unit gives good estimate of the stable weight of armor rubbles. Furthermore, the shape effect on wave forces and stability is significant; whereas, the shape effect of armor rubble on the stable weight is relatively small.

### 1. INTRODUCTION

The submerged breakwater is a nature-conscious coastal protection work which takes the essential role in providing an agreeable environment of safety in coastal areas. This structure creates a calm sea and scarcely harms the coastal scenery nor obstruct the utilization of the sea for recreational and residential developments. In the design of submerged breakwater, an accurate estimation of stable weight of armor unit is deemed necessary. The stable weight of a rubble structure such as the rubble-mound breakwaters (e.g., Hudson et al. 1958, 1959; Hedar 1986), composite rubble-mound breakwater (Brebner and Donnelly 1962), and artificial reef (Uda et al. 1989) were discussed and stability models were subsequently proposed. Most of the existing stability formulae are intended to correlate the stable weight with the wave height, and the relation between the stable weight and wave forces acting have not been discussed in detail. However, the stable weight of the armor unit depends largely on the acting wave forces; thus, it is necessary to relate the stability to the acting wave forces and its pertinent characteristics. Although there have been some studies

---

<sup>1</sup>Assoc. Professor, D. Eng., Dept. of Civil Eng., Nagoya Univ., Nagoya 464-01, JAPAN

<sup>2</sup>Graduate Student, M. Eng., Dept. of Civil Eng., Nagoya Univ., Nagoya, JAPAN

<sup>3</sup>M. ASCE, Professor, D. Eng., Dept. of Civil Eng., Nagoya Univ., Nagoya, JAPAN

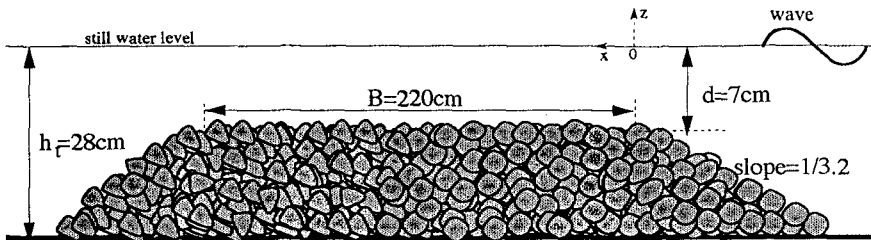


Figure 1: Schematic diagram of submerged wide-crown breakwater.

Table 1 Characteristics of sample armor stones.

CLASS	SHAPE	D (cm)	D / d	W (g)	S <sub>1</sub> /S <sub>2</sub>	L <sub>1</sub> /L <sub>2</sub>
A	sphere	2.47	0.353	19.6	1.0	1.0
	round-type				1.67	1.21
	flat-type				3.01	1.77
	edged-type				2.85	1.22
B	sphere	1.94	0.277	9.5	1.0	1.0
	round-type				1.62	1.48
	flat-type				3.14	1.43
	edged-type				1.87	0.98
C	sphere	1.65	0.236	6.2	1.0	1.0
	round-type				1.62	1.31
	flat-type				2.84	2.38
	edged-type				1.56	0.94

on wave forces acting on rubble stones of a rubble-mound slope breakwaters (Iwata et al. 1985; Tørum 1994), still the accumulated knowledge on wave force on rubble stones are very limited because of the complexity of the shape of stones. The present authors analyzed the wave force acting on a spherical armor unit which is an ideal shape of rubble stone, and then discussed and proposed a model for the stable weight in relation to the acting wave force (Mizutani et al. 1992; Rufin et al. 1993). This method, however, cannot be directly applied for the case of actual rubble stones without first clarifying the shape effect of rubble stone on stability and wave force. Hence, this paper aims to present the wave force and stability of armor stones in relation to the shape effect, and then develop a method of evaluating the stable weight of armor rubble of a submerged wide-crown breakwater.

## 2. EXPERIMENTAL SET-UP AND PROCEDURE

The stability tests and the laboratory observations of wave forces acting on spherical armor unit and armor rubble stones on a submerged breakwater were carried out using an indoor wave tank (25m long x 0.7m wide x 0.9 m deep). The model of the breakwater was prepared using spheres and then performed with one made of natural stones, as shown in Fig. 1. Regular waves with different wave periods ( $T = 1.0, 1.4, \text{ and } 1.8\text{s}$ ) were generated in this experiment.

For the stability measurement, the critical wave height of each sample of

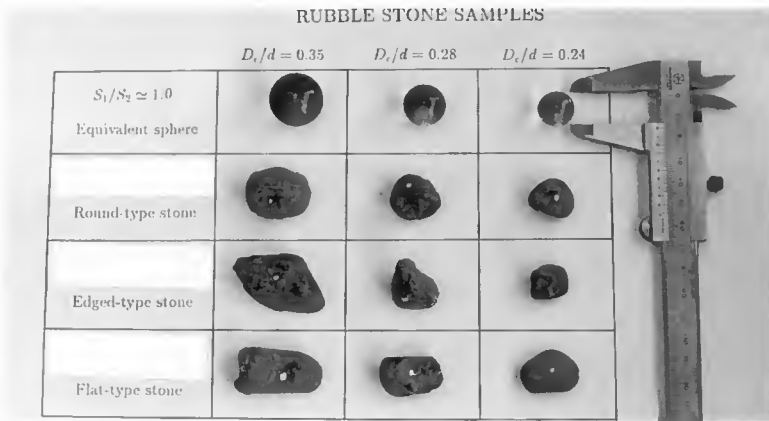


Figure 2: Stones samples.

armor unit in each wave period was determined for every designated locations on the submerged breakwater. The critical wave height is defined as the minimum wave height required to move a given sample of armor unit. The samples of armor units were spheres with  $D/d = 0.35, 0.28,$  and  $0.28$  and stones, as shown in Fig. 2, with the same volume with that of the equivalent sphere of three different shapes (round-type, flat-type, and edged-type), where  $D$  is the diameter of sphere and  $d$  is the crown water depth. Table 1 gives the characteristics of the sample armor units used in the investigation, where  $S_1$  and  $S_2$  are the maximum and minimum lengths, respectively, and  $L_1$  and  $L_2$  are the maximum tangential and normal lengths, respectively. The determination was made by generating series of experimental trials with different values of wave height until the critical wave height is attained. The armor sample was placed on the structure surface with the maximum cross-section parallel to the horizontal plane and the minimum cross-section normal to the wave incident direction.

For wave force measurement, the horizontal and vertical wave forces ( $F_x, F_z$ ) of each sample were measured for a given incident wave height ( $H_I$ ) and critical wave height conditions. The corresponding water surface elevations and horizontal and vertical water particle velocities ( $u$  and  $w$ ) were also measured. Table 2 gives the experimental conditions. The wave forces were measured for the same placement except for a very small gap between the wave force meter and the surface of the structure. In the measurement of wave force acting on rubble stones, a prototype of the actual stone of interest with exactly the same shape was prepared by plaster cast and used as sensor on the wave force meter.

### 3. WAVE FORCE ACTING ON ARMOR UNIT

Regardless of wave period, shape, and size of armor units, the nondimen-

Table 2 Experimental conditions.

	$h_t/L$	0.203	0.131	0.098
x/L	sloping side	-0.304	-0.203	-0.152
		-0.150	-0.102	-0.103
		-0.101	-0.051	-0.051
		0.0	0.0	0.0
	crown side	0.101	0.051	0.051
		0.203	0.102	0.103
		0.304	0.152	0.204
		0.506	0.203	0.308
		0.761	0.307	0.512
		1.017	0.508	0.767
		1.268	0.765	
		1.523	1.021	

dimensional maximum wave force,  $Fx_m/\rho g D^2 H_I$ , shows similar variation with the dimensionless distance,  $x/L$ , where  $\rho$  is the density of water,  $g$  is the gravitational acceleration,  $x$  is the horizontal distance referred from the leading crown-edge, positive in onshore direction, and  $L$  is the wavelength at the toe of the structure. As shown in Fig. 3,  $Fx_m/\rho g D^2 H_I$  increases with  $x/L$  and  $H_I/h_t$  on the slope ( $x/L < 0$ ) and attains a maximum value near the crown-edge (Rufin et al. 1994), where  $h_t$  is the still water depth at the toe of the structure. On the crown ( $x/L > 0$ ),  $Fx_m/\rho g D^2 H_I$  decreases rapidly for wave breaking condition; whereas,  $Fx_m/\rho g D^2 H_I$  decreases gradually for non-breaking condition. Therefore, the nondimensional maximum wave force,  $Fx_m/\rho g D^2 H_I$ , for non-breaking condition is larger than the wave breaking condition. This may be attributed to the disturbance due to the wave breaking and higher harmonic wave component generated on the crown. Similar tendency was observed for nondimensional maximum wave force in the vertical direction,  $Fz_m/\rho g D^2 H_I$ , however, the variation with  $x/L$  and  $H_I/h_t$  is not clear as compared with the horizontal wave force. Moreover, the figure shows that the onshore wave force is generally larger than the offshore wave force.

The shape effect of stones is not sensitive in the variations of nondimensional wave forces with  $x/L$ . However, shape effect is very significant on the magnitude of wave forces. Figure 4 gives the comparison of wave force among various shapes of armor unit. For the horizontal wave force, the wave force on round-type stone is almost the same magnitude with the equivalent sphere. The wave force on edged-type stone, however, is much larger than the sphere and round-type stone. For edged-type shape, flow separation takes place easier than the round-shape body because of the edges of stone, consequently, resulting to a larger drag force. On the other hand, the horizontal wave force on flat-type stone is generally small compared to the other types of stones. The method of placement wherein the smallest cross-sectional area faces the horizontal flow gives the flat-type stone the smallest projected area which results to a smaller horizontal wave force. However, the vertical wave force on flat-type stone is much larger than the other types of stone, because of very large projected area. This significant property is attributed to the variation of

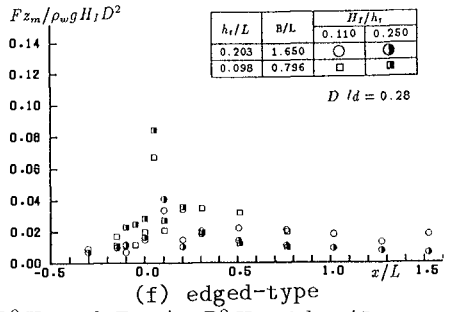
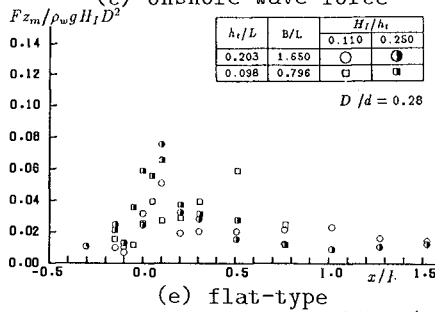
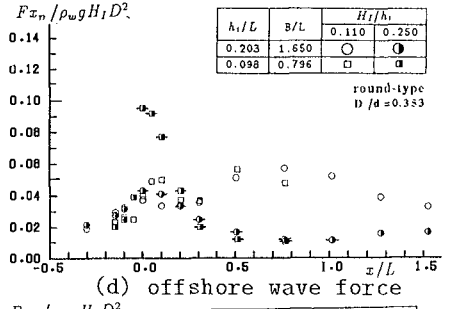
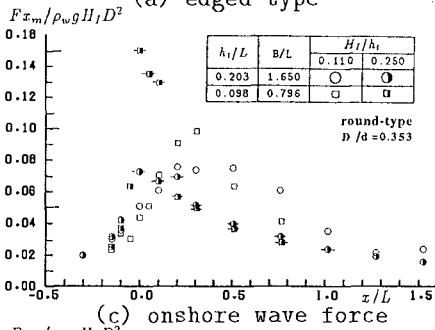
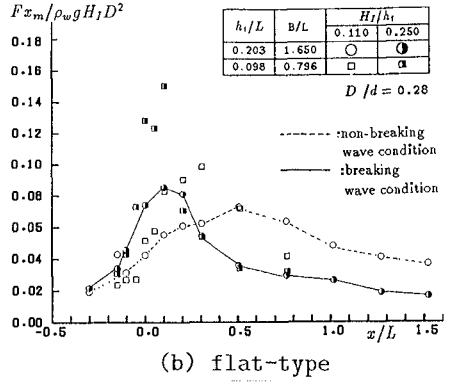
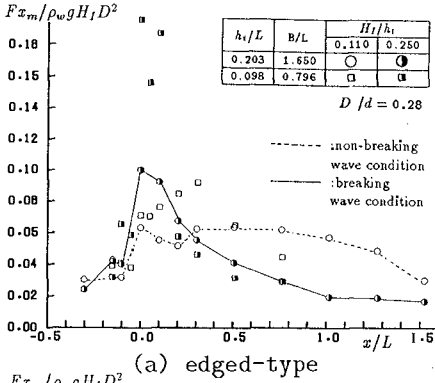


Figure 3: Variations of  $F_{x_m}/\rho_w g D^2 H_1$  and  $F_{z_m}/\rho_w g D^2 H_1$  with  $x/L$ .

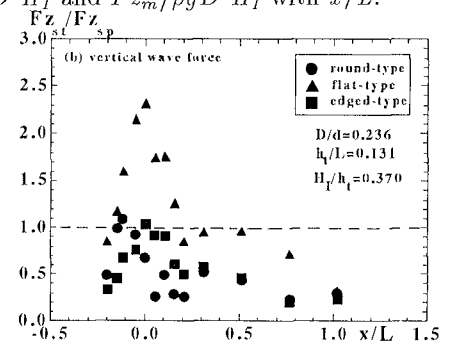
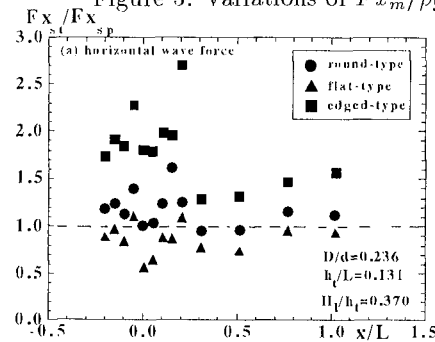


Figure 4: Shape effect of stones.

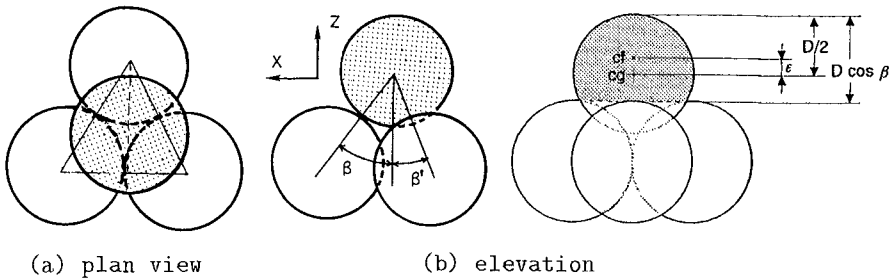


Figure 5: Arrangement of spherical units.

the cross-sectional area in the flow direction.

#### 4. STABILITY MODEL OF SPHERICAL ARMOR UNIT

The stability models for spherical armor unit were derived by the present authors (Mizutani et al. 1992); however, the proposed models were applicable only for a given experimental conditions and not suitable for the case of the actual rubble stones. Therefore, in this study, a more general stability model for spherical armor unit for various types of movements were derived in the following manner. By considering an element consisting of four spherical units of the most densely packed arrangement, as shown in Fig. 5, the possible movements of the sphere resting on top of the pyramid formed by the assemblage of these four spheres are rolling, sliding, and uplifting. For sliding and rolling movements, a maximum external force is required to move the sphere along the median line connecting the vertex of the triangle; whereas, a minimum external force is necessary to move the sphere along the median line connecting the base of the triangle. Furthermore, the case of the most movable arrangement of the exposed armor unit also depends on the direction of movement (onshore and offshore). Based on these methodologies, the theoretical models were developed for these two typical cases, CASE-I and CASE-II, as shown in Fig. 6. The uplifting motion was not observed in the experiment proper for the given samples of armor unit, thus, the succeeding models were derived based on rolling and sliding movements only.

By considering the balance of moments for rolling movement and balance of forces for sliding movement, as shown in Fig. 7, the following stability models for spherical armor unit on a submerged breakwater are summarized as follows:

- Stability model for offshore rolling (CASE-I)

$$W_1' \geq \{(\tan \beta)Fn - [1 + (2\epsilon/D)/\cos \beta] Ft\}_m / (\tan \beta - \tan \theta)(\cos \theta) \quad (1)$$

- Stability model for offshore rolling (CASE-II)

$$W_2' \geq \{(\tan \beta)Fn - 2[1 + (2\epsilon/D)/\cos \beta] Ft\}_m / (\tan \beta - 2 \tan \theta)(\cos \theta) \quad (2)$$

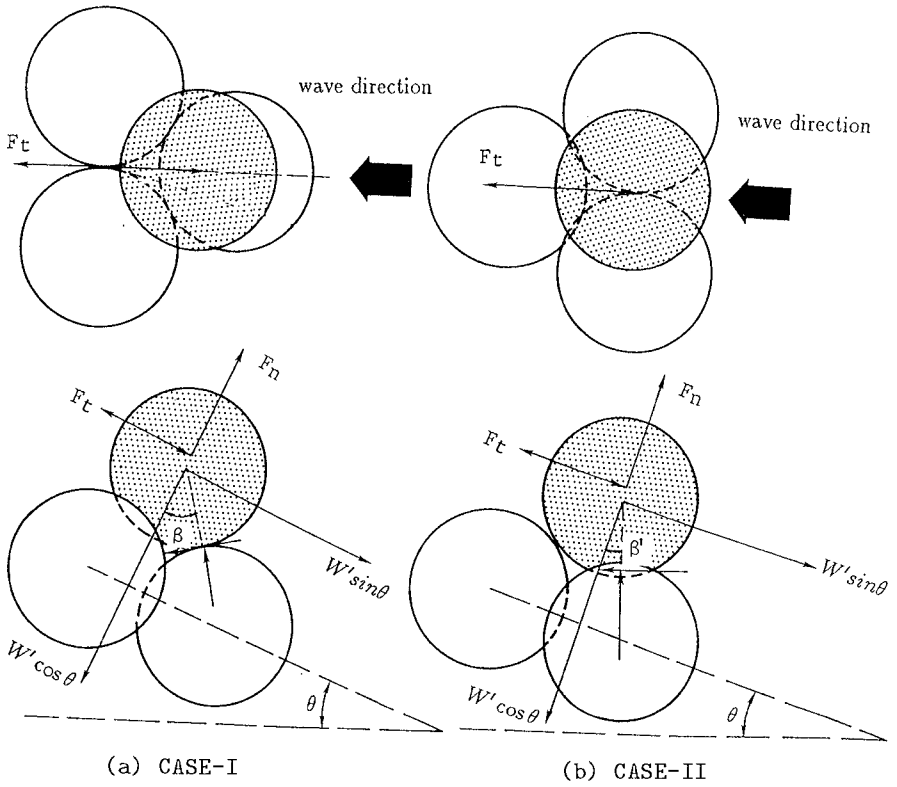


Figure 6: Methods of placement.

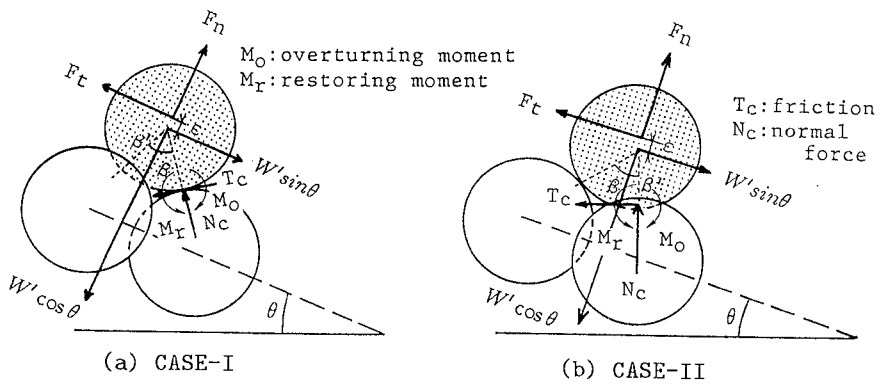


Figure 7: Balance of moments and forces.

- Stability model for onshore rolling (CASE-I)

$$W'_3 \geq \{(\tan \beta)Fn + 2[1 + (2\varepsilon/D)/\cos \beta]Ft\}_m / (\tan \beta + 2 \tan \theta)(\cos \theta) \quad (3)$$

- Stability model for onshore rolling (CASE-II)

$$W'_4 \geq \{(\tan \beta)Fn + [1 + (2\varepsilon/D)/\cos \beta]Ft\}_m / (\tan \beta + \tan \theta)(\cos \theta) \quad (4)$$

- Stability model for offshore sliding (CASE-I)

$$W'_5 \geq \frac{\{(\sin \beta + \mu \cos \beta)Fn - (\cos \beta - \mu \sin \beta)Ft\}_m}{(\cos \theta \sin \beta - \sin \theta \cos \beta) + \mu(\cos \theta \cos \beta + \sin \theta \sin \beta)} \quad (5)$$

- Stability model for offshore sliding (CASE-II)

$$W'_6 \geq \frac{\{(\sin \beta + 2\mu \cos \beta')Fn - (\cos \beta - \mu \sin \beta')2Ft\}_m}{(\cos \theta \sin \beta - 2 \sin \theta \cos \beta) + 2\mu(\cos \theta \cos \beta' + \sin \theta \sin \beta')} \quad (6)$$

- Stability model for onshore sliding (CASE-I)

$$W'_7 \leq \frac{\{(\sin \beta + 2\mu \cos \beta')Fn + 2(\cos \beta - \mu \sin \beta')Ft\}_m}{(\cos \theta \sin \beta + 2 \sin \theta \cos \beta) + 2\mu(\cos \theta \cos \beta' - \sin \theta \sin \beta')} \quad (7)$$

- Stability model for onshore sliding (CASE-II)

$$W'_8 \leq \frac{\{(\sin \beta + \mu \cos \beta)Fn + (\cos \beta - \mu \sin \beta)Ft\}_m}{(\cos \theta \sin \beta + \sin \theta \cos \beta) + \mu(\cos \theta \cos \beta - \sin \theta \sin \beta)} \quad (8)$$

where subscript  $_m$  indicates the maximum value,  $Fn$  and  $Ft$  are the normal and tangential wave forces, respectively,  $\beta$  and  $\beta'$  are the contact angles defined in Fig. 6,  $\mu$  is the coefficient of friction,  $\theta$  is the slope angle of the submerged breakwater ( $\theta = 0^\circ$  on the crown), and  $\varepsilon$  is the eccentricity and location of the center of action of wave force. In this study, the treatment of offshore rolling and offshore sliding for both CASE-I and CASE-II is the same with the work of Lee et al. (1990).

Figure 8 shows the concept of the stability conditions. The domain bounded by the critical stability lines is the stable range; thus, in the case that the trace of wave force is inside the domain, the armor unit is said to be stable. However, as the trace of wave force touches the critical stability lines, the corresponding incipient movement occurs. And beyond the critical stability lines, unstable state of the armor unit is attained.

The comparison between the calculated and experimental values of stable weight for CASE-I on the crown is shown in Fig. 9(a). By following the video-movement analysis, all movements were observed to be onshoreward rolling; thus, the corresponding critical weight given by Eq. 3 is used for the computed values. The calculated value, neglecting the eccentricity and friction, is obtained by substituting the time-varying wave forces into Eq. 3 and taking the maximum value, then, the maximum value for each run was plotted. Some scattering for each period was observed in the maximum wave force, and this



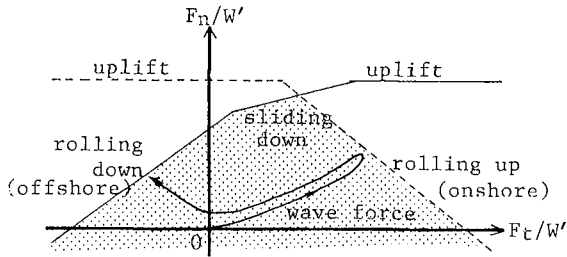


Figure 8: Concept of stability conditions.

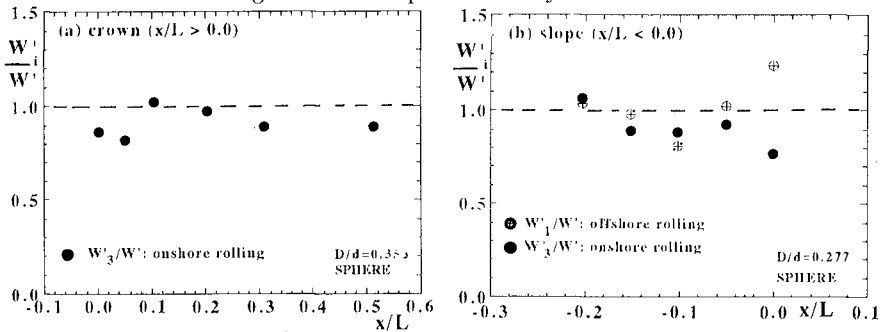


Figure 9: Estimated and experimental values for spherical armor unit.

scattering is significant in the movement of the armor unit. On the slope, as shown in Fig. 9(b), both onshore and offshore rolling movements were observed; thus, the calculated values are based on these two movements. These two directions of rolling movements occurred because on the slope, downward movement is likely to prevail; however, the onshore wave force is generally greater than the offshore wave force, as described in Fig. 3, thus, onshore movement is also evident. Although there are some discrepancies between the calculated and experimental values because of the non-uniformity of the slope of the structure, the calculated values generally agree well with the experimental value. Thus, the models derived in this study express well the stable weight of the spherical armor unit.

### 5. STABILITY MODEL OF ARMOR RUBBLE STONE

A straightforward application of the stability formulae of the spherical armor unit to the armor rubble stone is quite difficult because the shape effect and contact angle vary for a given stone. Thus, some modifications with theoretical consideration and engineering point of view are considered. In this study, only the physical quantities which has a major influence on the movement of the armor stone were included.

For rolling-type movement, the important quantities considered were the acting wave force and the moment-arm lengths. Representing the arm lengths

of the overturning and restoring moments by the maximum tangential and normal lengths, the following models were summarized and given as:

- Stability model for offshore rolling (CASE-I)

$$W'_1 \geq \frac{\{Fn - L_e S(1 + \varepsilon/L_2 K)Ft\}_m}{(\cos \theta - L_e S \sin \theta)} \quad (9)$$

- Stability model for offshore rolling (CASE-II)

$$W'_2 \geq \frac{\{Fn - 2L_e S(1 + \varepsilon/L_2 K)Ft\}_m}{(\cos \theta - 2L_e S \sin \theta)} \quad (10)$$

- Stability model for onshore rolling (CASE-I)

$$W'_3 \geq \frac{\{Fn + 2L_e S(1 + \varepsilon/L_2 K)Ft\}_m}{(\cos \theta + 2L_e S \sin \theta)} \quad (11)$$

- Stability model for onshore rolling (CASE-II)

$$W'_4 \geq \frac{\{Fn + L_e S(1 + \varepsilon/L_2 K)Ft\}_m}{(\cos \theta + L_e S \sin \theta)} \quad (12)$$

For sliding-type movement, the acting wave force, friction and contact angles were considered important. However, the accurate estimation of the contact angle is complicated for the case of the actual stone. Thus, in the computation, the contact angle can be assumed equal to zero for conservative estimation. The following sliding models are summarized and given as:

- Stability model for offshore sliding (CASE-I)

$$W'_5 \geq \frac{\{Fn(\sin \beta + \mu \cos \beta) - Ft(\cos \beta - \mu \sin \beta)\}_m}{(\cos \theta \sin \beta - \sin \theta \cos \beta) + \mu(\cos \theta \cos \beta + \sin \theta \sin \beta)} \quad (13)$$

- Stability model for offshore sliding (CASE-II)

$$W'_6 \geq \frac{\{Fn(\sin \beta + 2\mu \cos \beta') - 2Ft(\cos \beta - \mu \sin \beta')\}_m}{(\cos \theta \sin \beta - 2\sin \theta \cos \beta) + 2\mu(\cos \theta \cos \beta' + \sin \theta \sin \beta')} \quad (14)$$

- Stability model for onshore sliding (CASE-I)

$$W'_7 \geq \frac{\{Fn(\sin \beta + 2\mu \cos \beta') + 2Ft(\cos \beta - \mu \sin \beta')\}_m}{(\cos \theta \sin \beta + 2\sin \theta \cos \beta) + 2\mu(\cos \theta \cos \beta' - \sin \theta \sin \beta')} \quad (15)$$

- Stability model for onshore sliding (CASE-II)

$$W'_8 \geq \frac{\{Fn(\sin \beta + \mu \cos \beta) + Ft(\cos \beta - \mu \sin \beta)\}_m}{(\cos \theta \sin \beta + \sin \theta \cos \beta) + \mu(\cos \theta \cos \beta - \sin \theta \sin \beta)} \quad (16)$$

where  $L_e = L_2/L_1$ ,  $S = \cot \beta$ ,  $K = \cos \beta/2$ , and the relation between the contact angles,  $\beta$  and  $\beta'$ , is given by  $\tan \beta = 2 \tan \beta'$ ; for sphere,  $L_e = 1.0$ . In the above mentioned formulae,  $W'$  is the weight of stone in water, and for the weight of armor rubble stone in air,  $W$ , the following equation is given.

$$W = W' + \rho V = W' \left( 1 + \frac{\rho}{\rho_s} \right) \quad (17)$$

where  $V$  is the volume of stone and  $\rho_s$  is the density of stone.

## 6. APPLICATION OF STABILITY MODEL

The movements observed for armor stone were rolling and sliding with no uplifting movements. The type of movement depends largely on shapes of stones and location on the structure. On the crown, onshoreward rolling was generally observed for round-type and edged-type of stones. For the case of flat-type stones, onshoreward sliding was generally observed for  $D/d = 0.236$  and  $0.353$ ; whereas, for  $D/d = 0.277$  onshore rolling was always observed. Regardless of shape and size of stone, offshoreward movement was not observed on the crown. On the slope, only rolling motion was generally observed for round-type and edged-type of stones, the direction of movement was almost onshoreward because the onshore wave force is predominant over the offshore wave force. However, there are some cases that offshoreward movement was observed, since armor unit is easily moved in offshoreward direction (down the slope) due to gravitational effect.

The validity of the derived models was examined by comparing the weight of each sample with the estimated weight. Although there is no clear classification of CASE-I and CASE-II for the actual stones, comparison between these two arrangements is made for analysis.

For round-type stones on the crown, the model given by Eq. (11), as shown in Fig. 10(a), for onshoreward rolling for CASE-I generally gives a good estimate although small scattering of data was observed. Figure 10(a) also shows the comparison for the case of the edged-type of stones; the model based on CASE-I arrangement overestimates the actual value. This is attributed to the effect of interlocking between stones, thus, movement is relatively difficult for the same acting wave force. However, the model based on CASE-II arrangement can estimate well the stable weight of the edged-type stone. Therefore, the stable weight of the round-type and edged-type stones can be estimated by Eq. (11) and (12), respectively. The present results suggest that the shape effect is clearly recognized by referring to the arrangement of the spherical armor unit which is the basis of the models derived for rubble stones. Figure 10(b) gives the comparison of stable weight for onshoreward sliding, in this study,  $\mu = 0.60$  is used. The model based on the contact angle of sphere,  $\beta = 35.26^\circ$ , underestimates the actual values; whereas, the model with  $\beta = 0.0^\circ$  gives good agreement. Therefore, the model based on CASE-I for onshore sliding with  $\beta = 0.0^\circ$  can estimate well the stable weight of flat-type stone.

The onshore movements on the slope were also analyzed. Figure 11(a) shows the comparison between the actual value and the estimated weight based on CASE-I for round-type and edged-type of stones. Although the number of data is limited, the model estimate well the stable weight. The estimated weight based on CASE-II overestimates the stable weight. On the slope, the

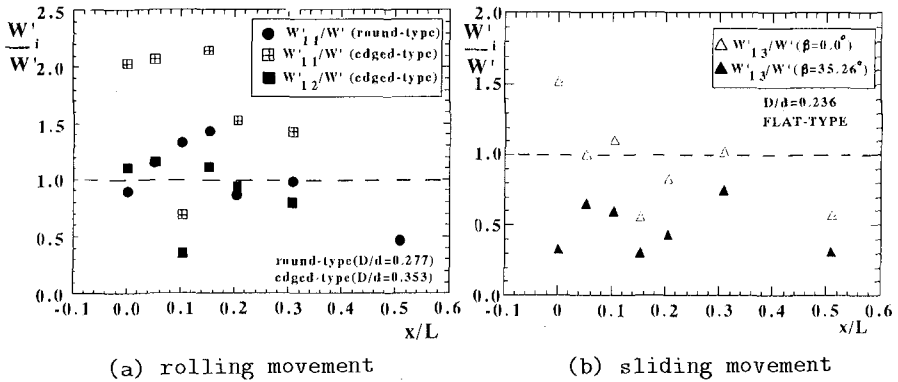


Figure 10: Estimated and experimental values for armor stones on the crown.

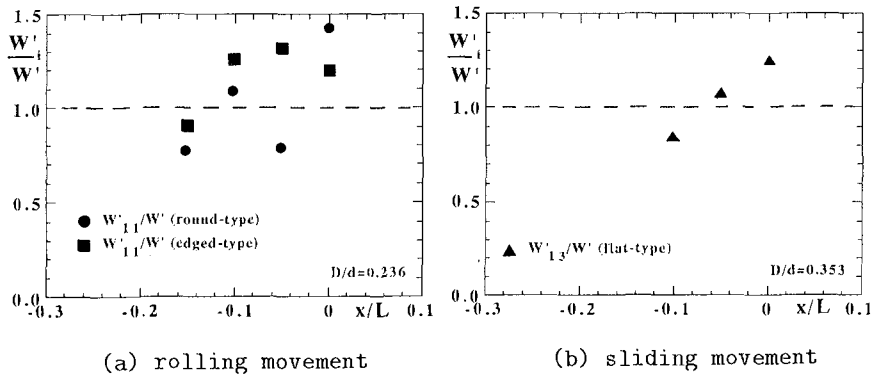


Figure 11: Estimated and experimental values for armor stones on the slope. shape effect of the edged-type stone was not so clear as in the case on the crown. This can be attributed to the contribution of the vertical wave force because on the slope the acting vertical wave force is almost upward when the onshoreward wave force takes its maximum value at incipient motion; consequently, the weight of stone is reduced, thereby, reducing the resistance against rolling. For flat-type stone, the model for offshoreward sliding based on CASE-I gives a good estimate of the stable weight, as shown in Fig. 11(b).

Summarizing these results, the recommended models for each shape of stone are given in Table 3.

7. SIMPLIFICATION OF STABILITY MODEL

The proposed models express the stable weight as a function of both the tangential and normal wave force components. Thus, it is convenient to express the stable weight as a function of only one wave force component. The orthogonal wave forces are correlated by a linear relationship as given in the following equation.

Table 3 Summary of recommended stability models.

STONE SHAPES	LOCATION	MOVEMENT	DIRECTION	STABILITY FORMULA	REMARKS
ROUND TYPE	SLOPE	ROLLING	ONSHORE	Equation 11	
			OFFSHORE	Equation 9	
	CROWN	ROLLING	ONSHORE	Equation 11	
FLAT TYPE	SLOPE	SLIDING	OFFSHORE	Equation 13	$\beta = 0.0^\circ$
		ROLLING	ONSHORE	Equation 11	
	CROWN	SLIDING	ONSHORE	Equation 15	$\beta = 0.0^\circ$
SLOPE		ROLLING	ONSHORE	Equation 11	
	OFFSHORE		Equation 9		
EDGED TYPE	CROWN	ROLLING	ONSHORE	Equation 12	

$$Fn_m = \phi Ft_m \tag{18}$$

where  $\phi$  is the coefficient. This assumption is based on the experimental results that the movement occurs at the phase that the tangential wave force takes almost a maximum value. Then, if the normal wave force at the phase is expressed in terms of the tangential wave force, the normal wave force can be eliminated. Based on the result, the coefficient  $\phi$  is taken equal to unity for engineering point of view. This means that the normal wave force is almost the same magnitude with the tangential wave force, a phenomenon which corresponds to the most dangerous condition for armor stability. This result was confirmed in some cases but in other cases, the vertical wave force is overestimated. However, the variations of the maximum wave force for each wave period exist even in the case of the regular wave train, and this effect has a significant contribution in the stability of armor unit. On the other hand, it is very difficult to estimate such variation of maximum wave force and mean value of the maximum wave force may be available as an input data. Consequently, the assumption,  $Fn_m \simeq Ft_m$ , does not overestimate the stable weight, as shown in Fig. 12, where  $W'(t)_m$  is the computed stable weight using the maximum time varying quantity of the right-hand side of the corresponding model, and  $W'(Ft)_m$  is the computed stable weight using the relation that the maximum normal is approximately equal to maximum tangential wave force.

Substituting the variation of maximum wave forces into the respective models, depending on the arrangement, the distribution of the stable weight of typical shape of stone along the submerged breakwater is obtained, as given in Fig. 13. It is noted that there is no significant differences among the three shapes of stones, although the shape effect was evident in wave force and stability. This implies that the shape effect of armor unit has a significant influence on wave force and moving limitations, but, for the case of stable weight, the shape effect due to the wave force and moving limitations cancel each other.

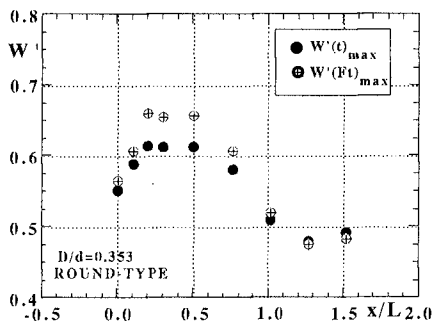


Figure 12: Validity of the assumption,  $F_{n_m} \simeq Ft_m$ .

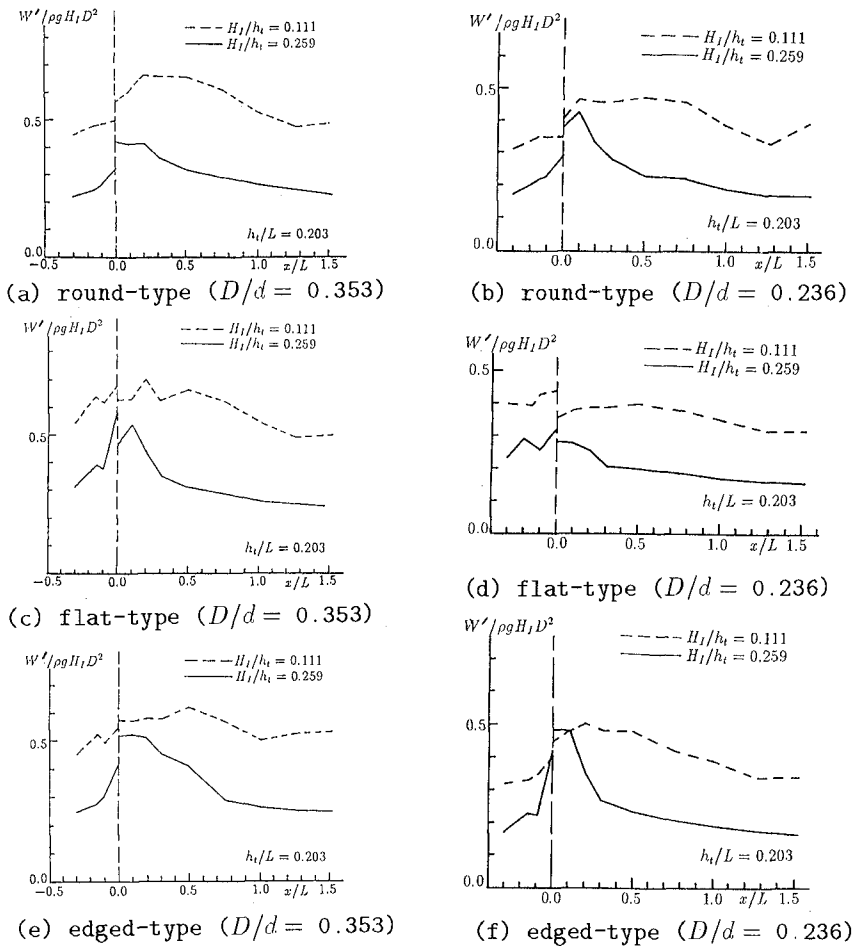


Figure 13: Stability distribution of armor stones.

## 8. CONCLUSIONS

Significant results are summarized as follows:

- (1) A general stability models were derived based on acting wave forces, moment-arm lengths and contact angles.
- (2) The vicinity around the crown-edge is revealed to be the most critical location on the submerged breakwater.
- (3) Large cross-sectional area enlarges the wave force.
- (4) To consider the moment-arm length and contact angle, the stability model for spherical armor unit can be applicable to the armor stone.
- (5) The stable weight is not so affected by the stone shape since the shape effect on the stability is offset by the shape effect of the acting wave force.

### ACKNOWLEDGMENT

The grant awarded by the Japan Society for the Promotional of Science (JSPS) to Mr. Teofilo Monge Rufin, Jr., one of the authors, is deeply appreciated. The contribution of Ms. Natsuko Totsuka is also acknowledged.

### REFERENCES

- [1] Brebner, A. and Donnelly, P. (1962). "Laboratory study of rubble foundations for vertical breakwaters," *Proc., 8th Coastal Engrg. Conf., ASCE*, pp. 408-429.
- [2] Hedar, P. A. (1986). "Armor layer stability of rubble-mound breakwaters," *J. of Waterway, Port, Coastal, and Ocean Engrg., ASCE*, Vol. 112, No. 3, pp. 343-350.
- [3] Hudson, R. Y. (1958). "Design of quarry-stone cover layers for rubble-mound breakwaters," *Technical report, Waterways Experiment Station Research*, No. 2-2.
- [4] Hudson, R. Y. (1959). "Laboratory investigation of rubble-mound breakwaters," *J. of Waterway, Port, Coastal, and Ocean Engrg., ASCE*, Vol. 85, pp. 93-121.
- [5] Iwata, K., Miyazaki, Y. and Mizutani, N. (1985). "Experimental study of the wave force acting on armour rubble of a rubble-mound slope," *Proc., Natural Disaster Science*, Vol. 7, No. 2, pp. 29-41.
- [6] Lee, S. W., McDougal, W. G., Sulisz, W., and Sollitt, C. K. (1990). "Stability of Rubble Toe," *Engineering Report, Department of Civil Engrg., OSU*, 117 pp.
- [7] Mizutani, N., Iwata, K., Rufin, T.M. Jr., and Kurata, K. (1992). "Laboratory investigation on the stability of a spherical armor unit of submerged breakwater," *Proc., 23rd Coastal Engrg. Conference, ASCE*, pp. 1400-1413.
- [8] Rufin, T.M. Jr., Mizutani, N., and Iwata, K. (1993). "Stability model of a spherical armor unit of a submerged breakwater," *Proc., 25th International Association for Hydraulic Research*, Vol. 4, pp. 190-197.
- [9] Rufin, T.M. Jr., Mizutani, N., Totsuka, N., Kurata, K., and Iwata, K. (1994). "Wave forces acting on armor unit of a submerged wide-crown breakwater," *Proc., 4th International Offshore and Polar Engrg., ISOPE*, Vol. 3, pp. 556-563.
- [10] Tørum, A. (1994). "Wave-induced forces on armor unit on berm breakwaters," *J. of Waterway, Port, Coastal, and Ocean Engrg., ASCE*, Vol. 120, pp. 251-268.
- [11] Uda, T., Omata, T., and Saito, T. (1989). "Design formula for weight of armor unit for an artificial reef," *Proc., Japanese Conference on Coastal Engrg., JSCE*, Vol.36, pp. 648-652 (in Japanese).

## CHAPTER 105

# Wave Induced Flow around Submerged Sloping Plates

Hitoshi Murakami<sup>1</sup>, Sadahiko Itoh<sup>2</sup>,  
Yoshihiko Hosoi<sup>3</sup> and Yoshiyuki Sawamura<sup>4</sup>

### Abstract

This paper deals with the hydraulic characteristics of two kinds of submerged plate type breakwaters. One is a plate with a gradual upward slope, the other is with a downward slope. The characteristics of the temporal and spatial wave induced flow and turbulence around a plate are discussed in detail on the basis of the result of the water particle velocity measured by the Laser Doppler Velocimeter. In addition, the effects of the plate length, the submerged depth of the crown and the inclination angle of a plate on the wave transmission, reflection and wave energy dissipation are discussed.

Finally it is suggested that a plate with a gradual upward slope is effective not only for the control of wave absorption but also for water purification.

### Introduction

For improvement of a much better environment in the coastal zone, various kinds of breakwaters have been designed in full consideration of the conservation of water quality, sediment and non-injury to the landscape. The artificial reef is a typical example of the breakwater designed for this purpose. However, it has been known that its crown width should

---

1.Prof., Dept. of Civil Eng., Univ. of Tokushima, Tokushima, 770, Japan.

2.Assoc. Prof., ditto.

3.Prof., Dept. of Social Systems Eng., Tottori Univ., Tottori, 680, Japan.

4.Kajima Corporation., Kagawa, 760, Japan.



be constructed widely in comparison with regular submerged breakwaters, if we expect the reduction of wave energy in an artificial reef. In covering the sea bed with the rubble mound in order to set up an artificial reef, the destruction of a good environmental condition of habitat would be a worry. Such fear will be removed in the case of submerged plate type breakwater.

In recent years, the characteristics of wave reflection and transmission in submerged sloping plate type breakwaters have been actively investigated experimentally and theoretically (Aoyama et al, 1988, Takahashi et al, 1989, Yu et al, 1989, 1991, Yamashita et al, 1990). Unfortunately, we have no information on the characteristics of wave induced flow and the turbulence around a plate, though it would be important to understand the motion of water particles and behavior of eddies not only from the hydraulic viewpoint but also from an ecological point of view.

Prior to this study, we have experimentally investigated the characteristics of the flow around both the vertical and horizontal plate type breakwaters (Murakami et al., 1992).

Two kinds of submerged sloping plate type breakwaters are chosen in this study. First, the characteristics of wave transmission, reflection and wave energy dissipation are investigated for the two kinds of breakwaters which comprise the plate with a gradual upward slope and one with a gradual downward slope. Second, based on the results of the two direction components of water particle velocities measured by the Laser Doppler Velocimeter, the characteristics of the flow and the turbulence around a plate are discussed.

## Experimental Method

A wave tank with a flap-type wave generator at one end, which was 15m long, 20cm wide and 30cm deep, was used as shown in Fig.1. The submerged plate models were placed at a distance of 9.15m from the wave generator.

For convenience, the plate models with a gradual upward slope were named the A-type and ones with a gradual downward slope the B-type. The rear edge of the plate was in water. It did not touch the sea bottom in all of the experiments. The submerged depth  $d$  was defined as the water depth from the front edge of the plate. The water depth  $h$  and the wave period  $T$  were kept at a constant of 15cm and 0.65sec, respectively. Consequently, the wave length  $L$  was 60cm.

The wave heights were measured at the points **a**, **b** and **c** to obtain the reflection and the transmission coefficients.

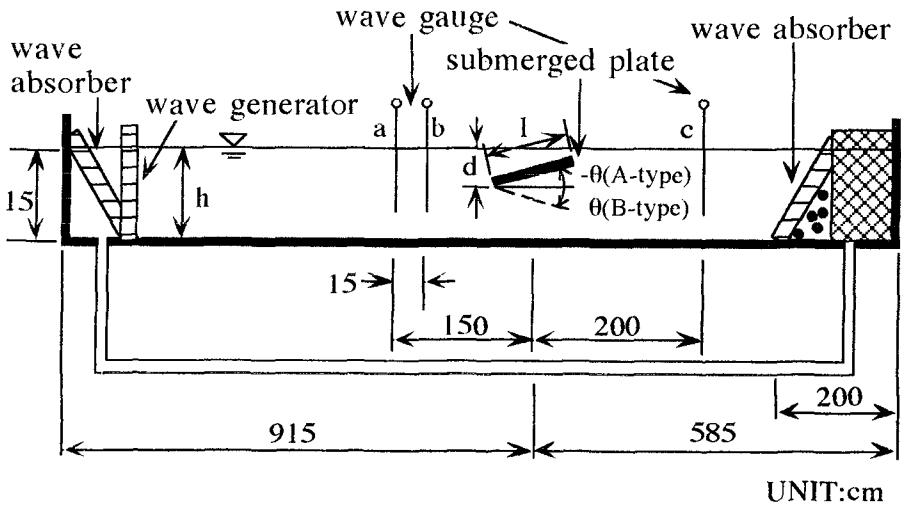


Fig.1 Experimental Apparatus

On the other hand, both the horizontal and the vertical water particle velocities were measured separately by the Laser Doppler Velocimeter (SYSTEM9100-3, KANOMAX) at 93-94 points around the plate. The change of water surface elevation was also measured at the same time above a measured point of the velocity.

Experimental conditions were shown in Table 1. In the table, the minus sign for the inclination angle of the plate  $\theta$  was assigned to the A-type, a plus sign to the B-type.

Table 1 Experimental Conditions

$T=0.65\text{sec}$ ,  $h=15\text{cm}$ ,  $L=60\text{cm}$ ,  $h/L=0.25$

1) Experiment of Wave Absorption    2) Experiment of Water Particle Velocity

H/L	0.029	0.062	0.075
d(cm)	1.5	3.0	4.5
d/h	0.1	0.2	0.3
l(cm)	15	20	30
l/L	1/4	1/3	1/2
$\theta(^{\circ})$	-10,-5, 0, 10, 20, 30, 40	-10,-5, 0, 10, 20, 30	-5, 0, 10, 20

H/L	0.062	
d/h	0.2	
l/L	1/3	1/2
$\theta(^{\circ})$	-10, -5, 0, 10, 20, 30	10

The effect of the relative plate length  $l/L$  and the relative submerged depth  $d/h$  on the wave energy dissipation have already been discussed for the horizontal plate (Murakami et al, 1992). The dimensions of the models were determined with reference to these studies in this paper.

## Analytical Method

The incident and the reflected wave heights were separated by Goda's method from the wave record at point **a** and **b** in Fig.1 (Goda et al, 1976). Using these results and the transmitted wave height, the coefficients of the transmission  $k_T$  and the reflection  $k_R$  were obtained. The wave energy dissipation rate  $\varepsilon$  was calculated by the following equation.

$$\varepsilon = 1 - k_T^2 - k_R^2 \quad (1)$$

Let's describe how to obtain the water particle velocity and the turbulent intensity at a measured point.

From the data of each velocity component which consists of the horizontal velocity  $U$  and the vertical one  $V$ , the data corresponding to a train of 30 waves were used for the analysis. Each averaged velocity component ( $U, V$ ) and each turbulent component ( $u' = U - \bar{U}, v' = V - \bar{V}$ ) at an arbitrary phase of a wave period were obtained as mentioned hereunder.

First, one wave with  $T=0.65$ sec was divided into 50 phases, the components of the velocity and the turbulence at each phase were obtained by calculating the average value of 30 waves at each phase. Second, the velocity ( $\sqrt{\bar{U}^2 + \bar{V}^2}$ ) and the turbulent intensity ( $\sqrt{u'^2 + v'^2}$ ) at a measured point were obtained by the composition of each component.

## Characteristics of Wave Absorption

### 1) Wave Profile Transformation

Fig.2(1) shows only one example of the spacial wave profile transformation with time in the case of  $l/L=1/3$ ,  $d/h=0.2$ ,  $\theta = -5^\circ$  in the A-type.

With the installation of the plate, the wave profile gradually changes with regard to time. By the wave breaking on the plate, the wave height decreases immediately. After that, the wave induced flow rolls beneath the plate. Then, an eddy with air bubbles can be observed there. Such patterns are periodically repeated.

The transmitted wave height is attenuated from this figure.

Fig.2(2) shows this in the case of the B-type. When an incident wave reaches right at the front edge of the plate, the wave profile is compulsorily

transformed there. Though the wave crest becomes sharp for a while, the wave does not break and the transmitted wave height does not decrease so much as in the A-type.

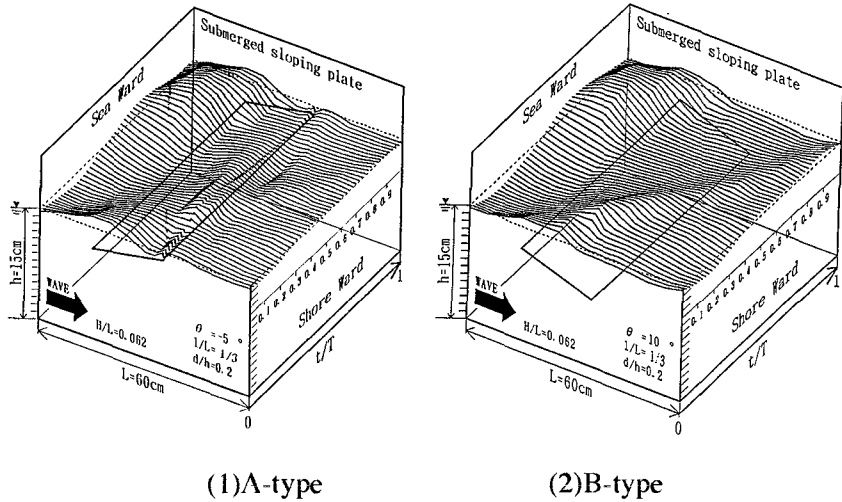


Fig.2 Wave Profile Transformation

**2) Characteristics of Transmission, Reflection and Wave Energy Dissipation**

Fig.3 shows the characteristics of the transmission coefficients  $k_T$  in  $d/h=0.2$ . The results in the A-type and the B-type are plotted in the minus and the plus region of the inclination angle  $\theta$ , respectively. The plate with  $\theta=0^\circ$  represents the horizontal plate.

In the A-type, the transmission coefficient  $k_T$  decreases with the increase of the inclination angle  $\theta$ . Such a tendency is remarkable as this relative plate length  $l/L$  increases.

In the case of  $l/L=1/2$ , the value of the  $k_T$  could be controlled 0.1 even for  $\theta=-5^\circ$ .

In the B-type, if the horizontal plate ( $\theta=0^\circ$ ) is inclined downward  $\theta=10^\circ$ , the value of the  $k_T$  increases steeply. However the effects of the  $l/L$  and the  $\theta$  on the  $k_T$  are not so remarkable in the range of  $\theta \geq 10^\circ$ .

Fig.4 shows the characteristics of the reflection coefficient  $k_R$  in  $d/h=0.2$ . It can be considered that there is no effect of the  $l/L$  on the  $k_R$  for each

type of plate .

In the A-type with a range of  $-10^\circ \leq \theta \leq 0^\circ$  , the  $k_R$  decreases with the increase of the  $\theta$  ,because the wave is easy to break on at the plate as the  $\theta$  increases. The  $k_R$  takes the small values 0.3-0.4 in this experiment.

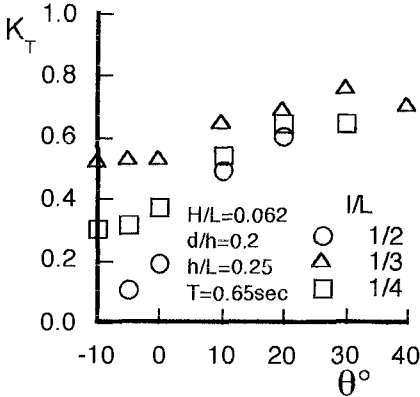


Fig.3 Transmission Coefficient

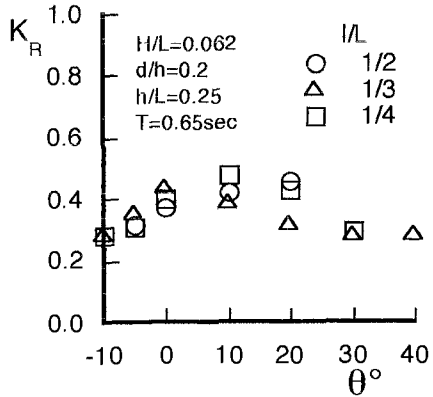


Fig.4 Reflection Coefficient

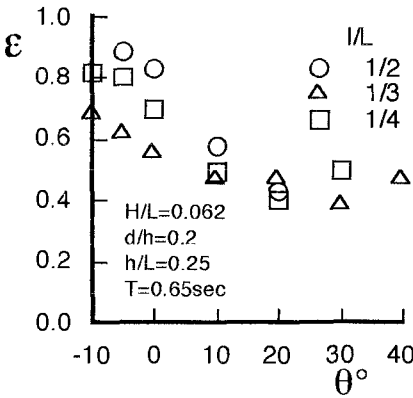


Fig.5 Wave Energy Dissipation Rate (d/h=0.2)

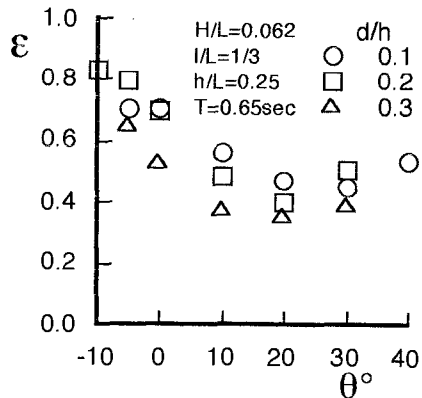


Fig.6 Wave Energy Dissipation Rate (I/L=1/3)

In the B-type, the  $k_R$  increases slightly with the increase of the  $\theta$  for  $I/L=1/2$ . Contrary to this , the tendency of the  $k_R$  decreases slightly for  $I/L=1/4$ . In this experiment, the  $k_R$  takes the values 0.3-0.45. These values of the  $k_R$  are not so big in comparison with the reflection coefficients in some other types of breakwaters.

Fig.5 shows the characteristics of the wave energy dissipation rate  $\varepsilon$  in  $d/h=0.2$ .

In the A-type with the range of  $-10^\circ \leq \theta \leq 0^\circ$ , the  $\varepsilon$  increases with the increase of both the  $\theta$  and the  $l/L$ . For  $\theta=-5^\circ$ , the incident wave energy is dissipated about 60% in the case of  $l/L=1/4$ , 80% in  $l/L=1/3$  and 90% in  $l/L=1/2$ .

It is effective for wave energy dissipation to incline the rear edge of the plate upward.

In the B-type with the range of  $0^\circ \leq \theta \leq 10^\circ$ , the  $\varepsilon$  decreases steeply with the increase of the  $\theta$  and with the decrease of the  $l/L$ . However, the values of the  $\varepsilon$  in the range of  $10^\circ \leq \theta \leq 40^\circ$  do not remarkably change regardless of the  $l/L$ . It means that effective dissipation of wave energy can not be expected regardless of the plate length, when the  $\theta$  exceeds a given value.

Fig.6 shows the effect of the relative submerged depth  $d/h$  on the  $\varepsilon$  in the case of  $l/L=1/3$ . The values of the  $\varepsilon$  in  $d/h=0.3$  are smallest of the three cases, the difference between the values of the  $\varepsilon$  in  $d/h=0.1$  and in  $d/h=0.2$  is not so big.

## Characteristics of Wave Induced Flow and Turbulence

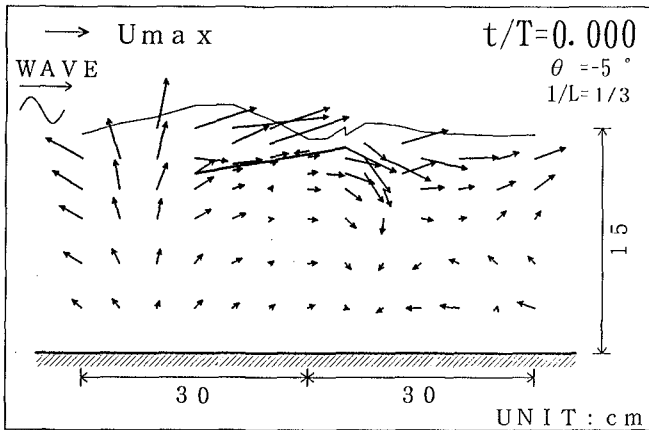
### 1) Spatial Distribution of Velocity and Turbulence at Arbitrary Phase

The spacial distribution of the mean velocity and turbulent intensity was obtained at every  $1/50$  phase of a wave period.

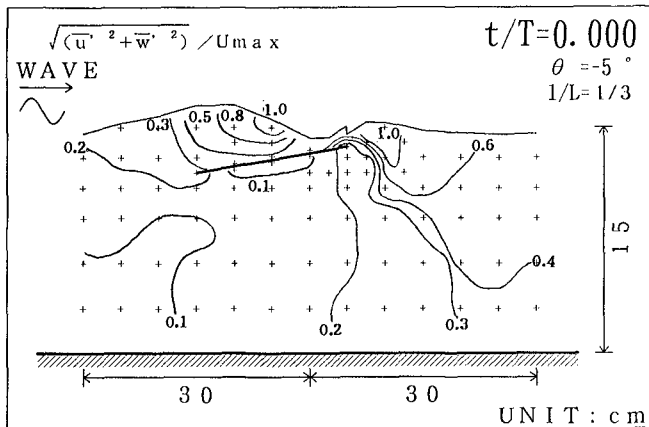
Fig.7 and Fig.8 show only two examples of the spacial distribution at the phases  $t/T=0$  and  $0.52$  of in the case of  $l/L=1/3$ ,  $d/h=0.2$ ,  $\theta=-5^\circ$  in the A-type.

The  $U_{\max}$  in a figure represents a maximum horizontal velocity at the still water surface calculated by the small amplitude wave theory. The value of  $U_{\max}=19.6$  cm/s is obtained in this experiment.

Pay attention to the upper figure of Fig.7. At this phase of  $t/T=0$ , the wave breaks intensely at the region from the front edge to the center part on the plate. Then the velocity at the forehead of the wave crest is about two times as large as the  $U_{\max}$ . The wave induced flow plunges into the rear part of the plate, and the shoreward flow is generated at the upper part of the inner basin overtopping the plate edge. However, the velocity along the back of the plate is very small in contrast to the velocity at the upper part of the plate.



(1) Velocity



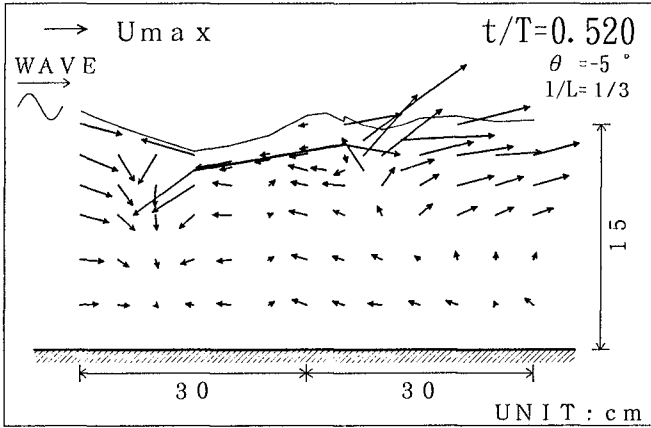
(2) Turbulent Intensity

Fig.7 A-type( $t/T=0$ )

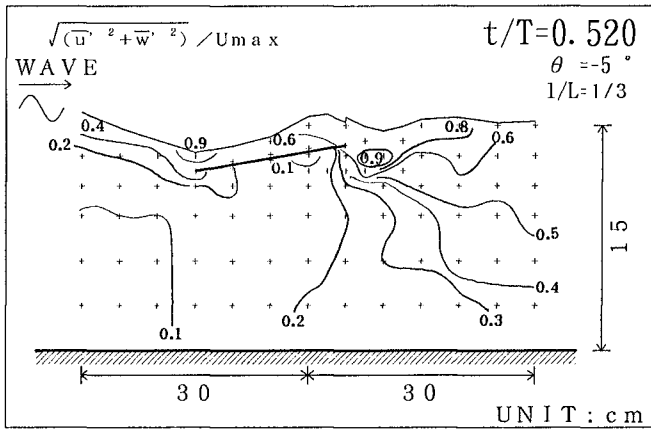
The values of turbulent intensity are shown by the nondimensional expression in the lower figure. It can be found that the large value of turbulent intensity appears at the forehead of the wave crest and at the rear edge of the plate where the overtopping flow plunges into it.

At the phase after the time of a half of a wave period  $t/T=0.52$ , the surge after a wave breaking climbs up the slope and jumps over the rear edge of the plate as shown in Fig.8. So, the region with a large velocity is

can be seen at the upper part of the inner basin. On the other hand, the seaward flow with a small velocity is generated at both sides of the plate. The direction and the size of these velocities near both edges are very complicated. As a consequence, comparative strong turbulence is generated there as in the lower figure. Generally, we can say the turbulence at the under region of the plate is very weak at any phase in the A-type.



(1)Velocity



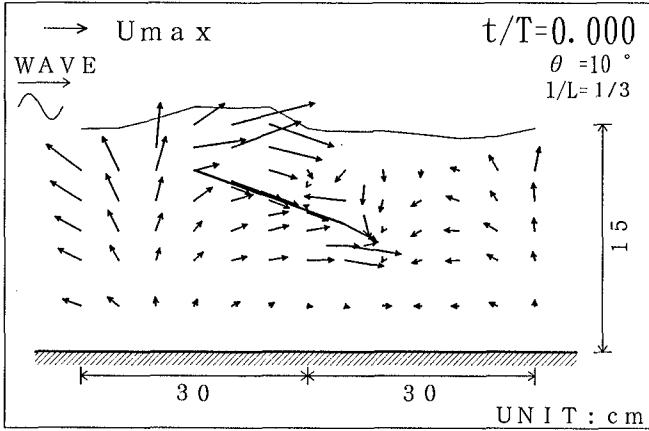
(2)Turbulent Intensity

Fig.8 A-type( $t/T=0.52$ )

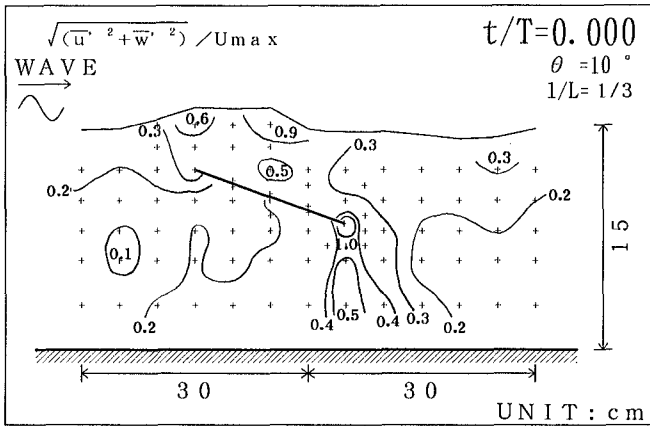
Fig.9 and Fig.10 show the spacial distribution in the case of  $1/L=1/3$ ,



$d/h=0.2, \theta =10^\circ$  in the B-type. At  $t/T=0$  as shown in Fig.9, the region with a large velocity exists at the upper part of the front edge of the plate.



(1) Velocity



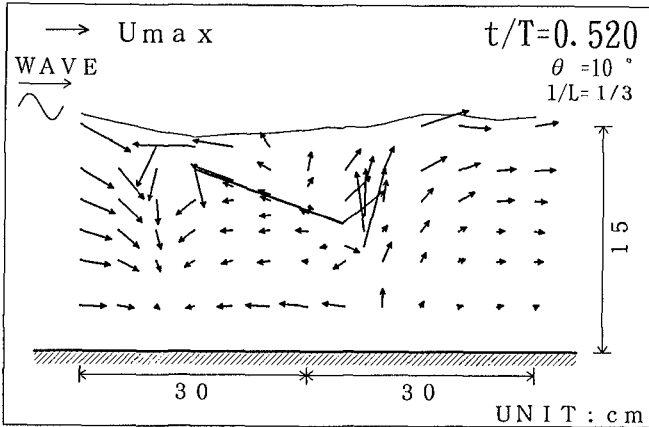
(2) Turbulent Intensity

Fig.9 B-type( $t/T=0$ )

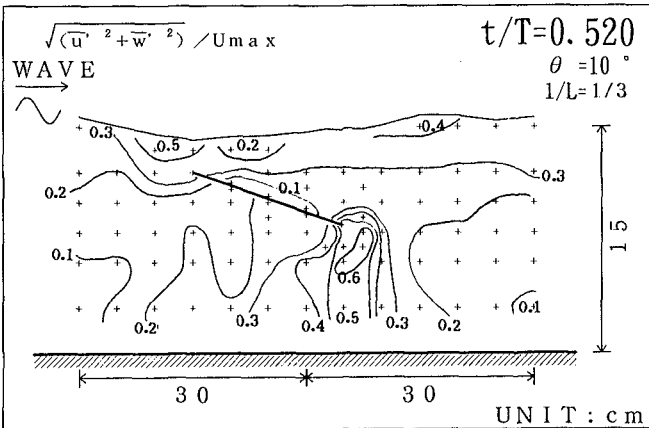
As the velocities along both sides of the plate are different, the turbulence due to the strong eddy is generated at the rear edge of the plate as shown in the lower figure.

At  $t/T=0.52$ , the upward flow with a large velocity is generated at the rear edge as in Fig.10. It could be observed that the eddy existing at the

lower part of the rear edge gradually expanded and moved upward. In the lower figure, we can see the result of the behavior of the eddy. It is noticeable that the influence of the turbulence extends to the lower part of the plate, though the turbulent intensity is not so strong.



(1)Velocity



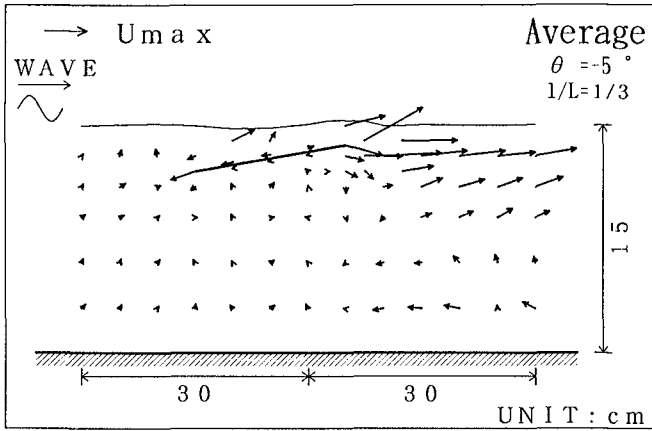
(2)Turbulent Intensity

Fig.10 B-type(t/T=0.52)

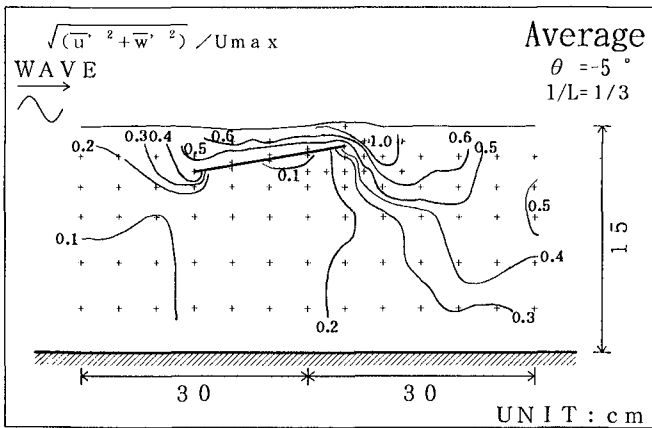
**2) Spatial Distribution of Averaged Value of Velocity and Turbulence of a Wave Period**

Fig.11 shows the spatial distribution of both the averaged velocity and

turbulent intensity of a wave period in the case of  $l/L=1/3$ ,  $d/h=0.2$ ,  $\theta = -5^\circ$  in the A-type.



(1)Residual Velocity



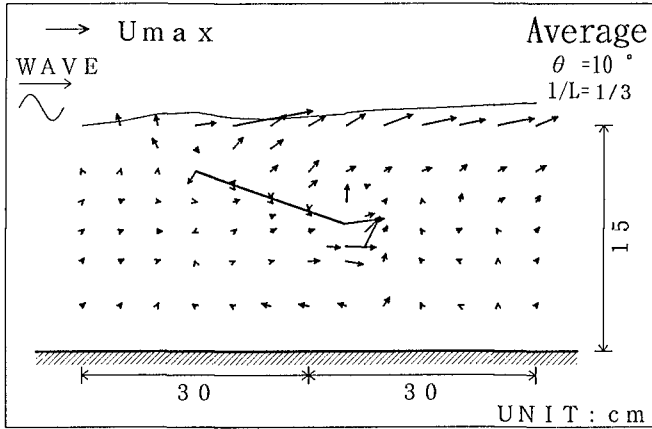
(2)Averaged Turbulent Intensity

Fig.11 A-type

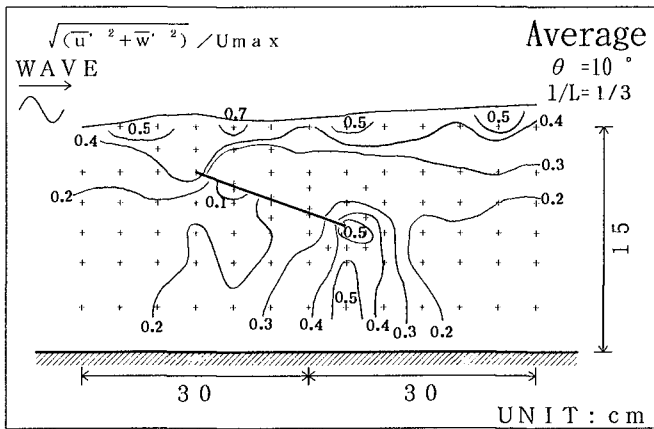
Each velocity vector in the upper figure means the residual velocity. The shoreward residual flow with comparative large velocities generated at the limited region of the upper part of the inner basin can be seen. Then, the strong turbulence can be found at the rear edge of the plate as in the lower figure. However, it is clear that strong turbulence is not generated

at the under region of the plate as already pointed out.

Fig.12 shows the case of  $l/L=1/3$ ,  $d/h=0.2$ ,  $\theta = 10^\circ$  in the B-type.



(1)Residual Velocity



(2)Averaged Turbulent Intensity

Fig.12 B-type

The shoreward residual flow is generated only at the region of the water surface behind the front edge of the plate. Furthermore, the complicated residual flow can be seen at the rear edge of the plate. It can be found that weak turbulence is scattered at the surface, the rear edge and at the bottom of the rear edge as shown in the lower figure.

Fig.13 shows the change of the flow rate  $Q$  through a cross section of the rear edge of the plate in the case of  $l/L=1/3$ ,  $d/h=0.2$  in the A-type with  $\theta=-5^\circ$  and the B type with  $\theta=10^\circ$ . The  $Q$  was calculated by the product of the averaged velocity in 5-6 points of the cross section and the water depth from the water surface to the bottom. Though the seaward flow is generated for a short time at some phases in the A-type, the one directional shoreward flow is almost always generated in both types of plates. It means that seawater with pure water quality flows into the inner basin through these types of breakwaters. Furthermore, if we suppose the reflected wave at a seawall in the A-type again acts upon an A-type plate, the seawater in the inner basin must flow out smoothly into the sea through the breakwater by the seaward residual flow. This is because the reflected wave seaward in the A-type corresponds to the incident wave shoreward in the B-type.

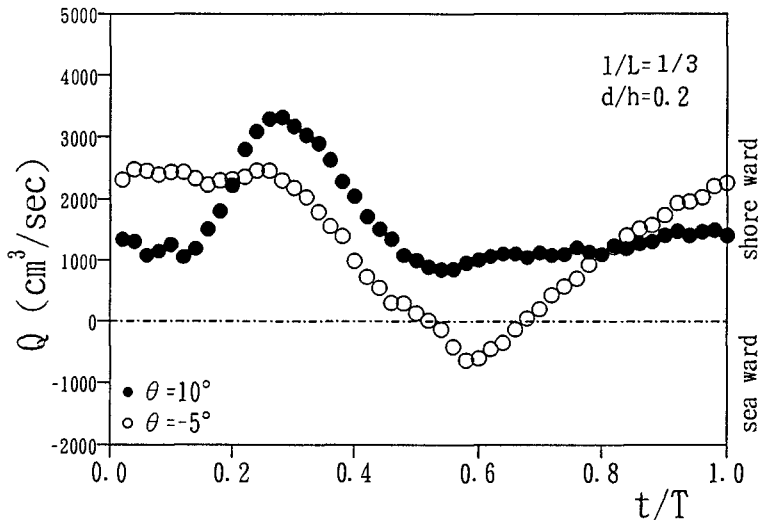


Fig.13 Change of Flow Rate

## Conclusion

The mechanism of wave absorption and the characteristics of wave induced flow around two kinds of submerged plate type breakwaters were discussed experimentally.

Results are summarized as follows.

1) it could be certified that the validity of a sloping plate type breakwater for wave absorption, especially a plate with a gradual upward slope is

effective for the control of wave absorption.

2) The behavior of temporal and spacial water particle velocity and turbulence around a plate type breakwater could be understood.

3) The submerged sloping plate is effective for water quality purification producing a one directional flow, regardless of the raising and lowering of the rear edge of the plate.

Through this knowledge, we could give information to make a good environmental habitat for aquatic biota.

### Acknowledgement

The authors would like to acknowledge the assistance of Miss Mika Masamoto who contributed her efforts in the accomplishment of many of the experiments.

### Reference

- 1) Aoyama,T., Izumiya,T.,Isobe,M. and A.Watanabe: A Study on Wave Control by a Submerged Plate, Proc. of 35th Conf. on Coastal Engrg., pp.507-511,1988 (in Japanese)
- 2) Goda,Y.,Suzuki,Y.,Kishira,Y. and O.Kikuchi:Estimation of Incident and The Reflected Waves in Random Wave Experiments, Technical Note of The Port & Harbour Research Institute, No.248, pp.1-24, 1976 (in Japanese)
- 3) Murakami,H.,Hosoi,Y.,Sawamura,Y. and R.Ikeda: Wave Induced Flow around Submerged Vertical and Horizontal Plates, Proc. of 39th Conf. on Coastal Engrg., pp.571-575, 1992 (in Japanese)
- 4) Takahashi,Y.,Moritaka,H.,Isobe,M. and A.Watanabe: A Study on A Sloped-Plate Breakwater Wave, Proc. of 36th Conf. on Coastal Engrg., pp.519-523, 1989 (in Japanese)
- 5) Yamashita,S.,Sakurai,S.,H.Takeuchi,K.,Uda,T. and A.Omata: A Practical Estimation of Wave Transmission and Wave-Induced Foree for An Offshore Breakwater with A Sloped Plate, Proc. of 37th Conf. on Coastal Engrg., pp.574-578, 1990 (in Japanese)
- 6) Yu,X.,Isobe,M. and A.Watanabe: Simulation of Nonlinear Wave Transformation over A Submerged Plate, Proc. of 36th Conf. on Coastal Engrg., pp.524-528, 1989 (in Japanese)
- 7) Yu,X.,Isobe,M. and A.Watanabe: Wave Force on Submerged Plate, Proc. of 38th Conf. on Coastal Engrg., pp.671-675, 1991 (in Japanese)

# Second-order wave interaction with arrays of vertical cylinders of arbitrary cross section

Keisuke Murakami\*      Akinori Yoshida†

## ABSTRACT

This paper proposes an approximate calculation method for the second-order wave interactions with arrays of vertical cylinders of arbitrary cross section. In mathematical formulations, the first- and the second-order boundary value problems are derived by perturbation method, and Green's Identity Formula is used to express the distribution of the velocity potentials on horizontal plane. Second-order water surface elevations near the cylinders and wave forces acting on the cylinders are computed, and the results are verified by comparing with wave tank experiments in the valid range of the Stokes second-order wave theory.

## 1. INTRODUCTION

Nonlinear wave interactions with structures are important under severe wave conditions, and the developments of a numerical method for calculating nonlinear wave forces and wave deformations are needed. A numerical calculation method of the second-order wave forces utilizing Hskind's reciprocal relationship has been proposed (e.g., Molin, 1979), and this method has been further applied to the case of plural vertical cylinders (e.g., Masuda et al., 1986). Nonlinear wave field near the structures, however, can not be calculated by this method because the second-order velocity potential in a fluid region is not determined. On the other hand, great efforts have been made to predict

---

\*Research Associate, Dept. of Civil Eng. Kyushu Univ., Hakozaki Higashiku Fukuoka 812, Japan

†Associate Professor, Ditto

the nonlinear wave field near the structure by solving the second-order boundary value problem. For examples, Yamaguchi and Tsuchiya(1974) derived a second-order solution of closed form for a vertical cylinder, Garrison(1979) proposed a numerical solution based on a source distribution method using Green's function. Recently, Kriebel(1987) proposed an analytical solution of the second-order diffraction problem for a single circular cylinder and Kim and Yue(1989) showed the complete second-order diffraction solution for an axisymmetric body. However, these methods are difficult to be applied to the case of plural cylinders of arbitrary cross section.

The main purpose of this study is to develop an approximate calculation method for the second-order interaction between water waves and the arrays of vertical cylinders of arbitrary cross section. The validity of the method are confirmed through comparison with experiments and other numerical results. In mathematical formulations, perturbation method is used to derive the first- and second-order boundary value problems, and Green's Identity Formula is also used to express the distribution of the velocity potentials on a horizontal plane(Ijima et al.,1974). A particular solution for scattered waves of the second-order problem is approximately expressed on the assumption that it has the same form of an eigenfunction in the vertical direction as that of the second-order Stokes solution.

## 2. FORMULATION OF THE BOUNDARY VALUE PROBLEM

### 2.1 General formulation

Fig.1 shows a coordinate system,  $x$  and  $y$  being the horizontal axes and  $z$  the vertical axis taken upward from the undisturbed still water surface. Fixed vertical cylinders of arbitrary cross section in water of uniform depth  $h$ , are subject to the incident waves with first-order wave amplitude  $\zeta_0$ , and angular frequency  $\sigma$ , propagating with an incident angle  $\theta$ , measured from positive  $x$  direction. It is assumed that the fluid is both inviscid and incompressible, and its motion is irrotational. The velocity potential  $\Phi(x, y, z, t)$  satisfy following Laplace equation in the whole fluid region.

$$\frac{\partial^2 \Phi}{\partial x^2} + \frac{\partial^2 \Phi}{\partial y^2} + \frac{\partial^2 \Phi}{\partial z^2} = 0 \quad (1)$$

The kinematic boundary condition and the dynamic boundary condition on the free water surface, and bottom boundary conditions are written as:

$$\frac{\partial \zeta}{\partial t} - \frac{\partial \Phi}{\partial z} + \frac{\partial \Phi}{\partial x} \frac{\partial \zeta}{\partial x} + \frac{\partial \Phi}{\partial y} \frac{\partial \zeta}{\partial y} = 0 \quad (z = \zeta(x, y, t)) \quad (2)$$

$$\frac{\partial \Phi}{\partial t} + g\zeta + \frac{1}{2} \left\{ \left( \frac{\partial \Phi}{\partial x} \right)^2 + \left( \frac{\partial \Phi}{\partial y} \right)^2 + \left( \frac{\partial \Phi}{\partial z} \right)^2 \right\} = Q \quad (z = \zeta(x, y, t)) \quad (3)$$



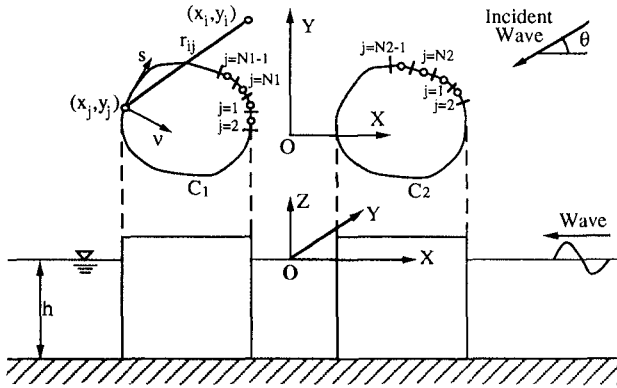


Fig.1 Definition sketch.

$$\frac{\partial \Phi}{\partial z} = 0 \quad (z = -h) \tag{4}$$

where  $Q$  is a constant and  $g$  is a gravity acceleration.

In order to obtain the first- and the second-order boundary value problems, perturbation method is employed. The velocity potential  $\Phi(x, y, z, t)$ , the water surface elevation  $\zeta(x, y, t)$ , and the constant value  $Q$  are expressed in power series by introducing a parameter  $\epsilon$  ( $\epsilon = k\zeta_0$ , where  $k$  is the incident wave number).

$$\left. \begin{aligned} \Phi(x, y, z, t) &= \frac{g}{k\sigma} Re \left[ \epsilon \phi_1^{(1)}(x, y, z) \exp(-i\sigma t) \right. \\ &\quad \left. + \epsilon^2 \left\{ \phi_2^{(0)}(x, y, z) + \phi_2^{(2)}(x, y, z) \exp(-i2\sigma t) \right\} \right] \\ \zeta(x, y, t) &= \frac{1}{k} Re \left[ \epsilon \eta_1^{(1)}(x, y) \exp(-i\sigma t) \right. \\ &\quad \left. + \epsilon^2 \left\{ \eta_2^{(0)}(x, y) + \eta_2^{(2)}(x, y) \exp(-i2\sigma t) \right\} \right] \\ Q &= \frac{g}{k} Re \left[ \epsilon Q_1 + \epsilon^2 Q_2 \right] \end{aligned} \right\} \tag{5}$$

The time independent component  $\phi_2^{(0)}$  in the second-order potential function does not contribute to the second-order wave forces and water surface elevation. Since the main purpose of this study is to develop the numerical calculation method of the second-order wave forces and wave height, we consider the time dependent component  $\phi_2^{(2)}$  only in the following formulations.

By expanding both Eqs.(2) and (3) in Taylor series about  $z=0$ , and substituting Eq.(5) into them, the first- and the second-order combined free surface boundary conditions are obtained.

## 2.2 First-order problem

The first-order boundary value problem is given as follows:

$$\nabla^2 \phi_1^{(1)}(x, y, z) = 0 \quad (6a)$$

$$\frac{\partial \phi_1^{(1)}}{\partial z} - \frac{\sigma^2}{g} \phi_1^{(1)} = 0 \quad (z = 0) \quad (6b)$$

$$\frac{\partial \phi_1^{(1)}}{\partial z} = 0 \quad (z = -h) \quad (6c)$$

The solution is obtained by separating the potential function  $\phi_1^{(1)}$  into the incident plane waves and the scattered waves. A general solution of Eq.(6a), which satisfies free surface boundary condition and bottom boundary condition simultaneously, is given as (Ijima et al., 1974)

$$\phi_1^{(1)}(x, y, z) = \{\varphi_{1I}(x, y) + \varphi_{1S}(x, y)\} \frac{\cosh k(z+h)}{\cosh kh} \quad (7)$$

In Eq.(7),  $\varphi_{1I}$  and  $\varphi_{1S}$  represent the potential of the first-order incident plane waves and the scattered waves respectively, and  $\varphi_{1I}$  is given as

$$\varphi_{1I}(x, y) = -i \exp \{-ik(x \cos \theta + y \sin \theta)\} \quad (8)$$

where  $i = \sqrt{-1}$  and  $k$  satisfies the following dispersion relationship.

$$\frac{\sigma^2 h}{g} = kh \tanh kh \quad (9)$$

$\varphi_{1S}$  must satisfy the following Helmholtz equation since  $\phi_1^{(1)}$  satisfies Laplace equation.

$$\nabla^2 \varphi_{1S}(x, y) + k^2 \varphi_{1S}(x, y) = 0 \quad (10)$$

## 2.3 Second-order problem

The second-order boundary value problem is given as follows:

$$\nabla^2 \phi_2^{(2)}(x, y, z) = 0 \quad (11a)$$

$$\frac{\partial \phi_2^{(2)}}{\partial z} - 4 \frac{\sigma^2}{g} \phi_2^{(2)} = \frac{i}{k} \left\{ \left( \frac{\partial \phi_1^{(1)}}{\partial x} \right)^2 + \left( \frac{\partial \phi_1^{(1)}}{\partial y} \right)^2 + \left( \frac{\partial \phi_1^{(1)}}{\partial z} \right)^2 \right\} + \frac{\eta_1^{(1)}}{2k} \left\{ \frac{\sigma^2}{g} \frac{\partial \phi_1^{(1)}}{\partial z} - \frac{\partial^2 \phi_1^{(1)}}{\partial z^2} \right\} \quad (z = 0) \quad (11b)$$

$$\frac{\partial \phi_2^{(2)}}{\partial z} = 0 \quad (z = -h) \quad (11c)$$

The second-order free surface boundary condition ,Eq.(11b), is nonhomogeneous because the quadratic forcing terms appear in the right hand side. The solution may be obtained by the separation of potential function  $\phi_2^{(2)}$  as

$$\phi_2^{(2)}(x, y, z) = \phi_{2I}(x, y, z) + \phi_{2L}(x, y, z) + \phi_{2F}(x, y, z) \tag{12}$$

where  $\phi_{2I}$  represents the second-order incident plane waves expressed as

$$\left. \begin{aligned} \phi_{2I} &= \varphi_{2I}(x, y) \frac{\cosh 2k(z + h)}{\cosh 2kh} \\ \varphi_{2I}(x, y) &= -\frac{3i}{8} \frac{\Gamma}{k \sinh^4 kh} e^{-i2k(x \cos \theta + y \sin \theta)} \end{aligned} \right\} \tag{13}$$

where  $\Gamma = \sigma^2 h/g$ .

In Eq.(12),  $\phi_{2L}$  represents a phase-locked wave which satisfies the nonhomogeneous free surface boundary condition and  $\phi_{2F}$  represents a free wave which satisfies the homogeneous free surface boundary condition. The boundary value problems of  $\phi_{2L}$ , and  $\phi_{2F}$  are obtained by a substitution of Eqs.(12) and (13) into Eqs.(11a),(11b) and (11c).

Firstly, the boundary value problem for  $\phi_{2L}$  is given as follows:

$$\nabla^2 \phi_{2L}(x, y, z) = 0 \tag{14a}$$

$$\frac{\partial \phi_{2L}}{\partial z} - 4 \frac{\sigma^2}{g} \phi_{2L} = \frac{i}{k} \left\{ \frac{3\Gamma^2 - k^2}{2} \varphi_{1s} (\varphi_{1s} + 2\varphi_{1I}) + \frac{\partial \varphi_{1s}}{\partial x} \left( \frac{\partial \varphi_{1s}}{\partial x} + 2 \frac{\partial \varphi_{1I}}{\partial x} \right) + \frac{\partial \varphi_{1s}}{\partial y} \left( \frac{\partial \varphi_{1s}}{\partial y} + 2 \frac{\partial \varphi_{1I}}{\partial y} \right) \right\} \quad (z = 0) \tag{14b}$$

$$\frac{\partial \phi_{2L}}{\partial z} = 0 \quad (z = -h) \tag{14c}$$

By assuming that the  $\phi_{2L}$  has the same form of an eigenfunction for z direction as the Stokes second-order solution has(Sabuncu et al.,1985), the particular solution of  $\phi_{2L}$  is approximately expressed as follows:

$$\phi_{2L}(x, y, z) = \gamma f(x, y) \frac{\cosh 2k(z + h)}{\cosh 2kh} \tag{15}$$

where  $\gamma$  and  $f(x, y)$  are given as follows:

$$\gamma = \frac{i}{2k^2 \tanh 2kh - 2 \tanh kh} \tag{16}$$

$$f(x, y) = \frac{3\Gamma^2 - k^2}{2} \varphi_{1s} (\varphi_{1s} + 2\varphi_{1I}) + \frac{\partial \varphi_{1s}}{\partial x} \left( \frac{\partial \varphi_{1s}}{\partial x} + 2 \frac{\partial \varphi_{1I}}{\partial x} \right) + \frac{\partial \varphi_{1s}}{\partial y} \left( \frac{\partial \varphi_{1s}}{\partial y} + 2 \frac{\partial \varphi_{1I}}{\partial y} \right) \quad (17)$$

Secondary, the boundary value problem for  $\phi_{2F}$  is given as follows:

$$\nabla^2 \phi_{2F}(x, y, z) = 0 \quad (18a)$$

$$\frac{\partial \phi_{2F}}{\partial z} - 4 \frac{\sigma^2}{g} \phi_{2F} = 0 \quad (z = 0) \quad (18b)$$

$$\frac{\partial \phi_{2F}}{\partial z} = 0 \quad (z = -h) \quad (18c)$$

The solution of Eq.(18a), which satisfies the homogeneous free surface boundary condition and bottom boundary condition simultaneously, can be expressed in much the same way as the first-order problem as

$$\phi_{2F}(x, y, z) = \varphi_{2F}(x, y) \frac{\cosh k^{(2)}(z + h)}{\cosh k^{(2)}h} \quad (19)$$

where  $k^{(2)}$  satisfies the following dispersion relationship.

$$\frac{(2\sigma)^2 h}{g} = k^{(2)} h \tanh k^{(2)} h \quad (20)$$

$\varphi_{2F}$  must satisfy the following Helmholtz equation since  $\phi_{2F}$  satisfies Laplace equation.

$$\nabla^2 \varphi_{2F}(x, y) + (k^{(2)})^2 \varphi_{2F}(x, y) = 0 \quad (21)$$

### 3. NUMERICAL CALCULATION METHOD

As shown in **Fig.1**, the boundaries  $C_1$  and  $C_2$  are defined as the intersection of still water surface and the vertical structures, and  $\nu$  as an unit vector normal to the boundary.  $X_i$  and  $X_j$  are the coordinates taken in the fluid region and on the boundary respectively. Since the potentials of the first-order scattered waves and the second-order free waves satisfy the Sommerfeld's radiation condition respectively, each potential at  $X_i$  can be expressed by means of Green's Identity Formula as follows (Ijima et al.,1974):

$$\varphi_{1S}(\mathbf{X}_i) = \alpha \oint_{C_1+C_2} \left\{ \varphi_{1S}(\mathbf{X}_j) \frac{\partial}{\partial \nu} H_0^{(1)}(kr_{ij}) - H_0^{(1)}(kr_{ij}) \frac{\partial}{\partial \nu} \varphi_{1S}(\mathbf{X}_j) \right\} ds \tag{22}$$

$$\varphi_{2F}(\mathbf{X}_i) = \alpha \oint_{C_1+C_2} \left\{ \varphi_{2F}(\mathbf{X}_j) \frac{\partial}{\partial \nu} H_0^{(1)}(k^{(2)}r_{ij}) - H_0^{(1)}(k^{(2)}r_{ij}) \frac{\partial}{\partial \nu} \varphi_{2F}(\mathbf{X}_j) \right\} ds \tag{23}$$

where  $r_{ij}$  represents a distance between  $\mathbf{X}_i$  and  $\mathbf{X}_j$  and  $H_0^{(1)}$  represent the first kind of Hankel function, and  $\alpha = -i/2$  ( $\mathbf{X}_i$  is on the boundary) and  $\alpha = -i/4$  ( $\mathbf{X}_i$  is in the fluid region)

For the first- and the second-order potential functions, no-flow conditions around the cylinders are written as follows:

$$\frac{\partial \phi_1^{(1)}}{\partial \nu} = 0 \quad (-h \leq z \leq 0) \tag{24}$$

$$\frac{\partial \phi_2^{(2)}}{\partial \nu} = 0 \quad (-h \leq z \leq 0) \tag{25}$$

By substituting Eq.(7) into Eq.(24) and Eq.(12) into Eq.(25), and by integrating Eq.(24) and Eq.(25) over the water depth after multiplying by eigenfunctions  $\cosh k(z+h)$  and  $\cosh 2k(z+h)$  respectively, the boundary conditions of  $\varphi_{1S}$  and  $\varphi_{2F}$  on  $C_1$  and  $C_2$  are derived as follows:

$$\frac{\partial \varphi_{1s}}{\partial \nu} = -\frac{\partial \varphi_{1l}}{\partial \nu} \tag{26}$$

$$\frac{\partial \varphi_{2F}}{\partial \nu} = -\frac{i}{4k\Gamma} \frac{1}{M_0} \frac{1}{\gamma} \frac{(k^{(2)})^2}{(2k)^2 - (k^{(2)})^2} \left( \frac{\partial \varphi_{2l}}{\partial \nu} + \gamma \frac{\partial f}{\partial \nu} \right) \tag{27}$$

where  $M_0 = (1 + 2k^{(2)}h / \sinh 2k^{(2)}h) / 2$

In order to obtain the numerical solutions of the integral equations written as Eqs.(22) and (23), the boundaries  $C_1$  and  $C_2$  are discretized into elements  $\Delta S_j$  of  $N_1$  and  $N_2$  numbers, and the coordinate  $\mathbf{X}_i$  is set on them. On each element, the potential and its normal derivative are assumed to be constant. By applying Eqs.(26) and (27) to Eqs.(22) and (23) respectively, the linear matrix equations for  $\varphi_{1s}$  and  $\varphi_{2F}$  are obtained as follows:

$$\sum_{j=1}^{N_1+N_2} \left( \overline{G_{ij}^{(1)}} - \delta_{ij} \right) \varphi_{1S}(\mathbf{X}_j) = - \sum_{j=1}^{N_1+N_2} G_{ij}^{(1)} \overline{\varphi_{1I}}(\mathbf{X}_j) \quad (i = 1 \sim N_1 + N_2) \tag{28}$$

$$\sum_{j=1}^N \left( \overline{G_{ij}^{(2)}} - \delta_{ij} \right) \varphi_{2F}(\mathbf{X}_j) = -\beta \sum_{j=1}^N G_{ij}^{(2)} \left\{ \overline{\varphi_{2I}}(\mathbf{X}_j) + \gamma \overline{f}(\mathbf{X}_j) \right\} \quad (i = 1 \sim N_1 + N_2) \tag{29}$$

$$\left. \begin{aligned} G_{ij}^{(1)} &= -\frac{i}{2} \int_{\Delta S_j} H_0^{(1)}(kr_{ij}) & \overline{G_{ij}^{(1)}} &= -\frac{i}{2} \int_{\Delta S_j} \frac{\partial}{\partial \nu} H_0^{(1)}(kr_{ij}) ds \\ G_{ij}^{(2)} &= -\frac{i}{2} \int_{\Delta S_j} H_0^{(1)}(k^{(2)}r_{ij}) & \overline{G_{ij}^{(2)}} &= -\frac{i}{2} \int_{\Delta S_j} \frac{\partial}{\partial \nu} H_0^{(1)}(k^{(2)}r_{ij}) ds \end{aligned} \right\} \tag{30}$$

where  $\overline{\varphi_{1I}}$ ,  $\overline{\varphi_{2I}}$  and  $\overline{f}$  mean a normal derivative of  $\varphi_{1I}$ ,  $\varphi_{2I}$  and  $f$  on the boundaries.

From Eq.(15),  $f(\mathbf{X}_i)$  must satisfy the following Helmholtz equation.

$$\nabla^2 f + (2k)^2 f = 0 \tag{31}$$

By assuming that  $\varphi_{2L}$  satisfies the same radiation condition as  $\varphi_{1s}$  and  $\varphi_{2F}$ ,  $f(\mathbf{X}_i)$  can be also expressed by means of Green's Identity Formula as follows:

$$f(\mathbf{X}_i) = \alpha \oint_{C_1+C_2} \left\{ f(\mathbf{X}_j) \frac{\partial}{\partial \nu} H_0^{(1)}(2kr_{ij}) - H_0^{(1)}(2kr_{ij}) \frac{\partial}{\partial \nu} f(\mathbf{X}_j) \right\} ds \tag{32}$$

From Eq.(32),  $\overline{f}(\mathbf{X}_j)$  can be computed without numerical differentiations of  $f(\mathbf{X}_j)$  on the boundaries.

The first-order potential function  $\varphi_1^{(1)}$  expressed in Eq.(7) is obtained by solving the linear matrix equation. After solving the first-order equation,  $\varphi_{2L}$  is determined from the first-order solution and thus  $\varphi_{2F}$  is obtained by solving the linear matrix equation given as Eq.(29). By applying these second-order solutions to Eq.(12), the second-order potential function  $\varphi_2^{(2)}$  is determined.

### 3. RESULTS OF CALCULATIONS

To verify the numerical calculation method, we conducted the wave tank experiments for single and double vertical circular cylinders. The vertical circular cylinders of radius  $a = 18.5\text{cm}$  are placed in the center of the wave tank of  $18\text{m}$  long and  $10\text{m}$  wide, and the water depth is maintained at  $h = 40\text{cm}$ .

Table-1 Incident wave conditions for single and double circular cylinders

Single Circular Cylinder			Double Circular Cylinder		
$kh$	$T(sec.)$	$\zeta_0/h$	$kh$	$T(sec.)$	$\zeta_0/h$
1.0	1.46	0.081	0.8	1.74	0.178
1.4	1.14	0.109	1.0	1.46	0.202
			1.4	1.14	0.179
			1.6	1.05	0.175

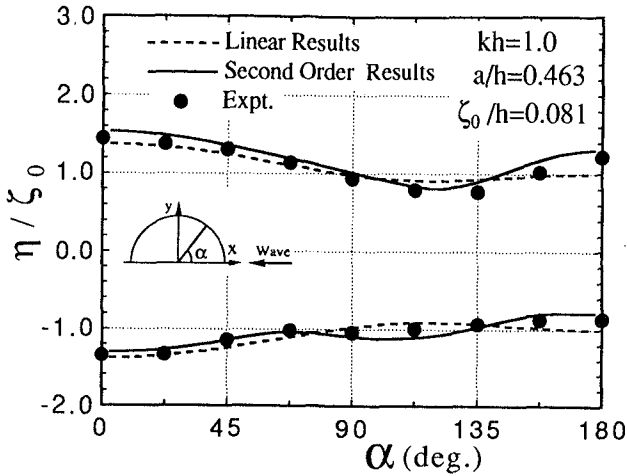


Fig.2 Wave runup and rundown around single circular cylinder.

Table-1 shows the incident wave conditions. The water surface elevations around the cylinders are measured by the wave gages. In the case of the double circular cylinders, the cylinders are placed in a row with spacing  $B = 1m$  normal to the incident wave direction.

Fig.2 and Fig.3 show the wave runup and rundown around the single cylinder for  $kh = 1.0$  and  $kh = 1.4$ . The incident wave propagates from positive  $x$  direction and  $\alpha$  is measured counterclockwise from positive  $x$  direction. In the experimental results, the secondary effects are observed at front side and rear side of the vertical cylinder and the second-order results show good agreements with experimental ones.

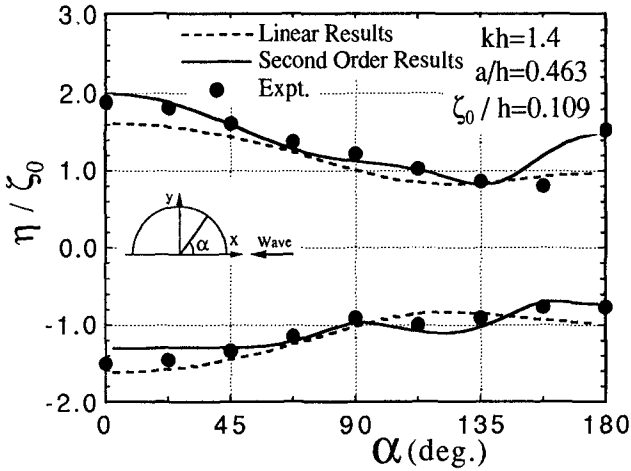


Fig.3 Wave runup and rundown around single circular cylinder.

Fig.4 and Fig.5 show the wave runup and rundown around the double cylinder for  $kh = 0.8$  and  $1.0$ . In the experiments, the waves become very steep between the cylinders and the wave patterns around the cylinders are more complicate than the case of single cylinder. The linear results are largely different from experimental ones especially at the front side( $\alpha = 0$ ), rear side( $\alpha = 180$ ) and inner side( $\alpha = 270$ ) of the cylinders. On the other hand, the second-order results show good agreements with experimental ones.

Fig.6 and Fig.7 show the computed maximum wave amplitude distribution around the double and the triple circular cylinders. The wave with  $kh = 1.0$  and  $\zeta_0/h = 0.1$  propagates from positive  $y$  direction normal to the row of the cylinders( $a/h = 0.5$ ,  $B/h = 2$ ;  $a$  is the cylinder radius and  $B$  is the space between cylinders) The second-order results show more complicated pattern than linear ones and secondary effects are clearly observed around the cylinders. The maximum differences of wave amplitude between linear results and second-order ones around the cylinders are about 20%.

Fig.8 shows the maximum wave forces acting on the single and double circular cylinders, and Fig.9 also shows the maximum wave forces acting on the center of the triple circular cylinders. The cylinders are placed in a row normal to the incident wave direction. The differences between linear results and second-order ones become small as the  $ka$  increase.



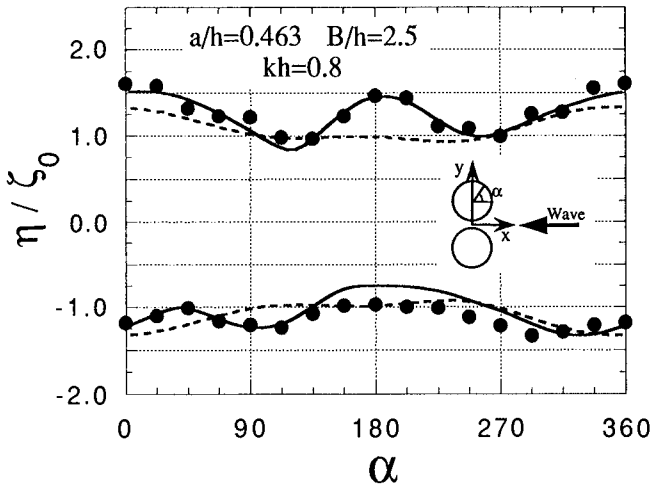


Fig.4 Wave runup and rundown around double circular cylinder.  
 - - - Linear Results, — Second-Order Results, ● Expt.

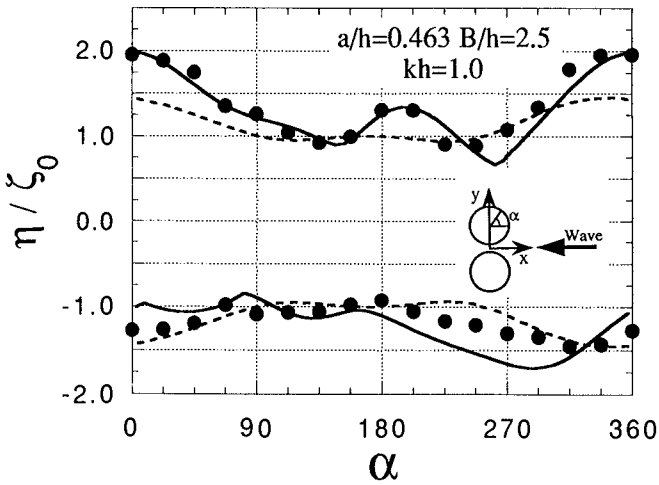


Fig.5 Wave runup and rundown around double circular cylinder.  
 - - - Linear Results, — Second-Order Results, ● Expt.

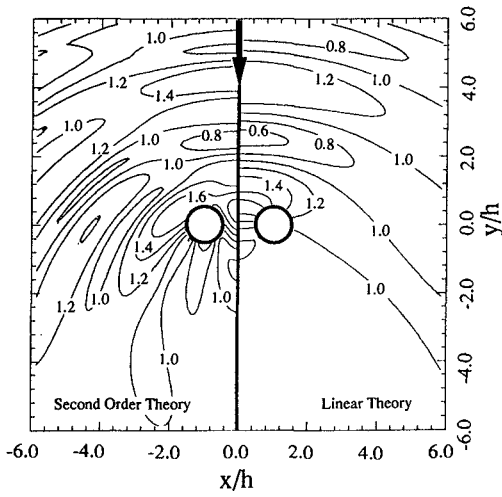


Fig.6 Maximum wave amplitude distribution near double circular cylinders.  
 $[B/h = 2, a/h = 0.5, \zeta_0/h = 0.1, kh = 1.0]$

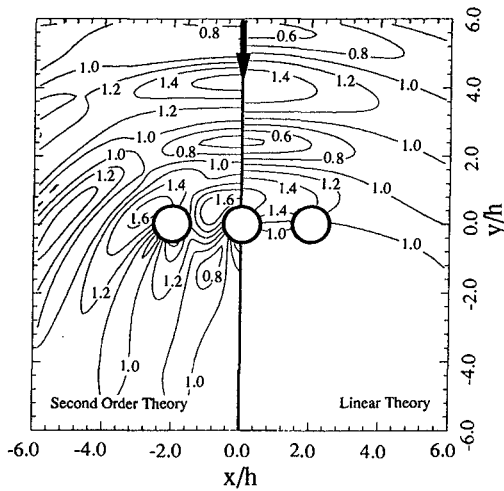


Fig.7 Maximum wave amplitude distribution near triple circular cylinders.  
 $[B/h = 2, a/h = 0.5, \zeta_0/h = 0.1, kh = 1.0]$

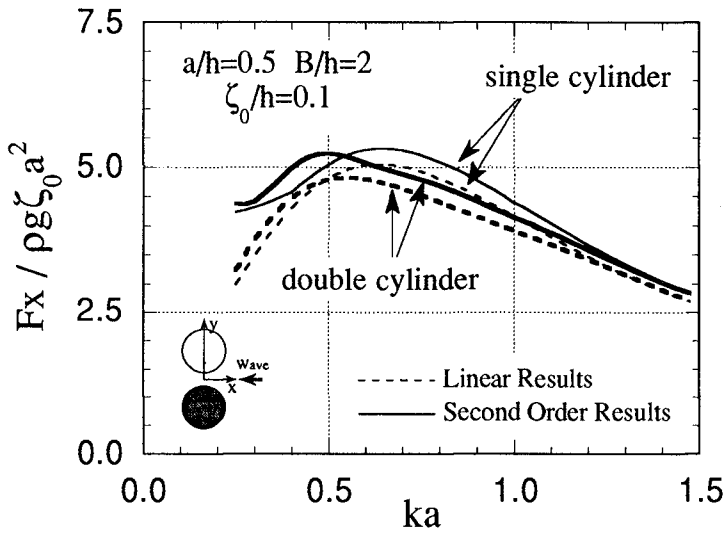


Fig.8 Maximum wave forces acting on double circular cylinders

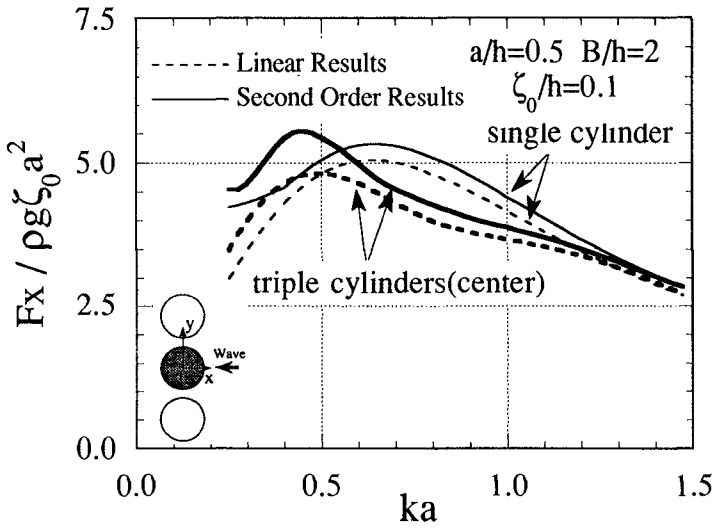


Fig.9 Maximum wave forces acting on triple circular cylinders

On the other hand, the differences become large as the  $ka$  decrease for  $ka < 0.5$ . The divergence of the present method in small value of  $ka$  ( $ka < 0.3$ ), small value of  $ka$  means large Ursell parameter in this case, is caused by the failure of the Stokes second-order theory (Isaacson, 1978). In  $0.6 < ka < 1.3$ , the wave forces acting on the single cylinder are always larger than those on the double cylinders and the center cylinder of the triple ones, but with increase of  $ka$ , the wave forces acting on those plural cylinders are converged to the value of single cylinder.

## 5. CONCLUSIONS

An approximate calculation method for the second-order wave interactions with array of vertical cylinders of arbitrary cross section is proposed by using both Green's Identity Formula and perturbation method in combination. The validity of the present method is confirmed by comparing the computed results with experimental ones. Though the present method includes approximation that the second-order potential function for phase-locked wave has the same form of an eigenfunction of the second-order Stokes solution, the nonlinear wave field and wave forces are estimated with good accuracy in the valid range of the Stokes second-order wave theory.

## References

- Garrison, C.J. (1979): Hydrodynamic loading of large offshore structures: Three dimensional source distribution methods, In numerical method in offshore engineering, Zienkiewicz, O., Lewis, R. and Stagg, K. (eds), John Wiley and Sons, pp. 97-140.
- Ijima, T., Chou, C.R. and Y. Yumura (1974): Scattering of waves by permeable and impermeable breakwater of arbitrary shape, Proc. JSCE, Vol. 228, pp. 31-42. (in Japanese)
- Isaacson, M. (1978): Nonlinear wave forces on large offshore structures, discussion, Proc. ASCE, Vol. 104, No. WW4, pp. 457-459.
- Kim, M.H. and Yue, D.K.P. (1989): The complete second-order diffraction solution for an axisymmetric body, Part 1. Monochromatic incident waves, J. Fluid Mech. 200, pp. 235-264.
- Kriebel, D.L. (1987): A second-order diffraction theory for wave runup and wave forces on a vertical circular cylinder, Ph.D. dissertation, University of Florida.
- Masuda, K., C. Sakai and W. Kato (1986): Study on nonlinear wave forces on plural vertical cylinder with arbitrary cross-section, J. Soc. Nav. Arch. Japan, Vol. 160, pp. 176-184 (in Japanese)

- Molin,B.(1979): Second-order diffraction loads upon three-dimensional bodies, Applied Ocean Res.,Vol.1,No.4,pp.197-202.
- Sabuncu,T. and Goren,O.(1985): Second-order vertical and horizontal wave forces on a circular dock, Ocean Eng.,Vol.12,No.4,pp341-361.
- Yamaguchi,M. and Y.Tsuchiya(1974): Nonlinear effect of waves on wave pressure and wave force on a large cylindrical pile, Proc. JSCE, Vol.229, pp.41-53. (in Japanese)

## CHAPTER 107

### HYDRODYNAMIC FORCES ON BOTTOM-SEATED HEMISPHERE IN WAVES AND CURRENTS

H. Nishida<sup>1</sup>, A. Tada<sup>2</sup> and F. Nishihira<sup>3</sup>

#### Abstract

The characteristics of hydrodynamic forces acting on a bottom-seated hemisphere in waves only, in currents only and in waves & currents are presented from the viewpoint of the design of an artificial reef. A large number of regular wave experiments were conducted in order to find the empirical formulas of the hydrodynamic coefficients for the bottom-seated hemisphere. It is shown that the proposed empirical formulas are sufficiently accurate for predicting the hydrodynamic forces. The effects of the normalized water depth and hemisphere spacing relative to its diameter are also elucidated experimentally.

#### Introduction

In order to provide a continued supply of marine products, the Japanese fishing industry has been shifting from fish catching to fish farming. Various artificial reefs have been used to attract fish by producing coherent eddies with upward flow as well as by providing hiding places for fish. Most of these reefs have rectangular shapes and caused tearing of fishing nets. In order to reduce entanglement of fishing nets, the authors have proposed bottom-seated hemispherical reefs. For the design of such a reef against waves and currents, the hydrodynamic forces acting on the reef need to be predicted.

=====  
<sup>1</sup> Research Engineer, Technical Research Institute, Nishimatsu Construction Co., Ltd., 2570-4, Shimotsuruma, Yamato, Kanagawa 242, Japan

<sup>2</sup> Senior Research Engineer, Technical Research Institute, Nishimatsu Construction Co., Ltd., 2570-4, Shimotsuruma, Yamato, Kanagawa 242, Japan

<sup>3</sup> Dr. and General Manager, Technical Research Institute, Nishimatsu Construction Co., Ltd., 2570-4, Shimotsuruma, Yamato, Kanagawa 242, Japan

### Hydraulic Experiments

Regular wave experiments were conducted in a wave flume which was 65m long, 1.0 m wide and 1.6 m high. The flume was capable of generating steady currents in both directions relative to the direction of wave propagation. As a first attempt, plastic hemispheres without any opening were used in the experiments. The experimental results presented herein may hence be of interest to researchers working on the design of quarry stone armor units. The three-dimensional hydrodynamic force acting on an individual hemisphere was measured using a three-component waterproof load cell with a water pressure adjustment. Fluid velocities at the location of the hemisphere were measured using a two-component electromagnetic current meter. Free surface oscillations above the hemisphere are measured using a capacitance wave gage. For limited tests, flow visualization was performed to examine the flow pattern and eddy formation using a laser and a high speed camera, as shown in Photo.1. A large number of tests were performed for a single hemisphere and three hemispheres in a row.

Fig.1 shows the experimental setup for three hemispheres, where  $X$ =horizontal coordinate taken to be positive in the direction of wave propagation with  $X=0$  at the center of the middle hemisphere;  $Z$ =vertical coordinate taken to be positive upward with  $Z=0$  at the still water level(SWL);  $h$ =water depth below SWL;  $H$ =height of incident regular waves whose period is denoted by  $T$ ;  $D$ =diameter of the hemisphere; and  $L_f$ =distance between the centers of two adjacent hemispheres. The experiments were conducted for the following conditions;

- 1)  $h=40,60$  and  $80$  cm
- 2)  $H=3.0,6.0$  and  $9.0$  cm
- 3)  $T=1.2,1.6,2.0,2.4$  and  $2.8$  sec
- 4)  $D=15.0$  and  $20.0$  cm
- 5)  $L_f/D=1.0,1.5,2.0,2.5$  and  $3.0$
- 6)  $U=\pm 5.0, \pm 10.0, \pm 20.0, \pm 30.0$  and  $\pm 40.0$  cm/sec

where  $U$ =depth-averaged steady current velocity which is negative for opposing currents.

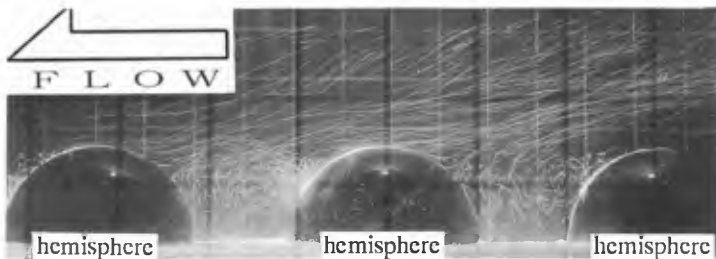


Photo.1 An example of flow visualization in currents only

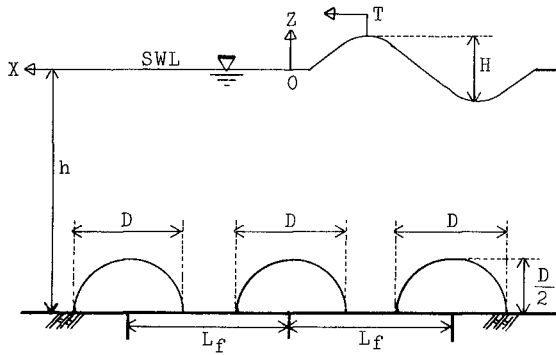


Fig.1 Experimental setup for three hemispheres

### Data Analysis

The measured horizontal and vertical hydrodynamic forces acting on the hemisphere are assumed to be expressed in the form proposed by Morison (Morison et al. 1950).

$$F_x = \frac{1}{2} \rho C_D \left( \frac{\pi D^2}{8} \right) (u + U) |u + U| + \rho C_M \left( \frac{\pi D^3}{12} \right) \frac{du}{dt} \quad (1)$$

$$F_{z_m} = \frac{1}{2} \rho C_L \left( \frac{\pi D^2}{8} \right) (u_m + U)^2 \quad (2)$$

where  $F_x$  = horizontal force ;  $\rho$  = fluid density ;  $u$  = oscillatory horizontal fluid velocity ;  $U$  = steady fluid velocity ;  $C_D$  = drag coefficient ;  $C_M$  = inertia coefficient ; and  $C_L$  = lift coefficient .The velocities  $u$  and  $U$  are at the location of the hemisphere. The constant values of  $C_D$  and  $C_M$  for each test were determined using the method of least squares (Reid 1957). The constant value of  $C_L$  was estimated such that the maximum vertical force  $F_{z_m}$  could be predicted by Eq.(2) accurately. This was because Eq.(2) with constant  $C_L$  did not reproduce the entire variation of  $F_z$  with respect to time  $t$  very well.

### Drag, Inertia and Lift Coefficients

The efforts for developing the empirical relationships for  $C_D$ ,  $C_M$  and  $C_L$  were separated into;

- single hemisphere in waves only
- single hemisphere in currents only
- single hemisphere in waves & currents
- middle hemisphere among three hemispheres in waves only
- middle hemisphere among three hemispheres in currents only



For these tests, the inertia force was generally dominant in Eq.(1) and the horizontal force was normally greater than the vertical force. In addition, it was judged that there was little scale effect on hemispherical models because the influence of Reynolds number  $Re=u_m D/\nu$  on the wave force coefficients were negligible under adopted experimental conditions, refer to Figs.2 and 3.

Fig.4 shows the relationship between the wave force coefficients and Keulegan-Carpenter number( $K.C.=u_m T/D$ ) for the single hemisphere in the water depth of 40 cm, where  $u_m$  is the maximum value of  $u$ . As shown in Fig.4,  $C_M$  in waves only is on the order of 1.35 and  $C_D$  in waves only varies with  $K.C.$  in a manner similar to a sphere (Jenkins and Inman 1976).

Eqs.(3), (4) and (5) are the empirical formulas of  $C_D$ ,  $C_M$  and  $C_L$  in waves only, respectively. They are statistically derived by means of the method of least squares.

$$C_D = 6.79 \cdot (K.C.)^{-0.89} \quad \text{for } U=0 \quad (3)$$

$$C_M = 1.35 \quad \text{for } U=0 \quad (4)$$

$$C_L = 3.3 \cdot (K.C.)^{-0.98} \quad \text{for } U=0 \quad (5)$$

Eqs.(6) and (7) are the empirical formulas of the drag and lift coefficients in currents only for the single hemisphere in the depth of 40 cm, respectively. The effect of Reynolds number  $Re=UD/\nu$  on these coefficients seems to be also negligible for the case of currents only as shown in Fig.5.

$$C_D = 0.48 \quad \text{for } u_m=0 \quad (6)$$

$$C_L = 0.8 \quad \text{for } u_m=0 \quad (7)$$

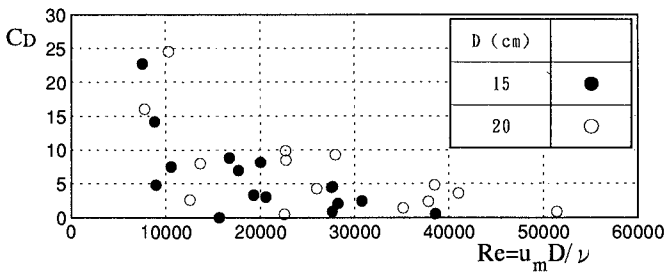


Fig.2 Drag coefficient  $C_D$  versus  $Re(=u_m D/\nu)$  in waves only

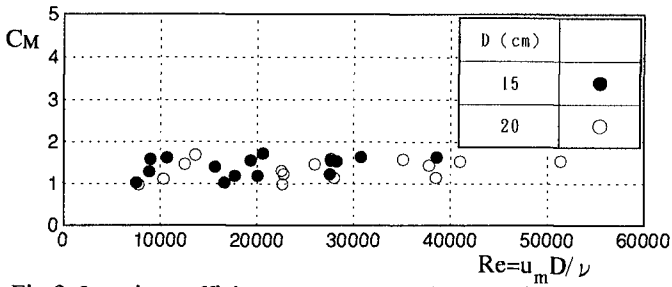


Fig.3 Inertia coefficient  $C_M$  versus  $Re(=u_m D/\nu)$  in waves only

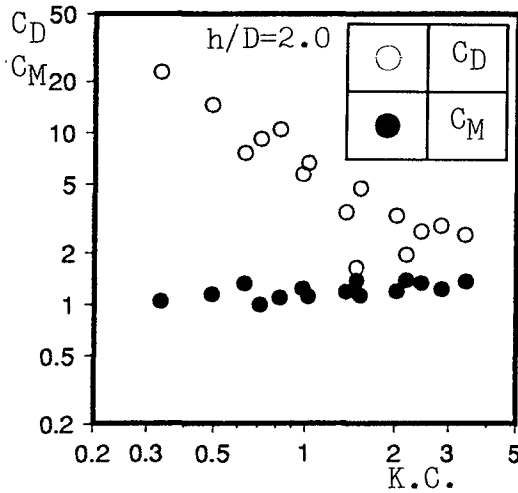


Fig.4 Drag coefficient  $C_D$ , inertia coefficient  $C_M$  versus  $K.C.$  in waves only

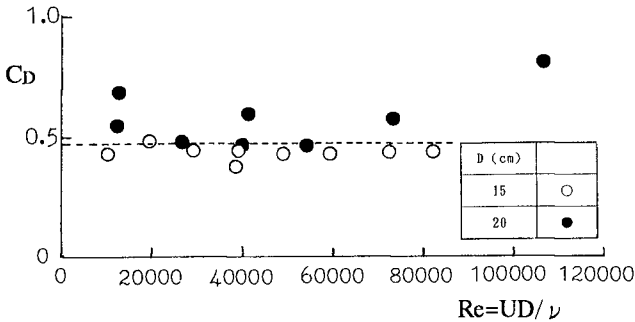


Fig.5 Drag coefficient  $C_D$  versus  $Re(=UD/\nu)$  in currents only

Fig.6 shows the relationship between  $C_D$  in waves & currents and the modified Keulegan-Carpenter number  $K=(|U|+u_m)T/D$  for the single hemisphere in fair currents for which  $U>0$  (Iwagaki et al . 1983). The water depth is 40 cm. The parameter  $\alpha$  shown in the figure is defined as  $\alpha=|U|/u_m$  and two solid lines in this figure indicate the empirical formulas of  $C_D$  in waves only [Eq.(3)] and in currents only [Eq.(6)] , respectively.  $C_D$  is slightly affected by  $K$  and  $\alpha$  and also approximately approaches 0.48 for large  $\alpha$ , corresponding to the value of  $C_D$  for currents only.

On the basis of these characteristics shown in Fig.6, the following empirical formula of  $C_D$  for the single hemisphere in waves & currents with  $U>0$  have been proposed;

$$C_D = 6.97 \cdot e^{-\beta} \cdot K^{-0.89} + 0.48(1 - e^{-\beta}) \text{ for } U>0 \quad (8)$$

with  $\beta = 0.019\alpha^2 + 0.99\alpha - 0.07$

When  $\alpha$  is equal to zero and  $K=K.C.$ , Eq.(8) yields almost the same value of  $C_D$  in waves only. On the other hand, this formula corresponds to  $C_D$  in currents only when  $\alpha$  tends to infinity. The broken lines in Fig.6 indicate Eq.(8) for  $\alpha$  in the range of 0.25 to 2.5. In order to evaluate the accuracy of Eq.(8), Fig.7 compares  $C_D$  calculated by Eq.(8) with  $C_D$  obtained from the experiments. It is realized that the former agrees fairly with the latter, regardless of  $\alpha$ .

Fig.8, for the case of water depth 40 cm, shows the relationship between the inertia coefficient in waves & currents and  $K$  for the single hemisphere in fair currents. It is obvious that  $C_M$  increases with increasing  $K$  in the region  $C_M>1.35$  , whereas  $C_M$  decreases with increasing  $K$  in the region  $C_M<1.35$ . Furthermore ,  $C_M$  decreases with increasing  $\alpha$  if  $K$  is assumed to be constant.

Considering the above characteristics, the following empirical formula of  $C_M$  as a function of  $\alpha$  and  $K$  is derived from the method of least squares.

$$C_M = 1.35 \cdot \exp \left[ 0.084(1.18 - \alpha)K \right] \text{ for } U>0 \quad (9)$$

Eq.(9) is equivalent to  $C_M$  in waves only if  $\alpha$  is equal to 1.18. Broken lines in Fig.8 indicate the above formula for  $\alpha$  in the range of 0.25 to 3.5. It is found that Eq.(9) coincides fairly with the experimental values.

The relationship between  $C_M$  calculated by Eq.(9) and  $C_M$  obtained from the experimental results is also shown in Fig.9. The reason why the accuracy of Eq.(9) is lower as the parameter  $\alpha$  becomes larger is that the drag force is more predominant than the inertia force and it is hard to estimate  $C_M$  accurately for large  $\alpha$ .

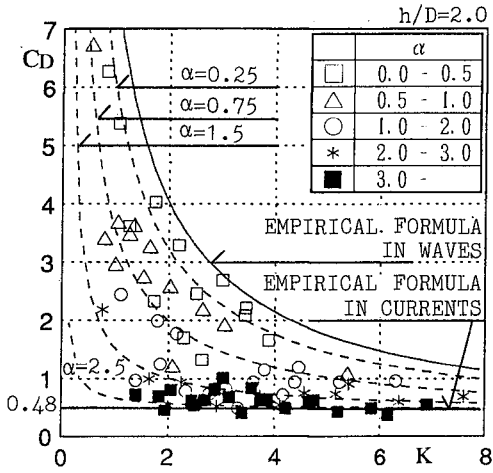


Fig.6 Drag coefficient  $C_D$  versus  $K$  in waves & currents(fair current)

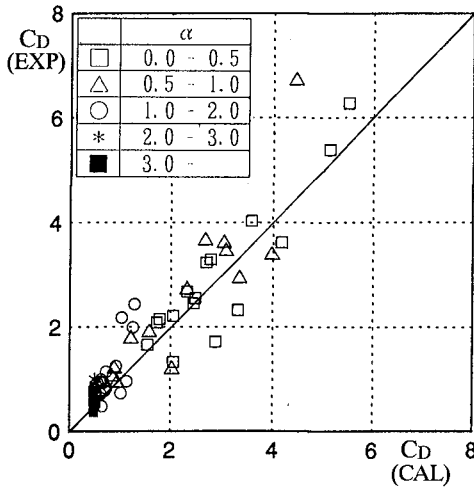


Fig.7 Drag coefficient  $C_D(\text{EXP})$  versus Drag coefficient  $C_D(\text{CAL})$

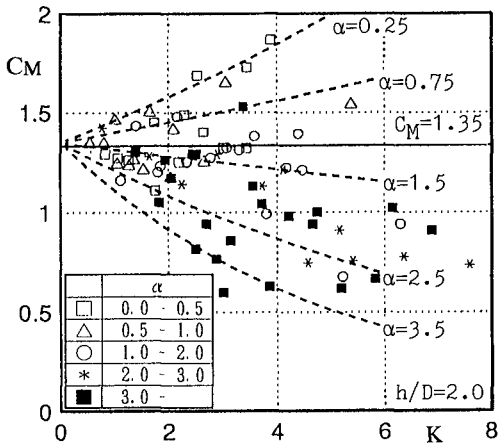


Fig.8 Inertia coefficient  $C_M$  versus  $K$  in waves & currents(fair current)

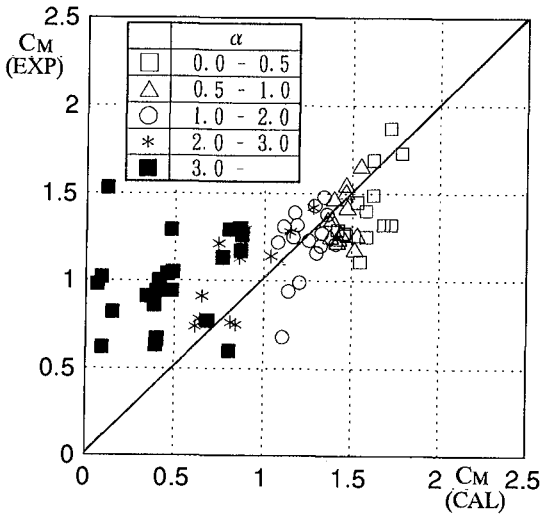


Fig.9 Inertia coefficient  $C_M$ (EXP) versus inertia coefficient  $C_M$ (CAL)

Fig.10 shows the relationship between  $C_L$  in waves & currents and  $K$  for the single hemisphere in the water depth of 40 cm . The variations of  $C_L$  with respect to these dimensionless parameters were similar to those associated with  $C_D$ . The following formula in fair currents is introduced.

$$C_L = 3.3 \cdot e^{-0.5\alpha} \cdot K^{-0.98} + 0.8(1 - e^{-0.5\alpha})^{0.16} \text{ for } U > 0 \quad (10)$$

The relationships between the hydrodynamic coefficients and  $K$  for the single hemisphere in adverse currents for which  $U < 0$  and  $\alpha$  are shown in Figs.11 and 12. Moreover, the following empirical formulas for adverse currents are derived using the same procedure .

$$C_D = 6.97 \cdot e^{-\beta} \cdot K^{-0.89} + 0.48(1 - e^{-\beta}) \text{ for } U < 0 \quad (11)$$

$$\text{with } \beta = -0.08\alpha^2 + 1.05\alpha - 0.1$$

$$C_M = 1.35 \cdot \exp \left[ 0.063(1.34 - \alpha)K \right] \text{ for } U < 0 \quad (12)$$

$$C_L = 3.3 \cdot e^{-0.6\alpha} \cdot K^{-0.98} + 0.8(1 - e^{-0.6\alpha})^{0.43} \text{ for } U < 0 \quad (13)$$

Those formulas should be reevaluated because free surface oscillations became larger and more irregular as waves propagated over a long distance in adverse currents.

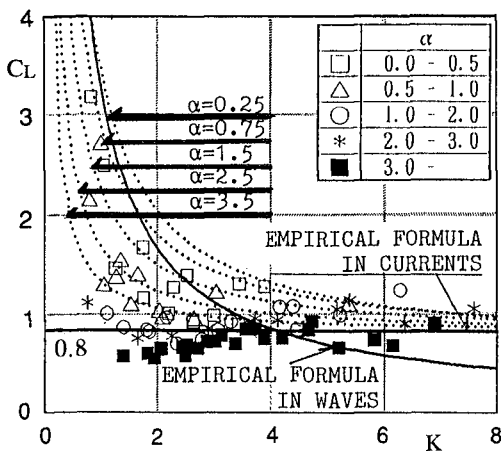


Fig.10 Lift coefficient  $C_L$  versus  $K$  in waves & currents(fair current)

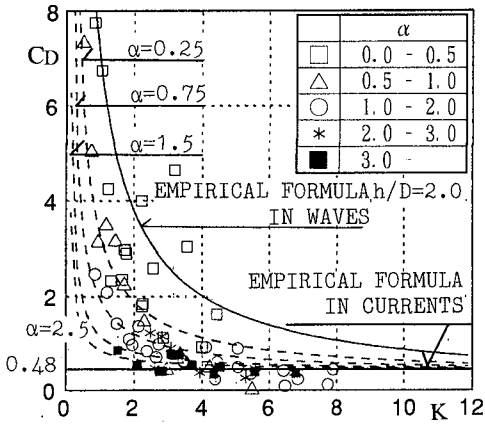


Fig.11 Drag coefficient  $C_D$  versus  $K$  in waves & current(adverse current)

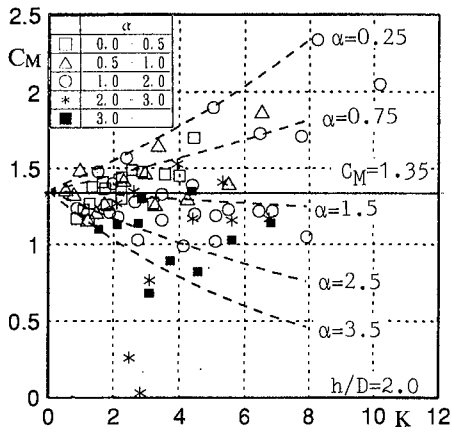


Fig.12 Inertia coefficient  $C_M$  versus  $K$  in waves & currents(adverse current)

Applicability of Empirical Formulas

The above experimental results were for the water depth of 40cm. It is very important to study the effect of the variation of water depth on  $C_D$  and  $C_M$  in waves & currents. Figs.13 and 14 show the effects of the water depth normalized by the diameter  $D$  on  $C_D$  and  $C_M$ , respectively. These coefficients are almost constant, regardless of the dimensionless parameter  $h/D$ . In other words,  $C_D$  and  $C_M$  in waves & currents are not practically affected by the effect of the water depth in the range  $h/D=2.0\sim 4.0$  tested here.

Fig.15 shows the relationship between the dimensionless  $C_{MG}/C_M$  and  $L_f/D$ , where  $C_{MG}$  is the inertia coefficient of the middle hemisphere among three hemispheres and  $L_f$  is defined in Fig.1.  $C_{MG}/C_M$  approximately approaches 1 for large  $L_f/D$ . The empirical formulas on the inertia coefficient proposed in this paper are valid for the range  $L_f/D > 2.0$ . The effect of the adjacent hemispheres on the drag coefficient was also negligible for  $L_f/D > 2.0$ .

Conclusions

The experimental results in this paper are summarized as follows;

- (1)The empirical formulas of  $C_D$  and  $C_M$  in waves & currents are derived using the modified Keulegan-Carpenter number  $K$  and the parameter  $\alpha$  indicating the current strength relative to the wave velocity. These formulas are accurate enough to estimate the hydrodynamic forces.
- (2)These hydrodynamic coefficients in waves & currents are not affected by the normalized water depth  $h/D$  in the range  $h/D=2.0\sim 4.0$ .
- (3)The empirical formulas proposed in this study are valid for the range  $L_f/D > 2.0$  for the conditions shown in Fig.1.

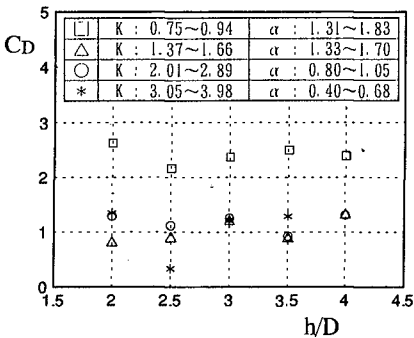


Fig.13 Drag coefficient  $C_D$  versus  $h/D$

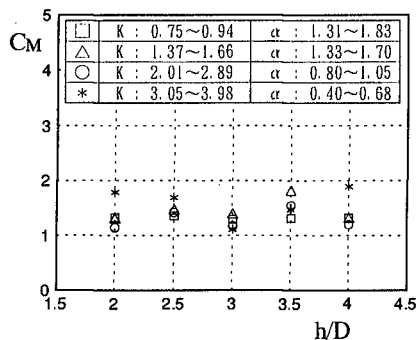


Fig.14 Inertia coefficient  $C_M$  versus  $h/D$



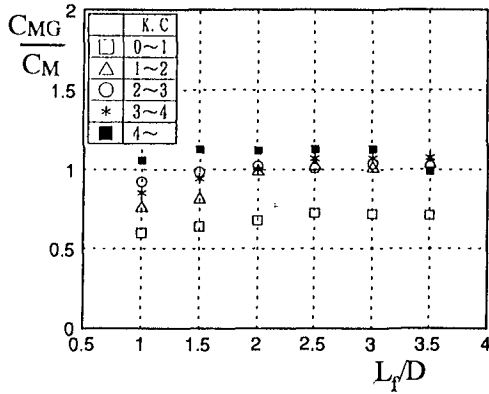


Fig.15  $C_{MG}/C_M$  versus  $L_f/D$

Acknowledgment

The authors would like to express their gratitude to Prof. Nobuhisa Kobayasi at the University of Delaware, whose insight and guidance were of great assistance in the preparation of this manuscript.

References

Iwagaki, Y., T. Asano and F. Nagai(1983)"Hydrodynamic forces on a circular cylinder placed in waves-current co-existing fields", Mem. Fac. Eng., Kyoto Univ., Vol.45, No.1, 11-23.

Jenkins, S.A. and Inman, D.L. (1976). "Forces on a sphere undere linear progressive waves ",Proc., 15th Int. Conf. on Coastal Eng., ASCE, 2413-2428.

Keulegan,G.H. and Carpenter, L.H.(1958). "Forces on cylinders and plates in an oscillating fluid." J. Res. Nat. Bur. Standards, 60(5), 423-440.

Morison ,J.R.,et al.(1950)."The forces exerted by surface waves on piles." Petroleum Trans., AIME, 189, 149-157.

Reid,R.O.(1957). "Correlation of water level variations with wave forces on a vertical pile for non-periodic waves." Proc., 6th Int. Conf. Coastal Eng., ASCE, 749-786.

## CHAPTER 108

# The Pressure Field due to Steep Water Waves Incident on a Vertical Wall

D.H.Peregrine<sup>1</sup> & M.E.Topliss<sup>2</sup>

### Abstract

The entrained air present when a wave impacts upon a vertical wall is modelled. A numerical boundary-integral method is applied, with appropriate initial conditions giving a prescribed surface profile and corresponding velocity potential, to model an overturning wave trapping a single air pocket between the oncoming wave front and the vertical wall. The resulting detailed computations provide suitable initial parameters for a simple theoretical model of the trapped air pocket as described in Topliss, Cooker & Peregrine (1992). The fundamental frequencies, and pressures on the impact wall due to the bubble can thus be estimated from the numerical computations. Video frames of small-scale experiments by Hattori & Arami (1992 and private communications) are also examined in detail and similar use of the model provides further pressure estimates. The resulting frequencies and maximum pressures are compared with the measured values. The peak pressures on the impact wall are within 30% of those measured and the frequencies are generally closer. Scaling with wave size is also discussed.

### Introduction

Much attention has been given to the peak pressures developed when storm waves meet sea walls and breakwaters, e.g. experimental studies by Kirkgöz (1991), Hattori & Arami (1992), Oumeraci & Partensky (1992) and theoretical studies by Cooker & Peregrine (1990,1992). These breaking-wave impacts can

---

<sup>1</sup>Professor of Applied Mathematics, School of Mathematics, Bristol University, University Walk, Bristol BS8 1TW, England. (*d.h.peregrine@bristol.ac.uk*)

<sup>2</sup>Research Student

have substantial aeration, either as air trapped at the wall or as pre-entrained air.

Aeration in wave impacts has been described in the laboratory experiments as either a cloud of small air bubbles in the water adjacent to the vertical structure or as a single air pocket trapped between the overturning wave and the impact wall. Numerical computations presented in this paper can simulate the motion of an overturning wave against a vertical structure on a finite depth, up until point of impact. This provides detailed data which can be used with theoretical analysis to describe the initial motion of an air pocket. Comparison of the analytic theory with the computations and experimental data, in particular that of Hattori & Arami (1992 and private communications) and Hattori, Arami & Yui (1994), has led to fairly good agreement with the various parameters. Three experimental data sets have been compared with computations that produce the same size air pockets.

The majority of experiments undertaken to study wave impact are performed in small-scale tanks and a discussion of scaling from model to prototype completes the paper.

## Numerical Method

The numerical method used in this paper for computing the unsteady two-dimensional motion of a water surface, including that for breaking waves, is described in Dold & Peregrine (1986) and Dold (1992).

The fluid is taken to be incompressible and the flow irrotational so that a velocity potential can be defined such that  $\mathbf{u} = \nabla\phi$  and  $\phi$  satisfies Laplace's equation with the fully nonlinear free surface boundary conditions. We have taken the pressure immediately above the free surface to be a constant and neglected surface tension.

The surface profile and velocity potential are prescribed on the free surface as initial data. The domain is reflected about the bed  $y = -h$  to form a symmetric image flow where a point on the upper free surface has an image on a lower free surface. The free surface boundary conditions are satisfied at the free surface which moves with time. The surface of the fluid is considered to be a smooth continuous profile approximated by a set of discrete points. A truncated Taylor series is used to perform explicit time-stepping. Cauchy's integral theorem is used to obtain a boundary integral equation for the evaluation of velocities and multiple derivatives of the surface motion. After the unsteady surface motion is calculated, the velocity and pressure beneath the surface can be evaluated at points over a rectangular grid. Variables are scaled accordingly:  $y^* = y/h$ ,  $x^* = x/h$ ,  $p^* = p/\rho gh$ ,  $t^* = t\sqrt{g/h}$ ,  $u^* = u/\sqrt{gh}$  and  $A^* = Ag$  where  $h$  is a chosen value and  $*$  represents the scaled variables.

## Computations for an overturning 'tanh' wave.

Using this boundary-integral method for a non-periodic surface, Cooker (1990) has described the motion of a wave overturning immediately before a vertical wall (with a finite depth), trapping a pocket of air against the wall. This was achieved by allowing two equal waves propagating in opposite directions towards each other to form a flow which is symmetric about a point. This is equivalent to a single wave approaching a vertical wall at this point. The initial data used obtained from a tanh expression describing a long wave of elevation:

$$u(x) = -\frac{1}{2}u_o \left\{ 1 + \tanh \left[ \frac{(x - x_o)}{s} \right] \right\} \quad (1)$$

where  $x_o$  is the initial centre of the wave,  $u_o$  is the initial maximum velocity, and  $s$  is a constant. The wave elevation is of the form  $\eta(x) = |u| + \frac{1}{4}u^2$  which gives a wave propagating towards the wall by shallow water theory. This long shallow water wave steepens and breaks as it propagates into water of constant depth, for an example see the surface profiles in figure 1. The computations have to stop just before the wave jet comes into contact with the wall and so the results only describe the motion immediately before impact.

Three examples have been studied of a wave overturning immediately in front of a vertical wall. Different initial positions of the wave give different size air pockets to illustrate the varying characteristics of the motion due to the volume of air trapped. In this section,  $h$  is the lowest water depth at the wall. Approximately 250-350 discretisation points were used for the surface of the wave. The wave is taken to have a large initial amplitude of 1.7 with  $s = 2.0$ , chosen to obtain large air pockets. Accuracy tests with more discretisation points have been very satisfactory. Surface profiles are presented for several timesteps and the pressure contours below the free surface have been evaluated in each case for the final computed time.

The first example (example 1) presented has an initial distance from the wall of  $x_o = 8.0$ .

The wave steepens and begins to overturn as it comes nearer to the wall as portrayed in the time history of the surface profiles in figure 1. The timesteps are reduced as the wave becomes steeper and the motion more violent. The computations stop just before impact with a small pocket of air is trapped between the wave front and the wall.

The pressure field at the final computed time shown in figure 2 has pressure contours in increments of 0.4. The thickened line represents the water surface. As well as high pressures at the foot of the wall, a region of much higher pressure is found just below the waterline with very tightly packed contour lines. Note that no direct impact between the water and the wall has yet occurred. The high pressures are spread over a substantial area of the fluid domain.

For a similar wave of amplitude 1.7, the initial distance of wave from wall

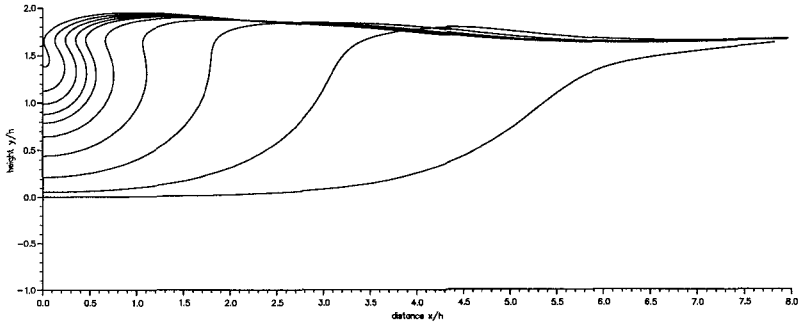


Figure 1: Surface profiles for a tanh waveform of amplitude 1.7, initial distance 8.0 at times 1.53, 2.81, 3.45, 3.77, 3.93 and 4.01 - 4.17 in steps of 0.04.

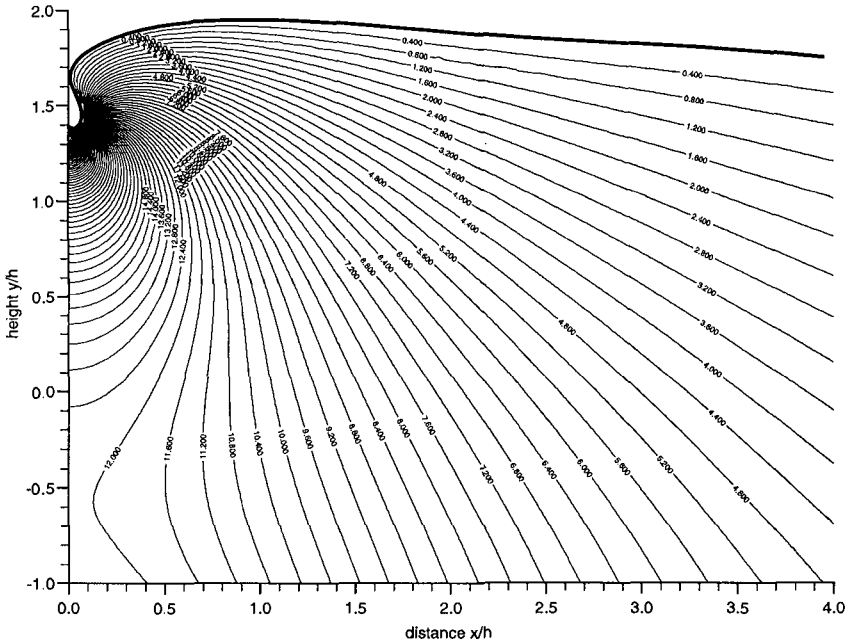


Figure 2: Pressure contours for a tanh waveform of amplitude 1.7, initial distance 8.0 at time 4.17 with increments of 0.4.

is now increased to  $x_o = 9.0$  in example 2. The time history of the surface profiles of the wave is displayed in figure 3. The waterline at the wall now lower and a larger amount of air is trapped. As can be seen in figure 4, the isobars, are at the same intervals, and show much lower pressures and pressure gradients than in example 1. Now the greatest pressures are at the bed.

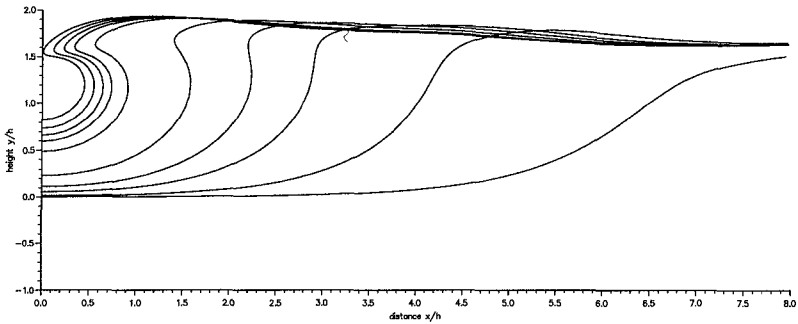


Figure 3: Surface profiles for a tanh waveform of amplitude 1.7, initial distance 9.0 at times 1.48, 2.76, 3.40, 3.72, 4.04, 4.36 and 4.44 - 4.56 in steps of 0.04.

Example 3 has a further increase of initial distance of the wave from wall to  $x_o = 10.0$ . The wave now overturns further from the wall and produces the largest air pocket. The surface profiles in figure 5 show the time history of the wave. Figure 6 shows the pressure distribution under the free surface for the final profile before impact has lower values than for the previous two examples. The pressure field is now in sharp contrast with the pressures of example 1, as the isobars are almost horizontal, indicating that pressures are not much in excess of hydrostatic. These three examples show that as the amount of air trapped increases, the pressures decrease and the characteristics of the pressure field change. Other examples have confirmed this trend.

The numerical data from the final computed times enables the characteristics of the three examples to be studied and compared. A representative set of numerical data includes the incident wave amplitude be  $H_o$ , the vertical height of the water above the bed after the final computational time be  $H$ , the vertical height of the water line in contact with the wall at the final computed time be  $H_w$ , and the vertical velocity, acceleration at this point be  $u_p, a_p$  respectively as shown in figure 7. The initial wave amplitude  $H_o$  is 1.7 in all three cases, but with three different size air pockets resulting from the original placing of the wave with regard to the wall. Let the horizontal velocity at the centre line of

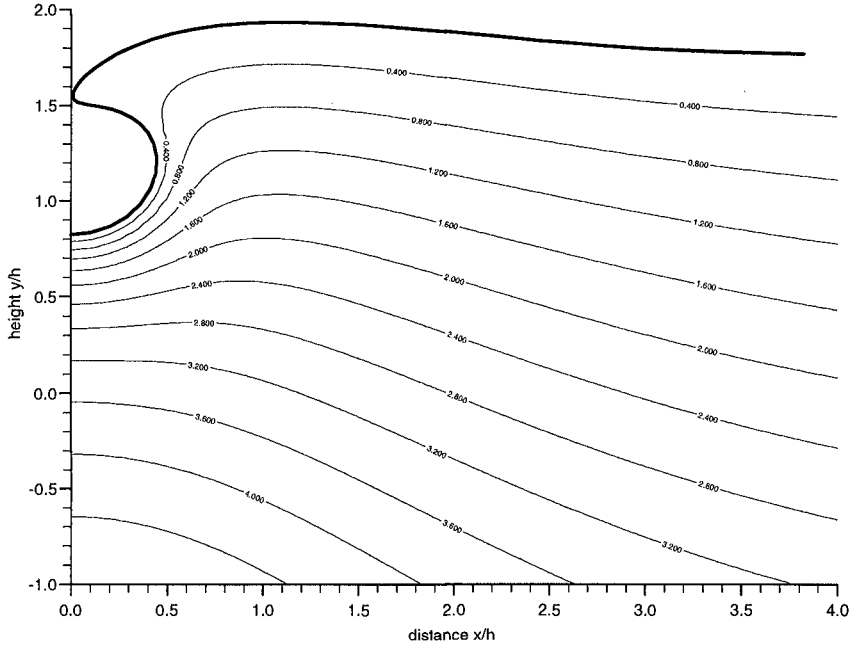


Figure 4: Pressure contours for a tanh waveform of amplitude 1.7, initial distance 9.0 at time 4.56 with increments of 0.4.

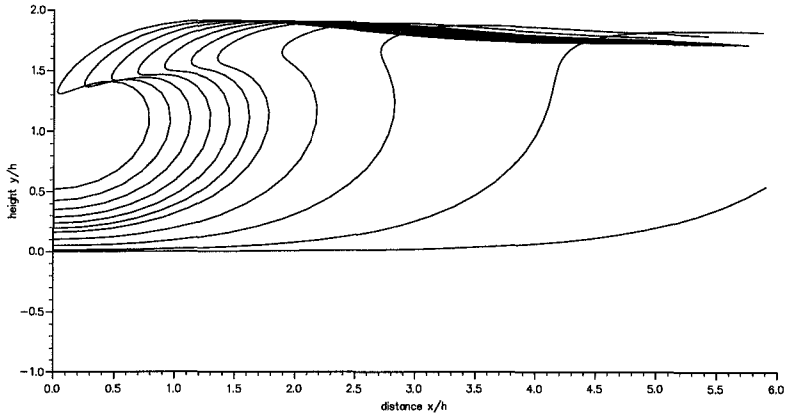


Figure 5: Surface profiles for a tanh waveform of amplitude 1.7, initial distance 10.0 at times 2.0, 3.28, 3.92, 4.24 and 4.44 - 4.92 at steps of 0.04.

the pocket be  $u_f$  and the horizontal velocity at the tip of the jet be  $u_t$ . The respective parameters for the three examples from the numerical results of the final computed time are shown in table 1. The horizontal velocity at the centre line of the bubble becomes much smaller as the radius of the pocket increases with the horizontal velocity of the tip of the jet not significantly altered. Thus in the first two examples, the velocity of the jet tip is larger than the velocity of the centreline as noted by Hattori, Arami & Yui (1994). In addition the upward velocity of the waterline at the wall decreases rapidly with the formation of larger pockets leading to the forward velocity  $u_f$  becoming greater than the upward velocity  $u_p$ .

For very small bubble sizes, large values are obtained for the vertical velocity and acceleration of the waterline. This shows an approach to the violent conditions reported by Cooker & Peregrine (1990) in their report of the "flip through" phenomenon. The vertical height of the waterline at the wall becomes much lower as the amount of air trapped increases resulting in the ratio  $H_w/H$  becoming smaller. These ratios are in agreement with those presented by Oumeraci, Klammer & Partenscky (1993).

## Comparison of numerical and experimental data

The numerical method for an overturning wave provides many parameters allowing different sizes of air pockets to be studied. Given experimental results,



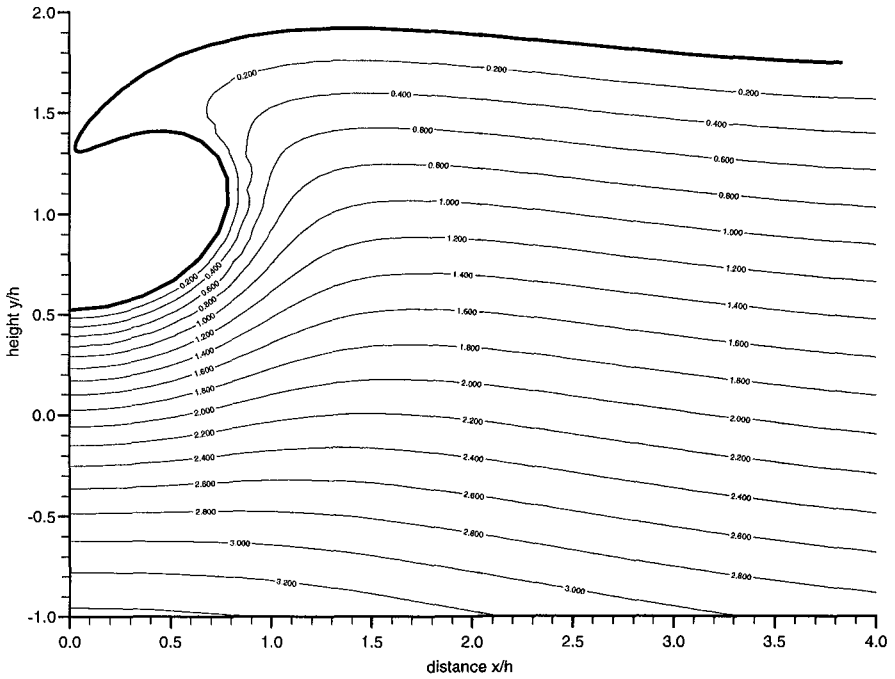


Figure 6: Pressure contours for a tanh waveform of amplitude 1.7, initial distance 10.0 at time 4.92 with increments of 0.2.

	Example 1	Example 2	Example 3
Wave amplitude $H_o$	1.7	1.7	1.7
Initial distance from wall	8.0	9.0	10.0
Pocket radius	0.071	0.445	0.784
Vertical height $H$	2.75	2.85	2.84
Vertical height $H_w$	2.390	1.823	1.522
Vertical velocity $u_p$	15.821	2.368	1.345
Vertical acceleration $a_p$	1700.7	10.93	4.09
Horizontal velocity $u_f$	5.35	2.69	1.99
Horizontal velocity $u_t$	3.06	2.81	2.77
Ratio $H_w/H$	0.869	0.640	0.536

Table 1: Comparison of dimensionless numerical data from the final computed times for the three tanh waveform examples.

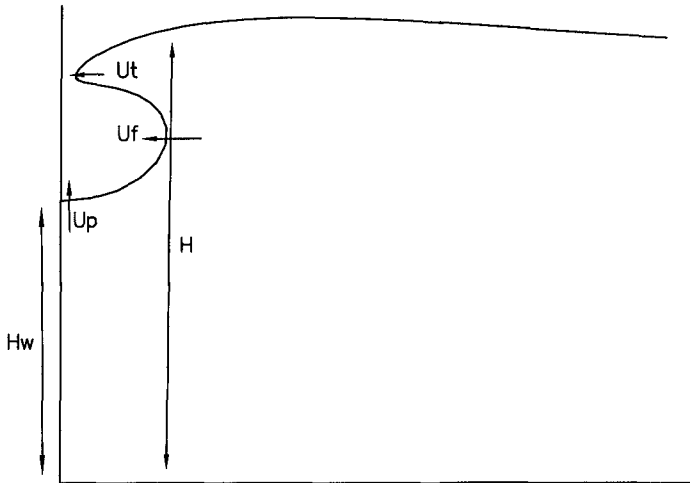


Figure 7: Parameters for an overturning wave

either with data showing the size of a trapped air pocket and its position under the free surface or photographs from which these parameters can be measured, a computation can be used to model the overturning wave by producing a resulting trapped air pocket of the same dimensions. We choose a computation to compare with an individual experiment by varying the initial wave height  $H_o$  and distance from the wall  $x_o$  until the computation gave a trapped air pocket which was a good match with the values for the radius  $r$ , the distance  $d$  of the bubble centre from the bed and the height  $H$  of the water after impact measured from the experimental data. We have compared with video frames from Hattori & Arami (1992). For a bubble nearer the bed than the free surface, a higher incident wave amplitude is required to obtain a correct  $d/H$  ratio. For a larger bubble, the initial distance of the wave from the wall needs to be increased as shown in the above examples. The numerical data for the final computed time gives values for the normal velocities around the curved surface which can then be averaged to give a radial velocity  $u_r$ .

The subsequent motion of the trapped air pocket has been modelled as a two-dimensional semi-circular bubble using Topliss, Cooker & Peregrine's (1992) result for the fundamental frequency. To a first approximation, it is

$$\omega^2 = -\frac{2\gamma p_o}{\rho_l a^2 \log\left[\frac{1}{4}(\pi a/H) \tan\left(\frac{1}{2}(\pi d/H)\right)\right]} \quad (2)$$

where  $\rho_l$  is the density of water,  $p_o$  the atmospheric pressure,  $\gamma$  the ratio of specific heats and  $\omega = 2\pi f$  where  $f$  is the fundamental frequency of the bubble. Once values for  $a, d, H$  and  $u_r$  have been obtained, either from a computation or, as in the next section, from experimental measurements, the frequencies and amplitudes of oscillation of the bubble can be predicted using equation 2, the linearised kinematic boundary condition,  $u_r = \omega\epsilon_o$ ,  $\alpha_o = a\epsilon_o\omega$  and the corresponding expression for maximum pressure,

$$p_{max} = -\rho\omega\alpha_o \log\left(\frac{\lambda a}{2} \tan(\lambda d)\right) \quad (3)$$

Hattori & Arami have provided us with many details of their experiments to investigate the importance of a trapped air pocket between the breaking wave and the wall. The experiments were undertaken in a small wave tank with a 1:20 bed slope to cause the wave to break. In each case the still water depth was five centimetres. High-speed video frames were taken of the fluid motion with simultaneous pressure histories. The experimental data sets with large clear trapped air pockets were chosen for comparison.

The histories of the pressure, measured on the impact wall immediately after impact exhibit three stages when air is trapped. Initially the pressure rises to a peak value and is followed by an interval of regular smooth oscillations, of decreasing amplitude. These oscillations are displayed with the same frequency in all six pressure gauges. This finally develops into a more confused signal, consisting of higher frequencies with lower amplitudes, and which carries on for an indefinite time.

The photographs show a cylindrical air pocket trapped between the wave front and the structure immediately after impact. In the video frames following the impact, it can be seen that the free surface rises and a thin jet of water shoots up the wall. We neglect this since it is usually much thinner than the bubble until a later stage and assume a flat surface in our models. The damped oscillations recorded by Hattori & Arami decay exponentially like  $e^{-\beta t}$ . The peak pressure is presented in the dimensionless form  $p^* = p/\rho g H_o$  where  $H_o$  is the incident wave height above the bed.

Three sets of experimental data on the formation of an air pocket by Hattori & Arami have been examined in detail. In each case measurements have been taken from the video frames to obtain values for  $a, d, H, u_f$ , where  $u_f$  is the forward velocity as previously defined. The bubble surface in the frames is not sufficiently well defined to take measurements around the surface and so the value obtained for  $u_f$  is used for the average radial velocity  $u_r$ . The video frames indicate a horizontal free upper surface at impact and so the computations of a tanh waveform should provide a good numerical model. For each of the cases studied, a table below shows the values of  $a, d, H$  and  $u_r$  obtained from both measuring the video frames of the experiments and from the corresponding computation. The table also gives the *estimated* values of  $f, \epsilon_o, \alpha_o$  and maximum

$p^*$  using the theoretical analysis for a semi-circular bubble and the measured values of peak pressure and oscillation frequency.

In experiment No. 132-3 the bubble radius was measured to be 7.5 mm from the video frames. Comparisons are made with a computation using a wave of initial dimensionless amplitude 8.0 and at an initial distance 6.5 from the impact wall. The corresponding dimensional value is 72 mm for wave height and there are comparable values for  $d$  and  $H$ . The radial velocity given by the numerical computations also gives agreement with that measured from the photographs. The top line in the table gives the maximum experimentally measured pressure and the frequency of its oscillation.

	$d$	$H$	$f$	$u_r$	$\epsilon_o$	$\alpha_o$	$p^*$
Hattori & Arami			190				38.1
From video	0.0295	0.066	221	1.0	0.00072	0.0075	43.5
Computation	0.0219	0.055	222.2	0.95	0.00068	0.0070	35.4

Table 2: Comparison of theory with experiment and computation for a pocket of radius 7.5 mm.

In experiment No. 172-3 the trapped air pocket, from the video frames, had radius 9.5mm. The computation producing a trapped pocket of the same size uses a wave of initial dimensionless height 5.0 and initial distance of 7.4, corresponding to 62 mm dimensional wave height .

	$d$	$H$	$f$	$u_r$	$\epsilon_o$	$\alpha_o$	$p^*$
Hattori & Arami			210				55.7
From video	0.029	0.063	186.5	1.1	0.00093	0.01	49.0
Computation	0.03	0.061	191.5	0.99	0.00082	0.0094	39.7

Table 3: Comparison of theory with experiment and computation for pocket of radius 9.5 mm.

The third data set, experiment No. 178-3, has the largest trapped air pocket, radius 20 mm, and produces the lowest pressures. The computation of initial dimensionless wave amplitude 7.0 with an initial distance from the impact wall of 9.0 corresponds to an incident wave height of 86 mm.

As can be seen from the comparisons, reasonable agreement is obtained between the experimental and theoretical results with larger bubble sizes producing lower frequencies. The measurements from the frames show that the lower surface rises more rapidly up the wall for a smaller pocket in agreement with the numerical computations. The damping of the oscillations appears to

	$d$	$H$	$f$	$u_r$	$\epsilon_o$	$\alpha_o$	$p^*$
Hattori & Arami			106				22.5
From video	0.026	0.067	99	0.8	0.0014	0.015	28.7
Computation	0.029	0.069	101.2	0.76	0.0012	0.015	20.0

Table 4: Comparison of theory with experiment and computation for a pocket of radius 20 mm.

be not as strong for the largest bubble and the oscillations last the longer. The slow rise of the pocket and mass of small bubbles in the video frame during the oscillations indicate little air loss initially through the surface of the water. The damping of pressure oscillations is yet to be modelled.

difference with Hattori & Arami	pressure from video	pressure from computation	frequency from video	frequency from computation
132-3	+12 %	-7 %	+16%	+17%
172-3	-12 %	-29 %	-11%	-9%
178-3	+22 %	-11 %	-7 %	-5%

Table 5: Comparison of the maximum pressure and oscillation frequency estimates for the three data sets.

The pressures predicted by the theory give reasonable agreement for both the experimental and computational parameters. Table 5 shows the differences in the pressures and frequencies estimated compared to those those measured by Hattori & Arami in each of the three experiments. The pressure differences are the percentage change between the peak pressures recorded in the data and the predicted values from the theory. Differences with those from the computations are all lower. The frequencies are generally closer to the experimental values.

## Scaling

Most experiments undertaken to investigate wave impact on vertical structures involve laboratory model-scale wave flumes. Scaling from model to prototype remains a complex and not fully understood problem. The number of parameters concerning the motion need to be identified and mathematical relationships established between the dimensionless scaling parameters.

When modelling the entrained air as either a single air pocket or a uniform bubbly mixture, expressions for the resonant frequencies have been obtained in

each case. Peregrine (1994) has suggested, to get order of magnitude estimates, a simpler approximation, similar to

$$\omega = (\gamma g H_a / C)^{1/2} \tag{4}$$

but without  $\gamma$ , where  $C$  is the volume of trapped air per unit length of wall ( $r^2$  for a single bubble or  $LH$  for a mixture of bubbles in a layer of width  $L$  at the wall),  $H_a$  is the hydrostatic head of water equal to atmospheric pressure. The comparison of this formula with  $\gamma=1.0$  (for isothermal bubbles) and 1.4 with the analytical expressions in each case is shown in figure 8. As can be seen

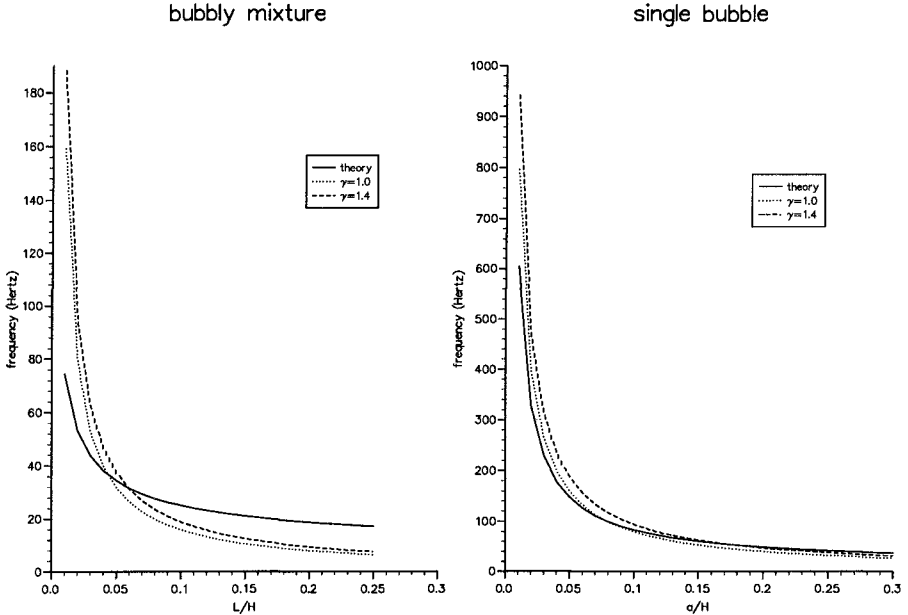


Figure 8: Comparison of the estimated fundamental frequencies, for a single cylindrical bubble with  $d/H=0.5$  (right) and for a column of bubbles next to a wall with  $\alpha=0.1$  (left).

from figure 8, the simplified formula presented by Peregrine is within a factor 2, particularly for the single air bubble, except for small pockets or very thin columns of bubbles.

Peregrine (1994) also presents a simple expression to estimate the maximum pressures:

$$\frac{p_{max}}{\rho g h} = \beta \left( \frac{h H_a}{C} \right)^{1/2} \tag{5}$$

where  $\beta$  is the fraction of the wall over which this impact occurs. For a reasonable ranges of  $\beta$ , 0.1 to 1.0, and  $C$ ,  $0.01 h^2$  to  $0.25 h^2$ , this gives

$$0.2 \left( \frac{H_a}{h} \right)^{1/2} \leq \left( \frac{p_{max}}{\rho g h} \right) \leq 10 \left( \frac{H_a}{h} \right)^{1/2}. \quad (6)$$

To assess these formulas, the maximum pressures for the three experimental data sets studied in have been evaluated using equation (5) with the data taken from the computational parameters and compared with the results obtained previously in tables 2, 3 and 4.

	$C$	$h$	$\beta$	$f$	$f$	$p^*$	$p^*$
	$m^2$	m		eq(2)	eq(4)	eq(3)	eq(5)
No 132-3	$(0.0075)^2$	0.072	0.27	222.2	212.2	35.4	30.8
No 172-3	$(0.0095)^2$	0.062	0.31	191.5	167.5	39.7	25.8
No 178-3	$(0.02)^2$	0.086	0.58	101.2	79.6	20.0	26.9

Table 6: Comparison of estimated frequencies and pressures evaluated earlier for the data sets from Hattori et. al. using the computational parameters, and the simple estimates for frequencies and maximum pressures given by Peregrine.

The maximum pressures predicted by equation (5) show agreement with those predicted by equation (3) to within 30 percent and thus this equation gives a very simple calculation for rough estimates. Looking at the range for the pressures given by equation (5), the values  $C = 0.01$ ,  $0.02$  and  $0.05 h^2$  are obtained for No 132-3, 172-3 and 178-3 respectively, giving  $p_{max}/\rho g h$  to be 3.2, 4.4 and 2.1  $(H_a/h)^{1/2}$  respectively, well within in the range given by (6).

## References

- COOKER, M.J. & PEREGRINE, D.H. (1990) Violent water motion at breaking wave impact. *Proc. 22nd Coastal Eng. Conf. A.S.C.E Delft* pp 1473-1486
- COOKER, M.J. & PEREGRINE, D.H. (1992) Wave impact pressure and its effect upon bodies lying on the sea bed. *Coastal Eng.* **18** pp 205-229
- DOLD J.W. (1992) An efficient surface-integral algorithm applied to unsteady gravity waves. *J. Comp. Phys.* **103**, 90-115.
- DOLD, J.W. & PEREGRINE, D.H. (1986) An efficient boundary-integral method for steep unsteady water waves. in *Numerical Methods for Fluid Dynamics II* (Eds. K.W.Morton & M.J.Baines), Oxford University Press. pp671-679.

- HATTORI, M. & ARAMI, A. (1992) Impact breaking wave pressures on vertical walls. *Proc. 23rd Coastal Eng. Conf. A.S.C.E.* Venice pp 1785-1798
- HATTORI, M., ARAMI, A. & YUI, T. (1994) Wave impact pressure on vertical walls under breaking waves of various types. *Coastal Eng.***22** pp 79-114
- KIRKGÖZ, M.S. (1991) Impact pressure of breaking waves on vertical and sloping walls. *Ocean Eng.***18** pp 45-59
- PEREGRINE, D.H. (1994) Pressure on breakwater: A forward look. *Int. Workshop on Wave Barriers in Deep Water*. Port & Harbour Res. Inst., Yokuska, 553-573
- SCHMIDT, R., OUMERACI, H. & PARTENSCKY, H.-W. (1992) Impact loads induced by plunging breakers on vertical structures. *Proc. 23rd Coastal Eng. Conf. A.S.C.E.* Venice pp 1545-1558
- TOPLISS, M.E., COOKER, M.J. & PEREGRINE, D.H. (1992) Pressure oscillations during wave impact on vertical walls. *Proc. 23rd Coastal Eng. Conf. A.S.C.E.* Venice pp 1639-1650



## CHAPTER 109

### RESULTS OF EXTENSIVE FIELD MONITORING OF DOLOS BREAKWATERS

D PHELP\*, S LUGER\*, A VAN TONDER\* and A HOLTZHAUSEN\*

#### ABSTRACT

The entrances to most of the ports in South Africa are protected by rubble mound breakwaters which have dolos armouring. As part of their maintenance programme, Portnet, the local Port Authority, has commissioned the CSIR to annually monitor the main breakwaters. A minimum of five years of photographic and other monitoring data have now been accumulated. This paper presents a brief description of the dolos breakwaters in South Africa, and the field monitoring techniques used to record the annual damage to the armouring. The results and analysis of the photographic monitoring are given in more detail. The application of these results are also presented, and some exciting new developments in breakwater monitoring are discussed.

#### INTRODUCTION

The conclusions of the report of the PIANC Working Group no. 12 on the Analyses of Rubble Mound Breakwaters, (PIANC, 1992), stated:

**'Finally, it is worth repeating that the experience of this working group has shown again, as others have found before us, that there is a great need for more detailed monitoring of existing rubble mound breakwaters including records of the wave conditions to which they are subjected in service. Collection and publication of data on this subject would greatly assist the advancement of engineering knowledge.'**

---

\* Ematek, CSIR, P O Box 320, Stellenbosch 7600 South Africa

The long-term stability of, and the intermittent storm damage to rubble-mound breakwaters are of considerable interest to the designers, builders and authorities responsible for maintenance. Depending on the severity of the wave attack, the breakwater armouring will deteriorate in time if not properly maintained. Gradual deterioration can often pass unnoticed until weak areas give way to major damage. Early detection of deterioration such as displaced, broken or lost armour units is therefore essential.

Annual monitoring of a breakwater provides an early warning system to identify any weak spots in the armouring which can then be repaired before the overall stability of the breakwater is threatened. The accumulation of data on damage which can be linked to the prevailing sea conditions during the monitoring period can also be used to improve breakwater design techniques and calibrate the design formulae which are mostly based on the results of hydraulic model tests. Breakwater monitoring also offers the potential for increasing our understanding of failure mechanisms associated with rubble-mound structures which are difficult to simulate accurately by way of physical model tests.

## DESCRIPTION OF BREAKWATERS

The seven harbours, where the breakwaters are monitored, are spread out along the east and south coast of South Africa, from Richards Bay in the north-east to Cape Town and Saldanha Bay in the south-west, as shown in Figure 1. All but one of these ports are protected by rubble mound breakwaters, which are covered with dolos armour units. Saldanha Bay, which is also monitored on an annual basis, lies in a large natural bay, and is protected by an artificial spending beach breakwater across the entrance to the bay.

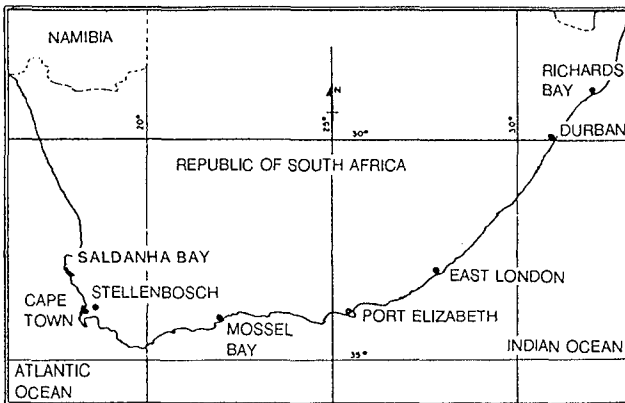


Figure 1. Location of Breakwaters

The main dolos breakwaters lie on the southern sides of the port entrance channels and the water depths at the toe of the breakwaters vary between 3 m and 15 m. The extreme wave conditions at most of the harbours are therefore depth limited. At the east coast ports the breakwaters have a dual function of reducing wave heights and preventing siltation in the entrance channels. At these ports maintenance dredging is necessary to intercept the littoral drift which is predominantly from south to north. Table I summarises the details of each of the dolos breakwaters (CSIR, 1981). The calculation of percentage damage, as given in the table, is described later in this paper.

Richards Bay has two dolos breakwaters, a shorter straight breakwater on the northern side and a longer curved breakwater on the southern side. East London, the only river port, is the oldest dolos structure which still has the original dolosse designed by Mr E Merrifield, the port engineer, in 1964. The main reason for the very high percentage damage to armouring on this breakwater, is that the dolosse were placed directly over randomly placed 35 ton blockwork. In some areas, there is only the blockwork left to protect the concrete mass-capping. Although the original breakwater was founded in 10 m water depth, a sand-bank, of 5 m depth, has formed just off-shore, which gives added protection from severe wave attack.

At the commencement of the regular monitoring programme for Portnet in 1989, a base-line damage status had to be calculated for those breakwaters which were already extensively damaged (specifically East London and Mossel Bay). This was done using a combination of visual inspection (of broken dolosse) and crane and ball survey. Cross-sectional plots compared the difference between the original as-built profiles and the existing profiles, and percentage damage was based on section areas.

Harbour	Length	No Dolosse	Year constructed	Monitored Years	Dolos size	Waiste ratio	Design Hs	Max % Damage	Average Damage
Richards Bay North	600 m	1000 (Head) 8800 (Trunk)	1973-1975	1987-1994	15t 5t	0,33 0,33	7,9 m	17% 16%	8,5% 6,5%
Richards Bay South	1400 m	2200(Head) 13400(Trunk)	1973-1976	1979-1994	30t 20t	0,36 0,33	7,9 m	10% 17%	3,9% 7,5%
Durban	585 m	2100	1982-1987	1989-1994	20 t	0,33	6,5 m	20%	6,1%
East London	600 m	2000	1964	1987-1994	18 t	0,34	8,5 m	71%	39%
Port Elizabeth	370 m	4600 (outer) 3700 (inner)	1978	1988-1994	10 t	0,31	6,4 m	7,5% 4,3%	3,4% 2,7%
Mossel Bay	200 m	2400 (outer) 1900 (inner)	1967-1969	1987-1994	5,4t 2,7t	0,33	5,2 m	37% 1,3%	28% 1,1%
Cape Town	500 m	2900	1988	1989-1994	25 t	0,355	7,5 m	16%	2,6%

Table I. Summary of Breakwater Damage

## MONITORING METHODS

Most of the breakwater monitoring methods, used by the CSIR in South Africa, are listed briefly below, together with descriptions of their usefulness and applicability. Detailed descriptions of these methods are available in various reports (CSIR, 1988a and Kluger, 1982).

- **Visual inspections** are useful for checking specific damage. The number of broken units per section of breakwater, and the type of break (important for structural analysis of armour units) can be checked visually but this is more time consuming than photographic methods and is not suitable for monitoring the entire slope. More broken units can usually be located using the visual method, and it is therefore useful at the start of a monitoring programme to get the base-line damage figures.
- **Close up photography** merely records the results of visual inspection and is useful for checking detailed progress of localised damage such as cracks in the mass capping. Camera type and position should be kept constant for good comparisons of subsequent photographs. Valuable information can also be obtained from photographs taken during extreme sea conditions. Areas of focused wave action can often be identified in this way, and related to the resulting damage to the breakwater. Aerial photography is normally not possible during storm events, but photographs, taken from the closest possible safe vantage point, have proven to be very useful.
- **Diver inspections** are just an extension of visual inspections to below water, provided visibility is good. Recording can be done by video or still photography but position fixing is more difficult and the whole operation more time consuming. This type of monitoring is normally only done if damage is already indicated by other methods such as crane and ball surveys.
- **Photographic surveys** from fixed positions to produce overlapping photographs covering the entire above-water condition of the breakwater (viewed at low spring tide) are the most useful and cost effective methods of breakwater monitoring. This method which involves the use of overlay techniques to check damage, should not be confused with photogrammetric survey methods, described below. The photographs may be taken from a boat (horizontal view), or crane or aircraft (vertical view), whichever is available. The helicopter was found to be most suitable, in that it could hover (wait for wave drawdown) and move quickly between monitoring stations. Position fixing of the helicopter is normally done by the use of Differential GPS, which is accurate to within 1m. The height can be set to suit the camera lens being used (the

greater the height, the better the accuracy, but once chosen, the equipment should be standardised for subsequent surveys). For South Africa's dolos breakwaters the above method was found to be generally adequate for monitoring the above-water damage to the armour units. A new development, however, is to substitute the helicopter photographs with video, which is equivalent to taking 25 images per second (at the TV frame rate of 25 Hz for the PAL standard).

- **Photogrammetric surveys** can also be done from a crane or aircraft, although position fixing of the camera is more critical and accurate benchmarks are required to properly reference each section of breakwater being stereographically photographed. This method is time consuming and expensive and is only used where very accurate three-dimensional recording of armour unit positions are required. This method is more applicable to the monitoring of small armour units or rock where the individual movements are more difficult to identify. As with the photographic surveys, a spring low tide and good wave drawdown are essential to get maximum exposure of the breakwater slope.

- **Crane and ball surveys** are used to monitor the breakwater profile (above and below water) at predefined intervals. A mobile crane is normally used to position the ball, and the level of the ball is measured from a theodolite station on the breakwater. The size of the ball which must obviously be kept constant from one survey to the next is normally around  $r = 1,14 V^{1/3} / \sin 45^\circ$  where  $r$  is the ball radius and  $V$  is the dolos volume. The above survey method was found to be the most successful in recording underwater damage, but the reach of the crane could be a limiting factor in the seaward extent of the survey. During construction of the breakwater, this method is essential to monitor the as-built rock and dolos profiles.

- **Seismic, sidescan sonar and bathymetric surveys** can be used to supplement the crane and ball survey by extending the monitoring seaward. Seismic profiling can even be used to check the profile of the original breakwater which may now be buried by sand. This detail is very important for the design of breakwater repairs including the toe berm. The survey equipment can be operated from either a crane or boat depending on the sea conditions adjacent to the breakwater. Provided visibility is good, any unusual features indicated by the above methods can be investigated by divers.

- **Standard tacheometric survey methods** may be used to accurately monitor levels of predetermined positions on the capping slab and specific armour units to identify general deterioration by settlement of the entire structure. Cracks in the capping slabs usually indicate settlement.

This method can be used to obtain cross section profiles by pre-marking (studs or drill holes) and surveying points up and down the breakwater slope. This survey data should be referenced to a stable benchmark located on shore.

Although a number of different breakwater monitoring methods have been listed above, not all these surveys, except possibly the photographic survey, need to be done on an annual basis. It is, however important that 'base-line' surveys using each of the different methods, listed above, are done as soon as possible after construction of the breakwater to provide a reference level to compare future damage against.

Other forms of monitoring which are complimentary to the breakwater monitoring techniques presented above, are:

- wave recording (by wave buoy - height, period and direction)
- bathymetric surveys around the breakwater to monitor toe erosion
- sediment sampling adjacent to the breakwater to check grain size
- water/sediment movement through the breakwater (dye tests)
- monitoring of concrete decay (possible alkali aggregate reaction)
- monitoring of cracks in capping slab (linked to settlement)

The results of these surveys are then linked to the breakwater damage analysis.

## ANALYSIS OF MONITORING DATA

Only the photographic survey will be described here, but the analysis principles are the same for the other methods of breakwater monitoring listed above. With the aim of the monitoring being the assessment of the deterioration of the breakwaters, the cumulative damage per monitoring station is calculated by comparing photographs taken before and after the monitoring period (usually annual) and adding the new damage to the previous cumulative damage per station. Provided the camera position and type of lens are kept constant for consecutive surveys, it is possible to use the overlay (or stereo-comparator) technique to quickly compare respective photographs to detect individual armour unit movements of less than 0,5 m. New, digital image analysis techniques are presently being investigated, and are presented later in this paper.

Both annual and cumulative damage are given in the monitoring reports. The visible damage has been categorised into three degrees of dolos movement (A) < 0,5 m, (B) 0,5 - 1,5 m and (C) > 1,5 m, (D) dolos breakage and (E) disappearance (loss) of the dolos from the visible slope. The damage per monitoring station, which normally cover 20 m to 25 m of breakwater length, are expressed as percentages, which are calculated by adding (C) + (D) + (E) and dividing by the total number of dolosse per station (N).

The movement of pieces of dolosse, which have already broken are also monitored, but do not contribute further to the damage calculation. In the same way, the smaller dolos movements (A) and (B) are recorded for information purposes, but do not contribute to the damage total. The movement history of a particular dolos is also tracked, so that the cumulative movement can be measured. Once this cumulative movement reaches more than 1,5 m (C), or  $h/2$  where  $h$  is the height of a dolos, it is then added to the damage total. Although some experts only consider prototype dolos breakage as 'damage', it was found that once a dolos had moved more than half its length ( $h/2$ ), the gap left by this movement often resulted in focused wave action, which in turn resulted in further damage (movement or breakage), especially under severe wave conditions. Monitoring results have shown that unrepaired localised damage causes an increase in the rate of damage in that localised area.

Because the main purpose of breakwater monitoring is to warn of potential failure areas which need to be maintained, it was decided to include these dolos movements (C), in the damage criteria given in the table. This theory is also more in line with the definition of damage of dolosse in scaled model tests, where movements more than  $h$  are generally recorded as damage (together with an observation of the number of rocking dolosse, to represent dolos breakage without displacement). The broken dolosse have however been listed separately to allow further analysis of damage, using dolos breakage as the only criteria.

It is recommended that the moved, broken or lost units be highlighted on the photographs which should be included in the monitoring report for easy reference. Weak areas or 'holes' in the armouring, which are more easily identified from photographs than in prototype, should also be highlighted to assist maintenance planning. When a hole is repaired with new units, the cumulative damage is reduced by the number of new units placed ( $n$ ), but when the new units are just added to the slope and are not particularly filling any 'holes', only the total number of units per section ( $N$ ) are increased.

The results of annual monitoring exercises at each port have been presented in reports issued to the port authority. The monitoring report also includes a brief description of the survey methods used, including camera details, and position and heights of camera stations to ensure continuity and ease of comparison for future monitoring. The wave data from wave buoys off each harbour, covering the monitoring period, are analyzed and included in each report so that annual damage can be linked to the prevailing sea conditions or significant storm events. Graphs are also plotted showing the rate of increase of damage per station which highlights those areas of the breakwater which may need urgent repairs.

## APPLICATION OF RESULTS

The results of these breakwater monitoring surveys have been found to be vitally important for a better understanding of, design of, and appropriate maintenance planning of dolos structures. Prototype monitoring results are presently being used for both structural (Zwamborn and Phelps 1989) and hydraulic damage analysis. The ultimate objective is to have sufficient prototype breakwater data (of dolos structures in this case), to combine with the recorded wave conditions, to create a basis for validating design formulae which are, thus far, predominantly based entirely on the results of small scale model tests.

Some of the uses to which these results have been applied in South Africa, include the following:

- **Planning of breakwater maintenance** - On-going maintenance is carried out on those breakwaters with permanently mounted breakwater cranes (Durban and East London have hammerhead cranes mounted on rails along the length of the mass-capping). At these ports it is economically feasible to carry out spot repairs, as needed and indicated by monitoring surveys. Gaps in the armouring are filled, and the percentage damage is kept low. For this purpose, a stockpile of spare dolosse is required at the root of the breakwater, within reach of the crane. As explained above, the damage at the East London breakwater was already high before the monitoring programme was started.

At other breakwaters, without permanent cranes, or spare dolosse, it is more feasible to let the damage rise to higher levels, before the planning of more major repairs. This critical level of damage depends on the importance of the breakwater in protecting the harbour entrance, and in the importance of the harbour itself. At Richards Bay, a major exporting port, planning for repairs to the southern breakwater commenced when the percentage damage per station exceeded 15 per cent. While at Mossel Bay, a small fishing harbour with a shallow water breakwater (-4 m), the maximum percentage damage per station was allowed to rise above 30 per cent before temporary repairs were done, and major repairs planned. As for East London, the damage to the Mossel Bay breakwater was already high when detailed monitoring commenced. Both dolos breakwaters are approximately 30 years old.

- **Age of breakwater vs damage (history of damage after construction)** - The Durban and Cape Town harbour breakwaters, which have been carefully monitored since construction, have shown that the initial 'settling in' of dolosse during the first major storm event, can result in more than double the normal annual damage. The rate of damage at any station, after initial settling-in, is generally related to the cumulative damage total at that station; this tended to increase after 20 per cent.



The damage history of the Port of Cape Town breakwater is shown in Figure 2, below. This graph is based on 6 years of monitoring data on the breakwater trunk, which consists of approximately 2 400 25 ton dolosse over a length of 500 m. The cumulative damage (movement and breakage, and breakage only) is plotted as a line graph against the left Y-axis, whilst the four worst storms (during the annual monitoring period) are plotted as bar graphs against the right Y-axis. The 1989 survey showed very high 'settling in' damage.

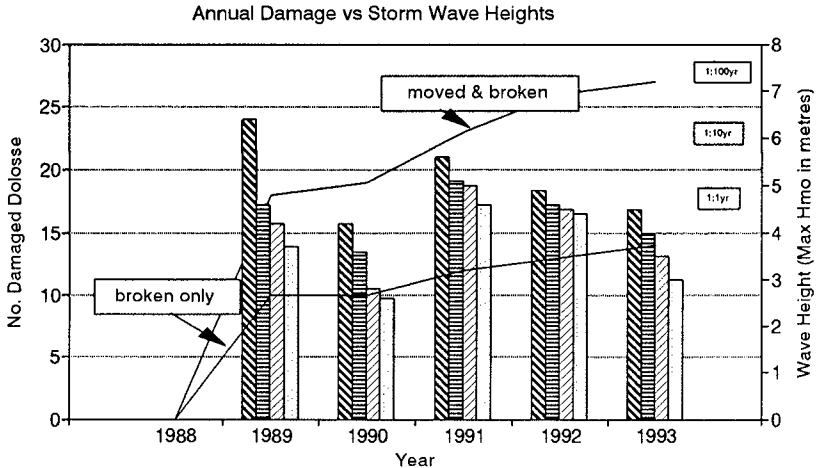


Figure 2. Damage History of Port of Cape Town Breakwater

- **Ratio of dolos movement vs breakage** - All visible dolos movements (above water) were recorded to within an accuracy of 0,1 m by the photographic survey method. Of all the recorded movements:
  - 52 per cent were less than 0,5 m,
  - 32 per cent were between 0,5 m and 1,5 m, and
  - 16 per cent were above 1,5 m

In this case, 1,5 m is approximately  $h/2$  where  $h$  is the height of a 25 ton dolos. This means that on average, only 16 per cent of all recorded dolos movements contribute to the recorded damage total. After the initial 'settling in' of the breakwater after construction, which normally involves a high percentage of small movements, approximately 55 per cent of the recorded movements, were new movements while 45 per cent had moved before. Besides rocking units, many dolosse move, or are displaced more than once, before becoming stable.

Based on a sample of 233 events (dolos movements including breakage), recorded on the Table Bay breakwater over a 5 year period:

- 75 per cent moved (without breakage) less than  $h/2$ , and
- 15 per cent moved more than  $h/2$  (also without breakage).
- 10 per cent of all the movements resulted in breakage.

Fewer than half the dolosse which moved more than  $h/2$ , actually broke, while some dolosse were seen to rotate up to  $270^\circ$  without breaking. Breakage of dolosse which had moved less than  $h/2$ , were usually the result of either rocking, impact from other dolosse or cold joints.

■ **Effect of rail reinforcing in dolosse** - The results of swing tests (with yield cushions) on 9 t dolosse using rail reinforcing (Zwamborn and Phelp, 1989) compared well with the results of monitoring the 25 t rail reinforced units which were used to repair the Cape Town breakwater (Zwamborn, Claassens and Van Tonder, 1990). The three types of rail reinforcement tested are shown in Figure 3. The test results showed that X-type rail reinforced dolosse could withstand approximately double the fall height, compared to unreinforced dolosse. A near design storm which occurred in July 1989, resulted in damage (as monitored photographically), of the same order as that predicted by the swing tests and hydraulic model tests, thereby validating the design.

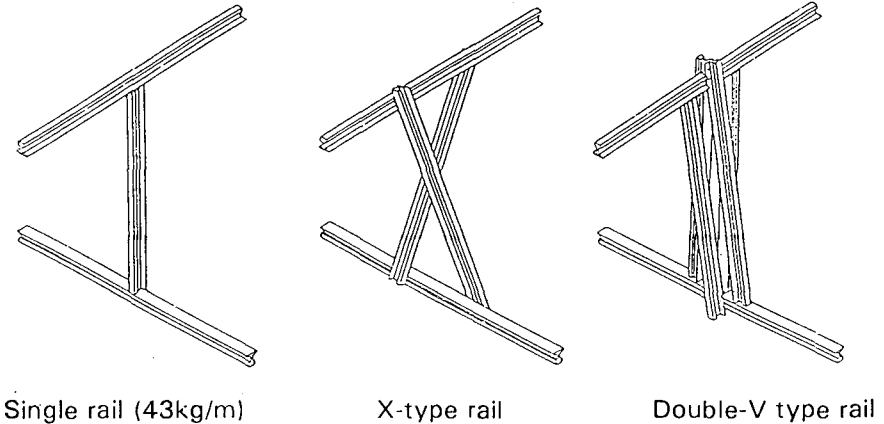


**Figure 3: Types of Rail Reinforcement**

Prototype reinforced units were observed to have moved more than  $h/2$  without breakage, and many of those units which did break, were still held together by the rail reinforcing, and thus continued to be functional in providing protection to the breakwater. Monitoring surveys of Cape Town breakwater revealed that rail reinforcing reduces both shank and fluke failure, but was not effective in reducing torsional failure (especially the double-V type, Figure 3). Torsional loading of reinforced dolosse tended to shatter concrete on the shank of the dolos, leaving the rails exposed. However, this is not considered too significant, because torsional failures constituted only 11 per cent of all observed dolos breakage (based on a sample of 357 broken dolosse).

■ **Improvement of dolos shape to reduce breakage** - As part of the breakwater monitoring exercises done in South Africa, a detailed study has been made of the number and type of broken dolos armour units, with a view to improving the shape to reduce breakage (Luger, 1993).

An analysis of these prototype dolos breakages has identified the fluke-shank intersection of the dolos as a region of structural weakness. Over 80 per cent of the dolosse breakages were found to originate from this point. Finite element analysis has been used in an attempt to improve the stress distribution in the dolos by modifying the dolos shape in the region of the fluke-shank intersection. Three of the shapes which have been analyzed are shown in Figure 4. This work is aimed at developing a dolos shape which is structurally superior to the existing shape, without significantly reducing the excellent hydraulic stability of the existing shape. The improved shape should be suitable for use on new projects as well as for the repair of existing breakwaters.

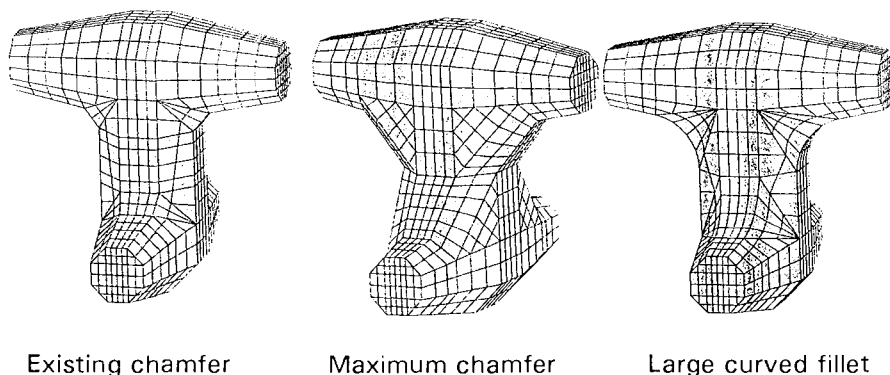


Figure 4: Evolution of Improved Dolos Shape

The continued monitoring of breakwaters where improved armour units are used will provide valuable data to determine the improved performance of the prototype units and confirm the theoretical advantages. The curved filleted dolos (Figure 4) are presently being used in the repair of existing breakwaters at Richards Bay and Mossel Bay, and in coastal protection works in Table Bay near the entrance to the Port of Cape Town. One advantage of using the improved dolosse for the repair of older dolos structures, is that there is still good interlocking between the new and old shaped units of the same weight.

■ **Effect of dolos size and waist ratio** - As a general rule, it was found that a larger waist ratio reduces the percentage of shank failure but increases the percentage of fluke failure. Independent of the waist ratio,

the introduction of even the smallest fillet, reduces breakage at the fluke/shank intersection. This was observed on some of the older breakwaters which have both dolosse with no fillet and dolosse with small rounded fillets and the original chamfer (SPM, 1984).

No relation could be found between breakwater damage and dolos size. It is the author's opinion however that dolosse, being slender units, are not suitable for deep water applications, and become structurally unstable above 35 ton to 40 ton, even with higher waist ratios. In South Africa, where most of the breakwaters lie in relatively shallow water, the dolos is still considered to be the most suitable armour unit.

■ **Calibration of site-specific model tests** - The Port of Richards Bay breakwaters, have been monitored by various techniques since completion in 1976, but regularly since 1987 using photographic survey from a mobile crane. The results of these surveys indicated that it was necessary to consider doing repairs to the 20 ton dolosse on the trunk of the south breakwater (CSIR, 1988b). Both 3D basin and 2D flume scale model tests were undertaken in 1991 to optimise the proposed breakwater repairs and check the effect of sand trap dredging adjacent to the breakwater (CSIR, 1992).

Because the breakwaters had already experienced storms with wave heights in excess of the 1:50 year design wave height of  $H_{mo} = 7,9$  m, it was decided to calibrate the 'design damage' in the model to equate the existing prototype damage. Each test consisted of a sequence of wave height steps from 2,5 m to 8,5 m in increments of 1,5 m, run for an equivalent of six hours (prototype) each. The model damage was determined using the photographic survey method to record dolos movements. These dolos movements were divided into the number of movements less than the height of a dolos ( $<h$ ) and the number of movements greater than the height of a dolos ( $>h$ ). The calibration factor  $0,4 (<h) + (>h)$  was found to give the best model approximation of prototype damage. Figure 5 shows the prototype and calibrated model damage for monitoring stations 5 to 17, which were spaced 25 m apart.

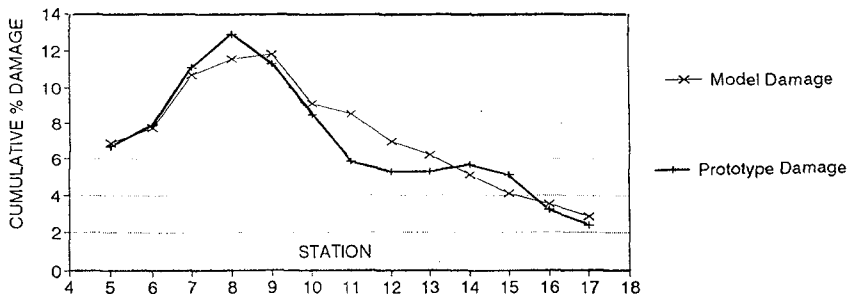


Figure 5: Prototype versus Calibrated Model Damage

By applying the same calibration factor to the model tests of different repair options, the expected design damage could be determined and the most effective repair option chosen.

Figure 5 also shows, both in model and prototype results, that the worst damage occurred between stations 7 and 9. Hydrographic surveys of the sand trap between 1977 and 1991 have shown that, almost since completion of the breakwater, the deepest area of the sand trap was located opposite stations 7 to 9 (Figure 6). This also coincided with the area where the sides of the sand trap were steepest and closest to the toe of the breakwater. One model test which was carried out with a larger deeper sand trap resulted in an increase in damage proportional to the extension of the sand trap, which indicated that the increased breakwater damage could be linked to the sand trap dredging (CSIR, 1992).

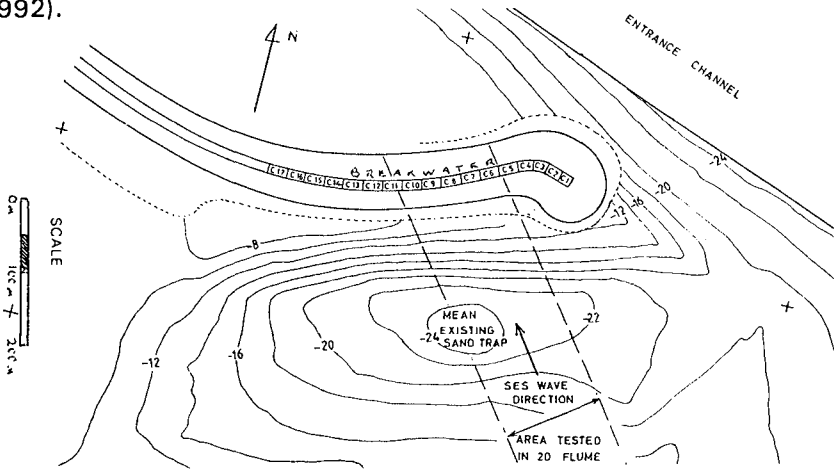


Figure 6: Mean Existing Sand Trap

## FUTURE DEVELOPMENTS

Future developments, in the field of breakwater monitoring, include improved correlation of damage with wave data, and video scanning for digital analysis, storage and presentation of monitoring results. The former involves the installation of directional wave recorders off the breakwaters. A brief description of the latter follows below:

A disadvantage of the photographic monitoring technique which is presented above, is the tedious manual comparison of photographs, even if the overlay or stereo comparator are used, to identify dolos movement and breakage. A recent new development is the replacement of the photograph of the breakwater by a digital image, captured by video recording or a live video camera signal. Flicker Optics<sup>1</sup> is a digital image processing technique which is then used to interlace, in real time, the image with a preview of the same breakwater station before the damage occurred. Any changes are then detected as a stroboscopic flashing of just that portion of the screen where the change has taken place.

A dynamogram (Figure 7) is then generated by simply subtracting the video image in which movement has been detected, from the initial or reference video image. The dolos that has moved shows up clearly while the background, which has not changed, is almost featureless. Three main areas of application of the above technique are as follows:

- Digitizing of archived photographic records (via CCD camera and frame grabbing card) for re-analysis and inclusion in a database.
- Aerial monitoring of prototype breakwater using video camera.
- Real time monitoring of scale model tests on breakwaters.

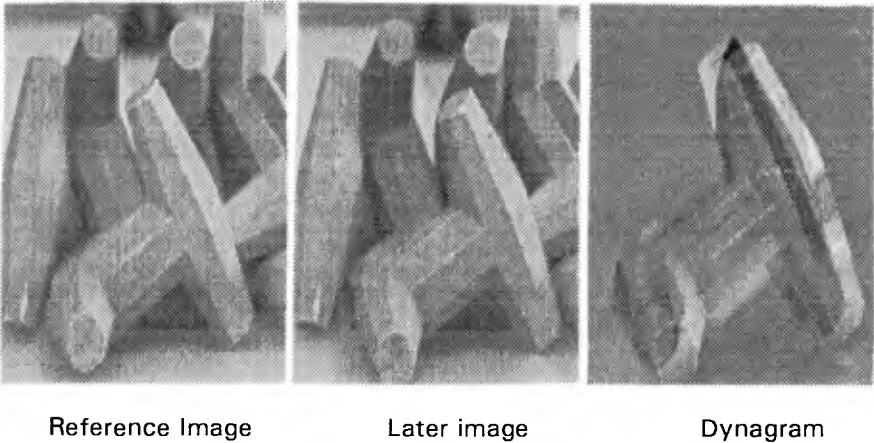


Figure 7. Digital Image Processing

Direct image subtraction assumes an invariant image geometry, illumination and reflectance. Initial testing of this new monitoring technique was carried out under ideal conditions, achievable in the laboratory at small scale. By real time video monitoring, even the small 'settling in' movements of the scaled dolosse were detected. For analysis of the photographic and prototype video record, however, the images need the following manipulation to overcome certain variables:

- Translation, rotation, scaling and warping to allow for errors in camera position (even with DGPS position fixing).
- Contrast stretching and histogram equalisation to allow for changes in illumination (sun and shadow) during consecutive surveys.
- Spatial intensity gradient image formats and edge detection techniques to allow for surface variation such as sea growth.

Advantages of digital images, include the ability to store only the necessary data (ie dolos movements and breakage), for the database and later presentation of survey results. By using a screen overlay grid and the cursor to scale known positions on the image, the dolos movements can be quantified. this information is then added to the data base.

## CONCLUSION

Breakwater monitoring in general, at South African ports and photographic monitoring in particular, have been successfully used as useful tools to identify damage, provide an early warning system (giving time for model tests of the repairs to be carried out) and assist in the planning of maintenance.

In this paper, the various methods of breakwater monitoring were covered and the use of monitoring results to calibrate model test results and improve repair designs were presented. Three projects involving two breakwater repairs and one new breakwater, soon to be undertaken, have been designed using mathematical and physical model tests, aided directly by the results of prototype breakwater monitoring. Ongoing monitoring of these structures will prove the performance of their design and of improvements made to the shape of the dolosse which are to be used.

## REFERENCES

- CSIR (1981)** Survey of dolos structures. *CSIR Report 385*. Stellenbosch, South Africa.
- CSIR (1988a)** Survey methods for breakwaters. *CSIR Report 8801*. Stellenbosch, South Africa.
- CSIR (1988b)** Richards Bay South breakwater evaluation of damage and proposals for repair. *CSIR Report EMA/C 88114*, Stellenbosch, South Africa.
- CSIR (1992)** Port of Richards Bay model study to optimise breakwater repairs. *CSIR Report EMAS-C 93049*, Stellenbosch, South Africa.
- Kluger (1982)** The monitoring of rubble mound breakwater stability using a photographic survey method by J W Kluger, *18th ICCE 1982*, Cape Town, South Africa.
- Luger (1993)** Increased dolos strength by shape modification by S Luger. Abstract for *24th ICCE 1994*, Kobe, Japan.
- PIANC (1992)** Analysis of rubble mound breakwaters. *Report of working group no. 12*. Brussels, Belgium.
- SPM (1984)** Shore Protection Manual. *U S Army CERC Vol. 2* U.S. Government Printing Office, Washington D.C.
- Zwamborn J and Help D (1989)** Structural tests on dolosse. *Seminar on stresses in concrete armour units*. Vicksburg U S A.
- Zwamborn J, Claassens H and Van Tonder A (1990)** Redesign, Repair and Monitoring of the Table Bay Main Breakwater. *27th International Navigation Congress* Section II Subject 3. Osaka, Japan.

## ACKNOWLEDGEMENTS

The author is indebted to Portnet for their support for the continued monitoring of the breakwaters at South Africa's seven major ports. G Hough and M J Alport of Space Physics Research Institute, University of Natal, are acknowledged for the digital (video) image analysis software. <sup>1</sup>Flicker Optics has a patent pending (December 1994).

## CHAPTER 110

# FAILURE OF RUBBLE MOUND STRUCTURES DUE TO THE STORM DURATION AND THE IRREGULARITY OF OCEAN WAVES

Cheong-Ro Ryu<sup>1</sup> and Hyeon-Ju Kim<sup>2</sup>

### Abstract

Failure mechanism and destruction processes of rubble mound structures under the irregular wave attack are discussed in considering with the effects of wave grouping, storm duration, and structural conditions using the model test results. In the analysis of the stability, a new irregular force parameter that affect the failure of rubble mound structures is defined by combining wave grouping characteristics, storm duration effects and wave-structure interaction mechanisms. Using the external force parameter, a modified rubble mound design formula is suggested, and its applicability is proved by the results of comparative studies with the conventional results.

### 1. Introduction

Wave climate, irregularities and uncertainty of ocean waves, and wave-structure interactions are the important parameters in the design of rubble mound structures. Remarkable efforts to develop design formulas of rubble mound structures considering irregular ocean waves have been made by Ryu and Sawaragi (1986), van der Meer (1988), and many of other researchers. Sawaragi et al. (1985) and Ryu et al. (1984) developed the design formula introducing the irregularity of ocean waves. Ryu and Sawaragi (1986) improved it considering allowable damage, material and/or block characteristics, spectral shape effects of ocean waves on the stability of rubble mound structures. Van der Meer (1988) proposed similar advanced design formula considering

---

<sup>1</sup> Professor, Ocean Engineering, National Fisheries University of Pusan,  
Pusan 608-737, Korea

<sup>2</sup> Graduate student, Ocean Engineering, National Fisheries University of Pusan



the storm duration, allowable damage, and the permeability of rubble mound structures. However, any of the results can't explain sufficiently the destruction mechanism and processes of rubble mound structures by the effects of storm duration and the irregularity of ocean waves including wave-structure interactions.

In the study, define a modified irregular force parameter that can consider the spectral shapes, wave-structure interactions and storm duration effects on the stability. Using the experimental data (Ryu, 1984), the destruction processes will be analyzed with the conception of storm duration effects, and combining the relation between the damage level increase and the irregular force parameter, a new design formula of rubble mound structures will be developed, and the applicability will be discussed by comparing with conventional results.

## 2. Conventional Design Formulas and Problems

The parameters considered in the conventional design formulas to estimate stable rubble weight ( $W$ ) for the monochromatic wave can be summarized as:

$$W = \begin{aligned} &f_1(H, \theta, \gamma_w, \gamma_s, f) \\ &+ f_2(T(L), \beta, D, P, i, h, \gamma_a, h_c) \\ &+ f_3(\dots) \end{aligned} \quad (1)$$

where  $H$  = wave height

$\theta$  = slope angle

$\gamma_w, \gamma_s$  = relative weight of sea water and cover material,  
respectively

$f$  = friction coefficient

$T(L)$  = wave period (length)

$\beta$  = incident wave angle

$D$  = allowable damage ratio (%)

$P$  = permeability coefficient

$i$  = slope of sea bottom

$h$  = water depth

$\gamma_a$  = thickness of cover layer

$h_c$  = crest height.

The most design formulas considered only the parameters in the  $f_1$  of Eq. (1), and the effects of parameters in  $f_2$  and  $f_3$  were introduced as a constant to correct the stability. Since the variety of the constant, the design results are varied by the career of designer and selection of design formula, however, the design rubble weight ( $W$ ) are presented to be proportional to the  $H^3$  (Ryu, 1984).

$$W \geq \alpha H^3 \tag{2}$$

where  $\alpha$  represents the proportional constant.

The variation of the design results will be largely increased, if the irregularity of ocean waves are introduced in the design concept. As shown in Fig. 1, the degree of rubble weight change can be pointed out as an important technical problem to develop a new design conception that minimize the scattering. In the figure, Ryu's (Ryu and Sawragi, 1986) and Meer's (van der Meer, 1988) formulas are to the irregular waves, and others are to the regular waves. It can easily found that the design rubble weights changed to 2 times or more due to the difference of coefficients and formulas.

In the case of irregular waves, following irregularity parameters of ocean waves should be considered additionally in Eq. (1).

$$W = f_{irr.} ( H_{1/n}, \xi_{1/n}, E_{sum} j(), Q_p, N, D, P, \theta, \phi, \gamma_w, \gamma_s, \dots ) \tag{3}$$

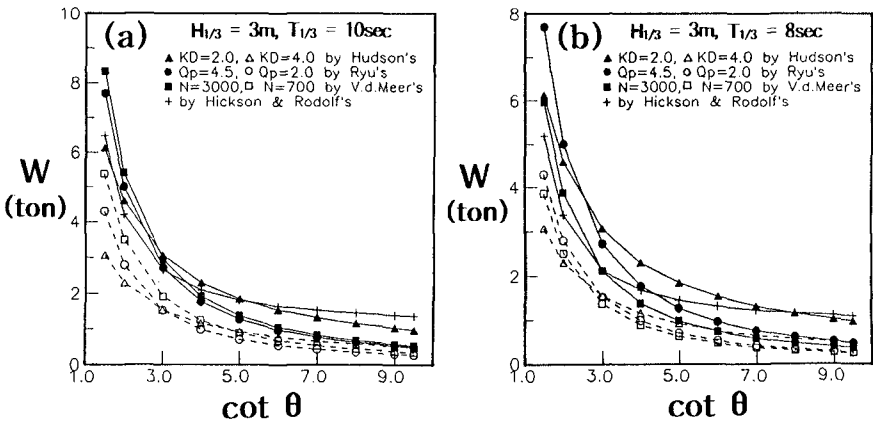


Fig. 1. Design weights of rubble units in relation to the slope angle by various formulas.

where  $H_{1/n}$  is the statistic wave heights,  $\xi_{1/n}$  the surf similarity parameter using  $1/n$  significant waves,  $Q_p$  the spectral peakedness parameter (Goda, 1985),  $N$  the number of incident waves,  $\phi$  repose angle of cover material.  $E_{sum}()$  denotes the concept of run-sum which is defined as the mean energy level of group formed waves as Eq. (7).

The representative design formula for irregular waves was proposed by parameterization of the effects of wave grouping/spectral shapes, wave periods/wave-structure interactions and the allowable damage level considering equilibrium slope formation as follows (Ryu and Sawaragi, 1986):

$$W_r \geq \left[ \frac{\gamma_w (6.15 Q_p + 20.0)}{\gamma_s^{1/3} (D + 30.1)} \frac{\tan \theta}{\tan \phi} \right]^{3/2} H_{1/3}^3 \quad (4a)$$

for the uniform slopes

$$W_r \geq \left[ \frac{\gamma_w (5.46 Q_p + 17.73)}{\gamma_s^{1/3} (D + 36.3)} \frac{\tan \theta'}{\tan \phi} \right]^{3/2} H_{1/3}^3 \quad (4b)$$

for the composite slopes

$$Q_p = \frac{2}{m_0^2} \int_0^\infty f S^2(f) df$$

in which  $W_r$  denotes the design rubble weight by Ryu's formula, allowable damage ratio  $D$  denotes percentage of eroded volume of cover layer to the total eroded volume until the damage level directly affects the stability of filter layer stones,  $m_0$  the zero-th spectral moment,  $S(f)$  the spectral density function,  $f$  the frequency.

Another design formula on irregular waves was proposed by van der Meer (1988) considering the permeability and storm duration etc. as follows:

$$W_v \geq \frac{\xi_m^{3/2} \gamma_s H_{1/3}^3}{[6.2 P^{0.18} (D_v / \sqrt{N})^{0.2}]^3 \left(\frac{\gamma_s}{\gamma_w} - 1\right)^3} \quad (5a)$$

for  $\xi_m < \xi_c$

$$W_v \geq \frac{\gamma_s H_{1/3}^3}{[P^{-0.13} (D_v/\sqrt{N})^{0.2} (\cot \theta)^{0.5} \xi_m]^3 \left(\frac{\gamma_s}{\gamma_w} - 1\right)^3} \quad (5b)$$

$$\text{for } \xi_m > \xi_c$$

where  $\xi_m$  is surf similarity parameter using mean wave period,  $D_v$  is the damage level defined by van der Meer (1988) that has the relation of  $D_v = 0.08 D$ . Eqs. (5a) and (5b) correspond to plunging and surging breakers, respectively classified with transition value of surf similarity parameter  $\xi_c$  given by

$$\xi_c = (6.7 P^{0.31} \sqrt{\tan \theta})^{\frac{1}{P+0.5}} \quad (6)$$

Though these design formulas are the most advanced, each has not included important parameters in Eq. (3). Ryu's formula (Ryu and Sawaragi, 1986) did not account for the effects of storm duration effect and structural permeability, and van der Meer (1988) neglected the wave grouping characteristics. To overcome before mentioned shortcomings and scatterings, the improved formula is needed to develop. It can be pointed out that such storm duration and wave grouping statistics is not clarified statistically as design parameters to introduce in actual design. However, it can be emphasized that the irregularities should be considered in the experiments on the stability and reliability check for the reasonable design.

### 3. Analysis of Available Data

#### 3.1 Experimental Features and Analysis

Destruction mechanism and damage processes are investigated used the results of hydraulic model tests in addition to previous works of Ryu (1984), and Ryu and Sawaragi (1986). The tests were carried out with 3 kinds of structural slopes 1:1.5, 1:2.0, 1:3.0 on a uniformly sloping beach of 1/40 with controlling the permeability of core layer to correct the scale effects. Irregular waves are generated with various spectral shapes of 200 cases. The destruction processes were

visualized simultaneously with incident waves by the 16 mm high speed cine camera (50 frames/sec) during the experiments.

Destruction mechanism is reanalyzed to investigate the effects of irregular wave parameters and correct the effects of resonance phenomena on the slope by introducing the tolerable destruction concept. And storm duration effect on destruction process is analyzed by measuring the destruction history to the irregular wave trains.

### 3.2 Analysis of Wave Irregularities as a Design Force Index

Waves used in the experiments were analyzed by wave by wave analysis and spectral analysis methods, and wave grouping parameters that is important to stability of rubble mound structures were evaluated. The wave grouping parameters such as run-length  $j(\ )$  and run-sum were defined same as Ryu (1984). The mean run-sum ( $E_{sum}$ ) is defined as the mean of energy-sum of group formed waves shown in Eq. (7). In the study, the mean run-sum of conditional run of  $\xi_o^*$  under the condition of significant wave height,  $E_{sum} j(\xi_o^*|H_{1/3})$  is introduced as a grouping parameter that affects to the stability. From the previous work by an author (Ryu and Sawaragi, 1985) on relations among the mean run-sum and  $Q_p$ , it can be estimated by the following formula.

$$E_{sum} j(\ ) = \sum_{j=1}^{\infty} \sum_{k=1}^{\infty} \frac{1}{8} \gamma_w H_k^2 / \sum_{j=1}^{\infty} N_{j(\ )} \quad (7)$$

$$E_{sum} j(\xi_o^*|H_c) = \gamma_w H_c^3 (0.04 Q_p + 0.13) \quad \text{for } H_c=H_{1/3} \quad (8)$$

$$\xi_o^* = \{1.5 \leq \xi_{1/3} \leq 2.5\} \quad (9)$$

$$\xi_{1/3}^* = \frac{\xi_{1/3}}{\xi_{max}} = \frac{\tan \theta / \sqrt{H/L_o}}{\tan \theta / \sqrt{(H/L_o)_{max}}} \quad (10)$$

where  $H_k$  ( $k=1,2,3,\dots$ ) is  $k$ -th wave of run-length  $j(\ )$ ,  $j(\ )$  denotes the run-length  $j$  of the run of  $(\ )$ ,  $N_j$  is number of wave group with the run-length  $j$ . The breaker types could be classified by surf-similarity parameters  $\xi$ , and the range of Eq. (9) makes the

resonance phenomena on the slope by wave by wave interaction.

Ryu and Sawaragi (1986) defined irregular force parameter [X] including wave grouping and resonance phenomena, and arranged the correlation with destruction ratio  $D(\%)$  as follows:

$$[X] = \left[ \frac{E_{sum} j(\xi_{ol}^* H_{1/3})}{\gamma_s l_a^2} \frac{\tan \theta}{\tan \phi} \right] \tag{11}$$

$$D(\%) = 153.8[X] - 30.1 \tag{12}$$

in which  $l_a$  is the characteristic length of stone/block. Eq. (12) did not consider the effects of storm duration and permeability of structures.

### 3.3 Analysis of Destruction Processes

Destruction mechanism and processes of rubble mound structures can be explained with combining the effects of storm duration time, resonance phenomena and wave force parameter [X] shown as Eq. (13). The contribution of the effects to the damage level illustrated schematically in Fig. 2.

$$D(\%) = AN^{0.25}[X] \tag{13}$$

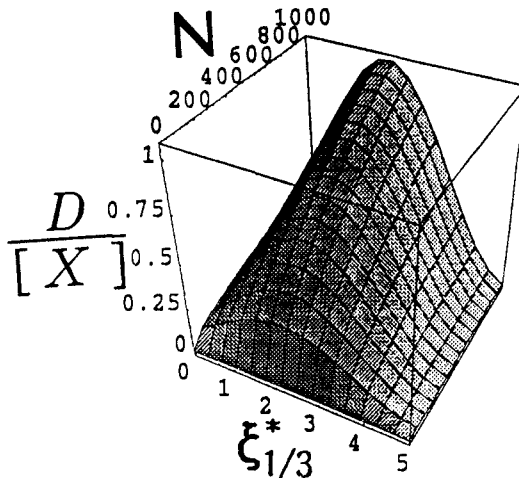


Fig. 2. Schematic definition of weighting function.

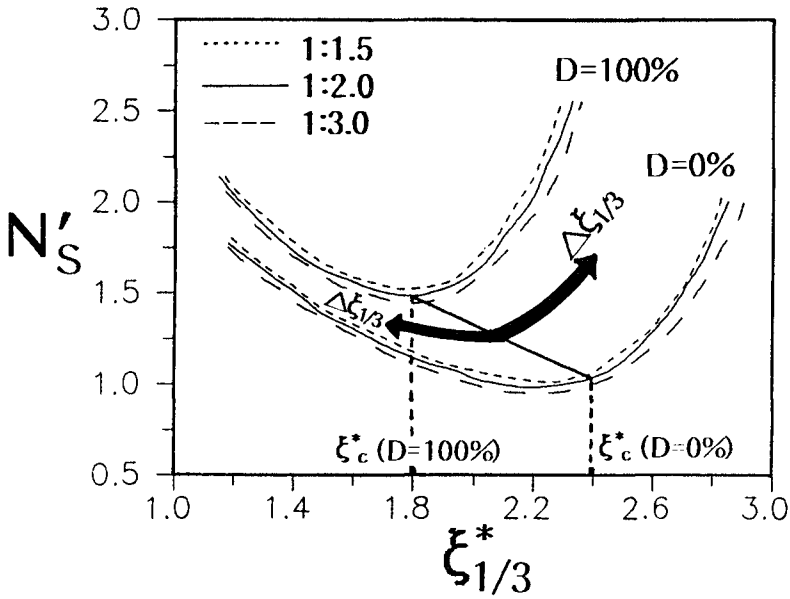


Fig. 3. Variation of modified stability number according to relative surf-similarity number.

Damage of rubble mound structures is strongly related with the waves in the range of  $1.5 < \xi_{1/3}^* < 2.5$  where the minimum point of modified stability number ( $N'_s$ ) is appeared as shown in Fig. 3. From Fig. 3 by Ryu and Sawaragi (1986), it can be pointed out that critical surf similarity parameter  $\xi_c^*$  with the minimum point of modified stability number decrease with the damage level increase.

$$N'_s = \frac{\gamma_w^{1/3} H_{D(\%)}}{(\gamma_{s/\gamma_w} - 1) W^{1/3}} \frac{\tan \theta}{\tan \phi} \tag{14}$$

where  $H_{D(\%)}$  is the design wave height for the damage level in percent  $D(\%)$ . In the case of tolerable destruction ratio  $D = 0\%$ , minimum point of  $N'_s$  located at about 2.3 of relative surf similarity parameter  $\xi_{1/3}^*$ , in  $D = 100\%$ , about 1.8. If the critical surf similarity parameter  $\xi_c^*$  can be assumed to be linearly changed according to tolerable damage ratio, it is represented as follows:

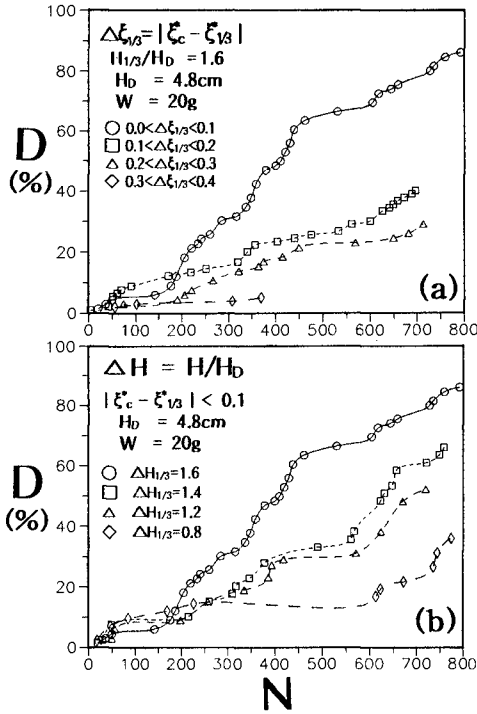


Fig. 4. Storm duration effects on the failure of rubble mound structures with the resonance indexes  $\Delta \xi_{1/3}^*$  (a) and  $\Delta H_{1/3}$  (b).

$$\xi_c^* = 2.3 - 0.005 D \tag{15}$$

Dimensionless damage level to irregular force parameter has a peak around critical surf similarity parameter  $\xi_c^*$  and decrease with increase of  $\Delta \xi_{1/3}^*$  ( $= \xi_c^* - \xi_{1/3}^*$ ) in Fig. 3. This was proved by investigating of the effects of the resonance indexes,  $\Delta \xi_{1/3}^*$  and  $\Delta H_{1/3}$  to the failure of rubble mound structures as shown in Fig. 4. In the figure, it is clarified that the damage level increase is affected by decrease of  $\Delta \xi_{1/3}^*$  and increase of  $\Delta H_{1/3}$  with the storm duration time  $N$ . Considering the characteristics, a weighting function was introduced as Eq. (16) by trial and error method with storm duration effect.

$$A = C_1 \cos\left(\frac{\xi_c^* - \xi_{1/3}^*}{2}\right) = C_1 \cos\left(\frac{(2.3 - 0.005 D) - \xi_{1/3}^*}{2}\right) \tag{16}$$



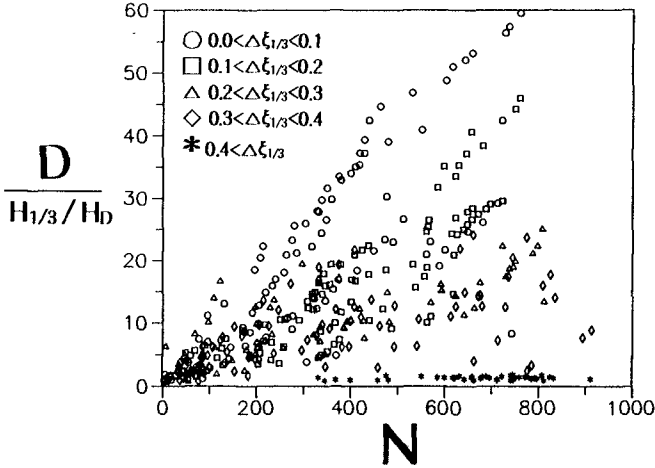


Fig. 5. Damage level increase of rubble mound structures according to the resonance indexes and the storm duration effects.

Combining Fig. 4(a) and (b), the damage level change due to storm duration under the condition of various  $\Delta\xi_{1/3}^*$  is shown in Fig. 5. It can be said that the severe damage will occur at smaller  $\Delta\xi_{1/3}^*$ .

Dimensionless damage level to the force parameter  $[X]$  and weight function  $A$  was compared versus the storm duration. The result of this analysis presented in Fig. 6. The variance of the results is considerable, however, if one wants to design more reliable structures considering uncertainty of damage processes, the upper limit of the figure will be applied, and the trend of damage increase whose resonance index is close to 0 can be presented as follows:

$$\frac{D}{A[X]} = C_2 N^{0.25} \tag{17}$$

Using the relations, the destruction processes can be summarized and formulated combining constants  $C_1$  and  $C_2$  to  $C$  as follows:

$$A N^{0.25} = C \cos\left(\frac{(2.3 - 0.005D) - \xi_{1/3}^*}{2}\right) N^{0.25} \tag{18}$$

where  $C$  is a constant of 0.194 from the data.

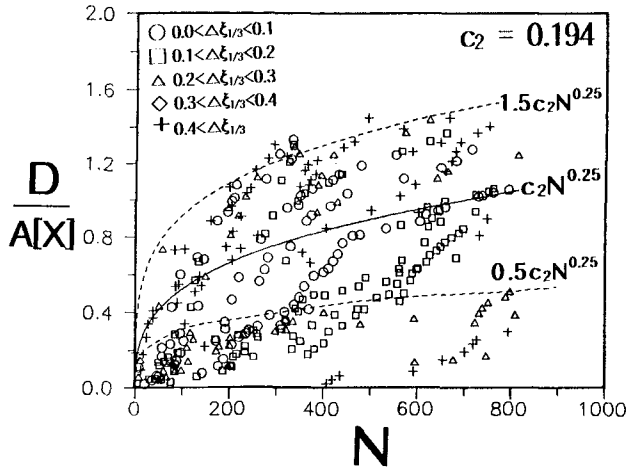


Fig. 6. Variation of damage level according to the storm duration.

### 4. Development of Design Formula

To develop a design formula considering the effects of irregularity of ocean waves and storm duration time on destruction processes as written in Eq. (18), the relationships between damage level ( $D$ ) and modified irregular force parameter  $[X]'$  were investigated by comparing with previous result used  $[X]$ . Fig. 7 shows the results,

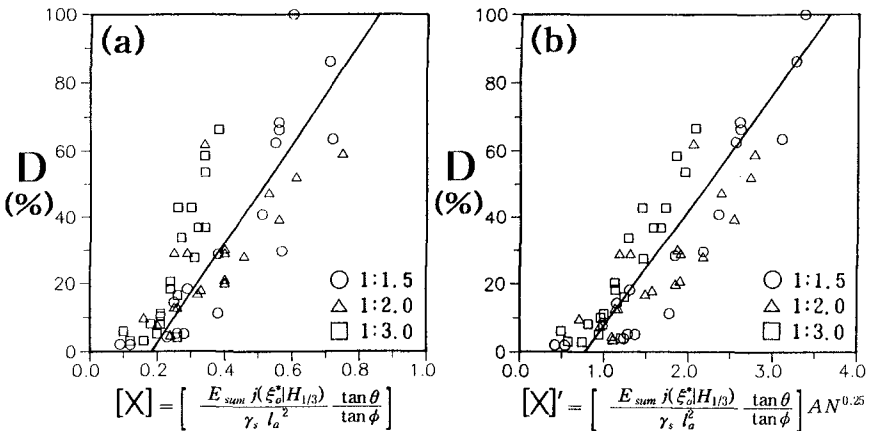


Fig. 7. Comparisons between failure characteristics with respect to the previous irregular force parameter (a) and the modified parameter (b).

and it can be clarified that the modified force parameter  $[X]'$  represents very well the damage processes than  $[X]$ . The correlation between the damage ratio and the new force parameter can be derived empirically as:

$$D = 29.84 [X]' - 5.82 \tag{19}$$

$$[X]' = A N^{0.25} [X] \tag{20}$$

By the relation, the formula to calculate the design weight of a rubble unit can be rearranged to as follow:

$$W_{new} \geq \left[ \frac{\gamma_w(1.19 Q_p + 3.88)}{\gamma_s^{1/3} (D/A N^{0.25} + 5.82)} \frac{\tan \theta}{\tan \phi} \right]^{3/2} H_{1/3}^3 \tag{21}$$

Using the new design formula and conventional formulas, the variation of design weight of a rubble unit is compared according to the storm duration under the same conditions of other parameters. Fig. 8 shows a typical example of variation of design weight of rubble unit. The design weight becomes heavier according to the longer storm duration, and the difference between new formula and others are significant by irregular wave conditions and allowable

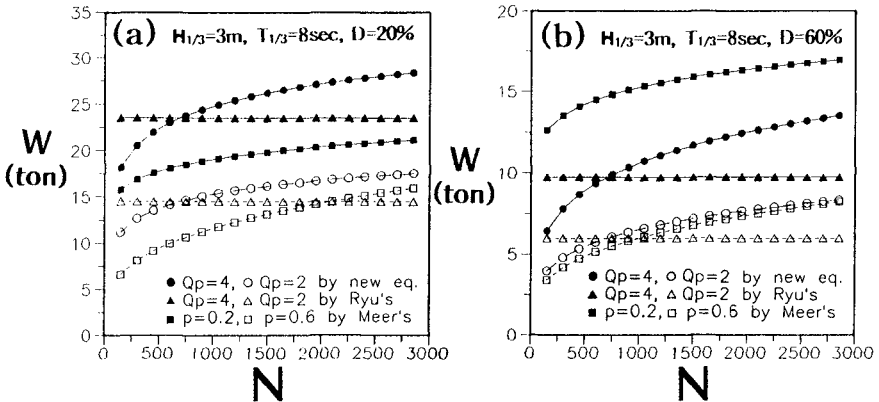


Fig. 8. An example of design weight of rubble unit in relation to storm duration.

damage level( $D$ ). This point out the importance of storm duration as well as the force parameter. It is emphasized that the wave grouping effects/spectral shape effects is one of the most important parameter in the new formula while neglected in van der Meer's formula.

Many researchers including authors pointed out the importance of permeability in rubble mound structures, but it is difficult to formulate using effective parameters on the stability. Kaku et al. (1991) developed a design formula using the experiments by van der Meer (1988), which was simplified as function of  $P$  and  $\xi_m$ , however, it has also problems for sensitivity analysis to the irregularity of waves.

To expand the new formula to the variable permeability, stability analysis parameter  $Q_s$  can be defined by combining the experimental results by author(1984) and van der Meer(1988).

$$Q_s = \frac{\xi_m \cot \alpha}{7.3 C_k^2 P^{0.36}} - 3.32 \quad (22a)$$

$$\text{for } \xi_m < \xi_c$$

$$Q_s = \frac{P^{0.26}}{0.19 C_k^2 \xi_m^{2P}} - 3.32 \quad (22b)$$

$$\text{for } \xi_m > \xi_c$$

where  $C_k$  denotes constant as introduced by Kaku et al. (1991). This formula represents the effect of  $Q_b$  to the stability in use of the new formula by introducing  $\xi_m$  and  $P$  of van der Meer's formula Eq. (5).

Stability analysis method could be formulated with regard to the storm duration, wave grouping characteristics, resonance phenomena and permeability, however, the parameters can not easily get in the field data. In future, field measurement to get a design parameter should be designated to satisfy the estimation of the force parameter, and the experiments should be designed to cover the effects. It is needed to consider the effects of crown height and wave-structures-soil interactions in the design.

These methods and data will be contributed to database as design constraints with numerical models on wave-structure interactions in the applications of the optimal design algorithm developed by Ryu et al.(1992).

## 5. Conclusions

Destruction processes of rubble mound structures are investigated by the hydraulic experiments considering irregularities of ocean waves and storm durations. The main results obtained in the study are:

- 1) From the analysis of destruction mechanism and its process, the effects of wave grouping and spectral shapes of irregular ocean waves, storm duration and wave-wave interaction on the slopes are emphasized as the important parameters in the analysis of stability of rubble mound structures.
- 2) The destruction processes are formulated empirically introducing the new irregular force parameter included the storm duration and resonance phenomena in addition to the irregular force parameter. And a modified design formula is proposed by rearranging the relationship between the damage level and the modified force parameter to calculate weight of rubble units.
- 3) By the comparative study with previous works, it can be emphasized that the new formula represents reasonably the effects of storm duration, wave irregularities, damage increasing processes, and wave-wave interaction on the slope. Applicability of the formula and research needs were discussed to the comprehensive optimal design algorithm of rubble mound structures.
- 4) The effect of permeability to the stability can be applied by a correct parameter to expand the use of the new formula.

## Acknowledgements

The financial support of the RCOID, National Fisheries University of Pusan, Korea, and critical discussions by Prof. Sawaragi, T. of Osaka University, Japan are gratefully acknowledged.

## References

- C. E. R. C. (1984): Shore Protection Manual, Vol. 2, US Army, CERC, pp. 7.202-7.243.
- Goda, Y.(1985): Random seas and design of maritime structures, Univ. of Tokyo Press, 323p.
- Kaku, S., N. Kobayashi and C. R. Ryu (1991): A design formula for mild rock slopes under irregular wave attack, Proc. 38th Japanese Conference on Coastal Engineering, JSCE, pp. 661-665. (in Japanese)

- Ryu, C. R. (1984): A study on the hydraulic optimal design of the rubble mound breakwaters, Thesis of Doctor of Eng., Osaka University, 165p. (in Japanese).
- Ryu, C. R. and T. Sawaragi (1986): A new design method of rubble mound structures, Proc. 20th ICCE, ASCE, pp. 2188-2202.
- Ryu, C. R., Y. Kang and J. Kim (1992): Optimal design of rubble mound structures under the irregular wave, Proc. of 23rd ICCE, ASCE, pp. 1503-1516.
- Sawaragi, T., C. R. Ryu and K. Iwata (1983): Consideration of the destruction mechanism of rubble mound breakwaters due to the resonance phenomena, Proc. 8th I.H.C., pp. 3.197-3.208.
- Sawaragi, T., C. R. Ryu and M. Kusumi (1985): Destruction mechanism and design of rubble mound structures by irregular waves, Coastal Engg. in Japan, JSCE, vol. 28, pp. 173-189.
- Van der Meer (1988): Rock slopes and gravel beaches under wave attack, Doctoral Thesis, Delft Univ. of Technology, 152p.

## CHAPTER 111

### BLOCK SUBSIDENCE UNDER PRESSURE AND FLOW

T. Sakai<sup>1</sup>, M. ASCE, H. Gotoh<sup>2</sup> and T. Yamamoto<sup>3</sup>

#### Abstract

The block subsides gradually into sandy bed under water pressure fluctuation. In actual coast the oscillatory flow also acts on the block. The block subsidence is reproduced qualitatively in a laboratory. The subsidence occurs even under the oscillatory flow. Under some combinations of water pressure fluctuation and oscillatory flow, the subsidence is larger than any of the subsidence under the pressure fluctuation only and the subsidence under the oscillatory flow only.

#### Introduction

In sandy coast armour blocks gradually subside into the bed. Fig.1 shows an example of the block subsidence and dispersion of an offshore breakwater off the west coast of Niigata facing the Japan Sea(Nakata, H. et al., 1991). There are several mechanisms proposed : for example, the rocking of the block and the porewater flow in the sand bed under the block.

One more explanation for this phenomenon is that the porewater pressure fluctuates due to the wave pressure, the vertical effective stress decreases at each wave trough phase, the block subsides slightly and it is repeated wave and wave. Already the subsidence was reproduced under a water pressure fluctuation in a laboratory(for example, Zen et al., 1990. See Fig.2). The behaviour of a sand bed during a block subsidence was observed in a laboratory(Nago et al., 1993. See Fig.3).

- 
- 1 Prof., Dept. of Civil Engrg., Kyoto Univ., Sakyo-Ku, Kyoto, 606, Japan.
  - 2 Res. Assoc., Dept. of Civil Engrg., Kyoto Univ., Sakyo-Ku, Kyoto, 606, Japan.
  - 3 Engineer, Hanshin Electric Railway Co. Ltd., Japan.

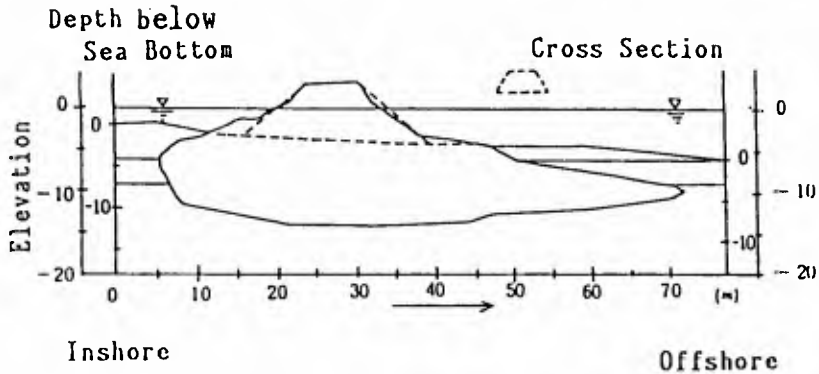


Fig.1 Subsidence and dispersion of block of offshore breakwater(Nakata, H. et al., 1991)

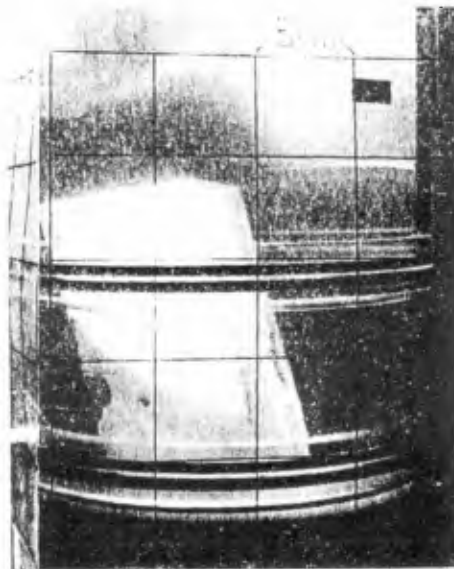


Fig.2 Reproduction of block subsidence due to water pressure fluctuation(Zen, K. et al., 1990)

In actual coasts, however, the oscillatory flow is also induced by waves and the scour around the blocks occurs. Here the subsidence of a model block on a sand bed is reproduced under a simultaneous action of a water pressure fluctuation and an oscillatory flow by a



laboratory experiment. The effects of the pressure and flow on the block subsidence are examined qualitatively.

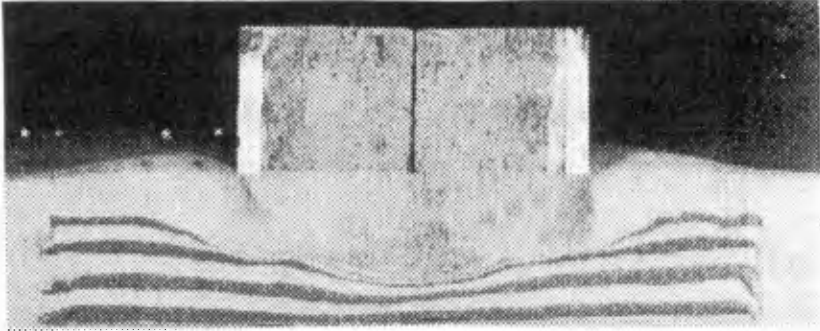


Fig.3 Behaviour of sand bed during block subsidence (Nago, H. et al., 1993)

### Experimental setup, procedure and conditions

#### experimental setup

An oscillatory tank, which can generate a water-pressure fluctuation and an oscillatory flow simultaneously, was used. It consists of a U-shaped tank (30cm x 30cm cross section) with both ends closed and

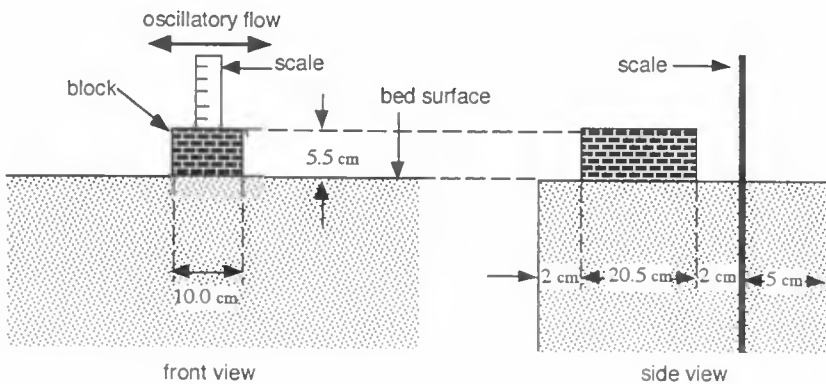


Fig.4 Experimental setup

a sand pit(200cm wide and 100cm deep) attached to the horizontal part of the tank.

The medium grain size of the sand was 0.25mm. A rectangular block(10cm wide, 5.5cm high and 20.5cm long) was set on the sand-bed surface(Fig.4).

#### experimental procedure and conditions

Three kinds of experiments were done, water-pressure fluctuation only, oscillatory flow only and both water-pressure fluctuation and oscillatory flow simultaneously. The periods of the pressure fluctuation and the oscillatory flow are same(3.0s and 6.0s). Fig.5 shows the combination of the total pressure fluctuation amplitude head and the average oscillatory flow amplitude for the case of wave period = 3.0sec. Fig.6 shows the combination for the case of wave period = 6.0sec. The phase between the pressure and the flow could not be controlled arbitrarily. It varied around 90 degrees. After 100 waves loaded, the amount of subsidence was measured.

The average head of water pressure was about 2.0m, the maximum total pressure-fluctuation amplitude head was 1.3m, and the maximum amplitude of oscillatory flow was 60cm/s. The void ratio of the sand bed was estimated several times during the experiment.

#### Experimental results

##### water-pressure fluctuation only

Fig.7 shows an increase of the amount of subsidence for the case of the period = 6.0sec and the total pressure fluctuation amplitude head = 141cm. Even after 300 waves(30min.) the subsidence continues.

Fig.8 shows a relation between the amount of subsidence after 100 waves and the total pressure-fluctuation amplitude head for the period = 3.0sec. The relation between the amount of subsidence and the total pressure fluctuation amplitude is roughly linear. The result for the period = 6.0sec shown in Fig.9 is nearly the same. No clear difference from that of the period = 3.0sec is seen.

##### oscillatory flow only

Under the oscillatory flow, the block was inclined generally. The amount of subsidence of the gravity center of the block was measured. Fig.10 shows a relation between the amount of subsidence after 100 waves and the average amplitude of oscillatory flow for the period = 3.0sec.

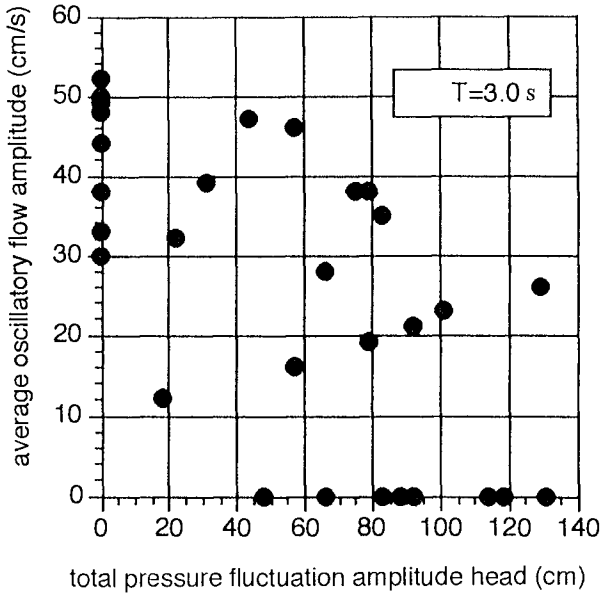


Fig.5 Combination of pressure fluctuation amplitude and oscillatory flow amplitude for wave period = 3.0sec

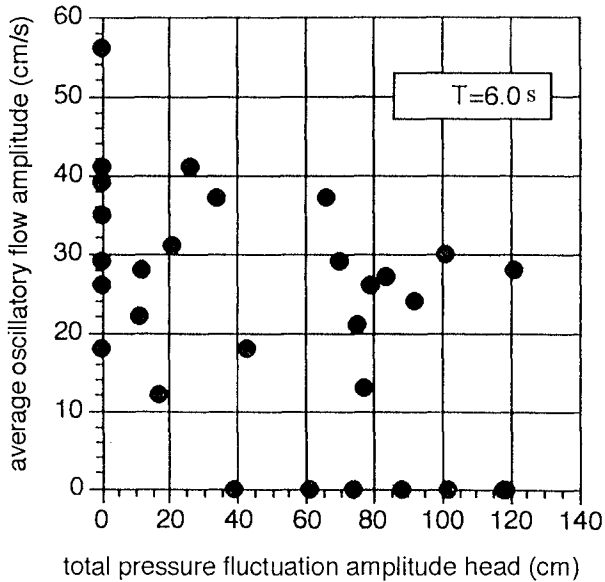


Fig.6 Combination of pressure fluctuation amplitude and oscillatory flow amplitude for wave period = 6.0sec

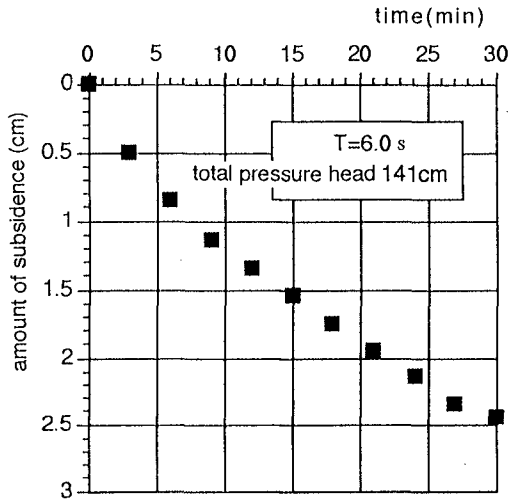


Fig.7 Increase of amount of subsidence in time

When the average oscillatory flow amplitude becomes larger than about 30cm/sec, the block begins to subside. The relation between the amount of subsidence and the flow amplitude is roughly linear. The result for the period = 6.0sec shown in Fig.11 is nearly the same. No clear difference from that of the period = 3.0sec is seen.

#### pressure fluctuation and oscillatory flow simultaneously

Fig.s 12 and 13 shows the amount of subsidence in the parentheses for the period = 3.0sec and 6.0sec respectively. The data on the horizontal axis are for the case of pressure fluctuation only. The data on the vertical axis are for the case of oscillatory flow only.

### Discussions

#### pressure fluctuation only

In the experiment of Zen et al.(1990), the width, height and length of the block were 6.9cm, 19.0cm and 6.9cm respectively(Table 1). The weight per unit area of the sand surface was 52.0g/cm<sup>2</sup> in the experiment of Zen et al., while it was 9.7g/cm<sup>2</sup> in this experiment. The void ratio of the sand bed, the period of pressure fluctuation and the total pressure fluctuation amplitude head were 0.80, 3.0sec and 566cm respectively. The amount of se after 100 waves was 0.5cm.

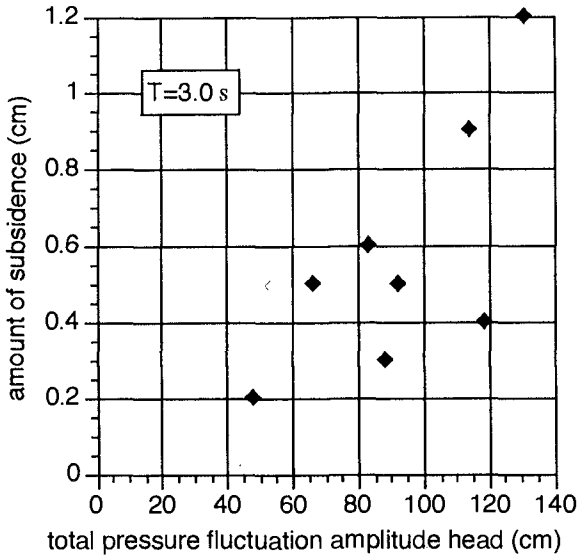


Fig.8 Amount of subsidence after 100 waves under pressure fluctuation only(wave period = 3.0sec)

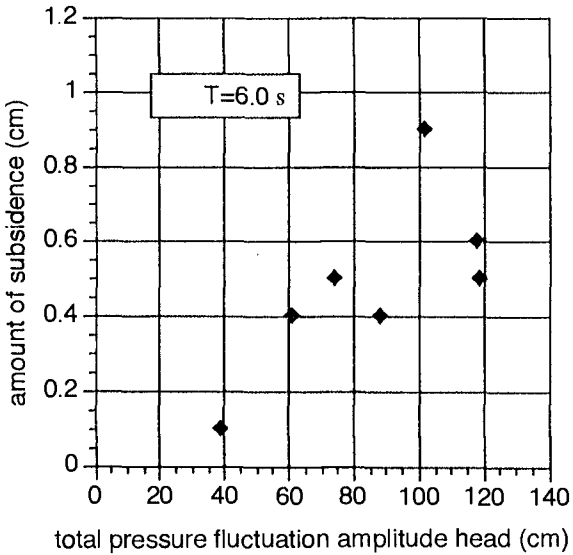


Fig.9 Amount of subsidence after 100 waves under pressure fluctuation only(wave period = 6.0sec)

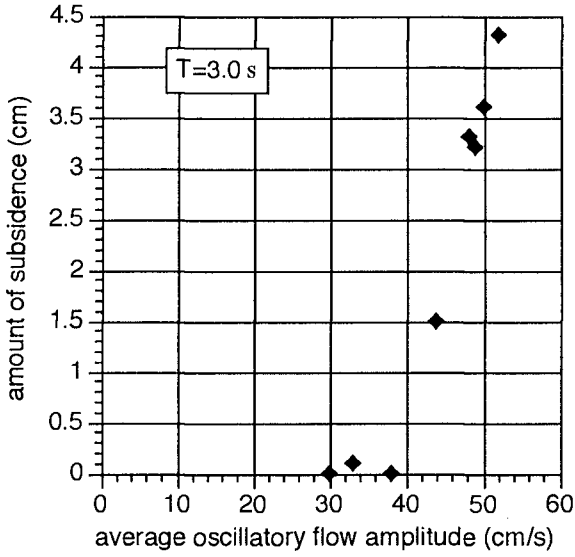


Fig.10 Amount of subsidence after 100 waves under oscillatory flow only(wave period = 3.0sec)

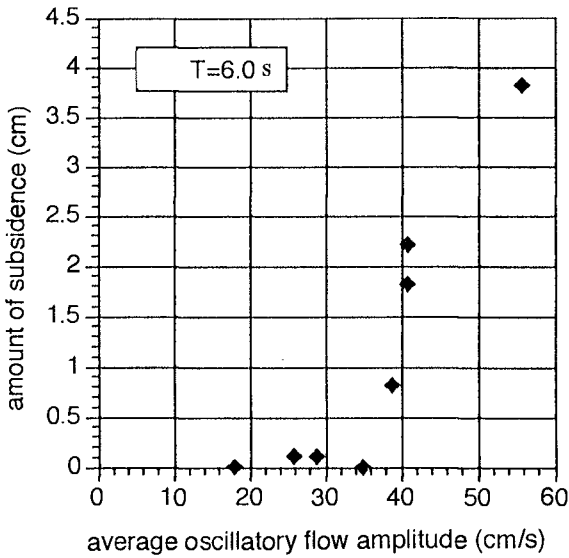


Fig.11 Amount of subsidence after 100 waves under oscillatory flow only(wave period = 6.0sec)

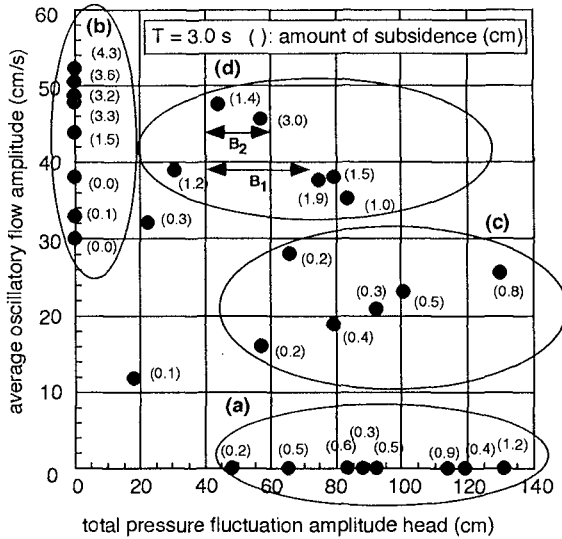


Fig.12 Amount of subsidence after 100 waves under both pressure fluctuation and oscillatory flow (wave period = 3.0sec)

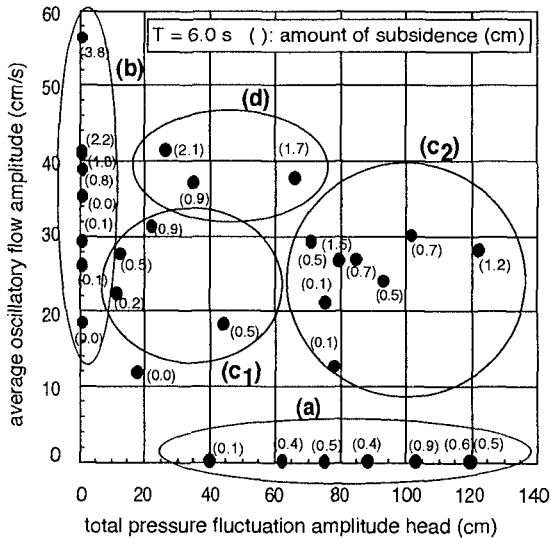


Fig.13 Amount of subsidence after 100 waves under both pressure fluctuation and oscillatory flow (wave period = 6.0sec)

Table 1 Comparison with Zen et al.'s experiment(1990)

	Zen et al.(1990)	this study
width(cm)	6.9	10.0
height(cm)	19.0	5.5
length(cm)	6.9	20.5
weight/bottom area (g/cm <sup>2</sup> )	52.0	9.7
void ratio	0.80	0.93
degree of saturation	high	low
period(sec)	3.0	3.0
total pressure amplitude head(cm)	566	131
subsidence(cm)	0.5	1.2

In this experiment, the amount of subsidence under total pressure fluctuation amplitude head of 131cm is 1.2cm. In the experiment of Zen et al., the amount of subsidence is less than half of that of this experiment under about 4 times larger pressure fluctuation. The void ratio of the sand bed of this experiment was 0.93 and fairly larger than 0.80 of the experiment of Zen et al. This is one reason of the large amount of subsidence of this experiment.

One more possible reason may be the low degree of saturation of porewater. The lower the degree of saturation of porewater, the larger the attenuation and the phase lag of the porewater pressure(Zen et al., 1990). It induces the larger decrease of the vertical effective stress under the wave trough.

#### pressure fluctuation and oscillatory flow simultaneously

For convenience' sake, the data in each figure of Fig.12 are divided into several groups. The group (a) consists of the data for the case of pressure fluctuation only. The group (b) consists of the data for the case of oscillatory flow only.

The scatter of data is large, but the following can be said. In the case of 3.0sec, the amount of subsidence under the pressure fluctuation and the oscillatory flow, the average flow amplitude of which is less than 35cm/sec, group (c), is roughly the same as that of group (a). In other words, under the average flow amplitude less than 35cm/sec, in which no subsidence occurs in group (b) of



oscillatory flow only, there is no effect of oscillatory flow on group (c).

In group (d), in which the average flow amplitude is larger than 35cm/sec, the amount of subsidence is larger than that of group (a) for the same pressure fluctuation amplitude. Some data show the amount of subsidence larger than any of those of the cases of the same pressure fluctuation only and the same oscillatory flow only.

In the case of 6.0sec shown in Fig.13, the similar trend is seen. There are the data in which the average flow amplitude is less than 35cm/sec and the total pressure fluctuation amplitude head is less than 40cm, group (c<sub>1</sub>). In the case of 3.0sec, there is no such data. Under the average flow amplitude less than 35cm/sec, in which no subsidence occurs in the case of flow only, the amount of subsidence is larger than that expected from the pressure fluctuation amplitude. This is one of the additive effects of the pressure fluctuation and the oscillatory flow.

### Conclusions

The amount of subsidence of a model block(10.0cm wide, 5.5cm high and 20.5cm long) on a sand bed was measured after 100 waves under a water pressure fluctuation and an oscillatory flow in a U-shaped oscillatory tank. The tank generated a water pressure fluctuation and an oscillatory flow simultaneously. The maximum total water pressure fluctuation head was 1.3m. The maximum average oscillatory flow amplitude was 60cm/sec. The period was 3.0sec and 6.0sec.

- (1) Under the water pressure fluctuation, the relation between the fluctuation amplitude and the amount of subsidence is roughly linear and independent on the period.
- (2) The amount of subsidence under the water pressure fluctuation is fairly large compared with that of Zen et al.(1990). This is thought to be due to the larger void ratio and the lower degree of saturation of the porewater.
- (3) Even under the oscillatory flow, the subsidence occurs. The relation between the flow amplitude and the amount of subsidence is roughly linear and independent on the period.
- (4) Under both the water pressure fluctuation and the oscillatory flow simultaneously, the subsidence is larger than any of the subsidence under the pressure

fluctuation only and the subsidence under oscillatory flow only for some combinations of the pressure and the flow.

#### Acknowledgment

A part of this investigation was supported by the Grant-in-Aid for Scientific Research of the Japanese Ministry of Education, Science and Culture, No. 03452211.

#### References

- Nago, H., Maeno, S. and Shimizu, Y.(1993), Visualization of sand bed displacement due to block subsidence under fluctuating water pressure, Proc. of Coastal Eng., JSCE, 40(1), 516-520(in Japanese).
- Nakata, H., Suzuki, M. and Kitayama, M.(1991), Observation on fluctuations of pore water pressure under high wave conditions, Proc. of GEO-COAST'91(International Conf. on Geotechnical Eng. for Coastal Development), Port and Harbour Inst., Japanese Ministry of Transport, 1, 615-620.
- Zen, K. and Yamazaki, H.(1990), Mechanism of wave-induced liquefaction and densification in seabed, Soil and Foundation, 30(4), 90-104.

## CHAPTER 112

# STABILITY OF ROCK ON BEACHES

by

Gerrit J. Schiereck, Henri L. Fontijn, Wout V. Grote, Paul G. J. Sistermans<sup>1</sup>

### ABSTRACT

Stability relations for rock on a mild slope are derived and compared with experimental results. It appears that for non-breaking waves the stability on a mild slope can be described with existing relations for stability on a horizontal bottom in oscillatory flow. For breaking waves, no existing relation can be used and a provisional empirical design rule was established. The results can be applied in designing outfall protections.

### 1. INTRODUCTION



Figure 1 Outfall protection

Pipelines on the sea bottom are usually protected in order to prevent damage by anchors or erosion. When a pipeline crosses a beach, it often lays in a dredged trench, see Figure 1, is covered with stones including a filter layer and is again covered with the original sand. The protection then acts as a last defence in case of severe wave attack on the beach. For the design of such a protection, which can be seen as an armour layer on a mild slope, no design rule is available at the moment.

---

<sup>1</sup>Delft University of Technology, Faculty of Civil Engineering,  
P.O. Box 5046, 2600 GA Delft

Much information is available on static stability of rock on steep slopes, as occurring at breakwaters and revetments, see e.g. Hudson (1959) or van der Meer (1988). Information is also available on static stability in oscillating flow on a horizontal bottom, see e.g. Sleath (1978) or Rance & Warren (1968), while Naheer (1977) investigated the stability under breaking solitary waves. For mild slopes much is known about dynamic stability, e.g. for sand and pebble beaches, where the profile is reshaped when conditions change. About static stability on mild slopes, which is a rather unusual combination in coastal engineering, practically nothing is known. At Delft University of Technology two studies were done (Sisternans (1993) and Grote (1994)) to find a static stability relation for rock on mild slopes which can be used as a design rule for outfall protections.

2. LOAD AND STRENGTH

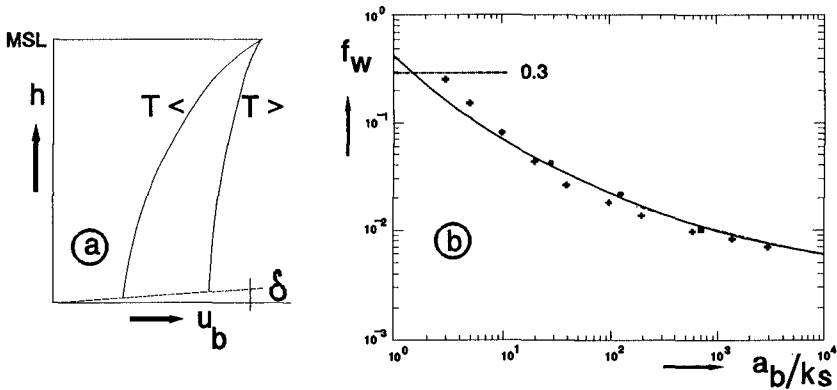


Figure 2 Orbital velocity and wave friction

The basic phenomenon in stability under waves on a mild slope, at least under non-breaking waves, is assumed to be the shear stress due to oscillatory flow:

$$\hat{\tau}_b = \frac{1}{2} \cdot \rho_w \cdot f_w \cdot \hat{u}_b^2 \tag{1}$$

with:

$$\hat{u}_b = \omega a_b = \frac{\omega H}{2} \frac{1}{\sinh kh} \tag{2}$$

$f_w$  and  $u_b$  depend on the wave height,  $H$  and period,  $T$ . Given a certain wave height, the longer the period, the larger the orbital velocity at the bottom,  $u_b$ , (Figure 2a).

With  $f_w$ , the friction coefficient, the relation is opposite: the shorter the period, the larger the friction coefficient, see Figure 2b, derived from Jonsson (1966) where  $f_w$  is given as a function of the orbital stroke at the bottom, related to the bottom roughness. This is caused by the fact that the boundary layer, ( $\delta$ , see Figure 2a) under a longer wave is more developed, leading to a lower velocity gradient, causing a smaller shear stress (given a certain velocity). In CUR/CIRIA (1991) an expression by Swart is given to describe the relation of Figure 2b:

$$f_w = \exp[-6 + 5.2 \left(\frac{a_b}{k_s}\right)^{-0.194}] \quad (f_{w \max} = 0.3) \quad (3)$$

For the stability relation between shear stress and stone dimensions, the critical Shields parameter, as adapted by Sleath (1978) for turbulent flow is:

$$\frac{\hat{\tau}_b}{(\rho_s - \rho_w) \cdot g \cdot d} = 0.056 \quad (4)$$

$d$  is the equivalent spherical diameter, in this paper approximated with  $d_{50}$ , the median sieve diameter, which is easily available and differs only a few percent from the spherical diameter. Equation (4) is partly based on experimental data by Rance & Warren (1968) from experiments in an oscillating flow tunnel. In this research, their results are, as an alternative for equation, (1), (3) and (4), described with:

$$\frac{a_b}{T^2 \Delta g} = 0.025 \left[\frac{a_b}{d}\right]^{-\frac{2}{3}} \quad (5)$$

In breaking waves, for the time being, the same mechanism is assumed to work. But due to a complete change in the velocity field and the turbulence in a breaking or broken wave, it can be expected that some amplification factor on the computational results has to be applied to fit experimental data.

### 3. EXPERIMENTS

#### Set up

Experiments were done in a wave tank (length 40 m, width 0.8 m, depth 0.9 m) at the Laboratory of Fluid Mechanics at Delft University of Technology (DUT). On the concrete surface of a slope 1:25, stones were laid with dimensions ranging from  $d_{50} = 7$  mm to 17 mm and densities ranging from 2400 to 2900 kg/m<sup>3</sup>. The width of the sieve curves of the stones ( $d_{85}/d_{15}$ ) used in the experiments was about 1.5. 3 to 4 layers of stone were used, in order to ascertain a proper roughness between

the stones and the slope. The difference with the geometry of a real pipeline cover, which has a filter layer under the top layer, is assumed to be negligible with respect to stability of the top layer.

The stones were laid in coloured strips of 0.2 m (in the wave direction) over the full width of the flume. By counting the number of stones displaced,  $n$ , after every test, the damage  $S$  was determined as a percentage of the total number of stones available in a strip:  $S = n * d_{s0}^2 / A$  (%). For every strip a relation between  $n$  and the wave height at the toe of the slope was established and from these curves, the level  $S = 0.5$  % was arbitrarily chosen as incipient motion.

The maximum number of waves in regular wave tests was 750. Irregular waves were generated according to a JONSWAP-spectrum; the number of waves was 2000 in irregular wave tests. The wave heights and spectra were determined at the toe of the slope. The water depth at that location varied from 0.7 m for regular waves to 0.6 m for irregular waves.

#### Scale effects

The flume in the laboratory is considered as a physical reality in itself, not as a model of some prototype with a scale 1:X. Computations are made for that reality and compared with the experimental results. However, in the end, the relations thus found have to be used for prototype circumstances. This is permissible only if no scale effects are present in the relations. Sources of scale effects in small flumes using water as a fluid, can be the viscosity of the water, the surface stress and air entrainment in breaking waves.

To avoid viscosity effects, the particle **Re**-number in the Shields-graph ( $u_* d / \nu$ ), should be more than about 600, indicating that the flow around the stones is turbulent. The minimum stone size of 7 mm was chosen to meet this demand.

Stive (1985) investigated the scale effects in breaking waves on a 1:40 slope and found no significant scale effects in wave heights and velocities on the slope for a wave height range from 0.1 to 1.5 m. The wave heights in the authors' experiments ranged from 0.1 m to 0.35 m.

## 4. COMPUTATIONS

Orbital velocities were computed with the linear wave theory. Although the circumstances on the slope are beyond the validity-range of this theory, LeMéhauté (1968) already showed that for orbital velocities at the bottom, the theory predicts measured values quite well. Figure 3 shows for various locations along the slope and wave steepnesses,  $s$ , in the authors' experiments, the comparison between

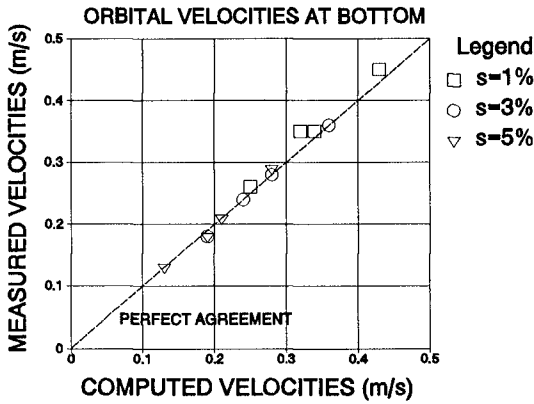


**Figure 3** Comparison computed and measured orbital velocities in DUT wave flume

computed and measured maximum orbital velocities at the bottom. The measured values are in the upslope direction, since it appeared from the experiments that the first movement of the stones is in upslope direction. The agreement between computed and measured values is remarkably good.

The wave heights on the slope were determined, applying the shoaling coefficient:

$$K_{sh} = \frac{1}{\sqrt{\tanh kh \left[ 1 + \frac{2kh}{\sinh 2kh} \right]}} \tag{6}$$

The water depth at the toe of the slope in the flume cannot be considered as deep water. Hence the local wave height is computed as:

$$H_L = K_{sh,L} * H_0 = K_{sh,L} * \frac{H_{Toe}}{K_{sh,Toe}} \tag{7}$$

For irregular waves the same procedure is followed, now with respect to a significant wave height,  $H_s$ , and a peak period of the wave spectrum,  $T_p$ .

Tests were done with various stone sizes. For each water depth along the slope, the (local) wave height for the threshold of motion for the stone dimensions in a certain test, and the corresponding wave height at the toe of the slope were determined with the above mentioned relations and compared with the measurements.

5. NON-BREAKING REGULAR WAVES

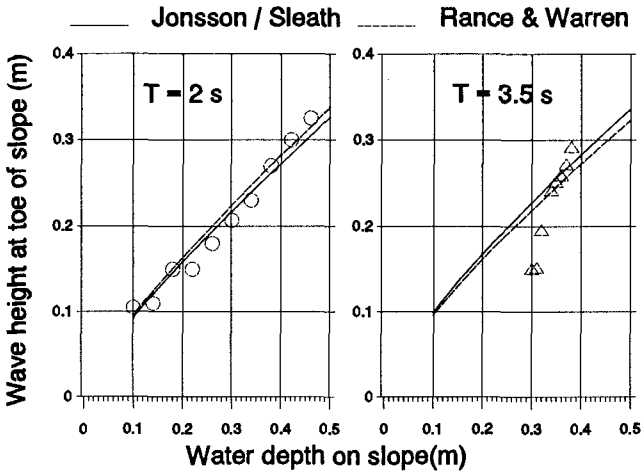


Figure 4 Wave height at toe of slope for incipient motion with constant T

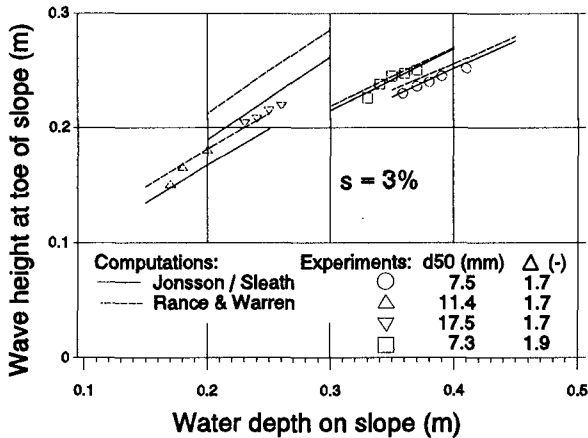


Figure 5 Wave height at toe of slope for incipient motion with constant  $s = 3\%$

Figure 4 shows the results for constant wave period (2 s and 3.5 s). The differences between the computation according to Jonsson/Sleath and Rance & Warren are small. The agreement for  $T = 2$  s is quite good. For  $T = 3.5$  s there is a deviation for water depths around 0.3 m. The wave steepness for which the threshold of



motion was determined was 1 % or less, and the corresponding wave appeared to be unstable in the flume: the waves fell apart into two separate waves. Figure 5 shows the stability for a constant steepness,  $s_r = H_r/1.56 \cdot T^2 = 3 \%$  and various stone sizes and densities. The difference between Jonsson/Sleath and Rance & Warren is again small for the smaller stones in relatively deep water. For larger stones the difference increases. This is caused by the fact that a large stone diameter gives a large friction coefficient,  $f_w$ , which is computed iteratively in Jonsson/Sleath.

In general it can be said that the assumed mechanism describes reasonably well the experimental results. In the following, all computations have been done with the method of Rance & Warren, being simpler than that of Jonsson/Sleath while the differences are small.

## 6. NON-BREAKING IRREGULAR WAVES

The stability mechanism in irregular waves does not differ from that in regular waves, but it is obvious that the higher waves cause the damage. In this research, the irregular wave field is described with a significant wave height and the peak period of the wave spectrum. From a first comparison between the results for regular and irregular waves, it appeared that, for incipient motion, in regular waves the wave height was about 50% higher than the significant wave height in irregular waves. Taking the Rayleigh-distribution as basis for the wave height distribution, this would mean that the 1% highest waves are responsible for the incipient motion ( $H_{1\%} \approx 1.5H_s$ ). In shallow water, the wave height distribution is going to deviate from the Rayleigh-distribution. An expression for this deviation is given by Stive, see CUR/CIRIA (1991). This expression is, however, independent of the wave period, while in the experiments the difference between regular and irregular waves was larger for lower wave steepness.

A magnifying factor for the significant wave height,  $K_I$ , is now defined with a lower limit 1 and an upper limit depending on the water depth and the wave period:

$$H_{ML} = K_I * H_{SL} = \left[ 1 + \text{Constant} * \tanh \left( \frac{H_M}{H_{S0}} \right) \right] * H_{SL} \quad (8)$$

$$= \left[ 1 + \text{Constant} * \tanh \left( \frac{0.14 * L * \tanh(kh)}{H_{S0}} \right) \right] * H_{SL}$$

$H_M$ , is the breaker height according to Miche, see CUR/CIRIA (1991). For the constant in  $K_I$ , a value 0.6 was chosen. The result is a magnifying factor for  $H_{SL}$  along the slope between 1 and 1.6 depending on the depth and the wave steepness.

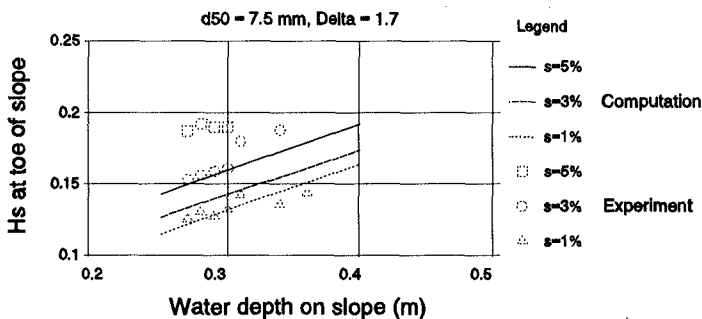


**Figure 6** Regular non-breaking waves,  $\Delta = 1.7$

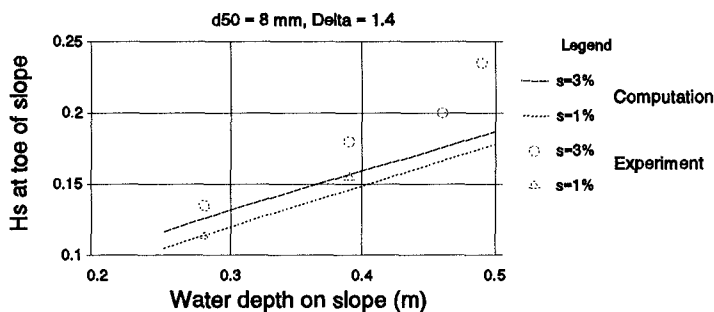


**Figure 7** Regular non-breaking waves,  $\Delta = 1.4$

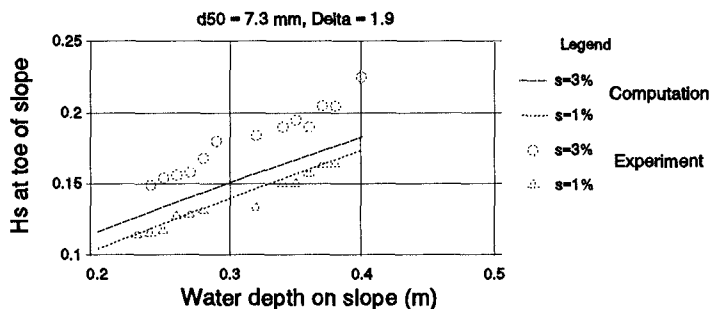


**Figure 8** Regular non-breaking waves,  $\Delta = 1.9$

Figure 6, Figure 7 and Figure 8 show the results for non-breaking irregular waves. It appears that for all stone densities investigated, the computations follow the trend

of the experiments rather well; the influence of the wave steepness, however, is underestimated. The constant (0.6) in  $K_1$  was chosen such that it fitted the experimental results for irregular waves with  $s = 1\%$ , being a practical lower limit for irregular waves. It appears that the representation of an irregular wave field with  $H_s$  and  $T_p$ , as used in shoaling computations, combined with the proposed magnifying factor,  $K_1$ , is too simple to describe correctly the whole process. For this first round, however, this is taken for granted, since the trend is indicated quite well and the final values to be used in the design rule are on the conservative side.

Note: The use of  $H_M$ , the local breakerheight according to Miche, seems somewhat peculiar in a formula for non-breaking waves. This is however deemed acceptable because, in an irregular wave field, there is a very gradual transition from non-breaking to breaking, while the mechanism at the point of breaking is not necessarily completely different. Moreover, the use of  $K_1$ , including  $H_M$ , has no other pretention than being a sensible way of curve-fitting.

## 7. BREAKING REGULAR WAVES

The assumed mechanism for the stability in breaking waves is again the shear stress under a wave. Starting with a given wave at the toe of the slope, the local wave parameters are computed and from these the stone diameter needed.

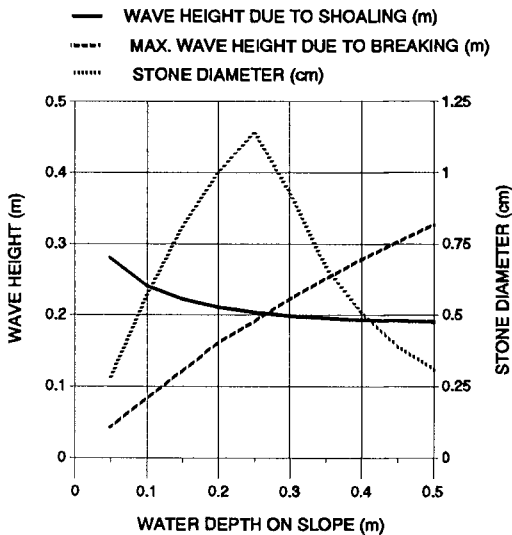
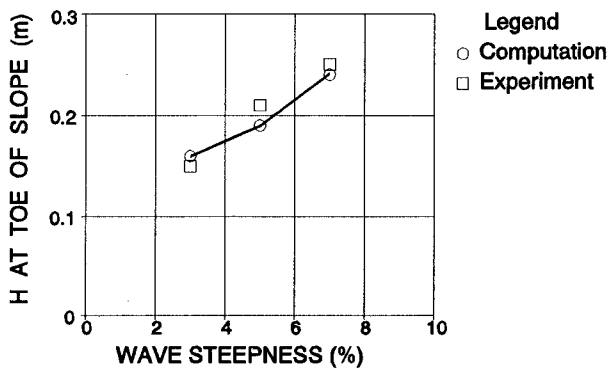


Figure 9 Computation of stone diameter in breaking wave

Figure 9 shows the computed wave heights due to shoaling and the breaker height according to Miche. The maximum of these two is used in the computation of the diameter, yielding a maximum value along the slope. It can be expected that this procedure will underestimate the necessary diameter, since the shape of the wave, the velocity field and the turbulence in a breaking or broken wave are unfavourable compared with non-breaking waves. Therefore, a second tuning parameter,  $K_B$ , comes in:

$$d_{\text{Breaking}} = K_B * d_{\text{Non-Breaking}} \quad (9)$$

The diameter that finally results from this procedure is taken as the diameter in breaking regular waves.



**Figure 10** Comparison measured and calibrated values for regular breaking waves

Figure 10 gives the results of the comparison between computation and experiment, in which the above mentioned procedure was performed in a reversed order and iteratively (starting with a given diameter, which is the case in a flume experiment, computing the local wave height for incipient motion and hence the wave height at the toe of the slope).  $K_B = 2$  is used in the figure, giving the best fit.

Here again it can be seen that a larger wave steepness leads to a more stable situation (larger wave height for incipient motion, see Figure 10). This can also be explained from the way of breaking of the waves. According to the common classification, all these waves belong to the spilling type ( $\xi < 0.4$ , see Battjes (1974)). There is, however, a gradual change in breaking characteristics and the lower the steepness of the waves in the experiments, the more they showed a

plunging behaviour. In a plunging breaker the bottom is attacked by a jet, giving a more unfavourable situation compared to a "real" spilling breaker. The energy dissipation in a plunging breaker is more concentrated than in a spilling breaker, see Figure 11.

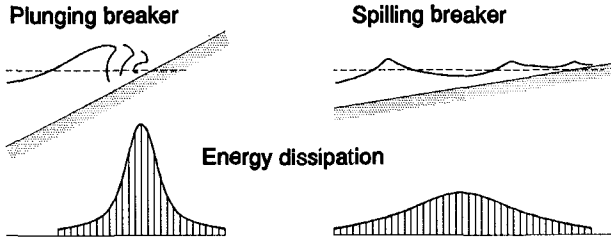


Figure 11 Energy dissipation in spilling and plunging breakers

### 8. BREAKING IRREGULAR WAVES

With a magnifying factor,  $K_i$ , for the irregularity of the waves and an amplification factor,  $K_B$ , to take the effect of breaking into account, the stability in breaking irregular waves is computed and the results are given in Figure 12.

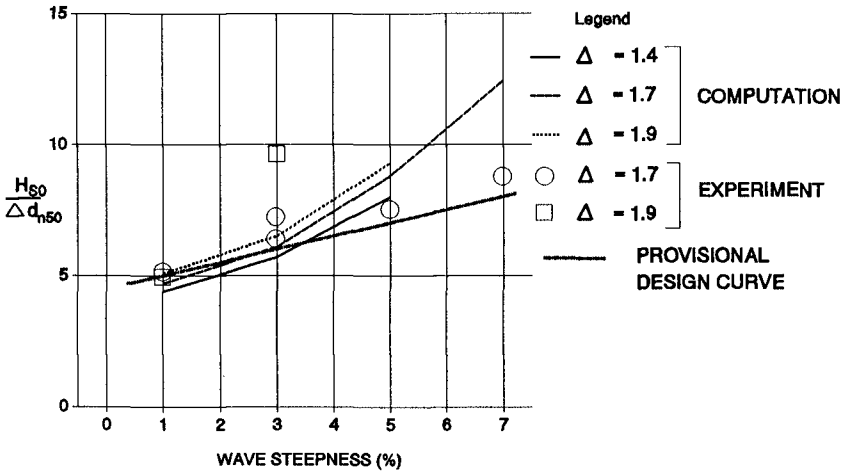


Figure 12 Comparison computed and measured values for irregular breaking waves

In this figure the stability is expressed as  $H_{S0} / \Delta d_{n50}$  in order to compare it with the stability of rock on breakwaters or revetments.  $H_{S0}$  is a fictitious deep water wave

height, derived from equation (7) in order to have an unambiguously defined wave height. The nominal diameter ( $d_{n50}$ ) is used instead of the sieve diameter because this is a more practical measure for large stones. The relation between  $d$  and  $d_n$  can be taken as an average for normal rock, see CUR/CIRIA (1991):  $d_n = 0.84*d$ .

From Figure 12 the following can be seen:

- The dimensionless parameter  $H/\Delta d$ , computed according to the procedure outlined above, still shows variation with  $\Delta$ . This means that either the mechanism assumed in the computation is not correct or the use of this dimensionless parameter is not allowed.
- The rather scarce data do not fit very well with the computations.
- Typical values of  $H/\Delta d$  for a wave steepness of 3 %, lie around 6 compared to 2 for revetments with steep slopes.

For the time being, the lower limit of the experimental results is taken as a conservative approach for a provisional design rule:

$$\frac{H_{s0}}{\Delta d_{n50}} = 4.5 + 50 * s_0 \quad (10)$$

The tendency of this result is conformable to van der Meer's equation for stability on steep slopes, see van der Meer (1988). For a given slope angle, van der Meer's equation for plunging breakers gives an increasing stability number  $H/\Delta d$  for an increasing wave steepness or a decreasing  $\xi$ . In Figure 13 both relations are given for a slope angle 1:25 (this is far beyond the range for which the van der Meer equations are valid, but it is just to show the mentioned tendency).

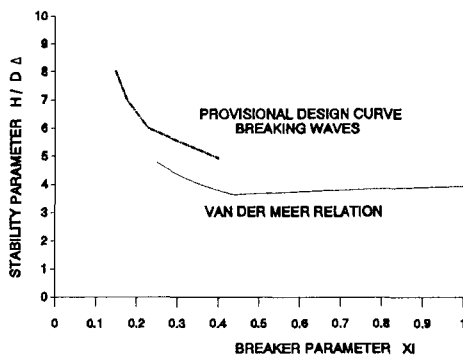


Figure 13 Comparison experimental results with van der Meer's equation

## 9. DESIGN RULE

The proposed design rule is now to be applied as follows:

- Start with the significant deep water wave height ( $H_{s0}$ ), measured or from equation (7) and a wave height measured at any relatively deep water location
- Compute the shoaling of  $H_{s0}$  along the slope with equation (6) using the peak period of the spectrum,  $T_p$
- Determine  $H_{ML}$  along the slope with equation (8)
- Compute the necessary diameter along the slope with equation (2) and (5)
- Compute the maximum diameter with equation (10)

Figure 14 gives the result for  $H_{s0} = 5$  m,  $T_p = 10$  s and  $\Delta = 1.65$ .

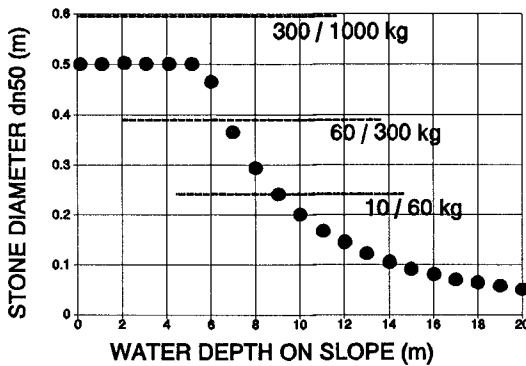


Figure 14 Design example

### NOTES:

- 1 Equation (10) expresses the stability as a function of the wave steepness,  $s$ . Since the stability is closely related to breaking, it would be more appropriate to relate the stability parameter  $H/\Delta d$  to the breaking parameter  $\xi$ . Only one slope was investigated (1:25). Using  $s$  instead of  $\xi$  is on the safe side for all slopes milder than 1:25, since a milder slope yields lower  $\xi$ -values leading to a more stable situation.
- 2 In the figure some limits of stone classes are given, which are common in the Netherlands. These are not essential, but are presented to show that for a practical case, a choice has to be made from material available.

## 10. RECOMMENDATIONS

The design rule, presented in the previous section, is the best approach available at the moment for stability of rock on mild slopes. Conservative choices had to be made; improvements are possible. Therefore the following is needed:

- A more complete description of the velocities and shear stresses on the slope in irregular waves. This can probably be obtained with a model that describes the behaviour of irregular waves on a slope, including bottom friction and breaking, see e.g. van der Meer (1990).
- A physical description of the breaker zone itself with a model that includes the shape of the waves, the velocity field and the turbulence. This could give more and better information on the attack on the slope than is possible with the orbital movement according to the linear wave theory.
- More systematic experimental data on stability in breaking waves, including other slope angles. In doing so, also an attempt can be made to make a better link between the relations in Figure 13, giving a complete picture of stability of rock on mild and steep slopes.

## SYMBOLS

A	surface area of coloured strips		m <sup>2</sup>
a <sub>b</sub>	orbital stroke at bottom		m
d <sub>n50</sub>	median nominal diameter of material	(d <sub>n50</sub> = (M <sub>50</sub> /ρ <sub>s</sub> ) <sup>0.33</sup> )	m
d <sub>50</sub>	median sieve diameter of material		m
f <sub>w</sub>	friction coefficient in waves		-
g	acceleration due to gravity		m/s <sup>2</sup>
H <sub>0</sub>	deep water wave height		m
H <sub>L</sub>	local wave height		m
H <sub>ML</sub>	maximum local wave height (Miche breaker height)		m
H <sub>S</sub>	significant wave height		m
h	waterdepth		m
K <sub>I</sub>	magnifying factor for irregular waves		-
K <sub>B</sub>	amplification factor for breaking waves		-
K <sub>sh</sub>	shoaling factor		-
k	wave number	(k = 2π/L)	1/m
k <sub>s</sub>	equivalent sand roughness	(k <sub>s</sub> = d <sub>50</sub> )	m
L <sub>0</sub>	deep-water wave length		m
M	mass		kg
n	number of displaced stones		-
S	damage		%



s	wave steepness	( $s = H/L_0$ )	%
$T_p$	peak wave period of spectrum		s
$u_b$	orbital velocity at bottom		m/s
$\alpha$	slope angle of structure		-
$\Delta$	relative mass density of material	( $\Delta = (\rho_s - \rho_w)/\rho_w$ )	-
$\rho_s$	mass density of material		kg/m <sup>3</sup>
$\rho_w$	mass density of water		kg/m <sup>3</sup>
$\xi$	breaker parameter	( $\xi = \tan \alpha \sqrt{H/L_0}$ )	-
$\hat{\tau}_b$	amplitude of bottom shear stress		N/m <sup>2</sup>
$\omega$	angular frequency	( $\omega = 2\pi/T$ )	1/s

## REFERENCES

- Battjes, J.A., 1974**, *Computation of set-up, longshore currents, run-up and overtopping due to wind-generated waves*  
PhD-thesis, Delft University of Technology, pp. 19
- CUR/CIRIA, 1991**, *Manual on the use of rock in coastal and shoreline engineering*, CUR Report 154/CIRIA Special Publication 83, Balkema, Rotterdam, pp. 197, 216, 217, 298
- Grote, W.V., 1994**, *Protection of outfall structures*  
MSc-thesis, Delft University of Technology
- Hudson, R.Y., 1959**, *Laboratory investigations of rubble mound breakwaters*  
WES Report, Vicksburg, USA
- Jonsson, I.G., 1966**, *Wave boundary layers and friction factors*  
Proc. 10th Conf. on Coastal Engineering, Tokyo, pp. 127-148
- LeMéhauté, B., 1968**, *Shallow water waves: A comparison of theories and experiments*, Proc. 11th Conf. on Coastal Engineering, London, pp. 86-107
- Meer, J.W. van der, 1988**, *Rock Slopes and Gravel Beaches under Wave Attack*  
Delft Hydraulics, Publication no. 396, The Netherlands
- Meer, J.W. van der, 1990**, *Extreme shallow water wave conditions*  
Delft Hydraulics, Report H 198, January 1990
- Naheer, E., 1977**, *Stability of bottom armorings under the attack of solitary waves*  
California Institute of Technology, Report no. KH-R-34, USA
- Rance, P.J., and Warren, N.F., 1968**, *The threshold of movement of coarse material in oscillatory flow*  
Proc. 11th Conf. on Coastal Engineering, London, pp. 487-491
- Sisternans, P.G.J., 1993**, *Stability of rock on beaches*  
MSc-thesis, Delft University of Technology
- Sleath, J.F.A., 1978**, *Measurements of bed load in oscillatory flow*  
Journal of the Waterway, Port, Coastal and Ocean Division, ASCE, Vol.104 no. WW4, pp. 291-307
- Stive, M.J.F., 1985**, *A scale comparison of waves breaking on a beach*  
Coastal Engineering, 9 (1985), pp. 151-158

## CHAPTER 113

### Short Term Wave Overtopping Rate of Block Armored Seawall

Tsunehiro Sekimoto\* Hiroshi Kunisu\* and Tsuyoshi Yamazaki\*

#### Abstract

The characteristics of short term over topping rate for a deepsea block armored seawall are investigated experimentally. Two series of experiments were conducted. One is a series that seawall has low crown height and a wave grouping effect is investigated. Another experiment is a series that it has a high crown height and slope effect of armor unit is studied. From these experiments, we have to consider the short term wave overtopping rate for the design of drainage facilities of deepsea structure such as an artificial island.

#### Introduction

Recently, Many ideas of offshore artificial island have been planning in Japan and many studies on a design method for deepsea seawall or deepsea breakwater have been started. In a concerning research, it is pointed out that excess wave overtopping maybe lead artificial island to ruin. Therefore it is very important in the construction of artificial island to estimate accurately of overtopping rate of seawall.

Usually, In order to estimate the wave overtopping rate, the Goda's diagrams (Goda, 1987) are used. This diagram illustrates the relationship between a mean overtopping and a crown height. It has been pointed out that short term overtopping rate is important for the design of drainage facilities behind the seawall (Kimura and Seyama, 1984). Moreover it is suggested that the short term overtopping rate become several ten times of mean wave overtopping rate and large amount of water comes into the drainage facilities in short time (Inoue et al., 1989).

---

\* Penta-Ocean Construction Institute of Technology, 1534-1 Yonku-cho Nishinasuno-machi Nasu-gun Tochigi 329-27 Japan

However, Goda's diagram is illustrated only for the time average of total overtopping quantity and this diagram dose not include an effect on the slope of block armor unit. In this study, we study the characteristics of short term wave overtopping rate on the block armored seawall experimentally.

**Experiments**

Experiments were conducted by using the wave flume with dimension of 0.6m in width, which is partly divided from a wave basin of 5m in wide, 34m in length and 1.2m in depth. At an end of basin, rubbles banked in 1: 5 slope in order to reduce reflected waves. The wave flume shows in Figure 1. Model seawall were set up in the flume.

Two series of experiments for the wave overtopping were carried out. In these experiments, it is supposed that a prototype water depth in front of the seawall is 22.5m. Considering the wave flume dimensions, the model scale of series one and two are assumed to 1/85.7 and 1/87.5 respectively.

One of two experiments is a series that seawall has low crown height and a wave grouping effect is investigated. A typical model section in Series-one is shown in Figure 2. Both a vertical and a block armored seawall are used in this series. The water depth in front of a model seawall was 26.3 cm. Sea bed slope in front of a model seawall is 1/100. The tetrapods (58.9g) were used as armored blocks and the same size blocks

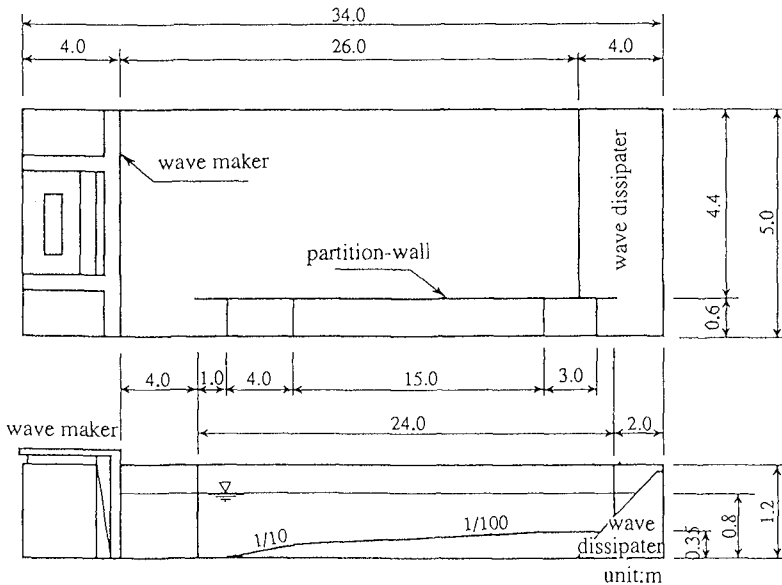


Figure 1 Experimental setup.

were used in all section. A crown height was 10.5 cm. It is 9m in prototype scale and the slope of armor units is 1:4/3.

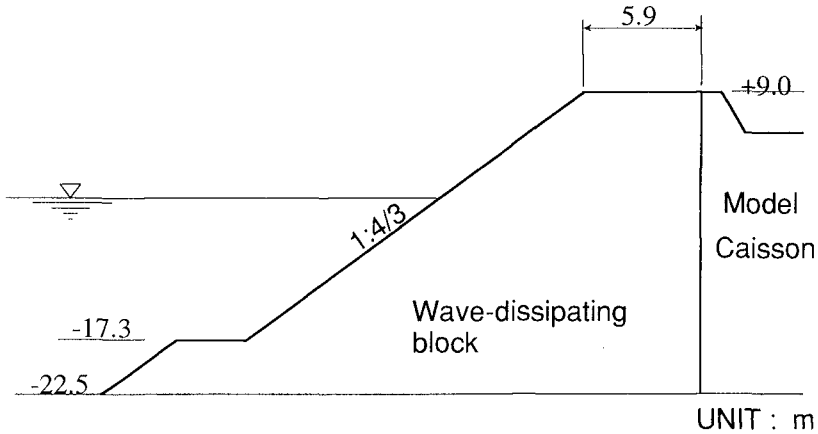


Figure 2 Typical model seawall (for series 1)

Irregular waves which have Wallops type spectrum were act on model seawall.

Wallops type wave spectrum is shown below.

$$S(f) = \beta H_{1/3}^2 T_p (T_p f)^{-m} \exp \left[ -\frac{m}{4} (T_p f)^4 \right] \quad (1)$$

$$\beta \equiv \frac{0.6238 m^{(m-2)/4}}{4^{(m-5)/4} \Gamma[(m-1)/4]} \left[ 1 + 0.7458(m+2)^{-1.057} \right] \quad (2)$$

$$T_p \equiv T_{1/3} / \left[ 1 - 0.283(m-1.5)^{-0.684} \right] \quad (3)$$

where  $m$  : Spectral shape factor,  $H_{1/3}$  : Significant wave height,  $T_{1/3}$  : Significant wave period,  $T_p$  : Peak wave period,  $\Gamma()$  : Gamma function.

The shape factor  $m$  become small, the bandwidth of wave spectrum becomes narrow, while the  $m$  is large, the band widths of wave spectra become wide. In the case that  $m$  is 5, Wallops type wave spectrum corresponds to Modified Bretschneider-Mitsuyasu type wave spectrum modified by Goda.

The experimental cases were shown in Table 1. In this series, 24 runs of experiment were conducted. The three types of spectral shape factor  $m= 3, 5$  and  $9$  were selected. The wave period was 1.73 second and

five kinds of wave height were used. The wave height normalized by the crown height were changed from 0.65 to 1.42.

Table 1 Experimental case for series 1.

$T_{1/3}(s)$	$H_{1/3}/h_c$	vertical seawall			block armored seawall		
		m=3	m=5	m=9	m=3	m=5	m=9
1.73 (16.0)	0.60	○	○	○	○	○	
	0.74	○	○	○	○	○	
	0.89	○	○	○	○	○	
	1.04	○	○	○	○	○	
	1.19	○	○		○	○	

Table 2 Experimental case for series 2.

$T_{1/3}$ (sec)	$H_{1/3}/h_c$	Slope of block armour units				
		1:4/3	1:1.6	1:1.8	1:2.0	1:2.5
1.28	0.456	○				
	0.548	○	○	○	○	○
	0.639	○	○	○	○	○
	0.684	○	○	○	○	○
	0.730	○				
	0.812	○	○	○	○	○
	0.913	○	○	○	○	○
1.71	0.456	○				
	0.548	○	○	○	○	○
	0.593	○				
	0.639	○	○	○	○	○
	0.684	○	○	○	○	○
	0.730	○				
	0.776	○				
	0.821	○	○	○	○	○
0.913	○	○	○	○	○	
2.14	0.456	○				
	0.548	○	○	○	○	○
	0.593	○				
	0.639	○	○	○	○	○
	0.684	○	○	○	○	○
	0.730	○				
	0.821	○	○	○	○	○
	0.913	○	○	○	○	○

Another experiment is a series that it has a high crown height and slope effect of armor unit is studied. Assuming an actual wave overtopping condition, the mean wave overtopping rate set below  $0.05\text{m}^3/\text{m}/\text{s}$  in prototype scale in the condition that the significant wave height normalized by crown height is 0.684, and significant wave period is 16s in this series. The crown height was 16 cm in experimental scale (it is 14m in prototype scale). Therefore these experiments were conducted under the relatively high crown height and low wave overtopping rate condition. The slopes of armor units which were used in the experiment were 1:4/3, 1:1.6, 1:1.8, 1:2.0 and 1:2.5. The tetrapods (36.8g) were used as armored blocks and the same size of block was used in all section. The Wallops type wave spectra were also used in this series. In this series, the shape factor of incident wave spectra is selected  $m = 5$ . The wave heights normalized by the crown height were changed from 0.46 to 0.91 and three wave periods 1.28s, 1.71s and 2.14s in experimental scale were used, which were 12s, 16s and 20s second in prototype scale respectively. Experimental condition is shown in Table 2. Eighty-four runs of experiments were conducted.

#### Short term over topping rate measurement.

In order to get the short term overtopping rate, a time dependent weight of water was measured using the measurement apparatus which was used by Sekimoto et al. (1994). This apparatus is consist of a water tank which was supported by four load-cells and was set just behind the seawall. The instantaneous wave over topping rate was defined as a change rate of water weight per unit time.

We defined a maximum wave overtopping rate as a maximum value of moving average of instantaneous overtopping rate over a time interval as shown below. The duration of average is to be  $n$  times significant wave period, where  $n$  is 1,3 and 5 in this study. Using this instrument, the short term wave overtopping rate can be measured accurately (Sekimoto et al., 1994).

$$q_n(t) = \frac{1}{nT_{1/3}} \int_{-nT_{1/3}/2}^{nT_{1/3}/2} q_i(t + \tau) d\tau \quad , n = 1, 3, 5 \quad (4)$$

$$q_{n-\max} = \text{Max}[q_n(t)] \quad (5)$$

where,  $q_i(t)$  : Instantaneous wave overtopping quantity,  $q_n(t)$  :  $n$ -waves mean overtopping rate,  $q_{n-\max}$  :  $n$ -waves maximum overtopping rate (short term wave overtopping rate),  $T_{1/3}$  : Significant wave period.

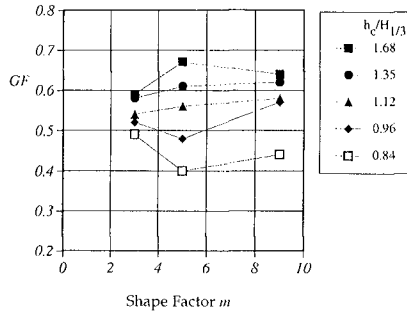


Figure 3 The relationship between spectral shape factor  $m$  and groupiness factor.

Results

Figure 3 shows the relationship between spectral shape factor  $m$  and groupiness factor. There is no clear relationship in both. In the case of high wave height, wave breaking is occurred and groupiness factor is relatively small.

In Figure 4, the mean wave overtopping rate normalized by wave height is plotted against the spectral shape factor  $m$ . In this figure, the wave height is measured on the position of seawall in the condition that the model seawall dose not set up. On the left hand side of this figure, the results of vertical wall type seawall are shown and on the right hand side the results of block armored seawall are shown. The mean wave overtopping rate have tendency of increase while spectral band width become narrow. However, this tendency is not so strong.

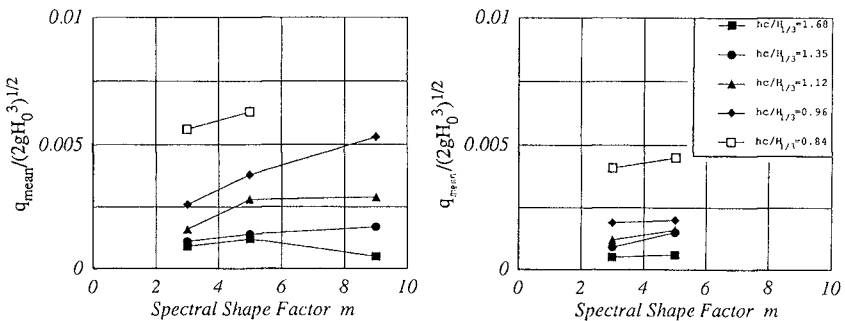


Figure 4 The relationship between the mean wave overtopping rate and the spectral shape factor.

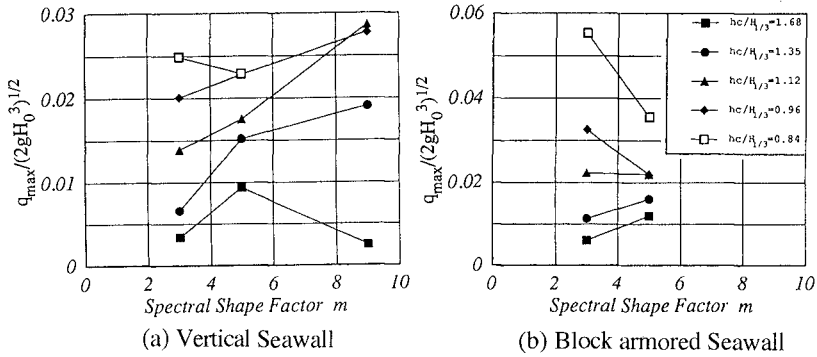


Figure 5 The relationship between the maximum wave overtopping rate and the spectral shape factor.

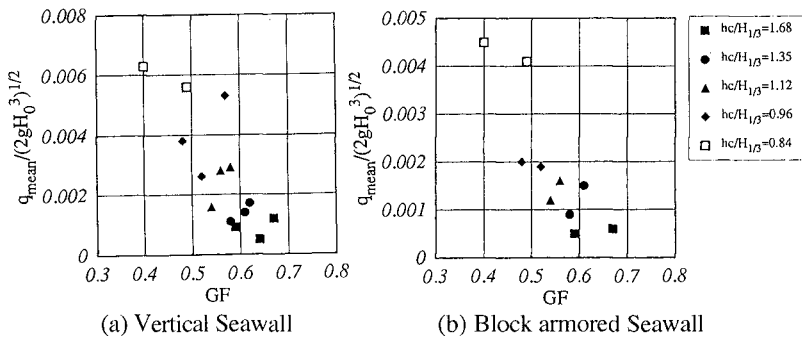


Figure 6 The relationship between the mean wave overtopping rate and the groupiness factor.

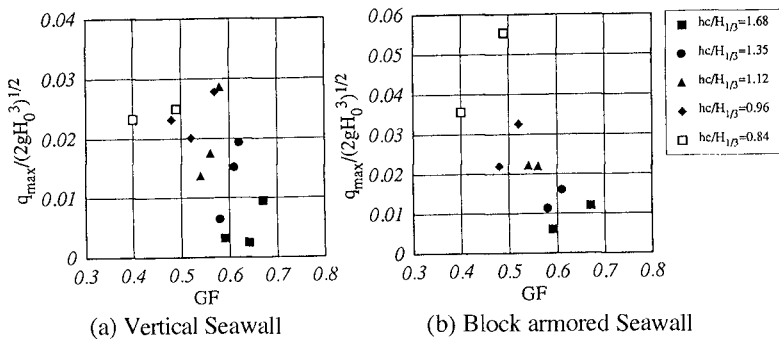


Figure 7 The relationship between the maximum wave overtopping rate and the groupiness factor.



Figure 5 shows the maximum wave overtopping rate in the same manner as Figure 4. The maximum wave overtopping seems depends on the shape factor except for the case of high waves. In the case of high wave height, wave breaking effect may be appeared.

The relationship between wave-overtopping rate and groupiness factor is compared in Figure 6 and Figure 7. On the left hand side of this figure, the results of vertical wall type seawall are shown and on the right hand side the results of block armored seawall are shown. The results show the strong relationship between both is available. In the case of the same wave height, the wave overtopping also increase as the wave groupiness increase.

We also compared the maximum wave height in a wave train with wave overtopping rate. The maximum wave height in this figure is measured at the location of model seawall before the model seawall was set up. The left-hand side and right-hand side of this figure are indicated in the same manner as previous figures.

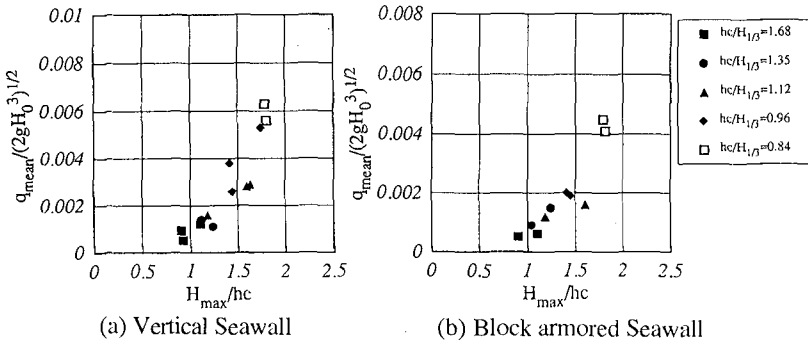


Figure 8 The relationship between the mean wave overtopping rate and the maximum wave height.

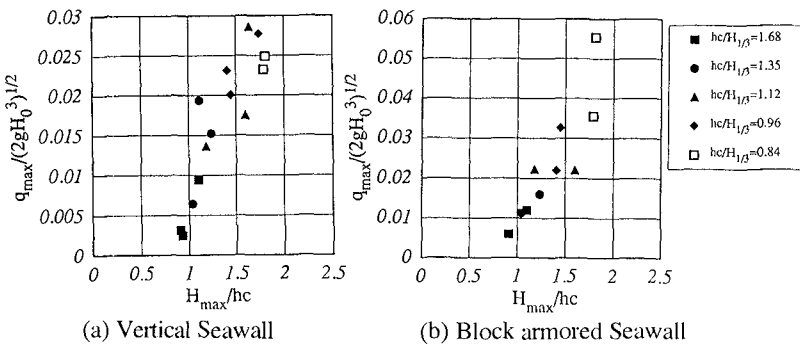


Figure 9 The relationship between the maximum wave overtopping rate and the maximum wave height.

Figure 8 shows the case of mean wave overtopping rate. The mean wave overtopping rate has one to one correspond to maximum wave height. In the results of maximum wave overtopping rate (Figure 9), we can clearly see the same relationship. This relationship is very natural and shows that once we know the maximum wave height in front of seawall, we can accurately estimate the wave overtopping rate not only the mean overtopping rate but also the short term wave overtopping rate.

Next, we investigated the slope effect on the wave over topping.

The relationship between the mean wave overtopping rate and an inverse of the slope in each wave period had investigated by Sekimoto et al. (1994). According to this study, the tendency of these relationships is similar to the results of Saville's runup experiment(1952). That is the mean overtopping rate is small when the slope is steep. As the slope becomes mild, the mean overtopping rate becomes large. The slope further becomes mild, the mean overtopping rate decreases.

This reason can be accounted for the wave deformation on the slope of blocks. In the case of steep slope, wave deformation does not occur on the slope because of the short slope length. As the slope becomes mild, the wave height increases due to wave shoaling. In the case that slope is further mild, the wave energy is dissipated due to the wave breaking on the slope and the energy loss in the armor units. In the case that the same wave act on the seawall, the mean overtopping rate has not same volume when the slope of armor units is not same. Especially in the case of the 1: 1.8 slope, the mean overtopping rate was seven times as large as that in the case of the 1: 2.5 slope.

We investigated the relationship between the maximum wave overtopping rate and the slope of armor unit in Figure 10. In this figure, the wave overtopping rate was indicated in prototype scale. The almost same relationship to the mean wave overtopping rate is available in this figure. However, the maximum wave overtopping rate is more variable quantity than the mean wave overtopping rate, in the sense of statistics.

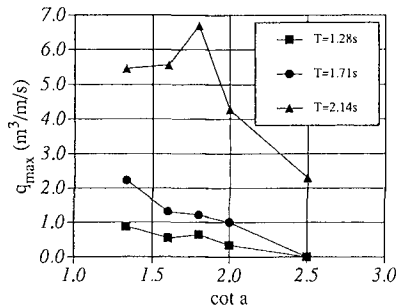


Figure 10 The relationship between the maximum wave overtopping rate and the slope of armor unit.

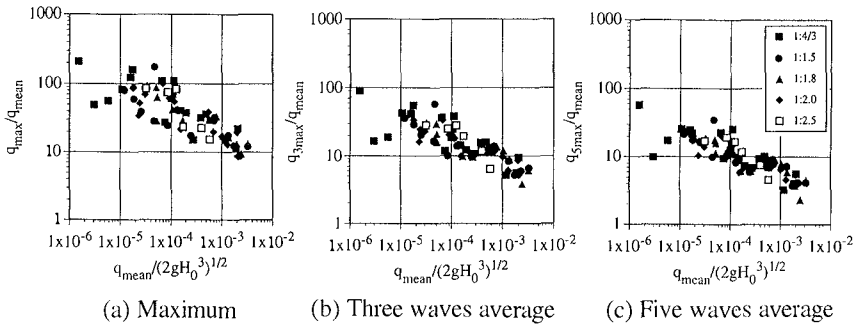


Figure 11 The relationship between the short term wave overtopping rate and the mean wave overtopping rate.

Therefore the maximum wave overtopping rate shows more complicated feature than mean wave overtopping rate.

Figure 11 shows the relationship between the short term wave overtopping rate and the mean wave overtopping rate. In this figure, vertical axis is the ratio of short term overtopping rate to the mean wave overtopping rate and horizontal axis is taken normalized mean wave overtopping rate. Three types of short term wave overtopping rate were taken in these figures. The  $q_{max}$  means the maximum wave overtopping rate which is the maximum value of the average of wave overtopping quantities during one wave. The  $q_{3max}$  means the maximum value of the average of wave overtopping quantities during three waves. The  $q_{5max}$  means during five waves.

From this figure, we find that the ratio becomes large as the mean wave overtopping rate becomes small. The maximum wave overtopping rate shows 10 to 170 times the mean wave overtopping rate. The maximum overtopping rate during three waves shows 5 to 100 times the mean wave overtopping ratio. The maximum overtopping rate during five waves indicated 3 to 50 times.

It shows that the large amount of water flows over seawall in short time and we have to consider short term wave overtopping in the design of drainage facilities just behind the seawall.

Figure 12 shows the relationship between the short term wave overtopping rates against the mean wave overtopping rate. The data of maximum overtopping rate during three waves were distributed from 0.333 to 0.8 times the maximum wave overtopping rate. In the case of maximum overtopping rate during five waves, it becomes from 0.2 to 0.5. It is natural that scattering of this ratio become small when the duration time for average is large. In the case of small rate of wave overtopping, the number of overtopped waves including the wave by which the maximum wave overtopping rate was occurred is only one. In the case of large rate of

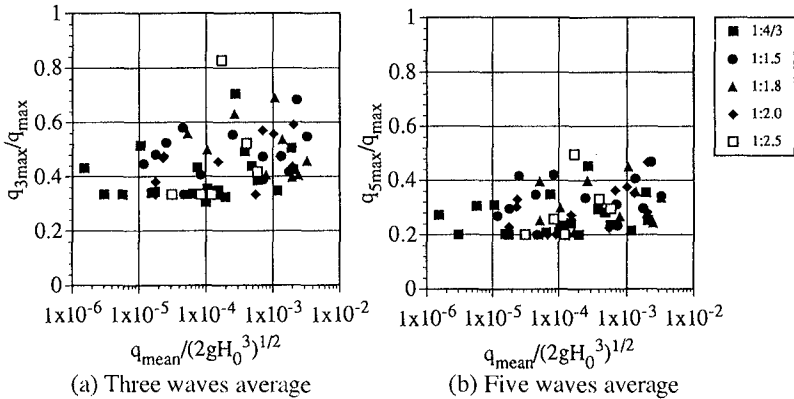


Figure 12 The relationship between the short term wave overtopping rates against the mean wave overtopping rate.

wave overtopping, the number of overtopped waves including the wave when the maximum wave overtopping rate was occurred is one to three.

## Conclusions

The main results obtained from this study were shown below.

(1) The mean wave overtopping rate is not so affected by the spectral band width in this experiment.

(2) The short term wave overtopping rate is affected by the spectral band width, except for the case that the wave breaking obviously occurred.

(3) The wave overtopping rate strongly related to the Groupiness Factor.

(4) The wave periods become longer, the short term wave overtopping rate become larger.

These results were similar to the case of mean overtopping rate.

(5) The maximum wave overtopping quantity, which is defined as the maximum value of wave overtopping for one wave, becomes more than 100 times of the mean wave overtopping rate in the case of high crown height. In the design of drainage facilities, it has to be considered that huge amount of water flows in short time.

(6) The mean overtopping rate and the maximum wave overtopping rate were clearly affected by the slope of block armor unit. This is a same tendency of previous experiments of Saville's wave run-up on composite slopes. The slope effect in the wave overtopping has to be considered in design of sea wall.

**References**

- Goda Y. (1987): Random Seas and Design of Maritime Structures, Univ. of Tokyo press, 323pp.
- Inoue M., H. Shimada and K. Tonomo (1989): Quantitative Study on Overtopping of Irregular Waves, Proc. Coastal Engineering, JSCE Vol.36, pp.618-622 (in Japanese).
- Kimura, A. and A. Seyama (1984): Statistical Properties of Short-Term Overtopping, Proc. 19th ICCE, pp.532-546.
- Saville, T., Jr. (1958): Wave run-up on composite slopes, Proc. 6th ICCE, pp.691-699.
- Sekimoto, T., H. Kunisu and T. Yamazaki (1994) : Slope Effect on Wave Overtopping Rate of Block Armored Seawall, Proc. Hydro-Port '94.

## CHAPTER 114

### Estimating the Sliding Distance of Composite Breakwaters due to Wave Forces Inclusive of Impulsive Forces

Kenichiro Shimosako<sup>1</sup>, Shigeo Takahashi<sup>2</sup>, Katsutoshi Tanimoto<sup>3</sup>

#### Abstract

Estimating the sliding distance is essential in the future probabilistic design of caisson breakwaters. In this paper, characteristics of the sliding phenomena are described, and a method based on the equivalent sliding forces to calculate the sliding distance is proposed. This calculation method is applicable for both impulsive and ordinary wave forces considering the shear force at the bottom of the caisson.

#### 1. Introduction

Composite type breakwaters consisting of a rubble mound foundation and upright section have several advantages over conventional rubble mound breakwaters, since they are more stable, can be constructed faster and easier, and also reduce wave transmission.

In the conventional design process of a composite breakwater, the sliding stability of the caisson is evaluated by the sliding safety factor (S.F.). However, even if the S.F. is below 1.0, the breakwater can still maintain its function if the sliding distance is small. Consequently, to ensure economical design, it is necessary to determine the expected sliding distance occurring in the return period of the caisson.

---

<sup>1</sup>Senior Research Engineer, Hydraulic Engineering Division, Port and Harbour Research Institute, Ministry of Transport, 3-1-1 Nagase, Yokosuka, 239 Japan

<sup>2</sup>Chief of Maritime Structures Laboratory, Hydraulic Engineering Division, Port and Harbour Research Institute, Ministry of Transport

<sup>3</sup>Professor, Faculty of Engineering, Saitama University, 255 Shimo-okubo, Urawa, 338 Japan

Ito, Fujishima, and Kitatani (1966) conducted the research on the stability of breakwaters and proposed the concept of the expected sliding distance. Horikawa, Ozawa, and Takahashi (1972) also discussed the expected sliding distance of high mound composite breakwater. However, it was difficult to estimate the wave pressure precisely, much more the sliding distance at that time.

Tanimoto, Kimura, and Miyazaki (1988) calculated the sliding distance based on the fourth order finite standing wave theory. This calculation is applicable for non-breaking wave conditions in deepwater area.

Goda (1974) developed a new wave pressure formula which included an impulsive pressure. This formula is quite useful and has become the standard method to obtain wave pressure against a vertical wall, although discrepancies arise under some impulsive pressure conditions. Takahashi, Tanimoto and Shimosako (1993, 1994b) proposed an impulsive pressure coefficient obtained by a re-analysis of the results of comprehensive sliding tests, which is introduced into the Goda pressure formula.

Takayama and Fujii (1991) carried out the probabilistic estimation of stability of sliding which considered the probabilistic property of wave height, wave pressure and friction coefficient between caissons and rubble mound. However, caisson's sliding distance was not included.

In order to estimate the caisson's sliding distance, the complex phenomena including the dynamic response of a breakwater caisson due to impulsive wave forces must be quantified. In the present study, model experiments with some non-linear FEM calculations to elucidate the characteristics of the dynamic response are described. A method is proposed to calculate the sliding distance, which is applicable for both impulsive and ordinary wave forces considering the shear force.

## 2. Present Design Method and Formulation of Caisson's Sliding

### Present Design Method

The design wave forces acting on the caisson's upright section can be obtained using the Goda pressure formula. The present design method for determining the sliding stability is shown as follows:

$$S.F. = \mu(W' - U) / P \quad (1)$$

The safety factor for sliding  $S.F.$  is represented by the ratio of the friction resistance  $\mu(W' - U)$  to the horizontal wave force  $P$ , where  $\mu$  is the friction coefficient between the caisson and rubble mound,  $W'$  is the caisson weight in water, and  $U$  is the uplift force. When  $S.F.$  is less than 1.0, the caisson is considered to be in an unstable condition. However, even if  $S.F.$  is less than 1.0, the breakwater can still maintain its function providing the sliding distance is small.

In order to optimize the design from an economical standpoint, we must determine the expected sliding distance occurring in the return period of the caisson. However, the sliding distance cannot be estimated using the present design method.

Equation of Motion of Caisson

Figure 1 shows the forces that act on the caisson when it is sliding.  $M_a$  is the added mass,  $F_R$  is the frictional resistance force, and  $F_D$  is the force related sliding velocity including the wave-making resistance force.

The equation of motion representing caisson sliding is presented as follows:

$$(W/g + M_a) \ddot{x} = P - F_R - F_D \tag{2}$$

where

$$F_R = \mu(W' - U) \tag{3}$$

In Eq.(2),  $P$  represents horizontal wave force, but the effective force producing caisson's sliding, that is the shear force at the caisson bottom,  $F_T$ , should be used instead of  $P$  in order to include the effect of dynamic response of caisson. Although the magnitude of impulsive pressure intensity is quite large, the shear force is greatly reduced due to the caisson's dynamic response which is discussed later. If wave pressure is not impulsive, the shear force is equal to the horizontal wave force.

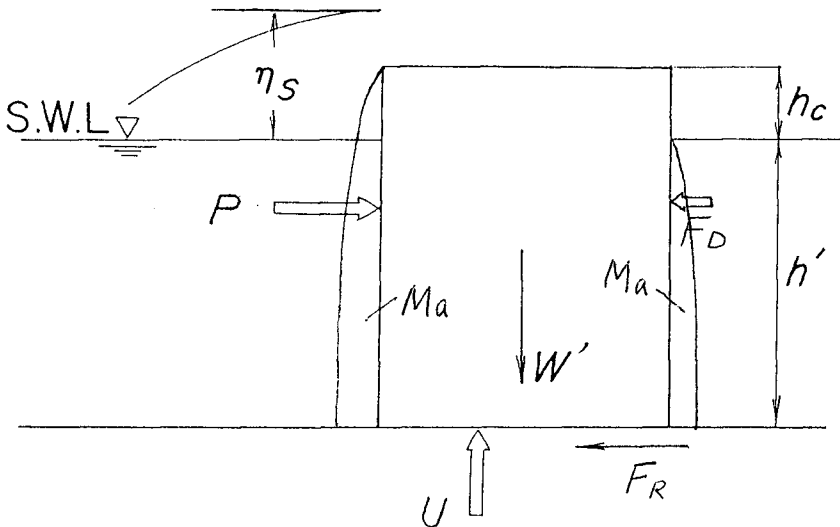


Figure 1 Forces acting on the caisson in sliding.



In our simplified sliding model, it is assumed that  $\mu$  is constant before and during sliding, and that  $M_a$  and  $F_D$  are small enough to be neglected. Consequently, Eq.(2) is rewritten as follows:

$$(W/g)\ddot{x} = F_T + \mu U - \mu W' \quad (4)$$

### Caisson's Dynamic Response due to Impulsive Wave Forces

The magnitude of impulsive pressure intensity is quite large, being several times that of ordinary wave pressure. However, the shear force at the caisson bottom, which is the effective pressure producing caisson sliding, is greatly reduced due to the caisson's dynamic response. Figure 2a shows the experimentally determined impulsive wave force  $P$ , inertia force  $m\ddot{x}_G$ , shear force  $F_T$ , and displacement  $x_G$ , where the peak shear force is about 80% of the peak impulsive force. The ratio of the peak shear force to the peak impulsive force varies according to the peak value and duration time of  $P$ . Note that the stability of the sliding is not dependent on  $P$  itself, but instead on  $F_T$ .

To reproduce the dynamic response of the caisson, we adopted a FEM calculation method named "the Bank Earthquake Analysis with Dynamic Water Pressure (BEAD)" (Uwabe, 1983). One advantage of the BEAD method is that it takes into account the pore water in the seabed and the surrounding water of the caisson. The equations utilized are a kind of Biot's equations. The BEAD program can simulate the behavior of the caisson, as well as that of the rubble mound and soil bed. The input data consists of the shear modulus, the Poisson ratio, and the permeability of the rubble mound and soil bed, as well as the input force on

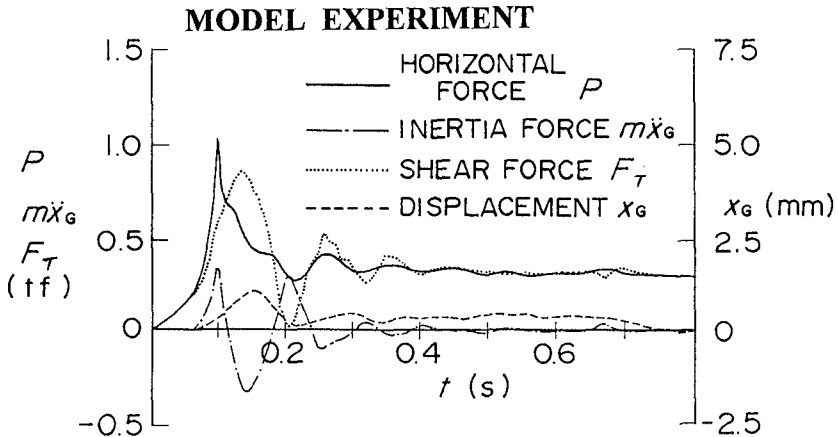


Figure 2a Experimental caisson response.

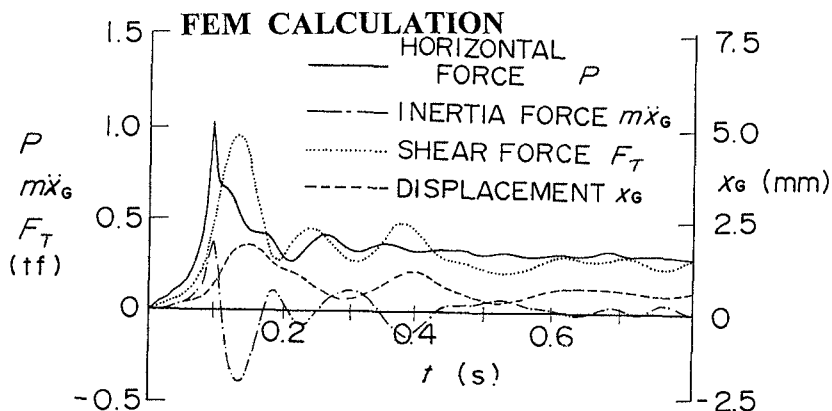


Figure 2b. Calculated caisson response.

the caisson. At each time step in the simulation, the acceleration, velocity, displacement, stress, and strain are evaluated. Figure 2b shows the corresponding FEM-calculated results using the same impulsive wave force, where good agreement is present with experimental results. (Takahashi, Tanimoto, and Shimosako, 1994a)

In actuality, sand bed and rubble mound are relatively soft in comparison with those of the model, and therefore, the dynamic response is much more significant. For instance, when applying the same impulsive force profile, the FEM-calculated ratio of the peak shear force to peak impulsive force under field conditions is about 40%, whereas about 75% in the 1/20 scale model.

#### Calculation Method of the Sliding Distance

The sliding distance of the caisson can be calculated by integrating the acceleration twice. Figure 3 shows the acceleration  $\ddot{x}$ , velocity  $\dot{x}$ , and displacement  $x$  over time.  $x$  can be calculated from Eq.(4) if the shear force  $F_T$ , uplift force  $U$ , friction coefficient  $\mu$ , caisson weight in water  $W'$  and in the air  $W$  are known. In the proposed model, we defined the equivalent sliding wave force  $F_s$  as follows:

$$F_s = F_T + \mu U \quad (5)$$

The time series of  $F_s(t)$  is considered to be a triangular pulse having a duration of  $\tau_0$ , which becomes smaller as the wave force increases. Figure 4 shows the time-dependent mathematical model used to simulate caisson displacement, where  $F_s(t)$  is defined as follows:

$$F_s(t) = \begin{cases} (2t/\tau_0) F_{Smax} & (0 \leq t < \tau_0/2) \\ 2(1-t/\tau_0) F_{Smax} & (\tau_0/2 \leq t < \tau_0) \\ 0 & (t \geq \tau_0) \end{cases} \quad (6)$$

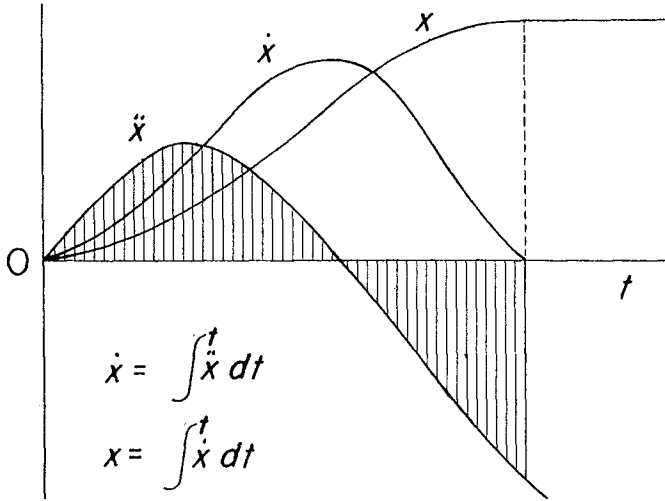


Figure 3 Acceleration, velocity, and displacement of the caisson.

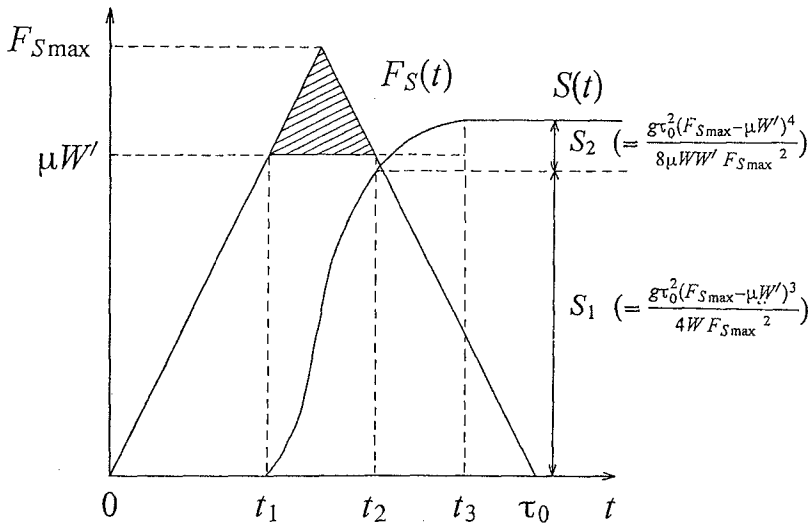


Figure 4 Proposed calculation model of the sliding distance.

The caisson begins to slide when  $F_s(t)$  becomes larger than  $\mu W'$ .  $S_1$  indicates the sliding distance while  $F_s(t)$  is larger than  $\mu W'$ , and  $S_2$  is that after  $F_s(t)$  becomes smaller than  $\mu W'$ . The total sliding distance  $S$  is evaluated as follows:

$$S = S_1 + S_2 = \frac{g\tau_0^2 (F_{S_{\max}} - \mu W')^3 (F_{S_{\max}} + \mu W')}{8\mu W' W' F_{S_{\max}}^2} \quad (7)$$

$F_{S_{\max}}$  can be obtained by the Goda pressure formula, but we still must determine  $\tau_0$  to evaluate  $S$ . We used theoretical analysis and model experiments to determine  $\tau_0$ . Consequently,  $\tau_0$  is represented as follows:

$$\tau_0 = k\tau_{0F} \quad (8)$$

$$k = 1/((\alpha^*)^{0.3} + 1)^2 \quad (9)$$

$$\alpha^* = \max \{ \alpha_1, \alpha_2 \} \quad (10)$$

$$\tau_{0F} = (0.5 - H/(8h))T \quad (0 \leq H/h \leq 0.8) \quad (11)$$

where  $\alpha_1$  is an impulsive pressure coefficient (Takahashi, Tanimoto and Shimosako, 1993),  $\alpha_2$  is a coefficient indicating the effect of impulsive pressure in Goda pressure formula,  $H$  is wave height,  $h$  is water depth, and  $T$  is wave period. In non-breaking wave,  $\tau_0$  is almost the same as  $\tau_{0F}$ , whereas for impulsive wave,  $\tau_0$  is 0.1~0.2 s in the model experiment. Note that  $\tau_0$  is determined based on the duration time of shear force. Actually, the duration time of impulsive pressure is much smaller than  $\tau_0$ .

### 3. Experiments

#### Experimental Procedure

Figure 5 shows a cross section of the caisson model which is made of synthetic acrylic plates and has its bottom comprised of a concrete slab that simulates the friction factor. Additional concrete blocks were placed in front of the caisson to generate impulsive wave pressures. Seven pressure transducers and a load cell are attached to the front plate to measure the applied wave pressure and force. Two acceleration meters and two displacement meters measure caisson movement. The caisson was mainly subjected to regular waves with a period  $T = 3.04$  s.

Sliding tests using both impulsive and non-breaking waves were conducted with the same caisson model and wave conditions. Based on the wave force, caisson weight was accordingly adjusted by putting lead weights inside it.

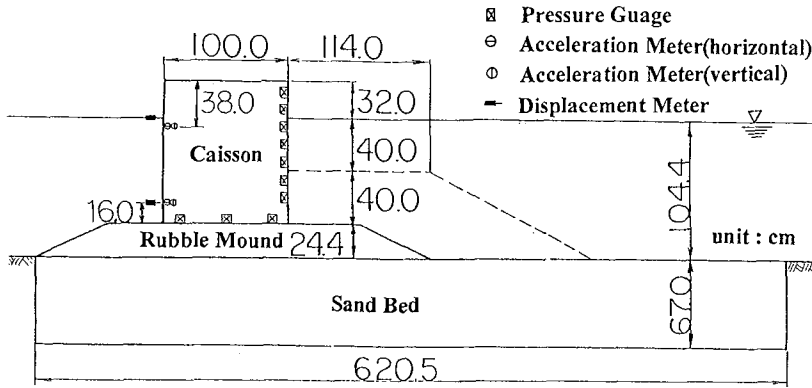


Figure 5 Cross section of the model experiment.

Sliding due to Non-breaking Wave Forces

Figure 6 shows typical recorded profiles of non-breaking wave.  $P$  is the horizontal wave force,  $U$  is the uplift force, and  $F_s$  is the equivalent sliding wave force as mentioned before.  $x_{GEXP}$  indicates the displacement of the caisson's center of gravity, while  $S_{CAL}$  is the calculated sliding distance.  $S_{CAL}$  is calculated from the measured  $F_{Smax}$  and  $\tau_0$  calculated from Eq.(8)-(11). The caisson starts to move before when  $F_s$  becomes larger than  $\mu W'$ . This is because  $x_{GEXP}$  includes the elastic displacement of rubble mound and soil bed. Actually, it is considered that the caisson starts to slide when  $F_s$  becomes larger than  $\mu W'$ , and it stops when  $x_{GEXP}$  is

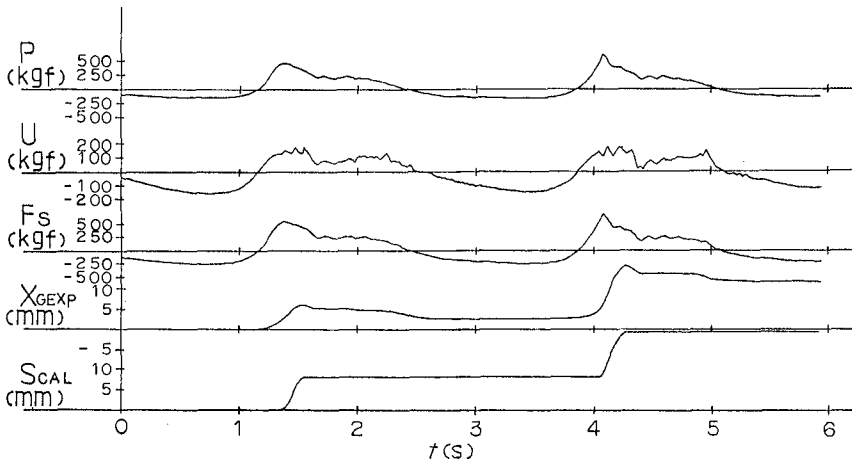


Figure 6 Recorded profiles of the non-breaking wave.

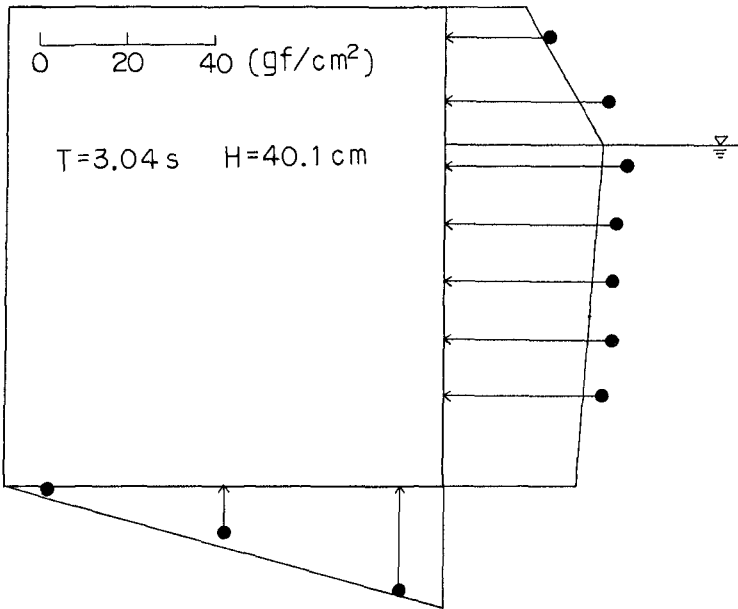


Figure 7 Wave pressure distribution of the non-breaking wave.

maximum. Notice that the elastic displacement continues until  $F_s$  becomes 0. Theresidual displacement of  $x_{GEXP}$  is slightly smaller than  $S_{CAL}$ .

Figure 7 shows a typical wave pressure distribution for a non-breaking wave as measured by a model experiment. The solid lines show the design wave pressure distributions calculated by the Goda pressure formula. Note the horizontal wave pressure distribution is almost uniform, except near the top of the caisson. In addition, the measured and calculated pressures indicate good agreement.

#### Sliding due to Impulsive Wave Forces

Figure 8 shows typical profiles recorded for an impulsive wave force hitting the caisson, where  $m\ddot{x}_G$  indicates the inertia force, and  $F_T$  is the shear force ( $= P - m\ddot{x}_G$ ). The peak value of  $F_T$  is smaller than that of  $P$ , and when  $m\ddot{x}_G$  is negative peak,  $F_T$  is larger than  $P$ . Displacement begins at the same time when impulsive pressure starts, and it peaks after  $P$  becomes smaller than  $\mu W'$ . The elastic motion is found just as non-breaking wave, however, it stops before  $F_T$  becomes 0. Therefore, the caisson does not move in the wave period, but the oscillation period of it. Good agreement is present between  $S_{CAL}$  and  $x_{GEXP}$ , although the residual displacement of  $x_{GEXP}$  is slightly smaller than  $S_{CAL}$ .

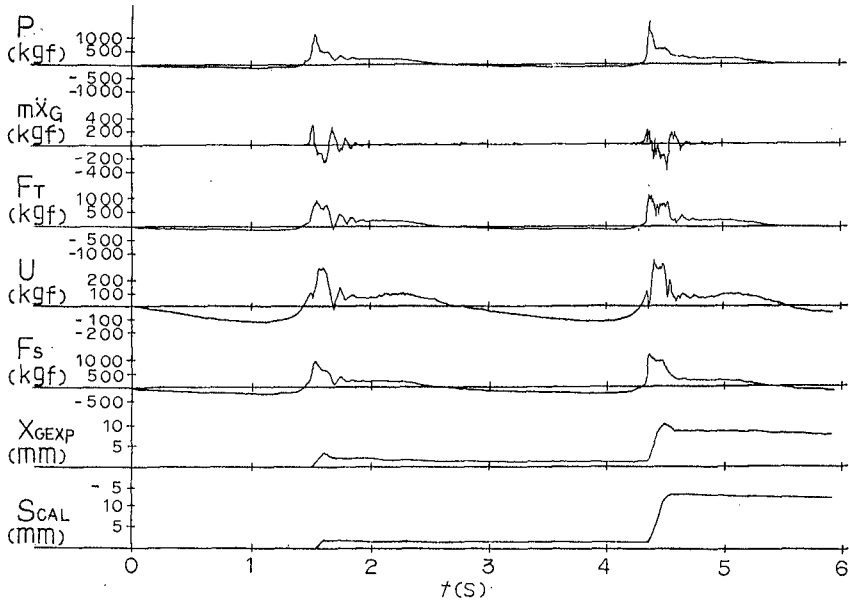


Figure 8 Recorded profiles of the impulsive wave.

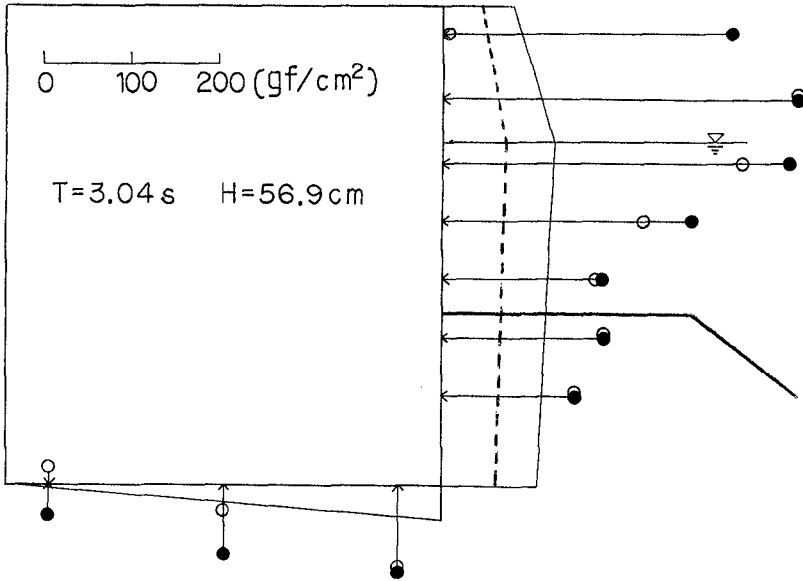


Figure 9 Wave pressure distribution of the impulsive wave.

Figure 9 shows a typical wave pressure distribution for an impulsive wave. The solid lines and the dotted lines are design wave pressure distributions calculated by the Goda pressure formula using and not using the "Impulsive Pressure Coefficient" respectively. Note the calculated value by the Goda pressure formula is much smaller than measured pressure. However, the shear force at the caisson bottom, which is the effective pressure producing caisson sliding, is greatly reduced due to the caisson's dynamic response as described before. The "Impulsive Pressure Coefficient" is determined based on the result of sliding experiments in order to represent the effective sliding force.

### Sliding Distance

Figure 10a compares the experimental and calculated results of sliding distance  $S$  versus the sliding safety factor  $S.F.$  for a non-breaking wave. Calculated results is obtained from the peak value of the measured equivalent sliding wave force  $F_s$  and the calculated of  $\tau_0$  (not measured  $\tau_0$ ). Note that the sliding distance increases as the sliding safety factor decreases, and also that good agreement exists between the experimental and calculated results.

In the present design method, the friction coefficient  $\mu$  is considered as 0.6. However, as  $\mu$  scatters in the experiment, the sliding distance  $S$  also scatters. Most of the experimental results are close to the calculations using  $\mu = 0.5 \sim 0.7$ .

Figure 10b shows the corresponding results for an impulsive wave. Notice it has almost the same general characteristics as the non-breaking wave. However, at the same sliding safety factor value, the sliding distance for the impulsive wave is smaller.

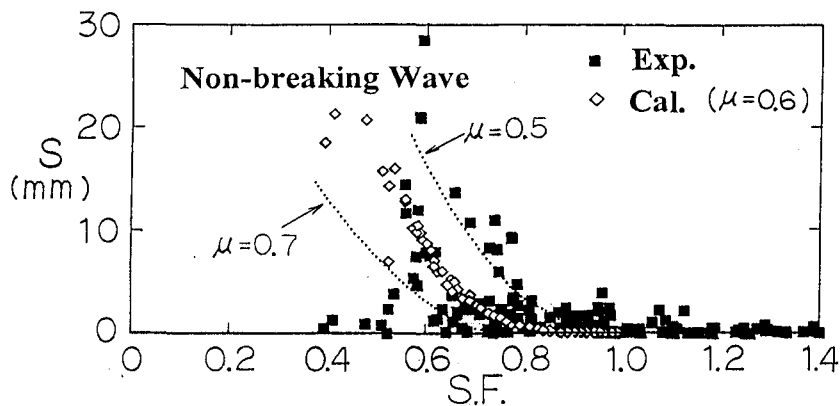


Figure 10a Sliding distance as a function of the sliding safety factor.  
( Non-breaking wave)



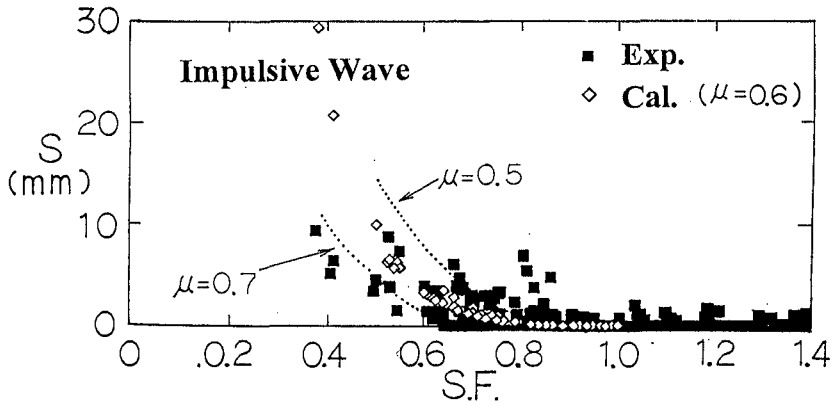


Figure 10b Sliding distance as a function of the sliding safety factor.  
( Impulsive wave)

#### 4. Estimation of Expected Sliding Distance

##### Calculation Procedure of Expected Sliding Distance

In the future breakwater designs, calculation method of expected sliding distance should be established to allow some sliding of the caisson. In that case, the proposed method should be extended to estimate the expected sliding distance.

Goda pressure formula with the impulsive pressure coefficient and the calculation model of the sliding distance can be applied as they were mentioned. In addition, all wave data during its return period are needed to calculate the expected sliding distance, and the probabilistic property of wave height, wave force, water level, friction coefficient, and caisson weight should be taken into consideration.

##### Sample Calculation

As a example, using 9-year wave data observed at a certain point, the expected sliding distance is calculated for a caisson breakwater. Figure 11 shows the cross section of the designed breakwater. The return period of the breakwater is usually 50 years, however, only 9-year observed wave data is used, and the fluctuation of wave force, friction coefficient, etc. are not considered.

Figure 12 shows the wave height distribution expressed in the form of probability density. Using the significant wave height, each wave height is reproduced according to the Rayleigh distribution. The number of waves which is larger than a certain wave height can calculate from this distribution. For instance, the number of waves which is larger than 12.1 m is 3.7, and that larger than 10.5 m is 36.3, where 12.1 m is the maximum significant wave height, and 10.5 m is the

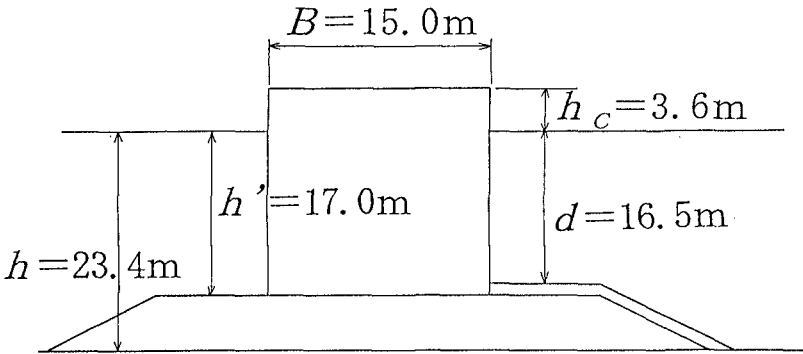


Figure 11 Cross section of the prototype calculation.

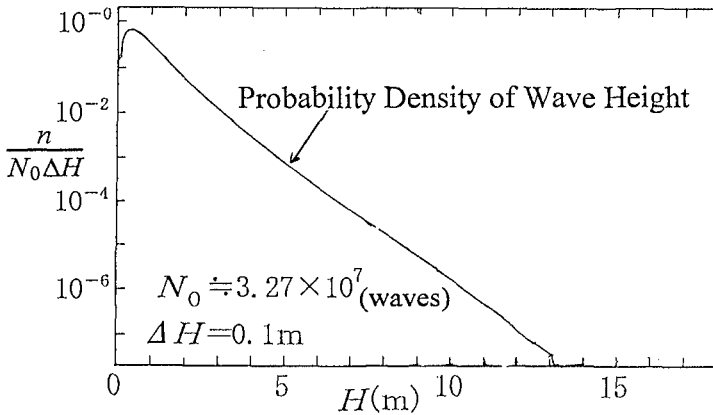


Figure 12 Probability density of wave height.

average value of the annual maximum significant wave heights for 9 years. The total number of waves during 9 years is almost 32.7 million.

Figure 13 shows the relation between wave height and sliding distance for one wave in various design wave heights. When the design wave height  $H_D = 12.1$  m and sliding safety factor  $S.F. = 1.0$ , the sliding distance at  $H = 18.0$  m is 72 cm.

The expected sliding distance for 9 years can be obtained using the sliding distance for one wave and the probability density of wave height. Figure 14 shows the relation between the design wave height and the expected sliding distance caisson for 9 years. The wave height distribution and the sliding distance for one wave are also shown in this figure. For instance, when the design wave heights  $H_D$  are 12.1 m and 10.5 m, the probable sliding distances are 0.6 cm and 45 cm, respectively.

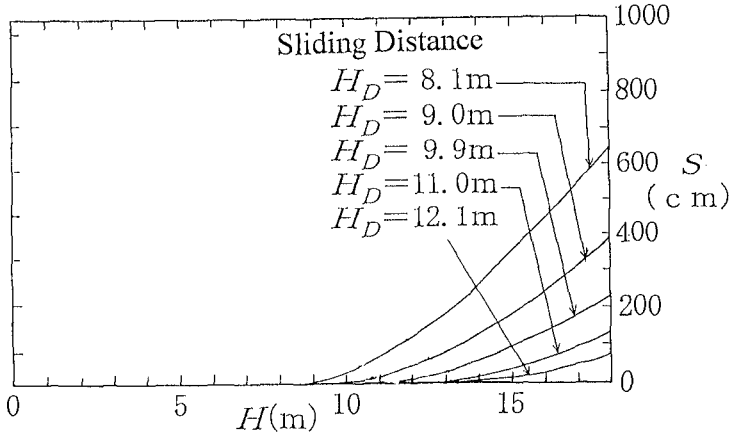


Figure 13 Sliding distance for one wave.

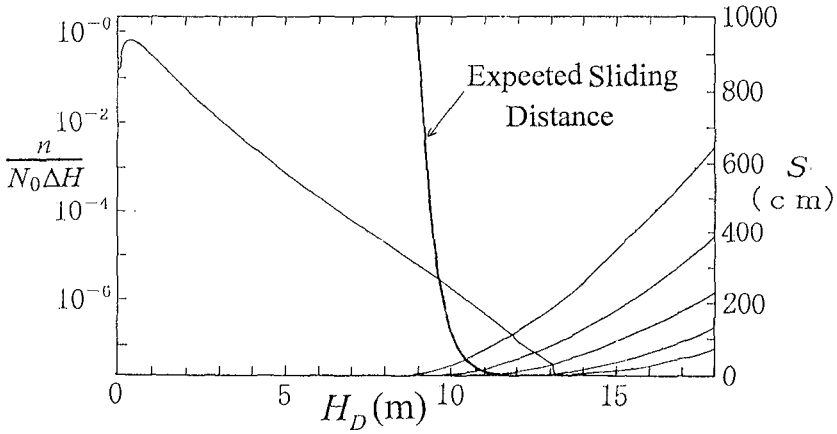


Figure 14 Expected sliding distance.

**5. Concluding Remarks**

A practical method was derived to estimate the sliding distance due to wave forces including impulsive ones. In future breakwater designs, probabilistic design method should be adopted to ensure economical considerations are optimized. Subsequent research will be directed at extending the proposed sliding model to estimate the sliding distance of the caisson during its return period considering the fluctuation of wave force, friction coefficient, and caisson weight.

**References**

- Ito, Y., M. Fujishima, and T. Kitatani (1966): On the stability of breakwaters, Rept. of Port and Harbour Research Institute, Vol.5, No.14, 134p (in Japanese).
- Goda, Y. (1974): A new method of wave pressure calculation for the design of composite breakwaters, Proc. of 14th Coastal Engineering Conference, ASCE, pp. 1702-1720.
- Horikawa, K., Y. Ozawa, and K. Takahashi (1972): Expected sliding distance of high mound composite breakwater, Proc. of Coastal Engineering, JSCE, Vol.17, pp.177-184 (in Japanese).
- Takahashi, S., K. Tanimoto and K. Shimosako (1993): Experimental study of impulsive pressures on composite breakwaters — Fundamental feature of impulsive pressure and the impulsive pressure coefficient —, Rept. of Port and Harbour Research Institute, Vol.31, No.5, pp.33-72 (in Japanese).
- Takahashi, S., K. Tanimoto and K. Shimosako (1994a): Dynamic response and sliding of breakwater caisson against impulsive breaking wave forces, Proc. of the International Workshop on Wave Barriers in Deepwaters, Port and Harbour Research Institute, pp362-401.
- Takahashi, S., K. Tanimoto and K. Shimosako (1994b): A Proposal of Impulsive Pressure Coefficient for Design of Composite Breakwaters, Proc. of the International Conference on Hydro-Technical Engineering for Port and Harbor Construction, pp489-504.
- Tanimoto, K., K. Kimura., and K. Miyazaki (1988): Study on stability of deep water breakwaters against waves (1st Rept.) — Wave forces on upright section of trapezoidal shape and its stability against sliding —, Rept. of Port and Harbour Research Institute, Vol.27, No.1, pp.3-29 (in Japanese).
- UWABE, T. (1983): Earthquake response and seismic design of composite type breakwater in deep sea, Proc. of 1983 Annual Research Presentations of Port and Harbour Research Institute, pp. 103-165 (in Japanese).

## CHAPTER 115

### BED SHEAR STRESS AND SCOUR AROUND COASTAL STRUCTURES

B.M. Sumer<sup>1</sup>, J. Fredsøe<sup>1</sup>, N. Christiansen<sup>1</sup> and S.B. Hansen<sup>1</sup>

#### Abstract

Two kinds of experiments were made: 1) Rigid-bed experiments and 2) erodible-bed experiments. In the former experiments, bed shear stresses were measured around three kinds of structures: 1) a vertical circular cylinder, 2) a cone-shaped structure and 3) the head of a breakwater (with and without side slopes). The results are presented in terms of amplification in the bed shear stress for the structures considered.

In the erodible-bed experiments, actual scour tests were carried out with the aforementioned structures. The results regarding the scour tests are related to the measured bed shear stress.

#### 1. Introduction

Considerable knowledge may be gained on scour around coastal structures by studying the bed shear stress on the unscoured bed, one of the hydrodynamic quantities directly related to scour.

The purpose of the present study is to investigate the bed shear stress around three kinds of coastal structures, namely a vertical pile, a cone-shaped structure and a breakwater, and to relate it to the resulting scour. The cone-shaped structure has been selected, to study the effect of side slopes on the complex vortex system responsible for scour around the structures. As regards the breakwater structure, attention is concentrated on the three-dimensional scour around the head of the breakwater.

---

<sup>1</sup> Institute of Hydrodynamics and Hydraulic Engineering (ISVA), Technical University of Denmark, 2800 Lyngby

## 2. Experiments

### 2.1. Bed-shear stress measurements

The experiments were conducted in a flume facility the size of  $26.5 \times 0.6 \times 0.8$  m. In most of the cases, the model structures were exposed to both waves and steady currents.

A two-component hot-film probe (DANTEC 55R46 spec.) was used in the experiments. The probe was flush-mounted with the rigid bed of the flume. It enabled the magnitude and the heading of the bed shear stress vector to be measured. The details about the probe and the other pertinent information have been reported elsewhere (Sumer et al., 1993).

Three kinds of structures were implemented in the tests (Fig. 1): 1) A vertical cylinder with a circular cross section (one with diameter  $D = 4$  cm and the other with  $D = 9$  cm), 2) a cone-shaped structure (one with  $\beta = 45^\circ$  side slope and the other with  $\beta = 30^\circ$  side slope; both with the same base diameter, namely  $D = 9$  cm), and finally 3) a breakwater with and without side slopes. In the case of the breakwater with side slopes, simulating a rubble-mound breakwater, the angle of the side slopes was  $45^\circ$ . The relatively high value of the side slope was due to experimental constraints. The base width of the breakwater was  $B = 3$  cm in the vertical wall breakwater case and  $B = 11.5$  cm in the rubble-mound case.

The bed shear stress measurements were supported in a few cases with velocity measurements where a one-component DANTEC Laser Doppler Anemometer was used.

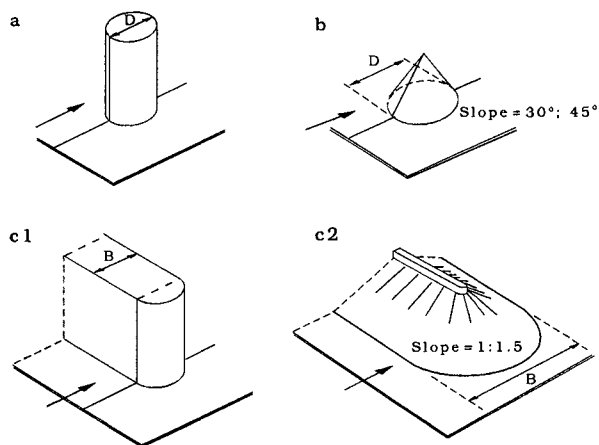


Fig. 1 Structures considered in the present study. a: Vertical cylinder. b: Cone ( $\beta = 30^\circ$  and  $45^\circ$ ). C1: Vertical-wall breakwater. C2: Rubble-mound breakwater (side slope = 1:1 in the bed shear stress meas., and 1:1.5 in the scour expts.).



## 2.2. Scour experiments

The scour processes around the structures were videotaped, using an underwater mini video camera in most of the cases. These experiments were carried out in three facilities, namely in a small scale flume (the same as that used in the bed shear stress measurements) and in two medium scale flumes (one with dimensions 28 × 4 × 1 m and the other 23 × 2 × 0.5 m).

In all the wave tests, the orbital velocity of the undisturbed flow at the bottom was measured. In the current tests, the undisturbed velocity profile over the depth was measured. Similar to the bed shear-stress measurements, three kinds of structures were used in the scour experiments: 1) Vertical circular cylinders, 2) cone-shaped structures and 3) breakwaters. Table 1 summarizes the test conditions of the scour experiments.

In the table,  $V$  is the mean flow velocity in the case of steady current and  $U_m$  is the amplitude of the orbital velocity at the bed in the case of waves, while  $U_f$  and  $U_{fm}$  are the corresponding friction velocities in the case of steady current and in the case of waves, respectively.  $\theta$  is the Shields parameter defined by

$$\theta = \frac{U_f^2}{g(s-1)d} \quad (1)$$

in which  $g$  is the acceleration due to gravity and  $s$  is the relative density of sand grains.  $U_f$  is replaced by  $U_{fm}$  in the case of waves. In the table,  $KC$ , the Keulegan-Carpenter number, is defined by

$$KC = \frac{U_m T}{D} \quad \text{or} \quad KC = \frac{U_m T}{B} \quad (2)$$

and  $Re$ , the Reynolds number,

$$Re = \frac{U_m D}{\nu} \quad \text{or} \quad Re = \frac{U_m B}{\nu} \quad (3)$$

From the table, it is seen that all the scour experiments were conducted under live-bed conditions,  $\theta > \theta_{cr}$ , in which  $\theta_{cr}$  is the critical value of  $\theta$  corresponding to the initiation of motion on the sand bed.

## 3. Results and discussion

### 3.1 Bed shear stress

#### Cylinder

The bed shear stress around a vertical cylinder placed on



a plane bed is increased due to the following three effects: 1) the contraction of streamlines near the structure 2) the horse-shoe vortex and 3) the vortex shedding (Fig. 2).

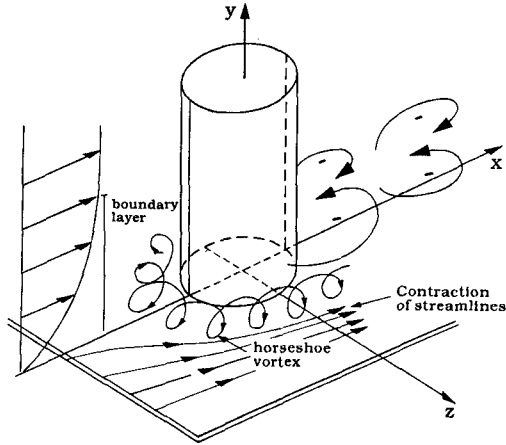


Fig. 2 Definition sketch. Near-bed flow structures around a vertical cylinder.

The mechanisms related to these effects and their role in the scour processes have been discussed in Breusers et al. (1977), Hjorth (1975), Baker (1979), Dargahi (1987) in steady current and Sumer et al. (1992) in waves.

Fig. 3 illustrates the distribution of the bed shear stress along the principal axes  $x$  and  $z$  in the case of steady current. In the figure,  $\alpha$  is the amplification in the bed shear stress

$$\alpha = \frac{\tau_0}{\tau_{0\infty}} \quad (4)$$

in which  $\tau_0$  is the bed shear stress and  $\tau_{0\infty}$  is that corresponding to the undisturbed flow. The figure includes also the results of Baker (1979) who obtained the bed shear stresses from the measured velocity profiles. (It is seen that the present results and the results of Baker agree fairly well despite the differences in the test conditions and in the flow environment). While Fig. 3b illustrates the amplification in  $\tau_0$  near the side edges of the cylinder due to contraction of the flow, Fig. 3a shows the amplification in  $\tau_0$  both in front of the cylinder (beneath the horse-shoe vortex) and at the rear side of the cylinder (in the lee-wake region).

It is seen that the increase in the bed shear stress near the cylinder can be as much as by a factor 10 or even larger. Similar results were obtained also by Hjorth (1975) (Fig. 4a).

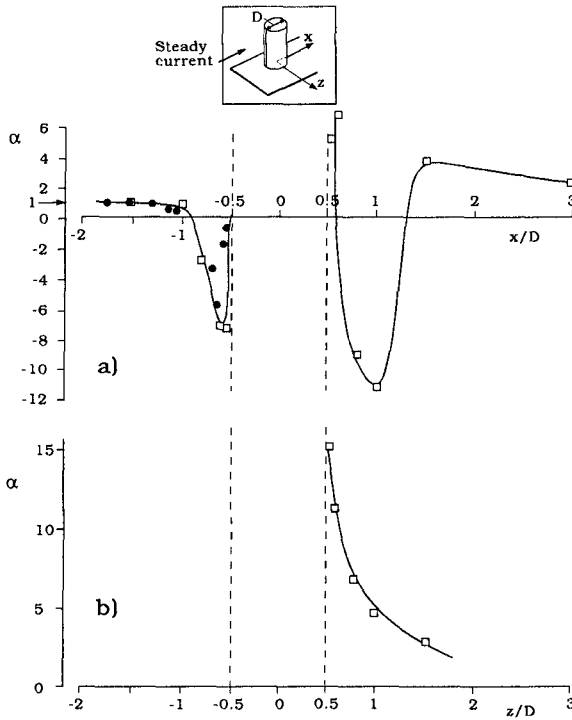


Fig. 3 Amplification in the shear stress along the principal axes  $x$  and  $z$  around a vertical cylinder. Squares: Present experiments (flow-depth,  $h = 40$  cm,  $D = 9$  cm and  $V = 8.7$  cm/s and  $Re = 7800$ ). Circles: Baker's (1979) experiments in air ( $D = 7.6$  cm,  $V = 51$  cm/s,  $D/\delta^* = 14.8$  and  $Re = 2610$ ,  $\delta^*$  being the displacement thickness of the boundary layer on the bottom).

Fig. 4 compares the distribution of the bed shear stress near the cylinder in the case of steady current (Hjorth, 1975) with that measured in the present study in the case of waves (where  $KC$ , the Keulegan-Carpenter number, is 10) while Fig. 5 gives a 3D illustration of the latter flow, at the phase value  $\omega t = 0$ , corresponding to the passage of the wave crest. In Fig. 4,  $\alpha$  is the amplification in the bed shear stress defined by

$$\alpha = \frac{|\bar{\tau}_0|}{\tau_{0\infty}} \quad ; \quad \text{steady-current case} \quad (5)$$

and

$$\alpha = \frac{Max|\bar{\tau}_0|}{\tau_{0m}} \quad ; \quad \text{wave case} \quad (6)$$

in which  $\tau_{0m}$  is the maximum value of the bed shear stress corresponding to the undisturbed flow.

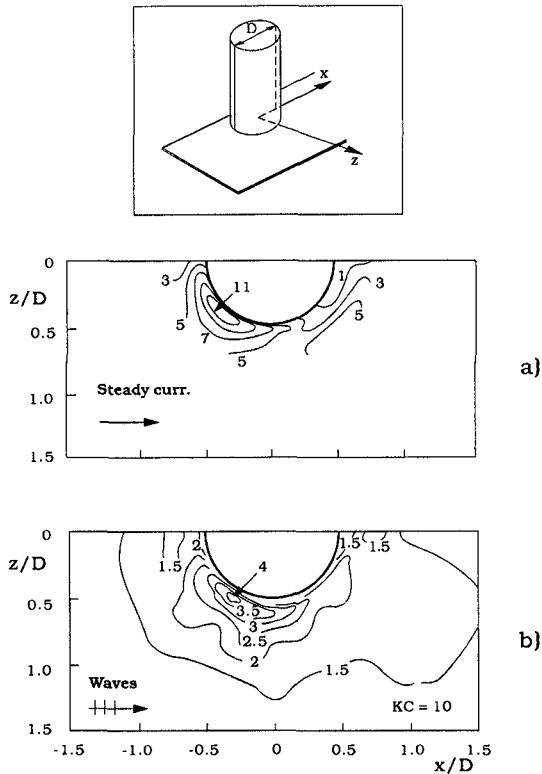


Fig. 4 Amplification in the bed shear stress. a: Steady current ( $D = 7.5$  cm,  $V = 30$  cm/s,  $h = 20$  cm) (from Hjorth (1975)). b: Waves ( $D = 4$  cm,  $U_m = 9.2$  cm/s,  $T = 4.4$  s,  $h = 40$  cm).

Fig. 4 indicates that, in the case of waves, the amplification factor is not as large as in steady currents; the increase in the bed shear stress with respect to its undisturbed value is only a factor 3-4 in the best condition. Measurements show that this is the case also for other  $KC$  numbers (up to  $KC = 100$ ), see Sumer et al. (1992). Fig. 6 depicts the distribution of amplification along the principal axes  $x$  and  $z$ . It seems that the measurements as regards the  $z$ -variation of  $\alpha$  apparently agree quite well with the potential-flow prediction (Fig. 6b).

As seen from Fig. 4, there is a factor 3 difference between the amplification in steady currents and that in waves. This may be attributed to the rather thin boundary layer developing

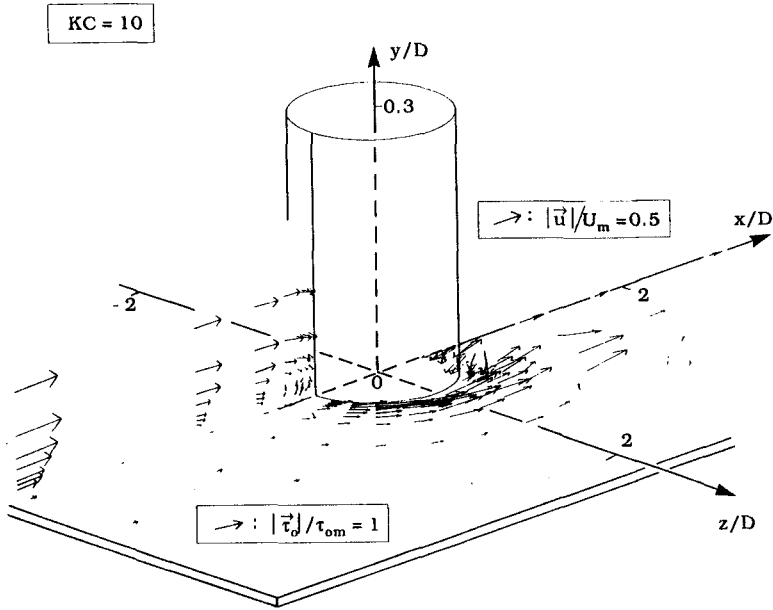


Fig. 5 Three-dimensional vector-diagram illustration of near-bed flow around a vertical circular cylinder at the phase value  $\omega t = 90^\circ$ , i.e. at the time of crest passing ( $D = 4$  cm,  $U_m = 9.2$  cm/s,  $T = 4.4$  s,  $h = 40$  cm).

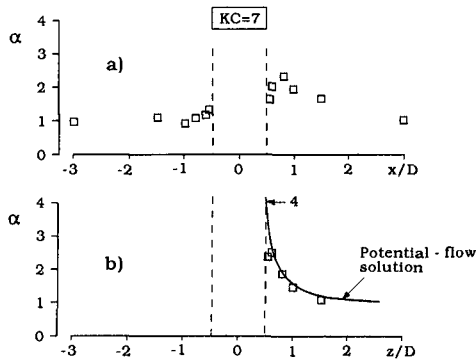


Fig. 6 Amplification in the bed shear stress around a vertical circular cylinder along the principal axes  $x$  and  $z$  ( $D = 9$  cm,  $U_m = 31.8$  cm/s,  $T = 1.9$  s,  $h = 40$  cm).

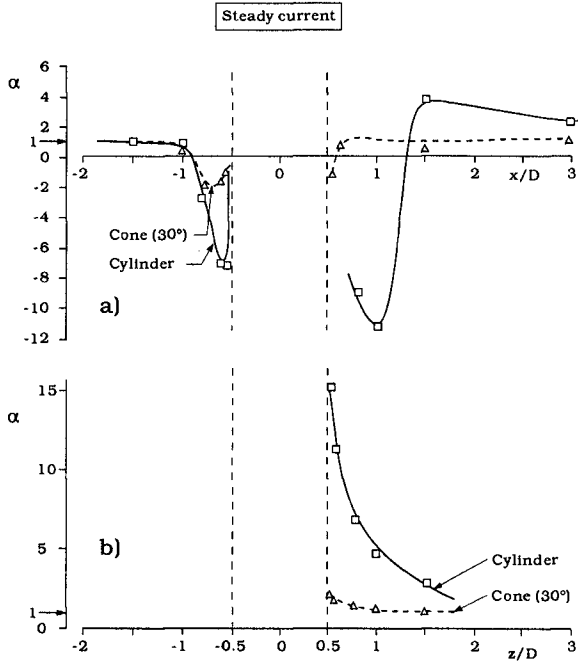


Fig. 7 Comparison of the bed-shear stress amplification around the cylinder and the cone. (Test conditions are the same as in Fig. 3 for the cylinder test. For the cone test:  $D = 9$  cm,  $V = 8.7$  cm/s,  $h = 40$  cm).

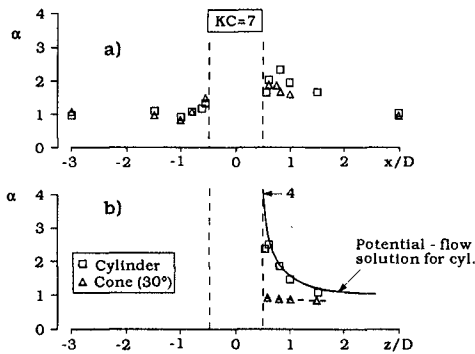


Fig. 8 Comparison of the bed-shear stress amplification around the cylinder and the cone. (Test conditions are the same as in Fig. 6 for the cylinder test. For the cone test:  $D = 9$  cm,  $U_m = 31.8$  cm/s,  $T = 1.9$  s,  $h = 40$  cm).

over the bed in the case of waves. The previously mentioned agreement between the measurements and the potential-flow prediction substantiates the latter argument. In the case of steady current, however, the combined action of the horse-shoe vortex and the contraction of flow near the side edges of the cylinder amplifies the bed shear stress tremendously, to give an  $\alpha$  value of  $O(10)$  (Figs. 3b and 4a). The strong presence of horse-shoe vortex in the steady-current situation accounts for also the large increase in the bed shear stress in front of the cylinder (Fig. 3a).

### Cone

Figs. 7 and 8 compare the cone results with the cylinder results along the principal axes  $x$  and  $z$ . It is clear that the net effect of side slopes (the cone case) is to decrease the bed shear stress. From the preceding figures, the following conclusions may be drawn.

1) Fig. 7a shows that  $\tau_0$  decreases by a factor of about 4 underneath the *horse-shoe* vortex (in the area extending over  $-1 \leq x/D \leq -0.5$ ) in the case of cone. (It is interesting to note that the horse-shoe vortex is still existent in the cone case, but its strength is greatly reduced with respect to the cylinder situation).

The decrease in  $\tau_0$  is due to the large decrease in the adverse pressure gradient which builds up at the upstream side of the structure and is known to be responsible for the formation of horse-shoe vortex. This decrease in the adverse pressure gradient is simply because of the favourable cone geometry.

It may be noticed that the cone and the cylinder results are almost identical in the case of waves at the upstream side of the structure (Fig. 8a). This is simply because no horse-shoe vortex exists for this KC number, not even in the case of cylinder (Sumer et al. (1992)). So, the results will obviously be the same. The 45°-cone experiments exhibited the same behaviour.

The results in Fig. 8a are not symmetric with respect to  $x = 0$  due to the asymmetry in waves.

2)  $\tau_0$  decreases considerably also near the *side edges* of the structure in the case of cone; this decrease is about a factor 10 in the steady-current situation (Fig. 7b), while it is a factor 2-3 in the case of waves (Fig. 8b). Two effects are responsible for this large decrease in  $\tau_0$ : 1) the contraction of streamlines near the side edges of the cone structure is rather small; and also, 2) the horse shoe vortex is rather weak in this case, as mentioned above.

3) Similar observations can be made also in the *lee-wake* area. Tremendous decrease (by an order of magnitude) takes place in  $\tau_0$  in this area ( $x \geq 0.5$ ) in the case of steady current (Fig. 7a), while practically no change takes place in the case of waves (Fig. 8a). This reduction in the bed shear stress

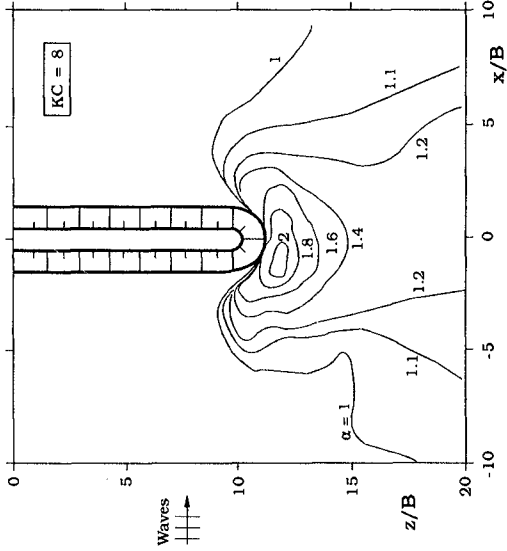
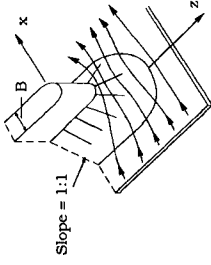


Fig. 10 Amplification in the bed shear stress around the head of a breakwater with side slopes. ( $B' \approx 11.5$  cm,  $U_m = 12$  cm/s,  $T = 1.3$  s,  $h = 40$  cm).

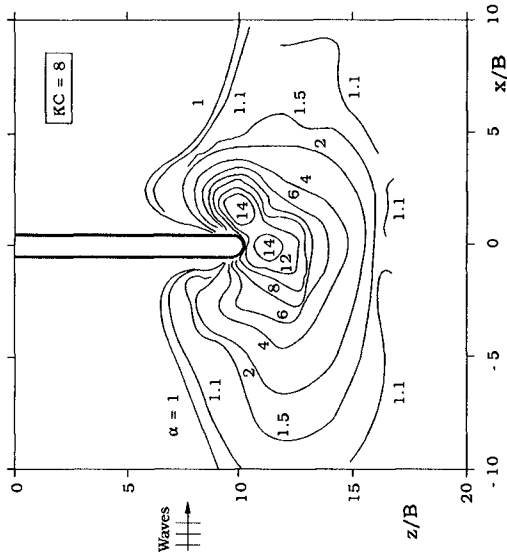
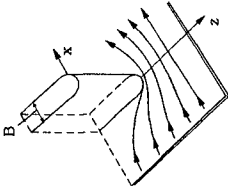


Fig. 9 Amplification in the bed shear stress around the head of a vertical-wall breakwater. ( $B = 3$  cm,  $U_m = 12$  cm/s,  $T = 1.3$  s,  $h = 40$  cm).

is obviously related to the rather weak occurrence of vortex shedding in the case of cone.

### Breakwater

Fig. 9 depicts the contour plot of the bed-shear-stress amplification,  $\alpha$ , in the case of vertical-wall breakwater for  $KC = 8$ . As seen, the  $\alpha$  values can be as high as 14 near the head of the breakwater. Similar behaviour was obtained for  $KC = 1$  where a value of about 10 was measured for the maximum value of  $\alpha$ .

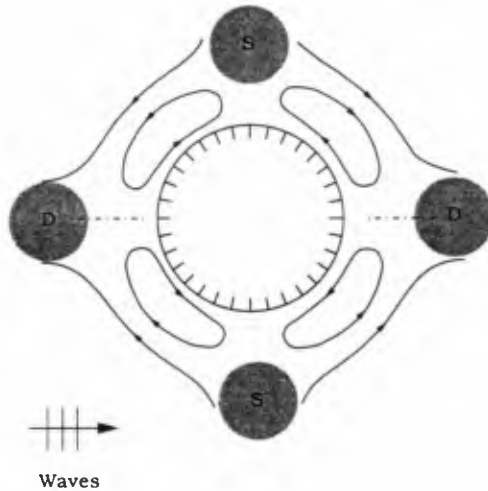


Fig. 11 Sketch illustrating the steady streaming around a large cylinder in waves. S: Scour. D: Deposition.

In a previous study undertaken at ISVA (Gökçe et al., 1994), the flow around the head of a vertical-wall breakwater was found to occur in the following three regimes: 1) Unseparated-flow regime when  $KC < 1$ , 2) separated-flow regime when  $1 < KC \leq 12$  and 3) separated-flow regime with a horse-shoe type vortex in front of the breakwater when  $KC \geq 12$ .

Since the tested  $KC$  numbers, namely  $KC = 1$  and  $8$ , are well below the  $KC$  number beyond which the horse-shoe vortex emerges, no horse-shoe vortex was present in the present tests. This means that the only factor behind the extensive increase in  $\tau_0$  at the head of the breakwater is the effect of flow contraction including the one experienced during the flow reversal where the separation vortex is washed around the breakwater. This explains why  $\alpha$  is a factor 3-4 larger in the present case (Fig. 9) than in the corresponding case of a circular cylinder (Fig. 4b) where the contraction effect is not as severe as in the case of breakwater.



Fig. 10 illustrates the effect of side slopes on the bed shear stress. The model used in the tests was exactly the same as that used in the vertical-wall breakwater tests (Fig. 9). The only difference is that the model was encircled with a sloping side wall on the bottom (as sketched in Fig. 10) with a slope 1:1. As seen, the effect is a large drop in the bed shear stress at the head of the breakwater. The maximum value of  $\tau_0$  is reduced by a factor 7 with respect to its value in the case of vertical-wall breakwater.

This large reduction is obviously related to the small flow contraction in the present case due to the geometry of the structure, similar to that when the structure is changed from a circular cylinder to a cone (Figs. 7b and 8b).

**3.2 Scour**

The scour data obtained in the case of cone (both with  $\beta = 30^\circ$  and  $45^\circ$ ) indicated that the smaller the side slope, the smaller the scour depth.

Secondly, it was apparent from the results that the scour depth in the case of cone ( $\beta = 30^\circ$  and  $45^\circ$ ) in steady current was one order of magnitude smaller than in the case of cylinder.

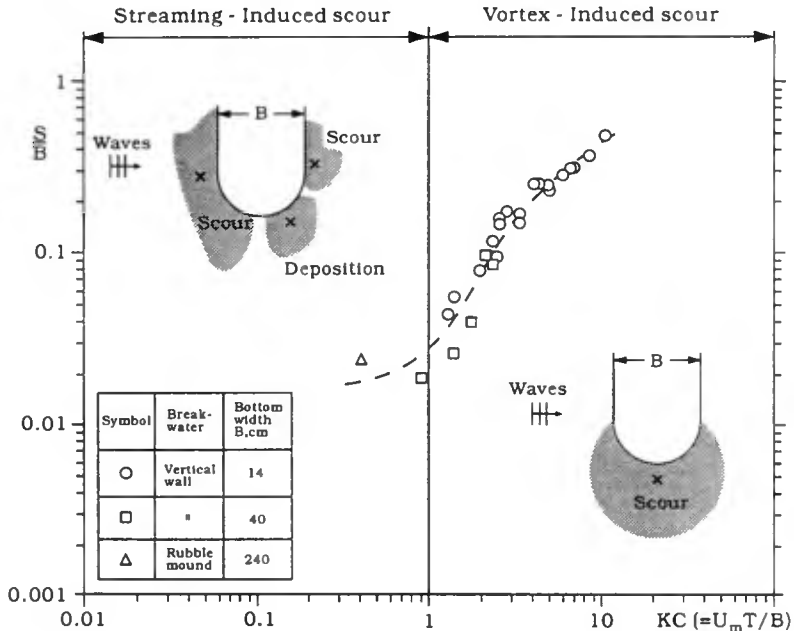


Fig. 12 Normalized scour depth at the head of breakwater as function of KC. For test conditions, see Table 1. x: Maximum scour or deposition

Thirdly, the cone results corresponding to the wave case have been compared with the cylinder scour reported in Sumer et al. (1992). It was found that, for KC numbers above 5, the cone scour is on average below the cylinder scour. For very small KC numbers ( $KC = O(5)$ ), however, the maximum scour depth appeared to be in the same order of magnitude as that measured in Sumer et al. (1992). This may be related to the not very extensive drop in the bed shear stress in the case of cone in waves (Fig. 8).

For extremely small KC numbers such as  $KC(1)$  (i.e., large structures), the scour is caused not by the vortex shedding but rather by various forms of steady streaming which build up around the structure. The steady streaming around a large cylinder is an example for this kind of streaming (Fig. 11). Here, the streaming is caused by the difference in the response of the cylinder boundary layer to the two successive half periods of the wave motion. This kind of steady streaming may cause a scour-and-deposition pattern around the structure, as sketched in Fig. 11.

The data related to the present breakwater-scour experiments are plotted in Fig. 12. As seen from the sketches in the figure, the scour hole occurring at the tip of the breakwater in the case of large KC-number situations disappears when KC becomes less than  $O(1)$ . Instead, a streaming-induced scour-and-deposition pattern forms around the breakwater head, in the way as described in the preceding paragraph. The disappearance of the scour hole at the tip of the breakwater is due partly to the unseparated flow regime and partly to the large reduction in the bed shear stress (cf. Figs. 9 and 10).

The scale effects in connection with both the flow-description experiments and the scour tests have been discussed elsewhere (in Sumer et al. (1992 and 1993) in conjunction with scour around vertical piles and in Gökçe et al. (1994) in conjunction with scour around the head of a breakwater).

#### 4. Conclusions

- 1) The bed shear stress around a vertical, circular cylinder is increased considerably (by a factor of 10) with respect to its undisturbed value when the cylinder is exposed to a steady current, while this increase is by a factor of 3-4 when it is exposed to waves.
- 2) For a cone-shaped structure, the increase in the bed shear stress near the structure is small, a factor of 2-4, regardless of the flow type (steady current or waves).
- 3) The increase in the bed shear stress around the head of a vertical-wall breakwater (which is exposed to waves) is a factor of 10 or so. When the breakwater is encircled at the bottom with a sloping side wall with a slope of 1:1, the increase in the bed shear stress is only a factor 2.
- 4) The scour depth around a cone-shaped structure is an order of magnitude smaller than in the case of cylinder struc-

ture in steady currents. In the case of waves, however, the scour depth appears to be smaller than that measured in the case of cylinder when  $KC > O(5)$ . For  $KC = O(5)$ , however, the cone scour is in the same order of magnitude as the cylinder scour.

- 5) Although the scour hole at the tip of the breakwater disappears in the case of rubble-mound breakwater (apparently due to the effect of the side slope), another mechanism, namely the steady streaming, may induce a scour-and-deposition pattern around the breakwater head.

#### Acknowledgement

This work was undertaken as part of MAST II "Monolithic (Vertical) Coastal Structures" and "Rubble Mound Breakwater Failure Modes" research programmes. It was funded jointly by the Danish Technical Research Council (STVF) under the programme "Marin Technique" and by the Commission of the European Communities, Directorate General for Science, Research and Development under MAST contracts No. MAS2-CT92-0042 and MAS2-CT92-0047.

#### Appendix. References

- Baker, C.J. (1979). The laminar horseshoe vortex. *J. Fluid Mech.*, Vol. 95, part 2, pp. 347-367.
- Breusers, H.N.C., Nicollet, G. and Shen, H.W. (1977). Local scour around cylindrical piers. *J. Hydr. Res.*, 15(3), pp. 211-252.
- Dargahi, B. (1987). Flow field and local scouring around a cylinder. *Hyd. Lab., the Royal Inst. of Technology, Stockholm, Sweden. Bulletin No. TRITA-VBI-137, iii + 230 p.*
- Gökçe, T., Sumer, B.M. and Fredsøe, J. (1994). Scour around the head of a vertical-wall breakwater. *Proceedings of the International Conf. on Hydro-Technical Engrg. for Port and Harbour Construction, Yokosuka, Japan, 19-21 Oct.*
- Hjorth, P. (1975). Studies on the nature of local scour. *Dept. of Water Resources Engineering, Lund Inst. of Technology, Univ. of Lund, Sweden, Bulletin Series A, No. 46.*
- Sumer, B.M., Christiansen, N. and Fredsøe, J. (1993). Influence of cross section on wave scour around piles. *ASCE, J. of Waterway, Port, Coastal and Ocean Engineering*, Vol. 119, No. 5, Sept./Oct., pp. 477-495.
- Sumer, B.M., Fredsøe, J. and Christiansen, N. (1992). Scour around vertical pile in waves. *ASCE, J. of Waterway, Port, Coastal and Ocean Engineering*, Vol. 118, No. 1, Jan./Feb., pp. 15-31.
- Sumer, B.M., Arnskov, M.M., Christiansen, N. and Jørgensen, F.E. (1993). Two-component hot-film probe for measurements of wall shear stress. *Experiments in Fluids*, Vol. 15, pp. 380-384.

## CHAPTER 116

# LABORATORY MEASUREMENT OF OBLIQUE IRREGULAR WAVE REFLECTION ON RUBBLE-MOUND BREAKWATERS

Charles TEISSON<sup>1</sup> and Michel BENOIT<sup>2</sup>

### Abstract

The present work aims to improve our knowledge of reflection coefficient of waves on a breakwater through a programme of laboratory tests. The experiments are conducted on a linear rubble-mound breakwater under random long-crested wave conditions. The wave signals are recorded through an array of 8 wave probes. Three wave reflection analysis approaches are applied and compared on the laboratory recorded data : Least-Squares Methods, Directional Analysis Methods, Modified Directional Analysis Methods. These methods are briefly presented, their assumptions are highlighted and their characteristics are discussed on numerical tests. The Directional Analysis Methods appear to be unable to properly model the superimposition of incident and reflected wave fields. When applied to laboratory experiments, the Least-Squares Methods and the Modified Directional Methods show concordant results, but nevertheless exhibit some differences. The effect of oblique incidence on reflection coefficient is then tentatively analysed.

### 1. INTRODUCTION

The reflection of waves on a marine or coastal structure is a rather complicated physical process to analyse, depending both from hydrodynamical conditions (wave steepness, wave period, wave obliquity,...) and characteristics of the structure (type of breakwater, slope of the reflective face, permeabilities of the various layers,...). The wave field in front of the reflective structure results from the superimposition of incident and reflected wave field and one has to use special analysis techniques in order to achieve the decomposition. The scope of the present work is to compare various such reflection analysis techniques on laboratory data.

In order to study the reflection coefficient of waves on a linear rubble-mound breakwater, a programme of laboratory tests in a long-crested random wave basin has been performed at Laboratoire National d'Hydraulique (LNH). These tests aimed to study the effects of the three following parameters on the reflection process : wave steepness, wave obliquity and mound slope. In order to determine the reflection coefficient of waves on the breakwater two problems have to be successively addressed and are briefly summarized hereafter.

---

1 Head of Maritime Group

2 Research Engineer — Maritime Group

EDF - Laboratoire National d'Hydraulique, 6, quai Watier 78400 CHATOU, FRANCE

- a. firstly a wave measurement system must be set up to record simultaneously several wave properties (elevation, pressure, velocities,..) at one or more locations. Such measuring devices may be co-located probes (e.g. Hughes, 1994) or wave probe arrays (e.g. Goda and Suzuki, 1976 ; Isaacson, 1991 ; Bird *et. al.*, 1994). In the present experiments we have only made use of an array of 8 wave gauges, recording the free-surface elevations.
- b. secondly a reflection analysis method must be used to proceed to the separation of incident and reflected components and determine the reflection coefficient. This problem has been addressed by several authors both for laboratory and field experiments (e.g. Mansard and Funke, 1980 ; Isobe and Kondo, 1984 ; Hashimoto and Kobune, 1987). There is however up to now no unique approach for the analysis of obliquely incident waves. The core of the present study is thus to compare three different approaches to model and analyse the wave field in front of the structure, namely :
  - \* Least-Squares Methods (section 2)
  - \* Directional Analysis Methods (section 3)
  - \* Modified Directional Analysis Methods (section 4)

All these methods are applied to the laboratory data (sections 6 and 7) recorded during the experiments described in section 5.

The present experiments have been conducted in the continuation of LNH tests on the effect of wave obliquity on breakwater stability (Galland, 1994).

## 2. THE LEAST-SQUARES METHOD (LSM)

This type of methods has been initially proposed by Goda and Suzuki (1976) for reflection analysis in a wave flume through two wave probes set up on the axis of the flume. The technique has been improved by Mansard and Funke (1980) for a linear array of three gauges. They provided spacing rules for the gauges and their method is now widely used for reflection analysis in random wave flumes. Recently Isaacson (1991) generalized the method to two-dimensional gauge arrays for basin experiments. Hughes (1994) also used this technique with a co-located gauge for oblique wave reflection measurement.

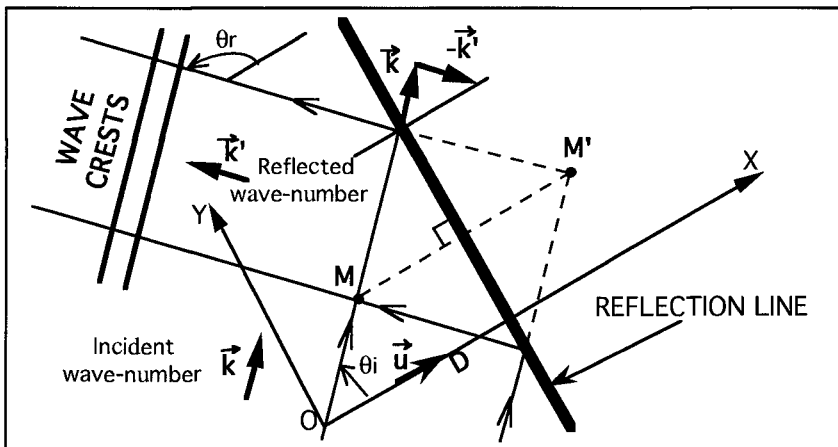


**Figure 1 :** Definition sketch for reflection analysis.

The main assumptions of this analysis approach are listed hereafter :

- > Both incident and reflected waves are long-crested and linear. The random wave fields are expressed using a linear superposition of numerous long-crested monochromatic components. For instance the incident wave field (referred by subscript i) reads (see figure 1 for definition sketch) :

$$\eta_i(M,t) = \sum_{j=1}^J A_j \exp(i.\omega_j.t) \exp(i.(-\vec{k}_j.\vec{OM} + \psi_j))$$

$A_j$  is the amplitude of the  $j$  component,  $\omega_j$  is the cyclic frequency,  $k_j$  is the wave-number given by the dispersion relation and  $\psi_j$  is the phase, which is generally assumed to be uniformly and randomly distributed over  $[0 ; 2\pi]$ .

- > Each component is assumed to reflect independently. In the following we thus focus on a particular component and drop the  $j$  subscript.
- > Frequency and wave-number remain unchanged during reflection.
- > The incident wave direction is assumed to be known and must be given as input to the method.
- > The incident and reflected wave directions are symmetrical :  $\theta_r = \pi - \theta_i$
- > The reflection coefficient is taken to be complex :  $R_j = C_{rj} \exp(i.\phi_j)$

The modulus  $C_{rj}$  is equal to the ratio of reflected and incident wave amplitudes and  $\phi_j$  is the phase lag during reflection.

By using these assumptions the resulting contribution of the component reads :

$$\eta(M,t) = A.\exp(i.\omega.t) . \left\{ \exp(i.(-\vec{k}.\vec{OM} + \psi)) + C_r.\exp(i.(-\vec{k}'.\vec{OM} + \psi - 2.k.D.\cos(\theta_i) + \phi)) \right\}$$

Through this approach we have only three unknown quantities at each frequency of analysis :

- the incident wave amplitude  $A$ .
- the modulus of reflection coefficient  $C_r$ .
- the phase lag during reflection  $\phi$ .

The analysis may thus be carried out from the measurements of only two wave gauges as in the wave flume, but it is preferable to increase the number of gauges (3 or more) and to perform a least-squares resolution of the system in order to improve the stability of results.

In order to study the effect of deviating from some of the above assumptions, several numerical tests have been performed prior to the experiments. For these numerical simulations we used the 3-gauges linear array presented on figure 2.

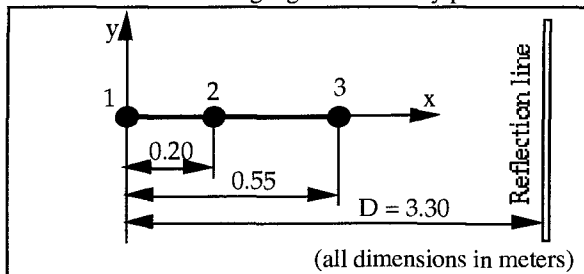


**Figure 2 :** Linear gauge array used for numerical simulations with LSM.

The numerical simulation characteristics (simulation method, wave period, water depth, time step, record duration,...) are identical to the ones used for the random wave laboratory experiments and presented in section 5.

We only report here some results related to the violation of the assumptions on incident and reflected directions to illustrate the sensitivity of the method :

— effect of wrong estimation of incident wave direction : Several simulations are performed with an actual incident wave direction varying from 0 to 60 degrees. For all these simulations the reflected wave direction is symmetrical of the incident direction. The direction given as input to the analysis method is however taken to be constant at a value of 0 degrees (figure 3-a), 30 degrees (figure 3-b) and 60 degrees (figure 3-c). Examination of results shows that the effect of a difference between actual and assumed incident directions is quite slight if both these directions are close to be normal to the reflection line (figure 3-a). In other words, one can assume an incident direction of 0 degrees for the analysis of wave fields with actual incidence up to 30 degrees : the resulting error is feeble. If the assumed direction is 30 degrees (figure 3-b) the actual incident direction must remain in the range  $[20^\circ ; 40^\circ]$  to keep reliable results. On the other hand, figure 3-c shows that almost no estimation error is allowed for the incident direction when working at large angles of incidence. These observations are largely explained by the fact that only the cosine of incident direction is used by the analysis method.

— effect of angular deviation during reflection : Several simulations are performed with an actual incident wave direction of 40 degrees. For all these simulations the incident direction taken for the analysis is equal to this value of 40 degrees (figure 3-d). The reflected wave direction is however no more symmetrical of the incident direction and there is an angular deviation during reflection. Figure 3-d shows the effect in the estimation of reflection coefficient and incident wave height of an angular deviation varying from -10 to +10 degrees. It appears that the sensitivity of estimated parameters is rather slight, at least at this value of incident direction.

These numerical tests (and additional ones, not reported here) lead to the conclusion that the method is quite stable, even if its basic assumptions are slightly violated. The effect of slightly misjudging the incident wave reflection for instance (say  $\pm 5$  to 10 degrees) is quite acceptable as long as the actual incident direction is lower than 45 degrees. At large angles of incidence however, great attention should be paid to the precise estimation of incident wave direction. The hypothesis that the incident and reflected wave directions are symmetrical is not very sensitive as long as angular deviations are lower than  $\pm 10$  degrees.

### 3. DIRECTIONAL WAVE ANALYSIS METHODS

In order to invoke less restrictive assumptions than the former approach, one may think to use (multi-)directional wave analysis methods. The LNH has acquired a good experience in this field, by implementing most of the available methods currently used in the world (Benoit, 1993). Very recently, these methods have been applied on laboratory simulated data for various types of recording systems : co-located or "single-point" gauges as well as probe array (Benoit and Teisson, 1994b). These tests have in particular shown that the gauge array has a unique resolving capability when associated with sophisticated methods (such as Maximum Entropy Method or Bayesian Directional Method) for severe bimodal test-cases.

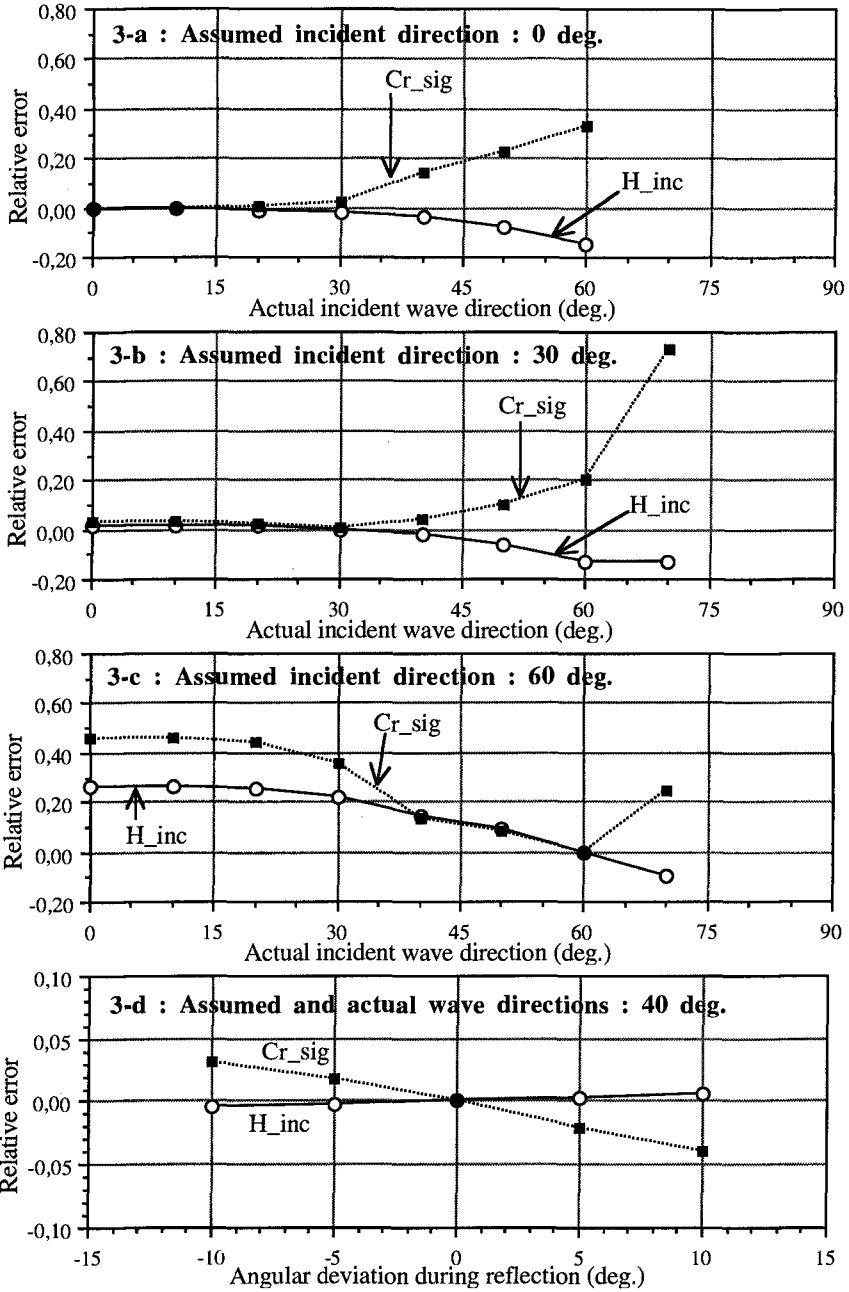


**Figure 3 : Results of numerical simulations with LSM.**



The theoretical background of the directional wave analysis is based on the following pseudo-integral relationship between the free-surface elevation field  $\eta(x,y,t)$  and the directional spectrum  $S(f,\theta)$  :

$$\eta(x,y,t) = \int_0^\infty \int_0^{2\pi} \sqrt{2.S(f,\theta).df.d\theta} \cdot \cos[2\pi ft - k.(x.\cos\theta+y.\sin\theta) + \varphi]$$

- The directional wave spectrum  $S(f,\theta)$  is a function of wave frequency  $f$  and direction of propagation  $\theta$  and is decomposed as :  $S(f,\theta) = E(f).D(f,\theta)$
- $E(f)$  is the 1D-variance spectrum and  $D(f,\theta)$  is the Directional Spreading Function (DSF) satisfying two important properties :

$$D(f,\theta) \geq 0 \text{ over } [0, 2\pi] \quad \text{and} \quad \int_0^{2\pi} D(f,\theta) d\theta = 1$$

- $\varphi$  is the phase, which is here assumed to be uniformly and randomly distributed over  $[0 ; 2\pi]$ .

By using an array of  $N$  wave probes, it is possible to record the sea-surface elevation at  $N$  different locations simultaneously (see figure 4).

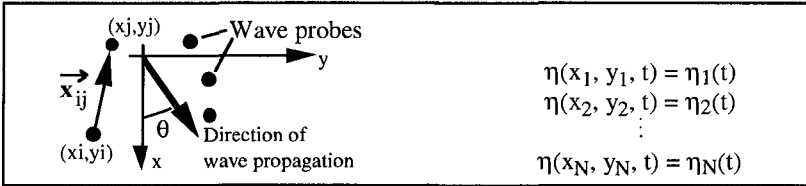


**Figure 4 :** Definition sketch for probe array configuration.

The computation of the cross-spectra  $G_{ij}(f)$  between each couple  $[\eta_i(t), \eta_j(t)]$  is performed by spectral analysis. The following relation yields between the measured complex cross-spectra  $G_{ij}(f)$  and the unknown directional spectrum  $S(f,\theta)$  :

$$G_{ij}(f) = C_{ij}(f) - i.Q_{ij}(f) = \int_0^{2\pi} S(f,\theta).exp(-i.\vec{k}.\vec{x}_{ij}) d\theta \quad i = 1, \dots, N \text{ and } j \geq i$$

The purpose of directional analysis is to solve the above inverse problem by considering the  $N.(N+1)$  real equations obtained from the cross-spectra  $G_{ij}(f)$  ( $j \geq i$ ). There is no unique way to deal with this awkward inverse problem and plenty of methods have been proposed (e.g. Benoit, 1993 ; Benoit and Teisson, 1994-b). Among them, the Maximum Entropy Method (MEM2) and the Bayesian Directional Method (BDM) are retained for this study as they have shown the highest resolving capabilities. They are only briefly presented hereafter. The reader is invited to consult the given references for more details.

— Maximum Entropy Method - version 2 (MEM2) (e.g. Kobune and Hashimoto, 1986 or Nwogu, 1989). This version is based on the definition of Shannon for the entropy function :

$$\chi = - \int_0^{2\pi} D(f,\theta).ln(D(f,\theta)) d\theta$$

This entropy has to be maximized under the constraints given by the cross-spectra. This results in a non-linear system of equations whose solutions are Lagrange multipliers  $\mu_I$  ( $I=1, \dots, N(N-1)+1$ ) and the estimate of DSF then reads :

$$D(f,\theta) = \exp \left\{ -1 + \sum_{I=1}^{N(N-1)+1} \mu_I \cdot q_I(\theta) \right\} \begin{cases} q_I(\theta) = \cos[\vec{k} \cdot \vec{x}_{ij}] & I = 1, \dots, N(N-1)/2 \\ q_I(\theta) = \sin[\vec{k} \cdot \vec{x}_{ij}] & I = N(N-1)/2+1, \dots, N(N-1) \\ q_I(\theta) = 1 & I = N(N-1)+1 \end{cases}$$

— Bayesian Directional Method (BDM) : (Hashimoto *et al.*, 1987). No *a priori* assumption is made about the spreading function which is considered as a piecewise-constant function over  $[0, 2\pi]$ . The unknown values of  $D(f,\theta)$  on each of the  $K$  segments dividing  $[0, 2\pi]$  are obtained by considering on one side the constraints of the cross-spectra and on the other side additional conditions on the smoothness of  $D(f,\theta)$ . Both these constraints are combined using an "hyperparameter" whose value may be computed by minimizing the ABIC (Akaike Bayesian Information Criterion). This method is quite difficult to implement, but its main features are to be model independent, data-adaptive and to consider the possibility that the recorded data may be contaminated by some noise.

In order to compute a reflection coefficient at each frequency of analysis with the directional analysis methods, one has first to integrate the computed DSF function over the range of incident directions on one hand and over the range of reflected directions on the other hand and then to compute the ratio of these values.

The application of directional analysis methods in the above described procedure is not fully well-founded in the sense that these methods are based on the assumption that the phases  $\phi$  are uniformly and randomly distributed over  $[0 ; 2\pi]$ , and thus that the directional spectrum  $S(f,\theta)$  is an homogeneous function. This assumption is however clearly violated close to a reflective structure because of the phase relationship between the incident and reflected components at each frequency. Isobe and Kondo (1984) provide a deeper discussion of this problem. Figure 8 shows an example of recorded 1D-variance spectra  $E(f)$  at various gauges of the array used for laboratory experiments. It is clearly noticeable that the sea-state can not be regarded as homogeneous and thus that the directional analysis methods may fail in the estimation of the DSF. Both MEM2 and BDM will however be tentatively considered when analysing laboratory data.

**4. MODIFIED DIRECTIONAL WAVE ANALYSIS METHODS**

In order to take into account the above remark on the phase relationship between incident and reflected components, Isobe and Kondo (1984) proposed to limit the determination of the directional spectrum to the range  $[0, \pi]$  and to modify the basic expression of the wave field in the following way :

$$\eta(x,y,t) = \int_0^\infty \int_0^\pi \sqrt{2 \cdot S(f,\theta)} \cdot df \cdot d\theta \cdot \{ \cos[2\pi ft - k \cdot (x \cdot \cos\theta + y \cdot \sin\theta) + \phi] + r(f,\theta) \cdot \cos[2\pi ft - k \cdot (x \cdot \cos\theta - y \cdot \sin\theta) + \phi] \}$$

In this expression the directional spectrum is an incident directional spectrum only, defined on  $[0, \pi]$  by using the definition sketch of figure 5. The directional reflection coefficient  $r(f, \theta)$  is an additional unknown, also defined on  $[0, \pi]$ . The main other assumptions of the above relationship are the following ones :

- the phase  $\varphi$  is assumed to be uniformly and randomly distributed over  $[0; 2\pi]$  for the incident spectrum only.
- the incident and reflected directions at each frequency are taken to be symmetrical, as for the LSM methods.
- the phase lag during reflection is assumed to be negligible.

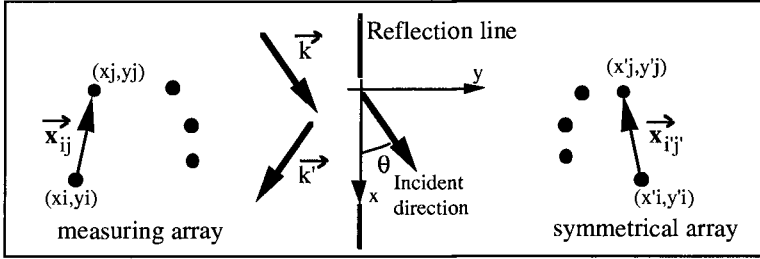


**Figure 5 :** Definition sketch for directional wave reflection.

By using the above expression and the definition sketch of figure 5, the inverse problem to be solved now reads :

$$G_{ij}(f) = \int_0^\pi S(f, \theta) \cdot \left\{ \exp(-i \cdot \vec{k} \cdot \vec{x}_{ij}) + r^2(f, \theta) \cdot \exp(-i \cdot \vec{k} \cdot \vec{x}_{ij}') \right. \\ \left. + r(f, \theta) \cdot \left[ \exp(-i \cdot \vec{k} \cdot \vec{x}_{i}') + \exp(-i \cdot \vec{k} \cdot \vec{x}_{j}') \right] \right\} d\theta \quad i = 1, \dots, N \text{ and } j \geq i$$

In order to solve this problem, two methods have been implemented at LNH and validated on numerical simulations :

- Modified Maximum Likelihood Method (Isobe and Kondo, 1984)
- Modified Bayesian Directional Method (Hashimoto and Kobune, 1987)

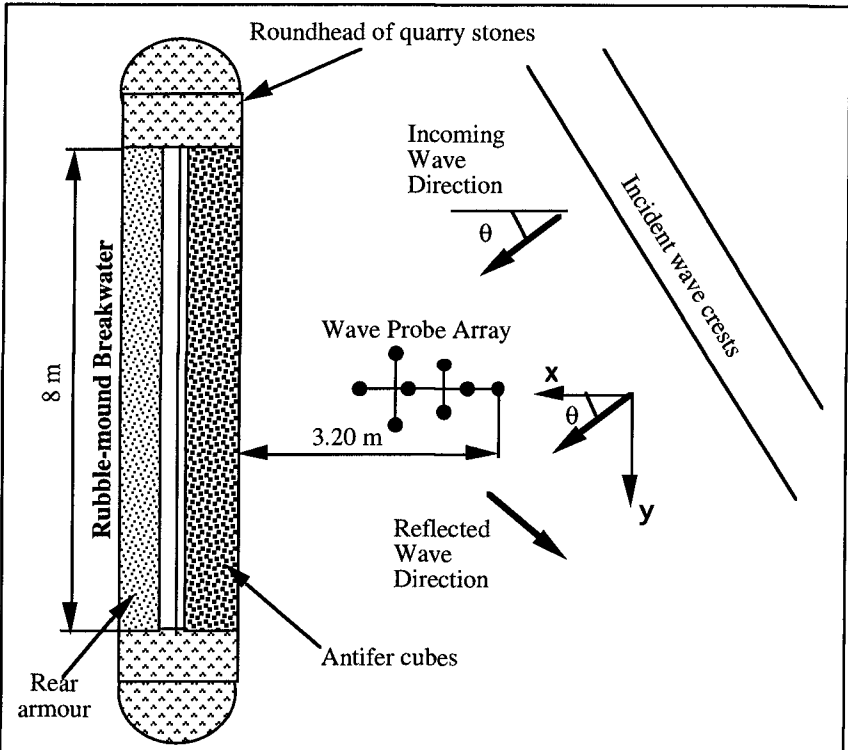
Numerical tests have shown that the MBDM is more powerful than MMLM, but it is also more difficult to implement and to operate (tuning, stability,...). Moreover both these methods assume that the distance from the gauge array to the reflection line is known, which is not always easy to insure (in particular in the case of a permeable slope). In this case, additional developments, such as the ones reported par Bird *et. al.* (1994), would be necessary.

**5. EXPERIMENTAL LAY-OUT AND TEST CONDITIONS**

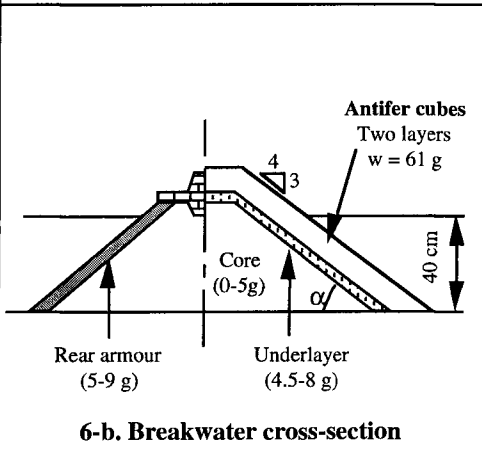
We only report here for clarity a brief description of experimental conditions and test parameters (see Teisson and Benoit (1994-a) for more details).

- Wave tank and wavemaker :

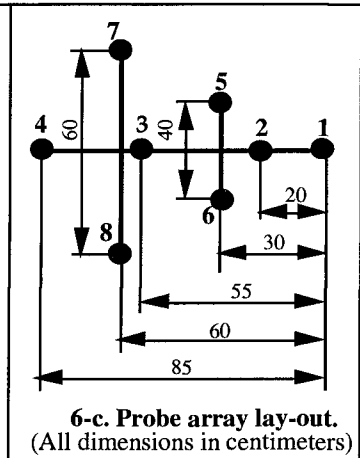
The experiments are performed in a semi-circular wave tank equipped with a 17 m long flap-type wavemaker. The wavemaker is able to rotate around the center of the breakwater in a range of  $[-90^\circ; +90^\circ]$  (see figure 6-a). It is computer monitored in order to produce regular or random waves according to a given energy spectrum. All tests have been conducted with a constant water depth of 0.40 m.



**6-a. Experimental set-up - Definition sketch**



**6-b. Breakwater cross-section**



**6-c. Probe array lay-out.**  
(All dimensions in centimeters)

**Figure 6 : General description of experimental conditions.**

— Breakwater description :

The breakwater is a 8 m long linear breakwater armoured with cubic blocs and terminated at each side by roundheads of quarry stones. The blocs are grooved Antifer-type cubes, laid on two layers (weight : 61 g ; density : 2.4). The core and filter-layers are reproduced following scaling rules used for this type of breakwater. The breakwater is designed to face without any damage all the test conditions of this study. In addition, the breakwater is almost never overtopped, so that no energy loss should occur through transmission by overtopping. An example of cross-section is presented on figure 6-b. In the present study we only report results of the 3/4 mound slope, but two other slope values have been tested (2/3 and 1/2) in order to study the effect of mound slope on wave reflection (Teisson and Benoit, 1994-a).

— Simulated wave characteristics :

During the various tests of this study a JONSWAP-type spectrum is used, with a peak enhancement factor of 3.3. Random waves sequences composed of about 1000 waves are generated. Five tests are considered with the following characteristics :

- \* The peak period used for the five tests is  $T_p=1.3$  s. The corresponding wavelengths are :  $L_p = 2.17$  m for the water depth of 0.40 m.  
 $L_{op} = 2.64$  m for infinite water depth.
- \* The significant wave height used for the five tests is  $H_s=0.06$  m. The corresponding value of steepness, defined as  $s_{op} = H_s/L_{op}$ , is 2.3 % and The surf-similarity parameter, defined as  $Ir_p = \tan \alpha / \sqrt{s_{op}}$ , is equal to 5.
- \* The incident wave direction is changed from one test to another and takes the values :  $0^\circ$ ,  $15^\circ$ ,  $30^\circ$ ,  $45^\circ$  and  $60^\circ$  successively.

— Wave probe arrangement and sampling characteristics:

An array of 8 resistive-type wave probes is used for each experiment. The probes lay-out is reported on figure 6-c. Several different probes combinations may be extracted from the whole array. The time series of free-surface elevation are recorded simultaneously with a sampling rate of 12.5 Hz and a duration of 819.2 s.

## 6. DETAILED ANALYSIS OF A PARTICULAR TEST (INCIDENT DIRECTION : $45^\circ$ )

In this section, the application of the various proposed reflection analysis methods on a particular test corresponding to an incident direction of  $45^\circ$  is presented and discussed in order to highlight the characteristics of the methods. Figure 7 shows both the incident spectrum and the significant reflection coefficient analysed by the various methods on this particular test.

— Least-Squares Methods (LSM) — figure 7-a :

Figure 7-a illustrates the results obtained with LSM by using on one hand only 3 wave probes (probes 1, 2 and 3) and on the other hand all the 8 probes of the array.

It is first noticeable that there is no great difference in the estimated incident spectra and reflection coefficients between the 3-probes array and the 8-probes array. Only at higher frequencies, the reflection coefficient computed from the 3-probes array appears to be somewhat higher than the one computed from the 8-probes array. In fact the 3-probes array is mainly designed for the peak frequency region of the spectrum and it is quite normal that its efficiency becomes somewhat lower as one moves away from this region. In addition, the reflection coefficient obtained from the 8-probes array is a little bit smoother than the one obtained from the 3-probes array, what may also indicate some more physical reliability. An important comment is thus that there is no need to use complex measuring devices

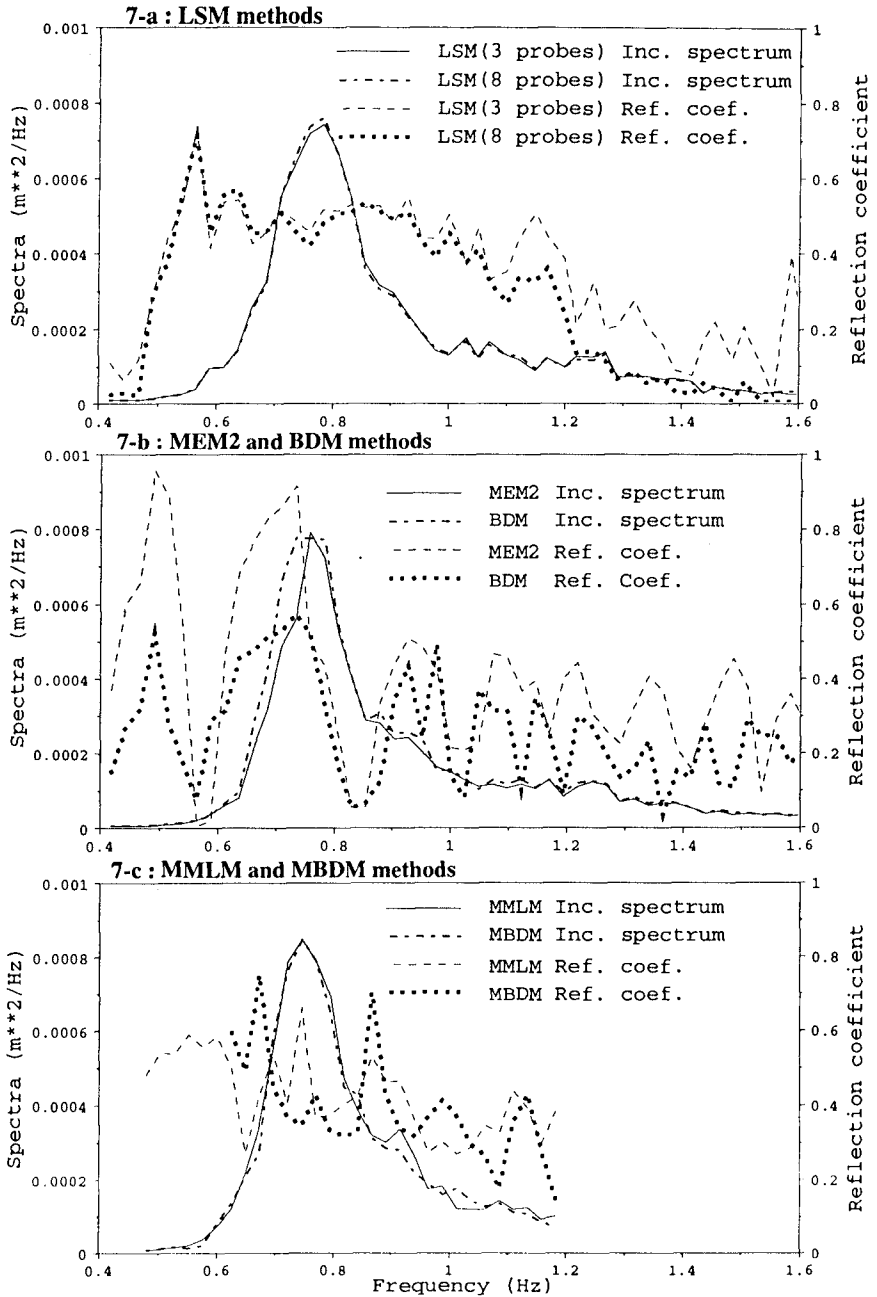


**Figure 7 :** Reflection analysis on a particular laboratory experiment (direction 45 deg).

with a lot of gauges for the LSM method and that stable estimates may be obtained from 3 probes. The explanation is clearly related to the fact that there are only few unknown parameters by using LSM, as discussed in section 2. On the other hand an important drawback of this method is the rather strong assumptions it requires in order to set this quite simple problem.

The value of the reflection coefficient is quite stable in the peak frequency region (between 45 and 50 %). This value seems in agreement with results of previous experiments performed in wave flumes (e.g. Seelig, 1983 ; Allsop and Hettiarachchi, 1988).

— Directional analysis methods (figure 7-b) :

The incident spectra obtained by MEM2 and BDM (figure 7-b) are in good agreement between each other and also compare quite well to the one obtained with LSM. Major discrepancies however appear when considering the reflection coefficients. Compared to the LSM estimates, the reflection coefficients computed both from MEM2 and BDM exhibit strong variations with frequency. These variations are quite similar for MEM2 and BDM estimates, except that their amplitudes are higher for the MEM2 method. Even if the mean value seems to keep a physical sense, the frequency dependency is definitely meaningless. This spurious behaviour of reflection coefficient is clearly related to the main shortcoming of this analysis approach that does not take into account the phase relationship between incident and reflected components, as discussed in section 3.

To illustrate that point, figure 8 shows the 1D-variance spectra recorded by various probes of the measuring array (see figure 6-c for the array geometry). It is clearly noticeable that the hypothesis of spatial homogeneity of energy is no more applicable and thus the directional analysis methods in their standard form do not seem to offer an obvious modelling approach for that kind of problems where reflection is quite important.

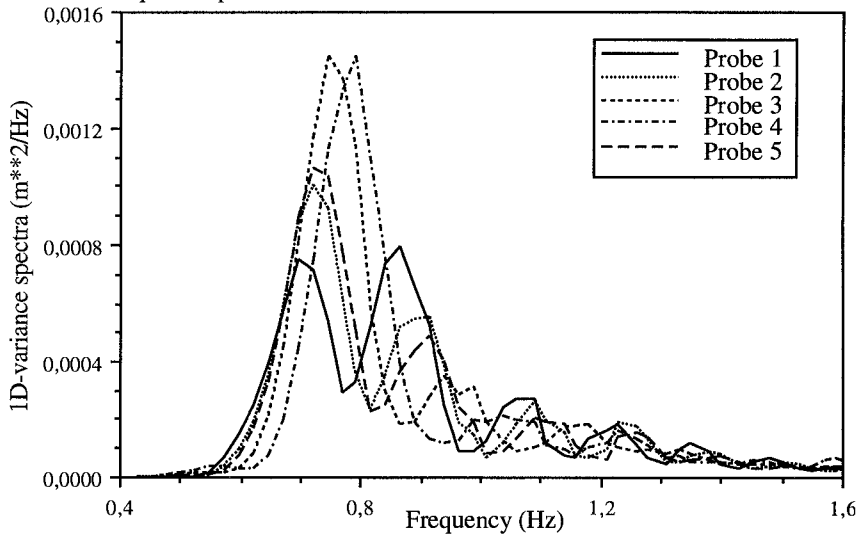


**Figure 8 :** 1D-variance spectra recorded at various gauges (direction 45°).

— Modified directional analysis methods (figure 7-c) :

The incident spectra obtained both from MMLM and MBDM are quite similar with each other and also compare quite well with the ones obtained from the previous methods. The reflection coefficients computed both from MMLM and MBDM show some oscillating behaviour, but clearly not as much as for the previous standard directional analysis methods. Their mean values are quite concordant, but appear to be a little bit lower than the ones obtained from the LSM methods (about 40 % here versus 45 % for LSM methods).

Even if they exhibit some deviation in absolute value of reflection coefficient, these methods seem to give converging results with the LSM methods. It must however be emphasized that the results obtained with the modified directional analysis methods might undoubtedly be improved by additional tests and developments. First of all, there are still work to be done on numerics (in particular with MBDM) in order to insure a more stable convergence towards the solution. Secondly, the effect of misjudging the distance from the array of gauges to the reflection line should received some attention (through numerical sensitivity tests for instance). It would be worthwhile to consider this distance as an additional unknown parameter of the problem. Finally, but this remark also holds for the standard directional methods, one may discuss the fact that we tried to apply directional approaches (and assume a continuous directional distribution of energy) to analyse long-crested waves (whose energy should be concentrated over one direction). This latter point could also be studied by additional numerical tests.

## 7. ANALYSIS OF A SERIES OF TESTS — EFFECT OF INCOMING DIRECTION

In this section, the results of the five tests described in section 5 are presented for the various analysis methods. We recall that only the incident direction changes from one test to another, in the range [0 ; 60 deg]. The reflection coefficients computed by all the methods are plotted as function of frequency on figure 9.

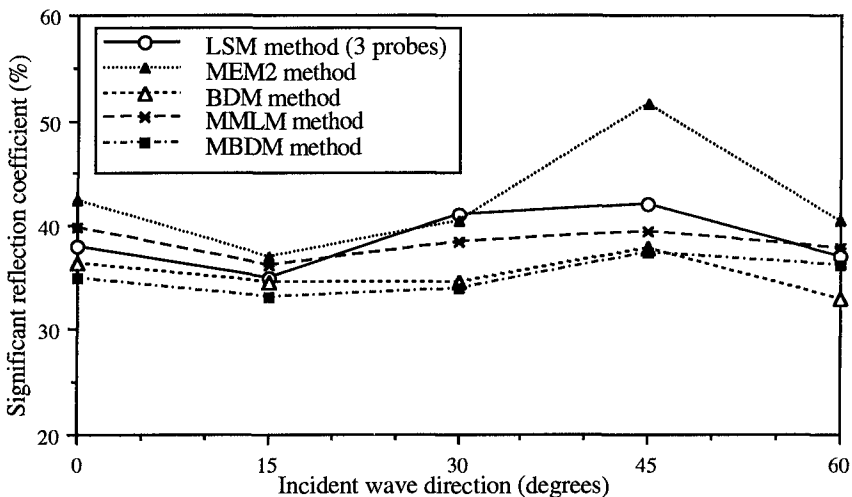


**Figure 9 :** Effect on incident wave direction on reflection coefficient.  
(Laboratory tests — Mound slope 3/4 — Wave steepness 2.3 %)



All methods indicate quite the same variations of reflection coefficient with incident wave direction, even if the range of variation of the reflection coefficient is quite feeble. Starting from normal incidence, the reflection coefficient decreases to become minimum at an incidence of about 15 degrees and then increases again to become maximum at an incidence of 45 degrees. For most of methods, the maximum value at 45 degrees is greater than the value obtained at normal incidence. For the incidence of 60 degrees, the reflection coefficient starts decreasing, but the results obtained at such large incidence have to be handled carefully because of the possible occurrence of Mach reflection which is not taken into account in the present analysis methods. This typical behaviour has been observed on the other tests, performed at different values of wave steepness and different mound slopes (Teisson and Benoit, 1994-a). Recent experiments performed by Juhl and Sloth (1994) in order to examine the effect of incoming direction on the amount of overtopping seem to confirm this trend, as the amount of overtopping appears to be maximum for an incidence of about 10 degrees.

## 8. CONCLUSIONS - FUTURE WORK

The main comments arising from this study are expressed hereafter :

- the Least-Squares Methods (LSM) seem to produce reliable results. This modelling approach requires rather strong assumptions, but it has been shown through numerical tests that this method is quite stable in its results even if one slightly departs from its assumptions.
- these Least-Squares Methods are quite easy to implement and to run. Furthermore, as there are only few unknown parameters in the problem, there is no need to use sophisticated arrays for wave measurement. A linear array of three wave probes or a co-located gauge recording 3 wave signals at the same location (Hughes, 1994) is sufficient for the analysis.
- the directional analysis methods MEM2 (Maximum Entropy Method - version 2) and BDM (Bayesian Directional Method) are not advised for this kind of problem where reflection is important. The relationship that exists between incident and reflected components violates the basic assumption of random phases needed by the methods and results in spurious variations of reflection coefficient with frequency. The mean value of reflection coefficient seems however to keep some physical sense.
- the modified directional analysis methods MMLM (Modified Maximum Likelihood Method) and MBDM (Modified Bayesian Directional Method) take into account the above mentioned phase relationship. Although they assume a continuous directional distribution of energy, these methods have been applied to the present tests performed with long-crested waves. The results seem concordant with the ones obtained from LSM methods, but these methods still need some developments to be fully efficient.

Based on these experiments, the LSM approach appears to be the obvious operational solution for laboratory experiments. The tests of the whole programme have been analysed with this method (Teisson and Benoit, 1994-a) and a typical variation of reflection coefficient with incoming direction has been highlighted. Future research interests will address the optimization of Modified Directional Analysis Methods, in order to study the sensitivity of the distance from the gauge array to the reflection line and possibly to incorporate this distance as an additional unknown parameter to the problem.

## 9. ACKNOWLEDGEMENTS

This study is a joint research program between EDF-Laboratoire National d'Hydraulique and the French Ministry of the Sea (Service Technique Central des Ports Maritimes et Voies Navigables — STCPMVN).

## 10. REFERENCES

- ALLSOP N.W.H., HETTIARACHCHI S.S.L. (1988) : Reflections from coastal structures. *Proc. 21st Int. Conf. on Coastal Eng. (ASCE), Vol 1, pp 782-794.*
- BENOIT M. (1993) : Extensive comparison of directional wave analysis methods from gauge array data. *Proc. 2nd Int. Symp. on Ocean Wave Measurement and Analysis (ASCE), pp 740-754, New-Orleans (USA).*
- BENOIT M., TEISSON C. (1994-a) : Laboratory study of breakwater reflection. Effect of wave obliquity, wave steepness and mound slope. *Proc. Int. Conf. "Waves : Physical and numerical modelling", pp 1021-1030, Vancouver (Canada).*
- BENOIT M., TEISSON C. (1994-b) : Laboratory comparison of directional wave measurement systems and analysis techniques. *Proc. 24th Int. Conf. on Coastal Eng. (ASCE), Kobe (Japan).*
- BIRD P.A., DAVIDSON M.A., BULLOCK G.N., HUNTLEY D.A. (1994) : Wave measurement near reflective structures. *Proc. of Coastal Dynamics'94 (ASCE), pp 701-711.*
- GALLAND J.C. (1994) : Rubble-mound breakwaters stability under oblique waves : an experimental study. *Proc. 24th Int. Conf. on Coastal Eng. (ASCE), Kobe (Japan).*
- GODA Y., SUZUKI Y. (1976) : Estimation of incident and reflected waves in random wave experiments. *Proc. 15th Int. Conf. on Coastal Eng. (ASCE), vol 1, pp 828-845.*
- JUHL J., SLOTH P. (1994) : Wave overtopping of breakwaters under oblique waves. *Proc. 24th Int. Conf. on Coastal Eng. (ASCE), Kobe (Japan).*
- HASHIMOTO N., KOBUNE K., KAMEYAMA Y. (1987) : Estimation of directional spectrum using the Bayesian approach and its application to field data analysis. *Report of the Port and Harbour Research Institute., vol 26, pp 57-100.*
- HASHIMOTO N., KOBUNE K. (1987) : Estimation of directional spectra from a Bayesian approach in incident and reflected wave field. *Report of the Port and Harbour Research Institute, vol 26, N°4, pp 3-33 (in Japanese).*
- HUGHES S. A. (1994) : Estimating laboratory oblique wave reflection. *Proc. Int. Conf. "Waves : Physical and numerical modelling", pp 206-215, Vancouver (Canada).*
- ISAACSON M. (1991) : Measurement of regular wave reflection. *Journal of Waterway, Port, Coastal and Ocean Eng., vol 117, N°6, pp 553-569.*
- ISOBE M., KONDO K. (1984) : Method for estimating directional wave spectrum in incident and reflected wave field. *Proc. 19th Int. Conf. on Coastal Eng. (ASCE).*
- KOBUNE K., HASHIMOTO N. (1986) : Estimation of directional spectra from maximum entropy principle. *Proc. 5th OMAE Symp., pp. 80-85, Tokyo (Japan).*
- MANSARD E.P.D., FUNKE E.R. (1980) : The measurement of incident and reflected spectra using a least squares method. *Proc. 17th Int. Conf. on Coastal Eng. (ASCE), vol 1, pp 154-172.*
- NWOGU O.U. (1989) : Maximum entropy estimation of directional wave spectra from an array of wave probes. *Applied Ocean Research, vol 11, N°4, pp 176-182*
- SEELIG W.N (1983) : Wave Reflection from Coastal Structures. *Proc. Int. Conf. on Coastal Structures (ASCE), Arlington (USA).*

## CHAPTER 117

# STONE MOVEMENT ON A RESHAPED PROFILE

G.R. Tomasicchio<sup>1</sup>, A. Lamberti<sup>2</sup>, F. Guiducci<sup>3</sup>

1 – Università di Perugia, Istituto di Idraulica, Loc. S. Lucia, 06125 Perugia, Italy

2 – Università di Bologna, Istituto di Idraulica, Viale del Risorgimento 2, 40136 Bologna, Italy

3 – ESTRAMED S.p.A., Via Campobello 6, 00040 Pomezia (Roma), Italy

### Abstract

Physical model tests were carried out aiming to provide information on armor stone movements in a berm breakwaters. The following items were examined: displacement threshold, frequency and length of stone displacements. Data were obtained from the observation of cumulative displacements at the end of each wave attack and from video records during the attacks; basic statistical analysis was performed. Threshold conditions, moving frequency and cumulative displacements are expressed as function of a modified mobility number, as stone mobility increases with both wave height and wave period.

Information on mobility and displacement is eventually used to estimate longshore transport and abrasion. The longshore model is based on the assumption that stones move during up- and down-rush in the direction of incident and reflected waves; the model compares favourably with experimental existing results. The abrasion model is based on a proportionality assumption between abrasion volume and abrasion work; the proportionality coefficient characterizing the stone material resistance to abrasion is derived from Latham and Poole mill abrasion tests.

### 1. Introduction

The berm breakwater concept, i.e. the conscious design of a rubble mound breakwater for dynamically stable conditions, is relatively new. The central idea is to maintain the profile stable in presence of extreme waves accepting some displacements, whose effect on the reshaped profile is irrelevant, and using rock armor of smaller size than required for a traditional (no movement) design criterium. In such a way available rock may be used in some cases where, according to the traditional design, this would not have been possible. Aiming to use available rock, even stones of poor quality may sometimes be used and were actually used (Sigurdarson & Viggosson, 1994) with satisfaction.

Berm breakwaters introduce some new shapes and variants to well known phenomena but also some completely new topics in breakwaters analysis.

In the first class we may include the strongly convex profile where breakers hit the armor layer and its high permeability caused by its greater thickness; these new

shapes require at least a verification of formulae and equivalence criteria used in the case of traditional breakwaters to estimate armor stability, reflection, wave run-up, overtopping and transmission.

In the second class we should include the reshaping process under eventually static or truly dynamic conditions, the abrasion or breakdown of sliding or colliding rock units and the longitudinal transport of mobile stones.

Run-up on a plane (uniform slope) impermeable surface or on a permeable rubble mound is experimentally well documented. Engineers, needing for an estimate of the behavior of more complex profiles, refer normally to the composite slope method proposed by Saville (1958). Herbich & al. (1963) pointed out the need for some correction for very wide berms; when the berm width is greater than 15% of the wave length its relative effectiveness in reducing wave run-up is strongly reduced. Pilarczyk (1990) describes similar results showing that the critical width is dependent on the breaker type. Van der Meer & Stam (1992) propose formulae describing wave run-up on rock slopes where run-up depends on the probability level (frequency of greater values), on the surf similarity parameter and on mound permeability. Ahrens & Ward (1991) express the reduction in run-up due to the berm as function of the berm geometry and observe that, while the reduction in run-up is modest, the improvement in stability of the revetments is substantial.

We have quoted just some of the information about run-up that can be found in the literature, as an example of how the knowledge of traditional breakwater behavior has been transferred to breakwaters with a relevant berm.

Among the other class of problems, the development of the dynamically stable seaward profile of a reshaping breakwater can be predicted by mathematical models based on extensive physical tests, cf. van der Meer (1988).

The movement of stones along the active profile is a peculiar characteristics of dynamic stability and this causes inherently some abrasion of stones and, when wave attack is oblique, some along-structure transport.

The effect of abrasion can nowadays be evaluated in a semi quantitative manner by the method proposed by Latham (1991) and included in CIRIA-CUR (1991) manual. The method is based on the similarity of armor units weight degradation in nature and in a standardized mill abrasion test (Latham & Poole, 1987); the scale factor for the conversion from milling time (measured as thousands of revolutions) to prototype time (measured as years) is given as the product of 9 factors accounting for: incident wave energy ( $\sim 10$ ), zone in the structure ( $\sim 10$ ), waterborne attrition agents ( $\sim 7$ ), mobility of armor in design condition ( $\sim 4-10$ ), size of the armor stones ( $\sim 2-10$ ), meteorological climate ( $\sim 5$ ), stone grading ( $\sim 2$ ), stone initial shape ( $\sim 2$ ), concentration of wave attack ( $\sim 2$ ); the numbers within parentheses are the measures of the ranges of possible factor values and therefore of the relative influence of the factor.

The along-structure transport  $S$  can nowadays be evaluated with the formula proposed by Van Hijum & Pilarczyk (1982) which may be written as:

$$\frac{S}{g \cdot D_{n50}^2 \cdot T_p} = 0.0012 \cdot \Delta^2 \cdot \frac{H_s \sqrt{\cos\beta}}{\Delta D_{n50}} \cdot \left( \frac{H_s \sqrt{\cos\beta}}{\Delta D_{n50}} - 7 \right) \cdot \sin\beta \quad (1)$$

The above equation was established in the range  $N_s := H_s/\Delta D_{n50} \simeq 12-27$  and is supposed to be usable in the range  $10 \div \infty$ , since when the mobility index is greater than 50 the formula becomes

$$S \simeq 0.0012 \cdot \pi \cdot H_s^2 \cdot c_{op} \cdot \sin 2\beta$$

i.e. similar to CERC formula.

The formula returns the volume transport rate; it gives anyways results of poor utility for actual berm breakwaters, since in almost every case  $N_s < 7$  and the formula returns no transport at all.

A second formula was proposed by Vrijling & al. (1991):

$$S = 4.8 \cdot 10^{-5} (H_0 T_0 - 100)^2 \quad (2)$$

The formula gives the along-structure transport measured as number of stones per wave and was verified in the range 100–400 of the mobility index used, i.e. in a range of mobility more representative of actual berm breakwaters. The absence of obliquity, for which the formula was criticized, may be interpreted as the effect of the range of the tested obliquity  $-25^\circ$  and  $50^\circ$ - wide but in the range of values where the sensitivity is irrelevant because the effect is maximum. The formula may be however easily adjusted including a factor  $\sin 2\beta$ .

The mobility index used in the formula  $-H_0 T_0$ , where  $H_0 := N_s$  and  $T_0 := T_p \sqrt{g/D_{n50}}$  is related to the more usual mobility number  $N_s$  by the trivial relation

$$H_0 T_0 = N_s \sqrt{2\pi N_s / (\Delta s_p)} \quad (3)$$

and, for the usual range of wave steepness ( $s_p \simeq 0.03$ ), the range of mobility where the formula was tested corresponds to  $N_s = 4-10$ .

If berm breakwaters are designed according to Burcharth & Frigaard (1987) recommendations ( $N_s \leq 3.5$  or  $4.5$  in the trunk under oblique and long or respectively steep waves;  $N_s \leq 3$  in the roundhead) the formula returns no transport at all and, as the one mentioned before, doesn't provide any information about the accepted "damage".

The present study:

- synthesizes physical model tests performed, cf. Tomasicchio & al. (1992) and Lamberti & al. (1994), aiming:
  - to determine conditions characterizing the incipient movement of stones along the dynamically stable profile,
  - to quantify stone movement frequency and amplitude for a sufficiently wide set of conditions and
  - to establish a relationship between movement characteristics and wave conditions in the range of mobility typical of a berm breakwater;
- shows how this information may be used in order to provide a longshore transport model calibrated in the mobility range typical of berm breakwaters, and to rationalize Latham method for the estimate of armor stone degradation.

## 2. Model tests

Physical model tests were performed using two different wave flumes, one at Danish Hydraulic Institute (DHI) and the others at ESTRAMED Pomezia Italy in 1993. The test set-up is described in more detail in Lamberti & al. (1994). The tests consisted in a reshaping phase carried out with the design wave attack, followed by stone movement measurements carried out with lower wave intensity. Profile surveys and video records were performed during the investigation. The offshore significant wave height used during reshaping was fixed at  $H_{so} = 0.18$  m; due to shoaling and breaking wave height incident on the structure differs somewhat from the offshore one; the significant height of waves incident on the structure  $H_s$  was systematically used as the wave intensity parameter. Armour stone size was chosen in order to give a mobility number  $N_s = H_s / \Delta D_{n50} \approx 3$  under the reshaping (design) conditions.

For all tests at DHI a fixed initial profile was used (fig. 1); the channel had a constant depth ( $h = 0.60$  m), the relative wave height was low ( $H_{so}/h < 0.3$ ) and waves broke essentially on the structure.

In the tests performed at ESTRAMED the channel presented a foreshore slope 1:20 from 0.60 m depth in the generating area to 0.34 m depth, followed by a more gentle 1:100 slope reaching  $h = 0.30$  m water depth at the structure toe; the range of offshore significant wave height is the same. Waves were moderately limited by water depth.

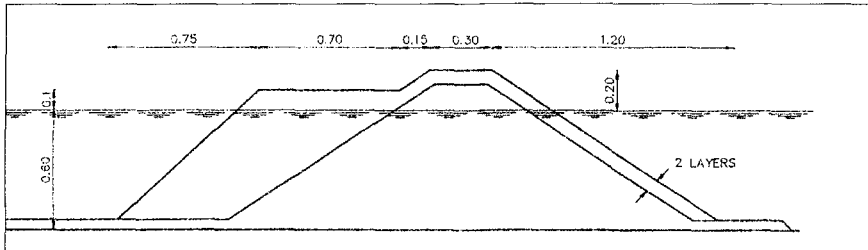


Fig. 1 As built structure in deep water

Each test series started with an initial reshaping phase of the berm-breakwater, composed by 6 wave attacks of 1000 waves each and reaching an almost equilibrium seaward profile of the breakwater. The phase was followed by further 1000 wave attacks of increasing intensity, starting at  $N_s \approx 2$  and increasing up to the reshaping wave conditions, aiming to analyze stone movements. During both phases irregular waves were used derived from a Pierson-Moskowitz spectrum with different significant wave steepness.

During the tests the offshore and the incident wave characteristics were measured and the reshaped profiles surveyed, as shown in fig. 2.

Data about displacements were obtained from two sources: video-records of individual stone movements during the wave attacks and observations of the cumulative displacements at the end of each wave attack.

The intensity of stone movements was experimentally defined through the number of stones displaced from the active profile: the convex part of the reshaped profile from the *step* to the *crest* (van der Meer, 1988).

Two non dimensional indexes are used because they naturally appear in the longshore transport and in the abrasion models: the traditional damage index  $N_{od}$ , defined as the ratio of the number of displaced stones to the number of the stones in a longitudinal line of the observation area, and the *surface damage level*  $S_s$ , defined similarly as the ratio of the number of displaced stones to the number of stones in the upper one grain layer in the active profile portion of the observation area.

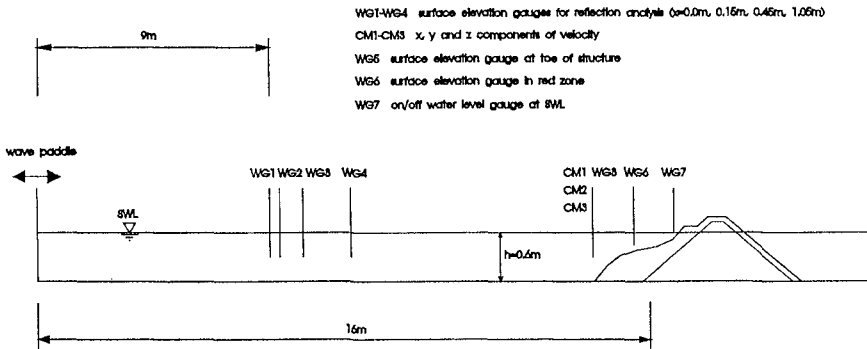


Fig. 2 Model test set-up in deep water

### 3. Threshold of movement

The threshold of stone movement along the reshaped profile was analyzed in deep and shallow water conditions. Movement on the profile is measured by the damage index:

$$N_{od} := N_d \cdot D_{n50} / B \quad , \quad (4)$$

or by the surface damage level:

$$S_s := N_d \cdot D_{n50}^2 / A \quad , \quad (5)$$

where  $N_d$ ,  $B$  and  $A$  are respectively: the number of stones displaced from the active profile at the end of the 1000 waves attack, the width of the observed area and the area itself.

Referring only to DHI model tests, small values of the damage, i.e.  $S_s < 0.05$  roughly corresponding to *zero damage* conditions of SPM (1984), were observed to depend mainly on the *stability number*  $N_s := H_s / \Delta D_{n50}$  with a minor but clearly observable influence of wave steepness. A good correlation was observed between damage and a modified stability number:

$$N_s^{**} \propto N_s \cdot s_m^{-1/5} \quad .$$

This relation suggests that the relevant wave intensity parameter obtained combining wave height and wave period is the onshore energy flux or the breaker height, cf. Lamberti & al. (1994) and Komar & Gaughan (1972).

The following tests showed that the same relation is satisfied for a berm breakwater also in shallow water conditions (see fig. 3) if as wave intensity parameter the incident wave height is considered, which has exceedence frequency almost equal to the frequency of stone movements, i.e. for practical purposes  $H_{1/50}$ .

In order to obtain a mobility index that accounts for the above mentioned observed phenomena and exhibits on average conditions the same values of the traditional stability number  $N_s$ , the following definition of the modified stability number is introduced.

$$N_s^{**} := \frac{H_{k0}}{C_k \Delta D_{n50}} \cdot \left( \frac{s_{m0}}{s_{mk}} \right)^{-1/5} \cdot (\cos \beta_0)^{2/5} \simeq \frac{0.89 \cdot H_{kb}}{C_k \Delta D_{n50}} \quad (6)$$

where  $H_k = H_{1/50}$ ,  $C_k = 1.55$ , i.e. the ratio  $H_{1/50}/H_s$  according to Rayleigh distribution of wave heights, and  $s_{mk} = 0.03$ . The last term includes the effect of wave obliquity according to the hypothesis that the onshore energy flux is the relevant wave intensity parameter.

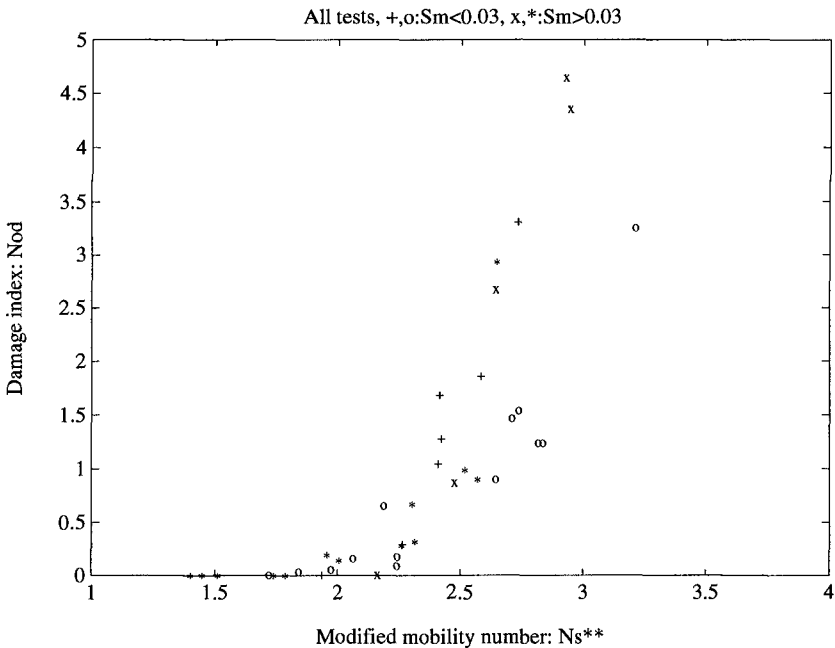


Fig. 3 The empirical relation between the damage in 1000 waves  $N_{od}$  and the modified stability number  $N_s^{**}$ . +, x : deep water; o, \* : shallow water.



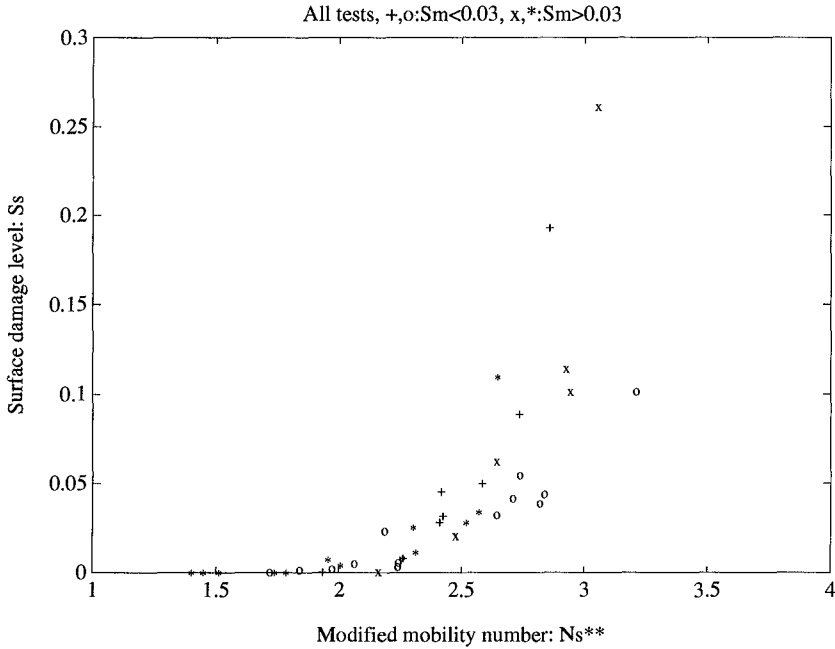


Fig. 4 The empirical relation between frequency of stone movement in 1000 waves  $S_s$  and the modified stability number  $N_s^{**}$ . +, x : deep water; o, \* : shallow water.

Strict threshold conditions correspond to  $N_s^{**} \simeq 2$ , or approximately to  $H_0T_0 \simeq 33$ . There is therefore a rather wide range of conditions where some stone movements occur below the threshold conditions of formulae (1) and (2).

#### 4. Stone mobility

An estimate of the frequency of stone movement can be obtained dividing the damage level by the length of the observation period ( $\simeq 1000$  waves).

The analysis of video records provided some simple statistical description of stone displacements; the mean and standard deviation of the interdisplacement period and of the displacement length were evaluated. The mean interdisplacement period resulted in good agreement with the global frequency derived before (frequency equal to the reciprocal of mean interdisplacement period).

Figure 5 shows the relation between the nondimensional mean displacement  $D_s^{**}$  and the modified mobility number  $N_s^{**}$  for deep water tests. In order to obtain a unique relation between the average displacement  $l_d$  scaled with the nominal stone

size and mobility the former should be multiplied by the square of the wave aspect ratio at structure toe (ratio between the vertical and the horizontal dimensions of the particle horbits). This factor includes the effect of both the water depth and the wave period. If the exponent was 1, the displacements would increase respect to wave height as the horizontal dimension of the horbits. The greater exponent was required for a complete compensation of shallow water effects.

The equations representing the average empirical correlation for mean damage level (frequency) and mean displacement length are:

$$N_{od} = 1.8 \cdot N_s^{**} \cdot (N_s^{**} - 2.0)^{2.2}, \text{ for } N_s^{**} > 2.0 \tag{7.1}$$

$$S_s = 0.14 \cdot (N_s^{**} - 2.0)^{2.2}, \text{ for } N_s^{**} > 2.0 \tag{7.2}$$

$$D_s^{**} := l_d t g h^2 (kh) / D_{n50} = 1.4 \cdot N_s^{**} - 1.3 \tag{8}$$

They represent a refinement of those published in Lamberti & Tomasicchio (1994), including more data on shallow water conditions.

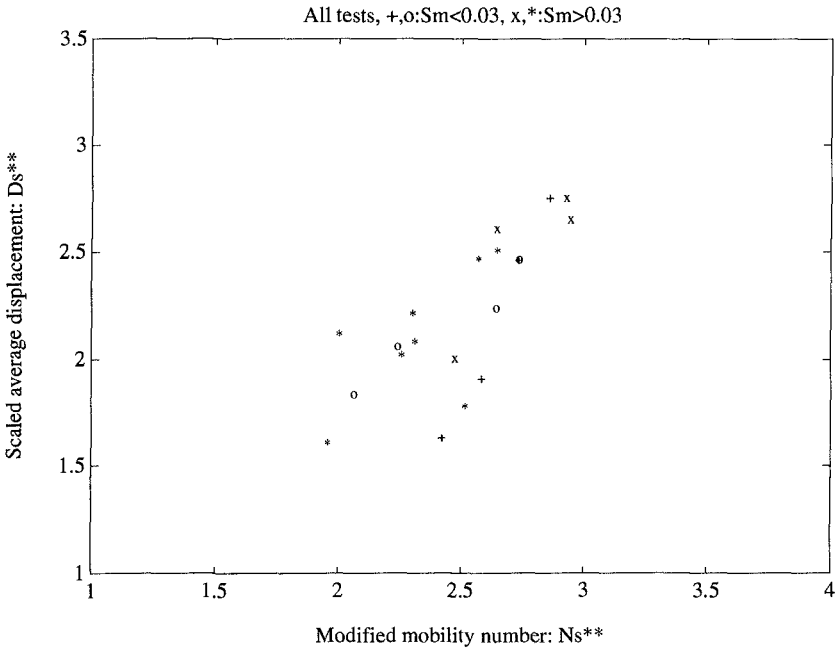


Fig. 5 The empirical relation between mean displacement length and the modified stability number  $N_s^{**}$ . +, x : deep water; o, \* : shallow water.

**5. The longshore transport model**

The two equations (7.1) and (8), or other similar ones giving the frequency and mean length of displacements, combined with the hypothesis that under oblique wave attack the displacement takes place in the direction of wave propagation, or an equivalent one, can be reworked in a long-structure transport formula for very low mobility levels, for which eq. (1) and (2) are not accurate.

A particle will pass through a certain control section in a small time interval  $\Delta t$ , if and only if it is removed from the updrift area of extension equal to the longitudinal displacement length  $l_d$  (if the intervall is small the probability of multiple movements is small of 2nd order, and the corresponding event may be treated as having 0 probability). The number of particle removed from this area is  $N_{od}$  in 1000 waves per one diameter long strip, i.e. the number of particles traversing the control section

$$S \cdot \frac{\Delta t}{T_m} = \frac{l_d \cdot \sin \beta_{kb}}{D_{n50}} \cdot \frac{N_{od} \Delta t}{1000 T_m}$$

i.e.:

$$S = \frac{l_d}{D_{n50}} \cdot \frac{N_{od}}{1000} \cdot \sin \beta_{kb} \tag{9}$$

where the characteristic wave obliquity at breaking point is evaluated from the wave characteristics at the measure point according to the procedure (the breaker index  $\gamma$  is set equal to 1.42 according to Komar & Gaughan, 1972):

$$H_{kb} = (H_k^2 \cdot c_g \cdot \cos \beta \cdot \sqrt{\gamma/g})^{2/5}$$

$$c_{kb} = \sqrt{g H_{kb} / \gamma}$$

$$\sin \beta_{kb} = \sin \beta \cdot c_{kb} / c$$

For the sake of simplicity we have assumed in the presentation that the length of displacements and the time between displacements are deterministic, but the result is asymptotically exact whichever are the distributions of the displacement length  $L_d$  and of the residence (between movements) time  $T_r$ , provided they are independent: the mean velocity of each mobile particle (time derivative of the mean particle position) is asymptotically  $E(L_d)/E(T_r)$ . The same relation is exact at any time if the event process of movements is Poissonian.

Fig. 6 shows the experimental data of Burcharth & Frigaard (1987) and van der Meer & Veldman (1992), interpreted according to the structure of formula (9). Fig. 7 shows the comparison between formula (9), which the substitutions corresponding to (7.1) and (8), and the experimental results. No calibration was necessary and the comparison is a verification of the approach. The four point which do not conform to the general trend refer to van der Meer data with 50° obliquity, for which no offshore equivalent conditions exist due to the great inshore obliquity.

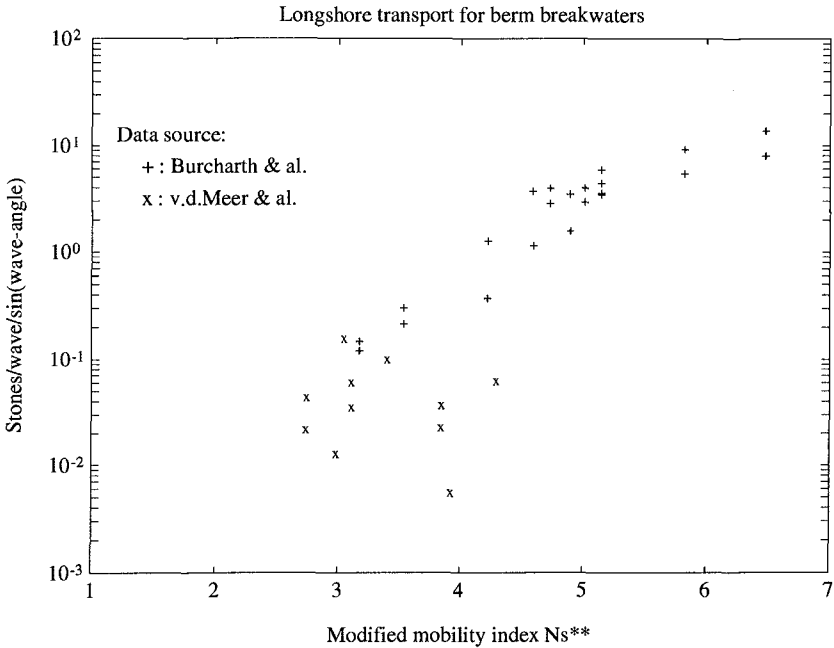


Fig. 6 Relation between the measured longshore transport at berm breakwaters and mobility.

## 6. The abrasion model

Information on mobility and displacement is eventually used to estimate armor stone abrasion for a given wave climate. The model is based on a proportionality assumption between abrasion volume and abrasion work, which is an ancient hypothesis due to Reye (1848) widely used in tribology; the proportionality coefficient, characterizing the stone material resistance to abrasion, may be easily derived from Latham and Poole mill abrasion tests.

The essence of Reye hypothesis is that between the two factors of the abrasion work, friction stress and sliding distance, a perfect compensation is possible: i.e. if both are altered but the product does not change so does erosion. Or when the energy is dissipated in the impacts, the hypothesis assumes that all the dissipated energy is spent for the disgregation of small volumes of material near the contact. In both cases it is evident that if the material resistance is greater than the applied local stress, part of the work may be converted into heat and not into abrasion. Some scale effects are therefore to be expected, since stress increase considerably with the size of the units while the material resistance remains unchanged.

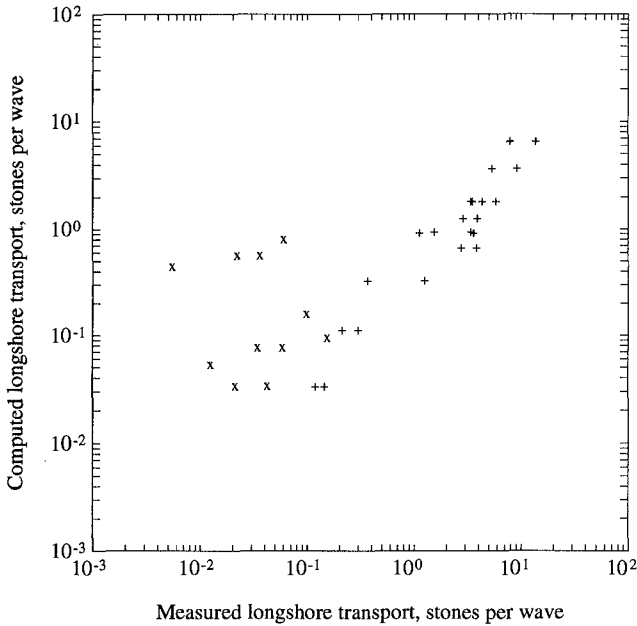


Fig. 7 Comparison between formula (9) and measured longshore transport in berm breakwaters

In the original Latham & Poole (1987) mill a  $\Phi$  176 mm cylinder is half-full with rock grains of size 25-32 mm submerged in water and is kept turning at 26-27 rpm speed (a second version of the mill -Latham, 1991- has  $\Phi$  195 mm and rotates at 33 rpm giving 1.5 higher abrasion per rotation); due to the internal friction the surface of the granular forms an angle with the horizontal equal to dynamic internal friction angle  $\varphi_d$ ; the gravity center results eccentric and the resisting moment, the work dissipated by abrasion per revolution  $\mathcal{L}_u$ , and the relative volume loss can be easily expressed

$$\begin{aligned}
 b &\simeq 4R/3\pi \cdot \sin\varphi_d \\
 \mathcal{L}_u &= W \cdot b \cdot 2\pi \simeq 8/3 \cdot (\rho_a - \rho_w)g \cdot V \cdot R \cdot \sin\varphi_d \\
 -\Delta V &= k \cdot \mathcal{L}_u \cdot N
 \end{aligned}
 \tag{10}$$

where  $b$  is the eccentricity of rock gravity center,  $W$  and  $V$  are respectively the submerged weight of the grains and their volume,  $\Delta V$  is the volume lost by abrasion and  $k$  is the proportionality constant characterizing rock material;  $1/k$  is homogeneous to a stress and is presumably proportional to material resistance. Combining the equations and assuming that during the test  $N = 1000$  revolutions are

carried out, since by definition  $k_s$  in this case is equal to the relative volume reduction, one obtains

$$l_{test} = 8/3 \cdot R \cdot N = 235 \text{ m (260 m in the 2nd version)}$$

$$-\Delta V/V \approx \ln \frac{V_0}{V} = k_s = k \cdot l_{test} \cdot (\rho_a - \rho_w)g \cdot \sin\varphi_d \tag{11}$$

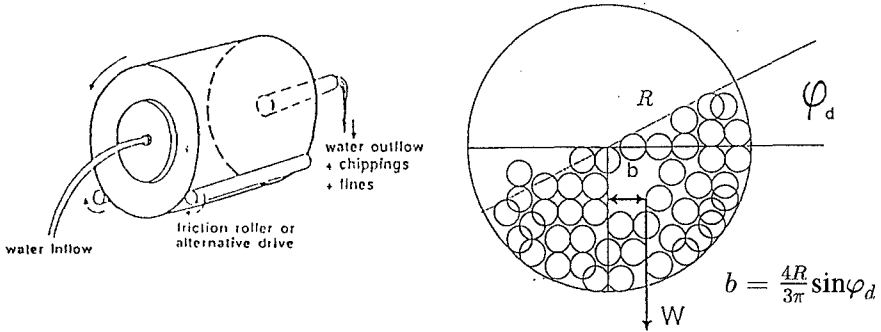


Fig. 8 Geometric scheme of Latham & Poole mill abrasion test

In prototype, a stone sliding for a length  $l$  over the profile having slope  $\alpha$  is accompanied by the dissipation work

$$\mathcal{L} = l \cdot (\rho_a - \rho_w)g \cdot V \cdot \cos\alpha \cdot \tan\varphi_d \approx l \cdot (\rho_a - \rho_w)g \cdot V \cdot \sin\varphi_d$$

since  $\cos\alpha/\cos\varphi_d \approx 1$ . According to Reye hypothesis and to relation (11) the relative loss of volume is

$$-\Delta V/V = k_s \cdot l/l_{test} \tag{12}$$

In the lifetime of the breakwater  $-L-$  the total displacement length of a stone on the active profile  $-l_L-$ , reminding that the damage level  $-S_s-$  was evaluated over 1000 wave periods, is

$$l_L = \int_0^L l_{avg}(t) \cdot S_s(t) \cdot \frac{dt}{1000T}$$

or, since no movement occurs if wave intensity is below threshold,

$$l_L = \sum_{\text{storms exceeding threshold}} l_{avg} \cdot S_s \cdot \frac{N_w}{1000} .$$

The number of storm exceeding threshold is in the case of practical interest great enough to assume the number of storms  $N_{st}$  deterministic and to approximate the sum by its expected value, and therefore

$$l_L = N_{st} \cdot E\left(l_{avg} \cdot S_s \cdot \frac{N_w}{1000} \mid \text{threshold is exceeded}\right)$$

Let  $\lambda$  be the mean frequency of storms and  $P_*$  the probability that a generic storm intensity  $h$  exceed threshold  $h_*$ , the expected number of storm is

$$N_{st} = \lambda_* \cdot L := \lambda \cdot L \cdot P_*$$

Let  $F_{H_s}(h)$  be the climatic distribution of storm wave height and let assume that the distribution has exponential behavior provided the threshold is exceeded:

$$F_{H_s}(h) \simeq 1 - \exp\left(-\frac{h-h_0}{h_1}\right) \quad \text{and} \quad P_* = \exp\left(-\frac{h_*-h_0}{h_1}\right)$$

The conditioned distribution, provided that the threshold is exceeded, has similar distribution with the parameter  $h_0 = h_*$ . Assuming finally for the sake of simplicity that both the number of waves per storm and the wave steepness are constant, that water is deep so that  $H_k/C_k = H_s$ , letting  $\xi$  be the running value of the modified mobility parameter and

$$\xi_1 := \frac{h_1(s_m/s_{mk})^{-1/5}}{\Delta D_{n50}} \quad (13)$$

the total displacement length in lifetime is

$$l_L = N_{st} \cdot N_w \cdot D_{n50} \cdot f_1(\xi_1) \quad (14)$$

where

$$f_1(\xi_1) := \int_{2.0}^{\infty} (1.4\xi - 1.3) \cdot 0.14\xi(\xi - 2.0)^{2.2} \cdot \exp\left(-\frac{\xi-2.0}{\xi_1}\right) \cdot \frac{d\xi}{1000\xi_1}$$

$$- \Delta V_L/V \simeq \ln \frac{V_0}{V} = k_s \cdot L \cdot \left[ \frac{\lambda_* \cdot D_{n50}}{l_{test}} \cdot N_w \cdot f_1(\xi_1) \right] \quad (15)$$

The function  $f_1$  may be approximated without any practical loss of accuracy as:

$$f_1(\xi_1) \simeq 0.0020 \cdot \xi_1^{3.0} \quad (16)$$

The factor in brackets in eq. (15) represents the conversion factor of lifetime into equivalent number of thousands of revolutions and should be equal to the reciprocal of Latham (1991) conversion factor  $X$ . Actually only some of the factors influencing stone degradation appear in our model; these are: 1-size, 4-incident wave energy, 9-mobility of armor in design concept.

Factor  $X_1$  is according to Latham (1991) directly proportional to the nominal diameter, whereas in our formula stone size acts as inversely proportional.

Factor  $X_4$  is also a scale factor as it is inversely proportional to wave height; it also represents the integrity of blocks.

Factor  $X_9$  depends on the ratio of the two mentioned scale parameters.

Actually the are at least two different scale effects: one for the external abrasion agents, such as chemical attack or waterborne attrition agents, and one for abrasion due to armor stone movement. The first type of abrasion acts on the surface of the stone and erodes a layer of thickness independent from stone size, and hence the scale effect on the relative lost volume is inversely proportional to its size; the factor representing the associated scale effect is  $X_1$ . In the second type, stresses on the contact among stones increase proportionally to stone or wave size, whereas the material resistance remains constant; this produces an effect on relative volume loss proportional to size and  $X_4$  is the factor representing this scale effect.

In any case since the two types of abrasion have different scaling factors and the effects are naturally added on stones, the effects should preferably be evaluated separately in the prototype and in the model. The model we propose can be used to evaluate one of the types of abrasion, provided the  $k_s$  values derived from small scale tests may be significant. For the other type existing statically stable breakwaters can provide useful information.

Example applications (Lamberti & Tomasicchio, 1994) show that Latham's method, including abrasion due to external agents, returns greater degradation of stones (one order of magnitude greater  $\Delta V_L/V$ ) but is less sensitive to mobility (half order of magnitude). Latham method is calibrated with the aid of several real world cases.

Some scale effects relative to Reye hypothesis are evident from the comparison between the 1st and the 2nd Latham mill: a factor 1.1 in the mill size or sliding length and 1.4 in peripheral velocity produces a factor 1.5 in abrasion intensity for the same material. This indication could suggest to scale up the degradation proportionally to the impact velocity scale, i.e. for a stone rolling on a mound, proportionally to the square root of the length scale. Since the length scale from the mill to reality is almost 100, the scaling would compensate approximately for the pointed out difference. More definite information is anyway required about the scale effects due to impact velocity and stress.

## 7. Conclusions

A careful analysis of stone mobility shows that:

- the wave height and wave period combination which describes properly stone mobility is the combination proportional to onshore energy flux ( $\propto H^2T$ ); according to the same concept also the effect of wave obliquity can be easily included in the wave intensity parameter; as a consequence a stability number modified respect to the traditional  $N_s$  is introduced.
- a wave height greater than the significant one should be used as wave height parameter in order to have comparable stability results in deep and shallow water conditions;
- the true threshold of stone movement corresponds to mobility conditions significantly lower than defined by previous researchers: in the range of mobility conditions typical of berm breakwater operation ( $N_s = 2 - 3$ ) the mobility is low but appreciable;
- relations are provided giving the non dimensional frequency of stone movements and their average length as function of the modified stability number.

The proposed longshore transport model, derived without any special calibration from frequency and length of displacements, gives results in good agreement with measurements performed on berm breakwater models.



The proposed conceptual method for the evaluation of armor stones abrasion on berm breakwater due to stone movement gives only reasonable results and requires some adjustment in order to account for the scale effects relative to impact velocities and stresses.

### Acknowledgments

The present study was partially supported by the research and technological development programme in the field of Marine Science and Technology (MAST) financed by the Commission of the European Communities, contract MAST-0032.

### References

- Ahrens J.P. & Ward D.L., 1991. *Performance of bermed breakwaters*, J. Waterway, Port, Coastal & Ocean Eng., ASCE, Vol.117, No 5, Sep/Oct. 1991.
- Allsop N.W.H., Briggs M.G., Denziloe T. & Skinner A.E., 1991. *Aldernay breakwater: the quest for a final solution*, Coastal structures and breakwaters, 6-8 Nov. 1991, London.
- Burcharth H.F. & Frigaard P., 1987. *Reshaping breakwaters. On the stability of roundheads and trunk erosion in oblique waves*, Aalborg Univ. Center, November 1987.
- CERC, 1984. *Shore Protection Manual*.
- CIRIA-CUR, 1991. *Manual on the use of rock in coastal and shoreline engineering*. CIRIA, London, Special Publication 83 - CUR, Gouda, Report 154.
- Hall K.R., Kao J. & Mulcahy M., 1991. *The influence of armour stone gradation on dynamically stable breakwaters*. Coastal structures and breakwaters, 6-8 Nov. 1991, London.
- Herbich J.B. & al., 1963. *Effect of berm on wave run-up on composite beaches*, J. of the Waterways and Harbors Division, May 1963
- Juhl J. & Jensen O.J., 1990. *Practical experience with berm breakwaters*, 1st Workshop MAST I, III B project, DHI.
- Kao J.S. & Hall K.R., 1990. *Trends in stability of dynamically stable breakwaters*, Proc. 22nd Int. Conf. on Coastal Eng., Delft, 1990.
- Komar P.D. & Gaughan M.K. (1972). *Airy wave theory and breaker height prediction*. Proc. 13th Coastal Eng. Conf., Vancouver, 405-418.
- Lamberti A. & Tomasicchio G.R., (1994). *Stone mobility and abrasion on reshaping breakwaters*. Proc. International Coastal Symposium, Höfn, Iceland, June 20-24.
- Lamberti A., Tomasicchio G.R. & Guiducci F., (1994). *Reshaping breakwaters in deep and shallow water conditions*. 24th Int. Conf. Coastal Eng., Kobe, Japan.
- Latham J.-P., 1991. *Degradation model for rock armour in coastal engineering*. Q. J. Eng. Geol., 24, 101-118.
- Latham J.-P. & A.B. Poole, 1987. *Pilot study of an aggregate abrasion test for breakwater armour stones*. Q. J. Eng. Geol., 20, 297-310.
- Norton P. & Holmes P., 1991. *Reshaping simulation model for dynamically stable breakwaters*, 1st Workshop MAST I, III B project, DHI.
- Pilarczyk K.W., 1990. *Design of seawalls and dikes- Including overview of the revetments*, Coastal Protection, 1990 Balkema, Rotterdam.
- Saville T. jr., 1958. *Wave runup on composite slopes*, Proc. 6th Int. Conf. Coastal Eng.

- Tomasicchio G.R., O.H. Andersen & P. Norton, 1992. *Measurements of individual stone movements on reshaping breakwaters*. CEC MAST-I Coastal Structures Final Workshop, LNEC Lisbon, 5-6 November 1992
- Van der Meer J.W., 1988. *Rock slopes and gravel beaches under wave attack*, TDU Ph.D. thesis.
- Van der Meer J.W. & Veldman J.J. 1992. *Singular points at berm breakwaters: scale effects, rear, round head and longshore transport*. Coastal Engineering, 17 (1992) 153-171
- Van der Meer J.W. & Stam C.J.M., 1992. *Wave runoff on smooth and rock slopes of coastal structures*, Proc. ASCE, J. Waterways Port Coastal & Offshore Eng., vol.118 WW5.
- Van Hijum E. & Pilarczyk K.W., 1982. *Equilibrium profile and longshore transport of coarse material under regular and irregular wave attack*, DH Publication No. 274, 1982.
- Vrijling J.K., Smitt E.S.P. & De Swart P.F., 1991. *Berm breakwater design-the longshore transport case: a probabilistic approach*, Coastal structures and breakwaters, 6-8 Nov. 1991, London.

## Notations

The following symbols and notations are used in the paper:

- $c$  = wave celerity, [ $m \cdot s^{-1}$ ];
- $c_g$  = group velocity, [ $m \cdot s^{-1}$ ];
- $C_k$  = ratio between the characteristic and significant wave height;
- $D_{nxx}$  = nominal diameter of armor stones corresponding to fractile  $xx\%$ :  
 $(W_{xx}/g\rho_a)^{1/3}$ , [m];
- $E()$  = expected value;
- $H$  = wave height, [m];
- $H_s$  = significant wave height, [m];
- $H_{1/n}$  = mean wave height of the  $1/n$  fraction of the highest waves;
- $L$  = wave length, [m];
- $L_d, l_d$  = length of displacement, stochastic variable and mean value, [m];
- $N_s$  = armor stone mobility (stability) number:  $H_s/\Delta D_{n50}$ , [];
- $N_s^{**}$  = modified stability number, [];
- $S$  = along-structure transport measured as bulk volume, [ $m^3 \cdot s^{-1}$ ], or as number of stones per wave, [];
- $s$  = wave steepness:  $H_s/L_o$ , [];
- $T$  = wave period, [s];
- $W_{xx}$  = weight of which  $xx\%$  by weight of the armor stones are smaller, [kg];
- $\beta$  = angle of wave attack (between wave front and shoreline), [];
- $\gamma$  = breaking index: ratio between breaking wave height and water depth, [];
- $\Delta$  = relative density of armor stones =  $(\rho_a - \rho_w)/\rho_w$ , [];
- $\rho_a$  = mass density of armor stones, [ $kg \cdot m^{-3}$ ];
- $\rho_w$  = mass density of water, [ $kg \cdot m^{-3}$ ];
- $\cdot_b$  = at wave breaking point;
- $\cdot_k$  = characteristic or effective value;
- $\cdot_m$  = relative to spectrum mean frequency;
- $\cdot_o$  = in offshore conditions;
- $\cdot_p$  = relative to spectrum peak frequency.

## CHAPTER 118

### THE LARGE SCALE DOLOS FLUME STUDY

George F. Turk and Jeffrey A. Melby<sup>1</sup>

**ABSTRACT:** In 1993, the U.S. Army Corps of Engineers, Waterways Experiment Station, Coastal Engineer Research Center conducted the Large Scale Dolos Flume Study (LSDFS) in order to investigate the structural response of concrete armor units. The study was primarily carried out in the large wave flume at the O.H. Hinsdale Wave Research Laboratory, Oregon State University. Over 300 model dolos units with a mass of 26 kg and a waist ratio of 0.32 were used. The units were cast from concrete. The instrumented dolosse were fitted with surface-mounted strain gages then subjected to a wide range of wave loading conditions. This strain gaging and the state-of-the-art data acquisition system increased the signal-to-noise ratio so that accurate measurements of static, quasi-static, wave-induced hydrodynamic, and unit-to-unit impact loading could be recorded. The LSDFS included a standard calibration series, static ramp tests, dry-land impact tests, and regular and irregular wave flume tests. Hydrodynamic instrumentation in the flume tests consisted of a very dense array of wave gages, current meters, runup-rundown gages, pore pressure transducers, hydrophones, digital video, and still photography in the nearshore zone. This paper presents previously unpublished details of the LSDFS specifically pertaining to instrumentation, calibration, dry-land impact tests, and some preliminary results of impact response captured in the flume tests.

### INTRODUCTION

Dolosse are the dominant concrete armor units used on U.S. rubble-mound structures. They continue to be specified for new breakwater construction and for rehabilitation. Recent surveys by Corps researchers of concrete-armored breakwaters indicate an urgent need for concrete armor repair and rehabilitation design guidance (Melby and Turk 1994a). But, despite many concrete armor structural investigations during the last 20 years, there is still a general lack of knowledge of dolos structural

---

1) Research Hydraulic Engineers, Coastal Engineering Research Center, USAE Waterways Experiment Station, Vicksburg, MS, 39180

response. This is partly because of the complexity of the response with both the loading and boundary conditions being stochastic and highly variable and the wave loads not being currently analytically solvable. The inadequate knowledge is also due to the lack of a high accuracy strain measurement system for concrete armor.

Past efforts to measure the structural response of dolosse have included the Crescent City Prototype Study (Howell 1986), where 38-tonne dolosse were internally structurally instrumented. The Crescent City study provided a valuable data set of wave-induced hydrodynamic loadings at prototype scale which was used to calibrate a strain amplifying load cell for measuring dolos structural response at small scale (Markle 1989). But no impacts were recorded during this study and the static data set was limited to the 15 dolosse that were sampled. Also, the static data may have drifted over the course of the measurement period due to long term differential curing of the concrete.

Numerous dolosse small scale model experiments have been conducted by Scott et al. (1986), Anglin et al. (1989), Markle (1989), Melby et al. (1989), and Burcharth et al. (1991). Most of these studies used a load cell developed by or similar to that of the Canadians. While these efforts have contributed to the understanding of dolos structural response, all have proven less than satisfactory in determining the maximum stresses in dolosse. The load cell was calibrated for response to hydrodynamic loading by Markle (1989). But small scale load cell structural investigations are subject to scale and modeling effects, as discussed by Melby and Turk (1994b). For instance, calibration for static response is difficult because the small scale units have different surface friction than prototype units and static strains in load cell instrumented units are so small that they are very unreliable. Also, calibration for impact stresses has been done using uninstrumented drop test results (Burcharth 1991). These tests define failure as a specific crack width and relate the height dropped that produced this crack width to concrete cylinder compressive test strength. There are a large number of factors contributing to the uncertainty in these tests including fatigue effects from ever increasing drop heights, failure occurring at different locations on the units, armor unit strength being very different than the cylinder strength, incorrect estimation of cylinder tensile strength, and the load cell unit responding dynamically entirely differently than an uncut unit.

The Coastal Engineering Research Center's Large Scale Dolos Flume Study (LSDFS) provided an effective solution for quantifying the maximum stresses in dolosse. By using large scale concrete models instrumented with surface-mounted strain gages, direct strain measurements were made. This limited the required assumptions concerning the concrete response and added a degree of control not possible in prototype investigations.

## **LARGE SCALE DOLOS FLUME STUDY OVERVIEW**

The purpose, goals, and experimental plan of the LSDFS, which began in 1991, are discussed in detail by Melby and Turk (1994b, 1994c) and will only be outlined herein. The large scale used was intended to minimize scale effects associated with flow forces, surface friction, materials, modeling, and instrumentation. The purpose of the study was to accurately and simultaneously measure dolos structural and hydrodynamic stability response. These data have been useful for verifying structural scaling criterion, developing design methods, and calibrating small scale model instrumentation. In addition, the results led to the development of a new concrete armor unit shape, the CORE-LOC™ (Melby and Turk 1995). The technology developed during this study for

constructing, instrumenting, and collecting data will hopefully be helpful in future physical structural modeling. Finally, the data set will provide calibration for several numerical models under development at the CERC.

Besides accurate structural measurements of dolos response, measurements of real-time dolos movement, incident and reflected waves, and water particle velocities in front of the slope were also sought from the study. Dynamic dry-land tests were conducted to quantify impact response, and validate scaling using impact drop tests under idealized conditions. Dry-land static ramp tests were conducted to measure static stresses found in the dolos for a wide range of boundary conditions and several positions in the armor layer.

### Model and Instrumentation Development

Approximately 300 concrete dolosse with a mass of 26 kg and a waist ratio of 0.325 were cast for the LSDFS (Figure 1). The most critical aspect of the LSDFS was the development of the Large Scale Instrumented Dolos (LSID). The LSID needed to be capable of detecting minute strains at a variety of locations on a dolos surface while maintaining integrity under the rigors of long-term underwater testing. Much discussion went into the planning of these units. Doubts were expressed that the strains produced, much of which would be below  $20 \mu\epsilon$ , would even be measurable. Noise levels of less than  $100 \mu\epsilon$  were at one time considered good. The option of using a cut section and strain amplifying instrumentation was discussed but ultimately rejected. A cut dolos with a metal pipe inserted between the sections does not respond dynamically like an uncut dolos. As discussed above, identification of an apparent elasticity is very difficult.

#### Dolos Concrete.

Concrete Type:	Type I Portland Cement
Aggregate:	Coarse Sand
Density:	$\rho = 2180 \text{ kg/m}^3$
Youngs Modulus:	$E = 29 \text{ GPa}$
Poisson Ratio:	$\nu = 0.46$
28-day Strength:	$f'_c = 54.8 \text{ MPa}$
Armor Unit Mass:	$M = 26 \text{ kg}$
Armor Unit Volume:	$V = 0.012 \text{ m}^3$

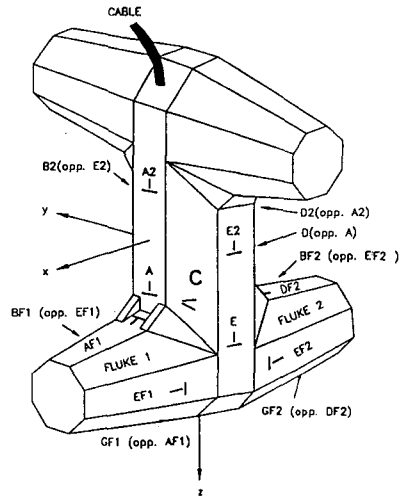


Figure 1. 26 kg instrumented dolos (LSID)

It was decided that surface-mounted strain gages, placed at up to 18 critical locations on the dolos shank and flukes (Figure 1), would be the the most successful instrumentation scheme. This scheme provided measurement of the exact surface strain

at the extreme fiber. Young's Modulus was determined from concrete cylinder sample tests, and Hooke's law applied to get a precise surface stress. Load cells generally measure two moments and a torque. Using these load-cells in small-scale dolosse, two moments and torque are determined as a function of voltage output by hanging weights off the end of the dolos. These gross responses are based on differencing the voltage across the wheatstone bridge circuit. For load cell instrumented units, a linear stress distribution must be assumed, with equal magnitudes of compressive and tensile strains at the extreme fibers. But Melby et. al. (1989) showed highly non-linear stress distributions in dolos shank sections under static loading, even for low stress levels, due to the abrupt changes in sectional shape. Therefore, the linear cross-sectional stress distribution assumption will always produce an unquantifiable error. In the LSDFS, by measuring the individual strains on opposite sides of a section, we can directly measure the compressive and tensile extreme fiber strains and use Hooke's Law to compute stress.

By casting the LSIDs out of sand aggregate concrete, the strain gages could be placed directly on the prepared concrete surface without concern that a gage would be placed on an undetected aggregate stone. But one of the compromises that had to be made was the need for extensive waterproofing and impact protection (Figure 2a) for the surface-mounted gages (Figure 2b). Dry-land tests showed that, if a LSID impacted another LSID on the waterproof covering, the impact strain amplitude could be attenuated by up to 40%. This was a great concern during the flume tests. Fortunately, rarely

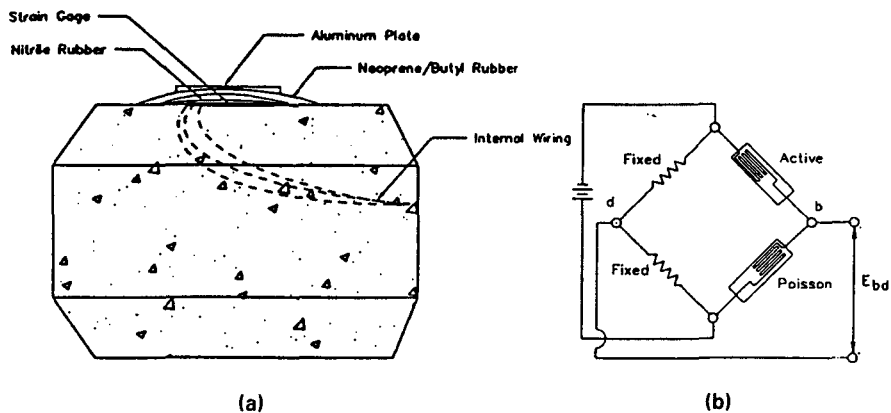


Figure 2. (a) Waterproofing and protection for (b) surface mounted strain gages

during the testing were impacts directly on the waterproofing evident. This was because the units generally impacted on the fluke ends, falling like a hammer. The waterproofing procedure was tedious and time consuming; but it was important because water intrusion into the instrumentation could cause gage drift and gage failure. Waterproofing integrity tests were done over the period of several weeks by soaking the LSIDs in tubs filled with water. During the waterproofing testing, the instrumentation showed minute and acceptable degrees of gage drift as shown in Figure 3.

The final strain gage layout consisted of 350  $\Omega$ , 1.25 cm foil gages set in a Wheatstone half bridge configuration (Figure 2b). By using a Poisson gage, signals were temperature compensated and amplified 10% to 30%. The waterproofed gages were capable of detecting strains on the surface of the concrete dolosse with a resolution of one

micro-strain ( $\mu\epsilon$ ) peak-to-peak and a variable range of around 1000  $\mu\epsilon$ . The high resolution was required for accurate measurement of strains due to static and hydrodynamic loads and the large ranges for measurement of static, quasi-static, and impact strains simultaneously. A total of seven dolosse were instrumented with up to 18 of these strain gages.

Other aspects of the model dolosse, instrumentation, and data acquisition system, including the details of molding the dolosse, the strain gaging development, and the data acquisition hardware specifications are given in Melby and Turk (1994c).

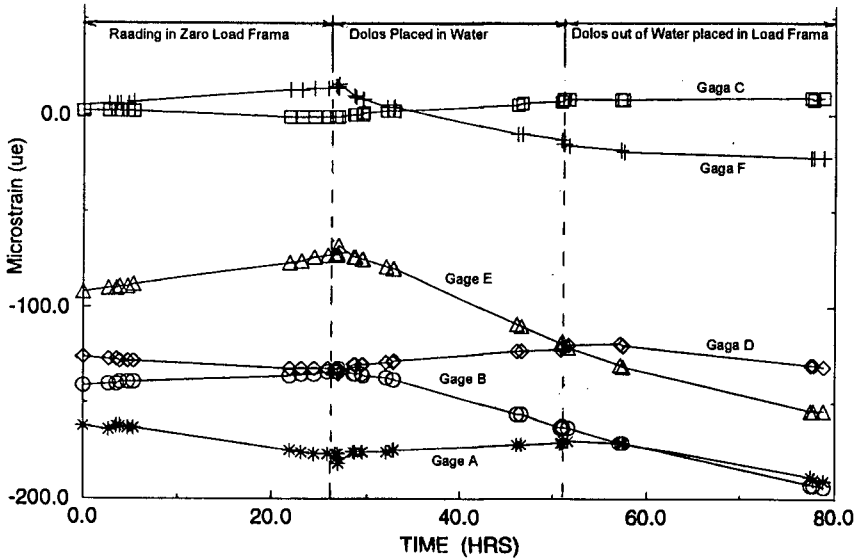


Figure 3. Typical waterproofing test results

### Dolos Calibration

The purpose of conducting an extensive bench test program for the instrumented dolosse was to check the strain gages and bridge circuitry and to quantify the amplification of the Poisson gages. By applying known torsion and bending moment loads to the dolos units and knowing the Young's Modulus, strain readings obtained from each of the bridge circuits were compared against theoretical values derived by combining simple beam theory and Hooke's Law. The strain was analytically calculated for bending as

$$\epsilon = \frac{FL}{0.0956d^3 E} \quad (1)$$

and for torsion as

$$\epsilon = \frac{16FL(1 + \mu)}{\pi d^3 E} \quad (2)$$

Here  $\epsilon$  is strain,  $F$  is the applied load,  $L$  is the moment arm,  $d$  is the distance between opposing faces of the dolos section,  $E$  is Young's Modulus, and  $\mu$  is the Poisson Ratio. Table 1 shows typical results of the static calibration, where measured strains were compared to analytically-calculated strains. The LSID measurements were at a maximum within 10% of the theoretical values.

Table 1. Typical results of dolos bench test

Load (N)	Bending Gage			Torsion Gage		
	Estimated Strain ( $\mu\epsilon$ )	Actual Strain ( $\mu\epsilon$ )	Percent Error (%)	Estimated Strain ( $\mu\epsilon$ )	Actual Strain ( $\mu\epsilon$ )	Percent Error (%)
45	4.1	4.5	+9.8	2.9	2.8	-3.6
67	6.2	6.5	+4.8	4.4	4.5	+2.3
89	8.3	8.5	+2.4	5.9	5.8	-1.7
134	12.4	11.5	-7.8	8.8	8.8	0
178	16.5	16	-3.1	11.7	11.8	+0.9
223	20.7	20	-3.5	14.7	14.8	+0.7
267	24.8	24.5	-1.2	17.6	17.8	+1.1
312	28.9	28	-3.2	20.6	20.5	-0.5

E = 29 Gpa , Moment Arm = 61 cm, Width of Shank = 13.8 cm

## Flume Setup

The OSU flume used for the LSDFS measured 104 m x 3.7 m and is 3.7 m deep (Figure 4a). The waves were generated by a flap-type wavemaker with active reflected wave suppression. The flume was fitted with an instrumentation carriage and had a configurable foreshore slope.

The flume instrumentation (Figure 4b) and data acquisition system included:

- 1) VAX-based 64-channel DAS
- 2) Time code generator linking all data acquisition devices with atomic clock
- 3) 4-three-axis current meters
- 4) 4-electro-resistive wave gages
- 5) 2-electro-resistive runup/rundown gages
- 6) 8- pore pressure transducers
- 7) 2-surface video cameras
- 8) 2-underwater video cameras
- 9) 2-underwater microphones
- 10) 2-35mm still cameras



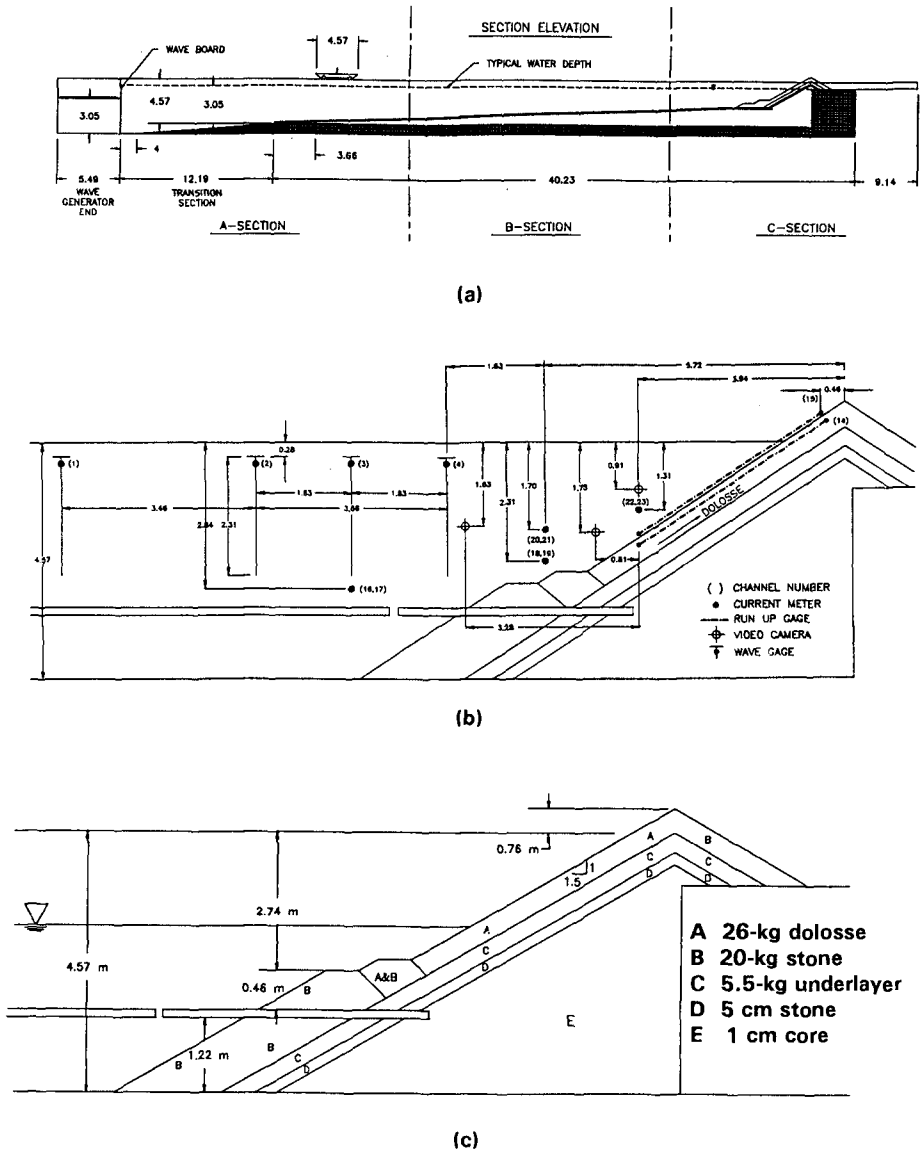


Figure 4. (a) Flume Layout. (b) Instrumentation. (c) Cross-section

Approximately 300 uninstrumented dolosse and up to seven LSIDs were placed on a 1V:1.5H structure slope (Figure 4c). The units were placed with a packing density of  $\phi = 0.83$ , a layer coefficient of  $K_{\Delta} = 0.94$ , and a porosity of  $P = 56\%$ . Using these parameters, 15 dolosses were placed per square meter of surface area.

## PRELIMINARY RESULTS

### Static Ramp and Dynamic Drop Tests

Results of the static ramp tests have been previously discussed in detail by Melby and Turk (1994b, 1994c). The ramp tests included 84 rebuilds on a 1V:1.5H slope. Strain measurements were taken with the slope flat, sloped, sloped and nested (vibrated), and flat again. The static ramp tests produced an overall non-dimensional static mean tensile stress,  $\sigma/\rho g C$ , of 15.2 with a standard deviation of 9.0, where  $g$  is the acceleration of gravity,  $\rho$  is the concrete density of  $2180 \text{ kg/m}^3$ , and  $C$  is the dolos fluke length of 43 cm.

The dynamic drop tests were conducted in the usual manner (Figure 5) with nine incremental centroidal drop heights from 0.035 to 1.98 cm. The dolosse were dropped on a structural concrete base over 1 meter thick. It was assumed that this base did not absorb an appreciable amount of energy.

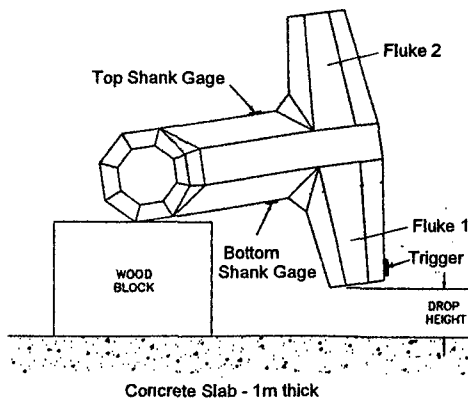


Figure 5. Standard drop test configuration

Two LSIDs were used (Figure 1) and 5 drops were performed at each of the nine heights on each end of the instrumented fluke. Figure 6 shows a typical impact signal recorded from the four gages located about the dolos shank. Figure 6(a) shows signals from gages A and D, located on the top and bottom of the shank. Here most of the vibrational energy is in the fundamental flexural vibration mode. Figure 6(b) shows signals from gages B and E, located on the sides of the shank where little straining occurs. These signals show that the dolos is in almost pure in-plane bending, with no out-of-plane bending or torsion introduced from the test procedures.

Figure 7a shows the maximum strains recorded during each drop from the four shank gages (gages A,B,D,E). In Figure 7, the abscissa is the ratio of the centroidal

drop height,  $h$ , to the dolos fluke length,  $c$ . Figure 7b shows maximum strains recorded from eight of the fluke gages (gages AF1,BF1,EF1,GF1,BF2,DF2,EF2,GF2). The raw data show consistent amounts of scatter between different drop heights. However, when observing the coefficient of variation (standard deviation divided by the mean), as plotted against the non-dimensional drop height (Figure 8), a greater degree of scatter becomes apparent at the lower drop heights. This is expected, as imperfections in the impacting face made accurate repeatability almost impossible for the smallest five drop heights

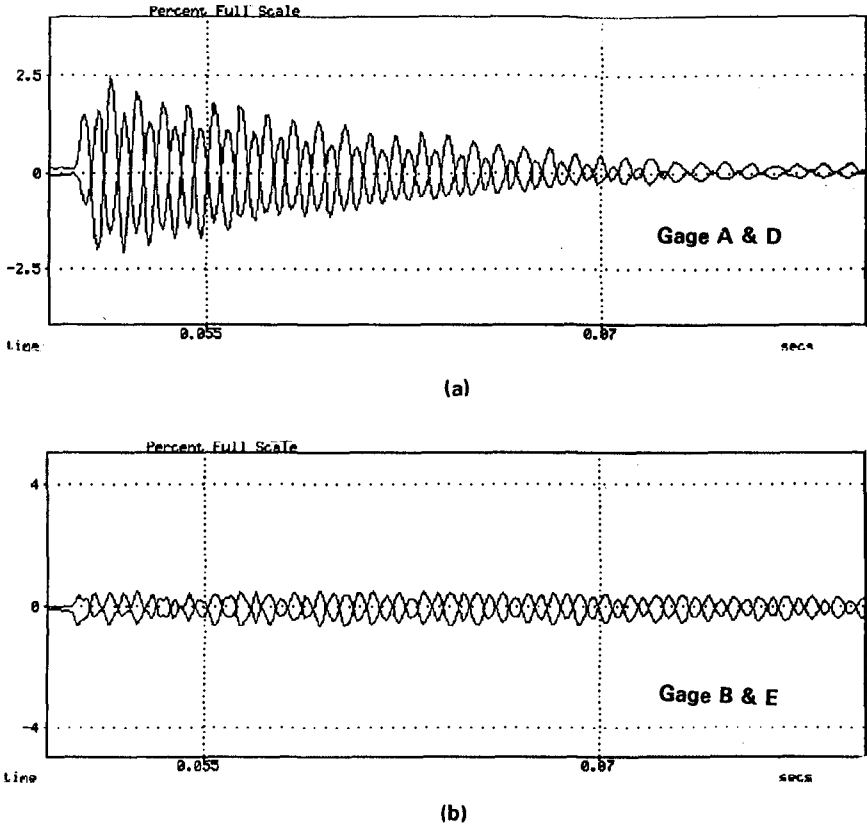


Figure 6. Typical impact signal. (a) signal from top and bottom gages. (b) signal from side gages

( $h/c = 0.0008$  to  $0.005$ ). But the region of interest in the drop tests is over those drop heights in the fully elastic range; in this case, the upper four drops. Figure 9 shows the results of a linear regression through these non-dimensional stresses as a function of the square root of the non-dimensional centroidal drop heights for both the shank and fluke. Theory indicates that the magnitude of impact stress is proportional to the square root of the drop height (Burcharth 1981, Melby and Turk 1994b), and these results support this impact scaling law reasonably well. The impact stresses found in the flukes also follow this scaling but are approximately 80% of those found in the shank.

The results indicate that impact stress scaling is proportional to the square root of the characteristic length scale, but the magnitudes of the impact stresses are significantly larger than those reported from prototype failure tests (Burcharth 1991). As discussed in Melby and Turk (1994b), this difference is very likely due to the weaknesses in uninstrumented prototype destructive dolos field tests, as discussed above. The prototype dolosse were dropped several times before cracks could be seen. Initial cracking and cylinder strength were used to define impact stress. Uncertainty in these tests can be due to scatter in levels and types of failure stresses, differences in the stiffness of the impacted bases for the various tests, failure stresses being not necessarily similar to test cylinder failure stresses, and assumptions about the actual strength and elasticity of the concrete at the time of the drop test.

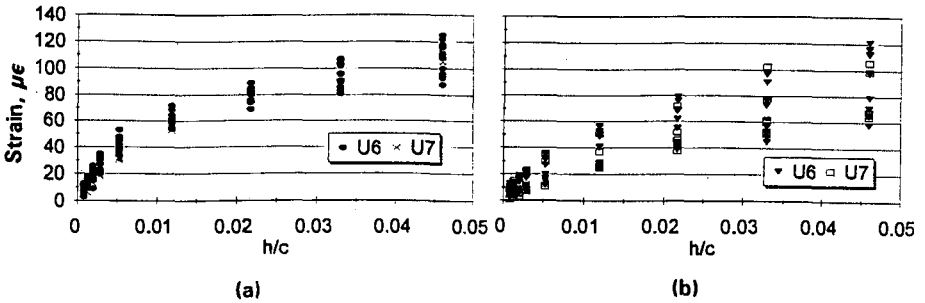


Figure 7. Record of all strains measurements from 9 drop heights. (a) Shank. (b) Fluke

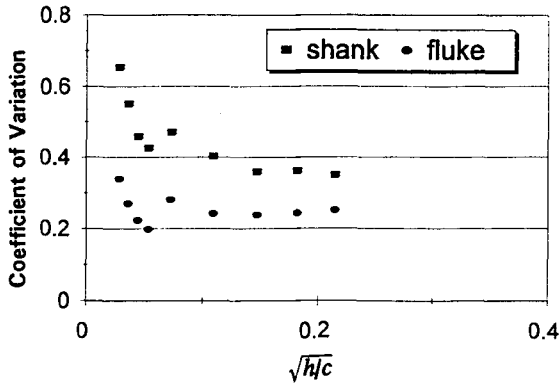


Figure 8. Coefficient of Variation for impact stresses in shank and fluke

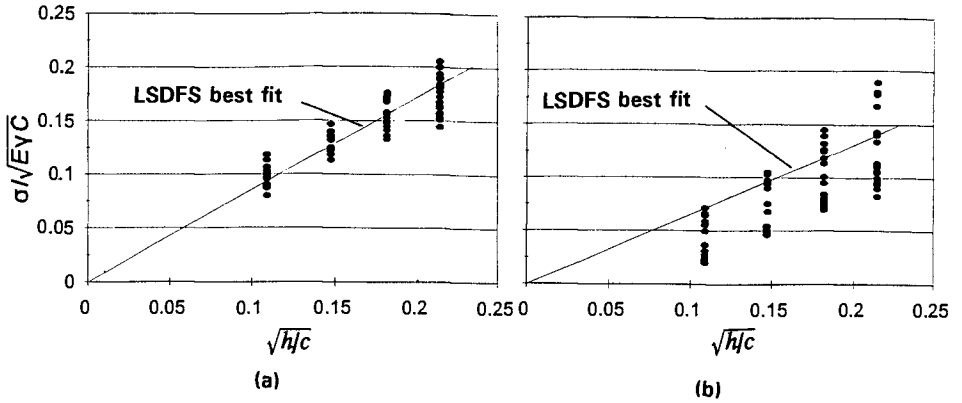


Figure 9. Nondimensional impact stress vs. Nondimensional centroidal drop height. (a) Shank. (b) Fluke

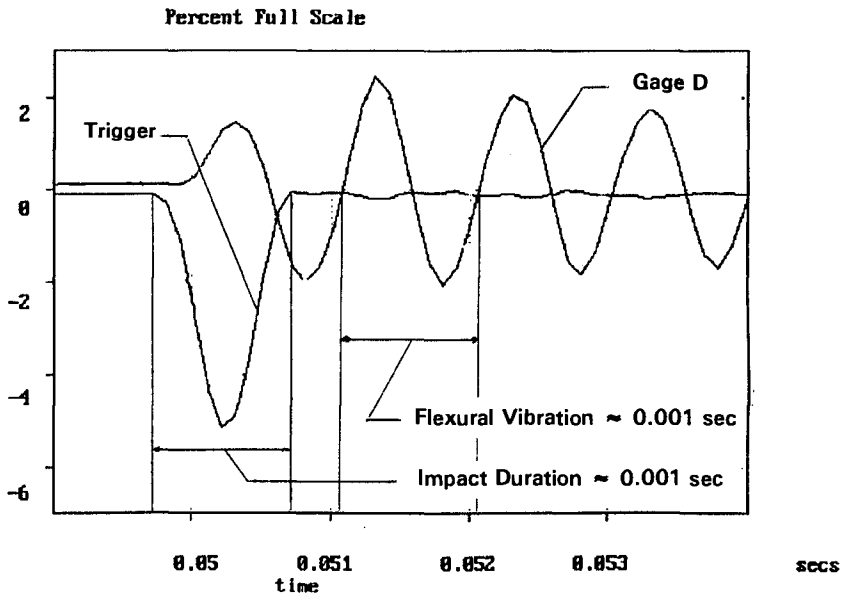


Figure 10. Comparison between impact duration recorded by trigger and flexural vibration recorded by top mounted strain gage (Gage D)

Melby and Turk (1994b) stated that the impact duration is governed predominately by the by the flexural response of the dolos. The impact duration was measured directly from a tip mounted strain gage. Figure 10 shows a raw data plot of an impact single from a drop height of 0.23 cm. The figure shows the duration of impact from the trigger to be nearly identical to the period of vibration recorded from a shank-mounted strain gage. This validates that the impact duration is governed by the flexural bending response of the unit and is equal to the inverse of the fundamental frequency of flexural vibration of the unit.

### Preliminary Flume Test Results

The intent of the flume tests was to quantify the maximum stresses in dolosse under wave loading. The model dolosse were sized based on small-scale model hydraulic stability tests results and the limitations of the wavemaker. The range of wave heights for the flume tests was chosen to produce a range of Hudson stability numbers,  $N_s$ , up to 4.6 ( $K_D$ 's up to 64). From the small-scale model testing, it was expected that dolos movement would achieve an upper limit of 4% rocking. In the small scale-tests, it was found that, at wave heights corresponding to  $N_s < 2.3$  ( $K_D < 8$ ), the dolosse generally do not move. At wave heights between  $N_s = 2.3$  and  $N_s = 2.9$ , dolosse that are not interlocked start to rock about on the slope. For  $N_s > 2.9$ , the movement of dolosse on slope becomes more unpredictable. Increasing the wave height may cause dolos to rock more violently, to move out of their original positions, groups of dolosse may become mobile, or the whole slope may slump.

The LSDFS dolosse, made from concrete, proved to be surprisingly more stable than their small-scale counterpart. Although it was previously felt that small scale models had little scale effects, the LSDFS tests showed dolosse stable up to  $N_s = 4.6$ . It was a rare case that 2% of the dolosse were rocking, and in general, for the more severe wave cases, only 1% rocking was observed. It was felt at the time that the higher surface friction on the large scale units caused the higher stability.

At present, a preliminary analysis of select records from the large volumes of impact data generated by the LSDFS (over 4 GB) has been accomplished. Impact response was recorded during 136 flume tests, and 10% of the impact records have been analyzed to-date. The records analyzed were from tests performed with monochromatic waves with periods ranging from 3 to 5 sec and wave heights to 1.4 m. The water depth for these tests was 1.5 meters.

Several plots are presented to show correlation, or the lack thereof, between impact stress and several typical wave parameters. In Figure 11a, the nondimensional impact stress,  $\sigma/(E\gamma C)^{1/2}$ , has been plotted against relative wave height,  $H/d$ , where  $H$  is incident wave height and  $d$  is depth. In general, one would expect the magnitudes of the impact stresses to increase with wave height; but little correlation has been found. Observing the tests, the authors noted that, for units with unstable boundary conditions, impacts occur at given wave particle velocities, regardless of the amount of incident wave energy. So, while it is certainly true that larger waves have more capacity for loosening stable armor units, waves below a given threshold have little capacity for loosening stable units and impact stresses will not, in general be a function of wave height. The data indicate that the stresses are related to the threshold of movement.

Figure 11b shows impact stress as a function of wave steepness,  $H/L_o$ , where  $L_o$  is the deep water wavelength. Stresses do not appear to be a function of the wave length.

Figure 11c shows impact stress as a function of Stability Number,  $N_s$ . This plot is similar to Figure 11a. The maximum stresses recorded were higher for the larger wave heights and higher stability numbers; but, in general, the mean stress and the mean stress plus one standard deviation was approximately the same for  $N_s$  between 3.0 and 5.0. Finally, the impact stresses are plotted as a function of the surf similarity parameter,  $\tan\alpha/(HL_o)^{1/2}$ , (Figure 11d), where  $\alpha$  is the structure slope angle. The effects of breaker

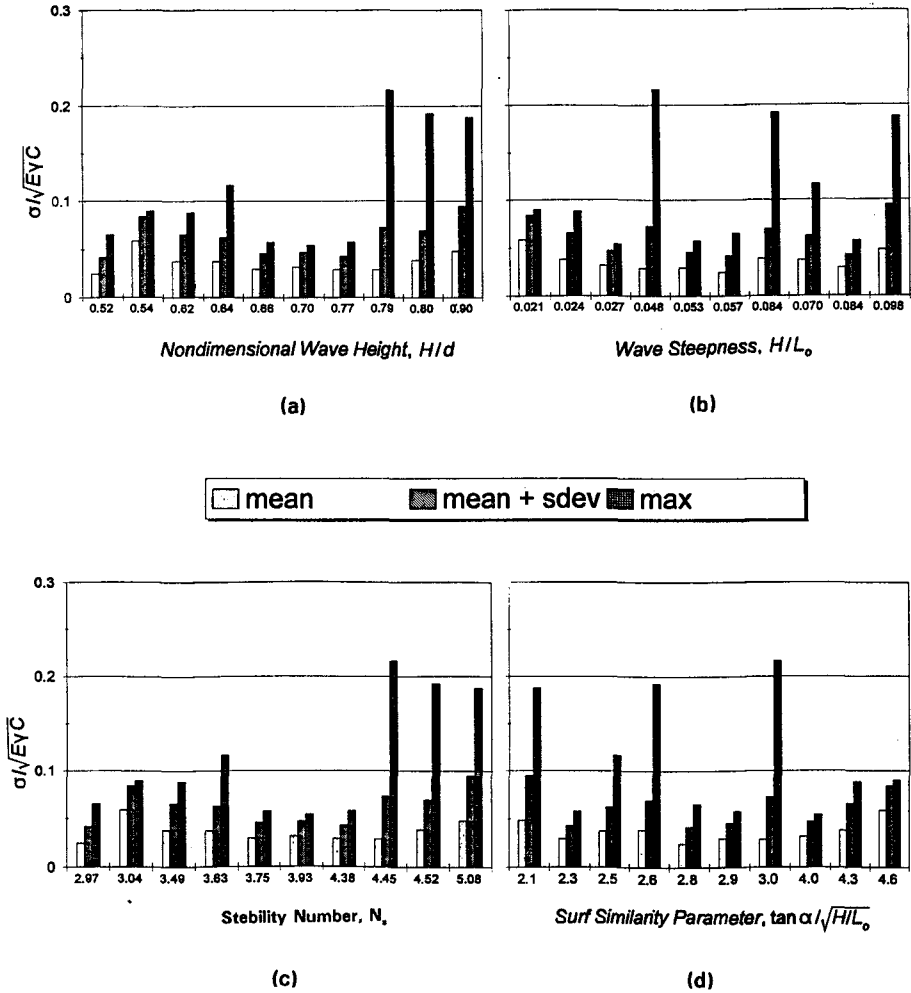


Figure 11. Nondimensional impact stress vs. (a) nondimensional wave height. (b) wave steepness. (c) Stability Number. (d) Surf Similarity Parameter.

type do not seem to effect the magnitudes of the impacts, with stress values approximately the same for both plunging and collapsing breakers.

At this point in the data analysis, trends are difficult to ascertain. It would be expected that large wave heights, plunging waves, and high energy content would all contribute to producing the largest impact stresses; but initial observations of the data do not show this to be the case. It seems that the magnitudes of the stresses are more predicated on the boundary conditions. The less stable the boundary conditions the more likely high impact stresses will occur, even in moderate wave conditions. This seems to allude to the fact that the integrity of a dolos armor slope is largely based on proper construction techniques, where no units are placed on slope without adjacent interlocking, as discussed by Melby and Turk (1994a).

This is made more significant by the magnitude of the impact stress over the broad range of wave conditions. While the tensile strength of concrete dolosse used in the LSDFS was approximately  $f't = 5.5$  MPa (or a nondimensional strength  $f't/(E\gamma C)^{1/2} = 0.34$ ), 12 dolosse were broken by wave action during the course of the experiment. Many dolos prototype structures have used concrete with tensile strengths around  $f't = 3.5$  MPa and have length scales of 5:1 to 8:1 relative to the LSDFS dolos. If the concrete strength for LSDFS has been scaled by these criteria and the impact scaling law, the reduced tensile strength for the LSDFS dolos would have been  $f't = 1.2$  to  $1.6$  MPa or  $f't/(E\gamma C)^{1/2} = 0.07$  to  $0.1$ . And in many cases, the mean impact stress plus standard deviation approaches or exceeds these values over the range of wave conditions. Also, in many of the records analyzed, the maximum stresses recorded are double this reduced tensile strength. The main point is, for unreinforced dolosse, unit-to-unit impact loading should not be permitted unless the resultant damage is deemed acceptable.

## SUMMARY AND CONCLUSIONS

The LSDFS allowed accurate measurement of structural response and quantification of the maximum stresses in dolosse for a wide range of boundary and loading conditions. The tests indicated that when a dolos nears its hydraulic stability threshold, at least 1%-2% of the units are rocking on slope. This rocking, and the associated unit-to-unit impact, produces impact stresses that, when combined with static and wave induced hydrodynamic stresses, can often be high enough to exceed the concrete strengths typically found in prototype dolosse. This can result in higher breakage levels than anticipated by conventional design. For even modest waves produced in the LSDFS, maximum tensile strains often exceeded  $80 \mu\epsilon$ . Scaled to prototype and converted to stress using Hookes Law and a dynamic modulus, these stresses would far exceed prototype concrete strength.

While data reduction and analysis of the substantial data set is ongoing, it is anticipated that these data will be incorporated into the Corps' probabilistic, reliability-based design program for concrete armor units, *PCARMOR*.

## ACKNOWLEDGEMENT

The work described in this paper was conducted as part of the Repair, Evaluation, Maintenance and Rehabilitation Research Program of the U.S. Army Engineer Waterways Experiment Station, US Army Corps of Engineers. The authors would like to express their gratitude to the following individuals for their contributions, comments,



and review of the LSDFS: Prof. Charles Sollitt, Oregon State University, Prof. Joseph Tedesco, Auburn University, Prof. Hans Burcharth of Aalborg University, Denmark, Mr. Joop Zwamborn from South Africa, and Prof. Fred Raichlen of the California Institute of Technology, Mr. Thomas Kendall, USAE San Francisco District, and Prof. Nobu Kobayashi of the University of Delaware. Permission to publish this paper was granted by the Chief of Engineers.

**REFERENCES**

- Anglin, C.D., et al., (1989). "The development of structural design criteria for breakwater armor units." *ASCE/WPCOE Sem. on Stres. in Conc. Ar. Un.*, ASCE, NY, NY.
- Burcharth, H.F., (1981). "Full-scale dynamic testing of dolosse to destruction." *Coastal Engr.*, Vol. 4
- Burcharth, H.F., et al., (1991). "On the determination of concrete armor unit stresses including specific results related to dolosse." *Coastal Engr.*, Vol. 15
- Howell, G.L., (1986). "A system for the measurement of the structural response of dolos armour units in the prototype." *The Dock and Harbor Auth.*,67(779)
- Markle, D.G., (1989). "Crescent city instrumented dolos model study," *ASCE/WPCOE Sem. on Stres. in Conc. Ar. Un.*, ASCE, NY, NY.
- Melby, J.A., et al., (1989). "An analytical investigation of static stresses in dolosse." *ASCE/WPCOE Sem. on Stres. in Conc. Ar. Un.*, ASCE, NY, NY.
- Melby, J.A. and G.F Turk, (1994a). "Concrete armor unit performance in light of recent research results." *ASCE/WPCOE Sem. on Case Histories of Design, Constr., and Maint. of Rubble Mound Struc.* ASCE, in publication
- Melby, J.A. and G.F Turk, (1994b). "Scale and modeling effects in concrete armor experiments," *ASCE Proc. 1st Int. Conf. on Role of L.S. Exp in Coas. Res.*, ASCE, NY, NY
- Melby, J.A. and G.F Turk, (1994c). "Large scale dolos flume study: Post-experiment report." *USAE WES TR-94-?*, in press, Vicksburg, MS, 39180
- Melby, J.A. and G.F Turk, (1995). "The CORE-LOC: optimized concrete armor." *Proc. 24th Int. Conf. on Coast. Engr.*, ASCE, NY, NY., in publication
- Scott, R.D., Turke, D.J., Baird, W.F., (1986). "A unique instrumentation scheme for measuring loads in model dolos units," *Proc. 20th Int. Conf. on Coast. Engr.*, ASCE, NY, NY.

**KEY WORDS:**

Rubble mound breakwater, concrete armor units, Dolosse, load-cell, strain gage

## CHAPTER 119

### **H<sub>o</sub> Parameter for Preliminary Design of Conventional Breakwater Structural Head. Data Analysis of Spanish North Coast Harbours**

\* Vicente Negro Valdecantos  
\*\* Ovidio Varela Carnero

\* Civil Engineer, Ph. D. Associate Professor. University of Madrid  
\*\* Civil Engineer, Ph. D. Head of Harbour Dpt. DRAGADOS.

### **SUMMARY**

The determination of the response of a Coastal Structures to waves is almost determined by model tests of using formulae fitted to model data. Using results of Aalborg University, 1987-88, and Collecting Spanish data from the North Coast, 1988, we approach for preliminary design the dimensionless wave height parameter,  $H_o$ , Van der Meer, 1988 for conventional breakwater, structural head, and start of damage and collapse of the structure.

The effect of wave length, storm duration, and the influence of the breakwater geometry, interlocking blocks and water depth will be include in the future for better calibration of Van der Meer parameter

### **1. INTRODUCTION**

The determination of the response of a Coastal Structure or a breakwater, trunk or head, to waves is almost always determined by model tests. Sometimes, Hydraulics Engineers use formulae fitted to model tests. The main problem depends on the stochastic nature of loads and random placement of the armour units in breakwater.

Brosen et al, 1974, demonstrated that the Hudson formula is not valid for complex interlocking types of armour blocks with respect the slope angle. Van der Meer, 1988, proposes the dimensionless wave height parameter,  $H_o$ ,  $H_s/\Delta D$ , to give the relationship between different structures and represents an important variable in a stability formula.

The agreement will be conclude:

$$\frac{u^2}{\Delta g D} \approx \frac{H_s}{\Delta D} = (\cotg \alpha \cdot K_D)^{1/3} = N_s$$

Shield parameter Van der Meer Hudson Brebner and Donelly

Using model tests of Aalborg University and collecting the Spanish Data, we approach for preliminary design the  $H_o$  parameter and

$$\frac{H^{2/3} \cdot L^{1/3}}{\Delta D}$$

for conventional breakwater, structural head, start of damage and collapse of the structure.

## 2. CLASSIFICATION OF RUBBLE MOUND STRUCTURES

Rubble mound structures can be classified by use of the static parameter,  $H_o$ ,

$$H_o = \frac{H_s}{\Delta D_{n50}}$$

where:

$H_s$  Significant wave height (m)

$\Delta$  Relative mass density (-)

$$\frac{\gamma}{\gamma_w} - 1 \quad \begin{array}{l} \gamma \text{ Specific weight of an individual unit (t/m}^3\text{)} \\ \gamma_w \text{ Specific weight of seawater (t/m}^3\text{)} \end{array}$$

$D_{n50}$  Nominal diameter (m)

Dynamically stable structures are characterized by the forming of a profile under wave attack. In this case, conventional breakwater can be classified with the combined wave height-wave period parameter  $H_o \cdot T_o$ , defined by,

$$H_o = \frac{H_s}{\Delta D_{n50}}, \text{ dimensionless wave height parameter}$$

$$T_o = T_m \cdot \sqrt{\frac{g}{D_{n50}}}, \text{ dimensionless wave period parameter}$$

As a simple remark, rubble mound structures can be classified (Fig. 1).

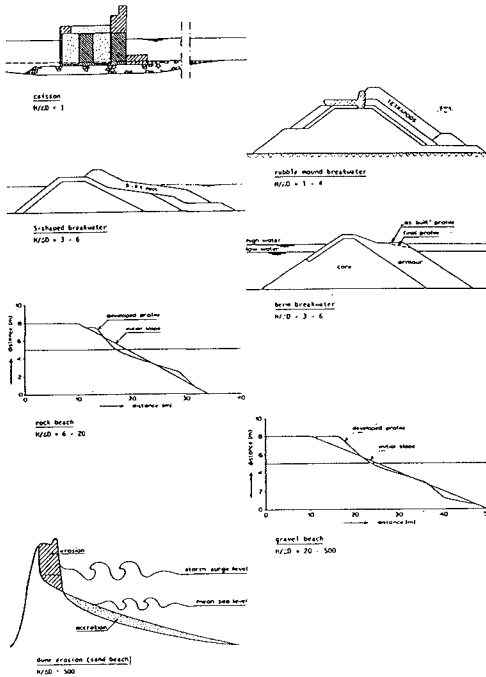


Fig. 1. Type of structure as a function of  $\frac{H}{\Delta D}$ , Van der Meer, 1988

- $H_o < 1$       Caissons, seawall, vertical breakwater. Instantaneous Failure.
- $1 < H_o < 4$       Conventional breakwater. Gradual Failure.
- $3 < H_o < 6$       Special breakwater, S shaped, berm

- $6 < H_o < 20$     Rock slopes. Nominal diameter relatively small.
- $15 < H_o < 500$     Gravel beaches.
- $H_o > 500$     Sand beaches.

The hydraulic stability can be classified including static and dynamic profiles,

- $H_o \cdot T_o < 100$     Static criteria
- $H_o \cdot T_o > 100$     Dynamic criteria

This classification is a great contribution to the total uncertainty of the coastal structures response and follows single estimation like Professor Suarez Bores 1968-74-78 and the evolution of breakwater structures, Goda and Tanimoto, 1991 (fig. 2).

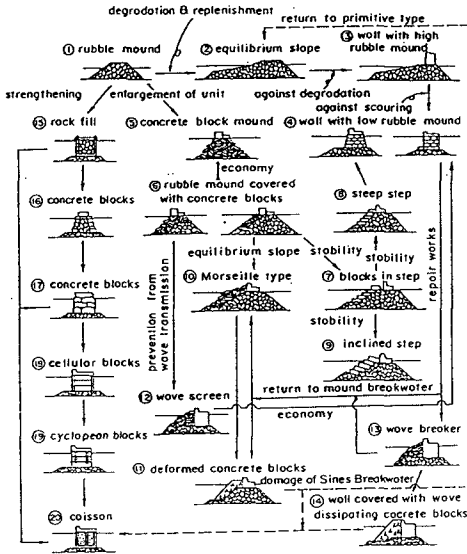


Fig. 2. Evolution of breakwater structures, Goda-Tanimoto, 1991

- Structural response and design
  - Deterministic
    - . Univariate:  $H_{1/n}$ , return period
    - . Multivariate:  $H_{1/n}$ , T, N, S, P, risk analysis
- Failure response
  - . Instantaneous failure
  - . Gradual failure
- Stochastic nature of the loads
  - . Conventional breakwaters,  $H_{1/n}$ . Gradual failure by the action of waves train.
  - . Rigid breakwaters,  $H_{max}$ , N - Collapse by the action of a single wave.
- Optimum design
  - . Risk analysis
  - . Economic analysis
  - . Stochastic analysis
  - . Multivariate risk analysis

Burcharth and Frigaard, Aalborg University, studied the front profile development, erosion and deformation of slopes, when exposed to oblique waves. Their range of tests correspond:

$$3,50 < H_0 < 7,10$$

the following stability factor values were proposed by Burcharth et al, 1988, for the start of significant transport of stones along the structures (angle of wave incidence  $\leq 30^\circ$ ).

	$\frac{H_s}{\Delta D_{n50}}$
. Trunks exposed to steep oblique waves	4,50
. Trunks exposed to long oblique waves	3,50
. Round heads	3

This research and study have been the basis to preliminary design of conventional breakwaters, structural head,  $1 < H_0 < 4$ , with a theoretical approach and using the long series of

Spanish Data from the North Atlantic Sea, the North Coast, and collecting model tests results.

### 3. DATA ANALYSIS AND ENGINEERING METHODS FOR PREDICTING THE DESIGN OF STRUCTURAL HEAD. START OF DAMAGE AND COLLAPSE OF THE STRUCTURE. SPANISH NORTH COAST EXAMPLES.

The waves reaching the Cantabrian Sea Coast, Spanish North Coast, are generated in the North Atlantic by the action of extratropical storm. The polar mass oscillations through the year define the path of the storms through the Bay of Biscay. Under such conditions, the winds are from West to North, including North West and NNW with the dominant gradient wind speed of 40 m/sg.

In that case, there are maximum frequency and intensities of waves, reaching values of significant wave height over ten meters with peak period of eighteen seconds. This is representative of the rough conditions in deepwater.

The studies reported here were done using the Spanish Data of conventional breakwaters, more than 100 ports and harbours, in the Cantabrian Sea Coast, and with a theoretical approach, obtained the following results,

Tetrápodos	2	"en desorden"	1,20	1,25	1,5
"	2	"	1,30	1,35	2,0
"	2	"	1,80	1,90	3,0
Tribars	2	"en desorden"	1,10	1,15	1,5
"	2	"	1,15	1,20	2,0
"	2	"	1,30	1,35	3,0
Dolos	2	"en desorden"	1,50	1,50	2,0
"	2	"	1,60	1,65	3,0
Cubo modificado	2	"en desorden"	-	1,55	1,5 a 3,0
Hexápodos	2	"en desorden"	1,65	1,35	1,5 a 3,0
Tribars	1	uniforme	1,60	1,60	1,5 a 3,0

Fig. 3. Coefficients for conventional breakwaters head



Type of Breakwater	Weight of the main armour layer (t)	Nominal Diameter (m)	Significant wave height (m)	H <sub>o</sub> (-)
Fuenterrabía, quarystone	9 t	1,50 m	5,00 m	2,04
Orio, blocks $\gamma = 2,80$	13 t	1,66 m	5,85 m	2,02
Getaria, quarystone	20 t	1,96 m	6,63 m	2,12
Bermeo, 1 <sup>a</sup> Phase	50 t	2,75 m	7,13 m	1,93
Bermeo, 2 <sup>a</sup> Phase	85 t	3,30 m	9,00 m	2,03
Bilbao, Punta Lucero	150 t	4,00 m	10,10 m	1,88
Lastres	40 t	2,55 m	6,80 m	1,98
Gijón	120 t	3,70 m	9,60 m	1,94
Candás (Failure)	27 t	2,25 m	4,95 m	1,64
San Esteban	125 t	3,70 m	8,75 m	1,77
Cudillero	60 t	2,92 m	8,00 m	2,04
Burela	72 t	3,10 m	7,45 m	1,79
San Ciprián	90 t	3,35 m	8,90 m	1,98
Cillero	28 t	2,25 m	6,25 m	2,06
Cariño, quarystone	12 t	2,05 m	5,00 m	1,96
Malpica	120 t	3,68 m	10,70 m	2,16
Lage	20 t	2,05 m	5,00 m	1,96
Finisterre	15 t	1,85 m	5,00 m	2,09
Panjón	5 t	1,28 m	3,18 m	1,85

Another conventional breakwaters were designed after this preliminary analysis in the Spanish North Coast. The results were:

Type of Breakwater	Weight of the main armour layer (t)	Nominal Diameter (m)	Significant wave height (m)	H <sub>o</sub> (-)
Zurriola, blocks	45 t	2,55 m	8,20 m	1,96
Cala Bens, La Coruña	125 t	3,75 m	10,00 m	1,98

The relative mass density coefficient ( $\Delta$ ) oscillate between 1,63 for quarrystone, 1,34 for concrete blocks, tetrapod, acropod ... etc, and 1.731 for high density natural blocks.

This analysis reported before is relation with the classic point of view for calculating head in conventional breakwater,

$$W_{\text{head}} = \text{Coefficient } (> 1,00) \times W_{\text{Hudson}}$$

The dimensionless coefficient accounts for all variables like (Fig. 3)

- Shape of the armour layer
- Number of units of the main armour layer
- Manner of placing armour layer
- Type of wave attacking structure (breaking or nonbreaking)
- Slope

Looking at the statistics of the present analysis and "only" for preliminary design in conventional breakwater head, start of damage, we can conclude in first step, fitting the model with nature test (Fig. 4-9),

$$H_o = \frac{H_s}{\Delta D_{Dn50}} \approx 2,00$$

Iribarren's model tests, 1965, presented in PIANC Congress Stockolm, demonstrated the evolution of a slope affected with groups of waves, obtaining the complete results of the evolution of damage in the armour layer of a conventional breakwater. The three phases are:

- Total stability
- Partial stability, start of damage
- Inestability, moderate damage to collapse of the structure

Stablishing the state of damage under the action of a monochromatic wave train, the slope is indefinite and the units of the main armour layer are quarrystone, concrete blocks and tetrapod (Fig. 10).

The results of damage levels with two diameter thick armour layer, Van der Meer, 1988, show the limits of the adimensional parameter  $S = A/D^2$ , a cross sectional eroded area, D nominal diameter of the armour layer (Fig. 11).

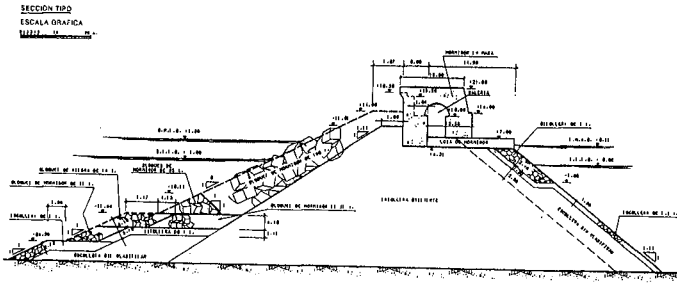


Fig. 4. Cross section Bilbao breakwater

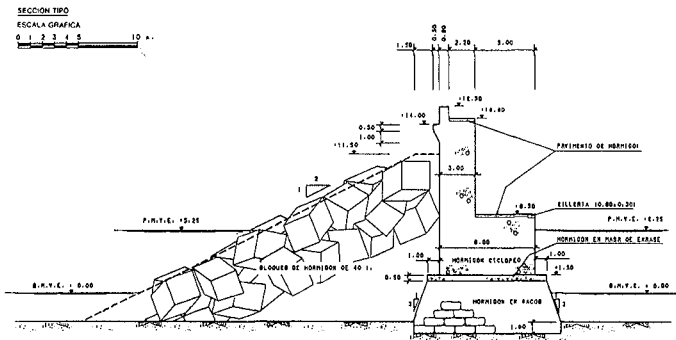


Fig. 5. Cross section Lastres breakwater

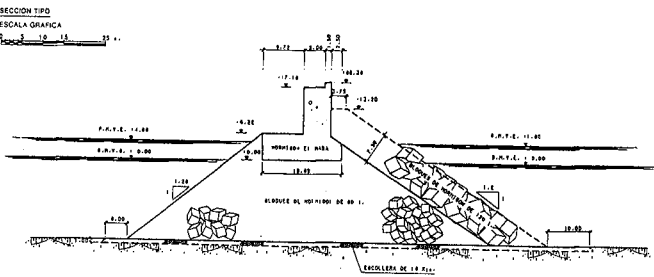


Fig. 6. Cross section principe de Asturias, Gijón breakwater

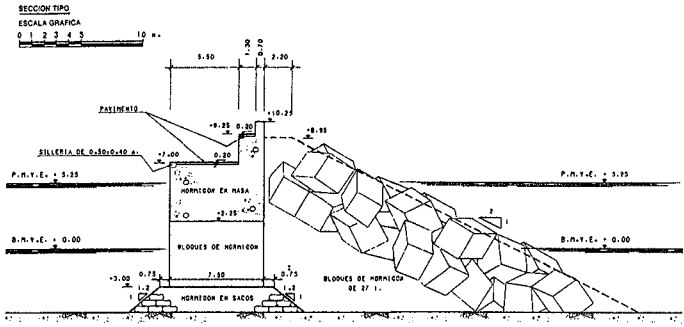


Fig. 7. Cross section Caudas breakwater

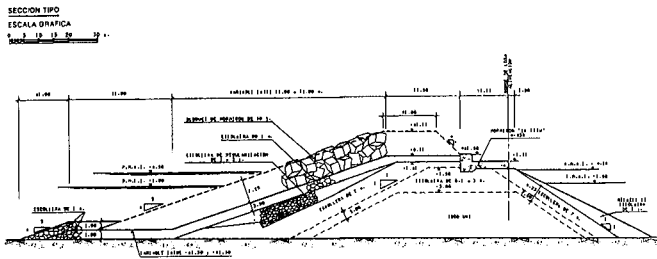
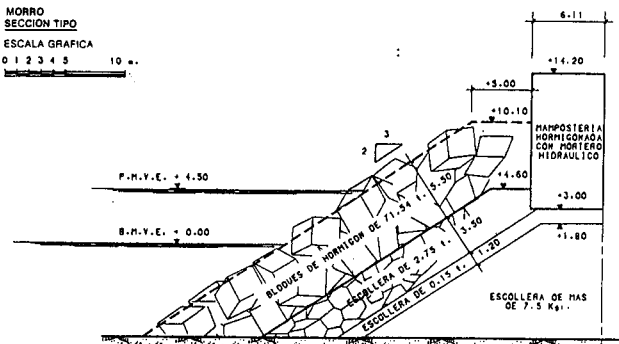


Fig. 9. Cross section San Ciprian breakwater

Type of armour layer	Slope	Damage Levels		
		Start of damage	Moderate damage	Filter visible
Stone armour layer	1,5/3,0	S = 2	S = 4/8	S $\geq$ 8/12
Block	1,5/2,0	Nod = 0	Nod=0,50/1,50	Nod = 2
Tetrapod	1,50/1	Nod = 0	Nod=0,50/1,00	Nod=1,50
Acropod	1,33/1,50	Nod = 0	---	Nod=0,50

Losada et al (1986) defined three hydrodynamic damage criteria,

1. Incipient damage
2. Iribarren's damage
3. Destruction

In order to be more precise, another stage of damage is included as a visual response, it is called incipient destruction, Vidal et al (1991). For a mound breakwater consisting of a main layer, secondary layer and core,  $P \approx 0,40$ , the definitions of the four damage criteria are as follows:

1. Initiation of damage. This level of damages defines the condition attained when a certain number of armour units are displaced from their original position to a new one at a distance equal to or larger than a unit length. Holes larger than average porous size are clearly appreciable.
2. Iribarren's damage. This damage occurs when the extension of the failure area on the main layer is so large that the wave action may extract armour units placed on the lower layer of the main armour layer.
3. Initiation of destruction. A small number of units, two or three, in the lower armour layer are forced out and the waves work directly on pieces of the secondary layer.
4. Destruction. Pieces of the secondary layer are removed. If the wave height does not change the mound will definitely be destroyed and it will cease to give the level of service defined in the design. It is called Filter visible.

As a consequence, for a preliminary design of mound breakwaters, and start of damage, we propose,

$$H_o = \frac{H_s}{\Delta D_{n50}} = 2,00$$

After the model tests performed by Iribarren, 1965, the medium relationship between the wave height of start of damage and the wave height of destruction or filter visible, is equal for stone armour layer, blocks and tetrapods and the value is 0,62.

Using the adimensional parameter for preliminary design and start of damage,  $H_o \approx 2,00$  and with the relation between the wave height start of damage and filter visible-destruction, the value of  $H_o$  will be,

$$\frac{H_{start\ of\ damage}}{H_{filter\ visible,\ destruction}} = 0,62$$

$H_o \approx 1,25$  Filter visible, collapse of structure thus, the following point will emphasized, with the concept of weight of the main armour layer,

$$W_{destruction} = \left(\frac{1}{0,62}\right)^3 W_{start\ of\ damage}$$

$$W_{destruction} = 4,10 W_{start\ of\ damage}$$

The results with oblique incidence do not show the same value for every Kind of armour piece, obtaining relation of 0,69 in rip-rap, armour layer with stone, and 0,73 with blocks and tetrapods.

However, the first analysis for a preliminary design can be consider stable.

The effect of wave length, storm duration, and the influence of the breakwater geometry, interlocking blocks, and water depth,

$$H_o = \frac{H_s}{\Delta D_{n50}} = 2,00 \quad \text{Start of damage}$$

$$H_o = \frac{H_s}{\Delta D_{n50}} = 1,25 \quad \text{Filter visible, destruction}$$

The effect of wave length, storm duration, and the influence of the breakwater geometry, interlocking blocks, and water depth, slope and other factors will be search in a future. Model test will provide the following conclusions,

$$H_o = \frac{H_s}{\Delta D_{n50}} = \frac{H_s^{2/3} \cdot L^{1/3}}{\Delta D_{n50}} = (\cot \alpha \cdot K_D)^{1/3} = N_s$$

$$\frac{H_s^{2/3} \cdot L^{1/3}}{\Delta D_{n50}} \cdot f(N)$$

where,

- L Wave length,  $\frac{1}{25} < \frac{d}{L} < \frac{1}{2}$  (m)
- N Number of active waves (-)
- $\alpha$  Slope of the breakwater ( $^\circ$ )
- $K_D$  Stability coefficient, Hudson (-)
- $N_s$  Stability coefficient, Brebner and Donelly (-)
- $H_o$  Van der Meer's parameter (-)
- $H_s$  Significant wave height (m)
- $D_n$  Nominal diameter (m)

$$Dn = \sqrt[3]{\left(\frac{W}{\gamma}\right)},$$

W Weight of an individual unit of the main armour layer (t)

$\gamma$  Specific weight of an individual unit (t/m<sup>3</sup>)

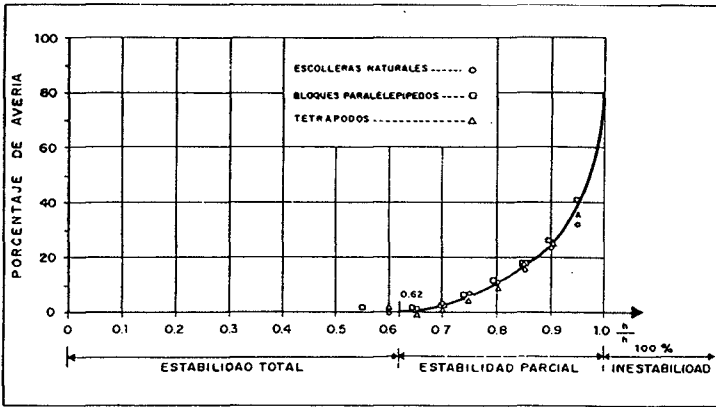


Fig. 10. Stability curve, Iribarren, 1965

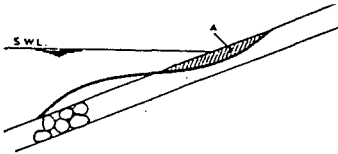


Fig. 11. Value of parameter "S", A cross sectional eroded area; D, nominal diameter of the armour layer

4. CONCLUDING REMARKS

According the model tests of Burcharth and Frigaard, and the data analysis and only for preliminary design and of no other more qualified information is available, the Spanish experience in the Cantabrian Sea Coast recommends for conventional breakwater, structural head, the value of the dimensionless wave height parameter  $H_o = H_s/\Delta D$ .



$$H_o = \frac{H_s}{\Delta D_{n50}} \approx 2,00 \quad \text{Start of damage}$$

$$H_o = \frac{H_s}{\Delta D_{n50}} \approx 1,25 \quad \text{Destruction, collapse}$$

The effect of wave length, storm duration, and the influence of the breakwater geometry, interlocking blocks and water depth are now in study and they will be include in the future as a function of L, N, D, H<sub>s</sub>, D, d and α.

## 5. REFERENCES

1. Inventario de Diques de Abrigo. Tomo I. MOPU. 1988.
2. Rock slopes and gravel beaches under wave attack. J.W. Van der Meer. Delft Hydraulics. 1.988.
3. Historical developments of breakwaters design. Y. Goda et al. I.C.E. 1991.
4. Análisis multivariado. P.S. Bores. 1980.
5. Random seas and design of maritime structure. Y. Goda. 1985.
6. Damage and repair work performed on some mound breakwaters in Spain. M. Losada et al. I.C.E. 1991.
7. Design innovation including recient research contributions. H.F. Burcharth. I.C.E. 1991.
8. On 3 - dimensional stability reshaping breakwaters. H.F. Burcharth y P. Frigaard. CERC. 1988.
9. Stability of Mound Breakwater's Head and Trunk. Vidal, C, Losada, M.A. y Medina, R. 1991. Journal of Waterway, Port, Coastal and Ocean Engineering. ASCE. Vol. 117. N° 6. Nov.Dec.

## CHAPTER 120

# Numerical Modelling of Breaking Wave Impacts on a Vertical Wall

N. T. Wu \*      H. Oumeraci †      H.-W. Partensky ‡

### Abstract

The impact processes on a vertical wall resulting from breaking waves are numerical simulated. Two dimensional incompressible viscous flow which is governed by the Navier-Stokes Equations and the continuity equation is solved by a finite difference scheme based on the Volume of Fluid (VOF) concept. Some comparisons with experimental results reveal that the present model is able to simulate the impact process with negligible air entrainment not only qualitatively but also quantitatively well. Although the impact pressure of a plunging breaker with non-negligible air entrainment can not be quantitatively well simulated by this model due to the restriction of the incompressible flow, the wave kinematics is still well simulated.

## 1 Introduction

Breaking waves represent the major cause for the damage of vertical face breakwaters. The stability of such structures is in fact a dynamic problem. The solution of this problem requires among others a detailed knowledge of the impact loading; i.e. the spatial and temporal distribution of the pressure induced by the breaking waves on the structure must be determined. To date, no theoretical approach for this problem is available. On the other hand, small-scale model investigations suffer from scale effects, so that no definite quantitative conclusions can be drawn. Even results from large-scale model tests recently conducted in super-wave tanks seem to be affected to some extent by scale effects. In addition, the use of such large facilities is so expensive and so time consuming that a reasonable parameter study cannot be effectively performed. Therefore, more attention has been paid within the last 15 years to numerical methods.

Most of the existing numerical model for the simulation of breaking wave impact loads are based on potential flow theory. These methods are however unable to describe the

---

\*Dr. -Ing., Tainan Hydraulics Laboratory, National Cheng Kung University, Tainan, Taiwan, R.O.C.

†Prof. Dr. -Ing., Univ. Professor, Techn. Univ. Braunschweig, Beethovenstr. 51a, 38106 Braunschweig, Germany

‡Prof. Dr. -Ing., Dr. phys., Prof. em. formerly Director of Franzius-Institut, Univ. Hannover, Germany

whole breaking and impact process due to the great distortion of the flow around the free surface interfaces which will not remain irrotational.

Therefore, the Volume of Fluid (VOF) (Nichols, et al., 1980) concept has been adopted here to develop a numerical model which can describe the complex free surface associated with breaking waves and the integral history of the impact pressures and forces on a vertical wall with a foreshore slope. The present paper is principally intended to present some of the results of the Ph.D. work of the first author. It will give a brief description of the developed viscous incompressible fluid model, but will particularly focus on the discussion of the results, as compared to experimental data and observations. Further developments of the model which are planned for the next years are finally outlined (air entrainment/ entrapment).

## 2 Governing Equations

A viscous incompressible 2D-flow is considered and the governing equations are the continuity equation:

$$\frac{\partial u}{\partial x} + \frac{\partial v}{\partial y} = 0 \quad (1)$$

and the Navier-Stokes Equations:

$$\frac{\partial u}{\partial t} + u \frac{\partial u}{\partial x} + v \frac{\partial u}{\partial y} = -\frac{1}{\rho} \frac{\partial p}{\partial x} + \nu \left( \frac{\partial^2 u}{\partial x^2} + \frac{\partial^2 u}{\partial y^2} \right) + g_x \quad (2)$$

$$\frac{\partial v}{\partial t} + u \frac{\partial v}{\partial x} + v \frac{\partial v}{\partial y} = -\frac{1}{\rho} \frac{\partial p}{\partial y} + \nu \left( \frac{\partial^2 v}{\partial x^2} + \frac{\partial^2 v}{\partial y^2} \right) + g_y \quad (3)$$

where:

$\rho, \nu$  are the density and the kinematic viscosity of the fluid, respectively.

$u, v$  are the velocity components in x and y direction, respectively.

$g_x, g_y$  are the x and y components of the gravitational acceleration.

p is for pressure and t is for time.

The computational domain and the boundary conditions are shown in Fig. 1. At the free surface, the pressure p should be continuous and p is therefore equal to the atmospheric pressure  $p_a$ . At the impermeable vertical wall, the free-slip condition ( $\frac{\partial v}{\partial x} = 0$ ) and the no-flux condition ( $u=0$ ) must be fulfilled.

For the inflow boundary conditions, any wave theory can be used to prescribe the surface elevation  $\eta(t)$  and the velocity components  $u(t)$  and  $v(t)$ . In this study, the linear wave theory, the second order solitary wave theory and the cnoidal wave theory of Keulegan and Patterson (Wiegel, 1960) are used. On the other hand, in order to keep the computational domain as small as possible, the weakly reflecting boundary condition (Delft Hydraulics, 1991) will be implemented. This allows the reflected wave to flow out the computational domain without inducing undesirable disturbance to the incident wave. The following free-slip condition for a slope is derived and considered in the model for the impermeable foreshore slope:

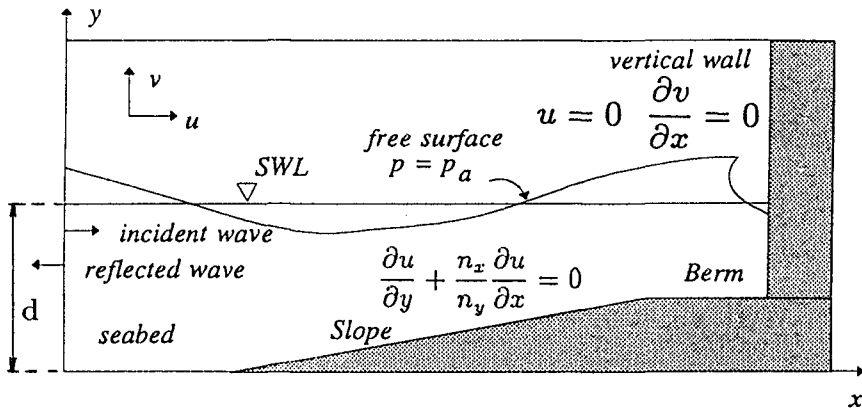


Figure 1: Computational Domain and Boundary Conditions

$$\frac{\partial u}{\partial y} + \frac{n_x}{n_y} \frac{\partial u}{\partial x} = 0 \tag{4}$$

where  $n_x$  and  $n_y$  are the components of the normal vector  $\vec{n}$  in  $x$  and  $y$  direction, respectively.

The governing equations are numerically solved by using a finite difference scheme incorporated with the Volume of Fluid (VOF) concept developed by Nichols et al. (1980) which deals with the free surface description. In this technique a function  $F(x,y,t)$  which describes the fractional volume of fluid in the mesh cells is included. The free surface can therefore be described according to the value of  $F$  in the mesh cells. Besides, the kinematic free surface boundary condition can be satisfied approximately by including the following transport equation of  $F$ :

$$\frac{\partial F}{\partial t} + \frac{\partial Fu}{\partial x} + \frac{\partial Fv}{\partial y} = 0 \tag{5}$$

Physically, this means that the  $F$  function moves with the flow motion.

### 3 Computational Results

#### Nonbreaking Waves

First of all, nonbreaking waves are numerically simulated in order to verify that the present model is able to simulate correctly nonbreaking waves not only qualitatively but also quantitatively. This will then offer a reasonable working platform for simulating the more complicated breaking waves. Two cases are considered for achieving this goal, namely, solitary wave run up on a vertical wall and the formation of standing waves.

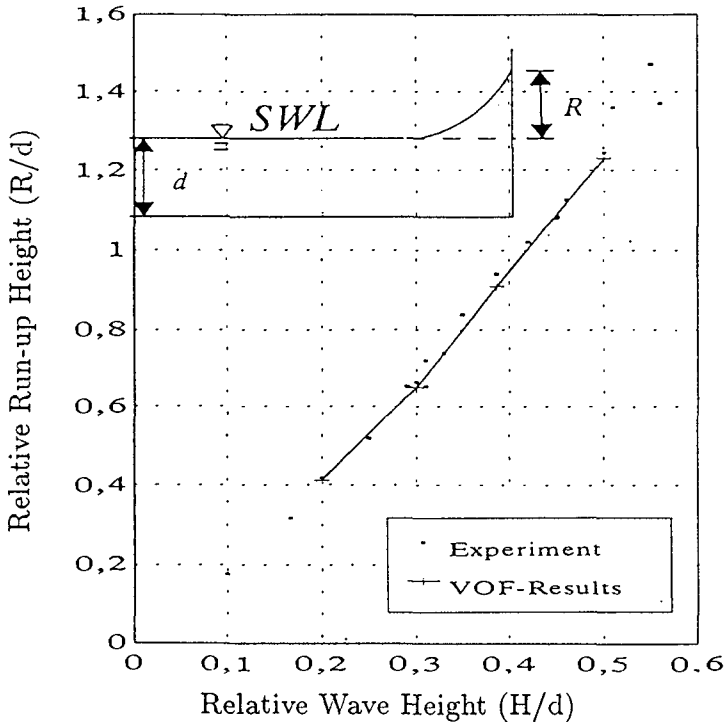


Figure 2: Comparison of Experimental and Computed Run-up Heights of Solitary Waves at a Vertical Wall

**Solitary Wave Run Up on a Vertical Wall**

Solitary waves propagating on a horizontal bed toward a vertical wall are first taken into account in order to verify that the free surface boundary condition is well handled in the present model. The second order solitary wave theory of Laitone(1960) is considered for incident waves. Solitary waves with relative wave heights  $H/d = 0.2, 0.3, 0.4$  and  $0.5$  are considered.  $H$  is the wave height and  $d$  the water depth.

The computed results for the relative run up height  $R/d$  of solitary waves for different wave heights are compared with the experimental results from Street and Camfield(1966) A very good agreement between the computational and experimental results is shown in Fig. 2.

**Standing Waves**

In order to verify that the weakly reflecting boundary condition is well implemented in the present model, incident waves propagating toward a vertical wall with and without a foreshore slope are therefore taken into account. Due to the impermeable vertical

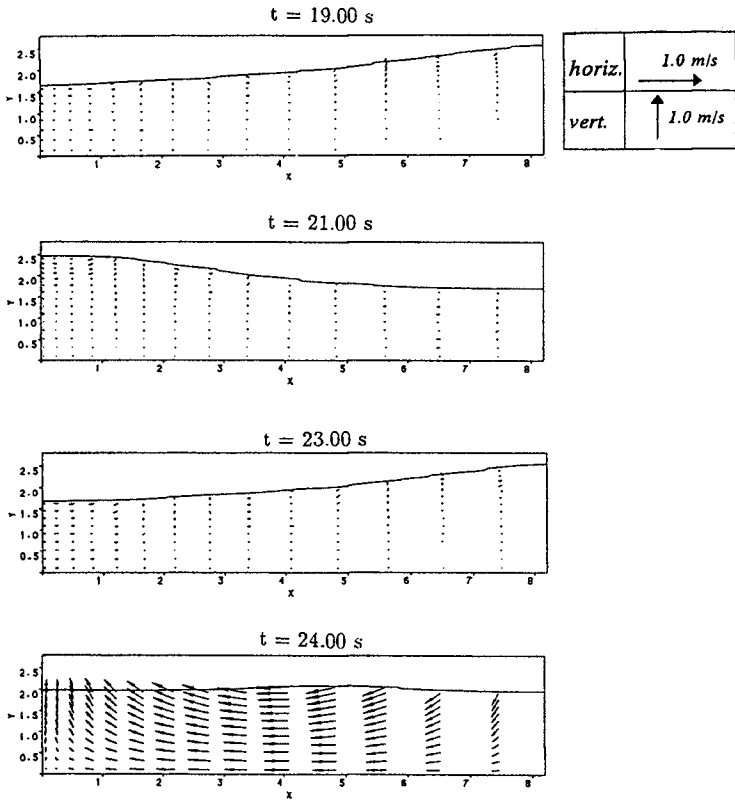


Figure 3: Numerical Simulated Standing Waves( $H=0.4 \text{ m}$ ,  $T=4.0 \text{ sec}$ ,  $d=2.0 \text{ m}$ )

wall, standing waves are expected to appear once the implemented weakly reflecting boundary condition can successfully let the reflected wave flow out the computational domain without inducing any unexpected re-reflection. The wave parameters used for this numerical test are:

- Incident Wave Height  $H = 0.4 \text{ m}$ ; Wave Period  $T = 4.0 \text{ sec}$ ; Water Depth  $d = 2.0 \text{ m}$

Airy wave theory is used for the incident waves. The wave length can be calculated as about  $16.2 \text{ m}$ . The computational domain is  $8.2 \text{ m} \times 2.8 \text{ m}$  and consists of a non-uniform grid with  $40 \times 20$  cells. The antinode is located at a distance  $nL/2$  ( $n=0,1,2, \dots$ ) from the vertical wall. Therefore, the second antinode should be located near the other side of the computational domain. The numerical simulated standing wave at times  $t=19.0$ ,  $21.0$ ,  $23.0$  and  $24.0$  second are shown in Fig. 3. It is seen that a standing wave with also 4 second of period appeared. On the other hand, the numerically simulated pressure distribution of a standing wave on a vertical wall is compared with the theoretical

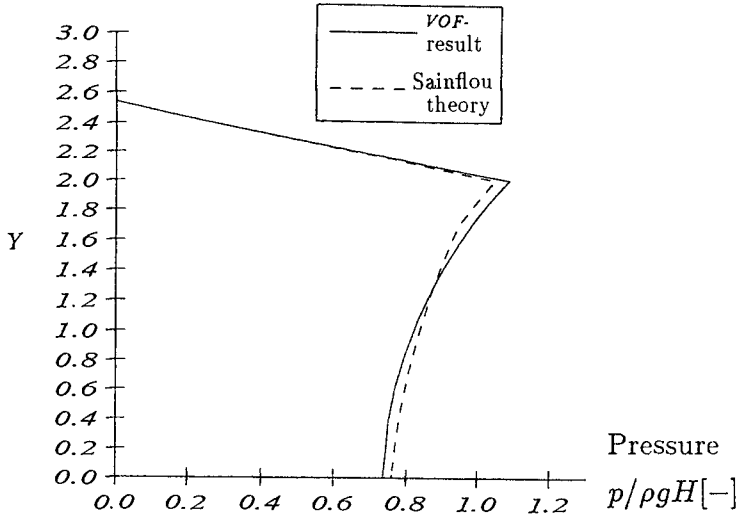


Figure 4: Pressure Distribution of Standing Wave on a Vertical Wall

results developed by Sainflou (Horikawa, 1978), and a very good agreement is shown as in Fig. 4.

### Breaking Waves

Four types of breaking waves impacting on a vertical wall are distinguished by Hattori et al. (1994):

- Flip-Through type breaker
- Impact of an almost vertical breaker front on the wall with a thin air layer
- Impact of a plunging breaker on the wall with a small air pocket
- Impact of a plunging breaker on the wall with a large air pocket

The four breaker types are shown as in Fig. 5 schematically. The term "Flip-Through" was first introduced by Cooker and Peregrine (1990). This kind of impact process contains either very few or no entrapped air and the impact pressure originates from the large flow acceleration due to the concentration of flow adjacent to the vertical wall. The impact process from (b) to (d) indicates an increasing air content.

These four types of breaking waves and the resulting pressure distribution on the vertical wall are numerically simulated. The experiments by Takahashi et al. (1983) are considered for comparison, since pictures of breaking processes at different stages were recorded which can be well compared with the numerical simulated breaking processes.

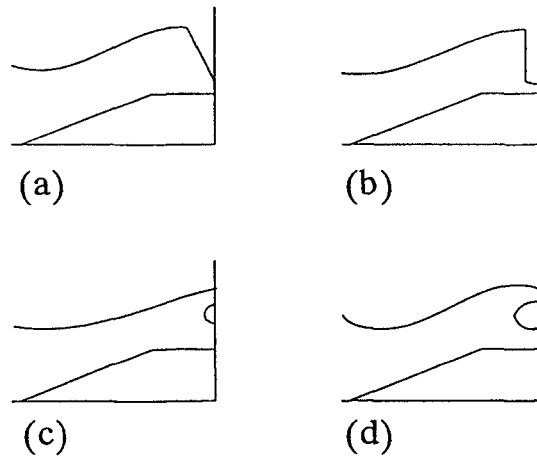


Figure 5: Schematized Breaker Types Simulated by the Numerical Model

Besides, different breaking wave impact can be systematically obtained in these experiments by simply changing the berm length in front of the vertical wall.

The wave parameters of the series of experiments which are also used for numerical simulation are

- Wave height  $H$  in front of the berm = 0.351 m
- Wave period  $T = 3$  sec
- Water depth  $d = 0.8$  m

The berm lengths considered in the numerical simulation are  $B = 0.25$  m, 0.50 m, 0.75 m and 1.25 m, respectively. The berm height is 0.5 m and the slope is 1:10. The computational domain is 7.0 m  $\times$  1.5 m and consists of a nonuniform grid with 150  $\times$  40 cells. The smallest cell width is 0.02 m and is located on the wall side and the smallest cell height is 0.02 m and is located on the mean water level.

The wave theory to be used in the numerical simulation corresponding to the wave parameters is the cnoidal wave theory. Among various existing mathematical description of cnoidal wave theories, the theory developed by Keulegan and Patterson (1940) is finally taken as the most appropriate, as recommended by Le Méhauté et al. (1968). The detailed mathematical description of the related components like the surface elevation  $\eta$ , the velocity components  $u$  and  $v$  etc. can be found in Wiegel(1960).

The first case to be considered is the "flip-through" type of breaking waves. The photographs recorded by Takahashi et al. (1983) refer to Photo 1(2) of the original paper. The numerical simulated breaking processes of flip-through with both of the free surface profile and velocity vector field are shown as in Fig. 6. Only a part of the computational domain is presented in this figure,  $x$  coordinate ranges from 3.5 m to 7.0 m and



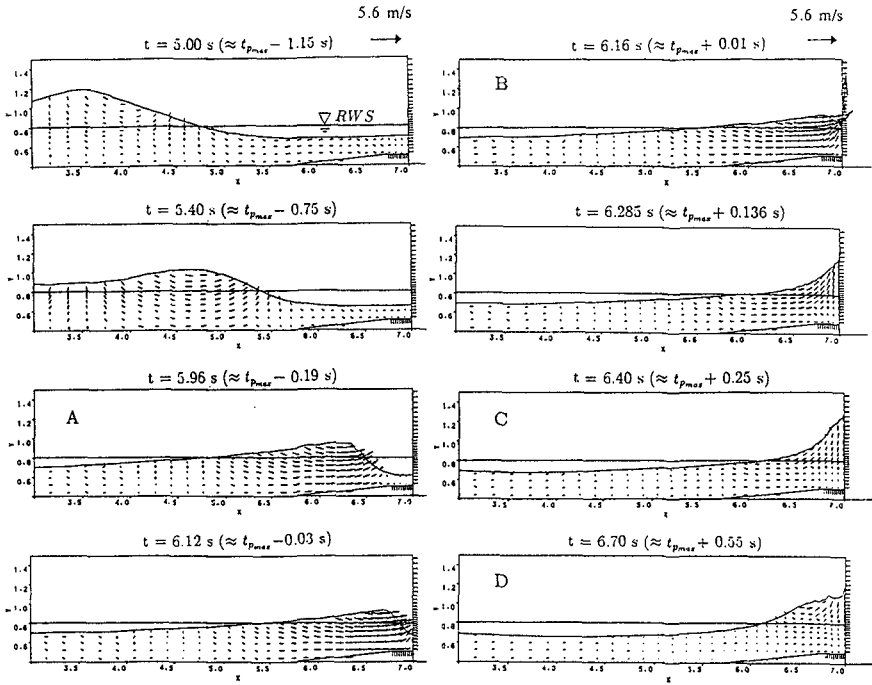


Figure 6: Computed Wave Profiles and Velocity Fields for the Flip-Through Breaker Type

the y coordinate ranges from 0.4 m to 1.5 m. After the comparison is made with the photographs taken by Takahashi et al. (1983), it is found that the numerical simulated flip through impact process agree qualitatively with the experiment.

The time history of the numerical simulated impact pressure is given in Fig. 7. The numerical simulated results agree not only qualitatively but also quantitatively well with the experimental results refer to Takahashi et al.(1983). The time history of the total force obtained by integrating the pressure distribution is shown as in Fig. 8. The characters A, B, C and D in Fig. 7 and 8 correspond to the A, B, C and D of the breaking wave processes shown in Fig. 6. It is worthwhile to mention that the point C in Fig. 8 which is the trough of the force history corresponds to the maximum run-up height of the impact process shown in Fig. 6. This phenomenon has already been pointed out experimentally by Mitsuyasu (1962) which also support the numerical simulated results.

For the other three breaker types, the numerically simulated free surface evolution of the other three breaking processes still agree qualitatively well with the photographs of the experiments. Fig. 9 is the numerical simulated breaking processes of the impact process-almost vertical breaker front with a thin air layer. The photographs of this

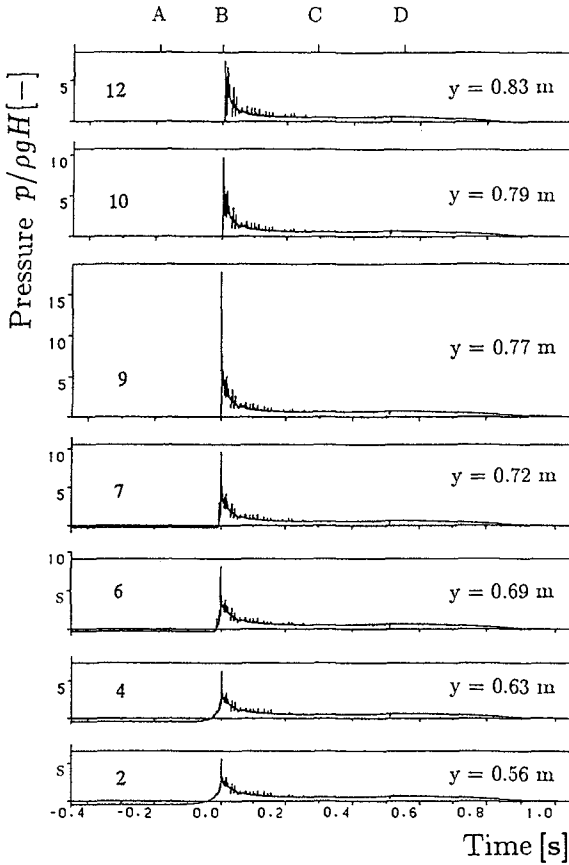


Figure 7: Computed Time History of Flip-Through Type Impact Pressure

impact process refer to Photo 1(3) of Takahashi et al. (1983). However, because the damping effect of the entrapped air can not yet be studied using the present model for incompressible flow, the resulting impact pressures of these three breaker types appear to be much larger than the experimental results and are not presented here. On the other hand, it is also found that the numerically simulated peak pressure can still be adjusted to the same order of magnitude with the experimental results once the impact velocity and breaker profiles obtained from the numerical simulation are used as the input data of Bagnold's formula which accounts for the damping effect of entrapped air. Fig. 10 are the numerical simulated free surface evolution of the plunging breaker type with small amount of air entrainment. The photographs of this impact process refer to the Photo 1(4) of Takahashi et al. (1983). Fig. 11 are the numerical simulated free surface evolution of the plunging breaker type with larger amount of air entrainment. The photographs of this impact process refer to Photo 1(5) of Takahashi et al. (1983).

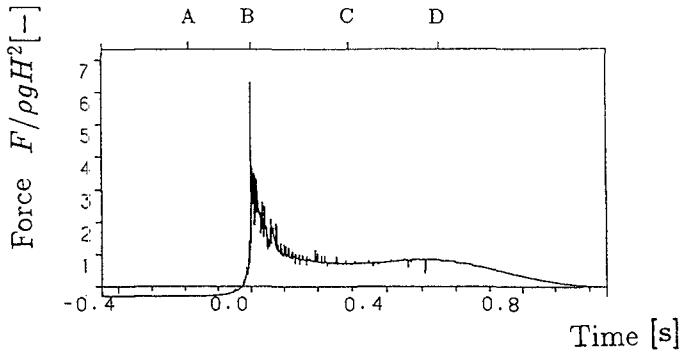


Figure 8: Computed Time History of Flip-Through Type Impact Force

On the other hand, in order to gain more insight of the computed wave kinematics of breaking waves, a comparison is made of the velocity distributions under wave crest around the breaking point. Besides, it is very difficult to define the exact breaking point during the breaking process since the free surface and velocity distribution rapidly change. It is therefore necessary to perform the comparison of experimental and numerical results under the consideration of both free surface and velocity distribution. However, this kind of measurement is rare due to the difficulty of getting an accurate velocity measurement and surface profile simultaneously. The experiment run by Iversen(1952) is still one of the most well known experiments which have considered both the surface profile and the velocity distribution. Fig. 12 shows the surface profile around the breaking point with the simultaneously observed velocity distribution. Fig. 13 shows the computed free surface around the breaking point and agrees also qualitatively well with Fig. 12. The quantitative comparison of the velocity distribution under a wave crest around breaking point is given in Fig. 14, also showing a good agreement. The X-coordinate represent the dimensionless velocity which is normalized by  $\sqrt{g\eta_b}$ ,  $\eta_b$  is the water depth under the wave crest. The Y-coordinate represent the relative depth  $Y/\eta_b$ ,  $Y=1.0$  indicates the wave crest,  $Y=0$  is on the bottom under the wave crest.

## 4 Discussion

The comparative analysis of the results of the computations may be summarized as follows:

- The basic tests of simulating non-breaking waves phenomena like the run up height of solitary waves on a vertical wall and the formation of standing waves have already proven that the present numerical model is able to correctly handling nonlinear waves and the weakly reflecting boundary.
- For flip-through breaker type (negligible air entrapment), the numerical results are qualitatively and quantitatively reliable with respect to the description of the breaker kinematics and to the subsequent impact loading on the vertical wall.

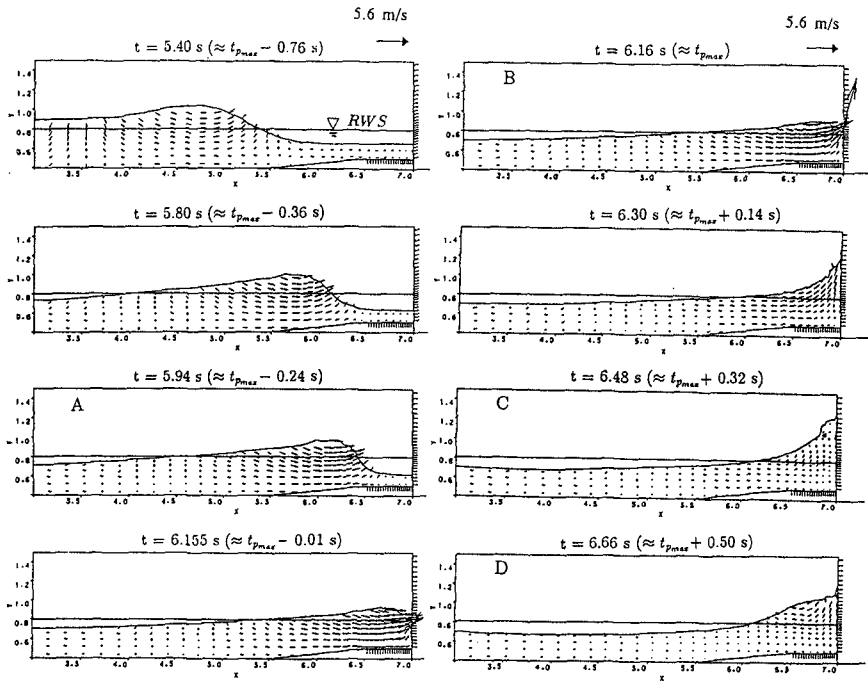


Figure 9: Computed Wave Profiles and Velocity Fields of Breaker Type- Almost Vertical Breaker Front with a Thin Air Layer

- For the last three breaker types with air entrapment in Fig. 5, the wave kinematics of the breakers is well simulated. However, the computed impact loading is much higher than the loading obtained from experiment. This result was expected since the numerical model cannot yet account for air entrapment (incompressible flow). However, by using the impact velocities and breaker profiles obtained from the numerical computation as input data into Bagnold's formula (Bagnold, 1939) which accounts for the damping effect of entrapped air, reasonable results are obtained for the magnitude of the peak impact loading.
- The last comparison is performed between the numerical simulation and the experiment done by Iversen(1952) for the velocity distribution under the wave crest around the breaking point; a quantitatively good agreement is also achieved.

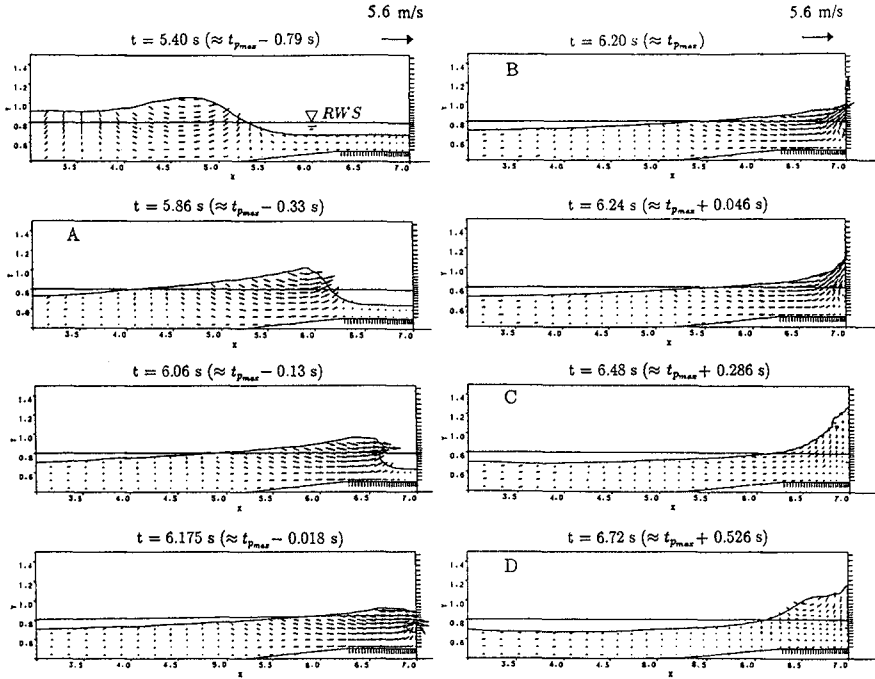


Figure 10: Computed Wave Profiles and Velocity Fields for Plunging Breaker with medium Entrapped Air Pocket

### 5 Concluding Remarks

The application of the VOF concept for the numerical solution of the governing equations and the development of further numerical schemes for the treatment of the boundary conditions have led to a powerful tool for the simulation of breaking and nonbreaking wave kinematics at and on a vertical structure with various foreshore geometries. The complete impact pressure and the resulting loading (impact) are also well simulated as far as the entrapped air is negligible. Corrective coefficients for the magnitude of the impact loading for the cases where air is entrapped in the breaker can be obtained from Bagnold's formula in which the impact velocity and the breaker profile during impact obtained from the numerical model are used as input data.

Further development of the model is directed towards accounting for the compressibility of air in order to obtain directly the proper magnitude of the impact loading in the case of plunging breakers with entrapped air.

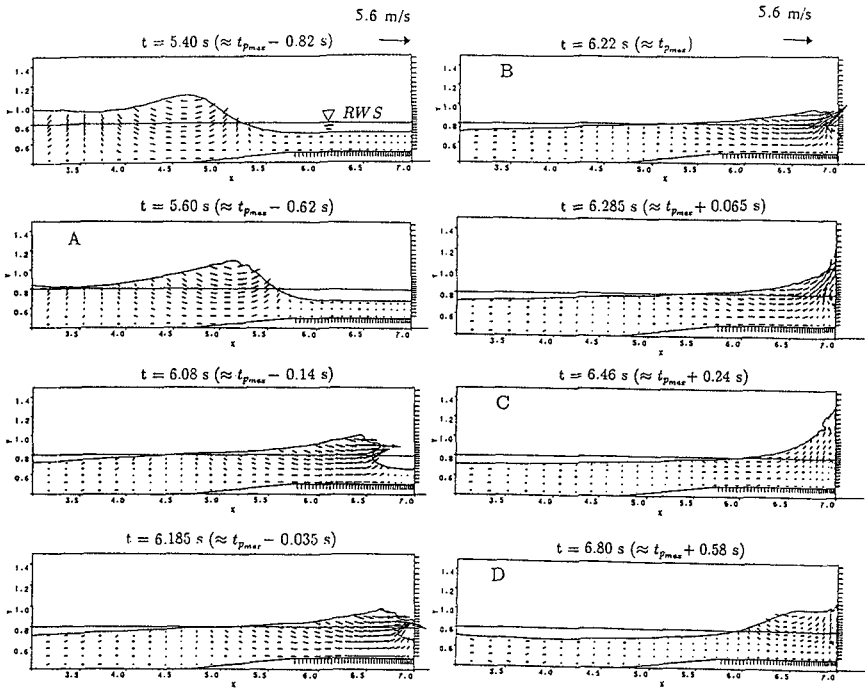


Figure 11: Computed Wave Profiles and Velocity Fields for Plunging Breaker with large entrapped airpocket

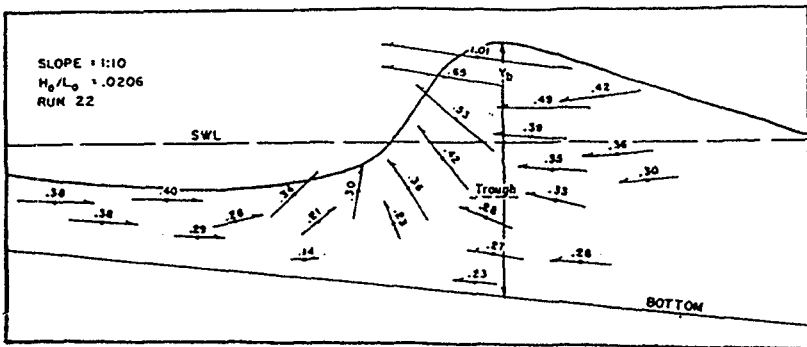


Figure 12: Surface Profile and Velocity Vectors around the Breaking Point Obtained from Experiments by Iversen(1953)

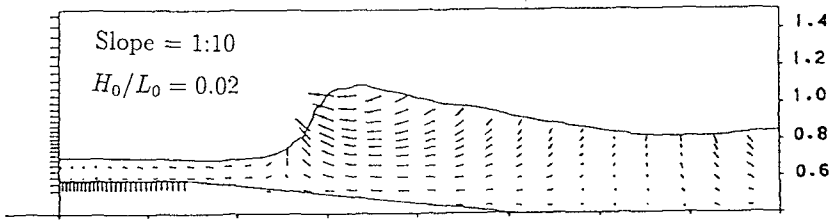


Figure 13: Surface Profile and Velocity Vectors around the Breaking Point Obtained from Numerical Simulation

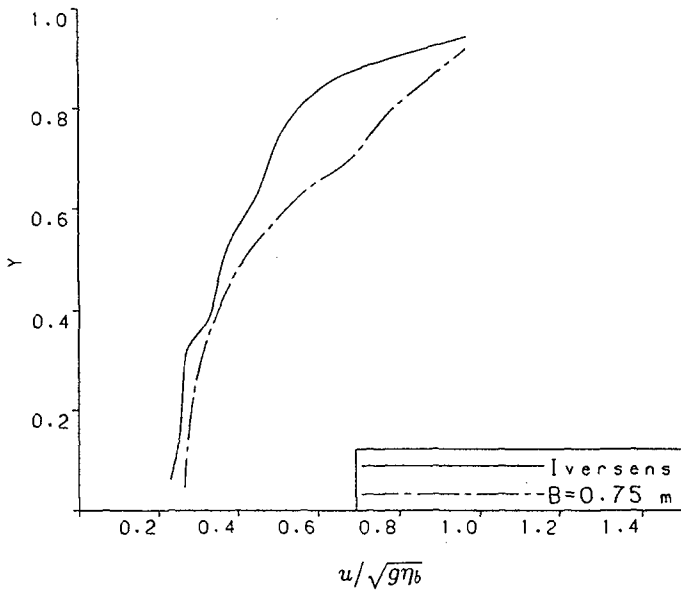


Figure 14: Comparison of Experiment and Numerical Simulation of Velocity Distribution under the Wave Crest of a Plunging Breaker

## 6 Acknowledgement

The first author is grateful to the Deutscher Akademischer Austauschdienst (German Scholarship Exchange Service) for awarding him the DAAD Scholarship which financially support his stay in Germany while the present study was done. The MAST II-Project MAS2-CT92-0047 supported by the EU which provided favorable research atmosphere for the development of this VOF-model is also appreciated.

## 7 References

1. Bagnold, R.A. (1939) Interim Report of Wave Pressure Research. J. Inst. Civil Engineers. Vol. 12, pp. 210-226.
2. Cooker, M. J. and Peregrine, D. H. (1990) Violent Water Motion at Breaking Wave Impact. Proc. 22nd Intl. Conf. on Coastal Engineering. Delft. pp. 164-176.
3. Cooker, M.J. and Peregrine, D.H. (1992) Wave Impact Pressure and its Effect upon Bodies lying on the Sea Bed. Coastal Engineering, 18. pp. 205-229.
4. Delft Hydraulics (1991) Skylla: Wave Motions in and on Coastal Structures- Feasibility Study in the Application of SAVOF- MAST G6.- Coastal Structures.
5. Hattori, M, Arami, A. Yui, T. (1994) Impact Wave Pressure on Vertical Walls under Breaking Waves of Various Types. Special Issue on Vertical Breakwaters, Coastal Engineering, Elsevier, Amsterdam.
6. Horikawa, K. (1978) Coastal Engineering- An Introduction to Ocean Engineering. University of Tokyo Press.
7. Iversen, H. W. (1952) Laboratory Study of Breakers. U.S. National Bureau of Standards, Circular No. 521 (Nov. 1952), pp. 9-31.
8. Keulegan, G. H. and Patterson, G. W. (1940) Mathematical Theory of Irrotational Translation Waves. J. Res. Natl. Bur. Std. 24.
9. Laitone, E. V. (1960) The Second Approximation to Cnoidal and Solitary Waves. J. Fluid. Mech., 9. pp. 430-444.
10. Le Méhauté, B., Divoky, D., Lin, A. (1968) Shallow Water Waves: A Comparison of Theories and Experiments. Proc. 11th Intl. Conf. on Coastal Engineering, pp. 86-107.
11. Mitsuyasu, H. (1962) Experimental Study on Wave Forces against a Wall. Coastal Engineering in Japan. Vol. 5. pp. 25-47.
12. Nichols, B.D.; Hirt, C.W.; Hotchkiss, R. S. (1980) SOLA-VOF- A Solution Algorithm for Transient Fluid Flow with Multiple Free Boundaries. Report LA-8355, Los Alamos Scientific Laboratory, University of California.
13. Street, R. L. and Camfield, F.E (1966) Observations and Experiments on Solitary Wave Deformation. Proc. 10th Intl. Conf. on Coastal Engrg, chapter 19, pp. 284-301.
14. Takahashii, S., Tanimoto, K., Suzumura, S. (1983) Generation Mechanism of Impulsive Pressure by Breaking Wave on a Vertical Wall. (in Japanese) Report of Port and Harbour Research Institute., Vol. 22, No. 4, pp. 3-31.
15. Wiegel R.L. (1960) A Presentation of Cnoidal Wave Theory for practical Application. J. Fluid Mech. 7, pp. 273-286.



## CHAPTER 121

### WIND EFFECTS ON RUNUP AND OVERTOPPING

by Donald L. Ward,<sup>1</sup> Christopher G. Wibner,<sup>2</sup> Jun Zhang,<sup>3</sup> and Billy Edge<sup>4</sup>

#### ABSTRACT

The maximum distance a wave may travel up the face of a coastal structure, or rate of overtopping if runup exceeds structure crest elevation, are critical parameters in planning and design of a coastal structure. Runup and overtopping are usually estimated by empirical equations based on physical model studies that do not include the effects of strong onshore winds that are typically present during design storm conditions. While it is generally assumed that onshore winds will increase runup and overtopping over no-wind conditions, there is currently no means of accurately calculating effects of these winds on runup and overtopping.

A joint research project by US Army Corps of Engineers and Texas A&M University (TAMU) is currently investigating wind effects on runup and overtopping of revetments and vertical walls through a series of physical model studies conducted in a combined wind/wave flume at TAMU. Initial tests measured runup and overtopping rates on a 1:3 smooth revetment for a range of incident monochromatic wave conditions, with wind speeds varying from no wind to maximum blower output. With the addition of wind, large increases in runup and overtopping were recorded over the no wind condition. The combined wind/wave spectrum recorded during tests with wind was then reproduced mechanically. Runup and overtopping were significantly higher during tests with

---

<sup>1</sup>Research Hydraulic Engineer, USAE Waterways Experiment Station's Coastal Engineering Research Center, Vicksburg, Mississippi

<sup>2</sup>Graduate student, Texas A&M University, College Station, Texas

<sup>3</sup>Assoc. Professor, Texas A&M University, College Station, Texas

<sup>4</sup>Head, Ocean Engineering Program, Texas A&M University, College Station, Texas

wind than during no-wind tests that reproduced the combined wind/wave spectrum.

The tests indicate that runup and overtopping estimates that do not include wind effects are underpredicting runup and overtopping on coastal structures. Continuing efforts in this study are aimed at quantifying prototype wind effects on runup and overtopping based on physical model results.

## BACKGROUND

The ability to accurately estimate potential runup and overtopping on a coastal structure is essential to structural and economic design of the structure. Although it may be desirable to construct shore-protecting structures with sufficient crest elevation to prevent overtopping, this is generally not economically feasible and overtopping rates must be considered. An analysis of runup heights and overtopping rates is necessary to determine structure crest elevations, design drainage systems, and estimate overtopping-induced damage levels for determining benefit/cost ratios. Typically, runup and overtopping are estimated from empirical equations that were developed from physical model studies (e.g., Weggel 1976, Ahrens and Martin 1985, Ahrens and Heimbaugh 1988, van der Meer 1988, van der Meer and Stam 1991, de Waal and van der Meer 1992, Schulz and Fuhrboter 1992, Ward 1992, Ward and Ahrens 1992, Yamamoto and Horikawa 1992), or determined directly from physical model studies. Numerical models have also been developed to estimate runup and overtopping (e.g., Kobayashi and Wurjanto 1989, Wurjanto and Kobayashi 1991, Kobayashi and Poff 1994); these numerical models are generally calibrated with physical model test results.

The typical design condition for a coastal structure is a severe storm accompanied by strong onshore winds, yet physical model tests on which runup and overtopping rates are based do not include wind effects. The Shore Protection Manual (1984) includes an equation for a wind correction factor that increases wave overtopping rates by up to 55%, but there is no data to support this equation. It is generally agreed that wind speeds greater than 50 km/hr may have a significant effect on runup and overtopping, but little research has been conducted to quantify wind effects (Sibul and Tickner 1956, Weggel 1976).

Resio (1987) divided action of winds on overtopping into two distinct physical processes: (1) increase of runup and overtopping due to wind energy input during the wave runup interval, and (2) advection by wind of water spray and splashing resulting from wave impact on coastal structures. The first process is the major cause for increase in runup and overtopping of mild-slope structures and the second is more important to vertical or steep-slope structures. A third process ignored in the previous studies is that onshore wind may generate onshore surface currents through the work of wind shear stresses and wind-induced wave breaking in the surf zone. This onshore surface current may greatly increase initial runup bore speed on the surface of revetments and consequently may increase runup heights and overtopping rates.

The influence of wind speed on runup and overtopping needs to be

determined. Because of very few laboratory and field measurements concerning wind effects on runup and overtopping, our knowledge of how wind may increase runup heights and overtopping rates is far from sufficient. If design wind conditions are found to have a significant effect on runup and overtopping rates, then a method of calculating runup and overtopping that accounts for wind is clearly needed. Funded by U.S. Army Corps of Engineers (USAE), a joint research program is being conducted by USAE Waterways Experiment Station's Coastal Engineering Research Center (CERC) and the Ocean Engineering Program of the Civil Engineering Department at Texas A&M University (TAMU). This paper presents some initial findings from this on-going study.

### OBJECTIVES

This study is evaluating effects of wind on runup and overtopping of coastal structures through physical model studies conducted in a combined wind/wave flume at TAMU.

Analysis of the data should lead to a better understanding of the physics of wind effects on coastal structures. Although it is not possible to fully describe mathematically the processes involved, such as wave breaking or flow through a porous media of randomly shaped, randomly placed armor units, a better understanding is sought of the energy transfers and physical processes involved.

Because of the difficulty of fully describing mathematically the processes involved, empirical equations will be developed to estimate runup and overtopping on coastal structures, including wind effects. This study hopes to provide design guidance for the range of conditions typically encountered in coastal structures design work, within the limitations of the test facility and test conditions.

### TEST FACILITY

Physical model tests are being conducted in a 36-m-long by 0.61-m-wide by 0.91-m-deep glass-walled wave flume equipped with a flap-type mechanical wave generator (Figure 1). The electrically-activated wave generator is capable of producing monochromatic wave trains as well as spectral wave trains through a computer-generated signal.

A blower is mounted above and at the far end of the wave flume, away from the wave generator. An intake manifold is located in front of the wave generator, therefore wind is pulled along the length of the flume and exhausts away from the wave generator. The entire flume is covered with removable panels to contain the wind. The blower is capable of producing an average wind velocity in the flume of 16 m/s over a water depth of 50 cm.

A plywood slope followed by a 2-m-long sealed overtopping basin are installed in the end of the flume away from the wave generator. Various extensions allow crest elevation of the slope to be varied. The current slope is set

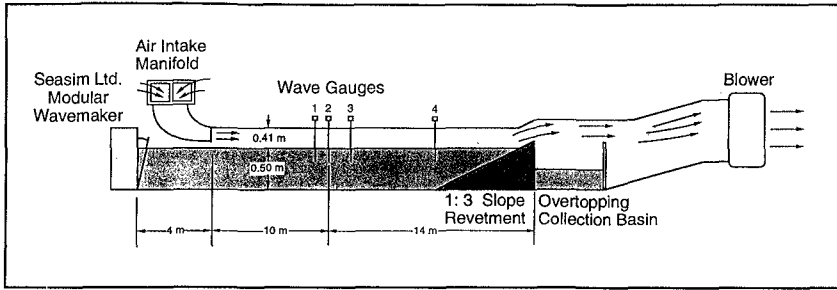


**Figure 1.** Wave flume test facility at Texas A&M University.

at 1:3 (V:H); other slopes will be installed at the conclusion of testing with the 1:3 slope. Runup on the slope is measured by two resistance gages mounted on the slope face, and by visual observation.

Three resistance wave gages are set in an array approximately mid-way between the wave generator and test slope, and a fourth gage is positioned at the toe of the slope. Gage spacing in the three-gage array is adjusted for different test periods to allow separation of incident and reflected wave trains using the method of Goda and Suzuki (1976).

#### TEST PARAMETERS

Table 1 lists parameters that will be varied in this study to provide design information covering a range of typical design conditions and to study separately the various effects of wind on runup and overtopping. The current test schedule includes revetment slopes of 1:1.5, 1:3, and 1:5, and of varying crest elevations to study both runup and overtopping rates. Overtopping of a vertical wall will also be studied. Two water depths are being tested, and two or three monochromatic wave heights at each of three wave periods. Greater wave height would have been preferred for the longer wave periods, but were limited by wave generator capability. Each combination of water depth and incident wave conditions will be tested without wind, then at 50%, 75%, and 100% of maximum blower output. Both smooth and rough revetments slopes will be tested, with rough slopes covered with armor stone in accordance with design guidance in the Shore Protection Manual (1984) and Engineering Manual 1110-2-1614, Design of Coastal Revetments, Seawalls, and Bulkheads (1985). At the completion of tests with monochromatic wave conditions, a series of tests will be conducted with irregular waves covering a range of wave heights and periods.

It should be emphasized that the testing program is still in its early phases. This paper presents results obtained only from the 1:3 smooth slope revetment with monochromatic wave conditions and a water depth of 50 cm. Each test was conducted twice; data shown in this paper is the average of the two tests.

Table 1. Ranges of test parameters planned for this study.

Wave Periods(s)	Wave Height(cm)	Revetment Slopes	Structures
1.0	5.0, 7.0, 10.0	1 : 1.5	* Smooth Slope Revetment
1.75	3.2, 5.4	*1 : 3.0	Rough Slope Revetment
2.5	2.2, 3.8	1 : 5.0	Vertical Wall
Water Depth(cm)	Wind Speed % of Fan Power	Revetment Heights above SWL (cm)	
*50.0	0 (0 m/s)	10.0	
	50 (8 m/s)	20.0	
	75 (12 m/s)	30.0	
	100 (16 m/s)		
65.0	0 (0 m/s)	10.0	
	50 (9 m/s)	20.0	
	75 (13 m/s)		
	100 (17 m/s)		* Results Presented

## RESULTS AND DISCUSSION

### Causes of wind effects on runup and overtopping

Wind affects runup and overtopping of coastal structures in several ways that are not reproduced in a typical wave flume (without wind generating capabilities). Beginning seaward of the structure, local winds may modify incident wave spectra through changes in direction or intensity and affect shoaling of wave trains as they approach shallow water. Wind-induced setup by onshore winds is also observed due to pressure gradients and wind shear at the air/water interface. Higher water levels due to setup result in higher runup both by raising the elevation at which runup begins and by allowing larger waves to reach the structure without breaking. As waves reach shallower water, onshore winds may cause a transfer of potential energy (wave height) to kinetic energy (surface current) through wind-induced wave breaking and through shear effects. Increased kinetic energy may cause higher initial velocities of the runup bore, which would result in greater runup heights. On the structure itself, onshore winds may create a favorable pressure gradient around the wave, and produce shear forces on the wave and runup bore. Finally, waves breaking on a coastal structure create large quantities of spray and on vertical structures may produce large vertical sheets of spray. On prototype structures the onshore winds carry spray over the structure, contributing to overtopping, but in most wave flumes the spray falls back into the flume seaward of the structure and is not measured as overtopping.

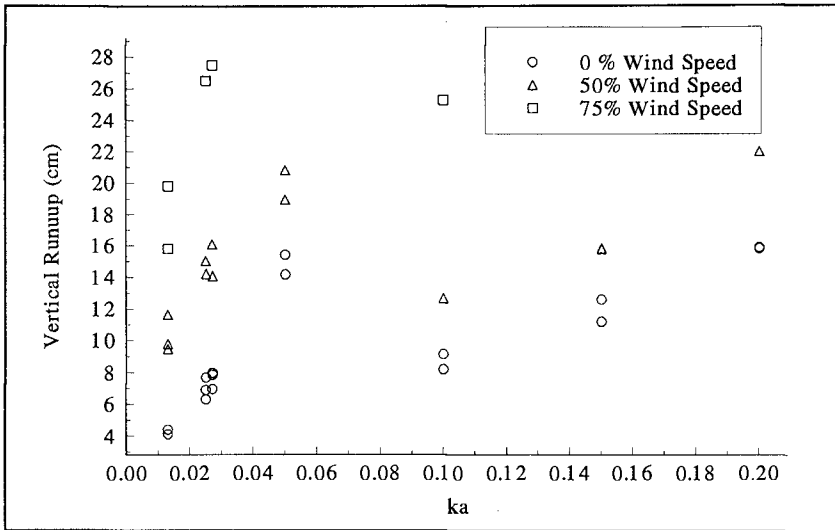
### Wave runup and overtopping results

A series of tests with monochromatic wave conditions was conducted to compare runup and overtopping rates without wind to runup and overtopping rates when wind of different intensities is added to monochromatic wave conditions. Mechanically-generated waves used in these tests had frequencies of 1.0 Hz, 0.57 Hz, and 0.40 Hz. Waves generated by wind had a frequency of about 2.0 Hz at the toe of the test revetment. Because the mechanically generated waves had a different frequency than waves generated by wind, the result was a bi-modal spectrum comprised of a sharp, low-frequency monochromatic peak for the mechanically generated wave and a broader, high-frequency peak for wind generated waves. In an exaggerated fashion, this is somewhat analogous to ocean swell nearing the coast and being acted upon by local winds.

The figures that follow in this text plot data collected from the wave flume study. The abscissa in all but one of the following figures is wave steepness defined as wave number,  $k$ , times wave amplitude,  $a$ . Wave number is defined as  $2\pi/L$ , where  $L$  is Airy wavelength determined from flume depth and wave period of the mechanically generated wave. Wave amplitude was determined as one-half the wave height of the mechanically generated wave. To simplify understanding the data these figures, wave steepnesses ( $ka$ ) used in these tests are given in ascending order in Table 2 along with wave period and wave height. All tests were conducted at a water depth of 50 cm.

Table 2. Wave steepness, period, and height for each set of test conditions presented in this paper.

$ka$	Wave Period (sec)	Wave Height (cm)
0.013	2.50	2.2
0.023	2.50	3.8
0.029	1.75	3.2
0.049	1.75	5.4
0.104	1.00	5.0
0.146	1.00	7.0
0.208	1.00	10.0



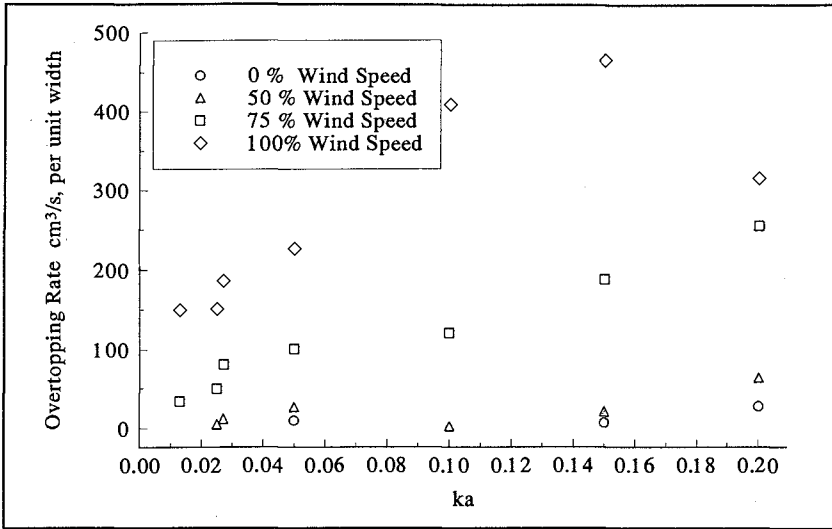
**Figure 2.** Maximum wave runup for various wind speeds tested.

Figure 2 plots maximum runup versus wave steepness for a range of wind

conditions. Because different revetment crest elevations were tested for the overtopping portion of this study, much of the runup data was collected from revetments with more than one crest elevations, which accounts for the paired data points shown in the figure. The ordinate in Figure 2 is maximum runup divided by wave height of the mechanically generated wave without wind effects. Maximum runup was determined visually by observing the runup bore. Small, narrow streams of runup that progressed considerably higher up the test revetment than the bulk of the runup bore were ignored, and an average maximum runup across the middle one-third of the flume was estimated. Wind speeds are presented as a fraction of the maximum blower speed. Average wind speeds for the two depths tested are shown in Table 1.

Figure 2 shows a dramatic increase in runup for tests with wind over tests without wind. This is hardly surprising because wind is introducing more energy into the system. Maximum wave heights occur when crests of a wave from each of the two wave trains coincide, producing a wave amplitude slightly greater than the sum of the individual wave heights (Zhang *et al.* 1992). Because maximum runup elevation is proportional to maximum wave height, increases in maximum runup elevation with addition of wind is expected.

Although crests of a wave from each wave train may coincide to produce a maximum wave height, it is just as likely that a wave trough from one wave train will coincide with a crest from the other wave train. The effect of the wind-generated wave train on overtopping rate, which is time-averaged, is therefore



**Figure 3.** Overtopping rate for different wind speeds tested (revetment height 10 cm above swl).

expected to be less significant than effect of wind on maximum runup. This is illustrated in Figure 3, which shows overtopping rates for a fixed revetment crest elevation of 60 cm (10 cm above swl). The 50% wind speed had little effect on overtopping rate, although larger increases were observed at 75% and 100% wind speeds. The sharp decrease in overtopping rate for maximum wind speed and wave steepness between 0.146 and 0.208 is noteworthy. The mechanically generated wave for  $ka = 0.208$  was a 1.0-sec, 10-cm wave (Table 2). At 100% wind speed, the 10-cm waves broke before reaching the revetment.

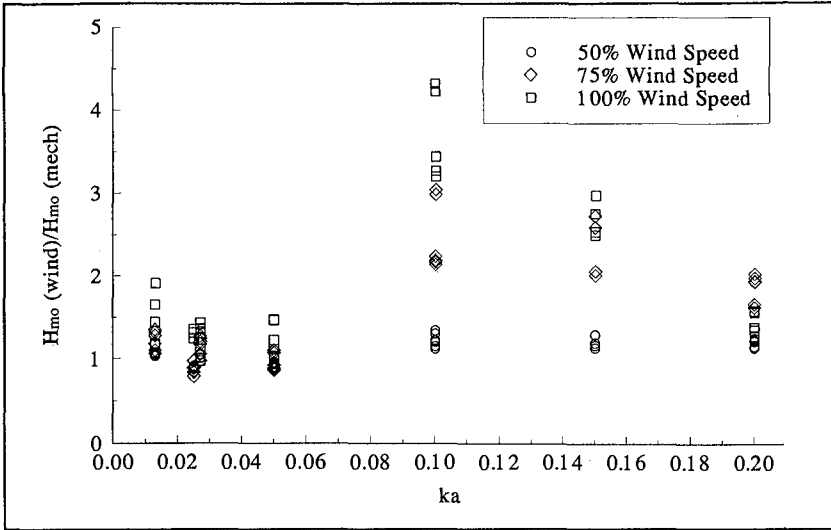
It is seen in Figure 3 that the increase in overtopping rate with wind is much greater for waves tested with a period of 1.0 sec ( $0.10 \leq ka \leq 0.20$ ) than for tests with wave periods of 1.75 sec or 2.5 sec. An explanation for this may be found in Figure 4.

Figure 4 shows the change in  $H_{m0}$  of the mechanically generated wave under the influence of wind. Because the frequency of wind waves ( $\approx 2$  Hz) differs significantly from frequencies of the 1.75-sec or 2.5-sec waves, wind is seen to have little effect on  $H_{m0}$ 's of the longer waves. However, the frequency of the wind waves is relatively close to the frequency of 1.0-sec waves, and wind energy is seen to have a significant effect on the  $H_{m0}$  of the 1.0-sec waves.

#### Mechanically reproducing a wind/wave spectrum

Assuming constant wind conditions, effects of wind on incident waves prior to shoaling may be accounted for by mechanically reproducing a fully developed





**Figure 4.** Wind effect on  $H_{mo}$  of mechanically-generated wave.

wind spectrum. This is the typical test condition for runup and overtopping in most wave flumes, but fails to account for wind effects during shoaling or wind effects at or near the structure.

To determine effects of wind on runup and overtopping at the structure, an attempt was made to mechanically reproduce the combined wind/wave spectrum. The wave record from the wave gage at the revetment toe (gage 4) taken during tests which included wind blowing over a mechanically-generated wave train was analyzed and the combined spectrum determined. The combined spectrum included a low-frequency wave from the mechanically-generated wave train, and a high-frequency wave generated by wind. Because high-frequency waves travel slower than low-frequency waves, the combined spectrum could be reproduced mechanically by generating a series of high-frequency waves and following with a series of low-frequency waves. When the low-frequency waves catch up with high-frequency waves, the combined spectrum is obtained. Trial and error was used to adjust the  $H_{mo}$ 's of the high- and low-frequency mechanically generated waves to match the combined wind/wave spectrum.

The wave generator was unable to reproduce the high frequency of wind waves ( $\approx 2$  Hz), therefore the frequency used was the highest frequency at which  $H_{mo}$  of the 50% wind could be reproduced. The 50% wind was chosen because the wave generator was capable of reproducing the wind wave at a higher frequency than it could reproduce larger wave heights generated by higher wind speeds. Figure 5 shows a mechanically-produced spectrum compared to the wind/wave spectrum. Except for the slightly higher frequency of wind waves, the two spectra are very similar.

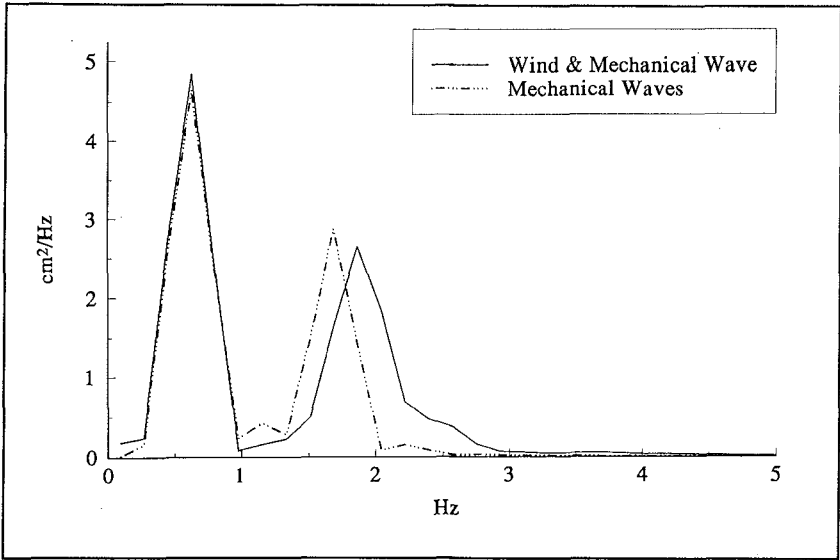


**Figure 5.** Comparison of energy spectra of wind/wave spectrum and mechanical reproduction of wind/wave spectrum.

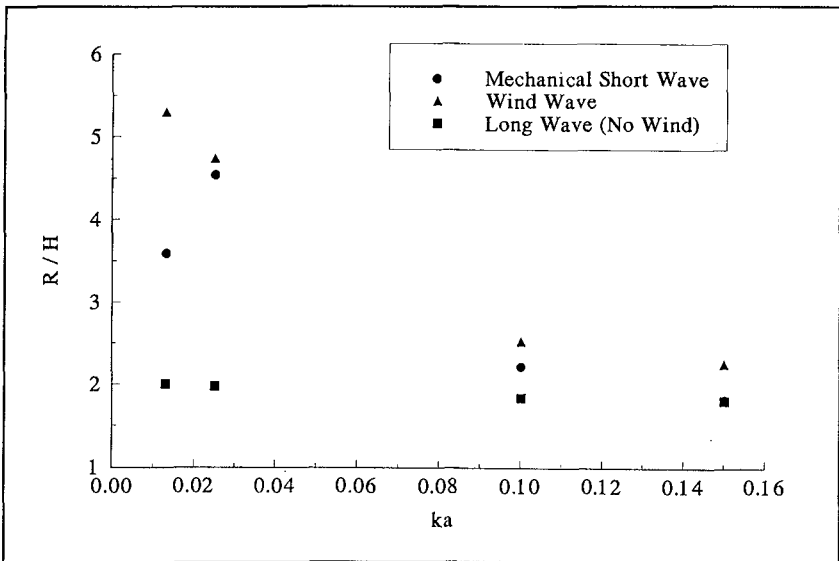


**Figure 6.** Maximum wave runup for no-wind condition, wind/wave condition, and mechanical reproduction of wind/wave condition (wind speed 50% of maximum).

Figure 6 shows runup information for the four tests reproduced mechanically. Runup data for mechanically-generated, low-frequency wave and for the combined wind/wave spectrum is the same as seen in Figure 2, but Figure 6 also plots runup from mechanically reproduced dual-peaked spectrum. Additional runup observed with wind is attributed to higher surface velocities due to wind-induced breaking and to wind effects on the runup bore.

Figure 6 clearly demonstrates that mechanically simulating wind waves fails to reproduce runup that will occur on prototype structures in the presence of onshore winds, and suggests that current formulae for estimating runup and overtopping of coastal structures therefore underestimate prototype runup and overtopping. However, until scaling relationships for a combined wind/wave experiment have been determined, and until relative effects of wind-induced setup in a wave flume and the prototype have been examined, it is not possible to quantify additional runup and overtopping that will occur on prototype structures.

#### Final comments

It is clear that wind affects runup and overtopping through a variety of processes and that mechanically reproducing a wind/wave spectrum will only account for some of the wind effects. Additional study is required to separate and quantify effects of wind due to the various processes involved.

In these tests, two key questions need to be answered before a relationship can be determined between model test results and real-world situations. First, the relationship between wind-induced setup in a wave flume and prototype wind-induced setup needs to be determined. Significant setup was observed during physical model tests with wind, which was seen to have an important effect on runup and overtopping. Second, a scaling relationship for runup and overtopping in a combined wind/wave environment needs to be determined. Waves, with gravity as the main restoring force to the inertial forces, are scaled by Froude's law. Wind effects, on the other hand, transfer energy to fluid through shear forces and are scaled by Reynold's law. To satisfy both Froude's law and Reynold's law in a single model requires either a centrifuge to increase gravitational effects in the model, or use of a "super fluid" to change viscous effects in the model. Neither of these options is practical for tests of this size.<sup>5</sup> Scaling relationships need to be explored to allow effects of wind and waves on runup and overtopping to be

---

<sup>5</sup>A large centrifuge is currently being constructed at WES to be completed in 1995. Test beds for the centrifuge will include a miniature wave flume approximately 2 m long equipped with a flap-type wave generator with spectral capabilities and a water-based fluid that can be mixed to obtain a range of kinematic viscosities. Although the centrifuge will be able to create up to 350 g's, the wave flume will be designed only for loads up to about 35 g's. A combined wind/wave environment in the flume could be obtained by redirecting wind created by movement of the wave flume through the air by the centrifuge.

considered separately and then hopefully they may be applied to prototype prototype coastal structures.

#### ACKNOWLEDGEMENT

The testing program reported herein is funded by the U.S. Army Corps of Engineers, and the authors gratefully acknowledge this support. Permission to publish this paper was granted by the Office, Chief of Engineers.

#### APPENDIX A: REFERENCES

- Ahrens, J.P., and Heimbaugh, M.S. 1988. "Approximate upper limit of irregular wave runup on riprap," Technical Report CERC-88-5, U.S. Army Engineer Waterways Experiment Station, Vicksburg, Mississippi.
- Ahrens, J.P., and Martin, F.T. 1985. "Wave run-up formulas for smooth slopes," *J. Waterway, Port, Coast. and Oc. Engrg.*, ASCE, 111(1), 128-133.
- de Waal, J.P., and van der Meer, J.W. 1992. "Wave runup and overtopping on coastal structures," *Proc. 23rd Coastal Engr. Conf.*, Venice, Italy, ASCE.
- Goda, Y., and Suzuki, T. 1976. "Estimation of incident and reflected waves in random wave experiments," *Proc. 15th Coast. Engr. Conf.*, Honolulu, Hawaii, ASCE.
- Kobayashi, N., and Poff, M.T. 1994. "Numerical model RBREAK2 for random waves on impermeable coastal structures and beaches," Research Report No. CACR-94-12, Center for Applied Coastal Research, Univ. of Delaware, Newark, Delaware.
- Kobayashi, N., and Wurjanto, A. 1989. "Numerical model for design of impermeable coastal structures," Research Report No. CE-89-75, Center for Applied Coastal Research, Univ. of Delaware, Newark, Delaware.
- Resio, D.T. 1987. "Assesment of wind effects on wave overtopping of proposed Virginia beach seawall", Tech. Memo to CERC., OCTI.
- Schulz, K.-P., and Führböter, A. 1992. "Full- and small-scale experiments of wave run-up and run-down on slopes with diefferent cover roughness," *Proc. 23rd Coastal Engr. Conf.*, Venice, Italy, ASCE.

- Sibul, O.J., and Tickner, E.G. 1956. "Model study of overtopping of wind-generated waves on levees with slopes of 1:3 and 1:6," Tech. Memo. No. 67, U.S. Army Corps of Engineers Beach Erosion Board, U.S. Government Printing Office, Washington, D.C.
- U.S. Army Engineer Coastal Engineering Research Center. 1984. *Shore Protection Manual*. U.S. Government Printing Office, Washington, D.C.
- U.S. Army Engineer Coastal Engineering Research Center. 1985. *Design of Coastal Revetments, Seawalls, and Bulkheads*. Engineering Manual 1110-2-1614, U.S. Government Printing Office, Washington, D.C.
- van der Meer, J.W. 1988. "Rock slopes and gravel beaches under wave attack," PhD thesis, Delft Technical University, Delft, The Netherlands (also published as Delft Hydraulics Communication No. 396)
- van der Meer, J.W., and Stam, C.-J.M. 1991. "Wave runup on smooth and rock slopes," Publication No. 454, Delft Hydraulics, Delft, The Netherlands.
- Ward, D.L. 1992. "Prediction of overtopping rates for irregular waves on riprap revetments," Miscellaneous Paper CERC-92-4, U.S. Army Engineer Waterways Experiment Station, Vicksburg, Mississippi.
- Ward, D.L., and Ahrens, J.P. 1992. "Overtopping rates for seawalls," Miscellaneous Paper CERC-92-3, U.S. Army Engineer Waterways Experiment Station, Vicksburg, Mississippi.
- Weggel, J.R. 1976. "Wave overtopping equation," Proc. 15th Coast. Engrg. Conf., Honolulu, Hawaii, ASCE, 3, 2737-2755.
- Wurjanto, A., and Kobayashi, N. 1991. "Numerical model for random waves on impermeable coastal structures and beaches," Research Report No. CACR-91-05, Center for Applied Coastal Research, Univ. of Delaware, Newark, Delaware.
- Yamamoto, Y., and Horikawa, K. 1992. "New methods to evaluate run-up height and wave overtopping rate," Proc. 23rd Coastal Engr. Conf., Venice, Italy, ASCE.
- Zhang, J., Randall, R.E., and Spell, C.A. 1992. "Component wave interactions and irregular wave kinematics," J. Waterway, Port, Coast. and Oc. Engrg., ASCE, 118(4), 401-416.

## CHAPTER 122

# Modelling of Wave Overtopping over Breakwater

F. Zhuang<sup>1</sup>, C. Chang<sup>2</sup>, J.J. Lee<sup>3</sup>

### Abstract

From a recent experimental study on the kinematics of wave overtopping on marine structure by Lee, Zhuang and Chang (1993) it was found that the overtopping wave generates a strong rotational velocity field in the shoreward region of the breakwater. The present study focuses on the development and the implementation of a numerical model for the generated velocity field in the vicinity of the shoreward face of the breakwater. The numerical model consists of two basic elements: The velocity field generated by using the potential flow theory utilizing boundary element method and the rotational velocity field generated by the separated flow of the overtopping waves as they leave the breakwater site using vorticity stream function formulation. The computational results at a region far away from the separation zone based on the potential flow theory (boundary element method) are used as specified boundary conditions for simulation in the vorticity stream function model. The numerical results have been compared with the experimental data revealing the rotational feature of the velocity field in the separated zone (shoreward region of the breakwater). The generated vortical motion remains in the separation region even when the wave has travelled to the region far away from the breakwater.

---

<sup>1</sup>Graduate Research Assistant, Department of Civil Engineering, University of Southern California, Los Angeles, CA 90089

<sup>2</sup>Postdoctoral Research Associate, Department of Civil Engineering, University of Southern California, Los Angeles, CA 90089

<sup>3</sup>Professor of Civil Engineering, University of Southern California, Los Angeles, CA 90089-2531, Member of ASCE.

## 1. Introduction

Interaction of nonlinear waves with marine structure such as the breakwater has been an important problem for coastal and ocean engineers. Among the many aspects of the interaction problem, wave overtopping may require more attention due to the complexity of the physical process and the lack of available predictive models. When the water depth at the breakwater site is quite close to the breakwater height, and the incident wave amplitude is large, a substantial wave overtopping can be expected.

In a recent experimental study on the kinematics of wave overtopping on marine structure by Lee, Zhuang and Chang (1993) some very fascinating results have been found. It was found that the overtopping wave constitutes a jet-like water mass impacting the shoreward region of the breakwater. This jet-like water mass induces strong vortices and large water particle velocities in both the horizontal and vertical direction. Moreover, the overtopping wave also generates waves in the shoreward region possessing significant wave energy with oscillatory wave trains. These two major conclusions have significant practical implications: The large rotational velocity field can remove the armor units of the breakwater and scour the bed. The generated waves could induce significant basin oscillations in the shoreward basin with resonant frequencies which are different from the incident wave frequencies. The present study focuses on the development and the implementation of a numerical model capable of generating the rotational velocity field in the vicinity of the shoreward face of the breakwater.

## 2. Experiments

Experiments involving propagation of solitary waves over various submerged breakwater configurations are conducted in a wave tank 15.2 meter long, 39.4 centimeter wide, and 61 centimeter deep. A programmable piston type wave generator is installed at one end of the tank and a sloping beach is installed at the other end of the tank to aid the wave dissipation for the purpose of reducing the waiting time between experimental runs. Two different breakwater configurations are used in the experiment. Three resistance type wave gauges are installed at desired locations to make simultaneous wave profile measurements.

The water particle velocities are measured using a portable four-beam, two-component, fiber optic Laser Doppler Velocimeter (LDV) manufactured

by TSI Inc.. Titanium Dioxide powder ( $\text{TiO}_2$ ) is used in the experiments as a seeding agent.

### 3. Numerical Models

Motivated by the findings in the experiment, the present paper will focus on the development and the implementation of a numerical model for modeling the generated velocity field in the vicinity of the breakwater as well as the wave field generated by the overtopping waves. The numerical model consists of two basic elements: The velocity field generated by using the potential flow theory and the rotational velocity field generated by the separated flow (vortices) of the overtopping waves as they leave the breakwater site. For the potential flow theory, the Boundary Element Method has been used. The nonlinear boundary condition at the free surface is satisfied in the numerical model to allow simulation of large amplitude waves. The transient non-rotational flow field obtained by the potential flow theory is combined with the time dependent rotational flow field due to vortices generated in the separation zone.

The potential flow theory formulation using boundary element method has been presented in Lee, Chang and Zhuang (1992). The rotational flow field in the vicinity of the shoreward breakwater is simulated with the governing equations for the vorticity stream function formulation of incompressible laminar flow. Figure 1 shows the computational domain for this rotational flow field (ABCDE). The governing equations are:

$$\frac{\partial \omega}{\partial t} + u \frac{\partial \omega}{\partial x} + v \frac{\partial \omega}{\partial y} = \nu \left( \frac{\partial^2 \omega}{\partial x^2} + \frac{\partial^2 \omega}{\partial y^2} \right) \quad (1)$$

$$\frac{\partial^2 \psi}{\partial x^2} + \frac{\partial^2 \psi}{\partial y^2} = \omega \quad (2)$$

where  $\omega$  is the vorticity vector;  $u, v$  are the horizontal and vertical components of the velocity vector, and  $\nu$  is the kinematic viscosity of the fluid. The boundary conditions in conjunction with the governing equations (1) and (2) are listed as follows:

A-B and A-E:

$$u = 0, \quad v = 0, \quad \psi = 0$$

B-C:

$$\frac{\partial \psi}{\partial y} = u, \quad \omega = \frac{\partial u}{\partial y} - \frac{\partial v}{\partial x}$$



C-D:

$$\frac{\partial \psi}{\partial x} = -v, \quad \omega = \frac{\partial u}{\partial y} - \frac{\partial v}{\partial x}$$

D-E:

$$\frac{\partial \omega}{\partial x} = 0, \quad \frac{\partial^2 \psi}{\partial x^2} = 0$$

For each time step, the particle velocity solution is collected along B-C and C-D from the computational results based on the boundary element method (potential flow theory). These are used as the boundary conditions for the vorticity stream function formulation, hereafter we refer it as combined rotational model. Equation (2) is solved using Successive Over Relaxation method. Equation (1) is then solved using Alternating Direction Implicit method. The same computational procedure is repeated over the successive time steps.

#### 4. Results and Discussion

The wave profile and the velocity vector field induced by an incoming solitary wave with various wave amplitude to water depth ratio over a submerged breakwater has been computed using the boundary element method presented by Lee, Chang and Zhuang (1992). Figure 2 presents computational results for the case of  $H/d=0.2$  for different time steps. The incident solitary wave is propagating from left to right. From Figure 2 it is seen that the transmitted waves contains oscillatory tails and the velocity field in the shoreward side of the breakwater does not show any rotational flow field based on this potential flow computation. As mentioned in Lee, Chang and Zhuang (1992) however, the experimental data agree well with the theory on the computed wave profiles and accompanying kinematics of the water particle in the region close to the free surface as well as in the region far away from the separation zone. However, the agreement between the experimental data and the results of the potential flow theory breaks down in the region near the separated zone. In fact, experimental evidence shows that as soon as the incident solitary wave passes over the breakwater, vortices are generated in the separation zone. These vortices are then formed to create a rotational flow field with both the horizontal and vertical components of the water particle velocity changing directions rapidly.

Figure 3 is a photograph taken in the experiment. It shows the generation of a vortex at the vicinity of the shoreward step of the breakwater, after the passage of the solitary wave over the breakwater. It is observed that a strong rotational flow field has been generated and the flow direction close to the shoreward breakwater surface is upward and seaward.

It is reasonable to expect that the computational results from the boundary element method based on the potential flow theory would fail at the separation zone due to its imposed assumption of inviscid fluid and irrotational condition. However, the computational results should be reasonably valid in the region far away from the separation zone. Therefore, our modelling strategy for the region near the separation zone is adopted as follows: As the incident wave propagates over the breakwater, the computed velocity field from the boundary element method in the regions BC and CD are used as input boundary condition for the rotational flow simulations based on equations (1) and (2). In this approach, the domain of computation is fixed thus the computational effort is greatly simplified.

Figure 4 presents the computed streamlines showing the process of the vortex generation at different time steps. As mentioned earlier the specific condition simulated is such that the crest of the breakwater is at one-half of the water depth. The wave height/water depth ratio is 0.3. The breakwater width is ten times the breakwater height. The domain of simulation for rotational flow computation is  $AC=DE=0.8d$ , and  $AE=CD=4d$ , where  $d$  is the still water depth. Figure 5 is the velocity vector field plot corresponding to the streamline plot presented in Figure 4. The results show that the vortex motion will remain eventhough the wave peak has travelled away from the breakwater. These aspects of the simulated results are in agreement with the experimental observation. A practical point to remember is that the rotational field so generated will induce more scouring capability in the shoreward region of the breakwater.

Figures 6 and 7 show the velocity time history at a location P (as indicated in the definition sketch included in Figure 1). The location P is at the vertical position one-half of the breakwater height and one-tenth of the depth from the breakwater shoreward surface. Included in the figure are the results of the potential flow theory (solution from boundary element method) shown in solid line. The results from the combined rotational model are shown in dotted line. The velocity time history obtained by using the Laser Doppler Velocimeter measurement are plotted using the star symbols. The ordinates in both figures are the velocity components normalized with

respect to  $\sqrt{gd}$  (the wave celerity in water depth  $d$ ). The abscissa is the real time normalized as  $t\sqrt{g/d}$ . Examining both Figure 6 and 7, it is seen that, at location P, both the combined rotational model and experimental data reveal that the horizontal velocity changes direction from positive to negative and vertical velocity changes the direction from negative to positive. That means the flow direction at that point changes from forward and downward to backward (seaward) and upward. It clearly shows that a vortical motion has been generated during the wave overtopping process. The present combined rotational model predicts this feature of particle movement and agree qualitatively well with the experimental data. As expected, the potential theory predicts only positive horizontal velocity and negative vertical velocity. Thus, according to the potential flow theory, the particles are always going forward and downward directions during the overtopping process, representing no rotational motion. The magnitude differences between the present model and the experimental data in the early stages of flow could be caused by the minor geometry differences of the breakwater (the experimental model breakwater has a slight slope at both seaward and shoreward side). Since the absolute value of the present model is smaller than the experimental data at the early stages of flow, it might be that the model computation was still warming up at the time. We plan to conduct more experimental measurements using the physical model breakwater with the exact geometry as the computation model. Another noticeable feature from the time history graph is the magnitude of the positive velocity and negative horizontal velocity, both are much greater than the particle velocities associated with an unmodified solitary wave. This feature of increased particle motion could contribute to the destabilization of the breakwater armor units in the shoreward face.

## 5. Conclusions

The major conclusions drawn from this study can be summarized as follows:

1. The combined potential flow theory and vorticity stream function formulation model describes the flow field quite well based on the comparison with the experimental data. It offers a tool for modelling the flow field in the vicinity of the shoreward region of the breakwater.
2. There is a vortex generated by the overtopping of solitary wave in the vicinity of the shoreward breakwater. The vortical motion remains

there even when the wave has travelled to the region far away from the breakwater. This vortical motion produces a velocity field which could cause significant scouring in the region close to the breakwater.

3. Because of the vortex motion, there is a relatively large velocity component in the upward and seaward direction. This velocity could produce a lifting force which could destabilize the armor units in the shoreward face of the breakwater.
4. The present combined rotational model can be easily implemented because of its time-saving feature. It only computes rotational flow field in a relatively small local domain, while the efficient potential theory using boundary element method offers the information away from the separation zone, where the irrotationality assumption is valid. Furthermore, this model can be extended to solve other wave-structure interaction problems.

### Acknowledgment

This study is supported by USC Foundation for Cross-Connection Control and Hydraulic Research. The LDV System is supported by NSF under Grant No. 8906898. The authors are grateful for the generosity of Dr. Fredric Raichlen for permitting them to conduct the experiments at Caltech's W.M. Keck Laboratory of Hydraulics and Water Resources.

### References

1. Fletcher, C.A.J., "Computational Techniques for Fluid Dynamics", Second Edition, Springer-Verlag, 1991.
2. Lee, J.J., Zhuang, F. and Chang, C., "Kinematics of Wave Overtopping on Marine Structure", Proceeding of the Second International Symposium on Ocean Wave Measurement and Analysis (Wave 93), July 25-28, 1993, New Orleans, Louisiana, pp. 821-834.
3. Lee, J.J., Chang, C. and Zhuang, F., "Interaction of Nonlinear Waves with Coastal Structures", Proceedings of the Twenty-Third International Conference on Coastal Engineering, ASCE, Venice, Italy, Oct. 4-9, 1992, pp. 1327-1340.

4. Raichlen, F., Cox, J.C. and Ramsden, J.D., "Inner Harbor Wave Conditions due to Breakwater Overtopping", Proceedings Coastal Engineering Practice '92, ASCE, March 1992.

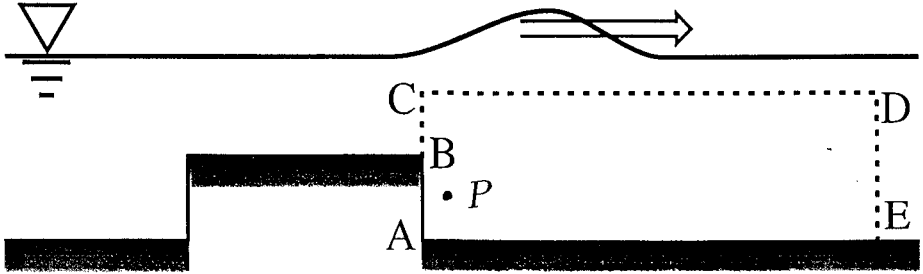


Figure 1: Sketch of the computational domain.

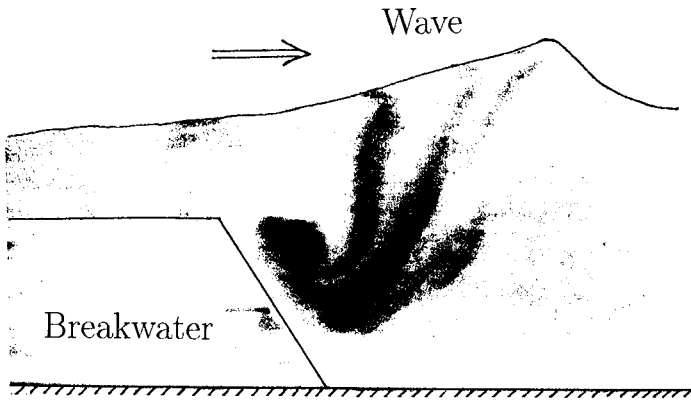


Figure 3: Photograph showing vortex generation by solitary wave propagating over a model breakwater in the experiment

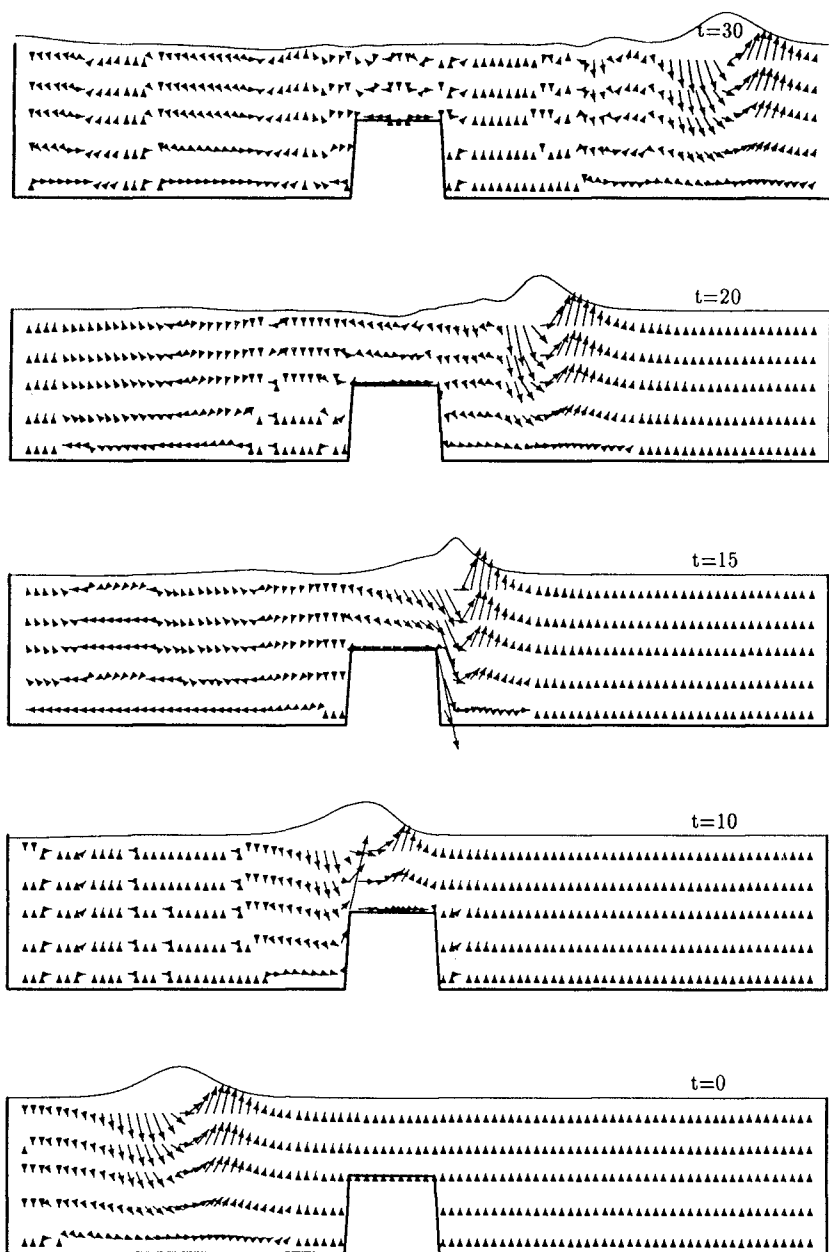
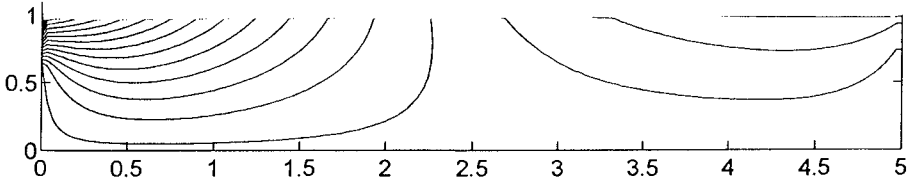
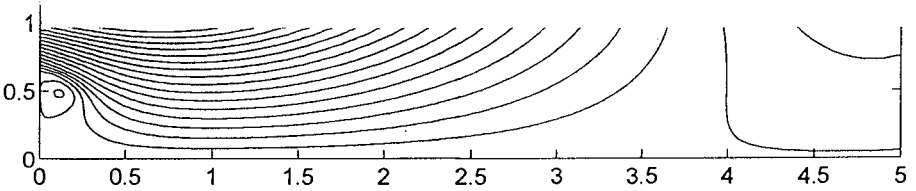


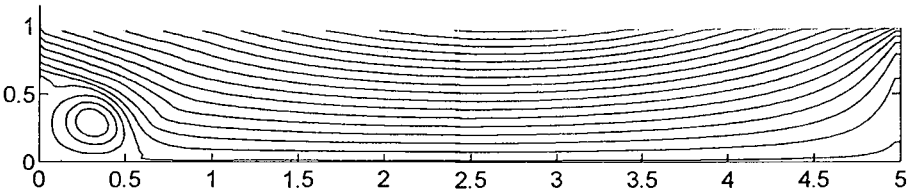
Figure 2: Velocity vector field at five time instants for the case of  $H/h=0.2$  solitary wave (based on the boundary element method of Lee, Chang and Zhuang (1992))



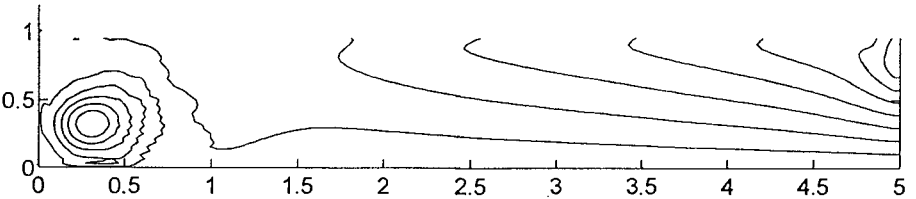
$t = 8$



$t = 12$



$t = 14$



$t = 18$

Figure 4: Streamlines at different time steps by the present model.

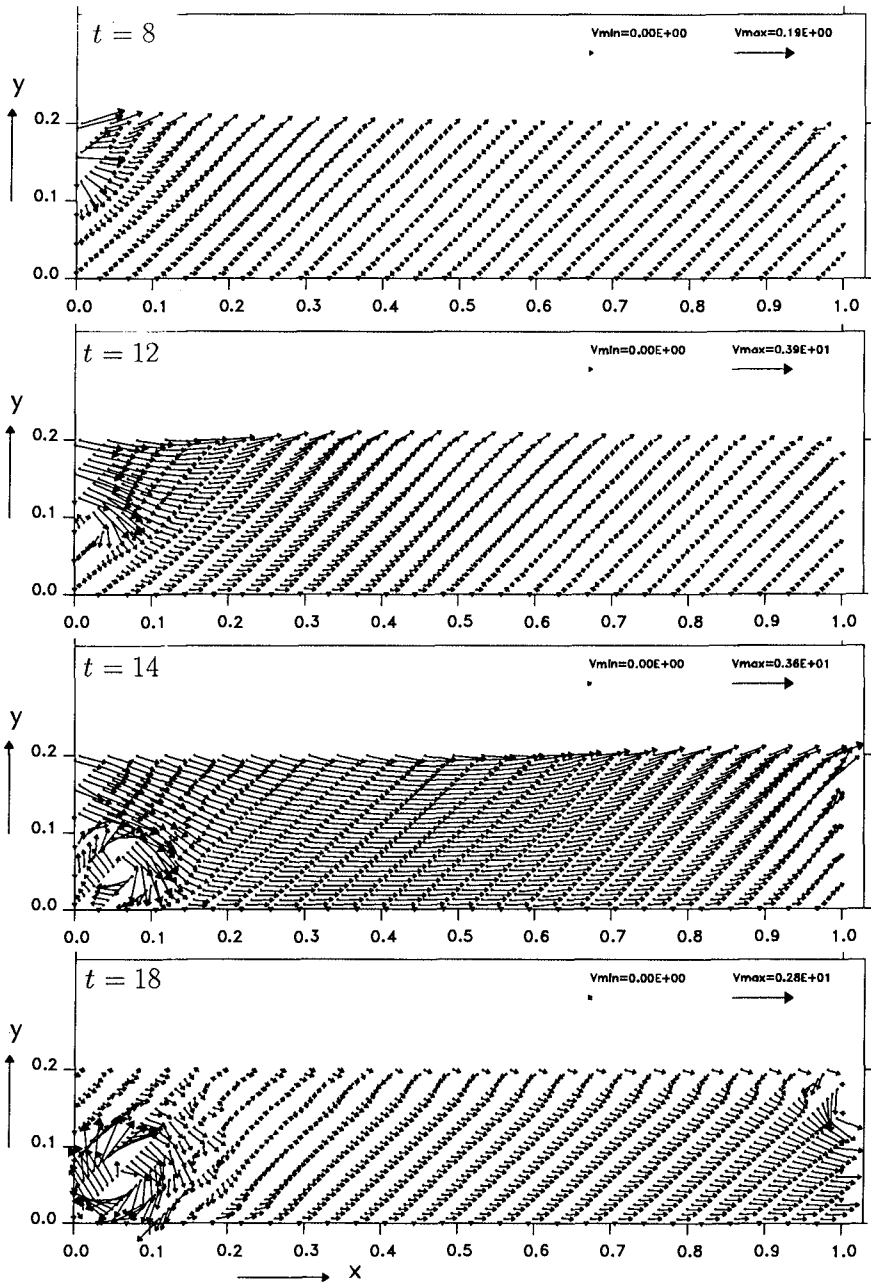


Figure 5: Velocity vector field at different time steps by the present model.



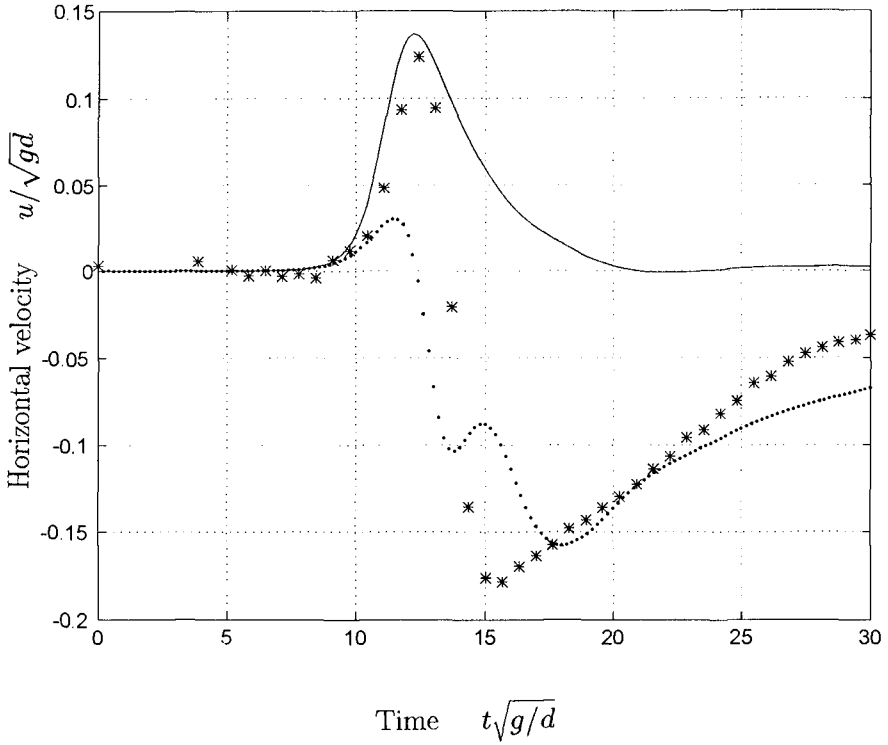


Figure 6: Comparison of horizontal water particle velocities at location P near the surface of the shoreward breakwater. The breakwater height to water depth ratio is 0.5 and the solitary wave height to water depth ratio is 0.3.

- present combined rotational model;
- potential flow theory using boundary element method;
- \* \* \* \* \* experimental measurements using Laser Doppler Velocimeter.

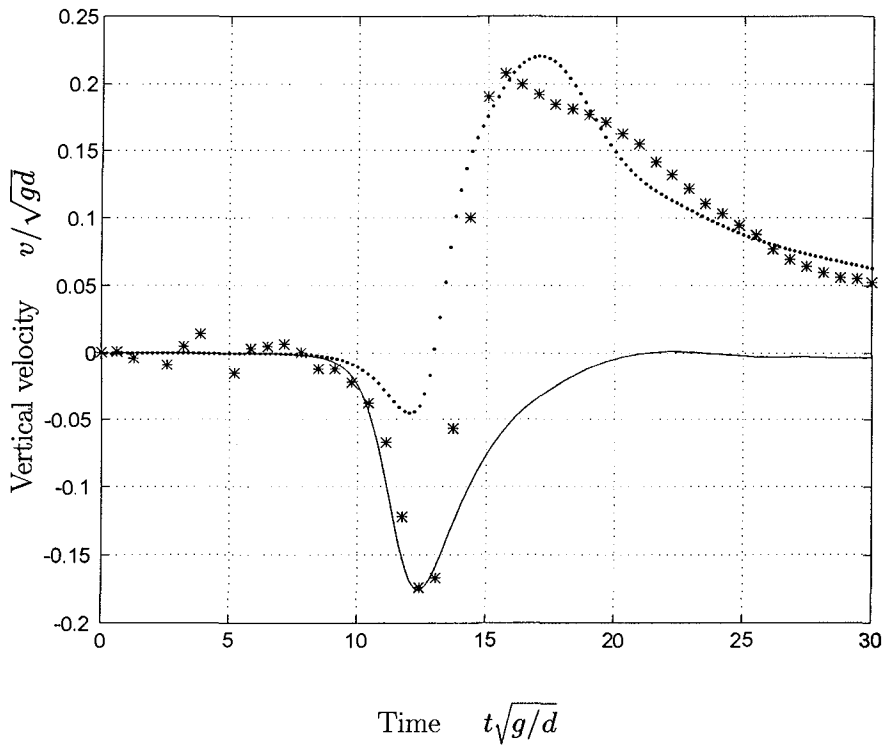


Figure 7: Comparison of vertical water particle velocities at location P near the surface of the shoreward breakwater. The breakwater height to water depth ratio is 0.5 and the solitary wave height to water depth ratio is 0.3.

- present combined rotational model;
- potential flow theory using boundary element method;
- \* \* \* \* \* experimental measurements using Laser Doppler Velocimeter.

## CHAPTER 123

# STRESSES IN TETRAPOD ARMOUR UNITS INDUCED BY WAVE ACTION

by

K. d'Angremond<sup>1</sup>, J.W. van der Meer<sup>2</sup> and C.P. van Nes<sup>1</sup>

### ABSTRACT

An extensive research program has been set up under the name of "*Rubble mound breakwater failure modes*". This research is part of the European MAST II project, (MARine Science and Technology) in which a number of universities and hydraulic institutes, from various countries in Europe, are participating.

In this study an analysis concerning the pulsating and impact portion of the tensile stresses inside tetrapod armour units is presented. The data has been obtained from a series of small scale model tests performed at Delft Hydraulics. Stresses have been measured using a load-cell technique developed and made available by Coastal Engineering Research Centre in association with Aalborg University Center.

For the tested area of the breakwater the following parameters only appeared to have influence on the stress distribution inside a leg of a tetrapod :

- significant wave height :  $H_s$
- water depth in front of the breakwater :  $h_{10c}$

Other parameters investigated which appeared to have no or a negligible influence on the stress distributions were:

- the fictitious wave steepness,  $s_{op}$
- the *location* of the tetrapod
- the *orientation* of the instrumented leg of the tetrapod.

---

<sup>1</sup> Delft University of Technology, P.O. Box 5048, 2600 GA Delft, The Netherlands,  
fax +31 15 78 5124

<sup>2</sup> Delft Hydraulics, P.O. Box 152, 8300 AD Emmeloord, The Netherlands,  
fax +31 5274 3573

## INTRODUCTION

In the late seventies, begin eighties a number of large breakwaters was severely damaged. The armour layer of these breakwaters consisted of slender concrete armour units, like dolosse or tetrapods.

It appeared that one of the main reasons of failure of these breakwaters was breakage of the armour units. Obviously, the mechanical strength of the armour units had been exceeded. The design of these breakwaters was actually based on extrapolation of experience from smaller or less exposed breakwaters.

New design methods, which not only take into account the hydraulic stability but the structural stability as well, are therefore needed. Especially for the slender armour unit types which are more vulnerable to breakage than the massive armour units.

## EARLIER RESEARCH

Two lines of research are identified on the determination of stresses in armour units. The first one, the CUR C70 investigation (1989, 1990), concentrated on movements or rocking of the armour units and the actual stresses in prototype armour units caused by those impacts.

The second line concentrated on describing the internal stresses of armour units by measuring the stresses directly inside the armour units. (Burcharth et al, 1993)

### *Rocking*

The impact momentum originating from collisions of rocking units can be described using the following parameters : (CUR C70, 1989)

- acceleration	a	[m/s <sup>2</sup> ]
- duration of impact	$\Delta t$	[s]
- development of acceleration in time	$\psi$	[-] (shape factor)
- mass	M	[kg]

The *integrated* signal of the accelerations,  $\int a \, dt$ , i.e. the impact *velocity*, can be scaled to prototype, using Froude, i.e.,  $\lambda_v = \lambda_L^{0.5}$ . (CUR C70, 1990) From this velocity, together with the mass of a prototype armour unit, the prototype impact momentum can be calculated. Further research was focused on the elasto-plastic behaviour of prototype colliding concrete units.

A design procedure based on the CUR C70 study results has been incorporated in the computer program, "ROCKING", using a full probabilistic approach. This takes into account the following elements:

- displacements, movements and impacts of armour units;
- impact velocities;
- impact behaviour;
- strength model.

For this probabilistic approach a Monte Carlo simulation has been used. The program calculates the number of broken units for a given combination of environmental conditions, armour unit characteristics and material properties. (Van der Meer and Heydra, 1990)

### *Direct method*

Whereas the CUR C70 approach concentrated on impact stresses due to rocking, Aalborg University Center investigated the behaviour of concrete armour units by directly measuring stresses in small scale models, not only measuring the loads or stresses caused by impacts but measuring the static and pulsating stresses as well.

Aalborg University Center has inserted a load cell in one of the two shank-fluke sections of a number of dolosse to investigate the stress distribution of dolosse. The dolos has been chosen because it was one of the types of armour units which caused the most problems when hydraulic stability and structural integrity were concerned.

Due to its slender form the dolos is vulnerable to breakage. Of all the component forces and moments, the two orthogonal bending moments,  $M_y$  and  $M_z$ , and torque,  $T$ , around the axial axis appear to be dominant. (Burcharth, 1991)

Beam theory has been used to calculate the maximum principal tensile stress at the surface,  $\sigma_T$ , using the cross sectional components moments as follows :

$$\sigma_T = \frac{\sigma}{2} + \sqrt{\left(\frac{\sigma}{2}\right)^2 + \tau^2} \quad (1)$$

where  $\sigma_T$  = maximum principal tensile stress [N/mm<sup>2</sup>]  
 $\sigma$  = normal stress [N/mm<sup>2</sup>]  
 $\tau$  = shear stress [N/mm<sup>2</sup>]

$$\sigma = \frac{\sqrt{M_y^2 + M_z^2}}{W_b} \quad \tau = \frac{T}{W_b/2} \quad (2)$$

where  $M_y$  = orthogonal bending moment [Nmm]  
 $M_z$  = orthogonal bending moment [Nmm]  
 $T$  = torque [Nmm]  
 $W_b$  = modulus of strain gauged cross section [mm<sup>3</sup>]

Failure is taken as the appearance of the first crack at the surface, i.e.

$$\sigma_T \geq S_T \quad (3)$$

where  $S_T$  = maximum tensile strength [N/mm<sup>2</sup>]

### PRESENT RESEARCH

In the present research, the method of measuring stresses in small scale units directly is used for the determination of stresses in tetrapod armour units induced by wave action. Model tests have been conducted in the 'Schedt' flume of Delft Hydraulics. This flume is 50 m. long, 1.0 m. wide and 1.2 m. deep.

#### Structural parameters

A 'standard' rubble mound cross section has been used, with a sloping foreshore of 1:50, Figure 1. The mass of the model tetrapods that have been used was 0.290 kg. The armour units were made of mortar with a mass density of  $\rho_a = 2307 \text{ kg/m}^3$ .

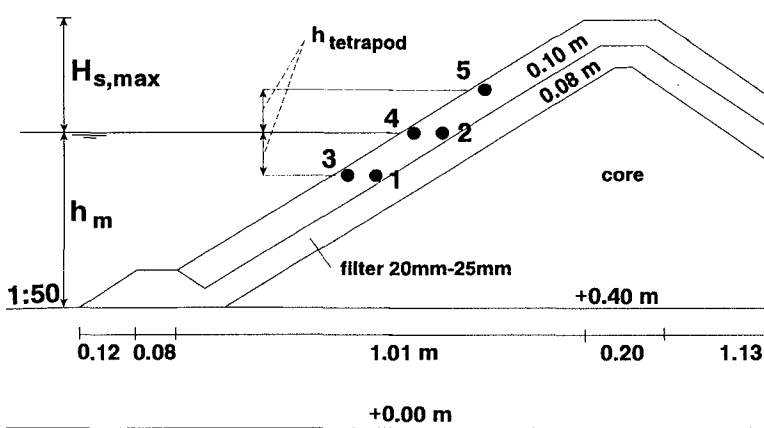


Figure 1 Cross section of model breakwater

#### Hydraulic parameters

Four different test series have been used, each consisting of 4 steps in which the significant wave height was increased. The spectrum used was a JONSWAP spectrum with a peak enhancement factor  $\gamma=4$ . For each repetition the same wave spectrum was used. In Table 1 an overview of the parameters is given.

The significant wave height,  $H_s$  and the wave steepness,  $s_{op}$ , given in Table 1 are the values near the wave board. The wave steepness is defined with the deep water wave length, i.e.

$$s_{op} = \frac{2\pi H_s}{gT_p^2} \quad (4)$$

- where  $H_s$  = significant wave height [m]  
 $g$  = gravitational acceleration [ $\text{m/s}^2$ ]  
 $T_p$  = peak period [s]

The relation between the 'deep' water significant wave height and the significant wave height at the toe of the structure has been determined before the actual model tests, without the structure present.

<i>variable</i>	<i>notation</i>		<i>range/value</i>	<i>remarks</i>
<i>mass</i>	$M$	[kg]	0.290	<i>tetrapods</i>
<i>mass density</i>	$\rho_a$	[kg/m <sup>3</sup> ]	2307	
<i>slope angle</i>	$\cot \alpha$	[-]	1.5	
<i>deep water depth</i>	$h$	[m]	0.70 and 0.90	<i>near the wave board</i>
<i>water depth at toe</i>	$h_m$	[m]	0.30 and 0.50	<i>at toe of structure</i>
<i>wave height</i>	$H_s$	[m]	0.10 - 0.25	<i>irregular, JONSWAP</i>
<i>wave period</i>	$T_p$	[s]	1.3 - 2.8	<i>peak period</i>
<i>wave steepness</i>	$s_{op}$	[-]	0.02 and 0.04	<i>near the wave board</i>
<i>number of waves</i>	$N$	[-]	200	
<i>location of tetrapod</i>		[-]	5	
<i>orientation of leg</i>		[-]	2	<i>perpendicular and parallel to slope</i>

**Table 1** Different parameters and their values or ranges

### Measurement of stresses

Five model tetrapods have been instrumented and calibrated by Aalborg University Center (Report 2<sup>nd</sup> workshop MAST 2, 1994) applying the same load-cell technique that was used for the dolos research. The instrumented tetrapods were able to record the bending moments in the critical cross section, i.e.,  $M_y$  and  $M_z$ . (Figure 2)

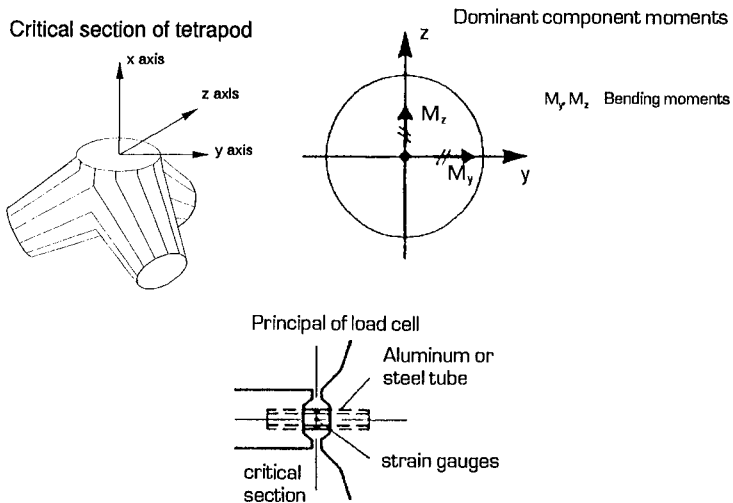


**Figure 2** Instrumented critical section of a tetrapod

Both the static and pulsating stresses as well as the impact stresses have been measured. In order to do so, the sample frequency of the instrumented tetrapods was set at 6000 Hz keeping well above the natural frequency of the instrumented leg of the tetrapod, which was approximately 800 Hz both in air and in water.

With 5 instrumented tetrapods on the model breakwater it was only possible to run 200 waves per significant wave height, i.e., 800 waves per test series, due to the enormous amount of data storage required (approx. 250 Mb/test)

### THE STRESS SIGNAL

Before starting with the analysis of the stresses, the stress signal itself will be discussed. Looking at a few examples of the stress signal, Figure 3, a number of conclusions can be drawn :

- the signal shows some noise; the instruments were sensitive for the influences from the mains.
- the base level or static stress is not constant. Obviously, the armour units sometimes move which causes a change in static stress. ( $\sigma_{static}$ )
- on top of this static stress a gradually fluctuating stress component can be identified, i.e. the pulsating stress. ( $\sigma_{puls}$ )
- the impacts are clearly recognizable. ( $\sigma_{impact}$ )
- within one wave period more than 1 impact may occur.

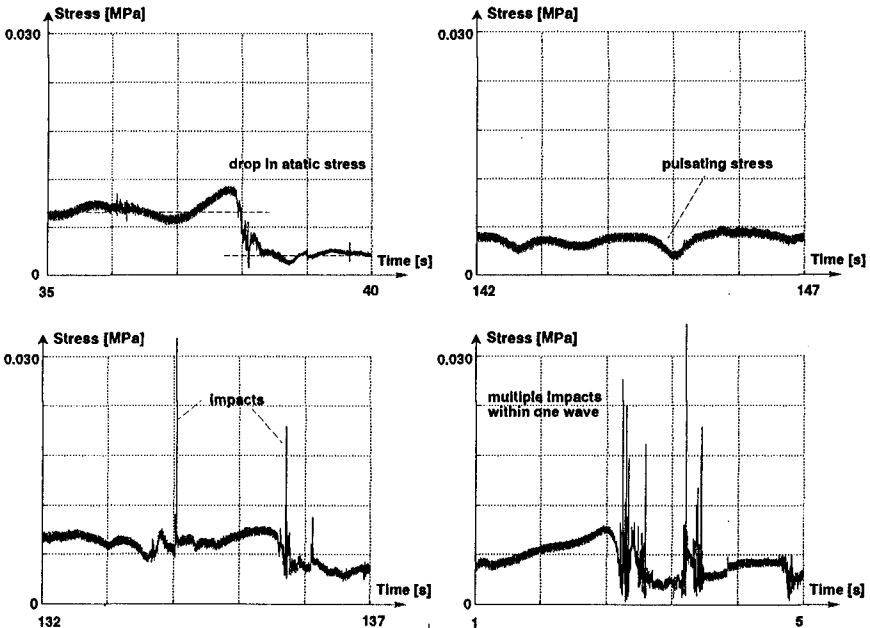


Figure 3 Examples of measured stress signals



Firstly, the noise was removed using a low-pass filtering technique. Together with the noise, the impacts are filtered as well.

Secondly, because of the fluctuations of the static stress, a moving average is needed in order to identify the local maximum value of the pulsating signal,  $\sigma_{puls,max}$ . This moving average was also determined using a low-pass filtering technique. Using the moving average as a reference, the treatment of the stress signal becomes more or less analogous to the analysis of a simple surface water wave.

Finally, the identification of the impacts was done by applying a high-pass filter technique on the raw stress signal which removed the lower frequencies, leaving the higher frequencies undisturbed.

### ANALYSIS OF STATIC AND PULSATING STRESSES

It appeared that only the wave height,  $H_s$ , the wave steepness,  $s_{op}$ , and the water depth,  $h_{toe}$  had influence on the combined maximum of the static and pulsating stress values, reducing the number of variables involved. In table 2 an overview of the found number of stress maxima is given.

<i>test series</i>	$H_{s,deep}$ [m]	$h_{toe}$ [m]	$s_{op}$ [-]	<i>Number of repetitions</i>	<i>Number of <math>\sigma_{puls,max}</math></i>	<i>Number of <math>\sigma_{impact}</math></i>	<i>N</i> [-]
1a	0.10	0.30	0.02	16	3474	615	3200
1b	0.15			16	3978	2157	3200
1c	0.20			19	4981	6010	3800
1d	0.25			22	5613	9340	4400
2a	0.10	0.30	0.04	21	4587	654	4200
2b	0.15			26	5602	1115	5200
2c	0.20			32	7041	2240	6400
2d	0.25			35	7906	3111	7000
3a	0.10	0.50	0.02	11	2409	14	2200
3b	0.15			12	2724	435	2400
3c	0.20			13	2921	509	2600
3d	0.25			14	3246	2604	2800
4a	0.10	0.50	0.04	10	2114	27	2000
4b	0.15			10	1988	203	2000
4c	0.20			13	2767	641	2600
4d	0.25			10	2393	1181	2000

**Table 2** *Number of found  $\sigma_{puls,max}$  and  $\sigma_{impact}$  for each combination of parameters*

On these 16 data-sets of stress values a Log Normal distribution has been fitted, giving typical plots like Figure 4. The Log Normal fit is described as follows :

$$f\left(\ln \frac{\sigma_{puls,max}}{\rho_a g D_n}\right) = \frac{1}{\sqrt{2\pi} \sigma_{LN}} \cdot e^{-\frac{1}{2} \cdot \left[ \frac{\ln\left(\frac{\sigma_{puls,max}}{\rho_a g D_n}\right) - \mu_{LN}}{\sigma_{LN}} \right]^2} \tag{5}$$

- where  $\sigma_{puls,max}$  = value of the maximum stress within a stress wave [MPa]
- $\rho_a$  = mass density of the armour units [kg/m<sup>3</sup>]
- $g$  = gravitational acceleration [m/s<sup>2</sup>]
- $D_n$  = nominal diameter of a tetrapod [m]
- $\mu_{LN}$  = average of Log Normal distribution [-]
- $\sigma_{LN}$  = standard deviation of Log Normal distribution [-]

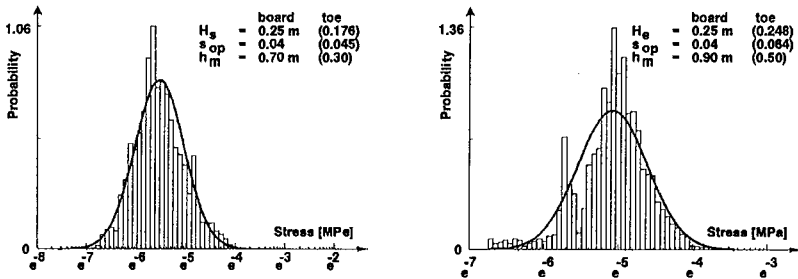


Figure 4 Two examples of fitted Log Normal distributions on data

The averages,  $\mu_{LN}$ , and the standard deviations,  $\sigma_{LN}$ , of the Log Normal distributions have been plotted as a function of the significant wave height and are given in Figure 5.

Although, the averages increases with increasing wave height, this increment is rather small. Therefore, the influence of the wave height is neglected and a horizontal line is assumed :

$$h_m = 0.30 \text{ m.} \quad \mu_{LN} = 1.10 \tag{5a}$$

$$h_m = 0.50 \text{ m.} \quad \mu_{LN} = 1.65 \tag{5b}$$

The standard deviation,  $\sigma_{LN}$ , seems to decrease somewhat with increasing wave height.

Again, a horizontal line is assumed, analogous to the research at Aalborg University Center. (Burcharth, 1993)

$$\sigma_{LN} = 0.53 \quad (6)$$

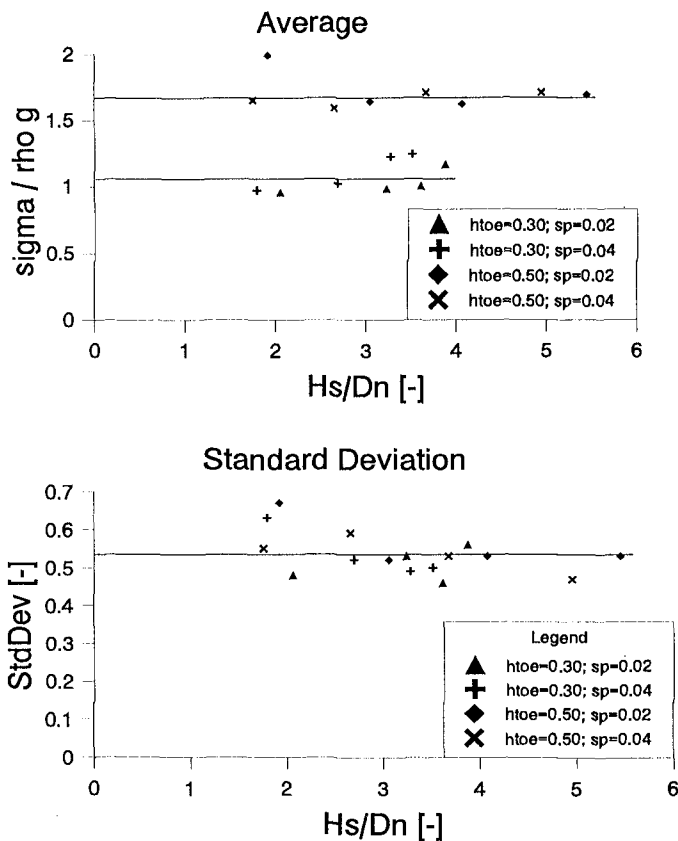


**Figure 5** The average and the standard deviation of the Log Normal fit as function of the wave height and the water depth

From these Figures, a number of conclusions can be drawn :

- the average,  $\mu_{LN}$ , of the Log Normal fit does not depend on the significant wave height. the water depth at the toe, however, does have influence on the combined static and pulsating stresses.
- the larger the water depth, the larger the combined static and pulsating stresses.
- the standard deviation,  $\sigma_{LN}$ , does not depend on both the significant wave height and the water depth at the toe.

## ANALYSIS OF IMPACT STRESSES

Before any statistical approach was applied to the impact stresses, a more detailed description of the physics was desired. Therefore, an effort has been made to answer the following questions :

- how many impacts can we expect within a test run?
- what are the orientations of these impacts?

Finally, the stress values itself, resulting from the concrete to concrete collisions have been described. This can be done in three different ways, i.e. :

- using all impact stress values and relate them to the number of impacts
- using the highest N impact stresses in a test run of N waves
- using the highest impacts stress value per wave and relate them to N waves

### Number of impacts

In Figure 6 the development of the number of impacts with increasing wave height is plotted for each tetrapod separately. Looking at Figure 6, it can be concluded that, firstly, the number of impacts increase with increasing wave height and, secondly, the number of impacts can vary substantially between two identical test series. Not only for the different locations investigated, but even for tetrapods at the same locations the number of impacts is quite different during subsequent tests.

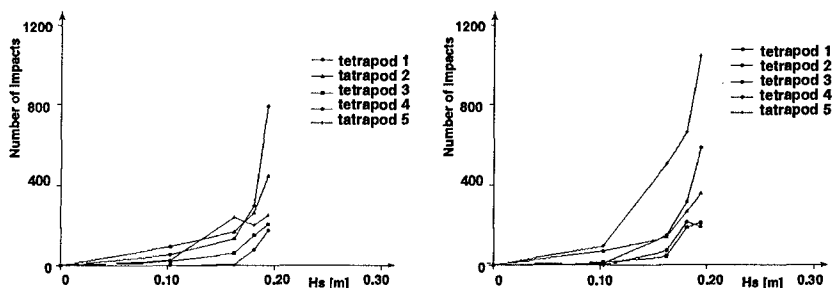


**Figure 6** Number of impacts as function of the significant wave height for two identical test series

Furthermore, it can be seen that for the larger values of the significant wave height, the number of impacts may exceed the number of waves. In the right plot of Figure 6, the tetrapod at location 5 received nearly up to 1000 impacts in 200 waves. This is clearly of importance when looking at fatigue of tetrapod armour units.

### Location of impacts

The next question concerned the location of the maximum tensile impact stress around the critical cross section. Taking the raw data signal which contains both the bending moments in X and Y direction, it is possible to obtain plots as presented in Figure 7.

From the plots it can again be seen that the number of impacts increases with increasing wave height. Secondly, the stress values become larger with increasing wave height. Finally, the scatter becomes larger.

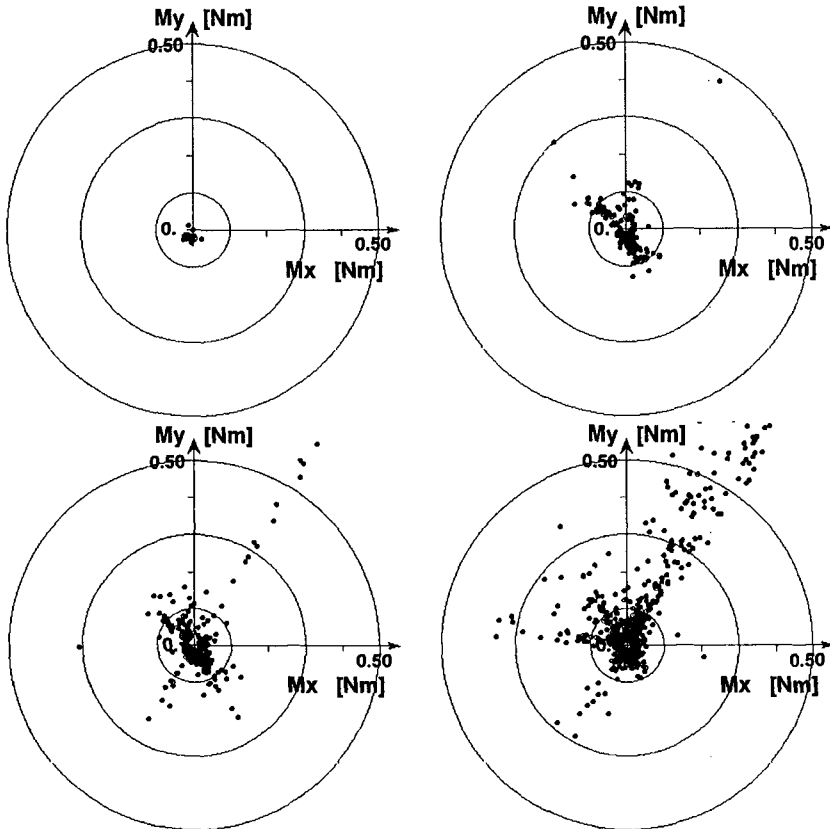


**Figure 7** Typical plots of development of orientation and size of the X and Y moment in a critical cross section of one tetrapod throughout a test series

Obviously, the armour unit was 'thrown around' the breakwater slope, hitting other tetrapods or being hit by others, resulting in a larger number of impacts from various directions. However, a number of main axes (1 to 3) are present. Again, this is important when looking at fatigue of the elements.

#### *Impact stresses*

Finally, a description of the actual impact stresses is needed. In Figure 8, two of the three earlier mentioned possible ways of presenting the impact stresses are given.

Firstly, in the left plot the stress levels of each test run are plotted that are exceeded by 1% of the total number of impacts in that test run. Secondly, in the right plot the 2nd highest stress value of each test run, i.e. 200 waves, is used. This stress value is given an exceedance value of 2/200.

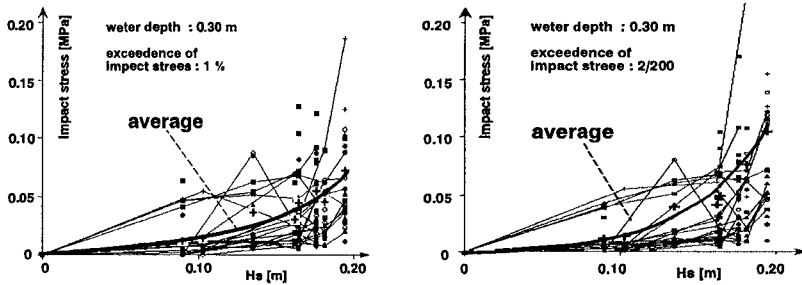


**Figure 8** Impact stresses related to number of impacts (left) and to number of waves (right)

Figure 8 clearly, shows the difference in stress level when plotting either the 1% exceeded stress level, which is related to the number of impacts, i.e. the length of the data-set, or plotting the 2/200 exceeded stress level, which is related to the length of the test run.

The solid line in both plots is calculated using a weighted average of these stress values using the number of points per test run over the total number of points in the vertical as the weight factor.

Conclusions, based on the obtained data-sets, that can be drawn on the impact stresses, are :

- with increasing wave height, the number of impacts, the scatter in the orientation of the impacts and the impact stress values increase as well.
- for the larger water depth, i.e.  $h_{loe} = 0.50$  m the impact stresses are larger than compared to the depth limited case. This is according to the combined static and pulsating stresses.

### PRELIMINARY DESIGN DIAGRAMS

Finally, combining the two descriptions, i.e., firstly, the Log Normal fit for the combined static and pulsating stresses and, secondly, the weighted average for the 1% exceeded impact stress level, it is possible to present very preliminary design diagrams for the stresses in tetrapod armour units exposed to wave action.

In Figure 9 the preliminary design diagrams are given for both the depth limited case as well as the deep water case, using the impacts stress levels related to the

number of impacts, i.e the solid line presented in the left plot of Figure 8.

The curved solid lines are the 1% exceeded impact stress levels for the prototype case of  $M = 20$  ton. From these Figures the more general conclusions can be drawn that the utmost care is recommended when applying tetrapods with a mass over 25 tons. For larger units it is advisable to reduce the permitted  $H_s/D_n$  values.

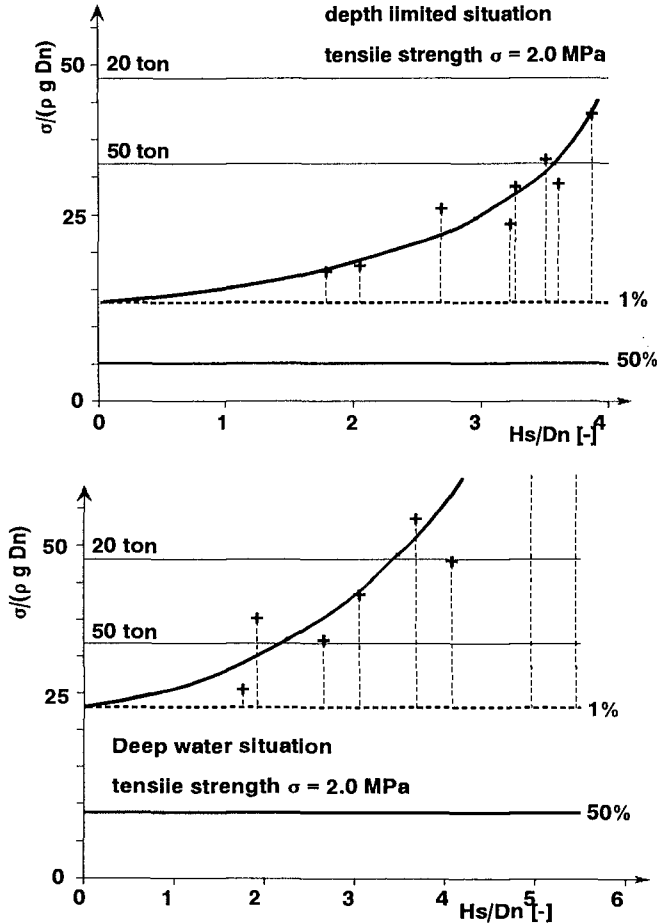


**Figure 9** Preliminary design chart for both the depth limited situation (top) and the not depth limited situation (bottom). 50% and 1% lines are stress level exceeded by the combined static and pulsating stress

However, because large differences between subsequent test runs have been observed under identical conditions, the randomness of the construction process of the breakwater must have large influence on the variation in stress level.

As the number of repetitions for each of the combinations of the parameters involved, i.e.  $H_s$ ,  $h_{toe}$ ,  $s_{op}$ , location and orientation, was rather small, it was not possible to derive trends between all individual variables and the accompanying stress distributions.

This means that further conclusions, concerning the influence of the individual parameters on the stress distributions, can only be drawn after performing a large number of tests, each test including a full reconstruction of the slope. However, before setting up such an extensive test program, it is recommended that a comparison is made between the method of measuring stresses in small scale armour units and the CUR C70 "Rocking" method.

#### REFERENCES

- Burcharth H.F., Howell, G.L. and Liu, Z., 1991. On the determination of concrete armour units stress including specific results related to dolosse. *Coastal Engineering, Vol. 15.*, pp. 129
- Burcharth, H.F., 1993. *Structural integrity and hydraulic stability of dolos armour layers.*, pp. 104
- CUR C70, 1989. Study group I "Investigation". Integration of stages 1-3. *Breakwaters. Strength of concrete armour units.* The Netherlands.
- CUR C70, 1990. Summary. *Breakwaters. Strength of concrete armour units.* (Dutch and English summary) The Netherlands.
- MAST 2 Rubble Mound Breakwater Failure Modes, Production and calibration of instrumented tetrapods, *Report 2<sup>nd</sup> workshop*, Bressanone, Italy
- Van der Meer, J.W. and Heydra, G., 1990. Rocking armour units: number, location and impact velocity. *Coastal Engineering, Vol. 15.*, pp. 38



## CHAPTER 124

# PORE PRESSURES IN RUBBLE MOUND BREAKWATERS

M.B. de Groot<sup>1</sup>, H. Yamazaki<sup>2</sup>, M.R.A. van Gent<sup>3</sup> and Z. Kheyri<sup>4</sup>

## ABSTRACT

Economic breakwater design requires knowledge of the wave induced pore pressures in the rockfill in view of sliding stability, filter requirements, wave transmission, wave overtopping and internal set-up. A mathematical model for the prediction of these pressures and the associated pore water flow has been developed. The model gives an integrated description of both external flow and internal flow. The sensitivity of the output to several input parameters and the validation of the external flow to model tests is discussed.

## 1. INTRODUCTION

Wave induced pore pressures influence the behaviour of rubble mound breakwaters in several ways. This may be relevant for the design. A numerical model, MBREAK/ODIFLOCS, has been developed for the prediction of pore water flow and pore pressures in the mound. Use is made of the progress made in the description of the external flow by Kobayashi and others (1987) and that made in the description of the internal flow by Barends and Hölischer (1988). The new model, however, gives an integrated description of both flow types. See Figure 1.

The paper will describe the relevancy of the pore pressures for the design, the basic features of the model, its potentials and its limitations. The results of a systematic series of calculations will be presented and the validation of the model with the help of measurements performed in flume tests, will be discussed.

---

<sup>1</sup> Delft Geotechnics, P.O. Box 69, 2600 AB Delft; <sup>2</sup> Port and Harbour Research Institute, Yokosuka; <sup>3</sup> Delft University; <sup>4</sup> I.H.E., Delft.

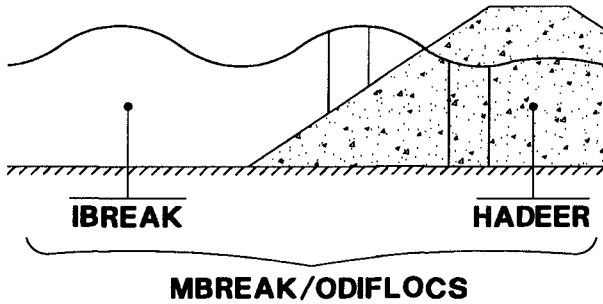


Figure 1 MBREAK/ODIFLOCS as a combination of two existing models

## 2 PORE PRESSURES AND DESIGN

Economic breakwater design requires knowledge of the wave induced pore pressures in the rockfill. Figure 2 illustrates five design features that may be influenced by the pore pressures and pore water flow:

- A) Sliding stability may be seriously affected by the combination of a high pressure head in the rock fill mass and the low pressure head at the slope during run-down.
- B) A three layer thick geometric filter is often needed underneath a rubble mound breakwater constructed at a sandy seabed, according to traditional filter design. More economic "hydraulic" filter design enables a reduction of the number of filterlayers where the pore pressure gradients are low (de Groot et al 1993).
- C) The wave climate inside any harbour basin partly depends on the wave transmission through the rubble mound, which mainly depends on the absorption of wave energy due to pore water flow.
- D) Wave overtopping also influences the wave climate in the harbour. It is greatly influenced by the discharge of water seeping into the mound during run-up, which discharge is an important feature of the pore water flow.
- E) The water table in any sandy back-fill may rise one or two meters due to wave induced internal set-up, depending on the flow characteristics inside the mound.

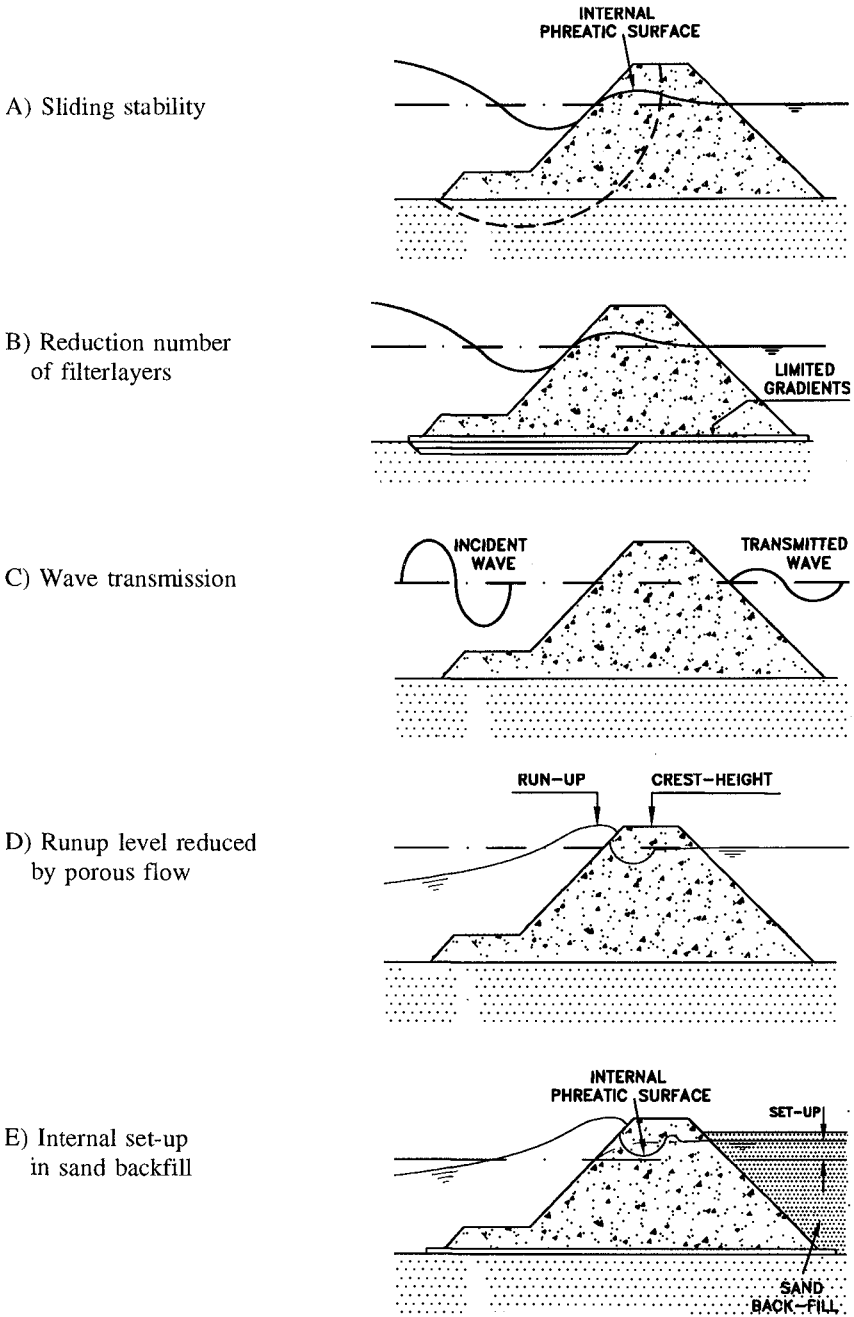


Figure 2 Breakwater design influenced by pore pressures

### 3. EXTERNAL AND INTERNAL FLOW

External and internal flow have much in common. Water level variations dominate both flow types. The pressure variations in vertical direction are roughly hydrostatic in most regions. The momentum in horizontal direction is determined in both flow types by inertia (including momentum convection), gravity (including pressure gradient) and friction.

There are, however, some important differences. Friction in the porous flow is much larger than friction in the external flow. Thus, the internal flow is dominated by friction and gravity; the external flow by inertia and gravity. The large friction limits the internal water velocities much more than the external velocities. As the water surface cannot move quicker than the water, also the motion of the internal phreatic surface is more limited than the motion of the external free surface. Thus, the friction causes a limited upward speed of the internal phreatic surface during uprush (Figure 3) and a limited downward speed during downrush. This yields the phenomenon of "disconnection" of the water surfaces: the point E where the external water surface meets the slope, is higher than the point I where the internal phreatic surface meets the slope during wave uprush (Fig.4A) and the other way around during downrush (Fig.4B)

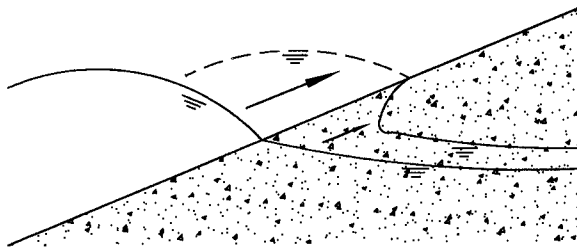


Figure 3 Speed difference between external and internal watersurfaces

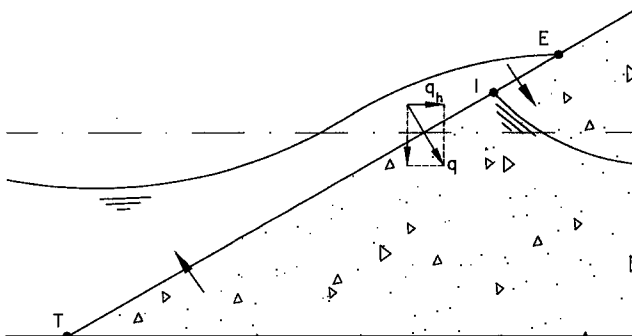


Figure 4A Water surfaces during maximum run-up

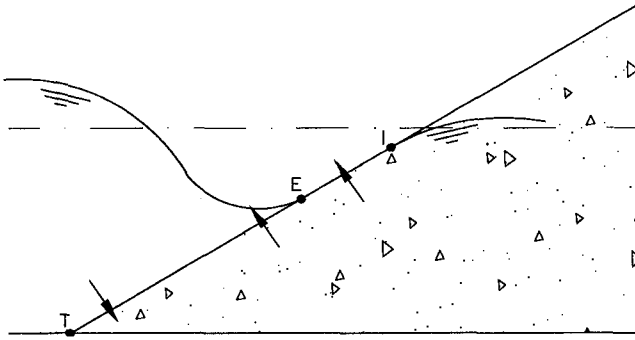


Figure 4B Water surfaces during maximum run-down

#### 4. MODEL DESCRIPTION

The above given flow characteristics enable both flow types to be largely described with long wave equations: for each flow type one storage equation and one equation for the momentum in horizontal direction. The coupling between both flow types requires a term to be added to the usual terms in each equation (Figure 5): an additional term in each of both storage equations for the infiltration discharge through the slope,  $q$ , and one in each of both momentum equations for the product of  $q$  with its horizontal component,  $q_h$ . Last term, however, can be neglected in many cases.

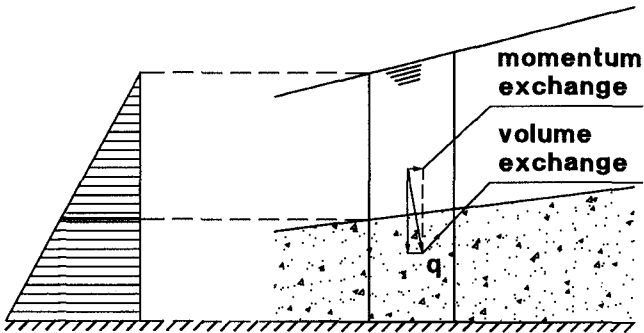


Figure 5 Coupling terms to be added to storage and momentum equations

At the seaward boundary of the external flow an incident wave is computed either with the Stokes second-order wave theory or the Cnoidal wave theory (Figure 6). The seaward boundary allows a reflected wave to leave the computational domain. This is calculated with the method of characteristics. This method allows water and momentum to leave the computational domain.

The modelling of the harbourside boundary of the external flow is based on work by Kobayashi et al. (1987). It uses a minimum waterdepth ("waterfilm") at the wave front above which level the slope is set dry.

The discharge through the slope,  $q$ , is a given boundary condition for the external flow, derived from the calculation of the internal flow. However, when point E is higher than point I (Fig. 4A),  $q$  between those points is the discharge of water freely falling through the partly saturated area. It is taken equal to the discharge which occurs when the downward head gradient equals unity. The water is supposed to reach the phreatic surface of the internal flow immediately.

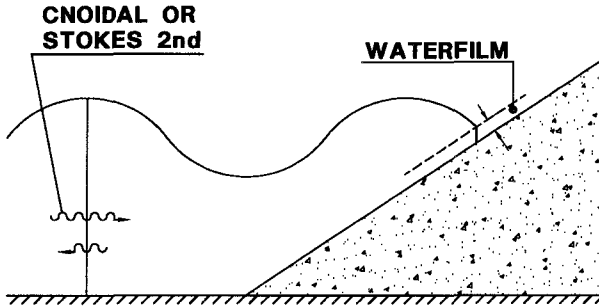


Figure 6 Modelling of the external flow

The slope between the toe, T, and point I makes up the seaward boundary of the internal flow. There the pressurehead is a given boundary condition, derived from the calculation of the external flow. When point E is lower than point I (Fig. 4B), then the head between those points is taken equal to the slope surface.

The harbourside boundary can be either an open boundary, allowing a wave to leave the calculation domain (Figure 7A) or a closed boundary at which a wave reflects completely (Figure 7B). A breakwater with a sand backfill can be modelled with last option.

Two or more layers with different stone sizes can be modelled. At the boundary between two layers disconnection can take place, just like at the external slope.

The water movement in and over a breakwater with limited crest height can be described with a special model option, allowing for the prediction of the wave radiating into the harbour by a combination of overtopping and penetration through the porous mound (Figure 7C).

Three different versions of the model have been made: 1) ODIFLOCS, 2) a one dimensional version of MBREAK and 3) a semi two-dimensional version of MBREAK. The numerical schemes of ODIFLOCS and MBREAK differ, as do certain minor assumptions about the flow properties. Version 3) is realised by alternately calculating the two-dimensional internal velocities with a stationary model with given phreatic surface, calculating the corresponding horizontal discharge and calculating the phreatic surface change with the one-dimensional model. Application of the different versions for the same situation yields a helpful tool to study the influence of numerical effects and particular assumptions.

A more extensive description of the different versions of the model can be found in (van Gent and Engering 1992); more about ODIFLOCS in (van Gent 1994).

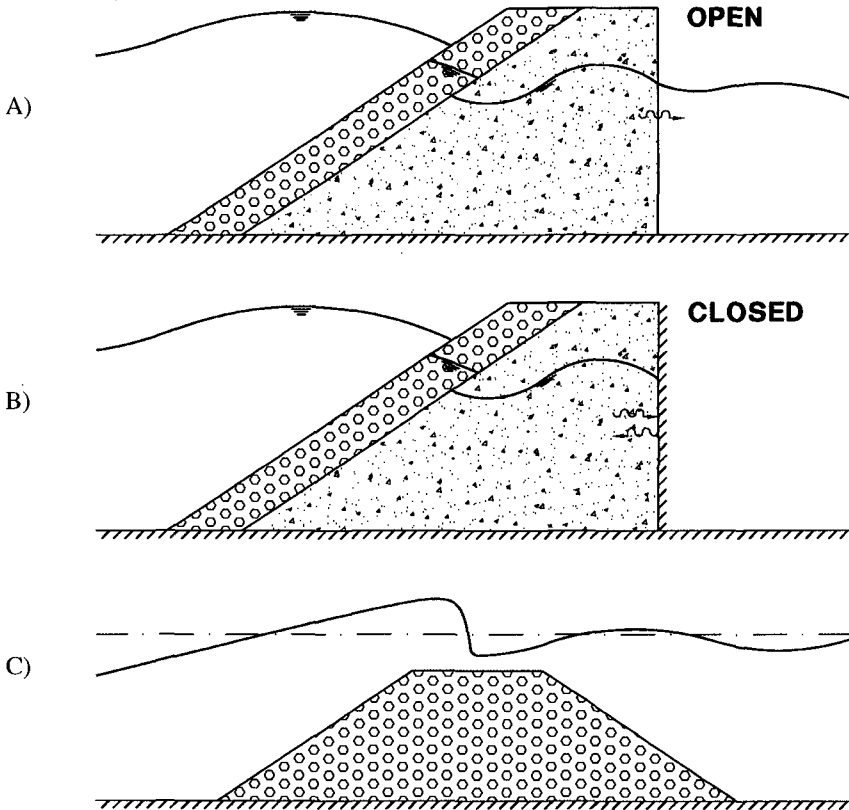


Figure 7 Different options for breakwater modelling

## 5 VALIDATION

The validation of the model started with an extensive sensitivity analysis for both model parameters and physical parameters. Application of the model requires assumptions concerning several model parameters, like the mesh size, the water film thickness, the maximum variation speed of the internal water level, the friction coefficients for the external and internal flow, the coefficient for added mass. Many calculations have been done in which these parameters have been varied to find out which parameter values would yield reasonable values.

The waterfilm thickness has a very large influence on many output parameters. An example is presented in Figure 8. It is seen that small values of the waterfilm thickness yield unreliable values of the run-down. An advise about the waterfilm thickness in proportion to the waveheight is formulated based on these results and a comparison with measurements of the run-down.

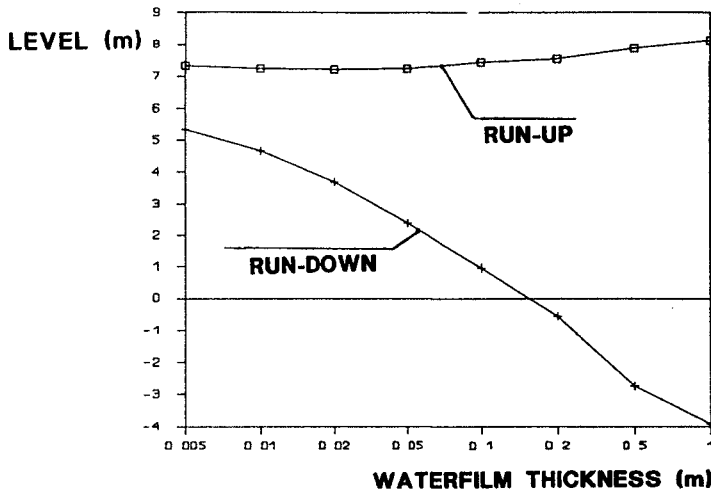


Figure 8 Influence of waterfilm thickness on run-up and run-down

Another important model parameter is related to the disconnection of the external and internal watersurface. A realistic limit to the speed of the internal watersurface must be selected. It can be shown that the maximum value of the downward speed equals the "free fall velocity" of the water, i.e. the downward water discharge per unit area occurring with a downward head gradient of unity, which means a pressure constant with depth. The upward watersurface speed may be more, because the effective upward gradient may reach higher values than unity during uprush (Hölscher et al 1988). Values up to 3 times the free fall velocity seem possible. A much higher limit yields the same results as no limit at all.

The external run-up and run-down, i.e. the highest level and the lowest



level of the points E of Figure 4, are hardly influenced by the limit to the internal watersurface speed. However, the internal run-up and run-down, i.e. the highest level and the lowest level of the points I of Figure 4, do depend a lot on this limit (Figure 9). It is of great interest to study this limit more in detail.

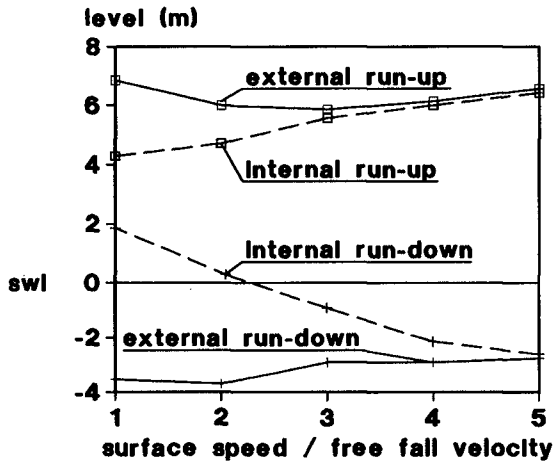


Figure 9 Influence of limit to internal water surface speed

Not only model input parameters have been varied during the sensitivity analysis, but also physical input parameters: the surf similarity parameter  $\xi$ , slope roughness, stone size, porosity, number of stone layers. Stone size and porosity determine the permeability of the rock fill. Its large influence on the external flow is illustrated in Figure 10 for a breakwater with impermeable core and permeable berm and for a completely impermeable berm breakwater (scaled to prototype dimensions). The thin lines show the water levels for the permeable breakwater at different moments during one wave. The thick lines represent their envelop. The envelop for the impermeable breakwater is indicated with interrupted lines. It is seen that the permeability of the breakwater has a large influence on the external head distribution, including run-up and run-down.

The relative influence of the different input parameters to one output parameter has been presented in Figure 11 as a kind of summary of the sensitivity analysis. The choice of the waterfilm thickness has the largest influence on output parameters like run-up level and discharge through the slope. Other important input parameters are the friction factors, the porosity the armour stone size and the wave period.

**WATER SURFACE LEVELS (m)**

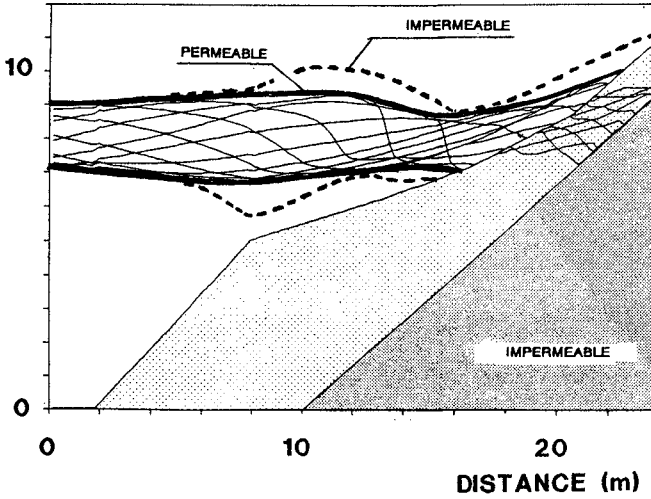


Figure 10 Influence of permeability on external water surfaces

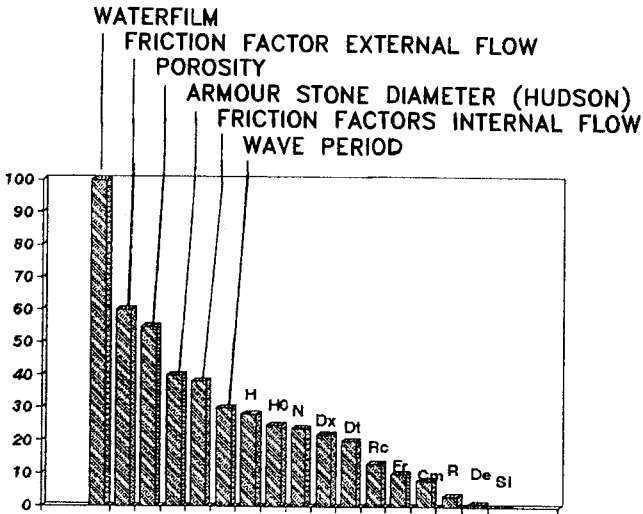


Figure 11 Relative influence of different input parameters to one output parameter

The effects of the parameter variation on the internal pore pressures and the external water movement, observed in these and other calculations, were qualitatively reliable. Whether they are quantitatively correct, however, can only be judged by comparison with model tests.

Many model test results are available on run-up values. Calculations made with MBREAK/ODIFLOCS for impermeable slopes for different values of the surf similarity parameter  $\xi$ , yield external run-up and run-down values which agree very well with model results. The same holds for the run-up values calculated for the breakwaters with permeable coverlayers tested by Ahrens (1975), as illustrated in Figure 12.

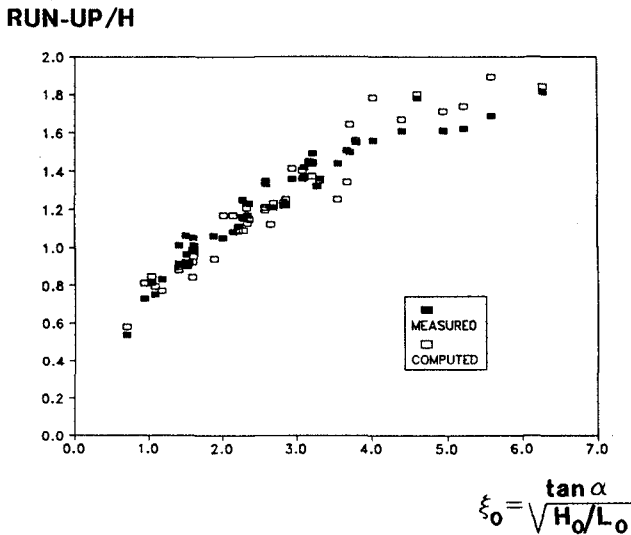


Figure 12 Run-up levels for breakwaters with permeable coverlayer

## 6 CONCLUSIONS

With MBREAK/ODIFLOCS a successful integration is realised of the mathematical modelling of the external flow on the slope of a rubble mound breakwater and the induced internal flow in the breakwater. Part of the success is due to the modelling of the disconnection between external and internal water surfaces. The sensitivity analysis made clear that many phenomena can be predicted qualitatively well. Run-up values can also be predicted fairly well. The further quantitative validation, however, is limited and requires more hindcasts to be made with the model for flume tests in which pore pressures have been measured.

## ACKNOWLEDGEMENTS

The model has been developed in the frame-work of the European MAST-G6-Coastal Structures project, co-sponsored by the Commission of the European Communities Directorate General XII (contract 0032-C). The sensitivity analysis is performed by close cooperation between the International Institute for Infrastructural, Hydraulic and Environmental Engineering (IHE) and Delft Geotechnics.

## REFERENCES

- Ahrens, J.P. (1975). "Large wave tank tests of riprap stability." *Technical Memorandum No. 5*. US Army Corps Eng., CERC, Ft. Belvoir, Va 22060.
- Barends, F.B.J., and Hölscher, P. (1988). "Modelling interior process in a breakwater." *Proc. of Breakwaters '88*, ICE, Design of breakwaters, Eastbourne, U.K., 49 - 58.
- Gent, M.R.A. van, and Engering, F.P.H. (1992). "The Modelling of Wave Action on and in Coastal Structures." *Proceedings of Final Overall Workshop of MAST G6-S Coastal Structures*. HR Wallingford, UK, Topic 1, Paper 1.2.
- Gent, M.R.A. van (1994). "The Modelling of Wave Action on and in Coastal Structures." *Coastal Engineering*, 22(3-4), 311 - 339.
- Groot, M.B. de, Bakker, K.J., and Verheij, H.J. (1993). "Design of geometrically open filters in hydraulic structures." *Filters in Geotechnical and Hydraulic Engineering*, Brauns, Heibaum & Schuler (eds). Balkema, Rotterdam, 143-154.
- Hölscher, P., Groot, M.B. de, and Meer, J.W. van der (1988). "Simulation of internal water movement in breakwaters." *Modelling Soil-Water-Structure Interactions*, Kolkman et al.(eds). Balkema, Rotterdam, 427-433.
- Kobayashi, N, Otta, A.K., and Roy, I. (1987). "Wave reflection and run-up on rough slopes." *J. of WPC & OE*, ASCE, 113(3), 282-298.

## CHAPTER 125

### WAVE ACTION ON AND IN PERMEABLE STRUCTURES

M.R.A. van Gent<sup>1</sup>, P. Tönjes<sup>2</sup>, H.A.H. Petit<sup>3</sup> and P. van den Bosch<sup>3</sup>

**ABSTRACT:** A numerical model that can simulate plunging waves on permeable structures is described. The 'Volume Of Fluid' method is used to solve the two-dimensional (2D-V) incompressible Navier-Stokes equations. After implementation of porous media flow for applications with permeable structures, the model has been verified by using several analytical solutions and by comparisons with physical model tests to study breaking waves on and inside permeable structures.

#### INTRODUCTION

Wave motion on permeable structures has often been studied using physical models. Small-scale physical modelling is influenced by scale effects while large-scale modelling is relatively expensive. Apart from this, measurements within breaking waves can be very complex. Therefore, numerical models simulating individual breaking waves are valuable design and research tools for studying wave motion on and inside coastal structures.

The description of breaking waves, the interaction with the porous part of permeable structures and the verification of the implementation of the most important phenomena involved, require a considerable amount of research of which some aspects are treated here. The numerical model described here (SKYLLA) was verified for breaking waves over a submerged bar, described in Van Gent *et al.* (1994-a). Other research concerning this numerical model, including the in- and outflow boundaries as well as the description of impermeable slopes were presented by Van der Meer *et al.* (1992) and Petit *et al.* (1994-b).

After a description of the numerical model and the method to solve the Navier-Stokes equations, adapted Navier-Stokes equations for porous media flow will be

---

1) Delft University of Technology, Department of Civil Engineering, P.O.Box 5048, 2600 GA Delft. 2) Rijkswaterstaat, Road and Hydraulic Engineering Division, P.O.Box 5044, 2600 GA Delft. 3) Delft Hydraulics, P.O.Box 152, 8300 AD Emmeloord, The Netherlands.

given. The implementation of these are validated using both analytical solutions and physical model tests. The physical model tests are performed with a Berm breakwater where surface elevations, velocities and pore-pressures are measured.

## NUMERICAL MODEL

Several models to simulate breaking waves have been made. For instance Vinje and Brevig (1981) used a potential flow model and modelled a plunging wave until the overturning wave hits the trough water. Sakai *et al.* (1986) applied the MAC-method to simulate breaking waves. Here, the 'Volume of Fluid' (VOF) method by Hirt and Nichols (1981) is used to solve the Navier-Stokes equations in two dimensions. This powerful method enables simulation of complex flow patterns including those where the free surface can become multiply connected. To achieve this, the treatment at the surface based on the adapted flux-method known as FLAIR by Ashgriz and Poo (1991), has been improved. Figure 1 shows that an overturning wave on an impermeable slope can be simulated by applying the Navier-Stokes equations solved using the VOF-method.

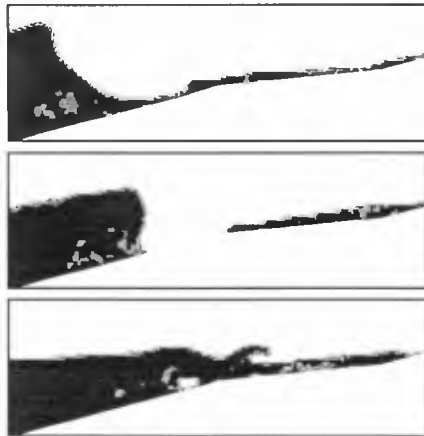


*Fig.1 Simulation of a breaking wave on an impermeable dike with a berm.*

The VOF-method is a method where for each cell the fluid fraction can vary between zero (empty) and one (full). Fluid fractions are transported between each cell and its surrounding cells. In Figure 2 the principle of the method is shown for the transport between two neighbouring cells. Based on the two fluid fractions of two neighbouring cells, a 'local surface' can be constructed. By using the velocity

and the time-step (varied based on the instantaneous stability and accuracy criteria), a part of the fluid is transported between these two cells. In the numerical model this is done using a non-equidistant staggered grid.

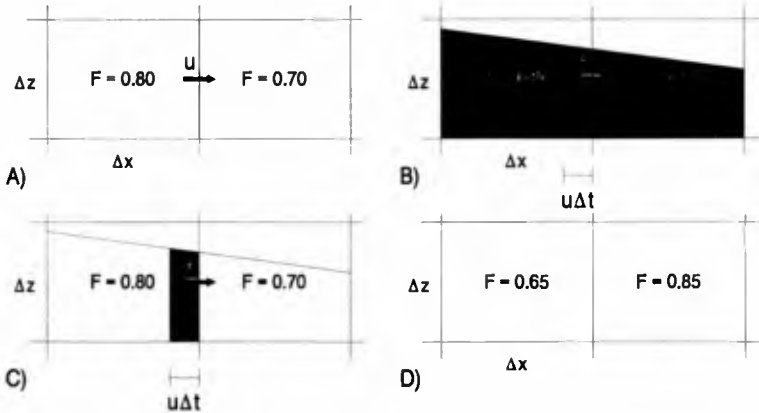


**Fig.2** Transport of fluid based on the VOF-method.

The velocity as used in the VOF-method is obtained from the discretisation of the Navier-Stokes equations. At impermeable slopes and at the free surface not all velocities necessary to discretise the equations are within the fluid domain. Figure 3 shows the required velocities for discretisation inside the fluid (A) and near the free surface (B). Boundary conditions are required to fill the lack of information at the free surface. For instance one can assume no gradient in the velocities at the surface or that the flow is irrotational at the surface.

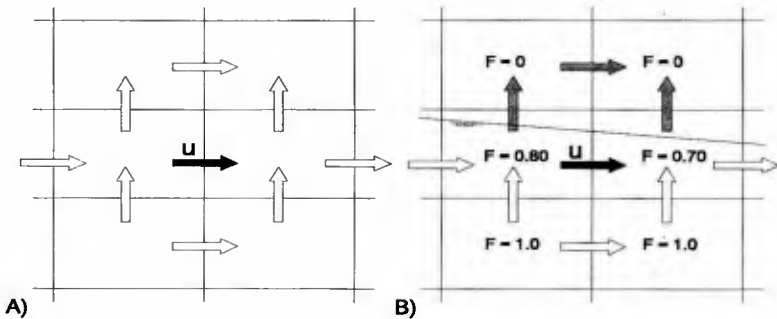


**Fig.3** Required information for discretisation of horizontal velocities.

Two open weakly-reflecting boundaries can be used at which regular wave trains can both be generated and absorbed. The incoming non-linear waves are based on the theory by Rienecker and Fenton (1981). The boundary for impermeable slopes are defined on sub-grid level which means that the slope can intersect cells (no 'stair-case' slope). At impermeable slopes no-slip or free-slip boundaries can be applied. In Van Gent *et al.* (1994-a) two weakly-reflecting boundaries were applied for wave breaking over a submerged bar schematised with a free-slip boundary. The comparison of these computed breaking waves with video images showed that plunging occurs at the same position as in the physical model tests. Although the decrease in wave height occurs somewhat quicker in the numerical model than in reality, the height of the transmitted wave is accurate. Here, after implementation of porous media flow, breaking waves on permeable structures will be verified.

## IMPLEMENTATION OF POROUS MEDIA FLOW

The VOF-method can also be applied for solving the wave motion inside permeable structures. The momentum equations, however, are different from those for the external wave motion. The Navier-Stokes/Reynolds equations for the external wave motion read:

$$\frac{\partial u}{\partial t} + \frac{\partial u^2}{\partial x} + \frac{\partial u w}{\partial z} + \frac{1}{\rho_w} \frac{\partial p}{\partial x} - \nu_t \left( \frac{\partial^2 u}{\partial x^2} + \frac{\partial^2 u}{\partial z^2} \right) + g_x = 0 \quad (1)$$

$$\frac{\partial w}{\partial t} + \frac{\partial u w}{\partial x} + \frac{\partial w^2}{\partial z} + \frac{1}{\rho_w} \frac{\partial p}{\partial z} - \nu_t \left( \frac{\partial^2 w}{\partial x^2} + \frac{\partial^2 w}{\partial z^2} \right) + g_z = 0 \quad (2)$$

where  $u$  and  $w$  are the velocities in the  $x$  and  $z$  direction respectively and  $\nu_t$  the eddy-viscosity for which a constant value will be used. Together with conservation of mass ( $\partial u/\partial x + \partial w/\partial z = 0$ ), which is satisfied by solving the Poisson equation, and boundary conditions, the VOF-method can then be applied yielding the external wave motion. For the internal wave motion adapted Navier-Stokes equations were derived (see Van Gent, 1991):

$$\frac{1+c_A}{n} \frac{\partial u}{\partial t} + \frac{1}{n^2} \left( \frac{\partial u^2}{\partial x} + \frac{\partial u w}{\partial z} \right) + \frac{1}{\rho_w} \frac{\partial p}{\partial x} + g_a u + g_b u \sqrt{(u^2+w^2)} + g_x = 0 \quad (3)$$

$$\frac{1+c_A}{n} \frac{\partial w}{\partial t} + \frac{1}{n^2} \left( \frac{\partial u w}{\partial x} + \frac{\partial w^2}{\partial z} \right) + \frac{1}{\rho_w} \frac{\partial p}{\partial z} + g_a w + g_b w \sqrt{(u^2+w^2)} + g_z = 0 \quad (4)$$

where  $u$  and  $w$  are both filter-velocities,  $a$  and  $b$  are dimensional friction coefficients and  $c_A$  is a coefficient to take the phenomenon *added mass* into account. Because filter/discharge velocities are used, the procedure to transport mass between the



cells, the VOF-method, does not require any adaptation. The discretisation (partial upwind scheme) and stability criteria are described in Van Gent *et al.* (1994-b). In the computational domain numerous regions with different properties can be selected and awarded a certain porosity and stone diameter. The permeable slopes are not, like for impermeable slopes, defined on sub-grid level which means that the properties cannot be varied within one cell. Permeable slopes can also be combined with impermeable regions. This implementation of permeable parts in this two-dimensional model, therefore, enables applications with breaking waves and other complex flow patterns for a very wide range of structure types. Here, some validation tests will be discussed. For some other applications see for instance Van Gent and Petit (1994).

## VALIDATION WITH ANALYTICAL SOLUTIONS

Several verifications of the implementation of porous media flow have been performed. Before the wave motion on and inside a permeable structure is verified using physical model tests, three comparisons with analytical solutions are carried out. The first case concerns a layer of water with a thickness  $L$  that is initially positioned above a dry permeable part, see Figure 4. At  $t=0$ , the layer of water starts entering the permeable part. For this simplified case of uniform flow entering a permeable part ( $-L < x_0 < 0$ ), the Navier-Stokes equations reduce to a set of one dimensional differential equations (Van Gent *et al.*, 1994-b) where  $u$  is the filter-velocity,  $n$  the porosity and  $x_0$  the position of the free surface, at  $t=0$ ,  $x_0=-L$ :

$$\frac{du}{dt} = \frac{-\frac{g}{n} (L + x_0) (a u + b u^2 - 1) - \left(\frac{1}{n^2} - 1\right) u^2 - g x_0}{\frac{L + x_0}{n^2} - x_0} \quad (5)$$

With  $dx_0/dt=u$ , this set of differential equations was solved using a fourth-order Runge-Kutta method with  $\Delta t=0.005$  s and  $\Delta x=0.05$  m while for the constants  $L$ ,  $n$ ,  $g$ ,  $a$ ,  $b$  the values 0.5 m, 0.5, 4 m/s<sup>2</sup>, 0 s/m and 16.9 s<sup>2</sup>/m<sup>2</sup> were used respectively (for  $g$ , 4 m/s<sup>2</sup> is taken instead of 9.81 m/s<sup>2</sup> to exaggerate the local maximum in Figure 4). After the layer has entered the permeable part, the differential equation reduces to:  $du/dt=ng(1-au-bu^2)$  for which an analytical solution was found:

$$u(t) = \left( u_1 - u_2 \frac{u(t_0) - u_1}{u(t_0) - u_2} e^{-bng(u_1 - u_2)(t - t_0)} \right) / \left( 1 - \frac{u(t_0) - u_1}{u(t_0) - u_2} e^{-bng(u_1 - u_2)(t - t_0)} \right) \quad (6)$$

where  $u_1=-a/2b + \sqrt{(a^2+4b)/2b}$ ,  $u_2=-a/2b - \sqrt{(a^2+4b)/2b}$  and  $u(t_0)$  is the initial velocity at  $t=t_0$  where  $t_0$  is the moment at which the whole layer of water has

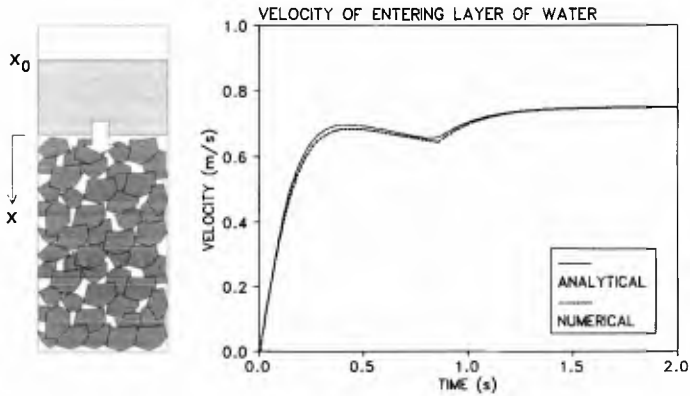


**Fig. 4** Comparison of numerical model results with solutions of simplified differential equations for the velocity of a layer of water entering a porous block.

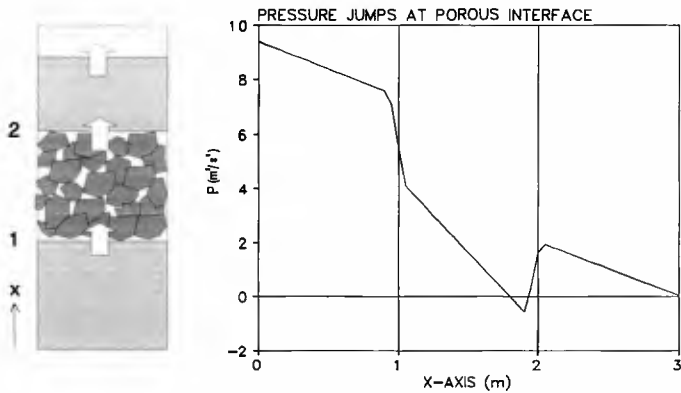


**Fig. 5** Calculated pressure jumps at the interfaces of a porous block with a steady flow.

entered the permeable part. Figure 4 shows the comparison of the numerical results and these solutions. At  $t=0$ , the velocity is zero, at  $t=0.435$  s a local maximum of  $u=0.6848$  m/s occurs and at  $t=0.850$  s ( $t_0$ ) the layer has entered the permeable part after which the velocity rapidly converges to the velocity 0.75 m/s. The difference between the numerical model results and the solutions of the set of simplified differential equations reaches a maximum of 0.0129 m/s at  $t=0.4$  s. As shown in Figure 4, the phenomenon is reproduced with good result.

A second verification concerns the flow through a saturated permeable block, see Figure 5. At  $x=0$  a constant inflow with a velocity of  $1\text{ m/s}$  is produced, between  $x=1\text{ m}$  and  $x=2\text{ m}$  a saturated permeable block is positioned. The pressure jumps at the porous interfaces ( $x=1\text{ m}$  and  $x=2\text{ m}$ ) can be determined analytically. Integrating the momentum equation for a uniform flow in the  $x$ -direction yields:

$$P(x_2 + \delta x) - P(x_2 - \delta x) = \left( \frac{1}{n^2} - 1 \right) u^2 - \delta x \left( g(au + bu^2 + 2) + \left( 1 + \frac{1 + c_A}{n} \right) \frac{\partial u}{\partial t} \right) \quad (7)$$

where  $x_2$  is the position of the outflow boundary ( $x=2\text{ m}$ ). The same procedure can be used at the inflow boundary ( $x=1\text{ m}$ ). The pressure jump is then equal to the one at the inflow boundary, except for the sign. Outside the stone the pressure is determined by  $\partial P/\partial x = -g$  while inside the stone the pressure gradient can be assessed through  $\partial P/\partial x = -g(au + bu^2 + 1)$ . In Figure 5 the comparison between the analytical solution and the numerical results is shown. Some arbitrary values for the constants  $n$ ,  $a$ ,  $b$  and  $g$  were used ( $0.5$ ,  $1\text{ s/m}$ ,  $0.75\text{ s}^2/\text{m}^2$  and  $2\text{ m/s}^2$  respectively). Because in the numerical model the pressure jumps are simulated in steps of  $3\Delta x$ ,  $\delta x = 3/2\Delta x$  is used in the analytical solution (Equation 7) for comparison with the numerical model results. The pressure jumps by the analytical solution and the numerical model results were  $2.4375\text{ m}^2/\text{s}^2$  and  $2.5065\text{ m}^2/\text{s}^2$  respectively. This comparison is again rather good. For  $\delta x \downarrow 0$ , the real analytical solution gives  $3\text{ m}^2/\text{s}^2$  to which the numerical model results will come close for smaller values of  $\Delta x$ .

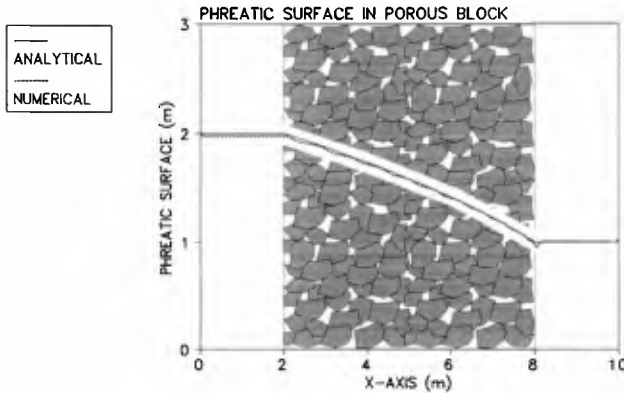


**Fig.6** Comparison of numerically computed phreatic surface and an analytical solution.

A third analytical solution has been compared with numerical model results. Now, a stationary flow through a rectangular block with only linear porous friction

( $b=0$ ) has been examined. Neglecting convection and assuming hydrostatic pressures and uniform flow over the depth, the solution for the phreatic surface is determined by  $h(x') = \sqrt{(H_1^2 - x'/L(H_1^2 - H_2^2))}$  where  $H_1$  is the free surface level at the inflow boundary (left in Figure 6),  $H_2$  is the free surface level at the outflow boundary and  $L$  the length of the permeable block (for Figure 6:  $x'=x-2$ ). Some arbitrary values for the constants  $n$ ,  $a$ ,  $L$  and  $g$  were used ( $0.2$ ,  $4.0$  s/m,  $6.0$  m and  $10$  m/s<sup>2</sup> respectively). The levels  $H_1$  and  $H_2$  were  $2.0$  m and  $1.0$  m respectively. In the numerical computation,  $\Delta x=0.1$  m has been used. The phreatic level was defined as the level where in the computation 50% of the cell was filled with water ( $F=0.5$ ). Differences between both phreatic surfaces at  $x=2, 4, 6$  and  $8$  m in Figure 6 were  $0.0233, 0.0206, 0.0105$  and  $0.0234$  m, respectively.

## VALIDATION WITH PHYSICAL MODEL TESTS

By means of the numerical model complex phenomena such as scale effects, wave transmission, the effects of non-stationary porous media flow, added mass and forces on stones can be studied. However, a verification with physical models must be performed first.

Non-stationary porous media flow tests have been performed in a U-tube tunnel. These measurements resulted in expressions for the porous media flow friction-coefficients  $a$ ,  $b$  and  $c_A$  in Equations 3 and 4, see Van Gent (1994). For the dimensional coefficients  $a$  and  $b$ , theoretically derived expressions are used:  $a = \alpha \cdot (1-n)^2/n^3 \cdot \nu/gD_{n50}^2$ ,  $b = \beta \cdot (1-n)/n^3 \cdot \nu/gD_{n50}$  and  $c_A = \gamma \cdot (1-n)/n$ . The physical model tests showed a dependency of  $\beta$  on the flow field, accounted for by including a dependency of  $\beta$  on the  $KC$ -number,  $\beta = \beta_c (1 + 7.5/KC)$ , where  $KC = \hat{U}T/nD_{n50}$  and  $\beta_c = 1.1$ . In the computations with the numerical model this has been included by estimating a representative filter-velocity  $\hat{U}$  beforehand and using the wave period for  $T$ .

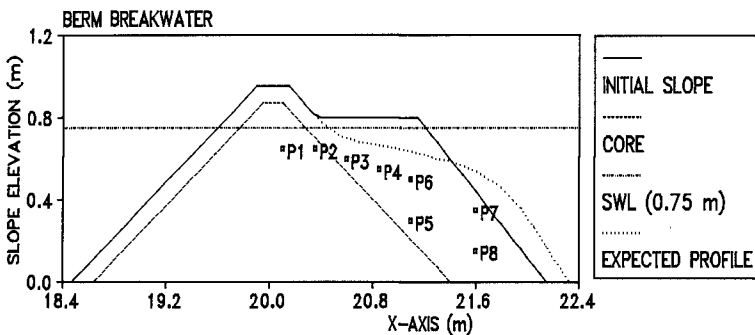


Fig. 7 Cross-section of the Berm breakwater in experimental set-up.

A second series of physical model tests was performed to verify the numerical model. A small-scale model of a Berm breakwater was used for this purpose. Figure 7 shows a sketch of the experimental set-up with the initially horizontal berm at a level of  $0.80\text{ m}$ , the still water level being  $0.75\text{ m}$ . All slopes were  $1:1.5$  except for the submerged seaward slope which was  $1:1.25$ . The size of the stone material was  $D_{n50}=0.0266\text{ m}$  in the cover layer and  $D_{n50}=0.0175\text{ m}$  in the core. The porosity of the two permeable parts were measured *in situ*, both giving  $n=0.417$ . Reshaping the seaward profile was achieved by four series of  $1000$  regular waves. After the last series, with the largest waves, the seaward profile was reshaped while the crest was heightened from  $0.95\text{ m}$  to  $1.00\text{ m}$ . Several series of regular waves were used to study the flow field. No reshaping took place during these tests. The flow field was recorded using a video, electro-magnetic flow meters (EMF), wave gauges and pressure transducers. The positions of the pressure transducers are indicated in Figure 7.

Surface elevations above the seaward slope were determined at ten points of time within a wave cycle for four series of regular waves:  $H=0.119\text{ m}$ ,  $T=1.5\text{ s}$ ;  $H=0.230\text{ m}$ ,  $T=1.5\text{ s}$ ;  $H=0.112\text{ m}$ ,  $T=2.1\text{ s}$  and  $H=0.217\text{ m}$ ,  $T=2.1\text{ s}$ . The computational domain in the numerical model started at  $4\text{ m}$  in front of the toe of the reshaped structure where the waves were generated at this weakly reflecting boundary by applying the method by Rienecker and Fenton (1981) using 16 Fourier-components. This method was adapted to deal with reflected waves as described in Petit *et al.* (1994-a). No net transport was allowed through this boundary. At the landward boundary again a weakly reflecting boundary was positioned at  $1.5\text{ m}$  behind the crest of the structure. In  $x$  and  $z$ -direction,  $270$  and  $80$  computational cells were used respectively. The computations were performed with a constant viscosity  $\nu_t=0.005\text{ m}^2/\text{s}$ . In the discretisation of the equations an up-wind fraction of  $0.2$  was used. Surface elevations were defined at positions of cells which were filled with fluid for  $50\%$ . After an adjustment time of six to eight waves to obtain a periodic computation, data was used for comparison with the measured properties.

Figure 8 shows comparisons of surface elevations for ten points of time for two wave conditions with a wave period of  $1.5\text{ s}$  (five surface profiles per graph with  $0.15\text{ s}$  in between two profiles). Only the surface elevations above the berm, where the waves are breaking, are shown since in the section in front of the structure only minor differences in wave height occur. Also for the two wave conditions with a wave period of  $2.1\text{ s}$ , as shown in Figure 9 ( $0.21\text{ s}$  in between two profiles), the comparisons for the five profiles in the first half of each wave cycle show good agreement (upper graph for each wave condition). In the second half of each wave cycle (lower graph for each wave condition) considerable air-entrapment occurs for the two highest waves. In the figures with measured surface elevations the position of entrapped air is indicated by the area in between the two lines of each surface profile. The comparisons with the computed results become rather complex in this part since the exact position of the free surface is not clear. However, the comparisons indicate that the decrease in wave height above the berm faster occurs

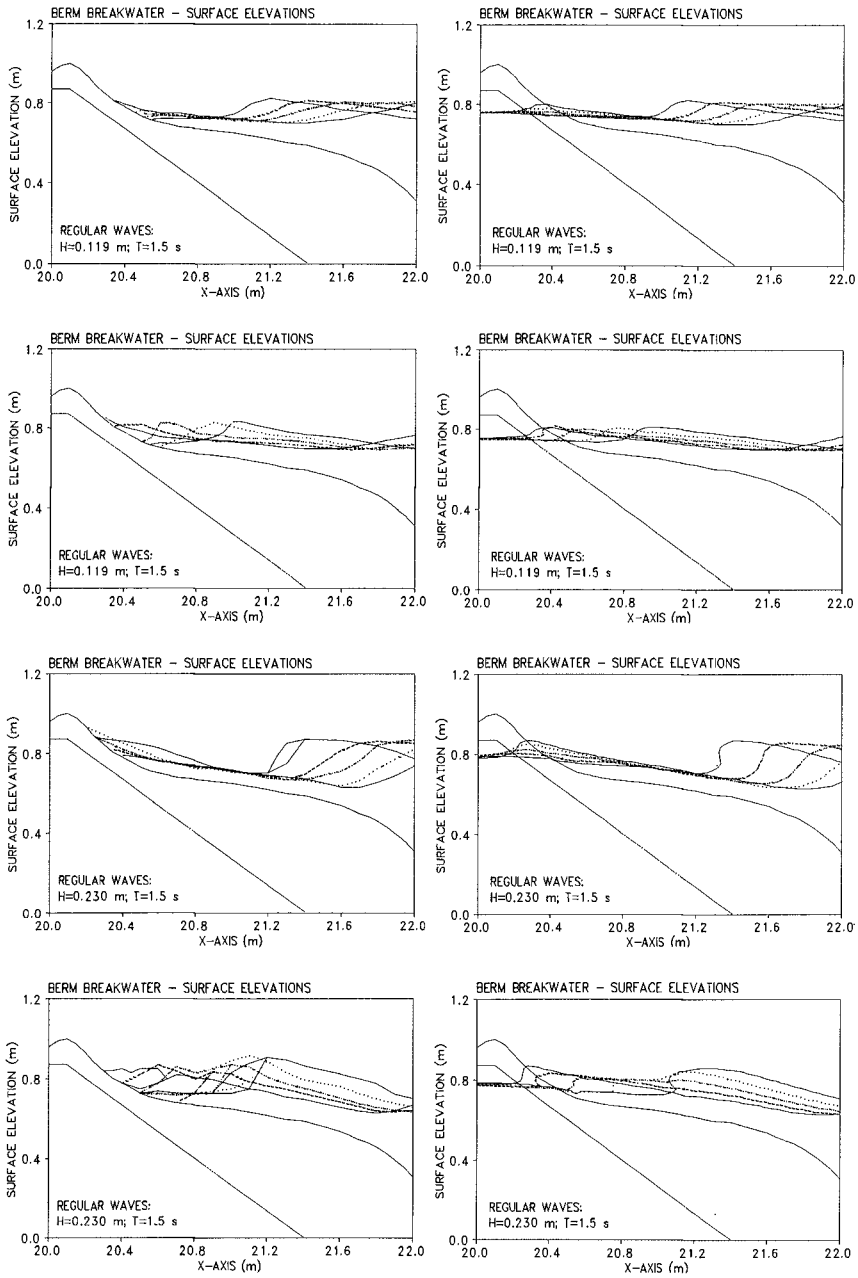


Fig.8 Comparison of measured (left) and computed (right) surface elevations.

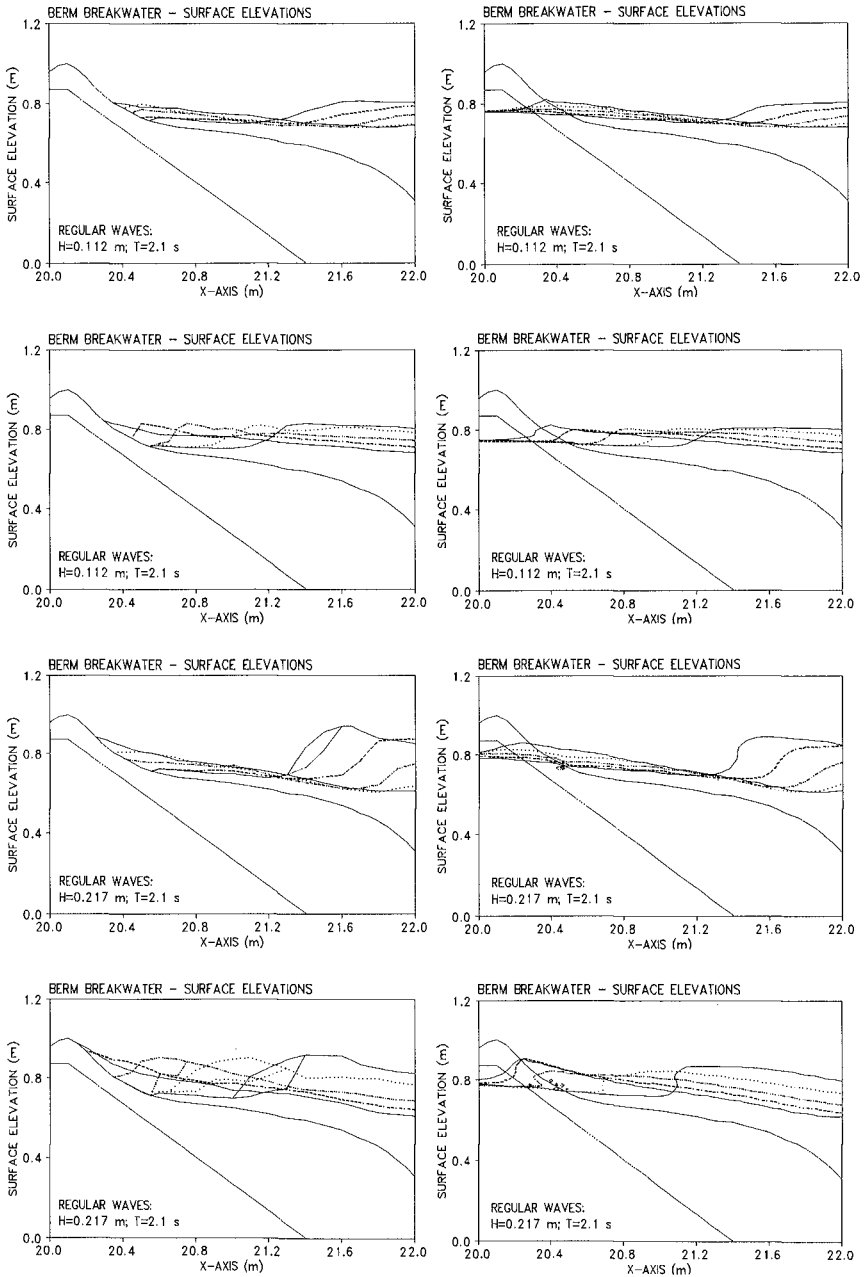
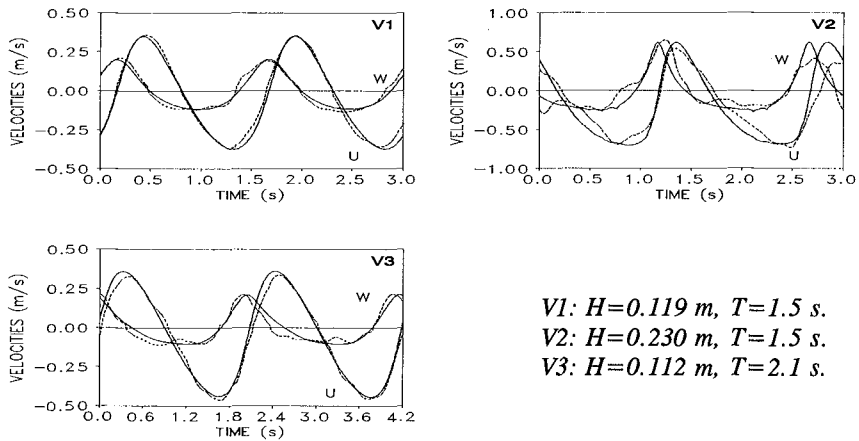


Fig.9 Comparison of measured (left) and computed (right) surface elevations.

in the computation than observed from the measurements. It seems as if this overestimated reduction in wave height, possibly due to a too large dissipation, leads to an underestimation of the run-up levels. For the two wave conditions with smaller waves, the comparisons are also rather good in the second half of the wave cycle.

For all four wave conditions  $H=0.119\text{ m}$ ,  $T=1.5\text{ s}$ ;  $H=0.230\text{ m}$ ,  $T=1.5\text{ s}$ ;  $H=0.112\text{ m}$ ,  $T=2.1\text{ s}$ ;  $H=0.217\text{ m}$ ,  $T=2.1\text{ s}$ , the computed run-up levels are too low compared with the measured run-up levels:  $0.07\text{ vs. }0.10$ ;  $0.14\text{ vs. }0.21$ ;  $0.08\text{ vs. }0.11$  and  $0.18\text{ vs. }0.27\text{ m}$ , respectively. All these values are relative to the average water levels in front of the structure during testing. The choice to define the surface elevations at the positions of cells that are filled with water for 50% instead of another percentage, might influence the computed run-up levels slightly. If for this definition positions of cells that are filled with water for 10% are regarded as surface elevations, the computed run-up levels might increase but not so much that they would fit to the measured run-up levels. The dissipation in the computed breaking process, by the description of the physical processes or by numerical dissipation, is assumed to cause these underestimated run-up levels.

Comparisons between measured and computed velocities were made. Because of air-entrainment the position closest to the crest without this difficulty was at  $x=21.6\text{ m}$ ,  $z=0.65\text{ m}$ . For three waves the comparisons for both the horizontal ( $u$ ) and the vertical ( $w$ ) velocities are shown in Figure 10. The comparison for the fourth wave ( $H=0.217\text{ m}$  and  $T=2.1\text{ s}$ ) was not possible because in the physical model this position was dry for some period within a wave cycle causing severe disturbance of the measured signal. The comparisons for the other three waves show accurate results for both the horizontal and vertical velocities.



**Fig.10** Comparison of velocities at  $x=21.6\text{ m}$  and  $z=0.65\text{ m}$ ; measured (dashed) and computed (lines).



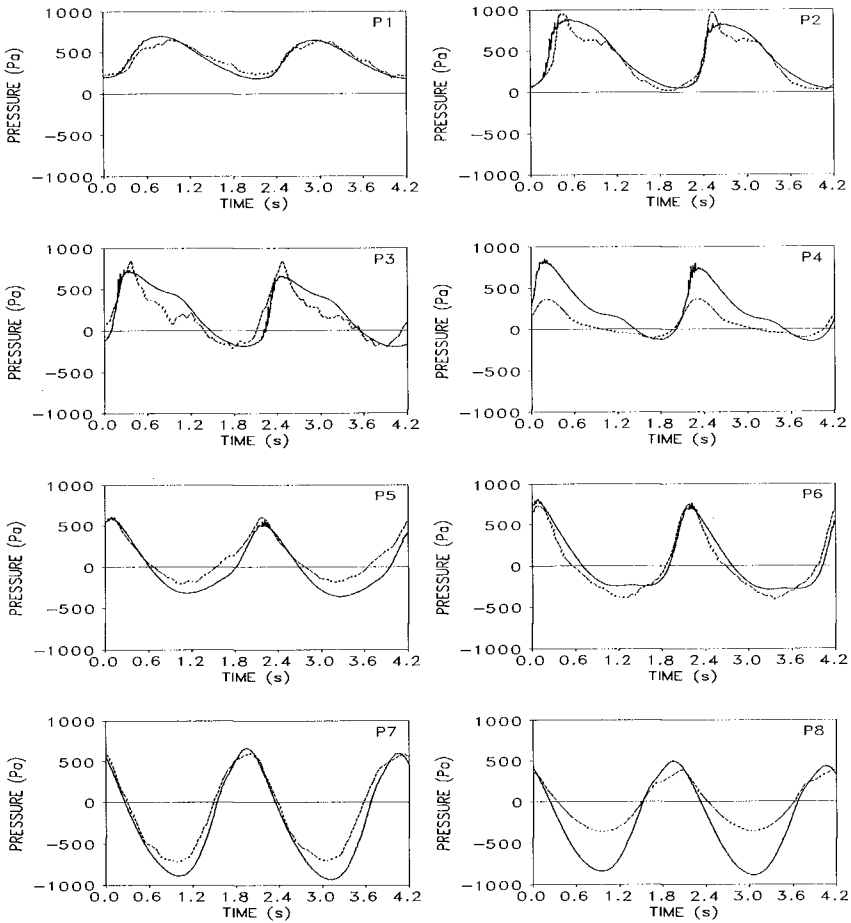


**Fig.11** Comparison of pressures; measured (dashed) and computed (lines),  $H=0.217$  m,  $T=2.1$  s.

Also comparisons between measured and computed pressures were made. Figure 11 shows the signals from the eight transducers and the computed pressures at the same positions. The positions of these transducers are shown in Figure 7. Transducer *P4* is positioned in between the transducers *P3* and *P6*. The recorded pressures by transducer *P4*, however, clearly deviate from those recorded by *P3* and *P6*. Because no decisive physical explanation can be given for these low pressures, estimated to be roughly 50% of the expected pressures for all analysed wave conditions, the signals of transducer *P4* are highly questionable. The comparisons with the other transducers are fairly accurate except for those with transducer *P8*.

Both the internal set-up as recorded by transducer *P1* (average level) and the internal wave height are reproduced with a high accuracy. The computed signals at positions just below the breaking waves, transducers *P2*, *P3* and *P6*, also show good correspondence with the measured signals although these measured signals show more higher-order fluctuations.

## CONCLUDING REMARKS

A numerical model solving the two-dimensional Navier-Stokes equations for simulating normally incident waves, including breaking waves, has been extended with porous media flow. The implementation of the combined external and internal wave motion on and inside permeable structures was successful as shown by comparisons with both analytical solutions and physical model tests. The model, now capable of providing a detailed flow description of breaking waves on permeable structures, will, however, be improved by including more sophisticated modelling of air-extrusion and turbulence. Furthermore, irregular waves will be implemented.

## ACKNOWLEDGEMENTS

The financial support by Rijkswaterstaat (Ministry of Transport, Public Works and Water Management, Road and Hydraulic Engineering Division) and by the Commission of the European Communities by way of the MAST-Berm Breakwater project (contract MAS2-CT94-0087) is gratefully acknowledged.

## REFERENCES

- Ashgriz, N. and J.Y. Poo (1991), *FLAIR: Flux line-segment model for advection and interface reconstruction*, J. of Comp. Physics Vol.39, pp.449-468.
- Gent, M.R.A. van (1991), *Formulae to describe porous flow*, Report MAST-G6 Coastal Structures, project 1 and Communications on Hydraulic and Geotechnical Engineering, ISSN 0169-6548 No.92-2, Delft University of Technology.
- Gent, M.R.A. van (1994), *Permeability measurements for the modelling of wave action on and in porous structures*, Proc. Coastal Dynamics'94, pp.671-685, Barcelona.
- Gent, M.R.A. van, J.P. de Waal, H.A.H. Petit and P. van den Bosch (1994-a), *SKYLLA: Wave motion in and on coastal structures; Verification of wave kinematics of waves breaking on an offshore bar*, Delft Hydraulics Report H1780.
- Gent, M.R.A. van, H.A.H. Petit and P. van den Bosch (1994-b), *SKYLLA: Wave motion in and on coastal structures; Implementation and verification of flow on and in permeable structures*, DELFT HYDRAULICS Report H1780.
- Gent, M.R.A. van, and H.A.H. Petit (1994), *Simulations of wave interaction with coastal structures*, Proc. Hydroinformatics'94, Vol.1, pp.141-146, IHE, Delft.

- Hirt, C.W. and B.D. Nichols (1981), *Volume of fluid method for the dynamics of free boundaries*, J. of Comp. Physics Vol.39, pp.201-225.
- Meer, J.W. van der, H.A.H. Petit, P. van den Bosch, G. Klopman and R.D. Broekens (1992), *Numerical simulation of wave motion on and in coastal structures*, Proc. ICCE'92, Vol.2, pp.1772-1784, Venice.
- Petit, H.A.H., P. van den Bosch and M.R.A. van Gent (1994-a), *SKYLLA: Wave motion in and on coastal structures; Implementation and verification of modified boundaries*, DELFT HYDRAULICS Report H1780.
- Petit, H.A.H., P. van den Bosch and M.R.A. van Gent (1994-b), *SKYLLA: Wave motion in and on coastal structures; Implementation of impermeable slopes and overtopping-boundary conditions*, DELFT HYDRAULICS Report H1780.
- Rienecker, M.M. and J.D. Fenton (1981), *A Fourier method for steady water waves*, J. of Fluid Mechanics, Vol.104, pp.119-137.
- Sakai, T., T. Muzutani, H. Tanaka and Y. Tada (1986), *Vortex formation in plunging breaker*, Proc. ICCE'86, Vol.1, pp.711-723, Taipei.
- Vinje, T. and P. Brevig (1981), *Numerical simulation of breaking waves*, Advances in Water Resources, Vol.4, pp.77-82.

## CHAPTER 126

### PROBABILISTIC CALCULATIONS OF WAVE FORCES ON VERTICAL STRUCTURES

J.W. van der Meer<sup>1)</sup>, K. d'Angremond<sup>2)</sup> and J. Juhl<sup>3)</sup>

#### ABSTRACT

In the past wave forces on vertical structures have been measured in a number of site specific projects at the Danish Hydraulic Institute and Delft Hydraulics. For nine selected cases, the data on forces and moments were re-analyzed, leading to an expression for reliability of Goda's formula for calculation of forces and moments on vertical breakwaters. Secondly, probabilistic level II design calculations were made using Goda's formula with the found reliability. It appears that the reliability of this formula has by far the largest influence on the probability of failure. Finally the influence of model tests on the probability of failure was studied. In that case the wave height has the largest influence on stability, which is usual for most coastal structures designs.

#### INTRODUCTION

Design of vertical breakwaters has for instance to take into account hydraulic, geotechnical and structural aspects. The wave forces exerted on a vertical structure depend on characteristics of the incident waves, type of structure, elasticity of the structure, air enclosure and the entrainment of dissolved air and foreshore characteristics

In a deterministic design approach, vertical breakwaters are designed based upon characteristic values of the load determining parameters. A safety factor is then introduced to allow for uncertainties. However, all parameters which are important

- 
- 1) Delft Hydraulics, P.O. Box 152, 8300 AD Emmeloord, The Netherlands, Fax +31-52743573
  - 2) Delft University of technology, P.O. Box 5048, 2600 GA Delft, The Netherlands
  - 3) Danish Hydraulic Institute, Agern Allé 5, 2970 Hørsholm, Denmark

for the wave loads on and the strength of a hydraulic structure are of a stochastic nature, ie a probability distribution can be assigned to each value of these parameters. Since the last decades methods for probabilistic design of hydraulic structures have been developed, taking into account the stochastic nature of the load determining parameters.

The formulae of Goda (1985) for wave forces on vertical structures is used worldwide. The distribution of wave pressures on a vertical structure can be calculated based on knowledge of structure geometry, seabed characteristics and wave parameters in front of the structure, see Figure 1, taken from Goda (1985).

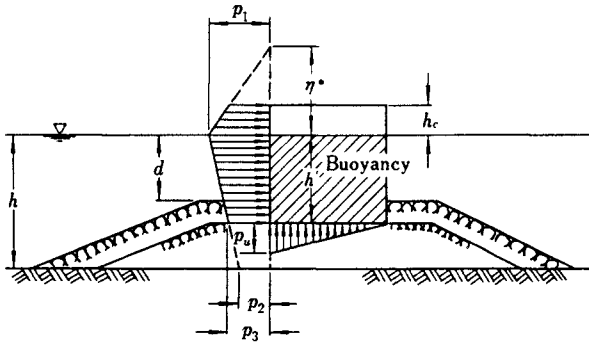


Figure 1 Distribution of wave pressures on a vertical structure, Goda (1985)

The design wave parameters are the maximum wave height in front of the structure,  $H_{\max}$ , and the corresponding wave period taken as the significant wave period,  $T_s$  (which is close to the peak wave period,  $T_p$ ). Goda (1985) states that: " $H_{\max}$  is the mean of the heights of the waves included in 1/250 of the total number of waves, counted in descending order of height from the highest wave. This definition yields the approximate relation  $H_{\max} = 1.8 H_{1/3}$  outside the surfzone". The formulae for pressures, total forces and moments, and definitions of symbols given in Fig. 1 can be found in Goda (1985) pp 115-119.

The present paper describes a re-analysis of model tests on various vertical structures carried out at the Danish Hydraulic Institute and Delft Hydraulics. Later two cases were added from CEDEX-CEPYC, Spain, and ENEL-CRIS, Italy. The reliability of Goda's formulae has been established by use of these practical cases by making comparisons of calculations and measurements. In a second stage, these data have been used for probabilistic level II calculations.

## RE-ANALYSIS

A total of eleven cases has been re-analyzed with respect to wave forces and moments on vertical structures. Details on caisson geometry, foreshore slopes, wave conditions and horizontal forces were stored in a database as presented in Juhl and Van der Meer (1992). The analysis of horizontal forces is also described in Juhl and Van der Meer (1992) with a summary in Van der Meer et al. (1992). Vertical forces and overturning moments were treated later by Bruining (1994).

The analyzed cases have been divided in three categories: vertical superstructure, inclined superstructure, and curved superstructure. In Figure 2, an example of each of these three categories is shown.

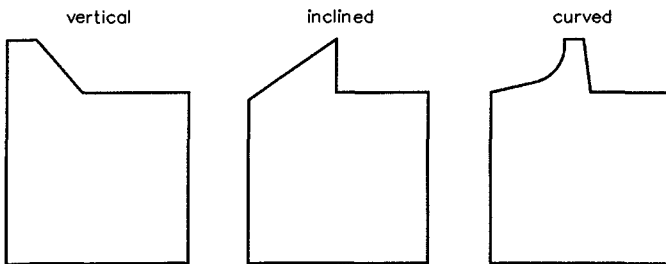


Figure 2 Examples of different superstructures

The significant and maximum wave heights in front of the vertical structure were calculated by Goda's formulae for transformation and deformation of random sea waves, Goda (1985) pp 71-87. Only total wave forces, measured by means of strain gauge based measuring equipment (eg a measuring frame or a dynamometer), are considered. This means that local wave impacts are not treated, as they cannot be measured by this measuring technique. It was assumed, however, that very fast local impacts would not influence the stability of a caisson and were therefore not interesting.

In all cases, wave trains with lengths of 1000-3000 waves were considered. Based on the recordings the horizontal and vertical forces and horizontal and vertical overturning moments at the heel of the caisson were tabulated, with exceedance frequencies of 0.1%, 0.4%, 1%, 2% and 5% respectively. In Figures 3-5 the measured horizontal forces,  $F_{0.4\%}$ , are compared with the horizontal forces calculated by Goda's formula,  $F_{Goda}$ . The cases with a vertical superstructure have been plotted in Figure 3, and the cases with an inclined or curved superstructure have been plotted in Figure 4. Due to the various structure geometries, foreshore slopes, wave characteristics, etc., a significant scatter in the measured wave forces was found.

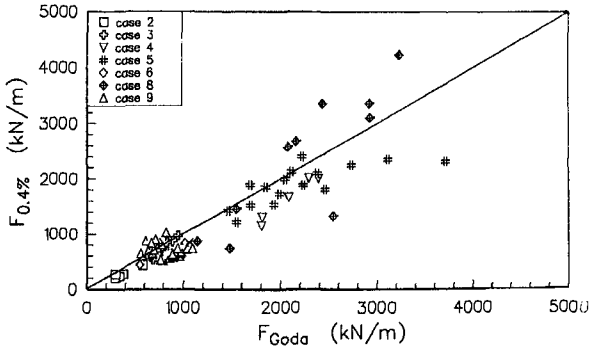


Figure 3 Measured and calculated horizontal wave forces; vertical superstructures

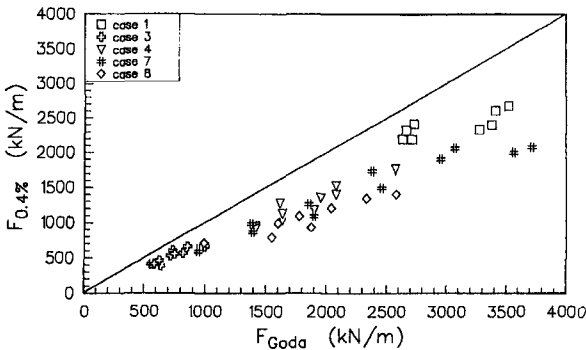


Figure 4 Measured and calculated horizontal wave forces; inclined and curved superstructures

From Figure 4, it is clear that for inclined and curved superstructures, the wave forces calculated by Goda’s formula are much higher than the measured forces. In the major part of those cases, the ratio between the calculated and measured force is in the order of 1.4-1.6. For inclined and curved superstructures, the maximum force on the superstructure occurs later than the maximum horizontal force on the vertical front. This phase difference in the forces led to the following modification of Goda’s formula for inclined and curved superstructures:

*The crest height should be determined at the transition from the vertical front to the inclined or curved superstructure.*

The horizontal forces,  $F_{Goda}$ , were re-calculated with a reduced crest height in accordance with the above-mentioned modification to Goda’s formula. The results are presented in Figure 5 and it is found that the ratio’s between calculated and measured forces are in the same order as found for the cases with a vertical superstructure.

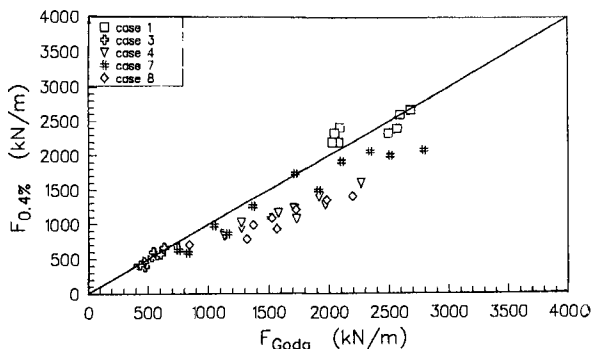


Figure 5 Measured and calculated horizontal wave forces; inclined and curved superstructures, ignoring the inclined or curved superstructure in the Goda force calculations

The average ratio between measured ( $F_{0.4\%}$ ) and calculated ( $F_{Goda}$ ) forces and moments was based on 134 data sets for horizontal forces and moments; 31 data sets were used for the uplift forces and moments and were treated in the same way as the horizontal forces. The average values of these ratios and the standard deviations, assuming a normal distribution, are given in Table 1.

		Ratio measured/calculated	Average	Standard deviation
Horizontal force	$F_h$	$r_{Fh}$	$\mu = 0.83$	$\sigma = 0.25$
Horizontal moment	$M_h$	$r_{Mh}$	$\mu = 0.75$	$\sigma = 0.40$
Vertical force	$F_b$	$r_{Fb}$	$\mu = 0.71$	$\sigma = 0.25$
Vertical moment	$M_b$	$r_{Mb}$	$\mu = 0.67$	$\sigma = 0.37$

Table 1 Comparison between measured and calculated forces and moments  
Measured = 0.4% exceedance; calculated = Goda

In all cases the ratio is smaller than one, which means an overprediction by the Goda formulae. The most important conclusion is that the standard deviations are large. The variation coefficients,  $\sigma/\mu$ , amount to 30-50%! It can be concluded that the Goda method gives only a rough estimation of the forces and moments.

Through a more in depth description of each of the cases, the following observations were made:

- Goda's formula is valid for caissons founded on a rubble mound berm well above the seabed. In a number of the tested cases, the caisson was founded at the seabed level. The results of some of these cases give the impression



that Goda's formula over-predicts the horizontal forces when the caisson is founded at the same level as the seabed;

- no general conclusions could be made on the influence of wave breaking on the foreshore or on the wave period (or wave steepness).

**EXCEEDANCE CURVE FOR THE HIGHEST FORCES**

Figure 6 shows an example of measured exceedance curves for the horizontal force. Through the five tabulated measured horizontal, but also vertical forces, with exceedance values of 5%, 2%, 1%, 0.4% and 0.1%, a two-parameter Weibull distribution was fitted for each test run (95 in total). This analysis resulted in an average shape parameter of 2.1 which corresponds closely to a Rayleigh distribution for the higher wave forces. The reliability of this factor 2.1 could be described by a standard deviation of 0.72. The average value for the vertical forces amounted to 2.35 with a standard deviation of 0.77. The conclusion was that, considering the large scatter, the distribution of the highest wave forces can be described by a Rayleigh distribution with a shape parameter of 2:

$$R(F) = e^{-\left(\frac{F}{a}\right)^2} \tag{1}$$

where R(F) is the exceedance probability and a the scale parameter. Results from using the Goda method were compared with measured 0.4% exceedance values. These ratio's have been given in Table 1. The Goda force is not equal to 1/250 = 0.4%, but equal to the average of the highest 1/250-th part of the forces. Now the shape of the force distributions has been found to be a Rayleigh distribution one can calculate the ratio between the average of the highest 1/250-part and the 0.4%. This ratio amounts to 1.084. With this factor the actual comparison between Goda and measured forces can be given as the average ratio's presented in Table 1, multiplied by 1.084. Table 2 gives the result.

		Ratio measured/calculated	Average	Standard deviation
Horizontal force	F <sub>h</sub>	Γ <sub>Fh</sub>	μ = 0.90	σ = 0.25
Horizontal moment	M <sub>h</sub>	Γ <sub>Mh</sub>	μ = 0.81	σ = 0.40
Vertical force	F <sub>b</sub>	Γ <sub>Fb</sub>	μ = 0.77	σ = 0.25
Vertical moment	M <sub>b</sub>	Γ <sub>Mb</sub>	μ = 0.72	σ = 0.37

Table 2 Comparison between the Goda method and measured values, both based on the average of the highest 1/250-th values

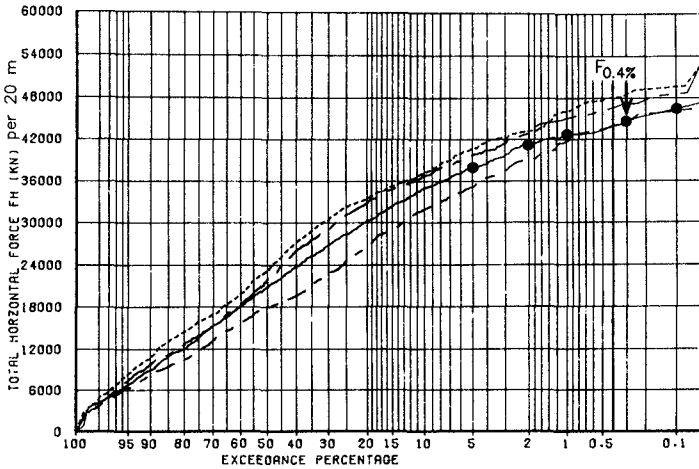


Figure 6 Example of measured distributions of horizontal forces

The most important force for stability is normally the horizontal force  $F_h$ . Based on the selected cases Goda overestimates this force by 10%. During a lecture Takayama (1994) gave the Japanese experience: based on 66 cases the average ratio amounted to  $\mu = 0.91$  with a standard deviation of 0.19. These values are in good agreement with those found for the horizontal force  $F_h$ , see Table 2.

The scale parameter in Equation 1 can be based on the Goda formula and on the found bias and reliability, given in Tables 1 or 2. With  $R(F_{0.4\%}) = 0.004$  substituted in Equation 1 the scale parameter  $a$  can be replaced using  $F_{0.4\%}$ :

$$R(F) = e^{-\left(\frac{2.35 F}{F_{0.4\%}}\right)^2} \tag{2}$$

With the factors  $r$  ( $r_{Fh}$ ;  $r_{Fb}$ ;  $r_{Mh}$ ;  $r_{Mb}$ , given in Table 1), which includes  $F_{0.4\%}$ , the formula becomes:

$$R(F) = e^{-\left(\frac{2.35 F}{r F_{Goda}}\right)^2} \tag{3}$$

Equation 3 can be seen as a design formula for the exceedance curve of the highest forces, based on Goda's method.

In reality the maximum wave force is related to the maximum number of waves during the sea state considered and not to the 0.4% or 1/250 wave only. Taking into account the actual maximum wave force based on the actual storm duration, a second factor,  $r_N$ , can be introduced:

$$r_N = \frac{F_{max}}{F_{0.4\%}} = \sqrt{\frac{\ln(1/N)}{\ln(0.004)}} \tag{4}$$

where  $N$  is the number of waves in the sea state. The design formula for the maximum wave force becomes then:

$$F_{max} = r \ r_N \ F_{Goda} \tag{5}$$

Figure 7 gives a graphical overall view of the above equations. It shows an example of a wave force exceedance curve. The horizontal axis has been plotted on a Rayleigh scale which means that a Rayleigh distribution becomes a straight line in this graph. Equation 3 gives the exceedance curve of the highest 5% of the wave forces. The calculated value for  $F_{Goda}$  has been drawn at 0.152%, which is equal to  $F_{1/250}$ , assuming a Rayleigh distribution. The difference between  $F_{Goda}$  and  $F_{0.4\%}$  is given by the ratio  $r$  from Table 1. The actual difference between  $F_{Goda}$  and the exceedance curve is given in Table 2. The 90% confidence levels can be calculated by taking into account the standard deviations given in Tables 1 or 2.

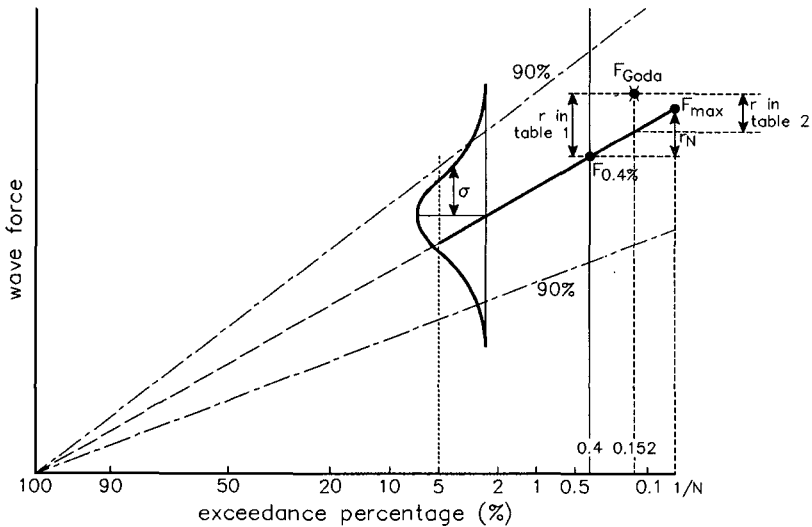


Figure 7 Distribution of horizontal forces (Weibull), including  $F_{Goda}$  and  $F_{max}$

The most right point on the curve in Figure 7 gives the maximum wave force  $F_{max}$  for an exceedance probability of  $1/N$ . The general conclusion is that the Goda formula gives, on average, a very good prediction of the maximum horizontal wave force for a storm duration of a few hours ( $N = 2000$  to  $3000$  waves).

## REFERENCE CASE FOR PROBABILISTIC CALCULATIONS

One test in one of the nine cases described in Juhl and Van der Meer (1992) will be taken as a reference (case 1, test 4F). Figure 8 gives a cross-section of the caisson. The parameters that are required for a calculation with the Goda formula are:

$$\begin{aligned} H'_0 &= 8.0 \text{ m (once per 50 years storm)} \\ T_p &= 15.4 \text{ s} \\ \text{Storm duration: } &8 \text{ hours (} N = 2550 \text{)} \\ h_{\text{sea}} &= 30.5 \text{ m} \\ h &= 19 \text{ m} \\ h_c &= 8 \text{ m, but inclined superstructure: } h_c = 1 \text{ m} \\ d &= 19 \text{ m} \\ \tan m &= 0.002 \end{aligned}$$

Furthermore a weight,  $W$ , of 5500 kN/m length and a friction coefficient,  $f$ , of 0.7 are assumed. Based on later communications with Takayama (1994) the Japanese experience on the friction coefficient can be summarized as follows. The design value is  $f = 0.6$ . Based on 42 cases on nearly prototype scale the average friction factor amounted to  $\mu = 0.64$  with a standard deviation of  $\sigma = 0.16$ .

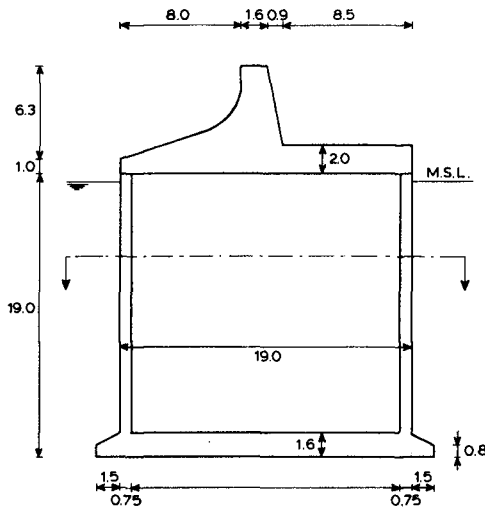


Figure 8 Cross-section of the caisson used for calculations

## PROBABILISTIC CALCULATIONS

In a probabilistic approach a reliability function,  $Z$ , should be given, which is in fact a design formula or design process. The two main failure mechanisms for a caisson are sliding and overturning. The reliability function for sliding becomes:

$$Z = (W - r_{Fb} r_N F_{b(Goda)}) f - r_{Fh} r_N F_{h(Goda)} \quad (6)$$

The first term describes the weight minus uplift force, multiplied by the friction coefficient. This gives the total friction resistance. The second term gives the maximum horizontal force.  $F_{b(Goda)}$  is the vertical force on the base of the caisson and  $F_{h(Goda)}$  is the horizontal force on the front side, both calculated by the Goda method described in Goda (1985) and depending on a large number of parameters.

A probabilistic approach with Equation 6 gives the probability that the caisson will slide during a (design) sea state. All calculations were made with a level II first-order second-moment (FOSM) with approximate full distribution approach (AFDA) method. General references on this aspect are Thoft-Christensen and Baker (1982), Hallam et al. (1977) and PIANC (1993). Calculations have been made for three cases: one for the design event, one for the life time of the structure and one including the results of physical model tests.

### Case 1: Calculations for the Design Event

In order to show the influence of the uncertainty of the Goda formula on the probability of failure a few different calculations have been made. One calculation has been made with only  $r$  and  $r_N$  as stochastic variables, another with  $f$  and  $W$  also as stochastic variables and finally one also including all the parameters in  $F_{Goda}$  as stochastic variables. The mean values and standard deviations of the normal distributions used in the calculations are shown in Table 3. The factor  $r_N$  is described by the number of waves,  $N$ , see Equation 4.

The probabilities of failure,  $P(f)$ , for the three calculations were 0.062, 0.086 and 0.097, respectively. These are the probabilities of failure during the (design) sea state of 1/50 years. All three probabilities are close, which means that the reliability of the Goda formula, by means of  $r_{Fb}$  and  $r_{Fh}$ , have by far the largest influence. In fact the influence of  $r_{Fh}$ , the reliability of the horizontal force, on the probability of failure amounted to 99%, 73% and 65% in the three calculations, respectively.

Parameter	Mean	Standard deviation	
$r_{Fh}$	0.83	0.25	calculation 1
$r_{Fb}$	0.71	0.25	
N	2550	127 (5%)	
f	0.7	0.1	calculation 2
W (kN/m)	5500	165 (3%)	
$H_0'$ (m)	8.0	0.4 (5%)	calculation 3
$T_p$ (s)	15.4	1.54 (10%)	
$h'$ (m)	19	0.57 (3%)	
$h_c$ (m)	1	0.03 (3%)	
$h_{sea}$ (m)	30.5	0.915 (3%)	
d (m)	19	0.57 (3%)	

Table 3 Parameters and values used for calculations.

### Case 2: Calculations for the Life Time of the Structure

More design information is obtained when not one (design) sea state is considered, but the whole wave climate by means of an extreme distribution for the wave heights. Taking the 1/50 years wave height as a reference (which was used for testing), such an extreme distribution can be established by means of an exponential distribution:

$$R(H_s) = e^{\frac{-(H_s - 5.1)}{0.51}} \quad (7)$$

In this case the once per year wave height is 5.1 m ( $R(H_s) = 1$ ) and the 1/50 years wave height becomes 8.0 m ( $R(H_s) = 0.02$ ).

With Equation 7 a probabilistic calculation gives the probability of failure per year instead of during the (design) sea state. Calculation 3 of case 1 above, where all parameters were treated stochastically, has been performed again, but now with the exponential distribution of the wave height (Equation 7) instead of the normal distribution for the 1/50 years wave height. This results in a probability of failure of 0.018 per year. The influence of  $r_{Fh}$  on the probability of failure amounted to 55% and of the wave height  $H_s$  to 17%.

The probability of exceedance for an X-year period can be obtained using:

$$P[Z < 0; X \text{ yr}] = 1 - (1 - P[Z < 0; 1 \text{ yr}])^X \quad (8)$$

With the above result of a probability of failure per year of 0.018 a graph can be drawn with the probability of failure as a function of the life time of the structure. The upper solid line in Figure 9 gives the result of above calculations. The proba-

bility of failure for a life time of 50 years is 0.60, considerably higher than for the 1/50 years sea state only (0.097). This is probably due to the fact that wave heights lower than the 1/50 years wave height increase the probability, but that also higher wave heights (with a lower probability of occurrence) increase the total probability.

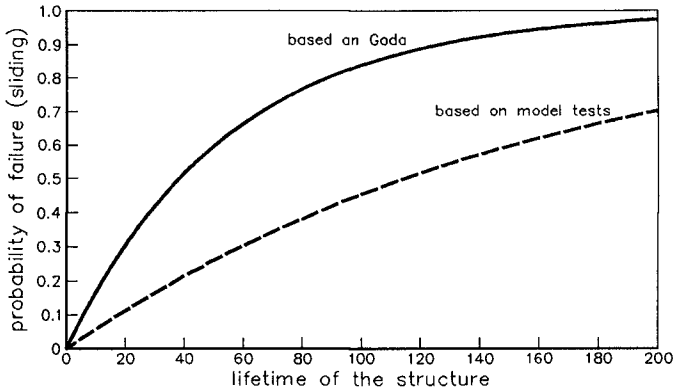


Figure 9 Probability of failure as a function of the life time of the structure

**Case 3: Use of Results of Physical Model Tests**

Until now the calculations were done for the Goda formula only, including the uncertainties of all the parameters. The large variation of the Goda formula by means of  $\sigma(r)$  has the largest influence on the failure probability. This variation is due to the large variety of structure geometries and foreshores that were present in the nine selected cases (see Juhl and Van der Meer (1992) and Bruining (1994)). This large variation can be eliminated by performance of physical model tests. In that case forces are measured for the specific structure geometry including all effects of the foreshore.

With respect to Equation 6 it means that the exact values of  $r_{Fh}$  and  $r_{Fb}$  are known (the bias) and the scatter of  $r_{Fh}$  and  $r_{Fb}$  is much smaller than  $\sigma(r) = 0.25$ . Further the ratio  $r_N$  (Rayleigh distribution or not) is also known. The same calculations can be done as in case 2, but now with  $r_{Fh}$  and  $r_{Fb} =$  measured value,  $\sigma(r) = 0.05$  (assumed) and  $r_N =$  measured value.

The following factors were determined by model tests. Between brackets the previous values, based on the Goda method only, are also given.

$$\begin{aligned}
 r_{Fh} &= 0.88 & \sigma &= 0.05 & (0.83; \sigma &= 0.25) \\
 r_{Fb} &= 0.67 & \sigma &= 0.05 & (0.71; \sigma &= 0.25) \\
 r_N (F_h) &= 1.21 & \sigma &= 0.05 & (1.19; \sigma &= 0.05) \\
 r_N (F_b) &= 1.11 & \sigma &= 0.05 & (1.19; \sigma &= 0.05)
 \end{aligned}$$

The calculations of case 2 were repeated with the new factors given above. The probability of failure per year amounted now to 0.006, a factor three lower than for case 2. The influence of the most important parameters for both cases (with and without model tests) on the probability of failure is given in Table 4.

With model tests	Without model tests
Probability of failure $p = 0.006$	Probability of failure $p = 0.018$
Influence of	
$r_{Fh}$ : 2%	$r_{Fh}$ : 55%
$f$ : 33%	$f$ : 15%
$H_s$ : 45%	$H_s$ : 17%
$T_p$ : 16%	$T_p$ : 10%

Table 4 Influence of main parameters on the probability of failure, with and without model tests

The influence of the wave height amounted now to 45% (this was 17% in case 2) and becomes the most important parameter, which is usual, see PIANC (1993).

With Equation 8 and the probability of failure per year of 0.006 the lower dashed line in Figure 9 was calculated. The probability of failure for a life time of 50 years becomes now 0.26 (this was 0.60 in case 2). Figures like Figure 9 can be used by designers. They have to decide which probabilities of failure to accept.

## CONCLUSIONS

The performed re-analysis of the data on wave forces on vertical structures for eleven selected cases gave the following results and conclusions:

- An inclined or curved superstructure results in much lower wave forces than a vertical superstructure. It was found that by ignoring the inclined/ curved superstructure in Goda's formula for horizontal forces (i.e. the crest height is determined as the transition from the vertical front to the inclined/curved superstructure) the force ratio's (calculated/measured) were in the same order of magnitude as for completely vertical structures
- In general, the horizontal forces calculated by Goda's formula are about 10% higher than the corresponding measured forces. This is in agreement with Japanese experience. However, a considerable scatter (standard deviation 0.25 on a ratio between measured and calculated force) is present due to the site specific differences, eg caisson geometry and foreshore slopes.
- The results indicate that Goda's formula over-estimates the horizontal wave forces on a caisson founded at the same level as the bottom of the foreshore, i.e. in the absence of a traditional rubble mound foundation.



Probabilistic calculations gave the following main results and conclusions:

- The Goda formula gives in fact a good (average) estimate of the maximum horizontal wave force when the sea state has a duration of some hours, including about 2000 - 3000 waves.
- Probabilistic calculations show that the reliability of (scatter around) the Goda formula by means of the factor  $r_{Fh}$  has by far the largest influence of all parameters on the probability of failure. Model tests are therefore advised in all cases and these will decrease this scatter and the influence on the failure probability.
- Design graphs of failure probability (of sliding or overturning) versus desired life time of the structure can be given as a result of probabilistic calculations.

## ACKNOWLEDGEMENTS

The work has been performed under a project of the Commission of the European Communities, called MAST-G6 Coastal Structures, project 0032 and was further funded by the Dutch Public Works Department. Acknowledged are CEDEX-CEPYC, Spain and ENEL-CRIS, Italy for providing data on cases 10 and 11.

## REFERENCES

- Bruining, J.W. (1994). *Wave forces on vertical breakwaters. Reliability of design formula*. Msc. Thesis, Delft University of Technology. Also Delft Hydraulics Report H 1903.
- Goda, Y. (1985). *Random seas and design of maritime structures*. University of Tokyo Press.
- Hallam, M.G., Heaf, N.I., and Wootos, I.R. (1977). *Rationalization of safety and serviceability factors in structural codes*. CIRIA Report No. 63, London.
- Juhl, J. and Van der Meer, J.W. (1992). *Quasi-static wave forces on vertical structures, re-analysis of data at Danish Hydraulic Institute and Delft Hydraulics Report*. Prepared for MAST G6-S Coastal Structures.
- PIANC (1993). *Analysis of rubble mount breakwaters*. Report of Working Group 12 of the Permanent Technical Committee II. Supplement to Bulletin No. 78/79 (1992). Brussels.
- Takayama, T. (1994). *Lecture on "The State-of-the-Art of composite type breakwaters in Japan"*. International Workshop on Coastal Hydrodynamics, Sediments and Structures, Pusan, Korea.
- Thoft-Christensen, P. and Baker, M.J. (1982). *Structural reliability theory and its applications*. Springer Verlag, Berlin.
- Van der Meer, J.W., Juhl, J. and Van Driel, G. (1992). *Probabilistic calculations of wave forces on vertical structures*. Proc. Final MAST G6-S Coastal Structures Workshop, Madrid.



# PART IV

## Coastal Processes and Sediment Transport



## CHAPTER 127

### Velocity and Pressure Boundary Conditions for Flow Over the Permeable Boundary of a Porous Medium

İsmail Aydın<sup>1</sup>

#### Abstract

Effect of permeability on pressure distribution over the permeable surface of a porous medium is investigated. Measured pressure distributions comparing impervious and permeable cases are presented. Flow of the free fluid over the permeable boundary and flow of the fluid in the porous medium are computed numerically, maintaining the interaction of the two flow fields through the boundary conditions at the permeable surface. Turbulence is modeled by a low Reynolds number  $k-\varepsilon$  model including a novel technique to model surface roughness effect eliminating the need for wall functions.

#### Introduction

The interaction between waves, currents and the loose boundary at the sea bottom is a basic question in the study of sediment transport mechanism. In most cases the loose boundary takes an undulated shape with a separating complex flow field on it. The direction and the rate of sediment transport is strongly related to the resulting geometry of the loose boundary and to the dynamics of the flow over the boundary.

Sand particles are removed from the loose boundary by the tangential and the pressure forces, then hold suspended by the vortex structures and carried forward or backward depending on overall flow pattern. In order to define the incipient motion of the sand particles and explain the sediment transport mechanism, a numerical solution of the flow field over the loose boundary is required. However, in such a numerical

---

<sup>1</sup> Assoc. Professor, Civil Engineering Department, METU, 06531 Ankara, Turkey

solution the boundary conditions for velocity and pressure on a permeable surface should be defined correctly.

Two different flow regions can be defined; flow of the free fluid over the permeable boundary and flow of the fluid within the porous medium of the loose boundary. These two flow fields are strongly interacting. The flow of the free fluid over the undulated surface induces a pressure variation along the common boundary of the two flow regions. This pressure variation and the traction forces acting on the common boundary excite the flow in the porous medium. The velocity, pressure and turbulence along the common boundary are affected by both flow regions.

In flows over a porous medium it is necessary to specify boundary conditions on the tangential and normal components of velocity of the free fluid at the permeable boundary. There exists an extensive analytical literature which describes coupled fluid motions satisfying the Navier-Stokes equations in the free fluid flow and some empirical set of equations in the porous medium with common boundary conditions at the permeable interface of the two flow regions.

Obviously, some uncertainty exists in definition of a true boundary for a permeable material. Therefore, it is useful to define a nominal boundary. In mathematical formulation, a smooth geometric surface is considered to represent the nominal boundary along the surface of the porous medium. The nominal boundary is located at a distance such that the volumetric flowrate between the impervious rough surface and a fictitious surface placed at the tip of roughness elements is equal to the volumetric flowrate between the fictitious surface and the nominal boundary. In numerical computations, hydrodynamic consequences of roughness and permeability are simulated on the nominal boundary.

## **Experiments**

The experiment reported here is designed to examine the nature of the pressure distribution on the nominal boundary of a permeable surface. Briefly, there is a two-dimensional steady flow between an impermeable rippled surface and a flat test surface opposite to the ripple (Fig.1). The ripple geometry is selected to induce a pressure variation on the test surface. Description of the ripple geometry is given in numerical model section. The test surface is either an impermeable flat plate or the permeable boundary of a saturated porous volume.

Three experimental cases are considered. In the first case the test surface is fitted by a smooth solid flat plate. Pressure measurements for this case are indicated as "Impervious" on the figures. In the second case the

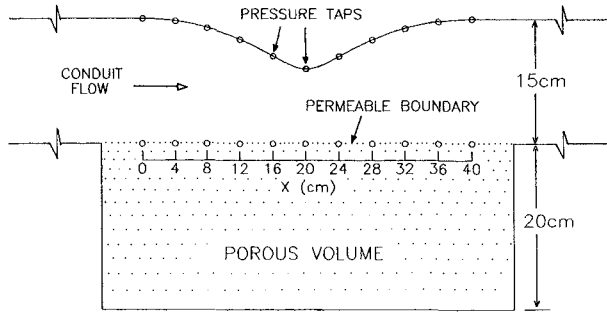


Fig.1 Experimental setup

test surface is fitted by a sieve screen and sand material is placed in the box indicated as "porous volume" in Fig.1. Hydraulic conductivity of the sand is measured to be 1.02 cm/s. Pressure measurements for this case are indicated as "Porous I". In the third case the sand material is replaced with another sample obtained from a different source. Hydraulic conductivity of this material is 1.07 cm/s, almost the same as in the second case. However, particle size distributions of the two sand materials are quite different. Pressure measurements for this case are indicated as "Porous II". The purpose of repeating the experiments with two different sand materials of approximately the same permeability is simply to verify experimental accuracy. Pressure distributions are measured for each case at about 25 different flowrates in the conduit. The maximum (centerline) velocity,  $U_m$ , in the conduit is varied between 50 ~ 250 cm/sec.

The measured pressure distributions at the test surface for the impervious and porous cases are shown in Fig.2 for three different flowrates. For  $U_m = 95$  cm/s, the difference between the pressures of the three test cases is negligible. Since the velocity is low, neither surface roughness nor permeability can affect the pressure distribution significantly. For  $U_m = 159$  cm/s, the pressures for the porous cases are less than the pressure for the impervious case at locations  $X \geq 16$  cm along the test surface. This pressure drop is due to the surface roughness effect of the sand material. When the flowrate is increased to  $U_m = 248$  cm/s the effect of surface roughness and permeability cancel each other and the resultant pressure distributions for the permeable cases are almost the same as the impervious case pressure distribution. At this high flowrate there is a larger pressure drop due to surface roughness effect of the permeable test surface but, permeability allowing flow into the porous medium from high pressure points and flow out of the porous medium from low pressure points, creates a counter effect to the contraction of flow section by the ripple on the

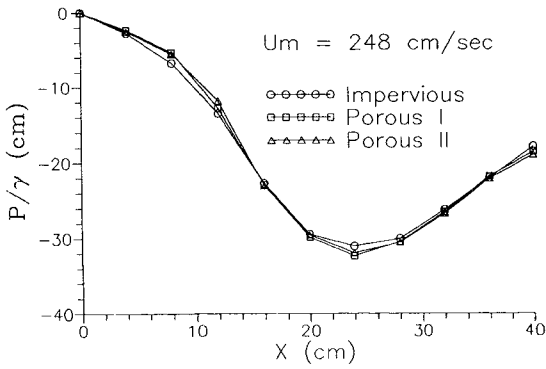
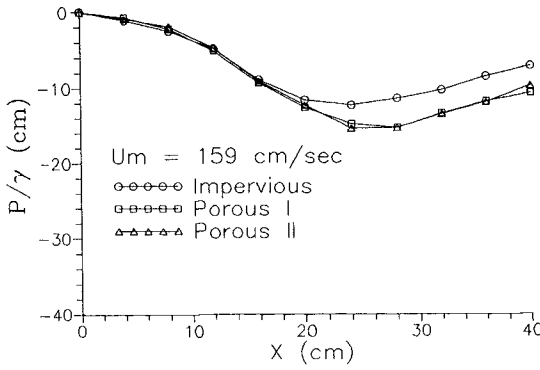
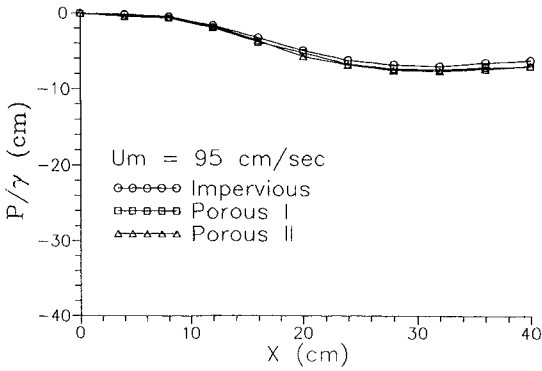


Fig.2 Comparison of pressure distributions along the test surface for flowrates  $U_m=95$ ,  $U_m=159$ , and  $U_m=248$  cm/s.

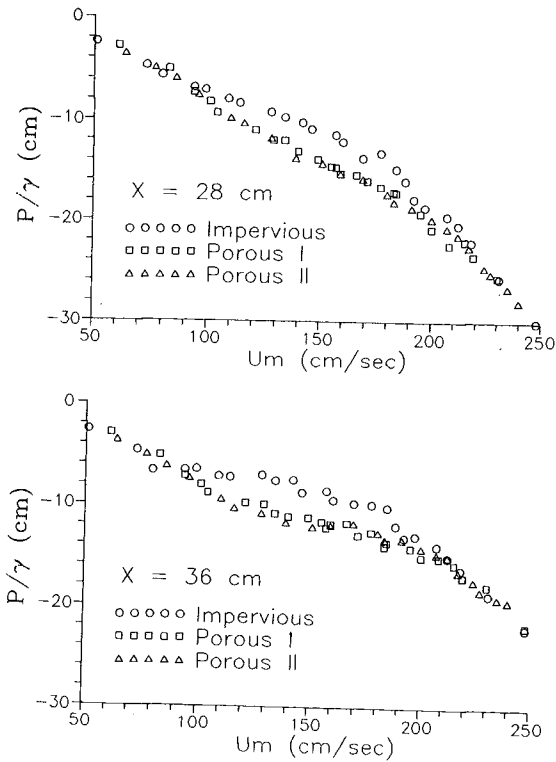


Fig.3 Comparison of pressures at fixed points  $X=28$  and  $X=36$  cm on the test surface as a function of flowrate in the conduit.

opposite side. In this way the pressure drop due to roughness effect is compensated by the relaxation introduced by permeability of the test surface.

This behavior can better be observed in Fig.3 where pressures at fixed points ( $x = 28$ ,  $x = 36$  cm) are compared as a function of flowrate. Pressure drop due to surface roughness can be recognized for  $U_m \geq 95$  cm/s and it is compensated by relaxation due to permeability for  $U_m \geq 190$  cm/s.

### Numerical Model

The flow of free fluid over the permeable boundary and the flow within the porous medium are solved simultaneously allowing interaction of the flow regions through the boundary conditions at the common boundary. Darcy law is assumed to govern the flow in the porous medium. The full



Navier-Stokes equations are solved in the region of free fluid flow and Laplace equation for pressure is solved in the porous medium.

A useful computational grid for the free fluid region is obtained from a conformal mapping between the physical plane ( $x, y$ ) and the computational plane ( $\xi, \eta$ ) defined by Eqns. (1) and (2)

$$x = \xi + c_m \frac{H}{2} \left[ \sin \alpha (\xi - \xi_1) e^{\alpha(\eta - \eta_1)} - \sin \alpha (\xi - \xi_2) e^{-\alpha(\eta - \eta_2)} \right] \quad (1)$$

$$y = \eta - \eta_1 - \eta_2 + c_m \frac{H}{2} \left[ \cos \alpha (\xi - \xi_1) e^{\alpha(\eta - \eta_1)} + \cos \alpha (\xi - \xi_2) e^{-\alpha(\eta - \eta_2)} \right] \quad (2)$$

$$\text{for } 0 \leq \xi \leq L, \quad 0 \leq \eta \leq \eta_1$$

where  $\alpha = 2\pi/L$ ,  $L = 40$  cm,  $H = 6$  cm,  $\eta_1 = -\eta_2 = 12$  cm,  $\xi_1 = 0$ ,  $\xi_2 = L/2$  and  $c_m = 1.023598$ . For  $\eta = \eta_1$  in Eqns. (1) and (2) the ripple geometry used in the experimental setup is obtained. The complete set of governing equations for the free fluid region in the computational plane are written as

$$\begin{aligned} \frac{1}{J} \frac{\partial u}{\partial t} + u_c \frac{\partial u}{\partial \xi} + v_c \frac{\partial u}{\partial \eta} &= \frac{\partial y}{\partial \xi} \frac{\partial \bar{P}}{\partial \eta} - \frac{\partial y}{\partial \eta} \frac{\partial \bar{P}}{\partial \xi} + \frac{\partial}{\partial \xi} \left( v_c \frac{\partial u}{\partial \xi} \right) + \frac{\partial}{\partial \eta} \left( v_c \frac{\partial u}{\partial \eta} \right) \\ &+ \frac{\partial v_t}{\partial \eta} \frac{\partial v}{\partial \xi} - \frac{\partial v_t}{\partial \xi} \frac{\partial v}{\partial \eta} \end{aligned} \quad (3)$$

$$\begin{aligned} \frac{1}{J} \frac{\partial v}{\partial t} + u_c \frac{\partial v}{\partial \xi} + v_c \frac{\partial v}{\partial \eta} &= \frac{\partial x}{\partial \eta} \frac{\partial \bar{P}}{\partial \xi} - \frac{\partial x}{\partial \xi} \frac{\partial \bar{P}}{\partial \eta} + \frac{\partial}{\partial \xi} \left( v_c \frac{\partial v}{\partial \xi} \right) + \frac{\partial}{\partial \eta} \left( v_c \frac{\partial v}{\partial \eta} \right) \\ &+ \frac{\partial v_t}{\partial \xi} \frac{\partial u}{\partial \eta} - \frac{\partial v_t}{\partial \eta} \frac{\partial u}{\partial \xi} \end{aligned} \quad (4)$$

$$\frac{\partial^2 \psi}{\partial \xi^2} + \frac{\partial^2 \psi}{\partial \eta^2} = - \left[ \left( \frac{\partial y}{\partial \eta} \frac{\partial v}{\partial \xi} - \frac{\partial y}{\partial \xi} \frac{\partial v}{\partial \eta} \right) - \left( \frac{\partial x}{\partial \xi} \frac{\partial u}{\partial \eta} - \frac{\partial x}{\partial \eta} \frac{\partial u}{\partial \xi} \right) \right] \quad (5)$$

$$\frac{\partial^2 \mathbf{P}}{\partial \xi^2} + \frac{\partial^2 \mathbf{P}}{\partial \eta^2} = -2\rho \mathbf{J} \left[ \left( \frac{\partial v}{\partial \xi} \frac{\partial y}{\partial \eta} - \frac{\partial v}{\partial \eta} \frac{\partial y}{\partial \xi} \right) \left( \frac{\partial u}{\partial \eta} \frac{\partial x}{\partial \xi} - \frac{\partial u}{\partial \xi} \frac{\partial x}{\partial \eta} \right) + \left( \frac{\partial u}{\partial \xi} \frac{\partial y}{\partial \eta} - \frac{\partial u}{\partial \eta} \frac{\partial y}{\partial \xi} \right)^2 \right] \quad (6)$$

where

$$\bar{\mathbf{P}} = \frac{\mathbf{P}}{\rho} + \frac{2}{3} \mathbf{k}, \quad \mathbf{u}_e = \mathbf{u} \frac{\partial y}{\partial \eta} - \mathbf{v} \frac{\partial x}{\partial \eta}, \quad \mathbf{v}_e = \mathbf{v} \frac{\partial x}{\partial \xi} - \mathbf{u} \frac{\partial y}{\partial \xi}, \quad \mathbf{v}_t = \mathbf{v} + \mathbf{v}_t,$$

$$\mathbf{u} = \mathbf{J} \left( \frac{\partial x}{\partial \xi} \frac{\partial \psi}{\partial \eta} - \frac{\partial x}{\partial \eta} \frac{\partial \psi}{\partial \xi} \right), \quad \mathbf{v} = \mathbf{J} \left( \frac{\partial y}{\partial \xi} \frac{\partial \psi}{\partial \eta} - \frac{\partial y}{\partial \eta} \frac{\partial \psi}{\partial \xi} \right),$$

$\mathbf{J}$  is Jacobian of coordinate transformation,  $\mathbf{v}_t$  is turbulent viscosity and  $\mathbf{k}$  is turbulent kinetic energy. In the porous medium the Laplace equation for pressure is written as

$$\frac{\partial^2 (\mathbf{P}/\gamma)}{\partial x^2} + \frac{\partial^2 (\mathbf{P}/\gamma)}{\partial y^2} = 0 \quad (7)$$

Pressures along the permeable boundary are obtained by integration of the momentum equations on the free fluid side and are supplied as boundary conditions of equation (7) for the potential flow in the porous medium. After solution of the Laplace equation for pressure, the velocity components due to porous media flow are computed. Tangential velocity on the permeable boundary is assumed to have two components. First component is the velocity induced due to the external tangential stress by the free fluid (Beavers and Joseph 1967, Saffman 1971, Taylor 1971) and the second is the velocity of porous media flow due to tangential pressure gradient. These two velocity components are combined to give the "slip velocity" at the permeable boundary.

$$\mathbf{u}_s = -\mathbf{K} \frac{\partial (\mathbf{P}/\gamma)}{\partial x} + \mathbf{c}_s \sqrt{\mathbf{K}\mu/\gamma} \left( \frac{\partial \mathbf{u}}{\partial y} \right)_{y=0} \quad (8)$$

where  $\mathbf{K}$  is hydraulic conductivity and  $\mathbf{c}_s$  is the slip velocity coefficient. In the literature slip velocity coefficient may take values between 0.1 ~ 4. In this study it is fixed as unity since the slip velocity has showed no control on the pressure distribution over the permeable boundary for the complete range of

values reported in the literature. The normal component of velocity is simply due to porous media flow and is named as the "seepage velocity" given by.

$$v_s = -K \frac{\partial(P/\gamma)}{\partial y} \quad (9)$$

The slip and seepage velocities are used as the boundary conditions for the momentum equations governing the free fluid flow.

In numerical computation of the free fluid flow a different technique is adopted. In Poisson equation for pressure (Eqn.6) divergence of velocity is not included, instead, the Poisson equation for the stream function (Eqn.5) is solved and velocities are recomputed from the stream function to enforce the continuity after solution of the momentum equations. Otherwise computations were not converging because of the added degree of freedom by the slip and seepage velocities at the permeable boundary.

Turbulent viscosity is obtained from a low Reynolds number  $k-\varepsilon$  model as described in (Aydın and Shuto 1988). This model allows a complete numerical solution starting from the boundary, eliminating the need for wall functions. When the wall functions are removed, a new model for the surface roughness is required. This is accomplished by introducing and additional viscosity due to surface roughness (Aydın, 1993). Roughness viscosity is defined in terms of a roughness length scale and the velocity gradient at the wall,

$$\nu_r = l_r^2 \left| \left( \frac{\partial u}{\partial y} \right)_{y=0} \right| \quad (10)$$

and the roughness length scale is given as

$$l_r = 0.4k_s f_r \quad (11)$$

where  $k_s$  is the equivalent sand roughness height and  $f_r$  is a function to express the turbulence level in terms of the roughness Reynolds number.

$$f_r = \frac{0.1}{\left[ 1 - \exp(-0.09R_k^{0.6}) \right]} \quad (12)$$

and

$$R_k = \frac{k_s u_*}{\nu} \quad (13)$$

In computations, turbulent viscosity at a point next to a boundary is equated to the roughness viscosity if  $\nu_t < \nu_r$ .

### Computations and Results

Pressure distributions for the first experimental case, the impervious boundary, are computed by the numerical model described above. Computed pressures are compared to experimental data at four different flowrates in Fig.4. In general computation and experiment agrees well, except the end points ( $X = 40$  cm). This is due to the uniform flow conditions imposed at the end of the computational domain which may be achieved at further downstream locations. Before computing the permeable cases, effects of surface roughness and permeability are studied separately. Pressure distributions on the test surface for  $U_m = 248$  cm/s using different  $k_s$  values are shown in Fig. 5. This figure indicates that the pressure drop along the test surface increases with the surface roughness. Fig. 6 shows pressure distributions for the same flowrate using different hydraulic conductivity values keeping  $k_s = 0$ . It is clearly observed that the increase in permeability reduces the pressure drop on the test surface.

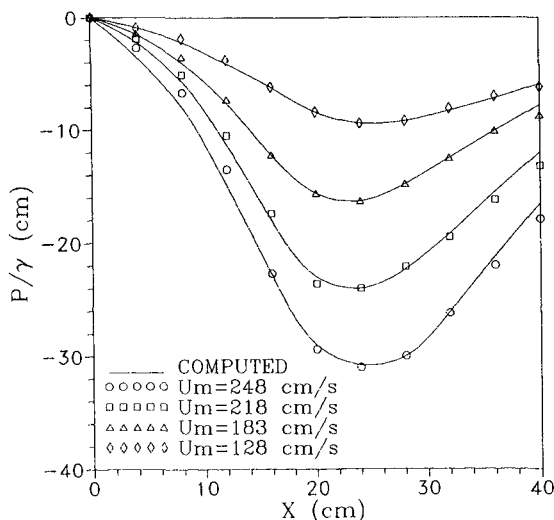


Fig.4 Comparison of computed and measured pressures along the test surface for impervious boundary.

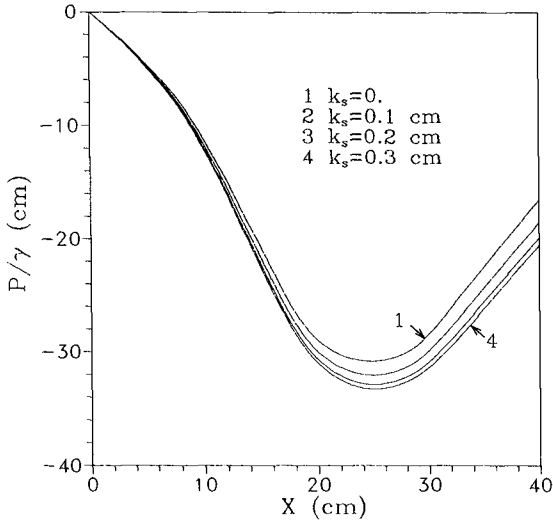


Fig.5 Pressure distributions along the test surface for different surface roughness values.

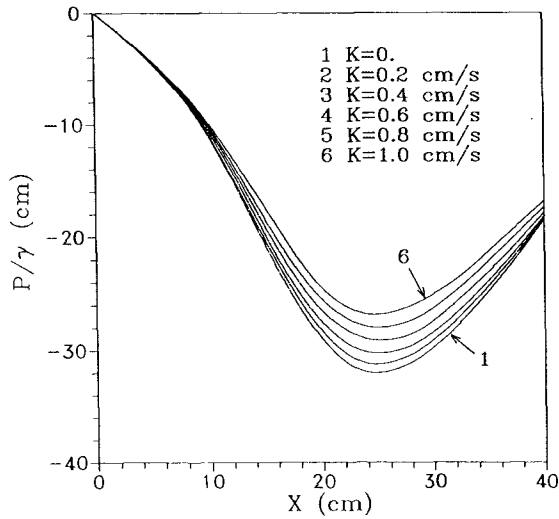


Fig.6 Pressure distributions along the test surface for different hydraulic conductivity values.

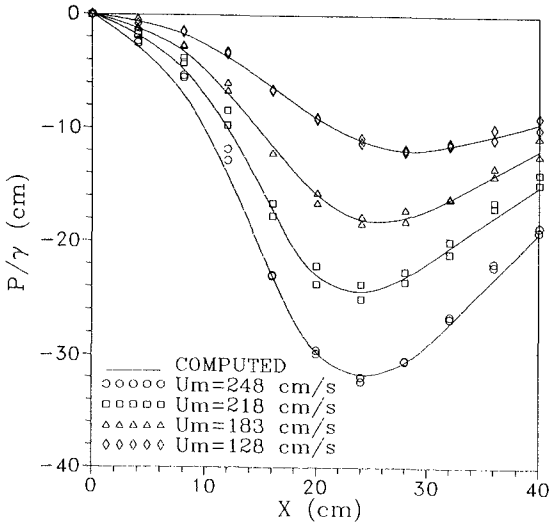


Fig.7 Comparison of computed and measured pressures along the test surface for permeable cases

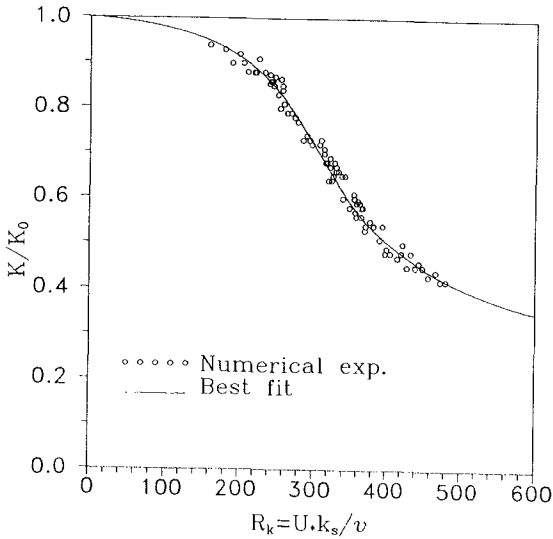


Fig.8 Hydraulic conductivity as a function of roughness Reynolds number along the test surface

The roughness model used in this study, as well as other models, represents the roughness effect due to surface irregularities. When the surface is permeable, the roughness effect will be increased by permeability since it allows turbulent fluctuations to enter into pores of the medium. On the other hand high turbulence due to free fluid flow near the boundary reduces permeability of the surface.

In this study the effect of permeability on roughness effect is ignored and dependence of permeability of a porous boundary to the turbulence level is investigated. Numerical model is forced to satisfy the experimentally measured pressures along the test surface for variable hydraulic conductivity at each computational node. Fig.7 shows a comparison of the measured and computed pressures for permeable test surface with variable hydraulic conductivity. Hydraulic conductivity values used to fit the measured pressures are shown in Fig.8 as a function of roughness Reynolds number. In this figure  $K_0$  represents the hydraulic conductivity for laminar flow conditions. As seen from the figure, hydraulic conductivity is reduced by turbulence when the hydrodynamically rough condition is reached and the reduction is about 50 % at a roughness Reynolds number of 400. However, in order to be able to give an expression of the relation between hydraulic conductivity and roughness Reynolds number, the effect of permeability on surface roughness should be clarified.

### Acknowledgement

The publication of the present paper is financially supported by the Ogawa Commemoration Fund of Japan.

### References

- Aydin, I. Shuto, N. (1988) An Application of  $k-\epsilon$  Model to Oscillatory Boundary Layers. **Coastal Eng. in Japan**, Vol. 30, No. 2, pp. 11-24.
- Aydin, I. (1993) Simulation of Rough Surfaces in Turbulent Flow Computation. **Proc. of 1<sup>st</sup> National Conf. on Computational Mechanics, Istanbul**, pp. 57-56.
- Beavers, G. S. and Joseph, D. D. (1967) Boundary Conditions at a Naturally Permeable Wall, **J. Fluid Mech.**, Vol. 30, part 1, pp. 197-207.
- Saffman, P. G. (1971) On the Boundary Condition at the Surface of a Porous Medium. **Studies in Applied Mech.**, Vol. 1. No. 2, pp 93-101.
- Taylor, G. I. (1971) A Model for the Boundary Condition of a Porous Material. Part I. **J. of Fluid Mech.**, Vol. 49, part 2, pp. 319-326.

## CHAPTER 128

# Physical Experiments on the Effects of Groins on Shore Morphology

Peyman Badiei<sup>1</sup>, J. William Kamphuis<sup>1</sup>, David G. Hamilton<sup>1</sup>

### Abstract

Physical mobile bed models were used to study the morphological effects of groins on an initially straight beach that was exposed to obliquely incident irregular waves. The tests were carried out at two different wave basins with the beach length of 8 and 28 m. A straight beach in the absence of groins was tested for each set of variables, then one or two impermeable surface piercing groins with different lengths were installed and tested. A detailed morphological and hydrodynamic data base was acquired which can be used for calibration and verification of numerical morphology models. Testing procedure and conditions are explained and typical results are presented along with a preliminary analysis which reveals the significant features of the evolution of beach bathymetry.

## 1. Introduction

Mobile bed models are widely used to study the problems dealing with morphological changes of coastal zones. The rapid growth in instrumentation technology has strengthened these models to provide more accurate and reliable results. The application of these models, however, is accompanied by problems associated with scale effects, boundary effects and operational errors discussed among others by Kamphuis (1991) and Hughes (1993). Kraus and Larson (1988) and Larson (1988) discuss examples of the application of large flumes in 2D morphology models to reduce the scale effects. The reduction of scale effects by using large basins, however, is not yet accomplished for a 3D model where wave induced longshore currents play a major role. In spite of these problems, mobile bed models are a unique way of providing a controllable environment for acquiring reliable data and insight into the physical processes.

---

<sup>1</sup> Department of Civil Engineering, Queen's University, Kingston, Ontario, Canada, K7L 3N6



In the present study a series of mobile bed *process models* (Kamphuis (1991)) were employed to investigate the effects of groins on the evolution of shore morphology under the attack of waves approaching with an angle towards the shoreline. These tests were carried out at the Queen's University Coastal Engineering Research Laboratory (QUCERL) and the Hydraulic Laboratory of the National Research Council of Canada (NRCC).

## 2. Objectives

This study attempts to understand the hydrodynamic and sediment processes near groins through the use of both physical and numerical models. The hydraulic model results provide a data base for the calibration and verification of a detailed numerical morphology model. The numerical model in turn will be used first to simulate the hydraulic model results and then to scale up to prototype, thus circumventing some of the shortcomings of the physical model. This paper presents the results of physical experiments.

A review of the very few mobile bed tests on groins reported in the literature (Barcelo (1968) and (1970), Price and Tomlinson (1968) and Hulsbergen et al (1978)) shows that no such comprehensive data base is at hand which can be used for the purpose of this study. The results of the available experiments have some common features; (1) tests were performed with regular waves, (2) they were restricted to one or two aspects and the overall impact of the groins was not investigated and (3) the data collection was limited to recording some parts of the overall process and many important details are lost.

Regular waves have concentrated energy around a single frequency, so they produce exaggerated offshore bar and strong currents (described by Hulsbergen et al (1978) as 'chaotic current patterns'). These effects which distort the test results and make the testing operation unmanageable were avoided in the present study by using irregular long crested waves. Moreover irregular waves have a closer resemblance to the waves in prototype. Detailed morphological data were collected along with measurements of hydrodynamic conditions (waves and currents). Because the changes in morphology made it difficult to perform sufficient steady state current measurements, a separate series of fixed bed tests were carried out at QUCERL basin to provide a more detailed hydrodynamic data base. The results of these tests will be discussed in a later paper. Finally, instead of looking at some specific features of morphological changes, within the framework of the variables of these tests (discussed in Section 3), all the important aspects of the groin impact on an initially straight beach were considered. During the tests and in the analysis of the results, special attention was given to the following morphological features:

1. The bar-groin interaction which affects the position of the breaker, the width of the surfzone, the reformation of the longshore current and the sediment transport distribution.

2. The extent and geometry of the accretion and erosion zones on either side of groin(s) which shows the length of the beach affected by the groin. In this regard the accretion and erosion pattern inside the groin bays are also very important.
3. The local scour holes or channels around the groin created by strong currents that are vital to the design of the groin structure.

### 3. Testing Procedure

Among the large number of parameters which could be varied in such tests, it was decided, due to practical limitations, to keep the following parameters constant. Based on a JONSWAP spectrum, irregular wave trains composed of 200 waves with a peak period of  $T_p = 1.15$  s and groupiness factor of  $G = 0.8$  were used. The mean diameter of the sand ( $D_{50}$ ) was 0.12 mm and the initial slope of the beach (m) was 0.1. The deep water wave angle  $\alpha$  and the ratio of  $S_g/L_g$  where  $S_g$  is the distance between the groins and  $L_g$  is the groin length measured from the still water line, were also constants. The variable quantities were the incident wave height  $H_s$ , the position and the number of groins and the ratio of  $L_g/L_b$  where  $L_b$  is the distance of the offshore bar (prior to the installation of any groin) measured from the still water line.

Table 1: QUCERL mobile bed tests summary

Test No.	Test Description	Target $H_s$ (cm)	Duration (hrs)	Estimate $L_g/L_b$	Groin Position (m)
QT1	Single Groin	Variable	---	----	----
QT2	Single Groin	6.0	25.2	1.0	Y = 4.50
QT3	Single Groin	6.0	22.0	0.9	Y = 4.50
QT4	Single Groin	6.0	26.0	1.12	Y = 4.50
QT5	Single Groin	6.0	28.0	0.95	Y = 4.50
QT6	Straight Beach	6.0	24.0	N/A	N/A
QT7	Straight Beach	6.0	24.0	N/A	N/A
QT8	Single Groin	6.0	12.0	0.5	Y = 8.25
QT9	Single Groin	6.0	12.0	1.0	Y = 8.25
QT10	Single Groin	6.0	16.0	1.5	Y = 8.25
QT11	Single Groin	8.0	14.0	1.0	Y = 8.25
QT12	Straight Beach	8.0	12.0	N/A	N/A
QT13	Single Groin	8.0	12.0	0.75	Y = 8.25

Table 2: NRCC mobile bed tests summary

Test No.	Test Description	Target $H_s$ (cm)	Duration (hrs)	Estimate $L_g/L_b$	Groin Position (m)
NT1	Straight Beach	8.0	12.0	N/A	N/A
NT2	Single Groin	8.0	12.0	1.0	Y = 15.50
NT3	Double Groin	8.0	12.0	1.0	Y=18.75 & 15.50
NT4	Double Groin	8.0	12.0	1.4	Y=20.25 & 15.50
NT5	Double Groin	8.0	12.0	0.8	Y=18.10 & 15.50
NT6	Double Groin	10.0	12.0	1.0	Y=20.50 & 15.50
NT7	Double Groin	6.0	12.0	1.0	Y=17.68 & 12.00

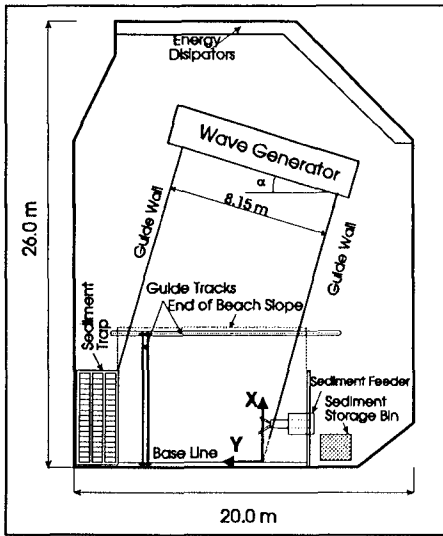


Figure 1: QUCERL Basin

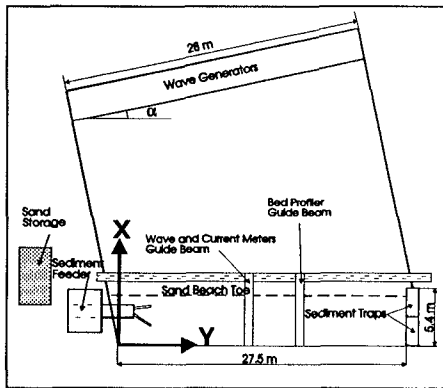


Figure 2: NRCC Basin

Tables (1) and (2) summarize the tests carried out at QUCERL and NRCC respectively. Here  $Y$  is the distance from the updrift wave guide shown in Figures 1 and 2.

At the beginning of each test the sandy beach was reshaped to a plane 1:10 slope. Then the beach was exposed to waves for four hours. At that time a clear offshore bar-trough/step formation (as defined by point 2 in Figure (23)) had developed. When groins were tested they were installed at this stage. The tests were continued thereafter in 2 hour cycles.

Figures 1 and 2 show the layout of the basins at QUCERL and NRCC respectively. Both basins had a closed updrift and an open downdrift boundary and the wave generators were raised above the floor so that water could flow underneath them. This measure according to Kamphuis (1977) would reduce circulation in the testing zone.

For an easier comparison with QUCERL, the NRCC results were transformed into their mirror image so that in all the test results the longshore current flows from right to left.

At QUCERL the angle  $\alpha$  of the wave generator was  $10^\circ$  in a water depth of 0.55 to 0.58 m and at NRCC this angle was  $11.6^\circ$  in a depth of 0.65 m

Wet sediment was fed to the updrift boundary at a rate calculated by the expression developed by Kamphuis (1991a) which yields 27.5, 48 and 74.4 kg/hr of submerged sand for 6, 8 and 10 cm wave heights respectively. This amount was divided into two parts fed separately to the swash zone and near the offshore bar/step. The sediment was trapped at the downdrift boundary and its submerged weight was measured by the loadcells connected to the traps. When the accumulated sand filled the traps it was recirculated into the storage bin near the feeder.

The Generalized Data Analysis Package (GEDAP) developed by NRCC was used for data acquisition. Waves and wave induced currents, submerged weight of the sand in the traps and bottom topography were measured during each two hour testing cycle. Sampling frequency in all these measurements was 20 Hz and sampling duration for waves and currents was 230 s which covered all the 200 waves with an average period of 1.15 s.

Fifteen capacitance type wave probes with 0.20 m spacing measured the wave height profile perpendicular to the shore line from offshore of the breaker up to a point near the still water line. Deep water wave probes (one at QUCERL and three at NRCC) measured the deep water waves.

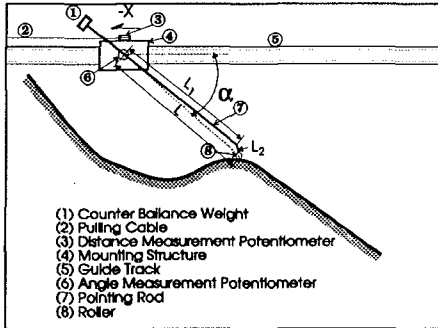


Figure 3: QUCERL Profiler

bed profiler manufactured by Delft Hydraulic Laboratory (Villaneuva(1989)) was used to survey the beach topography. In the other tests another bed profiler, designed and manufactured at QUCERL was used, shown in Figure 3. Here a roller (8) which was connected to the end of a pointing rod (7) followed the beach profile by simply resting on the sand. Knowing the length  $L$  and the angle  $\alpha$  which was measured by the reading of a potentiometer (6), the depth at each point was calculated. The distance in the  $X$  direction from the base line in (shown in Figure 1) was calculated from the readings of another potentiometer (3).

#### 4. Analysis of Morphological Data

The collected data along with the observations while performing the experiments are the basis of this first step of analysis. It should be mentioned that in the contour plots of the bathymetry and wave heights and the velocity vector plots of NRCC test results, the plotted distances in the  $X$  direction appear twice as large as the  $Y$  distances to make the plots clearer. Thus the angles of the velocity vectors are distorted.

##### 4.1. Straight Beach Tests

Four straight beach tests without any groins were performed as summarized in Tables 1 and 2. Comparing the results of these tests with the ones performed with

Electromagnetic (EM) bi-directional, sphere-headed current meters were used in both series of tests. Two current meters were used at QUCERL and maximum of four were used at NRCC. They were spaced at a distance greater than 0.25 m to avoid electrical interference. The time averaged velocities in  $X$  and  $Y$  directions were calculated from the measured time series and recorded.

In the first six tests at QUCERL and in all the NRCC tests the PV-07

groins allows the determination of the net effects of the groins. The contour plots of the beach bathymetry for tests QT7 after 14 hours and NT1 after 12 hours of testing are shown in Figures 4 and 5. The straight and parallel contour lines indicate that a straight and long beach was correctly modelled. The averages of three middle profiles (X = 3, 4 and 5 m) in QT7 and five middle profiles (X = 13.5, 15.5, 17.5, 19.5 and 21.5 m) in NT1 at different times are shown in Figures 6 and 7. These two Figures suggest that an equilibrium beach profile was not formed even after long hours of testing at QUCERL. They also show that smoother offshore bars were formed compared to the tests with regular waves reported by Larson(1988) and Kamphuis (1994). No build up of the offshore bar was observed after the first four hours of testing as opposed to Larson(1988). The smoother profile of the offshore bar formed by irregular waves is caused by the breaking of individual waves at different locations.

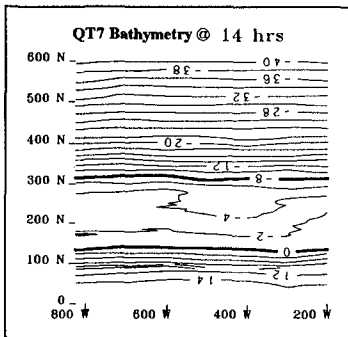


Figure 4:  $H_s = 6$  cm, no groins.

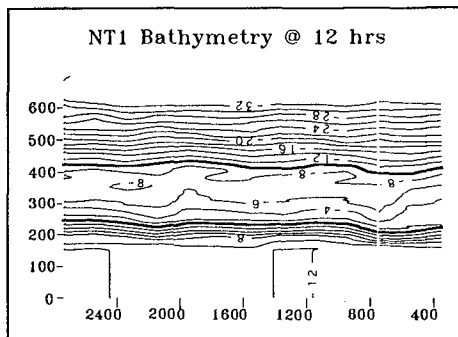


Figure 5:  $H_s = 8$  cm, no groins.

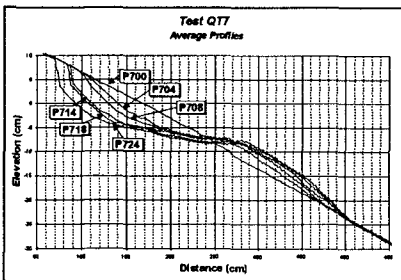


Figure 6: Average profiles in QT7

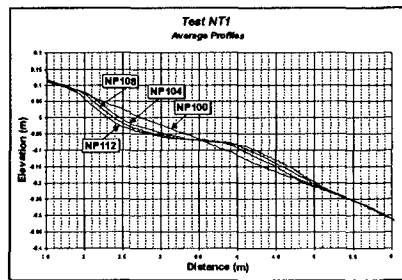
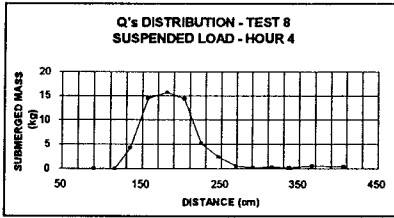


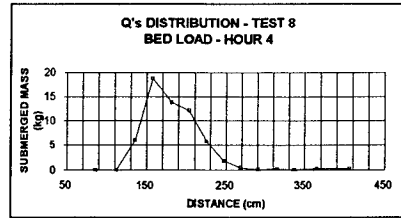
Figure 7: Average profiles in NT1

#### 4.2. Single Groin Near the Trap

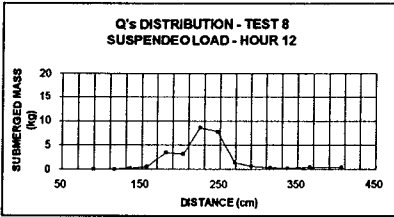
Five tests were performed in this group to monitor the changes in the cross shore distribution of sediment transport rate downdrift of the groin and to evaluate the updrift length of the beach affected by the groin. The details of measuring the



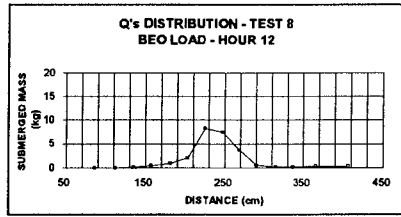
(a)



(b)

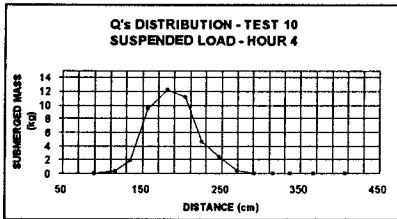


(c)

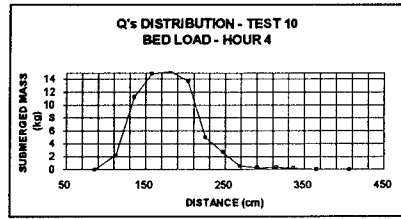


(d)

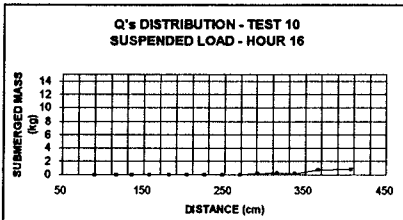
Figure 8: Cross shore sediment transport distribution at 4 and 12 hrs in QT8 with  $L_g/L_b = 0.5$



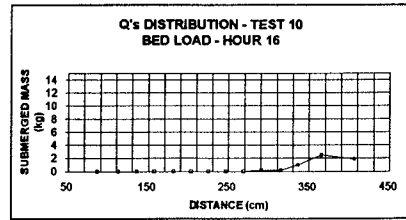
(a)



(b)



(c)



(d)

Figure 9: Cross shore sediment transport distribution at 4 and 16 hrs in QT10 with  $L_g/L_b = 1.5$

distribution of sediment transport rate at the sediment trap are explained in Kamphuis and Kooistra (1990). Figures 8 and 9 show typical examples of these distributions for

two extreme cases of  $L_g/L_b = 0.5$  and  $1.5$  (Tests QT8 and QT10 respectively). These Figures show the distributions at 4 hours with no groin and sometime after the groin was installed. In QT8 a considerable portion of the sand was bypassed into the trap. On the contrary in QT10, after 16 hours, practically no sediment was caught by the trap and all of the sediments were either accreted updrift of the groin or diverted offshore and created a shoal. Figure 8 shows an offshore shift of the peak of the longshore sediment transport rate, indicating that even a short groin deflects the longshore sediment flow.

Figure 10 presents the contours of QT10 at 4 and 16 hours. The still water line called  $L_0$  and the contour line with the closest depth to the breaker depth (here  $-8$  cm) called  $L_{br}$ , are highlighted. These lines are used to trace the evolution of beach bathymetry.  $L_{br}$  and  $L_0$  run almost parallel to each other during this test and both of

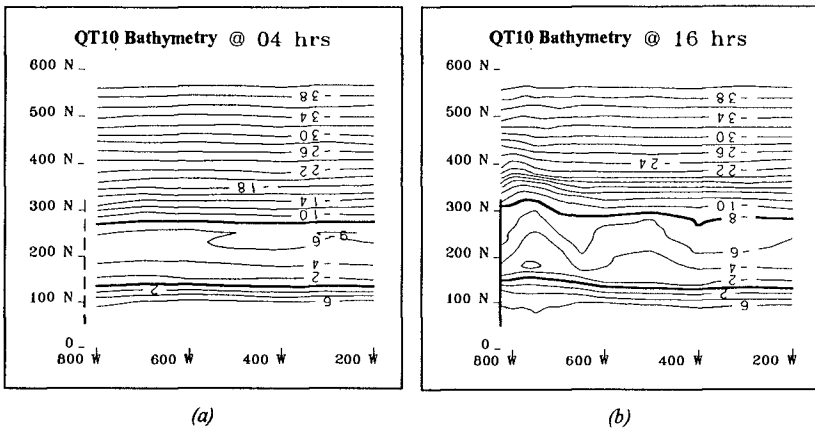


Figure 10:  $H_s = 6$  cm, groin at the sediment trap,  $L_g/L_b = 1.5$ .

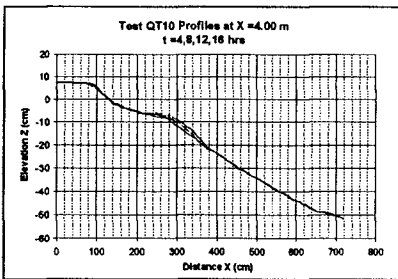


Figure 11: QT10 profiles at  $X=4$  m

them were deflected seaward by the groin.  $L_{br}$ , as shown in Figure 10 almost reached the head of the groin after 16 hrs.

Figure 11 shows that in QT10 the still water line at  $X=4$  m did not recede shoreward. The accretion caused by the groin at this location compensated the recession of the still water line,  $L_0$ , that was observed in the straight beach tests (discussed in Section 4.1). The distance of this point from the groin is almost equal to

that of the updrift boundary from the groin in QUCERL test with a groin in the middle of the basin. Evidently in these tests the groin affects the updrift boundary and the long beach condition updrift of the groin is not valid.

### 4.3. Groin(s) in the Middle of the Basin

#### 4.3.1. Single Groin in the Middle of the Basin

The contour plots of QT3 and NT2 shown in Figures 12 and 13 will be discussed as two examples in this group. Because the boundaries are affected by the groin, the contour pattern on either side of the groin in QT3 does not show the expected shape. Local effects near the groin such as the shift in  $L_0$  on either side of the groin, the deflection of  $L_{br}$  (depth 8 cm) to the offshore direction and the formation of a scour hole near the head of the groin are all well presented by this model, thus the results of this model are still useful as input to a numerical model. Nevertheless, to reduce the boundary effects, similar tests were carried out at NRCC and the result of the test with a single groin is shown in Figure 13 which shows a significant improvement. Here on the updrift side,  $L_0$  remained parallel to its original position far from the groin and advanced seaward close to the groin. Downdrift of the groin  $L_0$  receded shoreward except in the close vicinity of the groin and its direction was similar to that of  $L_0$  on the updrift side. The formation of a scour hole near the head of the groin was also quite obvious. In addition, a shoal was created in front of the groin which was due to the deposition of the deflected longshore sediment flow. Line  $L_{br}$  (depth -10 cm) runs parallel to  $L_0$  on the updrift side and remains parallel to its original alignment downdrift of the groin.

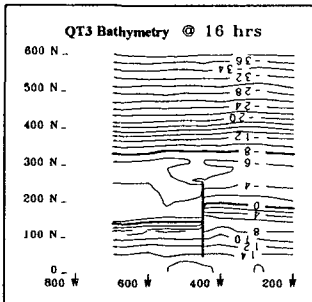


Figure 12:  $H_s = 6$  cm,  $L_g/L_b = 0.9$

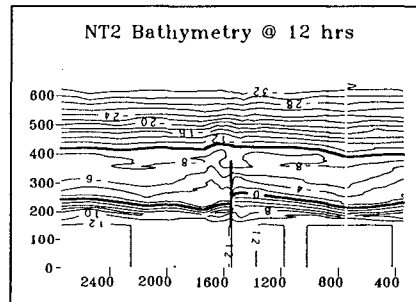


Figure 13:  $H_s = 8$  cm,  $L_g/L_b = 1$ .

#### 4.3.2. Double Groins in the Middle of the Basin

Figures 14-16 show the bathymetry of the tests with double groins with  $L_g/L_b = 0.8$  to 1.4 and  $H_s = 8$  cm at 12 hrs. Note that the updrift sides of Figures 13 and 14 are quite similar which is an indication of the repeatability of the tests. Two distinct shoals were formed offshore of the heads of the groins. These shoals were absent with short groins ( $L_g/L_b = 0.8$ , in test NT5).



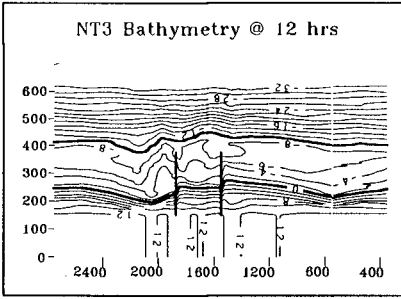


Figure 14:  $H_s = 8$  cm,  $L_g/L_b = 1$ .

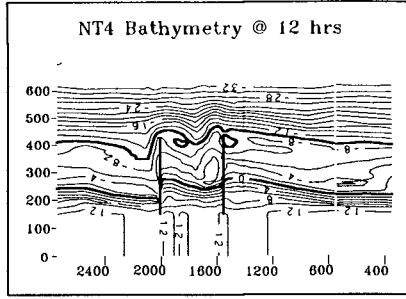


Figure 15:  $H_s = 8$  cm,  $L_g/L_b = 1.4$ .

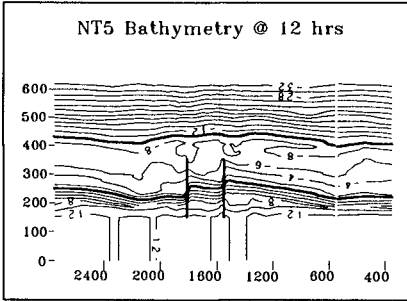


Figure 16:  $H_s = 8$  cm,  $L_g/L_b = 0.8$ .

The bypassed sediments collected downdrift near the groin and partly filled the zone eroded by the sediment transport rate deficit. This formed a depression zone (a ditch) at a distance downdrift of the groin. The ditch was closer to the groin with the longest groin (Figure 15) because the bypassing was small and was almost absent with shortest groin (Figure 16) due to increased bypassing. The contour line pattern on both sides of groins were similar with NT2.

The contour lines in the bay between the groins were more inclined and parallel to the incoming wave crests in NT4 where  $S_g$  was longer and little bypassing into the bay was allowed by the long groin.

Test NT6 with  $H_s = 10$  cm at 12 hrs is shown in Figure 17. The diversion of the more powerful longshore sediment flow caused a distinct offshore shoal, and more offshore contour lines were affected. Finally the topography of the low energy test NT7 at 12 hrs is presented in Figure 18.

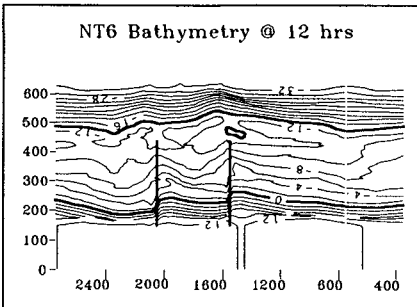


Figure 17:  $H_s = 10$  cm,  $L_g/L_b = 1$ .

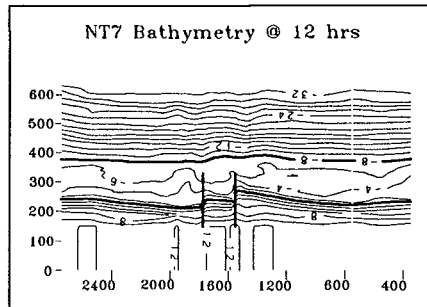


Figure 18:  $H_s = 6$  cm,  $L_g/L_b = 1$ .

In Figures 14-16  $L_{br}$  is the -10 cm contour line. With the short groin shown in Figure 16,  $L_{br}$  is almost unaffected by the groin.  $L_0$  in this case matches the expected pattern. In Figure 14 where  $L_g/L_b=1$ , the groin deflects  $L_{br}$  to some extent and for the case of the long groin shown in Figure 15,  $L_{br}$  is deflected considerably and runs almost parallel to  $L_0$  both updrift and downdrift of the groins. It is seen that the behaviour of  $L_{br}$  depends to a great extent, on the length of the groin.

#### 4.4. Net Morphological Changes Caused by Groins

As shown in Section 4.1 the bottom topographies in all the straight beach tests were continuously evolving and no equilibrium condition was reached. To differentiate between the bottom changes in a straight beach and that caused by the groin(s) the topographies of these two after the same duration of testing were subtracted from each other. Examples are shown in Figures 19-22. Here the dashed contour lines show the eroded zones and the solid lines represent the accreted areas. In all these figures it

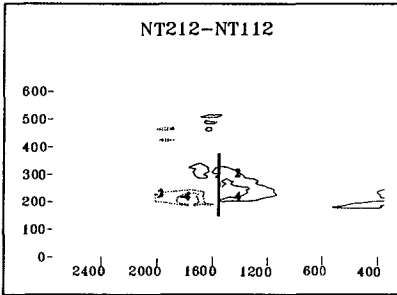


Figure 19: Net groin effect in NT2 at 12 hrs

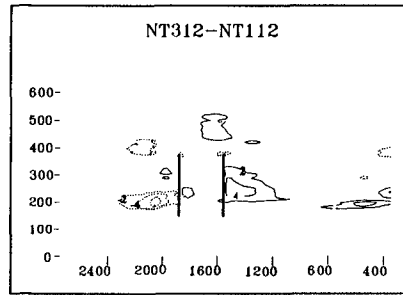


Figure 20: Net groin effect in NT3 at 12 hrs

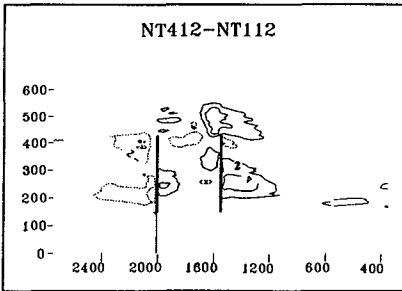


Figure 21: Net groin effect in NT4 at 12 hrs

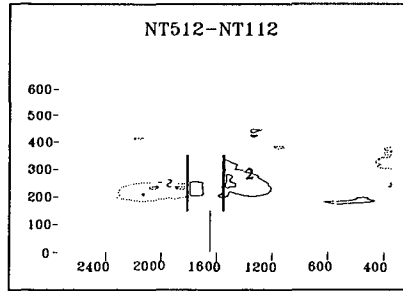


Figure 22: Net groin effect in NT5 at 12 hrs

is seen that the amount of net accretion caused by the groins is considerably more than the net erosion. This is possibly caused by the closeness of the downdrift boundary. It is not far enough from the groin to allow the erosion to compensate the accreted

volume updrift of the groin. The nonuniformity of the longshore current due to the circulation inside the basin could be another reason for this imbalance. The presence of offshore shoal is quite clear in Figures 20 and 21.

#### 4.5. Analysis of Characteristic Lines

The behaviour and evolution of the beach bathymetry can be studied by monitoring the changes in the positions of some *characteristic points* which define the geometry of the active zone of the beach profile. These points are defined in Figure 23. The offshore bar/step position is closely related to the breaker point and the beach head is located at the end of the wave uprush. The beach head and the offshore bar/step also define the boundaries of a *channel* in which most of the longshore sediment flow occurs. A FORTRAN code was written to detect the positions of these points based on the measured profiles.

The results of this analysis on the straight beach in test NT1 is shown in Figure 24. The process of beach profile lengthening in which beach head recedes and bar crest (offshore step) advances offshore is quite apparent if the characteristic lines of this test at different times are compared. It is also seen that the position of the bar crest (or the offshore step) and trough varied along the shore with a maximum difference of about 0.50 m in the X direction. A rip current which pushed the breaker and consequently the offshore bar/step away from the shore line is considered to be the cause of this behaviour. The formation of the rip currents in an experimental wave basin will be presented in more

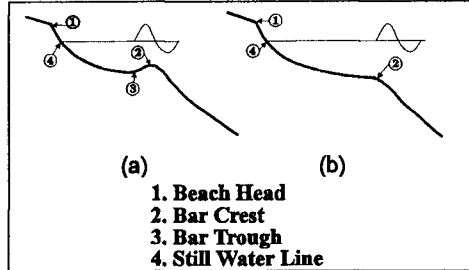


Figure 23: Definition of characteristic points

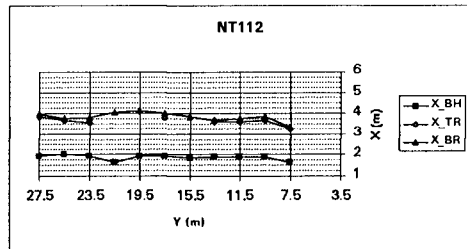


Figure 24: Characteristic lines for NT1 at 12 hrs

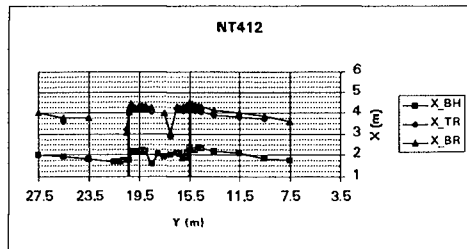


Figure 25: Characteristic lines for NT4 at 12 hrs

detail in a later paper. The comparison of  $L_0$  and  $L_{br}$  in Figure 15 and the bar/step and beach head characteristic lines in Figure 25 shows a similar pattern for the *channel* of longshore current in this test.

## 5. Wave and Current Data

To conduct these tests properly a large number of wave and current measurements within a short period of time were necessary to have a clear impression of waves and current patterns inside the testing zone which is unaffected by the changes in the movable bed. It was decided for practical reasons to perform limited measurements on waves and currents in these series of tests and use a fixed bed model later to acquire more detailed data on waves and currents. At NRCC more data acquisition channels were available, which provided a large number of simultaneous wave measurements. Thus the intensity of wave data within each test cycle was high enough as shown in Figure 26 to give a clear view of the wave pattern around the groins.

Typical results of wave and current measurements are presented in Figure 26 and 27.

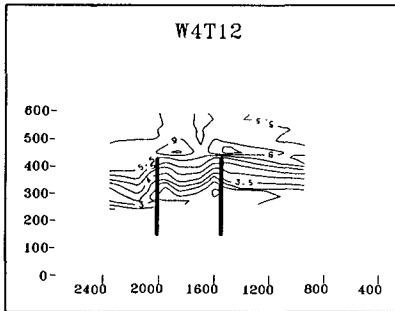


Figure 26:  $H_{ms}$  contours in NT4 at 12 hrs

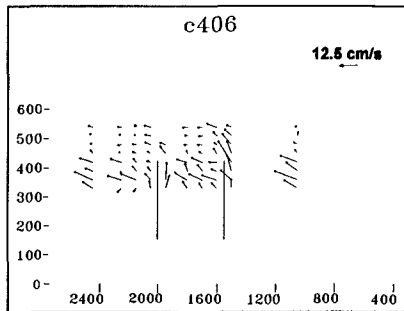


Figure 27: Velocities in NT4 at 6 hrs

## 6. Conclusions:

- Detailed morphological and hydrodynamic data were acquired in a set of mobile bed hydraulic model tests with and without groins
- At QUCERL the short distance of the boundaries from the groin prevented the simulation of a long beach on either side of a groin. The effects of the groin(s) on the boundaries were smaller in the tests at NRCC but not totally eliminated. However the boundary conditions in both series of these tests were measured and knowing these boundary conditions will permit the use of the collected data in a numerical model.

- Straight and parallel contour lines in straight beach tests both at QUCERL and NRCC indicate that a long straight beach was successfully modeled. Equilibrium beach profiles were not observed even after long hours of testing (maximum of 28 hours at QUCERL). In contrast to the tests with regular waves no pronounced offshore bar was formed and in most of the cases an offshore step was created instead of an offshore bar. No build-up of the offshore bar was observed after the first four hours of testing.
- The QUCERL tests with a groin at the trap showed that with a long groin, practically no sand was bypassed into the trap; the sediments were either accreted updrift of the groin or diverted offshore. A short groin on the other hand permitted some bypassing and simply deflected the peak of the longshore sediment transport rate offshore.
- The updrift accretion and downdrift erosion in the NRCC tests were quite similar to the expected pattern formed by groins on a straight and long beach. However, in these tests, the net erosion caused by the groin(s) was less than the net accretion which indicates that the downdrift boundary was not far enough from the groin.
- In the test with two long groins (NT4 ) the span of the bay was long enough and little bypassing was permitted so the contour lines inside the groin bay became parallel with the crests of the incoming waves. For the rest of the tests with double groins, the alignment of the contour lines ( $L_0$  in particular) did not change significantly inside the groin bay.
- The bypassing of sand created a shoal offshore of the head of the groin. The size of the shoal was proportional to the length of the groin. Longer groins diverted more sand offshore and created a more distinct shoal.
- The formation of a depression zone downdrift of the groin was also caused by sand bypassing. The depression zone which had the form of a ditch or a channel, was aligned with an angle to the groin and its location was farther from the groin when the groin was shorter. In prototype such a ditch will not be formed because of the variations in the wave condition. But its presence in these experiments with a persistent wave condition is essential to test the ability of a detailed numerical model to correctly simulate this process.
- The formation of a scour hole near the head of the groin is quite evident in all the tests both at QUCERL and at NRCC. The scouring channels however are not shown in the bathymetry plots because of the resolution of the surveying.
- The presence of rip currents in the NRCC basin was shown by the analysis of characteristic lines. Rip currents pushed the location of the breaker point and consequently the offshore bar/step away from the shore and caused changes in the position of characteristic points i.e. offshore bar/step, along the shore of a beach without groins.

## 7. References:

- Barcelo' J.P. (1968)**, "Experimental Study of the Hydraulic Behavior of Groyne System", Proc. 11th Coastal Eng. Conf. pp 326-548
- Barcelo' J.P. (1970)**, "Experimental Study of the Hydraulic Behavior of Inclined Groyne System", Proc. 12th Coastal Eng. Conf. pp 1020-1040
- Hughes S.A. (1993)**, "Physical Models and Laboratory Techniques in Coastal Engineering", Advanced Series on Ocean Engineering - Vol. 7, World Scientific Publishing.
- Hulshergen C.H., Bakker W.T., and Van Bochove G. (1976)**, "Experimental Verification of Groyne Theory", Proc. 15th Coastal Eng. Conf. pp 322-335
- Kamphuis J.W. (1977)**, Discussion on "Wave-Induced Circulation in Shallow Basins" By: Dalrymple R.A., Eubanks R.A., and Birkemeier W.A. (1977), J. of the Waterway , Port, Coastal and Ocean Eng., ASCE, Vol. 103, No. WW1, pp 570-571.
- Kamphuis J.W. and Kooistra J (1990)**, "Three Dimensional Mobile Bed Hydraulic Model Studies of Wave Breaking Circulation and Sediment Transport Processes", Proc. of Canadian Coastal Conference, Kingston, National Research Council of Canada, pp 363-386.
- Kamphuis J.W. (1991)**, "Physical Modelling", Chapter 21, Vol. 2, Handbook of Coastal and Ocean Engineering, Gulf Publishing.
- Kamphuis J.W. (1991a)**, "Alongshore Sediment Transport Rate", J. of Waterways , Ports, Coastal and Ocean Eng., ASCE, Vol. 117, No. 6, pp 624-640.
- Kamphuis J.W. (1995)**, "Comparison of Two-Dimensional and Three-Dimensional Beach Profiles" ,to be published in May 1995, J. of the Waterway , Port, Coastal and Ocean Eng., ASCE.
- Kraus N.C. and Larson M. (1988)**, "Beach Profile Change Measured in the Tank for Large Waves, 1956-1957 and 1962", Technical Report CERC-88-00, Coastal Engineering Research Center, U.S. Army Engineer Waterways Experimental Station, Vicksburg, MS.
- Larson M. (1988)**, "Quantification of Beach Profile Change", Department of Water Resources Engineering, Lund University of Science and Technology, Report No. 1008
- Price W.A. and Tomlinson K.W. (1968)**, "The Effect of Groynes on Stable Beaches", Proc. of 11th Coastal Eng. Conf. pp 518-525
- Villanueva, L.F. (1989)**, "A Novel Technique of Automatic Beach Profile Measurements", Proc. Workshop on Instrumentation, Burlington, Ontario, Canada

## CHAPTER 129

### Line-Modeling of Shoreface Nourishment.

by  
Willem T. Bakker<sup>1</sup>, Nico F. Kersting<sup>2</sup> and Hanz D. Niemeyer<sup>3</sup>

#### Abstract

Using line modeling, in the scope of the NOURTEC project a prediction is made concerning the behavior of the shoreface nourishment of Terschelling and an evaluation concerning the behavior of the combined supply on beach and shoreface at Norderney. Computations suggest smaller long-shore diffusivity on the upper beach than on the zone between NAP-1 m to -3 m for Terschelling and the inverse for Norderney (groynes!). Cross-shore diffusivity at Norderney appears to be much larger than at Terschelling. If further investigations substantiate those results, these lead to the conclusion, that shoreface nourishment at Norderney is still more preferable than at Terschelling.

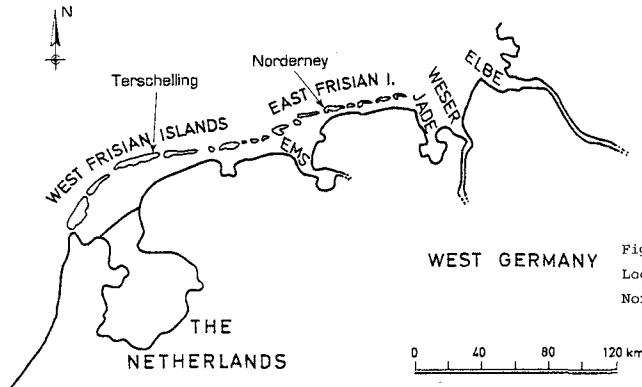


Fig. 1.  
Location Terschelling and  
Norderney

#### 1 Introduction

In the scope of the NOURTEC project (cf. Mulder et al., 1994) national coastal authorities in three different countries around the North Sea (Germany, the Netherlands

1 Netherlands Centre for Coastal Research (on secondment from Rijkswaterstaat, The Hague); Delft Univ. of Techn., Stevinweg 1, 2628 CN Delft, The Netherlands

2 Delft Univ. of Techn., Stevinweg 1, 2628 CN Delft, The Netherlands

3 Coastal Research Station Norderney, An der Mühle 5, D2982 Norderney, Germany

and Denmark) have carried out full-scale experiments with alternative coastal nourishment techniques: shoreface nourishment and combinations of shoreface and beach nourishment. These experiments are implemented under a range of environmental conditions. Extensive modelling and monitoring programmes form an essential part of the projects. The present paper deals with the prediction of the coastal behaviour with the aid of line models and comparison with prototype data for the Dutch and German supply: at Terschelling and Norderney (fig.1) respectively. In the future, also an analysis of the Danish supply will be given. A more detailed description of the investigations is given by Bakker & Kersting (1994) and by Kersting, Bakker & Niemeyer (1995) respectively.

## 2 Terschelling

### 2.1 Situation

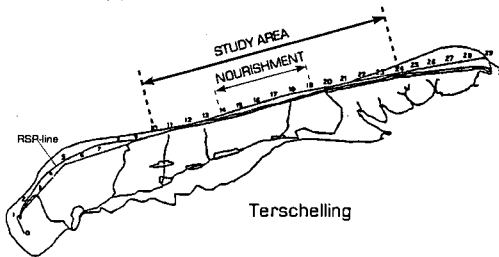


Fig.2 Location study area Terschelling

An underwater supply of ca. 2 Mm<sup>3</sup> has been carried out in spring and summer of 1993 on the Dutch Wadden isle of Terschelling. Fig. 2 shows the site. Three breaker bars are gradually moving seaward along the whole stretch; the motion is periodic.

Mutual distance between the breaker bars is 500 m; seaward propagation velocity is 50 m/year and period 10 years. Depth-averaged (between NAP + 3 m and NAP - 6 m; "NAP" denotes a level, which is about mean sea level) the area under consideration shows a coastal retreat of about 2.75 m/year.

### 2.2 Three-line model

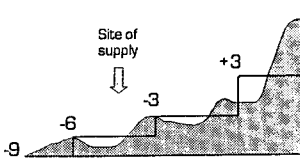


Fig.3. Schematization 3-line theory

Concerning the principles of line modeling is referred to the literature (Bakker, 1968a etc.). In the three-line model used the coastal zone is schematized in three zones (fig.3), which will be called: "beach", "inshore" and "deeper part".

In each zone it is assumed that all contour lines remain parallel and that the profile in this zone only moves horizontally. It is sufficient to compute only an average line in each zone, because it characterizes this zone. There is assumed to be a horizontal separation plane



between the zones. The sediment transport between the lines is assumed to be proportional to the difference between the equilibrium distance and the actual distance between the characterizing lines.

In the present application an initial equilibrium position (before any supply takes place) is assumed, where the three lines are straight and parallel (fig.4).

Distances  $y_{1,2,3}$ , are the deviations of the lines of the beach, inshore and deeper part, compared with this initial position. The y-value is computed by dividing the surplus volume in a zone (with respect to the initial position) by its height. In case  $y_1 = y_2 = y_3$ , the profile again is an equilibrium slope. If longshore transport could be neglected (see Appendix) the coast would tend to this equilibrium, if for instance originally sand on the inshore would have been supplied (fig.4).

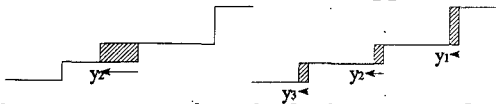


Fig.4. Definition  $y_1, y_2, y_3$

The process, sketched above results in cross-shore diffusion of sand. Adding longshore diffusion to the cross-shore diffusion, according to the approach of Pelnard-Considere (1954) and Bakker (1968a), the following dynamic equations can be derived:

$$\frac{dy_1}{dt} = \frac{s_1}{h_1} * \frac{\partial^2 y_1}{\partial x_1^2} - \frac{s_{y1}}{h_1} * (y_1 - y_2) \tag{1a}$$

$$\frac{dy_2}{dt} = \frac{s_2}{h_2} * \frac{\partial^2 y_2}{\partial x_1^2} + \frac{s_{y1}}{h_2} * (y_1 - y_2) - \frac{s_{y2}}{h_2} * (y_2 - y_3) \tag{1b}$$

$$\frac{dy_3}{dt} = \frac{s_3}{h_3} * \frac{\partial^2 y_3}{\partial x_1^2} - \frac{s_{y2}}{h_3} * (y_2 - y_3) \tag{1c}$$

On the lefthand side is the accretion of line of beach, inshore and deeper part respectively. On the righthand side the gradient of the longshore transport is determined by the constants  $s_1, s_2$  and  $s_3$  respectively; the cross-shore transport ("beach to inshore" and "inshore to deeper part") by  $s_{y1}$  and  $s_{y2}$  respectively.  $h_{1,2,3}$  denotes the depth allotted to the three zones. Fig 5 shows the diffusion of the (originally rectangular) supply shape in longshore direction in the course of time.

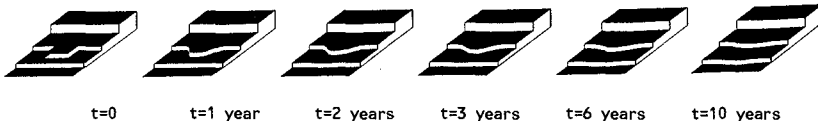


Fig. 5 Diffusion of supply

### 2.3 Coastal constants

**Cross-shore constants:** by the supply (between two breaker bars; fig.3) the breaker bars get an "antropogenic distortion". It is assumed, that by a diffusion process the sand, involved in this distortion will diffuse to the neighbouring breaker bars. Furthermore, it is assumed, that the velocity of diffusion is related to the time laps between the replacement of one bar by the next-landward bar. Per cycle, a certain percentage (determined by "engineering judgement") is retained; the rest of the sand is transported to the two adjacent breaker bars. The engineering judgement is based upon the solution of Smit (1987) for the cross-shore diffusion, reproduced in the Appendix. From his equations it can be derived, that in a period  $T_{01}$  (defined in the Appendix) the process of spreading the supply evenly over the profile is completed for almost 80 %. It does not seem illogical to assume, that the diffusion process to a similar rate is accomplished during the propagation period of the bars. The periods  $T_{01}$  and  $T_{02}$  are therefore chosen both equal to 10 years. With values for  $h_{1,2,3}$  (6 m, 3 m, 3 m; see fig.3), values of  $s_{y1}$  and  $s_{y2}$  of respectively .2 and .15 m/year are found. A higher cross-shore diffusivity at the upper part is found than at the lower part, which seems reasonable.

It is assumed, that processes, dominated by the diffusion of the supply can be linearly superponed to the natural longshore and cross-shore coastal processes. The latter processes are implemented by assuming an autonomous erosion of 2.75 m/yr for the zone between NAP -6 m and NAP + 3 m (derived from Van Vessem, 1992)

In the mathematical model it is assumed, that cross-shore transport of supply below a level of NAP -9m is negligible (during the time of consideration) compared to the transport above this level. Thus, in the model no period-averaged cross-shore transport is assumed by the periodical motion of the breaker bars as such.

To determine the **longshore constants** for the line-model use is made of the CERC-formula and the assumptions of Svasek (1968): the local sediment transport between two contour lines is proportional to the longshore component of the decrease of the energy flux between those two lines. For detailed description is referred to Svasek & Bijker (1969), Bakker et al. (1971), Ten Hoopen & Bakker (1974) and to Bakker et al. (1988).

Sloping shores (fig.6) have been assumed between terraces, separating beach, inshore and deeper zone; local height of the spilling breaker is taken proportional to local depth. Total wave climate has been taken into account, taking discrete wave classes, each defined by a certain wave height H, period T and direction  $\phi$  and a probability of occurrence:

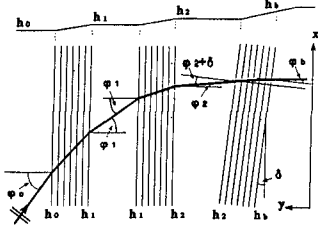


Fig.6 Schematization used for transport computations

$$S_{\phi} = S_{H,T,\phi} * P_r(H,T,\phi) \tag{2}$$

Fig. 7 shows the various classes of wave direction, translated into angles of incidence.

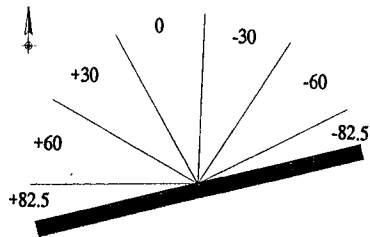


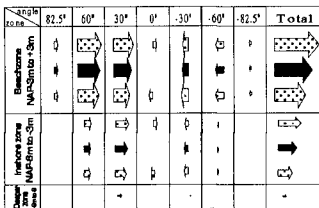
Fig.7. Directions of wave approach.

Vertical tide has been taken into account by schematizing it by a number of levels, combined with its probability of occurrence; furthermore it has been taken into account, that high waves from certain directions are

linked with water level rise (storm surge height).

The black arrows in fig.8 give the transport rates when all contour lines are parallel. Under those circumstances the method results in a total depth-integrated longshore transport for a certain H,T, $\phi$  as given by the

CERC-formula: 
$$S_{H,T,\phi} = .040 H_{b, sig}^2 n_b C_b \sin \phi_b * \cos \phi_b \tag{3}$$



	82.5°	60°	30°	0°	-30°	-60°	-82.5°	Total
+2°	43.42	500.4	431.4	40.53	-124.6	-84.63	-10.14	804.2
0°	40.55	478.3	387.3	0	-120.7	-87.91	-10.25	679.3
-2°	39.45	453.0	343.2	-40.53	-142.1	-90.54	-10.30	551.0
+2°	0.004	68.36	161.9	15.22	-38.16	-8.830	0	198.5
0°	0.004	67.57	148.5	0	-41.98	-8.818	0	165.3
-2°	0.004	66.30	134.4	-15.22	-45.56	-8.732	0	131.2
0°	0	0	5.518	0	-1.428	0	0	4.09

Fig.8 Transport rates along the three zones as function of angle of approach of the waves at deep water and the effect of  $\delta = 2^\circ$ .

Table 1. Transport rates ( $10^3 \text{ m}^3/\text{yr}$ ) Volumes of the arrows in fig.8 are proportional to numbers in table 1.

The columns in fig.8 denote the various angles of wave incidence; the 3 sets of 3 rows the 3 zones. The size of the arrows is proportional to the transport (weighted with its probability of occurrence) integrated over all classes of H and T. Probability of occurrence has been derived from SON, a measurement station in the vicinity of Schiermonnikoog. Wave data have been made available by Rijkswaterstaat (Roskam 1988). Calculated numerical values of transport rates (in thousands  $m^3/year$ ) are depicted in table 1 (the lines "0 degree "; for beach, inshore and deeper zone respectively).

For both upper zones the longshore transport has been computed three times for each wave direction: apart from assuming parallel depth contours also the angle of the beach (inshore) has been turned over an angle  $\delta$  with respect to the other contour lines. For instance: in fig 6 the angle of the beach is turned. The gray arrows in fig 8a show the effect, where  $\delta$  has been chosen  $\pm 2^\circ$ . Table 1 shows the numerical results.

The constants  $s_1$  and  $s_2$ , which can be shown theoretically (Pelnard Considere, 1954) to be the derivative of the longshore transport to the coastal direction (atan  $\partial y/\partial x$ ), are calculated from:

$$s_i = \frac{\sum_{+82.5^\circ}^{-82.5^\circ} S_i(\phi_i + \delta) - \sum_{+82.5^\circ}^{-82.5^\circ} S_i(\phi_i - \delta)}{2\delta} \quad (4)$$

## 2.4 Results

From the last column of table 1  $s_1$  is found by substitution of the total transport of  $804.2 \cdot 10^3$ , resp.  $551 \cdot 10^3$   $m^3/year$  for the terms in the numerator of (4) ( $\delta$  equals  $\pi/90$ ). A similar computation gives  $s_2$ ; then for  $s_1$ , resp.  $s_2$  values of  $3.63 \cdot 10^6$ , resp.  $0.964 \cdot 10^6$   $m^3/year/rad$  are found. A total transport of  $(697.3 + 165.3 + 4.09) \cdot 10^3 = .85 \cdot 10^6$   $m^3/year$  results.

It was found, that diffusivity in longshore direction along the deeper part could be neglected. Effect of curvature of the inshore on the coastal constant for the beach (the inshore turns more or less in the same way at the same time as the beach) has not been taken into account. Neglecting this effect can give a rather important over-estimate of the coastal constant of the beach (Bakker & Delver, 1986; Bakker et al., 1988). Another extreme (no longshore diffusion) is given by the formulae of Smit (1987) (Appendix)

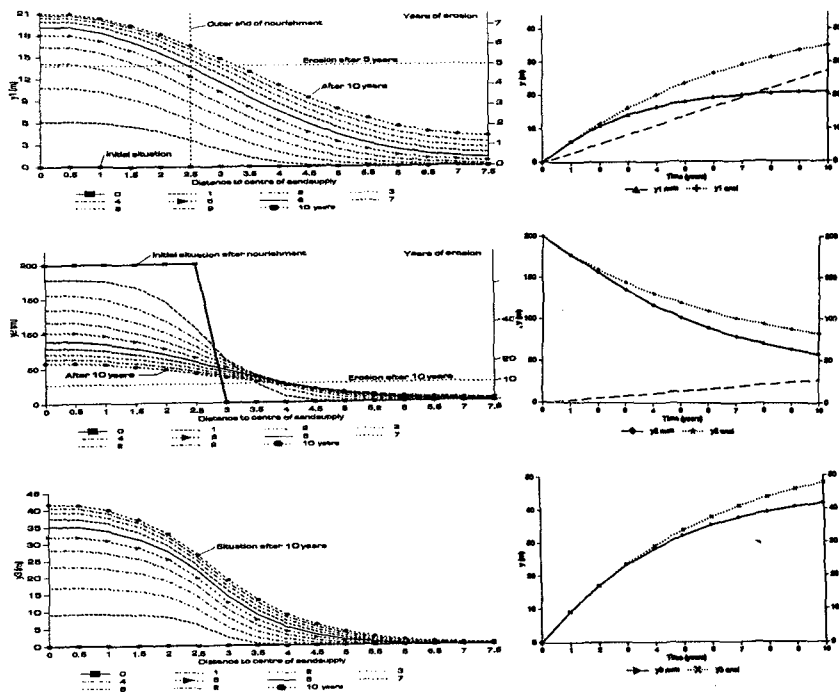


Fig 9a,b,c.Lines of beach, inshore and deeper part  $y_{1,2,3}$

Fig.10a,b,c Site of beach, inshore, deeper part in the course of time (in center of supply).

Fig 9 a,b,c shows (extreme high diffusivity) a plan view of the expected development of beach, inshore and deeper part (mind the different vertical scales). The autonomous erosion of the coast is depicted on the righthand side of the figure.

Fig.10a,b,c show the expected position (in the course of time) of the line of the beach, inshore and deeper part, in the center of the supply area.

Both extremes (no c.q. extreme longshore diffusivity) are shown, where autonomous erosion is not taken into account.

The positive direction denotes a more seaward position. The drawn lines show the development, if one ignores the autonomous coastal erosion. The beach would increase, the inshore (where the supply was applied at  $t=0$ ) would retreat from its exposed position. Finally, supply sand would spread evenly over the profile.

The interrupted lines in fig. 10 a,b,c show the rate of autonomous coastal erosion at the same scale, more exactly: the amount of cumulative supply, necessary to balance this kind of erosion.

During the time the drawn line lies above (c.q. below) the interrupted line, the beach, c.q. inshore has a more seaward (c.q. landward) position than just before the application of the supply.

It shows, that according to the computations the supply will stop the erosion of the beach during the order of a decennium, without causing considerable accretion.

### 3 Norderney

#### 3.1 Conditions at the site of supply.

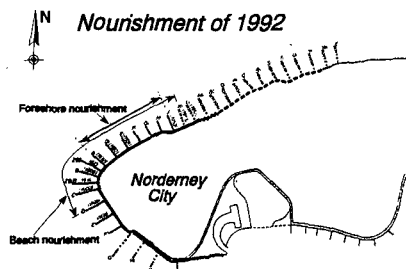


Fig.11 Combined beach and shoreface nourishment. Coastal protection.

Near the west point of the German Wadden island of Norderney, 450.000 m<sup>3</sup> of sand has been supplied in 1992 to the beach and the shoreface (fig. 11).

The seaward limit of the nourishment coincides with the 5 m depth contour. The coastline is protected by groynes, revetments and seawalls. For the largest part the area is inside the "Riffbogen" (bars formed by the outer delta).

Wave attack is important on the North West side.

At the South West side (Norderneyer Seegat) current dominates (cf. Thilo & Kurzak (1952), Luck (1977) and Niemeier (1986 a,b,c, 1990 and 1992)).

Since the first artificial nourishment (1.25 Mm<sup>3</sup> in 1951/52) (major) sand supply in this area and its vicinity was repeated 6 times (incl.1992). Fig. 12 shows the area of coastal nourishment in 1992: an amount of .5 Mm<sup>3</sup>, of which 50 % supplied above NN-1m (as NAP the level NN is about mean water level). Ca. 20% was supplied between NN-3m and NN-5m.

#### 3.2 Wave climate and wind set-up

The outer delta largely shelters the considered area from the deep water wave field. However, even more than at Terschelling, high waves and high surge levels are often linked together. Kersting et al.(1995) compute the sand transport using the SON deep water wave climate as well for Terschelling as for Norderney. However, storm surge

levels at Norderney are higher than at Terschelling. Thus, if Norderney would have been located near Terschelling, its (present) outer delta would give better protection; it would reduce wave height at the Westpoint shore more than in the present situation. Kersting et al. estimate that the effect of location on the surf height results (for the same wind, i.e. offshore wave height) in surge top water level rises, being 22% higher at Norderney than at Terschelling. They use as well theoretical considerations (Schalkwijk (1947) and Weenink (1958)) as well as analysis of the SON wind and wave data.

### 3.3 Sand transport computations

#### 3.3.1 Schematization

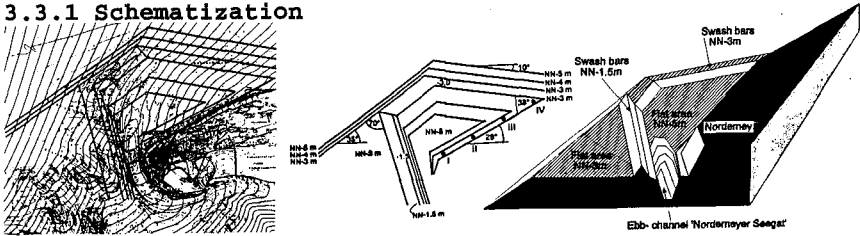


Fig.12a Refraction pattern

Fig.12b Schematization and points I to IV

Fig 12c Schematization (3D)

Investigations concern the coastal area with a length of ca 5 km between the tidal inlet and the site where the outer delta merges with the island (between point I to IV; fig 12b).

The wave climate on the inshore and the beaches in this area is strongly influenced by the bars of this outer delta. These bars reduce the energy of the incoming waves and also influence the propagation direction of the waves by refraction.

Fig 12b,c shows the schematization chosen; contour lines are schematized to sets of parallel straight lines. Furthermore, fig. 12a displays the real contour lines and a refraction diagram, from Niemeyer (1986), which indicates analogy in similarity of hydraulic response between schematization and prototype. Further research with respect to this aspect is proceeding. Convergence and divergence of wave rays are, in the schematization, partially taken into account: difference in direction of beach and inshore is implemented. However, the effect of the curvature of beach and inshore on the refraction coefficient is not taken into account. By the chosen schematization, the three parts of the outer delta together act as a convex lens, focussing the wave rays. From the refraction diagram of fig.12a the same picture arises. Because of this, a convex beach, making everywhere (about) the same angle with the wave crests will be stable, where for an offshore topography with totally

straight contour lines, parallel to the beach, a straight beach would have been stable. This explains the convex character of the Westend of the island.

Up to now, only the transport along the shore (beach and inshore) of the island has been calculated. The transport along the seaward shoreface of the outer delta will be calculated in the future. Again, the Svasek method of computation has been used (cf. ch.2 for literature). Effects of current are not taken into account.

Preliminary computations concerning diffusivity constants  $s_{1,2}$  have been carried out (for point IV; fig.12b) by varying the direction of beach or inshore as done in ch.2. Apart from this, diffusivity constants for Norderney will be calculated from measured data (sect.3.4)

### 3.3.2 Results

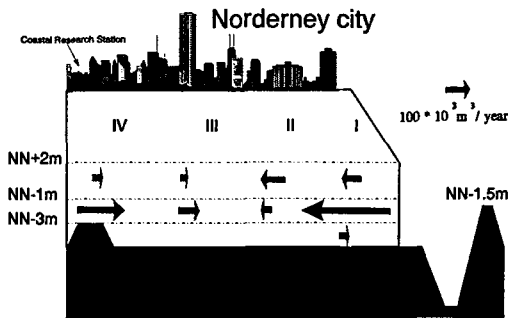


Fig.13 Transport capacity (without groynes) if the coast would be straight

Fig. 13 shows the calculated transport capacities in the points I to IV, which would occur, if the coastline would be straight. It shows, that accretion in the coastal area between points I and IV would result (according to the computations). Longshore diffusivity constants  $s_1$  and  $s_2$  in point IV are found of

$.6 \cdot 10^6$  and  $2.8 \cdot 10^6$   $m^3/year/rad$  for beach and inshore respectively. From the values calculated one would find, that a convex coast with a difference in coastal direction of ca.  $9^\circ$  to  $12^\circ$  between point I and point IV (fig.12b) would give a stable coast. The present difference in coastal direction is ca  $15^\circ$  which is more; thus erosion (as occurs) can be expected. For the computations is referred to Kersting et al. (1995). As accuracy is low, the result has only qualitative importance.

Because of the existing groynes the real transport, along the inshore, will be much less than the transport capacity. Bakker & Joustra (1970), comparing coastal erosion along the dutch coast before and after the construction of groynes, indicate, that groynes might reduce coastal transport with a factor of 4. This would reduce the value of  $s_2$  (in case of erosion) in the same way.



### 3.4 Line modeling

#### 3.4.1 Coastal constants; relation between curvature and erosion

Bakker (1968b) describes another way to find the coastal constants: from coastal measurements. Related are the data of volumetric change and curvature; the latter taken as difference of coastal direction  $\Delta\phi$  between left side and right side of the stretch. In order to obtain uniformity of data, a stretch of (only) 890 m (between groynes "A" and "H1") near the Western end of Norderney has been analyzed. Fig. 14 displays this relationship; from this figure Kersting et al. (1995) derive values of  $s_1=1.1*10^6$  and  $s_2=.9*10^6$  m<sup>3</sup>/year/rad. As for the first observation (encircled in fig.14b) leading to  $s_2$  the groynes will have been less effective (the supply extended further seaward than the groynes), this observation has been discarded, leading to  $s_2=.2*10^6$  m<sup>3</sup>/year/rad. Based upon fig. 14d,  $s_3$  has been taken zero. The constants  $s_{y1,2}$  (both assumed as 4 m/year) have been found by estimating  $T_{01}$  from the measurements and by iterative approximation, using the numerical three-line model (ch.2.2). Initial- and boundary conditions are imposed by prototype data.

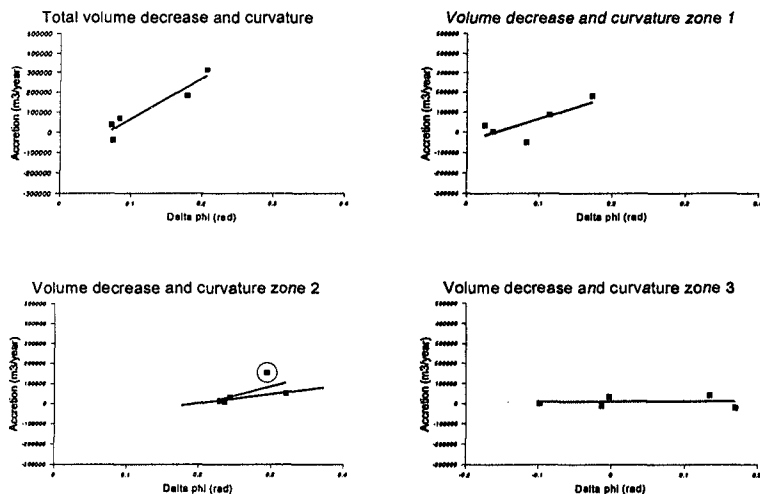


Fig.14a,b,c,d Volume decrease & curvature

#### 3.4.2 Results

In the Norderney case, " $y_{1,2,3}$ " will be defined as the surplus volume since the supply, (expressed in m<sup>3</sup>/m'/m

depth) between 2 successive separation planes (see fig.13). Comparison between measurement and computation show fig.15 ( $y_{1,2,3} = f(x); t$  as parameter) and 16 ( $y_{1,2,3} = f(t); x$  in the center of the field). For  $y_1$  and  $y_2$  good agreement is found;  $y_3$ , which in the model can only change because of cross-shore transport, appears to remain too large in the model. This suggests scour by current in the area below the groynes.

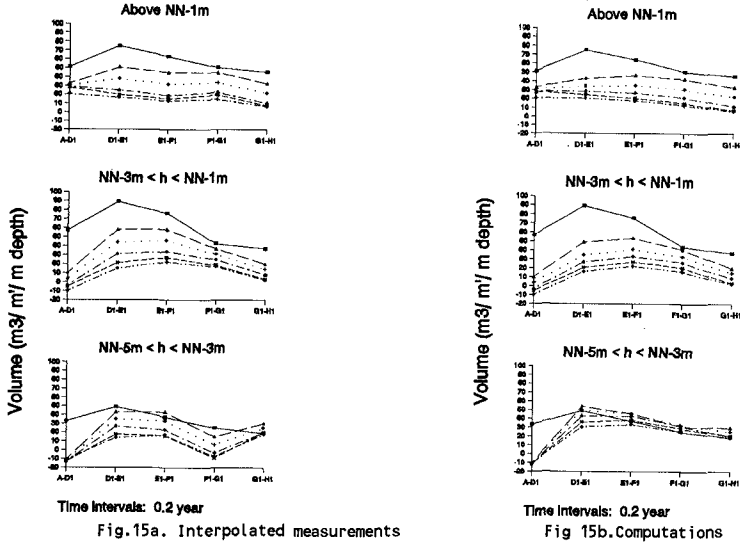


Fig.15a. Interpolated measurements

Fig 15b. Computations

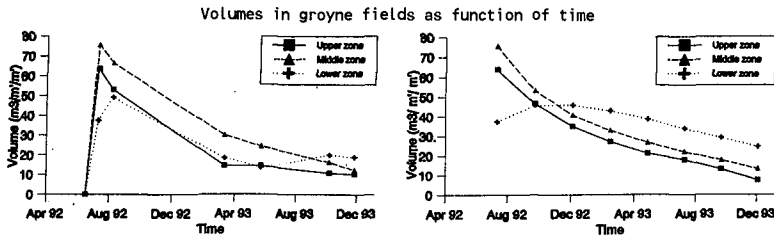


Fig 16a. Measured

Fig 16b. Computed

Volumes in central groyne section

#### 4 Discussion and conclusions.

##### 4.1 Terschelling

- Depending on the assumptions (of which the extremes are: "only cross-shore diffusivity" and "cross-shore plus unfavorable high value of longshore diffusion", a "life time" of the supply can be estimated, which varies respectively between 13 and 7 years (estimating the autonomous erosion as 2.75 m/year).

#### 4.2 Norderney

- Concerning Norderney only preliminary conclusions and some indications can be given. Comparing longshore coastal constants derived from transport formulae (sect.3.3) and from evaluation of topographic field data the  $s_2$ -value, found from those field data is lower than expected (even considering the effect of the groynes), where the  $s_1$ - value is considerably larger. The total of  $s_1+s_2$  is in the expected range.
- The coastal measurements indicate much larger longshore diffusivity on the beach (above NN - 1 m) than on the inshore (NN-3 m<h<NN-1 m).
- In the future effects of currents should be carefully examined, especially concerning the zone seaward of the groynes. For the three-line model (which is able to reproduce the development of beach and inshore rather well) underestimates (without current effects) the erosion of the deeper zone.

#### 4.3 General

- Comparison of coastal constants in general for various stretches of coast is given by Bakker et al. (1988). In that scope, the maximum values of the longshore diffusivity assumed for Terschelling are rather high: values of 1 to  $2 \cdot 10^6$  are more common. The cross-shore transport constants  $s_{y1,2}$  are (physically) strongly dependent upon the depth of the separation plane, as well on the schematization. Compared to the values, mentioned by Bakker et al. (1988), the cross-shore transport constants assumed for Terschelling are somewhat low. For instance, using Kalman filtering, de Vroeg (1987) finds  $s_y \approx 0.7$  m/year at NAP - .72m ( $T_{01} \approx 7$  years) for the Dutch Rijnland-coast. Compared to this, the value of  $s_{y1,2}$  of 4 m/year at NAP -3m ( $T_{01} = 0.4$  year and  $T_{02} = 0.25$  year) seems extremely high. Up to now,  $T_0$ -values of the order of 1 year were the smallest ever found (in Cadzand, CUR et al., 1986;  $s_y = 3$  m/year at NAP -2m). As in Norderney, in Cadzand a tidal channel is near to the coastal area. In the Norderney case, the wave attack is probably larger than in Cadzand.

Remarkable is the difference in character between the supplies of Terschelling and Norderney:.

- Supplying high on the beach instead of on the inshore would have been favorable for the Terschelling case if the costs of supplying on beach or inshore would have been equal. In Norderney however this is different because (most probably) the groynes largely reduce the longshore diffusivity of the inshore (compared to the beach).
- Probably the role of the deeper zone in Norderney will show to be more active (current effects near to the Norderneyer Seegatt) than at Terschelling.
- Different as well is the goal of both supplies, which emphasizes the importance of the offshore nourishment in Norderney: here the supply forms an essential part as a maintenance measure for the coastal protection by reducing the damage to the coastal defence works (sea-walls and groynes). This goal was formulated already in 1952 (Arbeitsgruppe Norderney); it has been shown to be very cost effective since then.

**Appendix. Smit's solution of the two-dimensional three-line problem.**

The dynamic equations for the cross-shore transport  $S_{y_i}$  between the layers (with  $i=1,2$ ) read:

$$S_{y_i} = s_{y_i}(y_i - y_{i+1}) \tag{A1}$$

Continuity ( $\Sigma(h_i \cdot y_i) = 0$ ) with  $i=1,3$  shows, that  $y_2$  is implicitly determined by  $y_1$  and  $y_3$ .

Continuity also yields:  $S_{y_1} = -h_1 \cdot dy_1/dt$        $S_{y_2} = +h_3 \cdot dy_3/dt$  (A2a,b)

Combination of (A1) and (A2a,b) leads to the vectorial equation:  $d\vec{y}/dt = \vec{A} \cdot \vec{y}$  (A3)

where  $\vec{y}$  is  $y_{1,3}$  and the matrix  $\vec{A}$  is  $(\alpha_{11} \dots \alpha_{22})$ , where:

$$\alpha_{11} = -\frac{s_{y_1} \cdot (h_1 + h_2)}{h_1 \cdot h_2} \quad \alpha_{12} = -\frac{s_{y_1} \cdot h_3}{h_1 \cdot h_2} \quad \alpha_{21} = -\frac{s_{y_2} \cdot h_1}{h_2 \cdot h_3} \quad \alpha_{22} = -\frac{s_{y_2} \cdot (h_2 + h_3)}{h_2 \cdot h_3} \tag{A4}$$

Displaying the solution gives a reason to define 5 timescales. Two of those are the time scales  $T_{01}$  and  $T_{02}$  of the two two-line systems: "beach + inshore" and "inshore + deeper part" (Bakker, 1968), equal to  $-1/\alpha_{11}$  and  $-1/\alpha_{22}$  respectively. The third one,  $T$ , is related to the other

diagonal of the matrix  $\vec{A}$ :  $T^2 = \frac{1}{\alpha_{12} \cdot \alpha_{21}} = \frac{h_2^2}{s_{y_1} \cdot s_{y_2}}$  (A5)

The last ones are  $1/\lambda_{1,2r}$  as occur in the solution of (A3):  $\vec{y} = \vec{K} e^{\lambda_1 t} + \vec{M} e^{\lambda_2 t}$  (A6)

where  $\vec{K} = (K_1, K_2)$  and  $\vec{M} = (M_1, M_2)$ , in which:

$$K_1 = -\frac{\alpha_{21}}{\lambda_2 - \lambda_1} y_{3b} + \frac{\lambda_2 + \frac{1}{T_{01}}}{\lambda_2 - \lambda_1} y_{1b} \quad M_1 = +\frac{\alpha_{21}}{\lambda_2 - \lambda_1} y_{3b} - \frac{\lambda_1 + \frac{1}{T_{01}}}{\lambda_2 - \lambda_1} y_{1b} \tag{A7a,b}$$

$$K_2 = \frac{1}{\alpha_{12}} \left( \lambda_1 + \frac{1}{T_{01}} \right) K_1 \quad M_2 = \frac{1}{\alpha_{12}} \left( \lambda_2 + \frac{1}{T_{01}} \right) M_1 \tag{A7c,d}$$

where  $y_{1b}$  and  $y_{3b}$  are the initial values of  $y_1$  and  $y_3$ .

**Acknowledgement:**

Support in the scope of Nourtec is acknowledged from: Rijkswaterstaat (RIKZ); Niedersächsischen Landesamt für Ökologie, Forschungsstelle Küste, Norderney, Delft University of Technology; financial support: DUT and the Commission of the EC (program MAST-II; contract MAS2-CT93-0049).

## References

- Bakker, W.T. (1968a) "The dynamics of a coast with a groyne system." Proc. 11th Conf. on Coastal Engng., London
- Bakker, W.T. (1968b) "A mathematical theory about sand waves and its application on the Dutch Wadden Isle of Vlieland" Shore and Beach
- Bakker, W.T. & D.Sj.Joustra (1970) "The History of the Dutch coast in the last century" Proc. 12th Conf. on Coastal Engng., Washington
- Bakker, W.T., H.G.H ten Hoopen & G.R.H.Grieve (1971) "Berekening van het zandtransport volgens de methode Svasek bij een strand en een vooroever, die een hoek met elkaar maken." (Computation of the sand transport according to the Svasek method, when beach and inshore make an angle with each other (in dutch) Rijkswaterstaat, Dir. for Water Management and Hydraulic Res., Dept. for Coastal Res. Study Rep WWK 71-18
- Bakker, W.T. & G.Delver (1986) "Coastal changes, caused by a shallow water sanddam in front of the Delfland coast." Delft University of Technology; Coastal Engineering Group.
- Bakker, W.T., C.v.d.Kerk & J.H. de Vroeg (1988) "Determination of coastal constants in mathematical line models." 2nd European Workshop on Coastal zones, as related to Physical Processes and Coastal Structures
- Bakker, W.T. & N.F.Kersting (1994) "Pilot study concerning the behaviour of coastal supply on the Dutch Wadden island of Terschelling." Delft University of Technology; Coastal Engineering Group.
- CUR, Rijkswaterstaat, Delft Hydr.Lab. (1986) Manual on Artificial Beach Nourishment.
- ten Hoopen, H.G.H & W.T.Bakker (1974) "Erosion problems of the Dutch Island of Goeree" Proc. 14th Int. Conf. on Coastal Engng., Copenhagen, 1974
- Kersting, N.F., W.T.Bakker & H.D.Niemeyer (1995) "Evaluation of a combined foreshore and beach nourishment at the German Wadden Island of Norderney." Delft University of Technology; Coastal Engineering Group and Coastal Research Station Norderney
- Kroon, A., P.Hoekstra, J.P.M.Mulder, D.Roelvink, K.T.Houman & B.G.Ruessink (1994) "Process-oriented monitoring of a shoreface nourishment; NOURTEC experiment at Terschelling, the Netherlands" Proc. 24th Int.Conf.on Coastal Engng., Kobe, Japan.
- Luck, G. (1977) "Inlet changes of the East Frisian Islands" Proc. 15th Int.Conf.on Coastal Engng., Honolulu
- Mulder, J.P.M., J.v.d.Kreeke, P.van Vessem (1994) "Experimental Shoreface Nourishment, Terschelling (NL)." Proc. 24th Int.Conf.on Coastal Engng., Kobe, Japan.
- Niemeyer, H.D. (1986) "Ausbreitung und Dämpfung des Seegangs im See- und Wattengebiet von Norderney" (Spreading and attenuation of swell around Sea and Wadden of Norderney, in german)
- Niemeyer, H.D. (1990) "Morphodynamics of tidal inlets" Course "Coastal Morphology" Delft University of Technology; Proc. COMETT-course
- Pelnaud Considere, R. (1954) "Essai de theorie a l'evolution des formes de rivages en plages de sable et de galets." Quatrieme Journees de l'Hydraulique, Paris 13-15 Juin 1954. Les Energies de la Mer Question 3
- Roskam, A.P. (1988) "Golfklimaten langs de Nederlandse kust" ( Wave climates along the dutch coast; in dutch) Rijkswaterstaat, Dienst Getijdewateren
- Schalkwijk, N.(1947) "A contribution of the study of storm surges on the Dutch coast." K.N.M.I. Med. & Verh. Series B, part 1, no.7
- Smit, E.S.P. (1987) "De rol van het sediment-dwarstransport in de ontwikkeling van de Hollandse kust." (The effect of cross-shore transport for the development of the Dutch coast; in dutch) Delft University of Technology; Coastal Engineering Group.
- Svasek, J.N. & E.W.Bijker (1969) "Two methods for determination of morphological changes induced by coastal structures." XXIInd Int.Nav. Congress Paris, Section II, item 4.
- Thilo, R. & G.Kurzak (1952) "Die Ursachen der Abbrucherscheinungen am West- und Nordwest-Strand der Insel Norderney" (the causes of erosion at the West- and North-West-beach of the island Norderney; (in German) Die Kuste
- van Vessem, P. (1992) "Morfologische analyse kustvak Terschelling, raai 13 tot 20." (Morphological analysis coastal area Terschelling; range 13 to 20; in dutch) Rijkswaterstaat, Tidal Waters Division
- de Vroeg, J.H. (1987) "The use of Kalman filtering for investigation of coastal behaviour." Delft University of Technology; Coastal Engineering Group.
- Weenink, M.P.H., (1958) "A theory and method of calculation of wind effect on sealevels in a partly enclosed sea, with special application to the southern coast of the North Sea." K.N.M.I. Med. & Verh. no.73

## CHAPTER 130

### Statistical Variations in Beach Parameter Change Rates for Walled and Non-Walled Profiles at Sandbridge, VA

John M. Hazelton<sup>1</sup>, David R. Basco<sup>2</sup>, Doug Bellomo<sup>3</sup>, Greg Williams<sup>4</sup>

#### Abstract

It has been argued that seawalls have a detrimental effect on the adjacent beach. These effects may only be noticeable over a period of years or may be short-term effects associated with storms or with seasonal transitions of the beach. Many theories on beach and seawall interaction have been speculative and have lacked actual field or laboratory evidence for their basis. This study uses four years of monthly and post-storm beach profile data to examine what influences the seawalls at Sandbridge, Virginia (USA) have on the adjacent beaches. Long-term effects of the seawalls are analyzed using fourteen years of profile data. Five parameters are defined to describe the subaerial beach profiles. Changes in the profile parameters in time are quantified using three methods of analysis.

#### 1. Introduction

Sandbridge, Virginia is the site for an ongoing investigation of seawall and beach interaction. The study area lies on the east coast of the United States. Sandbridge is located south of the Chesapeake Bay and north of the Virginia-North Carolina border, as depicted in Figure 1. The beach is used by local property owners, residents and tourists as a recreational area.

In August 1990 the Civil and Environmental Engineering Department at Old Dominion University (ODU) began a beach monitoring program at Sandbridge, Virginia. The purpose of the monitoring program was to examine the effects of seawalls on the adjacent beach. The monitoring program involves surveying 28 beach profiles at seawalls and dunes out to mean low water. Surveys are conducted once a month and after significant coastal storms. Results of the two year study may be found in Basco et al. (1992) and Bellomo (1993).

---

<sup>1</sup> Civil Engineer, EMC Engineering Services, Inc., Savannah, GA, 31412 (USA)

<sup>2</sup> Professor, Coastal Engineering Program, Old Dominion University, Norfolk, VA , 23529 (USA)

<sup>3</sup> Coastal Engineer, Dewberry and Davis, Inc., Springfield, VA (USA)

<sup>4</sup> Res. Hyd. Engr., CERC, Corps of Engineers, Vicksburg, MS, 39180 (USA)

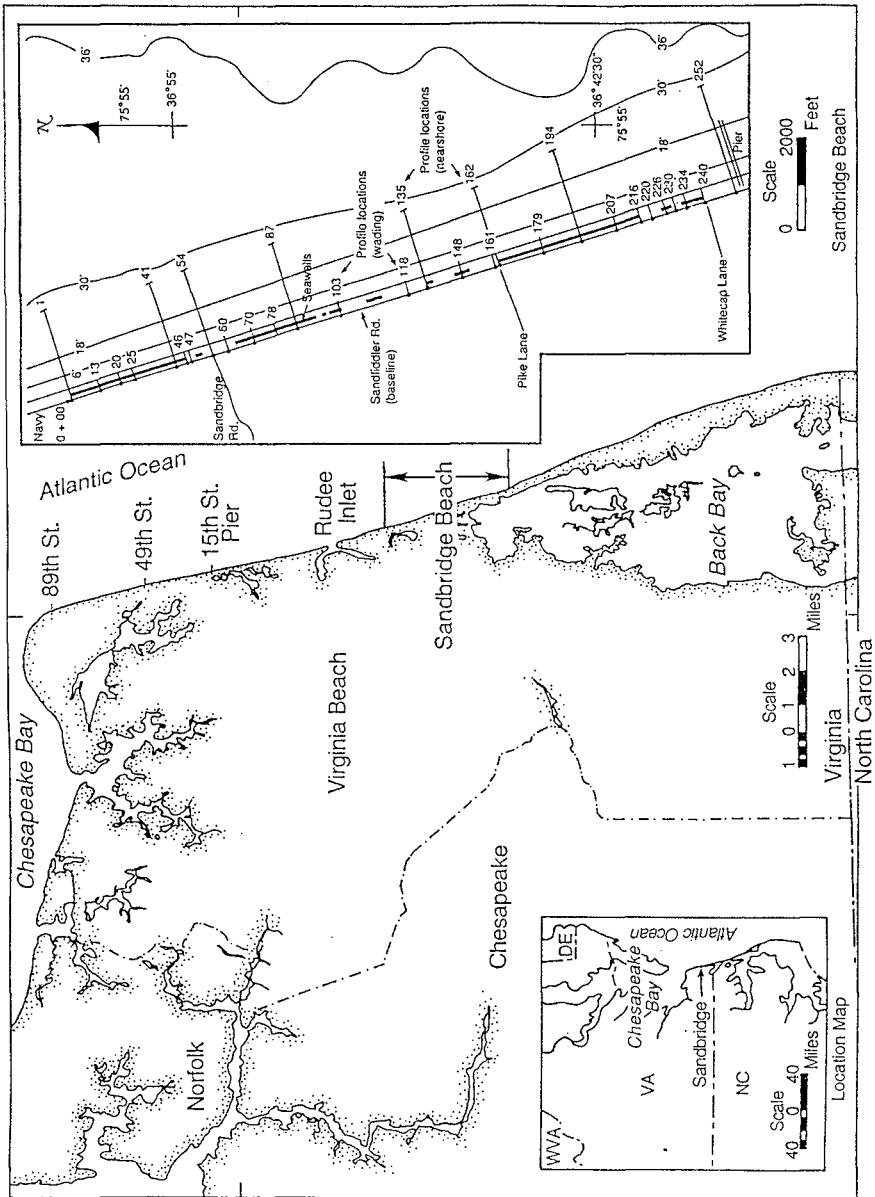


Figure 1. Location Map

The City of Virginia Beach began survey work at Sandbridge in 1980 with profiles at roughly 305 m intervals. Most profiles extend only out to wading depths, however some nearshore profiles (i.e. to depths of -8.0 meters) have been taken. The time between City surveys varies over the past 14 years. The Virginia Institute of Marine Science has also sponsored survey work at Sandbridge.

There are currently 2,350 profile-surveys at 53 locations collected during the last 14 years in the data base. Four of the profiles have had a seawall built during the period they were surveyed. Seven non-wall profiles have been surveyed before the boom in seawall construction in 1989.

The U.S. Army Engineer Waterways Experiment Station's Coastal Engineering Research Center (CERC) is sponsoring this study. This paper presents the preliminary results of what will be a five year study. They are also supporting two other beach and seawall interaction studies on United States beaches with one on the California coast and the second located at the eastern shore of Lake Michigan. It is anticipated that from the results of long-term field monitoring at three different locations, some facts will become clear regarding seawall and beach interaction.

## 2. Literature Survey

The Journal of Coastal Research (1988) Special Issue Number 4 entitled, "The Effects of Seawalls on the Beach", was specifically devoted to this topic. Included was a literature review by Kraus (1988) of beach and seawall interactions. Kraus concluded that there were no adverse effects of a seawall on the adjacent beach if a sediment supply exists.

Griggs et al. (1994) have described the results of seven years of monitoring beach and seawall interactions at Monterey Bay, California. They concluded that there were no significant long-term effects of the seawalls on the adjacent beach and the summer rebuilding of the beach was not influenced by the seawall. They found no difference between the winter profiles of the walled and non-walled beaches. At Monterey Bay the shoreline is stable and a steady sediment supply exists. This is different than at Sandbridge where a long-term, erosional trend exists.

### 3.0 Study Area Characteristics

Sandbridge, Virginia is quite literally a 'sand bridge' that is 7.7 km long and about 250 m wide at its narrowest point. Sandbridge separates the Atlantic Ocean to the east and the freshwater estuary Back Bay to the west. The long-term shoreline recession rate has been shown to vary linearly at Sandbridge from 1.1 m/yr at the north end, to 2.9 m/yr at the south end (Everts et al., 1983).

There are 4738 m of seawalls in 15 different sections along the Sandbridge shoreline. This is 62% of the oceanfront. The seawalls were built to protect septic tanks, driveway concrete slabs, and other property at ground level. The majority of the homes in the area are on piles above the one percent chance storm surge



elevation. Most of the walls are made of steel sheet-piles with others being constructed of timber. Short stretches of concrete and asphalt rubble revetments also exists along the Sandbridge shoreline.

Seawalls along the southern portion of Sandbridge have their base located within the tidal range during the summer months and below mean low water during the winter months. Seawalls along the middle and northern portion have their base above mean high water during the summer and within the tidal range during the winter months. The mean tidal range is 1.04 meters.

4.0 Parameter Definitions

To quantify profile "change" we have adopted five parameters as depicted in Figure 2. There are three section volume parameters, namely: landward volume ( $V_L$ ), seaward volume ( $V_S$ ), and total volume ( $V_T$ ), each carrying units of  $m^3/m$ . The area between the profile and the MLW line is calculated using the trapezoidal rule. To obtain a volume, this area is then multiplied by a unit length parallel to the beach. The different volumes (landward, seaward, and total) are calculated using different right and left hand boundaries. Landward volume is bounded on the left by the survey baseline. For a walled profile, the right hand boundary for landward volume is the wall itself. However, for a dune/beach profile, an imaginary partition is used as the landward right hand boundary. This imaginary partition is located at the same distance from the baseline as the nearby seawalls. Seaward volume is bounded on the left by the imaginary partition or seawall, and on the right by the intersection of the profile and the MLW line. The total volume is simply the sum of the landward and seaward volumes.

The berm elevation ( $E_B$ ) is measured in meters above the vertical datum. It is simply defined as the elevation of the profile at the seawall or imaginary partition, as shown in Figure 2. The shoreline position (P) is also shown in Figure 2. It is defined as the distance from the baseline, to where the profile intersects the MHW line.

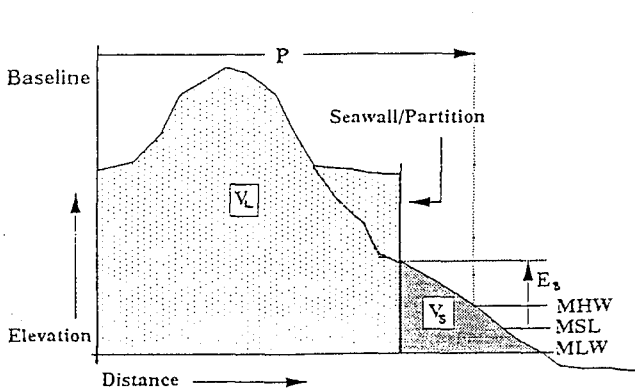


Figure 2 Definition Sketch

### 5.0 Methods of Analysis

Three basic methods have been devised to analyze changes in the profile parameters: (1) Individual Profile Method, (2) Simple Average Method and (3) Weighted Average Method. Each method uses an increasing number of profiles in their procedures and is useful in studying different topics of beach and seawall interaction. Linear regression was used to find the parameter rate of change for each method.

The weighted average method (WAM) used only 28 profile locations surveyed by ODU since August of 1990. The 28 profiles were separated into two categories, wall and non-wall profiles. Each wall profile was assigned a representative length of seawall along the beach. One wall profile is said to represent the conditions along this particular length of shore. The wall profile parameter is multiplied by the representative length. This is done for each wall profile. The sum of the representative lengths equals the total length of seawalls at Sandbridge, 4738 m. All of the weighted profile parameters were added together and then divided by 4738 m. The result is a single set of five weighted parameters ( $V_s, V_L, V_T, P$ , and  $E_B$ ) that represent all the wall profiles at Sandbridge. The same scheme was used with the dune profiles but with different representative lengths totaling 2953 m of non-walled beach.

For the simple average method (SAM) Sandbridge was divided into three reaches. The reasons for the division were due to differences in the baseline elevation and erosion rates along the Sandbridge shoreline. ODU profiles 1 to 54 were placed into the northern section, profiles 60 to 161 into the middle section and profiles 162 to 252 into the southern section. For each section the profiles were sorted again into wall and non-wall profiles. The data base has now been sorted into six categories. For each category, every profile had their parameters averaged together. The outcome is five parameters for a particular survey date representing either wall or dune profiles for each section.

For the individual profile method (IPM), the parameters were calculated for all surveys of a particular profile. This allows the profile history to be analyzed beyond the four years of ODU monitoring. The most significant benefit of the IPM was that parameter rates of change could be looked at before and after wall construction. An individual spreadsheet for each profile was created and contained the five parameters for every date that the profile was surveyed.

Seasonal variations of the profile parameters were studied using the results of the WAM. Seasonal trends can be mathematically modeled as a sinusoidal wave with a wave length of one year. The equation for the seasonal sine wave is given by:

$$Y = b + m(t) + (a)\sin(-2\pi(t-t_0)/365) \quad (1)$$

where:  $Y$  = parameter value ( $V_s, V_L, V_T, P$ , or  $E_B$ )  
 $b$  = parameter starting value, constant, at October 1990  
 $m$  = slope of best fit linear regression line  
 $t$  = time in number of days since January 1, 1900

$a$  = amplitude of sine wave

$t_0$  = start date October 1990

Linear regression was used to find the values of  $b$  and  $m$ . The amplitude,  $a$ , was found by using a value of the amplitude that gave the least variance between the measured WAM values and the predicted sine wave values,  $Y$ . Four years of WAM survey data were utilized in the analysis (October, 1990 to September, 1994). All values in the seasonal variation plots were subtracted by the parameter's linear regression intercept at October 1990. By using the "difference" values discrepancies between wall and dune profiles are more easily seen.

## 6. Beach and Seawall Interaction Hypotheses

To prove if the seawalls at Sandbridge are adversely affecting the adjacent beaches, three basic hypothesis were tested. The first hypothesis is that seawalls delay the recovery of the beach transition from winter to summer seasons. This hypothesis will be accepted or rejected by studying the weighted average volume seaward of the dune and wall profiles.

The second hypothesis is that the volume of sand in front of the walls erodes faster than the volumes in front of the partition for the dune profiles. This hypothesis will be accepted or rejected by comparing the rates of loss of volume seaward for the wall and dune profiles.

The third hypothesis is that the dune landward volumes are eroding at a faster rate because of sand being held back by adjacent seawalls. The volume of sand behind the wall is removed from the littoral system. This hypothesis will be tested by comparing the volume landward loss rates before and after seawall construction at the dune profile locations.

## 7.0 Results

### 7.1 Weighted Average Method

Results of the weighted average method are included in the plots of the seasonal variations in Figures 3 through 9. The solid dots represent the measured weighted average parameter difference. The heavy, solid line is the linear regression slope of the parameter rate of change using data from October, 1990 to September, 1994. The values of these four year, WAM slopes are summarized in Table 1. Also included in Table 1 are parameter rate of change using one, two and three years of data. There is some variability in the value of the parameter rate of change with an increasing number of years. The cause of this variability is that some winter seasons had more severe storms and some summers resulted in more beach recovery. By using the longest time span available, such inconsistencies are reduced. Parameter rate of change tends to decrease as the number of years used increased, except for the dune landward volume.

The null-hypothesis at the 95% confidence level was used to determine that the four year shoreline recession rate was statistically higher for the dune profiles. The volume seaward erosion rate was also statistically higher for the dune profiles. Berm elevation recession rates were found to be statistically the same for the wall and dune profiles.

### WAM Dune - Volume Seaward

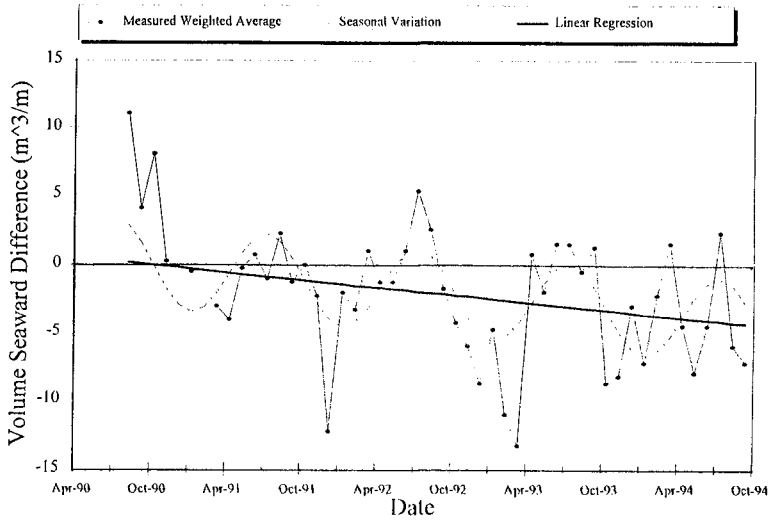


Figure 3 Dune Volume Seaward Seasonal Variations

### WAM Wall - Volume Seaward

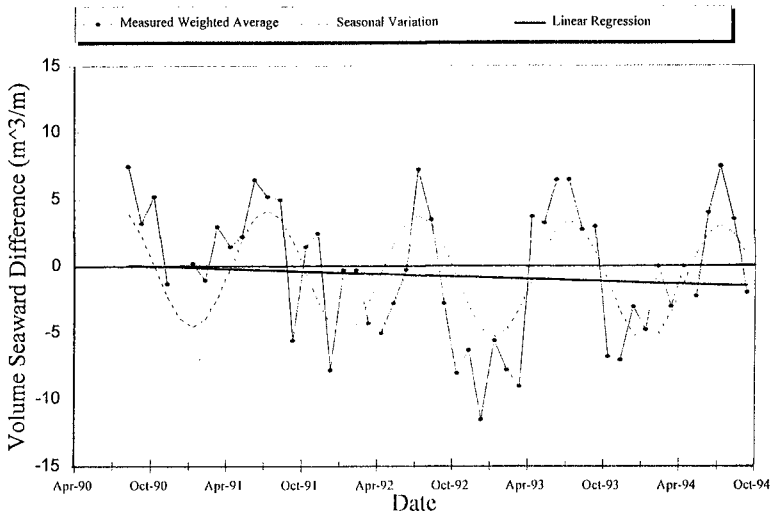


Figure 4 Wall Volume Seaward Seasonal Variations

The amplitude of the seasonal sine wave is larger for the wall profiles than for the dune profiles. This amplitude is one-half of the active volume of sand that builds in the summer and is removed in the winter. Active volumes for the dune and wall profiles are 6.2 m<sup>3</sup>/m in Figure 3 and 8.9 m<sup>3</sup>/m in Figure 4, respectively. The active seasonal volume of sand landward of the partition is 4.0 m<sup>3</sup>/m for the dune profiles as shown in Figure 5. Fluctuations in the seasonal berm elevation and shoreline position were found to be larger for the wall profiles than the dune profiles (see Figures 6, 7, 8 and 9).

These results suggest that the walls produce more seasonal variations causing lower winter profiles and more sand piled up in front of the walls in the summer than the duned sections. Dune and wall parameters reached their transition from winter to summer profiles in April and from summer to winter profiles in October. Volume seaward for the wall recovered before the dune in 1991 and simultaneously in 1993 and 1994. The dune recovered before the wall in 1992. Dune profiles achieved their winter profile before the wall in 1991 and simultaneously in 1990, 1992, 1993 and 1994. There is no evidence that walled sections recover at a later time than the duned sections.

### WAM Dune - Volume Landward

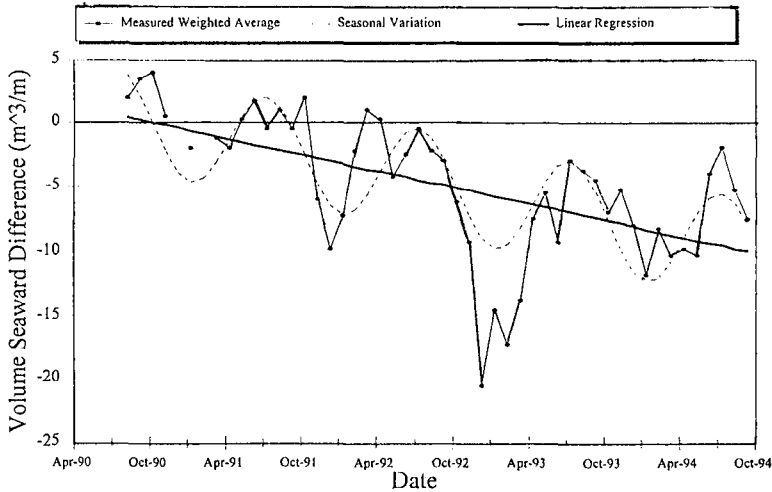


Figure 5 Dune Volume Landward Seasonal Variations

#### 7.2 Simple Average Method Results

Results from the simple average method are listed in Table 2. Column one is the section number and column two is the profiles used in that section. The third column is the percent of shoreline that is fronted with seawalls in that section. Column four is the profile parameter type. This table includes the parameter rate of change for each of the three sections in the last five columns.

### WAM Dune - Berm Elevation

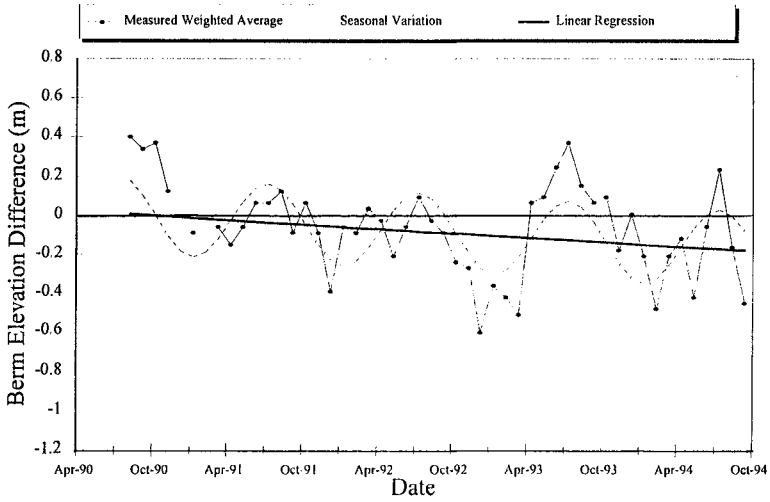


Figure 6 Dune Berm Elevation Seasonal Variations

### WAM Wall - Berm Elevation

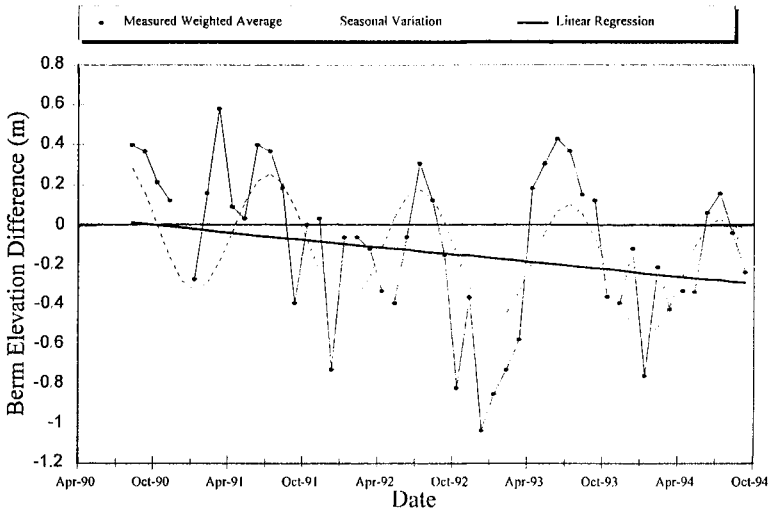


Figure 7 Wall Berm Elevation Seasonal Variations

### WAM Dune - Shoreline Position

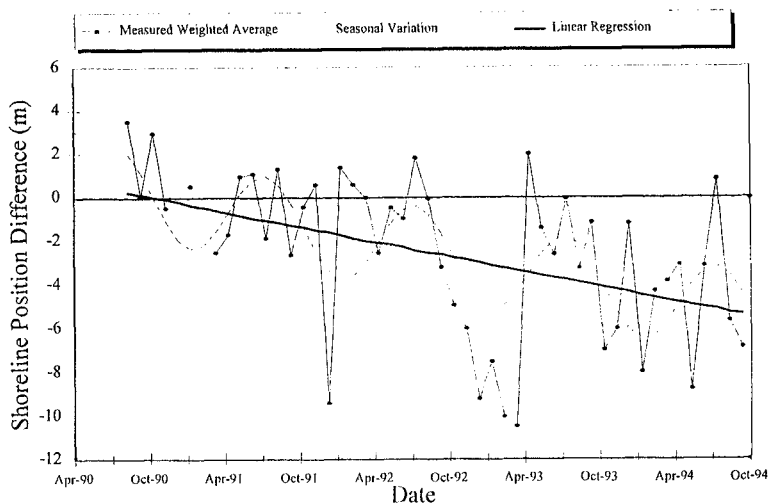


Figure 8 Dune Shoreline Position Seasonal Variations

### WAM Wall - Shoreline Position

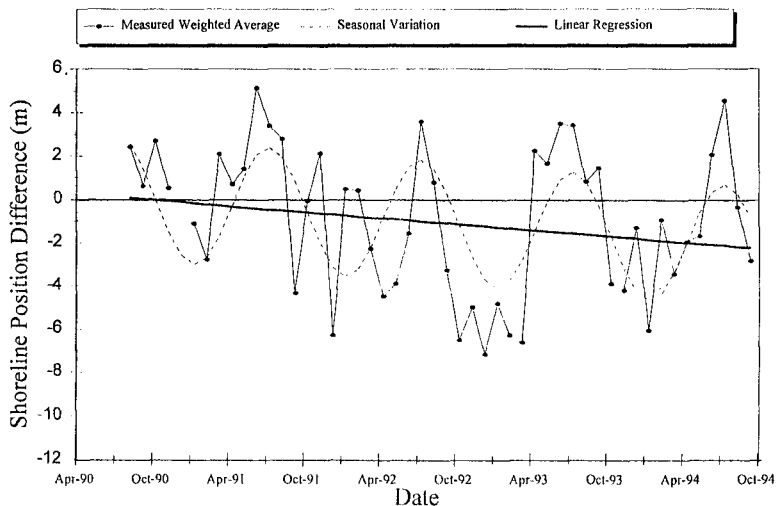


Figure 9 Wall Shoreline Position Seasonal Variations

WAM Beach Parameter	Wall	Dune	Difference
V(t) change rate (m <sup>3</sup> /m/yr) - 1 Year	0.14	-7.41	7.55
2 Years	-5.45	-5.18	-0.27
3 Years	-2.74	-5.00	2.26
4 Years	-1.71	-3.64	1.93
V(s) change rate (m <sup>3</sup> /m/yr) - 1 Year	-0.21	-4.70	4.49
2 Years	-2.93	-1.88	-1.05
3 Years	-0.94	-1.14	0.2
4 Years	-0.39	-1.10	0.71
V(l) change rate (m <sup>3</sup> /m/yr) - 1 Year	0.33	-2.54	2.87
2 Years	-2.60	-3.31	0.71
3 Years	-1.81	-3.86	2.05
4 Years	-1.33	-2.55	1.22
E(b) change rate (m/yr) - 1 Year	-0.07	-0.21	0.14
2 Years	-0.27	-0.13	-0.14
3 Years	-0.09	-0.03	-0.06
4 Years	-0.08	-0.05	-0.03
P change rate (m/yr) - 1 Year	-0.40	-2.25	1.85
2 Years	-2.51	-1.59	-0.92
3 Years	-0.90	-1.50	0.6
4 Years	-0.57	-1.38	0.81

Table 1. Weighted Average Method Parameter Rate of Change

Location	Profiles Used	Percent Walled	Profile Type	Parameter				
				V(t) (m <sup>3</sup> /m/yr)	V(s) (m <sup>3</sup> /m/yr)	V(l) (m <sup>3</sup> /m/yr)	E(b) (m/yr)	P (m/yr)
Section 1	1 to 54	79.5 %						
North			Wall	-2.6	1.9	-4.5	0.0	0.6
			Dune	-4.4	0.4	-4.8	-0.1	-0.8
Section 2	60 to 161	43.6 %						
Middle			Wall	0.7	0.8	-0.1	0.0	-0.2
			Dune	-0.4	-2.1	1.7	-0.1	-0.7
Section 3	162 to 252	73.3 %						
South			Wall	-4.6	-2.9	-1.7	-0.3	-1.7
			Dune	-4.6	-2.1	-2.5	-0.2	-1.5

Table 2 Simple Average Method Parameter Rate of Change  
from Oct. 1990 to Sep. 1994



The time span used in the regression analysis was from October 1990 to September 1994.

Section 3 experienced the largest total volume decrease of the three sections. Volume seaward loss and shoreline retreat were the highest for walled profiles in Section 3. The higher parameter change rates in Section 3 are due to the seawalls being located closer to the surf zone than the seawalls in Section 1 and 2.

### 7.3 Individual Profile Method Results

The parameter rates of change for each of the 28 profiles are provided in Table 3. Volume seaward and landward for profiles 1, 25, 161 and 252 have been plotted in time and are shown in Figures 10, 11, 12, and 13, respectively. Dune profile 1 is at the north end of Sandbridge and dune profile 252 is at the south end. These profiles have been regularly surveyed since October 1980 and have been the least affected by road maintenance, beach bulldozing and home construction. Both profiles show a significant increase in the loss rates of all parameters ( $V_T$ ,  $V_S$ ,  $V_L$ ,  $E_B$  and  $P$ ) after the construction of nearby seawalls in 1989. Profile 1 and 252 can be considered as control profiles in this study. The other dune profiles surveyed back to 1980 have seawalls to the north and south of them and have been modified by man. These other profiles have mixed results. The plot of dune profile 161 has a decrease in sand loss after a seawall was built 30 m to the south.

Profile 25 has been surveyed since 1980 and changed to a wall profile in the fall of 1988. Volume landward has a decreasing rate due to sand mechanically removed in the spring of 1994. The amount of sand decreased in front of the seawall after construction but has been increasing since then.

## 8.0 Conclusions

The hypothesis that erosion in front of the seawalls is greater than that on adjacent non-walled beaches was statistically found to be false. The hypothesis that seawalls inhibit the recovery of the beach after the winter storm season was also found to be false at Sandbridge. There is support for the hypothesis that the landward dune volume is eroding at a faster rate due to seawall construction on adjacent beaches. Complete details can be found in Hazelton (1994).

The seawalls at Sandbridge are performing exactly as they were intended to perform. They are protecting the infrastructure behind them from damage due to wave action. They were never intended to save the beach from erosion. The shoreline was receding well before the seawalls were constructed but now people have a reference point from which to judge the amount of retreat.

What is of concern in this study is the additional erosion caused by coastal armoring above the historic background erosion rates. The adverse effects of coastal armoring can be mitigated by nourishing the beach suffering from the increased erosion with sand so that the armoring has a neutral effect on the beach

Profile No.	Profile Type	Dates Used in Regression	No. of Years Used	No. of Survey Points	Volume Total (m <sup>3</sup> /m/yr)	Volume Seaward (m <sup>3</sup> /m/yr)	Volume Landward (m <sup>3</sup> /m/yr)	Berm Elevation (m/yr)	Shoreline Position (m/yr)
1 before	Dune	10/80 to 7/88	8	24	0.3	-0.5	0.8	0.0	-0.1
1 after	Dune	7/89 to 6/94	5	54	-11.4	-2.3	-9.0	-0.1	-1.4
13 before	EOW	5/91 to 4/93	2	26	-13.4	-1.0	-12.4	-0.3	-3.7
13 after	Wall	5/93 to 4/94	1	12	-23.8	-16.1	-7.6	-0.9	-9.7
20	Wall	10/90 to 9/94	4	49	1.1	-0.1	1.2	-0.1	-0.8
25 before	Dune	10/80 to 9/88	8	24	0.7	0.5	-0.2	0.1	0.0
25 after	Wall	10/90 to 9/94	4	52	-1.8	2.5	-4.4	0.1	1.0
41	Wall	10/90 to 9/94	4	53	2.7	2.0	0.7	0.0	0.6
46	EOW	10/90 to 9/94	4	50	6.1	2.6	3.6	0.0	0.8
47	Dune	10/90 to 9/94	4	49	-4.7	2.3	-6.9	-0.0	0.4
54	Dune	10/90 to 9/94	4	51	-4.0	-0.6	-3.4	-0.1	-1.7
60 before	Dune	10/80 to 7/85	4	17	-11.3	-6.2	-5.0	-0.5	-1.3
60 after	Dune	10/90 to 9/94	4	50	-6.1	-0.1	-6.0	-0.1	-1.3
70	Wall	10/90 to 9/94	4	51	-0.6	1.0	-1.7	-0.1	-0.1
74 before	Dune	10/80 to 9/88	7	30	-11.4	-0.8	-10.6	-0.4	-2.0
74 after	Wall	7/89 to 7/93	4	9	0.3	0.6	-0.4	0.2	0.5
78	Wall	10/90 to 9/94	4	53	3.9	1.6	2.2	-0.1	0.4
87	Wall	10/90 to 9/94	4	51	0.5	0.0	-0.4	0.0	0.0
103	EOW	10/90 to 9/94	4	48	-0.5	-2.1	1.6	0.0	-1.1
118	Dune	10/90 to 9/94	4	49	-14.6	-5.7	-8.9	-0.1	-2.8
135 before	Dune	10/80 to 9/88	8	24	4.3	1.4	2.9	0.1	1.1
135 after	Dune	10/90 to 9/94	4	53	6.1	1.3	4.8	0.1	-0.1
148	Wall	10/90 to 9/94	4	50	1.3	0.8	0.6	0.1	0.0
161 before	Dune	10/80 to 10/88	8	50	-4.6	-2.0	-2.6	-0.1	-1.0
161 after	Dune	10/90 to 9/94	4	54	-1.1	-0.7	-0.4	-0.0	-0.7
162	EOW	10/90 to 9/94	4	48	0.3	-0.6	0.9	0.0	-0.5
179	Wall	10/90 to 9/94	4	48	-4.9	-4.2	-0.7	-0.2	-2.1
194 before	Dune	10/88 to 9/89	1	18	-3.2	-2.1	-1.1	-0.3	-1.7
194 after	Wall	10/90 to 9/94	4	52	-3.2	-2.1	-1.1	-0.3	-1.7
207	Wall	10/90 to 9/94	4	49	-3.4	-2.2	-1.1	-0.2	-1.3
216 before	Dune	9/85 to 8/90	5	29	-7.6	-3.9	-3.7	-0.2	-2.6
216 after	EOW	10/90 to 9/94	4	53	-4.1	-1.3	-2.8	-0.2	-2.6
220 before	Dune	9/85 to 9/89	4	42	-16.4	-6.8	-9.6	-0.2	-3.0
220 after	Dune	10/90 to 9/94	4	53	-1.3	-0.2	-1.1	-0.0	-1.1
226	Wall	10/88 to 9/94	6	66	-3.9	-4.3	0.4	-0.2	-2.5
230	Dune	10/88 to 9/94	6	68	-7.8	-3.9	-4.0	-0.1	-2.2
234	Wall	10/90 to 9/94	4	49	-6.1	-3.4	-2.7	-0.1	-1.8
240	EOW	10/90 to 9/94	4	50	-6.6	-3.2	-3.4	-0.2	-1.9
252 before	Dune	10/80 to 9/88	8	47	-2.1	-2.9	0.9	0.1	-1.6
252 after	Dune	10/90 to 9/94	6	59	-7.6	-5.7	-1.8	-0.3	-2.8

Table 3. Individual Profile Method Results

Wall Profile No. 25 Sand Volume

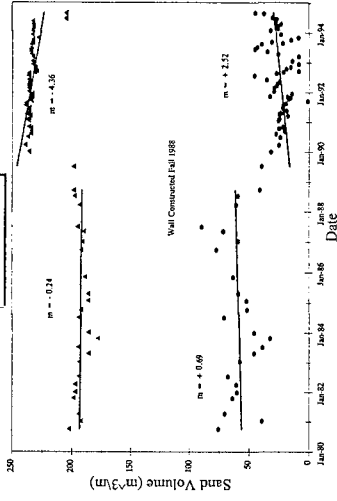


Figure 11 Wall Profile No. 25

Non-Wall Profile No. 252 Sand Volume

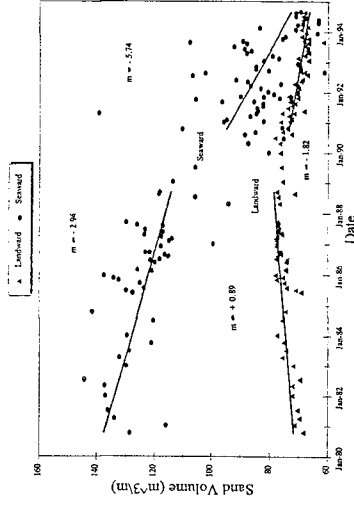


Figure 13 Wall Profile No. 252

Non-Wall Profile No. 1 Sand Volume

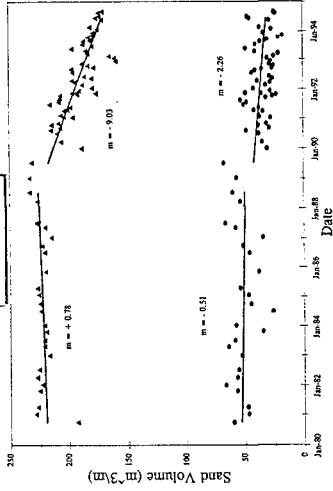


Figure 10 Non-Wall Profile No. 1

Non-Wall Profile No. 161 Sand Volume

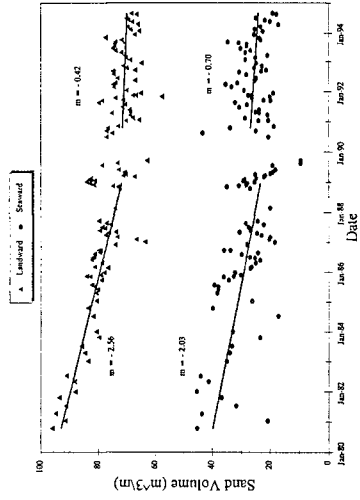


Figure 12 Non-Wall Profile No. 161

(Dean, 1986). Even with this mitigating nourishment, the historic background erosion will continue to erode the beach and the shoreline will eventually reach the seawall and no beach will exist.

Seawalls and beaches can only coexist with periodic beach nourishment for a beach experiencing high rates of historic erosion. A nourishment project has been planned for Sandbridge in the spring or summer of 1997. The seawalls can continue to provide protection to homes during periods of high waves and storm surges and tourist can also enjoy the wide summer beach. Subaerial beach monitoring at Sandbridge will continue until a nourishment project is completed after which full profile monitoring to closure depth will take place.

### Acknowledgments

This study has been supported by the U.S. Army Corps of Engineers, Coastal Engineering Research Center in Vicksburg, MS and was performed under the Work Unit entitled "Impacts of Coastal Armoring on Beaches". Permission was granted by the Chief of Engineers to publish this information. Some of the survey data used in the study was supplied by the City of Virginia Beach, VA and the Virginia Institute of Marine Science.

### References

- Basco, D.R., Bellomo, D.A. and Pollock, C. (1992) "Statistically Significant Beach Profile Change With and Without the Presence of Seawalls." *Proc., 23<sup>rd</sup> International Conference on Coastal Engineering*, Italy, Vol. 2, 1924-1937.
- Bellomo, D.A. (1993) "Statistical Variations in Beach Parameter Change Rates for Walled and Non-walled Profiles at Sandbridge, Virginia." Master of Science Thesis, Department of Civil and Environmental Engineering, Old Dominion University, Norfolk, VA.
- Dean, R.G. (1986) "Coastal Armoring: Effects, Principles and Mitigation." *Proc. 20<sup>th</sup> International Conference on Coastal Engineering*, Taiwan, Vol.2, 1843-1857.
- Everts, C.H., et al. (1983) *Shoreline Movements: Cape Henry, Virginia to Cape Hatteras, North Carolina, 1849-1980*, Rpt. No. 1, Tech. Rept. CERC-83-1, U.S. Army Coastal Engrg. Res. Ctr., Vicksburg, MS.
- Griggs, G.B., Tait, J.F., Corona, W. (1994) "The Interaction of Seawalls and Beaches: Seven Years of Field Monitoring Monterey Bay, California." *Shore and Beach*, 62(3), 21-28.
- Hazelton, J.M. (1994) "The Influence of Seawalls on Beach Response to Storms, Seasonal Transitions and Long-Term Erosion." Master of Science Thesis, Department of Civil and Environmental Engineering, Old Dominion University, Norfolk, VA.
- Kraus, N.C. (1988) "The Effects of Seawalls on the Beach: An Extended Literature Review." *J. of Coastal Research*, Spec. Iss., No. 4, Autumn, 1-28.

## CHAPTER 131

### A Bottom Boundary Layer Sediment Response to Wave Groups

J. Lee<sup>1</sup> , S. O'Neil<sup>1</sup>, K. Bedford<sup>2</sup>, and R. Van Evra<sup>3</sup>

#### Abstract

A field experiment measured *in situ* sediment resuspension in the bottom boundary layer. Spatially and temporally dense suspended sediment concentration profiles, three-dimensional velocities and pressures were obtained from a location with a flat, fine-sand bottom in Lake Erie in 1992. By use of a conceptual model, ten minute averaged near bottom sediment concentration is found to be proportional to significant wave orbital velocity and group wave parameters. The result attempts to clarify the ambiguity of using a monochromatic wave parameterization for bottom boundary layer model comparisons with measured data containing spectral wave conditions.

#### Introduction

Sediment transport models encompass many complex physical processes. Shear stresses exerted on the bottom, wave and current interactions and sediment concentration induced stratification are a few examples. Many bottom boundary layer models now have components which attempt to describe these processes. For certain flow regimes these models may accomplish the tasks of modeling natural phenomena.

Recently Bedford and Lee (1994) pointed out that

---

<sup>1</sup> Graduate Research Associate, Department of Civil Engineering, The Ohio State University, Columbus, OH 43210, U.S.A. (jkleee@glfs.eng.ohio-state.edu)

<sup>2</sup> Professor, The Ohio State University

<sup>3</sup> Senior Research Scientist, The Ohio State University

an external parameter in the Glenn and Grant (1987) model, the averaged wave orbital velocity,  $U_b$ , is one of the most sensitive input parameters required for calculating suspended sediment concentration profiles for a particular coastal bottom boundary layer in Mobile Bay, Gulf of Mexico. A monochromatic wave is used in this bottom boundary layer model for representing wave conditions. With reference to the spectral behavior of real waves, there has been a vigorous debate between researchers concerning the representative wave to be used for such sediment transport modeling. Obviously, a monochromatic wave formulation in the models makes it impossible to directly account for the randomness and nonlinearity of real waves.

It is believed that the nonsteady wave height variation in the surf zone generates the cross-shore component of radiation shear stress; any remnant wave height then contributes to group wave generation (Longuet-Higgins and Stewart, 1964). Grouping effects on near bottom sediment concentration were investigated by Hanes (1987), where he showed that longer period group waves (50 to 100 s) were more effective than shorter period group waves for enhancing sediment concentration. Sato (1992) performed laboratory experiments using bichromatic wave groups and showed enhanced suspended sediment concentrations due to an equivalent amount of monochromatic wave energy. But the question still remains as to how the wave grouping affects the amount of suspended sediment concentration, especially in the very near bottom.

In this paper, the authors will address the above question using a conceptual model of sediment entrainment by wave groups. First, a field experiment and data will be discussed. Then two methods of wave group analysis will follow, the run length method (Goda, 1985) and the envelope function method (List, 1991). Third, a conceptual model will be developed. Finally, group wave effects on the near bottom sediment concentration will be examined by the model and the validity of the monochromatic wave formulation will be tested.

### Field Experiment and Data

Fully automated sediment resuspension measurements were made near the southernmost part of Lake Erie from Oct. 20 to Oct. 28, 1992 (Figure 1). A galvanized steel tripod equipped with instruments and batteries (ARMS, the Acoustic Resuspension Measurement System) was situated on the flat fine sandy bottom in a water depth of 4.5m, 500m offshore. During the deployment, both

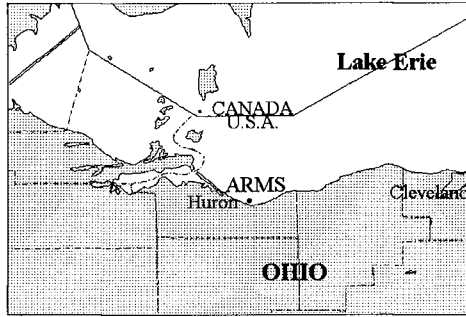


Figure 1. Map of *in situ* experiment site, Lake Erie, United States.

mild and weak storm events occurred and two 50 Mbytes data sets were collected. The suspended sediment concentration profiles are composed of 114 data points comprising a height of 132 cm above bottom (AB). Three-dimensional water particle velocities at the four heights ( 20, 50, 80, 110 cm AB) and the water pressure fluctuation at 212 cm AB were also obtained. The effective sampling rate of the acoustic concentration profiler was 1 Hz, the BASS (Benthic Acoustic Stress Sensor) current meters was 4 Hz and that of the pressure transducer was 4 Hz.

The flow characteristics of the two storms were extracted from the measured water surface fluctuations and velocity data. The first storm was mild, having a ten-minute averaged significant wave height of 56 cm. The second storm was very weak and not used in this analysis. The duration of the first storm spans almost 10 hours and is the data set analyzed in this paper. Figure 2 shows the significant wave orbital velocity,  $U_{bs}$ , calculated directly from the time trace of the orbital velocity,  $u_p(t)$ , at 20 cm AB, and the accompanying suspended sediment concentration at 5.2 cm AB.

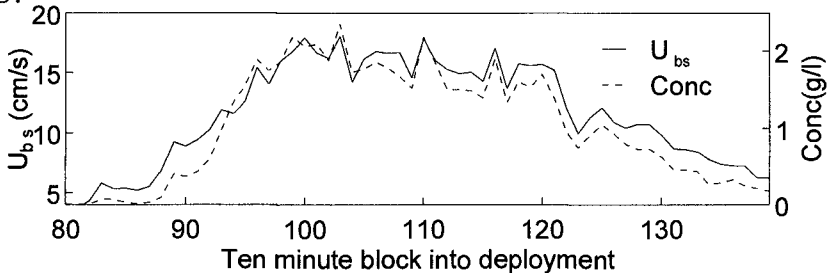


Figure 2.  $U_{bs}$  and suspended sediment concentration at 5.2 cm AB.

For subsequent wave group analysis, the wave orbital velocity time series,  $u_b(t)$  was examined as opposed to the conventional choice of the surface water fluctuation time series. This is similar to the choice of Hanes(1991) who used  $u_b^2(t)$  to do spectral wave group analysis.

### Wave Group Analysis and Correlation

Real waves exhibit two distinct spectral energy distributions. One comes from the incident waves, the other comes from group waves. The former can be represented by a statistical or spectral wave estimate. The latter may be characterized by group wave parameters. As the incident wave parameters, the  $U_{bs}$ , at 20 cm, is selected for analysis because the  $U_{bs}$  shows a higher correlation with the near bottom sediment concentration than does the significant wave height does. In Figure 2 the value of the correlation coefficient between  $U_{bs}$  and sediment concentration at 5.2 cm AB is 0.96 and that using significant wave height data is 0.95.

### Wave Group Parameterization

Two approaches are taken in the study of wave groups. Mase(1987) emphasized the necessity of more than two group wave parameters to characterize wave groups. One is the statistical investigation of *run length* and the other is the *envelope function*. The former is a measure of height exceedance duration and the latter is a measure of overall amplitude variability. In this paper the run length method by Goda (1985) and the envelope function method of List (1991) are used to parameterize the wave groups.

#### *Run Length Method*

Wave groups can be quantitatively described by counting the number of consecutive waves exceeding a threshold value (Goda, 1985). A succession of such high waves is called a run of high waves, and the number of waves is termed the run length, denoted by  $j_1$ . Another statistic is the measure of separation between the two consecutive groups denoted by  $j_2$ . Figure 3 depicts statistics  $j_1$  and  $j_2$ . The crest and trough velocity difference,  $v_i$ , and wave order number are defined similar to Goda (1985).

#### *Envelope Function Method*

The envelope function method (List, 1991) is a



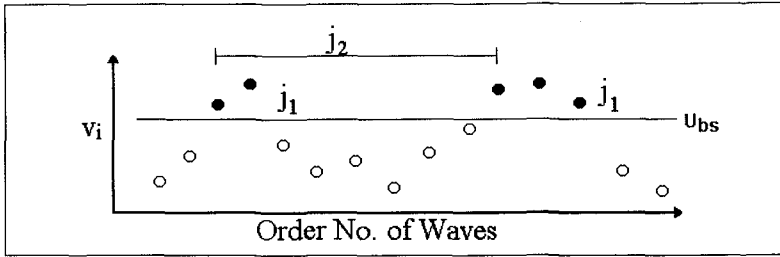


Figure 3. Schematic plot of the run lengths,  $j_1$  and,  $j_2$

method of obtaining the incident wave envelope,  $A(t)$  from the incident wave signal (Figure 4). The first procedure for determining  $A(t)$  is to high-pass filter the incident wave signal which removes the low-frequency or infra-gravity band waves. Then low-pass filtering of the envelope-related variance signal of  $A(t)$  gives the amplitude modulation of the incident waves. In this step the proper selection of a cutoff frequency for removing the incident waves is critical for obtaining a true envelope series. The final step is to multiply the envelope series by  $\pi/2$ . Using this final envelope function, the GF (Groupiness Factor) is defined as,  $GF=1.41S/A$  where  $S$  is the standard deviation of  $A(t)$  and  $A$  is the mean of  $A(t)$ .

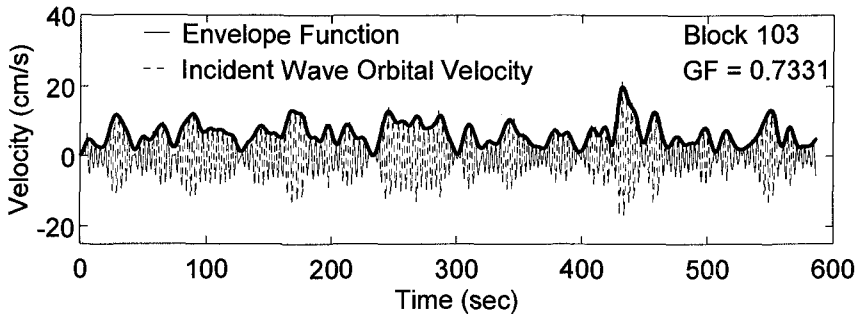


Figure 4. Wave envelope function,  $A(t)$

A Conceptual Model

*Implication of Run Length ( $j_1$  and  $j_2$ ) Value*

Figure 5 conceptually examines the near bottom sediment response to four different combinations of run length,  $j_1$ , and  $j_2$ . In this model only three dominant processes are considered: The entrainment rate as

parameterized by  $v_i$ , delayed settling by the group waves and sediment settling itself. From the simulations, the high  $j_1$  and low  $j_2$  combination of the upper left box in Figure 5 shows the most enhanced concentration of near bottom sediments. The high value of  $j_1$  enables sediment entrainment and the low value of  $j_2$  allows for the sediment already in suspension to remain there. However, a theoretical analysis by Ewing (1973) reveals that this type of flow field does not occur frequently.

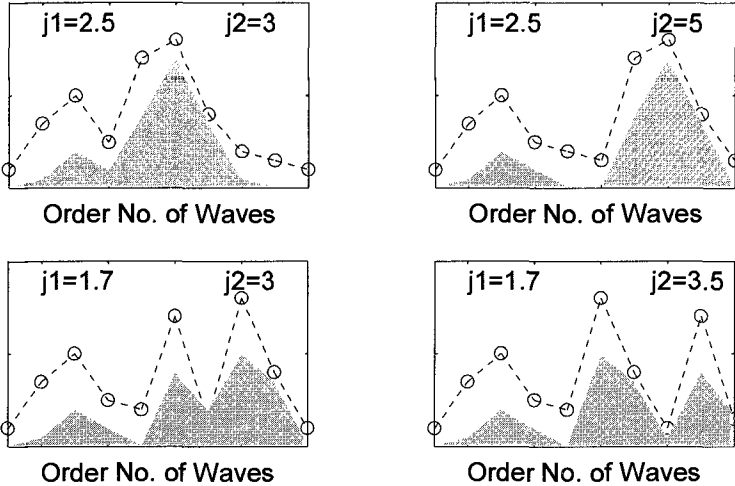


Figure 5. Sediment response due to the change of run length(-o-,  $v_i$  ; shadowed, sediment response)

*Implication of GF*

The groupiness factor defines the shape of the envelope function. High GF values indicate that the group wave envelope function possesses high temporal fluctuations. This high value of GF means a high value of the standard deviation when compared with the mean value of the envelope function  $A(t)$  (List, 1991). However, a high GF doesn't necessarily imply high sediment concentration because the probability of clustered high waves in time becomes rare. Figure 6 depicts this concept.

Results

The complete life cycle (10 hours) of a mild storm event in Lake Erie was measured. Consequently the

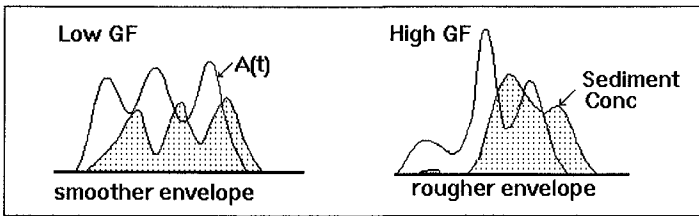


Figure 6. Sediment response due to the change of groupiness factor

evolution of wave groups and the resulting sediment response was completely recorded and analyzed. Run lengths  $j_1$  and  $j_2$  were estimated in 60, ten-minute blocks counted from the time of deployment. Figure 7 shows the changes in run length and the near bottom concentration at 5.2 cm AB.

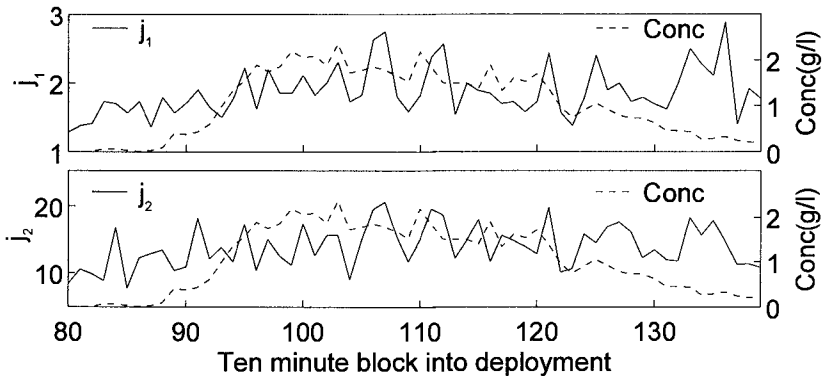


Figure 7. Run lengths,  $j_1$  and  $j_2$  compared with suspended sediment concentration at 5.2 cm AB

In the figure, the run lengths  $j_1$  and  $j_2$  weakly follow the storm pattern, i.e. spin up and spin down, over the storm period. The correlation coefficients between concentration at 5.2 cm AB and  $j_1$  and  $j_2$  are  $r_{j_1} = 0.32$  and  $r_{j_2} = 0.33$ , respectively.  $j_1$  and  $j_2$  show fluctuations even during the middle or equilibrium period of the storm.

Figure 8 shows the GF variation during the storm period and near bottom concentration at 5.2 cm AB. Although it loosely follows the storm pattern, it is hard to extract any significant correlation ( $r_{GF}=0.36$ ) between the GF and the near bottom concentration at 5.2 cm AB.

As indicated by the conceptual model group waves

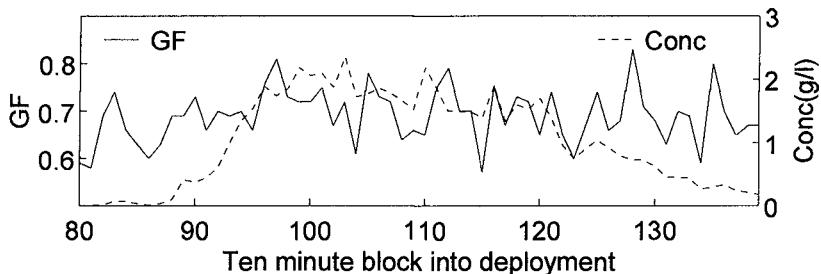


Figure 8. Groupiness factor(GF) compared with suspended sediment concentration at 5.2 cm AB

enhance the suspended sediment concentration by continuing entrainment of settling sediments which are already in suspension. To further see the effects of group waves we have to pick blocks with the same wave energy levels and compare only the suspended sediment concentration by group waves. In 10 hours of resuspension processes there are 5 pairs of comparable 10 minute blocks: 102 and 103; 107 and 108; 114 and 115; 119 and 120; and blocks 136 and 137. These pairs have very similar wave kinetic energy. Figure 9 summarizes the results.

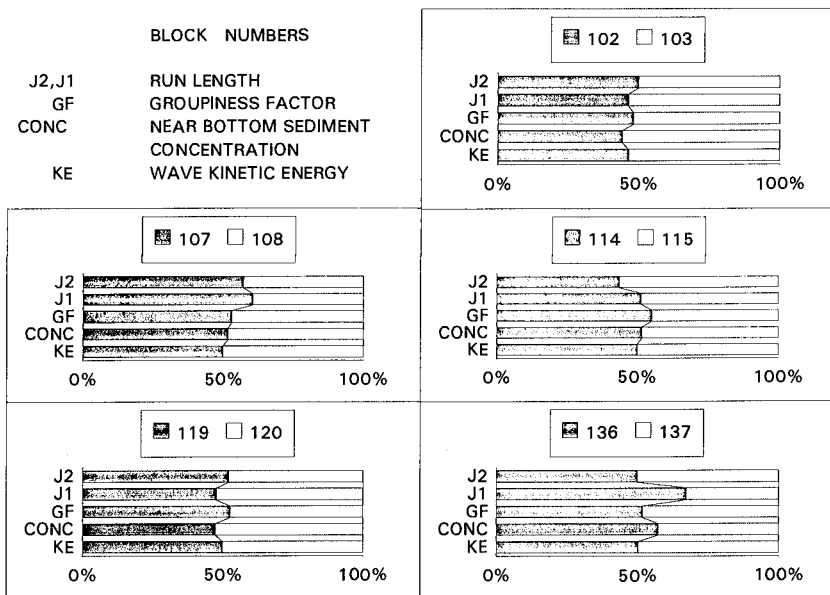


Figure 9. Test results of the conceptual model

From the first row of the upper right box, the combination of  $j_1(B102, \text{darker shadow bar}) < j_1(B103)$ ,  $j_2(B102) = j_2(B103)$ ,  $GF(B102) > GF(B103)$ . Thus the concentration of B102 is lower than that of B103. This case was also characterized by the conceptual model having lower concentration. In the second comparison, the group wave parameters of block 107 are bigger than those of block 108. Among them,  $j_1$  of block 107 shows the biggest difference. The result is higher concentration in block 107. It is noted that, even though the  $j_2$  of block 107 is bigger, the concentration of block 107 is higher. In other words, we can see the dominance of  $j_1$  in determining the amount of concentration. This idea is also suggested by the conceptual model. The third case examines how  $j_2$  can contribute to the enhancement of concentration.  $j_2$  of block 114 is far smaller than that of block 115, and results in a higher concentration. The fourth comparison in the bottom row, shows once again the dominance of  $j_1$  compared to GF.  $j_1$  of block 119 is smaller and results in a lower concentration. Also, a bigger  $j_2$  in block 110 helps to enhance the concentration. In the final comparison,  $j_1$  of block 136 is overwhelming. It leads to a much higher concentration. Again it shows the dominance of  $j_1$  in being the most effective group wave parameter in denoting enhanced concentration.

### Conclusions and Discussions

From the *in situ* measured data set we can verify the concepts of an enhanced near bottom suspended sediment concentration by group waves. Using the results obtained in this paper we can clarify some of the arguments in the study of sediment entrainment and resuspension due to both incident waves and group waves.

- i) Incident waves are the dominant forcing in determining the suspended sediment concentration at 5.2 cm AB.
- ii) Group waves may induce still higher concentration by delaying the suspended sediment settling.
- iii) The value of  $j_1$  governs the amount of enhanced sediment concentration and is the obvious indicator of group wave effects on the near bottom suspended sediment concentration.
- iv) The run lengths,  $j_1$  and  $j_2$ , are sufficient group wave parameters for describing enhanced sediment concentration. The GF(groupiness factor) is redundant.
- v) The monochromatic wave assumption in the bottom boundary layer models is correct to 96 percent

correlation coefficient when the significant wave orbital wave velocity is substituted for the monochromatic wave in a ten minute averaging period.

- vi) The remaining accuracy will be accounted for by group wave parameters particularly  $j_1$ .

### References

- Bedford, K. and J. Lee (1994). Near-bottom sediment response to combined wave-current conditions, Mobile Bay, Gulf of Mexico, *J. Geophys. Res.*, 99, 16,161-16,177.
- Ewing, J. (1973) Mean length of runs of high waves. *J. Geophys. Res.*, 78, 1933-1936.
- Hanes, D. (1991) Suspension of Sand Due to Wave Groups, *J. Geophys. Res.*, 96, 8911-8915.
- Glenn, S. and W. Grant (1987). A suspended sediment stratification correction for combined wave and current flows, *J. Geophys Res.*, 92, 8244-8264.
- Goda, Y. (1985) *Random Seas and Design of Maritime Structures*, University of Tokyo Press, Tokyo.
- List, J. (1991) Wave groupiness variations in the nearshore. *Coastal Eng.*, 15, 475-496.
- Longuet-Higgins, M. and R. Stewart (1964) Radiation stresses in water waves: a physical discussion, with applications, *J. Fluid Mech.*, 13, 481-504.
- Mase, H. (1989) Groupiness factor and wave height distribution, *J. Waterway, Port, Coastal, and Ocean Engineering*, 115, No.1, 105-121.
- Sato, S. (1992) Sand transport under grouping waves, *Proc. 23rd Int. Conf. Coastal Eng.*, paper 185.

## CHAPTER 132

### Geomorphological Analysis of a Beach and Sandbar System

Chen-Shan Kung<sup>1</sup>, Marcer Stive<sup>2</sup> and Geffery Toms<sup>3</sup>

#### Abstract

At Yunlin county a major development of over 10,000 ha of reclamation is being planned for port related industries. The development is taking place along a coast that bordered by Choshui river and the Wai-San-Ting sandbar. Detailed modeling using MIKE21 package with wave, flow and sediment transport modules were used to assess the morphological changes. Four such "relict" deltas were identified according to its ancient river courses. The decay of the sandbars was mostly independent due to the major discontinuities at sandbar headlands and tidal channels. The analysis of the complex morphological processes has provided an important insight into the probable impacts of coastal developments and guided the expensive and time-consuming model operations.

#### Introduction

At Yunlin county a major development of over 10,000 ha of reclamation is being planned for accommodating large scale port related industries and including a power plant and other developments. The reclamation, which covers shallow coastal areas along a 40 km length of coast, will be served by two new deep water ports.

The development is taking place along a stretch of coast that bordered in the North by Choshui river and in the South by the unique shoreline attached Wai-San-Ting sandbar. Wai-San-Ting, over 20 km long, is Taiwan's largest coast bar feature and morphologically is very active (Figure 1). Typhoons and a predominant NNE wind and wave climate approaching at very oblique angle to shore together with strong tidal currents are the main

---

<sup>1</sup>Sinotech Engineering Consultants Inc., 171 Nanking E. Road, Sec. 5, Taipei, Taiwan

<sup>2</sup>Delft Hydraulics, Emmeloord, The Netherlands

<sup>3</sup>Frederic R. Harris Inc., The Hague, The Netherlands

features shaping the existing coastline development.

During the six month winter period, the most frequently wave direction is NNE-N at offshore with 1.5-2 m in height, 5-6 second in period. In summer season, the most wave is coming from SSW direction with 0.5-1 m in height, 4.5-5.5 second in period. The tidal range is about 3-3.5 m in Yunlin coast with maximum current velocity of 1.5 m/s. Under these very rough sea conditions, a careful prediction is needed for the impacts' studies of the major reclamation project on the adjacent coast and sandbar systems for the Master plan study.

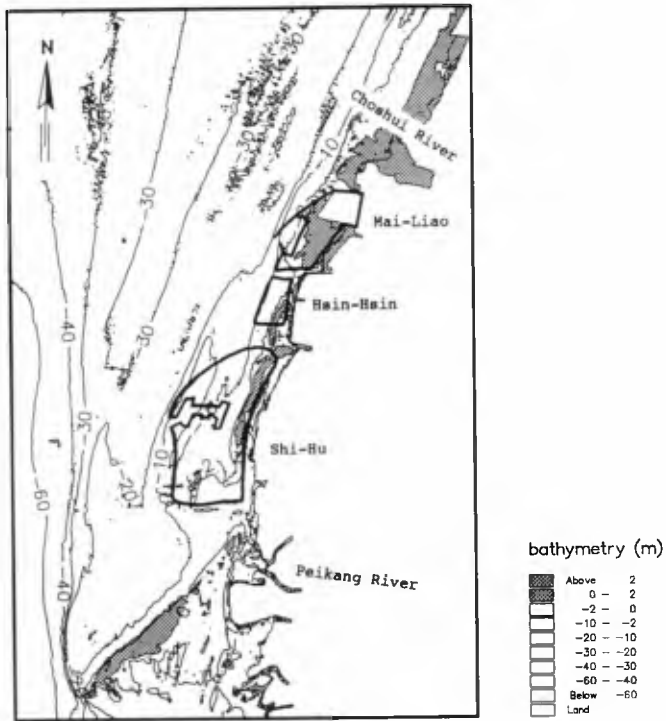


Figure 1 The Layout of Yunlin Offshore Industrial Estate in Yunlin Coast

Historical Development of Yunlin Coast

Most of the sediment between the shore and water depths of, say 20 to 30 m, originate from the various rivers and deposited in the last 100 to 300 years. At least four rivers have played an important role in the Yunlin coast, namely (from south to north) the Peikang river, the Old Huwei river, the New Huwei river and the Choshui



river. In the last 300 years, these four rivers were the tributary of the Choshui river system, the old river channel traces of these rivers are shown in figure 2. The first three mentioned rivers transported much more sediment in the last century than nowadays when they were the main channel of the Choshui river during the flood season.

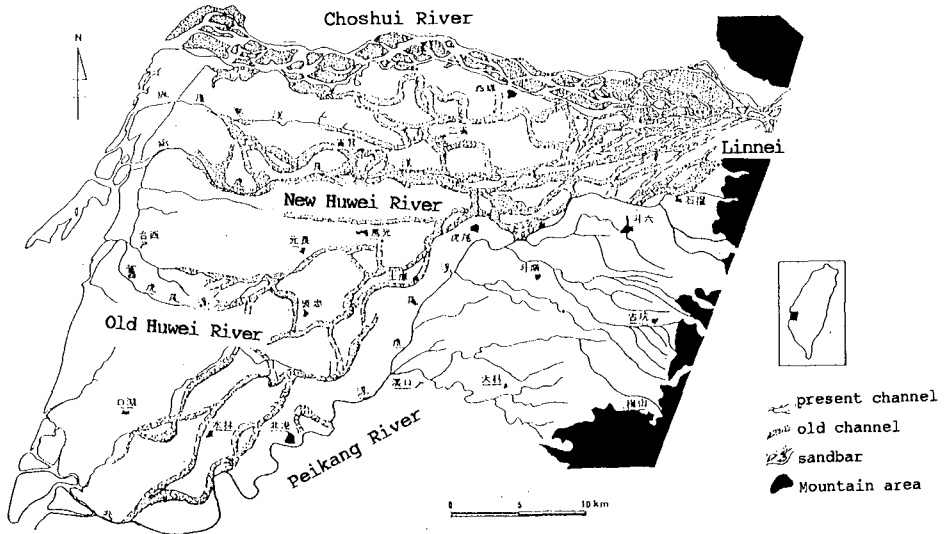


Figure 2 The old flow channel of Choshui river

In order to control the flood, several dikes and dams were constructed near the Linnei in 1911. The effect of these dikes was that the most of the drainage area of the Peikang river and the Old and New Huwei rivers were largely reduced. Their role as main sediment supplier to the coast stopped almost instantly. On the other hand, the Choshui rivers become the only sediment and water supplier to the coast. The consequence of this disturbance to the coast is the old river deltas are shrinking according to the reduction of the river sediment supply.

Figure 3 shows the historical development of the Wai-San-Ting coast line based on old map and remote sensing images. This historical movement of the sandbar system reflects this disturbance of the old Yunlin coast. The present-day coastal morphology still reflects the importance of the Peikang river and the Old Huwei river. The Wai-San-Ting and Pao-Zi-Liao sandbar are most likely the remnants of the deltas of these rivers. The disturbance of the old balance between river discharge and marine forces has results in significant morphological changes of these "relict" deltas. This is the more true for the wave dominated areas above, say, MSL -10 m. Due to the long morphological time scale at the sea bed below MSL -20 m, it still reflected the "old" situation of several decades ago. Wai-San-Ting has steadily moved southwards with

an average speed of 150 m/y. In the last two decades this southward movement took slowly rate of 75 m/y (Tsai and Huang, 1992). The orientation of depth contour of Wai-San-Ting has also undergone some changes. While the orientation of LW-line in 1932 was perpendicular to 305 degrees North, this is presently perpendicular to some 325 degrees North. This rotation took place mainly in the period among 1947 and 1972, the same period in which the largest southward movement occurred. The height of Wai-San-Ting has also undergone changes. In early time, Wai-San-Ting was a typical barrier coast, with heights above MSL along the entire coastline. Today, a lot of part of Wai-San-Ting is under the MSL.

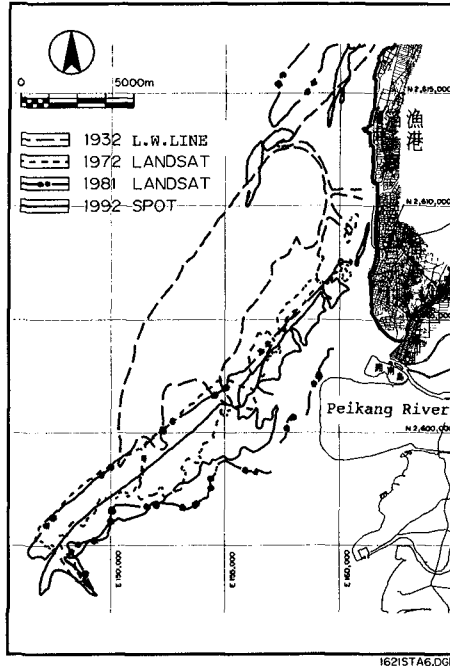


Figure 3 The historical changes of LW line of Wai-San-Ting

The Pao-Zi-Liao sandbar has undergone comparable changes in the last century like Wai-San-Ting: a steady southward movement (average above 100 m/y), its level being lowered in the last two decades, and a small westward rotation of 5 to 10 degrees. The general shape of the Pao-Zi-Liao has undergone significant changes. The sandbar has been broken up into separate bars that move southward and in a landward direction. The most southern sandbar has clearly become an isolated sand bar feature. The Pao-Zi-Liao sand bar system has degenerated more pronounced than Wai-San-Ting. Marine forces tend to disperse the sand bars and to smooth out the coast feature.

After the Linnei dike construction, the delta at Choshui river mouth becomes growing. The delta grows like a bow shape with strongly southward sediment transport. Due to the fish pond construction, the main stream of Choshui river changes toward to the north bank. The consequence of this disturbance is the sediment deposited at the north part of the delta during last two decades. After the construction of the Mailiao land reclamation (south of Choshui river mouth), the 10 meter's depth contour moved seawards. The MSL -20 m depth contour, on the other hand, did not follow this movement, which results in a steeping of the profile.

### Conceptual Model of Morphological Change

The above considerations reflect for a part the complexity of the area. A mix of physical processes determines the morphodynamic behavior of the sea bed, each with their own time and space scale. The complexity makes it virtually impossible to simply calculate the future development and the impact of reclamation. Uncertainty will always be part of such prediction, even with today's most advanced modeling tools, such as MIKE 21 (DHI, 1992) coastal hydrodynamic simulation system. Although state-of-the-art knowledge on the various physical processes has been incorporated in this model, this does not guarantee that the large-scale morphological developments are represented well. In order to assess the long term morphological changes in the Yunlin coast, a conceptual model is need. This conceptual model is based on good interpretation of historical data and information from recent measuring data. The conceptual model will indicates which questions have to be answered by the numerical model and the numerical model will aim at quantifying the conceptual model.

At Yunlin coast, the balance between river sediment transport and the onshore sediment transport is to a certain extent the dimension of a river delta. After the dike construction at Linnei, the Peikang river and Old Huwei river is lost its drainage function. Consequently, the sand bars and relict deltas start erosion under very rough wave climate. Since most of the wave energy comes from north to north-east directions, the direction of littoral transport will be southward. Although the coastline of Yunlin is straight, relatively large local gradients in the depth orientation occur. These local gradients in the orientation of the depth contour are caused by the presence of the old deltas along the coastline. These give rise to relatively large gradients in alongshore sediment transport, which results in morphological changes. The net southward littoral transport contributes to the net southward movement of sand bars and other morphological features.

Since the littoral transport is a function of incoming wave angle, the river delta will reach its equilibrium condition according its wave condition. Due to the prevailing north wave condition, the northern part of Wai-San-Ting delta coastline tends to erode, and the seaward part tends to accrete. Due to this erosion and accretion processes, the coastline of delta will be re-shaped, which causes the point of

maximum littoral transport to shift in downdrift direction. Hence, no limitation occurs to the seaward growth of the delta (Kung, 1993).

After the dike construction of Linnei, the erosion due to littoral transport is concentrated along the northern part of the coastline resulting in a steady rotating of Wai-San-Ting. Due to the sheltering effect of southward moving sand bars of Pao-Zi-Liao, the littoral transport at Wai-San-Ting as well as gradients in littoral transport, reduced and so the retreat of the coastline. Consequently, the rotation of Wai-San-Ting has remained more or less the same in the last two decades. The conceptual model of coast beach and sand bars morphological change in Yunlin coast is shown in figure 4.

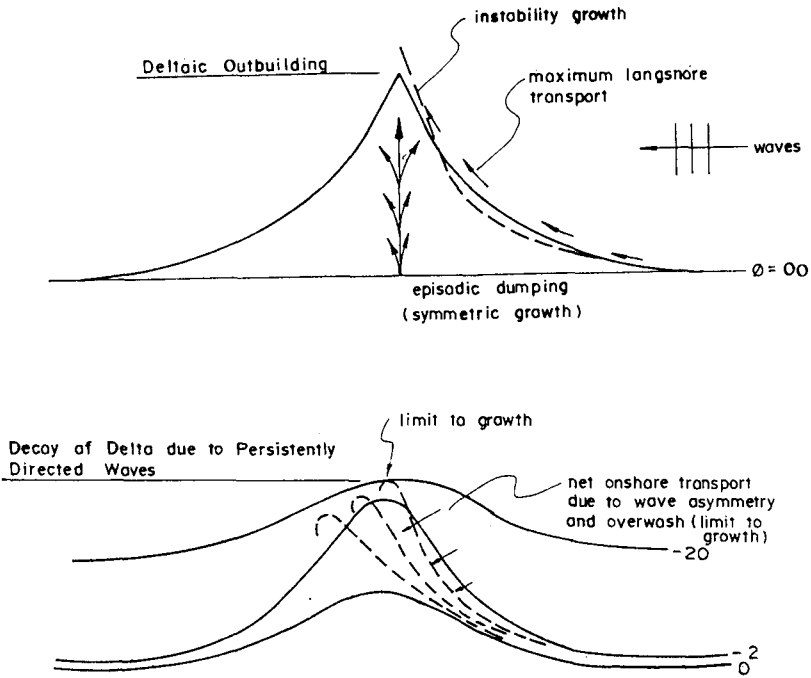


Figure 4 The conceptual model of morphological changes of "relict" deltas

Quantitative Analysis

The quantitatively analysis of morphological changes in Yunlin coast is initially concentrated on the geostatistical analysis. Natural variables such as grain size,

shoreline change, land form, length of coast is all function of natural forces. Due to the stochastic nature of nature forces, the natural variables are also have stochastic characteristics in space and time domain. In a geostatistical model of shore line change or grain size distribution can represent its spatial structure of the natural forces and it's controlling physical processes.

A semi-variogram of shore line change among 1932 and 1992 based on Yunlin coast data is given in figure 5 as an example of the geostatistical analysis. The results show that the characteristic length is 7.5 km for the shore line changing rate. The characteristic lengths of the shore line change rates are similar to different periods - this reflects the similar processes within last century. The characteristic lengths also reflect the largest length scale of the coastline evolution process. The distance between Choshui river mouth and New Huwei river mouth is about 8 km and the distance between New Huwei river mouth and Old Huwei river mouth is 7 km. The length of the Santiaolun sand bar is 8 km. The length of north part of Wai-San-Ting is 7 km and the length of south part is 15 km. The geostatistic analysis shows that the shore line changes within the elic delta region are correlated and the shore lines' changes on different delta are more or less independent. The characteristic length of the grain size distribution is also 7.5 km along the main tidal direction. This length scale is very close to the tidal velocity length in Yunlin coast. The analysis shows that the morphological changes at deep water part, say MSL -20 m, is dominated by tidal movement.

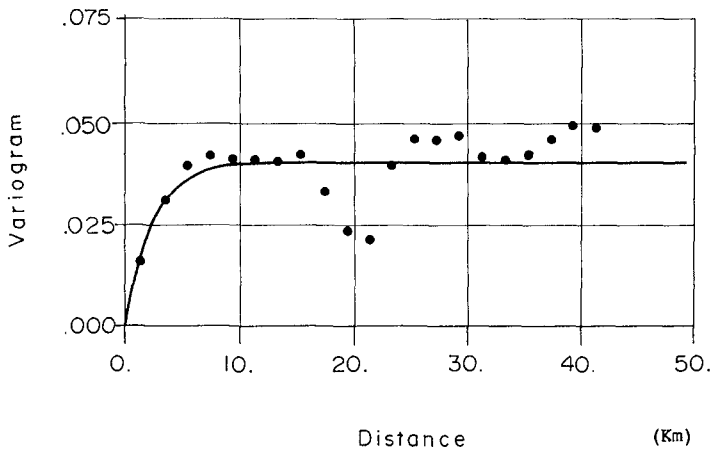


Figure 5 The semi-variogram of shoreline changing rate along Yunlin coast

The UNIBEST model (DH, 1991) was used for evaluating the longshore sediment transport rate along the Yunlin coast. The offshore wave climate was simulated by

using MIKE21 NSW package based on the local wave measurement data. The typical tidal motion was simulated by using MIKE21 HD model. The current velocity and wave information are used in the long shore sediment transport by using UNIBEST model. The result of the longshore sediment transport calculation is shown in figure 6. Due to the large ground water subtraction along the coast, the possible land subsidence rate along the Yunlin coast is also shown in figure 6.

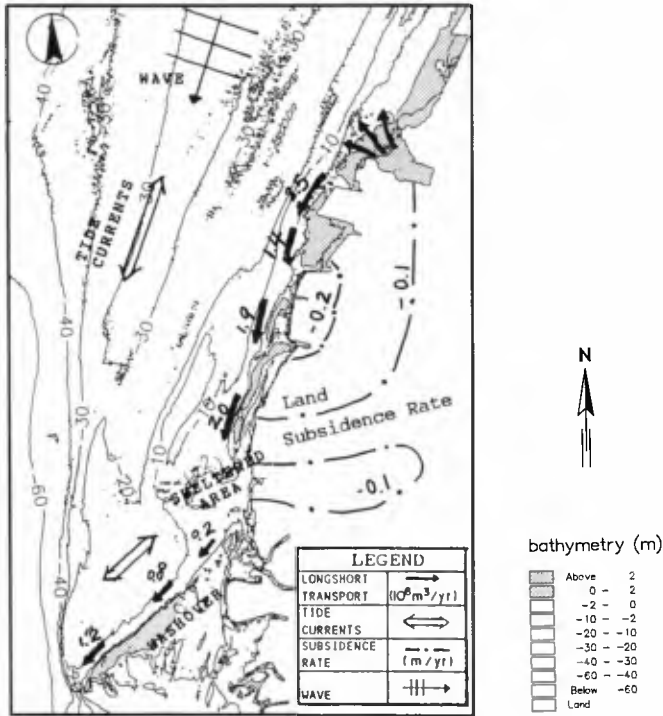


Figure 6 The longshore sediment transport rate of Yunlin coast

The longshore transport rate calculation shows that the local gradients of sediment transport exist at the tip of sand bar and along the Wai-San-Ting. The coast segment at south of Choshui river will be accretion due to the huge sediment supply from the river and south going littoral transport. The littoral transport rate is increased along the Santiaolun sand bar which imply the erosion of the sand bar. The littoral transport rate of the Wai-San-Ting is also gradually increasing along the southward direction. This local gradient implies the erosion of the Wai-San-Ting. The littoral transport rate is very minor at the north part of Wai-San-Ting due to the sheltering effect of

shelter by the Pao-Zi-Liao sand bar. The Pao-Zi-Liao sand bar its self has very huge littoral transport rate and gradient that means the significant morphological changes.

Does the Pao-Zi-Liao sand bar provide sediment transport to the Wai-San-Ting that is the main question on the impact assessment of the reclamation. If the Pao-Zi-Liao sand bar is the sediment supplier to the Wai-San-Ting, the reclamation will stop the sediment to the downstream area and causing more serious erosion. In order to answer this question, the more details two dimensional sediment transport simulation is need due to the complicated coast geometry and flow conditions. The well-known MIKE21 coastal hydrodynamic modeling system was used for analyzing the sediment transport capacity and initial movement of the coast sand near the Wai-San-Ting area. The 75 meter grid was used for balancing the computation time and the resolution. This gives around 4 grid point in the surf zone that provides reasonable accuracy for alongshore current simulation. Three different wave conditions was simulated by using NSW module which represents the wave climate of the area. The radiation stress field was used in the hydrodynamic simulation for calculation the velocity field under the tide and wave combination situation. The Engelund-Fredsoe formula (Engelund and Fredsoe, 1976) was used to calculated the sediment transport capacity at each grid point. The result of sediment transport capacity of Wai-San-Ting region is shown in figure 7.

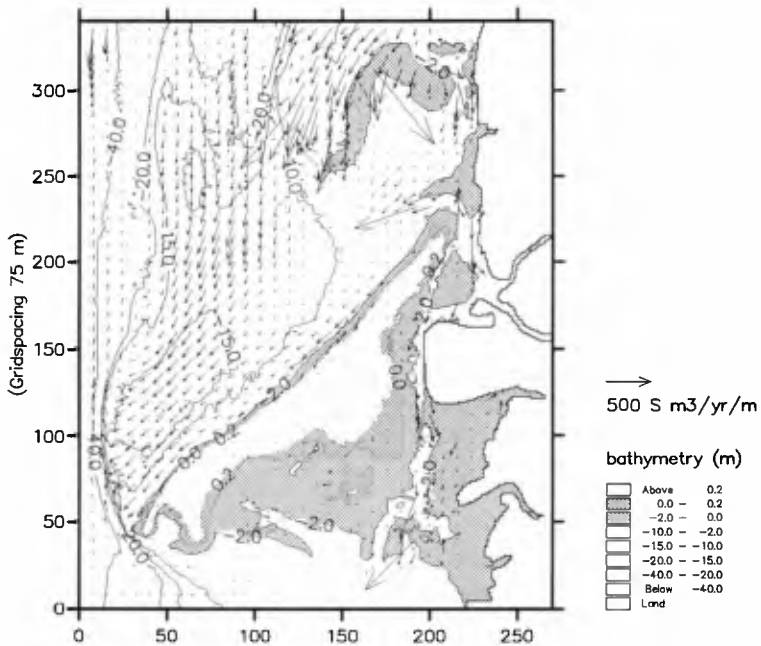


Figure 7 The sediment transport capacity near the Wai-San-Ting area

Results show that the sediment transport capacity is very small in the area between two sand bars due to the deeper water depth, stronger tidal current and the sheltering effect of Pao-Zi-Liao sand bar. Along the sand bars, the sediment transport capacity is much stronger that represent significant morphological changes along the sand bars. The sea bed initial movement of the sand bars is shown in figure 8. The result of simulation shows that two sand bars are evolution by itself. The migration of the Pao-Zi-Liao sand bar is toward to south-west and south. The sand bar does not provide sediment to the Wai-San-Ting that give quantitative explanation to the conceptual model.

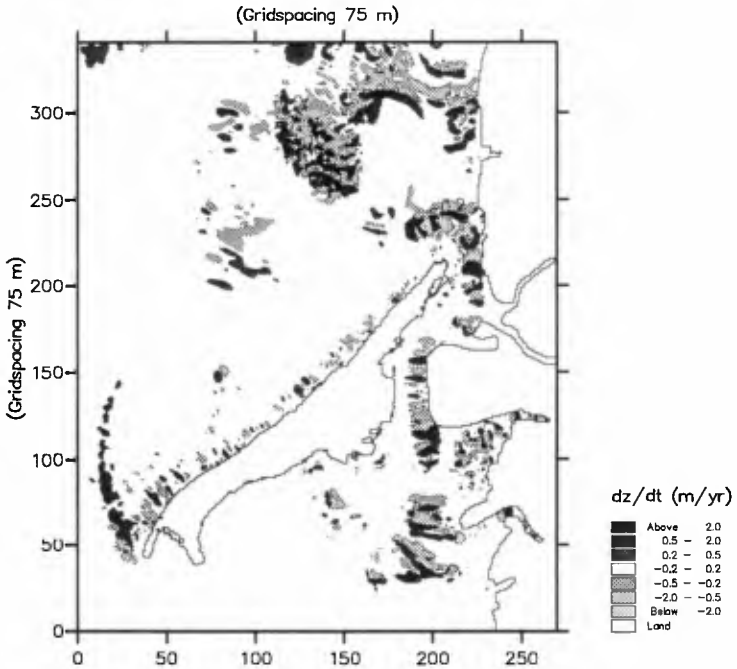


Figure 8 The sea bed initial moveemnt rate distribution of Wai-San-Ting area

Figure 9 shows the erosion and accretion area between the survey 1993 and 1994. The measurment bathymetry show similar erosion and accretion pattern among Pao-Zi-Liao and Wai-San-Ting sand bars. The maximum erosion rate is around 2m/year near the tips of the sand bars. The conceptual model and numerical model very well agree with the measurement data.



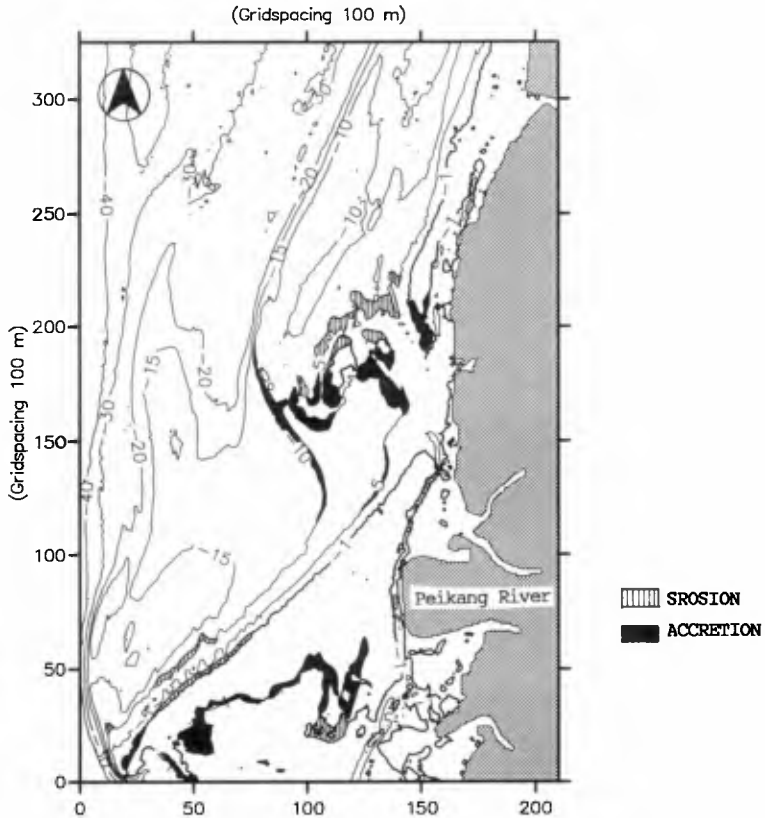


Figure 9 The erosion and accretion area among 1993 and 1994 bathymetry

### Discussion and Conclusion

A hypothesis concerning the historical morphological development of the coast and its present state in the ongoing coastal development process was formulated. Explanations to the questions concerning the origin and persistence of the main shoreline features were found in deeper water than the present surf zones. The -20 m contour marked the outer edge of very distinct historical features. The features were linked to the pathways of ancient river courses which deposited deltas over thousands of years. At the persistent and very oblique wave attack cut the original deltas to form the present day sandbars. Four such "relict" deltas were identified according to its river courses. Below -10 m the time scales of development and change were far larger

than those above -5 m, marking the difference between tide and wave dominated Zones. In the zone -5 to -10 m combined wave and tide effects dominate the processes.

Detailed modeling using MIKE21 package with wave, flow and sediment transport modules together with geostatistical analysis were used to assess key elements of the morphological hypothesis. Critical findings for the Yunlin coast morphological processes were:

(1) that the decay of the sandbars was mostly independent from the upstream coastal sediment supply due to the major discontinuities at sandbar headlands and tidal channels.

(2) That the deep water transport due to currents and waves outside the surf zone was not playing an important role in the development of the shoreline feature.

The analysis of the complex morphological processes has provided an important insight into the probable impacts of coastal developments and guided the expensive and time-consuming model operations. Many of the processes and investigations are common to other complex sandbar coasts worldwide.

#### Reference

DH, "User's manual of UNIBEST", Delft Hydraulics, 1991.

DHI , "MIKE21 User's Manual" , Danish Hydraulic Institute, 1992.

Engelund, F. and Fredsoe, J., "A sediment transport model for straight alluvial channels", *Nordic Hydrology*, 7, pp. 293-306, 1976.

Kung, C. S., "The morphological baseline study of Yunlin Offshore Industrial Estate Master Plan", Technical report, Sinotech, Taiwan, 1993.

Tsai, J.J and Huang, C.H, "The morphological changes of Wai-San-Ting in Yunlin coast," 14th Ocean engineering conference in Taiwan, pp. 498-504, 1992.

## CHAPTER 133

# Suspended Sediment Transport in Inner Shelf Waters During Extreme Storms

O.S. Madsen<sup>1</sup> T.A. Chisholm<sup>2</sup> and L.D. Wright<sup>2</sup>

### Abstract

The paper presents a simple model for the prediction of longshore and crossshore suspended sediment transport rates outside the surf zone in water depths less than 20 m or so. The model consists of a depth-resolving hydrodynamic component, which considers wind-induced currents in the presence of waves and includes the Coriolis effect. The hydrodynamic model component is coupled with a model for the mean suspended sediment concentration to produce a prediction of the depth-varying mean suspended sediment flux vector. In addition to specification of environmental conditions, *i.e.* waves and sediment characteristics as well as current driving forces (wind velocity and pressure gradient), the model requires three parameters:  $C_a$ , the wind-drag coefficient;  $k_N$ , the movable bed bottom roughness; and  $\gamma_0$ , the resuspension parameter. These three model parameters were determined (Madsen et al., 1993) from a subset of field data obtained in 13 m depth off Duck, North Carolina, during the severe “Halloween Storm” of 1991 and are used to perform a limited comparison between predicted and observed current velocity vectors and mean suspended sediment concentrations. The agreement is very encouraging and model prediction of an offshore loss of 22 m<sup>3</sup> sediment per m beach compares favorably with the loss of 27 to 54 m<sup>3</sup> obtained from beach profile surveys.

---

<sup>1</sup> R.M. Parsons Laboratory, Massachusetts Institute of Technology, Cambridge, MA 02139 USA

<sup>2</sup> Virginia Institute of Marine Science, College of William and Mary, Gloucester Point, VA 23062 USA

## Introduction

The importance of storms to coastal change has been documented extensively. Storm-driven processes are also known to dominate sediment transport on the inner shelf, *i.e.* outside the surf zone in water depths up to 20 m or so. However, very little quantitative information is available on near-bottom currents, bed shear stresses and sediment fluxes for the reliable prediction of sediment transport processes on the inner shelf which forms an important link between the extensively studied processes within the surf zone and deeper continental shelf waters.

Across the inner shelf currents are induced by wind and pressure gradients more so than by wave-associated radiation stresses. This paper presents a depth-resolving model for the wind-induced and pressure gradient driven (tidal) current in inner shelf waters along fairly straight coastlines. The bottom boundary condition for the current is specified in terms of the apparent bottom roughness experienced by currents in the presence of waves and is calculated from the theory of Madsen (1994). Since the determination of the apparent bottom roughness requires the current to be specified, an iterative solution procedure is necessary to solve for the depth-varying current velocity vector. In addition to wave-current interaction in the bottom boundary layer the model includes Coriolis effects, since crossshore sediment transport is sensitive to even minor changes of the current velocity vector's direction.

The current shear velocities and eddy viscosities obtained from the hydrodynamic model are used to predict the profiles of mean suspended sediment concentration. For the suspended sediment concentration the effect of waves is again manifesting itself through the specification of a reference concentration at the bottom. Mean suspended sediment fluxes are obtained from the product of current velocity and mean concentration, and integration over depth produces the total mean suspended sediment transport rate in the alongshore and crossshore directions.

The unique data set obtained during the severe "Halloween Storm" of 1991 is used to perform a limited comparison between observations and predictions by the hydrodynamic and sediment transport model. Although a small subset of this available field data set was used (Madsen et al., 1993) to determine empirical values for important model parameters (wind-drag coefficient, movable bed roughness, and resuspension parameter) this comparison is quite encouraging, as is the model's prediction of a net loss of sediment per meter beach during the entire "Halloween Storm" which is within a factor of two from the loss determined by beach profile surveys.

### The Depth-Resolving Hydrodynamic Model

Under the assumptions of slowly varying forcing in space and time the equations governing the depth-dependent current velocities,  $u = u(z)$  and  $v = v(z)$  of a constant density,  $\rho$ , fluid in the horizontal  $xy$ -plane may be written

$$\frac{Du}{Dt} \simeq 0 = -\frac{1}{\rho} \frac{\partial p}{\partial x} + fv + \frac{\partial}{\partial z} \left( \nu_t \frac{\partial u}{\partial z} \right) \quad (1)$$

$$\frac{Dv}{Dt} \simeq 0 = -\frac{1}{\rho} \frac{\partial p}{\partial y} - fu + \frac{\partial}{\partial z} \left( \nu_t \frac{\partial v}{\partial z} \right) \quad (2)$$

in which  $f = 1.45 \cdot 10^{-4} \sin(\text{latitude}) s^{-1}$  is the Coriolis Parameter,  $z$  is the vertical coordinate ( $z = 0$  at the bottom), the pressure gradients,  $\partial p/\partial x$  and  $\partial p/\partial y$ , are assumed independent of  $z$  corresponding to hydrostatic pressure distribution and  $\nu_t$  is a turbulent eddy viscosity.

Introducing the geostrophic current defined by

$$f\{U_g, V_g\} = -\frac{1}{\rho} \left\{ \frac{\partial p}{\partial y}, -\frac{\partial p}{\partial x} \right\} \quad (3)$$

multiplication of (2) by  $i = \sqrt{-1}$  followed by addition of (1) leads to a single governing equation

$$\frac{\partial}{\partial z} \left( \nu_t \frac{\partial W}{\partial z} \right) - ifW = 0 \quad (4)$$

in the complex velocity

$$W = (u - U_g) + i(v - V_g) \quad (5)$$

The complete analogy of (4) to the equation governing oscillatory turbulent bottom boundary layer for simple periodic waves, *e.g.* Eq. (4) of Madsen (1994), is noted. Here the Coriolis Parameter,  $f$ , replaces the radian frequency,  $\omega$ , and the imaginary part of the solution of (4) represents the  $y$ -component of the velocity whereas it, in the wave boundary layer case, is without physical significance.

In order to solve (4) it is first necessary to specify the turbulent eddy viscosity,  $\nu_t$ . Here we follow the suggestion of Madsen (1977) as did Jenter and Madsen (1989) by adopting an eddy viscosity which increases linearly with distance from a sheared boundary and is scaled by this boundary's shear velocity,  $u_* = \sqrt{\tau/\rho}$ . In the present case wind stress,  $\tau_s$ , acts on the free

surface,  $z = h$ , and a bottom stress,  $\tau_c$ , acts on the bottom  $z = 0$ . The resulting model for  $\nu_t$  therefore becomes

$$\nu_t = \begin{cases} \kappa u_{*c} z & \text{for } 0 < z < z_m \\ \kappa u_{*s} (h - z) & \text{for } z_m < z < h \end{cases} \tag{6}$$

in which  $\kappa =$  von Karman's constant ( $\kappa = 0.4$ ), and  $z_m$  is the distance above the bottom at which the transition from bottom to surface shear dominated turbulence is made. This level is chosen, as suggested by Madsen (1977), to be scaled by the relative magnitude of the two shear velocities, *i.e.*

$$z_m = \frac{u_{*c}}{u_{*s} + u_{*c}} h \tag{7}$$

With  $\nu_t$  given by (6) and (7) the general solution of (4) is obtained (Jenter and Madsen, 1989) in terms of zeroth order Kelvin functions

$$W = W_b = A_b (ber 2\sqrt{\zeta_b} + ibei 2\sqrt{\zeta_b}) + B_b (ker 2\sqrt{\zeta_b} + ikei 2\sqrt{\zeta_b}) \quad \text{for } 0 < \zeta_b < \zeta_{bm} \tag{8}$$

and

$$W = W_s = A_s (ber 2\sqrt{\zeta_s} + ibei 2\sqrt{\zeta_s}) + B_s (ker 2\sqrt{\zeta_s} + ikei 2\sqrt{\zeta_s}) \quad \text{for } 0 < \zeta_s < \zeta_{sm} \tag{9}$$

in which  $A_b, B_b, A_s$  and  $B_s$  are arbitrary complex constants, and the nondimensional vertical coordinates are given by

$$\zeta_b = \frac{zf}{\kappa u_{*c}} \quad \text{and} \quad \zeta_s = \frac{(h-z)f}{\kappa u_{*s}} \tag{10}$$

and  $\zeta_{bm}$  and  $\zeta_{sm}$  are the matching coordinates given by (10) with  $z = z_m$ .

The arbitrary constants in (8) and (9) are determined by the boundary condition at the surface

$$\left( \kappa u_{*s} \sqrt{\zeta_s} \frac{dW_s}{d(2\sqrt{\zeta_s})} \right)_{\zeta_s \rightarrow 0} = -\frac{1}{\rho} (\tau_{sx} + i\tau_{sy}) \tag{11}$$

in which the wind shear stress at the free surface is given by

$$\tau_s e^{i\phi_a} = \rho_a C_a U_a^2 e^{i\phi_a} = \tau_{sx} + i\tau_{sy} \tag{12}$$

with  $\rho_a$  being the air density,  $U_a$  the wind speed,  $\phi_a$  the wind direction measured from the x-axis and  $C_a$  is the wind-drag coefficient; and the turbulent no-slip condition at the bottom

$$W_b = -(U_g + iV_g) \quad \text{at} \quad \zeta_b = \zeta_{bo} = \frac{z_{oa}f}{k u_{*c}} \tag{13}$$

in which  $z_{oa}$  denotes the apparent bottom roughness, *i.e.* the bottom roughness experienced by the current in the presence of waves (Madsen, 1994).

The additional conditions are supplied by the requirement of continuity of velocity and shear stress at the matching level, *i.e.*

$$W_b(\zeta_b = \zeta_{bm}) = W_s(\zeta_s = \zeta_{sm}) \tag{14}$$

and

$$u_{*c} \sqrt{\zeta_{bm}} \frac{dW_b}{d(2\sqrt{\zeta_b})} \Big|_{\zeta_b = \zeta_{bm}} = -u_{*s} \sqrt{\zeta_{sm}} \frac{dW_s}{d(2\sqrt{\zeta_s})} \Big|_{\zeta_s = \zeta_{sm}} \tag{15}$$

in which the minus signs in (11) and (15) are the result of  $\zeta_s$  being proportional to  $(h - z)$  rather than  $z$ .

Formally the arbitrary constants may be obtained by sloving (11) through (15). Series expansions for the zeroth order Kelvin functions and their derivatives found in Abramowitz and Stegun (1972; Chapter 9) greatly facilitate this task. However, the vertical coordinate used in the lower (bottom) layer depends on the bottom shear stress,  $u_{*c} = \sqrt{\tau_c/\rho}$ , which is *a priori* an unknown. The same is true for the apparent bottom roughness which depends on wave-current interaction within the wave bottom boundary layer and hence needs a specification of the current characteristics before it can be determined (see Madsen, 1994). Finally, the pressure gradients need to be determined (or known) in order to solve the problem.

#### The Bottom Shear Velocity, $u_{*c}$

To overcome the problem of an initially unknown value of the bottom shear stress, we proceed in an iterative manner by assuming a value of  $u_{*c}$  to obtain the solution for  $W_b$  and subsequently evaluate the bottom shear stress from

$$\tau_c e^{i\phi_c} = \rho \kappa u_{*c} \sqrt{\zeta_{bo}} \frac{dW_b}{d(2\sqrt{\zeta_b})} \Big|_{\zeta_b = \zeta_{bo}} \quad (16)$$

which, since  $\tau_c = \rho u_{*c}^2$ , yields a "new" value of  $u_{*c}$ . When convergence has been achieved the angle  $\phi_c$  denotes the direction of the bottom shear stress and hence the direction of the near-bottom current velocity.

The Apparent Bottom Roughness,  $z_{oa}$

The evaluation of the apparent bottom roughness depends on the wave characteristics, the physical (movable bed) bottom roughness,  $k_N$ , and the current specification. The details of a spectral wave-current interaction model are presented by Madsen (1994). Here it suffices to mention that the wave motion is specified by a representative periodic wave of near-bottom orbital velocity amplitude,  $u_{br}$ , radian frequency,  $\omega_r$ , and direction of propagation  $\phi_{wr}$  (Eqs. (22), (23) and (24) in Madsen, 1994). From this information, along with  $k_N$  and an assumed current specified by its shear stress  $\tau_c$  and direction  $\phi_c$ , the solution of the wave-current interaction problem is detailed by Madsen (1994) and leads to a solution for the apparent bottom roughness obtained from Eq. (11) of Madsen (1994)

$$z_{oa} = \left( \frac{k_N}{30\delta_{wc}} \right)^{u_{*c}/u_{*r}} \delta_{wc} \quad (17)$$

in which  $\delta_{wc}$  and  $u_{*r}$  denote the wave bottom boundary layer thickness and the shear velocity based on the maximum combined wave-current bottom shear stress, respectively, and are defined by Eqs. (36) and (26) of Madsen (1994).

Specifying the no-slip condition for the current in terms of the apparent roughness  $z_{oa}$ , avoids the determination of the current velocity profile within the wave boundary layer. This information is, however, needed for the evaluation of suspended sediment flux immediately above the bottom. With general reference to Madsen (1994) for details, we merely state the proper form for the current velocity profile within the wave bottom boundary layer as

$$u + iv = \frac{u_{*c} u_{*c}}{u_{*r} \kappa} \ell n \frac{30z}{k_N} e^{i\phi_c} \quad (18)$$

valid for  $z < \delta_{wc}$  with  $\phi_c$  obtained from (16).



The Pressure Gradients,  $\partial p/\partial x$  and  $\partial p/\partial y$ 

It is consistent with the assumption of slow spatial variability to assume an essentially straight coastline. We therefore choose a coordinate system with a shore-parallel x-axis. Furthermore, limiting the model's application to water depths less than 10 to 20 m, corresponding to distances from shore of the order of at most 1 km or so, suggests that any crossshore depth-averaged current should be negligible.

For wind-dominated storm events the uniformity in the shore-parallel x-direction justifies the neglect of an alongshore mean surface slope and results in a pressure gradient of  $\partial p/\partial x \simeq 0$ . If the longshore mean surface slope cannot safely be assumed negligible an approximate methodology for obtaining an estimate of  $\partial p/\partial x$  to be used in conjunction with the steady depth-resolving model is presented by Chisholm (1993) and is outlined in Appendix A.

Imposing the negligible crossshore mean current on the general solution yields the condition

$$\int_0^h v dz \simeq \int_0^h \Im \{W + iV_g\} dz = 0 \quad (19)$$

from which the crossshore pressure gradient,  $\partial p/\partial y$ , may be determined with  $W$  given by (8) and (9). For the simplest model application (3) shows that  $V_g = 0$  since  $\partial p/\partial x \simeq 0$ .

## Solution Strategy

To apply the depth-resolving hydrodynamic model it is assumed that the representative periodic wave characteristics,  $u_{br}$ ,  $\omega_r$  and  $\phi_{wr}$  as defined by Madsen (1994) are known. From the wave conditions and knowledge of the bottom sediment characteristics the physical (movable bed) bottom roughness,  $k_N$ , may be estimated from, *e.g.* Wiberg and Harris (1994) for rippled bed or Madsen et al. (1993) for flat movable bed. The surface wind shear stress, is obtained from (12) with  $C_a$  estimated from, *e.g.* Wu (1982) or Madsen et al. (1993).

Assuming the wind to have a substantial longshore component an initial estimate of the bottom shear stress is obtained by considering the alongshore flow to be approximately described by as a Couette flow, *i.e.*  $\tau_c = \rho u_{zc}^2 \simeq \tau_s \cos \phi_a$ . With this shore-parallel current bottom shear stress "known" the wave-current interaction model by Madsen (1994) may be used to obtain a first estimate of the apparent bottom roughness,  $z_{oa}$ , from (17).

The depth-resolving hydrodynamic model may now be formally solved. The "unknown" crossshore pressure gradient,  $\partial p/\partial y$  (or  $U_g$ ), is obtained from

(19) and the bottom shear stress vector and shear velocity are upgraded by use of (16). We may now re-evaluate the apparent bottom roughness from (17) and continue the iteration until convergence has been achieved.

### The Mean Suspended Sediment Transport Model

The concentration of suspended sediment is described by the diffusion equation. Limiting the model's applicability to slowly varying conditions in space and time, *i.e.* disregarding variations over the timescale of the wave motion, the equation governing the mean suspended sediment concentration,  $c(z)$ , reads

$$\frac{Dc}{Dt} \simeq 0 = \frac{\partial}{\partial z} \left( \nu_s \frac{\partial c}{\partial z} \right) + \frac{\partial}{\partial z} (w_f c) \quad (20)$$

in which  $w_f (> 0)$  denotes the fall velocity of the sediment and  $\nu_s$  is the eddy diffusivity.

The eddy diffusivity is taken equal to the eddy viscosity used in the depth-resolving hydrodynamic model, *i.e.*  $\nu_s = \nu_t$  with  $\nu_t$  given by (6). The hydrodynamic model, however, did not explicitly include the description of the current profile in the immediate vicinity of the bottom, *i.e.* within the wave bottom boundary layer of thickness  $\delta_{wc}$ . Within the wave boundary layer the eddy viscosity and hence the eddy diffusivity is given by the wave-current interaction model (see Madsen, 1994) and we therefore have

$$\nu_s = \begin{cases} \kappa u_* r z & 0 < z < \delta_{wc} \\ \kappa u_* c z & \delta_{wc} < z < z_m \\ \kappa u_* s (h - z) & z_m < z < h \end{cases} \quad (21)$$

Integration of (20) leads to an expression for the vertical flux of suspended sediment which, by virtue of the steady state assumption, must be zero and the resulting equation becomes

$$\frac{dc}{dz} = -\frac{w_f}{\nu_s} c \quad (22)$$

To solve this equation with  $\nu_s$  given by (21) one boundary condition is needed.

### The Reference Concentration

We adopt the reference concentration,  $c_R$ , specified at a given elevation,  $z = z_R$ , within the wave boundary layer, *i.e.*  $z_R < \delta_{wc}$ , as our boundary

condition. Following Smith and McLean (1977) we assume the functional form of the mean reference concentration to be

$$c_R = \gamma_0 c_b \left( \frac{|\tau'_b|}{\tau_{cr}} - 1 \right) \quad \text{at} \quad z = z_R = 7d \quad (23)$$

in which  $c_b$  is the volume concentration of sediment in the bed,  $\tau'_b$  is the skin friction bottom shear stress due to the combined wave-current flow,  $\tau_{cr}$  is critical shear stress for initiation of motion (Madsen and Grant, 1976), and  $\gamma_0$  is the resuspension parameter. The functional form of (23) is supported by the simple bedload formula for saltating grains derived by Madsen (1991). Regarding the transport that takes place within the saltation layer as bedload (and therefore not to be included in the suspended load transport) the level at which the reference concentration is specified is taken as the top of the saltation layer which is approximated as  $z_R = 7d$ , with  $d$  being the diameter of the bottom sediment.

The skinfriction shear stress,  $\tau'_b$ , in (23) includes the contribution from wave motion. In fact, it is to be expected that  $|\tau'_b|$  is dominated by wave action with currents playing only a secondary role in the suspension of bottom sediments. Since the intended application of the present model is for stormy conditions, we shall assume wave-dominance and take

$$\tau'_b \simeq \tau'_w = \tau'_{wm} \cos(\omega_r t + \phi'_{\tau r}) \quad (24)$$

where  $\phi'_{\tau r}$  is a phase angle which, in the present context, is of no importance, and

$$\tau'_{wm} = \frac{1}{2} \rho f'_w u_{br}^2 \quad (25)$$

is the maximum skinfriction bottom shear stress of the representative periodic wave defined by Madsen (1994) evaluated for a bottom roughness equal to the mean diameter of the bottom sediment. Given the functional form of (23) it follows logically that the representative periodic wave defined by Madsen (1994), *i.e.* not the "significant wave", is the proper choice for the determination of the mean reference concentration in combined wave-current boundary layer flows.

Introduction of (24) in (23) therefore results in a relatively simple expression for the mean reference concentration for wave-dominated flows

$$c_R = \gamma_0 c_b \left( \frac{2}{\pi} \frac{\tau'_{wm}}{\tau_{cr}} - 1 \right) \quad \text{at} \quad z = z_R = 7d \quad (26)$$

with  $\tau'_{wm}$  given by (25) which is readily evaluated using formulas given by Madsen (1994). It is important to emphasize at this point that the empirical value of the resuspension parameter,  $\gamma_0$ , is intimately tied to the level,  $z_R$ , at which it is specified and to the particular theoretical model used to extrapolate actual concentration measurements from their level, to the chosen reference level. Wikramanayake (1992), using the present reference level obtained values of  $\gamma_0 = 2 \cdot 10^{-3}$  and  $2 \cdot 10^{-4}$  for rippled beds and flat movable beds, respectively. These values may be used for preliminary considerations, but it should be recognized that a great deal of uncertainty is associated with the specification of  $\gamma_0$ .

### The Mean Suspended Sediment Concentration

With the mean concentration governed by (22), the eddy diffusivity given by (21) and the reference concentration specified by (26) the solution for the mean suspended sediment concentration is readily obtained.

*Within the wave boundary layer,  $z_R < z < \delta_{wc}$  we obtain*

$$c = c_R \left( \frac{z}{z_R} \right)^{-\frac{w_f}{\kappa u_* r}} \quad (27)$$

*In the bottom layer of the water column,  $\delta_{wc} < z < z_m$ , integration of (21) and matching the concentration with (26) at  $z = \delta_{wc}$  gives*

$$c = c_R \left( \frac{\delta_{wc}}{z_R} \right)^{-\frac{w_f}{\kappa u_* r}} \left( \frac{z}{\delta_{wc}} \right)^{-\frac{w_f}{\kappa u_* c}} \quad (28)$$

*In the surface layer of the water column,  $z_m < z < h$ , the mean concentration is given by*

$$c = c_R \left( \frac{\delta_{wc}}{z_R} \right)^{-\frac{w_f}{\kappa u_* r}} \left( \frac{z_m}{\delta_{wc}} \right)^{-\frac{w_f}{\kappa u_* c}} \left( \frac{h - z_m}{h - z} \right)^{-\frac{w_f}{\kappa u_* s}} \quad (29)$$

### Mean Suspended Sediment Transport

The complex current velocity profile

$$u + iv = W + U_g + iV_g \quad (30)$$

is obtained from (3), (8) and (9), with (8) replaced by (18) within the wave boundary layer, for the three depth-intervals for which the mean concentrations of suspended sediments are given by (27) through (29). The depth-integrated complex suspended sediment flux vector is evaluated from

$$q_{sx} + iq_{sy} = \int_{z_R}^h (u + iv)cdz \quad (31)$$

### Extension of Model to Sediment Mixtures

The preceding presentation of the mean suspended sediment transport model treated the sediment as uniform, *i.e.* represented by a single size-class of diameter  $d$ . The model is formally extended to sediment mixtures consisting of several size-classes represented by diameter  $d_n$  for the  $n$ 'th size-class.

For mixtures the current velocity profiles are obtained with the mean sediment diameter,  $d_{50}$ , used to represent the sediment mixture in the evaluation of the movable bed roughness,  $k_N$ , and the skinfriction bottom shear stress. The reference concentration is obtained from (26) for the individual size-class with  $c_b$  and  $\tau_{cr}$  replaced by the values corresponding to the particular size-class,  $d_n$ . Finally, the concentration of each size class is obtained from (27) through (29) with  $w_f$  replaced by  $w_{fn}$  and the total mean concentration of suspended sediment is obtained by summation of the contributions from the individual size classes.

It is emphasized that the extension of the model to sediment mixtures, as presented above, is purely formal and based on a number of essentially unsubstantiated generalizations as well as several omissions. Thus, the generalization of the reference concentration formulation to mixtures, which follows the suggestion of Wiberg et al. (1994) is unsubstantiated. In fact, Wilcock and Southard (1988) present data on the initiation of motion of individual size-classes in a mixture that suggest the critical shear stress to be the same for all size-classes, in direct conflict with the proposed generalization. The formal extension of the model to sediment mixtures omits any consideration of armouring effects which ought to be included in a physically realistic manner to produce a complete model. At present the weaknesses of the proposed extension to sediment mixtures become part of the model and are reflected in the empirical determination of model parameters such as the resuspension parameter  $\gamma_0$ , obtained from this model.

### Model Application

The hydrodynamic and suspended sediment transport model presented in the preceding sections contains two parameters that are model-specific: the movable bed roughness,  $k_N$ , and the resuspension parameter,  $\gamma_0$ . These parameters and the wind-drag coefficient  $C_a$  were determined for an extreme storm event, the "Halloween Storm" of 1991, from a selected subset of field data obtained at the U.S. Army Corps' Field Research Facility (FRF) in 13 m water depth off Duck, North Carolina. For details of field experiments

and the data analysis, which produced values of  $k_N = 0.144 \text{ cm} \simeq 15 d_{50}$ ,  $\gamma_0 = 4.0 \cdot 10^{-4}$  and  $C_a = 5.0 \cdot 10^{-3}$ , the reader is referred to Madsen et al. (1993). Here it suffices to point out that a subset of five bursts of twenty three available were used to obtain the hydrodynamic parameters,  $k_N$  and  $C_a$ , whereas  $\gamma_0$  was obtained from analysis of three bursts of twelve available.

Adopting these parameters for the entire storm period, October 27 through November 1, 1991, with wind records from the FRF and augmenting our wave information by use of data from FRF's 8 m pressure sensor array (our tripod surcame to the elements around 18:00 h (EST) on October 30, 1991, when the significant wave height reached  $H_s \simeq 4.5 \text{ m}$  with a peak period of  $T_p \simeq 20 \text{ s}$ ) the required input for application of the model is available.

Figure 1 shows a comparison of predicted and measured longshore (southerly directed when positive) and crossshore (offshore directed when positive) currents at 29 cm above the bottom. The predicted relatively rapid increase in longshore current around 35 h, associated with a rapid increase in wind speed from about 7 m/s to about 16 m/s, precedes and exceeds the measured currents. The reason for this is most likely the neglect of unsteady effects in the hydrodynamic model formulation. Overall agreement between predicted and observed longshore currents is, however, considered acceptable and quite encouraging given the simplicity of the model. The agreement between predicted and observed crossshore currents is far less striking. Given, however, the very low crossshore current velocities the measurements are expected to be extremely sensitive to experimental errors, making detailed point-by-point comparison less meaningful.

Figure 2 shows a comparison of predicted and observed suspended sediment concentrations at 27 cm and 87 cm above the bottom. Considering the fact that only two of the twelve experimental observations at these elevations were used to determine  $\gamma_0$  the overall agreement between predicted and observed suspended sediment concentrations is very encouraging.

The model results presented in Figures 1 and 2 were obtained without inclusion of a longshore pressure gradient, *i.e.* taking  $\partial p / \partial x = 0$ . It is of practical interest to point out that the first model run, which was based on the initial estimate of  $z_{oa}$  obtained in the manner proposed above, yielded results that were practically indistinguishable from the results obtained after two and three iterations. Also, model runs were performed in which the longshore pressure gradient was estimated from tide records at Virginia Beach and Kitty Hawk, North Carolina, following the procedure described in Chisholm (1993). The inclusion of longshore tidal forcing resulted in only minor modifications of the longshore current of at most 5 cm/s and a negligible (less than 0.2 cm/s) effect on the crossshore velocity. This apparent success of the sediment transport model in its simplest form is, of course, a

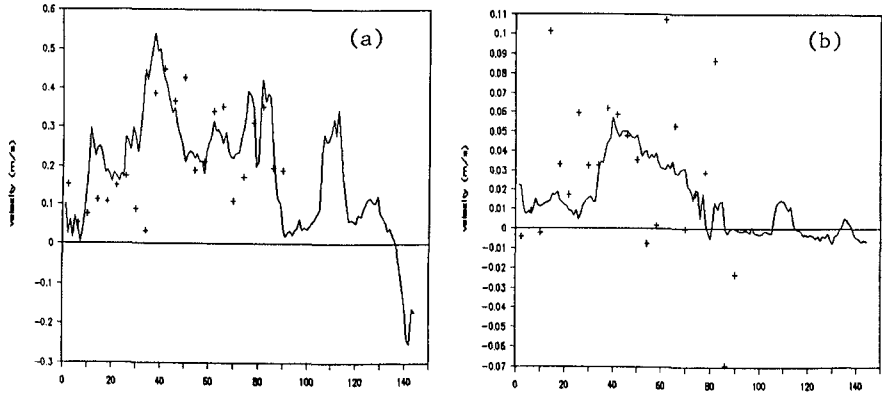


Figure 1: Comparison of measured (crosses) and predicted (full lines) long-shore, (a), and cross-shore, (b), velocities (m/s) 29 cm above the bottom as a function of time in hours from 0:00 on 27 October, 1991. Measurements at  $t = 58, 62, 66, 78$  and  $82$  hours used in model calibration to obtain  $k_N$  and  $C_a$ .

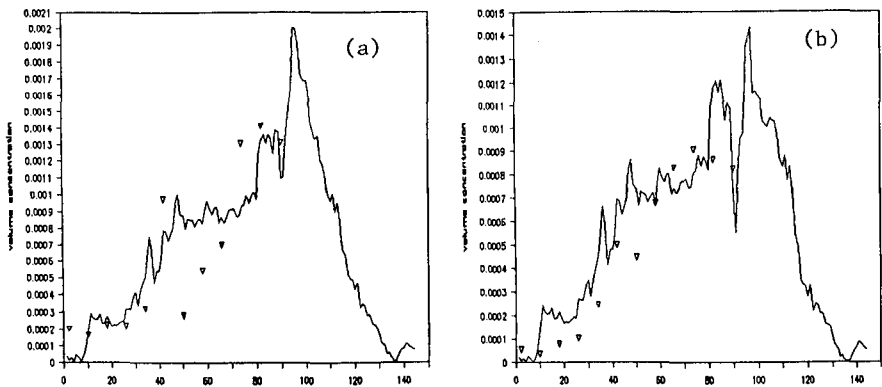


Figure 2: Comparison of measured (triangles) and predicted (full lines) mean suspended sediment concentration (volumetric) at 27 cm, (a), and 87 cm, (b), above the bottom as a function of time in hours from 0:00 on 27 October, 1991. Measurements at  $t = 58$  and  $66$  hours used in model calibration to obtain  $\gamma_0$ .

result of the specific nature of the extreme conditions encountered during the "Halloween Storm" and should not be interpreted to mean that longshore pressure gradients generally may be neglected.

### Conclusions

A relatively simple hydrodynamic model for currents induced in inner shelf waters extending from the surf zone to depths of 10 to 20 m along relatively straight coastlines was presented. The model includes Coriolis effect and wave-current interactions in the bottom boundary layer and predicts the current velocity profiles in both the longshore and crossshore directions.

The hydrodynamic model is coupled with a model for the prediction of the mean suspended sediment concentration to produce a mean suspended sediment transport model for inner shelf coastal waters.

The capabilities of the model were illustrated by its application to an extreme storm event, the "Halloween Storm", for which field data were available for comparison with model predictions. The limited comparison presented in this paper will be expanded upon in forthcoming publications. However, the comparison between predictions and observations presented here suggests an accuracy of within a factor of two to be achievable when the model is properly calibrated. This conclusion is further supported by computations of the net loss of sediment volume per meter of beach during the entire Halloween Storm. The model's predictions of a loss of about  $22 \text{ m}^3$  per meter compares favorably with losses of 27 and  $54 \text{ m}^3$  per meter beach obtained from profile surveys from before and after the "Halloween Storm" by the FRF along transects north of the FRF pier.

It is believed that the model presented here may serve the role of providing the important link between surf zone sediment transport processes and those in deeper waters of the continental shelf.

Acknowledgements This study was supported by the National Science Foundation, Marine Geology and Geophysics Grant OCE-9017828. Bill Birke-meier, Kent Hathaway, Chuck Long, and their colleagues at the U.S. Army Corps Field Research Facility (FRF) at Duck, NC, are thanked for retrieving the remains of our tripod, for providing the wave and wind data recorded by the FRF, and for their ongoing cooperation.

### References

- Abramowitz, M., I.A. Stegun (1972) *Handbook of Mathematical Functions*, National Bureau of Standards Applied Math Series, No. 55, pp. 379-509.
- Chisholm, T.A. (1993) Analysis of field data on near-bottom turbulent flows and suspended sediment concentrations, Eng. Thesis, Dept. Civil & Environmental Engineering, MIT.



- Jenter, H.L., O.S. Madsen (1989) Bottom stress in wind-driven depth-averaged coastal flows. *Journal Physical Oceanography* 19(7):962-974.
- Madsen, O.S. (1977) A realistic model of the wind-induced Ekman boundary layer. *Journal Physical Oceanography* 7(2):248-255.
- Madsen, O.S. (1991) Mechanics of cohesionless sediment transport in coastal waters. *Proceedings Coastal Sediments '91*, ASCE, Seattle. 1:15-27.
- Madsen, O.S. (1994) Spectral wave-current bottom boundary layer flows. *Proceedings 24th ICCE*, ASCE, Kobe, Japan.
- Madsen, O.S., W.D. Grant (1976) Quantitative description of sediment transport by waves. *Proceedings 15th ICCE*, ASCE, Honolulu. 2:1093-1112.
- Madsen, O.S., D.L. Wright, J.D. Boon, T.A. Chisholm (1993) Wind stress, bed roughness, and sediment suspension on the inner shelf during an extreme storm event. *Continental Shelf Research* 13(11):1303-1324.
- Smith, J.D., S.R. McLean (1977) Spatially averaged flow over a wavy surface. *Journal Geophysical Research* 82:1735-1746.
- Wiberg, P.L., C.K. Harris (1994) Ripple geometry in wave-dominated environments. *Journal Geophysical Research* 99(C1):775-790.
- Wiberg, P.L., D.E. Drake, D.A. Cacchione (1994) Sediment resuspension and bed armoring during high bottom stress events. *Continental Shelf Research* 14(10/11):1191-1220.
- Wikramanayake, P.N. (1992) Velocity profiles and suspended sediment transport for combined turbulent wave-current flows. Ph.D. Thesis, Dept. Civil & Environmental Engineering, MIT.
- Wilcock, P.R., J.B. Southard (1988) Experimental study of incipient motion in mixed-size sediments. *Journal Water Resources Research* 24(7):1137-1151.
- Wu, J.J. (1982) Wind-stress coefficients over sea surface from breeze to hurricane. *Journal Geophysical Research* 87:9704-9706.

#### Appendix A: Approximate Determination of $\partial p/\partial x$

If evidence of pronounced variations in mean water level along the coastal section under consideration is available, *e.g.* from tide gauge records, it may not be safe to assume the alongshore pressure gradient to be zero. To estimate the effect of a nonzero longshore pressure gradient it is assumed that an estimate of the mean surface slope, as a function of time, is available for the location of interest, *i.e.* the pressure gradient driving a longshore flow is given by  $\rho g \partial \bar{\eta} / \partial x$ . In the absence of any Coriolis forcing in the x-direction ( $V = 0$ ) the equation governing the depth-averaged longshore velocity  $U$  induced by the pressure gradient in water depth  $h$  is

$$\frac{\partial U}{\partial t} = -g \frac{\partial \bar{\eta}}{\partial x} - (C_b/h) |\bar{u}| U \quad (\text{A.1})$$

in which  $|\bar{u}|$  is the depth-averaged longshore velocity obtained from the depth-resolving model solution, *i.e.*

$$|\bar{u}| = \frac{1}{h} \int_0^h \Re\{W_{Ug}\} dz \quad (\text{A.2})$$

with  $W$  given by (8) and (9). Since model application is limited to water depths of 10 to 20 m or less, it is reasonable to assume that the longshore velocity is closely described by the logarithmic profile up to half-depth, *i.e.* up to  $z = h/2$ , and that the velocity at  $z = h/2$  is a close approximation to the depth-averaged total longshore velocity (wind-induced as well as pressure gradient driven). It follows from these considerations that the bottom drag coefficient,  $C_b$ , is related to the apparent bottom roughness  $z_{oa}$ , which is known from (16) of the depth-resolving model, through

$$\sqrt{C_b} = \frac{\kappa}{\ell n \frac{h}{2z_{oa}}} \quad (\text{A.3})$$

With  $|\bar{u}|$  and  $C_b$  known as functions of time from the depth-resolving model, (A.1) may be solved numerically for the given temporal variation of  $\partial \bar{\eta} / \partial x$ .

The solution for  $U$  obtained in this manner includes unsteady effects which were considered negligible in the depth-resolving model formulation. However, the exact same time-varying longshore velocity  $U$  could have been obtained from a steady form of (A.1) if the pressure gradient term,  $\frac{\partial \bar{\eta}}{\partial x}$  in (A.1) were replaced by an equivalent steady pressure gradient

$$-\frac{1}{\rho} \frac{\partial p}{\partial x} = \frac{C_b}{h} |\bar{u}| U \quad (\text{A.4})$$

Thus solving (A.1) for  $U$  and subsequent evaluation of (A.4) will produce a longshore pressure gradient which, when introduced in the steady depth-resolving model, will return practically the same estimate of the longshore pressure gradient driven velocity as obtained from (A.1). If the addition of the longshore pressure gradient determined from (A.4) leads to drastic modifications of the depth-resolving model's predictions of  $|\bar{u}|$  and  $C_b$  it may be necessary to use this procedure in an iterative manner until convergence has been achieved.

## CHAPTER 134

### SEA BED STABILITY ON A LONG STRAIGHT COAST

E. Damgaard Christensen<sup>1</sup>, R. Deigaard<sup>2</sup>, J. Fredsøe<sup>3</sup>

#### Abstract

A stability analysis is used to investigate the development of large-scale periodic bottom topographies on a straight uniform coast. The work is an extension of the work by Hino (1974) and (1976), and special attention is paid to improve and refine the description of the sediment transport. The effect of the bed slope on the bed load sediment transport turns out to be very important. Further, the behaviour of suspended sediment is described by introducing lag effects that modify the predictions of the wave length considerably.

#### 1 INTRODUCTION

A coast is often irregular. Even a long straight coast can be very non-uniform in the longshore direction. A longshore bar can be crossed by more or less regularly spaced rip channels or it may be sinuous. Lippmann and Holman (1990) have shown several examples of different configurations of a coast that on a large scale is almost straight.

Here the formation of large-scale periodic bottom topographies is investigated by applying a linear stability analysis. The basic idea is to give a uniform bed a small perturbation. This perturbation affects the hydrodynamics and the sediment transport which again influences the bed form. It is then investigated whether the perturbation will grow in time or die out. For several different perturbations the one with the fastest growth is the one that would be expected to be dominant if the coast was given a random perturbation.

The linear stability analysis is only valid for an infinitesimal small bed perturbations, but it is expected that some of the main features of the fastest growing perturbation would also be found in the coastal forms that actually emerge.

<sup>1</sup>Ph.D-student, <sup>2</sup>Associated Professor, <sup>3</sup>Professor: ISVA, Danish Technical University, DK-2800 Lyngby, Denmark

An investigation of this kind was carried out by Hino (1974) and (1976). Hino used a very simple model for the sediment transport, and the present work is an extension of that analysis, investigating the effect of more sophisticated sediment transport descriptions, including the effect of the bed slope, and the gradual adaption of the suspended load transport due to changing hydrodynamic conditions.

## 2 DESCRIPTION OF WAVES, CURRENTS AND SEDIMENT TRANSPORT

The analysis considers a uniform, plane (constant slope) coastal profile with a small perturbation. The geometry and coordinate system are shown in figure 1. The "breaker line" is here defined as the line where regular waves with a deep water wave height equal to the root-mean-square wave height for irregular waves at deep water would start to break.

The chosen models for waves, currents, and sediment transport are as simple as possible, yet still represent the relevant physical processes.

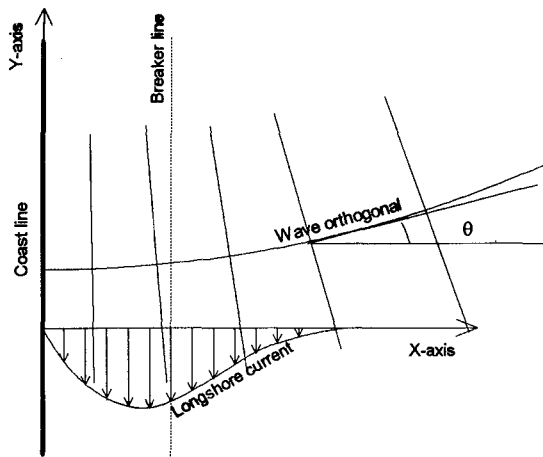


Figure 1 The figure shows the definition of the x and y-directions

### 2.1 Wave description

The waves are assumed to be irregular with Rayleigh-distributed wave heights. The breaking process is described by the theory of Battjes (1972), where the local wave height distribution is taken as the Rayleigh distribution where the wave heights are limited by the water depth:  $H_b = 0.8 h$ . This model is expected to give satisfactory results on a gently sloping, monotone beach profile. The assumption of irregular waves gives a smooth distribution of the driving forces and the longshore current distribution.

The waves are described by linear shallow water theory, which is expected to give a reasonable representation of the depth refraction and radiation stress variation in the surf zone. The wave conditions are specified at the breaker line  $x_b$  where uniform waves would start to break.

## 2.2 The current description

The current is described by the depth-integrated equations for conservation of mass and momentum:

Momentum in the x-direction:

$$\begin{aligned} \rho \frac{\partial u(h+\eta)}{\partial t} + \rho \frac{\partial (h+\eta)u^2}{\partial x} + \rho \frac{\partial (h+\eta)vu}{\partial y} + \frac{\partial s_{xx}}{\partial x} + \frac{\partial s_{xy}}{\partial y} = \\ -\rho g(h+\eta) \frac{\partial \eta}{\partial x} - \tau_{bx} \end{aligned} \quad (1)$$

Momentum in the y-direction:

$$\begin{aligned} \rho \frac{\partial v(h+\eta)}{\partial t} + \rho \frac{\partial (h+\eta)uv}{\partial x} + \rho \frac{\partial (h+\eta)v^2}{\partial y} + \frac{\partial s_{xy}}{\partial x} + \frac{\partial s_{yy}}{\partial y} = \\ -\rho g(h+\eta) \frac{\partial \eta}{\partial y} - \tau_{by} \end{aligned} \quad (2)$$

Mass conservation:

$$\frac{\partial (h+\eta)}{\partial t} + \frac{\partial u(h+\eta)}{\partial x} + \frac{\partial v(h+\eta)}{\partial y} = 0 \quad (3)$$

$u$  and  $v$  are the depth-averaged velocities,  $\eta$  is the mean surface elevation,  $h$  is the still water depth,  $s_{xx}$ ,  $s_{xy}$  and  $s_{yy}$  are the radiation stresses, and  $\tau_{bx}$  and  $\tau_{by}$  are the components of the bed shear stress.

The flow resistance is described by a simple model for the turbulent interaction between the current and the oscillatory wave boundary layer, Fredsøe (1981), see also Fredsøe and Deigaard (1992), pp 56-62. This gives a flow resistance represented by a logarithmic velocity profile, but with an increased bed roughness due to the wave boundary layer.

### 2.3 Sediment transport

The morphological development is described by the conservation equation for sediment:

$$(1-n)\frac{\partial h}{\partial t} = \frac{\partial q_{totx}}{\partial x} + \frac{\partial q_{toty}}{\partial y} \quad (4)$$

where  $q_{totx}$  and  $q_{toty}$  is the total sediment transport in x and y-directions and n the porosity.

One of the main purposes of this study has been to consider the influence of the sediment transport model on the morphological stability. Three approaches have been investigated.

#### The simple approach

As a first approach the sediment transport rate is taken to be proportional to the local current velocity. This is the model used by Hino (1974).

$$\mathbf{q}_t = C_s \mathbf{V} \quad (5)$$

where  $\mathbf{q}_t$  is the sediment transport vector and  $\mathbf{V}$  is the depth-averaged velocity. The coefficient  $C_s$  is taken to be constant.

#### The bed load transport model

The transport of sand is composed of bed load transport and suspended load transport, where the bed load transport  $q_b$  is determined by the local instantaneous bed shear stress, from the combination of waves and current.

The dimensionless bed load transport  $\Phi_b$  can be expressed as a function of the dimensionless bed shear stress, the Shields parameter  $\theta$ . The formula of Meyer-Peter and Müller (1948) has been applied:

$$\Phi_b = 8(\theta' - \theta_c)^{\frac{3}{2}} \quad (6)$$

$$\text{where } \Phi_b = \frac{q_b}{\sqrt{(s-1)gd^3}} \quad \text{and} \quad \theta = \frac{\tau_b}{(s-1)gd}$$

$\theta_c$  is the critical Shields parameter,  $\theta_c = 0.05$ , d is the grain diameter, and s is the relative density of the sediment.

If the bed is sloping, there is an additional down slope component of the sediment transport. When the transport is directed up (or down) the slope, gravity

gives a down slope force component that has to be added to the force from the shear stress, giving a correction to the critical Shield's parameter:

$$\theta = \theta_c - \alpha \frac{\partial h}{\partial x} \quad (7)$$

where  $\alpha$  is from 0.05 to 0.1 cf Fredsøe and Deigaard (1992).

When the transport is along the slope, the down slope component of the gravity deflects the direction of the transport by the angle  $\psi$ , which can be found as: (Engelund and Fredsøe 1982)

$$\tan \psi = \frac{1}{1.6\sqrt{\theta}} \frac{\partial h}{\partial y} \quad (8)$$

For an arbitrary angle between the bed shear stress vector and the strike of the slope the effect of a longitudinal and transverse slope is combined.

The bed load transport is determined by the instantaneous bed shear stress, and is then averaged over the wave period. The instantaneous bed shear stress is determined from the flow resistance model, using the wave friction factor  $f_w$  on the combination of the near-bed wave-orbital velocity and the mean flow velocity at the top of the wave boundary layer.

#### The suspended load transport

The suspended sediment moves away from the bed in the water column. When the hydrodynamic conditions change, it takes some time for the grains to be entrained in the water column or be deposited. Therefore, it takes some time/length for the suspended load transport to be adjusted to a variation in the hydrodynamic conditions.

The transport of the suspended sediment is calculated by the models of Fredsøe et al (1985) and Deigaard et al. (1986) which includes the turbulent interaction between the wave boundary layer and the current and takes the turbulence generated by wave breaking into account. For the suspended sediment transport calculations the modelling system Litpack of the Danish Hydraulic Institute has been applied.

The gradual adaptation of the transport to a gradient in the hydrodynamic conditions is represented by an adaptation length  $L_s$ , by which the transport lags behind the development in the forcing terms.  $L_s$  is estimated by the time it takes for a grain to settle from the concentration profile of suspended sediment:

$$L_s = \alpha \frac{z_c}{\omega_s} V_0 \quad (9)$$

where  $z_c$  is the height from the bed of the centroid of the sediment concentration profile,  $\omega_s$  is the settling velocity of the sediment and  $V_0$  is the mean flow velocity and  $\alpha$  is a coefficient, which is expected to be of the order 1.

### 3 ZERO ORDER SOLUTION AND FIRST ORDER EQUATIONS

The stability analysis is performed by using a perturbation method. First the equilibrium conditions for the longshore current and the set up are calculated. The equilibrium is perturbed, and the perturbed equations are found. Here the difference between the steady solution and the solution with a small perturbation is called the perturbed solution or the first order solution and the steady solution is called the zero order solution. If all types of perturbations of the bottom will die out in time, the equilibrium is stable. If the perturbation grows, the bed is unstable.

To calculate the zero order solution - the profile without any bed undulations - is actually a project by itself. It usually requires a detailed on offshore description including undertow etc. This cross shore sediment transport is considered to be unimportant for the further development of sand bed undulations, and for reasons of simplicity it has been assumed that a coast with a constant slope is an equilibrium profile for the bottom.

#### 3.1 The steady solution

The equations in section 2.1 are solved in the steady state. This means that  $U$ ,  $V$ ,  $\eta$ ,  $h$  only depends on  $x$ , because the initial conditions are described by parallel bottom contours and a constant slope of the bottom. By this  $U$  and all the derivatives with respect to  $y$  is equal to zero.

When the description of the waves given by Battjes (1972) is used, a smooth set up is found from equation (1). The set up is a function of the angle of the incoming waves, the percentage  $Q_b$  of the waves that break or have broken and the root-mean-square  $H_{rms}$  of the remaining waves.

The flow resistance is described by the simple model for turbulent interaction between the wave and current boundary layer, which gives an increased flow resistance for the flow expressed as an increase in the bed roughness. The flow resistance for the current is almost quadratic.

#### 3.2 First order equations

When the steady solution is found, the bed is given a little perturbation. This perturbation affects the hydrodynamics. The response time concept is applied. The idea behind the response time concept is that the bottom perturbation will cause immediate changes of the velocities in the  $x$ - and  $y$ -directions, but quick changes in the flow motion will not result in a response from the bottom. Thus the hydrodynamics are considered to be quasi-steady, and it is only the time variation of the bed level that is included in the description.



The total velocity field, water elevation, and water depth can be expressed by:

$$\left. \begin{aligned} U &= u'(x,y) \\ V &= V_0(x) + v'(x,y) \\ \eta &= \eta_0(x) + \eta'(x,y) \\ h &= h_0(x) + h'(x,y,t) \end{aligned} \right\} \quad (10)$$

The first order perturbed equations can be found by substituting (10) into (1)-(4). All terms of higher order than one will then be omitted. The zero order terms will automatically fulfill these equations and can be cancelled out. With this we obtain equations that only contain first order terms.

The gravitational acceleration  $g$  and the distance from the shore to the breaker line  $L_B$  are used to make the equations non-dimensional. The dimensionless variables are written,

$$x \rightarrow \frac{x}{L_B}, \quad k \rightarrow k \cdot L_B, \quad c \rightarrow \frac{c}{\sqrt{gL_B}}, \quad q \rightarrow \frac{q}{\sqrt{gL_B} L_B} \quad (11)$$

Each of the four differential equations can be put on a form as:

$$\begin{aligned} & \frac{\partial w_i}{\partial t} + A_{i1} \frac{\partial u}{\partial x} + A_{i2} \frac{\partial u}{\partial y} + a_i \mu + B_{i1} \frac{\partial v}{\partial x} + B_{i2} \frac{\partial v}{\partial y} + b_i \gamma \\ & + C_{i1} \frac{\partial \eta}{\partial x} + C_{i2} \frac{\partial \eta}{\partial y} + c_i \eta + D_{i1} \frac{\partial h}{\partial x} + D_{i2} \frac{\partial h}{\partial y} + d_i h + D_{i1}^* \frac{\partial^2 h}{\partial x^2} + D_{i2}^* \frac{\partial^2 h}{\partial y^2} + D_{i12}^* \frac{\partial^2 h}{\partial x \partial y} = 0 \end{aligned} \quad (12)$$

where  $i$  is the number of equation.  $w_i$  is the variable that is derived with time in the equation,  $w_4 = h$ , for the other variables this term is cancelled out due to the response time concept. The coefficients in (12) depends on the zero order solution and the description of the sediment transport.

#### 4 SOLVING THE EQ. BY FINITE DIFFERENCES

The equations are solved numerically by finite differences. When the assumption of periodic conditions in the  $y$ -directions is applied, the dependent variables can then be written as:

$$u = U(x) \exp(iky) \quad (13)$$

$$v = V(x) \exp(iky) \quad (14)$$

$$\eta = Z(x) \exp(iky) \quad (15)$$

$$h = H(x) \exp(pt +iky) \quad (16)$$

Figure 2 shows a sketch of how the finite difference scheme is applied. The node points are distributed over three times the width of the breaking zone. The

start of the breaking zone is defined as the line where regular waves with a wave height equal to  $H_0$  would start to break.

In figure 2  $x_b$  is the distance from the coast line at still water level to the start of the "breaking line".  $x_i$  is the distance between the still water line and the actual water line. The total width of the breaking zone  $L_b$  is thus the sum of  $x_i$  and  $x_b$ .

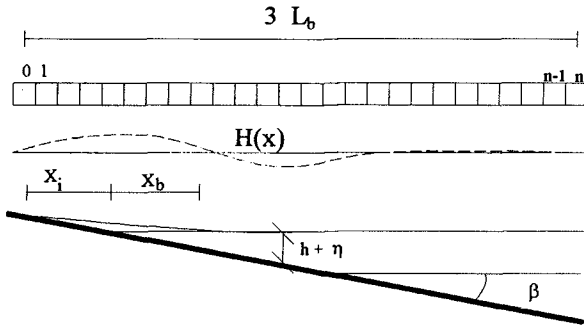


Figure 2 Sketch of the finite difference approximation. The points are distributed over three times the width of the "breaking zone"  $L_b$

Solution method

The expressions in (13) to (16) are substituted into (12) by which four ordinary differential equations for  $U, V, Z$  and  $H$  are obtained. These are solved by introducing second or fourth order finite difference approximations for the derivatives of  $U, V, Z$  and  $H$ . For node points at the boundaries forward/backward finite differences are used, and for the node points at 2 and  $n-2$  second order finite differences are used for terms that are not given on the boundary. As boundary conditions  $U, V, Z$  and  $H$  are set equal to 0 at the right boundary (deep water), and  $U$  is set equal 0 at the coast line,  $x = -x_i$ , see figure 2.

With this, a matrix-equation is found:

$$\underline{Ax} = \underline{px} \tag{17}$$

The vector  $x$  has the dimension  $4(n-1)$  and it has the form:

$$x = (U_1, U_2, \dots, U_{n-2}, U_{n-1}, V_1, V_2, \dots, V_{n-2}, V_{n-1}, Z_1, Z_2, \dots, Z_{n-2}, Z_{n-1}, H_1, H_2, \dots, H_{n-2}, H_{n-1})$$

$px$  is a vector that originates from the terms derived with respect to time in (12).

$$px = (0, 0, \dots, 0, 0, 0, \dots, 0, 0, 0, \dots, 0, 0, pH_1, pH_2, \dots, pH_{n-2}, pH_{n-1})$$

By use of gauss-elimination equation (17) is transformed to an eigenvalue problem for  $H$ .

Matrix  $\underline{A}$  contains of 16 sub-matrices. These are named  $A_i, B_i, C_i, D_i$ :

$$\underline{A} = \begin{pmatrix} A_1 & B_1 & C_1 & D_1 \\ A_2 & B_2 & C_2 & D_2 \\ A_3 & B_3 & C_3 & D_3 \\ A_4 & B_4 & C_4 & D_4 \end{pmatrix} \quad (18)$$

The matrices  $A, B, C$  and  $D$  contains elements, respectively, for  $U, V, Z$  and  $H$ . The index refers to the equations. 1 for the x-momentum, 2 for y-momentum, 3 for conservation of mass and 4 for conservation of sediment. When the matrix  $\underline{A}$  has been calculated, it is reduced to a triangular matrix except the last submatrix  $D_4$ . The form of the matrix-equation is now:

$$\begin{pmatrix} A_1^* & B_1^* & C_1^* & D_1^* \\ 0 & B_2^* & C_2^* & D_2^* \\ 0 & 0 & C_3^* & D_3^* \\ 0 & 0 & 0 & D_4^* \end{pmatrix} \begin{pmatrix} U \\ V \\ Z \\ H \end{pmatrix} = -p \begin{pmatrix} 0 \\ 0 \\ 0 \\ H \end{pmatrix} \quad (19)$$

The matrices'  $A_1^*, B_2^*$  and  $C_3^*$  are all upper triangular matrices. It is only possible to obtain a solution to equation (19) when  $H$  is a solution to the eigenvalue problem defined by following equation:

$$D_4^* \cdot H = -pH \quad (20)$$

(20) is complex in both matrix, vector, and eigenvalue. It is solved by use of standard procedures for complex eigenvalue problems. The solution to the eigenvalue problem gives  $n-1$  eigenvalues  $\lambda_1, \dots, \lambda_{n-1}$ . Each of the eigenvalues defines a solution to the eigenvalue problem, which also give  $n-1$  eigenvectors  $H_1 \dots H_{n-1}$ .

It is now possible to find the solution that gives the fastest growth rate of the bed perturbation that is determined by the largest real part of  $p_i = -\lambda_i$ , cf. eq. (16). When the eigenvector  $H_i$  for the fastest growing mode has been found, the solution for  $U, V$  and  $Z$  are found by using back substitution.

The calculations are made for several different values of  $k$  in order to determine the wave number  $k$  that gives the largest real part of  $p$  and thus the fastest growing perturbation. This bar pattern is expected largely to be the bed form that actually emerges.

Another result that comes from the eigenvalue problem is the migration velocity, which is:

$$c_h = \frac{-Im(p)}{k} \quad (21)$$

## 5 RESULTS

As can be seen in fig. 3 the simple sediment transport model does not give a maximum for the growth factor  $\text{Re}(p)$ . Fig. 4 shows the most unstable bed configuration for different values of  $k$ . It can be seen that as  $k$  increases the bars are situated closer to the coastline.

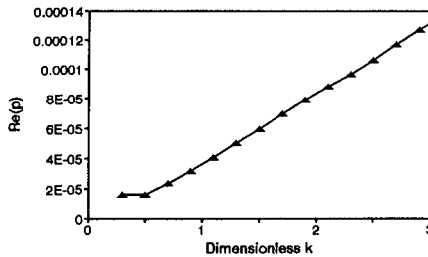


Figure 3 The real part of the growth factor  $p$  as a function of the wave number  $k$ . The simple sediment transport model was used.  $H_b=3$  m,  $T=10$  s,  $\beta = 2.5^\circ$  and  $\theta_b = 10.0^\circ$ .

For large longshore wave numbers the bed forms are thus embedded in the nearshore region where the longshore current is growing linearly with the distance from the shoreline, see figure 4. Under these conditions there is no lower limit for the wave length of the most unstable perturbation and the stability analysis cannot predict the emerging of a bed topography.

An explanation for this behaviour is as follows. When the bars are situated closer to the coast line, the area of a bar is decreased as  $k^{-2}$ , whereby the amount of sediment needed for the instability mechanism is reduced with  $k^{-2}$ . Close to the coast line the zero order velocity profile is almost linear and the sediment transport is proportional to the zero order velocity. The sediment transport hereby reduces by  $\sim k^{-1}$  as the bars are situated closer to the coast line. This gives:

$$\text{Re}(p) \propto k^{-1}/k^{-2} = k$$

This agrees with the result shown in figure 3.

When the bed load transport model is used a maximum for  $\text{Re}(p)$  is found, see figure 5. The dimensionless wave number  $k$  is found to be around 1.0 to 1.2 for waves for an incoming angle at the breakerline between  $8^\circ$  and  $12^\circ$ . For lower angles the wave number  $k$  becomes very small for the maximum of  $\text{Re}(p)$ . For  $\theta_b = 0^\circ$  it is impossible to get any results due to the use of a quadratic resistance law which also has influence on the results for small angles of  $\theta_b$ .

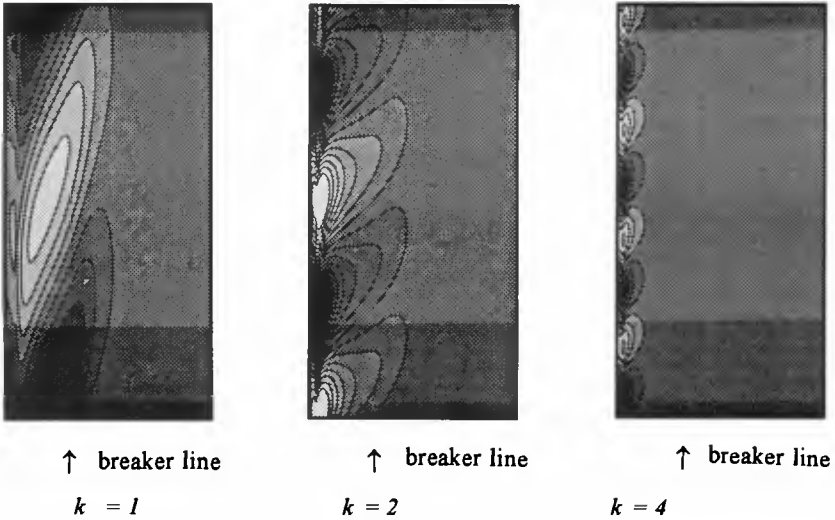


Figure 4 An example of the perturbation  $h$ , for three different wave numbers  $k$ ,  $H_b = 3$  m,  $T = 10$  m,  $\beta = 2.5^\circ$  and  $\theta_b = 10.0^\circ$ .

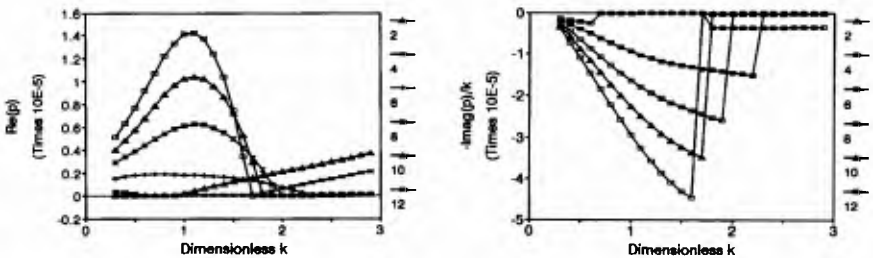


Figure 5 The real part of the growth factor  $p$  and the translation celerity as a function of the wave number  $k$  for six different angles. The bed load model was used.  $H_b = 3$  m,  $T = 10$  s,  $\beta = 2.5^\circ$

Illustrations of the 1. order bed topography, 1. order velocity field and the "total" meandering current are shown in figure 6. The orientations of the bars disagree with the one seen on the photo in figure 7. On the photo the bars propagate from the coastline obliquely in the same direction as the current, the opposite is the case in the stability analysis. In another case, illustrated by a photo of Short (1994), the orientation of the bed forms agree with the present stability analysis. Johnson et al. (1994)

modelled the current and morphological changes around an offshore breakwater for obliquely incoming waves. At the downstream side of the breakwater some bars developed that had the same orientation as those in the present study. It has not been possible to find a final explanation for the determination of the orientation.

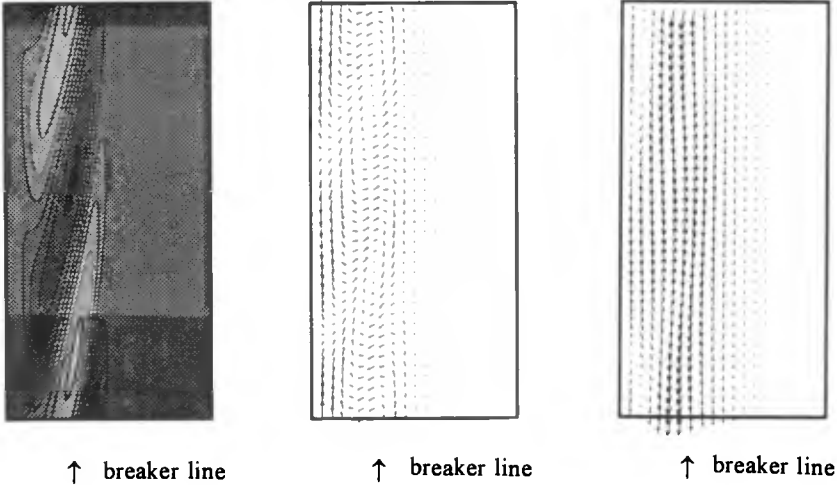


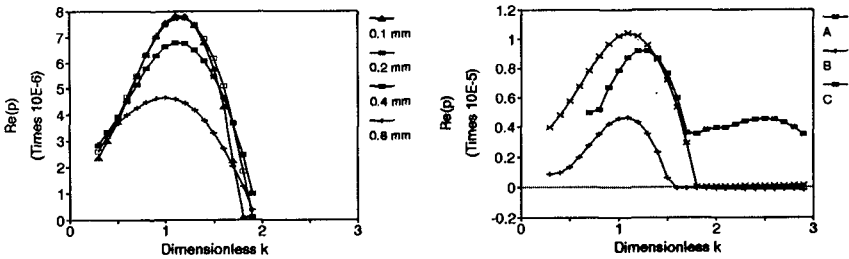
Figure 6 An example of the perturbation  $h$ , the 1. order current and the "total" (0. and 1. order) meandering current.  $\theta_b = 8.0^\circ$ ,  $k = 1.2$ ,  $H_b = 3$  m,  $T = 10$  m and  $\beta = 2.5^\circ$ . For the meandering current the maximum of  $h$  was set to 2 m. The scoured area is shown by the light colour



Figure 7 A photo of large periodic bottom topographies at the island Sylt, Wadden Sea Denmark/Germany, H. Dette (1994).

Figure 8a shows the dependence on the grain size. When the grain size increases the maximum of  $Re(p)$  decreases and the wave length of the most unstable perturbation increases.

The perturbation of the bed modifies the wave field. This influences on the radiation stresses and hereby on the hydrodynamics and the sediment transport. A comparison between the effects coming from the bed slope, the modification of the wave field due to the perturbation and the current is shown in figure 8b. When the modification of the wave field due to the perturbation is excluded the lowest curve is obtained where the maximum is situated at the same wave number  $k$  as for the full bed load model. When the effect of the bed slope and the effect of the modified wave field are excluded, the maximum for  $Re(p)$  is situated at a larger wave number  $k$ . Here a maximum is obtained in contrast to the simple model. This shows that a more refined model for the sediment transport gives a maximum even if the bed slope is not taken into account.



8a

8b

Figure 8 The figure shows the dependency of the grain size - 8a -, and the stability curve when the slope and/or the modification of the wave field are excluded - 8b. A: no slope and no modification of the wave field, B: no modification of the wave field, C: the full bed load model

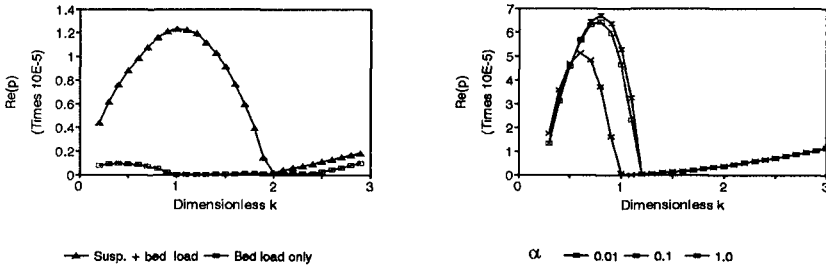


Figure 9 Here the suspended load is included, the figure on the left hand side is found for  $\theta_b = 5.0^\circ$  and for the figure at the right hand side  $\theta_b = 10^\circ$ .  $H_b = 3$  m,  $T = 10$  m and  $\beta = 2.5^\circ$ .

Figure 9 shows the results when the suspended load is incorporated. For  $\theta_b = 5.0^\circ$  the maximum for  $\text{Re}(k)$  moves to a bigger dimensionless  $k$ , while we get the opposite result for  $\theta_b = 10^\circ$ . When the suspended load becomes dominant, it moves the maximum of  $\text{Re}(p)$  to a lower dimensionless  $k$ , and the growth rate increases.

For  $\theta_b = 10^\circ$  the effect of a phase lag is shown too. This has a stabilizing effect on the growth rate especially with big wave numbers.

## 6 CONCLUSIONS

A linear stability analysis has been used to investigate the formation of large scale periodic bottom topographies. In the analysis the effects from the slope due to the perturbation of the bed are incorporated.

When a simple sediment transport formulation is used, taking the sediment transport to be proportional to the velocity, a maximum on the stability curve is not found, and the instability of the bed forms increases with the alongshore wave number.

The bed slope affects what kind of topography that will emerge and gives a spacing between the rips of about six times the width of the breaking zone. By including the suspended load this distance decreases for small angles of the incoming waves and increases for large angles. The phase lag in the suspended load gives a smaller growth rate and a longer length of the bar.

The modification of the wave field, due to the perturbation, increases the growth rate and gives a smaller bar length.

The stabilizing effects are the slope of the bed, large grain size and phase lag in the suspended load transport. The destabilizing effects are the longshore current, and the modification of the wave field due to the perturbation of the bed. Refraction and diffraction have not been investigated. These mechanisms could have an effect on the stability of the bars.

The resulting topography has been compared to field investigations and shows that the orientation of the bars sometimes but not always is the same as in this stability analysis.

## ACKNOWLEDGEMENT

This work was founded jointly by the Danish Technical Research Council under the programme "Marin Teknik" and by the Commission of the European Communities, Directorate General for Science, Research and Development under MAST contract no. MAS2-CT92-0024 under the programme CSTAB.



## REFERENCES

- Deigaard R., Fredsøe J., and Brøker Hedegaard I. (1986): "Suspended sediment in the surf zone" *Journal of Waterway, Port, Coastal and Ocean Engineering*, ASCE, Vol. 112, No. 1, pp 115 - 128
- Dette H. Private communications, (1994)
- Engelund F. and Fredsøe J. (1982): "Hydraulic theory for alluvial rivers", *Advances in Hydrosience*, Vol 13 pp 183-215
- Fredsøe J., Andersen O. H. and S. Silberg (1985): "Distribution of suspended sediment in large waves", *J. of Waterway, Port, Coastal and Ocean Engineering* Vol. 111, No 6, pp 1041-1059
- Fredsøe J. and R. Deigaard (1992): "Mechanics of Sediment Transport in Coastal Regions", World Scientific, Singapore, 369 pages
- Hino M. (1974): "Theory of formation of rip-current and cuspidal coast", *Proc. 14th Int. Conf. on Coastal Eng., Copenhagen*, Vol 1, page 901-919
- Hino M. (1976): "Rip-current and coastal topography", *Proc. 15th Int. Conf. on Coastal Eng., Honolulu*, Vol 1, pp 1326-1341
- Johnson H. K., Brøker I and Zysermann J. A. (1994): "Identification of relevant processes in coastal morphological modelling", *24th Int. Conf. on Coastal Eng., Kobe, Japan, Book of Abstracts*, pp 448-449
- Lippmann T. C. and Holman R. A. (1990): "The spatial and temporal variability of sand bar morphology", *J. of Geophysical Research* Vol. 95, No C7, pp 11575-11590, July 15
- Meyer-Peter, E and Müller, R. (1948): "Formulas for bed-load transport", *Rep. 2nd Meet. Int. Assoc. Hydraul. Struct. Res., Stockholm 1948*, pp 39-64
- Short, Andrew D. (1994): *Coastal Photograph*, *Jour. of Coastal Research*, Vol 10 nr. 1, page 250

## CHAPTER 135

### The Response of Gravel Beaches in the Presence of Control Structures

T T Coates<sup>1</sup>, N Dodd<sup>1</sup>

#### Abstract

Much of the research on beach control structure concentrates on sand beaches. Relatively little work has been done on gravel beaches though they are important features along temperate and sub-arctic coastlines, particularly in the UK. Until recently attempts to manage these beaches and to control erosion have relied on traditional approaches such as timber groynes, designed by past experience and engineering judgement. To improve this situation HR Wallingford have undertaken a programme of flume and wave basin physical model studies followed by the development of numerical models and design guidelines.

The most recent phase of this programme has been an investigation of beach response to detached breakwaters. This work was undertaken at a scale of 1:50 in a mobile bed, random wave basin. The breakwaters varied in length, crest elevation and distance offshore. The sea conditions varied in wave period and water level. Measurements were taken of wave heights around the structure, beach planshape development and longshore transport rates. For each breakwater configuration and sea condition an efficiency value has been derived which relates the longshore transport rate in the presence of the structure to the potential open beach rate. These efficiency values can be used to tune breakwater dimensions to the actual long term drift rates of a specific beach, thereby providing a stable beach.

This paper briefly reviews some of the previously published work, then discusses the major findings of the recent model tests and suggests methods for applying the results. The results are, at present, only applicable to a limited range of sea and beach conditions, but it is anticipated that the approach will be developed for general application. The findings are also related to a recently completed detached breakwaters and beach recharge scheme on the UK south coast.

---

<sup>1</sup>HR Wallingford, Howbery Park, Wallingford, Oxon, OX10 8 BA, UK

## Introduction

Detached breakwaters, unlike groynes, have not been used for beach control in the UK until quite recently. Existing design guidelines are based on experience in other areas of the world, with the most recent publication being the CERC Technical Report "Engineering Design Guidance for Detached Breakwater as Shoreline Stabilization Structures ". The majority of research and experience available relates to sand beaches in microtidal environments (range  $< 2\text{m}$ ) with shore normal wave attack, and are therefore not directly applicable to many UK situations. In addition, much of the research concentrates on determining the shape and extent of the beach development in the lee of the structures; this approach only considers the symptoms and not the causes, as it does not directly consider the sediment transport regime at the design site.

A number of morphodynamic models are available which go some way towards predicting sand beach response. Unfortunately these models are not applicable to the shingle beaches found along much of the UK coastline. To improve this situation HR Wallingford undertook an ongoing research programme, utilizing physical models, with the aim of developing design tools and guidelines.

Powell (1990) investigated the response of shingle beaches to random waves in a flume at a scale of 1:17. The physical model results were used to develop a parametric model which predicts beach response to wave and water level conditions. This work was extended to a large scale (1:17) wave basin study in which the hydrographic conditions included oblique long crested random waves (Coates and Lowe, 1993). Modifications to the original parametric model were derived which accounted for beach profile response under oblique waves. In addition, the cross-shore distribution of longshore transport along an open shingle beach was derived; this distribution was used by Brampton and Goldberg (1991) in conjunction with Powell's parametric model to improve an earlier one-line beach plan shape model (Brampton and Motyka, 1985).

Brampton and Goldberg's model was able to predict beach plan shape development in the presence of groynes, but the authors recognised that the model over-simplified a number of aspects relating to beach response. This response was investigated by further physical modelling at a scale of 1:17 and, more recently, in a different facility at a scale of 1:50 (Coates and Lowe, 1994; Coates, 1994a; Coates, 1994b). Some of the results of the larger scale model have been incorporated into a new mathematical model (Huang, 1993) which includes an improved method of predicting profile development within a groyne field as well as transport over and around groynes. The smaller scale study investigated beach response within a multiple groyne system and it is this work that is described in this paper. The approach adopted was to investigate sediment transport, rather than morphological development, in the lee of single breakwater, followed by a preliminary investigation of beach response to pairs of breakwaters.

### Model studies

The test programme was conducted at HR Wallingford in a 23m by 24m wave basin with a maximum working depth of 0.4m. The model was designed at an undistorted scale of 1:50, according to Froude's relationships. The basin was equipped with:

- a 15m long, mobile wave paddle capable of generating waves at up to 45° relative to the beach;
- nine wave monitoring probes;
- an oblique angle camera;
- a manual sediment recirculation system.

The model layout is illustrated in Figure 1. It was designed to simulate a typical UK sand lower/shingle upper beach. The lower portion of the beach was constructed from a rigid moulding at a slope of 1:50. The upper portion comprised a mobile bed formed of crushed and graded anthracite coal formed at an initial slope of 1:7½ with a crest above the limit of wave action.

The mobile bed was designed to be similar to those used in previous model studies within the programme and to simulate typical UK beaches. The scaling relationships used in selecting the model beach material are based on a well established method which attempts to satisfy three criteria: the permeability, which governs slope, the relative magnitude of onshore or offshore movement, which determines whether erosion or accretion will occur, the threshold velocity of particle motion.

The methods published by Yalin (1963) which relate slope to a non-linear function of the voids Reynolds Number are used to satisfy the permeability requirement. The fall velocity parameter  $H_b/wT$  proposed by Dean (1973) is used to satisfy the onshore/offshore criteria while the relationship of Komar and Miller is used for the threshold of motion. At the model scale of 1:50, an assumed prototype  $D_{50}$  of 15mm and a density of 2.65T/m<sup>3</sup> then the required model sediment should have a  $D_{50}$  of 2.5mm and a density of 1.41T/m<sup>3</sup>. Anthracite coal has a density of 1.39T/m<sup>3</sup> and can be obtained in a range of grades. It is therefore an appropriate material for use as the mobile bed.

The sea condition variables were restricted to wave steepness (S) and water level (SWL). All tests were run with a 2m  $H_s$  wave height and a 30° offshore wave direction. Wave steepness values were either 0.02 (swell) or 0.06 (storm) and water levels varied from 3.0m to 4.5m relative to the initial beach toe (each test was run at a fixed SWL). Wave induced currents were investigated in a single test using  $S = 0.02$  and a range of water levels from 1m to 4m. Tidal currents were not investigated.

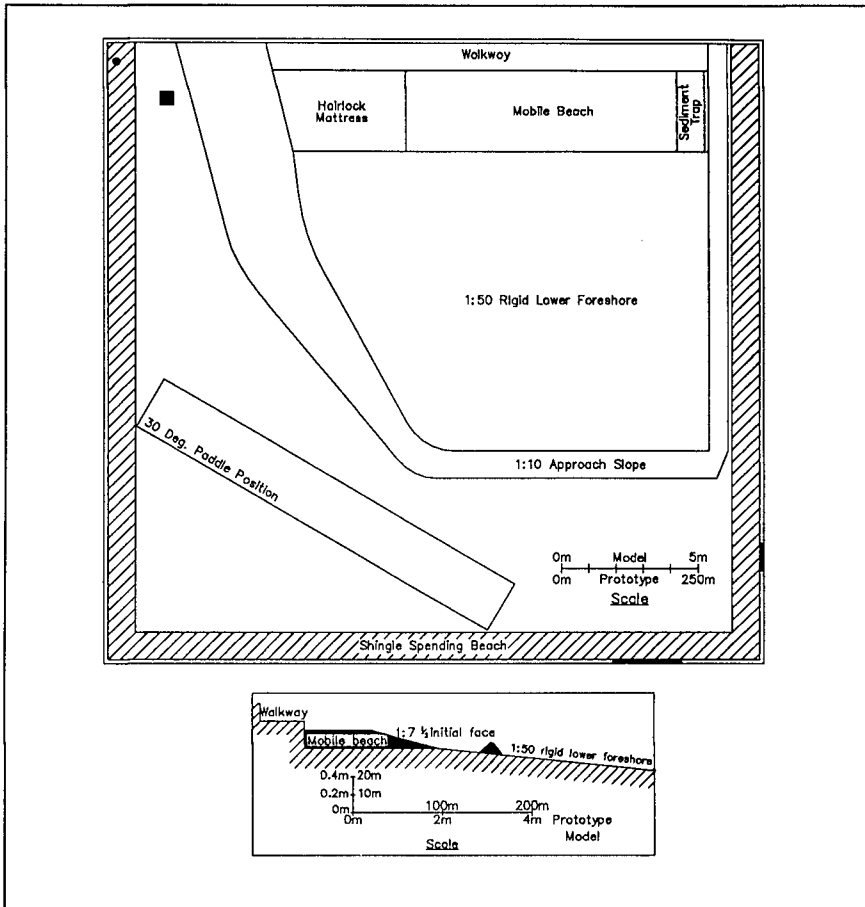


Figure 1 The wave basin facility

The test programme concentrated on single breakwaters. Structural variables included crest length ( $L_c$ ), freeboard ( $R_c$ ), offshore distance ( $X_s$ ). A short series of tests was run at the end of the programme to investigate pairs of structures. These tests investigated the influence of gap length ( $G_s$ ). A total of 34 tests were run, with an average duration of 2-3 days.

The basic structural design comprised a crest width of 4m, side slopes of 1:2 along the body of the structure and slopes of 1:3 at the ends. The rock grading was selected for minimal damage. The initial median rock weight was 6.55 tonne, with a linear grading from  $W_0 = 4.0$  tonne to  $W_{100} = 9.1$  tonne. During construction larger rocks were preferentially placed in the areas of potential damage, based on the findings of earlier research (Jones & Allsop, 1993). Figure 2 indicates the

breakwater layout and the variables. Table 1 summarizes the structural variables.

**Table 1** Structural variables

Length (m)	Distance offshore (m)	Crest elevation (m)	Gap length
60	120	4.5	N/A
60	90	3.5	60 & 90
60	90	4.5	N/A
90	150	4.5	N/A
90	120	3.5 & 4.5	N/A
90	90	3.5 & 4.5	N/A
90	60	4.5	N/A
120	120	3.5 & 4.5	N/A
120	90	4.5	N/A

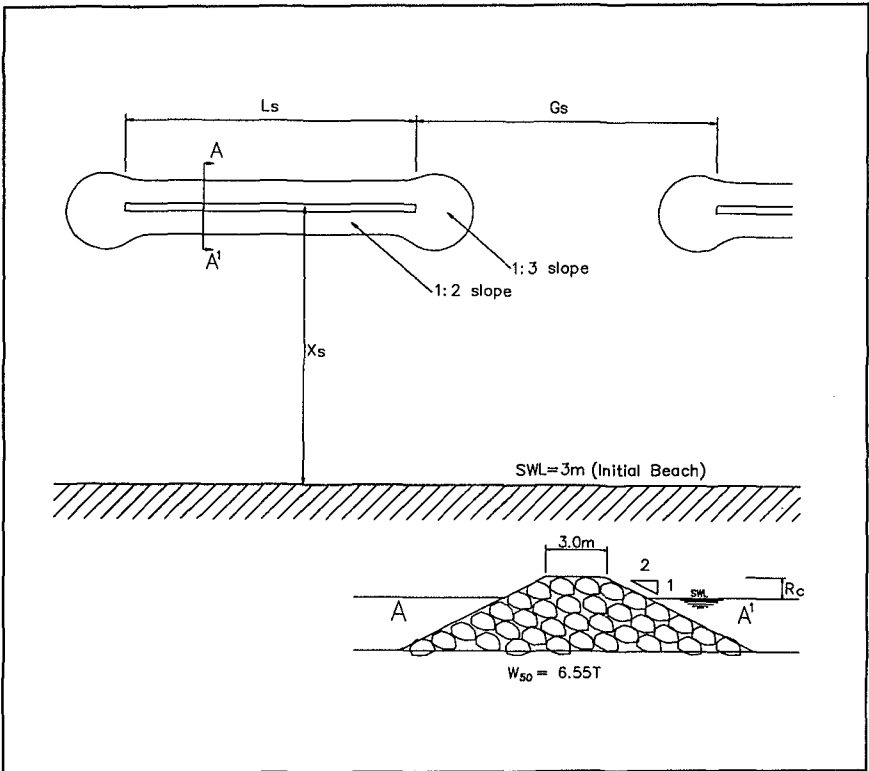


**Figure 2** Basic breakwater layout

During calibration, the model was run with an open beach, fed by an unlimited supply of sediment. The transport rates and cross-shore distribution of transport were measured for each wave and water level combination. The transport rates were used to determine standard sediment input rates for all subsequent tests; these are referred to as the *calibrated* rates.

Test procedures included:

- continuous monitoring of downdrift sediment output;
- regular measurement of the cross-shore position of the crest, SWL and toe on 12 section lines to monitor planshape developments;
- regular overhead photographs of beach development; and
- measurement of wave heights seaward and landward of the breakwater.

The terms salient, tombolo, efficiency, potential drift rate and actual drift rate are used in the discussions. Salient refers to the seaward development of the beach in the lee of the breakwater; if this development reaches the breakwater at the water line then the salient is referred to as a tombolo. Efficiency, denoted as  $\eta$ , refers to the ratio of output drift relative to the potential or calibrated open beach drift for the model beach under a given sea state as expressed by the equation

$$\eta = \left( 1 - \frac{Q_o}{Q_p} \right) \times 100$$

where  $Q_p$  is the potential drift rate for a beach under a given set of wave and water level conditions and  $Q_o$  is the output drift rate immediately downdrift of the structure. Potential and actual drift rates are important in relation to breakwater design. The potential drift rate is the volume of beach material that the incident wave condition could move along an open beach if the supply of material is unlimited - in the model this is the calibrated input rate. The actual drift rate on a given beach is often much less than the potential rate due to a lack of available material or the influence of artificial structures or channels; erosion of the foreshore often occurs as a result of the difference between these two rates.

Tests were run in two stages. During the initial stage the beach was supplied with drift material at the calibrated rate. This material was transported into the lee of the breakwater where a percentage was deposited to form a salient, while the remainder was transported to the downdrift sediment trap. When the downdrift transport rate stabilized after 12,000 to 16,000  $T_m$  then the second stage commenced. The updrift sediment input position moved to a point immediately updrift of the breakwater, and the input rate was reduced to the stabilized output rate of stage 1.

Assuming that this rate had been properly defined, then no further material accreted at the salient and the output equalled the new input. Stage 2 continued for about 12,000  $T_m$  or until the input/output equilibrium was confirmed. The relationship between the stabilized output and the original calibrated input was then

used to determine the efficiency of the particular structure.

### Discussion of results

The test results are presented in a series of figures. Figures 3-8 illustrate the influence of various seastate or structural variables on breakwater efficiency. The lines join directly comparable data points to illustrate the strongest relationships. Where several similar lines are presented on the same plot, they indicate the influence of secondary variables. Figure 9 presents a summary plot combining all of the structure variables.

### *Effect of test duration on efficiency and beach development*

The standard test procedure was followed during all tests except the first test, which was run with a constant input at the calibrated rate for over  $100,000T_m$ . The test was continued until a tombolo had built out to the breakwater and transport had resumed along the seaward face. Although this final result was not of use to the establishment of a  $\eta$  value, it did serve to illustrate the potential impact of a breakwater that is too effective relative to the actual beach drift rate. The structure efficiency reached a stable level of 86% after about  $20,000 T_m$ , but as the beach continued to develop  $\eta$  increased to almost 100%. This increase in efficiency over time is an important consideration in design, as a structure that is too effective will block longshore transport, causing downdrift erosion until the beach has built out sufficiently to allow bypassing to occur.

### *Effect of wave steepness on efficiency*

Tests were run with wave steepnesses of 0.02 and 0.06. Figure 3 illustrates that the structures were about 30% more efficient under shorter period waves.

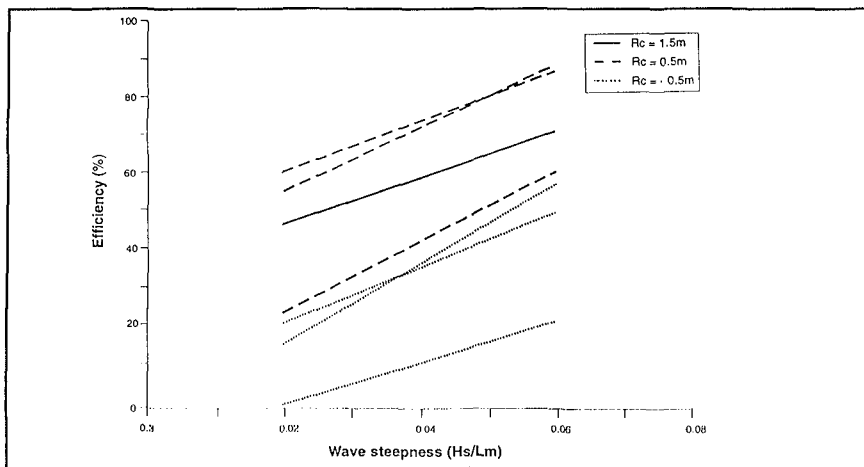


**Figure 3** Effect of wave steepness on efficiency



### *Effect of offshore distance ( $X_s$ ) on efficiency*

$X_s$  was measured from the structure centre line to the 3m contour line on the initial standard beach. Most of the tests were run with  $X_s$  values either 90m or 120m with only one test run with each of 60m and 150m.

Figure 4 illustrates that structures set at 60m, 90m and 120m had very similar impacts on efficiency. The only distance which showed a significant effect was 150m, which caused a substantial decrease in efficiency.

Insufficient data was collected for low and high values of  $X_s$  to establish any definite trends, however it is apparent that over the limited range of 90m and 120m  $X_s$  is not a dominant factor.

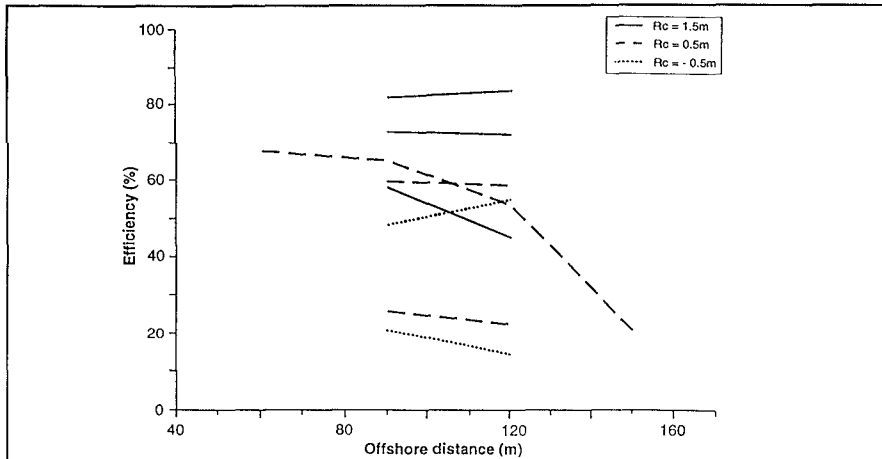


**Figure 4** Effect of cross-shore location of breakwater on efficiency

### *Effect of freeboard ( $R_c$ ) on efficiency*

$R_c$  is the difference in elevation from the structure crest to SWL. Changes in  $R_c$  influence the amount of wave energy that can pass over or through the breakwater. By varying both the structure crest elevation, from 3m to 4m, and the SWL from 3.0m to 4.5m,  $R_c$  values from -0.5m to 1.5m were tested. Figure 5 illustrates the effect of  $R_c$  on  $\eta$ . The results suggest that  $R_c$  is an important factor in beach response to breakwaters.

It is apparent from Figure 5 that  $R_c$  has a non-linear effect on efficiency.  $\eta$  increased by 30 - 40% as  $R_c$  increased from -0.5m to 0.5m. As  $R_c$  increased further to 1.5m then  $\eta$  only increased by 10 - 30% with the higher values being associated with the shorter structure lengths.

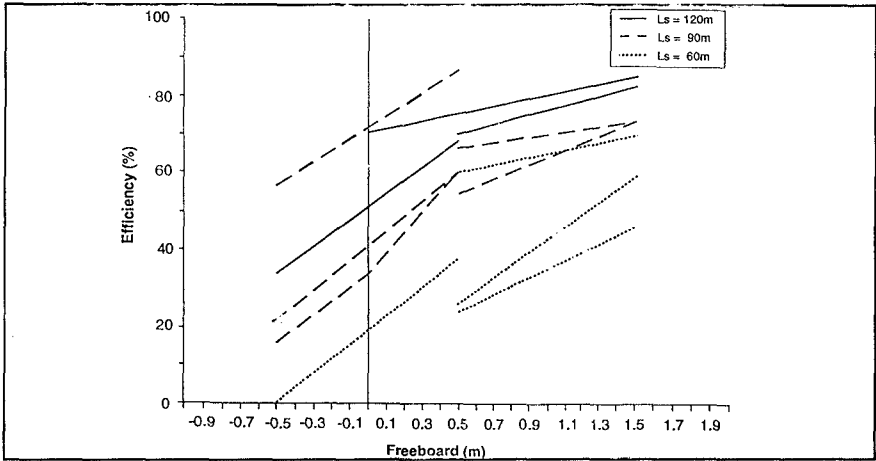


Figure 5 Effect of freeboard on breakwater efficiency

*Effect of crest length ( $L_s$ ) on efficiency*

$L_s$  values of 60m, 90m and 120m were tested and were found to be an important factor in determining beach response. Figure 6 illustrates the relationship between  $L_s$  and efficiency, with the lines joining data points of equal  $R_c$ .

Beach response to  $L_s$  was again non-linear. Changes in  $L_s$  from 60m to 90m resulted in efficiency increases of between 20 - 40% while changes from 90m to 120m resulted in increases of only 10 - 20%.

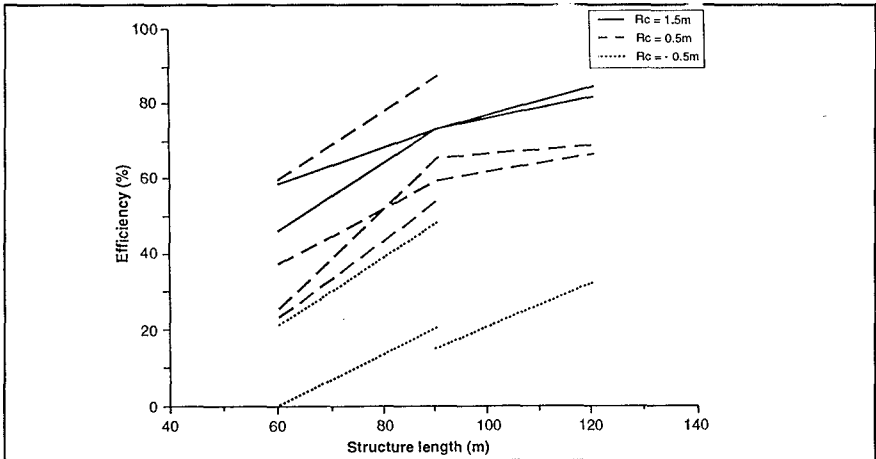
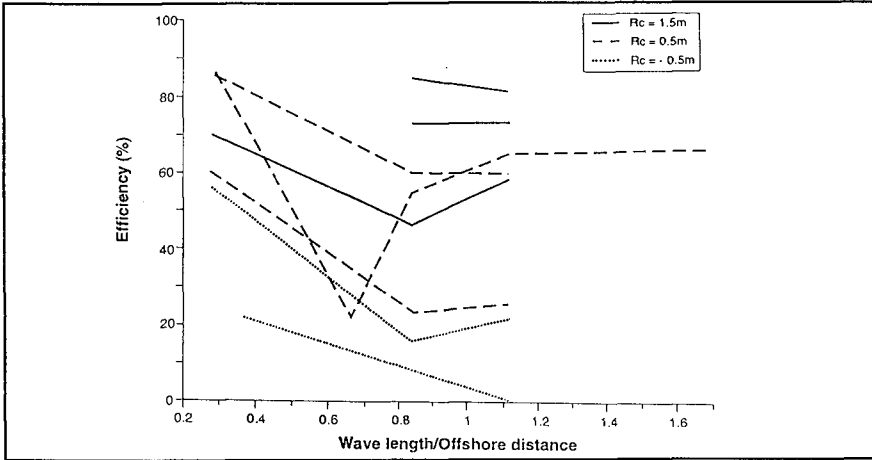


Figure 6 Effect of structure length on breakwater efficiency

*Relationship between wave length and structural dimensions*

The model data for wave steepness (or wave length),  $X_s$  and  $L_s$  were further investigated in combinations to determine any relationships. Figure 7 illustrates the influence of  $L_m/X_s$  on  $\eta$ . There are insufficient results to form any definite conclusions but the figure suggests that  $\eta$  may reach a minimum when  $0.4 < L_m/X_s < 0.9$ .



**Figure 7** Effect of wave length relative to offshore distance of structure on breakwater efficiency

Figure 8 illustrates the influence of  $L_m/L_s$  on  $\eta$ . Though the results show some scatter, there is an obvious trend of decreasing  $\eta$  with increases in  $L_m/L_s$ .

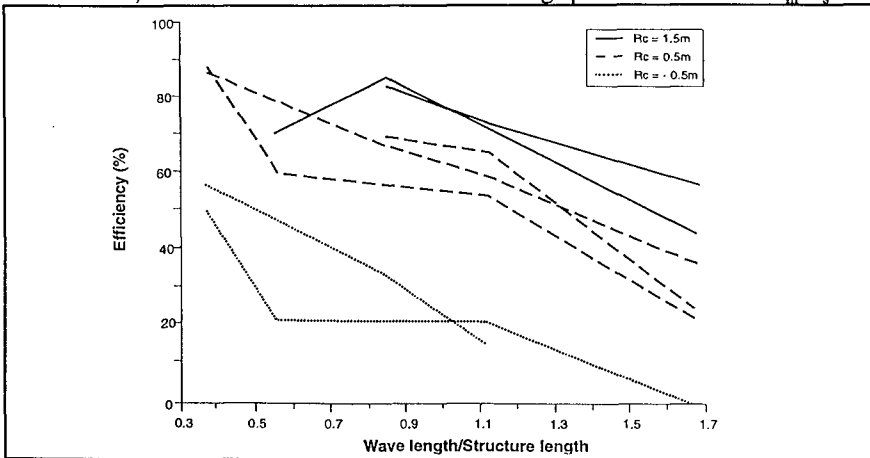


**Figure 8** Effect of wave length relative to structure length on breakwater efficiency

### Combined influence of structural variables

The individual effects of length, offshore distance and freeboard are combined into a single efficiency contour plot in Figure 9. The data set for the plot was extended by combining both the swell and storm values using the relationship  $\eta$  (swell) =  $\eta$  (storm) - 30; the plot is therefore set out for wave steepnesses of 0.02, and is only applicable to 2m  $H_s$  waves.

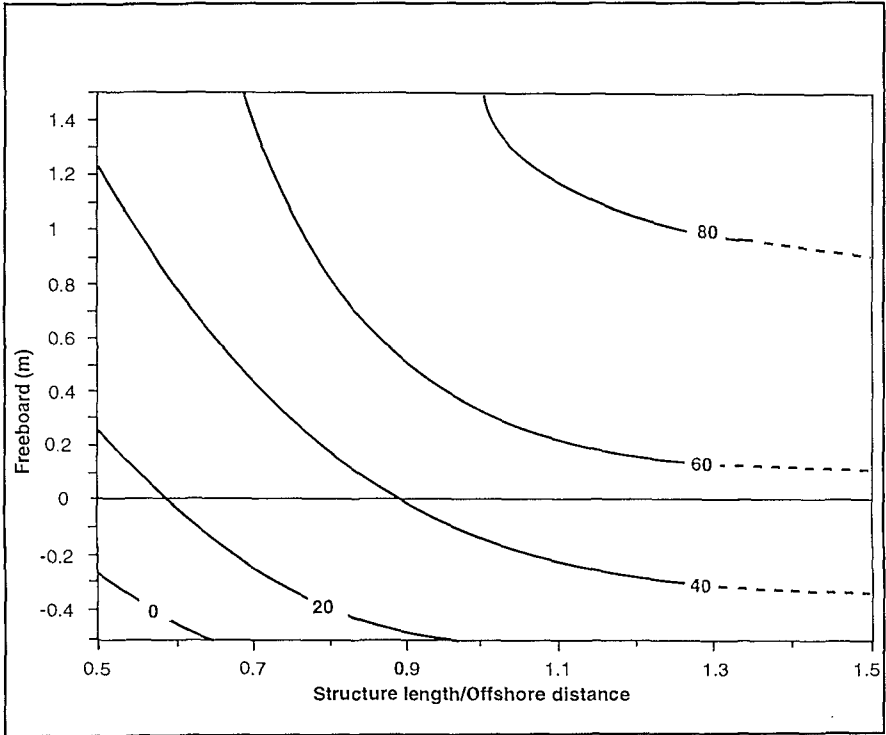


**Figure 9** Contour plot of efficiency relative to structure variables for a single detached breakwater (Data points corrected for a single wave steepness of 0.02)

The contour plot can be used to determine the optimum combination of structural dimensions for a given situation. Although the model variables were limited, the method used to obtain the contour plot could be extended to form a full set of design plots for detached breakwaters. Alternatively, the information derived from the study could be used to calibrate existing numerical models which predict wave energy distribution in the lee of structures, although at present none of the available models are able to fully simulate wave/structure interactions.

### Wave induced currents

Titanium dioxide was used as a neutrally buoyant tracer to monitor currents

along the model beach and in the lee of the breakwaters. This work was subjective only.

Tracer was injected in the lee of a 90m breakwater during swell wave conditions with a range of water levels. Wave induced currents transported dye from the updrift beach and the immediate downdrift beach to the head of the beach salient. From this point the dye was transported intermittently seaward around the down drift end of the breakwater. The intermittent currents had a period of about 10 - 15 seconds (model), equivalent to 8 - 12 incident wave periods. The seaward current reached strong peak velocities, particularly at water levels of between 1m and 3m. Currents at higher water levels were less well defined.

These results qualitatively support available field observations. Further field work should be undertaken as areas of potential rip currents or deposition will be important to breakwater design.

#### *Results of paired breakwater tests*

Only three tests of breakwater pairs were carried out as a post-script to the single structure study. Variables included only gap width ( $G_s$ ) and freeboard ( $R_c$ ). The results are insufficient for rigorous analysis, but the following observations can be made.

As might be expected, a larger gap width resulted in a slightly lower efficiency, while a change of freeboard from +0.5 to -0.5 resulted in a substantial drop. Comparison against single structures indicated that two emergent 60m long breakwaters with a 60m gap have a  $\eta$  value approximately equal to a single 60m structure, indicating that the efficiency data collected for the single breakwaters may be applicable to multiple structures if appropriate gap widths can be determined. However, when submerged the pair of structures became significantly more effective than a single submerged structure suggesting that the relationships may not be straight forward.

#### Design applications

The results of the model study are not yet sufficient to form the basis of a design method for detached breakwaters. Only a limited number of conditions were tested, the programme concentrated on single structures and no field verification has been undertaken. However, a number of useful guidelines can be derived which will be of use to coastal engineers and managers.

Most shingle beaches in the UK are of a type known as shingle upper/sand lower, and are subjected to high wave energy within meso (range 2m - 4m) or macro (range < 4m) tidal environments with the potential for substantial storm surges. It is these beaches which are considered here.

Detached breakwaters affect the beach by altering the inshore wave climate. Waves approaching the beach are either reflected from the structure, overtop the structure (usually breaking in the process) or diffract into the lee. The wave energy in the lee is less than on the open beach and therefore sediment which is transported along the open beach may be deposited. The percentage of deposition relative to the potential drift, for a sea condition close to those tested, can be derived from Figure 9. Efficiency at different tidal levels can be derived from the plot by varying  $R_c$  and  $X_s$ . If the actual open beach drift rate and the potential open beach drift rate can be derived from numerical modelling, desk studies and field measurements then the optimum layout can be derived.

The optimization may be based on factors apart from sediment transport efficiency. These might include cost of materials, cost of stabilizing the substrate, visual impact, navigational safety, desirability of providing safe mooring for small craft and possible use as an amenity platform for activities such as fishing. The design method assumes a strongly dominant drift direction. Substantial drift reversals driven by waves of lower energy than the design waves will cause material to be deposited in the lee of the breakwater from where it will not be eroded by subsequent conditions. This process will lead to tombolo formation and downdrift erosion. If this situation is likely then groynes may be more appropriate structures.

No single design will be satisfactory under the diversity of conditions found on most beaches, but satisfactory compromises should be possible.

### Conclusions

Shingle beach response in the presence of detached breakwaters was investigated using a 1:50 mobile bed physical model as part of an ongoing coastal research programme at HR Wallingford. The study concentrated on single detached rubble mound structures, but concluded with a brief series of tests on pairs of structures. Structural variables included length, crest elevation, distance offshore and gap width. The sea conditions only varied in wave steepness and water level.

The study conclusions are as follows.

- 1 The modelling work that has been completed provides a substantial data base for use in further physical modelling of single or multiple structures and for the development and calibration of numerical models based on wave transformation in the lee of breakwaters.
- 2 Breakwaters can be used to stabilize an existing or recharged beach where the natural drift has a strong dominant direction and both the potential and actual drift rates can be determined. Successful design depends on matching the breakwater geometry to the actual natural drift under the dominant wave and water level condition. Breakwaters on beaches with high gross transport, but

low nett transport are likely to cause unwanted areas of scour and accretion, as the structures can only be designed correctly for one drift direction.

- 3 An efficiency contour plot was derived from the study which relates the structure length/offshore distance ratio to freeboard. Application of this plot is limited as the range of sea conditions tested was restricted and no field verification data is available. However it provides a useful first step in developing design guide lines and can be used to optimize structural geometry with respect to construction costs and other design factors.
- 4 The relationships of efficiency with structure length ( $L_s$ ) and freeboard ( $R_c$ ) were clearly established.  $R_c$  is dominant when the structure crest is submerged due to the high level of wave energy transmission through and over the structure.  $L_s$  becomes the dominant factor as  $R_c$  increases above zero.
- 5 The influence of the offshore distance of the structures ( $X_s$ ) was less conclusive. Most tests were run with an  $X_s$  of 90m or 120m. These distances were too similar to show any distinct trend. Comparison of efficiency with the ratio of wave length to offshore distance ( $L_m/X_s$ ) suggests that there may be an efficiency minimum when the ratio is between 0.4 and 0.9. However the available data set is insufficient to confirm this possibility.
- 6 Tests on wave induced currents showed the potential for strong rip currents around the downdrift end of the breakwaters. The currents observed were intermittent at periods associated with 8 - 12 incident waves. They were also dependant on the depth of water in the lee of the structure, with peak currents being observed at depths of between 1m and 3m.
- 7 Breakwater efficiency also appears to be dependant on the size of the beach salient. As the salient extends out towards the structure the efficiency increases due to more of the wave energy being dissipated on the beach and less being available for transport. This applies particularly to structures with a large freeboard where the transmitted energy level is low. It is therefore important not to over design structures initially, but to allow for minor modifications after construction based on monitoring results.
- 8 The study did not investigate the potential for deposition of sand and fines in the lee of the structures, nor the influence of strong nearshore tidal currents. These aspects need further work.

### Acknowledgements

Much of the research on which this paper is based was funded by the UK Ministry of Agriculture, Fisheries and Food under Research Commissions on Flood

Defence. The authors are grateful for advice from J D Simm. The compilation of this paper was supported by HR Wallingford.

### References

Brampton A H and Motyka J M (1985). Modelling the plan shape of shingle beaches. Lecture Notes on Coastal and Estuarine Studies, Vol 12, Springer Verlag, Berlin.

Brampton A H and Goldberg D G (1991). Mathematical model of groynes on shingle beaches. HR Wallingford Report SR 276.

Chadwick, A J, Fleming, C, Simm, J and Bullock, G N (1994). Performance evaluation of offshore breakwaters - A field and computational study. Coastal Dynamics '94 Conf, Barcelona, pp 950-961.

Coates T T (1994a). Physical modelling of the response of shingle beaches in the presence of control structures. Coastal Dynamics '94, Barcelona, pp924 - 937.

Coates T T (1994b). The response of shingle beaches in the presence of control structures. HR Wallingford Report SR 387.

Coates T T and Lowe J P (1993). Three-dimensional response of open and groyned shingle beaches. HR Wallingford Report SR 288.

Dean, R G (1973). Heuristic models of sand transport in the surf zone. Conference on Engineering Dynamics in the Coastal Zone.

Huang Z (1993). Mathematical model of shingle beaches with a groyne system. HR Wallingford Report IT 399.

Jones, R J and Allsop, N W H (1993), Stability of rock armoured beach control structures. HR Wallingford Report SR 289.

Komar, P D and Miller, M C (1973). The threshold of sediment movement under oscillatory water waves. J. Sediment Petrol., 43: 1101 - 10.

Powell K A (1990). Predicting short term profile response of shingle beaches. HR Wallingford Report SR 219.

Powell, K A (1992). Study of dissimilar sediment. MAFF Conf. of River and Coastal Eng., Loughborough, UK.

Yalin, S (1963). A model shingle beach with permeability and drag forces reproduced. Proc. 10th IAHR Congress 1963. London p.169.



## CHAPTER 136

### The Role of Rollers in Surf Zone Currents

William R. Dally<sup>1</sup>, M. ASCE, and Daniel A. Osiecki<sup>2</sup>

#### Abstract

Employing a recently developed model for the creation and evolution of the aerated region of breaking waves, the relative importance of the roller in driving and mixing cross-shore and longshore currents is explored. Modeling results using linear wave theory confirm that in the mean balances of mass, momentum, and energy, the roller plays a role comparable to (and sometimes greater than) the underlying organized wave motion. It also appears that the roller is responsible for the landward shift of the peak cross-shore and longshore current observed in laboratory and field measurements, and is as important as the net convective acceleration in cross-shore mixing of the longshore current.

#### Introduction and Background

In the investigation and modeling of nearshore circulation, it has long been suspected that a significant role is played by the aerated region of the breaking wave (see e.g. Svendsen, 1984). However, a lack of understanding and modeling capabilities of the "roller" itself has thus far stymied attempts to clarify its importance in the mean mass, momentum, and energy balances of the surf zone.

---

<sup>1</sup>Associate Professor, Ocean Engineering Program, Florida Institute of Technology, 150 W. University Blvd., Melbourne, FL 32901, U.S.A

<sup>2</sup>Graduate Research Assistant, Ocean Engineering Program, Florida Institute of Technology, 150 W. University Blvd., Melbourne, FL 32901, U.S.A

A model that describes the growth, evolution, and decay of the breaking wave roller has recently been developed by Brown (1993) and Dally and Brown (1995). This model, annotated below, calculates the time-averaged cross-sectional area of the roller (essentially its mass flux) as a function of position in the surf zone. The roller model has a single fitting coefficient, which has been calibrated by including roller terms in the equations for the mean mass and momentum balances, and then tuning comparisons to data for cross-shore currents from a single wave channel experiment. With the calibration coefficient held fixed, additional comparisons to set-up and undertow data from other experiments reported in the literature are very favorable. Of particular note is a greatly improved ability to model the cross-shore structure of set-up and currents in the transition region of the outer surf zone.

The purpose of the present investigation is, by employing the calibrated and verified roller model, to examine in detail the role played by the rollers in driving set-up and cross-shore and longshore currents. Of specific interest is the magnitude of the roller mass and momentum fluxes relative to the familiar expressions for Stokes Drift and Radiation Stress components, as derived from linear wave theory.

#### Overview of the Roller Model

Based on a depth-integrated, period-averaged energy balance, Dally and Brown (1995) propose a governing equation for the creation and evolution of the aerated region of a breaking wave that is normally incident to the beach. Generalizing this model for the obliquely incident situation, but assuming longshore uniformity, yields

$$\frac{\partial}{\partial x} (F_w \cos \alpha) + \frac{\partial}{\partial x} \left( \frac{1}{2} \rho_r c^2 \cos^2 \alpha \frac{A}{T} \right) = -\rho_r g \beta_D \frac{A}{T} \quad (1)$$

where  $x$  is the cross-shore coordinate (directed onshore),  $F_w$  is the period-averaged energy flux associated with the organized wave motion,  $\alpha$  is the local wave angle relative to shore-normal,  $\rho_r$  is the mass density of the roller (including air),  $A$  is the cross-sectional area of the roller (including air),  $T$  is the wave period,  $g$  is gravity, and  $\beta_D$  is a dissipation coefficient related to the angle of inclination of the roller as it rides the face of the wave.  $\beta_D$  is the primary calibration factor for the model, for which a value of 0.1 has been established by Brown (1993).

In Dally and Brown (1995) it is noted that the dependent variable in Eq.(1) is essentially the period-averaged mass flux in the roller  $\rho_r A/T$ . This obligingly

circumvents the need to specify/model the mass density of the aerated roller  $\rho_r(x)$ . Consequently, the volume flux of water in the roller in the direction of wave propagation,  $Q_r$ , and the momentum flux in the roller,  $M$ , are given by

$$Q_r = \frac{\rho_r A}{\rho T} \quad (2)$$

$$M = \rho_r c \frac{A}{T} = \rho Q_r c \quad (3)$$

Snell's Law is used to provide the local wave angle, and the boundary condition that  $A=0$  at the breaker line is adopted. Using linear wave theory and the wave height decay model of Dally, Dean, and Dalrymple (1985) to compute  $F$  and  $c$ , Figures 1 and 2 present results for the evolution of the volume and momentum fluxes. These quantities are nondimensionalized by their maximum values, which are found well landward of the point of incipient breaking, indicating the end of the transition region.

#### Two-Layer Governing Equations for Cross/Longshore Currents

Laboratory measurements of cross-shore flows (e.g. Nadaoka and Kondoh, 1982), and field measurements of longshore flows (e.g. Rodriguez, et al., 1994) clearly indicate that strong vertical gradients in mean discharge exist at the wave trough level. The cross-shore discharge switches from onshore-directed flow above the trough level (i.e. the Stokes Drift and roller mass flux), to offshore-directed below the trough level (i.e. the undertow) as required due to the presence of the shoreline. Although the longshore discharge does not change directions, it decays from a nearly depth-uniform current below the trough (see Visser, 1991) to zero at the wave crest level. That is, it appears that the most salient vertical structure in the mean horizontal discharge can be represented by splitting the flow in the vicinity of the wave trough level.

A complete set of governing equations for a two-layer (2D-H) current field, which includes terms associated with the roller, has been developed by Dally (1994). For the situation of longshore uniformity and steady currents, the period-averaged, depth-averaged conservation of mass reduces to

$$\frac{\partial}{\partial x} [U(h+\bar{\eta})] + \frac{\partial Q_{wx}}{\partial x} + \frac{\partial Q_{lx}}{\partial x} = 0 \quad (4)$$

in which  $U$  is the depth-averaged cross-shore current,  $h$  is

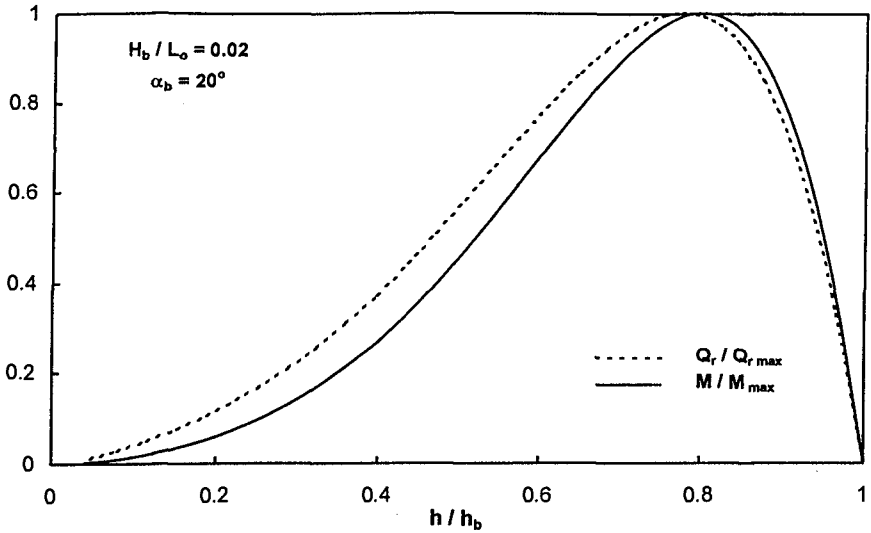


Figure 1 - Dimensionless volume ( $Q_r$ ) and momentum fluxes ( $M$ ) in the roller from numerical solution of Eq.(1), for a breaker angle of  $20^\circ$ .

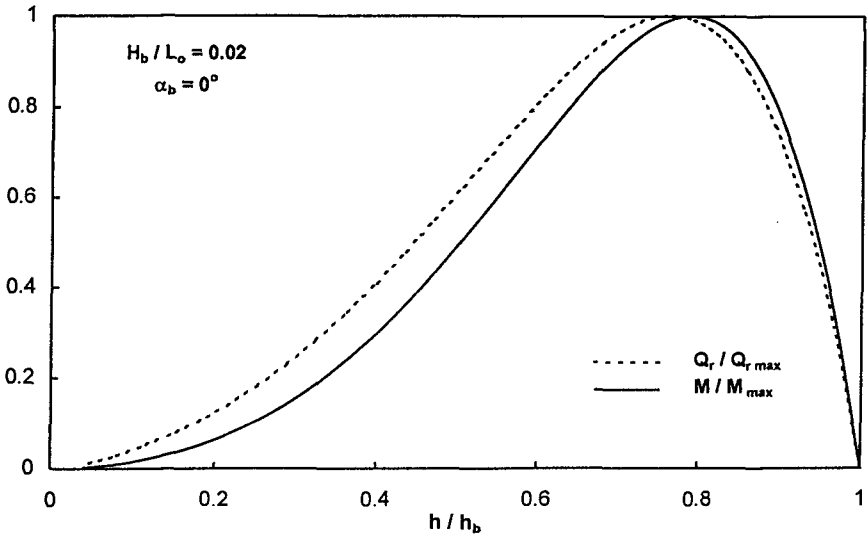


Figure 2 - Same as Figure 1. Breaker angle of  $0^\circ$ .

the still water depth,  $\bar{\eta}$  is the mean water elevation, and  $Q_{wx}$  and  $Q_{rx}$  are the mean volume fluxes associated with the organized wave motion and the roller, respectively, projected in the x direction. The period-averaged, depth-averaged momentum equations for the x and y directions are

$$\lambda \frac{\partial}{\partial x} [\rho U^2 (h + \bar{\eta})] + \frac{\partial S_{xx}}{\partial x} + \frac{\partial M_{xx}}{\partial x} + \rho g (h + \bar{\eta}) \frac{\partial \bar{\eta}}{\partial x} = - \overline{\tau_{bx}} \quad (5)$$

and

$$\lambda \frac{\partial}{\partial x} [\rho UV (h + \bar{\eta})] + \frac{\partial S_{xy}}{\partial x} + \frac{\partial M_{xy}}{\partial x} = - \overline{\tau_{by}} \quad (6)$$

where V is the depth-averaged longshore current,  $S_{xx}$ ,  $S_{xy}$ ,  $M_{xx}$ , and  $M_{xy}$  are the Radiation Stress and roller momentum flux components, and  $\overline{\tau_b}$  is the mean bed stress. In this formulation the first terms in Eqs. (5) and (6) are parameterizations of the net convective acceleration associated with the vertical structure of the currents, in which  $\lambda$  is an empirical coefficient. Although the importance of the net convective acceleration to the cross-shore mixing of the longshore current has been explored by Svendsen and Putrevu (1994), this mechanism is not yet well-resolved. However, for the immediate purpose of examining the influence of the roller on the currents, the parameterized form is adequate.

Adopting the quadratic bed stress model:

$$\begin{aligned} \overline{\tau_{bx}} &= \rho \frac{f}{8} \overline{u_b (u_b^2 + v_b^2)^{1/2}} \\ \overline{\tau_{by}} &= \rho \frac{f}{8} \overline{v_b (u_b^2 + v_b^2)^{1/2}} \end{aligned} \quad (7)$$

in which  $u_b$  and  $v_b$  are the total instantaneous velocities at the bed, and the Darcy-Weisbach friction factor f is related to Manning's n by (see Smith, et al., 1993)

$$f = \frac{8gn^2}{(h + \bar{\eta})^{1/3}} \quad (8)$$

and a value of  $0.019 \text{ sm}^{-1/3}$  is used herein.

### Results and Discussion

Neglecting set-up and currents for the moment, and once again using linear wave theory and the breaker model of Dally, et. al (1985) to drive Eq.(1), the volume flux, energy flux, and momentum flux terms of Eqs.(4), (5), and

(6) can be calculated, and their relative magnitudes examined. In Figures 3 and 4, nondimensional quantities defined as

$$\begin{aligned}
 Q'_x &= \frac{Q_r}{Q_w} \\
 F' &= \frac{\frac{1}{2} \rho Q_r c^2 \cos^2 \alpha}{F_w \cos \alpha} \\
 M'_{xx} &= \frac{\rho Q_r c \cos^2 \alpha}{S_{xx}} \\
 M'_{xy} &= \frac{\rho Q_r c \sin \alpha \cos \alpha}{S_{xy}}
 \end{aligned} \tag{9}$$

are plotted versus relative still-water depth for a planar beach of 1/30 slope, with  $H_b/h_b = 0.8$ , and breaker angles of  $20^\circ$  and  $0^\circ$ . It appears that once the roller is fully developed,  $Q_r$  and  $M_{xy}$  are nominally  $1\frac{1}{2}$  times greater than  $Q_w$  and  $S_{xy}$  computed from linear wave theory, whereas  $M_{xx}$  and  $F_r$  are respectively 1 and  $\frac{1}{2}$  times the magnitude of  $S_{xx}$  and  $F_w$ .

To include set-up and currents, the complete system of five equations (energy, Snell's Law, mass, x-momentum, and y-momentum) and five unknowns ( $Q_r$ ,  $\alpha$ ,  $U$ ,  $V$ , and  $\bar{\eta}$ ) are solved numerically. Results for wave decay, set-up and undertow are shown in Figure 5 for  $0^\circ$  angle of incidence. Note that the maximum set-down and maximum cross-shore current are shifted landward of the breakpoint, in qualitative agreement with observations (e.g. Bowen, Inman, and Simmons, 1968). Dally and Brown (1995) present a comparison of similar model results to set-up and undertow laboratory data from the literature, in which it was discovered that quantitative agreement could be achieved if Stream Function wave theory was used to specify the quantities associated with the organized motion.

In contrast to Figure 5, Figure 6 displays results of the model if all roller terms are neglected (the problem reduces to four equations and four unknowns, with wave heights specified by the Dally, et al. breaker model). It is clear that the roller terms are responsible for the transition region.

Figures 7 and 8 are generated for a breaker angle of  $20^\circ$ , and a landward shift in the peak longshore current, due to the roller, is also evident. The convective acceleration is responsible for the longshore current found seaward of the breaker line, and the value for the coefficient  $\lambda$  has been chosen as 0.2 to produce a

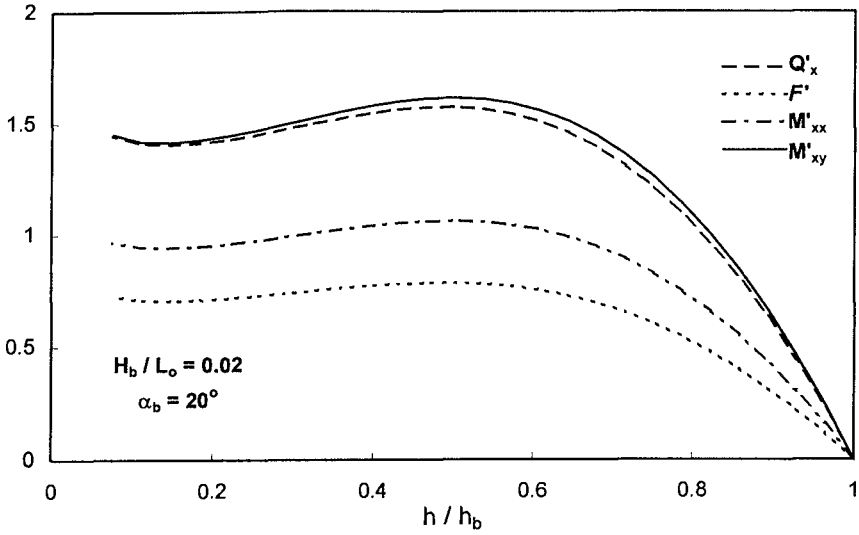


Figure 3 - Evolution of dimensionless volume, energy, and momentum flux components, defined in Eq.(9), for a breaker angle of  $20^\circ$ .

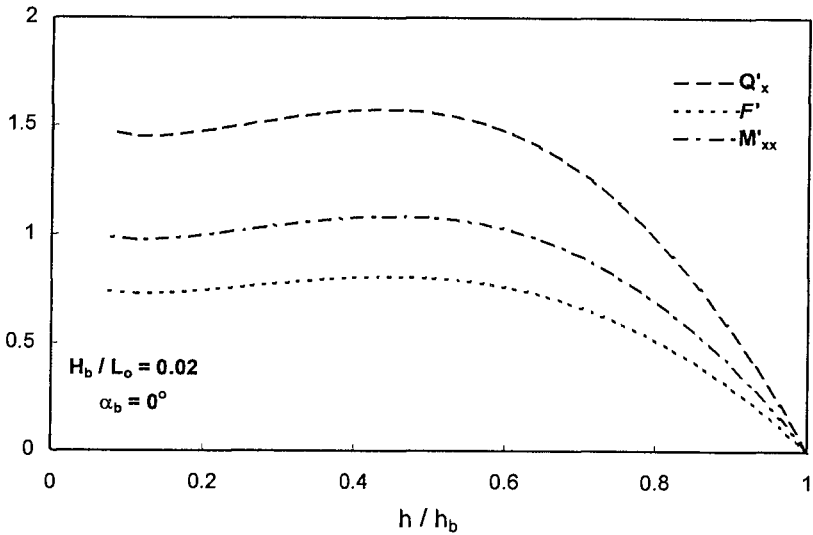


Figure 4 - Same as Figure 3. Breaker angle of  $0^\circ$ .

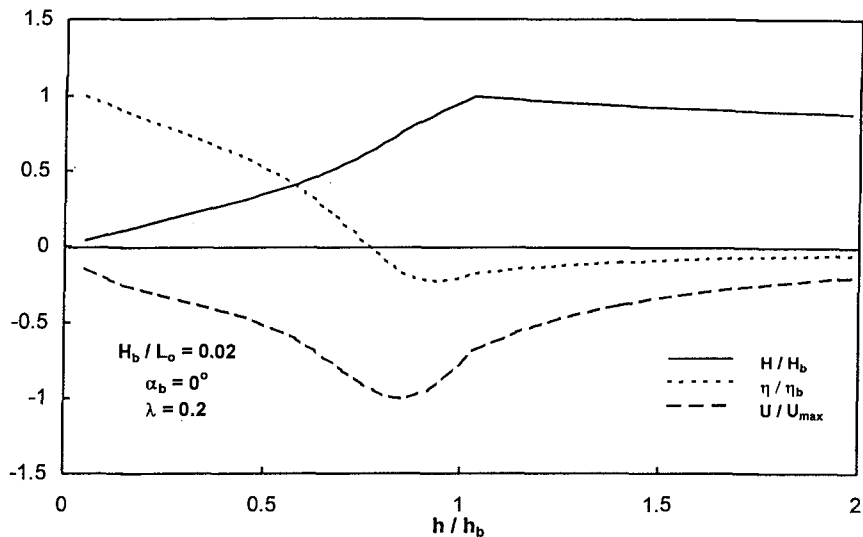


Figure 5 - Dimensionless wave height, set-up, and cross-shore current generated by numerical solution to Eqs. (1), (4), (5), and (6), for a breaker angle of  $0^\circ$ .

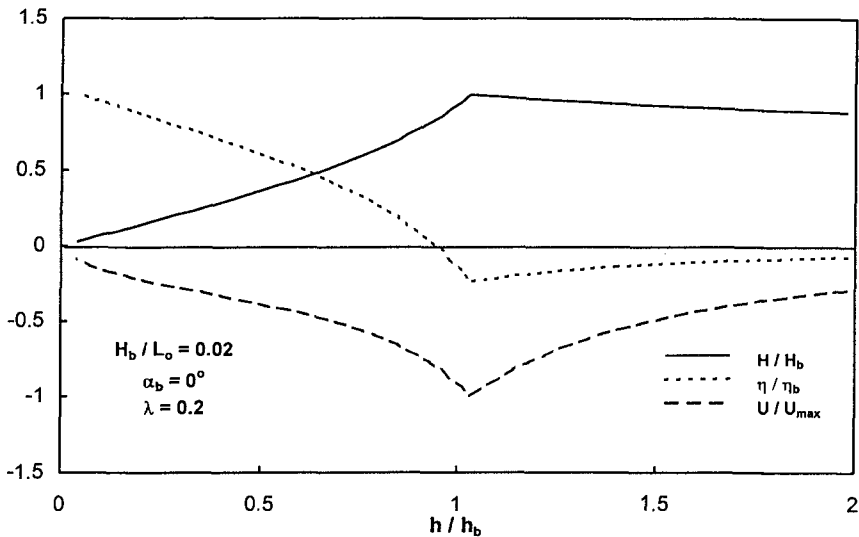


Figure 6 - Same as Figure 5, but roller terms neglected.



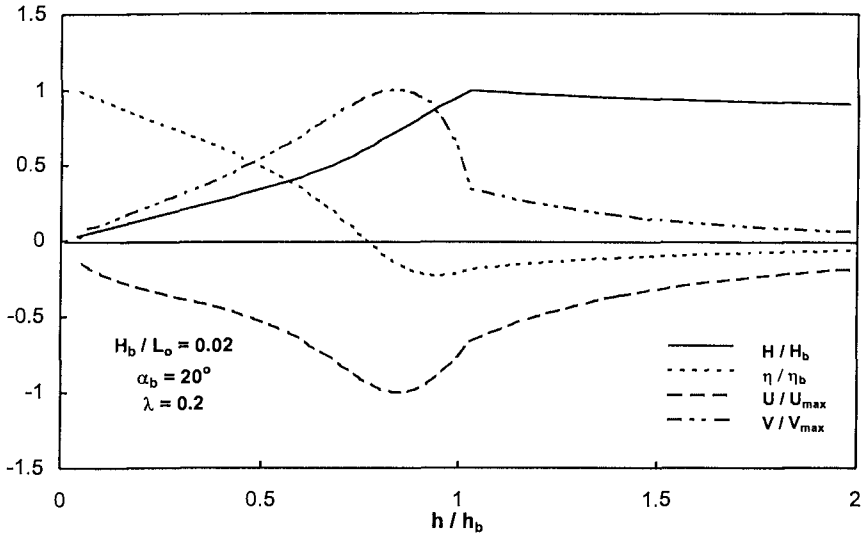


Figure 7 - Dimensionless wave height, set-up, cross-shore current, and longshore current generated by numerical solution to Eqs. (1), (4), (5), and (6), for a breaker angle of  $20^\circ$ .

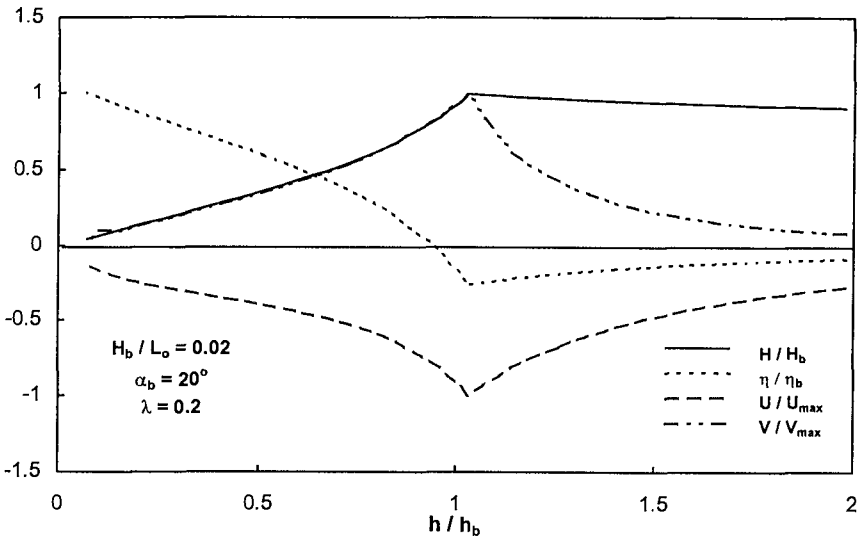


Figure 8 - Same as Figure 7, but roller terms neglected.

reasonable tail. Inside the surf zone, it appears that the roller is as important as the convective acceleration in determining the cross-shore structure of the longshore current. In comparing Figure 5 with Figure 7, altering the breaker angle does not change the cross-shore structure of the dimensionless set-up or undertow.

### Conclusions

By utilizing the very simple roller model developed by Dally and Brown (1995), the long-suspected role played by the aerated region in driving and mixing surf zone currents is confirmed. Because Dally and Brown (1995) found the net convective acceleration to be negligible in the cross-shore momentum balance, it can be concluded that the roller is almost solely responsible for the observed landward shift in set-up and peak cross-shore current.

The roller also appears to contribute significantly to the landward shift in the peak longshore current, as well as to cross-shore mixing in the surf zone. In light of the findings of Svendsen and Putrevu (1994), it is reasonable to conclude that the momentum flux associated with the roller is significantly more important to the horizontal structure of the currents than the turbulent mixing (Reynolds Stress) associated with the wake left behind.

The modeling results also indicate that the roller could be of importance comparable to the net convective acceleration associated with the vertical structure of the currents (Svendsen and Putrevu, 1994); however, a more precise assessment awaits closer study of the vertical structure of the currents. Svendsen and Putrevu (1994) assume it is vertical structure in the longshore current that leads to mixing, where comparison of the laboratory measurements of Nadaoka and Kondoh (1982) for undertow to those of Visser (1991) for the longshore current indicate that it is actually the undertow that is more depth-dependent.

Finally, it is stressed that all of the modeling done herein utilizes linear wave theory to represent the organized wave motion. In light of the findings of Dally and Brown (1995) for set-up and undertow driven by normally incident waves, it is anticipated that Stream Function, or another suitable nonlinear wave theory, will be required to achieve satisfactory comparisons of the model to longshore currents observed in the laboratory and field.

References

- Bowen, A. J., D. L. Inman, and V. P. Simmons, Wave 'set-down' and set-up, J. Geophys. Res., 73(8), 2569-2577, 1968.
- Brown, C. A., Modelling of cross-shore currents in the surf zone, M. S. Thesis, Dept. Oceanography, Ocean Engineering, and Environmental Science, Florida Institute of Technology, 1993.
- Dally, W.R., Development of governing equations for wave, wind, and tide-driven currents for numerical modeling of the Sebastian Inlet system, report to the Sebastian Inlet Tax District Commission, 30pp.
- Dally, W.R. and Brown, C.A., A modeling investigation of the breaking wave roller with application to cross-shore currents, subm. to J. of Geophys. Res., 1995.
- Dally, W.R., R.G. Dean and R.A. Dalrymple, Wave height variation across beaches of arbitrary profile, J. of Geophys. Res., 90(C6), 11,917-11,927, 1985.
- Longuet-Higgins, M. S., Longshore currents generated by obliquely incident waves - 2, J. of Geophys. Res., 75(33), 6790-6801, 1970.
- Nadaoka, K. and T. Kondoh, Laboratory measurements of velocity field structure in the surf zone by LDV, Coastal Eng. Jpn., 25, 125-145, 1982.
- Rodriguez, A., A. Sanchez-Arcilla, F. Collado, V. Gracia, and M.G. Coussirat, Waves and currents at the Ebro Delta surf zone: measured and modelled, presentation at the 24th ICCE (see Book of Abstracts, 268-269), 1994.
- Smith, J. M., M. Larson, and N. C. Kraus, Longshore current on a barred beach: field measurements and calculation, J. Geophys. Res., 98(C12), 22,717-22,731, 1993.
- Svendsen, I. A., Mass flux and undertow in a surf zone, Coastal Eng., 8, 347-365, 1984.
- Svendsen, I.A., and U. Putrevu, Nearshore mixing and dispersion, Proc. Royal Soc. Lon., 445, 561-576, 1994.
- Visser, P.J., Laboratory measurements of uniform longshore currents, Coastal Eng., 15, 563-593, 1991.

## CHAPTER 137

### THREE DIMENSIONAL MORPHOLOGY IN A NARROW WAVE TANK: MEASUREMENTS AND THEORY

Robert G. Dean<sup>1</sup> and Tae-Myoung Oh<sup>2</sup>

#### ABSTRACT

Results are described from movable and fixed bed wave tank tests to examine the characteristics and causes of three dimensional beach profiles occurring in a narrow wave tank. The movable bed tests demonstrated a strongly repeatable sequence in which both the hydrodynamics and sediment transport patterns were two-dimensional over the initial stages of testing; however, after approximately 200 to 240 minutes, a horizontal circulation appeared and strengthened and resulted in a narrow channel incised adjacent to one of the tank walls. This circulation was reminiscent of a rip current system and resulted in a net landward transport of sediment. During the later stages of profile evolution, an equilibrium was reached in which the profile was steeper and the channel adjacent to the wall persisted. The fixed bed tests were conducted to examine, under controlled conditions, the mechanisms and causes of the horizontal circulation. Tests were carried out specifically to examine generation and maintenance mechanisms for rip currents and edge waves. One set of the fixed bed tests induced a jet into the surf zone and examined its interaction with incident waves. The interaction was found to exert a torque which was counter to that of the induced jet and thus would reduce its circulation. Edge wave mechanisms were examined in the second set of fixed bed tests by generating incident waves with the wave period corresponding to the edge wave length equal to twice the width of the tank for various edge wave modes. No indication of edge waves were found in the experiments. It is concluded that the sequence of profile evolution documented in the movable bed model tests is most likely caused by a long term instability and is reminiscent of and may be representative of the beach recovery stages from a storm profile.

---

<sup>1</sup>Chairman and Graduate Research Professor, <sup>2</sup>Ph. D. Recipient, Department of Coastal and Oceanographic Engineering, University of Florida, Gainesville, Florida 32611

## INTRODUCTION

The nearshore coastal zone is characterized by complex hydrodynamic and sediment transport processes. With few exceptions, three-dimensional hydrodynamic flows occur in the natural system that are associated with three-dimensional bathymetry, including beach cusps, rip currents and some bar morphologies. There has been considerable conjecture and debate in the literature as to the formation mechanisms of the three-dimensional morphology in nature and the necessary conditions for their occurrence under laboratory conditions. It is generally considered that experiments conducted in a narrow wave tank will be free of three-dimensional circulation and morphology and this raises the question of how narrow a tank must be to preclude the formation of such features.

Various mechanisms and causes have been advanced for three-dimensional features in nature, including, for beach cusps: edge waves (Komar, 1973 and Guza and Inman, 1975) and instabilities (Werner and Fink, 1993); for rip currents: combinations of edge waves with synchronous incident waves (Bowen, 1969 and Bowen and Inman, 1969), wave current interaction (Dalrymple and Lozano, 1978), instabilities (Hino, 1974) and topographic control (Dalrymple, 1978); for nearshore three-dimensional features: interaction of edge waves with incident waves (Holman and Bowen, 1982).

The motivation for the experiments presented here resulted from tests in which three dimensional hydrodynamics were found to occur. This led to the program described herein in which experiments were conducted to investigate the causes of and mechanisms associated with the three dimensional features.

## EXPERIMENTS

The experiments were conducted in both movable and fixed bed wave tank facilities.

### Movable Bed Experiments

All experiments commenced from an initially planar beach with 1:18 slope. The tank is 15.5 m long, 0.9 m high and 0.6 m wide. The median sand size was 0.21 mm with a sorting coefficient of 0.58 and a fall velocity of approximately 2.3 cm/sec. The water depth in the horizontal portion of the wave tank was 0.275 m. Regular waves with a height of 0.11 m and a period of 1.5 sec were used. Profile evolution was documented by three lines measured along the tank centerline and at quarter points across the tank width. The profiles were measured manually with a point gage and are denoted, B1, B2 and B3 with B2 being located along the tank centerline. A total of six experiments was conducted with the conditions summarized in Table 1. The experiments are referred to as: (1) Reference Test (Experiment MT01), (2) Repeat Tests (Experiments MT02 and

Table 1

## Movable Bed Experiment Conditions and Objectives

Exp. No.	Duration (min)	Water Table Level (cm)	Objectives
MT01	0-476	0.0	Reference Test
MT02	0-407	0.0	Repeatability Test
MT03	0-545	0.0	Repeatability Test
MT04	0-821	0.0	Perturbations in Bar Topography
	(0-69)	0.0	(No Change)
	(69-138)	0.0	(Bar Trough Deepened)
	(138-352)	0.0	(Asymmetric Offshore Scour Area)
	(352-821)	0.0	(Half of Bar Crest Removed)
MT05	0-1166	+11.0	Initially 3-D Berm. Elevated Water Table Level
MT06	0-1166	+16.5	Higher Water Table

MT03), and (3) Perturbation Tests (Experiments MT04, MT05, and MT06); results are presented below.

Experiments MT01, MT02 and MT03 - These experiments were all conducted with the same general conditions and the results were approximately the same confirming the general repeatability of the tests. A bar formed rapidly as shown in Figure 1. At times ranging from 210 to 270 minutes, the profile appeared to become stable. However, soon after this time, a weak horizontal circulation appeared in the tank. The circulation became stronger and a depth variation across the tank was soon evident with a narrow channel approximately 5 cm deeper than the adjacent bathymetry through the bar on the tank side with the seaward flowing currents. At this stage, the horizontal circulation was quite reminiscent of a rip current cell in nature. The morphological response to this horizontal circulation was quite surprising. It was expected that the horizontal circulation would result in a net seaward transport of sediment; however, the contrary happened. Substantial landward transport occurred with a considerable portion of the material originating from seaward of the bar. As summarized in Figure 2 for Experiment MT03, the bar moved landward during the later times

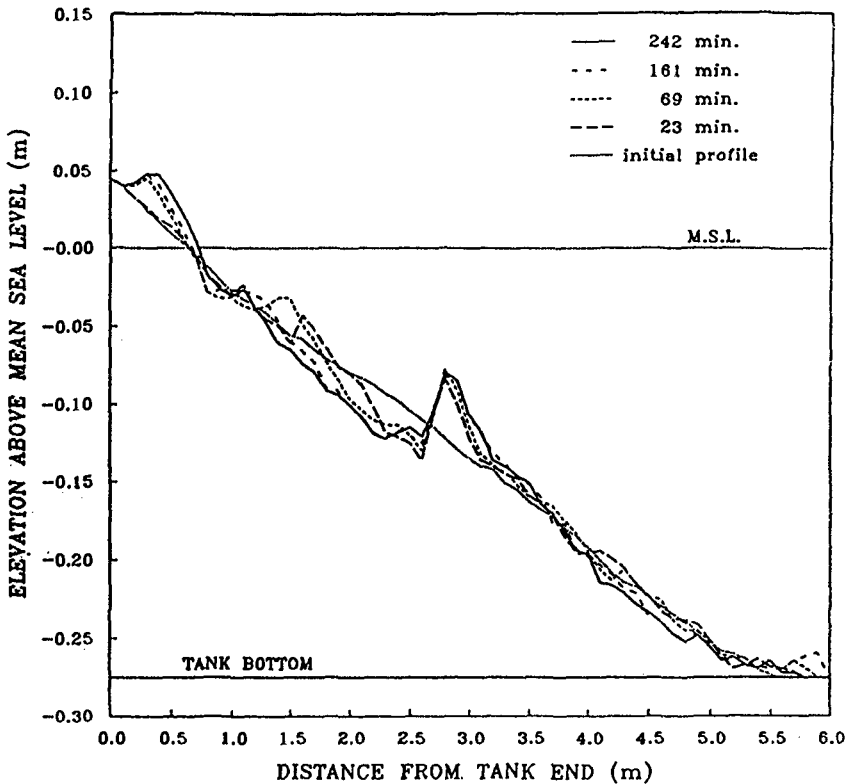
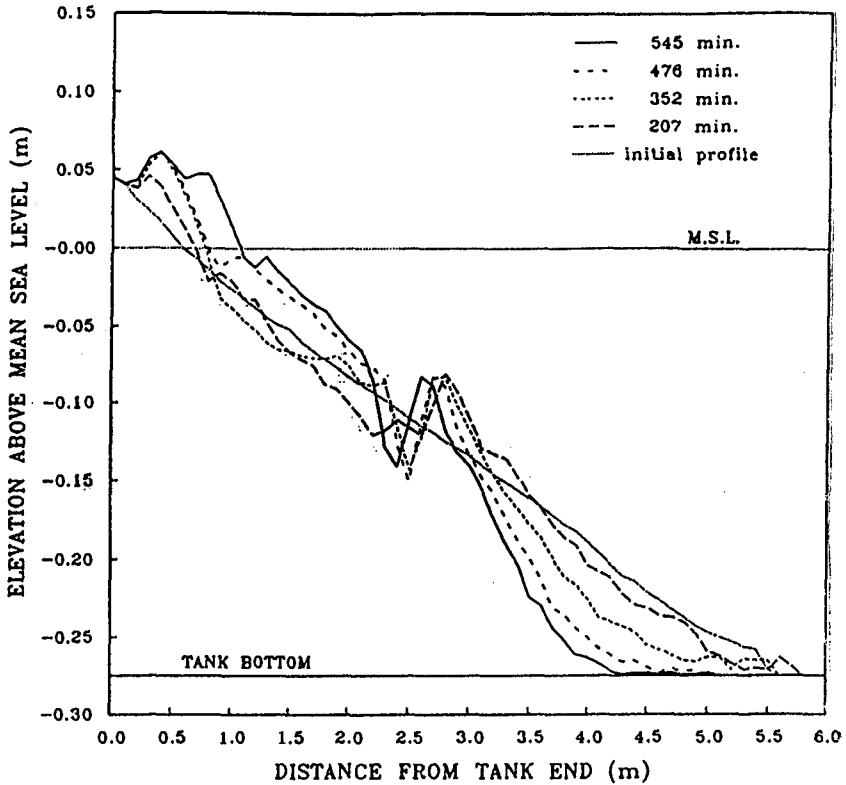


Figure 1. Mean profile evolution during early stages of Experiment MT01. Elapsed times = 0, 23, 69, 161, and 242 minutes. Note that the profile approached an equilibrium at 242 minutes.

of the experiment and the beach built seaward. At this time, the profile was essentially two-dimensional except for a narrow channel at one side of the wave tank. The remaining experiments in the movable bed tests were conducted to attempt to clarify the causes and mechanisms associated with the results, especially the circulation and transport patterns.

Experiment MT04 - In an attempt to clarify the processes, perturbations were introduced artificially into the morphology to observe the response. The experiment commenced as for the three experiments described earlier and the profile evolution was approximately the same. At a time of 70 minutes, a two-dimensional perturbation to the profile was induced by deepening the bar trough by approximately 4 cm with the sand placed seaward of the bar. The run was then recommenced and it was found that by 140 minutes, the profile had essentially returned to the pre-modification conditions. After 140 minutes, the seaward area



**Figure 2.** Mean profile evolution during Experiment MT03. Elapsed times = 0, 207, 352, 476 and 545 minutes. Note rapid change during 476 to 545 minutes with the landward movement of the bar and advancement of the beach face.

of the bar was intentionally modified from a two-dimensional to a three-dimensional area with approximately the same mean profile as before. It was expected that this modification would change the breaking and circulation characteristics over the bar region. Weak horizontal circulation occurred in the wave tank and was reinforced by a sedimentary feedback. This reinforced three-dimensional circulation transported sands from the higher perturbed area to the area immediately landward of the bar trough, and from there to the lower perturbed area seaward of the bar, resulting in a return to the pre-modified two-dimensional area at a time of 210 minutes. However, during this time, the three-dimensional flow remained too weak to cause onshore sand transport from the area seaward of the bar; hence, the profile remained nearly stable until 300 minutes at which time the bar had rotated by approximately 20 degrees. Here it is worthwhile to note that the circulation direction varied from experiment to experiment. The horizontal circulation strengthened from 300 minutes to 350



minutes and a three-dimensionality in the profile and a net onshore sand transport commenced. At 350 minutes, half of the bar crest was removed from the side of the tank with the channel present and this material was placed in the landward trough, resulting in a monotonic profile over one-half the tank width. This perturbation reinforced the three-dimensional morphology which had appeared in the tank. Within an hour, the morphology returned to its pre-perturbation condition. No additional perturbations were imposed during this experiment. During the remainder of the run, the subsequent profile evolution was approximately the same as in the three experiments described earlier. Sand was transported landward and the profile became nearly two-dimensional with the exception of a fairly deep channel adjacent to one of the side walls.

Experiment MT05 - Experiment MT05 differed from earlier tests in that a constant water level of +11.0 cm was maintained in the berm and the tests commenced with a cross-tank perturbation in the beach face of approximately 4 cm vertically. The elevated water table in the berm was maintained by a siphon and weir arrangement from an excavation in the berm. The reader is referred to Oh (1994) for the details. The perturbed beach face returned to two-dimensionality within the first 23 minutes. During the remainder of the testing, it was found that the evolution was surprisingly similar to those of previous tests, including the appearance of horizontal circulation between 210 and 240 minutes, bar rotation and landward transport of sand, and formation of a fairly deep (6 cm relative to the adjacent bottom) channel adjacent to one side wall. This experiment was extended to 1028 minutes and the profile stabilized at nearly two-dimensional conditions with relative minor seaward and landward oscillations of the bar position. No substantial effect of the elevated water table was evident which led to a decision to investigate this effect further in Experiment MT06.

Experiment MT06 - The berm water table level was maintained at + 16.5 cm in this experiment. One difference between this and previous experiments was that there was some indication that the higher water table accelerated the sequence found in previous experiments. Additionally, it appeared that the higher water table may have resulted a somewhat milder equilibrium profile slope.

Summary of Movable Bed Model Tests - Taken in their aggregate, the six movable bed model tests demonstrated a repeatable sequence as follows. During the initial stages, a two-dimensional bar formed that was stable against induced perturbations. After approximately 240 to 300 minutes a weak horizontal circulation commenced and strengthened gradually. This circulation, reminiscent of a rip current circulation, caused rotation of the bar and a relatively deep channel to be incised adjacent to one of the tank side walls. Associated with the horizontal circulation was a net landward transport of sediment, an advancement of the shoreline and a steepening of the profile. During the later stages of testing, the profile was reasonably two-dimensional except for the channel adjacent to one side of the wave tank. Finally, the only noticeable effects of elevated water tables

in the berm were to cause a slightly increased rate at which the sequence of profile evolution occurred and a possibly somewhat milder equilibrium profile slope.

### Fixed Bed Model Tests

The purpose of the fixed bed model tests was to investigate possible causes and mechanisms of known three-dimensional surf zone phenomena. Specifically, experiments were conducted to clarify the role of wave-current interaction versus wave sediment interaction in the observed rip currents and to determine whether edge waves were likely to have been caused in the movable bed model tests by periodic waves. The fixed bed wave tank is 20 m long, 0.6 m wide, and 1.5 m high and has a uniform slope of 1:20.

Rip Current Tests - One of the rip current theories is that the incident waves provide a reinforcing mechanism, eg. Dalrymple and Lozano (1978). Other investigators (LeBlond and Tang, 1974) have concluded that this interaction would be negative. Bowen (1969) and Bowen and Inman (1969) have attributed the cause of rip currents to the interaction of synchronous incident and edge waves. Hino (1974) has suggested an instability mechanism. A thorough review of rip current mechanisms has been provided by Dalrymple (1978).

A jet with discharge distributed over the water depth was directed into the surf zone as shown in planform in Figure 3. Two current strengths and wave heights were tested. Two approaches were followed to investigate the interaction of waves and currents. The first was direct and consisted of suspending a freely rotating spindle with eight vanes into the surf zone and monitoring its rotations by video. This apparatus will be referred to as a "vorticity meter" in the following discussion and is shown as "V. M." in Figure 3. Results of these tests are shown in Figure 4 in which the rotation under various sequences and combinations of waves and currents are presented. Test F101 involved only the jet and it can be seen that the vorticity meter rotated in a counterclockwise direction at a fairly constant rate. Test F102 involved only waves and there was essentially no rotation. For Test F103, the jet was operated continuously and the wavemaker was activated from  $t=60$  sec to  $t=130$  sec. It is seen that during the time that the waves affected the nearshore system, there was a counter rotation of the vorticity meter (the cumulative rotation changed from a negative to positive slope). After cessation of the waves, the vorticity meter commenced rotating in a counter clockwise direction at the same rate as prior to wave commencement. In the initial stages of Test F104, waves were operated alone during which no rotation of the vorticity meter occurred. After a time, the current was started and the vorticity meter rotated in accordance with the jet induced momentum. Later still in this experiment, the jet was stopped and the rotation ceased.

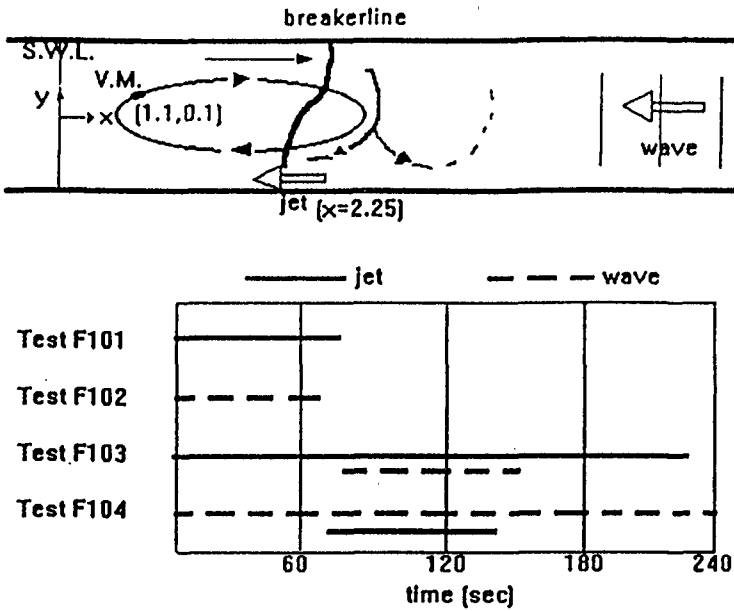
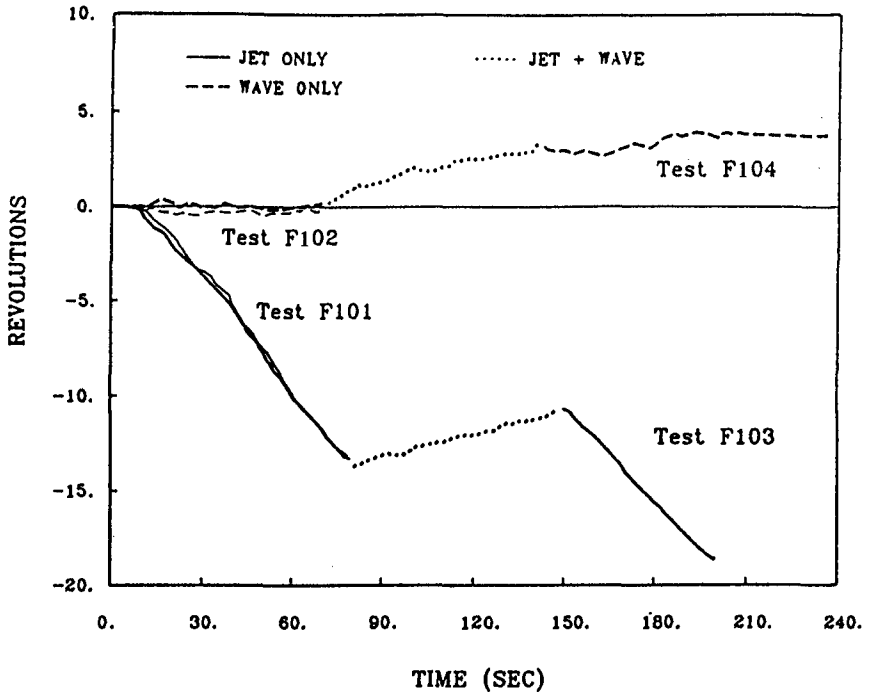


Figure 3. Schematic diagram of the vorticity measurement tests with a description of conditions for each test.

The second approach to documenting and interpreting the interaction of the waves and induced currents was through measurement of the wave height and direction fields. An example of the wave height field for the presence of the jet and a 9 cm wave height is shown in Figure 5. It is seen as expected that the wave height was enhanced in the vicinity of the seaward flowing current. The radiation stresses associated with the larger wave heights are believed to be responsible for the tendency of the waves to reduce the circulation induced by the jet. In addition to wave heights, wave crest orientations were documented by video, but are not presented here. The wave height and direction fields were used in conjunction with the mean vorticity equations to examine the driving torque due to the interaction. Due to space limitations, these equations will not be presented here; however, it was found, consistent with the vorticity meter results, that the interaction of the waves and currents exerted a torque that was counter to the induced current.

Edge Wave Tests - Experiments were conducted to evaluate the effects of edge waves by generating incident waves of the period associated with an edge wave length,  $L_r$ , of twice the width of the tank,



**Figure 4.** Cumulative rotation at a point within the surf zone as influenced by the jet and waves. Positive rotation corresponds to a counter-clockwise rotation of the vorticity meter.

$$T = \sqrt{\frac{2 \pi L_r}{g \sin[(2n + 1) \beta]}}$$

where  $g$  is gravity,  $\beta$  is the uniform beach slope and  $n$  is the mode of the edge waves. For the tank width of 0.6 m, the periods tested are given in Table 2.

Table 2

Required Incident Wave Periods for Synchronous Edge Wave Generation

n	0	1	2	3	4	5	6	7	8	9	10
T (sec)	3.92	2.27	1.76	1.50	1.33	1.21	1.13	1.06	1.01	0.97	0.94

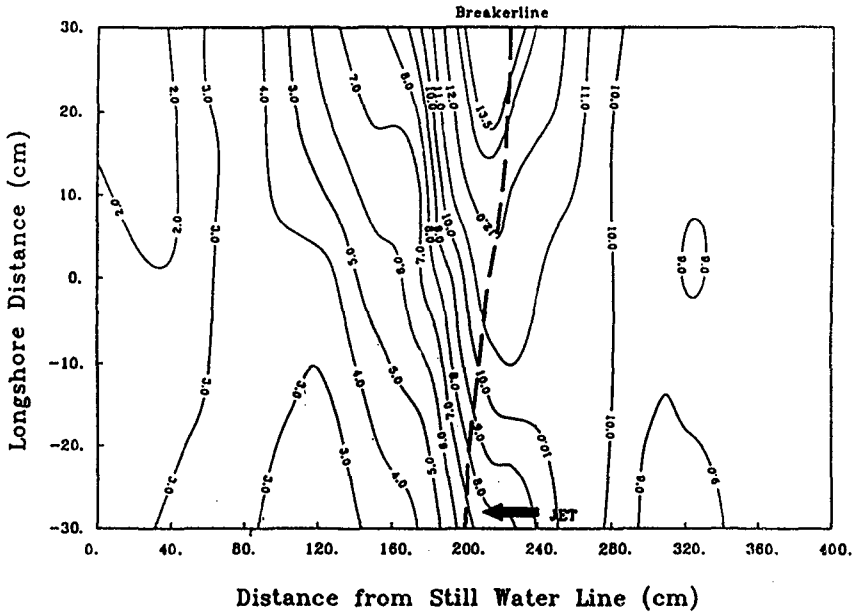


Figure 5. Wave height distribution in the presence of a jet-induced current when  $H_0 = 9$  cm (Test F222). Wave heights are in cm. Note higher wave heights due to both refraction by current and wave-current interaction.

During these tests, the wave height was set to result in both surging and plunging breaking conditions. Initially, a smaller wave height causing surging breaking wave conditions was generated and continued for ten minutes while the wave tank was monitored visually for edge waves. After ten minutes the wave height was increased such that plunging breaking wave conditions occurred and the run was extended for an additional ten minutes. During all these experiments, no evidence of edge waves was observed.

### INTERPRETATION

The results of the tests requiring interpretation are: (1) The onset of the three-dimensional circulation after the profiles had reached a state of quasi-stability and (2) The onshore transport of sediment by the circulation that was reminiscent of a rip current. Prior to offering an interpretation, it is worthwhile to note the strong repeatability of the experiments and that the fixed bed tests demonstrated that interaction of waves and induced circulation tended to reduce the circulation rather than reinforce it. Additionally, the direction of the induced circulation varied from experiment to experiment. At any time, there are forces that tend to incise channels through the bar and other processes that tend to fill in any lower portions of the bar. The stability of the two-dimensional nature of

the profile for the early stages of the evolution from an initially planar form is believed to be due to the fact that the sand is quite mobile during this time and thus any increase in depth over the bar is rapidly filled by the available sand due to its high mobility. After some time, the profile approaches a quasi-equilibrium state and the sand is less in transit and becomes more consolidated and less mobile. On a subaerial beach, this transition from a poorly consolidated condition to a more consolidated condition is evident when, for a number of hours after accretion of a beach, the pressure due to walking will result in a depression of a centimeter or so into the beach surface. Later, after the waves have consolidated the surface, the sand is less mobile and deforms less in response to surface pressures. Returning to the wave tank results, after the material on the profile surface becomes less mobile, a local deepening of the bar will not be filled in so readily due to less material being readily available for this process. Since the local depression is more efficient hydraulically, the channel deepens gradually until a depth is reached which both relieves the mass transport within the surf zone and results in side slopes that preclude further deepening. With a substantial portion of the mass transport return flow now occurring through the deepened channel, the seaward forces that were present over the bar due to the return flow are reduced resulting in a predominance of the onshore transport processes and the occurrence of a net landward sediment transport, an advancement of the shoreline and deepening of the portions of the profile seaward of the bar. This mechanism is very similar to that of shoreline recovery through ridge and runnel systems and associated breaks in the bar through which the return flow (rip currents) of the mass transport occurs.

### SUMMARY AND CONCLUSIONS

Both movable and fixed bed wave tank tests were conducted to investigate beach profile evolution and the causative hydrodynamic mechanisms. The movable bed experiments demonstrated a repeatable sequence in which, starting from a planar bed, an offshore bar was formed and the profile appeared to approach a quasi-stable two-dimensional form after approximately 200 to 240 minutes. Following this initial stage, a weak three-dimensional circulation appeared and increased in strength causing the bar to rotate. A narrow and relatively deep channel developed adjacent to one of the side walls as a result of this circulation which is reminiscent of a rip current system. The circulation caused substantial net onshore sediment transport and resulted in significant shoreline advancement. During two of the movable bed model tests, the profile was intentionally perturbed and the processes resulted in the profile soon being returned to the form consistent with the evolutionary time without the perturbation. Effects of increased water table elevation were small and resulted in somewhat smaller evolutionary time scales and possibly a milder equilibrium beach slope.

Fixed bed tests were conducted to investigate possible mechanisms that could cause the horizontal circulation experienced. It was found that the interaction of incoming waves with an incoming jet exerted a torque counter to and thus would suppress the circulation by the jet induced circulation. Additionally, experiments especially configured to excite synchronous edge waves were not successful leading to the conclusion that edge waves were not important in driving the circulatory system.

It is concluded on a preliminary basis that the evolution observed, including the appearance of three-dimensional circulation and the associated transport are relevant to the transformation of a two-dimensional bar system in nature to a three-dimensional form and the subsequent migration of the bar to the shoreline and its recovery. The instability mechanism proposed by Hino (1974) is supported by the experiments. If further testing confirms the mechanisms identified in these experiments, a substantial contribution to the clarification of the physics of the nearshore zone will have resulted.

#### REFERENCES

- Bowen, A. J. (1969) "Rip Currents. Part 1: Theoretical Investigation", Jour. of Geophys. Res., Vol. 74, No. 23, pp. 5467-5478.
- Bowen, A. J. and D. L. Inman (1969) "Rip Currents. Part 2: Laboratory and Field Observations", Jour. of Geophys. Res., Vol. 74, No. 23, pp. 5479-5490.
- Dalrymple, R. A. (1978) "Rip Currents and Their Causes", Proc. Sixteenth Inter. Conf. on Coast. Engrg., ASCE, Hamburg, Germany, pp. 1414-1427.
- Dalrymple, R. A. and C. J. Lozano (1978) "Wave-Current Interaction Models for Rip Currents", Jour. of Geophys. Res., Vol. 83, pp. 6063-6071.
- Guza, R. T. and D. L. Inman (1975) "Edge Waves and Beach Cusps", Jour. of Geophys. Res., Vol. 80, pp. 2997-3012.
- Hino, M. (1974) "Theory on Formation of Rip-Current and Cuspidal Coast" Proc. Fourteenth Inter. Conf. on Coast. Engrg., ASCE, Copenhagen, Denmark, pp. 901-919.
- Holman, R. A. and A. J. Bowen (1982) "Bars, Bumps and Holes: Models for the Generation of Complex Beach Topography", Jour. of Geophys. Res., Vol. 87, pp. 457-468.
- Komar, P. D. (1973) "Observations of Beach Cusps at Mono Lake, California", Geol. Soc. of Amer. Bull., Vol. 84, pp. 3593-3600.

LeBlond, P. H. and G. L. Tang (1974) "On Energy Coupling Between Waves and Rip Currents", *Jour. of Geophys. Res.*, Vol. 79, pp. 811-816.

Oh, T. M. (1994) "Three-Dimensional Hydrodynamics and Morphology Associated with Rip Currents", Ph. D. Dissertation, Department of Coastal and Oceanographic Engineering, University of Florida, Gainesville, FL.

Werner, B. T. and T. M. Fink (1993) "Beach Cusps as Self-Organized Patterns", *Science*, Vol. 260, pp. 968-971.



## CHAPTER 138

### Numerical Simulation of Finite Amplitude Shear Waves and Sediment Transport

Rolf Deigaard<sup>1</sup>, Erik Damgaard Christensen<sup>1</sup>,  
Jesper Svarrer Damgaard<sup>2</sup> and Jørgen Fredsøe<sup>1</sup>

#### Abstract

The shear instability of a uniform longshore current and the fully developed shear waves are studied in the numerical hydrodynamic model MIKE-21. The effect of the shear waves on the sediment transport, the cross-shore momentum transfer and mean velocity profile and the dispersion of suspended or dissolved matter is studied. The strength of the shear waves is calculated for a varying flow resistance and a varying momentum exchange coefficient. The formation of shear waves can be suppressed by modest rip channels in a longshore bar.

#### Introduction

Shear waves or far infra gravity waves is a phenomenon which was first observed by Oltman-Shay et al. (1989) from field measurements of wave-driven currents along an almost uniform coast. By analysing the correlation between simultaneous current measurements from different locations it was found that variations in the longshore current were actually a wave motion. The observed waves were only found in connection with a longshore current, propagating in the flow direction with a celerity of about half the maximum longshore current velocity. The observed wave lengths were so small when considering the wave periods that no theory for surface gravity waves can explain the dispersion relation for these waves. Therefore they were termed "far infra gravity waves".

---

1 Institute of Hydrodynamics and Hydraulic Engineering (ISVA), Building 115,  
Technical University of Denmark, DK-2800 Lyngby, Denmark

2 H.R. Wallingford, Howbery Park, Wallingford, Oxon Ox10, 8BA, U.K.

The formation of these waves was explained by Bowen and Holman (1989) as the result of an instability of an initially uniform longshore current. A linear stability analysis showed that the crossshore gradient (shear) in the longshore velocity profile is the cause of the instability, similar to the instability of a free shear layer. The instability of a uniform longshore current was apparently first noted by Hino (1974), who had to disregard the unsteady terms in the hydrodynamic equations in order to describe the morphological instability of a uniform sand coast. Since the paper of Bowen and Holman (1989) more refined stability analyses have been performed e.g. Dodd and Thornton (1990) and Svendsen & Putrevu (1992). One of the most important stabilizing factors is the flow resistance due to bed friction, which may cause a longshore current to be stable, analogous to a Hele-Shaw flow.

A linear stability analysis, as the ones listed above, assumes the deviation from the steady, uniform longshore current to be infinitely small and the strength of the shear waves cannot be predicted. By considering a situation very close to a neutrally stable longshore current, a non-linear perturbation analysis has been made (Dodd and Thornton, 1992), which can describe a stationary situation with shear waves. For situations which are far from neutral stability chaotic behaviour may occur, and it is not certain that analytical methods can describe such flows satisfactorily.

The formation of shear waves is strongly dependent on the coastal topography e.g. the presence of longshore bars cf. Svendsen & Putrevu (1992). The stability analyses consider a uniform coastal profile. It is not known if shear waves are formed on a non-uniform coast as for example a longshore bar with rip channels.

### The present study

The purpose of this study is to investigate some properties of shear waves by use of a numerical hydrodynamic model, that simulates the unsteady wave driven currents along a coast. The hydrodynamic model used is MIKE-21 developed by the Danish Hydraulic Institute. The model solves the complete, unsteady depth integrated flow equations. In this way it is possible to make a simulation of the fully developed shear waves on a longshore current driven by waves breaking on a given topography.

An example of a topography is given in Fig. 1 that shows a cross section of a long straight uniform coast. The profile is barred, composed of a plane profile with a slope of  $\tan(\beta) = 1:33.3$ , superposed by a bar with a shape described by a Gaussian function. The still water depth is given by

$$D(x) = D_p(x) - (D_p(x) - D_c) \exp\left(-\chi \frac{(x - x_c)^2}{x_c^2}\right) \quad (1)$$

where  $D_p(x)$  is the plane profile:

$$D_{\rho}(x) = D_0 - x \tan(\beta) \quad (2)$$

$x$  is the cross-shore coordinate. The parameters  $D_c$  and  $x_c$  determine the still water depth over the bar crest and its position.  $\chi$  determines the width of the bar. A similar bar profile was applied in the stability analysis by Svendsen & Putrevu (1992). For the profile in Fig. 1  $D_c$  is 1.5 m,  $x_c$  is 200 m, and  $\chi$  is equal to 30.

### *The wave description*

The wave conditions are modelled by the MIKE-21 NSW module, which describes refraction and breaking of irregular waves with directional spreading. The wave heights are assumed to be Rayleigh-distributed, and the wave breaking is described by the model of Battjes and Janssen (1978). The wave modules are run for a rectangular modelling domain of 400 m  $\times$  3600 m with the long side parallel with the coast line, which is situated at the east boundary. Constant boundary conditions are prescribed at the west boundary: Significant wave height  $H_s = 3.0$  m, mean wave period  $T_m = 9.0$  s, wave direction  $\alpha_0 = 45^\circ$  relative to the coast normal.

The north and south boundary conditions assume uniform wave conditions along the coast. The simulation is run on a grid  $\Delta x = 1.0$  m and  $\Delta y = 5.0$  m. Results from the wave module are shown in Fig. 1. The wave breaking is seen to reduce the wave height at the bar and at the shore line. The shore-normal radiation stress  $S_{yy}$  and the shear radiation stress  $S_{xy}$  vary according to the variation in wave height and direction.

### *The hydrodynamic simulation*

The wave module gives the basis for calculating the radiation stress field, and by differentiation of the radiation stresses, the forcing from the waves is determined. The wave-driven flow is simulated by the hydrodynamic module MIKE-21, which solves the depth-integrated equations for conservation of mass and momentum.

The flow resistance is described by the Manning formula, and the bed shear stress  $\tau_b$  is calculated as

$$\frac{\tau_b}{\rho} = \frac{gV^2}{M^2 h^{1/3}} \quad (3)$$

where  $M$  is the Manning number, which is determined by the bed roughness,  $\rho$  is the density,  $g$  is the acceleration of gravity,  $V$  is mean flow velocity and  $h$  is the water depth.

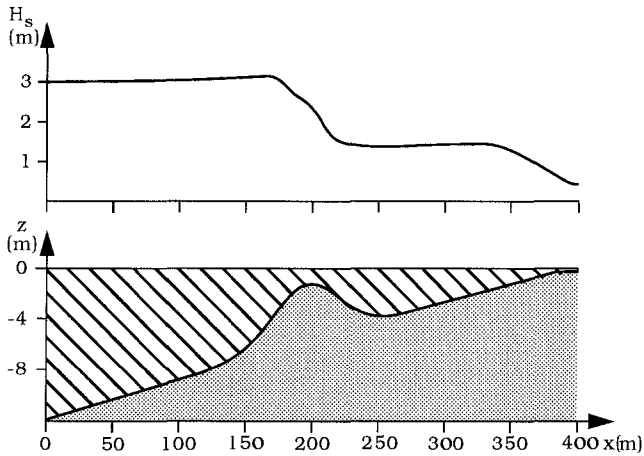


Figure 1. Bottom: coastal profile. Top: Simulated wave height variation across the profile.

The boundary conditions for the hydrodynamic simulations are specified at the offshore boundary, where the water level is kept constant, and at the upstream and down-stream boundary, where the flux is specified with a distribution across the profile corresponding to a uniform longshore current. The grid size for this hydrodynamic simulation is  $\Delta x = 2\text{m}$ ,  $\Delta y = 4\text{m}$ . The time step is  $\Delta t = 1.25\text{s}$  and the simulation period is 3.0 h. In order to avoid a surge caused by the wave set up, the soft start facility is used, increasing the driving forces gradually from zero to the steady state conditions during a period of 2000s. The topography and the boundary conditions have thus been designed - as closely as possible - to give a steady, uniform longshore current after the warm up period. It appears, however, that the instability mechanism creates an unsteady meandering motion of the longshore flow, which is similar to the shear waves observed by Oltman-Shay et al. (1989).

Figure 2a shows a vector plot of the velocity field at the downstream point of the modelling area at time  $t = 3200$  s and  $5200$  s. Fig. 2b shows the instantaneous water surface elevation along the bar crest for fully developed shear waves. The instability mechanism can clearly be seen, the shear waves become visible at some distance from the upstream boundary. They grow in amplitude to reach an approximately uniform level.

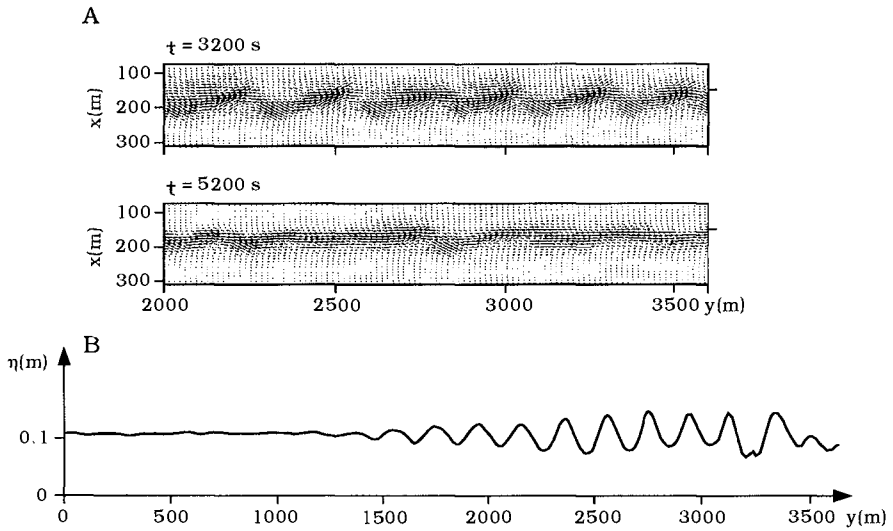


Figure 2. A: Vector plots of the velocity field at the downstream part of the bar. B: Water surface elevation along the bar crest, fully developed shear waves.

Figure 3 shows time series of the longshore and the cross-shore velocity. The time series are taken in the point on the bar crest, 125 m from the downstream boundary. The period of the shear waves is approximately 200s and the wave length is 190 m, giving a phase velocity of 0.95m/s, which is about 55% of the maximum longshore velocity speed. It is seen that the oscillations have all the characteristics of the shear waves observed in the field measurements and described by the perturbation analyses. It has been attempted to make a faster growth of the instabilities by making an abrupt change in the topography near the upstream boundary. It was found that the irregular topography did not enhance the formation of the shear waves significantly.

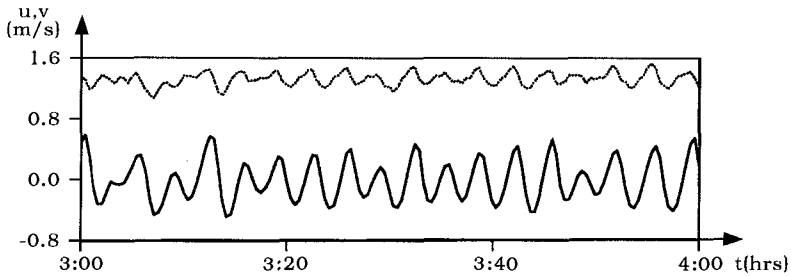


Figure 3. Time series of longshore (dotted line) and cross-shore (full drawn line) velocities at the bar crest.

### The sediment transport

Based on the results from the wave module and the hydrodynamic module, MIKE-21 can calculate the instantaneous sediment transport rate in every grid point of the hydrodynamic model. The sediment transport is calculated on basis of the water depth, the wave-averaged flow velocity, the wave height, period and direction and the wave breaking. The sediment transport model is based on the model by Fredsøe et al. (1985) including the effect of breaking waves according to the model by Deigaard et al. (1986). Fig. 4 shows the distribution of the calculated longshore sediment transport across the coastal profile. The time-averaged transport at a distance of 125m from the downstream boundary is shown together with a calculation corresponding to the steady uniform conditions that would be found if shear waves were not found. It can be seen that the formation of shear waves causes a reduction in the calculated longshore sediment transport of about 17% compared to the result that would be obtained by assuming steady uniform longshore current.

Due to the non-linearity of the hydrodynamics and the sediment transport the time average of the cross-shore sediment transport deviates from zero. Fig. 5 shows the time averaged cross-shore transport across the profile. The distribution is closely related to the distribution of the driving forces, i.e. the longshore current velocity profile. It tends to modify the bar profile, removing the material from the front of the bar and depositing it offshore and at the crest of the bar. The maximum cross-shore transport rate is of the order  $1 \text{ m}^3/\text{m hr}$ , which is not negligible compared to other contributions.

### Conditions close to neutral stability

The stabilizing mechanisms which may prevent the formation of shear waves in the model are the bed shear stress and the horizontal momentum exchange, modelled as a turbulent eddy viscosity term. In all runs (except when specifically mentioned) the momentum exchange coefficient  $E$  has been specified as zero.

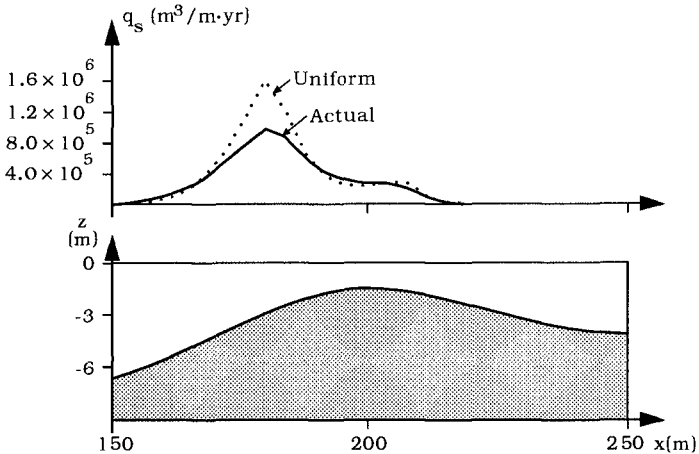


Figure 4. The distribution of the time mean longshore sediment transport,  $q_s$ , across the bar profile. Full drawn line: actual value; dotted line: assuming steady uniform conditions.

### *The flow resistance*

The dependence of the shear waves on the flow resistance has been investigated by varying the Manning number in the example considered above. For a very large flow resistance (small Manning numbers) the longshore current is steady and uniform, but at a certain value ( $M = 21.75 \text{ m}^{1/3}/\text{s}$  in the present case) shear waves are formed with an increasing intensity for increasing Manning numbers. The intensity of the shear waves is characterized by the standard deviation of the velocity fluctuations at the bar crest. The variation of the intensity with the Manning number is illustrated in Fig. 6. It may be noted that the flow resistance in Fig. 6 corresponds to very large bed roughnesses. A  $M$  of  $21.75 \text{ m}^{1/3}/\text{s}$  corresponds to a hydraulic bed roughness of 2.5 m, a  $M$  of  $25 \text{ m}^{1/3}/\text{s}$  corresponds to 1.1 m,  $30 \text{ m}^{1/3}/\text{s}$  to 0.37 m and  $35 \text{ m}^{1/3}/\text{s}$  to 0.17 m. The actual flow resistance will depend on the physical bed roughness and on the turbulent interaction between the wave boundary layer and the current, which will cause an increase in the flow resistance

compared to a pure current situation. This mechanism has not been considered in details in the present study.

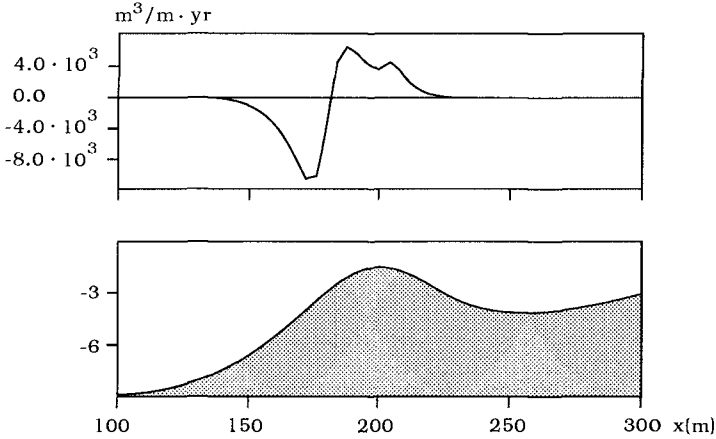


Figure 5. The distribution of the time-mean cross-shore sediment transport.

In this investigation shear waves have not been formed on a constant slope beach. A longshore current on a bar is expected to be more unstable, because it has two shear zones and can move freely onshore as well as offshore. For a given coastal profile the stability of a longshore current will depend on the formulation of the flow resistance and the distribution of the driving force ( $\partial s_{xy}/\partial x$ ) across the profile. For small deviations,  $u$  and  $v$ , from the uniform longshore current  $V_0$ , the shear stress can be linearized to give:

$$\bar{\tau}_b = \frac{\rho g}{M^2 h^{1/3}} \bar{V} |\bar{V}| = \frac{\rho g}{M^2 h^{1/3}} \left\{ \frac{u}{V_0 + v} \right\} \sqrt{u^2 + (V_0 + v)^2} \approx \tag{4}$$

$$\frac{\rho g}{M^2 h^{1/3}} \left\{ \frac{V_0 u}{V_0^2 + 2 V_0 v} \right\} = \left\{ \begin{matrix} 0 \\ \tau_{b0} \end{matrix} \right\} + \tau_{b0} \left\{ \frac{u/V_0}{2v/V_0} \right\}$$

where  $\tau_{b0}$  is the bed shear stress corresponding to  $V_0$ .  $\tau_{b0}$  is thus identical with the driving force. For given wave conditions  $\tau_{b0}$  is constant, and the flow resistance for the perturbations is proportional to  $M^{-1}$  or the Chezy coefficient. This flow resistance has many similarities to the 'strong current case' considered by Dodd



(1994). The assumption of irregular waves and the use of the Battjes and Jansen (1978) model for wave breaking give a rather smooth distribution of the driving force and the mean longshore current across a plane beach, which may give a rather weak instability mechanism.

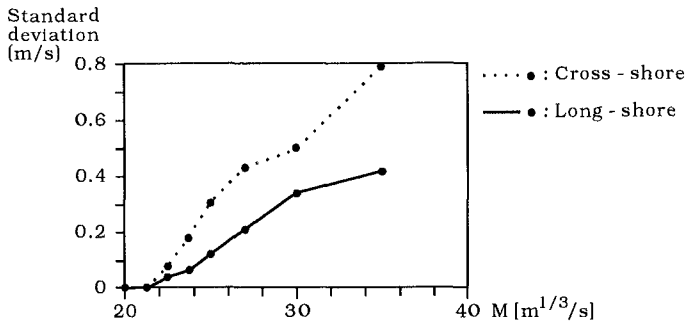


Figure 6. The intensity of the shear waves as function of the Manning number. Full drawn line: longshore velocity, dotted line: cross-shore velocity.

#### *The stabilizing effect of the momentum exchange coefficient*

The dependence of the shear waves on the momentum exchange coefficient has been illustrated by runs similar to the runs with variable flow resistance. The Manning number is kept at  $M = 25 \text{ m}^{1/3}/\text{s}$ , which gave shear waves for  $E = 0 \text{ m}^2/\text{s}$ . Fig. 7 shows the intensity of the shear waves as a function of  $E$ .  $E$  is constant over the entire modelling area. The intensity of the shear waves is seen to decrease with increasing  $E$ , until a very low level is reached at  $E = 0.1 \text{ m}^2/\text{s}$ . An increase in  $E$  may stabilize the flow in two ways: by giving a more smooth velocity distribution of the longshore current or directly by dampning the fluctuations. In the present case with a very smooth distribution of the driving force across the profile it is expected that the latter mechanism is the most important.

#### The exchange of momentum caused by the shear waves

The shear waves cause a redistribution of the momentum across the coastal profile, analogous to the Reynolds stresses in a turbulent flow. The momentum balance is considered at a location where the shear waves are fully developed. If there is no momentum exchange, the driving and the retarding forces are in

balance, and the time-averaged bed shear stress will be identical to the radiation stress gradient  $\partial S_{xy}/\partial x$ .

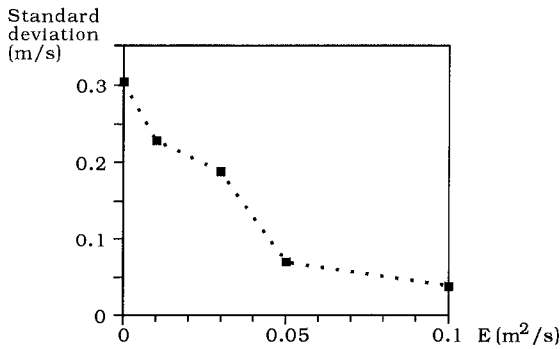


Figure 7. The intensity of the shear waves as function of the momentum exchange coefficient E.

The cross shore momentum transport due to the shear waves can be calculated as

$$\overline{\rho Duv} \quad (5)$$

where an overbar signifies a time average.

Fig. 8 gives examples of "phase plots" showing the traces of the velocity vectors at three locations: at the bar crest, 40 m offshore and 40 m inshore of the crest. It is clearly seen that the correlation between the longshore and cross-shore velocity fluctuations give a non-zero cross-shore flux of momentum (defined by eq. 5) at the crest and - more pronounced - at the offshore location. At the inshore location the momentum transfer is apparently zero. Traces made at locations further offshore than the three shown here are similar to the inshore trace without any momentum transfer.

Fig. 9a shows the distribution across the coastal profile of the three elements in the momentum balance:

$$-\frac{\partial S_{xy}}{\partial x} = \bar{\tau}_b + \frac{\partial}{\partial x} \overline{\rho Duv} \quad (6)$$

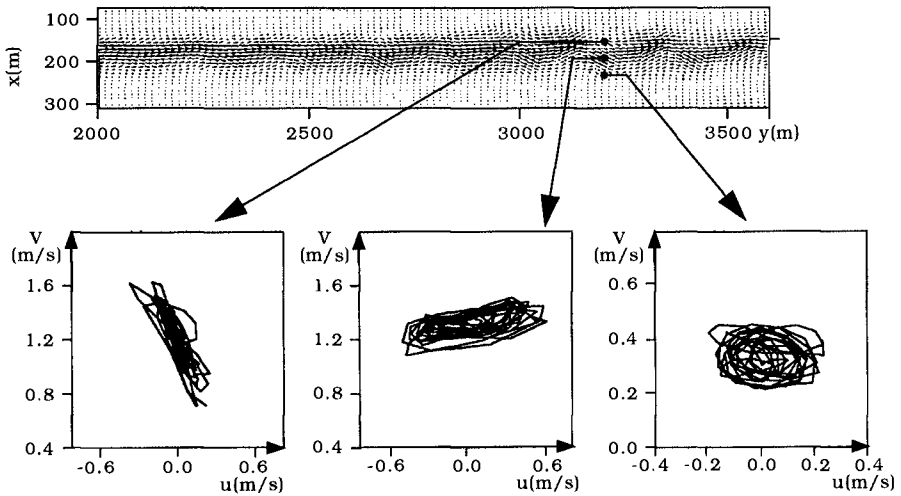


Figure 8. "Phase plots" showing the traces of the current velocity vectors at three locations.  $v$  is the longshore velocity and  $u$  is the cross-shore velocity.

It can be seen that the distribution of the mean bed shear stress is more smooth than the driving force, and the redistribution of the momentum corresponds to the transfer by the shear waves. Fig. 9b shows the mean velocity profile at this cross section together with the velocity distribution corresponding to a steady uniform longshore current. The reduction in the peak of the mean bed shear stress due to the shear waves is closely related to the reduction in the peak of the longshore velocity and the reduction in the sediment transport illustrated in Fig. 4.

In longshore current models the momentum exchange is often modelled by an eddy viscosity term. The maximum of the momentum transfer defined by Eq. 5 is close to the point of maximum gradient in the mean longshore current. The magnitude of the momentum transfer by the shear waves can be illustrated by the eddy viscosity that would be necessary to give a similar transfer of momentum. In the example considered this equivalent eddy viscosity  $E_{eq}$  is found to be

$$E_{eq} = \max(D\bar{u}\bar{v})/\max\left(D\frac{d\bar{V}}{dx}\right) \approx 0.7 \text{ m}^2/\text{s} \quad (7)$$

This is a very large value, considering for example the drastic effect of a much smaller eddy viscosity on the flow regime, cf. Fig. 7.

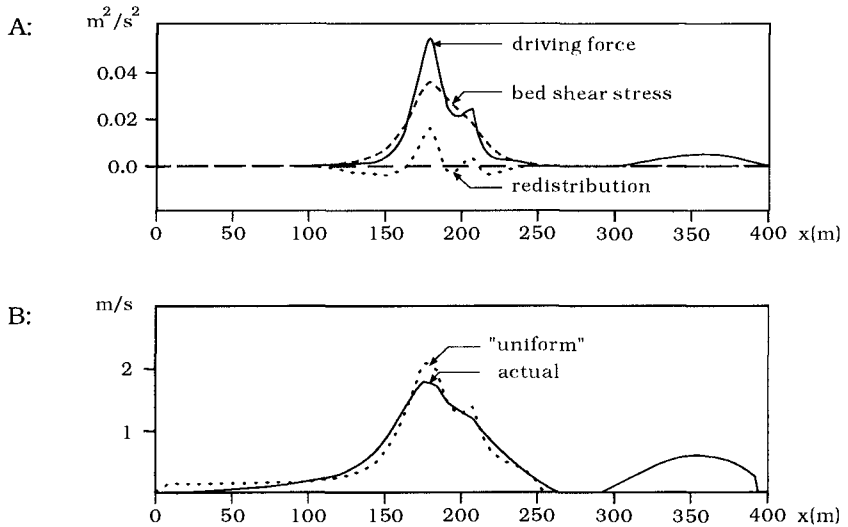


Figure 9. (A) full drawn line:  $\partial(S_{xy}/\rho)/\partial x$  broken line:  $\bar{\tau}_b/\rho$ , dotted line:  $\partial(D\bar{u}\bar{v})/\partial x$ . (B) Time mean longshore velocity. Full drawn line: actual velocity, dotted line: assuming steady, uniform conditions.

### Longshore non-uniformity of the coastal topography

The bar has been made non-uniform in the longshore direction by giving it a sinusoidal perturbation, representing very weak rip channels. The shear waves have been analysed for varying amplitudes of the perturbation. The strength of the shear waves is characterized by the standard deviation of the velocity fluctuations at the bar crest. Fig. 10 shows the strength of the shear waves as a function of the amplitude of the perturbation of the bar in the profile of Fig. 1. The longshore wave length of the perturbation is 400m. It is seen that the non-uniformity of the bar effectively suppresses the shear waves and that they have disappeared completely for an amplitude of 0.4 m.

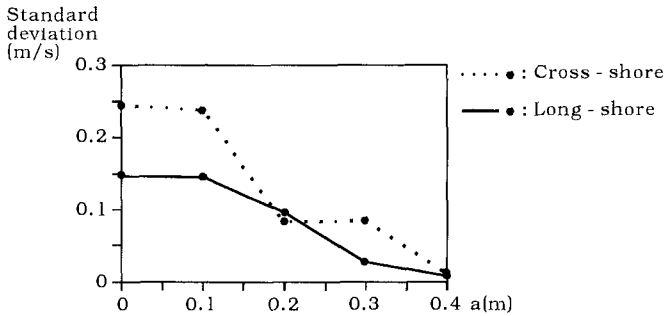


Figure 10. The strength of the shear waves as function of the amplitude of the perturbation of the bar.

### Dispersion by shear waves

In addition to the exchange of momentum, the shear waves are effective for dispersing suspended or dissolved matter in the surf zone. This is illustrated by a simulation with the advection-dispersion module of MIKE-21. The hydrodynamic simulation corresponds to the example considered previously. A constant source is placed at the bar crest near the upstream boundary. The dispersion coefficient has been specified to be zero. Figure 11 shows the instantaneous concentration field of the released matter. It can be seen that the plume is deformed by the shear waves and broken up in unconnected units - 'cat eyes', which are also observed in flow visualizations of shear layers. In the case where the source is located at a point offshore of the point of maximum mean longshore current velocity, the "cat eyes" will be formed around another row of vortices.

### Conclusions

Shear waves can be simulated in a numerical model for wave-driven currents. The simulations can be used to study the formation of shear waves and the properties of the fully developed shear waves.

The shear waves are found to be effective in the cross shore exchange of momentum and matter. They reduce the longshore sediment transport and causes a cross shore transport. The present simulation can be improved in a number of ways, e.g. by including wave-current interaction in the description of the flow resistance and by including the effects of time-and-space lag in the description of the sediment transport.

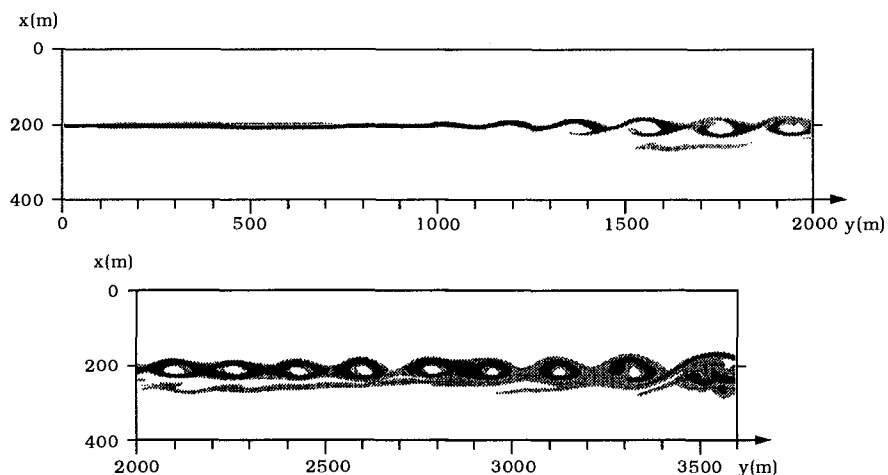


Figure 11. Dispersion of suspended material discharged at the bar crest.

### Acknowledgements

This work was founded jointly by the Danish Technical Research Council under the programme "Marin Teknik" and by the Commission of the European Communities, Directorate General for Science, Research and Development under MAST contract no. MAS2-CT92-0027 under the programme "G8 Coastal Morphodynamics".

The mathematical model MIKE-21 has been made available by the Danish Hydraulic Institute (DHI).

### References

Battjes, J.A. and Janssen, J.P.F.M., 1978: Energy loss and set-up due to breaking in random waves. Proc. 16th Int. Conf. on Coastal Eng., Hamburg, ASCE 1979, Vol. 1, pp. 569-587.

Bowen, A.J. and Holman, R.A., 1989: Shear instabilities of the mean longshore current. 1. Theory. J. Geophys. Res. 94(C12), pp. 18.023-18.030.

Deigaard, R., Fredsøe, J. and Hedegaard, I.B., 1986: Suspended sediment in the surf zone. *J. Waterway, Port, Coastal and Ocean Eng.* Div., ASCE, 112(1), pp. 115-128.

Dodd, N., 1994: On the destabilization of a longshore current on a plane beach: Bottom shear stress, critical conditions, and onset of instability. *J. Geophys. Res.* 99(C1), pp. 811-824.

Dodd, N. and Thornton, E.B., 1992: Longshore current instabilities: growth to finite amplitude. *Proc. 23rd Int. Conf. on Coastal Eng., Venice, ASCE 1993, Vol. 3*, pp. 2655-2668.

Fredsøe, J., Andersen, O.H. and Silberg, S., 1985: Distribution of suspended sediment in large waves. *J. Waterway, Port, Coastal and Ocean Eng.*, ASCE, 111(6), pp. 1041-1059.

Hino, M., 1974: Theory of formation of rip-current and cuspidal coast. *Proc. 14th Int. Conf. on Coastal Eng., Copenhagen, ASCE 1975, Vol. 1*, pp. 901-919.

Oltman-Shay, J., Howd, P.A. and Birkemeier, W.A., 1989: Shear instabilities of the mean longshore current. 2. Field observations. *J. Geophys. Res.* 94(C12), pp. 18.031-18.042.

Putrevu, U. and Svendsen, I.A., 1992: Shear instabilities of longshore currents: a numerical study. *J. Geophys. Res.* 97(C5), pp. 7283-7303.

## CHAPTER 139

### BEACH NOURISHMENT AND DUNE PROTECTION

Hans H. Dette<sup>1</sup> and Arved J. Raudkivi<sup>2</sup>

#### ABSTRACT

The environmentally favoured method of beach maintenance by nourishment with sand raises the question of minimization of the average annual sand requirement. In the following sand loss estimation models are compared to field data. A concept for protection of the dry beach and dune areas against erosion during stormtides is discussed as a means of reducing the required sand volumes for the beach maintenance.

#### INTRODUCTION

Sand beaches play a rapidly increasing part for general holiday and weekend activities. Consequently, the "stability" of beaches receives more and more attention. A stable sand beach assumes under a constant wave action an equilibrium form on which the hydrodynamic forces are in equilibrium with the resistance forces of sand grains to movement. The shore normal net movement of sand ceases on such a profile and the amount of sand mobilized by the wave action has a minimum. Large disturbances can be caused to the dynamic equilibrium conditions (average due to usual wave conditions) by the erosion due to heavy storms and storm tides. The sand carried by the storm waves from the high beach into the usual surf zone is after the storm "surplus" to the requirements and has to be redistributed, i.e. in the amount of loss increases.

#### BEACH NOURISHMENT

Beach nourishment is regarded today as the environmentally acceptable method of beach protection. The need for nourishment may arise from a number of causes. For example, an island may lose its beach by littoral transport that is carried beyond the ends of the island and is not returned to the beach; i.a. an open sand system. Likewise a reduction of sediment supply to a coast, by whatever cause, will lead to local erosion that may have to be counteracted by nourishment.

---

<sup>1</sup> Leichtweiß-Institute, Technical University of Braunschweig, POB 3329, 38023 Braunschweig, Germany

<sup>2</sup> University of Auckland, New Zealand, 7 Coates Rd., Howick, Auckland, New Zealand



Nourishment itself also disturbs the dynamic equilibrium of the underwater profile and leads to increased losses. The extent of the disturbance depends on the grain size of sand used in nourishment relative to the native beach sand and on the coastwise extent of the beach fill.

Detle et al. (1994) introduced the assumption that for a two-dimensional beach fill, Fig. 1, the erosion rate under constant energy flux is proportional to the volume. Hence, the eroded volume is

$$V(t) = k_2 e^{-k_1 t} = V_0 e^{-k_1 t} \tag{1}$$

for  $V(t) = V_m$  at  $t = 0$ . A renourishment is required when  $V(t) = V$  and the required volume is

$$V_n = V_m (2^{T_r/T_h} - 1) \tag{2}$$

where  $V_n$  is the volume of nourishment per m,  $V_m$  the minimum volume under an equilibrium profile (Fig. 2),  $T_r$  the renourishment interval and  $T_h$  is the half-life of the beach fill when  $V(t = T_h) = V_0 / 2$ .

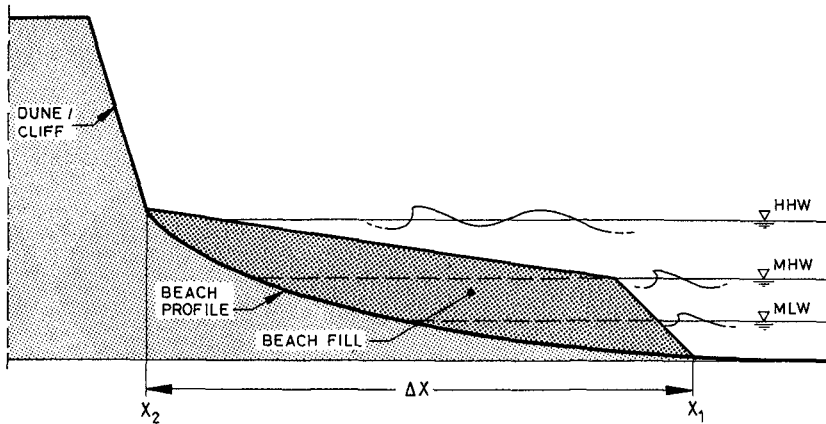


Fig. 1 Cross-section of beach nourishment (schematic).

According to eqn (2) the required renourishment volume,  $V_n$ , at a constant  $V_m$  is a function of  $T_r$  and  $T_h$  only. Consequently, the same condition can be maintained with a shorter repetition interval,  $T_r$ , and smaller volume of beach fill,  $V_n$ , or with larger volumes at longer intervals.

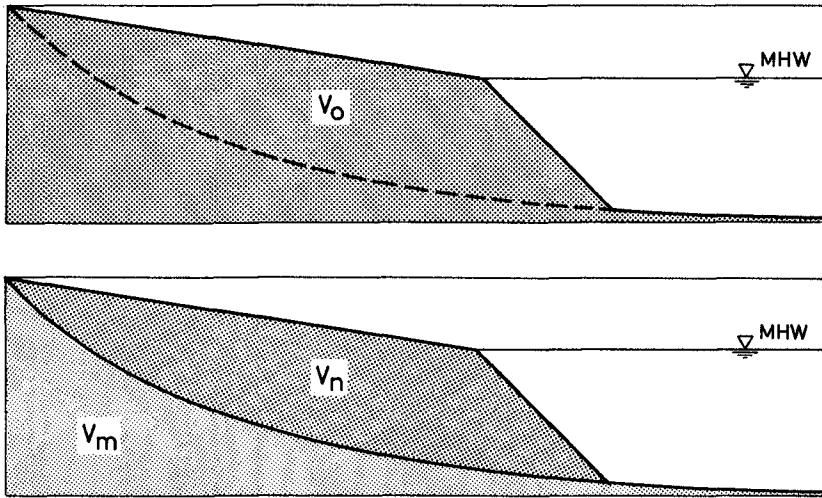


Fig. 2 Definition of volumes  $V_0$ ,  $V_m$  at  $t = 0$  after placement of the beach fill (schematic)

The average required rate of sand supply is  $Q_n = V_n / T_r$  or

$$Q_n = \frac{V_m}{T_r} (2^{T_r/T_h} - 1) \tag{3}$$

The rate increases exponentially with  $T_r$ . Conversely,  $Q_n$  goes to minimum if  $T_r$  goes to zero, i.e. a continuous nourishment. Whether a continuous nourishment (according to demand) is practicable is another matter that is not further discussed here, except to say that hydraulic conveyance as sand by - passing has been used for a long time.

Expressing the rate of required nourishment as a ratio of  $Q_n(T_r)$  to  $Q_{min}$  as

$$\alpha = \frac{2^{T_r/T_h} - 1}{(T_r/T_h) \ln 2} \tag{4}$$

shows that both the required beach fill volume (eqn (2)) and the average sand supply rate increase exponentially with repetition interval, Table 1.

$T_r / T_h$	$V_n / V_m$	$\alpha$
0	0	1
1/2	0,41	1,20
1	1	1,44
3	7	3,37
5	31	8,94

Table 1 Dimensionless beach fill volumes  $V_n / V_m$  and average dimensionless annual sand requirement as a function of the ratio of nourishment interval to the half life of the fill,  $T_r / T_h$ .

The result also indicates that for a given  $V_m$ , which is a function of the wave climate and grain size of the beach material, the minimum required sand supply rate occurs at  $T_r = 0$ , i.e. continuous supply.

The deduction is that the optimum supply rate  $Q > Q_{min}$ , is a compromise between practical requirements and aspects that affect the half-life.

Dean (1983) showed on the basis of the Pelnard-Considère (1956) equation that the length of the beach fill,  $l$ , affects the loss rate as

$$(t_p)_2 = (t_p)_1 \frac{l_2^2}{l_1^2} \frac{H_{b1}^{5/2}}{H_{b2}^{5/2}} \tag{5}$$

where  $t_p$  is time required for a percentage  $p$  of the fill volume to be lost,  $H_b$  is the breaker height and subscripts 1 and 2 refer to particular fills.

FIELD DATA

Data are available from six beach nourishment sites on the island of Sylt in the North Sea (by the courtesy of ALW Husum). The coast is a high energy coast with a mean annual shore normal energy flux of ca. 30 000 kWh per m beach. The data from Westerland are plotted in Fig. 3. The volumes were recorded as those above the 4 m datum below mean sea level.

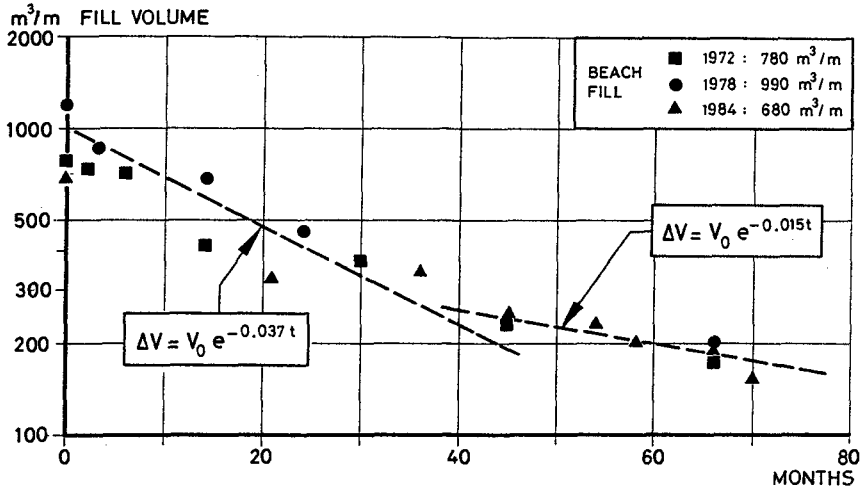


Fig. 3 Decay of repeated beach fill volumes in front of coastal structures at Westerland; Sylt/North Sea

The data show that the initial rate of decrease of the beach fill volume tends to support the exponential loss concept according to eqn (1). However, after about 2.5 to 3 years the slope changes appreciably and the data approach another exponential loss rate. Similar behaviour is illustrated by the data from the other five sites along the southern half of the coastline, Fig. 4. Although the scatter of data points for the reduced loss rate is substantial, the trend is unmistakable.

The relationships like eqn (5) are difficult to verify because although the fill profiles are known as a function of time the amounts of material brought into the study area by littoral transport are essentially unknown. At Westerland the three fills had different lengths. The 1972 fill was in the form of a peninsula into the surf zone with 1 ~ 350 m, extending about 250 m seaward at mean sea level. In 1978 an about 1 km long beach fill of 80 m width and in 1984 one of 1.5 km were placed. Assuming that the wave height remained the same eqn (5) indicates that the time to lose the same percentage of sand from the 1984 fill volume should be approximately 18 times that of 1972. Even for the similar fills of 1 km about 1.5 km lengths the ratio should be 2.25, yet Fig. 3 indicates that the volume was halved in approximately in the same length of time.

An additional feature of the field data is that the seaward slope of the beach fill has a strong effect on the loss of material during storms from the normally dry beach as illustrated by Fig. 5 for two successive winters with comparable storm tide histories.

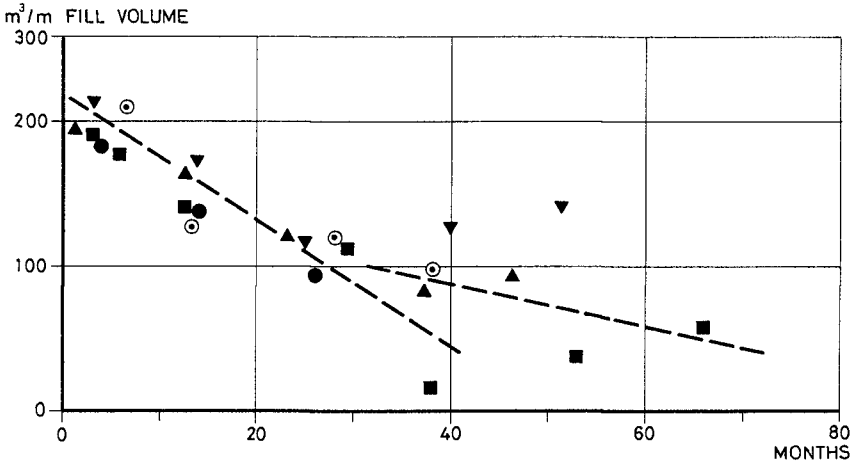


Fig. 4 Decay of beach fill volumes at 5 sites in front of dunes at the west coast of Sylt/North Sea

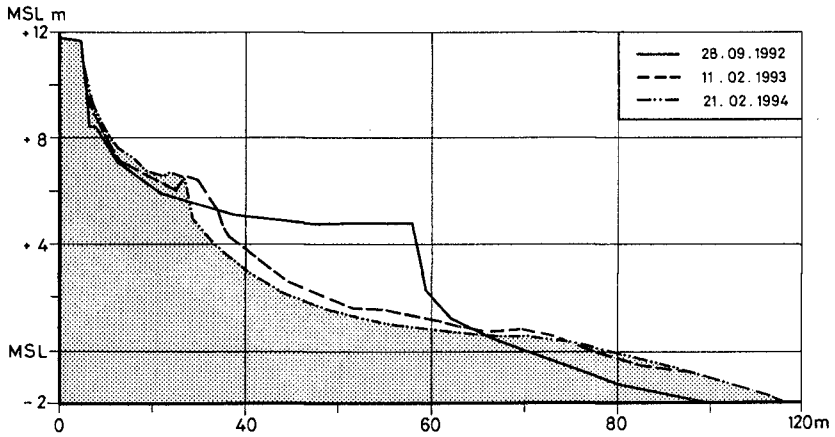


Fig. 5 Erosion of dry beach by storm tides on the west coast of Sylt

Peak water levels above MSL were 2.86 m and 3.25 m in 1993 and 1994, respectively with residence times above 2.0 m of ca. 50 and 80 hours respectively. The flat slopes with reduced losses are well described by the Dean-type relationship

$$h = A x^n \quad (6)$$

Apparently, when the waves are able freely run up and down the slope the losses are minimized.

## DUNE PROTECTION

Substantial quantities of sand can be eroded by storm tides from the usually dry beach zone. Steep storm waves at raised water level transport large quantities of sand shore normal to the usual surf zone. Locally these quantities can reach 200 m<sup>3</sup>/m. For example, the 1990 storms eroded 1.8 x 10<sup>6</sup> m<sup>3</sup> of sand from the west coast of Sylt, averaging ca. 60 m<sup>3</sup>/m for the coastline. In many instances only a fraction of this sand is brought back to the beach face by subsequent wave action. The restoration of the dry beach and dune by wind-borne sand transport too is a slow process. Especially in open sand systems most of the "surplus" sand in the every day surf zone can be lost in littoral transport after the storm, i.e. carried beyond the ends of the island and lost from the local sand system. On an out of equilibrium underwater profile the amount of sand mobilized by the daily wave action is higher and hence also the amounts transported currents.

Consequently, for an efficient management of beach nourishment volumes and for the protection of dry beach/dune the uncontrolled transfer of large volumes of sand into the surf zone during severe storms should be avoided. Raudkivi (1989) proposed a method of reduction of the sand loss with the aid of geotextile membrane, Fig. 6.

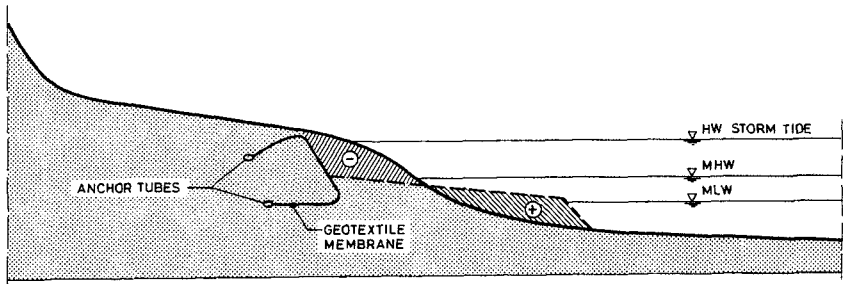


Fig. 6 Damage limitation of the dry beach and dune by a storm tide with the aid of a geotextile membrane (schematic)

The sand seaward of the membrane may be eroded during a storm or a sequence of storms but that behind it is protected. The membrane usually is called in action only a few days in a year and is thus not comparable to a seawall. If the membrane is uncovered the sand cover has to be restored from the lower beach. The location of the membrane is a matter of optimization. Too near to the water's edge the frequency of maintenance increases, too far the amount of sand lost increases.

In general, an uncontrolled erosion of the high beach leads to an erosion escarpment. In the sand behind the escarpment (or dune) the wave impacts maintain a water table in the sand that is a little higher than the local mean water level at the escarpment. At each wave trough a step is created in the water level, Fig. 7, and the sand starts to drain. The outflow of water concentrates at the level of water in front of the escarpment and carries sand with it. This leads to an undercutting of the sand face which tends to slide down in layers. The loose sand is rapidly dispersed by waves and the process repeats itself.

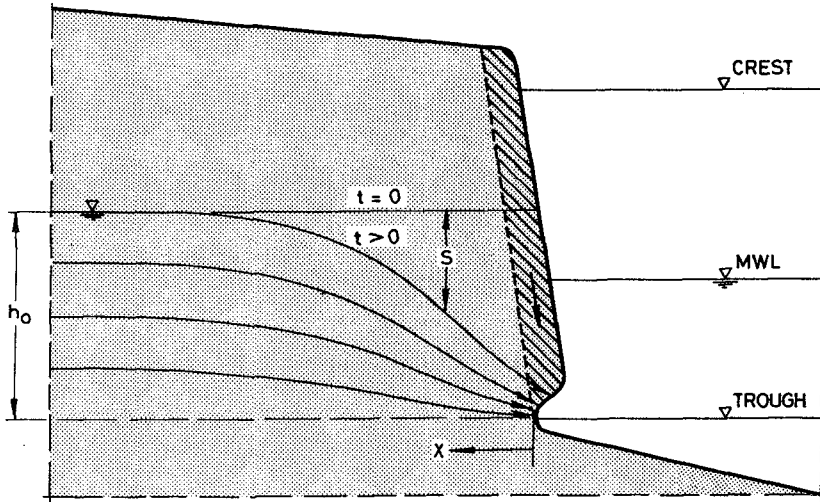


Fig. 7 Drainage and undercutting of a sand face due to wave action (schematic)

The problem of drainage through a "vertical" face was treated by Nguyen and Raudkivi (1983). Fig. 8 shows the propagation of the phreatic surface back from the sand face. The drawdown,  $s$ , at a distance  $x/h_0$  is expressed in terms of a

dimensionless time  $\tau$  as

$$s = h_0 [1 - G(x/h_0, \tau)]$$

$$\tau = \left( \frac{K}{S_v h_0} \right) t \tag{7}$$

where  $K$  is the permeability of sand (m/s),  $S_v$  is the volume of water retained in the pore space ( $S_v < n$  the porosity) and  $t$  is time.

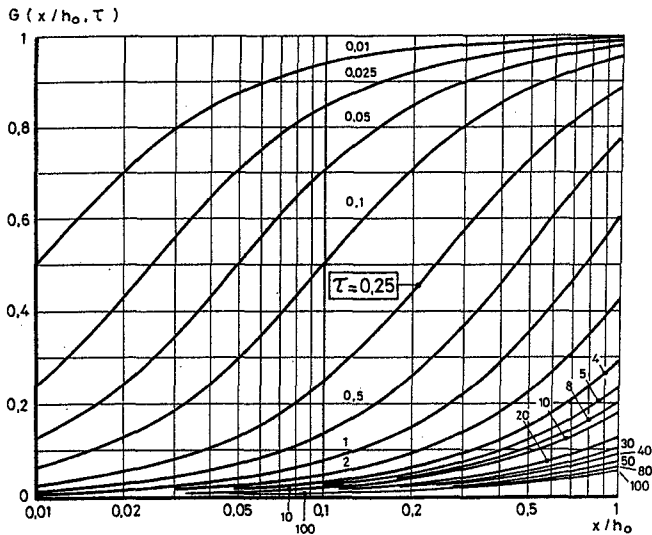


Fig. 8 Movement of the phreatic surface by drainage through a vertical face (Nguyen and Raudkivi, 1983)

The order of magnitude of the term  $(k/S_v h_0)$  is ca  $10^{-4}$ . Hence, already at  $\tau = 0.01$  the position of the phreatic surface corresponds to that at ca 2 minutes. Consequently, the water surface translation are confined to the immediate vicinity of the sand face, within a fraction of  $h_0$ , i.e. ca 10 to 20 %.

The membrane serves to restrain the sand grain during the drainage periods and to prevent the undercutting. The main requirement, apart from required tensile strength, weathering and abrasion properties, is that it must enable free flow of water, i.e. it must be more permeable than the sand. This is achieved by using an "opening size" in the membrane of about  $d_{65}$  of the sand.



During the wave impacts the wave forces are taken by the sandgrains and the membrane is stressed only by the through flow of water. The pressure waves attenuate in the sand very rapidly due to the air in the voids and in the water, c.f. studies by Nago and Maeno (1987). Consequently, any liquefaction of sand is confined to the immediate vicinity of the sand face.

A system of membranes as shown in Fig. 9 was tested in the Large Wave Flume in Hannover (Führböter, et al. 1991). Fig. 10 shows the initial profile and that after 15 hrs subject to monochromatic waves of 6 - 9 secs with wave heights most of the time 1.0 m and up to 1.3 m. The deformations of the installed membrane were generally less than 10 cm.

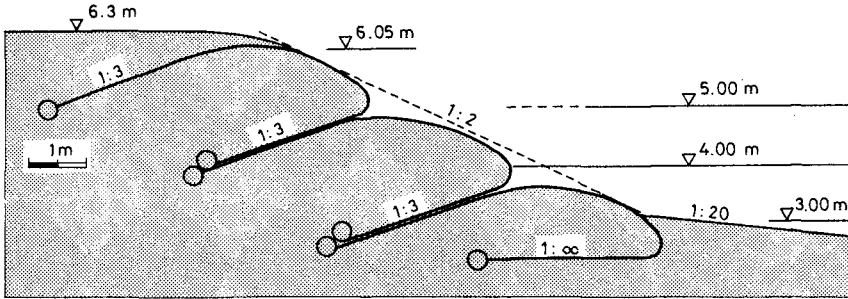


Fig. 9 Cross-section of the three-layered membrane tested in the Large Wave Flume in Hannover

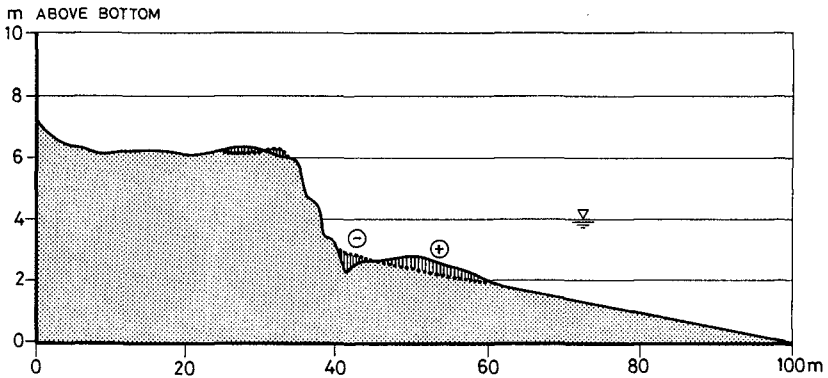


Fig. 10 Membrane after 15 hours of wave attack with waves up to 1.3 m height in the Large Wave Flume

The membrane limits the management of beach nourishment volumes to those required to maintain the surf zone under normal sea conditions, i.e. to the supply of sand to replace that lost from the system by the daily littoral transport. The membrane preserves all the sand in the high beach and dune.

About 2 km of such a membrane (two layers) were installed as hurricane protection 1992/93 in Fiji and 300 m in the three layers in a dune in front of a building at the dune's edge on Sylt 1991 (Fig. 11). Both have performed according to expectations.



Fig. 11 Uncovered geotextile membrane in front of a dune after called in action during a storm surge (photo: Raudkivi, 1994)

#### ACKNOWLEDGMENT

This work was undertaken as part of the MAST G 8 Research Programme - Coastal Morphodynamics. It was funded partly by the Commission of the European Communities. Directorate General for Science, Research and Development under Contract MAS 2-CT 92-0027, partly by the German Ministry of Research and Technology (BMFT).

## REFERENCES

- Dean, R. G. (1983) Principles of beach nourishment. Handbook of coastal processes and erosions, P. D. Komar, ed., CRC Press, Boca Ratan, Fla., 217 - 231.
- Detle, H. H., Führböter, A. and Raudkivi, A. J. (1994) Interdependence of Beach Fill Volumes and Repetition Intervals. Journal of Waterway, Port, Coastal and Ocean Engineering, Vol. 120, No 6.
- Führböter, A., Raudkivi, A. J., Dette, H. H. and Dierken, H. (1991) Untersuchungen zur Begrenzung der Ausräumung des hohen Strandes vor Dünen über die Dauer von Sturmfluten. Bericht Nr. 721, Leichtweiss-Institute, Techn. Univ. Braunschweig, Germany.
- Nago, H. and Maeno, S. (1987) Pore pressure and effective stress in a highly saturated sand bed under water pressure variation on its surface. Natural Disaster Science, Vol. 9, No 1. 23 - 25.
- Nguyen, V. U. and Raudkivi, A. J. (1983) Analytical solution for transient two-dimensional unconfined ground water flow. Hydrological Sciences Journal, Vol. 28, No 2, 209 - 219.
- Pelnard-Considère, R. (1956) Essai de théorie de l'évolution de formes de rivage en plages de sable et de galets". 4th Journées de l'Hydraulique, Les Energies de la Mer, Question III, Raport No 2, Paris, France, (in French).
- Raudkivi, A. J. (1989) Untersuchungen zur Optimierung des Küstenschutzes auf Sylt. Bericht des Amtes für Land- und Wasserwirtschaft Husum (not published).

## CHAPTER 140

# PROFILE CHANGE OF A SHEET FLOW DOMINATED BEACH

Mohammad Dibajnia <sup>1</sup>, Takuzo Shimizu <sup>2</sup> and Akira Watanabe <sup>3</sup>

### Abstract

A new and detailed model for predicting the profile change of a real beach is presented. The model is based on the sediment transport formula of Dibajnia and Watanabe (1992) and therefore incorporates, explicitly, the asymmetry of the near-bottom orbital velocity and the undertow into the transport of bottom sediment. Its applicability is examined by using the data of beach profile change obtained from prototype scale laboratory experiments as well as field measurements. It is shown that quite accurate profile simulation is possible when the details of the flow field and transport mechanism are considered.

## 1. Introduction

An important phenomenon concerned in short-term prediction of nearshore bottom topography changes is the formation and disappearance of longshore bar systems. It is now clear that during storms, usually the shoreward sheet flow sediment transport due to large waves faces the seaward transport of the undertow in a region close to the breaking point and makes a bar. This bar in turn, may be washed out by the undertow of some larger waves and move to deeper waters, or it could be forced by the shoreward transport of other waves to move into shallower waters and form a smaller bar or recover the beach. Also we know that under field conditions, sheet flow movement is the predominant transport mode

---

<sup>1</sup>Associate Professor, Dept. of Civil Eng., Univ. of Tokyo, Bunkyo-ku, Tokyo 113, Japan.

<sup>2</sup>Penta-Ocean Construction Co. Ltd., 2-2-8 Koraku, Bunkyo-ku, Tokyo 112, Japan.

<sup>3</sup>Professor, Dept. of Civil Eng., Univ. of Tokyo, Bunkyo-ku, Tokyo 113, Japan.

over a significant part of the nearshore area including both inside and outside of the surf zone.

In the present study a numerical model for simulating the profile transformation of a real beach is presented. The model is based on sediment transport formula of Dibajnia and Watanabe (1992) which incorporates the asymmetry of near bottom orbital velocity and superimposed currents into estimating the sheet flow sand transport rates. The formula is extended here to cover suspended load as well as bed load transports. Applicability of the model is confirmed through comparison of the simulated profiles with those obtained from prototype scale laboratory experiments and field data. A new formulation for estimating the return flow velocity in the field is also presented.

## 2. Experimental and Field Data

Kajima *et al.* (1982) investigated on-offshore beach profile changes under regular waves in a prototype scale wave flume for a variety of incident wave, bottom slope, and grain size conditions. Two of their experimental cases, corresponding to extreme conditions of erosion and accretion, are selected to be tried against the present model. The conditions for each case are shown in Table 1. In this table  $\tan \beta$  is the initial bottom slope,  $d_{50}$  the median grain size of beach material,  $T$  the wave period, and  $H_0$  the deepwater wave height.

CASE	$\tan \beta$	$d_{50}$ mm	$T$ s	$H_0$ m	Breaker form
3-3	5/100	0.27	12.0	0.65	plunging
3-4	5/100	0.27	3.1	1.62	spilling

Table 1: Experimental conditions

The field measurement data are those reported by Kuriyama (1991) and have been obtained at Hazaki Oceanographical Research Facility (HORF) which belongs to the Port and Harbour Research Institute of the Japanese Ministry of transport and is located at Kashima beach, Ibaraki Prefecture, Japan. The average bottom slope at the site is about 1/60 and the median grain size,  $d_{50}$ , is 0.18 mm. The field investigations have been conducted from the 12th to 26th of September 1988, during which a strong storm has occurred. Profile survey data at the beginning and end of this period are given. Time histories of the offshore significant waves at a mean depth of about 24 m and those of wave height, bottom elevation, tidal level, and cross-shore steady current at a point inside the surf zone, P145, are also reported. The graphical data are transferred to digital data with an interval of two hours by using a digitizer and are used and demonstrated in the present paper.

### 3. Elements of The Model

#### 3.1 Calculation of the wave field

For regular waves, the time-dependent mild-slope equations and numerical scheme of Watanabe and Dibajnia (1988) are used. The equations can take care of wave shoaling, reflection, breaking, and energy dissipation in cross-shore direction. Location of the breaking point is calculated with the generalized breaker index diagram proposed by Watanabe *et al.* (1984).

As for the calculation of the waves in the field, the method proposed by Isobe (1987) for irregular waves is applied. This model is based on an energy conservation equation which contains a breaking dissipation term. The equation which can take care of wave shoaling, breaking, and energy dissipation in cross-shore direction reads:

$$\frac{d}{dx}(Ec_g) = -\frac{5}{2}P_B E \sqrt{\frac{g}{h}} \sqrt{\frac{\alpha_{1/3} - \alpha_r}{\alpha_s - \alpha_r}} f_d(kh) \tan \beta \quad (1)$$

in which  $E$  is the total wave energy,  $x$  the cross-shore distance,  $g$  the acceleration of gravity,  $\alpha$  the ratio of water particle velocity at the wave crest to the wave celerity,  $c_g$  the group velocity,  $f_d$  a function of the wave number  $k$  and the water depth  $h$  given by Isobe (1987), and  $\tan \beta$  the local bottom slope. Values of  $c_g$  and  $f_d$  should be calculated by using the peak frequency of the spectrum.  $\alpha_r = 0.135$  and  $\alpha_s = 0.4(0.57 + 5.3 \tan \beta)$  are the values of  $\alpha$  for broken waves recovered in a uniform depth region and for breaking waves on a uniform slope, respectively (see Dibajnia and Watanabe, 1988). In the above equation  $P_B$  is the breaking probability and is obtained from the following relation

$$P_B = \left\{ 1 + 2.004 \left( \frac{\alpha_b}{\alpha'_{1/3}} \right)^2 \right\} \exp \left[ -2.004 \left( \frac{\alpha_b}{\alpha'_{1/3}} \right)^2 \right] \quad (2)$$

where  $\alpha_b$  is the critical value of  $\alpha$  for breaking and  $\alpha'_{1/3}$  is the value of  $\alpha$  if the waves continue to shoal without breaking. By using  $P_B$ , Equation (1) can be used for both outside and inside of the surf zone.

For both regular and irregular waves, the change in the position of shoreline due to the setup of mean water level (and tides) is incorporated through applying a moving boundary technique which allows a variable grid size at the shoreline.

#### 3.2 Estimation of the near-bottom velocity profile

In reality, waves are nonlinear due to finite depth and asymmetric due to the bottom slope. Despite recent developments in applying Boussinesq equations to predicting the relevant properties of waves over the whole nearshore region, an empirical method is applied in the present study to estimate the near-bottom

velocity profiles. This is because that only information about significant wave height and period of the incident waves are available for the field case. Isobe and Horikawa (1981), based on laboratory experiments, proposed empirical formulas for estimation of velocity profile properties of normally incident waves on a beach with uniform slope up to the point of breaking. The validity of their relations for estimation of velocity profile of prototype-scale shoaling waves over an erodible bed has been verified by Maruyama *et al.* (1983). In the absence of a reliable theory or formulation for breaking waves, in the present work the method of Isobe and Horikawa (1981) is applied to the surf zone region as well as the offshore region. It has been shown in a separate paper (Dibajnia *et al.*, 1992) that inside the surf zone, the method of Isobe and Horikawa gives reasonable results for spilling breakers, but fails to predict the velocity profile of plunging breakers accurately.

The method is also applied to estimating the asymmetry of orbital velocity profile at the bottom for irregular waves by using values of the significant wave height and period. According to the experimental study of Sato *et al.* (1988), the asymmetry of velocity profile in the surf zone is less than those in the offshore and in the breaking region. Therefore, the estimated velocity profiles inside the surf zone are modified gradually from the breaking point to the shoreline.

### 3.3 Calculation of the undertow

Undertow is the name given to the average seaward return flow found below wave trough level. It balances the mass flux carried shoreward by breaking waves including the effect of the surface roller. Despite its simple qualitative description, a general mathematical formulation of the undertow and its vertical distribution is difficult and not yet available. For regular waves over simple bottom profiles, Okayasu *et al.* (1990) took the mass balance approach and presented a model based on the experimental results and the assumption that following the breaking, the wave energy is transferred to the roller or large vortices, is kept by them for a while, then is conveyed to the small structure turbulence and is dissipated. The time-dependent mild-slope equations of Watanabe and Dibajnia (1988) were used to estimate the rate of energy transfer. The model showed good agreement with the experiments, however, its application to more general cases is not straightforward.

A simple model based on the assumption that the mass flux of a bore propagating shoreward is proportional to the square of the wave height was presented by Sato *et al.* (1988). By assuming that the corresponding return flow is uniform over the local mean water depth,  $D$ , the steady component of near-bottom velocity was estimated as

$$U = U_w + U_b + U_e \quad (3)$$

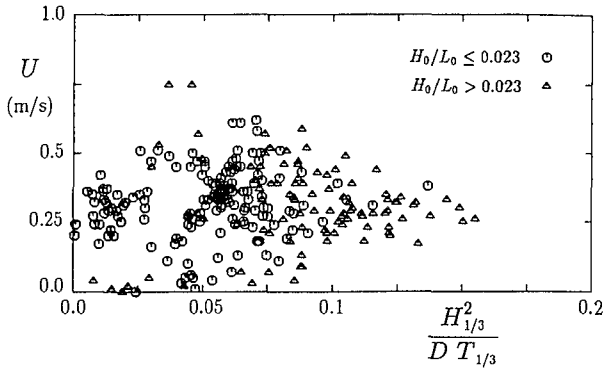


Figure 1: Undertow velocity measured at the point P145 versus Eq. (4).

in which  $U_b$  is the undertow velocity given as

$$U_b = -A \frac{H^2}{D \cdot T} \quad (4)$$

,  $U_w$  the offshore flow compensating the onshore mass flux due to the irrotational wave motion,  $U_e$  the Eulerian mass transport velocity at the edge of the laminar boundary layer,  $T$  the wave period,  $H$  the wave height, and  $A$  a nondimensional coefficient of the order of unity. These two models are used here for calculating the undertow velocity of regular waves.

For the irregular waves in the field, in order to examine the applicability of Eq. (4) to estimating the undertow velocity caused by breaking, values of the significant wave height,  $H_{1/3}$ , and the mean water depth measured at the point P145, together with the values of the significant wave period,  $T_{1/3}$ , of offshore waves are substituted into Equation (4) and the results are compared with the measured values of the cross-shore mean current velocity at P145 as shown in Fig. 1. A large scatter is observed and it is hard to define a value for the coefficient  $A$ . Those data with a deepwater wave steepness greater than 0.023 are shown by triangle symbols. It may be seen that these data are more or less separated from the others. On the other hand, it is expected that the undertow velocity varies with the beach slope. From these two points one may conclude that the undertow velocity should depend on the surf similarity parameter,  $\xi = \tan \beta / \sqrt{H_0/L_0}$ , which is often used to classify the breaker types. Thus, the return flow velocity should vary with the breaker type, as it is indeed a breaking generated process. Also, using the bottom slope at the breaking point,  $(\tan \beta)_b$ , would be more appropriate than  $\tan \beta$ . Figure 2 shows the results of such an analysis when  $\xi_b = (\tan \beta)_b / \sqrt{H_0/L_0}$  is used instead of  $\xi$ . In this figure it is assumed, considering the incident waves, that during the first half of the measurement period the waves were breaking in deeper waters on a slope of 1/60 because they were large (see Fig. 8), and during the second half they were breaking on the bar closer to the



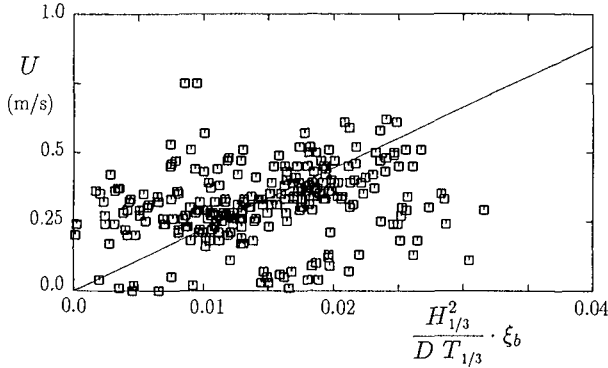


Figure 2: Undertow velocity measured at the point P145 versus Eq. (5).

shore with a slope of about 1/25. It can be seen that the data show a good trend which may be written as

$$U_b = -22 \frac{H_{1/3}^2}{D \cdot T_{1/3}} \cdot \xi_b \tag{5}$$

The next problem regarding the undertow of irregular waves is about its distribution in cross-shore direction. In case of regular waves there is a certain breaking point which controls the distribution. For irregular waves, however, there is not such a point and at any location some of the waves may break because waves of different heights and periods are involved. At each point it is only this breaking portion of the waves which contributes to the generation of the undertow. Thus, considering the ratio of the energy of the broken waves to the total wave energy we may write

$$U = -22 \left( 1 - \frac{E}{E'} \right) \frac{H_{1/3}^2}{D \cdot T_{1/3}} \cdot \xi_b \tag{6}$$

for irregular waves. Here,  $E$  is the total wave energy, and  $E'$  the total wave energy of an imaginary case in which the same waves shoal without breaking. P145 is a point inside the surf zone where all the waves are expected to break and hence  $E/E' \simeq 0$ . At other locations, however, because of irregularity only part of the waves may break and it is only this breaking portion of the waves which is taken into account.

### 3.4 Sediment transport rate

The sediment transport formula of Dibajnia and Watanabe (1992) is used. This formula has been made for the transport under sheet flow conditions, but is extended here to be able of estimating the suspended load and bed load transport

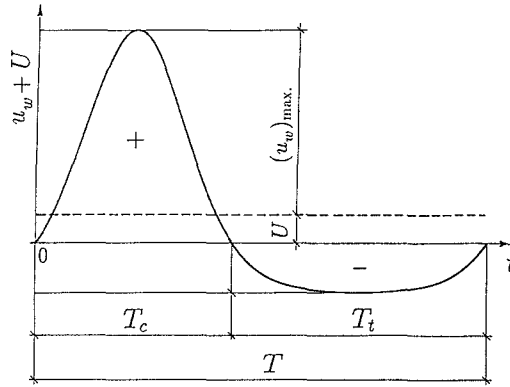


Figure 3: Definitions for the near-bottom velocity profile.

rates as well. The nondimensional net transport rate,  $\Phi_s$ , is obtained by

$$|\Phi_s| = \frac{q_s(1 - \epsilon)}{Wd} = 0.001 \cdot \text{sign}(\Gamma) \cdot |\Gamma|^{0.55} \tag{7}$$

where

$$\Gamma = \frac{u_c T_c (\Omega_c^3 + \Omega_t^3) - u_t T_t (\Omega_t^3 + \Omega_c^3)}{(u_c + u_t)T} \tag{8}$$

in which  $u_c$  and  $u_t$  are the equivalent sinusoidal velocity amplitudes of positive and negative portions of the near-bottom velocity profile including the steady current (Fig. 3), respectively, and are defined as

$$u_c^2 = \frac{2}{T_c} \int_0^{T_c} (u_w + U)^2 dt \quad \text{and} \quad u_t^2 = \frac{2}{T_t} \int_{T_c}^T (u_w + U)^2 dt \tag{9}$$

with  $T_c$  and  $T_t$  being their corresponding time durations, respectively, and  $u_w$  the near-bottom orbital velocity. Values of  $\Omega_j$  in Eq. (8) are obtained as follows.

$$\left\{ \begin{array}{l} \text{if } \omega_j \leq \omega_{\text{critical}} \\ \text{if } \omega_j > \omega_{\text{critical}} \end{array} \right\} \left\{ \begin{array}{l} \Omega_j = \omega_j \cdot \frac{2WT_j}{d} \\ \Omega_j' = 0 \\ \Omega_j = \omega_{\text{critical}} \cdot \frac{2WT_j}{d} \\ \Omega_j' = (\omega_j - \omega_{\text{critical}}) \cdot \frac{2WT_j}{d} \end{array} \right. \tag{10}$$

with

$$\omega_j = \frac{1}{2} \frac{u_j^2}{sgWT_j} \tag{11}$$

In the above relations  $q_{\text{net}}$  is the net volumetric transport rate,  $\epsilon$  the sediment porosity,  $d$  the sediment grain size,  $W$  the sediment fall velocity,  $s = (\rho_s - \rho)/\rho$  where  $\rho$  and  $\rho_s$  are the densities of water and sediment, respectively, and the

subscript  $j$  should be replaced by either  $c$  or  $t$ . It should be mentioned that the factor 2 in relations (10) has been mistakenly omitted in the original paper of Dibajnia and Watanabe (1992).

In order to extend this formulation to estimate suspended load and bed load transport rates, we note that in the actual phenomenon at the sea bottom there is a transition region between the rippled bottom of suspended load and the flat bed of sheet flow. Over this region, the ripple height decreases, and the net transport rate changes its direction from the seaward suspended load to the shoreward sheet flow. Furthermore, experimental results show that  $\omega_{\text{critical}} = 1$  for sheet flow transport (Dibajnia and Watanabe, 1992), while  $\omega_{\text{critical}} = 0.03$  for the transport over ripples (Suzuki *et al.*, 1994). Therefore, by gradually changing the critical value of  $\omega$  from unity to a value of 0.03, an effect similar to the above phenomenon can be simulated. Thus

$$\omega_{\text{critical}} = 1 - 0.97\sqrt{\Lambda} \quad (12)$$

in which the parameter  $\Lambda$  is given by

$$\Lambda = \left[ 1 - [(\Psi_{\text{rms}} - 0.2)/0.4]^2 \right] \cdot \min(1, 2\lambda/d_0) \quad (13)$$

where  $\Psi_{\text{rms}}$  is the Shields number estimated in terms of the root mean square of near bottom velocity profile,  $\lambda$  the ripple wavelength, and  $d_0$  the orbital diameter of water particle displacement at the bottom. In this relation it is assumed that the transition from rippled bed to flat bed occurs in a parabolic manner as the Shields number increases from 0.2 to 0.6. For  $\Psi_{\text{rms}} > 0.6$ , which corresponds to the sheet flow condition,  $\Lambda$  should be set equal to zero. When  $\Psi_{\text{rms}} < 0.2$  then  $\Lambda = 1.0$ . The last term takes care of the fact that when  $d_0$  is much larger than  $\lambda$  on a rippled bed, the net transport rate should be in onshore direction. The functional form of Eq. (13), however, needs further varification. Also, the limiting values of the Shields number in this equation should be modified if Eq. (7) is to be tried against laboratory data on net sediment transport rate.

## 4. Results and Discussion

### 4.1 Prototype scale laboratory experiments

Profile change simulation of each experimental case is conducted for 15 hours of wave action and with both of the undertow models of Okayasu *et al.* (1990) and Sato *et al.* (1988), Eq. (3). Longer time durations are not tried because of the decrease in the accuracy of these models over complicated topographies. It is assumed that the undertow velocity is uniform over the local depth. In both of the models, the calculated steady currents are multiplied by hyperbolic functions in a region from the transition point to a point which is ten times of the breaking depth far from the breaking point in the offshore direction, so as to assume values of zero in the offshore region. The position of transition point is estimated by the

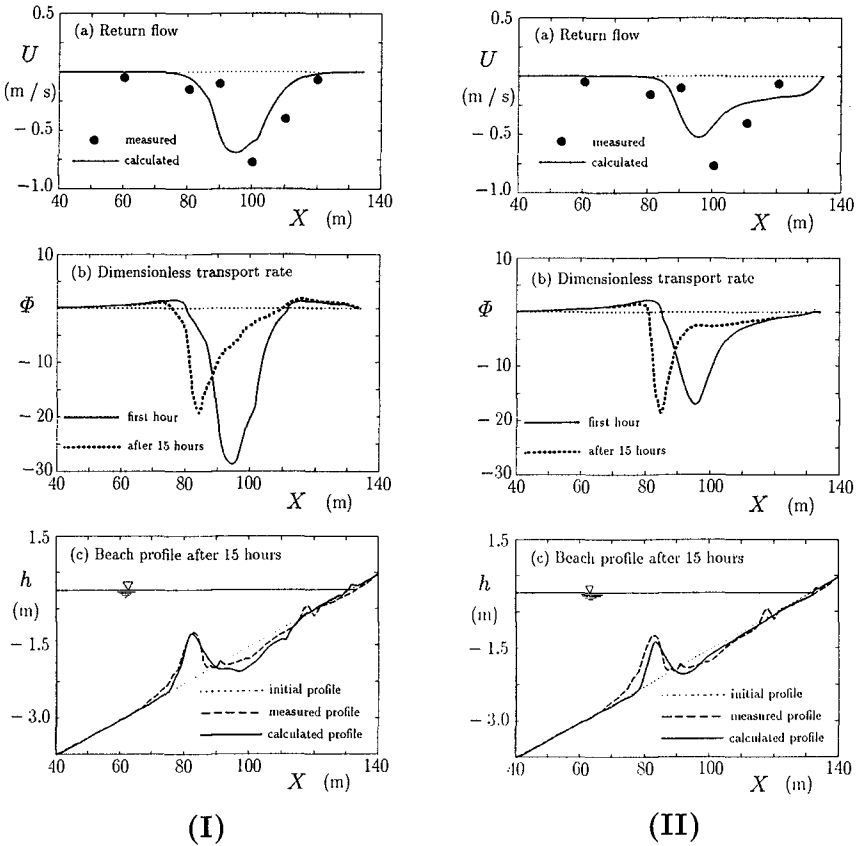


Figure 4: Simulation results for Case 3-4 with the undertow model of (I) Sato *et al.* and (II) Okayasu *et al.*.

formula of Okayasu *et al.* (1990). Steady current velocities obtained by the model of Sato *et al.* are multiplied by a hyperbolic function also in the region between the transition point and shoreline in order to obtain a more realistic distribution.

Figures 4 and 5 show the numerical simulation results and their comparison with the measurements. It is observed that the return flow calculated by Sato *et al.*'s model (with  $A = 4$ ) agree well with the experimental data for case 3-4. It should be noticed that this case has a breaker of spilling form. Therefore, the method of Isobe and Horikawa for calculation of near-bottom velocity profile is supposed to give reasonable profiles. As a result it is seen that the development of bottom profile and the position of bar are fairly well simulated. When the model of Okayasu *et al.* is applied to this case, also reasonable results are obtained.

On the other hand, the model of Sato *et al.* considerably underestimates the

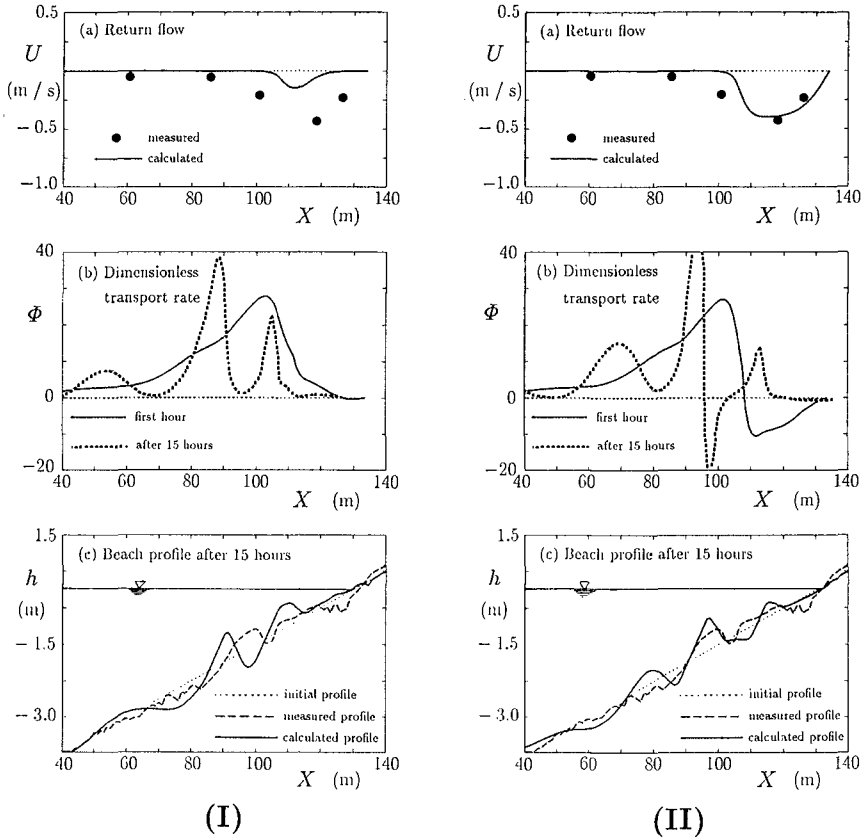


Figure 5: Simulation results for Case 3-3 with the undertow model of (I) Sato *et al.* and (II) Okayasu *et al.*.

undertow velocity of case 3-3. The performance of Okayasu *et al.*'s model in this case is better and the resulting profile is more acceptable. Strong reflection appears in the calculation of wave field for case 3-3. This reflection has much affected the transport rate distribution and consequently the profile change, specially in the offshore region. Figure 6 shows the resulting beach profile for the same case as that of Fig. 5(II) when reflected waves are removed from the wave field. A remarkable improvement is observed. In general, from the above results it is clear that the simulation of beach profile is quite sensitive to the estimation of the flow field, particularly the steady current velocity and its cross-shore gradients or distribution.

#### 4.2 Field measurements

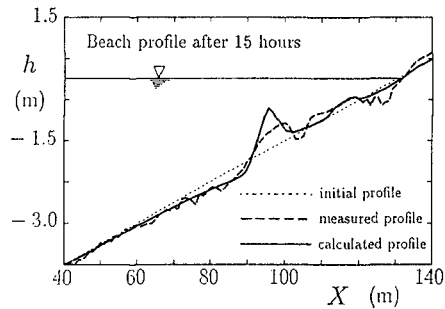


Figure 6: Simulation results for Case 3-3 when reflection is removed (undertow model of Okayasu *et al.*).

The model described in Sec. 3 is now applied to simulating the beach profile change which has occurred during the field measurements reported by Kuriyama (1991). Using the offshore incident wave data as the input, the wave field and its corresponding profile change are calculated every two hours.

In order to examine the sensitivity of the results on the method of estimating the undertow, at first the following equation is used for estimation of the return flow and its distribution:

$$U = -A \left( 1 - \frac{E}{E'} \right) \frac{H_{1/3}^2}{D \cdot T_{1/3}} \quad (14)$$

The best agreement between the calculated and measured final profiles is obtained when  $A = 5.6$  as shown in Fig. 7. It is seen that the general features of the

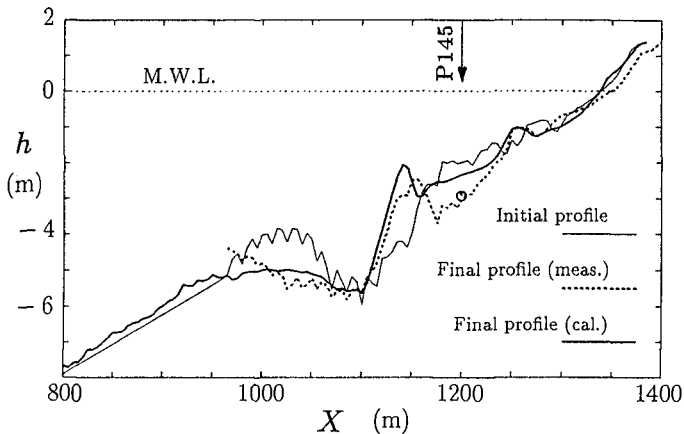


Figure 7: Beach profile change by using Eq. (14) with  $A = 5.6$ .

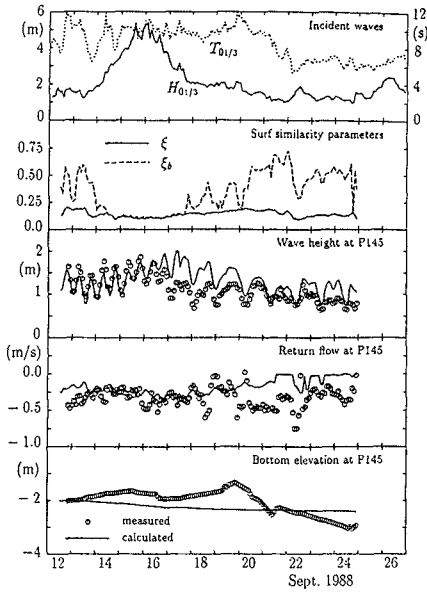


Figure 8: Time histories of deepwater incident waves, surf similarity parameter, and wave height, undertow velocity, and bottom elevation at P145.

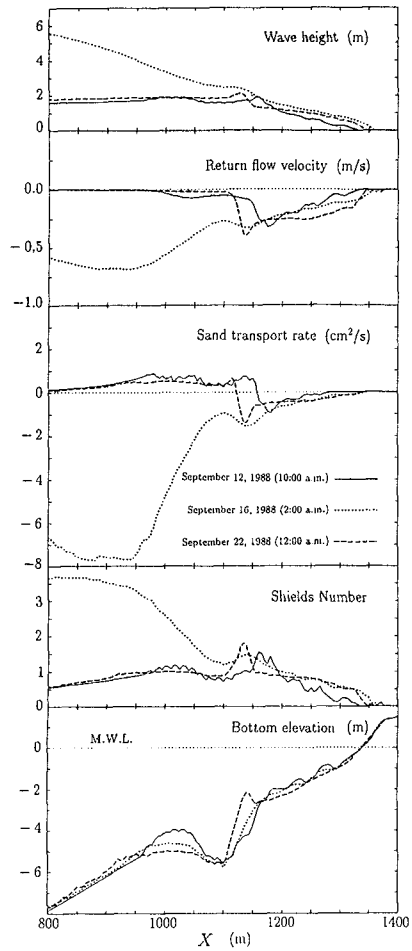


Figure 10: Calculation results at three different times.

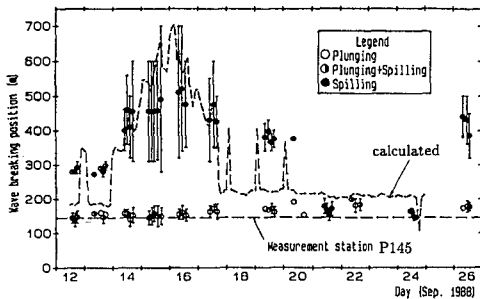


Figure 9: Calculated and observed breaking positions.

profile evolution, such as disappearance of the offshore bar and movement of the nearshore bar are well simulated. More details of the calculation results of this case are given in Figures 8 to 10. In Fig. 8 time variations of the deepwater incident waves and of the surf similarity parameters  $\xi$  and  $\xi_b$  are given. Also the calculated time variations of the wave height, undertow, and bottom elevation at the point P145 are plotted and compared with the measurements. The agreement between calculated and measured wave height is quite good. Estimated values of the undertow show good agreement with the measurements only during the large wave conditions when the values of  $\xi$  are nearly same as  $\xi_b$ , as was discussed in Sec. 3.3. Prediction of the bottom elevation at P145 is not satisfactory. This is attributed to the errors in estimating the cross-shore distribution of return flow, three dimensional effects, and also partly to the neglect of breaking induced turbulence. Figure 9 shows the comparison between calculated and measured breaking points. Calculated results are shown by a dashed line and are plotted on Fig. 6(2) of Kuriyama (1991). A breaking point in the calculations is defined when  $\alpha'_{1/3} = \alpha_b$  which gives  $P_B = 0.4$ . Considering the breaking of irregular waves, this is likely to correspond to the offshore limit of the breaking zone.

In Fig. 10 some of the calculation results at three different times are given. It can be seen that values of the Shields number are usually greater than 0.5 over a large portion of the domain, indicating that sheet flow is the dominant transport mode. Large values of undertow, offshoreward transport rate, and Shields number are observed for the waves of Sept. 16, 1988. It is around this time that the offshore bar disappears and it is well simulated by the model. The large waves on the other hand, have less effect on the nearshore profile, and the change in the nearshore region is mainly occurred after the storm is finished.

As for the next case, Equation (6) is used for calculating the undertow. Figure 11 shows the time variation of the undertow velocity and its comparison with the measurements at the point P145. In Fig. 12 the result of profile simulation

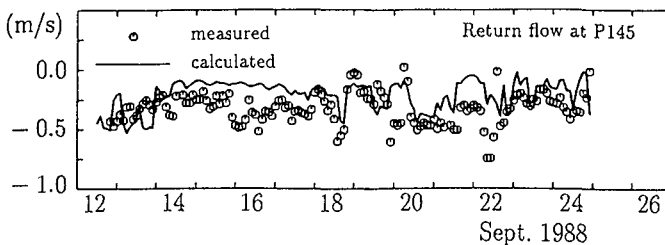


Figure 11: Undertow velocity at the point P145 using Eq. (6).

is given. Although an improvement in the estimation of the undertow velocity is observed, but the resulting beach profile does not show an improvement. The reason is attributed to the errors in estimation of cross-shore distribution of the undertow, determination of the bottom slope at the breaking point, effect of alongshore variation in the flow field and the existence of rip currents, and the



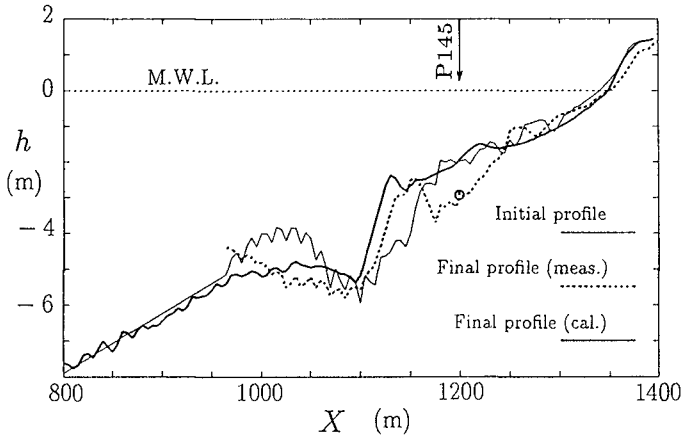


Figure 12: Beach profile change by using Eq. (6).

neglect of breaking induced turbulence. Further study on modelling of the flow field is thus required for more improvements.

## 5. Conclusions

A new and detailed model of beach profile change is presented. It incorporates, explicitly, the asymmetry of the near-bottom orbital velocity and the undertow, into the transport of bottom sediment. The model is examined by using the data of beach profile change obtained from prototype scale laboratory experiments as well as field measurements. It is shown that quite accurate profile simulation is possible when the details of the flow field and transport mechanism are considered.

The results show strong dependency on the distribution and magnitude of the undertow velocity. For further improvements, accurate and general models for estimation of the near-bottom orbital velocity profile in the surf zone and for undertow velocity are required. The so-called swash transport is not included in the present model and therefore the profile change around the shoreline is not well simulated. Modelling of the swash zone is left for a future study.

## References

- Dibajnia, M., and A. Watanabe 1992: Sheet flow under nonlinear waves and currents, *Proc. 23rd Int. Coastal Eng. Conf., ASCE*, pp. 2015-2028.
- Dibajnia, M., T. Shimizu, and A. Watanabe 1992: Profile change of a sheet flow dominated beach, *Proc. 39th Japanese Annual Conf. on Coastal Eng., JSCE*, pp. 301-305 (in Japanese).
- Isobe, M., 1987: A parabolic equation model for transformation of irregular

- waves due to refraction, diffraction and breaking, *Coastal Eng. in Japan*, Vol. 30, No. 1, pp. 33-47.
- Isobe, M., and K. Horikawa 1981: Change in velocity field in and near the surf zone, *Proc. 28th Japanese Annual Conf. on Coastal Eng., JSCE*, pp. 5-9 (in Japanese).
- Kajima, R., T. Shimizu, K. Maruyama, and S. Saito 1982: Experiments on beach profile change with a large wave flume, *Proc. 18th Int. Coastal Eng. Conf., ASCE*, pp. 1385-1404.
- Okayasu, A., A. Watanabe, and M. Isobe 1990: Modeling of energy transfer and undertow in the surf zone, *Proc. 22nd Int. Coastal Eng. Conf., ASCE*, pp. 123-135.
- Sato, S., M. Fukuhama, K. Horikawa 1988: Measurements of near-bottom velocities in random waves on a constant slope, *Coastal Eng. in Japan*, Vol. 31, No. 2, pp. 219-228.
- Suzuki, k., A. Watanabe, M. Isobe, and M. Dibajnia 1994: Experimental study on transport of sediment with mixed-grain size due to oscillatory flow, *Proc. 41st Japanese Annual Conf. on Coastal Eng., JSCE*, pp. 356-360 (in Japanese).
- Watanabe, A., and M. Dibajnia 1988: A numerical model of wave deformation in surf zone, *Proc. 21rd Int. Coastal Eng. Conf., ASCE*, pp. 578-587.
- Watanabe, A., T. Hara, and K. Horikawa 1984: Study on breaking condition for compound wave trains, *Coastal Engineering in Japan, JSCE*, Vol. 27, pp. 71-82.

## CHAPTER 141

### A NONLINEAR SURF BEAT MODEL

Zhili Zou<sup>1</sup> and Nicholas Dodd<sup>2</sup>

#### Abstract

A nonlinear, short-wave-averaged (surf beat) model is presented. The model is based on that of Roelvink (1993), but the numerical techniques used in the solution are based on the so-called weighted-averaged flux (WAF) method (eg Watson et al, 1992), with time-operator splitting used for the treatment of some of the source terms. This method allows a small number of computational points to be used, and is particularly efficient in modelling breaking long waves. The short-wave (or primary-wave) energy equation is solved using a more traditional Lax-Wendroff technique. Results of validation indicate that the model performs satisfactorily in most respects.

#### Introduction

There are two classical characteristic time-scales in a system of waves: that of the individual waves and that of the wave groups. On the time scale of the wave group the short-wave averaged momentum flux ("radiation stress") and mass flux ("wave-induced mass flux") vary slowly. This variation in time and space of radiation stress and mass flux generates long waves with periods and wavelength similar to the group periods and lengths. These long waves may travel with the wave groups or they may be released as free waves if the wave groups forcing them change rapidly, e.g. due to breaking in the surf zone. The free waves either escape to deep water ("leaky modes") or are trapped at the shoreline by refraction as "edge waves". These long waves are often collectively called infragravity waves or "surf beat".

---

<sup>1</sup>Dalian University, Dalian 116024, China

<sup>2</sup>Coastal Group, HR Wallingford, Howbery Park, Wallingford, OX10 8BA, UK.

In the recent decades numerous observations have shown that the energy at surf beat frequencies can be substantial, and in some cases even exceed that of the short waves (Wright et al, 1982). Likewise, the shoreline amplitudes arising from infragravity waves can be comparable to the run-up height of short waves (Guza and Thornton, 1982; 1985). The importance of low-frequency motion for the nearshore dynamics can be inferred from the fact that natural sedimentary coasts often exhibit morphological features (bars and cusps) with length scales considerably in excess of those of the wind waves. This is found to be particularly pronounced in very shallow water. The effect of surf beat on morphology was found to increase offshore transport and to move bars in a seaward direction while reducing their amplitude (Roelvink, 1993). Recent work done at HR Wallingford (Bowers, 1992) highlighted the need for accurate numerical modelling of surf beat: physical model experiments using realistic short crested waves demonstrated the importance of surf beat as well as incident set-down in causing long waves inside harbours. This surf beat is produced by groups of waves breaking on the shoreline surrounding the harbour. Due to the large length of shoreline needed for realistic modelling of the generation of surf beat in a physical model, an efficient mathematical model of surf beat generation would be far more cost effective than extensive additional coastline moulding in a physical model together with additional lengths of wave-maker. The work in this report has been undertaken as a first step in meeting this need in that only cross-shore wave modes are considered.

In the early sixties Longuet-Higgins and Stewart developed the concept of "radiation stress", by which they explained how groups of high waves are accompanied by a depression of the mean water surface. In other words, groups of short waves force a long wave, which is known as the set-down or the bound long wave. This concept successfully explained many of the early observations of surf beat, and forms the basis of many subsequent surf beat models.

In one of the earliest such models, Symonds et al. (1982) assume that within the inner surf zone, the short waves are "saturated", meaning that the variations on wave group scale have vanished and the radiation stress gradients are constant in time. Outside the surf zone, they assume that the horizontal variation of radiation stress is negligible (and thereby do not include the effect of bound waves). In the transition region, the breaking-point moves back and forth; in this region there is a radiation stress gradient varying in time. This gradient acts as a local forcing, comparable to a wave maker which generates waves both in the onshore direction and (with opposite sign) in the offshore direction. The onshore directed wave is subsequently reflected off the beach and interferes with the offshore directed wave. Depending on the dimensionless width of the surf zone, the relative phase of the two free outgoing wave components change, resulting in an enhancing or damping of the total free wave radiated from the surf zone. The fact that such an amplitude variation with the dimensionless surf zone width exists was confirmed in laboratory experiments by Kostense(1984); however, the

quantitative agreement between the model and experiments was not entirely convincing.

Schäffer and Svendsen (1988) improved this model concept by including the forcing outside the surf zone responsible for the bound long waves. In their model this forcing is reduced in the surf zone but does not vanish completely since they relax the rigid assumption of a saturated inner surf zone. Schäffer and Jonsson (1990) compared this model with Kostense's (1984) data and found considerably better agreement; remaining discrepancies can be ascribed to the lack of bottom friction and the use of linearized equations in their model.

Roelvink (1993) developed a nonlinear surf beat model based on short-wave averaged mass and momentum conservation equations (Phillips 1977). To get the radiation stress, a mean short wave energy transportation equation was solved simultaneously, which included the effect of variation of mean water level on the energy evolution. Numerical results for incident bichromatic waves agreed with the Kostense (1984) data to different degrees depending on the bottom friction coefficient used. For incident irregular waves, a narrow band assumption was used to overcome the difficulty of determining the group velocity of irregular waves, which is needed in the calculation of radiation stress. Comparisons of numerical results with Van Leeuwen's (1992) (random) experimental data showed good agreement. This model was then applied to the study of the effect of surf beat on cross-shore beach morphology.

The numerical models mentioned above are all based on the 'wave-averaged' approach, i.e. averaging the mass and momentum conservation equations over a short wave period and using the concept of radiation stress to express the short-wave momentum flux. The disadvantage of this approach is that questionable assumptions are made about the validity of linear theory for the propagation of breaking waves within the surf zone. An alternative to this is to use short-wave-resolving models to study the full wave motion, including the generation processes of low frequency wave. This is usually done using either the nonlinear shallow water wave equations (in the inner surf zone) or the Boussinesq equations (or both). Whilst being more satisfactory from a theoretical point of view, this approach obviously involves considerably more computational time and expense than the wave-averaged approach. In this work we therefore chose to follow the wave-averaged route.

### Equations of motion

The shallow-water wave equations for the conservation of mass and momentum (in 1-D) can be written (in so-called conservation form, and in the absence of bottom friction) as

$$d_t + (du)_x = 0 \quad (1)$$

$$(du)_t + (u^2d + \frac{1}{2}gd^2)_x = gdh_x \quad (2)$$

where  $u$  is the depth-averaged fluid velocity,  $d$  is the total water depth,  $g$  the gravitational acceleration constant, and  $h$  the still water depth ( $x$  is the offshore coordinate, and  $\zeta = d-h$  is the free surface elevation). The term on the right, arising from the bottom slope w.r.t.  $x$ , is referred to as a source term. These equations resolve the primary wave motion. In order to exclude this type of motion, the original equations must be time as well as depth averaged. This results in a similar continuity equation (see below), but additional terms appear in the momentum equation. To treat these properly we start from the momentum equation of Phillips (1977) describing time and depth-averaged 1-D motion,

$$\frac{\partial}{\partial t} \int_{-h}^{\zeta} \rho u \, dz + \frac{\partial}{\partial x} \int_{-h}^{\zeta} (\rho u^2 + p) \, dz - p_b \frac{d}{dx} h + \bar{\tau}_b = 0 \quad (3)$$

where  $\rho$  is water density, and  $p$ ,  $p_b$  are pressure and pressure at the bottom respectively, and an overbar denotes an average over a short wave period. The following decomposition is made:

$$u = U + u' \quad (4)$$

where  $U$  is the long wave velocity and  $u'$  is the fluctuating component (due to the primary waves). We define

$$d = h + \zeta \quad (5)$$

so that  $d$  now denotes a mean total depth. Following Roelvink (1993) we define fluxes

$$Q_t = \int_{-h}^{\zeta} u \, dz \quad (6)$$

and

$$Q_w = \int_{-h}^{\zeta} u' \, dz \quad (7)$$

We introduce the velocity  $V$  such that

$$V = \frac{Q_t}{d} = U + \frac{Q_w}{d} \quad (8)$$

and after some manipulations, and using the shallow water assumption, the final continuity and momentum equations are arrived at:

$$\frac{\partial}{\partial t}d + \frac{\partial}{\partial x}(Vd) = 0 \tag{9}$$

$$\frac{\partial}{\partial t}(Vd) + \frac{\partial}{\partial x} [ dV^2 + \frac{1}{2}gd^2 ] = gd\frac{\partial h}{\partial x} - \frac{\partial}{\partial x}[\frac{S_{xx}}{\rho}] + \frac{\partial}{\partial x}[\frac{Q_w}{d}]^2 - \frac{\bar{\tau}_b}{\rho} \tag{10}$$

It can be seen that these equations have a similar form on the left hand side to (1) and (2). We use this correspondence to apply similar flux-conservative techniques to the solution of the wave-averaged equations (see below). The final equation to consider is the equation describing the transformation of short wave energy. It is the variation in this energy that will drive the incoming bound waves. Assuming (Roelvink, 1993) that the characteristic short wave frequency is constant in space and time we get an energy equation of the form

$$\frac{\partial E}{\partial t} + \frac{\partial}{\partial x}(c_g E) = -D \tag{11}$$

In the model, the radiation stress,  $S_{xx}$ , and the primary-wave-induced flux,  $Q_w$ , are represented by the expressions of Longuet-Higgins & Stewart (1964); bottom shear stress is represented in the usual quadratic form.  $D$ , representing the short wave decay due to breaking, is formulated using both the method of Roelvink (1993) and of Battjes & Janssen (1978). In the runs performed so far there has been little difference between the two methods. In view of this we chose Roelvink's method,

$$D ( E , d ) = \left\{ 1 - \exp \left[ - \left( \frac{H}{\gamma d} \right)^n \right] \right\} 2 \alpha f_p E \tag{12}$$

it being rather simpler. Here, following Roelvink we take  $\alpha = 1.0$  and  $n = 10$ . The parameter  $\gamma$  will vary depending on the type of wave being studied. Its value is given in each case studied.  $f_p$  is the characteristic measure of the (constant) frequency. For waves other than monochromatic waves we take it to be an average of the constituent frequencies. Using linear theory it can be shown that

$$H = \sqrt{8E/(\rho g)} \tag{13}$$

so the system is now closed.

Numerical methods

In the WAF method applied to the shallow-water wave equations the equations are solved in so-called flux-conservative form (eg (1) and (2)). Both the original shallow water wave equations and the surf beat model equations can be written in the same flux-conservative vector formulation

$$\underline{U}_i + \underline{F}_x = \underline{S} \quad (14)$$

where  $\underline{U}$  represents the conserved quantities, and  $\underline{F}$  represents the flux of these quantities. The term  $\underline{S}$  is the so-called source term, and it is this term that differs depending on whether the equations are just depth averaged or both depth and time averaged. This vector equation is solved in finite-difference form, using fluxes at intermediate locations:

$$\underline{U}_i^{n+1} = \underline{U}_i^n + \frac{\Delta t}{\Delta x} ( \underline{F}_{i-1/2} - \underline{F}_{i+1/2} ) + \underline{S}_i \Delta t \quad (15)$$

where  $t = n\Delta t$  is the initial time, and  $t = (n+1)\Delta t$  is the time at which we want to find a solution. The flux, which is found by solution of the local Riemann problem at each cell, is then averaged over the cell width at the half time level, and a total-variation-diminishing adjustment is made by means of upwinding, in order to reduce spurious oscillations. The slope term can cause problems with accuracy, but these are circumvented by making an appropriate transformation, thus allowing it to be incorporated into the local Riemann problem solution (see Watson et al. (1992) for details). The boundary condition at the seaward end allows waves to propagate out of the solution domain without reflection, and the shoreline is defined as the position at which the depth decreases below a specified amount.

For the surf beat problem, we can decompose the source term into the slope term and an additional term

$$S^* = - \frac{\partial}{\partial x} \left( \frac{S_{xx}}{\rho} \right) + \frac{\partial}{\partial x} \left( \frac{Qw^2}{d} \right) - \frac{\bar{\tau}_b}{\rho} \quad (16)$$

The problem caused by this additional term can be solved by applying the time-operator splitting (TOS) method. Firstly we solve the following equations to get an intermediate solution  $d^*$  and  $V^*$ :

$$\frac{\partial}{\partial t} d^* + \frac{\partial}{\partial x} ( V^* d^* ) = 0 \quad (17)$$

$$\frac{\partial}{\partial t} ( V^* d^* ) + \frac{\partial}{\partial x} [ V^{*2} d^* + \frac{1}{2} g d^{*2} ] = g d^* h_x \quad (18)$$

These equations have the same form as (1) and (2), so they can be solved using the same method for solving those equations, including the treatment of seaward and shoreline boundary conditions. Secondly we solve the equations:

$$d_t = 0 \quad (19)$$

$$V_t = S^* \quad (20)$$



starting with the intermediate solutions. This is the solution to equations (9) and (10) given by the TOS method. The accuracy of this solution is first order (Watson et al 1992), which is lower than that of equations (1) and (2). This decrease of accuracy due to TOS method was remedied by using a transformation similar to that of Watson et al (1992), but differing by the quantity  $S^*$ . Thus, at each time step and for the difference calculation at each grid point we transform the problem into a reference frame that is accelerating at the rate

$$a^* = -gh_x + S^* \quad (21)$$

In this frame the new variables are

$$\xi = x - \frac{a^*}{2} t \quad (22)$$

$$\tau = t \quad (23)$$

$$W = V - a^* t \quad (24)$$

$$D = d \quad (25)$$

Substitution of (22)-(25) into (9) and (10) gives

$$D_\xi + (WD)_\xi = 0 \quad (26)$$

$$W_\xi + WW_\xi + gD_\xi = 0 \quad (27)$$

Once the solution of the (26) and (27) has been found (using the same method as for (1) and (2)), the solution of (9) and (10) can be effected by using relations (22)-(25). The solutions so obtained,

$$d(x,t) = D\left(x - \frac{a^*}{2}\Delta t^2, t\right) \quad (28)$$

$$V(x,t) = W\left(x - \frac{a^*}{2}\Delta t^2, t\right) + a^*\Delta t \quad (29)$$

provide the basis for the modification of the TOS method by inclusion of the second order terms. Thus, noting that

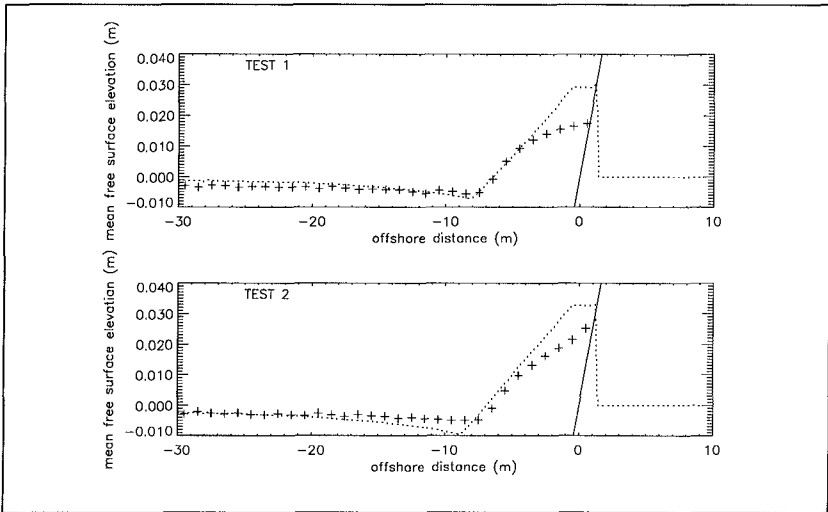


Figure 1. Mean surface elevation from model and experiments (Stive, 1983). Crosses from experiments. (a) Test 1 (b) Test 2.

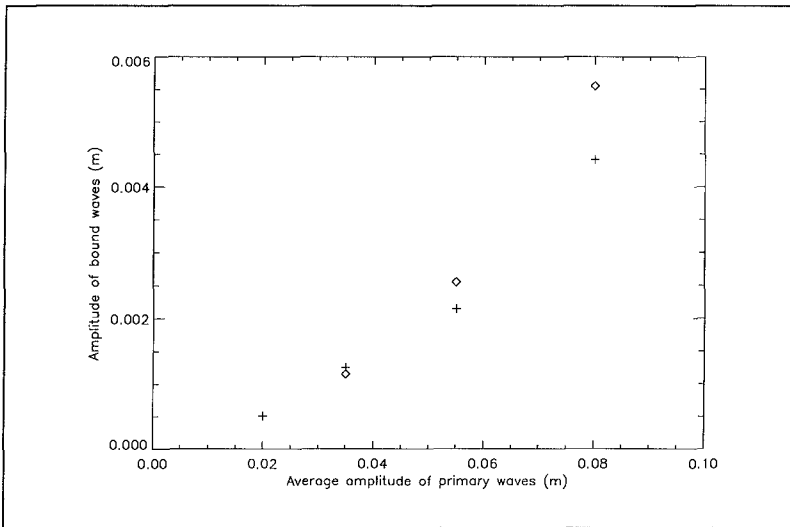


Figure 2. Amplitude of bound waves vs primary wave amplitude. Diamonds from experiments (Kostense, 1984). Crosses from model.

$$d^*(x,t) = D\left(x + \frac{1}{2}gh_x\Delta t^2, t\right) \quad (30)$$

$$V^*(x,t) = W\left(x + \frac{1}{2}gh_x\Delta t^2, t\right) - gh_x\Delta t^2 \quad (31)$$

the final solutions of the surf beat model are

$$d(x, (n+1)\Delta t) = d^*(x, (n+1)\Delta t) - \frac{\partial d^*}{\partial x} (\frac{1}{2} S^* \Delta t^2) \quad (32)$$

$$V(x, (n+1)\Delta t) = V^*(x, (n+1)\Delta t) - \frac{\partial V^*}{\partial x} (\frac{1}{2} S^* \Delta t^2) + S^* \Delta t \quad (33)$$

During the numerical calculation discussed above, the short wave energy equation (11) should be solved simultaneously to give the value of energy  $E$  for the calculation of radiation stress  $S_{xx}$  and short wave mean flux  $Q_w$ . A one-step second-order Lax-Wendroff difference scheme was used to solve the equation.

### Results

The surf beat model has so far been validated only by comparison with monochromatic (Stive, 1983) and bichromatic wave tests (Kostense, 1984). Both of these tests were performed on plane beaches.

Two tests were examined in Stive's data, corresponding to spilling and plunging breaker types: Test 1 (spilling; wave height = 0.145m, period = 1.79s), and Test 2 (plunging; wave height = 0.145m, period = 3.00s). The flume consisted of a flat bed section of depth 0.70m (continuing for a length of 10m) and then a non-erodible constant slope of 1:40. In Figure 1(a) and 1(b) the mean free surface elevation in the two cases is compared with the model result. It can be seen in Fig. 1(a) that in the first case modelling is generally good everywhere other than at the shoreline, where the mean shoreline is clearly overpredicted (this is equally true of Test 2). To obtain accurate modelling of the region of the breaker point

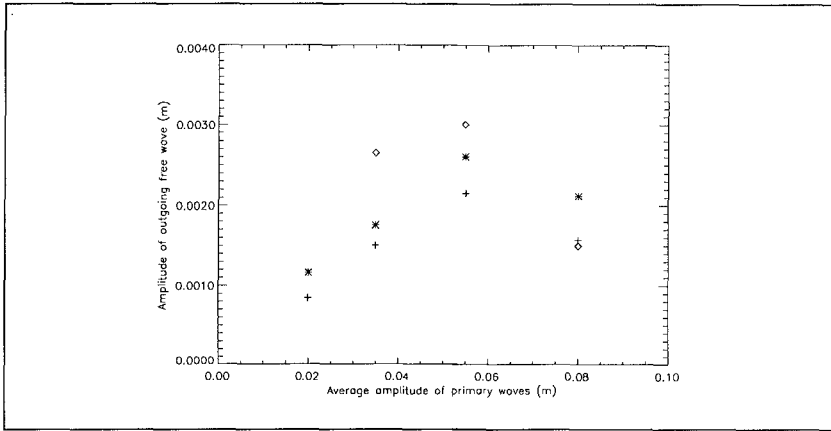


Figure 3. Amplitude of free waves vs primary wave amplitude. Diamonds = experiments (Kostense, 1984). Asterisks = model ( $f_w=0.01$ ). Crosses = model ( $f_w=0.05$ ).

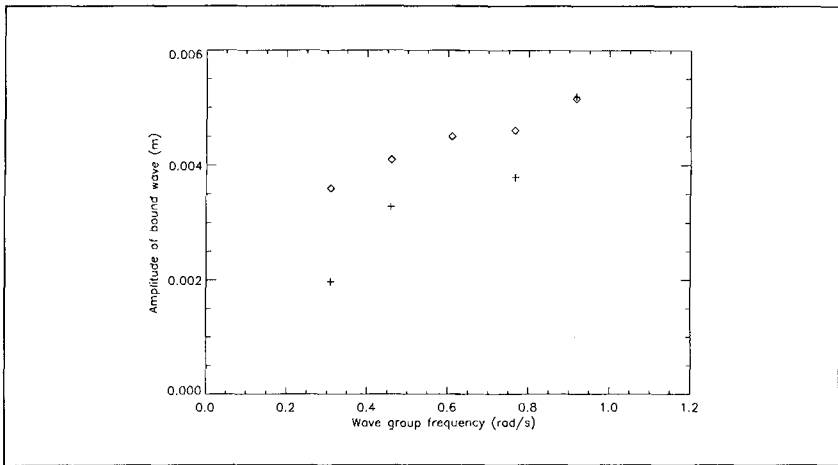


Figure 4. Amplitude of bound waves vs group frequency. Diamonds = experiment (Kostense, 1984). Crosses = model.

in Test 1, a value of  $\gamma = 0.88$  was used. The same value gave the best fit for Test 2, but in this case modelling clearly is not as good. It is not clear why modelling in this region should be inferior for Test 2. The model of Thornton & Guza (1983) of wave height decay, on which the model of Roelvink is based, works well for plunging as well as spilling breakers.

In the tests of Kostense (1984), the primary waves were made up of two frequencies generated in a water depth of 0.50m which broke on a plane cemented beach of a 1:20 slope after travelling over a horizontal stretch. Figures 2 and 3 are, respectively, the variation of the bound wave amplitude and the reflected free wave (out-going) amplitude vs the primary wave amplitude  $\zeta_1$  with  $\zeta_2/\zeta_1 = 0.2$ . and  $\Delta\omega = 0.772$ , which corresponds to series C in Kostense's experiments. Figures. 4 and 5 are, respectively, the variation of the bound wave amplitude and the reflected free wave (out-going) amplitude vs the wave group frequency  $\Delta\omega$  with  $\zeta_2/\zeta_1 = 0.2$  ( $\zeta_1 = 0.055\text{m}$  and  $\zeta_2 = 0.011\text{m}$ ), which corresponds to series A in Kostense's experiments ( $\gamma = 0.88$ ). The procedure of the calculation to simulate the experiments is as follows. For a given set of primary waves, the model is run until transients are no longer present in the solution domain. The surface elevation time series are then split into three components, viz. the incoming bound wave, the reflected free wave and an incoming free wave. The incoming free wave is negligible since it is not generated and the seaward boundary condition allows the reflected free wave to propagate out of the model area. The amplitudes of the incoming bound wave and the reflected free wave are determined by harmonic analysis as done in Kostense's experiments. Although more points are required for a more conclusive comparison to be made, Fig. 2 seems to show the bound wave amplitude increasing approximately quadratically, as expected. In fact, apart from one point the position of which seems slightly anomalous, results are very similar to those of Roelvink, as we would expect. The comparison with experiment is quite good. In Fig. 3 we perform a similar kind of comparison to that of Roelvink, by using two different values of bottom friction coefficient,  $f_w = 0.05$  and  $0.01$ . A similar trend is found with regard to the dependence of the amplitude of the outgoing free wave on the average amplitude of the primary waves. The comparison is not as good as for the incoming bound wave. This is not surprising since the reflected free wave will only emerge after the processes of short wave breaking and run-up have taken place and we only use linear theory to describe highly nonlinear processes in these regions. Nevertheless, the agreement is good in parts. The agreement in Fig. 4 is reasonably good (dependence of the bound wave on the group frequency), although it appears to deteriorate for lower values of the wave group frequency. The agreement in Fig. 5 is less than satisfactory at present. The experimental results clearly show a peak in the response at around 0.6 rad/s. More analysis needs to be done here if the interference patterns of Roelvink (1993) are to be reproduced.

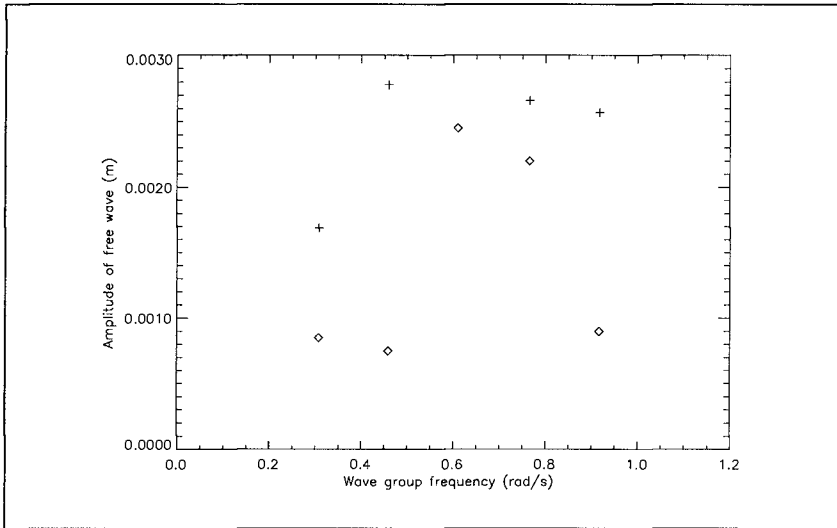


Figure 5. Amplitude of free waves vs group frequency. Diamonds = experiments (Kostense, 1984). Crosses = model.

### Conclusions

A nonlinear surf beat model based on the same approach as that of Roelvink (1993) has been presented. It uses a novel (for this application) numerical scheme for its solution, which is highly efficient, especially for the case when long waves break. The comparisons done so far indicate that it performs reasonably well, but further validation is required, especially for random waves. The advantage of a nonlinear model over a linear surf beat model is that we do not have to identify beforehand the mechanism by which the free waves are generated, as is the case for linear models (eg, Symonds et al, 1982). Certain parameters are still present in the model however (unavoidably so), some of which must be calibrated for different types of applications.

### Acknowledgements

This work was carried out as part of the G8 Coastal Morphodynamics research program. It was jointly funded by the Commission of the European Communities, Directorate General for Science, Research and Development, under contract MAS2-CT92-0027; and by Hydraulics Research Wallingford Ltd. The authors would like to thank both these bodies for their support.

### References

- Battjes, J. A. and Janssen, J.P.F.M. (1978). Energy loss and set-up due to breaking in random waves. Proc. 16th Int. Conf. on Coastal Eng., ASCE, 569-587.
- Bowers, E. C. (1992). Physical models of harbours: the proving with field data of a model of Shoreham Harbour with a new type of wave-maker generating short crest waves. HR Report SR 335.
- Guza, R. T. and Thornton, E.B. (1982). Swash oscillations on a natural beach. J. Geophys. Res., 87, C1, 483-491.
- Guza, R. T. and Thornton, E.B. (1985). Observations of surf beat. J. Geophys. Res., 90, C2, 3161-3171.
- Longuet-Higgins, M. S. and Stewart, R.W. (1964). Radiation stresses in water waves; a physical discussion, with applications. Deep Sea Res., Vol.11, 529-562.
- Kostense, J. K. (1984). Measurements of surf beat and set-down beneath wave groups. Proc. 19th Int. Conf. on Coastal Eng., pp. 724-740, ASCE, New York.
- Phillips, O.M. (1977). The dynamics of the upper ocean. 2nd Edition, Cambridge Univ. Press.
- Roelvink, J.A. (1993). Surf beat and its effect on cross-shore profiles. Ph.d Thesis, Delft Hydraulics.
- Schäffer, H.A. and Svendsen, I.A. (1988). Surf beat generation on a mild-slope beach. Proc. 21st I.C.C.E., 1058-1072.
- Schäffer, H.A. and Jonsson, I.G. (1990). Theory vs. experiments in 2-dimensional surf beats. Proc. 22nd I.C.C.E., 1131-1143.
- Stive, M.J.F. (1983). Two-dimensional breaking of waves on a beach. Delft Hydraulics Report, M 1585, part 1.

Symonds, G., Huntley, D.A. and Bowen, A.J. (1982). Two-dimensional surf beat: long wave generation by a time-varying breakpoint. *J. Geophys. Res.*, Vol. 87, no. C1, 492-498.

Thornton, E.B. and Guza, R.T. (1983). Transformation of wave height distribution. *J. Geophys. Res.*, 88, 5925-5938.

Van Leeuwen, P.J. (1992). Low frequency wave generation due to breaking wind waves. Ph.D. Thesis, Delft University of Technology.

Watson, G., Peregrine, D.H. and Toro E.F. (1992). Numerical solution of the shallow-water equations on a beach using the weighted average flux method. *Computational Fluid Dynamics'92*. Ch. Hirsch et al (eds.), Elsevier, 495-502.

Wright, L. D., Guza, R.T. and Short, A.D. (1982). Surf zone dynamics on a high energy dissipative beach. *Mar. Geol.*, 45, 41-62.



## CHAPTER 142

### PIV Measurements of Oscillatory Flow over a Rippled Bed.

Earnshaw, H.C.,<sup>1</sup> Bruce, T.,<sup>2</sup> Greated, C.A.<sup>1</sup> & Easson, W.J.<sup>2</sup>

This paper presents results of a study of the kinematics of planar oscillatory flow over a rippled sea bed. The flows are mapped using Particle Image Velocimetry (PIV), a flow measurement technique yielding accurate, full field maps of an instantaneous velocity field. The practical implementation of the PIV method for this study is described, and flow maps presented for amplitude of oscillation to ripple length ratios of 0.8, 1.2 and 1.8. The generation of vortices at the ripples and their subsequent trajectories is described. Finally, the vortex strengths for the three flow regimes are investigated.

### Introduction

This paper presents detailed experimental velocity measurements of oscillatory flow over a rippled bed. The main motivations for the work are to validate numerical models (eg Block, 1993, Perrier, 1993) and eventually to help in the development of models for the prediction of sediment transport. Full field instantaneous velocity data is obtained using Particle Image Velocimetry (PIV). Existing studies using point measurement techniques (eg Sato et al, 1984 and Ranasoma and Sleath, 1992) have shown flow over a rippled bed to be very complex and turbulent but with coherent structures, primarily in the vortex shedding process (see fig. 1). By the very nature of these methods the details of this complex and constantly changing flow are lost. The numerical modelling of sediment transport over a rippled sandy bed requires accurate knowledge of the flow kinematics above the bed. Through the application of the PIV technique we hope to provide this information.

### Experiments

The tests were carried out in a towing tank six metres long, a metre wide with a water depth of half a metre. Because of the way the PIV systems are set up

---

<sup>1</sup>Fluid Dynamics Unit, Department of Physics & Astronomy, The University of Edinburgh, Edinburgh, EH9 3JZ, Scotland

<sup>2</sup>Department of Mechanical Engineering, The University of Edinburgh, Edinburgh, EH9 3JL, Scotland

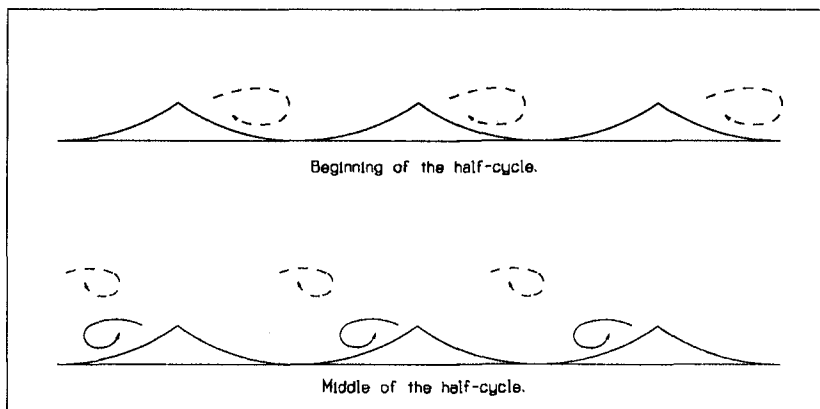


Figure 1: The vortices from the previous half-cycle are swept up and over the crests of the ripples as the flow accelerates from right to left and the new lee vortices form in the troughs.

in Edinburgh it is easier to have the light sheet coming in from underneath the tank and to suspend the ripples above, as shown in fig. 2. Rather than using an oscillatory flow over stationary ripples the ripple bed was oscillated in still water. There are several advantages to doing the experiment this way round: it allows a wider variation of amplitude of oscillation and ensures there is no externally imposed shear or turbulence as well as making the experiment physically easier. The ripples were attached upside down to a computer controlled trolley which could then oscillate them in initially still water. Three amplitudes of oscillation,  $a$ , corresponding to  $a/L = 0.8, 1.2$  and  $1.8$  (where  $L$  is the ripple length) were used giving maximum velocities of 131, 196 and 294 mm/s respectively. The time period,  $T$ , for all tests was 8.46s and pictures were taken of one of the central ripples at nine phases,  $\omega t$ , of oscillation from  $0^\circ$  to  $180^\circ$ . Parameters were chosen within the EU MAST G8-M program to facilitate comparisons between the modellers and experimentalists in the group.

The ripples were solid and pre-formed from styrofoam. Again the EU MAST G8-M program decided on a 'standard' ripple shape and size. This is a sharp crested ripple (not as realistic as a rounded crest but generally easier for numerical work) 22 cm long from crest to crest and 35 mm high from crest to trough. The ripple shape was approximated to an arc of radius 19cm.

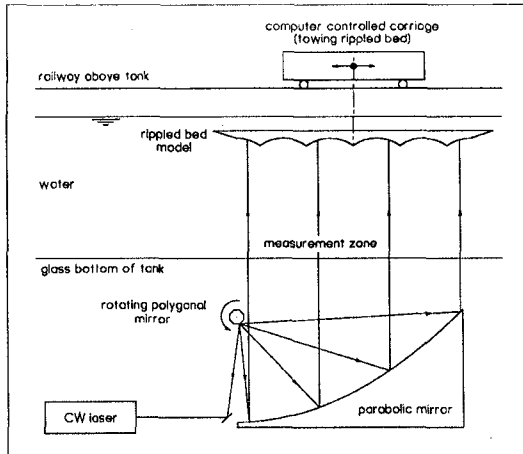


Figure 2: Ripple bed attached to the trolley above the wave tank with a scanning beam system under it

### Particle Image Velocimetry

Particle Image Velocimetry (PIV) is well documented; for a general overview see Adrian, 1991, and for applications in the field of coastal engineering see Greated et al, 1992 and Quinn et al, 1993. The advantages of PIV are that it is a non-intrusive technique and therefore does not in any way interfere with the flow and that it provides simultaneous full field data. Briefly, the flow is seeded with small, neutrally buoyant particles which scatter light and follow the flow accurately. A light-sheet is generated to illuminate the flow stroboscopically using a scanning beam system as shown in figure 2 (see also Gray et al, 1991). Typical scan rates are of the order of a millisecond. The area of interest is then photographed with a long enough camera exposure time to ensure that multiple images of each of the seeding particles are captured on the same negative. By looking at the separation of successive images of each particle a full picture of the magnitude and direction of velocity at each point in the flow can be built up.

In oscillating flows two difficulties are encountered when applying PIV. Directional ambiguity occurs because there is no way of telling which of the multiple images came first and zero and near-zero velocities cannot be measured as the images are too close together to be discriminated by the analysis system. To overcome these two problems a known shift velocity was superimposed onto the flow field such that the multiple images always occurred on the same side of the original particle thus resolving both the above problems. This technique is analogous to frequency shifting in LDA. The simplest way of including a shift velocity is to move the camera during the exposure, achieved here by mounting the cam-

era on a computer controlled turntable; the shutter is triggered when the camera is perpendicular to the tank (Bruce & Easson, 1992). The shift velocity is later subtracted from the analysed negative to reveal the true flow field.

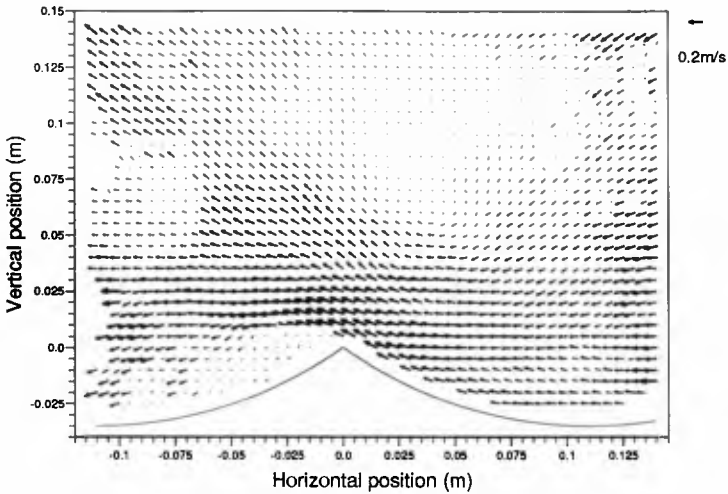


Figure 3: Velocity map for  $a/L=0.8$ ,  $T=8.46s$  and  $\omega t=30^\circ$ .

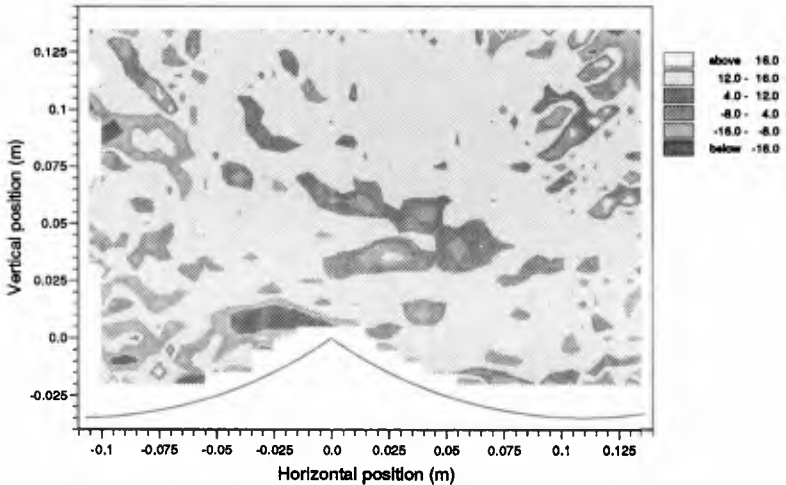


Figure 4: Vorticity plot for  $a/L=0.8$ ,  $T=8.46s$  and  $\omega t=30^\circ$ .

### Results and Discussion

The sequences of pictures were obtained for each of the three amplitudes and show the evolution of the flow over half-cycles, where one half-cycle runs from  $0^\circ$  when the bed is stationary through  $90^\circ$  at maximum velocity to  $180^\circ$  when the

bed is momentarily stationary again. Detailed information about the generation of vortices, their trajectories and their decay can be obtained from the data.

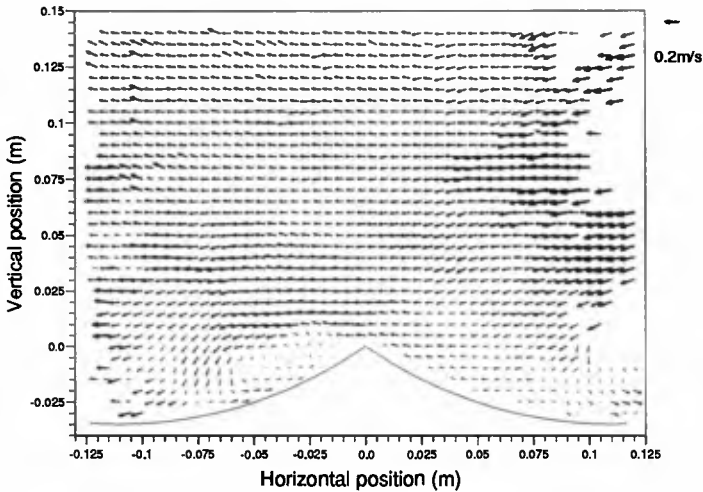


Figure 5: Velocity map for  $a/L=0.8$ ,  $T=8.46s$  and  $\omega t=120^\circ$ .

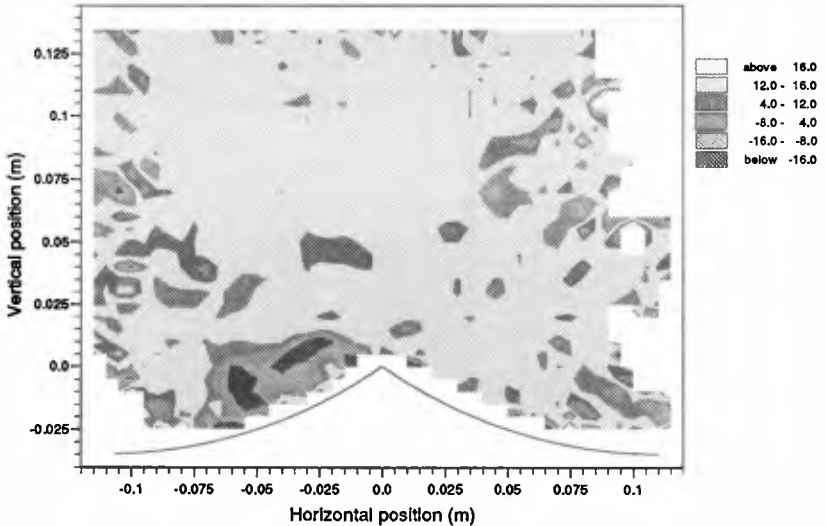


Figure 6: Vorticity plot for  $a/L=0.8$ ,  $T=8.46s$  and  $\omega t=120^\circ$ .

Figure 3 shows a typical measured velocity field and figure 4 its derived vorticity contour plot. These are for the slowest oscillation,  $a/L=0.8$ , at phase  $30^\circ$

that is, just after the bed begins to move. The bed is accelerating from left to right, so the flow appears as right to left. The black areas on the vorticity plot correspond to areas of high negative vorticity, the colour lightens to a neutral grey background and then to areas of increasingly positive vorticity. A vortex, ejected from the crest of this ripple in the previous half-cycle, is now travelling up and away from the bed, above and to the right of the crest, whilst a new vortex is just being formed immediately to the left of the crest.

Later in the half-cycle (figure 5 and figure 6) the lee vortex has grown considerably whilst the positive vortex has dissipated a lot of its energy and has been swept across by the main flow.

These flow fields have been compared (Perrier, 1993) with the results of numerical models, in particular the Discrete Vortex Model developed by Danish Hydraulic Institute (DHI), Technical University of Denmark (ISVA) and Laboratoire National d'Hydraulic, France (LNH). Qualitative agreement was noted in the formation, shedding and trajectories of the vortices. Quantitative comparisons of the spatial flow fields are now possible for the first time. One way of approaching this would be to look more closely at the vortices and try to measure their positions and strengths as functions of time.

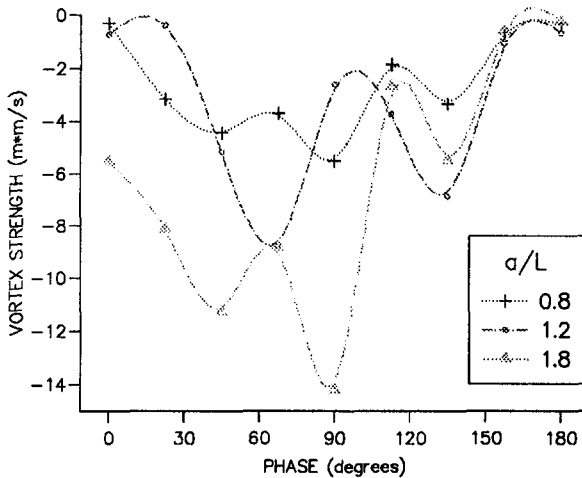


Figure 7: Plot showing vortex strength varying with phase for each of the three amplitudes of oscillation.

As a preliminary study the developing lee vortex has been looked at more closely. Calculations of vortex strength were made by imposing a boundary, defined by a lower vorticity level, on the vortex and summing the vorticity over all

the discrete points within the boundary. Figure 7 shows the variation of vortex strength through the half-cycles for each of the three amplitudes of oscillation. The data is rather scattered and the method needs a lot more thought but as a first calculation it does show roughly the trends expected. The negative vorticity increases towards  $90^\circ$ , corresponding to the flow's maximum velocity, and decreases again as the flow slows down at the end of the half-cycle. The faster, stronger flows generate more vorticity.

### Concluding Remarks and Future Work

These new measurements give a lot more detail than previous point measurements and have shown the expected vortices in the right places. Qualitatively they agree with previous experiments and with numerical models.

One of the main problems with these experiments is the question of the repeatability of the flow from one period to the next. Successive pictures are not taken in the same oscillation due to the camera's finite wind-on time. One sequence of pictures is taken over several oscillations. One of the next things to be done is to check how repeatable the flow is from cycle to cycle. It has been suggested that the spikes in the vortex strength curves may be due to the effect of the positive vortices moving across the field and therefore affecting the calculations of negative vortex strength. Again this possibility needs to be tested. The next step is to develop a method of quantifying the information in the pictures so the results will be of help in predicting the sediment transport over ripples.

### Acknowledgement

This work has been carried out as part of the MAST G8-M Coastal Morphodynamics research programme. It was funded by the Commission of the European Communities Directorate General for Science, Research and Development under contract N<sup>o</sup>. EC MAST-II OCT 92 0027.

### References

1. Adrian, R.J., (1991) Particle-Imaging Techniques for Experimental Fluid Mechanics. *Ann. Rev. Fluid Mech.* 23:261-304.
2. Block, M., (1993) University of Wales, Bangor. Private Communication.
3. Bruce, T. & Easson, W.J., (1992) The Kinematics of Wave Induced Flows Around Near-bed Pipelines. *Proc. 23rd Int. Conf. Coastal Eng.* 229:2990-2998.
4. Gray, C., Greated, C.A., McCluskey, D.R. & Easson, W.J., (1991) An Analysis of the Scanning Beam PIV Illumination System. *Journal of Physics (Measurement Science and Technology)*, 2, pp717-724.

5. Greated, C.A., Skyner, D.J. & Bruce, T., (1992) Particle Image Velocimetry (PIV) in the Coastal Engineering Laboratory. *Proc. 23rd Int. Conf. Coastal Eng. 15:212-225.*
6. Perrier, G. Institute of Hydrodynamic and Hydraulic Eng., (1993) Technical University of Denmark. Private Communication.
7. Quinn, P.A., Skyner, D.J., Gray, C., Greated, C.A. and Easson, W.J., (1993) A Critical Analysis of the Particle Image Velocimetry technique as applied to Water Waves. *In Flow Visualization and Image Analysis. Ed. F.T.M Nieuwstadt. Kluwer Academic Publishers, Dordrecht, The Netherlands.*
8. Ranasoma, K.I.M and Sleath, J.F.A., (1992) Velocity Measurements Close to Rippled Beds. *Proc. 23rd Conf. Coastal Eng. 2383-2396.*
9. Sato, Minura & Watanabe, (1984) Oscillatory Boundary Layer Flow over Rippled Beds. *Proc. 16th Conf. Coastal Eng. 2293-2309.*



## CHAPTER 143

# SHEAR INSTABILITY OF LONGSHORE CURRENTS: EFFECTS OF DISSIPATION AND NON-LINEARITY

Albert Falqués, Vicente Iranzo and Miquel Caballería <sup>1</sup>

### Abstract

The effect of bottom friction and turbulent lateral mixing on shear instability of the longshore current is investigated. Transition conditions for this instability as a function of non-dimensional parameters related to the basic current, topography, bottom friction and lateral mixing are found. A direct nonlinear numerical simulation of shear instability is presented. The basic flow is found to be supercritical and the amplitude of shear waves can reach at least 20% of the basic flow. A small increase in the period due to non-linearity is also found. Preliminary results suggest that far from criticality there is an important contribution of the instability to the mean flow. Some applications to field and laboratory experiments are discussed.

### 1. Introduction

In the presence of a significant wave-driven longshore current, low frequency oscillations in the current that are not due to gravity waves may appear. These oscillations, called far infragravity waves (FIG waves) because their frequency is lower than the infragravity edge waves of the same wavenumber, were first observed by Oltman-Shay et al. (1989) as strong fluctuations in the time series of longshore and cross-shore velocity components. They appear as a meandering in the current that propagates downflow. According to the spectral analysis performed by Oltman-Shay and co-workers, they are almost non-dispersive with a phase speed proportional to the peak mean longshore current,  $c \sim 0.5 - 0.7 V_{max}$ . Their period and wavelength in natural beaches are

---

<sup>1</sup> *Departament de Física Aplicada, Universitat Politècnica de Catalunya, 08034 Barcelona, Spain*

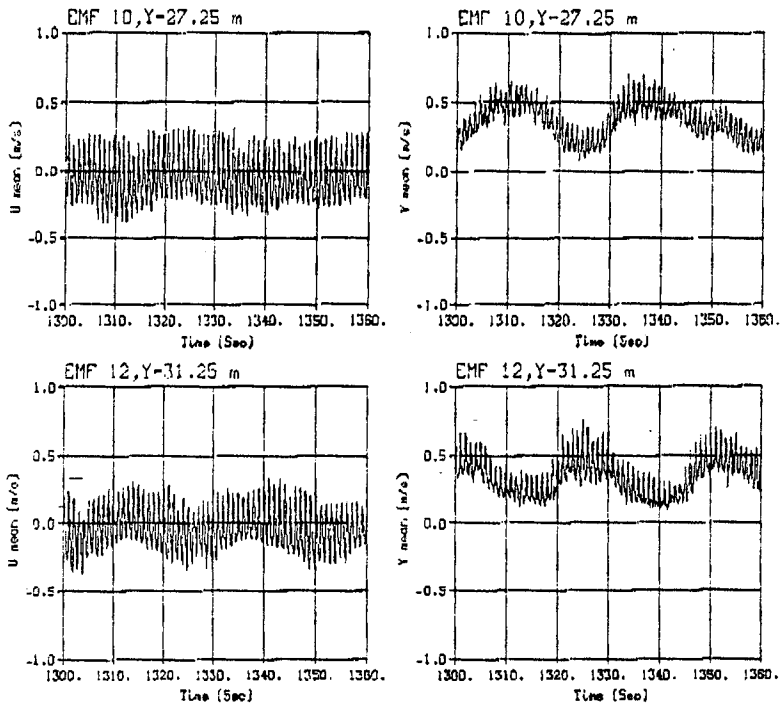


Figure 1: Time series of cross-shore (left) and longshore (right) components of the current at two alongshore locations. LIP experiment M19, from Reniers et al. 1994.

of the order of  $10^2$  sec. and  $10^2$  m. respectively. More recently, experiments have been conducted in a wave basin (Delft Hydraulics facilities, LIP project M19) in order to observe FIG waves in a laboratory beach. Preliminary analysis of data in the case of a barred beach profile (Reniers et al., 1994) indicates the presence of FIG waves of a period and a wavelength of about 25 sec. and 8 m. respectively. Time series of alongshore and cross-shore components of the current for two different current-meters in two different alongshore positions are shown in Fig.1. The incoming waves of a period of 1 sec. and strong low frequency oscillations with a period of about 25 sec. may be seen. The amplitude of these oscillations in comparison with the peak longshore current is of the order of 20% for the cross-shore component and 35% for the longshore component. These amplitudes are of the same order of magnitude as those observed by Oltman-Shay et al. (1989) at Duck (USA).

Bowen and Holman (1989) proposed a theoretical explanation for the FIG waves based on an instability mechanism of the mean longshore current. According to their theory, the longshore current may be unstable because of the shear and this instability may generate growing disturbances that progress downflow or shear waves. Their theory was developed using a very simplified analytical model that succeeded in giving the main features of the instability and matched the experimental results of Oltman-Shay et al. reasonably well. Nevertheless, their model has a number of limitations such as unrealistic geometry, inviscid flow, rigid lid and linearized governing equations and several improvements are therefore necessary in order to analyze the instability mechanism in more realistic conditions. This has been done by Dodd et al. (1992), Putrevu and Svendsen (1992), Deguchi et al. (1992), Dodd (1994), Dodd and Thornton (1992) and Falqués and Iranzo (1994).

The first aim of the present contribution is to find general transition conditions for shear instability as a function of some non-dimensional parameters involving the longshore current, the topography of the beach, the bottom friction and the lateral mixing. The second aim is to show how the linear stability analysis can be applied to any particular beach, handling actual cross-shore profiles of longshore current, bathymetry, bottom friction and eddy viscosity. Furthermore, the linear analysis can explain the initial growth and propagation of small amplitude shear waves but cannot describe properly the finite amplitude shear waves actually observed in Nature. In particular, the linear theory cannot predict the amplitude of such shear waves. This requires a nonlinear stability analysis which is our third goal.

The importance of shear instability lies in several factors. The theoretical models for the longshore current are usually based on an equilibrium between the driving forces from the incoming wave field and dissipative forces from bottom friction and lateral mixing. But the possibility of instability in such an equilibrium solution indicates that the matter is not so simple and that in some cases the longshore current may have a dynamic behaviour quite far from this equilibrium. Moreover, as several authors have pointed out (see Putrevu and Svendsen, 1992) shear instability can be a mixing factor in the surf zone which is quite stronger than the mixing due to wave induced turbulence.

## 2. Linear Analysis

We consider the shallow water equations for momentum and mass conservation with a lateral momentum diffusion given by  $\nu(x)$ :

$$\frac{\partial v_i}{\partial t} + v_j v_{i,j} + g\eta_{,i} = -\frac{c_d}{\zeta} |\bar{v}| v_i + \frac{1}{\zeta} S_{i,j} + \frac{1}{\zeta} [\nu \zeta (v_{i,j} + v_{j,i})]_{,j} \quad i = 1, 2 \quad (1)$$

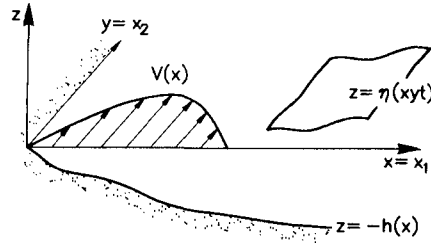


Figure 2: Coordinate system and geometry.

$$\frac{\partial \eta}{\partial t} + [\zeta v_j]_{,j} = 0 \tag{2}$$

Here,  $x = x_1$  and  $y = x_2$  are the cross-shore and long-shore coordinates (see Fig.2) and repeated indexes are assumed to be summed. The derivative with respect to  $x_i$  has been indicated by the subindex  $,i$ . The total depth is  $\zeta = \eta + h$ , where  $h(x)$  stands for the still water depth and  $\eta(x, y, t)$  for the free surface elevation. We assume a quadratic bottom friction with a  $c_d(x)$  coefficient and  $S_{ij}$  are the radiation stresses.

We consider a basic undisturbed state which is a steady solution of equations (1)-(2) given by  $v_1 = 0, v_2 = V(x), \eta = \bar{\eta}(x)$ , where  $V(x)$  is the longshore current and  $\bar{\eta}(x)$  the wave set up/down. Then we superpose on the basic flow a small perturbation of the form

$$e^{ik(y-ct)}(u(x), v(x), \eta(x))$$

and upon linearization of the shallow water equations, (1)-(2), we obtain the eigenproblem:

$$ik(V - c)u + c_d V u + g \eta_x = 2\nu_x u_x + \nu(2u_{xx} - k^2 u + ikv_x + 2\frac{\bar{\zeta}_x}{H} u_x + ik\frac{V_x}{\bar{\zeta}} \eta) \tag{3a}$$

$$V_x u + ik(V - c)v + 2c_d V v + ik g \eta = \nu_x(v_x + iku) + \nu(v_{xx} - 2k^2 v + iku_x - \frac{\bar{\zeta}_x V_x}{\bar{\zeta}^2} \eta + \frac{V_x}{\bar{\zeta}} \eta_x + \frac{\bar{\zeta}_x}{\bar{\zeta}}(v_x + iku)) \tag{3b}$$

$$(\bar{\zeta} u)_x + ik\bar{\zeta} v + ik(V - c)\eta = 0 \tag{3c}$$

where the subindex  $x$  indicates differentiation with respect to  $x$ . The eigenvalue,  $c = \omega/k = (\omega_r + i\omega_i)/k$ , is the phase speed, which may be complex. The period and the wavelength are given by  $T = 2\pi/\omega_r$  and  $\lambda = 2\pi/k$ . The total depth is given by  $\bar{\zeta} = h(x) + \bar{\eta}(x)$ . In these linearized equations any perturbation in the radiation stresses has been neglected.

Given any set of current, bathymetry, bottom friction and viscosity profiles, and for any wavenumber,  $k$ , Equations (3) can be solved numerically by using spectral expansions. The details of the numerical procedure can be seen in Falqués and Iranzo (1992, 1994) or Iranzo and Falqués (1992). In that way the  $k - \omega_r$  and the  $k - \omega_i$  curves, that is, the dispersion and the instability curves can be computed. The basic flow is unstable if there is some wavenumber with positive growthrate,  $\omega_i > 0$ , and stable otherwise. The fastest growing wavelength in the linear theory, FGM, can be determined as the maximum in the  $k - \omega_i$  curve. Although shear waves observed in experiments have a finite amplitude and therefore need a nonlinear analysis, this wavelength, and its corresponding period that can be obtained from the dispersion line, are expected to give some estimate of the observed wavelength and period. This kind of analysis is presented here in two different ways: i) using analytical profiles to find general properties of shear instability, ii) using measured profiles for some particular beach.

The motivation for the first aim is as follows. For many Fluid Mechanics stability problems such as Rayleigh-Bénard convection and Couette flow, there are non-dimensional parameters say Reynolds number, Rayleigh number, etc. governing the transition between stability and instability and the sequence of bifurcations arising from the basic flow (Drazin and Reid, 1981). So far, transition conditions as a function of non-dimensional parameters have been lacking for shear instability of the longshore current. The latter stability problem has two dissipative sources, namely, bottom friction and eddy viscosity, which stabilize the flow. Our aim is to find two non-dimensional parameters related to bottom friction, viscosity, the current and the topography that govern stability. In such a way, transition lines in the plane of both parameters will be obtained and these lines will allow for a rough prediction of stability or instability for a wide class of beaches. For this purpose we will consider a basic current profile given by

$$V(x) = ax \exp(-(bx)^3) \quad (4)$$

This profile was suggested by Bowen and Holman (1989) and used by Falqués and Iranzo (1994). It can be an equilibrium solution of Equations 1-2 for a suitable radiation stress distribution. The parameters  $a, b$  are related to the maximum backshear and to the width of the current trough  $l_0 = 0.69/b$  and  $f_s = 0.79a$  where  $l_0$  is the offshore distance of the peak of the current and  $f_s$  is the maximum backshear, that is, the maximum shear at the sea-face of the current profile. Many realistic current profiles can be roughly fitted by (4) for suitable values of  $a$  and  $b$ . Concerning topography, we will consider the most simple situation, that is, plane sloping beach. Also, we will neglect the wave set-up/down which, regarding stability analysis, gives just a small correction on the total depth,  $\bar{\zeta}(x)$ . These simplifications allow us to handle only one parameter related to the bathymetry which is the beach slope,  $\beta$ . So, we assume

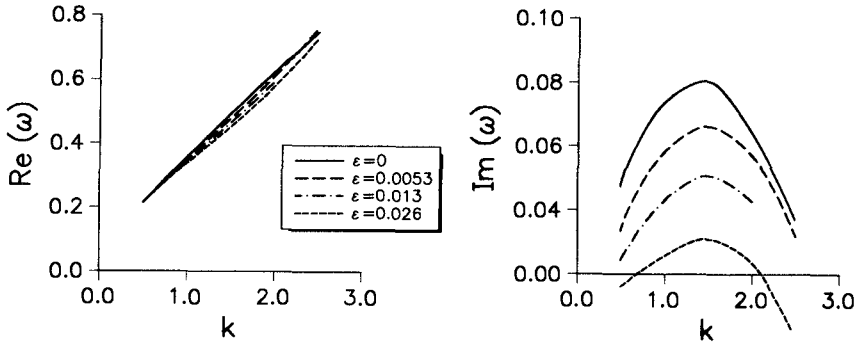


Figure 3: Dispersion (left) and instability (right) curves for  $F = 0.3, c_d = 0, x_b/l_0 = 1.6, \alpha l_0 = 3.5$  and for several maximum eddy viscosities.

$\bar{\zeta}(x) = h(x) = \beta x$ . Concerning lateral mixing, we consider (see Deguchi et al., 1992)

$$\nu(x) = \nu_m(h(x)/h(x_b))^{3/2} \quad \text{if } x \leq x_b \tag{5a}$$

$$\nu(x) = \nu_m e^{-\alpha(x-x_b)} \quad \text{if } x \geq x_b \tag{5b}$$

Finally, a uniform bottom friction coefficient,  $c_d$ , has been assumed. Equations (3) have been scaled using the cross-shore lengthscale of the current and its maximum backshear in such a way that we have taken  $b^{-1} = 1.45l_0$  as lengthscale and  $a^{-1} = 0.79f_s^{-1}$  as timescale. After this scaling the non-dimensional parameters in the equations are the maximum Froude number of the basic flow,  $F = (V(x)/\sqrt{gh(x)})_{max} = 0.63a/\sqrt{\beta gb}$ , the frictional parameter,  $c_d/\beta$ , and the non-dimensional maximum eddy viscosity,  $\epsilon = \nu_m/f_s l_0^2$ , which plays the role of a reciprocal Reynolds number,  $Re^{-1}$ . Concerning lateral mixing, two more parameters appear: the position of the maximum viscosity in comparison with the maximum in the current,  $x_b/l_0$ , and the non-dimensional offshore gradient,  $\alpha l_0$ .

Typical instability and dispersion lines are shown in Figure 3 for increasing viscosity from  $\epsilon = 0$  up to  $\epsilon = 0.026$ , with no bottom friction and for  $F = 0.3$ . The wavenumber  $k$ , and the complex frequency  $\omega$  have been scaled to  $b$  and  $a$ . In accordance with previous work, the dispersion relations are quite linear. The general trends we have found are that increasing bottom friction and/or eddy viscosity results in a decrease in growthrates,  $\omega_i$ , and in a small decrease in frequencies. An increase in Froude number decreases instability too. This may be because for high Froude number shear instability feeds surface gravity

modes so that instability is weakened. These general characteristics may have some exception regarding viscosity. When the eddy viscosity distribution has its maximum around the maximum in the current profile and has a strong offshore decay (large  $\alpha$ ) an increase in eddy viscosity can result in a larger growthrate. If  $\epsilon$  goes on increasing, this trend is reversed and stability is finally reached. This behaviour can be understood by considering that viscosity has two opposite effects: it dampes instability but also has a diffusive effect which propagates perturbations and therefore favours instability. Then, when  $\nu_m$  increases from a very small value the viscosity in the sea face of the current profile still remains negligible at the beginning, whereas it reaches significant values at the shore face of the profile. Since the source of the instability is mainly located in the sea face (in the region where the backshear is maximum) the damping effect is therefore negligible. On the other hand, the diffusive effects at the shore face can be important. If  $\nu_m$  continues to increase, the values of  $\nu(x)$  near the maximum backshear become large enough so that the damping effect become dominant. This is in contrast with the effects from bottom friction. Dodd (1994) found that there may be destabilizing effects due to bottom friction (curvature terms) but that the overall effect was a stabilizing one. In line with his results, we also find that the overall influence of bottom friction on shear instability is always a stabilizing one.

In any case, for each set of values of  $F, x_b/l_0, \alpha l_0$  and for each  $c_d/\beta$  we find a critical value of  $\epsilon$  such that instability requires lower values. We thus obtain a stability diagram in the  $\epsilon - c_d/\beta$  plane with transition lines that bound stability and instability regions. These lines are shown in Fig.4 for  $F = 0.14, F = 0.3$  and  $F = 0.89$ . We have set  $x_b/l_0 = 1.6$  and  $\alpha l_0 = 3.5$ . Very small sensitivity has been observed to the latter two parameters, except for the case  $x_b/l_0 \simeq 1$  and large  $\alpha l_0$  described above, which is not very realistic because  $x_b$  is usually expected to be offshore of the maximum in the current. As can be seen in Fig.4, for small Froude number instability is almost insensitive to Froude number. However, for high values some sensitivity appears and the stability region is widened.

Some experimental data sets have also been plotted in Fig. 4. This is not an easy job as only crude estimates of  $c_d, \nu$  are available, the actual current profiles are usually rather far from (4) even for suitable  $a, b$  and we have to rely on a mean beach slope,  $\beta$ . Though these limitations result in large error bar we think that the diagram can be useful in giving a rough prediction of stability or instability. Four data sets have been represented: Duck (USA), Leadbetter (USA), wave-basin experiment (LIP project M19, The Netherlands) and Trabucador (Ebro Delta, Spain). The experimental information was taken from Dodd et al. (1992), Reniers et al. (1994) and Redondo et al. (1994). The lateral mixing was estimated according to Deguchi et al. (1992). The most stable situation corresponds to Leadbetter beach and indeed no evidence of shear waves was found at this site. On the other hand, the diagram predicts

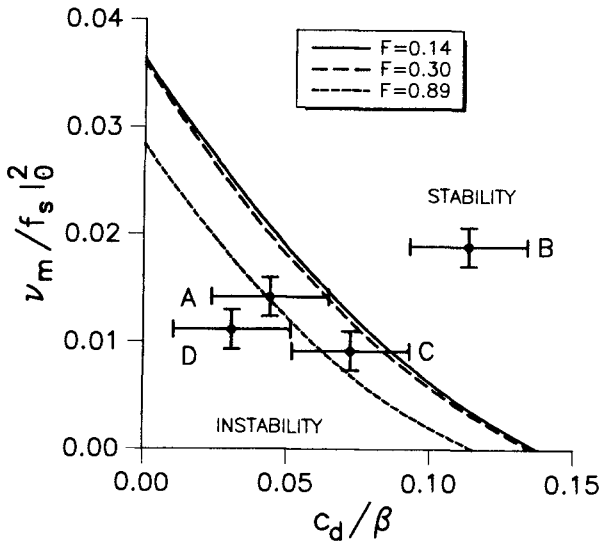


Figure 4: Transition lines for  $x_b/l_0 = 1.6$ ,  $\alpha l_0 = 3.5$  and for three Froude numbers. Four experimental data sets have also been plotted: A:Duck (USA); B:Leadbetter (USA); C:Wave-basin experiment LIP project M19; D:Trabucador (Spain).

instability for Duck data set in agreement with observations (the maximum Froude number did not exceed 0.3). The Trabucador data set also leads to instability according to the model. A complete data analysis is not yet available (Delta'93 campaign). However, a preliminary inspection indicates the presence of low frequency oscillations that might be shear waves. Regarding the wave basin experiment, the maximum Froude number reached  $F = 0.7$ , so the corresponding box in the diagram would match the transition line that would be somewhere in between the  $F = 0.3$  and the  $F = 0.89$  lines. Therefore, no conclusive analysis can be made by this way in this case and a detailed numerical simulation for the actual  $V(x)$ ,  $\zeta(x)$ ,  $c_d(x)$  and  $\nu(x)$  profiles is necessary. In any case, if we want a more accurate prediction of instability, with the period and wavelength of the shear waves, this computation for the actual profiles is needed. This kind of analysis has been made for Trabucador Beach, and for the wave basin experiment. Although a detailed analysis of the results of this latter experiment is under way, some preliminary results are already available. For instance, measurements from the longshore array of currentmeters for one of the tests with barred beach indicated the presence of shear waves with a period of approximately 25sec. and a phase speed of 0.33m/s, giving rise to a wavelength of 8.3m. In this case, a dominant mode with a wavelength of  $2\pi/k = 7.3m$  and a



period of  $2\pi/\omega_r = 27\text{sec.}$  was obtained from the numerical model. Experiments and theory were thus found to be in a fairly good agreement.

### 3. Nonlinear Stability

Only a preliminary study of the nonlinear shear instability is currently available, and a much more detailed analysis is under way. For this preliminary study, some assumptions have been made: plane sloping topography, uniform bottom friction and viscosity coefficients, a basic current given by (4) and the rigid lid assumption, that is, the vertical fluxes are much smaller than the horizontal ones (Bowen and Holman, 1989). Falqués and Iranzo (1994) showed that rigid lid hypothesis was a suitable one for low Froude number so that for  $F$  up to 0.6 only a correction less than 12% was necessary in growth rates. Therefore, rigid lid assumption is not a severe restriction for natural beaches. A further assumption regarding the mean flux that will be specified later on has been taken into account. The mass conservation equation (2) and the rigid lid hypothesis allow us to use a streamfunction for the perturbation,  $\psi(x, y, t)$ , defined by:

$$v_1 = \frac{1}{h} \frac{\partial \psi}{\partial y} \quad , \quad v_2 = V(x) - \frac{1}{h} \frac{\partial \psi}{\partial x} \quad (6)$$

Then, by taking the curl of the momentum equations (1) we end-up with a single governing equation which is

$$C \frac{\partial \psi}{\partial t} = \mathcal{M}\psi + \mathcal{N}(\psi) \quad (7)$$

where the linear operators  $C$  and  $\mathcal{M}$  are given by

$$\begin{aligned} C\psi &= \frac{1}{h} \left( \frac{h_x}{h} \psi_x - \Delta \psi \right) \\ \mathcal{M}\psi &= -VC\psi_y + \psi_y CV + \frac{c_d V}{h^2} (2\psi_{xx} + \psi_{yy} + 2(\frac{V_x}{V} - 2\frac{h_x}{h})\psi_x) + \\ &+ \nu \left( (\frac{h_x}{h})_x (C\psi + \frac{2}{h} \psi_{yy}) + \frac{h_x}{h} (C\psi)_x + \Delta(C\psi) \right) \end{aligned}$$

and the nonlinear operator  $\mathcal{N}$  is given by

$$\mathcal{N}(\psi) = \frac{1}{h} (\psi_x C\psi_y - \psi_y (C\psi)_x + \frac{h_x}{h} \psi_y C\psi)$$

The subindices  $x, y$  mean derivative with respect to  $x$  or  $y$  and the operator  $\Delta$  is the 2D horizontal Laplace operator. The operator  $C$  applied to  $\psi$  gives the vertical component of the vorticity. Hereafter, the scaling introduced in Section 2 is used. Equation (7) has to be solved in the domain  $x, y \in (0, +\infty)$   $\times$   $(-\infty, +\infty)$ . However, for technical reasons the cross-shore domain has been

cut off at some suitable offshore position,  $x = l$ . A comparison between the spectrum of the linear part of (7) and the spectrum of (3) solved without this restriction shows that the error remains very small if  $l$  is large enough compared to the width of the current. A suitable value has been  $l = 6$ . The boundary conditions at the shoreline and far offshore are:

$$\psi = \psi_x = 0 \quad x = 0, x = l \tag{8}$$

Periodicity conditions with respect to some basic wavelength,  $\lambda_0 = 2\pi/K_0$ , have been used as boundary conditions regarding the longshore coordinate. The boundary conditions at  $x = l$  just mean vanishing cross-shore and longshore velocity perturbations far offshore. Concerning the shoreline the matter is not so simple because of the singularity coming from  $h(0) = 0$ . The set of boundary conditions chosen at  $x = 0$  ensures a bounded velocity field at the shoreline and it means vanishing mass transport.

Equation (7) has been solved numerically using a spectral Chebyshev-Fourier expansion

$$\psi(x, y, t) = \sum_{k=-n}^{k=n-1} \sum_{j=0}^m a_{kj}(t) T_j(x) e^{ikK_0 y} \tag{9}$$

where  $T_j(x)$  are Chebyshev polynomials. After spatial discretization which is performed by Galerkin projection concerning  $y$  and by collocation concerning  $x$ , Equation (7) reads as a set of  $2n$  vector ordinary differential equations (one for each alongshore Fourier mode)

$$\hat{C}_k \frac{d\vec{a}_k}{dt} = \hat{M}_k \vec{a}_k + \vec{N}_k(\vec{a}_{-n} \dots \vec{a}_0 \dots \vec{a}_{n-1}) \quad k = -n, \dots, n-1 \tag{10}$$

where the  $(m+1) \times (m+1)$  matrices  $\hat{C}_k, \hat{M}_k$  and the vector functions  $\vec{N}_k$  are the discrete versions of operators  $C, M, N$  for each Fourier mode,  $k$ , and where  $\vec{a}_k = (a_{0k}, a_{1k}, \dots, a_{mk})$  stands for the  $m+1$  Chebyshev coefficients of the Fourier mode  $k$ . The equations corresponding to each Fourier mode are coupled only because of their nonlinear terms,  $\vec{N}_k$ . Time discretization proceeds by using a semi-implicit Euler scheme

$$(\hat{C}_k - \delta t \hat{M}_k) \vec{a}_k^{\tau+1} = \hat{C}_k \vec{a}_k^\tau + \delta t \vec{N}_k(\vec{a}_{-n}^\tau \dots \vec{a}_{n-1}^\tau) \quad k = -n, \dots, n-1 \tag{11}$$

Given the solution  $\vec{a}_k^\tau$  at time step  $\tau$ , Eq.11 is linear in  $\vec{a}_k^{\tau+1}$  and can be easily solved. More details and references on numerical spectral methods applied to coastal dynamics may be seen in Falqués and Iranzo, (1992, 1994) or in Iranzo and Falqués (1992).

Some sensitivity tests concerning the parameters of the numerical model were made. The model proved to be quite robust and the values of  $m = 40, n = 8, \delta t = 0.01$  were found to be suitable for the preliminary study made up to

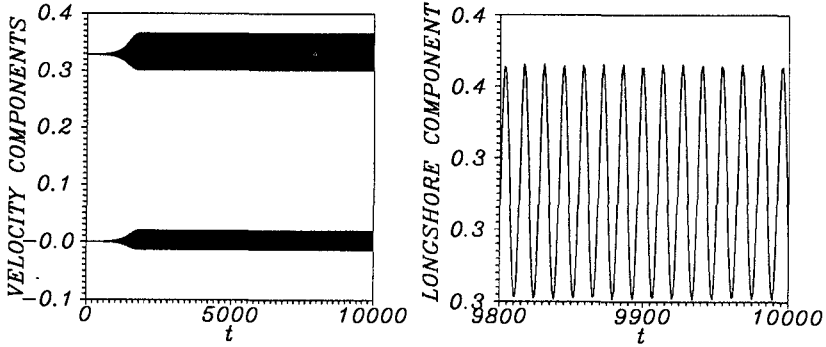


Figure 5: Time evolution from a small initial perturbation for  $\epsilon = 0.053, \mu = 11.1$ . Time series of cross-shore and longshore velocity components (left) and final steady oscillation in the longshore component (right).

now. Owing to the linear theory outlined in Section 2 the control parameters for instability are the frictional parameter,  $\mu = \beta/c_d$ , and the non-dimensional viscosity,  $\epsilon = \nu_m/f_s l_0^2$ . Time evolution from some initial perturbations has been computed for several values of  $\epsilon, \mu$ . For any  $\epsilon$ , a critical value  $\mu_c$  was found to exist such that below it all the perturbations tend to vanish whereas above it the perturbations grow. At the beginning this growth is nearly exponential but then a saturation is reached and a final oscillatory solution is obtained. For  $\mu$  slightly higher than  $\mu_c$  its period is very close to the period predicted for the linear theory. The critical value,  $\mu_c$ , coincides with that given by the linear analysis. For instance, for  $\epsilon = 0.053$  the transition occurs at  $\mu_c = 10.0$ . One test slightly above critical conditions ( $\mu = 11.1$ ) is shown in Fig. 5. These results show that shear instability of the longshore current gives rise to a supercritical Hopf bifurcation and are in line with the weakly nonlinear analysis carried out by Dodd and Thornton (1992). Far from criticality the behaviour may be quite complicated: an energy transfer between Fourier modes occurs, the FGM mode may be no longer dominant, the final steady wave may be modulated... A further increase in  $\mu$  leads to a blow-up of the numerical model. For  $\epsilon = 0.053$  this occurs for  $\mu > 20$  and may be due to numerical instabilities that might be due in turn to a further bifurcation in the physical problem. This is currently being investigated. An example of the strongly nonlinear behaviour is shown in Figure 6 by means of a time evolution from a small initial perturbation for  $\epsilon = 0.053, \mu = 20$ . In this test, the basic wavenumber has been chosen to be  $K_0 = 0.467$ , that is, one third of the FGM (linearly dominant) which is 1.4. This means that the FGM mode corresponds to  $k = 3$  so that the simulation uses two subharmonics in addition to the superharmonics. As we can see, the first mode to grow significantly is  $k = 3$ . Apparently, it reaches a saturation.

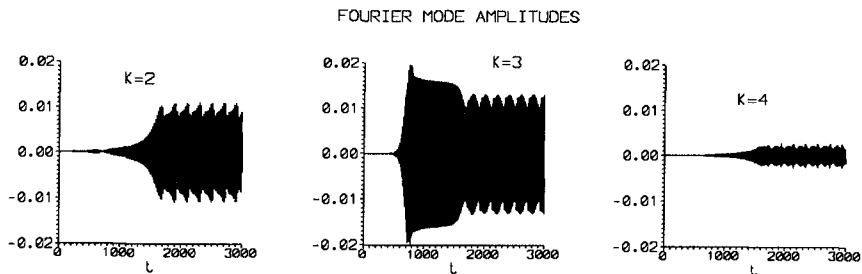


Figure 6: Time evolution of the FGM,  $k = 3$ , its subharmonic  $k = 2$  and its superharmonic  $k = 4$  from a small initial perturbation for  $\epsilon = 0.053$ ,  $\mu = 20$ . The basic wavenumber is  $K_0 = 0.467$ .

However, it slowly loses part of its energy by feeding the other modes, specially the  $k = 2$  subharmonic and the  $k = 0$  mode. Finally, the other modes reach a saturation and a final steady modulated oscillation in all modes starts. The time unit in all these plots is the timescale defined in Section 2 and based on the maximum backshear of the basic flow. For natural beaches, 10 units may be of the order of  $1min$ . Therefore, our numerical time series of 10000 time units would represent a real time of 16 hours. This is quite enough for shear wave simulation.

According to the numerical experiments performed some preliminary properties of finite amplitude shear waves can be summarized. For each set of values of  $\mu, \epsilon$  the final finite amplitude shear waves has been computed from several initial conditions and no sensitivity to the initial conditions has been found except in the parameters range where the numerical model blows up. As expected, the flow pattern corresponding to the perturbation for near critical conditions is very similar to the linear eigenfunction although some asymmetry between crests and troughs can be noticed. However, far from criticality the streamlines are quite different from the linear ones, showing a strong mean flow component (Fig. 7). This component comes from the 0 Fourier mode and means a correction on the mean flow due to the instability. Because of the boundary conditions at the shoreline (8) the mean alongshore discharge due to the perturbation vanishes,  $\psi(l, y, t) - \psi(0, y, t) = 0$ . This is an unphysical constraint on the mean flow and has been taken because of technical reasons concerning the boundary conditions and the numerical procedures. Work is under way in order to relax this constraint by considering boundary conditions (8) only for  $k \neq 0$ . However, the present results already suggest that the mean flow component of the perturbation is not very important for near critical

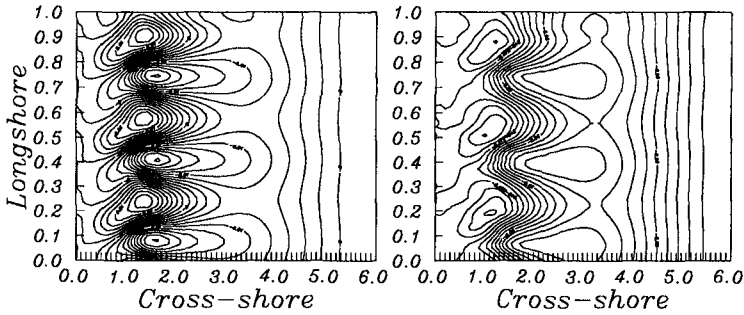


Figure 7: Streamlines of the perturbation, (A): near critical conditions ( $\epsilon = 0.053, \mu = 11.1$ ), (B): strongly nonlinear ( $\epsilon = 0.053, \mu = 20.0$ ).

conditions but can have a strong influence far from criticality. The amplitude of shear waves can be defined, for instance, as the fluctuation in the cross-shore component in comparison with the mean longshore current. This ratio has been plotted in Figure 8 as a function of the control parameter  $\mu$  for  $\epsilon = 0.053$ . This provides us with a bifurcation diagram for shear instability. Notice that this amplitude can reach 20%, that is, the same order of magnitude as the amplitudes measured at Duck (Oltman-Shay et al., 1989) or in the LIP experiment (Reniers et al., 1994). This is in contrast with the weakly nonlinear analysis of Dodd and Thornton (1992), where only amplitudes of about 0.07% were obtained. The curve stops when the numerical model breaks down. Intriguingly, this occurs roughly when the amplitude of shear waves reaches the maximum value observed in experiments,  $u/V_{max} \sim 0.2$ . The relationship between the final amplitude and the linear growthrate is shown in Figure 9. In qualitative agreement with the weakly nonlinear theory a small nonlinear correction on the period of the shear waves has been found. The relative increase, shown in Figure 9, can reach 6%.

#### 4. Conclusions

Analytical profiles for the current, eddy viscosity and bottom friction coefficient, and a mean beach slope have been used to investigate the general trends for shear instability of the longshore current. The overall influence of bottom friction and lateral mixing is a stabilizing effect and a small decrease in the frequency of shear waves. However, for some eddy viscosity profiles this trend is not monotone and an increase in viscosity may eventually result in

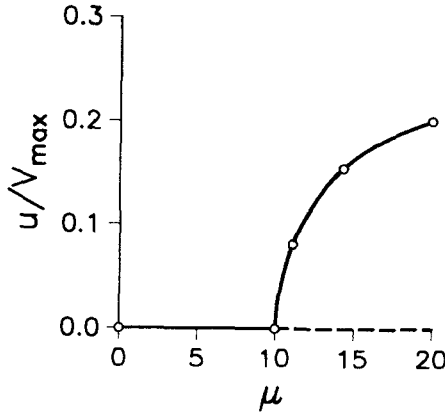


Figure 8: Bifurcation curve showing the amplitude of the crossshore fluctuation in the current with respect to the mean longshore current for  $\epsilon = 0.053$ .

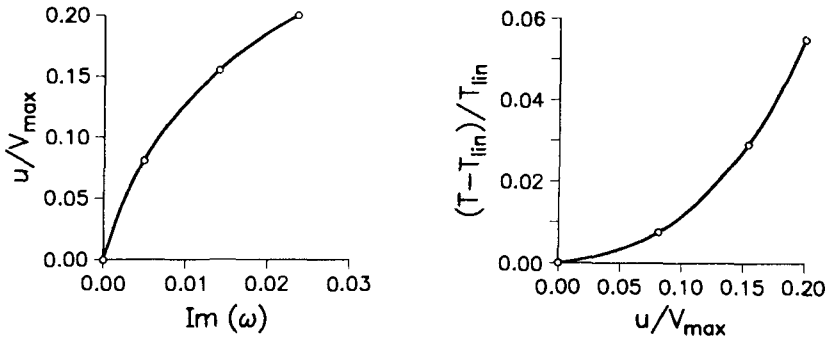


Figure 9: Left: amplitude of the final shear wave as a function of the linear growthrate. Right: Relative increase in the period of the shear wave as a function of the amplitude. ( $\epsilon = 0.053$ ).

larger growthrates. An instability diagram as a function of two non-dimensional parameters related to bottom friction, lateral mixing, the current and the bathymetry has been presented. This diagram allows for a rough prediction of shear stability characteristics for any beach and has been found to compare fairly well with four experimental data sets. A more accurate study of shear instability for a given situation requires the use of the actual profiles. This has been done for a wave basin experiment and a good agreement between numerical modelling and measurements has been found. A nonlinear numerical simulation has also been conducted. In accordance with the weakly nonlinear theory (Dodd

and Thornton, 1992) shear instability has been found to give finite amplitude waves through a supercritical Hopf bifurcation. However, the amplitudes are larger than the weakly nonlinear ones and reach at least 20% of the mean current. A small nonlinear correction on the period has also been found. Far from critical conditions shear waves can exhibit a complicated behaviour, with a modulation and with a flow pattern rather different from that predicted by the linear theory. Preliminary results suggest that for the strongly nonlinear situation there can be an important contribution of instability to the mean current.

## References

- Bowen A.J. and Holman R.A., 1989. *Shear instabilities of the mean longshore current, 1. Theory*, J.Geophys.Res. 94, C12, 18023-18030.
- Deguchi I., Sawaragi T. and Ono M., 1992. *Longshore current and lateral mixing in the surf zone*. Proc.23th Int.Conf.Coastal Eng., 202, p.2642-2654.
- Dodd N., Oltman-Shay J. and Thornton E.B., 1992. *Shear instabilities in the longshore current: a comparison of observations and theory*, J.Phys.Oceanog. 22, 1, 62-82.
- Dodd N. and Thornton E.B., 1992. *Longshore current instabilities: growth to finite amplitude*. Proc.23th Int.Conf.Coastal Eng., 203, p.2655-2668.
- Dodd N., 1994. *On the destabilization of a longshore current on a plane beach: Bottom shear stress, critical conditions, and onset of instability*, J.Geophys.Res., 99, C1, 811-824.
- Drazin P.G. and Reid W.H., 1981. *Hydrodynamic Stability*. Cambridge University Press.
- Falqués A. and Iranzo I., 1992. *Edge waves on a longshore shear flow*, Phys.Fluids A, 4 (10), 2169-2190.
- Falqués A. and Iranzo I., 1994. *Numerical simulation of vorticity waves in the near-shore*, J.Geophys.Res., 99, C1, 825-841.
- Iranzo V. and Falqués A., 1992. *Some spectral approximations for differential equations in unbounded domains*, Comp.Meth.Appl. Mech.Eng., 98, 105-126.
- Oltman-Shay J., Howd P.A. and Birkemeier W.A., 1989. *Shear instabilities of the mean longshore current, 2. Field observations*, J.Geophys.Res. 94, C12, 18031-18042.
- Putrevu U. and Svendsen I.A., 1992. *Shear instability of longshore currents: A numerical study*, J.Geophys.Res. 97, C5, 7283-7303.
- Redondo J.M., Rodriguez A., Bahia E., Falqués A., Gracia V., Sánchez-Arcilla A. and Stive M.J.F., 1994. *Image analysis of surf zone hydrodynamics*, Coastal Dynamics'94, p.350-365.
- Reniers A.J., Battjes J.A., Falqués A. and Huntley D.A., 1994. *Shear-wave laboratory experiment*, Proc.Int.Symposium: waves - physical and numerical modelling, vo.1, 356-365.

## CHAPTER 144

### Interpretation of Shoreline Position from Aerial Photographs

John S. Fisher<sup>1</sup>  
Margery F. Overton<sup>2</sup>

#### Abstract

A review of some of the potential sources of error associated with the use of aerial photographs to map shoreline change is presented. The influence of both tides and waves in the estimation of the position of the wet sand line on the subaerial beach is included. The use of the relatively new digital photogrammetry as applied to shoreline mapping is discussed and suggested as having the potential for being a superior method for this application.

#### Introduction

Aerial photographs have been used extensively to determine shoreline positions and erosion rates. Several different features on the beach and backshore have been used as reference lines, including the bluff or dune line, the seaward vegetation line, and the water line. The latter is usually defined as the wetted line where there is a marked contrast between the wet and dry sand. This latter feature is sometimes referred to as the "wet sand line", or the "high water line". Various investigators have described formalized methods for using this line to monitor shoreline change, including Stafford (1971), Dolan et al. (1978), and Leatherman (1983). Each of these methods share basically similar techniques which include the identification of the wet sand line, the digitizing of the line, and the measurement of change, either relative to an earlier shoreline position, or relative to a reference line offshore.

---

<sup>1</sup>Professor, Department of Civil Engineering, North Carolina State University, Box 7908-NCSU, Raleigh, NC 27695-7908

<sup>2</sup>Associate Professor, Department of Civil Engineering, NCSU



Once the shoreline position has been determined, the rate of erosion (or accretion) can be computed by determining the change between two or more shorelines over a known period of time.

It is well recognized that the use of aerial photographs in combination with the wet sand line has inherent inaccuracies. When dealing with erosion rate these errors can be reduced by simply using a relatively long period between dates of photography. As an example, consider the case where the error in identification of shoreline position for each date is  $\pm 50$  ft. If the time between photo sets is 10 years, then the maximum potential error is 10 ft/yr (100 ft divided by 10 years). However, if the time between these photos is 50 years, this error is reduced to 2 ft/yr. Thus, where possible, one should attempt to maximize the time between photo dates. In North Carolina, where only two dates are used to determine shoreline erosion rates, a minimum of forty years between dates is usually employed.

The above discussion also makes it clear why one must be extremely careful to minimize errors when using aerial photographs and the wet sand line to compute short term erosion rates (i.e., less than 10 years).

In partial recognition of the potential errors associated with this technique to measure shoreline change rates, some investigators use multiple dates of photography and either a linear regression, or some other statistical technique to model the rate of change. The advantage of using a series of dates is that the errors associated with any one date is reduced. A discussion of the pros and cons of these different statistical tools for computing shoreline change rates is beyond the scope of this paper. For the analysis which follows we will assume that this rate is computed by simply looking at the difference beyond two dates. This is sometimes referred to as the "end point method".

#### Sources of Error

The process of measuring shoreline change from aerial photographs has several potential sources of error:

1. distortions in the photographs,
2. the georeferencing of "permanent features",
3. human error in measuring and digitizing,
4. corrections for tides, and
5. corrections for wave setup and runup.

Crowell, et al. (1991) present a thorough review of mapping accuracy as applied to shoreline change. Of particular interest in this review is the discussion of the errors associated with the aerial photos (including distortion and corrections for camera angle) and the procedures used to tie the photos to the ground.

In order to fix the aerial photograph in space it is necessary to georeference it to known features. The degree to which this is done with accuracy will of course have a significant impact on the overall accuracy of the analysis. For example, if USGS topographic maps are used to georeference the photos, one is limited to the accuracy of these maps; approximately +/- 40 ft. This error can be reduced if ground referenced points are surveyed at the site using traditional means, or GPS. One can reasonably reduce this error to +/- 1-2 ft (or less) with careful survey techniques.

The actual procedure by which the photos are digitized will also effect the probable error. For many investigations of shoreline change the photos are enlarged and the shoreline digitized directly. While this technique is relatively fast and inexpensive, it does not take advantage of the higher accuracy available from using photogrammetric techniques and analytical stereoplotters. While the former is more time consuming, it nonetheless will yield far better measurements of shoreline position as determined from the wet sand line. We estimate that a careful operator on an analytical stereoplotter can consistently determine shoreline position to within +/- 5 ft with surveyed ground control for the georeferencing. This is in contrast to an estimated error of +/- 50 ft using the more conventional techniques of digitizing directly from the photographs and USGS topographic maps for control. These error estimates represent a combination of the error involved in both georeferencing, identifying the wet dry line, and human error in digitizing this line.

Thus, for the determination of the rate of shoreline change for a period of 50 years between photographs, the larger of these two potential errors (+/- 50 ft) could produce an error in rate of up to 2 ft/yr. Alternatively, the lesser error would be 0.2 ft/yr. Depending upon the particular application, this may justify the additional effort required by the use of the analytical stereoplotter for the measurements.

In addition to the errors associated with the photographs, (georeferencing, and digitizing), one must also consider the dynamics of the wet sand line itself. Both the tide and the waves will influence this line. Consider first the influence of the tide. Most shoreline

mapping applications that the authors are aware of have not attempted to make corrections for tide. Generally the time of the photographs is dictated by the logistics of the aircraft and the lighting requirements. At best, some mapping programs attempt to collect the photographs on consistent points on the tide curve, e.g., spring low, mean, spring high, etc. For the historical photographs one generally accepts what is available, and in many cases the time of the photograph relative to the tide may not be known or obtainable.

The magnitude of the error introduced by not correcting for tide can be easily estimated. This error will be a function of the tidal range, the slope of the beach, and the time of the aerial photograph. As an example, consider a beach where the tidal range is 3 ft, the beach slope is 1:20, and the two photographs are taken at high and low tide respectively. The maximum probable error introduced by not correcting for the tide is 60 ft. This error means that if there had been no real change in shoreline position, the analysis would nonetheless have yielded a 60 ft change due to the tidal difference. If the time between the two photographs is 50 years, then this translates into an error of 1.2 ft/yr.

A similar argument can be made for the effect of wave runup and setup on the interpretation of shoreline change. In this case the wave conditions at the time of the aerial photograph will influence the position of the wet sand line. The slope of the beach, wave height, and wave period will all contribute to the relative shoreline position. For example, if one uses a simple model for wave runup, and a beach slope of 1:20, then a relatively small change in wave height and period will produce horizontal differences in shoreline position of approximately 80 ft. In terms of the previously assumed time between photographs of 50 years, this yields a difference in rate of change of 1.6 ft/yr. Again, as with the example for tide, the failure to correct for wave runup will introduce an apparent change in the position of the wet sand line even though there has not been any actual erosion or accretion of the beach.

#### Summary of Potential Errors

It is clear from the previous discussion that the potential errors in computing the rate of shoreline change from aerial photographs can be significant. Even if one is willing to use ground surveys to control the photographs and photogrammetric techniques to map the position of the wet sand line, there are still the problems associated with waves and tide. The correction for the tide would require some knowledge of the beach slope, and thus some minimum ground measurements at the time of the photographs.

Correction for waves would require this beach profile as well as an estimate of the wave conditions at the time of the photographs. The only alternative is to recognize that the potential for these errors exists, and therefore the interpretation of the data must include reasonable estimates of these errors. The actual error will of course depend upon the techniques employed and the specific conditions at the site.

### Digital Photogrammetry

Many of the problems described above can be eliminated by the use of digital photogrammetric techniques to map shoreline change. Digital photogrammetry is a process by which a three dimensional representation of the shoreline is mapped from a pair of stereo aerial photographs. This can be accomplished with an analytical stereoplotter, or alternatively, with the newer techniques using computer controlled scanners to digitize the aerial photographs. There are a number of commercial vendors for these digital systems. We are currently working with a series of products developed by Intergraph Corporation.

As with the more conventional techniques, it is still necessary to have accurate ground control in order to have an accurate model of the beach. However, in place of mapping the wet sand line, it is possible to define the shoreline as a particular datum, such as the mean high water line, or mean lower low water, etc. Since there is a 3-D model of the subaerial beach for each date of photography, there no longer is a need to correct for either tide or waves. In addition, since digital photogrammetry can achieve relatively high resolution (on the order of +/- 0.5 ft), the computation of the rate of shoreline change, even for short time periods, can be reasonably determined.

We are currently working with the Intergraph system to determine both its utility and economics when used to measure shoreline change. The results of this investigation will be presented in future publications.

### Conclusions

Aerial photographs will continue to be an important tool in the determination of shoreline change, and in the prediction of future shoreline positions. There are a number of sources of potential error in the current techniques. However, as long as these errors are understood, these techniques can continue to be employed. It is anticipated that the use of digital photogrammetry will, in time, replace today's technology, and thereby

provide a far superior mechanism for determining shoreline change from aerial photographs.

### Acknowledgments

This research is currently being supported by grants from the North Carolina Division of Emergency Management, the North Carolina Department of Transportation, the North Carolina Division of Coastal Management, and the Kenan Institute for Engineering, Science, and Technology. The assistance of Intergraph Corporation is also greatly appreciated in this research. Mr. Johnny Martin provided significant help in this research.

### References

- Crowell, Mark, Leatherman, S.P., and Buckley, M.K. (1991). "Historical shoreline change: error analysis and mapping accuracy." *Journal of Coastal Research*, Vol.7, 839-852.
- Dolan, Robert, Hayden, B., and Heywood, J. (1978). "New photogrammetric method for determining shoreline erosion." *Journal of Coastal Engineering*, Vol.2, 21-39.
- Leatherman, S.P. (1983), "Shoreline mapping: a comparison of techniques." *Shore and Beach*, Vol. 51, 28-33.
- Stafford, D.B., and Langfelder, J. (1971), "Air photo survey of coastal erosion." *Photogrammetric Engineering*, Vol.37, 565-575.

## CHAPTER 145

### SETTLING COLUMNS PARAMETRIC TESTS APPLIED TO COASTAL SEDIMENT CONSOLIDATION

Stéphane GALLOIS<sup>1</sup>, Alain ALEXIS<sup>1</sup>, Pierre THOMAS<sup>1</sup>

#### ABSTRACT

This paper presents a set of devices and a study both experimental and original in order to determine the influence of various parameters on the sedimentation-consolidation process of soft soils. We use this system to investigate the behaviour of a natural estuarine mud. A series of tests is performed, in which each test differs from the reference test in the value of only one parameter. We give a synthesis allowing the comparison of the action of each parameter on the mud behaviour. This systematic parametric experimental study builds an original data base, which is obviously necessary to validate theoretical modelization.

#### 1. INTRODUCTION

The behaviour of cohesive sediments is one of the main components of coastal engineering processes. These sediments are in an intermediate state between solid and liquid. Their theoretical study requires geotechnical or hydraulical modelization, both conceived with their own approach. We have proposed (ALEXIS et al., ICCE' 93) a unification of consolidation theories, pointing out the interest of the use of Gibson's law. The application of these theoretical models requires the knowledge of constitutive relationships (permeability, effective stress) of the muddy material. In this paper, we are proposing an original and experimental set of devices and study in order to determine the influence of various parameters on the sedimentation-consolidation process.

#### 2. EXPERIMENTAL SET

Our topic is to perform experiments characterised by :  
- One-Dimension-Vertical experimentation by means of

---

<sup>1</sup>Civil Engineering Laboratory E.C.N.I.U.T. St. NAZAIRE  
BP 420, F 44606 St-NAZAIRE CEDEX (FRANCE)

instrumented settling columns.

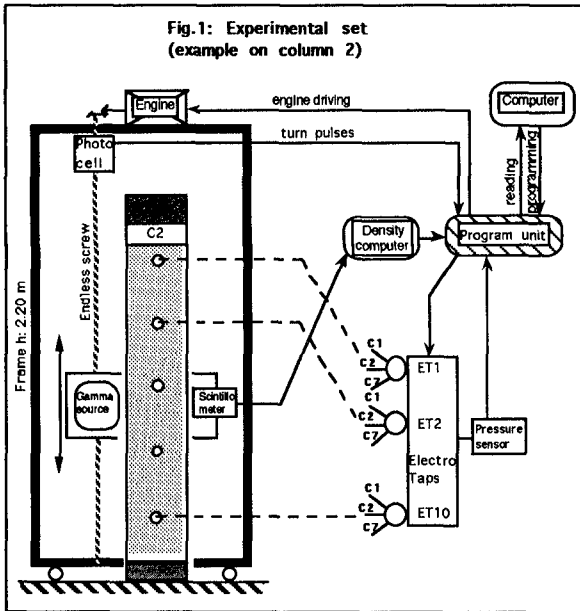
- No-disturbance of the evolutive material which is a natural mud with a natural estuarine water.
- Continuous tracking of its evolution.
- Simultaneous measurements on several columns under different conditions.

Our bibliographic research has shown the present lack of convenient experimental set.

So, we propose an original experimental set in order to reach these aims.

This experimental set needs a particular environment of the experiments to reduce the biochemical evolution of mud : the set is in a blind climatized room, the temperature is 10 degrees Celsius.

The experimental set (fig.1) is composed of a servo gammadensimetric bench and 7 columns in different conditions with acquisition, piloting and delayed processing.



The bench is 2.2 meters high.

It is shiftable for simultaneous measurements on the 7 columns.

It also uses a driving engine for moving the gammadensimeter which consists of a gamma source and its scintillometer.

The experiments require a localisation set by photocell

and 10 pressure locations for each columns.

By means of an hydraulic network, these pressure locations are connected to a unique pressure sensor by pipes via electrotaps.

These phases of acquisition, piloting, and delayed processing require a specific programmation and adaptation of program unit for the measurement and acquisition of density, pressure, position and also for piloting the driving engine and the electrotaps.

This system has several specificities:

- *experimentation systematisation*: simultaneous measurements on seven parallel columns, shifting the movable gammadensimeter to each column. All the columns are connected by plastic pipes to the pressure sensors through the set of electrotaps.

- *specific procedure*: the adjustment of the number of measurements enables the compromise between accuracy and speed: profile duration can vary from 2 min (continuous profiles) to 20 min (step by step profiles) in order to identify the mud behaviour during the initial stage of the process and to obtain a good accuracy in the final phase as well.

- *search of reliability*: the use of a unique pressure sensor allows the avoiding of drift errors and the obtaining of automatic pore pressure profiles throughout the whole experiment.

### 3. EXPERIMENTAL STUDY

#### 3.1 Experimental method

The phenomenon is characterized by its complexity because of :

- superposition of spatial and time evolutions.
- large variations of evolution with geometric conditions and composition of material.
- numerous interactions between characteristics.

So, we propose an experimental methodology.

We have 2 steps of procedure :

- on line for measurement acquisition and also for concentration and pore pressure profiles performing
- and delayed processing of profiles evolution.

So, we tackle this parametric study by changing only one parameter at a time experimentally with respect to one reference case. Our experimental approach is quite similar to partial derivative approach.

There are 16 instants of measurements in a geometrical progression of ratio 2.

Among the numerous characteristics governing the cohesive soils settling, the basic parameters are initial concentration ( $c_0$ ), initial height ( $h_0$ ), fines



proportion (less than 63  $\mu\text{m}$  in size) and organic matter content (ignition loss).

We are using a reference case and 4 other cases.

The reference case is performed with natural mud (LL=65%, PI=18%, OM=13%),  $h_0=1.50$  m,  $c_0 = 90$  g/l, temperature 10°C, natural water. In the 4 other cases, the changed parameter value is respectively:  $h_0=0.75$  m (half height),  $c_0 = 180$  g/l (double concentration), 100% fines, 0% organic matter.

At last, we will obtain 10 000 recorded data issued from measurements of position, density and pressure.

### 3.2 Results

We propose a full synthesis of our measurements results which allows the comparison between the respective influences of studied parameters upon the evolution of profiles of concentration and pore pressure concentration on the one hand, and on constitutive relationships on the other. We have chosen to present concentration profiles and permeability as examples.

#### a) General influence of parameters

A great deal of information (fig. 2 and 3) are induced by the observation of the following three special aspects of concentration profiles: soil-water interface downing speed, behaviour during sedimentation ("vertical" part of the profiles) and shape of the curve in the deposit (lower part of each profile).

These 2 figures show the concentration profiles in 5 cases, at 3 instants.

The comparative analysis of these curves and of their slopes give a lot of informations.

- The similarity of the first parts of reference curve and fines only curve implies that the influence of fines particles governs interface downing speed, and it also implies the lack of size segregation of particles during downing.

- in the highest part of profiles, the concentration is lower than initial concentration, so there is probably a swelling, that is a local decreasing of concentration.

- this hypothesis is confirmed by the importance of non-verticality of first part of double concentration profiles.

- consolidation is slowed by the thickness of deposit and by the organic matter. This can be explained in terms of draining path length and of draining speed of pore pressure.

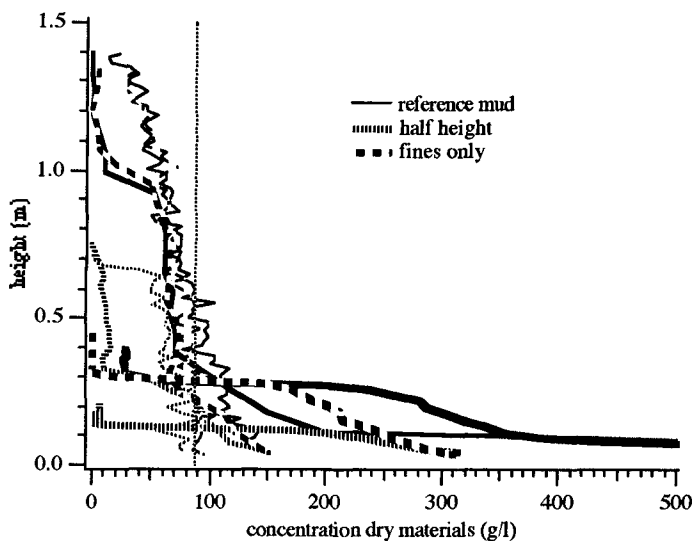


Fig.2: Concentration profiles at  $t=5$  min, 3h and 192 h in the cases reference, fines and half height

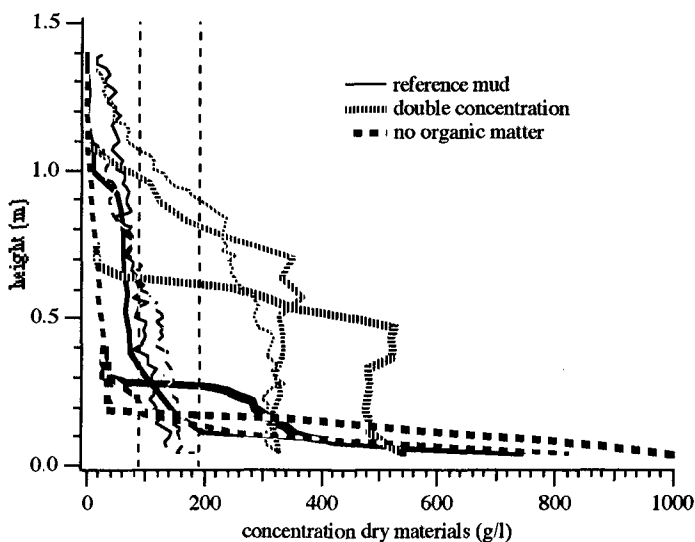


Fig.3: Concentration profiles at  $t=5$  min, 3h and 192 h in the cases reference, double concentration and no organic matter

We propose, also, a set of measurements of excess pore pressure profiles (fig.4).

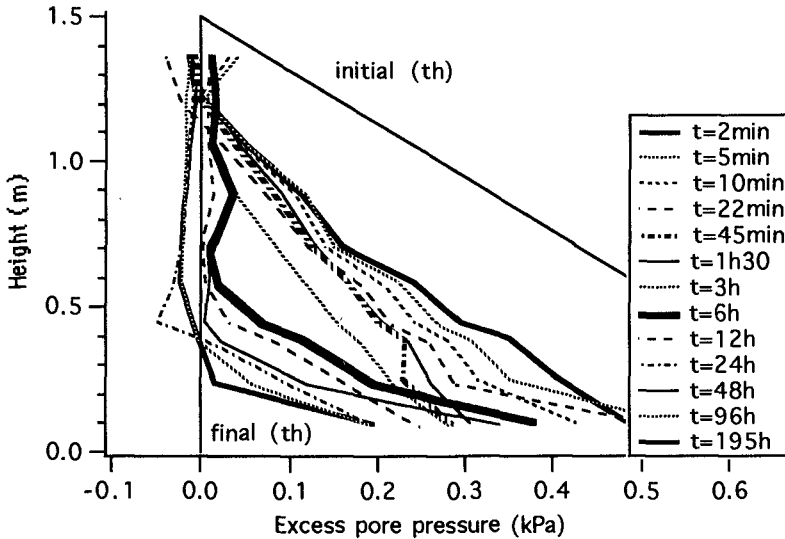


Fig.4: Evolution of excess pore pressure profiles with time

These measurements are original but quite delicate to carry out.

The figure represents the evolution with time of pore pressure excess above hydrostatic pressure for the different pressure locations.

It appears a quite regular dissipation of pore pressure.

During initial phase, there is a fast evolution of pore pressure and during final phase, after 6 hours, there is a slow evolution curves in the deposit.

We specify that accuracy is about 20 Pascal and that salinity generates a complex geochemical behaviour so, there is an instability of curves around zero over pore pressure.

#### b) Application to constitutive laws

These different results can be applied for a better knowledge of constitutive laws.

We can use density or pore pressure measurements to obtain new parameters, at each measurement point.

Density measurements give us void ratio  $e$ .

By means of an integration of profile, we can obtain total stress  $\sigma$  at each point.

The profile evolution with time gives us settling velocity  $v_s$

Pore pressure measurements  $u$  drive us to effective

stress  $\sigma'$  which is the difference between total stress and pore pressure.

Pore pressure profiles  $u$  give us hydraulic gradient  $i$ .

Then, we can determine permeability :  $k$

So, we obtain 3 essential parameters : effective stress  $\sigma'$ , permeability  $k$  and void ratio  $e$ .

Their linkage is the main part of constitutive laws study.

First, we apply that way of research to permeability.

In figure 5, we propose a set of dots, corresponding to 4 cases material at 3 instants (33 mn., 9h., 72h.).

At each instant, we can draw an average curve between the corresponding dots, whatever their case.

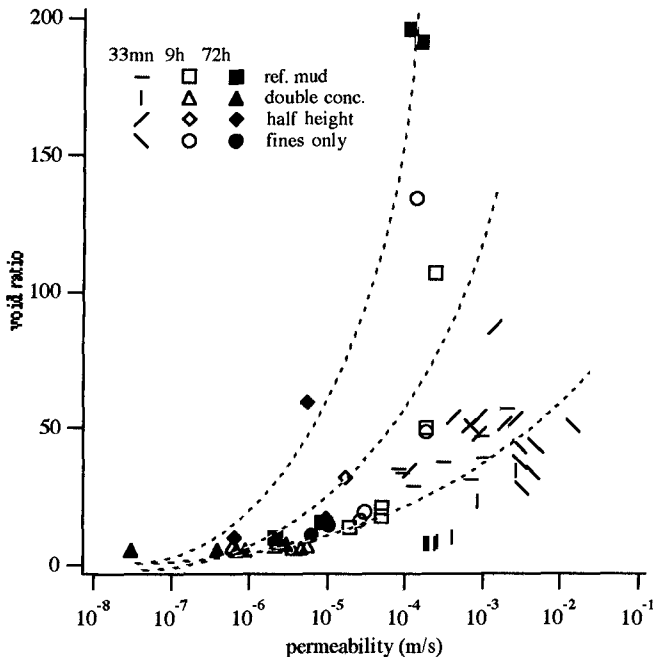


Fig 5 Evolution of permeability with time and void ratio

We observe that permeability decreases with time, for a constant void ratio. So, the permeability is not constant with time. This new and original result underlines the limits of validity of Darcy's law as a flow law through very little consolidated cohesive sediments.

Otherwise, we can remark the good agreement of fines

permeability values with references permeability values. We can deduce that fine fraction probably governs the mixture permeability.

The measurements in non-organic mixture, not shown here, are always close to the lowest curve. So, the permeability of non-organic mixture does not depend on time.

Second, we apply that way of research to effective stress.

Figure 6 represents effective stress and void ratio for the reference case at each instant.

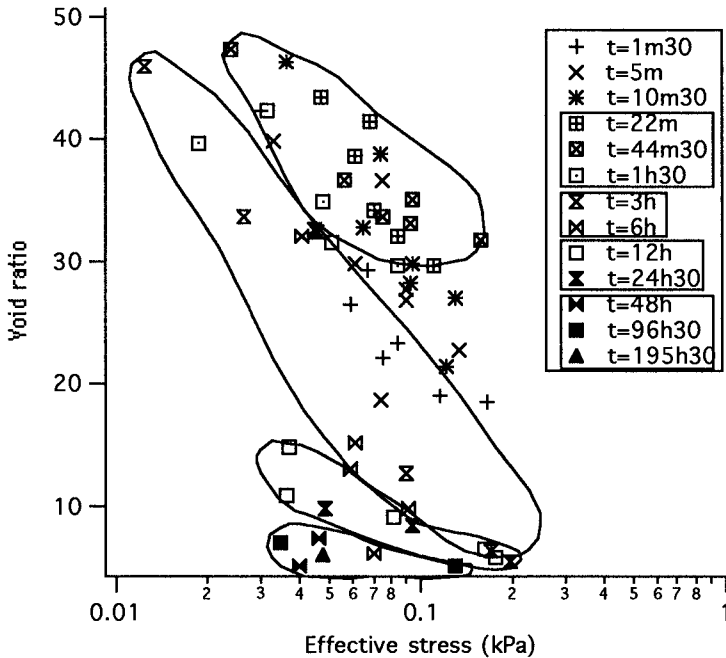


Fig.6: Evolution of effective stress with void ratio and time (reference case)

We must specify that relative accuracy decreases with the decrease of effective stress because of the way of obtention of effective stress by difference between total stress and pore pressure.

We can observe gathering dots for 4 instants ranges.

Results show clearly that effective stress increases while void ratio decreases.

From 20 minute, and for a constant effective stress, void ratio decreases with time.

It is an original result : effective stress depends not only on void ratio but also on time, probably by means

of strain rate which is linked to the variation of the derivative ratio with time : $\dot{\epsilon}$ .

That creeping phenomenon could be introduced in sedimentation-consolidation process and we could research later a relation between effective stress, void ratio and derivative of void ratio with time.

#### 4. CONCLUSION

Cohesive sediments are complex materials.

Their specific behaviour implies the complexity of their study.

In this paper, we have proposed :

- an original experimental set including an automatic gammadensimetric bench.
- a systematic approach by changing only one parameter at a time.
- numerous measurements to create a data base.

Our results give the different evolution of concentration profiles for different cases of materials and tests conditions. They give also the evolution of permeability with time and so, the limits of Darcy's law for sedimentation-consolidation modelling.

At last, our results give the evolution of effective stress with time. This evolution implies a possibility of creeping during sedimentation-consolidation process.

These conclusions drive us to a significant progress in the knowledge of cohesive sediment and in the formulation of its behaviour in order to model sedimentation-consolidation process.

Now, new aims could be defined for further studies as : the research of a new flow law (for instance velocity in function of void ratio and hydraulic gradient) and of a new approach of effective stress.

#### 5 - ACKNOWLEDGEMENTS

The present research on consolidation is undertaken as part of the MAST European program Coastal Morphodynamics (contract n°035).

#### 6 - REFERENCES

- ALEXIS, A., P. BASSOULET, P. LE HIR & C. TEISSON (1992). Consolidation of soft marine soils: unifying theories, numerical modelling and in situ experiments. *Proc. of the 23rd International Conference on Coastal Engineering ICCE'92, Venice, Italy*. ASCE, Ed. B.L. Edge, 2949-2961.
- ALEXIS A., P. THOMAS, S. GALLOIS (1993). Tassement des sédiments cohésifs, Contrat Européen MAST. IUT St Nazaire, France, Jan. 1993, pp 134.

## CHAPTER 146

### Sediment-Cloud Based Model of Suspension over Ripple Bed due to Wave Action

Hitoshi Gotoh<sup>1</sup>, Tetsuro Tsujimoto<sup>2</sup> and Hiroji Nakagawa<sup>3</sup>

#### ABSTRACT

Sediment cloud, which is released periodically from the crest of ripples, plays a very important role in suspension over a ripple bed under the wave action. By considering the special role of the sediment cloud, suspension is divided into two subprocesses: (i) the transition process from bed-load motion to suspension as the entrainment of the sediment cloud; and (ii) the diffusion process of suspended sediment released from the sediment cloud. The trajectory of the sediment cloud is calculated by Lagrangian approach in the flow field solved by k- $\epsilon$  model of turbulence. The suspended sediment concentration is simulated by solving a diffusion equation which has the source term due to sediment cloud.

#### INTRODUCTION

Since an important role of sediment cloud on the suspension over a ripple bed was recognized from the experiment with the aid of the visualization technique (Sunamura, Bando and Horikawa (1978); Sawamoto and Yamaguchi (1979)), the model of the suspension using the characteristics of the sediment cloud began to be investigated. Sunamura (1980) proposed a formula of the sediment discharge by defining the net sediment discharge as the amount of the sediment transported more than 1.5 times of a ripple's wave length in the offshore direction. Hayakawa, Tani and Wakui (1985) applied a Lagrangian model to the suspension due to wave action over a ripple bed, by assuming the scale of sediment cloud after the experiment and solving the flow field by the Stokes's second order approximation. Swamoto and Yamaguchi

<sup>1</sup>Research Associate, Department of Civil Engineering, Kyoto University, Yoshida Honmachi, Sakyo-ku, Kyoto, 606, Japan

<sup>2</sup>Associate Professor, Department of Civil Engineering, Kanazawa University, 2-40-20, Kodatsuno, Kanazawa, 920, Japan

<sup>3</sup>Professor, Division of Environmental Engineering, Kyoto University, Yoshida Honmachi, Sakyo-ku, Kyoto, 606, Japan

(1979) divided the flow field into two layers: (i) the "vortex layer" in which the transport by sediment cloud is predominant; and (ii) the "diffusion layer" in which the diffusion by turbulence is predominant. They estimated the one-cycle averaged turbulent intensity and the one-cycle averaged concentration of suspended sediment, based on their two layer model.

The applicability of a k-ε model of turbulence to the oscillating flow over a ripple bed was confirmed by comparing the prediction by the model to the body of the experimental data. Sato, Uehara and Watanabe (1986) performed the numerical simulation of oscillating boundary layer on the basis of the k-ε model with the equation of vorticity. They also simulated the trajectory of a suspended particle by a Lagrangian approach. Tsujimoto, Hayakawa, Ichiyama and Fukushima (1991) calculated the suspended sediment concentration by coupling the k-ε model with the diffusion equation of suspended sediment.

Sediment suspension in the oscillating flow is characterized by two factors: (i) the complexity of flow field; and (ii) the response of a suspended particle to the change of the flow field. The factor (ii) is divided into two processes: (a) the transition process from bed-load motion to suspension as the entrainment of the sediment cloud, and (b) the diffusion process of suspended sediment released from the sediment cloud. Although this hierarchical structure of sediment behavior makes the transport process more complicated, Sawamoto & Yamaguchi's model of two layer, "vortex layer & diffusion layer," which is the one-cycle averaged model, gives a good suggestion to explain this complexity. In this study, Sawamoto & Yamaguchi's model is developed to the unsteady condition, by regarding the sediment cloud as a moving source of diffusion.

The structure of the model is schematically shown in Fig. 1. The transition process by the motion of sediment cloud (subprocess (a)) is simulated by tracing the trajectory of sediment cloud in the flow field solved by a k-ε model; while the diffusion process of suspended sediment released from the sediment cloud (subprocess (b)) is simulated on the basis of the Murphy's diffusion equation (1984) with the sediment source term which expresses the generation of the sediment due to the sediment cloud. The former is treated by the Lagrangian model which can estimate the detailed motion of the suspension; while the latter by the Eulerian model more conveniently than Lagrangian one. This model can be regarded as a fusion of the Eulerian model and the Lagrangian one by considering their advantages.

EXPERIMENT

The experiment was conducted in U-tube type oscillating

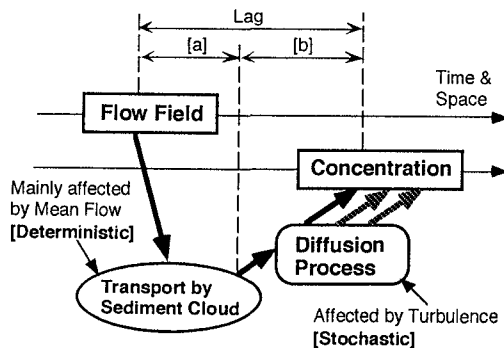


Figure 1 Constitution of the model



water tunnel with a movable bed illustrated in Fig.2. The equipment was made of acrylic resin, and the working section was 180cm long, 20cm high and 20cm wide. The access to the working section was provided by the hatches located above the central part of the water tunnel. The driving mechanism is installed to maintain the oscillation. The pump system was connected with the water tunnel at the both ends of the horizontal section, to generate the uni-directional flow. The motion of the sediment cloud was recorded by a CCD video camera from the side of the working section. The time series of the concentration of sediment near the bottom was measured by an optical turbidity meter. The test particle was a natural sand with the specific gravity 2.65 and the diameter 0.26mm. Experimental condition is shown in Table 1.

In an oscillation-current coexisting flow, the asymmetry of the flow field and that of the sediment transport due to the existence of the current bring the asymmetric ripple profile: the upstream-side slope is steeper than the downstream-side slope. The geometrical parameters of the ripple in the experimental condition is included in the range of the body of the experimental data in the wave-current coexisting flow by Watanabe, Sakinada and Isobe (1989).

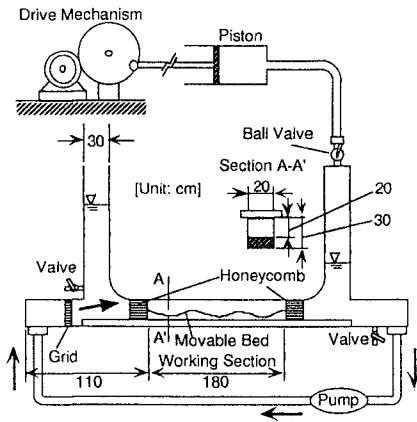


Table 1 Experimental condition

Period of oscillation $T$ (s)	2.6
Amplitude of the mean velocity $U_w$ (cm/s)	19.0
Current velocity $u_c$ (cm/s)	6.2
Ripple wavelength $L_r$ (cm)	12.0
Ripple waveheight $H_r$ (cm)	2.1
Ripple steepness $H_r/L_r$	0.175
Ripple symmetry	asymmetric
Propagating velocity of the ripple (cm/s)	-1.67

Figure 2 Oscillating water tunnel

## GOVERNING EQUATIONS OVER RIPPLE BED

### *Orthogonal curvilinear coordinate over ripple bed:*

Sawamoto (1978) proposed the orthogonal curvilinear system for the symmetric ripples. Tanaka and Syuto (1984) modified the Sawamoto's system to express the asymmetric profile of ripples. The relation between the Cartesian coordinate  $(x,y)$  and the orthogonal curvilinear coordinate system  $(\xi,\eta)$ , based on Tanaka & Syuto's method, is introduced to make a conformal mapping over the ripple bed as follows:

$$\left. \begin{aligned} x &= \xi - H_r \sum_{j=1}^N a_{rj} \exp(-k_r j \eta) \sin(k_r j \xi + \theta_{rj}) \\ y &= \eta + H_r \sum_{j=1}^N a_{rj} \exp(-k_r j \eta) \cos(k_r j \xi + \theta_{rj}) \end{aligned} \right\} \quad (1)$$

where  $H_r$ =ripple wave height;  $k_r$ =ripple wave number ( $=2\pi/L_r$ ); and  $L_r$ =ripple wave length. The empirical parameter  $a_{rj}$ ,  $\theta_{rj}$  are determined by trial and error. The agreement between the measured ripple profile and Eq. 9 is fairly good as shown in Fig. 3.

*Governing equations:*

The governing equations in the orthogonal curvilinear coordinate  $(\xi, \eta)$  is given as follows:

$$h_1 h_2 \frac{\partial \phi}{\partial t} + \frac{\partial}{\partial \xi} \left( h_2 U_{OR} \phi - \Gamma_\phi \frac{h_2}{h_1} \frac{\partial \phi}{\partial \xi} \right) + \frac{\partial}{\partial \eta} \left( h_1 V_{OR} \phi - \Gamma_\phi \frac{h_1}{h_2} \frac{\partial \phi}{\partial \eta} \right) = h_1 h_2 S_\phi(\xi, \eta) \quad (2)$$

$$h_1 \equiv \sqrt{\left( \frac{\partial x}{\partial \xi} \right)^2 + \left( \frac{\partial y}{\partial \xi} \right)^2} ; h_2 \equiv \sqrt{\left( \frac{\partial x}{\partial \eta} \right)^2 + \left( \frac{\partial y}{\partial \eta} \right)^2} \quad (3)$$

where  $\phi$ =variable;  $\Gamma_\phi$ =coefficients of apparent viscosity; and  $S_\phi$ =source terms, and they are summarized in Table 2. The parameters and variables in Table 2 are as follows:  $U_{OR}, V_{OR}$ = mean velocity components in  $\xi, \eta$  directions, respectively;  $P$ =mean pressure;  $\rho$ =mass density of fluid;  $\Gamma$ =effective viscosity;  $\nu$ =kinematic viscosity;  $\nu_t$ = kinematic eddy viscosity;  $G$ =production of turbulent energy;  $w_0$ =terminal fall velocity of sediment particle;  $S_{cl}$ =source term due to the sediment cloud; and  $\Gamma_{sx}, \Gamma_{sy}$ = the coefficient of diffusion in the streamwise and vertical direction. The empirical constants are set at the recommended values by Launder and Spalding (1974) as follows:  $C_\mu=0.09$ ,  $C_{1\epsilon}=1.44$ ,  $C_{2\epsilon}=1.92$ ,  $\sigma_k=1.0$  and  $\sigma_\epsilon=1.3$ .

Although the governing equations are standard ones which are frequently used for the unsteady flow simulation, the present simulation is characterized by the sediment source term  $S_{cl}$  and its estimation mentioned later in detail. In some previous simulations, the buoyancy term, which represents the effect of suspended sediment on the flow field, is introduced into the equations of flow field. In this study, the concentration is set at the suffi-

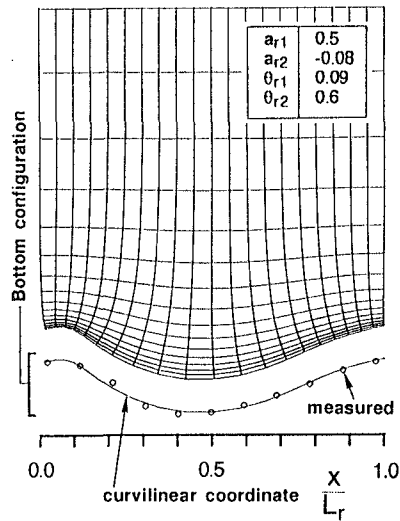


Figure 3 Grids for the calculation

Table 2 Terms in governing equations

$\phi$	$\Gamma_\phi$	$S_\phi$
$U_{OR}$	$v + v_t$	$S_U = -\frac{1}{h_1} \frac{\partial}{\partial \xi} \left( \frac{P}{\rho} \right) + \frac{1}{h_1^2} \frac{\partial v_t}{\partial \xi} \frac{\partial U_{OR}}{\partial \xi} + \frac{V_{OR}}{h_1^2 h_2} \frac{\partial v_t}{\partial \xi} \frac{\partial h_1}{\partial \eta}$ $+ \frac{1}{h_1 h_2} \frac{\partial v_t}{\partial \eta} \frac{\partial V_{OR}}{\partial \xi} - \frac{U_{OR}}{h_1 h_2^2} \frac{\partial v_t}{\partial \xi} \frac{\partial h_1}{\partial \eta}$
$V_{OR}$	$v + v_t$	$S_V = -\frac{1}{h_2} \frac{\partial}{\partial \eta} \left( \frac{P}{\rho} \right) + \frac{1}{h_1 h_2} \frac{\partial v_t}{\partial \xi} \frac{\partial U_{OR}}{\partial \eta} - \frac{V_{OR}}{h_1^2 h_2} \frac{\partial v_t}{\partial \xi} \frac{\partial h_2}{\partial \xi}$ $+ \frac{1}{h_2^2} \frac{\partial v_t}{\partial \eta} \frac{\partial V_{OR}}{\partial \eta} - \frac{U_{OR}}{h_1 h_2^2} \frac{\partial v_t}{\partial \eta} \frac{\partial h_2}{\partial \xi}$
$k$	$v + \frac{v_t}{\sigma_k}$	$S_k = G - \epsilon$
$\epsilon$	$v + \frac{v_t}{\sigma_\epsilon}$	$S_\epsilon = \frac{\epsilon}{k} (C_{1\epsilon} G - C_{2\epsilon} \epsilon)$
$C$	$\frac{\Gamma_s}{S_c}$	$S_{co} = \frac{1}{h_2} \frac{\partial}{\partial \eta} (w_0 C) + S_{cl}$
$G = v_t \left[ 2 \left\{ \left( \frac{1}{h_1} \frac{\partial U_{OR}}{\partial \xi} + \frac{V_{OR}}{h_1 h_2} \frac{\partial h_1}{\partial \eta} \right)^2 + \left( \frac{1}{h_2} \frac{\partial V_{OR}}{\partial \eta} + \frac{U_{OR}}{h_1 h_2} \frac{\partial h_2}{\partial \xi} \right)^2 \right\} \right.$ $\left. + \left( \frac{1}{h_2} \frac{\partial U_{OR}}{\partial \eta} - \frac{V_{OR}}{h_1 h_2} \frac{\partial h_2}{\partial \xi} + \frac{1}{h_1} \frac{\partial V_{OR}}{\partial \xi} - \frac{U_{OR}}{h_1 h_2} \frac{\partial h_1}{\partial \eta} \right) \right]$		

ciently low level at which the effect of the suspended sediment on the flow field is negligibly small, or the clear water flow assumption can be applied. By substituting Eq. 1 into Eq. 3,  $h_1=h_2(=h_{fq})$ .

**Boundary conditions and procedure of simulation:**

The wall function is applied at the bottom boundary, or the logarithmic law of the mean velocity at the lowest point of the grid. The turbulent energy and its dissipation rate at the lowest grid point are calculated based on the local equilibrium assumption.

At the top boundary, an axial symmetric condition is applied for  $U, k$  and  $\epsilon$ . The periodic boundary condition is applied for  $U, k$  and  $\epsilon$  between the both side boundaries. The present simulation does not require the boundary condition of concentration at the bottom, which is usually employed in the calculation of the concentration, because the sediment source term is added in the present simulation. Therefore, the concentration profile can be evaluated by the present simulation without giving the sediment concen-

tration at the reference level.

The governing equations are discretized by SIMPLE algorithm by Patankar and Spalding (1972), and the calculation was conducted based on TEACH code (Gosman and Ideriah (1976)). For the conversion assessment of the flow field, the following conditions are subjected: (i) the summation of the absolute residual in each cell of a continuity equation is less than 1% of the flow discharge in the streamwise direction; (ii) the absolute residual in each cell of a mean flow equation is less than 1% of the total momentum at the inflow boundary.

The procedure of the present simulation are as follows: (i) to solve the flow field ; (ii) to simulate the motion of the sediment cloud by Lagrangian method in the flow field solved in the process (i); (iii) to evaluate the sediment source term in the equation of concentration based on the trajectories of the sediment cloud determined in the process (ii); and (iv) to solve the equation of concentration in the flow field determined in the process (i) with the sediment source term evaluated in the process (iii).

### SOLUTION OF FLOW FIELD

The characteristics of the calculated flow field are discussed at the phase  $2\pi/5$  and  $7\pi/5$ . The change of the bulk mean velocity at the inflow boundary is given in the cosine pattern, hence the velocity in the current direction is maximum at the phase  $2\pi$ , and the velocity against the current direction is maximum at the phase  $\pi$ .

The calculated mean velocity field at the phase  $2\pi/5$  and  $7\pi/5$  are shown in Fig. 4. The vortex due to the separation is found in the lee side of ripples at the phase  $2\pi/5$ ; while the vortex is not clearly simulated at the phase  $7\pi/5$ . The asymmetric ripple profile affects strongly on the flow field.

Figure 5 shows the calculated distribution of the turbulent energy. At the phase  $2\pi/5$ , the high value area is recognized along the outer edge of the vortex due to the separation; while at the phase  $7\pi/5$ , the high energy area due to the vortex is not found. The non-uniformity of the turbulent energy in the streamwise direction at the phase

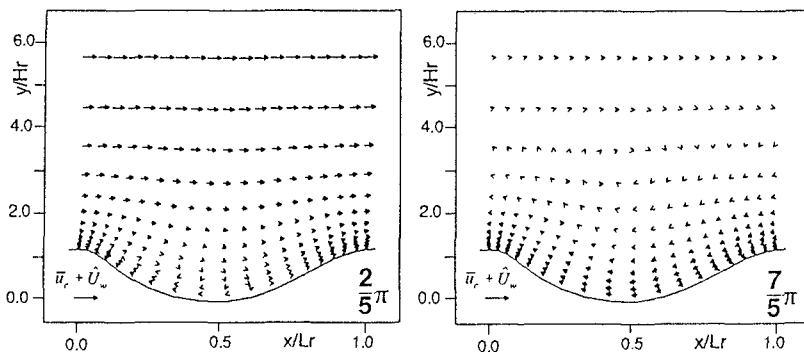


Figure 4 Mean velocity vector

$2\pi/5$  is smaller than that at the phase  $7\pi/5$ , hence the contour lines at the phase  $7\pi/5$  become more parallel to the bottom profile than those at the phase  $2\pi/5$ . Fig. 6 shows the calculated energy dissipation, and Fig. 7 shows the calculated kinematic eddy viscosity. Their asymmetric distributions due to the asymmetric bottom profile are found in both figures. The calculated results suggest the drastic change of the kinematic eddy viscosity, which are usually used to estimate the coefficient of the diffusion of suspended sediment.

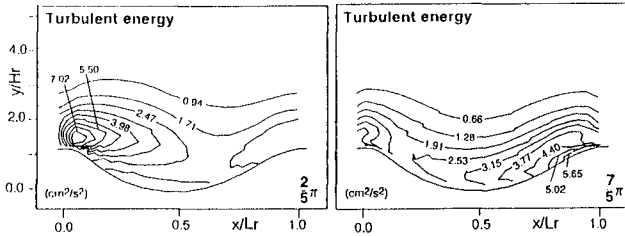


Figure 5 Distribution of turbulent energy

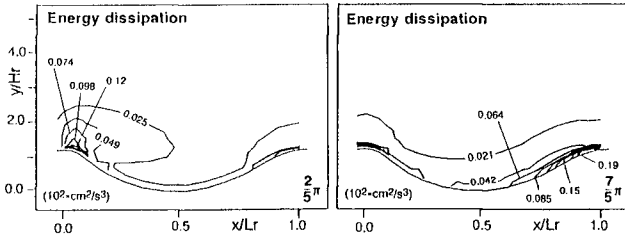


Figure 6 Distribution of energy dissipation

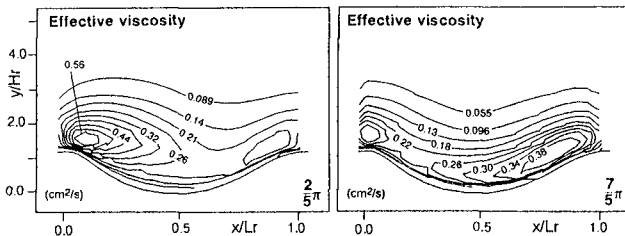


Figure 7 Distribution of kinematic eddy viscosity

SIMULATION OF SEDIMENT CLOUD MOTION

*Simulation model:*

The sediment cloud was defined only qualitatively in the previous studies as the mixture of sediment and fluid which is apparently like a cloud; while the quantitative

definition of the sediment cloud is not clear because the boundary between the sediment-fluid mixture and the surrounding fluid is ambiguous. In order to clarify the qualitative definition of the sediment cloud, it is here idealized as follows: a "kernel" exists at the central part of the cloud in which the all of the sediment transported by the cloud is contained. The kernel is not affected by the turbulence, hence the trajectory of the kernel is a deterministic one ruled by the mean velocity filed.

Here, the kernel is approximated by the rigid cylinder. By neglecting a rotating motion of the cylinder, the equation of the motion of the kernel is written as follows:

$$\rho \left( \frac{\sigma_{cl}}{\rho} + C_M \right) A_2 d_{cl}^2 \frac{d\mathbf{u}_{cl}}{dt} = -\frac{1}{2} C_D \rho A_1 d_{cl} |\mathbf{u}_{cl} - \mathbf{u}_f| (\mathbf{u}_{cl} - \mathbf{u}_f) + \rho (1 + C_M) A_2 d_{cl}^2 \frac{d\mathbf{u}_f}{dt} - \rho \left( \frac{\sigma_{cl}}{\rho} - 1 \right) \mathbf{g} A_2 d_{cl}^2 \quad (4)$$

where  $\mathbf{u}_{cl}$ =velocity vector of the kernel;  $\mathbf{u}_f$ =velocity vector of the surrounding fluid;  $\mathbf{g}$ =gravitational acceleration;  $d_{cl}$ =diameter of the kernel;  $C_M$ =added mass coefficient;  $\sigma_{cl}$ =density of the kernel; and  $A_1, A_2$ =one- and two dimensional geometrical coefficients. The drag coefficients  $C_D$  is given by

$$C_D = C_{D\infty} + \frac{24}{R_e} \quad ; \quad R_e = \frac{d_{cl} |\mathbf{u}_{cl} - \mathbf{u}_f|}{\nu} \quad (5)$$

Although the coefficient  $C_{D\infty}$  depends on the shape of the particle,  $C_{D\infty}$  sets 0.4 in this study. It is smaller than that of cylinder, because the real kernel is not a rigid body.

Equation 4 is applicable to the orthogonal curvilinear coordinate  $(\xi, \eta)$  only with the modification of the gravity term as follows:

$$\begin{bmatrix} g_\xi \\ g_\eta \end{bmatrix} = \frac{1}{h_{\eta q}^2} \begin{bmatrix} \frac{\partial y}{\partial \eta} & -\frac{\partial x}{\partial \eta} \\ -\frac{\partial y}{\partial \xi} & \frac{\partial x}{\partial \xi} \end{bmatrix} \begin{bmatrix} 0 \\ g \end{bmatrix} = \begin{bmatrix} -\frac{1}{h_{\eta q}^2} \frac{\partial x}{\partial \eta} g \\ \frac{1}{h_{\eta q}^2} \frac{\partial x}{\partial \xi} g \end{bmatrix} \quad (6)$$

Following the definition of the kernel mentioned above, the velocity of the surrounding fluid in Eq. 4 is given by the mean velocity of the flow field. By considering that the sediment cloud is generated by the vortex due to the separation, the diameter of the kernel  $d_{cl}$  is related to the scale of the vortex, or the ripple wave height as follows:

$$d_{cl} = \beta_{dcl} H_r \quad ; \quad \beta_{dcl} = 0.1 \quad (7)$$

Here, the kernel is treated by the deterministic equations, hence the probabilistic aspect of the suspension, namely the random motion of the suspended sediment should not be included in the kernel. In general, the number of the random suspended sedi-

ment increases with the distance from the center of the sediment cloud. Hence, the kernel with small diameter is adopted in this study.

The mass density of the kernel  $\sigma_{cl}$  is given in a following form.

$$\sigma_{cl} = \sigma \frac{q_{scl}}{q_{cl}} + \rho \left( 1 - \frac{q_{scl}}{q_{cl}} \right) \tag{8}$$

where  $q_{cl}$ =volume of the sediment cloud; and  $\sigma$ =density of sand. The volume of the contained sediment  $q_{scl}$  is estimated in a following manner. The volume of the sediment released from the sediment cloud (kernel) per unit time is assumed to be proportional to the volume of the contained sediment. Hence, the volume of contained sediment in the kernel is given by following equation .

$$\frac{q_{scl}}{q_{scl0}} = \exp \left( -\frac{\zeta_{cl}}{\beta_{cl} T_D} \right) ; \quad \zeta_{cl} = t - t_{cl0} \tag{9}$$

where  $q_{scl0}$ =initial volume of the contained sediment;  $T_D$ =life time of the sediment cloud;  $\beta_{cl}$ =the empirical constant; and  $t_{cl0}$ =starting time of the sediment cloud, or the time at which the main stream changes their direction. An observation of the motion of sediment clouds in the experiment suggested that the life time of the sediment cloud approximately coincides the period of the oscillation; and that the diffusion is active in the half period of oscillation from  $t_{cl0}$  to the time when the central position of the cloud is difficult to determine. By considering these results of the observation,  $T_D$  and  $\beta_{cl}$  are set  $T_D=T$ , (=period of oscillation); and  $\beta_{cl}=0.2$ . By setting  $\beta_{cl}=0.2$ , the volume of the contained sediment after a half period from  $t_{cl0}$  is about 10% of the initial volume of the contained sediment.

*Trajectory of the sediment cloud:*

Figure 8 shows the simulated trajectory of the kernel with the experimental data. In the simulation, the initial position of the kernel is determined by the experiment. The experimental data were obtained as a following manner: (i) the motion of the sediment cloud was recorded by a CCD video camera from the side wall of the water tunnel; (ii) the position of the center of the sediment cloud, which was defined as the position with the highest concentration of sediment by a visual judgment, in

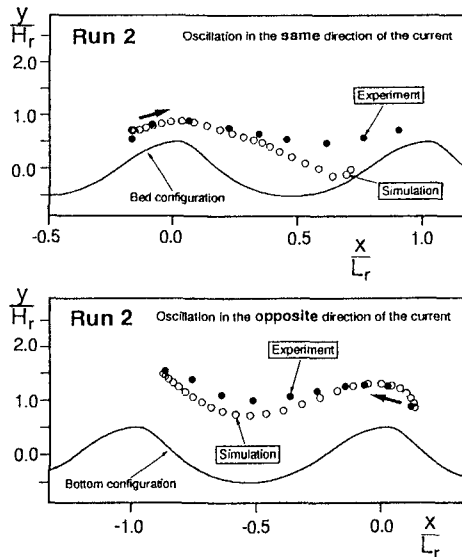


Figure 8 Trajectory of the kernel of sediment cloud

each 1/10 seconds was determined; (iii) the deterministic trajectory was determined by averaging the trajectories given in the process (ii).

When the oscillation occurs in the opposite direction of the current, the agreement between the simulation and the experiment is fairly good. While, under the oscillation in the same direction of the current, the result of the simulation deviates from the experimental result after the cloud passes the trough of the ripple. The concentration of the sediment decreases with the increase of the travelling time of the cloud, hence the reliability of the experimental results, which depends on the concentration, decreases with the increase of the travelling time of the cloud. Furthermore, the volume of the contained sediment decreases with the increase of the travelling time of cloud, therefore the role of the kernel as a source of the sediment in the diffusion equation becomes less important with the travelling time of cloud. Hence the deviation of trajectory never bring a severe error in the simulation explained in the following chapter.

### SIMULATION OF SUSPENSION

#### *Estimation of the source term:*

The sediment source term found in Murphy's diffusion equation are estimated as follows:

$$S_{cl}(\xi, \eta, t) = -\chi_{cl}(\xi, \eta, t) \frac{dq_{scl}}{dt} \quad (10)$$

Where  $\chi_{cl}(\xi, \eta, t)$  = the distribution of the suspended sediment around the center of the sediment cloud, and the uniform distribution is here supposed. Then,  $\chi_{cl}(\xi, \eta, t)$  is written as follows:

$$\chi_{cl}(\xi, \eta, t) = \begin{cases} 1 & \text{when } (\xi, \eta) = (\xi_{cl}, \eta_{cl}) \\ 0 & \text{other} \end{cases} \quad (11)$$

where  $(\xi_{cl}, \eta_{cl})$  = the location of the center of the sediment cloud.

#### *Estimation of the diffusion coefficient:*

Although the diffusion coefficient of suspended sediment is usually estimated by assuming it's similarity to the kinematic eddy viscosity, the motion of the suspended sediment is affected not only by the fluid motion, the characteristics of the variation of which is represented by the kinematic eddy viscosity; but also by the response of the particle to the change of the surrounding fluid motion. Tsujimoto and Nakagawa (1986) proposed the estimation of the diffusion coefficient on the basis of the similarity between the diffusion equation and the continuous expression of the random walk model. In this section, the diffusion coefficient is estimated based on the Tujimoto and Nakagawa's method.

By considering the equilibrium state of the random walk of suspended sediment in the vertically one-dimensional infinite space, the following relation is obtained.



$$\frac{E[\zeta^2]}{2} \frac{\partial f_s}{\partial y} = E[\zeta] \cdot f_s \quad (12)$$

where,  $f_s$ =probability density of existing height of suspended sediment, and  $\zeta$ =vertical deviation of suspended sediment during  $\Delta t$ .  $\Delta t$ =time step of random walk. On the other hand, the one-dimensional diffusion equation in a steady state which is written as follows:

$$\varepsilon_s \frac{dC_s}{dy} = -w_0 \cdot C_s \quad ; \quad C_s = C_m \cdot f_s \quad (13)$$

where  $C_m$ =depth-averaged concentration of suspended sediment. By comparing Eqs. 12 and 13 to each other, and supposing the relation  $E[\zeta]=w_0\Delta t$ , the diffusion coefficient can be written as follows:

$$\varepsilon_s = \frac{E[\zeta^2]}{2\Delta t} = \frac{E[\zeta]^2 + \sigma_\zeta^2}{2\Delta t} = \frac{w_0^2\Delta t}{2} + \frac{\sigma_\zeta^2}{2\Delta t} \quad (14)$$

The magnitude of the deviation of the suspended sediment during  $\Delta t$ ,  $\sigma_\zeta$ , is given in a following form, by introducing one-dimensional Markovian process to express the characteristics of the turbulence.

$$\sigma_\zeta^2 = 2k_{os}^2\sigma_v^2 \left[ \Delta t \cdot T_L - \Delta t^2 \left\{ 1 - \exp\left(-\frac{\Delta t}{T_L}\right) \right\} \right] \quad (15)$$

where  $\sigma_v$ =the standard deviation of the surrounding fluid velocity during  $\Delta t$ , and  $k_{os}$ =the parameter of the particle's response. Finally, by substituting Eq. 15 into Eq. 14, the turbulent Schmidt number  $S_c$  is written as follows:

$$\frac{1}{S_c} \equiv \frac{\varepsilon_s}{v_t} = \frac{\varepsilon_s}{\sigma_v^2 T_L} = \frac{1}{2} \left( \frac{w_0}{\sigma_v} \right)^2 \Xi_s + k_{os}^2 \{ 1 - \Xi_s (1 - e^{-\Xi_s}) \} \quad ; \quad \Xi_s = \Delta t / T_L \quad (16)$$

In the homogeneous turbulent flow, the Lagrangian time scale  $T_L$  can be written in the following form through a dimensional consideration as follows:

$$T_L \cong \frac{3v_t}{2k} \quad (17)$$

The Lagrangian time scale can be related to the parameters of the flow field by Eq. 17.

Figure 9 shows the distribution of turbulent Schmidt number estimated by Eq. 16 with the time step of the simulation  $\Delta t=0.01$  s. At the phase  $2\pi/5$ , at which the separation occurs, the spatial non-uniformity is strong; while at the phase  $7\pi/5$ , the spatial non-uniformity is small, or the contour line is almost parallel to the bottom configuration. Although Eq. 16 is derived by assuming the diffusion in the one-

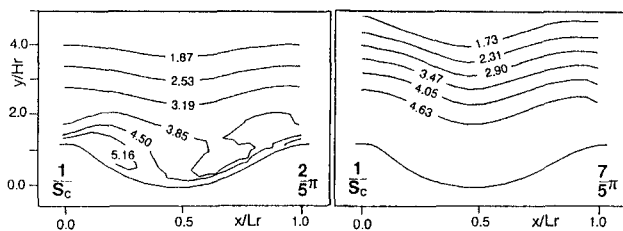


Figure 9 Distribution of the turbulent Schmidt number

dimensional uniform field  $(-\infty, \infty)$ , the fundamental mechanism of the motion of suspended sediment: the characteristics of the response of suspended sediment to the turbulence; and the fundamental characteristics of the turbulent flow field are included in this equation. Therefore, the estimation of the diffusion coefficient based on Eq. 16 is better than the usual way of estimation, in which a linear proportionality is assumed between kinematic eddy coefficient and the diffusion coefficient.

## RESULTS OF SIMULATION AND DISCUSSION

Figure 10 shows the result of the simulation on the distribution of the concentration of suspended sediment. The value on each contour line implies the relative concentration to the initial concentration of the kernel ( $=C_{c0}$ ), and the phase shown in each figure is the phase of the bulk mean flow. Although the experiment shows that many of bed-load particles are entrained into the separation zone and high density sediment is recognized in the separation zone; the present simulation never treats the sediment in the separation zone as suspended sediment, the definition of which is the sediment in a random motion. Because the motion of the sediment in a separation zone is strongly ruled by the motion of vortex, and it is rather deterministic. Therefore, the high concentration region is not found at the phase  $2\pi/5$  in the simulation, in which the separation is found in the lee side of ripples.

The sediment cloud propagating in the opposite direction to the current (leftward in Fig. 9), which emerges at the phase  $3\pi/5$ , moves in the upstream direction (leftward in Fig. 9) with generating high density suspended sediment, and then it reaches the region above the steep slope of the upstream neighboring ripple (right-hand side mild slope in Fig. 9) at the phase  $4\pi/5$ . At the phase  $\pi$ , the sediment cloud exists above a trough of ripple, and it plays a role to push the contour lines up. At the phase  $6\pi/5$ , high concentration region due to the sediment cloud is not found clearly, and the concentration is almost uniform in the horizontal direction. While the sediment cloud propagating in the same direction to the current (rightward in Fig. 9), which emerges at the phase  $7\pi/5$  above the mild slope of the ripple, reaches the region above the steep slope in the downstream neighboring ripple. At the phase  $9\pi/5$ , the high-concentration region extends to the downstream direction. At the phase  $2\pi$ , the contour lines are almost parallel to each other, and the concentration profile is approximately uniform in the horizontal direction.

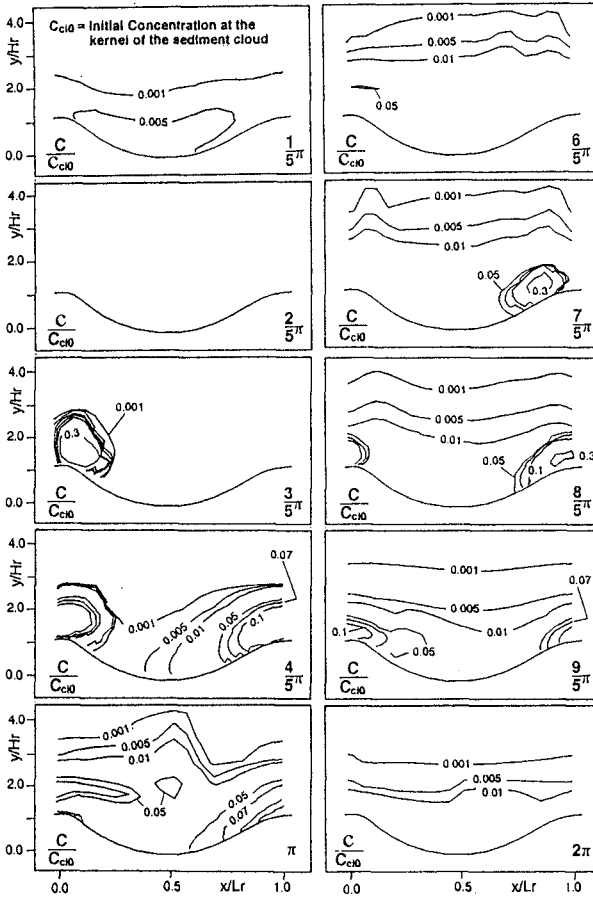


Figure 10 Concentration distribution of suspended sediment

From the phase  $2\pi$  to  $2\pi/5$ , the deposition of the sediment is promoted and the contour lines move in the downward direction, because the sediment cloud, or the source of sediment, does not exist; while, from the phase  $7\pi/5$  to  $2\pi$ , the speed of the downward motion of the contour lines is suppressed due to the existence of the sediment cloud. Although the sediment cloud moving in the same direction of the current is smaller than that moving in the opposite direction to the current, it plays a role to maintain the high-concentration region which is generated by the motion of the sediment cloud moving in the opposite direction of the current.

Figure 11 shows the comparison between the simulated time series of the concentration and that obtained by the experiment at the two points: [A] the concentration

at the point near the crest located within the trajectory of the sediment cloud; and [B] the concentration at the point near the trough. The initial volume of the contained sediment is determined to fit the peak of the concentration of the Fig.10 [A]. Although the peak-phase of the simulation is smaller than that of experiment, the relative height of the second peak to the first peak is simulated fairly well in Fig. 10 [A]. Fig. 10 [B] shows that, at the trough, the fundamental features of the experimental results are simulated: the existence of the first peak and the gradual transition from the first to the second peak.

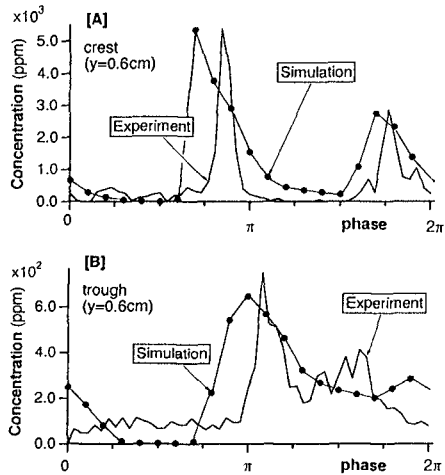


Figure 11 Time series of concentration

### CONCLUSION

The results obtained in this study are summarized as follows:

(1) The oscillation-current coexisting flow over a ripple bed is numerically simulated by a  $k-\epsilon$  model of turbulence. The result of the simulation shows that an asymmetry of the bottom-neighboring structure of the flow is induced clearly from a slight asymmetry of the ripple profile.

(2) To simulate the motion of the sediment cloud as the moving source of the suspended sediment in the field of the diffusion, the existence of a kernel is supposed at the central part of the sediment cloud. The motion of the kernel is simulated based on the equation of motion of a rigid cylinder. The result of the simulation agrees well with the experiment of the trajectory of sediment cloud.

(3) The turbulent Schmidt number is estimated on the basis of the similarity between the stochastic model of the suspension and the diffusion model. The spatial non-uniformity of the Schmidt number indicates the importance of the improvement of previous method which requires an assumption of a linear proportional relation between the kinematic eddy viscosity and the diffusion coefficient.

(4) The concentration profile is simulated by Murphy's diffusion equation with sediment source term, to connect a Lagrangian approach of the motion of sediment cloud with an Eulerian approach based on the diffusion equation. From the results of the simulation, the important role of the sediment cloud on the diffusion of suspended sediment over a ripples is clarified.

### ACKNOWLEDGMENT

The authors express their sincere gratitude to Messrs. Masaru Senba & Mikihiro

Watanabe (former Graduate Students, Kyoto University) for their help in the experiment.

#### APPENDIX-REFERENCES

- Gosman, A. D. and Ideriah, J. K. (1976). "TEACH-T, A general computer program for two-dimensional, turbulent, recirculating flows." Dept. of Mech. Eng., Imperial College of Tech., London, S. W. 7.
- Hayakawa, N., Tani, M. and Wakui, M. (1985). "Mechanism of sand transport and transport rate over sand ripples due to wave action." *Proc. 32th Japanese Conf. on Coastal Eng.*, 288-292, (in Japanese).
- Lauder, B. E. and Spalding, D. B. (1974). "The numerical computation of turbulent flow." *Computer method in applied mech. and Eng.*, Vol. 3.
- Murphy, P. J. (1984). "Equilibrium boundary condition for suspension", *Jour. Hydraul. Eng. ASCE*, Vol. 111, No. 1, 1613-1640.
- Patankar, S. V. and Spalding, D. B. (1972). "A calculation procedure for heat, mass and momentum transfer in three-dimensional parabolic flows." *Int. Jour. Heat Mass Transfer*, Vol. 15, 1787.
- Sato, S., Uehara, H. and Watanabe, A. (1986). "Numerical simulation of the oscillatory boundary layer flow over ripples by a  $k-\epsilon$  turbulence model." *Coastal Eng. in Japan, JSCE*, Vol. 29, 65-78.
- Sawamoto, M. (1978). "The conformal mapping of the semi-infinite region over a wavy boundary." *Proc. JSCE*, Vol. 216, 29-35.
- Sawamoto M. and Yamaguchi S. (1979). "Theoretical modeling on wave entrainment of sand particles from rippled beds." *Proc. JSCE*, Vol. 288, 107-113, (in Japanese).
- Sunamura, T., Bando, T. and Horikawa, K. (1978). "An experimental study of sand transport mechanism and rate over asymmetrical sand ripples." *Proc. 25th Japanese Conf. on Coastal Eng.*, 250-254, (in Japanese).
- Sunamura, T. (1980). "A laboratory study on-offshore transport of sediment and a model for eroding beaches." *Proc. 17th Coastal Eng. Conf., ASCE*, 1051-1070.
- Tanaka, H. and Syuto, N. (1984). "Experimental study on an oscillatory flow combined with a steady motion over a wavy wall." *Proc. 31th Japanese Conf. on Coastal Eng.*, 301-305, (in Japanese).
- Tsujimoto, G., Hayakawa, N., Ichiyama, M., Fukushima, Y. and Nakamura, Y. (1991). "A study on suspended sediment concentration and sediment transport mechanism over rippled sand bed using a turbulence model." *Coastal Eng. in Japan, JSCE*, Vol. 34, No. 2, 177-189.
- Tsujimoto, T. and Nakagawa, H. (1986). "Saltation and suspension." *Proc. 3rd Int. Symp. on River Sedimentation*, Mississippi, USA, 777-786.
- Watanabe, A., Sakinada, M. and Isobe M. (1989). "Ripple formation and sand transport rate in a wave-current coexisting system." *Proc. Coastal Eng.*, Vol. 36, 229-303, (in Japanese).

## CHAPTER 147

# Wave Overtopping and Sediment Transport over Dunes

Mark W. Hancock<sup>1</sup> and Nobuhisa Kobayashi, M. ASCE<sup>2</sup>

### Abstract

Experiments were conducted on a sand beach to represent occurrences of minor to major dune overtopping by varying the spectral peak period of incident irregular waves. Both water overtopping and sand overwash rates were measured. The experimental results were compared to existing empirical formulas for equilibrium beach slopes (Kriebel, Kraus, and Larson, 1991), cross-shore sediment transport (Kraus and Mason, 1993), and irregular wave reflection (Seelig, 1983) from sand beaches. Scale and non-equilibrium effects were found to be important causes of discrepancies between predicted and measured values. Additionally, an empirical formula for the overtopping of coastal structures (De Waal and Van der Meer, 1992) was compared with overtopping measurements for the experimental dune. The empirical formula of De Waal and Van der Meer gave order-of-magnitude estimates, but could not account for the effects of the profile evolution within each test. The measured average volumetric sediment concentration was found to be independent of the normalized overtopping rate and varied by only a factor of two.

### Introduction

Wave overtopping of dunes and barrier islands has been investigated in the past using site-specific field data (e.g., Holland *et al.*, 1991). However, the quantitative understanding of the overwash process remains rudimentary, partly because of the difficulties associated with field measurements during storms. At present, there is no predictive method to generalize the findings of site-specific field data. A knowledge of the overwash process is necessary for establishing a realistic boundary condition for existing beach and dune erosion models. For example, the simple empirical model of Kriebel (1990) simulates only offshore transport at the crest of the remnant dune and does not simulate the landward transport of sand due to overwash. The latest version of the storm-induced beach erosion model SBEACH (Wise and Kraus, 1993) allows for the landward transport of sand due to dune overwash, but prediction is based on simple geometric arguments related to the runup exceedance of the dune and the transport magnitude at the landward

---

<sup>1</sup>Frederic R. Harris, Inc., 300 East 42nd St., New York, NY 10017

<sup>2</sup>Center for Applied Coastal Research, Department of Civil Engineering, University of Delaware, Newark, DE 19716

boundary of the surf zone.

## Experimental Setup and Procedures

The experiment to collect data on the overwash of a subaerial dune was conducted in the tow tank located in the basement of DuPont Hall at the University of Delaware and is detailed in Hancock (1994). The tow tank is 30 m long, 2.44 m wide and 1.5 m deep. Figure 1 shows the tank layout. Irregular waves were generated using a piston-type wave paddle. A gravel beach was located 25 m away from the paddle to absorb waves and reduce the effects of re-reflection from the paddle. A 9.7 m long divider wall was constructed 0.61 m from one of the tow tank side walls. The dune overwash experiment was conducted in the 0.61 m wide flume. Figure 2 shows a detail of the experimental setup, including wave gage placement, at the beginning of each test, where  $d_t$  = water depth below still water level (SWL) at gage 1;  $d_s$  = water depth below SWL at the toe of the dune;  $H_c$  = positive crest height of the subaerial dune above SWL;  $m$  = slope of the seaward dune face;  $d_p$  = water depth of the horizontal bottom in front of the wave paddle; and  $B_c$  = horizontal distance between the dune crest and the seaward edge of the basin used to collect the overtopped water and overwashed sand. The height of the collection basin was 53 cm and was less than  $(d_p + H_c)$ . The initial beach profile was limited to a 1:23.5 slope, corresponding to the fixed beach tests on irregular wave overtopping over a 1:2 smooth revetment conducted by Poff and Kobayashi (1993a).

Five moveable bed tests for spectral peak periods,  $T_p$ , of 1.2, 1.4, 1.6, 1.8, and 2.0 seconds were conducted to represent occurrences of minor to major dune overwash. These tests will herein be referred to as tests MH1, MH2, MH3, MH4, and MH5 to distinguish them from further tests which will be conducted using the same facilities and procedures. Each test consisted of a series of runs, where each run duration was 325 seconds. A test was terminated when it appeared that further runs would expose the collection basin wall directly to wave action. Data

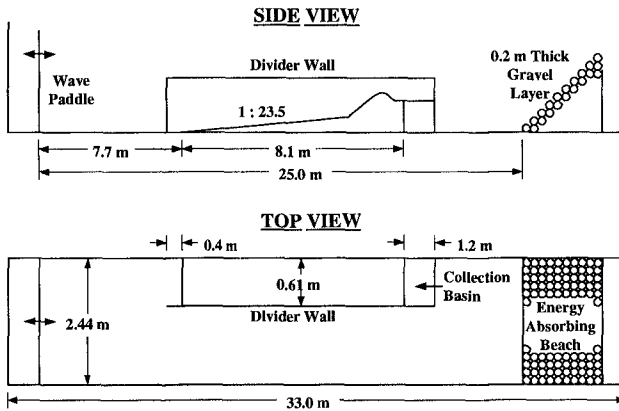


Figure 1: Layout of the Tow Tank

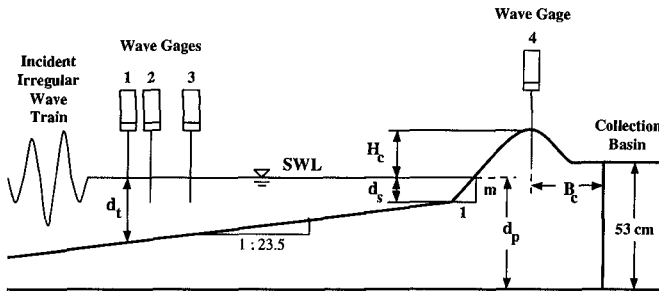


Figure 2: Experimental Setup

from the four wave gages were recorded during every test run. At the end of each test run, the volumes of overtopped water and overwashed sand in the collection basin were measured. The total volume of water collected was found by adding the volume of water pumped out of the collection basin to the volume of water held in the pores of the overwashed sand. The overtopping rate,  $\bar{Q}_w$ , and overwash rate,  $\bar{Q}_s$ , were determined by dividing the total volume of water and the volume of sand (no voids), respectively, by the test duration and flume width.

Beach and dune profiles were taken before each test and after runs of noticeable profile change. Three cross sections along the beach were profiled. One profile was taken at a distance of 20 cm from the plywood wall, another along the center line, and the last 20 cm from the tow tank wall. The average of these three profiles was calculated and this average profile was assumed to be uniform across the flume. The initial profile of a test was taken over the entire length of the beach at intervals of 10 cm. After runs of interest, profiles were taken from the seaward edge of the collection basin to a point of no net sediment transport, which was approximately 250 cm from the basin edge. Depths were sampled at an interval of 1 cm in order to distinguish smaller bed features such as ripples created by the wave action. The cross-shore variation of the net sediment transport rate,  $\bar{q}_s$ , for each test run was calculated using the continuity equation of sediment and the measured profiles starting from the seaward location of no profile change. The value of  $\bar{q}_s$  at the landward boundary corresponds to the net sediment transport rate into the collection basin and should be equal to the average overwash rate  $\bar{Q}_s$  for the same duration calculated from the collected sand.

The sand used in this experiment was well-sorted with a median diameter,  $d_{50}$ , of 0.38 mm. The measured value for the specific gravity,  $s$ , was 2.66, which falls within the expected range for quartz sand. The measured value for sediment proposity,  $n_p$ , was 0.41, which is reasonable for beach sand. The fall velocity,  $w$ , of the sediment was measured to be 5.29 cm/sec.

The parameters specified to the wave generation program (Poff and Kobayashi, 1993b), which accounts for the effect of directional random wave refraction, were  $d_p$  = water depth below SWL at the wave maker;  $d_t$  = water depth below SWL at gage 1;  $(H_{mo})_p$  = spectral estimate of the significant wave height at the water depth  $d_p$ ;  $T_p$  = spectral peak period at the water depth  $d_p$ ;  $\gamma$  = peak enhancement



factor of the TMA spectrum at the water depth  $d_p$ ;  $s_{max}$  = maximum value of the directional spreading parameter at the water depth  $d_p$ ;  $\alpha$  = predominant incident wave direction at the water depth  $d_p$ ; and  $m_t$  = bottom slope at the water depth  $d_t$ . The input parameters used for each test are shown in Table 1.

Table 1: Wave Generation Input Parameters

<i>Test</i>	MH1	MH2	MH3	MH4	MH5
$T_p$ (sec)	1.2	1.4	1.6	1.8	2.0
$d_p$ (cm)	46.5	46.5	46.5	46	45.5
$d_t$ (cm)	44.3	43.4	44.8	43.7	43.2
$(H_{mo})_p$ (cm)	12.5				
$\gamma$	3.3				
$s_{max}$	10.0				
$\alpha$ (deg)	0.0				
$m_t$	1/23.5				

The initial dune profile geometry for each test was held as nearly constant as possible. However, some variability occurred due to the difficulties of manipulating significant quantities of sand. The still water level in each test was determined by matching the initial dune crest elevations of all the tests. The dimensions of the initial dune profiles for each test are given in Table 2 and are defined in Figure 2.

Table 2: Initial Dune Profile Geometry

<i>Test</i>	MH1	MH2	MH3	MH4	MH5
$d_s$ (cm)	19.0	18.5	20.0	18.5	18.0
$H_c$ (cm)	12.9	12.3	12.5	12.5	12.3
$m$	3.32	3.32	3.27	3.45	3.26
$B_c$ (cm)	40.0				

## Experimental Results

The measured time series and spectra of the incident and reflected waves varied very little from one test run to another. This implies that the incident and reflected waves were almost unaffected by the beach profile changes during each test. The mean of the measured spectral estimates of the significant wave height was 12.47 cm, which is nearly identical to the  $H_{mo}$  value of 12.5 cm specified to the wavemaker. The standard deviation of the measured  $H_{mo}$  values was 0.26 cm. The spectral peakedness parameter,  $Q_p$ , decreased with increased spectral peak period,  $T_p$ .  $Q_p$  ranged from a mean value of 5.4 in test MH1 with  $T_p = 1.2$  sec, to

a mean value of 3.1 in test MH5 with  $T_p = 2.0$  sec. Similarly, the spectral correlated parameter,  $\kappa$ , decreased with increased  $T_p$ , with a high mean value of 0.64 for test MH1 and a low mean value of 0.41 for test MH5. The average run length,  $\bar{j}$ , remained relatively constant throughout the experiment, with  $1.30 \leq \bar{j} \leq 1.87$ .

In general, the reflection coefficient,  $\bar{r}$ , tended to increase slightly with increasing spectral peak period. Within each test, the trend was that the measured value for  $\bar{r}$  decreased as the overtopping rate,  $\bar{Q}$ , increased. The values of  $\bar{r}$  ranged from 0.195 to 0.305. The values of  $\bar{Q}$  approximately doubled from test to test as  $T_p$  was increased by 0.2 sec. In each test,  $\bar{Q}$  increased during the initial runs before becoming a nearly constant value for the remainder of the runs, as can be seen in Figures 3 and 4. The normalized overtopping rates,  $\bar{Q}/(H_s\sqrt{gH_s})$  with  $H_s =$  significant wave height, ranged from 0.0 in run 1 of test MH1 to 0.00625 in run 4 of test MH5. Unlike the average overtopping rate, the measured average overwash rate trend varied significantly between tests. In test MH1,  $\bar{Q}_s$  increased during the initial runs before assuming a constant value over the final runs, as shown in Figure 3. Test MH2 displayed a similar trend in the initial runs, but after obtaining a peak value in run 3,  $\bar{Q}_s$  decreased appreciably before maintaining a nearly steady value. In tests MH3, MH4, and MH5, the value of  $\bar{Q}_s$  was relatively high in the first run, peaked in the second run, and then decreased with each remaining run. This trend is shown in Figure 4. The measured values of  $\bar{Q}_s/(wd_{50})$  ranged from 0.0 in run 1 of test MH1 to 1.82 in run 2 of test MH5. The qualitative and quantitative trends of the average sediment concentration in volume were similar for each test. The calculated values for  $\bar{Q}_s/\bar{Q}$  tended to decrease as each test progressed, with the exception of test MH1, and ranged from 0.023 to 0.056.

The parameters used to describe the dune profile evolution were selected following the examples of the equilibrium beach profile presented by Kriebel, Kraus, and Larson (1991) and the equivalent slope for a coastal structure with a berm presented by De Waal and Van der Meer (1992). Many of the profile parameters

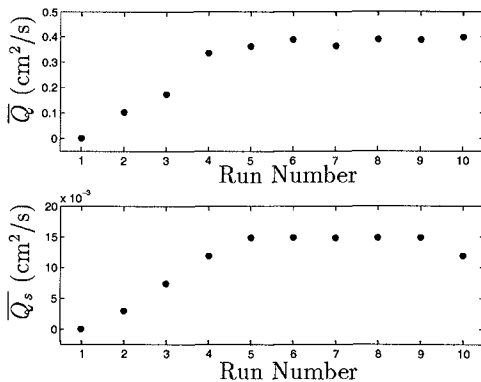


Figure 3: Overtopping Rate,  $\bar{Q}$ , (Top) and Overwash Rate,  $\bar{Q}_s$ , (Bottom) for MH1 with  $T_p = 1.2$  sec.

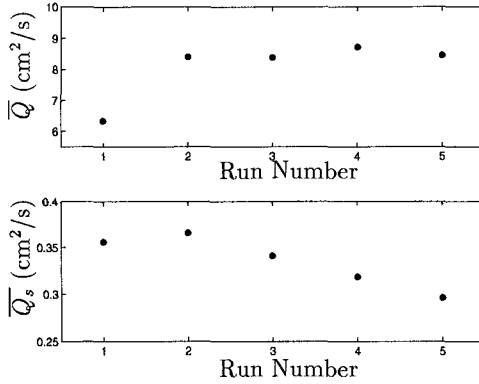


Figure 4: Overtopping Rate,  $\bar{Q}$ , (Top) and Overwash Rate,  $\bar{Q}_s$ , (Bottom) for MH5 with  $T_p = 2.0$  sec.

are defined in Figure 5 where  $x$  = positive-seaward horizontal coordinate with an origin where the still water level (SWL) intersects the beach;  $d_s$  = depth relative to SWL below which there is effectively no profile change;  $H_s$  = depth below SWL equal to the average significant wave height between two measured profiles;  $B_s$  = horizontal distance from the dune crest to the depth  $H_s$ ;  $h$  = depth below SWL at a distance  $x$  seaward of the origin of the horizontal coordinate;  $H_c$  = dune crest height above SWL;  $m$  = fitted slope of the dune face from the crest to a point slightly below SWL; and  $B_c$  = horizontal distance from the dune crest to the edge of the collection basin. The concept of an equilibrium profile of the form  $h = Ax^{2/3}$  was introduced by Bruun (1954), where  $h$  is the depth at a distance  $x$  offshore from the still water shoreline and  $A$  is the profile scale factor. For this analysis,  $A$  was found by fitting the two-thirds power profile to each measured profile. An additional parameter examined was the equivalent beach slope for wave runup and overtopping,  $m_e$ , expressed as

$$m_e = \frac{H_s + H_c}{B_s} \quad (1)$$

The dune profile evolutions for tests MH1 and MH5 are shown in Figures 6 and 7. For all of the test runs,  $d_s$  was greater than  $H_s$ , probably because these tests corresponded to a high dune and a large storm surge. Also, the crest height was always greater than  $(53 - d_p)$  cm, which is the height of the collection basin above SWL. In each test, the fitted dune face slope and equivalent beach slope decreased as the profiles evolved. The range of  $m$  was 0.23-0.31 and the range of  $m_e$  was 0.11-0.30. The measured  $B_s$  values increased as the toe of the evolving beach advanced seaward and  $B_c$  went to zero. The initial value for  $B_s$  was about 84 cm in each test and the final values ranged from 173 cm in test MH1 to 119 cm in test MH5. In general, the steep dune was transformed to a more gentle beach by the waves. The fitted values of  $A$  ranged from 0.9 to 1.2 cm<sup>1/3</sup> and decreased slightly as the tests with shorter spectral peak periods, and correspondingly longer durations, progressed. Kriebel, Kraus, and Larson *et al.* (1991) used field data

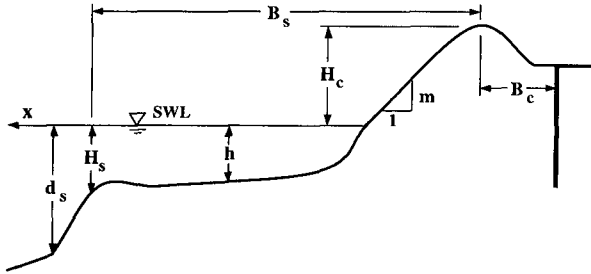


Figure 5: Definition Sketch for Profile Parameters

to obtain the following equation for the equilibrium value of  $A$ :

$$A \approx 2.25 \left( \frac{w^2}{g} \right)^{1/3} \tag{2}$$

where  $w$  is the sediment fall velocity and  $g$  is gravitational acceleration. Equation 2 is applicable for a water temperature of approximately 20° C and  $1 \leq w \leq 10$  cm/sec. The measured  $w$  of the sand used in this experiment was 5.29 cm/sec, which yields  $A = 0.69 \text{ cm}^{1/3}$  for an equilibrium profile. This  $A$  value is significantly less than the fitted  $A = 0.9\text{-}1.2 \text{ cm}^{1/3}$  values, probably because the measured profiles were not in equilibrium and the experiment was a small-scale test.

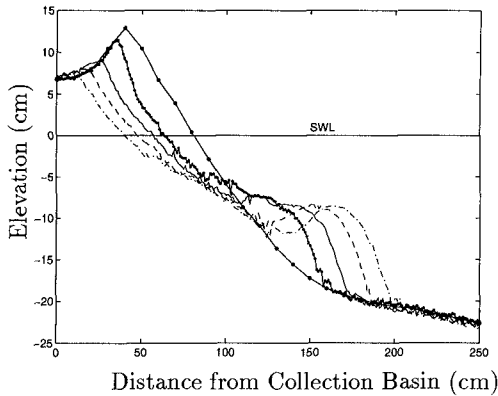


Figure 6: Dune Profile Evolution with Initial Profile (—●—) and Profiles after Run 1 (---), Run 3 (—), Run 6 (---), and Run 10 (-.-) for MH1 with  $T_p = 1.2$  sec.

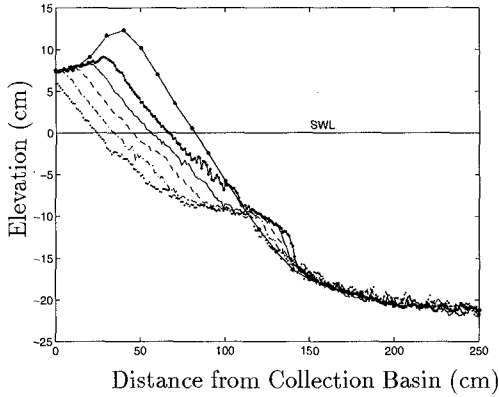


Figure 7: Dune Profile Evolution with Initial Profile (—●—) and Profiles after Run 1 (— — —), Run 2 (— — —), Run 3 (— — —), Run 4 (— · —), and Run 5 (· · · ·) for MH5 with  $T_p = 2.0$  sec.

The calculated net cross-shore sediment transport rates,  $\bar{q}_s$ , which is positive onshore, as a function of the distance from the collection basin for run 1 of tests MH1, MH3, and MH5 are shown in Figure 8. It is apparent from the figure that there was an appreciable seaward transport of sand at the base of the dune during the first run of each test. The magnitude of this seaward transport decreased with increased  $T_p$ . The landward transport of sand observable at the dune crest was increased in the tests with larger  $T_p$ . In all of the tests, the amplitude of

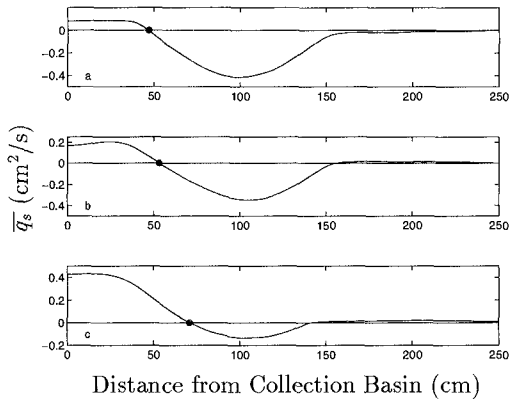


Figure 8: Average Cross-Shore Sediment Transport Rates During the First Run of a) Test MH1, b) Test MH3, and c) Test MH5.

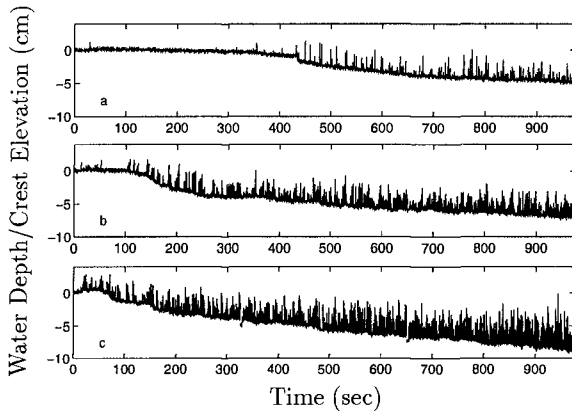


Figure 9: Gage 4 Time Series for a) Test MH1, b) Test MH2, and c) Test MH3.

$\bar{q}_s$  between two measured profiles was appreciably smaller after the initial run. The landward transport of sand dominated after the initial run in tests MH4 and MH5.

The time series recorded by gage 4 for the first three runs of tests MH1, MH3, and MH5 are shown in Figure 9. During these early runs, it is easy to distinguish a defined baseline between overtopping events. This baseline corresponds to the time-dependent dune crest elevation relative to the initial dune elevation. In test MH1, essentially no overtopping occurred during the first 400 sec of the test. This period of limited overtopping is shorter in test MH3 and non-existent in test MH5. Once large overtopping events occurred on a regular basis, the sand elevation at gage 4 began to decrease approximately linearly with time. The location of the baseline at the end of three runs in each test demonstrates the increased erosion at the location of gage 4 as  $T_p$  increased.

## Analyses of Experimental Results

### Beach Slope

Kriebel, Kraus, and Larson (1991) reanalyzed the field data of Sunamura (1984) in terms of the sediment fall velocity,  $w$ , and proposed the following expression for the equilibrium foreshore slope,  $m$ :

$$m = 0.15 \left( \frac{wT}{H} \right)^{1/2} \quad (3)$$

Kriebel (1990) suggested that the root-mean-square wave height,  $H_{rms}$ , at breaking be used for  $H$  in Equation 3 since Sunamura did not specify this quantity for random waves. For the present analysis, the wave period  $T$  was taken to be the significant wave period,  $T_s$ .

Although the measured slopes tended to decrease as each test progressed, as already discussed, the empirical  $m$  values determined using Equation 3 remained nearly constant, with  $0.13 \leq m \leq 0.15$ , and significantly underpredicted the beach slope. Kriebel, Kraus, and Larson (1991) remarked that their analysis of field data

gave much smaller beach slopes for given  $H/(wT)$  than those observed during the small-scale tests of Dalrymple and Thompson (1976). Additionally, the empirical  $m$  values are based on an equilibrium profile. Neither the stage of the profile evolution nor memory effects can be incorporated in the parameter  $(wT_s)/H_{rms}$ . Therefore, the empirical formula presented by Kriebel, Kraus, and Larson (1991) is too simplistic to incorporate the scale and non-equilibrium profile effects of the beach evolution in this experiment.

### Cross-Shore Sediment Transport

Using field data, Kraus and Mason (1993) extended the profile parameter,  $\mathbf{P}_s$ , developed by Dalrymple (1992) to irregular waves:

$$\mathbf{P}_s = \frac{gH_{os}^2}{w^3T_p} = 26,500 \quad (4)$$

where  $H_{os}$  is the deep-water significant wave height and  $T_p$  is the spectral peak period. Offshore sediment transport was observed to occur for  $\mathbf{P}_s$  values significantly greater than 26,500.

The values of  $\mathbf{P}_s$  measured in the present experiment ranged from a high average value of 939 in test MH1 to a low average value of 553 in Test MH5. Because  $\mathbf{P}_s$  is inversely proportional to the spectral peak wave period, the onshore transport of sediment is expected to increase as  $T_p$  increases. This prediction is proven correct by Figure 8. All of the calculated  $\mathbf{P}_s$  were much less than the threshold value of  $\mathbf{P}_s = 26,500$  determined by Kraus and Mason. This would seem to indicate exclusively onshore transport of sand in this experiment. However, both onshore and offshore sediment transport are observable in Figure 8. In particular, significant bar formation occurred in test MH1 as evidenced in Figure 6. It is uncertain whether overwash occurred in the field measurements of Kraus and Mason, but it is expected that overwash would act to increase the landward transport of sand. Equation 4 does not include the slope effect on the direction of net sediment transport. Therefore, the probable reasons that offshore sediment transport occurred despite the small  $\mathbf{P}_s$  values are that this experiment was a small-scale test and that the initial foreshore slopes were rather steep.

### Irregular Wave Reflection

Seelig (1983) proposed that the average reflection coefficient,  $\bar{r}$ , for irregular waves could be expressed as

$$\bar{r} = \frac{\alpha\xi_p^2}{\xi_p^2 + \beta} \quad (5)$$

where  $\xi_p$  is the irregular wave surf similarity parameter defined as

$$\xi_p = \frac{m_i}{\sqrt{\frac{2\pi H_s}{gT_p^2}}} \quad (6)$$

with beach slope  $m_i$  at the still water intercept, significant wave height  $H_s$ , and spectral peak period  $T_p$ . Seelig recommended that for smooth slopes  $\alpha = 1.0$  and  $\beta = 5.5$ .

Figure 10 is a plot of the measured reflection coefficients of each test versus the irregular wave surf similarity parameter values found from the measured  $T_p$  and

$H_s$ . Three lines corresponding to  $\alpha = 0.65$ ,  $\alpha = 0.85$ , and  $\alpha = 1.05$  in Equation 5 are plotted in the top portion for comparison. Using  $\alpha = 1.0$  appears to be a reasonable value to conservatively estimate  $\bar{r}$ . The bottom portion of Figure 10 shows a linear least-squares fit of the data. The formula for this fit is

$$\bar{r} = 0.106 \xi_p + 0.075 \quad \text{for } 1.10 \leq \xi_p \leq 2.01 \quad (7)$$

The data points display low scatter, with a standard deviation of 0.03.

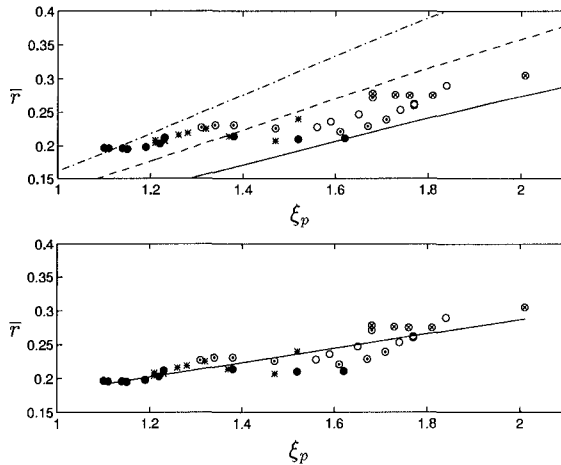


Figure 10: Reflection Coefficient,  $\bar{r}$ , versus Irregular Wave Surf Similarity Parameter,  $\xi_p$ , for Tests MH1 ( $\bullet$ ), MH2 ( $*$ ), MH3 ( $\odot$ ), MH4 ( $\square$ ), and MH5 ( $\otimes$ ). Top Plot includes the Empirical Formula of Seelig (1983) for  $\alpha = 0.65$  (—),  $\alpha = 0.85$  (---), and  $\alpha = 1.05$  (-.-). Bottom Plot includes Least-Squares Data Fit (—).

### Irregular Wave Overtopping

The empirical formulas of De Waal and Van der Meer (1992) for the prediction of irregular wave runup and overtopping on coastal structures were compared to experimental results for dune overtopping. Since De Waal and Van der Meer did not have beach test data, their formulas are examined in the context of their applicability to the dune overtopping experiment. Their formula for predicting the 2%-runup,  $R_2$ , which corresponds to the runup with an exceedance probability of 2%, is

$$\frac{R_2}{H_s} = 1.5 \gamma_f \gamma_h \gamma_\beta \xi_{p,eq} \leq 3.0 \gamma_f \gamma_h \gamma_\beta \quad (8)$$

where  $\xi_{p,eq}$  is a breaking parameter based on an equivalent slope and modified by the influence factors  $\gamma_f$  for roughness effects,  $\gamma_h$  for shallow water effects, and  $\gamma_\beta$  for oblique wave attack effects. Since the present experiment involves only normally incident waves,  $\gamma_\beta = 1.0$ . Also,  $\gamma_f$  is assumed to be approximately 1.0 since a sand beach may be treated as a smooth slope.



The form of  $\gamma_h$  suggested by De Waal and Van der Meer, and modified here for application to dunes, is

$$\gamma_h = \begin{cases} 1 - 0.03 \left(4 - \frac{d_s}{H_s}\right)^2 & \text{for } 1 \leq \frac{d_s}{H_s} \leq 4 \\ 1 & \text{for } \frac{d_s}{H_s} \geq 4 \end{cases} \quad (9)$$

where  $d_s$  is the water depth at the toe of the dune as shown in Figure 5. They suggested an expression for  $\xi_{p,eq}$  including berm effects, but for the present analysis it is assumed that  $\xi_{p,eq} = \xi_e$ , where

$$\xi_e = m_e T_p \sqrt{\frac{g}{2\pi H_s}} \quad (10)$$

with  $m_e$  = equivalent slope as defined in Equation 1. Equation 10 implies that wave runup is affected by the beach profile from the water depth  $H_s$  to the dune crest height,  $H_c$ , as shown in Figure 5. The simplified form of the normalized 2%-runup used in the dune analysis is, therefore,

$$\frac{R_2}{H_s} = 1.5 \gamma_h \xi_e \leq 3.0 \gamma_h \quad (11)$$

De Waal and Van der Meer proposed that the mean overtopping rate,  $\bar{Q}$ , was related to a "shortage in crest height",  $R_* = (R_2 - H_c)/H_s$ . By fitting about 500 data points from various overtopping tests, they came up with the following expression for the normalized overtopping rate,  $Q_*$ :

$$Q_* = \frac{\bar{Q}}{\sqrt{gH_s^3}} = 8 \times 10^{-5} \exp(3.1 R_*) \quad (12)$$

They observed a large data scatter, so that Equation 12 should be considered an order-of-magnitude estimate only.

The influence of the shallow water effects remained nearly constant throughout the present experiment with an average value of 0.82. However, the breaking parameter,  $\xi_e$  decreased as each test progressed and tended to increase with  $T_p$ , as is expected from Equation 10. The measured range of  $\xi_e$  was 0.48-1.77. The values of  $R_2/H_s$  and  $R_*$  followed the same qualitative trend as  $\xi_e$ , with  $0.60 \leq R_2/H_s \leq 2.11$  and  $-0.02 \leq R_* \leq 1.25$ . The predicted decrease of  $R_2/H_s$  due to the decrease of  $m_e$  is greater than the measured decrease of the normalized crest height  $H_c/H_s$ . As a result, the predicted  $Q_*$  decreased as each test progressed and ranged from 0.7 to 38.7. However, as shown in Figures 3 and 4, the measured average overtopping rates increased in the early runs before becoming nearly constant. The equivalent slope,  $m_e$ , for dunes and coastal structures appears to be different in light of the opposite trend. A plot of the measured ( $\ln Q_*$ ) versus  $R_*$  is shown in Figure 11. For comparison, Equation 12 is plotted in the top portion of Figure 11. It is apparent that the formula of De Waal and Van der Meer significantly underpredicts the dune overtopping rate in all but the first runs of the tests. However, the predicted values are within an order of magnitude of the measured results. A linear regression analysis of the data is shown in the bottom portion of Figure 11 and yields

$$Q_* = 3.35 \times 10^{-4} \exp(2.82 R_*) \quad \text{for } -0.02 \leq R_* \leq 1.25 \quad (13)$$

The slope of the fitted line is very close to that found from Equation 12 indicating a similar data trend, but the magnitude of  $Q_*$  found from Equation 13 is about four times greater. Bounding lines plotted for  $(2.0 \times Q_*)$  and  $(0.5 \times Q_*)$  show that there is a data scatter of a factor of about 2. Although the tests tend to fall along the fitted line, it is apparent that there are data trends within each test. Therefore, the stage of the dune profile evolution is an important factor that can not be accounted for in Equations 12 and 13.

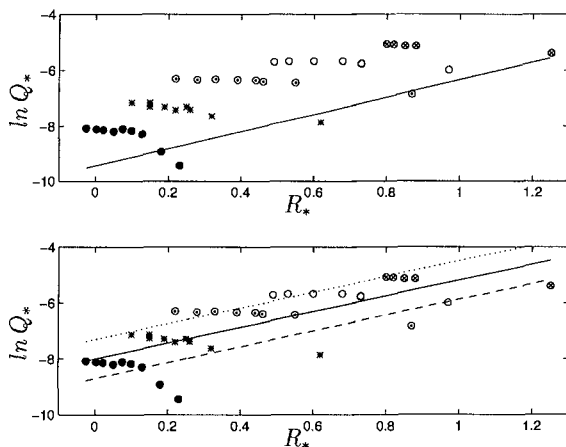


Figure 11: Natural Log of the Non-dimensional Overtopping Rate,  $Q_*$ , versus Non-dimensional 2% Runup Exceedance,  $R_*$ , of Tests MH1 ( $\bullet$ ), MH2 ( $*$ ), MH3 ( $\odot$ ), MH4 ( $\circ$ ), and MH5 ( $\otimes$ ). Top Plot includes the Empirical Formula of De Waal and Van der Meer (1992) (—). The Bottom Plot includes a Least-Squares Data Fit  $\ln(Q_*)$  (—),  $\ln(2Q_*)$  ( $\cdots$ ), and  $\ln(0.5Q_*)$  ( $---$ ).

### Irregular Wave Overwash

The average volumetric sediment concentration,  $\overline{C}_s$ , is defined as

$$\overline{C}_s \equiv \frac{\overline{Q}_s}{\overline{Q}} \quad (14)$$

which is the ratio of the sediment (no voids) overwash rate,  $\overline{Q}_s$ , to the water overtopping rate,  $\overline{Q}$ . Figure 12 shows a plot of  $\overline{C}_s$  versus  $Q_*$ . It is apparent that no relationship exists between the two parameters in this experiment. The value of  $\overline{C}_s$  did tend to decrease as the profile evolved in all of the tests except test MH1. Nevertheless, the range of  $\overline{C}_s = 0.023$ - $0.056$  is surprisingly narrow in this experiment. Therefore, if  $\overline{C}_s$  remains approximately constant,  $\overline{Q}_s$  can be predicted for estimated  $\overline{Q}$ .

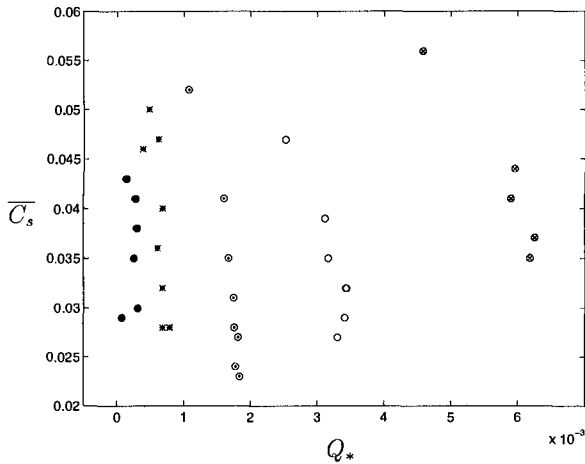


Figure 12: Average Volumetric Sediment Concentration,  $\overline{C}_s$ , versus Non-dimensional Overtopping Rate,  $Q_*$ , in Tests MH1 (●), MH2 (\*), MH3 (○), MH4 (○), and MH5 (⊗)

## Conclusions

A range of minor to major occurrences of overtopping was produced in the laboratory by increasing the spectral peak period of incident waves. Both overtopping and overwash rates were measured. Scale and non-equilibrium profile effects were found to be important factors in causing discrepancies between predicted and measured beach slopes. Scale effects and initially steep dune slopes appear to have increased the offshore transport of sediment. A linear relation between the irregular wave surf similarity parameter and the average reflection coefficient was shown to be adequate for this experimental range. The empirical formula of De Waal and Van der Meer (1992) for coastal structures gave order-of-magnitude estimates of the overtopping rate but could not account for variations due to the dune profile evolution. The experimental sediment concentration was found to be independent of the normalized overtopping rate and varied by only a factor of two in the range of 0.023-0.056. This implies that a reasonable estimate of the overwash rate may be easily determined from an accurate prediction of the overtopping rate. The proposed empirical formulas for irregular wave reflection and overtopping rate will need to be verified using large-scale experiments.

## Acknowledgement

This work was sponsored by the U.S. Army Research Office, University Research Initiative, under contract No. DAAL03-92-G-0016. The first author would like to acknowledge funding provided by the National Defense Science and Engineering Graduate Fellowship and American Society for Engineering Education.

## References

- Bruun, P. (1954). "Coast erosion and the development of beach profiles." Beach Erosion Board, Tech. Memo, No. 44.
- Dalrymple, R.A. (1992). "Prediction of storm/normal beach profiles." *J. Wtrwy. Port, Coast., and Oc. Engrg.*, ASCE, 118(2), 193-200.
- Dalrymple, R.A. and Thompson, W.W. (1976). "A study of equilibrium beach profiles." *Proc. 15th Coast. Engrg. Conf.*, ASCE, 1277-1296.
- De Waal, J.P. and Van der Meer, J.W. (1992). "Wave runup and overtopping on coastal structures." *Proc. 23rd Coast. Engrg. Conf.*, ASCE, 2, 1758-1771.
- Hancock, M.W. (1994). "Experiments on irregular wave overtopping and overwash of dunes." Thesis submitted for the degree of Master of Civil Engineering, Univ. of Delaware, Newark, DE.
- Holland, K.T., Holman, R.A., and Sallenger, A.H., Jr. (1991). "Estimation of overwash bore velocities using video techniques." *Coastal Sediments '91*, ASCE, 489-497.
- Kraus, N.C. and Mason, J.M. (1993). Discussion of "Prediction of storm/normal profiles." *J. Wtrwy. Port, Coast., and Oc. Engrg.*, ASCE, 119(4), 468-470.
- Kriebel, D.L. (1990). "Advances in numerical modeling of dune erosion." *Coastal Engineering*, 14, 2304-2317.
- Kriebel, D.L., Kraus, N.C., and Larson, M. (1991). "Engineering methods for predicting beach profile response." *Proc. Coastal Sediments '91*, ASCE, 557-571.
- Poff, M.T., and Kobayashi, N. (1993a). "Effects of toe depth and slope roughness on wave overtopping." *Proc. of the Hilton Head Intl. Coast. Symp.*, 1, 115-120.
- Poff, M.T., and Kobayashi, N. (1993b). "Computer program for refraction of directional random waves." *Res. Report No. CACR-93-04*, Ctr. for Appl. Coast. Res., Univ. of Delaware, Newark, DE.
- Seelig, W.N. (1983). "Wave reflection from coastal structures." *Proc. Coastal Struc. '83*, ASCE, 961-973.
- Sunamura, T. (1984). "Quantitative prediction of beach-face slopes." *Geol. Soc. of America Bulletin*, 95(2), 242-245.
- Wise, R.A. and Kraus, N.C. (1993). "Simulation of beach fill response to multiple storms, Ocean City, Maryland." *Proc. Coastal Zone '93, Coast. Beach Nourish. Engrg. and Mgmt. Considerations*, ASCE, 133-147.

## CHAPTER 148

### SEDIMENT TRANSPORT OVER RIPPLES IN WAVES AND CURRENT

G. Perrier<sup>1-3</sup>, E.A. Hansen<sup>2</sup>, C. Villaret<sup>3</sup>, R. Deigaard<sup>1</sup> and J. Fredsøe<sup>1</sup>

#### ABSTRACT

Numerical simulations are presented for the flow and the dynamics of non-cohesive sediment over 2D ripples in waves and current. For this purpose, a model based on a discrete vortex approach using the "cloud-in-cell" concept has been applied. The hydrodynamic model drives a Lagrangian model for the suspended sediment.

The characteristic vorticity structures prevailing in the vicinity of ripples are accurately replicated and sediment suspension mechanisms are successfully described. Thus, the sediment transport resulting from asymmetrical waves and combined waves and current can be predicted. Especially, the wave-related component of the transport opposes the maximum free stream velocity and contributes significantly to the total transport. In the present work, the effect of the wave-induced drift is not included.

#### INTRODUCTION

A detailed understanding of flow kinematics and suspension mechanisms of non-cohesive sediments in waves and current situations is of great interest to coastal engineers because of its importance in sediment transport predictions.

When the seabed is plane, the suspension of sediment is governed by turbulent diffusion. But when ripples occur on the bed, the prevailing process becomes convection. At each half-cycle of the oscillation, coherent vorticity structures are formed in the lee side of the ripple and trap sediment. At flow reversal, these sediment laden vortices are shed into the flow, thus giving rise to suspension.

In the field of non breaking regular waves, experimental investigations have been conducted for flows over 2D ripples (Sato *et al.*, 1984; Ranasoma and Sleath, 1992). In connection with the hydrodynamics, experimenters have studied sediment dynamics (Sleath, 1982). For asymmetrical waves, few experiments exist (Sato and Horikawa, 1986). For combined waves and current flows, whereas comprehensive experiments over flat beds are rather numerous, fewer are available for rippled beds (Murray, 1992; Villaret and Latteux, 1992).

<sup>1</sup>) ISVA, Building 115, Technical University of Denmark, DK 2800 Lyngby, Denmark

<sup>2</sup>) Danish Hydraulic Institute, Agern Allé 5, DK 2970 Hørsholm, Denmark

<sup>3</sup>) Laboratoire National d'Hydraulique, 6 Quai Watier 78401 Chatou, France

To model the flow over ripples, different methods have been developed : vorticity-stream function formulation with finite difference and spectral methods (Blondeaux and Vittori, 1990), classical turbulence models : K- $\epsilon$  (Tsujiimoto *et al*, 1991), or K-L (Huynh Thanh, 1990), and discrete vortex methods by Longuet-Higgins (1981), Block (1994) and Hansen *et al* (1994).

To model sediment suspension, the common approach is based on the turbulent diffusion equation where the sediment diffusivity relies on various assumptions (Fredsoe and Deigaard, 1992). Nevertheless, in the case of rippled beds, convection becomes the prevailing process. The diffusion assumption has been used by Tsujimoto (1991) coupled with his K- $\epsilon$  model, but most of the other models are based on a Lagrangian particle tracking (Blondeaux and Vittori, 1990; Block, 1994; Hansen *et al*, 1994).

In this study, a discrete vortex approach is adopted to achieve a 2D model for the flow, the sediment suspension mechanisms and the resulting net transport. After a brief presentation of the model, hydrodynamic calculations are performed for an oscillatory flow over fixed ripples. Then, the complete model is used to study the asymmetrical wave case and the combined sine waves and current case. Experimental conditions are listed in appendix.

## PRESENTATION OF THE DISCRETE VORTEX MODEL

The discrete vortex model (DVM) developed by ISVA-DHI is designed to compute complex instationary flows interacting with structures or stationary seabeds. The model relies on a discretization of vorticity in "vortices" and concentration in "particles" combined with a finite difference method. A detailed description is presented in Hansen *et al* (1994).

### The hydrodynamical model.

The model is based on a vorticity-stream function formulation:

$$\text{Poisson equation :} \quad \nabla^2 \psi = -\omega \quad [1]$$

$$\text{Vorticity transport equation :} \quad \frac{d\omega}{dt} = \nu \nabla^2 \omega \quad [2]$$

( $\psi$  is the stream function,  $\omega$  the vorticity and  $\nu$  the kinematic viscosity).

Using an operator splitting method, the vorticity transport equation [2] is split into :

$$\text{a convection equation :} \quad \frac{\partial \omega}{\partial t} + u \frac{\partial \omega}{\partial x} + v \frac{\partial \omega}{\partial y} = 0 \quad [3]$$

$$\text{and a diffusion equation :} \quad \frac{\partial \omega}{\partial t} = \nu \nabla^2 \omega \quad [4]$$

The convective transport is then modelled by moving the individual vortices with the velocity field ( $u, v$ ), while the diffusive transport is described by adopting a random walk technique : at each time step  $\Delta t$ , vortices are moved with a random displacement following a Gaussian distribution characterised by the standard deviation :

$$\sigma = \sqrt{2\nu \Delta t} \quad [5]$$

The Poisson equation [1] is solved on a curvilinear finite difference grid by an Alternative Direction Implicit method. The grid is generated from a solution to the Laplace equation describing a periodic potential flow over ripples.

*Cloud-in-cell technique.*

To obtain the vorticity field from the set of vortices, a cloud-in-cell technique is used to distribute the circulation of the vortices in each cell as vorticity on the four grid points at the cell corners.

*Boundary layer model at the surface.*

Vorticity can only be generated by shear forces acting on physical surfaces. On these boundaries, a turbulent boundary layer model based on the integrated momentum equation (Fredsoe, 1984) gives the time development of the boundary layer and hence, determine the strength and the motion of vortices within this zone.

*Merging method.*

To limit the growth of the number of vortices and to get a feasible calculation, a merging procedure is introduced : when two vortices with opposite signs come closer to each other than the sum of their radii, they combined into one single vortex.

*Computational domain and boundary conditions.*

In the computations, the bed is assumed stationary and a time-independent domain is used. In most of the presented simulations, the horizontal length of the domain is two ripple lengths. Vertically, various discretizations have been used. For the wave-alone case, where the vorticity is confined in the near-bed layer, a stretched net is adopted, with a height chosen so that vortices do not reach the top boundary. In the wave-current case, the boundary layer develops over the entire depth. As non-physical boundaries are difficult to represent in this kind of model, a symmetrical domain with ripples at the top has been chosen in order to satisfy the symmetry condition on the center line. In some facilities such as shallow tunnels, a real domain covering the entire depth can be used.

No-slip conditions are applied on physical boundaries while a simple stream line condition ( $\psi = \text{constant}$ ) is used at the top for the wave-alone case. To drive the flow, the time-dependent water discharge is imposed via the stream function. Besides, spatial periodicity between the two lateral boundaries is prescribed.

**The sediment transport model.**

The total sediment transport is divided into two contributions : bed load and suspended load. In the present model, it is assumed that the ripple shape is stationary and that the presence of suspended sediment does not affect the hydrodynamics. The two components of the sediment transport are modelled as follows.

\* The bed load transport rate  $Q_b$  along the ripple is modelled with the Meyer-Peter and Müller formula corrected for the slope effect :

$$\frac{Q_b}{\sqrt{(s-1)gd_{50}^3}} = 8 \left[ \theta - \theta_c \left( 1 + \frac{1}{\tan \varphi} \frac{dy_b}{dx_b} \right) \right]^{3/2} \quad [6]$$

where  $\theta$  is the local instantaneous Shields parameter,  $\theta_c$  the critical Shields parameter,  $s$  the relative density of the sediment,  $g$  the gravity,  $\varphi$  the angle of repose of the sediment,  $d_{50}$  the mean grain diameter and  $(x_b, y_b)$  are the bed coordinates.

\* The suspended sediment is discretized in computational "particles" containing a certain amount of sediment. They are characterised by their mass and their fall velocity.

The generation of these particles at the ripple surface involves two different mechanisms :

- The action of shear stresses on the bed produces a local erosion and thus creates new suspended particles. To model this, a source of sediment is located at the level  $y^*_o=2d_{50}$  ( $y^*$  is the coordinate normal to the ripple surface). Its strength  $Q_d$  is determined as a source term in the local turbulent diffusion equation in order to satisfy the bed-concentration formula of Zyserman and Fredsøe (1994) :

$$c_b(y^*_o=2d_{50}) = \frac{0.331 (\theta-0.045)^{1.75}}{1 + \frac{0.331}{0.46} (\theta-0.045)^{1.75}} \quad [7]$$

The mass of the particles is then derived from  $Q_d$ . To account for the grain sorting effect, the settling velocity is based on the mean grain diameter of the suspended fraction  $d_{50,susp}$ , fraction defined as sediment with a settling velocity  $w_s < 0.8 u_f$  where  $u_f$  is a characteristic friction velocity at the crest.

- Due to the recirculation zone downstream of the crest, the bed load is ejected into the flow at the separation point as described by Sleath (1982). This contribution is modelled by calculating  $Q_b$  at the location of maximum Shields parameter upstream of the separation. Then, a new particle is introduced just above the separation point with a mass derived from  $Q_b$  and a fall velocity based on the mean grain diameter of the bed material  $d_{50}$ .

Similarly to the hydrodynamic model, the continuity equation for the suspended sediment concentration [8] is tackled in a Lagrangian fashion.

$$\frac{dc}{dt} = w_s \frac{\partial c}{\partial y} + \nabla \cdot (\epsilon_s \nabla c) \quad [8]$$

where  $c$  is the concentration,  $w_s$  the settling velocity and  $\epsilon_s$  the sediment diffusivity. The motion of the sediment suspended over vortex ripples is dominated by convection except in the boundary layer along the ripple surface where the turbulent diffusion becomes important. Therefore, sediment particles are assumed to follow the flow paths with a fall component.

Inside the boundary layer, the motion normal to the ripple surface due to turbulent diffusion is modelled by a random walk method in the same manner as for the vorticity. Here, the standard deviation is :

$$\sigma_s = \sqrt{2\epsilon_s \Delta t_s} \quad [9]$$

where the sediment diffusivity  $\epsilon_s$  is assumed to be equal to the eddy viscosity  $\nu_t$  which has a linear variation within the boundary layer :

$$\epsilon_s = \nu_t = \kappa u_f y^* \quad [10]$$

where  $u_f$  is the local instantaneous friction velocity given by the boundary layer model,  $\kappa$  is the Von Karman's constant and  $\Delta t_s$  is the time step for sediment typically much smaller than the hydrodynamical time step  $\Delta t$ .

### Discretization parameters.

The computational grid presents 50 potential lines along a ripple length. The hydrodynamical time step is  $T/360$  (where  $T$  is the wave period) and the sediment time step is  $\Delta t_s = \Delta t/10$ . Numerical independence of the solution has been tested.



## Results processing.

After a transient regime of at least 20 cycles, any variable  $z(x,y,t)$  is decomposed into a mean (time-averaged) component  $Z$ , a periodic (phase-averaged) component  $z_w$  and a fluctuating component  $z'$ . Averaging is performed over at least 20 cycles :

$$z(x,y,t)=Z(x,y)+z_w(x,y,t)+z'(x,y,t) \quad [11]$$

Variables are then spatially averaged along horizontal lines with at least 50 points per ripple wave length. In the following angle brackets will denote space-averaged and an overbar or a capital time-averaged.

Assuming turbulent fluxes to remain small, the time and space averaged horizontal flux of suspended sediment,  $F_s = \overline{\langle u(x,y,t)c(x,y,t) \rangle}$  is found to be made of two components :

$$F_s = F_c + F_w \quad [12]$$

where  $F_c = \langle U(x,y) \rangle \langle C(x,y) \rangle$ , the current flux, represents the advection of the mean concentration by the mean velocity and  $F_w$ , the wave flux comes out from the non-zero covariance between periodic components  $u_w$  and  $c_w$ . The model provides  $F_s$  and  $F_c$ ,  $F_w$  is then obtained by subtraction.

To compute total suspended transport rates, two different methods can be used :

- Eulerian method : depth-integration of the fluxes profiles gives the transport rate  $Q_s$  and its two components  $Q_c$  and  $Q_w$ . This method is the one utilised in experiments. Particular attention must be paid to the lower integration limit and the large gradients in the near-bed region.

- Lagrangian method : the transport rate  $Q_s$  is directly computed from each "particle" contribution.

The total transport rate  $Q_t$  is the sum of the transport rate for the bed load and the transport rate for the suspended load calculated with the Lagrangian method :

$$Q_t = Q_b + Q_s \quad [13]$$

In the model, all the variables are made non-dimensional with the length scale  $L_r$  and the time scale  $L_r/U_w$  (where  $L_r$  is the ripple length and  $U_w$  the wave velocity amplitude). At the crest location  $x=0$  and at mid ripple height  $y=0$  whereas  $y_c$  denotes the vertical coordinate relative to the crest level. The positive direction ( $x>0$ ) will refer as the direction of maximum free stream velocity. As only phase-averaged and time-averaged results will be presented throughout the paper, the notation  $z$  will be used for  $Z+z_w$ .

## HYDRODYNAMIC COMPARISON

Detailed LDA velocity measurements were carried out by Ranasoma (92) over stabilised ripples fixed on a rig oscillating in a closed tank. The experiment covered various combinations of beds and oscillations. In the following, a comparison is presented for the selected test 2a with ripples in equilibrium with the flow. The ratio between wave orbital amplitude and ripple wave length  $a/L_r=0.78$  is in the range of vortex ripples, or orbital ripples as classified by Wiberg and Harris (1994). The simulated ripple shape is averaged from the measured bed profile. The initial time corresponds to maximum negative free stream velocity  $U_\infty$  relative to the bed as illustrated on figure 1.

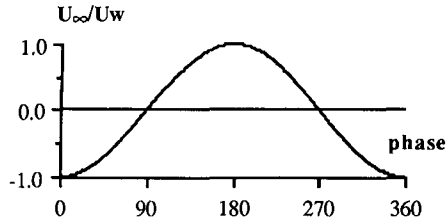
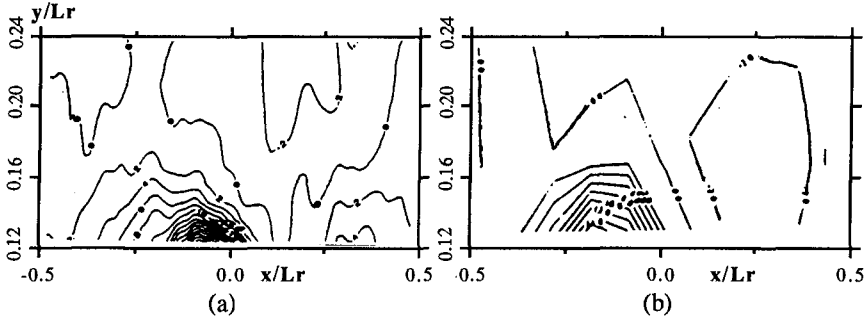
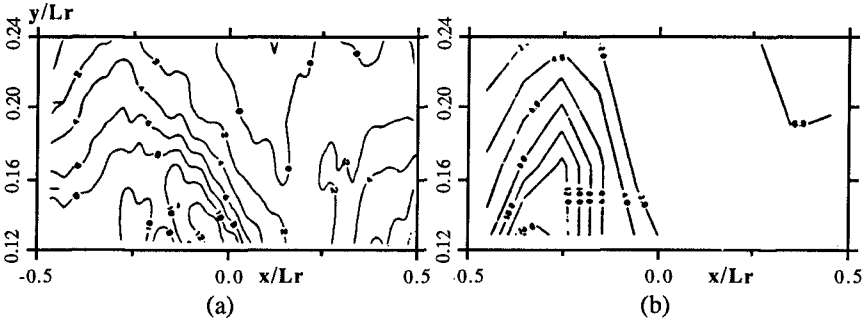


Fig. 1. Free stream velocity history.  
Experiment of Ranasoma (1992).

The agreement between computed and measured vorticity fields at two "key" phases demonstrates the ability of the hydrodynamic model to reproduce the important flow features. The vortex formation is well predicted (intensity, size and core location) whereas small differences appear before flow reversal : in the calculation, the core of the vortex appears closer to the crest and its spatial extent is larger. The convection and the decay of the ejected vortex agree with measurements, its location after one half-cycle is only slightly higher in the calculation : fig (2.1) shows the vortex shed one half-cycle before from the neighbouring ripple which is about to pass over the crest.



2.1. Phase=7°



2.2. Phase=64°

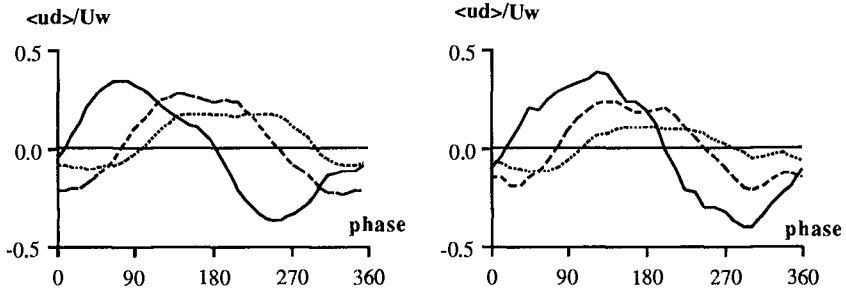
Computed

Measured

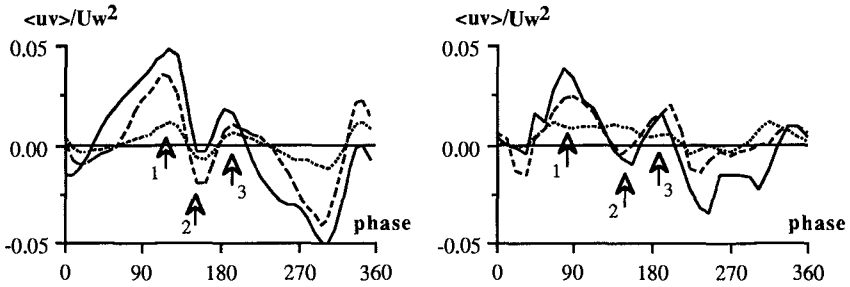
Fig. 2. Non-dimensional vorticity field at 2 phases.  
Experiment of Ranasoma (1992).

The time-evolution of the space-averaged horizontal defect velocity (velocity relative to the free stream)  $\langle u_d(x,y,t) \rangle = \langle u(x,y,t) \rangle - U_\infty(t)$  and momentum  $\langle u(x,y,t)v(x,y,t) \rangle$  is plotted on figure 3. The velocity amplitude is in good agreement close to the bottom ( $y_c=1\text{mm}$ ) but the simulation assesses a slower decay with elevation, which is consistent with the higher location of vortices. There is a phase shift between computed and measured profiles close to the bottom ( $y_c=1\text{mm}$ ) for velocity extrema. This is associated with the location of the vortex core closer to the crest in the simulation resulting in a slightly earlier "sweep" on the bed. The momentum curves exhibit three peaks per half-cycle, each peak connected to a particular flow structure as described by Ranasoma (1992) :

- Peak (1) : the vortex sweep close to flow reversal throws upwards accelerated fluid from the crest and brings down still fluid above the trough.
  - Peak (2) : the vortex is now located in the trough. Its circulation carries up slow-moving fluid above the trough and brings down fast-moving fluid above the crest.
  - Peak (3) : the vortex has arrived above the crest of the neighbouring ripple. The combined effects of the vortex circulation, the local spatial acceleration at the crest and the separation zone in formation bring up more positive momentum from the crest than bring down negative momentum above the trough.
- The model fits well the general peak structure. The only significant discrepancies are observed for the peak (1) : it occurs slightly later in the simulation the amplitude is relatively larger.



Computed Measured  
 Fig. 3.1. Space averaged non-dimensional defect horizontal velocity.  
 (solid :  $y_c=1\text{mm}$ ; dashed :  $y_c=9\text{mm}$ ; dotted :  $y_c=20\text{mm}$ ). Experiment of Ranasoma (1992).



Computed Measured  
 Fig. 3.2. Space averaged non-dimensional momentum.  
 (solid :  $y_c=4\text{mm}$ ; dashed :  $y_c=9\text{mm}$ ; dotted :  $y_c=20\text{mm}$ ). Experiment of Ranasoma (1992).

The hydrodynamical model appears to be in very good agreement with the experiment. The slight differences are not significant.

**SEDIMENT TRANSPORT IN ASYMMETRICAL WAVES**

A series of experiments in a water tunnel with a sandy bed under asymmetrical Stokes and cnoidal wave conditions have been carried out by Sato and Horikawa (1986).

In the following, the simulation of the selected test C2-12 is presented. In this test, the driving free stream velocity signal (Fig. 4) is based on a third-order cnoidal wave with an asymmetry parameter  $U_w/\dot{U}=0.72$  and a zero time-averaged value. The ratio  $a/L_r=1.3$  and the measured ripple is  $2D$  with an asymmetry parameter  $L_u/L_r=0.65$ . The simulated ripple is "smoothed parabolic" : parabolically shaped troughs with a crest smoothed over 10 % (Fig. 5). The mean sand grain diameter is  $d_{50}=0.18\text{mm}$ . As the height of the tunnel is only about twice the ripple length, it has been chosen to use the whole height as a computational domain taking a flat smooth boundary at the top.

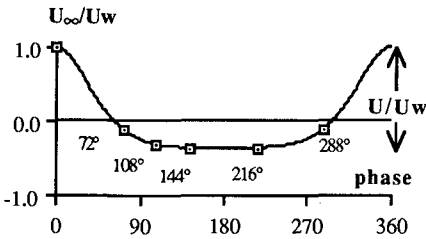


Fig. 4. Free stream velocity history.

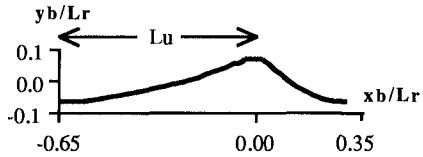


Fig. 5. Ripple shape.

Experiment of Sato and Horikawa (1986).

A snap-shot of the particles distribution is shown after flow reversal on figure (6) and the time evolution of the concentration field over a complete wave-cycle is displayed on figure (7) for 5 phases. On the steep flank of the ripple, a sand cloud forms with a large input of sediment from the crest during the short positive part of the cycle. At flow reversal, this cloud is ejected over the crest and travels in the negative direction. While convected, the cloud undergoes some diffusion and a large part of the trapped sediment falls down on the bed. During the longer negative part of the cycle, the flow motion is slow and no sand cloud formation is observed on the mild flank of the ripple, the friction velocity being too small and the slope too mild to get a sand cloud. Thus, a strong asymmetry exists between the two parts of the wave cycle resulting in a negative transport.



Fig. 6. Computed particles distribution at 108°. Experiment of Sato and Horikawa (1986).

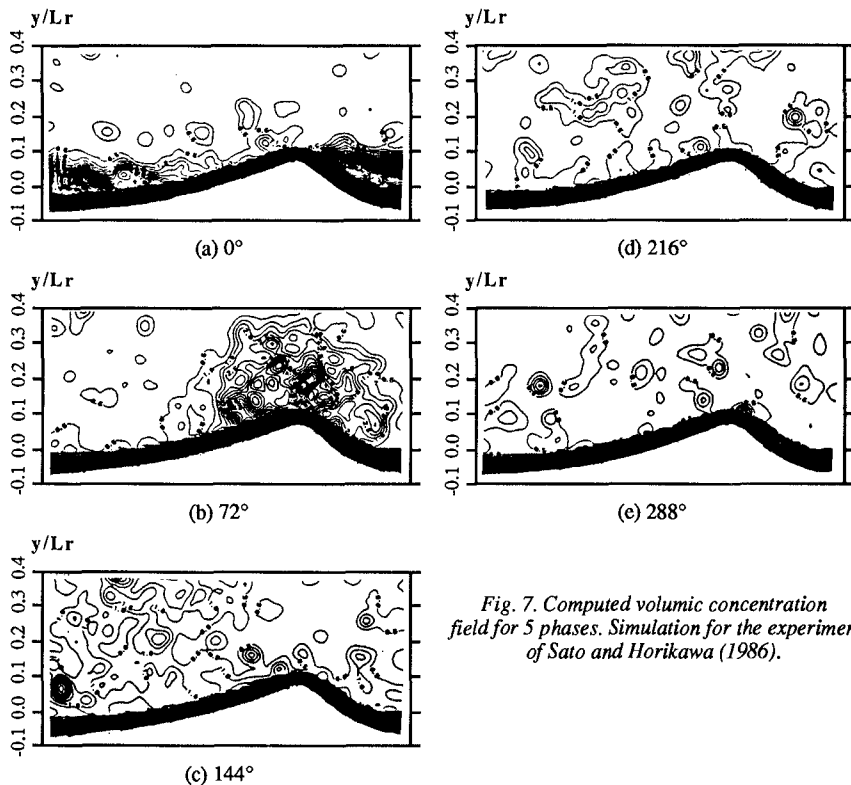
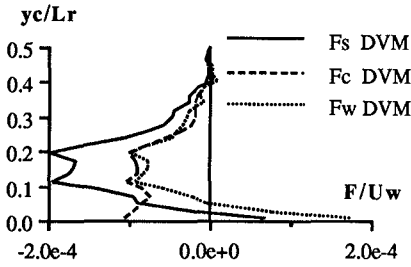


*Fig. 7. Computed volumic concentration field for 5 phases. Simulation for the experiment of Sato and Horikawa (1986).*

The computed horizontal suspended sediment fluxes (Fig. 8) reveal that the transport occurs only in a layer  $0.5 L_r$  thick. Because of the return current in the bottom part,  $F_c$  is negative down to the crest level. The wave flux  $F_w$  is negative above the level  $y_c = 0.06 L_r \approx 0.4 H_r$  (where  $H_r$  is the ripple height) as a result of sand cloud convection processes in this region and becomes positive below. The total suspended flux is then negative except very close to the bottom.

Three representative tests for 2D ripples have been used for simulations with an increasing degree of asymmetry and flow severity. The agreement (Table 1) is close with only a small underprediction for weaker flow conditions (S3-03).



Test	Qt/Lr/Uw * 10 <sup>-4</sup>		
	DVM	Exp	Ratio
S3-03	-0.2	-0.5	0.4
C2-12	-1.0	-1.5	0.7
C3-37	-1.1	-1.4	0.8

Fig. 8. Computed non-dimensional horizontal suspended sediment fluxes profiles. Experiment of Sato and Horikawa (1986).

Table 1. Non-dimensional net sediment transport rates. Experiment of Sato and Horikawa (1986).

**SEDIMENT TRANSPORT IN COMBINED WAVES AND CURRENT**

In the following, two different simulations for combined waves and current are presented : experiment of Murray (1992) in a tunnel and experiment of Villaret and Latteux (1992) in a wave flume. As far as sediment transport is concerned, wave flumes and tunnels are not totally equivalent. Indeed, in a flume the presence of a wave propagating in the positive direction induces vertical velocities and an horizontal drift positive at the bottom and negative in the outer flow. This effect that might change bottom processes is not included in the model.

The value of the proper free stream current  $U_c$  to prescribe is obtained by data fitting on the space and time averaged horizontal velocity profile.

**Combined waves and current in a tunnel.**

Murray used a set of various hydraulic conditions essentially in the sheet flow regime. However, one test (WCS1) presented a rippled bed. Here, the parameter  $a/L_r=6.57$  is out of the range of classic vortex ripples and is classified as anorbital by Wiberg and Harris (1994) : the ripple shape does not depend on the wave orbital amplitude but rather on the grain diameter  $d_{50}$ . The measured ripple shape is more 3D than 2D with no asymmetry reported. In the model, we choose a symmetric "smoothed parabolic" shape as a first approximation. The sand is fine with a mean grain diameter  $d_{50}=0.14\text{mm}$ .

The time and space averaged horizontal velocity and concentration are shown on figure (9). The two-slope velocity profile is well reproduced with a break of slope at  $y/L_r \approx 0.5$  and only a slight underprediction in the lower part. The concentration profile is correct both in terms of bottom concentration and slope. Very close to the bed, the model predicts an increase in the concentration but no data points are available at these lower levels. At high elevations, the small overestimation is not significant for such low concentrations.

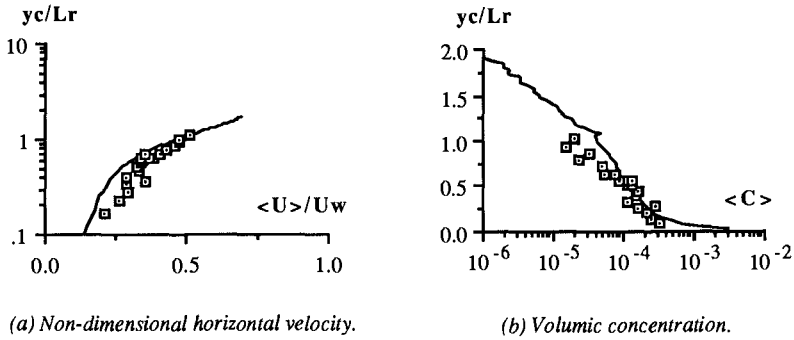


Fig. 9. Time and space averaged profiles.  
 solid line : DVM; squares: Experiment of Murray (1992)

The total suspended sediment flux profile  $F_s$  and the two contributions  $F_c$  and  $F_w$  presented on figure (10) appear to be in very good agreement with data. The strong reduction of the total flux by the negative wave contribution is properly predicted by the model at least above the level  $y_c/L_r=0.2$ . As we get closer to the bottom, current and wave contributions become strongly positive with a reversal of  $F_w$  at about one ripple height above the crest level. This behaviour has previously been observed by Vincent and Green (1990) for large scale ripples in the field.

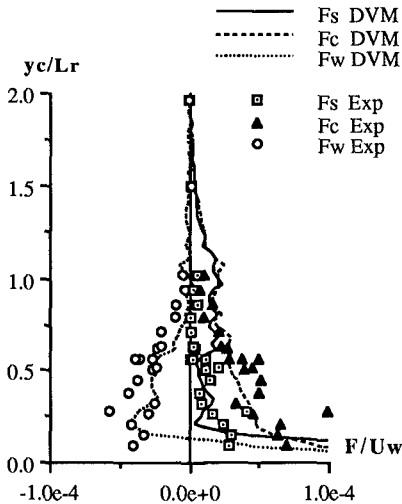


Fig. 10. Non-dimensional horizontal suspended sediment fluxes profiles.  
 Experiment of Murray (1992).

$Q/L_r/U_w \cdot 10^{-5}$	DVM	Exp	Ratio
<b>Bed load</b>			
$Q_b$	0.5	*	*
<b>Suspended load (Eul)</b>			
$Q_s$	2.6	1.3	2.0
$Q_c$	3.9	4.1	0.9
$Q_w$	-1.3	-2.8	0.5
<b>Suspended load (Lag)</b>			
$Q_s$	7.0	*	*
<b>Total load</b>			
$Q_t$	7.5	*	*

Table 2. Non-dimensional transport rates.  
 Experiment of Murray (1992).  
 (\* : unavailable)

To obtain transport rates, Murray used a linear extrapolation of the fluxes from the last measurement point ( $y_c/L_r=0.09$ ) down to the averaged bed level ( $y=0$ ) where  $F=0$  and then performed a depth-integration. Table 2 shows that the same Eulerian method applied to model results gives an overprediction of  $Q_s$  by a factor 2. The current contribution  $Q_c$  agrees with data while the wave contribution  $Q_w$  is underpredicted. Once considered the shape of the flux  $F_w$  profile, the reason of the discrepancy is clearly the reversal for the lower levels. The Lagrangian method gives a larger (2.7 times) transport rate because it takes indirectly account of the very large positive transport beneath  $y_c/L_r=0.09$ . The proportion of bed load in the total load is predicted as only 6.6%.

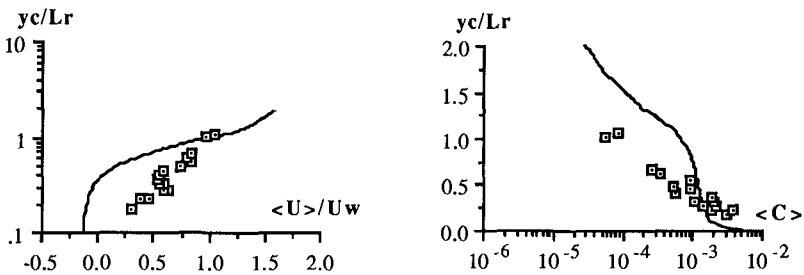
### Combined waves and current in a flume.

Villaret and Latteux (1992) have carried out combined waves and current experiments in a flume. For the selected test, the current followed the wave and the wave-induced drift is about 1 or 2 cm/s at the bottom for a velocity amplitude  $U_w=34$  cm/s. The other differences with the previous tunnel experiment are a larger current :  $U_{c1}/U_w=1.0$  for Villaret and Latteux (1992) whereas  $U_{c1}/U_w=0.5$  for Murray (1992) ( $U_{c1}$  is the current at  $y_c/L_r=1.0$ ), a finer sand ( $d_{50}=0.09$ mm) and a smaller ratio  $a/L_r=1.9$ , at the upper range of the vortex ripples regime and classified as suborbital by Wiberg and Harris (1994). The ripple was 2D but no asymmetry was reported. In the model, we use a symmetric "smoothed parabolic" shape.

The computed horizontal velocity deviates significantly from data (Fig. 11.a). The model exhibits a two-slope profile with a break of slope at  $y/L_r=0.5$  and a larger apparent roughness with even negative velocity in the near-bed wave-current boundary layer where data shows rather large positive velocities. The discrepancy at the bottom is a result of the wave drift present in the experiment but not included in the simulation.

In contrast with flat beds, the increase in the current-wave ratio  $U_c/U_w$  from the simulation of Murray (1992) to Villaret and Latteux (1992) results in a larger apparent roughness. Actually, the regime is closer to vortex ripples and the flow asymmetry is larger. Hence, shed vortices strongly reduce the velocity.

In spite of the correct bottom concentration, the calculated profile appears too steep in its lower part (Fig. 11.b.). The two-layer structure is rather pronounced attesting the large-scale mixing in the lower layer dominated by vortex convection.



(a) Non-dimensional horizontal velocity.

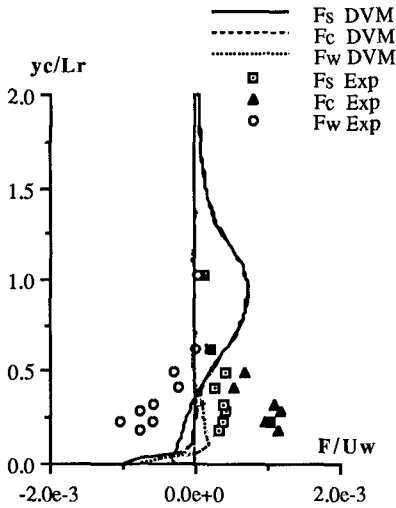
(b) Volumic concentration.

Fig. 11. Time and space averaged profiles.  
solid line: DVM; squares : Experiment of Villaret and Latteux (1992).



As a direct consequence of these discrepancies, the computed fluxes profiles (Fig. 12) exhibit a completely different pattern from data. At higher elevations where the concentration is overestimated,  $F_s$  and  $F_c$  exhibit maxima, while at lower levels where a return flow is predicted, fluxes disagree in amplitude and direction.

Villaret and Latteux (1992) computed  $Q_s$  from the fluxes profiles,  $Q_t$  from sand budget and  $Q_b$  by subtraction. They used a constant extrapolation of the fluxes from the last measurement point ( $y_c/L_r=0.18$ ) down to the crest level ( $y_c=0$ ) and then performed a depth-integration. The same Eulerian method is used here. As the flux  $F_s$  is small in the near-bed layer, the two methods for obtaining  $Q_s$  give similar results (Table 3). Nevertheless, the rather close agreement with data is not meaningful when the discrepancies in fluxes profiles are considered. The bed load is underpredicted and accounts for only 10% of the total transport compared to roughly 20% in the experiment.



$Q/Lr/U_w * 10^{-4}$	DVM	Exp	Ratio
<b>Bed load</b>			
$Q_b$	0.2	0.5	0.4
<b>Suspended load (Eul)</b>			
$Q_s$	2.1	1.6	1.3
$Q_c$	2.0	2.6	0.8
$Q_w$	0.1	-1.0	-0.1
<b>Suspended load (Lag)</b>			
$Q_s$	2.0	*	*
<b>Total load</b>			
$Q_t$	2.2	2.1	1.1

Fig. 12. Non-dimensional horizontal suspended sediment fluxes profiles. Experiment of Villaret and Latteux (1992).

Table 3. Non-dimensional transport rates. Experiment of Villaret and Latteux (1992). (\* : unavailable)

**DISCUSSION OF THE RESULTS AND CONCLUSIONS**

A numerical model based on a discrete vortex approach has been developed to study flow and sediment processes over rippled beds. It has been tested for a representative experiment in clear oscillatory flow and three different configurations where the free stream asymmetry induces a transport of sand in the near-bed region.

As far as hydrodynamics are concerned, the model provides a consistent prediction of the processes in the near-bed layer dominated by coherent vorticity structures. For the wave-alone case, the experiment of Ranasoma (1992) with fixed ripples has been used as a validating test. The model is able to describe rather accurately the mechanisms of generation, ejection and convection of vortices. For

combined waves and current, the model predicts a two-layer flow structure in accordance with the experimental data of Murray (1992) in tunnel.

The consistent qualitative picture of suspension processes and the good agreement of concentration profiles found by Hansen *et al* (1994) for the wave-alone case are extended here to the case of asymmetric waves and combined waves and current in tunnel. Especially, the large-scale mixing resulting from vortex shedding generates a rather uniform concentration in the ripple-influenced near-bed layer.

Regarding suspended sediment transport, detailed flux profiles provide much more information than depth-integrated transport rates. The particularity of such unsteady flows is to give rise to a wave flux in addition to the current flux. The total suspended sediment flux is then the sum of these two contributions. The current flux is always in the direction of the local current (negative for asymmetrical wave and positive for combined waves and current) whereas the wave flux opposes the direction of the maximum free stream velocity at most levels. This results from the convection of sand-laden vortices generated during the positive flow, shed into the flow at reversal and convected backwards during the negative flow. In the near-bed region, the wave flux reverses and becomes strongly onshore. This behaviour is thought to be the result of the larger amount of sand picked up from the crest during the positive flow. The fluxes data of Murray (1992) provides a successful quantitative comparison for the vortex-dominated region but no data is available to understand clearly near-bed mechanisms.

The evaluation of suspended sediment transport rates has proven the importance of the choice of the lower limit for depth-integration when the fluxes exhibit large increases close to the bed.

A discrepancy between model results and experimental data arises for combined waves and current in a flume (Villaret and Latteux, 1992). Progressive waves induce vertical velocities and a drift positive at the bottom and negative above. The absence of this physical feature in the modelling results in a conspicuous two-layer structure with a large underestimation of the horizontal velocity and a steep concentration profile in the near-bed region, whereas in the experiment the wave drift produces much more gradual profiles. The resulting computed fluxes disagree with experiment not only in magnitude but also in direction. This simulation demonstrates the need to include in the model the effect of wave propagation.

In such unsteady flows, the assumption of a steady-state ripple can be discussed. Indeed the ripple deforms locally during the wave cycle : a small volume of sand moves back and forth in the crest region and forms at each half-cycle a small cliff downstream of the crest which disappears at flow reversal (Sleath, 1982). In the simulations with sediment, the selected shape, "smoothed parabolic", is representative of the experimental bed shape (Fredsoe and Deigaard, 1992) and changing the length of the smoothed crest region has only a small influence on bottom processes. It appears from experiments that the bed is less affected by the superposition of a current on sine waves than by the wave asymmetry. Therefore, symmetric ripples have been used for combined waves and current simulations. Beside its stationary shape, the migration of the ripple is neglected based upon experiments. Nevertheless, the large increase in the computed wave flux close to the bed could be partly due to this unrepresented characteristics.

As a general conclusion, the study has demonstrated the ability of the model to replicate hydrodynamical and sediment mechanisms when the water motion induced by waves can be reckoned as oscillatory.

## Acknowledgements.

This work was founded jointly by the Danish Technical Research Council under the program "Marin Teknik", the G8 Coastal Morphodynamics program under EC contract MAST2-CT92-0027 and by the French Sea State Secretary S.T.C.P.M.V.N.

## Appendix : Experimental conditions.

Experiment Facility	Motion	Test	$U_w$ (cm/s)	$U_w/\bar{U}$	$T$ (s)	$a/L_r$	$U_c/U_w$	$H_j/L_r$	$Re=U_w L_r/\nu$	$d_{50}$ (mm)
Ranasoma (92) Oscillatory rig	W	2A	20.3	0.5	2.41	0.78	-	0.18	18000	0.41
Sato (86) Tunnel	Asym W	S3-03	39.3	0.63	4.0	1.60	-	0.16	48000	0.18
		C2-12	40.6	0.72	3.0	1.30	-	0.14	38000	0.18
		C3-37	67.0	0.83	5.0	1.25	-	0.15	120000	0.18
Murray (92) Tunnel	W+C	WCS1	41.3	0.5	10.0	6.57	0.38	0.15	36000	0.14
Villaret Latteux (92) Flume	W+C	40	34.0	0.5	2.0	1.91	0.43	0.12	36800	0.07

## References.

- Block, M.E. (1994). Wave generated flow over sand ripples and the resulting entrainment and suspension of sediment. *PhD Thesis. Univ. Col. North Wales.*
- Blondeaux, P. and G. Vittori (1990). Oscillatory flow and sediment motion above a rippled bed. *Proc. 22nd ICCE*, pp 2186-2199.
- Fredsøe, J. (1984). Turbulent boundary layer in wave and current motion. *J. Hydr. Eng., ASCE*, 110(8), pp 1103-1120.
- Fredsøe, J. and R. Deigaard (1992). Mechanics of coastal sediment transport. *Advanced Series on Ocean Engineering. Vol. 3. World Scientific.*
- Hansen, E. A., J. Fredsøe and R. Deigaard (1994). Distribution of suspended sediment over wave-generated ripples. *J. Waterway, Port, Coastal and Ocean Eng., ASCE*, 120(1), pp 37-55.
- Huynh Thanh S. (1990). Etude numérique de la couche limite turbulente oscillatoire générée par l'interaction houle-courant en zone côtière. *PhD Thesis. INPG Grenoble.*
- Longuet-Higgins M. S. (1981). Oscillating flow over steep sand ripples. *J. Fluid Mech.*, 107, pp 1-35.
- Murray P. B. (1992). Sediment pick-up in wave-current flow. *PhD Thesis. Univ. Col. North Wales.*
- Ranasoma K. I. M. (1992). Measurements in combined oscillatory and steady flow over rippled beds. *PhD Thesis. Cambridge.*
- Sato S., N. Mimura and A. Watanabe (1984). Oscillatory boundary layer flow over rippled beds. *Proc. 19th ICCE*, pp 2293-2309.
- Sato, S. and K. Horikawa (1986). Laboratory study on sand transport over ripples due to asymmetric oscillatory flows. *Proc. 20th ICCE*, pp 1481-1495.
- Sleath J. F. A. (1982). The suspension of sand by waves. *J. Hydr. Res.*, 20(5), pp 439-452.
- Tsujimoto G., N. Hayakawa, M. Ichiyama, Y. Fukushima and Y. Nakamura (1991). A study on suspended concentration and sediment transport mechanism over rippled sand bed using a turbulence model. *Coastal. Eng. Japan*, 34(2), pp 177-189.
- Villaret, C. and B. Latteux (1992). Transport of fine sand by combined waves and current : an experimental study. *Proc. 23rd ICCE*, pp 2500-2512.
- Vincent C. E. and M. O. Green (1990). Field measurements of the suspended sand concentration profiles and fluxes and of the resuspension coefficient  $\gamma_0$  over a rippled bed. *J. Geophys. Res.*, 95(C7), pp 11591-11601.
- Wiberg P. L. and C. K. Harris (1994). Ripple geometry in wave-dominated environments. *J. Geophys. Res.*, 99(c1), pp 775-789.
- Zyserman, J. and J. Fredsøe (1994). Data analysis of bed concentration of suspended sediment. *J. Hydr. Eng., ASCE*, vol 120(9), pp 1021-1042.

## CHAPTER 149

### In-Situ Determination of the Critical Bed-Shear Stress for Erosion of Cohesive Sediments

Erik-Jan Houwing and Leo C. van Rijn<sup>1</sup>

#### Abstract

A new in-situ erosion meter has been developed to measure the in-situ bed-shear strength of cohesive beds. It is assumed that the current velocity, at initiation of motion of the toplayer of the bed, can be used to compute the critical bed-shear stress. This critical shear stress is the characteristic parameter which can define different types of sediment beds.

The in-situ measurements show that the test results are determined by the prevailing hydrodynamic conditions in the field (wave activity) and recent depositions rather than by physical and biological parameters.

#### Introduction

It is commonly accepted that the strength of the inter-tidal mud flats is strongly influenced by physical-, biological- and chemical- parameters (see Amos et al., 1992; Verreer et al., 1986). Until now it is not possible to measure these parameters separately and predict the resulting strength of the bed. The best way to handle this problem is to measure the critical shear stress for erosion of the top layer of the bed. By this, all shear strength related parameters are captured in one overall parameter: the critical shear stress corresponding to the erosion of the top layer of the bed (defining the maximum shear strength of the top layer of the bed). These tests can be performed in the laboratory either by using kaolinite beds or by samples of natural beds which have to be taken from the field. Both types of tests do not seem to reflect the natural conditions of in-situ beds properly. For this reason in-situ measurements have to be carried out in order to determine the erosive resistance of cohesive sediment. Several in-situ instruments have been developed already (Amos et al., 1992a; Williamson, 1994; Gust, 1994; Cornelisse

---

<sup>1</sup>Institute for Marine and Atmospheric Research Utrecht, Utrecht University, PO Box 80115, 3508 TC Utrecht, The Netherlands.

et al., 1994). Until now, the techniques used are not accurately enough to determine the parameters controlling the entrainment of cohesive sediments. One of the major problems is that differences are found in the stresses generated by the instruments in comparison with the real values in nature (Gust, 1994). Furthermore, the measurement results are often biased and the measurement results of the available erosion instruments show significant differences. This is mainly caused by differences in the settings of the instruments (Cornelisse et al., 1994).

The in-situ Erosion Flume, presented herein, is developed to measure the shear resistance of the top layer of cohesive beds. Like most of the flume-systems the shear stress on the bed is exerted by an adjustable unidirectional flow. The shear stress exerted by the adjusted current velocity was calibrated in the laboratory. The results of the ISEF measurements will give the maximum shear strength of the top layer of the bed and is an overall representation of shear strength related parameters.

This article describes the development of the ISEF, the reproductivity tests in the laboratory and the field measurements on cohesive beds in the salt marsh region in the Netherlands Wadden Sea.

### In-Situ Erosion Flume (ISEF)

The in-situ Erosion Flume is a circulating flow system in the vertical plane. It consists of a lower horizontal test section, two bend sections and an upper section where the flow is generated by a propeller (see figure 1).

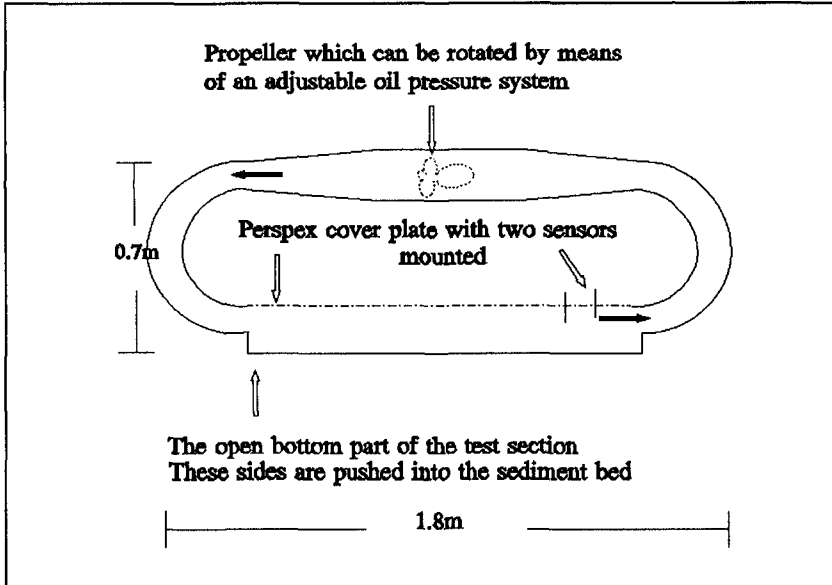


Fig.1 The in-situ erosion flume (ISEF).

The horizontal test section and the two bend sections have a rectangular cross-section with a height of 0.1 meter and a width of 0.2 meter. The bottom part of the horizontal test section is open over a length of 0.9 and a width of 0.2 meter. When the Erosion Flume is resting on the sediment bed properly, the surface of the bed will be in line with the steel bottom plates of the flume on both ends of the horizontal section. The total weight of the erosion flume is about 50 Kg. The total volume of water in the flume is 100 liter.

The propeller can be rotated at various speeds by means of an adjustable oil pressure system. The flow velocity in the horizontal section is measured with a small disc-type electro-magnetic flow meter (EMF) placed at 0.55 meter from the entrance of the horizontal test section. The measuring point is at 0.075 meter below the covering plate of the test section, which is 0.025 meter above the bed surface. The suspended sediment concentration is measured by means of an optical monitor.

The erosion process of sediment particles of the bed is related to the prevailing bed-shear stress.

The bed-shear stress can be determined from the measured velocity profile assuming a logarithmic distribution in vertical direction, which reads as:

$$u_z = \frac{u_*}{\kappa} \ln\left(\frac{z}{z_0}\right) \quad (1)$$

in which:

$u_z$  = flow velocity at height  $z$  above the bed (m/s),  $u_* = (\tau_b/\rho)^{0.5}$  = bed-shear velocity (m/s),  $\tau_b$  = bed-shear stress (Pa),  $\rho$  = fluid density ( $\text{kg/m}^3$ ),  $\kappa$  = constant of von Karman (0.4) (-),  $z$  = height above the sediment bed (m),  $z_0 = 0.033 k_s + 0.11\nu/u_*$  = zero-velocity level (m),  $k_s$  = effective bed roughness height of Nikuradse (m), and  $\nu$  = kinematic viscosity coefficient ( $\text{m}^2/\text{s}$ ).

Based on Eq.(1) the bed-shear stress can be expressed as:

$$\tau_b = \rho \kappa^2 u_z^2 \left[ \ln\left(\frac{z}{z_0}\right) \right]^{-2} \quad (2)$$

An equilibrium flow will not be established in the ISEF because of the short length of the test section. This means that the velocity distribution in the near-bed region of the horizontal section might deviate slightly from the logarithmic distribution. Introducing a calibration coefficient  $\alpha$  (close to unity) to account for this effect, and using the maximum velocity  $u_m$  at the upper edge of the boundary layer ( $\delta$ ) above the bed, Equation (2) can be expressed as:

$$\tau_b = \rho \kappa^2 (\alpha u_m)^2 \left[ \ln \left( \frac{\delta}{0.033 k_s + 0.11 \nu \left( \frac{\tau_b}{\rho} \right)^{-0.5}} \right) \right]^{-2} \quad (3)$$

The  $\alpha$ -coefficient was determined by measuring velocity profiles above a flat bed of moving (non-cohesive) sand and gravel particles at conditions just beyond the initiation of motion (Houwing and van Rijn, 1992). The  $\alpha$ -coefficient varies from 0.9 to 0.74 as function of an increasing Reynolds number. The boundary layer thickness ( $\delta$ ) was found to be about 0.025 m. In field situations, the hydrodynamic conditions just above the cohesive bed lies within the hydraulic smooth regime. Therefore, an  $\alpha$ -coefficient of 0.9 is recommended to determine the bed-shear stress. The velocity should be measured at a height of 0.025 meter above the bed.

### Reproduction measurements

Reproduction tests are essential for a correct interpretation of data and to know whether the experimental results are reliable (see Cornelisse et al., 1994). Changes in test results should be due to changes in bed composition rather than to differences in the setting of the erosion meter. It is expected that, in case of the ISEF, erosion will appear more easily along the edges of the test section as here the bed might be slightly disturbed. Besides that, small undulations on top of the bed will lead to small velocity variations thus increasing erosion on that specific location.

Cornelisse et al. (1994) found that the areal size of the test section is crucial for the reproductivity of the erosion instruments. The spatial variations in the bed properties and the turbulent stresses are averaged out when the erodible area is larger. They found a linear relationship between the reproduction error and the areal surface which reads as:  $R = 796 * A^{-0.528}$ , based on 13 tests carried out with four different erosion meters. The surface area of the test section of the ISEF measures 1800 cm<sup>2</sup> and the resulting error R is calculated to 15%.

In order to investigate the reproduction error of the ISEF three laboratory tests have been carried out similar to the tests performed with a laboratory carousel (de Jong, 1991). For each test a new bed is constructed in the test section of the ISEF. The bed consists of kaolinite and is formed by sedimentation in still fresh water. The mean density of the kaolinite bed is in the order of 350 kg/m<sup>3</sup>.

The current velocity in the ISEF is increased in steps of one hour during each experiment. The sediment concentrations are determined by means of the optical sensor. The output of the optical sensor is calibrated in situ based on pumped samples. The results of the tests show a good reproductivity (Fig. 2) and the error for the reproductivity tests is estimated to 20 % which is in agreement with the calculated 15%. The rate of erosion per exerted shear stress is up to 3 times higher for the ISEF in comparison with the test results performed by de Jong. This is probably due to a lower mean density of the initial bed used in the ISEF (350 vs 400 kg/m<sup>3</sup>).

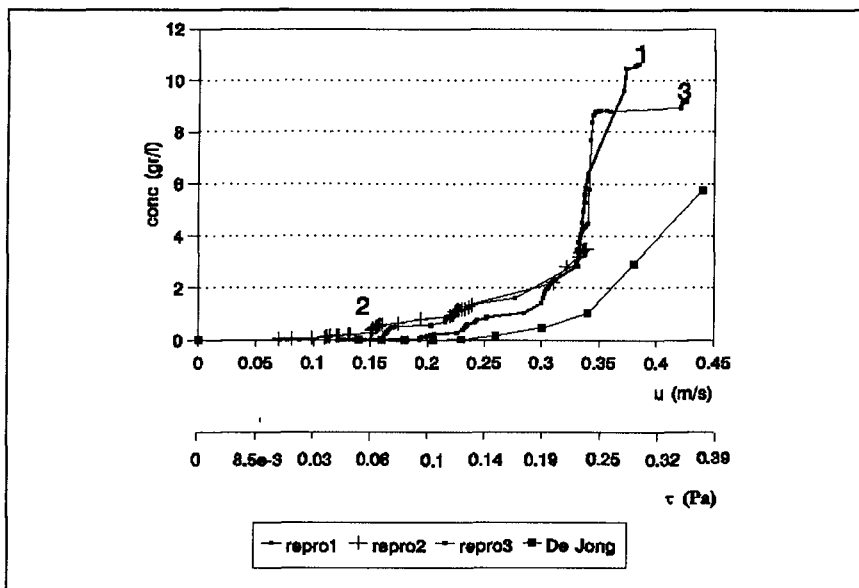


Fig.2 Reproduction of erosion tests.

### Field measurements

The in-situ field measurements are carried out in one specific area in the salt marshes along the main coast of the Netherlands Wadden Sea. The field site is surrounded by brushwood groynes and measures 400 x 400 meter. The tide is diurnally and most of the time the field area is inundated during high water. Mean water depth lies in the order of 1 meter. The area develops into the salt marsh in landward direction and is bounded in seaward direction by low tidal flats. The bed sediment in this area can be classified as cohesive sediment. It consists of well sorted very fine sand ( $d_{50}=80\mu\text{m}$ ;  $d_{90}=100\mu\text{m}$ ;  $d_{10}=65\mu\text{m}$ ) and contains between 20 to 30 % material smaller than  $50\mu\text{m}$ .

Small variations can be found within the field area ranging from  $d_{50}\approx 75\mu\text{m}$  close to the groynes to  $d_{50}\approx 90\mu\text{m}$  near the windward side of the groynes. The density of the top layer of the bed (first 5 mm) varies from  $1050\text{ kg/m}^3$  in less consolidated regions to  $1300\text{ kg/m}^3$  in the better consolidated regions. The increase in consolidation is found going towards the salt marsh and can be contributed to the decrease in frequency in tidal flooding and to a better dewatering of the bed. The bed density is measured with use of a cylinder of 2.5 cm in diameter. This cylinder is pushed into the bed and the sediment core is pushed out carefully and slices of 5 mm thick are cut accurately. The bed density is measured in this way till 3 cm beneath the surface with a 5 millimeter interval (figure 3).



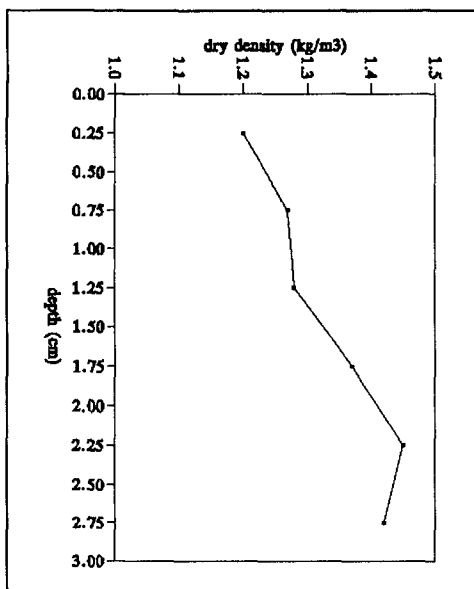


Fig. 3 Example of bed density as function of depth

The samples are weighted in order to obtain the wet bulk density, dry bulk density, moisture content and voids ratio.

The results from the ISEF-measurements will give the maximal shear strength of the top-layer of the bed for that specific location. Comparison with other ISEF-measurements will show how the erosion resistance of the bed will change both in time and in space.

Several in-situ field measurements distributed throughout the field area have been performed during the autumn and winter period of 1993 and the summer period of 1994. Five measurements are discussed here forming two identical groups where in each group the measurements are recorded for two consecutive days. Group 1 is formed by ISEF-1 and ISEF-3 and the tests are carried

out during autumn on 13 and 14 October 1993. The second group is formed by ISEF-5, -6 and -7 and is carried out during summer on 7 and 8 June 1994.

ISEF-1 is carried out in the middle of the field area where the bed is inundated twice a day (mean water depth during high water is around 1 meter) and ISEF-3 is carried out close to the salt marsh where the bed is less frequently flooded (mean water depth is about 0.15 meter). The differences in bed density, grain size and mud content ( $d_{50} < 50 \mu\text{m}$ ) are given in Table 1.

Measurement ISEF-5 is carried out on the same spot as ISEF-1: in the middle of the field area. ISEF-6 and -7 are carried out more to the west in the field area where the bed is sheltered by the groynes. Here, the bed is less consolidated and contains a higher percentage of mud.

ISEF-6 and ISEF-7 are carried out close to each other on one day. The difference between both tests is that in case of ISEF-7 the fluffy top layer, of about 5 mm thickness, is removed by a scraper exposing the underlying undisturbed bed. The bed parameters are shown in Table 1.

The ISEF is placed carefully on the sediment bed. The current velocity in the ISEF is tuned accurately during the measurements until the top layer of the bed starts to erode. It is tried to follow the same procedure during each measurement. The first minutes of the test the velocity is adjusted to 0.05 m/s. The current velocity is then increased by steps of 0.05 m/s. Each step lasts as long as one hour or until at least the erosion of the bed is arrested (concentrations become constant in time). In the latter case the exerted shear stress equals the

strength of the bed at that particular depth ( $z$ ):  $\tau_b = \tau_{s(z)}$ . With help of equation (3) the shear stress is computed. The results of the ISEF measurements are shown in figure 4 to 8.

Table 1. ISEF-measurements and bed parameters. The bed parameters are measured in the upper 5 millimeter of the bed. The grain size is computed from the fall velocity distribution from the sediment samples. The mud content is determined by filtering the sediment samples through a 50  $\mu\text{m}$  filter. The standard deviation (STD) is the deviation around the mean ( $\sigma_{n-1}$ ) calculated from five samples ( $n=5$ ).

	$d_{50}$ ( $\mu\text{m}$ )	$d_{90}/d_{10}$ (-)	mud cont (%)	Bulkdens ( $\text{kg}/\text{m}^3$ )	STD	Drydens ( $\text{kg}/\text{m}^3$ )	STD
ISEF-1	80	1.85	15	1.74	0.15	1.15	0.14
ISEF-3	76	1.55	25	1.75	0.09	1.23	0.11
ISEF-5	80	1.86	15	1.82	0.02	1.20	0.07
ISEF-6	74	1.55	25	1.60	0.13	1.01	0.17
ISEF-7	76	1.98	25	1.77	0.13	1.17	0.19

All figures show an increase in erosion of the top layer of the bed at an increasing current velocity (increasing shear stress). At low velocities erosion of the bed is non linear and erosion is arrested after a while indicating that the exerted stress equals the bed shear strength at that level. At high current velocities erosion is linear (see figure 4). It is apparent that in all cases, except for ISEF-3, most linear erosion starts around an exerted velocity of 0.20 m/s (figures 4 to 8).

One of the major problems is to measure the bed density of the top mm's of the bed which is one of the basic parameters for the bed shear strength. The amount of erosion of the bed can be recalculated to erosion depth, assuming that the measured bed density of the first 5 mm of the bed is also characteristic for the top layer of the bed. If erosion occurred equally over the entire test section (1800  $\text{cm}^2$ ), the erosion depth is limited to  $10^{-4}$  millimeter. This is not in agreement with visual observations after each test. Here it is found that at the end of the test the erosion depth can be as high as one centimetre. This difference can first of all be ascribed to the fact that the calculations are based on the mean bed density while it can be expected that the top millimeter of the bed measures a much lower density. Second, erosion of the bed will not always happen throughout the entire surface but will often be confined to patches in the test section where erosion resistance is lowest. This means that it is of major importance to measure the bed density with a much smaller interval and on a much more accurate way than in the present study.

The results of the tests show that the relationship between the exerted shear stress and the erosion rate is poor. This can be expected as in nature the composition of the bed and the density of the bed varies strongly in depth.

### Conclusions and recommendations

The laboratory and the in-situ field measurements of the ISEF show realistic results in respect to the results of other researchers. The laboratory tests show that the reproducibility of the ISEF is reasonably good. The in-situ measurements based on the ISEF measures the minimum exerted shear stress at initiation of erosion of the bed leading to the maximum bed shear strength.

The ISEF measures erosion of the top-layer of the bed due to the uni directional current only. It is found that due to wave propagation mud-beds can weaken and the bed shear strength decreases as result (Mehta, 1988). The ISEF-measurements, in this respect, will overpredict the maximal bed shear strength.

It is expected that the moment of erosion of the top layer of the bed will strongly be determined by the composition of the bed, the bed density and biological activity in the top layer of the bed (for instance the presence of diatoms). The test results have shown that if variation in sand-mud composition, bed density, grainsize distribution and biologic activity in the top layer of the bed is relatively small, the strength of the top layer of cohesive beds at different locations tend to be constant.

The strength of the top layer of the bed of intertidal mudflats are determined by the governing (preceding) hydrodynamic conditions. Wave action, especially in very shallow water depth, remoulds the bed sediment. This effect is visual in the field to several cm beneath the bed surface, depending on the wave heights. The top layer of the bed was found to have approximately constant shear strength' on a small spatial scale. The strength of the top layer of intertidal mud flats, in this case, is determined rather by the prevailing hydrodynamic conditions (wave activity) and recent depositions than by physical and biological parameters. Interdisciplinary research of physicist and biologists is needed in order to investigate the variation in shear strength of the top layer of intertidal mudflats properly. It is wise to choose research locations which differs in great extend in shear strength-related parameters. The ISEF is useful to characterize different types of cohesive sediment beds. More thorough investigation is possible if the bed density can be measured on a small vertical scale (millimeters). For this purpose the acoustic density meter which is developed by Delft Hydraulics can be recommended (Verbeek and Cornelisse, 1994).

More thorough investigation is possible if the in-situ pumped suction samples are analyzed with respect to grain size distribution during test procedure. In this way it is possible to separate the moment of resuspension of the fraction  $d < 50\mu\text{m}$  from the moment the sand fraction  $d > 50\mu\text{m}$  is resuspending.

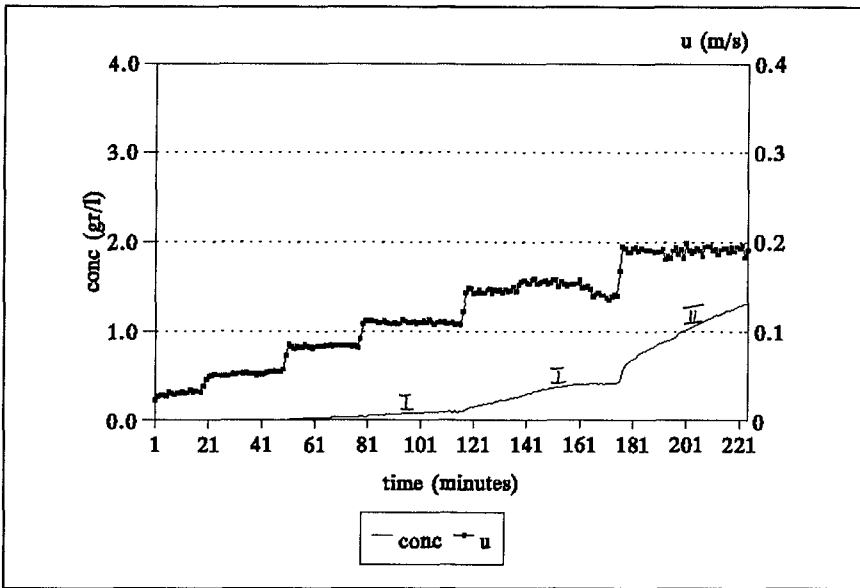


Fig.4 Measurement ISEF-4. I indicates non-linear erosion. II indicates linear erosion.

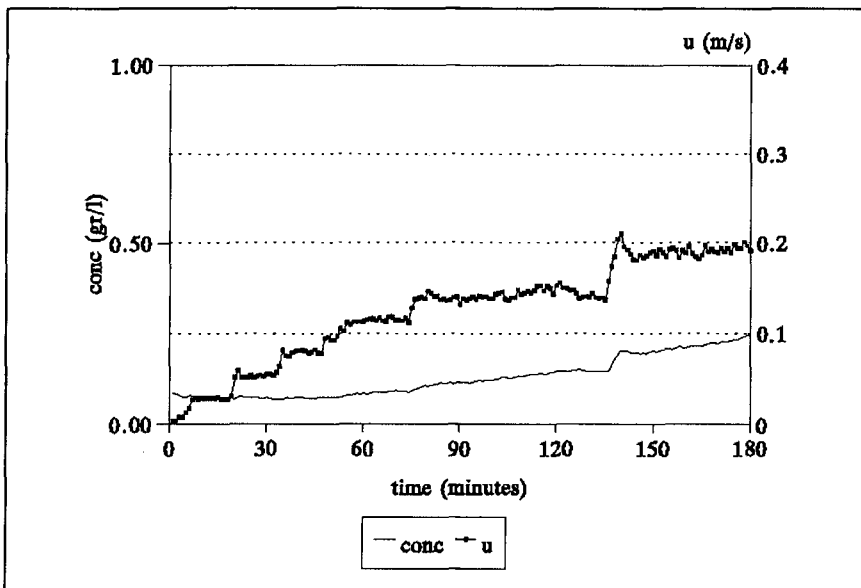


Fig. 5 Measurement ISEF-3.

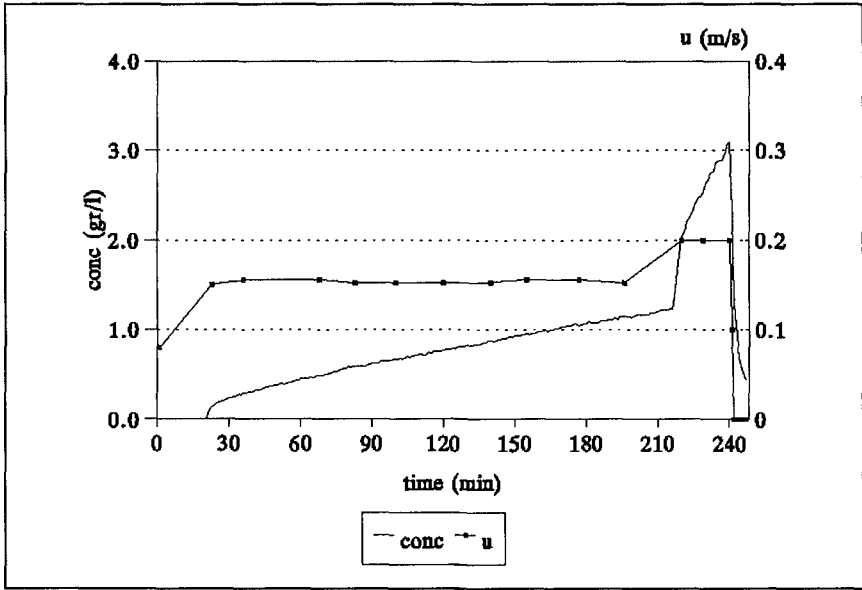


Fig. 6 Measurement ISEF-5.

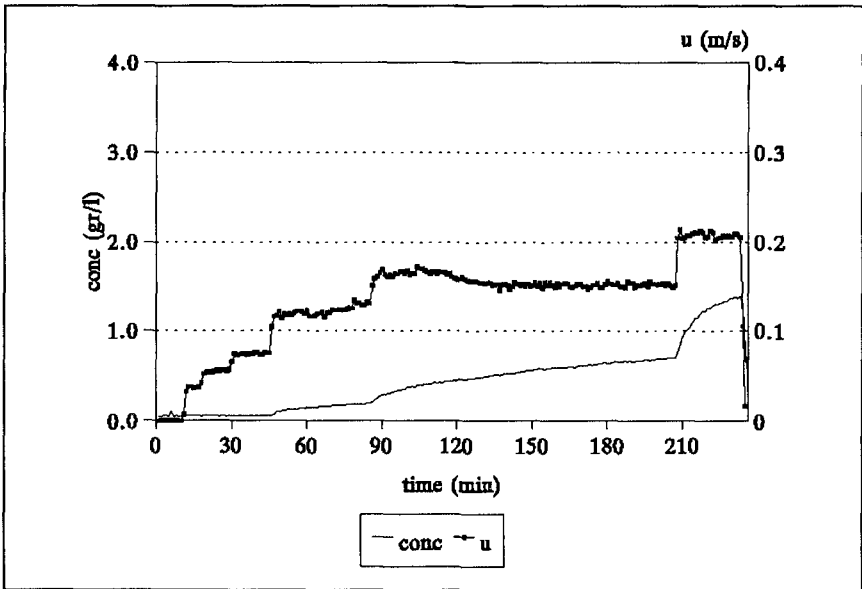


Fig. 7 Measurement ISEF-6.

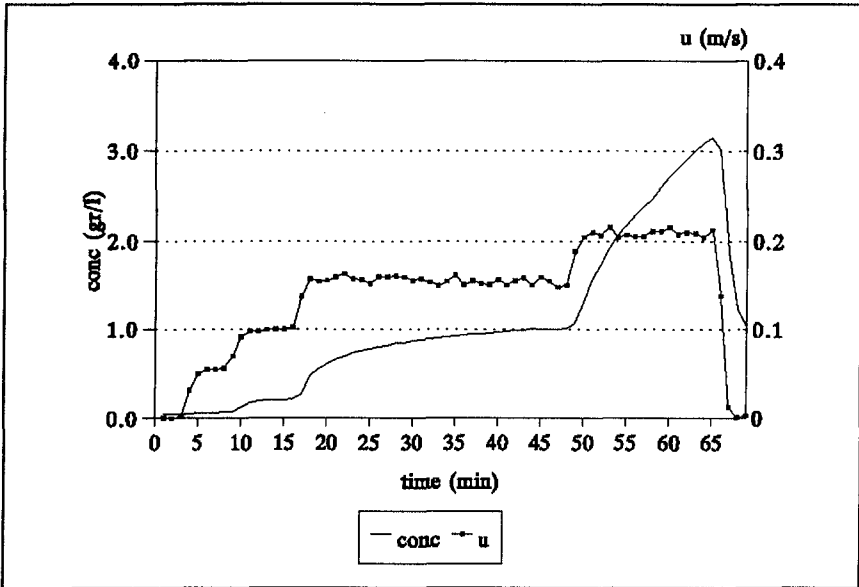


Fig. 8 Measurement ISEF-7.

References

- Amos, C.L., G.R. Daborn and H.A. Christian (1992). In-situ erosion measurements on fine-grained sediments from the Bay of Fundy. Marine Geology, 108, 175-196.
- Amos, C.L., J. Grant, G.R. Daborn and K. Black (1992a). Sea Carousel- A benthic, annular flume. Estuarine, Coastal and Shelf Science, 34, 557-577.
- Cornelisse, J.M., H.P.J. Mulder, H. Williamson et al. (1994). On the development of instruments for in situ erosion measurements. 4th Nearshore and Estuarine Cohesive Sediment Transport Conference INTERCOH'94, Wallingford, England.
- Houwing, E.J. and L.C. van Rijn (1992). In situ erosion Flume (EROSF): determination of bedshear stress and erosion of a kaolinite bed. Internal report, IMAU.
- Jong, P. de (1991). Reproduction-research carrousel (in Dutch). Internal report Delft Hydraulics, note z161-94.
- Mehta, A.J. and E. Partheniades (1982). Resuspension of deposited cohesive sediment beds. Proc. 18<sup>th</sup> ICCE, ASCE, 1569-1588.
- Mehta, A.J. (1988). Laboratory studies in cohesive sediment deposition and erosion. In: Dronkers, J. and W. van Leussen (eds.). Physical processes in Estuaries. Springer Verlag, Berlin, 427-445.
- Verbeek, H. and J.M. Cornelisse (accepted). Consolidation of dredged sludge, measured by an acoustic densitometer. Australian Journal of Marine and Freshwater Research.
- Verreet, G., J. van Goethem, W. Viaene et al. (1986). Relations between physico-chemical and rheological properties of fine-grained muds. Proceedings of the Third International Symposium on River Sedimentation, River Sedimentation, volIII, 1637-1646.
- Williamson, H.J. (1994). Recent Field Measurements of erosion shear stress using ISIS. 4th Nearshore and Estuarine Cohesive Sediment Transport Conference INTERCOH'94, Wallingford, England.

## CHAPTER 150

# Control of Cross-shore Sediment Transport by a Distorted Ripple Mat

Isao Irie\*    Nobuyuki Ono†    Seiya Hashimoto‡  
Satoshi Nakamura§    Keisuke Murakami¶

## ABSTRACT

A method to control cross-shore sediment transport by a distorted ripple mat which is the artificial ripples of distorted cross section has been studied through hydraulic experiments and numerical simulation. First of all, the relative importance of factors affecting cross-shore sediment transport on fixed bed ripples and the condition on which sediment is definitely transported on-shoreward are obtained. Based on this condition, experiments with movable bed are carried out to see how efficiently the distorted ripple mat can be utilized in stabilizing natural/artificial beaches. Furthermore, a numerical model of beach profile change in which effects of ripple distortion are considered has been developed and beach stabilizing effects of the mat are also reproduced numerically.

## INTRODUCTION

Recently, the needs of preventing beach erosion without installing such bulky structures as offshore or submerged breakwaters have increased so as to keep a beautiful view and to enable various maritime recreational activities. In order to prevent people's lives and properties from natural disasters, sandy beach needs to be expanded so that land behind is efficiently protected even with the

---

\*Professor, Dept. of Civil Eng. Kyushu Univ., Hakozaki Higashiku Fukuoka 812, Japan

†Graduate Student, Ditto

‡Former Graduate Student, Ditto

§Graduate Student, Ditto

¶Research Associate, Ditto



temporary retreat of shoreline under severe storm waves. The idea of supplying sediment from other sources to fulfill those demands, however, will become very difficult to be adopted as the general shore protection methods in the future because every coast is more or less suffering from the shortage of sediment and cannot afford to supply for other coasts. The supply from land sources will also have by itself limitation. The expected sea level rise in coming century will make the situation more serious. Thus, the shore protection measures utilizing sandy beach can be established only when beach expansion is carried out on self sufficiency bases, that is to say, some measures must be developed to preserve shoreline through sediment supply from beaches themselves, probably from offshore sources. Controlling cross-shore sediment transport by a distorted ripple mat composed of precasted concrete blocks could be one of the hopeful measures to fulfill those demands, but no positive study seems to be carried out since the study by Innian et.al. (1972). In the present paper, effectiveness of the distorted ripple mat in stabilizing natural/artificial beaches has been studied by hydraulic experiments and numerical simulation.

### Methods of Experiments on Sediment Movement Velocity

Artificial ripples of fixed bed of different distortion as shown in **Figure 1** were set in two dimensional wave channel whose length, width and height is  $28m$ ,  $0.3m$  and  $0.5m$  respectively. The length of installation of fixed bed ripples was  $3m$  and the average water depth was  $27cm$ . The length and height of sinusoidal ripples in **Figure 1** was originally determined from the ripple dimensions of preliminary experiments with movable bed, in which standard waves of  $8cm$  in height and  $1.5$  sec. in period were acted on the horizontal movable bed composed of sediment  $0.16mm$  in median diameter (settling velocity  $W = 1.6cm/s$  at  $20^\circ C$ ). In the troughs of the fixed bed ripples shown in **Figure 1**, sediment of the same diameter as the movable bed experiments were placed with a certain volumes and the same waves were acted. After the wave action,

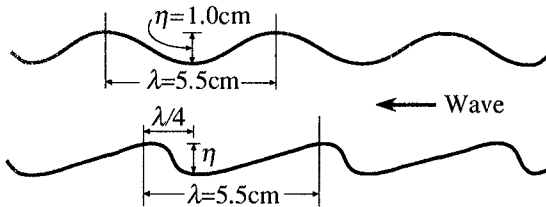


**Fig.1** Shape and scale of fixed bed ripples

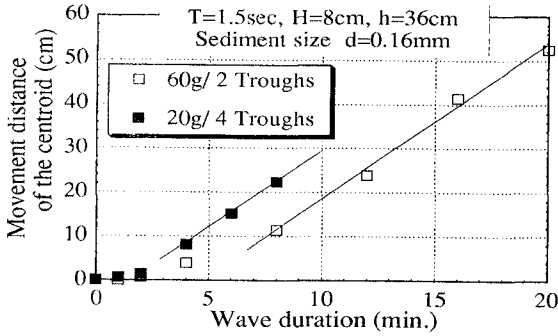


Fig.2 Movement of the centroid of sediment placed on the fixed bed ripples

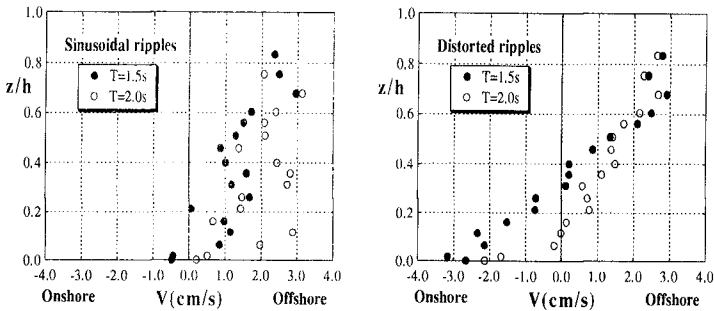


Fig.3 Vertical distribution of mean velocity for sinusoidal ripples and distorted ripples

sediment of each trough of ripples was sucked up by a nozzle and weighed by drying. From the change of horizontal distribution of sediment, movement of its centroid is obtained. As shown in **Figure 2** in which sediment movement is traced for sinusoidal ripples, the velocity of centroid movement becomes constant after a certain time of wave action and more time is required as the volume of sediment per one trough of ripples increases. The steady state of centroid movement is considered that the ratio of suspended part and settled part of sediment has attained equilibrium condition and thus the centroid movement velocity is nothing but the average movement velocity of suspended sediment. **Figure 3** shows the velocity profiles measured by a magnetic type current meter when waves of 8cm in height and 1.5 or 2.0 sec. in period are acted on sinusoidal ripples (Left) and distorted ripples (Right). It is seen that for distorted ripples, the mean velocity is onshoreward within the range of 0.2~0.3 of relative water depth above the bottom whereas it is mostly offshoreward in sinusoidal ripples. Distortion of ripples clearly creates onshore

current near the bottom and this feature could be utilized for controlling cross-shore sediment transport.

### Factors Affecting Cross-shore Sediment Transport

The velocity and direction of cross-shore sediment transport on fixed bed ripples may largely depend on the relative magnitude of vortices formed on the onshore/offshore side of a ripple. As shown in **Figure 4**, three factors are picked up as the dominant factors determining the relative magnitude of vortices, that is, the unsymmetry of wave crest height and trough depth  $S_1 = (H_c - H_b)/H$ , the tilt of wave profile  $S_2 = (L_R - L_F)/L$  (related to the bottom slope  $\tan \beta$ ), and the distortion of ripples  $S_3 = (\lambda_R - \lambda_F)/\lambda$  (negative in the figure). The mean velocity of sediment placed on the fixed bed ripples is considered to be expressed (Irie et al., 1993),

$$V_g^* = \sum a_i S_i \quad (i = 1, 2, 3) \tag{1}$$

where  $V_g^*$  is nondimensional form of the mean velocity of sediment movement  $V_g$  which is positive offshoreward, that is,  $V_g^* = (V_g/U_m)(W/U_m)(h/\eta)$  in which  $U_m$ ,  $W$ ,  $h$  and  $\eta$  are the maximum orbital velocity at the bottom, the settling velocity of sediment, the water depth and the height of ripples respectively. The coefficients  $a_1$ ,  $a_2$  and  $a_3$  are determined empirically through the experiments with fixed bed ripples by changing wave characteristics (for the wave height  $H = 8\text{cm}$ ,  $T = 1.0 \sim 2.0$  sec.), the bottom slope ( $0 \sim 1/15$ ) and the rate of distortion of ripples (for  $\lambda = 5.5\text{cm}$  and  $\eta = 1.0\text{cm}$ ,  $\lambda_R = 0 \sim \lambda/4$ ). According to the experiments,  $a_1 = 0.044$ ,  $a_2 = -0.028$  and  $a_3 = 0.033$ , respectively. **Figure 5** shows the correlation of the mean velocity of sediment movement  $V_g$  between hydraulic experiments and calculation using Eq.(1). As shown in the Figure, the correlation coefficient was 0.91, indicating satisfactory validity of the empirical equation.

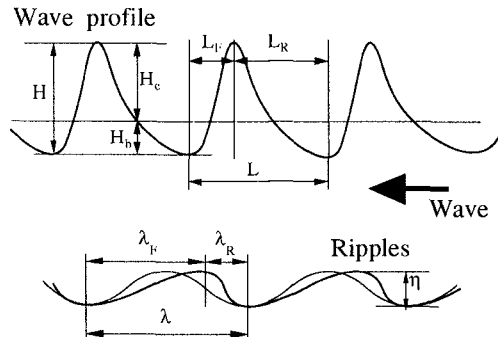


**Fig.4** Definition of dimensions

The criteria of onshore/offshore sediment movement when the distortion of fixed bed ripples is  $\lambda_R = \lambda/4$  ( $\lambda = 5.5\text{cm}, \eta = 1\text{cm}$ ) are examined by Monte Carlo Method using Eq.(1). **Figure 6** shows the result of calculation where the direction and extent of sediment movement are shown with respect to the bottom slope and relative wave height. The figure depicts that definite onshore sediment movement is expected if the relative wave height  $H/h$  is less than 0.5 (corresponding to the offshore zone) although it varies with the bottom slope  $\tan \beta$ .

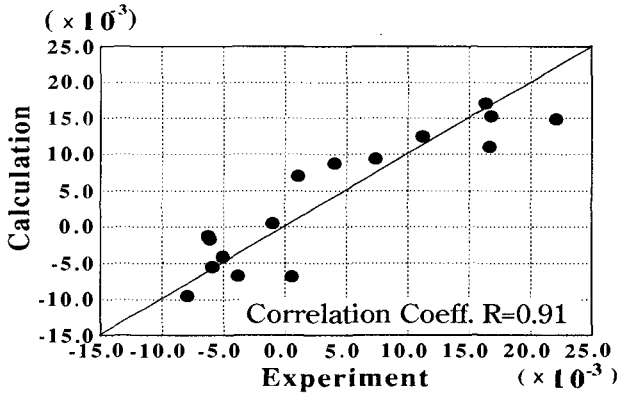


**Fig.5** Comparison of  $V_g/U_m$  between calculation and experiments

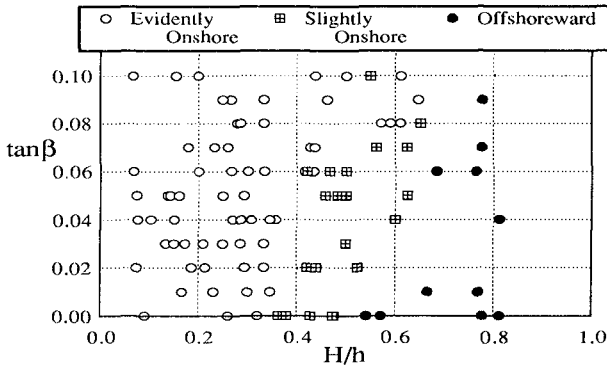


**Fig.6** Criteria of onshore movement

**Effectiveness of Distorted Ripple Mat**

A distorted ripple mat made by precasted concrete blocks is developed as shown in **Figure 7**. As shown in the figure, one end of a unit block is

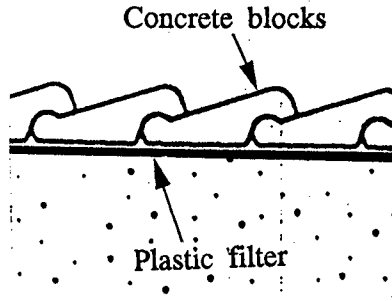


Fig.7 Distorted ripple mat

piled on the end of the other block and the plastic filter is stuck on the bottom face of the block, and thus it flexibly adapts itself to the change of movable bed and no settlement is expected. The surface profile of the distorted ripple mat is made to have the distortion characteristics of  $\lambda_R = \lambda/4$ , which corresponds to the maximum distortion in preserving strength of the concrete blocks. The effectiveness of the distorted mat in controlling cross-shore sediment transport is examined by movable bed experiments, where the distorted ripple mat was set in the offshore zone based on the results of **Figure 6**. **Figure 8** shows one result of small scale experiment carried out as the preliminary experiment in a wave flume 4m in length, 15cm in width and 20cm in height. The bed material used was glass beads with 0.08mm in diameter. After the action of waves of 2cm in height and 0.9 sec. in period, an equilibrium beach was formed and a distorted mat whose scale was almost 1/3 of the blocks shown in **Figure 7** was set in the offshore zone and waves were acted again. Sediment was supplied intermittently for beach fill at the location just onshore of the distorted mat. The distorted ripple mat checked the offshore sediment movement effectively, and most of the supplied sediment moved onshoreward and finally, as seen in the figure, a new beach is formed. **Figure 9** shows the medium scale experiment; the same scale as the experiments shown from **Figure 1** to **Figure 6**. An equilibrium beach was formed by acting waves of 8cm in height and 1.6 sec. in period on the initial each slope of 1/5 in the surf zone and 1/20 in the offshore zone. A distorted ripple mat was set in a limited range of the offshore as shown in the figure and waves were acted again. Sediment was supplied just onshore side of the distorted ripple mat. Movement of sediment can be more easily detected by spatially integrating bottom profile change onshoreward from the offshore point where no significant change takes place. The result of calculation of the present experiments is shown on the bottom of **Figure 9**. From the figure, the direction of net sediment movement on the distorted ripple mat is seen to be definitely onshoreward in spite of much sand

supply on the onshore side of it. Because of the strong effect of distorted ripple mat, the bottom is scoured just offshore side of the mat although a portion of scoured sediment is offshoreward which is considered to have caused because the initial profile was not completely in equilibrium.

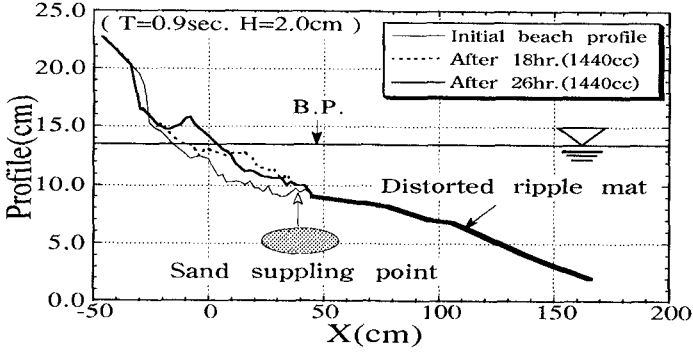


Fig.8 Beach fill by dumping (small scale experiments)

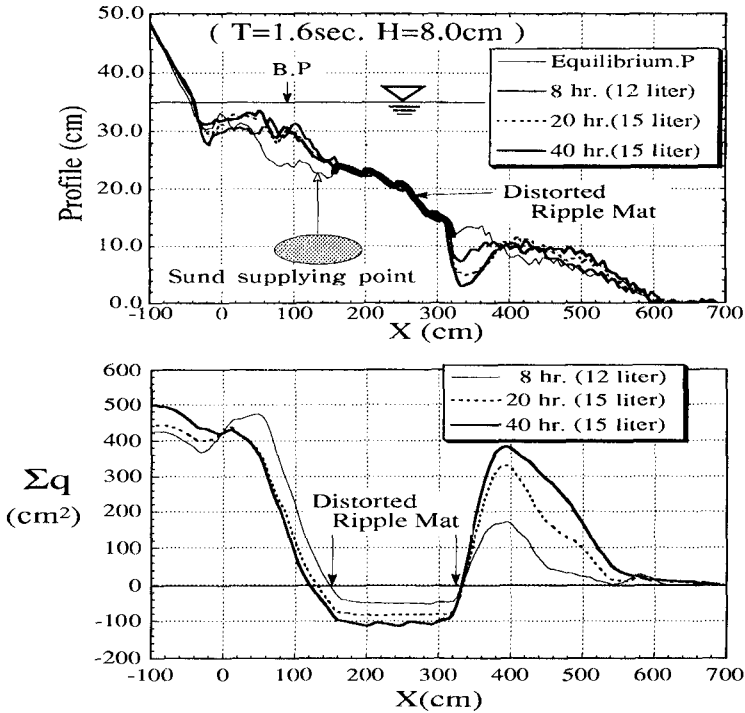


Fig.9 Beach fill by dumping (medium scale experiments)

## Reproduction by Numerical Calculation

A numerical model of beach profile change has been developed by taking consideration of the effects of ripple distortion on cross-shore sediment transport. In Eq.(1), the average velocity of sediment movement  $V_g$  on fixed bed ripples could be considered to represent also the velocity of suspended part of sediment on movable bed if the rate of distortion of ripples  $S_3$  is same as the one of movable bed. Thus the transport rate of suspended part of sediment in one pitch length of ripples can be obtained by multiplying  $V_g$  with the potential rate of sediment suspension. Here, we give;

$$QSS = \lambda \int C dz \quad (2)$$

$$VSG = V_g \quad (3)$$

where  $\lambda$  is the pitch length of ripples and  $C$  is the density of potential suspension of sediment at the height  $z$ . In the present study,  $C$  is obtained by the suspension formula by Skafel et.al.(1984). The important phenomena not included in the fixed bed ripples are the movement by bed shear at the surface of ripples on onshore and offshore phase of orbital velocity. As shown in **Figure 10**, sediment entrained by bed shear near the tips of ripples will be transported onshore or offshore up to the range of orbital length  $d_0$  and during this process, the entrained sediment will be partly enrolled in the rear vortices of ripples at a rate, say,  $R$  as shown by the shaded parts in the figure. The enrolled parts could be considered to contribute directly to suspended sediment whereas the rest of sediment will settle down on the bottom during half period. In finite amplitude waves, the characteristics of orbital velocity is different between onshore phase and offshore phase and thus the rate of bed shear transport is different between both phases. The rate of bed shear transport  $\Phi(t)$  is obtained from Madsen and Grant(1976) as follows:

$$\Phi(t) = 40\Psi^3(t) \quad (4)$$

where  $\Psi(t)$  is the Shields Number. In **Figure 10**, we define;

$QBO$  :Integration in space and time of sediment volume transported by bed shear and settled on the bottom on onshore phase (related to the rate of vortex enroll= $R$ )

$QBF$  :ditto but on offshore phase (also related to the rate of vortex enroll= $R$ )

**Figure 10** indicates that the centroids of  $QBO$ ,  $QBF$  and  $QSS$  have moved by the distance,  $XGL$ ,  $XGR$  and  $XBG$  in one period. Further we denote;

$VBG$  :Average movement velocity of ( $QBO + QBF$ )

$VT$  :Total average movement velocity of ( $QBO + QBF + QSS$ )

The following equation is formulated(Hashimoto et.al.,1993);

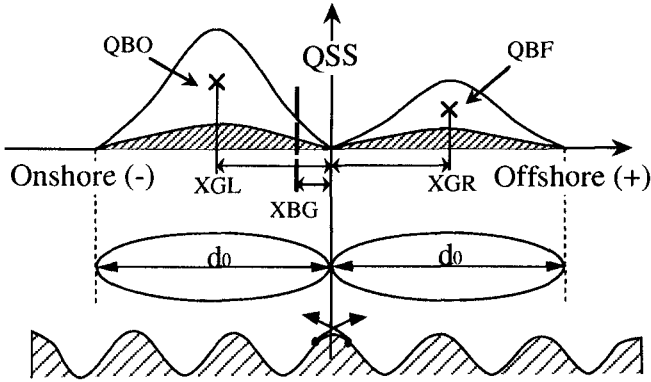


Fig.10 Onshore/Offshore sediment movement by bed shear

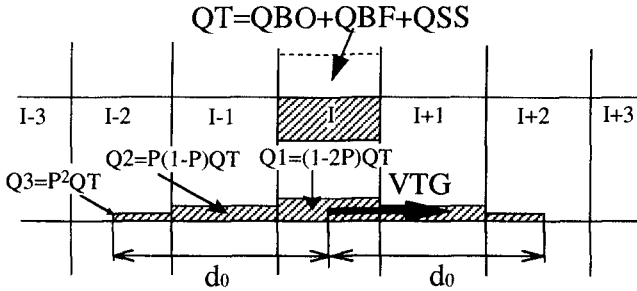


Fig.11 Movement and expansion of sediment in a ripple pitch length during one period of waves

$$(QBO + QBF + QSS) \times VT = (QBO + QBF) \times VBG + QSS \times VSG \quad (5)$$

Defining  $QT = QBO + QBF + QSS$ ,

$$VT = (QBO + QBF)/QT \times VBG + QSS/QT \times VSG \quad (6)$$

The total average movement velocity  $VT$  should be modified by the effect of gravity, that is, the local bottom slope  $\theta$ . Defining the modified velocity to be  $VTG$ ,

$$VTG = VT + J \cdot \sin \theta \quad (7)$$

where  $J$  is the empirical constant value.



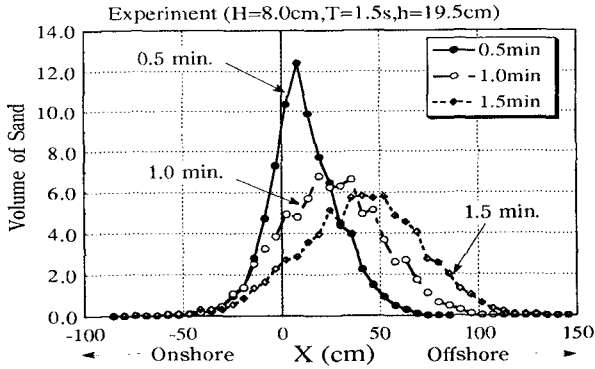


**Fig.12** Movement and expansion of sediment placed on the trough of sinusoidal ripples of fixed bed(experiment)

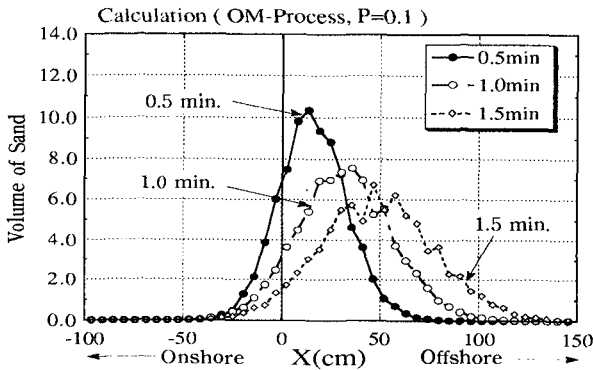


**Fig.13** Movement and expansion of sediment placed on the trough of sinusoidal ripples of fixed bed(calculation)

As shown in **Figure 11**, the total volume  $QT$  in one pitch length of ripples is considered to move with the modified velocity  $VTG$  and scattered at a rate  $P$  in the range of orbital length  $d_0$  during one period. Further, this movement in one pitch of ripples is assumed to take place at random throughout the profile and each ripple experiences only one time during one period. This idea enabled to calculate dispersion process of sediment due to wave action. **Figure 12** shows the scattering process of sediment placed on the trough of sinusoidal ripples of fixed bed (at  $X = 0$  in the figure) by wave action, and the results of numerical calculation in the same condition is shown in **Figure 13**. The rate of dispersion  $P$  was selected to be 0.1 empirically. The process of sediment dispersion seems to be reproduced satisfactory. Another important feature of

the present model is the adoption of equilibrium profile. Natural beaches could be considered to be in quasi-equilibrium on long term basis. Once the beaches experience a certain impact of change such as excavation or beach filling, the beach profile change will take place being governed by the hydraulic condition in equilibrium state. In the present study, the equilibrium condition is given by the following condition.

$$VTG = VT + J \cdot \sin \theta = 0 \tag{8}$$

Here, two empirical constant values, that is,  $R$  in definition of  $QBO$  and  $QBF$ , and  $J$  in Eq.(8) could be determined if another definitive equation is available in addition to Eq.(8). In the present study,  $R$  and  $J$  were determined by comparing the beach profile change calculated by substituting a trial value of  $R$  and  $J$  (on the condition that Eq.(8) is satisfied) with movable bed experiments. As shown in **Figure 14**, initial equilibrium profile is given from laboratory experiments.

$$Z = 0.184X^{0.81} \tag{9}$$

The horizontal axis is divided into average ripple pitch length and sediment movement only in the offshore zone is calculated.

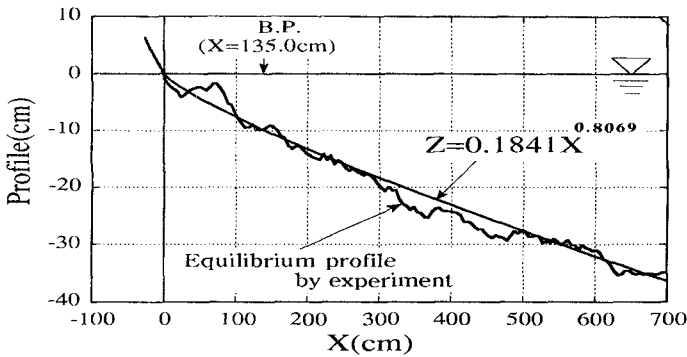


**Fig.14** Equilibrium profile used as the initial condition

**Effectiveness of Distorted Ripple Mat by Numerical Calculation**

Effectiveness of distorted ripple mat is reproduced by numerical model explained above. **Figure 15** shows the idea in calculation. Suppose the original beach profile is  $AFBC$  in the figure. We consider the case when the profile is partly excavated as  $AFGH$  and calculate resulting change of profile. We

secondly calculate the change of profile when most steep part  $FG$  is protected by the distorted ripple mat. This calculation would also correspond to the case when the original beach  $AFBC$  is filled to form  $ADEBC$ , that is to say, the beach fill is cut at half way  $E \sim B$  and thus it is examined whether or not the filled beach can be preserved by the distorted ripple mat. The results of calculation are compared with experiments and actual initial profile and excavation section are shown in **Figure 16**.

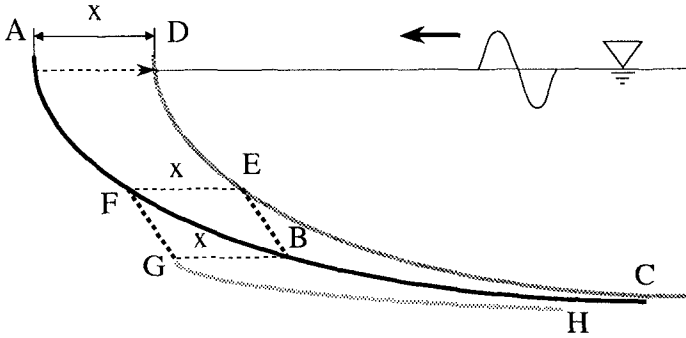


**Fig.15** Conception showing that beach cut  $AFGH$  is virtually same as beach fill  $ADEBC$

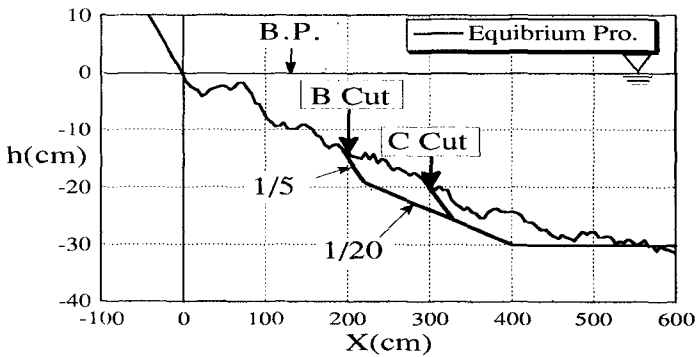


**Fig.16** Method of beach cut

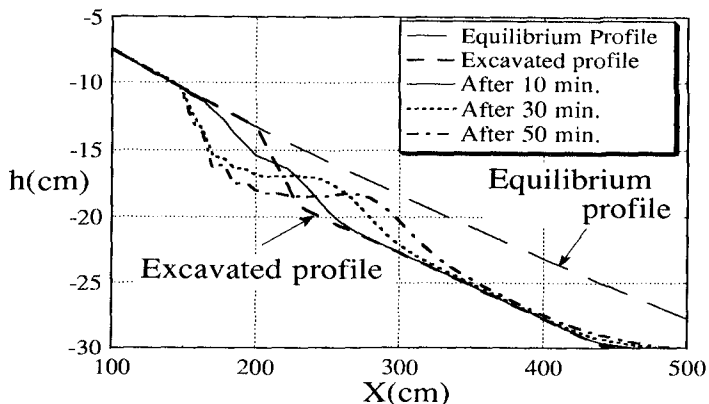


Fig.17 Deformation of the slope by calculation without distorted ripple mat

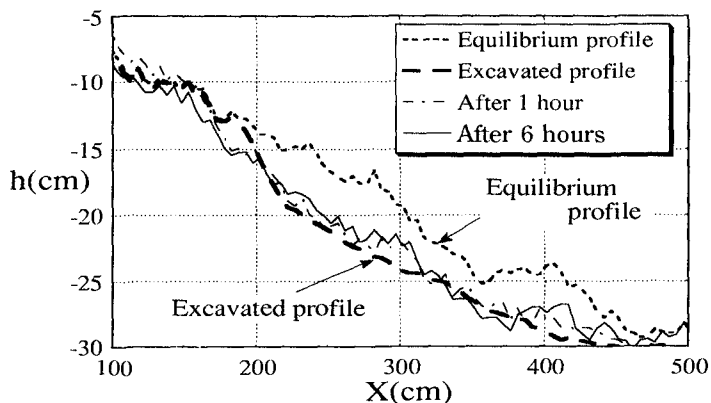


Fig.18 Deformation of the slope by experiments without distorted ripple mat

Figure 17 is the result of calculation when steep slope face is not protected and Figure 18 is the result of experiments. The steep face is rapidly collapsed by wave action in both cases. Figure 19 and 20 show the result when the steep slope is protected by the distorted ripple mat for the case of calculation and experiments respectively. The initial profile is seen to be almost preserved even after 3 ~ 4 hours of wave action for both cases. This is because offshore sediment movement is checked by the distorted ripple mat and only the local minor change took place.

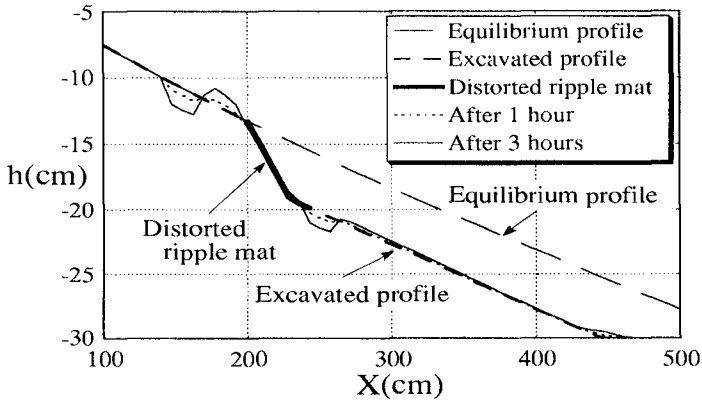


Fig.19 Stabilized slope by calculation with distorted ripple mat

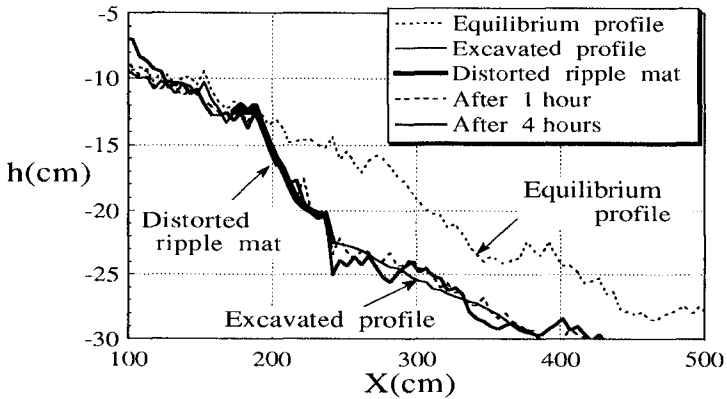


Fig.20 Stabilized slope by experiments with distorted ripple mat

## Conclusions

Three factors, that is, the unsymmetry of wave crest height and trough depth, the distortion of wave profile and the distortion of ripples are the dominant factors affecting cross-shore sediment transport on fixed bed ripples. In the present distortion of ripples, definite onshore sediment movement is expected if the relative wave height  $H/h$  is less than 0.5, depicting that the distorted ripple mat is effective only in the offshore zone. The effectiveness of the distorted ripple mat is confirmed by both experiments with movable bed and numerical calculation.

## References

- Goda, Y. (1964): Wave forces on a vertical circular cylinder, experiments and proposed method of wave force computation, Rept. of PHRI, No. 8, 74p
- Inman, D.L. and E.B. Tunstall (1972): Phase dependent roughness control of sand movement, Proc. 13th ICCE, pp. 1155-1171
- Irie, I., N. Ono, K. Murakami, S. Hashimoto and S. Nakamura (1993): Control of cross-shore sediment transport by a distorted ripple mat, Proc. of 40th Japanese Conf. on Coastal Eng., JSCE, pp. 561-565 (in Japanese)
- Hashimoto, S., I. Irie, K. Murakami, N. Ono and H. Kojima, (1993): Numerical calculation of beach profile change by Monte Carlo Method, Proc. of 40th Japanese Conf. on Coastal Eng., JSCE, pp. 366-370 (in Japanese)
- Madsen, O.S., and W.D. Grant (1976): Quantitative description of sediment transport by wave, Proc. 15th Coastal Eng. Conf., ASCE, pp. 1093-1112
- Skafel, M.G. and B.G. Krishnappan (1984): Suspended sediment distribution in wave field, J. of Waterway, Port, Coastal and Ocean Eng., ASCE, Vol. 110, No. 2, pp. 215-230

## CHAPTER 151

### HOW MUCH VELOCITY INFORMATION IS NECESSARY TO PREDICT SEDIMENT SUSPENSION IN THE SURF ZONE?

Bruce E. Jaffe<sup>1</sup>, David M. Rubin<sup>1</sup>, and Asbury Sallenger, Jr.<sup>2</sup>

#### ABSTRACT

The time-dependent response of sediment suspension to water velocity was explored by modeling field measurements collected in the surf zone during a large storm. Both linear and nonlinear input-output models were formulated with water velocity as input and suspended-sediment concentration as output. A sequence of past velocities (velocity history), in addition to velocity from the same instant as the measurement of suspended-sediment concentration, were used as input. The velocity-history length was allowed to vary. The models also incorporated a lag between input (instantaneous velocity or velocity history) and output (suspended-sediment concentration).

Instantaneous horizontal water velocity, or velocity to a power, does not contain enough information to predict suspension in the surf zone. Unlike steady uniform flow, more than one velocity is necessary to parameterize pick-up and mixing of sediment into the water column. Using a velocity history improves predictions of suspension by more fully specifying flow conditions (including accelerations and changes in accelerations) responsible for suspension.

Suspension in the future is better predicted than suspension at the same instant as velocity measurements. Incorporating such a lag between velocity and concentration improved predictions, with optimum lag time increasing with elevation above the sea bed (from 1.5 seconds at 13 cm to 8.5 seconds at 60 cm for linear models). These lags are largely due to the time for an observed flow event to effect the bed and mix sediment upward.

Nonlinear models relating suspension to velocity do better than linear models using the same velocity history. Nonlinear models are able to exploit changing relationships between suspension and velocity history for different wave shapes. For the environmental conditions of our study, the optimal model (correlation coefficient of 0.58) used 3 seconds of velocity history (approximately one-quarter wave period) and a 1.5 second lag to predict suspension.

---

<sup>1</sup> U. S. Geological Survey, 345 Middlefield Rd., Menlo Park, CA 94025

<sup>2</sup> US Geological Survey, Center for Coastal Geology, 600 4th St. South, St. Petersburg, FL 33701

## INTRODUCTION

Models for sediment suspension in the surf zone are based on models developed for streams and the continental shelf. Additions of time-varying pick-up and mixing of sediment into the water have been the major changes to fluvial or continental shelf models to make them usable in the surf zone. For stream flow, a mean velocity (raised to a power) is used to determine the steady driving force for suspension. Two velocities, a mean velocity and a maximum orbital velocity, are used to determine the forcing for suspension in continental shelf sediment transport models (Smith, 1977; Grant and Madsen, 1979; Glenn and Grant, 1987). It is not obvious how much velocity information is necessary to predict suspension in the surf zone or if velocity alone is a good predictor for suspension.

There are many complexities that make it difficult to use first principles of physics to formulate models for sediment suspension. For example, it is not obvious how to model suspension in a reversing flow with velocity asymmetries caused by irregular waves. In this paper, we use a method developed by researchers studying nonlinear systems, input-output modeling, to determine which velocity information is important to predict sediment suspension. The goal of this study is to guide us in formulation of improved models.

## METHODS

The ability to predict sediment suspension from flow velocity was evaluated using input-output modeling of field measurements. Input-output modeling, employing one time series of forcing input and a simultaneous series of output response, has been described by Hunter and Theiler (1992). In this study, input is a single near-bed flow velocity or a sequence of velocities (velocity history) and output is suspended-sediment concentration.

The techniques applied in this paper are based on techniques that have been developed recently for forecasting nonlinear, nonperiodic, time series and spatial patterns (Livezey and A. G. Barnston, 1988; Farmer and Sidorowich, 1989; Sugihara and May, 1990; Casdagli, 1991; Casdagli et al., 1992; Rubin, 1992). The procedure requires splitting a time series into two parts. One part, the learning set, is used to learn the relations between input and output variables. The other part of the time series, the testing set, is used to test the predictive ability of relations determined from the learning set. Predictions are made by searching the learning set for conditions where the recent velocity history approximates the velocity history of a predictee from the testing set, and then using the concentration response of these nearest neighbors in the learning set to predict the concentration of the predictee. The general approach is outlined below; details of the computational algorithm are given by Casdagli (1991) and Rubin (1992).

The approach in this study is to relate concentration  $C$  to a sequence of velocities ( $U_t^n$  through  $U_{t+1-m}^n$ ) in the learning set by solving

$$C_t = a_0 + \sum_{i=1}^m a_i U_{t+1-i}^n \quad (1)$$

where  $m$  is the number of velocity measurements that are used to predict each  $C$ ,  $n$  is an integer, and  $t$  is time.



Eq (1) can be used for both linear and nonlinear modeling. For linear models,  $a_0$  through  $a_m$  are evaluated a single time for the entire learning set. The values of  $a_0$  through  $a_m$  are then substituted in eq (1), and each predictee velocity sequence from the testing set is substituted in eq (1) to predict concentration. The resulting model is a global, linear, multiple regression.

For nonlinear models,  $a_0$  through  $a_m$  are re-evaluated for each prediction using a subset of observations in the learning set. To solve eq (1) requires a minimum of  $m+1$  observations from the learning set, but any greater number of observations can be used. For each solution, the  $k$  observations that are most similar to each predictee sequence are used to solve eq (1). For example, if concentration is being related to a sequence of 2 successive velocity measurements, then to make a single nonlinear prediction, the entire learning set is searched to find the 3 sequences of 2 successive velocities that are closest to the predictee sequence. Eq (1) is used to solve for  $a_0$  through  $a_2$  using these 3 nearest-neighbor velocity sequences and the 3 corresponding observed concentrations in the learning set. Those values of  $a_0 \dots a_2$  and the velocities of the predictee sequence are then substituted in eq (1) to predict concentration.

Closeness of sequences is measured using least squares, and those sequences that are most similar to the predictee sequence are known as nearest neighbors. Ranking of neighbors can be visualized in two ways: (1) similarity of velocity sequences in a time series or (2) distance in velocity space. Determination of nearest neighbors can be visualized as matching a segment of velocity time series by sliding a  $m$ -point window through the time series (Fig. 1a). The most similar velocity sequences (evaluated by the squared differences between individual points in the two sequences) are defined to be the nearest neighbors. Alternately, nearest neighbors can be visualized by plotting each velocity sequences as a single point in velocity space. For a two-point sequence, the axes of velocity space are the two successive velocities (Fig. 1b). The nearest neighbor to a velocity sequence (represented as a single point) is the nearest point. Note this is computationally equivalent to the squared difference in individual dimensions. The three nearest neighbors to point A in Figure 1b are points B, C, and D.

Because  $a_0$  through  $a_m$  are re-evaluated for each prediction in nonlinear modeling, nonlinear relations between concentration and velocity can be learned and exploited for forecasting, even though eq (1) is purely linear. The advantage of using a small subset of observations (or small neighborhood) in the learning set is that the nonlinear structure of the data can be approximated most precisely using small linear pieces; the resulting model (called a local linear model) is thus more sensitive to the specific flow conditions (Fig. 2a). In contrast, the advantage of using all the observations in the learning set (a global model) is that noise reduction is greater (Fig. 2b). In the present study, we know that sediment response to forcing by velocity is nonlinear but are using the forecasting technique to learn if the system is noise-free enough that nonlinear models outperform linear models and if the nonlinearity is more complicated than  $U^n$  or  $|U|^n$ .

In addition to varying the number of nearest neighbors used to make forecasts, we can vary the number of velocity measurements (velocity history) used to predict each concentration. This velocity history can be as low as 1 point (where instantaneous concentration is related only to the simultaneously observed velocity), but increasing the velocity history to values greater than 1 can improve modeling accuracy in several ways. First, additional dynamic properties of the forcing flow can be identified. For example, with a single velocity observation, only velocity is known; with a second sequential velocity observation, acceleration can also be determined; and with a longer sequence of velocity measurements, wave shape can be identified.

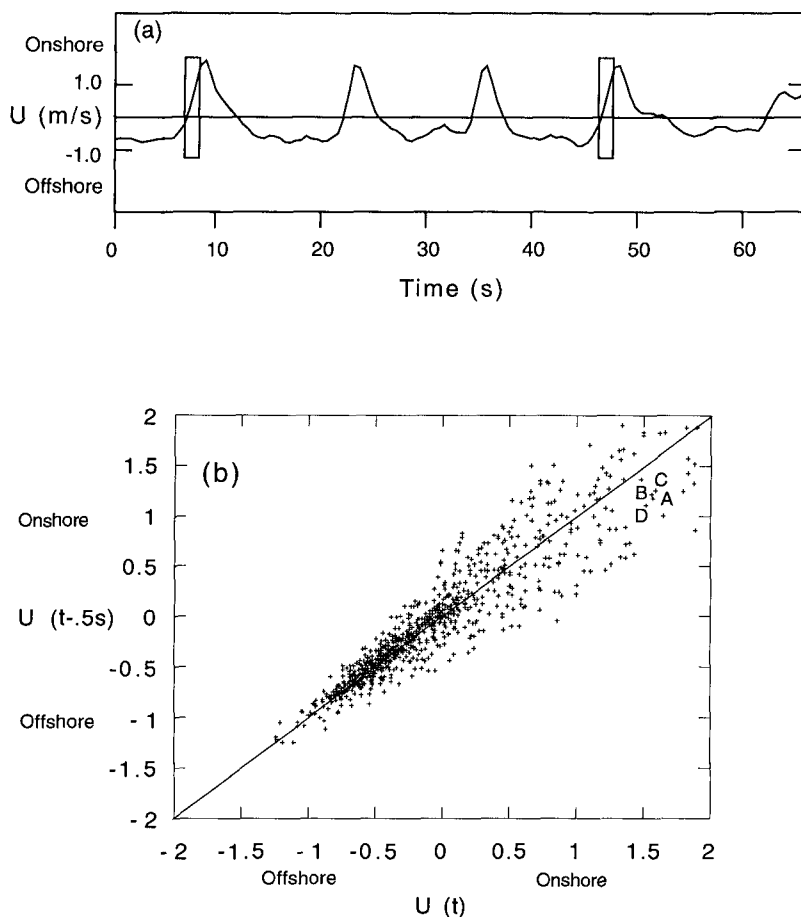


Figure 1. Two methods of visualizing selection of nearest neighbors. (a) Sliding a window the width of the velocity sequence through a time series to select similar sequences. (b) Distance in velocity space. In this case a two point sequence can be represented by a single point having coordinates given by velocity and velocity from the previous time step. The nearest neighbors to point A are points B, C, D. In both cases, the difference between sequences (a) or the distance between neighbors (b) is defined by  $\sum_{i=1}^m (U_{t+1-i} - U_{t_s+1-i})^2$ , where  $m$  is the number of points in the velocity sequence,  $U$  is the velocity in the testing set,  $U_l$  is the velocity in the learning set, and  $t$  and  $t_s$  are the times of the last point in the velocity sequences in the testing and learning set, respectively.

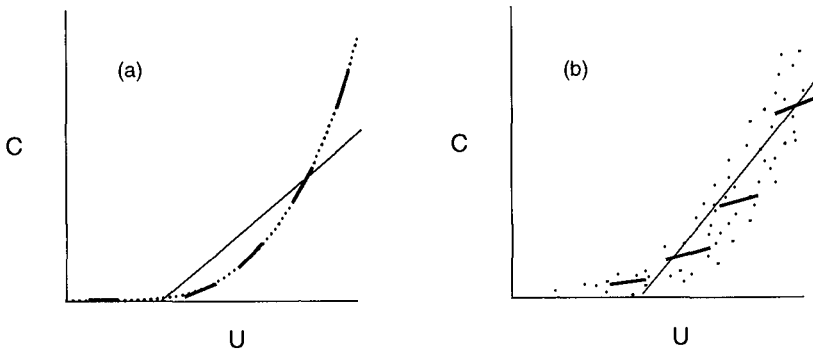


Figure 2. Comparison of modeling results for hypothetical steady flow transport data. Dots are data points; light lines are global linear model predictions; dark lines are local linear model predictions. For noise-free data (a), local linear models can learn the nonlinear relation between concentration,  $C$ , and velocity,  $U$ , by looking at local pieces of the curve, thereby outperforming a global linear model. For example, a threshold velocity for suspension can be predicted by a local linear model. For noisy data (b), the global linear model outperforms local linear models because of the greater noise reducing capability of the global model. These examples are based on one-dimensional models (concentration is predicted from a single value of velocity). In the case of surf-zone transport, concentration is predicted from a sequence of velocities, and the relations can not be displayed as easily. Instead, the capability of each model is quantified by the correlation coefficient for the predictions.

Second, because of the time required for settling to occur, concentration in a decelerating flow depends on previous velocities (those that caused suspension of sediment that has not yet had time to fall to the bed). If the velocity history used to predict concentration is extended too far into the past, however, forecasts become degraded because the early velocities have increasingly little relevance to the later concentration.

In applying these forecasting techniques, a large number of models are evaluated, each employing a different number of nearest neighbors  $k$ , a different number of velocity measurements  $m$  used for each forecast, a different exponent of the velocity  $n$ , or a different time from the end of the velocity sequence to the time for which concentration is forecast (lag). The models are evaluated by the correlation coefficient between predicted and observed concentrations.

## FIELD EXPERIMENT

Sediment suspension was measured during a large cooperative field experiment investigating the morphologic response of the nearshore to storms conducted at the U. S. Army Corps of Engineers Field Research Facility (FRF) at Duck, North Carolina (see Mason et al., 1984, for a description of the experiment). The FRF is located on a long straight beach with well-sorted fine sand ( $\sim 0.15$  mm median diameter) in the offshore.

As part of this experiment, the U. S. Geological Survey deployed an underwater sea sled (Sallenger et al., 1983) equipped with instruments to measure

waves, currents, sediment suspension, and profile change. Waves were measured using a pressure sensor and horizontal currents were measured at 3 elevations (0.5, 1.0, and 1.75 m above the bed) using 2.5-cm-diameter electromagnetic current meters. Suspended-sediment concentration was measured at 5 elevations (0.10, 0.13, 0.19, 0.31, and 0.61 m above the bed) using optical backscatter sensors (OBS, Downing et al., 1981). The nearshore profile was measured using an infrared range-finder sighting on prisms mounted on a 10 m mast as the sled was pulled offshore and onshore by a winch and lines and a system of blocks. The sled was moved to measurement locations where 34.1 minutes of data were collected at 2 Hz from each sensor.

## RESULTS AND DISCUSSION

Data reported in this paper were collected at one mid-surf-zone station, 100 m offshore, during the waning stages of a large extra-tropical cyclone on October 13, 1982. Offshore significant wave height was 1.6 m, and peak period was 12 s during data collection. Significant wave height at the measurement location was 1.7 m (water depth of 3.6 m). Mean currents at 0.5 m above the sea bed were directed obliquely offshore, with a 0.11 m/s cross-shore component and a 0.12 m/s longshore component. Significant orbital velocities at 0.5 m above the bed were 0.85 m/s in the cross-shore direction and 0.36 in the longshore direction. Waves were asymmetrical, with stronger, short-duration onshore flows and weaker, longer-duration offshore flows. Maximum cross-shore velocity was 2.12 m/s, directed onshore. The bed configuration was calculated to be within the planar-bed regime of Komar and Miller (1975).

### *Using instantaneous velocity to predict suspension*

A time series of suspension and horizontal water velocity (Fig. 3) shows intense suspension (referred to as suspension events by Downing, 1983; Jaffe and Sallenger, 1992) occurs irregularly. A scatter plot of concentration 19 cm above the sea bed versus cross-shore velocity (squared, to remove the sign and to make the relation between flow and concentration more in agreement with what is known for steady flow) 50 cm above the sea bed shows a lack of correlation between suspended sediment concentration and instantaneous velocity (Fig. 4). High concentrations can occur at zero velocity because sediment suspended earlier has not yet settled. Low concentrations can occur at high velocities because sediment suspended at the bed has not yet mixed high enough into the water column to reach the elevation of the sensor. The correlation between instantaneous concentration and cross-shore velocity squared is very poor, with a correlation coefficient of -0.02. Correlations between the instantaneous concentration and velocity to a higher power are also poor (Fig. 5). Other instantaneous velocity measures, longshore velocity or speed, are also poor predictors of suspension (Jaffe and Rubin, in preparation; Jaffe, 1993). More than instantaneous velocity is needed to predict sediment suspension.

### *Acceleration as a Predictor for Suspension*

Acceleration/deceleration effects on bottom turbulence have been observed by other researchers. Increased turbulence during flow deceleration was observed by Schubauer and Skramstad (1947) in the laboratory. Gordon (1975) found increased Reynolds stresses during deceleration in tidal flow (Fig. 6). Hanes and Huntley (1986) and Osborne and Greenwood (1993) measured increasing suspension during

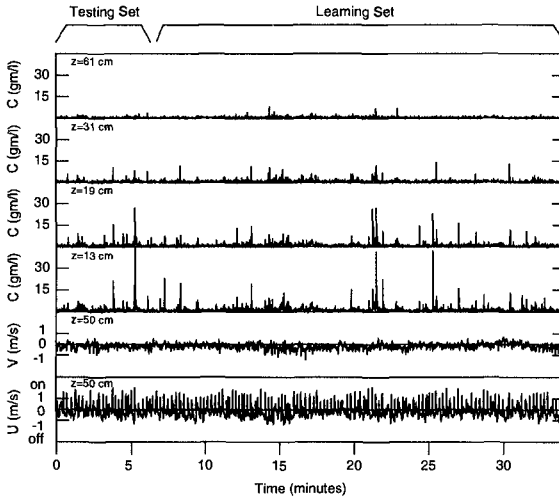


Figure 3. Time series of cross-shore velocity ( $U$ ) and longshore velocity ( $V$ ) at 50 cm above the sea bed, and suspended sediment concentrations ( $C$ ) at 4 elevations above the sea bed (13, 19, 31, and 61 cm above the sea bed). For this time series, the testing set used in the modeling is the first 6.66 minutes (800 points) of the time series. The learning set is the measurements from 6.66 minutes to 34.1 minutes (3295 points). Intensity of suspension decreases with elevation above the bed. Note the short-lived periods of intense suspension (suspension events) throughout the record.

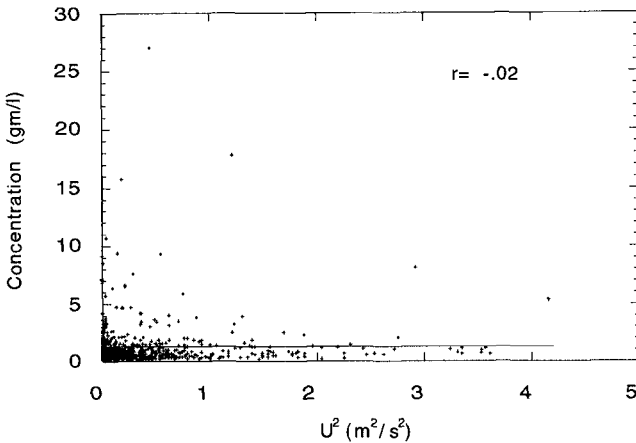


Figure 4. Scatter plot of concentration at 19 cm above the sea bed versus the cross-shore velocity squared at 50 cm above the sea bed. The correlation coefficient for a linear regression (global model) is -0.02. Note the high concentrations occurring at low velocities.

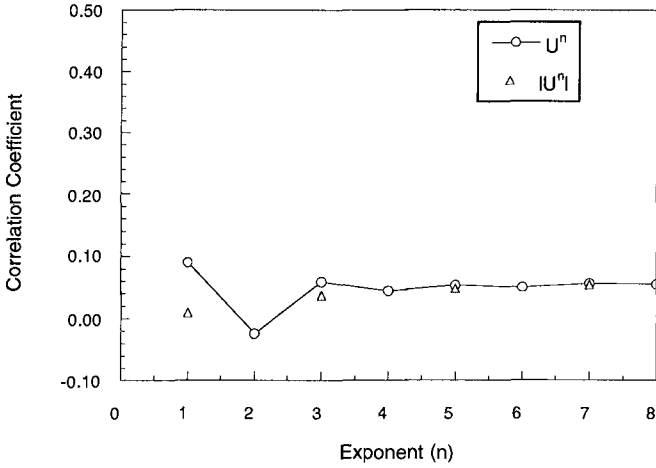


Figure 5. Correlation coefficient versus exponent of velocity. Correlation coefficients are for a linear model using instantaneous velocity raised to a power to predict concentration at 19 cm above the bed. The velocity and absolute value of velocity raised to a power are plotted for odd powers. Linear models using instantaneous velocity as input are not able to predict concentration well.

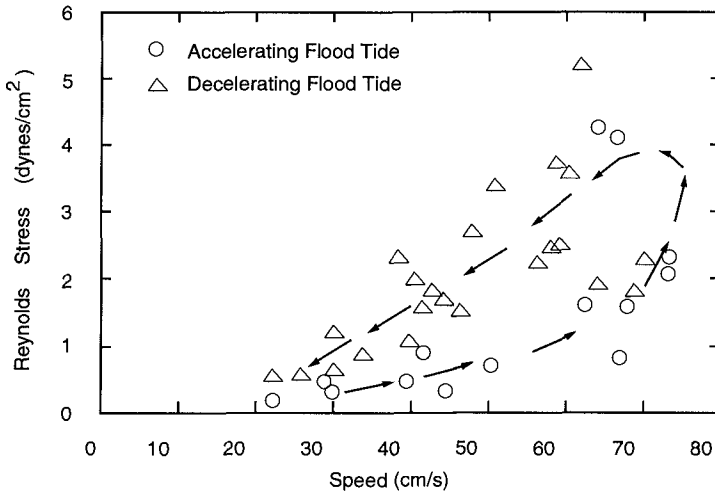


Figure 6. Reynolds stress versus flow speed for flood tidal flows. Note that stresses are greater during decelerating flow than accelerating flow for the same speed. Figure from Gordon, 1975.

flow deceleration over bedforms. Conley and Inman (1992) found sediment pluming events (in which sediment was lifted on the order of 10 cm into the water column) occurred during the decelerating phase of some waves over plane beds (Fig. 7).

We tested to determine if suspension was correlated with instantaneous acceleration. Sediment concentration was not well correlated ( $r=0.12$ ) with acceleration at the same instant (Fig. 8). Higher concentrations tended to occur during decelerating flow than accelerating flow. Onshore accelerating flows tended to have higher concentrations than offshore accelerating flows. Highest concentrations occurred during decelerating onshore flows under the wave crest. High concentrations also occurred at low accelerations and after flow reversals. Similar to instantaneous velocity, instantaneous acceleration was a poor predictor for suspension. However, the tendency for higher concentrations during flow deceleration indicates that it is important to include acceleration in the input for a model of sediment suspension.

#### *Using a Sequence of Velocities to Predict Suspension*

A velocity history contains more information about the state of the flow (and possibly about forces causing suspension) than a single velocity. In the previous two sections, instantaneous velocity and acceleration were found to be poorly correlated with suspension. More information is contained if two velocity points are used to define the flow (Fig. 1b). For example, a two-point velocity sequence contains information about magnitude and direction of instantaneous velocity and magnitude and sign of acceleration. Seven different flow regimes can be delineated by regions in a velocity space plot of a two-point velocity sequence (Fig. 9a). The diagonal line in Figures 1b and 9a indicate no accelerations; points off this line indicate either accelerating or decelerating flow. Contours of concentration plotted in two-point velocity space (instantaneous velocity and velocity 0.5 seconds earlier) are ordered and show that high concentrations occurred for some sequences of two velocities (Fig. 9b). For example, high concentrations occurred for decelerating strong onshore flows (A in Fig. 9b).

Longer velocity histories give information about persistence of strong flows, acceleration history, flow reversals, and wave shape, all of which could be important in predicting suspension. A representative time series of cross-shore velocity (Fig. 10) illustrates how irregular waves have different velocity sequences even where instantaneous velocities and accelerations are similar.

To test whether more information about suspension is contained in earlier flows, differing lengths of velocity histories were used as input to models. Correlations increased as more velocity history was included to relate velocity to suspension until reaching a maximum of 0.42 at a velocity history length of about one wave period. Correlation coefficients for nonlinear models were maximum (0.48) at about one-half wave period of velocity history (Jaffe and Rubin, in preparation; Jaffe, 1993). The increase in predictability primarily results from a more complete description of flow conditions causing suspension. Improved predictions were also the result, in part, of including a lag effect.

#### *Lag between Velocity and Suspension*

Because modeled concentration was measured 19 cm above the sea bed, a lag between the flow inducing suspension and the concentration response would be expected (to allow time for sediment to be carried up into the water column). Models incorporating such a lag performed better than models that did not. For a linear

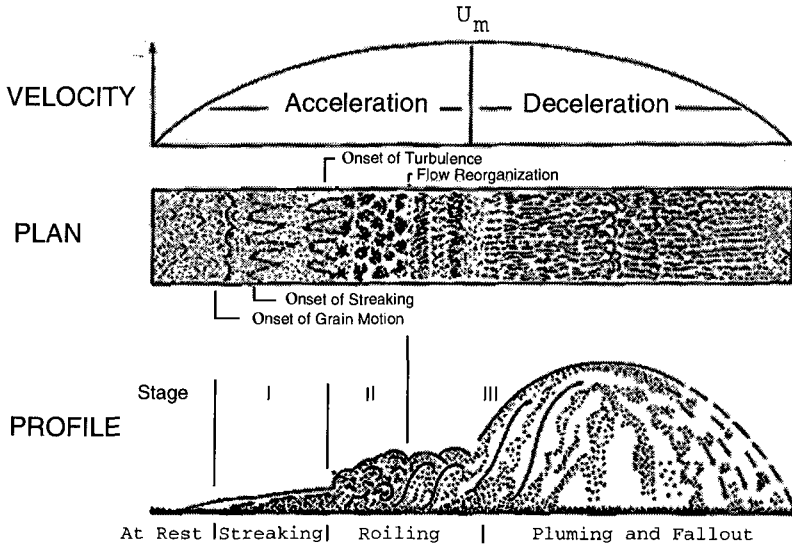


Figure 7. Sediment plume rising above the bed during decelerating flow under a wave crest. Figure from Conley and Inman, 1992.

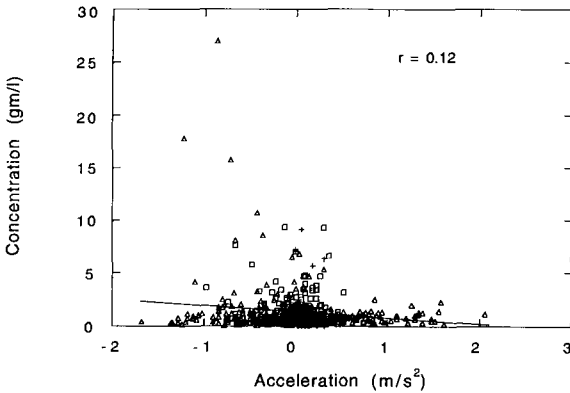


Figure 8. Concentration at 19 cm above the bed versus cross-shore flow acceleration. Triangles are onshore flows; squares are offshore flows; crosses are for periods where flow reversed. Highest concentrations occurred during decelerating (negative sign) onshore flows.



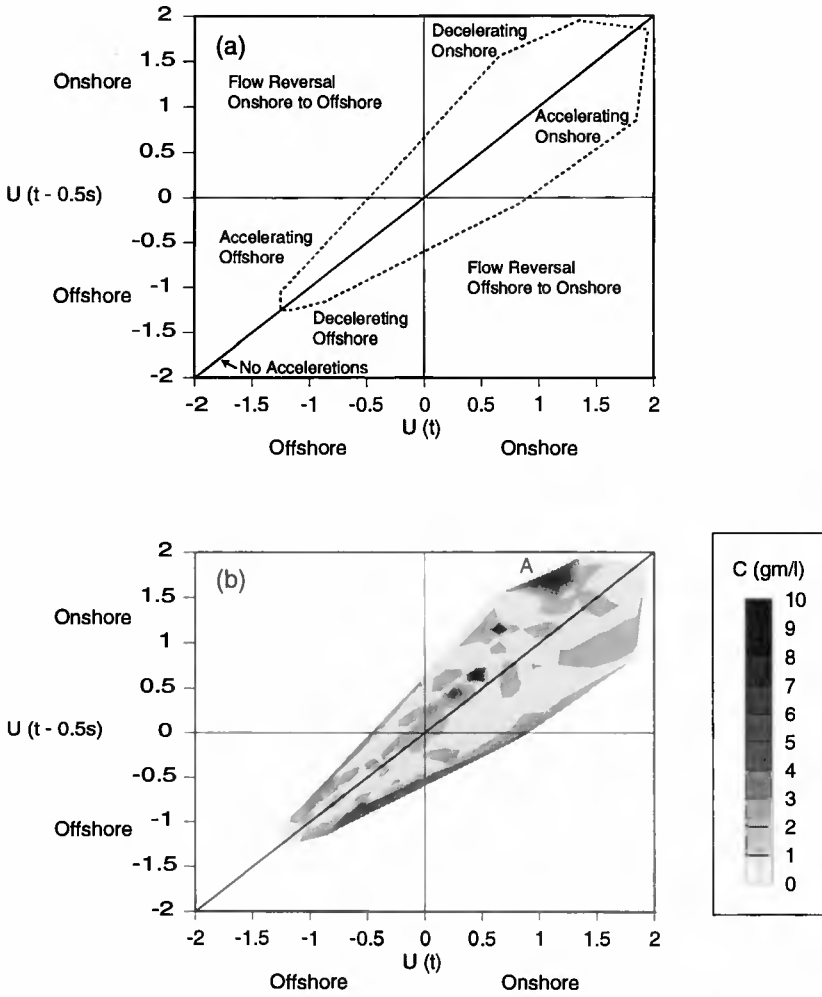


Figure 9. (a) Seven different flow regimes in a velocity space plot of a two-point velocity sequence (b) Concentration contours plotted in velocity space (instantaneous velocity and velocity from the previous time step). See Figure 1b for data density. High concentrations occurred for decelerating strong onshore flows (e.g., point A).

model with instantaneous cross-shore velocity squared as input, peak performance was obtained using velocity to predict concentration 1.5 seconds later (Fig. 11). This lag increased with elevation above the bed, increasing to 8.5 seconds at 61 cm above the bed (Jaffe and Rubin, in preparation; Jaffe, 1993). Nonlinear models and models using a velocity history also performed better when including a lag. An additional cause for a lag would be a sediment pick-up response lagging the velocity. This could occur if turbulence at the sea bed took time to build or its structure changed with time (e.g., response to flow reversal).

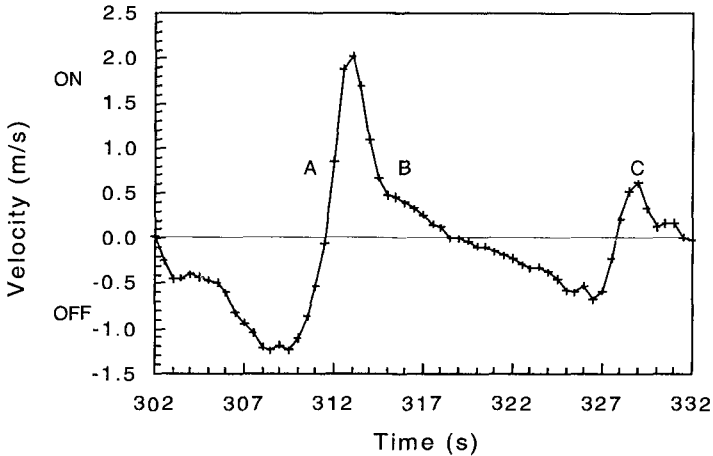


Figure 10. Time series of cross-shore velocity at about 300 s into the record (Fig. 3) illustrating why a velocity history is necessary to fully specify flow conditions. Points A, B, and C have similar instantaneous velocities, but different accelerations and are preceded by different velocities.

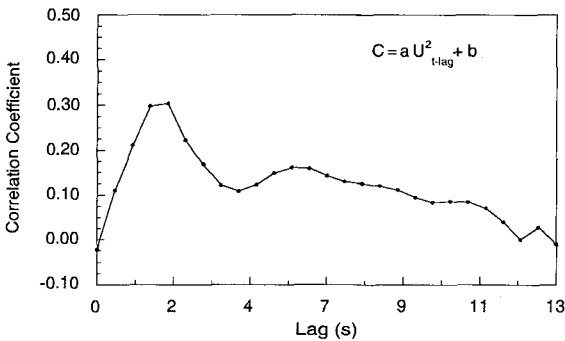


Figure 11. Correlation coefficient versus lag time between input (a single cross-shore velocity squared) and output (concentration 19 cm above the sea bed). A positive lag is concentration later than velocity. Models perform better when a lag time is included primarily because they account for the time it takes to mix sediment up into the water column.

*Best model*

Incorporating lag and velocity history into a nonlinear model gave the best predictions for suspension. Addition of nonlinearity allows differing relationships between velocity and concentrations for different velocity sequences (e.g., flow under differing wave shapes). The optimal model (correlation coefficient of 0.58) used 3 seconds of velocity history (approximately one-quarter wave period) and a 1.5 second lag to predict suspension. This nonlinear model was able to predict the suspension event at 312 seconds (Fig. 12). Just as important, suspension events were not predicted for waves between 320 and 350 seconds.

Mean concentration and cross-shore suspended sediment flux were well predicted by this model. Observed and predicted mean concentration was 1.12 and 1.11 gm/l, respectively. Observed and predicted cross-shore flux at 19 cm above the bed was 37.1 and 34.3 gm/m<sup>2</sup>/s onshore, respectively. The good agreement between predicted and observed flux was largely due to good predictions for high concentration. Low concentrations were not predicted as well; but, because their phasing relative to the wave orbital velocity is more random than high concentrations (Jaffe and Sallenger, 1992), errors in predictions were diminished by fluxes in opposite directions canceling resulting in a low contribution to net flux.

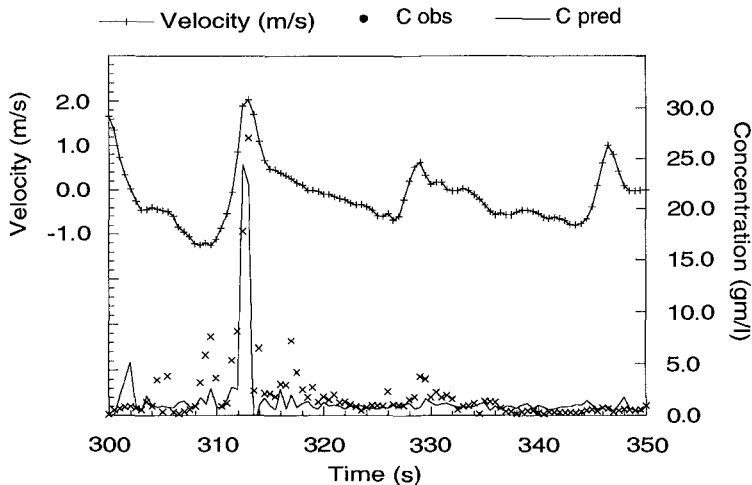


Figure 12. Time series of cross-shore velocity 50 cm above the sea bed and predicted and observed suspended sediment concentration 19 cm above the sea bed. Concentrations were predicted using the best model found through exploratory modeling, a local linear model with an input of 3 seconds of velocity squared, decimated to one point every 1.5 seconds, and a time lag of 1.5 seconds. This nonlinear model was able to predict high concentrations that occurred at 310 seconds into the record. Intermediate concentrations before and after highest concentrations are not well predicted. Correlation coefficient for 794 predicted/observed values is 0.58.

## CONCLUSIONS

- (1) Instantaneous horizontal water velocity, or velocity to a power, does not contain enough information to predict suspension in the surf zone. Unlike steady uniform flow, more than one velocity is necessary to parameterize the pick-up and mixing of sediment into the water column.
- (2) Instantaneous acceleration predicts suspension better than instantaneous velocity, but neither of the instantaneous models performs as well as models using a sequence of velocities. A sequence of past velocities (a velocity history) improves predictions of suspension by more fully specifying flow conditions (including accelerations and changes in accelerations) responsible for suspension.
- (3) Suspension in the future is better predicted than suspension at the same instant as velocity measurements. These lags are largely due to the time for an observed flow event to effect the bed and mix sediment upward.
- (4) Nonlinear models relating suspension to velocity do better than linear models using the same velocity history. Nonlinear models are able to exploit relationships between suspension and velocity history that change for different wave shapes. For the environmental conditions of this study, the optimal model used 3 seconds of velocity history (approximately 1/4 wave period) and a 1.5 second lag to predict suspension.

## ACKNOWLEDGMENTS

BEJ would like to thank his Thesis committee, Gary Griggs (Chair), Bob Anderson, and Ed Thornton for their help during the early stages of this work. This manuscript was improved by the reviews of Guy Gelfenbaum and John Dinger. We wish to thank the personnel at the Army Corps of Engineers Field Research Facility in Duck, North Carolina for their excellent help with the experiment.

## REFERENCES

- Casdagli, M., Chaos and Deterministic Versus Stochastic Nonlinear Modeling, *J. of Royal Statistical Soc. B*, 54, 303-328, 1991.
- Casdagli, M., Des Jardins, D., Eubank, S., Farmer, J. D., Gibson, J., Hunter, N. F. and Theiler, J., Nonlinear modeling of chaotic time series: Theory and application, in *Applied Chaos* edited by J. Kim and J. Stringer, Wiley, New York, 1992.
- Conley, D. C. and Inman, D. L., Field observations of the fluid granular boundary layer under near breaking waves, *J. of Geophys. Res.*, 97 (C6), 9631-9643, 1992.
- Downing, J. P., Sternberg, R. W., and Lister, C. R. B., New instrumentation for the investigation of sedimentary processes in the shallow marine environment, *Mar. Geol.*, 42, 19-34, 1981.
- Downing, J. P., Field studies of suspended sand transport, Twin Harbors Beach Washington, *Ph.D. thesis*, 121 pp., Univ. of Washington, Seattle Washington, 1983

- Farmer, J. D. and Sidorowich, J. J., Exploiting Chaos to Predict the Future and Reduce Noise, in *Evolution, Learning, and Cognition*, edited by Y. C. Lee, World Scientific, New York, 1989.
- Glenn, S. M. and Grant, W. D., A suspended-sediment stratification correction for combined wave and current flows, *J. Geophys. Res.*, 92, 8244-8264, 1987.
- Grant, W. D., and Madsen, O. S., Combined wave and current interaction with a rough bottom, *J. Geophys. Res.*, 84 (C4), 1797-1808, 1979.
- Gordon, C. M., Sediment entrainment and suspension in a turbulent tidal flow, *Mar. Geology*, 18, M57-M64, 1975.
- Hanes, D. M. and Huntley, D. A., Continuous measurements of suspended sand concentration in a wave dominated nearshore environment, *Cont. Shelf Res.*, 6 (4), 585-596, 1986.
- Hunter, N., and Theiler, J., Characterization of nonlinear input-output systems using time series analysis, in *Proceedings of the 1st Experimental Chaos Conference*, edited by S. Vohara, M. Spano, M. Schlesinger, L. Pecora, and W. Ditto, pp. 54-60., World Scientific, Singapore, 1992.
- Jaffe, B. E., and Sallenger, A. H., Jr., The contribution of suspension events to sediment transport in the surf zone, *Proceedings of the 23rd International Coastal Engineering Conference, ASCE*, 3, 2680-2693, 1992.
- Jaffe, B. E., Episodic transport of sediment in the nearshore, *Ph.D. thesis*, 172 pp., Univ. of California, Santa Cruz, California, 1993.
- Jaffe, B. E., and Rubin, D. M., Using nonlinear forecasting to learn the magnitude and phasing of time-varying sediment suspension in the surf zone, in preparation.
- Komar, P. D., and Miller, M. C., The initiation of oscillatory ripple marks and the development of plane-bed at high shear stresses under waves, *J. Sed. Petrol.*, 45, 697-703, 1975.
- Livezey, R. E. and Barnston, A. G., Operational Multifield Analog/Antianalog Prediction System for United States Seasonal Temperatures, Part 1, System Design and Winter Experiments, *J. Geophys. Res.*, 93 (D9), 10953-10974, 1988.
- Mason, C., Sallenger, A. H., Holman, R. A., and Birkemeier, W. A., Duck82- A coastal storm processes experiment, *Proceeding of the 19th International Coastal Engineering Conference, ASCE*, 2, 1913-1927, 1984.
- Osborne, P. D. and Greenwood, B., Sediment suspension under waves and currents: time scales and vertical structure, *Sedimentology*, 40, 599-622, 1993.
- Rubin, D. M., Use of forecasting signatures to help distinguish periodicity, randomness, and chaos in ripples and other spatial patterns, *Chaos*, 2 (4), 525-535, 1992.
- Sallenger, A. H., Jr., Howard, P. C., Fletcher, C. H., and Howard, P. A., A system for measuring bottom profile, waves and currents in the high-energy nearshore environment, *Mar. Geol.*, 51, 63-76, 1983.
- Schubauer, G. B. and Skramstad, H. K., Laminar boundary layer oscillations and stability of laminar flow, *National Bureau of Standards Research Paper 1772*, 69-78, 1947.
- Smith, J. D., Modeling of sediment transport on continental shelves. In: Goldberg et al. (Editors), *The Sea*, Wiley Interscience, New York, 6, p. 539-577, 1977.
- Sugihara, G. and May, R. H., Nonlinear Forecasting as a Way of Distinguishing Chaos from Measurement Error in Time Series, *Nature*, 344, 734-741, 1990.

## CHAPTER 152

### BEACH PROFILE SPACING: PRACTICAL GUIDANCE FOR MONITORING NOURISHMENT PROJECTS

Timothy W. Kana, Ph.D., and Christopher J. Andrassy, P.E.<sup>1</sup>

#### ABSTRACT

A search of the literature shows there are no established standards for the spacing of profiles for postnourishment monitoring. One standard that appears to apply in the United States relates to construction surveys. Most recent nourishment projects use prefill and postfill profiles at 100-foot (ft) [ $\sim 30$  meter (m)] spacing for payment purposes. Rarely is this close spacing duplicated in subsequent monitoring surveys. How accurately does such spacing reflect the actual volume of fill remaining?

Four sets of closely spaced profile surveys to closure were performed over a two-year period following the 1991 Hunting Island, South Carolina, nourishment project. Fill volumes remaining within the project area were computed to closure depth using the average-end-area method. The complete dataset at 100-ft (30 m) spacing provided the basis of comparison. Volume calculations were performed for the possible combinations of profiles at greater spacings up to 1,200 ft (365 m). The normalized results show the expected increase in error as profile spacing increases. However, the variation was generally less than  $\pm 3$  percent up to spacings of 500 ft ( $\sim 150$  m). At 1,000 ft ( $\sim 365$  m), the error band spanned 20 percent of the project volume. The Hunting Island dataset provides guidance for minimum profile spacing for nourishment projects with highly varying fill sections or irregular shoreline morphology. Spacings of 400-500 ft (120-150 m) provided a reasonably accurate result. Accuracy was greatly reduced at longer spacings. Longer nourishment projects, involving less variable fill volumes, likely can be evaluated at somewhat longer spacing with comparable accuracy. However, a disadvantage of surveying only the minimum number of profile lines is the error introduced if even one line has to be discarded from the dataset because of field survey errors.

---

<sup>1</sup>CSE Coastal Science & Engineering, Inc., PO Box 8056 Columbia SC 29202

**INTRODUCTION**

A critical aspect of beach nourishment is postproject monitoring. Periodic surveys are typically performed to determine the amount of fill remaining and establish quantitative loss rates. Beach and inshore profiles--shore-perpendicular transects from the backshore to depth of closure--are the principal database. There are no established standards for the spacing of profiles. A search of the literature shows a wide range of profile spacing, sometimes dictated by project length and economics, other times a function of the interest of the designers and owners. The more profiles obtained, the more detailed and, presumably, accurate the result. One standard that appears to apply in the United States relates to construction surveys. Most recent nourishment projects use prefill and postfill profiles at 100-foot (ft) [ $\sim 30$  meter (m)] spacing for payment purposes. Rarely is this close spacing duplicated in subsequent monitoring surveys.

Example profile spacings are given in Table 1. A typical spacing for routine beach monitoring or postproject evaluation appears to be 1,000 ft ( $\sim 300$  m), or greater. The State of Florida, for example, has one of the best established networks of profiles which are monitored at a frequency of less than once every three years (Bokuniewicz and Tanski, 1991). The State

**TABLE 1.** Typical profile spacing for beach monitoring. [Sources: Bokuniewicz and Tanski (1991), Kana and Andrassy (1993), Stauble and Grosskopf (1993).]

• Pre and Post Construction:	100 ft (30 m)
• Project Monitoring:	> 1,000 ft (300 m)
• Statewide Surveys:	
◦ Florida	1,000 ft (300 m)
◦ South Carolina	1,500 ft (450 m)
◦ New Jersey	6,500 ft (2,000 m)
◦ New York (proposed)	2,000 ft (600 m)
<i>Example Projects</i>	
Myrtle Beach (SC)	1986 750 ft (semiannual)
Ocean City (MD)	1988 1,000 ft (quarterly)

of South Carolina surveys wading depth profiles on  $\sim 1,500$  ft (450 m) spacing twice per year. The 1986 Myrtle Beach (South Carolina) nourishment project (Williams and Kana, 1987) and the 1991 Ocean City (Maryland) project (Stauble and Grosskopf, 1993) have been monitored yearly or more frequently using profiles at 700-1,000 ft (215-300 m) spacing, respectively. How accurately does such spacing reflect the actual volume of fill remaining?

To investigate that question, the authors performed four sets of profile surveys over a two-year period following the 1991 Hunting Island, South Carolina, nourishment project. Hunting Island is a 4.2-mile (7-kilometer) long barrier island bounded by large tidal deltas (Fig. 1). Background erosion rates are exceedingly high at around 25 cubic yards per foot per year (cy/ft/yr) [62.5 cubic meters per meter per year

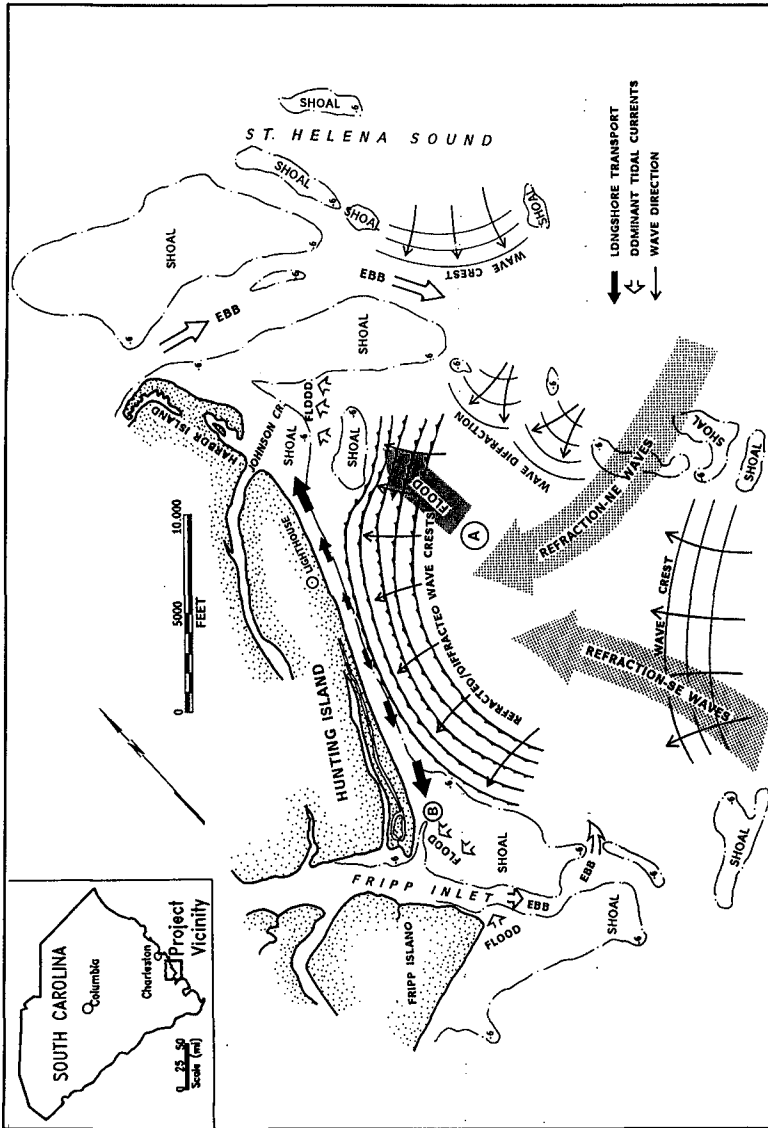


FIGURE 1. General model of coastal processes producing refraction and diffraction around shoals and sand transport away from the center of Hunting Island. Shoals are defined by the -6 ft (-1.8 m) mean low water contour as depicted on U.S. National Ocean Survey Chart No. 11513 (after CSE, 1990).



( $m^3/m$ ) (USACE, 1977; CSE, 1990). Historical surveys in connection with earlier nourishment projects indicate that as the center of the island erodes, sediment is transported toward both ends of the island. This pattern of sediment transport appears to be controlled by wave refraction and diffraction around and through ebb-tidal delta shoals associated with St. Helena Sound, Johnson Creek, and Fripp Inlet.

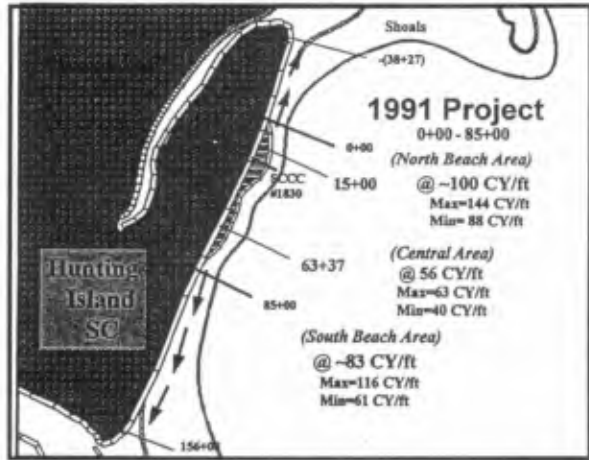
Hunting Island has been nourished five times since 1968. The first four projects were engineered by the U.S. Army Corps of Engineers and were completed in 1968, 1971, 1975, and 1980 (Table 2). The 1991 project was sponsored by the South Carolina Department of Parks, Recreation and Tourism with all funding by the state. The project involved excavation of sediment from an offshore borrow area by hydraulic dredge and placement along an ~8,500 ft (2,600 m) reach in the center of Hunting Island. Mean grain size on the beach averaged 0.20 millimeter (mm) diameter before the 1991 project. Grain size in the borrow area averaged 0.22 mm diameter. The contractor (Great Lakes Dredge & Dock Company) mobilized equipment the first week of February 1991 and completed the project on 24 March 1991, 44 days after pumping began. The pay volume was based on surveys in the borrow area with a total pay volume not to exceed 755,000 cy as per terms of the contract.

**TABLE 2.** Beach nourishment projects along Hunting Island. [Sources: USACE (1977); CSE (1991).]

[\*NOTE: USACE stations for the 1968-1980 projects run north and south from the vicinity of the lighthouse (e.g., 50+00N is 5,000 ft north; 97+00S is 9,700 ft south of the lighthouse). Total length of Hunting Island is about 21,000 ft ( $\pm 4$  miles), ranging from  $\pm 70+00N$  to  $\pm 140+00S$ .]

Project*	Construction Dates	Volume (cy)	Limits of Placement	Net Unit Cost (\$/cy)	Total Cost (\$)	
1968	Feb-Dec'68	750,000	50+00N to 50+00S*	0.58	435,178	
1971	May-Dec'71	761,324	50+00N to 50+00S	0.70	534,000	
1975	Apr-Jun'75	612,974	60+00N to 30+00S	1.58	971,540	
1980	Jan-May'80	1,412,692	24+60N to 97+00S	1.60	2,267,201	
	Subtotal	3,536,990		\$1.19/cy	\$4,207,919	
1991	Feb-Mar'91	757,644	7+00 to 85+00	\$3.80/cy	\$2,876,250	
<b>GRAND TOTAL</b>				<b>4,294,634</b>	<b>\$1.65/cy</b>	<b>\$7,084,169</b>

The 1991 project concentrated the fill at two localities (Fig. 2). One bulge in the fill was constructed along a recreational beach access ~1.4 miles (2.3 km) from the north end of the island. The second bulge was centered at the midpoint of the island. Unit fill volumes ranged from a low of 40 cy/ft (100 m<sup>3</sup>/m) between the two "bulges" to highs of about 140 cy/ft (350 m<sup>3</sup>/m) and 110 cy/ft (275 m<sup>3</sup>/m) at the north and south ends of the project, respectively.



### Profile Surveys

Profiles at 100-ft (30-m) spacing were

surveyed to the estimated depth of closure along the Hunting Island project area. Closure depth was defined based on negligible profile change for available surveys, as well as morphological evidence of nearly flat slopes with distance from shore and the initial presence of mud at the surface of the substrate (Fig. 3). Closure depths range from 11 ft to 12 ft (3.3 m to 3.7 m) below mean sea level in this mesotidal setting [mean tide range equals 6.7 ft (2.05 m)]. Profiles were analyzed for unit-volume change. Fill volumes remaining within the project area were computed the traditional way by extrapolating unit volumes after each survey over representative shore lengths using the average-end-area method. Four reference lenses were developed as follows:

- 1) *Backshore to mean high water* — At Hunting Island, this is represented by the +10 ft to +3.2 ft (+3 m to +1 m) NGVD\* contour and corresponds to the dry beach. \*NGVD — National Geodetic Vertical Datum of 1929 which in South Carolina is approximately 0.5 ft (0.15 m) below present mean sea level.
- 2) *Intertidal beach* — From mean high water (MHW) to mean low water (MLW) [-2.2 ft -0.67 m) NGVD].
- 3) *Wading zone* — From MLW to -5.0 ft (-1.5 m) NGVD.
- 4) *Lower foreshore* — From -5.0 ft NGVD to -12.0 ft (-3.65 m) NGVD.

FIGURE 2. Vicinity map of the 1991 Hunting Island nourishment project fill limits between station 0+00 and 85+00 (stationing in feet divided by 100).

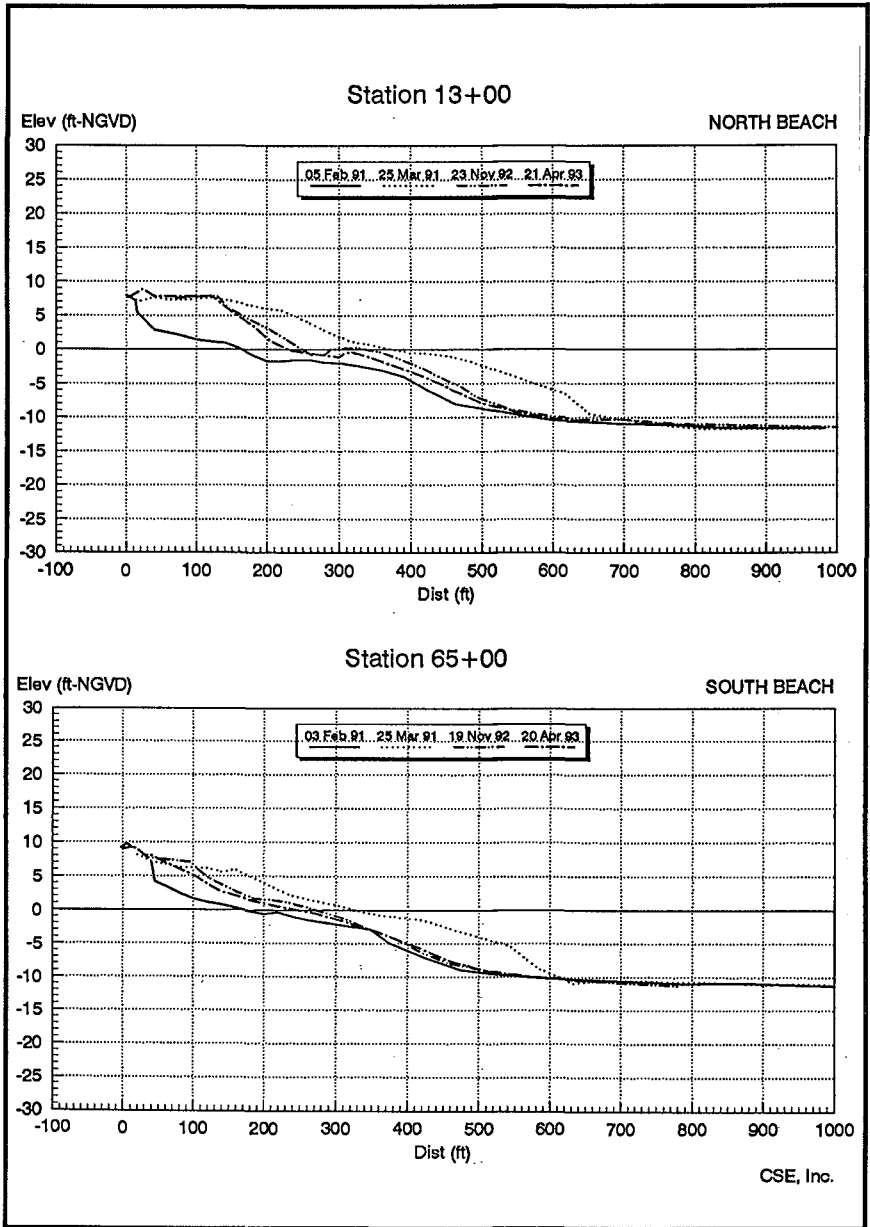


FIGURE 3. Representative profiles to closure along North Beach and South Beach before and after the March 1991 nourishment (after Kana and Andrassy, 1993).

In addition to the above contour boundaries, certain cross-shore boundaries were prescribed in the analysis. In general, the starting distance for volume calculations is at the prenourishment scarp in the backshore. The seaward limit is generally prescribed at a point within 100 ft seaward of the base of the fill.

Unit volumes (quantity of sand per unit length of shoreline between given contour intervals) and unit-volume changes between prenourishment and postnourishment surveys were computed for all profiles. The variation in unit volumes before and after nourishment within the Hunting Island project area is given in Figure 4. With minor exceptions, the quantity of sand in the profile was less than 200 cy/ft (500 m<sup>3</sup>/m) [to -12.0 ft (-3.65 m) NGVD] before nourishment (February 1991) and ranged from 250 cy/ft (625 m<sup>3</sup>/m) to 350 cy/ft (875 m<sup>3</sup>/m) after nourishment (April 1991). North Beach and South Beach, by design, received the most fill. Erosion rates for the 1991 project as well as earlier projects have been exceedingly high. North Beach, in general, retained the most sand. Higher loss rates are evident at the ends of the project, particularly south of station 73+00. The average trend in unit sand volume by contour interval, retained within the project area since nourishment, is illustrated in Figure 5. These loss rates have averaged 20-25 cy/ft/yr (50-62.5 m<sup>3</sup>/m/yr) and are nearly the same as loss rates reported after the 1971 and 1975 beach fills (USACE, 1977).

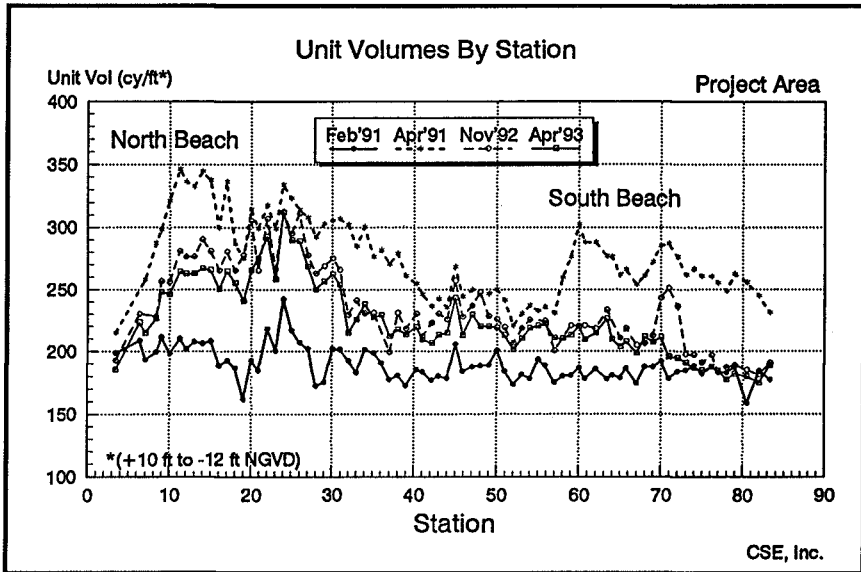
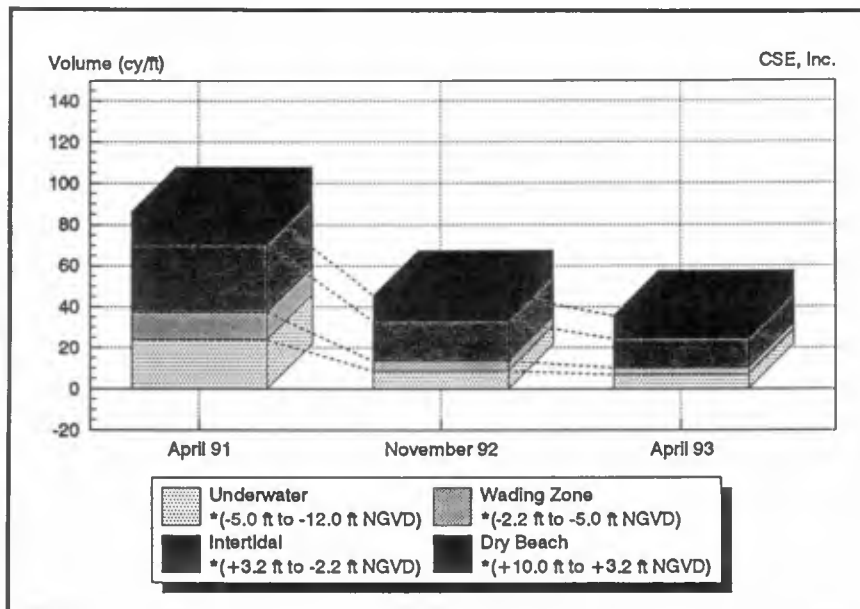


FIGURE 4. Variation in sand volume per foot of shoreline by profile station and date within the project area. Computation boundaries are from the foredune-scarp to -12.0 ft (-3.65 m) NGVD.



**FIGURE 5.** Average unit-volume beach change since nourishment (February 1991) as a function of contour interval\* within the Hunting Island project area (stations 3+42 to 83+31). Note: Higher loss rate for lower beach lenses is thought to be related to variations in grain size along the profile. After Kana and Andrassy (1993).

Interestingly, the loss rate for the upper beach lenses was much lower than the underwater lenses. The dry beach to MHW (lens 1) within the project area retained 70 percent of the fill through April 1993. The intertidal beach (MHW to MLW) retained about 45 percent of the fill two years later. These two zones comprise the primary recreational zone of the beach. In contrast, the underwater lenses (mean low water to closure) retained only 27 percent by April 1993. These cross-shore variations in the rate of beach fill losses produced a steepening of the mean profile slope along the intertidal beach (see Fig. 3). Krishnamohan et al. (1993) theorize this results from the presence of a minor coarse fraction in the borrow sediments which was selectively deposited along the backshore during construction.

**Profile Spacing Criteria**

It is apparent profile spacing can increase for a given accuracy as the variance of individual profile volumes approaches the mean profile volume of a dataset. This is illustrated conceptually in Figure 6. The ideal case is where standard deviation of unit volume change is zero and all profiles in the dataset yield the exact mean volume

change. In this case, one profile line can accurately define the performance of the nourishment project. For this to occur in the field is nearly impossible, however, given the uncertainty in placement of underwater volumes, variations in sediment quality, discharge rates, and the inherent natural variation in profile geometry. More commonly, the initial condition after nourishment will show considerable variations in actual volumes, even where fill volumes are designed to be uniform.

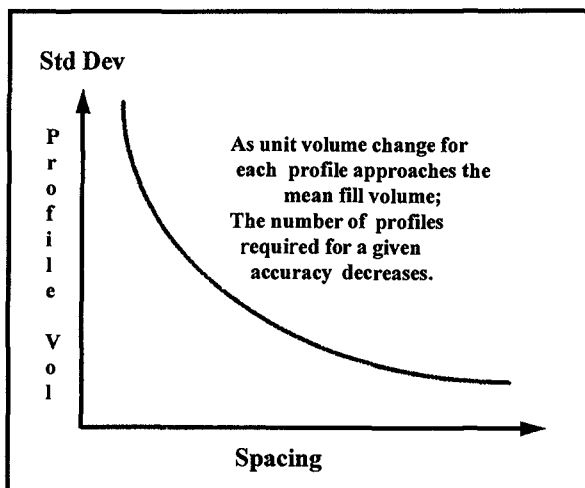


**FIGURE 6.** Conceptual model of the relationship of profile volume variance to profile spacing. For projects where the variance of profiles is high, more closely spaced are required to yield the "true" volume change.

The Hunting Island 1991 profile dataset, in addition to yielding a certain but unknown variance due to normal problems in controlling fill placement, included a planned variation in fill volumes. Thinnest sections designed for the center reach of the project area involved an average of only 56 cy/ft (140 m<sup>3</sup>/m). In contrast, the north and south bulges involved average sections of 100 cy/ft (250 m<sup>3</sup>/m) and ~83 cy/ft (207 m<sup>3</sup>/m), respectively, as shown in Figure 2. This yielded a standard deviation in profile volume change for pre and postconstruction surveys (all profiles) of approximately  $\pm 25$  cy/ft (62 m<sup>3</sup>/m). Profile variance is also reflected in the unit volumes from station to station (see Fig. 4).

### Postproject Surveys and Profile Analysis

Pre and postnourishment surveys at 100 ft (30 m) spacing provided the basis for the initial fill volume calculation. For the 1991 Hunting Island project, payment was based on borrow area surveys rather than beach surveys. Results in the borrow area confirmed an excavation volume of 757,644 cy (579,219 m<sup>3</sup>). The initial postconstruction beach surveys confirmed an in-place volume of 715,766 cy (547,209 m<sup>3</sup>) (CSE, 1991a). This latter volume represents 94.5 percent of the excavated quantity and is considered a satisfactory result based on the confirmed mud content of 5 percent in the borrow area (CSE, 1991b).

For purposes of evaluating project performance using various profile spacings, it was assumed the entire set of profiles at 100 ft (30 m) spacing for each of three postproject surveys yielded the true sand volume change on the beach compared to pre-nourishment conditions. Volume calculations were then performed for the possible combinations of profiles at greater spacings up to 1,200 ft (365 m). There are two possible combinations using profiles at 200-ft (61-m) spacing (i.e., odd-numbered stations and even-numbered stations). At 300-ft (91-m) spacing, there are three combinations and so on up to 1,200-ft (365-m) spacing. Adjacent unnourished areas were also surveyed but at a minimum profile spacing of 500 ft (152 m). By convention, the end surveys within the project area were applied in each analysis to provide a uniform shoreline length for comparison. Thus, the two profiles at each end of the project will not necessarily be spaced the same distance as the chosen profile spacing. Because of earlier surveys at variable spacing and a desire to match profile lines, certain stations were offset slightly from 100 ft (30 m) spacing. In practice, this is common because of obstructions which prevent backshore monuments from being placed at uniform distances along the shoreline.

Table 3 and Figures 7 and 8 provide results of the analysis. It can be seen that as the profile spacing increases, the range of computed sand volume changes also increases. As Table 3 shows, the normalized volume change (as a percentage of the result for all profiles in April 1991) varied by only  $\pm 3$  percent up to spacings of 500 ft. At 800 ft, the error band increased to about  $\pm 5$  percent; at 1,000 ft, the error band spanned about  $\pm 10$  percent.

It can also be seen the percentage error reduces by April 1993 (two years post-project) when compared to the original fill volume. However, this also reflects the smaller volume being compared. If the April 1993 data are normalized against the result for all profiles in April 1993, the percent difference at 1,000-ft spacing is on the order of  $\pm 12$  percent. For a project involving about one-half million cubic yards (cubic meters), this equates to a possible range from 440,000 cy (cm) to 560,000 cy (cm), computed from various profile spacings.

**TABLE 3.** Sand volume change as a function of the number of profiles for the Hunting Island project area (stations 3+42 to 83+31). Transition profiles 0+00 to 3+42 and 83+31 to 85+00 are excluded in profile spacing analysis, but are included in references to the initial fill volume in this paper. [\*Compared to Feb'91 pre-nourishment; volumes in cy.]

Profile Spacing (ft)	Change in Sand Volume*			% Apr'91 — All Data		
	Apr'91	Nov'92	Apr'93	Apr'91	Nov'92	Apr'93
100	688,044	364,310	283,684	100.0	52.9	41.2
200	687,984	370,606	282,083	100.0	53.9	41.0
200	686,356	356,774	285,632	99.8	51.9	41.5
300	676,274	360,192	280,030	98.3	52.4	40.7
300	674,053	367,858	290,556	98.0	53.5	42.2
300	704,369	369,914	279,689	102.4	53.8	40.6
400	684,518	382,628	282,995	99.5	55.6	41.1
400	678,568	368,531	276,713	98.6	53.6	40.2
400	683,294	334,328	282,873	99.3	48.6	41.1
400	689,316	365,819	282,873	100.2	53.2	41.1
500	690,362	380,933	279,081	100.3	55.4	40.6
500	692,609	362,730	292,520	100.7	52.7	42.5
500	681,282	342,794	276,787	99.0	49.8	40.2
500	671,701	355,069	284,679	97.6	51.6	41.4
500	692,414	364,361	279,572	100.6	53.0	40.6
600	692,291	366,586	273,499	100.6	53.3	39.8
600	673,749	345,906	298,219	97.9	50.3	43.3
600	678,468	366,565	276,200	98.6	53.3	40.1
600	703,348	372,565	283,572	102.2	54.1	41.2
600	666,795	393,747	283,185	96.9	57.2	41.2
600	666,339	356,257	276,462	96.8	51.8	40.2
800	663,282	371,372	260,967	96.4	54.0	37.9
800	669,662	335,324	283,120	97.3	48.7	41.1
800	649,346	321,921	255,955	94.4	46.8	37.2
800	671,164	368,586	277,771	97.5	53.6	40.4
800	696,087	389,739	298,181	101.2	56.6	43.3
800	703,751	343,752	311,129	102.3	50.0	45.2
800	688,300	392,952	285,210	100.0	57.1	41.5
800	681,566	395,918	284,233	99.1	57.5	41.3

[continued . . .]



TABLE 3. (continued)

Profile Spacing (ft)	Change in Sand Volume*			% Apr'91 — All Data		
	Apr'91	Nov'92	Apr'93	Apr'91	Nov'92	Apr'93
1,000	605,373	390,369	276,788	88.0	56.7	40.2
1,000	662,836	306,811	292,476	96.3	44.6	42.5
1,000	660,298	363,351	284,311	96.0	52.8	41.3
1,000	704,117	396,662	307,580	102.3	57.7	44.7
1,000	736,092	412,425	290,777	107.0	59.9	42.3
1,000	729,360	387,250	283,878	106.0	56.3	41.3
1,000	680,873	356,546	241,304	99.0	51.8	35.1
1,000	646,969	352,494	271,981	94.0	51.2	39.5
1,000	654,105	321,139	271,866	95.1	46.7	39.5
1,000	613,281	329,670	259,566	89.1	47.9	37.7
1,200	684,896	352,287	290,984	99.5	51.2	42.3
1,200	637,199	339,229	281,853	92.6	49.3	41.0
1,200	606,005	381,766	270,707	88.1	55.5	39.3
1,200	651,454	345,424	263,448	94.7	50.2	38.3
1,200	659,058	347,853	316,214	95.8	50.6	46.0
1,200	680,001	377,555	277,574	98.8	54.9	40.3
1,200	704,075	388,157	268,647	102.3	56.4	39.0
1,200	710,351	445,059	284,561	103.2	64.7	41.4
1,200	697,919	311,538	271,016	101.4	45.3	39.4
1,200	701,185	362,156	265,173	101.9	52.6	38.5
1,200	664,103	347,339	288,246	96.5	50.5	41.9
1,200	579,424	353,125	271,109	84.2	51.3	39.4

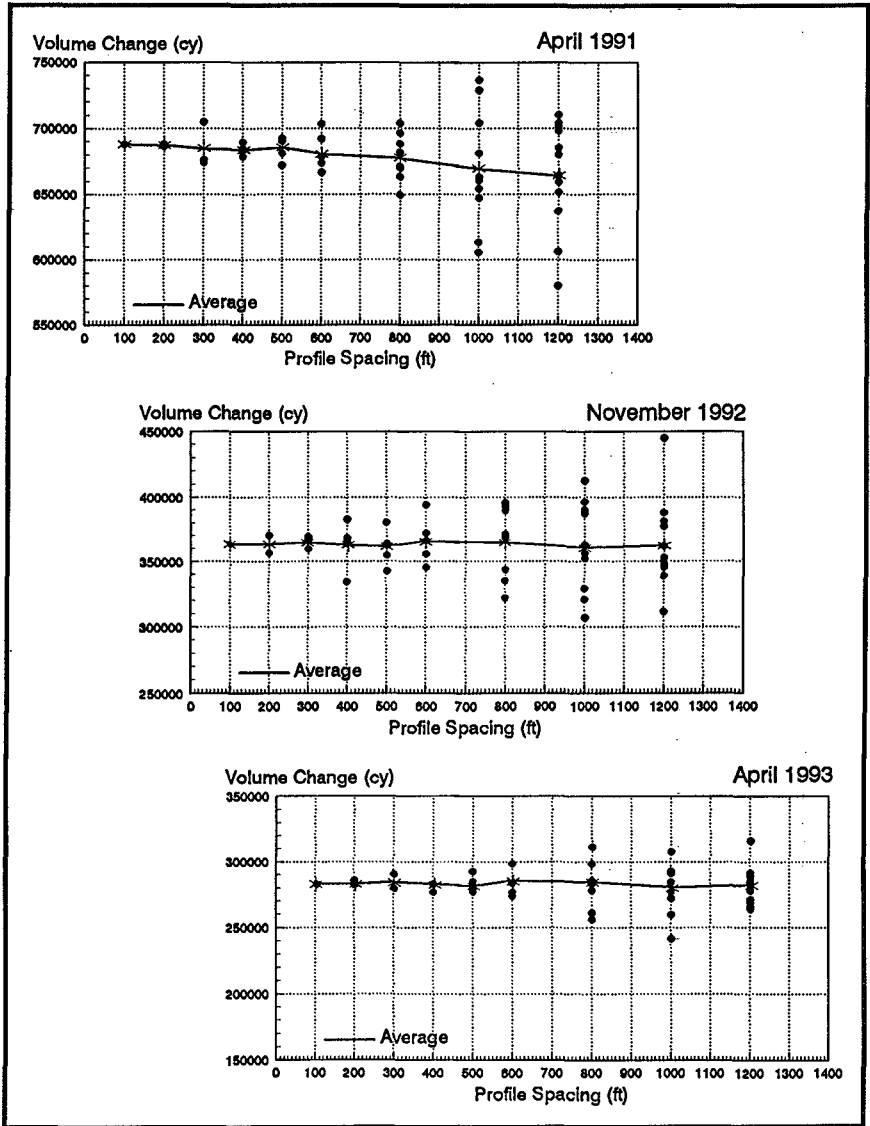


FIGURE 7. Computed sand volume changes since nourishment as a function of profile spacing for April 1991 (upper), November 1992 (middle), and April 1993 (lower) in the project area (stations 3+42 to 83+31). Averages are arithmetic and are not weighted for minor variations in profile spacing or for the fact that the ends of most profile pairs will not equal the nominal spacing, as explained in the text. After Kana and Andrassy (1993).

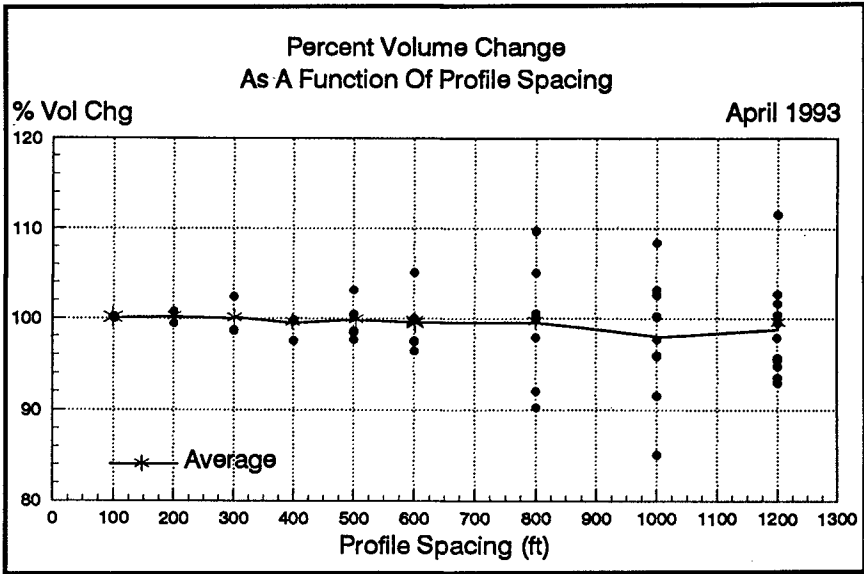


FIGURE 8. Normalized volume changes as a function of profile spacing for a post-nourishment survey of 90+ lines to closure at Hunting Island, South Carolina.

DISCUSSION

The Hunting Island dataset is somewhat unusual because of the project's short length and highly variable fill volumes (by design). A longer project with uniform fill volumes could probably be monitored at longer spacings. But in areas where rhythmic features are common along the shoreline (e.g., shoreline salients and offshore bars) or fill volumes are variable, the Hunting Island results provide some rules of thumb. In this case, profile spacings of 400-500 ft (120-150 m) appear to represent the practical limit for accurate results. Given the common uncertainty in performance because of no or few previous projects at most nourishment sites, initial monitoring should be performed in as much detail as possible. Errors of a few percentage points or less should be a requirement for all postproject surveys. Consider that a common goal of nourishment is restoration of a dry sand beach. The authors' experience suggests the upper portion of the profile which should contain the visible high-tide beach represents a small part of the profile volume. Variations in sand volume of 20-30 percent (the possible result from surveys involving large profile spacings) could mean the difference between a project yielding a viable high-tide beach and one that is not viable. With considerable debate regarding nourishment project performance, detailed profiling is one of the few means for objective analysis. Monitoring should favor as detailed a profile survey as possible.

Few datasets are available to develop any firm guidelines for profile spacing yet, but based on results of the recent Hunting Island nourishment project, it would appear profile spacings of less than 500 ft are required for a confident analysis of performance. The authors believe this will hold true for most large nourishment projects.

The suggested rule of thumb should be tested with additional datasets as they become available, but it provides a reasonable guide for most projects. Obviously, the main advantage of minimizing the number of profiles is lower expense of surveys. However, a disadvantage of surveying the fewest lines possible is the error due to profile spacing introduced if even one transect has to be discarded from the dataset because of field survey error.

## ACKNOWLEDGMENTS

This study was sponsored by the South Carolina Coastal Council, South Carolina Department of Parks, Recreation and Tourism, and the U.S. Army Corps of Engineers, Coastal Engineering Research Center (CERC) (contract DACW39-92-C-0110). Field surveys in 1991 were performed by Great Lakes Dredge & Dock Company.

## REFERENCES

- Bokuniewicz, H., and J. Tanski. 1991. Development of a coastal erosion monitoring program for the south shore of Long Island, New York. Proc. Workshop for Long Island Regional Planning Board, SUNY Stony Brook, N.Y., 67 pp.
- CSE. 1990. Erosion assessment and beach restoration alternatives for Hunting Island, South Carolina. Feasibility Study for South Carolina Department of Parks, Recreation and Tourism. Coastal Science & Engineering, Inc. (CSE), Columbia, S.C., 66 pp. + app.
- CSE. 1991a. Hunting Island State Park 1991 beach nourishment project. Survey Report No. 1 to South Carolina Department of Parks, Recreation & Tourism, Columbia; CSE, Columbia, S.C., 26 pp. + appendices.
- CSE. 1991b. Geotechnical studies for the Hunting Island beach nourishment project. Survey Report for South Carolina Department of Parks, Recreation and Tourism. CSE, Columbia, S.C., 35 pp. + appendices.
- Kana, T.W., and C.J. Andrassy. 1993. Hunting Island State Park: 1991 beach nourishment project. Survey Report No. 3, for the South Carolina Coastal Council and South Carolina Department of Parks, Recreation and Tourism; CSE, Columbia, S.C., 32 pp. + appendices.
- Krishnamohan, R., T.W. Kana, and C.J. Andrassy. 1993. Comparison of geotechnical properties of beach fill versus borrow area sediments for the fifth Hunting Island (SC) beach nourishment project. Tech. Report, Contract DACW39-92-C-0110, USACE, WES, Vicksburg, Miss. CSE, Columbia, S.C., 48 pp. + appendices.
- Stauble, D.K., and W.G. Grosskopf. 1993. Monitoring project response to storms: Ocean City, Maryland, beachfill. *Shore & Beach*, Vol. 61(1), pp. 23-33.
- USACE. 1977. Hunting Island Beach, South Carolina: project evaluation and proposals for FY 1977 construction. Unpublished manuscript, U.S. Army Corps of Engineers, Charleston District, 37 pp.
- Williams, M.L., and T.W. Kana. 1987. Beach nourishment at Myrtle Beach, South Carolina: an overview. In Proc. Coastal Sediments '87, ASCE, N.Y., pp. 1106-1120.

## CHAPTER 153

# WATERTABLE OVERHEIGHT DUE TO WAVE RUNUP ON A SANDY BEACH

Hong-Yoon KANG, Peter NIELSEN<sup>1</sup> and David J. HANSLOW<sup>2</sup>

### Abstract

Watertable overheight in beaches due to waves is investigated through laboratory experiments and field tests. Infiltration from wave runup onto the exposed beach creates a significant lifting of the coastal watertable. The infiltration velocity distribution is obtained from both the laboratory and field conditions. The inland overheight for the steady state (regular waves and no tide) is found to be  $0.62 \tan \beta \sqrt{H_o L_o}$  and that for the unsteady state (irregular waves) is estimated as  $0.55 \tan \beta \sqrt{H_{oRMS} L_o}$ .

### Introduction

The time averaged watertable in beaches stands considerably above the mean sea level due to waves and tidal effects. This is of practical importance for the stability of coastal structures, for the operation of coastal sewage disposal systems and for the accretion/erosion of the beach. The elevated watertable in coastal areas also influences hydrology, e.g., agricultural and soil conservation activities. The main factors for the overheight above the mean sea level are waves and tides as seen in Figure 1 (Nielsen et al. 1988; Aseervatham et al., 1993; Kang and Nielsen, 1994).

This figure shows the watertable variation in wells just landward of the high water mark on two beaches north of Sydney. Both beaches are subject to the same tidal influences, but only Palm beach is exposed to the ocean waves while Pittwater beach is protected from wave action. The data clearly demonstrates that the wave activity is a significant factor affecting the coastal

---

<sup>1</sup>Department of Civil Engineering, University of Queensland, Brisbane, Australia 4072. (Fax) +61 7 365 4599

<sup>2</sup>Coast and Flood Policy Branch, NSW Public Works, Sydney 2001, Australia

watertable elevation. In this case, the waves raise the watertable by up to 0.7m compared to the protected beach. The overheight inside the protected beach is due to the tide acting on a sloping beach face as explained by Nielsen (1990).

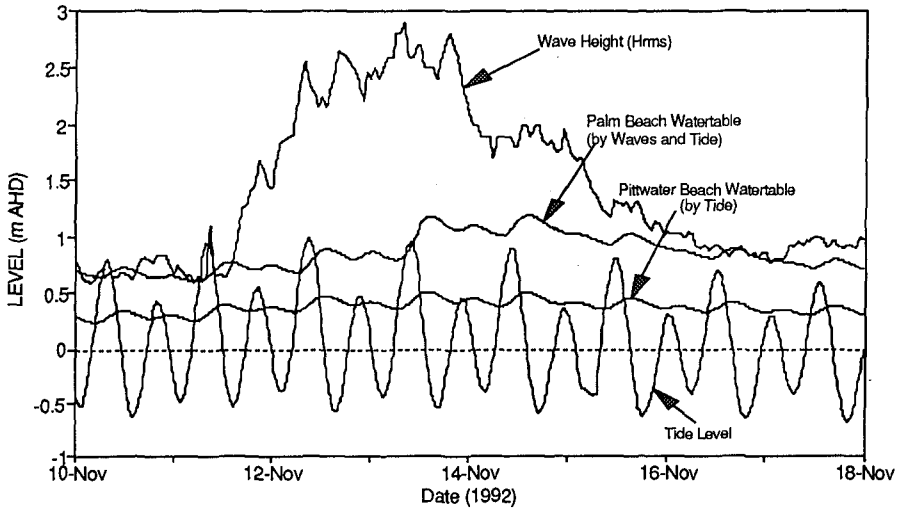


**Figure 1.** Field data showing the significant lifting of the watertable due to waves and tides.

This paper describes the infiltration of water due to wave runup which creates a significant lifting of the coastal watertable. The steady state asymptotic inland overheights are investigated under controlled wave conditions with different beach sands in a wave flume without tides. This overheight is compared with the field data.

### **Infiltration from wave runup**

The effect of infiltration due to wave runup is clearly visible from the measured watertable profiles shown in Figure 2. The watertable profiles exhibit humps due to wave runup infiltration between the shoreline and the runup limit. These humps are particularly noticeable during the rising tide.

To model the watertable in the area between the shoreline and the runup limit, a modified Boussinesq equation (1) which includes the runup infiltration effect must be used

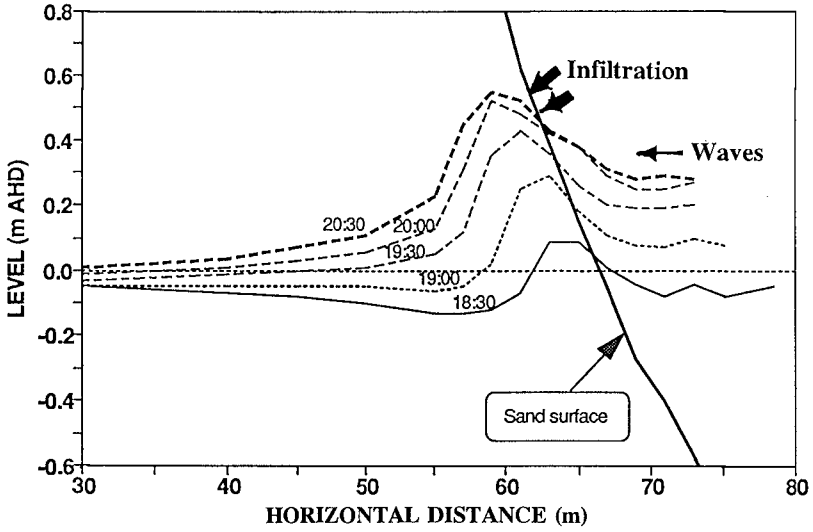


**Figure 2.** Watertable profiles measured on the rising tide at Kings Beach, Queensland, Australia.

$$\frac{\partial \eta}{\partial t} = \frac{KD}{n} \frac{\partial^2 \eta}{\partial x^2} + \frac{U_f(x,t)}{n} \tag{1}$$

where  $\eta$  denotes the watertable height averaged over a few surf beats,  $K$  is the hydraulic conductivity,  $D$  the aquifer depth,  $n$  the specific yield and  $U_f$  the infiltration velocity. For pure regular waves forcing without tidal effects, the situation may be considered quasi-stationary. Thus equation (1) becomes

$$\frac{\partial^2 \eta}{\partial x^2} = - \frac{U_f(x)}{KD} \tag{2}$$

This steady situation is achieved experimentally in a wave flume.

From these equations,  $U_f$  can be derived from measured watertable profiles. Two examples are shown in Figure 3. This Figure represents the smoothed relative infiltration velocity distributions against the relative shorenormal distance from the field and laboratory data. Infiltration velocity  $U_f$  is obtained by the Finite Difference Method. The normalised infiltration velocity has a maximum approximately 2/3 of distance from the shoreline to the runup

limit for the field data and halfway between the shoreline and the runup limit for the laboratory data. Both the distributions show similar trends, but the magnitudes are different. This difference is possibly due to the assumed value of  $n=0.3$  (for field) being too large, and it seems because field is unsteady with waves running onto dry sand or  $K$  is not correctly determined.

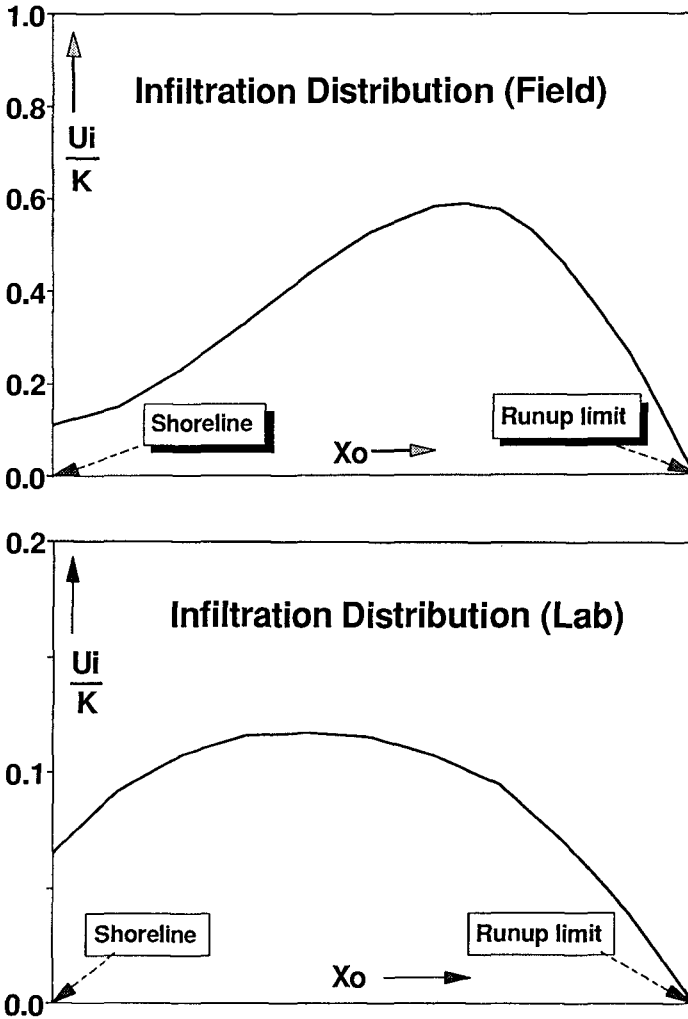


**Figure 3.** Relative infiltration velocity as a function of non-dimensional shore-normal distance. These infiltration velocity values were obtained through equation (1) for the field data (unsteady state) and equation (2) for the laboratory data (steady state).



The general nature of  $U_1$  may be expressed by

$$U_1(x) = \begin{cases} C_1 \frac{K}{n} f(x) & \text{for } x_s \leq x \leq x_R \\ 0 & \text{for } x > x_R \end{cases} \quad (3)$$

where  $f(x)$  denotes the function of shorenormal distance  $x$ ,  $x_s$  and  $x_R$  the horizontal coordinate of the shoreline and the runoff limit respectively and  $C_1$  a dimensionless infiltration coefficient.

Substituting this expression of  $U_1$  into the equation (2), the watertable overheight  $\eta$  will be independent of  $K$  and thus independent of sand size. This fact is verified by the laboratory data in Figure 4.

### Steady state inland overheight due to waves

Flume experiments were carried out to investigate the watertable response due to wave runoff without tidal effects. Sands of two different sizes ( $d_{50}=0.18\text{mm}$  and  $0.78\text{mm}$ ) were used. The relative steady state inland overheight is plotted against the relative runoff height in Figure 4.

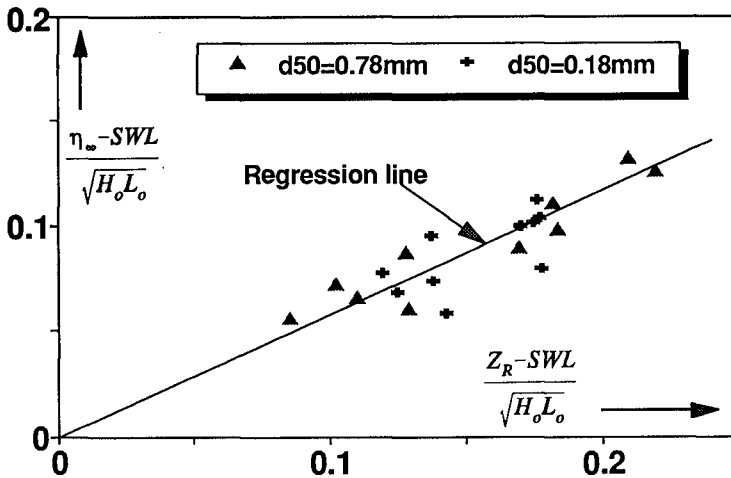


**Figure 4.** The relative inland overheight against the relative runoff height in a steady state.

From the regression analysis for both sand sizes, the steady state inland overheight above the still water level ( $\eta_{\infty}$ -SWL) is obtained as

$$\eta_{\infty}\text{-SWL} = 0.62(Z_R\text{-SWL}) \quad (4)$$

where  $Z_R$ -SWL is the runup height above the still water level. As mentioned earlier, the laboratory data in Figure 4 verify that the watertable overheight is independent of sand size and thus independent of the hydraulic conductivity  $K$ . In analogy with Hunt's (1959) formula for the runup of regular waves, equation (4) can then be written as

$$\eta_{\infty}\text{-SWL} = 0.62 \tan\beta \sqrt{H_o L_o} \quad (5)$$

where  $\tan\beta$  is the beachface slope. The data in Figure 4 represent deep water wave heights ranging from 60mm and 180mm, periods ranging from 1.5sec to 2.9sec and aquifer depths ranging from 370mm to 440mm.

### Runup distributions for irregular waves

It is natural to expect that the  $U_I$ -distribution is closely related to the runup distribution. In general the runup distribution has been found to be of the Rayleigh type. That is

$$P(Z_R > Z) = \exp\left[-\left(\frac{Z - Z_{100}}{L_R}\right)^2\right] \quad (6)$$

where  $Z_{100}$  is the highest level transgressed by 100% of the waves during the recording interval,  $L_R$  is the vertical runup scale of the distribution, see e.g. Nielsen and Hanslow (1991). Furthermore Saville (1962) and Battjes (1971) suggested that individual runup percentiles  $R_n$  correspond to the same wave height percentile through 'the principle of equivalency' which is based on Hunt's (1959) formula for the regular wave runup

$$R_n = Z_n\text{-SWL} = \tan\beta \sqrt{H_{on} L_o} \quad (7)$$

where  $Z_n$  is the level transgressed by  $n$  percent of waves and  $H_{on}$  the height exceeded by  $n$  percent of the deep water waves. The vertical runup scale  $L_R$  for irregular waves, which is RMS runup according to the Rayleigh distribution, can then be estimated in terms of  $H_{oRMS}$  value by

$$L_R = R_{RMS} = \tan\beta \sqrt{H_{oRMS} L_o} \quad (8)$$

where  $H_{oRMS}$  is the deep water root mean square wave height.

Relative runup height for regular waves and relative vertical runup scale for irregular waves were plotted together against beachface slope  $\tan\beta$  in Figure 5. This comparison is due to the concept that the runup length scale  $L_R$  for irregular waves plays a somewhat similar role to that of  $Z_R$  for regular waves. Both the field and laboratory runup data show the increasing function of the beachface slope.

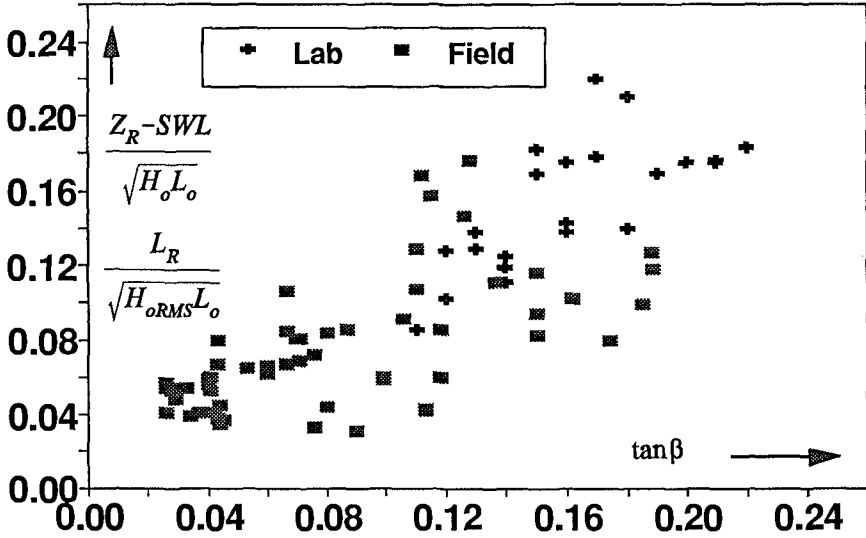


Figure 5. Comparison of runups for regular waves and irregular waves.

**Overheight for irregular waves**

The  $U_r$ -distribution due to irregular waves will be different from that due to regular waves. The reason is that while all of the regular waves run up to the same level, the runup limit, the individual waves in a train of irregular waves all reach different levels.

Field data of the watertable overheight due to waves are plotted in Figure 6. It is clearly seen that the overheight is an increasing function of the parameter  $\tan\beta\sqrt{H_{oRMS}L_o}$  which is the runup height of the RMS wave according to Hunt's formula (1959). This correlation corresponds to the overheight due to regular waves being proportional to  $\sqrt{H_o L_o}\tan\beta$ , see Figure 4. The lower group of data in the Figure 6 corresponds to a period when the exposed beach (Palm beach)

watertable does not increase much even though the RMS wave height is increasing. This is mainly due to refraction.

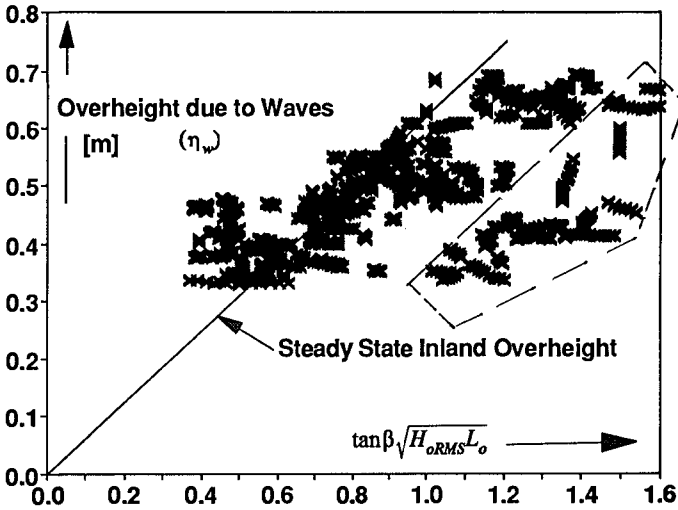


Figure 6. Watertable overheights due to waves : The differences in watertable levels between the exposed Palm Beach and the protected Pittwater Beach.

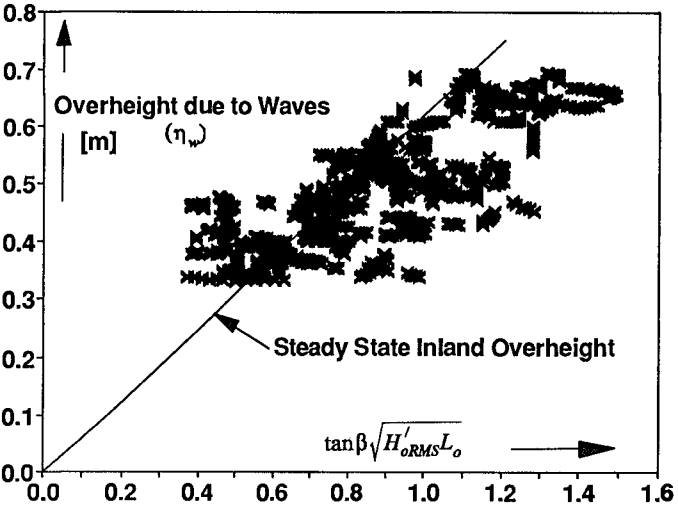


Figure 7. Watertable overheights due to waves : The differences in watertable levels between the exposed Palm Beach and the protected Pittwater Beach. The same data are used as shown in Figure 6, but refraction is accounted for by using  $H'_{oRMS}$  instead of  $H_{oRMS}$ .

After including the effect of refraction, the same data as shown in Figure 6 are plotted in Figure 7. That is, the equivalent perpendicular deep water RMS wave height  $H'_{oRMS}$  is used

$$H'_{oRMS} = K_r H_{oRMS} = \sqrt{\cos\alpha_o} H_{oRMS} \quad (9)$$

where  $K_r$  is the refraction coefficient and  $\alpha_o$  wave angle between the deep water wave crest and the shoreline. It is seen that the inclusion of refraction improves the correlation.

Figure 7 shows that the watertable overheight due to waves  $\eta_w$  is well correlated with  $\tan\beta\sqrt{H'_{oRMS}L_o}$ . linear regression gives

$$\eta_w = 0.55\sqrt{H'_{oRMS}L_o} \tan\beta \quad (10)$$

and with the vertical scale  $L_R$  of the runup distribution given by

$$L_R = 0.80\tan\beta\sqrt{H_{oRMS}L_o} \quad (11)$$

based on the data from the present study and Nielsen & Hanslow (1991), this gives ( $\alpha_o$  was not known for all data sets)

$$\eta_w = 0.69L_R \quad (12)$$

which corresponds qualitatively to the regular wave result, see Figure 5.

## Conclusions

1. There is a significant lifting of the coastal watertable due to the infiltration from wave runup.
2. The infiltration velocity from the field and laboratory data has a maximum value roughly midway between the shoreline and the runup limit.
3. For regular waves and no tide, steady state inland watertable overheight ( $\eta_w$ -SWL) was found to be  $0.62\tan\beta\sqrt{H_oL_o}$  for both coarse and fine sand sizes and thus independent of the hydraulic conductivity  $K$ .

4. For irregular waves with tides, the inland overheight due to waves  $\eta_w$  is estimated by  $0.55 \tan \beta \sqrt{H'_{\text{ORMS}} L_o}$  and the relation  $\eta_w = 0.69 L_R$  was found.
5. Use of the equivalent perpendicular deep water RMS wave height  $H'_{\text{ORMS}}$  gives better estimation of watertable overheight.

### References

- Aseervatham, A.M., H.Y. Kang and P. Nielsen (1993). Groundwater movement in beach watertables. *Proc. 11th Australasian Conf. on Coastal and Ocean Engng, IEAust*, pp. 589-594.
- Battjes, J.A. (1971). Runup distributions of waves breaking on slopes. *Journal of Waterways, Port, Coastal and Ocean Engineering, ASCE, 97WW1*, pp. 91-114.
- Hunt, I.A. (1959). Design of seawalls and breakwaters. *Proc. ASCE, V85, WW3*, pp. 123-152.
- Kang, H.Y. and P. Nielsen (1994). Wave runup and the coastal watertable. *Proc. International Conference on Hydraulics in Civil Engineering, IEAust*, pp. 283-286.
- Nielsen, P., G.A. Davis, J. Winterbourne and G. Elias (1988). Wave setup and the watertable in sandy beaches, *Tech. Rep., 88/1, Coast and Rivers Branch, PWD, Sydney, Australia*, pp. 1-62.
- Nielsen, P. (1990). Tidal dynamics of the water table in beaches, *Water Resources Research, Vol.26 No.9, September*, pp. 2127-2134.
- Nielsen, P. and D.J. Hanslow (1991). Wave runup distributions on natural beaches, *Journal of Coastal Research, 7(4)*, pp. 1139-1152.
- Saville, T. (1962). An approximation of wave runup frequency distribution, *Proc. 8th International Conference on Coastal Engineering, ASCE*, pp. 48-59.

## CHAPTER 154

### A model for cross shore sediment transport

Irene Katopodi and Nikos Kitou<sup>1</sup>

#### Abstract

In this paper a mathematical model for the computation of the cross shore sediment transport for random waves is presented. The model consists of the hydrodynamic, the suspended sediment transport and bed load modules. The suspended sediment concentration is computed with the use of the wave-averaged convection diffusion equation. The vertical structure of both the wave-induced current and suspended sediment concentration are modelled with the use of quasi-3d techniques. Mechanisms for the offshore transport (undertow) and the onshore transport (Lagrangian transport, transport due to wave asymmetry) are included. The model is tested against an experiment with random waves at prototype scale.

#### Introduction

The computation of the sediment transport, being an essential element in the understanding and ultimately the control of the morphological processes is a subject that has received a lot of attention in the last decades. Still, the complexity of the various phenomena has not allowed for predictions accurate enough for the design and maintenance of coastal works. This is one reason for the wide variety of existing mathematical models (for a review, see Roelvink and Brøker, 1993).

In the present model the hydrodynamic and the sediment transport parts are an extension of the work of Katopodi et al (1992) where the wave driven current and the suspended sediment concentration were computed with quasi-3D analytical/numerical methods. Thus the vertical distributions of the velocity and concentration were retained at a computer cost almost similar to that of depth-averaged models. Moreover, with the use of the convection-diffusion equation the horizontal variation of the concentration was resolved, a factor that it is believed to have an important impact to the bed level changes (see Katopodi and Ribberink, 1992). The model is extended for random waves and the Lagrangian drift is incorporated to account for the wave transport.

For the bed load two alternatives based on the formula of van Rijn (1985) were tried, a wave averaged and an interperiod formulation. The latter can take into account the wave asymmetry. The bed slope effect is included in both formulations.

---

1. Democritus Univ. of Thrace, Dept. of Civil Eng., 67100 Xanthi, Greece

Moreover, wave heights, set-up, wave-mean velocities and (total) sediment transport are compared with experimental data from the Delta Flume experiment (S.-Arcilla et al, 1994) conducted in prototype conditions.

### Hydrodynamics

The wave heights are computed from of the wave energy equation.

$$\frac{\partial E_f}{\partial x} = - D_b - D_f \quad (1)$$

where:  $E_f$ ,  $D_f$ , and  $D_b$  are the energy flux, the dissipation due to bottom friction and the dissipation due to breaking.

Battjes and Janssen (1978) proposed a formulation for  $D_b$  proportional to the fraction of breaking waves  $Q_b$ . They also derived the fraction of breaking waves from a simple parameterization of the breaking wave height distribution from a Rayleigh distribution.

The current velocities are computed using the quasi-3D model of de Vriend and Stive, (1987) as modified by Ribberink and de Vriend (1989) to take into account the wave boundary layer effects. This model is based on a profile function technique combined with a 2DH current formulation. The current is divided into a primary component and a number of secondary components due to the vertical nonuniformities of the various driving forces. The effects of wave breaking, bottom dissipation and boundary layer streaming are included. The velocity profile is given as a sum of components due to the various driving forces:

$$U(\zeta) = U_1(\zeta) + U_2(\zeta) + U_3(\zeta) + U_4(\zeta) + U_5(\zeta) \quad (2)$$

where  $U_1(\zeta)$ ,  $U_2(\zeta)$ ,  $U_3(\zeta)$ ,  $U_4(\zeta)$  and  $U_5(\zeta)$  are the primary current, the secondary current due to surface shear stress, the secondary current due to secondary bottom shear stress, the near-bottom drift due to spatial variation of the orbital velocity and the near-bottom drift due to the boundary layer respectively.

The wave and the current model were tested against the Delta Flume'93 experiment (see S.-Arcilla et al., 1994) conducted in the Delta Flume of Delft Hydraulics. The flume dimensions are length 225m, width 5m and depth 7m. The experiment included tests with two geometries, i.e. equilibrium parabolic Dean-type profile with and without a dune, and three "dynamic states", i.e. near-equilibrium, erosive and accretive conditions. The hydrodynamic model is tested against test 1A (profile without a dune, near equilibrium conditions). Narrow banded random waves were used and the wave characteristics were  $T=4.83$  s and  $H_{rms} = 0.62$  m. The  $D_{50}$  of the sand was 0.2 mm. The bed configuration after two hours of wave action is used for the calculations, see Fig. (2). The bed roughness is taken 1cm.

In Fig. (1a) the root-mean-square wave height computed with the model is shown together with measurements conducted with wave height meters. We can see that the overall agreement is rather good.

In Fig. (1b) the computed fraction of breaking waves is presented. Two major peaks can be seen before and after 150m. A third extreme peak appears near the shoreline ( $Q_b=1$ ). As explained by Battjes and Janssen (1978) the wave model is not valid in this region but the solution in the rest of the domain is not contaminated. Nevertheless, the unnatural



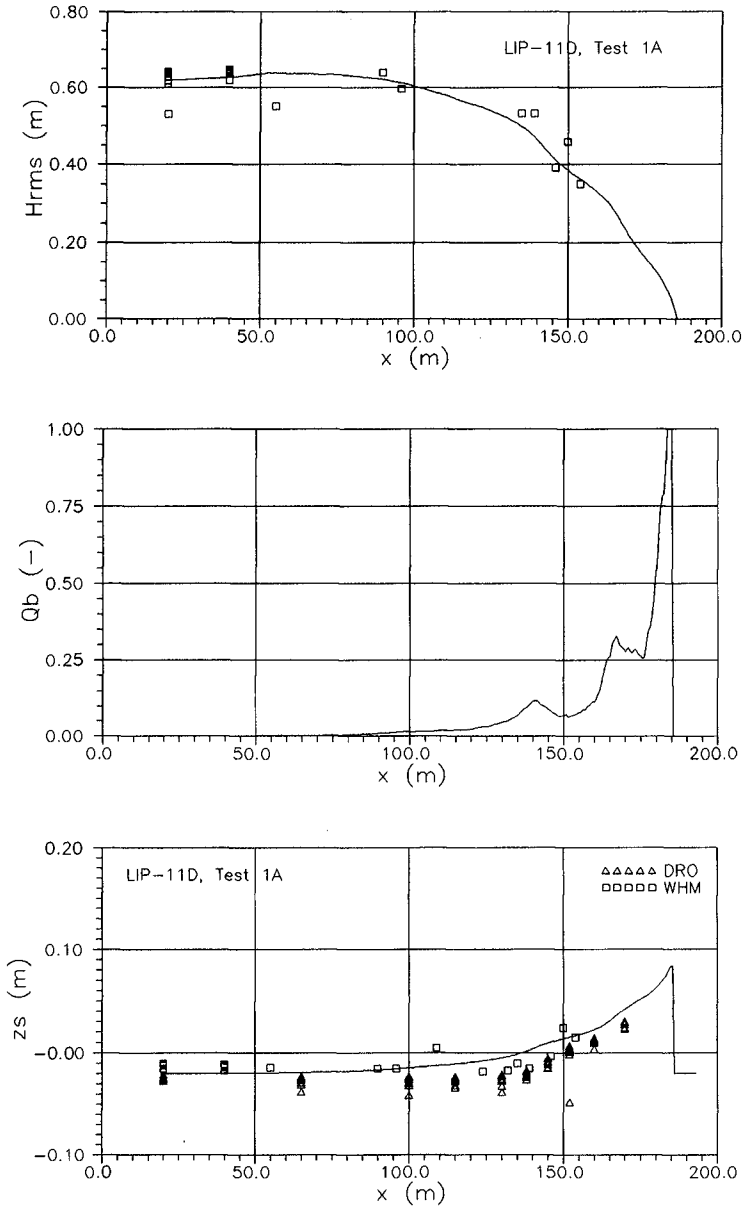


Fig.1 a) Wave height, b) Fraction of breaking waves, c) Set-up

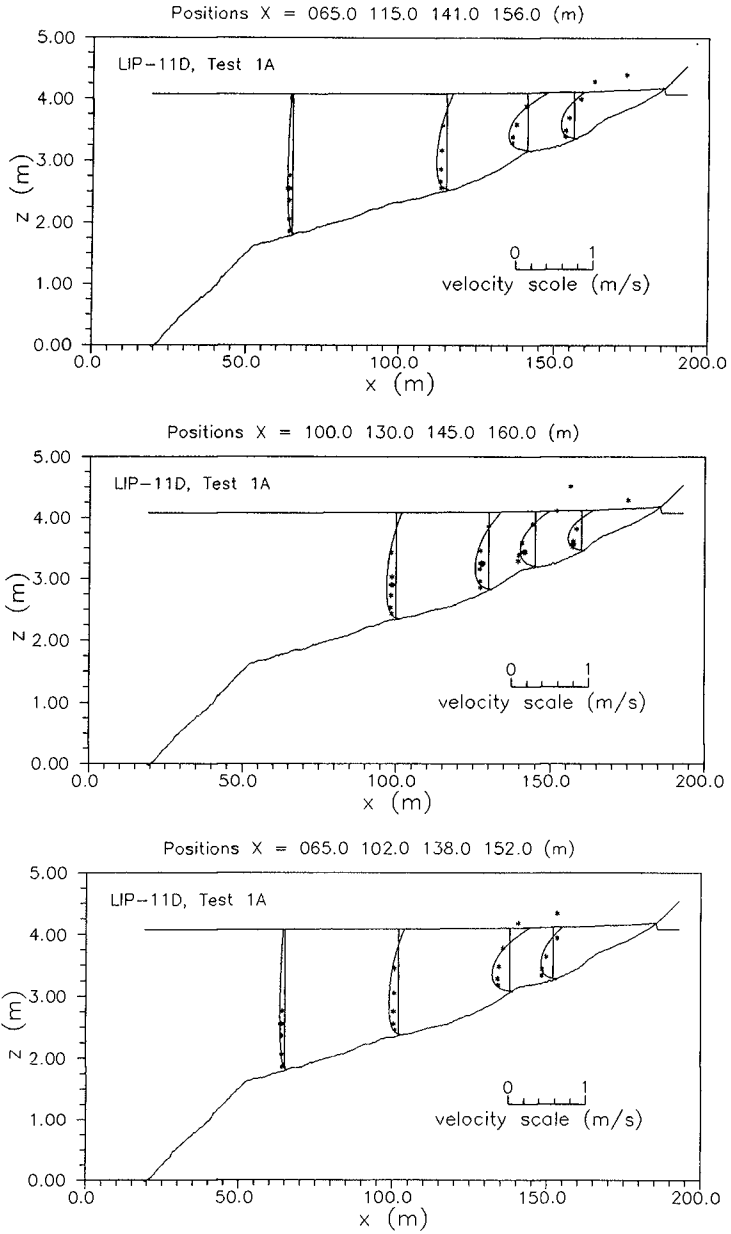


Fig.2 Velocity profiles

behaviour of  $Q_b$  close to the shoreline has a local impact in all the quantities that are computed in the following (e.g. set-up, bed shear stress, undertow, suspended sediment transport, bed load).

In Fig. (1c) the computed set-up is depicted together with measurements from wave height meters (WHM) and pressure sensors (DRO). The latter are considered more accurate (S.-Arcilla et al, 1994). We can see that the set-up is somewhat overpredicted by the model, owing to the formulation of the driving forces in the depth averaged momentum equation (set-down was excluded, see de Vriend and Stive, 1987).

In Fig. (2) the computed horizontal velocity profiles are shown together with the measurements conducted with two component electromagnetic flow meters in several cross sections. The model overpredicts the velocities in all cross-sections. In the main body of the water (under the wave trough) the curvature of the computed profiles is larger than in measurements that tend to have a more uniform profile over the depth. Yet the results are encouraging once certain aspects of the hydrodynamic model can still be improved. Of course the measurements between trough and crest should not be compared with the model due to the partial presence of the water at the sensors during the wave cycle.

### Sediment transport

The total sediment transport is the sum of the suspended sediment and the bed load transport. The suspended sediment transport is computed with the model of Katopodi et al. (1992) where the wave-induced transport caused by the Lagrangian velocity is added. The bed load is modelled with a) the formula of van Rijn (1985) derived for wave averaged transport and b) the same formula applied here for instantaneous transport during the wave cycle. In principle, the instantaneous (or interperiod) formula can take into account the wave asymmetry.

### Suspended sediment transport.

The suspended sediment is computed in terms of the suspended concentration and of the velocity. For the suspended sediment concentration the model of Katopodi and al (1992) is used (see also Katopodi and Ribberink, 1992). This model is based on an asymptotic solution (Galappatti and Vreugdenhil, 1985) of the wave averaged 3D convection diffusion equation. The model uses the mixing coefficient and the near-bed reference concentration of van Rijn (1986).

The depth averaged convection diffusion equation (Katopodi et al, 1992), reads:

$$\bar{c}_e = (1 + V_T + V_X)\bar{c} + T_A \frac{\partial \bar{c}}{\partial t} + L_X \frac{\partial \bar{c}}{\partial x} - T_A \frac{\partial}{\partial x} \left( \epsilon_x \frac{\partial \bar{c}}{\partial x} \right) \quad (3)$$

with

$$T_A = \frac{\gamma_{21}}{\gamma_{11}} \frac{h}{w_s}, \quad L_X = \left( \sum_{i=1}^n \bar{U}_i \frac{\gamma_{22,i}}{\gamma_{11}} \right) \frac{h}{w_s} \quad (4)$$

$$V_T = \left( \beta \frac{\gamma_{23}}{\gamma_{11}} + \frac{\gamma_{24}}{\gamma_{11}} \right) \frac{1}{1+\beta} \frac{\partial z_s}{\partial t} \frac{1}{w_s} \quad (5)$$

$$V_x = \sum_{i=1}^n \left( \frac{\partial}{\partial x} (\bar{U}_i h) \frac{\gamma_{25,i}}{\gamma_{11}} \right) \frac{1}{w_s} \quad (6)$$

where  $\bar{c}$  and  $\bar{c}_e$  are the depth averaged and the equilibrium concentration,  $\bar{U}_i$  the depth averaged horizontal velocities, and  $w_s$  the sediment fall velocity. The coefficients  $\gamma_{ij}$  depend only on the explicit knowledge of the vertical mixing coefficient, the fall velocity and the normalized velocity profiles and are computed before the solution of (3). The coefficient  $\beta$  is the reference level normalized by the depth  $h$ . The index  $i$  denotes the number of similarity profiles that constitute the undertow velocity ( $i=1-5$ ) and the Lagrangian drift ( $i=6$ ).

Equation (3) describes the adjustment of the depth averaged concentration to its equilibrium value. The parameters  $TA$  and  $LX$  are characteristic scales in time and space of this adjustment process (adaptation time, adaptation length). The terms  $VT$  and  $VX$  arise from the vertical coordinate transformation and from the inclusion of the vertical velocities that are computed via the continuity equation, respectively.

The above equation has been derived for "concentration" bed boundary condition (the concentration at the reference level is assumed to adapt immediately to equilibrium conditions). A similar equation holds for "gradient" bed boundary condition (the near-bed vertical gradient of the concentration adapts immediately to equilibrium conditions).

The suspended sediment transport, equation (7), actually is computed in terms of the depth averaged velocity (undertow plus Lagrangian) and concentration and of already computed coefficients (cf Katopodi and Ribberink, 1992).

$$S_x = h \int_0^1 U c \, d\zeta - h \int_0^1 \varepsilon_x \frac{\partial c}{\partial x} \, d\zeta \quad (7)$$

After equation (3) has been solved for  $\bar{c}$ , the vertical concentration profile, if desired, can be constructed in terms of already known profile functions (see Katopodi and Ribberink, 1992).

The effect of the Lagrangian velocity on the sediment particles is incorporated in the model to account for the wave induced transport. In progressive waves there is a net forward motion of the water particles related to the mass carried forward by the wave crests plus the mass deficiency carried backwards by the troughs (Longuet-Higgins, 1969). As a consequence there is also a net forward sediment transport over the wave cycle. In the computation of the concentration the Lagrangian velocity profile is incorporated as a sixth profile:

$$U_L(z) = \omega k \frac{H^2}{8} \frac{\cosh 2k(z+h)}{\sinh^2 kh} \quad (8)$$

where  $\omega$  is the wave angular frequency,  $k$  the wave number,  $H$  the wave height,  $h$  the water depth and  $z$  the vertical coordinate positive upwards the mean water level.

The integral of the above expression (8) over the depth yields the wave mass flux. Although the undertow profile and the Lagrangian profile are in volumetric balance for a steady state cross-shore case, the

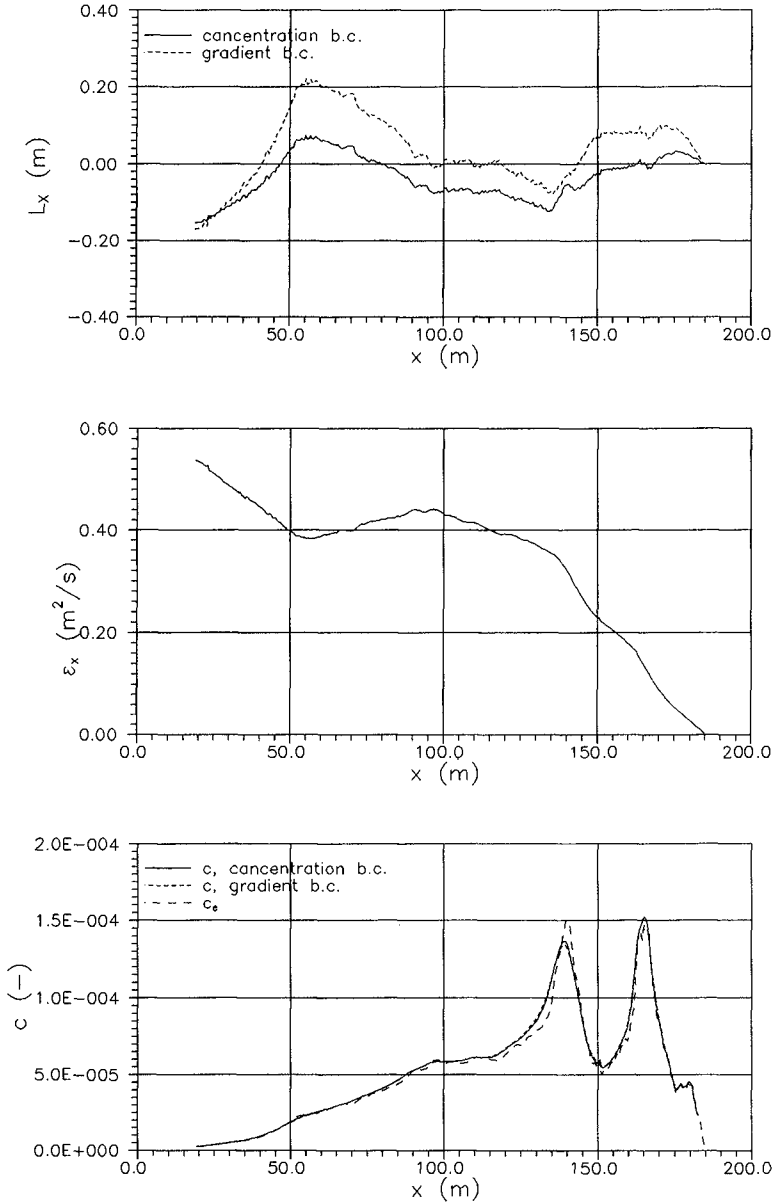


Fig.3 a) Adaptation length, b) horizontal eddy viscosity  
c) Depth-averaged concentration

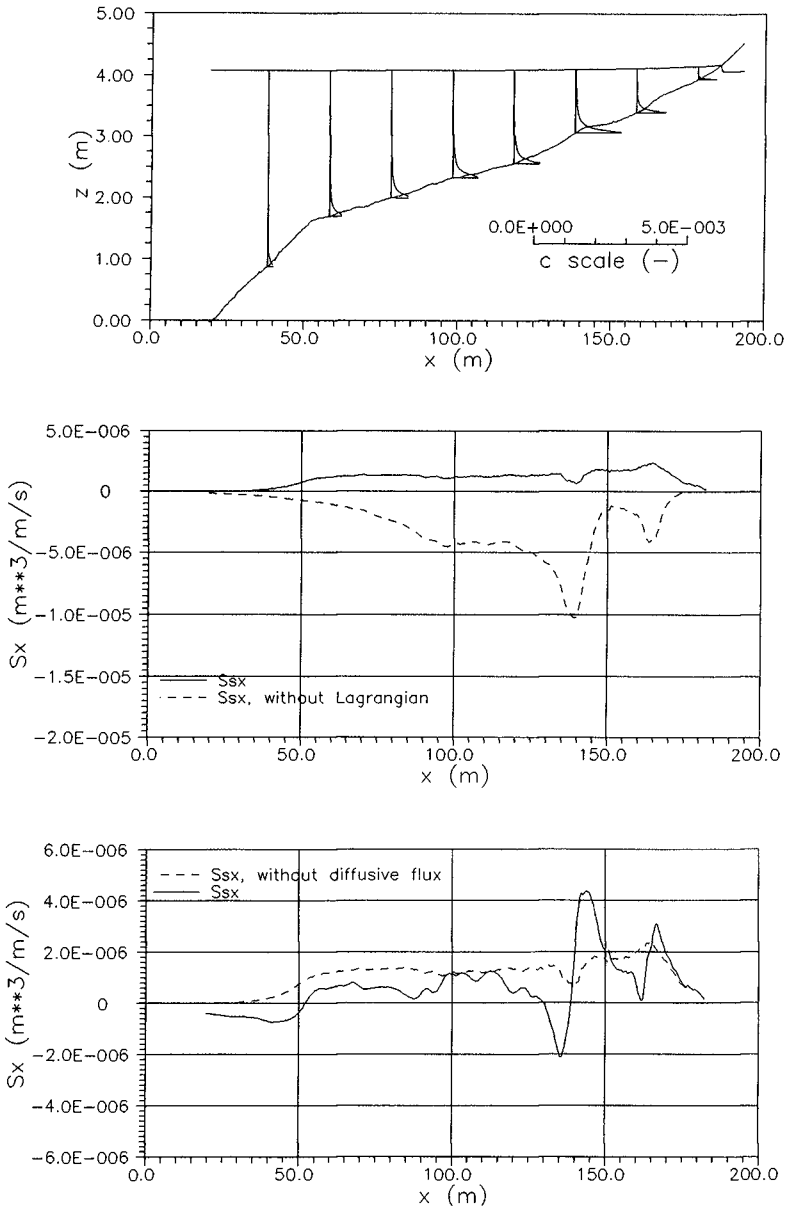


Fig.4 a) Concentration profiles along the flume.  
 b) Suspended sediment transport (with and without Lagrangian),  
 c) Suspended sediment transport (with and without diffusive part)

resultant sediment transport is not. The sign and the magnitude of the suspended sediment transport depends on the local profile shapes of undertow, Lagrangian drift and concentration.

In Fig. (3a) the adaptation length along the flume is shown for concentration and for gradient bed boundary conditions. The magnitude of the adaptation length is smaller than the space step (0.5m) and as a result the concentration is expected to be close to equilibrium (cf Katopodi and Ribberink, 1992). In Fig. (3b) the horizontal eddy viscosity for the computation of the concentration is shown (Katopodi et al, 1992).

Fig. (3c) presents the depth averaged non-equilibrium concentration for the two bed boundary conditions as well as the equilibrium concentration. Very small differences exist between the equilibrium and the non-equilibrium concentrations, as expected from the magnitude of the adaptation length. Clearly, the concentration adapts immediately to local conditions. The concentration presents two major peaks and a smaller spurious peak near the shore line.

In Fig. (4a) the profiles of the concentration are shown at various cross-sections along the flume. Not much concentration is in suspension and most of it is concentrated near the bottom.

In Fig. (4b) the suspended sediment transports computed with only the wave mean velocity and with the inclusion of the Lagrangian velocity are presented. It is clear that the Lagrangian transport is in the onshore direction and has such a strong influence on the transport that it reverses the sign of the wave mean transport everywhere in the flume.

Fig. (4c) depicts the suspended sediment transport computed with only the first term (convective transport) of equation (7) and with the second term (diffusive transport) also included. The impact of the diffusive transport is strong especially in zones with large horizontal gradients of the concentration (e.g. see the concentration peaks in Fig. 3c).

### Bed Load

For the computation of the bed load two formulations have been tried. One wave averaged and one interperiod. For the wave averaged formulation the formula of van Rijn (1985) was used:

$$\dot{S}_b = (\Delta g D_{50}^3)^{1/2} 0.053 \frac{1}{D_*^{0.3}} T^{2.1} \text{sign}(\dot{\tau}_{cw}) \quad (9)$$

where

$$T = (|\dot{\tau}_{cw}| - \tau_{cr}) / \tau_{cr} \geq 0, \quad \dot{\tau}_{cw} = \mu_c \dot{\tau}_c + \mu_w \dot{\tau}_w$$

with  $\dot{\tau}_{cw}$  the combined bed shear stress for currents and waves as function of  $\dot{\tau}_c$ ,  $\dot{\tau}_w$  the current related and wave related bed shear stress respectively. The critical shear stress for the initiation of motion (Shields) is denoted by  $\tau_{cr}$ .  $D_*$  is the dimensionless particle parameter which is function of the median particle diameter  $D_{50}$ ,  $\Delta$  is the relative apparent density of the bed material and  $g$  the acceleration of gravity.

The formula of van Rijn involves the significant wave height in the calculation of the orbital velocity. In our model  $H_s$  is computed as a function of  $H_{rms}$  and  $Q_b$ .

In the above formulation the waves are used as a stirring mechanism while the current transports the sediment. The formula was chosen because

it contains the same parameters as the reference concentration we used for the suspended sediment part and because it has well proved its validity for unidirectional flows. Of course wave asymmetry can not be implemented.

In asymmetric waves during a short fraction of the wave cycle, strong forward velocities occur transporting big amounts of sediment while during a longer fraction weak backward velocities transport small amounts of sediment. Over the whole wave cycle there is a net forward transport. For short waves (high frequencies) it can be assumed that the asymmetry effect on the sediment transport is concentrated close to the bottom (no time for the concentration to fill the water column) and as such it can be incorporated in the bed load only. For longer waves (low frequencies) the asymmetry transport should be considered for the whole depth. Near the shore the waves are asymmetric.

In order to be able to account for interperiod effects such as the wave asymmetry, following an idea of Ribberink and de Vriend (1989), the same formula (van Rijn) was also used in interperiod mode for the calculation of the instantaneous transport. The only difference now is that the wave related shear stress and consequently the dimensionless shear stress parameter  $T$  as well as the transport are functions of time and vary during the wave cycle. The bed load transport is computed by numerical integration of the instantaneous transport over the wave period.

It is understood that the formula of van Rijn has been calibrated to compute convective wave averaged transport but the use of unidirectional flow formulae for instantaneous transport has been suggested and verified before (see Ribberink and de Vriend, 1989). An additional advantage of the formula of van Rijn is that it is provided with a threshold of motion.

At first the interperiod formula was used for sinusoidal waves to check the tendencies of the bed load transport in relation to the wave averaged formula and the order of magnitude of the transport. Then, a form of asymmetry was added by using non-linear second order Stokes waves.

$$U_{orb}(t) = U_1 \cos(\omega t) + U_2 \cos(2\omega t) \quad (10)$$

In order to avoid a secondary maximum in the trough of the orbital velocity the second harmonic was bounded by the relation  $U_2 \leq U_1/5$ .

Another element taken into account in the bed load formulation is the bed slope effect. This mechanism which is present in nature plays an important role in the morphodynamic computations because it stabilizes the solution by giving the computed bed slope the natural limit of the slope of the bed material internal friction.

In the formulation chosen (see e.g. Fredsøe and Deigaard, 1992) the critical bed shear stress is scaled by a factor  $\alpha_s$  that takes into account the relation of the bed slope to the slope of the internal friction.

$$\alpha_s = \frac{\tan \phi}{\cos \beta (\tan \phi \pm \tan \beta)} \quad (11)$$

where  $\phi$  is the angle of internal friction, property of the bed material and  $\beta$  is the local bed slope. The sign (+) holds for downsloping motion of the water while the sign (-) holds for upsloping motion. In our computations the critical shear stress was taken  $0.18 \text{ N/m}^2$  and  $\phi = 25$  degrees (sand with small amount of organic material).



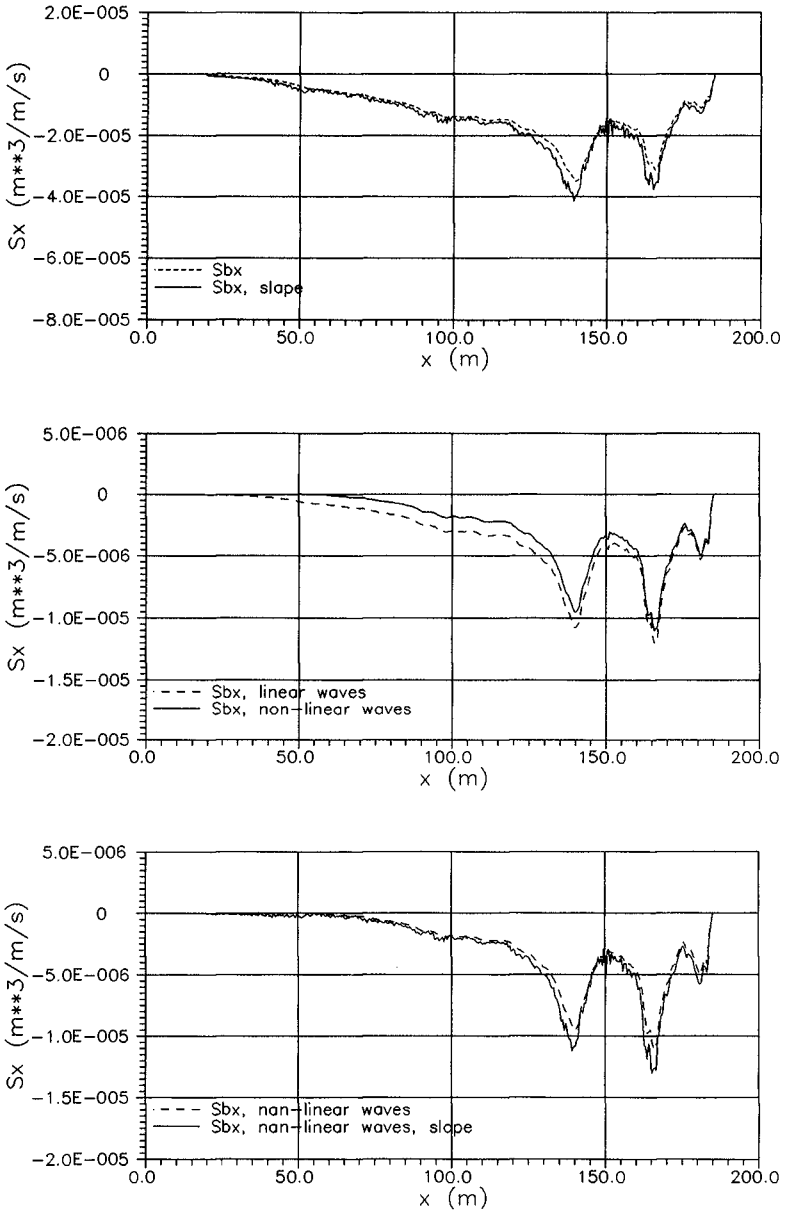


Fig.5 a) Bed load with and without slope effect (wave-averaged formula),  
 b) Bed load (interperiod formula with sin and Stokes waves),  
 c) Bed load with and without slope effect (Stokes waves)

Although the above formula has a clear meaning in instantaneous mode, it was used also for the wave-averaged formulation once the formula is equipped with the threshold of motion in the parameter  $T$ .

In Fig. (5a) the bed load transport computed with the wave-averaged formula with and without the bed slope effect is shown. Fig. (5b) presents the interperiod bed load transport computed with sinusoidal and with Stokes waves. Fig. (5c) shows the slope effect on the bed load for Stokes waves. The magnitude of the transport in the interperiod formulations is smaller than that of the wave averaged one. The tendencies though are similar as well as the positions of the bed load maxima. It looks encouraging to calibrate the formula for instantaneous use. For Stokes waves the effect of the wave asymmetry is clear compared with sin waves, especially in the offshore region where we have some onshore transport. In general, the presence of the wave asymmetry tends to add onshore transport. The bed load including the slope effect has a noisy shape but it looks that exactly this immediate reaction to the bed slope is needed for the correct computation of the bed level changes.

#### Total load

The total load is the sum of the suspended and the bed load. The total transport is presented for the wave averaged (Fig. 6a) and for the non-linear interperiod bed load formulation (Fig. 6b). We can see that the suspended transport is a small fraction of the total transport, something expected from the computation of the concentration once there is not much sand in suspension. In the interperiod formulation the suspended transport moves the main peak somewhat offshore and results in onshore transport from 50 to 70 m.

In Fig. (7a) the total transport computed with the wave averaged and the interperiod non-linear formulation is shown.

Fig. (7b) shows the measured (total) transport as derived from the measured bed levels at different times of the experiment. The transport estimated from the bed level changes between 02-07, 07-12 and 02-12 hours of the experiment is shown.

As previously mentioned, test 1A was designed to be near equilibrium and it was successful at that. The max difference in bed level between hours 02 and 12 (wave action of 10 hours) was 15 cm locally at the main bar while in most of the flume it was of the order of 1-2 cm. Such small changes would not have an important impact on the hydrodynamic and the sediment transport computations. Thus, although in our model we used the bed configuration after 02 wave hours in the experiment, the computed quantities were compared with all data regardless of the time taken. The transport estimated by such small differences contains large uncertainties. This is why we included in Fig. (7b) all three curves.

The averaged formulation seems to underpredict the transport in the deepest part of the flume (from 0 to 80m) and to overpredict (factor of 2) the transport in the region before breaking (say from 80 to 155m). The peak at 165 m is reproduced at the correct location and agrees rather well in magnitude. The peak at 145 m is shifted about 7 m offshore and its magnitude is clearly overpredicted. The small peak near the shore owes its presence to the unrealistic values of  $Q_b$ .

The interperiod model clearly underpredicts the transport. Again the two peaks in the surf zone are reproduced and the overall shape of the

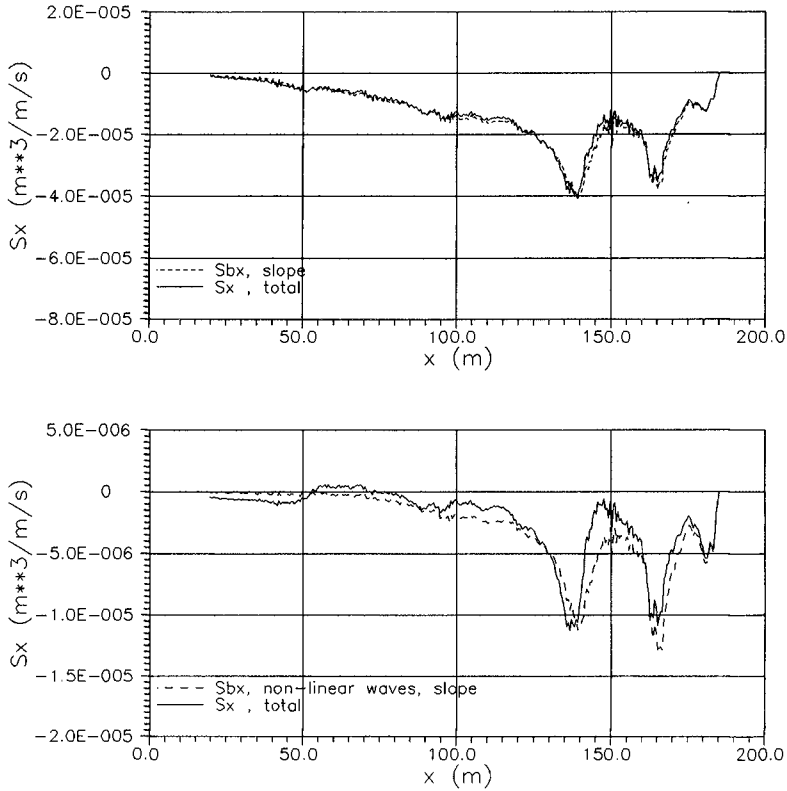


Fig.6 a) Total and bed load (wave-averaged formula),  
 b) Total and bed load (interperiod formula with Stokes waves)

transport seems to be captured. The shape can be seen more clearly in Fig. (6b). The interperiod model, although with the wave kinematics rather crudely included, seems to be promising if a new calibration of the van Rijn formula is performed.

### Conclusions

A model of cross-shore sediment transport for random waves has been presented. The model consists of the hydrodynamics module, the suspended sediment and the bed load modules. In the suspended sediment module Q-3d velocities and Q-3d concentrations are coupled in a unified formulation while the bed load includes bed slope and wave asymmetry effects.

The behaviour of the hydrodynamic model, in comparison with the Delta Flume data, was rather good. Future improvements would concern correction of the wave model near the shore and the bed shear stress formulation.

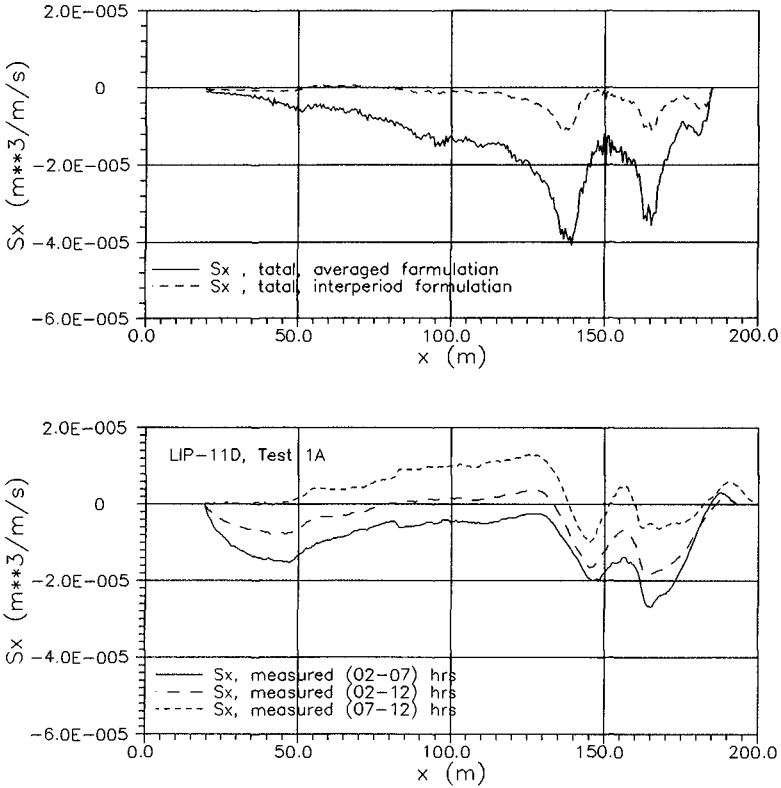


Fig.7 a) Total load (wave-averaged and interperiod formula),  
b) Total load (measured)

In the suspended sediment module, the inclusion of the Lagrangian transport was a very important step. The adaptation length for the case examined was very small (and the suspended sediment concentration almost in equilibrium), but this not always the case. The suspended sediment concentrations, although small, should be compared with experimental data.

The wave asymmetry, taken into account in the bed load, was rather conceptually modelled. The wave kinematics should be improved using a suitable wave theory.

The inclusion of the bed slope effect in the bed load is expected to have an important influence on the bed level changes.

The total load was rather good and it is expected to improve as the different modules improve.

Although the model needs certain improvements it has the advantage of integrating most of the components of the cross-shore sediment transport. The swash zone transport, although an important element (see Briand and

Kamphuis, 1993), is not taken into account but before any attempt to include it, the present model has to be improved in the coast line region.

The model should be tested for other dynamic states that would show its capabilities and limitations, starting from tests 1B and 1C of the Delta Flume experiment.

Future research will concern formulation of the model for oblique wave incidence and the coupling of the different modules through the sediment balance equation to yield the bed level evolution.

### Acknowledgment

This work was carried out as part of the MAST G8 Coastal Morphodynamics research programme. It was funded by the Commission of European Communities, Directorate General for Science, Research and Development, under MAST contract no. MAS2-CT92-0027.

### Appendix I. References

- Battjes, J.A. and Janssen, J.P., 1978.  
Energy Loss and Set-up due to Breaking of Random waves, Proc. 16th ICCE, ASCE, pp. 569-588.
- Briand H.M.G. and Kamphuis, J.W., 1993.  
Sediment transport in the surf zone: a quasi-3D numerical model. Coastal Engineering, Vol. 20, pp 135-156.
- Fredsøe, J. and Deigaard, R., 1992.  
Mechanics of Coastal Sediment Transport. World Scientific, Singapore.
- Galappatti, R. and Vreugdenhil, C.B., 1985.  
A depth integrated model for suspended sediment transport. J. Hydr. Res. Vol. 23, No. 4, pp. 359-377.
- De Vriend, H.J. and Stive M.J.F., 1987.  
Quasi-3D modelling of nearshore currents. Coastal Engineering, Vol. 11, pp. 565-601.
- Katopodi, I. and Ribberink, J.S., 1992.  
Quasi-3D modelling of suspended sediment transport by currents and waves Coastal Engineering, Vol.18, pp. 83-110.
- Katopodi, I., Kitou, N. and de Vriend, H.J., 1992.  
Coupling of a quasi-3D model for the transport with a quasi-3D model for the wave induced flow. Proc. 23rd ICCE, Venice, ASCE, pp. 2150-2163.
- Longuet-Higgins, M.S., 1969.  
On the transport of mass by time varying ocean currents. Deep Sea Research, Vol. 16, pp. 431-447.
- Ribberink, J.S. and de Vriend, H.J., 1989.  
VOORDELTA morphological study, Report H526, Delft Hydraulics.
- Roelvink, J.A. and Brøker, I., 1993  
Cross-shore profile models. Coastal Engineering, Vol.21, pp. 163-191.
- S.-Arcilla, A., Roelvink, J.A., O'Connor, B.A. and Himénez, J.A., 1994.  
The Delta Flume'93 Experiment. Proc. Coastal Dynamics'93, Barcelona, Spain, ASCE, pp. 488-502.
- Van Rijn, L.C., 1985.  
Two-dimensional vertical mathematical model for suspended sediment transport by currents and waves. Delft Hydraulics, Report H461/Q250/Q242
- Van Rijn, L.C., 1986.  
Sedimentation of dredged channels by currents and waves. J. of Waterway Port Coastal and Ocean Eng., Vol.112, No.5, pp. 541-559.

## NUMERICAL MODELLING OF FLOW OVER RIPPLES USING SOLA METHOD

Hyoseob Kim <sup>1</sup>, Brian A. O'Connor <sup>2</sup> and Youngbo Shim <sup>3</sup>

### ABSTRACT

In order to simulate flow over ripples more accurately than existing approaches, a modified MAC scheme (called SOLA) proposed by Hirt et al.(1975) was adopted in the present study. Primitive equations composed of velocities and pressure were directly solved instead of the usual vorticity and velocity potential function. The governing equations were the Reynolds momentum equations in the x and z directions and the water continuity equation. The driving force was assumed to be the acceleration of the wave orbital movement just above the wave boundary layer. A mixing length hypothesis was adopted to describe the time-and-space varying turbulent eddy viscosity and the shear stress. An explicit difference method was used to solve the equations on a regular grid. The model showed good result when applied to Sato's(1987) laboratory data. The model was applied to a series of ripple tests, using similar hydraulic conditions to Sato, to study the effect of bed ripple steepness and asymmetry. Only a small effect was found on vortex movement and flow characteristics, although a clear offshore vortex movement was found.

### INTRODUCTION

An example of the seabed shows that it is mostly covered by ripples or dunes. Waves or currents affect the generation of ripples directly or indirectly. It is widely known that the flow or sediment transport mechanism in shallow waters is closely related to the ripple parameters. It is an important step to understand the flow over ripples in order to accurately predict the sediment transport and the resulting seabed level change.

Bed material movement over ripples in the wave direction is so complicated that the wave-induced sediment transport rate or direction cannot be simply predicted by empirical formulae. Micro-scale research within the ripple length should help the understanding of sediment transport over ripples. Interesting features related to ripples have been

---

<sup>1</sup>Civil and Environmental Engineering Department, Kookmin University, 861-1 Chongnung-dong, Songbuk-ku, Seoul, Korea

<sup>2</sup>Civil Engineering Department, Liverpool University, P.O.Box 147, Liverpool, L69 3BX, U.K.

<sup>3</sup>Civil Engineering Department, Sung Kyun Kwan University, Chunchun-dong, Changan-ku, Suwon, Korea

reported by previous researchers. For example, vortex generation and its contribution to the suspended sediment transport has been well described by previous laboratory or numerical works.

After Bagnold's(1946) pioneering investigation on flow over ripples, laboratory experiments on the flow or sediment movement over ripples have been carried out by Du Toit and Sleath(1981), Sato(1987), Horikawa and Ikeda(1990), Ranasoma and Sleath(1992), and Horikawa and Mizutani(1992). Numerical modelling works have also been undertaken to examine flow or sediment movement over ripples. One ripple length has usually been used as the computational domain of the models. Existing numerical models have adopted the procedure of solving a vorticity equation and a velocity potential function. The existing models can be classified into two groups, an Eulerian grid group, and a Lagrangian discrete vortex method group. Typical models of the former type include Sato S.(1987), Blondeaux and Vittori(1991), Huynh-Thanh and Temperville (1990), and Sato Y. and Hamanaka(1992), while typical models of the latter type include Hansen et al.(1992). The method of solving the vorticity equation is known to have some merits. For example, the continuity equation is automatically satisfied and the pressure need not be solved. However, it has a problem in assigning adequate boundary values at rigid boundaries which is not easy because of the rapidly varying vorticity near them. Once the vorticity field is obtained, the velocity potential function should be solved from the Poisson equation. This procedure involves an iteration step, and produces numerical error, which is a negative aspect of this approach. Model results of the vorticity type proposed by previous investigators have shown rather poor agreement with measured experimental data sets upto the present. Therefore, it is proposed to adopt a method to solve the primitive velocities and pressures instead of the vorticity and velocity potential functions, and compare the two methods.

In the present study, the primitive variables are solved by an existing SOLA method to simulate flow over ripples. A mixing length hypothesis in the zero-equation turbulence closure was adopted to express time-and-space varying turbulent eddy viscosity. The SOLA approach is composed of explicit finite difference schemes. The present model uses a regular grid so that an arbitrary rigid bed boundary geometry can be easily expressed and modified by the rectangular grid points.

The present model is applied to synthetic situations to examine the effect of ripple steepness and non-uniform ripple shape.

## **MODEL DESCRIPTION**

### **Governing Equations**

We have four basic equations for incompressible fluid dynamics, i.e. water continuity and the Reynolds momentum equations in three directions. To simplify the problem, a two-dimensional vertical situation was assumed so that the gradient terms in the y direction disappear in the equations. Then, the governing equations are the water continuity and two Reynolds

momentum equations in the  $x$  and  $z$  directions:

- Continuity Equation

$$\frac{\partial \bar{u}}{\partial x} + \frac{\partial \bar{w}}{\partial z} = 0 \quad (1)$$

- Momentum Equations

$$\begin{aligned} \frac{\partial \bar{u}}{\partial t} + \bar{u} \frac{\partial \bar{u}}{\partial x} + \bar{w} \frac{\partial \bar{u}}{\partial z} \\ = -\frac{1}{\rho} \frac{\partial \bar{p}}{\partial x} + \left( \frac{\partial(\overline{u'u'})}{\partial x} + \frac{\partial(\overline{u'w'})}{\partial z} \right) + \nu \left( \frac{\partial^2 \bar{u}}{\partial x^2} + \frac{\partial^2 \bar{u}}{\partial z^2} \right) \end{aligned} \quad (2a)$$

$$\begin{aligned} \frac{\partial \bar{w}}{\partial t} + \bar{u} \frac{\partial \bar{w}}{\partial x} + \bar{w} \frac{\partial \bar{w}}{\partial z} \\ = -\frac{1}{\rho} \frac{\partial \bar{p}}{\partial z} + \left( \frac{\partial(\overline{u'w'})}{\partial x} + \frac{\partial(\overline{w'w'})}{\partial z} \right) - g + \nu \left( \frac{\partial^2 \bar{w}}{\partial x^2} + \frac{\partial^2 \bar{w}}{\partial z^2} \right) \end{aligned} \quad (2b)$$

where,  $x, z$  are horizontal and vertical cartesian coordinates, respectively;  $u, w$  are the instantaneous velocity components in the  $x, z$  directions, respectively;  $\bar{u}, \bar{w}$  are the time-mean velocity components in the  $x, z$  directions, respectively;  $u', w'$  are the turbulent fluctuation velocity components in the  $x, z$  directions, respectively;  $\bar{p}$  is the pressure;  $g$  is the acceleration due to gravity; and  $\nu$  is the kinematic viscosity.

The momentum equations are further simplified, firstly, by ignoring the molecular viscosity. Secondly, the turbulent normal stresses are included in the pressure terms. The Reynolds stress term  $\overline{u'w'}$  requires a turbulent closure to complete the system.

### Turbulent closure

Boussinesq's eddy viscosity concept was adopted in the present study. The turbulent stress was assumed to be proportional to the mean-velocity gradients, that is:

$$-\overline{u'w'} = \nu_t \left( \frac{\partial \bar{u}}{\partial z} + \frac{\partial \bar{w}}{\partial x} \right) \quad (3)$$

Prandtl's mixing-length hypothesis was also applied to express the time and space varying turbulent eddy viscosity. Prandtl's mixing length hypothesis relates the eddy viscosity to the local mean velocity gradient and involves a single unknown parameter, the mixing length  $l_m$  as follows:

$$\nu_t = l_m^2 \cdot \left| \frac{\partial \bar{u}}{\partial z} + \frac{\partial \bar{w}}{\partial x} \right| \quad (4)$$

where  $\nu_t$  is the turbulent eddy viscosity,  $l_m$  is the mixing length ( $= \kappa l_{sb}$ ),  $\kappa$  is the von Karman constant, and  $l_{sb}$  is a length scale. In the present model,  $l_{sb}$  is assumed to be the shortest distance from the calculation point to the solid boundaries.



## Boundary conditions

Three kind of boundary conditions were applied in the present model. A zero velocity condition was used at the rigid bottom boundary, and a periodic condition in a ripple length was used at the two side boundaries. At the top boundary a zero shear stress condition was applied where no influences are assumed to be reached at the height of two ripple lengths.

The solution of the Reynolds equations yields velocity and pressure distribution in the flow field. When a submerged structure is exposed to fluid motion, non-uniform pressure distribution occurs adjacent to the structure. In solving the Reynolds equation, this pressure distribution gets into trouble. The MAC(Marker-And-Cell) method was proposed by Welch et al.(1965) at Los Alamos Scientific Laboratory(LASL) of the University of California to treat the problem. After then, the SMAC was proposed by Amsden et al.(1970) and the SOLA by Hirt et al.(1975) at LASL. The SOLA scheme uses a simple method to calculate the pressure by adjusting the tentative velocities iteratively until changes are within a given tolerance in the whole computational domain.

## MODEL VERIFICATION

The present model with the SOLA method was tested against Sato's(1987) laboratory results for non-uniform waves, and asymmetric ripple geometry (Case 7), in order to examine its validity. The ripple had asymmetric geometry with a round crest. The ripple length was 12 cm; the ripple height was 2 cm. The generated waves were close to the Stokes third order wave; first, second, and third harmonics of the near bed orbital velocity amplitude were -29.5, -7.611, and -1.416 cm/s, respectively. Sato's(1987) asymmetric ripple profile was tested, which had a round crest shape.

The spatial increments in the x, z directions were both 0.25 cm. The time increment was 1/800 of the wave period of 2 seconds. The parameter which controls the accuracy of the continuity equation in the SOLA method was chosen to be sufficiently small. The CPU required for the execution of five real wave periods was typically 7200 seconds on a CRAY-2S/YMP machine.

## Flow Field

The vorticity or the shear stress are directly related to the flow information. The model should be able to reproduce the flow fields first. The calculated and measured velocity fields were found to match reasonably well for the whole wave period. Fig. 1 shows the calculated velocities at the wave phase of  $19\pi/10$ (see Fig.10), and Fig. 2 shows the measured velocities at the wave phase of  $3\pi/10$  of Sato's experiment as same phase with this study. The present model results reproduces the correct position and size of the vortex. The above phase is for the flow reversing time, and clearly shows the newly-generated vortex over the ripple trough. It should be mentioned that the present model results show

better agreements with the laboratory experimental data sets than the previous vorticity model results, although the previous models are not systematically assessed in the present work.

### **Vertical Distribution of horizontal velocities**

Fig. 3 shows that the calculated horizontal velocity profile over the ripple trough at the wave phase of  $19\pi/10$  agrees well with the measured values for Sato's experimental conditions. The present model also reproduced the correct position and size of the wave-induced vortex throughout the wave period. The horizontal velocity profile agrees well with the measured one above the level of about half a ripple height from the ripple trough, while the agreement becomes less good near the ripple surface. This would partially be due to the unsatisfactory presentation of the smooth seabed shape with the regular grid.

### **Residual Currents**

Since the residual flow is the secondary flow, it is expected that the agreement between calculated and measured residual flow may not be so good as that of the primary flow. The calculated and measured residual currents (wave period average velocities) are shown in Figs. 4 and 5 respectively. Sato's laboratory wave condition was close to the Stokes third order wave theory, and the order of magnitude of the measured residual current over ripples was about 0.1 cm/s in the offshore direction. The calculated residual current shows similar magnitude and direction, although the separated small circulation cell just next to the ripple crest shows a slightly different pattern from the measured one. The reason for the deviation may eventually be the boundary treatment techniques, which require further investigation.

### **Vorticity Contours**

The vortex (circulation cell) was well reproduced by the present model at the lee of the ripple crest at the wave phase of  $19\pi/10$  in Fig. 6. The calculated vorticity field gives reasonable agreement on the vorticity magnitude with the Sato's laboratory experiment shown in Fig. 7. The secondary vortex proposed by Blondeaux et al.(1991) was also well reproduced by the present model just over the ripple surface.

### **Effect of Sharp Crest Shape**

In order to examine the effect of ripple crest shape (round and sharp), the present model was applied to a sharp crested ripple profile. The ripple crest shape of Sato's Case 7 experiment was modified from a round to a sharp shape for the present numerical test, while all the other parameters for the experiment were retained. The calculated flow field for the sharp crested ripple at the wave phase of  $19\pi/10$  is shown in Fig. 8. The position of the vortex centre is higher, and the area occupied by the vortex is larger than that for the round crested ripple case, as expected. The inter-wave-period (IWP) variation of the maximum absolute vorticities over the round and sharp crested ripples are shown in Fig. 9, which

reveals that the maximum absolute vorticities for the sharp-crested ripple were larger than those for the round crested ripple.

**MODEL APPLICATION**

**Application Conditions**

In order to examine the effect of ripple steepness and ripple asymmetry on the flow over ripples, the present numerical model was applied to various artificial conditions. The model run conditions were the water depth of 40 cm; the wave height of 15 cm; the wave period of 2 seconds. The waves were assumed to be the Stokes third order waves, i.e. the near-bed wave orbital velocity was obtained from the following equation(refer to Fig. 10)

$$u_{\infty} = c ( F_1 \cdot \cos \omega t + F_2 \cdot \cos 2\omega t + F_3 \cdot \cos 3\omega t ) \tag{ 5 }$$

where  $u_{\infty}$  is the near-bed wave orbital velocity outside the wave boundary layer.  $c$  is the wave celerity.  $F_1, F_2,$  and  $F_3$  are the constants in the Stokes third order wave.  $g$  is the acceleration due to gravity.  $k$  is the wave number ( $k = 2\pi/L$ ).  $\omega$  is the angular frequency ( $\omega = 2\pi/T$ ).  $h$  is the water depth.  $a$  is the wave amplitude.  $L$  is the wave length.  $T$  is the wave period. The coefficients of equation (5) can be obtained from following relationships:

$$c^2 = \frac{g}{k} \cdot \tanh(kh) \cdot \left( 1 + a^2 k^2 \frac{8 \cosh^4(kh) - 8 \cosh^2(kh) + 9}{8 \sinh^4(kh)} \right) \tag{ 6 }$$

$$F_1 = \frac{a k}{\sinh(kh)} \tag{ 7a }$$

$$F_2 = \frac{3}{4} \frac{a^2 k^2}{\sinh^4(kh)} \tag{ 7b }$$

$$F_3 = \frac{3}{64} \frac{a^3 k^3 \{13 - 4 \cosh^2(kh)\}}{\sinh^7(kh)} \tag{ 7c }$$

$$a = \left( \frac{H}{2} \right) / \left[ 1 + a^2 k^2 \frac{3 \{8 \cosh^6(kh) + 1\}}{64 \sinh^6(kh)} \right] \tag{ 8 }$$

where  $H$  is the wave height.

The ripple dimensions (length and height) were calculated from Nielsen's(1981) empirical formulae. The ripple profile for the given ripple dimensions was obtained from the following equations proposed by Sleath(1974):

$$x = X_c - (\eta/2) \sin(2\pi X_c / \lambda) \tag{ 9a }$$

$$z = (\eta/2) \cos(2\pi X_c / \lambda) \tag{ 9b }$$

where  $X_c$  is the parameter for a curvilinear coordinate;  $x, z$  are the horizontal and vertical cartesian coordinates, respectively; and  $\eta, \lambda$  are the

ripple height and the ripple length, respectively.

In order to examine the effect of ripple steepness and asymmetry, a fixed ripple length was chosen. The wave height of the ripple ( $\eta$ ) varied between 1.0 and 2.0 cm, and the longer half of ripple length ( $\lambda_1$ ) varied between 4.5 to 6.3 cm. Ripple geometries for the tests are given in the following table:

**Table 1** Ripple geometries for numerical tests

Run Case	Ripple Length (cm)				Height (cm)		Remarks
	$\lambda_1$	$\lambda_2$	$\lambda$	$\lambda_1/\lambda$	$\eta$	$\eta/\lambda$	
RS-1					1.00	0.11	Variation of Ripple Steepness
RS-2					1.25	0.14	
RS-3	4.5	4.5	9.0	0.5	1.50	0.17	
RS-4					1.75	0.19	
RS-5					2.00	0.22	
RA-1	4.50	4.50		0.50	1.50	0.17	Variation of Ripple Asymmetry
RA-2	4.95	4.05		0.55			
RA-3	5.40	3.60	9.0	0.60			
RA-4	5.85	3.15		0.65			
RA-5	6.30	2.70		0.70			



$\eta$  : Ripple height  
 $\lambda$  : Ripple length  
 $\lambda_1$  : Longer half length of ripple  
 $\lambda_2$  : Shorter half length of ripple

## Application Results

Fig. 11 shows the typical flow pattern at a wave phase for case RS-5. Fig. 11 confirms the fact that the near-bed flow turns its direction before the ambient flow (outside the wave boundary layer) turns its direction. Existing one-dimensional vertical wave boundary layer models have also produced the phase shift between the ripple-length-averag boundary layer flow and the outside boundary layer flow. However, the two-dimensional vertical model can track the detailed movement of vortices which directly affect the sediment transport in suspension or as bed load.

### 1) Vertical distribution of horizontal velocities

Fig. 12 (a) shows the vertical distribution of horizontal velocities over the ripple trough at the wave phase of  $18\pi/10$  for various ripple steepnesses, and Fig. 12 (b) for various ripple asymmetry. The centre of the strong vortex generally positions at the ripple crest level. Another weak vortex at the two ripple height is also seen in Fig. 12. The vertical distribution of horizontal velocities for various cases is nearly the same at the upper part above two ripple heights ( $2.0\eta$ ) from the ripple trough.

If the ripple is steep, the level of the vortex centre is generally high at

the wave phase of  $18\pi/10$ . However, if the wave period is not long enough, the vortex cannot grow sufficiently to fill the ripple space between the two crests.

Fig. 12 (b) shows that the position of the vortex centre and the vertical distribution of horizontal velocities are almost the same for various ripple asymmetry. The ripple asymmetry seems not to affect the vortex movement very much.

## 2) Time variation of horizontal velocities

The time variation of horizontal velocities at ripple crest is shown in Figs. 13 (a) and (b). At the ripple crest the horizontal velocities show little difference for various ripple steepness or asymmetry. In contrast to the ripple crest, the velocities at the ripple trough surface for various ripple steepness, see Figs. 13 (c), produces the double peak time variation of horizontal velocity. This pattern is closely related to the vortex motion over the ripple trough.

## 3) Track of vortex

Bagnold(1946) briefly described the track of a vortex over the ripples. Longuet-Higgins(1981) presented the vortex motion by time series using his discrete vortex model. He proposed that the vortex would reach upto the level of  $2.5\lambda$  when the water particle excursion length ( $d_0$ ) is  $1.5\lambda$  from his discrete vortex model results.

In the present study, the track of the separated vortex from the ripple crest was calculated for the case RS-3, see Fig. 14. The calculated movement of the two vortices generated in the onshore and offshore directions is not symmetric due to the asymmetry of the wave orbital velocity in both directions. The vortex generated at the lee side of the ripple crest moves about  $2.5\lambda$  in the onshore direction and disappears, i.e. the vorticity approaches zero after about a wave period time. On the other hand, the vortex generated at the front side of the ripple crest moves about  $3.0\lambda$  in the offshore direction and turns its direction. It disappears after about one and half wave periods.

The movement of the vortex generated at the lee side of the ripple crest for case RS-3 can be divided into 3 phases. The first phase is the generation phase. This starts at the wave phase of about  $3\pi/10$ . The vortex centre moves slightly upwards by the strong offshore ambient wave orbital velocity and slightly sinks down at the wave phase of  $7\pi/10$  due to the weak wave orbital velocity until the wave phase of  $11\pi/10$ . The second phase is the rising phase by the change of the wave orbital velocity direction. During the second phase, the vortex departs from the ripple trough by the onshore return flow. The third phase is the free vortex phase. The rising phase between the wave phase of  $3\pi/10$  and  $11\pi/10$  produces the two peak time variation of horizontal velocity at the ripple trough surface, see Fig. 13 (c).

The behaviour of the vortex generated at the front side of the ripple

crest shows quite different behaviour, i.e. asymmetric movement to the former pair vortex, see Fig. 14. The movement of the vortex generated at the front side of the ripple crest can also be divided into 3 phases. The vortex rises from the wave phase of  $15\pi/10$  to  $19\pi/10$ . The vortex starts to turn its direction at the wave phase of  $19\pi/10$  by the outside return flow. The distance moved is about  $3.0\lambda$ .

#### 4) Vorticity

The vorticity contours for the wave phase of  $19\pi/10$  are shown in Fig. 15. It is interesting to note that the smaller the ripple steepness ( $\eta/\lambda$ ), the larger the vorticity of the separated vortex as shown in Fig. 16 (a) and the maximum vorticity of the separated vortex for all cases was between  $33\text{--}38 \text{ sec}^{-1}$ . If the ripple became steeper, the area occupied by the vortex was expanded. The ripple surface provides higher energy dissipation rate due to the strong bed shear stress which may reduce the vorticity at the vortex centre. On the other hand, ripple asymmetry (cases RA-1 to 5) shows little effect on the vorticity of the separated vortices, see Fig. 16 (b).

The maximum vorticity is shown in Fig. 17 for various ripple steepness and asymmetry at a wave phase of  $15\pi/10$ .

The time variation of maximum vorticity on the ripple surface is presented in Fig. 18 for the cases of ripple steepness and asymmetry variation. In this figure, (+) value indicates the clockwise vorticity.

#### 5) Bottom shear stress

Longuet-Higgins(1981) derived a horizontal velocity distribution for oscillatory laminar boundary layer from the Navier-Stokes equation. Bottom shear stress for oscillatory laminar boundary layer can be derived from that formula, and the phase different between the bottom shear stress and the water particle velocity outside the oscillatory laminar boundary layer is known to be  $45^\circ$ .

In the present study, the bottom shear stress can be calculated from the mixing length assumption, i.e. the multiplication of the mixing length squared and the gradient of vertical velocity as follows:

$$\frac{\tau_b}{\rho} = l_m^2 \left| \frac{\partial \overline{u_p}}{\partial n} \right| \left( \frac{\partial \overline{u_p}}{\partial n} \right) \quad (10)$$

where  $l_m$  is the mixing length ( $l_m = \alpha \cdot l_{sb}$ ),  $l_{sb}$  is the shortest distance from the calculation point to the solid boundaries,  $\alpha$  is the von Karman's constant(0.4),  $u_p$  is the velocity parallel to the solid boundary surface, and  $n$  is the normal direction to the solid boundary.

The time variation of bottom shear stress divided by the density ( $\tau_b/\rho$ ) and water particle velocity(non-scale) at the ripple crest is shown in Fig.

19. Jonsson and Carlsen(1976) proposed that that the phase shifts between the wave orbital velocity and the bed shear stress are  $18^\circ$  and  $31^\circ$  in the onshore and offshore directions, respectively, for a rough turbulent flow over a flat bed with relatively small roughness. The phase differences for the turbulent flows are smaller than that ( $45^\circ$ ) for the laminar flow.

The present model results show that the phase shift between the bottom shear stress and the water particle velocity for the test cases are between  $16^\circ$  and  $40^\circ$ . The value varied depending on the vortex strength. The steeper the ripple, the bigger the phase difference. For the less steep ripple of case RS-1, the phase shift was  $16^\circ$  and  $30^\circ$  in the onshore and offshore directions, respectively. For the steep ripple of case RS-5, the phase shift was  $25^\circ$  and  $40^\circ$  in the onshore and offshore directions, respectively. The ripple asymmetry gives little influence on the phase shift between the bottom shear stress and the water particle velocity.

## CONCLUSIONS

A numerical model is proposed here to obtain the wave-induced turbulent flow information over ripples. The present model directly solves primitive velocities and pressure from the continuity and Reynolds momentum equations. The calculation of pressure term followed the existing technique, SOLA. The turbulence was modelled by a mixing length zero-equation closure. A regular model grid was chosen for the present model.

The numerical model was firstly verified using Sato's laboratory experimental conditions. The model results generally agree well with the measured values in the velocity field, vorticity, and the residual flow field.

The model was then applied to various situations to assess the importance of ripple steepness and asymmetry. In order to examine the effect of ripple steepness and asymmetry, the waves were assumed to be Stokes third order waves. The two vortices generated in the onshore and offshore directions move in a different manner due to the asymmetry of the wave orbital velocity. It moves  $2.5\lambda$  in the onshore direction, and  $3.0\lambda$  in the offshore direction. The vorticity becomes very small after about 1.5 wave periods.

The smaller the ripple steepness, the larger the vorticity for the separated vortex. If the ripple became steeper, the area occupied by the vortex was expanded. The ripple surface provides higher energy dissipation rate due to the strong bed shear stress which may reduce the vorticity at the vortex centre.

The time variation of horizontal velocity at the ripple trough surface shows two peaks, which become clearer for steeper ripples because of the strong vorticity. The two peaks can only be explained by the vortex movement.

The phase differences between the wave orbital velocities outside the

wave boundary layer and the bottom shear stresses at the ripple crest are shown to be about  $30^\circ$  on average. The phase difference slightly varies depending on the vortex strength at the ripple crest.

Judging from the model results, ripple asymmetry gives only a small influence on the vortex movement or the flow characteristics over the ripples.

## ACKNOWLEDGEMENTS

The authors are grateful for financial assistance from the Commission of the European Directorate General for Science, Research and Development under Contract No. MAS2-CT92-0024C. The present work was also undertaken as part of the research project, "The numerical modelling of sediment transport taking account of wave boundary layer characteristics" granted by Cray Research Inc., and System Engineering Research Institute, KIST.

## REFERENCES

- Amsden, A.A. and Harlow, F.H. 1970. The SMAC Method-A numerical Technique for calculating incompressible fluid flows. Los Alamos Scientific Laboratory of the Univ. of California
- Bagnold, R.A. 1946. Motion of Waves in Shallow Water Interaction Between Wave and Sand Bottoms. Proc., Royal Society of London, Series A, Vol. 187.
- Blondeux, P. and Vittori, G. 1991. Vorticity dynamics in an oscillatory flow over rippled bed. J. of Fluid Mech., Vol. 226, pp 257-289.
- DuToit, C.G. and Sleath, J.F.A. 1981. Velocity measurement close to rippled beds in oscillatory flow, J. of Fluid Mech., Vol. 112, pp 71-96.
- Hansen, E.A., Fredsoe, J. and Deigaard, R. 1992. Distribution of suspended sediment over wave-generated ripples. J. of Waterway, Port, Coastal, and Ocean Engineering Vol. 120. No1. ASCE. pp 37-55
- Hirt, C.W., Nichols, B.D. and Romero, N.C. 1975. SOLA-A numerical solution algorithm for transient fluid flows. Los Alamos Scientific Laboratory of the Univ. of California
- Horikawa, K. and Ikeda, S. 1990. Characteristics of oscillatory flow over ripple models, 22nd Coastal Engineering Conference, ASCE, pp 661-694
- Horikawa, K. and Mizutani, S. 1992. Oscillatory flow behavior in the vicinity of ripple model, 23rd Coastal Engineering Conference, ASCE, pp 2122-2135
- Huynh-Thanh, S. and Temperville, A. 1990. A numerical model of the rough turbulent boundary layer in combined wave and current interaction, 22nd Coastal Engineering Conference, ASCE, pp 853-867
- Jonsson, I.G. and Carlsen, N.A. 1976. Experimental and theoretical investigations in an oscillatory turbulent boundary layer, J of



Hydraulic Research

Longuet-Higgins, M.S. 1981. Oscillating flow over steep sand ripples, *J. of Fluid Mech.*, Vol 107, pp 1-35

Nielsen, P. 1981. Dynamics and geometry of wave-generated ripples, *J. Geophys. Res.*, Vol 86, No C7., pp 6467-6472

Ranasoma, K.I.M. and Sleath, J.F.A. 1992. Velocity measurements close to rippled beds, 23rd Coastal Engineering Conference, ASCE, pp 2383-2396

Sato, S., 1987. Oscillatory boundary layer flow and sand movement over ripples. Ph.D. Thesis, The University of Tokyo, Tokyo, Japan.

Sato, Y. and Hamanaka, K. 1992. Quasi-turbulent boundary layer of oscillatory flow over ripples, 23rd Coastal Engineering Conference, ASCE, pp 2424-2437

Sleath, J.F.A. 1974. Mass Transport over a Rough Bed, *J. of Marine Research*, pp 13-24

Welch, J.E., Harlow, F.H., Shannon, J.P. and Daly, B.J. 1965. The Mac Method A computing technique for solving viscous, incompressible, transient fluid-flow problems involving free surfaces. Los Alamos Scientific Laboratory of the Univ. of California

FIGURES

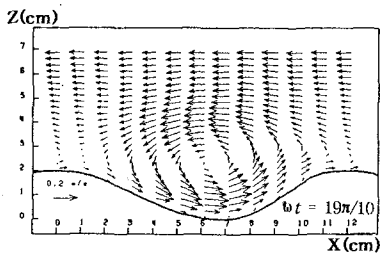


Fig. 1 Calculated flow field over a round crest

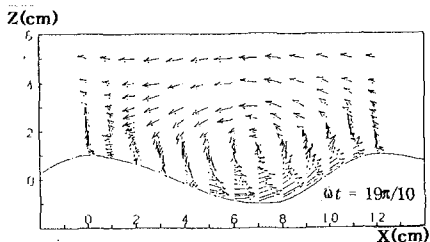


Fig. 2 Measured flow field over a round crest(after Sato, 1987)

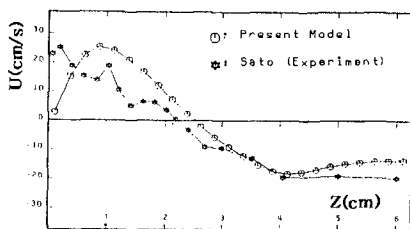


Fig. 3 Comparison of horizontal velocities over a ripple trough

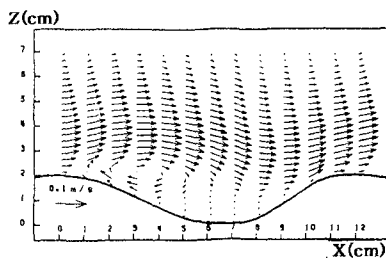


Fig. 4 Calculated residual flow field over a round crest

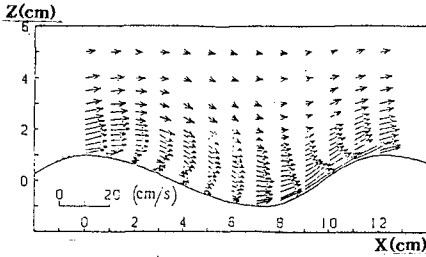


Fig. 5 Measured residual flow field over a round crest (after Sato, 1987)

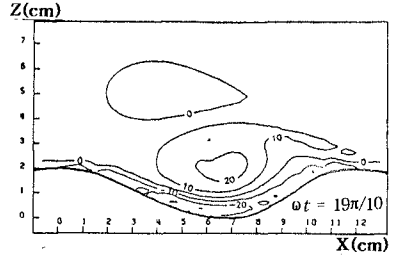


Fig. 6 Calculated vorticity over a round crest

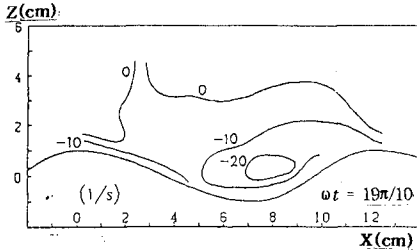


Fig. 7 Measured vorticity over a round crest (after Sato, 1987)

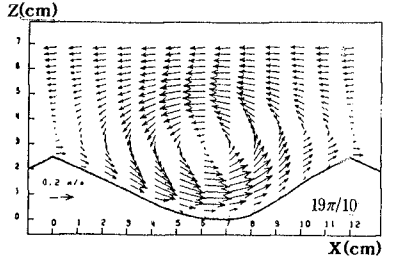


Fig. 8 Calculated flow field over a sharp crest

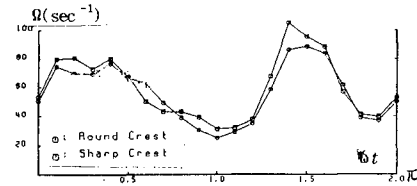


Fig. 9 IWP variation of maximum vorticity over round and sharp crests

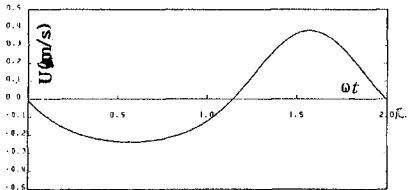


Fig. 10 Wave orbital velocity profile

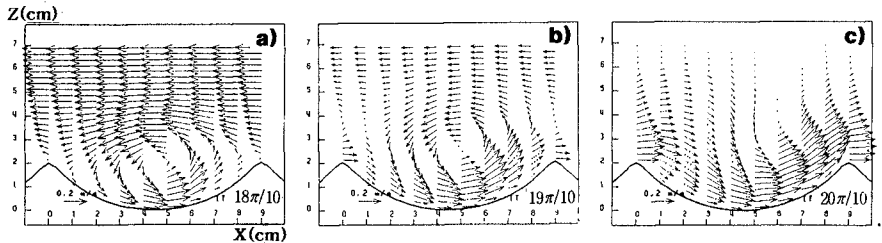


Fig. 11 The process of return flow

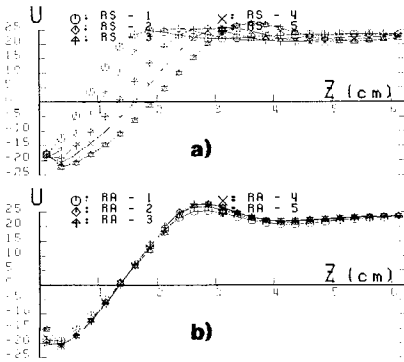


Fig. 12 Vertical distribution of horizontal velocity at the wave phase of  $18 \pi/10$

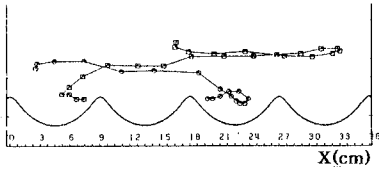


Fig. 14 Track of vortex centre

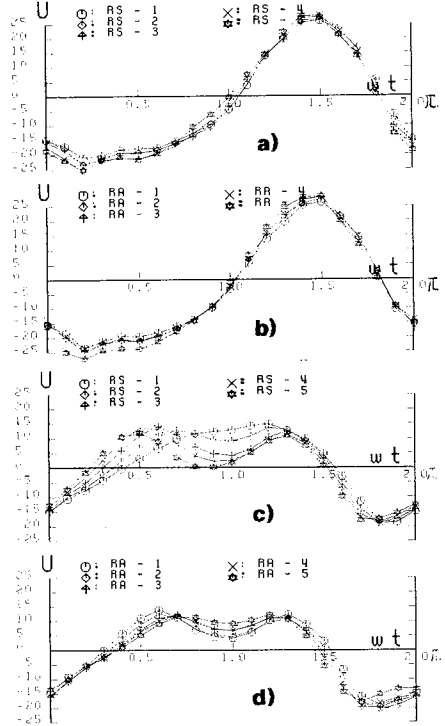


Fig. 13 IWP variation of horizontal velocity over a ripple crest and trough

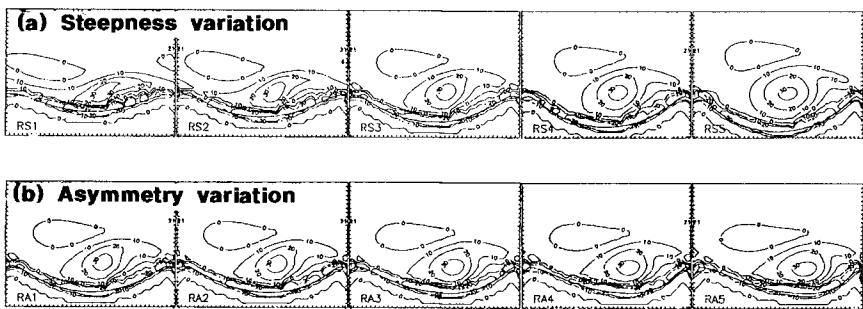


Fig. 15 Vorticity for each computational condition at the wave phase of  $19 \pi/10$

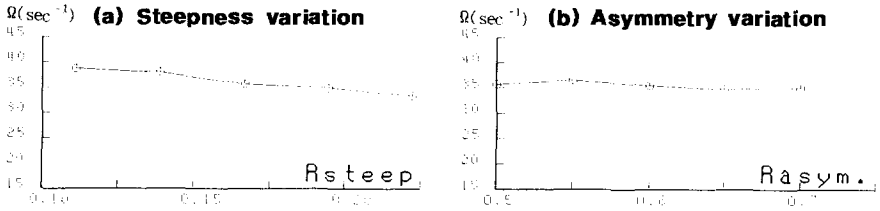


Fig. 16 Vorticity for the separated vortex at the wave phase of  $19\pi/10$

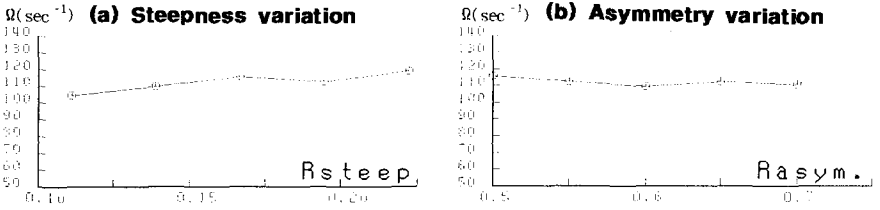


Fig. 17 Maximum vorticity at the wave phase of  $15\pi/10$

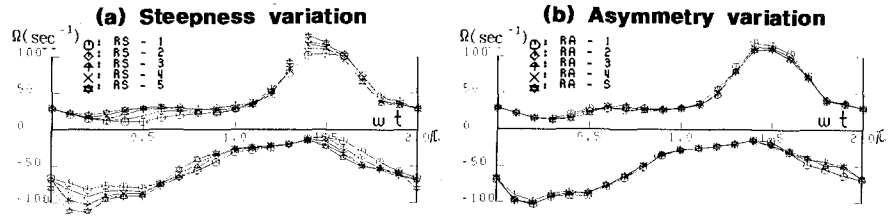


Fig. 18 IWP variation of maximum vorticity

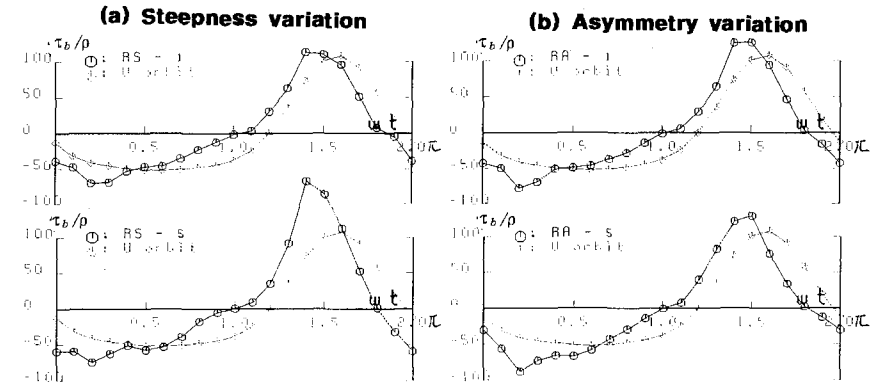


Fig. 19 IWP variations of bed shear stress for each computational condition

## CHAPTER 156

### Swash Dynamics under Obliquely Incident Waves

Nobuhisa Kobayashi<sup>1</sup>, and Entin A. Karjadi<sup>2</sup>

**ABSTRACT:** A horizontally two-dimensional, numerical model is developed for predicting the time-dependent free surface elevation and fluid velocities in the swash and surf zones under obliquely incident waves. The assumptions of shallow water waves with small incident angles are made to simplify the continuity and momentum equations and reduce computational efforts considerably. The developed numerical model allows gradual alongshore variations of the bathymetry and the incident regular or irregular waves at its seaward boundary. The numerical model is compared with available regular wave data of alongshore uniformity as an initial assessment of the model. The wave height, setup and runup are predicted well. The numerical model with the bottom friction factor calibrated previously for swash oscillations predicts the magnitude of longshore current but can not reproduce the longshore current profile probably because it does not model the transition zone and lateral mixing.

#### INTRODUCTION

A quantitative understanding of swash hydrodynamics and sediment transport on beaches under obliquely incident waves is essential for the design of shoreline erosion mitigation measures such as sand bypassing and beach nourishment. Field and laboratory measurements on the distribution of longshore sediment transport across the surf zone indicated that the distribution was generally bimodal with peaks in the swash and breaker zones (e.g., Bodge and Dean 1987; Kamphuis 1991). Bodge and Dean (1987) observed that the relative significance of the peaks shifted from the breaker zone peak to the swash zone peak as the surf varied from spilling to collapsing conditions. They found that longshore sediment transport in the swash zone might account for at least 5% to over 60% of the total drift. Knowledge of longshore sediment transport in the swash zone is important for the design of a sand bypassing system such as the system based on a jet pump deployed in the swash zone at Indian River Inlet, Delaware (Clausner et al. 1991).

Ryrie (1983) developed a time-dependent numerical model for longshore fluid motion along a straight shoreline with a plane slope generated by obliquely incident monochromatic waves with a small angle of incidence. The numerical model was not compared with any data. The numerical model developed herein is formulated

---

<sup>1</sup>Prof., Dept. of Civ. Eng., and Assoc. Dir., Ctr. for Applied Coast. Res., Univ. of Delaware, Newark, DE 19716, USA.

<sup>2</sup>Ph.D. Student, Ctr. for Applied Coast. Res., Univ. of Delaware, Newark, DE 19716, USA.

unlike that of Ryrie (1983) such that it will be applicable to beaches of arbitrary geometry under obliquely incident random waves. Approximate two-dimensional governing equations under the assumptions of shallow water waves with small angles of incidence are derived from the three-dimensional continuity and Reynolds equations (e.g., Rodi 1980) in a manner similar to the derivation of Kobayashi and Wurjanto (1992) of approximate one dimensional equations from the two-dimensional continuity and Reynolds equations. It should be noted that the mechanical energy equation for turbulent flow can be derived from the continuity and Reynolds equations and that the energy equation for turbulent flow is generally associated with the conservation of heat energy (e.g., Rodi 1980).

### TIME-DEPENDENT NUMERICAL MODEL

The cartesian coordinate system  $(x', y', z')$  is defined as  $x'$  = horizontal coordinate normal to the overall orientation of the shoreline;  $y'$  = horizontal coordinate normal to the  $x'$ -axis; and  $z'$  = vertical coordinate with  $z' = 0$  at the still water level (SWL). The prime indicates the physical variables that will be normalized later. Limiting to waves in shallow water, the coordinates  $x'$ ,  $y'$  and  $z'$  are normalized by  $\sigma H'$ ,  $\sigma H'/\theta_c$  and  $H'$ , respectively, where  $H'$  = incident wave height;  $\theta_c$  = reference incident wave angle in radian; and  $\sigma = T'\sqrt{g/H'}$  with  $T'$  = incident wave period and  $g$  = gravitational acceleration. The corresponding fluid velocity components  $u'$ ,  $v'$  and  $w'$  in the  $x'$ ,  $y'$  and  $z'$  directions are normalized by  $\sqrt{gH'}$ ,  $\theta_c\sqrt{gH'}$  and  $H'/T'$ , respectively. The normalized continuity and Reynolds equations are then simplified under the assumptions of  $\sigma^2 \gg 1$  and  $\theta_c^2 \ll 1$  for shallow water waves with small angles of incidence. The simplified equations are integrated from the bottom to the instantaneous free surface using the kinematic bottom and free surface boundary conditions as well as the boundary conditions of zero normal and tangential stresses at the free surface.

The derived continuity and horizontal momentum equations for  $\sigma^2 \gg 1$  and  $\theta_c^2 \ll 1$  are expressed in the following normalized forms (Kobayashi and Karjadi 1995)

$$\frac{\partial h}{\partial t} + \frac{\partial}{\partial x}(hU) = 0 \quad (1)$$

$$\frac{\partial}{\partial t}(hU) + \frac{\partial}{\partial x}(C_1 hU^2) = -h \frac{\partial \eta}{\partial x} - f|U|U \quad (2)$$

$$\frac{\partial}{\partial t}(hV) + \frac{\partial}{\partial x}(C_2 hUV) = -h \frac{\partial \eta}{\partial y} - f|U|V \quad (3)$$

The normalized variables without the prime in these equations are defined as

$$t = \frac{t'}{T'} ; x = \frac{x'}{\sigma H'} ; y = \frac{y'}{\sigma H'/\theta_c} ; h = \frac{h'}{H'} ; \eta = \frac{\eta'}{H'} \quad (4)$$

$$U = \frac{U'}{\sqrt{gH'}} ; V = \frac{V'}{\theta_c \sqrt{gH'}} ; f = \frac{1}{2} \sigma f' ; \sigma = \frac{T'\sqrt{gH'}}{H'} \quad (5)$$

where  $t$  = time;  $h$  = instantaneous water depth;  $\eta$  = instantaneous free surface elevation above SWL;  $U$  = depth-averaged value of the cross-shore velocity  $u$ ;  $V$  = depth-averaged value of the longshore velocity  $v$ ;  $f'$  = bottom friction factor used to express the bottom shear stress in terms of  $U$  and  $V$ ; and  $\sigma$  = ratio between the

cross-shore and vertical length scales. The momentum correction coefficients  $C_1$  and  $C_2$  equal the depth-averaged values of  $(u/U)^2$  and  $(uv/UV)$ , respectively. It is noted that the vertical momentum equation yields essentially hydrostatic pressure in shallow water. Eqs. (1) and (2) with  $C_1 = 1$  are the same as those used previously for predicting the setup and runup of normally incident waves (Kobayashi and Wurjanto 1992). The assumption of  $C_1 = 1$  was suggested to result in an error on the order of 10%. The assumption of  $C_2 = 1$  in (3) may also be made to compute  $V$  using (3) for the temporal and spatial variations of  $U$  and  $h$  computed using (1) and (2). For the case of  $\theta_c^2 \ll 1$ , the dominant cross-shore fluid motion is not affected by the secondary longshore fluid motion varying more slowly in the longshore direction. Furthermore, the variations in the  $y$ -direction appear only in the term  $\partial\eta/\partial y$  in (3) and along the seaward boundary of the computation domain. The alongshore momentum equation (3) is more sensitive to the gradual alongshore variability. In short, the assumption of  $\theta_c^2 \ll 1$  reduces computational efforts considerably and eliminates difficulties associated with lateral boundary conditions for general two-dimensional computations.

The instantaneous quantities  $h, U$  and  $V$  in (1)–(3) include both oscillatory and mean quantities. The time-averaged continuity equation corresponding to (1) yields  $\overline{h\bar{U}} = 0$  to satisfy the condition of no flux into the assumed impermeable beach where the overbar denotes time averaging. The time-averaged momentum equation corresponding to (2) with  $C_1 = 1$  and  $f = 0$  corresponds to the conventional cross-shore momentum equation used to compute wave setup  $\bar{\eta}$  (Kobayashi et al. 1989). The time-averaged alongshore momentum equation corresponding to (3) with  $C_2 = 1$  can be written as

$$\frac{\partial}{\partial x} S_{xy} = -f|U|\bar{V} - \bar{h} \frac{\partial \bar{\eta}}{\partial y} - \frac{1}{2} \frac{\partial}{\partial y} \left[ \overline{(\eta - \bar{\eta})^2} \right] \quad (6)$$

with

$$S_{xy} = \overline{hUV} = \overline{hU(V - \bar{V})} \quad (7)$$

If the setup  $\bar{\eta}$  and the variance  $\overline{(\eta - \bar{\eta})^2}$  related to the root mean square wave height do not vary in the alongshore direction, (6) is similar to the conventional alongshore momentum equation that assumes  $\bar{U} = 0$ . The gradual alongshore variations of the wave setup and variance are as important as the bottom friction and the cross-shore gradient of the alongshore radiation stress  $S_{xy}$  for a small angle of wave incidence. The dispersion or lateral mixing term due to the vertical variations of  $u$  and  $v$  (e.g., Rodi 1980) is neglected in (6) because of the assumption of  $C_2 = 1$  employed here. Svendsen and Putrevu (1994) discussed the vertical variations of the mean velocities  $\bar{u}$  and  $\bar{v}$  and attributed the lateral mixing due to the nonlinear interaction between  $\bar{u}$  and  $\bar{v}$ . The dispersion terms arise from the nonlinear interaction between  $(u - U)$  and  $(v - V)$  integrated over the depth in conventional turbulent flow analyses (e.g., Rodi 1980).

Fig. 1 shows the finite difference grid of constant grid sizes  $\Delta x$  and  $\Delta y$  used in the numerical model. The cross-shore coordinate  $x$  is taken to be positive landward and the alongshore coordinate  $y$  is positive in the downwave direction with  $y = 0$  at the upwave boundary. The seaward boundary of the computation domain is located at  $x = 0$  along the  $y$ -axis. The time step size  $\Delta t$  is allowed to vary in the same way

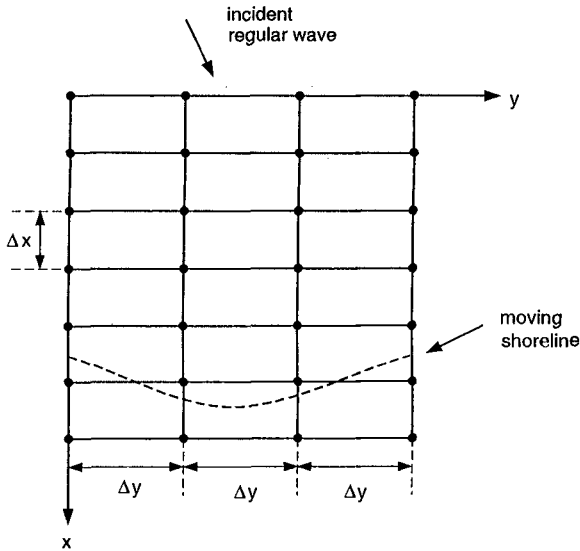


Figure 1: Finite Difference Grid for Numerical Model

as in the existing one-dimensional numerical model RBREAK2 (Kobayashi and Poff 1994) where  $\Delta t$  is reduced in a semiautomated manner whenever numerical difficulties occur at the moving shoreline. The initial time  $t = 0$  for the computation marching forward in time is taken to be the time when the incident wave train arrives at  $x = 0$  and there is no wave action in the region  $x \geq 0$  and  $y \geq 0$ .

For the known values of  $h$ ,  $\eta$ ,  $m = hU$  and  $q = hV$  at the time level  $t$ , the values of these variables at the next time level  $t^* = (t + \Delta t)$ , which are denoted by the asterisk, are computed in sequence. The value of  $(h - \eta)$  is the normalized depth below SWL which is known for the specified bottom elevation. First, along each of the shore-normal lines at  $y = (i - 1)\Delta y$  with  $i = 1, 2, \dots, I$  where  $I$  is the number of the shore-normal lines,  $h^*$  and  $m^*$  are computed by solving (1) and (2) using the explicit dissipative Lax-Wendroff method (e.g., Richtmyer and Morton 1967) together with the seaward and landward boundary conditions employed in RBREAK2 (Kobayashi et al. 1987, 1989). The obliquely incident wave train at the seaward boundary is specified as input. The computation along each shore-normal line is actually made using RBREAK2. Second, along each of the shore-normal lines at  $y = (i - 1)\Delta y$  with  $i = 2, 3, \dots, (I - 1)$ ,  $q^*$  is computed using (3) together with the computed  $h^*$  and  $m^*$  where  $\partial\eta/\partial y$  in (3) is approximated by a central finite difference based on the values of  $\eta^*$  at the two adjacent lines. Use is made of the MacCormack method (MacCormack 1969) which is a simplified version of the Lax-Wendroff method and has been used successfully for the computation of unsteady open channel flows with hydraulic jumps (e.g., Gharangik and Chaudhry 1991).  $q^*$  is set zero landward of the shoreline node computed by RBREAK2. The seaward boundary condition for  $q^*$  is based on the characteristic equation derived from (3) as explained by Kobayashi and



Table 1: Incident Waves at Seaward Boundary  $x' = 0$ 

Expt. No.	$\tan \theta'$	$d'_i$ (cm)	$T'$ (s)	$H'$ (cm)	$\theta_i$ (deg)	$\sigma$	$\theta_c^2$	$\xi$
2	0.101	21.1	1.00	9.5	26.0	10.2	0.206	0.409
3	0.101	21.3	1.00	8.7	14.2	10.6	0.061	0.428
4	0.050	18.5	1.02	7.9	13.9	11.4	0.059	0.227
5	0.050	18.2	1.85	9.0	12.9	19.3	0.051	0.385

Karjadi (1995).

When the beach profile and incident wave conditions are uniform in the longshore direction, it is sufficient to compute  $h(t, x)$ ,  $\eta(t, x)$  and  $m(t, x) = h(t, x) U(t, x)$  along the three lines at  $y = 0$ ,  $\Delta y$  and  $2\Delta y$  and  $q(t, x) = h(t, x) V(t, x)$  along the line at  $y = \Delta y$ . The computed  $\eta$  along the three lines are used to ensure the alongshore uniformity of the mean and variance of  $\eta$  used in (6). Even if the beach profile and incident wave conditions vary gradually alongshore, the developed numerical model will be applicable for the computation of the gradual longshore variations of  $h$ ,  $m$  and  $q$  by choosing a larger value of  $I$ , provided that lateral boundary conditions do not affect  $h$ ,  $m$  and  $q$  in the computation domain.

### COMPARISON WITH AVAILABLE REGULAR WAVE DATA

Visser (1991) conducted eight monochromatic wave experiments on 1:10 and 1:20 slopes and presented detailed data on uniform longshore currents, local wave heights, angles of wave incidence, wave setup and runup. The numerical model is compared with four experiments for which the seaward boundary location can be taken to be in relatively shallow water seaward of the breaker line. Table 1 lists the experiment number used by Visser (1991) and the slope and incident wave characteristics specified as input to the numerical model where  $\tan \theta' =$  uniform slope;  $d'_i =$  water depth below SWL at the seaward boundary located at  $x' = 0$ ;  $T' =$  wave period;  $H' =$  incident wave height at  $x' = 0$ ;  $\theta_i =$  angle in degrees of wave incidence at  $x' = 0$ ;  $\sigma =$  ratio between the cross-shore and vertical length scales defined in (5);  $\theta_c =$  reference incident wave angle in radian taken to be  $\theta_i$  in radian; and  $\xi =$  surf similarity parameter given by  $\xi = \sigma \tan \theta' / \sqrt{2\pi}$ . For these experiments, plunging breakers were observed. The assumptions of  $\sigma^2 \gg 1$  and  $\theta_c^2 \ll 1$  may be appropriate except for Experiment 2 with  $\theta_c^2 = 0.206$ . The only empirical parameter involved in the numerical model is the bottom friction factor  $f'$  in (5) where  $f' \simeq 0.05$  has been used for predicting wave runup on smooth slopes in small-scale experiments (e.g., Kobayashi et al. 1989). The value of  $f' = 0.05$  is used here for both cross-shore and alongshore fluid motions.

The obliquely incident regular wave train  $\eta'_i(t', y')$  at  $x' = 0$  for the small angle  $\theta_i$  in radian is assumed to be in the following dimensional form

$$\eta'_i(t', y') = \text{periodic function of } \left( \frac{t'}{T'} - \frac{y'}{L'/\theta_i} \right) = \frac{1}{T'} \left( t' - \frac{y'}{C'/\theta_i} \right) \quad (8)$$

in which  $L'$  and  $C' = L'/T'$  are the wavelength and phase velocity in the water depth

$d'_t$ . Eq. (8) accounts for the phase or time lag along the alongshore coordinate  $y'$ . The periodic function in (8) is specified using Stokes second-order or cnoidal wave theory depending on the value of Ursell parameter (Kobayashi et al. 1987).

The normalized grid sizes  $\Delta x$  and  $\Delta y$  in Fig. 1 need to be chosen to be small enough to resolve breaking waves in the surf and swash zones. For these experiments of alongshore uniformity, it is sufficient to use the three cross-shore lines at  $y = 0$ ,  $\Delta$  and  $2\Delta y$  in Fig. 1. The value of  $\Delta x$  is selected to be on the order of 0.01, corresponding to 200 grid spacings between the seaward boundary and the still water shoreline. The value of  $\Delta y$  is chosen to be the same as  $\Delta x$  to yield the same spatial resolution in the normalized coordinates. A limited sensitivity analysis has indicated that the computed results remain essentially the same as long as  $\Delta y$  is on the order of  $\Delta x$  or less.

First, the detailed computed results for Experiment 2 are presented as an example. The temporal and cross-shore variations of the free surface elevation  $\eta$ , the depth-averaged cross-shore velocity  $U$ , and the depth-averaged alongshore velocity  $V$  are stored along the center line at  $y = \Delta y$ . The temporal variations of  $\eta$ ,  $U$  and  $V$  for the duration  $0 \leq t \leq 300$  at  $x = 0$  (at the seaward boundary),  $x = 0.509$  (immediately seaward of the breaker line),  $x = 0.770$  (in the outer surf zone),  $x = 1.550$  (in the inner surf zone), and  $x = 2.265$  (in the swash zone) are shown in Figs. 2, 3 and 4, respectively. The cross-shore fluid motion represented by  $\eta$  and  $U$  computed using (1) and (2) becomes periodic fairly quickly for  $t \gtrsim 20$  as has been the case with the previous one-dimensional computations for beaches (e.g., Kobayashi et al. 1989). The alongshore fluid motion represented by  $V$  computed using (3) becomes periodic very slowly especially in the vicinity of the breaker line. The very slow response of the alongshore fluid motion is qualitatively consistent with the analytical result of Ryrie (1983) for the periodic solution development as well as the experimental procedure adopted by Visser (1991) who made measurements one hour after the start of the wave maker. In light of Fig. 4, the time averaging denoted by the overbar in the following is performed for the duration  $200 \leq t \leq 300$ .

The computed cross-shore variations of  $\bar{\eta}$ ,  $\eta_{rms}$ ,  $\bar{U}$ ,  $U_{rms}$ ,  $\bar{V}$  and  $V_{rms}$  for Experiment 2 are shown in Fig. 5 where the root-mean-square values representing the magnitude of the oscillatory components are defined as

$$\eta_{rms}^2 = \overline{(\eta - \bar{\eta})^2} ; U_{rms}^2 = \overline{(U - \bar{U})^2} ; V_{rms}^2 = \overline{(V - \bar{V})^2} \quad (9)$$

For example, if  $\eta = 0.5 \cos(2\pi t)$ ,  $\bar{\eta} = 0$  and  $\eta_{rms} = 1/\sqrt{8} = 0.35$ . The normalized uniform slope is indicated by the dashed-dotted straight line in the top figure in Fig. 5. The upper limit of the wave setup  $\bar{\eta}$  is the maximum runup elevation on the slope above SWL because  $\bar{h} \geq 0$  in the region wetted by water. The increase of  $\bar{\eta}$  and the decrease of  $\eta_{rms}$  in the surf and swash zone are approximately linear. On the other hand,  $U_{rms}$  decreases slowly in the surf zone and rapidly in the swash zone.  $\bar{U}$  is negative and represents the cross-shore return current as explained by Kobayashi et al. (1989). The longshore current  $\bar{V}$  is dominant in the surf zone and the oscillatory component  $V_{rms}$  decreases approximately linearly in the surf and swash zone.

Fig. 6 shows the computed cross-shore variations of the normalized quantities in-

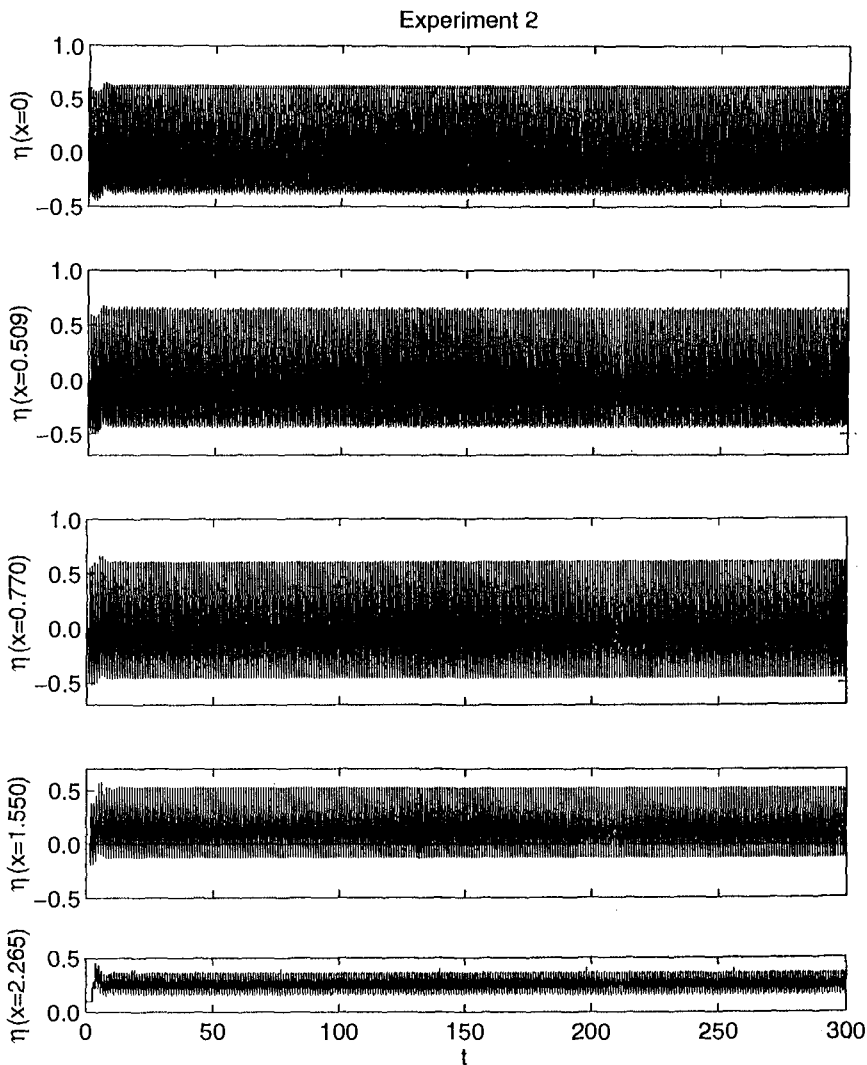


Figure 2: Computed Temporal Variations of Free Surface Elevation  $\eta$  at  $x = 0, 0.509, 0.770, 1.550$  and  $2.265$ .

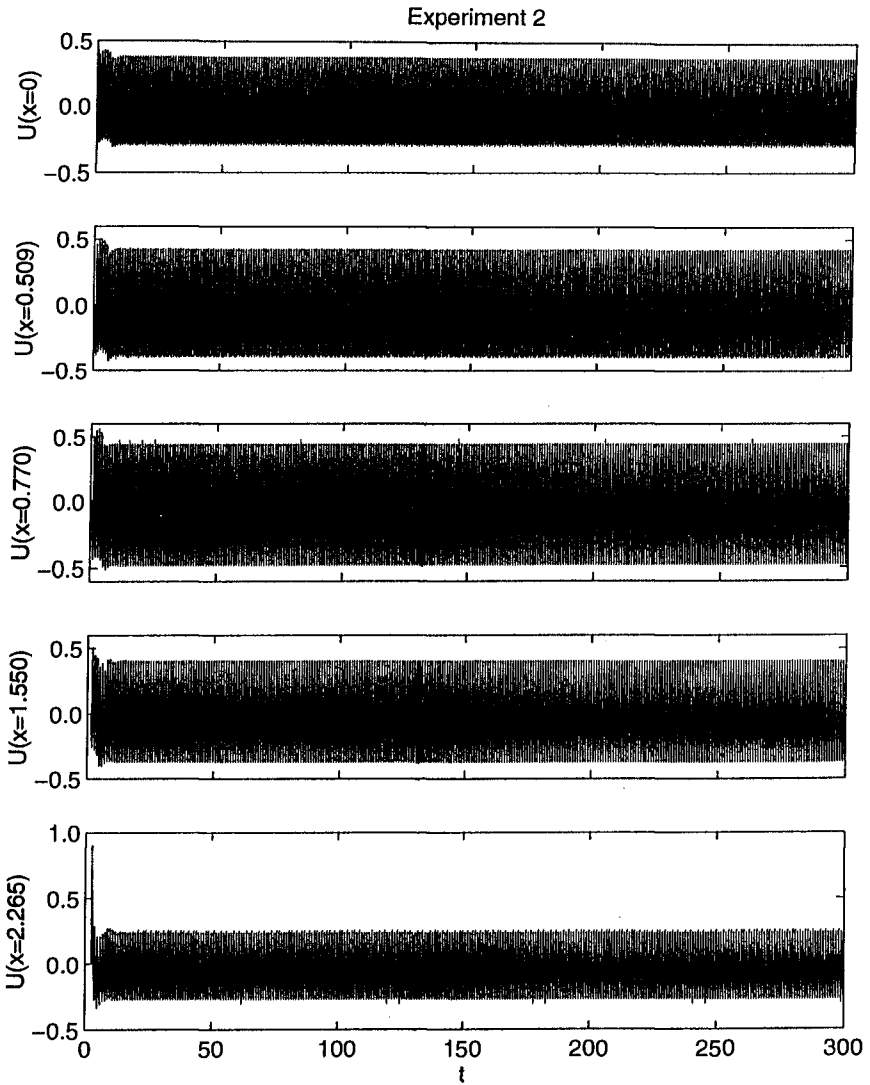


Figure 3: Computed Temporal Variations of Cross-Shore Velocity  $U$  at  $x = 0, 0.509, 0.770, 1.550$  and  $2.265$ .

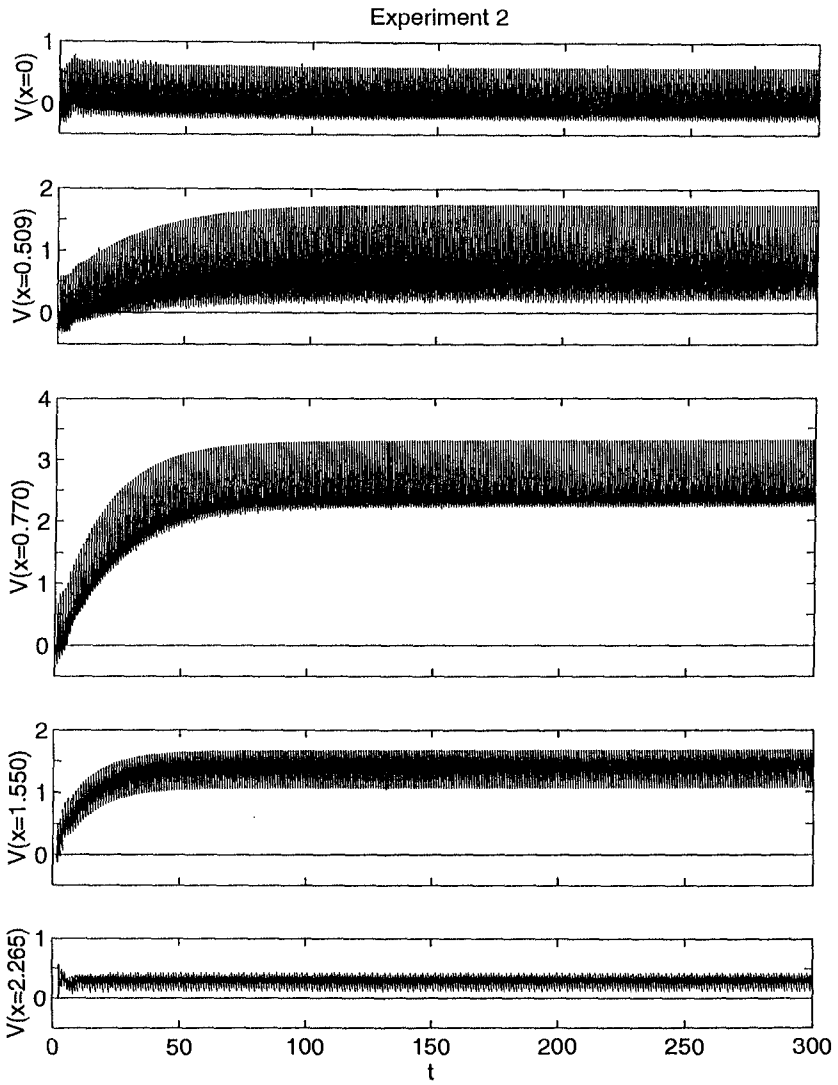


Figure 4: Computed Temporal Variations of Alongshore Velocity  $V$  at  $x = 0, 0.509, 0.770, 1.550$  and  $2.265$ .

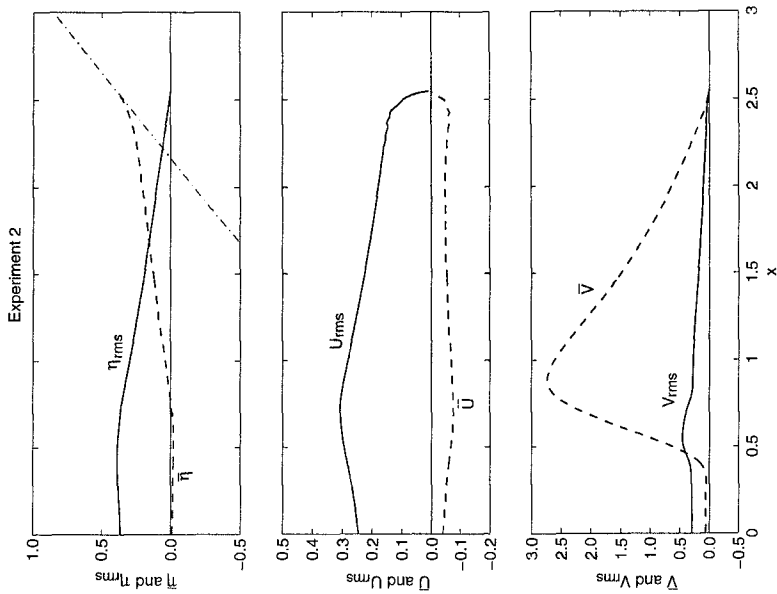


Figure 5: Cross-Shore Variations of  $\bar{\eta}$ ,  $\eta_{rms}$ ,  $\bar{U}$ ,  $U_{rms}$ ,  $\bar{V}$  and  $V_{rms}$

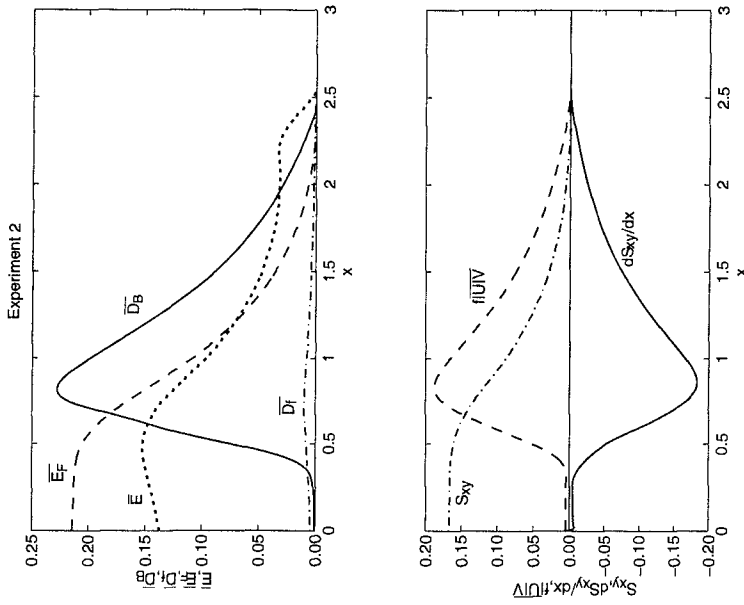


Figure 6: Time-Averaged Cross-Shore Wave Energy and Alongshore Momentum Balances.

volved in the time-averaged cross-shore wave energy equation (Kobayashi and Wurjanto 1992) and the time-averaged alongshore momentum equation (6) where  $\bar{E}$  = specific energy per unit horizontal area;  $\bar{E}_F$  = energy flux per unit width;  $\bar{D}_f$  = energy dissipation rate due to bottom friction per unit horizontal area;  $\bar{D}_B$  = energy dissipation rate due to wave breaking per unit horizontal area;  $S_{xy}$  = alongshore radiation stress given by (7); and  $f|\bar{U}|\bar{V}$  = alongshore bottom shear stress. The top figure in Fig. 6 indicates that the energy dissipation due to wave breaking is dominant and does not occur suddenly in this numerical model which does not account for wave breaking explicitly (Kobayashi and Wurjanto 1992). For these experiments of alongshore uniformity, the computed alongshore gradients of the mean and variance of  $\eta$  are negligible and the time-averaged alongshore momentum equation (6) reduces to  $dS_{xy}/dx = -f|\bar{U}|\bar{V}$ . The bottom figure in Fig. 6 shows that  $S_{xy}$  decreases monotonically in the surf and swash zones. The computed cross-shore variations of  $dS_{xy}/dx$  and  $-f|\bar{U}|\bar{V}$  are essentially the same where  $f|\bar{U}|\bar{V}$  is plotted to distinguish the two curves.

Fig. 7 compares the measured and computed cross-shore variations of the normalized local wave height  $H$  for each of the four experiments listed in Table 1. The agreement is very good in view of no adjustable parameter included in this numerical model to initiate wave breaking. However, it should be stated that this numerical model can not predict wave shoaling without wave breaking over a long distance (Kobayashi et al. 1989).

Fig. 8 compares the measured and computed cross-shore variations of the normalized wave setup  $\bar{\eta}$  together with the normalized uniform slope indicated by the dotted line for each of the four experiments. The agreement is good in the swash zone but the computed mean water level rises too rapidly landward of the breaker line as was the case with the previous comparison by Kobayashi et al. (1989). The numerical model does not predict the transition zone of constant wave setback whose effects on surf zone hydrodynamics were reviewed and elaborated by Nairn et al. (1990).

Table 2 shows the comparisons of the measured and computed maximum setup and runup for the four experiments. The computed maximum setup and runup correspond to the mean and maximum shoreline elevations, respectively, measured by hypothetical wires placed parallel to the above the uniform slope at elevations of 1, 5 and 10 mm,

Table 2: Measured and Computed Maximum Setup and Runup

Expt. No.	Maximum Setup				Runup			
	Computed			Meas.	Computed			Meas.
	1mm	5mm	10mm		1mm	5mm	10mm	
2	0.34	0.29	0.26	0.29	0.38	0.35	0.35	0.43
3	0.34	0.28	0.25	0.31	0.38	0.35	0.35	0.47
4	0.19	0.17	0.17	0.20	0.20	0.20	0.21	0.24
5	0.28	0.23	0.21	0.27	0.31	0.29	0.29	0.34

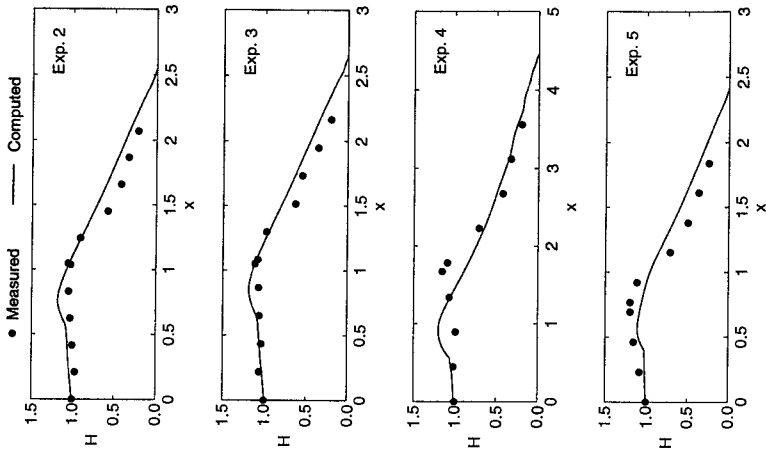


Figure 7: Measured and Computed Local Wave Height  $H$  for Four Experiments.

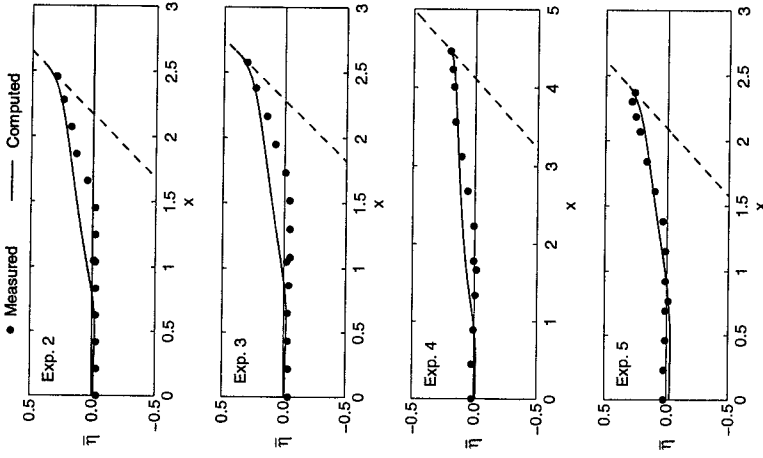


Figure 8: Measured and Computed Wave Setup  $\bar{\eta}$  for Four Experiments.



whereas the actual measurements were made visually. The computed results are not very sensitive to the wire elevations and in fair agreement with the measured values except that the numerical model with the bottom friction factor  $f' = 0.05$  slightly underpredicts the visually measured runup. It is also noted that the swash oscillations in the regular wave experiments are very narrow in comparison to swash oscillations on natural beaches that tend to be dominated by low-frequency motions (Guza and Thornton 1982; Holman and Sallenger 1985).

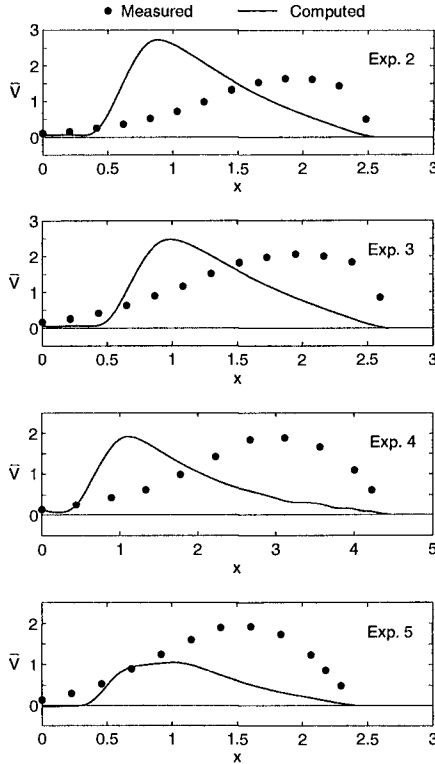


Figure 9: Measured and Computed Longshore Current  $\bar{V}$  for Four Experiments.

Finally, Fig. 9 compares the measured and computed cross-shore variations of the longshore current  $\bar{V}$  for the four experiments. The numerical model with  $f' = 0.05$  predicts the magnitude of  $\bar{V}$  but can not predict the shape of  $\bar{V}$  probably because the numerical model based on (3) with  $C_2 = 1$  does not include lateral mixing (dispersion) and it can not predict the transition zone as shown in Fig. 8. Comparing the similar agreement for Experiments 2 and 3 whose incident wave conditions are listed in Table 1, it may be concluded that  $\theta_c^2 = 0.206$  may still be regarded to be much less than unity. Visser (1984) and Nairn et al. (1990) showed it necessary to delay the initiation of the influence of energy dissipation on the generation of longshore currents until the landward limit of the transition zone. These shortcomings of the numerical model

may be serious for longshore currents generated by regular waves but are much less apparent for irregular waves due to irregular wave breaking and generation of low-frequency motions as presented by Kobayashi and Karjadi (1995) who compare the numerical model with available field data on longshore currents (Thornton and Guza 1986).

## CONCLUSIONS

A horizontally two-dimensional, time-dependent numerical model is developed for predicting swash and surf hydrodynamics under obliquely incident waves. The assumptions of shallow water waves with small incident angles are made to reduce computational efforts significantly and eliminate difficulties associated with lateral boundary conditions. Under these assumptions, the dominant cross-shore fluid motion along each cross-shore line is computed first using the existing one-dimensional numerical model. The secondary alongshore fluid motion, which may vary slowly in the alongshore direction, is then computed using the computed free surface elevation and cross-shore fluid velocity. The developed numerical model is compared with available data for obliquely incident regular waves. The numerical model is shown to predict the wave height, setup and runup well, although it can not model the transition zone. This implies that the existing one-dimensional model for normally incident waves can be used to predict the cross-shore variations of the free surface elevation for obliquely incident waves with small incident angles. The numerical model with the bottom friction factor calibrated previously for swash oscillations predicts the magnitude of longshore current fairly well but can not reproduce the longshore current profile probably because it does not include the transition zone and lateral mixing. The utility of the developed time-dependent model in comparison to conventional time-averaged models with several adjustable parameters (e.g., Nairn et al. 1990) is not apparent for the compared regular wave data for which the swash zone is narrow and the oscillatory alongshore velocity is small relative to the longshore current.

## ACKNOWLEDGEMENTS

This work was supported by the U.S. Army Research Office, University Research Initiative, under Contract No. DAAL03-92-G-0116 and by the NOAA Office of Sea Grant, Department of Commerce, under Grant No. NA85AA-D-SG033 (SG95 R/OE-18).

## REFERENCES

- Bodge, K. R., and Dean, R. G. (1987). "Short-term impoundment of longshore transport." *Proc. Coastal Sediment '87*, ASCE, 1,468-483.
- Clausner, J. E., Gebert, J. A., Rambo, A. T., and Watson, K. D. (1991). "Sand bypassing at Indian River Inlet, Delaware." *Proc. Coastal Sediments '91*, ASCE, 1,1177-1191.
- Gharangik, A. M., and Chaudhry, M. H. (1991). "Numerical simulation of hydraulic jump." *J. Hydraulic Eng.*, ASCE, 117(9),1195-1211.
- Guza, R. T., and Thornton, E. B. (1982). "Swash oscillations on a natural beach." *J. Geophys. Res.*, 87(C1),483-491.

- Holman, R. A., and Sallenger, Jr., A. H. (1985). "Setup and swash on a natural beach." *J. Geophys. Res.*, 90(C1),945-953.
- Kamphuis, J. W. (1991). "Alongshore sediment transport rate." *J. Wtrwy. Port Coast. Oc. Eng.*, ASCE, 117(6),624-640.
- Kobayashi, N., DeSilva, G. S., and Watson, K. D. (1989). "Wave transformation and swash oscillation on gentle and steep slopes." *J. Geophys. Res.*, 94(C1),951-966.
- Kobayashi, N., and Karjadi, E. A. (1995). "Obliquely incident irregular waves in surf and swash zones." Submitted to *J. Geophys. Res.*
- Kobayashi, N., Otta, A. K., and Roy, I. (1987). "Wave reflection and runup on rough slopes." *J. Wtrwy. Port Coast. Oc. Eng.*, ASCE, 113(3),282-298.
- Kobayashi, N., and Poff, M. T. (1994). "Numerical model RBREAK2 for random waves on impermeable coastal structures and beaches." *Res. Rpt. No. CACR-94-12*, Ctr. for Applied Coastal Res., Univ. of Delaware, Newark, Del.
- Kobayashi, N., and Wurjanto, A. (1992). "Irregular wave setup and run-up on beaches." *J. Wtrwy. Port Coast. Oc. Eng.*, ASCE, 118(4),368-386.
- MacCormack, R. W. (1969). "The effect of viscosity in hypervelocity impact cratering." *Pap. 69-354*, Am. Inst. Aeronaut. and Astronaut., New York, N.Y.
- Nairn, R. B., Roelvink, J. A., and Southgate, H. N. (1990). "Transition zone width and implications for modelling surf zone hydrodynamics." *Proc. 22nd Coastal Eng. Conf.*, ASCE, 1, 68-81.
- Richtmyer, R. D., and Morton, K. W. (1967). *Difference Methods for Initial-Value Problems*. Interscience, N.Y.
- Rodi, W. (1980). *Turbulence Models and Their Application in Hydraulics*. Intl. Assoc. for Hydraul. Res., Delft, The Netherlands.
- Ryrie, S. C. (1983). "Longshore motion generated on beaches by obliquely incident bores." *J. Fluid Mech.*, 129,193-212.
- Svendsen, I. A., and Putrevu, U. (1994). "Nearshore mixing and dispersion." *Proc. Roy. Soc. Lond.*, A(445), 561-576.
- Thornton, E. B., and Guza, R. T. (1986). "Surf zone longshore currents and random waves: field data and models." *J. Phys. Oceanogr.*, 16,1165-1178.
- Visser, P. J. (1984). "Uniform longshort current measurements and calculations." *Proc. 19th Coastal Eng. Conf.*, ASCE, 2, 2192-2207.
- Visser, P. J. (1991). "Laboratory measurements of uniform longshore currents." *Coastal Eng.*, 15,563-593.

## CHAPTER 157

# WAVE RUN-UP AND SEA-CLIFF EROSION

S.-M. Shih<sup>1</sup>, P. D. Komar<sup>2</sup>, K.J. Tillotson<sup>2</sup>,  
W.G. McDougal<sup>3</sup> and P. Ruggiero<sup>3</sup>

### Abstract

Studies have been undertaken along the Oregon coast to better understand the processes involved in sea cliff erosion in order to develop improved predictions of the susceptibilities of properties to wave attack. A model has been developed that includes evaluations of extreme water elevations measured by tide gauges, calculations of wave run-up levels due to major storms, and a documentation of beach morphology variations that affect the wave run-up and determine the elevation of the junction between the beach and toe of the sea cliff. The occurrence of erosion depends on the combined water levels compared with the beach/cliff junction. All of these factors vary with time and also spatially along the coast. A program has been initiated to measure wave run-up on Oregon beaches ranging from reflective to dissipative in order to test the model predictions.

### Introduction

The erosion of sea cliffs backing beaches generally depends on the run-up of large waves generated by a major storm, superimposed on elevated water levels due to tides and other processes that affect water elevations (storm surge, etc.). Critical is the total level achieved by the water compared with the elevation of the junction between the beach and face of the sea cliff. These factors vary with time, tending

---

<sup>1</sup>Institute of Oceanography, National Taiwan Univ., Taipei, Taiwan

<sup>2</sup>College of Oceanic & Atmos. Sciences, Oregon State Univ., Corvallis, OR 97331

<sup>3</sup>Ocean Engineering, Oregon State Univ., Corvallis, OR 97331

to reach extremes during the winter months so that the susceptibilities of properties to erosion are greatest in that season. The factors can also vary spatially along the length of coast, particularly the morphology of the beach and the degree of protection it offers to the sea cliff from wave attack.

In order to evaluate the susceptibilities of coastal properties on sea cliffs to wave erosion, it is necessary to make quantitative assessments of: (1) potential mean-water elevations due to tides, storm surges, and other processes, (2) the most extreme run-up levels of storm-generated waves, and (3) expected elevations of the beach/cliff junction. The application in this paper is to the Oregon coast, but the techniques can be used on other coastlines, employing wave and water-level data specific to those areas. In this paper we report on analyses of extreme mean-water levels measured by a tide gauge, on calculated wave run-up elevations due to major storms, on a program that has been initiated to measure wave run-up on a variety of Oregon beaches to test the extreme predictions, on efforts to document the beach morphology variations that affect wave run-up and determine beach/cliff junction levels, and on efforts to apply the analyses in coastal-zone management decisions such as the establishment of set-back distances.

## Study Site

Erosion has been common along the Oregon coast due to the high energy of the wave climate and the dynamic behavior of its beaches. Much of this erosion has occurred in sea cliffs backing beaches, of concern in that many communities are sited on uplifted marine terraces that are suffering from sea-cliff recession. The erosion has been episodic, associated with the occurrence of extreme storms, but it also has been spatially variable. This spatial variation is due in part to the tectonic setting of Oregon, which has resulted in different rates of coastal uplift (Komar and Shih, 1993). In general, the southern part of the coast and the northern-most part near the Columbia River are rising faster than the present rate of sea level rise, while the north central stretch has minimal uplift and therefore is experiencing a sea-level transgression due to the global rise in sea level. This coast-wide pattern of relative sea-level change is reflected in the degree of sea

cliff erosion. However, there are also more local controls which include the volume of sand on the fronting beach and the corresponding ability of the beach to act as a buffer between the sea cliffs and storm waves (Shih and Komar, 1994). The north-central portion of the Oregon coast, where erosion has been greatest, is segmented into a series of littoral cells by large headlands, which effectively isolate the stretches of beach within each cell. Sources and losses of sand to the series of littoral cells are highly variable, and this has controlled the amount of sand on the beach and the elevation of the beach/cliff junction. As a result, there tends to be differences in susceptibilities of properties to erosion between the series of littoral cells. It is this high spatial as well as temporal variation in the susceptibilities of properties to erosion that has made it important to develop analysis techniques that can assist in rationally evaluating those susceptibilities.

## Model Development and Process Evaluations

### *The Basic Model*

The model is illustrated in Figure 1. The probability of water reaching the base of a sea cliff backing the beach is dependent on water-elevation factors which include:

1. The tide level within its predicted harmonic cycle;
2. Processes such as storm surge, water temperatures, and the occurrence of an El Niño that produce departures of the mean water level from the predicted tidal elevations;
3. Set-up induced by waves breaking on the beach;
4. The frequency and elevations achieved by the run-up of individual waves above the mean set-up level.

Important to the induced erosion of sea cliffs is the comparison between elevations achieved by the water due to these combined processes ( $H_T + \bar{\eta} + R$  in Figure 1), and the elevation of the junction of the beach face with the sea cliff ( $H_J$ ). Wave-induced property erosion will not occur unless the elevation of the water exceeds the elevation of the beach/cliff junction ( $H_T + \bar{\eta} + R > H_J$ ). Implementation of the model to evaluate the susceptibilities of sea cliffs and associated properties to erosion depends on the ability to quantitatively evaluate the processes that govern water and beach elevations.

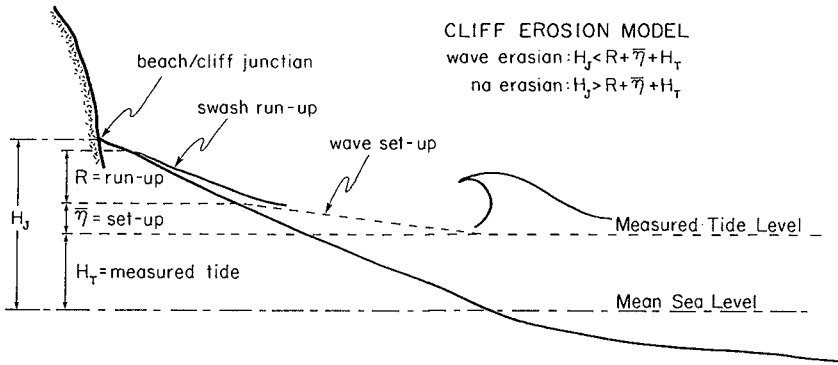


Figure 1: The basic model for the quantitative assessment of the susceptibilities of sea cliffs to wave-induced erosion.

### **Extreme Water Levels**

From the above list of water-level factors, it is apparent that tides are generally an important process controlling water elevations on the beach and thus the probability of waves reaching the toe of the cliff. Water-level elevations resulting solely from tide-generating forces are predictable, but there can be significant departures from those predictions due to a number of oceanic and atmospheric processes. The analyses presented here are based on the tide-gauge records from Yaquina Bay on the central Oregon coast. Measurements from that gauge span a sufficient number of years for projections of extreme water-elevations expected within a 100-year time frame.

The yearly extreme high tides recorded at the Yaquina Bay tide gauge have been analyzed to construct the probability curves of extreme water levels shown in Figure 2. The measurements were modeled by the General Extreme Value distribution (Shih, 1992). The results are expressed in terms of recurrence intervals of the water-level elevations, but can also be expressed as the probability of occurrence of a specified level during a given year. Based on the measured water levels, the projected 100-year elevation is about 2.5 meters above mean sea level (MSL). A similar analysis of the predicted yearly extreme tides yields a curve that is displaced well

below that based on measured tides, Figure 2, and yields a projected 100-year predicted tidal elevation of about 2.0 meters, some 50 cm lower than that based on the measured extreme tides.

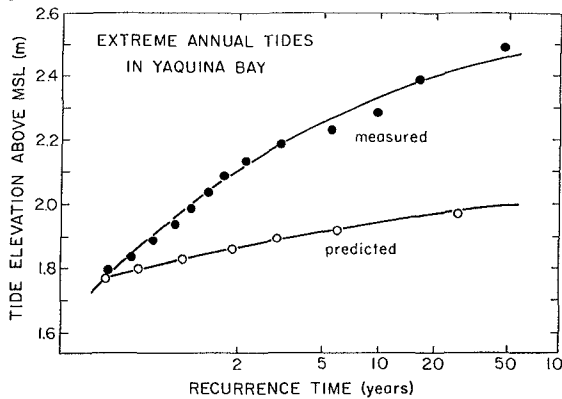


Figure 2: Analyses of extreme predicted and measured tides based on the yearly maximum elevations recorded on the tide gauge in Yaquina Bay on the central Oregon coast.

The results demonstrate that there are significant differences between predicted and observed extreme tides, with the measured elevations typically being 10's of centimeters higher. This demonstrates the importance of the oceanic and atmospheric processes such as storm surge, water temperatures, etc., that can raise water levels well above predicted tidal elevations. It is important to account for the causes of the differences between the measured versus predicted tides in order to improve our basic understanding of the processes. Detailed analyses of these processes are still underway, but the broad seasonal variations are apparent. Higher water levels occur during the winter off the Oregon coast due to the generally warmer water temperatures (upwelling during the summer makes the water colder and denser, depressing the water-surface level); typically, mean-water elevations are about 20 cm higher during the winter than in the summer (Huyer et al., 1983). A particularly important phenomenon affecting extreme water levels is the occurrence of an El Niño; for example, the 1982-83 El Niño raised water levels by approximately 15 cm above the previously measured high levels for the winter months, on the



order of 35 cm above the average measured levels for those months (Huyer et al., 1983; Pittock et al., 1982).

There can also be daily fluctuations in mean water elevations such as those due to a storm surge as low-pressure fronts cross the coast. This factor has been investigated for only a few specific storms that resulted in property erosion along the Oregon coast (McKinney, 1976). In those few cases the maximum increases in water elevations attributable to storm surge were less than 20 cm. This small magnitude, compared with other coastal areas, results because the storms either crossed the coast too fast to develop a sizable wind set-up of the water, or the extreme waves of the storm were generated by a large fetch but not by extreme winds. More study of storm surge on the Oregon coast is needed, since it still exerts an important control on the total elevation of the water, and thus on the occurrence of sea cliff erosion; furthermore, there may be circumstances when storms do give rise to more significant storm surges on the Oregon coast.

### ***Storm Waves and Run-up Levels***

The second component in the cliff-erosion model is the evaluation of wave run-up associated with major storms. An assessment of this factor requires a good documentation of the deep-water wave climate and a capacity to calculate wave run-up elevations on beaches for those wave conditions.

A variety of wave-data sources is available for the Oregon coast upon which to base projections of extreme-wave parameters, which in turn can be used to calculate extreme run-up elevations. The data sources include the deep-water buoy data of the Coastal Data Information Program (CDIP) of the Scripps Institution of Oceanography, and from the National Data Buoy Program (NDBP) of NOAA. Those buoy-measurement programs began only in the 1980s, and in themselves do not provide a sufficiently long record upon which to base extreme-wave projections. Important in this respect are wave data derived from the microseismometer system operated by Oregon State University at the Marine Science Center in Newport. This system has been in operation since 1971, yielding measurements of significant wave heights and periods four times each day. Direct comparisons between buoy and microseismometer measurements demonstrate that the seis-

momometer yields good data for significant wave heights, while the periods are systematically too large (Tillotson, 1995; Tillotson and Komar, in review). Wave data are also available for the 20-year period from 1956 to 1975, derived from the daily wave hindcasts of the Wave Information Study (WIS) of the U.S. Army Corps of Engineers. Unfortunately, the WIS wave heights are systematically 30% too high in comparison with the direct measurements. An attempt was made to recalibrate the WIS data in order to make it more compatible with the wave climate based on the direct measurements, but the results then yielded too few storm-wave conditions based on a threshold of the significant wave height being greater than 6 meters, the limit used in the extreme-wave analyses. Therefore, the extreme-wave analyses had to rely on the combined measurements of the deep-water buoys (specifically the CDIP buoy offshore from Bandon, Oregon), and the wave data derived from the microseismometer system (Tillotson, 1995; Tillotson and Komar, in review). The data base thereby consists of 23 years of daily wave measurements, during which 24 storms were identified as having deep-water significant wave heights equal to or greater than 6 meters. The largest measured deep-water significant wave height was 7.3 meters, while extreme-wave analyses yielded a wave height of 7.8 meters for the 50-year projection, and a less reliable value of 8.2 meters for the 100-year projection. If a 5-meter wave height is used to define "storms" rather than 6 meters, then the projected 50-year and 100-year wave heights are respectively 8.2 and 8.8 meters.

This established deep-water wave climate has been used to calculate extreme run-up elevations on Oregon beaches backed by sea cliffs. There is a considerable literature derived from studies of wave run-up on structures such as jetties and on natural beaches; Douglass (1990) provides a recent review, and van der Meer and Stam (1992) have undertaken a synthesis of the extensive laboratory results. The analysis approach used here is based mainly on the field measurements of Holman and Sallenger (1985) at the Field Research Facility, Duck, North Carolina, and in particular on the results of Holman (1986) derived from his reanalysis of the data to evaluate extreme run-up elevations. Holman analyzed run-up in terms of the mean run-up level, the significant level (elevation of the

highest one-third), the 2% exceedence elevation, and the absolute maximum run-up elevation achieved during a 20-minute measurement record. In our predictions, we have used the 2% exceedence, denoted by  $R_{2\%}$ . Similar to earlier studies, Holman (1986) found that this run-up elevation can be predicted by the relationship

$$\frac{R_{2\%}}{H_s} = C\xi \quad (1)$$

where  $H_s$  is the deep-water significant wave height,  $C = 0.90$  is an empirical constant established by the measurements, and  $\xi$  is the dimensionless Iribarren number defined as

$$\xi = \frac{S}{(H_s/L_o)^{1/2}} \quad (2)$$

where  $S$  is the slope of the beach face and  $L_o$  is the deep-water wave length given by  $L_o = (g/2\pi)T^2$  where  $g$  is the acceleration of gravity and  $T$  is the wave period. Combining the above equations yields

$$R_{2\%} = CS(H_s L_o)^{1/2} = C \left( \frac{g}{2\pi} \right)^{1/2} S H_s^{1/2} T \quad (3)$$

for the run-up elevation as a function of the deep-water significant wave height and period, and of the beach slope. Equation (3) accounts for the total run-up elevation due to the presence of waves, that is, it combines the wave-induced set-up which raises the elevation of the mean shoreline, and the swash elevation of individual waves beyond that mean shoreline. If analyzed independently, the set-up and swash elevations both have predictive equations like the above relationships, but the coefficients in equation (3) are respectively  $C = 0.35$  and  $0.55$ , which sum to the  $0.90$  coefficient.

Equation (3) has been used to calculate expected run-up elevations associated with the 24 storms during the past 23 years. Here the calculation depends on the wave period during the storms, as well as the wave heights. This emphasizes the importance of storms in that, as is commonly found, there is a broad positive correlation between significant wave heights and periods (Tillotson, 1995; Tillotson and Komar, in review), which combine in equation (3) to yield the most extreme run-up elevations on Oregon beaches during the past 23 years. Those calculated  $R_{2\%}$  values for the 24 storms have been subjected to an extreme-value analysis using the Automated

Coastal Engineering System (ACES) developed by the U.S. Army Corps of Engineers. Assuming a beach-face slope of  $S = 0.03$ , an approximate average for the Oregon coast, the projected 50-year run-up level is  $1.87 \pm 0.15$  meters, while the less reliable 100-year projection is  $1.97 \pm 0.17$  meters (Tillotson, 1995). These magnitudes for the extreme wave run-up are comparable to the total tidal excursion on the Oregon coast, and are much larger than water-level enhancements resulting from storm surge, etc. The calculations, therefore, reconfirm the importance of run-up during storms being a major factor in causing sea-cliff erosion.

### ***Beach Morphology and Elevations***

The elevation of the beach/cliff junction,  $H_j$  (Fig. 1), can vary from one beach to another due to the total quantities of sand within the littoral cells, and with the grain size of the beach sediment. The grain-size dependence has been demonstrated by Shih and Komar (1994) in a study of the Lincoln City littoral cell on the central Oregon coast. This cell is unusual in that there is a pronounced and systematic longshore variation in sediment grain sizes and thus in the beach morphology, ranging from dissipative to reflective systems. The coarser-sand reflective beaches have higher beach/cliff junction elevations, probably resulting from the higher levels that can be achieved by run-up during storms due to the slope dependence  $S$  in the run-up relationships. Furthermore, the coarser-sand beaches undergo larger profile changes through the seasons, and also experience greater profile shifts during individual storms as compared with the finer-sand beaches. Rip currents on the coarser-sand beaches tend to erode larger and deeper embayments into the berm, and this in particular can lower the elevation of the beach/cliff junction, thereby locally and temporally increasing the susceptibility of the property to erosion.

The analyses have established that a critical component to the development of cliff erosion models is the determination of the beach/cliff junction elevation and how it depends on the total quantities of sand on the beach, the coarseness of the sediment, and on factors such as the occurrence of a rip-current embayment that locally lowers the elevation. This

component has been particularly important to the occurrence of cliff erosion episodes along the Oregon coast.

### Measurements of Wave Run-up

In order to test the model that combines water elevations with calculated wave run-up levels, and to better understand the processes involved in sea-cliff erosion, we have begun a program to measure wave run-up on a number of beaches. Swash run-up is measured using the video techniques developed by Holman and Sallenger (1985). This includes beach profile surveys of the swash zone, and the video recording of the run-up signal during high tides, with markers placed on the beach for geometric transformations. The time series of vertical run-up signals were then extracted from the two-dimensional video intensity signal using the beach profile elevations and known geometric positions of the markers. The highest run-up levels achieved during 50-second time intervals were sub-sampled from a 70-minute run-up time series digitized at 1 Hz, giving a total of 82 data points of run-up maxima; a long sampling interval and time series were necessary due to the strong infragravity component in the run-up. The run-up maxima were then analyzed to determine the maximum run-up ( $R_{\max}$ ) achieved during the 70-minute measurement interval, the 2% exceedence statistic ( $R_{2\%}$ ), the 33% "significant" exceedence ( $R_{1/3}$ ), and the mean run-up elevation ( $\bar{R}$ ); all of these measurements include the set-up elevation.

Thus far, three sites along the Oregon coast have been included in the measurement program, representing different degrees of beach sand volumes and buffering capacities, and different beach sand grain sizes and morphologies ranging from strongly dissipative to reflective. The results from the three beaches are given in Figure 3, where all elevations are with respect to mean sea level as established by surveying from nearby bench marks. The tide levels shown are for the times of run-up measurements. At Beverly Beach the maximum run-up exceeded the beach/cliff junction elevation, and the extreme swash was observed to surge up the face of the cliff. Beverly Beach is located within a littoral cell that is deficient in sand volume, and this in part is reflected in the low level of its beach/cliff junction elevation (4.1 meters, MSL) compared

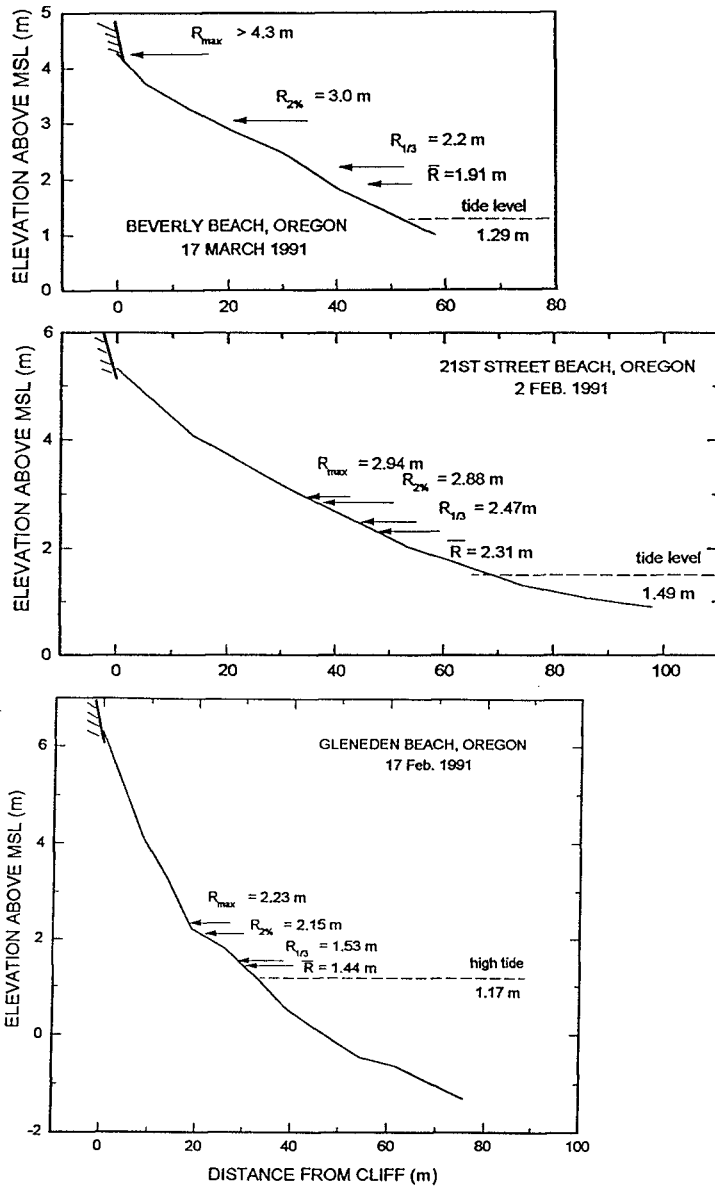


Figure 3: Measurements of wave run-up elevations on three beaches along the Oregon coast, where all elevations are referenced to mean sea level (NGVD).

with the other two beach locations included in Figure 3 (elevations of 6.2 and 5.3 meters, MSL). This difference in part also results from the contrasting grain sizes of the sediments on these three beaches. The lower beach/cliff junction elevation at Beverly Beach, has resulted in a high frequency of wave run-up reaching the toe of the cliff, and in substantially greater erosion compared with most other locations on the Oregon coast.

The other two beach locations included in the run-up measurements, Gleneden Beach and 21st Street Beach, are within the Lincoln City littoral cell (Shih and Komar, 1994). Gleneden Beach is coarser grained and has the steeper slope so it is reflective (summer) to intermediate (winter), while the beach at 21st Street is composed of fine sand and is always dissipative. During the times of run-up measurements, Figure 3, the swash did not reach the beach/cliff junctions at either location, and this is generally the case as cliff erosion is a relatively rare event within the Lincoln City littoral cell due to the large quantities of sand on the beaches. In that cell, rip currents play a particularly important role in locally reducing the beach/cliff junction elevation,  $H_j$ , during the occasions of episodic erosion.

The run-up measurements can be analyzed to test the model predictions, specifically the predicted elevation achieved by the calculated  $R_{2\%}$  run-up level superimposed on the measured tide, compared with the measured results. Although the measurements thus far have not included extreme-storm conditions, the comparisons can still provide a test of the model. The comparisons for the three data sets of Figure 3 are given in Table 1.

Table 1: Model and Measurement Comparisons

Location	Date	Tide (MSL) (meters)	$H_s$ (m)	T (sec)	$R_{2\%}$ + Tide Calc.	Meas.
Gleneden	2/2/91	1.17	1.56	13.1	2.04	2.15
21st Street	2/17/91	1.49	2.76	13.1	2.31	2.88
Beverly Beach	3/17/91	1.29	3.47	14.2	2.47	3.00

In each comparison in Table 1, the predicted water elevation is lower than the measured elevation, the difference ranging from about 10 to 50 cm. This difference results from the calculated  $R_{2\%}$  using equation (3), versus the measured run-up elevation, since the measured tidal elevation is the same in both calculated and measured total water levels in Table 1. This suggests that equations (1) and (3) based mainly on the measurements of Holman and Sallenger (1985) and Holman (1986) at the Field Research Facility, Duck, North Carolina, will need to be revised for the present application to run-up on Oregon beaches. Such a revision at this stage is premature, as we presently have only the three measurement sets shown in Figure 3. A primary objective of our ongoing research is to obtain more run-up data on a greater variety of beaches, at which time refinements in the model calculations can be made.

### Summary and Discussion

The application of the sea-cliff erosion model to the Oregon coast has shown that the predicted tides, elevations of mean water levels due to a variety of processes, and wave run-up during major storms can all be contributing factors to the erosion. Also important is the morphology of the beach, and in particular the elevation of the beach/cliff junction. In some littoral cells on the Oregon coast, this junction elevation is low due to the paucity of sand on the beach, allowing elevated water levels to frequently reach the toe of the sea cliff, resulting in more rapid erosion. In other littoral cells there are sufficient volumes of sand on the beach that it generally can act as a buffer between the water and sea cliff. In those cells rip currents at times cut embayments into the beach and locally lower the beach/cliff junction elevation so that cliff erosion results; the erosion is therefore extremely episodic and spatially variable.

Although the model thus far has been useful in a broad examination of sea-cliff erosion variability along the Oregon coast and in accounting for the susceptibilities of properties to erosion in the various littoral cells, refinements based on additional field data are needed. This is the objective of our on-going research. In particular we are focusing on the video collection of more run-up data on a greater variety of beaches in order to re-calibrate the run-up equations so that they



provide improved predictions. The measurements are also being analyzed to determine the proportions of infragravity versus incident-wave energy so as to provide a better understanding of the dynamics of wave run-up. In that connection, our continuing research is expanding to obtain measurements of water depths and celerities of the bores leading up to the swash, as well as properties of the resulting run-up. The measurements will be used to test and refine models of run-up dynamics and elevation predictions, and to improve the design of shore-protection structures used to reduce sea-cliff erosion.

## Acknowledgments

This work is a result of research supported by the NOAA Office of Sea Grant, Department of Commerce, under Grant # NA81AA-D000086, Project R/CP-24.

## References

- Douglass, S.L. (1990) *Estimating runup on beaches: A review of the state of the art*: C.R. CERC-90-3, U.S. Army Engr. Waterways Experiment Station, Vicksburg, Miss.
- Holman, R.A. (1986) Extreme value statistics for wave run-up on a natural beach: *Coastal Engineering*, 9: 527-544.
- Holman, R.A., and A.H. Sallenger (1985) Set-up and swash on a natural beach: *Journal of Geophysical Research*, 90 (C1): 945-953.
- Huyer, A., W.E. Gilbert, and H.L. Pittock (1983) Anomalous sea levels at Newport, Oregon, during the 1982-83 El Niño: *Coastal Oceanography and Climatology News*, 5: 37-39.
- Komar, P.D., and S.-M. Shih (1993) Cliff erosion along the Oregon coast: A tectonic — sea level imprint plus local controls by beach processes: *Journal of Coastal Research*, 9: 747-765.
- McKinney, B.A. (1976) *The spring 1976 erosion of Siletz Spit, Oregon, with an analysis of the causative wave and tide conditions*: M.S. thesis, Oceanography, Oregon State University, Corvallis, 66 pp.
- Pittock, H.L., W.E. Gilbert, A. Huyer, and R. Smith (1982) *Observation of sea level, wind and atmospheric pressure at Newport, Oregon, 1967-1980*: Data Report 98, College of Oceanography, Oregon State University, Corvallis.

- Shih, S.-M. (1992) *Sea-Cliff Erosion on the Oregon Coast: From Neotectonics to Wave Run-up*: Ph.D. thesis, Oregon State University, Corvallis, 135 pp.
- Shih, S.-M., and P.D. Komar (1994) Sediments, beach morphology and sea cliff erosion within an Oregon coast littoral cell: *Journal of Coastal Research*, 10: 144-157.
- Tillotson, K.J. (1995) *Wave Climate and Storm Systems on the Pacific Northwest Coast*: M.S. thesis, Oceanography, Oregon State Univ., Corvallis.
- Tillotson, K.J., and P.D. Komar (in review) The wave climate of the Pacific Northwest (Oregon & Washington): A comparison of data sources: *Journal of Coastal Research*.
- van der Meer, J.W., and C.-J. M. Stam (1992) Wave runup on smooth and rock slopes of coastal structures: *Jour. of Waterway, Port, Coastal and Ocean Engineering*, Amer. Soc. Civil Engrs., 118: 534-550.

## CHAPTER 158

### MEASUREMENT OF PARAMETERS, DIRECTION AND RATE OF BEDFORM MIGRATION

R. D. KOS'YAN, I. S. PODYMOV

#### Abstract

Special sensor was developed in the Southern Branch of of the P.P. Shirshov Institute of Oceanology, Russian Academy of Sciences Oceanology Institute, able to register variations of sediment layer thickness in any point of interest on reservoir, sea, channel or river bottom under any hydrodynamic conditions.

Uninterrupted information on geometry, rate and direction of migration of bedforms (ripples, ridges, dunes, bars) in the chosen point of underwater slope can be obtained in the following manner. Three or more sensors are placed by a diver on bottom in a horizontal plane in apieces of equilateral triangle on metal girder. The construction is put deeper into ground to 20-25 cm. Distance between sensors and their spatial orientation are set beforehand. Height and "period" of sand bedforms are found from time variations of sediment layer thickness above any of the sensors. Rate and directions of their migration are calculated by time of bedform crest transit above sensors. Sand wave length is calculated from its "period" and migration rate. A series of laboratory and field experiments has been performed for the purpose of clearing up a sensor working capacity, calibrating and work methods.

#### Introduction

Migration of sand microforms caused by surface waves, wave currents or channel flows plays an important role in cross-shore, longshore and channel sediment transport. This component of overall sediment transport has not been studied, as reliable instruments for continuous measurement of bedform geometry are still lacking.

Geometry parameters of bedforms are usually measured by divers (Manual..., 1975; Kos'yan, 1983; 1987; Miller, Komar, 1980; Dingler, 1974). The diver descends to bottom in calm or slightly wavy weather and while moving along a set route, measures bedform parameters and estimates their shape and spatial orientation in the certain points.

Observation of bedform dynamics by divers has certain disadvantages: information is interrupted, as measurements during storm are not possible; data on rate and direction of

---

The Southern Branch of the P.P. Shirshov Institute of Oceanology, Russian Academy of Sciences. Gelendzhik-7, 353470 RUSSIA

bedform migration can not be obtained; diving works are laborious and expensive.

Method of repeat photography of the same bottom portion from a fixed point (Gizejewski et al., 1982) is used more rarely. Under storm observation of bottom sand layer dynamics seems possible only by measurements taken from rigid trestle bridges, piers and tramways. In other cases the data reflect only post-storm bottom variations.

Uninterrupted information on geometry, rate and direction of migration of bedforms (ripples, ridges, dunes, bars) in the chosen point of underwater slope can be obtained with the use of special sensors.

Such sensor was developed in the Southern Branch of the P.P. Shirshov Institute of Oceanology (Kos'yan, Podymov, 1993; 1994), able to register variations of sediment layer thickness in any point of interest on reservoir, sea, channel or river bottom under any hydrodynamic conditions.

### General description

The sensor (we named it sand level gauge) is destined for the investigation of physical aspects of solid particle movement near the bottom, specifically for measuring velocity of formation and shift of bottom accumulative forms, when studying the dynamics of sea sediments on the shelf and the engineer research for the creation of hydrotechnical constructions, etc.

It is an electron-mechanic device for the determination of instantaneous value of the bottom sediment thickness in a selected point. A method of fixation of sediment pressure on the outer metal diaphragm of the gauge, caused by above sediment thickness variations, is realized in this device. Its technical characteristics are in the table 1.

Table 1. Sea level gauge technical characteristics.

- diameter of a sensible weight accounting membrane	0.1 m
- maximum measured weight	5 kg
- sensibility	0.0002 m
- change of initial value of output signal, when temperature changes in operating range	$< \pm 0.1\%/10^0 \text{C}$
- non-linearity of the output signal according to absolute value	$< 0.7\%$
- time constant	$< 0.1 \text{ sec.}$
- maximum sediment thickness above the sensor during measuring (depends on "arch" effect)	0.25 m
- maximum admissible shift of the membrane during measuring	0.0003 m
- supply voltage	$\pm 15 \text{ V}$
- utilized current (without current load)	$< 0.0005 \text{ A}$
- utilized current (when output signal is the maximum one)	$< 0.0025 \text{ A}$
- output signal	$0 \div 0.02 \text{ A}$
- range of operating temperature	$+1^0 \text{C} \div +80^0 \text{C}$

The structural scheme of the sand level gauge (Fig.1) includes tensoresistive bridge (1), electronic module of signal formation (2) and electronic module of current formation (3).

Tensoresistive bridge represents four tiny semiconducting tensoresistors, which are placed on a single sapphire backing. Tensobridge is constructed in such a way, that a change of environment temperature is equally inherited to every tensoresistor. In addition computer access of resistors according to their parameter identity let to minimize an error connected with the bridge out-of-balance caused by environment temperature change. Electronic module of signal formation fulfills the stabilization of voltage, which feeds the tensometric bridge, and chooses a out-of-balance signal with the help of circuits of differential amplification. Electronic module of current formation passes the out-of-balance signal to the point of data storage and processing.

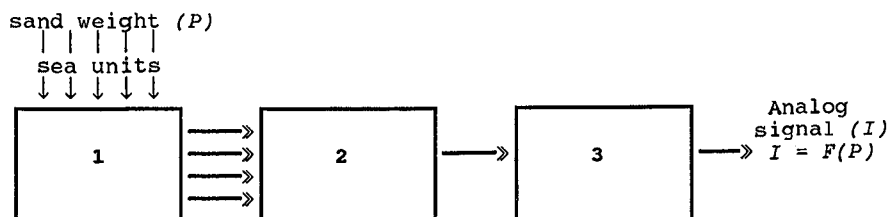


Fig. 1. The structural scheme of the sand level gauge.

The device is made as a cylindrical casing, inside of it a manometric unit and dynamometer connected kinematically are placed, and a compensating load-bearing element as well, which effects upon the manometer.

The sand level gauge is used in the following manner. One sensor or a group of sensors are deepened into bottom sediments at the depth of 15-20 cm in the selected point of the shelf. The ground surface above the sensor is flattened. The pressure of sediment cover recorded at the moment of installation is assumed as an initial one.

Shift of accumulative bottom forms (ripples, ridges, dunes) through any point of the bottom causes a periodic change of the sediment mass in this point. When a wave crest is passing, the pressure on the external membrane increases, changing the pressure distribution in and provokes the out-of-balance of the bridge system, which is formed by tensoresistors. When a wave trough is passing, the same effects occur, but the sign of out-of-balance becomes a contrary one. Periodic changes of the water static pressure caused by waves or tide cycles are not displayed in the sensor reading as far as they are completely compensated.

Finally, the gauge secures continuous high-grade measuring of the bottom sediment thickness in a wide range of changing static pressure. Thus, a quantitative information about accumulative bottom form movement can be obtained. And then a velocity of its movement under any hydrodynamic conditions can be calculated. An important feature of the gauge is the isolation of dynamometric assembly from external membrane

(Fig.2), that makes easier the compensation of the parameters of the sensor temperature error.

The appearance of the sand level gauge is given in Fig.3.

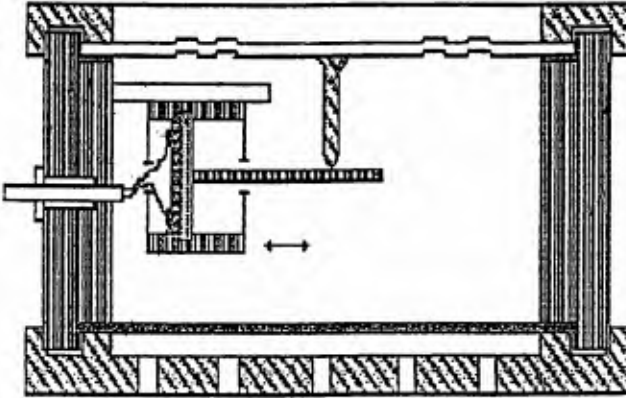


Fig. 2. The cross-section of the sand level gauge construction.

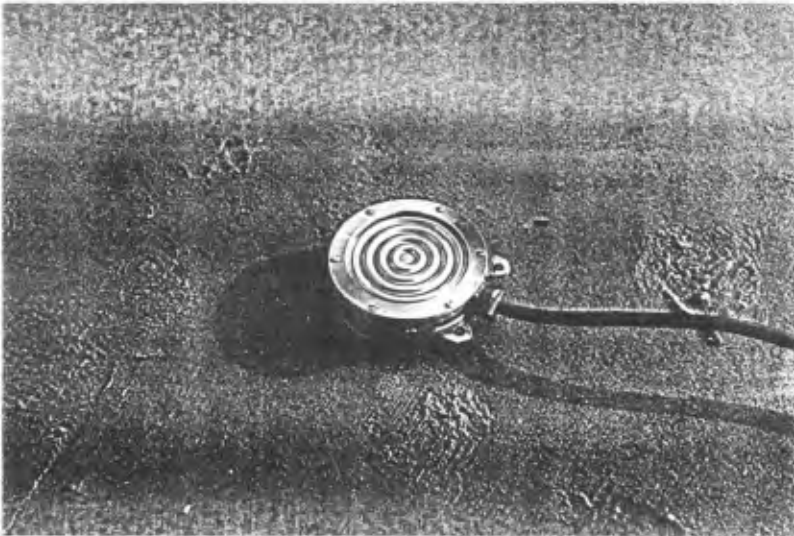


Fig. 3. The appearance of the sand level gauge.

### Communication and data playback

The sand level gauge is connected with the point of the data storage and processing by 4-core cable. Supply voltage  $\pm 15V$  and a midpoint are transmitted by 3 cable lines. A separate line brings an information signal as a current, which depends on the bottom sediment thickness. An electronic module of current formation is made as a self-tuning current loop with negative feedback, parameters of which do not depend within certain limits on the cable length and resistance. Analog information signal is converted into binary code with the help of dodecadischarge analog-to-digital converter of successive approximation. Output signal of the sand level gauge converted into binary code is being recorded on magnetic carrier of the computer with necessary discreteness.

For the purpose of clearing up a sand level gauge working capacity, calibrating and work methods a series of laboratory and field experiments has been performed.

### The laboratory experiment

The main task of the laboratory experiment is to determine the dependence of sand pressure poured on the sensor under the water on the thickness of sand cover and to assess the influence of different kinds of sand upon the "arch" effect.

Electronic units have not been used in order to eliminate their influence on the transmitting parameters of the sensor. A stable supply voltage fed directly the tensometric bridge. Out-of-balance voltage was recorded by digital voltmeter.

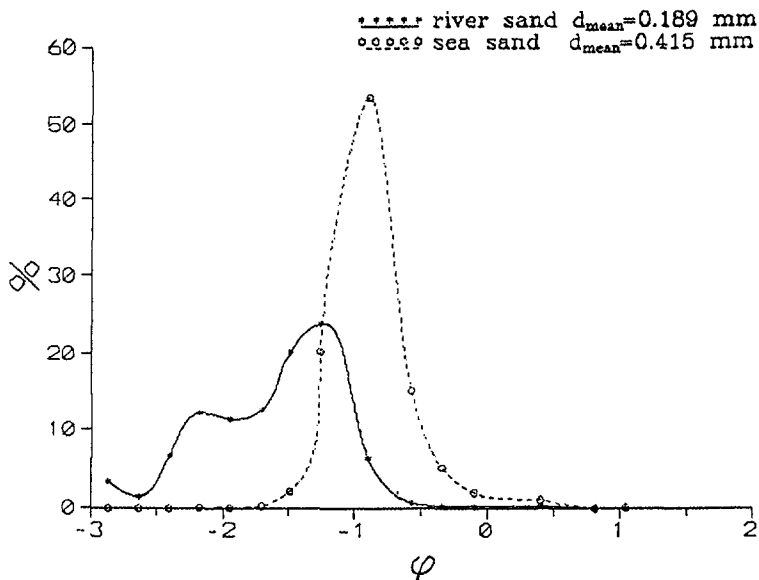


Fig. 4. Grain-size distribution curves for beach and bank kinds of sand, which were used for calibration.

Two kinds of natural sands were used in the experiment. Below they are marked as beach sand and bank sand. According to the data of mineralogical analysis 90% of beach sand are quartz and feldspar with density ( $\rho_s$ ) of  $2.65 \text{ g/cm}^3$ . A mineralogical analysis of the bank sand has not been done but this type of sand contained a considerably large amount of clay. The assessment of the particle form has not been done. Curves of the particle distribution according to their size ( $\Phi = -\log_2 d$ ),  $d$  is a particle diameter) for both kinds of sand are given in Fig.4. Their mean diameter ( $d_{\text{mean}}$ ) is given in the same figure.

The calibrating of the sand level gauge was performed in the tank, which volume was 50 l and the height - 470 mm. The sensor was placed on the bottom of the tank, and then a portion of sand was added. At first the thickness of sand layer covering the membrane of the sensor was 20 mm. The sand layer thickness was recorded continuously. Out-of-balance signal of the tensobridge was fixed by digital voltmeter for every portion of sand. The tank was vibrated after every sand supplement. Then, the vibration was stopped, and 5 minutes later, the thickness of the sand layer above the sensor and a value of analog out-of-balance signal were measured. In the course of calibration simultaneously with sand a small amount of water was added into the tank. The calibration was done firstly for beach sand and then for bank sand. Measuring was stopped, when the tank was brimful with sand.

The check of temperature stability of the sensor work was carried out in this experiment too. Measuring in water without sand has shown that output signal of the sensor remains to be stable one with an error 0.1%, when water temperature changes from  $10^\circ$  to  $30^\circ\text{C}$ .

The check of water static pressure on the value of the out-of-balance signal was performed in another experiment. For this purpose the sensor was being slowly lowered from the trestle-bridge to the depth of 5 m. Out-of-balance signal of the tensobridge did not change.

The results of the sensor calibrating for beach and bank sands are given in Fig.5. As it is seen in diagrams, a good coincidence for different kinds of sand and a high linearity of the characteristics of out-of-balance signal  $U$  on the sand layer thickness  $D$  above the sensor can be observed only when the sand layer thickness is not more than 220 mm. When the sand layer is more thick, the linearity of the dependence is true only for beach sand. Diagram  $U(D)$  for bank sand becomes distorted and its slope. The character of the change of the curve slope points to the reduction of the sand layer thickness influence on the pressure given to sensor. Probably it can be explained by the fact that clay, present in sand, binds sand particles and forms interstitial layers of a high strength. Those layers prevent the pressure to pass from the upper layers to the lower ones. We named as an "arch" effect the phenomenon of distortion of pressure. It is evident, that any loose sediments have an "arch" effect. But the value of layer thickness, from which it begins to display, is a characteristic peculiarity of every definite kind of sediments.

The analysis of the laboratory experiment data shows that, when laboratory calibration data are used for the processing of field measurements, the depth of the sensor immersion into sediments must not exceed 220 mm. But it does not exclude the



possibility of the sensor use in the conditions different from laboratory ones. Only the calibrating *in situ* for every kind of sediment and conditions is necessary.

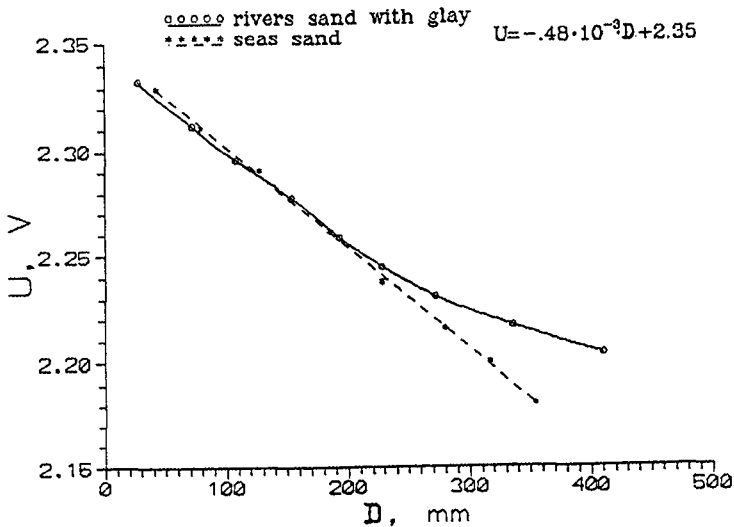


Fig. 5. Calibration curves for different kinds of sand.

Laboratory test of the sand level gauge was carried out in a wave flume. This flume was 61m length, 0.8m in width and about 0.7m height (Kos'yan, Onishchenko, Philippov, 1988).

Test consisted in the comparison of bed form height  $H$  with  $D$ , measured with the help of the sensor. For this purpose the sand level gauge was buried into sand at the depth of 15 cm in immediate proximity to a glass wall of the flume in such a way that an observer can define exactly the bed form position relative to the sensor. While changing the wave producer period of oscillation during 1-2 s we managed to create sand ripples 6 cm high and to move them along the longitudinal axis of the flume. Fig.6a. shows the measuring data of two ripples which have passed just above the sensor during the laboratory experiment.

#### Full-scale experiment

Field test of the sand level gauge was carried out in the course of international experiments on the Shkorpilovtsy (Bulgaria) testing-ground.

Field test consisted in the recording of the change of bed form height during a storm and in comparison of the sand level gauge reading with the data obtained by divers. The sensor was buried into bottom sediments at the depth of 15 cm in the point

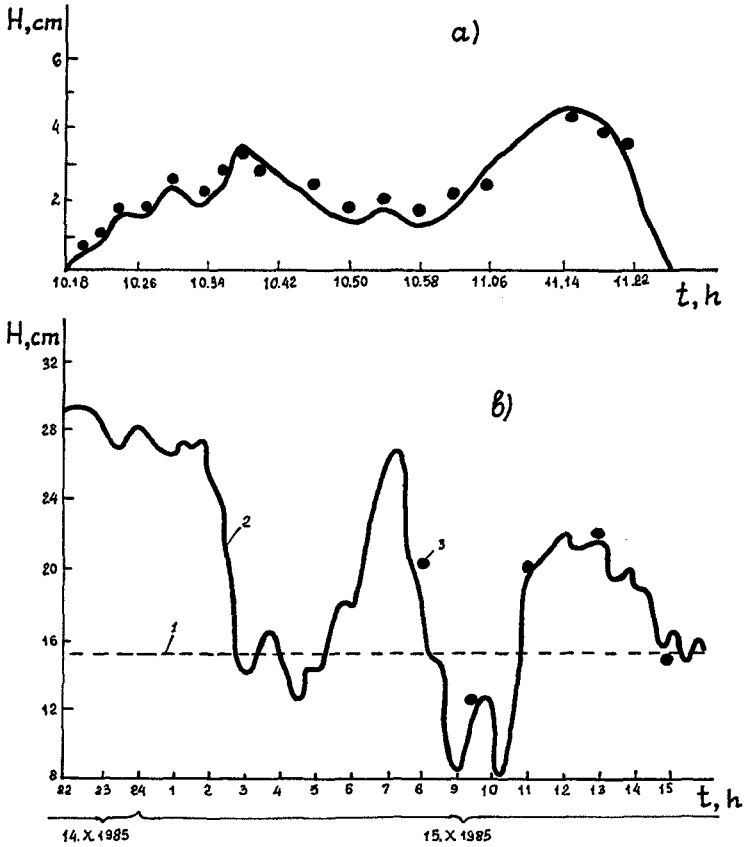


Fig. 6. The results of the change of sediment layer thickness. a - laboratory study, b - field study: 1 - sediment level above the sensor before the storm; 2 - change of bottom relief, measured with the help of the sensor; 3 - change of bottom relief ( $H$ ) observed visually.

where the sea was 4 m deep. Recording equipment was installed on the trestle and it was connected with the sensor by means of shielded cable. There was obtained uninterrupted three day recording of the change of sand layer thickness above the sensor, and at the same time six control measurements of bed

form height were made by divers. The comparison of the sand level gauge reading with the data obtained by divers has shown that the results conform within the accuracy of diver measuring (1-2 cm).

Fig.6b. shows a nature of the change of bottom level at the depth of 4 m during 24 hours in the phase of the storm stabilization. Underwater visual observation confirmed the reliability of instrumental information about little known picture of bed forms near the wave breaking zone. Large sand waves, 14-16 cm high, are covered by ripples, which height ranges from 1 to 4 cm. And the largest ripples are in the troughs of sand waves.

The most intensively sand level gauges were used in joint with the Low Sacsonian Coastal Research Center field investigations in Germany in Autumn, 1994, when complex lithodynamic study in the coastal zone of the Norderney island was done.

Synchronous fluctuations of orbital velocity, suspended sediment concentration and risings of free surface were studied. While measuring it was very important to fix continuously the distance between sensors and eroded bottom. For this purpose under the equipment we buried sensor into sand. It gave us a chance to find sought distance in any moment of measuring. Control measurements of maximum bottom relief deformation during the whole period of observation were done with the help of metal pin with mobile plate. We measured the length of pin from its top to the bottom and then determined changes of bottom level during the time period between measurements. When sand near the pin was washed out, the plate, put on it, dropped.

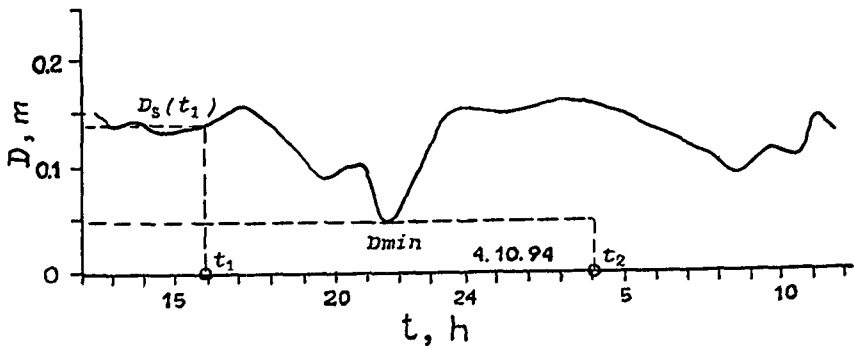


Fig. 7. The comparison of measuring of an active layer thickness with the help of sand level gauge and metal mobile plate.

When bottom erosion changed into aggradation, the washer was covered with sediments and showed the most low level of the bottom during the period between measurements.

A comparison of the data obtained by measuring of the

bottom form deformation by means of sand level gauge and by classic method, i.e. by measuring with the help of metal pins and plates, was made in the course of lithodynamic investigations. The results of one such a comparison are given in Fig.7 (measuring was done during 12 hours). The technique of obtaining these results, was the following: during the low tide, when a place, where the sensor has been installed, was drained, a metal pin was hammered into sand at the distance of 1 m from the sensor. A heavy flat mobile plate with a hole in its center was put on this pin. The plate dropped along the pin and lied down the sand surface. Necessary measurements were made after a tide cycle, when the place of the pin positioning was drained again. It was supposed that if a deformation of the bottom profile would take place, then the thickness of an active layer in this place could be determined with the help of the mobile plate. If the sediment accumulation was the first stage of the bottom deformation, which was replaced by erosion and then by accumulation again, the quantitative information about the first accumulation was lost. Full line in Fig.7 shows the bottom profile in the measuring point, obtained with the help of the sand level gauge. Here,  $t_1$  is the time of metal plate placing on sand;  $t_2$  is the time of measuring of the depth of the plate sinking.

Introduced notations have the following sense:

$\Delta D_s = D_s(t_1) - D_{min}$  is the thickness of an active layer for the time period  $t_1 - t_2$  according to sensor data. The initial process of accumulation has not taken into account as far as it is not fixed by plate. As it is seen;  $\Delta D_s = 8.5$  cm.

$\Delta D_p$  is the thickness of an active layer, obtained with the help of the plate. According to the results of measuring  $\Delta D_p = 8.0$  cm.

As it is seen from the comparison, the difference is not more than 0.5cm.

While measuring a bench mark pin was used for the absolute tie of the surface sand level to the environment. The sensor position was fixed not by the depth of its burying, but by the distance from the top of the bench mark pin. In such a manner the the recording of sand surface relative to the top of the bench mark pin was done.

As a typical example Fig.8 shows a fragment of 7-day recording of sand surface level relative to the top of the bench mark pin. This fragment was obtained by measuring with sand level gauge (interrupted line). Gaps in the line correspond to low tide, when the place of the sensor positioning was drained, and measurements were not done.

In this figure, level of sand surface measured by a rule from the top of the shelf mark pin in the moments of complete discharge in the point of the sensor installation is marked by small circles. Vertical lines show the thickness of active layer during the period of two measurements, obtained with the help of mobile plates.

### Discussion

The results of the laboratory calibrations and full-scale tests testify to the sand level gauge fitness for the investigation of the physical aspects of solid particle movement in the near bottom water layer, especially for the measuring of

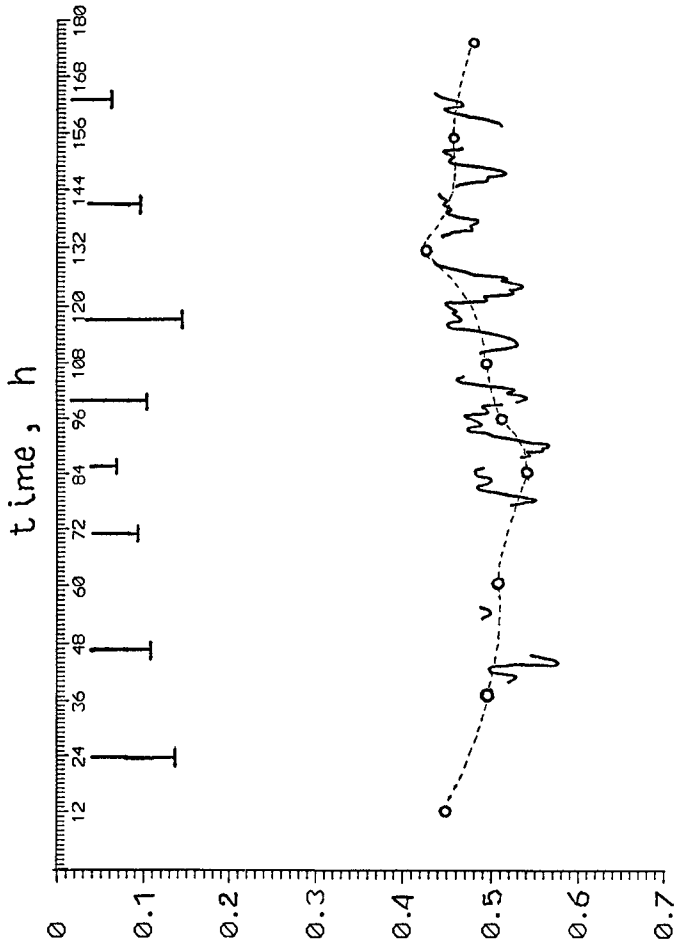


Fig. 8. A typical example of temporal change of the surface sand level and the thickness of an active layer.

the rate of accumulative form formation and shift, when studying the dynamics of sea sediments on the shelf.

Uninterrupted information on geometry, rate and direction of migration of bedforms (ripples, ridges, dunes, bars) in the chosen point of underwater slope can be obtained in the following manner. Three or more described sensors are placed by a diver on bottom in a horizontal plane in apieces of equilateral triangle on metal girder. Distance between sensors and their spatial orientation are set beforehand. Height and "period" of sand bedforms are found from time variations of sediment layer thickness above any of the sensors. Rate and directions of their migration are calculated by time of bedform crest transit above sensors. Sand wave length is calculated from its "period" and migration rate.

The above sensors can be used for routine monitoring of raceway, harbor and river channel silting, and for continuous observation on dynamics of bedforms (ripples, ridges, dunes, bars) under any hydrodynamic conditions in zones practically inaccessible for other observation techniques.

### References.

Dingler J.R. Wave-formed ripples in nearshore sands: Ph. D. Thes. San. Diego, 1974. 136 p.

Gizejewski E., Ronevich P., Roschenko V., Rudowski S. Microforms of the Black Sea coastal zone in the area of experimental testing ground Interaction of atmosphere, hydrosphere and lithosphere in the coastal zone ("Kamchia-78). Sofia. 1982. Bulg. Ac. Sci. Publ. P.223-234 (in Russian).

Kos'yan R.D. Results of lithodynamic research in the nearshore zone on the north African shelf. Moscow. 1983. Reprint. N 5402-83. 64 p. (in Russian).

Kos'yan R.D. About ripple formation and existence under wave action in the coastal zone. Water resources. 1987. N 1. P. 52-60 (in Russian).

Kos'yan R.D., Onischenko E.L., Philippov A.P. About measuring of variability of bottom sand layer thickness in different basins. Meteorology and hydrology. 1988. N 5. P.131-135 (in Russian).

Kos'yan R.D., Podymov I.S., Measurement of sediment erosion and accumulation on a studied nearshore area. Proc. of the International Conference "Sediment Transport Mechanism in Coastal Environments and Rivers. EUROMECH 310". Le Havre, France, 1993, p.133-135.

Kos'yan R.D., Podymov I.S., Sand level gauge. Russian patents NN 94033291, 94033292. 1994.

Manual on research and calculation methods of sediment transport and coast dynamics when engineering research is being done. Moscow. Gidrometeoizdat publ. 1975. 238 p. (in Russian).

Miller M.C., Komar P.D. A field investigation of the relationship between oscillation ripple spacing and the near-bottom water orbital motions J. Sediment. Petrol. 1980. Vol. 50. P. 183-191.

## CHAPTER 159

### Breach Growth Research Programme and Its Place in Damage Assessment for a Polder

Arie W. Kraak<sup>1</sup>, Wim T. Bakker<sup>2&3</sup>, Jan van de Graaff<sup>3</sup>,  
Henk J. Steetzel<sup>4</sup>, Paul J. Visser<sup>3</sup>

#### Abstract

In the Netherlands the Technical Advisory Committee on Waterdefences (TAW) is developing a new safety philosophy, in which safety levels will be expressed in terms of risk of flooding. At present safety levels are expressed in terms of probability of exceedance of a certain water level. Risk is here defined as the product of probability of failure and expected damage. In order to be able to assess the expected damage, the flooding discharges in case of a dike failure have to be determined. These flooding discharges largely depend on the process of breach growth. The TAW has started a study on the breach growth mechanism, which is carried out by means of a step by step approach. Firstly laboratory experiments have been carried out to investigate the essential features of the total process. Mathematical models have been developed that describe the different phases of the breach growth process as observed in the laboratory. Recently a large field experiment has taken place in order to validate the mathematical models. So far, all research on breach growth has been focussed on sand-dikes and dunes, which implicitly means that the models are upper bound approaches. In next phases of the research programme breach growth in dikes containing less erosive materials such as clay will be investigated.

---

<sup>1</sup>) Ministry of Transport, Public Works and Water Management, Department of Road and Hydraulic Engineering, P.O.Box 5044; 2600 GA Delft, The Netherlands.

<sup>2</sup>) Ministry of Transport, Public Works and Water Management, National Institute for Coastal and Marine Management, P.O.Box 20907; 2500 EX Den Haag.

<sup>3</sup>) Technical University of Delft, Department of Civil Engineering, P.O. Box 5048; 2600 GA Delft.

<sup>4</sup>) Delft Hydraulics, P.O. Box 152; 8300 AD Emmeloord.

Introduction

The research described in this paper has been carried out for the Technical Advisory Committee on Water Defences (TAW). This committee is a permanent advisory board for the Dutch Minister of Transport, Public Works and Water Management on all technical aspects of flood defences in the Netherlands. Research is carried out by order of the Road and Hydraulic Engineering Division of the Ministry. The results are supportive to the advises of the TAW. The gained knowledge is published in technical reports and guides with practical design standards.

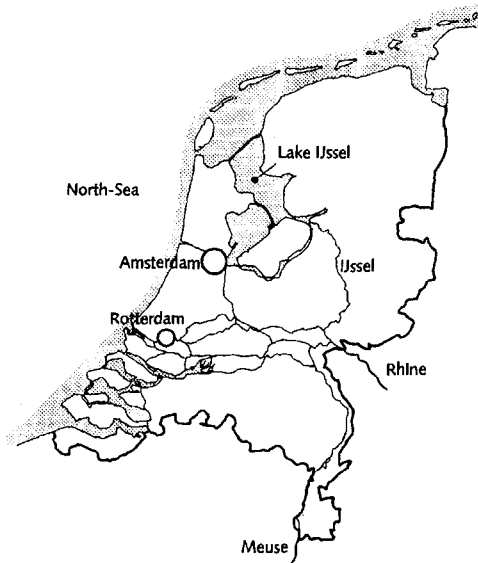


Fig. 1. The Netherlands.

A large part of the Netherlands is several meters below mean sea level, lake level and flood levels of the rivers Rhine, Meuse and IJssel [fig. 1]. To protect the Netherlands from flooding, a system of 53 so-called dike ring areas has been defined. Each dike ring area is in fact a polder protected by flood defences such as dikes, dunes and special constructions (for instance sluices and storm surge barriers). About 1600 km of dikes, 300 km of dunes and hundreds of special constructions protect the low lying country.



### History of design standards

In Dutch flood protection history the 1953 disaster plays a crucial role and marks a change in approach to flood defence standards. Before 1953 dikes were built based on a level of 0.5 meter above the highest known flood level with a surcharge for wave run-up. This experienced based approach became fatal in 1953. A major part of the south-west of the Netherlands was flooded due to a unexpected high flood level with a return period of 300 years. The damage was enormous: 1853 people were killed; direct economical loss was approximately 14% of the Dutch GNP. Flooding of the economical more important and more densely populated central part of Holland could just be avoided. Directly after this disaster the government installed the so-called Delta-committee which had to recommend about measures to avoid such a disaster in the future. Partly based on an analysis of the economical values of the dike ring area of the central part of Holland, the committee concluded that a design water level with a frequency of exceedance of once in 10,000 years should be appropriate. Under design conditions each dike section should be absolutely safe. Since absolute safety is per definition not achievable, this absolute criterion was translated in a criterion for overtopping: less than 2% of the number of incoming waves were allowed to cause overtopping. For the rest of the Netherlands similar safety levels were derived: depending on the relative economical importance flood defences of other dike ring areas should have a design water level with a frequency of exceedance of 1/4000 or 1/1250 per year.

### Present approach

The present approach is based on the work of the Delta-committee. The safety standards in terms of a certain water level exceedance frequency are still up to date. However throughout the years several adaptations have been made, especially to the design methods. The 2% run-up criterion for instance has been translated into an equivalent overtopping criterion of 0.1, 1.0 or 10 l/m/s depending on the expected strength of the inner slope. For other mechanisms such as geotechnical failure, additional design criteria have been developed. All criteria are related to individual cross section of the dike. No correlations are considered. Only for certain dike ring areas which are situated in the transition regime where a combination of high tides and river discharges cause design water levels, an approach has been followed in which for the overtopping mechanism correlations between individual dike sections are dealt with [TAW/CUR, 1991]. For dunes it was noticed that an

overtopping criterion based on a certain water level was not appropriate. For the determination of the safety of dunes a totally different approach has been chosen for that reason. A probabilistic design standard has been developed in which several stochastic parameters, such as water level, wave height and grain size were taken into account. The safety level has been expressed in terms of probability of failure per dune section. This probability was chosen to be a factor 10 smaller than the water level exceedance frequency of 1/10,000 per year [TAW/CUR 1988].

In general the present approach is not a uniform design method and can be referred to as a 'dike section overloading approach'. In fig. 2 this approach is indicated. On the vertical axis the load  $S_0$  (for example the overtopping discharge) is given. On the horizontal axis the strength (for example expressed in terms of resistance to erosion of the inner slope). In general failure will occur if the load exceeds the strength.

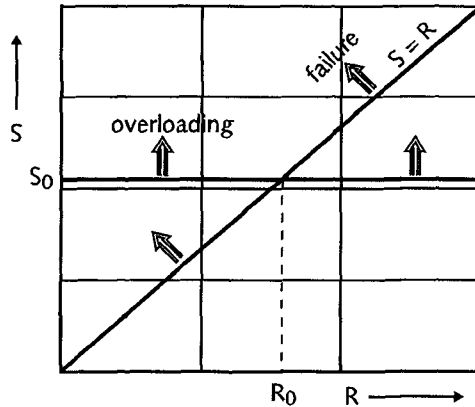


Fig. 2. Overloading approach.

This is the area above the diagonal line. The horizontal line refers to the overloading approach in which the probability that the strength is smaller than an expected value  $R_0$  is not considered.

Thus, features of the present approach are:

- safety levels are partly based on economical analysis (1953 situation);
- probabilistic description of the hydraulic load only (water level

- exceedance frequency);
- deterministic approach of the strength in terms of allowable overtopping rates (0.1, 1.0 or 10 l/m/s);
- a dike section approach: no correlations between dike/dune sections are considered;
- several kinds of merely deterministic approaches for other failure mechanisms like geotechnical failure;
- probability of failure approach for dune sections.

### Future approach

The TAW has decided to aim at a general overall consistent design philosophy. This new approach is referred to as the inundation risk approach. In this approach safety levels will be expressed in terms of risks. Risk is here defined as the value of probability of inundation times the expected damage in case of inundation:

$$R = P_f * D$$

$$R = \text{risk}$$

$$P_f = \text{probability of failure (inundation)}$$

$$D = \text{damage in case of failure}$$

Risk can be expressed in for instance monetary units and/or loss of lives. Load as well as strength will be dealt with in a probabilistic way. Correlations between dike sections will be accounted for. Polders with high values at risk should have a relatively lower probability of inundation than others. In this approach two separate tracks of development have to be distinguished. The first one is the assessment of the risk itself. The other one is the assessment of an acceptable risk level. The former is discussed here.

Several issues have to be investigated. In general the following steps can be distinguished:

- estimation of the probability of failure of the flood defence system;
- estimation of the inundation process in case of failure;
- analysis of the expected damage (material and immaterial) in case of inundation.

For the estimation of the probability of failure all possibly known (physical) causes of failure have to be gathered and arranged

systematically in a so-called fault tree. The top event of the tree is inundation. The branches are all possible failure mechanisms such as overtopping, sliding, erosion of revetments, piping etc. For each mechanism a mathematical model is developed. By means of either Monte Carlo analysis, other level III or level II analysis, the probability of the top event (inundation) is estimated. Of course for the parameters which are involved in the several models statistical information has to be gathered to estimate the distribution function and values for its parameters such as mean value and standard deviation. Much knowledge is already developed on this aspect of the inundation risk approach. Several mathematical models for the description of the failure mechanisms are available now [TAW/CUR, 1990].

For the analysis of the expected damage in case of failure floodings of the past have been analysed. This information is reproduced in mathematical relationships of the inundation parameter (such as inundation depth) and the expected damage as a percentage of the total value of an object. In fig. 3 such a relation is shown for damage to households in relation to inundation depths. In fig. 4 a similar curve is shown for casualties [TAW/CUR, 1990]. It is obvious that for the use of this type of relations a good estimate of the inundation parameters is important. These parameters depend heavily on the flood discharges in case of dike failure. However, knowledge of the flood discharges as a result of dike breaching is poor. Most information is based on eye-witness reports of breach growth events in the past. This information is very difficult to gather and also difficult to relate to the hydraulic and geotechnical conditions of the dike itself. Indeed, this kind of data is extremely unreliable. An example of the result of eye-witness information of the past is shown in fig. 5. From this and other similar figures it can be estimated that the velocity of the widening of a breach, ranges from 0.5 m to 50 m per hour [TAW-C/Delft Hydraulics, 1993b]. From sensitivity analysis it is known that an uncertainty of a factor 10 in the breach widening velocity gives at least a factor  $\sqrt{10}$  in uncertainty of the water level inside the polder and in the time that certain waterlevels are reached [TAW-C/Delft Hydraulics, 1993c]. This leads to an overall uncertainty in the expected damage. This uncertainty in the process might also influence disaster management strategies in which evacuation of inhabitants of a polder is an essential part.

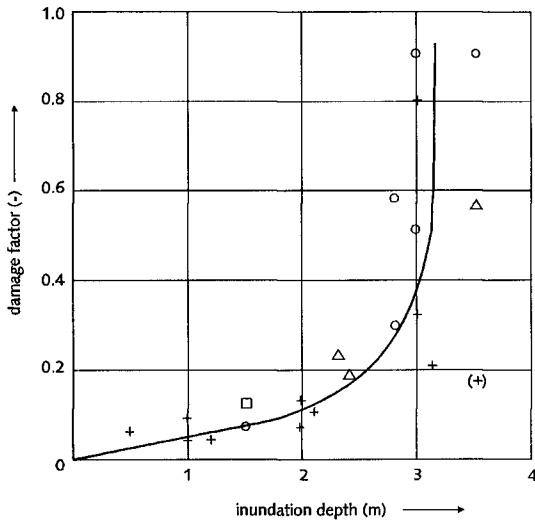


Fig. 3. Damage factor (1.0=100%) for houses and farms as a function of the inundation depth [TAW/CUR, 1990].

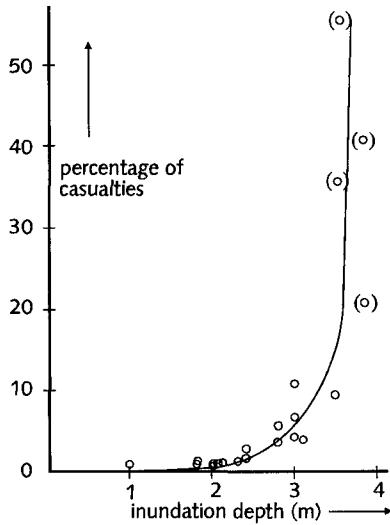


Fig. 4. Percentage of persons drowned (proportion of the population) as a function of the inundation depth [TAW/CUR, 1990].

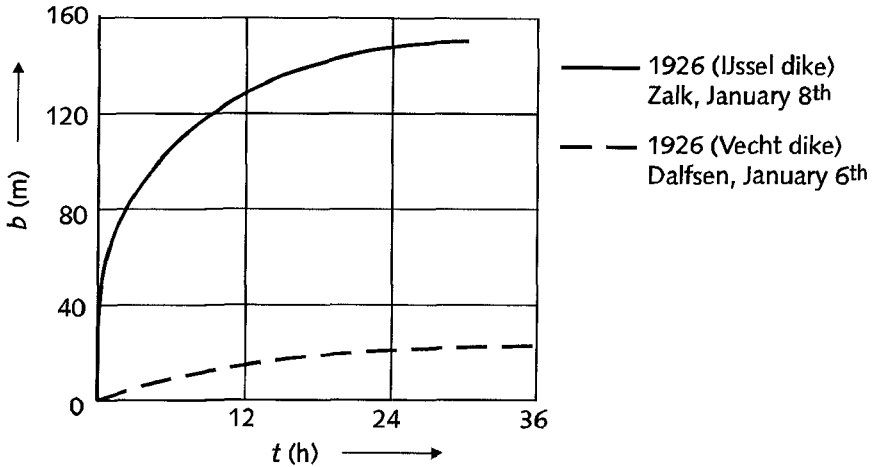


Fig. 5. Development of the breach width as a function of time, based on eye-witness reports.

#### Set up of research programme

To overcome this lack of knowledge the TAW decided in the late eighties to develop a breach growth model which determines flood discharges as a result of initial failure of a flood defence (dunes and dikes). In 1989 an unexpected opportunity occurred to observe a breach growth process in a sand-dike, which was temporarily built in a small tidal inlet (het Zwin) in the Netherlands [Visser et al. 1990]. There was hardly any time for preparation, so the experiment didn't provide many data. However, photographs and video provided sufficient information to start modelling and were helpful in setting up laboratory test series on breach growth. Being aware of the complexity of the process it was decided to start with sand-dikes first. This would provide an upper bound of the process as other materials are expected to be less erosive. It would also provide a good estimation of the processes expected in case of breaching of dunes.

From the Zwin experiment in 1989 it was learned that the process could well be separated in some typical phases. The first phases are described

as the erosion process of the inner slope and the lowering of the crest of the dike, which are two-dimensional processes [Steetzel et al 1992]. This was investigated first in the Schelde-flume at Delft Hydraulics [TAW-C/Delft Hydraulics, 1993a]. After these experiments it was decided to investigate the so-called isolated widening of the breach in the Schelde-basin of Delft Hydraulics. This provided information on the stepwise sliding of the edges of the breach [TAW-C/Delft Hydraulics, 1993b]. During this series an additional experiment was done to investigate the fully three dimensional process. However, this provided only little information because of the limitation of the basin bottom. Mainly for this reason, and also to verify the results obtained in small scale situations, an other prototype experiment was carried out in October 1994 in the Zwin. This time more preparation time was available and extensive measurements were carried out on all relevant aspects of the breach growth process, such as current velocities, waterlevels, scour hole dimensions and of course the development of the breach itself.

### Future research

In 1995 much effort will be put into the finishing of the mathematical modelling for breach growth in sand-dikes and dunes [Visser, 1994]. By means of a sensitivity study, it will be decided which aspects have to be investigated in more detail and which priorities have to be given. Future research will at least be focussed on breaching in dikes composed of less erosive materials.

### Conclusions

As a conclusion it can be pointed out that:

1. Breach growth development is an essential factor in an inundation risk analysis.
2. Breach growth research by means of step by step approach turned out to be an effective way to unravel the complex process.
3. An upper bound model, directly applicable for sand dunes, will be available in the near future (1995)
4. Future research will be focussed on dikes containing less erosive materials.

### References

Steetzel, H.J. and Visser, P.J. (1992). Profile development of dunes due to overflow. *Proc. 22nd Int. Conf. Coastal Eng. Venice, Italy.*

TAW/CUR (1988). Guide to the assessment of the safety of dunes as a sea defence, *report 140.*

TAW/CUR (1990). Probabilistic design of flood defences, *report 141.*

TAW/CUR (1991). Guidelines on the design of river dikes, part 2, tidal rivers.

TAW-C/Delft Hydraulics (1993a). Investigations on breach growth, results of 2DV model tests. *Research report H1242 part II (in Dutch)*

TAW-C/Delft Hydraulics (1993b). Investigations on breach growth, results of 2DH/3D model tests. *Research report H1242 part III (in Dutch).*

TAW-C/Delft Hydraulics (1993c). Breach growth, pragmatic modelling of the widening of a breach, *Research report H1242 part IV (in Dutch).*

Visser, P.J., Vrijling, J.K. and Verhagen, H.J. (1990). A field experiment on breach growth in sand-dikes. *Proc. 22nd Int. Conf. Coastal Eng., Delft, The Netherlands.*

Visser, P.J. (1994). A model for breach growth in sand-dikes. *Proc. 24th Int. Conf. Coastal Eng., Kobe, Japan.*



## CHAPTER 160

### SWASH ZONE WAVE CHARACTERISTICS FROM SUPERTANK

David L. Kriebel<sup>1</sup>

#### ABSTRACT

Measured values of shoreline wave setup and shoreline wave heights are summarized from the SUPERTANK Laboratory Data Collection Project. Water surface elevation time-series in the swash zone were measured by capacitance wave gages that were partially buried in the sand beach. As a result, wave measurements were obtained on the actively eroding/accreting beach-face where little data has traditionally been available. Results presented in this paper include examples of wave transformation across the entire beach profile. Mean water level and wave height conditions at the still water shoreline are then summarized for 19 sets of random wave conditions tested during the first two weeks of the SUPERTANK Project.

#### INTRODUCTION

Despite recent progress in the study of wave transformation across the surf zone, relatively little is known about wave properties near the shoreline or in the swash zone. Most measurements of wave transformation have focussed on the incipient breakpoint and the mid to outer surf zone where there is sufficient water depth to operate various surface-piercing or bottom-mounted wave gages. Wave measurements in the swash zone are generally more difficult to make and, as a result, are not as widely available. One approach used to measure waves in the swash zone has involved remote time-lapse photography of the time-varying runup, e.g. Holman and Sallenger (1985). Another approach, used to record time-series of water surface elevations at specific locations across the swash zone, has involved filming waves as they propagate past reference stakes driven into the beach-face, e.g. Carlson (1984). In contrast, Waddell (1973) and Sonu et al. (1974) present some of the only data available based on use of electronic surface-piercing wave gages to record time-series of water surface elevations in the swash zone.

---

<sup>1</sup>Ocean Engineering Program, U.S. Naval Academy, Annapolis, MD 21402

In this paper, some results of extensive swash zone wave measurements are presented from the SUPERTANK Laboratory Data Collection Project. As part of the SUPERTANK Project, twenty-six wave gages were used to document wave transformation across a sandy beach profile in a large wave tank. Of these, ten capacitance-based wave gages were specifically designed to measure wave transformation in the inner surf zone and swash zone where the beach face was intermittently submerged and exposed. The objective of this paper is to present results of these measurements for wave setup and for wave heights in the swash zone. Examples are first shown for wave transformation across the entire profile; then, values measured at the still water shoreline are discussed as a way of summarizing the extensive swash zone measurements.

## DESCRIPTION OF EXPERIMENTS

The SUPERTANK Laboratory Data Collection Project took place during the summer of 1991 in the in the large wave tank at Oregon State University. The tank is 104 m long and 3.6 m wide. A sand beach with a median grain size of 0.22 mm was placed in the tank with an "equilibrium" form (concave-upward) having a length of about 75 m and a maximum water depth of 3.05 m. A total of 66 different wave conditions, 70 percent using irregular waves, were then tested over almost 129 hours of wave action during the seven-week long project. In general, wave heights ranged from 0.2 to 1.0 meters and wave periods ranged from 3 to 8 seconds. A thorough documentation of the entire SUPERTANK project is given by Kraus and Smith (1994) while a review of the wave transformation measurements is presented by Kriebel and Smith (1994).

Mean water levels and wave transformation measurements were obtained using 26 wave gages between the wavemaker and the runup limit on the sand beach. Of these, 16 resistance wire wave gages were used to record wave properties between the wavemaker and the mid surf zone while 10 capacitance wave gages were used in the inner surf zone and swash zone. The resistance gages were separated at 3.7 meter intervals while the capacitance gages were spaced at 0.9 to 1.8 meter intervals to obtain better resolution in the swash zone. One capacitance gages was normally located close to the still water shoreline, which evolved from run to run as the beach eroded or accreted.

As illustrated in Figure 1, the capacitance wave gages consisted of a single loop of Teflon-insulated 20-gauge copper wire which was lightly twisted so that both ends of the wire were attached to one terminal at the base of a PVC electronics housing. The electronics housing was attached to a stainless steel support frame that was then attached to the side wall of the wave tank. The bottom of the sensing wire loop was attached to the support frame by a non-conductive rubber band in order to maintain a constant tension in the sensing wire. Sensing wires with lengths of 0.91 to 1.83 meters were used.

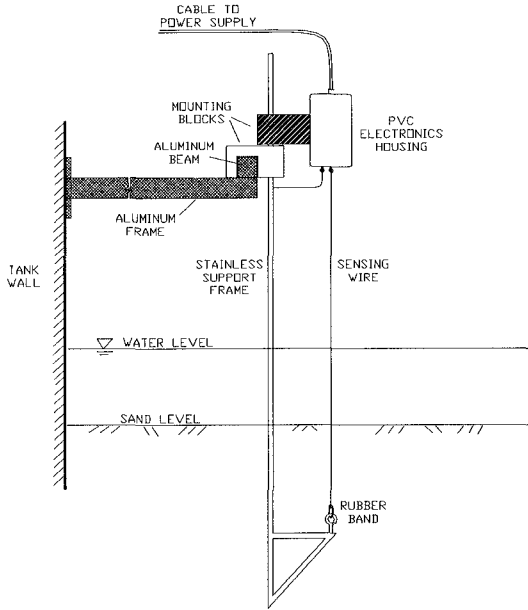


Figure 1. Illustration of capacitance wave gage used in the SUPERTANK Project.

The capacitance wave gages were partially buried in the sand beach and could record the wave uprush and downrush as well as the saturated sand bed elevation if the bed was exposed in between successive swash events. Water surface elevations and wave heights were measured relative to either: (1) the still water level if the gage was located seaward of the still water shoreline where the sand bed was not exposed at the beginning of the test, or (2) the wet sand surface if the gage was located landward of the still water shoreline where the sand bed was exposed at the start of the test. As a result, the mean wave setup on the exposed beach-face was measured as the increase in the mean (time-averaged) water level above the initial sand bed elevation at the start of the test.

After the mean water level was identified and removed from the wave record, the remaining time-series was subjected to low and high-pass filtering with a filter cut-off at one-half of the peak wave frequency of the target wave spectrum input into the wavemaker. Following this filtering, three time series were available for subsequent analysis: (1) the original or total wave record, (2) the high-frequency wave record containing the wavemaker frequencies and higher harmonic components, and (3) the low-frequency wave record containing wave group and tank seiching frequencies.

Wave heights were determined for each of these three time-series based on both time-domain and frequency-domain analyses. Standard zero-crossing analysis was used to define statistical wave height parameters such as  $HRMS$ ,  $H_{1/3}$ ,  $H_{1/10}$ , and  $H_{MAX}$ . In the swash zone, these wave heights were determined as the vertical height between each wave crest and the exposed sand bed. Standard spectral analysis was then performed to define the zero-moment wave height. Once again, three values were determined as  $HMO$ ,  $HMOL$ , and  $HMOH$  based on the total, low, and high frequency wave records respectively. Based on the filtering, conservation of wave energy requires that the relationship between the various zero-moment wave heights be given as  $HMO = (HMOL^2 + HMOH^2)^{1/2}$ .

## EXAMPLES OF WAVE HEIGHT TRANSFORMATION

Selected results showing typical beach profiles from the SUPERTANK Project are shown in Figure 2, while examples of dimensionless wave transformation across these beach profiles are shown in Figures 3, 4, and 5.

Beach profiles in the SUPERTANK Project varied continuously in response to the incident wave conditions. The initial profile, depicted in Figure 2a, was placed in a concave-upward shape in accordance with equilibrium beach profile concepts. As the experiments proceeded, the initial shoreline receded, the beach face steepened, a bar developed offshore, and the surf zone widened, as illustrated in Figure 2b. This profile is typical of conditions following erosive wave conditions. The profile in Figure 2c is then typical of conditions following accretionary wave conditions in which the bar-trough system was smoothed.

In Figures 3, 4, and 5, dimensionless mean water levels and dimensionless wave heights are plotted against the dimensionless "depth" across the profile. Seaward of the still water shoreline, the initial water depth is considered positive. Landward of the still water shoreline, the "depth" is considered negative when the initial sand bed elevations are above the still water level. The reason for using this format is that the wave transformation can then be shown continuously across the surf zone, to the still water shoreline (depth equal to zero), and across the swash zone to the runup limit. In all cases, the local "depth" is normalized by the significant wave height  $HMO_0$ , measured in 3.05 m of water at the first wave gage nearest the wavemaker.

Results shown in Figures 3 through 5 were obtained from tests using irregular waves having three values of wave steepness,  $HMO_0/L_0$ , equal to 0.005, 0.01, and 0.04, all for TMA spectra having a peak enhancement factor of 3.3. The first case, with the lowest steepness, had a significant wave height,  $HMO_0$ , equal to 0.5 m and a peak period,  $T_p$ , of 8 seconds. The second case then had  $HMO_0 = 0.64$  m and  $T_p = 6$  seconds, while the third case had  $HMO_0 = 0.57$  m and  $T_p = 3$  seconds. The beach profile in each case was similar to that shown in Figure 2b, although conditions at the end of tests with the lowest steepness were more similar to those in Figure 2c.

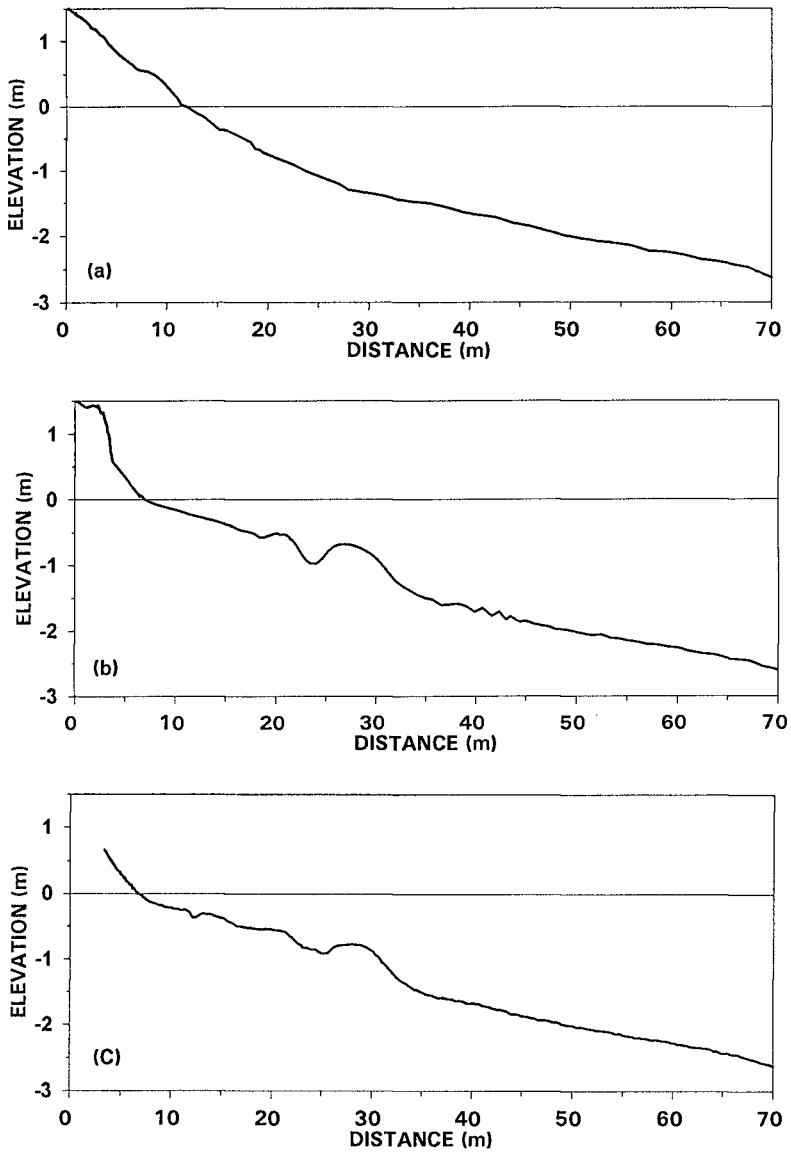


Figure 2. Typical beach profiles: (a) initial profile, (b) profile after erosive wave conditions, and (c) profile after constructive wave conditions.

Figure 3 shows the normalized wave setup and setdown, defined as ratio of the local mean water level,  $\mathcal{S}$ , to the offshore significant wave height. For the three values of wave steepness, the setdown seaward of the breakpoint is fairly consistent, reaching a maximum of 3 to 5 percent of the incident significant wave height. Setup inside the surf zone and in the swash zone is a much stronger function of wave steepness. The maximum setup near the shoreline ranges between 10 and 20 percent of the incident significant wave height and is larger for the lower steepness waves.

Figure 4a shows the normalized total wave heights, defined as ratio of the local zero-moment wave height relative to the value measured offshore near the wavemaker. For the highest steepness, wave heights decrease slightly between the wavemaker and the dominant breakpoint (at a relative depth of about 1.4) due to the selective breaking of the largest waves in the spectrum. Waves then continue to diminish across the surf and swash zones to the runup limit where the relative depth is  $-0.75$ . For the lower steepness wave conditions, significant wave heights increase by more than 20 percent between the wave maker and the dominant breakpoint due to shoaling effects. Throughout the surf and swash zones, these lower steepness waves produce greater relative wave heights. At the still water shoreline, wave heights are still about 40 to 60 percent of the offshore values and is largest for the smallest wave steepness.

Figure 4b and 4c then show the normalized wave heights for the high and low frequency portions of the wave spectrum respectively. In the offshore region, the low-frequency wave heights are found to be fairly small ( $0.1$  to  $0.2 H_{M00}$ ) and the high frequency waves are dominant. Near the shoreline and in the swash zone, however, the low frequency wave heights are generally the same magnitude, or larger than, the high frequency wave heights. In the three cases shown, high-frequency wave heights at the shoreline are only about 20 to 50 percent of the offshore zero-moment wave height while the low frequency wave heights are 25 to 35 percent of the offshore height. For the two cases with the highest wave steepness, low-frequency wave components have more energy than high-frequency wave components in the vicinity of the shoreline.

Based on visual observations and on spectral analysis, these low-frequency motions are mostly coherent standing waves. Unlike the high-frequency waves in Figure 4b, which are mainly progressive and which show large gradients in the swash zone due to breaking, the low-frequency waves in Figure 4c exhibit these gradients due to the presence of a reflected wave antinode at the sloping shoreline. These low-frequency waves experience strong growth between the breakpoint and the shoreline and may be the result of forced incident wave groups, long-wave generation by the moving breakpoint, and/or long-wave generation by swash zone wave interactions, all augmented by tank seiching and re-reflection of long waves by the wavemaker. The wavemaker was operated with reflection-compensation to absorb reflected waves at the dominant wave frequency but not at these long-wave frequencies.

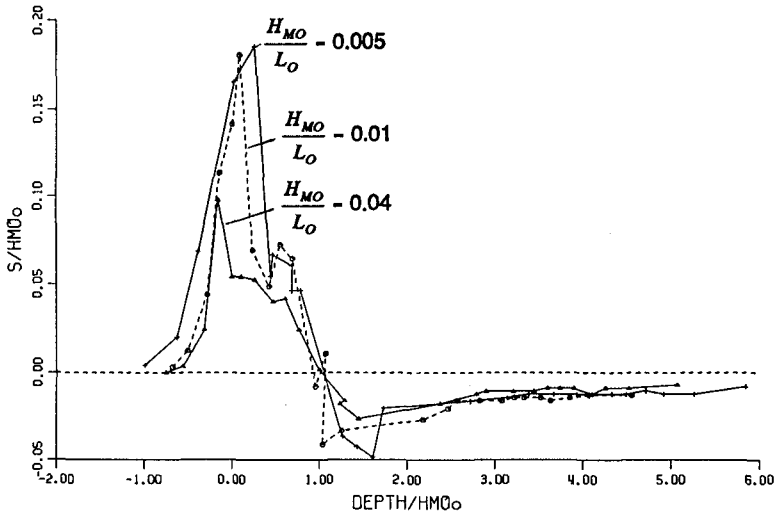


Figure 3. Dimensionless wave setup for three values of random wave steepness.

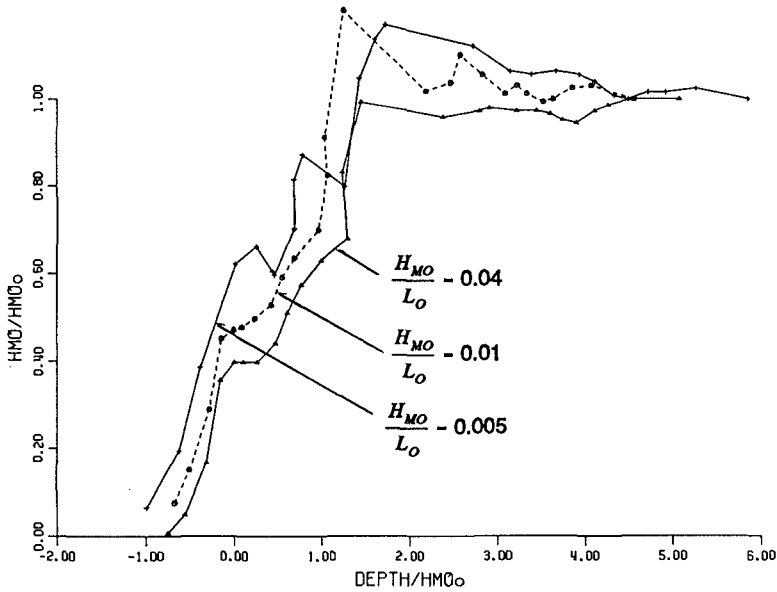


Figure 4. Dimensionless wave heights for three values of wave steepness: (a) based on total or unfiltered wave record

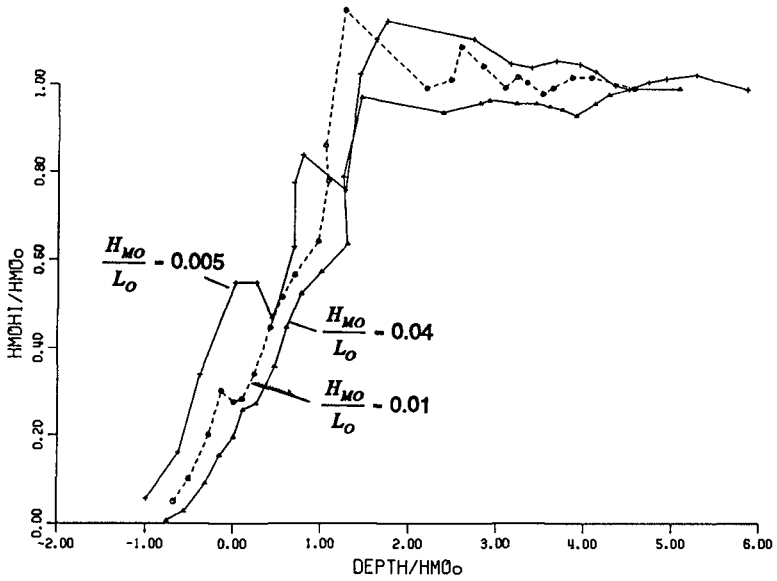


Figure 4. (b) based on high-pass filtering at one-half of the peak frequency.

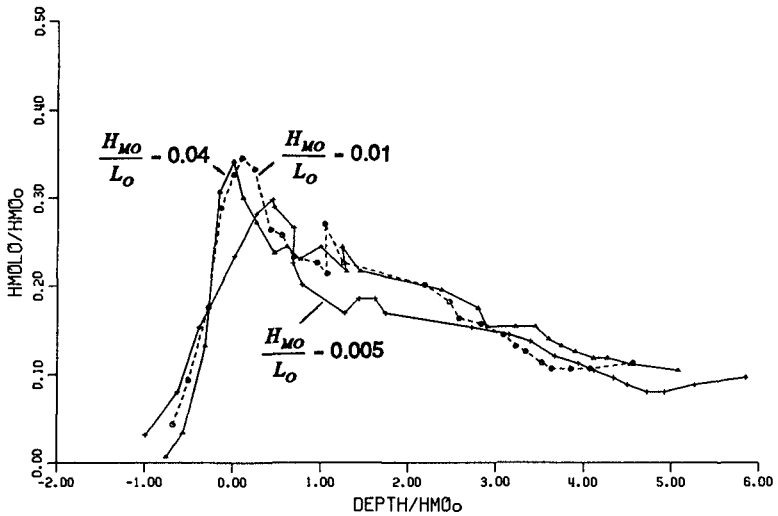


Figure 4. (c) based on low-pass filtering at one-half of the peak frequency.



One interesting result of these measurements is that, despite the effect of the reflective wavemaker boundary, there appears to be a strong correlation between the low-frequency and high-frequency wave heights. Figure 5 shows the ratio between the low- and high-frequency zero-moment wave heights as measured at each wave gage. This ratio is extremely consistent and well-behaved across the entire offshore region from the wavemaker to the mid surf zone. In this region, the ratio of low-to-high frequency wave heights increases from approximately 0.1 near the wavemaker to approximately 0.3 near the bar crest to nearly 0.5 in the inner surf zone. Although there is a slight trend toward increasing ratios for higher values of wave steepness, this ratio is similar for each of the three conditions.

At the shoreline, the ratio of low-to-high frequency wave heights is then a strong function of wave steepness, varying from about 0.5 for the lowest steepness, to about 1.2 for the middle steepness, to about 2.0 for the highest steepness. Thompson and Briggs (1993) considered the same ratio and concluded that the long-wave heights may reach a maximum of about 1.2 times the short-wave heights at the shoreline based on field data from Duck, North Carolina, for conditions where the spectral wave steepness was about 0.01. This seems to be confirmed by the laboratory data, however, the SUPERTANK data suggests that this growth in low-frequency wave components relative to the rapidly decaying high-frequency components depends strongly on the incident wave steepness so that no simple generalization is possible.

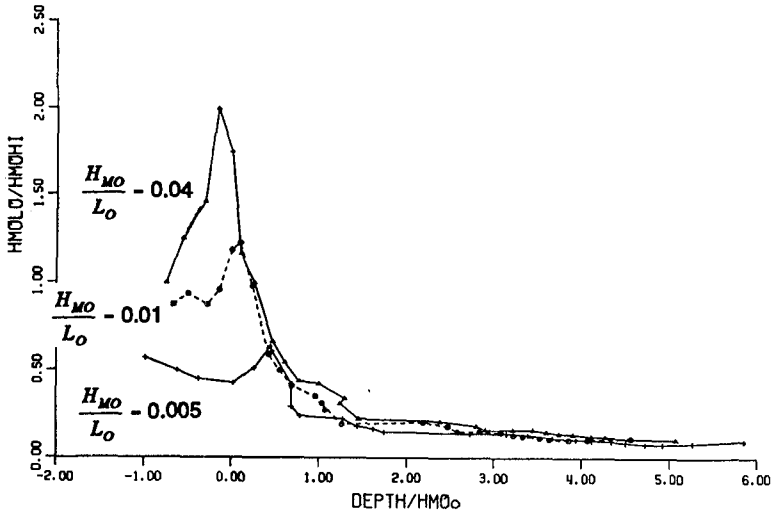


Figure 5. Ratio of locally-measured low-frequency significant wave height to high-frequency significant wave height based on filtering at one-half of the peak frequency.

## SUMMARY OF SHORELINE SETUP AND WAVE HEIGHTS

In order to summarize additional data from the SUPERTANK Project, the remainder of this paper will present results of wave setup and wave height parameters measured at the still water shoreline in 19 tests conducted with irregular waves over the first two weeks of the experiment. Figures 6 through 8 show normalized wave setup and zero-crossing wave heights as determined from the total wave record, the high-pass wave record, and the low-pass wave record. Results are based on linear interpolation between wave gages located either side of the still water shoreline. In each figure, values of shoreline setup and wave height are normalized by the offshore zero-moment wave height,  $HM_{0o}$ , and the normalized results are plotted against the incident wave steepness,  $(HM_{0o}/L_o)^{1/2}$ .

Figure 6 shows results for the normalized wave setup at the shoreline. Results from the SUPERTANK Project appear consistent with other lab and field data in which maximum wave setup at the shoreline is generally in the range of 0.15 to 0.2 times the offshore significant wave height. For example, Greenwood and Osborne (1990) suggest a ratio of 0.19 based on field data from Lake Huron. The SUPERTANK data also show a clear trend toward decreasing wave setup for increasing wave steepness, as also found in the literature. In this case, the wave setup ranges between 0.21  $HM_{0o}$  for the lowest wave steepness tested to about 0.11  $HM_{0o}$  for the highest wave steepness tested.

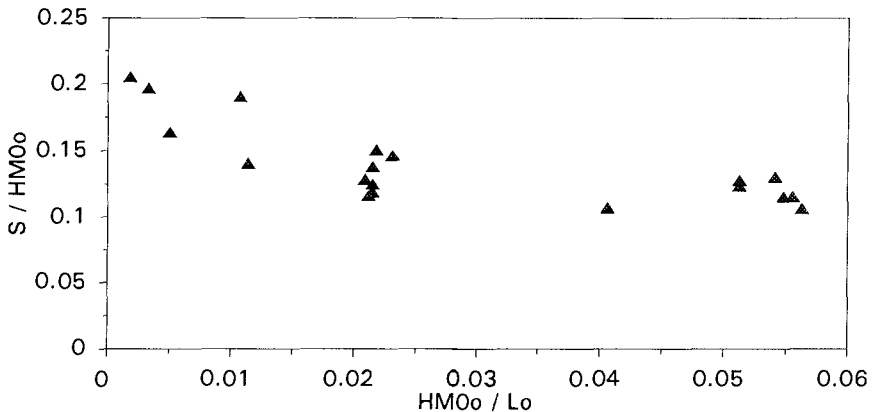


Figure 6. Normalized wave setup at the shoreline from SUPERTANK data.

Figure 7 shows the energy-based zero-moment wave heights at the shoreline,  $HMO_s$ , relative to the offshore zero-moment wave height,  $HMO_o$ , as a function of incident wave steepness. Figure 7a shows the total wave height at the shoreline, while Figures 7b and 7c show the high and low frequency wave height components at the shoreline respectively. As shown in Figure 7a, the wave height at the shoreline can vary between about 40 and 80 percent of the offshore value for the extreme wave steepness tested. While these shoreline wave heights decrease as wave steepness increases, there is little variation for values of steepness above 0.02.

The high and low frequency wave heights at the shoreline, shown in Figures 7b and 7c, show opposing functional dependencies on wave steepness. For the lowest values of steepness, low-frequency wave heights are small, about 0.2  $HMO_o$ , while high frequency wave heights are dominant, up to 0.7  $HMO_o$  or so. As the wave steepness increases, however, low frequency wave heights increase up to about 0.4  $HMO_o$  while high frequency wave heights decrease dramatically to about 0.2  $HMO_o$ . As a result, for the higher values of steepness, the low frequency wave height components (low frequency energy content) is actually twice as large as the high frequency wave components. A reversal in which wave energy band is dominant occurs at a wave steepness of about 0.01.

As shown in Figure 5, the ratio of low-to-high frequency wave height components is fairly stable across the surf zone but shows large differences in the swash zone. Figure 8 then shows this ratio at the shoreline as a function of wave steepness. As discussed previously, high frequency wave heights dominate for the lowest wave steepness tested and the ratio of low-to-high frequency wave heights is about 0.5 or less. Above a steepness of 0.01, however, the low frequency wave heights dominate the swash zone motions such that the ratio of low-to-high frequency wave heights is greater than unity. While there is significant scatter in the data, the ratio is in the range of 1.5 to 2.0 for the highest values of wave steepness which were highly energetic and highly erosive wave conditions.

At the still water shoreline, there is initially zero water depth until the mean water level rises due to wave setup. As a result, the ratio of wave height to still water depth at the shoreline is infinite unless wave setup is considered. With wave setup, the ratio of wave height to water depth (setup) is finite and this ratio is shown in Figure 9 for all 19 data sets. As shown, the ratio of total zero-moment wave height to wave setup at the shoreline is in the range of 3 to 4 and is insensitive to wave steepness. In contrast, the ratio of wave height to water depth in the surf zone is commonly assumed to be approximately one. Based on the SUPERTANK data, the significant wave height at the shoreline is given by  $HMO_s = 3.3 S$  on average. Consideration of the high and low frequency significant wave heights separately does not produce results that are as well-behaved, but on average the high frequency significant height at the shoreline is 2.0 times the wave setup while the low frequency wave height is 2.5 times the setup.

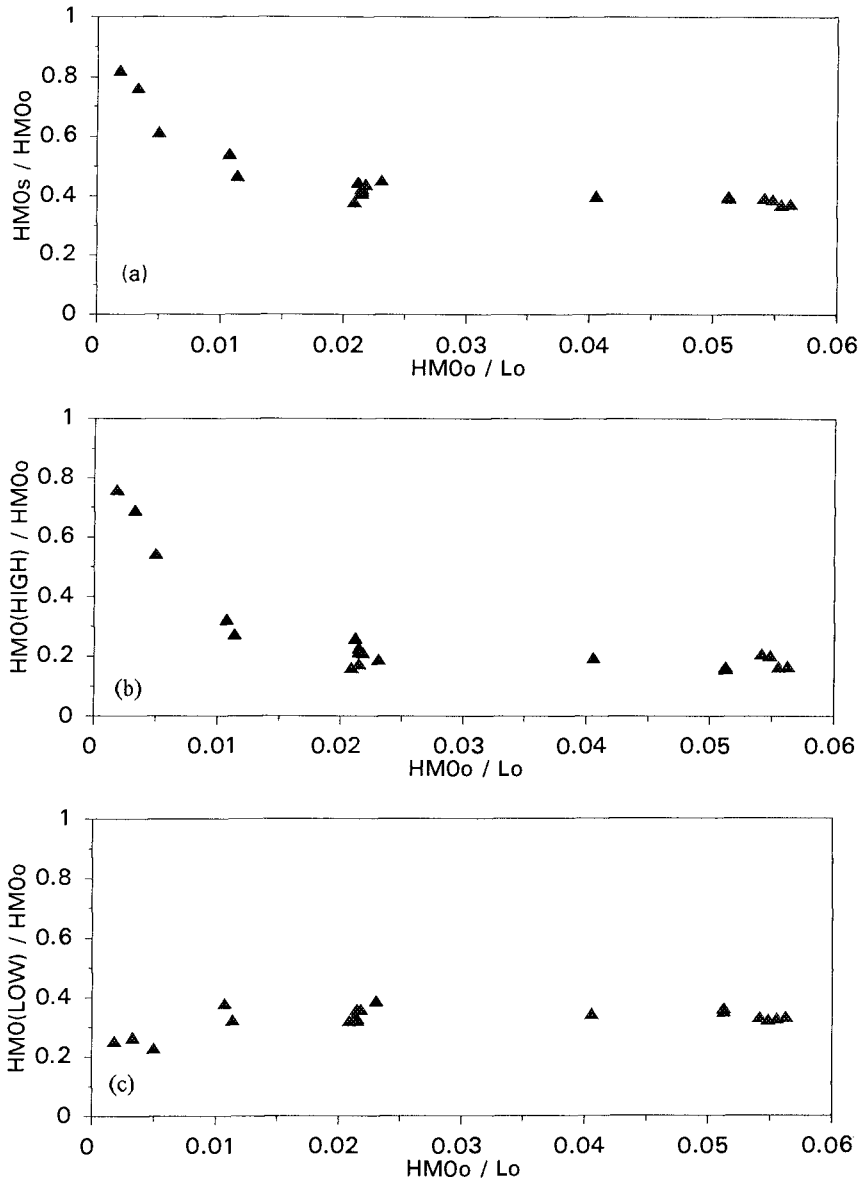


Figure 7. Normalized zero-moment wave heights at the shoreline: (a) total wave height, (b) high-frequency wave height, (c) low-frequency wave height.

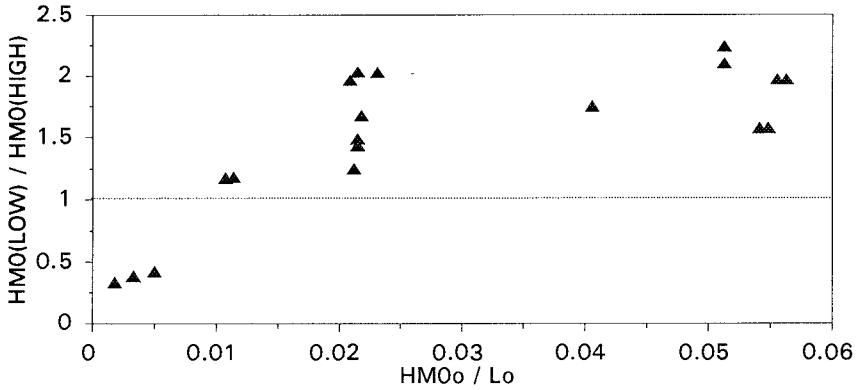


Figure 8. Ratio of low-to-high frequency wave heights at the still water shoreline.

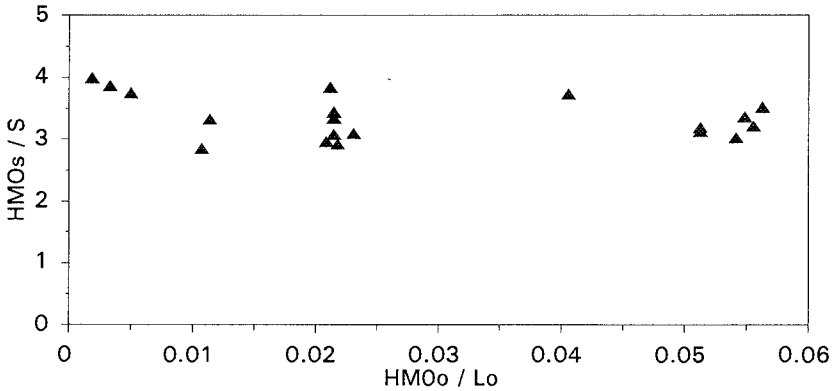


Figure 9. Ratio of significant wave height to mean water depth (setup) at shoreline.

As a final consideration, statistical wave height parameters at the shoreline, obtained from a zero-crossing analysis of the total wave record, are shown in Figure 10. This gives  $HRMS$ ,  $H_{1/3}$ , and  $H_{MAX}$  measured at the shoreline, all normalized again by the offshore zero-moment wave height. For the lowest values of wave steepness, it is found that statistical wave heights are a strong function of wave steepness. For these conditions,  $HRMS$  at the shoreline can be 0.4 to 0.5 times  $HMO_o$ ,  $H_{1/3}$  can typically be 0.5 to 0.7  $HMO_o$ , and  $H_{MAX}$  can typically be 0.7 to 1.1  $HMO_o$ . At the other extreme, for the highest values of wave steepness, wave heights are not strong functions of steepness and  $HRMS$ ,  $H_{1/3}$ , and  $H_{MAX}$  are about 0.2, 0.3, and 0.5 to 0.6 times  $HMO_o$ , respectively.

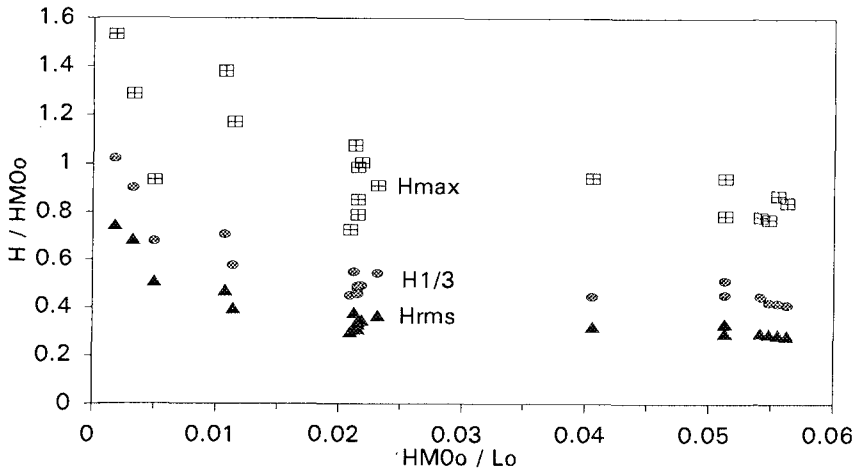


Figure 10. Shoreline wave height parameters based on zero-crossing analysis.

## CONCLUSIONS

This paper has presented selected results of wave setup and wave height measurements from the SUPERTANK Data Collection Project. The main objective of the measurements was to document wave transformation across the beach profile at all locations between the wavemaker and the wave runup limit. This required use of capacitance wave gages, partially buried in the sand beach, to document mean water levels and time-varying wave heights in the swash zone where the initial sand bed elevation was above the still water level of the wavetank.

Several examples have been presented of the random wave transformation across the beach profile for various wave steepness conditions. These measurements show that wave properties in the swash zone are well-behaved despite the fact that waves in this region are intermittently occurring bores that do not propagate on a finite water depth. Results are then shown for wave setup and wave heights at the still water shoreline where the initial water depth is zero.

In the analysis, the wave record is filtered into separate low and high frequency components. In the offshore region, the high frequency (incident band) wave components dominate and low frequency components (wave group and tank seiching frequencies) are small. In the inner surf zone and swash zone, the high frequency components diminish due to breaking while the low frequency components grow and reach a maximum amplitude at the still water shoreline.

For low incident wave steepness, the high frequency portion of the wave spectrum, containing the intended peak frequency of the spectrum and higher harmonics, dominates in the swash zone and is usually larger than the long standing waves at the shoreline. In contrast, for high incident wave steepness, the low frequency portion of the spectrum dominates at the shoreline and in the swash zone. While this paper has documented the characteristic heights of these long wave components, it does not address the possible generation mechanisms for these waves.

## ACKNOWLEDGEMENTS

This work was supported by the Coastal Engineering Research Center of the U.S. Army Corps of Engineers. The author was also supported by a Presidential Young Investigator Award from the National Science Foundation.

## REFERENCES

- Carlson, C.T., 1984, "Field Studies of Run-Up on Dissipative Beaches," Proc. 19th Intl. Conf. on Coastal Engineering, ASCE, pp. 399-414.
- Greenwood, B., and Osborne, P., 1990, "Vertical and Horizontal Structure in Cross-Shore Flows: An Example of Undertow and Wave Set-up on a Barred Beach," Coastal Engineering, Vol. 14, pp. 543-580.
- Holman, R. A., and Sallenger, A. H., "Setup and Swash on a Natural Beach," J. Geophysical Research, Vol. 90, No. C1, pp. 945-953.
- Kraus, N. and Smith, J., 1994, "SUPERTANK Laboratory Data Collection Project, Volume 1," Waterways Experiment Station, U.S. Army Corps of Engineers, Tech. Rpt. CERC-94-3, 274 pp.
- Kriebel, D.L., and Smith, J.M., 1994, "Wave Transformation Measurements at SUPERTANK," Proc. Coastal Dynamics '94 Conf., ASCE, Barcelona, pp. 233-247.
- Sonu, C., Pettigrew, N., and Fredericks, R., 1974, "Measurement of Swash Profile and Orbital Motion on the Beach," Proc. Ocean Wave Measurement and Analysis Conf., ASCE, pp. 621-638.
- Thompson, E. and Briggs, M., 1993, "Surf Beat in Coastal Waters," Waterways Experiment Station, U.S. Army Corps of Engineers, Tech. Rpt. CERC-93-12, 66 pp.
- Waddell, E., 1973, "Dynamics of Swash and Implication to Beach Response," Coastal Studies Institute, Louisiana State University, Tech. Rpt. No. 139, 49 pp.

## CHAPTER 161

### MORPHOLOGICAL MONITORING OF A SHOREFACE NOURISHMENT NOURTEC Experiment at Terschelling, The Netherlands

Aart Kroon\*, Piet Hoekstra\*, Klaas Houwman\* and Gerben Ruessink\*

Netherlands Center for Coastal Research (NCK)

- \* Institute for Marine and Atmospheric Research Utrecht, Utrecht University, P.O.Box 80.115, 3508 TC Utrecht, The Netherlands.

#### *Abstract*

The morphological behaviour of a shoreface nourishment site is studied. The originally observed patterns in bar development before the nourishment are disturbed by the extra volume of sediment in the cross-shore profile. Attention is focused on the morphological development of the nearshore bars and troughs after the nourishment.

After almost a year, the bar at the landward site of the nourishment showed a reversal in bar behaviour in comparison with the natural conditions as described by Ruessink and Kroon (in press). The bar was slightly moving landward and was growing in height, whereas a similar bar at this position within a non-nourished environment would move seaward and reduce in height. The bar at the seaward side of the nourishment is quickly adjusting itself to the situation before the nourishment.

The bar behaviour after the nourishment is accompanied by a redistribution of the sediments over the profiles. The net amount of sediment losses in the nearshore area is negligible. This also means that the nourished volume of sediments is still available in the central part of the nourishment area. Longshore movements of the nourished volume are in the order of 400 m to the east over a period of about a year, and are not observed in the cross-shore profiles with a longshore spacing of 1000 m.

#### *Introduction*

The coastline of the northern part of the Netherlands consists of a chain of barrier islands alternating with tidal inlets. The beaches and nearshore zones of these barrier islands are composed of sandy sediments. The central parts of the barrier islands do suffer from erosion over the last decades. At Terschelling (figure 1) the shoreline of the central part of this barrier island retreated over the last decades with an average, annual rate of 2.5 to 3 m.year<sup>-1</sup>, which means an average, annual volumetric loss of 110.000 m<sup>3</sup> of sediment within the nearshore zone.



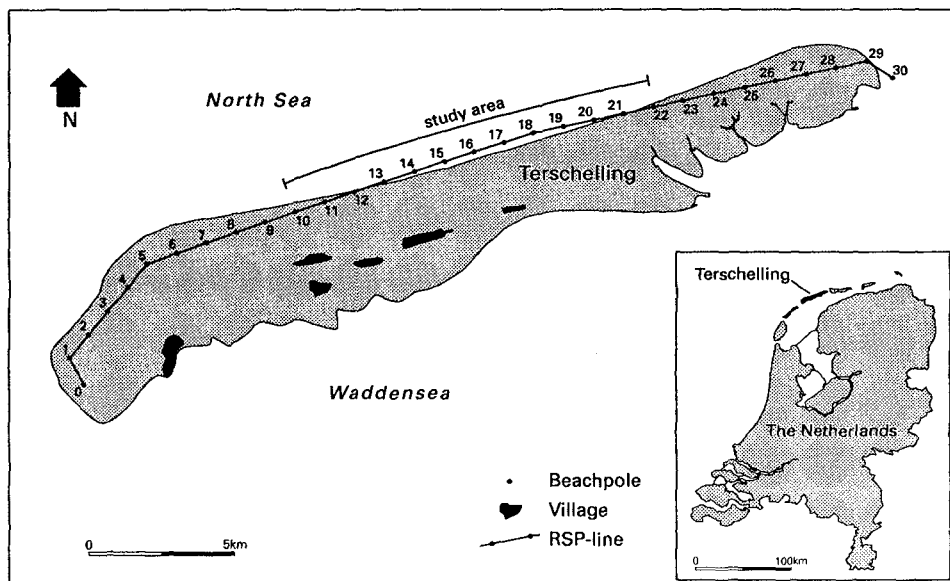


Figure 1 Location of the study area

Since the seventies, the eroding coastal stretches along the Dutch coast are mainly defended by beach nourishments. However, in the early nineties other kinds of soft engineering structures are considered. This resulted in the decision to execute another type of nourishment in 1992, a shoreface nourishment consisting of a submerged volume of sediment filling up a trough between two shore-parallel bars in the outer nearshore zone. Hereby, the design of the shoreface nourishment has to guarantee the same degree of safety as the other measures of shore protection. This means that the artificial volume of sediments must be beneficial for the coastal system for at least period of 10 years.

The scientific EC-MAST2 programme NourTEC has the objective to describe and explain the behaviour of this shoreface nourishment. The behaviour of the nourishment is analyzed in different phases. An evaluation of the behaviour before the nourishment is made by studying the evolution of the barred morphology in the nearshore zone over the last decades (Ruessink and Kroon, in press). The hydrodynamic processes and sediment properties in the barred nearshore zone just prior to the nourishment have been subject of study within a relatively small field campaign ( $T_0$ ; Hoekstra et al., 1994). The behaviour of the barred morphology and the morphodynamics after the nourishment is studied since 1993 by means of detailed process-oriented measurement campaigns.

In this paper, the morphological behaviour of the nourishment site is studied. Attention is paid to the morphological development of the nearshore bars and troughs after the nourishment. These observations are then compared with the natural behaviour of these bars in cross-shore and longshore direction before the nourishment (Ruessink and Kroon, in press). In addition, the sediment budgets within the cross-shore profiles along the nourishment site are computed.

### *Study area and previous results*

The shoreface nourishment is situated at the north coast of the barrier island Terschelling, The Netherlands (figure 1). This north coast of Terschelling is facing the semi-enclosed North Sea and is made of a sandy shoreface, beaches and dunes.

The morphology of the nearshore zone, defined as the upper shoreface, is characterized by two or three nearshore bars. The width of the nearshore zone is about 1400 m and the mean slope is about 1:180. The shoreface nourishment is placed in a trough between two shore-parallel nearshore bars at a depth of -5 to -7 m below mean sea level. The length of the nourishment in a longshore direction is 4.4 km. The median grain size ( $D_{50}$ ) of the sediments in the intertidal zone is about 200 to 250  $\mu\text{m}$ . At the seaward side of the shoreface nourishment site, at a water depth of about 10 m, the median grain size is reduced to about 160 to 180  $\mu\text{m}$ .

The morphological behaviour of the multiple bar system in the nearshore zone of Terschelling, The Netherlands between 1965 and 1993 is analyzed in Ruessink and Kroon (in press). Herein, both the cross-shore and longshore tendencies of the bar behaviour before the nourishment are described. The morphodynamical development of the nearshore bars over the last decades results in the following tendencies:

- The net cross-shore migration of the nearshore bars is in a seaward direction and shows different behaviour with distance offshore. Close to the shore, the volume of the bar is small and the behaviour is quite chaotic, hardly showing any net tendency (stage 1). Further offshore the nearshore bars constantly migrate in a seaward direction until the outer margin of the barred nearshore area (stage 2). At this position the outer nearshore bar declines (stage 3).  
The plane view of the bar is changing from crescentic to straight in an offshore direction. Overall, the bar feature has a 'life-cycle' of about 12 to 15 years;
- The net longshore migration of the nearshore bars is in an eastward direction with an average rate between 800 and 1250  $\text{m}\cdot\text{year}^{-1}$  over the period 1975 - 1993.

The general hydrodynamic conditions are mainly determined by the processes related to the waves and tides. The sea and swell waves are coming from the North Sea from western to northern directions. The mean annual significant offshore wave height is about 1.5 m and has a period of about 6 to 8 s. The highest waves are incident from the west to northwest and have a significant height of about 5 to 6 meter and a period of 10 to 15 s. The wave-related undertow and the longshore and cross-shore wind-driven currents are of major importance in the nearshore zone of Terschelling (Hoekstra et al., 1994). The tides are semi-diurnal and have a neap-tide range of 1.2 m and a spring-tide range of 2.8 m (meso-tidal). The tidal current ellipses in the nearshore are shore-parallel oriented and the eastward flowing flood currents exceed the westward flowing ebb currents.

### *Methods of analysis*

#### **Data set**

The present data set consists of five soundings carried out in lines perpendicular to a longshore reference line which connects the beach poles (the RSP-line, see figure 1). These soundings were executed in April 1993 (just before the nourishment), November 1993 (after the nourishment), January, April, and June 1994. The length of the cross-shore profiles is about 2000 m, and always covers the zone between the beach and the

lower shoreface at -10 m NAP. The longshore spacing between the studied profiles is 1000 m. The cross-shore profiles in the nourishment area are used to describe the morphological development in a morphometric and a volumetric sense.

### Morphometric analysis

The quantitative description of the cross-shore profiles in a morphometric way requires a mean profile equation to which the single measured profiles at different time steps are compared. This mean cross-shore profile equation is determined in two steps. The first step concerns the computation of the mean of all the measured cross-shore profiles at one location over the period 1964 to 1993 (dataset Ruessink and Kroon, in press). This mean cross-shore profile can not be used as a reference profile because it still contains some barred features, due to the limited amount of profile measurements in comparison to the 'life-cycle' of the system. The second step concerns the fit of a mathematical expression to the computed mean profile. An exponential curve fitting procedure was chosen for the nearshore profile between the beach and the lower shoreface. This exponential curve is expressed by:

$$d = d_0 \cdot [1 - e^{-ax}] \quad (1)$$

in which

- d = computed depth of the average profile below NAP [m]
- $d_0$  = depth at the location where the slope of the bed is almost zero [m]
- a = coefficient [ $m^{-1}$ ]
- x = horizontal coordinate, positive in seaward direction [m]

In the Terschelling case, the  $d_0$ -value is 8.7 and the a-value is 0.0018 (see also Ruessink and Kroon, in press).

The residual profile, which is defined as the individual measured profile minus the fitted profile is used for the description of the bar morphology. The dimensions of the bar features are defined in figure 2. The studied dimensions are the depth of the bar crest to NAP ( $d_c$  in m), the position of the bar ( $P_c$  in m), the height of the crest of the bar ( $h_b$  in m) and the width of the bar ( $W_b$  in m) (figure 2).

### Volumetric analysis

The volumetric analysis of the cross-shore profiles is executed in several successive steps. The first step is the determination of the seaward boundary of the dynamic part of the nearshore. This boundary must be located seaward of the closure depth of the cross-shore profiles (see Kroon, 1994). At Terschelling, the location of the -8 m depth contour in the cross-shore profiles matches this requirement.

Thereafter, the sediment volume between the measured cross-shore profile and the -8 m depth is computed across the profile. These computed sediment volumes are determined in a cumulative way from the seaward boundary towards the beach. The trends in the cumulative sediment volumes are finally compared along the nourishment site. Three volumes are hereby selected:

- the nearshore zone, defined as the area between the 0m and -8m depth contour. The width of the nearshore zone was constant for each profile location during the 1993 to 1994 period;
- the seaward half of this nearshore zone;
- the seaward quarter of this nearshore zone.

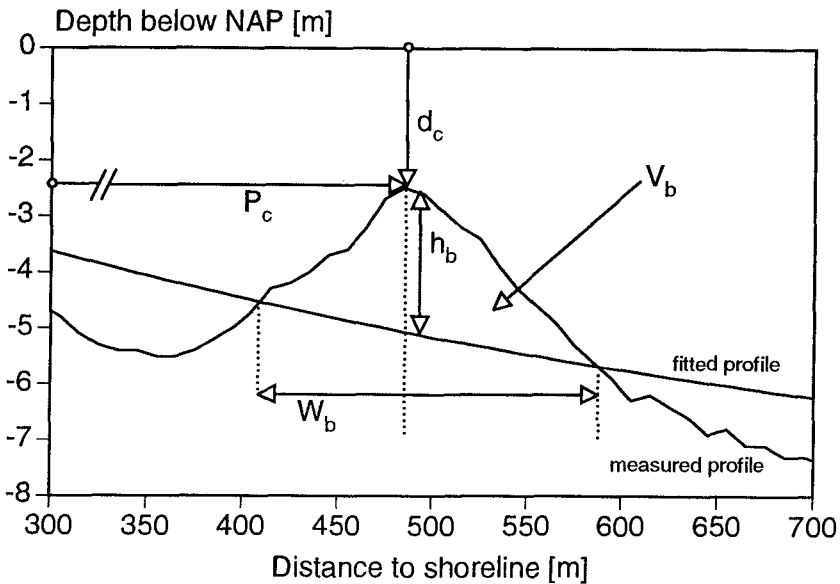


Figure 2 Definition sketch of morphometric variables

### Results

#### Morphological development after the nourishment

The overall characteristics of the nearshore zone along the nourishment site are summarized in Table 1. The width of the nearshore zone slightly increases from the central nourishment area (profile 16) to the western (profile 13) and eastern (profile 19) side.

Table 1 Bar characteristics profile 17

time	distance offshore [m]	bar crest depth [m]	bar crest height [m]
April 1993	597 - 1077	3.6 - 5.7	2.1 - 1.7
November 1993	607 - 912	3.8 - 4.4	1.9 - 2.7
January 1994	546 - 922	3.5 - 4.6	1.9 - 2.4
April 1994	562 - 978	2.7 - 5.2	2.9 - 2.0
June 1994	530 - 922	2.5 - 5.2	2.8 - 1.9

The cross-shore profile behaviour at several locations along the nourishment site are presented in figure 3.

At about 800 m west of the nourishment (profile 13), the positions of the nearshore bars are almost stable in time. The trough between the two outer bars is slowly filling up from -7 to -5.5 m NAP.

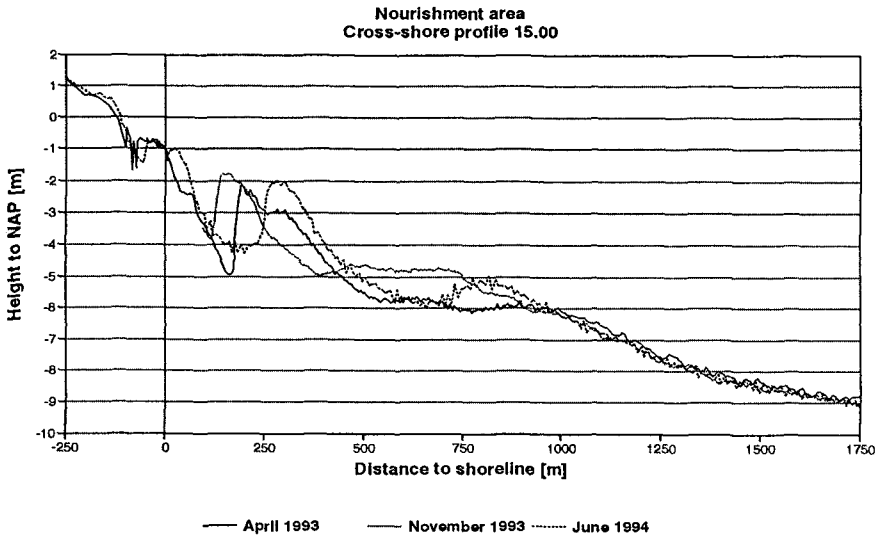
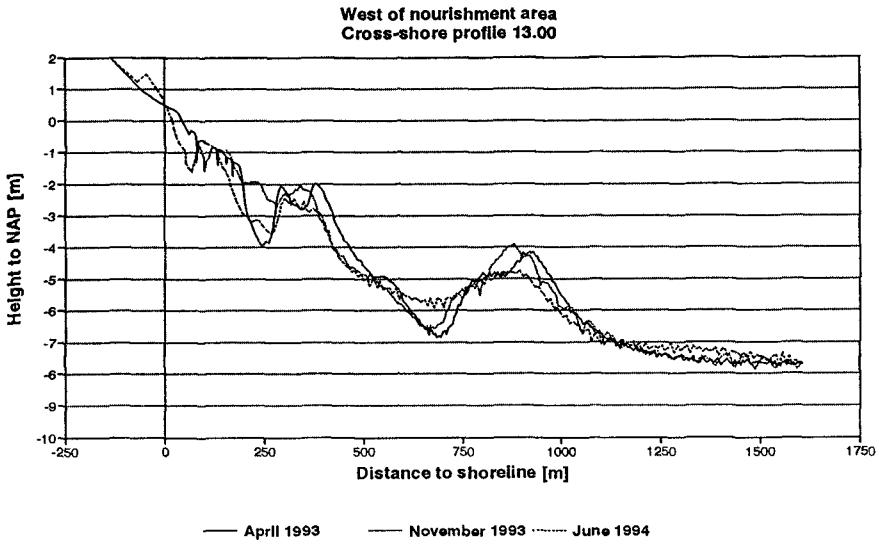


Figure 3 Cross-shore profiles

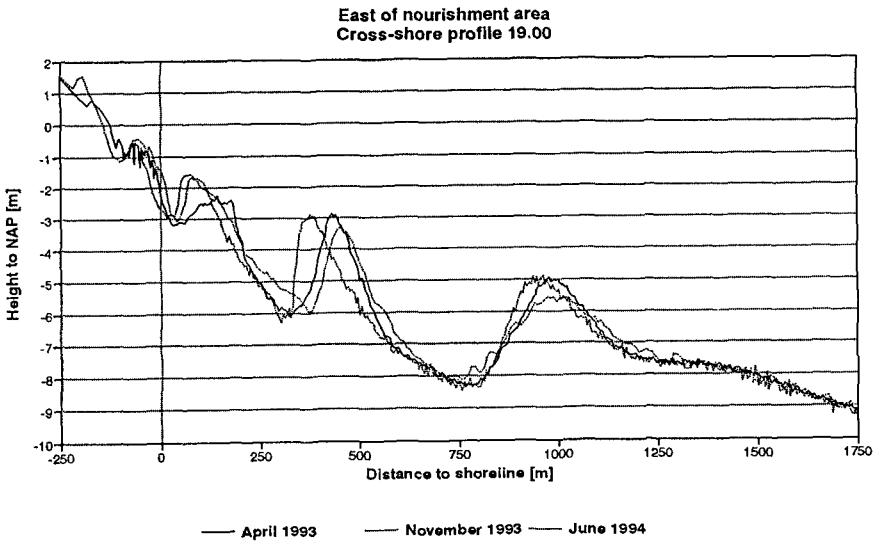
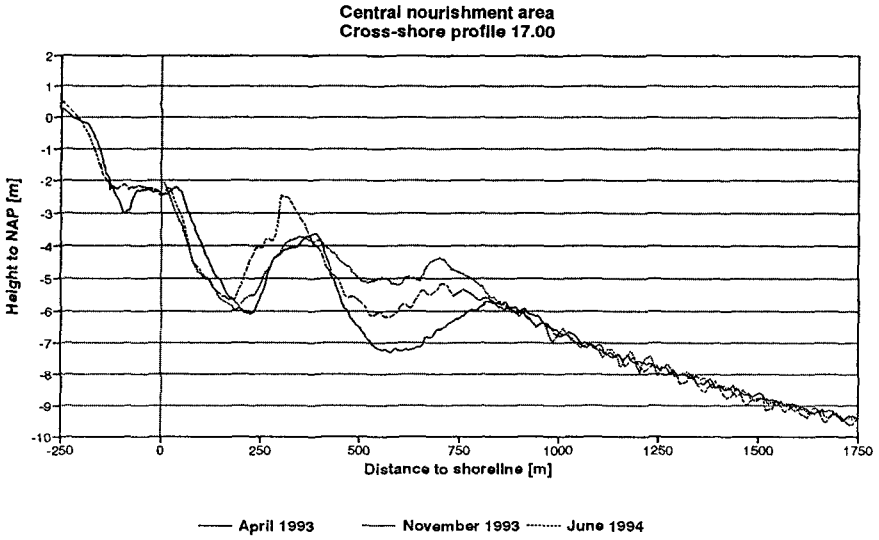


Figure 3 Cross-shore profiles (continued)

At about 800 m east of the nourishment (profile 19), the position of the most seaward, nearshore bar hardly changes in time. The landward located nearshore bar is moving onshore over a distance of about 50 m between April and November 1993, followed by a seaward shift over the same distance between November 1993 and June 1994.

At the central part of the nourishment area (profile 17), the nourished volume of sediment in the trough between the two outer nearshore bars is easy to trace. The morphological developments in this cross-shore profile can be summarized in three phases:

- filling up of the trough in the nourishment period (April November 1993);
- development of a barred topography at the nourishment site. The outer bar is reduced in height, the trough is increased in depth and the inner bar is increased in volume in a landward direction;
- the bar topography is even more pronounced. The most seaward bar is further reduced in height, while the landward bar at the nourishment site is increasing in height to a value of -2.5 m NAP. The offshore position of this bar crest is stable over the January to June 1994 period.

At the western part of the nourishment (profile 15), the morphological development of the bars is more complex. Before the nourishment, the outer nearshore bar had just disappeared, due to the longshore migration of a bar attachment point that came from the west (Ruessink and Kroon, in press). This means that the morphological development of bars in the cross-shore profile can be better studied at profile 17 where the longshore movements of sediment volumes are only caused by the nourishment in the 1993-1994 period.

For the central part of the nourishment (profile 17), the morphometric variables of the bar topography in time are presented in figure 4. The different lines in this figure represent the successive nearshore bars in the period 1964 to 1994. The two nearshore bars before the nourishment (bar 4 and bar 5 in figure 4) have changed in one large double crested bar (see figure 5). However, for the comparison of the bar behaviour with the autonomous behaviour before the nourishment, both crests are regarded as two bars.

The distance to the shoreline of the inner bar crest (5 in figure 4a) in time is almost constant. The distance to the shoreline of the outer bar crest (4 in figure 4a) is reduced with about 100 m as a result of the nourishment (difference between April and November 1993). Thereafter, the position of the outer bar crest is quite constant in time.

The depth of the inner bar crest to NAP subsequently decreases after the nourishment (5 in figure 4b). The depth of the outer bar crest to NAP is decreasing during the nourishment period (4 in figure 4b) and increasing in the period after the nourishment.

The relation between the bar crest depth and the distance to the shoreline for the autonomous system is presented in figure 6a. According to the three stages of bar behaviour as defined by Ruessink and Kroon (in press), both the inner and the outer crest are in stage 2. This means that the crests should normally have a seaward migrating tendency. However, as a result of the increased volume of sediment due to the nourishment, both the inner and outer crest are firstly moving in the direction of the first stage. The reversal of this tendency to an expected offshore migration has already started at the outer crest position (see April to June 1994).

The relation between the bar height and the distance offshore is presented in figure 6b.

The height of the inner crest of the bar is obviously deviating from the previously observed patterns: the crest is located at greater heights than has ever been recorded in the past (Ruessink and Kroon, in press). The outer crest of the bar is positioned at a location where the observed relation in the autonomous behaviour was weak.

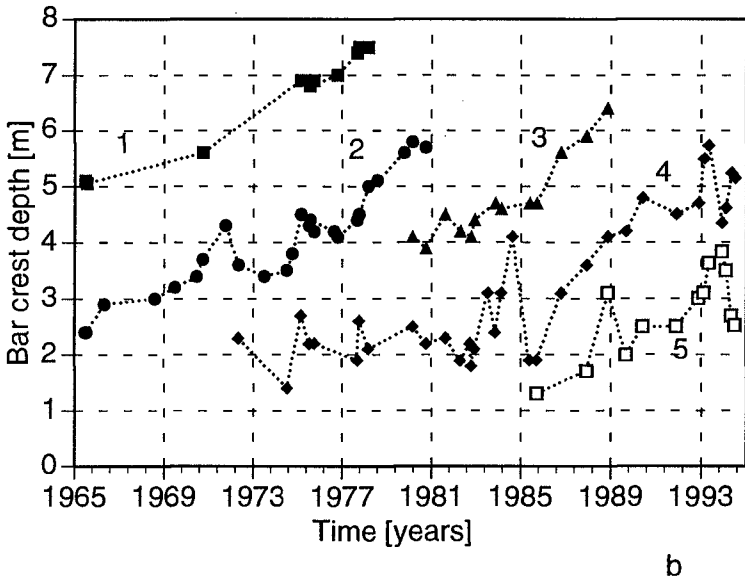
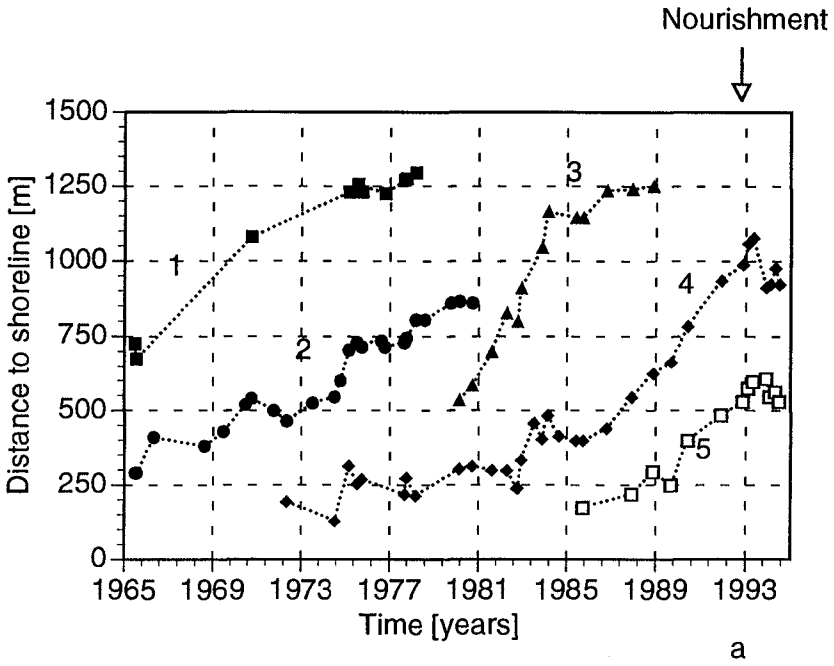


Figure 4 Position of bar crests (a) and depth of bar crests (b) in time



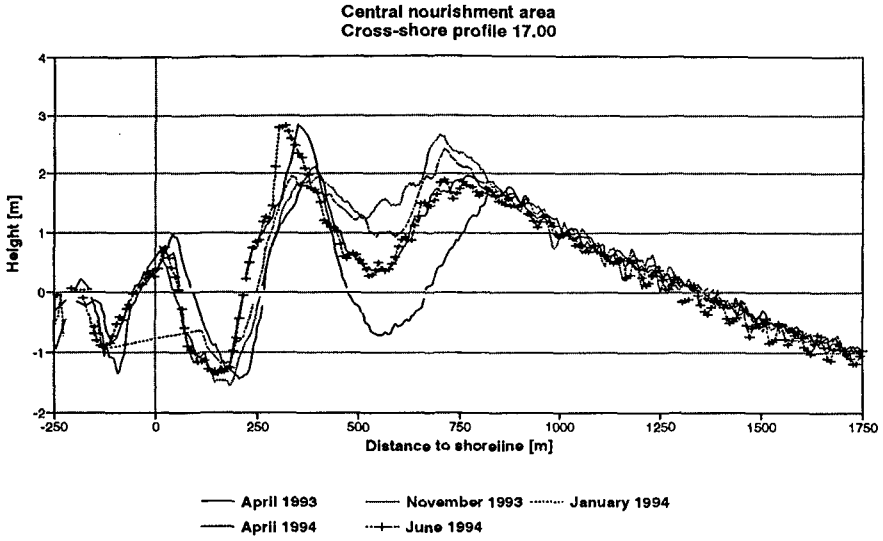
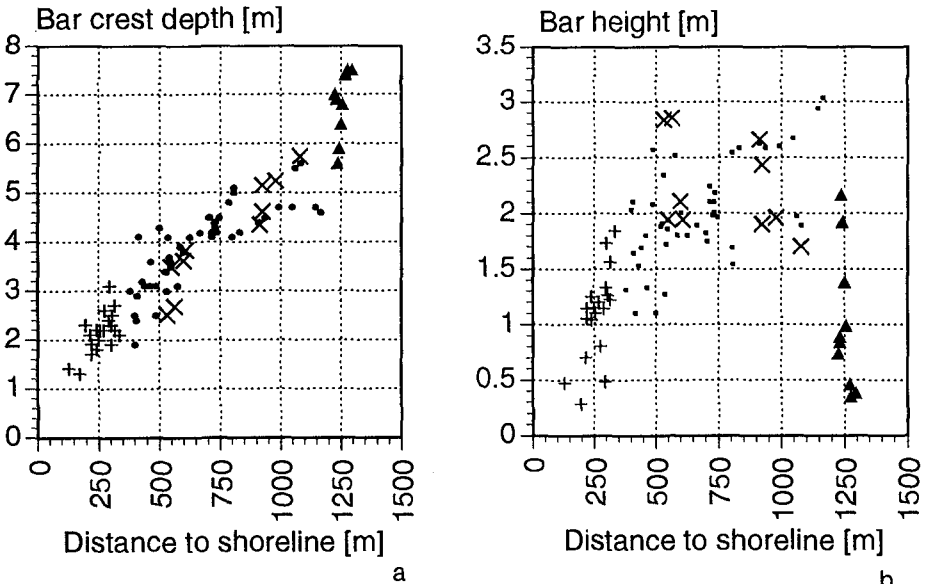


Figure 5 Detailed bar developments using residual profile 17



+ stage 1	• stage 2	▲ stage 3	X double crest
-----------	-----------	-----------	----------------

Figure 6 Position of the bar crests versus bar height (a) and depth of bar crest (b)

Longshore patterns in bar behaviour are observed. The development of the bar patterns in the cross-shore profiles over the nourishment site do suggest a shift in the bar variables towards stage 1. The nourishment will thus increase the duration of stage 2. The relation between the development of the bar pattern at the central part and those at the western and eastern sides of the nourishment area are still not clear. The alongshore shift of the nourishment volume can not be measured with an alongshore profile spacing of 1000m. Detailed soundings in the area have shown a eastward shift of the sediment volume of about 400 m over the period November 1993 to June 1994.

### Volumetric development

The cumulative sediment volumes within the cross-shore profiles are shown in figure 7.

At about 800 m west (profile 13.00) and east (profile 19.00) of the nourishment, the differences in sediment volumes are not influenced by the nourishment. At profile 14.00, there is an overall decrease in the sediment volume over the 1993 to 1994 period. At profile 19.00, the cumulative sediment volumes are almost constant.

At the central part of the nourishment area (profile 17), the sediment volume is increased between April and November 1993, due to the nourishment. Thereafter, there is a slight decrease in the sediment volume.

The spatial distribution of the cumulative sediment volumes in the cross-shore profiles is presented in figure 8. The volumetric changes within the nearshore zone, defined as the area between the 0m and -8m depth contour, are showing an increase of sediment volume after the nourishment in the central part of the nourishment (compare 1 and 2 for profile 15 to 18 in figure 8a), followed by an almost constant volume after this period. At the western end of the nourishment area (profile 14), this tendency is not observed.

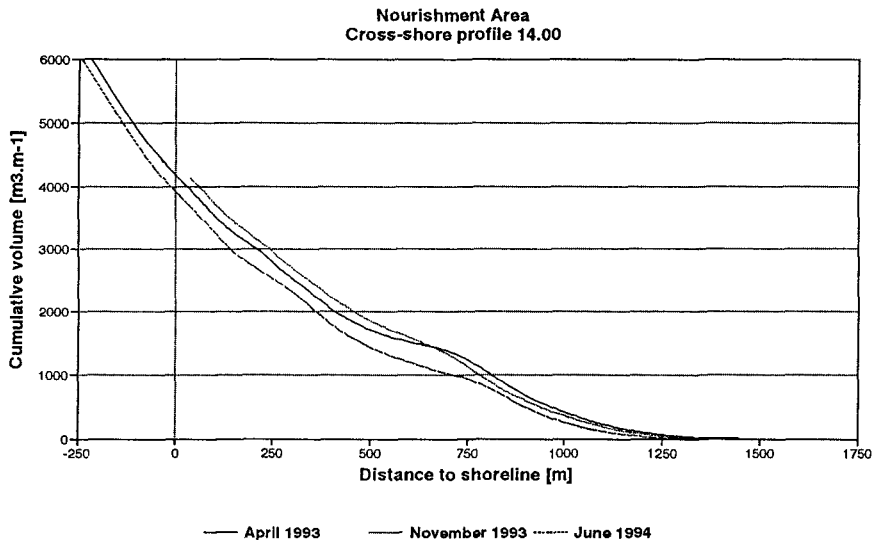


Figure 7 Cumulative sediment volumes at certain cross-shore profiles

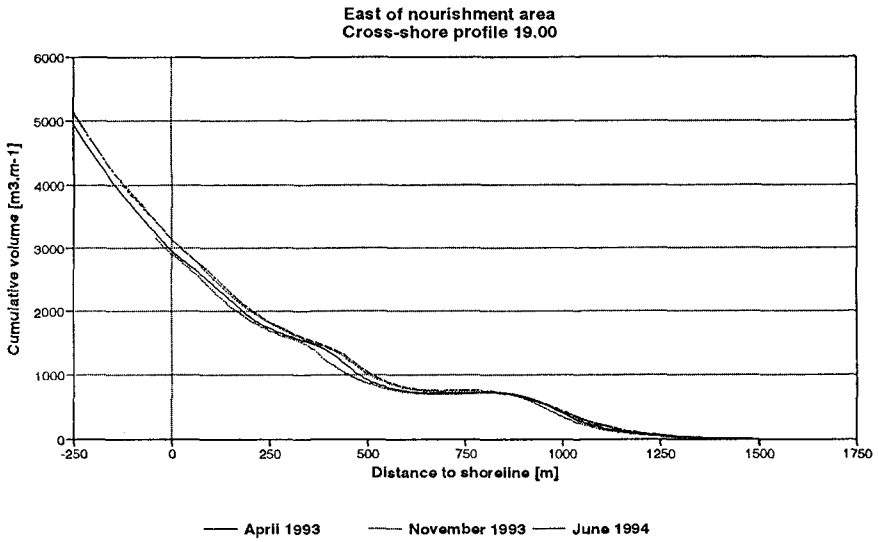
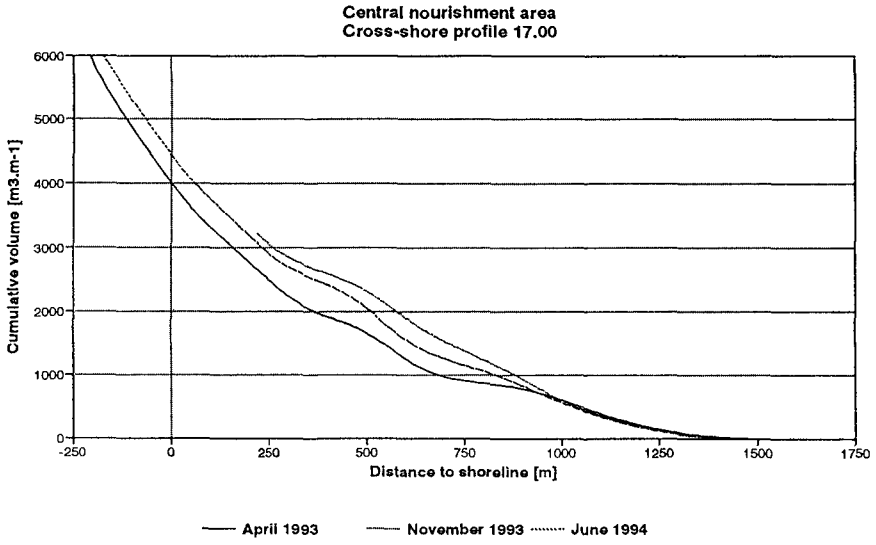


Figure 7 Cumulative sediment volumes at certain cross-shore profiles (continued)

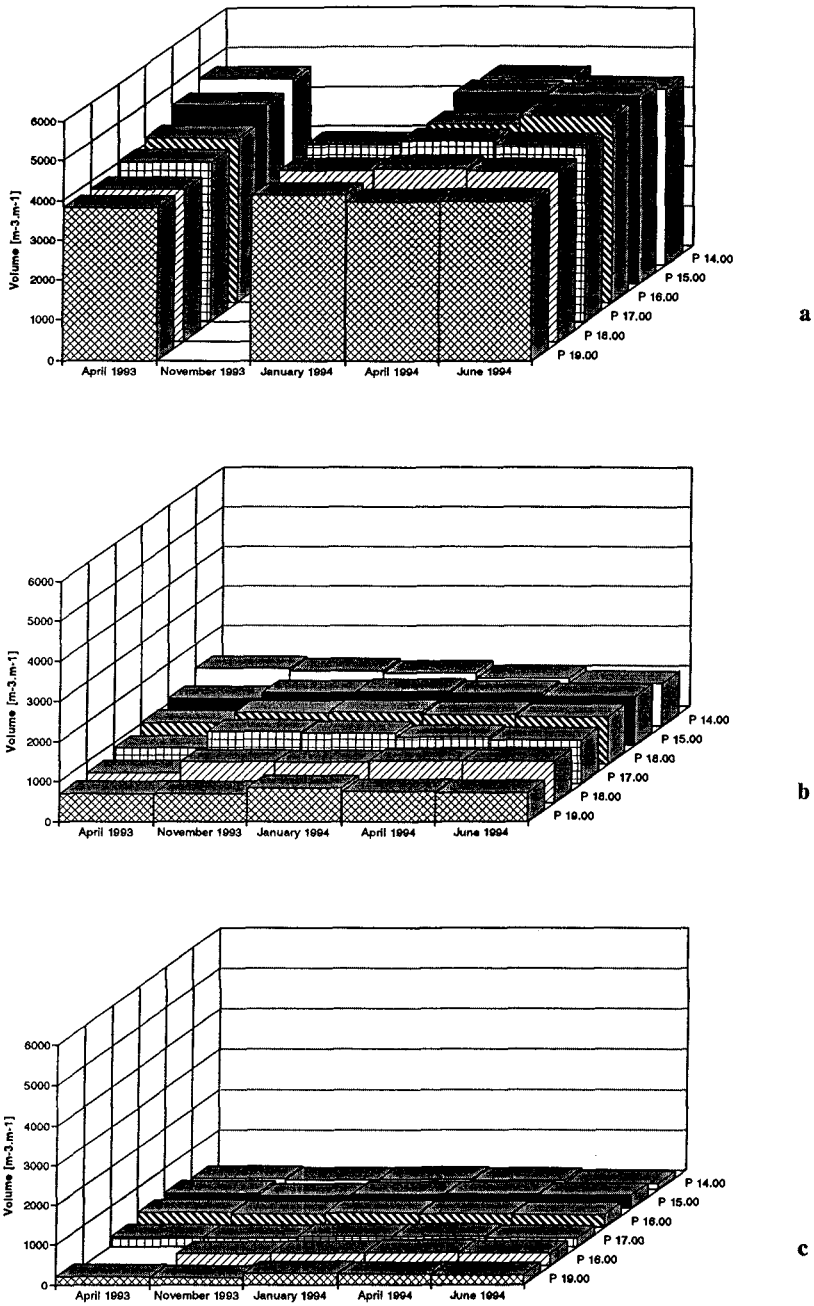


Figure 8 Spatial distribution of nearshore sediment volumes: a. nearshore area, b. seaward half, c. seaward question.

The influence of the nourishment is even better to see in the volumes of the seaward half of the nearshore zone (figure 8b). It is obvious that the nourishment is effective in the central area (profile 15 to 18). The western area (profile 14) is rather complex. The influence of the nourishment is interfering with the longshore migration of a bar attachment point from the west.

The spatial pattern of the cumulative sediment volumes in the seaward quarter of the nearshore zone is presented in figure 8c. The changes in volumes are negligible small over the period April 1993 to June 1994.

### *Discussion*

The morphological development of the breaker bars in the central nourishment area consists of three phases:

- the pattern of the bars and troughs are disturbed in the nourishment period. The trough between the two outer bars is filled up, and the bar topography has changed in a shore platform with two small undulations at the landward and seaward side. The total volume of sediment in the cross-shore profile between the -8 m to the 0 m depth contours has increased with about  $450 \text{ m}^3 \cdot \text{m}^{-1}$ ;
- just after the nourishment, the profiles are quickly adjusting to the former bar and trough topography. The outer bar crest depth and trough depth are increasing and the inner bar crest depth is decreasing. However, along the nourishment the total volume in the cross-shore profiles between the -8 m to the 0 m depth contours is almost constant, which implies a redistribution of the sediment over the nearshore part of the profile;
- in the period between January and June 1994, the bar and trough topography becomes more pronounced. This is especially the case for the inner bar. The crest of this bar is further growing in height and the depth of the crest is now at about -2.5 m NAP. However, according to the morphometric relations for the natural bars in the period 1964 to 1993, the inner bar must be out of equilibrium and may be flattened off. The behaviour of the outer bar is already typical for stage 2 again. The total volume in the cross-shore profile between the -8 m to the 0 m depth contours is almost constant. The small changes in bar patterns are thus made by the redistribution of sediments over the cross-shore profile.

The observed patterns in time are still not related to the observed hydrodynamics. The observed adaptations of the cross-shore profile to the pre-existing bar morphology is however within the time-span of a month. This means that the modulating mechanisms of the barred topography immediately act upon the disturbed profile.

The increase in the height of the inner bar in the period January to June 1994 may be partly caused by the onshore directed sediment transport by wave-asymmetry processes. However, this remark is still very tentative and will be verified in the next future in two steps by:

- analyzing detailed process-oriented field measurements (see Hoekstra et al., 1994). These measurements are used to verify different wave-, tide- and wind-related processes over the barred cross-shore profile;
- analyzing the type of combined wave- and tidal-sequences over this period (see Kroon, 1994). The analysis of the sequences of the waves (e.g. storm-related events) will be executed in order to understand the representativeness of the observed period within the average, long-term wave climate.

The combined morphometric and volumetric analysis of the cross-shore profiles in the nourishment areas has clearly shown that significant changes in the cross-shore bar and trough patterns may occur with hardly any changes in the nearshore volume over the same period.

The disturbed pattern of the cross-shore morphology due to the nourishment is quickly adjusted. These adjustments, striving to attain a new type of quasi-equilibrium are good indicators of the morphodynamics of the bars on the longer term.

### *Conclusions*

The morphological development of the nearshore bars and troughs after the nourishment is showing the following aspects:

- the disturbed bar morphology caused by the nourishment is quickly adjusting itself to the previously observed pattern. The bar pattern in the central part of the nourishment area is already back within a month after the completion of the works. The former trough at the position of the nourished volume has a similar time of adjustment;
- the bar and trough morphology is still out of dynamic equilibrium. The inner bar crest is growing in height and almost stable at its position, at a location where the previous observed patterns in bar behaviour would suggest a seaward migration and with an almost constant height. The nourishment volume has thus decreased the rate and even reversed the pattern of bar behaviour.

The overall behaviour of the nourishment volume over the year 1993 to 1994 is showing the following aspects:

- after November 1993, no significant net change in sediment volume at the studied cross-shore profiles along the nourishment are observed;
- the only transport of the nourished sediment volume is observed in an eastward longshore direction. This can be expected because the major components of the wind-, wave-, and tide-driven currents are also directed towards the east;
- despite the lack of net changes in the nearshore sediment volumes, there is a redistribution of sediments within the nearshore zone which may be coupled to the behaviour of the bars.

### *Acknowledgements*

This work was carried out as part of the project NOURTEC: Innovative Nourishment Techniques Evaluation. It was funded jointly by the Ministry of Transport, Public Works and Water Management in the Netherlands and by the Commission of the European Communities, Directorate General for Science, Research and Development under the Marine Science and Technology programme contract no. MAS2-CT93-0049. All sounding data were kindly made available by *Rijkswaterstaat*, National Institute for Coastal and Marine Management (RIKZ) of the Dutch Ministry of Transport, Public Works and Water Management.

### *References*

- Hoekstra, P., Houwman, K.T., Kroon, A., Van Vessem, P. and Ruessink, B.G., 1994. The Nourtec experiment of Terschelling: process-oriented monitoring of a shoreface nourishment (1993-1996). *Proc. Coastal Dynamics'94*, ASCE, 402-416.
- Kroon, A., 1994. Sediment transport and morphodynamics of the beach and nearshore zone near Egmond, The Netherlands. PhD-thesis, Utrecht University, 275 pp.
- Ruessink, B.G. and Kroon, A., in press. The behaviour of a multiple bar system in the nearshore zone of Terschelling, the Netherlands: 1965-1993. *Marine Geology*

## CHAPTER 162

### Numerical Model for Longshore Current Distribution on a Bar-Trough Beach

Yoshiaki KURIYAMA<sup>1</sup>

#### Abstract

A numerical model for the time-averaged nearshore current in the surf zone is developed to simulate the longshore current distribution on a bar-trough beach that has a peak velocity shoreward of the bar crest. Momentum fluxes due to mass transport under broken waves, which are ignored in other models, are included in the present model. The validity of the model is verified with field data.

#### 1. Introduction

There are two patterns of the time-averaged longshore current distribution on a bar-trough beach. One has a peak velocity seaward of the bar crest, and the other has the peak shoreward of the bar crest. Kuriyama and Ozaki (1993) measured longshore current velocities in the field when a single bar-trough system was formed and waves broke over the bar. They showed that eighty-five percent of the measured longshore current distributions have peak velocities shoreward of the bar crests, whereas fifteen percent have peaks seaward of the bar crests.

The seaward peak can be reproduced by one-dimensional models of the longshore current where the driving force of the longshore current is the cross-shore gradient of radiation stress (Ebersole and Dalrymple, 1980; Larson and Kraus, 1991) because the gradient is largest seaward of a bar crest owing to the large dissipation of wave energy due to wave breaking. On the other hand, the shoreward peak cannot be reproduced by the one-dimensional models. Church and Thornton (1993) and Smith et al. (1993) have recently developed one-dimensional numerical models for the longshore current that include the effect of turbulence due to wave breaking on the driving force through consideration of the surface roller. Although the peak velocities predicted by their models are located shoreward of the peaks predicted by previous

---

1) Senior Research Engineer, Port and Harbour Research Institute  
Nagase 3-1-1, Yokosuka, Kanagawa 239, JAPAN

models, the peaks predicted by their models are still located seaward of the peaks measured in the field. Symonds and Huntley (1980) showed that the longshore gradient of wave setup can cause a shoreward peak. The shoreward peak, however, was sometimes observed when the longshore gradient of the wave setup was small.

The objective of this study is to develop a numerical model that reproduces the shoreward peak in the longshore current even when the longshore gradient of the wave setup is small. It is assumed that the momentum fluxes due to mass transport under broken waves generate the shoreward peak, and the resultant momentum fluxes are introduced into a previous nearshore current model. Longshore current distributions predicted by the present model are compared with those measured in the field.

## 2. Numerical Model

The present model consists of two computationally distinct numerical models: a wave height transformation model and a nearshore current model.

### 2.1 Wave height transformation model

The present model for wave height transformation is based on the Karlsson's model (1969) for directional random waves, which is based on the balance of wave energy. I introduce a wave energy dissipation term as Takayama et al. (1991) did. The energy equation of a wave component with the frequency of  $f$  and the direction of  $\theta$  is expressed as

$$\begin{aligned} \frac{\partial(D_s V_x)}{\partial x} - \frac{\partial(D_s V_y)}{\partial y} + \frac{\partial(D_s V_\theta)}{\partial \theta} &= -D, \\ D_s &= S(f, \theta) \delta f \delta \theta, \\ V_x &= C_g \sin \theta, \quad V_y = C_g \cos \theta, \\ V_\theta &= \frac{C_g}{C} \left( -\cos \theta \frac{\partial C}{\partial x} - \sin \theta \frac{\partial C}{\partial y} \right), \end{aligned} \quad (1)$$

where  $D_s$  is the wave energy,  $S$  is the directional wave spectral density,  $\delta f$  is the frequency band width,  $\delta \theta$  is the directional band width,  $C_g$  is the group velocity,  $C$  is the celerity, and  $D$  is the wave energy dissipation rate. The values of  $D_s$ ,  $C_g$ ,  $C$  and  $D$  are defined for a wave component. The co-ordinate system used in this paper is shown in Figure 1. The positive direction of the  $y$ -axis is seaward. The wave direction is defined relative to the shoreward direction and positive counterclockwise. The vertical axis extends upward.

The principle of the dissipation term proposed by Dally et al. (1985) is used in the present model because the dissipation term can reproduce the wave height stabilization in a uniform depth, which is like the wave transformation over a trough.



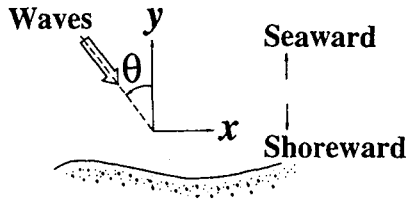


Figure 1 Definition sketch of co-ordinate system.

Modification of the dissipation term by Dally et al., which is for one-dimensional monochromatic waves, yields Eq. (2) for a wave component of directional random waves.

$$D = \frac{K}{h} (D_s C_g - D_s \frac{E_s}{E} C_g), \tag{2}$$

$$E_s = \frac{1}{16} \rho g (H_{1/3})_s^2, \quad (H_{1/3})_s = \Gamma h.$$

where  $(H_{1/3})_s$  is the stable significant wave height,  $h$  is the still water depth,  $E$  is the total wave energy, the sum of  $D_s$ ,  $E_s$  is the total energy where the wave height is stable after wave breaking, and  $K$  and  $\Gamma$  are dimensionless empirical coefficients.

I assume that  $K$  and  $\Gamma$  are functions of the beach slope,  $\tan \beta$ , and express them with Eqs.(3) and (4) because the wave energy dissipation in the surf zone is affected by the beach slope. These functions were obtained on the basis of the calculations of the wave height transformation in the surf zone for offshore wave steepness of 0.02 by Goda (1975).

$$K = 1.7 \times 10^\alpha, \quad \alpha = -0.857 \log_{10}(1/\tan \beta) + 0.219. \tag{3}$$

$$\Gamma = -0.14 \log_{10}(1/\tan \beta) + 0.56. \tag{4}$$

The significant wave height,  $H_{1/3}$ , and the principal wave direction,  $\theta_p$ , are calculated by

$$H_{1/3} = 4.0 \sqrt{m_0}, \quad m_0 = \int_0^\infty \int_{-2\pi}^{2\pi} D_s d\theta df. \tag{5}$$

$$\theta_p = \int_0^\infty \int_{-2\pi}^{2\pi} \theta D_s d\theta df / m_0. \tag{6}$$

The significant wave period,  $T_{1/3}$ , is assumed to be equal to that in deep water.

## 2.2 Nearshore current model

### a. Momentum equation

The movements of water particles, which have the maximum orbital velocity of  $v_m$  due to waves, are assumed as shown in Figure 2. Water particles above the wave trough level,  $d_w$ , are transported by the depth and time-averaged nearshore current;  $U$  and  $V$  are the longshore and cross-shore components of the nearshore current velocity. The particles are also transported shoreward by mass transport due to waves at the angle of  $\theta$  and the velocity of  $V_u$ . Water particles below the wave trough level are transported by the nearshore current, and transported seaward at the velocity of  $V_l$  of the return flow, which is perpendicular to the shore. The mass of water transported shoreward by the mass transport is assumed to be equal to that transported seaward by the return flow.

Under the assumptions, the cross-shore flux of the longshore momentum in the surf zone,  $M_w$ , is expressed as

$$\begin{aligned}
 M_w = & \frac{\rho}{T} \int_0^T \int_{d_w}^{\eta} \{ [U + (V_u + v_m \cos \sigma t) \sin \theta_p] \\
 & \{ V + (V_l + v_m \cos \sigma t) \cos \theta_p \} \} dz dt \\
 & + \frac{\rho}{T} \int_0^T \int_{-h}^{d_w} \{ (U + v_m \cos \sigma t \sin \theta_p) \\
 & (V + V_l + v_m \cos \sigma t \cos \theta_p) \} dz dt,
 \end{aligned} \tag{7}$$

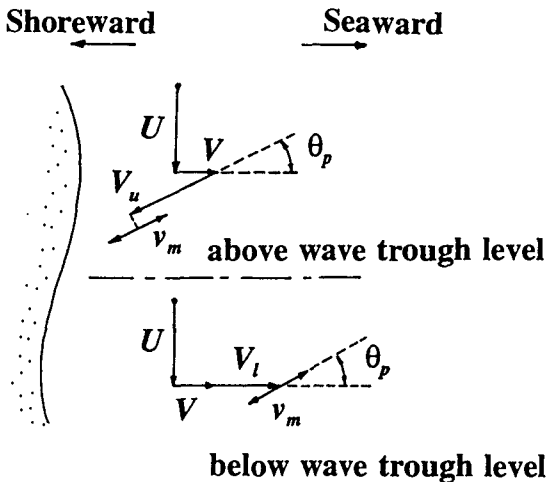


Figure 2 Definition sketch of the assumed movements of water particles above and below the wave trough level.

where  $\rho$  is the density of sea water,  $T$  is the wave period,  $\eta$  is the elevation of water surface,  $z$  is the upward elevation relative to the mean water level,  $\sigma$  is the angular frequency. The value of  $T_{1/3}$  is used as  $T$  in the calculation.

Equation (7) becomes

$$\begin{aligned}
 M_w = & \frac{\rho}{T} \int_0^T \left\{ \int_{-h}^{\eta} U V dz \right. \\
 & + \int_{-h}^{\eta} v_m^2 \cos^2 \sigma t \sin \theta_p \cos \theta_p dz \\
 & + U \left( \int_{d_r}^{\eta} V_u \cos \theta_p dz + \int_{-h}^{d_r} V_l dz \right) \\
 & \left. + \int_{d_r}^{\eta} (V_u^2 + V V_u) \sin \theta_p \cos \theta_p dz \right\} dt.
 \end{aligned}
 \tag{8}$$

The first and second terms on the right-hand side of Eq.(8) represent the momentum flux due to the nearshore current and a radiation stress, respectively. The third term is equal to zero because the mass of water transported shoreward is assumed to be equal to that transported seaward. The fourth term is the cross-shore flux of the longshore momentum due to mass transport by waves.

In most previous models for the nearshore current, the fourth term is neglected because the effect of the mass transport due to unbroken waves on the nearshore current is small. However, the mass flux under broken waves is several times of that calculated with a formula for unbroken waves (Nadaoka and Kondoh, 1982). This means that a momentum flux due to mass transport under broken waves is much greater than that under unbroken waves. Therefore I consider that the momentum fluxes due to mass transport under broken waves are significant for the prediction of the longshore current distribution on a bar-trough beach, and introduce the fluxes into a previous model.

The fourth term,  $M_{bl}$ , becomes Eq.(9) with a surface roller model proposed by Svendsen (1984) as shown in Figure 3; in his model, a water particle in the surface roller is transported shoreward with the celerity,  $C$ ,

$$M_{bl} = \rho P_b e (-C \cos \theta_p + V) C \sin \theta_p,
 \tag{9}$$

where  $e$  is the time-averaged thickness of the surface roller, and  $P_b$  is the fraction of breaking waves, which is introduced for random waves. The value of  $e$  is assumed as

$$e = C_A H_{1/3}^2 / L,
 \tag{10}$$

in which  $C_A$  is a dimensionless coefficient, and  $L$  is the wavelength for the wave period of  $T$ .

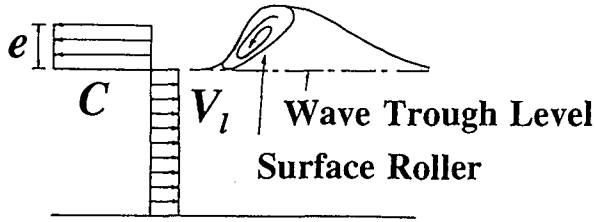


Figure 3 Definition sketch of the vertical distribution of time-averaged cross-shore velocity in a surface roller model by Svendsen (1984).

The cross-shore flux of the cross-shore momentum due to broken waves,  $M_{b2}$ , and the longshore flux of the longshore momentum,  $M_{b3}$ , are obtained in a similar way for the value of  $M_{b1}$ ; these are described by

$$M_{b2} = \rho P_b e C^2 \cos^2 \theta_p + (d_r + h) V_i^2. \quad (11)$$

$$M_{b3} = \rho P_b e (C \sin \theta_p + 2U) C \sin \theta_p. \quad (12)$$

The value of  $V_i$  is expressed as Eq.(13), which is derived by Kuriyama(1991) on the basis of Svendsen's model (1984).

$$V_i = \left( C \frac{m_0}{h^2} + P_b C_A \frac{H_{1/3}^2}{hT} \right) \cos \theta_p. \quad (13)$$

Finally, the horizontal momentum equations in the present model for the nearshore current, which contains the momentum fluxes due to surface rollers, are represented by

$$\begin{aligned} \frac{\partial U}{\partial t} + U \frac{\partial U}{\partial x} + V \frac{\partial U}{\partial y} + F_x - L_x + R_x + g \frac{\partial \bar{\eta}}{\partial x} + M_x &= 0, \\ \frac{\partial V}{\partial t} + U \frac{\partial V}{\partial x} + V \frac{\partial V}{\partial y} + F_y - L_y + R_y + g \frac{\partial \bar{\eta}}{\partial y} + M_y &= 0, \end{aligned} \quad (14)$$

$$\begin{aligned}
 L_x &= \frac{\partial}{\partial x} \left( \epsilon \frac{\partial U}{\partial x} \right) + \frac{\partial}{\partial y} \left( \epsilon \frac{\partial U}{\partial y} \right), \quad L_y = \frac{\partial}{\partial x} \left( \epsilon \frac{\partial V}{\partial x} \right) + \frac{\partial}{\partial y} \left( \epsilon \frac{\partial V}{\partial y} \right), \\
 R_x &= \frac{1}{\rho(\bar{h} + \bar{\eta})} \left( \frac{\partial S_{xx}}{\partial x} + \frac{\partial S_{yx}}{\partial y} \right), \quad R_y = \frac{1}{\rho(\bar{h} + \bar{\eta})} \left( \frac{\partial S_{xy}}{\partial x} + \frac{\partial S_{yy}}{\partial y} \right), \\
 M_x &= \frac{1}{\rho(\bar{h} + \bar{\eta})} \left( \frac{\partial M_{bx}}{\partial x} + \frac{\partial M_{by}}{\partial y} \right), \quad M_y = \frac{1}{\rho(\bar{h} + \bar{\eta})} \left( \frac{\partial M_{by}}{\partial x} + \frac{\partial M_{bx}}{\partial y} \right),
 \end{aligned}
 \tag{15}$$

where  $\bar{\eta}$  is the elevation of the mean water level,  $F_x$  and  $F_y$  are the bottom friction terms,  $L_x$  and  $L_y$  are the lateral mixing terms,  $S_{xx}$ ,  $S_{xy}$ , and  $S_{yy}$  are the radiation stress components, and  $\epsilon$  is a lateral mixing coefficient. The subscripts  $x$  and  $y$  denote the values in the  $x$ -direction and  $y$ -direction.

b. Fraction of breaking waves

Seaward of a bar crest, I assume that the fraction of breaking waves is a function of wave height-water depth ratio as Thornton and Guza (1983) did, and represent it by Eq.(16) with a dimensionless coefficient,  $\gamma$ , which is the wave height-water depth ratio in the surf zone, where all waves are broken.

$$P_b = (H_{1/3} / (\gamma \bar{h}))^4. \tag{16}$$

I introduce the effect of beach slope into the calculation of  $\gamma$  because the wave energy dissipation in the surf zone depends on beach slope. The value of  $\gamma$  is assumed as Eq.(17) on the basis of the calculations of the wave height in the surf zone for offshore wave steepness of 0.02 by Goda (1975).

$$\gamma = 0.68 \exp(4.2 \tan \beta). \tag{17}$$

Shoreward of a bar crest, the fraction of breaking waves is assumed as

$$\begin{aligned}
 P_b &= (P_b)_{bar}, & y_{bar} - 10 < y \leq y_{bar}, \\
 P_b &= (P_b)_{bar} - 0.014(y - y_{bar} + 10)^2, & y \leq y_{bar} - 10,
 \end{aligned}
 \tag{18}$$

where  $(P_b)_{bar}$  is the fraction of breaking waves at the bar crest, and  $y_{bar}$  is the offshore distance at the bar crest. According to visual observations, waves break even shoreward of a bar crest. This means that the fraction of breaking waves does not decrease rapidly from a bar crest although the value predicted by Eq.(16) decreases rapidly from the bar crest. Thus, the fraction of breaking waves shoreward of a bar crest is assumed to be constant near the bar crest and to decrease shoreward proportionally to the square of the distance from the shoreward limit of the constant

$P_b$  zone. The coefficients of Eq.(18) were determined on the basis of visual observation data (Kuriyama and Ozaki, 1993); the units of  $y$  and  $y_{bar}$  are meters.

Near the surf zone shoreward of a trough, Eq.(16) is used again where  $P_b$  estimated by Eq.(16) is larger than that by Eq.(18).

c. Surface roller area parameter,  $C_A$

I assume that  $C_A$  changes according to the development and decay of the surface roller although it is treated as a constant value by Svendsen (1984), because a constant  $C_A$  cannot represent the disappearance of the surface roller in a trough. The development and decay of the surface roller are assumed to be proportional to the fraction of wave breaking; the maximum value of  $C_A$  is determined to be 4.0 on the basis of the field data obtained by Kuriyama (1991). Finally,  $C_A$  is expressed as

$$C_A = 4.0 P_b. \quad (19)$$

d. Radiation stress, bottom shear stress and lateral mixing

The radiation stresses of directional random waves are calculated by Eq.(20) proposed by Yamaguchi(1988).

$$\begin{aligned} S_{xx} &= \int_0^\infty \int_{-\pi/2}^{\pi/2} \rho g \left\{ \frac{C_g}{C} \sin^2 \theta + \left( \frac{C_g}{C} - \frac{1}{2} \right) \right\} D_s d\theta df, \\ S_{xy} = S_{yx} &= \int_0^\infty \int_{-\pi/2}^{\pi/2} \rho g \frac{C_g}{C} \cos \theta \sin \theta D_s d\theta df, \\ S_{yy} &= \int_0^\infty \int_{-\pi/2}^{\pi/2} \rho g \left\{ \frac{C_g}{C} \cos^2 \theta + \left( \frac{C_g}{C} - \frac{1}{2} \right) \right\} D_s d\theta df. \end{aligned} \quad (20)$$

Equation (21) (Nishimura, 1982; Nishimura, 1988) is used for the calculation of the bottom shear stresses,  $F_x$  and  $F_y$ . The value of 0.005 is used as the friction coefficient,  $C_f$ .

$$\begin{aligned} F_x &= \rho C_f \left\{ \left( W + \frac{w_b^2}{W} \sin^2 \theta_p \right) U - \frac{w_b^2}{W} \sin \theta_p \cos \theta_p V \right\}, \\ F_y &= \rho C_f \left\{ \frac{w_b^2}{W} \sin \theta_p \cos \theta_p U - \left( W + \frac{w_b^2}{W} \cos^2 \theta_p \right) V \right\}, \\ W &= \left\{ \sqrt{U^2 + V^2 + w_b^2} + 2(U \sin \theta_p - V \cos \theta_p) w_b \right. \\ &\quad \left. + \sqrt{U^2 + V^2 + w_b^2} + 2(U \sin \theta_p - V \cos \theta_p) w_b \right\} / 2, \\ w_p &= 2(v_m)_b / \pi, \quad (v_m)_b = \frac{\pi H_{1/3}}{T \sin(2\pi h/L)}. \end{aligned} \quad (21)$$

The lateral mixing coefficient proposed by Battjes (1975) is used in the present model. This coefficient is given by

$$\epsilon = Mh \left( \frac{D_{total}}{\rho} \right)^{1/3}, \quad (22)$$

where  $D_{total}$  is the total wave energy dissipation rate and  $M$  is a dimensionless coefficient. Lateral mixing is probably related to turbulence; the turbulence due to breaking waves is much larger than that due to non-breaking waves. Hence, the degree of the lateral mixing in a trough is expected to be smaller than that in the surf zone located shoreward of the trough. Although the lateral mixing coefficient proposed by Longuet-Higgins (1970) is widely used, it seems to be inappropriate for the prediction of the longshore current on a bar-trough beach because the coefficient proposed by Longuet-Higgins, which is proportional to the distance from the shoreline, does not reproduce the difference between the lateral mixing in a trough and that in the shoreward surf zone. On the other hand, the lateral mixing coefficient proposed by Battjes reproduces the difference because it is based on the wave energy dissipation due to wave breaking. Thus, in the present model, I adopt the lateral mixing coefficient proposed by Battjes.

### 3. Model Comparisons with Measurements

The significant wave heights and the longshore current velocities predicted by the present model are compared with the values measured at Hazaki Oceanographical Research Facility (HORF), which is a field observation pier of 427m in length on the Kashima-nada coast of Japan facing to the Pacific Ocean. Water surface elevations were measured with ultrasonic wave gages before and after the measurement of the longshore current. A spherical float having a diameter of 0.2m was used to measure time-averaged longshore current velocities 1m below the water surface. This method with the float was confirmed to be useful for the measurement of the time-averaged longshore current velocity by calibrations with an electromagnetic current meter; there is a strong correlation between the time-averaged longshore current velocity measured by the float and that measured by the current meter (Kuriyama and Ozaki, 1993).

#### 3.1 Calculation conditions

The calculation results for three cases, on March 24, 28 and April 4, 1989, are compared with the measurements. Figure 4 shows the topographic map of the vicinity of the HORF on March 31; this topography is used in the calculations for the three cases because the beach profile changes from March 24 to April 4 were small. The topography was almost uniform alongshore although scour occurred around the tip and the middle of the HORF,  $y=380\text{m}$  and  $y=200\text{m}$ , where piles are concentrated. The calculation areas extend from the shorelines to  $y=650\text{m}$ , and alongshore from  $x=-320\text{m}$  to  $x=320\text{m}$ .

In the calculations of wave height transformation, the grid distances in  $x$ -direction and  $y$ -direction are 10m. The numbers of frequency components and directional components are 10 and 35, respectively. The wave heights,  $(H_{1/3})_{obs}$ , the wave periods,

$(T_{1/3})_{ob}$ , the principal wave directions,  $(\theta_p)_{1/3}$ , and the spreading parameters,  $(s_{max})_{ob}$ , input at the offshore boundaries are listed in Table 1. The Bretschneider-Mitsuyasu frequency spectrum and the Mitsuyasu-type spreading function are given at the offshore boundaries.

In the calculations of wave energy dissipation, a beach slope below 1/100 and that over 1/10 are replaced by values of 1/100 and 1/10, respectively, because Eqs.(3) and (4) are valid for the beach slopes from 1/100 to 1/10.

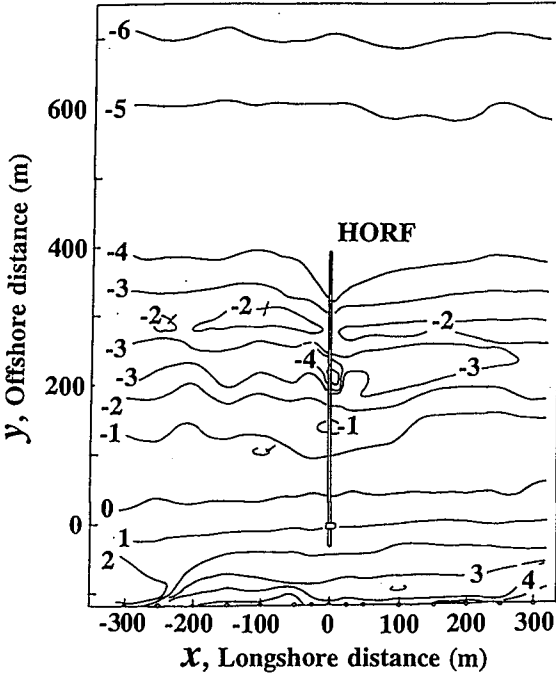


Figure 4 Topographic map of the vicinity of the HORF.

Table 1 Offshore boundary conditions

Case	Date	$(H_{1/3})_{ob}$	$(T_{1/3})_{ob}$	$(\theta_p)_{ob}$	$(s_{max})_{ob}$
1	March 24	3.20m	11.20s	-20.0°	90
2	March 28	2.47m	8.86s	-25.0°	40
3	April 4	2.03m	8.40s	-10.0°	45



The nearshore currents are calculated with the horizontal momentum equations, Eqs.(14) and (15), and the continuity equation by the ADI (Alternating Direction Implicit) method. The calculations are done for 4000 time step with a step length of 0.4s; the grid distances are 10m.

The nearshore current velocities are assumed to be equal to zero at the offshore boundaries and at the shorelines. The nearshore current velocities and the mean water levels at the side boundaries are assumed to be equal to the values at internal grid points next to the side boundaries.

The longshore flux of the longshore momentum,  $M_{b3}$ , is neglected in the calculations of the nearshore current because the nearshore currents preliminarily calculated by a previous model are almost uniform alongshore.

### 3.2 Wave height

Figure 5 shows the predicted significant wave heights and the values measured at the HORF. The solid lines show the values predicted by the present model, and the closed circles show the values measured before and after the measurements of the longshore current. The predicted values agree well with the measured values except for the data near the shorelines.

Causes of the small disagreement of calculated and measured values near the shorelines are supposed to be infragravity waves and the increase of water depth due to wave setup. When an offshore wave height is large, the amount of wave setup and the infragravity wave height are large near the shoreline. Infragravity waves and the increase of water depth due to wave setup, however, are not taken into account in the present model although the gradient of mean water level is considered in the nearshore current model. Disregard of the two factors results in the disagreement of calculated and measured values near the shorelines.

### 3.3 Nearshore current

Figure 6 shows a comparison of the longshore current velocities measured at the HORF with those predicted by the present model and by a previous model, which does not include momentum fluxes due to mass transport under broken waves; the velocities on March 24 and 28 were predicted with  $M=5$  and those on April 4 were predicted with  $M=10$ . Seaward of the bar crests, the values predicted by the present model and by the previous model increase shoreward; both agree with the measured values. Shoreward of the bar crests, however, the values predicted by the present model and the measured values increase toward shore whereas the values predicted by the previous model decrease. Consequently the longshore current velocities over the troughs predicted by the present model agree well with the measured values whereas the values predicted by the previous model do not.

The Longshore current velocities predicted by a quasi-present model where the fraction of breaking waves shoreward of the bar crest is estimated with Eq.(16) are also shown in Figure 6. The peaks in velocity predicted by the quasi-present model are located at the bar crests, shoreward of the peaks predicted by the previous model and seaward of the peaks measured at the HORF and predicted by the present model.

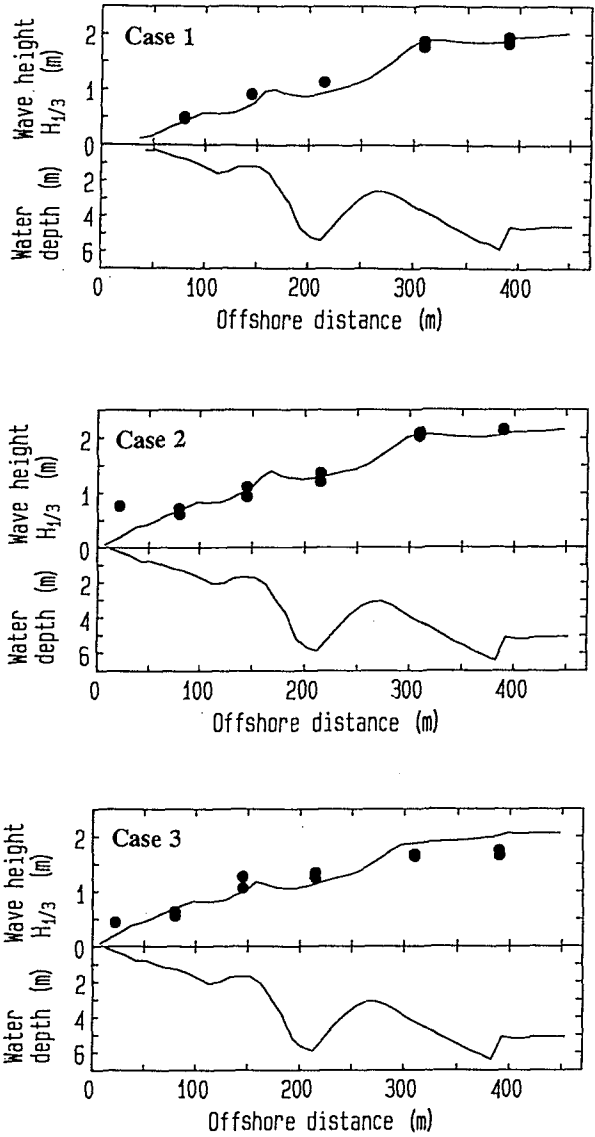


Figure 5 Comparison of the significant wave heights measured at the HORF (circles) with those predicted by the present model.

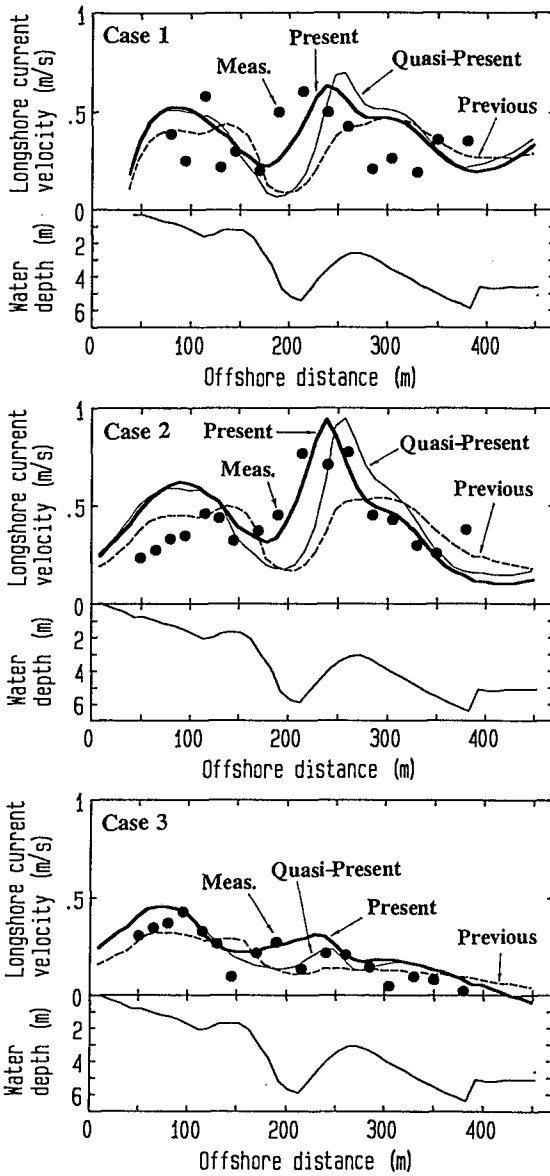


Figure 6 Comparison of the longshore current velocities measured at the HORF (circles) with those predicted by the previous model (broken lines), by the quasi-present model (thin solid lines), and by the present model (thick solid lines).

#### 4. Discussion and Conclusions

Let us assume that an incident wave angle and the longshore current velocity are positive. Shoreward of a bar crest, the cross-shore flux of the longshore momentum due to the surface roller decreases with travel shoreward owing to the decay of the roller. This decrease means that the cross-shore flux of the longshore momentum transported into a unit volume is larger than that transported out of the volume. Consequently the longshore current velocities calculated by the present model are larger than those calculated by the previous model.

On the other hand, seaward of the bar crest, the cross-shore flux of the longshore momentum due to the surface roller increases with travel shoreward owing to the development of the surface roller. Thus the longshore current velocities calculated by the present model are smaller than those calculated by the previous model. As a result, the longshore current distribution calculated by the present model has a peak velocity shoreward of the bar crest.

The longshore current distributions predicted by the quasi-present model have peaks at the bar crests, seaward of the peaks predicted by the present model because the surface roller calculated by the quasi-present model with Eq.(16) decays rapidly from the bar crest whereas the roller calculated by the present model with Eqs.(16) and (18) propagates without decay near the bar crest, and then gradually decays.

The longshore current distributions on a bar-trough beach predicted by the present model agree with the field measurements, which have peaks in velocity shoreward of the bar crests, better than the distributions predicted by the other two models. The agreement shows that the fraction of breaking waves predicted by Eq.(18) is reasonable shoreward of a bar crest and the momentum fluxes due to mass transport under broken waves are significant for the prediction of the longshore current.

#### Acknowledgement

The author would like to thank Mr. Yasushi Ozaki for analyzing field data. Further acknowledgement is extended to Dr. Nicholas C. Kraus, Director of Conrad Blucher Institute, Texas A&M University -Corpus Christi, for his useful comments that improved this paper.

#### References

- Battjes J. A. (1975): Modeling of turbulence in the surf zone, Symp. on Modeling Techniques, ASCE, pp.1050-1061.
- Church J. C. and E. B. Thornton (1993): Effects of breaking wave induced turbulence within a longshore current model, Coastal Eng., 20, pp.1-28.
- Dally W. R., R. G. Dean and R. A. Dalrymple (1985): Wave height variation across beaches of arbitrary profile, J. Geophys. Res., Vol.90, No.C6, pp.11,917-11,927.
- Ebersole B. A. and R. A. Dalrymple (1980): Numerical modeling of nearshore circulation, Proc. 17th Coastal Eng. Conf., pp.2710-2725.

- Goda Y. (1975): Irregular wave deformation in the surf zone, Coastal Eng. in Japan, Vol.18, pp.13-26.
- Karlsson T. (1969): Refraction of continuous ocean wave spectra, J. Waterways and Harbors Div., Proc. of the ASCE, Vol.95, No.WW4, pp.437-448.
- Kuriyama Y. (1991): Investigation of cross-shore sediment transport rates and flow parameters in the surf zone using field data, Rep. of the Port and Harbour Res. Inst., Vol.30, No.2, pp.3-58.
- Kuriyama Y. and Y. Ozaki (1993): Longshore current distribution on a bar-trough beach -Field measurements at HORF and numerical model-, Rep. of the Port and Harbour Res. Inst., Vol.32, No.3, pp.3-37.
- Larson M. and N. C. Kraus (1991): Numerical model of longshore current for bar and trough beaches, J. Waterway, Port, Coastal, and Ocean Eng., Vol.117, No.4, ASCE, pp.326-347.
- Longuet-Higgins M. S. (1970): Longshore current generated by obliquely incident waves, 1&2, J. Geophys. Res., Vol.75, No.33, pp.6778-6801.
- Nadaoka K. and T. Kondoh (1982): Laboratory measurements of velocity field structure in the surf zone by LDV, Coastal Eng. in Japan, Vol.25, pp.125-146.
- Nishimura H. (1982): Numerical simulation of the nearshore circulation, Proc. 29th Japanese Conf. on Coastal Eng., JSCE, pp.333-337. (in Japanese)
- Nishimura H. (1988): Computation of nearshore current, Nearshore Dynamics and Coastal Process - Theory, Measurements and Predictive Models - (ed. by K. Horikawa), University of Tokyo Press, pp.271-291.
- Smith J. M., M. Larson and N. C. Kraus (1993): Longshore current on a barred beach: Field measurements and calculation, J. Geophys. Res., Vol.98, No.C12, pp.22717-22731.
- Svendsen I. A. (1984): Mass flux and undertow in a surf zone, Coastal Eng., 8, pp.347-365.
- Symonds G. and D. A. Huntley (1980): Waves and currents over nearshore bar systems, Proc. of Canadian Coastal Conf., pp.64-78.
- Takayama T., N. Ikeda and T. Hiraishi (1991): Practical computation method of directional random wave transformation, Rep. of the Port and Harbour Res. Inst., Vol.30, No.1, pp.21-67. (in Japanese)
- Thornton E. B. and R. T. Guza (1983): Transformation of wave height distribution, J. Geophys. Res., Vol.88, No.C10, pp.5925-5938.
- Yamaguchi M. (1988): A numerical model of nearshore currents due to irregular waves, Proc. of 21st Coastal Eng. Conf., ASCE, pp.1113-1126.

## CHAPTER 163

### PREDICTION OF BEACH PROFILE CHANGE AT MESOSCALE UNDER RANDOM WAVES

Magnus Larson<sup>1</sup>

**ABSTRACT:** A mesoscale model is presented to calculate the average net cross-shore transport rate and beach profile evolution under random waves. Cross-shore transport formulas for random waves are derived by superimposing the transport from individual waves, which belong to an ensemble that represents the random wave field. The transport relationships for individual waves are based on experiments with monochromatic waves in large wave tanks. The model is validated using beach profile data from the SUPERTANK Laboratory Data Collection Project and three different types of profile evolution events are studied, namely equilibrium erosion with bar formation, berm flooding, and the impact of breaking waves on an offshore mound. Berm flooding includes the erosion of a well-developed summer berm and the erosion of an artificially constructed foredune, and the offshore mound tests encompass narrow- and broad-crested mounds.

#### INTRODUCTION

On a natural beach the random properties of the waves have a major influence on the evolution of the bottom topography. Monochromatic waves typically break in a narrow region across the profile, where incipient breaking of individual waves is a weakly random process that tends to slightly shift the location of the break point back and forth. A random wave field, however, consists of individual waves with different height, period, and direction, implying wave breaking all across the profile. The more evenly distributed forcing of random waves across shore tends to produce a profile with less pronounced morphological features as compared to monochromatic

---

<sup>1</sup> Coastal Engineering Laboratory, Department of Civil Engineering, University of Tokyo, 7-3-1 Hongo, Bunkyo-ku, Tokyo 113, JAPAN (Associate Professor on leave from Department of Water Resources Engineering, University of Lund, SWEDEN).

waves (Larson and Kraus 1989, 1994). Also, in a random wave field individual waves that are potentially constructive or destructive to the beach could exist simultaneously, which makes it more difficult to assess the net effect on the profile evolution (Mimura et al. 1986). Thus, when applying numerical beach profile change models to field conditions the effect of random waves on the profile development should be included through a realistic description of the hydrodynamics and net cross-shore transport rate.

Numerical models of beach profile change may be classified according to the characteristic scale employed in resolving the fluid and sediment motion. Models which attempt to describe scales of motion in time and space compatible with individual waves belong to the class of microscale models, whereas mesoscale models focus on resolving scales of motion that are the result of many waves (Larson and Kraus 1994, 1995). The numerical models by Kriebel and Dean (1985) and Larson and Kraus (1989) are examples of mesoscale models, where the local cross-shore flow pattern is not computed, and the net transport rate is derived directly from the variation in wave properties across shore. These models simulate the effect of random waves by transforming a statistical wave height measure as a monochromatic wave. Such an approach is expected to primarily reproduce the overall beach response and the details of the profile evolution will be less well predicted. For example, if the impact of a storm is simulated the total amount of material moved, including erosion on the foreshore and deposition at an offshore bar, may be in agreement with measurements, whereas the detailed shape of the bar and erosion scarp on the foreshore could differ more. Thus, treating a representative wave measure as a monochromatic wave may characterize the total forcing the profile is exposed to; however, local cross-shore variations in the forcing will be accurately described to a lesser extent.

The main objective of this paper is to present a mesoscale model to predict the net transport rate and resulting beach profile change under random waves. The randomness of the wave field is included from the start in the development of the model equations, and predictive formulas are obtained in terms of simple statistical wave properties. These properties are calculated using the random wave decay model by Larson (1995). The method of superimposing the effect of individual waves is employed for calculating the average net transport rate for a random wave field. The net transport rate distribution for individual waves is estimated from the relationships presented by Larson and Kraus (1989), which involves schematizing the beach profile into different transport regions depending on the wave characteristics. The contribution from individual waves is summed up taking into account if the wave is breaking, non-breaking, or in the swash. Profile measurements from the SUPER-TANK Laboratory Data Collection Project (Kraus et al. 1992) are used to validate the model, including such events as foreshore erosion and bar formation, berm flooding, and the transport at an offshore mound. Because the net transport rate and profile evolution are described at the mesoscale, a robust model is obtained that has potential for describing long-term profile response including seasonal changes. The

model allows the specification of long-term wave statistics as input which is needed to reproduce seasonal changes.

## THEORETICAL CONSIDERATIONS

### Wave Model

A successfully employed technique for modeling the decay of random waves in the surf zone is to calculate wave transformation for individual wave components in the probability density function (pdf) or spectrum, and determine the wave characteristics in the surf zone by superposition of the effect of the individual wave components (Mase and Iwagaki 1982, Dally 1992). Such a simulation technique may be computationally intensive but does not rely on any inferences about the pdf or spectrum in the surf zone (Battjes and Janssen 1978, Thornton and Guza 1983). Larson (1995) presented a model which requires the transformation of a single representative wave only; this model produces results identical or similar to a simulation that involves many wave components.

In the present profile change model, the wave transformation is described by the following equations (Larson 1995),

$$\frac{d}{dx}(F_{rms} \cos\theta) = \frac{\kappa}{d}(F_{rms} - F_{stab}) \quad (1)$$

in which,

$$F_{rms} = \frac{1}{8} \rho g H_{rms}^2 C_g \quad (2)$$

$$F_{stab} = \frac{1}{8} \rho g [(1-\alpha)H_n^2 + \alpha\Gamma^2 d^2] C_g \quad (3)$$

where  $H_{rms}$  is the root-mean-square (rms) wave height for breaking and non-breaking waves,  $H_n$  the rms wave height for non-breaking waves,  $\alpha$  the ratio of breaking waves,  $C_g$  the group velocity,  $\theta$  the incident wave angle,  $\rho$  the density,  $g$  the acceleration of gravity,  $d$  the water depth,  $x$  a cross-shore coordinate pointing offshore, and  $\kappa$  ( $=0.15$ ) and  $\Gamma$  ( $=0.40$ ) empirical coefficients as given by Dally et al. (1985). The wave number conservation equation and the cross-shore momentum equation are solved in parallel with Equations 1-3 to yield the wave properties and the mean water elevation across the profile.

In general,  $H_{rms}$  is obtained by employing numerical methods; this requires the specification of  $H_n$  and  $\alpha$  at each point across shore. For a beach profile with a depth that increases monotonically with distance offshore  $H_n$  and  $\alpha$  may be computed



directly from the local pdf, which is transformed from the offshore boundary neglecting wave breaking and truncated at the depth of incipient breaking for an individual wave. However, for a non-monotonic beach profile, such as a barred profile, an empirical closure relationship must be added to model how  $\alpha$  is affected by wave reforming (Larson 1995). In the latter case, the non-breaking waves may consist of waves that have never been breaking (unbroken waves) and waves that were breaking but have reformed at some seaward point. A Rayleigh pdf is assumed to describe the variation in wave height in the offshore, and the sea is taken to be narrow-banded in frequency and direction.

**Cross-Shore Sediment Transport Model**

Relationships for the net cross-shore transport rate developed by Larson and Kraus (1989) for monochromatic waves were generalized to random waves by treating the random wave field as a collection of individual waves. Under the assumptions of linearity in transport and no interactions, the transport rate distribution generated by random waves was obtained by computing the distribution for each individual wave and then averaging over all waves according to,

$$\bar{q} = \frac{1}{N} \sum_{i=1}^N q_i \tag{4}$$

where  $\bar{q}$  is the average net transport rate at  $x$ ,  $N$  is the number of individual waves, and  $q_i$  the transport rate for wave  $i$  at  $x$ . Different transport relationships are employed depending on if a wave is breaking, non-breaking, or in the swash.

Breaking waves. If the relationship developed by Larson and Kraus (1989) for the net transport rate under breaking waves is substituted into Equation 4, the following expression is obtained for the average transport rate  $\bar{q}_b$ ,

$$\bar{q}_b = \frac{1}{N} \sum_{i=1}^N K \left[ D_i - (D_{eq} - \frac{\epsilon}{K} \frac{dh}{dx}) \right] \tag{5}$$

where  $D$  is the wave energy dissipation per unit water volume due to wave breaking and  $D_{eq}$  its equilibrium value (Dean 1977),  $h$  the profile elevation, and  $K$  and  $\epsilon$  empirical transport coefficients from the monochromatic transport relationship. In developing Equation 5 further, an assumption has to be made regarding the partitioning of the average energy dissipation between erosional and accretionary waves at all points across shore. The random wave model will predict the average energy dissipation; however, no information is obtained on the amount of dissipation that contributes to onshore and offshore transport, respectively. The simplest approach is to assume that each breaking wave at a specific water depth transports similar magnitudes of material, which leads to the following equation (Larson and Kraus 1994),

$$\bar{q}_b = K\xi \left[ \bar{D} - \alpha \left( D_{eq} - \frac{\epsilon}{K} \frac{dh}{dx} \right) \right] \tag{6}$$

where  $\bar{D}$  is the average energy dissipation per unit water volume as given by the random wave model. The function  $\xi$  automatically provides the direction of the transport and weights the influence of the erosional and accretionary waves based on the empirical criterion by Larson and Kraus (1989),

$$\xi = 2 \frac{e^{-\frac{1}{M} \frac{H_{rms0}}{L_o} \left( \frac{wT}{H_{rms0}} \right)^3}}{e^{-\left( \frac{H_{bo}}{H_{rms0}} \right)^2}} - 1 \quad -1 \leq \xi \leq 1 \tag{7}$$

where  $H_{rms0}$  is the deepwater rms wave height,  $H_{bo}$  the wave height at incipient breaking transformed backwards to deep water,  $w$  the sediment fall speed,  $T$  the wave period,  $L_o$  the deepwater wavelength, and  $M$  ( $=0.00070$ ) an empirical coefficient.

Non-breaking waves. The net transport rate seaward of the break point of an individual wave is assumed to decay exponentially with distance offshore (Larson and Kraus 1989). For a random wave field, the contribution to the transport rate from non-breaking waves is estimated to,

$$\bar{q}_u = \frac{1}{N} \sum_{i=1}^n q_{bi} e^{-\lambda_i(x-x_{bi})} \tag{8}$$

where  $n$  is the number of non-breaking waves at  $x$ ,  $x_b$  the breakpoint location,  $q_b$  the transport rate at incipient breaking, and  $\lambda$  an exponential decay coefficient, the latter two variables evaluated at  $x_b$ . Equation 8 sums the contributions to the transport rate from all waves that break landward of  $x$ . The coefficient  $\lambda$  depends on the median grain size and the incipient breaking wave height as for transport by monochromatic waves. Equation 8 is most easily solved by dividing the profile shoreward of  $x$  in a number of grid cells  $n_s$  and adding together the contribution from each cell to the transport rate at  $x$ . Such a method to approximate Equation 8 yields,

$$\bar{q}_u = \sum_{j=1}^{n_s} q_{bj} e^{-\lambda_j(x-x_{bj})} \Delta \alpha_j \tag{9}$$

where  $\Delta \alpha_j$  represents the increase in the ratio of breaking waves in cell  $j$ , which has a length  $\Delta x$  (index  $j$  denotes the grid cell number as opposed to  $i$  that denotes the number of the wave). In Equation 9,  $q_{bj}$  and  $\lambda_j$  must be estimated at all shoreward locations before the transport rate can be calculated.

**Swash waves.** The average net transport rate at a specific location  $x$  in the swash may be obtained by superimposing the transport from all waves that run up passed this location using the equation proposed by Larson and Kraus (1995),

$$\bar{q}_r = \frac{1}{N} \sum_{i=1}^{n_r} q_{si} \left( \frac{h-R_i}{h_s-R_i} \right)^{1.5} \frac{\tan\beta}{\tan\beta_s} \tag{10}$$

where  $q_s$  is the transport rate at the shoreward end of the surf zone located at  $x_s$  where the elevation is  $h_s$  and the beach slope  $\beta_s$ ,  $h$  and  $\beta$  are the elevation and local beach slope at  $x$ , respectively,  $R$  is the runup height, and  $n_r$  is the number of waves that run up passed  $x$ . Equation 10 involves summing transport contributions from all waves that have runup heights exceeding the elevation where the average transport rate is calculated. Based on Equation 10,  $\bar{q}_r$  is approximated in a similar manner to  $\bar{q}_u$ ; the profile shoreward of  $x$  is divided in  $n_{sr}$  grid cells, each cell having a length of  $\Delta x$ , and the contribution to  $\bar{q}_r$  from each cell is summed up to yield,

$$\bar{q}_r = \sum_{j=1}^{n_{sr}} q_{sj} \left( \frac{h-R_j}{h_s-R_j} \right)^{1.5} \frac{\tan\beta}{\tan\beta_s} \Delta\rho_j \tag{11}$$

where  $\Delta\rho_j$  is the change along  $\Delta x$  in the ratio of waves that run up passed  $x$  and  $j$  denotes the grid cell number as before. The pdf for the runup height (needed to calculate  $\Delta\rho_j$ ) may be derived using a transformation for individual wave components in the Rayleigh pdf, where each component is assumed to have a runup height which depends upon the surf similarity parameter (Battjes 1974). The corresponding distribution function  $F(R)$  is obtained by integrating the pdf to yield,

$$F(R) = 1 - e^{-\left(\frac{R}{R_{rms}}\right)^{\frac{2}{1-b/2}}} \tag{12}$$

where  $R_{rms}$  is defined as,

$$R_{rms} = a (\tan\beta_s \sqrt{L_o})^b H_{rmso}^{1-b/2} \tag{13}$$

and  $a$  ( $=1.47$ ) and  $b$  ( $=0.79$ ) are empirical coefficients that determine the functional dependence on the surf similarity parameter (Larson and Kraus 1989).

**VALIDATION OF RANDOM PROFILE CHANGE MODEL**

Profile data from the SUPERTANK Laboratory Data Collection Project (Kraus et al. 1992) were employed to examine the predictions of the model for cross-shore transport and profile change under random waves. First, the random wave model was used to calculate wave transformation in the surf zone, and then the net cross-shore transport rate distribution was determined based on the calculated wave

properties. Finally, the equation for sediment volume conservation was employed to compute depth changes.

Three different types of profile evolution tests were investigated: (1) equilibrium erosion, (2) berm flooding, and (3) waves breaking on an offshore mound. The equilibrium erosion tests involved bar development under random waves, where the profile change decreased with elapsed time as the profile approached an equilibrium configuration under the influence of a steady random wave field. Berm flooding encompassed tests where the foreshore was exposed to marked wave action, including berm and foredune erosion. Two tests were studied involving transport at an offshore mound; one mound was narrow-crested and the other mound was broad-crested. Table 1 summarizes the SUPERTANK Tests used in the model validation in terms of Test number, profile survey time, and wave conditions. The sand used in the tank had a median grain size of 0.22 mm during all SUPERTANK tests and the standard water depth employed in the tank was 3.05 m. The wave conditions in Table 1 represent target values and the generated values were slightly different (the measured wave conditions at the most seaward wave gage were used as input to the model).

Table 1. SUPERTANK Tests used in the present study.				
Profile Event	Test No.	Time of survey	H <sub>rms</sub> (m)	T <sub>p</sub> (s)
Equilibrium erosion	ST_10	910805: 900 910806: 1100	0.57	3.0
Berm flooding	ST_90	910828: 700, 1120	0.49	3.0
	ST_A0	910828: 1500, 1637	0.49	3.0
Offshore mound	ST_J0	910908: 1100, 1610	0.49	3.0
	ST_K0	910912: 700, 1220	0.49	3.0

The preliminary calculations indicated that the initial rate of profile change was satisfactorily reproduced, whereas the development of the equilibrium profile shape was slower than expected and the shape too flat. For example, SUPERTANK Test ST\_10 indicated an evolution towards a barred equilibrium profile under random waves that the model did not reproduce because of small, but significant transport rates even after long time periods. To improve the description in the model of the approach to equilibrium, Equation 6 was modified according to,

$$\bar{q}_b = K\xi \left[ \bar{D} - \alpha^p \left( D_{eq} - \frac{e}{K} \frac{dh}{dx} \right) \right] \quad (14)$$

where  $p$  is an empirical power less than one. The power  $p$  may be considered as a means of taking into account that the transport rate for an individual wave is typically

overestimated in the averaging process. Because  $p < 1$ , the effect on the profile development in parts of the profile where most of the waves are breaking is minor; however, if only few waves are breaking the effect of introducing  $p$  is marked. The quantity  $\alpha^p > \alpha$  effectively produces a profile that is steeper than if the  $p$  is not introduced. In all calculations discussed in this paper a value of  $p = 0.5$  was employed based on trial calculations with several different  $p$ -values, where comparisons were made with SUPERTANK measurements.

The values of the empirical transport coefficients in Equation 14 used in all simulations were  $K = 2.0 \cdot 10^{-6} \text{ m}^4/\text{N}$  and  $\epsilon = 0.0002 \text{ m}^2/\text{s}$ . The value of  $K$  agrees well with the optimum value determined by Larson and Kraus (1989) for profile evolution under monochromatic waves in large wave tanks, who found an overall  $K$ -value of about  $1.6 \cdot 10^{-6} \text{ m}^4/\text{N}$ . However,  $\epsilon$  determined for monochromatic waves is larger than for random waves, mainly because the profile slopes tend to grow steeper for monochromatic waves and a larger value is needed on  $\epsilon$  to reduce this growth in slope. The similar coefficient values found on the  $K$ -value for monochromatic and random waves support the approach to superimpose the contribution from many individual waves to derive the transport rate distribution under random waves.

### Equilibrium Erosion

In Test ST\_10 random waves were employed until a near-equilibrium profile shape developed that had a distinct breakpoint bar in the offshore ( $H_{rms} = 0.57 \text{ m}$ ,  $T_p = 3.0 \text{ s}$ ). Figure 1 displays the calculated and measured profile after 400 min of wave action together with the initial profile. The calculated profile agrees quite well with the measurements, especially on the foreshore and on the seaward side of the bar. The largest discrepancies are found in the trough region, where the measurements show a more marked trough than what the model predicts. This is probably due to the oversimplification of directly relating the transport rate to the energy dissipation. The calculated average energy dissipation is a fairly smooth function across shore, which produces a smooth evolution of the bottom topography. In reality, at incipient breaking there is a pronounced local impact on the bottom, especially for plunging breakers, that could induce a marked peak in the transport rate and enhance trough development. If a large number of the waves break in approximately the same location, a marked trough could appear that the model does not reproduce.

In order to verify that the model predicted the development of an equilibrium profile for random waves, a simulation was performed using the conditions for Test ST\_10 during a period of 7 days. Figure 2 displays the calculated profile at selected times, clearly showing the decrease in profile change with time elapsed. An equilibrium profile has almost developed after 3.5 days with a pronounced bar feature in the offshore.

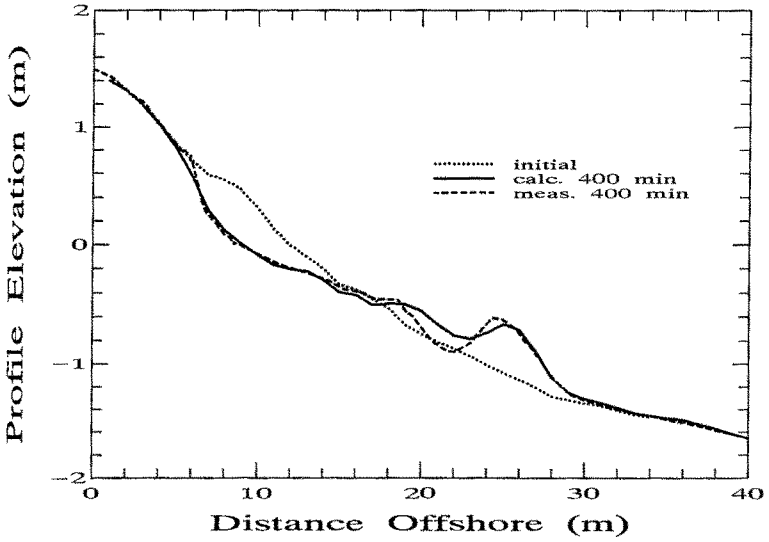


Figure 1. Comparison between measured and calculated profile from SUPER-TANK Test ST\_10 after 400 min of wave action.

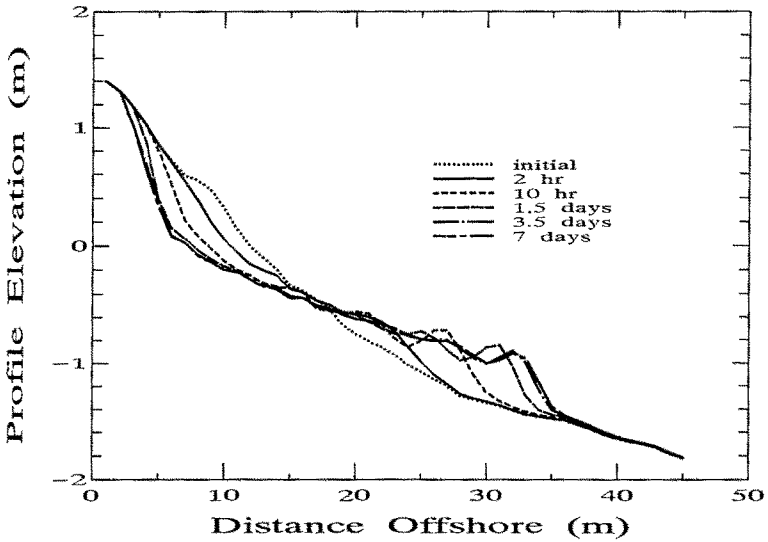


Figure 2. Calculated profiles at selected times for conditions as given by SUPERTANK Test ST\_10.

### Berm Flooding

SUPERTANK Tests ST\_90 and ST\_A0 focused on the foreshore response to random waves. In Test ST\_90 the foreshore consisted of a well-developed berm that was flooded and exposed to erosive wave conditions ( $H_{rms} = 0.49$  m,  $T_p = 3.0$  s). Test ST\_A0 involved a small foredune that was quickly eroded away by the waves (same wave conditions as Test ST\_90). In both these tests the water level in the tank was 3.35 m. Figure 3 displays a comparison between calculated and measured profile for ST\_90 after 50 min of wave action together with the initial profile (only the portion of the profile where any change was recorded is displayed). The model prediction somewhat underestimates the rapid response of the foreshore; in the test material was moved seaward and deposited about 10 m from the shoreward end of the tank. Also, the deposition of material occurred more evenly along the profile than what the model predicts, and the calculations tend to produce a more pronounced depositional feature. However, the overall agreement is satisfactory, which supports the transport relationship employed on the foreshore (Equation 10).

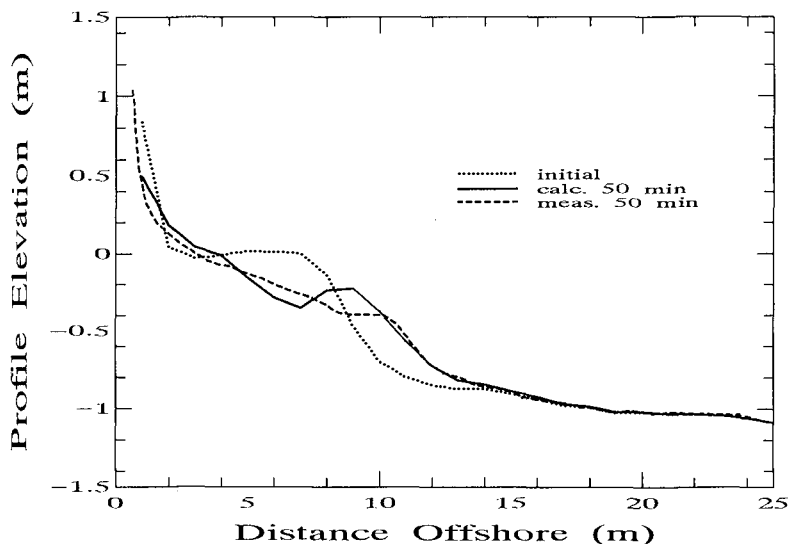


Figure 3. Comparison between measured and calculated profile from SUPERTANK Test ST\_90 after 50 min of wave action.

In Test ST\_A0 the constructed foredune eroded away very rapidly and after 10 min of wave action the foredune was completely flattened. Figure 4 shows a comparison between the model prediction and the measured profile after 10 min together with the initial profile. The calculated profile response is almost as rapid as

the measured response, and the resulting profile shape is well predicted. The transport rate formula employed in the swash zone produces onshore transport if the local slope is negative, which is the case on the shoreward side of the foredune in the beginning of Test ST\_A0. Material is thus moved by the model from the foredune both in the shoreward and seaward direction, speeding up the flattening of the foredune.

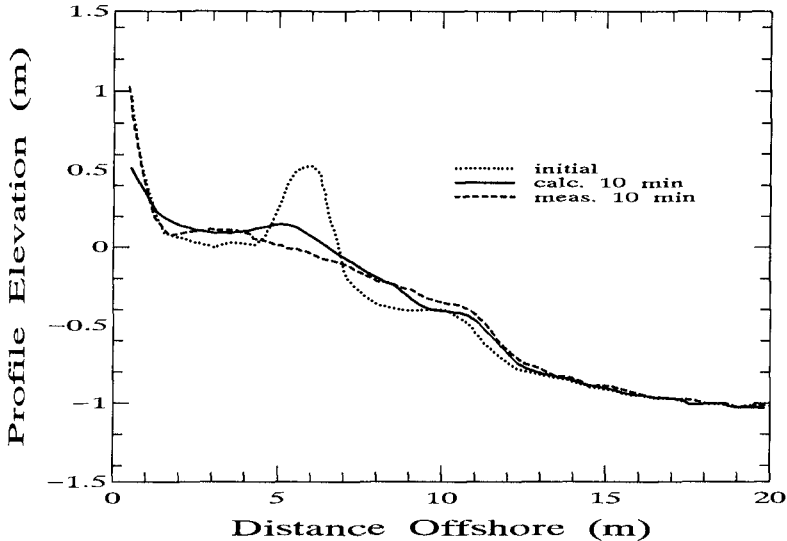


Figure 4. Comparison between measured and calculated profile from SUPER-TANK Test ST\_A0 after 10 min of wave action.

### Offshore Mound

Tests ST\_J0 and ST\_K0 were carried out to investigate the response of an offshore mound to random waves if a large portion of the waves broke on the seaward side of the mound. For Test ST\_J0 the mound was narrow-crested, whereas a broad-crested mound was constructed for ST\_K0. The target wave conditions were identical to Tests ST\_90 and ST\_A0. A large portion of the waves broke and dissipated energy on the mound, and the effect on the foreshore of the waves that were severely broken by the mound was minor. Thus, Figure 5 shows only the profile evolution around the mound for Test ST\_J0, and Figure 6 displays the corresponding region for Test ST\_K0.

The narrow-crested mound deflated during wave action with some transport in the shoreward direction, although most of the material moved offshore (Figure 5). The model cannot represent such complex transport conditions and, in the model



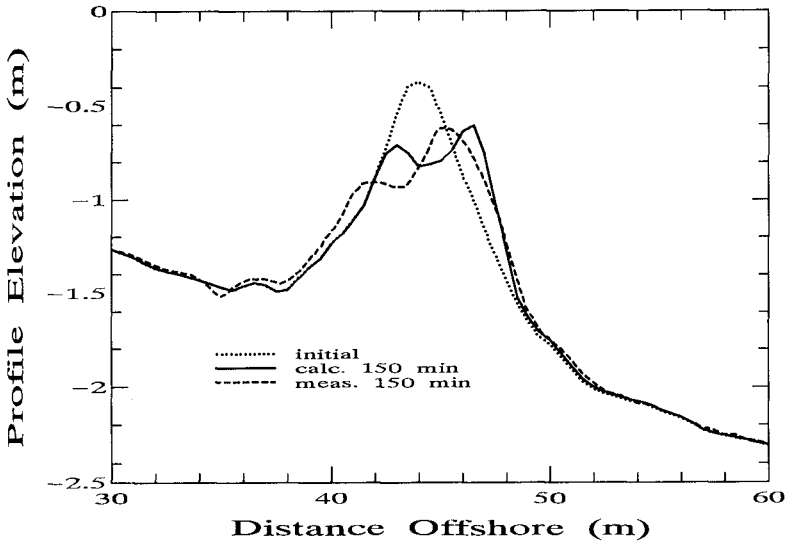


Figure 5. Comparison between measured and calculated profile from SUPER-TANK Test ST\_J0 after 150 min of wave action.

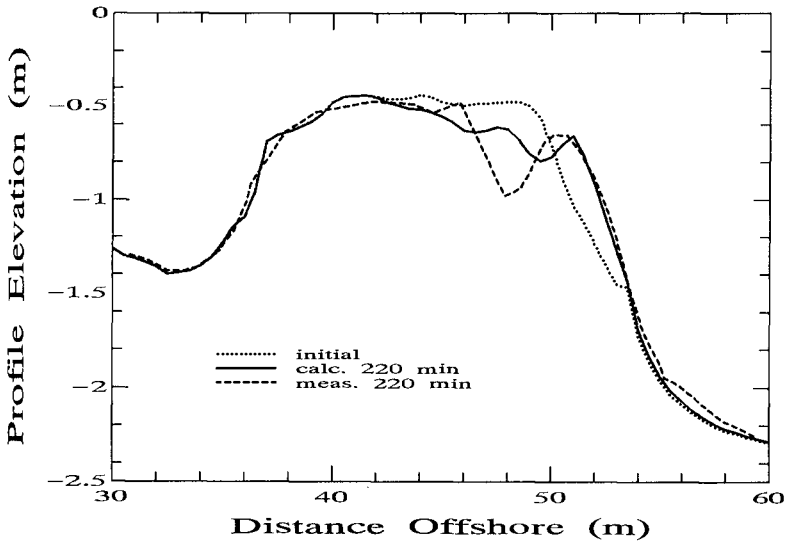


Figure 6. Comparison between measured and calculated profile from SUPER-TANK Test ST\_K0 after 220 min of wave action.

predictions, material only moved offshore. Thus, the profile development on the seaward side of the mound is reproduced by the model, whereas the model predicts no change on the shoreward side. The model was able to predict the profile response somewhat better for the broad-crested mound (Test ST\_K0), because little material was pushed onshore by the waves on the shoreward side of the mound (Figure 6). The seaward shape of the mound is well predicted by the model; however, the measurements show a pronounced trough close to the seaward end of the mound that is absent in the calculations. This trough is most likely caused by the complex wave transformation occurring locally at the mound and which the random wave model is unable to represent.

### CONCLUDING REMARKS

The model discussed in this paper represents one of the first attempts to consistently treat random waves in all components of a beach profile change numerical model. Previous approaches to model the profile evolution under random waves have typically involved using statistical wave measures in equations primarily developed for monochromatic waves; these models have not considered the random properties of the waves at the outset of deriving the predictive equations. The new model eliminates the problem related to selecting an equivalent monochromatic wave that reproduces a specific cross-shore phenomenon. The root-mean-square wave height is identified as the characteristic wave to be used in calculating the profile evolution under random waves with the present model.

Comparison with measured profile change under random waves from the SUPERTANK Laboratory Data Collection Project supported the technique of linearly superimposing the transport from individual waves to derive transport rate formulas for random waves. The model validation included such profile evolution events as equilibrium erosion with bar formation, berm flooding, and the impact of breaking waves on an offshore mound. In the mound tests the agreement between the model predictions and the measurements was less good compared to the other tests; this is mainly attributed to the difficulties of accurately predicting the across-shore wave properties over the mound with the random wave model. Also, the effect of the velocity asymmetry in shoaling, non-breaking waves on the mound is not described by the profile model.

After being generalized to random waves, the equation to predict the net sand transport rate in the swash zone derived by Larson and Kraus (1994) modeled profile change on the foreshore satisfactorily during erosional conditions. The model faithfully reproduced the rapid flattening of a foreshore dune indicating that the complex net transport rate distribution, where onshore transport on the shoreward side of the foredune prevailed, was well predicted. However, the model was not evaluated for accretionary conditions, and some modification might be needed regarding the local slope term to obtain a realistic description of berm build-up on the foreshore.

The net transport rate distribution under random waves was derived without specific assumptions about the properties of the random wave field; thus, wave statistics representative for longer time periods could be used as input to the model and long-term predictions of the transport rate and profile evolution may be possible. The characteristic time scale of the profile response discussed in this paper implied that a Rayleigh pdf was a good description of the variation in wave height for the time step employed. For long-term simulations the wave statistics would have to be described by other distributions, but the calculations of the net transport rate and profile evolution could be handled within the framework of the present model. However, because the present model mainly predicts the profile response to breaking waves, additional terms that describe the transport due to non-breaking waves may have to be included to achieve a realistic profile evolution.

### ACKNOWLEDGEMENTS

The SUPERTANK Laboratory Data Collection Project was conducted at the O.H. Hinsdale Wave Research Laboratory, Oregon State University, under the direction of Dr. Nicholas C. Kraus. The SUPERTANK data are courtesy of Dr. Kraus, formerly CERC, now at the Conrad Blucher Institute, Corpus Christi State University. The support from the Japan Society for the Promotion of Science for the research visit of ML to the University of Tokyo is gratefully acknowledged, as well as the assistance from all members of the Coastal Engineering Laboratory during his stay. The research presented in this paper was conducted under the Calculation of Cross-Shore Sediment Transport and Beach Profile Change Processes Work Unit 32530, Shore Protection and Restoration Program, Coastal Engineering Research Center, U.S. Army Engineer Waterways Experiment Station. Contract coordination was provided by the European Research Office of the US Army in London under contract DAJA45-93-C0013.

### REFERENCES

- Battjes, J.A. (1974). "Surf similarity." *Proceedings of the 14th Coastal Engineering Conference*, American Society of Civil Engineers, 466-480.
- Battjes, J.A. and Janssen, J.P.F.M. (1978). "Energy loss and setup due to breaking of random waves." *Proceedings of the 16th Coastal Engineering Conference*, American Society of Civil Engineers, 569-587.
- Dally, W.R. (1992). "Random breaking waves: Field verification of a wave-by-wave algorithm for engineering application." *Coastal Engineering*, 16, 369-397.
- Dally, W.R., Dean, R.G., and Dalrymple, R.A. (1985). "Wave height variation across beaches of arbitrary profile." *Journal of Geophysical Research*, 90 (C6), 11917-11927.

Dean, R.G. (1977). "Equilibrium beach profiles: U.S. Atlantic and the Gulf Coasts." Department of Civil Engineering, Ocean Engineering Report No. 12, University of Delaware, Newark, DE.

Kraus, N.C., Smith, J.M., and Sollitt, C.K. (1992). "SUPERTANK Laboratory Data Collection Project." *Proceedings of the 23rd Coastal Engineering Conference*, American Society of Civil Engineers, 2191-2204.

Kriebel, D.L. and Dean, R.G. (1985). "Numerical simulation of time-dependent beach and dune erosion." *Coastal Engineering*, 9, 221-245.

Larson, M. (1995). "Model for decay of random waves in the surf zone." *Journal of Waterway, Port, Coastal and Ocean Engineering*, (in press).

Larson, M. and Kraus, N.C. (1989). "SBEACH: Numerical model for simulating storm-induced beach change, Report 1: Empirical foundation and model development." Technical Report CERC-89-9, US Army Engineer Waterways Experiment Station, Coastal Engineering Research Center, Vicksburg, MS.

Larson, M. and Kraus, N.C. (1994). "Cross-shore sand transport under random waves at SUPERTANK examined at mesoscale." *Proceedings of Coastal Dynamics '94*, American Society of Civil Engineers, 204-219.

Larson, M. and Kraus, N.C. (1995). "Prediction of cross-shore sediment transport at different spatial and temporal scales." *Marine Geology*, (in press).

Mase, H. and Iwagaki, Y. (1982). "Wave height distribution and wave grouping in surf zone." *Proceedings of the 18th Coastal Engineering Conference*, American Society of Civil Engineers, 58-76.

Mimura, N., Otsuka, Y., and Watanabe, A. (1986). "Laboratory study on two-dimensional beach transformation due to irregular waves." *Proceedings of the 20th Coastal Engineering Conference*, American Society of Civil Engineers, 1393-1406.

Thornton, E.B. and Guza, R.T. (1983). "Transformation of wave height distribution." *Journal of Geophysical Research*, 88 (C10), 5925-5938.

## CHAPTER 164

# A QUASI-3D SURF ZONE MODEL

Jung Lyul Lee<sup>1</sup> and Hsiang Wang<sup>2</sup>

### ABSTRACT

This paper presents theoretical circulation patterns in both cross-shore and longshore directions on the plane beach slope. In the model an amended form of radiation stress which is consistent with the wave energy flux in the wave-current coexisting field is presented. Comparison of theoretical surf zone properties with laboratory experiments showed good agreements. Finally, a quasi-three dimensional model suitable for the entire nearshore zone is presented by linking the depth-integrated properties with vertical profiles.

### 1. INTRODUCTION

A prominent feature in the nearshore zone is the wave-induced current. It is commonly accepted that the primary driving force is the wave-induced radiation stress first introduced by Longuet-Higgins and Stewart (1961). Modeling this circulation has advanced considerably since the earlier development by Noda et al. (1974) and Ebersole and Dalrymple (1979). Both of these earlier models were driven by a wave refraction model with no current feedback. In recent years, coupled wave-induced circulation models have also been developed (Yoo and O'Connor, 1986; Yan, 1987; and Winer, 1988). All these models depth-uniform circulation patterns and can, therefore, be classified as two-dimensional. They are not suitable for surf zone where current is vertically non-uniform. This feature is particularly prominent in the cross-shore direction because the onshore mass transport produced by the depth-varying momentum flux has to be compensated by the return flow due to the depth-uniform set-up force. This driving mechanism was first suggested by Dyhr-Nielsen and Sorensen (1970) and treated

---

<sup>1</sup>Ocean Engineering Division, Korea Ocean Research and Development Institute, P.O. Box 29, Ansan 425-600, Korea

<sup>2</sup>Coastal and Oceanographic Engineering Department, University of Florida, Gainesville, FL 32611

analytically by Dally (1980). Effort has since been made to produce cross-shore circulation patterns inside the surf zone such as the undertow model developed by Svendsen (1984), Buhr-Hansen and Svendsen (1984) and more recently, by Okayasu et al. (1988) and Yamashita and Tsuchiya (1990). It is only natural to attempt to develop circulation models that can address both horizontal and vertical variations in the nearshore zone. So far the effort is still few. De Vriend and Stive (1987) recently formulated a nearshore circulation model by employing a quasi-3D approach. At present, this approach is attractive from both theoretical and computational point of view.

One of the handicaps of all the existing depth-varying models whether cross-shore models or three-dimensional models is the pre-requisite on the large number of empirical coefficients that have to be assigned. This severely limits their application as one must be confident on the behavior of these coefficients under various natural conditions. Recently, Lee (1993) presented a formulation on current-wave interaction problems. In there, the radiation stress term in the momentum equation is amended, and two new conservation equations governing intrinsic wave frequency and wave action are introduced. In this paper, this new formulation is utilized to develop a depth-varying circulation model. The difference between the new model and the existing models is quite significant. First of all, since radiation stress is the primary driving force for circulations an amended formula alters this force. Secondly, the new model has stronger theoretical basis and requires fewer empirical coefficients owing to the fact the model must satisfy the additional governing equations. An analytical model for a straight shoreline of uniform slope is introduced first to explore the nature of the model and to facilitate comparisons. A general version suitable for the entire nearshore zone is then developed by linking the depth-integrated properties with depth-varying models. The numerical technique is briefly addressed and examples are given.

## 2. HORIZONTAL CIRCULATION MODEL

The governing equations for the horizontal circulation model are obtained after depth integration and wave-averaging. In order to protect from losing the Eulerian mean quantities at the mean water level, the depth integration is taken prior to wave-averaging them. The strong presence of turbulence is a prominent feature in surf zone. Consequently, the fundamental equations governing the fluid motion should also include the turbulent effects. This is usually accomplished with the introduction of Reynolds stresses by time averaging over the turbulent fluctuations.

### 2.1 Depth-Integrated and Time-Averaged Equation of Mass

Integrating the continuity equation for incompressible fluid over depth and employing the kinematic boundary conditions on the free surface and on the bottom, we get

$$\frac{\partial \eta}{\partial t} + \frac{\partial}{\partial x} \int_{-h}^{\eta} u dz + \frac{\partial}{\partial y} \int_{-h}^{\eta} v dz = 0 \quad (1)$$

Now let the turbulence-averaged velocity vector,  $\mathbf{U}(u, v, w)$ , and the surface elevation,  $\eta$ , be decomposed into mean current and wave fluctuation, which will be distinguished by the subscript  $c$  and  $w$ , respectively; thus,

$$\mathbf{U} = \mathbf{U}_c + \mathbf{U}_w, \quad \eta = \eta_c + \eta_w \quad (2)$$

where  $\mathbf{U}_w$  and  $\eta_w$  are the residual wave fluctuation which can be removed through the process of wave-averaging, and  $\mathbf{U}_c$  and  $\eta_c$  are the time-averaged value of velocity. The velocity at a particular water level with a mean position of  $(\mathbf{x}_1, z_1)$  is  $\mathbf{U}(\mathbf{x}_1, z_1 + \xi)$ , where  $\xi$  is a location of the vertical trajectory being up and down with the residual wave fluctuation at  $\mathbf{x}_1$ .

Then, we obtain the wave-averaged value of velocity,  $\mathbf{U}_c$ , as

$$\mathbf{U}_c(\mathbf{x}_1, z_1) = \frac{1}{T} \int_0^T \mathbf{U}(\mathbf{x}_1, z_1 + \xi) dt$$

Substituting Eq. (2) and taking the wave-average after expanding in a Taylor series at  $\eta = \eta_c$ , Eq.(1) can be simplified as

$$\frac{\partial \eta_c}{\partial t} + \frac{\partial}{\partial x} \int_{-h}^{\eta_c} u_c dz + \frac{\partial}{\partial x} (\overline{\eta_w u_w})_{\eta_c} + \frac{\partial}{\partial y} \int_{-h}^{\eta_c} v_c dz + \frac{\partial}{\partial y} (\overline{\eta_w v_w})_{\eta_c} = 0 \quad (3)$$

The wave components are given by linear progressive wave theory as follow:

$$\frac{\partial \eta_c}{\partial t} + \frac{\partial}{\partial x} \int_{-h}^{\eta_c} u_c dz + \frac{\partial}{\partial y} \int_{-h}^{\eta_c} v_c dz + \frac{1}{\rho} \left[ \frac{\partial M_x}{\partial x} + \frac{\partial M_y}{\partial y} \right] = 0 \quad (4)$$

where the  $x$  and  $y$  components of mass flux are defined as

$$M_x = \frac{E' k_x}{\sigma}, \quad M_y = \frac{E' k_y}{\sigma} \quad (5)$$

and  $E'$  is defined as  $\rho g H^2 / 8$ . The mass flux terms are considered the mass transport above the mean water level.

## 2.2 Depth-Integrated and Time-Averaged Equations of Momentum

Assuming that no horizontal viscous stress exist, the horizontal momentum equation in the  $x$  direction is integrated over depth to yield

$$\begin{aligned} & \frac{\partial}{\partial t} \int_{-h}^{\eta} u dz + \frac{\partial}{\partial x} \int_{-h}^{\eta} u u dz + \frac{\partial}{\partial y} \int_{-h}^{\eta} u v dz \\ & = \frac{1}{\rho} \left[ -\frac{\partial}{\partial x} \int_{-h}^{\eta} p dz + p|_{\eta} \frac{\partial \eta}{\partial x} + p|_{-h} \frac{\partial h}{\partial x} + \tau_{Wx} - \tau_{Bx} \right] \end{aligned} \quad (6)$$

where  $\tau_{Wx} = \tau_{zx}|_{\eta}$  is a wind stress in the  $x$  direction and  $\tau_{Bx} = \tau_{zx}|_{-h}$  is the bottom friction. Substituting  $\mathbf{U}$  and  $\eta$  defined in Eq. (2), the time-averaged

quantities is also obtained by expanding  $\eta$  in Taylor series at the mean water level,  $\eta_c$ ,

$$\begin{aligned} & \frac{\partial}{\partial t} \int_{-h}^{\eta_c} u_c dz + \frac{\partial}{\partial x} \int_{-h}^{\eta_c} u_c^2 dz + \frac{\partial}{\partial y} \int_{-h}^{\eta_c} u_c v_c dz + \frac{\partial}{\partial x} \int_{-h}^{\eta_c} \overline{u_w^2} dz + \frac{\partial}{\partial y} \int_{-h}^{\eta_c} \overline{u_w v_w} dz \\ & + \frac{\partial}{\partial t} (\overline{\eta_w w_w})|_{\eta_c} + \frac{\partial}{\partial x} (2\overline{\eta_w u_c u_w})|_{\eta_c} + \frac{\partial}{\partial y} (\overline{\eta_w (u_c v_w + v_c u_w)})|_{\eta_c} \\ & = \frac{1}{\rho} \left[ -\frac{\partial}{\partial x} \int_{-h}^{\eta_c} p dz + \bar{p}|_{-h} \frac{\partial h}{\partial x} + \overline{\tau_{Wx}} - \overline{\tau_{Bx}} \right] \end{aligned} \quad (7)$$

where the pressure at the free surface was assumed to be zero and then the total pressure is given as

$$p = \bar{p} + p_w = -\rho \overline{u_w^2(z)} + \rho g(\eta_c - z) + \rho g \eta_w K_p(z) \quad (8)$$

where  $K_p$  is the pressure response factor given by linear wave theory,

$$K_p = \frac{\cosh k(h+z)}{\cosh k(h+\eta_c)} \quad (9)$$

Substituting Eq (8), finally, the depth-integrated and time-averaged momentum equation in the  $x$  direction is obtained;

$$\begin{aligned} & \frac{\partial}{\partial t} \int_{-h}^{\eta_c} u_c dz + \frac{\partial}{\partial x} \int_{-h}^{\eta_c} u_c^2 dz + \frac{\partial}{\partial y} \int_{-h}^{\eta_c} u_c v_c dz \\ & + \frac{1}{\rho} \frac{\partial S_{xx}}{\partial x} + \frac{1}{\rho} \frac{\partial S_{yx}}{\partial y} + g(h + \eta_c) \frac{\partial \eta_c}{\partial x} - \frac{\overline{\tau_{Wx}}}{\rho} + \frac{\overline{\tau_{Bx}}}{\rho} = 0 \end{aligned} \quad (10)$$

The momentum equation in the  $y$  direction can be similarly obtained,

$$\begin{aligned} & \frac{\partial}{\partial t} \int_{-h}^{\eta_c} v_c dz + \frac{\partial}{\partial x} \int_{-h}^{\eta_c} u_c v_c dz + \frac{\partial}{\partial y} \int_{-h}^{\eta_c} v_c^2 dz \\ & + \frac{1}{\rho} \frac{\partial S_{xy}}{\partial x} + \frac{1}{\rho} \frac{\partial S_{yy}}{\partial y} + g(h + \eta_c) \frac{\partial \eta_c}{\partial y} - \frac{\overline{\tau_{Wy}}}{\rho} + \frac{\overline{\tau_{By}}}{\rho} = 0 \end{aligned} \quad (11)$$

For the case of linear progressive wave and mild slope, the radiation stress terms can be expressed in terms of wave characteristics as

$$S_{xx} = E' \left[ n(\cos^2 \theta + 1) - \frac{1}{2} + 2 \cos \theta \frac{u_s}{C} \right] \quad (12)$$

$$S_{xy} = S_{yx} = E' \left[ \sin \theta (n \cos \theta + \frac{u_s}{C}) + \cos \theta \frac{v_s}{C} \right] \quad (13)$$

$$S_{yy} = E' \left[ n(\sin^2 \theta + 1) - \frac{1}{2} + 2 \sin \theta \frac{v_s}{C} \right] \quad (14)$$

where  $n = Cg/C$  and  $u_s$  and  $v_s$  are the time-averaged current velocity at mean water level. It is noted here that the definition of the radiation stress differs from that given by Longuet-Higgins and Stewart (1961) with the additional advective



terms. The amended form of radiation stress has been proven to be consistent with the wave energy flux in the wave-current coexisting field by Lee (1993).

**3. VERTICAL CIRCULATION MODEL FOR STRAIGHT SHORE-LINE**

For the case of straight shoreline and parallel offshore contours the cross-shore and longshore components are decoupled. This simplifies the mathematical manipulation considerably.

**3.1 Theoretical Undertow Model**

The vertical circulation in the  $x$ - $z$  plane is treated as quasi-steady. Since there is no  $y$ -direction (longshore) variation, the turbulence-averaged momentum equation in the  $x$ -direction (onshore) integrated from any level  $z$  to the mean water level can be written as

$$\frac{\partial}{\partial x} \int_z^\eta uudz - uw|_z = \frac{1}{\rho} \left[ -\frac{\partial}{\partial x} \int_z^\eta pdz + p(\eta) \frac{\partial \eta}{\partial x} + \tau_{zx}|_\eta - \tau_{zx}(z) \right] \tag{15}$$

where the shear stress is assumed to be expressed in the form

$$\tau_{zx} = \rho \nu_t \frac{\partial u}{\partial z} \tag{16}$$

with  $\nu_t$  defined as the total kinematic viscosity, which is composed of both eddy and molecular viscosities in the vertical direction. The shear stress at free surface,  $\tau|_\eta$ , is assumed only due to wind stress  $\tau_W$ . Separating the velocity into the current and wave components and taking time-average, Eq. (15) becomes

$$\nu_t \frac{\partial u_c}{\partial z} |_z = -\frac{\partial}{\partial x} \int_z^{\eta_c} (\overline{u_w^2} - \overline{w_w^2}) dz - \frac{g}{2} \frac{\partial \overline{\eta_w^2}}{\partial x} + \frac{\partial}{\partial x} (2\overline{\eta_w u_c u_w})|_{\eta_c} - g(\eta_c - z) \frac{\partial \eta_c}{\partial x} + \frac{\overline{\tau_{Wx}}}{\rho} \tag{17}$$

The convective term of the mean current was assumed to be small enough compared to the rest. In shallow water, the first term on the right hand side becomes

$$\frac{\partial}{\partial x} \int_z^{\eta_c} (\overline{u_w^2} - \overline{w_w^2}) dz = g \frac{(\eta_c - z)}{(\eta_c + h)} \frac{\partial}{\partial x} \left[ (\cos^2 \theta + 1) \frac{H^2}{8} \right] \tag{18}$$

and the second term reduces to,

$$\frac{g}{2} \frac{\partial \overline{\eta_w^2}}{\partial x} = \frac{g}{16} \frac{\partial H^2}{\partial x} \tag{19}$$

The fourth term can be determined by the depth-integrated equation of momentum, Eq. (10), under the following assumptions; 1) the flow is in steady state, and 2) the effect of squared mean current are negligible. Then, Eq.(10) becomes

$$\frac{\partial \eta_c}{\partial x} = -\frac{1}{\rho g(h + \eta_c)} \left[ \frac{\partial S_{xx}}{\partial x} - \overline{\tau_{Wx}} + \overline{\tau_{Bx}} \right] \tag{20}$$

Substituting Eqs. (18-20) into Eq. (17) and introducing non-dimensional variable,  $z' = (\eta_c - z)/(\eta_c + h)$ , results in,

$$-\frac{\nu_t}{\eta_c + h} \frac{\partial u_c}{\partial z'} \Big|_{z'} = z' \left\{ \frac{g}{16} \frac{\partial H^2}{\partial x} - 2g \frac{\partial}{\partial x} \left( \cos \theta \frac{u_s H^2}{C} \frac{H^2}{8} \right) - \frac{\overline{\tau_{Wx}}}{\rho} + \frac{\overline{\tau_{Bx}}}{\rho} \right\} - \frac{g}{16} \frac{\partial H^2}{\partial x} + 2g \frac{\partial}{\partial x} \left( \cos \theta \frac{u_s H^2}{C} \frac{H^2}{8} \right) + \frac{\overline{\tau_{Wx}}}{\rho} \quad (21)$$

According to the above equation, we can estimate the shear stress at the mean water level,

$$-\frac{\nu_t}{\eta_c + h} \frac{\partial u_c}{\partial z'} \Big|_{\eta_c} = -\frac{g}{16} \frac{\partial H^2}{\partial x} + 2g \frac{\partial}{\partial x} \left( \cos \theta \frac{u_s H^2}{C} \frac{H^2}{8} \right) + \frac{\overline{\tau_{Wx}}}{\rho} \quad (22)$$

and the shear stress at the bottom,

$$-\frac{\nu_t}{\eta_c + h} \frac{\partial u_c}{\partial z'} \Big|_{-h} = \frac{\overline{\tau_{Bx}}}{\rho} \quad (23)$$

Now we assume that the turbulent motions originating from the surface wave breaking is governed by an constant eddy viscosity, and that the boundary layer remains thin. Then, the above equation can be solved explicitly to give the following solution,

$$u_c(z') = u_s + C_{x1} z'^2 + C_{x2} z' \quad (24)$$

where

$$C_{x1} = -\frac{\eta_c + h}{2\varepsilon_z} \left\{ \frac{g}{16} \frac{\partial H^2}{\partial x} - 2g \frac{\partial}{\partial x} \left( \cos \theta \frac{u_s H^2}{C} \frac{H^2}{8} \right) - \frac{\overline{\tau_{Wx}}}{\rho} + \frac{\overline{\tau_{Bx,tb}}}{\rho} \right\} \quad (25)$$

$$C_{x2} = -\frac{\eta_c + h}{\varepsilon_z} \left\{ -\frac{g}{16} \frac{\partial H^2}{\partial x} + 2g \frac{\partial}{\partial x} \left( \cos \theta \frac{u_s H^2}{C} \frac{H^2}{8} \right) + \frac{\overline{\tau_{Wx}}}{\rho} \right\} \quad (26)$$

where  $\varepsilon_z$  implies the constant eddy viscosity which will be estimated in Section 3.3. According to this equation, the mean flow pattern inside the surf zone in the main region is essentially parabolic. The analytical solution for a plane beach is presented to simplify mathematical operation and to facilitate comparisons with data.

The profile given by Eq. (24) contains 3 physical parameters, the surface current, the eddy viscosity and the bottom friction. One of them can be eliminated by constraint that, in the cross-shore direction, the net flow has to be equal to zero for a steady case, or

$$\int_{-h}^{\eta_c} u_c dz + \frac{M_x}{\rho} = 0 \quad (27)$$

where  $M_x$  is wave-induced mass flux. Eliminating  $\tau_b$  from Eqs.(24-26) and (27), the coefficients can be rewritten as

$$C_{x1} = 3(\bar{u} - u_s) - \frac{3}{2} \frac{\eta_c + h}{\varepsilon_z} P, \quad C_{x2} = \frac{\eta_c + h}{\varepsilon_z} P \quad (28)$$

where

$$P = \frac{g}{16} \frac{\partial H^2}{\partial x} - 2g \frac{\partial}{\partial x} \left( \cos \theta \frac{u_s H^2}{C} \right), \quad \bar{u} = -\frac{M_x}{\rho(\eta_c + h)} = -\frac{g \cos \theta H^2}{8 C(\eta_c + h)} \quad (29)$$

### 3.2 Theoretical Longshore Current Model

The longshore current profile can be obtained in a similar manner. For a straight shoreline, the surface gradient as well as the radiation stress gradient in the  $y$ -direction can be neglected. Again, neglecting the convective term of the mean current, the momentum equation in the  $y$  direction yields,

$$\frac{\partial}{\partial x} \int_z^{\eta_c} \bar{v}_w \bar{u}_w dz + \frac{\partial}{\partial x} (\bar{\eta}_w \bar{v}_c \bar{u}_w)|_{\eta_c} + \frac{\partial}{\partial x} (\bar{\eta}_w \bar{u}_c \bar{v}_w)|_{\eta_c} = \frac{1}{\rho} \left[ \bar{\tau}_{W_y} - \rho \nu_t \frac{\partial v_c}{\partial z} \Big|_z \right] \quad (30)$$

Since the second and third terms become zero (Lee, 1983), Eq. (30) is reduced to

$$\frac{\partial}{\partial x} \int_z^{\eta_c} \bar{v}_w \bar{u}_w dz = \frac{\bar{\tau}_{W_y}}{\rho} - \nu_t \frac{\partial v_c}{\partial z} \Big|_z \quad (31)$$

In shallow water, the LHS becomes

$$\frac{\partial}{\partial x} \int_z^{\eta_c} \bar{v}_w \bar{u}_w dz = \frac{(\eta_c - z)}{(\eta_c + h)} \frac{\partial}{\partial x} \left[ g \cos \theta \sin \theta \frac{H^2}{8} \right] \quad (32)$$

by linear wave theory. Substituting Eq. (32) into Eq. (31) gives the following:

$$-\frac{\nu_t}{\eta_c + h} \frac{\partial v_c}{\partial z'} \Big|_{z'} = -z' \frac{\partial}{\partial x} \left[ g \cos \theta \sin \theta \frac{H^2}{8} \right] + \frac{\bar{\tau}_{W_y}}{\rho} \quad (33)$$

Integrating Eq.(33) with respect to  $z'$  with introduction of depth-independent  $\varepsilon_z$  we obtain,

$$\bar{v}(z') = v_s + C_{y1} z'^2 + C_{y2} z' \quad (34)$$

where

$$C_{y1} = \frac{\eta_c + h}{2\varepsilon_z} \frac{\partial}{\partial x} \left[ g \cos \theta \sin \theta \frac{H^2}{8} \right], \quad C_{y2} = -\frac{\eta_c + h}{\varepsilon_z} \frac{\bar{\tau}_{W_y}}{\rho} \quad (35)$$

Or, alternatively,  $C_{y1}$  can be expressed in terms of radiation stress as

$$C_{y1} = \frac{\bar{\eta} + h}{2\varepsilon_z} \frac{1}{\rho} \frac{\partial S_{xx}}{\partial x} \quad (36)$$

For steady longshore current, the depth-integrated radiation stress is balanced by the bottom friction under no wind. The depth-averaged mean longshore current is given by,

$$\bar{v} = v_s + \frac{C_{y1}}{3} + \frac{C_{y2}}{2} \quad (37)$$

### 3.3 Estimation of Surface Velocity and Eddy Viscosity

The solutions for cross-shore and longshore current profiles will be complete if the surface velocity and eddy viscosity are determined. Lee (1993) has shown that the surface current can be determined semi-analytically by virtue of wave action and intrinsic frequency conservation equations; both of them are surface conditions. The solutions briefly summarized here.

The surf zone is assumed to be coherent in that the essential wave-like periodic motion is retained and is quasi-steady when time-averaged over wave period. In this case, the wave action and wave frequency conservation equations are, respectively,

$$\nabla_h \cdot \left( \mathbf{U}_s \frac{H^2}{\sigma_s} \right) = 0, \quad \nabla_h \cdot (\mathbf{U}_s \sigma_s) = 0 \quad (38)$$

Here  $\sigma_s$  denotes  $\sigma$  inside the surf zone. The wave energy equation is modified to reflect dissipation,

$$\nabla_h \cdot \left[ (\mathbf{Cg} + \mathbf{Cg}_D + \mathbf{U}_s) \frac{H^2}{\sigma_s} \right] = 0 \quad (39)$$

with  $\mathbf{Cg}_D$  representing a dissipation velocity. Eliminating a  $\mathbf{U}_s$  term of Eq. (39) based on the first equation of Eqs.(38), the cross shore component of Eq. (39) provides

$$H = \frac{\beta_H}{(Cg_{Dx} - Cg_x)} \quad (40)$$

and also the surface currents are obtained,

$$u_s = \beta_C (Cg_{Dx} - Cg_x), \quad v_s = \beta_L (Cg_{Dy} - Cg_y) \quad (41)$$

with  $\beta$ 's the constants of proportionality. They further assume on two-dimensional beaches of uniform slope that the dissipation inside the surf zone is dominated by the influence of the initial condition at the breaking point and  $\mathbf{Cg}_D$  to be equal to  $-\beta \mathbf{Cg}_b$ . The above equations can then be written as

$$H = \frac{\beta_H}{\cos \theta (\beta Cg_b - Cg)}$$

$$u_s = \beta_C \cos \theta (\beta Cg_b - Cg), \quad v_s = \beta_L \sin \theta (\beta Cg_b - Cg) \quad (42)$$

Thus, the wave height and surface currents are determined explicitly. Figure 1 shows the comparison of wave height variation in the surf zone between the present theory and the laboratory data by Horikawa and Kuo (1966). Figure 2 compares the theory with the laboratory longshore current data measured by Visser (1991).

The vertical eddy viscosity for both cross-shore and longshore components is treated as the same and is estimated from the longshore mean current strength. From Section 3.2 we can obtain,

$$\frac{\overline{\tau_{By,tb}}}{\rho} = \frac{6\varepsilon_z}{\bar{\eta} + h} (\bar{v} - v_s) \tag{43}$$

In a flow field where the turbulent-induced stress dominates the bottom friction, the bottom stress can be approximated by,

$$\frac{\overline{\tau_{By,tb}}}{\rho} \approx \frac{\sin \theta}{C_a} D \tag{44}$$

where  $C_a = \omega/k$  and  $D$  is the local rate of energy dissipation. Based on Eq.(39),  $D$  can be expressed as

$$D = -\nabla \cdot [\beta C g_b \frac{K}{k} \frac{\omega}{\sigma_s} E']$$

Eliminating the bottom stress term from Eqs.(43) and (44), an expression for the eddy viscosity is obtained,

$$\frac{\varepsilon_z}{\bar{\eta} + h} = \frac{\sin \theta D}{6 C_a \rho (\bar{v} - v_s)} \tag{45}$$

which relates the eddy viscosity to the the mean longshore current strength. In the following computation we simply assume that mean longshore current strength is proportional to the surface current strength, that is,

$$\bar{v} = \gamma v_s \tag{46}$$

with  $\gamma$  the ratio of mean current to the surface current. Therefore, the eddy viscosity can be simplified as the following explicit expression,

$$\frac{\varepsilon_z}{\eta_c + h} = -\frac{1}{24(1 - \gamma)\beta_L} \frac{|u_{orb}|}{(1 - Cg/(\beta C g_b))} \frac{\partial}{\partial x} (\cos \theta H) \tag{47}$$

### 3.4 Data Comparisons

In this subsection, each theoretical solution is compared with data measured on the plane beach of uniform slope. Wind stress effect is omitted in the solutions.

#### Undertow Model

The velocity profile is calculated by Eq. (24). Four parameters are to be designated; they are,  $\gamma$ : the ratio of mean current to surface current;  $\beta$ : the dissipation coefficient;  $\beta_C$ : the cross-shore current coefficient; and  $\beta_L$ : the longshore current coefficient.

Figure 3 shows the comparisons of the computed vertical profiles of the cross-shore current with those measured by Buhr-Hansen and Svendsen (1984). The

test conditions were: slope = 1:34.25;  $H_o = 0.12m$  and  $T=1$  sec. The parameters used in the computations are:  $\beta = 1.17$ ;  $\beta_C=0.07$ ;  $\beta_L=5.0$  and  $\gamma=0.982$ . The limiting wave height at breaking point is determined by the Miche's criterion with  $\kappa=0.78$ . Figure 4 plots the profile changes across the untire surf zone using the same paramters as given above. In order to examine the effect of the advection term, the results when the term is neglected are also represented as dotted lines in Figure 5. The effect seems to show the significant deviation from the measurements as it is close to the shoreline under the same input condition. However, the difference also seems to show the overall agreement with the experiments by small reduction of the  $\gamma$  value as shown in Figure 5.

### Longshore Current Model

Figure 6 shows the comparasions between computed profiles and the laboratory data measured by Visser (1991). The test conditions were: slope=1 : 10,  $H_o = 9.6cm$ ,  $T = 1sec$  and  $\theta_o = 16.4^\circ$ . The values of parameters are as follows;  $\beta=1.2$ ,  $\beta_L=5.0$ , and  $\gamma=0.96$ . It is seen that  $\gamma$  plays an important role. A maximum value 1 results in a uniform longshore current profile whereas a value 2/3 results in a no-slip bottom velocity. From the comparisons with experimental data, a value near 0.95 is suggested. Figure 7 plots the longshore current profile variations across the surf zone.

Figure 8 illustrates the three-dimensional current profiles inside the surf zone using the same conditions as Figure 5 with the exception that the input wave is oblique at  $10^\circ$  in deep water clockwise to the shoreline normal. The three-dimensional current forms a clockwise spiral from top to bottom.

### 3.5 Model Adoption for General 3-D Topography

The theoretical models so far developed are for parallel contours. For irregular bathymetries, getting the surface velocity as the surface boundary condition might be ineffective for modelling, so the bottom shear stress in terms of depth-averaged current is considered as the boundary condition instead of the surface velocity. For the prediction of a longshore current this alternative way gives the exactly same result. For that of the undertow, however, this will give the different result. The bottom shear stress suggested by Longuet-Higgins (1970) is now modified for both cross-shore and longshore directions by

$$\overline{\tau_{B,ib}} = \rho F_w |u_{orb}| \gamma \bar{U} \quad (48)$$

where  $F_w$  can be estimated in terms of wave characteristics as

$$F_w = \frac{\beta}{4\gamma\beta_L} \frac{\nabla \cdot (\mathbf{KH}/k)}{(\beta - Cg/Cg_b)} \quad (49)$$

When the bottom shear stress given in Eq. (49) is applied as a boundary condition instead of the surface velocity, three coefficients of the undertow model,  $C_{x1}$ ,  $C_{x2}$

and  $u_s$ , are written by

$$C_{x1} = -\frac{\eta_c + h}{2\varepsilon_z}(P + \overline{\tau_{Bx,tb}}) \tag{50}$$

$$C_{x2} = \frac{\eta_c + h}{\varepsilon_z}P \tag{51}$$

$$u_s = \bar{u} - \frac{C_{x1}}{3} - \frac{C_{x2}}{2} \tag{52}$$

The result is shown in Figures 9-10 for the same experimental conditions as used by Buhr-Hansen and Svendsen (1984) given in Section 3.4. The ‘S.B.C.’ indicates the full theory obtained by the surface boundary condition, and the ‘B.B.C.’ indicates the approximate theory obtained by the bottom shear stress with neglecting the advection term. The full theory was obtained by  $\gamma=0.982$ , the approximate theory by  $\gamma=0.978$ . The comparison with experiments is still in agreement. Therefore, instead of the boundary condition given by surface currents, the bottom shear stress is used in the practical model for the complicated bathymetry, and the advection terms are omitted.

**4. QUASI THREE-DIMENSIONAL MODEL**

The depth-integrated horizontal model is now combined with the vertical theoretical model to a quasi-3D model. This quasi-3D model looks promising since it provides three-dimensional information at almost the same cost of a two-dimensional horizontal model although it produces the relatively simple variation of vertical profile.

Even for the general topography, velocity variation with respect to depth may be approximated as the function of parabola of 2nd order.

$$u_c = C_{x1}z'^2 + C_{x2}z' + C_{x3} \tag{53}$$

$$v_c = C_{y1}z'^2 + C_{y2}z' + C_{y3} \tag{54}$$

where  $C_1$ ,  $C_2$  and  $C_3$  are expressed in terms of wave characteristics and current quantities such as  $H$ ,  $h + \eta_c$ ,  $Q$ (depth integration of velocity vector), and  $\overline{\tau_W}$ :

$$C_{x1} = -\frac{\eta_c + h}{2\varepsilon_z} \left\{ \frac{g}{16} \frac{\partial H^2}{\partial x} - \frac{\overline{\tau_{Wx}}}{\rho} + \frac{\overline{\tau_{Bx,tb}}}{\rho} \right\} \tag{55}$$

$$C_{x2} = -\frac{\eta_c + h}{\varepsilon_z} \left\{ -\frac{g}{16} \frac{\partial H^2}{\partial x} + \frac{\overline{\tau_{Wx}}}{\rho} \right\} \tag{56}$$

$$C_{x3} = \frac{Q_x}{\eta_c + h} - \frac{C_{x1}}{3} - \frac{C_{x2}}{2} \tag{57}$$

$$C_{y1} = -\frac{\eta_c + h}{2\varepsilon_z} \left\{ \frac{g}{16} \frac{\partial H^2}{\partial y} - \frac{\overline{\tau_{Wy}}}{\rho} + \frac{\overline{\tau_{By,tb}}}{\rho} \right\} \tag{58}$$

$$C_{y2} = -\frac{\eta_c + h}{\varepsilon_z} \left\{ -\frac{g}{16} \frac{\partial H^2}{\partial y} + \frac{\overline{\tau_{Wy}}}{\rho} \right\} \tag{59}$$

$$C_{y3} = \frac{Q_y}{\eta_c + h} - \frac{C_{y1}}{3} - \frac{C_{y2}}{2} \quad (60)$$

Substituting Eqs. (53) and (54) into the convective acceleration terms yields

$$\int_{-h}^{\eta_c} u_c^2 dz = \left[ \frac{Q_x^2}{(h + \eta_c)^2} + T_{xx} \right] (h + \eta_c) \quad (61)$$

$$\int_{-h}^{\eta_c} u_c v_c dz = \left[ \frac{Q_x Q_y}{(h + \eta_c)^2} + T_{xy} \right] (h + \eta_c) \quad (62)$$

$$\int_{-h}^{\eta_c} v_c^2 dz = \left[ \frac{Q_y^2}{(h + \eta_c)^2} + T_{yy} \right] (h + \eta_c) \quad (63)$$

where

$$T_{xx} = \left[ \frac{4C_{x1}^2}{45} + \frac{C_{x2}^2}{12} + \frac{C_{x1}C_{x2}}{6} \right] \quad (64)$$

$$T_{xy} = T_{yx} = \left[ \frac{4C_{x1}C_{y1}}{45} + \frac{C_{x2}C_{y2}}{12} + \frac{C_{x1}C_{y2}}{12} + \frac{C_{x2}C_{y1}}{12} \right] \quad (65)$$

$$T_{yy} = \left[ \frac{4C_{y1}^2}{45} + \frac{C_{y2}^2}{12} + \frac{C_{y1}C_{y2}}{6} \right] \quad (66)$$

Substituting into Eq. (10) leads to the following  $x$ -directional modified momentum equation:

$$\begin{aligned} \frac{\partial Q_x}{\partial t} + \frac{\partial}{\partial x} \left[ \frac{Q_x^2}{h + \eta_c} + (h + \eta_c)T_{xx} \right] + \frac{\partial}{\partial y} \left[ \frac{Q_x Q_y}{h + \eta_c} + (h + \eta_c)T_{xy} \right] \\ + \frac{1}{\rho} \frac{\partial S_{xx}}{\partial x} + \frac{1}{\rho} \frac{\partial S_{yx}}{\partial y} + g(h + \eta_c) \frac{\partial \eta_c}{\partial x} - \frac{\overline{\tau_{wx}}}{\rho} + \frac{\overline{\tau_{Bx}}}{\rho} = 0 \end{aligned} \quad (67)$$

The modified momentum equation of  $y$  direction from Eq. (11)

$$\begin{aligned} \frac{\partial Q_y}{\partial t} + \frac{\partial}{\partial x} \left[ \frac{Q_x Q_y}{h + \eta_c} + (h + \eta_c)T_{yx} \right] + \frac{\partial}{\partial y} \left[ \frac{Q_y^2}{h + \eta_c} + (h + \eta_c)T_{yy} \right] \\ + \frac{1}{\rho} \frac{\partial S_{xy}}{\partial x} + \frac{1}{\rho} \frac{\partial S_{yy}}{\partial y} + g(h + \eta_c) \frac{\partial \eta_c}{\partial y} - \frac{\overline{\tau_{wy}}}{\rho} + \frac{\overline{\tau_{By}}}{\rho} = 0 \end{aligned} \quad (68)$$

As noted below, the bottom friction consists of turbulent shear stress and bottom frictions due to viscous and streaming flows, which can be expressed as

$$\overline{\tau_B} = F_w |u_{orb}| \bar{U} + F_c |u_{orb}| (\mathbf{U}_{B,tb} + \mathbf{U}_{strm}) \quad (69)$$

where  $\mathbf{U}_{B,tb}$  represents the bottom velocity induced by turbulent flow and  $\mathbf{U}_{strm}$  is the streaming velocity in the oscillatory boundary.

The continuity equation results in the same equation as before.

$$\frac{\partial \eta_c}{\partial t} + \frac{\partial}{\partial x} (Q_x + M_x) + \frac{\partial}{\partial y} (Q_y + M_y) = 0 \quad (70)$$



5. CONCLUSION

The surface advective terms were added to the conventional radiation stress by taking Taylor series expansion at the mean water level. The resulting radiation stress was proven by Lee (1993) to be consistent with the wave energy flux in the wave-current coexisting field.

The surface properties obtained from the surf zone model enabled us to develop the theory for the vertical circulation model which had suffered obscurity of boundary conditions. In addition, the friction coefficient and eddy viscosity applicable to the turbulent flow in a surf zone have been estimated in terms of energy dissipation. The developed model yielded the theoretical results comparable with laboratory experiments.

Based on the examination of the theoretical model for vertical profiles of currents in steady state, a quasi-three dimensional circulation model suitable for the entire nearshore zone is developed by linking the depth-integrated properties with the vertical profiles.

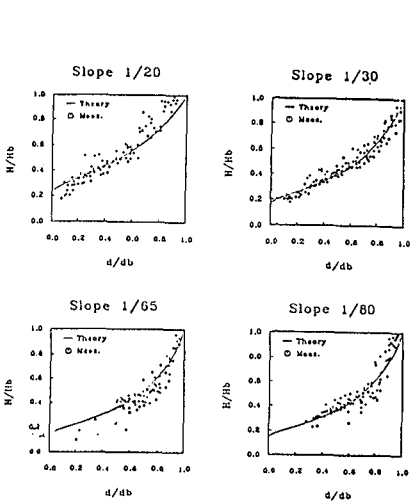


Fig. 1. Comparison with laboratory experiments presented by Horikawa and Kuo (1966).

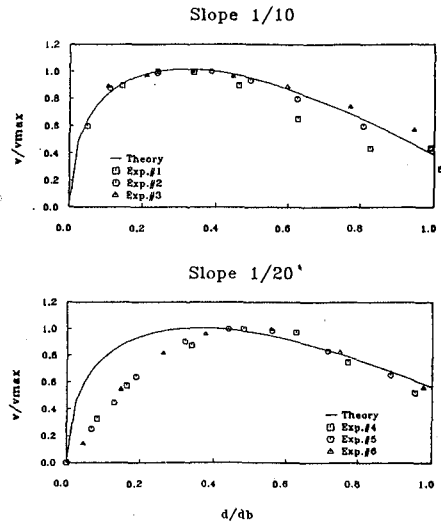


Fig. 2. Comparison of longshore current with laboratory experiments presented by Visser (1991).

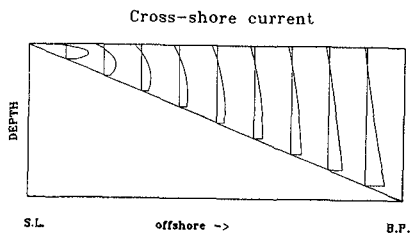


Fig. 3. Vertical profiles of cross-shore current.

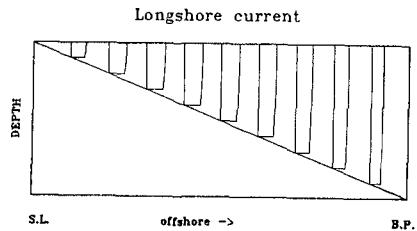


Fig. 6. Vertical profiles of longshore current.

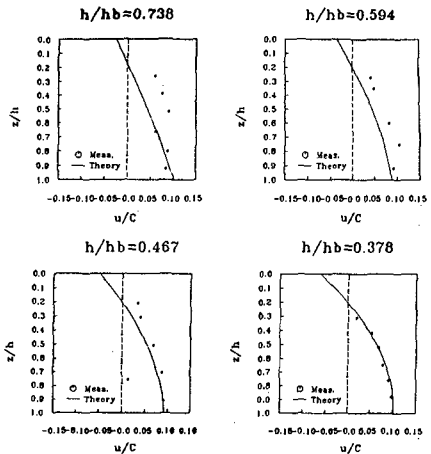


Fig. 4. Comparison with experiments presented by Hansen and Svendsen (1984).

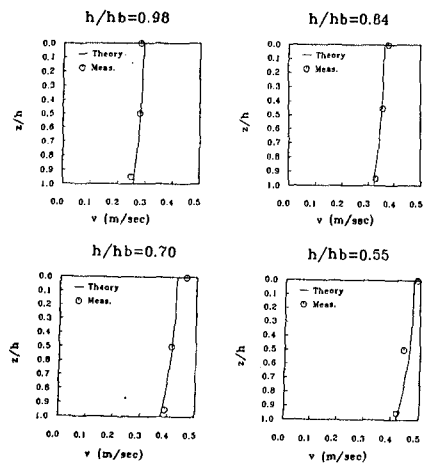


Fig. 7. Comparison with experiments presented by Visser

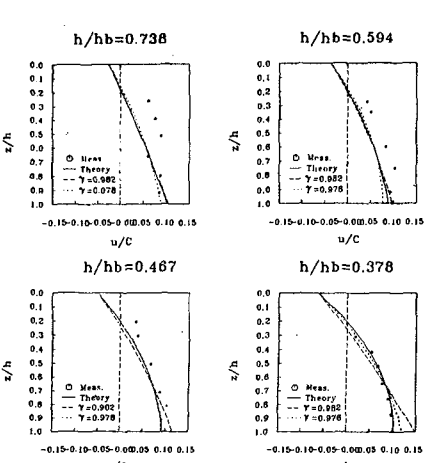


Fig. 5. Effect of the advection term in the undertow model.

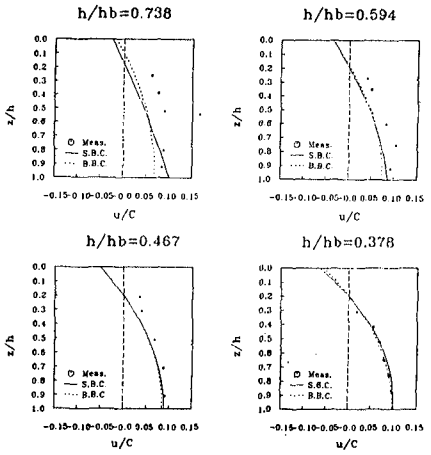


Fig. 10. Comparison with experiments presented by Hansen and Svendsen (1984).

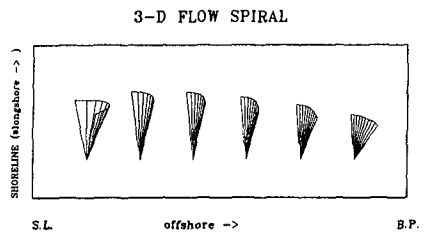


Fig. 8. Combined three-dimensional profiles.

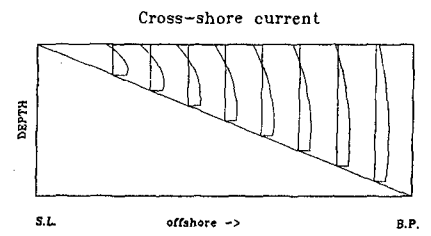


Fig. 9. Vertical profiles of cross-shore current by using bottom shear stress.

## REFERENCES

- Buhr-Hansen, J. and Svendsen, I.A. 1984. "A theoretical and experimental study of undertow," Proc. 19th ICCE, ASCE.
- Dally, W.R. 1980. "A numerical model for beach profile evolution," Master's Thesis, Civil Eng., Univ. of Delaware, Dept., Newark.
- De Vriend, H.J., and Stive, M.J.F. 1987. "Quasi-3D modelling of nearshore currents," Coastal Eng., 11: 565-601.
- Dong, P., and Anastasiou, K. 1991. "A numerical model of the vertical distribution of longshore currents on a plane beach," Coastal Eng., 15: 279-298.
- Ebersole, B.A., and Dalrymple, R.A. 1979. "A numerical model for nearshore circulation including convective accelerations and lateral mixing," Ocean Engineering Report No. 21, Dept. of Civil Eng., Univ. of Delaware, Newark, Delaware.
- Horikawa, K., and Kuo, C.T. 1966. "A study of wave transformation inside the surf zone," Proc. 10th ICCE, ASCE, Tokyo, 217-233.
- Lee, J.L. 1993. "Wave-current interaction and quasi-3D modelling in nearshore zone," Ph.D. Dissertation, Coastal and Oceanographic Engineering Department, University of Florida, Gainesville.
- Longuet-Higgins, M.S. 1970. "Longshore currents generated by obliquely incident sea waves, I," J. Geophys. Res., 75(33): 6778-6789.
- Longuet-Higgins, M.S. and Stewart, R.W. 1961. "The changes in amplitude of short gravity waves on steady non-uniform currents, J. Fluid Mech., 10:529-549.
- Nielson, D.M., and Sorensen, T. 1970. "Sand transport phenomena on coasts with bars," Proc. 12th ICCE, ASCE, pp.855-866.
- Noda, E., Sonu, C.J., Rupert, V.C., and Collins, J.I. 1974. "Nearshore circulation under sea breeze conditions and wave-current interactions in the surf zone," Tetra Tech Report TC-149-4.
- Okayasu, A., Shibayama, T., and Horikawa, K. 1988. "Vertical variation of undertow in the surf zone," Proc. 21st ICCE, ASCE, pp.478-491.
- Svendsen, I.A. 1984. "Wave heights and set-up in a surf zone," Coastal Eng., 8: 303-329.
- Svendsen, I.A., and Lorenz, R.S. 1989. "Velocities in combined undertow and longshore currents," Coastal Eng., 13: 55-79.
- Svendsen, I.A., and Putrevu, U. 1990. "Nearshore circulation with 3-D profiles," Proc. 22nd ICCE, ASCE, pp.241-254.
- Visser, P.J. 1991. "Laboratory measurements of uniform longshore currents," Coastal Eng., 15: 563-593.
- Winer, H.S. 1988. "Numerical modeling of wave-induced currents using a parabolic wave equation," Ph.D dissertation, Coastal and Oceanographic Engineering Department, Univ. of Florida, Gainesville.
- Yamashita, T, Tsuchiya, and Suriamihardja, D.A. 1990. "Vertically 2-D nearshore circulation model," Proc. 22nd ICCE, ASCE, pp.150-163.
- Yan, Y. 1987. "Numerical modeling of current and wave interaction on an inlet-beach system," Technical Report No. 73, Coastal and Oceanographic Engineering Department, Univ. of Florida, Gainesville.
- Yoo, D., and O'Connor, B.A. 1986. "Mathematical modeling of wave-induced nearshore circulations," Proc. 20th ICCE, ASCE, pp.1667-1681.

## CHAPTER 165

### QUANTIFICATION OF LONGSHORE TRANSPORT IN THE SURF ZONE ON MACROTIDAL BEACHES

Field experiments along the western coast of Cotentin (Normandy, France)

Franck Levoy<sup>1</sup>, Olivier Monfort<sup>1</sup>, H el ene Rousset<sup>1</sup> and Claude Larssonneur<sup>1</sup>

**ABSTRACT :** Many *in situ* measurements of hydrodynamic parameters and sediment transport in the surf zone have been carried out on the beaches of the western coast of Normandy. The vertical and cross-shore distributions of the sediment transport induced by breaking waves have been identified in a set of various hydrodynamic conditions. Several longshore sediment transport formulas have been devised. The comparison between measured and computed transport rates enables choice of the best formulation according to the hydrodynamic context. This formulation emphasizes the indirect effect of tidal fluctuations on the wave characteristics and the sediment transport processes.

### INTRODUCTION

For engineering purposes, the prediction of long term evolution of a sandy coastline requires insight into sediment circulation on beaches, specially sand movement along coasts where oblique waves induce longshore currents.

Many formulas exist to calculate the longshore sediment transport in the surf zone, but they have been defined for microtidal environments from experimental research. The goal of this paper is to present field results in a very specific tide dominated environment and to evaluate the performance of some empirical formulas in these hydrodynamic conditions.

---

(1) University of CAEN, Centre R egional d'Etudes C ot ieres, Laboratoire de G eologie Marine, 54 Rue Charcot, 14530 LUC-SUR-MER, FRANCE

**PROJECT SITE**

In order to prevent erosion that was affecting the west coast of Cotentin Peninsula, the local government authorities decided to implement in 1989 a research programme aimed at elaborating a global coastal defence policy (Levoy F., Avoine J., 1991).

Field studies, carried out in the framework of this project constitute the R.O.M.I.S. program, a French acronym for Réseau d'Observations et de Mesures In Situ (field observations and measurements system). The main goals of this program were to understand how sediments responds to various hydrodynamic conditions. It was applied from the Cape Carteret to Mont-Saint-Michel Bay, in a macrotidal area, where the tidal range decreases from 15 m in the South to 12 m in the North during high spring tides (Fig. 1).

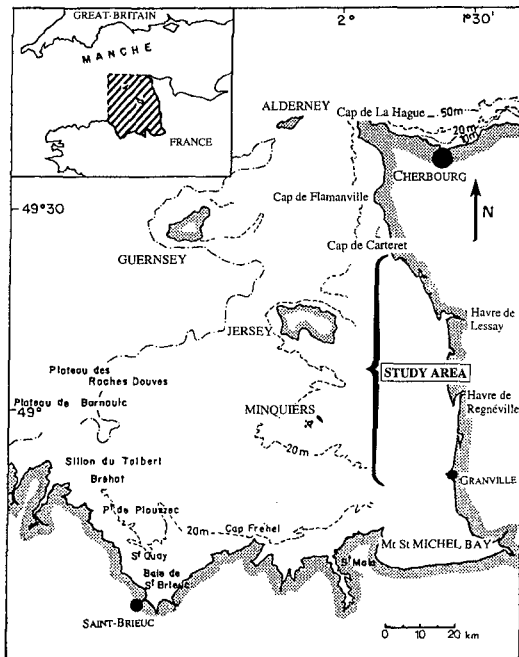


Figure 1. Location map of the study site

Open to the west offshore area, the western coast of Cotentin is exposed to long waves coming from North Atlantic Ocean. The propagation of these waves is affected by a complex bathymetry with numerous shoals and islands. The annual significant wave height in the north of the study area is about 4.2 metres. The attenuation coefficient of waves crossing the Channel island barrier reaches 0.7. The

modal breaker height varies from 0.7 to 0.9 m and Dean's parameter,  $\Omega$  ( $H_b/W_s.T$ ) from 4 to 1.5.

This coast is characterized by a wide tidal flat with a steeper high tidal zone. At high tide, the upper foreshore behaves like a microtidal beach and long waves or, frequently, wind-waves induce opposite residual longshore movements, materialized by opposite spits near small inlets. In the surf zone, plunging breakers are often observed on a steeper beach slope. At mid-tide, spilling breakers take place on a smooth slope.

## MEASUREMENT TECHNIQUES

To quantify the longshore sediment transports, 19 field experiments were carried out under the R.O.M.I.S program. Several parameters were recorded at different locations (table 1):

(1) dynamic parameters:

- tidal variations,
- tidal and wave induced currents with EMC and dye injections,
- on the lower part of the beach, wave characteristics ( $H_s$ ,  $T_p$ ,  $T_s$ , direction of propagation...) with S4DW from Interocean Corporation,
- breaker height with a graduated rod,
- wind conditions.

(2) morphological parameters and sediment characteristics:

- beach slopes with surveys at low tide using an electronic theodolite and infrared-ray distance meter,
- grain-size.

CAMPAIGN	date	time	$H_b$ (m)	$T_p$ (s)	$L_p$ (m)	Gamma parameter	beach slope tan beta	grain size of the beach Md (m)	grain size in the trap Md (m)	Alpha degree	Q measured kg/m/mn
PORSLD10	26.2.91	17:45	1.25	9.9	75.37	0.95	0.04	0.0002555	0.000166	14	3.20
PORSLD1E	27.2.91	17:12	1.35	13.7	95.85	0.99	0.026	0.0002555	0.000175	24	16.00
GOUCOU1B	17.4.91	11:00	0.5	4.6	29.82	0.96	0.0618	0.00051	0.0002	67	0.13
GOUCOU1C	18.4.91	8:40	0.75	3.4	17.93	0.78	0.1016	0.000662	0.00035	22	3.35
COUHAU1	15.5.91	19:40	0.65	3.4	17.77	0.78	0.0636	0.000243	0.000175	22	0.13
GERCRE1A	10.6.91	19:45	1.2	4.5	25.35	0.68	0.0185	0.000243	0.000163	19	0.32
GERCRE1B	11.6.91	17:00	0.6	9.6	42.81	0.55	0.0164	0.000243	0.000175	1	0.05
GERCRE1C	11.6.91	18:25	0.7	10.4	71.68	0.67	0.0195	0.000243	0.000181	3	0.06
GERCRE	13.6.91	20:00	1.1	10.8	76.68	0.78	0.0195	0.000243	0.000187	6	0.14
GERCRE1F	13.6.91	21:00	1.25	13	101.35	0.57	0.0613	0.000243	0.000187	12	1.30
GERCRE2	5.11.91	17:30	0.7	10	63.35	0.5	0.0175	0.000213	0.000181	9	0.40
GOUCOU2A	11.3.92	13:00	1.02	14.5	89.23	0.77	0.055	0.00035	0.000186	6	2.30
BARCAR2A	1.4.92	18:35	0.94	9.6	58.45	0.65	0.021	0.00038	0.000164	27	2.10
COUHAU2	29.4.92	20:30	0.87	4.1	20.9	0.78	0.0737	0.00038	0.000194	21	2.10
PORSLD2	23.5.92	17:15	0.79	3.8	20.38	0.64	0.0373	0.000316	0.000223	12	0.27
SPHJUZ	22.10.92	18:05	0.66	4	22.11	0.62	0.0262	0.000465	0.000268	7	1.70
LINSMB2	18.11.92	17:15	0.91	6	29.08	0.81	0.0524	0.00037	0.000296	42	37.60
SJTDRA2A	12.1.93	11:14	0.79	16.4	118.92	0.99	0.0539	0.00035	0.000355	40	35.80
SJTDRA2B	14.1.93	12:08	1.07	9.6	65.73	1.08	0.0539	0.00035	0.000235	25	10.60

Table 1. Characteristics of the field experimentation conditions

Sediment transport was measured in the breaker zone with streamer traps (Rosati J.D & al., 1990). Cross-shore distribution, with 3 or 4 traps perpendicular to the shoreline, and vertical distribution of sand fluxes, with 4 streamers on a single trap permit to calculate an integrated rate across the breaker zone. The duration of the runs varies from about 5 to 15 minutes on the mid tidal or high tidal zone, with typically one person carrying one trap. The sediment transport rates (Fig. 2) were calculated using the numerical method defined by Kraus and al (1989).

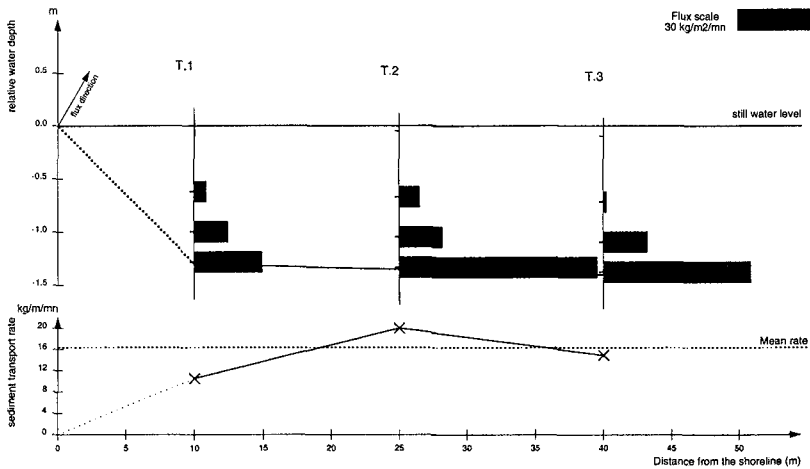


Figure 2. Example of results obtained from runs using sand traps in the surf zone

Various hydrodynamic and morphosedimentary conditions were observed during the experiments. The breaker height varied from 0.5 m to 1.35 m, the peak period, from 3.4 to 16.4 seconds, the  $\gamma$  parameter, from 0.5 to 1.08 and the beach slope from 0.016 to 0.1. The grain size on the beaches increased from the mid-tide beach to the upper foreshore, between 0.210 to 0.510 mm.

**RESULTS**

The first part of the field experiments consisted in measuring the hydrodynamics conditions.

**Breaker and longshore current characteristics:**

The breaker height, measured about 4 metres above the mean sea water level was always greater than the significant wave height on the lower foreshore, about 2 metres under the MSWL. The factor between these parameters varied from 2 to 1.15 when offshore wave conditions increased. During a typical semi-diurnal tidal cycle,

the large variability of wave height induced a large variability of breaker wave characteristics (Fig. 3).

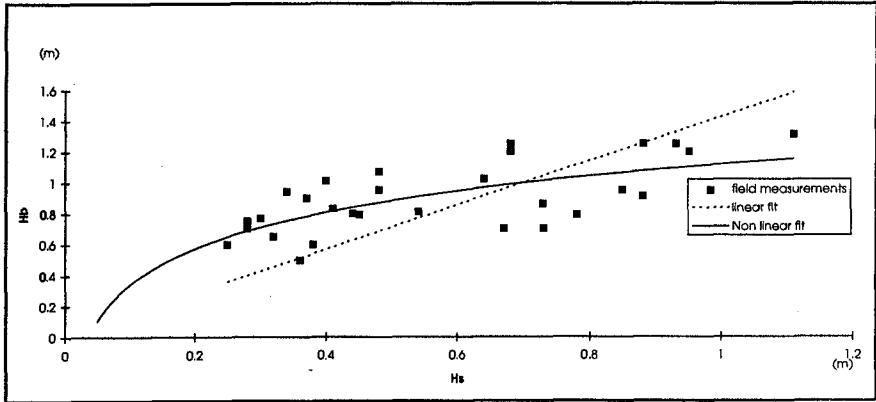


Figure 3. Significant wave height versus breaker height

The measurements confirmed the relationship between the  $\gamma$  parameter (breaker height to water depth ratio) and the beach slope ( $\tan \beta$ ). The modification of the slope along the beach profiles induced a temporal evolution of the  $\gamma$  parameter during a tidal cycle with a constant modification of the breakers characteristics (Fig.4).

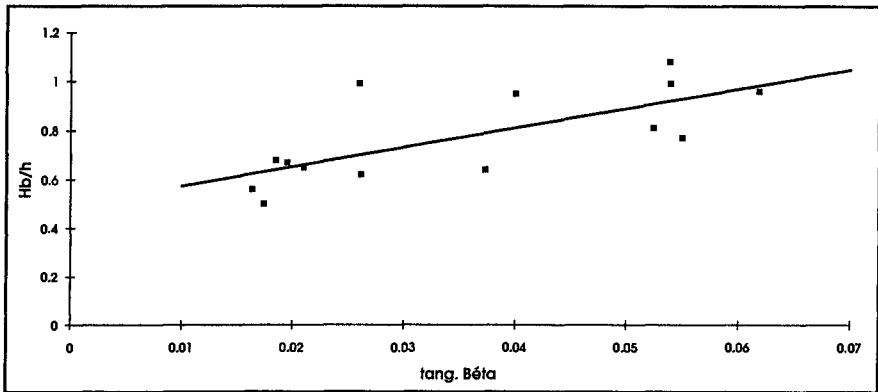


Figure 4.  $\gamma$  parameter versus beach slope

Some LST formulas use the longshore current velocity. The comparison between the calculated and the measured longshore velocities with some classical



formulations did not give satisfactory results (Fig. 5). Most of the results were overpredicted. The best agreement between measured and calculated longshore currents was obtained with the Van Rijn formula (1990), derived from the Longuet-Higgins formula (1970). The empirical coefficient of this formulation was found to be equal to 5 in the field experiments (Fig. 6).

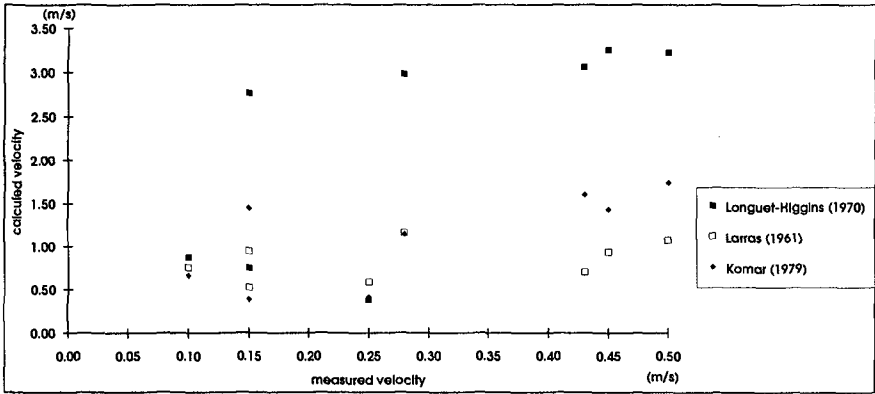


Figure 5. Comparison between measured and calculated longshore velocities with various formulations

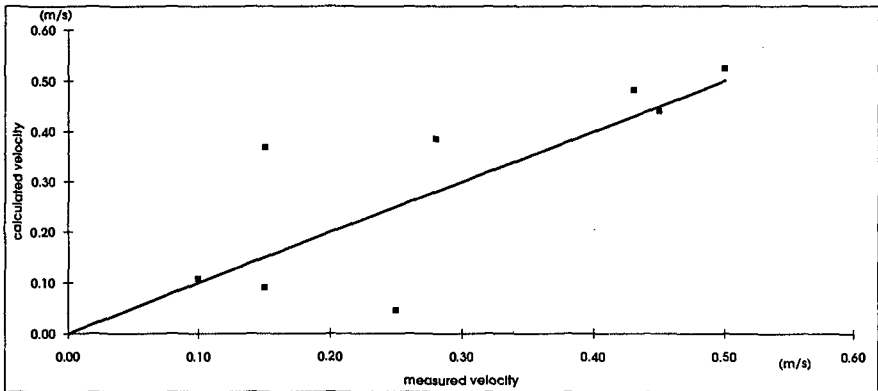


Figure 6. Measured and calculated velocities of longshore currents with modified Van Rijn formula (empirical coefficient=5)

**Vertical and cross-shore distributions:**

The vertical distributions of sand fluxes were best fitted with an exponential relationship, like the one described by Rosati and al (1991). The correlation coefficient, 0.67, was smaller than those obtained in American programs (0.9 during SUPERDUCK, 0.79 at Ludington), but the hydrodynamics and beach conditions observed along the western coast of the Normandy vary a lot, with specially long and wind-wave conditions (Fig. 7).

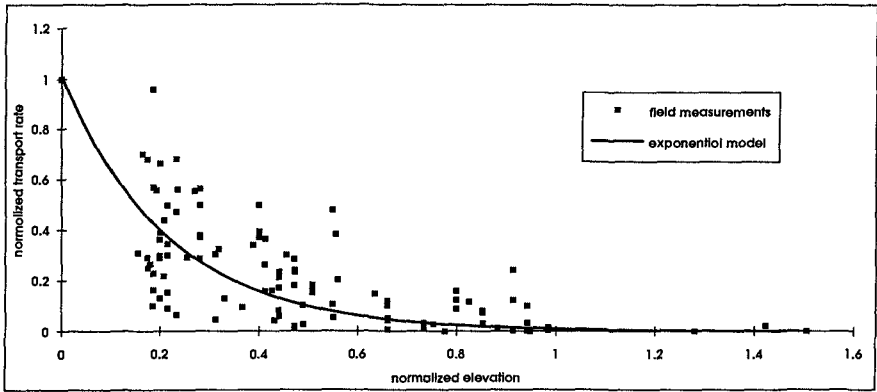


Figure 7. Vertical distribution of longshore sediment transport in the surf zone

In fact, there were two types of vertical sediment distributions in the surf zone:

- with long wave periods, suspended sediment transport dominated (Fig.8a),

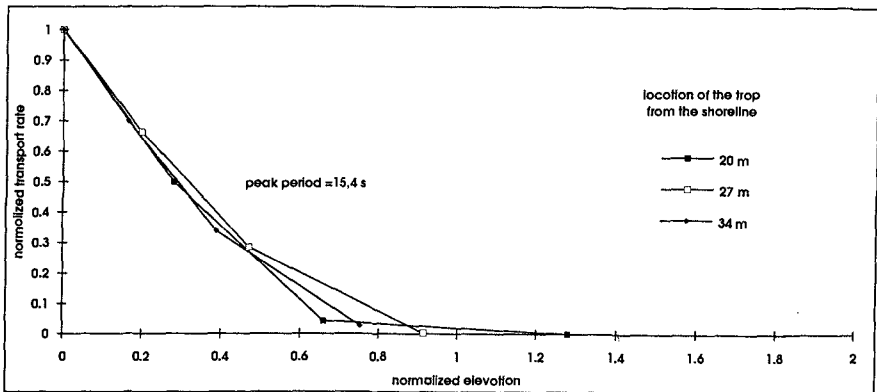


Figure 8a. Vertical distribution of longshore sediment transport during long wave conditions

- with short wave conditions, the bed-load transport became higher (Fig. 8b).

The bi-modal wave climate in the English Channel explains the dispersion of vertical distribution of sediment transport rates in the surf zone.

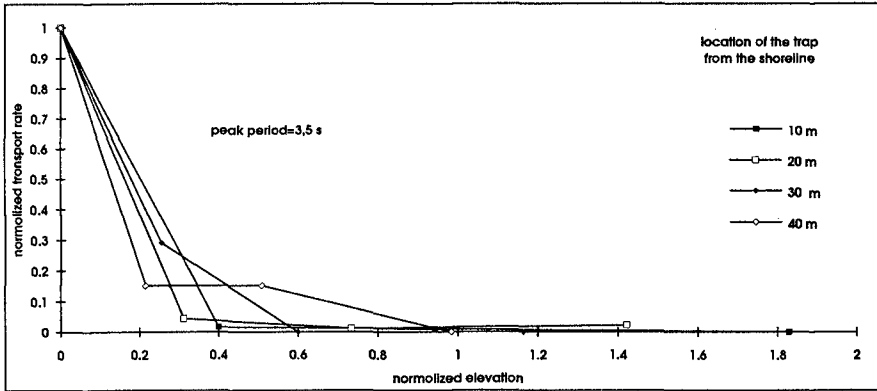


Figure 8b. Vertical distribution of longshore sediment transport during wind-wave conditions

For the cross-shore sediment transport distribution in the surf zone, two kinds of peak locations were observed (Fig. 9):

- first, in the swash zone ( $0.15 < X/X_b < 0.35$ ), the normalized sediment transport rate sometimes attained 3 or 4 times the mean longshore sediment transport rate integrated over the width of the breaker zone. These movements were measured during wind-wave conditions, acting on steep beaches with small or medium breaker height.

-the second peak, more classical, was observed near the breakerline ( $0.6 < X/X_b < 0.7$ ). The sediment transport rate was lower than in the swash zone and more homogeneous over the entire surf zone. These circulations were observed during long wave conditions at mid-beach level.

However, as opposed to Kamphuis' experimental investigations (1991), these two kinds of distributions were recorded independently, showing the narrow relationship between the hydrodynamic conditions and the transport processes.

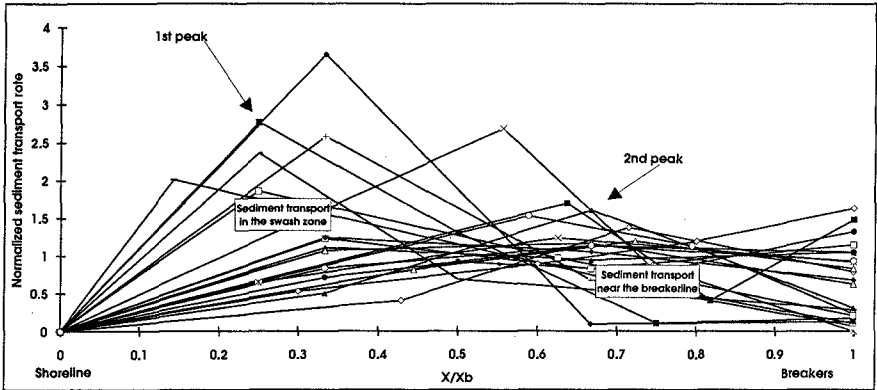


Figure 9. Cross-shore distribution of the longshore sediment transport in the surf zone

### Grain size gradients in the surf zone

The traps used to calculate the sediment transport rate allowed collection of sand grains at several locations in the surf zone. Grain sizes of the bed were used to compare the ground sedimentary stock and the moving materials (Fig. 10).

During long wave conditions and large breaker height, with a well-sorted sediment on the beach, the moving sand grain size was lower than the beach grain size. The vertical and transversal distributions of the grain size were very close. Good mixing of the sediment was observed.

With wind-wave conditions, vertical and transversal grain size gradients appeared. The gradients were more important with a badly sorted sediment on the beach than with a well-sorted material. With bed-load processes prevailing during short wave conditions, only fine sediments were trapped in the upper layer of water. Between the bed and the water surface, the grain size was noted to vary from 1 to 2.

Even with a well-sorted sediment on the beach floor, a transversal gradient was identified. The coarser sediments were located in the swash zone, according to the cross-shore distribution of the sediment transport rate. The finer grain sizes, with a median diameter lower than that of the beach sand, were observed in suspension near the breakerline.

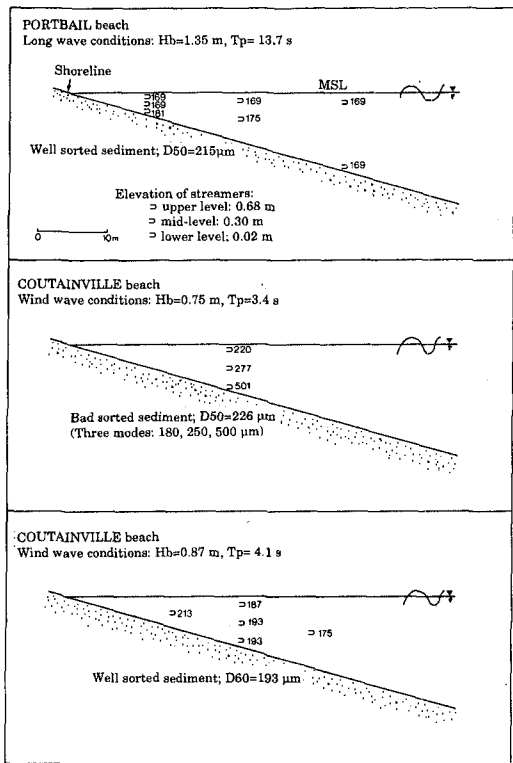


Figure 10. Grain sizes in the surf zone in various hydrosedimentary conditions

**Comparison between measured and calculated rates**

Several L.S.T. formulas were compared with results coming from in situ measurements. Two methods of calculation were used:

- Integral method:

(1) 1986' Kamphuis formula:

$$Q = 1,28 \cdot \frac{H_b^{3,5}}{D_{50}} \cdot \tan\beta \cdot \sin 2\alpha_b$$

with: Q= sediment transport rate (kg/s),

Hb= breaker height (m)

D50= median grain size (m),

tanβ= beach slope

αb = incident wave angle.

(2) 1990' Kamphuis formula:

$$Q = 0,0013 \cdot \left(\frac{H_b}{L_p}\right)^{-1,25} \cdot \tan\beta^{0,75} \cdot \left(\frac{H_b}{D_{50}}\right)^{0,25} \cdot \sin^{0,6} 2\alpha_b \cdot \frac{\rho \cdot H_b^3}{T_p}$$

with:

Q= sediment transport rate (kg/s),

L<sub>p</sub>= peak wave length according to the peak period T<sub>p</sub> (m),

(3) 1982' Kraus formula

$$Q = \frac{A}{\gamma_b \cdot \tan\beta} \cdot H_b^2 \cdot V_l$$

with:

Q= sediment transport rate (m<sup>3</sup>/s),

γ<sub>b</sub>= H<sub>b</sub>/H<sub>t</sub>, H<sub>t</sub> is the mean water depth,

V<sub>l</sub>= longshore current velocity (m/s),

A= empirical coefficient equal to 0.00038

- Local method:

(4) 1989' Van Rijn Formula

In most cases, all these formulas overpredicted the sediment transport rates, especially when the transport was weak. The ratios between computed and measured rates were very high with the Kamphuis formulas, even though the second formulation improved the result (Fig. 11).

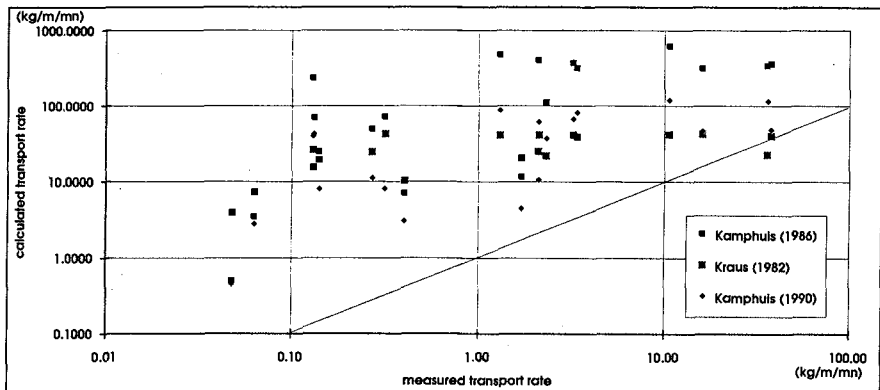


Figure 11: Comparison between measured longshore sediment transport rate and calculated rate with the Kamphuis and Kraus formulas.

Best agreement (factor of 1 to 3) was obtained in high energy condition, when the measured rate was greater than about 35 kg/m/mn. But under 5 kg/m/mn, the 1990' Kamphuis formula overpredicted with a factor of 10 and sometimes more for small sediment movements.

Kraus and Van Rijn formulas gave the best prediction of L.S.T. (Fig.12). But it was necessary to adapt the formulation to the hydrodynamical context (Fig. 13):

- on the upper part of beaches, when  $\gamma$  parameter was higher than 0.78 and incidence angle between the wave crests and the shoreline direction was greater than 25 degrees, a factor of about 2 was found between calculated and measured rates. In these cases, LST rates were greater than 10 kg/m/mn.

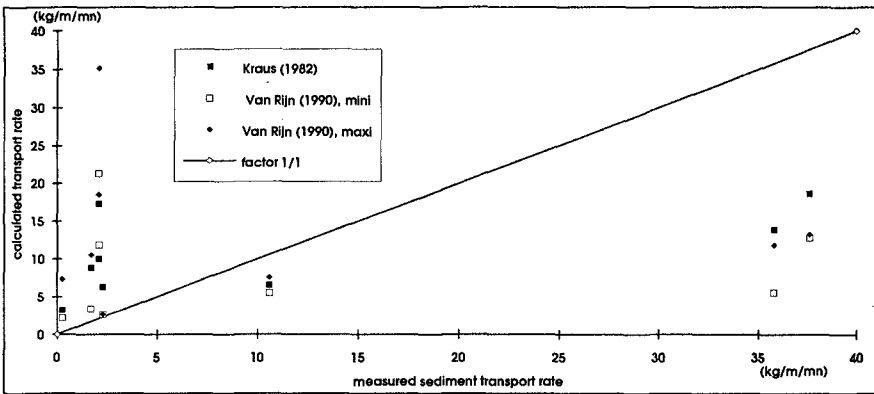


Figure 12. Comparison between longshore sediment transport rate and calculated rate with Van Rijn and Kraus formulas.

- when wave crest incidence angle was lower than 25 degrees and  $\gamma$  parameter lower than 0.78, the LST rate, in our experiments, was smaller than 5 kg/m/mn. In these cases, formulas overpredicted sediment movements (factor of 5).

A new formulation is proposed to calculate LST rates, taking into account the important variability of the wave approach incidence to the coast and the modification of  $\gamma$  parameter during the tidal cycle.

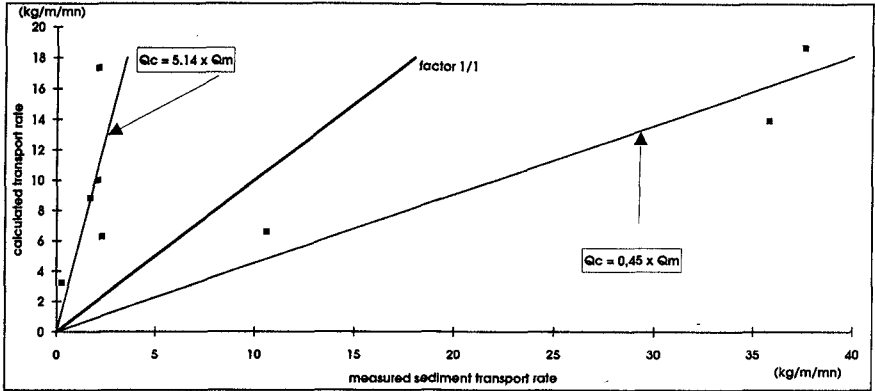


Figure 13. Comparison between measured longshore sediment transport rate and calculated rate with Kraus formula (the longshore velocities were deduced from field measurements)

Table 2 summarizes the results obtained along the western coast of Normandy. It is necessary to underline the relationship between the tidal level, the beach slope and the breaker type. For each beach state, a new empirical coefficient derived from the Kraus formula can be calculated. But the factor between these two coefficients is about 10. As a result of this, in calculating a global longshore sediment transport, there is an important discrepancy between the upper and the midforeshore rate. This discrepancy is not realistic.

Tidal level	Beach state	Breaker type	Empirical coefficient
high tide	reflective	plunging	$8.36 \cdot 10^{-4}$
mid-tide	dissipative	spilling	$0.73 \cdot 10^{-4}$

Table 2

**CONCLUSIONS**

(1) Several longshore sediment transport formulas have been tested and compared to our field experiment results. The Kraus formula gives the best agreement between the rates computed and the calculated values, during a large set of hydrodynamic conditions. But, it will be necessary to test other formulations in this kind of environment (S.P.M...).

(2) A local adaptation of the empirical coefficient is necessary to adapt the Kraus formulation to the regional hydrodynamic conditions. On macrotidal beaches, the tidal fluctuations, firstly, and the wave climate, secondly, induce a great temporal variability of several parameters in the surf zone. The breaker type, at different levels of the tidal cycle, connected to the beach slope and the water depth, is a parameter



which controls the sediment transport rate. The bi-modality of the wave frequency also induces two kinds of vertical and cross-shore sediment transport distributions, modifying the global sediment movement.

(3) Lots of field data will be necessary to reduce the factor between the new empirical coefficients. Their values should be defined taking into account, quantitatively, parameters that include the breaker type and the tidal fluctuation. The use of a combination between the RTR parameter defined by Masselink and Short (1994) and the  $\Omega$  parameter should be a new way improving modelling of LST on a concave and wide beach profile such as that of macrotidal beaches.

## ACKNOWLEDGEMENTS

This work aimed at defining a global policy of protection of the coastline of Normandy against storm effects was undertaken as a part of the ROMIS program. It was funded by the Conseil Général de la Manche, the Conseil Régional de Basse-Normandie and the Secrétariat d'Etat à la Mer. Our thanks to Edward Anthony for improving the English of the paper.

## REFERENCES:

- Kamphuis J.W., Davies M.H., Nairn R.B. & Sayoa O.J., 1986. « Calculation of littoral sand transport rate », *Coastal Engineering*, 10, 1-21.
- Kamphuis J.W., 1990. « Alongshore Sediment Transport Rate », *Proc. 22nd Coastal Eng. Conf. ASCE*, 2402-2415.
- Kraus N.C., Isobe M., Igarashi H., Sasaki T.O. and Horikawa K., 1982. « Field experiments on longshore sand transport in the surf zone », *Proc. 18th Coastal Eng. Conf.*, ASCE, 969-988.
- Kraus N.C., Gingerich K.J. & Rosati J.D., 1989. « DUCK85 surf zone sand transport experiment », *U.S. Army Corps of Engineers, technical report 89-5*, 48 p.
- Levoy F., Avoine J., 1991. « Quantitative approaches to coastal sediment processes, Field measurements to estimate sediment transport in a high-energy coastal area », *Proc. Coastal Sediments '91*, Seattle, June 1991, (published separate from proceedings), ASCE.
- Longuet-Higgins M.S., 1970. « On the longshore currents generated by obliquely incident sea waves », *Jour. Geophys. Review*, 75, 6778-6801.

Masselink G., & Short A.D., 1993. «The effect of tide range on beach morphodynamics and morphology: a conceptual beach model », *Journal of coastal research*, 9, n°3, pp 785-800.

Rosati J.D., Gingerich K.J., and Kraus, N.C., 1990. « SUPERDUCK Surf zone sand transport experiment », *Technical Report CERC-90-10, Coastal Engineering Research Center*, U.S. Army Engineer Waterways Experiment Station, Vicksburg, MS.

Rosati J.D., Gingerich K.J., Kraus N.C., Smith J.McK. & Beach R.A., 1991. « Longshore sand transport rate distribution measured in Lake Michigan », *Coastal Sediment '91*. vol.I. 156-169.

Van Rijn L.C., 1989. « Handbook Sediment Transport by Currents and Waves », Delft Hydraulics. 307 p.

Van Rijn L.C., 1990. « Principles of fluid flow and surface waves in rivers, estuaries, seas and oceans », Delft Hydraulics. *Aqua Publications*, Amsterdam. 335 p.

# CHAPTER 166

## A THREE DIMENSIONAL MODEL FOR WAVE INDUCED CURRENTS

BIN LI and ROGER J MADDRELL

SIR WILLIAM HALCROW & PARTNERS LTD, BURDEROP PARK,  
SWINDON, WILTSHIRE, SN4 0QD, UK

### 1 Introduction

In this paper, a three-dimensional model which is based on the Navier-Stokes equations is developed. The finite volume method and a time-splitting technique are used to solve the equations. Longshore and crossshore currents induced by waves are reproduced by the model and the results are compared with existing experimental data.

### 2 Governing Equations

If, apart from the wave-induced orbital motion, the current involves no strong vertical accelerations, the time-mean pressure can be approximated by:

$$p = p_h - \rho \langle w_w^2 \rangle \quad (1)$$

in which  $p$  is pressure;  $p_h$  is hydrostatic pressure

$$p_h = \rho g(\eta - z) \quad (2)$$

$\rho$  is mass density of the fluid;  $w_w$  vertical component of the wave orbital velocity;  $\langle \dots \rangle$  averaged over one wave cycle.

If, in addition, the Boussinesq-hypothesis is adopted to model the Reynolds stress terms, the wave-and turbulence-averaged horizontal momentum equations can be written as:

Momentum equations:

$$\frac{\partial u}{\partial t} + u \frac{\partial u}{\partial x} + v \frac{\partial u}{\partial y} + w \frac{\partial u}{\partial z} = -\frac{1}{\rho} \frac{\partial p}{\partial x} + \frac{\partial}{\partial x} (v_h \frac{\partial u}{\partial x}) + \frac{\partial}{\partial y} (v_h \frac{\partial u}{\partial y}) + \frac{\partial}{\partial z} (v \frac{\partial u}{\partial z}) + W_x \quad (3)$$

$$\frac{\partial v}{\partial t} + u \frac{\partial v}{\partial x} + v \frac{\partial v}{\partial y} + w \frac{\partial v}{\partial z} = -\frac{1}{\rho} \frac{\partial p}{\partial y} + \frac{\partial}{\partial x} (v_h \frac{\partial v}{\partial x}) + \frac{\partial}{\partial y} (v_h \frac{\partial v}{\partial y}) + \frac{\partial}{\partial z} (v \frac{\partial v}{\partial z}) + W_y \quad (4)$$

Continuity equation:

$$\frac{\partial u}{\partial x} + \frac{\partial v}{\partial y} + \frac{\partial w}{\partial z} = 0 \quad (5)$$

where  $u$ ,  $v$  and  $w$  are the velocities in the  $x$ ,  $y$  and  $z$  directions, respectively;  $P$  is pressure;  $W_x$  and  $W_y$  are the radiation stress terms in the  $x$  and  $y$  directions, respectively. These radiation stress components will be discussed in the next section.

### 3 Radiation Stresses

The radiation stress formulae are:

$$W_x = -\frac{\partial}{\partial x} (\langle u_w^2 \rangle - \langle w_w^2 \rangle) - \frac{\partial}{\partial y} (\langle u_w v_w \rangle) \quad (6)$$

$$W_y = -\frac{\partial}{\partial x} (\langle u_w v_w \rangle) - \frac{\partial}{\partial y} (\langle v_w^2 \rangle - \langle w_w^2 \rangle) \quad (7)$$

and it should be noted that

$$\frac{\partial}{\partial z} (\langle u_w w_w \rangle) = 0 \quad \text{and} \quad \frac{\partial}{\partial z} (\langle v_w w_w \rangle) = 0 \quad (8)$$

due to the phase shift between  $(u_w, w_w)$  and  $(v_w, w_w)$ , where  $\langle \dots \rangle$  means time average.

Formulae for the depth averaged radiation stresses are also given here because they will be used later on when the time splitting technique is applied.

$$S_{xx} = \int_{z_b}^{\langle z_s \rangle} \rho (\langle u_w^2 \rangle - \langle w_w^2 \rangle) dz + \frac{1}{2} \rho g \langle (z_s - \langle z_s \rangle)^2 \rangle = [N(\cos^2 \theta + 1) - 1] E \quad (9)$$

$$S_{yy} = \int_{z_b}^{\langle z_s \rangle} \rho (\langle v_w^2 \rangle - \langle w_w^2 \rangle) dz + \frac{1}{2} \rho g \langle (z_s - \langle z_s \rangle)^2 \rangle = [N(\sin^2 \theta + 1) - 1] E \quad (10)$$

$$S_{xy} = S_{yx} = \int_{z_b}^{\langle z_s \rangle} \langle \rho u_w v_w \rangle dz = [N \sin \theta \cos \theta] E \quad (11)$$

where  $N$  is the ratio of the wave group velocity to the wave phase speed.

The water surface roller induced by wave breaking has not been taken into account in the above expressions. If the surface roller due to wave breaking is taken into account, the corresponding stresses can be explicitly expressed as (Svendsen, 1984):

$$\tau = -\frac{1}{h} \frac{\partial}{\partial x} (7 \frac{h}{L} E) \quad (12)$$

where  $L$  is the wave length at wave breaking and it is assumed that the roller induced stress is in the cross-shore direction.

#### 4 Numerical Modelling

The three dimensional model for wave induced currents is governed by the equations given in section 2. Due to the complicated nature of the model, efficient numerical schemes are definitely required to reduce run times as much as possible. In this section, we will use the time splitting technique and the finite volume method to solve the equations.

##### 4.1 Application Of The Time Splitting Method

From the governing equation for wave induced currents it is understood that the surface variation is a function of  $x$  and  $y$ , but not  $z$ . The radiation stresses below wave trough level are hardly varying with  $z$ . First, we introduce depth averaged velocities,

$$\bar{u} = \frac{1}{h} \int_{z_b}^{z_s} u dz \quad \text{and} \quad \bar{v} = \frac{1}{h} \int_{z_b}^{z_s} v dz \tag{13}$$

Then the original governing equations can be split into two main parts. The first part corresponds to water surface set-up and set-down and the mean movement of the wave-induced current:

$$\frac{\partial \eta}{\partial t} = - \int \left( \frac{\partial u}{\partial x} + \frac{\partial v}{\partial y} \right) dz \tag{14}$$

$$\frac{\partial u}{\partial t} = -g \frac{\partial \eta}{\partial x} - \frac{1}{\rho h} \frac{\partial S_{xx}}{\partial x} - \frac{1}{\rho h} \frac{\partial S_{xy}}{\partial y} - \tau \tag{15}$$

$$\frac{\partial v}{\partial t} = -g \frac{\partial \eta}{\partial y} - \frac{1}{\rho h} \frac{\partial S_{xy}}{\partial x} - \frac{1}{\rho h} \frac{\partial S_{yy}}{\partial y} \tag{16}$$

Defining

$$(u', v') = (u, v) - (\bar{u}, \bar{v}) \tag{17}$$

yields

$$\frac{\partial \eta}{\partial t} + \frac{\partial \bar{u} h}{\partial x} + \frac{\partial \bar{v} h}{\partial y} = 0 \tag{18}$$

$$\frac{\partial \bar{u}}{\partial t} = -g \frac{\partial \eta}{\partial x} - \frac{1}{\rho h} \frac{\partial S_{xx}}{\partial x} - \frac{1}{\rho h} \frac{\partial S_{xy}}{\partial y} - \tau \tag{19}$$

$$\frac{\partial \bar{v}}{\partial t} = -g \frac{\partial \eta}{\partial y} - \frac{1}{\rho h} \frac{\partial S_{xy}}{\partial x} - \frac{1}{\rho h} \frac{\partial S_{yy}}{\partial y} \tag{20}$$

The second part involves solving for the velocity field

$$\frac{\partial u}{\partial t} + u \frac{\partial u}{\partial x} + v \frac{\partial u}{\partial y} + w \frac{\partial u}{\partial z} = \frac{\partial}{\partial x} (v_h \frac{\partial u}{\partial x}) + \frac{\partial}{\partial y} (v_h \frac{\partial u}{\partial y}) + \frac{\partial}{\partial z} (v \frac{\partial u}{\partial z}) + W_x + RS_x \tag{21}$$

$$\frac{\partial v}{\partial t} + u \frac{\partial v}{\partial x} + v \frac{\partial v}{\partial y} + w \frac{\partial v}{\partial z} = \frac{\partial}{\partial x} (v_h \frac{\partial v}{\partial x}) + \frac{\partial}{\partial y} (v_h \frac{\partial v}{\partial y}) + \frac{\partial}{\partial z} (v \frac{\partial v}{\partial z}) + W_y + RS_y \tag{22}$$

$$w = - \int_{-h}^z \left( \frac{\partial u}{\partial x} + \frac{\partial v}{\partial y} \right) dz \tag{23}$$

where  $RS_x$  and  $RS_y$  are depth averaged radiation stresses

$$RS_x = -\frac{1}{\rho h} \frac{\partial S_{xx}}{\partial x} - \frac{1}{\rho h} \frac{\partial S_{xy}}{\partial y} \quad (24)$$

$$RS_y = -\frac{1}{\rho h} \frac{\partial S_{xy}}{\partial x} - \frac{1}{\rho h} \frac{\partial S_{yy}}{\partial y} \quad (25)$$

The first set of the equations is used to obtain the mean velocity field and the water surface elevation, while the second one to obtain the depth-varying velocities  $u$ ,  $v$  and  $w$ . Both sets of equations can be expressed based on time splitting as follows (from  $ndt$  to  $(n+1)dt$ ):

At the first step

$$\bar{u}^n = \frac{1}{h} \int_{-h}^{\eta^n} u^n dz \quad (26)$$

$$\bar{v}^n = \frac{1}{h} \int_{-h}^{\eta^n} v^n dz \quad (27)$$

and

$$u' = u^n - \bar{u}^n \quad (28)$$

$$v' = v^n - \bar{v}^n \quad (29)$$

then

$$\frac{\eta^{n+1} - \eta^n}{\Delta t} + \frac{\partial \bar{u}^{n+\frac{1}{2}}}{\partial x} + \frac{\partial \bar{v}^{n+\frac{1}{2}}}{\partial y} = 0 \quad (30)$$

$$\frac{\bar{u}^{n+\frac{1}{2}} - \bar{u}^n}{\Delta t} = -g \frac{\partial \eta^{n+1}}{\partial x} - \frac{1}{\rho h} \frac{\partial S_{xx}}{\partial x} - \frac{1}{\rho h} \frac{\partial S_{xy}}{\partial y} - \tau \quad (31)$$

$$\frac{\bar{v}^{n+\frac{1}{2}} - \bar{v}^n}{\Delta t} = -g \frac{\partial \eta^{n+1}}{\partial y} - \frac{1}{\rho h} \frac{\partial S_{yx}}{\partial x} - \frac{1}{\rho h} \frac{\partial S_{yy}}{\partial y} \quad (32)$$

$$u^{n+\frac{1}{2}} = \bar{u}^{n+\frac{1}{2}} + u' \quad (33)$$

$$v^{n+\frac{1}{2}} = \bar{v}^{n+\frac{1}{2}} + v' \tag{34}$$

At the second step, we have

$$\frac{u^{n+1} - u^{n+\frac{1}{2}}}{\Delta t} + U_i^{n+\frac{1}{2}} \frac{\partial u^{n+1}}{\partial X_i} = \frac{\partial}{\partial x} (v_h \frac{\partial u^{n+1}}{\partial x}) + \frac{\partial}{\partial y} (v_h \frac{\partial u^{n+1}}{\partial y}) + \frac{\partial}{\partial z} (v \frac{\partial u^{n+1}}{\partial z}) + W_x + RS_x \tag{35}$$

$$\frac{v^{n+1} - v^{n+\frac{1}{2}}}{\Delta t} + U_i^{n+\frac{1}{2}} \frac{\partial v^{n+1}}{\partial X_i} = \frac{\partial}{\partial x} (v_h \frac{\partial v^{n+1}}{\partial x}) + \frac{\partial}{\partial y} (v_h \frac{\partial v^{n+1}}{\partial y}) + \frac{\partial}{\partial z} (v \frac{\partial v^{n+1}}{\partial z}) + W_y + RS_y \tag{36}$$

$$w^{n+1} = - \int_{-h}^z (\frac{\partial u^{n+1}}{\partial x} + \frac{\partial v^{n+1}}{\partial y}) dz \tag{37}$$

The two sets of equations given above will be solved by different methods. The depth averaged equations will be treated by the alternating direction implicit method (ADI) and governing equations for the depth-varying velocities will be solved by the finite volume technique.

#### 4.2 ADI Solver

It is well known that the Alternative Direction Implicit method, or ADI, has been widely used in two dimensional flow problems. It is used here to solve the depth averaged equation set. Hence, we have:

First step:

$$\frac{\eta^{n+\frac{1}{2}} - \eta^n + \frac{\partial \bar{u}^{n+\frac{1}{2}}}{\partial x} h}{\Delta t} = - \frac{\partial \bar{v}^n}{\partial y} h \tag{38}$$

$$\frac{\bar{u}^{n+\frac{1}{2}} - \bar{u}^n + g \frac{\partial \eta^{n+\frac{1}{2}}}{\partial x}}{\Delta t} = - \frac{1}{\rho h} \frac{\partial S_{xx}}{\partial x} - \frac{1}{\rho h} \frac{\partial S_{xy}}{\partial y} - \tau \tag{39}$$

Second step:

$$\frac{\eta^{n+1} - \eta^{n+\frac{1}{2}} + \frac{\partial \bar{v}^{n+\frac{1}{2}}}{\partial y} h}{\Delta t} = - \frac{\partial \bar{u}^{n+\frac{1}{2}}}{\partial x} h \tag{40}$$

$$\frac{\bar{v}^{n+\frac{1}{2}} - \bar{v}^n + g \frac{\partial \eta^{n+1}}{\partial y}}{\Delta t} = - \frac{1}{\rho h} \frac{\partial S_{yx}}{\partial x} - \frac{1}{\rho h} \frac{\partial S_{yy}}{\partial y} \tag{41}$$

It is clear that the solution process presented here is exactly the same as that for a two dimensional flow model like, for example, tidal model. The equations above satisfy the continuity equation from which the water surface variable is obtained.

#### 4.3 Coordinate Transformation

The purpose of the transformation is to restructure the vertical coordinate viz:

$$\sigma = \frac{z - z_b}{\eta - z_b} \quad (42)$$

Using this relationship, the water column at any location between water surface and the sea bottom is transformed into a layer of thickness 1. This transformation introduces additional terms into the equations of motion. However, most of the additional terms introduced by the stretching are contained in the horizontal diffusion terms. Since horizontal diffusion is generally small compared to the vertical diffusion and horizontal advection, only the leading terms need to be retained in general. The derivatives can be obtained as follows:

$$\frac{\partial \sigma}{\partial z} = \frac{1}{h} \quad (43)$$

$$\frac{\partial}{\partial z} = \frac{1}{h} \frac{\partial}{\partial \sigma} \quad (44)$$

$$\frac{\partial^2}{\partial z^2} = \frac{1}{h^2} \frac{\partial^2}{\partial \sigma^2} \quad (45)$$

$$\frac{\partial}{\partial t} = \frac{\partial}{\partial t} + \frac{\partial \sigma}{\partial t} \frac{\partial}{\partial \sigma} \quad (46)$$

$$\frac{\partial}{\partial x} = \frac{\partial}{\partial x} + \frac{\partial \sigma}{\partial x} \frac{\partial}{\partial \sigma} \quad (47)$$

$$\frac{\partial}{\partial y} = \frac{\partial}{\partial y} + \frac{\partial \sigma}{\partial y} \frac{\partial}{\partial \sigma} \quad (48)$$

$$\frac{\partial^2}{\partial x^2} = \frac{\partial^2}{\partial x^2} + \text{higher order terms} = \frac{\partial^2}{\partial x^2} \quad (49)$$

$$(50)$$



$$\frac{\partial^2}{\partial y^2} = \frac{\partial^2}{\partial y^2} + \text{higher order terms} \sim \frac{\partial^2}{\partial y^2}$$

$$\frac{\partial \sigma}{\partial x} = -\frac{1}{h} (\sigma \frac{\partial \eta}{\partial x} + (1-\sigma) \frac{\partial z_b}{\partial x}) \tag{51}$$

$$\frac{\partial \sigma}{\partial y} = -\frac{1}{h} (\sigma \frac{\partial \eta}{\partial y} + (1-\sigma) \frac{\partial z_b}{\partial y}) \tag{52}$$

In general from the transformation formulae given above one can derive the governing equations in the new coordinate system. However, it is convenient to define a vertical velocity as

$$w^* = \frac{\partial \sigma}{\partial t} + u \frac{\partial \sigma}{\partial x} + v \frac{\partial \sigma}{\partial y} + w \frac{\partial \sigma}{\partial z} \tag{53}$$

We can finally obtain the momentum equations in x and y directions:

$$\frac{\partial u}{\partial t} + u \frac{\partial u}{\partial x} + v \frac{\partial u}{\partial y} + w^* \frac{\partial u}{\partial \sigma} = \frac{\partial}{\partial x} (v_h \frac{\partial u}{\partial x}) + \frac{\partial}{\partial y} (v_h \frac{\partial u}{\partial y}) + \frac{1}{h^2} \frac{\partial}{\partial \sigma} (v \frac{\partial u}{\partial \sigma}) + W_x^* + RS_x^* \tag{54}$$

$$\frac{\partial v}{\partial t} + u \frac{\partial v}{\partial x} + v \frac{\partial v}{\partial y} + w^* \frac{\partial v}{\partial \sigma} = \frac{\partial}{\partial x} (v_h \frac{\partial v}{\partial x}) + \frac{\partial}{\partial y} (v_h \frac{\partial v}{\partial y}) + \frac{1}{h^2} \frac{\partial}{\partial \sigma} (v \frac{\partial v}{\partial \sigma}) + W_y^* + RS_y^* \tag{55}$$

where the radiation stress terms with a star mark use values of the new coordinate. In the time-splitting scheme, the equations are

$$\frac{u^{n+1} - u^{n+\frac{1}{2}}}{\Delta t} + U_i^* \frac{\partial u^{n+1}}{\partial X_i} = \frac{\partial}{\partial x} (v_h \frac{\partial u^{n+1}}{\partial x}) + \frac{\partial}{\partial y} (v_h \frac{\partial u^{n+1}}{\partial y}) + \frac{1}{h^2} \frac{\partial}{\partial \sigma} (v \frac{\partial u^{n+1}}{\partial \sigma}) + W_x^* + RS_x^* \tag{56}$$

$$\frac{v^{n+1} - v^{n+\frac{1}{2}}}{\Delta t} + U_i^* \frac{\partial v^{n+1}}{\partial X_i} = \frac{\partial}{\partial x} (v_h \frac{\partial v^{n+1}}{\partial x}) + \frac{\partial}{\partial y} (v_h \frac{\partial v^{n+1}}{\partial y}) + \frac{1}{h^2} \frac{\partial}{\partial \sigma} (v \frac{\partial v^{n+1}}{\partial \sigma}) + W_y^* + RS_y^* \tag{57}$$

where  $U^*$  is the vector velocity in the new coordinate system and

$$U_i^* \frac{\partial}{\partial X_i} = u \frac{\partial}{\partial x} + v \frac{\partial}{\partial y} + w^* \frac{\partial}{\partial \sigma}$$

It should be noted that the vertical velocity in the old coordinate system is calculated by

$$w^{n+1} = - \int_{-h}^* (\frac{\partial u^{n+1}}{\partial x} + \frac{\partial v^{n+1}}{\partial y}) dz \tag{58}$$

where no transformation is required.

#### 4.4 Application Of The Finite Volume Method

After transforming the momentum equations into a new coordinate system where the calculation domain is in regular form, the finite volume method is a suitable numerical solver due to its excellent conservation characteristics. The details of this method have been very well described by Patankar in his book (Patankar 1977). The discretization equation for velocity  $u$  is:

$$a_p u_p = a_E u_E + a_W u_W + a_N u_N + a_S u_S + a_T u_T + a_B u_B + b \quad (59)$$

where indexes E,W,N,S,T and B mean the east,west,north,south,top and bottom neighbours respectively, P means central point, and

$$a_E = D_e A (|P_e|) + [F_e, 0] \quad (60)$$

$$a_W = D_w A (|P_w|) + [F_w, 0] \quad (61)$$

$$a_N = D_n A (|P_n|) + [F_n, 0] \quad (62)$$

$$a_S = D_s A (|P_s|) + [F_s, 0] \quad (63)$$

$$a_T = D_t A (|P_t|) + [F_t, 0] \quad (64)$$

$$a_B = D_b A (|P_b|) + [F_b, 0] \quad (65)$$

$$a_p^o = \frac{\Delta x \Delta y \Delta \sigma}{\Delta t} \quad (66)$$

$$b = S_c \Delta x \Delta y \Delta \sigma + a_p^o u_p^o \quad (67)$$

$$a_p = a_E + a_W + a_N + a_S + a_T + a_B + a_p^o \quad (68)$$

where  $S_c$  is the source term including contributions from radiation stresses. The flow rates and conductances are defined as

$$F_e = u_e \Delta y \Delta \sigma \quad D_e = \frac{v_{he} \Delta y \Delta \sigma}{\Delta x} \quad (69)$$

$$F_w = u_w \Delta y \Delta \sigma \quad D_w = \frac{v_{hw} \Delta y \Delta \sigma}{\Delta x} \quad (70)$$

$$(71)$$

$$(72)$$

$$F_n = v_n \Delta \sigma \Delta x \quad D_n = \frac{v_{hn} \Delta \sigma \Delta x}{\Delta y}$$

$$F_s = v_s \Delta \sigma \Delta x \quad D_s = \frac{v_{hs} \Delta \sigma \Delta x}{\Delta y}$$

$$F_t = w_t^* \Delta x \Delta y \quad D_t = \frac{v_t \Delta x \Delta y}{h^2 \Delta \sigma} \quad (73)$$

$$F_b = w_b^* \Delta x \Delta y \quad D_b = \frac{v_b \Delta x \Delta y}{h^2 \Delta \sigma} \quad (74)$$

The Peclet number  $P$  is to be taken as the ratio of  $F$  and  $D$ ; thus,  $P_e = F_e/D_e$ , and so on. The power-law formulation is used here, that is

$$A(|P|) = \{0, (1-0.1|P|)^2\} \quad (75)$$

which means taking the largest of the values in the brackets. More details can be found in Patankar's book.

### 5 Boundary Conditions

Wave breaking on the water surface produces extra momentum. Svendsen (1984) introduced the concept of the surface roller which actually takes into account the effect of wave breaking. The formulae derived by him have been used by many researchers. The essential point of Svendsen's idea is that the surface roller contains a certain amount of shoreward directed momentum, which causes a return flow below the wave trough in the offshore direction. According to his work, the flux induced by the water surface roller can be related to the wave energy. If linear wave theory is used, the wave induced mass flux including the water surface roller contribution can be written as

$$M = \left(1 + \frac{7h}{L}\right) \frac{E}{\rho c} \quad (76)$$

where  $h$  is the water depth,  $L$  is the wave length,  $c$  is the wave celerity,  $E$  is the wave energy density. Actually this formula has already been given in section 3 when discussing radiation stresses. However, in the calculation domain, we need to define a boundary at the water surface, and assumptions are required to tackle this requirement. Here it is assumed that:

1. The thickness of the surface layer is approximately equal to the wave height.
2. The time-averaged velocity in the layer is uniform and it is

$$u_s = \left(1 + \frac{7h}{L}\right) \frac{E}{\rho c} / (\langle \eta_s \rangle - z_{tr}) = \left(1 + \frac{7h}{L}\right) \frac{E}{\rho c} / H \quad (77)$$

3. The mean water surface is located halfway between the wave crest and the wave trough.

The momentum equations solved by the finite volume method are actually only applied to the area below the wave trough. The velocity at the wave trough is

then known from assumption (2) made above, which can be used as the boundary condition at the water surface.

The boundary condition at the sea bottom should include the effects of the wave oscillatory velocities. Liu and Dalrymple (1977) derived a formula for the bottom shear stress under the condition of a weak current and large incident wave angle. Their formula is used here.

## 6 Model Tests And Discussions

Aspects of model stability are considered first before verification tests are carried out. The model is a combination of two sub-models: the first is the ADI model and the second is the finite volume based model for the advection terms. It is well known that the ADI model is stable and accurate if the Courant number is not very large (usually less than 4). On the other hand, the finite volume method used in this paper is also a stable numerical solver. The power-law formula proposed by Patankar (1972) can ensure unconditional stability. It can therefore be concluded that the wave-induced current model is stable.

The model proposed in this paper is tested against available experimental data. The model includes the time variable, and a steady state solution can be obtained if the model is run for a sufficiently long period. Of course for a problem like the simulations of tidal flow, the model can quickly reach a three-dimensional velocity field. Before the model performance was compared against experimental data, a series of numerical tests were undertaken for some simple cases in order to ascertain the capabilities of the model. The cases include horizontal channel flow and a plane beach with a constant slope. As a rough criterion for accessing the model performance, continuity of the flow must be satisfied. After these numerical experiments had been done successfully, the experimental data presented by Stive and Wind (1982,1986) were used to test whether the model could predict cross-shore circulation and water surface set-up.

The experiments were conducted in a wave flume 55m long, 1m wide and 1m deep. A plane, concrete beach with a 1:40 slope was installed. Two experiments have been reported by Stive and Wind in 1982 and in 1986. In the first experiment, two test conditions were used. The first of these was also used for the experiment carried out in 1986. The experimental results from the first test of the first experiment and of the second experiment are used for testing the model. For more details for these experiments the interested reader can consult the original papers.

Comparisons of the results of the model presented in this paper against Stive and Wind's experimental data for water level set-up and cross-shore circulation are shown in figures 1 to 4. In the case of the water surface set-up, it is clear that the agreement between the experimental data and the computational results is reasonable. The velocity distribution over the water depth obtained from the model is plotted against the experimental data. The trend of both experimental and computational results is the same, however, there are obvious differences. If the results from other models are considered, for example, Stive and Wind's model (1986) and Svendsen's model (1986), the results from the present model are acceptable. Some reasons for such differences between the experimental data and the model results are as follows.

1). Wave breaking is a nonlinear process. Although Svendsen (1984) presented

a formula dealing with the surface roller and the results from this formula is reasonable, a much more detailed description is really required.

2). The eddy viscosity formula used in the present model can be improved if the turbulence in the surf zone is better described. It is well known that the turbulent processes in the surf zone are far from understood. Bottom friction is another subject which many researchers are still studying. The bottom friction formula used in the present model is only one of the many available formulae.

3). Wave-current interaction is ignored in the present model and it is ignored in all existing wave-induced current models. How to incorporate wave-breaking into wave-current interaction is a problem which has yet to be tackled.

4). The calculated velocities at water surface are smaller than the values of the experimental data which is probably caused by the inaccurate simulation of the air-water mixture at the surface. Improvement is under way.

From the above statements it can therefore be concluded that the wave-induced current problem is so complicated that numerical results are only rough estimates of the true solutions.

#### REFERENCES

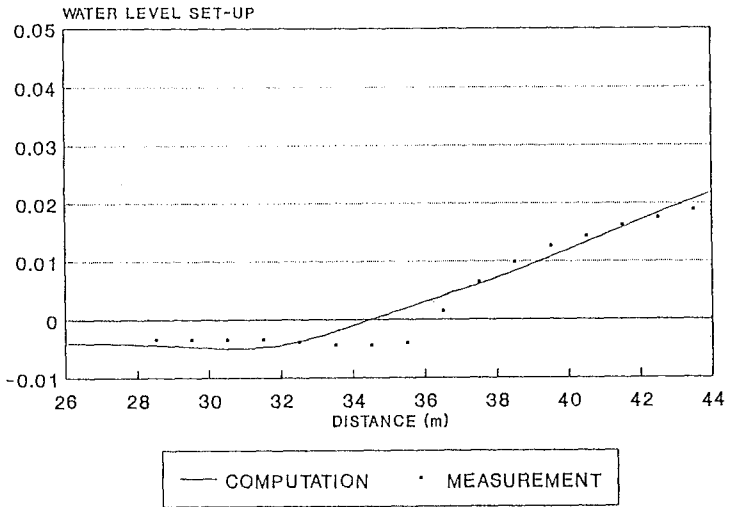
Patankar, S.V., 1977. Numerical Heat Transfer and Fluid Flow, Hemisphere Publishing Corporation.

Stive, M.J.F. & Wind, H.G., 1982. 'A study of radiation stress and set-up in the nearshore region', Coastal Engineering, Vol 6: 1-25.

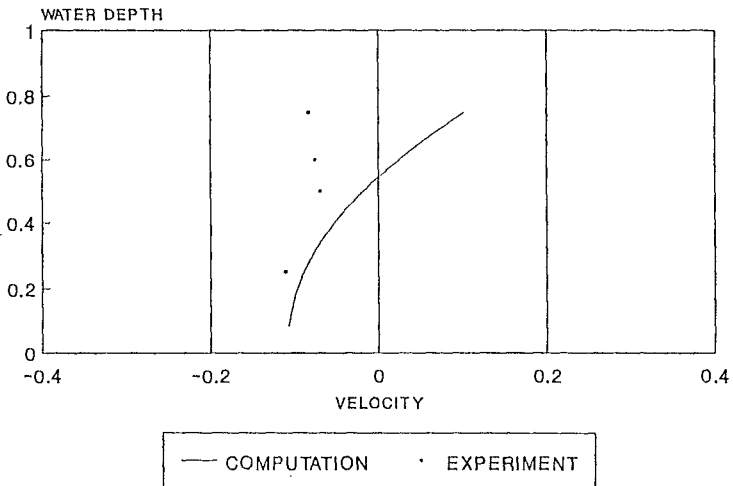
Stive, M.J.F. & Wind, H.G., 1986. 'Cross-shore mean flow in the surf zone', Coastal Eng., Vol. 10: 235-240.

Svendsen, I.A., 1984. 'Wave heights and set-up in a surf zone', Coastal Engineering, Vol. 8: 303-329

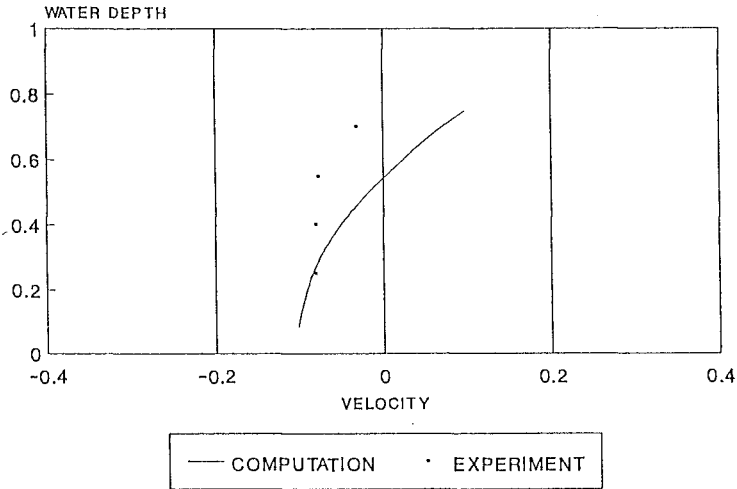
COMPUTATIONAL RESULTS FROM 3-D  
WAVE-INDUCED CURRENT MODEL



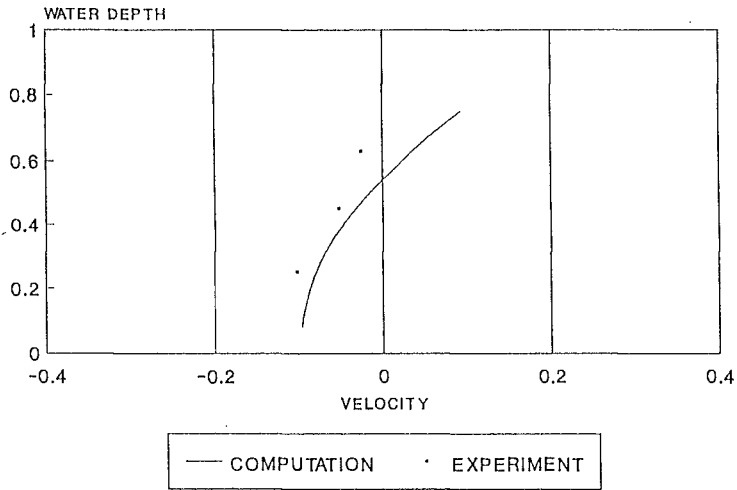
RESULTS FROM 3-D WAVE-INDUCED  
CURRENT MODEL  
X = 36.5 (m)



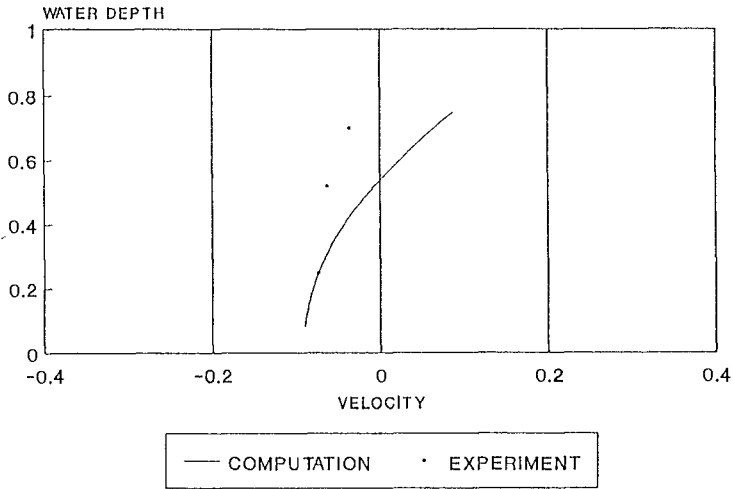
RESULTS FROM 3-D WAVE-INDUCED  
CURRENT MODEL  
X = 37.5 (m)



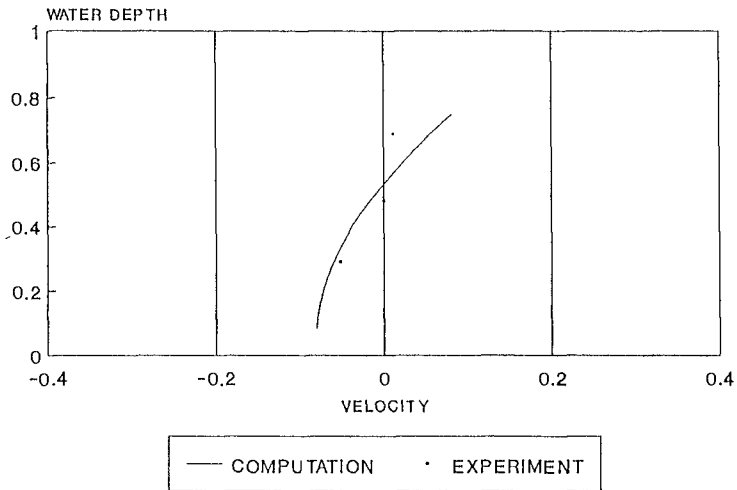
RESULTS FROM 3-D WAVE-INDUCED  
CURRENT MODEL  
X = 38.5 (m)



RESULTS FROM 3-D WAVE-INDUCED  
CURRENT MODEL  
X = 39.5 (m)



RESULTS FROM 3-D WAVE-INDUCED  
CURRENT MODEL  
X = 40.5 (m)





## CHAPTER 167

### INFLUENCE OF OFFSHORE BANKS ON THE ADJACENT COAST

N.J. MacDonald and B.A. O'Connor<sup>1</sup>

#### Abstract

A numerical model has been used to study the influence of offshore sand banks on the wave climate along a stretch of the Belgian coast. Results of the model have been interpreted to provide predictions of wave height under several scenarios, assuming that the banks do not respond quickly to changes in the local hydrodynamic environment. Results show that the sand banks afford substantial protection to the coast and that this effect may be reduced as a result of rising mean sea level and dredging.

#### Introduction

As part of the EC MAST II Programme, the Circulation and Sediment Transport Around Banks (CSTAB) project has brought together coastal engineers, oceanographers and geologists from five European countries to study of the role of sand banks in the processes and development of the nearshore hydrodynamic and littoral environment. The CSTAB project, scheduled to run between 1992 and 1995, is centred around an ambitious field programme measuring hydrodynamics and sediment dynamics in a typical linear sand bank system off the Belgian coast.

The field study site, which includes the inter-tidal and surf zones of the adjacent beach as well as the offshore sand banks, covers an area of approximately 400 km<sup>2</sup>. Since this entire region cannot be covered completely in a field study, computer models are being used to provide the necessary additional information to link together the various field campaigns and to provide a valuable predictive capability. This paper describes the application of a wave climate computer model to quantify the influence of offshore sand

---

<sup>1</sup> Dept. of Civil Eng., Univ. of Liverpool, PO Box 147, Liverpool L69 3BX, UK

banks on the adjacent coast.

### **Sand banks and the coast**

Large linear sand banks are a feature of many continental shelves throughout the world (Off, 1963). These sand banks occur in both tide and wave-dominated coastal seas, and in most instances, do not appear as lone features but as part of a regional group. The sand banks being investigated in the present paper are part of the Flemish Banks, which are situated on the Belgian coastal shelf in the southern North Sea. This bank system can be described, broadly, as a group of linear sand banks of the order of 10 to 20 km in length, 1 km in width and 10 to 20 m in height. A comprehensive review of the Flemish Banks has been presented by de Moor (1989).

One of the effects of offshore sand bank systems is to shelter the adjacent coast. This is believed to result primarily from the increased frictional drag on storm surges and increased friction on, and breaking of, the larger short-period storm waves. This latter feature has also been investigated by Tucker et al. (1983) who studied wave attenuation over a sand bank on the East Anglian coast of the UK. Using measurements taken by two wave rider buoys, they found negligible attenuation for small waves and a saturation level for larger waves determined by the breaking conditions over the bank.

If existing sand banks were reduced in size, or removed altogether from a system, the coast would experience a significant increase in the amount of wave energy reaching it. This would result in intensified erosion of the shoreline and the possible necessity to reinforce existing coastal defences. Sand banks also significantly modify the regional distribution of wave energy impacting on the coast. The local wave height field is determined by interaction with the local currents and the shoaling, refraction and diffraction which results from the reaction of the propagating waves to changes in bottom bathymetry. Changes in the offshore depths, either actual morphological changes or as a result of water level variation, could have serious implications for individual locations along the coast far beyond that expected for the coast in general.

The size and orientation of the sand banks may also change with long-term changes in mean sea level providing sufficient material is available. However, the time scale at which the banks can react may be very long. A number of linear sand bank systems, such as the Celtic Banks, were at one time active but are now moribund, having been unable to respond to rapid changes in sea level. De Vriend (1990) and van de Meene (1994) have both noted that, while the smaller-scale features on the sand banks (such as sand waves or smaller) can react quite rapidly, the morphological time scale of sand bank development is on the order of decades to centuries. In the present work

the bathymetric features are assumed to be unaffected by any change in mean sea level which may result due to climate change.

### **Climate Change**

Recently, studies have indicated that the growth in the level of greenhouse gases in the atmosphere can lead to a gradual increase in mean global temperature. One consequence of a gradual increase in mean global temperature is a rise in mean sea level (MSL). Pirazzoli (1989) found the rate of increase of MSL for the North Sea to be 1.0 to 1.5 mm/year. This was confirmed for the southern North Sea by Jensen et al. (1990) who calculated an average MSL rise of 1.2 mm/year across 12 tidal recording stations over a 100 year period. Jensen et al. (1990) also found some evidence to suggest that MSL increases may be accelerating.

Warrick and Oerlemans (1990) have presented sea level predictions based on a compilation of existing results and new computations. Their High, Best and Low predictions, for the Business-as-Usual scenario are given in Fig. 1. There is considerable spread in the three estimates given - a 20 cm rise in MSL could be realized anytime from 2020 to 2070 - but, all do show a gradually accelerating rise in MSL. For the purpose of the present paper, this Best Estimate will be used to relate simulation water levels to future dates.

Increased MSL will have serious consequences for coastal regions. A higher MSL will result in a general retreat of the shoreline and will allow larger waves to penetrate further inshore. An increase in MSL will also lead to larger tidal ranges because of the decreased frictional losses. This increase in tidal range will result in higher high water levels which will permit even larger waves to penetrate inshore than would be expected from increases in MSL alone.

Another possible consequence of climate change is increased storminess for some locations. Mitchell et al. (1990) have indicated that, while tropical disturbances may increase in frequency, the mid-latitudes may experience reduced storminess as a result of a decrease in the polar to equatorial mean temperature gradient.

### **The Bathymetric Grid**

Surveys from the Belgian Service of Coastal Harbours, were collected to model the region from the banks to the shore in very fine detail. Over 100 000 bathymetric values, with an average separation distance of 5 m, were used to generate the finite difference grid of the area. A contour plot of depths for this grid at the present-day MSL is shown in Fig. 2. The grid is 201 x 181 with a grid spacing of 100 m in both dimensions. The grid has its origin at

(51°07'30"N, 2°40'00"E) and its positive y-axis is aligned at 327° so that the alongshore side, or x-axis, is roughly parallel to the coast.

### The Numerical Model

Due to the size of the area being modelled it was decided to employ a wave-period averaged computer model since this type of model is not restricted to a limiting number of solution points per wavelength. The model selected was a simplified version of the WC2D model which is based on the work Yoo and O'Connor (1986) but which has been substantially improved since its initial development. The model has been validated against numerous laboratory and field results (Yoo and O'Connor, 1986; Yoo and O'Connor, 1988) as well as against wave rider measurements at Flemish Banks taken during the CSTAB field programme (O'Connor, 1993) where computed wave heights were within 5% of measured.

Wave kinematics are obtained through solution of a combined refraction-diffraction kinematic conservation equation for linear surface waves:

$$\frac{\partial K_i}{\partial t} + C_g \frac{K_j}{k} \frac{\partial K_i}{\partial x_j} + \frac{\sigma G}{2h} \frac{\partial h}{\partial x_i} + \frac{C_g}{2kA} \left[ \frac{1}{A} \frac{\partial A}{\partial x_i} \left( \frac{\partial^2 A}{\partial x_j^2} \right) - \frac{\partial}{\partial x_i} \left( \frac{\partial^2 A}{\partial x_j^2} \right) \right] = 0 \quad (1)$$

where  $K_i$  is the wave number vector,  $i=\{x,y\}$ ,  $k$  is the wave separation factor,  $h$  is the depth,  $A$  is the wave amplitude,  $\sigma$  is the wave frequency,  $C_g$  is the group velocity and  $G = 2kh/\sinh 2kh$ . The second term of Eq. (1) describes the advection of wave number, the third describes the effects bottom slope and the final term permits diffraction of the wave field. Since the forcing, and consequently the solution, of the model is steady, the first term in Eq. (1) is retained only as a iteration parameter. An approximate non-linear solution is achieved through use of the non-linear dispersion relation of Hedges (1976).

The wave dynamics are obtained from the combined refraction-diffraction wave energy conservation equation for linear surface waves:

$$\frac{\partial A}{\partial t} + \frac{1}{2A} \frac{\partial}{\partial x_i} \left( A^2 C_g \frac{K_i}{k} \right) + F_b A^2 = 0 \quad (2)$$

The final term in Eq. (2) has been introduced to include the effects of frictional dissipation. The calculation of  $F_b$  using an improved Bijker approach is described in O'Connor and Yoo (1988).

The numerical scheme is a simple explicit formulation with upwinding methods employed for the advection terms. The solution is obtained on a

staggered grid in an iterative approach until a steady-state solution is achieved. Boundary conditions of wave amplitude and wave direction must be supplied at the offshore boundary. At the side boundaries a radiation boundary condition is applied and at the shoreline all energy must be dissipated through breaking.

### **Application to the study site**

Three MSLs were selected: the present-day; +0.25 m; +0.50 m. According to Warrick and Oerlemans (1990), the latter two MSLs relate to the years 2040 and 2075. These levels were used in tests with four wave climates and five wave directions (see Tables 1 and 2). Analyses of a wave hindcast performed for this location by the UK Meteorological Office (pers. comm.) show that wave climates A through D have rates of occurrence of 1.36%, 0.72%, 0.24% and <.01% for the sectors between directions 1 to 5, respectively. No account was made of any tidal effects in the present work.

A  $k_s$  value of 10 cm was used for the roughness height for the area. This value was used to take into account the sub-grid scale bed features, such as the sand waves, mega-ripples, and ripples, that are known to occur on the sand banks in this area.

### **Results**

A simple illustration of the effectiveness of the sand banks in protecting the coast can be seen from the cross-shore transformation characteristics of the model for the present-day bathymetry and for the case where the sand banks do not exist. This is most easily done in a one-dimensional test, so as to eliminate any influence of longshore variability in the bathymetry. For the present-day situation, the wave height field produced by the model for normal wave approach on the two-dimensional bathymetry was averaged between 5 km and 15 km in the alongshore direction from a line 2 km from the coast to the offshore boundary. These were compared with the results of the model for an equivalent plane slope (see Fig. 3). Figure 4 shows the ratios of present-day wave height with banks to plane slope wave height for wave climates A through D. The sheltering effect of the sand bank system is clearly visible in each of the four wave climates. The results also indicate that the sand banks have a greater influence on the larger wave climates, with reductions in wave height approaching 30% a distance 2 km offshore. Clearly, the longer waves are influenced by the bottom bathymetry over a much larger fetch.

When examining the effects of sea level rise on the entire system it is more informative to examine the full two-dimensional results. A typical result of the simulation is shown in Fig. 5. Here a contour plot of wave height is presented for the present-day MSL and an increase of 0.5 m for condition D3 ( $H=5.0$  m,  $T=9.0$  s,  $\theta=327^\circ$ ). Although both patterns of contour lines are

complex, it is evident from their rhythmic pattern that the sand banks have a significant effect on the wave climate in the region. While there are substantial losses in energy over the domain, especially in the shallower regions, there are areas of increased wave height due to the focusing. The sheltering effects of the sand banks are discernible by the decrease of wave height over each successive bank. The increase in MSL has the effect of permitting larger waves to progress further shoreward, as is most evident in the nearshore zone.

Substantial alongshore variation in the change in wave height due to increased MSL was found in most tests. Figure 6 shows the percentage change in wave height for condition 4B along a line 1 km offshore for the two increased MSLs. Under an assumption of a 0.5 m rise in MSL, the resulting increase in wave height varies from 8% to 25%. This alongshore non-uniformity in wave height is reduced to 8% to 10% when the results for all tests are averaged together, as is shown in Fig. 7. The results for the entire domain, see Fig. 8, shows a general pattern of increasing wave height towards the shoreline. Individual wave climates also exhibited some variation, as shown in Fig. 9, where the results for the line 1 km offshore are plotted against projected dates.

In order to illustrate some possible consequences of the effects of offshore dredging on the adjacent coast, a hypothetical dredged region was constructed within the bathymetric grid. This area is delineated by the dashed line in Fig. 10. The depth was reduced to a constant 10.25 m below present MSL over this region, corresponding to approximately  $1.5 \times 10^6$  m<sup>3</sup> of material removed.

A typical contour plot of the change in wave height is shown in Fig. 11 for condition C5. The influence of the increase of depth is apparent almost immediately and extends over a large area, although the differences away from the direct shadow zone are minute. The effect towards the shore is again dependent upon the wave climate. Figures 12a and 12b show the alongshore distribution of the change in wave height for each of the wave climates from directions 1 and 5, respectively. In both cases the wave height immediately behind the dredging site has decreased, while it has increased to either side. In both cases the larger wave climates are affected for a greater distance along the coast.

## Conclusions

Nearshore sand bank systems protect the coast by dissipating wave energy offshore. Rising sea levels, however, will lessen their effectiveness and permit larger waves to reach the coast. For the sea level rise scenario used in the present work, wave heights at a line 1 km off the Belgian coast was

predicted to increase by the order of 10% by 2075. The effects closer to the surf zone may be greater, as increases in wave energy were generally found to get larger towards the shore.

Substantial variation in the change in wave climate along the coast was noted in all tests, although this effect was modulated when tests from several directions were combined. The situation with regards to the sediment dynamics in these locations will more extreme, however, due to the highly non-linear relationship of sediment transport with wave height.

The illustration of possible consequences from the extraction of sediment from the top of an offshore bank showed that in each case the wave height immediately behind the dredging site was decreased while it increased to either side.

### **Acknowledgements**

This work was funded as part of the MAST II Programme by the Commission of the European Union under contract MAS2-CT92-0024.

### **References**

- de Moor, G., 1989. Maintenance of the Flemish Banks. In: J.P. Henriët and G. de Moor (Editors), *Quaternary and Tertiary Geology of the Southern Bight, North Sea*. Belgian Geological Survey, Brussels: 185-216.
- De Vriend, H.J., 1990. Morphological processes in shallow tidal seas. *Coastal Estuarine Studies*, 38: 276-301.
- Hedges, T.S., 1976. An empirical modification to linear wave theory. *Proc. Inst. Civil Engs.*, 61: 575-579.
- Jensen, J., Mügge, H-E. and Schönfeld, W., 1990. Development of water level changes in the German Bight, an analysis based on single value time series. In: B.L. Edge (Editor), *Proc. Twenty Second Inter. Coastal Engrg. Conf.*, 1: 2839-2851.
- Mitchell, J.F.B., Manabe, S., Meleshko, V. and Tokioka, T., 1990. Equilibrium climate change - and its implications for the future. In: Houghton, J.T., Jenkins, G.J., and Emphraums, J.J. (Editors), *Climate Change: The IPCC Scientific Assessment*. Cambridge University Press, Cambridge, pp. 365.
- O'Connor, B.A. and Yoo, D., 1988. Mean bed friction of combined wave-current flow. *Coastal Engineering*, 12: 1-21.

O'Connor, B.A., 1993. Mid-term report in circulation and sediment transport around banks, Project MAS2-CT92-0024. Liverpool University, Liverpool.

Off, T., 1963. Rhythmic linear sand bodies caused by tidal currents. Bull. Am. Soc. Petrol. Geol., 47: 324-341.

Pirazzoli, P.A., 1989. Recent sea-level changes in the North Atlantic. In: D.B. Scott (Editor), Late Quaternary Sea-Level Correlation and Applications.

Tucker, M.J., Carr, A.P. and Pitt, E.G., 1983. The effect of an offshore bank in attenuating waves. Coastal Engineering, 7: 133-144.

Warrick, R., and Oerlemans, J., 1990. Sea level rise. In: Houghton, J.T., Jenkins, G.J., and Emphraums, J.J. (Editors), Climate Change: The IPCC Scientific Assessment. Cambridge University Press, Cambridge, pp. 365.

Yoo, D. and O'Connor, B.A, 1986. Mathematical modelling of wave-induced nearshore circulations. In: B.L. Edge (Editor), Proc. Twentieth Coastal Engrg. Conf., 3: 1667-1682.

Yoo, D. and O'Connor, B.A, 1988. Diffraction of waves in caustics. J. Waterway, Port, Coastal and Ocean Engrg., A.S.C.E., 114: 715-731.

Van de Meene, J.W.H., 1994. The Shore-Face Connected Ridges Along the Central Dutch Coast. Nederlandse Geografische Studies, Utrecht, 222 pp.

Table 1 Test wave climates

Climate	H (m)	T (s)
A	1.0	4.0
B	2.0	6.0
C	3.0	7.0
D	5.0	9.0

Table 2 Test wave directions

Direction	°N
1	347°
2	332°
3	327°
4	322°
5	307°



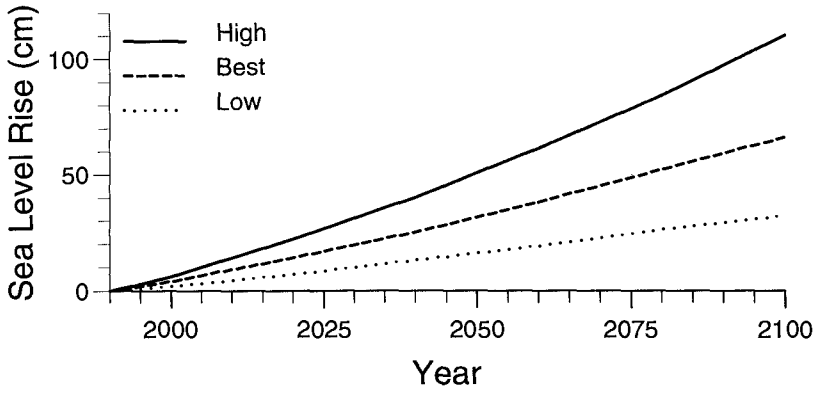


Figure 1 Predicted MSL Rises (after Warrick and Oerlemans (1990)).

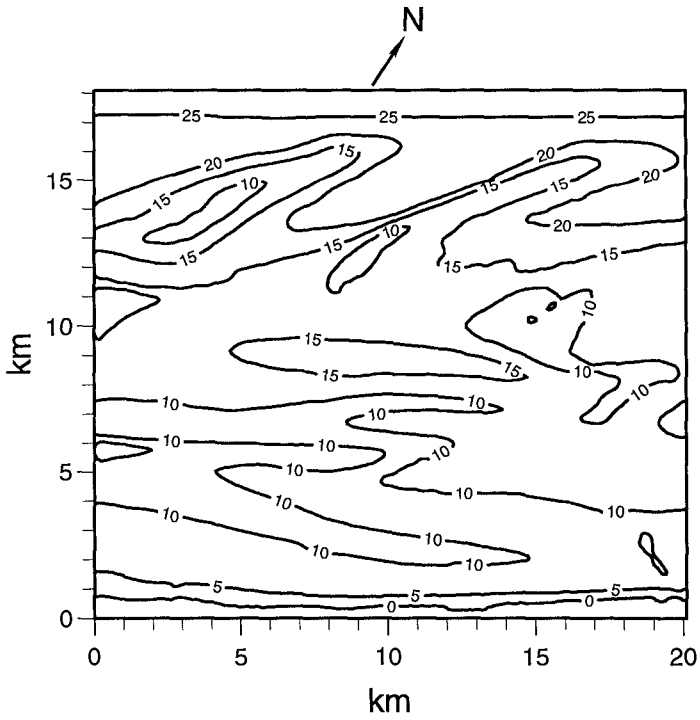


Figure 2 Bathymetric grid (m).

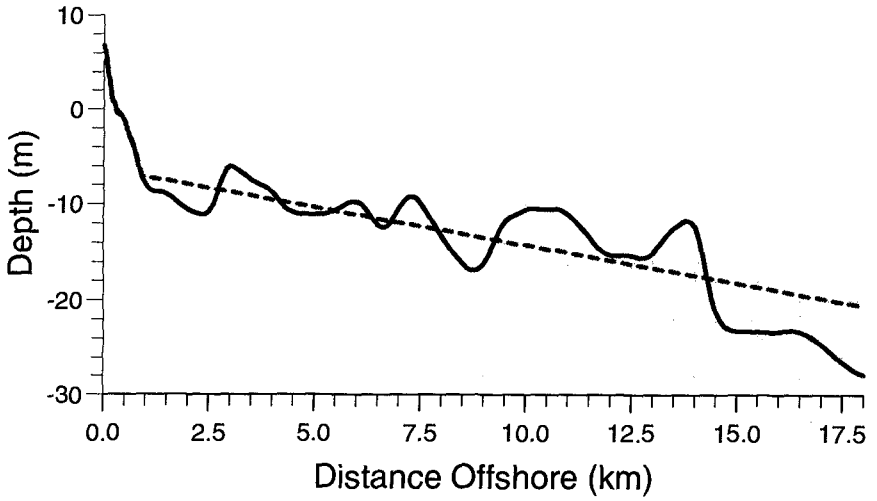


Figure 3 Actual cross-shore bathymetry and equivalent slope.

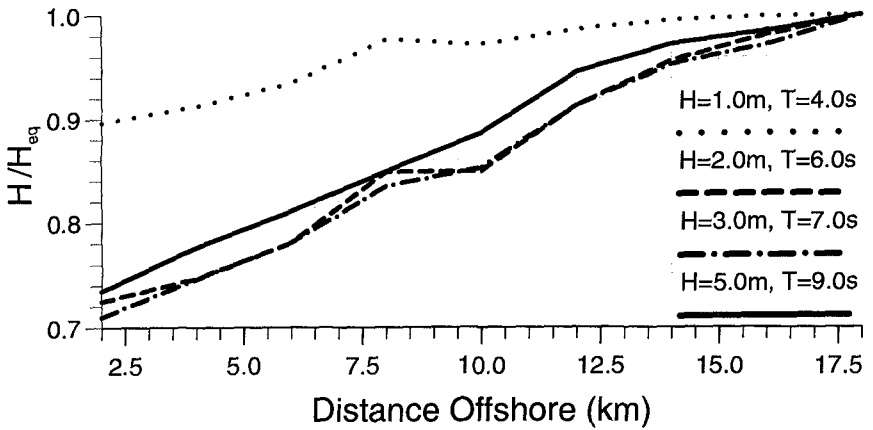


Figure 4 Cross-shore to equivalent slope wave height ratio.

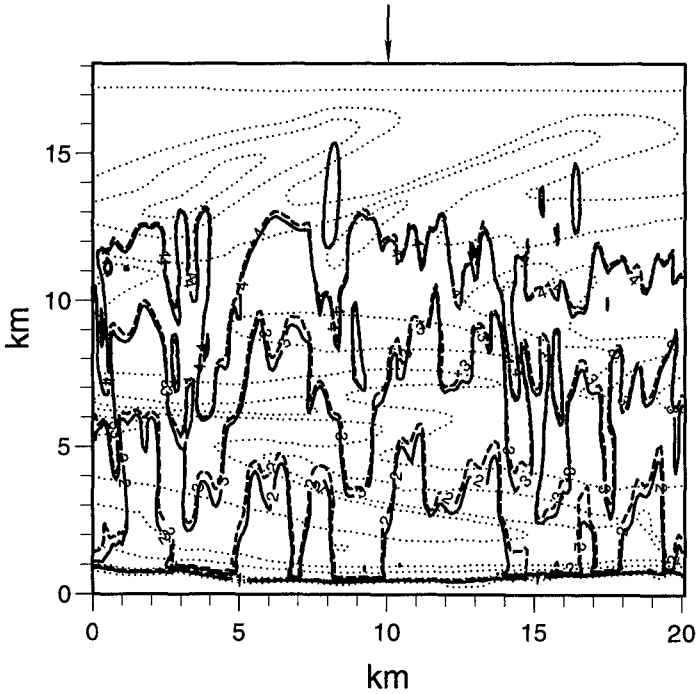


Figure 5 Wave height (m), condition D3. Present-day MSL,-----; MSL+0.5m,———.

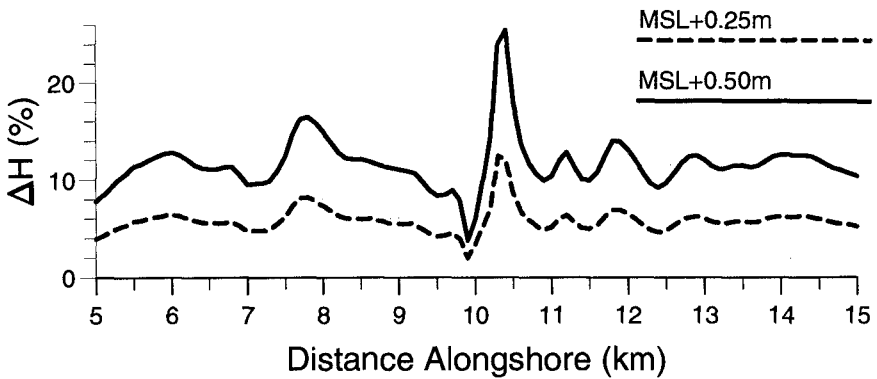


Figure 6 Alongshore wave height change at  $y=1\text{km}$ , condition 4B.

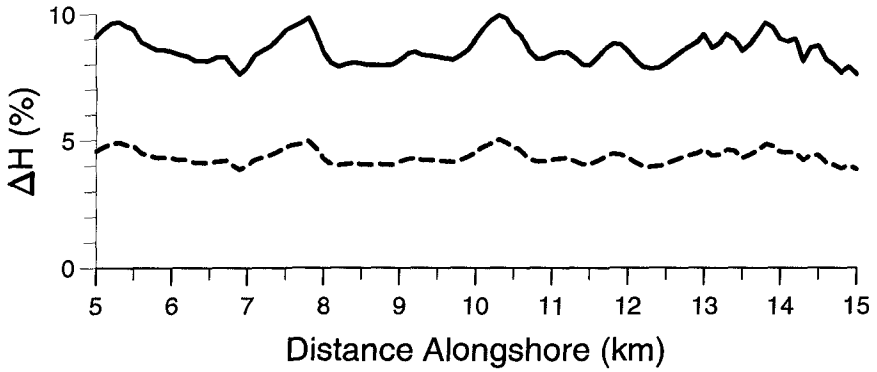


Figure 7 Alongshore wave height change at  $y=1$  km, all conditions MSL+0.5m. (see Fig. 6 for key).

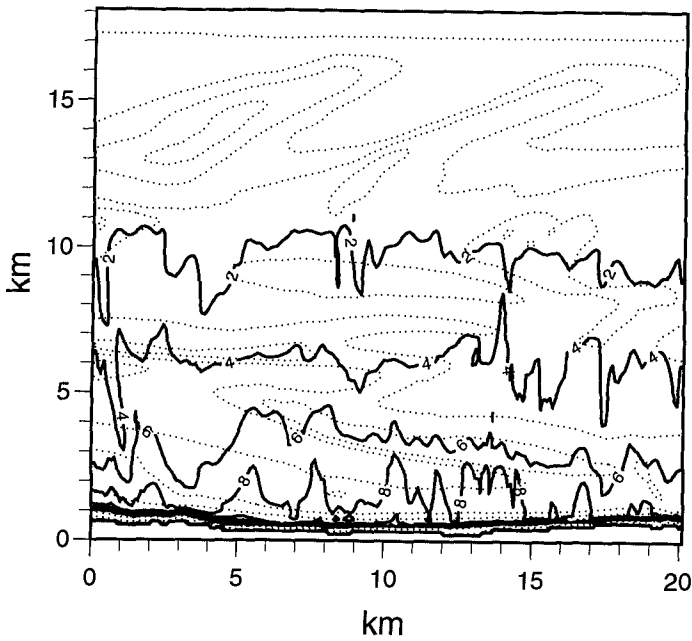


Figure 8 Wave height change (%), all conditions. MSL + 0.5 m.

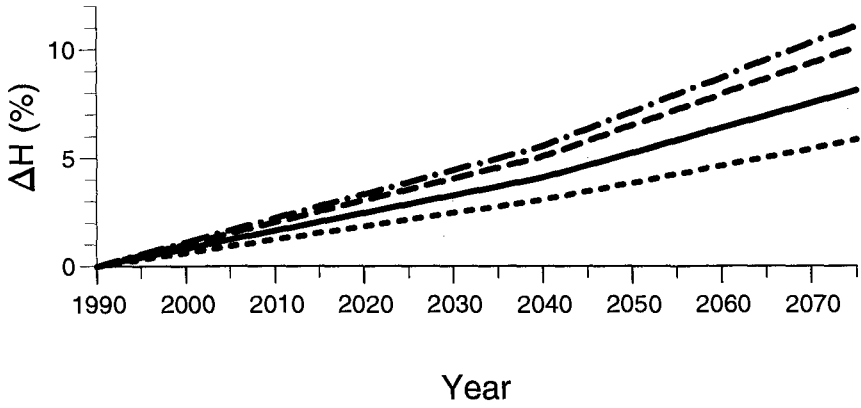


Figure 9 Wave height change at  $y=1$  km, all directions averaged.  
(see Fig. 4 for key)

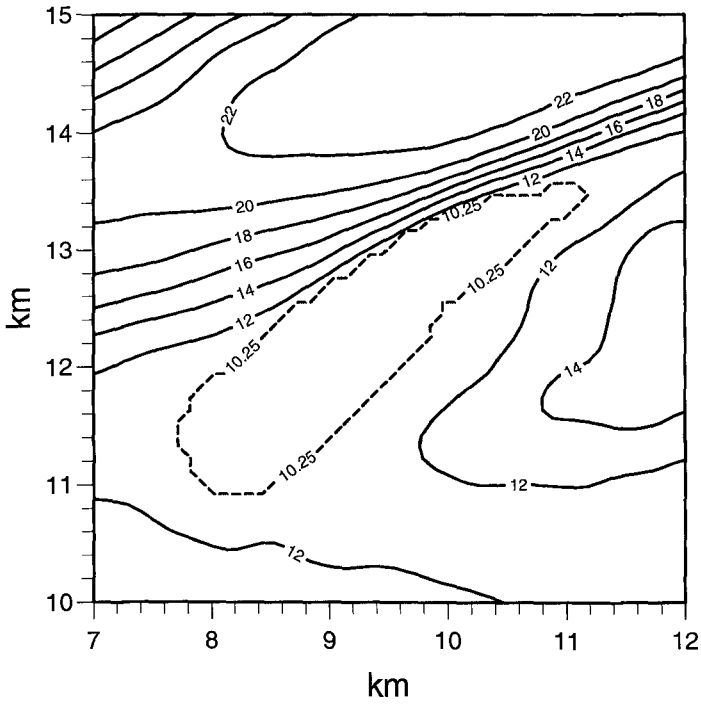


Figure 10 Dredged region of bathymetric grid (m).

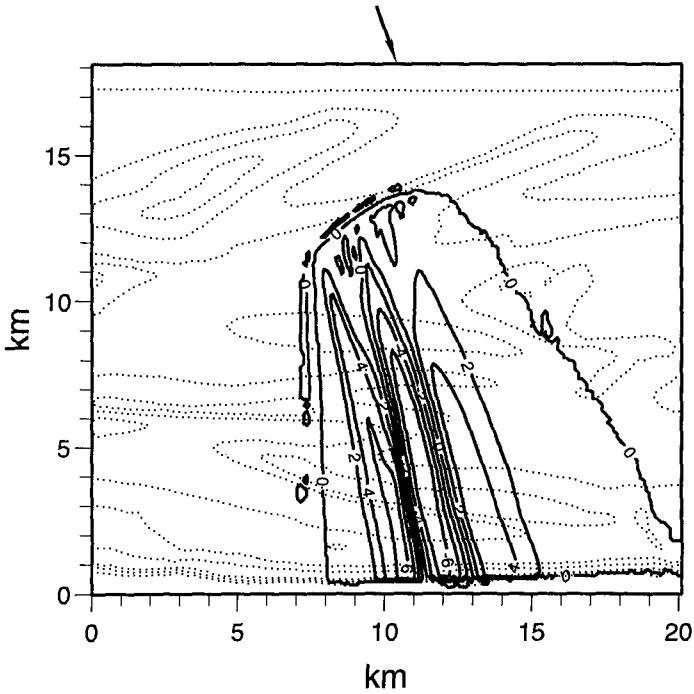


Figure 11 Wave height change (%), condition C5, due to dredging.

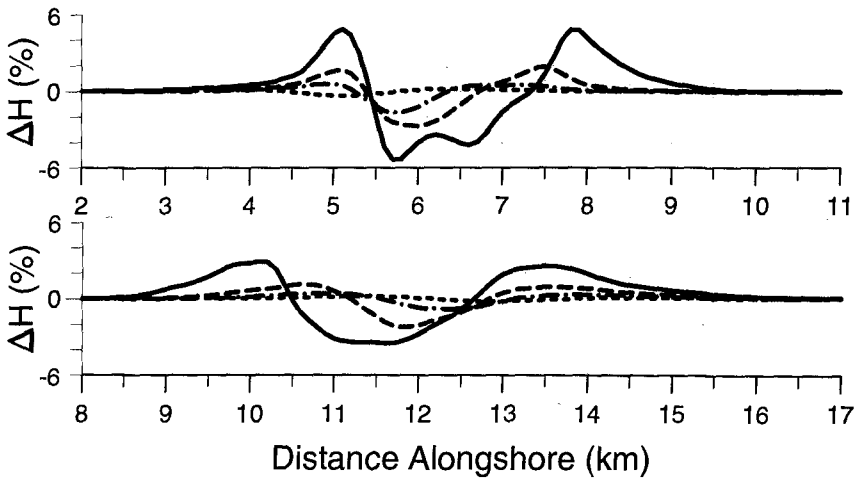


Figure 12a-b Alongshore wave height change at  $y=1$  km.  $a=347^\circ$ ,  $b=307^\circ$ .  
(see Fig. 4 for key)

## CHAPTER 168

### WAVE RUNUP ON COMPOSITE-SLOPE AND CONCAVE BEACHES

R. H. Mayer<sup>1</sup> and D. L. Kriebel<sup>1</sup>

#### ABSTRACT

Laboratory experiments were carried out for regular and irregular wave runup over non-uniform beach profiles, including both bi-linear and concave "equilibrium" beach profiles. Measured runup is shown to be substantially less than that predicted by the Hunt Formula if the exposed beach-face slope is used to define the typical beach slope. More accurate runup estimates are obtained using Saville's hypothetical slope concept; and, Saville's method is integrated with the Hunt Formula to provide simple analytical estimates of wave runup over complex beach topography.

#### INTRODUCTION

One problem encountered when predicting wave runup on open-coast beaches is the dilemma of how to define the beach slope for use in runup predictive formulas. Most runup design methods have been developed from laboratory tests conducted on uniform beach slopes. For field application, however, where beaches are generally concave in shape, and where offshore sand bars or complex beach berms may exist, the appropriate slope for use in runup calculations is never clear. On natural beaches, different definitions of beach slope can typically differ by a factor of two or three such that runup estimates can vary by a similar amount.

The purpose of this paper is to present a computationally-simple method for calculating wave runup on beaches with composite-slopes or concave shapes. This study consists of two main parts: (1) development of an analytical method for predicting runup on composite-slope or concave beaches and (2) an experimental evaluation of this methodology based on small-scale laboratory tests of wave runup for both regular and random waves.

---

<sup>1</sup> Ocean Engineering Program, U.S. Naval Academy, Annapolis, MD 21402

The analytical approach used in this paper integrates two widely-used methods of predicting wave runup: (1) the Hunt Formula, developed by Hunt (1959) for predicting runup of regular waves on coastal structures with a uniform slope and, (2) the "effective" slope method of Saville (1958), which defines an appropriate average slope for use in predicting runup on composite-slope structures. By combining these analytically, a simple quadratic equation is obtained for wave runup that can be solved in closed form for simplified geometries. This solution is then verified by comparison to wave runup measured in over 340 small scale laboratory tests conducted at the U.S. Naval Academy in both regular and irregular waves.

## BACKGROUND

Most methods of predicting wave runup on open-coast beaches are variations of the Hunt Formula, proposed by Hunt (1959), and rewritten by Battjes (1974) as

$$\frac{R}{H_o} = \frac{\tan\beta}{\sqrt{H_o/L_o}} = \xi \quad (1)$$

where  $H_o$  is the deep water wave height,  $L_o$  is the deep water wave length,  $\tan\beta$  is the tangent of the beach slope, and where  $\xi$  is the surf-similarity parameter which is defined by  $\tan\beta/(H_o/L_o)^{1/2}$ . Battjes (1974) showed that the dimensionless runup is generally equal to  $\xi$  over the range from  $0.1 < \xi < 2.3$  for regular waves acting on uniform, smooth, and impermeable laboratory beaches with slopes typical of many natural beach slopes.

For irregular waves, Battjes (1971) also obtained reasonable predictions of the median runup by using the Hunt Formula expressed in terms of the median wave height. Mase (1989) defined the surf similarity parameter in terms of the deep water significant wave height and, based on analysis of laboratory tests on uniform impermeable slopes, developed empirical correlations between  $\xi$  and the mean runup, the significant runup, as well as other runup parameters. Holman (1986) developed graphical correlations between runup and the surf similarity parameter, again defined by the significant wave height, based on field measurements over complex barred beach profiles.

A discrepancy can be found, however, between the field results of Holman and the laboratory results of Mase. Mase (1989) found that the significant runup measured in his small-scale laboratory tests on smooth plane slopes was approximately twice as large as values measured in the field by Holman (1986). Mase speculates that his expression provides an upper bound to the scattered field data and further attributes the overprediction to the use of smooth impermeable slopes in the laboratory tests. It is our belief, however, that there is a more fundamental cause of this discrepancy related to the effect of beach profile geometry.



This contradiction between laboratory and field values for runup may be partly explained by considering the bi-linear profile in Figure 1a. As pointed out by Hunt (1959), the Hunt Formula will not accurately predict the runup of regular waves on this profile if either the beach-face slope  $m$  or the submerged surf zone slope  $s$  is used. Predictions based on the beach-face slope dramatically over-estimate runup while predictions based on the surf zone slope under-estimate the runup. Hunt (1959) suggested an empirical weighted average of the two slopes  $m$  and  $s$  for bi-linear geometries, but a more general method is required for more complex beach geometries, such as the concave beach profile in Figure 1b.

The most widely-used method for predicting runup over complex geometries was proposed by Saville (1957). Saville suggested that runup predictions over arbitrary geometries should use a hypothetical average or "effective" slope of the entire active surf zone, extending between the wave break point and the runup limit. This approach, however, is cumbersome to apply. It requires a time-consuming iterative solution in which: (1) a runup limit is assumed, (2) an average slope is calculated from the breakpoint to the assumed runup limit, (3) the runup is estimated using this average slope in empirical design curves, (4) the calculated runup is compared to the assumed value. If necessary, the new runup limit is then used to define a new effective slope and the process is repeated until the runup converges on a stable value.

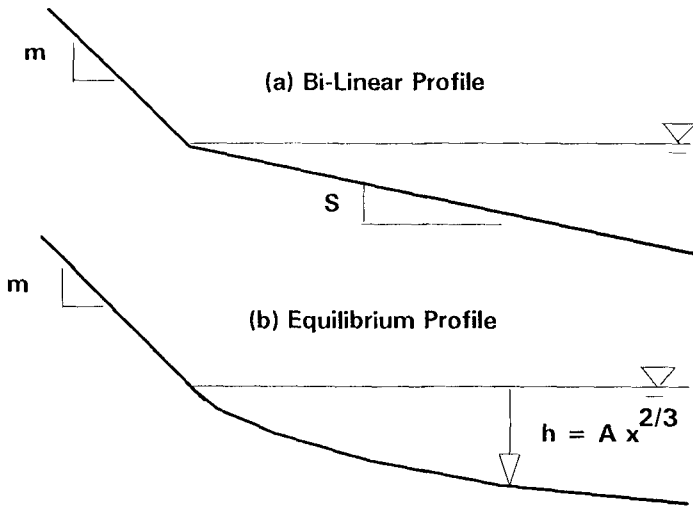


Figure 1. Illustration of idealized beach profiles: (a) bi-linear composite-slope profile and (b) concave equilibrium beach profile.

## INTEGRATED RUNUP METHOD

In this study, the Hunt Formula and the Saville effective slope concept are integrated into one general runup equation for application to open-coast beaches. Because the Hunt Formula is known to describe runup for linear beach slopes, the numerous design curves which are traditionally used with Saville's effective slope method are not required. As a result, the iterative solution procedure recommended by Saville can be avoided, and a single expression for runup on composite-slope and concave beaches is found that can be solved analytically or numerically.

Beach geometries considered in both the analytical and experimental phases of this study are depicted in Figure 1. These include: (1) a bi-linear profile and (2) a concave profile given by the "equilibrium" profile form of Dean (1977). In each case, the exposed beach-face slope is assumed to be linear and the tangent of this slope is denoted by  $m$ . The surf zone is then either represented by a linear slope,  $s$ , or by a concave equilibrium profile form following the theory of Dean (1977) where the depth  $h$  is related to the distance offshore by the relationship  $h=Ax^{2/3}$  in which  $A$  is a parameter relating the general slope of the beach to sediment characteristics.

It is assumed that the physical mechanisms of wave runup are represented by the Hunt Formula in equation (1) which, in dimensional form is given by

$$R = \tan\beta \sqrt{H_o L_o} \quad (2)$$

Following Saville's hypothetical slope concept,  $\tan\beta$  is then defined as the average slope between the incipient breakpoint and the runup limit. As illustrated in Figure 2, this may be quantified numerically as

$$\tan\beta = \frac{R + h_b}{X_R + X_b} \quad (3)$$

where  $h_b$  is the incipient breaking depth,  $X_b$  is the horizontal distance from the shoreline to the breakpoint, and  $X_R$  is the horizontal distance to the runup limit. By combining the expression for average slope in equation (3) into the Hunt Formula in equation (2), a single equation for the wave runup is found in the form

$$R = \frac{R + h_b}{X_R + X_b} \sqrt{H_o L_o} \quad (4)$$

Note that the runup appears on both sides of equation (4) and, in fact, it appears in both the numerator and denominator on the right-hand-side since the horizontal runup limit  $X_R$  is related to the vertical runup limit  $R$  by the slope of the beach face as  $X_R=R/m$ . As a result, equation (4) can be solved for the runup  $R$  in two ways.

For general application over arbitrary beach geometries, equation (4) can be solved iteratively in the form

$$R_{i+1} = \frac{R_i + h_b}{X_{R_i} + X_b} \sqrt{H_o L_o} \tag{5}$$

where the subscripts  $i$  and  $i+1$  denote old and new values in the iteration process. In this approach, the distances  $X_R$  and  $X_b$  are determined directly from the known (measured) beach geometry at each step in the iterative solution. Although perhaps not apparent, equation (5) is much simpler to apply than the traditional effective slope method of Saville (1958) because there is no need to look up runup values from design curves. As a result, this method has the advantage that it could be added to any existing numerical model for surf zone hydrodynamics or sediment transport.

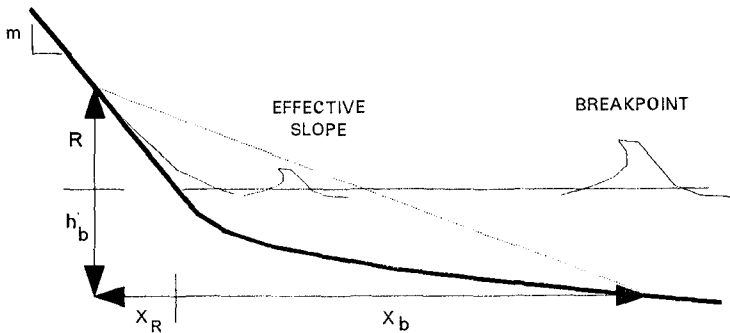


Figure 2. Definition of effective slope for idealized beach profiles.

For idealized open-coast conditions, one way to simplify equation (4) is to assume a uniform beach-face slope,  $m$ , as depicted in Figure 1. The horizontal runup excursion is then related to the vertical runup by  $X_R=R/m$  and equation (4) gives

$$R = \frac{R + h_b}{R + mX_b} m \sqrt{H_o L_o} \tag{6}$$

This suggests that the runup over a concave beach profile will always be less than runup over a uniform planar beach. For concave beach profiles, the breaking depth  $h_b$  is always smaller than the depth of a uniform slope projected out to the breakpoint,  $mX_b$ . The ratio  $(R+h_b)/(R+mX_b)$  is then always less than unity and the runup is less than that predicted by the Hunt Formula using the beach-face slope,  $m$ .

Further interpretation indicates that if the breakpoint is near the still water shoreline (shore-break conditions), then as expected

$$R = m \sqrt{H_o L_o} \quad (7)$$

In contrast, if the breakpoint is far offshore so that the surf zone is very wide, then equation (6) simplifies to the Hunt Formula based on the surf zone slope as

$$R = \frac{h_b}{X_b} \sqrt{H_o L_o} \quad (8)$$

For most other conditions however, the solution will lie in between these limits and is may be determined by first rewriting equation (6) as a quadratic equation

$$R^2 + R m ( X_b - \sqrt{H_o L_o} ) - h_b m \sqrt{H_o L_o} = 0 \quad (9)$$

An analytical solution for wave runup over non-uniform beach profiles is then found to be given by the solution of the quadratic equation

$$R = \frac{m}{2} ( X_b - \sqrt{H_o L_o} ) \left[ -1 + \sqrt{1 + \frac{4 h_b \sqrt{H_o L_o}}{m ( X_b - \sqrt{H_o L_o} )^2}} \right] \quad (10)$$

Interpretation of equation (10) is somewhat difficult but approximate solutions can be found by applying series expansions or by solving equation (9) subject to assumptions regarding the magnitude of each term. Space limitations prevent a full presentation of these results but, in general, results show that the runup is between the limits suggested in equation (7) and (8). For storm conditions, it can be shown that runup is actually given more closely by equation (8) than equation (7), suggesting that the average surf zone slope, not the average beach-face slope, is most appropriate for runup predictions when the wave conditions are energetic.

## EXPERIMENTAL EVALUATION OF INTEGRATED RUNUP METHOD

Over 340 wave tank tests have been conducted in order to verify the integrated approach of combining the Hunt Formula with the Saville effective slope concept in equation (10). Laboratory tests were conducted in the wave basin at the U.S. Naval Academy which is 13 meters long and 5.4 meters wide. Model beach profiles, having shapes depicted in Figure 1, were constructed of smooth impermeable PVC plastic sheets placed on top of an aluminum frame mounted inside a 7.5 meter long and 0.6 meter wide test channel installed in the wave basin. Water depths in the basin were generally kept at 24 centimeters.

Regular and irregular wave tests were conducted on uniform plane slopes and on bi-linear profiles as depicted in Figure 1a. Seven combinations of slopes  $m$  and  $s$  were tested for regular waves while two combinations were tested for irregular waves. Tests were next conducted on equilibrium profiles, depicted in Figure 1b, for regular waves only. In these tests, water levels were varied since, according to the hypothetical slope concept, runup for given wave conditions should be greater when the water level is elevated due to the steeper average slope of the surf zone.

Waves were generated by a piston-type wavemaker and, because of the lack of reflection compensation in the short wave basin, test durations were kept relatively short. In regular wave tests, typically 10 to 20 waves were generated for each combination of wave height and period. For each beach configuration, 20 combinations of  $H$  and  $T$  were tested producing 20 values of wave steepness. For irregular waves, tests were conducted in short "bursts" of about 30 waves. Ten such 30-wave sets were used for each combination of significant wave height and peak period tested so that about 300 waves were obtained for each wave spectrum tested. For each structure geometry, ten values of  $H_s$  and  $T_p$  were used producing 10 values of spectral wave steepness. All random wave tests used JONSWAP wave spectra with a peak enhancement factor of 3.3

Because the goal of this study was to evaluate the integrated runup solution in equation (10), measurements in each laboratory experiment included: (1) incident wave height and period, (2) breaking depth  $h_b$ , (3) surf zone width  $X_b$ , and (4) wave runup. Input to equation (10) consisted of the first three, with incident waves converted to equivalent deep water values. For irregular waves, measurement of input parameters was rather complicated since the breakpoint changes from one random wave to the next. Both the wave runup and the location of each breaking wave were recorded on video tape. Breaker depth was then determined from the observed surf zone width based on the known geometry.

### *Regular Waves on Bi-Linear Profile*

Results of tests conducted with regular waves on bi-linear beach profiles are shown in Figure 3. Each figure shows the normalized runup plotted as a function of the deep water wave steepness on a log-log scale so that the theoretical solutions plot as a straight line. In each figure, three theoretical predictions are shown: (1) the Hunt Formula based on the beach face slope  $m$  from equation (7), (2) the Hunt Formula based on the surf zone slope  $s$  from equation (8), and (3) the integrated runup method using the effective slope concept from equation (10). Though not shown, tests conducted on a uniform beach profile confirmed that both equation (10) and the Hunt Formula gave identical results in good agreement with the measured runup values for plane slopes.

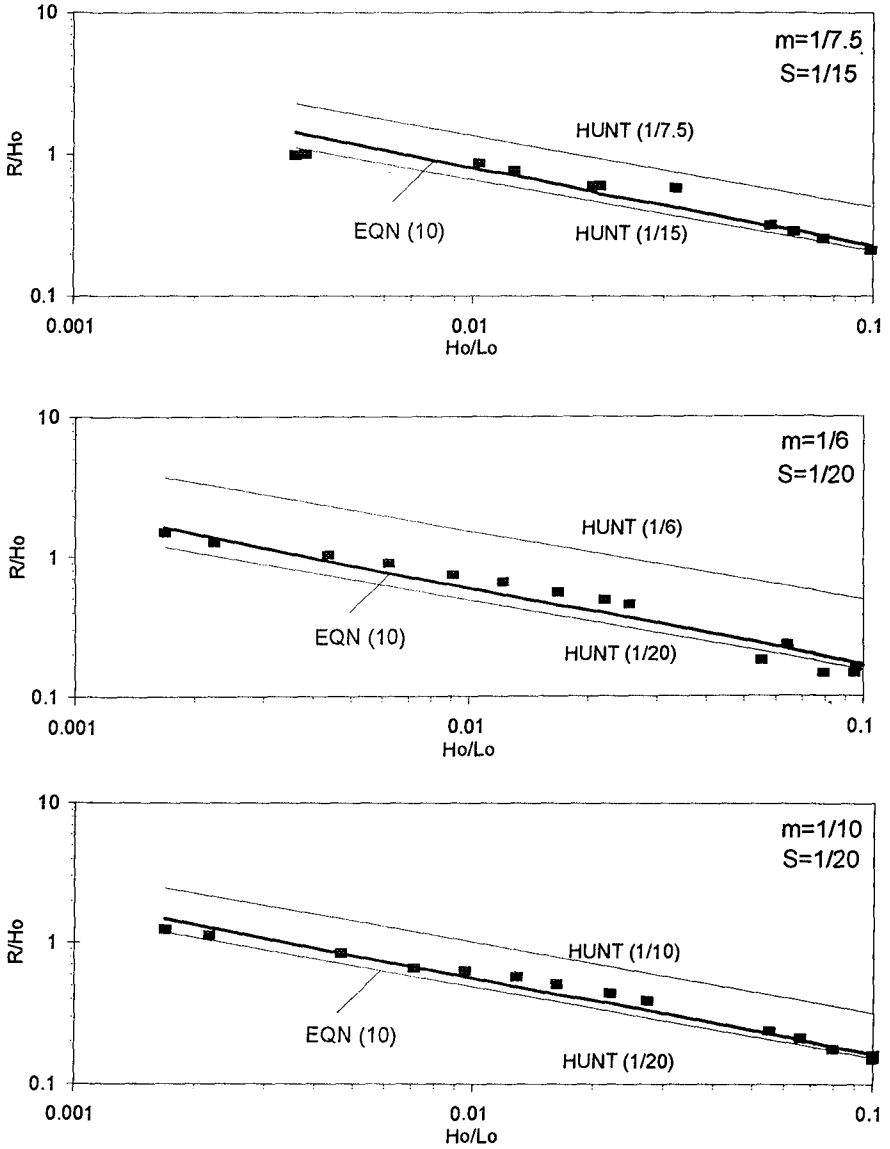


Figure 3. Comparison of measured and predicted runup for bi-linear beach profiles.

Figure 3a shows results for a bi-linear profile with a surf zone slope of 1-on-15 and a beach-face slope of 1-on-7.5. Figures 3b and 3c then show similar results where the surf zone slope was equal to 1-on-20, and where the beach-face slope was 1-on-6 and 1-on-10 respectively. In almost all cases, the measured runup (shown by solid squares) falls between the two limiting predictions based on the Hunt Formula using slopes  $m$  and  $s$ . It can be seen that the integrated method based on the effective slope concept provides a much better prediction in good agreement with the data.

These results suggest that the proposed method - integrating the Hunt Formula with Saville's effective slope concept - is capable of providing a simple unified description of regular wave runup on bi-linear beach profiles. For all 140 tests conducted on bi-linear profiles in this study, the Hunt Formula, based on the traditional use of the exposed beach-face slope  $m$ , over-estimates the runup by an average of 92%. Use of the surf zone slope,  $s$ , gives improved predictions but consistently underestimates the runup with an average error of 20%. The integrated method was found to predict runup to within an average error of 13.5%, although it also was somewhat biased toward under-estimating the runup.

### *Regular Waves on Equilibrium Profiles*

Results of tests conducted with regular waves on equilibrium profiles are shown in Figure 4. In these tests, a single equilibrium profile slope parameter was used with  $A = 0.088 \text{ m}^{1/3}$ . As depicted in Figure 2b, a linear beach-face slope was then joined to this concave equilibrium profile at a depth where the slopes matched. Two linear beach-face slopes were tested, but results in this paper are only shown for one slope,  $m=1/8$ . In Figure 4, three tests results are then shown, corresponding to three different water levels. Figure 4a shows results for a "mean" water level based on a 24.1 cm water depth in the wave basin. Figure 4b then shows a "high" water level condition based on a water depth of 30.4 cm, while Figure 4c shows a "low" water level condition based on a depth of 18.7 cm.

Each figure again shows the normalized runup plotted as a function of the deep water wave steepness on a log-log scale so that the Hunt Formula plots as a straight line. For equilibrium profiles, it is found however that neither the measured runup (solid squares) nor the predicted runup (open squares) based on the integrated method plots as a straight line with the same slope as the Hunt Formula. The reason for this is that, for any given value of wave steepness, the runup depends on the exact values of breaking depth and surf zone width. Because these vary nonlinearly on the concave beach profile based on the equilibrium profile shape  $h=Ax^{2/3}$ , the solution is then a unique function of  $h_b$  and  $X_b$ .

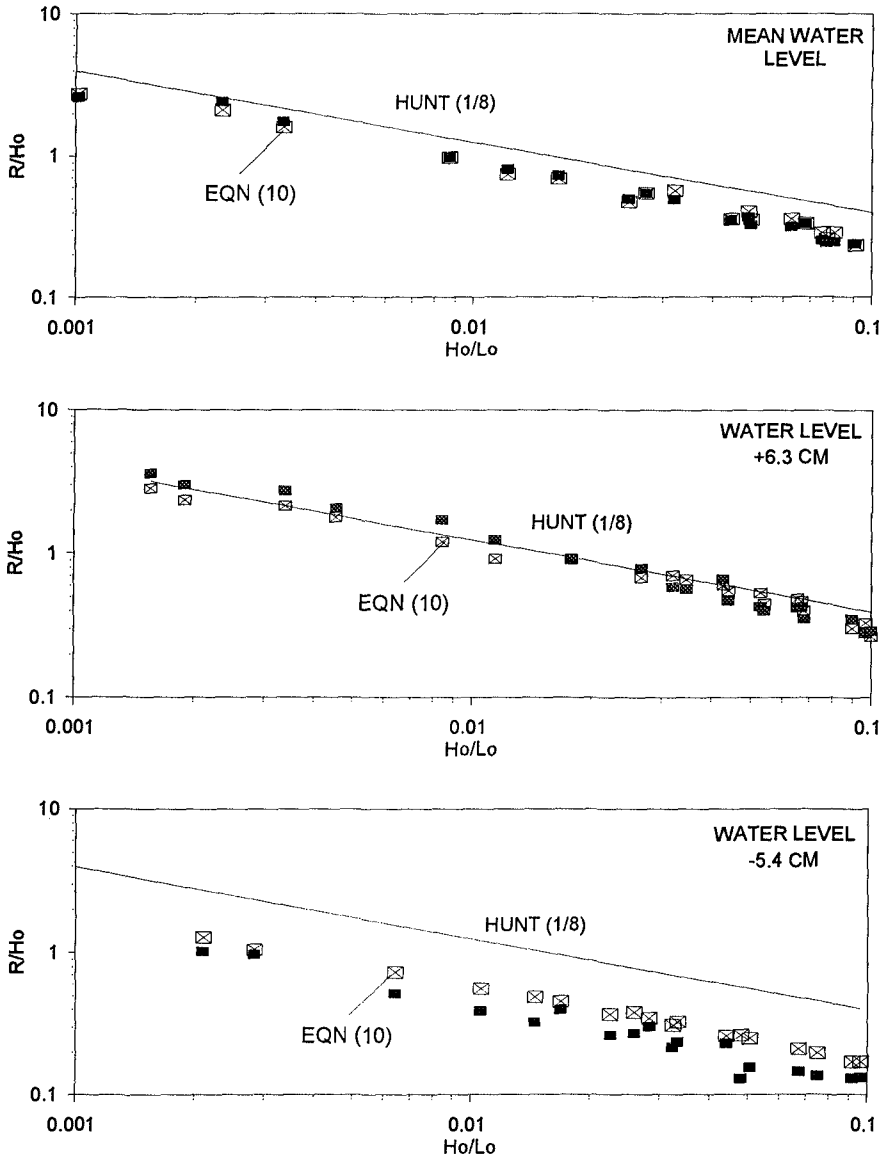


Figure 4. Measured and predicted runup over concave equilibrium profiles with  $m=1$ -on-8: (a) normal water level, (b) high water level, and (c) low water level.



For the mean water level condition, in Figure 4a, predictions based on equation (10) are in excellent agreement with measured values. Both are significantly below predictions from the Hunt Formula using the exposed beach-face slope. The difference is most pronounced for high steepness conditions where, in these experiments, the waves are relatively large and break far offshore yet produce relatively small runup so that the effective slope across the surf zone is fairly small.

In Figure 4b, for "high" water level conditions, measured and predicted runup agree much more closely with values predicted by the Hunt Formula using the beach-face slope. With the elevated water level, most waves now break on, or close to, the uniform beach-face slope so that the entire surf and swash zones are confined to the linear beach-face slope. Only in a few cases, with large waves having higher steepness, did waves break offshore on the concave portion of the profile so that runup was less much than expected from the Hunt Formula.

In contrast, Figure 4c for "low" water levels shows a large reduction in runup for essentially the same wave conditions used in the previous two tests. This is the result of the incipient break point being located far offshore over the concave portion of the profile. Measured runup is far below that predicted by the Hunt Formula using the beach-face slope of 1-on-8. Predictions based on the integrated method are in much better agreement but are somewhat higher than measured values. Figures 4b and 4c illustrate a strong dependence of runup on the profile geometry and water level that is rarely discussed in the literature. This should not be overlooked, however, as the measured values in this study show that runup may differ by about a factor of two over the range of water levels tested.

#### *Irregular Waves on Bi-Linear Profiles*

The integrated runup method in equation (10) was evaluated for irregular wave runup using statistical wave and runup parameters. Since most previous expressions for random wave runup have correlated statistical runup parameters to the incident significant wave height, a similar approach was used in this study. Incident wave conditions were described by both the mean and significant values for wave height and period. The mean and significant values for breaking depth and surf zone width were also determined from the video tape data of breaking waves. With these values as input, equation (10) was then used to predict the mean and significant runup values for comparison to the measured runup statistics.

Results of this analysis confirmed the results of Battjes (1971) that the mean runup could be predicted quite well using the mean wave conditions. Equation (10) gave quite good results when mean wave height, mean breaking depth, and mean surf zone width were used without use of any empirical coefficients. Use of the significant wave height in equation (10) produced runup estimates that were substantially below the measured significant runup. These results seem to indicate that the mean wave

conditions describe the best average slope across the surf zone for use in runup predictions according to the Saville hypothetical slope method. Use of significant wave conditions produced a flatter average slope since the significant breakpoint is located much farther offshore. In the integrated runup method, this smaller effective slope produces smaller runup estimates that do not agree with the measured values.

Examples of runup predictions using the integrated method in equation (10) based on mean wave statistics are shown in Figure 5. Dimensionless mean runup, defined as mean runup normalized by mean deep water wave height, is plotted against the mean wave steepness, defined as the mean wave height divided by deep water wavelength calculated by linear wave theory using the mean wave period of the random sea. In Figure 5a, results are shown for a baseline test on a planar beach profile having a 1-on-15 slope. These results confirm the ability of the Hunt Formula, and the integrated method which is identical to the Hunt Formula for a planar slope, to predict the mean random wave runup on uniform plane slopes. The results are in contrast to the findings of Mase (1989), however, who found that the Hunt Formula did not describe runup on plane slopes.

Figures 5b and 5c then show results for irregular wave runup on bi-linear profiles. It is evident that use of the Hunt Formula based on the exposed beach-face slope gives large over-estimates in the mean wave runup. Use of the integrated method, with the average slope defined by the mean breakpoint and the mean runup limit, then gives much better results. When the results in Figure 5 are analyzed, it is found that the Hunt Formula based on the linear beach-face slope gives an average error of 93% while the use of the Hunt Formula coupled with the Saville effective slope concept gives an average error of just 12%. As with regular waves, the integrated method tends to be slightly biased toward under-estimating the runup.

Additional subjects of concern for design are the distribution of runup about the mean value and the extreme runup statistics. In this study, it has been found that, while incident waves and breaking depths are described quite well by the Rayleigh distribution, the runup distribution is wider than the Rayleigh distribution with both more small runup events and more very large runup events. As a result, the assumption of a Rayleigh distribution for runup is not valid over composite-slope beaches.

Results of this study indicate that the ratio between the significant runup and the mean runup is between 1.5 and 2.0, with an average of about 1.8. In contrast, the Rayleigh distribution would suggest a ratio of 1.6. Similarly, the ratio between the average of the largest ten-percent of the measured runup events to the mean runup varied between about 1.8 and 2.7 with an average of about 2.25. The Rayleigh distribution would suggest a ratio of 2.0. In general, no specific functional dependence was found between these ratios and either wave steepness or the surf similarity parameter, although there was a general trend toward greater ratios for the higher-steepness, more energetic waves.

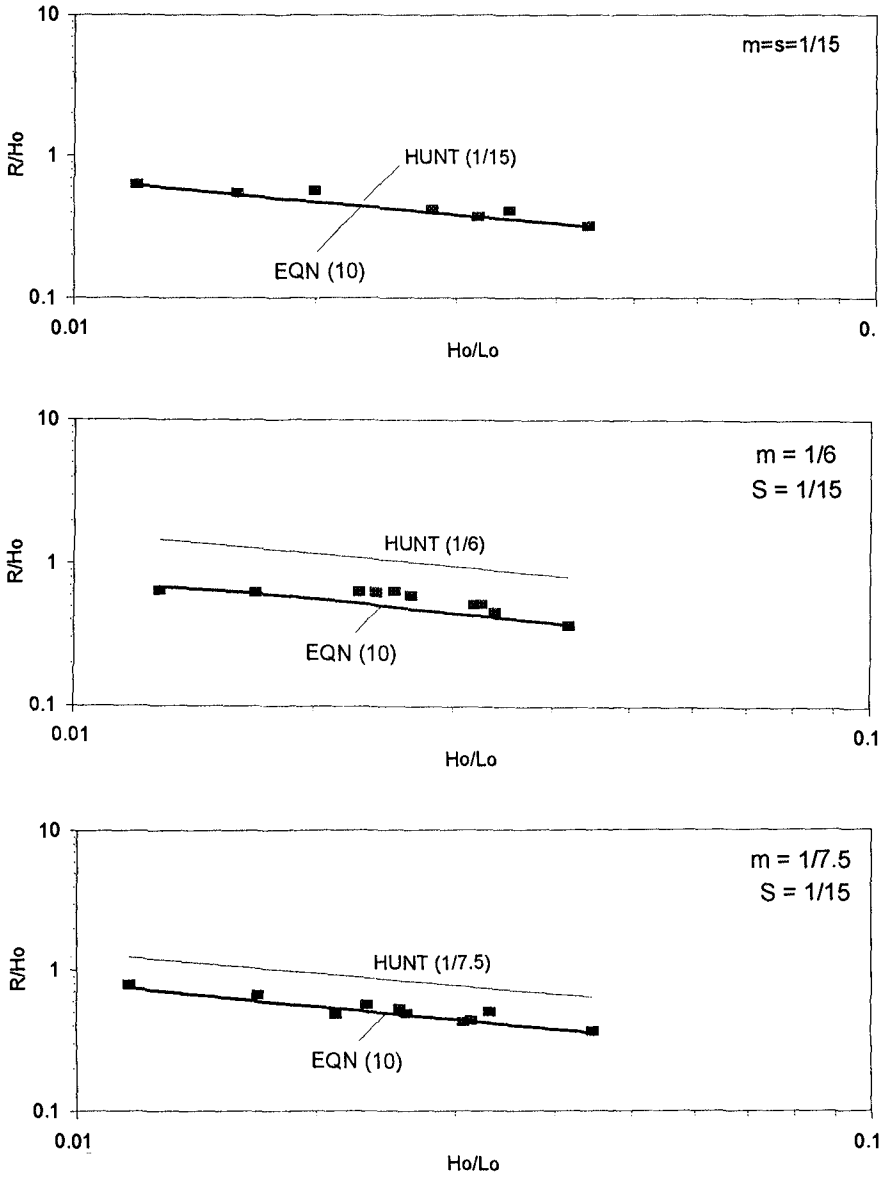


Figure 5. Comparison of measured and predicted runup of irregular waves on (a) linear profile and (b) bi-linear profiles. All wave heights are mean values.

### Alternative Integrated Runup Method

The integrated runup method presented above works well but is complicated by the requirements that: (1) the breakpoint of incident waves must be determined *a priori* and (2) the runup limit is initially unknown and enters the description of the effective beach slope. An alternate effective slope concept of de Waal and van der Meer (1992) overcomes these difficulties by defining the effective slope between points on the profile that are a distance of  $H_o$  above and below the still-water level. For a bi-linear beach profile, the effective slope according to de Waal and van der Meer is given by  $\tan\beta = 2ms/(m+s)$  and the runup based on the Hunt Formula is then

$$R = \frac{2mS}{m+S} \sqrt{H_o L_o} \quad (11)$$

Results of equation (11) for the mean runup are shown in Figure 6. Also shown are the predictions from the integrated method in equation (10) and from the empirical equations of Mase (1989). As shown, the method of de Waal and van der Meer produces results that have approximately the same average error as obtained using the Saville effective slope concept. The method of Mase over-estimates the runup severely primarily since it is based on planar uniform slopes.

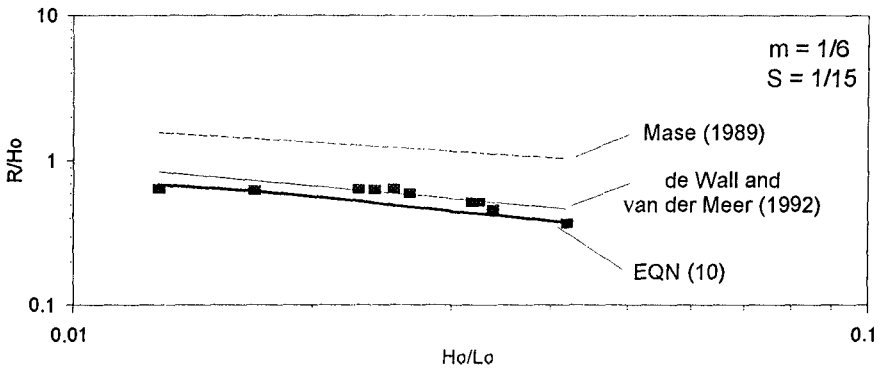


Figure 6. Comparison of measured and predicted mean runup in random waves from various prediction methods.

### CONCLUSIONS

This paper has included two main parts: (1) the development of a simple integrated method for predicting runup on composite-slope beaches and (2) the experimental verification of this integrated approach in both regular and irregular waves. It has been shown that by combining the Hunt runup formula with the Saville

effective slope concept, an analytical solution is obtained for runup over idealized bi-linear and equilibrium beach profiles. The solution can also be obtained by iterative methods for use in existing numerical models for surf zone hydrodynamics or beach profile change to estimate the runup over more complicated beach geometries.

The integrated method demonstrates that runup over concave and bi-linear beach profiles is less than would be expected from the Hunt Formula based on use of the exposed beach-face slope. Laboratory tests conducted on impermeable smooth slopes tend to verify the analytical solution for both bi-linear beaches and concave equilibrium beaches in both regular and random waves. While additional work on extreme runup statistics in random waves is needed, preliminary results indicate that the integrated method can be applied directly using the mean incident wave height to estimate the mean runup.

### ACKNOWLEDGEMENTS

The authors acknowledge the support of the Coastal Engineering Research Center of the U.S. Army Waterways Experiment Station. Laboratory tests were carried out with the assistance of Ensigns Mark Vannoy, Greg Selfridge, Monty Hasenbank, Tom Mayne, and Gillian Brest van Kempen.

### REFERENCES

- Battjes, J.A., 1971, "Run-up Distributions of Waves Breaking on Slopes," *J. Waterways, Harbors and Coastal Engr. Div.*, ASCE, Vol. 97, pp. 91-114.
- Battjes, J.A., 1974, "Surf Similarity," 14th Intl. Conf. Coastal Engr., pp. 466-480.
- De Waal, J.P. and van der Meer, J.W., 1992, "Wave Runup and Overtopping on Coastal Structures," *Proc. 23rd Intl. Conf. on Coastal Engineering*, pp. 1758-1771.
- Dean, R.G., 1977, "Equilibrium Beach Profiles: U.S. Atlantic and Gulf Coasts, Ocean Engineering Report No. 12, University of Delaware, Newark, DE..
- Holman, R.A., 1986, "Extreme Value Statistics for Wave Runup on a Natural Beach," *Coastal Engineering*, Vol. 9, No. 6, pp. 527-544.
- Hunt, I.A., 1959, "Design of Seawalls and Breakwaters," *J. Waterways and Harbors Div.*, ASCE, Vol. 85, No. WW3.
- Mase, H., 1989, "Random Wave Runup Height on Gentle Slope," *J. Waterway, Port, Coastal, and Ocean Engineering*, ASCE, Vol. 115, No. 5, pp. 649-661.
- Saville, T., 1958, "Wave Run-up on Composite Slopes," 6th Intl. Conf. Coastal Engr., pp. 691-699.

## CHAPTER 169

### Simulation of nearshore wave current interaction by coupling a Boussinesq wave model with a 3d hydrodynamic model

ROBERTO MAYERLE, ANDREAS SCHRÖTER and WERNER ZIELKE <sup>1</sup>

#### ABSTRACT

This paper describes a deterministic modelling system under development at the Institute of Fluid Mechanics in Hannover to simulate three dimensional wave induced currents and the morphological evolution in the nearshore region. It is basically a coupling of a 2d Boussinesq wave model which predicts the wave motion along the horizontal direction with a 3d hydrodynamic, sediment transport and morphodynamic models that simulate the time averaged wave induced currents and the associated changes in the bathymetry due to sediment transport. It is intended to improve the understanding of morphological processes, investigate the impact of sea level rises due to climate change, study extreme events and assess in the selection of cost effective measures for coastal protection. Results of a demonstration of the simulation of the wave induced currents along a nearshore region in the Baltic Sea are shown.

#### 1. INTRODUCTION

Along the coast it is possible to distinguish between the erosion processes due to mean hydraulic conditions, that has an impact on large time scales (seasons, years), and due to extreme hydraulic conditions, that are restricted to small time scales (hours to days). Beach and dune erosion at large time scales are usually due to net positive, longshore sediment transport gradients. Short term erosion takes place occasionally during less frequent extreme events such as storms and hurricanes and the significant profile changes are restricted to the upper part of the coastal profile.

On the other hand, the morphological evolution in the nearshore region is the result of highly complicated three dimensional processes that combine tur-

---

<sup>1</sup>Institute of Fluid Mechanics and Computer Applications in Civil Engineering, University of Hannover, Appelstr. 9 A, D-30167 Hannover, Germany

bulent, oscillatory (wave) and current motion. In particular within the breaker zone the turbulence generated by wave-breaking is intensive. A number of hypotheses have been formulated to describe the process of bar formation within the surf zone. Although it may involve several mechanisms, the most reasonable explanation relates to the wave driven circulation currents in the vertical plane known as undertow. If a movable bed with constant slope is exposed to waves, a bar will develop close to the point of wave breaking. This is due to the sediment transport within the breaker zone being directed away from the coast due to the undertow. Besides, intensive wave breaking generates high turbulence levels causing large amounts of sediment to suspend, thus being the transport of this suspended sediment the predominant transport mechanism under such conditions.

Until recently most of the numerical model simulations in the nearshore region have been carried out using 2d models. Although in some cases it is possible to capture the main patterns with depth or laterally averaged models, only part of the sediment transport is taken into account, i. e. either the longshore or the cross-shore sediment transport is captured. In other words the models describe either the transport along with time and depth averaged currents, or the transport due to waves and vertical circulations in a more or less cross-shore profile. In more complex situations, it makes little sense and neither transport should be neglected.

Nowadays, there are a number of numerical models under development for short term coastal profile evolution for direct incoming waves. An intercomparison among six models developed with different degrees of refinement and empiricism was carried out by Hedegaard et al., 1992. The models were tested against experimental results obtained at the large wave flume in Hannover in a pure 2d depth vertical case. The results showed that it is relevant to go to full or quasi 3d modelling of currents and suspended sediment to be able to judge where the major research efforts should be spent in the years to come (Roelvik and Brøker, 1993).

The 3d modelling system under development is intended to handle short term events in the nearshore region and to reproduce wave induced currents and the associated changes in the bathymetry adequately. It is also to improve the understanding of morphological processes, investigate the impact of sea level rises due to climate changes, study extreme events and assess in the selection of cost effective measures for coastal protection. With the improvements in computer efficiency and algorithm performance, process-based or deterministic wave modelling in the time domain are within reach. However, unless the wave phenomena in the horizontal direction is properly simulated there is little gain in going to three dimensional modelling. As linear wave models do not apply well in the nearshore region, the proposed modelling system is a coupling of a 2d nonlinear time discrete Boussinesq wave model with a 3d hydrodynamic and sediment transport models. The wave model computes the wave field along the horizontal direction whereas the 3d model is responsible for the time averaged wave induced currents and the associated changes in the bathymetry due to sediment transport. The suggestions proposed by Svendsen and Lorenz (1989) in solving a modified set of the Navier-Stokes equations for three dimensional wave induced currents were followed. The radiation stresses, wave set-up and wave trough level needed for the solution of these equations result from the

application of the wave model. A description of the approach adopted and a demonstration of the simulation of the wave induced currents along a small stretch on the German coast in the Baltic Sea are presented.

## 2. APPROACH

The three dimensional wave induced currents are described by a set of modified Navier-Stokes and the continuity equations that are solved respectively for the velocities along the horizontal plane and vertical. The velocities along each direction ( $x$ ,  $y$  and  $z$ ) are replaced by three contributions respectively: the mean (current) component ( $U$ ,  $V$  and  $W$ ); a purely periodic component correspondent to the wave motion ( $u_w$ ,  $v_w$  and  $w_w$ ) and a turbulent velocity fluctuation ( $u'$ ,  $v'$  and  $w'$ ) as follows:

$$\left. \begin{aligned} u &= U + u_w + u' \\ v &= V + v_w + v' \\ w &= W + w_w + w' \end{aligned} \right\} \quad (1)$$

The resulting set of modified Navier Stokes equations (Svendson and Lorenz, 1989) are:

$$\frac{\partial U}{\partial t} + \frac{\partial U^2}{\partial x} + \frac{\partial UV}{\partial y} + \frac{\partial UW}{\partial z} + \frac{\partial(\overline{u_w^2} - \overline{w_w^2})}{\partial x} + \frac{\partial \overline{u_w v_w}}{\partial y} + \frac{\partial \overline{u_w w_w}}{\partial z} = -g \frac{\partial b}{\partial x} - \frac{\partial(\overline{\tilde{u}'^2} - \overline{\tilde{w}'^2})}{\partial x} - \frac{\partial \overline{\tilde{u}' v'}}{\partial y} - \frac{\partial \overline{\tilde{u}' w'}}{\partial z} \quad (2)$$

$$\frac{\partial V}{\partial t} + \frac{\partial V^2}{\partial y} + \frac{\partial UV}{\partial x} + \frac{\partial VW}{\partial z} + \frac{\partial(\overline{v_w^2} - \overline{w_w^2})}{\partial y} + \frac{\partial \overline{u_w v_w}}{\partial x} + \frac{\partial \overline{v_w w_w}}{\partial z} = -g \frac{\partial b}{\partial y} - \frac{\partial(\overline{\tilde{v}'^2} - \overline{\tilde{w}'^2})}{\partial y} - \frac{\partial \overline{\tilde{u}' v'}}{\partial x} - \frac{\partial \overline{\tilde{v}' w'}}{\partial z} \quad (3)$$

In the equations  $t$  is the time,  $g$  is the acceleration due to gravity and  $b$  is the wave set-up. The superscripts  $\tilde{\phantom{x}}$  and  $\bar{\phantom{x}}$  have been used to denote respectively ensemble-averaging and averaging over a wave period. The terms  $\partial U^2/\partial x$  and  $\partial V^2/\partial y$  represent the momentum flux from the cross-shore and long-shore currents whereas the  $UV$ -term represents the coupling between the two current components. The  $\overline{u_w^2} - \overline{w_w^2}$  and  $\overline{v_w^2} - \overline{w_w^2}$  are the wave radiation stress components. The  $\partial/\partial x$ -component is one of the key elements in the driving mechanism for the undertow although it is generally small in comparison to other components such as the pressure term  $\partial b/\partial x$ . The  $\overline{u_w v_w}$  is the tangential radiation stress term responsible for creating the longshore flow  $\partial \overline{u_w v_w}/\partial x$  and the crossshore flow  $\partial \overline{u_w v_w}/\partial y$ . The terms  $\partial \overline{u_w w_w}/\partial z$  and  $\partial \overline{v_w w_w}/\partial z$  represent the horizontal stresses created by the oscillatory wave components. The remaining terms are the Reynolds' stresses.

The vertical velocity is obtained by solving the continuity equation similarly to the approach used by Pechon, 1992:

$$\frac{\partial U}{\partial x} + \frac{\partial V}{\partial y} + \frac{\partial W}{\partial z} = 0 \quad (4)$$



The equations are applied only within the central layer, from the bottom boundary layer to the wave trough level. Above the wave trough level, where there is water only part of the time, a current velocity component cannot be defined. Their solution assumes knowledge of the oscillatory wave motion to determine the radiation stresses and to define the wave set-up elevation and the wave trough level. An eddy viscosity model based on the mixing length is used for computing the Reynolds stresses. At the bottom, a partial slip boundary condition related to the logarithmic law is used. At the wave trough level, the wave induced currents are computed similarly to the other nodes located within the central layer, since it is also within the water body. The pressure distribution is assumed uniform along the vertical and the radiation stresses come from the application of the wave model.

### 3. MODELLING SYSTEM

The modelling system includes a wave module that computes the wave related quantities (wave trough level, wave set-up and radiation stress) and 3d hydrodynamic, sediment transport and morphodynamic modules responsible respectively for the three dimensional wave induced currents, sediment transport (bed plus suspended loads) and bed evolution.

The wave module is based on an extended form of the Boussinesq wave equations with improved dispersion and shoaling properties in deeper water (Schröter et al., 1994). Refraction, diffraction, reflection and interaction of the different directions of incoming waves and components are included (Prüser and Zielke, 1990). Short and long water waves of arbitrary shape with high resolution up to depth to wave length ratio of about 1.5 can be handled adequately. It should be stressed that although the equations are solved for the depth averaged wave induced currents along the horizontal directions, a vertical velocity distribution is implicit in the derivation of the Boussinesq equations. A parabolic and linear distribution along the vertical apply respectively for the horizontal and vertical velocities. Besides, since the resulting velocities are already wave induced components, the current component contribution needs to be subtracted in order to determine the oscillatory wave motion and thus the radiation stress distribution along the vertical.

The hydrodynamic module uses a numerical model originally developed at the Center for Computational Hydrosience and Engineering in Oxford, USA. The first author participated in the development, improvement and verification of the model. It was originally developed to solve two Navier-Stokes for the velocities along horizontal directions, the kinematic condition on free surface for the surface elevation and the flow continuity equation for the vertical velocity component (Wang et al., 1992). The model was changed to solve the modified set of Navier-Stokes and continuity equations from the bottom to the wave trough level. It uses quadrilateral structured grids with constant number of nodes along the vertical. Along the horizontal the grid system is kept throughout the simulation whereas along the vertical it adjusts itself to the changes in the wave trough level and bathymetry.

In the sediment transport module, the total load is obtained by adding bed to suspended loads. The bed load is based on empirical equations and the suspended load results from the solution of the convection-diffusion equation.

The influence of the waves on the sediment transport is included. The morphodynamic module or the bed evolution module is assumed to be governed by the sediment continuity equation.

The wave induced currents and the associated changes in the bathymetry are obtained in successive steps using alternatively the wave, hydrodynamic and morphodynamic modules (Figure 1). Along the horizontal directions the grid system is kept the same. A constant number of nodes throughout the domain is defined along the vertical direction for the three dimensional simulations. The simulations for a given bathymetry begin with the wave module and are carried out until the changes in the time integrated wave related quantities are no longer significant. Then the time averaged radiation stresses (at every node within the three dimensional domain), wave set-up elevation and wave trough level are determined. Next, a nearly steady state three dimensional wave induced current is computed below the wave trough, for the same bathymetry, by the hydrodynamic module. In the sediment transport module the total sediment transport is evaluated. Finally, the resulting wave induced currents are used to compute the bed elevation changes by the morphodynamic module. Once the bed evolution anywhere in the domain is significant, the wave module is recalled and updated wave related quantities are determined for the new conditions. This sequence is carried out repeatedly advancing the solution in time.

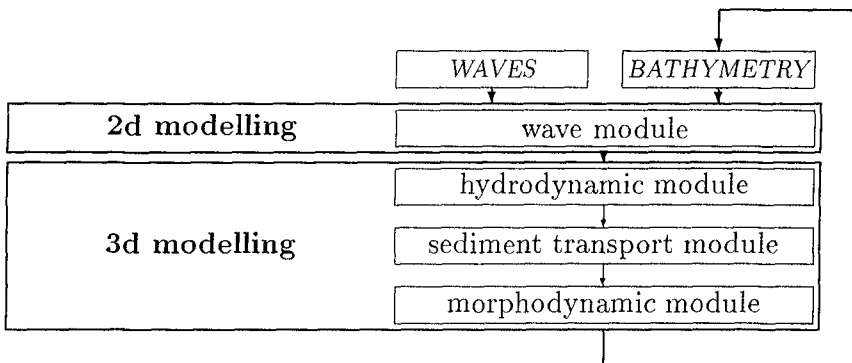


Figure 1. Modelling system.

#### 4. DEMONSTRATION

Results of a demonstration of the modelling system to the simulation of three dimensional wave induced currents without sediment transport along a nearshore stretch were carried out to show its applicability. The domain simulated (300m longshore by 120m cross-shore) is a small stretch on the German coast in the Baltic Sea (Figure 2) with two lines of groynes (150m apart) normal to the coastal line. The bathymetry was defined from five cross-shore profiles. Wave conditions measured in June 1992 at three gauges located in the center, just upstream of the simulated domain were considered in the simulations. The estimated wave spectrum used in the simulations is shown in Figure 3. Wave

lengths from 15m to 70m and mean water depths from 0.2m to 2.9m were observed. The simulations were carried out for the conditions described above. Only wave induced currents without sediment transport were considered.

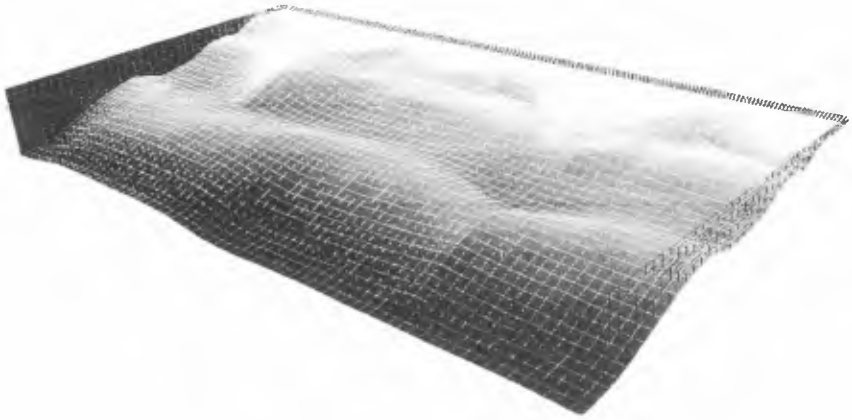


Figure 2. Bathymetry of the simulated domain.

*ENERGY DENSITY* [ $\text{m}^2/\text{Hz}$ ]

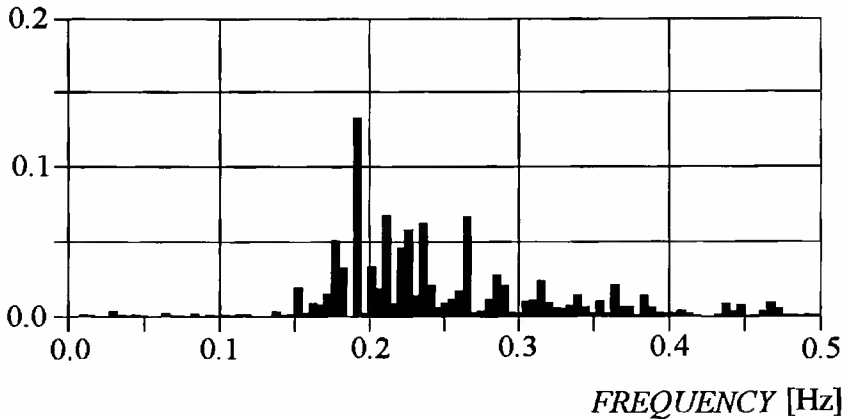


Figure 3. Measured spectrum of the incoming waves.

The simulations with the wave module (Boussinesq model) were carried out for 500s. Results at this time level are shown in Figure 4. Experience shows that at least 10 nodes are required per wave length in order to capture the main wave phenomena properly. Therefore, a highly refined finite difference grid with 152 by 292 nodes ( $\Delta x = \Delta y = 1\text{m}$ ) in conjunction with time steps equal to 0.1s were used. The information needed to define the three dimensional domain and to solve Eqns. 2 to 4 were obtained by averaging the results obtained in the application of the wave module from the time levels 250s to 500s.

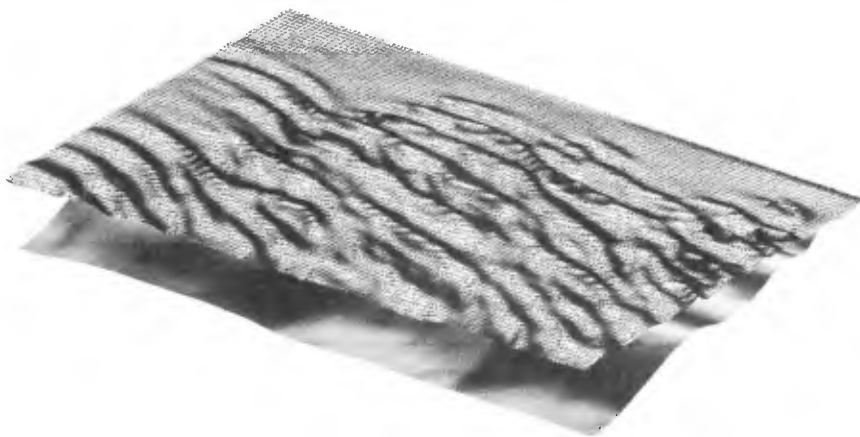


Figure 4. Simulated waves with the Boussinesq wave model.

The three dimensional simulations used a slightly coarser grid along the horizontal directions. The domain was defined by 73 x 38 nodes respectively along the longshore and cross-shore directions. A 4m grid spacing was considered along the horizontal directions. Along the vertical, 10 nodes were placed from the bottom to the elevation of the wave trough level. On the sides of the domain, total slip boundary conditions were used. Results of a quasi-steady state wave induced current field are shown in Figures 5 to 7. In Figures 5 and 6 the resulting three dimensional wave induced currents respectively at the bottom and at the elevation of the wave trough level are shown. Although the circulations are mainly along the horizontal directions, vertical circulations are also present. Notice that in the vicinity of the sand bank the velocities are directed seawards especially near to the bottom.

The tracks of several particles released from two different velocity profiles (see Figures 5 and 6) are shown in Figure 7 to illustrate the highly three dimensional conditions in the vicinity of the sand bank. Although it is difficult to judge without direct comparisons with measurements whether the resulting wave induced currents were adequately captured, it can be seen that they are highly three dimensional.



Figure 5. Three dimensional wave induced currents at the bottom.

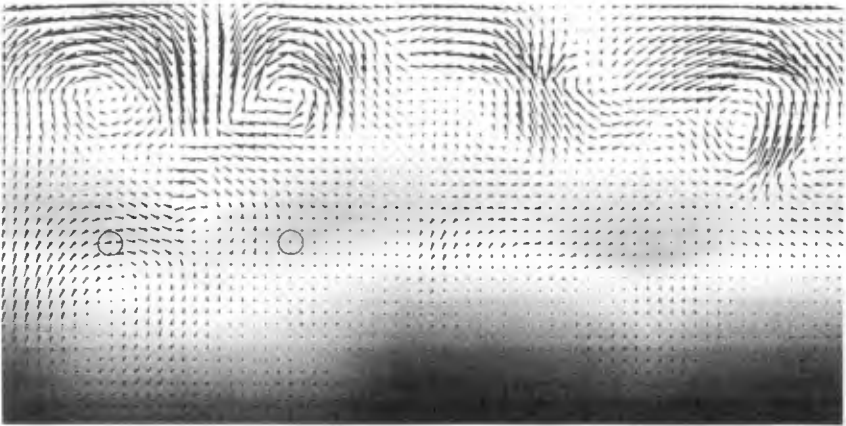


Figure 6. Three dimensional wave induced currents at the wave trough level.

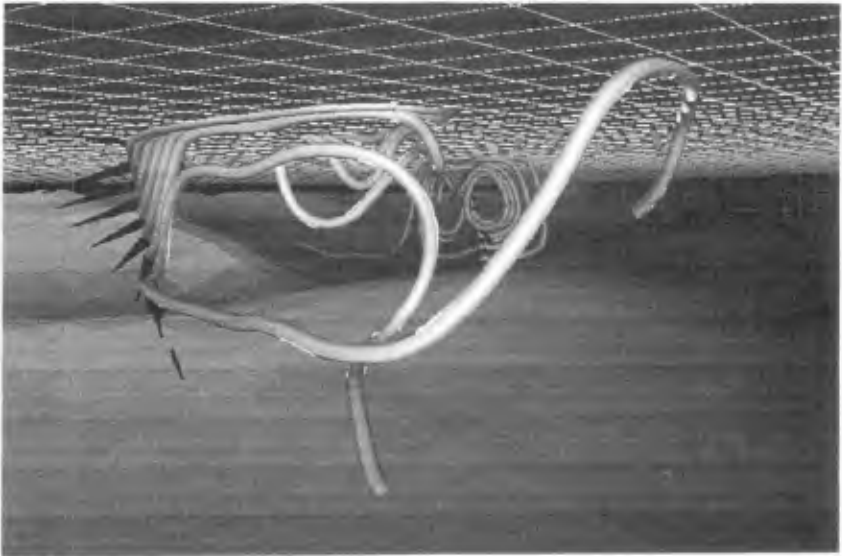


Figure 7. Particle tracks.

## 5. CONCLUSIONS

This paper shows the results of a simulation of a stretch on the German coast using a 3d deterministic wave modelling system under development. The results show the models ability in describing highly complicated conditions within the surf zone. The coupling of a Boussinesq wave model with a 3d model implemented with a set of modified Navier-Stokes equations enables the most important wave phenomena of interest to the coastal engineer to be captured. Further improvements and verifications of individual models, treatment of boundary conditions and of the layer between wave trough and wave crest, incorporation of hydrodynamic pressure, improvements to the sediment transport module as well verifications of the modelling system with three dimensional measurements are envisaged.

## 6. ACKNOWLEDGEMENTS

This work is part of the project SFB205 TP B4 sponsored by the German Research Association (*Deutsche Forschungsgemeinschaft*). The authors would like to thank Mr. F. Behrendt for his assistance in the preparation of the figures with an Application Control Environment based on AVS/UNIRAS Visual Systems(Germany) and Dr. Schönfeldt of the Zingst Maritime Observatory - Leipzig University for providing the measurements.

## 7. REFERENCES

Hedegaard, I. B., Roelvink, J. A., Southgate, H., Pechon P., Nicholson, J. and Hamm, L. *Intercomparison of coastal profile models*. International Conference on Coastal Engineering, Delft 1992

Pechon, P. *Numerical modelling of wave-driven currents and sediment transport in the surf-zone*. Electricite de France, Internal Report HE-42/92-15, 1992.

Prüser, H.-H. and Zielke, W. *Irregular waves on a current*. International Conference on Coastal Engineering, Delft 1990.

Roelvik, J. A. and Brøker, I. *Cross-shore profile models*. Coastal Engineering, 21, 163-191, 1993

Schröter, A., Mayerle, R. and Zielke, W. *Optimized dispersion characteristics of the Boussinesq wave equations*. Proceedings of the International Symposium: Waves-Physical and Numerical Modelling. University of British Columbia, Vancouver, Canada, August 1994.

Svenson, I. A. and Lorenz, R. S. *Velocities in combined undertow and longshore currents*. Coastal Engineering, 13, 55-79, 1989.

Wang, S. S. Y., Hu, K. K. and Mayerle, R. *3d free surface flow modeling by efficient finite element method*. In ASCE, editor, Hydraulic Engineering, 1021-1029, August 1992.

## CHAPTER 170

### EXPERIMENTAL RESULTS OF WAVE TRANSFORMATION ACROSS A SLOPING BEACH

Constantine D. Memos<sup>1</sup>, Member ASCE

#### Abstract

Experiments have been conducted to investigate the transformations of the wave characteristics induced by a uniformly decreasing sea bed. These transformations were recorded on both the frequency and the time domain representations of random wave trains. The coastal zone upwind of severe breaking was studied. Among the findings it is noted the tendency of the spectrum width parameter to decrease at a slowing rate as the waves propagate on shoaling waters. Also, the correlation coefficient between wave heights and periods seems to inversely follow the variations of a measure of the wave heights. A mathematical model has been developed based on existing results for shoaling, wave breaking and decay. This model applicable to a wide area of the surf zone predicts adequately the evolution of the joint probability between wave heights and periods provided by the experimental results.

#### Introduction

Wind wave modeling in the surf zone and the transitional waters is of central importance to coastal engineering. Albeit, shallow water waves in coastal areas are much more complex to model compared to waves in deep water. The transformations of random waves propagating into shallow water are governed by various processes, that are usually described by the source terms in an energy-balance equation. Apart from the wind action on the sea surface, the dissipation due to "white capping" and the nonlinear wave-wave interactions, factors that influence wave propagation in deep water, shallow water waves are additionally affected by processes such as shoaling, refraction, diffraction, reflection, bottom friction and wave breaking due to depth limitation.

---

<sup>1</sup> Civil Engineering Department, National Technical University of Athens, Greece.



Depth-controlled shoaling and wave breaking play a dominant role in modifying the waves as they travel across the beach. The depth-induced wave breaking affects the whole frequency band in a way similar to the shoaling process. In fact, breaking can be regarded as the final stage in a combined shoaling/breaking transformation. This transformation can be tracked either on the frequency spectrum of the incoming waves or on the relevant statistics of wave heights and periods based on the representation of the wave train in the time domain.

The latter representation contains more information on the statistical structure of the sea state and seems to suit better the probabilistic approach to the design of coastal defences.

### Existing Results

Various approaches have been used in the past to investigate and model the transformations to the probability density function (pdf) of the wave heights induced by wave shoaling/breaking due to depth limitation. The earlier models (Collins, 1970; Battjes, 1972; Kuo, 1974; Goda 1975) describe shoaling as only dependant on the local water depth. The common idea of all local-depth models is to cut off the portion of the wave height pdf beyond a breaker height controlled by water depth.

Collins and Battjes used a sharp cut-off of the Rayleigh pdf with all broken waves having heights equal to the breaker height  $H_b$ . Kuo and Kuo assumed the broken waves to have some height smaller than  $H_b$  after breaking and produced a sharply truncated Rayleigh pdf renormalized to unity. Goda's approach constitutes a refined version of the previous methods in that wave breaking occurs with linearly varying probability over a range of wave heights  $H_{b1}$  to  $H_{b2}$ , resulting in a distribution with a gradual cut-off around  $H_b$ . Figure 1 illustrates the above assumptions as regards the modification of the wave height pdf due to wave breaking.

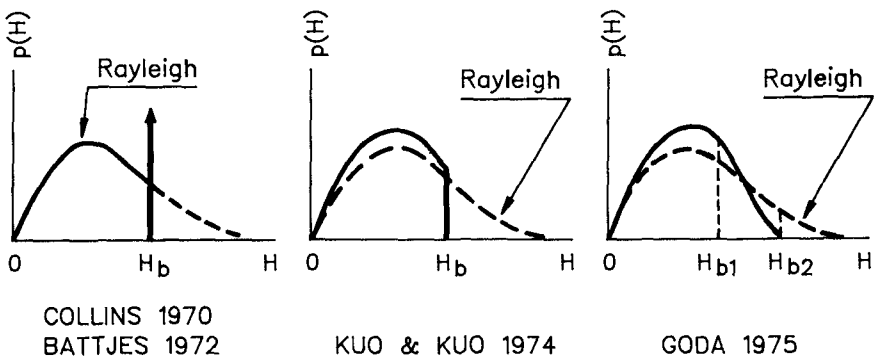


Fig.1 Modification of wave height pdf due to wave breaking

A second type of models (Battjes & Janssen, 1978; Thornton & Guza, 1983; Battjes and Beji, 1992) are based on integrating the energy-flux balance equation with wave height as it is transformed by the shoaling process along a path starting in deep water. Models applying the energy-flux balance calculate wave heights by employing the energy dissipation due to a bore, to model the shallow-water wave breaking. This involves a bore dissipation function adjusted through a variable parameter to each individual breaker type.

To simplify the analysis both types of models assume that the waves are narrow-banded in frequency, so that all wave heights of the distribution are associated with the same average frequency. Therefore, starting in deep water, the wave heights are described by the single parameter Rayleigh pdf, which is modified accordingly as the waves propagate over the shoaling beach.

A further method to tackle the problem of random wave shoaling is the wave-by-wave analysis, that permits more realistic inclusion of the physics of the process. This approach selects randomly offshore waves from a known joint distribution between heights and periods, transforms individual waves and then reassembles the wave heights into probability distributions across the surf zone. In fact recent studies indicate that much of the behavior of random waves in the surf zone can be represented by the behavior of a set of individual regular waves (Dally and Dean, 1986; Ebersole 1987; Dally 1990; etc). Dally (1992) presented such a method by using as input the joint pdf of wave heights and periods proposed by Longuet-Higgins (1983). However, this density function is limited mainly to narrow banded spectra. It is noted that a simpler technique employing only the characteristic wave height and the wave period at peak has been suggested by Kamphuis (1994), avoiding the computations for many regular waves as originally proposed. However, this approach is suited rather for the spectral representation than for the joint pdf of the waves.

### Scope of Present Research

Motivation for the present investigation was provided by recent results regarding the joint pdf of wave heights and periods applicable to the more realistic broad banded power spectrum (Memos & Tzanis, 1994). The scope of this research is to study experimentally the transformations on the time and frequency domain incurred during the initial phases of shoaling in the transitional water depths prior to intense breaking. Also, a synthetic model on the joint pdf of shoaling/breaking waves in a wider zone of a uniformly sloping bed is presented along with some initial results.

The experiments have been conducted in the 50 m-long random wave flume of Imperial College, London and the data analysis was performed at the Technical University of Athens.

### Experimental Set-up

The experiments aimed at studying the behavior of random unidirectional waves propagating over a beach of decreasing depth and they were carried out in a 50m-long random wave flume. The set-up allowed data collection at probes placed over a flat beach sloping at 5.5%, while the water depth was kept around 1m over the horizontal bed of the flume (Fig. 2).

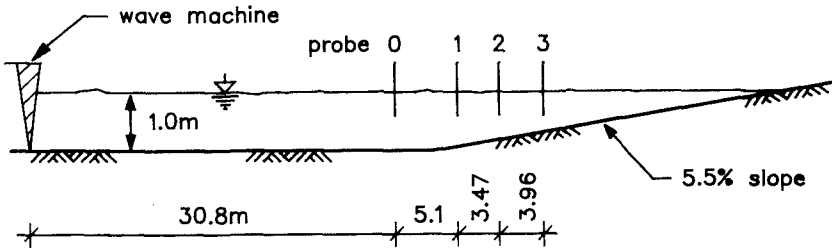


Fig.2 Experimental set- up

The random wave machine spanned the 2.78 m wide flume and was fed with signals of prescribed spectral characteristics. The data were collected from twin wire probes through an analog-to-digital converter. In all 27 runs were carried out, each one having a different input signal.

The transitional waters and outer surf zone was mainly investigated, where wave breaking and set-up occurred at low percentages, thus excluding the significant effect of wave reforming, which could otherwise "contaminate" the results of the present study of the shoaling process. Also, in this region the bed friction effect was rather reduced and could easily be ignored.

The investigation of the transformations referred to both the frequency and the time domain representations of the wave train.

### Main Findings and Discussion

The main results related to the transformation of the power spectrum across the outer surf zone are based on results of 4 representative experimental runs. These findings are the following:

- (a) In general the peak frequency of the input spectrum did not change significantly after the waves have travelled for 31m from the wave machine to the first probe. Also, the peak energy density and the frequency at peak tend to be stable as the waves propagate over the beach. This happened in all 27 runs. The shape of the spectrum around the peak was found to be

stable, too. It is noted that since we are studying the outer surf zone, with little wave breaking the spectrum tends to increase slightly in energy prior to major dissipation due to intense wave breaking.

The above stability of the shape of the spectrum and of the frequency at peak have been reported also by other researchers (Cai et al., 1992; Resio, 1987; etc).

- (b) A systematic modification of the rear face of the spectrum was taking place as the waves propagated into shallower waters. This is due to conservative non-linear effects in accordance with Kitaigorodskii's modification of the tail of the spectrum in shallow water behaving there like  $f^{-3}$  rather than  $f^{-5}$ , where  $f$  the frequency (Bouwes and Komen, 1983).
- (c) A transfer of energy to the forward face of the spectrum was also noticed. This, has again been verified by other investigators (Mase & Kirby, 1992; Resio, 1987).
- (d) A second peak is usually being developed at twice the peak frequency of the spectrum, presumably due to bound waves (Bendykowska and Werner, 1989; Memos, 1990; etc.).

All points mentioned previously can be observed in Fig. 3.

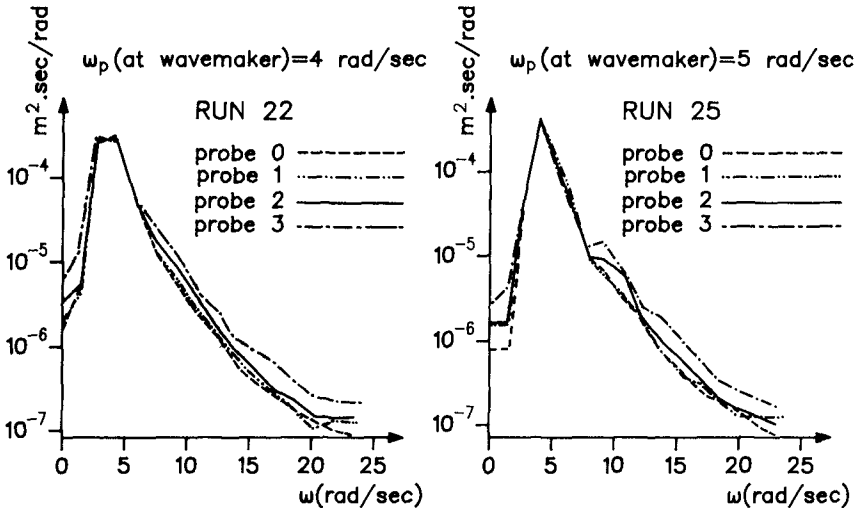


Fig. 3 Modification of wave energy spectrum

- (e) A systematic narrowing of the spectrum established by the decrease of spectral width  $\epsilon$  as the waves propagate from deep water toward the surf zone was detected (Fig. 4). It appears that a lower limit of  $\epsilon$  around 0.4 is reached at the most innershore probe, regardless of the initial width of the input spectrum (with  $\epsilon > 0.4$ ). This seems to be a new result.

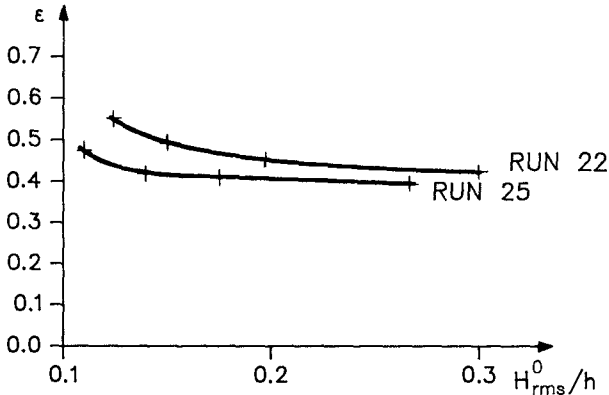


Fig. 4 Variation of bandwidth parameter  $\epsilon$  across the beach

Referring to the variation of wave heights and periods across the slope, the following points can be made for the time domain representation of the waves:

- (f) No major deviation of the wave heights pdf from the Rayleigh distribution occurs within the considered zone. Only a small redistribution of energy seems to take place around the peak of the pdf of wave heights (Fig. 5). This has been reported, also, by Thornton & Guza (1983).
- (g) A mild increase of the mean wave period with wave propagation was also detected (Fig.6).
- (h) The joint pdf of wave heights  $H$  and periods  $T$  showed an overall stability in line with the stability displayed by the energy spectrum. This can be seen in Fig. 7, where the corresponding joint pdfs for the 4 locations have been plotted for one run. However, a trend of more  $H$ - $T$  pairs accumulating close to the modal values was uncovered by estimating the double integral  $\int \int p dHdT$  for, say,  $p > 1.0$ . The results for 2 runs shown in Fig. 8 exhibit this tendency. This accumulation can also be verified in the marginal distribution of wave heights along the mean period, as shown in Fig. 9.

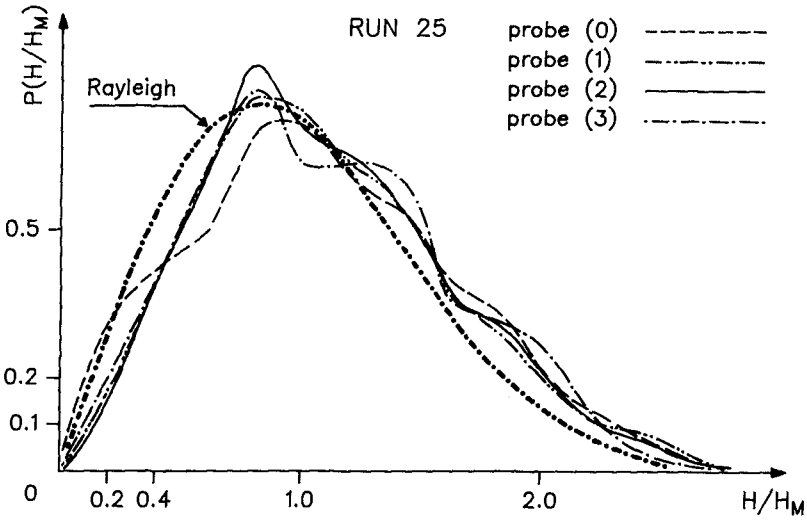


Fig. 5 Evolution of wave height distribution

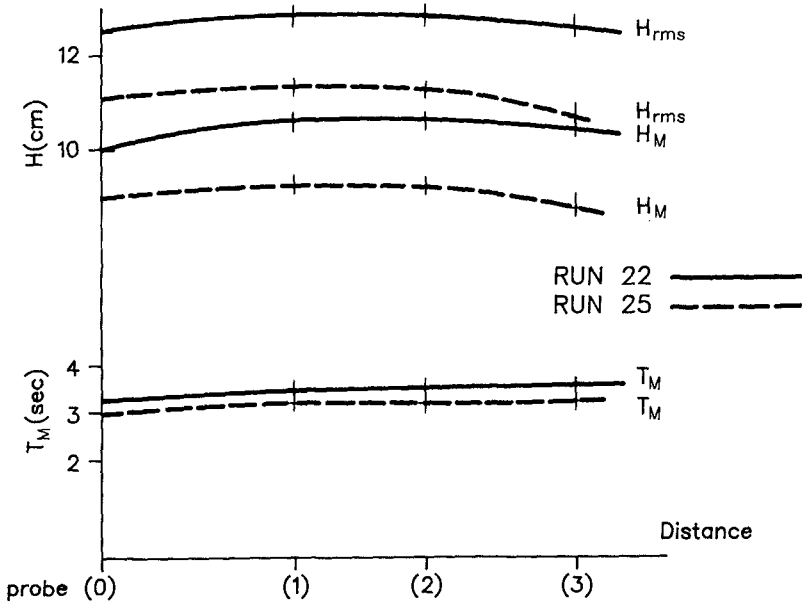


Fig.6 Variation of wave height and period across the beach

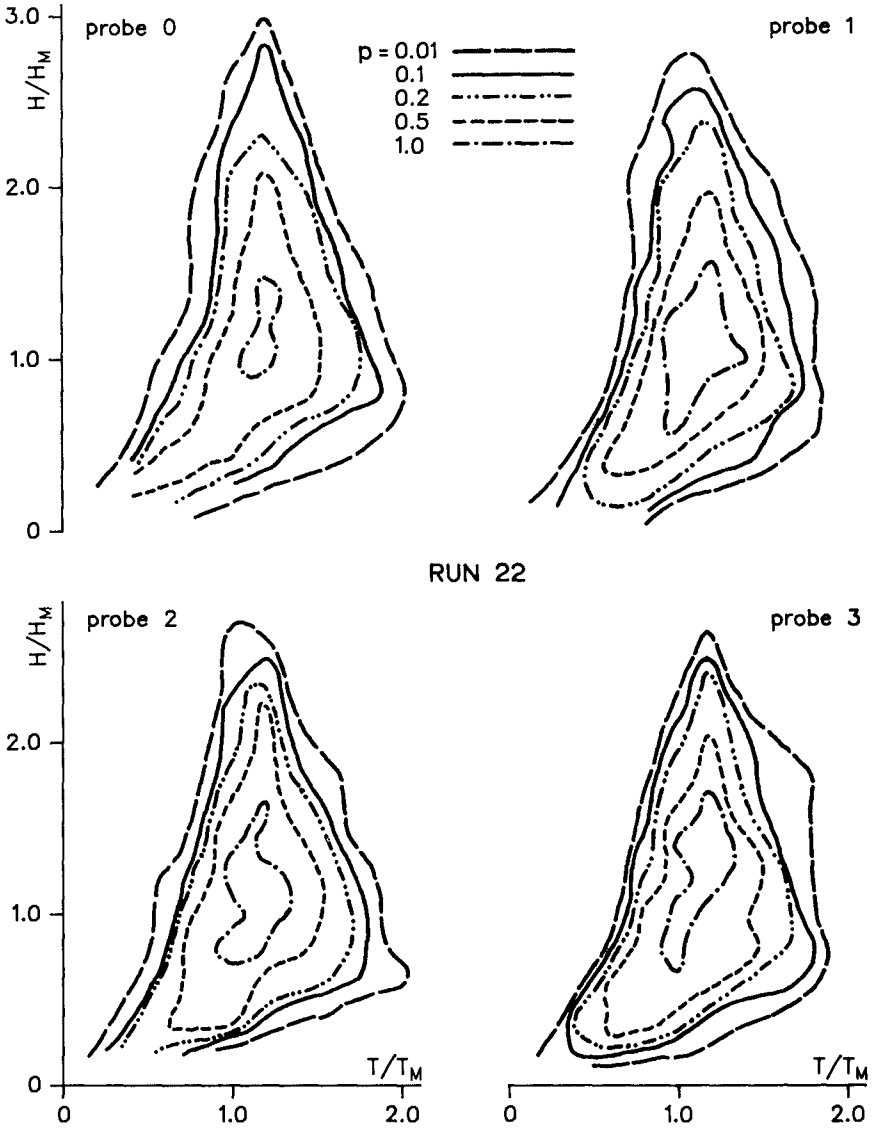


Fig. 7 Joint pdf of H-T at 4 gauges

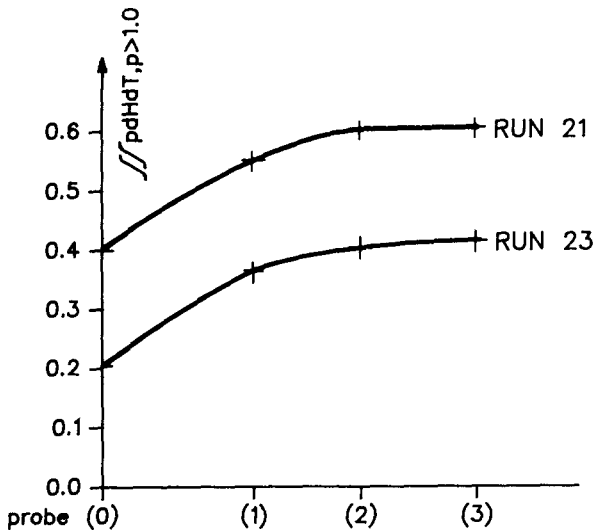


Fig. 8 Higher probabilities for higher waves

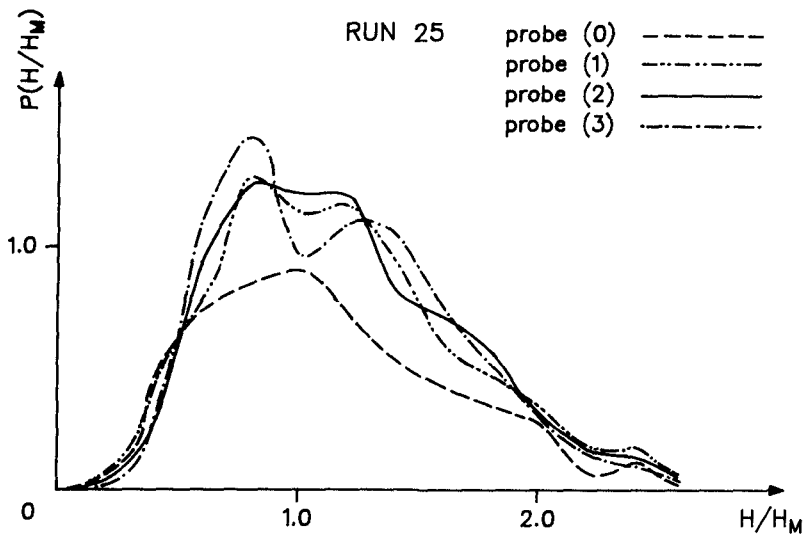


Fig. 9 Marginal distribution of H along the mean period

- (i) The variation of the correlation coefficient  $r$  between wave heights and periods can be seen in Fig. 10. A similar trend with that of the



spectrum bandwidth parameter  $\varepsilon$  can be observed, the difference lying in that  $r$  reaches a minimum value within the outer surf zone under examination. This seems to correspond to the variation of the wave heights over the slope. For decreasing  $H$  we obtain increasing  $r$  and vice versa (cf Figs 6 and 10).

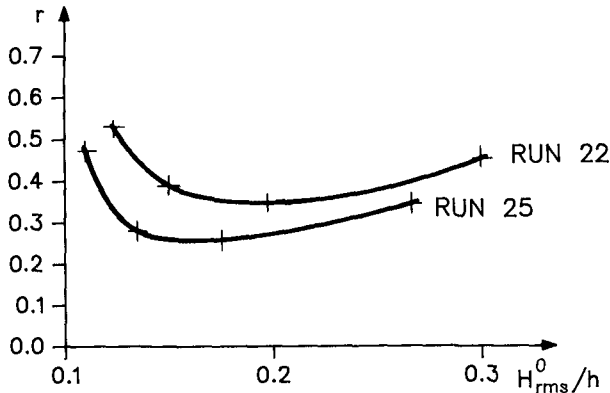


Fig. 10 Variation of  $r(H,T)$  across the beach

This relation can be said that is generally valid in wind waves: for large enough wave heights the inherent correlation between heights and periods becomes looser and the extreme wind waves are in general associated with a narrow band of periods. The same phenomenon is also demonstrated in the scatter diagrams of short term wave heights and periods, which are nearly symmetrical for large wave heights with respect to a vertical axis, implying little correlation between  $H$  and  $T$ .

Based on the experimental data the relationship between the variation of  $r$  and wave height is depicted in Fig. 11, which clearly shows that indeed there exists a kind of law between the two variables.

The horizontal axis denotes the relative increase of the wave height in terms of  $\Delta\bar{H}/\bar{H}$ ,  $\bar{H}$  mean value, and the vertical gives the variation  $\Delta r$ . A main feature of the graph is that for an increase in  $\bar{H}$  we have a corresponding decrease in  $r$ , and vice versa, as already noted previously.

#### A Simple Wave Shoaling/Breaking Model

A mathematical model based on existing results for depth-induced shoaling, wave breaking and decay has been developed to check the experimental data. The wave-by-wave approach, referred to previously, has

been applied. It is noted that this technique is better suited for the surf zone rather than the transitional waters where our experiments were confined. However, its performance in such depths was quite acceptable, as it will be shown later.

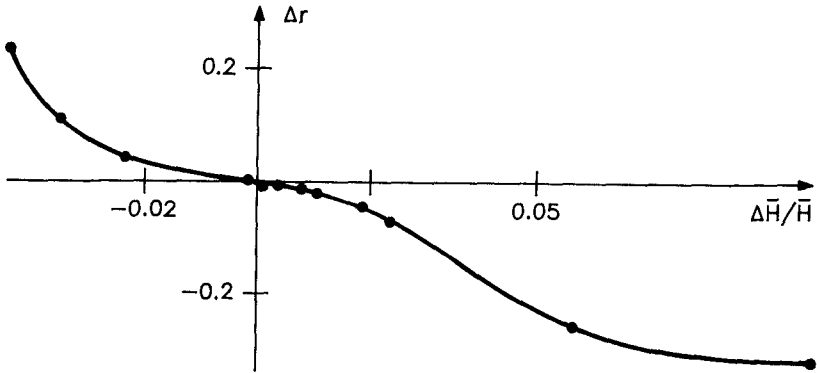


Fig.11 Relation between  $\Delta\bar{H}$  and  $\Delta r$ .

Cnoidal wave theory has been assumed to apply for the shoaling process and as a good first approximation the record at probe (0) was assumed to represent deep water conditions. Following Shuto (1974) as modified by Goda (1975), the shoaling transformations given below were taken into account.

$$H = H_0 K(h), \quad h \geq h_1 \tag{1}$$

$$H = H_0 K(h_1)(h_1/h)^{2/7}, \quad h_2 \leq h \leq h_1 \tag{2}$$

where  $H_0, L_0$  deep-water wave height and wavelength

$H, L$  wave height and wavelength at depth  $h$

$$K(x) = 1/\{ [1+(4\pi x)/L \sinh(4\pi x/L)] \tanh(2\pi x/L) \}^{1/2} \tag{3}$$

$$h_1^2 = 0.209 H_0 L_0 K(h_1) \tag{4}$$

$$h_2 = 0.8 h_1 \tag{5}$$

When  $h < h_2$ , then solution of the following equation provides the shoaling coefficient  $K_1 = H/H_0$

$$K_1(\sqrt{K_1 - B}) - C = 0 \tag{6}$$

where  $B = 1.382h/h_0 (H_0/L_0)^{1/2}$  (7)

$C = C_2 (L_0/h)^{3/2} / (2\pi H_0/L_0)^{1/2}$  (8)

$C_2 = 3.693 K(h_1) (h_2/L_0)^{3/2} [(0.558 H_0/L_0)^{1/2} - h_2/L_0]$  (9)

The breaking criterion proposed by Weggel (1972) has been assumed. This reads as follows

$$\frac{H_b}{L} = (1/7) \tanh \left[ \frac{7h_b}{L} \frac{b}{1+\alpha(h_b/gT^2)} \right] \tag{10}$$

where  $H_b$  wave height at breaking

$T$  wave period

$\alpha = 43.75 [1-\exp(-19m)]$  (11)

$b = 1.56 / [1+\exp(-19.5 m)]$  (12)

$m$  bed slope

$h_b$  still water depth at incipient breaking.

Finally, wave decay after breaking has been included in the model after Dally et al. (1985) as follows.

$$\frac{H}{H_b} = \left[ (1+c)(h/h_b)^{(G/m)-0.5} - c(h/h_b)^2 \right]^{1/2} \tag{13}$$

where  $H$  the height of the decaying wave

$$c = \frac{\Gamma^2}{m[(2.5)-(G/m)]} (h/H)_b^2 \tag{14}$$

$G$  decay coefficient ( ~0.2 or lower)

$\Gamma \sim 0.35 \div 0.40$

Applying the above synthetic model to the experimental conditions mentioned earlier and taking as deep water conditions those recorded at probe (0), joint pdfs at locations (1), (2) and (3) can be produced for direct comparison with the experimental data. Figure 12 contains the model results for run 22 which are comparable with the experimental results shown in Fig. 7.

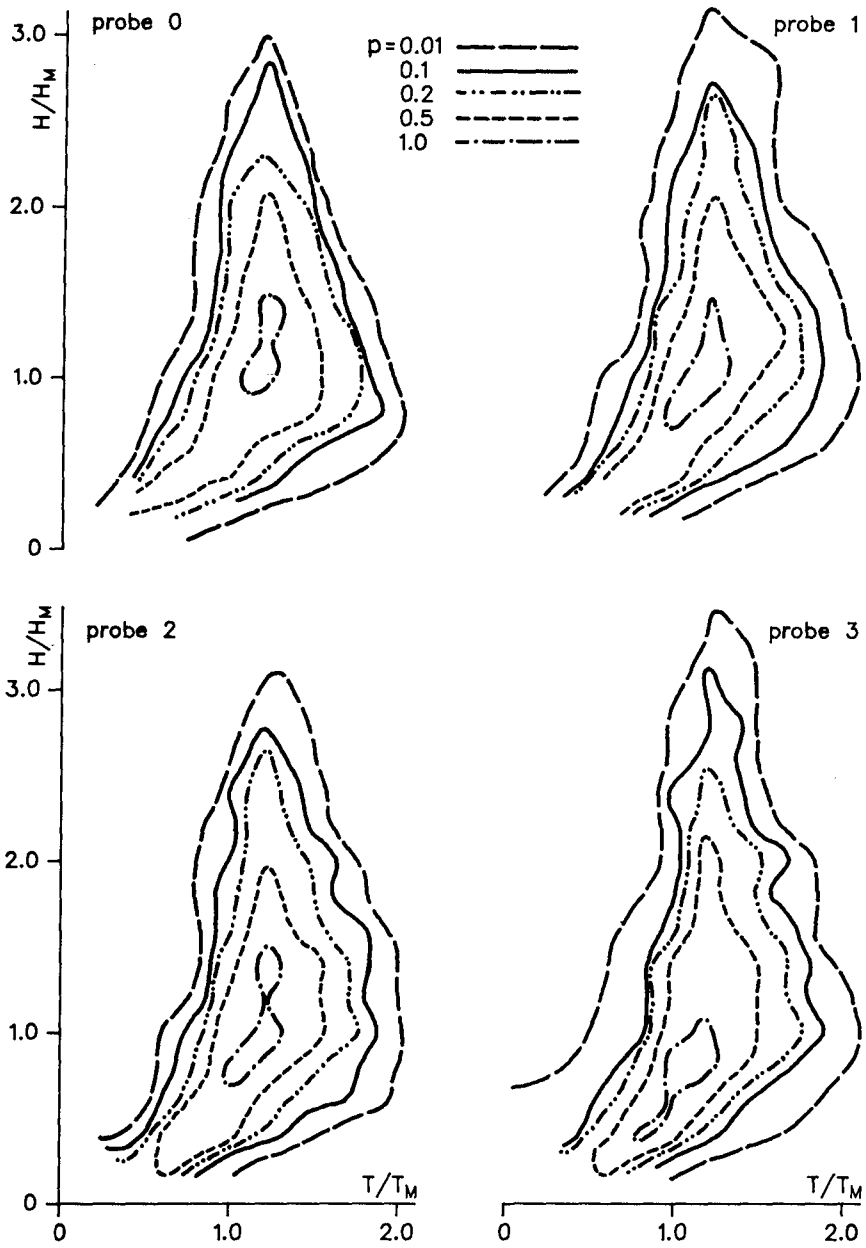


Fig. 12 Model results for run 22

The model results verifies the observed only slight variability of the joint probability structure, as the waves propagate over the sloping bed.

Agreement between the two sets of results is quite acceptable, despite the fact that the wave-by-wave technique is better suited for the surf zone inshore of probe (3), as noted above. Results for other runs indicate the same trend and agree similarly well with experimental data.

### Conclusions

Focusing on the new findings of the present research, we can conclude that the variations of both the bandwidth parameter  $\epsilon$  and the correlation coefficient  $r$  between wave heights and periods across the outer surf zone, follow a trend resulting from a general law governing the correlation between wave heights and periods for large heights. The correlation coefficient  $r(H,T)$  is closely related to the variations of a measure of the wave height across the beach, while the decrease of  $\epsilon$  seems to flatten out within the surf zone.

Also, that a synthetic model developed on existing results can adequately predict the variation of the joint probability density function between waveheights and periods in the outer surf zone of a sloping beach. Improvement of the model is currently underway by abolishing the assumption that the deep water conditions occur at probe (0) and, also, by assuming Stokian waves of the 3rd order rather than cnoidal waves for the shoaling part of the process. This description of the waves may suit better a transitional zone of deeper waters as those present in the experiments.

### Acknowledgments

My thanks are due to Dr K. Anastasiou of Imperial College for helping with the experiments and for providing the original of figure 3. Also, to K. Tzanis of National Technical University of Athens for performing the computations.

### References

1. Battjes, J.A., (1972). Set-up due to irregular waves. Proc. 13th Conf. Coast. Eng., pp. 1993-2004.
2. Battjes, J.A., and S.Beji (1992). Breaking waves propagating over a shoal. Proc. 23rd Conf. Coast. Eng., vol. 1, pp. 42-50.
3. Battjes J.A., and J.P.E.M. Janssen (1978). Energy loss and set-up due to breaking of random waves. Proc. 16th Conf. Coast. Eng., pp 569-587.
4. Bendykowska, G., and G. Werner (1989). Shallow water wave spectra, Their dispersion, transformation and spectral characteristics. Bul. No. TRITA-VBI-142, Royal Institute of Technology, Stockholm.
5. Bouwes, E., and G.J. Komen (1983). On the Balance Between Growth and Dissipation in an Extreme Depth-Limited Wind-Sea in the Southern

- North Sea. J. Phys. Ocean., vol. 13, pp. 1653-1658.
6. Cai, M., D.R. Basco, and J. Baumer (1992). Bar/trough effects on wave height probability distributions and energy losses in surf zones. Proc. 23rd Conf. Coast. Eng., vol. 1, pp. 103-115.
  7. Collins, J.I. (1970). Probabilities of breaking wave characteristics. Proc. 12th Conf. Coast. Eng., pp. 399-412.
  8. Dally, W.R. (1990). Random breaking waves: A closed-form solution for planar beaches. Coastal Eng., vol. 14, pp. 233-263.
  9. Dally, W.R. (1992). Random breaking waves: field verification of a wave-by-wave algorithm for engineering application. Coastal Eng., vol. 16, pp. 369-397.
  10. Dally, W.R. and R.G. Dean (1986). Transformation of random breaking waves on surf beat. Proc. 20th Conf. Coast. Eng., vol. 1, pp. 109-123.
  11. Ebersole, B.A. (1987). Measurements and prediction of wave height decay in the surf zone. Proc. Spec. Conf. Coast. Hydrodyn., ASCE, pp. 1-16.
  12. Goda, Y. (1985). Random Seas and Design of Maritime Structures, Univ. of Tokyo Press.
  13. Kamphuis, J.W. (1994). Wave Height from Deep Water through Breaking Zone. J. Waterw., Port, Coast. and Ocean Eng., vol. 120, No.4, pp. 347-367.
  14. Kuo, C.T., and S.T. Kuo (1974). Effect of Wave Breaking on Statistical Distribution of Wave Heights. Proc. Civ. Eng. Oceans, vol. 3, pp. 1211-1231.
  15. Longuet-Higgins, M.S. (1983). On the joint distribution of wave periods and amplitudes in a random wave field. Proc. R. Soc. London, Ser. A, vol. 389, pp. 241-258.
  16. Mase, H., and J.T. Kirby (1992). Hybrid Frequency-Domain KdV Equation for Random Wave Transformation. Proc. 23rd Conf. Coast. Eng., vol. 1, pp. 474-487.
  17. Memos, C.D. (1990). On the Shoaling/Breaking of Random Waves. 3rd Europ. Workshop Coast. Zones, pp. 2.1-2.20.
  18. Memos, C.D., and K. Tzanis (1994). Numerical Results on the Joint Probability of Heights and Periods of Sea Waves. J. Coastal Eng., vol. 22, pp. 217-236.
  19. Resio, D.T. (1987). Shallow-Water Waves. I: Theory. J. Waterw., Port, Coast. and Ocean Eng., vol. 113, No.3, pp. 264-281.
  20. Thornton, E.B., and R.T. Guza (1983). Transformation of Wave Height Distribution. J. Geophys. Res., vol. 88, No. C10, pp. 5925-5938.

## CHAPTER 171

### A RELATIVE INTERCOMPARISON BETWEEN VARIABLE WAVE SHOALING, BREAKING AND TRANSITION ZONE FORMULATIONS

G P Mocke, F Smit<sup>1</sup>

#### **Abstract**

The description of nearshore structural and sedimentary dynamics is highly dependant on a quantification of the nearshore wave regime, which is subject to bathymetry induced transformation effects. Assuming straight and parallel bottom contours, computed wave heights and water levels using variable wave shoaling, incipient breaking, wave decay and transition zone formulations are compared with measurements.

#### **1 Introduction**

Waves approaching the shoreline undergo transformations due to shoaling and refraction effects. The most significant such transformation, however, occurs coincident with the breaking process, where a dramatic change in wave form occurs. Associated with wave height decay is an internal transition from predominately oscillatory, irrotational motion to a highly rotational state where breaker generated turbulent kinetic energy (TKE) is strongly dissipated.

As reviewed by Ham *et al* (1993), complex numerical methods have been relatively successfully applied to the highly non-linear shoaling region. However, in order to have more efficient tools for engineering application a number of analytical formulations have been proposed. In the present study a comparison is made between linear theory and two of the simplest such formulations, namely first order cnoidal and parametrized solutions proposed by Isobe (1985) and Swart (1978) respectively. For defining the onset of wave breaking, the earlier criteria of Weggel (1972) is compared with formulations of Moore (1982) and Larson and Kraus (1989).

Energy dissipation in a breaking wave is often formulated (Battjes and Janssen, 1978) as being equivalent to that across an hydraulic jump. An alternative approach proposed by Dally *et al* (1984) relates the rate of energy dissipation to the excess of energy between the actual and a stable wave energy flux. Despite generally favourable wave height comparisons with measured values, a consistent lag between the maximum gradient of wave energy and that of setup and return flows has been

---

<sup>1</sup> Research Engineers, CSIR, P O Box 320, Stellenbosch 7599, South Africa

observed (Roelvink and Stive, 1989).

Such findings relate primarily to the manifestation of a transition zone immediately after breaking across which waves undergo transformation into turbulent bores. Svendsen (1984) defined the extent of this zone to be equivalent to the area of near constant mean water level. It was proposed by Basco and Yamashita (1986) that the width of this zone would vary in relation to the surf similarity parameter.

Svendsen (1984) incorporated the effect of the transition zone in the energy conservation formulation by including a storage term representing an initial conversion of organized wave motion into forward momentum flux in the roller. A similar term proposed by Roelvink and Stive (1989) considers a local imbalance of production and dissipation of TKE. Drawing on the concept (Svendsen, 1984) of a surface roller "riding" on a wave front, Nairn *et al* (1990) incorporate a relation proposed by Deigaard and Fredsoe (1989) whereby dissipation is modelled as the work performed by a shear stress at the interface between the roller and the organized wave motion. In a fundamentally different approach Okayasu *et al* (1990) incorporate a term representing the initial transfer of kinetic energy to organized large vortices before subsequent conversion to dissipative TKE for an evaluation of the various transition zone relations.

Lacking explicit measurements of energy dissipation rates in the surfzone, the present study deduces the cross-shore distribution of this parameter through an inverse modelling approach that draws on measurement of surfzone TKE.

## 2 Experimental Data

The experimental cases discussed are primarily confined to measurements of regular waves over planar bottom slopes. Test conditions for these cases are summarized in Table 1. The set of measurements constitutes a total of 14 test cases with breaking conditions ranging from weakly spilling to strongly plunging.

For each of the data parameters considered, a root mean square error  $e$  denoting the deviation of predictions from measurements is computed. This statistical parameter, along with a computed bias  $b$  are defined as follows:

$$e = \frac{1}{N} \left[ \sum_{i=1}^N (X_{pred,i} - X_{meas,i})^2 \right]^{\frac{1}{2}} \quad (1)$$

$$b = \frac{1}{N} \sum_{i=1}^N (X_{pred,i} / X_{meas,i}) \quad (2)$$



**Table 1** Beach slopes and deepwater wave characteristics of various laboratory experiments used in model simulations

Test	slope	H <sub>o</sub> (m)	T (s)	H <sub>o</sub> /L <sub>o</sub>	breaker type
Hansen & Svendsen B	1:34	0.103	1.00	0.0710	spilling
Hansen & Svendsen E	1:34	0.098	1.25	0.0440	spilling
Hansen & Svendsen H	1:34	0.099	1.67	0.0240	spilling
Hansen & Svendsen I	1:34	0.091	1.67	0.0220	plunging
Hansen & Svendsen K	1:34	0.080	1.67	0.0190	plunging
Hansen & Svendsen L	1:34	0.070	1.67	0.0170	plunging
Hansen & Svendsen N	1:34	0.066	2.00	0.0110	plunging
Hansen & Svendsen P	1:34	0.071	2.50	0.0080	plunging
Hattori & Aono 1	1:20	0.030	1.00	0.0210	plunging
Hattori & Aono 3	1:20	0.029	1.60	0.0080	plunging
Nadaoka & Kondoh 1	1:20	0.216	1.32	0.0792	spilling
Nadaoka & Kondoh 5	1:20	0.219	2.34	0.0257	plunging
Stive 1	1:40	0.159	1.79	0.0320	spilling
Stive 2	1:40	0.142	2.99	0.0100	plunging

### 3 Wave Shoaling

Transformed wave heights and water levels ( $\eta$ ) are defined by the 1-D depth-averaged energy and momentum conservation equations:

$$\frac{\partial}{\partial x} (EC_g) = -D_b \tag{3}$$

$$\frac{\partial S_{xx}}{\partial x} = -\rho g d \frac{\partial \bar{\eta}}{\partial x} \tag{4}$$

where E is the wave energy, C<sub>g</sub> the group velocity, D the energy dissipation and S<sub>xx</sub> the radiation stress. In addition to linear wave theory, an adaptation (Isobe, 1985) of the first order cnoidal theory is considered:

$$EC_g = \rho g H^2 (gd)^{\frac{1}{2}} f_2$$

$$\text{with } f_2 = \text{func}(U_s) \sim \frac{32}{15(3U_s)^{\frac{1}{2}}} \left( 1 - \frac{15}{(3U_s)^{\frac{1}{2}}} + \frac{20}{U_s} \right) \text{ for } U_s \gg 1 \tag{5}$$

$$\text{and } U_s = \frac{gHT^2}{d^2}$$

as well as the vocoidal theory of Swart (1978):

$$EC_g = (e_p + e_k) \rho g H^2 n C, \quad \text{with } e_p \text{ and } e_k = \text{func} \left( \frac{H}{d}, \frac{L}{d} \right) \quad (6)$$

Computed wave height and mean water level variations were compared for several laboratory experiments. An example of such a comparison against the measurements of Stive (1980) is shown in Figure 1. Figure 2 presents a comparative summary of statistical errors for both wave height and water levels in the shoaling region. Results of the error and bias calculations for wave heights and mean water levels for the experimental data simulated are summarized in Figure 3.

No pre-breaking measurements for either the Hattari and Aono(1985) or Nadaoka and Kondoh (1982) cases were available and comparisons could thus not be made. For the rest of the test cases the cnoidal technique provided the best overall estimates of both wave height and mean water levels in most cases. The vocoidal theory, on the other hand, seemed to fare the worst of the three theories tested. However even though the deviation is highest across the shoaling region, the vocoidal theory provided the closest estimation of both wave height and mean water level at the breaking point for most of the test cases. The bias calculations indicated that the linear theory both estimates wave height and overpredicts setdown. The cnoidal theory performs slightly better in estimating both wave height and mean water levels, whilst the vocoidal theory tends to overestimate both these parameters slightly.

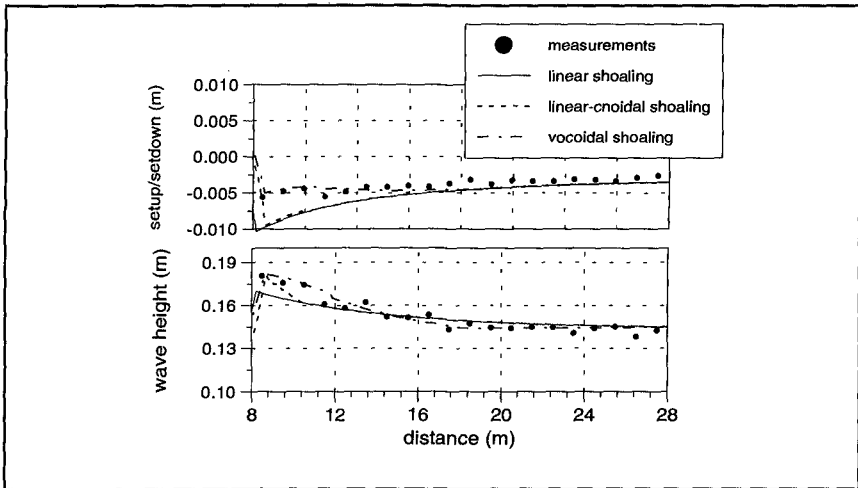


**Figure 1** Comparison between different shoaling techniques for Stive Test 1

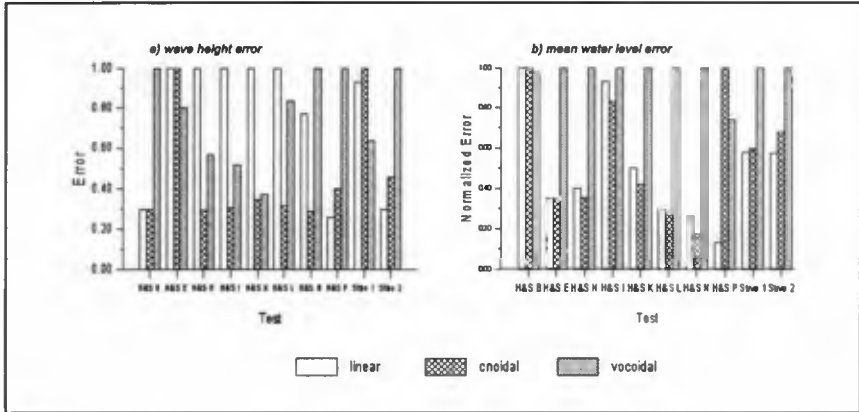


**Figure 2** Normalized root mean square errors for wave heights and mean water levels in the shoaling region

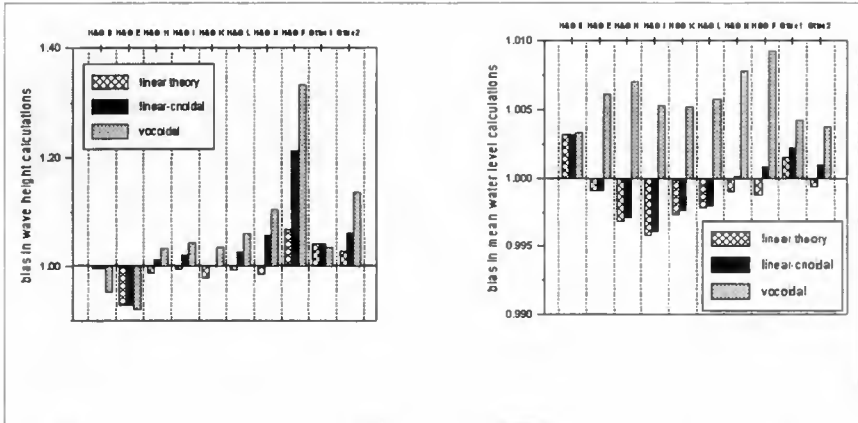


**Figure 3** Bias statistics for wave heights and mean water levels in the shoaling region

#### 4 Wave Breaking

##### *Incipient Breaking*

Three relatively well-established breaking criteria were assessed, namely the criterion of Weggel (1972),

$$\frac{H_b}{d_b} = b_m - a_m \cdot \frac{H_b}{gT^2} \tag{7}$$

where  $H_b$  = wave height at breaking,  $d_b$  = water depth at breaking

$$a_m = 43.8 (1.0 - e^{-19m}), \quad b_m = \frac{1.56}{1.0 + e^{-19.5m}}$$

$m$  = bottom slope

Moore (1982),

$$\frac{H_b}{d_b} = b_m - a_m \cdot 0.083 \left( \frac{H_0}{L_0} \right)^{0.8} \quad (8)$$

and Larson and Kraus (1989):

$$\frac{H_b}{d_b} = 1.14 \zeta^{0.21} \quad (10)$$

with  $\zeta$  = surf similarity parameter =  $m \left( \frac{H_0}{L_0} \right)^{-\frac{1}{2}}$

An example of a comparison for a case of Hansen and Svendsen (1979) is presented in Figure 4. The results for all the test cases indicate that there is very little difference between the 3 breaking criteria. The Larson-Kraus (1989) criterion tends to predict the breaking point in slightly deeper water than either the Moore (1982) or Weggel (1972) criteria. For all intents and purposes the oldest and probably most established of the criteria, namely that of Weggel, seems perfectly adequate to use. The Weggel criterion has the advantage of using only local information in determining the breaking position as the deep water wave steepness does not have to be known. This implies that a wave transformation model using the Weggel criterion can be run using input conditions at any point seaward of the breaker zone.

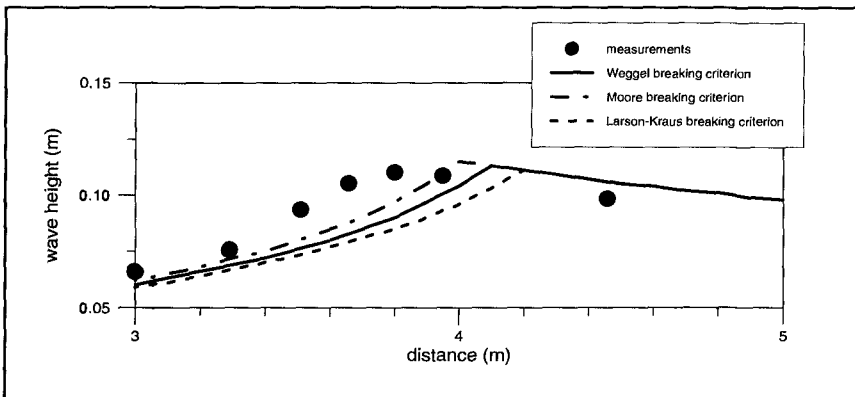


**Figure 4** Comparison between breaking criteria for Hansen and Svendsen Case N

**Wave Decay**

With the steady state conservation of wave energy flux described by equation (3) it is necessary to quantify the rate of energy dissipation  $D_b$  due to breaking, which is the dominant energy dissipation mechanism in the surfzone. Considering an equivalence to a hydraulic jump the average breaking wave dissipation per unit area has been expressed for random waves by Battjes and Janssen (1978).

In the event of regular waves the above formulation reduces to the bore dissipation expression of Stive (1984):

$$D_b = A_b \frac{\rho g c}{4} \frac{H^3}{d} \quad (10)$$

where  $A_b$  should ideally be greater than unity so as to compensate for the tendency of the hydraulic jump formulation to underestimate wave breaker dissipation.

Dally *et al* (1984) propose a simple algorithm that models waves as undergoing energy dissipation at a rate equivalent to the excess of energy above some stable limit. This approach, which has been referred to as the excess-energy (EE) concept, has been formulated as follows:

$$D_b = \frac{\kappa}{d} [ ECg - F_s ] \quad (11)$$

where  $\kappa$  = decay coefficient  $\sim 0.15 - 0.2$   
 $F_s$  = stable wave energy flux =  $\frac{1}{8} \rho g H_s^2 Cg$   
 $H_s$  =  $\Gamma d$ , (with  $\Gamma \sim 0.35 - 0.40$ )

Both approaches were applied over the whole surfzone using standard coefficients ( $A_b = 1$ ,  $\kappa = 0.15$ ,  $\Gamma = 0.4$ ). The possible reformation of waves was incorporated in the model using a stable wave definition, as proposed by Horikawa and Kuo (1966). An example of results obtained from the two formulations is presented in Figure 5. Relative wave height and water level error and bias statistics are charted in Figures 6 and 7 respectively.

The results indicate that using standard parameters the bore model generally describes the wave height change through the surfzone slightly better than the EE model, with the bias calculations showing the latter tends to underestimate breaker dissipation. An exception to this is in the case of plunging breakers (H&S Case P, H&A Case 3, Stive Case 2) where the bore expression tends to underestimate dissipation rates. However, either of the models can be made to fit the plane slope measurements well using slight parameter adjustments. In the event of a highly irregular bathymetry, particularly under random waves, a limited sensitivity analysis shows neither method to be entirely adequate. As has been previously observed the problem in this regard relates primarily to the effect of wave reformation over trough features. This is

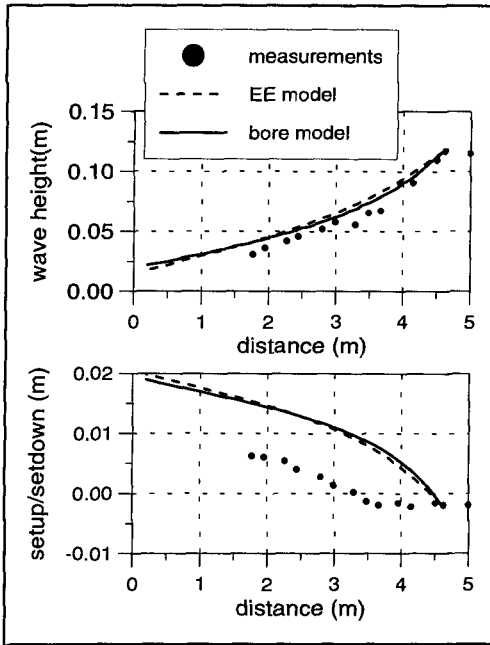


**Figure 5** Comparison between wave heights and mean water levels with the EE and bore breaker models (H&S, Case K)

reflected in an incorrect estimate of the percentage of broken waves, as found by Mocke *et al* (1994) in an inverse modelling exercise using undertow and suspended sediment measurements.

The comparison of calculated mean water levels with measurements indicated quite clearly that the use of the momentum equation as defined in equation (4) is not able to describe the setup in the surfzone adequately at all. This serves to underline the importance of including the transition zone and the "lag" effect on the setup in the formulation.

**5 The Transition Zone**

**Transition zone length**

Defining the transition zone length ( $l_t$ ) as the distance from the breakpoint to a point of

abrupt change in mean water level slope Nairn *et al* (1990) (hereafter NRS) use a data set of laboratory experiments to define the following empirical relation:

$$\begin{aligned}
 l_t &= 0.556 m_b L_b \zeta_b^{-1.465} && \text{for } \zeta_b \geq 0.05 \\
 &= 0 && \text{for } \zeta_b < 0.05
 \end{aligned}
 \tag{12}$$

Zhang and Sunamura (1990) (hereafter ZS) use visual laboratory observations for assessing the process described by Nadaoka *et al* (1989) of a progressive transition from strongly two-dimensional vortices at breaking to oblique vortices. Adapting a temporal relation proposed by the authors, an equivalent expression in terms of distance results:

$$l_t = \left[ 0.02 \frac{H_b}{g T^2 m} \left( \frac{H_b L_b}{\nu T} \right)^{\frac{1}{3}} + 0.12 \right] T c
 \tag{13}$$

Also using visual laboratory observations Okayasu *et al* (1990) (hereafter OWI) define the transition point as the position of roller establishment:

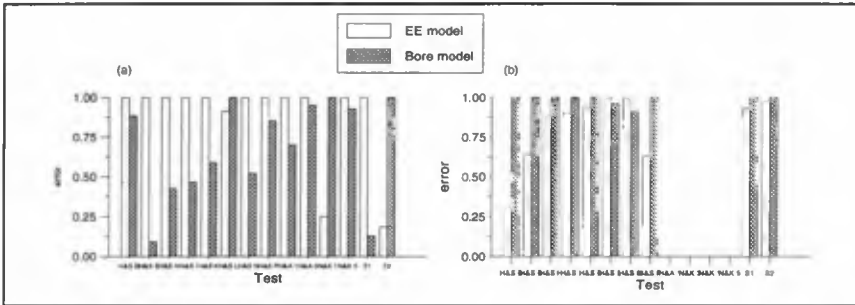


**Figure 6** Normalized root mean square errors for (a) wave height and (b) mean water levels using the EE and bore breaker decay models

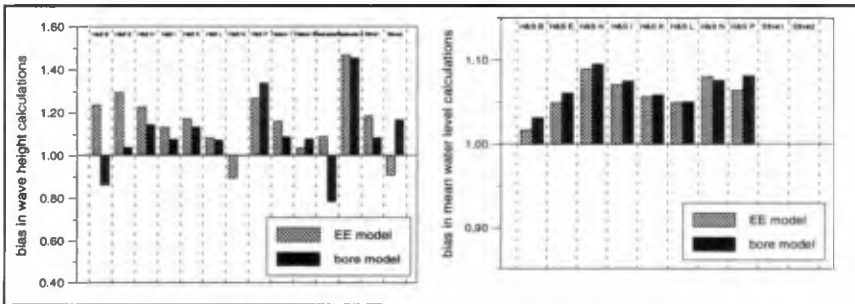


**Figure 7** Bias in a) wave heights and b) water levels for breaker decay models

$$l_t = \left( \frac{1}{m} + 4 \right) d_b \tag{14}$$

Quantifying the transition zone length as the area of depressed setdown the above relations are compared to our experimental data set in Figure 8. Being the only formulation based on a similar definition of the transition zone the NRS (1990) expression not surprisingly provides the closest correspondence to measurements. The ZS definition, however, also provides a relatively close comparison. The more qualitatively determined OWI scale, however, tends to consistently predict a transition zone distance that extends beyond the point of change in setup slope. Lacking a more explicit definition of the transition zone, it is impossible at this juncture to make a relative judgement on the proposed relations. So as to assure a certain level of consistency between the comparisons that follow, the empirical NRS relation is considered to define the transition zone length within each formulation.

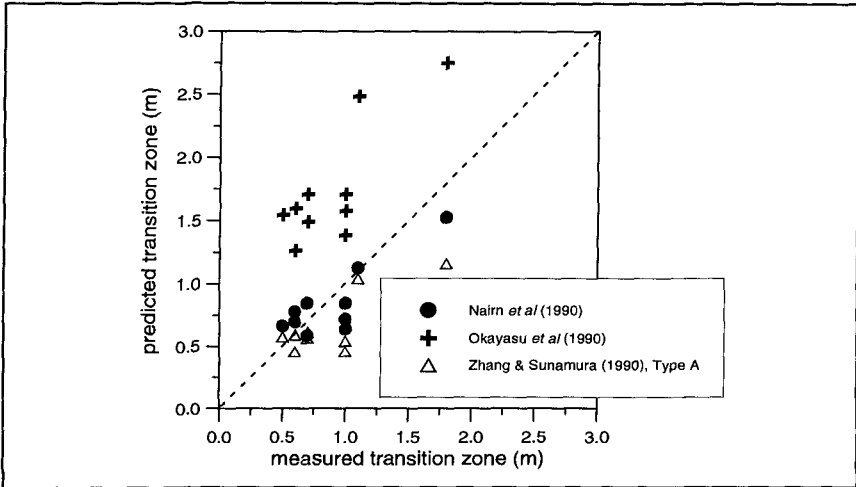


**Figure 8** Comparison between measured transition zone lengths and predicted lengths using different empirical transition zone length formulations

**Analytical formulations**

In recent years attention has been focussed on obtaining an analytical formulation to describe the contribution of the transition zone after the onset of breaking. These formulations all include the inclusion of a lag/storage term in the energy conservation equation. Our previous equations (3) and (4) are therefore adapted to the form below:

$$\frac{\partial}{\partial x} (E_w C_g) + \Gamma_x = D_b \tag{15}$$

$$\frac{\partial}{\partial x} S_{xx} + M_r + \rho g d \frac{\partial \bar{\eta}}{\partial x} = 0, \tag{16}$$

where  $\Gamma_x$  = lag/storage term  
 $M_r$  = additional momentum flux term

Where the additional energy and momentum equation terms have been formulated as follows by the various investigators:

**Svendsen (1984):**

$$\Gamma_x = \frac{\partial}{\partial x} E_r c \text{ and } M_r = \frac{\partial}{\partial x} (2E_r) \tag{17}$$

where  $E_r$  = roller energy =  $\rho \frac{Ac}{2T}$ , and  $A$  = roller area  $\sim 0.9H^2$



**Roelvink and Stive (1989):**

$$\Gamma_x = \frac{\partial}{\partial x} \beta_r k d c, \quad D_b = -\rho \beta_d k^{\frac{3}{2}}, \quad \text{and } M_r = \frac{\partial}{\partial x} \beta_s \rho k d \quad (18)$$

with  $\beta_r = \beta_d = 1$  and  $\beta_s = 0.22$  and  $k = \text{turbulent kinetic energy}$

**NRS:**

$$\Gamma_x = \frac{\partial}{\partial x} E_r c, \quad D_b = -2\beta g \frac{E_r}{c} \quad \text{and } M_r = \frac{\partial}{\partial x} (0.22 E_r) \quad \text{with } \beta = 0.1 \quad (19)$$

**OWI:**

$$\Gamma_x = \frac{\partial}{\partial x} E_v c_g, \quad D_b = \frac{\partial}{\partial x} E_t c_g, \quad \text{and } M_r = \frac{\partial}{\partial x} \left( \frac{5}{3} E_v \right) \quad (20)$$

where  $E_v = \text{energy of organized vortices}$ ,  $E_t = \text{total wave energy} = E_v + E_w$

OWI proposed that the energy transferred to the vortices is dissipated over a "dissipation distance" proportional to the water depth. Comparisons between the analytical formulations of Svendsen, NRS and OWI were carried out on Stive (1980) case 1. Figure 9 depicts the calculated energy dissipation ( $D_b$ ) and gradient in energy flux ( $\partial EC_g / \partial x$ ) across the surfzone using the three formulations. It may be remarked that both terms are non-zero prior to the breakpoint for the OWI case. This is because energy transfer in the OWI model starts at a position slightly seaward of the breaking point primarily as a means of avoiding an abrupt energy step, and associated numerical instabilities, across this point.

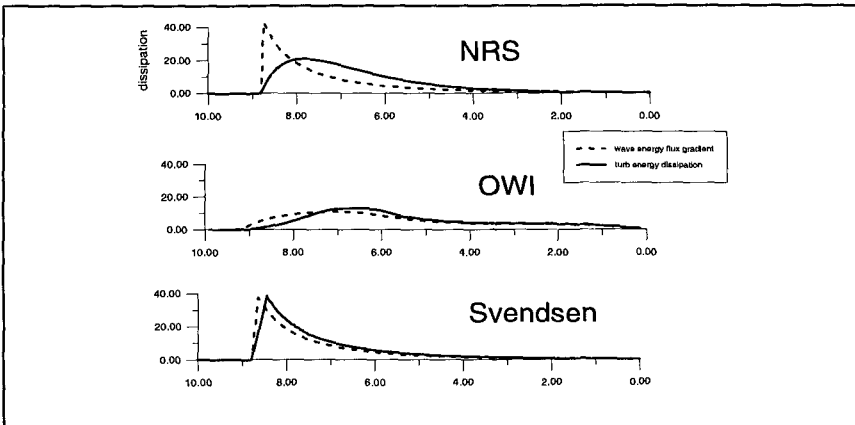


**Figure 9** Calculated gradient in energy flux and energy dissipation for Stive Case 1 using the Svendsen, Nairn *et al* and Okayasu *et al* analytical transition zone formulations

In Figure 10 is shown the computed setup distributions for the same test case. As may be seen from a comparison with the setup computed without transition zone effects, the Svendsen relation shows negligible improvements. Although the other relations are found to be somewhat more satisfactory, comparisons with measurements are found to be generally inadequate. It is difficult to pursue the

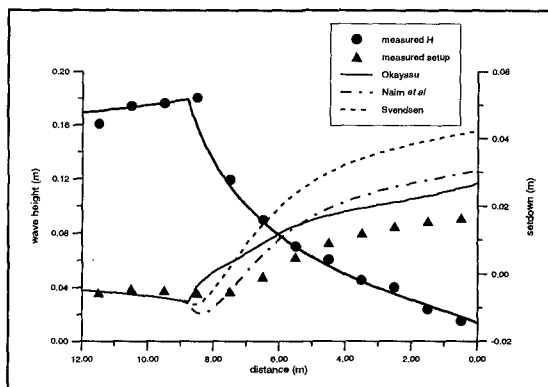


**Figure 10** Comparison between setup calculated for Stive Case 1 using different analytical transition zone formulations

analysis in terms of setup measurements as inadequacies may exist in both the adapted energy and momentum relations. Lacking explicit energy dissipation measurements reference is made to available TKE measurements.

#### ***Depth-dependant TKE***

In employing a two equation ( $k, \epsilon$ ) turbulence model as described in Mocke (1991),  $D_b$  rates as determined by the various methods are imposed as a near surface production source of TKE. Considering a dominant diffusion/dissipation balance, computed turbulent intensities for the formulations of OWI and NRS are compared with computations lacking a transition effect. Comparisons with measurements from Stive 1 are shown in Figure 11.

With the breakpoint at approximately  $X = 9$  m, limited transition effects appear to be necessary for the three inner measurement stations. At  $X = 7.5$  m, however, turbulence intensities tend to be overpredicted with the OWI relation showing the most favourable lag effects. Although no measurements were made at  $X = 8.5$  m, the significant discrepancy between predictions at this point immediately following breaking is apparent, with the OWI relation once again showing the most lag effects. Similar findings were observed comparisons against for case 2 of Stive (1980) as well as for the eddy viscosity estimates of OWI.

#### ***Depth averaged TKE***

Further comparative analyses have been made using depth average/equation ( $k-l$ ) and two equation ( $k, \epsilon$ ) turbulence closure modelling. The details pertaining to this approach are comprehensively described in Mocke *et al* (1993). Referring once again to Stive case 1 measurements, depicted in Figure 12 are comparisons between

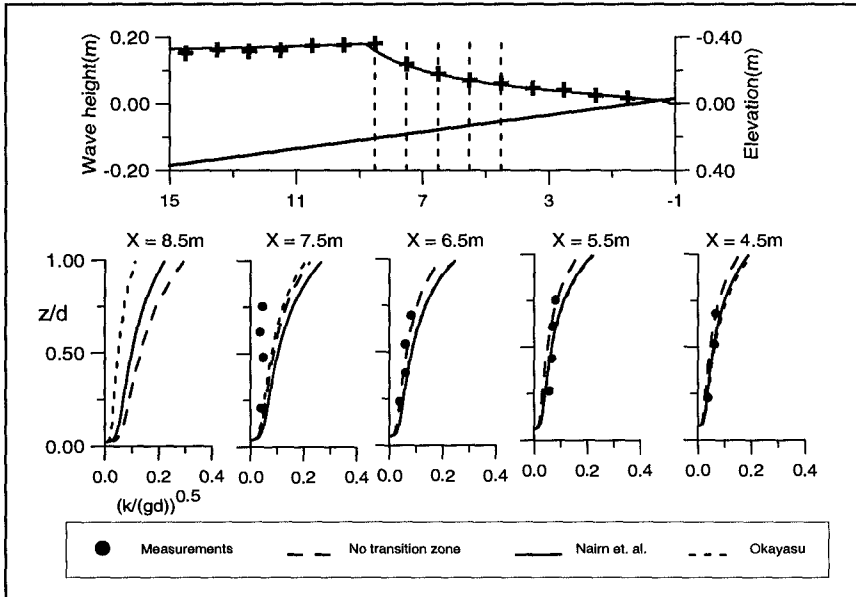


**Figure 11** Comparison between TKE profiles through the surfzone using the NRS and OWI transition zone formulations

simulations and estimates of depth averaged TKE.

Note the discernible lag after breaking in the increase in TKE, an effect not reflected in simulations made without consideration of transition zone effects. Although the OWI relation provides for more lag influence than the NRS expression, neither approach satisfactorily represents the measurements.

Examining the NRS expression we note that a fundamental assumption is that the effective roller slope used for determining the dissipation rate remains constant throughout the full extent of the surfzone. This assumption inherently assumes no roller development area nor any changes in the form of this feature throughout the surf zone. In an effort to more closely reflect the physical reality, transformation effects are incorporated by artificially varying the roller slope factor  $\beta$  in the cross-shore direction. A limited sensitivity analysis shows a variation of  $\beta$  from 0.01 to 0.07 within the NRS relation provides an improved estimate of the measurements under consideration.

## Conclusions

The comparison between the different shoaling techniques indicates that the first order cnoidal technique provides the closest approximation of wave heights and mean water levels in most of the test cases. However the vocoidal theory provides the

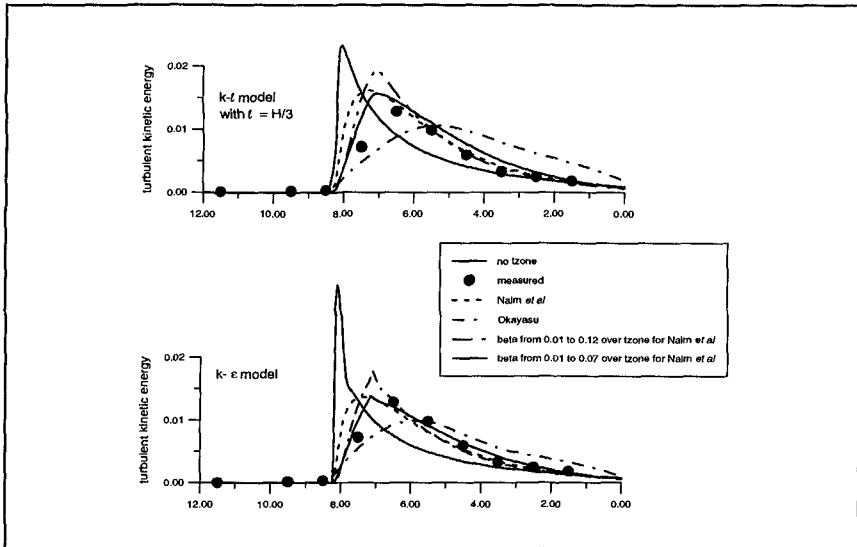


**Figure 12** Calculated depth averaged TKE using the Naim *et al* and Okayasu transition zone formulations compared to measurements

closest estimate of wave height and setdown at the breaking point itself. The comparison between the different incipient breaking criteria indicated that there is little to choose between them, and the Weggel criterion, which has the advantage of requiring only local information, is adequate for most applications.

The EE and bore models were found to provide reliable wave decay predictions for regular waves over simple geometries. Simulations not discussed here however reflect previous findings of inadequate predictions for more complex cases. Many of the integral surfzone processes associated with breaking are furthermore not satisfactorily predicted without incorporation of transition zone effects following initiation of breaking. The formulation of Okayasu *et al* (1990), which attempts to quantify an initial transfer of energy to organized large vortices, appears to be physically and empirically the most appropriate approach. An adaptation of the Naim *et al* (1990) formulation to reflect a changing bore configuration, however provides the best correspondence with measured turbulence intensities.

## References

- Basco, D R and Yamashita, T (1986). Toward a Simple Model of breaking Transition Region in Surfzones. *Proceedings of the 20th International Conference on Coastal Engineering*.
- Battjes, J A and Janssen J P F M (1978). Energy Loss and Set-up due to Breaking of Random Breaking Waves. *Journal of Geophysical Research*, Vol.90, pp. 9159-9167.
- Dally, W R, Dean, R G and Dalrymple, R A (1984). A Model for Breaker Decay on Beaches. *Proceedings of the 19th Conference on Coastal Engineering*, ASCE.
- Deigaard, H J and Fredsoe, J (1989). Shear Stress Distributions in Dissipative Water Waves. *Coastal*

- Engineering*, Vol.13, pp. 357-378.
- Ham, L, Madsen P A and Peregrine, H (1993). Wave Transformation in the Nearshore Zone: A Review. *Coastal Engineering*, Vol. 21, pp. 5-39.
- Hansen, J B and Svendsen, I A (1979). Regular Waves in Shoaling Water - Experimental Data. *Series Paper No. 21*, University of Denmark.
- Hattori, M and Aono, T (1985). Experimental Study on Turbulence Structures Under Breaking Waves. *Coastal Engineering in Japan*, Vol. 28, pp. 97 - 116.
- Horikawa, K and Kuo, C T (1966). A Study of Wave Transformation Inside the Surf Zone. *Proceedings of the 10th International Conference on Coastal Engineering*, Vol. 1, ASCE.
- Isobe, M (1985). Calculation and Application of First-order Conoidal Wave Theory. *Coastal Engineering*, Vol. 9, pp. 309-325.
- Kajima R, Takao, S, Kohki, M and Saito, S (1983). Experiments on Beach Profile Change with a Large Wave Flume. *Proceedings of 18th Coastal Engineering Conference*, ASCE.
- Larson, M and Kraus, N C (1989). SBEACH: Numerical Model for Simulating Storm-induced Beach Change, Report 1: Empirical Foundation and Model Development. *Technical Report CERC-89-9*, US Army Engineer Waterways Experiment Station, CERC.
- Mocke, G P (1991). Turbulence Modelling of Suspended Sediment in the Surf Zone. *Coastal Sediments '91*, ASCE, Seattle.
- Mocke, G P, Smit, F and Engelbrecht, L (1993). Wave Breaker Turbulence in the Modelling of Coastal Hydrodynamics and Sediment Transport. *5th Intl. Symposium on Refined Flow Modelling and Turbulence Measurements*, IAHR, Paris.
- Mocke, G P, Reniers, A and Smith, G (1994). A Surfzone Parameter Analysis on LIP 1D Suspended Sediment and Return Flow Measurements. *Coastal Dynamics '94*, Barcelona, ASCE.
- Moore, B D (1982). Beach Profile Evolution in Response to Changes in Water Level and Wave Height. M.Sc. Thesis. University of Delaware.
- Nadaoka, K, Hino, M and Koyano, Y (1989). Structure of Turbulent Flow Field under Breaking Waves in the Surf Zone. *Journal of Fluid Mechanics*.
- Nadaoka, K and Kondoh, T (1982). Laboratory Measurements of Velocity Field Structure in the Surf Zone by LDV. *Coastal Engineering in Japan*, Vol. 25, pp. 125 - 145.
- Nairn, R B, Roelvink, J A and Southgate, H N (1990). Transition Zone Width and Implications for Modelling Surfzone Hydrodynamics, *22nd Intl Conf on Coastal Engineering*, ASCE.
- Okayasu, A, Watanabe, A and Isobe, M (1990). Modelling of Energy Transfer and Undertow in the Surf Zone, *Proc 22nd Intl Conf on Coastal Engineering*, ASCE, pp. 123-135.
- Roelvink, J A and Stive, M J F (1989). Bar-generating Cross-shore Flow Mechanisms on a Beach. *Journal of Geophysical Research*, Vol.94, pp. 4785-4800.
- Stive, M J F (1980). Two Dimensional Breaking of Waves on a Beach. *Report on Laboratory Investigations*, parts I - III, Delft Hydraulics Laboratory.
- Stive, M J F (1984). Energy Dissipation in Breaking Waves on Gentle Slopes. *Coastal Engineering*, Vol. 8, pp. 99-127.
- Svendsen, I A (1984). Wave Heights and Set-up in a Surf Zone. *Coastal Engineering*, Vol. 8, pp. 303-329.
- Swart, D H (1978). Vocoidal Water Wave Theory, Volume 1: Derivation. *CSIR Report No 357*, National Research Institute for Oceanology.
- Weggel, J R (1972). Maximum Breaker Height. *Journal of the Waterways, Harbours and Coastal Engineering Division*, ASCE, Vol.98, WW4.
- Zhang, D and Sunamura, T (1990). Conditions for the Occurrence of Vortices Induced by Breaking Waves. *Coastal Engineering in Japan*, Vol. 33, No. 2, pp. 145-155.

## CHAPTER 172

### Analysis of Coastal Processes at Toronto Islands

R.B. Nairn, R.D. Scott, C.D. Anglin and P.J. Zuzek<sup>1</sup>

#### Abstract

The paper summarizes the analysis of the coastal processes which have been responsible for the evolution of the Toronto Islands sand spit feature. Both natural and artificial influences have created a situation of a rapidly evolving landform. The purpose of the study was to evaluate the feasibility of rebuilding a school near the shoreline of this rapidly evolving feature. Several different techniques were employed to evaluate the changes including: shoreline recession rate estimates, lake bed surface change comparisons, sediment budget calculations and alongshore and cross-shore sediment transport calculations. These techniques were combined to develop a descriptive model of the changes in order to forecast future changes to the landform over the next 100 years.

#### Introduction

This paper summarizes the findings of an investigation of erosion processes at Gibraltar Point on the Toronto Islands situated along the northwest shore of Lake Ontario in Canada. The Toronto Islands Nature School is located at Gibraltar Point and the future safety of this location with respect to erosion and flooding hazards is dependent on the future evolution of the Gibraltar Point landform. The Toronto Board of Education has plans to construct a new school on and just west of the location of the existing school. The purpose of the study was to investigate the potential future erosion hazards at Gibraltar Point and the implications for constructing a new school at the existing location.

The following sections of the paper provide: an overview of the geomorphology of the Toronto Islands feature including the background of the problem; a description of the analyses used to prepare a representative nearshore wave climate; a review of the historic changes in the shoreline position; an interpretation of changes to the lake bed; an explanation of the descriptive model of the changing landform including future projections; and study findings.

---

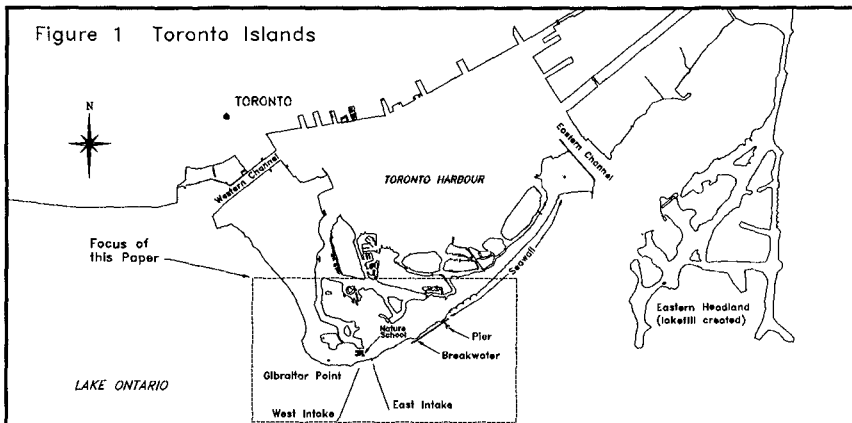
<sup>1</sup> - Baird & Associates, 221 Lakeshore Rd E, Oakville, ON, Canada L6J 1H7  
tel: 905 845 5385, fax: 905 845 0998, Internet: Oakville@Baird.com

### Study Background and Regional Coastal Geomorphology

The City of Toronto is located on the north shore of Lake Ontario and was founded at this location in 1793 because of the presence of a 9 km long sand spit that provided excellent natural protection for a large harbour (see Figure 1).

A geomorphologic review found that the Toronto Islands feature is a complex (compound) recurved sand spit that has formed and developed over the last 3500 to 5000 years as a result of the following factors: stabilization of the existing lake level ( $\pm 2$  m) over the last 3500 years; a dominant northeast to southwest directed sediment transport; a continuous supply of sediment from the erosion of the Scarborough Bluffs to the east (estimated to be 30,000 m<sup>3</sup>/yr on average); the presence of an underlying shallow and gently sloping bedrock shoreface platform; and the presence of a significant re-entrant angle in the shoreline orientation (i.e. an embayment). This type of feature is characterized by a progressive extension in the direction of the dominant sediment transport (i.e. to the southwest at this site). The ability of the spit to continue its southwestward growth depended on a continued supply of sediment, both to build the subaerial part of the feature, and essentially, to extend the offshore shelf southwestwards.

The continued extension of the spit to the southwest combined with a severe storm event in 1852 resulted in a breach near the location of the present day Eastern Channel. The breach in the spit expanded between 1852 and 1882 to an extent that threatened the future potential for harbour development at Toronto and the associated economic development. In response to this situation, the Toronto Harbour Commissioners embarked on an ambitious plan to stabilize the naturally formed Eastern Gap to create a navigation channel of controlled width and depth. These plans resulted in the construction of the Eastern Channel jetties which were completed in 1892. In order to protect the shore of the islands from future erosion and potential breaching, a seawall and breakwater were constructed over a length of 2.5 km extending westward from the west jetty.



Sand which continued to move along the shore from east to west was deposited in the Eastern Channel. Records show that on average 25,000 cubic metres of sand was dredged from the channel and dumped offshore on an annual basis

between 1896 and 1965. This suggests that most of the annual supply volume of 30,000 cubic metres was prevented from reaching the shore and lake bed of the Islands feature to the west of the Eastern Channel. This situation has resulted in erosion with 1 to 2 m of lake bed lowering offshore of the seawall immediately to the west of the channel. Therefore, the supply of sediment to Gibraltar Point, although mostly cut off at the Eastern Channel, was probably compensated in part by the erosion of the lake bed offshore of the seawall.

The Eastern Headland (also known as the Leslie Street Spit) is a 5 km long artificial spit feature located immediately east of Toronto Islands that has been created through lakefilling (see Figure 1). The spit was originally created to form a protected outer harbour; however, it has also been used as a dump site for construction refuse (mostly concrete rubble from downtown construction projects), and as a confined disposal facility for contaminated dredge spoil from the harbour area. The construction of the headland was initiated in the early 1960's, and although still ongoing today, its greatest offshore extent was reached by 1978.

The headland has two important impacts on the regional coastal processes. First, the historic rate of sediment supply from the east, which had been severely reduced by the construction of the Eastern Channel jetties and subsequent dredging, was eliminated completely with the construction of the headland. The Eastern Channel has only been dredged once since 1965. The second and most important impact of the Eastern Headland has been the modification of the nearshore wave climate through sheltering the eastern half of the Islands from the easterly storm waves. Detailed wave transformation analyses (discussed below) revealed that the zone of influence of appreciable sheltering probably extends no further west than the Centre Island pier at the east end of the Centre Island seawall (refer to Figure 1). The headland does not have a significant impact on the waves which reach Gibraltar Point.

The Toronto Islands Water Filtration Plant is located just east and inland of the Nature School in the Gibraltar Point area. While the intake lines for this facility date back to the late 1800's, the two existing intake lines were completed in the early 1950's. Each line extends almost 1 km offshore and consists of a pipe confined by two steel sheet pile walls, which in places extend up to 2 m above the adjacent lake bed. The eastern intake line has an associated steel sheet pile groyne structure at the shoreline which appears to have been constructed in the late 1940's. These structures act to impede the alongshore transport of sediment.

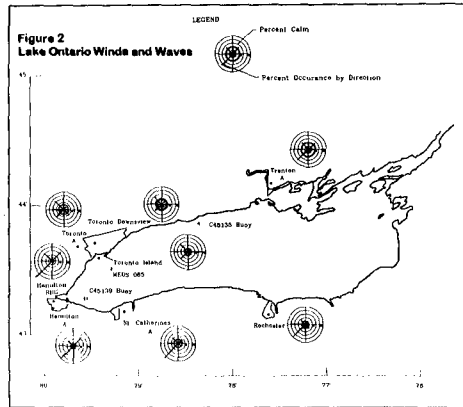
#### Development of a Nearshore Wave Climate

A wind-wave hindcast was performed to develop an estimate of the long term offshore wave climate at the Toronto Islands. A 1D parametric hindcast model based on the approach of Donelan (1980) was used. Research by Skafel and Bishop (1993) has shown that the available 2D dynamic hindcast models do not give superior results to the 1D models when estimating wave conditions on the Great Lakes. A considerable effort was devoted to assessing wind data input for the hindcast model. Overwater wind speeds for a 35 year hindcast period were determined from comparison of several land based wind data records to available overwater wind data records (Figure 2 shows available wind and wave data for Lake Ontario).

The use of a combined wave refraction / diffraction model was vital to the assessment of the nearshore wave climate at Toronto Islands due to the nature of the underwater topography and the influence of the artificial Eastern Headland. The



REF/DIF 1 model developed by Kirby and Dalrymple (1983), which is based on a parabolic approximation of the mild slope equations, was utilized. Model runs were performed for a range of representative wave directions, heights and periods.



Due to its position at the west end of Lake Ontario, the most severe storms are generated by easterly winds over a 250 km fetch. The maximum significant wave height during the 35 year hindcast period was estimated to be 5.6 m with a peak period of 12 s and a direction just north of east. The prevailing winds are from the southwest and the maximum significant wave height from this direction during the hindcast period was 4 m with a period of 10 s. The considerable year to year variability in the ratio of east to southwest storm events, as well as variations in overall annual wave energy, have an important influence on the pattern of morphologic response.

The level of Lake Ontario has an average seasonal fluctuation of about 0.6 m. There is also considerable long term variability with a 2 m difference between the maximum spring high level and the minimum winter low level.

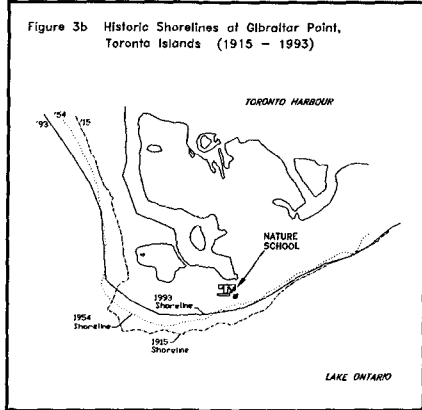
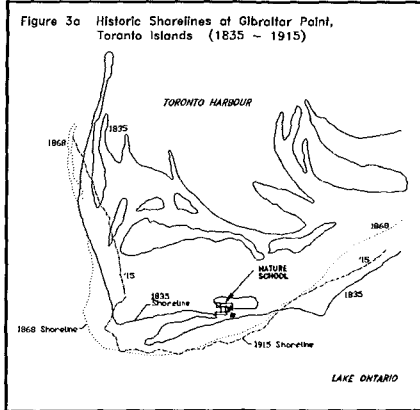
### Change in Shoreline Position

There is a wealth of information on the position of the Toronto Islands shoreline dating back to the initial European settlement in 1793. The accuracy of this information varies considerably; however at the very least, each map or aerial photo provides a snap shot giving some indication of the evolving nature of the Toronto Islands feature at a point in time.

For those sources of data which have an acceptable degree of accuracy, intercomparisons may be made between the different snap shots allowing for the calculation of shoreline recession rates for the various periods. Under the Shoreline Policy of the Province of Ontario, potential hazard areas must be determined in part from an estimate of the shoreline position in 100 years time based on historic shoreline recession rates.

A summary of some of the historic shoreline positions in the Gibraltar Point area that have been corrected for lake level variations are shown in Figures 3a and b. From the shoreline changes between 1835 and 1915 given in Figure 3a, it is evident that between 1835 and 1868 the south facing section of the shoreline moved lakeward

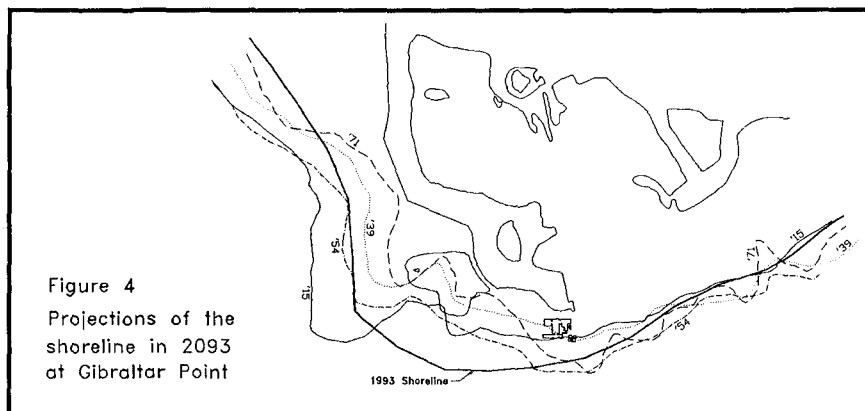
(i.e. the Islands deposit was growing). Between 1868 and 1915 the depositional trend was reversed, possibly due to the influence of the updrift breach. Figure 3b shows that after 1915, erosion was experienced along the south facing shore with deposition along the west facing shore. In the vicinity of the School, and to the east, the shoreline apparently was stable during the period from 1954 to 1993. However, this finding should be considered with caution owing to the highly eroded state of the 1954 shoreline as caused by the abnormally high lake levels in 1951 and 1952.



In summary, the trend of shoreline change cannot be described as a linear process over the period from 1835 to the present. Prior to 1868, the south facing part of the shore was accreting and since at least 1939 the shore has been eroding. Furthermore, short term and temporary changes to the shoreline position caused by the rapid response of the nearshore profile to storm conditions can obscure long term trends that are based on these snap shots.

Under the Provincial Shoreline Policy, one part of the definition of hazard lands (where development is restricted) relates to those areas which will be threatened by erosion within 100 years time. As noted above, the Policy requires that the position of the 100 year shoreline be established through linear extrapolation of historic shoreline recession rates (with a minimum time span of 35 years between snap shots of shoreline position). For the purposes of these investigations, the 100 year shoreline has been established through extrapolating recession rates for all available periods in order to provide a range of results. Two recent surveys were used as a basis of comparison against historic shoreline positions: a 1988 aerial survey and a 1993 ground survey (only the latter set of comparisons are presented in this paper).

The 100 year shoreline position projections, based on a comparison of historic and 1993 shoreline position's, are presented in Figure 4. Generally, these results feature three different zones of shoreline change consisting of deposition along the north part of the west facing shore, dramatic erosion around the strongly curved point and relatively minor changes for the remainder of the south facing shore. As expected, for the shortest comparison period (1971 to 1993) the 100 year position features the greatest variability while the 100 year projection from the earliest shoreline in the comparison (1915) is distinguished by the least alongshore variability. If the process of erosion was linear, it would be reasonable to assume that the 100 year projection based on the latter comparison was the most reliable.



However, a close review of the shoreline positions offshore of the School reveals a distinct difference between projections based on pre- and post- 1940's data. The 1915 and 1939 projections of the 100 year shoreline pass directly through the School site, whereas the more recent projections produce a 100 year shoreline offshore of the existing School. Here it may be postulated that the groyne and intake lines which were constructed for the Filtration Plant in the late 1940's have had an important effect on the shoreline in this area. Therefore, since the effect of this change is not reflected over the full comparison period with the historic shorelines prior to the 1940's, these results do not provide realistic projections of future conditions. In addition, the 100 year projection based on the comparison of the 1954 and 1993 shoreline positions may also be misleading. This result suggests that the shoreline offshore of the School will remain stable or even accrete over the next 100 years. However, it should be recalled that the 1954 shoreline may have been in a temporary highly eroded state. Therefore, any recession rates calculated through comparison to the 1954 shoreline may underestimate future erosion.

In summary, there are several problems with 100 year shoreline projections which assume linear extrapolation. These include the following issues at this site: the erosion process is not linear in time; considerable changes to the regional processes have occurred over the last 100 years; the erosion process will not be linear in the future, as shoreline and lake bed changes will alter the pattern of future change which is related to the transport and redistribution of sediment; existing shoreline protection at Gibraltar Point will not last for the 100 year projection period and obscures the future predictions; the 100 year projections also assume that other structures such as the groyne and the intake lines will be maintained in the future; snap shots of shoreline position may reflect temporary and reversible changes to shoreline position which are not indicative of long term trends, the questionable 1954 shoreline projection is an example of this problem.

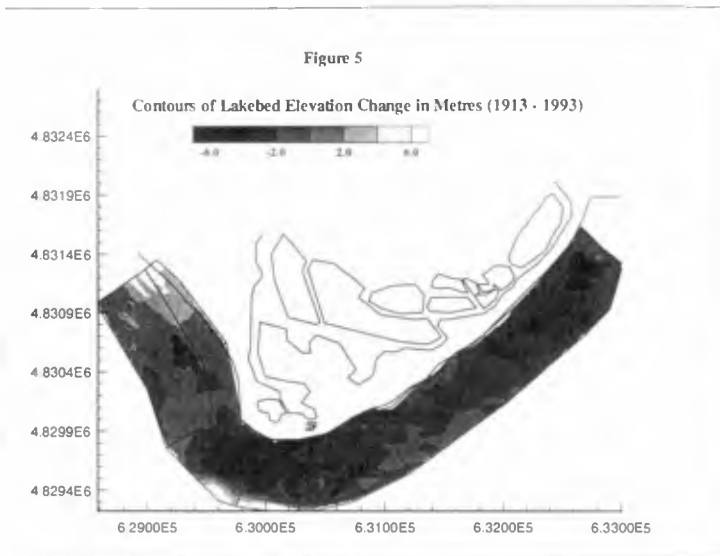
Nevertheless, the 100 year projection results do provide some general findings which are pertinent to this investigation. The strongly curved part of Gibraltar Point has been and probably will continue to be the focus of greatest erosion. The pattern of erosion changed sometime in the 1940's, possibly related to the construction of the groyne and intake lines for the Filtration Plant, such that the shoreline east of the School became more stable.

### Changes in Lake Bed Levels and Sediment Budget

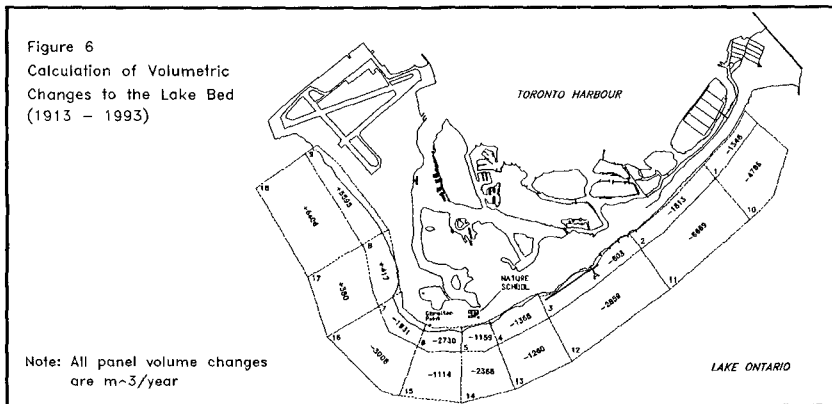
There is extensive information on the water depths offshore of the Toronto Islands dating back to 1793. Comparisons of changes in the lake bed levels between the various bathymetric snap shots provide a more comprehensive perspective of the changing nature of the Toronto Islands feature than does the shoreline change data. The interpretation of long term trends in lake bed change are not obscured by temporary lake level related changes in shoreline position or the effects of structures.

The complexity of an investigation of the temporal change in an irregular three dimensional surface (i.e. the lake bed) is such that the full value of this information in developing an understanding of the problem is seldom realized. Therefore, the bathymetric change data was considered in four different ways, providing the greatest opportunity of maximizing the value of this information.

Contours of lake bed elevation change were prepared by subtracting one lake bed surface from another. This procedure was completed for five separate time periods between 1913 and 1993. Figure 5 provides the results for the full 1913 to 1993 period, and gives an overview of the findings. The outer boundary of the comparison area varies in depth between 6 and 8 m. There is a pronounced erosional zone all around Gibraltar Point with the highest erosion rates found immediately offshore of the western extremity of the Point (i.e. where the shoreline curvature is at a maximum). Up to 5 m of lake bed lowering has occurred in places. Aside from the heavy deposition offshore of the north part of the west facing shoreline and the transition between this zone and Gibraltar Point, the only other relatively stable section of lake bed is a zone located between the groyne (and the east intake line) and the west end of the breakwater. Offshore of the seawall, erosion is prevalent. There is also evidence of deposition off the southwest corner of the shelf which suggests some of the eroded sediment has been lost offshore of the shelf.



The second approach of considering the evolution of the lake bed surface is based on calculations of volumetric change for various "panels". The panels have been selected on the basis of available lake bed information and to describe sections of lake bed which have similar trends of erosion or deposition. This exercise was completed for five different snapshots, one example is provided in Figure 6 for the full period from 1913 to 1993. There are two tiers of panels corresponding to an inshore set and an offshore set separated by the 3 to 4 m depth contour. The volume change estimates for the inner Panels 1 to 9, while showing much variation between periods, reveal some consistent trends. There is sediment sink in Panel 9 offshore of the north section of the west facing shore. Also, Panels 5 and 4 (offshore of the School and the adjacent panel to the east) often feature either lower erosion rates than neighbouring panels, or even deposition.



A comprehensive sediment budget analysis can be applied to the '13-'93 period based on volume change calculations for all of the panels around the shore. As explained earlier, this area now represents a confined littoral cell. For the 80 year period, there was a net loss of  $1,620,000 m^3$  of sediment from the area covered by the panels, or a little over  $20,000 m^3/yr$  on average. While a significant amount of this sediment may have been transported beyond the ends of the panel area (i.e. northwest of Panels 9 and 18, and northeast of Panels 1 and 10), it is likely that a significant proportion of the sediment has been lost offshore beyond the outer boundary of the panels and perhaps over the shelf at the edge of the wide platform which surrounds the Islands feature. Referring to Figure 5, a zone of deposition along the outer edge of Panels 15 and 16 may represent the growth of the shelf caused by the deposition of the sediment that has been transported offshore.

Another manner of interpreting the changes to the lake bed surface through time is to plot the changing position of selected depth contours. The 2, 4 and 6 m contours were selected for this exercise. In addition, by comparing the historic position of the contours to 1993 as a base year, "recession rates" for the contours may be calculated and projected to determine the 100 year position of the contour lines. It is again cautioned that these are linear extrapolations of a non-linear process.

Figure 7a shows the changing position of the 2 m contour around Gibraltar Point. Between 1951 and 1993, the 2 m contour position has remained relatively

stable everywhere east of the west intake line, whereas west of this point this contour has moved rapidly inshore. The recession rates of the 2 m contour line offshore of the Point for the 1951 to 1993 period reach almost 5 m/yr. This is much higher than the long term rate of shoreline recession of about 1.5 m/yr in this area. Figure 7b gives the 100 year projections for the position of the 2 m contour; these also indicate that the severity of erosion may be far greater than is indicated by the projections of the shoreline position. The erosion of the nearshore zone is outpacing the recession of the shoreline, probably as a result of shoreline structures and vegetation (including the root systems of large trees) which delay the shoreline erosion. The fact that the profile shape is changing from convex to concave also helps to explain the differential recession rates between the shoreline and the 2 m contour.

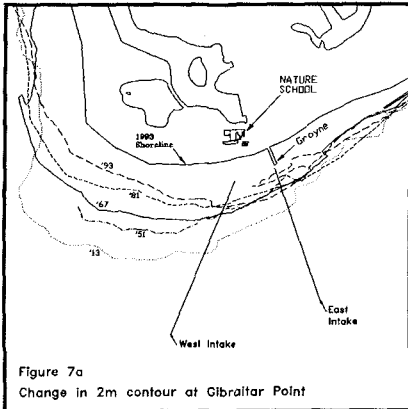


Figure 7a  
Change in 2m contour at Gibraltar Point

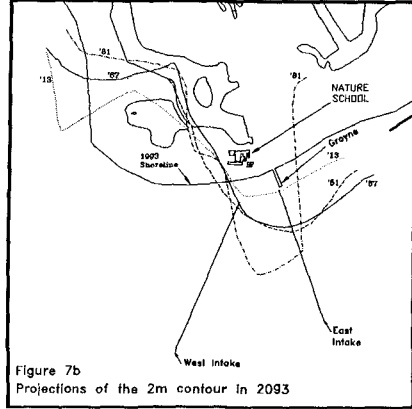


Figure 7b  
Projections of the 2m contour in 2093

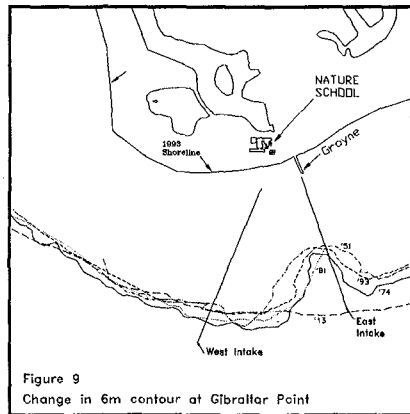
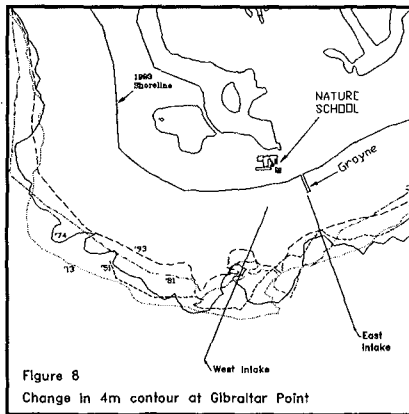
Interestingly, the 100 year projections of the 2 m contour in the vicinity of the School are in much closer agreement (i.e. for the various snap shot comparisons) than were the shoreline projections. The projections highlight the role of the intake lines in stabilizing the position of the 2 m contour.

The 4 m contour has receded inshore considerably at Gibraltar Point, mostly since 1951, although at a slower rate than the 2 m contour, with average rates of about 1.5 m/yr (see Figure 8). Offshore of the Point, there was minimal erosion between 1913 and 1951. Considering the recession of the 4 m contour was initiated about the same time that the intake lines were constructed, it is possible that the lines, by intercepting westward moving sediment, may have accelerated the erosion of the lake bed offshore of the Point.

There are several interesting features of the changing position of the 6 m contour line (see Figure 9). Starting from a point between the intake lines and moving to the west, the 6 m contour has been completely stable in position over the last century owing to the fact that this contour marks the transition from onshore erosion to offshore deposition. The 6 m contour delineates a pronounced depression or canyon around the east intake line that developed over the period between 1913 and 1951. The canyon represents a zone where the intake line acts as a total littoral barrier.

Representative profiles were also plotted for the midpoint of each of the lake bed panel sections. Around Gibraltar Point, these plots revealed the changing nature

of the feature from a depositional zone with a pronounced convex profile to an erosional zone with the related concave profile shape.



### Sediment Transport Predictions

The observed patterns of erosion and deposition that have been discussed in the previous sections have resulted from the transport and redistribution of sediment (e.g. sand). Sediment is transported by the effects of waves and the associated steady currents both in an alongshore direction and in a cross-shore direction. This section presents a brief summary of the results of numerical simulations of these sediment transport processes which were aimed at developing an improved understanding of why the observed changes have occurred and what may happen in the future.

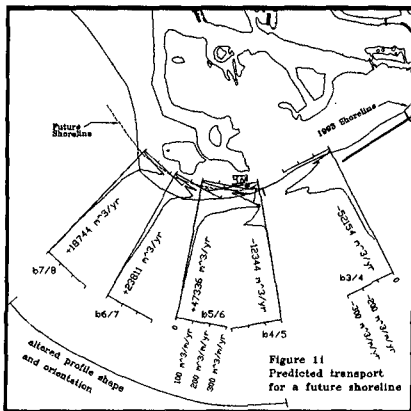
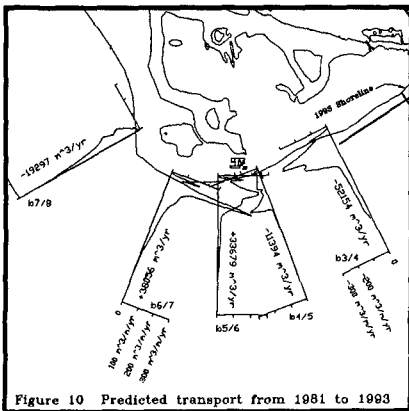
The COSMOS-2D numerical model of coastal processes has been applied to simulate the alongshore and cross-shore sediment transport. This numerical model is based on a deterministic quasi-2D representation of the actual physical processes which result in the transport of sand on a profile or cross-section of the lake bed. The calculation scheme is based on a time-averaged finite difference approach for random wave conditions. A comprehensive description of the model is given in two companion papers: Nairn and Southgate (1993) and Southgate and Nairn (1993).

Estimates of average annual alongshore transport have been made for several profiles around the exposed shore for three separate intervals within the hindcast period (i.e. '58 to '67, '67 to '81, '81 to '93). The alongshore transport estimates were made at the boundaries between the panels to determine the sediment transport entering and exiting each panel. An extensive set of sediment samples indicated that a D50 of 0.2 mm would be representative of the average lake bed conditions. An example of the results for the period from 1981 to 1993 is shown in Figure 10. The profile name indicates the panel boundary (i.e. b6/7 is the boundary between Panels 6 and 7) and the annual average sediment transport rate is given for each of the profiles. The distribution of alongshore transport across the profile is also depicted in the figure, providing an indication of the sediment transport pathways along the shore.

For each of the three periods, the alongshore transport estimates indicate that Panel 7, located offshore of Gibraltar Point, is a divergent zone for net sediment transport. In other words, sand is moving out of this panel at each boundary. This

type of situation results in high erosion rates with a potential annual loss of sediment from the panel equal to the sum of the outgoing amounts at each boundary. The neighbouring Panel 6 to the east, which together with Panel 7 represents the zone of highest observed erosion, has incoming sediment on the west boundary (b6/7) and outgoing sediment on the east boundary (b5/6) for each period. The difference between these two values is usually small, however, it must be recognized that the full potential value at b6/7 may not be realized with the net result being that Panel 6 is probably subject to ongoing erosion due to the alongshore redistribution of sediment from west to east (in other words, the divergent zone may extend into Panel 6).

Panel 5, located offshore of the School, is predicted to be a convergent zone (i.e. with incoming sediment at each boundary) and deposition would be expected to occur. It was noted earlier that Panel 5 features relatively low observed erosion rates compared to adjacent panels. Part of the basis for predicting that Panel 5 is a depositional zone relates to the prediction of potential transport from the east (i.e. at b3/4 and b4/5). Concerning the b3/4 prediction, it is likely that this is considerably overestimated since the offshore breakwater will partially restrict the movement of sand supplied from the east. Also at b4/5, the alongshore transport is influenced by the presence of the groyne and the intake line for the Filtration Plant a factor which also restricts the transport along the shore. In addition, the supply of sediment from the east is now derived from the erosion of the lake bed offshore of the seawall and breakwater, and with time, this source of sediment will be exhausted as deep concave profiles develop next to these structures (this outcome has already been observed along a large section of the eastern part of the seawall).



As the alongshore transport redistributes the sediment through the erosion of Gibraltar Point and deposition along the southwest shore and offshore of the School, the shape of the shoreline changes and this in turn effects the rate at which sediment can be transported by waves. In other words, there is a feedback system whereby the waves alter the shoreline and lake bed, and these changes in turn alter the waves and therefore the sediment transport. In order to assess how future changes to the shoreline shape may influence the future patterns of alongshore transport, estimates were made for a future shoreline position as determined from the shoreline projections discussed earlier. Revised profile shapes were also considered based on the amount of shoreline recession dictated by the assumed future shore position. The future shoreline position and the revised estimates of alongshore transport at each of the panel



boundary profiles are presented in Figure 11. The 1981 to 1993 waves were used, so these results are best compared to those given in Figure 10.

Only Profiles b4/5 through to b7/8 have been modified. Reviewing the results, there is only a minor change in the estimates for Profiles b4/5 and b5/6, but the net transport at b6/7 is halved and the transport at b7/8 has changed direction from west (or clockwise) to east. These findings suggest that in the future the zone of highest "erosional stress" due to alongshore transport will be shifted or extended from Panel 7 (current position) to the east into Panel 6 and to the west into Panel 8. However, the zone immediately offshore of the School (i.e. Panel 5) will remain a zone of deposition as long as the supplies from the west and east are maintained.

A rough estimate may be made of the remaining supply of sediment which may be available from ongoing erosion of the lake bed as a source for westward directed transport reaching Panel 5 offshore of the School. It was determined that the potential transport rate of 23,500 cubic metres per year could be sustained for another 28 years. This calculation suggests that the future supply of sediment to the panel offshore of the School from erosion of the lake bed to the east may be exhausted in 25 to 50 years.

Sediment transport calculations were performed to investigate the influence of the Filtration Plant intake lines and associated groyne structure. It was determined that neither the intake lines nor the groyne represent a significant impediment to alongshore transport under the June 1994 snap shot conditions. However, additional model tests indicated that the groyne helps to maintain a small fillet beach during storm conditions and thus the stability of the shore to the east, and similarly, the intake lines appear to act as submerged groynes helping to hold the 2 m contour offshore at this location, particularly during storm conditions (while along the adjacent shore to the west, the 2 m contour has continued to recede inshore). It is anticipated that with the ongoing erosion of the lake bed offshore of the 2 m contour in the vicinity of the intake lines, the stability of the lines could be threatened in about 50 years from now.

Next, the role of cross-shore transport in the reshaping of the Gibraltar Point feature was considered. Of primary concern is the potential for permanent loss of sediment from the nearshore to offshore locations. The COSMOS numerical model provides a description of the cross-shore sediment transport rates for a nearshore profile. In preliminary tests it was found that only the largest waves result in appreciable offshore loss of sediment (i.e. sediment which is transported beyond the edge of the shelf). Therefore, an input wave file with a relatively small number of representative wave conditions (about 20) could be prepared for the calculation of cross-shore sediment transport at each profile. The offshore loss rates for the entire hindcast period and the sub-periods were then estimated based on the product of the total duration for each representative wave condition and the offshore loss rate determined through the COSMOS simulations. Calculations were made for both the 1993 profile shape and the estimated future profile shape that may exist in 50 to 100 years time. The offshore loss rate over the wave hindcast period (1954 to 1993) was determined to be  $5.06 \text{ m}^3/\text{m}/\text{yr}$  with the 1993 profile shape. For a future profile shape with a flatter slope based on continued shoreline recession, the predicted offshore loss rate was  $3.65 \text{ m}^3/\text{m}/\text{yr}$  representing a 30% reduction from the current rate. As a check on the validity of these estimates, the 1951 to 1993 average loss rate for Panel 15 (i.e. the offshore segment of Profile 6) was found to be  $2860 \text{ m}^3/\text{yr}$ , or about  $5.5 \text{ m}^3/\text{m}/\text{yr}$ , which corresponds well to the calculated rate of  $5.06 \text{ m}^3/\text{m}/\text{yr}$ .

In summary, in the vicinity of Gibraltar Point, alongshore transport processes are causing a redistribution of sand from the Point to the north part of the west facing shore and also towards the area of the intake lines. Thus, the Point is a zone of divergent sediment transport while the area of the intake lines is a zone of convergent sediment transport. Also, there is an ongoing offshore loss of sediment due to cross-shore transport processes. This situation is related to the change in the profile shape from a convex form (which developed when the Point was a depositional feature) to a concave form which is consistent with the present eroding condition.

### Descriptive Model of the Morphodynamics

A descriptive model was developed to relate quantitatively the observed changes in the Gibraltar Point feature to coastal processes, particularly the alongshore and cross-shore transport of sediment which are the driving forces of change at this location. Another aspect of the model is the temporal and spatial schematization which are required to simplify a continually evolving and complex three dimensional problem. From a temporal perspective, the last 35 years were subdivided into three periods ('58-'67, '67-'81 and '81-'93) in part related to the availability of data and also to identify three quite different periods of response. The spatial schematization is based on the "panel" descriptions presented earlier, which consist of an inner and an outer ring of panels, again in part related to data availability and also to identify unique zones of lake bed change. This approach was inspired by the work of Stive and deVriend (1994). As a check on the validity of the descriptive model, the historic observations of change may be compared to the predictions from the model. In essence, the descriptive model is no more than the application of a sediment budget to past changes (with the aid of sediment transport estimates to explain these changes) and the projection of the future sediment budget for periods of 50 and 100 years from the present based on future estimates of sediment transport and sediment supply.

Figure 12 provides a summary of the descriptive model of the evolving morphology at Gibraltar Point over the last 35 years which illustrates the relative magnitude of the incoming and outgoing sediment transport components along with the transfer between the two sections (i.e. the arrows are drawn to represent the relative magnitude of the transport components). This model explains why the west section (Panels 6/7 and 15/16) is eroding at a much greater rate than the east section (Panels 4/5 and 13/14). These transport patterns and associated lake bed changes also translate to shoreline erosion, with the shore along Panels 6 and 7 experiencing high recession rates and the shoreline along Panels 4 and 5 being relatively stable.

Figure 13 provides a summary of the expected pattern of sediment redistribution in the next 50 years (i.e. 1993 to 2043). The offshore loss rates have been reduced to about 70% of the current rate based on the calculations described earlier. The outgoing alongshore transport along the northwest boundary was found to be almost the same as the '81-'93 value, and therefore, is left unchanged. The incoming transport at the east boundary of the east section has been significantly reduced to reflect the remaining supply of sediment available from erosion of the lake bed in Panels 3/12 and 4/13. With the future evolution of the shoreline, the transfer of sediment between the east and west sections is predicted to be reduced to about 25% of the current rate, resulting in a projected transfer of 2,500 cubic metres per year. The expected changes in the second half of the next century (i.e. 2043 to 2093) were also completed but are not presented here. The only difference in the various incoming and outgoing components from the 1993 to 2043 period is that it the supply of transport

from the east will be exhausted by the second half of the next century, thus eliminating incoming sediment on the east boundary of the east section.

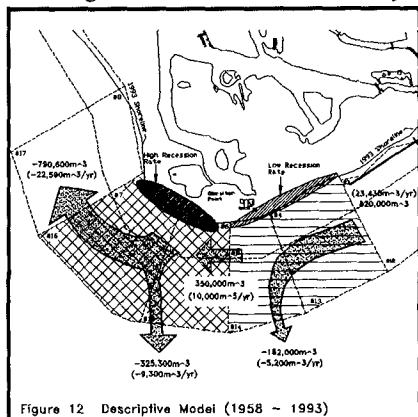


Figure 12 Descriptive Model (1958 - 1993)

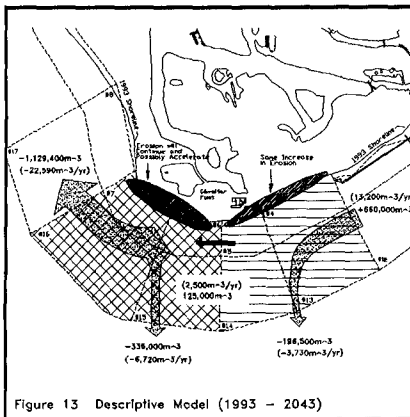


Figure 13 Descriptive Model (1993 - 2043)

For the west section of Gibraltar Point (i.e. Panels 6/7 and 15/16), the findings suggest there will only be a slight decrease in overall sediment loss over the next 100 years. As noted earlier, the shoreline recession has been outpaced by the erosion of the lake bed. The lag in the response of the shoreline is due presence of ad hoc protection structures and natural vegetation, but is also partly explained by the change from a convex to concave profile shape. With the failure or removal of the shore protection structures, it is anticipated that accelerated shoreline recession will occur. Therefore, the linear projections of future shoreline position, if anything, may underestimate the potential shoreline erosion along the inner boundary of Panels 6 and 7.

The results also point to increasing erosional stress on the lake bed of the east section of Gibraltar Point (i.e. Panels 4/5 and 13/14 offshore of the School) through the next 100 years. The analysis presented earlier showed that a linear extrapolation of the historic rate of recession of the 4 m contour over the next 100 years would destabilize the currently stable deposit offshore of the School (i.e. bracketed by the two intake lines, the shoreline and the 2 m contour line). Considering that the descriptive model projects that the erosional stress will be increased in the future, the linear projections may underestimate the future erosion of the lake bed and the future shoreline recession.

The intake lines, which help to stabilize the shoreline and nearshore lake bed offshore of the School, will be increasingly threatened with the projected lake bed lowering. It was noted above that based on the projected rate of recession for the 4 m contour, the stability of the steel sheet piles on either side of the intake pipes would be threatened in 50 to 100 years time. The predictions from the descriptive model suggest that the linear projections underestimate the future lake bed erosion and therefore, the stability of the intake lines could be jeopardized in 50 years time, or possibly less.

### Findings and Concluding Remarks

The findings of shoreline comparisons, which give the projected position of the shoreline in 100 years time based on a linear extrapolation of historic rates, were ambiguous with respect to the security from erosion hazards of the existing Nature

School position. Some projections indicated that the School position may be satisfactory after accounting for 100 years of erosion, while others found the existing School location would be completely eroded in 100 years time. This investigation revealed serious shortcomings in the method of linearly extrapolating historic shoreline recession rates to determine future shoreline positions.

In a review of historic and recent lake bed changes, there were both positive and negative implications with respect to the safety of the School position. On the positive side, the lake bed offshore of the School out to the 2 m depth contour and bracketed by the intake lines has been relatively stable over the last 50 years. Also, the section of lake bed to the east of the intake lines has experienced much less erosion than the lake bed offshore of Gibraltar Point or offshore of the seawall further to the east. However, the continued lowering of the lake bed offshore of the 2 m contour in the vicinity of School over the last 50 years has a very negative implication to the future stability of the shoreline in this area. The various ways of depicting the changes to the three dimensional lake bed surface each provided valuable insight to the nature of the evolving morphology.

The descriptive model of the evolution of Gibraltar Point has shown that erosion of the lake bed offshore of the School will be accelerated in the future. Therefore, the currently stable deposit offshore of the School and inshore of the 2 m depth contour will be destabilized, possibly in less than 50 years time. This outcome will allow the erosion of the shoreline in the vicinity of the School to accelerate. Therefore, the linear estimates of the 100 year shoreline position will underestimate the future shoreline recession. In other words, the existing School position will be susceptible to erosion hazards in less than 100 years time.

The application of a fully deterministic model of changing morphology over a 100 year period was considered to be unrealistic given the current state of our understanding of the processes. As an alternative, the descriptive model extends the traditional sediment budget approach by accounting for possible changes in future sediment transport rates to provide a highly schematized projection of future changes to the morphology of the Gibraltar Point feature.

### References

- Donelan, M.A. (1980). "Similarity Theory Applied to the Forecasting of Wave Heights, Periods and Directions". Proceedings of the Canadian Coastal Conference, National Research Council, Canada. pp. 47-61.
- Kirby, J.T. and Dalrymple, R.A., (1983). "A Parabolic Equation for the Combined Refraction-Diffraction of Stokes Waves by Mildly Varying Topography". *J. of Fluid Mech.*, 136. pp. 543-566.
- Nairn, R.B. and Southgate, H.N. (1993). "Deterministic Profile Modelling of Nearshore Processes. Part II. Sediment Transport and Beach Profile Development". *Coastal Eng.* 19. Elsevier. pp. 57-96.
- Skafel, M.G. and Bishop, C.T. (1993). "Validity of Wave Direction Predictions". Canadian Coastal Conference, Vancouver. Vol. 1. pp. 81-94.
- Southgate, H.N. and Nairn, R.B. (1993). "Deterministic Profile Modelling of Nearshore Processes. Part I. Waves and Currents". *Coastal Engineering* 19. Elsevier. pp. 27-56.
- Stive, M.J.F. and DeVriend, H.J. (1994). "Modelling Shoreface Profile Evolution". Submitted for Special Issue Marine Geology on Large Scale Coastal Behavior.

## CHAPTER 173

### STABILITY AND MANAGEMENT OF AN ARTIFICIAL BEACH

Naofumi Shiraishi<sup>1</sup>, Hoiku Ohhama<sup>2</sup>, Taiji Endo<sup>3</sup> and Patricia G. Peña-Santana<sup>4</sup>

#### ABSTRACT

An example of an artificial beach constructed for recreational purposes is presented. The beach stability and its impact on the marine environment is discussed. Also, the beach maintenance and management during almost 20 years is reported.

#### 1. INTRODUCTION

The venue of the 1975 Ocean Expo-75 was in Okinawa, and for this event an artificial beach was constructed to show the "Expo Beach" marine exposition. This was one of the first artificial beaches to be built for recreational purposes in Japan. Since then, the Ocean Expo Commemorative Park Management Foundation has been in charge of management and maintenance for the public beach. In this paper, first the beach characteristics are described, then the impact of the artificial beach on the marine environment, and the stability of the beach are discussed based on measurement campaigns performed at the site, before and after the beach construction. And finally, the beach maintenance and management programs necessary to preserve it as an attractive recreational facility are reported.

#### 2. EXPO BEACH DESCRIPTION

The artificial beach "Expo Beach" is located in the northern part of Okinawa, Japan. It is laid out in a north-south direction above a natural coral reef, with a maximum width of about 1 km at the north of the beach. At the place where the structures were built, the reef width is about 0.5 km, and this gradually decreases to 0.1 km at the southernmost end. The reef elevation around the

---

<sup>1</sup>Chairman, Nippon Tetrapod Co. Ltd., Tokyo, Japan

<sup>2</sup>Managing Director, Ocean Expo Commemorative Park Management Foundation, Okinawa, Japan

<sup>3</sup>Director, Nippon Tetrapod Co. Ltd., Tokyo, Japan

<sup>4</sup>Research Engineer, Nippon Tetrapod Co. Ltd., Tsuchiura, Japan

beach structures is D.L.  $\pm 0 \sim +0.3$  m, and at the reef edge the elevation is D.L.  $+0.5 \sim +1.0$  m. Outside the reef, the slope varies from  $1/3$  to  $1/5$  from north to south, the average water depth is 30 m and this goes down to 60 m in some areas. To the north of the beach there are some notorious reef discontinuities; among these, the most pronounced is located about 200 m from the beach north-headland; here the minimum width is at the reef edge, and this gradually expands inside the reef. A sketch of the reef and the beach layout are shown in *Figure 1*.

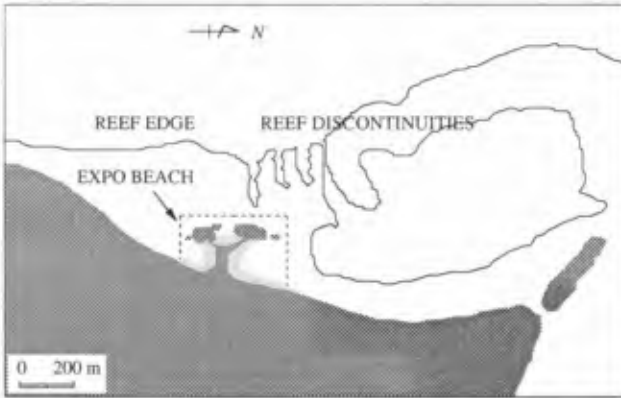


*Fig. 1.* Beach and reef layout

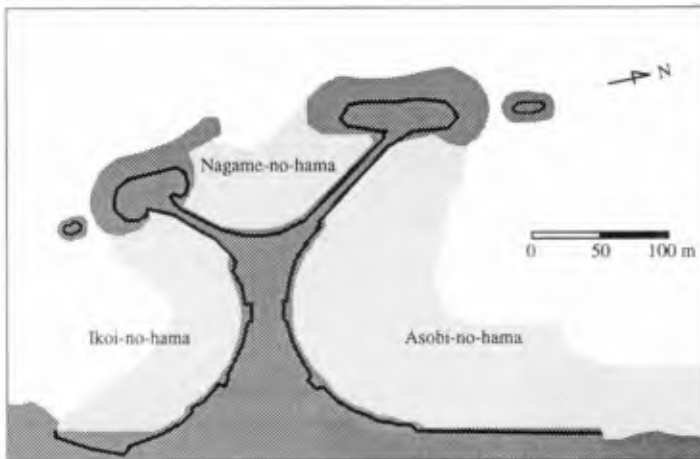


*Fig. 2.* Plan view of the artificial beach

For the beach design, a length of about 400 m was available, and to make the best use of this, a "Y" shape was selected for the beach layout, as shown in *Figure 2*. Consequently, the total beach length became about 900 m, and this

was then divided accordingly into three beaches named Ikoi-no-hama, Nagame-no-hama and Asobi-no-hama. These are located on the left, top and right sides of the "Y", respectively. The widths of the beaches are approximately 28 m in the Ikoi-no-hama and Nagame-no-hama, and 44 m in Asobi-no-hama.

In *Figure 3* a typical design cross section of the beaches is shown.



*Fig. 3.* Typical design cross section of the beach

Each beach was designed to fulfill a different main purpose. That is, Ikoi-no-hama was designed to be safely used by young children who just wanted to play in the water, rather than swim. Nagame-no-hama was designed for those who would like to contemplate the seascape scenery. And, finally, Asobi-no-hama was designed for swimmers.

Relatively shallow water depths were therefore accepted for the Ikoi-no-hama and Nagame-no-hama beaches design; but for the Asobi-no-hama beach, deeper water depths were desired to satisfy the swimmers. For this purpose, the sea bottom material was removed to increase depth by 1.0 m. A sand layer of about 20 cm was then spread over this dredged zone. Hence, 80 cm were added to the water depth here; and for the M.W.L. depths of about 1.9 m were ensured for the swimmers in an area of 10 672 m<sup>2</sup>, that is about 9 to 10 times the size of a standard swimming pool. The total volume of extracted rock for this purpose was 14 010 m<sup>3</sup>.

*Table 1* summarized some of the design characteristics of the artificial

*Table 1.* Characteristics of the artificial beach

Characteristic	Amount
total beach area	64 000 m <sup>2</sup>
stones for protection	36 000 m <sup>3</sup>
pedestrian area	7 100 m <sup>2</sup>
green area	4 000 m <sup>2</sup>
changing rooms and showers	400 m <sup>2</sup>
sand nourishment area	42 000 m <sup>2</sup>
sand nourishment volume	56 000 m <sup>3</sup>
sand mean diameter	0.5 ~ 0.7 mm
sand specific weight	2.8

beach, which have remained unchanged throughout the years. The sand nourishment volume shown in *Table 1* was used to fill the beach during its construction, and no surcharge has been necessary since then.

### 3. IMPACT ON THE MARINE ENVIRONMENT

Before the artificial beach was constructed, there was no beach development at the site. A comparison of field studies performed at that time, and those done during the almost 20 years thereafter have allowed an assessment of the beaches marine environmental impact. These field studies are mainly related to the velocity field, wave and tide climate, water quality and marine ecology, and are described in this section.

#### 3. 1. Velocity field

Results obtained from field measurements carried out before and after the artificial beach was constructed are shown in *Table 2*. The measurements of 1973 were performed before the beach construction by taking aerial photographs, at fixed intervals, of buoys deployed in front of the zone destined for the beach. The rest of the results shown in *Table 2* are from measurements taken after the beach construction. The latter results were obtained from measurements at two stations located inside the reef, one at the south of the beach, and the other at its north. The south station was located almost at the same place for all measurement campaigns. The north station, however, was set closer to the beach, outside any notorious reef discontinuity, for the campaigns of 1974 and 1975, and for the campaigns of 1985 and 1986, it was located inside a reef discontinuity. The measurements performed after the beach construction were taken about 50 cm below the water level.

*Table 2.* Current velocity

Year	Velocity during ebb tide (m/s)	Velocity during flood tide (m/s)	Wind velocity (m/s)
1973	0.30 - 0.40	—	—
1974	0.07 - 0.18	0.06 - 0.17	7.0
1975	0.05 - 0.20	0.02 - 0.12	3.5 - 6.0
1985	0.05 - 0.35	0.03 - 0.55	5.0
1986	0.03 - 0.10	0.02 - 0.50	2.0 - 3.0

*Table 2* shows that the respective velocity values are of the same order of magnitude, and that the higher velocities are related to higher wind velocities. It should be noticed, however, that the maximum velocity values were found inside the greatest reef discontinuity, schematized in *Figure 1*. Because during the 1974 and 1975 campaigns the north station was set outside this zone, smaller current velocity values were reported here even though the corresponding wind velocities



were higher, when compared with those values reported from the campaigns of 1985 and 1986.

From measurements taken at other stations, it was found that the maximum velocities reported were obtained at the narrow part of the greatest reef discontinuity. In 1973, velocities ranging from 0.6 to 1.0 m/s during the ebb tide, and in 1986, 0.85 m/s during the flood tide were measured. Relatively high velocities were also found close to the north-headland, where there is another discontinuity; in 1975, velocities of 0.6 m/s were found during both ebb and flood tides, at a station located between the north-headland and the promontory located nearby; and in 1986, velocities of 0.55 m/s during the flood tide were reported to be just in front of this headland.

### 3. 2. Wave and tide climate

The deep water wave conditions used for the beach design are wave height  $H_0 = 7.2$  m, wave period  $T = 12.0$  s, with a SW wave direction. The computed significant wave height in front of the beach, at the depth 2.5 m for H.W.L., is  $H_{1/3} = 1.5$  m.

The results of wave conditions measured before and after the beach was constructed are summarized in *Table 3*.

*Table 3.* Wave conditions

Year	Significant wave		Maximum wave		Wave direction
	$H_{1/3}$ (m)	$T_{1/3}$ (s)	$H_{\max}$ (m)	$T_{\max}$ (s)	
1974	0.21	7.0	0.31	6.8	SW
1985	0.60	6.0	0.65	6.0	NW, SW
1986	0.61	5.1	1.28	2.9	SW

In 1974, the measurements were performed from January to March, and in 1985, during November. In the latter period, two stations were considered, one about 150 m at the SE of the south-headland, and the other about 1 000 m at the NE of the north-headland. The measurements in 1986 were performed in September, during a typhoon. Two stations were selected, one inside the reef, about 200 m at the SE of the north-headland, and the other outside, about 400 m at the E of the same headland. Outside the reef, the significant wave height during the typhoon was 1.88 m, and its related wave period 9.2 s, and the maximum wave height and related period were 3.08 m and 2.5 s, respectively.

Field observations performed outside and inside the reef show that the wave height inside the reef was significantly decreased from the wave height outside; for instance during the typhoon reported in 1986, the wave height inside the reef was about 30% of the wave height outside.

The wave conditions are influenced by the tide as follows: for H.W.L. waves

of longer period and greater height appear, and of shorter period and smaller height for L.W.L. The tide levels of H.H.W.L., H.W.L., M.W.L. and L.W.L. are +2.40 m, +1.90 m, +1.10 m and  $\pm 0.00$  respectively.

### 3. 3. Water quality

Water quality monitoring has shown that the composition of the water inside and outside the reef is similar, so it is presumed that there is enough water circulation inside the reef.

Water quality monitoring is performed twice a year since 1979, once during the Spring time and the other during the Summer. It has been found that the respective average temperatures are about 22 and 28°C. In *Table 4* some results are shown from samples taken before the beach was constructed, in December 1973, and afterwards. In this table, NCB means number of coliform bacteria groups, MPN means most probable number, and the transparency is determined by the secchi disk depth.

*Table 4.* Water components of the artificial beach

Year	Season	NCB MPN/100 ml	Hexane extracts	COD mg/l	Secchi disk depth
1973	Winter	—	—	0.0 ~ 1.3	≈0.3 m
1980	Spring	17.0	not present	0.7	≈0.3 m
	Summer	25.0	"	0.9	≈0.3 m
1985	Spring	0.2	"	0.7	all depth
	Summer	6.0	"	0.8	all depth
1989	Spring	1.1	"	0.5	≈1.5 m
	Summer	0.3	"	0.9	≈1.5 m
1991	Spring	0.3	"	0.4	≈1.0 m
	Summer	0.8	"	0.3	≈1.0 m
1992	Spring	1.5	"	1.0	≈1.0 m
	Summer	0.0	"	0.8	≈1.0 m
1993	Spring	0.0	"	0.6	all depth
	Summer	2.0	"	0.8	all depth

The Japanese standards for water quality at bathing beaches are shown in *Table 5*.

Comparing the measured values with these standards, it is observed that before 1985 the water quality was good, and thereafter it has improved, and it is now considered to be of very good quality.

Furthermore, in addition to the water quality characteristics shown in *Table 4*, the concentrations of elements such as cadmium, arsenic, chromium, mercury, lead, and phosphorus were analysed, and it was found that the amounts

Table 5. Japanese standards for water quality of bathing beaches

Quality	NCB MPN/100 ml	Hexane extracts	COD mg/l	Secchi disk depth
very good	2	not present	≤2.0	≥1.0 m
good	100	not present	≤2.0	≥1.0 m
moderate	1 000	rarely detected	2.0	<1.0 m
bad	>1 000	always present	—	—

detected in the samples were under the acceptable limits so as to be harmless to humans.

### 3. 4. Marine ecology

The marine fauna inside the reef consists mainly of deer's horn coral (*Acropora sp.*). During and just after the beach construction was completed, three campaigns to determine the life expectancy of the corals were carried out. The campaigns took place in November 1974, and April and September of 1975. The mortality rates of the corals at seven stations were determined. Results from the April 1975 campaign show values of the coral's mortality rates that lie between those rates measured during the November 1974 and September 1975 campaigns. Results from these two last campaigns are shown in *Figure 4*.

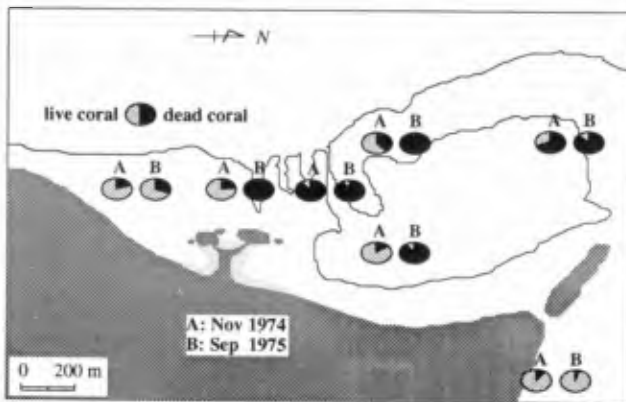


Fig. 4. Coral's mortality rates

In *Figure 4* is observed that particularly for the stations in front of the beach, the mortality rate increased notoriously. One reason for this was indeed the pollutants derived from the beach's construction. The main reason, however, was the sudden proliferation of a marine creature called crown-of-thorns (*Acanthaster*

*planci*) which feeds on coral. This creature came from a nearby island directly in front of the beach. A campaign to remove part of this species was conducted to preserve the coral reef communities. In 1986, field studies showed that in front of the beach, the coral's mortality rate was less than 30%, and that the prevalent environmental conditions then were also found to be favorable for their steady reproduction.

#### 4. BEACH TOPOGRAPHY CHANGE AND BEACH STABILITY

Nineteen years have passed since the artificial beach was constructed and no re-nourishment has been necessary.

The initial beach slope was 1/15, and it has presently changed as follows: in Nagame-no-hama it is 1/14, in Asobi-no-hama 1/30 and in Ikoi-no-hama 1/32. The wave and current effects on Nagame-no-hama have been the most significant ones; as expected during the design phase. That is to say, the actual state of the beach is now just as predicted. The wave and current effects on Asobi-no-hama and Ikoi-no-hama are weak and therefore their slopes are mild. These slopes had been established in a couple of years after the beach construction. It is surmised therefore that all the beaches are stable.

Once a year, in February, bed profiles have been measured during the last 10 years and the necessary amount of sand to be moved for the beaches' restoration has been determined. Then, in March, the beaches' configuration is restored. The amount of sand moved for the beaches restoration during five years is shown in *Table 6*. And, in *Table 7* the amount of sand moved for each beach during four years is shown.

*Table 6.* Amount of sand moved during the beaches restoration

Year	1990	1991	1992	1993	1994
<b>Amount of sand moved (m<sup>3</sup>)</b>	3 403	5 611	4 321	3 182	2 242

*Table 7.* Amount of sand moved for each beach restoration, in m<sup>3</sup>

Year	1990	1992	1993	1994
<b>Ikoi-no-hama</b>	1 204	1 198	1 668	436
<b>Nagame-no-hama</b>	362	423	541	528
<b>Asobi-no-hama</b>	1 837	2 700	973	1 278

From *Table 6* it is seen that during the five years shown here, the amount of sand moved for the restoration of the beach configuration represents about 5 to 10% of the sand volume used for the beach nourishment.

From *Table 7* it is seen that only for the Nagame-no-hama beach's restoration the sand volume moved is roughly similar each year, whereas for the Ikoi-no-hama and Asobi-no-hama beaches, the amount of sand moved is more irregular.

Table 8. Amount of sand moved during the beach restoration in 1994

Beach	Removed sand (m <sup>3</sup> )	Filled sand (m <sup>3</sup> )
Ikoi-no-hama	249	187
Nagame-no-hama	198	330
Asobi-no-hama	674	604

It seems that the amounts of sand moved for these two last beaches are somehow influenced by the volume moved in the previous year.

In Table 8 the amount of sand removed or used to fill each beach for its restoration in March 1994 is shown; this is schematized in Figure 5. In this figure the negative values of thickness refer to the sand removed, and the positive values correspond to the sand filling.

Figure 5 shows that in Ikoi-no-hama there was sand transport from the middle part of the beach to both its ends, but mainly to its closest land end. In the Nagame-no-hama, the sand transport is offshore, so sand should be returned onshore for its restoration. In the Asobi-no-hama, the sand transport is from the beach ends towards the middle part. During its restoration, sand should be therefore removed from the middle and returned to its ends.

The yearly restoration of the beach similar to that shown in Figure 5 contributes to maintain the beach stability in a functional way.

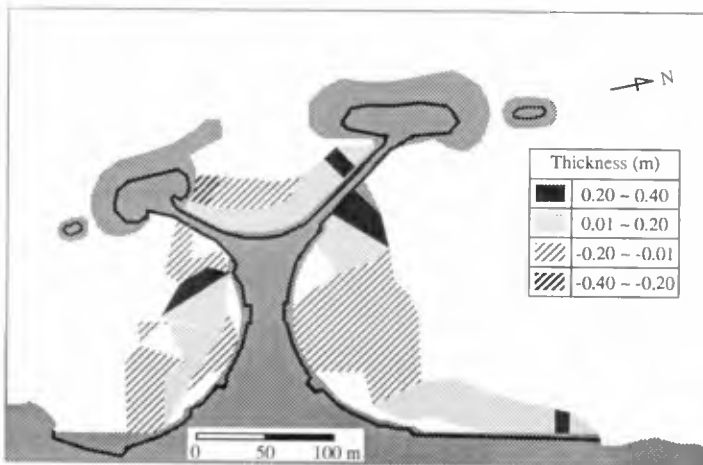


Fig. 5. Sand moved for the beach restoration in 1994

## 5. BEACH MAINTENANCE AND MANAGEMENT

To protect the environment, the beach is cleaned 250 times each year, and in the water itself, the cleaning is performed 60 times per year. The main problem concerning the environment is the proliferation of seaweeds. The seaweeds that reproduce in the reef are transported to the beach by waves and currents, and since they present an unattractive view to bathers, they are removed periodically.

For the beach restoration, which is performed in March, a bulldozer is used.

The artificial beach is open to the public every year from the first of April to the last day of October. In *Table 9* three year data is shown of the yearly number of visitors to the beach, and from these, the number who used the beach to swim.

*Table 9.* Visitors and bathers using the beach

Year	1990	1991	1992
Visitors	138 484	154 061	350 921
Bathers	86 620	79 536	132 068

*Table 9* reveals that for three consecutive years there has been a continuous increase in the number of visitors and bathers. This may be accredited to the beach maintenance described herein which makes it an attractive recreational facility.

Finally, it may be added that the annual maintenance cost, which includes the beach cleaning and restoration programs, is about fifteen million yen.

## 6. CONCLUSIONS

It is concluded that after the nearly two decades that the artificial beach "Expo Beach" has existed, the facility has to all extents and purposes retained its natural environment unchanged. Yearly restoration of the beach configuration by using only the sand transported by waves and currents effects, *i.e.* without any sand renourishment, has proved enough to maintain the beach stability in a functional way. This task together with the periodical beach cleaning have preserved this artificial beach as a pleasant recreational facility.

Furthermore, the stated artificial beach was constructed on a coral reef which gave a firm foundation for coastal structures.

The study of the stability, maintenance and management of the artificial beach "Expo Beach" is a good example to consider when similar beach construction projects are planned.

## ACKNOWLEDGEMENTS

The authors wish to express their thanks to Mr. H. Maesato of the Ocean Expo Commemorative Park Management Foundation and Mr. T. Yabushita of Nippon Tetrapod Co. for providing us field data, and to Dr. K. Horikawa, President of Saitama University, for his comments on the manuscript.

## REFERENCES

- Association of the International Ocean Expo in Okinawa (1975): Field Study on the Artificial Beach of the Ocean Expo Commemorative Park, Part II, Report of the Association of the International Ocean Expo in Okinawa, 153 p. (in Japanese).
- Association of the International Ocean Expo in Okinawa (1976): Field Study on the Artificial Beach of the International Ocean Exhibition in Okinawa, Report of the Association of the International Ocean Expo in Okinawa, 106 p. (in Japanese).
- Ocean Expo Commemorative Park Management Foundation (1975): Proceedings of the Expo Beach, Ocean Expo Commemorative Park Management Foundation, 194 p. (in Japanese).
- Ocean Expo Commemorative Park Management Foundation (1986): Environmental Study on the Ocean Expo Commemorative Park, Part I, Report of the Okinawa Development Department, 220 p. (in Japanese).
- Ocean Expo Commemorative Park Management Foundation (1987): Environmental Study on the Ocean Expo Commemorative Park, Part II, Report of the Okinawa Development Department, 241 p. (in Japanese).
- Yabushita, T., and T. Nakamura (1976): Design and construction of the artificial beach for the Ocean Expo-75 in Okinawa, Proc. 23th Japanese Conf. on Coastal Eng., JSCE, pp.591-596 (in Japanese).

## CHAPTER 174

# SUSPENDED SEDIMENT PARTICLE MOTION IN COASTAL FLOWS

Peter Nielsen<sup>1</sup>

### Abstract

The motion of suspended sediment particles is discussed with the aim of determining which aspects are important and which ones can be neglected when the goal is to model coastal sediment transport. It is shown that the key lies in the structure of the flow, i e, vortices versus wave orbital motion, rather than in details of the drag law. With a proper description of the flow structure the most important phenomena can be modelled under simple assumption that the sediment velocity is everywhere the sum of the local, instantaneous fluid velocity and the still water settling velocity of the sediment:  $u_s = u + w_o$ . Guide lines are also given for dealing with sediment in numerical models. This paper considers only non-cohesive particles in thin suspensions where the interaction of sediment particles can be safely neglected.

### Introduction

To model the transport of (suspended) sediment one must first understand the way in which suspended particles move with the flow. For many years, this was however considered to be too difficult. - The turbulence was filed away as "complicated" and little progress was made with respect to the motion of suspended particles in organised flows because it was assumed that the general non-linearity of the of drag forces would have to be accounted for in the first approximation.

Recent research has however shown that simple kinematic considerations suffice to describe the most important aspects of suspended particle motion. For example, the important difference between vortices and wave motion, which is illustrated in Figure 1, can be understood through the simple kinematic model

$$u_s = u + w_o. \quad (1)$$

which expresses the assumption that the sediment particle velocity vector  $u_s$  can at all

---

Reader, Department of Civil Engineering, University of Queensland, Brisbane, AUSTRALIA 4072, fax: +61 7 365 4599, e-mail: nielsen@civil.uq.oz.au



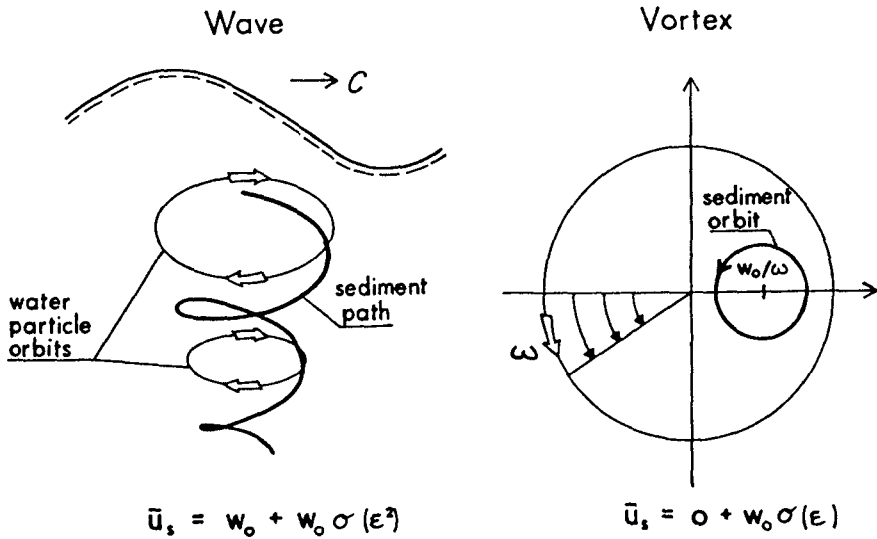


Figure 1: Although vortices and wave motion both have closed elliptical fluid orbits, their influence on suspended sediment are quite different. Vortices will practically eliminate the settling velocity while the effect of wave motion is small of order  $\epsilon^2$  (Equation 2).

times be obtained by adding the still water settling velocity  $w_o$  to the local fluid velocity vector  $u$ .

Under the assumption (1) it can be shown that sediment particles can be trapped along closed paths in most types of vortices as illustrated in figure 3. On the other hand, a wave motion with elliptical fluid orbits has no effect:  $\bar{u}_s = w_o$ , see e.g Nielsen (1992). No consideration of the linear/non-linear nature of the fluid forces is needed to explain these differences. What is important however, is the nature of the organised flow structures like vortices. The essential difference between the vortices and the wave motion in this respect is that the vortices are inhomogeneous while the wave motion is (approximately) homogeneous.

In the following we shall consider, and as far as possibly quantify, the various mechanisms which affect the motion of sediment particles.

### Non-linear Drag

It has long been realised that if the fluid drag force on the particle is non-linear then

this will affect the mean vertical velocity of a particle that settles through a vertically oscillating flow. The effect will be a delay compared to settling through still water.

Several numerical studies, e.g. Ho (1964) and Murray (1970) have been conducted on this effect and an analytical solution was given by Nielsen (1979, 1992). The effect has also been shown experimentally by Ho (1964) who monitored the settling of single particles inside a water filled container which was shaken as a whole in the vertical direction but not stirred. Other types of experiments, which include stirring of the fluid, are not suitable for showing the effect of non-linear drag because the other effects such as vortex trapping and/or fast tracking are likely to dominate in such flows.

The perturbation solution of Nielsen (1979, 1992) shows that the reduction in settling velocity due to quadratic drag on a particle in vertically oscillating fluid with amplitude  $R$  and angular velocity  $\Omega$  is approximately given by

$$\bar{w} = w_o \left[ 1 - \frac{1}{16} \left( \frac{R\Omega^2}{g} \right)^2 \right] \tag{2}$$

showing that the effect the effect is small of order  $\epsilon^2$  where

$$\epsilon = \frac{1}{g} \left| \frac{du}{dt} \right| \tag{3}$$

The solution (2) is compared to Ho's (1964) data in Figure 3. Note that in near-bed coastal flows  $\epsilon \lesssim 1/6$  (Bagnold 1946) and that Equation (2) with  $\epsilon = 1/6$  gives a delay of only  $0.002w_o$ , which is clearly negligible.

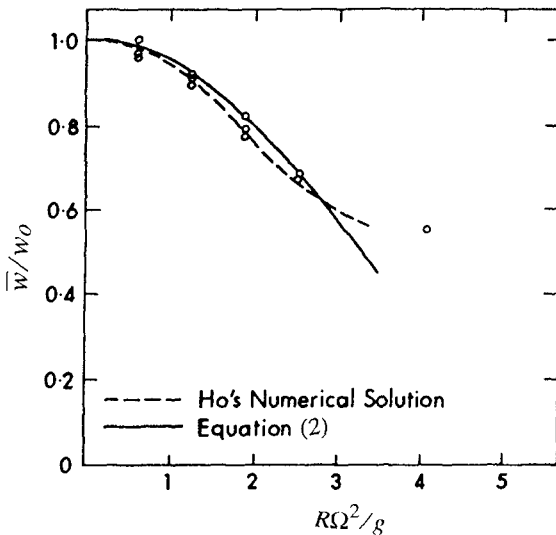
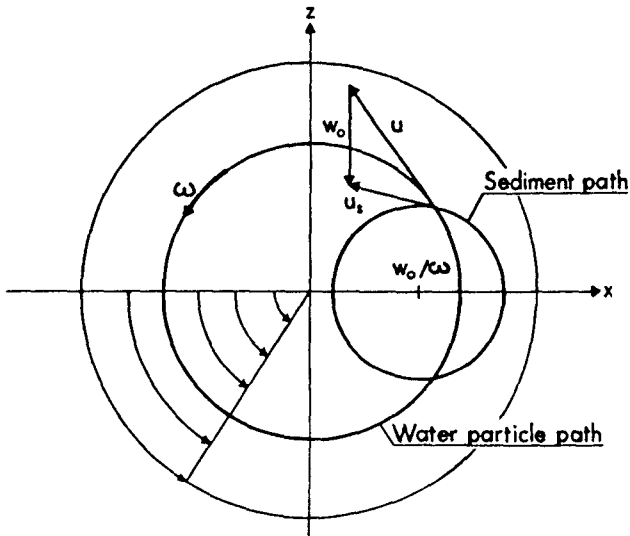


Figure 3: The settling delay due to non-linear drag is well described by equation (2) and it is seen that the effect is insignificant when the fluid accelerations are small compared to  $g$ . This is always the case near the bottom in a wave motion.

### Vortex trapping

An effect which can cause much greater delay to sediment settling is the trapping in vortices. If a particle is trapped in a vortex for ever, its settling velocity is obviously eliminated. The potential for vortex like flows to trap particles and bubbles was probably first noted by Stommel (1949) who considered the motion of particles inside a box shaped convection cell. However, this motion is much more complicated mathematically than that of a circular solid body vortex. Tooby et al (1977) and Nielsen (1979) considered the latter and showed that if a sediment particle moves in accordance with the assumption (1) in such a vortex it can be trapped for ever on any circular orbit around the point where the fluid velocity balances its still water settling velocity, and the orbit angular velocity is that of the vortex, cf Figure 3.



*Figure 3:* A sediment particle with settling velocity  $w_o$  can, under the assumption (1) be at rest at the point  $(w_o/\omega, 0)$  or move along any circle around this point with the angular velocity of the vortex motion. See also the photograph by Tooby et al (1977).

In a simple forced vortex the sediment paths are circles around the point  $P_o$  where the fluid velocity is equal and opposite to  $w_o$ . In Rankine vortices and irrotational vortices, the closed sediment orbits still exist in the vicinity of  $P_o$  but they are not circular. See e g Nielsen (1992).

The fact that also irrotational vortices can trap sediment shows that the essence

of the effect is not that the flow is rotational. Rather, it lies in the inhomogeneity of the flow. In fact, the trapping effect is a special case of the loitering effect which is discussed below.

### **Centrifugal effects**

The assumption (1) and hence the solution shown in Figure 3 is valid if the fluid accelerations are small in the sense that

$$\varepsilon = \frac{1}{g} \left| \frac{d\mathbf{u}}{dt} \right| \ll 1 \quad (4)$$

At order  $\varepsilon^1$  another interesting feature of particle motion in flow with eddies becomes apparent. Due to centrifugal effects a heavy particle in a vortex will spiral outwards from the closed path shown in Figure 3 and as a result, sand particles will tend to become concentrated in the border areas between eddies. This concentration effect was noticed by Maxey & Corrsin (1986) through a computer simulation, but the essence of it, i.e., the centrifugal drift of heavy particles towards the edge of the vortices was quantified already by Nielsen (1979) who showed that the time scale  $T_{sp}$  of the spiralling process is given by

$$T_{sp} = \left[ \frac{1}{r} \frac{dr}{dt} \right]^{-1} = \frac{g}{w_o \Omega^2} \quad (5)$$

where  $r$  is the distance from the vortex centre and  $\Omega$  is the angular velocity of the vortex, see also Nielsen (1992) p 186. The centrifugal effect also affects bubbles, but since they are lighter than water, they spiral inwards. This makes the trapping mechanism particularly efficient for bubbles.

### **Fast tracking between vortices**

The fact that dense particles will spiral out towards the vortex boundaries can lead to fast tracking of small, dense particles in strong turbulence. The reason, as shown in Figure 4, is that the particle speed along the preferred tracks is the maximum vortex velocity which may be much larger than the particles still water settling velocity.

The result of this fast tracking is an increase in effective settling velocity  $\bar{w}$  which is theoretically unlimited: the relative, effective settling velocity is proportional to the relative turbulence intensity for strong turbulence. For grid turbulence the factor of proportionality is approximately 0.3

$$\frac{\bar{w}}{w_o} \approx 0.3 \frac{\sigma}{w_o} \quad (6)$$

where  $\sigma$  is a typical turbulent velocity, see Figure 5. A perfectly regular and steady array of vortices would lead to a factor of about 0.4,

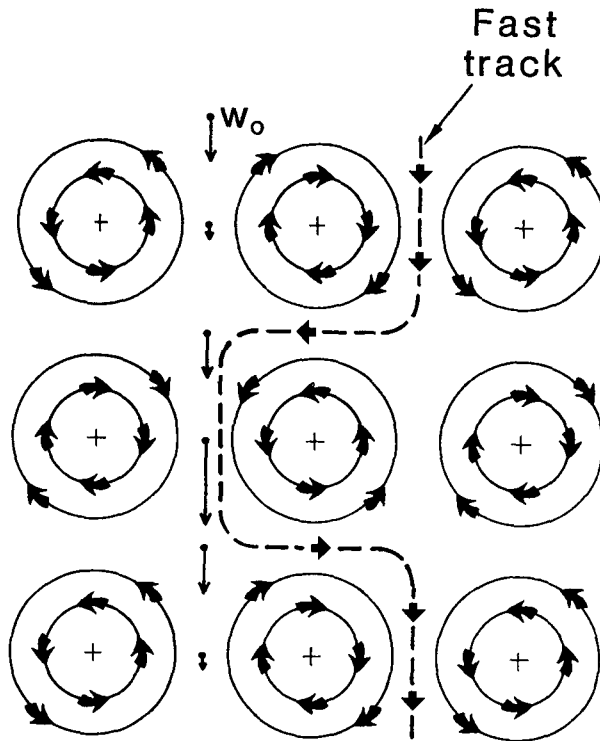


*Figure 4:* Due to centrifugal effects, sediment particles will get concentrated along the boundaries between vortices and experience a settling velocity increase if the vortices are persistent enough and strong enough.

A sceptic is of course justified in asking whether the behaviour of particles in a highly artificial flow field as the one in Figure 4 has any relevance to sediment motion in natural turbulence. The answer from experimental evidence is that it has. The available data from grid turbulence experiments is shown in Figure 5 but also experiments in steady open channel flow by Jobson & Sayre (1970) show the fast tracking effect. The Jobson & Sayre experiments show up to a factor 2 increase in

settling velocity for fine sand [ $w_o = 1.1\text{cm/s}$ ] and a more moderate increase of only a few percent for coarse sand [ $w_o = 6.3\text{cm/s}$ ] - a picture which is in qualitative agreement with that of the grid turbulence data.

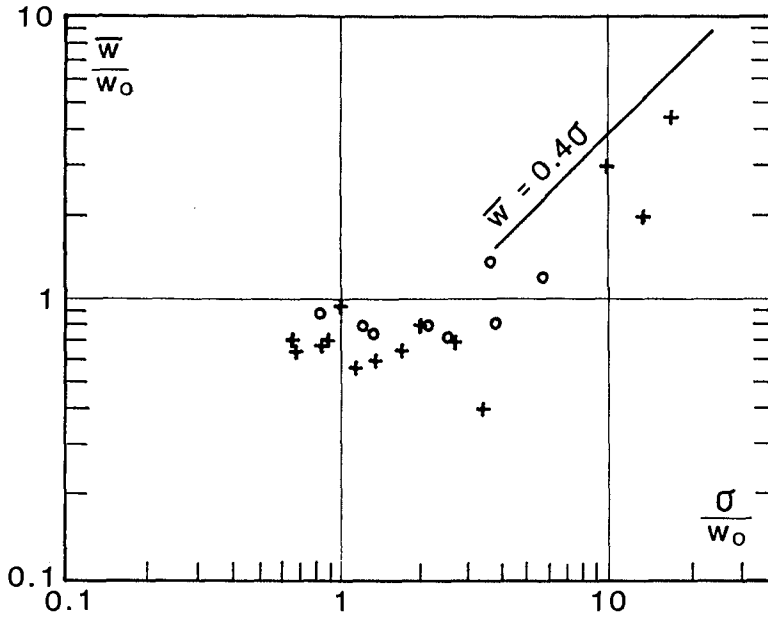


Figure 5: Measured change in settling velocity due to grid turbulence. For weak turbulence the effect is generally a settling velocity decrease due to the loitering effect and trapping, while strong turbulence results in a (theoretically unlimited) increase. + Murray (1970), o Nielsen (1993).

### Trapping or fast tracking?

In the two previous sections we have seen that vortices can have two opposite, strong effects on the settling of particles. The particles can be trapped inside a vortex or they can be fast tracked along the boundaries of vortices. The question then naturally arises: *Which effect is going to be dominant?*

The answer is that if the sand is fed into the vortex while it is being formed such as it happens with the lee vortices on a rippled sand bed, see e.g. Bijker et al (1976). Then it is going to be trapped for a while and will travel with the vortex for some considerable distance without settling out.

On the other hand, there is no chance of a heavy particle coming from the outside of a vortex and getting onto one of the "trapping" closed trajectories inside. Sediment particles which settle towards a vortex will get swept past the potential

trapping area of the vortex as illustrated in Figure 4. See also Nielsen (1992) Figure 4.6.3.

### **The general loitering effect**

Considering the particle which settles along the vertical symmetry line between the vortices in Figure 4 it can be seen that that even though the spatial average of its velocity ( $\mathbf{u} + \mathbf{w}_o$ ) is  $\mathbf{w}_o$ , the time averaged velocity will be less than  $\mathbf{w}_o$ . Hence particles will settle more slowly through an inhomogeneous flow field than through still (or uniformly flowing) water. This is because the particle spends more time (loiters) with the fluid which moves opposite to its settling velocity.

The loitering effect was quantified by Nielsen (1992, 1993) for a special example and it was shown how this effect might slow the settling of particles in random walk simulated, "structureless" turbulence. That is, while the loitering effect is due to the non-uniformity of the flow field, it is not necessary to deal explicitly with the flow structure.

The loitering represents the essential reason why vortices delay settling while a (almost) uniform wave motion, does not. - Figure 1.

### **Sediment in wave motions**

With coastal engineering applications in mind, it is natural to ask whether a pure wave motion will delay the settling of sediment or the rise of bubbles significantly. It is very difficult to give a complete answer to this. However, for the simple velocity field of a linear shallow water wave

$$\mathbf{u} = \begin{pmatrix} u \\ v \end{pmatrix} = \begin{pmatrix} \frac{Hc}{2h} \cos(\omega t - kx) \\ \frac{H\omega z}{2h} \sin(\omega t - kx) \end{pmatrix} \quad (7)$$

the possible effect must be as small as effect of non-linear drag i.e. without significance. In Equation (7)  $H$  is the wave height,  $h$  the water depth,  $c$  the wave celerity,  $\omega$  the angular velocity and  $k$  the wave number.

The equation of vertical motion of a small (with linear drag) particle can be conveniently written as

$$\frac{dw_r}{dt} + \frac{\alpha g}{w_o} w_r + \frac{\partial w}{\partial t} = -\alpha g - \alpha \frac{dw}{dt} \quad (8)$$

where  $w_r$  is the vertical velocity relative to the fluid and  $\alpha = \frac{s-1}{s+C_m}$ ,  $s$  being the relative density of the sediment and  $C_m$  being the added mass coefficient (approximately 0.5 for nearly spherical particles).

If the expression above is inserted for  $w$ , this gives

$$\frac{dw_r}{dt} + \frac{\alpha g}{w_o} \left[ 1 + \frac{H\omega w_o}{2hg} \sin \omega t \right] w_r \approx -\alpha g - \alpha \frac{\omega^2 H z}{2h} \cos \omega t \quad (9)$$

Here it seems safe to neglect the second term in the bracket since its typical magnitude for sand in waves is  $10^{-3}$ . This small term represents the effect of the vertical non-uniformity of the wave motion.

Then, by writing the relative velocity  $w_r$  in terms of the still water settling velocity  $w_o$ :  $w_r = w_o + w_I$  and using

$$z = h - w_o t [1 + O(\epsilon)] \quad (10)$$

we get the following equation for  $w_I$

$$\frac{dw_I}{dt} + \frac{\alpha g}{w_o} w_I \approx -\alpha \frac{\omega^2 H z}{2h} [h - w_o t] \cos \omega t \quad (11)$$

The solutions to this equations are of the form  $A \cos(\omega t + \phi) + B t \cos(\omega t + \psi)$  showing that at the first level of approximation there is no net change of the settling rate due to the wave motion.

Any net change of the settling velocity is thus either due to the non-uniformity mentioned above or due to non-linear drag. In both cases its magnitude will be of the order  $10^{-3} w_o$  for sand in wave motions.

### Sediment in numerical models

For the purpose of dealing with sediment particles in numerical models it is useful to note that the sediment velocity can be written as

$$\mathbf{u}_s = \mathbf{w}_o + \mathbf{u}(t - \delta_t) + w_o \mathbf{O}(\epsilon^2) \quad (12)$$

where  $\mathbf{O}(\epsilon^2)$  denotes a vector function of magnitude  $\epsilon^2$ . The time lag is given by  $\delta_t = w_o/g$  for small particles that settle under the laminar drag law and  $\delta_t = w_o/2g$  for larger particles that settle with quadratic drag, see Nielsen (1979, 1992).

The use of the approximation

$$\mathbf{u}_s \approx \mathbf{w}_o + \mathbf{u}(t - \delta_t) \quad (13)$$

is thus usually justified in natural sediment transport processes and it is very convenient because it does not require explicit consideration of the particle dynamics at all. All



that is needed is a stored value  $u(t-\delta_t)$  of the local fluid velocity at a previous time.

### Frequency response

The expression (13) corresponds to a linear frequency response function  $F(\omega)$  defined by

$$u_s - w_o = F(\omega) U e^{i\omega t} \quad (14)$$

for the dynamic part of the velocity of a particle that moves in a homogeneous, simple harmonic flow  $u(t) = U e^{i\omega t}$ . In terms of the time lag quantified above this frequency response function is given by:

$$F(\omega) = \frac{1}{1 + i\omega\delta_t} \quad (15)$$

and a corresponding gain function is

$$G(\omega) = \frac{1}{\sqrt{1 + (\omega\delta_t)^2}} \quad (16)$$

### Conclusions

The considerations above cover the behaviour of suspended sediment particles in small concentrations where particle-particle interactions can be neglected and the analytical approximations are obtained using perturbation expansions in the parameter  $\epsilon = \frac{1}{g} \left| \frac{du}{dt} \right|$ .

It has been shown that the most important aspects of the motion of such sediment can be understood on the basis of the simple assumption  $u_s = u + w_o$  which is valid for  $\epsilon \rightarrow 0$ .

It has also been shown that the settling delay due to drag non-linearity is negligible (about  $10^{-3} w_o$ ) for sand in wave motions and that the effect of non-uniformity of the wave motion is likely to be equally small.

Vortices can have two strong but opposite effects on the settling of sediment: *Trapping inside the vortices* and *fast tracking between vortices*. The former occurs only when the sand is fed into the vortex during the vortex formation as it happens with lee vortices behind sharp-crested bedforms. Fast tracking occurs when the sediment is settling through a field of vortices. Both of these effects are limited to situations where the typical vortex velocities  $u_v$  are large compared to  $w_o$ . Trapping is possible as long as  $u_v > w_o$ . Fast tracking is not dominant unless  $u_v/w_o \geq 4$ . For

smaller vortex strengths, the particles tend to cut through the vortices (see the illustrations of Maxey & Corrsin (1986)) and doing so they are delayed through the loitering effect and/or trapping.

Numerical modelling of particles in flows where  $\epsilon^2 \ll 1$  can be done very easily using equation (13) which does not require explicit consideration of the particle dynamics.

### **References**

- Bagnold, R A (1946): Motion of waves in shallow water: Interaction between waves and sand bottoms. *Proc roy Soc Lond, Vol A 187*, pp 1-15.
- Bijker, E W, E van Hijum & P Vellinga (1976): Sand transport by waves. *Proc 15th Int Conf Coastal Eng, ASCE*, pp 1149-1167.
- Ho, H W (1964): *Fall velocity of a sphere in an oscillating fluid*. Ph D thesis, University of Iowa, Iowa City.
- Jobson, A M & W W Sayre (1970): Vertical transfer in open channel flow. *J Hydraulics Div, A S C E, Vol 96*, pp 703-724.
- Maxey, M R & S Corrsin (1986): Gravitational settling of aerosol particles in randomly orientated cellular flow fields. *J of the Atmospheric Sciences, Vol 75*, pp 1112-1134.
- Murray, S P (1970): Settling velocities and diffusion of particles in turbulent water. *J Geophysical Res, Vol 75*, pp 1647-1654.
- Nielsen, P (1979): *Some basic concepts of wave sediment transport*. Series Paper No 20, ISVA, Technical University of Denmark, 160pp.
- Nielsen, P (1992): *Coastal bottom boundary layers and sediment transport*. World Scientific, Singapore, 324pp.
- Nielsen, P (1993): Turbulence effects on the settling of suspended particles. *J Sedimentary Petrology, Vol 63, No 5*, pp 835-838.
- Stommel, H (1949): Trajectories of small bodies sinking slowly through convection cells. *J Mar Res, Vol 8*, pp 24-29.
- Tooby, P F, G F Wick, & J D Isacs, (1977): The motion of a small sphere in a rotating velocity field: A possible mechanism for suspending particles in turbulence. *J Geophys Res, Vol 82, No 15*, pp 2096-2100.

# SUBJECT INDEX

Page number refers to first page of paper

- Aeration, 1895  
Aerial photographs, 1998  
Air entrainment, 1496  
Airport runways, 2683  
Aquatic plants, 142  
Armor units, 918, 958, 986, 1001, 1061,  
1090, 1143, 1157, 1227, 1388, 1412,  
1426, 1439, 1511, 1541, 1568, 1625,  
1641, 1713  
Artificial islands, 1568  
  
Barrier islands, 181, 2222, 2417, 2886,  
3251, 3491  
Bathymetry, 871  
Beach erosion, 315, 609, 1197, 1880,  
1934, 2070, 2252, 2340, 2380, 2434,  
2449, 2571, 2683, 2726, 2943, 3208,  
3393, 3478, 3491  
Beach nourishment, 1359, 1797, 1934,  
2100, 2222, 2395, 2668, 2886, 3016,  
3208, 3491, 3507, 3548, 3564, 3579  
Beaches, 540, 1157, 1782, 1812, 1880,  
2115, 2325, 2395, 2449, 3167, 3378  
Bed load, 3360  
Bed load movement, 2513  
Bed ripples, 635, 1975, 2013, 2043, 2070,  
2140  
Bed roughness, 300  
Bedforms, 2185  
Benefit cost analysis, 3237  
Berms, 1075, 1343, 1625, 2252, 2712,  
3594  
Blocks, 932  
Boundary conditions, 272, 442, 594, 886,  
1770  
Boundary element method, 871, 1241,  
1700  
Boundary layer, 594, 1827  
Boundary layer flow, 384, 2527  
Breaking waves, 219, 330, 399, 412, 511,  
525, 594, 609, 1101, 1255, 1312,  
1496, 1553, 1672, 1739, 1895, 1961,  
2252, 2282, 2365, 2461, 2503, 2557,  
2583, 2813, 2856, 3167  
Breakwaters, 272, 525, 791, 1016, 1030,  
1046, 1101, 1255, 1269, 1298, 1343,  
1359, 1373, 1397, 1412, 1426, 1439,  
1454, 1580, 1595, 1625, 1657, 1700,  
1754, 1880, 2583, 2653, 2668, 2871,  
3167, 3208, 3420, 3564, 3608  
Buoyant jets, 3045  
Buried pipes, 1553, 2571, 3099  
  
Caissons, 1030, 1046, 1255, 1298, 1373,  
1580  
Calibration, 207  
Case reports, 3491, 3507, 3564, 3579,  
3594  
Channel bends, 128  
Channels, waterways, 128, 3002, 3060,  
3139, 3533  
Circular channels, 1373  
Climatic changes, 3193, 3251, 3462  
Coastal engineering, 1, 1837  
Coastal management, 3579  
Coastal morphology, 142, 1782, 1797,  
1837, 1906, 2100, 2207, 2222, 2252,  
2340, 2417, 2513, 2871, 3126, 3223,  
3251  
Coastal processes, 57, 2380, 2406, 3237,  
3335  
Coastal structures, 511, 2476, 3154, 3167,  
3522, 3564  
Cohesionless sediment, 2043, 2406  
Cohesive sediment, 2004, 2058, 3060  
Collisions, 3030  
Comparative studies, 3208  
Composite structures, 1030  
Computer analysis, 1090  
Computer models, 2311  
Concrete, 1426, 1641  
Concrete blocks, 1269  
Conical bodies, 1595  
Consolidation, soils, 2004, 2902  
Construction, 3594  
Coral reefs, 609  
Cost effectiveness, 1412  
Cross sections, 1130  
Currents, 113, 384, 565, 624, 1484, 2476,  
2503  
Cylinders, 973, 1115, 1212

**Volume 1 1-1196**

**Volume 2 1197-2416**

**Volume 3 2417-3614**

- Dam breaches, 2755
- Damage assessment, 2197
- Damage estimation, 1412
- Damage patterns, 1001, 1090, 1157, 1657
- Deep water, 12, 412, 455, 579, 973, 1343, 3608
- Deltas, 2542
- Design, 1327, 1359
- Digital mapping, 1998
- Dikes, 1075, 1169, 2197, 2639, 2755, 3350
- Dilution, 3045
- Discrete elements, 192
- Dispersion, 3071
- Displacements, 1255, 1625
- Distribution, 3086
- Distribution patterns, 192
- Dolos, 958, 1388, 1426, 1511, 1641
- Drainage systems, 1568, 2571
- Dredge spoil, 2928, 3305, 3507, 3579
- Dredging, 2972, 3002, 3016, 3060, 3139, 3393, 3533
- Dunes, 1934, 2028, 2197, 2434, 2488, 2755, 2770
- Earthquakes, 886
- Eddy viscosity, 384
- Embankments, 1130
- Energy dissipation, 635, 1454, 2557
- Energy losses, 761
- Entrainment, 3071
- Entropy, 232, 340
- Environmental impacts, 3178
- Erosion, 2058, 2170, 2488, 2542, 2639, 3360
- Erosion control, 1880, 1934, 2070, 2155, 2683, 2712, 3193, 3208, 3378, 3491
- Estuaries, 2004, 3060, 3178, 3281, 3408, 3533
- Failure modes, 1388, 1713
- Failures, 1526, 1657, 1754, 3350
- Field investigations, 540, 719, 1946, 2028, 2513, 3522
- Field tests, 665, 689, 945, 1269, 2115, 2610, 2799
- Filters, digital, 168
- Finite element method, 746, 871, 1388
- Fish habitats, 3420
- Fisheries, 1484, 3447, 3478
- Flocculation, 3060
- Flood control, 3126, 3193
- Flooding, 2197, 2755, 3154
- Flow characteristics, 27
- Flow measurement, 1975
- Flow patterns, 1770
- Flow rates, 98, 1975, 2058, 2085
- Flow simulation, 2140
- Flow visualization, 861, 3045
- Fluid flow, 98
- Fluid-structure interaction, 1115
- Flumes, 86, 1641, 1880, 2843, 2913
- Free surfaces, 86
- Frequency analysis, 12
- Frequency response, 207
- Friction, 1983
- Friction factor, 565, 986
- Geomorphology, 1837
- Global warming, 3462
- Grasses, 2639
- Gravel, 1880
- Gravity waves, 86, 579, 635, 1919, 3071
- Greens function, 442
- Groins, structures, 1157, 1327, 1782, 2668, 3564
- Harbor engineering, 791, 806
- Harbor structures, 3507
- Harbors, 871, 2987
- Hydraulic models, 1001, 1182, 1197, 1269, 2987, 3447
- Hydraulic performance, 918, 1373
- Hydraulic properties, 1454
- Hydraulic roughness, 2871
- Hydraulics, 2902
- Hydrodynamic pressure, 973, 1484
- Hydrodynamics, 861, 1849, 1919, 2282, 2340, 2741, 3099, 3432
- Hydrologic aspects, 3251
- Impact loads, 958, 3522
- Impulsive loads, 1580
- Indonesia, 609, 821
- Inlets, waterways, 2943, 3432
- Instrumentation, 42
- Japan, 1, 247, 674, 886, 1016, 1046
- Jetties, 2799

- Kinematics, 540
- Laboratory tests, 42, 98, 128, 168, 650,  
689, 776, 1075, 1101, 1143, 1157,  
1212, 1241, 1284, 1610, 1641, 1782,  
1946, 2115, 2325, 2449, 2461, 2476,  
2488, 2843, 2856, 3295
- Lagoons, 2928, 3223
- Lagrangian functions, 2828
- Lakes, 2380, 3281
- Land reclamation, 2972, 3178, 3305
- Landslides, 821
- Laycred soils, 3360
- Lift, 1115, 3099
- Linear analysis, 285
- Liquefaction, 2698, 3350
- Littoral currents, 27, 1895, 1919, 1983,  
2237, 2267, 2282, 2297, 2503, 2741
- Littoral deposits, 1327
- Littoral drift, 2513, 2595, 2625, 2726,  
2799, 2943, 2972, 3478, 3507
- Long waves, 455, 791, 847, 886, 1961
- Marshes, 3548
- Mass transport, 86, 2828, 2913
- Mathematical models, 1241, 1727, 2125,  
2197, 2350, 2755, 2928, 3223
- Measuring instruments, 42, 207
- Meteorological data, 79
- Mining, 3335, 3393
- Mixing, 3071, 3281
- Model accuracy, 57, 2595
- Model analysis, 57
- Model studies, 1880, 2770
- Model tests, 1030, 1061, 1182, 1197, 1298
- Model verification, 901, 1961, 2595, 2610,  
2785, 3223
- Monitoring, 1511, 1812, 2100, 2222,  
2799, 2886, 3522, 3579
- Monsoons, 3378
- Mooring, 791, 847
- Movable bed models, 300, 1782, 1906,  
2972
- Mud, 2004, 2913, 3266, 3360, 3408
- Navier-Stokes equations, 511, 1739, 2297
- Navigation, 3139, 3533
- Nearshore circulation, 68, 207, 272, 330,  
1895, 2237, 2267, 2340, 2365, 2461,  
2583, 2610, 2741, 3420
- Netherlands, 2886, 3193, 3208, 3350
- Nonlinear analysis, 157, 285, 427, 467,  
1961
- Normal stress, 986
- North Sea, 261, 1359, 1797
- Numerical calculations, 427
- Numerical models, 27, 79, 113, 157, 192,  
272, 442, 467, 511, 689, 746, 776,  
806, 821, 871, 886, 1016, 1672, 1700,  
1739, 1880, 1919, 1946, 1983, 2043,  
2070, 2140, 2155, 2237, 2311, 2434,  
2503, 2542, 2557, 2610, 2653, 2741,  
2785, 2843, 2871, 3086, 3295, 3305,  
3420
- Ocean mining, 3393
- Ocean waves, 232, 340, 806, 1526
- Offshore engineering, 2928
- Offshore structures, 1115
- Oscillations, 847, 1255, 2987
- Oscillatory flow, 1541, 1553, 1975, 1983,  
3408
- Outfall sewers, 1553, 3045, 3071, 3564
- Overtopping, 511, 918, 1016, 1030, 1046,  
1130, 1182, 1373, 1568, 1687, 1700,  
2028, 2639, 3154
- Oxygen content, 3447
- Oxygenation, 3167
- Particle motion, 2406
- Permeability, 1101
- Perturbation, 746, 973, 1469
- Photogrammetry, 1998
- Photographic analysis, 1511
- Plates, 1312, 1454
- Plunging flow, 1739
- Polders, 2197
- Pollution, 3071
- Pore pressure, 932, 1727, 2698, 3111
- Pore water pressure, 3030, 3369
- Porous media, 635, 1770
- Porous media flow, 1739
- Ports, 1197, 3608
- Portugal, 3608
- Pressure distribution, 1770
- Probabilistic methods, 1754, 3154
- Probability density functions, 482
- Probability distribution, 247, 356, 482,  
497
- Progressive waves, 86

- Prototypes, 1016  
 Public safety, 1016, 1046  
 Random waves, 192, 272, 285, 300, 370,  
     412, 427, 482, 553, 565, 579, 704,  
     719, 1130, 1157, 1610, 2125, 2252,  
     2843  
 Recreation, 2395  
 Recreational facilities, 2668  
 Reefs, 1484  
 Regression models, 247  
 Rehabilitation, 3594, 3608  
 Research, 1  
 Residence time, 553  
 Residual strength, 2639  
 Return flow, 1101  
 Revetments, 932, 1001, 1269, 1687  
 Rip currents, 2583  
 Riprap, 3320  
 Risk analysis, 3154  
 Rivers, 3002, 3126, 3295  
 Rotational flow, 861  
 Rubble-mound breakwaters, 918, 958,  
     986, 1001, 1061, 1090, 1182, 1227,  
     1397, 1511, 1526, 1610, 1713, 1727,  
     3594  
 Salinity, 2928, 3533  
 Sand, 3360  
 Sand transport, 2557  
 Sandbars, 157, 1837, 1865, 2222, 2311,  
     2325, 2571, 2712, 2770, 2856, 3126,  
     3548  
 Scale effect, 1143, 2668, 2770  
 Scour, 1284, 1595, 3320  
 Scouring, 1212  
 Sea cliffs, 2170  
 Sea floor, 3111, 3139, 3320, 3369  
 Sea level, 2115, 2311, 2340, 3193, 3462  
 Sea state, 247  
 Sea walls, 1046, 1130, 1169, 1496, 1568,  
     1672, 1812, 3154, 3335  
 Sediment concentration, 1827, 2085, 2125,  
     2476, 2813  
 Sediment deposits, 2185, 3305  
 Sediment transport, 27, 98, 142, 300, 370,  
     525, 1212, 1327, 1770, 1827, 1837,  
     1849, 1865, 1906, 1919, 1946, 1975,  
     2028, 2043, 2070, 2125, 2140, 2185,  
     2282, 2406, 2503, 2513, 2527, 2595,  
     2625, 2770, 2785, 2799, 2843, 2871,  
     2902, 2928, 2928, 2972, 3295, 3360,  
     3478  
 Sedimentation, 2004, 3002, 3139  
 Sensors, 2185, 2799  
 Settling velocity, 3408  
 Shallow water, 261, 330, 370, 455, 467,  
     482, 665, 704, 731, 761, 1212, 1343,  
     1849, 2350, 2928, 3281  
 Shape, 1343, 1388, 1439, 1625  
 Shear stress, 98, 565, 594, 986, 1595,  
     2058  
 Shear waves, 1919  
 Shellfish, 3086, 3420  
 Ship motion, 791, 847, 871  
 Ships, 3030  
 Shoaling, 12, 467, 594, 2365  
 Shock, 1075  
 Shore protection, 142, 3237, 3335  
 Shoreline changes, 1327, 1782, 1812,  
     1837, 1906, 1946, 1998, 2380, 2610,  
     2625, 2653, 2683, 2726, 2755, 2785,  
     2813, 2943, 3178, 3295, 3335, 3378,  
     3393, 3462, 3478  
 Silts, 2902, 3060  
 Simulation models, 821, 3266  
 Sliding, 1580  
 Slope stability, 1553  
 Slopes, 315, 746, 1075, 1568, 1865, 2325,  
     2350, 3167  
 Soil mechanics, 2902, 3030  
 Soil permeability, 2902, 3111  
 South Africa, 1511  
 Spatial distribution, 579, 674  
 Spectral analysis, 12, 68, 384, 731  
 Spits, coastal, 2380, 2726, 3478  
 Stability, 918, 932, 1061, 1143, 1227,  
     1397, 1426, 1439  
 Stability analysis, 1865  
 Standing waves, 3369  
 State-of-the-art reviews, 1, 832  
 Statistical analysis, 674  
 Statistical data, 832  
 Statistics, 79  
 Stones, 1553, 1625  
 Storm surges, 901, 2170, 2434  
 Storms, 79, 261, 1526, 1849, 1934, 2843,  
     3491, 3608  
 Stratification, 3360  
 Stratified flow, 3447

- Strength, 1388  
 Stress distribution, 1713  
 Structural response, 832, 1412, 1641  
 Structural strength, 958  
 Submerged discharge, 3320  
 Subsidence, 1541  
 Surf beat, 399, 689, 1961  
 Surf zone, 98, 315, 399, 553, 1895, 1934,  
     2085, 2155, 2237, 2267, 2282, 2350,  
     2503, 2513, 2542, 2712, 2813, 2856  
 Surface roughness, 1169  
 Surface waves, 467, 635, 3111  
 Suspended load, 3360  
 Suspended sediments, 1827, 1849, 1865,  
     2013, 2043, 2085, 2125, 2406, 2476,  
     2527, 2770, 2813, 3002, 3016, 3281  
 Suspended solids, 3408  
  
 Tensile stress, 1713  
 Three-dimensional flow, 370  
 Three-dimensional models, 871, 901,  
     1227, 2267, 2297, 2340, 2461, 2741,  
     3432  
 Tidal currents, 2282, 3281  
 Tidal hydraulics, 861  
 Tidal marshes, 3251  
 Tidal waters, 181, 2417, 3533  
 Tides, 3462  
 Time dependence, 272, 285, 553, 635  
 Tin, 3393  
 Tombolo, 1197, 2653  
 Topography, 272, 746, 1212, 1865, 1946,  
     2325, 2557, 2610, 3126  
 Transport rate, 2785, 2828, 2913, 2972  
 Tsunamis, 821, 886  
 Turbidity, 3016  
 Turbulence, 98, 861, 901, 2712, 3281  
 Turbulent boundary layers, 300, 384  
 Turtles, 3491  
 Two-dimensional analysis, 3447  
 Two-dimensional flow, 27  
 Two-dimensional models, 1030, 2155  
 Typhoons, 1, 219, 674, 2434  
  
 Ultrasonic testing, 624  
 Undertow, 330, 399, 2125, 2610, 2712,  
     2785  
 Uplift pressure, 932, 1298  
  
 Velocity profile, 86  
  
 Vertical cylinders, 1284, 1469, 1595  
 Vibration, 1115  
 Vibration analysis, 455  
 Viscoelasticity, 2913  
 Viscoplasticity, 2913  
 Viscosity, 3408  
 Vortices, 113, 525, 1115, 1975, 2140,  
     2856  
  
 Water content, 3266  
 Water depth, 261, 1343  
 Water flow, 1373  
 Water level fluctuations, 2170  
 Water levels, 2365, 3533  
 Water pollution, 3178  
 Water pressure, 1541  
 Water quality, 2395  
 Water surface profiles, 455, 624, 704,  
     1469  
 Water table, 2115, 2449, 2571  
 Water waves, 455  
 Waterfront facilities, 901  
 Wave action, 315, 918, 1001, 1061, 1212,  
     1227, 1269, 1739, 1934, 2013, 2058,  
     2639, 2698, 2712, 3016, 3045, 3099,  
     3266, 3522  
 Wave attenuation, 1312, 2913  
 Wave climatology, 181, 247, 1526, 2311  
 Wave crest, 356, 497, 540  
 Wave damping, 142, 609  
 Wave diffraction, 128, 285, 442, 973  
 Wave energy, 609, 761, 791, 806, 1454,  
     2698  
 Wave forces, 330, 1046, 1075, 1115, 1298,  
     1312, 1439, 1469, 1484, 1496, 1580,  
     1754  
 Wave generation, 68, 168, 650, 704, 776  
 Wave groups, 689, 776, 832, 847, 945,  
     1526, 1568, 1827, 1961, 2828  
 Wave height, 79, 181, 192, 247, 261, 356,  
     370, 399, 412, 497, 579, 609, 674,  
     746, 1016, 1101, 1182, 1241, 1397,  
     1657, 1754, 2155, 2207, 2311, 2350,  
     2365, 2488, 2698, 2828, 2987, 3266,  
     3608  
 Wave measurement, 42, 57, 207, 232, 624,  
     731, 776, 806, 832, 1610, 1906, 2207  
 Wave pressure, 1312, 1541  
 Wave propagation, 157, 168, 181, 232,  
     665, 1241

- Wave reflection, 128, 168, 442, 719, 945,  
1241, 1610, 2434
- Wave refraction, 68, 285, 442
- Wave runup, 27, 315, 399, 553, 689, 761,  
776, 821, 886, 1169, 1687, 1727,  
2115, 2155, 2170, 2207, 2325, 2488,  
2557, 2571, 2583
- Wave spectra, 12, 42, 68, 232, 340, 370,  
384, 467, 482, 497, 624, 665, 719,  
731, 806, 2843
- Wave tanks, 128, 650, 1469, 1880, 1906,  
2207, 2449
- Wave velocity, 427, 525, 540, 565, 986,  
1046, 1454, 2527
- Waves, 113, 2476
- Wind, 57
- Wind direction, 79, 3447
- Wind speed, 79, 261, 330, 1687
- Wind waves, 12, 68, 181, 232, 330, 665,  
731, 761, 901, 945, 2350



## AUTHOR INDEX

Page number refers to first page of paper

- Ahn, K., 482  
Akeda, S., 3420  
Alexis, A., 2902  
Alcxis, Alain, 2004  
Allsop, N. W. H., 918, 1130, 1157, 3154  
Alvarez, J., 3579  
An, Nguyen Ngoc, 2913  
Andrassy, Christopher J., 2100  
Anglin, C. D., 2380  
Aono, Toshio, 12  
Asai, Tadashi, 232, 847  
Asano, Toshiyuki, 27  
Aydin, Ismail, 1770
- Badiei, Peyman, 1782  
Baird, W. F., 3608  
Bakker, Willem T., 1797  
Bakker, Wim T., 2197  
Balzano, Andrea, 2928  
Barnes, T. C. D., 776  
Barthel, Volker, 791  
Basco, David R., 1812  
Battjes, J. A., 157  
Bedford, K., 1827  
Beji, Serdar, 427  
Bellomo, Doug, 1812  
Benoit, Michel, 42, 1610  
Bergmann, Hendrik, 553, 1075  
Bertotti, Luciana, 57, 79  
Besley, P., 918  
Bezuijen, Adam, 932  
Blomgren, Sten H., 1327  
Boccotti, Paolo, 945  
Bodge, Kevin R., 2943  
Booij, N., 68, 261  
Bouws, E., 261  
Brandt, Günther, 181  
Briggs, Michael J., 806  
Brøker, I., 2871  
Brøker, Ida, 2958  
Bruce, T., 1975  
Burcharth, Hans F., 958
- Caballería, Miquel, 1983  
Carnero, Ovidio Varela, 1657  
Cavaleri, Luigi, 57, 79  
Chacaltana, J. T. Aquije, 973  
Chang, C., 1700  
Chang, Chen-Yue, 3045
- Chang, Hsien-Kuo, 2972  
Chaplin, John R., 1115  
Chen, Xinjian, 3281  
Chen, Yih-Far, 3045  
Chen, Z., 3223  
Chilo, Bruno, 1090  
Chin, Ikuo, 3478  
Chisholm, T. A., 1849  
Chou, C. R., 2987  
Christensen, E. Damgaard, 1865  
Christensen, Erik Damgaard, 1919  
Christensen, Morten, 168  
Christiansen, N., 1595  
Chyan, Jih-Ming, 3045  
Ciešlikiewicz, Witold, 86  
Coates, T. T., 1880  
Collado, F. R., 2542  
Cornett, Andrew, 986  
Cornett, Andrew M., 1001  
Coussirat, M. G., 2542  
Covarsi, Manuel F., 3564  
Cox, Daniel T., 98  
Cummins, I., 113
- da Silva, A. F. Teles, 973  
Daemrich, Karl-Friedrich, 2828  
Dally, William R., 1895  
Dalrymple, Robert A., 128  
Damgaard, Jesper Svarrer, 1919  
d'Angremond, K., 1713, 1754  
Daniil, E. I., 3167  
Davidson, D. D., 3608  
Davies, Michael H., 1001  
de Gerloni, M., 1030  
De Groot, M. B., 1727  
de Groot, Maarten B., 3350  
de Quirós, Fernando Bernaldo, 3237  
de Ronde, J. G., 261  
de Ronde, John G., 761  
de Ruig, J. H. W., 3208  
de Vriend, Huib J., 594  
Dean, Robert G., 1906, 2449, 3491  
Deguchi, Ichiro, 370, 2476, 3002  
Deigaard, R., 1865, 2043  
Deigaard, Rolf, 1919, 2583  
Dette, Hans H., 1934  
Dette, Hans-H., 2843  
Dette, Hans-Henning, 553  
Dibajnia, Mohammad, 1946

- Dijkman, Michiel, 3522  
 Dodd, N., 1880  
 Dodd, Nicholas, 1961  
 Dowd, Millard, 3491  
 Drago, Michele, 540  
 Dubi, Alfonse, 142
- Earnshaw, H. C., 1975  
 Easson, W. J., 1975  
 Easson, William J., 525  
 Edge, B. L., 3608  
 Edge, Billy, 1687  
 Edge, Billy L., 3491  
 Eldeberky, Y., 157, 261  
 Endo, Taiji, 2395  
 Endoh, Kimihiko, 1016, 1046
- Falqués, Albert, 1983  
 Ferier, P. G. P., 261  
 Fernandez, Joaquin, 3594  
 Fisher, John S., 1998, 2488  
 Foda, Mostafa A., 3099  
 Fontijn, Henri L., 1553  
 Franco, C., 918  
 Franco, L., 1030  
 Fredsøe, J., 1595, 1865, 2043  
 Fredsøe, Jørgen, 1919  
 Frigaard, Peter, 168  
 Fujima, Koji, 1115  
 Fukushima, Masahiro, 2571  
 Furuta, Goichi, 861
- Gal, J. Andorka, 261  
 Galland, J.-C., 1061  
 Gallois, Stéphane, 2004  
 Gärtner, Joachim, 181  
 Giménez, Marcos H., 192  
 Glaser, Detlef, 181  
 Goda, Yoshimi, 1241  
 Goldenbogen, Roland, 3251  
 Gomez, Daniel, 3594  
 Gomez-Pina, G., 3579  
 Gómez-Pina, Gregorio, 3507  
 Goto, Chiaki, 12  
 Gotoh, H., 1541  
 Gotoh, Hitoshi, 2013  
 Gracia, V., 2542  
 Grass, Tony J., 565  
 Greated, C. A., 1975  
 Greated, Clive A., 540
- Grote, Wout V., 1553  
 Grüne, Joachim, 181, 1075  
 Gudmestad, Ove T., 86  
 Guiducci, F., 1343, 1625  
 Guiducci, Franco, 1090
- Hamilton, David G., 1782  
 Han, W. Y., 2987  
 Hancock, Mark W., 2028  
 Hanes, Daniel M., 3016  
 Hansen, E. A., 2043  
 Hansen, N.-E. Ottesen, 3030  
 Hansen, S. B., 1595  
 Hanslow, David J., 207, 2115  
 Hanson, Hans, 1327  
 Hanzawa, Minoru, 1143  
 Hara, Koji, 2461  
 Hardaway, C. Scott, 2653  
 Harkins, Gordon S., 806  
 Harris, J. M., 300  
 Harshinie, Karunarathna G., 689  
 Hashida, Misao, 219  
 Hashimoto, Noriaki, 232, 624, 847  
 Hashimoto, O., 1197  
 Hashimoto, Seiya, 2070  
 Hata, Sadakatsu, 2571  
 Hatada, Yoshio, 247, 674  
 Hattori, Masataro, 1101  
 Hattori, Takeshi, 704  
 Hayashi, Kenjiro, 1115  
 Hazelton, John M., 1812  
 Herbert, D. M., 1130  
 Hibbert, Kevin, 207  
 Higaki, Futoshi, 1115  
 Higano, Junya, 3086  
 Hoekstra, Piet, 2222  
 Holthuijsen, L. H., 68, 261  
 Holtzhausen, A., 1511  
 Holtzhausen, A. H., 1388  
 Hosoi, Yoshihiko, 1454  
 Houwing, Erik-Jan, 2058  
 Houwman, Klaas, 2222  
 Hsu, Tai-Wen, 2972  
 Hujii, Atsushi, 1046  
 Hwang, Kyu-Nam, 2488  
 Hwung-Hweng, Hwung, 3045
- Ikeno, Masaaki, 3320  
 Imamura, Fumihiko, 821, 886  
 Iranzo, Vicente, 1983

- Iric, Isao, 2070  
 Ishii, Toshimasa, 272  
 Isobe, Masahiho, 719  
 Isobe, Masahiko, 272, 285, 2785, 3266  
 Ito, Kazunori, 847  
 Ito, Masahiro, 1143  
 Ito, Yoshiki, 624  
 Itoh, Sadahiko, 1454  
 Iwagaki, Yuichi, 1, 1143  
 Iwata, Koichiro, 1212, 1439  
 Izumi, Tatsuhisa, 3378  
  
 Jaffe, Bruce E., 2085  
 Janssen, Hans, 3522  
 Jensen, Anders, 2958  
 Jensen, Frerk, 181  
 Johnsen, John, 2958  
 Johnson, Hakeem, 2871  
 Johnson, Patrick, 3491  
 Jones, R. J., 918, 1157  
 Juang, Jea-Tzyy, 1169  
 Juhl, J., 1754  
 Juhl, Jørgen, 1182  
  
 Kabling, Michael B., 2557  
 Kaczmarek, L. M., 300  
 Kaihatsu, Sumio, 1269  
 Kaiser, Ralf, 181  
 Kamata, A., 1197  
 Kamphuis, J. William, 1782  
 Kana, Timothy W., 2100  
 Kang, Hong-Yoon, 2115  
 Karjadi, Entin A., 2155  
 Katoh, Kazumasa, 315  
 Katopodi, Irene, 2125, 2527  
 Kawaguchi, T., 1197  
 Kawata, Yoshiaki, 330  
 Kersting, Nico F., 1797  
 Kheyryuri, Z., 1727  
 Kim, Chang-Je, 1212  
 Kim, Hyeon-Ju, 1526  
 Kim, Hyoseob, 2140  
 Kim, Kyu Han, 2476  
 Kim, Taerim, 340  
 Kimura, A., 497  
 Kimura, Akira, 356  
 Kimura, Katsutoshi, 1227  
 Kirby, James T., 128  
 Kitou, Nikos, 2125  
 Kittitanasuan, Wudhipong, 1241  
  
 Kiyokawa, Tetsushi, 650  
 Klammer, P., 1255  
 Klammer, Peter, 1298  
 Klatter, Leo, 3522  
 Kobayashi, Akio, 847  
 Kobayashi, Masonori, 1269  
 Kobayashi, Nobuhisa, 98, 1373, 2028,  
 2155  
 Kobayashi, Tomonao, 861, 1284  
 Koelewijn, Ria, 2527  
 Kohlhase, Søren, 1298  
 Kojima, Haruyuki, 1312  
 Komar, P. D., 2170  
 Koole, R., 3071  
 Koontanakulvong, Sucharit, 3002  
 Kortenhaus, Andreas, 1298  
 Kos'Yan, R. D., 2185  
 Kraak, A. W., 3208  
 Kraak, Arie, W., 2197  
 Kraus, Nicholas C., 1327  
 Kriebel, D. L., 2325  
 Kriebel, David L., 2207  
 Kroon, Aart, 2222  
 Kung, Chen-Shan, 1837  
 Kunisu, Hiroshi, 1568  
 Kunz, H., 3533  
 Kunz, Hans, 3251  
 Kuriyama, Yoshiaki, 2237  
 Kusuda, Tetsuya, 3408  
 Kuwabara, S., 3420  
 Kuwahara, Hisami, 3086  
 Kwon, J. G., 370  
  
 Lamberti, A., 1343, 1625  
 Larson, Magnus, 2252  
 Larssonneur, Claude, 2282  
 Lastrup, Christian, 1359  
 Law, Adrian W. K., 3099  
 Lee, Dal Soo, 1373  
 Lee, J., 1827  
 Lee, J. J., 1700  
 Lee, Jung Lyul, 2267  
 Lee, Tsong-Lin, 3369  
 Levoy, Franck, 2282  
 Li, Bin, 2297, 3548  
 Liberatore, Gianfranco, 525  
 Lin, Li-Hwa, 340, 2770  
 Lindenberg, Jaap, 3350  
 Lindo, Mark H., 3594  
 Lintrup, Morten, 2928

- Liu, Shuxue, 731  
 Liu, Zhou, 958  
 Longo, Sandro, 2527  
 Luger, S., 1511  
 Luger, S. A., 1388
- MacDonald, N. J., 2311  
 Maddrell, Roger, 3548  
 Maddrell, Roger J., 2297  
 Madsen, Holger Toxvig, 1359  
 Madsen, O. S., 1849  
 Madsen, Ole Secher, 384  
 Madsen, P. A., 399  
 Madsen, Per A., 2583  
 Magda, Waldemar, 3111  
 Magoon, O. T., 3608  
 Mano, A., 3126  
 Mansard, E., 3608  
 Mansard, E. P. D., 832, 1397  
 Mansard, Etienne, 791, 986  
 Mansard, Etienne P. D., 1001  
 Manzenrieder, Helmut, 3139  
 Masc, Hajime, 635  
 Matsumi, Y., 1397  
 Matsumoto, Akira, 442  
 Matsunaga, Nobuhiro, 219  
 Matsuoka, Michio, 442  
 Matsutomi, Hideo, 886  
 Mayer, R. H., 2325  
 Mayerle, Roberto, 2340  
 McDougal, W. G., 2170  
 Meadowcroft, I. C., 3154  
 Medina, Josep R., 192, 1412  
 Melby, Jeffrey A., 1426, 1641  
 Memos, Constantine D., 2350  
 Miura, H., 2698  
 Miyaike, Yoshihito, 1212  
 Miyamoto, Y., 3420  
 Mizui, Hiroyuki, 219  
 Mizumoto, T., 1197  
 Mizutani, Norimi, 1439  
 Mocke, G. P., 2365, 3335  
 Møller, Jacob Steen, 2958  
 Monfort, Olivier, 2282  
 Mori, Nobuhito, 412  
 Moutzouris, C. I., 3167  
 Mulder, J. P. M., 2886  
 Murakami, Hiroshi, 1143  
 Murakami, Hitoshi, 1454  
 Murakami, Keisuke, 1469, 2070
- Muraoka, Kohji, 3178  
 Muraoka, Kouji, 3447
- Nadaoka, Kazuo, 427, 650  
 Nagai, Toshihiko, 232, 624, 847  
 Nagao, M., 3126  
 Nairn, R. B., 2380  
 Nakagawa, Hiroji, 2013  
 Nakagawa, Yasuyuki, 427  
 Nakamura, Satoshi, 2070  
 Nakamura, Tetuya, 1312  
 Nakatsuji, Keiji, 3178, 3447  
 Nemoto, Kenji, 1143  
 Nielsen, Peter, 207, 2115, 2406  
 Niemeyer, Hanz D., 181, 1797, 2417  
 Nishi, Ryuichiro, 2434  
 Nishida, H., 1484  
 Nishihira, F., 1484  
 Nishimura, Hitoshi, 442  
 Nishimura, Tsukasa, 861  
 Nochino, Masao, 455  
 Nwogu, Okey, 467
- Ochi, M. K., 482  
 O'Connor, B. A., 300, 2311  
 O'Connor, Brian A., 2140  
 Oda, Kazuki, 3305  
 Oda, Kenji, 1284  
 Oh, Tae-Myoung, 1906, 2449  
 Ohhama, Hoiku, 2395  
 Ohta, T., 497  
 Ohta, Takao, 356  
 Ohyama, Takumi, 650, 871  
 Okayasu, Akio, 98, 2461  
 O'Neil, S., 1827  
 Ono, Masanobu, 2476, 3002  
 Ono, Nobuyuki, 2070  
 Oshiro, Shinichi, 609  
 Osiecki, Daniel A., 1895  
 Osmond, Bill, 3548  
 Oumeraci, H., 1255, 1672  
 Oumeraci, Hocine, 1298  
 Overton, Margery F., 1998, 2488  
 Owen, M. W., 1130
- Park, Woo Sun, 1373  
 Partenscky, H.-W., 1255, 1672  
 Péchon, Philippe, 2503  
 Peerbolte, E. Bart, 3193  
 Peña, Carlos, 3564

- Peña-Santana, Patricia G., 2395  
 Peregrine, D. H., 776, 1496  
 Perrier, G., 2043  
 Petit, H. A. H., 511, 1739  
 Petti, Marco, 525, 540  
 Phelp, D., 1511  
 Phelp, D. T., 1388  
 Pluijm, M., 3208  
 Podymov, I. S., 2185  
 Presti, A. Lo, 2625  
 Prieto, J., 2542  
 Pruszek, Zbigniew, 2513  
 Putrevu, U., 2741  
  
 Quinn, Paul A., 525, 540  
  
 Ramadan, Khaled A. H., 2527  
 Ramírez, Jose L., 3507  
 Raudkivi, Arved J., 1934  
 Reeve, D. E., 3154  
 Ribberink, Jan S., 2527  
 Ris, R. C., 68  
 Rodriguez, A., 2542  
 Roelvink, J. A., 3223  
 Rousset, H el ene, 2282  
 Rubin, David M., 2085  
 Ruessink, Gerben, 2222  
 Rufin, Teofilo Monge, Jr., 1439  
 Ruggiero, P., 2170  
 Ruiz, Luis Felipe Vila, 3237  
 Rutledge, J., 1397  
 Ryu, Cheong-Ro, 1526  
  
 Sakai, Hiroyuki, 1101  
 Sakai, T., 1541  
 Saleh, Wameidh M., 565  
 Sallenger, Asbury, Jr., 2085  
 S anchez-Arcilla, A., 2542, 2625  
 S anchez-Carratal a, Carlos R., 192  
 Sancho, F. E., 2741  
 Sand, S. E., 832  
 Sasaki, Hiroshi, 624  
 Sato, Michio, 2434, 2571  
 Sato, Shinji, 2557  
 Sawamoto, M., 3126  
 Sawamura, Yoshiyuki, 1454  
 Sawaragi, Toru, 2476, 3002  
 Sch affer, H. A., 399  
 Sch affer, Hemming A., 2583  
 Schicreck, Gerrit J., 1553  
 Schmeltz, Edward J., 3594  
 Schoonees, J. S., 2595, 2668  
 Schroeder, Ernst, 3251  
 Schr oter, Andreas, 2340  
 Sch utttrumpf, Holger, 553  
 Scott, R. D., 2380  
 Seiffert, J. W. W., 2639  
 Sekimoto, Tsunehiro, 1568  
 Shen, Daoxian, 3266  
 Sheng, Y. P., 3432  
 Sheng, Y. Peter, 3281  
 Shiba, Kazuhiko, 2785  
 Shibata, Takao, 847  
 Shibayama, Tomoya, 2461, 2813, 2913, 3295  
 Shigematsu, Takaaki, 3305  
 Shih, S.-M., 2170  
 Shim, Youngbo, 2140  
 Shimizu, Takao, 3320  
 Shimizu, Takuzo, 1946, 2610  
 Shimosako, Kenichiro, 1580  
 Shinoda, Seirou, 704  
 Shiraishi, Naofumi, 2395  
 Shuto, Nobuo, 821, 886  
 Sierra, J. P., 2625  
 Sigemura, Toshiyuki, 1115  
 Simons, Richard R., 565  
 Simonsen, B. C., 3030  
 Sistermans, Paul G. J., 1553  
 Sloth, Peter, 1182  
 Smit, F., 2365  
 Smith, G. G., 3335  
 Smith, G. M., 2639  
 S orensen, O. R., 399  
 S orensen, Ole R., 2583  
 Stansberg, Carl Trygve, 579  
 Steetzel, Henk J., 2197  
 Sterndorff, M. J., 3030  
 Stive, Marcel J. F., 594, 761  
 Stive, Marcer, 1837  
 Stoutjesdijk, Theo P., 3350  
 Sueyoshi, Toshiaki, 3178  
 Sugihara, Yuji, 219  
 Suh, Kyung Duck, 2653  
 Sulaiman, Dede M., 609  
 Sumer, B. M., 1595  
 Sunamura, Tsuguo, 2856  
 Svendsen, I. A., 2741  
 Swan, C., 113, 3071  
 Swart, D. H., 2668, 3335

Syamsudin, Abdul R., 2683

Tada, A., 1484

Takahashi, S., 2698

Takahashi, Shigeo, 1016, 1046, 1227,  
1580

Takahashi, Tomoharu, 624

Takahashi, Tomoyuki, 821, 886

Takayama, Tomotsuka, 624

Takeba, Ken, 635

Tamashita, Takao, 901

Tanaka, Masahiro, 650

Tanimoto, Katsutoshi, 689, 1227, 1580

Tehrani, Mehrdad M., 565

Teisson, Charles, 42, 1610, 2503

Theron, A. K., 2595

Thomas, P., 2902

Thomas, Pierre, 2004

Tillotson, K. J., 2170

Ting, Francis C. K., 2712

Toba, E., 3579

Tobikik, Isao, 847

Togashi, Hiroyoshi, 746

Tolman, H. L., 261

Tomasicchio, G. R., 1343, 1625

Toms, Geffery, 1837

Tonder, A. van, 1388, 1511

Tönjes, P., 511, 1739

Tøorum, Alf, 142

Topliss, M. E., 1496

Torfs, Hilde, 3360

Toue, Takao, 847

Tsai, Ching-Piao, 3369

Tsuchida, Mitsuru, 871

Tsuchiya, Toshito, 609

Tsuchiya, Yoshito, 2683, 3378, 3478

Tsujimoto, Tetsuro, 2013

Tsuru, Masahito, 2610

Tsutsui, Shigeaki, 609

Turk, George F., 1426, 1641

Uda, Takaaki, 2726

Ujii, Hisayoshi, 3320

Valdecantos, Vicente Negro, 1657

van de Graaff, Jan, 2197

van de Kreeke, J., 2886

van den Bosch, P., 511, 1739

van der Lem, J. C., 3208

van der Meer, J. W., 1030, 1713, 1754,

2639

Van Dongeren, A. R., 2741

Van Evra, R., 1827

van Gent, M. R. A., 511, 1727, 1739

van Nes, C. P., 1713

van Rijn, Leo C., 2058

van Vessem, P., 2886

van Vledder, Gerbrant Ph., 761

Verhagen, L. A., 665

Villaret, C., 2043

Visser, Paul J., 2197, 2755

von Lany, P. H., 3154

Vongvisessomjai, Suphat, 3393

Walstra, D. J. R., 3223

Wang, Hsiang, 340, 2267, 2434, 2770,  
2843

Wang, Xu, 2770

Ward, Donald L., 1687

Watanabe, Akira, 272, 719, 1946, 2610,  
2785, 3266

Watson, G., 776

Weggel, J. R., 3608

Whalin, R. W., 3608

White, Thomas E., 2799

Wibner, Christopher G., 1687

Williams, Greg, 1812

Wind, Herman G., 3193

Winyu, Rattanapitikon, 2813

Woltering, Stefan, 2828

Wright, L. D., 1849

Wu, N. T., 1672

Wu, Yongjun, 2843

Yamada, Akiko, 3295

Yamada, Minoru, 3478

Yamaguchi, Masataka, 247, 674

Yamamoto, Koji, 2726

Yamamoto, Masato, 1143

Yamamoto, S., 2698

Yamamoto, T., 1541

Yamamoto, Yoshimichi, 689

Yamanishi, Hiroyuki, 3408

Yamashita, Takao, 609, 2683, 3378

Yamauchi, Kazuaki, 3320

Yamazaki, H., 1727

Yamazaki, Tsuyoshi, 1568

Yan, Yixin, 3060

Yang, David W., 3594

Yano, K., 3420

- Yassuda, E. A., 3432  
Yassuda, Eduardo A., 3281  
Yasuda, Takashi, 412, 704  
Yen, Kai, 3060  
Yokoki, Hiromune, 719  
Yoon, Jong Seong, 3447  
Yoshida, Akinori, 1312, 1469  
Yoshioka, Hiroshi, 609, 901  
Young, I. R., 665  
Ysuchiya, Yoshito, 901  
Yu, Hong-Sun, 1212  
Yu, Xiping, 746  
Yu, Yuxiu, 731  
Zeidler, Ryszard B., 2513, 3462  
Zeng, Xiaochuan, 3060  
Zhang, Da Ping, 2856  
Zhang, Jun, 1687  
Zhuang, F., 1700  
Zielke, Werner, 2340  
Zou, Zhili, 1961  
Zuzek, P. J., 2380  
Zyserman, J. A., 2871

VOLUME 3

TRAD

# Coastal Engineering 1994

Proceedings of the  
twenty-fourth international conference

October 23-28; 1994  
Kobe, Japan

Conference held under the auspices of the  
Coastal Engineering Research Council of the  
American Society of Civil Engineers

Organized by the Japan Society of Civil Engineers

Edited by Billy L. Edge



Published by the  
American Society of Civil Engineers  
345 East 47th Street  
New York, New York 10017-2398



## ABSTRACT

This proceedings contains over 200 papers presented at the 24th International Conference on Coastal Engineering which was held in Kobe, Japan, October 23-28, 1994. The book is divided into six parts: 1) Characteristics of coastal waves and currents; 2) long waves and storm surges; 3) coastal structures; 4) coastal processes and sediment transport; 5) coastal, estuarine and environmental problems; and 6) case studies. The individual papers include such topics as the effects of wind, waves, storms and currents as well as the study of sedimentation and beach nourishment. Special emphasis is given to case studies of completed engineering projects. With the inclusion of both theoretical and practical information, these papers provide the civil engineer and related fields with a broad range of information on coastal engineering.

Coastal engineering 1994: proceedings of the twenty-fourth international conference, October 23-28, 1994, Kobe, Japan  
edited by Billy L. Edge.

p. cm.

"Conference held under the auspices of the Coastal Engineering Research Council of the American Society of Civil Engineers; organized by the Japan Society of Civil Engineers (JSCE)." Papers presented at the 24th International Conference on Coastal Engineering.

Includes index.

ISBN 0-7844-0089-X

1. Coastal engineering—Congresses. 2. Ocean waves—Congresses. 3. Shore protection—Congresses. I. Edge, Billy L. II. Coastal Engineering Research Council (U.S.) III. Doboku Gakkai. IV. International Conference on Coastal Engineering (24th: 1994: Kobe, Japan)

TC203.5.C6184 1995

95-18653

627.58—dc20

CIP

The Society is not responsible for any statements made or opinions expressed in its publications.

Photocopies. Authorization to photocopy material for internal or personal use under circumstances not falling within the fair use provisions of the Copyright Act is granted by ASCE to libraries and other users registered with the Copyright Clearance Center (CCC) Transactional Reporting Service, provided that the base fee of \$2.00 per article plus \$.25 per page copied is paid directly to CCC, 222 Rosewood, Drive, Danvers, MA 01923. The identification for ASCE Books is 0-7844-0089-X/95 \$2.00 + \$.25. Requests for special permission or bulk copying should be addressed to Permissions & Copyright Dept., ASCE.

Copyright © 1995 by the American Society of Civil Engineers,  
All Rights Reserved.

Library of Congress Catalog Card No: 95-18653

ISBN 0-7844-0089-X

Manufactured in the United States of America.

# CONTENTS

## PART I

Plenary Session THE PRESENT AND FUTURE OF COASTAL ENGINEERING IN JAPAN.....	1
<i>Yuichi Iwagaki</i>	
Chapter 1 ON THE CHARACTERISTICS OF ONE-DIMENSIONAL SPECTRA AND NON-DIMENSIONAL PARAMETERS OF WIND WAVES.....	12
<i>Toshio Aono, Chiaki Goto</i>	
Chapter 2 SWASH MOTION DUE TO OBLIQUELY INCIDENT WAVES.....	27
<i>Toshiyuki Asano</i>	
Chapter 3 LABORATORY COMPARISON OF DIRECTIONAL WAVE MEASUREMENT SYSTEMS AND ANALYSIS TECHNIQUES .....	42
<i>Michel Benoit, Charles Teisson</i>	
Chapter 4 ACCURACY OF WIND AND WAVE EVALUATION IN COASTAL REGIONS.....	57
<i>Luciana Bertotti, Luigi Cavaleri</i>	
Chapter 5 A SPECTRAL MODEL FOR WAVES IN THE NEAR SHORE ZONE.....	68
<i>R.C. Ris, L.H. Holthuijsen, N. Booij</i>	
Chapter 6 WIND VARIABILITY AND EXTREMES STATISTICS.....	79
<i>Luigi Cavaleri, Luciana Bertotti</i>	
Chapter 7 MEAN FLUX IN THE FREE SURFACE ZONE OF WATER WAVES IN A CLOSED WAVE FLUME.....	86
<i>Witold Cieslikiewicz, Ove T. Gudmestad</i>	
Chapter 8 VERTICAL VARIATIONS OF FLUID VELOCITIES AND SHEAR STRESS IN SURF ZONES .....	98
<i>Daniel T. Cox, Nobuhisa Kobayashi, Akio Okayasu</i>	

Chapter 9	
VORTICITY EFFECTS IN COMBINED WAVES AND CURRENTS.....	113
<i>I. Cummins, C. Swan</i>	
Chapter 10	
WAVES IN AN ANNULAR ENTRANCE CHANNEL .....	128
<i>Robert A. Dalrymple, J.T. Kirby</i>	
Chapter 11	
WAVE DAMPING BY KELP VEGETATION.....	142
<i>Alfonse Dubi, Alf Tørum</i>	
Chapter 12	
NONLINEAR COUPLING IN WAVES PROPAGATING OVER A BAR.....	157
<i>Y. Eldeberky, J.A. Battjes</i>	
Chapter 13	
AN ABSORBING WAVE-MAKER BASED ON DIGITAL FILTERS .....	168
<i>Peter Frigaard, Morten Christensen</i>	
Chapter 14	
WAVE CLIMATE STUDY IN WADDEN SEA AREAS .....	181
<i>Ralf Kaiser, Günther Brandt, Joachim Gärtner, Detlef Glaser, Frerk Jensen, H.D. Niemeyer, Joachim Grüne</i>	
Chapter 15	
FALSE WAVES IN WAVE RECORDS AND NUMERICAL SIMULATIONS.....	192
<i>Marcos H. Giménez, C.R. Sánchez-Carratalá, J.R. Medina</i>	
Chapter 16	
MEASURING WAVES WITH MANOMETER TUBES .....	207
<i>David J. Hanslow, P. Nielsen, K. Hibbert</i>	
Chapter 17	
QUANTITY OF SPRAY TRANSPORTED BY THE STRONG WIND OVER BREAKING WAVES .....	219
<i>Nobuhiro Matsunaga, Misao Hashida, Hiroyuki Mizui, Yuji Sugihara</i>	
Chapter 18	
EXTENSION OF THE MAXIMUM ENTROPY PRINCIPLE METHOD FOR DIRECTIONAL WAVE SPECTRUM ESTIMATION .....	232
<i>Noriaki Hashimoto, Toshihiko Nagai, Tadashi Asai</i>	

Chapter 19	
A REGRESSION MODEL FOR ESTIMATING SEA STATE PERSISTENCE .....	247
<i>Yoshio Hatada, Masataka Yamaguchi</i>	
Chapter 20	
THE MAXIMUM SIGNIFICANT WAVE HEIGHT IN THE SOUTHERN NORTH SEA .....	261
<i>L.H. Holthuijsen, J.G. de Ronde, Y. Eldeberky, H.L. Tolman, N. Booij, E. Bouws, P.G.P. Ferier, J. Andorka Gal</i>	
Chapter 21	
IMPROVED BOUNDARY CONDITIONS TO A TIME-DEPENDENT MILD-SLOPE EQUATION FOR RANDOM WAVES .....	272
<i>Toshimasa Ishii, Masahiko Isobe, Akira Watanabe</i>	
Chapter 22	
TIME-DEPENDENT MILD SLOPE EQUATIONS FOR RANDOM WAVES .....	285
<i>Masahiko Isobe</i>	
Chapter 23	
MODELLING MOVEABLE BED ROUGHNESS AND FRICTION FOR SPECTRAL WAVES .....	300
<i>L.M. Kaczmarek, J.M. Harris, B.A. O'Connor</i>	
Chapter 24	
DIFFERENCE BETWEEN WAVES ACTING ON STEEP AND GENTLE BEACHES .....	315
<i>Kazumasa Katoh</i>	
Chapter 25	
WAVE BREAKING UNDER STORM CONDITION .....	330
<i>Yoshiaki Kawata</i>	
Chapter 26	
APPLICATION OF MAXIMUM ENTROPY METHOD TO THE REAL SEA DATA .....	340
<i>Taerim Kim, Li-Hwa Lin, Hsiang Wang</i>	
Chapter 27	
PROBABILITY OF THE FREAK WAVE APPEARANCE IN A 3-DIMENSIONAL SEA CONDITION .....	356
<i>Akira Kimura, Takao Ohta</i>	

Chapter 28	
ON THE JOINT DISTRIBUTION OF WAVE HEIGHT, PERIOD & DIRECTION OF INDIVIDUAL WAVES IN A 3-DIMENSIONAL RANDOM SEAS.....	370
<i>J.G. Kwon, Ichiro Deguchi</i>	
Chapter 29	
SPECTRAL WAVE-CURRENT BOTTOM BOUNDARY LAYER FLOWS.....	384
<i>Ole Secher Madsen</i>	
Chapter 30	
TIME DOMAIN MODELLING OF WAVE BREAKING, RUNUP AND SURF BEATS .....	399
<i>Per A. Madsen, O.R. Sørensen, H.A. Schäffer</i>	
Chapter 31	
ORTHONORMAL WAVELET ANALYSIS FOR DEEP-WATER BREAKING WAVES .....	412
<i>Nobuhito Mori, Takashi Yasuda</i>	
Chapter 32	
A FULLY DISPERSIVE-NONLINEAR WAVE MODEL AND ITS NUMERICAL SOLUTIONS .....	427
<i>Kazuo Nadaoka, Serdar Beji, Yasuyuki Nakagawa</i>	
Chapter 33	
A GENERALIZED GREEN-FUNCTION METHOD FOR WAVE FIELD ANALYSIS .....	442
<i>Hitoshi Nishimura, Michio Matsuoka, Akira Matsumoto</i>	
Chapter 34	
COUPLED VIBRATION EQUATIONS FOR IRREGULAR WATER WAVES.....	455
<i>Masao Nochino</i>	
Chapter 35	
NONLINEAR EVOLUTION OF DIRECTIONAL WAVE SPECTRA IN SHALLOW WATER .....	467
<i>Okey Nwogu</i>	
Chapter 36	
NON-GAUSSIAN PROBABILITY DISTRIBUTION OF COASTAL WAVES .....	482
<i>M.K. Ochi, K. Ahn</i>	

Chapter 37	
PROBABILITY CHARACTERISTICS OF ZERO-CROSSING WAVE HEIGHT .....	497
<i>Takao Ohta, Akira Kimura</i>	
Chapter 38	
NUMERICAL SIMULATION AND VALIDATION OF PLUNGING BREAKERS USING A 2D NAVIER-STOKES MODEL.....	511
<i>H.A.H. Petit, P.Tönjes, M.R.A. Van Gent, P. Van Den Bosch</i>	
Chapter 39	
WAVE VELOCITY FIELD MEASUREMENTS OVER A SUBMERGED BREAKWATER .....	525
<i>Marco Petti, Paul A. Quinn, Gianfranco Liberatore, William J. Easson</i>	
Chapter 40	
VELOCITY FIELD MEASUREMENTS AND THEORETICAL COMPARISONS FOR NON-LINEAR WAVES ON MILD SLOPES .....	540
<i>Paul A. Quinn, Marco Petti, Michele Drago, Clive A. Greated</i>	
Chapter 41	
THE CONCEPT OF RESIDENCE TIME FOR THE DESCRIPTION OF WAVE RUN-UP, WAVE SET-UP AND WAVE RUN-DOWN .....	553
<i>Holger Schüttrumpf, Hendrik Bergmann, Hans-Henning Dette</i>	
Chapter 42	
BOTTOM SHEAR STRESSES UNDER RANDOM WAVES WITH A CURRENT SUPERIMPOSED.....	565
<i>Richard R. Simons, Tony J. Grass, Wameidh M. Saleh, Mehrdad M. Tehrani</i>	
Chapter 43	
EFFECTS FROM DIRECTIONALITY & SPECTRAL BANDWIDTH ON NON-LINEAR SPATIAL MODULATIONS OF DEEP-WATER SURFACE GRAVITY WAVE TRAINS .....	579
<i>Carl Trygve Stansberg</i>	
Chapter 44	
SHEAR STRESSES AND MEAN FLOW IN SHOALING AND BREAKING WAVES .....	594
<i>Marcel J.F. Stive, Huib J. De Vriend</i>	

Chapter 45		
PREDICTION OF THE MAXIMUM WAVE ON THE CORAL FLAT .....	609	
		<i>Dede M. Sulaiman, Shigeaki Tsutsui, Hiroshi Toshioka, T. Yamashita, S. Oshiro, Y. Tsuchiya</i>
Chapter 46		
DEVELOPMENT OF A SUBMERGED DOPPLER-TYPE DIRECTIONAL WAVE METER .....	624	
		<i>Tomotsuka Takayama, Noriaki Hashimoto, Toshihiko Nagai, Tomoharu Takahashi, Hiroshi Sasaki, Yoshiki Ito</i>
Chapter 47		
BRAGG SCATTERING OF WAVES OVER POROUS RIPPLED BED .....	635	
		<i>Hijime Mase, Ken Takeba</i>
Chapter 48		
NON-REFLECTIVE MULTI-DIRECTIONAL WAVE GENERATION BY SOURCE METHOD .....	650	
		<i>Masahiro Tanaka, Takumi Ohyama, Tetsushi Kiyokawa, Kazuo Nadaoka</i>
Chapter 49		
THE GROWTH OF WIND WAVES IN SHALLOW WATER .....	665	
		<i>L.A. Verhagen, I.R. Young</i>
Chapter 50		
ESTIMATION OF TYPHOON-GENERATED MAXIMUM WAVE HEIGHT ALONG THE PACIFIC COAST OF JAPAN BASED ON WAVE HINDCASTING .....	674	
		<i>Masataka Yamaguchi, Yoshio Hatada</i>
Chapter 51		
RUN-UP OF IRREGULAR WAVES ON A GENTLY SLOPING BEACH .....	689	
		<i>Yoshimichi Yamamoto, Katsutoshi Tanimoto, Karunarathna Harshinie</i>
Chapter 52		
SOLITON-MODE WAVEMAKER THEORY AND SYSTEM FOR COASTAL WAVES .....	704	
		<i>Takashi Yasuda, Takeshi Hattori, Seirou Shinoda</i>
Chapter 53		
ON A METHOD FOR ESTIMATING REFLECTION COEFFICIENT IN SHORT-CRESTED RANDOM SEAS .....	719	
		<i>Hirumune Yokoki, Masahiko Isobe, Akira Watanabe</i>

Chapter 54	
THE DIRECTIONAL WAVE SPECTRUM IN THE BOHAI SEA.....	731
<i>Yuxiu Yu, Shuxue Liu</i>	

Chapter 55	
IRREGULAR WAVES OVER AN ELLIPTIC SHOAL.....	746
<i>Xiping Yu, Hiroyoshi Togashi</i>	

Chapter 56	
PERFORMANCE OF A SPECTRAL WIND-WAVE MODEL IN SHALLOW WATER.....	761
<i>Gerbrant Ph. van Vledder, John G. de Ronde, Marcel J.F. Stive</i>	

## PART II

Chapter 57	
THE GENERATION OF LOW-FREQUENCY WAVES BY A SINGLE WAVE GROUP INCIDENT ON A BEACH.....	776
<i>Gary Watson, Timothy C.D. Barnes, D. Howell Peregrine</i>	

Chapter 58	
INFLUENCE OF LONG WAVES ON SHIP MOTIONS IN A LAGOON HARBOUR.....	791
<i>Volker Barthel, Etienne Mansard</i>	

Chapter 59	
RESONANT FORCING OF HARBORS BY INFRAGRAVITY WAVES.....	806
<i>Gordon S. Harkins, Michael J. Briggs</i>	

Chapter 60	
NUMERICAL SIMULATION OF THE 1992 FLORES TSUNAMI IN INDONESIA: DISCUSSION ON LARGE RUNUP HEIGHTS IN THE NORTHEASTERN FLORES ISLAND.....	821
<i>Fumihiko Imamura, Tomoyuki Takahashi, Nobuo Shuto</i>	

Chapter 61	
A COMPARATIVE EVALUATION OF WAVE GROUPING MEASURES.....	832
<i>E.P.D. Mansard, S.E. Sand</i>	

Chapter 62	
RELATIONSHIP OF A MOORED VESSEL IN A HARBOUR AND LONG WAVE CAUSED BY WAVE GROUPS.....	847
<i>Toshihiko Nagai, N. Hashimoto, T. Asai, I. Tobiki, K. Ito, T. Toue, A. Kobayashi, T. Shibata</i>	



Chapter 63  
 COHERENT STRUCTURE OF TIDAL TURBULENCE IN A ROTATING  
 SYSTEM OF OSAKA-BAY ..... 861  
*Tsukasa Nishimura, Tomonao Kobayashi, Goichi Furuta*

Chapter 64  
 DEVELOPMENT OF A PARTIALLY THREE-DIMENSIONAL MODEL  
 FOR SHIP MOTION IN A HARBOR WITH ARBITRARY BATHYMETRY ..... 871  
*Takumi Ohyama, M. Tsuchida*

Chapter 65  
 THE MEASURED AND COMPUTED HOKKAIDO NANSEI-OKI  
 EARTHQUAKE TSUNAMI OF 1993 ..... 886  
*Tomoyuki Takahashi, Nobuo Shuto, Fumihiko Imamura,  
 Hideo Matsutomi*

Chapter 66  
 QUASI-THREE-DIMENSIONAL MODEL FOR STORM SURGES AND  
 ITS VERIFICATION ..... 901  
*Takao Yamashita, Yoshito Tsuchiya, Hiroshi Yoshioka*

### PART III

Chapter 67  
 ANALYSIS OF PRACTICAL RUBBLE MOUNDS ..... 918  
*N.W.H. Allsop, R.J. Jones, P. Besley, C. Franco*

Chapter 68  
 FRICTION AND CLAMPING FORCES IN WAVE LOADED PLACED  
 BLOCK REVETMENTS ..... 932  
*Adam Bezuijen*

Chapter 69  
 A FIELD EXPERIMENT ON THE INTERACTION  
 WAVES-REFLECTING WALL ..... 945  
*Paolo Boccotti*

Chapter 70  
 THE APPLICATION OF LOAD-CELL TECHNIQUE IN THE STUDY  
 OF ARMOUR UNIT RESPONSES TO IMPACT LOADS ..... 958  
*Hans F. Burcharth, Zhou Liu*

Chapter 71	
STEEP WAVE DIFFRACTION BY A SUBMERGED CYLINDER.....	973
<i>J.T. Aquije Chacaltana, A.F.T. da Silva</i>	
Chapter 72	
WAVE STRESSES ON RUBBLE-MOUND ARMOUR .....	986
<i>Andrew M. Cornett, Etienne Mansard</i>	
Chapter 73	
DAMAGE ANALYSIS FOR RUBBLE-MOUND BREAKWATERS .....	1001
<i>Michael H. Davies, Etienne P.D. Mansard, Andrew M. Cornett</i>	
Chapter 74	
NUMERICALLY MODELING PERSONNEL DANGER ON A PROMENADE BREAKWATER DUE TO OVERTOPPING WAVES .....	1016
<i>Kimihiko Endoh, Shigeo Takahashi</i>	
Chapter 75	
WAVE OVERTOPPING ON VERTICAL AND COMPOSITE BREAKWATERS.....	1030
<i>L. Franco, M. de Gerloni, J.W. van der Meer</i>	
Chapter 76	
AN INVESTIGATION OF THE WAVE FORCES ACTING ON BREAKWATER HANDRAILS .....	1046
<i>Atsushi Hujii, Shigeo Takahashi, Kimihiko Endoh</i>	
Chapter 77	
RUBBLE MOUND BREAKWATER STABILITY UNDER OBLIQUE WAVES: AN EXPERIMENTAL STUDY .....	1061
<i>J.-C. Galland</i>	
Chapter 78	
WAVE LOADS ON SEADYKES WITH COMPOSITE SLOPES & BERMS .....	1075
<i>Joachim Grune, Hendrik Bergmann</i>	
Chapter 79	
COMPUTERISED METHODOLOGY TO MEASURE RUBBLE MOUND BREAKWATER DAMAGE.....	1090
<i>Bruno Chilo, Franco Guiducci</i>	

Chapter 80	
WAVE BREAKING OVER PERMEABLE SUBMERGED BREAKWATERS .....	1101
	<i>Masataro Hattori, Hiroyoki Sakai</i>
Chapter 81	
WAVE FORCES ACTING ON A VORTEX EXCITED VIBRATING	
VERTICAL CYLINDER IN WAVES .....	1115
	<i>Kenjiro Hayashi, Futoshi Higaki, Koji Fujima,</i> <i>Toshiyuki Sigemura, John R. Chaplin</i>
Chapter 82	
OVERTOPPING OF SEA WALLS UNDER RANDOM WAVES .....	1130
	<i>D.M. Herbert, N.W.H. Allsop, M.W. Owen</i>
Chapter 83	
STABILITY OF HIGH-SPECIFIC GRAVITY ARMOR BLOCKS .....	1143
	<i>Masahiro Ito, Y. Iwagaki, H. Murakami, K. Nemoto, M. Yamamoto,</i> <i>M. Hanzawa</i>
Chapter 84	
ROCK ARMoured BEACH CONTROL STRUCTURES ON	
STEEP BEACHES .....	1157
	<i>R.J. Jones, N.W.H. Allsop</i>
Chapter 85	
EFFECT ON ROUGHNESS TO IRREGULAR WAVE RUN-UP.....	1169
	<i>Jea-Tzyy Juang</i>
Chapter 86	
WAVE OVERTOPPING OF BREAKWATERS UNDER OBLIQUE WAVES.....	1182
	<i>Jørgen Juhl, Peter Sloth</i>
Chapter 87	
CONSTRUCTION OF OFFSHORE FISHING PORT FOR PREVENTION	
OF COASTAL EROSION .....	1197
	<i>Takeshi Kawaguchi, O. Hashimoto, T. Mizumoto, A. Kamata</i>
Chapter 88	
TOPOGRAPHICAL CHANGE AROUND MULTIPLE LARGE	
CYLINDRICAL STRUCTURES UNDER WAVE ACTIONS.....	1212
	<i>Chang-Je Kim, Koichiro Iwata, Yoshihito Miyaike, Hong-Sun Yu</i>

Chapter 89	
STABILITY OF RUBBLE MOUND FOUNDATIONS OF COMPOSITE BREAKWATERS UNDER OBLIQUE WAVE ATTACK .....	1227
<i>Katsutoshi Kimura, Shigeo Takahashi, Katsutoshi Tanimoto</i>	
Chapter 90	
ANALYSIS OF NONLINEAR COEFFICIENTS OF REFLECTION AND TRANSMISSION OF WAVES PROPAGATING OVER A RECTANGULAR STEP .....	1241
<i>Wudhipong Kittitanasuan, Yoshimi Goda</i>	
Chapter 91	
OSCILLATORY MOTIONS AND PERMANENT DISPLACEMENTS OF CAISSON BREAKWATERS SUBJECT TO IMPULSIVE BREAKING WAVE LOADS.....	1255
<i>P. Klammer, H. Oumeraci, H.-W. Partenscky</i>	
Chapter 92	
HYDRAULIC CHARACTERISTICS AND FIELD EXPERIENCE OF NEW WAVE DISSIPATING CONCRETE BLOCKS (ACCROPODE) .....	1269
<i>Masanori Kobayashi, Sumio Kaihatsu</i>	
Chapter 93	
EXPERIMENTAL STUDY ON DEVELOPING PROCESS OF LOCAL SCOUR AROUND A VERTICAL CYLINDER.....	1284
<i>Tomonao Kobayashi, Kenji Oda</i>	
Chapter 94	
WAVE-INDUCED UPLIFT LOADING OF CAISSON BREAKWATERS .....	1298
<i>Andreas Kortenhaus, Hocine Oumeraci, Søren Kohlhase, Peter Klammer</i>	
Chapter 95	
LINEAR AND NONLINEAR WAVE FORCES EXERTED ON A SUBMERGED HORIZONTAL PLATE.....	1312
<i>Haruyuki Kojima, A. Yoshida, T. Nakamura</i>	
Chapter 96	
MODERN FUNCTIONAL DESIGN OF GROIN SYSTEMS.....	1327
<i>Nicholas C. Kraus, Hans Hanson, Sten H. Blomgren</i>	
Chapter 97	
RESHAPING BREAKWATERS IN DEEP AND SHALLOW WATER CONDITIONS.....	1343
<i>A. Lamberti, G.R. Tomasicchio, F. Guiducci</i>	

Chapter 98	
DESIGN OF BREAKWATERS AND BEACH NOURISHMENT .....	1359
<i>Christian Laustrup, Holger Toxvig Madsen</i>	
Chapter 99	
CIRCULAR CHANNEL BREAKWATER TO REDUCE WAVE OVERTOPPING AND ALLOW WATER EXCHANGE .....	1373
<i>Dal Soo Lee, Woo Sun Park, Nobuhisa Kobayashi</i>	
Chapter 100	
INCREASED DOLOS STRENGTH BY SHAPE MODIFICATION .....	1388
<i>S.A. Luger, D.T. Phelp, A. Van Tonder, A.H. Holtzhausen</i>	
Chapter 101	
INFLUENCE OF WAVE DIRECTIONALITY ON STABILITY OF BREAKWATER HEADS .....	1397
<i>Y. Matsumi, E.P.D. Mansard, J. Rutledge</i>	
Chapter 102	
COST-EFFECTIVENESS OF D-ARMOR BREAKWATER .....	1412
<i>Josep R. Medina</i>	
Chapter 103	
THE CORE-LOC: OPTIMIZED CONCRETE ARMOR .....	1426
<i>Jeffrey A. Melby, George F. Turk</i>	
Chapter 104	
STABILITY OF ARMOR STONES OF A SUBMERGED WIDE-CROWN BREAKWATER .....	1439
<i>Norimi Mizutani, Teofilo Monge Rufin, Jr., Koichiro Iwata</i>	
Chapter 105	
WAVE INDUCED FLOW AROUND SUBMERGED SLOPING PLATES .....	1454
<i>Hitoshi Murakami, Sadahiko Itoh, Yoshihiko Hosoi, Yoshiyuki Sawamura</i>	
Chapter 106	
SECOND-ORDER WAVE INTERACTION WITH ARRAYS OF VERTICAL CYLINDERS OF ARBITRARY CROSS SECTION .....	1469
<i>Keisuke Murakami, Akinori Yoshida</i>	
Chapter 107	
HYDRODYNAMIC FORCES ON BOTTOM-SEATED HEMISPHERE IN WAVES AND CURRENTS .....	1484
<i>Hidenori Nishida, A. Tada, F. Nishihira</i>	

Chapter 108	
THE PRESSURE FIELD DUE TO STEEP WATER WAVES INCIDENT ON A VERTICAL WALL .....	1496
<i>D.H. Peregrine, M.E. Topliss</i>	
Chapter 109	
RESULTS OF EXTENSIVE FIELD MONITORING OF DOLOS BREAKWATERS.....	1511
<i>D. Phelps, S. Luger, A. Van Tonder, A. Holtzhausen</i>	
Chapter 110	
FAILURE OF RUBBLE MOUND STRUCTURES DUE TO THE STORM DURATION AND THE IRREGULARITY OF OCEAN WAVES .....	1526
<i>Cheong-Ro Ryu, Hyeon-Ju Kim</i>	
Chapter 111	
BLOCK SUBSIDENCE UNDER PRESSURE AND FLOW .....	1541
<i>T. Sakai, H. Gotoh, T. Yamamoto</i>	
Chapter 112	
STABILITY OF ROCK ON BEACHES.....	1553
<i>Gerrit J. Schiereck, Henri L. Fontijn, Wout V. Grote, Paul G.J. Sijm</i>	
Chapter 113	
SHORT TERM WAVE OVERTOPPING RATE OF BLOCK ARMORED SEAWALL .....	1568
<i>Tsunehiro Sekimoto, Hiroshi Kunisu, Tsuyoshi Yamazaki</i>	
Chapter 114	
ESTIMATING THE SLIDING DISTANCE OF COMPOSITE BREAKWATERS DUE TO WAVE FORCES INCLUSIVE OF IMPULSIVE FORCES .....	1580
<i>Kenichiro Shimosako, S. Takahashi, K. Tanimoto</i>	
Chapter 115	
BED SHEAR STRESS AND SCOUR AROUND COASTAL STRUCTURES .....	1595
<i>B.M. Sumer, J. Fredsøe, N. Christiansen, S.B. Hansen</i>	
Chapter 116	
LABORATORY MEASUREMENT OF OBLIQUE IRREGULAR WAVE REFLECTION ON RUBBLE-MOUND BREAKWATERS.....	1610
<i>Charles Teisson, Michel Benoit</i>	

Chapter 117	
STONE MOVEMENT ON A RESHAPED PROFILE .....	1625
<i>G. Roberto Tomasicchio, A. Lamberti, F. Guiducci</i>	
Chapter 118	
THE LARGE SCALE DOLOS FLUME STUDY.....	1641
<i>George F. Turk, Jeffrey A. Melby</i>	
Chapter 119	
H <sub>0</sub> PARAMETER FOR PRELIMINARY DESIGN OF CONVENTIONAL BREAKWATER STRUCTURAL HEAD: DATA ANALYSIS OF SPANISH NORTH COAST HARBOURS .....	1657
<i>Vincente Negro Valdecantos, Ovidio Varela Carnero</i>	
Chapter 120	
NUMERICAL MODELLING OF BREAKING WAVE IMPACTS ON A VERTICAL WALL .....	1672
<i>N.T. Wu, H. Oumeraci, H.-W. Partensky</i>	
Chapter 121	
WIND EFFECTS ON RUNUP AND OVERTOPPING .....	1687
<i>Donald L. Ward, Christopher G. Wibner, Jun Zhang, Billy L. Edge</i>	
Chapter 122	
MODELLING OF WAVE OVERTOPPING OVER BREAKWATER.....	1700
<i>F. Zhuang, C. Chang, J.J. Lee</i>	
Chapter 123	
STRESSES IN TETRAPOD ARMOR UNITS INDUCED BY WAVE ACTION....	1713
<i>Kees d'Angremond, J.W. van der Meer, C.P. van Nes</i>	
Chapter 124	
PORE PRESSURES IN RUBBLE MOUND BREAKWATERS.....	1727
<i>M.B. de Groot, H. Yamazaki, M.R.A. van Gent, Z. Kheyruri</i>	
Chapter 125	
WAVE ACTION ON AND IN PERMEABLE STRUCTURES.....	1739
<i>M.R.A. van Gent, P. Tönjes, H.A.H. Petit, P. Van Den Bosch</i>	
Chapter 126	
PROBABILISTIC CALCULATIONS OF WAVE FORCES ON VERTICAL STRUCTURES.....	1754
<i>J.W. van der Meer, K. d'Angremond, J. Juhl</i>	

## PART IV

Chapter 127	
VELOCITY AND PRESSURE BOUNDARY CONDITIONS FOR FLOW OVER THE PERMEABLE BOUNDARY OF A POROUS MEDIUM.....	1770
<i>Ismail Aydin</i>	
Chapter 128	
PHYSICAL EXPERIMENTS ON THE EFFECTS OF GROINS ON SHORE MORPHOLOGY.....	1782
<i>Peyman Badiei, J. William Kamphuis, David G. Hamilton</i>	
Chapter 129	
LINE-MODELING OF SHOREFACE NOURISHMENT.....	1797
<i>Willem T. Bakker, Nico F. Kersting, Hanz D. Niemeyer</i>	
Chapter 130	
STATISTICAL VARIATIONS IN BEACH PARAMETER CHANGE RATES FOR WALLED & NON-WALLED PROFILES AT SANDBRIDGE, VA.....	1812
<i>John M. Hazelton, David R. Basco, D. Bellomo, G. Williams</i>	
Chapter 131	
A BOTTOM BOUNDARY LAYER SEDIMENT RESPONSE TO WAVE GROUPS .....	1827
<i>J. Lee, S. O'Neil, K. Bedford, R. Van Evra</i>	
Chapter 132	
GEOMORPHOLOGICAL ANALYSIS OF A BEACH AND SANDBAR SYSTEM.....	1837
<i>Chen-Shan Kung, Marcer Stive, Geffery Toms</i>	
Chapter 133	
SUSPENDED SEDIMENT TRANSPORT IN INNER SHELF WATERS DURING EXTREME STORMS.....	1849
<i>O.S. Madsen, T.A. Chisholm, L.D. Wright</i>	
Chapter 134	
SEA BED STABILITY ON A LONG STRAIGHT COAST.....	1865
<i>E. Christensen, R. Deigaard, J. Fredsoe</i>	
Chapter 135	
THE RESPONSE OF GRAVEL BEACHES IN THE PRESENCE OF CONTROL STRUCTURES .....	1880
<i>T.T. Coates, N. Dodd</i>	



Chapter 136	
THE ROLE OF ROLLERS IN SURF ZONE CURRENTS .....	1895
<i>William R. Dally, Daniel A. Osiecki</i>	
Chapter 137	
THREE DIMENSIONAL MORPHOLOGY IN A NARROW WAVE TANK: MEASUREMENTS AND THEORY .....	1906
<i>Robert G. Dean, Tae-Myoung Oh</i>	
Chapter 138	
NUMERICAL SIMULATION OF FINITE AMPLITUDE SHEAR WAVES & SEDIMENT TRANSPORT .....	1919
<i>Rolf Deigaard, Erik Damgaard Christensen, Jesper Svarrer Damgaard, Jørgen Fredsøe</i>	
Chapter 139	
BEACH NOURISHMENT AND DUNE PROTECTION .....	1934
<i>Hans H. Dette, Arved J. Raudkivi</i>	
Chapter 140	
PROFILE CHANGE OF A SHEET FLOW DOMINATED BEACH .....	1946
<i>Mohammad Dibajnia, Takuzo Shimizu, Akira Watanabe</i>	
Chapter 141	
A NONLINEAR SURF BEAT MODEL .....	1961
<i>Zhili Zou, Nicholas Dodd</i>	
Chapter 142	
PIV MEASUREMENTS OF OSCILLATORY FLOW OVER A RIPPLED BED....	1975
<i>H.C. Earnshaw, T. Bruce, C.A. Greated, W.J. Easson</i>	
Chapter 143	
SHEAR INSTABILITY OF LONGSHORE CURRENTS: EFFECTS OF DISSIPATION AND NON-LINEARITY .....	1983
<i>Albert Falqués, Vincente Iranzo, Miquel Caballería</i>	
Chapter 144	
INTERPRETATION OF SHORELINE POSITION FROM AERIAL PHOTOGRAPHS .....	1998
<i>John S. Fisher, Margery F. Overton</i>	

Chapter 145	
SETTLING COLUMNS PARAMETRIC TESTS APPLIED TO COASTAL SEDIMENT CONSOLIDATION.....	2004
<i>Stephane Gallois, Alain Alexis, Pierre Thomas</i>	
Chapter 146	
SEDIMENT-CLOUD BASED MODEL OF SUSPENSION OVER RIPPLE BED DUE TO WAVE ACTION .....	2013
<i>Hitoshi Gotoh, Tetsuro Tsujimoto, Hiroji Nakagawa</i>	
Chapter 147	
WAVE OVERTOPPING AND SEDIMENT TRANSPORT OVER DUNES.....	2028
<i>Mark W. Hancock, Nobuhisa Kobayashi</i>	
Chapter 148	
SEDIMENT TRANSPORT OVER RIPPLES IN WAVES AND CURRENT .....	2043
<i>Gilles Perrier, Erik Asp Hansen, C. Villaret, Rolf Deigaard, Jorgen Fredsøe</i>	
Chapter 149	
IN-SITU DETERMINATION OF THE CRITICAL BED-SHEAR STRESS FOR EROSION OF COHESIVE SEDIMENTS.....	2058
<i>Erik-Jan Houwing, Leo C. van Rijn</i>	
Chapter 150	
CONTROL OF CROSS-SHORE SEDIMENT TRANSPORT BY A DISTORTED RIPPLE MAT.....	2070
<i>Isao Irie, N. Ono, S. Hashimoto, S. Nakamura, K. Murakami</i>	
Chapter 151	
HOW MUCH VELOCITY INFORMATION IS NECESSARY TO PREDICT SEDIMENT SUSPENSION IN THE SURF ZONE? .....	2085
<i>Bruce E. Jaffe, David M. Rubin, Asbury Sallenger, Jr.</i>	
Chapter 152	
BEACH PROFILE SPACING: PRACTICAL GUIDANCE FOR MONITORING NOURISHMENT PROJECTS.....	2100
<i>Timothy W. Kana, Christopher J. Andrassy</i>	
Chapter 153	
WATERTABLE OVERHEIGHT DUE TO WAVE RUNUP ON A SANDY BEACH.....	2115
<i>Hong-Yoon Kang, P. Nielsen, D.J. Hanslow</i>	

Chapter 154	
A MODEL FOR CROSS SHORE SEDIMENT TRANSPORT .....	2125
<i>Irene Katopodi, Nikos Kitou</i>	
Chapter 155	
NUMERICAL MODELLING OF FLOW OVER RIPPLES USING SOLA METHOD.....	2140
<i>Hyoseob Kim, Brian A. O'Connor, Youngbo Shim</i>	
Chapter 156	
SWASH DYNAMICS UNDER OBLIQUELY INCIDENT WAVES .....	2155
<i>Nobuhisa Kobayashi, Entin A. Karjadi</i>	
Chapter 157	
WAVE RUN-UP AND SEA CLIFF EROSION .....	2170
<i>S.-M. Shih, P. Komar, K.J. Tillotson, W.G. McDougal, P. Ruggiero</i>	
Chapter 158	
MEASUREMENT OF PARAMETERS, DIRECTION AND RATE OF BEDFORM MIGRATION .....	2185
<i>Ruben D. Kos'yan, I.S. Podymov</i>	
Chapter 159	
BREACH-GROWTH RESEARCH PROGRAMME AND ITS PLACE IN DAMAGE ASSESSMENT FOR A POLDER.....	2197
<i>Arie W. Kraak, W.T. Bakker, J. van de Graaff, H.J. Steetzel, P.J. Visser</i>	
Chapter 160	
SWASH ZONE WAVE CHARACTERISTICS FROM SUPERTANK .....	2207
<i>David L. Kriebel</i>	
Chapter 161	
MORPHOLOGICAL MONITORING OF A SHOREFACE NOURISHMENT NOURTEC EXPERIMENT AT TERSCHELLING, THE NETHERLANDS.....	2222
<i>Aart Kroon, Piet Hoekstra, Klass Houwman, Gerben Ruessink</i>	
Chapter 162	
NUMERICAL MODEL FOR LONGSHORE CURRENT DISTRIBUTION ON A BAR-TROUGH BEACH .....	2237
<i>Yoshiaki Kuriyama</i>	

Chapter 163	
PREDICTION OF BEACH PROFILE CHANGE AT MESOSCALE UNDER RANDOM WAVES .....	2252
<i>Magnus Larson</i>	
Chapter 164	
A QUASI-3D SURF ZONE MODEL .....	2267
<i>Jung Lyul Lee, Hsiang Wang</i>	
Chapter 165	
QUANTIFICATION OF LONGSHORE TRANSPORT IN THE SURF ZONE ON MACROTIDAL BEACHES .....	2282
<i>Franck Levoy, Olivier Monfort, Helene Rousset, Claude Larssonneur</i>	
Chapter 166	
A THREE DIMENSIONAL MODEL FOR WAVE INDUCED CURRENTS .....	2297
<i>Bin Li, Roger J. Maddrell</i>	
Chapter 167	
INFLUENCE OF OFFSHORE BANKS ON THE ADJACENT COAST .....	2311
<i>N.J. MacDonald, B.A. O'Connor</i>	
Chapter 168	
WAVE RUNUP ON COMPOSITE-SLOPE AND CONCAVE BEACHES .....	2325
<i>Robert H. Mayer, D.L. Kriebel</i>	
Chapter 169	
SIMULATION OF NEARSHORE WAVE CURRENT INTERACTION BY COUPLING A BOUSSINESQ WAVE MODEL WITH A 3D HYDRODYNAMIC MODEL .....	2340
<i>Roberto Mayerle, Andreas Schröter, Werner Zielke</i>	
Chapter 170	
EXPERIMENTAL RESULTS OF WAVE TRANSFORMATION ACROSS A SLOPING BEACH.....	2350
<i>Constantine D. Memos</i>	
Chapter 171	
A RELATIVE INTERCOMPARISON BETWEEN VARIABLE WAVE SHOALING, BREAKING AND TRANSITION ZONE FORMULATIONS .....	2365
<i>G.P. Mocke, F. Smit</i>	

Chapter 172	
ANALYSIS OF COASTAL PROCESSES AT TORONTO ISLANDS.....	2380
<i>R.B. Nairn, R.D. Scott, C.D. Anglin, P.J. Zuzek</i>	
Chapter 173	
STABILITY AND MANAGEMENT OF AN ARTIFICIAL BEACH.....	2395
<i>Naofumi Shiraiishi, Hoiku Ohhama, Taiji Endo,</i> <i>Patricia G. Pena-Santana</i>	
Chapter 174	
SUSPENDED SEDIMENT PARTICLE MOTION IN COASTAL FLOWS.....	2406
<i>Peter Nielsen</i>	
Chapter 175	
LONG-TERM MORPHODYNAMICAL DEVELOPMENT OF THE EAST FRISIAN ISLANDS AND COAST .....	2417
<i>Hanz D. Niemeyer</i>	
Chapter 176	
FIELD OBSERVATION AND NUMERICAL SIMULATION OF BEACH AND DUNE SCARPS.....	2434
<i>Ryuichiro Nishi, Michio Sato, Hsiang Wang</i>	
Chapter 177	
EFFECTS OF CONTROLLED WATER TABLE ON BEACH PROFILE DYNAMICS .....	2449
<i>Tae-Myoung Oh, R.G. Dean</i>	
Chapter 178	
LABORATORY EXPERIMENTS ON 3-D NEARSHORE CURRENTS AND A MODEL WITH MOMENTUM FLUX BY BREAKING WAVES.....	2461
<i>Akio Okayasu, Koji Hara, Tomoya Shibayama</i>	
Chapter 179	
SUSPENDED SEDIMENT CAUSED BY WAVES AND CURRENTS .....	2476
<i>Masanobu Ono, Kyu Han Kim, Toru Sawaragi, Ichiro Deguchi</i>	
Chapter 180	
DEVELOPMENT OF A DUNE EROSION MODEL USING SUPERTANK DATA.....	2488
<i>Margery F. Overton, John S. Fisher, Kyu-Nam Hwang</i>	

Chapter 181	
NUMERICAL MODELLING OF THREE-DIMENSIONAL WAVE-DRIVEN CURRENTS IN THE SURF-ZONE.....	2503
<i>Philippe Péchon, Charles Teisson</i>	
Chapter 182	
SEDIMENT TRANSPORT IN VARIOUS TIME SCALES .....	2513
<i>Zbigniew Pruszek, Ryszard B. Zeidler</i>	
Chapter 183	
SEDIMENT TRANSPORT UNDER (NON)-LINEAR WAVES AND CURRENTS .....	2527
<i>Jan S. Ribberink, Irene Katopodi, Khaled A.H. Ramadan, Ria Koelewijn, Sandro Longo</i>	
Chapter 184	
WAVES AND CURRENTS AT THE EBRO DELTA SURF ZONE: MEASUREMENTS AND MODELLING .....	2542
<i>A. Rodriguez, A. Sánchez-Arcilla, F.R. Collado, V. Gracia, M.G. Coussirat, J. Prieto</i>	
Chapter 185	
A NUMERICAL SIMULATION OF BEACH EVOLUTION BASED ON A NONLINEAR DISPERSIVE WAVE-CURRENT MODEL .....	2557
<i>Shinji Sato, Michael B. Kabiling</i>	
Chapter 186	
AN EXPERIMENTAL STUDY ON BEACH TRANSFORMATION DUE TO WAVES UNDER THE OPERATION OF COASTAL DRAIN SYSTEM.....	2571
<i>Michio Sato, Sadakatsu Hata, Masahiro Fukushima</i>	
Chapter 187	
WAVE BREAKING AND INDUCED NEARSHORE CIRCULATIONS .....	2583
<i>Ole R. Sørensen, Hemming A. Schäffer, Per A Madsen, Rolf Deigaard</i>	
Chapter 188	
ACCURACY AND APPLICABILITY OF THE SPM LONGSHORE TRANSPORT FORMULA.....	2595
<i>J.S. Schoones, A.K. Theron</i>	

Chapter 189	
FIELD VERIFICATION OF A NUMERICAL MODEL OF BEACH TOPOGRAPHY CHANGE DUE TO NEARSHORE CURRENTS, UNDERTOW AND WAVES .....	2610
<i>Takuzo Shimizu, Masahito Tsuru, Akira Watanabe</i>	
Chapter 190	
AN ATTEMPT TO MODEL LONGSHORE SEDIMENT TRANSPORT ON THE CATALONIAN COAST .....	2625
<i>J.P. Sierra, A.I. Presti, A. Sánchez-Arcilla</i>	
Chapter 191	
EROSION AND OVERTOPPING OF A GRASS DIKE LARGE SCALE MODEL TESTS .....	2639
<i>G.M. Smith, J.W.W. Seiffert, J.W. van der Meer</i>	
Chapter 192	
CALCULATION OF TOMBOLO IN SHORELINE NUMERICAL MODEL .....	2653
<i>Kyung Duck Suh, C. Scott Hardaway, Jr.</i>	
Chapter 193	
BEACH IMPROVEMENT SCHEMES IN FALSE BAY .....	2668
<i>D.H. Swart, J.S. Schoonees</i>	
Chapter 194	
BEACH EROSION IN KUTA BEACH, BALI & ITS STABILIZATION .....	2683
<i>Abdul R. Syamsudin, Yoshito Tsuchiya, Takao Yamashita</i>	
Chapter 195	
FUNDAMENTAL CHARACTERISTICS OF A NEW WAVE ABSORBING SYSTEM UTILIZING SAND LIQUEFACTION .....	2698
<i>Shigeo Takahashi, S. Yamamoto, H. Miura</i>	
Chapter 196	
LABORATORY STUDY OF SURF-ZONE TURBULENCE ON A BARRED BEACH .....	2712
<i>Francis C.K. Ting</i>	
Chapter 197	
BEACH EROSION AROUND A SAND SPIT—AN EXAMPLE OF MIHONO-MATSUBARA SAND SPIT .....	2726
<i>Takaaki Uda, Koji Yamamoto</i>	

Chapter 198	
SHORECIRC: A QUASI 3-D NEARSHORE MODEL .....	2741
<i>A.R. Van Dongeren, F.E. Sancho, I.A. Svendsen, U. Putrevu</i>	
Chapter 199	
A MODEL FOR BREACH GROWTH IN SAND-DIKES .....	2755
<i>Paul J. Visser</i>	
Chapter 200	
SCALING EFFECTS ON BEACH RESPONSE PHYSICAL MODEL .....	2770
<i>Xu Wang, Li-Hwa Lin, Hsiang Wang</i>	
Chapter 201	
A NUMERICAL MODEL OF BEACH CHANGE DUE TO SHEET-FLOW .....	2785
<i>Akira Watanabe, Kazuhiko Shiba, Masahiko Isobe</i>	
Chapter 202	
FIELD TESTS OF RADIATION-STRESS ESTIMATORS OF LONGSHORE SEDIMENT-TRANSPORT .....	2799
<i>Thomas E. White</i>	
Chapter 203	
SUSPENDED SEDIMENT CONCENTRATION PROFILES UNDER NON-BREAKING AND BREAKING WAVES .....	2813
<i>Rattanapitikon Winyu, Tomoya Shibayama</i>	
Chapter 204	
MASS TRANSPORT AND ORBITAL VELOCITIES WITH LAGRANGEIAN FRAME OF REFERENCE .....	2828
<i>Stefan Woltering, Karl-Friedrich Daemrich</i>	
Chapter 205	
CROSS-SHORE PROFILE MODELLING UNDER RANDOM WAVES .....	2843
<i>Yongjun Wu, H-H Dette, H. Wang</i>	
Chapter 206	
MULTIPLE BAR FORMATION BY BREAKER-INDUCED VORTICES: A LABORATORY APPROACH .....	2856
<i>Da Ping Zhang, Tsuguo Sunamura</i>	
Chapter 207	
IDENTIFICATION OF SOME RELEVANT PROCESSES IN COASTAL MORPHOLOGICAL MODELLING .....	2871
<i>Hakeem Johnson, Ida Brøker, Julio A. Zyserman</i>	



Chapter 208	
EXPERIMENTAL SHOREFACE NOURISHMENT, TERSCHELLING, (NL) .....	2886
<i>J.P.M. Mulder, J. van de Kreeke, P. van Vessem</i>	

## PART V

Chapter 209	
IMPORTANCE OF PERMEABILITY IN THE SEDIMENTATION CONSOLIDATION PROCESS.....	2902
<i>Alain Alexis, P. Thomas</i>	

Chapter 210	
WAVE-CURRENT INTERACTION WITH MUD BED .....	2913
<i>Nguyen Ngoc An, T. Shibayama</i>	

Chapter 211	
ON RESIDUAL TRANSPORT IN SHALLOW TIDAL BASINS .....	2928
<i>Andrea Balzano</i>	

Chapter 212	
THE EXTENT OF INLET IMPACTS UPON ADJACENT SHORELINES .....	2943
<i>Kevin R. Bodge</i>	

Chapter 213	
THE SPREADING OF DREDGING SPOILS DURING CONSTRUCTION OF THE DENMARK-SWEDEN LINK.....	2958
<i>Ida Brøker, John Johnsen, Morten Lintrup, Anders Jensen, Jacob Steen Møller</i>	

Chapter 214	
EXPERIMENTAL STUDIES ON THE EFFECT OF THE DREDGING ON CHANG-HWA RECLAMATION AREA, TAIWAN .....	2972
<i>Tai-Wen Hsu, Hsien-Kuo Chang</i>	

Chapter 215	
OSCILLATIONS INDUCED BY IRREGULAR WAVES IN HARBOURS .....	2987
<i>C.R. Chou, W.Y. Han</i>	

Chapter 216	
MECHANISM AND ESTIMATION OF SEDIMENTATION IN BANGKOK BAR CHANNEL.....	3002
<i>Ichiro Deguchi, Toru Sawaragi, Masanobu Ono, Sucharit Koontanakulvong</i>	

Chapter 217	
TURBIDITY & SUSPENDED SEDIMENT ASSOCIATED WITH BEACH NOURISHMENT DREDGING .....	3016
<i>Daniel M. Hanes</i>	
Chapter 218	
SOIL MECHANICS OF SHIP BEACHING .....	3030
<i>N.-E. Ottesen Hansen, B.C. Simonsen, M.J. Sterndorff</i>	
Chapter 219	
THE DILUTION PROCESSES OF ALTERNATIVE HORIZONTAL BUOYANT JETS IN WAVE MOTION .....	3045
<i>Hwung-Hweng Hwung, Jih-Ming Chyan, Chen-Yue Chang, Yih-Far Chen</i>	
Chapter 220	
STUDY ON THE BEHAVIORS OF THE COHESIVE SEDIMENT IN THE YANGTZE ESTUARY .....	3060
<i>Xiaochuan Zeng, Yixin Yan, Kai Yen</i>	
Chapter 221	
DISPERSION OF POLLUTION IN A WAVE ENVIRONMENT .....	3071
<i>R. Koole, C. Swan</i>	
Chapter 222	
MODEL OF BIVALVE ON/OFFSHORE MOVEMENT BY WAVES .....	3086
<i>Hisami Kuwahara, Junya Higano</i>	
Chapter 223	
INITIAL GAP IN BREAKOUT OF HALF-BURIED SUBMARINE PIPE DUE TO WAVE ACTION .....	3099
<i>Adrian W.K. Law, M.A. Foda</i>	
Chapter 224	
ANALYTICAL SOLUTION FOR THE WAVE-INDUCED EXCESS PORE-PRESSURE IN A FINITE-THICKNESS SEABED LAYER.....	3111
<i>Waldemar Magda</i>	
Chapter 225	
RESPONSE CHARACTERISTICS OF RIVER MOUTH TOPOGRAPHY IN WIDE TIME SCALE RANGE .....	3126
<i>A. Mano, M. Sawamoto, M. Nagao</i>	

Chapter 226	
HALF-LIFE PERIOD OF SEDIMENTATION—MODEL TEST ON A SCALE 1:1 .....	3139
<i>Helmut Manzenrieder</i>	
Chapter 227	
RISK ASSESSMENT FOR COASTAL AND TIDAL DEFENCE SCHEMES.....	3154
<i>I.C. Meadowcroft, P.H. von Lany, N.W.H. Allsop, D.E. Reeve</i>	
Chapter 228	
WATER OXYGENATION IN THE VICINITY OF COASTAL STRUCTURES DUE TO WAVE BREAKING .....	3167
<i>C.I. Moutzouris, E.I. Daniil</i>	
Chapter 229	
ENVIRONMENTAL ASSESSMENT OF HYPOTHETICAL LARGE-SCALE RECLAMATION IN OSAKA BAY, JAPAN.....	3178
<i>Keiji Nakatsuji, Toshiaki Sueyoshi, Kohji Muraoka</i>	
Chapter 230	
FLOOD AND EROSION CONTROL IN THE CONTEXT OF SEA-LEVEL RISE.....	3193
<i>E. Bart Peerbolte, Herman G. Wind</i>	
Chapter 231	
OFFSHORE BREAKWATERS VERSUS BEACH NOURISHMENTS— A COMPARISON.....	3208
<i>M. Pluijm, J.C. van der Lem, A.W. Kraak, J.H.W. de Ruig</i>	
Chapter 232	
MORPHOLOGICAL MODELLING OF KETA LAGOON CASE .....	3223
<i>J.A. Roelvink, D.J.R. Walstra, Z. Chen</i>	
Chapter 233	
COST-BENEFIT ANALYSIS OF SHORE PROTECTION INVESTMENTS.....	3237
<i>L. Felipe Vila Ruiz, Fernando Bernaldo de Quirós</i>	
Chapter 234	
PARAMETRIZATION FOR CONCEPTUAL MORPHODYNAMIC MODELS OF WADDEN SEA AREAS .....	3251
<i>Ernst Schroeder, R. Goldenbogen, H. Kunz</i>	

Chapter 235	
MUD TRANSPORT AND MUDDY BOTTOM DEFORMATION BY WAVES .....	3266
<i>Daoxian Shen, Masahiko Isobe, Akira Watanabe</i>	
Chapter 236	
WAVE-INDUCED SEDIMENT RESUSPENSION AND MIXING IN SHALLOW WATERS.....	3281
<i>Y. Peter Sheng, X. Chen, E.A. Yassuda</i>	
Chapter 237	
A NUMERICAL MODEL FOR BEACH DEFORMATION AROUND RIVER MOUTH DUE TO WAVES AND CURRENTS.....	3295
<i>Tomoya Shibayama, Akiko Yamada</i>	
Chapter 238	
DEVELOPMENT OF A NUMERICAL SIMULATION METHOD FOR PREDICTING THE SETTLING BEHAVIOR & DEPOSITION CONFIGURATION OF SOIL DUMPED INTO WATERS .....	3305
<i>Kazuki Oda, Takaaki Shigematsu</i>	
Chapter 239	
PLANE DESIGN OF “SPAC”; COUNTERMEASURE AGAINST SEABED SCOUR DUE TO SUBMERGED DISCHARGE AND LARGE WAVES .....	3320
<i>Takao Shimizu, Masaaki Ikeno, Hisayoshi Ujiie, Kazuaki Yamauchi</i>	
Chapter 240	
MODELLING AND ANALYSIS TECHNIQUES TO AID MINING OPERATIONS ON THE NAMIBIAN COASTLINE .....	3335
<i>G.G. Smith, G.P. Mocke, D.H. Swart</i>	
Chapter 241	
ENGINEERING APPROACH TO COASTAL FLOW SLIDES .....	3350
<i>Theo P. Stoutjesdijk, Maarten B. de Groot, Jaap Lindenberg</i>	
Chapter 242	
EROSION OF LAYERED SAND-MUD BEDS IN UNIFORM FLOW.....	3360
<i>Hilde Torfs</i>	
Chapter 243	
STANDING WAVE INDUCED SOIL RESPONSE IN A POROUS SEABED .....	3369
<i>Ching-Piao Tsai, Tsong-Lin Lee</i>	

Chapter 244	
EROSION CONTROL BY CONSIDERING LARGE SCALE COASTAL BEHAVIOR .....	3378
<i>Yoshito Tsuchiya, Takao Yamashita, Tatsuhisa Izumi</i>	
Chapter 245	
SHORELINE EROSION DUE TO OFFSHORE TIN MINING .....	3393
<i>Suphat Vongvisessomjai</i>	
Chapter 246	
BEHAVIORS OF FLUID MUD UNDER OSCILLATORY FLOW .....	3408
<i>Hiroyuki Yamanishi, Tetsuya Kusuda</i>	
Chapter 247	
FORMATION OF HABITATS FOR BIVALVES BY PORT AND HARBOR STRUCTURES .....	3420
<i>Kenji Yano, S. Akeda, Y. Miyamoto, S. Kuwabara</i>	
Chapter 248	
USE OF THREE-DIMENSIONAL HYDRODYNAMICS MODEL FOR TIDAL INLETS STUDIES .....	3432
<i>E.A. Yassuda, Y.P. Sheng</i>	
Chapter 249	
STUDY OF UPWELLING PHENOMENA OF ANOXIC WATER "A-OSHIO" ....	3447
<i>Jong Seong Yoon, Keiji Nakatsuji, Kouji Muraoka</i>	
Chapter 250	
SEA LEVEL RISE AND COAST EVOLUTION IN POLAND .....	3462
<i>Ryszard B. Zeidler</i>	

## PART VI

Chapter 251	
FORMATION OF DYNAMICALLY STABLE SANDY BEACHES ON AMANOHASHIDATE COAST BY SAND BYPASSING .....	3478
<i>Ikuo Chin, Minoru Yamada, Yoshito Tsuchiya</i>	
Chapter 252	
THE RECONSTRUCTION OF FOLLY BEACH .....	3491
<i>Billy L. Edge, Millard Dowd, Robert G. Dean, Patrick Johnson</i>	

Chapter 253	
THE COMPLEMENTARY INTERACTION BETWEEN BEACH NOURISHMENT AND HARBOUR MANAGEMENT: FOUR CASES IN SPAIN .....	3507
<i>Gregorio Gómez-Pina, Jose L. Ramírez</i>	
Chapter 254	
WAVE IMPACTS ON THE EASTERN SCHELDT BARRIER EVALUATION OF 5 YEARS FIELD MEASUREMENTS .....	3522
<i>Leo Klatter, Hans Janssen, Michiel Dijkman</i>	
Chapter 255	
SALINITY & WATER LEVELS IN THE WESER ESTUARY DURING THE LAST HUNDRED YEARS—ANTHROPOGENIC INFLUENCES ON THE COASTAL ENVIRONMENT .....	3533
<i>Hans Kunz</i>	
Chapter 256	
REVIEW OF SOME 30 YEARS BEACH REPLENISHMENT EXPERIENCE AT DUNGENESS NUCLEAR POWER STATION, UK .....	3548
<i>Roger Maddrell, Bill Osmond, Bin Li</i>	
Chapter 257	
PROJECT, WORKS AND MONITORING AT BARCELONA OLYMPIC BEACHES .....	3564
<i>Carlos Peña, Manuel F. Covarsi</i>	
Chapter 258	
SANTA CRISTINA BEACH NOURISHMENT WORKS AND MONITORING PROGRAM .....	3579
<i>Eduardo Toba, G. Gomez-Pina, J. Alvarez</i>	
Chapter 259	
DESIGN & CONSTRUCTION OF AN EXTENDED BERM BREAKWATER AT PORT OF HAINA, DOMINICAN REPUBLIC .....	3594
<i>David W. Yang, Mark H. Lindo, Edward J. Schmeltz, Joaquin Fernandez, Daniel Gomez</i>	
Chapter 260	
REHABILITATION OF THE WEST BREAKWATER— PORT OF SINES .....	3608
<i>Orville T. Magoon, J.R. Weggel, B.L. Edge, E. Mansard, R.W. Whalin, W.F. Baird</i>	

Subject Index .....3615  
Author Index .....3621

## CHAPTER 175

### LONG-TERM MORPHODYNAMICAL DEVELOPMENT OF THE EAST FRISIAN ISLANDS AND COAST

Hanz D. Niemeier<sup>1</sup>

#### Abstract

The morphology of the East Frisian Islands and Coast has experienced enormous changes in the course of the last centuries. The resedimentation of medieval sturm bays has played a dominant role within these morphodynamical processes which could no longer only be credited to the impacts of littoral drift. Reconstructions of former coastal morphology have been used to quantify the long-term development of significant parameters for the tidal basins of the East Frisian Wadden Sea. Additionally also the tidal volumes for situations since 1650 could be determined. On this basis the long-term stability of common empirical relationships was checked.

#### Introduction

The East Frisian Islands and Coast are part of the Frisian Wadden Sea which ranges from the eastern part of the Dutch across the German to the southern part of the Danish North Sea coast (fig. 1) and consist of a chain of seven barrier islands separated by tidal inlets from each other through which the tidal basins with intertidal areas and supratidal salt marshes are filled and emptied during each tidal cycle. The tidal range is about 2,5 m and the yearly mean offshore significant wave height is about 0,7 to 1,0 m. It is therefore a mixed energy tide-dominated coast according to the classification of HAYES [1975]. The littoral drift is predominantly eastward directed.

The East Frisian Islands and Coast have been performed at the end of the holocene transgression [KRÜGER 1911; LÜDERS 1951; STREIF 1990] and have experienced enormous morphological changes since then. Though no detailed information is available for that time firstly a superposition of human impacts on this natural development is expected to have been effective when the mainland coast was closed consecutively against the sea by constructing sea dykes since the beginning of this millenium [HOMEIER 1969]. Later on and particularly for the last 350 years the morphological behaviour of the East Frisian Islands and Coast is well documented by the horizontal position of the morphologically representantive markers tidal low and high water lines, dune foot and border lines of supratidal salt marshes [HOMEIER 1962]. Additionally there is even information with lesser accuracy on certain areas available concerning situations until more than 600 years ago (fig. 2). The migration of tidal inlets and barrier islands

-----  
<sup>1</sup>Coastal Research Station of the Lower Saxonian Central State Board for Ecology  
Fledderweg 25, 26506 Norddeich/East Frisia, Germany



has been superimposed interactively by further large scale human impacts interfering with the natural processes. In the course of the last centuries the two most important ones have were:

1. Artificial acceleration of re sedimentation of the medieval storm surge bays at the mainland coast in respect of land reclamation and afterwards consecutively executed partial enclosures of these areas by dyking.
2. The fixation of the four migrating ones of the six tidal inlets separating the East Frisian barrier islands since the middle of the 18th century in order to protect there developing holiday and health resorts.

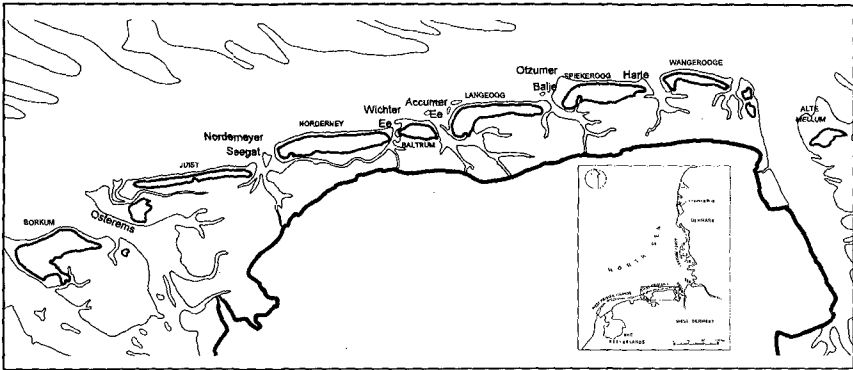
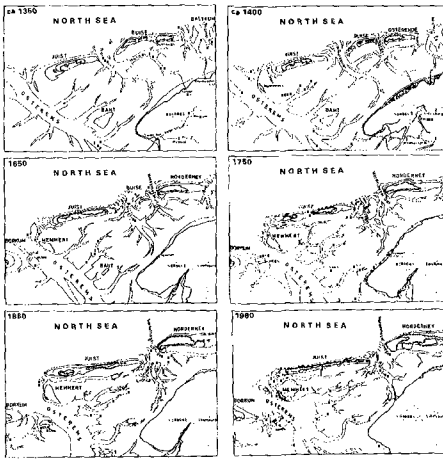


Figure 1. East Frisian Islands and Coast with inserted overview of the North Sea



These large scale morphodynamical processes have mainly taken place in the western and eastern part of the East Frisian Wadden Sea whereas the tidal inlet Accumer Ee and its basin in the central part have remained rather stable in the course of the recent centuries. Beside geological boundary conditions it is also remarkable that in this area no large storm surge bay was ever existent. A detailed knowledge about the background of these developments is of high interest. Not only for improving backward directed process knowledge but also for the development of long-term prognostic tools like empirical morphodynamical models. In order to create a data basis for this purpose the charts containing historical reconstructions of coastal morphology elaborated by HOMEIER [1962] and hydrographic charts have been transferred into a Geographical Information System (GIS) which is used as a database for further evaluation and parametrization.

Figure 2. Reconstruction of the western East Frisian Wadden Sea since 1350 by HOMEIER [1964]

## Extension and enclosure of medieval storm surge bays

### Ley Bay

The Ley Bay ever got its largest extension due to the erosional effects of the catastrophic storm surges of the 14th century and especially due to those of the "First Dyonysis Surge" in 1374 [HOMEIER 1972]. The storm surges in that time were very effective in respect of eroding the flooded areas after dyke failures as their soil consisted predominantly of very erodible peat. Due to that fact the losses of land to the sea were much higher than usual, the extension of the bay did afterwards not fit with the hydrodynamical boundary conditions in order to reestablish a morphodynamical equilibrium. This imbalance caused sedimentation leading to the rise of salt marshes at the borders of the bay supported and accelerated by interfering human reclamation works. These processes changed the system again resulting in further sedimentation [NIEMEYER 1984, 1991b]. The rise of salt marshes allowed a subsequent reclamation and partial enclosures of formerly lost areas (fig. 3). In the course of the centuries the areal extensions of the enclosures decreased until the beginning of this century. But in recent years the advanced tools then available in coastal engineering made even the dyking of intertidal flats possible and not only of those areas which had already reached the stage of supratidal salt marshes. These measures interfered with hydrodynamical-morphological interactions to a much higher extent than the dyking of salt marshes.

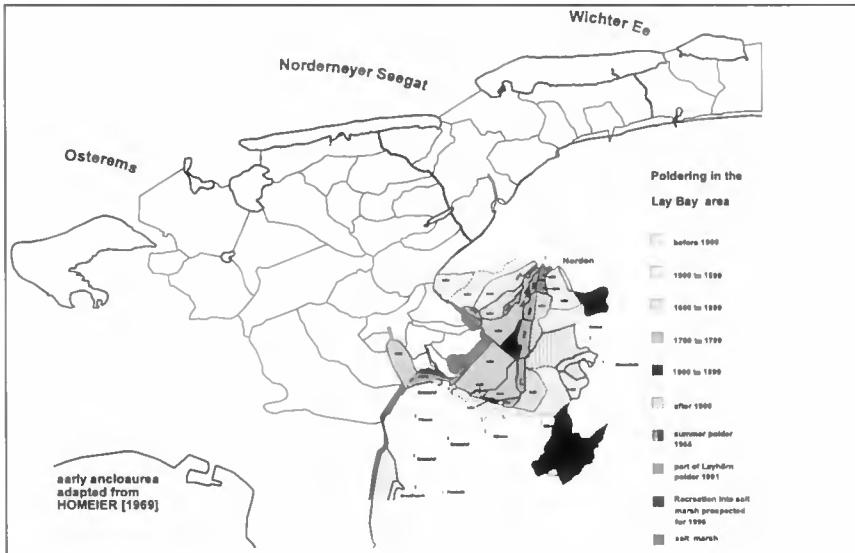


Figure 3. Partial enclosures of the Ley Bay during the last six centuries

### Harle Bay

The Harle Bay already existed at the beginning of dyke construction at the end of the last century. It was silting up and the dyking of growing salt marshes is reported for the 12th and 13th century [HOMEIER 1969, 1979]. In the middle of the 14th century an unknown number of subsequently following storm surges caused the destruction of dyke lines and created erosion in the flooded areas. But the enlarged size of the tidal basin was not in tune with the dynamical equilibrium and in particular the higher intertidal areas silted up due to the absence of waves

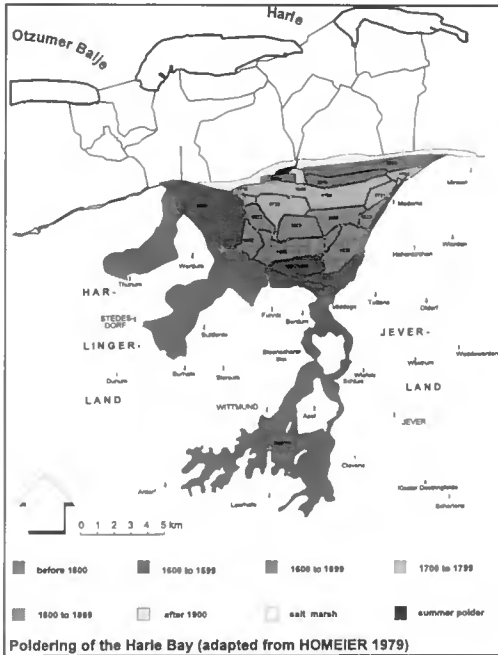


Figure 4. Partial enclosures of the Harle Bay

with sufficient energy to prevent siltation and the subsequent growth of supratidal salt marshes. The nearly continuous silting up occurred since then was followed by partial enclosures of the emerged supratidal salt marshes. More than 50% of the bay area had already been reclaimed at the end of the 16th century and two hundred years later only small remnants of the formerly large Harle Bay existed which mostly were reclaimed until the end of the 19th century. The Harle Bay had disappeared totally and a closed straight coastline was established (fig. 4).

**Morphodynamical impacts of storm surge bay enclosures**  
General remarks

The enclosure of medieval storm surge bays has lead to the following consequences: reduction of basin area, of basin volume, of tidal basin volume and of ebb delta volume in order to provide the basin's requirements for sedimentation. All these changes provoked

additionally changes of local wave climate in the basin leading to a further increase of sedimentation, resulting reduction of tidal volume and again sedimentation until a new equilibrium stage was achieved [NIEMEYER 1991b]. In areas where only small storm surge bays had been created as i. e. g. in the basin of the tidal inlet Accumer Ee in the central part of the East Frisian Wadden Sea (fig. 1) morphodynamical changes during the last centuries have been less dramatic than in those where storm surge bays performed a quantitatively remarkable part of the total basin area.

Western East Frisian Wadden Sea

In comparison to its present total area of about 334 km<sup>2</sup> the basin of the tidal inlet Osterems has experienced a remarkable reduction of about 100 km<sup>2</sup> since the 14th century due to the numerous partial enclosures (fig. 3). Surprisingly the total basin area has nearly remained unchanged since 1650 (tab. 1) whereas more than 40 km<sup>2</sup> have been reclaimed in the Ley Bay during that period (fig. 5). This development and the morphodynamical processes in the remaining parts of the offshore areas must have substantially interacted. A comparison of the situations of 1650 and 1960 using the historical maps evaluated by HOMEIER [1962] makes evident that the basin of the tidal inlet Osterems has compensated nearly all its losses by an eastward extension of its watershed against the basin of the tidal inlet Norderneyer Seegat which can probably be explained by the remarkably larger tidal volume of the Osterems tidal basin. This process cannot be explained due to the direction of the littoral drift, because the migration of the tidal inlet Osterems [HOMEIER & LUCK 1977; STEPHAN 1994] is counterdirectional. This development is in tune with the increase of relative area and respectively tidal volume in the

eastern part of its basin which performs nowadays its largest subsystem. These facts indicate strongly that the morphodynamical processes due to the migration of the tidal inlet Osterems (fig. 5) could be credited to the silting-up and consecutively reclamation by partial enclosures of the Ley Bay.

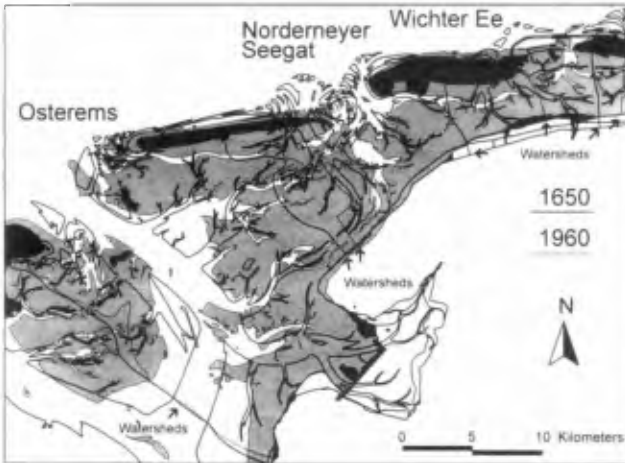


Figure 5. Morphological development of the tidal inlets Osterems, Norderneyer Seegat, Wichter Ee, of their basins and watersheds between 1650 and 1960 (reconstruction from HOMEIER [1962])

Indirectly also the eastern shift of the watershed between the Osterems and Norderneyer Seegat basins is remarkably influenced by that and not only a consequence of littoral drift. Even the migration of the tidal inlet Norderneyer Seegat must at least partly be regarded as a consequence of the consecutive reduction of the Ley Bay superimposing here littoral drift effects. This statement is contradictory to the qualitative migration models of LUCK [1977] for tidal inlets of the Norderneyer Seegat and Harle type basing on reconstructions of HOMEIER [1962, 1964] and being causally supplemented by NIEMEYER [1990] considering hydrodynamical impacts on ebb deltas and barrier islands. The explanation of migration processes by LUCK [1977] is still very useful in order to provide insight into processes which happened in the past but their cyclic character is doubtful due to regarding littoral drift as steering force of inlet migration. Considering the impact created by the areal reduction of the Ley Bay on primarily the shift of watershed between Osterems and Norderneyer Seegat basin and secondarily on the migration of the tidal inlet Norderneyer Seegat itself a continuation of inlet migration at the same scale could -even in the case of no human interference- not be expected because after the large areal reduction of the Ley Bay an important steering force has nearly disappeared.

The consequences of the migration of the Nordemeyer Seegat for its ebb delta and respectively for the sediment balance on the beaches on the island of Norderney have been described as well as the measures to preserve the coast line and to combat erosion there [LUCK 1977; NIEMEYER 1990, 1991a; KUNZ 1991]. Moreover inlet migration and subsequent morphological changes have also had remarkable impacts on the adjacent mainland coastline [NIEMEYER 1990]: The gradual disappearance of the remnants of the former island of Buise and the reunification of the two inlets to a wider channel with wider spread swash bars in its ebb delta rendered as well possible the impact of higher wave energy up to the opposite mainland coast as the accompanying extension of sublittoral areas between the inlet and the coast (fig. 6). In 1650 there was a broad stretch of supratidal salt marshes in front of the mainland dykes. In 1750 the

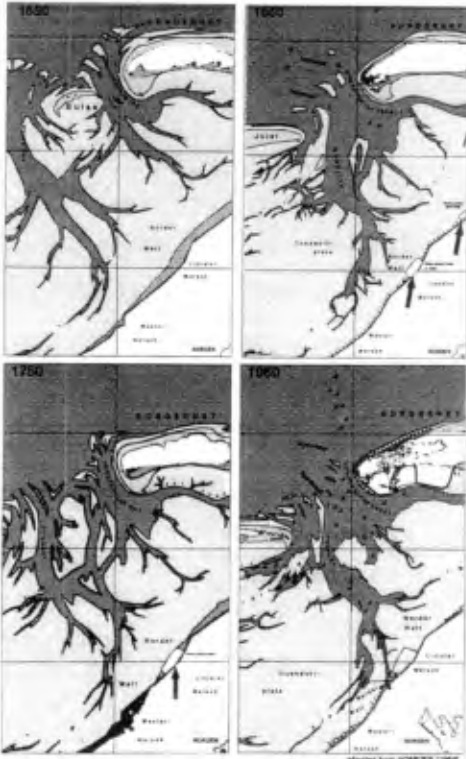


Figure 6. Impact of tidal inlet migration between Juist and Norderney in the period from 1650 to 1860 on the adjacent mainland coast (reconstruction from HOMEIER [1962]) → polders

polder and of a second one which had been erected at the beginning of the 19th century. Both were flooded during the storm surge of 1825 and had afterwards to be abandoned. Starting about 1860 the tidal inlet was successfully fixed by the construction of groynes ranging across the eastern slope of its deep channel.

The areal losses of the Osterems tidal basin have been compensated by an eastward shift of its watershed at the cost of that one of the Nordermeyer Seegat. The same process repeated itself in the interaction of the basins of the Nordermeyer Seegat and of the Wichter Ee (fig. 5): Again the basin with the larger volume shifted the watershed between both remarkably into eastern direction between 1650 and 1860. The western shore of the island of Baltrum experienced in the same period enormous erosion and moved more than 4 km eastward. Since the eastern watershed of the Wichter Ee tidal basin did not shift to the same extent into eastern direction as the western one the basin area was enormously reduced (tab. 1). The differences in the eastward shift of the western and the eastern watershed of the Wichter Ee tidal basin indicate also the impact of the partial enclosures in the Ley Bay on the morphodynamical processes of the tidal inlets and basins in its eastern neighbourhood.

salt marshes in front of the mainland dyke of the Westermarsch had disappeared and a coastline retreat had become necessary after the dyke breaches during the storm surge of 1717. On the one hand the shadow effect of the remnants of the former island of Buisse was no longer effective. On the other had the migration of the inlet channels and of their tributaries led to the superposition of wave systems entering via Buissegat and Norderneyer Gat from the North Sea into that coastal area. Easter of this area the salt marshes in front of the dyke of the Linteler Marsch must have been sufficiently stable in order to encourage people to build a polder. In 1860 the inlets Buissegat and Norderneyer Gat merged to a one-inlet-system called Nordermeyer Seegat. The consequences are primarily a less pronounced ebb delta with smaller shallows being spread wider. The higher concentration of tidal energy effects also a relative increase of sublittoral areas in the basin close to the inlet. Secondly this allows in tune with the wider inlet the input of higher wave energy into the basin upto the mainland coast. Particularly the eastern part of the regarded area has lost shelter due to the morphological changes of the ebb delta and the inlet. The resulting effect is the total disappearance of salt marshes there and as well the destruction of the 1750 already existing

### Eastern East Frisian Wadden Sea

Another example of subsequent consequences of the enclosure of a medieval storm surge bay becomes evident regarding the tremendous relative reduction of the basin area of the tidal inlet Harle since the middle of the 14th century due to the land reclamation in the area of the former Harle Bay leading finally to its total enclosure. The reduction of basin area and corresponding tidal volume initialized consequently as well a decrease of cross-sectional area and width of the tidal inlet as of the seaward extension and volume of the ebb delta (fig. 7). This process was accompanied by an eastward migration of the tidal inlet Harle, an erosion and retreat of the eastern shore of the island of Wangeroog, a remarkable eastward extension of the island of Spiekeroog and a corresponding shift of the watershed between the tidal basins of the Otzumer Balje and Harle, whereas the eastern watershed of the Harle tidal basin did not move remarkably within the same period. A comparable eastward shift of the latter one was probably impossible because the neighbouring Jade estuary with its much higher tidal volume and resulting kinetic energy hampered such a reaction. Since also the watershed between the basins of the Accumer Ee and Otzumer Balje has migrated easterly to a much lesser extent than that one between the Otzumer Balje and the Harle, the basin area of the latter one experiences a large reduction while the Otzumer Balje basin's area increases significantly. Correspondingly the island of Spiekeroog enlengthened by more than 4 km or more than 80 % (fig. 7).

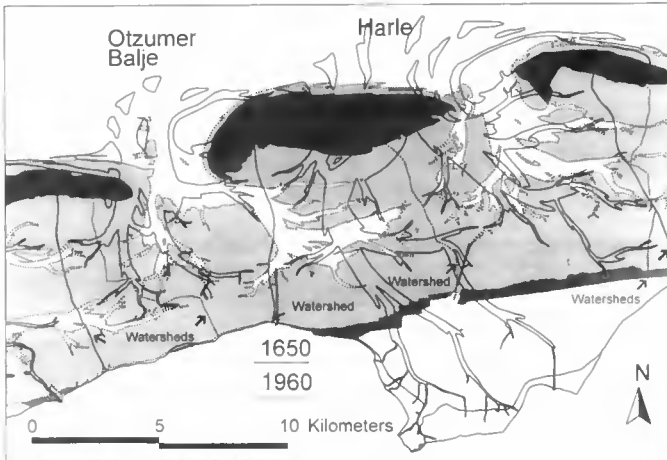


Figure 7. Morphological development of the tidal inlets Otzumer Balje and Harle, of their basins and watersheds between 1650 and 1960 (reconstruction from HOMEIER [1962])

This differences in inlet, ebb delta, island and migration are not explainable by littoral drift though not counterdirectional. But it is evident that the reduction of area and tidal volume of the Harle basin is intensively steered by the silting up of the Harle Bay. Therefore this must be regarded as the major steering impact for the enormous morphodynamical changes in this area.

#### **Quantittative change of characteristic basin parameters**

##### Total basin areas $A_b$

The total area of the tidal basins in the East Frisian Wadden Sea experienced a reduction of more than 13 % between 1650 and 1860 and afterwards fluctuated around a value of 85 % of the 1650 existing area (fig.8, tab. 1). The losses must mainly be credited to the reduction of the

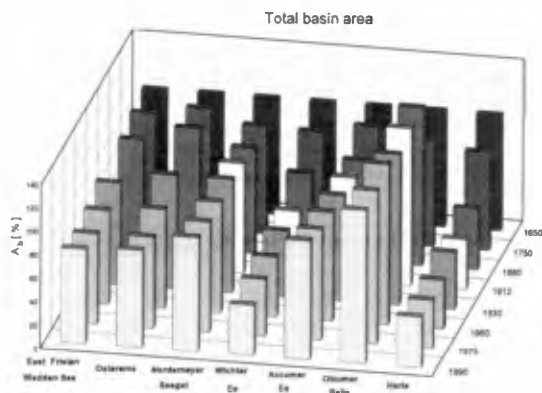


Figure 8. Relative development of total basin areas  $A_b$  (in percentages) in the East Frisian Wadden Sea

storm surge bays, particularly to that of Ley and Harle Bay with an reclaimed area of more than 80 km<sup>2</sup> during that period. Corresponding to the already described morphodynamical development of the western East Frisian Wadden Sea the basin areas of the Osterems and of the Norderneyer Seegat experienced maximal losses of about 10 % being later reduced to about 5 % whereas the basin area of the Wichter Ee was reduced by more than 55 % (fig. 8, tab. 1). The total reduction of the three basin areas is some what larger than the corresponding reduction of the Ley Bay between 1650 and

1960, but this could probably be explained by a phase shift of morphodynamical adaption to former silting up of bay areas.

		1650	1750	1860	1912	1930	1960	1975	1990
East Frisian Wadden Sea	$A_b$ [10 <sup>6</sup> ·m <sup>2</sup> ]	835,00	806,37	755,54		723,83	666,28	637,72	669,54
	$A_b$ [%]	100,00	96,57	90,48		100,00	79,79	76,37	80,18
Osterems		358,32	372,76	371,70		348,26	301,20	276,52	296,22
		100,00	104,03	103,73		97,19	84,06	77,17	82,67
Norderneyer Seegat		109,83	101,79	99,31	103,44	100,00	103,28	102,70	106,47
		100,00	92,67	90,48	94,18	96,96	94,04	93,51	96,94
Wichter Ee		53,93	49,16	38,93	30,27	51,10	27,20	25,93	23,09
		100,00	91,17	72,20	56,13	55,82	56,13	100,00	42,82
Accumer Ee		100,21	99,69	87,01	88,88	90,20	92,25	94,30	101,54
		100,00	99,47	88,88	88,69	90,01	92,05	94,10	101,32
Otzumer Balje		56,90	51,29	77,53	76,82	73,50	78,17	74,57	74,47
		100,00	90,14	136,25	135,00	129,17	137,38	131,04	130,87
Harle		155,80	131,68	81,06	66,37	75,27	64,18	63,70	67,75
		100,00	84,52	52,03	42,60	48,31	41,20	40,89	43,49

Tab. 1 Total basin areas 1650 - 1990

The basin area of the Accumer Ee has remained in the same order of magnitude independently from the enormous morphodynamical developments both in the western and eastern neighbourhood of that area. In the eastern East Frisian Wadden Sea the tidal basin area of the Otzumer Balje increased by about 30 % between 1650 and 1960. This increase was compensated by losses of basin area of the Harle of more than 45 % (fig.8, tab. 1). The total loss of area for both basins is also higher than the correspondingly reclaimed areas in the Harle Bay. But here also the same explanation fits as for the western part of the East Frisian Wadden Sea. The area of partial enclosures was until the end of the 19th century only an indirect measure of long term silting up, because in that time dykes were only built on supratidal salt

marshes which had been silted up earlier. In connection with the phase shift of morphodynamical adaption this quantitative differences must not necessarily be inconsistent with the basic idea. Moreover the phase shift of morphodynamical adaption of the seaward basin area to bay reduction becomes i. e. g. evident by the response of the Harle basin with a remarkable areal decrease until 1912 (fig. 8, tab. 1) whereas the most partial enclosures had already been carried out at the end of the 18th century (fig. 4).

Sublittoral and Intertidal basin areas  $A_{sl}$  and  $A_i$

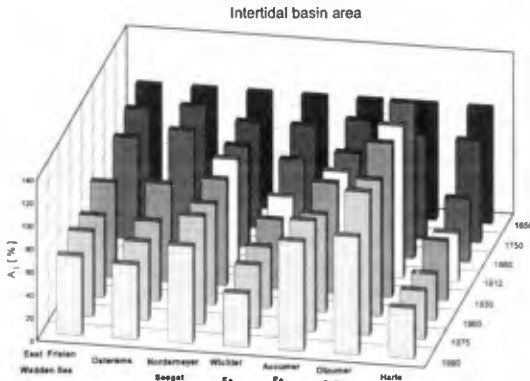


Figure 9. Relative development of intertidal basin areas  $A_i$  (in percentages) in the East Frisian Wadden Sea

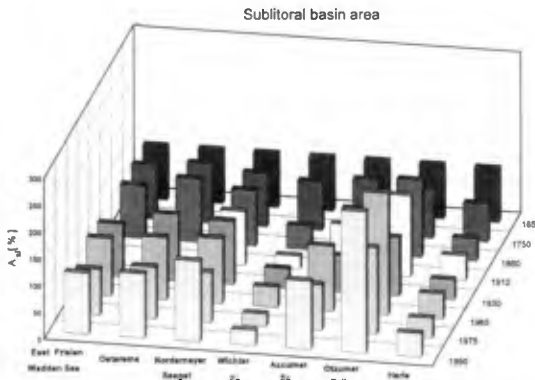


Figure 10. Relative development of sublittoral basin areas  $A_{sl}$  (in percentages) in the East Frisian Wadden Sea

The intertidal areas of the East Frisian Wadden Sea have both absolutely and relatively much more decreased (fig. 9, tab. 2) than the total basin areas (fig. 8, tab. 1). Correspondingly the sublittoral areas have as well absolutely as relatively increased (fig. 10, tab. 3). But this tendency is not uniform for all tidal basins: It is valid for those ones with as a small reduced total area like Osterems and Nordermeyer Seegat, a nearly constant one like Accumer Ee or even enlarged one like Otzumer Balje. Contradictory in those basins which total area experienced reduction like those ones of the Wichter Ee and the Harle the tendency is different. In the Harle basin both intertidal and sublittoral areas have experienced nearly the same amount of relative reduction whereas in the Wichter Ee basin the sublittoral areas have been relatively more reduced than the intertidal ones (fig. 9, tab. 2; fig. 10, tab. 3). In total the tendency of reduction for the intertidal areas being evident until 1960 has been substituted by a fluctuation of less than 3 % since then (fig. 9, tab. 2) which is generally in tune with the development of the total basin areas (fig. 8, tab. 1).

Contradictory the until 1930 rather stable figures for the sublittoral basin areas tend to fluctuate more significantly since then (fig. 10, tab. 3). Partly this effect might also be caused by changes in the seaward boundary of the basins for the different surveys due to the chosen determination of the seaward inlet cross-section for computations.



		1650	1750	1860	1912	1930	1960	1975	1990
East Frisian Wadden Sea	$A_i [10^6 \cdot m^2]$	623,35	596,07	548,41		515,86	439,63	458,02	428,60
	$A_i [\%]$	100,00	95,02	87,98		82,76	70,53	73,48	68,76
Osterems		242,28	245,48	235,76		205,60	166,85	164,30	156,81
		100,00	101,32	97,01		84,86	68,87	67,81	64,72
Norderneyer Seegat		84,86	80,95	77,54	82,35	81,65	77,65	82,90	74,61
		100,00	90,27	87,43	92,85	92,07	80,95	93,47	84,13
Wichter Ee		43,90	40,15	30,52	27,87	26,48	23,40	23,82	20,29
		100,00	91,45	78,64	63,48	60,32	53,31	54,26	46,22
Accumer Ee		80,52	80,95	70,88	71,30	77,00	68,32	80,95	76,34
		100,00	99,29	88,03	88,55	95,63	84,86	96,32	94,81
Otzumer Balje		46,86	42,19	63,15	61,70	62,60	55,39	58,40	47,96
		100,00	90,02	134,76	131,66	133,58	118,20	124,61	102,34
Harle		121,10	107,36	66,55	50,57	62,53	48,01	51,04	52,59
		100,00	88,66	54,96	41,76	51,63	39,64	42,15	43,43

Tab. 2: Intertidal basin basin areas 1650 - 1990

		1650	1750	1860	1912	1930	1960	1975	1990
East Frisian Wadden Sea	$A_{sl} [10^6 \cdot m^2]$	211,63	210,29	207,13		207,97	226,65	179,92	240,93
	$A_{sl} [\%]$	100,00	99,37	97,87		98,27	107,10	85,02	113,84
Osterems		116,04	127,28	135,94		142,66	134,35	112,22	139,41
		100,00	109,69	117,15		122,94	115,78	96,71	120,14
Norderneyer Seegat		21,14	28,94	21,77	21,09	24,85	25,64	19,80	31,86
		100,00	98,54	102,96	99,75	117,52	121,25	93,65	150,68
Wichter Ee		10,02	9,02	4,41	2,40	3,62	3,79	2,33	2,80
		100,00	89,94	44,00	23,94	36,12	37,84	23,25	27,94
Accumer Ee		19,69	19,74	16,13	17,58	13,20	23,93	19,74	25,20
		100,00	100,23	81,92	89,28	67,01	121,50	85,03	127,95
Otzumer Balje		10,04	9,10	14,37	15,12	10,90	22,77	16,17	26,51
		100,00	90,70	143,20	150,62	108,59	226,90	161,08	264,07
Harle		34,70	24,32	14,50	15,80	12,74	16,17	12,66	15,16
		100,00	70,10	41,79	45,55	36,73	46,62	36,49	43,69

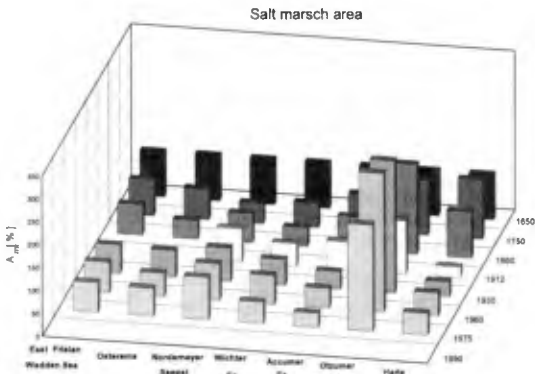
Tab. 3: Sublittoral basin areas 1650 - 1990

### Supratidal salt marsh areas $A_{sm}$

The interactions of hydro- and morphodynamics in the storm surge bays created favourable boundary conditions for the growth of supratidal salt marshes as described before. But these were more and more dyked by subsequent partial enclosures. The deceleration of silting-up due to the reduction of the bays' oversize effected primarily also a deceleration of salt marsh (fig. 3 + 4). Though only insufficient data are available for the time before 1650 the areal development of salt marshes from then still reflects that process (fig. 11, tab. 4): The total area of supratidal salt marshes in the East Frisian Wadden Sea has been reduced from 1650 to 1750 by about 20 % and then again until 1860 by another 12 %. The decrease between 1860 and 1930 has again decelerated to less than 5 % even followed by an increase of nearly 4 % until 1960. The subsequent reduction of about 5 % until 1975 has growth and secondarily in tune with partial enclosures a reduction of existing salt marsh areas been a consequence of the

enclosures of salt marshes by construction of new dykes due to the guidelines for coastal safety established after the catastrophic storm surge of 1962 seawardly of the old ones.

Regarding the tidal basins separately the developments do not reflect the same uniform tendency (fig. 11, tab. 4): The Osterems tidal basin has lost nearly 60 % of its supratidal salt marsh areas between 1650 and 1860, particularly due to the partial enclosures in the Ley Bay. But it regained about until 1975 about 20 %, particularly to salt marsh growth in the Ley Bay in spite of executed partial enclosures in the same period. The initial losses of salt marsh areas in the tidal basin of the Norderneyer Seegat have already been explained as a consequence of inlet migration and changes of local wave climate with a decrease of about 55 % from 1650 to 1750. But already between 1750 and 1860 the continuous losses (fig. 6) were overcompensated by salt marsh growth in other areas of the basin. Since then salt marshes areas have increased until 1975. The losses of supratidal salt marsh areas in the tidal basin of the Wichter Ee must



particularly be regarded as a consequence of the enormous reduction of its total basin area which is also evident for the changes between 1960 and 1975. The pursued reduction of salt marshes in the tidal basin of the Accumer Ee since 1650 must be primarily credited to the seaward movement of dyke lines whereas the continuous growth of salt marsh areas in the tidal basin of the Oztumer Balje is particularly a consequence of the described extension of its total basin area since 1650.

Figure 11. Relative development of salt marsh basin areas  $A_m$  (in percentages) in the East Frisian Wadden Sea

		1650	1750	1860	1912	1930	1960	1975
East Frisian Wadden Sea	$A_m [10^6 \text{ m}^2]$	45,59	36,24	30,60		86,90	30,26	29,22
	$A_m [\%]$	100,00	79,49	67,12		62,51	66,37	64,09
Osterems		16,96	11,47	6,82		9,93	8,65	10,23
		100,00	67,63	40,21		58,55	51,00	60,32
Norderneyer Seegat		5,85	2,61	3,70	4,06	4,23	4,06	5,36
		100,00	44,69	63,34	2,70	72,72	79,53	92,02
Wichter Ee		5,05	2,78	2,78	2,52	2,78	3,23	2,11
		100,00	53,95	41,71	48,88	55,56	62,74	46,84
Accumer Ee		6,74	5,05	4,90	4,06	2,54	2,52	2,11
		100,00	80,98	72,72	60,22	37,63	43,31	31,28
Oztumer Balje		2,10	2,52	4,14	2,42	6,06	6,37	4,87
		100,00	120,50	197,44	115,44	289,27	303,87	231,90
Harle		8,80	11,40	8,89	2,01	2,88	4,45	4,22
		100,00	129,57	101,09	22,80	32,69	50,58	48,01

Tab. 4: Salt marsh areas 1650 - 1975

The reduction after 1960 is an effect of the dyking of salt marshes. Between 1750 and 1912 salt marsh areas in the tidal basin of the Harle have as well decreased as the total basin area due to re-sedimentation and partial enclosures of the Harle Bay. Until 1960 then a certain growth appeared in tune with the stabilization of the tidal basin which only experienced a slight reduction after 1960 due to dyking of salt marshes.

### Evaluation of tidal volumes

The parametrization of Wadden Sea areas in the framework of the project WADE was carried out in order to establish empirical relationships between these parameters describing morphodynamical equilibrium conditions. A parametrization of morphological parameters like areas must be sufficient for that purpose, the evaluation of hydrodynamical parameters is additionally necessary for reaching the aim. The most common hydrodynamical parameter used in empirical morphodynamical relationships is the tidal volume. The evaluation of tidal volumes for defined areas is no problem if detailed surveys or maps are available and the representative tidal high and low water peaks are known. But in the case of the reconstructed historical coastal morphology of 1650, 1750 and 1860 by HOMEIER [1962] there are only the contour lines of mean tidal high and low water and the border lines of the supratidal salt marshes available. Furthermore measurements of tidal water levels providing reliable data have been carried out in the East Frisian Wadden Sea since the end of the 19th century (fig. 14). Therefore the evaluation of tidal volumes for these dates requires extra efforts.

The substitution of complex tidal basin morphology by only mean high and low water contour lines has been exercised by WALTHER [1972] in order to avoid enormous computational efforts without the aid of modern computers:

$$V_T = TR \cdot (A_b + A_{sl}) / 2$$

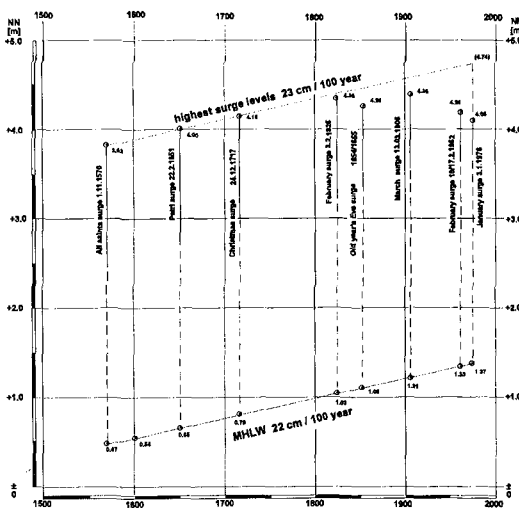


Figure 12. Reconstructed historical mean high tide and storm surge water levels and long-term trends, island of Wangeroog, tidal inlet Harle [LÜDERS 1977]

Since there is nothing reported about the accuracy of this method a calibration test for recent data sets was carried out with the data of all six East Frisian tidal basins from the surveys of 1960, 1975 and 1990. Surprisingly the deviation from data being evaluated with the aid of a GIS was on the average about 6 % (fig. 12) which is in the same or even in a lower order of magnitude as the measuring accuracy of data from hydrographic surveys. Based on these results the method of WALTHER [1972] is a suitable tool for the evaluation of tidal volumes for the situations of 1650, 1750 and 1860 for the reconstructed coastal morphology. In order to keep the data comparable the tidal volumes for the surveys since 1912 were also determined by the same method.

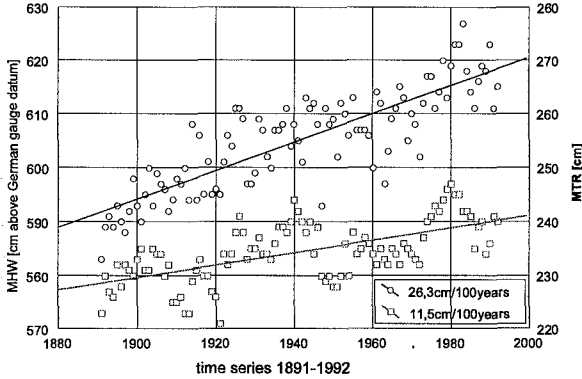


Figure 13. Yearly mean high water levels and tidal ranges since 1896 and corresponding mean trends, island of Norderney, tidal inlet Norderneyer Seegat

Beside the before mentioned data of tidal water levels there are also reconstruction of historical mean higher water and storm surge levels available. A very valuable data set has been elaborated by LÜDERS [1977] for the island of Wangerooge at the shore of the tidal inlet Harle (fig. 1) based on historical levellings being transferred to present datum and metric scale (fig. 13). These long-term data set has nearly the same rising velocity as that one being measured in the course of the last 100 years at the tidal gauge at the island of Norderney in

the tidal inlet Norderneyer Seegat (fig. 1 + 14). The measured data make also a parallel increase of tidal range with rising high water levels evident (fig. 14). Referring to the documented rise of high water levels since 1570 it is reasonable that the tidal range has increased since then by nearly the same order of magnitude as for the last century. Based on this assumption the tidal volumes for the morphological situations of 1650, 1750 and 1860 have been evaluated by taking into account an increase of tidal range between 1650 and 1900 of 10 cm per century (fig. 15, tab 5). This figure is used in order to consider the long-term tendency of tidal boundary conditions of the morphodynamical development in the investigation area. The evaluated tidal volumes are quantitative not very sensitive against a possible inaccuracy of  $\pm 5$  cm/century, the fluctuation of the tidal volumes is therefore less than 2,5 %.

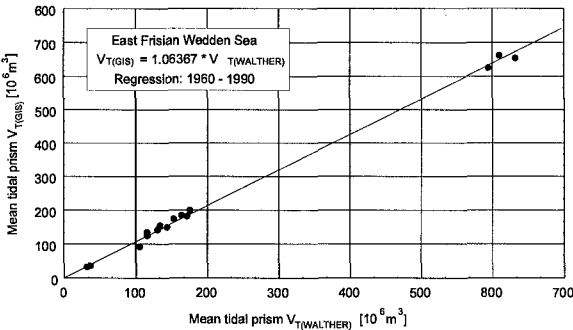


Figure 14. Comparison of tidal volumes computed with a GIS from detailed morphological maps and evaluated by the method of WALTHER [1972]

The tidal volumes of the tidal basins in the East Frisian Wadden Sea have in total remained nearly constant over the regarding the long-term development. The increase of tidal range measured since the end of the 19th century (fig.14) and expected to have also occurred with a similar coincidence to the rise

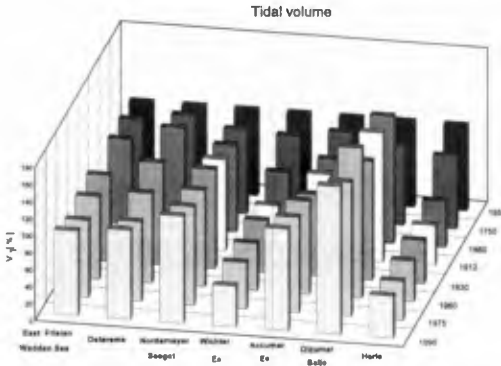


Figure 15. Relative development of tidal volumes (in percentages) of the tidal basins in the East Frisian Wadden Sea

of mean tidal high water since the 16th century (fig. 13) has compensated the reduction of basin areas. For the midterm development of the last decades with nearly stable total basin areas the tidal volume has not experienced a remarkable increase whereas the tidal range has also increased during this period (fig. 14); for 1975 even a significant reduction occurred (fig. 15, tab. 5) which can partly be explained by the reduction of the total basin areas (fig. 8, tab.1). According to the reduction of total areas the

		1650	1750	1960	1912	1930	1960	1975	1990
East Frisian Wadden Sea	$V_T [10^6 \text{ m}^3]$	1135,35	1149,22	1131,64		1141,33	1105,40	1032,77	1133,23
	$V_T [\%]$	100,0	101,2	99,07		100,0	97,36	90,97	99,81
Osterems		498,08	550,04	583,79		594,01	524,83	466,48	524,93
		100,0	110,4	117,2		119,5	105,3	93,66	105,3
Norderneyer Seegat		134,25	131,82	136,22	142,58	156,30	152,12	155,58	169,45
		100,0	98,19	101,4	106,2	110,4	113,3	115,8	126,2
Wichter Ee		65,55	62,54	48,76	37,40	40,13	36,57	35,89	31,72
		100,0	95,54	74,39	57,06	61,22	55,79	54,75	48,39
Accumer Ee		131,90	137,34	123,78	129,35	126,66	145,22	148,25	158,42
		100,0	104,1	93,84	98,07	96,03	110,4	112,4	120,1
Oztumer Balje		76,98	72,48	114,88	116,30	107,61	135,77	121,58	134,29
		100,0	94,15	149,2	151,0	139,7	176,3	157,9	174,4
Harle		228,59	195,01	124,22	108,06	116,62	110,89	104,99	114,41
		100,000	85,31	54,34	47,27	51,02	48,51	45,93	50,05

Tab. 5: Tidal volumes of the East Frisian Wadden Sea tidal basins 1650 - 1990

tidal volumes of the Wichter Ee and Harle have decreased significantly. Correspondingly the tidal volume of the Oztumer Balje has increased overproportional in respect of other tidal basins. The Accumer Ee has in 1990 a tidal volume which is 20 % higher than 1650, whereas the total basin areas for both dates are nearly constant. The tidal volume of the Osterems has experienced remarkable fluctuation which are generally in tune with the development of its basin areas. That one of the Norderneyer Seegat has generally increased. The fairly reduction of its basin areas must have been compensated partly by the increase of tidal range. Furthermore the shape of the basin and the relation of intertidal and sublittoral areas might have been of importance.

Long term stability of empirical relations

The morphological changes in the East Frisian Wadden Sea [HOMEIER 1962, LUCK 1977] has decelerated enormously in the course since the middle of the last century and particularly

since the beginning of this one. The fixing of four of the six inlets since the beginning of this century and particularly the coincidently nearly finished re-sedimentation and land reclamation in the areas of the medieval storm surge bays has effected that development. Therefore morphodynamical changes in the East Frisian Wadden Sea occur not only self-evidently on much lower time scales but also on smaller length scales leading to a morphodynamical quasi-equilibrium, which in the long run is expected to be only temporarily. But nowadays a mid-term dynamical equilibrium could be assumed which is expressed by a number of well-established semi-empirical relationships being evaluated on a data basis with sufficient density for that purpose. That method for a functional parametrization of morphodynamical processes has proved as a success for coastal research and for coastal engineering planning since decades [O'BRIEN 1931; WALTHER 1972; EYSINK 1979, 1991; NIEMEYER 1991]. One of the important relationships describing a morphodynamical equilibrium is that one between total basin area and tidal volume which has been introduced by EYSINK [1979] and was used in the framework of the Dutch coastal defense study as a tool for the estimation of the impacts of an accelerated relative sea-level rise.

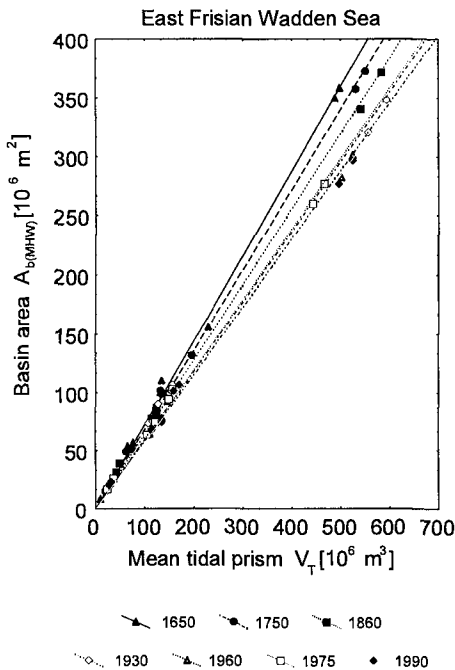


Figure 16. Correlation of total basin areas  $A_b$  and tidal volumes  $V_T$  since 1650

In order to get a deeper insight into those documented long-term morphodynamical processes occurring at the East Frisian coast since 1650 these relationship has also been adapted to the evaluated parameters being available for all situations from 1650 to 1990 beside that one of 1912 for which not a complete data set was available. Though the incorporated assumption of a dynamical equilibrium could not be assumed as valid for the situations between 1650 and 1860 the relation e. g. between tidal volumes and intake areas of the basins are for all situations rather strict (fig. 16). In respect of the experience gained from recent data [EYSINK 1979, 1991] this result is not trivial, because these data sets incorporate also a variation in tidal range due to its regional differences. Looking at the data sets from 1960, 1975 and 1990 including also the sub-systems of the tidal basins for the same parametrization for the East Frisian Wadden Sea this effect is evident only for the larger values of 1990 (fig. 17). A first explanation of this discrepancy is the only use

of data for mid-term developments: As tidal ranges varies to a much lesser extent than for the long-term time scale, statistical scattering is of the same or even bigger order of magnitude than the structural differences due to tidal range variation.

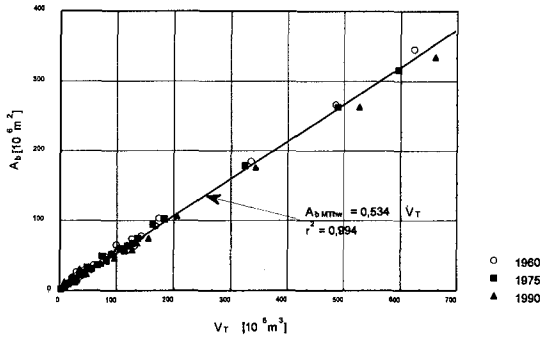


Figure 17. Correlation of basin areas and tidal volumes for the tidal basins and subsystems in the East Frisian Wadden Sea (surveys 1960, 1975, 1990).

Further emphasis will be laid on finding a reliable explanation and detecting the mechanism steering that process. The solution to this problem is of high importance because these relations provide the basis for conceptual or empirical model like the Box-model of VAN DONGEREN & DE VRIEND [1994] being up to now the only promising tool for morphodynamical modelling of future mid- and long-term development. A successful treatment will therefore deliver a valuable basis not only for current problems with structural erosion but also for the foreca-

sting of prospected long-term morphodynamical processes due to changing boundary conditions like an expected acceleration of relative sea-level rise.

An obvious explanation would be a change of hydrodynamical boundary condition. Considering that possibility the changes of tidal range over the time were taken into account though no measured data before 1891 were taken into consideration and the figures for 1860, 1750 and 1650 were evaluated on the basis of an assumption. But this assumption is regarded as rather sound and in every case as a sufficient basis to look for indications for a qualitative change of empirical relationships for morphodynamics: The data reflect a pronounced correlation of the factor a of the relationship

$$A_b = a \cdot V_T$$

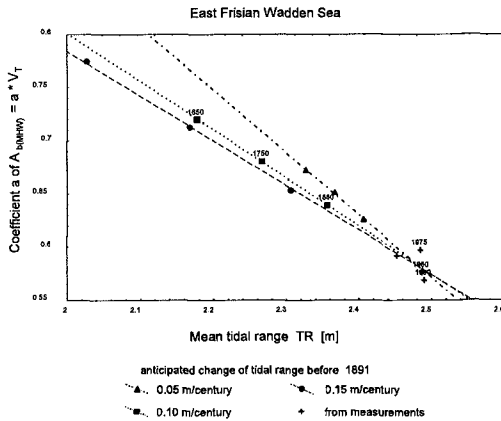


Figure 18. Correlation of the coefficient a from  $A_b = a \cdot V_T$  with tidal range TR

and tidal range range TR (fig. 18). Obviously those correlations depend particularly on the anticipated change of tidal range before 1891. In order to estimate the effect of a misjudgement a variation of  $\pm 5$  cm per century is taken additionally into consideration. The result makes evident that the tendency of the correlation is still evident (fig. 18). Therefore it must be concluded that for long term investigations in the same area the variation of the tidal range must be taken into consideration in order to describe the relationship between total basin areas and tidal volumes with sufficient accuracy.

## Conclusions

The resedimentation of storm surge bays at the East Frisian mainland coast has been a major steering impact of morphodynamical processes in five of the six tidal basins of the East Frisian Wadden Sea during the last centuries. As well the shifting of basin watersheds, the migration of inlets as the changes in size and position of the barrier islands can no longer only be credited to littoral drift. Furthermore they could not be regarded as a cyclic process which would have continued without the fixing of tidal inlets since the middle of the last century.

A reliable quantitative approximation of tidal volumes is also possible for the reconstructions of historical coastal morphology of Wadden Sea areas. The accuracy of these figures is sufficient for use in the framework of empirical relationships used for empirical and conceptual morphodynamical modeling. It has become evident that relationships being used for empirical or conceptual modeling which have been established for data sets covering only a period of a few decades or even less could not in every case be regarded as valid for long-term periods like centuries. This was demonstrated for the well known relationship of tidal basin areas and tidal volumes which is in the long run dependent on tidal range variations.

## Acknowledgements

This work was carried out in the framework of the Dutch-German research project WADE (Wadden Sea Morphological Development in respect of an accelerated relative sea-level rise). The German part is sponsored by the GERMAN FEDERAL MINISTRY FOR RESEARCH AND TECHNOLOGY (BMFT) under contract no. MTK 0508. The author is very grateful to the assistance he got from colleagues of the CRS Section of Coastal Hydrodynamics: H. Alberts, R. Goldenbogen, T. Hartkens, R. Kaiser, W. Liebig, M. Puschmann and E. Schröder transferred the reconstructions of historical coastal morphology and recent maps into the GIS, extracted data and elaborated graphics. Finally it is urgently necessary to stress the fact that this kind of investigation was only possible on the basis of the reconstruction of historical coastal morphology being carried out successfully by the author's late colleague Hans HOMEIER between 1949 and 1980.

## References

- EYSINK, W.D. [1979]: Morphologie van de Waddenzee. Waterlooppkundig Laboratorium, Rap. H 1336
- EYSINK, W.D. [1991]: Morphologic response of tidal basins to changes. Proc. 22nd Int. Conf. Coast. Eng. Delft, ASCE, New York
- HAYES, M.O. [1975]: Morphology and sand accumulation in estuaries. *in*: L. E. Cronin (ed.): Estuarine Research, Vol. 2, Academic Press, New York
- HOMEIER, H. [1962]: Historisches Kartenwerk 1:50000 der niedersächsischen Küste. Jber. 1961 Forsch.-Stelle f. Insel- u. Küstenschutz, Bd. 13
- HOMEIER, H. [1964]: Beiheft zu: Niedersächsische Küste, Historische Karte 1:50 000 Nr. 5. Forsch.-Stelle f. Insel- u. Küstenschutz
- HOMEIER, H. [1969]: Der Gestaltwandel der ostfriesischen Küste im Laufe der Jahrhunderte. *in*: J. Ohling (Hrsg.): Ostfriesland im Schutze des Deiches, Bd.2, Eigenverlag, Delichacht Krummhörn
- HOMEIER, H. [1972]: Beiheft zu: Niedersächsische Küste, Historische Karte 1:50 000 Nr. 4. Forsch.-Stelle f. Insel- u. Küstenschutz
- HOMEIER, H. [1979]: Die Verlandung der Harlebucht bis 1600 auf der Grundlage neuerer Befunde. Jber. 1978 Forsch.-Stelle f. Insel- u. Küstenschutz, Bd. 30
- HOMEIER, H. & LUCK, G. [1977]: Untersuchungen zur Nordstrandentwicklung von Borkum als Grundlage für den Inselnschutz. Jber. 1976 Forsch.-Stelle f. Insel- u. Küstenschutz, Bd. 28
- KRÜGER, W. [1911]: Meer und Küste bei Wangeroog und die Kräfte die auf ihre Gestaltung einwirken. Zeitschr. t. Bauwesen, Jg. 1911
- KUNZ, H. [1991]: Protection of the island of Nordemey by beach nourishments, alongshore structures and groynes. Proc. 3<sup>rd</sup> Conf. Coast & Port Eng. i. Devel. Countr., Mombasa/Kenya
- LUCK, G. [1977]: Inlet changes of the East Frisian islands. Proc. 15th Int. Conf. o. Coast. Eng. Honolulu, ASCE, New York
- LÜDERS, K. [1951]: Die Entstehung der Ostfriesischen Inseln und der Einfluß auf den geologischen Aufbau der ostfriesischen Küste. *in*: Probleme d. Küstenforsch. i. südlich. Nordseegebiet, Bd. 5
- LÜDERS, K. [1977]: Wangerooch heft'n hooge Toren, ... Jber. 1976 Forsch.-Stelle f. Insel- u. Küstenschutz, Bd. 30
- NIEMEYER, H.D. [1984]: Hydrographische Untersuchungen in der Leybucht zum Bauvorhaben Leyhörn. Jber. 1983 Forsch.-Stelle f. Insel- u. Küstenschutz, Bd. 35
- NIEMEYER, H.D. [1990]: Morphodynamics of tidal inlets. Civ. Eng. Europ. Course Prog. o. Cont. Educ. Coast. Morph., Syll. Delft Univ. o. Tech. Int.-Int. Civ. Eng.
- NIEMEYER, H.D. [1991a]: Field measurements and analysis of wave-induced nearshore currents. Proc. 22nd Int. Conf. o. Coast. Eng. Delft, ASCE, New York
- NIEMEYER, H.D. [1991b]: Case study Ley Bay: an alternative to traditional enclosure. Proc. 3<sup>rd</sup> Conf. Coast & Port Eng. i. Devel. Countr., Mombasa/Kenya
- O'BRIEN, M. P. [1931]: Estuary tidal prisms related to entrance areas. ASCE, Civ. Eng., Vol. 1, No. 8
- STEPHAN, H.-J. [1994]: Dünenabbrüche am Nordweststrand der Insel Borkum. Ber. Forsch.-Küste
- STREIF, H. [1994]: Das ostfriesische Küstengebiet - Nordsee, Inseln, Watten und Marschen. Samml. geolog. Führer 57, Gebr. Borntraeger, Berlin/Stuttgart
- VAN DONGEREN, A. & DE VRIEND, H. [1993]: A model of morphological behaviour of tidal basins. Coast. Eng., Vol. 22, Nos. 3,4
- WALTHER, F. [1972]: Zusammenhänge zwischen der Größe der ostfriesischen Seegaten mit ihren Wattgebieten sowie den Gezeiten und Strömungen. Jber. 1971 Forsch.-Stelle f. Insel- u. Küstenschutz, Bd. 23



## Field Observation and Numerical Simulation of Beach and Dune Scarps

Ryuichiro Nishi<sup>1</sup>, Michio Sato<sup>1</sup>, and Hsiang Wang<sup>2</sup>

### ABSTRACT

Beach and dune scarps are prominent erosional features and probably interfere with post-storm beach profile recovery because of wave reflection on the scarp face during high tide and reduced swash height. As examples, beach and dune scarps, created by typhoon waves on the Pacific Coast and on the East China Sea Coast in Kagoshima Prefecture, were investigated. The highest scarp elevation on these coasts were found to be approximately to 7 m on the Pacific Coast and 10 m on the East China Sea Coast. Following the field observation, a numerical study was conducted to study the generation of scarps.

### INTRODUCTION

A sandy beach and dune will be vulnerable to storm waves and storm surge when a severe storm approaches to a coastal zone. These high waves will change cross-shore profile significantly and cause shoreline recession. Following beach and dune erosion by a storm, a beach profile recovery process will take place under the incidence of ordinary waves. This process probably correspond to a ordinary profile suggested by Johnson (1949). Regarding cross-shore profile recovery, it is mentioned by Kriebel (1986) that "Time scales of beach profile recovery are highly variable. It is generally known that recovery processes occur on much slower time scales than erosion. As observed by Meyer (1936); " the time required for the bar to move shoreward under normal conditions is four to six times as long as to form the bar during storm conditions." Recovery typically occurs over time scales of several days to several months. In some extreme cases, recovery may take on the order of several

---

<sup>1</sup> Dept. of Ocean Civil Engineering, Kagoshima University, 1-21-40 Korimoto, Kagoshima-shi 890, JAPAN

<sup>2</sup> Dept. of Coastal and Oceanographic Engineering, 336 Weil Hall, University of Florida, Gainesville, Florida 32611, U.S.A.

years due to the infrequent onshore motion of sand in deeper water. On the other hand, observations immediately after the peak of a storm indicate that a large portion of the eroded volume may recover within one to two days, seemingly accelerated by elevated water levels and fairly energetic but constructive wave conditions." The study at Ocean City, Maryland by Randall and Kraus (1993) also suggested that large amount of profile recovery occurred during the last part of storm condition.

The recovery process depends on the wave condition during and after the storm, as well as on the post-storm beach profile such as scarps and longshore bar features, because the cross-shore profile interacts with a wave transformation and effects the resulting cross-shore sediment transport rate. Beach and dune scarps are significant erosional features and probably retard post-storm recovery by ordinary waves, because some of the low steepness waves with constructive force under the normal circumstance have undermined a foot of scarp and reflected by a vertical scarp face during high tide. As an example, the dune scarp was caused by the Typhoon 9119 in Kashiwabara beach, Kagoshima in 1991. The height of dune scarp was nearly 7 m according to the Minami Nippon Daily Newspaper. Once these scarp features are generated by storm waves, potential risk for properties behind the dune/beach will increase, because there is either only a narrow beach or no beach at all to dissipate incident wave energy and to resist destructive forces of successive storms. Since the average annual wave height along Japan Coast has increased in the last decades and the sediment supply from river is decreasing due to the structures placed in river, again it seems that the rate of beach profile recovery might be slower compared to the last decades. Therefore, from an engineering point of view, it is important to collect the data of erosional features and antecedent recovery process for the purpose of improving shore-protection and coastal management. It is also recognized that dunes have several functions, such as (i) serving as soft structures against storm surge and severe wave attack including tsunami waves, (ii) filtering effect of wind blown sand and salt by the coastal forest on and behind the dune, (iii) sediment source to the foreshore and longshore bar in a severe storm condition, (iv) a habitat and nesting area for sea animals and vegetation, (v) a setback area for the sea-level rise as well as storm surge, and (vi) a recreational area for local residents and tourists, etc. Therefore, proper dune management is very important.

Regarding numerical studies of dune erosion, there are several numerical methods, from two dimensional to quasi-three dimensional, to predict the dune erosion quantitatively. (Vellinga (1983, 1986), Kriebel and Dean (1984, 1985), Stieve and Battjes (1984), Sargent and Birkemeier (1985), Larson and Kraus (1989, 1990), Kriebel (1990), Wang and Miao (1992), Steetzel (1993), etc.) However, there is very little knowledge of physical processes on the beach and dune erosion and resulting scarps under a severe storm condition. (For instance, Kana (1977), Vellinga (1986), and Fisher (1986)). It is necessary to obtain enough physical knowledge on dune erosion process, however it is almost impossible to obtain a data set of beach and dune profile evolution just before and during the storm activity in the natural condition. Therefore, field surveys are usually carried out between and after storms.

Strictly speaking, the beach profile after the storm contains an information of beach profile recovery, since the waves may have high constructive force in the last part of storm period according to several beach profile predictors, for instance Kraus et al. (1991).

In the current study, field observations were conducted to study the geomorphological features of dune and beach scarps, and generation of scarp by storm waves. Based on these field observations, a numerical study has been carried out to simulate the scarps.

## FIELD OBSERVATION OF SCARPS

The coast line of Kagoshima Prefecture, which exceeds 2200 kms, suffered extensive damage by two of the biggest typhoons in this century, one in 1991 and the other in 1993. Due to these recent and successive severe typhoons, beach and dune scarps have been generated along the Fukiage coast which extends about 30 km south to north on the East China Sea, and along the Shibushi coast which extends about 8.2 km on the Pacific Coast in Kagoshima. The locations of these two coasts are shown in Fig. 1.

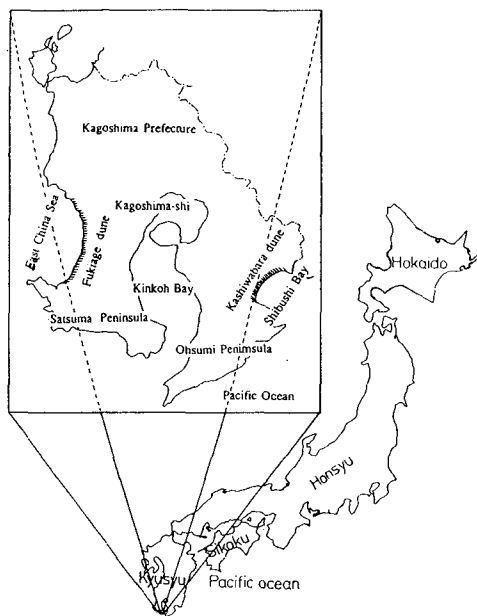


**Fig. 1. Locations of study areas**

### Cross-shore processes

The maximum height of dune scarp at Fukiage Beach was nearly 10 m, and an initial stage of dune scarping is shown in Fig 2. It can be seen that the dune has a steep seaward slope, and has a vertical face at the foot of the dune which was truncated by waves. Other field surveys have been carried out at Kashiwabara Beach on the Pacific Ocean Coast. Since dune scarp, beach nourishment, and beach scarp after the nourishment have alternatively appeared in this study area, the physical processes in this coast are probably particularly attractive from coastal engineering view point. Therefore, scarps in this area are mainly discussed in this paper. General characteristic of this coast are shown by a series of photographs, and then the longshore distribution of scarps will be discussed based on the field data.

Dune scarps at Kashiwabara Beach caused by Typhoon 9119 is shown in Fig 3. The photograph was taken one year after the Typhoon 9119, thus the foot of the dune is partially filled by onshore sediment transport. The height of dune scarp just after the Typhoon was about 7m according to the local newspaper (Minami Nippon Daily News), and the height of scarp shown in Fig. 3 was about 5 m. Because the shoreline and the crest of the dune regressed further landward, there was little foreshore remaining to dissipate wave energy. As a result, part of the coastal forest on and behind the dune was damaged by the collapse of dune and by the wind-blown salt. To protect the coastal forest and properties, a beach nourishment project was carried out in the beginning of 1993. The nourishment project area shown in Fig. 4 extends 2 km to cover the highly eroded beach. A few months after the beach nourishment project, storm waves caused by one of the biggest typhoons in this century, Typhoon 9313, for which the lowest pressure was 914 hp(mb), affected the project area, and produced beach scarps which extended along the whole nourished beach. Beach scarps in the central area of the project is shown in Fig. 5. In contrast to the nourished beach, there was little beach scarp at the neighboring natural beach. This difference probably arose from the fact that the nourished nearshore beach profiles was much steeper than the natural or equilibrium beach profile. The field survey showed that the maximum height of beach scarp was close to 3m where the shoreline retreated significantly landward. In addition, it was noted that the most severe damage was located in the same area as that of the heaviest dune scarp area produced by preceding Typhoon 9119 which caused a maximum of 7 m dune scarp.

To reduce further beach and dune erosion by an antecedent typhoon, it is necessary to accurately estimate the beach and dune profile before and after the typhoon. Then, the behavior of the dune and beach profile under the action of another storm can be predicted. Unfortunately, in the present case, beach profile data before the typhoon was not available to the authors and the field data were collected only after the generation of dune and beach scarps.

Field observations showed that swells with low steepness during high tide easily reach to the foot of scarp and undermine the vertical scarp face, while a low steepness swell has the constructive force in general. Following the undermining, the



**Fig. 2. Small dune scarp at Fukiage Beach**



**Fig. 3. Dune scarped by Typhoon 9119 at Kashiwabara Beach, 1992  
(Photograph taken one year after the typhoon)**



**Fig. 4. Beach nourishment at Kashiwabara Beach in 1993.**



**Fig. 6. Moment of collapsing (the sand blocks are falling)**

vertical layer of sand above the scoured foot loses support and collapses around the foot of scarp, and is deposited at the foot with an angle of repose. Fig. 6 shows the moment of collapsing of a scarped face. The block of sand which is in motion can be seen in the middle of the figure. The sand deposited at the foot of the scarp is transported offshore by successive waves and probably supplies sand to enhance the generation of longshore bar. This cross-shore process repeats itself at the end of wave attack during high water level. Thus, beach scarp plays a role as a moving boundary for the wave and moving sediment source for which a sand layer with a certain thickness is cut from the scarp face at distinct moments in time. It is also expected that the cross-shore sediment transport rate has a peak at the position of scarp during the collapse of the scarp face. This kind of process was also noted by Vellinga (1986) that " The first series of waves reaching the dune front causes erosion and a consequent lowering of the beach just in front of the dunes. After a number of waves the foot of the dune is eroded to such an extent that the dune front becomes unstable. Then, a slice of sand of between 0.2 and 2.0 m thick

(depending on the height and form of the dune) slides down, forming a pile of sand at the foot of the dune. This volume of sand is then gradually eroded by the waves. After some 50 to 100 waves, the pile of sand is cleared away and a new dune front instability occurs. In course of time it takes longer and longer before the pile of sand is removed. The rate of dune erosion decreases with time."

**LONGSHORE PROCESSES**

In contrast to the ordinary dune erosion which is two dimensional, scarp on this beach shows a longshore curved distribution. To see a planform, the beach width, defined as a length from the vegetation line to the crest of the scarp, is shown in Fig.7. In addition, the height of beach scarp is shown in Fig. 8. There is a T-

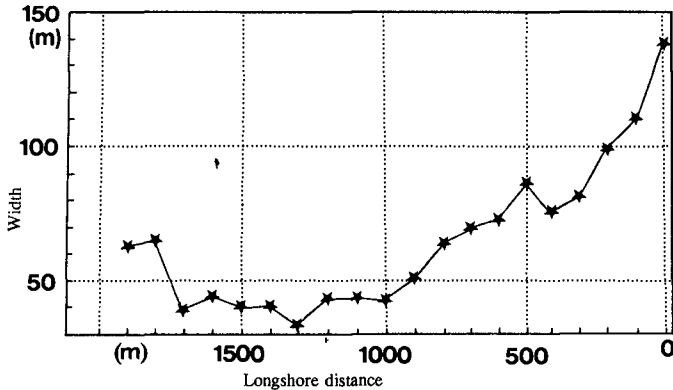


**Fig. 7. Width of the beach at Kashiwabara Beach**

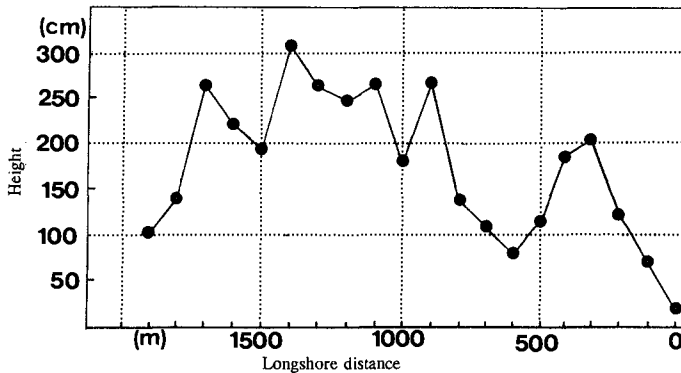


**Fig. 8. Height of the beach scarp**

shaped groin at the south end ( $x=0$  m) for which the longshore sediment transport further south is blocked at this boundary. It is seen that the beach is wider around the groin ( $x=0$ m), gradually decreasing in width to the north, and reaches a minimum width of 35 m at the location of  $x=1300$  m. Because of the narrow width of the beach in this area, waves break just near the dune and occasionally strong winds scatter the blown salt around the coastal forest. As a result, the coastal forest at this location has been damaged and many pine trees have withered. Also, the height of beach scarp was a maximum of 3 m around the area where the beach was the narrowest, and it was smallest at both the north and the south sides of the nourishment project area. It is noted that the position of the highest beach scarp caused by Typhoon 9313 was consistent with the position of the highest dune scarp caused by the Typhoon 9119.

## NUMERICAL TESTS

Based on the knowledge gained with the above field surveys, a numerical study was conducted to examine the cause of erosion and the generation of dune and beach scarps. Regarding numerical modeling of dune erosion, Vellinga (1983,1986), Kriebel and Dean (1984, 1985), Kriebel (1990) and other researchers have proposed two-dimensional cross-shore models. Here the SBEACH model (Larson and Kraus, 1989, 1990) has been applied to simulate dune and beach scarps. Because waves on a natural beach are random and their wave height distribution in offshore region might be expressed by the Rayleigh distribution, a simple model for the beach profile evolution due to random waves is also applied to simulate the dune erosion. Due to space limitation, the SBEACH model is only briefly reviewed.

### *SBEACH model*

The main structure of this model is composed of three sub-programs, (1) wave transformation, (2) cross-shore sediment transport, and (3) profile change calculated from conservation equation for bed material as the same in the other two-dimensional models. This model can be classified as semi-open model which uses an equilibrium beach profile concept. In contrast to the equilibrium concept which was originally developed by Dean (1977), Moore (1982) and Kriebel and Dean (1984), the SBEACH model simulates the generation of bar-trough features, avalanching, and some beach profile recovery. The wave transformation calculation is based on the model proposed by Dally (1984) and Dally et al. (1985 a,b) which is shown by Eq.(1).

$$\frac{\partial}{\partial x} (F \cdot \cos \theta) + \frac{\partial}{\partial y} (F \cdot \cos \theta) = \frac{\kappa}{d} (F - F_s) \quad (1)$$

where,  $F$  is the energy flux of progressive wave,  $\theta$  is the incident wave angle,  $x, y$  are coordinates normal and parallel to the coast respectively,  $\kappa$  is an empirical decay coefficient, and  $d$  is the total water depth which is the sum of still-water depth  $h$  and the mean water level  $\eta$ . In the present study, the wave angle is restricted to normal



incidence, so that the  $y$  component is negligible.  $F_s$  is the energy flux of a stable wave. The mean water level  $\eta$  is computed as follows;

$$\frac{\partial S_{xx}}{\partial x} = -\rho g d \frac{\partial \eta}{\partial x} \quad (2)$$

where,  $S_{xx}$  is the radiation stress,  $\rho$  is the density of the water, and  $g$  is the acceleration due to the gravity.

The cross-shore sediment transport rate in the surf zone is a type of energy dissipation model for which the transport rate is proportional to the difference between the actual wave dissipation per unit water volume,  $D$ , and the energy flux in equilibrium condition,  $D_{eq}$ . The local slope term is also added to the transport rate to account for the slope effect as shown :

$$q = K(D - D_{eq} + \frac{\epsilon}{K} \frac{\partial h}{\partial x}) \quad (3)$$

where,  $q$  is the net cross-shore sediment transport rate,  $K$  is an empirical coefficient for the sediment transport, and  $\epsilon$  is an empirical coefficient,  $h$  is a still water depth. To compute the depth change (profile change) in a time increment  $\Delta t$ , conservation equation for bed material is used as;

$$\frac{\partial h}{\partial t} = \frac{\partial q}{\partial x} \quad (4)$$

## NUMERICAL RESULTS

Because the natural beach with mild foreshore slope showed less damage compared to the nourishment area in Kashiwabara beach, the effect of beach slope on the generation of scarps was studied, first. Regular waves were applied for a plane beach with 1/10, 1/15, 1/20 uniform slope, respectively. Numerical results of the beach profile evolution and resulted scarps are shown in the Fig. 9 for regular waves with height 2.3 m and period 6.0 sec. It is seen that the shoreline was retreated as the wave duration increased, and sediment which was eroded around the shoreline was transported offshore to generate a longshore bar. The resulting scarped face migrated shoreward, while the shoreline retreated. It is clearly seen that the steeper is the initial beach profile, the higher is the resulting beach scarp. It appears that the numerical predictions agrees qualitatively with the field data.

Second, a composite dune-beach profile was used to generate dune scarp under a steady storm surge condition. It meant that the storm surge level did not vary in time. A 1-m and 2-m steady storm surge was added to the still water level.

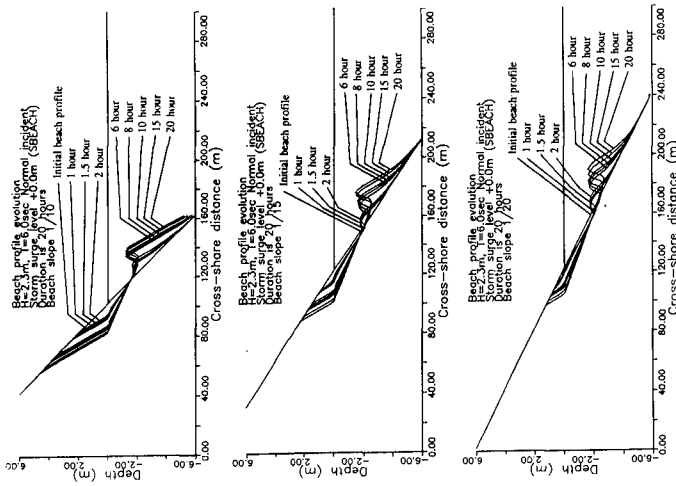


Fig. 9. Calculated beach profile evolution on beaches of different slope

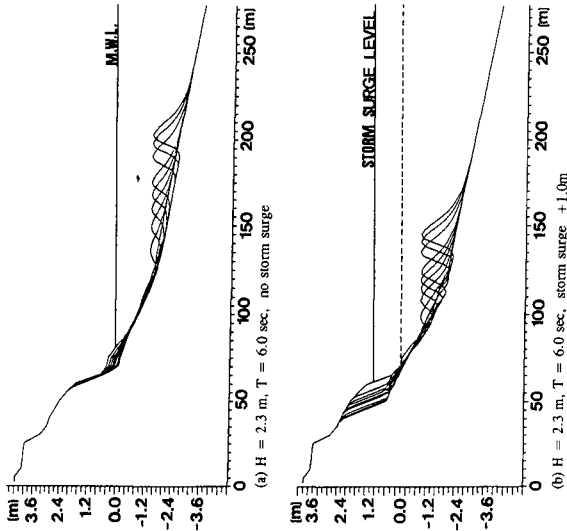


Fig. 10. Dune erosion during storm surge

Numerical results for the case of no increase in water level, and 1-m increase in water level during the storm are shown in Fig. 10. It is seen that longshore bars were generated by waves and migrated offshore with the passage of time. Corresponding to the migration of longshore bars, the sediment around the shoreline was transported offshore and then the dune erosion started. The resulting dune scarp became higher, while the cross-sectional area of dune erosion widened with time. In addition, it is clear that the larger the increase in water level due to storm surge, the higher the dune scarp for these cases. This is interpreted that the slope of the dune face is usually steep compared to the foreshore slope, so the slope where the stormy waves act probably is steeper during a high increase in water level. Therefore, the dune profile is eroded much more and as a result higher dune scarp appears.

Since the dune material is usually finer than the beach material, it is more easily carried away by the storm waves. However, the effect of different grain sizes between beach and dune is not taken into account in the present study. Vegetation also functions to strengthen a dune face, but its role is not taken into account in the present study.

As shown in Fig. 7 and Fig. 8, the beach scarp in this study area exhibits a longshore curved shape in terms of height and width. This curvature was perhaps caused by a negative gradient of longshore sediment transport. However, there was little shoreline progress along the coast even at the T-shaped groin just after the Typhoon 9113, though storm waves caused a significant beach erosion at the central area of nourished beach. It is expected that if the longshore sediment process mainly governs the topography change at this area, the area beside the groin should prograde or a part of the beach should widen, but there is little evidence to show such shoreline changes in this study area. Therefore, it is believed as a first step of the research that the longshore curved beach scarp was probably caused by an incident wave field which has a longshore uneven wave height, caused by an artificial island in front of the study area and dredging hole in the offshore region, and is mainly manifested in the cross-shore sediment transport. It is noted that this assumption need to be verified by a bathymetry data covering the area from the dune to beyond the depth of closure for considering the sand budget and a direction of sediment movement. However, such data were not available for this study.

The uneven longshore wave height distribution was calculated by eq. (5)

$$H(y) = H_1 + H_2 \sin^2 \left( \frac{2\pi}{400} y \right) \quad (5)$$

where,  $H(y)$  is the wave height at shoreline position  $y$ ,  $H_1$  was set to be 1.0 m, and  $H_2$  was set to be 3.0 m. Based on this wave height distribution, beach profile evolution and scarp were computed at 50 m spatial intervals alongshore. Fig. 11 shows a numerical result for this case. In accordance with the field data, the

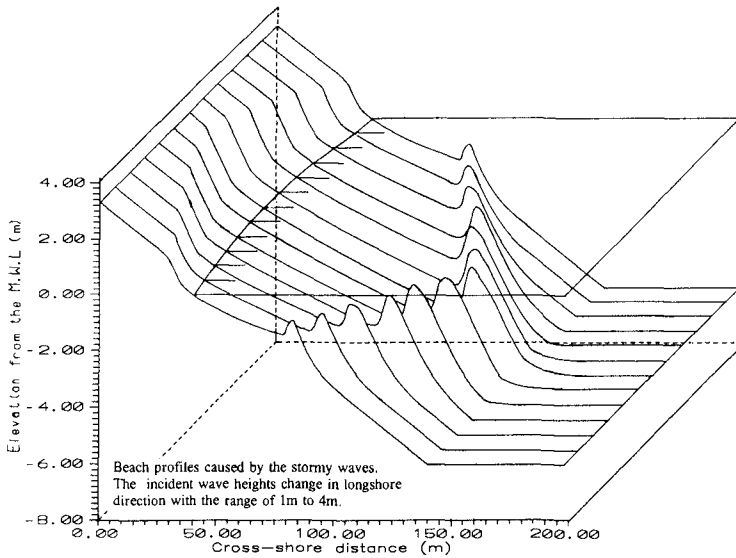


**Fig. 11. Longshore curved scarping calculated by numerical model**

numerical result shows a longshore curved scarp as well as curved longshore bar. The height of the beach scarp in the central region is the highest corresponding to the height of incident wave height. The crest line of the scarp also shows a curved longshore distribution.

## CONCLUDING DISCUSSION

The general characteristics of the dune and beach scarps at the Fukiage beach and the Kashiwabara Beach, Kagoshima, were investigated in field surveys. Dune scarp caused by the Typhoon 9119 and beach scarp by the Typhoon 9313 show similar longshore curved distribution. It was observed that once a vertical scarp face was generated, the waves directly attacked the scarp face during high water and undermined the foot of the scarp. As a result, blocks of sand collapsed, deposited at the foot of the scarp and was transported offshore by successive waves. This is a straight-forward process and agreed well with a set of physical model data by Dette et al. (1992). In addition, there was little evidence to show that the negative gradient of longshore sediment transport dominated the scarp generation in this study area. It was also shown by a numerical study that the steeper is the beach face the higher is the resulting scarp.

The sediment budget in the study area should be confirmed in the future. It is expected that the direct measurement of scarp generation and the recovery process at the foot of scarp are required for further investigations. The estimation of the sand movement in the offshore region and depth of closure due to extreme typhoons is

also necessary, because it could be a source of onshore sediment transport during the beach profile recovery. Although it is not discussed in this paper, there is a man-made island of 192ha area and also a dredging area near the study site which strongly affect local wave fields and result in the change of planform of the beach. Before the Typhoon 9119, the planform of the beach was significantly changed by a construction of the man-made island and was narrowed especially around the area where dune and beach scarp had been generated by severe storm waves. Thus, a further study of the wave field affected by islands can help the proper coastal management at this area.

### **Acknowledgements**

The authors would like to express their special thanks to Prof. Nicholas C. Kraus at the Conrad Blucher Institute for Surveying and Science, Texas A&M university - Corpus Christi, for his kind comments and recommendation. The authors also appreciate Mr. Iwamoto, Mr. Ikeda, and other members of the Coastal Engineering Lab. at the Department of Ocean Civil Engineering, Kagoshima University. This study was partially supported by the research grants of the Ministry of Education, Japan and by Kagoshima National University.

### **References**

- Dally, D.L., 1984: Suspended sediment transport and beach profile evolution, *Journal of Waterway, Port, Coastal and Ocean Engineering*, Vol. 110, No. 1, ASCE, pp.15-33.
- Dally, W.R., Dean, R.G., and Dalrymple, R.A., 1985 a: Wave height variation across beaches of arbitrary profile, *Journal of Geophysical Research*, Vol. 90, C6, pp.11917-11927
- Dally, W.R., Dean, R.G., and Dalrymple, R.A., 1985 b: A model for breaker decay on beaches, *Proceedings of the 19th International Conference on Coastal Engineering*, ASCE, pp.82-98
- Dean, R.G., 1977: Equilibrium beach profiles: U.S. Atlantic and Gulf coasts, *Ocean Engineering Report No. 12*, Department of Civil Engineering, University of Delaware, Newark, Delaware
- Dette, H., 1992: Personal communication
- Johnson, J.W., 1949: Scale effect in hydraulic models involving wave motion, *Transactions, American Geophysical Union*, Vol. 30, Number 4, 1949, pp.517-525.
- Fishier, J.S., 1986: Field measurements of dune erosion, *Proceedings of the 20th Conference on Coastal Engineering*, ASCE, pp.1107-1115.
- Kana, T. W., 1977: Beach erosion during minor storm, *Journal of the Waterway, port, Coastal and Ocean Division*, Vol. 103, No. WW4, ASCE, pp.
- Kraus, N.C., Larson, M., and Kriebel, D.L., 1991: Evaluation of beach erosion and accretion predictors, *Coastal Sediments '91*, ASCE, pp.572-587.

Kriebel, D.L., and Dean, R.G., 1984: Beach and dune response to severe storms, Proceedings of the 19th International Conference on Coastal Engineering, ASCE, pp.1584-1599.

Kriebel, D.L. and Dean, R.G., 1985: Numerical simulation of time-dependent beach and dune erosion. Coastal Engineering, 9, pp.221-245

Kriebel, D.L., Dally, W.R., and Dean, R.G., 1986: Beach profile response following severe erosion events. UFL/COEL-86/016, Coastal and Oceanographic Engineering, University of Florida, Gainesville, Florida.

Kriebel, D.L., 1987: Beach recovery following Hurricane Elena. Coastal Sediments '87, ASCE, pp.990-1005

Kriebel, D.L., 1990: Advances in numerical modeling of dune erosion. Proceedings of the 22nd International Conference on Coastal Engineering, ASCE, pp.2304-2317

Kriebel, D.L., Kraus, N.C., and Larson, M., 1991: Engineering methods for predicting beach profile response, Coastal Sediments '91, ASCE, pp.557- 571

Larson, M., and Kraus, N.C., 1989: SBEACH: Numerical model for simulating storm-induced beach change. Report 1. Empirical foundation and model development. Technical Report, CERC-89-9, U.S. Army Engineering Waterways Experiment Station, Coastal Engineering Research Center, Vicksburg, Mississippi.

Larson, M., and Kraus, N.C., 1990: SBEACH: Numerical model for simulating storm-induced beach change. Report 2. Numerical formulation and model tests. Technical Report CERC-89-9, U.S. Army Engineering Waterways Experiment Station, Coastal Engineering Research Center, Vicksburg, Mississippi.

Meyer, R., 1936: A model study of wave action on beaches, M.S. Thesis, Dept. of Engineering, Univ. of California, Berkeley, California.

Moore, B.D., 1982: Beach profile evolution in response to changes in water level and wave height. A thesis submitted to the faculty of the University of Delaware in partial fulfillment of the requirements for the degree of Master of Civil Engineering, Newark, Delaware.

Randall A.W. and Kraus N.C., 1993: Simulation of beach fill response to multiple storms, Ocean City Maryland, Beach Nourishment Engineering and Management Considerations, Edit Donald K. Stauble and Nicholas C. Kraus, ASCE, p245.

Sargent, F. E. and Birkemeier, W. A., 1985: Application of the Dutch method for estimating storm-induced dune erosion, Instructional Report CERC-85-2, U.S. Army Engineering Waterways Station, Coastal Engineering Research Center, Vicksburg, Mississippi.

Steetzel, H.J., 1993: Cross-shore transport during storm surges, Delft Hydraulics -111, ISSN 0920-9808.

Stive, M.J.F., and Battjes, J.A., 1984: A model for offshore sediment transport, Proceedings of the 19th International Conference on Coastal Engineering, ASCE, pp.1420-1436

Vellinga, P., 1983: Predictive computational model for beach and dune erosion during storm surges, Proc. Conference on Coastal Structures '83, ASCE, pp. 806- 819.

Vellinga, P., 1986: Beach and dune erosion during storm surges, Delft hydraulics Communication No. 372.

Wang, H., and Miao, G. 1993. A time-dependent nearshore morphological response model. Proceedings on the 23rd International Conference on Coastal Engineering, ASCE, pp.432-446

## CHAPTER 177

# EFFECTS OF CONTROLLED WATER TABLE ON BEACH PROFILE DYNAMICS

Tae-Myoung Oh<sup>1</sup> and Robert G. Dean<sup>1</sup>

### ABSTRACT

The purpose of this study is to improve general understanding of beach profile dynamics as affected by the interaction between the beach profile and the water table level within the beach by presenting the results of laboratory and numerical studies. Two series of laboratory experiments were conducted in “large” and “small” wave tank facilities. Special attention was given to elevated water table levels to investigate whether or not erosion of the beach face is enhanced. The results of the large wave tank experiments demonstrated a surprising influence of beach water table on profile dynamics including changes in the bar region. Although the experiments in the small wave tank used correctly scaled sand, it was found that the effects documented in the large scale tests could not be duplicated. Furthermore those results were supported by numerical simulation of the internal flow inside the beach. One possibility for the difference is that the sand in the large scale tests was more poorly-sorted than that in the small scale experiments.

### INTRODUCTION

For a permeable beach, we would expect an internal flow within the beach, which might be driven by the mean pressure due to the ground water table level inside the beach and/or wave induced set-up. If the mean pressure gradient is large enough to stabilize or destabilize the sand particles, it may affect the sand transport and resulting profile evolution.

Attempting to demonstrate the effect of percolation, Bagnold (1940) prevented free percolation through the sand by placing an impermeable steel plate just below the sloping beach surface. The thin layer of the sand above the plate was at once removed as soon as waves attacked, resulting in erosion of the beach.

Grant (1948) noted, by observations of the fluctuations in the width and slope of beaches in southern California, that the position of the ground water table

---

<sup>1</sup>Coastal and Oceanographic Engineering Department, University of Florida, Gainesville, FL 32611



within the beach played an important role on deposition and on erosion of the foreshore and backshore. He suggested that a higher water table than mean sea level accelerated beach erosion, and conversely, a lower water table might result in pronounced aggradation of the beach. Emery and Foster (1948) found that the escape of water from the lower part of the beach may exert an appreciable upward force on the sand particles, sufficiently large to destabilize them, resulting in erosion of the beach.

Based on possibilities of beach stabilization, test installations of the beach drain system have been conducted in the laboratory and in the field; this approach consists of burying a pipeline along the beach to maintain the water table level at a lower one than the mean sea level by pumping.

Machemehl, French and Huang (1975) conducted laboratory experiments to determine the effects of a sub-sand filtering system on the stability of a beach profile, which consisted of well pipes buried perpendicular to the shoreline and pumping  $136.3 \text{ cm}^3/\text{s}/(\text{m of beach})$ . The results showed that the drain system caused deposition on the beach face and stabilized the sand at the offshore zone by inducing a flow into the beach, but it had a negligible effect in the breaking zone since turbulence by wave breaking was too strong to be controlled by the drain system.

Kawata and Tsuchiya (1986) performed laboratory experiments to examine the effects of beach drain for the case of solitary and regular waves on the beach face. With a relatively fine sand for the solitary wave tests, the beach face was much steeper with pumping than non-pumping cases. With much coarser sand for the regular wave cases, it was recognized that the pumping system was effective under storm wave conditions by reducing the sand transport, thus stabilizing the beach near the shoreline.

Terchunian (1988) reported on a prototype beach drain system installed along 180 m of the beach at Sailfish Point on Hutchinson Island, Florida. The system had been in operation over two years and beach profiles were taken monthly to determine the efficiency of the system. The system appeared to result in a stabilization of the beach as moderate accretion occurred while the updrift and downdrift beaches showed erosion.

However, the interaction mechanism of beach drain system is not obvious since some laboratory results appeared to result in no significant effects of water table levels on the beach profile changes. Bruun (1989) claimed that the method ought to be more effective in mild conditions than storm conditions as the velocities (and energy levels) are far higher in the surf zone during a storm. Ogden and Weisman (1991) performed two-dimensional laboratory experiments to assess the effectiveness of a beach drain system on stabilization. Tests were carried out with a very fine sand (median diameter of  $0.145 \text{ mm}$ ) under irregular waves. Even with a fairly long duration of waves, they could not find any significant differences in the final profiles. They suggested that the beach drain would not be effective where there is a negligible tide.

This paper presents the results of laboratory studies to investigate the effects of controlled water table on beach profile dynamics. To achieve this goal, two series of experiments were conducted in "large" and "small" wave tanks at three different water table levels while the other factors (e.g., wave height, wave period, water depth, initial beach slope, etc.) were fixed to constant values with regular waves. The water table levels included : (a) normal water table level which is the same as mean sea level, (b) a higher level and (c) a lower level than the mean sea level. Special attention was given to elevated water table levels to investigate whether or not erosion of the beach face is enhanced. The results of numerical studies are also presented to simulate the internal flow inside the beach and to understand the interaction mechanism.

### LARGE WAVE TANK EXPERIMENTS

The first experiment was conducted in the "large" wave tank facility of the Department of Coastal and Oceanographic Engineering at the University of Florida, which is approximately 36 *m* long, 1.8 *m* wide and 1.8 *m* deep. A long partition has been constructed along the tank center line dividing it into two channels each of 0.9 *m* width. A planar beach was formed with initial slope 1:18 and composed of poorly-sorted fine sand with a median diameter of 0.24 *mm* and a sorting coefficient of about 1.0. (At first, the beach was considered as composed of well-sorted fine sand with a median diameter of 0.2 *mm* and a sorting coefficient of 0.5. However, it was found that the fine sand was underlain by well-sorted coarse sand with a mean diameter of 0.4 *mm*, which appeared to affect the overall permeability of the beach.) Regular waves with a period of 2.0 *seconds* and height of 0.16 *m* were generated. The water depth at the toe of the beach slope was 0.47 *m* at mean sea level. Details are provided in Oh and Dean (1992).

The experiment was conducted at three different water table levels, which were regulated sequentially to: (1) normal water table level which was the same as mean sea level (1.5 *hours*), (2) a higher level (+11.0 *cm* during 2.0 *hours*) and (3) a lower level than the mean sea level (-11.0 *cm* during 1.5 *hours*). The duration of each test with the same water table level was determined based on an assessment that the beach profiles were near equilibrium and would not significantly change beyond this test duration. Throughout the test program, the beach profiles were monitored at one-half hour intervals.

The higher water table (at 1.5 *hours*) was established by raising the entire water level in the wave tank and allowing the ground water table to equilibrate with no waves acting. The tank water level was then lowered and the water table level in the beach was maintained by excavating a small depression in the berm below the desired water level, which was then maintained by filling periodically with a hose. For the lower water table, the procedure described above was followed except that water was siphoned out of the excavated hole in the beach berm to maintain the desired level.

### SMALL WAVE TANK EXPERIMENTS

A total of 8 "small" wave tank experiments was carried out (1) to evaluate the repeatability of the large wave tank experiments and (2) to illustrate beach profiles that would have occurred if the water table had not been altered or regulated with different sequences from the first experiment. This tank is 15 m long, 0.9 m high and 0.6 m wide, and is equipped with a piston type wavemaker with a mechanically controlled motion and with one glass wall panel and one steel wall.

Table 1 lists the experiment identification number, total wave run duration, water table level condition, and a brief description of each experiment. The experiments were scaled from the large wave tank experiment according to the fall velocity parameter (Dean, 1985) for a well-sorted fine sand with mean diameter of 0.21 mm and a sorting coefficient of 0.5 with a length scale of 1:1.7, and the waves were modelled according to the Froude relationship. Regular waves with a period of 1.5 sec and a height of 11.0 cm (rather than 9.5 cm as would be required by scaling) were used due to wavemaker limitations, and were measured by a capacitance-type wave gage. Figure 1 presents a schematic diagram of the initial profile and other experimental details.

Table 1: Description of Small Wave Tank Experiments

Exp. No.	Water Table Level		Note
	Duration(min)	Level(cm)*	
SW01	230	0.0	Reference test
SW02	230	+6.5	High water table level
SW03	230	-6.5	Low water table level
SW04	0-69	0.0	Repeat test of Large wave tank experiment
	69-161	+6.5	
	161-230	-6.5	
SW05	0-69	0.0	Effect of sequence of changing water table level
	69-161	-6.5	
	161-230	+6.5	
SW06	0-69	0.0	Elevated water table level
	69-545	+11.0	
SW07	0-1166	+16.5	Elevated water table level
SW08	0-890	-11.0	Lowered water table level
	890-2201	+11.0	Elevated water table level

\* Zero refers to the mean sea level (MSL). Hence, positive value represents the water table level above MSL.

The desired water table level in the berm was maintained by excavating 2-D depressions across the tank. These excavations were connected to a constant

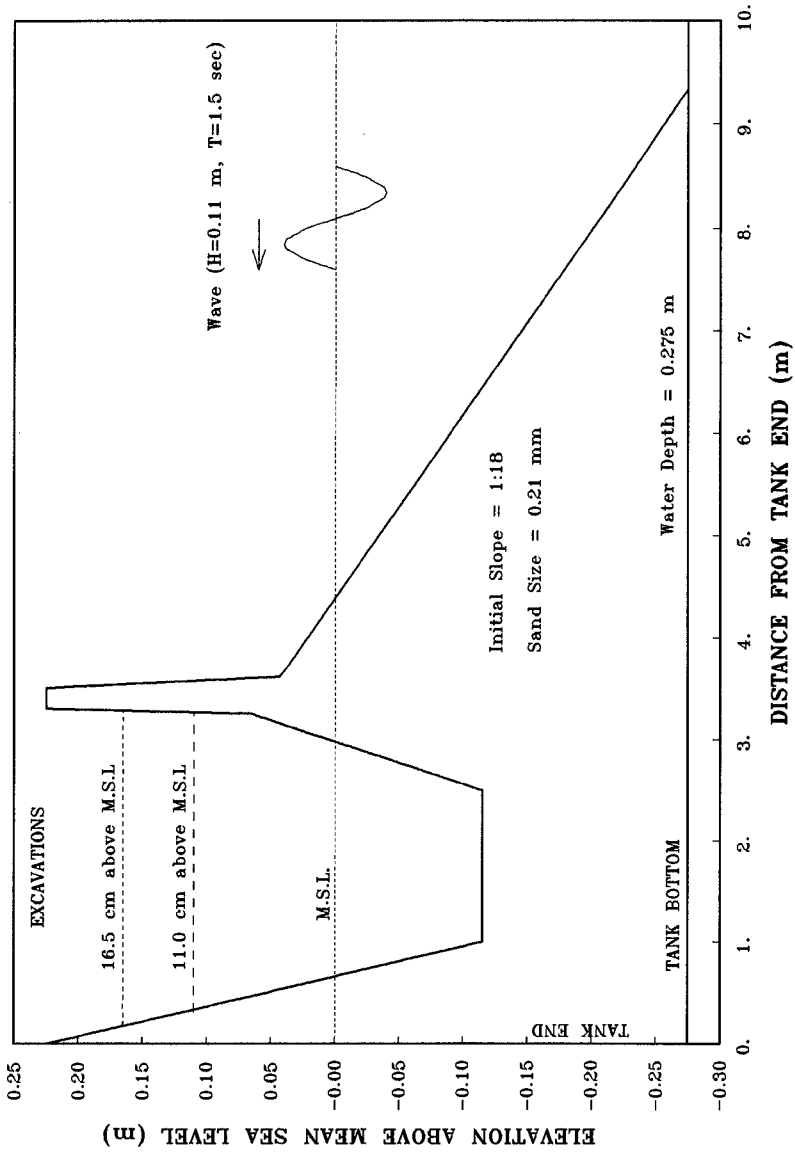


Figure 1: Schematic Diagram of the Initial Profile and Other Experimental Details

head reservoir through plastic tubes so that water was siphoned out of or into the excavated holes to maintain the desired water table level. During the experiments, this method worked very well. However, bubbles appeared sometimes inside the tubes due to prolonged experimental duration; at which time, they were removed by allowing a small amount of flow from the excavated holes to the reservoir, or vice versa.

### INTERACTION MECHANISM

Consider a sand particle, as shown in Figure 2, on the bed which has a slope  $\theta$  and experiences a lift force  $F_L$ , a portion of which is due to an upward or inward flow perpendicular to the sand surface.

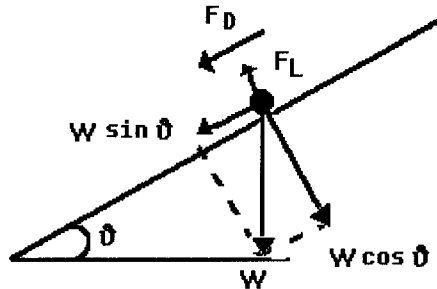


Figure 2: Free Body Diagram for a Sediment on a Sloping Bed with an Internal Flow System

The critical Shields parameter for motion downslope can be written as;

$$\frac{W \sin \theta + F_D}{W \cos \theta - F_L} = \tan \phi_s \quad (1)$$

where,  $W$  is the submerged weight of the sediment,  $\theta$  is the bed slope,  $\phi_s$  is the angle of repose of the sediment, and  $F_D$  is the drag force acting on the particle. The lift force component due to the flow out of bed,  $F_L'$ , can be expressed as;

$$F_L' = \frac{u}{K} \rho g V \quad (2)$$

in which,  $u$  is the average flow velocity perpendicular to the sand surface,  $K$  is the hydraulic conductivity (or permeability),  $\rho$  is the mass density of water,  $g$  is the gravitational acceleration, and  $V$  is the volume of the sediment. Finally, the critical Shields parameter,  $\psi_c$ , as affected by both the bed slope and the internal flow system, can be given as;

$$\frac{\psi_c}{\psi_{c0}} = \cos \theta \left[ 1 - \frac{\tan \theta}{\tan \phi_s} - \frac{u/K}{(s-1) \cos \theta} \right] \quad (3)$$

where,  $\psi_{c0}$  represents the critical Shield parameter on the impermeable bed with no slope, and  $s$  is the ratio of mass densities of sediment to water. In order to reduce the effective weight of the sand particles and therefore their stability, hence, the upward flow velocity should be sufficiently large or local slopes of the beach should be quite steep, where the sand particles had marginal stability.

### NUMERICAL MODELING

Considering a beach of uniform porosity with internal flow velocity that obeys Darcy's law, the internal flow system is governed by the Laplace equation;

$$\nabla^2 \phi = 0 \quad (4)$$

where,  $\phi$  is the hydraulic head defined as;

$$\phi = z + \frac{p}{\rho g} \quad (5)$$

in which,  $z$  is the elevation from the tank bottom,  $p$  is the pressure,  $\rho$  is the mass density of water, and  $g$  is the gravitational acceleration. Equation (4) can be solved efficiently by the Boundary Integral Equation Method (BIEM) if the proper boundary conditions are given at the tank bottom, beach profile, seepage face, phreatic surface inside the beach and lateral ends of tank. The transient state can be included in Equation (4) through the time-varying boundary conditions at the beach profile and phreatic surface; however, steady-state was considered in this paper. If  $\phi$  is known, then the internal flow velocity can be computed from Darcy law;

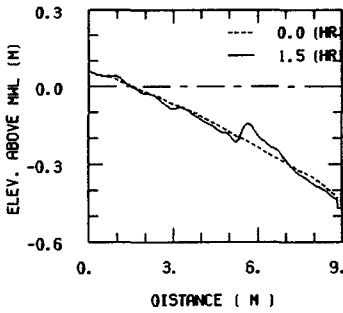
$$\mathbf{u} = -\mathbf{K}\nabla\phi \quad (6)$$

where,  $\mathbf{u}$  is the average velocity across a given area of sand, and  $K$  is the hydraulic conductivity. In this paper, hydraulic conductivity was measured by using a permeameter based on constant/variable method, and was found to be 0.022 cm/sec for the sediment used in the small wave tank experiments.

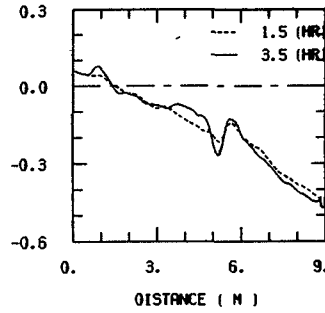
### RESULTS AND DISCUSSIONS

As illustrated in Figure 3, the results of the large wave tank experiments demonstrated a surprising influence of beach water table on profile dynamics including changes in the bar region. Figure 3 shows the profiles during normal, higher and lower water table levels. During normal water level, sand was transported both onshore and offshore resulting in deposition at the berm and at the bar, and the profiles were approaching an equilibrium. As soon as the higher level was established, however, very large changes occurred at the bar crest with relatively smaller changes at the bar trough; the bar started to move landward rapidly at the initial

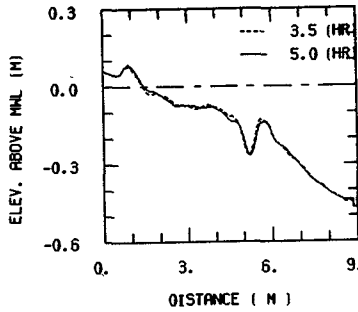
stages and stayed stationary at the later times. During the higher level, sand was transported onshore and deposited at the berm and at the depositional area located immediately landward of the bar trough. The increased water table level caused a strong landward transport, which is contradictory to previous studies that higher water table level enhances erosion. However, there was erosion immediately seaward of the berm. Also it can be seen that relatively small changes occurred with the lower water table level. The only noticeable trend was a limited deposition in the scour hole at the base of the beach face.



(a) NORMAL WATER TABLE



(b) HIGHER WATER TABLE



(c) LOWER WATER TABLE

Figure 3: Profiles during Normal, Higher and Lower Water Table Levels in the Large Wave Tank Experiment

Based on the results of the large scale tests, the following can be concluded: (1) the effect responsible for the changes in the profiles appeared to be a destabilization of the bottom particles in areas of pre-existing marginal stability with the eroded particles transported to stable areas, (2) the increased water table appeared to be effective far offshore, which was somewhat surprising, and (3) the lowered water table appeared to result in a much more stable beach by introducing a downward flow into the beach and the resulting effects were much less.

Although the experiment in the small wave tank used correctly scaled sand, it was found that the effects documented in the large scale tests could not be duplicated. In fact, all of the various small scale test results were nearly the same up to a testing time in excess of 3 *hours*. Based on the conclusions drawn above, several possible causes can be considered: (1) effects of coarser sand layer overlain by fine sands in the large wave tank experiments, (2) more poorly-sorted sand in the large scale tests than that in the small scale tests, (3) different wave height from that required by scaling, and (4) microorganisms inside the beach under prolonged submergence, which may influence the sand permeability. Other possibilities could be explained by the numerical studies.

As shown in Figure 4, calculations demonstrated that a small upward flow of water emerged through a porous sand bed, which is driven by wave-induced set-up only within a linear beach. However, the magnitude of the ratio  $\frac{u}{K}$  appears too small to reduce the effective stability of the sand particles. Even with a fairly steep beaches, as shown in Figure 5, the effect of upward flow was not significant although the overall stability of the bottom particles on the steep beaches was reduced due to the effect of the slope. Higher water table levels intensified the magnitude of the internal flow, as shown in Figure 6; however, the effect of upward flow appeared to be small compared with the effects of steep slope. Hence, these results of the small scale tests suggested that the altered water tables had no effects on the beach profile dynamics, which is contradictory to the conclusions from the large scale experiments. More definite conclusions can be reached only by further research including a more comprehensive comparison of numerical modeling results with measurements.

## CONCLUSIONS

Based on the present laboratory and numerical studies, the following conclusions and recommendations are described.

Large scale tests demonstrated that upward flow of water emerged through a porous sand bed due to both the higher water table level and wave-induced set-up and appeared to destabilize the bottom particles in areas of pre-existing marginal stability with the eroded particles transported to stable areas. However, the effects documented in the large wave tank experiments were not verified by the small scale experiments even with the correctly scaled sand. Furthermore, numerical results on the steady-state beach system supported the small scale test results. Several possible reasons were suggested, which need further study.



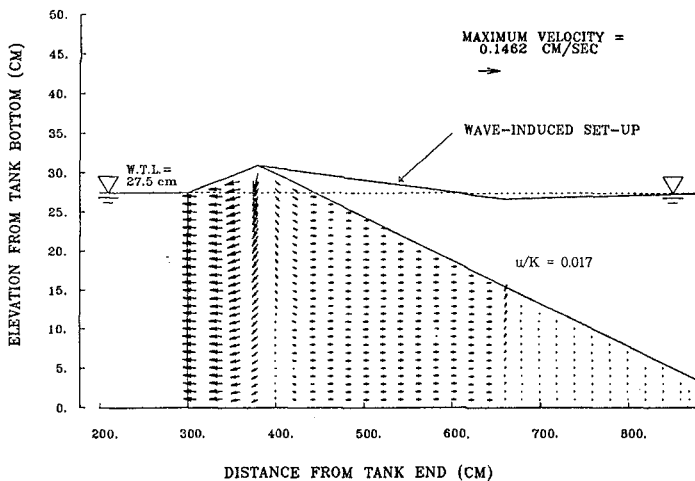


Figure 4: Internal Flow by Wave-Induced Set-Up within a Beach of Uniform Slope

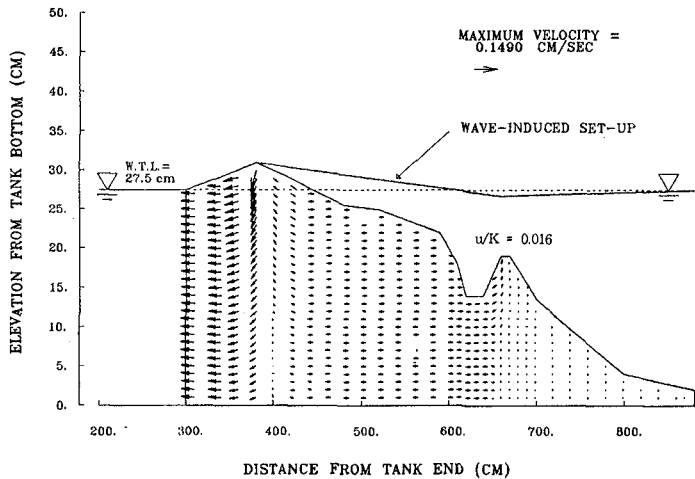


Figure 5: Internal Flow by Wave-Induced Set-Up for a Typical Beach Profile

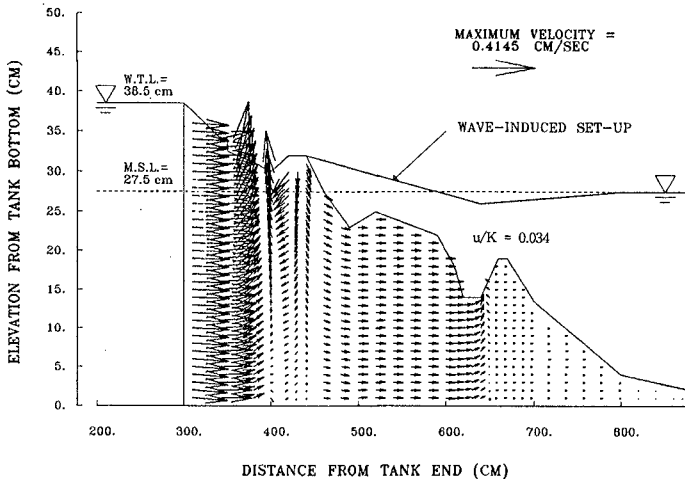


Figure 6: Internal Flow by Wave-Induced Set-up and Elevated Water Table Level for a Typical Beach Profile

There is a substantial need for additional carefully controlled laboratory experiments with different range of sediment sizes and sorting (thus permeabilities) from the present experiments. The numerical modeling should be improved to include the transient state boundary conditions and the effects of coarser sand layer overlain by fine sands as in the large scale tests.

#### REFERENCES

- Bagnold, R.A. (1940), "Beach Formation by Waves; Some Model Experiments in a Wave Tank", *Inst. Civil Engineers Jour.*, Paper No. 5237, pp. 27-53.
- Bruun, P. (1989), "Coastal Drain: What Can It Do or Not Do?", *J. Coastal Research*, 5(1), pp. 123-125.
- Dean, R.G. (1985), "Physical Modeling of Littoral Processes", in *Physical Modeling in Coastal Engineering*, ed. by R.A. Dalrymple, pp. 119-139.
- Emery, K.O. and J.F. Foster (1948), "Water Tables in Marine Beaches", *J. Marine Research*, 7, pp. 644-654.
- Grant, U.S. (1948), "Influence of the Water Table on Beach Aggradation and Degradation", *J. Marine Research*, 7, pp. 655-660.

- Kawata, Y. and Y. Tsuchiya (1986), "Application of Sub-Sand System to Beach Erosion Control", Proc. 20th International Coastal Engineering Conference, ASCE, Taiwan, pp. 1255-1267.
- Machemehl, J.L., T.J. French and N.E. Huang (1975), "New Method for Beach Erosion Control", Proc. Civil Engineering in the Oceans, III, ASCE, University of Delaware, pp. 142-160.
- Ogden, M.R. and R.N. Weisman (1991), "Beach Stabilization Using Drains - An Experimental Model Study", Proc. Coastal Sediment '91, ASCE, pp. 1955-1969.
- Oh, T.M. and R.G. Dean (1992), "Beach Face Dynamics as Affected by Ground Water Table Elevations", UFL/COEL-92/004, Coastal and Oceanographic Engineering Department, University of Florida, Gainesville, Fl, 35 pp.
- Terchunian, A.V. (1988), "Performances of the STABEACH@ System at Hutchinson Island, Florida", Proc. Beach Preservation Technology 89, Univ. of Florida, Florida Shore and Beach Preservation Association and American Shore and Beach Preservation Association, Fl., pp. 229-238.

## CHAPTER 178

### LABORATORY EXPERIMENTS ON 3-D NEARSHORE CURRENT AND A MODEL WITH MOMENTUM FLUX BY BREAKING WAVES

Akio Okayasu<sup>1</sup>, Koji Hara<sup>2</sup> and Tomoya Shibayama<sup>3</sup>

#### Abstract

Laboratory experiments are performed in a wave basin to investigate the characteristics of three dimensional distribution of the nearshore current. Direction and amplitude of the nearshore current significantly change along the vertical axis and have spiral distribution. A quasi 3-D model which gives the 3-D distribution of nearshore current is proposed. Momentum flux due to the large vortexes formed on the front face of breaking waves is included in the model to evaluate the depth averaged current. The model is examined with the experimental results.

#### 1. Introduction

In order to predict the sediment transport or material diffusion in the coastal field, 3-D structure of nearshore currents should be considered. Recently, some models for the 3-D distribution of nearshore current were presented. De Vriend and Stive (1987) investigated the vertical distribution of nearshore current on a beach uniform in the alongshore direction. Svendsen and Lorenz (1989) presented a model for 3-D nearshore current by composing cross-shore and alongshore velocities. Sanchez-Arcilla *et al.* (1992) proposed a quasi 3-D model by combining a 2-DH nearshore current model and an 1-DV undertow model. However, few comparisons were done with measured velocity. The actual 3-D characteristics of nearshore current is not clarified yet.

---

<sup>1</sup> Research Associate, Department of Civil Engineering, Yokohama National University, Hodogaya, Yokohama 240, Japan. E-mail: okayasu@coast.cvg.ynu.ac.jp

<sup>2</sup> Civil Engineering Division, Taisei Corporation, Shinjuku, Tokyo 163-06, Japan

<sup>3</sup> Associate Professor, Department of Civil Engineering, Yokohama National University. Hodogaya, Yokohama 240, Japan. E-mail: tomo@coast.cvg.ynu.ac.jp

Visser (1984) measured alongshore current in a basin which simulated an infinite beach in the alongshore direction. In general, it is difficult to control the side boundaries to obtain a uniform current field in the alongshore direction, which may not be necessary as far as the primary purpose is to examine numerical models with the data. In the present study, velocity measurements were performed in a closed laboratory basin to obtain vertical profiles both for cross-shore and alongshore currents in the surf zone for three different beach topographies. The importance of undertow for nearshore circulation was confirmed. The characteristics of the 3-D structure of nearshore currents has been investigated from the measured profiles.

In the surf zone, the mass flux by the organized large vortices (surface rollers) formed in the front face of the waves must be taken into account to evaluate the cross-shore current in 2-DV plane (see *e.g.* Svendsen, 1984). It is considered that momentum flux by the large vortices is also significant. In the present paper, a 2-DH model is proposed in which the momentum flux due to the large vortices is included to evaluate the two dimensional current field. This 2-DH nearshore current model is expanded to a quasi 3-D model by coupling with an 1-DV undertow model which gives vertical distribution of cross-shore component of nearshore current. The model is examined with the experimental results.

## 2. Experiments on 3-D nearshore current distribution

### 2.1 Experimental arrangement

A 9 m by 9 m wave basin was used for the experiments. This wave basin had a 1/20 slope which was uniform in the alongshore direction, and a regular wave generator which could generate obliquely incident waves. The 1/20 slope had a 1.05 m of 1/3 slope at the toe. Steal wave guides were placed on the slope along the wave propagation direction in order to control current patterns to be relatively simple and stable. Figure 1 shows the plan and side views of the wave basin.

The experiments were performed under 3 different conditions which were, Case 1: obliquely incident waves (wave angle;  $\alpha = 10$  deg) + plain slope, Case 2: normal incident waves + circular shoal, and Case 3: normal incident waves + rectangular shoal. The diameter of the circular shoal in Case 2 was 100 cm and the water depth at the top of the shoal was 8.0 cm. The length and width of a top horizontal bed on the rectangular shoal in Case 3 were 120 cm and the water depth there was 4.0 cm. The distances between the wave guides at the both sides of the test sections were 530 cm for Case 1 and 400 cm for Cases 2 and 3. The experimental conditions are listed in Table 1. In the table,  $h_i$  is the still water depth at the offshore constant depth region,  $T$  the wave period,  $H_i$  the incident wave height.

### 2.2 Data acquisition and processing

Table 1 Experimental conditions

case	beach type	$h_i$ (cm)	$T$ (s)	$H_i$ (cm)	$\alpha$ (deg)
1	plain slope	49.7	1.33	5.5*	10
2	circular shoal	49.0	1.36	4.8	0
3	rectangular shoal	49.0	1.20	7.0	0

\* estimation

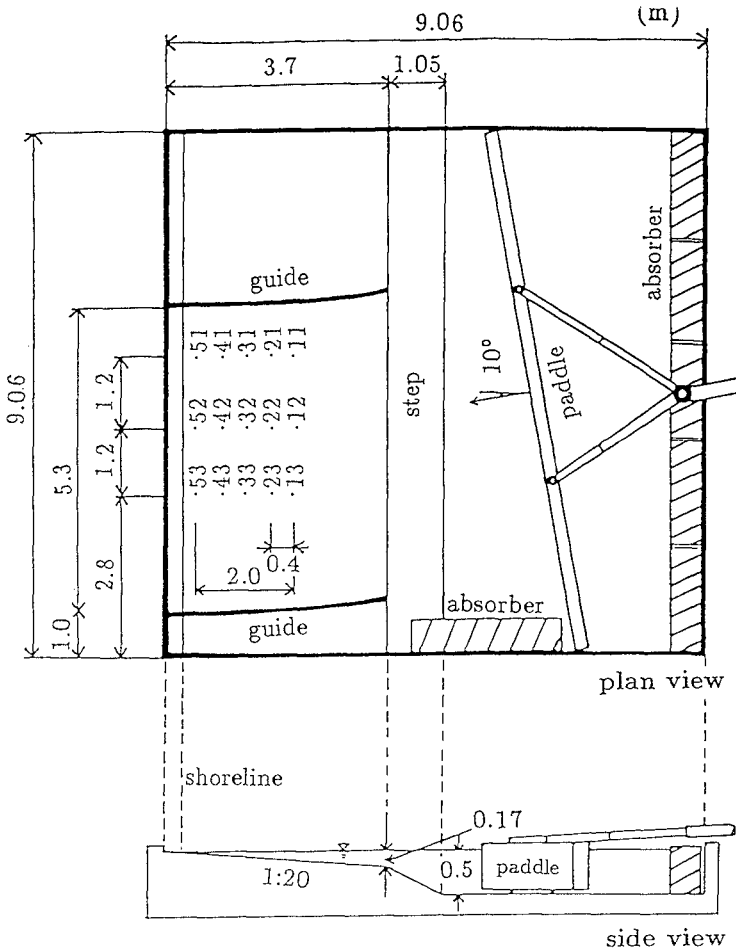


Fig. 1 Plan and side views of the wave basin (Case 1).

Cross-shore and alongshore components of velocity were independently measured by using an optic-fiber laser Doppler velocimeter (FLV). The currents were measured on 15 to 28 vertical measuring lines which located both inside and outside of the surf zone. Water surface elevation was separately measured by a capacitance type wave gage at the same locations. 5 to 16 measuring points were arranged from 2mm above the bottom to the wave crest level along each measuring line to obtain velocity profiles. The arrangement of the measuring lines for Case 1 is shown in Fig. 1.

Since the FLV used in the experiment was for one-component of the velocity vectors, velocity measurements were done twice for cross-shore and alongshore directions at each measuring point by rotating the optics. The velocity was measured over 10 wave periods with data rate of about 50 data per second.

The steady current component,  $\bar{u}$  and  $\bar{v}$ , of the velocity was calculated by integrating the measured instantaneous cross-shore and alongshore velocities,  $u(x, y, z; t)$  and  $v(x, y, z; t)$  over 10 wave periods and dividing by the total measuring time. At the measuring points above the wave trough level,  $u$  (or  $v$ ) was assumed to be 0, if no datum was found for more than 0.1 second.

### 2.3 Experimental results

Comparisons between the depth averaged velocity and the velocity close to the bottom are shown in Figs 2 and 3 for Cases 1 and 2, respectively. The contribution by undertow to the bottom velocity can be obviously seen in both cases. The figures show that even if the depth-averaged velocity can be predicted well, it should not be enough to evaluate the bottom shear stress or the sediment transport rate.

Figure 4 shows vertical profiles of cross-shore and alongshore steady current  $\bar{u}$  and  $\bar{v}$  at measuring lines in the central section for Case 1. The measuring line 12 located just before (offshore side) the breaking point and 52 was around the still water shoreline. As for the cross-shore direction, the profiles look similar to those observed for undertow in two dimensional wave flumes (see *e.g.* Okayasu *et al.*, 1988), and are shifted by the depth averaged velocity.

In the alongshore direction, the measured velocity is almost constant over the depth. However, since velocity near the bottom show the influence by the bottom boundary layer, the distributions look similar to the log profile in general. Above the wave trough level, velocity shows less value than that below, because the instantaneous velocity was not integrated while the measuring point was out of the water. The results shown here are different from those by Visser (1984) in which the profiles showed linear distributions. From the figures, it can be said that it is possible to evaluate the 3-D distribution of nearshore currents by composing the cross-shore and alongshore currents which are separately obtained.

Figure 5 shows examples of 3-D distribution of nearshore current for Case 1. The point No. 13 located around the breaker line, No. 42 was at the middle

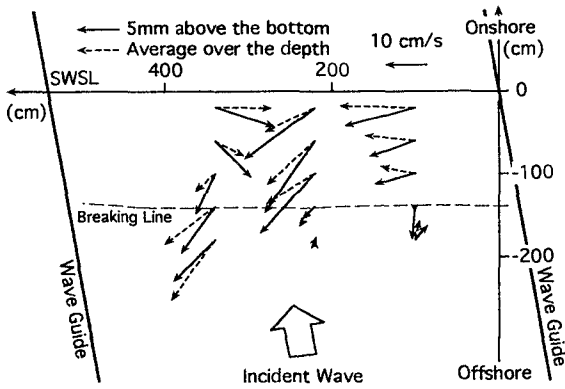


Fig. 2 Depth averaged and near-bottom velocity for Case 1.

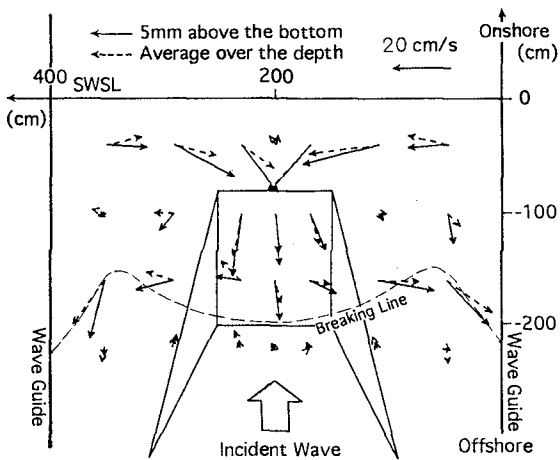


Fig. 3 Depth averaged and near-bottom velocity for Case 2.

of the inner region of the surf zone. The velocity vectors of nearshore current change the direction significantly along the vertical axis, and have spiral distributions. The figure also indicates the existence of strong onshore current above the trough level which should contribute to the lateral mixing of the sea water as well as the undertow.

### 3. Quasi 3-D nearshore current model with momentum flux by large vortexes

A quasi 3-D nearshore current model proposed in the present study can be divided into three parts which are 1) calculation for wave field, 2) calculation for 2-DH current field, and 3) calculation for vertical distribution of the



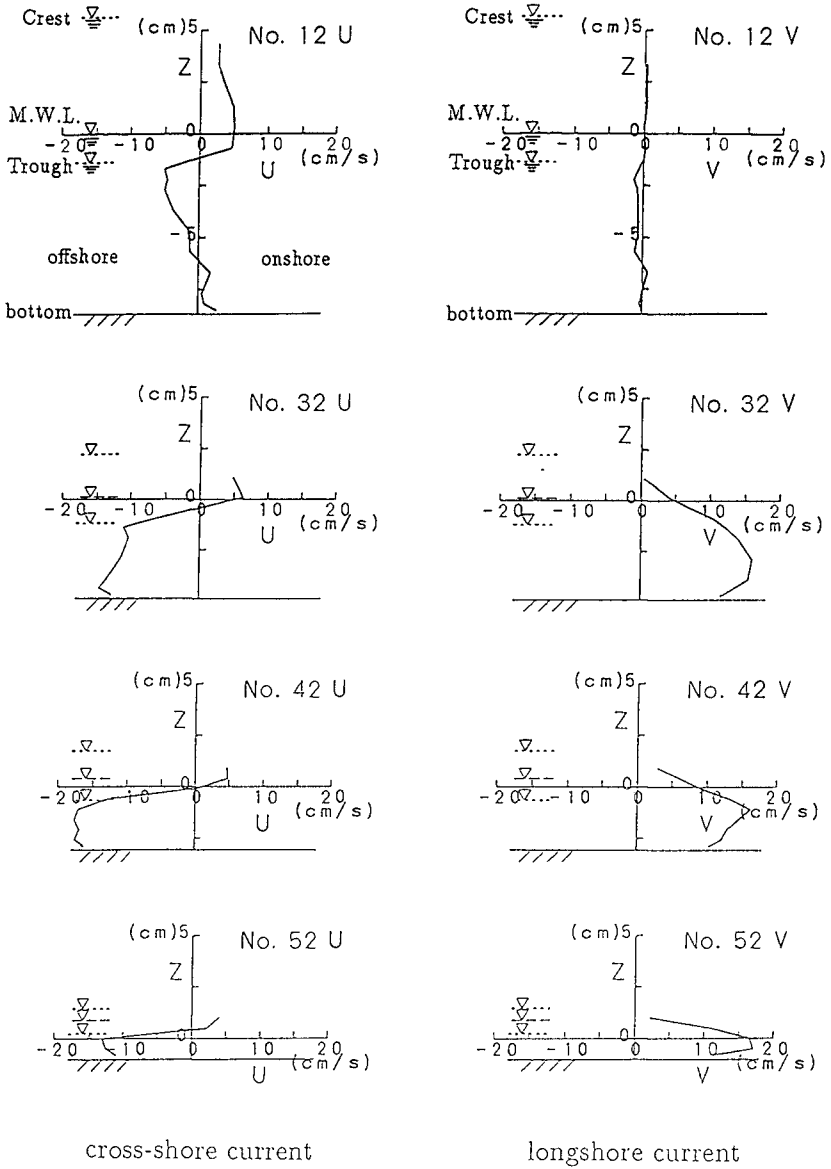


Fig. 4 Vertical distributions of cross-shore and alongshore current (Case 1).

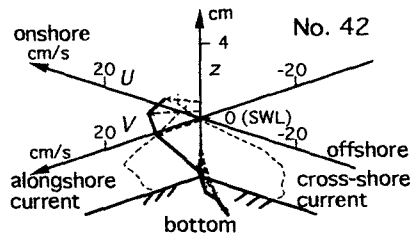
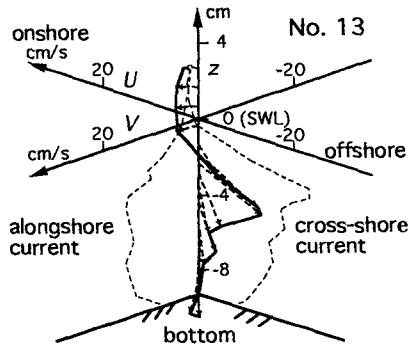


Fig. 5 3-D distribution of nearshore current (Case 1).

current. For the wave and current fields, a 2-DH model which is similar to one proposed by Ohnaka *et al.* (1988) is used. In the current model, both of the momentum flux by wave motion and the momentum flux due to the large vortexes formed on the front face of breaking waves are considered as driving forces to induce the nearshore current. In the wave field calculation, as the wave-current interaction is considered, the shoreline change is predicted with an iteration process between wave and current field calculations.

The depth averaged current in the wave propagation direction is expanded on the vertical axis to obtain the undertow profile by using a method proposed by Okayasu *et al.* (1990). In the direction normal to the wave propagation direction, constant value is given for vertical distribution of the current as found in the experimental results shown in the previous section. Finally, 3-D distribution of the nearshore current is obtained by composing those profiles with an assumption that the interaction between them is negligible as described in Svendsen and Lorenz (1989)

### 3.1 2-DH wave-current model

In order to evaluate the wave field, the following time-dependent mild slope equation in which wave-current interaction is taken into account is used after

Ohnaka *et al.* (1988):

$$m \frac{\partial \zeta}{\partial t} + \nabla \cdot (\mathbf{U}\zeta) + \nabla \cdot (n\mathbf{Q}) = 0 \quad (1)$$

$$\frac{\partial \mathbf{Q}}{\partial t} + \omega c^2 \nabla \frac{\partial \zeta}{\partial \sigma} + f_D \mathbf{Q} = 0 \quad (2)$$

$$m = 1 + \frac{\sigma}{\omega} (n - 1), \quad n = c_g/c \quad (3)$$

in which  $t$  is the time,  $\nabla$  the differential operator in horizontal directions,  $\zeta$  the surface elevation,  $\mathbf{Q}$  the flow rate by waves,  $\mathbf{U}$  the steady current,  $c$  the phase velocity vector,  $c_g$  the group velocity vector and  $f_D$  the attenuation factor by wave breaking.  $\omega$  is the angular frequency without current and  $\sigma$  the relative angular frequency with current. Since the calculation procedures are also similar to those by Ohnaka *et al.*, only the differences will be described hereafter.

The breaking point is determined by using the ratio of water particle velocity to wave celerity. Isobe (1987) approximated the ratio of it at the breaking point by the following formula:

$$\begin{aligned} \left(\frac{\hat{u}}{c}\right)_b &= 0.53 - 0.3 \exp\left(-3\sqrt{\frac{h_b}{L_0}}\right) \\ &+ 5(\tan\beta)^{3/2} \exp\left\{-45\left(\sqrt{\frac{h_b}{L_0}} - 0.1\right)^2\right\} \end{aligned} \quad (4)$$

where  $\hat{u}$  is the horizontal velocity at the still water level,  $c$  the celerity,  $h$  the mean water depth,  $L_0$  the deep-water wavelength,  $\tan\beta$  the bottom slope and subscript  $b$  denotes the quantity at the breaking point.

The attenuation factor  $f_D$  by wave breaking is expressed as

$$f_D = \alpha_D \tan\beta \sqrt{\frac{g}{h} \left(\frac{\hat{Q} - Q_r}{Q_s - Q_r}\right)} \quad (5)$$

which was given by Watanabe and Dibajnia (1988). In Eq. (5),  $\alpha_D$  is a parameter which linearly increases from 0 to 2.5 around the breaking point, then takes a constant value 2.5 in the inner region (see Okayasu *et al.*, 1990). The bottom slope  $\tan\beta$  is the average value of the bottom slope near the breaking point,  $g$  the acceleration of gravity,  $\hat{Q}$  the amplitude of the flow rate.  $Q_s$  and  $Q_r$  are  $\hat{Q}$  on constant slope and for wave recovery zone, respectively.

After calculation of the wave field, the current field and the wave setup are evaluated by using wave momentum flux. The obtained current field is

feedback to the wave field calculation and an iteration process is done until the steady solution can be obtained both for the wave and current fields.

The following basic equations are used to solve the current field:

$$\frac{\partial \bar{\zeta}}{\partial t} + \nabla U(h + \bar{\zeta}) = 0 \quad (6)$$

$$\frac{\partial \mathbf{U}}{\partial t} + (\mathbf{U} \cdot \nabla) \mathbf{U} + \mathbf{F} - \mathbf{M} + \mathbf{R} + g \nabla \bar{\zeta} = 0 \quad (7)$$

in which  $\mathbf{F}$  is the bottom friction term,  $\mathbf{M}$  the horizontal mixing term and  $\mathbf{R}$  the radiation stress term. In the calculation, momentum flux due to the organized large vortexes (surface rollers) formed on the front face of breaking waves is taken into account as described in the next section.

### 3.2 Effect of large vortexes on nearshore circulation

Okayasu *et al.* (1990) proposed a 1-D (cross-shore) wave breaking model in which energy flux due to large vortexes formed near the wave crests is taken into account to evaluate the energy dissipation by wave breaking. In the model, the wave energy is once transferred to the energy of large vortexes before changing to the turbulence energy. The momentum flux by these large vortexes affects the balance of the mean water level, the setup. In the 2-DH field, the influence on the momentum balance should appear on the nearshore current field. In the present model, the effect of the momentum flux due to large vortexes are investigated by coupling with a numerical nearshore current model in the following manner.

It is assumed, as Okayasu *et al.* (1990) did in the breaking process, that the energy of waves,  $E_w$ , dissipates to turbulence through the energy of large vortexes,  $E_v$ . If the energy transfer from waves to large vortexes is irreversible, the energy transfer rate  $T_B$  can be expressed as

$$T_B = -\nabla \cdot (c_g E_w) \quad (8)$$

in which  $c_g E_w$  is the energy flux by wave motion. The organized large vortexes propagate with the wave crests. Since the phase velocity  $c$  is nearly equal to the group velocity  $c_g$  in the surf zone, the energy flux by the large vortexes can be approximated by  $E_v c_g$ , which satisfies the following equation:

$$\nabla \cdot (c_g E_v) = T_B - D_B. \quad (9)$$

where  $D_B$  is the dissipation rate per unit area through turbulence by wave breaking.

In the model of Okayasu *et al.*, energy transferred from wave motion to large vortexes at a certain location equally dissipates over the dissipation length,  $l_d$ , which is determined by the local water depth. As the large vortexes

move with the wave crests, the energy transfer process must be considered along the wave propagating direction. However, the energy of large vortexes in the present model is calculated by using  $x$ -components as follows with assumptions that the angle of the wave propagation is very small to the  $x$ -axis in the calculating grids and the change of the angle within the length  $l_d$  is also negligible:

$$T_{Bx} = -\frac{\partial c_{gx} E_w}{\partial x} \quad (10)$$

$$D_{Bx} = \int_{-\infty}^x t_d(x, x') dx' \quad (11)$$

$$\frac{\partial(c_{gx} E_w)}{\partial x} = T_{Bx} - D_{Bx} \quad (12)$$

where  $c_{gx}$  is the  $x$ -component of  $c_g$ .  $t_d$  is evaluated after Okayasu *et al.* (1990).

By assuming the internal velocity distribution in a vortex, the momentum flux due to organized large vortexes,  $S_v$ , can be evaluated from  $E_v$  as follows:

$$S_v = \frac{5}{3} E_v. \quad (13)$$

The total radiation stress including the additional radiation stress due to  $S_v$  in the horizontal plane can be described as

$$\left. \begin{aligned} S_{xx} &= S'_{xx} + S_v \cos^2 \alpha \\ S_{yy} &= S'_{yy} + S_v \sin^2 \alpha \\ S_{xy} &= S'_{xy} + \frac{1}{2} S_v \sin 2\alpha \end{aligned} \right\} \quad (14)$$

where  $S'_{xx}$ ,  $S'_{yy}$  and  $S'_{xy}$  are radiation stresses due to pure wave motion and  $\alpha$  the angle of wave propagation to the  $x$ -axis. The influence by the organized vortex motion to the wave motion is neglected here.

### 3.3 Vertical distribution of undertow

The vertical distribution of cross-shore current is evaluated by the undertow model proposed by Okayasu *et al.* (1990). It is assumed that the large vortexes are formed along the wave crest lines and move to the wave propagating direction in which the undertow is also considered.

In this model, the undertow profile is essentially determined by the energy dissipation rate at that location. The cross-shore component of nearshore current only shifts that fixed profile to the positive or negative direction. Therefore, even if the magnitude of cross-shore component of nearshore current is comparable to that of undertow, the interaction between them which should exist in nature is not considered. In the present cases, the nearshore current is not so strong. However, if it is large, such influence must be taken into account.

In the direction normal to the wave propagation direction, no depth dependent velocity component is given to the steady current obtained by the 2-DH nearshore current model.

#### 4. Comparisons with measured values

The calculated nearshore current is compared with the measured values for Case 1. Sinusoidal waves which have the wave period,  $T = 1.33$  s and the wave height,  $H = 5.5$  cm are given along  $x$ -axis at the offshore boundary of the computational domain. The shoreline boundary makes an angle of 10 degree to  $y$ -axis. The bottom slope is 1/20, the grid space is 8 cm for both of  $x$  and  $y$ -axes. The side boundaries are treated as perfect reflective straight boundaries.

##### 4.1 Comparisons of 2-DH current field

Figures 6 (a) and (b) show the 2-D nearshore current which are calculated by the conventional model and the present model, respectively. Arrows with broken lines show the measured steady current averaged over the total depth. For both figures, the small clockwise circulation which can be seen at the left upper corner of the measured field is not predicted by the models. This may be because of the straight side boundaries and unevenness of the bottom of the basin which could not be controlled enough at the measurements.

The calculated alongshore current in Fig. 6 (b) is larger than that in Fig. 6 (a). This shows that the increment of the momentum flux by wave breaking has a considerable effect on the nearshore circulation. It can be seen that the model with the momentum flux by large vortexes generally gives the better estimates.

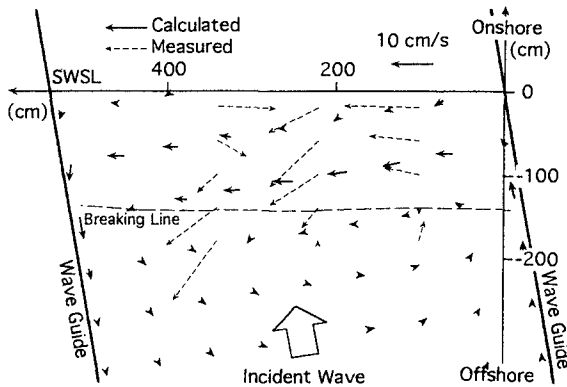
Figures 7 (a) and (b) give comparisons between calculated and measured currents at 5 mm above the bottom. Figure 7 (a) is for the model without the large vortexes by wave breaking and Fig. 7 (b) is for the present model. Figure 7 (b) gives the better agreement. It can be said that the influences both by the large vortexes and the three dimensionality due to undertow should be considered for the estimation of the near bottom velocity.

##### 4.2 3-D distribution of nearshore current

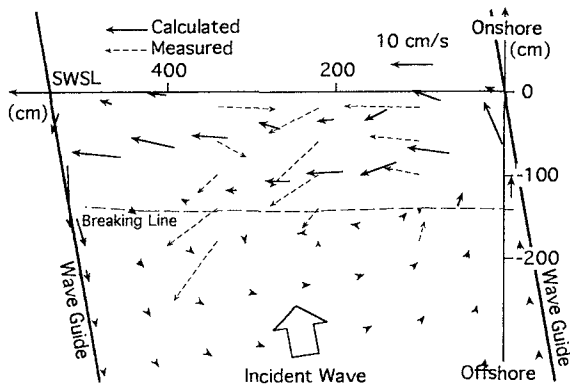
The calculated and measured profiles of cross-shore current are shown in Fig. 8. The location is denoted by the measuring point shown in Fig. 1. The profiles are well estimated here, but the general agreement is strongly dependent on the accuracy of the 2-DH model.

Figure 9 gives the 3-D distribution of calculated and measured nearshore currents in the middle of the surf zone. The calculated values are only obtained below the wave trough level. However, it can be concluded that the present model estimates the 3-D distribution of nearshore current well in this region.

#### 5. Conclusions



(a) Calculation without momentum flux due to large vortexes

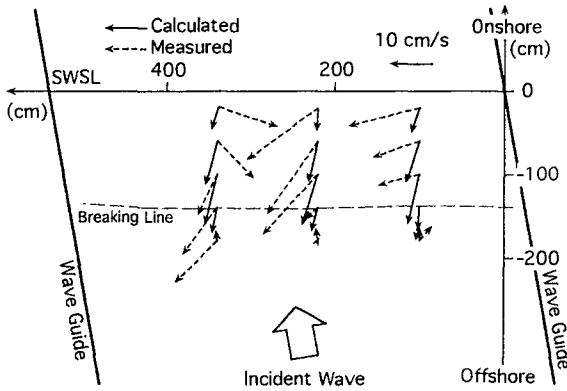


(b) Calculation with momentum flux due to large vortexes

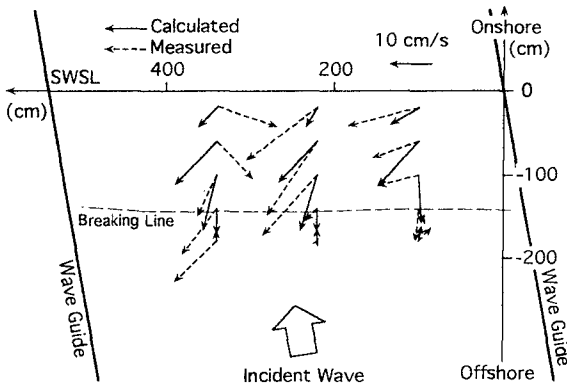
Fig. 6 Measured and calculated depth averaged nearshore current (Case 1).

In the present study, laboratory experiments were performed on nearshore current induced by regular waves in a wave basin. Characteristics of three dimensional distribution of the nearshore current was investigated. A model was proposed in which momentum flux due to large vortexes formed on the front face of breaking waves was included to evaluate two dimensional current field in the basin. This 2-DH nearshore current model was expanded to a quasi 3-D model by coupling with an 1-DV undertow model which gave vertical distribution of cross-shore component of the nearshore current. The model was examined with the experimental results. The conclusions of the present study are as follows.

- 1) Direction and amplitude of the nearshore current significantly change along



(a) Calculation without momentum flux due to large vortexes



(b) Calculation with momentum flux due to large vortexes

Fig. 7 Measured and calculated near-bottom velocity (Case 1).

the vertical axis and have spiral distribution. It is necessary to consider the vertical distribution of nearshore current to evaluate near bottom velocity in the surf zone.

- 2) Profiles of cross-shore currents look similar to those observed in 2-DV wave flumes. Alongshore currents take almost constant values over the depth. Therefore, it may be possible to evaluate the 3-D distribution of nearshore currents by composing the cross-shore and alongshore currents which can be separately obtained.
- 3) Momentum flux by the large vortexes of breaking waves causes significant change on the nearshore current field. A 2-DH numerical model in which this additional momentum flux is taken into account improves the



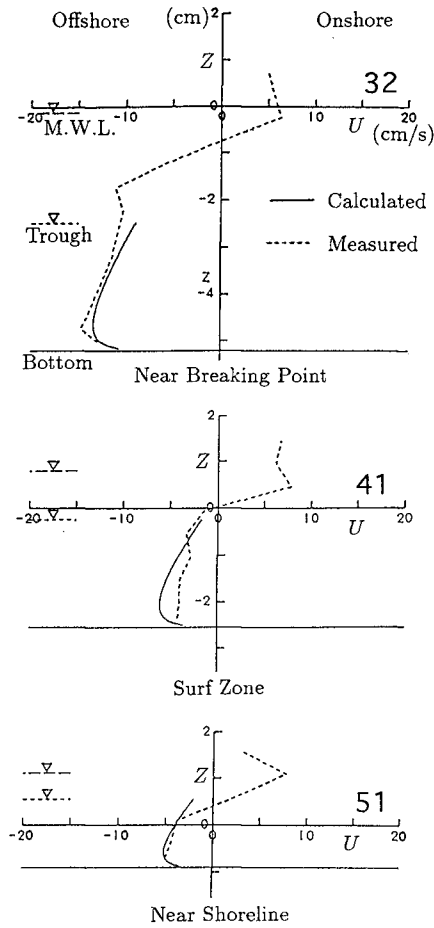


Fig. 8 Measured and calculated profiles of cross-shore current.

estimation of the nearshore current field.

- 4) A quasi 3-D nearshore current model presented in this paper can predict the 3-D distribution of nearshore current below the wave trough level.

**References**

De Vriend, H.J. and M.J.F. Stive 1987: Quasi-3D modeling of nearshore currents, *Coastal Eng.*, Vol. 11, pp.565-601.

Isobe, M. 1987: Parabolic equation model for transformation of irregular waves due to refraction, diffraction and breaking, *Coastal Eng. Japan*, Vol. 30, No.1, pp.33-47.

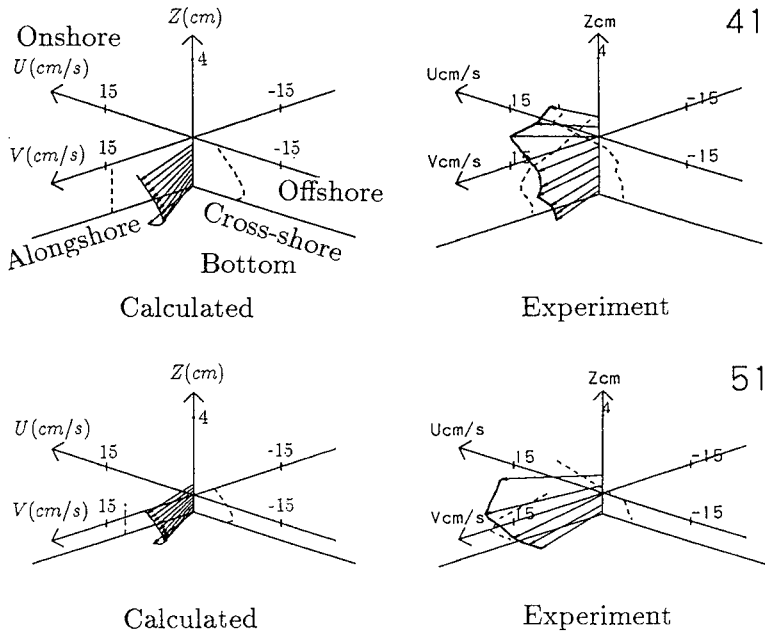


Fig. 9 Measured and calculated 3-D distribution of nearshore current.

- Ohnaka, S., A. Watanabe and M. Isobe 1988: Numerical modeling of wave deformation with a current, *Proc. 21st Int. Conf. Coastal Eng.*, pp.5393-407.
- Okayasu, A., T. Shibayama and K. Horikawa 1988: Vertical variation of undertow in the surf zone, *Proc. 21st Int. Conf. Coastal Eng.*, pp. 478-491.
- Okayasu, A., A. Watanabe and M. Isobe, 1990: Modeling of energy transfer and undertow in the surf zone, *Proc. 22nd Int. Conf. Coastal Eng.*, pp.123-135.
- Sanchez-Arcilla, A., F. Collado and A. Rodriguez 1992: Vertically varying velocity field in q-3D nearshore circulation, *Proc. 23rd Int. Conf. Coastal Eng.*, pp.2811-2824.
- Svendsen, I.A., 1984: Mass flux and undertow in a surf zone, *Coastal Eng.*, Vol. 8, pp.347-365.
- Svendsen, I. A. and R. S. Lorenz 1989: Velocities in combined undertow and longshore currents, *Coastal Eng.*, Vol. 13, pp.55-79.
- Visser, P. J. 1984: Uniform longshore current measurements and calculations, *Proc. 19th Int. Conf. Coastal Eng.*, pp.2192-2207.
- Watanabe, A. and M. Dibajnia 1988: A numerical model of wave deformation in surf zone, *Proc. 21st Int. Conf. Coastal Eng.*, pp.578-587.

## CHAPTER 179

### SUSPENDED SEDIMENT CAUSED BY WAVES AND CURRENTS

Masanobu Ono<sup>1)</sup>, Kyu Han Kim<sup>2)</sup>, Toru Sawaragi<sup>3)</sup> and  
Ichiro Deguchi<sup>4)</sup>

#### **Abstract**

A procedure to estimate vertical diffusion coefficient and reference concentration of time averaged suspended sediment concentration caused by waves and current are discussed based on experimental results obtained in a laboratory.

It is found that the non-dimensional diffusion coefficient normalized by the product of shear velocity  $u^*$  and the equivalent roughness  $k_s$ , is more closely related to the Shields' number when the shear velocity is evaluated by using the equivalent roughness where the effect of ripple geometry is taken into account. The reference concentration is not a unique function of the sediment Shields' number. Incident wave period has also influence on the reference concentration.

#### **Introduction**

Waves and currents around coastal structures and navigation channels have large spatial gradients that cause non-equilibrium sediment transport. In the analysis of topographic changes around these obstacles, we have to take into account the effect of non-equilibrium property of sediment transport. Especially, non-equilibrium property of suspended sediment rather than that of bed load plays very important role. Because it takes bed particles a little time to adopt themselves to the new surroundings and there is an instantaneous adjustment to equilibrium state in the very vicinity of the bottom.

To evaluate suspended sediment transport rate based on an advection-diffusion equation, we have to know both concentration and transporting velocity. The authors have already developed highly accurate numerical procedure for solving the advection-diffusion equation by applying a split-operator approach (Komatsu, et al., 1985). The accuracy of the numerical procedure deeply depends on a boundary

<sup>1)</sup>Research Assoc., <sup>3)</sup>Prof., and <sup>4)</sup>Assoc. Prof., Dept. of Civil Engineering, Osaka University, Yamada-oka, Suita-city, Osaka 565, Japan

<sup>2)</sup>Assis. Prof., Dept. of Civil Engineering, Kwan-Dong University, Korea

condition at the bottom (reference concentration or vertical sediment flux at the bottom) and diffusion coefficient. Until now, many studies have been conducted about suspended sediment due to waves in equilibrium state. Only a few have been carried out about the non-equilibrium suspended sediment concentration and the effect of current superposed on waves.

The aim of this study is to investigate the effect of current on suspended sediment, especially the reference concentration and the vertical diffusion coefficient of suspended sediment, through experiments.

### **Typical example of topographic change caused by non-equilibrium sediment transport**

First of all, we briefly examine the characteristics of non-equilibrium suspended sediment concentration measured in an experiment and an applicability of the numerical procedure for predicting non-equilibrium sediment concentration. Figure 1 shows the typical example of non-equilibrium suspended sediment transport caused by waves and current.

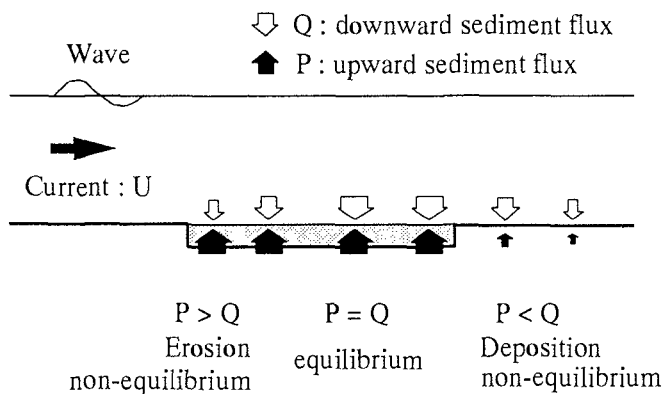


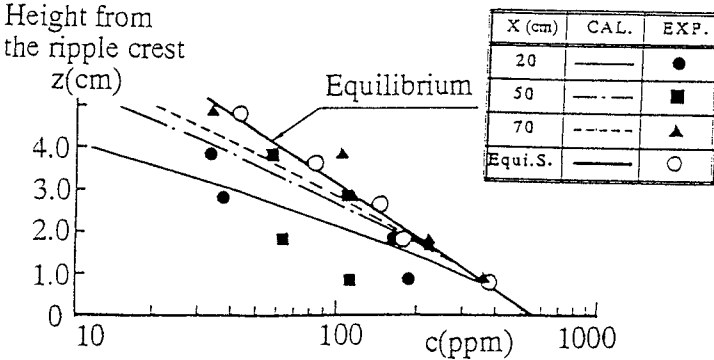
Fig. 1 Typical example of non-equilibrium suspended sediment transport

The waves and current are in the same direction on a horizontal bottom where a part of the bottom was replaced by a movable bed. Around the both sides of the movable bed, non-equilibrium suspended sediment transport takes place due to the unbalance of upward and downward sediment flux. Near the upstream end of the movable bed, only upward transport occurs and there is little settling flux and water depth increases. Near the downstream end of the movable bed, there is no upward sediment flux and only settling flux exists. It is needless to say that the water depth decreases there.

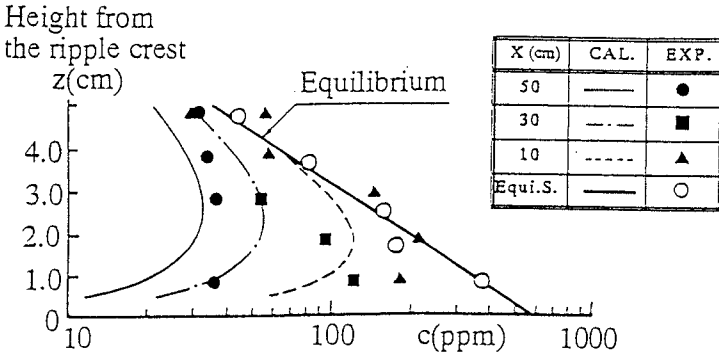
To predict non-equilibrium suspended sediment concentration numerically, the details of which I will mention later, we have to give reference concentration and diffusion coefficient. We should fundamentally use reference concentration and diffusion coefficient for suspended sediment under the non-equilibrium condition.

However, there are various degree of non-equilibrium property and it is difficult to obtain universal expression of reference concentration and diffusion coefficient under the non-equilibrium condition. Then we tentatively use those values obtained from the experiment under the equilibrium condition.

Figure 2 shows the comparisons of measured and calculated distribution of suspended sediment concentration. Fig.(a) is the non-equilibrium state near the upstream end of the movable bed. Fig.(b) is the results near the downstream end of the movable bed. x axis is taken positive in the direction of waves and currents from the edge of upward movable bed.



(a) Distribution of non-equilibrium sediment concentration near the upstream end of the movable bed



(b) Distribution of non-equilibrium sediment concentration near the downstream end of the movable bed.

Fig. 2 The comparisons of the numerical results and measured value of the vertical distribution of non-equilibrium suspended sediment concentration. (h=20cm, D=0.012cm, U=17cm/sec, T=1.25sec, H=6cm)

In spite of the usage of reference concentration and diffusion coefficient of equilibrium condition, the numerical results coincide with the measured results relatively well. So we can judge that we can predict non-equilibrium suspended

sediment concentration by applying the split operator approach provided that we can give the reference concentration and diffusion coefficient even under the equilibrium state.

### **Experiments for diffusion coefficient and reference concentration of equilibrium suspended sediment concentration**

Experiments were carried out in two two-dimensional wave tanks of different size. Length, depth and width of a large tank were 30m\*1.9m\*1.8m and those of a small tank were 30m\*0.9m\*0.7m. Two kinds of bed materials of mean diameter  $D=0.012\text{cm}$  and  $0.035\text{cm}$  were used to make a movable bottom of the length 3m (in a small tank) and 6m (in a large tank). All experiments were conducted on a horizontal bottom of water depth between 10cm to 40cm. The range of wave height was 5cm to 20cm and wave period was 1second to 2.5seconds. In the small tank experiments, we generated current in the direction of wave propagation. The relative magnitude of current and wave  $U/u_b$  varied from 0 to 0.9, where  $U$  is the depth averaged velocity of current and  $u_b$  is the water particle velocity at the bottom due to waves. Some parts of the experiments were conducted by generating irregular waves of Bretschneider-Mitsuyasu type frequency spectrum.

Suspended sediment concentration was measured by using an optical sensor and sampling of sediment laden water. Figure 3 shows an examples of vertical distributions of time averaged suspended sediment concentration measured at the crest and the trough of the ripple.

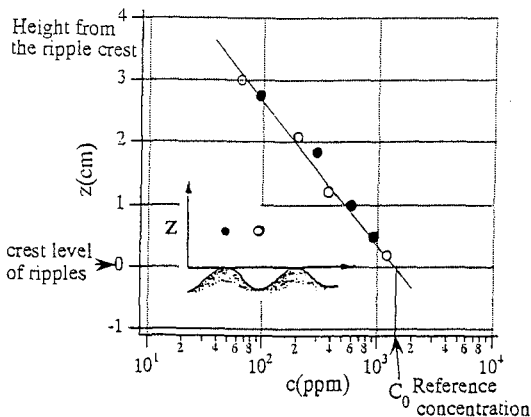


Fig. 3 Examples of vertical distributions of time averaged suspended sediment concentration measured at the crest and the trough of the ripple. ( $h=20\text{cm}$ ,  $D=0.012\text{cm}$ ,  $T=1.5\text{sec}$ ,  $H=6\text{cm}$ )

As has already been pointed out by many researchers, there is not any significant difference between the vertical distribution of time averaged concentration

measured on the crest and that measured at the trough and the time averaged concentration of suspended sediment became a log-linear vertical distribution. This implies that the diffusion coefficient of suspended sediment  $\kappa_z$  becomes constant through the depth.

In the figure, our methods to determine diffusion coefficient and reference concentration from experimental results are also illustrated. We evaluated diffusion coefficient from the vertical distribution of suspended sediment concentration and the relation shown by Eq.(1) that is derived from the usual one-dimensional diffusion equation in a steady state.

$$\kappa_z = -\frac{w_f z}{\log(c/C_0)} \quad (1)$$

where  $\kappa_z$  is the diffusion coefficient,  $w_f$  is the settling velocity.

The value of reference concentration  $C_0$  was determined from concentration at the crest level of ripples.

In the analyses of the diffusion coefficient and reference concentration, the experimental results obtained by other researchers that have already been published in journals and proceedings are also used together with our experimental results.

### Estimation of bottom shear stress and shear velocity under wave-current coexisting field

The diffusion coefficient and reference concentration are deeply related to a bottom shear stress or friction velocity under wave-current coexisting field. Equation (2) is our expression of the bottom shear stress  $\tau_{cw}(t)$  due to waves and current derived by solving a turbulent boundary layer equation (Deguchi, 1995) where the maximum shear velocity  $u_{cw}^*$  is given by Eq.(3).

$$\begin{aligned} \tau_{cw}(t) &= \tau_c + \tau_w(t) \\ &= \rho u_c^{*2} + \rho \hat{u}_{bp} \sqrt{\kappa \sigma z_0 u_{cw}^*} (R_{wp}^{\prime 2} + I_{wp}^{\prime 2})^{1/2} \cos(\sigma t - \psi') \quad (2) \\ \psi' &= \tan^{-1}(I_{wp}' / R_{wp}') \end{aligned}$$

$$\frac{u_{cw}^*}{u_b} = \frac{u_c^*}{u_b} + \sqrt{\kappa \left( \frac{z_0}{a_b} \right) \left( \frac{u_{cw}^*}{u_b} \right) (R_{wp}^{\prime 2} + I_{wp}^{\prime 2})^{1/2}} \quad (3)$$

$$R_{wp}' = 1 - \frac{\ker' q_0 \ker q_0 + \kei' q_0 \kei q_0}{(\ker q_0)^2 + (\kei q_0)^2}, \quad I_{wp}' = \frac{\ker' q_0 \kei q_0 + \kei' q_0 \ker q_0}{(\ker q_0)^2 + (\kei q_0)^2}$$

where  $q_0 = 2\{z_0 / (\kappa u_{cw}^* / \sigma)\}^{1/2}$ ,  $u_c^*$  is the bottom shear velocity due to current,  $z_0$  is the height of roughness element,  $\sigma$  is the angular frequency,  $\kappa$  is the Karman's constant and  $\ker$  and  $\kei$  are the real and the imaginary parts of the modified Bessel Functions of 2nd. kind,  $\ker'$  and  $\kei'$  are the derivatives of  $\ker$  and  $\kei$ , respectively.

The depth-averaged velocity  $U$  is calculated by integrating the steady velocity between  $z=z_0$  and  $h$ . From this relation, the bottom shear velocity  $u_c^*$  with respect to the mean current is expressed by Eq.(4)

$$\frac{u_c^*}{u_b} = \frac{1}{2} \left\{ -\left(\frac{\alpha_2}{\alpha_1}\right)\left(\frac{u_{cw}^*}{u_b}\right) + \sqrt{\left(\frac{\alpha_2}{\alpha_1}\right)^2\left(\frac{u_{cw}^*}{u_b}\right)^2 + 4\kappa\left(\frac{U}{u_b}\right)\left(\frac{u_{cw}^*}{u_b}\right)\frac{h-z_0}{\alpha_1}} \right\} \quad (4)$$

$$\alpha_1 = h \ln(\delta_w/z_0) - \delta_w + z_0 \quad \alpha_2 = h \ln(h/\delta_w) - h + \delta_w$$

where  $\delta_w$  is the thickness of wave boundary layer.

Figure 4 illustrates the comparison of measured and calculated distribution of mean current. Solid line is the calculated vertical distribution of mean current velocity without waves and the broken line is the calculated velocity profile in the case of wave and current coexisting field. Open and closed circles in the figure are the time averaged measured velocity in the cases of no waves and wave-current coexisting field.

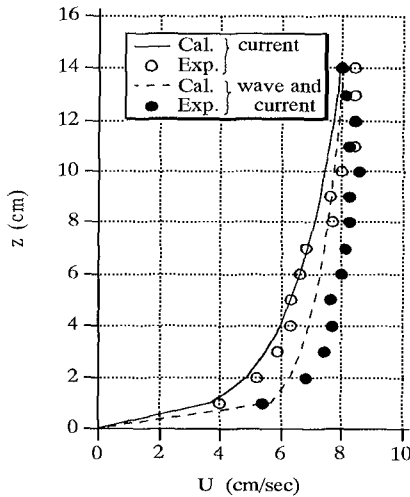


Fig. 4 Vertical distribution of mean current velocity in the case of wave and current coexisting field. ( $h=20\text{cm}$ ,  $D=0.012\text{cm}$ , current,  $U=7.0\text{cm/sec}$ ; wave and current : $T=1.5\text{sec}$ ,  $H=6\text{cm}$ ,  $U=7.5\text{cm/sec}$ )

The velocity was measured by an electromagnetic current meter. It is found that the calculated velocity profile reproduce the measured profile. It is also found that the presence of waves increases the kinematic eddy viscosity that results in the steep velocity profile.

**Results and discussion**

**(1) Diffusion coefficient**

Here we examine the expression of diffusion coefficient based on the continuity equation of suspended sediment concentration that is expressed by Eq.(5).



$$\frac{\partial c}{\partial t} + \frac{\partial}{\partial x}(cu_s) + \frac{\partial}{\partial z}(cw_s) = 0 \quad (5)$$

We decompose the variables in Eq.(5) into steady part, wave and turbulent components and express each component by using an over bar(-), subscript p and (') as follows:

$$c = \bar{c} + c_p + c'$$

$$u_s = \bar{u}_s + u_{sp} + u_s' \quad (6)$$

$$w_s = -\bar{w}_f + w_{sp} + w_s'$$

Substituting these components into Eq.(5) and taking time average, we obtain Eq.(7)

$$\frac{\partial \bar{c}}{\partial t} + \frac{\partial}{\partial x}(\overline{cu_s}) - \frac{\partial}{\partial z}(\overline{cw_s}) = \frac{\partial}{\partial x} \left( \kappa_x \frac{\partial \bar{c}}{\partial x} \right) + \frac{\partial}{\partial z} \left( \kappa_z \frac{\partial \bar{c}}{\partial z} \right) \quad (7)$$

where the diffusion coefficient is expressed by Eqs.(8) and (9).

$$\kappa_x = -(\overline{c_p u_{sp}} + \overline{c' u_s'}) / \frac{\partial \bar{c}}{\partial x} \quad (8)$$

$$\kappa_z = -(\overline{c_p w_{sp}} + \overline{c' w_s'}) / \frac{\partial \bar{c}}{\partial z} \quad (9)$$

The first term of Eq.(7) is neglected in a steady state. We assume here that horizontal gradient of mean current velocity is negligibly small and all variables are uniform in x-direction. Then Eq.(5) becomes a usual one dimensional diffusion equation.

On the other hand, Schmidt number is usually defined as Eq.(10)

$$\text{Schmidt number} = \varepsilon_z / \kappa_z \quad (10)$$

where  $\varepsilon_z$  is the kinematic eddy viscosity. It is often assumed that the order of Schmidt number is unity. If we adopt this assumption, the diffusion coefficient can be expressed in the same way as the kinematic eddy viscosity. We used the following form of the kinematic eddy viscosity as shown in Eq.(11) to solve the boundary layer equation:

$$\varepsilon_z \approx \kappa u_{cw}^* l \quad (11)$$

where  $l$  is the length scale.

According to this expression, we assume that the velocity scale and length scales of the diffusion coefficient be the shear velocity  $u^*$  and equivalent roughness  $k_s$ . The value of  $u^*$  depends on the expression of  $k_s$ . In the following, we will examine the relation between non-dimensional diffusion coefficient and Shields' number calculated by using two different expression of  $k_s$ , Eq.(12) and (13). Eq. (13) is proposed by Nielsen(1992) includes the effect of ripple geometry.

$$l = k_s = 2.5D \quad (12)$$

or

$$k_s = 8\eta^2 / \lambda + 5\phi_D D \quad (13)$$

Fig.5 is the result obtained by using Eq.(12) where we assume that the value of  $k_s$  is a unique function of  $D$ .

The vertical axis is the diffusion coefficient normalized by dividing measured diffusion coefficient by the product of  $u^*$  and  $k_s$ . The horizontal axis is grain roughness Shields' number  $\phi_D$  defined by Eq.(14).

$$\phi_D = u^{*2} / (\sigma' gD) \tag{14}$$

where  $u^{*1}$  is the shear velocity calculated by using Eq.(12),  $\sigma'$  is the immersed grain density,  $g$  is the gravity acceleration. In this case plotted data scatters in a wide range.

Author	Symbol	$U/u_b$	$\alpha=D/(f_w T)$	$wD/v$
Present study	I.W.	●	0	0.37-1.40
Present study	R.W.	○	0	0.22-0.31
Nielsen(1986)	R.W.	+	?	0.44
Staub et al.(1984)	O.F.	×	0	0.12-0.16
Tanaka et al.(1973)	R.W.C.	□	0	0.25-0.32
		■	0.1- 0.5	0.21-0.30
		▣	0.5- 0.9	0.17-0.24
		▤	-0.1- -0.5	0.23-0.30
		▥	-0.5- -0.9	0.16-0.20
Present study	R.W.C.	△	0	0.16-0.19
		▲	0.2-0.4	0.15-0.18
		▴	0.4-0.7	0.13-0.17
		▵	0.7-0.9	0.11-0.15
Nakato et al.(1977)	O.F.	◇	0	0.27-0.47
Hayakawa et al.(1983)	O.F.	◇	0	0.15-0.19
Nielsen(1984)	F	◆	?	0.07-0.19

I.W.: Irregular waves, R.W.: Regular waves, O.F.: Oscillatory flow,  
R.W.C.: Regular waves and currents, F: Field

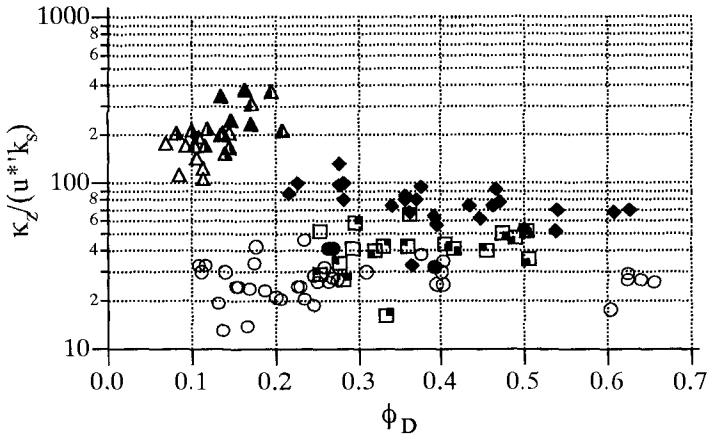


Fig. 5 Relation between non-dimensional diffusion coefficient and grain roughness Shields' number

Fig.6 shows the relation between non-dimensional diffusion coefficient and ripple roughness Shields' number  $\phi_\eta$ .

The vertical axis is again the non-dimensional diffusion coefficient and the horizontal axis is the ripple roughness Shields' number  $\phi_\eta$  defined by Eq.(15).

$$\phi_\eta = u^{*2} / (\sigma' gD) \tag{15}$$

where  $u^*$  is the shear velocity calculated by using Eq.(13).

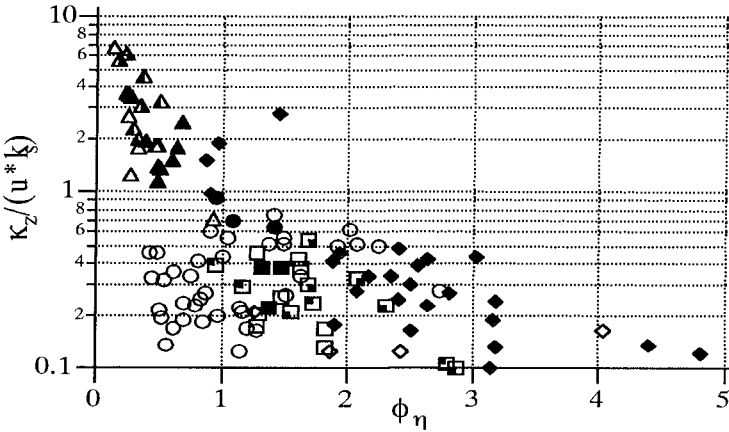


Fig. 6 Relation between non-dimensional diffusion coefficient and ripple roughness Shields' number

In this case, the scattering of data becomes small when compared with the data shown in Fig.(5). This implies that the length scale of the diffusion coefficient depends on vortex formation around ripples.

In the figure, the results obtained in the irregular wave experiments are also shown. The bottom shear velocity is calculated by using wave characteristics with respect to the rms wave height.

It was reported that there were no regular ripples on the bottom and sheet flow transport just begun in the case where ripple roughness Shields' number is greater than three. When  $\phi_\eta$  is larger than 0.7, the non-dimensional diffusion coefficient varies from 0.1 to 0.6. In the region where  $\phi_\eta$  is smaller than 0.7, non-dimensional diffusion coefficient increases a little with the increases in the value of  $U/u_b$ . In this region, waves have not large power to bring sediment into suspension and contribution of current to suspension becomes relatively large. However, it required further investigation about turbulence generated by ripples and diffusibility of suspended sediment to quantitatively estimate the value of diffusion coefficient.

**(2)Reference concentration**

We have already proposed semi-empirical expression for predicting reference concentration based on energetic consideration. The outline of the derivation of the expression for reference concentration are shown below.

We assumed that a part of the turbulent energy of vortex generated in the ripple trough is used to bring sediment into suspension. Tunstall and Inmen (1975) evaluated the kinematic energy of vortex formed in the trough of ripples that is expressed by Eq.(16) (see Fig. 7)

$$Ev = 2.26\rho(\Gamma/2\pi)^2 \tag{16}$$

where  $\Gamma$  is the strength of vortex circulation and is given by Eq.(17).

$$\Gamma / 2\pi = 0.39u_b\eta \tag{17}$$

The work  $W_v$  that is required to keep suspended sediment of the concentration  $C_0$  in the vortex whose diameter  $r_v$  is estimated by Eq.(18)

$$W_v = \rho C_0 \sigma' g w_f (T/2) r_v^2 \tag{18}$$

where  $r_v$  is expressed by the relation of Eq.(19).

$$r_v = 0.6\eta \tag{19}$$

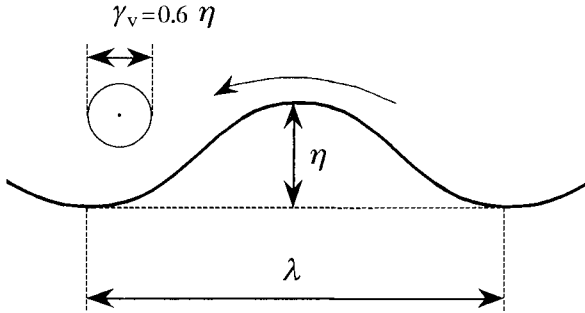


Fig. 7 Vortex generated on the ripple

We further assume that a part of  $E_v$  is used to keep sediment into suspension.

$$W_v \propto E_v \tag{20}$$

This leads to the following expression for  $C_0$ .

$$C_0 = \beta u_b^2 / (\sigma' g w_f T) \tag{21}$$

where  $\beta$  is the empirical coefficient.

When we replace  $u_b$  by using a shear velocity, we can finally obtain the expression of the reference concentration

$$C_0 = 0.49(\alpha \phi_D)^{1.77} \tag{22}$$

$$\alpha = D / (f_w w_f T)$$

where  $f_w$  is Jonsson's friction factor and  $T$  is wave period.

Figure 8 shows the relation between measured reference concentration  $C_0$  and grain roughness Shields' parameter  $\phi_D$ .

Straight lines in Fig.8 are the reference concentrations calculated from Eq.(22) for the various values of  $\alpha$ . In the figure, expression of reference concentration proposed by Fredsøe et al.(1978) is also shown. Measured reference concentration increases with the increase of the value of  $\alpha$  as was predicted by Eq.(22).

Measured reference concentration caused by wave and current decreases with the increase in the value of  $U/u_b$ . A ripple geometry was deformed into asymmetry by the presence of current. Significant suspended sediment cloud was generated only once within one wave period from the steep side of the ripple. Consequently, time

averaged concentration at the bottom (reference concentration) decreases when current exists.

To figure out the reference concentration in the presence of current, further investigation is required about asymmetrical property of generated ripples and flow field on them.

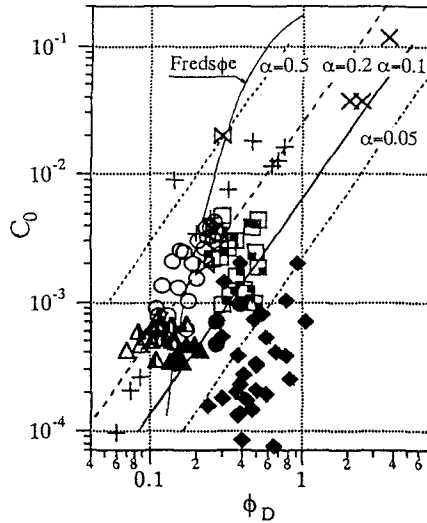


Fig. 8. Relation between measured reference concentration  $C_0$  and grain roughness Shields' parameter  $\phi_D$ .

## **Conclusions**

Characteristics of the vertical diffusion coefficient and the reference concentration of time averaged suspended sediment concentration caused by waves and current are examined based on the experimental results obtained in laboratory.

It is found that the non-dimensional diffusion coefficient normalized by the product of the shear velocity and the roughness element is closely related to the ripple roughness Shields' number when the shear velocity is evaluated using the relative roughness that includes the effect of ripple geometry. When ripple roughness Shields' number is larger than 3, ripples lose their two-dimensional shape and the non-dimensional diffusion coefficient becomes small.

Current superimposed on waves deforms ripple shape into asymmetry and the reference concentration of suspended sediment caused by waves and current decreases with the increase in the relative magnitude of current  $U/wb$ . The reference concentration is not a unique function of the sediment Shields number and incident wave period also influence the reference concentration as was expected from the energetic consideration shown in the paper.

## **Reference**

- Deguchi, I., 1995, Waves, wave-induced currents and sediment transport, in "Coastal Engineering-Waves Beaches and Wave-Structure Interactions-", Edited by. T. Sawaragi, Elsevier Science B.V. (in printing).
- Fredsoe, J., O.H. Andersen and S. Siberg, 1978, Distribution of suspended sediment in large waves, Proc. ASCE, Vol.110, No.ww2, pp.215-230.
- Hayakawa, N., G. Tsujimoto and H. Hashimoto, 1983, Velocity distribution and suspended sediment concentration over large scale ripple, Coastal Eng. in Japan, Vol.26, pp.91-100.
- Komatsu, T., F.M. Holly, Jr., N. Nakashiki and K. Ohguchi, 1985, Numerical calculation of pollutant transport in one and two dimensionals, JHHE, Vol.3, No.2, pp.15-30.
- Nakato, T., F.A. Locher, J.G. Glove and J.F. Kennedy, 1977, Wave entertainment of sediment from rippled bed, Proc. ASCE, Vol.103, No.ww1, pp.83-99.
- Nielsen, P., 1984, Field measurements of time averaged suspended sediment concentrations under waves, Coastal Engineering, Vol.8, pp.21-72.
- Nielsen, P., 1986, Suspended sediment concentrations under waves, Coastal Engineering, Vol.10, pp.23-31.
- Nielsen, P., 1992, Coastal bottom boundary layers and sediment transport, Advanced Series on Ocean Engineering, Vol.4, 324p.
- Sawaragi, T., I. Deguchi, M. Ono and K.S. Bae (1991), Numerical simulation for shoaling process of navigation channel, Int'l. Sympo. on Natural Disaster Reduction and Civil Engineering, JSCE, pp.117-126.
- Tanaka, N., H. Ozawa and A. Ogasawara, 1973, Experiments on sand movement by waves and currents, Rept. Port and Harbour Res. Inst., Vol.12, No.4, pp.2-22 (in Japanese).
- Tunstall, E.B. and D.L. Inman, 1975, Vortex generation by oscillatory flow over rippled surface, J.G.R., Vol.80, No.24, pp.3475-3484.

## CHAPTER 180

### Development of a Dune Erosion Model using SUPERTANK Data

Margery F. Overton<sup>1</sup>

John S. Fisher<sup>2</sup>

Kyu-Nam Hwang<sup>3</sup>

#### Abstract

A model predicting dune erosion under storm conditions has been developed using data from SUPERTANK laboratory experiments. In this model, the swash approach is applied with the basic assumption that the volume eroded from the dune is a function of the swash force acting on the dune. The swash force is characterized with swash parameters, specifically the swash height, the swash velocity and the swash period. For given storm conditions, the model predicts wave height variation across-shore, swash height variation on the beach face, swash velocity, swash period, swash forces and finally volume eroded at the dune. Predictions of swash parameters and dune erosion are compared with measurements from SUPERTANK laboratory experiments.

#### Introduction

A lot of effort has been made to develop a prediction model for dune erosion by storm events and the resulting beach profile. An extensive research program for the process of dune erosion due to wave impact was started by Fisher and Overton (1984). Their approach for the process of dune erosion is based on the interaction of the wave swash and the dune. This approach treats the dune erosion phenomenon as a time-dependent process in which a series of successive uprushes attack the dune face. Each individual uprush erodes a finite volume of sand which in turn is deposited on the eroding beach.

Currently, the most important achievement in the development of a dune erosion model due to wave impact is the experimental observation of the linear

---

<sup>1</sup> Associate Professor, Department of Civil Engineering, North Carolina State University, Box 7908, Raleigh, NC 27695-7908.

<sup>2</sup> Professor, Dept. of Civil Engineering, NCSU.

<sup>3</sup> Graduate Research Assistant, Dept. of Civil Engineering, NCSU.

relationship between swash force and dune erosion. This linear relationship has been confirmed through field measurements (Fisher et al., 1986) and laboratory experiments (Overton et al., 1988). Therefore, it is possible to predict the dune erosion from this relationship if the swash force is known for the given storm conditions. However, limited knowledge of swash parameters, which are identified as swash height, swash velocity and swash period, has discouraged the development of a quantitatively (or even qualitatively) reliable predictive model.

It is therefore highly instructive to understand qualitatively the hydrodynamics of the swash zone in terms of waves generated by storms outside the surf zone. These waves commonly serve as an input for the prediction of transformed waves in the surf zone. For this purpose, a set of experiments designed to simulate dune erosion under storm conditions at prototype scale was conducted in the large wave tank at the O. H. Hinsdale Wave Research Laboratory, Oregon State University as part of SUPERTANK Laboratory Data Collection Project. Through the analysis of SUPERTANK laboratory data for the swash parameters, an attempt is made in this study to produce useful information regarding hydrodynamics in the swash zone, and to develop a predictive model for dune erosion by wave impact.

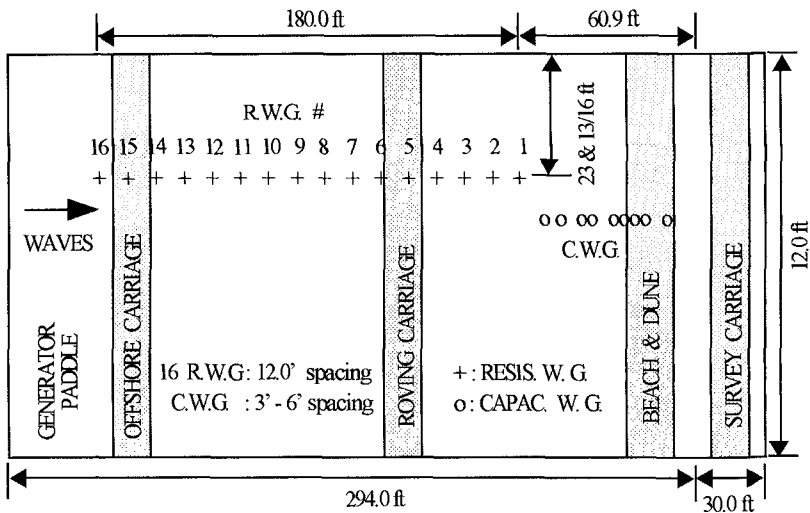


Figure 1. Configuration of flume and location of wave gages.

**Laboratory Experiments**

The experiments were designed to simulate dune erosion under storm conditions at prototype scale. Flume configurations with the locations of wave gages are shown in Figure 1. A dune of 5 ft height was constructed with fine sands



of median grain sizes,  $d_{50}$ , of 0.23 mm. A vibrating compactor was used to consolidate the artificial dune. Sixteen resistance wave gages designed at OSU (Dibble and Sollitt, 1989) were used to obtain wave data across-shore and ten capacitance type wave gages were placed on the beach in front of the dune to collect swash data. The OSU data acquisition system sampled the wave gages at a rate of 16 Hz. The pre- and post-test beach and dune profile were surveyed. Additionally, dune position was documented by a 35 mm camera before, during and after each experiment. Each photograph of the dune included the profile of the dune face and a 2 ft by 2 ft standard grid to determine scale.

Thirteen experiments were successfully conducted. The design conditions of each test are given in Table 1. The design wave heights,  $H$ , ranged from 1.640 ft to 2.625 ft while the wave periods,  $T$ , ranged from 3 sec to 6 sec. The duration of the tests,  $T_d$ , ranged from 10 minutes to 30 minutes and the water level (WL) varied from 9.5 ft to 11.0 ft. The water level is defined as the distance from the original bottom of the flume to the still water surface.

Test #	$T_d$ (min)	$T$ (sec)	$H$ (ft)	WL (ft)	Test #	$T_d$ (min)	$T$ (sec)	$H$ (ft)	WL (ft)
1	10	3.0	2.625	9.5	8	20	3.0	2.297	10.5
2	20	3.0	2.625	9.5	9	20	3.0	2.297	10.5
3	30	4.5	2.625	9.5	10	20	4.5	2.297	10.5
4	30	6.0	2.625	9.5	11	20	4.5	2.297	10.5
5	30	4.5	2.297	10.5	12	20	4.5	2.297	10.5
6	30	6.0	2.297	9.5	13	20	6.0	1.640	11.0
7	30	3.0	1.640	9.5					

Table 1. List of Experimental Design Parameters.

Using a standard Fourier Transform, frequency domain analyses were performed on the SUPERTANK hydrodynamic data collected in the prebreaking and breaking zone. The wave parameters calculated from frequency domain analyses are *rms* and significant wave height. Both time domain analyses and frequency domain analyses were performed on the time history of the water surface variation in the swash zone. The swash parameters calculated from time domain analyses are mean value of swash height, swash peak height, swash velocity, swash period. The representative swash heights calculated from the power spectra are *rms* and significant swash height.

Typical features of an individual swash recorded during the experiment are given in Figure 2. Height of swash is defined as the difference between the background height and the height of the plateau before the start of the backwash. The velocity of the leading edge of the swash (or swash velocity,  $V_{sw}$ ) is determined by identifying the time at which the swash hits the first and the second probes on

the beach. The swash period  $T_{sw}$  of an individual swash is defined as the time between the initial swash hits.

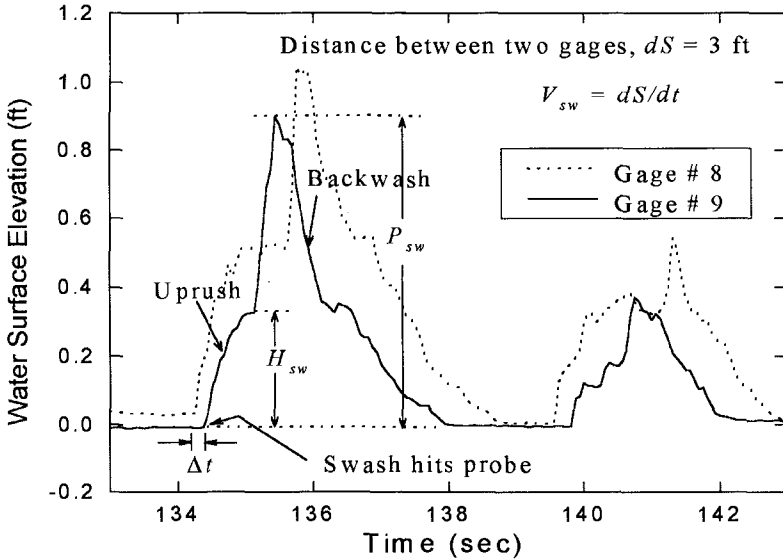


Figure 2. Definition of swash parameters.

Survey data was used to determine the dune and beach profiles for each test. A polynomial smoothing method was applied to the survey data to obtain the depth data equally spaced in the horizontal direction. Specific volume eroded at the dune,  $Q_e$ , was determined from the before and after profiles of the dune face as recorded on 35 mm film, and checked with survey profiles of the beach and dune. In order to differentiate between beach erosion and dune erosion, the initial face of the dune was used to define the seaward extent of the dune.

An individual swash force acting on the dune is defined as

$$F_{swi} = \rho V_{swi}^2 H_{swi} \quad (1)$$

where  $\rho$  is the density of the water,  $H_{swi}$  is an individual swash height and  $V_{swi}$  is the swash velocity. While quantifying the force for an individual swash is possible using (1), it is not always possible to measure the amount eroded due to that loading. One possible way is to use the "summing-up" method by Overton et al. (1988), in which the summation of the force in a given interval of time versus the volume of eroded in the same time interval becomes the quantity evaluated. Each individual swash force was determined by (1) and summed up to obtain the total swash force,  $F_{sws}$ , for a given duration of time. Linearity between dune erosion and swash force was examined. Figure 3 shows the estimated data and the best linear

fit line with a  $R$ -squared value of 0.90. An apparent linear relationship exists between dune erosion and swash force.

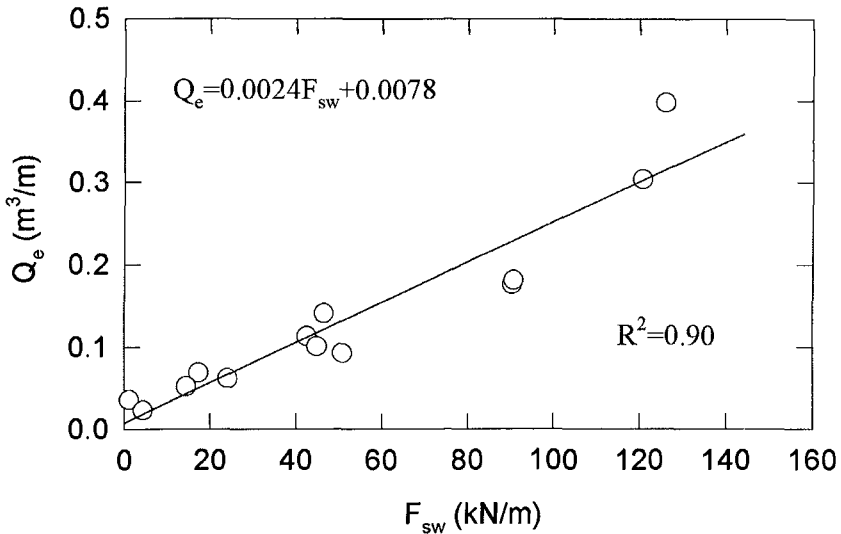


Figure 3. Linearity of dune erosion as a function of swash force.

### Modeling of Swash Parameters

Swash parameters required for the prediction of dune erosion are the swash height, swash velocity, and swash period. In the current stage of modeling dune erosion due to wave impact, individual swashes (or waves) are not considered. Instead, statistically representative swash parameters (e.g., mean, rms and significant swash) are used to develop the prediction model.

A beach profile in the cross-shore direction is divided into three regions: the prebreaking zone, surf zone, and swash zone. In order to predict the swash height in the swash zone with a given condition in deep water, it is necessary to predict the cross-shore variation of wave height in the prebreaking and surf zone. Linear wave theory has been used to determine wave height across-shore from deep water to the initial break point of waves. Wave height transformation in the surf zone has been calculated by applying the breaking wave dissipation model by Thieke and Sobey (1990).

#### Modeling of Wave Height

Several models have been developed to predict surf zone wave height variation, based upon the conservation of energy equation (Battjes and Janssen; 1978, Dally, et al.; 1985, and Stive; 1984). The steady-state, depth-integrated

equation governing the energy balance for waves propagating directly towards shore is simply

$$\frac{\partial F}{\partial x} = -D \tag{2}$$

where  $F$  is the wave energy flux,  $x$  is the distance along the propagation path, and  $D$  is the rate of energy dissipation per unit plan area due to breaking.

Thieke and Sobey (1990) established a form of a predictive equation for the breaking wave dissipation as

$$D = f_{bw} \omega E \tag{3}$$

where  $f_{bw}$  is a dimensionless breaking wave dissipation coefficient,  $\omega$  is the spectral peak frequency and  $E$  is the wave energy. Adopting a simple direct partition estimator yields an expression for  $f_{bw}$ :

$$f_{bw} = \alpha \left( 1 + \frac{H_m^2}{H_{rms}^2} \right) \exp \left( - \frac{H_m^2}{H_{rms}^2} \right) \tag{4}$$

where the coefficient  $\alpha$  is of order  $1/\pi$  (or perhaps  $H_b/(\pi h)$ ),  $H_m$ , a local limiting wave height, is order of  $0.83h$  and  $H_{rms}$  is the root-mean-square wave height.

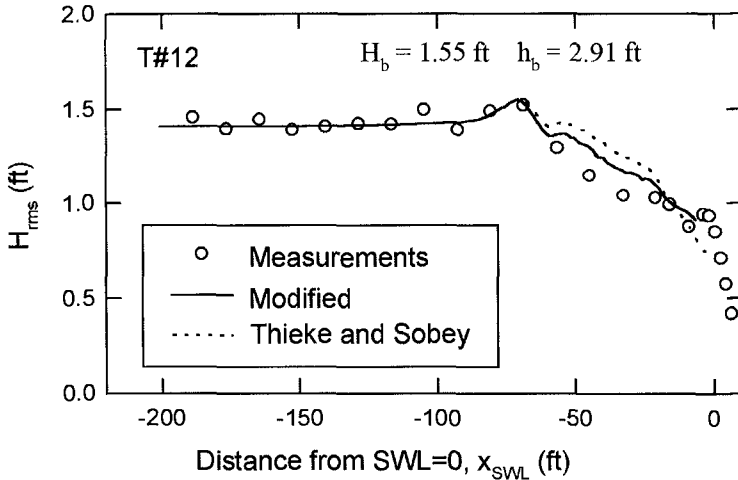


Figure 4. Measured and predicted wave height variation in the prebreaking and breaking zone.

Predictions by Thieke’s model for wave height variation in the surf zone are shown in Figure 4 as a dotted line. The measured  $rms$  wave height has been computed by  $2\sqrt{2}\sigma$  ( $\sigma$  is a spectral estimate of the standard deviation of the water surface). While the trend predicted by Thieke’s model is physically reasonable, the model underpredicts significantly the wave height near the swash zone. In order to obtain more accurate predictions of the wave height near the swash zone, a modification to Thieke’s model has been made to decrease the breaking wave

dissipation near the swash zone. Calibrating the predicted wave heights (by Thieke's model) to the measurements, the quantity of the coefficient  $\alpha$  in (4) was computed for all 13 tests. By scaling arguments it can be shown that Thieke's model is improved when the coefficient  $\alpha$  is related to  $H_b$ ,  $h_b$ , and  $H_o$  by the following expression :

$$\alpha = 0.8 \frac{H_o}{H_b} + \left( 23.06 \frac{H_b}{h_b} - 5.79 \right)^{-1} \frac{H_b}{H_o} \quad (5)$$

where  $H_b$ ,  $h_b$ , and  $H_o$  are the initial breaking wave height, the corresponding depth, and deepwater wave height, respectively. Note that prediction of wave height in the middle of the surf zone (beach profile section between -50 and -30 ft of xSWL) was sacrificed to obtain the best prediction near the swash region. It was necessary since the wave height predicted at the end of the surf zone is used as an initial value for the prediction of swash height in the swash zone. The model predictions with the modified coefficient  $\alpha$  are shown as a solid line in Figure 4. Near the swash zone, agreement between predicted and measured wave height is excellent.

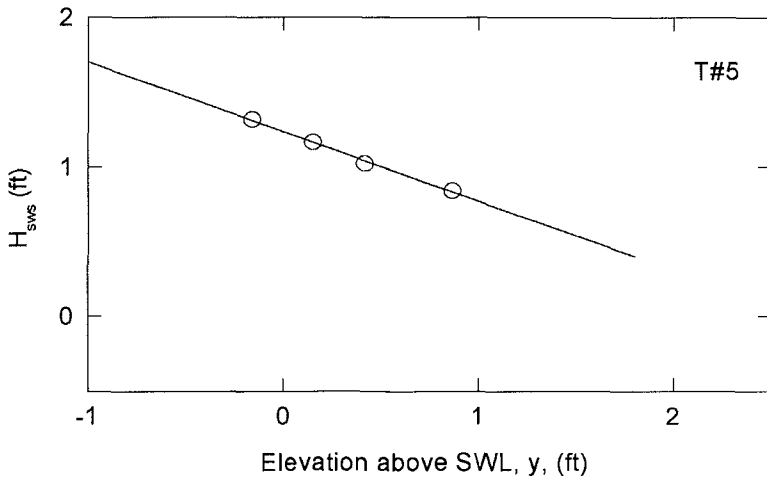


Figure 5. Significant swash height variation on a beach face for Test #5.

#### Modeling of Swash Height

Since the swash phenomena in nature is so complicated, no attempt has been made to express, in a simple manner, the swash height variation on a beach face. Figure 5 shows the measured significant swash height ( $H_{sws}$ ) variation versus beach face elevation ( $y$ ) for Test #5. The elevation of beach face represents the positive elevation above the still water level (SWL) and the negative elevation below it. The most important experimental observation is that the swash height decreases linearly with beach face elevation, which is apparent in all 13 tests. This

linearity of the swash height on the beach face plays a key role in establishing a model for swash height variation.

Applying boundary conditions of i)  $H_{sws} = 0$  at  $y = y_{max}$  and ii)  $H_{sws} = H_{swso}$  at  $y = 0$ , this linearity yields a prediction model for the swash height :

$$1 - \frac{H_{sws}}{H_{swso}} = \frac{y}{y_{max}} \quad (6)$$

where  $H_{swso}$  represents a significant swash height at  $y=0$  and  $y_{max}$  is the beach face elevation where a significant swash height becomes zero.

Note that if  $y_{max}$  is known for a given deep water wave condition, (6) becomes an initial value problem and can be used directly to compute the swash height for a given elevation. In order to quantify  $y_{max}$  for each test, the left side of (6) was computed with the measured swash height and plotted with  $y$ . The best linear fit lines (crossing the origin) to the measured data allow determination of  $y_{max}$  for each test. The significant swash height at  $y=0$ ,  $H_{swso}$ , for each test has been determined by the interpolation of the measured swash height.

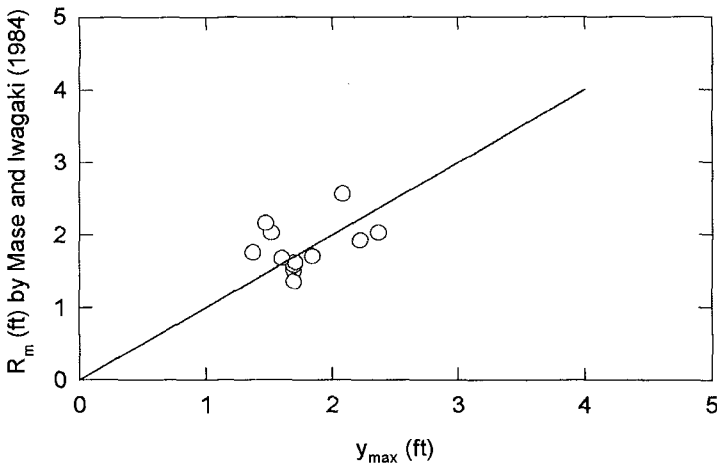


Figure 6. Comparison of  $y_{max}$  with the mean runup height by Mase et al. (1984).

Since  $y_{max}$  can be physically interpreted as a representative runup height for irregular waves climbing on the beach, it would be valuable to examine  $y_{max}$  with respect to the existing models for runup heights. Mean run-up heights for each test were computed from the runup height equation proposed by Mase and Iwagaki (1984). The comparisons between  $y_{max}$  and the computed runup heights are shown in Figure 6. It is noticed that  $y_{max}$  appears to matches roughly with mean runup heights  $R_m$  by Mase et. al (1984), as  $y_{max}$  deviate by at most a factor of 2 from  $R_m$ .

The swash height variation in the swash zone was predicted using (6). The comparisons between the measured and the predicted swash height variation in the swash zone for Test # 5 are shown in Figure 7. The solid line represents the predicted swash height variation using  $R_m$  computed from runup equation by Mase et. al (1984).

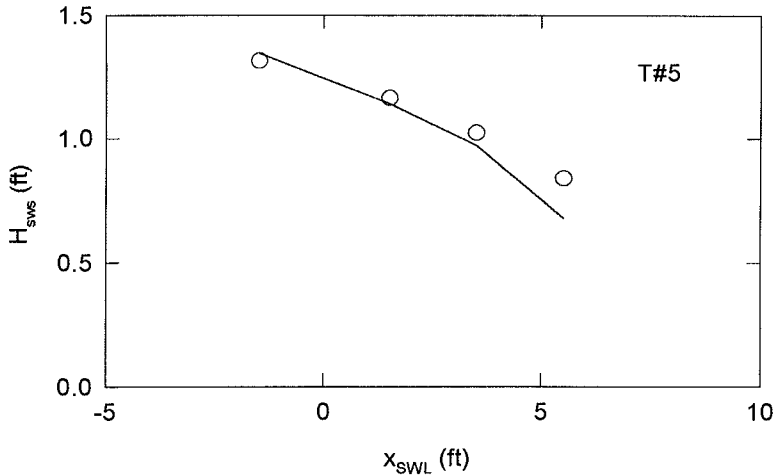


Figure 7. Comparison between predicted and measured swash heights for Test #5.

#### Swash Velocity Model

In order to develop a prediction model for swash velocity, it is assumed that it is possible to idealize the water particle as a solid particle which retains its identity. Thus, a particle of swash height,  $H_{sw}$ , is considered to move up and down the beachface as a solid particle would. If the normally incident waves are considered, a force balance implies

$$m \frac{dV_{sw}}{dt} = -mg \sin \theta - \frac{f}{8} \frac{m}{H_{sw}} |V_{sw}| V_{sw} \quad (7)$$

where  $m$  is a mass of the water particle,  $V_{sw}$  is a swash velocity,  $g$  is the gravitational acceleration,  $\theta$  is the beach slope and  $f$  is a friction factor. For simplicity, a frictionless planar beach is assumed. Eliminating common terms and applying initial conditions of  $V_{sw} = V_{sw0}$  at  $x=y=0$  (where  $x$  is the distance in the water particle translation direction from the location of  $SWL=0$ ), simple integration of this equation yields

$$V_{sw} = \sqrt{2g(y_{\max} - y)} \quad (8)$$

where  $y$  is the elevation positive from SWL.

The swash velocity for each test has been predicted from (8). The comparisons between the measured and the predicted velocity are given in Figure 8. Note that the predicted velocity matches well with the measured significant velocity.

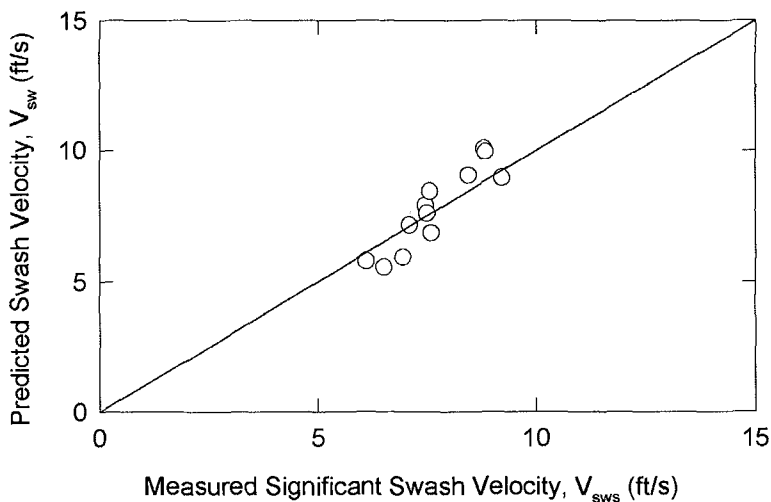


Figure 8. Comparison of the predicted swash velocity to the measured swash velocity.

#### Modeling of Swash Period

In order to develop a prediction model for swash period, a possible simple method is to apply a model which predicts the probability of wave overtopping for offshore structures. Since the probability of runup can be expressed as  $T_{sw0}/T_{sw}$ , the runup prediction model becomes

$$T_{sw} = T_{sw0} \exp \left[ \left( \frac{y}{R_{rms}} \right)^2 \right] \quad (9)$$

assuming that the runup height on natural beaches has a Rayleigh distribution. In (9),  $T_{sw0}$ , and  $T_{sw}$  are the initial swash period at  $y=0$ , and the swash period at any elevation of  $y$ , respectively, and  $R_{rms}$  is the *rms* value of runup height.

Note that in order to apply (9) for the prediction of swash period, it is necessary to express both  $T_{sw0}$  and  $R_{rms}$  in terms of known deepwater wave conditions or swash variables. It is possible to express  $T_{sw0}$  with  $T_o$  using the laboratory data by Mase and Iwagaki (1984). They indicated that the ratio of the number of deep water waves to the number of runup waves,  $N/N_o$  (or  $T_o/T_{sw0}$ ), varies nonlinearly with the deep water wave condition, expressed as the Iribarren number. Fitting a second order polynomial to their experimental data yields



$$\alpha = \frac{T_o}{T_{sw0}} = 0.69 \xi^{(0.42 - 0.08 \ln \xi)} \quad (10)$$

where  $T_o$  is the deepwater wave height and  $\xi$  is the Iribarren number (or surf similarity parameter). From the analysis of the laboratory measurements, Hwang (1995) also gives a linear relationship between  $R_{rms}$  and  $y_{max}$  :

$$y_{max} = 1.65 R_{rms} \quad (11)$$

From (10) and (11), the swash period is given as

$$T_{sw} = \frac{T_o}{\alpha} \exp \left[ \left( \frac{1.65 y}{y_{max}} \right)^2 \right] \quad (12)$$

A comparison between the predictions and the measurements for the swash period is shown in Figure 9. The predictions for the swash period are in good agreement with the measurements.

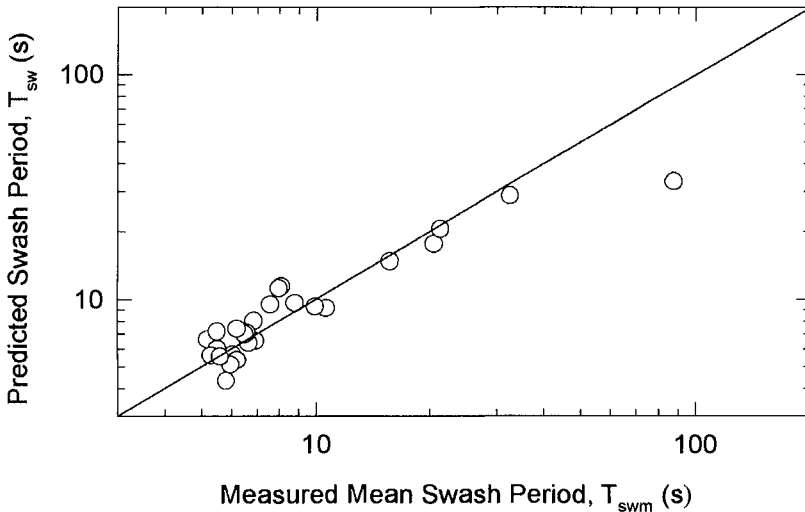


Figure 9. Comparison of the predicted to the measured swash period.

#### Modeling of Swash Force

Previously, the summing-up method has been used to relate the swash force to the volume eroded at the dune. However, applying this method directly to the prediction model for dune erosion is computationally intensive since each swash has to be computed and summed up for each time step (usually 20 minutes). An alternative approach is to use statistically representative swash parameters, such as mean, *rms* and significant values. As an example, a swash force by mean parameters may be defined as

$$F_{swm} = \rho \frac{T_d}{T_{swm}} V_{swm}^2 H_{swm} \quad (13)$$

where subscript  $m$  represent the mean values of the swash height, the swash velocity, and the swash period. Note that the ratio  $T_d/T_{swm}$  in (13), which represents the number of swash hit at the dune face, is introduced to scale the total swash force for a given duration of test.

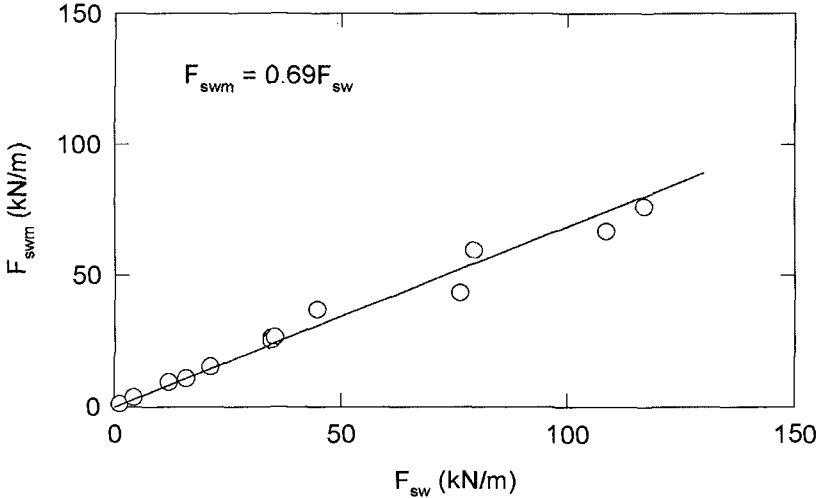


Figure 10. Relationship between  $F_{swm}$  and  $F_{sw}$ .

The swash force by mean parameters was computed with the measured mean swash parameters for each test. Comparisons of the swash force using (13) with total swash force ( $F_{sw}$ ) obtained by summing-up method are shown in Figure 10. It is interesting to notice that swash force defined by mean swash parameters is linearly related with the swash force by the summing-up method. The linear relationship obtained by the best fit line is

$$F_{swm} = 0.69F_{sw} \quad (14)$$

### Predictive Model for Dune Erosion

The dune erosion model predicts the volume eroded at the dune due to wave impact. The model consists of an input data routine, prebreaking zone wave height routine, surf zone wave height routine, swash zone hydrodynamics routine, dune erosion routine, and an output routine. As initial input data, the model requires the deepwater wave conditions and initial beach and dune profile data. Linear wave theory is used to determine the wave height from deepwater or a specified water depth offshore to the breaking point. Shoreward of the breaking

point, a modified form of Sobey's prediction model is used to compute the wave height. The swash zone hydrodynamics routine computes each statistically representative swash height, swash velocity, and swash period. Once the swash parameters are determined, the corresponding swash force is computed and used to calculate the volume eroded at the dune.

In order to determine the wave heights across-shore, the model uses an explicit solution scheme in which quantities known at a specific grid point are used to determine corresponding quantities at the next grid point. Propagation of individual waves is not described by the model.

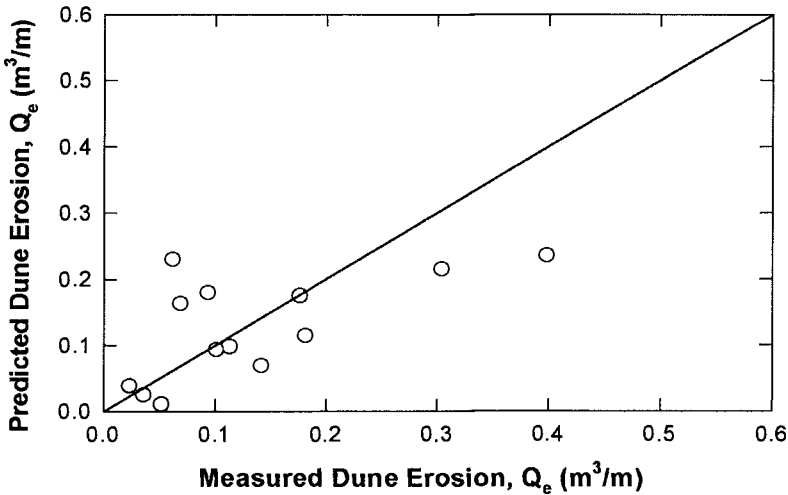


Figure 11. Comparison of predicted dune erosion to the measured dune erosion using predicted  $R_m$  from runup equation.

Dune erosion was simulated for all 13 tests using the data from SUPERTANK laboratory experiments. Data used for each prediction were the significant wave height at Gage #14, peak spectral wave period at Gage #14, mean wave period at Gage #14, beach and dune profile, test duration, and dune toe location. Assuming that  $y_{max}$  can be replaced by runup height, the runup height equation proposed by Mase and Iwagaki (1984) was used for the computation of  $y_{max}$  which was required for the prediction of all swash parameters (swash height, swash velocity and swash period). Comparisons of model predicted dune erosions with measurements for all 13 tests are shown in Figure 11. It is easily noticed that the prediction of dune erosion by model is not successful. The model predictions deviate by as much as a factor of 4 from the measured dune erosion.

Since the runup height equation has been used for the prediction of  $y_{max}$ , a slight modification to the model was made to check the effect of the runup height on the prediction of dune erosion. Instead of calculating the runup height and using it as  $y_{max}$ , the measured  $y_{max}$  was used for the simulation of swash force and dune erosion for each test. Predictions of dune erosion using the measured  $y_{max}$  are shown in Figure 12 and compared with the measured dune erosion. It is obvious that predictions are much improved, as the model predictions deviate by at most a factor of 2 from the measured values.

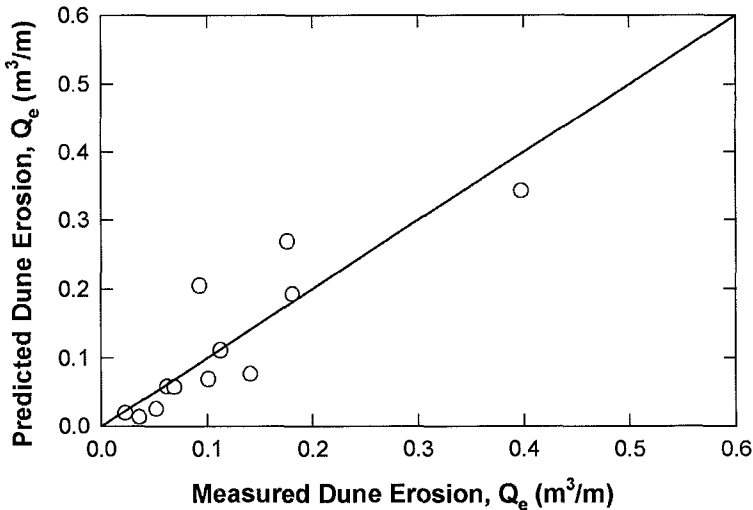


Figure 12. Comparison of predicted dune erosion to the measured dune erosion using the measured  $y_{max}$ .

Clearly,  $y_{max}$  is a significant factor and plays an important role in the prediction of dune erosion. Consequently, it is concluded that quantitatively good prediction for dune erosion can be obtained by improving the ability of prediction of  $y_{max}$ .

## Conclusions

A simulation model has been developed using SUPERTANK experimental data to predict dune erosion due to wave impact. The analysis of the laboratory data confirmed an apparent linearity between swash force and dune erosion. With a modification of Sobey's model, predictions of wave height variation in the surf zone were improved, especially near the swash zone. Swash height, swash velocity, and swash period predicted by the model agreed well with the laboratory measurements. However, the model predicted dune erosion with limited success. An uncertainty in the value of  $y_{max}$  is the primary cause which led to the failure of

the prediction of dune erosion. The results indicate that improvement in the dune erosion model will depend upon more reliable estimates of runup height.

### References

- Battjes, J. A., and Janssen, J. P. F. M. 1978. "Energy Loss and Set-up Due to Breaking of Random Waves", *Proceedings of the 16th Coastal Engineering Conference*, ASCE, Vol. 1, pp 569-587.
- Dally, W. R., and Dean, R. G., and Dalrymple, R. A. 1985. "Wave Height Variation Across Beaches of Arbitrary Profiles", *Journal of Geophysical Research*, Vol. 90, No. 6, pp 11917-11927.
- Dibble, T. L., and Sollitt, C. K. 1989. "New Designs for Acoustic and Resistive Wave Profiles", *Proceedings*, Workshop on Instrumentation for Hydraulic Laboratories, IAHR.
- Fisher, J. S., and Overton, M. F. 1984. "Numerical Model for Dune Erosion Due to Wave Uprush", *Proceedings of the 19th Coastal Engineering Conference*, ASCE, pp 1553-1558.
- Fisher, J. S., Overton, M. F., and Chisholm, T. 1986. "Field Measurements of Dune Erosion", *Proceedings of the 20th Coastal Engineering Conference*, ASCE, pp 1107-1115.
- Hwang, K. 1995. "Predictive Model for the Dune Erosion and Swash Hydrodynamics", *Ph.D. Dissertation* in preparation, North Carolina State University, Raleigh, NC.
- Mase, H., and Iwagaki, Y. 1984. "Run-Up of Random Waves on Gentle Slopes", *Proceedings of the 19th Coastal Engineering Conference*, ASCE, pp 593-609.
- Overton, M. F., Fisher, J. S., and Young, M. A. 1988. "Laboratory Investigation of Dune Erosion", *Journal of Waterway, Port, Coastal and Ocean Engineering*, ASCE, Vol. 114, No. 3, pp 367-373.
- Stive, M. J. F. 1984. "Energy Dissipation in Waves Breaking on Gentle Slopes", *Coastal Engineering*, Vol. 8, pp 99-127.
- Thieke, R. J., and Sobey, R. J. 1990. "Cross-shore Wave Transformation and Mean Flow Circulation", *Coastal Engineering*, Vol. 14, pp387-415.

## CHAPTER 181

### Numerical Modelling of Three-Dimensional Wave-Driven Currents in the Surf-Zone

Philippe Péchon<sup>1</sup> and Charles Teisson<sup>1</sup>

#### Abstract

The numerical modelling of time-averaged three-dimensional currents due to breaking waves is presented. The basic equations and the closures are described. The driving terms in the momentum equations are the radiation stresses derived from "organised" velocity of waves and the roller contribution. The model is validated on measurements collected in a flume. The application to the case of a rectilinear beach with oblique incidence wave displays a helicoidal circulation. In the situation of a detached breakwater with a normal wave, depth-integrated currents show two large symmetrical cells in the lee of the structure whereas streamlines near the bottom converge spirally toward the centres of the eddies.

#### Introduction

Longshore currents induced by breaking waves are often assumed to be responsible for changes in the shoreline plan-shape on extend of some kilometres (Horikawa 1988 , Southgate 1987 , Péchon, 1982). However the action of cross-shore currents have to be taken into account for the prediction of detailed bathymetry variations, for instance when appraising the impact nearby coastal structures (Hansen and Svendsen 1984 , Okayasu 1989).

A compound system is being developed to simulate wave, current and sediment transport patterns for the design of coastal projects. The module for time-averaged wave-driven 3D-currents is presented ; the physical concept and applications are described. In this article we focus on the wave-driven currents due to breaking phenomena exclusively. The wave is assumed to be regular and the wave pattern is supposed to be known here, resulting from the wave module of the system.

---

<sup>1</sup> Laboratoire National d'Hydraulique, Electricité de France  
6, quai Watier, 78400 Chatou, France

## The Three-Dimensional current model

### The equations

For sake of clarity the Navier-Stokes equations are considered in the case of a two-dimensional motion in a flume :

$$\begin{aligned}\frac{\partial u}{\partial t} + \frac{\partial u^2}{\partial x} + \frac{\partial uw}{\partial z} &= -\frac{1}{\rho} \frac{\partial p}{\partial x} \\ \frac{\partial w}{\partial t} + \frac{\partial uw}{\partial x} + \frac{\partial w^2}{\partial z} &= -\frac{1}{\rho} \frac{\partial p}{\partial z} \\ \frac{\partial u}{\partial x} + \frac{\partial w}{\partial z} &= 0\end{aligned}$$

where  $u$ ,  $w$  are the horizontal and vertical components of the instantaneous velocity,  $p$  is the pressure. The viscous molecular terms are neglected in the highly turbulent environment.

As it is proposed in Svendsen and Lorentz (1989), the velocity is separated into three contributions : a mean current ( $U$ ,  $W$ ), a purely periodic current ( $u_w$ ,  $w_w$ ) corresponding to wave motion, and turbulent fluctuations ( $u'$ ,  $w'$ ). The time-averaged equations reads, the overbar indicating averaged quantities :

$$\begin{aligned}\frac{\partial U}{\partial t} + \frac{\partial U^2}{\partial x} + \frac{\partial UW}{\partial z} + \frac{\partial \overline{u_w^2}}{\partial x} + \frac{\partial \overline{u_w w_w}}{\partial z} &= -\frac{1}{\rho} \frac{\partial \bar{p}}{\partial x} - \frac{\partial \overline{u'^2}}{\partial x} - \frac{\partial \overline{u' w'}}{\partial z} \\ \frac{\partial U}{\partial x} + \frac{\partial W}{\partial z} &= 0\end{aligned}$$

and the vertical momentum equation leads to (Stive and Wind, 1982) :

$$\bar{p} = \rho g (\bar{\xi} - z) - \rho \overline{w'^2} - \rho \overline{w_w'^2}$$

where  $\bar{\xi}$  is the free surface level. By substitution in the momentum equation :

$$\frac{\partial U}{\partial t} + \frac{\partial U^2}{\partial x} + \frac{\partial UW}{\partial z} + \frac{\partial (\overline{u_w^2 - w_w^2})}{\partial x} + \frac{\partial \overline{u_w w_w}}{\partial z} = -\frac{1}{\rho} \frac{\partial \bar{\xi}}{\partial x} - \frac{\partial (\overline{u'^2 - w'^2})}{\partial x} - \frac{\partial \overline{u' w'}}{\partial z}$$

The derivative  $\partial (\overline{u_w^2 - w_w^2}) / \partial x$  is the wave radiation stress. The term  $\partial \overline{u_w w_w} / \partial z$  created by waves is also considered whereas the term  $\partial (\overline{u'^2 - w'^2}) / \partial x$  is neglected except in the roller. Dropping the time derivative term, the 2 DV equations reduce to :

$$\begin{aligned}\frac{\partial U^2}{\partial x} + \frac{\partial UW}{\partial z} + \frac{\partial (\overline{u_w^2 - w_w^2})}{\partial x} + \frac{\partial \overline{u_w w_w}}{\partial z} &= -g \frac{\partial \bar{\xi}}{\partial x} - \frac{\partial \overline{u' w'}}{\partial z} + t \\ \frac{\partial U}{\partial x} + \frac{\partial W}{\partial z} &= 0\end{aligned}$$

where  $t$  is the contribution of the roller of the breaking waves,  $t = -\partial \overline{u'^2} / \partial x$ .

**The closures**

The terms which depends on the periodic current of breaking waves are expressed in function of the input wave characteristics and the energy dissipation (Longuet-Higgins 1970, Dingemans et al 1986, Deigaard and Fredsoe 1989) :

$$\frac{\partial (\overline{u_w^2 - w_w^2})}{\partial x} = \frac{1}{\rho h} D$$

with  $D$  : energy dissipation  
 $C$  : wave celerity  
 $h$  : mean water depth

$$\frac{\partial \overline{u_w w_w}}{\partial z} = \frac{1}{2\rho h} D$$

It is noted that the contribution of non-breaking waves in the expression of the radiation stress is not included here. Apart from the roller, Reynolds stresses are given using the eddy viscosity concept :

$$\overline{u'w'} = -v_t \frac{\partial U}{\partial z}$$

A uniform turbulence viscosity distribution is adopted, following Svendsen et al (1987) :

$$v_t = Mh \left(\frac{D}{\rho}\right)^{1/3} \text{ The constant } M \text{ is taken to be } 0.03$$

The contribution of the roller in the term  $-\overline{\partial u'^2} / \partial x$  can be expressed by approximating the horizontal velocity profile as suggested by Svendsen (1984) :

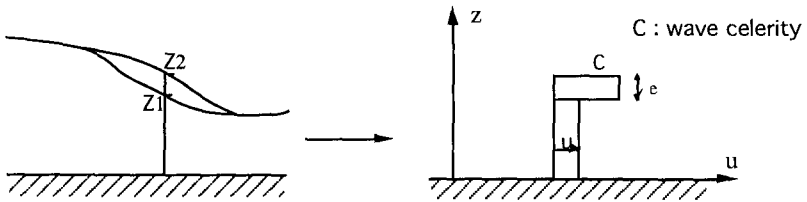


Fig.1 Vertical profile of velocity in the surfzone

He proposed :  $\bar{e} = 0.9 H^2 / L$  with  $H$  : wave height  
 $L$  : wave length

$$\text{So we obtain } \int_{z_1}^{z_2} u'^2 dz = C^2 \bar{e} = 0.9 \frac{C^2}{L} H^2$$

The time-averaged entrainment force  $t$  due to the roller is specified uniform from the wave trough to the mean water level, on a layer thickness of  $H/2$ . It follows :

$$t = - \frac{2}{H} \frac{\partial}{\partial x} \left( 0.9 \frac{C^2 H^2}{L} \right) = - \frac{1.8}{HT} \frac{\partial C H^2}{\partial x}$$



Introducing the flux of energy  $E_f$ , in shallow water :

$$E_f = \frac{1}{8} \rho g H^2 C_g \approx \frac{1}{8} \rho g H^2 C$$

$$t = \frac{14}{\rho g} \frac{D}{HT} \quad \text{where } D = -\frac{\partial E_f}{\partial x} \text{ energy dissipation}$$

$T$  : wave period

### *The exchanges of momentum and mass through the surface*

In quasi-3D models (Wind and Stive 1987, Sanchez-Arcilla et al. 1992) the equations are generally solved from the bottom to the trough level and a shear stress is specified at the boundaries. Moreover the mass flux above trough level is given as an input.

Since the present model is fully three-dimensional, the time-averaged equations have to be solved from the bottom to the mean water level. The total flux of momentum due to breaking waves which is introduced in the computational domain is specified through the radiation stresses distributed over the water column and the force  $t$  on a thickness  $H/2$ . It follows that it is not relevant to impose any additional shear stress at the surface in this model ; so the shear stress is set to zero.

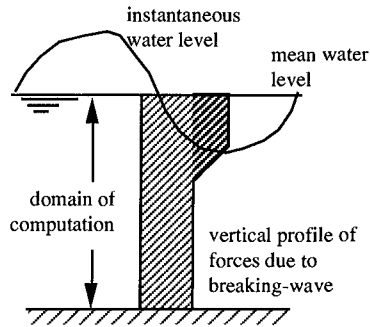


Fig. 2 Vertical distribution of forces

In nature the wave-induced mass-flux above the mean water level is not nil in and out the surf-zone and the horizontal variation of this quantity induce also mass flux through the time-average surface. Walstra et al (1994) take this effect into account in a 2DV model by adding a term in the continuity equation and they allow vertical velocities through the surface boundary. Since this type of circulation occurs for breaking as well as non-breaking waves, we chosen here to solve it separately with a Boussinesq type model which reproduces it automatically. This part is not presented in this paper.

## **Applications**

### *Cross-shore currents in a flume*

The numerical model has been applied with standard parameters to the case of a flume which had been investigated on a physical model (Buhr-Hansen and Svendsen, 1986).

The bottom profile is parabolic (fig. 3). The generated wave is regular with a period of 2.0 s and at the breaking point the wave height is 0.17 m and the still water depth is 0.20 m. The wave field specified in the numerical model is the one measured on the experimental set-up.

The computed undertow added to the mean currents due to wave motion has been compared to measurements collected in the surf-zone. In this case the currents due to wave motion (non-breaking contribution) is estimated with a non-linear wave theory (analytical solution of Serre equations) depending on the wave height. The numerical results were in good agreement with measured velocities.

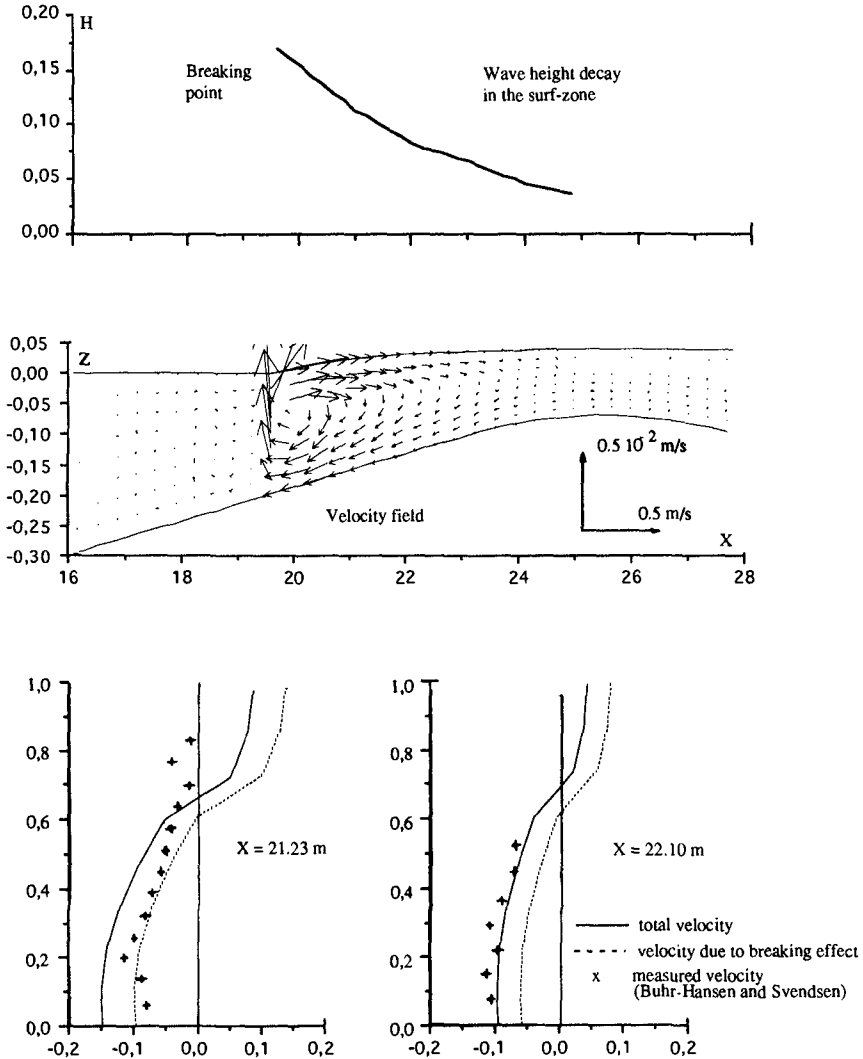


Fig. 3 Wave-driven currents in a flume  
Comparison with measurements

**Three-dimensional circulation along a rectilinear beach.**

The studied domain had a constant bottom slope equal to  $2/100$ , the off-shore water depth was 9.0 meters. The wave height at the deeper limit was 2.0 m, the period 8.0 s and the incidence  $25^\circ$  (fig. 4). All boundaries were closed in this test, with a slipping condition.

Wave propagation was computed with a simple refraction model and the decay in the surf-zone was deduced from the energy equation where the energy dissipation in the bore is assumed to be similar to an hydraulic jump one.

In this situation an helicoidal wave-driven flow occurs in the domain (fig. 5) and the velocity near the bottom is oriented offshore. This qualitative result is confirmed by field observations (Ingle 1966) but measurements are not available for validation. Moreover it is pointed out that the "non-breaking contribution" of wave motion is not included in this result.

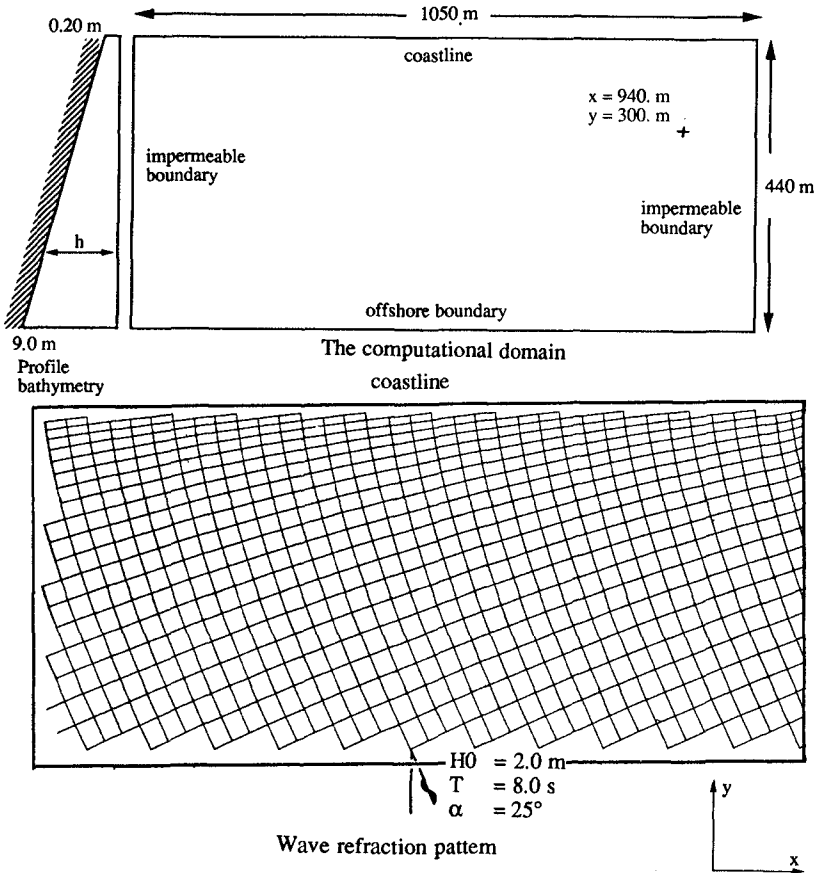


Fig. 4 Wave propagation along a rectilinear coast

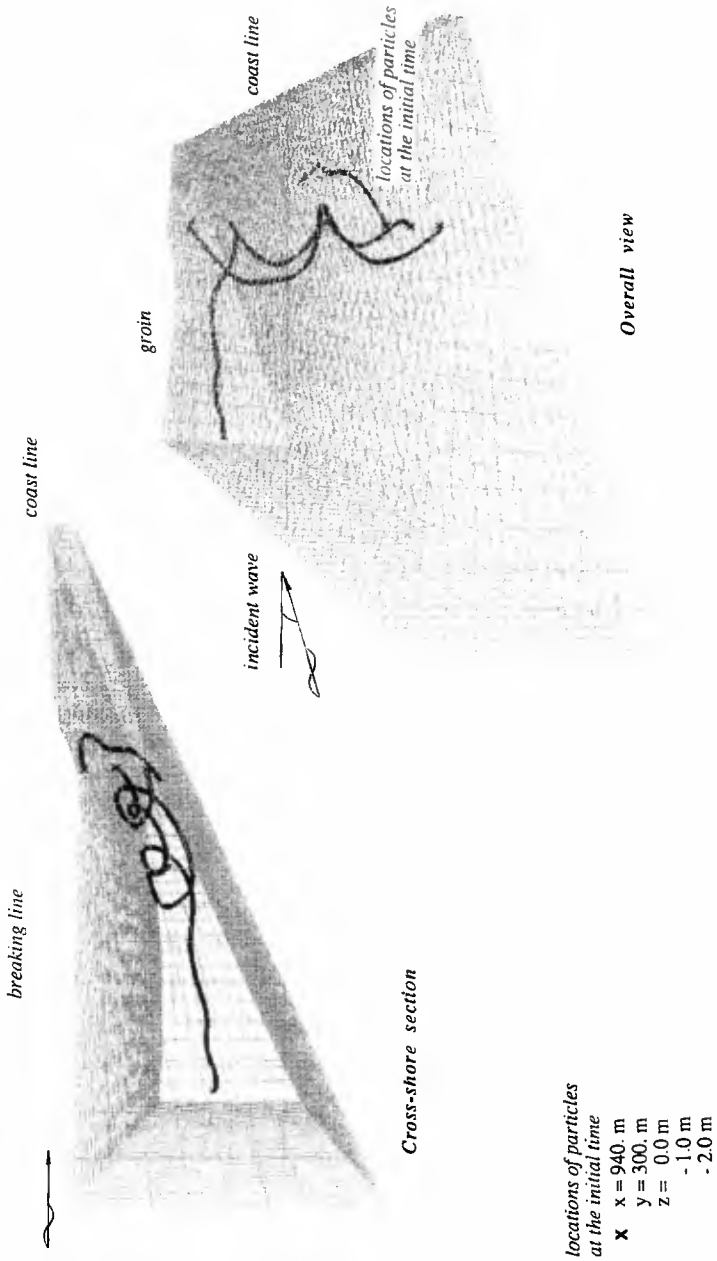


Fig. 5 Currents induced by breaking waves - Particle tracks

### *Currents near a the detached breakwater*

The bottom slope is constant and equal to 3/100. The still water depth is 5.0 meters at the off-shore frontier and it is 0.5 meter at the shoreline. The off-shore boundary is open while the three others are closed and combined with slipping conditions. The detached breakwater is 100 meters long and it is located at 100 meters from the shoreline. The still water depth at the toe of the structure is 3.5 meters.

The wave at the open boundary is 2.5 meters high, its period is 8.0 seconds and its incidence is normal to the coast. For this preliminary simulation the wave field is schematised, the wave-driven terms are nil in the lee of the structure and the wave height decay elsewhere in the surf-zone is given by a formula. Of course this wave field is very crude but the aim of this test is to display vertical heterogeneity of the velocity pattern. A more accurate computation of the wave field is planned in the future.

The depth-averaged flow pattern shows two large and symmetrical eddies behind the breakwater (fig.6). The maximum velocity reaches 1.5 m/s. In order to see three-dimensional effects, particles tracks computed with the bidimensional velocity fields near the bed, near the surface and with depth-averaged one are also visualised on figure 6. The streamlines near the bottom are oriented toward the centre of the eddy while the others describe large cells. This difference between the depth-averaged and the near-bed flow patterns is crucial for sediment transport modelling.

### **Conclusion**

The computation of time-averaged wave-driven currents in the surf-zone for schematical 3D cases gives satisfying qualitative results. The model have already been compared successfully with measurements collected in experimental flumes but additional validation tests are needed in three-dimensional situations.

The wave pattern in practical studies can be complex and its prediction requires a sophisticated wave model, especially if hydrodynamic results are used to determine sediment transport. It can be provided by bidimensional infragravity wave models (based on Boussinesq or Serre equations) which also simulate wave height decay in the surf-zone (Hamm et al. 1993, Karambas et al. 1992, Schäffer et al. 1992). The total velocity in the surf zone is the combination of the three-dimensional currents induced by breaking waves and the instantaneous wave velocity. However some care have to be taken in the summation of the two velocity fields because the current resulting from the wave model also partly includes the breaking effect. So the component which comes from breaking in the wave model must be subtract before adding the two velocity fields.

### **Acknowledgements**

This work was carried out as part of the G8 Coastal Morphodynamics research programme. It was funded partly by the Service Central Technique du Secrétariat d'Etat à la Mer and the Commission of the European Communities, Directorate General for Science, Research and Development, under contract n° MAS2-CT92-0027.

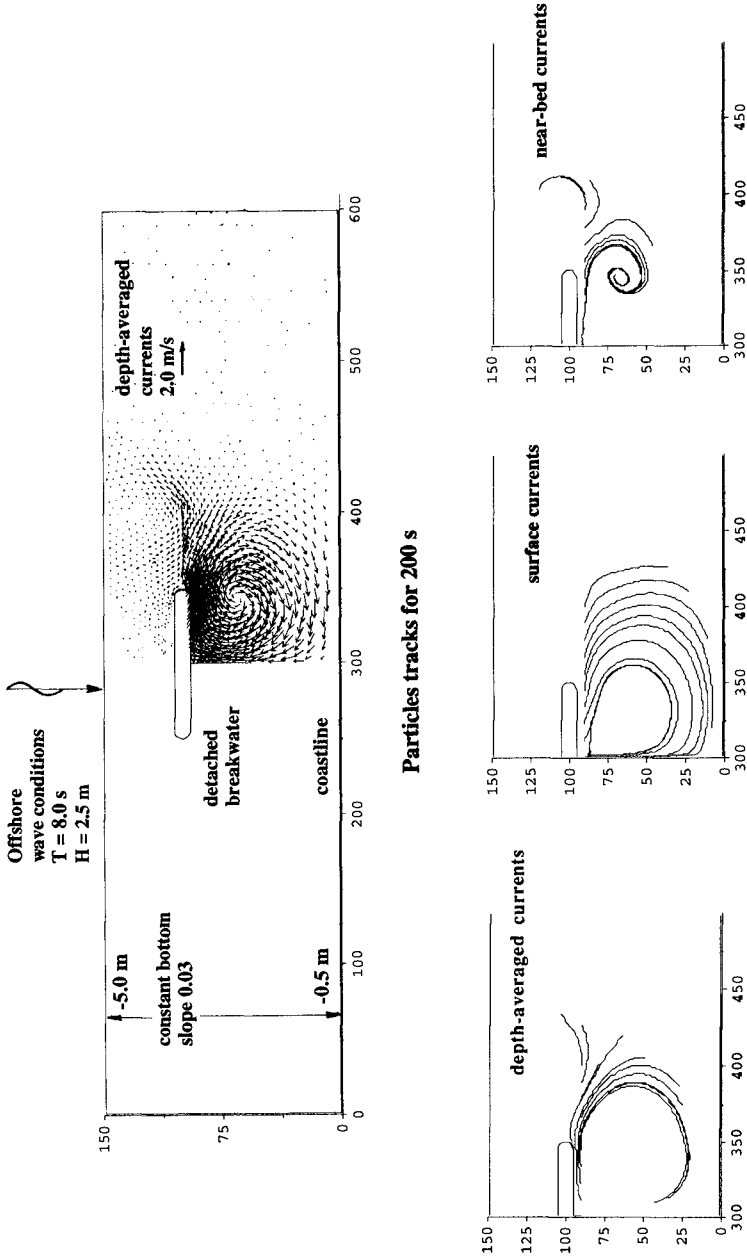


Fig. 6 Circulations near a detached breakwater

## References

- Buhr Hansen, J. and Svendsen, I.A.(1984). A theoretical and experimental study of undertow. International Conference on Coastal Engineering : 2246-2262.
- Buhr Hansen, J. and Svendsen, I.A.(1986). Experimental investigation of the wave and current motion over a longshore bar. International Conference on Coastal Engineering.
- De Vriend, H.J. and Stive M.J.F (1987). Quasi-3D modelling of nearshore currents. Coastal Engineering, 11, 5 & 6 : 565-601.
- Dingemans, M.W., Stive M.J.F., Bosma, J., De Vriend, H.J., and Vogel J.A., Directional nearshore wave propagation and induced currents, Coastal Engineering, ASCE : p 1092-1106.
- Hamm, L., Madsen, P. A. and Peregrine, D. H., 1993. "Wave transformation in the nearshore zone : A review ", Coastal Engineering, Vol. 21, 1-3 : 5-39.
- Hervouet, J-M., Janin, J-M. , Lepointre, F. and P  chon, P. (1993). TELEMAR-3D : A finite element software to solve 3D free surface flow problems. International Conference on Hydrosience and Engineering.
- Horikawa, K. (1988). Nearshore Dynamics and Coastal processes. Ed.University of Tokio Press.
- Ingle, X. (1966). The movement of beach sand , Development in sedimentology , Ed. Elsevier.
- Karambas, Th. and Koutitas, C., 1992. "A breaking wave propagation model based on the Boussinesq equations". Coastal Engineering.Vol. 18,1-19.
- Longuet-Higgins, M.S., 1970. "Longshore currents generated by obliquely incident sea waves," Journal of Geophysical Research, Vol. 75 : 6778-6801.
- Okayasu, A. (1989). Characteristics of turbulence structure and undertow in the surf-zone. Phd Thesis, University of Tokio.
- P  chon, P. (1982). Modelling of sea-bed evolution under waves action. International Conference on Coastal Engineering : 1149-1160.
- P  chon, P. (1992). Numerical modelling of wave-driven currents and sediment transport in the surf-zone. Internal report EDF-LNH HE42/92.15.
- Southgate, H. (1987). A one-dimensional model of wave-current interaction. ASCE Speciality Conference on Coastal hydrodynamics : 79-92.
- Sanchez-Arcilla,A., Collado, F. and Rodriguez, A., 1992. "Vertically varying velocity field in Q-3D nearshore circulation," International Coastal Engineering Conference. pp. 2811-2824.
- Sch  ffer, H.A., Madsen P.A. and Deigaard, R., 1992. A two-dimensional surf-zone model based on the Boussinesq equations, International Coastal Engineering Conference : 576-589.
- Svendsen, L.A., 1984. "Waves heights and set-up in a surf zone". International Coastal Engineering Conference : 303-329.
- Svendsen, I.A., Sch  ffer, H.A. and Buhr Hansen, J., 1987. "The interaction between the undertow and the boundary layer flow on a beach," Journal of Geophysical Research, vol 92, n   C11.
- Svendsen, I.A. and Lorenz, R.S. (1989). Velocities in combined undertow and longshore currents. Coastal Engineering, 13 : 55-79.
- Walstra, W., Piepers, M., Roelvink, J.A. and Stelling, G.S. (1994) 2DV Modelling of surfzone currents. Book of abstracts, Mast G8M, Gregynog.

## Sediment Transport in Various Time Scales

Zbigniew PRUSZAK & Ryszard B. ZEIDLER<sup>1</sup>

### Abstract

Some basic sediment movement characteristics such as critical velocities of motion, bed load layer thickness, as well as local and overall sediment transport have been measured in field at Lubiatowo, Poland.

The survey was carried out in a multi-bar (4–5 bars) Polish coastal zone with the medium grain diameter  $D_{50}$  from 0.2 to 0.25 mm. Irydium glass grains tracer, close in size to the natural sand, has been used. The investigations embodied 8 hydrodynamical situations in various climates of waves and currents.

For oblique wave incidence it has been found that local intensity of longshore sediment transport can reach 40–100 kg/(m h) under storm conditions, strongly dependent on local bed topography. The overall sediment transport rate across the entire surf zone can exceed  $7 \cdot 10^{-3}$  m<sup>3</sup>/s under storm conditions. For weak wave motion the bed surface layer of sediment transport has a thickness of several grain diameters, while it may be even 4–6 cm thick during storms. Vertical distributions of sediment concentration beneath of bed surface are identified. Transport rates are related to the product of squared breaker height and longshore velocity. Annual time series of sediment transport are presented.

### 1 INTRODUCTION

Coastal zone is characterized by intensive sediment transport and considerable morphodynamic changes. Because of its importance as an interface of the atmosphere, the sea, the land and engineering structures, its dynamics should be well understood.

Some primary quantities describing sediment transport in the coastal zone include critical speeds of incipient movement, thickness of the bedload layer and velocity distribution within this layer, and the resulting bedload transport rate.

For the purposes of this study, we distinguish short-term changes (hours, at most days) mainly associated with a single storm, meso-scale ones (weeks or months) and long-term changes (years or decades). In this paper, emphasis is placed on the first and third scale.

---

<sup>1</sup>Assoc.Prof. and Prof.; Polish Academy of Sciences' Institute of Hydro-Engineering *IBW PAN* 7 Kosciarska, 80-953 Gdansk, Poland



Field studies provide a reliable background for understanding coastal processes and drawing conclusions on various estimates of sediment transport quantities. Numerical models are still inaccurate and require validation based on field measurements.

This paper describes results of recent field studies, thus expanding the earlier investigations by Pruszk & Zeidler (1992). The sediment transport experiments were carried out at the IBW PAN Coastal Research Facility off Lubiato.

## 2 FIELD DATABASE

The Coastal Research Facility (CRF) at Lubiato is situated on the southern Baltic beach and shore of transitional nature, which experiences neither accretion nor erosion in long time scales. The short-term variability of shore processes is evidenced by cyclic occurrence of erosion bays or accretion cusps every 30 years (Pruszk 1993).

The shore at Lubiato is dissipative mild slope one with conspicuous four bars about 110, 190, 370 and 650 m from shoreline (Fig. 1). An ephemeral unstable bar is sometimes visible close to the shoreline (some 30–40 m away). The median grain diameter  $D_{50}$  varies between 0.2 and 0.25 mm. The littoral drift is substantial since the net annual wave momentum flux is oriented obliquely to the shoreline. Wave breaking in the Lubiato surf zone is pronounced at a few locations, identified with underwater bars. During average storms the significant wave reaches the height  $H_s \approx 2\text{--}3.5$  m with the period  $T$  from 5 to 7 s at the seaward boundary on the depth of 7 m. As a result of the subsequent transformation, the mean wave height falls to 1–1.5 m on the depth of 2–3 m (about the second and third bars) while the mean wave period becomes 4–5 s.

Along with parameters of wind, waves, currents and other hydrologic factors, topographic features have been measured at Lubiato since 1983 on a 2.7-km beach and nearshore zone extending some 800 m from shoreline. The beach profiles have been arranged every 100 m, and have been recorded every four weeks. Subaqueous profiles extending to about 100 m from shoreline have been measured systematically every four weeks since 1991.

In our tracer studies of sediment transport we have been using iridium glass grains close in size to the natural sand. The half-life period of the radioisotope is 74.4 days.

The 1993–1994 field campaign included *inter alia* the disposal of six tracer batches at six different locations of the Lubiato coastal zone, as depicted in Figure 1. The disposal points were chosen so as to monitor the three characteristic subareas of the coastal zone shown in Figure 1, as already pursued by Pruszk & Zeidler (1992).

The sediment transport investigations were carried out in two series in autumn 1993 and spring 1994. Simultaneous measurements of waves, currents and wind were conducted during the radioisotopic studies. The measurements were continued regularly every three hours at two locations of the surf zone denoted by D1 and D2 in Figure 1. An exemplary record of wind, waves and currents along and across shore is given in Figure 2.

Ninety four core samples 40 cm in length were taken from the sea bed. The samples originate from various areas coupled with the movement of tracer plumes. The samples were analysed in 2-cm layers by the use of a very sensitive scanner. Both location and intensity of the radiotracer in plumes was measured from a boat with a special monitoring and recording apparatus. Examples of

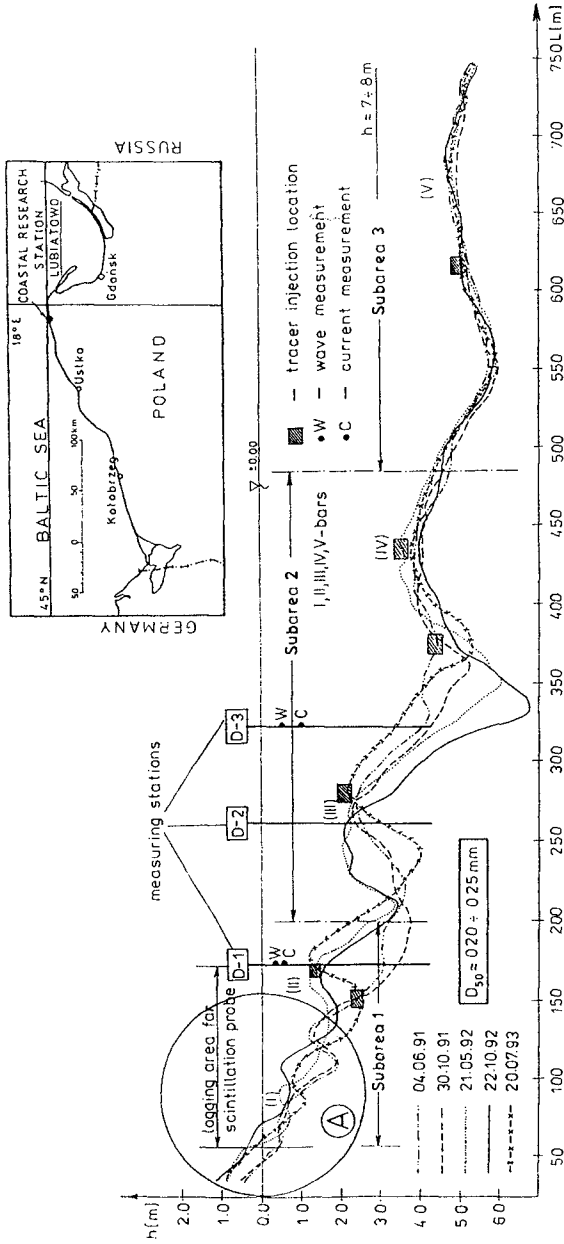


Figure 1. CRF Lubiatowo, bottom topography and measuring arrangements.

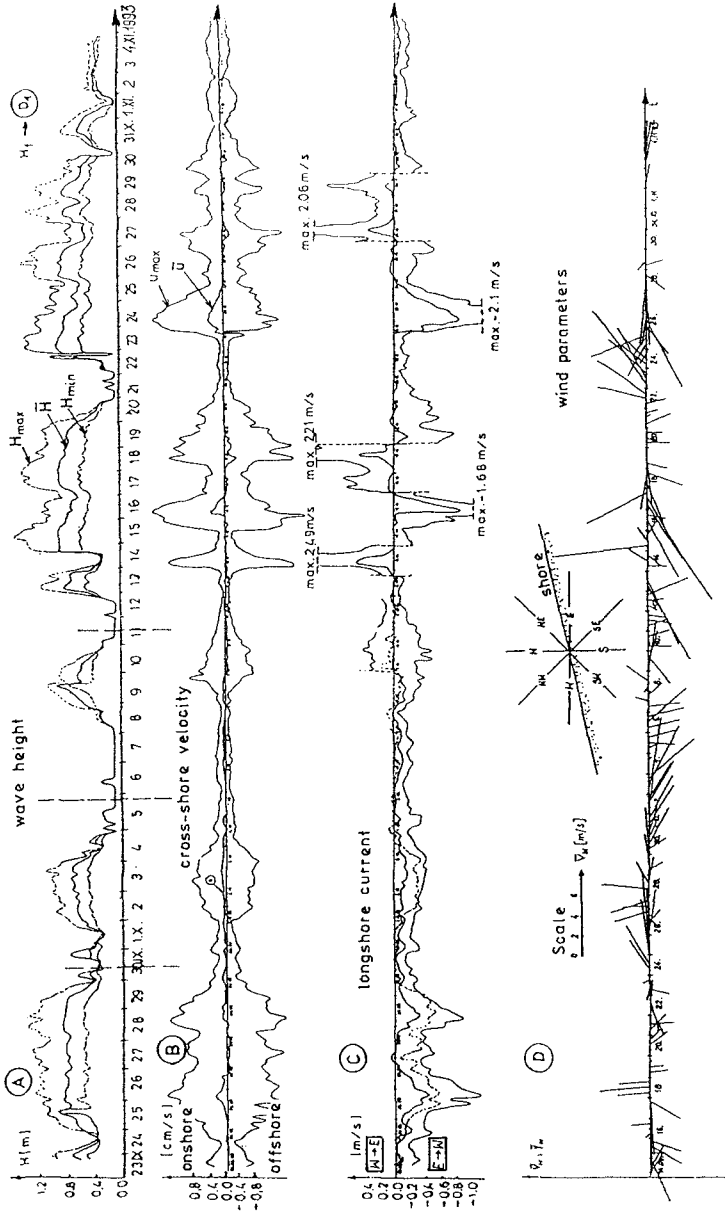


Figure 2. Wind, wave height, cross-shore and longshore velocity at CRF Lubiatowo during the 1993 field studies.

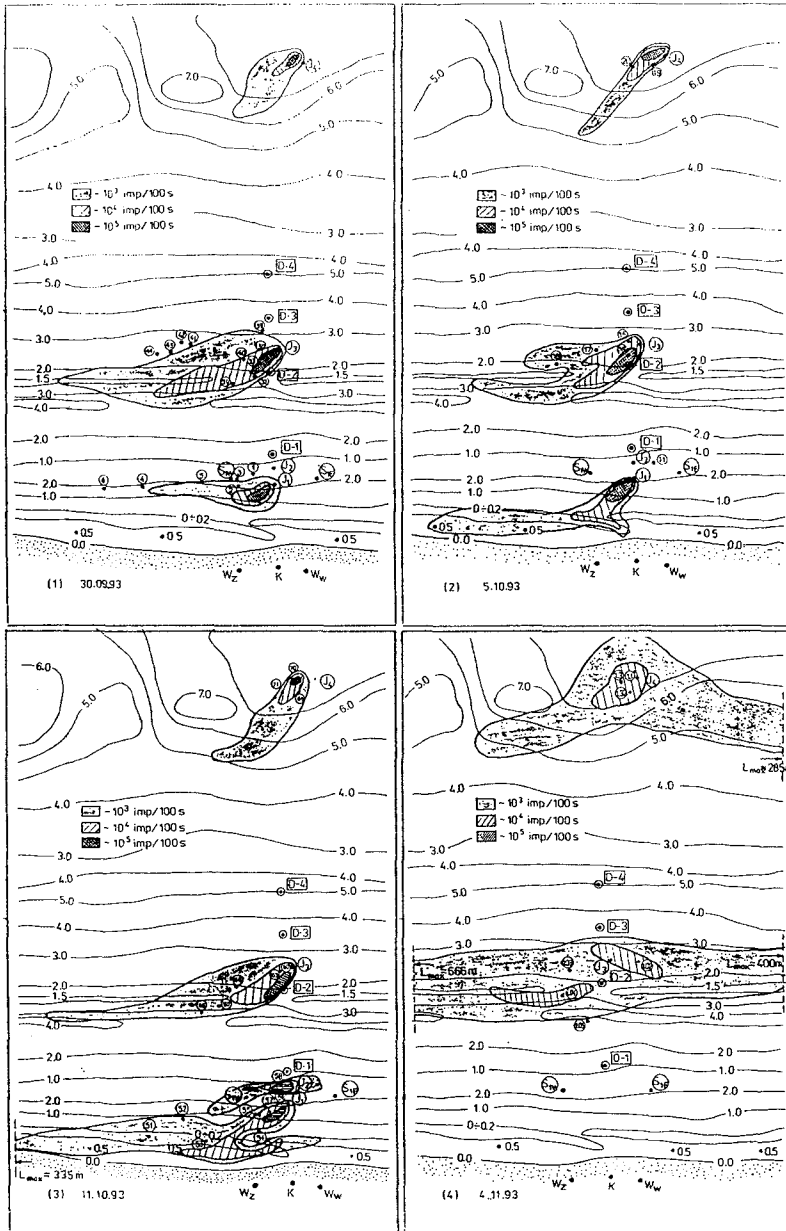


Figure 3. Radiotracer plumes at CRF Lubiato, fall 1993; (52) etc. tracer sampling location, (imp) - pulse; (I) - injection spot; (S) - sand trap

subsequent locations of 3-4 plumes out of total six are shown in Figure 3 for the first measurement series of autumn 1993.

Simultaneously with the observations and measurements of the radio-tracer, measured at two locations of the surf zone were suspended loads up to 2 m above sea bed, at stations denoted by  $S_{1E}$ ,  $S_{1W}$  and  $S_4$ , as in Figure 3. The suspended load was measured separately for longshore and cross-shore directions. Tracer grains were identified in every sample.

### 3 SEDIMENT MOVEMENT FIELD STUDY

#### 3.1 Critical velocities

Two primary thresholds of sediment transport can be identified under waves and currents:

- incipient motion of single grains  $V_{cr}^{(1)}$
- critical velocity of bulk transport identified with the movement of the bed-load layer having the thickness  $a$ , i.e.  $V_{cr}^{(2)}$ .

From recent investigations, including those by Pruszek & Zeidler (1988), it is known that the motion of single grains having the median diameter  $D_{50}=0.10-0.25$  mm and the density  $\rho_s=2650$  kg/m<sup>3</sup> occurs at  $V_{cr}^{(1)} \approx 8-12$  cm/s. In exceptional cases coupled with local bathymetry and random disturbances of wave motion, those velocities can be smaller than 8 cm/s or greater than 12 cm/s, up to 20 cm/s.

The other sediment transport threshold lies at  $V_{cr}^{(2)} \approx 40-50$  cm/s or even 20 cm/s for fine particles having  $D_{50}=0.08-0.10$  mm. The bulk motion of sediment grains can obviously occur in layers of different thickness. It can be assumed that the incipient motion occurs in a thin layer of a few sand grains when the flow velocity reaches about 30-40 cm/s, and it is fully developed at currents reaching 50-70 cm/s, when the moving layer of sediment is considerably thicker.

#### 3.2 Sand grain speed

Once the critical velocity  $V_{cr}^{(1)}$  is surpassed, the sediment is likely to move in a very thin surficial layer. The grain speed at the mud line  $v_{ml}$  will depend on the intensity of water flow. As the latter increases, the grain speed will also change but the sediment at the mud line will move much faster than that beneath. The bulk motion of sediment in the deeper layers is much slower than the mud line velocity  $v_{ml}$  as illustrated in Figure 4. Sediment grains participating in the mud line motion are much more mobile and their speeds exceed that of the deeper layers by a factor of two and more.

The discrimination of the bed surface layer at mud line and bulk transport of sediment grains is schematized on the right hand side of Figure 4. The experimental relationships between the mean grain speed and water velocity for the two distinct sediment layers are shown on the left hand of the same drawing. In our analysis of sediment transport characteristics in the above layers, we have followed the distinction of three characteristic subareas of the coastal zone having different hydrodynamic and morphodynamic conditions, as identified at CRF Lubiatowo by Pruszek & Zeidler (1992), cf. Figure 1.

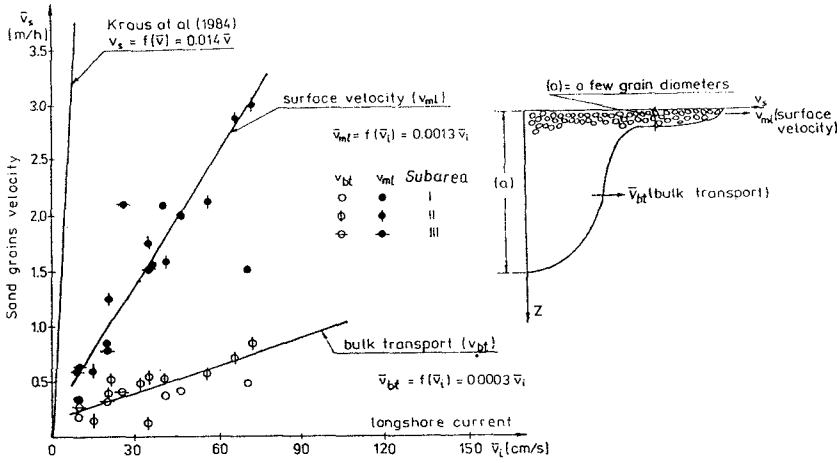


Figure 4. Mean longshore sediment speed versus velocity of longshore current

The mean longshore mud line velocity of sediment grains within the entire active cross-shore profile is given as follows:

$$\overline{v_{ml}} = 0.0013 \overline{V_i} \tag{3.1}$$

while the bulk transport velocity reads

$$\overline{v_{bt}} = 0.0003 \overline{V_i} \tag{3.2}$$

where  $\overline{V_i}$  = longshore current velocity averaged over respective subarea ( $i = 1, 2$  or  $3$ ).

The sediment transport velocities obtained for the Polish conditions of the South Baltic are smaller by an order of magnitude than those given by Kraus et al. (1982). The discrepancy indicates that such relationships are regional and depend on local parameters. It should be noted that the grain speed given by Kraus et al. (1982) is presented as a function of the longshore current velocity averaged across the entire shore profile, not a specific subarea, as in our analysis.

### 3.3 Bedload layer thickness

Examples of a few vertical distributions of the radiotracer in the three subareas of motion are presented in Figure 5. Zero denotes that the radioactivity of the selected layer was smaller than 600 pulses/100 s, that is below the natural background of sea bed activity. Upon thorough analysis of the obtained distributions one can identify stratification of sediment transport in sea bed. Major concentrations of the radiotracer occur at the mud line and seldom deeper than about

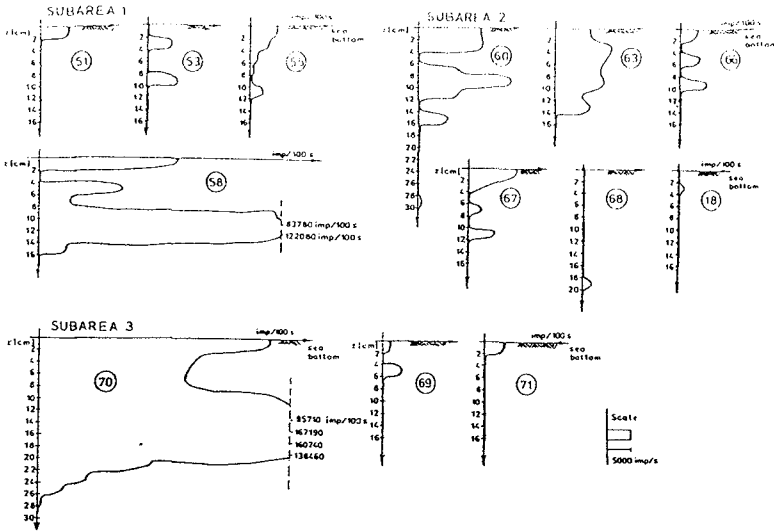


Figure 5. Vertical distributions of bedload as judged from the 1993 tracer studies at CRF Lubiatowo; (imp) pulses.

15 cm below mud line. It was only in one case that tracer concentration of 640 pulses/100 s was detected 30 cm below bed surface (sample No. 70). In that case the sample was taken in the immediate vicinity of the disposal point, and the initial radioactivity was rather high. The results and the analysis suggest that it is only during storms that the bed surface layer of moving sediment exceeds 2 cm in thickness, while the latter can be assessed at a few or several grain diameters for average waves, whereas the maximum thickness of 4-6 cm could be expected at very severe storms. The thickness of the bedload layer also depends on local bed topography. Considerable differentiation of the thickness is noted about an underwater bar crest.

It should be emphasized that the values given above refer to the active bedload layer in which all moving sediment grains are in motion at the same time and move in the same direction.

From our recent and earlier investigations it can be concluded that the bedload layer thickness corresponds to the estimate given by Kraus et al. (1982):

$$a = 0.027 H_b \tag{3.3}$$

in which  $H_b$  = breaker height at a depth of 2-3 m (about the second bar).

### 3.4 Sediment transport

#### 3.4.1 Cross-shore transport

Sediment transport rate can be computed by the following formula:

$$q = q_{ml} + q_{bt} = (\rho_s - \rho)(\bar{v}_{ml}a_{ml} + \bar{v}_{bt}a_{bt}) \tag{3.4}$$

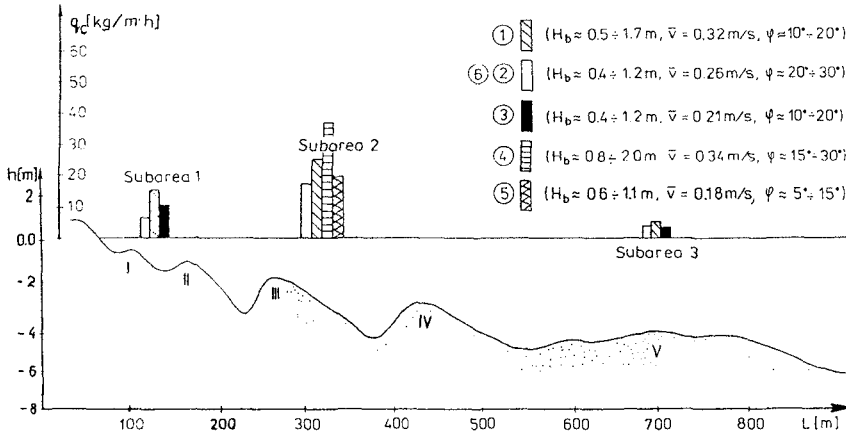


Figure 6. Cross-shore distribution of cross-shore sediment transport rate in five classes of waves.

where  $\bar{v}$  denotes time-averaged sand speed (either along or across shore), the index *ml* denotes mud line and *bt* stands for bulk motion.

The most intensive net cross-shore transport occurs at the second and third bar in the cases of average or high waves, as illustrated in Figure 6. The sediment transport rate at crests of those bars can reach 25 kg/(m h) during storm phases. Local maxima can even amount to 35-40 kg/(m h). The transport rate decreases in the seaward direction and for the average wave conditions it is about 5-10 kg/(m h) in subarea 3. For the predominant oblique wave incidence it can be assumed that a local ratio of cross-shore transport rate to the longshore one oscillates about 1:3-1:4. However, it should be noted that the above mean values can deviate substantially from instantaneous rates because of the high variability of sediment transport.

It has been found that the cross-shore transport in the troughs between bars is negligible, so that practically all grains move about bar crests. The resulting movement of sediment in the cross-shore direction can be coupled with the displacement of bar crests. The latter can be both landward and seaward.

### 3.4.2 Longshore sand transport (local)

The longshore sediment transport depends on the nature and intensity of waves and currents and on local topography. In local terms, the sediment transport is a function of sand grain speed  $v$  and the thickness of transport layer  $a$ , and can be approximated as follows:

The cross-shore variability of the longshore sediment transport rate computed by Equation 3.4 is illustrated in Figure 7 for a few selected wave-current cases. The most intensive longshore sediment transport appears to occur at sec-



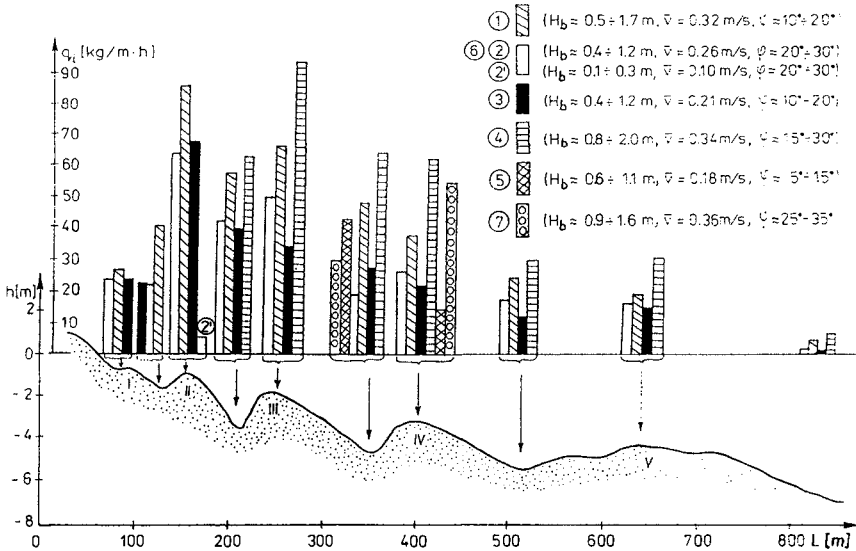


Figure 7. Cross-shore distribution of longshore sediment transport rate in five classes of waves.

ond and third bars, and decreases both seawards and shorewards. It is worthwhile to note the existence of a relatively high sediment transport in between bars, particularly in areas of the prevailing wave breaking, in our case again about second and third bars. This finding is not widespread, and contrary arguments on the low importance of the troughs in the overall longshore sediment transport have often been raised. In many instances, particularly at smaller wave incidence angles, the longshore sediment transport rate between bars is of the same order as that on bars. In some situations the troughs did not permit cross-shore spreading of sediment, especially if they were deeper and steeper.

By and large, the longshore sediment transport under weak waves (breaking between second bar and shoreline, with breaker height much lower than 1 m) occurs only in subarea 1, and its rate does not exceed 5-8 kg/(m h). As the wave height increases (wave breaking between third bar and shoreline, mean breaker height slightly below 1 m), the longshore sediment transport occurs in a wider surf zone and extends up to the fifth bar at maximum. Depending on local longshore current and wave parameters, the longshore sediment transport rate may vary between 5-30 kg/(m h) in subareas 1 and 2 and 0-15 kg/(m h) in subarea 3.

The longshore sediment transport rate increases substantially under storm conditions, when waves break far away from shoreline and at many locations across the surf zone, with the mean breaker height above 1 m. Hence in subarea 1 the local magnitude of  $q_s$  reaches 100 kg/(m h) and varies from 40 to 100 kg/(m h) about bars. In subarea 2 the longshore transport is similar, but often even exceeds the earlier magnitude. In subarea 3 the transport rate decreases considerably, and falls to 30 kg/(m h) about the fifth bar. Further seawards one observes transport rates falling to 5-10 kg/(m h) at depths of 6-7 m. Obviously, the transport rate can be higher under extreme storms. In general, the longshore transport rate during storms is a few times greater than at average waves.

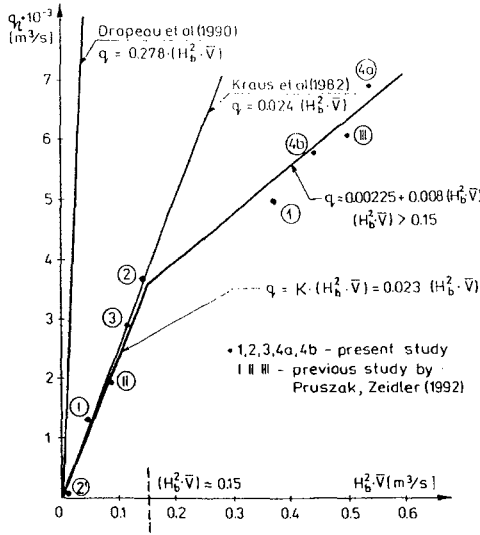


Figure 8. Dependence of littoral drift rate on the product  $H_b^2 \bar{V}$ .

3.4.3 Littoral drift rate

From our experiments and the analysis of the obtained data it follows that the littoral drift rate i.e. the overall longshore transport rate across the coastal zone (assumed 950 m wide for the purposes of this study) reaches  $3-7 \cdot 10^{-3} \text{ m}^3/\text{s}$  under conditions of intensive waves approaching the shore at angles from 10 to  $30^\circ$ . Of course, local unit transport rates vary across the shore, as pointed out above. If waves are very high and conspicuously oblique then the transport rate can exceed  $7 \cdot 10^{-3} \text{ m}^3/\text{s}$ , while at lower waves under our conditions the transport rate varied from  $0.35 \cdot 10^{-3}$  to  $2.3 \cdot 10^{-3} \text{ m}^3/\text{s}$ .

The overall longshore transport rate can be presented as a function of  $H_b^2 \cdot \bar{V}$ , where  $\bar{V}$  represents the mean longshore velocity of water. It appears that the relationships between the sediment transport rate and that quantity (Fig. 8) can be approximated by two straight lines. For smaller values of the quantity  $H_b^2 \cdot \bar{V} = 0-0.15$ , thus small and medium waves, the function  $q = f(H_b^2 \cdot \bar{V})$  reads:

$$q_l = K(H_b^2 \cdot \bar{V}) = 0.023(H_b^2 \bar{V}) \tag{3.5}$$

For higher waves and storms, with  $H_b^2 \cdot \bar{V} > 0.15$  the function is as follows:

$$q_l = q_0 + K_1(H_b^2 \cdot \bar{V} - 0.15) = 0.00225 + 0.008(H_b^2 \bar{V}) \tag{3.6}$$

It seems that the above relationships can be used for the forecast of the overall longshore transport rate in short time scales.

Upon comparison of the results obtained under this study and our earlier investigations (Pruszek & Zeidler 1992), versus other sources of data, one can say that the formula must be site specific. From investigations by Drapeau et al.

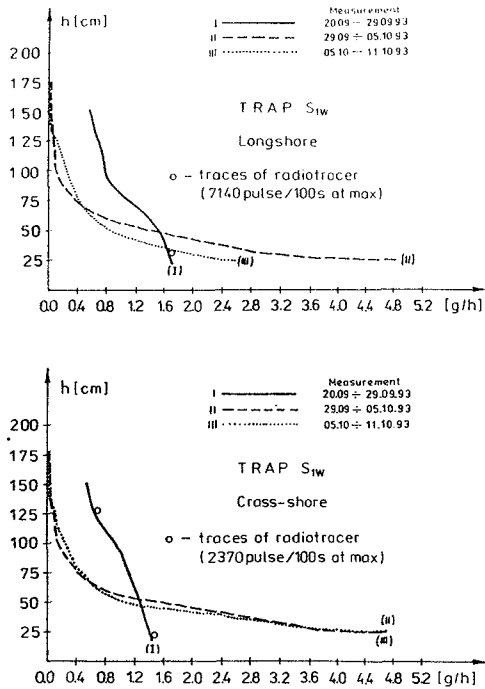


Figure 9. Vertical distributions of sediment concentration in sand traps; trap slots aligned along shore (upper) and across shore (lower).

(1990) carried out in the North Atlantic in the presence of strong tides it follows that the proportionality factor  $K$  in Equation 3.5 is 0.278. On the other hand, Kraus et al. (1982), under mesotidal conditions, obtained  $K=0.024$ . It may be seen that this proportionality factor coincides with ours up to  $H_b^2 \cdot \bar{V}=0.15$ , while a conspicuous deviation is noted for higher values of that parameter, i.e. higher waves.

### 3.4.4 Suspended sediment

The concentration of suspended sediment is higher in subarea 1, with predominant wave breaking and high turbulence, than in subarea 3. Under storm conditions (cf. Fig. 2), the sediment was picked up from the sea bed in subarea 1 to reach the free surface. In cases of less intensive waves (situations II and III) the sediment was kept in suspension up to 1-1.2 m above bed, that is middepth at the investigated location (Fig. 9).

The radioactive tracer was disposed of some forty metres away from sand traps. It was found at different elevations up to 1.3 m above bottom. This indicates that the radiotracer moves not only as bedload but also in suspension, quite high above sea bed. The proportions between bedload and suspended load are difficult to define as they depend on many factors such as intensity of wave mo-

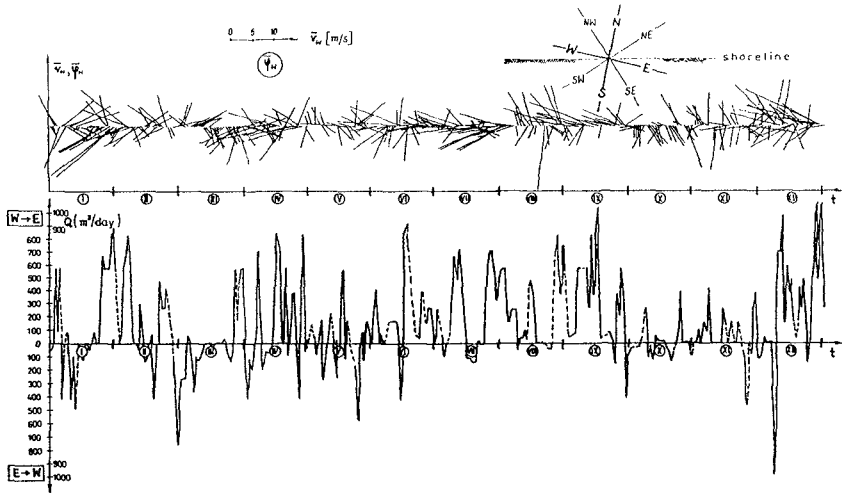


Figure 10. Annual time series of wind (upper) and the resulting littoral drift rate (lower).

tion, circulation and currents, local topography and sediment properties. From different observations and estimates, including those with radiotracers, it can be assessed that about 70-80% of total transport belongs to bedload under weak wave conditions, or even about 100% in exceptional cases. On the other hand, storm conditions bring about intensive suspension, and bedload and suspended load become of the same order, whilst suspended load can clearly predominate under very intensive storm conditions. The latter structure is typical of the surf zone, about wave breaking line and on small depths. On greater depths bedload seems to prevail. It should also be added that suspension is usually preceded by bedload.

### 3.4.5 Mesoscale sediment transport

From many observations and investigations it appears that major effects of the longshore sediment transport are noted in time scales counted in days, months and even years. Our field studies provide a certain insight into the yearly structure of the longshore sediment transport. If one averages over a day the causative sequence of events bringing about the sediment transport (wind, waves, currents, sediment transport), then one obtains a picture permitting conclusions on the yearly structure of sediment transport rates. This is illustrated below and in Figure 10 where both wind input and the resulting sediment transport itself are shown. It should be recollected that only causes, not sediment transport itself are measured in the yearly series. The sediment transport rate was computed from Equations 3.5-3.6.

From our computations and the distributions shown in Figure 10 it appears that although daily transport rates can exceed  $1000 m^3/day$  (across the entire surf zone), the resulting mean net monthly rate is only  $4000 m^3/month$ , corresponding

to the mean annual rate of 50000 m<sup>3</sup>. It is also visible that the yearly course of sediment transport is stepwise: some 25% of the mean monthly amount of sediment transported can be derived from a single storm.

#### 4 CLOSING REMARKS

Upon comparison of our results with other investigations and findings it can be concluded that many sediment transport formulae are site specific, or depend on particular environmental properties embedded in those formulae. Hence from studies by Drapeau et al. (1990) for the North Atlantic and strong tidal effects it appears that the parameter  $K$  is 0.278. Kraus et al. (1982) conclude that  $K$  is 0.024 for a nontidal shore with a single bar. On the other hand, from our measurements for the Polish Baltic conditions the coefficient is identical with Kraus's if the characteristic quantity  $H_b^2 \bar{V} < 0.15$  predominates, while it deviates considerably if that quantity is above 0.15, i.e. for intensive wave conditions. The observations, measurements and conclusions drawn for the two ranges of  $H_b^2 \bar{V}$  above and below 0.15 add an interesting message to the linkage between sediment transport rate and its causes.

No matter how approximate and incomplete, the annual distribution of sediment transport rate shown in Figure 10 for the Polish Baltic conditions contains an important information on the stepwise nature of sediment transport. The estimates shown can be regarded as typical of the southern Baltic.

It is worthwhile to emphasize our finding that the sediment transport between bars can be quite conspicuous particularly at locations of the most frequent wave breaking (our bars II and III) This is contrary to the widespread belief that the sediment transport in troughs is much less important than that on bar crests.

#### LITERATURE

- Drapeau G., B.Long & J.W.Kamphuis (1990), Evaluation of radioactive sand tracers to measure longshore sediment transport rates. *Proceed. 22nd ICCE*, Delft, ASCE, 2710–2723.
- Kraus N.C., M.Isobe, H.Igarashi, T.O.Sasaki & K.Horikawa (1982), Field experiments on longshore sand transport in the surf zone. *Proceed. 18th ICCE*, Cape Town, ASCE, 969–988.
- Pruszek Z. & R.B.Zeidler (1988), Estimates of cross-shore bedload and bed changes. *Proceed.21st ICCE*, Malaga, ASCE, 1174–1787.
- Pruszek Z. & R.B.Zeidler (1992), Beach changes and sediment movement in the surf zone. *Proceed.23rd ICCE*, Venice, ASCE, 2370–2382.
- Pruszek Z. (1993), The analysis of beach profile changes using Dean's method and empirical orthogonal functions. *Jour. Coastal Eng.*, 19, 245–261.

#### *Acknowledgements*

This study has been carried out under a scientific programme 4S 401 023 04 sponsored by the Polish Committee for Scientific Research *KBN*, which is gratefully acknowledged. The first author expresses his gratitude to the *Stefan Batory Foundation* who granted him the *Soros* scholarship and sponsored his travel to Kobe.

## CHAPTER 183

### SEDIMENT TRANSPORT UNDER (NON)-LINEAR WAVES AND CURRENTS

Jan S. Ribberink<sup>1)</sup>, Irene Katopodi<sup>2)</sup>, Khaled A.H. Ramadan<sup>3)</sup>,  
Ria Koelewijn<sup>4)</sup> and Sandro Longo<sup>5)</sup>

#### Abstract

Two series of experiments were carried out in the Large Oscillating Water Tunnel of Delft Hydraulics, which was recently extended with a recirculation flow system. Combined wave-current boundary layer flows were studied with a mobile sand bed in the sheet flow regime. Detailed intra-wave concentration and velocity measurements were carried out and revealed a three-layer system, i.e. a pick-up layer, a sheet flow layer and a suspension layer. In the suspension layer time-lag effects of the sediment concentration led to sediment fluxes in upstream direction. The suspended sediment was more confined to the near-bed region than according to diffusion theories, most likely due to turbulence damping. The horizontal time-dependent and net sediment fluxes were concentrated in the sheet flow and pick-up layer. Measured net sediment transport rates could be described as a linear relation with the third-order velocity moment  $\langle U^3 \rangle$  near the bed.

- 
- 1) Senior research officer, Delft Hydraulics, P.O. Box 152, 8300 AD Emmeloord, The Netherlands and: Delft University of Technology (Netherlands Centre of Coastal Research)
  - 2) Scientific officer, Democritus University of Thrace, Department of Civil Engineering, 67100 Xanthi, Greece
  - 3) Research officer, Hydraulics & Sediment Research Institute, P.O. Box 13621, Delta Barrage, Egypt
  - 4) M.Sc. student, Delft University of Technology, Fac. of Civ. Eng., Hydr. Eng. Section, P.O. 5048, 2600 GA Delft, The Netherlands
  - 5) Researcher, University of Florence, Department of Civil Engineering, via S.Marta 3, 50139 Florence, Italy

### Introduction

The understanding of the physical processes near the sea bed in combined wave-current flows plays an essential role in the description of the sediment transport in the coastal zone. A general lack of basic knowledge on the interaction between waves, currents, sediments and the sea bed in the combined wave-current boundary layer exists. The validity of various mathematical models can hardly be assessed due to the low number of measurements available, especially at prototype scale (Horikawa, 1988). The present study is focused on the boundary layer processes in the case of high bed-shear stress conditions (Shields parameter  $> 0.6$ ). In this regime the sea bed is plane with sheet flow and suspension as the dominating transport modes. A research programme is concentrated around the Large Oscillating Water Tunnel of Delft Hydraulics in which the wave-induced near bed oscillatory flow and sediment transport phenomena can be simulated in the scale of nature (1:1). The present research is a follow-up of earlier work by Ribberink and Al-Salem (1994) and Al-Salem (1993) whom collected a large series of data on the sediment dynamics in mainly asymmetric oscillatory flow conditions. They verified and developed several mathematical models for the description of the observed phenomena. In 1992 the tunnel was extended with a recirculation flow system (see Figure 1) which enabled the superposition of net currents to the oscillatory flow. During a first experimental programme the behaviour of the tunnel flow and the various bedform regimes were investigated in regular wave-current conditions (Ramadan, 1993).

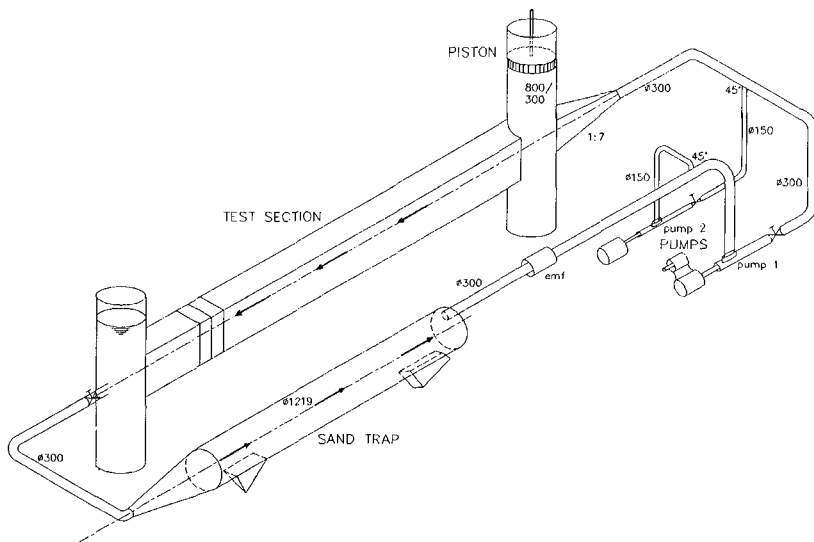


Figure 1 The Large Oscillating Water Tunnel with its recirculation system

In the present paper the main results of two experiment series (series C and E) are presented. Series C was focused on the influence a net current superimposed on asymmetric (second-order Stokes) waves on time-averaged quantities such as the suspended load and the net sediment transport rate.

During series E detailed time-dependent (intra-wave) measurements were carried out in the suspension layer and the sheet flow layer in a number of sinusoidal wave/net current combinations.

The main objectives of the experiments were: i) to increase the understanding of the wave-current boundary layer processes in the case of mobile sandy beds, and ii) to obtain a number of datasets to be used for the development of sediment transport models.

For the complete experimental results, reference is made to the original data reports, i.e. Ramadan (1993), Ribberink (1994) and Katopodi et al (1994).

### Experimental set-up and programme

The Large Oscillating Water Tunnel (LOWT) has the shape of a vertical U-tube with a long rectangular horizontal section and two cylindrical risers on either end. The desired oscillatory water motion inside the test section is imposed by a steel piston in one of the risers. The other riser is open to the atmosphere. The test section is 14 m long, 1.1 m high and 0.3 m wide. A 0.3 m thick sand bed can be brought into the test section, leaving 0.8 m free for the oscillatory flow above the bed. The range of the oscillatory velocity amplitudes is 0.2-1.8 m/s and the range of periods is 4-15 s. The LOWT, extended with a recirculation flow system for the generation of a steady current, is shown in Figure 1. The maximum capacity of the two pumps is 100 l/s and 20 l/s. The maximum superimposed mean current velocity in the test section is 0.5 m/s. The two risers are used as sand traps, moreover the recirculation system is provided with a 12 m long pipe sand trap.

As a follow-up of previous research with asymmetric (second-order Stokes) waves (Ribberink and Al-Salem, 1994), a series of experiments was conducted (series C) with asymmetric waves combined with following and opposing currents (following current = a positive current in the direction of the crest half wave cycle motion). In total 10 conditions were investigated. Series C was mainly aimed at the measurement of time-averaged concentrations and sediment transport rates. Each condition was repeated 3-5 times. Each test started with a flat horizontal sand bed. Table 1 gives the main flow characteristics of series C, i.e. the pump discharge  $Q$ , the mean current velocity in the test section  $\langle U \rangle$ , the root mean square velocity of the oscillatory flow part  $\tilde{U}_{rms}$  and the wave period  $T$ . Sand was used with characteristics  $D_{10} = 0.15$  mm,  $D_{50} = 0.21$  mm and  $D_{90} = 0.32$  mm.

Detailed time-dependent measurements were carried out during series E for four sinusoidal wave/net current conditions (see Table 2). From E1 to E4 the oscillatory velocity amplitude  $\hat{U}$  decreases but the net current velocity increases in such a way that the third-order velocity moment  $\langle U^3 \rangle$  of the horizontal oscillatory flow (above



the wave boundary layer) is approximately constant. This choice was based on the linear relation between the net transport rate and  $\langle U^3 \rangle$  as found by Al-Salem (1993) for only (asymmetric) waves. During 5 series of experiments different measuring techniques were used and 115 tests (tunnel runs) were carried out using the same sand as for series C.

Exp.	Net current		Oscillatory flow	
	Q (m <sup>3</sup> /s)	$\langle U \rangle$ (m/s)	$\hat{U}_{rms}$	T (s)
C1	0	0	0.56	6.5
C2	0.012	0.05	0.56	6.5
C3	0.072	0.3	0.55	6.5
C4	0.036	0.15	0.56	6.5
C5	0.096	0.4	0.55	6.5
C9	0	0	0.56	6.5
C10	0.096	0.4	0.8	6.5
C11	0	0	0.8	6.5
C12	0.024	0.1	0.8	6.5
C13	0.096	0.4	0.8	6.5

Table 1 Experimental conditions series C (sheet flow)

Exp.	Net current		Oscillatory flow	
	Q (m <sup>3</sup> /s)	$\langle U \rangle$ (m/s)	$\hat{U}$ (m/s)	T (s)
E1	0.036	0.15	1.6	7.2
E2	0.048	0.20	1.35	7.2
E3	0.072	0.30	1.10	7.2
E4	0.096	0.40	0.9	7.2

Table 2 Experimental conditions series E (sheet flow)

Suspended sediment concentrations in the range of 0.1 - 50 g/l were measured with a transverse suction technique for time-averaged values (series C, E) and an optical infra-red light extinction technique OPCON for time-dependent values (series E).

The large (time-dependent) concentrations in the sheet flow layer ( 100-1600 g/l) were measured with an electro-resistance technique CCM (series E).

Time-dependent velocities were measured with a 2 component forward-scatter laser-doppler flow meter LDFM for mainly clear water (series C, E), an electro-magnetic flow meter EMF in the suspension layer (series C,E) and a high-speed video technique HSV for grain velocities in the sheet flow layer (series E). Net sediment transport rates were measured with a mass-conservation technique using sand trap volumes and measured bed-level changes. For more detailed information about the techniques, reference is made to Katopodi et al (1994).

Suspended sediment

During the 10 series C and 4 series E conditions totally 81 time-averaged concentration profiles were measured with the transverse suction technique in the layer between 1-1.5 cm and 25 cm above the bed.

In Figure 2 all suspended concentration profiles of series E are plotted on a log-log x-y scale. The straight best-fit lines imply a vertical distribution according to the following power-law:

$$\frac{\langle C(z) \rangle}{C_a} = \left( \frac{z_a}{z} \right)^\alpha$$

where  $C_a$  is a reference concentration at the level  $z_a$  and the power  $\alpha$  is a concentration decay parameter.

Despite the different combinations of waves and currents during series E, the best-fit lines are almost parallel, indicating that the power  $\alpha$  is almost constant ( $1.9 < \alpha < 2.4$ ).

Also for the series C experiments the power-law distribution (1) fitted well with the measurements. The concentration decay parameter  $\alpha$  varied between  $1.6 < \alpha < 2.3$ .

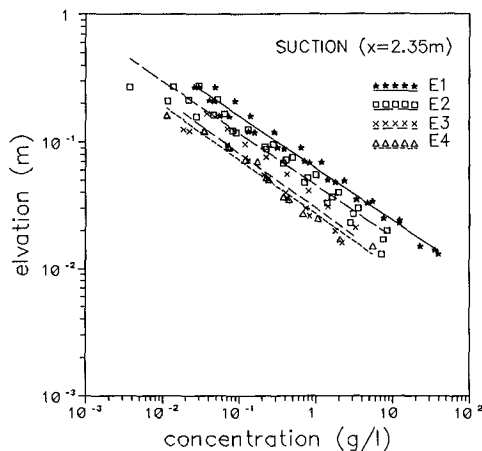


Figure 2 Time-averaged concentration profiles of suspended sediment, series E

Ribberink and Al-Salem (1994) found the same power-law form for a large number of waves-only cases in the sheet flow regime (same sand). The power  $\alpha$  was almost constant ( $\alpha \approx 2.1$ ) in a wide velocity range ( $U_{rms} = 0.3-1.2$  m/s). Figure 3 shows power  $\alpha$  as a function of the maximum Shields number  $\theta'_{max}$  (maximum value during the wave cycle) for the 'waves alone' measurements and the new 'waves + currents' measurements.

$\theta'_{max}$  is computed on the basis of the maximum bed-shear stress during the wave cycle according to:

$$\theta'_{max} = \frac{\tau'_{b,max}}{(\rho_s - \rho) g D_{50}}$$

Herein  $\tau'_{b,max} = 0.5 \rho f_{cw} (\langle U \rangle + \hat{U})^2$  with the combined wave-current friction factor according to the theory of Jonsson (1966) using  $k_s = D_{50}$  as bed roughness height. The measured values of  $\langle U \rangle$  at  $z = 10$  cm above the bed are used as input for the formulation.

Figure 3 shows that all measured values of  $\alpha$  (for waves alone and waves + currents) scatter around  $\alpha = 2$ , showing no relation with the Shields number.

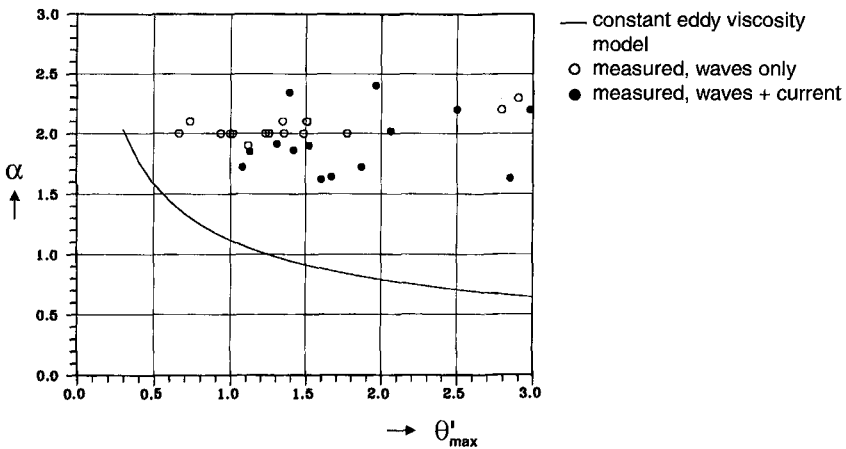


Figure 3 Concentration decay parameter  $\alpha$  vs. maximum Shields number

In the case of a time-invariant sediment mixing or diffusion coefficient increasing linearly with distance above the bed, diffusion models for suspended sediment generate a similar power-law distribution for the time-averaged concentration (see Ribberink and Al-Salem, 1994). However, the models generally lead to decreasing values of  $\alpha$  (= Rouse number) for increasing Shields numbers. This is due to an increasing turbulent or sediment mixing coefficient with increasing bed-shear stress. The full line in Figure 3 represents the theoretical solution of the Rouse number. It is shown that the measured concentration decay is always greater than the theoretical decay and shows no relation with the Shields number.

Apparently, the suspended sediment is more confined to the near-bed region than the theory predicts. Moreover, the result indicates the increasing importance of turbulence damping above the mobile bed (sheet flow layer) for increasing Shields numbers.

The measured time-dependent behaviour of the suspended sediment concentrations during experiment E1 is shown in Figure 4. In the lower part ensemble-averaged concentrations measured with OPCON are shown during one wave cycle at three elevations near the bed. The upper part shows the time-dependent horizontal velocity (at  $z = 20$  cm) as well as the vertical position of the piston driving the oscillatory flow.

It can be observed that the concentration exhibits two peaks that roughly coincide with the maximum downstream and upstream velocities. Due to the asymmetry of the flow (downstream velocity amplitude  $>$  upstream velocity amplitude) the two peaks are not of equal magnitude. Two other generally smaller concentration peaks occur near the moments of flow reversal. Similar peaks were observed by Al-Salem (1993) for waves only. A possible explanation for their existence may be found in turbulence generation due to shear instabilities in the bottom boundary layer (see Foster et al, 1994).

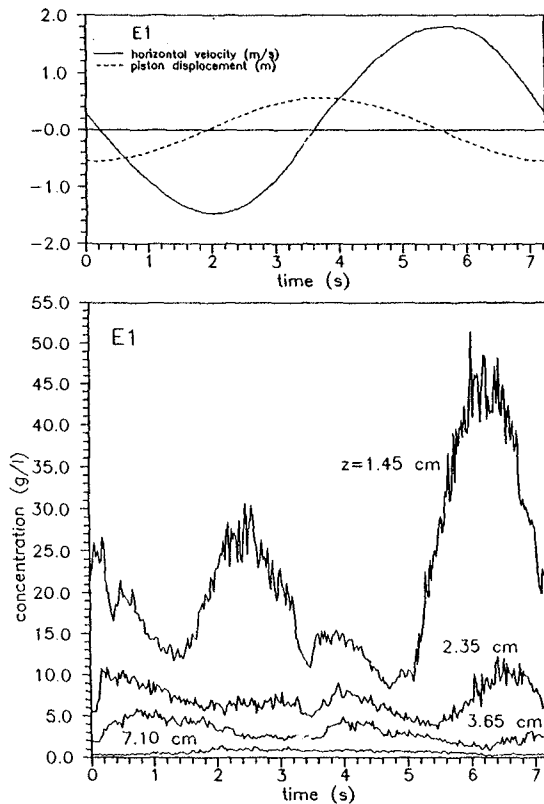


Figure 4 Time-dependent suspended sediment concentrations, E1

With increasing distance above the bed the concentration decays rapidly and the concentration maxima occur at a later moment (time lag effect). At higher elevations

the maximum concentrations occur even after the next flow reversal, indicating history effects from a previous half wave cycle.

From E1 to E4 the flow asymmetry increases due to an increasing net current velocity/oscillatory velocity ratio (see Table 2). Simultaneously, the concentration measurements show an increasing history effect of the 'downstream' half cycle during the 'upstream' half cycle. Moreover, the concentration peaks at flow reversal become less dominant. For more detailed results, see Katapodi et al (1994a).

### Sheet flow

At lower elevations near the bed ( $z < 1$  cm) the sheet flow layer is entered with very large sediment concentrations (100-1600 g/l). Time-dependent concentration measurements were carried out with the CCM. The CCM was brought into the test section from below through the sand bed in order to minimize possible flow disturbance. The lower part of Figure 5 shows ensemble-averaged concentrations (E1) at various elevations around  $z = 0$ . The elevation  $z = 0$  is defined as the mean bed elevation before/after the experiment (without sediment motion). The upper part of Figure 5 shows the time-dependent velocity at  $z = 20$  cm.

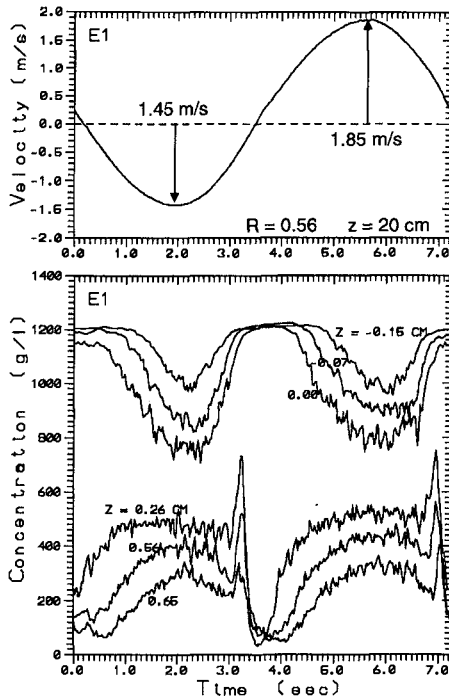


Figure 5 Time-dependent concentrations in the sheet flow layer, E1

Two layers with different behaviour can clearly be observed, i.e. a pick-up layer with minimum concentrations in phase with maximum velocities and a sheet flow layer with maximum concentrations in phase with maximum velocities. In the pick-up layer two phases occur during each wave cycle with no sediment motion and maximum sand concentration (settled sand, near  $U = 0$ ), which are both followed by a phase with lower concentrations due to the vertical pick-up of grains. In the sheet flow layer ( $z > 0$ ) the phase behaviour is opposite, reflecting the exchange of sand with the pick-up layer (see also Al-Salem, 1993). Near the moments of flow reversal large concentration peaks with a short duration occur, which are probably related with similar peaks as observed in the suspension layer somewhat later in time (see Figure 4). In general, all series E experiments show very small phase shifts between the concentration peaks at different elevations, indicating that time-lag effects are of minor importance in these near-bed layers.

The concentrations in the sheet flow layer do not show the asymmetry of the two half cycles as observed in the suspension layer of E1. However, for E2...E4 the increasing flow asymmetry effect becomes also visible in the sheet flow layer.

Figure 6 shows the complete time-averaged concentration profile on a log-linear x-y scale for all layers of E1 obtained from the CCM, OPCON and SUCTION measurements. The approximate positions of the suspension layer ( $C < 100$  g/l), the sheet flow layer ( $C > 100$  g/l) and the pick-up layer are indicated.

In the upward direction the concentration profile shows the transition from a convex shape (pick-up layer) to a concave shape (suspension layer), reflecting the presence of different physical mechanisms of the mixing process.

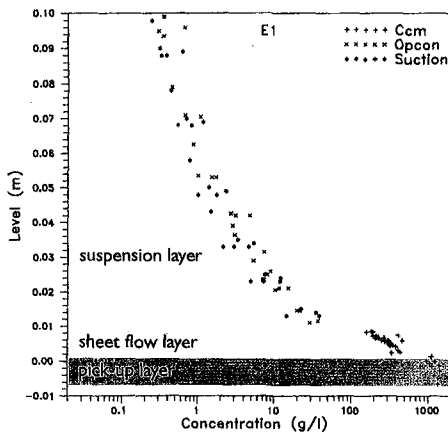


Figure 6 Time-averaged concentration profile of E1, a three-layer system

A high-speed video camera (500 frames/s) was focused through the glass side wall 2 cm inside the test section on a vertical image of 1.55 x 2.15 cm parallel to the oscillatory flow direction. A time counter on the video image was synchronized with

the piston motion. Two different particle tracking techniques were applied to measure the grain velocities at a number of phases of the cycle at several elevations above the bed.

Figure 7 shows measured horizontal grain velocity profiles of E1. Large velocity gradients occur especially in the sheet-flow and pick-up layer.

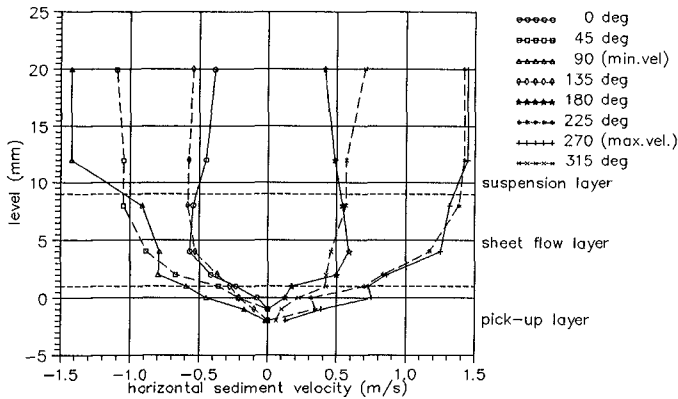


Figure 7 Horizontal grain velocity profiles of E1 (obtained with high-speed video)

#### Sediment fluxes and net sediment transport rates

By multiplication of the horizontal velocities  $U(z,t)$  (LDFM, EMF) and concentrations  $C(z,t)$  (OPCON), time-dependent horizontal sediment fluxes  $\phi(z,t)$  were calculated in the suspension layer. The same was done in the sheet flow layer using the horizontal grain velocities (HSV) and the concentrations (CCM). The result of this analysis for experiment E1 is shown in Figure 8, using a log-linear x-y scale (with  $\phi = \pm 10^{-3}$  m/s as separation between negative and positive fluxes). The dimensionless volume concentration is used for the flux computation, and thus the sediment flux unit is m/s.

Maximum fluxes occur at the moments of maximum downstream and upstream velocity (above the wave boundary layer) in the sheet flow layer. Deeper into the sheet flow and pick-up layer the fluxes gradually reduce. A very strong reduction of the fluxes occurs in the suspension layer. The net horizontal sediment fluxes over the wave cycle were computed by time-averaging, making distinction between a current related and a wave related contribution, according to:

$$\langle \phi(z,t) \rangle = \langle U(z,t) \cdot C(z,t) \rangle = \phi_c + \phi_w$$

$$\phi_c = \langle U(z,t) \rangle \cdot \langle C(z,t) \rangle$$

$$\phi_w = \langle \tilde{U}(z,t) \cdot \tilde{C}(z,t) \rangle$$

Herein  $\tilde{U}$  and  $\tilde{C}$  represent the periodic parts of  $U$  and  $C$  after subtracting the wave-mean values  $\langle U \rangle$  and  $\langle C \rangle$  respectively. The distinction between  $\phi_c$  and  $\phi_w$  was only possible in the suspension layer where the mean velocity  $\langle U \rangle$  could be computed with a reasonable accuracy.

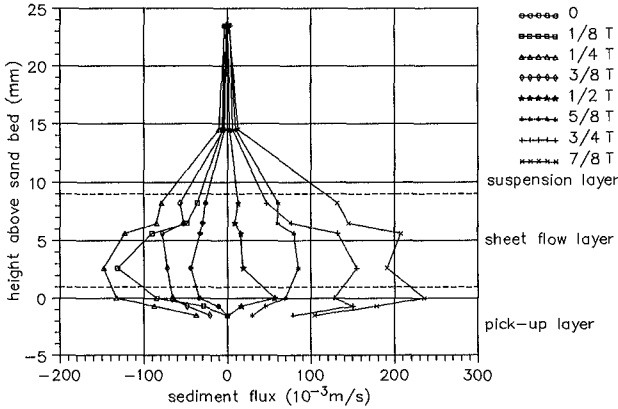


Figure 8 Time-dependent horizontal sediment flux profiles, E1

Figure 9 shows the computed net sediment flux profiles of the suspension layer of E1.

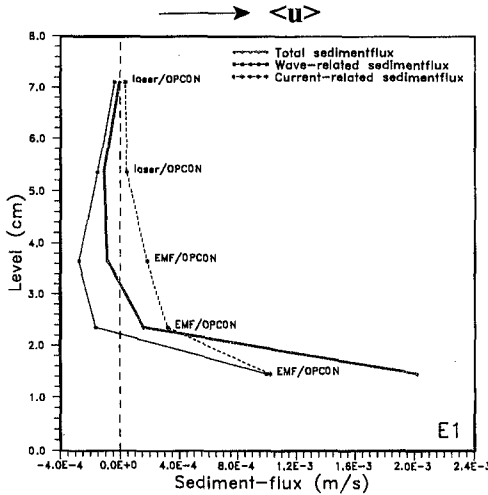


Figure 9 Net horizontal sediment flux profiles in the suspension layer, E1



It can be observed that due to time lags of  $\tilde{C}$  with respect to  $\tilde{U}$  (phase differences) a negative wave related flux is present at elevations  $z > 2$  cm. However, this negative contribution is almost compensated by the positive contribution of the current-related flux (the latter is positive by definition). Closer to the bed ( $z < 2$  cm) both contributions become positive and a relatively large positive total net flux results, showing a strong increase in the direction of the bed.

The complete total net horizontal flux profile for E1 is shown in Figure 10. In comparison with Figure 9 the scale of the horizontal axis had to be changed considerably (factor 10), due to the large magnitude of the net fluxes in the sheet flow and pick-up layer. The fluxes in the suspension layer can now hardly be recognized, indicating their minor importance for the total net sediment transport rate.

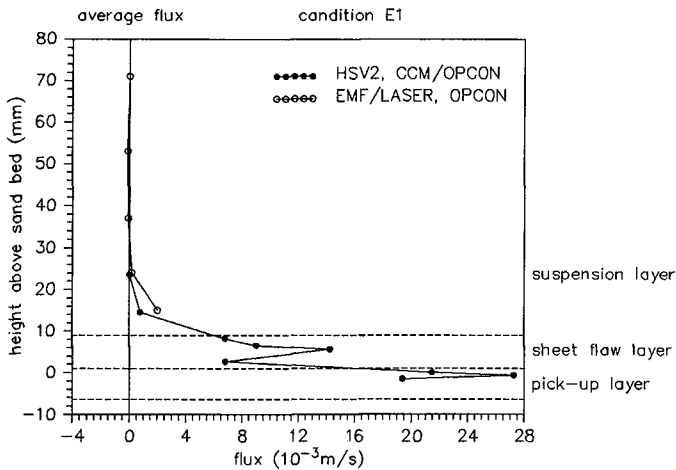


Figure 10 Total net horizontal sediment flux profile, E1

The fluxes in the sheet flow and pick-up layer show a considerable scatter, which is mainly caused by the low number of measured grain velocities per wave cycle in combination with a low accuracy of the grain velocity measurements. Vertical integration of the flux profile was carried out to estimate the total net sediment transport rate during E1. The obtained transport rate ( $120 \cdot 10^{-6} \text{ m}^2/\text{s}$ ) agreed reasonably well with the (relatively accurate) total net transport rate as obtained with the mass conservation technique ( $92.4 \cdot 10^{-6} \text{ m}^2/\text{s}$ ).

Also the experiments E2...E4 confirmed the result of experiment E1, namely that the net transport rate is mainly concentrated in the sheet flow and the pick-up layer. Even for E4 with the greatest net current the contribution of the suspension layer to the total net transport rate is minor. The previously mentioned relatively small

suspended sediment mixing above the mobile bed, most likely caused by turbulence damping effects of the sheet flow layer, is responsible for this phenomenon.

The results are only valid for the investigated conditions. It is expected that for finer sand, an increased current dominance (with respect to the waves) and in cases with rippled beds the importance of suspended sediment will strongly increase.

Al-Salem (1993) showed that in case of asymmetric 2<sup>nd</sup> order Stokes waves the net sediment transport is also concentrated in the sheet flow layer (same sand). Ribberink and Al-Salem (1994) showed that the net sediment transport can be described with a linear function of  $\langle U^3 \rangle$ , i.e. the third-order moment of the horizontal velocity above the wave boundary layer.

The measured net sediment transport rates of the series C and the series E experiments (totally 69 tunnel runs) were used to verify this relation in the case of combined waves and currents. The result is shown in Figure 11.

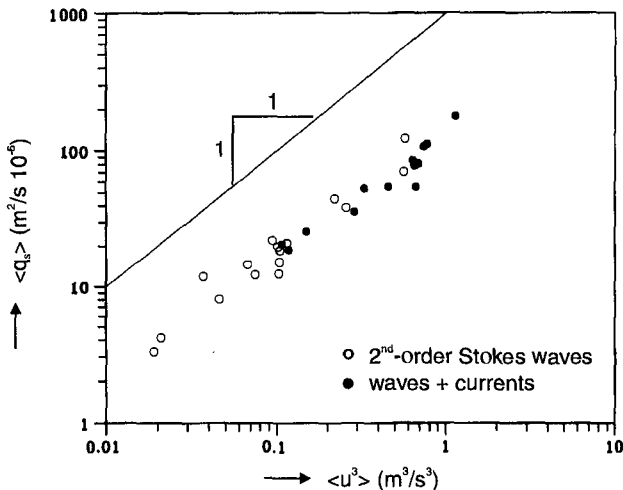


Figure 11 Measured net sediment transport rates vs. velocity moments  $\langle U^3 \rangle$

As the net current velocity is a function of the elevation above the bed and the velocity moment is computed on the basis of measured velocities, a choice was made for  $z = 10$  cm (series C) and  $z = 20$  cm (series E). Both elevations are above the wave boundary layer. The influence of the difference in the selected elevation (10 or 20 cm) on Figure 11 appeared to be minor.

The 'wave+current' cases in Figure 11 show approximately the same correlation between  $\langle q_s \rangle$  and  $\langle U^3 \rangle$  as the previous 'waves alone' cases.

The reasonable success of this relation (for this sand type and the selected experimental conditions) can be explained by the concentration of the sediment

transport near the bed (sheet flow layer) and the quasi-steady character of the transport process in this layer.

### Conclusions

Two experimental studies were conducted in the Large Oscillating Water Tunnel of Delft Hydraulics which was recently extended with a new recirculation system. Detailed time-dependent measurements were carried out in the combined wave current boundary layer in sheet flow conditions (series E) using a number of measuring techniques, among them a high-speed video technique for the measurement of grain velocities in the sheet flow layer. Series C concerned time-averaged measurements near the bottom. The datasets obtained can be used for the verification and development of boundary layer flow and transport models. In the present study a first analysis of the experimental results was presented.

The main conclusions are:

1. The time-dependent measurements of series E revealed a three layer transport system, viz. a pick-up layer, a sheet flow layer and a suspension layer with:
  - 4 concentration peaks per wave cycle in the sheet flow and suspension layer, (2 main peaks related to the maximum downstream and upstream velocities and 2 peaks near flow reversal),
  - increasing phase lags for increasing elevation in the suspension layer and almost no phase lags in the sheet flow and pick-up layer.
2. The time-averaged suspended sediment concentration profiles showed a similar negative power distribution as found during previous experiments with only waves. The concentration decay parameter  $\alpha$  appeared to be almost constant ( $\approx 2$ ) for all experiments (waves alone and waves + currents). The measured concentration decay near the bed was larger than the predicted decay of a theoretical diffusion model (with a time-invariant diffusion coefficient) and did not show the expected decrease for increasing Shields numbers. This is probably caused by turbulence damping effects above the mobile bed (sheet flow layer).
3. Using the time-dependent velocity and concentration measurements horizontal time-dependent and time-averaged sediment fluxes were computed and analyzed. The horizontal fluxes were concentrated in the sheet flow and pick-up layer near the bed. The contribution of the suspension layer to the total net flux appeared to be minor.
4. Due to the quasi-steady character of the transport process in the sheet flow and pick-up layer the measured net sediment transport rates of series C and series E showed a similar linear relation with  $\langle U^3 \rangle$  as obtained during previous experiments with asymmetric waves and no current.

### Acknowledgements

The series C experiments were carried out in the framework of the Coastal Genesis research programme in the Netherlands and were funded by the Ministry of Transport and Public Works (Directorate General Rijkswaterstaat).

The series E experiments were part of the European programme "Access to Large-scale Facilities and Installations" and were funded by the Commission of the European Communities, Directorate General for Science, Research and Development, contract no. GE1\*-CT91-0032 (HSMU). The research was executed by a European team with members, apart from the authors, also P. Ruol, C. Lodahl, A. Crosato and H. Wallace. The data analysis and reporting was partly done in the framework of the MAST G8, Coastal Morphodynamics research programme of the Commission of the European Communities, contract no. MaS2-CT92-0027. The assistance of M. Janssen with the computation of the sediment fluxes is greatly acknowledged.

### References

- Al-Salem, A.A. (1993). Sediment transport in oscillatory boundary layers under sheet-flow conditions, Ph. D. Thesis, Delft University of Technology.
- Horikawa, K. (ed) (1988). Nearshore dynamics and Coastal Processes, University of Tokyo Press, Tokyo, 522 pp.
- Jonsson, I.G. (1966). The friction factor for a current superimposed on waves, Basic Research-Progress Report No. 11, Technical University of Denmark, pp 1-12.
- Katopodi, I., J.S. Ribberink, P. Ruol, R. Koelewijn, C. Lodahl, S. Longo, A. Crosato and H. Wallace (1994). Intra-wave sediment transport in an oscillatory flow superimposed on a mean current, Delft Hydraulics Data report, H 1684, Part III, August.
- Katopodi, I., J.S. Ribberink, P. Ruol and C. Lodahl (1994a). Sediment transport measurements in combined wave current flows, Proc. Coastal Dynamics '94, Barcelona, Spain, ASCE, pp. 837-851.
- Ramadan, K.A.H. (1994). Time-averaged sediment transport phenomena in combined wave-current flows, M.Sc. Thesis, IHE Delft, Delft Hydraulics Report H1889.11, Part I, January.
- Ribberink, J.S. (1994). Time-averaged sediment transport phenomena in combined wave-current flows, Delft Hydraulics, Data-Report H1889.11, Part II, December.
- Ribberink, J.S. and A.A. Al-Salem (1994). Sediment transport in oscillatory boundary layers in cases of rippled beds and sheet flow, J. of Geoph. Res., Vol. 99, No. C6, pp. 12707-12727, June 15.

## CHAPTER 184

### WAVES AND CURRENTS AT THE EBRO DELTA SURF ZONE: MEASUREMENTS AND MODELLING

Rodriguez,A.; Sánchez-Arcilla,A.; Collado,F.R.;  
Gracia, V. Coussirat M.G. and Prieto J. <sup>1</sup>

#### Abstract

The wave incidence and the wave-induced circulation in the surf zone (SZ) is studied from both experimental and numerical point of view. The *DELTA'93* experiments were carried out in the Trabucador bar of the Ebro Delta, in the Spanish mediterranean coast. The emphasis of *DELTA'93* was on the SZ vertical flow structure, measuring simultaneously undertow and longshore current in a barred profile. The numerical simulation with *NEARCIR* Q3D model assumes longshore uniformity and stationarity. The wave decay, 2DH currents and 1DV undertow and longshore currents are modelled. The agreement is quite reasonable as can be seen in the included figures.

#### Introduction

The Ebro delta, one of largest in the Mediterranean, is located on the Spanish coast, 200 Km Southwest of Barcelona (figure 1). As in many other deltas of the world, the Ebro delta is experiencing a severe erosion due to the nearly total reduction of solid river discharges associated to dam construction (Jimenez and S.-Arcilla, 1993). Because of this there is an important monitoring activity around the deltaic coastline from which hydrodynamic, morphodynamic and meteorological data have been extracted to support the surf-zone campaign, which is the main object of this paper.

The data recorded during the surf-zone campaign, which took place along the Trabucador bar, will be described in this paper, together with some references to the wealth of previously recorded information along the deltaic coastline. The numerical model used to simulate surf-zone processes and to gain insight into the physics at the Ebro delta surf-zone during the time of the campaign, is the *NEARCIR* model presented in (S.-Arcilla et al., 1990/1992). This Q3D model works at the current time-scale and is structured into three modules:

---

<sup>1</sup> Lab. Ing. Marítima , L.I.M., Univ. Politécnic de Cataluña, U.P.C.  
Av. Gran Capitàn s/n, 08034 Barcelona, Spain.

- i. Wave Propagation Module (based on the kinematic conservation principle and the wave action balance equation).
- ii. Depth Uniform Current Module (based on the 2DH rigid-lid mass and momentum equations).
- iii. Depth Varying Current Module, including the Bottom Boundary Layer (this module is briefly described for completeness within this paper).

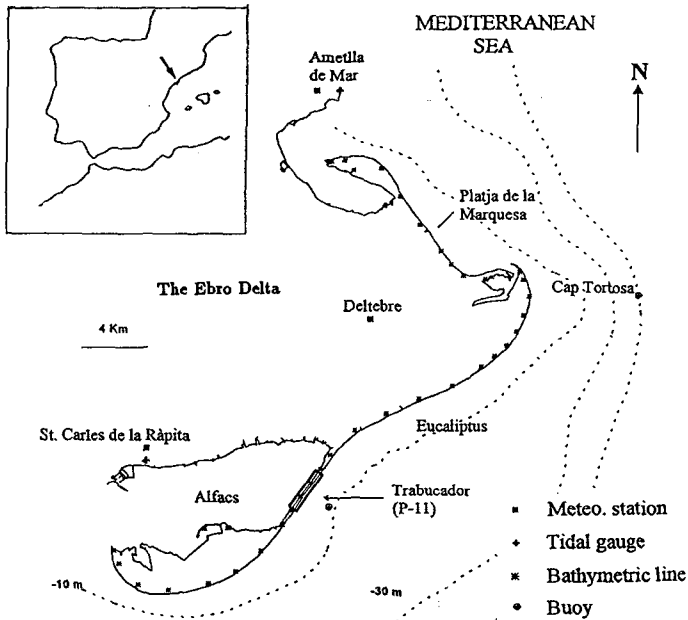


Figure 1. The Ebro Delta

### DELTA '93 Field Experiments

The motivation for this campaign was the lack of detailed 3D data on surf-zone hydrodynamics in a microtidal environment. The campaign was thus focussed on the 3D structure of wave-induced circulation, i.e. on the simultaneous vertical structure of shore-normal (undertow) and shore-parallel (longshore current) flows. Because of this, and trying to avoid excessive complexities and/or unknowns, it was decided to look for an alongshore uniform beach subject to unidirectional waves and a time interval without significant wind.

Based on these considerations and because of the availability of previously recorded field data, the Trabucador bar in the Ebro delta was selected as the most suitable coastal stretch to carry out the surf-zone field exercise. The campaign was centered around the beach profile P11 (see figure 1). The obtained field data include bathymetry, shoreline, wave data outside and inside the SZ, mean water levels across the SZ, and the associated velocity fields (both

horizontal and vertical structure).

The bathymetry in the field site is shown in figure 2. Only relatively modest bottom variations were recorded during the three days of the campaign, which allows assuming a steady bottom geometry for the hydrodynamic analyses. The wave climate was recorded at 50 m and 7.5 m water depth by means of two directional wave rider buoys recording 20 minutes every 3 hours. An Etrometa step wave-gauge was located at the beach sledge, which was used to monitor hydro- and morphodynamic conditions across the surf-zone from the shoreline down to 2.5 m water depth. A BW video camera, placed at 20 m height, was used to record SZ images from which, after digital image processing, information on wave direction, breaking intensity, etc. could be obtained. An X-band radar was also used to measure mean surface roughness (mean wave height) and low-frequency oscillations of the mean water level in the SZ and adjacent nearshore area.

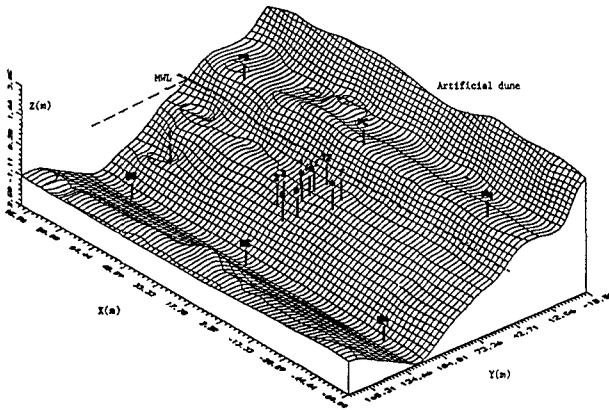


Figure 2. The Trabucador bar bathymetry (P11) for 16/December/93.

Some wave field characteristics plus 2DH circulation and mixing patterns derived from the video images using the developed digital processing technique have been presented in Redondo et al. (1994). This technique allows to quantify the time and space evolution of sea surface tracers (foam, dyes and Lagrangian buoys) and the horizontal mixing properties associated to dye spots.

The vertical structure of horizontal instantaneous velocities was measured with six electromagnetic current meters (Delft Hydraulics-S type) placed in a vertical pole at the sledge, see figura 3. The vertical spacing of the electromagnetic sensors (ems) range from 0.10 to 0.20 m above the bottom up to maximum level of 0.80 m above the bottom, with a sampling rate of 20 Hz allowing therefore to measure some macroturbulence features. Simultaneously with the velocities, the local water level evolution was measured at the same vertical with the step wave-gauge mentioned above (sampling rate 4 Hz). The MWL was computed by averaging the free surface time series, while crest and trough

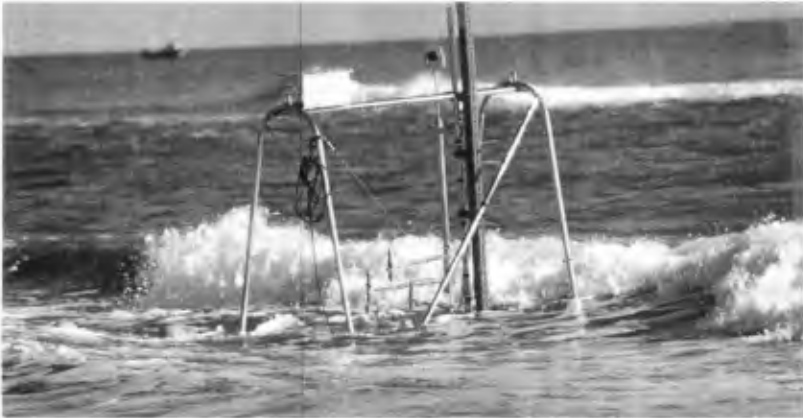


Figure 3. Movable Sledge with: 6 EMS, 1 WG, 3 OBS, 1 COMPASS, Data-Logger and 1 Optic-Prism).

levels were obtained as the mean of the upper "1/3" series of individual crest and trough values. The crests and troughs were obtained after numerically filtering the original water-surface series to remove the effect of long waves and other alien-phenomena.

### Waves: Measurements and Modelling

#### Wave Features

Table 1 summarizes the 5 cases measured during the *DELTA'93* experiments.

Cases	Date	I. E. L.	Spectra	$T_p$ (s)	Sea State	Test n.
I	26/05/93	High	doubled-peak	$T_{p1}$ 18 $T_{p2}$ 3	unsteady	-
II	15/12/93	Low	wide	7.5	Q-steady	NT1-NT4
III	16/12/93 a.m.	Medium-High	sharp	6.0	Q-steady	NT5-NT7
IV	16/12/93 p.m.	Medium	sharp	5.5-7.0	unsteady	NT8-NT12
V	17/12/93	Low	wide	7.5	steady	-

Table 1: Measured conditions I.E.L.: Incident wave energy level; Spectra: type of wave spectra;  $T_p$ : wave period; Test n.: Test number

In this paper only cases III and IV, measured during 16th December 1993, are considered for an in-depth analysis because they were the most complete cases with strong enough wave-induced currents. There are several potential sources of error, such as the linear interpolation in directional wave data recorded every



3 hours by the buoy (to have time correspondance with the wave gauge data recorded every half-hour), the spreading in wave direction given by the buoy or those inherent to the measurement equipment and processing techniques. In spite of this, there was reasonable agreement between the surf-zone spectra from wave-gauge and video images data, showing a good correspondance of frequencies or dominant periods. The comparison between wave angles from the video (VTR) and the ems is not finished because of the large amount of data-processing necessary to obtain a mean angle of wave incidence. The incident wave conditions during the 16th December 1993 (outside and inside the SZ) are summarized in tables 2 and 3. Hrms (m) is the root mean square wave height, Tp(s) is the wave period,  $\theta_m$  is the mean angle of wave incidence, X is the crossshore coordinate,  $h$  is the mean water depth and  $U$ - $V$  (m/s) are the depth-averaged cross- and alongshore velocity components at different sledge positions (test) inside the surf-zone.

Wave incident conditions (DWR)				
Test	Hrms (m)	Tp(s)	$\theta_m$	GMT
5	.61	6.0	177.0	10:04
6	.60	6.1	175.3	10:55
7	.59	6.3	173.0	12:05
8	.50	5.7	179.5	14:07
9	.44	5.4	183.3	15:07
10	.43	5.4	180.6	15:46
11	.425	5.6	176.1	16:20
12	.42	5.8	171.9	16:51

Table 2: Incident wave conditions at *dwr* position (1500 m offshore,  $h$ :7.5m) during 16/December/93.

Hydrodynamic measurements in the SZ						
Test	Hrms	Tp(s)	X(m)	$h$ (m)	$V^*$	$U^*$
5	.47	7.1	87.9	1.29	.48	.15
6	.38	7.1	73.2	0.80	.88	.19
7	.31	8	65.1	0.70	.66	.13
8	.41	7.1	93.5	1.34	.23	.08
9	.40	7.1	79.8	0.70	.62	.24
10	.33	7.1	74.0	0.68	.60	.16
11	.27	8	69.5	0.60	.46	.11
12	.18	8	60.0	0.38	.28	.10

\* (mean below wave trough level  $z_{tr}$ )

Table 3: Hydrodynamic conditions from *WG* and *ems*

An image processing technique, still under development, has also been used to evaluate the acrossshore distribution of the intensity of wave breaking,  $Q_b$ . From an image threshold intensity associated to breaking, the breaking wave distribution acrossshore can be determined for a time series of beach profile transects derived from the video record. The processing technique is able to reproduce some of the features of the acrossshore evolution of the fraction of breaking waves, as derived from e.g. the Battjes and Janssen (1978) (hereinafter

BJ'78) model (figure 4).

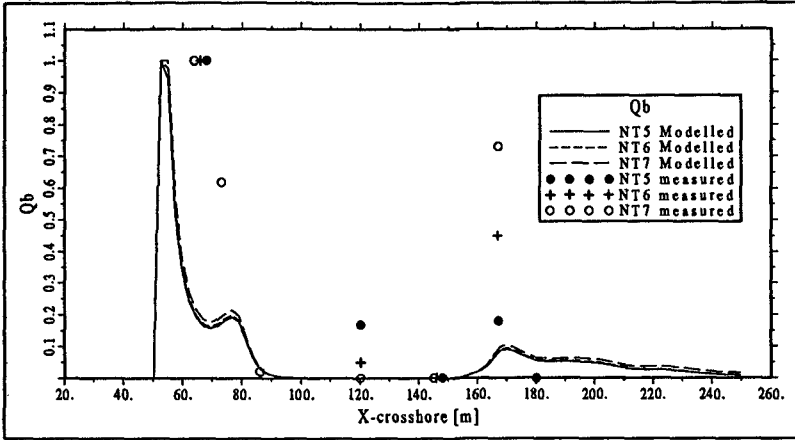


Figure 4. Measured and computed Qb for case III (around 100 waves)

Wave Propagation

The wave conditions for cases III and IV were quasi-stationary, although in this latter case a transient component was also apparent (see test 8 in figure 5). Wave decay due to breaking has been modelled using the BJ'78 approach for random waves (neglecting bottom dissipation). In spite of the lack of perfect stationarity the obtained results are quite reasonable (figure 6). The single value used for the dissipation parameter  $\alpha$ , leads to overestimating the higher wave values near the shore. Moreover, in this shoreline region, the shoaling process dominates over the breaking-induced decay which yields some oscillations in the cells of the computational domain close to the shoreline (not appreciable in figure 6).

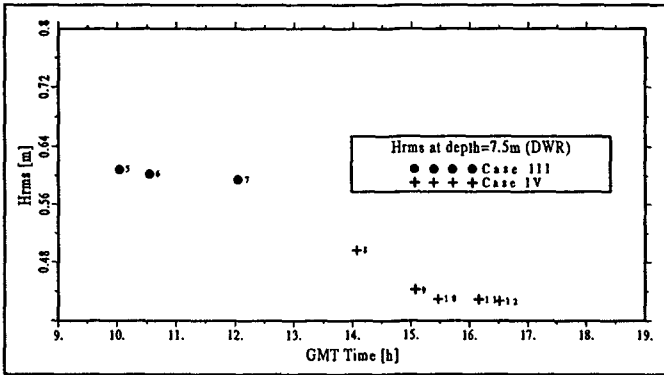


Figure 5. Wave height (Hrms) at 7.5 m depth from DWR

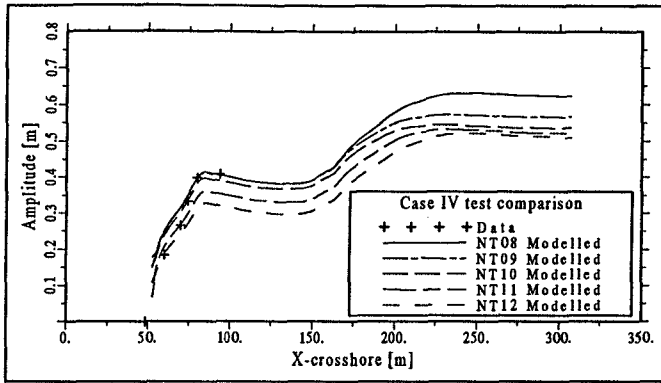


Figure 6. Wave decay Case IV. The different lines correspond to the varying conditions at the offshore boundary corresponding to the SZ-test time.

To achieve a reasonable setup prediction, a general sea level rise due to storm-surge has to be assumed in the field data. This general sea level rise has been estimated in 15cm and 8cm for cases III and IV respectively, using an iterative process. The resulting setdown/up predictions are reasonable although the fit is far from perfect. There is not yet a satisfactory explanation for this mean water level behaviour (figure 7). The predictions of the angle of wave incidence are in general acceptable (see figure 8), although numerical results overpredict systematically the experimental data from the ems. The origins for this could be the procedure used to derive an angle of wave incidence from the ems data, the spreading in wave angle given by the directional buoy (which is quite high when compared to the accuracy of the computations) or wave current interaction effects which have not been considered in this preliminary analysis.

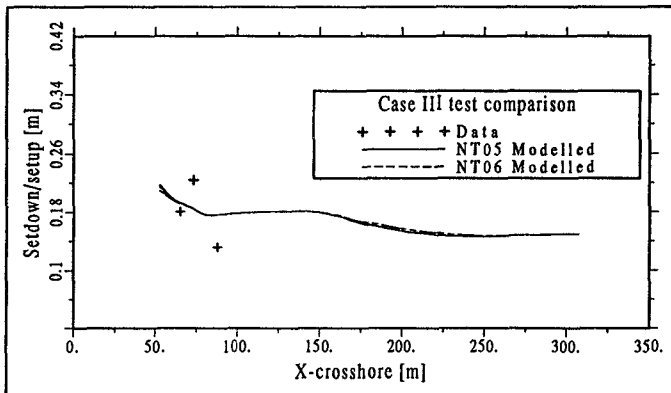


Figure 7. Wave setdown/setup for Case III.

Apart from the incident wind waves, there was evidence of stationary long waves with a period of around 40 s in the water surface time series. This long period pulsations are more clear in the spectral and moving average analysis of the velocity time series, both for the longshore and undertow components. These pulsations were uncoupled for longshore and cross-shore currents in most

of the measured tests. The longer period oscillations and the macroturbulence features are still being processed and will not be further discussed in this paper.

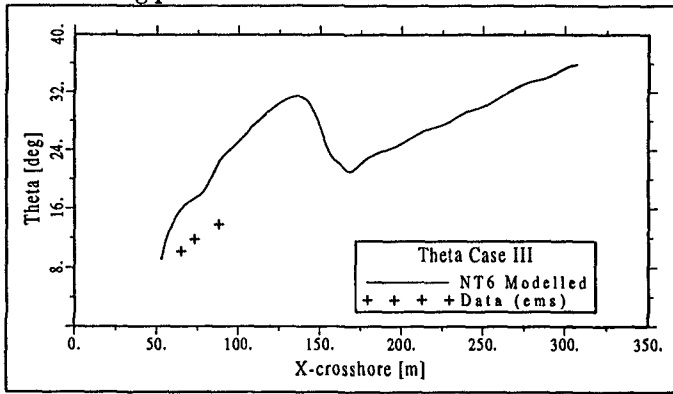


Figure 8. Incident wave angles for Test 6, Case III

The current measurements have shown the coexistence of a strong longshore current with a clear undertow crossshore distribution. The general pattern of measured data agree with the expected 3D "helicoidal" current structure shown in figure 9. Additionally it was observed the maxima for cross- and longshore components located at roughly the same across-shore coordinate.

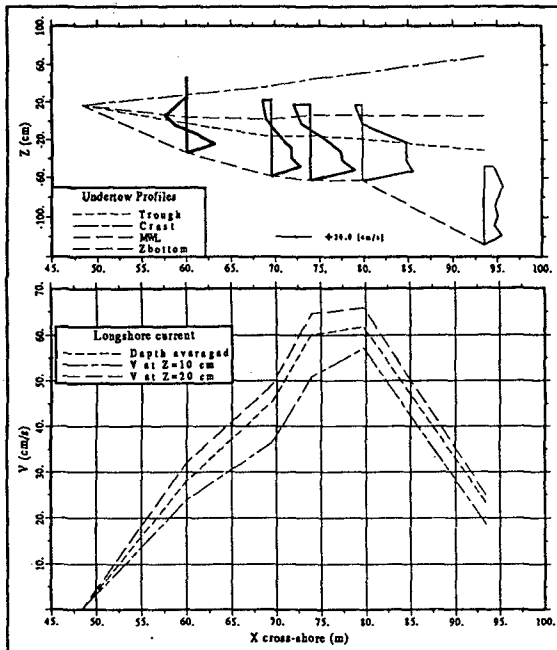


Figure 9. Measured 3D current field structure for Case IV.

### Depth Averaged Currents

The velocity data were obtained after debugging, compass-correction and quality controls applied to the "raw" time series. The mean (referring to time and depth average) current values were calculated after time and vertical averaging over the series length (from 20 to 40 minutes depending on the record) and from the bottom up to the highest sensor (always below trough level).

Eulerian (ems) and Lagrangian (buoys and dye-spots) current velocities have been compared for the same time and space intervals, showing reasonable agreement even though the potential sources of error are different for each type of measurements. The main sources of error include the dye-spot location in the vertical, inaccuracies of the pixel-coordinates transfer function, ditto for the ems-orientation, limitations of the scale range and those inherent to the processing/filtering technique.

The 2DH currents have been modelled assuming an alongshore uniform beach which implies a mass balance restriction per profile. The bottom shear stress is modelled using a standard linear expression and the horizontal eddy viscosity coefficient follows the De Vriend and Stive (1987) (hereinafter DVS'87) proposal. These values agree well with the experimental data obtained from the processing of dye dispersion images (see Rodriguez et al, 1995). The numerical domain extends up to the shoreline, considering dynamically the "dry-flood" problem in that region.

The obtained results are quite reasonable (see figure 10) with two maxima roughly in the region of the two bars present in the profile. The mean cross-shore flux, obtained using the external mass flux closure submodel of DVS'87, is acceptable only in some regions. This point must be clearly improved in the future, from which better longshore current predictions can be expected.

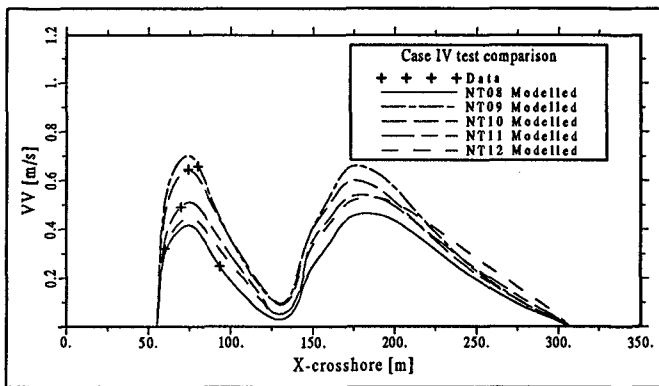


Figure 10. Longshore currents for Case IV. The different lines correspond to the hydrodynamics conditions of fig. 6.

### 1DV Structure of Currents

The vertical flow structure during *DELTA'93* was monitored with six ems

placed at 0.1, 0.2, 0.3, 0.4, 0.6 and 0.8 m above the bottom, at a single vertical pole located at the sledge. Measurements above  $z_{tr}$  were used to estimate the mass flux during the "wet intervals". Measurements below  $z_{tr}$  were used to characterize the vertical profiles of longshore and cross-shore currents, outside the bottom boundary layer (BBL).

The undertow profiles show a maximum near the bottom as expected according to previous experimental information (see e.g. Okayasu, 1989 or Smith et al., 1992). The longshore current profiles below  $z_{tr}$  show a mildly increasing trend upwards rather than a constant value.

The 1DV module, described in S.-Arcilla et al. (1992), splits the total current velocity vector into depth uniform,  $\vec{u}$ , and depth varying,  $\vec{u}'$ , components. The crest-to-trough layer is not solved because it is considered exclusively via its interaction with the middle layer at trough level through the imposition of the appropriate boundary conditions. The BBL model is inspired on the one proposed by Fredsøe (1984), whose solution leads to algebraic expressions of logarithmic form that have been here parameterized to achieve an economic solution. The middle layer equations are solved using a power series approximation,  $\sum_1^N a_i z^i$ , to reproduce the vertical variation of  $\vec{u}$ .

It can be shown theoretically (S.-Arcilla et al, 1992) that the middle layer equation may not converge under certain conditions. Because of that, in general, the profile obtained consists of a first logarithm within the BBL, from  $z_o$  up to  $z_b$ , ( $z_b - z_o = \delta_m$ ), a second one up to a given  $z_l$  level, and from this level to  $z_{tr}$  the power series  $a_i z^i$ .

The "optimal"  $z_l$  level to achieve an efficient convergence and to avoid artificial profile distortions is here considered to be  $z_l \simeq 0.2z_{tr}$ . The trough level  $z_{tr}$  has been estimated as:

$$z_{tr} = \max [0.8h; h - 0.5H_{rms}]$$

The  $\vec{u}$  model needs three main external closure submodels to determine the  $\vec{u}$  profile: a) the shear stress  $\langle \tau_{tr} \rangle$  at trough level, b) the mass flux over this level,  $\langle \bar{Q}_s \rangle$ , and c) the eddy viscosity vertical distribution,  $\nu_t(z)$ .

For the case of longitudinal uniformity, the mean cross-shore velocity  $\bar{u}$  is obtained using a  $Q_s$  expression similar to the one proposed in DVS'87. This expression, which is given by:

$$\langle Q_{sx} \rangle = (1.0 + 7.0 Q_b \frac{h}{L}) \frac{E}{\sigma} K_x$$

does not fit well the experimental  $\bar{u}$  (see figure 11). In the  $\langle Q_{sx} \rangle$  formula  $Q_b$  is a measure of the breaking intensity,  $h$  is the water depth,  $L$  the wave length,  $E$  the wave energy density,  $\sigma$  the wave frequency and  $K_x$  the  $x$  component of the wave number vector.

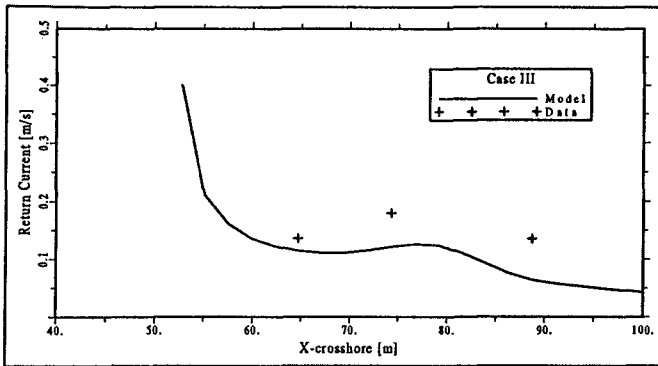


Figure 11. Crest-to-trough mass flux calculated according to DVS'87 and measured mean flow values (across-shore distribution)

The closure model for  $\langle \vec{\tau}_{ir} \rangle$  uses the general expression proposed by Deigaard (1993), which extends the 1-dimensional expression obtained in Deigaard and Fredsøe (1989). The closure model for the eddy viscosity allows either a constant or a parabolic form for  $\nu_t$ . The resulting expression is made up of two terms, the first one corresponding to the current induced eddy viscosity (similar to the one proposed in e.g. Coffey and Nielsen (1984)) and the second one corresponding to the breaking induced eddy viscosity similar to the value proposed by DVS'87 and Battjes (1983).

The resulting undertow profiles for cases III and IV are obtained with a constant  $\nu_t$  and  $N = 20$  in the middle layer equations, see figures 12 and 13. The continuous line represents the modelled undertow using as mean return flow the experimental value, while the dashed line represents the modelled undertow with an analytically calculated mean mass flux. It is apparent that the model fits much better the measured vertical structure when the experimental mean mass flux is used. The obtained fit is quite satisfactory even though there are no data from the bottom boundary layer.

The values above trough level, also indicated in the figures, have only been used to calculate the mean mass flux. Points I and II, physically "unrealistic", have been disregarded. No explanation for these two points is available. It can be, thus, concluded that most of the profiles show a good agreement between experimental and modeled values in the middle layer. This agreement is also reasonable near the bottom, although there is a small trend to underestimate measured current values in the lower part of the water column.

The corresponding longshore current vertical profiles for cases III and IV are shown in figures 14 and 15. The model results, which are preliminary, have been obtained using a parabolic power series. The solution with the complete power series is now being tested although the fit appears to be reasonable enough with the second order approach.

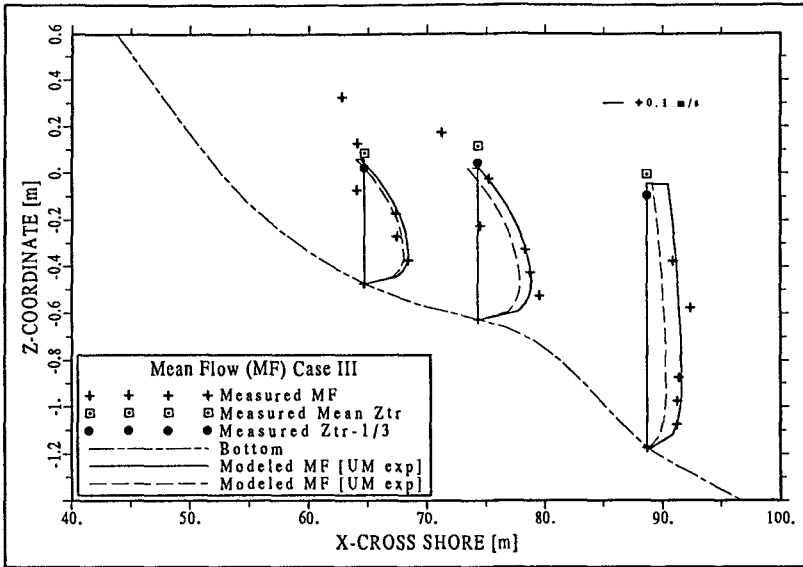


Figure 12. Undertow measured and modeled for Case III.

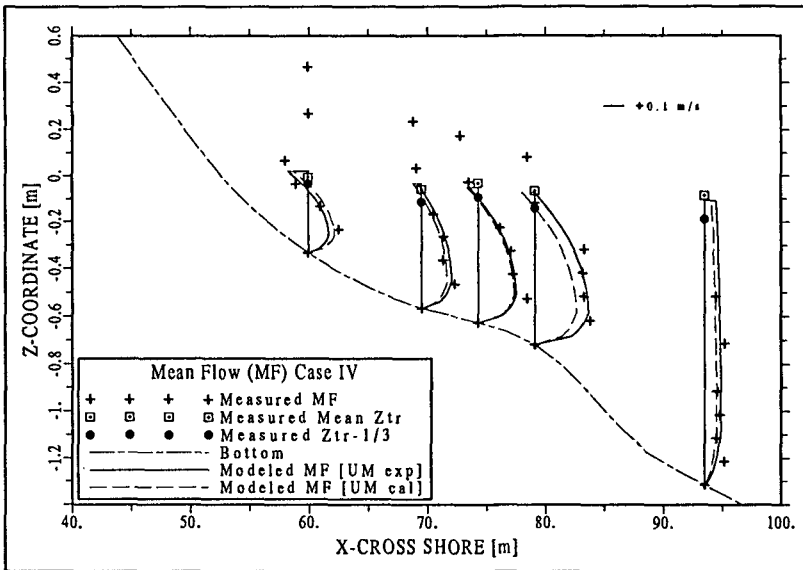


Figure 13. Undertow measured and modeled for Case IV.



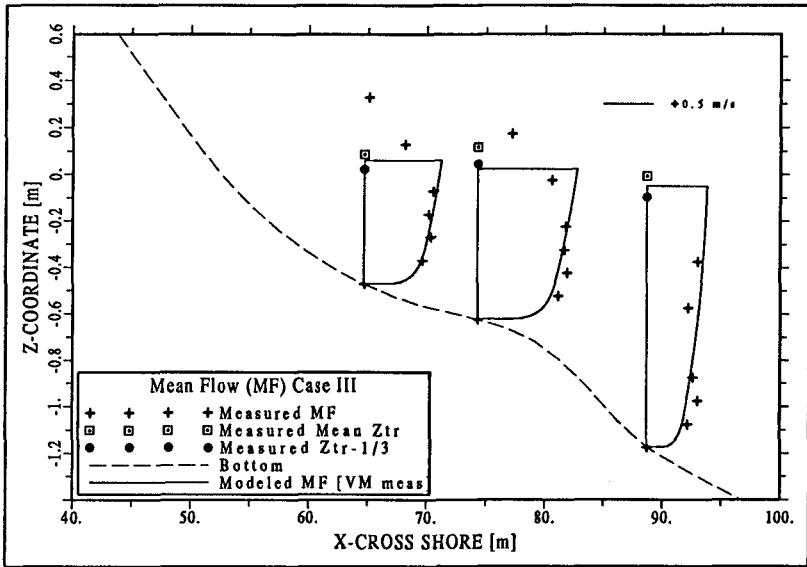


Figure 14. Longshore currents measured and modeled for Case III, (note rotated longshore profiles from the  $z-y$  to the  $z-z$  plane).

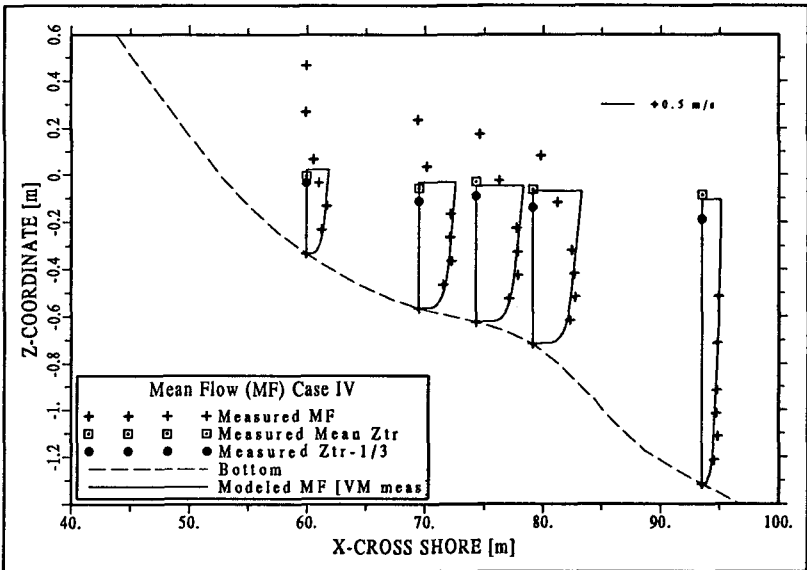


Figure 15. Longshore currents measured and modeled for Case IV.

### Final Remarks

The *DELTA'93* field campaign is a modest field effort with respect to other experimental studies (e.g. DUCK, SUPERDUCK, NSTS, B-BAND, EGMOND, C2S2, NERC, DELILAH, etc.). The emphasis of *DELTA'93* was on the SZ vertical flow structure since the Mediterranean sea is an adequate environment to study this kind of processes, due to its microtidal range and medium wave energy-level characteristics.

The developed methodology works successfully eventhough there were some difficulties to define what was the still water level and what was the mean water level due to setup, setdown and storm surge. The identification of different flow modes (e.g. splitting up between low frequency, high frequency and current type motions) needs to be careful due to the non-negligible dependence on the filtering/processing techniques.

Long period pulsations are clear in the spectral analysis of the velocity time series, both for the longshore and undertow components. These pulsations were uncoupled for longshore and cross-shore currents in most of the tests.

The general pattern of measured data in the SZ agree with the expected 3D "helicoïdal" current structure (figure 9). The maxima for cross- and longshore components happen at roughly the same across-shore coordinate.

The undertow profiles show a maximum near the bottom and the longshore current profiles below  $z_{tr}$  show a mildly increasing trend upwards rather than a constant value.

A good estimation of  $Q_b$  from video images needs time series longer than 100 waves period.

The disipation model have showed difficulties in the fitting of the measured data when it was applied in the considered domain.

With respect to the modelling effort a general conclusion is the inherent limitation of field data to accurately validate numerical models. These numerical models always simulate a much simplified situation with respect to the field one, which precludes any definite and accurate validation conclusions for the time being.

In the wave modelling part there were in general good agreement with a slight overpredicted wave heights and some decay/shoaling oscillations near the shoreline. The main trouble with respect to the depth-averaged current modelling were the current overpredictions near the shoreline because of the decay oscillations just mentioned.

The 1DV model showed a good enough fitting of the vertical profiles, although the mass flux submodel should be improved due to its sistematic underpredictions. It was also noted a slight trend to underestimate the current values near the bottom.

### Acknowledgements

This work was undertaken as part of the Surf Zone Research project of LIM-UPC. It was funded jointly by the Programa de Clima Marítimo PCM-MOPTMA and the Ministerio de E. y C. (DGICYT) of Spain, with some support from the MAST-II G8M Project of the E.U. We want to thank the research staff of LIM-UPC, particularly J Gomez, J Sospedra and all those who endured the field work. Thanks are also due to G Voulgaris and MA Tenorio from Southampton University for their OBS and radar; and to MJF Stive and JM Redondo for their helpful collaboration "before, during and after" the experiments.

### References

- Battjes J. (1983) Surf zone turbulence. *Proc. 20th IAHR Cong.*, Moscow.
- Battjes J. and Jansen J. (1978) Energy loss and set-up due to breaking of random waves. *Proc. ICCE*, ASCE, pp 569-587.
- Coffey F. and Nielsen P. (1984) Aspects of Wave Current Boundary Layer Flows. *Proc. ICCE*, ASCE, pp 2232-2245.
- Deigaard R. and Fredsøe J. (1989) Shear stress distribution in dissipative water waves. *Coastal Engineering*, 13, pp. 357-378.
- Deigaard R. (1993) A note on the three dimensional shear stress distribution in a surf zone. *Coastal Engineering*, 20, pp. 157-171.
- De Vriend H. and Stive M.J.F. (1987) Quasi-3D modelling of nearshore currents. *Coastal Engineering*, 11, pp 565-601.
- Fredsøe J. (1984) The turbulent boundary layer in Wave-Current Motion, *J.H.E*, ASCE, Vol 110, N° 8, pp 1103-1120.
- Jiménez J. and Sánchez-Arcilla A. (1993) Medium-term coastal response at the Ebro delta, Spain. *Marine Geology*, 114, pp. 105-118.
- Okayasu A. (1989) Characteristics of turbulence structure and undertow in the surf zone. Ph.D. thesis, University of Tokio, Japan.
- Redondo J., Rodriguez A., Bahía E., Falqués A., Gracia V., Sánchez-Arcilla A. and Stive M.J.F. (1994). Image Analysis of Surf-Zone Hydrodynamics. *Proc. Coastal Dynamics 94*, ASCE, pp. 350-365.
- Rodriguez A., Sánchez-Arcilla A., Redondo J., Bahía E., and Sierra, J.P. (1995), Pollutant dispersion in the nearshore region: modelling and measurements. *Int.Jour. Water Sc. and Tech.*, IAWQ, (in press).
- Sánchez-Arcilla A., Collado F., Lemos C. and Rivero F. (1990) Another quasi-3D model for surf-zone Flows. *Proc. ICCE*, ASCE, Delft, pp. 316-329.
- Sánchez-Arcilla A., Collado F. and Rodriguez A. (1992) Vertically varying velocity field in Q3D nearshore circulation. *Proc. ICCE*, ASCE, Venice, pp. 2811-2824.
- Smith J.M., Svendsen I. and Putrevu, U. (1992) Vertical structure of the nearshore current at Delilah: measured and modeled. *Proc. ICCE*, ASCE, Venice, pp. 2825-2838.

# A numerical simulation of beach evolution based on a nonlinear dispersive wave-current model

Shinji Sato<sup>1</sup> and Michael B. Kabiling<sup>2</sup>

## ABSTRACT

A numerical wave model based on the Boussinesq equation was extended to the computation of two-dimensional wave-current field including diffraction, refraction and wave breaking. The energy dissipation due to wave breaking was modeled by a momentum mixing term using eddy viscosity. Beach deformation was estimated based on the wave-current field simulated in the nearshore region. Energetics-based equations were used to estimate the total sediment transport in the cross-shore and longshore directions. The model applicability was confirmed with laboratory experiments.

## 1. INTRODUCTION

In the nearshore region, where water depths are shallow and amplitudes are relatively large, waves are highly nonlinear characterized by asymmetric orbital motion of the water particle. This nonlinearity becomes increasingly dominant with decreasing water depth. Hence, it is expected that numerical models based on the linear wave theory will not provide an accurate simulation of the nearshore wave phenomenon. Moreover, since the nearshore current is caused by the gradient of nonlinear radiation stress, it cannot be estimated simultaneously with the wave variables in linear wave models.

The Boussinesq equation can be considered as one of the valid nonlinear dispersive wave theories for finite amplitude wave transformation. The nearshore currents generated by the wave action can also be determined from nonlinear wave computation using the Boussinesq equations. The performance of the Boussinesq equations in 1-D wave transformation was evaluated by Madsen and Warren (1984)[10], Abbott *et al.* (1984)[1], and McCowan (1987)[13]. It was noted that Boussinesq equations with various forms of the dispersion terms generally performed well in the shallow water region. Madsen *et al.* (1991)[11] also presented a method of extending the validity of the Boussinesq equations to deeper water. The use of the Boussinesq equations was extended to the surf zone by more recent researches by Schäffer *et al.* (1992)[16], Karambas *et al.* (1992)[8] and Sato *et al.*

---

<sup>1</sup> Dr. Eng., Coastal Engineering Division, Public Works Research Institute, Ministry of Construction, 1 Asahi, Tsukuba, 305, JAPAN

<sup>2</sup> Dr. Eng., MBK Engineering, 444 Jupiter St., San Fernando Subdivision, San Fernando, Pampanga, 2000, PHILIPPINES

(1992)[15]. It was shown that with the use of an appropriate additional term expressing the momentum mixing due to wave breaking, the Boussinesq equations give reasonable results even inside the surf zone. However, most of the previous works in this area have been confined to 1-D wave modeling.

In this study, the nonlinear dispersive wave model based on the Boussinesq equation is extended for wave transformation in two horizontal dimensions. A new breaking criterion using the ratio of the water particle velocity at the crest surface to the wave celerity for three-dimensional wave field is presented. A momentum mixing term is introduced to simulate the energy dissipation due to wave breaking and thus extend the use of the Boussinesq equations into the surf zone. These two factors extended the wave-current model application into the surf zone. A beach run-up sub-model similar to that used by Iwasaki and Mano (1979)[5] was added to extend the model application up to the swash zone. It also allowed for the estimation of the beach deformation beyond the initial shoreline. Results from the numerical computations are compared with previous theoretical works and with existing laboratory data.

## 2. WAVE AND CURRENT MODELING

### 2.1. Governing equations

The Boussinesq equations for 2-D incompressible flow applicable for a horizontal or mildly sloping bottom are used as the basis for the governing equations. Additional momentum mixing terms  $M_{Dx}$  and  $M_{Dy}$  were added into the Boussinesq equations to simulate the energy dissipation due to wave breaking inside the surf zone. Another term was also added to include the effect of the bottom friction. The governing equations thus read:

$$\frac{\partial \eta}{\partial t} + \frac{\partial Q_x}{\partial x} + \frac{\partial Q_y}{\partial y} = 0 \tag{1}$$

$$\frac{\partial Q_x}{\partial t} + \frac{\partial}{\partial x} \left( \frac{Q_x^2}{d} \right) + \frac{\partial}{\partial y} \left( \frac{Q_x Q_y}{d} \right) + g d \frac{\partial \eta}{\partial x} \tag{2}$$

$$= \frac{1}{3} h^2 \left( \frac{\partial^3 Q_x}{\partial x^2 \partial t} + \frac{\partial^3 Q_y}{\partial x \partial y \partial t} \right) - \frac{f_w}{2 d^2} Q_x \sqrt{Q_x^2 + Q_y^2} + M_{Dx}$$

$$\frac{\partial Q_y}{\partial t} + \frac{\partial}{\partial x} \left( \frac{Q_x Q_y}{d} \right) + \frac{\partial}{\partial y} \left( \frac{Q_y^2}{d} \right) + g d \frac{\partial \eta}{\partial y} \tag{3}$$

$= \frac{1}{3} h^2 \left( \frac{\partial^3 Q_x}{\partial x \partial y \partial t} + \frac{\partial^3 Q_y}{\partial y^2 \partial t} \right) - \frac{f_w}{2 d^2} Q_y \sqrt{Q_x^2 + Q_y^2} + M_{Dy}$

where as shown in Fig. 1,  $Q_x(x,y,t) = \bar{u}_x d$  and  $Q_y(x,y,t) = \bar{u}_y d$  are the depth-integrated flow rates in the x-axis and y-axis directions respectively,  $\bar{u}_x = \bar{u}_x(x,y,t)$  and  $\bar{u}_y = \bar{u}_y(x,y,t)$  are the depth-averaged water particle velocities in the x-axis and y-axis directions respectively,  $d(=h + \eta)$  is the total water depth,  $h = h(x,y)$  is the still water depth,  $\eta = \eta(x,y,t)$  is the water surface elevation,  $g$  is the acceleration due to gravity,  $f_w$  is the bottom friction coefficient, and  $M_{Dx}$  and  $M_{Dy}$  are the momentum correction terms in the x-axis and y-axis directions respectively.

An Alternating Direction Implicit (ADI) finite difference scheme with a double sweep algorithm on a staggered rectangular grid region was used in the wave-current computations. In all

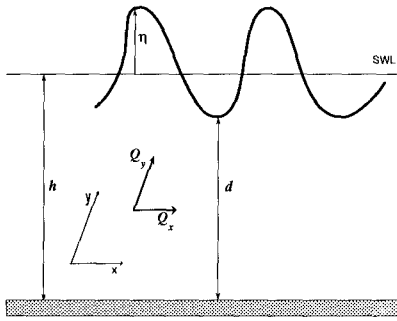


Figure 1 Definition sketch of a typical wave profile.

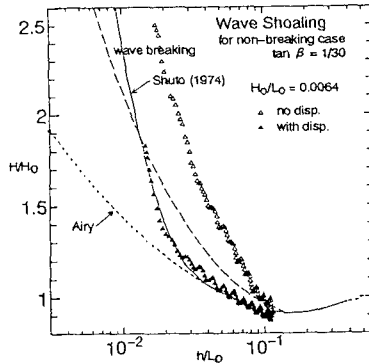


Figure 2 Wave shoaling under 1-D non-breaking wave computations.

computations, monochromatic first-order cnoidal waves were generated at the incident boundary. The incident boundary was set as an absorbing boundary which allowed the reflected waves to pass through freely. An absorbing boundary was defined by solving the radiation problem along this boundary. The computation started from still water and continued until both wave and current fields reached equilibrium state. The time required to reach the equilibrium was about 40 wave periods in the present computations.

### 2.2. Wave shoaling

To verify the numerical scheme, 1-D non-breaking wave computations ( $M_{Dx} = M_{Dy} = 0$ ) were performed on a rectangular region where the onshore boundary was set as an absorbing boundary which allowed the non-breaking waves to pass through freely. The still water depths at the incident and onshore boundaries were set to  $0.12L_0$  and to just below the wave breaking limit respectively. Numerical computations for bottom slope  $\tan\beta = 1/30$  to  $1/20$  were made with incident wave condition  $H_0/L_0 = 0.0064$  where  $H_0$  and  $L_0$  are the deep water wave height and wavelength respectively.

Figure 2 shows the ratio of the wave height to the deep water wave height  $H/H_0$  for computations with and without the dispersion terms. The small undulations were caused by small amounts of wave reflection arising from the bottom slope as well as the onshore boundary. The values of  $H/H_0$  from nonlinear non-dispersive wave computations overestimate wave shoaling. In contrast, those from nonlinear dispersive wave computations adhere closely to the theoretical curve presented by Shuto (1974)[17]. This indicates the importance of including the dispersion terms in nonlinear wave computations. These results confirmed the capability of the Boussinesq wave model for wave shoaling up to the breaking limit.

### 2.3. Two-dimensional wave breaking criterion

In order to establish an appropriate 2-D wave breaking criterion for nonlinear dispersive waves in a multi-directional wave field, the ratio of the water particle horizontal velocity at the surface of wave crest  $u_{max}$  to the wave celerity  $c$  at the breaking point was investigated. The aim of the investigation is to determine the critical ratio at incipient wave breaking.

The wave celerity  $c$  was taken to be equal to the celerity in the direction of the maximum horizontal water particle velocity  $u_{max}$  which occurs at the crest surface. The ratio  $u_{max}/c$  was thus

estimated by:

$$\frac{u_{smax}}{c} = \frac{|\vec{k} \cdot \vec{u}_{smax}|}{\sigma} \quad (4)$$

where  $\vec{k}$  is the wave number vector and  $\sigma$  is the angular frequency. The wave number  $\vec{k}$  was determined from the gradient of the phase lag  $\Phi$ . The phase lag was estimated from the Fourier analysis of the computed water surface elevation  $\eta(t)$ . A quadratic vertical distribution of the horizontal velocity was assumed. Based on the investigation, the critical values of  $u_{smax}/c$  was found to be in the range  $0.4 \leq u_{smax}/c \leq 0.70$  depending on the bottom slope and incident wave condition.

## 2.4. Energy dissipation due to wave breaking

Significant amount of energy is dissipated by the turbulence generated by the breaking of waves. Several momentum correction models have been proposed so far to simulate wave damping in the surf zone (e.g., Karambas and Koutitas, 1992, Schäffer *et al.*, 1992). Watanabe and Dibajnia (1988)[21] presented a numerical wave model based on the linear wave theory. It computes wave transformation by using a set of time-dependent mass and momentum conservation equations that are equivalent to the mild-slope equations. The functional form of  $M_D$  that was used in the wave transformation computations from this linear wave model for which results well agree with laboratory data is:

$$M_D = -f_D \cdot Q = -\alpha_D \tan \beta \sqrt{\left(\frac{g}{\bar{d}}\right) \left(\frac{\hat{Q} - Q_r}{Q_s - Q_r}\right)} \cdot Q \quad (5)$$

where  $f_D$  is an energy dissipation coefficient,  $Q$  is the discharge per unit width,  $\alpha_D$  is a coefficient which is 2.5 inside the surf zone and zero elsewhere,  $\tan \beta$  is the bottom slope,  $\bar{d}$  is the mean total depth,  $\hat{Q}$  is the amplitude of discharge per unit width,  $Q_s$  is the wave induced flow rate inside the surf zone, and  $Q_r$  is the flow rate amplitude of recovered waves. Based on the experimental data of Isohe (1986)[4] and Maruyama and Shimizu (1986)[12] respectively,  $Q_s$  and  $Q_r$  can be estimated as:

$$Q_s = 0.4 (0.57 + 5.3 \tan \beta) \sqrt{g \bar{d}^3} \quad (6a)$$

$$Q_r = 0.135 \sqrt{g \bar{d}^3} \quad (6b)$$

Wave breaking however, involves strong turbulence and momentum mixing particularly at the front face of the wave. The energy dissipation is a direct result of the diffusion of momentum in the surf zone. It is therefore necessary to use a more appropriate form of  $M_D$  that can better describe these phenomena. Sato *et al.* (1992)[15] presented an energy dissipation term that was proportional to the diffusion of the momentum. The following formulation of  $M_{Dx}$  and  $M_{Dy}$  by Sato *et al.* (1992) in terms of an eddy viscosity  $\nu_B$  was used to describe the momentum exchange due to turbulence.

$$M_{Dx} = \nu_e \left( \frac{\partial^2 Q_x}{\partial x^2} + \frac{\partial^2 Q_x}{\partial y^2} \right) \quad (7a)$$

$$M_{Dy} = \nu_e \left( \frac{\partial^2 Q_y}{\partial x^2} + \frac{\partial^2 Q_y}{\partial y^2} \right) \quad \text{with} \quad \nu_e = \nu_n + \nu_l \quad (7b)$$

The functional form of  $\nu_B$  was analogically deduced from Eq. (5). By assuming sinusoidally varying  $Q$ , the form of  $\nu_B$  for long waves becomes:

$$\nu_B = \frac{\alpha_D g \bar{d} \tan \beta}{\sigma^2} \sqrt{\left(\frac{g}{\bar{d}}\right) \left(\frac{\hat{Q} - Q_r}{Q_s - Q_r}\right)} \quad (8)$$

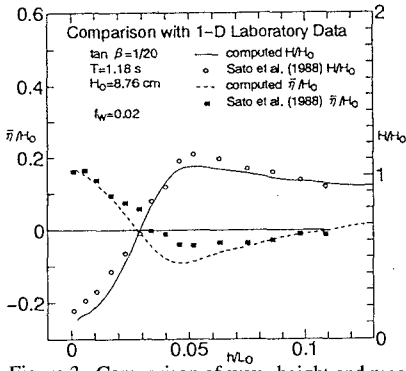


Figure 3 Comparison of wave height and mean water surface.

The form of  $\nu_b$  in Eq. (8) is consistent with Eq. (5). Sato *et al.* (1992) confirmed that the momentum mixing model given by Eq. (8) is capable of simulating the tilting of the wave profile as the wave propagates into shallow water.

Equation (8) is used only in the surf zone and the eddy viscosity  $\nu_b$  is zero outside the surf zone. However, this will result in the appearance of enormously large velocities at sharp corners of structures located outside the surf zone. These large velocities occur in places where there is a sudden difference in wave height and mean water level. They are likely to occur in sharp corners like at the tip of a detached breakwater. To avoid these large

velocities, additional viscosity is introduced. An appropriate form for this additional viscosity  $\nu_l$  is found to be similar to that proposed by Longuet-Higgins (1970)[9] and is given by

$$\nu_l = 0.016 l \tan \beta \sqrt{g d} \tag{9}$$

where  $l$  is the horizontal distance from the shoreline. The magnitude of  $\nu_l$  is set to be much smaller than  $\nu_b$  so as not to cause additional wave damping.

### 2.5. One-dimensional wave transformation

Data from a series of 1-D laboratory experiments conducted in a wave flume by Sato *et al.* (1988)[14] were used to verify the wave transformation capability of the present model in the surf zone. In one wave flume experiment, the instantaneous surface elevation and the near-bottom velocity at several points were measured along a line in the direction of the wave propagation. The bottom slope was  $\tan\beta= 1/20$ , the still water depth at the incident boundary  $h_i = 40$  cm, the monochromatic incident wave period  $T = 1.18$  s and the incident wave height  $H_o = 8.76$  cm.

The computed non-breaking wave heights as well as the mean water level  $\bar{\eta}$  well agree with the measurements as shown in Fig. 3. With the inclusion of the momentum mixing terms into the Boussinesq equations, the computed  $H/H_o$  in the surf zone also agree well with the measured  $H/H_o$ . From the profile of  $\bar{\eta}/H_o$ , it can be seen that the model is capable of simulating the wave set-down before wave breaking and the subsequent wave set-up after wave breaking.

The computed instantaneous water surface elevation  $\eta(t/T)$  and near-bottom velocity  $u_b(t/T)$  were compared with the measurements. Figures 4(a) and 4(b) show  $\eta$  and  $u_b$  respectively at two measuring points located before and after wave breaking. In these figures,  $t$  denotes the time within one wave period and  $x$  is the horizontal distance from the still water shoreline.

The best agreement between computation and measurement seems to occur before wave breaking. This is expected since the Boussinesq theory has been proven to be a valid nonlinear wave theory for non-breaking water waves. Inside the surf zone, there is a good agreement of the computed  $\eta$  with the data. The computed near-bottom velocity  $u_b$  also agrees fairly with the data. The slight deterioration in model accuracy in the surf zone may be due to three reasons. First, the Boussinesq theory may not be valid for such strongly nonlinear dispersive waves where wave nonlinearity and wave dispersion do not have the same order of magnitude. Second, strong turbulent mixing generated by wave breaking cannot be well simulated by the simple eddy viscosity approach that uses a constant



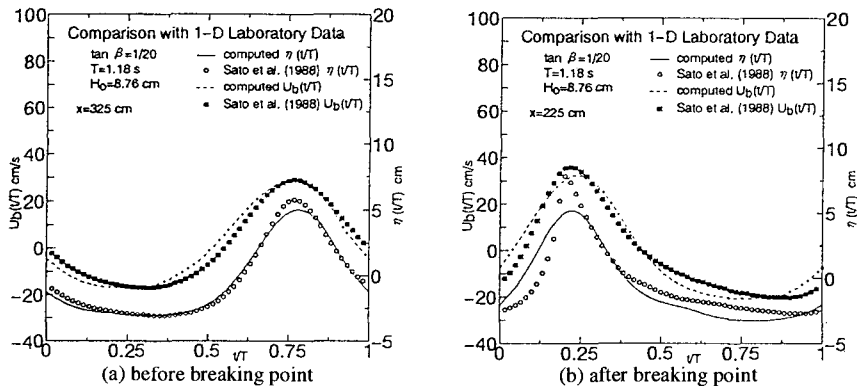


Figure 4 Time history of water surface elevation  $\eta(t/T)$  and near-bottom velocity  $u_b(t/T)$ .

eddy viscosity value for one wave period. Third, the assumption of a nearly horizontal slope may have caused this inaccuracy. In spite of these, the model can be regarded to be applicable in the region outside the surf zone and fairly accurate within the surf zone.

### 3. BEACH DEFORMATION MODELING

#### 3.1. Total sediment transport equations

Two sediment transport equations were used by Kabiling and Sato (1993)[7] in modeling 3-D beach deformation. The first of which was used to simulate the sediment transport due to the current. It can be expected therefore that cross-shore sediment transport will not be simulated. On the other hand, the second model based on the Bailard (1981)[2] equations, was seen to be inaccurate around the breaking point. To improve the accuracy in estimating sediment transport around the breaking point and at the same time to include the sediment transport due to asymmetric oscillatory motion of nonlinear waves during one wave period, another set of energetics-based sediment transport equations is needed.

The bed load and suspended sediment equations were formulated to include a threshold value for the initiation of sediment transport. In the case of bed load transport, this threshold value can include the effect of wave breaking on the bed load transport. The bed load transport  $\bar{q}_b(t)$  at any time  $t$  was formulated as:

$$\frac{\bar{q}_b(t)}{\sqrt{(\rho_s/\rho - 1)gD_s^3}} = \alpha_b |\Psi(t)|^a [\max(\Psi(t) - \Psi_c, 0)]^b \cdot \frac{\bar{u}_b(t)}{|\bar{u}_b(t)|} \tag{10a}$$

where  $\alpha_b$ ,  $a$  and  $b$  are parameters that need calibration,  $\Psi_c$  is the critical Shield's parameter for the initiation of bed load transport,  $\bar{u}_b(t)$  is the near-bottom velocity at time  $t$ ,  $\rho_s$  is the density of the sediment particle, and  $\rho$  is the density of water.

Investigations by Kabiling and Sato (1993) on their second sediment transport model based on Bailard (1981) equations revealed that the overestimation of the total sediment transport at the breaking point was mainly coming from the estimation of the suspended sediment transport which was modeled in terms of the near-bottom velocity raised to the fifth power. This can be corrected by

expressing suspended sediment transport as a function of near-bottom velocity raised to less than the fifth power. Furthermore, it was revealed that the first sediment transport model by Kabiling and Sato (1993) was able to simulate the suspended sediment transport. This leads one to adopt a form for the present suspended sediment transport equation in the form:

$$\frac{\bar{q}_s(t)}{w_s D_s} = \alpha_s [\max(\Psi(t) - \Psi_c, 0)]^p \cdot \frac{\bar{u}_b(t)}{|\bar{u}_b(t)|} \tag{10b}$$

where  $\bar{q}_s(t)$  is the suspended sediment transport rate,  $w_s$  is the sediment particle fall velocity, and  $\alpha_s$  and  $p$  are parameters that also need calibration. Equation (10b) is different from the second sediment transport by Kabiling and Sato (1993) since it is expressed as a function of the instantaneous near-bottom velocity. This will result in the inclusion of the effect of nonlinear waves on the suspended sediment transport. In both Eqs. (10a) and (10b), the Shield's parameter is estimated using the Jonsso (1966)[6] friction coefficient:

$$\Psi(t) = \frac{f_w}{2} \frac{[\bar{u}_b(t)]^2}{(\rho_s / \rho - 1) g D_s} \tag{11}$$

The total sediment transport in the present model is estimated by the summation of Eqs. (10a) and (10b). Sediment transport rate in the swash zone was overestimated due to the large velocity moments from highly nonlinear waves that are usually found in this zone. The direction of the net sediment transport was also seen to have been always in the offshore direction which indicated that the offshore rush was larger than the onshore rush. This may be due to the big difference in the water depth during onshore and offshore rushing of the shoreline. During the offshore rush, total water depth is less than that during the onshore rush so larger velocities will result during the offshore rush. In order to avoid unrealistic erosion, sediment transport rate in the swash zone was linearly interpolated between the sediment transport at the still water shoreline and the zero sediment transport at the maximum beach run-up point.

To calculate the local bottom elevation change due to the sediment transport, the sediment conservation equation proposed by Watanabe *et al.* (1986) is used. The sediment conservation equation is given by

$$\frac{\partial h}{\partial t} = - \frac{\partial z}{\partial t} = \frac{1}{1 - \lambda_v} \{ \nabla \cdot (\bar{q} + \epsilon |\bar{q}| \nabla \cdot h) \} \tag{12}$$

where  $z$  is the bottom elevation,  $\lambda_v (=0.4)$  the sediment porosity, and  $\epsilon$  is a coefficient that reflects the effect of local bottom slope on the sediment transport.

### 3.2. Two-dimensional beach deformation

Watanabe *et al.* (1980)[19] measured the change in beach topography in a wave flume. In one set of the experiments, the initial bed slope was  $\tan \beta = 1/20$  and the sediment mean diameters were  $D_s = 0.2$  and  $0.7$  mm respectively. Monochromatic incident wave periods were 1.0, 1.5, and 2.0 s while wave steepness varied from 0.006 to 0.073. The beach was exposed to wave action for a period of one hour. At the end of this period, the beach profile was measured and the cross-shore sediment transport rate was computed based on the measured beach deformation.

One-dimensional wave computations for six cases were done. Based on the computed velocity field, Eqs. (10a) and (10b) with Eq. (12) were used to estimate the beach deformation for each case. The values of the parameters in Eqs. (10a) and (10b) were  $\alpha_s = 1.0$ ,  $a = 0.5$ ,  $b = 1.0$ ,  $\alpha_x = 3.5$ ,  $p = 1.0$ , and  $\Psi_c = 0$ . Since surf zone beach deformation is of prime interest in the present study, the

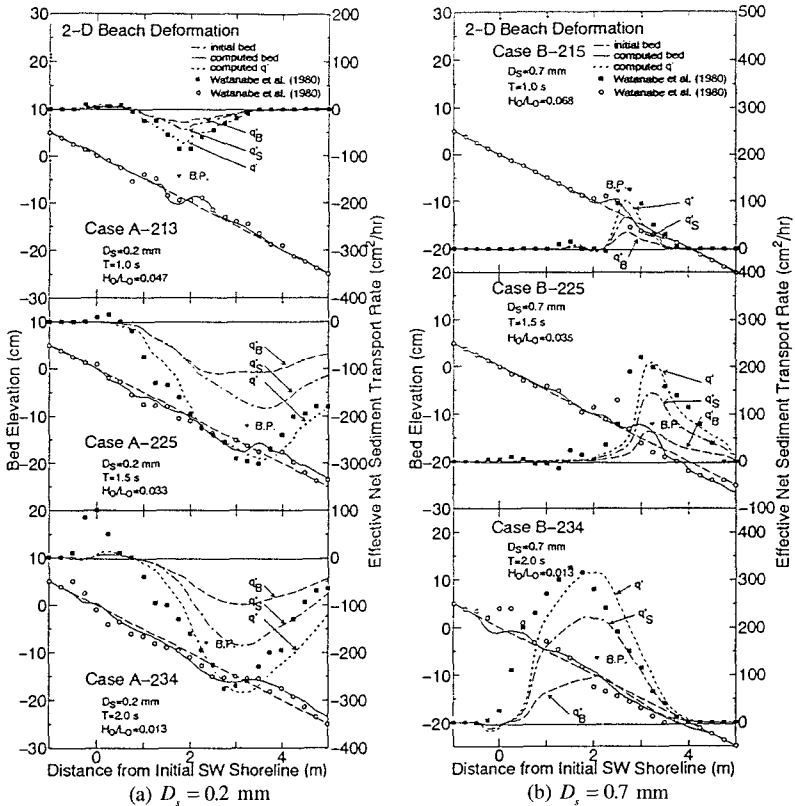


Figure 5 Computed bed elevations and cross-shore effective net sediment transport rates.

values of  $a$  and  $b$  were such as to make the bed load proportional to  $u_b^3$ . The beach deformation time step  $\Delta t'_e$  was estimated following Watanabe *et al.* (1986):

$$\Delta t'_e \leq \min \left\{ \frac{1}{2} \frac{\Delta x^2}{\varepsilon |\bar{q}_x|_{\max}}, \frac{1}{2} \frac{\Delta y^2}{\varepsilon |\bar{q}_y|_{\max}} \right\} \quad (13)$$

where  $\Delta x$  and  $\Delta y$  are the grid spacing in the x-axis and y-axis respectively,  $\bar{q}_x$  and  $\bar{q}_y$  are the net total sediment transport rates in the x-axis and y-axis respectively and  $\varepsilon = 4.0$ .

(1) Fine Sediment

Figure 5(a) shows the computed bed elevation, cross-shore net bed load  $q'_b$ , suspended sediment  $q'_s$ , and total sediment  $q'$  transport rates (which are positive in the onshore direction) for  $D_s = 0.2$  mm and  $\tan\beta = 1/20$  (Cases A-213, A-225 and A-234). The closed triangle indicates the computed location of the breaking point. When compared with the measured beach topography (open circle) and computed net sediment transport rate (closed square) of Watanabe *et al.* (1980), the

magnitude of the computed beach deformation and sediment transport rates have the same order of magnitude. This confirmed the values of the parameters used in Eqs. (10a) and (10b).

The direction of the sediment transport as computed by Watanabe *et al.* (1980) was generally offshore. Sand ripples were observed during the experiment which indicated the predominance of suspended sediments. The direction of sediment transport was simulated correctly by the present model with suspended sediment transport accounting for approximately 60% of the maximum total sediment transport which occurred at the breaking point. Unfortunately, this cannot be confirmed with the data since the contributions of bed and suspended load cannot be separated in the laboratory experiment. The location of the breaking point was correctly estimated by the wave model and generally was between the initial and final measured location of the breaking point.

## (2) Coarse Sediment

Computation results for Cases B-215, B-225 and B-234 where  $D_s = 0.7$  mm are shown in Fig. 5(b). When compared with measurements of Watanabe *et al.* (1980), it can be seen that the computed beach deformation and net sediment transport rates are also consistent. The computed sediment transport was onshore-directed which is consistent with those computed by Watanabe *et al.* (1980). Watanabe *et al.* (1980) noted that the bed load was predominant in cases where  $D_s = 0.7$  mm. At this sediment size, the computations in this study still indicate the predominance of the suspended sediment. This renders inconclusive the investigation on whether the present sediment transport model can simulate properly the proportion of bed load and suspended sediment transports.

## 3.3. 3-D beach deformation

In a 3-D beach deformation laboratory experiment, Watanabe *et al.* (1986)[20] measured the wave heights, currents, and beach deformation around a detached breakwater. Sand with a median grain diameter of 0.2 mm was placed on a 4 m long by 7.2 m wide wave basin with an initial slope of  $\tan\beta = 1/20$ . A 1.5 m long and 0.5 m high model detached breakwater was placed parallel and 1.8 m offshore from the initial shoreline. Monochromatic waves with period and wave height  $T = 0.87$  s and  $H_s = 4.5$  cm respectively were incident normal to the initial shoreline. The bottom topography was measured at  $t = 0:00, 2:37, 5:05$  and  $6:55$  (hr:min). The location of the breaker line was determined from overhead photographs taken near the middle of each time duration while the wave height and current fields were measured from  $t = 0:00$  to  $2:37$ ,  $t = 2:37$  to  $5:05$ , and  $t = 5:05$  to  $6:55$ .

To verify the wave-current model performance under steeper bottom slopes and to verify the 3-D beach deformation model, numerical results were compared with measurements from this experiment. Two-dimensional numerical computations on a half-width of the wave basin were done. The uniform grid spacing was  $\Delta x = \Delta y = 4$  cm, the computation time step was  $\Delta t = 0.035$  s, and the bottom friction coefficient was estimated from the Jonsson (1966) friction factor formula. The incident boundary was set as an open boundary while the adjacent side boundaries were fully reflecting boundaries.

### (1) Breaker Line

The computed breaker line location at  $t = 0:00$  is shown in Fig. 6 taken at quasi-steady state that was achieved after 40 wave periods. In Fig. 6, it can be seen that the general location of the computed breaker line agrees with the measurements of Watanabe *et al.* (1986). Simulation by the present wave-current model was particularly good in the region behind the breakwater. This confirmed the applicability of the 2-D wave breaking criterion in a predominantly 2-D wave field.

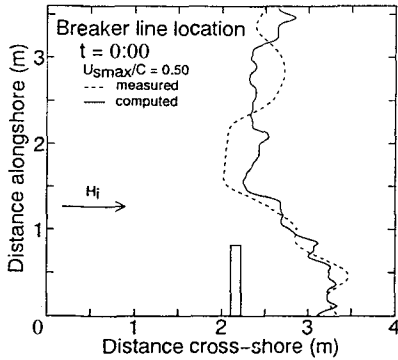


Figure 6 Comparison of breaker line location.

topography at  $t = 2:37$ , the second 2-D wave-current computation followed by the second 3-D beach deformation computation were made and results were compared with measurements during the period  $t = 2:37$  to 5:05.

The wash zone sediment transport was found to have been largely overestimated by the model as was discussed in 2-D beach deformation modeling. Hence, the sediment transport vector in the wash zone was linearly interpolated between those at the still water shoreline and maximum beach run-up point. The computed beach topographies are shown in Figs. 7(a) and 7(b). Compared with the laboratory measurements, it can be seen that the accretion behind the breakwater was simulated well. The alternate pattern of erosion and accretion in front of the breakwater was also simulated as well as the erosion at the tip of the breakwater. Some discrepancies still exist particularly at the region beyond the tip of the breakwater where the measured erosion was simulated at about 1 m onshore. When the computed and measured breaker line locations are compared, it can be observed that in this region, the computed breaker line was located onshore by roughly the same amount. This may explain the discrepancies in this region. This is further reinforced by the fact that both the measured and computed breaker lines are located along the steepest change in their respective bottom topographies. Moreover, the instantaneous near-bottom velocity may not have been estimated accurately in the region.

Comparing with results from the simple sediment transport model by Kabiling and Sato (1993), the present model simulated the beach topography change due to asymmetric nonlinear waves in the region bounded by  $x > 2.0$  m and  $y > 1.5$  m where  $x$  is the cross-shore distance from the incident boundary and  $y$  is the alongshore distance. In this region, erosion was simulated in the offshore side of the breaker line while accretion was simulated on the onshore side of the breaker line. In general, the measurements were qualitatively simulated by the present model and computations are consistent in magnitude particularly in the region located behind the breakwater.

### (3) Wave Height and Nearshore Currents

The wave height and currents computed from the bottom topography at  $t = 2:37$  are shown in Figs. 8 and 9 respectively. These figures show results from computations started from still water conditions. The currents are the time average of the computed velocity field over one wave period. Agreement with measurements was improved over those presented by Kabiling and Sato (1993). The

### (2) Beach Deformation

Equations (10a) and (10b) were used to estimate the 2-D sediment transport based on the computed 2-D velocity field. The parameters used in Eqs. (10a) and (10b) were  $\alpha_B = 1.0$ ,  $a = 0.5$ ,  $b = 1.0$ ,  $\alpha_S = 3.5$ ,  $p = 1.0$ , and  $\Psi_r = 0$ . These values are similar to those used in 2-D beach deformation in the previous section. Equation (12) was then applied to calculate the 3-D beach deformation. The time step in the beach deformation computation was estimated by Eq. (13) with  $\varepsilon = 4.0$ .

The first 2-D wave-current computation followed by the first 3-D beach deformation computation gave results that were compared with measurements during the period  $t = 0:00$  to 2:37 (hr:min). Using the newly computed beach

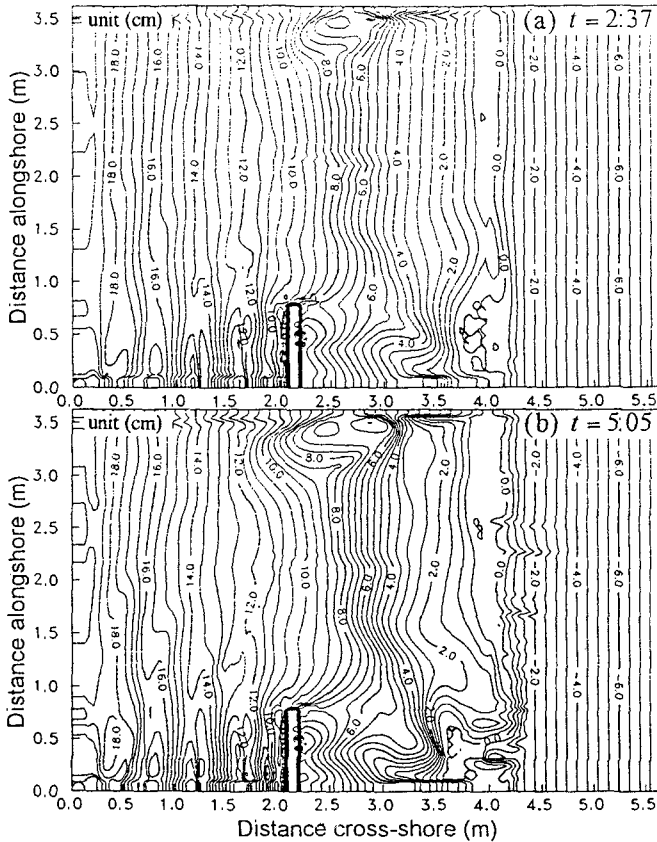


Figure 7 Computed beach topographies.

computed wave height shown in Fig. 8 exhibits an overall agreement with the measured wave height particularly in the surf zone. This can be observed by comparing Fig. 8 with Fig. 5.10 in Horikawa (1988)[3]. The nearshore circulation pattern behind the breaker was simulated well by the present model as seen upon comparison of Fig. 9 with Fig. 5.10 in Horikawa (1988). The computed current magnitude was found to be consistent with the observed nearshore circulation pattern.

## 4. CONCLUSIONS

A two-dimensional nonlinear dispersive wave-current model was presented on the basis of the Boussinesq equations. The wave breaking criterion that is based on the ratio of water particle velocity at the surface of the wave crest to the wave celerity was found to accurately predict the breaker line location for a three-dimensional wave field. The correction terms that were introduced into the momentum equations were found to sufficiently simulate the wave decay caused by the

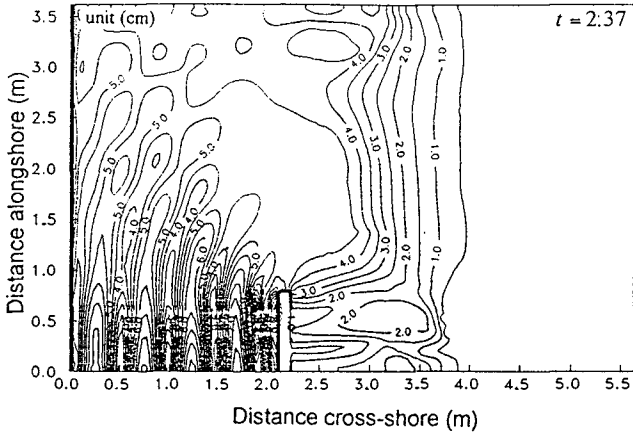


Figure 8 Computed wave height after initial beach topography change.

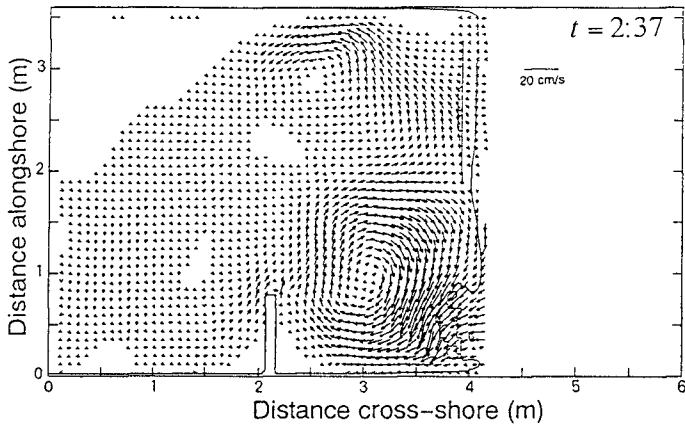


Figure 9 Computed currents after initial beach topography change.

momentum mixing and strong turbulence at the front face of the breaking wave. The wave set-up and set-down as well as the nearshore current have been simultaneously simulated by the model. The temporal variation of water surface elevation and near-bottom velocity was accurately estimated outside the surf zone. The accuracy of the estimation in the surf zone was slightly impaired. This can be caused by the use of a constant eddy viscosity during one wave period, the limited accuracy of the Boussinesq theory to weakly nonlinear and weakly dispersive waves, and by the assumption of a nearly horizontal bottom.

Beach evolution around a detached breakwater was estimated on the basis of the computed wave-current field. There was a general agreement and consistency with laboratory data of the 3-D beach deformation simulation result. The accretion behind the breakwater was simulated. The present sediment transport model was found to simulate surf zone sediment transport in the cross-shore and longshore directions including that caused by asymmetric wave motion. However, the present model was still seen to be unable to simulate the sediment transport in the swash zone.

## REFERENCES

- [1] Abbott, M.B., A.D. McCowan and I.R. Warren (1984): Accuracy of short wave numerical models, *J. Hydraulic Eng.*, Vol. 110, No. 10, pp. 1287-1301.
- [2] Bailard, J.A. (1981): An energetics total load sediment transport model for a plane sloping beach, *J. Geophys. Res.*, Vol. 86, No. C11, pp. 10938-10954.
- [3] Horikawa, K., Ed. (1988): *Nearshore Dynamics and Coastal Processes*, University of Tokyo Press, p. 311.
- [4] Isobe, M. (1986): A parabolic equation model for transformation of regular waves due to refraction, diffraction and breaking, *Coastal Eng. in Japan*, Vol. 30, No. 1, pp. 33-47.
- [5] Iwasaki, T. and A. Mano (1979): Numerical computations of two-dimensional run-ups of tsunamis due to Eulerian description, *Proc. 26th Japanese Conf. Coastal Eng.*, pp. 70-74 (*in Japanese*).
- [6] Jonsson, I.G. (1966): Wave boundary layers and friction factors, *Proc. 10th Int. Conf. Coastal Eng.*, pp. 127-148.
- [7] Kabilig, M. B. and S. Sato (1993): Two-dimensional nonlinear dispersive wave-current model and three-dimensional beach deformation model, *Coastal Eng. in Japan*, Vol. 36, No. 2, pp. 195-212.
- [8] Karambas, T.V. and C. Koutitas (1992): A breaking wave propagation model based on the Boussinesq equations, *Coastal Eng.*, Vol. 18, pp. 1-19.
- [9] Longuet-Higgins, M.S. (1970): Longshore currents generated by obliquely incident sea waves, *J. Geophys. Res.*, Vol. 75, No. 33, pp. 6778-6801.
- [10] Madsen, P.A. and I.R. Warren (1984): Performance of a numerical short-wave model, *Coastal Eng.*, Vol. 8, pp. 73-93.
- [11] Madsen, P.A., R. Murray and O.R. Sørensen (1991): A new form of the Boussinesq equations with improved linear dispersion characteristics, *Coastal Eng.*, Vol. 15, pp. 371-388.



- [12] Maruyama, K. and T. Shimizu (1986): Simulation model for wave deformation considering interaction of waves and a beach, *Proc. 33rd Japanese Conf. Coastal Eng.*, pp. 109-113 (*in Japanese*).
- [13] McCowan, A.D. (1987): The range of application of Boussinesq type numerical short wave models, *Proc. 22nd IAHR Cong.*, pp. 378-384.
- [14] Sato, S., M. Fukuhama and K. Horikawa (1988): Measurements of near-bottom velocities in random waves on a constant slope, *Coastal Eng. in Japan*, Vol. 31, No. 2, pp. 219-229.
- [15] Sato, S., M. Kabiling and H. Suzuki (1992): Prediction of near-bottom velocity history by a nonlinear dispersive wave model, *Coastal Eng. in Japan*, Vol. 35, No. 1, pp. 68-82.
- [16] Schäffer, H.A., R. Deigaard and P. Madsen (1992): A two-dimensional surf zone model based on the Boussinesq equations, *Proc. 23rd Int. Conf. Coastal Eng.*, pp. 576-589.
- [17] Shuto, N. (1974): Nonlinear long waves in a channel of variable section, *Coastal Eng. in Japan*, Vol. 17, pp. 1-12.
- [18] Sunamura, T. and K. Horikawa (1974): Two-dimensional beach transformation due to waves, *Proc. 14th Int. Conf. Coastal Eng.*, pp. 920-938.
- [19] Watanabe, A., Y. Riho and K. Horikawa (1980): Beach profiles and on-offshore sediment transport, *Proc. 16th Int. Conf. Coastal Eng.*, pp. 1106-1121.
- [20] Watanabe, A., K. Maruyama, T. Shimizu and T. Sakakiyama (1986): Numerical prediction model of three-dimensional beach deformation around a structure, *Coastal Eng. in Japan*, Vol. 29, pp. 179-194.
- [21] Watanabe, A. and M. Dibajnia (1988): A numerical model of wave deformation in surf zone, *Proc. 21st Int. Conf. Coastal Eng.*, pp. 578-587.

# An experimental study on beach transformation due to waves under the operation of coastal drain system

Michio Sato\*, Sadakatsu Hata\*\* and Masahiro Fukushima\*

## ABSTRACT

The performance of a coastal drain system was investigated experimentally. When the drain pipe was buried in the seaward area of a shoreline, the system was most effective. When the discharge is large, the drain system could accumulate a large amount of sediments on a beach face even under erosive wave conditions without drainage. The flow toward shore induced by drainage seemed to play an important role.

## INTRODUCTION

The coastal drain system has been publicized to be a new effective soft approach to coastal erosion control and beach restoration that has no impact on human activity and the environment (Parks,1989; Vesterby,1991). However, there seemed to have been negative view on the performance of it e.g. Bruun(1989). Moreover, this system does not seem to have enough physical basis which enables us to design optimum system.

The purpose of this study is to investigate experimentally the function, performance and optimum location to install of a coastal drain system.

The results showed that this system has a potential ability to accumulate a large amount of sediments on a beach even under storm wave conditions and it protects the landward area of the drain pipe at the worst.

The reason the system work has been explained by relating effects of drain to the net sediments carried due to runup-down wash processes of waves on a beachface. Our experimental results showed, however, that the flow toward the shore generated by drain in surf zone carried suspended sediment and migrated a bar toward the beachface and seemed to play the most important role.

## EXPERIMENTS

A series of experiments was carried out using a wave basin of 26.7m long, 14m wide and 1.2m deep (Figure 1) to take a survey of the performance of coastal drain system by comparing the beach profile of drained part with the one of part where

---

\* Dept. of Ocean Civil Engineering, Faculty of Engineering, Kagoshima University.,  
Korimoto 1-21-40, Kagoshima-shi, 890, JAPAN

\*\* Kyushu Electric Power Co.,Ltd.

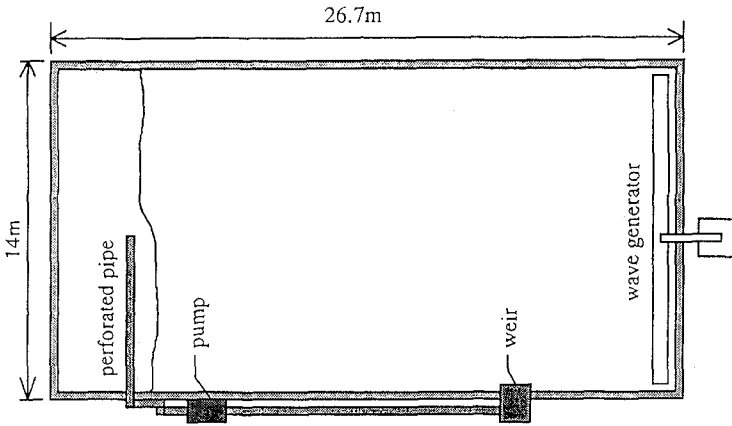


Figure 1. Experimental Setup

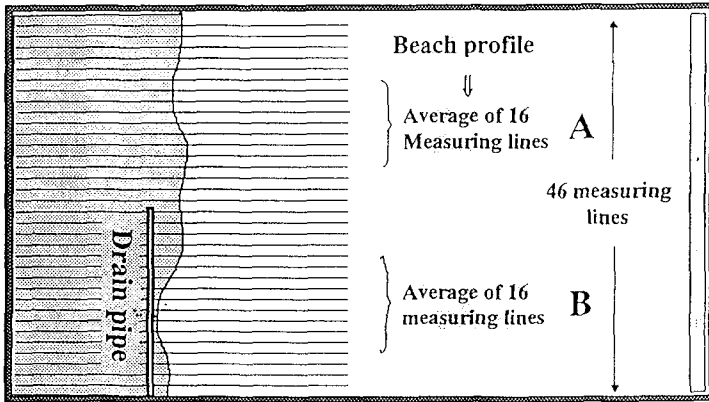


Figure 2. Measuring lines

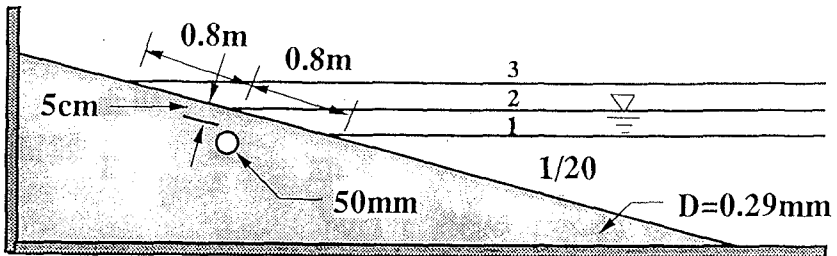


Figure 3. Cross section of the beach.

the system was not installed. The beach profile of each side was obtained as the mean profile of 16 measuring lines perpendicular to the initial shoreline(Figure 2).

A drain pipe of 7m long was installed under the beachface of the left half of the beach parallel to the shoreline. The diameter of the pipe was 50mm. Filter sheet of 10mm thickness was bound round the pipe. Then, the pipe was buried under the beach face of 1/20 slope. The initial covering was 50mm (Figure 3).

The dependence of the performance on location of the system was investigated to find optimum location to install by changing the relative location of the drain pipe from landward to seaward of the shoreline. Water depth was changed to change the relative location of the system from the shoreline instead of changing the location of the system itself.

The experimental conditions are shown in Table 1. According to the classified laboratory beach profiles by Sunamura and Horikawa, runs 2,3 and 6 are expected to produce erosive beach profiles of Type I and runs 4 and 5 were expected to produce accretive profiles of Type III(Figure 4).

Table 1 Experimental conditions

Run No.	Wave Period	Wave Height	C	Type	Location
1	2.0sec	10cm	7.3	II	1
2	1.0	10	11.6	I	1
3	1.0	10	11.6	I	2
4	2.0	5	3.7	III	2
5	2.0	5	3.7	III	3
6	1.0	10	11.6	I	3

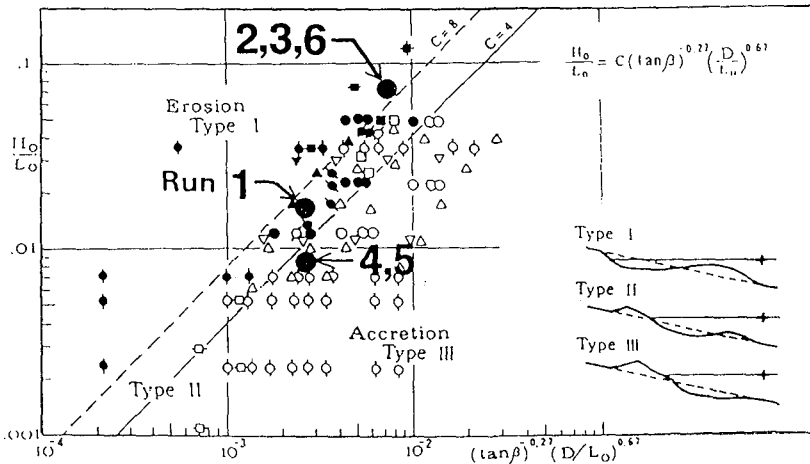


Figure 4. Classified laboratory beach profiles(Sunamura and Horikawa, 1974)

The pump used was 2.2kw and the discharge was 0.33l/sec/m when the covering was 50mm. This discharge was equivalent to about 4 percent of flux that balances with the mass transport of the wave,  $E/\rho C$  ( $E$ : wave energy density;  $\rho$ : density;  $C$ : wave celerity). The velocity of water infiltrated into the bottom was about 2 percent of the settling velocity of the bottom sediments ( $d_{50}=0.29\text{mm}$ ).

As the discharge of the drain system for the experiments mentioned above was relatively small and invariable, we used a small wave flume of 13m long, 0.4m wide and 0.4m deep to investigate the dependence of the performance of a coastal drain system on discharge (Figure 5). Discharge of the drain system installed in the flume was variable by changing the engine speed and larger (maximum discharge was 1.6 l/sec/m).

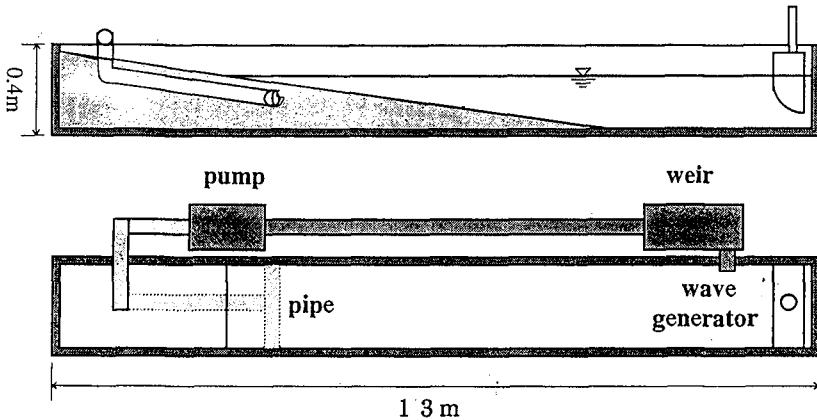


Figure 5 Experimental set-up

## RESULTS AND DISCUSSION

Figure 6 is one of the experimental results under accretive wave conditions. The ordinate  $\Delta d$ , is the net change of the bottom level from the initial beach profile (Figure 7). Black circles in the figure denote the relative location of drain pipe from the shoreline (left vertical dashed line; another vertical dashed line indicates the wave breaking point). The profiles of upper part of the beach face could not be obtained by the surveys after 18 and 24 hours wave action because the berms of drained side developed too high to measure using our profiler. These results showed that the drain system enhanced accretion.

Figure 8 is one of the results under erosive wave conditions. The profiles of drained side after 18, 24 and 36 hours wave action show accretion on beach face in spite of the erosion in the rest side. This accretion ceased and turned into erosion as the erosion in the inshore region proceeded. However, the drainage reduced the erosion. Figure 9 shows the difference of shoreline change with time between the drained

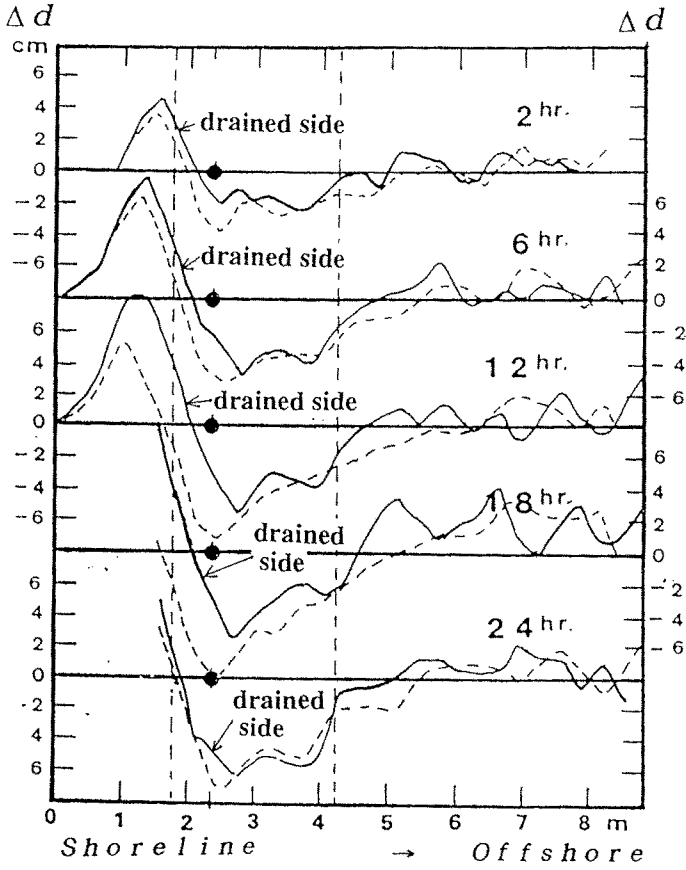


Figure 6 Result under accretive wave condition

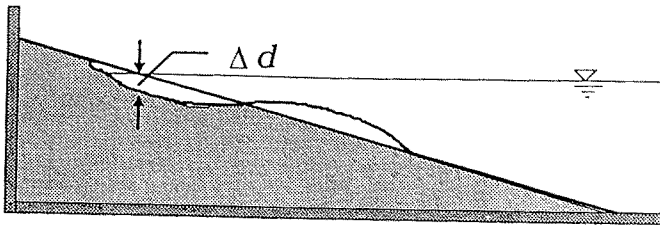


Figure 7 Definition of  $\Delta d$

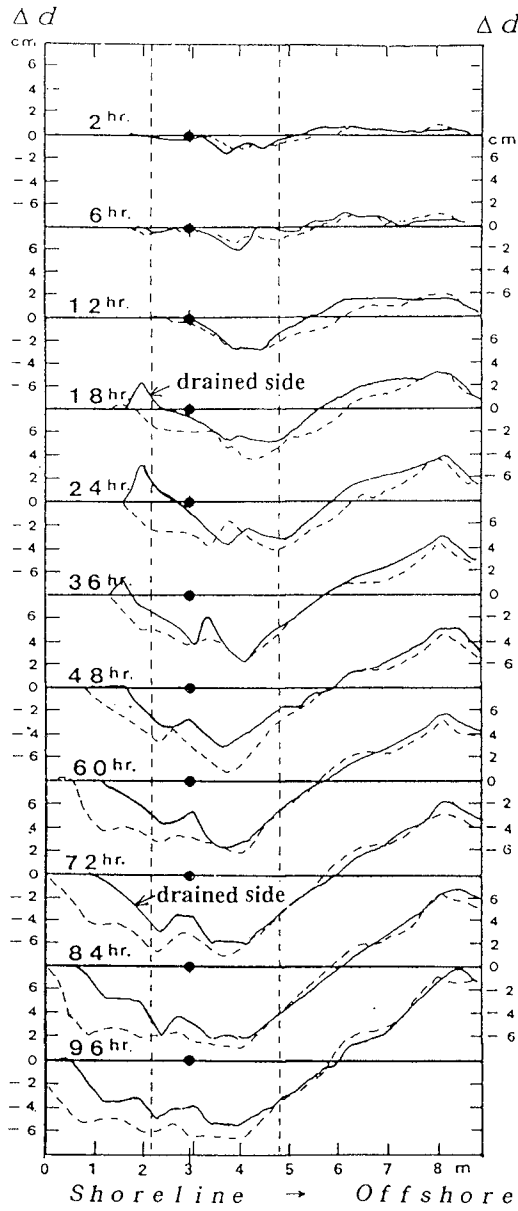


Figure 8 Result under erosive wave condition

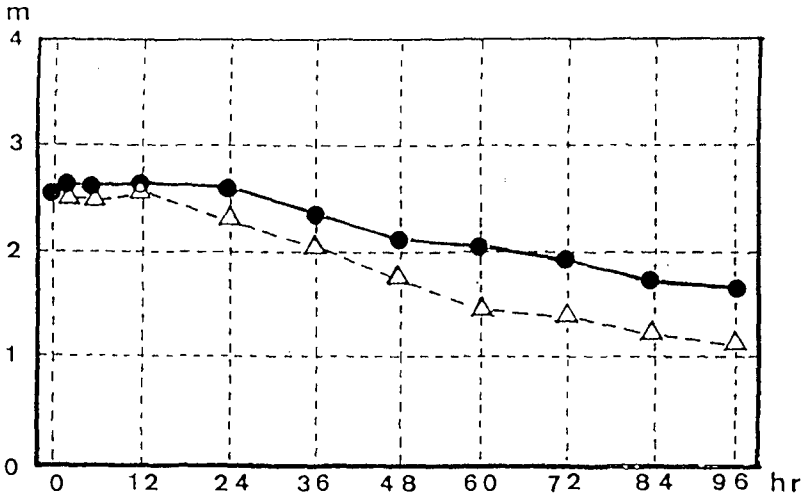


Figure 9 Changes of shoreline

side(full line) and the rest(dashed line). The ordinate is the distance of shoreline from a reference point on the back shore. This figure shows the retrogression speed of the became smaller by drainage.

These experimental results confirmed that a coastal drain system advances accretion of sediments on the beach face under accretive wave conditions and retards beach erosion under erosive wave conditions even if the discharge is not so large.

**Effect of location of the drain pipe**

Next, we consider the dependence of performance of a coastal drain system on the location of the drain pipe.

Figure 10 shows the comparisons of beach changes between drained side and the rest due to twelve hours accretive wave action. The best results were obtained when the drain pipe was installed in the seaward of the shoreline.

Figure 11 is a result of twelve hours erosive wave action. In this figure, there was no discernible difference between the two beach profiles. However, the difference became discernible after twenty-four hours wave action(Figure 12). This result also shows that seaward of a shoreline is the best to install. As we quitted the experiment for the case of landward installation after eighteen hours elapsed, results of two locations were depicted in Figure 12. Examination of the result after eighteen hours wave action did not affect the above conclusion.

When the system was installed at a shoreline or somewhere landward of beach face, we were impressed to see visually the infiltration of runup waves into the beach and sheet-like sediments left and piled up on a berm for accretive wave conditions. For erosive wave conditions, however, the erosion of inshore zone was retarded most for the cases of seaward installation.



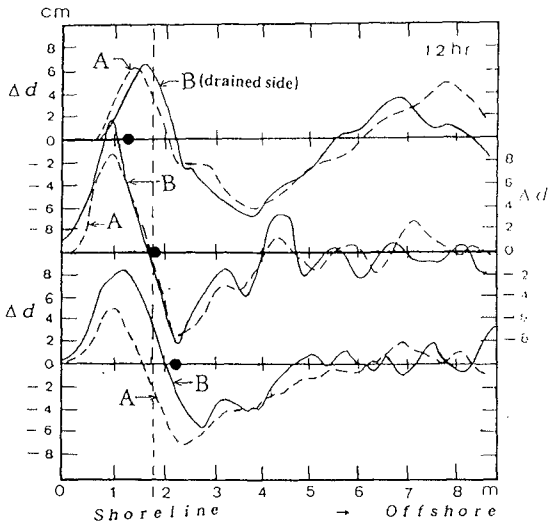


Figure 10 Comparison of beach change among three locations of drain pipe after 12 hours accretive wave action

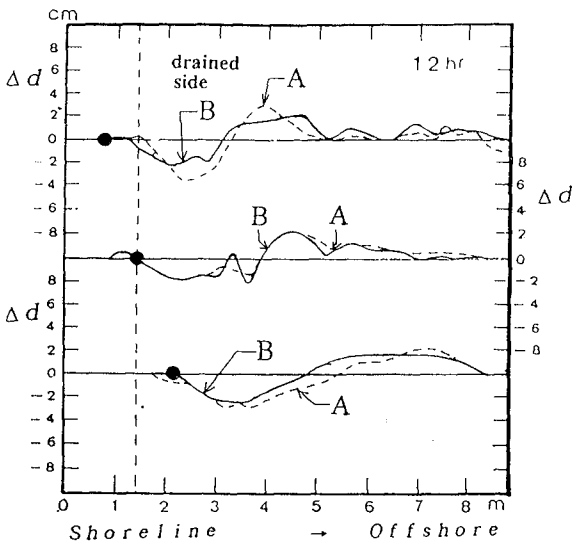


Figure 11 Comparison of beach change among three locations of drain pipe after 12 hours wave action

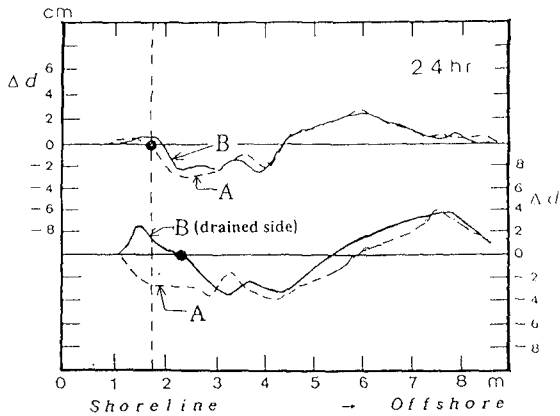


Figure 12 Comparison of beach change among two locations of drain pipe after 24 hours wave action

### Effect of discharge

As the discharge of the drain system for the experiments mentioned so far could not be changed, we used a small wave flume to investigate the dependence of the performance on discharge. Discharge of the drain system installed in the flume was controllable by changing the engine speed and the maximum discharge was 1.6 l/sec/m. As the discharge increases, the system becomes effective even for storm wave conditions. Figure 13 is an example of such cases. Figure 13 (a) shows the change of beach profile when the drain system was not operated. Just seaside part from the shoreline and offshore part were eroded and sediments from both parts formed a bar. When the discharge was 0.4 l/sec/m, there was no erosion of the part just seaside of the shoreline (b). For the case of 0.7 l/sec/m discharge, accretion of sediments in the inshore area resulted on a large scale after two hours' wave action. Observations of the sediment motion showed that a large amount of suspended sediments of the offshore zone moved toward the shore and a bar which was formed at the same location as the cases (a) and (b) in early stage grew and migrated to the shore with time.

The function of a coastal drain system has been regarded as the reduction of sediments which are carried away by backwash than are brought to the beach face by uprush. It is because drainage lowers the water table and intensifies downward percolation of wave runup which lessens water runs down than runs up.

However, our results revealed the idea that, when a shoreward flow induced by the drain system overcame the wave induced flow component to offshore like undertows, the system became effective even under erosive wave conditions without the coastal drain system. In any case, the shoreward flow seemed to play an important part when a drain pipe is buried in seaside area of a shoreline.

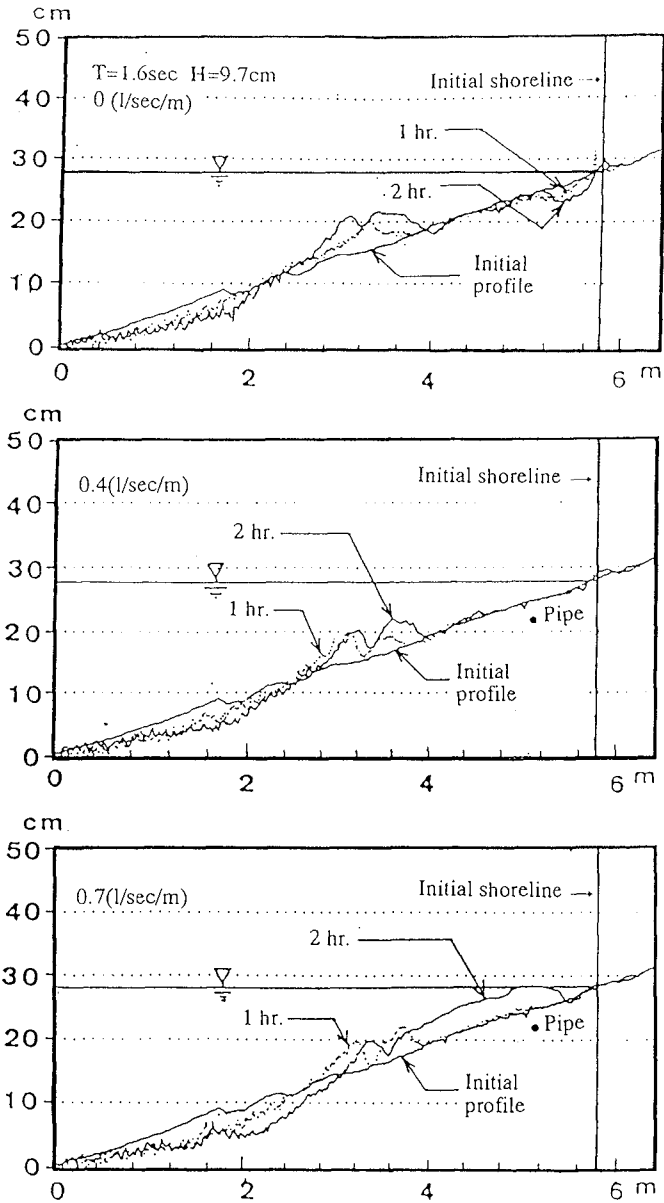


Figure 13 Changes of beach profile with discharge

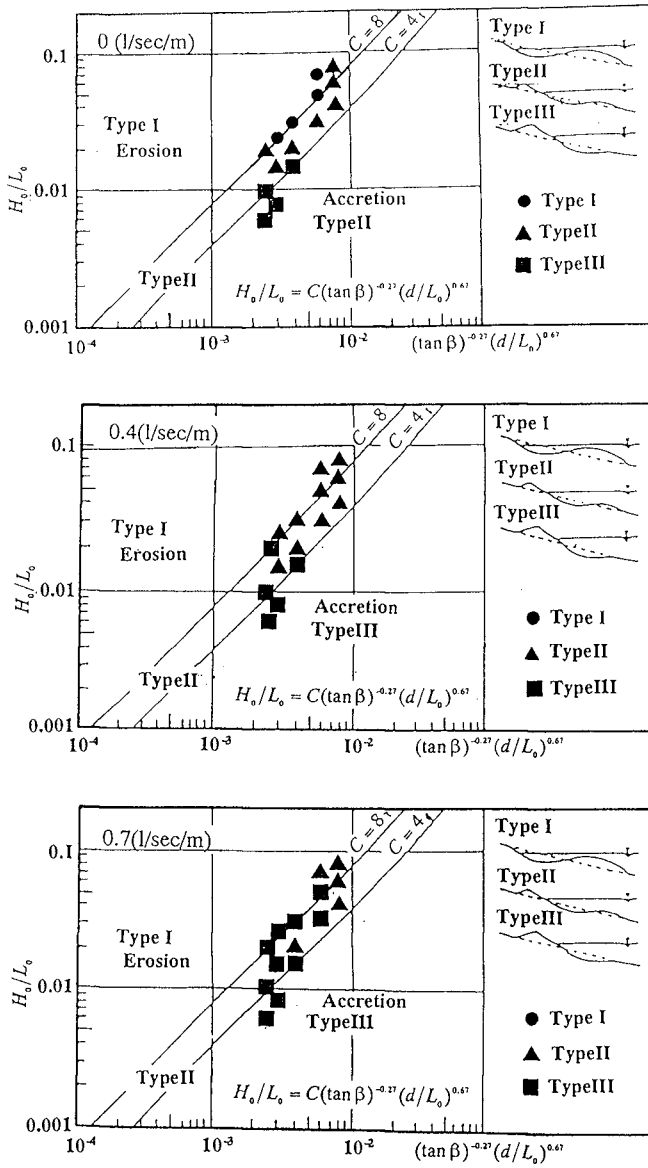


Figure 14 Change of beach type with discharge

Figure 14 shows the change of classified beach profiles with discharge. We can see that some of Type I profiles changed into Type III as the discharge increased. This shows that the coastal drain system has a potential ability to coastal erosion control.

### CONCLUSION

The performance, function and optimum location to install of a coastal drain system was investigated experimentally.

From the experimental results, it was confirmed that a coastal drain system advances accretion of sediments on the beachface for accretive wave conditions and retards beach erosion for erosive wave conditions.

Comparisons of the performance among three installation locations showed that seaward area of a shoreline was most appropriate for the installation.

As the discharge increases, the system becomes effective even for storm wave conditions.

The flow toward shore induced by drainage in the surf zone carried suspended sediments and migrated a bar toward the beach face and seemed to play the most important role.

### ACKNOWLEDGMENTS

This work was supported in part by a grant from the Yonemori Seishin Ikuseikai Foundation.

### REFERENCES

- Parks, J.M.: Beachface dewatering : A new approach to beach stabilization, THE COMPASS, Vol.66, No.2, pp.65-72, 1989
- Vesterby, H.: Coastal drain system - a new approach to coastal restoration, Proc. of the 1st. Conf. on Geotech. Eng. for Coastal development, pp.651-654, 1991
- Bruun, P.: The coastal drain: What can it do or not do ?, Jour. of Coastal Research, 5-1, pp.123-125, 1989

## CHAPTER 187

### WAVE BREAKING AND INDUCED NEARSHORE CIRCULATIONS

Ole R. Sørensen †, Hemming A. Schäffer†, Per A. Madsen†, and Rolf Deigaard‡

#### ABSTRACT

Wave breaking and wave induced currents are studied in two horizontal dimensions. The wave-current motion is modelled using a set of Boussinesq type equations including the effects of wave breaking and runup. This is done without the traditional splitting of the phenomenon into a wave problem and a current problem. Wave breaking is included using the surface roller concept and runup is simulated by use of a modified slot-technique. In the environment of a plane sloping beach two different situations are studied. One is the case of a rip channel and the other concerns a detached breakwater parallel to the shoreline. In both situations wave driven currents are generated and circulation cells appear. This and many other nearshore physical phenomena are described qualitatively correct in the simulations.

#### 1. INTRODUCTION

State of the art models for wave driven currents are based on a splitting of the phenomenon into a linear wave problem, described e.g. by the mild-slope equation, and a current problem, described by depth-integrated flow equations including radiation stress. Wave-current interaction effects such as current refraction and wave blocking may be included in these systems by successive and iterative model executions.

A more direct approach to the problem would be the use of a time domain Boussinesq model which automatically includes the combined effects of wave-wave and wave-current interaction in shallow water without the need for explicit formulations of the radiation stress. In the present work this direct approach is used in the study of wave-induced current phenomena in two horizontal dimensions.

The drawback of traditional Boussinesq models is that they cannot reproduce the effects of wave breaking. This precludes the modelling of surf conditions and thus the primary cause of wave driven currents. Prüser (1991) and Kabling and Sato (1993) have modelled the effects of wave breaking by

---

† International Research Center for Computational Hydrodynamics (ICCH), Danish Hydraulic Institute, Agern Allé 5, DK-2970 Hørsholm, Denmark

‡ Institute of Hydrodynamics and Hydraulic Engineering (ISVA), Technical University of Denmark, DK-2800 Lyngby, Denmark

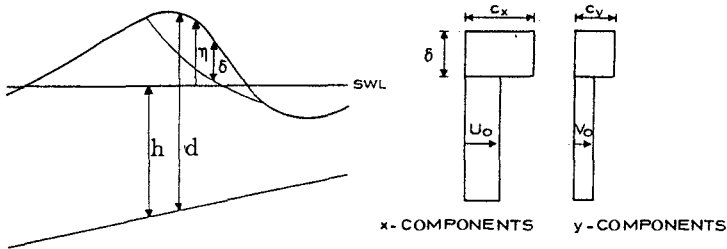


**Figure 1** Cross-section and components of assumed velocity profile of a breaking wave with a surface roller.

including eddy viscosity terms in the equations. In general this approach tends to smear out the effects of breaking over the whole wave cycle. Thus basic physical phenomena like, for example, the pronounced vertical asymmetry in breaking waves may not be reproduced.

Schäffer et al. (1992, 1993) incorporated wave breaking in a Boussinesq model by assuming a redistribution of momentum as a surface roller develops, taking the roller to be a passive bulk of water moving with the wave celerity. Accordingly, the vertical distribution of the horizontal velocity was approximated by the simple profile shown in Fig. 1. This was originally suggested by Svendsen (1984). Based on the idea of Deigaard (1989) the surface rollers were identified by a simple geometrical method. Despite the rather simple approach the results for e.g. wave height decay and set-up were promising. This work continues in two directions. One is confined to cross-shore processes (Madsen et al., 1994) while the other (present paper) deals with obliquely incident waves and wave induced circulations.

A number of coastal wave phenomena, such as the generation of infragravity waves, are sensitive to the conditions at the shoreline. For example, a natural beach tends to reflect most energy at low frequencies, while energy in the high frequency range is almost fully dissipated. Reproducing this as well as many other physical phenomena in a numerical model requires a runup condition allowing for a moving boundary. In the present model the formulation of such a shoreline boundary condition is based on a modified version of the slot-technique described by Tao (1983). This method is described in Madsen et al. (1994).

## 2. WAVE BREAKING AND RUNUP IN A BOUSSINESQ MODEL

### 2.1. Governing equations

Assuming the simplified velocity profile shown in Fig. 1 to be valid in case of wave breaking, the following modified version of the Boussinesq equations appear

$$\frac{\partial p}{\partial t} + \frac{\partial}{\partial x} \left( \frac{p^2}{d} \right) + \frac{\partial}{\partial y} \left( \frac{pq}{d} \right) + \frac{\partial R_{xx}}{\partial x} + \frac{\partial R_{xy}}{\partial y} + gd \frac{\partial \eta}{\partial x} + \psi_1 + \frac{\tau_x}{\rho} = 0 \quad (1a)$$

$$\frac{\partial q}{\partial t} + \frac{\partial}{\partial y} \left( \frac{q^2}{d} \right) + \frac{\partial}{\partial x} \left( \frac{pq}{d} \right) + \frac{\partial R_{yy}}{\partial y} + \frac{\partial R_{xy}}{\partial x} + gd \frac{\partial \eta}{\partial y} + \psi_2 + \frac{\tau_y}{\rho} = 0 \quad (1b)$$

Here  $(p, q)$  is the depth integrated velocity in the Cartesian coordinate system  $(x, y)$ ,  $d = h + \eta$  is the instantaneous depth and  $\eta$  is the surface elevation. The definition of the surface roller terms are

$$R_{xx} \equiv \delta \frac{(c_x - \frac{p}{d})^2}{1 - \frac{\delta}{d}} \quad (2a)$$

$$R_{xy} \equiv \delta \frac{(c_x - \frac{p}{d})(c_y - \frac{q}{d})}{1 - \frac{\delta}{d}} \quad (2b)$$

$$R_{yy} \equiv \delta \frac{(c_y - \frac{q}{d})^2}{1 - \frac{\delta}{d}} \quad (2c)$$

as derived by Schäffer et al. (1992, 1993). Here  $\delta = \delta(x, y, t)$  is the thickness of the surface roller determined in a heuristic geometrical way as given below. Components of the wave celerity are denoted  $c_x$  and  $c_y$ .

The terms denoted  $\psi$  are dispersive Boussinesq type terms which in shallow water may be taken from Peregrine (1967). Here we use the version derived by Madsen et al. (1991) and Madsen and Sørensen (1992):

$$\begin{aligned} \psi_1 \equiv & - \left( B + \frac{1}{3} \right) h^2 \left( \frac{\partial^3 p}{\partial x^2 \partial t} + \frac{\partial^3 q}{\partial x \partial y \partial t} \right) - Bgh^3 \left( \frac{\partial^3 \eta}{\partial x^3} + \frac{\partial^3 \eta}{\partial x \partial y^2} \right) \\ & - h \frac{\partial h}{\partial x} \left( \frac{1}{3} \frac{\partial^2 p}{\partial x \partial t} + \frac{1}{6} \frac{\partial^2 q}{\partial y \partial t} + 2Bgh \frac{\partial^2 \eta}{\partial x^2} + Bgh \frac{\partial^2 \eta}{\partial y^2} \right) \\ & - h \frac{\partial h}{\partial y} \left( \frac{1}{6} \frac{\partial^2 q}{\partial x \partial t} + Bgh \frac{\partial^2 \eta}{\partial x \partial y} \right) \end{aligned} \quad (3a)$$

$$\begin{aligned} \psi_2 \equiv & - \left( B + \frac{1}{3} \right) h^2 \left( \frac{\partial^3 q}{\partial y^2 \partial t} + \frac{\partial^3 p}{\partial x \partial y \partial t} \right) - Bgh^3 \left( \frac{\partial^3 \eta}{\partial y^3} + \frac{\partial^3 \eta}{\partial x^2 \partial y} \right) \\ & - h \frac{\partial h}{\partial y} \left( \frac{1}{3} \frac{\partial^2 q}{\partial y \partial t} + \frac{1}{6} \frac{\partial^2 p}{\partial x \partial t} + Bgh \frac{\partial^2 \eta}{\partial x^2} + 2Bgh \frac{\partial^2 \eta}{\partial y^2} \right) \\ & - h \frac{\partial h}{\partial x} \left( \frac{1}{6} \frac{\partial^2 p}{\partial y \partial t} + Bgh \frac{\partial^2 \eta}{\partial x \partial y} \right) \end{aligned} \quad (3b)$$

as valid for a wider range of water depths using  $B = 1/15$ .

Bottom friction is modelled using

$$(\tau_x, \tau_y) \equiv \rho \frac{\sqrt{p^2 + q^2}}{C^2 d^2} (p, q) \quad (4)$$

where  $C = Md^{1/6}$  is the Chezy resistance ( $m^{1/2}/s$ ),  $M$  being the Manning number. This formulation is very simplified and does not represent the effect of turbulent interaction between oscillatory boundary layers and the mean flow.



The equation for conservation of mass is unchanged

$$\frac{\partial \eta}{\partial t} + \frac{\partial p}{\partial x} + \frac{\partial q}{\partial y} = 0 \quad (5)$$

## 2.2. Determination of the surface roller

The determination of the surface roller  $\delta(x, y, t)$  (see Fig. 1) is made as described in detail by Schäffer et al. (1992) and summarized below, beginning with the case of only one horizontal dimension.

Breaking sets in when and where the local slope exceeds a certain value  $\tan \phi_B$  and the actual point is taken as the instantaneous toe of a surface roller. At the given instant, the roller is then taken to be constituted by the water above the tangent of angle  $\phi_B$  starting at the roller toe and going in the direction opposite of wave propagation. After incipient breaking the procedure is the same except now decreasing angles  $\phi = \phi(t)$  are used in place of  $\phi_B$ . The system keeps track on the age of each surface roller and applies a value given by

$$\tan \phi(t) = \tan \phi_0 + (\tan \phi_B - \tan \phi_0) \exp \left[ -\ln 2 \frac{t - t_B}{t_{1/2}} \right] \quad (6)$$

Here  $\phi_0$  is the terminal value of  $\phi(t)$ ,  $t_B$  is the time of incipient breaking and  $t_{1/2}$  is the half time for  $\tan \phi(t)$ . The following values were used in all the results presented below:  $\phi_B = 20^\circ$ ,  $\phi_0 = 10^\circ$  and  $t_{1/2} = T/10$  where  $T$  is a typical period of the waves. After the determination of the surface roller in each time step,  $\delta$  is multiplied by a shape factor  $f_\delta$  prior to the inclusion in the governing equations. A value of  $f_\delta = 2$  was used.

In two horizontal dimensions the toe of the roller becomes a curve instead of a single point and the tangent becomes a set of generating lines determined by the instantaneous local angle  $\phi(t)$ . Whereas  $\phi(t)$  in the one-dimensional case is constant within each roller, it is allowed to have a lateral variation in the two-dimensional case. This lateral variation of  $\phi(t)$  within each surface roller must be allowed since, for example, when oblique regular waves break on an alongshore uniform beach both the initial and the final stage of the breaking process will be represented within the same roller. The lateral variation of  $\phi(t)$  is allowed for by keeping track on the surface roller age along the orthogonal to the roller toe curve. Thus, between each pair of generating line used for the roller determination,  $\phi(t)$  decays according to (6).

## 2.3. Solution technique

The differential equations are discretized using a time-centered implicit scheme with variables defined on a space-staggered rectangular grid. The method is based on the Alternating Direction Implicit algorithm. For more details of the solution procedure reference is made to Abbott et al. (1978, 1981, 1984), McCowan (1978, 1984) and Madsen et al. (1991, 1992).

The finite-difference approximation of the spatial derivatives is generally a straight-forward mid-centering. However, in the present work we have treated the nonlinear convective terms somewhat differently. The use of high-order central schemes for the discretization of convective terms is known to introduce non-physical oscillations in regions with large gradients of the convected variable. Typically these appear around corners of structures e.g. at the tip of

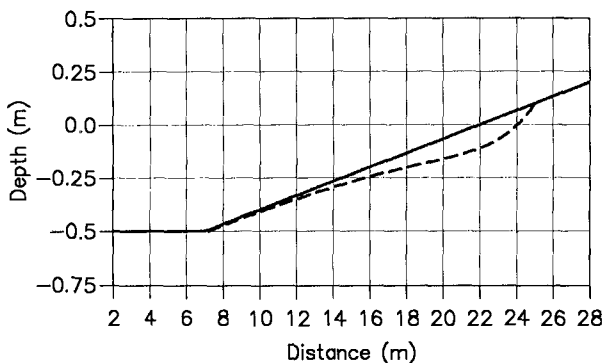


**Figure 2** Beach profiles for the rip channel test. (—): along a plane beach section and (- - -): along the rip channel.

a breakwater, in regions of strong wave-induced circulations, and in the bore-like stage in the inner surf zone. The classical first-order upwinding scheme is non-oscillatory, but introduces an unacceptable artificial diffusion. Higher-order upwinding schemes significantly reduce this diffusion, but still overshoots and undershoots may occur in the solution.

A number of oscillation-free schemes have been proposed in the literature, especially within the field of compressible flows with strong shocks. A disadvantage of these schemes is that they increase the computational cost significantly. For this reason a more simple approach has been used here: a first-order upwinding scheme is applied in sharply varying regions, that is in regions where the depth-integrated velocity is non-monotonic, and elsewhere second-order (quadratic) upwinding is applied.

### 3. NUMERICAL SIMULATIONS

In principle, the model can be used for a wide range of coastal phenomena. However, since the inclusion of wave breaking is more or less based on the spilling-breaker assumption, it is primarily suited for mild slopes and rather steep waves.

We have chosen two different situations with waves normally incident on a plane sloping beach but with some alongshore non-uniformity to trigger nearshore circulation. In the first example a rip channel is present while the other concerns a detached breakwater parallel to the shoreline. In both examples the bathymetry has a crossshore line of symmetry. In case of normally incident unidirectional waves the numerical computation was only made in half of the region in question. This reduced the computational cost, but precluded possible instabilities of currents along the line of symmetry.

#### 3.1. A plane beach with a rip channel

The first example is chosen according to laboratory experiments reported by Hamm (1992). The wave basin was 30m by 30m and the bathymetry was a plane sloping beach of 1:30 with a rip channel excavated along the centerline. The profiles of the rip channel and the plane beach is shown in Fig. 2. Two of

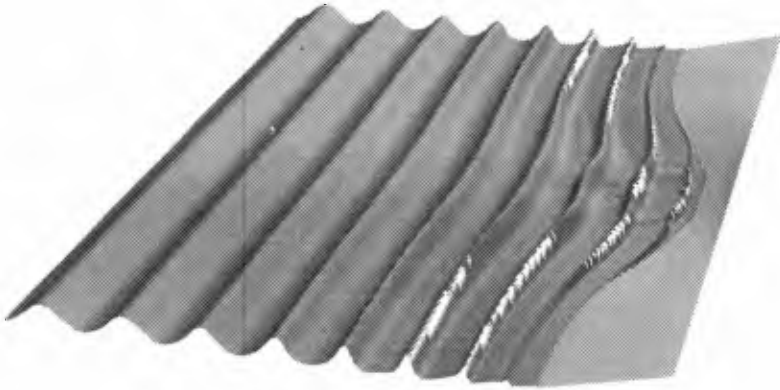


**Figure 3** Birds view of the free surface elevation for the rip channel case with regular waves. The surface rollers are shown in white.

Hamm's test cases were modelled numerically. In the first test the waves were regular with a period of 1.25s and a wave height of 0.07m and unidirectional with normal incidence. In the second test the incident waves were multidirectional and irregular and sampled from a JONSWAP spectrum with a peak period of 1.25s and a significant wave height of 0.07m and with a directional spreading corresponding to a  $\cos^6 \theta$ -distribution. In both cases a Manning number of  $72\text{m}^{1/3}/\text{s}$  was used in the bed friction term. The grid spacing was 0.05m and the time step 0.01s.

For the regular-wave case a birds view of the surface elevation (in a sub-domain) is shown in Fig. 3. The surface rollers are shown in white. Due to the increased depth and due to depth refraction by the rip channel incipient breaking occurs comparatively close to shore along the centerline. Here the setup is quite small and the larger setup appearing away from the rip channel gives an alongshore gradient in the mean water surface forcing a current towards the centerline. Here the flows from the two sides join to form a rip current and two symmetrical circulation cells appear.

The effect of the rip current on the wave height counteracts the effect of depth refraction and hence incipient breaking starts locally at the centerline. The rip current also causes a small local oscillation in the wave crest occurring at the same place. These phenomena also show up in a video of the experiment kindly supplied by Hamm.

A vector plot of the depth-integrated velocity averaged over one wave period is shown in Fig. 4. A subdomain is shown in order to focus one of the circulation cells which has developed. A pronounced rip current is seen along the centerline of the bathymetry i.e. at the top of the figure.

Figure 5 shows the cross-shore variation of the rip current computed as the time-average of the velocity below the roller,  $U_0$ . For reasons of symmetry the rip current was bound to be directed exactly perpendicular to the shore. In Hamm's experiments the measured rip current showed a significant deviation from this direction. It is unclear whether this was due to imperfections in the supposedly symmetrical experiment or if instabilities of the rip current could

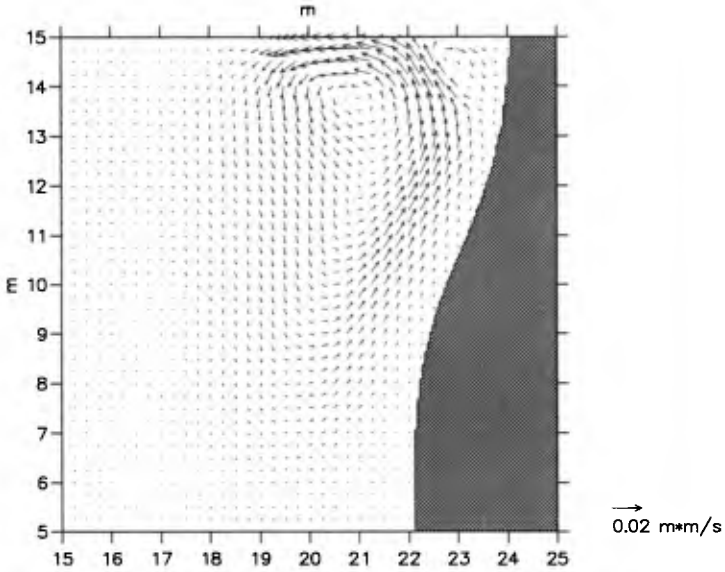


**Figure 4** Depth-integrated velocity for the situation shown in Fig. 3 focusing on a circulation cell.

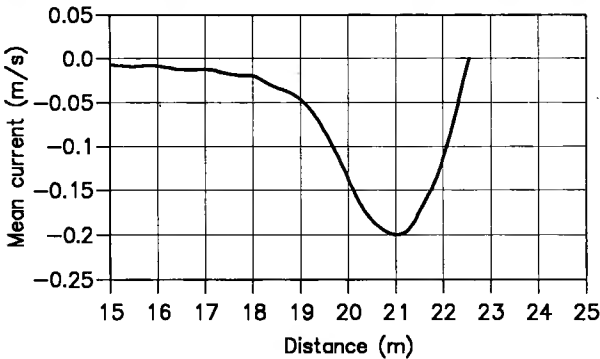


**Figure 5** Rip current along the rip channel for the regular-wave case.

be responsible. With regard to the order of magnitude of the rip current speed, agreement was found between the numerical simulation and the experimental results.

Figure 6a shows the wave height at some distance from the rip channel where the beach is a plane slope. A similar plot but along the excavated beach at the centerline is shown in Fig. 6b. The measurements of Hamm are included for comparison and the agreement is quite good. The large variation of the rip

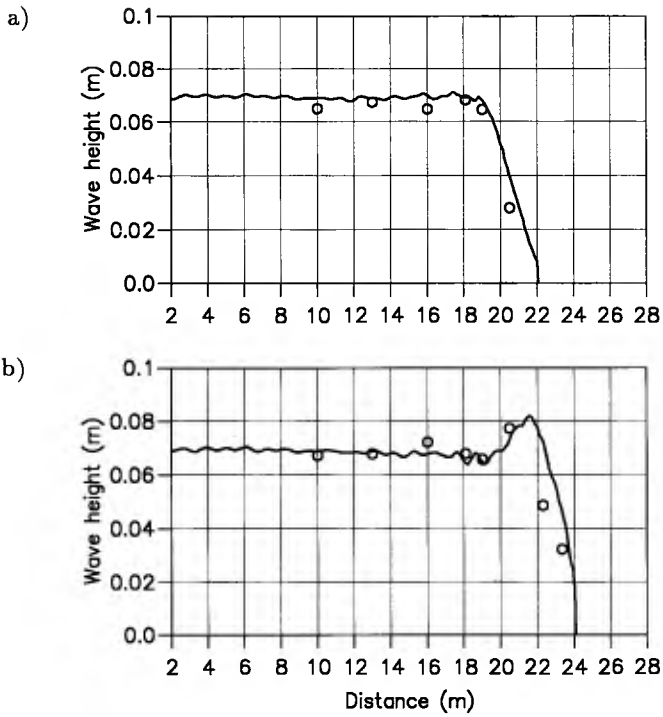


**Figure 6** Comparison of the cross-shore wave height variation for the regular wave case of the rip channel case a) along a plane beach section and b) along the rip channel. (—): numerical simulation, (o): measurements by Hamm (1992).

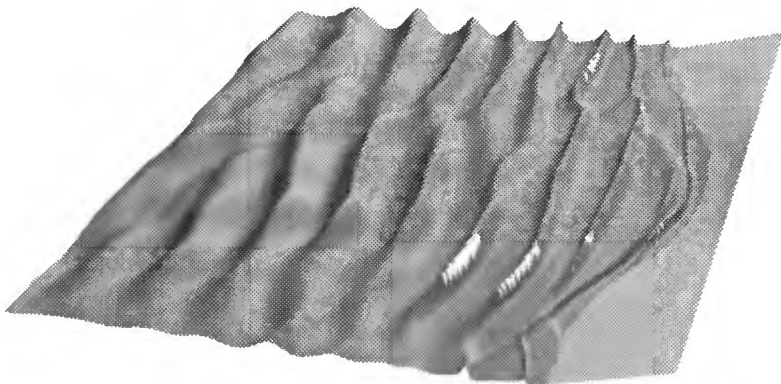


**Figure 7** As Fig. 3, but for the case of irregular multidirectional waves.

current (see Fig. 5) is seen to cause a pronounced increase in the wave height in Fig. 6b.

Figure 7 shows a birds view of the surface elevation for the multidirectional irregular-wave case. The duration of this simulation was too short to give confidential statistics precluding comparison of significant wave height and average velocities with the experimental values.

### 3.2. *A plane beach with a detached breakwater*

The second example concerns a plane sloping beach of 1:50 with a 300m long detached breakwater placed at a still water depth of 6m i.e. 300m from the shore. Regular, unidirectional waves of normal incidence, a period of 8s and a wave height of 2m were generated at a depth of 10m. The computational domain extended 700m offshore and 600m alongshore from the line of symmetry and the seaward side of the breakwater was treated as land. The grid spacing was 1m and the time step was 0.08s. Bed friction was modelled using a Manning number of  $32\text{m}^{1/3}/\text{s}$ .

A birds view of the elevation is shown in Fig. 8. Again, surface rollers are shown in white. The diffraction around the breakwater gives the expected oscillations in the wave height along the wave crests, see Fig. 9 for the wave height variation. This further results in scattered incipient breaking, but the surface rollers quickly merge extending the breaking process to cover the long crested wave. In the simulation the roller disappears before the waves reach the shore. This is an unwanted side effect of a spatial smoothing which for reasons of stability was applied in the vicinity of the swash zone. Note the nonlinear cross-wave pattern close to the shore in lee of the breakwater.

The depth-integrated velocity averaged over one wave period is shown in Fig. 10. The maximum current speed behind the breakwater is approximately 0.7m/s and it occurs about 80m from the shoreline near the edge of the breakwater. In addition to the expected circulation cell, a local phenomenon resembling thin rip currents appears further away from the breakwater. This is more pronounced in Fig. 11 showing the time-average of the velocity below the roller,  $(U_0, V_0)$ . This velocity field includes the depth averaged undertow. The thin rip currents may be caused by the lateral variation of the wave height as created by the diffraction around the breakwater. However, this remains to be studied further.

### ACKNOWLEDGEMENT

This work has been financed mainly by the Danish National Research Foundation and partly by the Commission of the European Communities, Directorate General for Science, Research, and Development under MAST contract No. MAS2-CT92-0027.

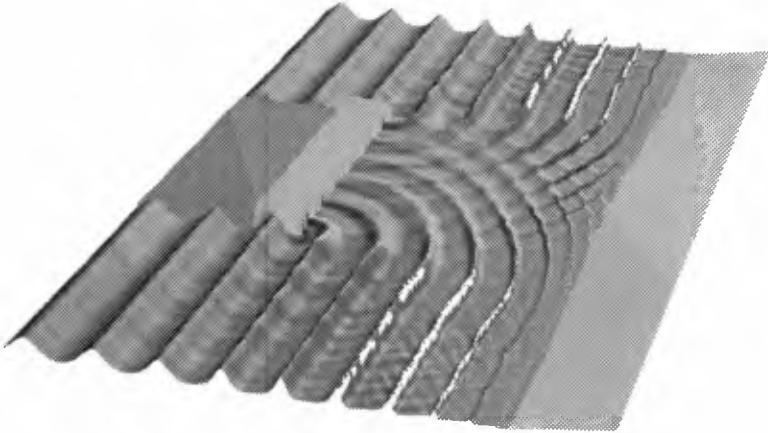


**Figure 8** Birds view of the free surface elevation for the detached break-water case with regular waves. The surface rollers are shown in white.

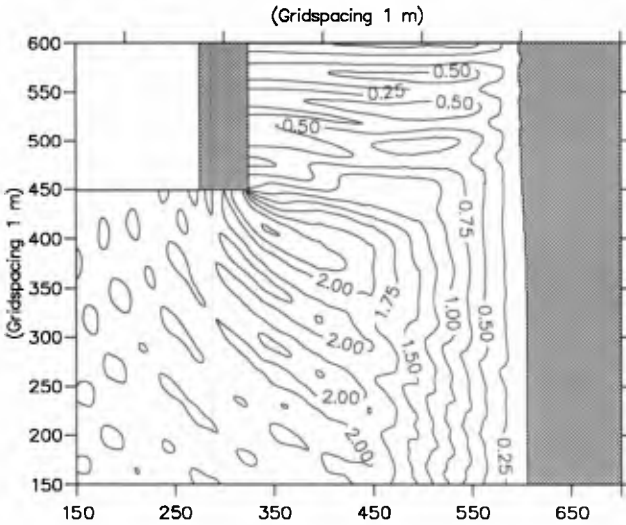


**Figure 9** Wave height variation for the situation in Fig. 8, showing only half of the region.

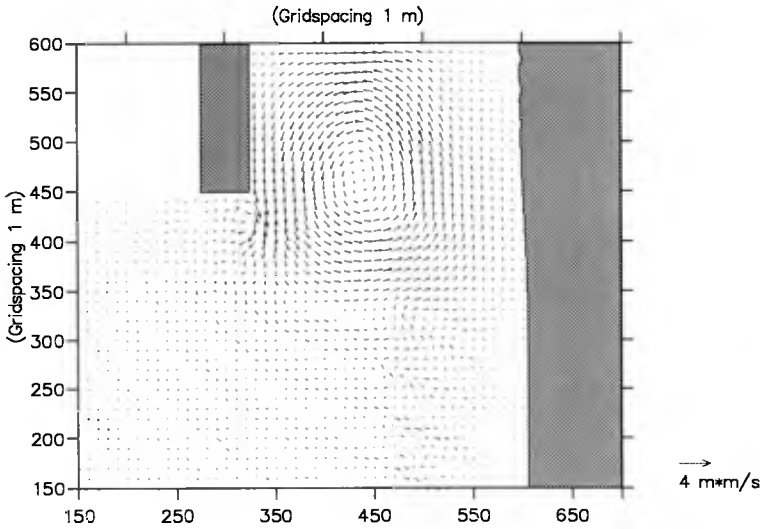


**Figure 10** Time-averaged and depth-integrated velocity corresponding to Fig. 9.

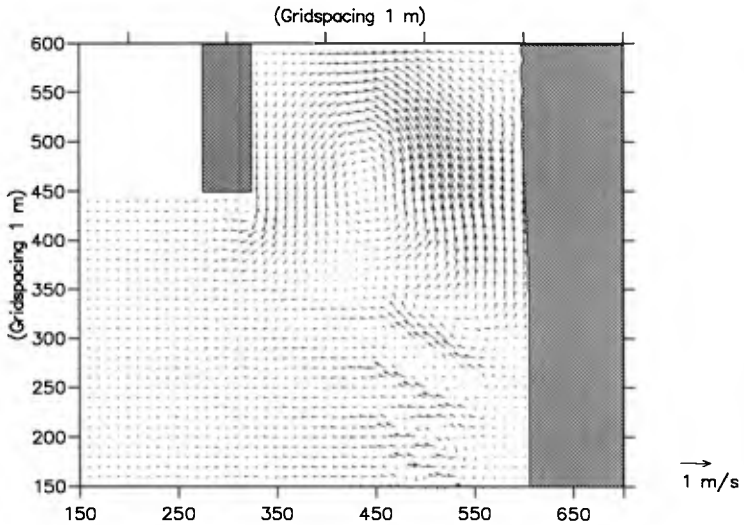


**Figure 11** Time-average of the velocity beneath the surface rollers corresponding to Fig. 10.



## REFERENCES

- Abbott, M. B., H. M. Petersen and O. Skovgaard (1978). On the numerical modelling of short waves in shallow water. *J. Hydraul. Res.*, **16**(3), 173-203.
- Abbott, M. B., A. D. McCowan and I. R. Warren (1981). Numerical modelling of free-surface flows that are two-dimensional in plan. In: *Transport Models for Inland and Coastal Water*, Symp. Predictive Ability, Academic Press, New York, N.Y.
- Abbott, M. B., A. D. McCowan and I. R. Warren (1984). Accuracy of short wave numerical models, *J. Hydraul. Engrg.* **110**(10), 1287-1301.
- Deigaard, R. (1989). Mathematical modelling of waves in the surf zone. Prog. Rep. 69, ISVA, Technical University of Denmark, Lyngby, 47-59.
- Hamm, L. (1992). Directional nearshore wave propagation over a rip channel: and experiment. Proc. 23rd Int. Conf. Coastal Eng., Venice Italy, 1992, ASCE, New York, 1993.
- Kabiling, M. B. and S. Sato (1993). Two-dimensional nonlinear dispersive wave-current and three-dimensional beach deformation model. *Coastal Engrg. in Japan* **36**, 196-212.
- Madsen, P. A., R. Murray and O. R. Sørensen (1991). A new form of the Boussinesq equations with improved linear dispersion characteristics. Part 1. *Coastal Engrg.* **15**, 371-388.
- Madsen, P. A. and O. R. Sørensen (1992). A new form of the Boussinesq equations with improved linear dispersion characteristics. Part 2. A slowly-varying bathymetry. *Coastal Engrg.* **18**, 183-204.
- Madsen, P.A., O.R. Sørensen, and H.A. Schäffer (1994). Time domain modelling of wave breaking, runup, and surf beats. This conference.
- McCowan, A. S. (1978). Numerical simulation of shallow water waves. Proc. 4th Austr. Conf. Coastal and Ocean Eng., Adelaide, Australia.
- McCowan, A. S. (1984). Developments in numerical short wave modelling. Proc. 5th Austr. Conf. Coastal and Ocean Eng., Perth, Australia.
- Peregrine, D. H. (1967). Long waves on a beach. *J. Fluid Mech.* **27**(4), 815-827.
- Prüser, H.-H. (1991). Zur Interaktion von Wellen und Strömung im flachen Wasser. *Report No. 30*, Institut für Strömungsmechanik und elektronisches Rechnen im Bauwesen, Universität Hannover.
- Schäffer, H.A., R. Deigaard, and P.A. Madsen (1992). A two-dimensional surf zone model based on the Boussinesq equations. Proc. 23rd Int. Conf. Coastal Eng., Venice Italy, 1992, ASCE, New York, 1993.
- Schäffer, H.A., P.A. Madsen, and R. Deigaard (1993). A Boussinesq model for waves breaking in shallow water. *Coastal Engineering*, Vol. 20, 185-202.
- Svendsen, I. A. (1984). Wave heights and setup in a surf zone. *Coastal Engrg.*, **8**(4), 303-329.
- Tao, J. (1983). Computation of wave run-up and wave breaking. Internal Report, 40 pp, Danish Hydraulic Institute.

## CHAPTER 188

### ACCURACY AND APPLICABILITY OF THE SPM LONGSHORE TRANSPORT FORMULA

by

J S SCHOONEES\* and A K THERON\*

#### ABSTRACT

The ability to predict the time-averaged longshore sediment transport rate accurately is essential for many coastal engineering applications. Because the longshore transport formula in the Shore Protection Manual (SPM; US Army, Corps of Engineers, 1984) is possibly the most widely used, it is important to know its accuracy. The aim of this paper is therefore to investigate the accuracy and applicability of this formula (the SPM formula). In addition, a number of variations to this formula are presented; these are also tested against a comprehensive data set. Finally, the SPM formula is re-calibrated and guidance is given regarding the use of this formula for coarse bed material.

#### INTRODUCTION

The ability to predict the time-averaged longshore sediment transport rate accurately is essential for the design of breakwaters at harbour entrances, navigation channels and dredging requirements, beach improvement schemes incorporating groynes, detached breakwaters and beach fill as well as for the determination of the stability of inlets and estuaries.

Because the longshore transport formula in the Shore Protection Manual (SPM; US Army, Corps of Engineers, 1984) is possibly the most widely used, it is important to know its accuracy. The aim of this paper is therefore to investigate the accuracy and applicability of this formula (the SPM formula). In addition, a number of variations to this formula have been presented; these will also be tested against a comprehensive data set. Finally, the SPM formula is re-calibrated and guidance is given regarding the use of this formula for coarse bed material.

---

\* Research Engineers, CSIR, P O Box 320, Stellenbosch, 7599, South Africa

The data considered in this paper are only for particulate (non-cohesive) sediment (including sand, gravel and shingle) being transported alongshore from the swash zone across the surf zone to deep water. Only bulk (total rate across the shore) and not local transport rates are considered. These bulk rates include both the bedload and suspended load. Only field data are used because of possible scale effects in laboratory investigations and/or because regular waves were used. Furthermore, the ultimate aim is to be able to predict longshore transport accurately in the field (Komar, 1988).

The data are not meant to provide average long-term data at (a) specific site(s). It is rather assumed that if a longshore transport formula is capable of accurately predicting transport rates for the data sets given herein, it can be used with reasonable confidence at similar sites to determine the long-term longshore sediment budget if representative wave and other input parameters are available. It would of course be even better to have site-specific calibration data before calculating average long-term transport rates.

Previous studies where a few longshore transport formulae have been tested against data are Swart (1976), Fleming *et al.* (1986) and Kamphuis *et al.* (1986). Schoonees (1994) evaluated 51 formulae against an extensive data base. This paper reports the findings of the above-mentioned study with regard to the SPM formula and variations thereof. Two of the most important papers on the development of the SPM formula are Komar and Inman (1970) and Komar (1988). The latter study in which the dependency of the SPM formula on sediment grain size, beach slope and wave steepness was investigated, is partially revised here with a bigger data base.

## DATA

Schoonees and Theron (1993) compiled and reviewed almost all the available field data on longshore transport. They used a point rating system to assess the quality of the data in detail. Two data sets, namely Data Sets 1 and 2, were extracted from the data contained in Schoonees and Theron (1993) together with their point ratings.

Data Set 1 containing 123 data points, consists of data where all the required parameters are available. Table 1 summarizes this data set and gives the point ratings in percentages according to Schoonees and Theron (1993). Data Set 2 includes Data Set 1 and contains other measurements totalling 240 data points. These other measurements are usually where only values of the energy flux factor, the longshore transport rate and the median grain size are available. Table 2 lists the sources of Data Set 2.

It is important to note that the data ranges of the particular Data Set 1 are:

0,058	<	$H_{bs}$ (m)	<	3,400
2,32	<	$T_p$ (s)	<	16,60
0,30	<	$\theta_b$ ( $^\circ$ )	<	35,00
0,0070 (=1/142,9)	<	beach slope	<	0,1380 (=1/7,2)

0,154	<	$D_{50}$ (mm)	<	15,000
600	<	$S$ ( $m^3/year$ )	<	14 793 000

From the above values it is clear that the data ranges of this data set (and therefore also Data Set 2) are quite wide. Most conditions encountered on natural beaches are covered and the data were collected on beaches from a variety of sites from around the world. These give credibility to the conclusions drawn in this comparison with data.

**FORMULAE**

One of the earliest longshore transport formulae and perhaps the best-known method, the **SPM formula** (SPM = Shore Protection Manual) is given in US Army, Corps of Engineers (1984):

$$S = K_1 P_{ls} \quad (m^3/yr)$$

- where  $K_1 = 1289 (m^4/(W.yr))$  for prototype beaches
- $P_{ls} =$  wave energy flux factor using the significant wave height in the calculation. (W/m)
- $= E_b n_b C_b \sin \theta_b \cos \theta_b$

- with  $E =$  wave energy density
- $= \rho g H_{bs}^2 / 8$
- $\rho =$  density of sea water ( $kg/m^3$ )
- $g =$  gravitational acceleration ( $m/s^2$ )
- $H_{bs} =$  significant breaker wave height (m)
- $n_b = 0,5 (1 + (4\pi d_b / L_b) / (\sinh 4\pi d_b / L_b))$

- and  $d_b =$  breaker depth (m)
- $L_b =$  wavelength at the breaker line (m)
- $C_b =$  wave celerity at the breaker line (m/s)
- $= (L_b / T_p)$

- and  $T_p =$  peak wave period
- $\theta_b =$  wave incidence angle at the breaker line

An alternative formulation of the SPM is:

$$I = K_s P_{ls}$$

$$= K_r P_{lr}$$

with  $I =$  immersed weight longshore transport rate  
 $P_r =$  energy flux factor using the root-mean square breaker height  
 where  $K_s = 0,5$  (0,78) = 0,39 if the significant breaker height is used in  $P_s$   
 $K_r = 0,78$  if the root-mean-square breaker height ( $H_{brms}$ ) is used in  $P_r$

Development of the SPM formula was done, among others, by the Scripps Institute of Oceanography (1947), Watts (1953), Caldwell (1956), Inman and Bagnold (1963), Komar (1969), Komar and Inman (1970) and Komar (1988).

Swart (1976) adapted the coefficient  $K_1 = 1289$  to be a function of the median grain size ( $D_{50}$ ). His version of the SPM formula which appears to differ from the SPM formula given above because of several implications, is

$$S = K_2 P_{ls} \quad (m^3/yr)$$

where  $K_2 = 1876 \log_{10} (0,00146 / D_{50})$   
 ( $D_{50}$  in m)

This equation together with a relationship proposed by Bruno *et al* (1981) will be shown later. Komar (1988) maintained that there is no significant relationship between  $K_1$  and  $D_{50}$ . This issue will be discussed further based on all the data.

Kamphuis and Readshaw (1978) and Vitale (1981) investigated whether  $K_1$  is a function of the surf similarity parameter (or Iribarren number)  $\xi_b$ :

$$\xi_b = \frac{\tan \alpha}{(H_{brms} / L_o)^{0,5}}$$

where  $\tan \alpha =$  bottom slope in the surf zone

$$H_{brms} = H_{bs} / \sqrt{2}$$

$$L_o = \text{deep-sea wavelength}$$

Vitale (1981) used a mean wave height (measured in relatively deep water) instead of  $H_{brms}$ . To prevent the need for calculation of the wave height at the breaker line, it was decided to use the relationship proposed by Kamphuis and Readshaw (1978) and Readshaw (1979), namely:

$$K_p' = 0,7 \xi_b \quad \text{for } 0,4 < \xi_b < 1,4 \\ \text{(say for } \xi_b < 1,4)$$

$$1,24 \quad \text{for} \quad \xi_b \geq 1,4$$

with  $Q_s$  (kg/s) =  $K_p' P_{ls} / 2g$

and  $S$  =  $\frac{31\,557\,600 Q_s}{(1-p) \rho_s} \quad (m^3/yr)$

- where  $p$  = porosity of the sediment (assumed to be 0,4 for sand)
- $\rho_s$  = density of the sediment (usually 2650 kg/m<sup>3</sup> for sand)
- and 31 557 600 = number of seconds in one year

**Bailard** (1981) generalized the Bagnold (1963, 1966) energetics-based stream model. After integrating the local time-averaged longshore transport rate, Bailard (1984) obtained the following alternative equation for  $K_1$ , (called  $K_3$ ) valid for both model and prototype applications:

$$K_3 = 0,05 + 2,6 \sin^2 2\theta_b + 0,007 u_{mb} / w$$

- where  $w$  = fall velocity of the sediment grains
- $u_{mb}$  = 0,5  $\gamma (g d_b)^{0,5}$
- and  $\gamma$  = breaker index = 0,8

Bailard (1985) adds another term the equation for  $K_3$ , namely,  $0,0096 \tan \alpha$ . However, choosing a very high value of the beach slope ( $\tan \alpha$ ) of 0,2, it is clear that the estimated maximum value of this term is about 0,0019. For  $\tan \alpha = 0,04$ , a typical value, the term is only 0,00038. Because its contribution to  $K_3$  is negligible, this term was omitted. Furthermore:

$$I = 0,5 K_3 P_{ls}$$

and  $S = \frac{31\,557\,600 I}{(\rho_s - \rho) g (1 - p)} \quad (m^3/yr)$

Watts (1953) empirically related the longshore transport rate to the wave energy flux factor. The **Watts formula** in SI units is:

$$S = 2223 P_{ls}^{0,9}$$

Similarly, **Caldwell** (1956) obtained his formula (given here in SI units):

$$S = 2505 P_{ls}^{0,8} \quad (m^3/yr)$$

## EVALUATION OF FORMULAE

### Method of Testing

The results of the testing of the formulae will be presented in a number of ways in order to facilitate interpretation. These are:

- \* A plot of the predicted longshore transport rates ( $S_p$ ) versus the measured rates ( $S_m$ ).
- \* The relative standard error of estimate ( $\sigma$ ) was calculated (Kamphuis, *et al*, 1986):

$$\sigma = \sqrt{\sum_{i=1}^n \left[ \frac{(\log S_{p,i} - \log S_{m,i})^2}{n-1} \right]^{0.5}}$$

where  $n$  = number of data points  
 $i$  = number of the particular data point

- \* The discrepancy ratio ( $r_d$ ) (Van Rijn, 1984) and its distribution were determined.

$$r_{d,i} = S_{p,i} / S_{m,i}$$

A histogram of the percentage occurrence versus  $r_d$  gives this distribution.

(The residuals ( $e_i = S_{m,i} - S_{p,i}$ ) were computed and plotted against  $S_p$  to check whether there is a systematic trend in the residuals, or not - these are not shown. Refer to Schoonees (1994)).

### Results

Table 3 lists the relative standard error of estimate ( $\sigma$ ) and the percentage occurrence of the discrepancy ratio ( $r_d$ ) within certain limits for the formulae. For example, the percentage of the predicted transport rates for which the discrepancy ratio falls between 0,5 and 2 or between 0,25 and 4 can be read from this table.

Figures 1 and 2 show the predicted longshore transport rates ( $S_p$ ) versus the measured rates ( $S_m$ ) for the SPM and the SPM, Kamphuis and Readshaw formulae respectively. The histogram of the discrepancy ratios for the SPM, Kamphuis and Readshaw formula is contained in Figure 3. Refer to Schoonees (1994) for similar figures of the other formulae. Note that in these figures  $m^3/yr$  means  $m^3/yr$ .

### Discussion

A first impression when examining Figures 1 and 2 and Table 3 is that considerable scatter exists in the predicted longshore transport rates. Based on this particular data set, the SPM, Kamphuis and Readshaw formula gives the best answer of the six formulae over the full range of measured longshore transport rates ( $\sigma=0,515$ ;  $r_d$  between 0,5 and 2: 65,0%). Even so this formula tends to underpredict high transport rates (Figure 2). This is an area of concern because at a particular site, most

of the longshore transport occurs during a few storms so that it is important to predict high transport rates accurately.

It is interesting to note that the SPM formula, perhaps the best known and most used predictor, does not fare very well. Although one can argue that its poor performance at low transport rates (Figure 1) can be attributed to a lack of an incipient motion criterion, it is still clear that it over-predicts in the range  $1,5 \times 10^4 \text{ m}^3/\text{year}$  to  $1,5 \times 10^6 \text{ m}^3/\text{year}$ . What is, however, comforting is that for high transport rates ( $> 1,5 \times 10^6 \text{ m}^3/\text{year}$ ) the SPM predicts transport rates accurately. That is, for the few data points in this range. However, two of the oldest formulae, namely, the Caldwell and Watts methods, also do not have an incipient motion criterion but both appear to be more accurate than the SPM and the SPM and Swart formulae (compare  $\sigma=0,579$  (Caldwell) and  $0,685$  (Watts) to  $0,708$  (SPM) and  $0,720$  (SPM and Swart)). In fact, adapting the SPM formula for grain size (SPM and Swart method) caused a slight decrease in the accuracy of the predictions. The similar answers of these two predictors can, however, merely indicate that most of the data points were collected for grain sizes between  $0,2 \text{ mm}$  to  $0,4 \text{ mm}$  as indeed found by Schoonees and Theron (1993). In this grain size range the SPM and Swart formula gives very similar answers to the SPM formula.

It is interesting to note that the original SPM, Kamphuis and Readshaw formula was only calibrated against laboratory data and therefore no field data of Data Set 1 were used in its derivation. The second-best formula (Caldwell's) only used a few of the data points, especially when compared to the 41 points of Data Set 1 included in the calibration of the SPM formula.

#### FURTHER CALIBRATION OF THE SPM FORMULA

One can argue that the SPM formula is not applicable for coarse-grained sediment which are included in Data Set 1. In addition, the data points for which only  $S$  and  $P_b$  are available, should also be used.

Figure 4 shows the data in Data Set 2 with a distinction being made between fine - ( $D_{50} < 1 \text{ mm}$ ) and coarse-grained ( $D_{50} > 1 \text{ mm}$ ) sediment. It is clear from this figure that except for some minor overlap, two different populations of points are apparent. For the fine-grained sediment (206 data points) the best fit relationship is:

$$I = 0,20 P_b \quad (1)$$

$(R^2 = \text{coefficient of determination} = 0,72)$

Considerable scatter is evident. If the recommendation by Schoonees and Theron (1993) is followed whereby only data in their higher category (point rating 60% and better) is used (Tables 1 and 2), 46 data points are retained. Figure 5 illustrates the result while the equation is:

$$I = 0,41 P_b \quad (R^2 = 0,77) \quad (2)$$



or  $I = 0,82 P_r$  (i.e.  $K_r = 0,82$ )

Unfortunately, the scatter is not significantly reduced and the range of  $P_b$  values is much smaller. In comparing Equations 1 and 2, it is clear that the elimination of the lower quality data, more than doubled the value of  $K_r$ .  $K_r = 0,82$  is an increase of the value of 0,57 proposed by Komar (1988) based on 70 of the data points in Data Set 1. The value in the original formula is 0,78 which is derived from 41 data points (US Army, Corps of Engineers, 1984). Kraus *et al.* (1982) found  $K = 0,58$  based on their data and those of Komar (1969), which are 25 data points. It would of course be even better to have site-specific calibration data before calculating longshore transport rates. The foregoing illustrates the great uncertainties involved in using the SPM formula and in view of this we recommend that the SPM, Kamphuis and Readshaw formula preferably be used.

Both Swart (1976) and Bruno *et al.* (1981) presented relationships between  $K_s$  and  $D_{50}$ . Figure 6 shows these relationships together with the data having median grain sizes below or equal to 1 mm. From this figure it is clear that a single relationship between  $K_s$  and  $D_{50}$  will not explain all the scatter shown in Figures 4 and 6. The same applies if the settling velocity instead of the median grain size is used. Although this correlates with the finding of Komar (1988), the authors believe that a longshore transport formula must contain either  $D_{50}$  or the settling velocity. It is also evident from Figure 6 that neither of the relationships by Swart and Bruno *et al.* are generally valid. The relationship by Bruno *et al.* (1981) almost forms an upper envelope to the values.

Returning to Figure 4, a very approximate line through the coarse-grained sediment is:

$$I = 0,01 P_b \quad (R^2 = 0,11) \quad (3)$$

Because of the considerable scatter in the data and the very low  $R^2$ , this equation should only be used to obtain a rough order of magnitude of the longshore transport rate. For these coarse-grained data as well, no single relationship between  $K_s$  and  $D_{50}$  (figure not shown) will explain all the scatter shown in Figure 4. Clearly, further work is required. For example, an incipient motion criterion (see e.g. Chadwick, 1989, Brampton and Motyka, 1984 and Van Hijum and Pilarczyk, 1982) is necessary.

## CONCLUSIONS

The data ranges of Data Sets 1 and 2 are quite wide and as such, cover most conditions encountered on natural beaches.

Of the six formulae (SPM formula and variations thereof), tested against Data Set 1, the SPM, Kamphuis and Readshaw method fared the best. The standard error of estimate for this method was 0,515 while 65,0% of the time, the discrepancy ratio ( $r_d$ ) fell between 0,5 and 2.

By using only the data from Data Set 2 that fall in the higher (better) category of Schoonees and Theron (1993) - 46 data points -, the best fit relationship for sand ( $D_{50} < 1$  mm) is:

$$I = 0,41 P_{ls} \quad (R^2 = 0,77)$$

Unfortunately, significant scatter is still evident (Figure 5). It was also found that no single relationship between  $K_s$  and the median grain size (or the settling velocity) will explain all the scatter in the data. In view of the uncertainties involved in using the SPM formula it is recommended that the SPM, Kamphuis and Readshaw formula preferably be used.

For coarse grained sediment ( $D_{50} > 1$  mm) 34 data points were available which yielded an approximate relationship:

$$I = 0,01 P_{ls} \quad (R^2 = 0,11)$$

Because of the considerable scatter evident in Figure 4 and very low  $R^2$ , this equation should only be used to obtain an order of magnitude of the transport. Again, no single relationship between  $K_s$  and the median grain size (or settling velocity) will explain all the scatter in the data.

#### REFERENCES

- Adachi, S., Sawaragi, T. and Ogo, A., 1959. The effects of coastal structures on the littoral sand drifts. Coastal Engineering in Japan, Vol. 2 : 85 - 98.
- Bagnold, R.A. (1963). Mechanics of marine sedimentation. The sea, Vol. 3, The earth beneath the sea. Hill, M.N. (Ed.). Inter-science Publ., New York, pp. 507-528.
- Bagnold, R.A. (1966). An approach to the sediment transport problem from general physics. U.S. Dept. of the interior, Geological Survey Prof. Paper 422-1. 37 pp.
- Bailard, J.A., 1981. "An energetics total load sediment transport model for a plane sloping beach," J. Geophysical Res., Vol. 86, no. c11, pp 10938-10954.
- Bailard, J.A. (1984). A simplified model for longshore sediment transport. 19 I(ternational Conf. on Coastal Eng, Houston, Texas, Vol 2: 1454-1470.
- Bailard, J.A. (1985). Simple models for surfzone sediment transport. NCEL technical note N-1740. Naval Civil Eng. Lab., Port Hueneme California.
- Bijker, E.W., 1968. Littoral drift as a function of waves and current. Proc. 11th International Conf. on Coastal Eng., ASCE, London. Vol 1 : 415-435.
- Bodge, K.R., 1986. Short-term impoundment of longshore sediment transport. Ph.D. thesis, University of Florida, Gainesville. 346 pp.
- Brampton A and Motyka J M (1984). Modelling the plan shape of shingle beaches. Estuarine Studies, Vol. 12, Springer Verlag.
- Bruno, R.O., Dean R.G., Gable, C.G. and Walton, T.L., 1981. Longshore sand transport study at Channel Islands Harbor, California. Technical paper no. 81-2, CERC, U.S. Army Corps of Engineers, Fort Belvoir. 48pp.
- Caldwell, J.M., 1956. Wave action and sand movement near Anaheim Bay, California. U.S. Army, Beach Erosion Broad, Tech. Memorandum 68. 21pp.
- Castanho, J., 1966. Rebentação das ondas e transporte litoral. Laboratorio Nacional de Engenharia Civil, Lisbon, Paper No. 275. (in Portuguese) 278pp.
- Chadwick, A.J., 1989. Field measurements and numerical model verification of coastal shingle transport. Advances in Water Modelling and Measurement, Palmer, M H (ed.), BHRA,

- Cranfield, Bedford.
- Chang, T.T. and Wang, Y.H., 1978. Field verification of sediment transport model. Proc. 26th Specialty Conf. of Hydraulics Div., ASCE, University of Maryland, Maryland. pp. 737-744.
- Dean, R.G., 1978. Review of sediment transport relationships and the data base. Proc. of a workshop on coastal sediment transport with emphasis on the National Sediment Transport Study, DEL-SG-15-78. Sea Grant College Program, Univ. of Delaware, Newark, Delaware, pp. 25-39.
- Dean, R.G., Berek, E.P., Bodge, K.R. and Gable, C.B., 1987. NSTS measurements of total longshore transport. Proc. of Coastal Sediments '87, New Orleans, Louisiana, Vol. 1 : 652-667.
- Dean, R.G., Berek, E.P., Gable, C.G. and Seymour, R.J., 1982. Longshore transport determined by an efficient trap. Proc. 18th International Conf. on Coastal Engineering, ASCE, Cape Town. Vol. 2 : 954-968.
- Delorme, J.-L., 1981. Erosion des côtes due à des travaux portuaires et mesures visant à y remédier. Permanent International Association of Navigation Congresses, Edinburgh (in French). Vol. 5 : 771-797.
- Duane, D.B. and James, W.R., 1980. Littoral transport in the surf zone elucidated by a Eulerian sediment tracer experiment. J. Sedimentary Petrology, Vol. 50 (No. 3) : 929-942.
- Fairchild, J.C., 1977. Suspended sediment in the littoral zone at Ventnor, New Jersey, and Nags Head, North Carolina. U.S. Army, Coastal Eng. Research Center, Fort Belvoir, Report TP 77-5. 97pp.
- Fleming, C A, Pinchin, B M and Nairn R B (1986). Evaluation of models of nearshore processes. 20 Intern. Conf. on Coastal Eng., ASCE, Taipei, Taiwan, Volume 2: 1116-1131.
- Gable, C.B., 1981. Report on data from the nearshore sediment transport study experiment at Leadbetter Beach, Santa Barbara, California, Jan-Feb, 1980. Institute of Marine Resources, University of California, IMR Report No. 80-5.
- Hou, H., 1988. Study of shelf waves vs. sand drift in NW coast of Taiwan. Proc. 21st International Conf. on Coastal Eng., ASCE, Malaga. Vol.2 : 1152-1165.
- Hou, H., Lee, C. and Lin, L., 1980. Relationship between alongshore wave energy and littoral drift in the midwest coast at Taiwan. Proc 17th International Conf. on Coastal Eng., ASCE, Sydney. Vol. 2 : 1255-1274.
- Inman, D.L. and Bagnold, R.A. (1963). Littoral processes. The Sea, Vol. 3, The earth beneath the sea. Hill, M.N. (Ed.) Interscience Publ., New York, pp. 529-551.
- Inman, D.L., Zampol, J.A., White, T.E., Hanes, D.M., Waldorf, B.W. and Kastens, K.A., 1980. Field measurements of sand motion in the surf zone. Proc. 17th International Conf. on Coastal Eng., ASCE, Sydney. Vol. 2 : 1215-1234.
- Ishihara, T., Iwagaki, Y. and Murakami, M., 1958. On the investigation of beach erosion along the north coast of Akashi Strait. Coastal Eng. in Japan, Vol. 1 : 97-109.
- Kamphuis, J W and Readshaw, J S (1978). A model study of alongshore sediment transport rate. 16th International Conf. on Coastal Eng, Hamburg. Vol. 2: 1656-1674.
- Kamphuis, J.W., Davies, M.H., Nairn, R.B. and Sayao, O.J., 1986. Calculation of littoral sand transport rate. Coastal Engineering, Vol. 10 : 1-21.
- Kana, T.W., 1977. Suspended sediment transport at Price Inlet, S.C. Proc. of Coastal Sediments '77. Charleston. pp. 366-382.
- Kana, T.W. and Ward, L.G., 1980. Nearshore suspended sediment load during storm and post-storm conditions. Proc. 17th International Conf. on Coastal Eng., ASCE, Sydney. Vol. 2 : 1158-1173.
- Knoth, J.S. and Nummedal, D., 1977. Longshore sediment transport using fluorescent tracer. Proc. of Coastal Sediments '77, Charleston. pp. 383-398.
- Komar, P.D., 1969. The longshore transport of sand on beaches. Ph.D thesis, Scripps Institute of Oceanography, University of California, San Diego.
- Komar, P.D., 1988. Environmental controls on littoral sand transport. 21st International Conf. on Coastal Eng., ASCE, Malaga. Vol. 2 : 1238-1252.
- Komar, P.D. and Inman, D.L., 1970. Longshore sand transport on beaches. J. Geophys. Res., Vol. 76 (No. 30) : 5914-5927.

- Kooistra, J. and Kamphuis, J.W., 1984. Scale effects in alongshore sediment transport rates. Canadian Coastal Sediment Study, Report No. C2S2-13. Kingston.
- Kraus, N.C., Isobe, M., Igarashi, H., Sasaki, T.O. and Horikawa, K., 1982. Field experiments on longshore sand transport in the surf zone. Proc. 15th International Conf. on Coastal Eng., Cape Town, ASCE, Vol. 2 : 969-988.
- Lee K.K., 1975. Longshore currents and sediment transport in west shore of Lake Michigan. Water Resources Research. Vol. II, No. 6 : 1029-1032.
- Laubscher, W.I., Schoonees, J.S. and Swart, D.H., 1989. A calibrated longshore sediment transport model for Richards Bay. CSIR Report EMA-C 89121, Ematek, Stellenbosch.
- Moore, G.W. and Cole, J.Y., 1960. Coastal processes in the vicinity of Cape Thompson, Alaska. Geologic investigations in support of Project Chariot in the vicinity of Cape Thompson, Northwestern Alaska - Preliminary Report. Final Report U.S. Geol. Survey Trace Elements Investigations, Report No. 753.
- Nicholls, J.N. and Wright, P., 1991. Longshore transport of pebbles: Experimental estimates of K. Proc. of Coastal Sediments '91, ASCE, Seattle. Vol. 1 : 920-933.
- Readshaw, W.J.S. (1979). A model study of alongshore sediment transport M.Sc. thesis, Dept. of Civil Engineering, Queen's University, Kingston.
- Sato, S., 1962. Sand movement at Fukue Coast in Atsumi Bay, Japan, and its observation by radioactive glass sand. Coastal Eng. in Japan, Vol. 5 : 81-92.
- Sato, S. and Tanaka, N., 1966. Field investigation on sand drift at Port Kashima facing the Pacific Ocean. Proc. 10th International Conf. on Coastal Eng., ASCE, Tokyo. Vol. 1 : 595-614.
- Schoonees, J S (1994). Longshore sediment transport in terms of the applied wave power concept. PhD thesis, University of Stellenbosch, Stellenbosch (in preparation).
- Schoonees, J S and Theron, A K (1993). Review of the field data base for longshore sediment transport. Coastal Engineering 19:1-25.
- Scripps Institute of Oceanography (1947). A statistical study of wave conditions at five locations along the California Coast. University of California, San Diego, Wave Report no. 68.
- Sireyjol, P., 1964. Communication sur la construction du port de Cotonou (Dahomey). Proc. 9th International Conf. on Coastal Eng., ASCE, Lisbon, (in French) pp. 580-595.
- Swart, D H (1976). Predictive equations regarding coastal transports. 15th International Conf On Coastal Eng, Honolulu, Hawaii. Vol 2: 1113-1132.
- U.S. Army, Corps of Engineers, 1984. Shore Protection Manual, Volumes I and II, Coastal Engineering Research Center, Vicksburg.
- Van Hijum, E and Pilarczyk, K W (1982). Equilibrium profile and longshore transport of coarse material under regular and irregular wave attack. Publikasie Nr 274. Delft Hidroulika-laboratorium, Delft, Holland.
- Van Rijn, L.C. (1984). Sediment transport, Part I: Bed load transport. J. Hydr. Eng., ASCE, Vol. 110 (10): 1431-1456.
- Vitale, P. (1981). Movable-bed laboratory experiments comparing radiation stress and energy flux factor as predictors of longshore transport rate. U.S. Army Coastal Eng. Res. Center, Fort Belvoir, Miscellaneous Report No. 81-4. 94 pp.
- Voitsekhovich, O.V., 1986. Longshore sediment transport - generalized relations and observation data. Ukrainian State Planning, Surveying, and Scientific-Research Institute of Water-Management Construction. Translated from Vodnye Resursy, No. 5, September - October, 1986, pp. 108-115.
- Wang, Y-H and Chang, T.H., 1978. Littoral drift along bayshore of a barrier island. Proc. 16th International Conf. on Coastal Eng., ASCE, Hamburg. Vol. 2 : 1614-1625.
- Watts, G.M., 1953. A study of sand movement at South Lake Worth inlet, Florida. U.S. Army, Beach Erosion Board, Tech. memo No. 42. 24 pp.

**TABLE 1: DATA SET 1**

Data set no.	Reference(s)	Location	No of points	Point rating (%)
1	Caldwell (1956)	Anaheim Bay California	5	46
2	Watts (1952)	South Lake Worth	3	42
4	Adachi <i>et al</i> (1959)	Miyazu Japan	8	24
5	Moore and Cole (1960)	Cape Thompson Alaska	1	50
6	Delorme (1981)	North & Central Africa	5	49
8	Sireyjol (1964)	Cotonou Benin	1	51
9	Castanho (1966)	Lobito Angola	2	52
10	Fairchild (1977)	Ventnor (NJ) Nags Head (NC)	2	36 37
12	Bijker (1968)	Ivory Coast Abidjan	1	19
13	Komar and Inman (1970)	El Moreno & Silver Strand	11	62
14	Duane and James (1980)	Point Mugu California	1	56
16	Lee (1975)	Lake Michigan	8	57
17	Kana (1977)	Price Inlet South Carolina	25	48
18	Bruno <i>et al</i> (1981)	Channel Islands Harbour	18	55, 67
21	Inman <i>et al</i> (1980)	Torrey Pines California	2	64
22	Kana and Ward (1980)	Duck North Carolina	2	57
23	Gable (1981) Dean <i>et al</i> (1982)	Leadbetter Santa Barbara	9	68
28	Kooistra and Kamphuis (1984)	Pointe Sapin Canada	2	60, 71
29	Bodge (1986)	Duck North Carolina	8	56,57,61
32	Voitsekhovich (1986)	Ros. Pri. Kin. Black Sea	39	58
33	Chadwick (1989)	Shoreham Sussex England	7	57,60

**TABLE 2: DATA SET 2**

Data Set 1 plus the following data:

Data set no.	Reference(s)	Location	No of points	Point rating (%)
3	Ishihara <i>et al</i> (1958)	North Akashi Miyazu	10 7	37
7	Sato (1962)	Fukue, Atsumi Japan	5	61
11	Sato and Tanaka (1966)	Port Kashima Japan	2	58
15	Hou <i>et al</i> (1980)	Taichung Harbour Taiwan	4	57
19	Chang and Wang (1978) Wang and Chang (1978)	Santo Rosa Island (Bayside)	35	55
20	Knoth and Nummedal (1977)	North Bull Island	5	52
24	Dean <i>et al</i> (1987)	Rudee inlet Virginia	3	63
25	Nicholls and Wright (1991)	Southern England H. Bury Long Beach Hurst Castle Spit	6	48
26	Kraus <i>et al</i> (1982)	Shi. Hir. Aji. Oar. Japan	12	63
30	Laubscher <i>et al</i> (1989)	Richards Bay South Africa	5	54
34	Hou (1988)	Lin-Kou Northwest Taiwan	1	58

**TABLE 3: RELATIVE STANDARD ERROR OF ESTIMATE ( $\sigma$ ) AND PERCENTAGE OCCURRENCE OF THE DISCREPANCY RATIOS ( $r_d$ ) FOR EACH FORMULA**

NAME OF FORMULA	NUMBER OF DATA POINTS	$\sigma$	PERCENTAGE OCCURRENCE OF $r_d$ BETWEEN:	
			0,5 and 2	0,25 and 4
SPM	119	0,708	42,0	58,0
SPM and Swart	119	0,720	42,0	58,0
SPM, Kamphuis and Readshaw	123	0,515	65,0	95,1
SPM and Bailard (bulk transport rate)	119	0,741	46,2	66,7
Watts	123	0,685	42,2	65,0
Caldwell	123	0,579	56,1	75,6

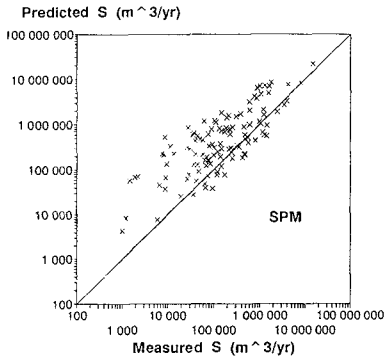


Figure 1: Predicted longshore transport rates versus measured rates for the SPM formula.

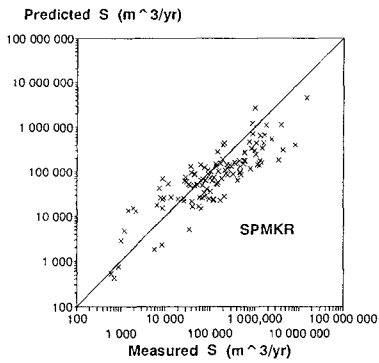


Figure 2: Predicted longshore transport rates versus measured rates for the SPM, Kamphuis and Readshaw formula.

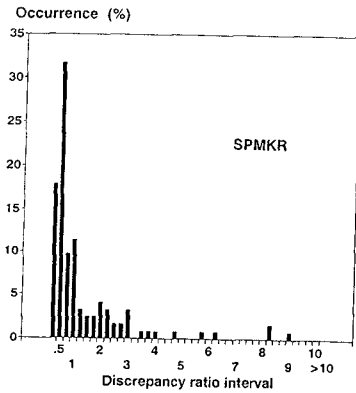


Figure 3: Histogram of the discrepancy ratios for the SPM, Kamphuis and Readshaw formula.

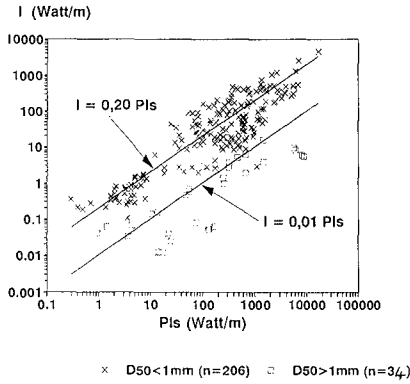


Figure 4: Immersed weight longshore transport rate ( $I$ ) versus wave energy flux factor ( $P_b$ ) for Data Set 2.

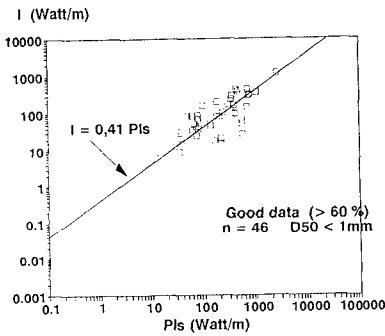


Figure 5:  $I$  versus  $P_b$ , only for data with a point rating of 60% or more.

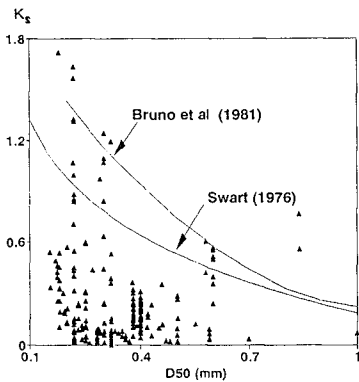


Figure 6: Coefficient ( $K_s$ ) in  $I = K_s P_b$  versus median sediment diameter ( $D_{50}$ ).



## CHAPTER 189

# FIELD VERIFICATION OF A NUMERICAL MODEL OF BEACH TOPOGRAPHY CHANGE DUE TO NEARSHORE CURRENTS, UNDERTOW AND WAVES

Takuzo Shimizu <sup>1</sup>, Masahito Tsuru <sup>1</sup> and Akira Watanabe <sup>2</sup>

### ABSTRACT

A practical method for estimating the undertow velocity and its direction is developed and verified on the basis of field measurement data. It is found that a simple vector addition of nearshore current and undertow gives a good approximation.

The actual bottom topography change during a year is simulated by the 3-D beach evolution model taking into account the cross-shore sediment transport due to waves and undertow as well as the transport due to nearshore currents. The results of both measurements and calculations show that the sediment transport due to nearshore current is predominant and the contribution of cross-shore sediment transports is cancelled for a long-term beach evolution.

### INTRODUCTION

The sediment transport due to nearshore currents plays a predominant roll on the long-term beach evolution and the contribution of cross-shore sediment transports due to waves and undertow is usually cancelled for a long period beyond approximately a year. In many cases for prediction of long-term beach topography changes due to construction of a coastal structure, only the sediment transport due to nearshore currents is taken into account. The shoreline model based on this concept is also widely used in practice. Therefore, the 3-D beach evolution model which treats only the sediment transport due to nearshore currents, can be regarded as an improved version of the shoreline model, which has

---

<sup>1</sup>Penta-Ocean Construction Co. Ltd. , 2-2-8 Koraku, Bunkyo-ku, Tokyo 112, Japan.

<sup>2</sup>Professor, Dept. of Civil Eng., Univ. of Tokyo, 7-3-1 Hongo, Bunkyo-ku, Tokyo 113, Japan.

an advantage of predicting the spatial beach topography changes.

In recent years, we have applied the 3-D beach evolution model based on this concept to many practical problems and presented a few attempts to quantitatively demonstrate its field applicability through comparisons with the actual topographical changes around harbors (e.g. Shimizu et al., 1990). It is well known, on the other hand, that the offshoreward sediment transport due to undertow in the surf zone and the onshoreward sediment transport due to sheet flow movement outside the surf zone causes a considerable beach profile change and form a bar during the storm. Most of the previous studies on the undertow and its effects on beach profile changes have been conducted mainly through laboratory experiments and are not thoroughly discussed on the basis of field measurement data.

In this study, at first, we discuss the undertow velocity and its direction through comparisons between the field measurement data and the calculated nearshore currents and, then, discuss their practical estimation method. We also try to simulate the actual bottom topography changes during approximately a year by taking into account the cross-shore sediment transport due to waves and undertow as well as the sediment transport due to nearshore currents.

## FIELD INVESTIGATION

Fig. 1 shows the bottom topography of the investigation site and the calculation area which is 0.9km long in the alongshore direction and 1.0km long in the cross-shore direction with the grid spacing of 12.5m. The field investigation site is located at the end of a sandy pocket beach. The bottom slope is approximately 1/40. A part of the shore is bounded directly by the sea cliff, and the bottom slope is steep near the shoreline. The bottom contours are straight and parallel to the shoreline outside the harbor, and they extend offshoreward like a tongue around the harbor entrance owing to extreme accretion caused by nearshore currents. The seabed material is well-sorted fine sands in the nearshore region where the water depth is less than 10m, and the grain diameter is approximately 0.35mm.

The field observation was carried out over a period of approximately one month during the winter stormy season, in order to obtain the data for verification of the numerical models for estimation of nearshore waves and currents. At Points 1 to 4 with the water depth of about 5m, the mean currents including nearshore currents and undertow and principal wave direction were measured at the level of 0.7m above the bottom by using electro-magnetic current meters. At Points 2 and 4, nearshore waves were also measured by pressure sensors attached to the electro-magnetic current meters. The incident wave conditions were also measured at Point 0 with the water depth of 20m by using a combination of an ultrasonic wave gauge and an electro-magnetic current meter. Data were recorded with the sampling interval of 0.5 seconds during 10 minutes every 2 hours. The pressure fluctuations obtained by a pressure sensor were converted into water

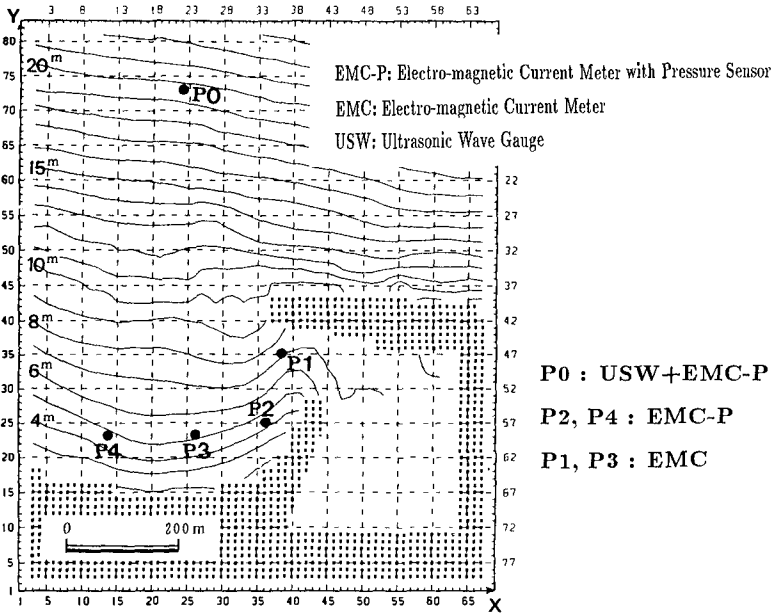


Fig. 1 Bottom topography and calculation area of investigation site.

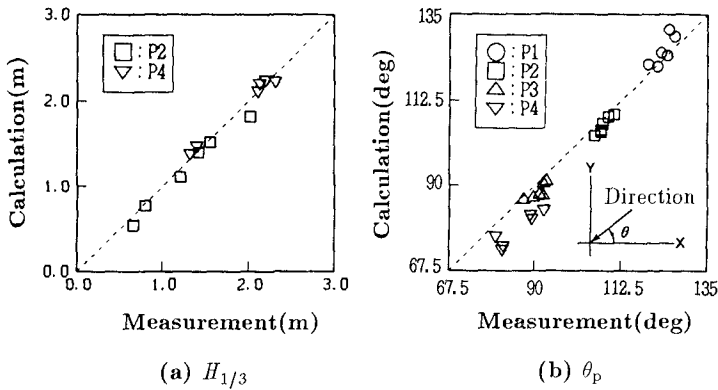


Fig. 2 Comparisons between the measured and the calculated significant wave heights and principal directions.

surface motion on the basis of the small amplitude wave theory. During the observation, storm waves greater than 3m in significant wave height attacked twice. The maximum significant wave height was 4.2m and its period was 9.6s.

## VERIFICATION OF WAVE MODEL

### The Employed Wave Model

The parabolic-type equation model proposed by Isobe(1987) is employed in this study to properly estimate the wave field around the harbor entrance where combined diffraction and refraction occur. This basic equation is derived from the mild slope equation and the energy dissipation term due to wave breaking is included. The parabolic-type equation model has advantages that much computational time can be saved owing to the forward stepping scheme, and then, treatment of multi-directional irregular waves is easy. Random waves are described as a superposition of component regular waves with different frequencies and directions.

In order to improve the accuracy of calculating the wave transformation for a wide range of propagation directions of component waves, a curvilinear coordinate system is introduced. In this model, the curvilinear coordinates are defined from the peak frequency and the peak direction of the directional wave spectrum. In a shadow region, additional wave rays are radiated from the tip of the breakwater. The applicabilities of the model to the actual wave field over complicated bottom topographies were verified through comparisons with field measurement data (Shimizu et al., 1992, 1994).

### Comparison of Wave Height and Direction

In order to compare the calculations with the measurements, the incident wave conditions measured at Point 0 are classified into three cases in accordance with the wave height level ( $H_{1/3}$  (P0):  $\sim 2.0\text{m}$ ,  $2.0 \sim 3.0\text{m}$ ,  $3.0\text{m} \sim$  ) and two cases of wave direction, the righthand side and the lefthand side directions to that perpendicular to the shoreline. For totally six cases of incident wave conditions, the mean values of significant wave height and principal direction were calculated at all measurement points. And these values were adopted as the field verification data. The numerical calculations were also conducted for the mean significant waves of these six cases, using the Bretschneider-Mitsuyasu frequency spectrum and the Mitsuyasu-type directional distribution function.

Fig. 2 (a) and (b) show the comparisons between the measured and the calculated significant wave heights and principal directions. The calculations of both significant wave height and principal direction by the parabolic-type equation model show fairly good agreements with the measurements.

## VERIFICATION OF UNDERTOW AND NEARSHORE CURRENT MODEL

**Field Observation Results**

Fig. 3 (a) shows an example of the comparisons between the measured steady component vectors of near-bottom velocity and the calculated nearshore current vectors under the same wave condition with the significant wave height of 3.5m. The bold vectors are measurements and illustrated in a different scale from the calculated vectors. In calculating the nearshore current field of random waves, the radiation stress is evaluated as for a regular wave with the equivalent wave energy and the principal direction.

During the storm, the wave-induced nearshore circulation develops around the harbor entrance behind the main breakwater. Extreme accretion around the harbor entrance is caused mainly by this nearshore circulation. Around the harbor entrance, the calculated nearshore current field satisfactorily reproduces the observed dominant nearshore circulation.

On the contrary, at Point 4 where there is no influence of diffraction due to breakwater, when the significant wave height becomes larger than 2m and

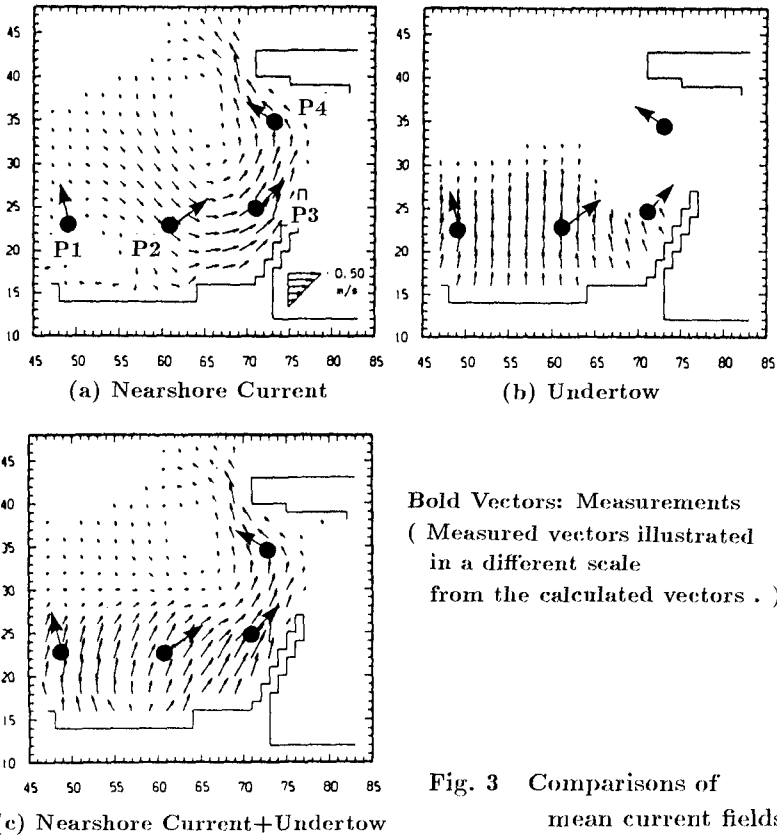


Fig. 3 Comparisons of mean current fields.

the measurement point is involved in the surf zone, the remarkable offshoreward mean currents occur and the velocity becomes larger than 0.3m/s. Even at Point 3 where the nearshore circulation occur, the mean current vector slightly inclines offshoreward. The sensors of the electro-magnetic current meters were installed at the level of 0.7m above the bottom and at the water depth of about 5m and, then, they were always located under the trough level. The observed offshoreward mean current, therefore, seems to be due to undertow.

**Estimation Method of Undertow**

The undertow velocity is estimated as the sum of the return flows compensating for the onshore mass flux due to breaking bores and due to irrotational wave motion and the Eulerian mass transport velocity. We adopt the following rough estimation of the undertow velocity due to breaking bores after Sato et al.(1988).

$$U_b = -A \frac{H^2}{d \cdot T} \tag{1}$$

where  $A$  is a nondimensional coefficient,  $H$  the wave height,  $d$  the water depth and  $T$  the wave period. For random waves, assuming that only breaking waves contribute to generation of return flow,  $H^2$  is replaced by the breaking wave energy  $E_b/(\rho g/8)$ .

$$\frac{E_b}{\rho g/8} = \int_{x_b}^{\infty} H^2 p(\xi) d\xi = H_{rms}^2 \cdot P_b \tag{2}$$

$$P_b = (1 + x_b^2) \exp(-x_b^2) \tag{3}$$

where  $x_b = H_b/H_{rms}$  and  $P_b$  is the probability of wave breaking which is estimated by assuming the Rayleigh distribution for individual waves. The root mean square wave height  $H_{rms}$  is estimated by not taking into account the wave breaking. The breaking wave Height  $H_b$  is evaluated by using the appropriate coefficient value, 0.14 in the wave breaker indices for regular waves proposed by Goda(1970). If the breaking wave energy estimated by this equation becomes larger than that estimated by the parabolic equation model with the additional term of energy dissipation due to wave breaking, the breaking wave energy is set to be the value estimated by the parabolic equation model.

In this study, it is assumed that the near-bottom mean current vector can be estimated by a simple vector addition of the nearshore current vector and the undertow vector after Svendsen and Lorenz(1989). The undertow vectors are given in the opposite direction of the local wave propagation.

**Comparison of Undertow Due to Breaking Bores**

Fig. 4 shows the relationship between the measured undertow velocity due to breaking bores  $U_b$  and the estimated values of  $(H^2/d \cdot T)$ , in order to calibrate the nondimensional coefficient  $A$ . The nearshore current vectors are given by the numerical calculations. The measured undertow velocity due to breaking bores  $\vec{U}_b$  is evaluated by extracting the calculated nearshore current vector  $\vec{U}_c$ , the calculated return flow vector due to irrotational wave motion  $\vec{U}_w$  and the calculated

Eulerian mass transport velocity  $\vec{U}_e$  from the measured steady component vector of near-bottom velocity variation  $\vec{U}_m$ .

$$\vec{U}_b = \vec{U}_m - \vec{U}_c - (\vec{U}_w + \vec{U}_e) \quad (4)$$

The appropriate value of nondimensional coefficient  $A$  is found to be 5.6 through comparisons of the calculations with the measurements. This result is the same as the value obtained by Sato et al.(1988).

Fig. 5 shows the examples of the calculated cross-shore distributions of the significant wave height  $H_{1/3}$ , the breaking wave energy  $E_b$  and the undertow velocity  $U$  under the incident wave conditions with the significant wave height of 2.6m and 3.5m. The calculation results show that the undertow velocity increases exponentially and has a peak in the surf zone. The calculated wave heights and undertow velocities agree well with the measurements at Point 4.

### Comparison of Mean Current

Fig. 3 (a) to (c) show the calculated mean current fields of nearshore current, undertow and the vector addition of both currents. Not only the nearshore circulation around the harbor entrance, but also the measured mean currents due to combined undertow and nearshore current are reproduced well by the simple vector addition. At Points 1 and 2 in the shadow region of the breakwater, the undertow velocity is small. At Points 3 and 4, on the other hand, where the incident waves directly attack, the undertow must be taken into account in order to properly estimate the mean current field during a storm.

Fig. 6 (a) and (b) show the comparisons between the measured and the calculated mean current velocities and between the measured and the calculated mean current directions at all measurement points. The open symbols indicate the calculations of only nearshore current, and the solid symbols indicate the calculations of a vector addition of nearshore current and undertow.

The calculations are the results conducted for the mean values of the incident significant waves observed at Point 0 for six cases in accordance with the incident wave height levels and the principal wave directions. The measurements are the mean values for six cases at each point. By a simple vector addition of nearshore current and undertow, both the calculated mean current velocity and its direction show fairly good agreements with the measured ones. The method for estimating the near-bottom mean current in the surf zone employed in this study is a simple and primitive, but it has enough accuracy for practical use.

## VERIFICATION OF BEACH EVOLUTION MODEL

In order to verify the field applicability of the 3-D beach evolution model. We tried to reproduce the long-term topography changes around the harbor entrance during a year. Before completion of the construction of breakwaters, the bottom contours are parallel, and after the completion, they stretched like a tongue along

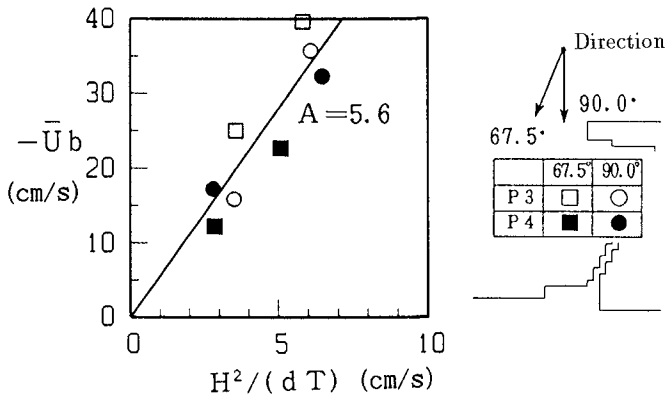


Fig. 4 Relationships between the undertow velocity due to breaking bores  $U_b$  and  $(H^2/d \cdot T)$ .

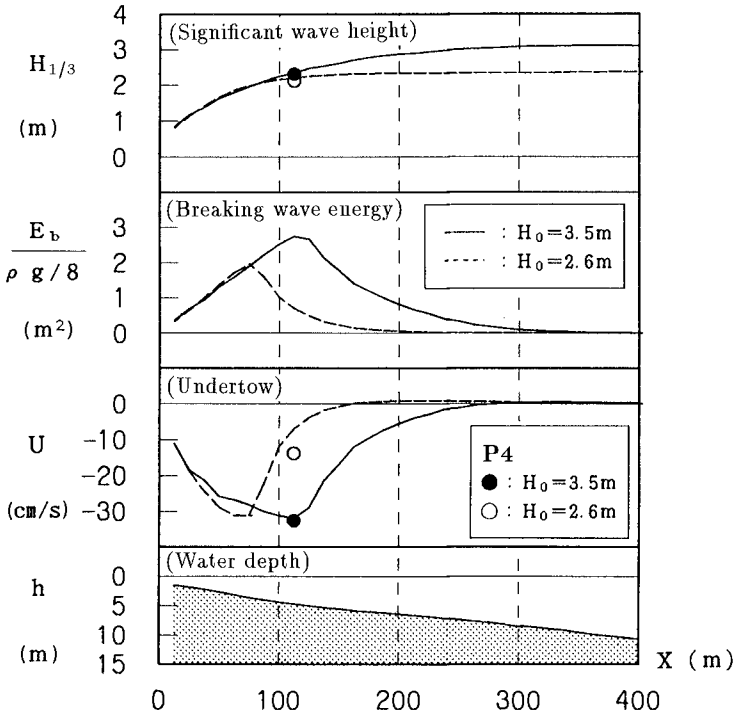


Fig. 5 Distributions of  $H_{1/3}$ ,  $E_b$  and  $U$  (Undertow).



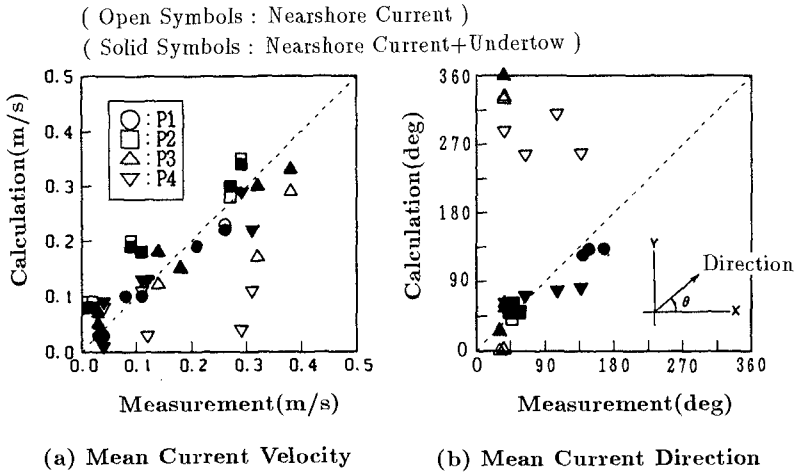


Fig. 6 Comparisons between the measured and the calculated mean current velocities and directions.

the sub-breakwater to the harbor entrance mainly owing to the nearshore circulation.

**Sediment Transport Formula**

The local sediment transport rate formula employed in this study is the formula proposed by Watanabe et al.(1986). The formula for local sediment transport rate under combined wave-current action is formulated so as to be consistent with previous studies on both longshore drift and cross-shore sediment transport. The transport rate  $\vec{q}$  is divided into  $\vec{q}_c$  due to mean currents and  $\vec{q}_w$  due to waves. These formulas are based on the power model concept and assume that the sediments set in motion by the excess shear stress under combined wave-current action are transported with both mean currents and wave motion into the respective directions.

$$\vec{q}_c = A_c(\tau - \tau_c)\vec{U}/\rho g \tag{5}$$

$$\vec{q}_w = A_w F_D(\tau - \tau_c)\vec{u}_b/\rho g \tag{6}$$

where  $A_c$  and  $A_w$  are nondimensional coefficients,  $\vec{U}$  the current velocity vector,  $\vec{u}_b$  the maximum near-bottom orbital velocity vector,  $F_D$  a direction function for wave-induced net transport,  $\tau$  the maximum bottom shear stress in a wave-current coexistent system,  $\tau_c$  the critical shear stress for the onset of the general movement,  $\rho$  the water density, and  $g$  the gravity acceleration.

After Watanabe et al.(1991), the direction function for wave-induced net cross-shore sediment transport is set to be +1 for the onshoreward movements under

the Shields parameter less than 0.2 of the upper limit of bed load and larger than 0.5 of the onset of sheet flow movement, and is set to be -1 for the offshoreward movements of suspended load over ripples under the Shields parameter between 0.2 and 0.5. The bottom shear stress for a wave-current coexistent system is evaluated by the friction law proposed by Tanaka and Shuto(1981). The critical shear stress is calculated from the critical value of the Shields parameter, which is 0.11 for fine sands and 0.06 for coarse sands according to Watanabe et al.(1980).

The coefficient  $A_w$  in the formula for the transport due to wave action is related to another coefficient  $B_w$  in the formula for the wave-induced net sediment transport rate  $q_w$  proposed by Watanabe(1982), which is expressed as follows:

$$\phi = B_w(\psi - \psi_c)\psi^{1/2} \quad (7)$$

where  $\phi = (1 - \lambda_v)q_w/w_0D$  is a dimensionless net transport rate,  $D$ ,  $w_0$  and  $\lambda_v$  are the diameter, settling velocity and porosity of the sediment,  $\psi = \tau/(\rho_s - \rho)gD$  is the dimensionless shear stress or the Shields parameter,  $\rho_s$  and  $\rho$  are the densities of sediment and water, and  $\psi_c$  is the critical value of  $\psi$  for the onset of general movement of sediment.

The coefficient  $A_w$  is related to  $B_w$  as follows:

$$A_w/B_w = w_0\sqrt{f_w/2} / \{(1 - \lambda_v)s\sqrt{sgD}\} \quad (8)$$

where  $f_w$  is the wave friction factor.

In the previous studies under the field conditions conducted by Watanabe et al.(1991), the value of  $B_w$  is considered to be approximately 3.0 to 5.0, though the coefficient must be calibrated in the field application. In this study, the value of  $B_w$  is set to be 2.0 after several tries and errors, and the value of  $A_w$  changes depending on local wave conditions and properties of sea-bed material. The value of  $A_c$  is set by multiplying the value of  $A_w$  by 10.0 after Watanabe et al.(1991).

### Reproduction of Beach Topography Change

The numerical simulation was performed under a simply modelled series of wave conditions by repeating the calculations of waves, mean currents and beach topography changes. The wave conditions during the calibration period of approximately a year were replaced by the simply modelled four series of storms with the significant wave height larger than 2m as shown in Fig. 7. This modelled series of waves have the same occurrence frequency in total as that of the observed wave climate data.

Fig. 8 (a) shows the measured topographical changes and Fig. 8 (b) shows the calculated bottom topography changes by taking into account only the sediment transport due to nearshore currents. Remarkable accretion around the harbor entrance and erosion around Point 3 and at the tip of the breakwater due to nearshore circulation are reproduced satisfactorily. The results of both measurements and calculations show that the sediment transport due to nearshore current is predominant for the long-term beach evolution and that the contributions of

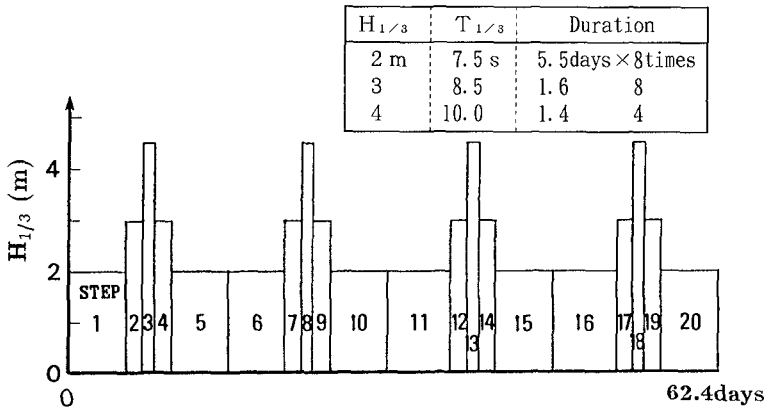


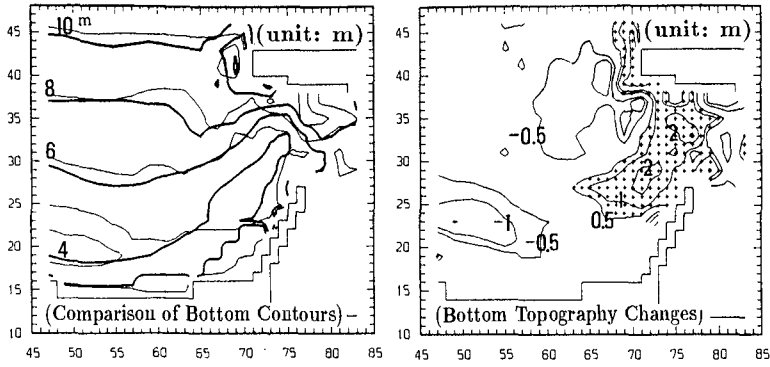
Fig. 7 Simply modelled series of incident wave conditions.

both the offshoreward sediment transport due to undertow and the onshoreward transport due to sheet flow are cancelled for a long-term beach profile change.

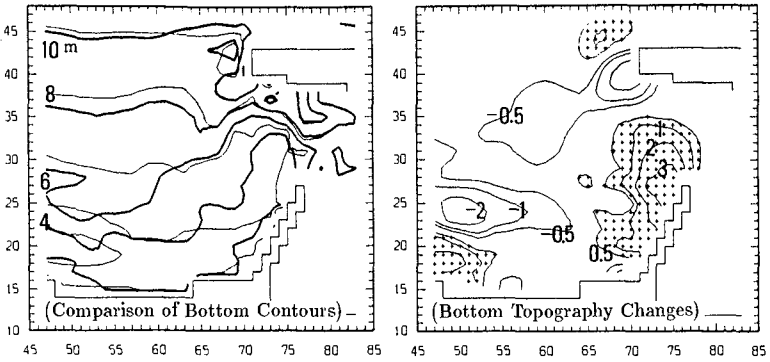
The difference between calculation and measurement is that the calculated result does not show such a sharp extension of the tongue-shaped bottom contours, for example the 4m contour, compared with the measurements. This fact suggests that the nearshore circulation is sharper and the width of fast current is narrower in the field than they are expected. In numerical calculation, however, it is difficult to reproduce such a sharp circulation as observed in the field, owing to the numerical diffusion.

Fig. 8 (c) shows the calculated bottom topography changes by taking into account the cross-shore sediment transport due to waves and undertow in addition to the transport due to nearshore currents. Around the harbor entrance, accretion due to nearshore current is reproduced well. In the area where waves attack directly and the cross-shore sediment transport is active during the storm, however, the measured topography changes are not reproduced well. In numerical calculation, the topographical changes due to cross-shore sediment transport is not cancelled even after a year.

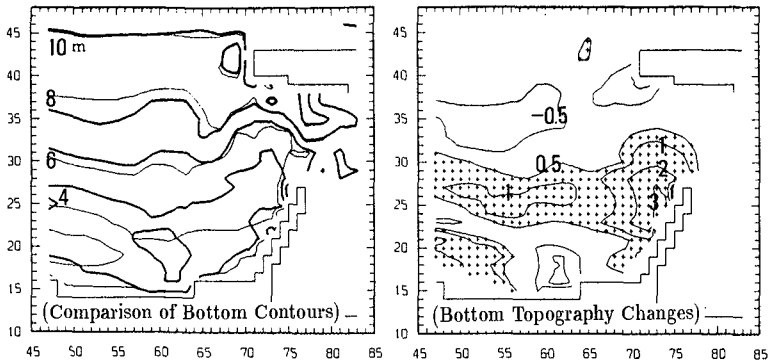
We, therefore, tried to investigate more precisely the calculation results. Fig. 9 shows the examples of calculated bottom topography changes after 3rd to 5th step during the decreasing period of the wave height. The upper figures show changes during each step, and the lower ones show the cumulative changes from the initial topography. The eroded area during 3rd step with the largest wave height is accreted during 4th step. And the eroded area during 4th step is accreted during 5th step. The eroded area near the shore due to severe waves is, thus, gradually buried and the accreted area moves onshoreward during the decreasing period of the storm. These results suggests that the wave-induced transport due to sheet flow and the flow-induced sediment transport due to undertow play an



(a) Measurement



(b) Calculation (Nearshore Current)



(c) Calculation (Nearshore Current+Undertow+Wave)

Fig. 8 Comparison of the calculated bottom contours and bottom topography changes during a year with the measured ones. (Fine Line: Initial Contour; Bold Line: Contour After a Year)

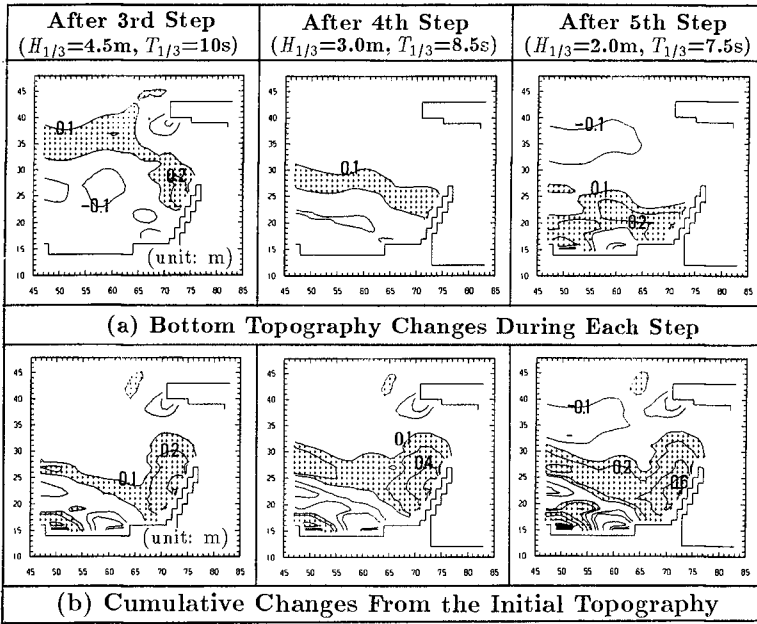


Fig. 9 Examples of calculated bottom topography changes by taking into account the sediment transport due to nearshore currents, undertows and waves.

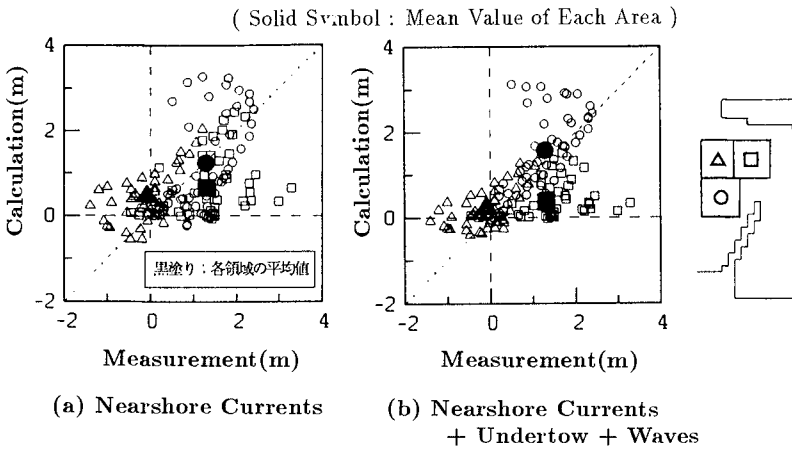


Fig. 10 Comparisons between the measured and the calculated bottom elevation changes.

important role in the short-term beach profile change.

The above tendencies of the actual beach profile change can be reproduced well by numerical simulation. However, the reason for disagreement of final topography after a year is that the modelled series of waves are not given continuously and the duration of each step is not appropriate. In order to properly estimate the beach profile changes due to cross-shore sediment transports, more detailed modelling of the storm is needed.

Fig. 10 shows the comparisons between the measured and the calculated bottom elevation changes. The solid symbols indicate the mean values in each area and the open symbols indicate those at each calculation point. Although the results at each point scatter a lot, the averaged values of each area around the harbor entrance show reasonable agreements in both cases.

## CONCLUSIONS

The results of this study are summarized as follows:

- (1) The parabolic equation model has a fairly good accuracy for estimating the random wave transformation such as combined diffraction, refraction and wave breaking.
- (2) The undertow was clearly observed through the field investigation. A simple vector addition of the nearshore current vector and the undertow vector has enough accuracy for practical use for estimating the near-bottom mean current in the surf zone.
- (3) For a long-term beach evolution, the measurement showed that beach profile changes due to cross-shore sediment transports were cancelled and the beach evolution can be reproduced satisfactorily by taking into account only the sediment transport due to nearshore currents. Further investigations are, however, needed for properly estimating the short-term beach profile changes due to waves and undertow as well as the long-term beach evolution due to nearshore currents.

## REFERENCES

- Goda, Y., 1970: A synthesis of breaker indices, *Trans. Japan Soc. Civil Engrs.*, Vol.2, Part2, pp.227-230.
- Isobe, M., 1987: A parabolic equation model for transformation of irregular waves due to refraction, diffraction and breaking, *Coastal Eng. in Japan*, Vol. 30, No. 1, JSCE, pp.33-47.
- Sato, S., M. Fukuhama and K. Horikawa, 1988: Measurements of near-bottom velocities under random waves on a constant slope, *Coastal Eng. in Japan*, Vol. 31, No. 2, JSCE, pp.219-229.

- Shimizu, T., H. Nodani and K. Kondo, 1990: Practical application of the three-dimensional beach evolution model, *Proc. 22nd Int. Conf. on Coastal Eng.*, ASCE, pp.2481-2494.
- Shimizu, T., A. Ukai and M. Isobe 1992: Field verification of numerical models for calculation of nearshore wave field, *Proc. 23rd Int. Conf. on Coastal Eng.*, ASCE, pp.590-603.
- Shimizu, T., A. Ukai, Y. Kubo and M. Shimada, 1994: Field applicability of wave models to estimating the wave fields outside and inside a harbor, *Proc. HYDRO-PORT'94*, pp.303-315.
- Svendsen, I.A. and R.S. Lorenz, 1989: Velocities in combined undertow and longshore currents, *Coastal Eng.*, Vol.13, pp.57-79.
- Tanaka, H. and N. Shuto, 1981: Friction coefficient for a wave-current coexistent system, *Coastal Eng. in Japan*, Vol.24, JSCE, pp.105-128.
- Watanabe, A., Y. Riho and K. Horikawa, 1980: Beach profile and on-offshore sediment transport, *Proc. 17th Int. Conf. on Coastal Eng.*, pp.1106-1121.
- Watanabe, A., 1982: Numerical models of nearshore currents and beach deformation, *Coastal Eng. in Japan*, Vol.25, JSCE, pp.147-161.
- Watanabe, A., K. Maruyama, T. Shimizu and T. Sakakiyama, 1986: Numerical prediction model of three-dimensional beach deformation around a structure, *Coastal Eng. in Japan*, Vol.29, JSCE, pp.179-194.
- Watanabe, A., T. Shimizu and K. Kondo, 1991: Field application of a numerical model of beach topography change, *Proc. of Coastal Sediments '91*, ASCE, pp.1814-1828.

## CHAPTER 190

### AN ATTEMPT TO MODEL LONGSHORE SEDIMENT TRANSPORT ON THE CATALAN COAST

J.P. Sierra, A. Lo Presti and A. Sánchez-Arcilla <sup>1</sup>

#### Abstract

In this work, the main variables involved in one-line shoreline evolution models have been identified and typical values for them have been found for different zones of the Catalan Coast. These values have been employed in a shoreline evolution model. The model has been calibrated in several points of the Catalan Coast, adjusting the free parameters in a longshore sediment transport formula. Taking into account the quality of the results, the model seems to be an efficient tool for medium term coastal engineering purposes.

#### 1. Introduction

The estimation of longshore transport rates is an important problem in coastal engineering, in order to predict shoreline changes when coastal structures are constructed and to consider shore protection methods without unexpected effects.

Beach changes are controlled by wind, waves, currents, sediment nature and water level among other variables, which are necessary data to estimate these changes. Given the complexity of beach processes, efforts should be made to identify and analyze all relevant physical data needed for an efficient evaluation and interpretation of beach evolution.

Many often these data are not available in the target site. This situation increases the number of unknowns which must be obtained by reasonable estimates or by adaptation and extrapolation from other projects on similar or adjacent coasts. These assumptions should be considered when interpreting computed results because they could induce erroneous or misleading estimated beach changes.

However, sometimes, the methods used for predicting longshore transport rates and beach evolution, over a medium-term period of time (several years),

---

<sup>1</sup> Laboratori d'Enginyeria Marítima (LIM/UPC), Universitat Politècnica de Catalunya. C/ Gran Capitán s/n, mòdul D-1, 08034 Barcelona, SPAIN.



fail in their predictions because the input parameters are not computed for local conditions and corrective procedures are not taken into account.

As an example, the Catalan Coast, located in the Mediterranean Sea, presents distinctive features from other coastal areas like Atlantic or Pacific ones. Among these features, we can mention beach slopes, grain size, tidal range (which is practically negligible) or the wave climate, which presents storms of smaller intensity than other zones due to the limited fetches.

For this reason, the input variables to predict longshore sediment transport rates and shoreline evolution should be expressed in terms of local parameters and conditions.

Therefore, the main goals of this paper are the characterization of input variables for shoreline models in terms of Catalonian coastal features and the application of the obtained results to the Catalan Coast in order to calibrate a shoreline evolution model.

## 2. Data employed

The Catalan Coast has a total length of 580 Km, 270 of them being sandy beaches. The northern part shows a predominance of rocky cliffs and reefs. In the central and southern areas, sandy beaches are dominant.

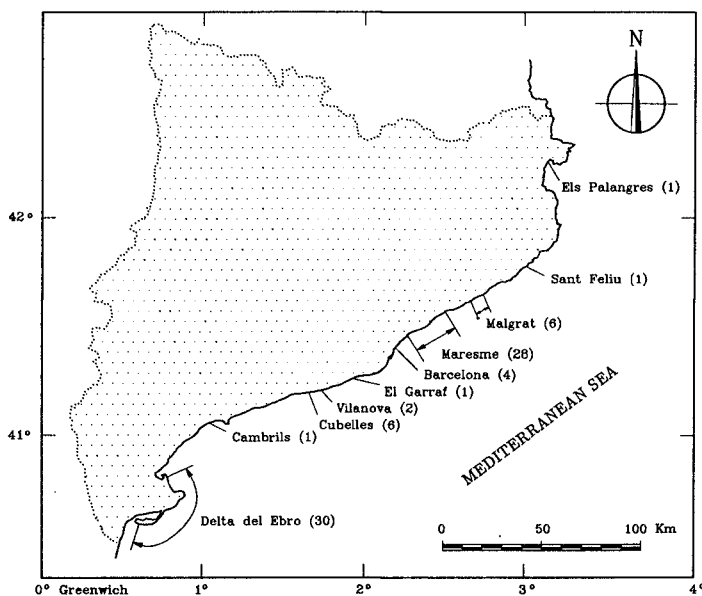


Figure 1. Location of the 82 beach profiles.

In this work, 82 beach profiles from the Catalan Coast have been used. These profiles are representative of 105.2 Km of beach (37.6% of the total length). In figure 1, the profile locations are shown.

The profile data have been obtained from several field measurement campaigns. Some of them are described in Serra et al. (1989, 1990) and Jiménez et al. (1992).

### 3. Variables characterization

The main variables involved in one-line shoreline evolution models are beach profile shape, closure depth, wave climate, sea level changes, sediment size, boundary conditions and interaction with coastal structures.

The boundary conditions and coastal structures will be defined in each individual case to be studied. On the other hand, sea-level fluctuations at geological and intermediate time scales have not been taken into account. Shorter recurrence intervals which are related to climatic effects, as e.g. daily tides, are practically negligible on the Mediterranean Sea, because tidal ranges are very small in this area (order of 20-30 cm). Other episodic events will not be considered either.

In this section, attention will be focused on the other mentioned variables and their characteristics along the Catalan Coast will be analyzed.

#### 3.1. Depth of closure

The depth of closure can be defined as the limit depth for appreciable longshore transport. It is a fundamental parameter in shoreline evolution models but it is difficult to quantify it.

Several expressions for the computation of the closure depth have been proposed. As an example, the Hallermeier (1978, 1981) expression has been widely used since it provides a guidance for the estimated closure depth:

$$d_{,e} = 2.28 H_e - 68.5 \left( \frac{H_e^2}{g T_e^2} \right) \quad (1)$$

where  $H_e$  is the wave height exceeded 12 hours a year,  $T_e$  is the associated wave period and  $d_{,e}$  is the estimated closure depth.

If possible, it would be better to determinate the closure depth from beach profile changes at the site, but the scarcity and accuracy of data is the main difficulty to estimate this parameter which has a statistical nature.

Based on the field measurements available from multiple profile surveys made over a 5 year period through the Catalan Coast, the depth of closure was estimated following a similar approach to the one employed by Kraus and Harikai (1983) on Oarai Beach. In this approach the closure depth was evaluated

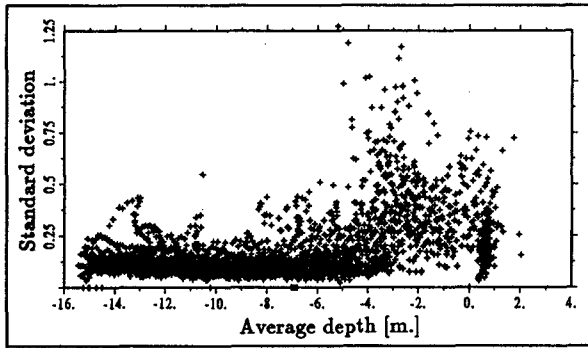


Figure 2. Depth changes

plotting the standard deviation of the measured depth values versus the average depth for the overall studied area, as it is shown in figure 2.

It can be observed that the most important deviations occur in depths shallower than 5.5-6 meters. On the other hand, if the closure depth is computed employing the Hallermeier expression (1) fed with the wave data from three existing buoys in the zone (as it will be explained later), the obtained values are of the same order of magnitude, as it can be seen in table 1.

Buoy	$H_e$	$T_e$	$d_{se}$
Tordera	3.5	7.3	6.4
Llobregat	3.2	7.4	5.9
Ebro	3.8	7.0	6.6

Table 1. Closure depths from Hallermeier expression

### 3.2. Beach profiles

The second analyzed variable is the beach profile shape. The aim here is the obtention of an analytical expression which provides the best possible representation of the equilibrium beach profile in the Catalan Coast.

Bruun (1954) based on the analysis of beach profiles for the North Sea and California Coast, developed an empirical equation with a potential function which relates water depth  $h$  and shoreline distance  $y$ .

$$h = A y^B \quad (2)$$

Later on, Bruun and other authors found theoretical justifications for this expression. Dean (1976, 1977), centering his study on linear wave theory and assuming that the ratio of breaking wave height to water depth is constant, justified from three different points of view this potential form for the equilibrium beach profile. He found a value of  $2/5$  or  $2/3$  for the exponent  $B$  and showed that the aforementioned equation with  $B = 2/3$  is consistent with uniform wave energy dissipation per unit volume across the surf zone. Other authors, who also adopted this equation, suggested a potential relationship between the shape parameter  $A$  and the grain size (Moore 1982, Hanson and Kraus, 1989).

The wide spread use of this profile equation, together with its simplicity, led to its application to numerous beaches, which present quite different characteristics from the beaches of United States Atlantic Coast. For this reason, the first step consisted in the evaluation of the Bruun-Dean expression fit to measured data. It was observed that this equation over-predicts depths, specially when the  $A$  parameter values of Moore (1982) are used (see figure 3).

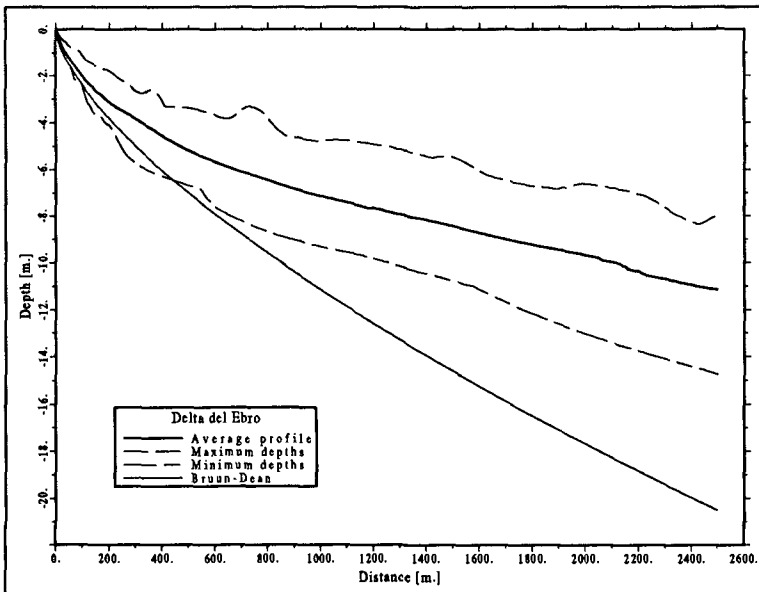


Figure 3. Bruun-Dean profile vs measured data in Ebro Delta area

Considering that the combination of the Bruun-Dean type profile with  $A$  values from Moore (1982) was not suitable for the available data, the following step consisted in the use of an inductive approach to find alternative expressions for the beach profile (Lo Presti, 1994; Sierra et al., 1994). The aim was to improve the fit with respect to the aforementioned equation for the Catalan Coast and to avoid an infinite slope at the shoreline.

This analysis of beach profile shapes was carried out with a purely statistical approach, without any in-depth analysis of the underlying physics. No attempt was made to relate the new profile expressions to the beach morphology or boundary conditions because of the limited number of surveyed profiles. The obtained expressions can be useful in the characterization of beach profiles for site-specific applications. It should be stressed that no attempt is here made to predict the actual beach shape parameters.

The selection of alternative expressions is based on the previous knowledge of general profile shapes. Two alternative expressions have been proposed for the equilibrium beach profile.

i) Exponential equation:

$$e^z = A(y + C)^B \quad (3)$$

ii) Rational equation:

$$z = \frac{y}{A + By} \quad (4)$$

Both equations will be compared with the power-law (potential) expression:

$$z = Ay^B \quad (5)$$

where  $z$  is the water depth,  $y$  the distance to the shoreline and  $A$ ,  $B$  and  $C$  are parameters to be determined.

In order to find the best fit curve, a suitable transformation of variables has been carried out followed by a straight line regression analysis using the least squares method. The curve that provides the best fit to the measured data is the one which shows the minimum vertical distance (or prediction error) to them.

Taking into account the prediction errors of the expressions, in the major part of the 82 profiles it has been observed that both proposed expressions (exponential and rational) fit better to the measured data than power-law equations. Moreover, the differences in fit quality between both expressions are minimal, as it can be observed in figures 4 and 5. These figures show, as an example, the fit of the three expressions to two different measured beach profiles. A potential expression with  $B = 2/3$  has also been plotted and referred with (D). The measured beach profiles are drawn with continuous line.

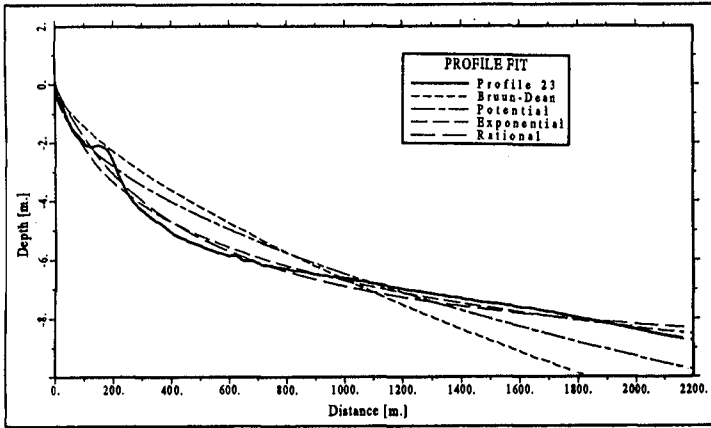


Figure 4. Fit of one profile in Ebro Delta area

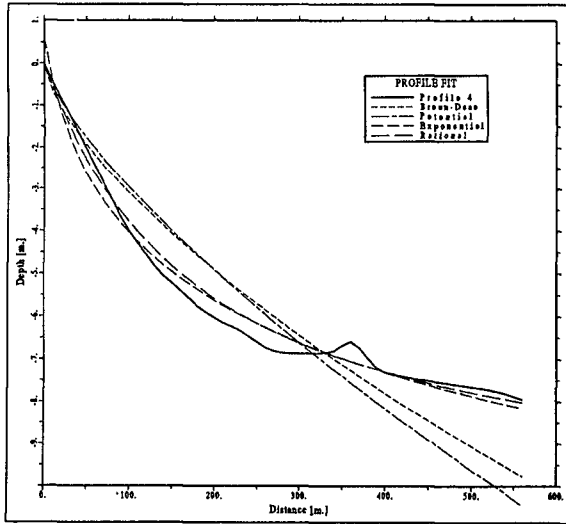


Figure 5. Fit of one profile in Maresme area

### 3.3. Sediment size

The next studied variable was the sediment size. In this case, the aim was to find relationships between the parameters of the analyzed beach profile and

the sediment diameter.

For the exponential equation no predictive relation was found. On the other hand, a poor relationship (with a correlation coefficient  $r = 0.50$ ) between the  $A$  parameter of the potential expression and the gran size appears to exist (see figure 6), while a reasonable relationship ( $r = 0.82$ ) between the  $A$  parameter of the rational equation and the sediment diameter  $D_{50}$  was found (figure 7).

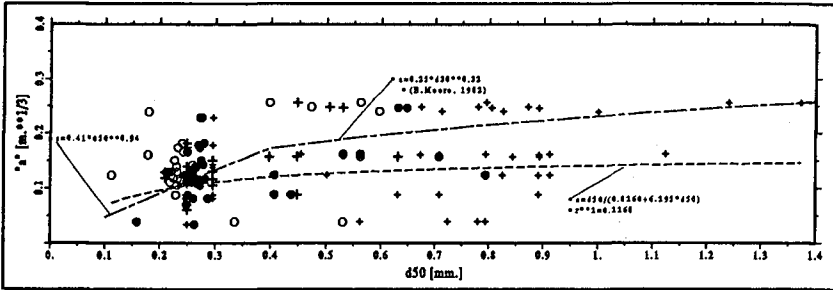


Figure 6. Relationship between  $A$  and  $D_{50}$ . Potential equation.

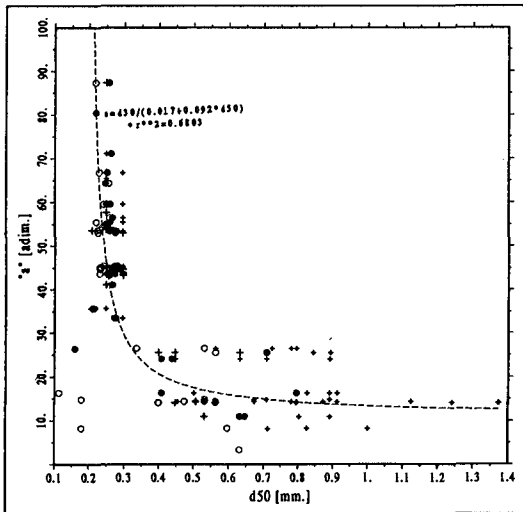


Figure 7. Relationship between  $A$  and  $D_{50}$ . Rational equation.

### 3.4. Wave data

As it is well known, waves are generally the most important external factor taking part in beach evolution at a short/medium time scale, while the variables before studied are beach parameters which graduate its response to wave action. For this reason, a good definition of waves characteristics in the studied zone is necessary in order to perform an adequate modelling.

In this work, different sets of wave data were used. The monitoring program of the Regional Authorities for the Catalan Coast includes 3 offshore buoys, one of which is directional and began to operate in June 1990. The other two buoys entered in service in May 1984. In figure 8, the three buoys locations are shown. Visual data (since 1950) are available too.

For obvious reasons of space limitation, a detailed analysis of the wave data can not be included here. As a summary of the available information, it can be said that the wave heights recorded by the three buoys present similar trends because the distances among them are relatively short (about 100 km).

Since the Catalan Coast is the West boundary of the Occidental Mediterranean basin, it is opposite to the coasts of France, Italy, Africa and some islands, and as a consequence the maximum fetch on this coast is about 750 Km. Due to this restriction in the fetch magnitude, the waves acting on this zone have a limited energy, as it was mentioned before. The most energetic storms are those coming from NE or E.

The directions of the most frequent waves change along the Catalan Coast. In the southern part, near the Ebro Delta, there are three predominant directions (with almost 80% of the occurrences) according to both visual and recorded data: NW, S and the sector comprised between E and NE. In the northern and central parts, there is no recorded directional information and the only source are visual data. According to this data, the waves are more uniformly distributed in all directions, with two predominant sectors: NE-E (about 40% of the events) and SW-W (about 28%).

## 4. Shoreline evolution modelling

### 4.1 Model description

After all the necessary variables were characterized and their typical values defined, a numerical simulation of beach changes produced by spatial and temporal differences in longshore sediment transport was carried out at several areas of the Catalan Coast. In order to predict the shoreline evolution, a model was developed following Hanson and Kraus (1989). It is an one-line model and therefore it only considers longshore transport.

Several longshore sediment transport expressions have been used in the model. The most frequently employed was the Ozasa and Brampton (1980) one:



$$Q_t = (H^2 C_g)_b \left[ a_1 \sin 2\alpha_{b_s} - a_2 \cos \alpha_{b_s} \frac{\partial H_b}{\partial x} \right]_b \quad (6)$$

in which  $H$  is the significant wave height (in m),  $C_g$  is the wave group celerity (in m/s),  $b$  is a subscript denoting wave breaking,  $\alpha_{b_s}$  is the angle between breaking waves and the local shoreline and  $a_1$ ,  $a_2$  are adimensional parameters given by:

$$a_1 = \frac{K_1}{16 \left[ \frac{\rho_s}{\rho} - (1-p)(1.416)^{5/2} \right]} \quad (7)$$

$$a_2 = \frac{K_2}{8 \left[ \frac{\rho_s}{\rho} - (1-p) \tan \beta (1.416)^{5/2} \right]} \quad (8)$$

where  $K_1$ ,  $K_2$  are calibration parameters,  $\rho_s$  is the sand density,  $\rho$  is the water density,  $p$  is the porosity and  $\tan \beta$  is the average bottom slope from the shoreline to the closure depth.

This formula is a modification of the well-known CERC expression, with an additional term in order to consider wave height gradients alongshore. The free parameters ( $K_1$  and  $K_2$ ) were calibrated as a function of the net volume changes between successive historical coastlines at several beaches on the Catalan Coast. The average shoreline trend for each historical line was estimated, to avoid misinterpretations due to seasonal variability.

Successive analyses were made to characterize sequential order and discretization fineness effects, particularly concerning wave angles. It was concluded that the effect of wave angle variation is very important because of nonlinearities. A small change in wave angle produces greater differences in beach evolution than small changes in wave height.

A sensitivity analysis of the coastline discretization size was carried out too. The importance of both discretizations (spatial and temporal) was analyzed. It was found (within engineering accuracy bounds) that small changes in the spatial discretization parameter ( $\Delta x$ ) do not give rise to significative differences in the results, if the stability condition (given by the Courant number) is satisfied.

On the other hand, changes in the temporal discretization parameter ( $\Delta t$ ) do not originate differences in the results, if the stability condition is preserved and provided that wave directions remain unaltered when a different discretization is adopted.

#### 4.2. Case study

As an example of the model performance, one of the analyzed cases will be

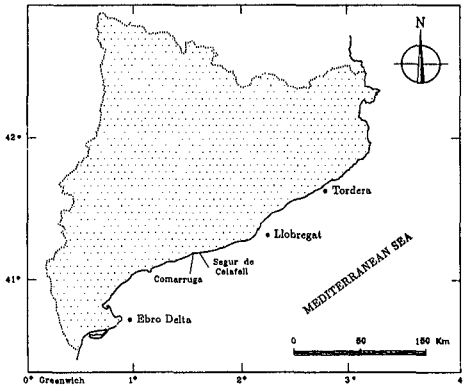


Figure 8. Comarruga-Calafell beach and buoys locations

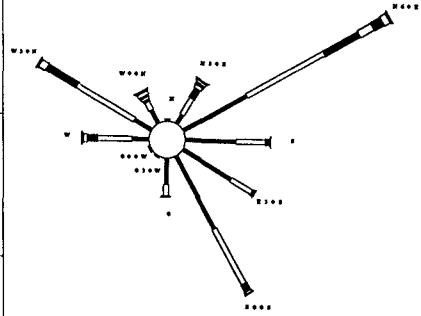


Figure 9. Wave climate for the simulated beach

described here. It deals with the beach between Comarruga and Calafell whose location is shown in figure 8.

This coastal stretch is a sandy beach with a length of 13 km. Originally it was in a relative dynamic equilibrium and the shoreline was approximately a straight line. The bottom contours were also approximately straight and parallel lines. In this zone, there was a rather large gross longshore sediment transport (about 200,000 m<sup>3</sup>/year) but the net rate of longshore transport was practically negligible (about 10,000 m<sup>3</sup>/year).

In the middle seventies two offshore marinas were constructed here, without taking into account the littoral dynamics and the important gross sediment transport existing in the area. The construction of both marinas induced important changes in the longshore sediment transport conditions and a tombolo was generated between the shoreline and each marina.

Shoreline position data were available immediately before and four years after the construction of the marinas. Using this data set, the one-line model was calibrated simulating the generation of both tombolos.

The main problem was the lack of recorded wave data during the tombolos formation. The necessary wave climate to feed the model was taken from the directional buoy wave data. This directional buoy provides wave parameters (height, period and direction among others) every 3 hours. The available wave data were from the nineties while the simulation period was from the seventies. It is nevertheless hoped that the recorded wave data are representative of average conditions in the zone so that they can be adopted to perform the simulation. A summary of the wave climate is shown in figure 9.

The selected boundary conditions were of pinned-beach type on both sides,

because the simulation bounds were enough far from the studied zone. This means that the transport rate gradients are zero and as a consequence the shoreline at these points does not move.

For other problem variables like closure depth, sediment size and beach profile shape, local values following the methodology described before were adopted. Correspondingly, a closure depth of 6 meters was employed in this case. The adopted grain diameter, obtained averaging several samples was  $D_{50} = 50$  mm. With this value, a profile of the rational type was derived taking into account the curve shown in figure 7. Therefore the only unknowns of the problem were the parameters  $K_1$  and  $K_2$  of the longshore sediment transport expression. These parameters were calibrated following a trial and error procedure. It was found that the more suitable values were  $K_1 = 0.3$  and  $K_2 = 0.7$ .

The value found for  $K_1$  is much smaller than the value of  $K_1 = 0.77$  originally determined by Komar and Inman (1970), although several authors have recommended in more recent works a decrease of the  $K_1$  magnitude. On the other hand, the value of  $K_2$  seems too large. This is probably due to the difficulty in reproducing with accuracy the behaviour of the marinas since they are coastal structures with a complex geometry.

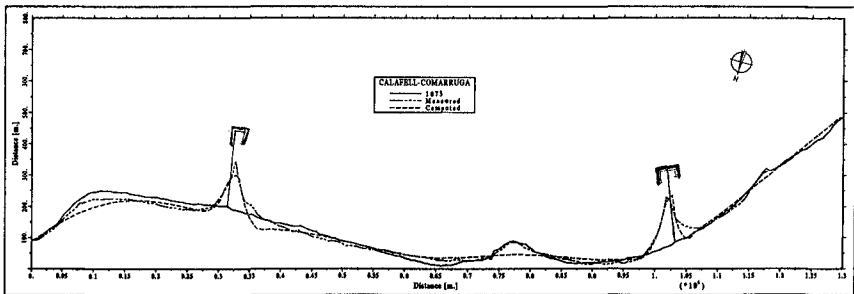


Figure 10. Model calibration in terms of shore-line evolution

The obtained prediction of shoreline evolution is shown in figure 10. A reasonable agreement between measured and predicted shoreline positions can be observed. It is also noticeable that the model reproduces the tomboles at the proper locations.

Finally, a sensitivity analysis of the  $K_1$  parameter was carried out, as shown in figure 11. In this figure, the deviations between measured and predicted

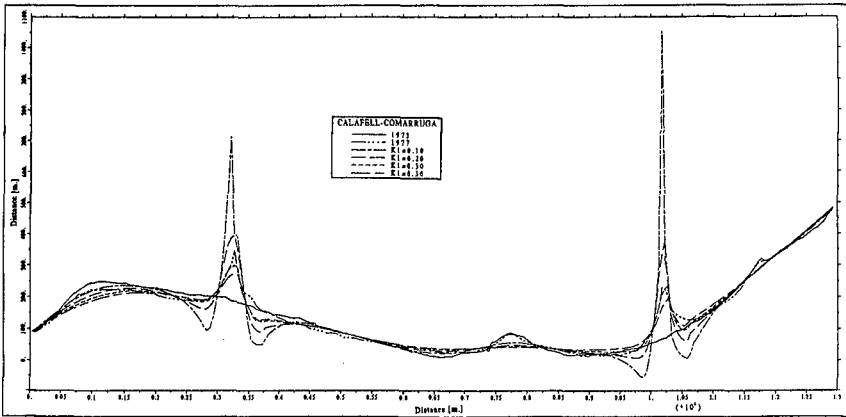


Figure 11. Sensibility analysis of  $K_1$

shorelines for other  $K_1$  values can be seen.

## 5. Summary and conclusions

The essential variables involved in shoreline evolution models have been identified and corresponding typical values have been determined for different zones of the Catalan Coast. The improved description of the relevant physical data in terms of local values is very important in order to reduce the number of unknowns involved in beach evolution simulation.

On the other hand, two new expressions for equilibrium beach profiles have been tested, one of exponential type and the other one with a rational form. Both expressions give an improved fit in most of the measured profiles on the Catalan Coast with respect to other state of the art expressions.

Finally, a shoreline evolution model has been calibrated for different areas of the Catalan Coast, employing local values for the variables involved in the process. The calibration was carried out adjusting the free parameters of a longshore transport formula and finding their most suitable values.

## References

- Bruun, P. (1954). "Coast Erosion and the Development of Beach Profiles". *Beach Erosion Board, Tech. Memo. no. 44*, 108 p.
- Dean, R.G. (1976). "Equilibrium Beach Profiles and Response to Storms". *Proc. 15th Conf. on Coastal Eng., Honolulu, Hawaii*.

- Dean, R.G. (1977). "Equilibrium beach profiles: U.S. Atlantic and Gulf Coasts". *Dep. Civil Eng. and College Marine Studies, Univ of Delaware, Tech. Rep. no. 12, 45 p.*
- Hallermeier, R.J. (1978). "Uses for a calculated limit depth to beach erosion". *Proc. 16th Conf. on Coastal Eng., ASCE, pp. 1493-1512.*
- Hallermeier, R.J. (1981). "Profile zonation for seasonal sand beaches from wave climate". *Coastal Engineering, vol. 4, pp. 253-277.*
- Hanson, H. and N.C. Kraus (1989). "Genesis: Generalized model for simulating shoreline change". *U.S. Army Corps of Eng., CERC, Tech. Rep. no. 89-19, 185 p.*
- Jiménez, J.A., V. Gracia, M.A. García and A. Sánchez-Arcilla (1992). "Análisis y propuesta de soluciones para estabilizar el Delta del Ebro: Balance sedimentario y esquemas de transporte". *Technical report LT-3/4, D.G. Ports i Costes, Generalitat de Catalunya.*
- Komar, P.D. and D.L. Inman (1970). "Longshore sand transport on beaches". *Journal of Geophysical Research, vol. 73, no. 30, pp. 5914-5927.*
- Kraus, N.C. and S. Harikai (1983). "Numerical model of the shoreline change at Oarai Beach". *Coastal Engineering, vol. 7, pp. 1-28.*
- Lo Presti, A. (1994). "Modelado del transporte longitudinal de sedimentos. Aplicación a la costa catalana". *Ph. D. Thesis, Catalonia Univ. of Tech., Barcelona, 355 p.*
- Moore, B. (1982). "Beach Profile Evolution in Response to Changes in Water Level and Wave Height". *M.S. Thesis, Dep. of Civil Eng., Univ. of Delaware, Newark.*
- Ozasa, H. and A.H. Brampton (1980). "Mathematical modelling of beaches backed by seawalls". *Coastal Engineering, vol. 4, pp. 47-64.*
- Serra, J., A. Calafat, M. Canals, J.L. Casamor and J. Sorribas (1989). "Seguiment de l'evolució de les platges del Maresme. Anys 1987 i 1988". *Technical report, D.G. Ports i Costes, Generalitat de Catalunya.*
- Serra, J., J. Sorribas, A. Calafat and M.A. García (1990). "Anàlisi del comportament de les platges regenerades al Maresme. Memoria anual (Set. 1989-Jul. 1990)". *Technical report, D.G. Ports i Costes, Generalitat de Catalunya.*
- Sierra, J.P., A. Lo Presti and A. Sánchez-Arcilla (1994). "Equilibrium beach profiles on the Catalan Coast". *Proc. Coastal Dynamics'94. ASCE, pp. 432-445.*

## CHAPTER 191

### EROSION AND OVERTOPPING OF A GRASS DIKE LARGE SCALE MODEL TESTS

G.M. Smith<sup>1)</sup>, J.W.W. Seijffert<sup>2)</sup> and J.W. van der Meer<sup>1)</sup>

#### ABSTRACT

A comprehensive test series at full-scale was performed on a grass dike to obtain quantitative information on the wave loading, erosion rate, residual strength and overtopping under design storm conditions. The purpose was to establish design and assessment criteria for this type of dike, which exists in many places in The Netherlands. The particular dike tested exhibited, in general, a considerable resistance to erosion. However, such a non-homogeneous surface is subject to weak spots which can erode very quickly. The most critical region, where the wave loading is the highest, has been identified. The residual strength of the underlying layer of clay is defined as the time it takes for erosion to progress through the entire layer and expose the sand core of the dike. For the dike tested, the residual strength of the 0.8 m thick clay layer is estimated to be 10 hours under design conditions. Measurements of the average overtopping rate and the volumes per overtopping wave were compared to existing formulae, developed from the results of small-scale tests. The comparison was favourable, indicating that scale effects are not substantial for these quantities.

#### INTRODUCTION

Along many rivers and some sections of sea coast in The Netherlands a grass dike protects the low-lying polder land. Interest in grass dikes is growing, as a result of increasing environmental, economic and aesthetic concerns. In spite of this, no method was available to assess the strength of a grass layer for design or repair

---

1) DELFT HYDRAULICS, P.O. Box 152, 8300 AD Emmeloord, The Netherlands

2) Dutch Ministry of Public Works, Road and Hydraulic Engineering Division, P.O. Box 5044, 2600 GA Delft, The Netherlands

purposes. In recent years the strength characteristics of a grass dike have been systematically studied in order to answer the following questions: Is the strength mostly determined by the grass itself, the root system or the underlying soil? How does the grass layer behave during long-term wave and current loading and how long does it take before the grass layer can be considered to have failed? What is the residual strength of the dike, ie. how long does it take, after failure of the grass layer, until the sand core of the dike becomes exposed?

In 1992 a large-scale testing programme was created in order to answer these questions. By also measuring the overtopping rate, these tests then also provided the opportunity to compare recently derived overtopping formulae with full scale measurements. The aim of the study was:

1. to study the behaviour of the water motion (velocity, pressure distribution, layer thickness and runoff) over the grass slope.
2. to measure the erosion resistance of the grass layer.
3. to measure the average overtopping rate and the overtopping volume per wave, for a wide range of wave and water level conditions.
4. to measure the residual strength of the underlying layer of clay.

The project was commissioned by the road and hydraulic engineering division of the Dutch Ministry of Public Works and was performed by DELFT HYDRAULICS, Delft Geotechnics and the Agricultural University of Wageningen.

The tests were performed in de Delta Flume of DELFT HYDRAULICS. This flume is 250 m long, 5 m wide, 7 m deep. Waves can be generated up to 3 m in height. With this facility waves occurring under design storm conditions for the north coast of Holland could therefore be generated.

## TESTING SETUP

For this project a section of an existing sea dike was excavated and transported to DELFT HYDRAULICS. This was achieved by cutting a total of 16 blocks out of the grass and clay covering layer out of the dike. Each block measured 2.5 m x 2.5 m x 1 m thick (Photo 1).

The dike section was reconstructed in de Delta Flume and consisted of an outer slope (sea side) of 1:4, a 2 m wide crest at a height of 7 m above the flume bottom and an inner slope (land side) of 1:2.5 (see Figure 1 and Photo 2). The grass section of the dike was located in the centre 2.5 m of the flume, with 1.25 m wide concrete sections on either side. The inner slope consisted of grass from the crest down to an elevation of 3.5 m and below that of concrete to a height of 2.5 m. Behind this slope was the overtopping container, which had a capacity of 17 m<sup>3</sup>. The grass was placed only in the middle of the flume for three reasons:



Photo 1 Excavation of sections from the dike



Photo 2 Dike in the Delta Flume prior to testing



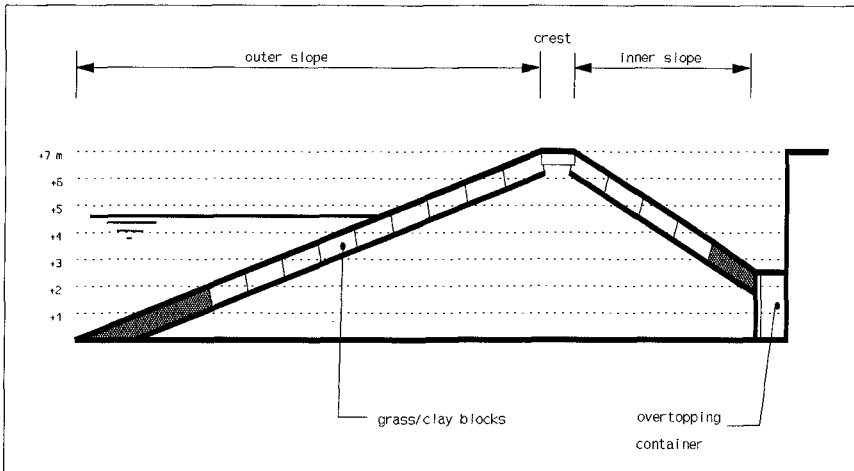


Figure 1 Cross-section of the dike in the Delta Flume

1. Fewer sections were needed to be excavated from the dike and placement in the flume was facilitated due to access from the sides. This also reduced the possibility of damage during placement.
2. Instruments could be easily attached to the concrete sections of the slope.
3. The concrete section of the slope served as a smooth reference for wave runup measurements.

In order to prevent interaction of the water on the concrete and grass sections of the dike, 0.45 m high wooden partitions were placed in between and sealed water-tight.

### Condition of the grass in the flume

Approximately 16 m of the dike was located inside the hall of the facility (only part of the flume is located within a hall). The inside section (the outer slope, from the toe to an elevation of 6 m) received therefore less light than would occur under natural conditions. This, in conjunction with relatively high temperatures (25 to 30°C), caused the condition of the grass to deteriorate. In order to minimize this, twenty special 400 Watt lamps were hung 1 m above the grass slope. The lamps burned about 16 hours per day, following the natural day-night cycle. The grass reacted well to this measure and had grown about 30 cm before preparations for the tests were completed. The Agricultural University of Wageningen performed a detailed inspection of the vegetation and root network before testing commenced. The vegetation cover was in good condition and had a high covering density.

## Instrumentation

A large number of instruments was placed on and in the dike. For measurements of the water motion on the slope 6 electro-magnetic velocity meters (EMV's), 2 runup meters (one on the grass and one on the concrete), 3 water layer thickness meters and 30 pressure transducers were used. In order to measure the pore water pressure response in the clay, Delft Geotechnics inserted 32 pore pressure transducers into the clay layer. These transducers were inserted at various depths below the surface via the sides of the grass/clay blocks. In order to measure the rate of erosion due to wave attack the elevation of a large number of points on the grass surface was regularly surveyed.

The overtopping rate was measured via a water level gauge located in the overtopping container. This container consisted of three separate sections to ensure that only the overtopping water from the grass section was accumulated and measured. The number of overtopping waves was determined from the runup meter, which extended to the crest elevation of the dike.

## TESTING PROGRAMME

To achieve the three main aims of the study, three test series were performed: erosion, overtopping and residual strength.

### Erosion tests

This series consisted of seven tests. The purpose of these tests was to obtain information about the behaviour of the water motion on the slope before and after breaking and about the erosion resistance of the grass layer itself.

The first five tests were of short duration and were performed with relatively small regular and irregular waves. These tests were intended to provide information about the water motion without damaging the grass layer. For the interpretation of the measurements of the erosion rate, differentiation was made between the average rate and hole development. On average, the erosion process progresses relatively slowly and is more or less evenly distributed over the surface. Hole development occurs after the erosion has locally progressed through the root layer. The sixth and seventh erosion tests provided information over both types of erosion.

The sixth test was performed with irregular waves having  $H_S = 1,4$  m and  $T_P = 4.7$  s and a water level of 4.8 m (Photo 3). These are the conditions for a design storm along the northern Dutch coast. During the test the waves were interrupted several times for inspections and surveying of the grass surface. After 9 hours of wave attack a hole 0,75 m in diameter and 0,12 m deep was noted 1 m under the still water level (SWL). After 1 more hour of wave attack the hole was measured again and then again after a second hour. The hole had in that time grown to a diameter of 1 m and a depth of 0.15 m (Photo 4).



Photo 3 Erosion test 6:  $H_S = 1.4$  m,  $T_P = 4.7$  s



Photo 4 Erosion test 6: Damage after 11 hours of testing

In order to obtain more information about the average erosion rate, it was decided to continue the test for at least another several hours. To prevent the hole from becoming so large as to affect the other measurements and the subsequent test series, it was repaired and protected from further erosion. After a total of 17 hours of wave loading a second hole had appeared 0.5 m under the SWL. This hole was 0.8 m in diameter and had a depth of 0.11 m. This was the location of the heaviest wave loading, where the most damage was expected to occur. This was the end of the test; the surface was inspected in detail and then repaired and protected for the remaining tests.

The seventh erosion test was performed with small irregular waves ( $H_S = 0.75$  m;  $T_p = 3.4$  s) and a lower water level (3.5 m). This lower part of the slope had not been subjected to much wave loading and was considered to still be in the original condition. The purpose of this test was to obtain information over the influence of the wave height on the erosion rate. The test was carried out in the same manner as test number 6, except the inspections and surveys of the surface were made every 4 hours instead of every hour due to the slower erosion rate. After 20 hours of wave loading the test was stopped. No serious erosion had occurred (Photo 5).



Photo 5 Condition after erosion test 7

The results of the erosion measurements of these two tests led to the definition of 3 erosion zones over the slope. The most erosion (both hole development and the highest average erosion rate) was concentrated to a depth of  $(0.3H_S)$  to  $(0.6H_S)$  under the SWL. This is defined as zone 1 (see Figure 2). Between the SWL and a depth of  $0.3H_S$  (zone 2), the average erosion rate was half of that in the first zone.

No hole development occurred in this second zone. In the third zone, above the SWL, practically no erosion was noted.

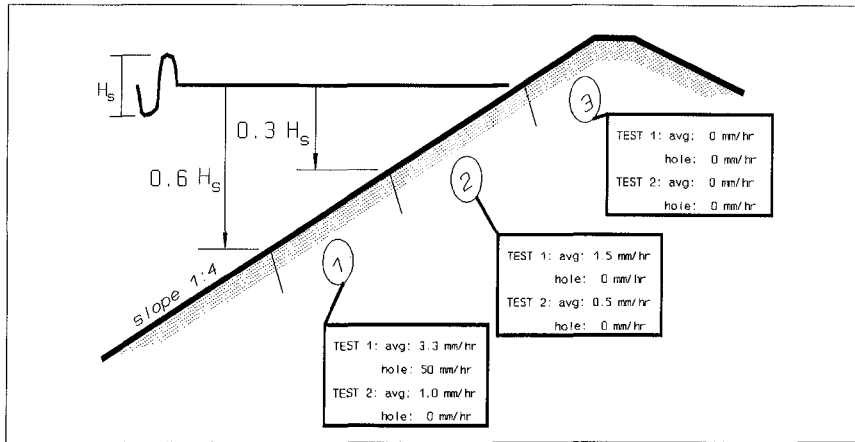


Figure 2 Defined erosion zones

The results showed clearly that the strength of this particular grass dike lay in the root network which was between 5 and 10 cm thick. It was also noted that the average erosion rate was proportional to about the square of the significant wave height (see Figure 3).

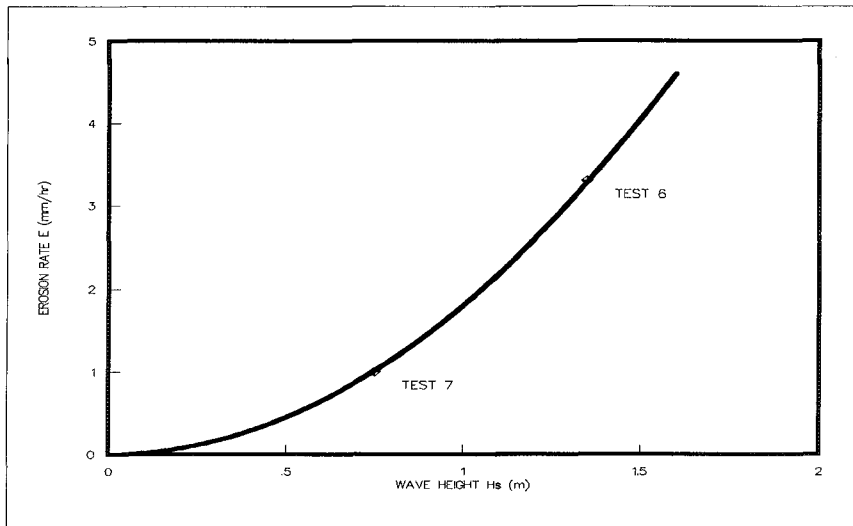


Figure 3 Erosion rate ( $E$ ) as function of  $H_s$

Based on these measurements a preliminary model has been developed which allows one to estimate the maximum allowable duration of continuous wave loading before a certain depth of erosion is achieved (Meijer and Verheij, 1994). An example is given in Figure 4 wherein lines of 5 mm and 50 mm erosion are shown. Of course, based on only two tests, this model is very limited. However, more tests have recently been performed with other wave heights on a wide range of different vegetation and subsoil characteristics and it is meant to expand the model with the new information.

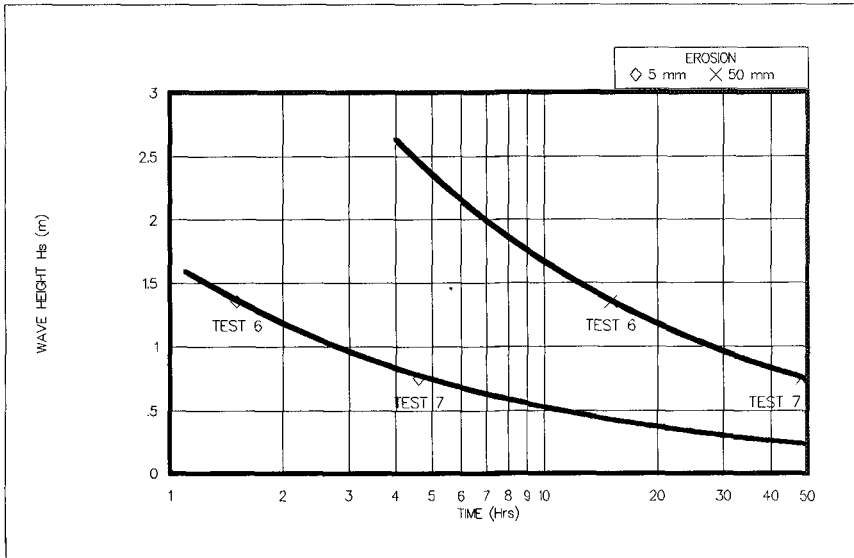


Figure 4 Loading duration for erosion of  $d = 5$  mm and  $d = 50$  mm

### Overtopping tests

In this series twelve tests were performed with irregular waves. The purpose was twofold:

1. to give a visual impression of average overtopping rates from 0.1 to 25 l/s/m, under typical conditions for sea dikes (large freeboard and large waves) as well as for river dikes (low freeboard and small waves). A video presentation of the differing conditions was made. During some of the tests an observer stood on the crest of the dike to experience the force of the overtopping water under the various conditions. This was performed for the practical purpose of setting a criterion for the safe performance of dike inspections and repairs during a storm.

2. to compare the predictions of overtopping formulae, developed from small-scale tests, with large scale measurements. Formulae for both the average overtopping discharge and the overtopping volumes per wave and maximum overtopping volume were tested.

The observer on the crest noted that for an average overtopping discharge of 25 l/s/m ( $H_s = 1.8$  m,  $T_p = 4.7$  s and freeboard  $R_c = 1.8$  m) the force of most of the overtopping waves (green water, acting mostly on the observer's legs) was not large enough to cause a loss of balance. However, twice in 15 minutes the spray from the waves (acting over the full height of the observer) did have sufficient force to cause him to lose his balance. If it is also considered that during real storm conditions a high wind speed is also present, it must be concluded that performance of inspection or repair work during these conditions is not possible. This conclusion is also extended to conditions leading to an average discharge of 10 l/s/m.

### Comparison of measurements to existing formulae

#### *Average overtopping rate:*

The most widely applied formula for the average overtopping discharge is (Van der Meer and Janssen, 1994):

$$Q = A \exp(-BR) \quad (1)$$

For this formula the parameters  $Q$ ,  $R$ ,  $A$ ,  $B$  are dependent on the breaker parameter as follows:

for  $\xi_{op} < 2$  (breaking waves):

$$Q_b = \frac{q}{\sqrt{gH_s^3}} \sqrt{\frac{s_{op}}{\tan \alpha}}; \quad R_b = \frac{R_c}{\gamma_f H_s} \frac{\sqrt{s_{op}}}{\tan \alpha}; \quad A = 0.06; \quad B = 5.2 \quad (2a)$$

for  $\xi_{op} > 2$  (non-breaking waves):

$$Q_n = \frac{q}{\sqrt{gH_s^3}}; \quad R_n = \frac{R_c}{\gamma_f H_s}; \quad A = 0.2; \quad B = 2.6 \quad (2b)$$

with

- $Q_b, Q_n$  = dimensionless overtopping discharge [-]
- $b$  = subscript for breaking waves
- $n$  = subscript for non-breaking waves
- $A, B$  = regression coefficients [-]

$q$	= average overtopping discharge, per metre length of dike	$[m^3/s/m]$
$g$	= acceleration due to gravity	$[m/s/s]$
$R_c$	= crest freeboard	$[m]$
$H_s$	= significant wave height	$[m]$
$R_b, R_n$	= dimensionless crest freeboard	$[-]$
$\xi_{op}$	= breaker parameter = $\tan \alpha / \sqrt{s_{op}}$	
$s_{op}$	= wave steepness = $2\pi H_s / (gT_p^2)$	$[-]$
$\gamma_f$	= reduction factor for roughness	$[-]$

Analysis of the runup measurements for the grass slope indicate that the  $\gamma_f$  value is, on average, between 0.8 and 0.9. It is dependent on the length of the grass, etc.

Figure 5 shows that for the higher overtopping rates the measured data points compare favourably to the predicted values.

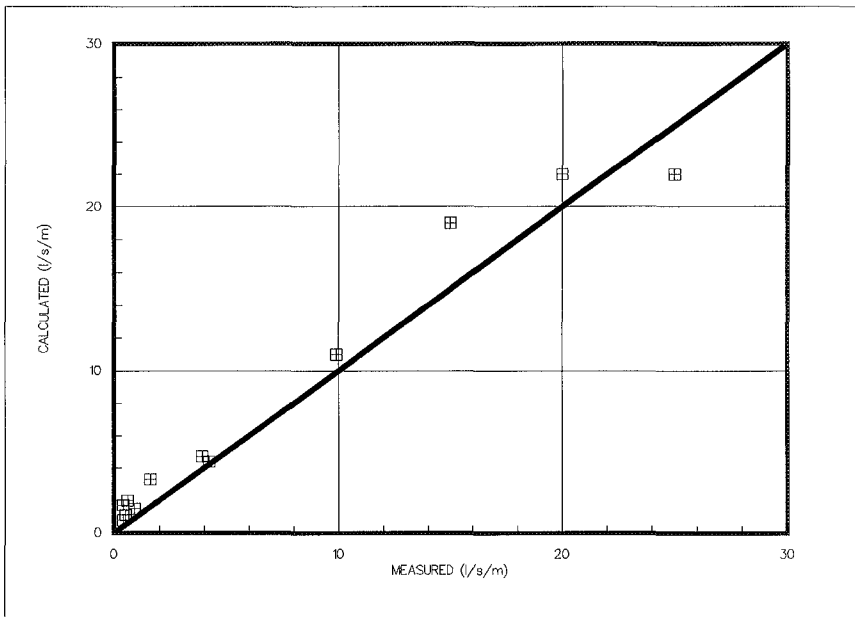


Figure 5 Measured and calculated average overtopping discharges

#### *Overtopping rates per wave:*

The average overtopping discharge does not give an indication of how much water can be expected to overtop the crest by a particular wave. The maximum volume per wave can be more than 10 times higher than the average discharge. In Van der Meer and Janssen (1994) a formula is presented to calculate the overtopping volumes per wave, based on the probability distribution of the overtopping volumes of individual waves (a Weibull distribution). The volume per wave is based on the



average overtopping discharge. From this approach the maximum overtopping volume from a group of  $N$  waves can be predicted with

$$V_{\max} = a [\ln(N_{ov})]^{4/3} \quad (3)$$

where

$V_{\max}$	= maximum overtopping volume in a single wave	$[m^3]$
$N_{ov}$	= number overtopping waves = $N/P_{ov}$	$[-]$
$N$	= number of incoming waves	$[-]$
$P_{ov}$	= probability of wave overtopping	$[-]$
$a$	= scale factor in the Weibull distribution = $0.84 qT_m/P_{ov}$	$[-]$
$T_m$	= average wave period = storm duration / $N$	$[s]$
$q$	= average overtopping discharge, per m length of dike	$[m^3/s/m]$

The probability of overtopping  $P_{ov}$  can be calculated with

$$P_{ov} = \exp \left[ - \left( \frac{R_c / H_s}{c} \right)^2 \right] \quad (4)$$

The coefficient  $c$  follows from the assumption that the runup distribution follows a Rayleigh distribution. The value of  $c$  can be calculated with

$$c = 0.81 \gamma_f \xi_{op} \text{ with a maximum of } c = 1.62 \gamma_f \quad (5)$$

The relation between the maximum volume in one wave and the average overtopping discharge is shown in Figure 6. In this figure the calculated line is based on a wave height of 1 m. The data points are for differing wave conditions. For average discharges of less than 10 l/s/m the wave heights were all approximately 1 m. For the higher rates the wave heights were approximately 1.5 m, which is why the data points fall above the calculated line.

It can therefore be generally concluded that the formulae developed on the basis of small scale tests are representative of prototype conditions.

### Residual strength test

The residual strength of a dike is defined as the capacity of the underlayers to withstand wave and current loading after the top protection layer has failed. For a grass dike the top protection layer is the top 5 to 10 cm layer where the grass and root network is concentrated. The underlayer is the approximately 1 m thick layer of clay which covers the sand core of the dike. The residual strength is expressed in terms of the time it takes, after failure of the grass layer (the development of a hole), for the sand core to become visible.

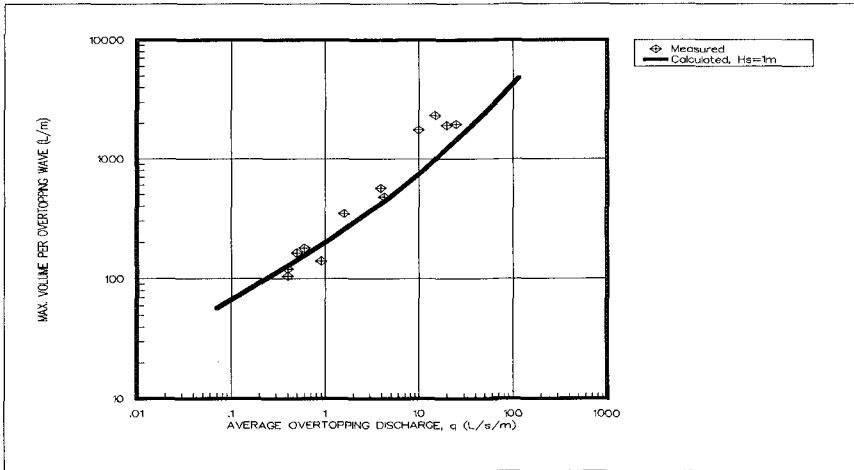


Figure 6 Maximum overtopping volume in a single wave as a function of the average overtopping discharge

This last test was performed after all erosion and overtopping tests were completed. The wave conditions for this test were identical to those for the sixth erosion test (design wave conditions). At the location of the wave impact, the grass and root layer had already been fully eroded away during the first two test series. Therefore, this test was considered to give a measurement of the residual strength of the clay layer alone. At the start of the test the clay layer was about 0.8 m thick.

After 4 hours of wave loading an under water inspection of the slope was carried out. It was noted that a large hole 0.4 m deep had appeared just under the still water line, along the edge of the grass/clay section of the dike. After 1 more hour of loading this hole had expanded to the full depth of the clay layer and the test was stopped. Photo 6 shows the results.

The growth of this hole must most likely be attributed to edge-effect and these results cannot be interpreted as the behaviour of a pure clay surface. This can be considered representative, however, for a dike with a transition from grass to a "hard" cover layer such as asphalt or a block revetment. Based on these measurements, the residual strength would be (conservatively) estimated at 5 hours.

Measurements of other sections of the surface that were not disturbed by this hole can be used to get an indication of the erosion rate of the clay. These measurements showed 0.25 m erosion over the 5 hours of testing or 0.05 m/hr. This compares extremely well with the results from erosion tests 6 and 7: the erosion rate, which can be compared to that for hole development, as well as the location of the erosion agreed with the values for zone 1. This value leads to an estimation of the residual strength as being 16 hours. Based on these two results the residual strength of this 0.8 m thick clay layer is estimated to be about 10 hours.



Photo 6 Condition after residual strength test

#### REFERENCES

- Van der Meer, J.W. and J.P.F.M. Janssen, 1994. Wave runup and overtopping at dikes. To be published in ASCE. Wave forces on inclined and vertical wall structures. Ed. Z. Demirbilek.
- Meijer, D.G. and H. Verheij, 1994. Grass dikes - Analysis of measurements from large scale tests. DELFT HYDRAULICS draft report Q1584 (in Dutch).

## CHAPTER 192

# Calculation of Tombolo in Shoreline Numerical Model

Kyung Duck Suh<sup>1</sup>, Associate Member, ASCE, and C. Scott Hardaway<sup>2</sup>

### Abstract

An algorithm is developed that is capable of calculating the formation of a tombolo in the lee of an offshore breakwater in a shoreline numerical model by inversely applying the method proposed in 1985 by Hanson and Kraus for constraining the shoreline not to retreat landward of a seawall. The algorithm is linked to a shoreline numerical model which uses curvilinear coordinates that follow the shoreline. The project of six segmented breakwaters at Chippokes State Park, Virginia is reported. The developed model is applied to the simulation of the shoreline change during the first nine months after construction of the Chippokes breakwaters.

## 1 Introduction

Offshore breakwaters have been used as a means to protect beaches against severe erosion. The wave-induced longshore currents generated behind the breakwaters deposit sediments in the sheltered area to build a new morphological shape called a salient. Sometimes the salient grows until its apex reaches the breakwater to form a tombolo. A number of numerical models has been developed for predicting shoreline change in the vicinity of coastal structures. However, there are few numerical models that can simulate the formation of tombolos. Most of the numerical models stop computation when the computed shoreline reaches the breakwater or predict outgrowth of the salient

---

<sup>1</sup>Principal Research Engineer, Ocean Engineering Division, Korea Ocean Research & Development Institute, Ansan P.O. Box 29, Seoul 425-600, Korea; formerly Marine Scientist at Virginia Institute of Marine Science.

<sup>2</sup>Marine Scientist, Department of Physical Sciences, School of Marine Science, Virginia Institute of Marine Science, The College of William and Mary, Gloucester Point, VA 23062, USA.

seaward of the breakwater. Perlin (1979) has proposed a method for handling the formation of a tombolo. Unfortunately, however, he could not find a well-documented data set to test his model for the case of tombolo formation.

In the present study, a numerical shoreline evolution model is developed to permit the formation and growth (or decay) of tombolos in the lee of impermeable offshore breakwaters. Hanson and Kraus (1985) have proposed a method for constraining the shoreline for the case of a seawall in a shoreline numerical model, which corrects the longshore sediment transport rates so as not to allow the shoreline to retreat landward of a seawall. In the present model, the method of Hanson and Kraus is borrowed for the calculation of tombolo formation in the lee of offshore breakwaters, the inverse of the problem of a seawall. The project of six segmented breakwaters at Chippokes State Park, Virginia reported in Hardaway et al. (1988) is summarized, and the developed model is applied to the simulation of the shoreline response during the first nine months after construction of the breakwaters.

## 2 Numerical Model

Advanced knowledge of waves and currents and the resulting sediment transport, associated with the increased capacities of large high-speed computers and improved numerical modeling algorithms, has made it possible to apply such complex models as a multi-line model (Perlin and Dean 1985) or general 3-D topographical change models (Wang et al. 1975; Watanabe 1982) to numerical modeling of shoreline problems. However, due to the relatively accurate prediction of the shoreline change with less computational effort, shoreline models have been widely used. In this section, a shoreline numerical model is developed using the curvilinear coordinates that follow the shoreline, as done in LeBlond (1972), Uda (1983), and Kobayashi and Dalrymple (1986). The use of a curvilinear coordinate system may be more advantageous than the Cartesian coordinate system for the situation in which the shoreline orientation is deviated largely from the straight shoreline as on a tombolo behind an offshore breakwater.

### 2.1 Shoreline change model

The curvilinear coordinate system used in the present model is shown in Fig. 1 along with some other notations. The symbol  $s$  denotes the coordinate following the shoreline whose positive direction points to the right when facing seaward. The coordinate pair  $(x_s, y_s)$  gives the location of an arbitrary point on the curved shoreline in terms of a Cartesian coordinate system.

$$\vec{m} = \left( \frac{\partial x_s}{\partial s}, \frac{\partial y_s}{\partial s} \right) = (\cos \theta, \sin \theta) \quad (1)$$

is the unit tangential vector to the shoreline in the direction of increasing  $s$ ,

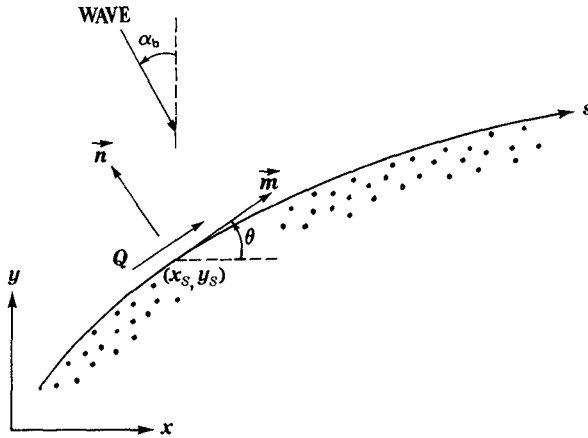


Fig. 1. Curvilinear coordinate system and definition of model variables.

$$\vec{n} = \left( -\frac{\partial y_s}{\partial s}, \frac{\partial x_s}{\partial s} \right) = (-\sin \theta, \cos \theta) \tag{2}$$

is the seaward unit normal vector to the shoreline, and  $\theta$  is the angle between  $\vec{m}$  and the  $x$ -axis which is measured counterclockwise from the positive  $x$ -direction. In the figure,  $Q$  is the volumetric longshore sediment transport rate, and  $\alpha_b$  is the breaking wave angle between the wave crest and the  $x$ -axis which is measured counterclockwise from the positive  $x$ -direction.

Assume that the point,  $(x_s, y_s)$ , moves perpendicular to the shoreline, so that

$$\left( \frac{\partial x_s}{\partial t}, \frac{\partial y_s}{\partial t} \right) = e \vec{n} \tag{3}$$

in which  $e$  is the rate of shore-normal movement of shoreline. Using the notation of complex variables,

$$z_s = x_s + iy_s \tag{4}$$

in which  $i = \sqrt{-1}$ , and expressing  $e$  as

$$e = -\frac{1}{D} \frac{\partial Q}{\partial s} \tag{5}$$

(3) can be written as

$$\frac{\partial z_s}{\partial t} = -\frac{1}{D} \frac{\partial Q}{\partial s} \exp \left[ i \left( \theta + \frac{\pi}{2} \right) \right] \tag{6}$$

in which  $D$  is the depth of profile closure at which no measurable change in bottom elevation occurs. If  $\theta$  is very small, the real part of this equation states that the shoreline does not move in the  $x$ -direction and the imaginary part reduces to the sediment continuity equation of traditional shoreline models using the Cartesian coordinate system.

A widely-used expression for the longshore sediment transport rate in places where diffraction dominates is that proposed by Ozasa and Brampton (1980):

$$Q = \Gamma H_b^{5/2} \left[ K_1 \sin(2\delta_b) - K_2 \frac{\partial H_b}{\partial s} \cot \beta \cos \delta_b \right] \quad (7)$$

in which

$$\Gamma = \frac{\sqrt{g}}{16(s_s - 1)(1 - p)\sqrt{\kappa}} \quad (8)$$

and

$$\delta_b = \alpha_b - \theta \quad (9)$$

is the breaking wave angle relative to the shoreline under the assumption that the breakerline and the shoreline are locally parallel, and  $g$  = gravitational acceleration;  $s_s$  = specific gravity of sediment relative to fluid;  $p$  = porosity of sediment;  $\kappa$  = ratio of wave height to water depth at breaking;  $H_b$  = breaking wave height;  $\tan \beta$  = beach slope;  $K_1, K_2$  = empirical longshore sediment transport coefficients. The first term in (7) describes the sediment transport rate produced by obliquely incident waves, whereas the second term describes the transport due to a longshore gradient of breaking wave height, which has been found to be of great importance in cases where diffraction dominates. The beach slope is calculated by the empirical formula proposed by Sunamura (1984) for given breaking wave height, wave period and sand grain size.

A number of studies has been performed to determine the coefficient  $K_1$ . A value of  $K_1 = 0.77$  was originally determined by Komar and Inman (1970), and a decrease from 0.77 to 0.58 was recommended by Kraus et al. (1982). The second transport coefficient,  $K_2$ , has not received great attention of researchers. Ozasa and Brampton (1980) used  $K_2 = 3.24K_1$ . Hanson and Kraus (1989), however, recommended that the value of  $K_2$  is typically 0.5 to 1.0 times that of  $K_1$ .

One of the basic assumptions of shoreline numerical models is that the beach has a constant depth of profile closure throughout the model area, within which erosion or accretion of beach occurs. In this study, the expression proposed by Hallermeier (1983) is adopted with a deep water wave height,  $H_o$ , in place of the extreme wave height for an annual seaward limit of profile change:

$$D = \frac{2.9H_o}{(s_s - 1)^{1/2}} \quad (10)$$

In the model, the greatest  $H_o$  during the simulation period is used for calculation of  $D$ .

## 2.2 Breaking wave model

The sediment continuity equation, (6), can be solved for the shoreline position,  $z_s$ , if the wave heights and angles along the breakerline are given. In the present model, the wave condition (height, period and angle of incidence) at the location of the breakwaters is given as input data and the wave deformation in the lee of the breakwaters is computed. It is assumed that the wave condition is constant along the line connecting the breakwaters and its longshore extensions to the lateral boundaries. This assumption will be appropriate if the offshore bottom topography does not deviate drastically from straight and parallel contours, the offshore distances of the breakwaters are almost constant, and the longshore distance of the model area is not too long.

The three major phenomena which alter the wave in the lee of the breakwaters are refraction, diffraction and shoaling. In the present model, it is assumed that all these wave phenomena occur independently, so that the breaking wave height,  $H_b$ , can be calculated by

$$H_b = K_D K_R K_S H_B \quad (11)$$

in which  $H_B$  = wave height at the location of breakwaters, and  $K_D, K_R, K_S$  = coefficients of diffraction, refraction, and shoaling. The diffraction analysis used in this model is based on the theory of Penney and Price (1952). The method of determining the refraction and shoaling coefficients and the breaking wave angle closely follows that of Kraus (1982).

## 2.3 Finite-difference equations

An explicit finite-difference method is used to solve (6), (7) and (9) numerically for the wave condition computed along the shoreline. The location and orientation of the shoreline and the breaking wave angle are defined at the nodal points, and the longshore transport rate is defined between the nodal points, as shown in Fig. 2. The sediment continuity equation, (6), at the  $i$ th point can be expressed as the following finite-difference form:

$$z'_i = z_{s_i} + \frac{\Delta t}{D} \left[ \frac{Q_{i-1} - Q_i}{\frac{1}{2}(\Delta s_i + \Delta s_{i-1})} \right] \exp \left[ i \left( \frac{\theta_i + \theta_{i-1}}{2} + \frac{\pi}{2} \right) \right] \quad (12)$$

in which  $\Delta t$  is the time step. The prime denotes the quantity being solved for the next time step and the unprimed quantities are known quantities at the present time step. The quantities,  $\Delta s_i$ ,  $\theta_i$ , and  $Q_i$ , are computed by

$$\Delta s_i = \left[ (x_{s_{i+1}} - x_{s_i})^2 + (y_{s_{i+1}} - y_{s_i})^2 \right]^{1/2} \quad (13)$$

$$\theta_i = \tan^{-1} \left( \frac{y_{s_{i+1}} - y_{s_i}}{x_{s_{i+1}} - x_{s_i}} \right) \quad (14)$$



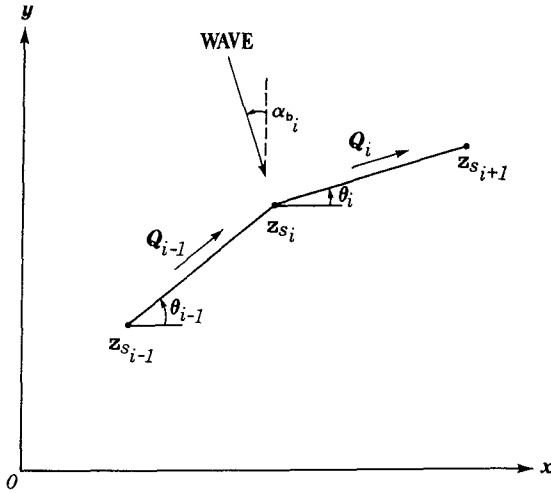


Fig. 2. Finite-difference representation of shoreline and associated transport around  $i$ th point.

and

$$Q_i = \Gamma \left( \frac{H_{b_i} + H_{b_{i+1}}}{2} \right)^{5/2} \cdot \left[ K_1 \sin(2\delta_{b_i}) - K_2 \frac{H_{b_{i+1}} - H_{b_i}}{\Delta s_i} \left( \frac{\cot \beta_i + \cot \beta_{i+1}}{2} \right) \cos \delta_{b_i} \right] \quad (15)$$

in which

$$\delta_{b_i} = \frac{\alpha_{b_i} + \alpha_{b_{i+1}}}{2} - \theta_i \quad (16)$$

The explicit finite-difference scheme becomes unstable for a large time step  $\Delta t$ . As done in Kraus and Harikai (1983) for a Cartesian coordinate system, an approximate stability criterion for small  $\delta_{b_i}$  can be obtained as

$$\Delta t \leq \frac{1}{2} \frac{(\Delta x_s)^2}{\epsilon} \quad (17)$$

in which  $\epsilon = 2K_1\Gamma H_b^{5/2}/D$ . This stability criterion can give the first approximation of the time step for stable solution. If the computed shoreline shows saw-tooth instability, a smaller time step will be needed. Such an instability can be suppressed by smoothing shoreline orientation, longshore transport rate, and shoreline position as done in Uda (1983), but the smoothing process of shoreline position introduces an error in the conservation of sand as  $\Delta x$  increases.

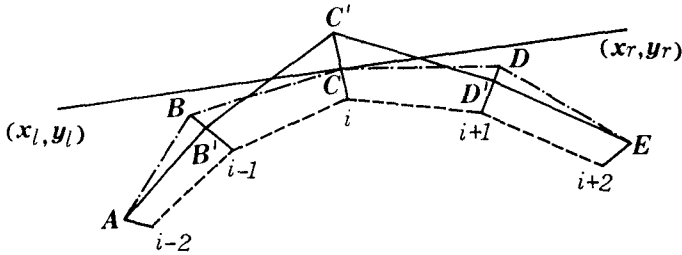


Fig. 3. Illustration of tombolo calculation.

### 2.4 Calculation of tombolo

When the shoreline reaches an impermeable offshore breakwater, its offshore movement should stop there. But a numerical model that does not recognize the presence of the breakwater may calculate shoreline positions located seaward of the breakwater. Thus, at each time step the calculated shoreline position should be examined to determine if any point has moved seaward of the breakwater. If so, the point should be pulled back to the location of the breakwater. Hanson and Kraus (1985) proposed a method to incorporate a seawall constraint in a shoreline numerical model. The method permits a grid point to move landward of the position of a seawall in the initial computation, and then adjusts the longshore transport rates near that point so as to pull it back to the location of the seawall while preserving sediment volume. In the present study their method is applied inversely for the calculation of tombolo formation in the lee of offshore breakwaters.

Consider the discretized shoreline position as shown in Fig. 3. The dashed line denotes the shoreline position at the present time step, and the solid line and dash-dotted line denote the uncorrected and corrected shoreline positions, respectively, at the next time step. In Fig. 3, the  $i$ th point moved seaward of the breakwater to reach the point  $C'(x'_{s_i}, y'_{s_i})$ . We want to pull it back to the point  $C(x_{s_i}, y_{s_i})$ , which is the intersection of the breakwater and the line passing the points  $C$  and  $C'$ . The equation of the breakwater whose tips are located at  $(x_l, y_l)$  and  $(x_r, y_r)$  is

$$y = (x - x_l) \tan \theta_B + y_l \tag{18}$$

in which  $\theta_B$  is the angle between the breakwater and the  $x$ -axis which is measured counterclockwise from the positive  $x$ -direction. The equation of the line passing the points  $C$  and  $C'$  is

$$y = (x'_{s_i} - x) \cot \frac{\theta_{i-1} + \theta_i}{2} + y'_{s_i} \tag{19}$$

in which  $\theta_i$  and  $\theta_{i-1}$  are as defined in Fig. 2, and  $-\cot\{(\theta_{i-1} + \theta_i)/2\}$  represents the slope of the line passing the points  $C$  and  $C'$ . The location of the point  $C$  is then calculated as the intersection of the lines expressed by (18) and (19).

The advance of the shoreline position from  $C$  to  $C'$  results in a fictitious (nonphysical) transport of sand from either one or both sides of the  $i$ th point. The fictitious transport rate of sand,  $\Delta Q_{fic}$ , contributed to move the shoreline position from  $C$  to  $C'$  can be calculated by putting  $z_{s_i}$  for the point  $C$  and  $z'_{s_i}$  for the point  $C'$  in (12) as

$$\Delta Q_{fic} = \frac{D(\Delta s_i + \Delta s_{i-1})}{2\Delta t} \exp \left[ -i \left( \frac{\theta_i + \theta_{i-1}}{2} - \frac{\pi}{2} \right) \right] (z'_{s_i} - z_{s_i}) \quad (20)$$

The amount  $\Delta Q_{fic}$  must be subtracted from the computed transport rates ( $Q_{i-1}$  and/or  $Q_i$ ) depending on their directions as follows:

$$\left. \begin{aligned} Q_{i-1}^c &= Q_{i-1} - \Delta Q_{fic} \frac{Q_{i-1}}{Q_{i-1} - Q_i} \\ Q_i^c &= Q_i - \Delta Q_{fic} \frac{Q_i}{Q_{i-1} - Q_i} \end{aligned} \right\} \text{ if } Q_{i-1} \geq 0 \text{ and } Q_i \leq 0 \quad (21)$$

$$Q_{i-1}^c = Q_{i-1} - \Delta Q_{fic} \text{ if } Q_{i-1} \geq 0 \text{ and } Q_i > 0 \quad (22)$$

$$Q_i^c = Q_i + \Delta Q_{fic} \text{ if } Q_{i-1} < 0 \text{ and } Q_i \leq 0 \quad (23)$$

The superscript  $c$  denotes the corrected transport rates. The new position of the point  $B$  and/or  $D$  is then calculated using the corrected transport rates. If the new point,  $B$  or  $D$ , is computed to move seaward of the breakwater, it is pulled back to the location of the breakwater using the same procedure as above. Finally, it should be mentioned that in the present model, if any two adjacent shoreline points touch the breakwater, the transport rate between these points is set to zero.

### 3 Chippokes State Park Breakwater Project

The six segmented breakwaters at Chippokes State Park are located on the southern shore of Cobham Bay in the James River, one of the tributary estuaries of Chesapeake Bay, Virginia (Fig. 4). Chippokes is a recreational and historic state park as well as a model farm. The site is characterized by high (12 m) eroding fastland banks composed of a lower unit of shelly, fossiliferous, fine to coarse sand overlain by an upper layer of slightly muddy, fine to medium sand.

The preconstruction beach at Chippokes was a curvilinear strand of sand about 7.5 m wide from MHW to the base of the bank. The beach itself consists of well sorted, shelly sand derived from the eroding bluff. The mean diameter of the beach sand averaged from six sediment samples is 0.44 mm (medium sand). The shoreline at Chippokes faces almost due north and has an average fetch of about 4.8 km. Long fetch exposures of 9.3 km and 14.8 km occur to NNE and NW directions, respectively. Net longshore transport here is eastward but with seasonal fluctuations and on-offshore movement. The seasonal wave climate favors northerly winds in winter and southwesterly winds in summer. Mean seasonal winds generate limited waves across the

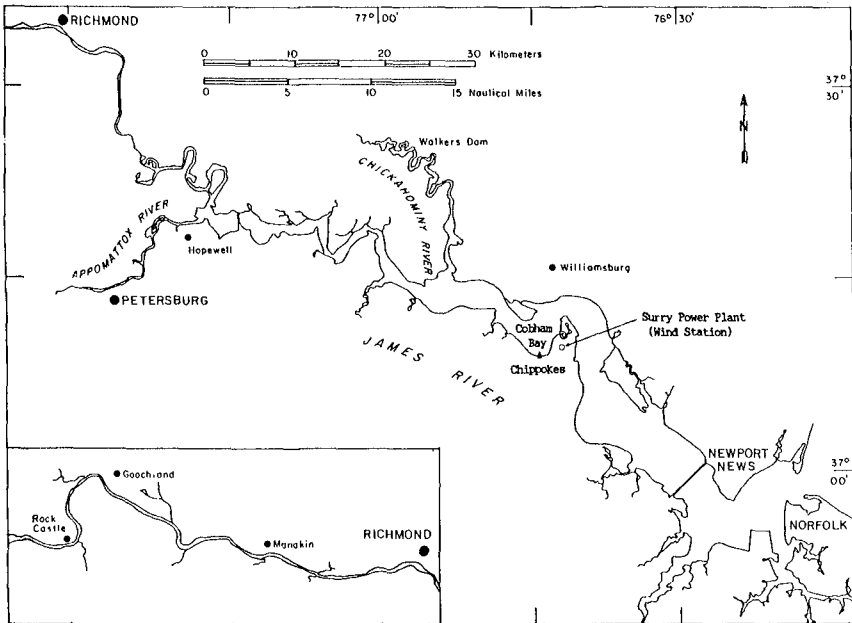


**Fig. 4. Location map of Chippokes State Park Breakwaters, Virginia.**

river. Extratropical and tropical storms with the associated storm surges are the main forces causing movement of beach sand and shoreline erosion. Mean tidal range is 58 *cm*.

The goal of the project was to design a system which would permit tombolos to form utilizing the existing volume of sand on the beach such that with time a stable backshore would develop and protect the base of the high banks. A system of six rubble mound breakwaters with a length to gap ratio of 1:1.5 was constructed in June 1987. The crest lengths are 15 *m* and gaps are 22.5 *m*. The centerline of the breakwaters is approximately 9 *m* from the initial MHW line. The water depth below MHW at the location of breakwaters varies between 0.75 and 0.87 *m*.

A baseline (*x*-axis in Fig. 5) was established using a transit. From this, 33 profile lines were determined and surveys performed using a rod and level. Profile measurements were made in July 28 and November 12, 1987 and February 23, 1988. Aerial photography was done every three months between September 2, 1987 and March 9, 1988. The photographs were used along with the profile data to create shoreline position maps.

Fig. 5 shows the measured shoreline change (dashed lines) from June 1987

to March 1988 along with the computed results. The position of MHW was used to track beach changes. Sand began accumulating and migrating toward each breakwater unit as cusped spits formed almost immediately after construction. The characteristic double salients evolved behind each breakwater by September 1987. Sediment for the salients was derived from the adjacent embayments. By March 1988 all the bays showed signs of filling. Especially obvious are the accumulation of sand on the west end of the system and marked loss of sand on the east. One would infer a net west to east movement of sand along this portion of the reach.

## 4 Model Application

The developed numerical model was applied to the simulation of the shoreline change near the Chippokes State Park Breakwaters for the first nine months (from June 1987 to March 1988) after construction.

### 4.1 Wave hindcast

There are no available wave data near the project site for the simulation period. Therefore, input wave data at the location of the breakwaters were hindcasted from wind data measured at Surry power plant located about 2.8 km ENE of the project site (see Fig. 4). The wind data included speed and direction every one hour. Assuming that the wave direction corresponds to the wind direction, as seen in Fig. 4, the project site is affected by the wind blowing within the directional window fanning from  $320^\circ$  to  $20^\circ$  measured clockwise from the north. It is also assumed that in order to generate the wave field that affects the shoreline change, wind should blow for more than three hours (i.e., more than three consecutive observations) within the directional window. The average wind speed and direction for the period were calculated by vector-averaging the observations given every one hour. A constant wind field corresponding to the averaged wind speed and direction was assumed for that period.

The significant wave height and period at the location of the breakwaters were computed using the model of Kiley (1989), which is essentially a shallow water estuarine version of the quasi-empirical wind wave prediction model developed by Bretschneider (1966) and modified by Camfield (1977). The model includes variation in water depth, the effect of surrounding land forms on the computation of the effective fetch, wave growth due to wind stress and wave decay due to bottom friction and percolation. The wave angle at the location of the breakwaters is determined by Snell's law assuming that the offshore bottom contours are straight and parallel to the  $x$ -axis and the deep water wave direction (at the center of the river) is the same as the wind direction.

The weight-averaged (by duration of each wave condition) values of significant wave height and period, and wave angle at the location of breakwaters

are 12.2 *cm*, 1.43 *s*, and 1.33°, respectively, indicating very short small waves and net eastward longshore transport rate. The highest wave during the simulation was 21 *cm* high with 2.0 *s* period. Waves of 0.5 to 0.7 *m* height with 2.5 to 3.0 *s* period have been observed on April, 13, 1988. In this area, these types of events occur every two to three years but slightly lesser events occur even more frequently. Total duration of the simulation is 568 hours so that the percent of calm is 90 %.

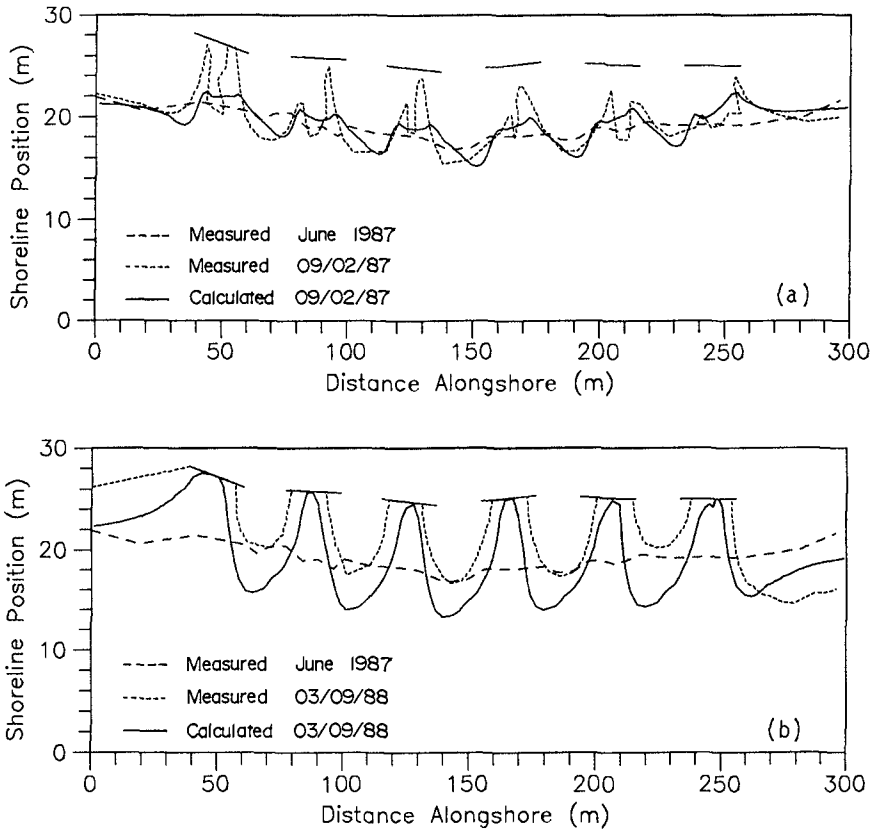


**Fig. 5. Comparison between measurement and computation of shoreline change near Chippokes State Park Breakwaters, Virginia; (a) September 1987, (b) March 1988.**

## 4.2 Simulation

The initial shoreline in June 1987 in Fig. 5 was discretized by  $\Delta x = 1.524 \text{ m}$  ( $5 \text{ ft}$ ) to give about 10 points behind each breakwater and 195 points ( $296 \text{ m}$ ) for the shoreline reach shown in Fig. 5.  $\Delta t = 90 \text{ s}$  was used. All the water depths and shoreline position in the model are with respect to MHW level, since the shoreline position in the report of Hardaway et al. (1988) is presented in terms of MHW line. The water level was assumed to be fixed at the MHW level. The coordinates of the breakwater tips were taken as the shoreward corners of the bases of the breakwaters.

The shoreline change in the areas far from the project site is not available. Therefore, the model area was extended to both sides by  $100 \text{ m}$  and fixed boundary conditions were used at both ends. The offshore distances of the initial shoreline in the extended areas were assumed to be the same as those at the end points of the initial shoreline in Fig. 5. The shoreline change in the extended areas is not shown in Fig. 5.

The longshore sediment transport coefficient  $K_1 = 0.77$  was used as suggested by Komar and Inman (1970).  $K_2 = K_1$  was used tentatively. The calculated depth of profile closure is  $0.52 \text{ m}$ .

Fig. 5 shows the computed (solid lines) shoreline changes in September 2, 1987 and March 9, 1988 along with the measurement (short-dashed lines). The initial shoreline position is also given by long-dashed lines. The formation of double salients in September 1987 is predicted by the model, even though it is not so clear as in the measurement. The model calculated smaller tombolos and more prominent erosion behind the gaps compared to those in the measurement in March 1988. This may be due to the addition of sediment to the system by runoff and bluff erosion as reported in Hardaway et al. (1988), which was not included in the present model that assumes zero on-offshore transport of sediment.

## 4.3 Decay of tombolos

Sometimes tombolos are built artificially as a means to protect beaches as in Elm's Beach, Maryland (Hardaway and Gunn 1989), for example. If the project is not designed properly, the tombolos can be reduced to salients. In order to test how the model works for such a situation, the model was run for 48 hours of  $H_B = 7.9 \text{ cm}$ ,  $T = 1.16 \text{ sec}$ , and  $\alpha_B = 0^\circ$  (the mildest wave condition used in the previous simulation) with the computed shoreline in March 9, 1988 as the initial condition. The result is shown in Fig. 6. For the mild wave condition, the tombolos reduced to salients and accretion occurred in the embayments.

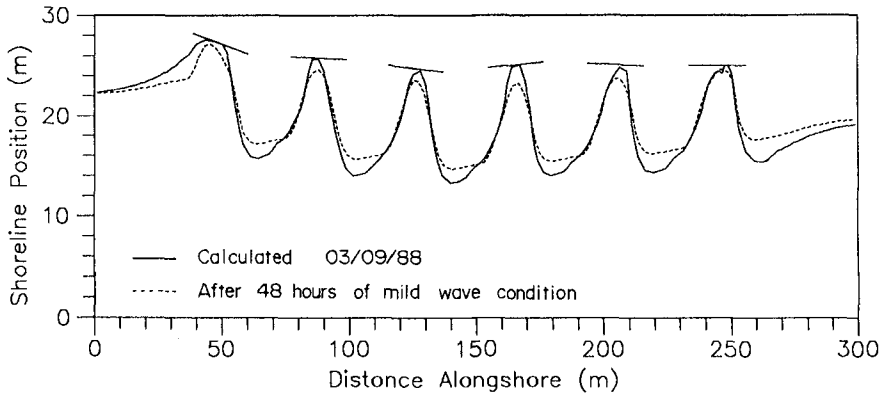


Fig. 6. Test for decay of tombolos.

## 5 Conclusion

The present study has proposed an algorithm that is capable of calculating the growth and decay of tombolos in the lee of offshore breakwaters in a shoreline numerical model. The algorithm permits a grid point to move seaward of an offshore breakwater in the initial computation, and then adjusts the longshore transport rates near that point so as to pull it back to the location of the breakwater while preserving sand volume. The neighboring shoreline positions are recalculated using the adjusted longshore transport rates. Even though in this study the algorithm was used along with a shoreline numerical model which uses curvilinear coordinates that follow the shoreline, it could be easily modified for the use in traditional shoreline models using Cartesian coordinate system.

The project of six segmented breakwaters at Chippokes State Park, Virginia has been reported. The developed model was applied to the simulation of the shoreline change during the first nine months after construction of the Chippokes breakwaters. The present model, which does not include cross-shore transport, predicted smaller tombolos and more embayment erosion compared to measurement at the Chippokes project site, where sediment was added to the system by runoff and bluff erosion. The model was applied for offshore breakwaters in an estuary with very short small waves, and applications in open coasts may be needed to fully examine the performance of the model.



## Acknowledgements

The authors acknowledge the financial support from the Norfolk District, U.S. Army Corps of Engineers and the Virginia Department of Conservation and Recreation. The first author was partly supported by Korea Ocean Research and Development Institute under Project No. BSPE 00223.

## References

- Bretschneider, C.L. (1966). "Wave generation by wind, Deep and shallow water." In: *Estuary and Coastline Hydrodynamics* (Ed. A.T. Ippen). McGraw-Hill, New York, 133-196.
- Camfield, F.E. (1977). "A method for estimating wind-wave growth and decay in shallow water with high values of bottom friction." *Tech. Aid CETA 77-6*. Coast. Engrg. Res. Center, Fort Belvoir, Virginia.
- Hallermeier, R.J. (1983). "Sand transport limits in coastal structure design." *Proc. Coast. Structures '83*, ASCE, 703-716.
- Hanson, H. and Kraus, N.C. (1985). "Seawall constraint in shoreline numerical model." *J. Wtrwy., Port, Coast. and Oc. Engrg.*, ASCE, 111(6), 1079-1083.
- Hanson, H. and Kraus, N.C. (1989). "GENESIS: Generalized model for simulating shoreline change; Report 1, Technical reference." *Tech. Rep. CERC-89-19*. Coast. Engrg. Res. Center, Waterways Experiment Station, Vicksburg, Miss.
- Hardaway, C.S. and Gunn, J.R. (1989). "Elm's Beach breakwater project - St. Mary's County, Maryland." *Proc. Beach Preservation's Technology '89*, Florida Shore and Beach Preservation Association, 147-160.
- Hardaway, C.S., Thomas, G.R., Moustafa, M.S.J. and Li, J.-H. (1988). "Chesapeake Bay Shoreline Study - Interim Report." Virginia Inst. of Marine Sci., Gloucester Point, Virginia.
- Kiley, K. (1989). "Estimates of bottom water velocities associated with gale wind generated waves in the James River, Virginia." *Unpublished manuscript*. Virginia Inst. of Marine Sci., Gloucester Point, Virginia.
- Kobayashi, N. and Dalrymple, R.A. (1986). "Erosion of unprotected causeway due to waves." *Res. Rep. No. CE-86-58*, Dept. of Civil Engrg., Univ. of Delaware, Newark, Delaware.
- Komar, P.D. and Inman, D.L. (1970). "Longshore sand transport on beaches." *J. Geophys. Res.*, 75(30), 5914-5927.

- Kraus, N.C. (1982). "Pragmatic calculation of the breaking wave height and wave angle behind structures." *Proc. 29th Japanese Coast. Engrg. Conf.*, 95-99 (in Japanese).
- Kraus, N.C. and Harikai, S. (1983). "Numerical model of the shoreline change at Oarai beach." *Coast. Engrg.*, 7, 1-28.
- Kraus, N.C., Isobe, M., Igarashi, H., Sasaki, T. and Horikawa, K. (1982). "Field experiments on longshore sand transport in the surf zone." *Proc. 18th Coast. Engrg. Conf.*, ASCE, 969-988.
- LeBlond, P.H. (1972). "On the formation of spiral beaches." *Proc. 13th Coast. Engrg. Conf.*, ASCE, 1331-1345.
- Ozasa, H. and Brampton, A.H. (1980). "Mathematical modelling of beaches backed by seawalls." *Coast. Engrg.*, 4(1), 47-63.
- Penney, W.G. and Price, A.T. (1952). "The diffraction theory of sea waves and the shelter afforded by breakwaters." *Phil. Trans. Roy. Soc. London*, A 244, 236-253.
- Perlin, M. (1979). "Predicting beach planforms in the lee of a breakwater." *Proc. Coast. Structures '79*, ASCE, 792-808.
- Perlin, M. and Dean, R.G. (1985). "3-D model of bathymetric response to structures." *J. Wtrwy., Port, Coast. and Oc. Engrg.*, ASCE, 111(2), 153-170.
- Sunamura, T. (1984). "Quantitative predictions of beach-face slopes." *Geological Soc. of America Bull.*, 95, 242-245.
- Uda, T. (1983). "Predictive model of planform change of a spit at a river mouth." *Coast. Engrg. in Japan*, 26, 137-150.
- Wang, H., Dalrymple, R.A. and Shiau, J.C. (1975). "Computer simulation of beach erosion and profile modification due to waves." *Proc. Symp. Modeling Technique*, ASCE, 1369-1384.
- Watanabe, A. (1982). "Numerical models of nearshore currents and beach deformation." *Coast. Engrg. in Japan*, 25, 147-161.

## CHAPTER 193

### BEACH IMPROVEMENT SCHEMES IN FALSE BAY

by

D H Swart\* and J S Schoonees\*\*

#### ABSTRACT

A physical sediment model was used to design two beach improvement schemes in False Bay near Cape Town. Different layouts of T, L and detached breakwaters were tested to determine their effect on the beach and how they improved bathing conditions. Although caution was exercised to eliminate scale effects, it was found to be necessary to minimize their influences. A method was devised to do so which proved successful. It was found that equilibrium shoreline positions were reached after 4 years (prototype time). Sand feeding after construction will be necessary to minimize the deleterious effects of the breakwaters on the adjacent beaches.

#### INTRODUCTION

False Bay which is a large, partly protected bay (ca 35 km x 35 km) is situated near Cape Town, South Africa (Figure 1). The study site covered about 8 km of coastline from Strandfontein to Kapteinsklip alongshore (Figure 1) and up to the -20 m to mean sea level (MSL) contour. False Bay provides beach recreational facilities for the nearby metropolitan area of Cape Town.

The CSIR was commissioned to undertake studies on recreational schemes proposed for the north shore of False Bay. A tidal pool was built at Strandfontein as Phase 1 of this project. Phase 2 consists of beach improvement schemes at Kapteinsklip and Middelbank. The aim of this latter phase is to provide safe bathing beaches using groynes. At present the major part of the coast is rather unsafe for bathing mainly because of steep

---

\* Division director and \*\* Research engineer, CSIR, P O Box 320, 7599 Stellenbosch, South Africa.

beach profiles. The client laid down specific criteria to ensure safe bathing, e.g. a uniform flat beach slope and the absence of rock and strong rip currents. Further requirements were that a safe bathing beach forms soon after completion of the structures and that the adjacent coastline must not be adversely affected in the long term. This paper deals with the design of these beach improvements schemes using a physical sediment model.

Based on the expected number of visitors and bathers and assuming that 10 bathers per metre distance alongshore can be accommodated, it was stipulated that 1 200 m and 2 000 m of safe bathing beach must be provided at Kapteinsklip and Middelbank respectively.

Waves were recorded in about 20 m of water using two Waverider buoys. During the one year recording period, the mean significant wave height at the Waveriders was 1,2 m with a mean peak wave period of 11,1 s. The tides in the False Bay area are semi-diurnal with a mean spring tidal range of 1,6 m. From quarterly surveys it was found that the average median sand grain size on the beach is 0,45 mm. A best estimate of the gross longshore transport rate is 387 000 m<sup>3</sup>/year while the net longshore transport is eastbound and about 145 000 m<sup>3</sup>/year (CSIR, 1983). More details about the characteristics of the site can be found in Schoonees and Möller (1982) and CSIR (1983, 1988).

The mobile bed model which was about 100 m by 35 m, had a horizontal length scale of 1/20 and a vertical scale of 1/50 (giving a distortion of 2,4). The model sediment was sand with a median grain size ( $D_{50}$ ) of 0,315 mm. Calibration of shoreline evolution was carried out using results from aerial photography. This yielded a sedimentological time scale of 24 h of waves in the model being equivalent to 1 year in prototype. The wave climate was schematized into five cycles comprising quasi-irregular waves from both the westerly and easterly sectors. Schoonees and Möller (1982) and CSIR (1988) discusses the design and calibration of this model in detail.

The values of parameters given below are prototype values unless specified otherwise.

## TEST SERIES

### General

The authorities plan to implement the Kapteinsklip beach improvement scheme first followed by Middelbank some four years later. Because of the

time and cost involved, it was decided to run most of the tests for four years. This was found to be sufficient to reach an equilibrium coastline at the groynes as will be discussed later.

### **Programme**

The groyne layouts for the Kapteinsklip scheme, the A series, are shown in Figure 2a. Figure 2b illustrates the groynes tested in the Middelbank area. T, L and detached breakwaters were modelled. In addition, a zero test (Test A5) was conducted to determine the behaviour of the model without any structures. Having built in the 4 year shoreline condition (of an L groyne) at Kapteinsklip, another zero test (Test B3) was run; in this case for the Middelbank scheme. This test also served the purpose of showing shoreline response over 8 years at Kapteinsklip because the initial shoreline was the 4 year condition.

### **Scale Effects**

The effect of varying the number of cycles of westerly and easterly waves to make up one representative year was investigated. Both 5 and 10 cycles were tested. It was found that there was very little difference in coastline evolution between using 5 or 10 cycles. The easier and cheaper option of 5 cycles was therefore chosen.

Sediment samples were taken during Test B3 at different cross-shore and longshore locations to investigate the variation in  $D_{50}$  over time. No consistent tendencies and therefore scale effects due to sorting were found.

Rocky areas must be accurately represented in the model. Because they limit the availability of sand, rocky areas have a profound effect on coastline evolution if they are present. Care, therefore, should be exercised to survey them in detail so that they can be modelled correctly.

Three different scale effects were present in the results. These are diffraction effects causing the longshore transport to be incorrectly simulated, onshore sediment transport and the formation of cusps. For each of these, a factor was determined such that the shoreline response could be modified to account for these scale effects.

Because it was a distorted model, only refraction or diffraction could be reproduced correctly. Refraction was chosen to be of more importance and thus diffraction had to be corrected for. This was done as follows:

- Diffraction coefficients were determined from diffraction diagrams (US Army, Corps of Engineers, 1977) along a line in the lee of the groynes and parallel to the shore. This was done for the diffraction in the model and for the case where diffraction would have been correctly

simulated. From these, the incident wave characteristics and by assuming Snell's law, the breaker conditions were calculated.

- The longshore transport rates were then computed at different positions along the shore for both diffraction cases. The formulae by Engelund, Hansen and Swart and the SPM adapted by Swart (Swart, 1976a and b) were used. The Schoonees (1986) method was used to account for a gradient in breaker height.
- Volume changes per time were derived from the difference in longshore transport rates. These yielded the diffraction factor,  $k_{dif}$ . Following this procedure for westerly and easterly waves, weighted mean diffraction factors were determined along the beach. These varied around 1,0 (from 0,5 to 2,0). A factor of 1,0 means that the rate of shoreline change was predicted correctly in the model. These factors were almost always positive which means that the model predicted accretion and erosion to occur in the correct locations.

To account for onshore sand transport, mean beach profiles found in the model during Test A5 (a zero test) were computed after 1, 2, 3 and 4 years. A cross-shore sediment transport model (Swart, 1974) was calibrated for both model and prototype beaches. Thereafter the model was used to predict the onshore transport correction factor ( $k_{dwa}$ ) for different wave heights.

$$k_{dwa} = \text{(predicted distance that the coastline changed under model conditions, scaled to prototype size) / (predicted distance that the coastline changed in prototype conditions)}$$

An analysis of the cusps found in the zero tests (Figure 3) yielded a mean cusp factor ( $k_{str}$ ) of 2,0. The ratio of the distance to the apex of the cusp to the distance to the new mean shoreline position without the cusp is  $k_{str}$ . This factor was taken to be 2,0 if a cusp was present or 1,0 if not. This could be done because adaptations of the coastline position were only done at or close to the apex of cusps if they were present.

Adaptation of the coastline changes to account for these three scale effects were done as follows:

$$\begin{aligned} V_m &= V_{dwa,m} + V_{dif,m} \\ \text{and } V_p &= V_{dwa,p} + V_{dif,p} \\ \text{where } V &= \text{volume accreted or eroded} \end{aligned}$$

and subscripts      dwa =      onshore transport

dif = diffraction  
 m = model  
 and p = prototype

Furthermore:  $k_{dif} = V_{dif,m} / V_{dif,p}$   
 $k_{dwa} = V_{dwa,m} / V_{dwa,p}$

Substituting these equations it is possible to obtain  $V_p$  as a function of  $V_{dwa,m}$ ,  $V_m$ ,  $k_{dif}$  and  $k_{dwa}$ . Assuming that the distance over which the shoreline changes horizontally is directly proportional to  $V$  (which model results confirmed) and incorporating  $k_{str}$ , the result is:

$$a_p = a_{dwa,m} \left( \frac{1}{k_{dwa} \cdot k_{str}} - \frac{1}{k_{dif}} \right) + a_m / k_{dif}$$

This relationship was used to modify the measured model responses. It should be noted that the model was designed using preliminary (visually estimated) wave data. While the model was being constructed, the wave recordings were carried out. If the measured wave characteristics are used to compute the vertical scale in the same way as explained in Schoonees and Möller (1982), the vertical scale would have been 1/75 (instead of 1/50) giving a distortion of 1.6. This would definitely affect the cross-shore transport and possibly also the formation of cusps, thus influencing (hopefully reducing) the scale effects in the model.

### Test Results and Discussion

Figures 4a and b show the original model results of Test A4 and the model response of this test corrected for the above-mentioned scale effects respectively. Note that the adaptation of the results were only done in the lee of the L groyne and not to the right of the groyne. The corrected shoreline response of Test B3 which started with the 4 year condition of Test A4, is illustrated in Figure 4c. Shoreline variations over a period of 8 years were thus modelled. From these figures it can be seen that most shoreline changes occurred within 2 or 3 years after construction of the groynes. Equilibrium is reached after 4 years. The same was found of the coastline evolution in the other tests. This is in accordance with what has been found in the field in Israel (Nir, 1982), Japan (Toyoshima, 1976) and Brittain (Barber and Davies, 1985). Thereafter the shoreline fluctuates slightly around the equilibrium position (Figure 4c).

Detailed wave and current measurements were done in order to quantify the improvement in bathing conditions. Figures 5a and b show wave height contours and current velocities for regular westerly waves at the end of Test A6. The comfort of beach users will be improved by the schemes

because the beaches will be wider and will vary less in width over time. Bathing safety will be substantially enhanced because of the reduction in wave action and the associated reduction in current velocities. However, a varying wave climate will be provided along the beach from calm areas to enough wave action for the more adventurous swimmer. In addition, the beach slopes will be flatter and most of the rock will be covered by sand. Rock pinnacles which will still be exposed will have to be removed. To limit the return flow (out of gaps between groynes) due to wave overtopping, it was recommended that the crest height of the groynes be +2 m to MSL. An analysis of prototype schemes around the world and the tidal ranges occurring at those sites, also indicated this crest height to be realistic.

To minimize the effect of the schemes on the adjacent coastline, it was recommended that sand feeding be carried out with compatible sand. This should be done once and up to the equilibrium shoreline position after the construction of the groynes is complete.

Kamphuis (1975) presents an equation to calculate the sedimentological time scale. In this formula the factor  $M$  should be 1 for perfect agreement. By analysing a number of studies he showed  $M$  to vary between 0,35 and 14,6. For this study  $M = 1,48$ , which is in good agreement with the theoretical and empirical values.

### **Proposed Schemes**

Figure 6a presents the proposed scheme at Kapteinsklip. Together with the predicted equilibrium coastline position, areas are shown where additional beaches can be created using sand nourishment. In Figures 6b and c two alternatives are given for the Middelbank scheme. For both the schemes at Kapteinsklip and Middelbank, the required length of safe bathing beach will be obtained. Sand feeding is strongly recommended to minimize the effect on the adjacent beaches. Building each of these schemes in phases in order to limit the initial expenditure, was also considered and found to be viable (CSIR, 1989).

### **CONCLUSIONS**

A physical sediment model is an effective tool to apply to investigations of coastline evolution following the construction of groynes. Clients and designers can see what happens during tests. However, these models are expensive to build and operate.

Scale effects are normally present in studies using mobile bed models. Caution should be exercised to minimise these. In this study the important scale effects were found to be the result of diffraction effects, onshore sand transport and cusps. A method was devised and applied successfully to minimize these scale effects. To achieve this, it is essential to conduct (a)



zero test(s) by which the model behaviour without structures can be quantified. It was also found that rocky areas should be built in accurately because they can have a profound effect on beach evolution.

In accordance with field observations worldwide it was found that most shoreline changes occurred within the first 2 to 3 years after groyne construction. Equilibrium shoreline positions are reached after about 4 years. An independent check on the sedimentological time scale confirmed its accuracy.

The T, L and detached breakwaters proposed for the beach improvement schemes (Figures 6a - c) will improve bathing conditions significantly. Sand feeding after construction is necessary to minimize the deleterious effects of the groynes on the adjacent beaches.

### **ACKNOWLEDGEMENT**

The authors gratefully acknowledge Messrs Frank van Dulm, André Leith, Willie Daniels, Henry Davids and Koos Möller for their meticulous operation of the model.

### **REFERENCES**

- Barber, P C and Davies, C D (1985). Offshore breakwaters - Leasowe Bay. Proceedings of the Institution of Civil Engineers, Part 1, Volume 77: 85-109.
- CSIR (1983). False Bay: Field data report. CSIR Report C/SEA 8219/1,2 and 3, Stellenbosch. (In Afrikaans).
- CSIR (1988). False Bay: The hydraulic design of beach improvement schemes with a physical sediment model. CSIR Report EMA-C 8886, Stellenbosch (in Afrikaans).
- CSIR (1989). Improved beach amenities along the False Bay coast between Strandfontein and Mhandi. CSIR Report EMA-C 8940, Ematek, Stellenbosch.
- Kamphuis, J W (1975). The coastal mobile bed model. C E Research Report No 75. Dept Civil Engineering, Queens University, Kingston, Ontario.
- Nir, Y (1982). Offshore artificial structures and their influence on the Israel and Sinai Mediterranean beaches. 18 Intern. Conf. on Coastal Eng., ASCE, Volume 3: 1837-1856, Cape Town.
- Schoonees, J S (1986). Breaker wave characteristics and longshore sediment transport along a bay. M.Eng. Thesis, University of Stellenbosch, Stellenbosch.

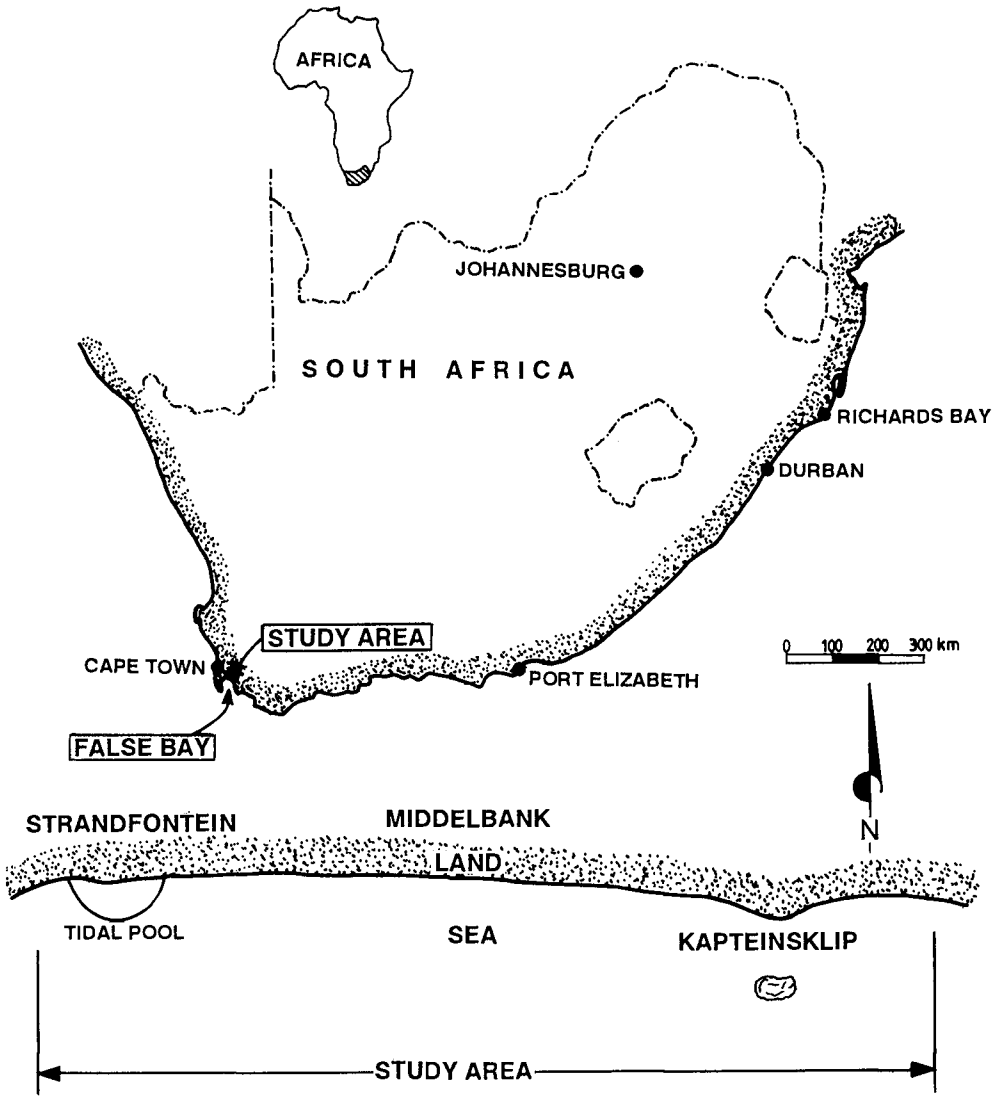


FIGURE 1: LOCATION MAP

Schoonees, J S and Möller, J P (1982). Design and calibration of False Bay sediment model. 18 Intern. Conf. on Coastal Eng., ASCE, Vol. 2: 1161-1180, Cape Town.

Swart, D H (1974). Offshore sediment transport and equilibrium beach profiles. Delft Hydraulics Laboratory Publication No 131, Delft.

Swart, D H (1976a). Coastal sediment transport. Computation of longshore transport. Report R968, Part 1, Delft Hydraulics Laboratory, Delft.

Swart D H (1976b). Predictive equations regarding coastal transports. 15 Intern. Conf. on Coastal Eng., ASCE, Vol. 2: 1113-1132, Honolulu, Hawaii.

Toyoshima, O (1976). Changes of sea bed due to detached breakwaters. 15 Intern. Conf. on Coastal Eng, ASCE, Volume 2: 1572-1589, Honolulu, Hawaii.

United States Army, Corps of Engineers (1977). Shore Protection Manual. Volumes I, II and III. Fort Belvoir, Virginia.

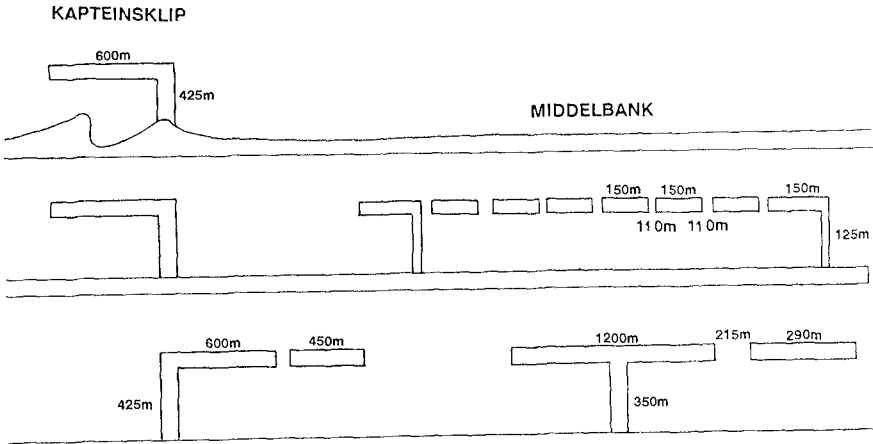


FIGURE 2b: GROYPE LAYOUTS AT MIDDELBANK

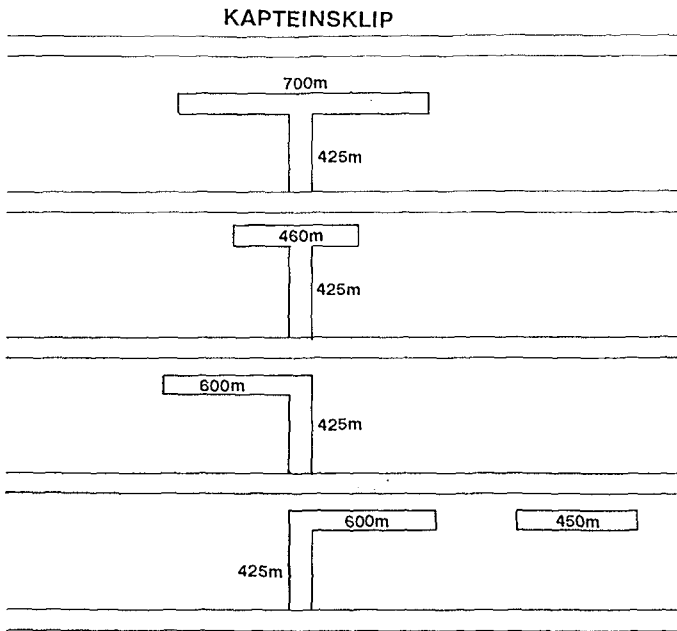


FIGURE 2a: GROYPE LAYOUTS AT KAPTEINSKLIP

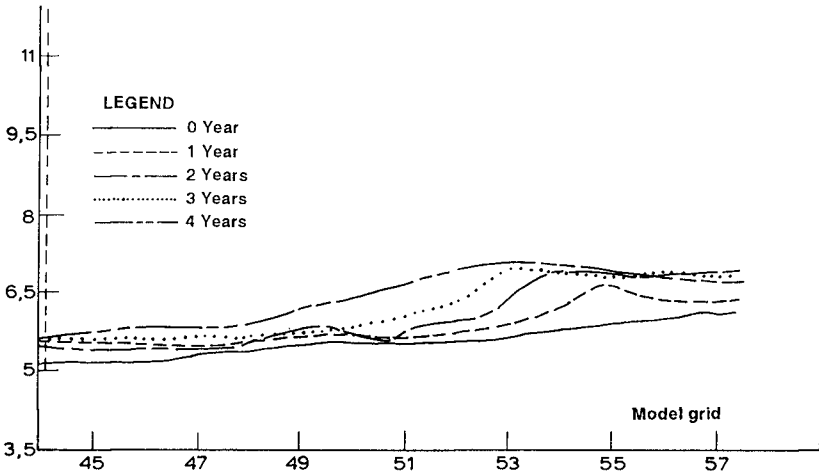


FIGURE 3: COASTLINE CHANGES DURING A ZERO TEST (A5)

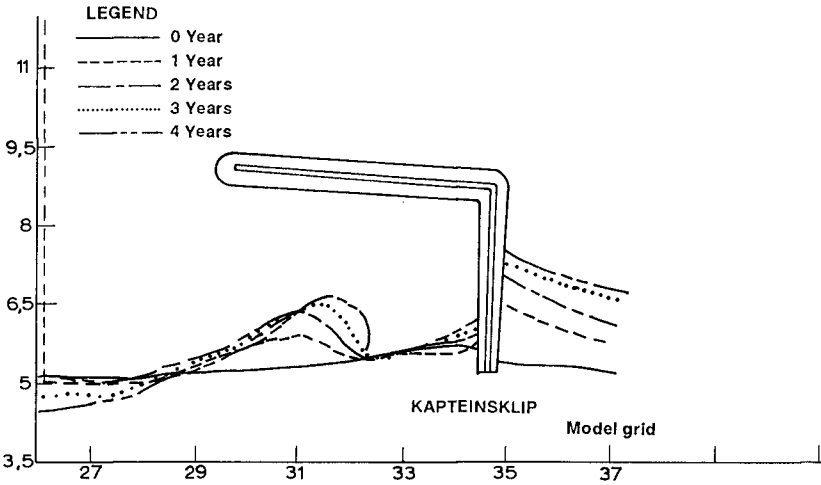


FIGURE 4a: COASTLINE CHANGES DURING TEST A4  
(NOT CORRECTED FOR SCALE EFFECTS)

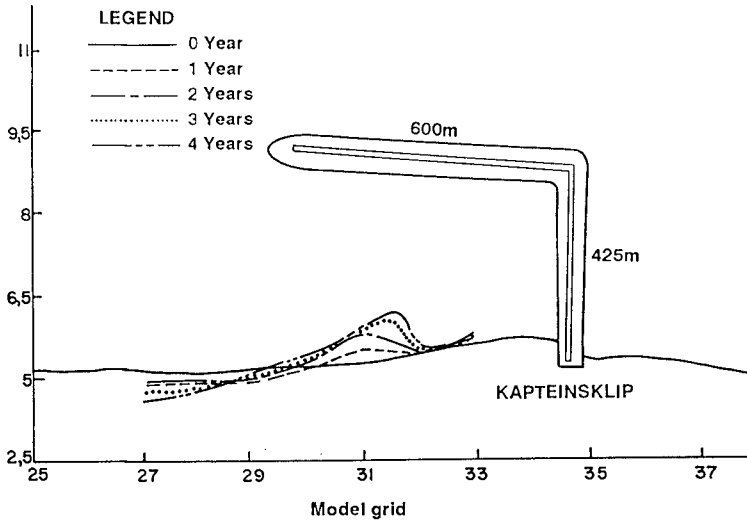


FIGURE 4b: COASTLINE CHANGES DURING TEST A4  
(CORRECTED FOR SCALE EFFECTS)

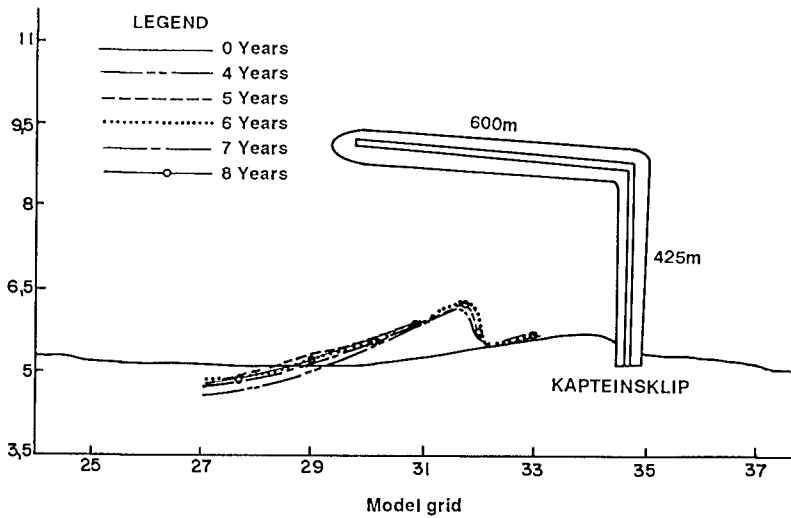


FIGURE 4c: COASTLINE CHANGES DURING TEST B3  
(CORRECTED FOR SCALE EFFECTS)

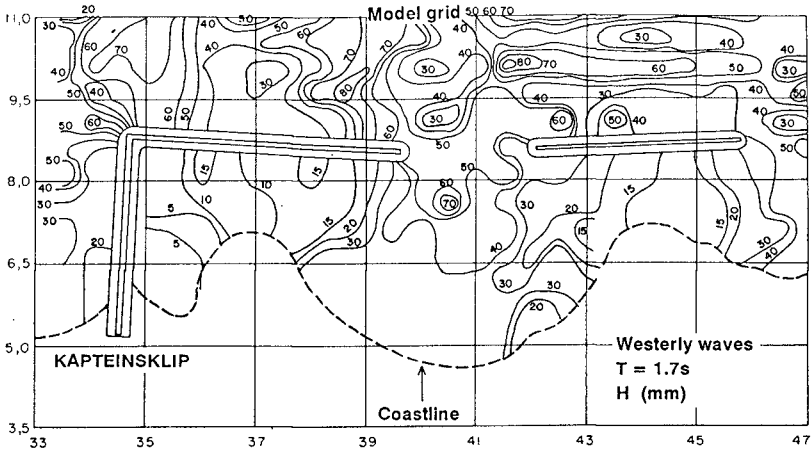


FIGURE 5a: WAVE HEIGHT CONTOURES

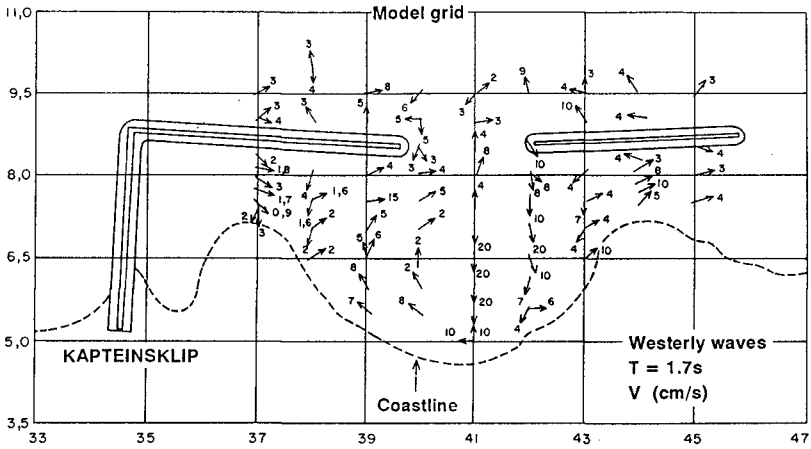


FIGURE 5b: CURRENT VELOCITIES

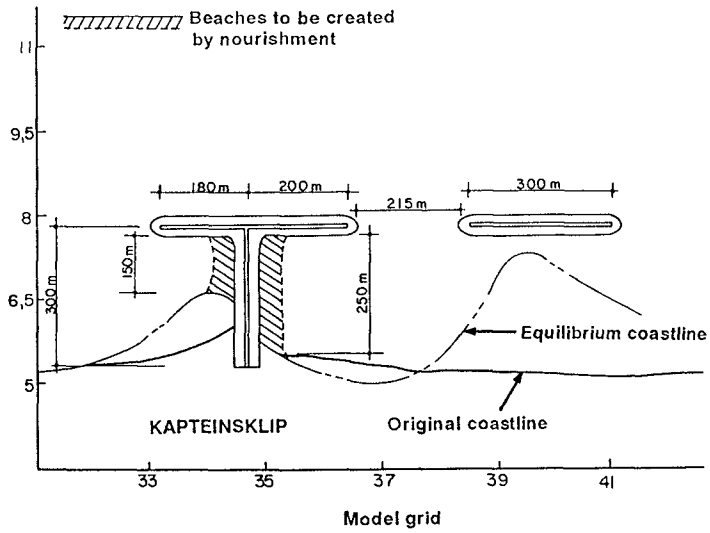


FIGURE 6a: PROPOSED LAYOUT AT KAPTEINSKLIP

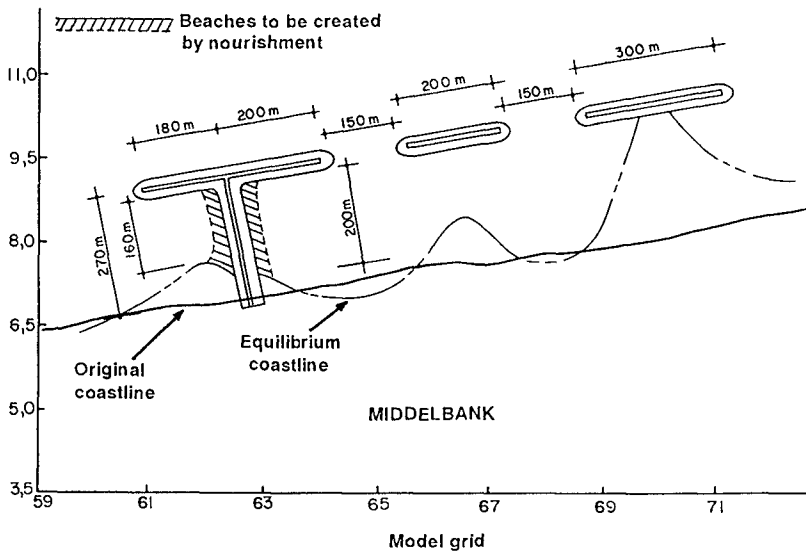


FIGURE 6c: A PROPOSED LAYOUT AT MIDDELBANK



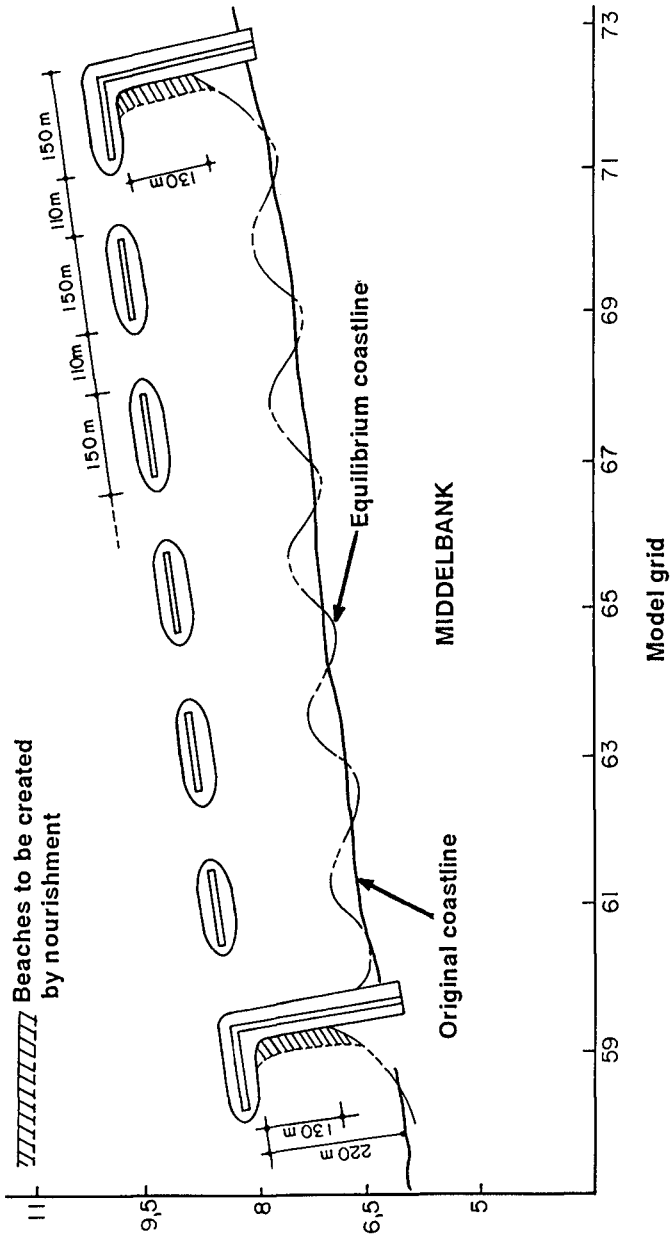


FIGURE 6b: A PROPOSED LAYOUT AT MIDDELBANK

## CHAPTER 194

# BEACH EROSION IN KUTA BEACH, BALI AND ITS STABILIZATION

Abdul R. Syamsudin<sup>1</sup>, Yoshito Tsuchiya<sup>2</sup>, M. ASCE and Takao Yamashita<sup>3</sup>

### Abstract

Due to the construction of an airport runway, severe beach erosion has taken place on the Kuta beach, a coral-sand beach in Bali. Introducing the most effective wave for beach change in terms of wave transformation on a coral reef, the long-term shoreline change is predicted with changing the positions for the boundary conditions to be used as headlands for stabilizing the beach in the large scale coastal behavior. We could find a possibility of stabilizing the beach against beach erosion by constructing three headlands at the positions found. In this beach, a very small amount of sediment source can only be produced from the activity of sea animals. On the basis of the long-term shoreline change and the theory of the formation of static stable beaches, therefore, a methodology for coral-sand beach stabilization was proposed, and parts of this were constructed. Further improvement for the headlands is needed, but as of 1989, a static stable coral-sand beach has been well-formed between the headlands.

### INTRODUCTION

Acceleration of beach erosion throughout the world is now recognized as being due to the way humans have developed and utilized coastal zones and river basins. Many attempts have been made to control beach erosion, but in the long term none have succeeded in stabilizing sandy beaches that are being eroded. Due to current development of coral reef beaches, severe beach erosion has taken place in coral-sand beaches in Bali. One of them is the Kuta beach as shown in Figure 1, facing the Bali straight. Since, in 1968, an airport runway was constructed on the coral flat in this

---

<sup>1</sup>Director, Hydraulic Laboratory, Research Institute for Water Resources Development, Agency for Research & Development, Ministry of Public Works of Indonesia, Bandung, Indonesia.

<sup>2</sup>Professor Emeritus, Kyoto University & Professor, Meijo University, Tenpaku-ku, Nagoya 467, Japan.

<sup>3</sup>Instructor, Disaster Prevention Research Institute, Kyoto University, Uji, Kyoto 611, Japan.

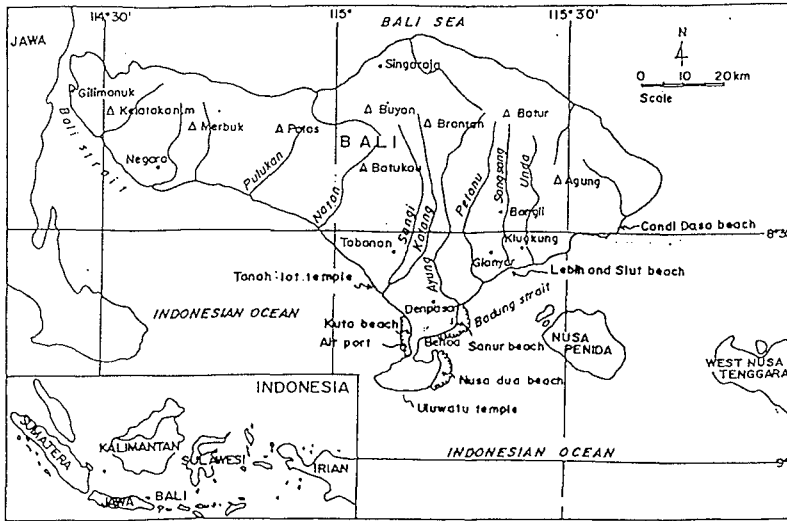
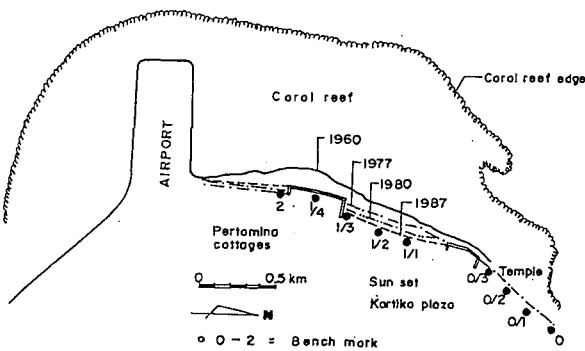
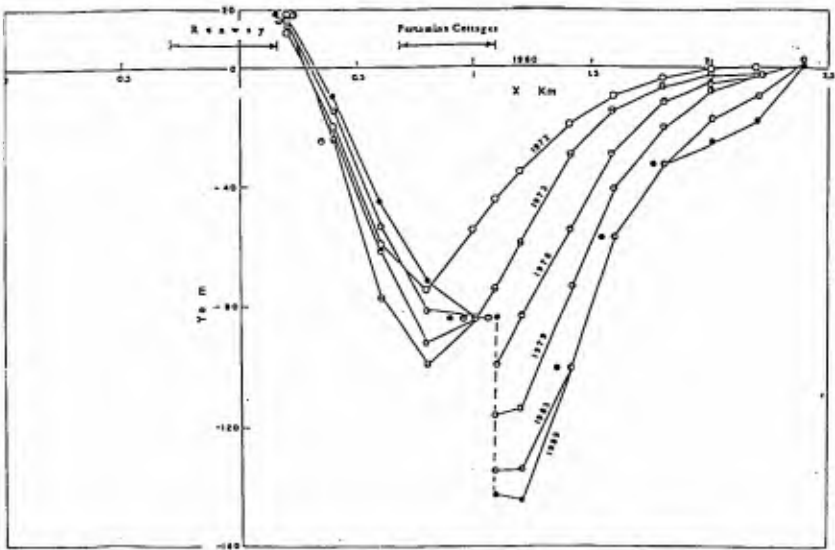


Figure 1. Location of the Kuta beach in Bali island.

beach severe beach erosion began to take place near the runway and has propagated widely on the northern beach (Figure 2 and Photo. 1). Some countermeasures were taken locally, but beach erosion continues to extend northward. In 1975, an UNDP team (Tsuchiya, Yahya and Syamsudin, 1976, and Tsuchiya, 1987) surveyed first the beach erosion problem, and many international advisors also conducted. Recently, an international joint investigation has been carried out with close cooperation between both the Research Institute for Water Resources Development, Agency for Research & Development, Ministry of Public Works of Indonesia and the Disaster Prevention Research Institute, Kyoto University, Japan (Tsuchiya, Syamsudin & Yamashita, 1993). In Figure 1(a), the sorelines measured in 1960, 1977, 1980 and 1987 are shown, and in the figure (b) the distance is taken from the end of the runway in the north direction. Note that severe shoreline retreat has taken place in front of Pertamina Cottages, and that a foreland was formed near the end of runway. Photo. 1



(a) Alongshore shoreline change.



(b) Alongshore and temporary change in shoreline.  
Figure 2. Shoreline changes in the Kuta beach since 1960.



Photo. 1. Severe beach erosion near Pertamina Cottage on the Kuta beach taken in 1975.

also clearly shows severe beach erosion by which trees were fallen near Pertamina Cottages.

In Bali island, two prevailing winds, westerly and easterly exist by which waves are generated. Figure 3 shows refraction diagrams of the wave with a period of 15sec, in which the small bounded area shows the Kuta beach. Due to westerly winds, swells are incident from SW to WSW directions, but no effective waves due to easterly winds. A twin mode appears in frequency distributions of coral-sand on the beach. The sediment sizes decrease northward. Figure 4 shows sedimentation cells in the

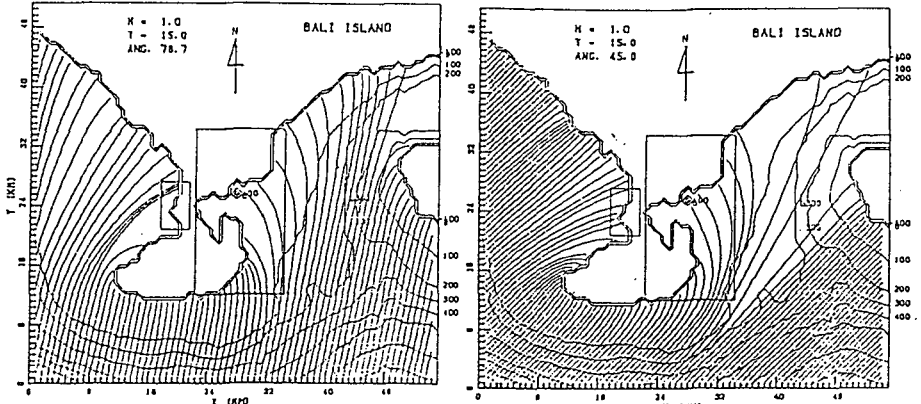


Figure 3. Wave refraction diagrams off the southern part of Bali island.

beach, that was schematically shown using coral-sand characteristics, in which the arrows indicate the possible directions of onshore and longshore sediment transport. Before the construction of the runway there existed a sedimentation cell in equilibrium, but after the construction it was changed by the runway. Note that the main sediment source is only due to coral-sand production from the activity of sea

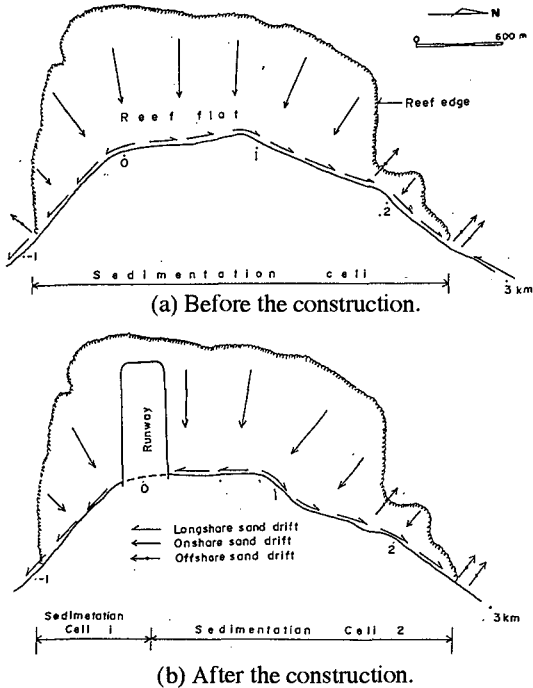


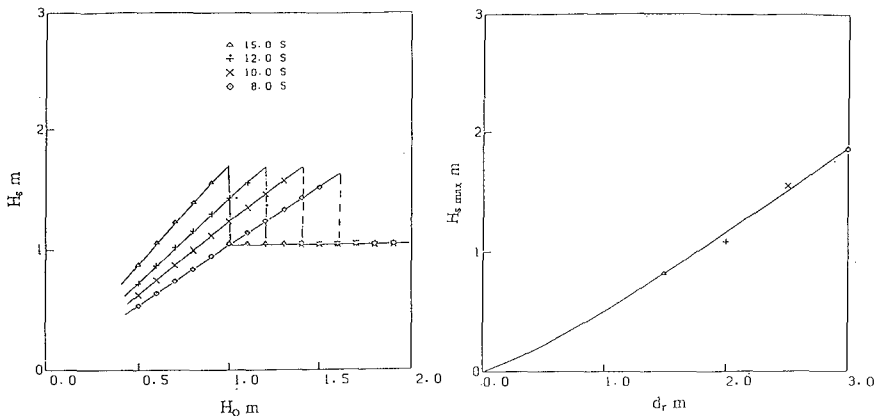
Figure 4. Sedimentation cells formed before and after the construction of the airport runway.

animals and that the northward predominant direction of longshore sediment transport exists. These facts result in severe beach erosion since the airport runway was constructed, especially in the northern area of the beach.

In this paper, we first introduce the most effective wave for beach change in relation to the wave transformation on a coral reef, and second predict long-term shoreline changes with changing the positions for the boundary conditions to be used as headlands for stabilizing the beach against erosion. Third, taking into account an existing small amount of sediment source in the coral-sand beach, a methodology for coral-sand beach stabilization using headlands must be proposed on the basis of long-term shoreline change and the theory of the formation of static stable sandy beaches (Tsuchiya, Chin & Wada, 1993, and Tsuchiya, 1994). Since parts of the proposed headlands were constructed, a coral-sand beach has been well-formed between the headlands. Its plane configuration is compared satisfactorily with the stable one.

### THE MOST EFFECTIVE WAVE FOR BEACH CHANGE

No continuous wave observations in Bali have been carried out and no available wave data can be used. In the prediction of shoreline change, we must specify what wave does effectively influence on the beach change. Incident waves onto coral flats are subjected to the water depth on a coral flat (Takayama, Koyama & Kikuchi, 1977, Tsukayama, Nakaza & Gakiya, 1989, and recently Nelson, 1994) and wave set-up on the flat (Seeling, 1982). Wave transformation in the offshore region on a coral reef can be calculated by the usual method, but on the coral flat we must introduce wave damping due to breaking of the propagating wave and bottom friction. Introducing Battjes' bore model (1974) into the conservation of wave energy flux a wave damping



(a) Dependency to deep water wave height      (b) Dependency to water depth  
 Figure 5. Changes of the wave height at shore with an increase in the deep water wave height and the maximum wave height in relation to the water depth on a coral flat.

model due to breaking is derived and compared satisfactorily with experimental data by Tsuchiya, Syamsudin and Yamashita (1993). Thus, wave transformation on a coral reef was calculated in terms of wave refraction, shoaling, and damping due to breaking and bottom friction to estimate the wave height near the coral-sand beach in

relation to the deep water wave height. Figure 5 (a) shows the relation between the wave height ( $H_s$ ) near the coral-sand beach and the deep water wave height ( $H_0$ ), in which the numerals show the wave period, resulting in clearly a maximum wave height ( $H_{smax}$ ) independent of the wave period. Figure 5(b) shows the relation between the maximum wave height ( $H_{smax}$ ) and the water depth ( $d_r$ ) on the coral flat, that clearly indicates a linear relation independent of the wave period. In the evaluation of the water depth on the coral flat for estimating the maximum wave height, wave set-up must be superimposed on the high tide.

The total rate of longshore sediment transport plays the most important role in the shoreline change. By introducing the longshore sediment transport rate, therefore, the wave height changes were calculated with changing wave period as shown in Figure 6, in which the upper two curves indicate the effective wave heights that representatively were calculated by linear and nonlinear wave theories, and the lower shows the dependency of the relative total rate of longshore sediment transport on the wave period. There exists a maximum total rate of longshore sediment transport at the wave period of about 14sec, but the wave height is nearly constant. The wave having the period and the maximum wave height can be used as the most effective wave in the coral-sand beach process in the Kuta beach. But, the incident angle of the wave should be assumed to be SW in the calculation.

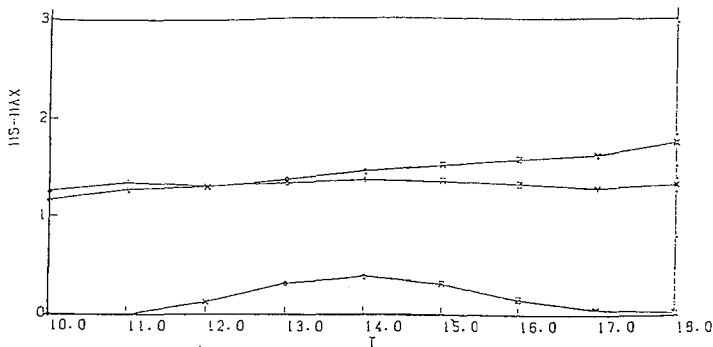


Figure 6. Changes in the maximum wave height and the relative longshore sediment transport rate with the wave period at a central position of the Kuta beach.

## WAVE TRANSFORMATION, NEARSHORE CURRENTS AND LONG-TERM SHORELINE CHANGE

### Wave refraction and nearshore currents on the coral reef

Transformation of the most effective wave respectively was calculated by the usual methods of wave ray and mild-slope equation (Yamashita, Tsuchiya, Matsuyama & Suzuki, 1990). Figure 7 shows the wave ray diagram that was calculated under the high tide condition including an effect of wave set-up. In the figure, the thick line indicates the wave concentration clearly exist at two locations in the northern beach where severe beach erosion has taken place. This fact was understood more exactly in wave height distributions obtained by the method of mild-slope equation (Syamsudin, 1993). Introducing the result of wave fields into the equations of nearshore currents, nearshore currents on the coral flat also were calculated as shown in Figure 8. The result demonstrates that there appear remarkable

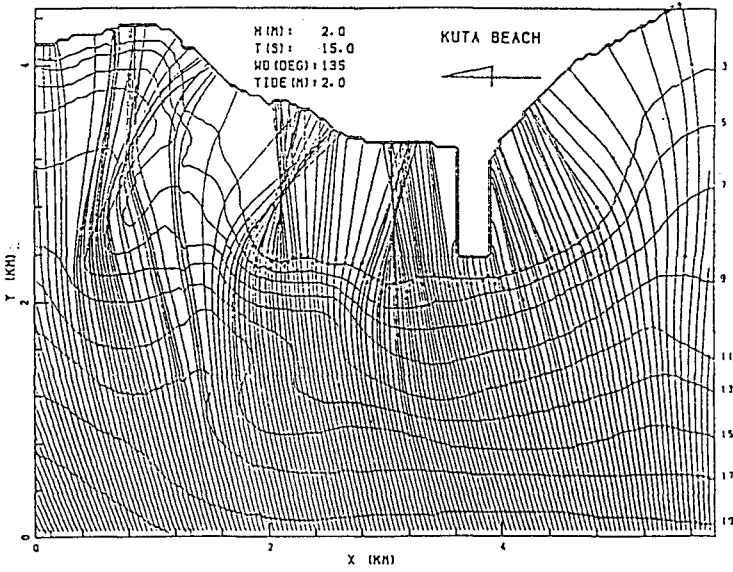


Figure 7. Wave ray diagram of the most effective wave in the Kuta beach.

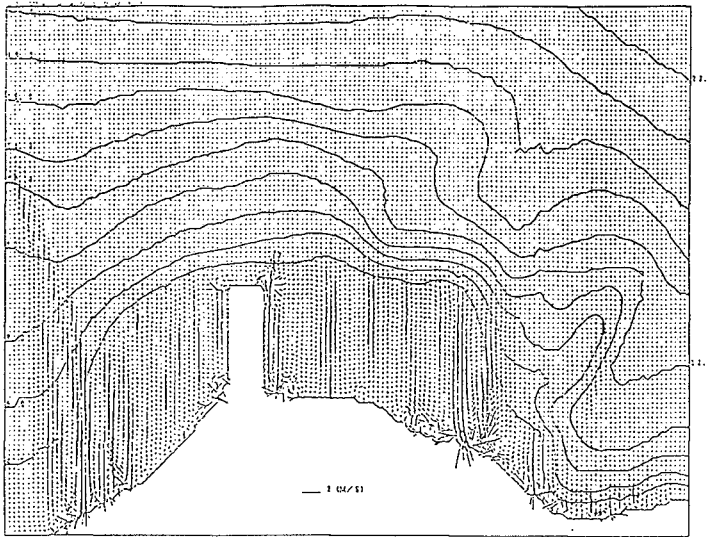


Figure 8. Nearshore currents on the coral flat in the Kuta beach.

nearshore circulation cells that are formed near the end of the runway and locations

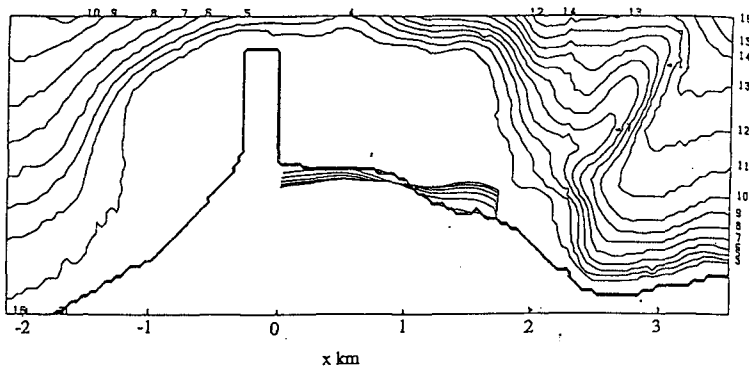


where waves concentrate. Unfortunately, we could not find direct influence of the runway on the nearshore circulation. It may be necessary for obtaining more realistic results to change the incident angle of the wave a little southward.

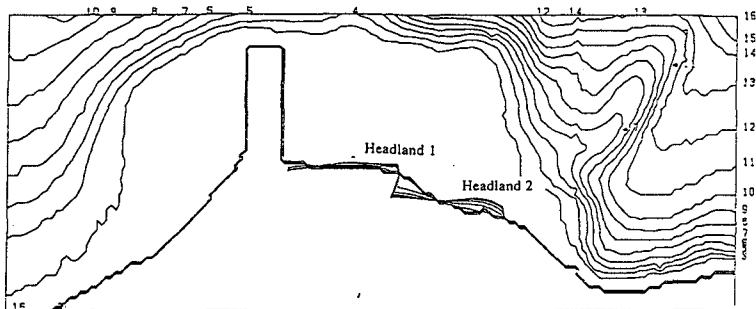
**Prediction of long-term shoreline change under boundary conditions**

As previously stated, we can not estimate the annual duration of the most effective wave. We must investigate whether the beach can be stabilized by some boundary conditions for shoreline change in the long-term shoreline change. In the prediction of long-term shoreline change, therefore, no use of the wave duration is necessary for the prediction.

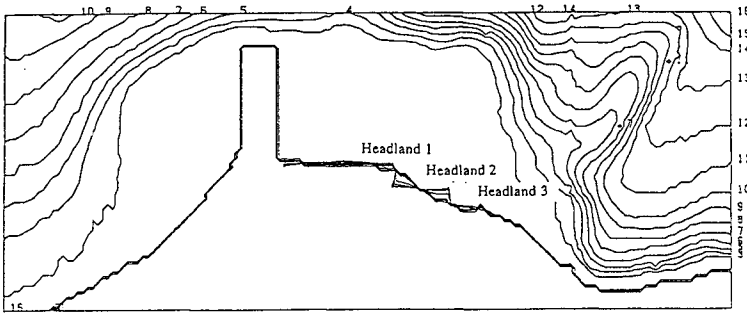
Applying the long-term shoreline change prediction model (Yamashita, Tsuchiya, Matsuyam & Suzuki, 1990, and Tsuchiya, Yamashita, Izumi & Tottori, 1993), we predict the long-term shoreline changes in the Kuta beach in order to find the most suitable locations of man-made boundary conditions, as headlands for stabilizing the entire beach. The single, two and three boundary conditions respectively are given as headland 1, headland 2, and headland 3, and no wave diffraction by the boundary conditions are included in the prediction. Figures 9 and 10 show the predicted results, in which the solid curves between the headlands indicate shoreline change at intervals of the total run indicated in hours. Figure 10 shows the more detailed expression for the shoreline changes shown in Figure 9. When the single boundary condition was given at the central location of the beach, as shown in Figures 9 (a) and 10 (a), due to



(a) In the case of single boundary condition.



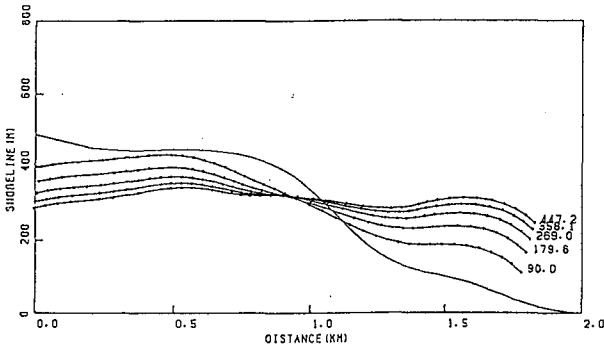
(b) In the case of two boundary condition.



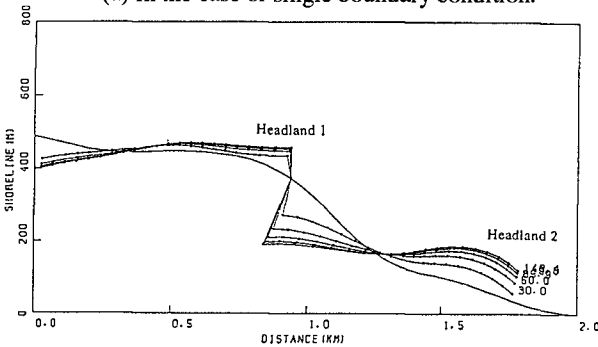
(c) In the case of three boundary condition.

Figure 9. Long-term shoreline changes predicted under the single, two and three boundary conditions, respectively.

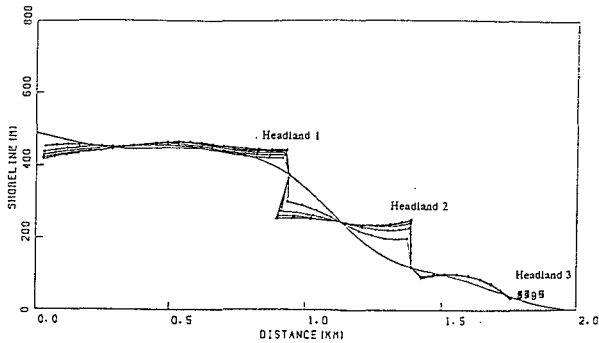
northward longshore sediment transport, severe shoreline retreat takes place widely near the end of the runway. In contrast, shoreline accretion occurs severely further down coast. In the case of two boundary conditions, as shown in Figures 9 (b) and 10 (b), little shoreline retreat takes place widely between the end of the runway and the headland 1, but shoreline retreat occurs down coast from the headland 2, resulting in



(a) In the case of single boundary condition.



(b) In the case of two boundary condition.



(c) In the case of three boundary condition.

Figure 10 Detailed expression of long-term shoreline changes predicted under the single, two and three boundary conditions, respectively.

remarkable shoreline accretion further down the coast to the headland 2. If shoreline change is predicted for the coast down the headland 2, shoreline retreat may take place there. If wave diffraction by the headland 2 is included in the prediction, shoreline change rate may reduce down coast.

Finally, when three headlands are given, as shown in Figures 9 (c) and 10 (c), there appears a nearly same tendency of shoreline change as the second case, but magnitude of shoreline change becomes lesser than the second. We recognize that little shoreline change takes place between the headlands 2 and 3, making the shoreline near the headland 3 continued the original one naturally.

## METHODOLOGY FOR CORAL-SAND BEACH STABILIZATION AND ITS APPLICATION

### The principal methodology for coral-sand beach stabilization

Beach erosion takes place locally due to change in the sedimentation cell on a coral reef beach, and extends more widely down coast in the direction of longshore sediment transport. In coral-sand beaches, there exists a natural system of the formation process of coral-sand beaches surrounded by the coral flats. The system is governed biologically and also in the nearshore dynamics on coral flats. The sediment sources are generally due to mainly 1) the activity of coral and other sea animals, producing a very little sediment source into the coral-sand beach, and partially 2) sediment sources from rivers if flowing into the coral flat. As previously stated in the sedimentation cell, the Kuta beach has only the sediment source that are produced from the activity of sea animals. To stabilize the beach against erosion, therefore, we must first consider its formation process of the coral-sand beach and the long-term shoreline change along the entire beach in the large scale coastal behavior. Second, we must investigate whether the beach can be stabilized by some boundary conditions for beach change. When we found the most suitable positions for the boundary conditions necessary for stabilizing the beach in the large coastal behavior, based on the theory of the formation of static stable sandy beaches (Tsuchiya, Chin and Wada, 1993, and Tsuchiya, 1994), we can establish a principal methodology for coral-sand beach stabilization.

As shown in Figure 3, the predominant waves are incident nearly normal to the coral-

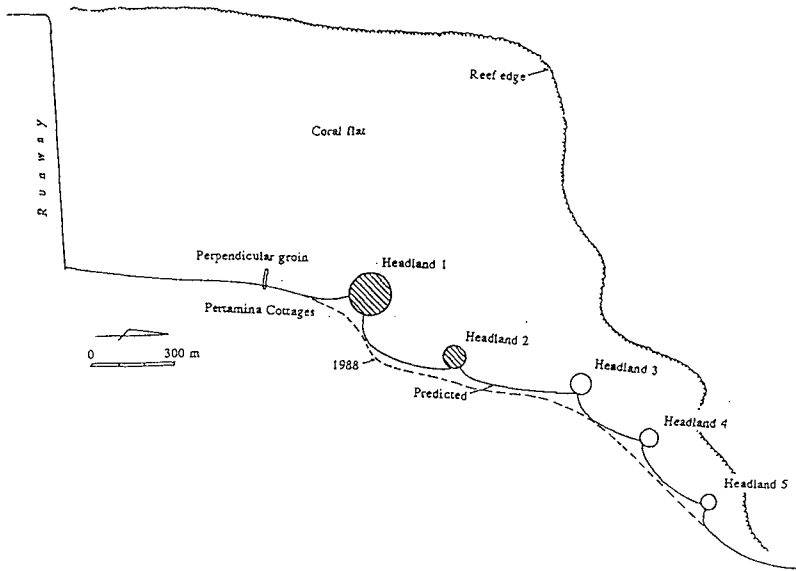


Figure 11. A methodology for coral-sand beach stabilization proposed for the Kuta beach.

sand beach. In relation to the formation of the convex coral reef, the coral-sand beach is formed convex offshore by a very little sediment source from the sea animals production (Tsuchiya, 1987). As only a little sediment source maintains the Kuta beach, into which no river flows, static stable beaches must be formed on the basis of the theory of the formation of stable sandy beaches (Tsuchiya, Chin & Wada, 1993, and Tsuchiya, 1994). The theory recognizes that, when two boundary conditions for shoreline change are given at the ends up and down costs, a stable sandy beach can be formed in relation to longshore sediment transport. When no longshore sediment transport is given from up coast, a static stable sandy beach is formed between the boundaries. In other words, no longshore sediment transport exists along the beach formed. Therefore, a series of head-

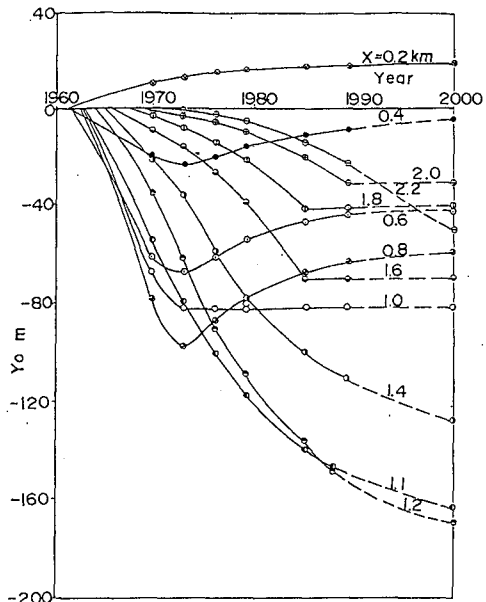


Figure 12. Temporary change in shoreline at several locations on the Kuta beach.

lands that constitute the boundary conditions for shoreline change can then be spaced suitably so as to produce a series of well-stabilized coral-sandy beaches.

As previously shown in Figures 9 (c) and 10 (c), we have found a possibility for stabilizing the beach against beach erosion by constructing three boundary condition for shoreline change at the specified locations shown in the figure. In other words, when three headlands are constructed at the locations, the long-term shoreline change along the entire beach becomes an equilibrium state, in which a static stable coral-sand beach is formed. We can not construct a mathematical headland having no wave diffraction and deflection. Therefore, we must experience to construct it practically. A methodology for coral-sand beach stabilization was proposed as shown in Figure 11, in which the three headlands are to be constructed, and two others, but smaller may be needed to compensate for the direct effect of the headland 3 on shoreline change. A small groin shown in the figure was constructed before the application of the proposed methodology, to remove a cusped foreland formed near the runway.

### Application of the proposed methodology

Among the headlands, the headlands 1 and 2 had been constructed independently with concrete-filled concrete piles in 1985 and 1988, respectively. The respective headlands are of groin and offshore breakwater type. Due to the local circumstance of Indonesia, therefore, these headlands have too steep slopes to reduce wave reflection. No beach nourishment was carried out between the headlands. Figure 12 shows the shoreline change after the construction of the runway. Referring to Figures 2 and 12,

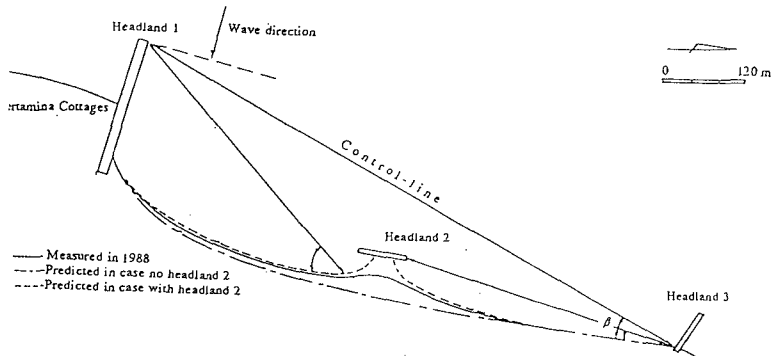


Figure 13. Shoreline changes after the construction of headlands 1 and 2 in comparison with the shoreline configuration for the static stable sandy beach.

severe shoreline retreat has taken place after the construction of the runway, but after the construction of the headlands the shoreline positions tend to approach equilibrium ones. Figure 13 shows the shoreline change between the headlands, comparing it with the static stable shoreline configuration that was obtained by an empirical relation of equilibrium bay configuration (Hsu, Silvester & Xia, 1987). The shoreline is approaching to the final shape of shoreline. Photo. 2 (a) and (b) show actual views of the formation of coral-sand beach between the headlands 1 and 2, in which (a) and (b) respectively were taken in the north and south directions in 1989. In Photo. 2 (a), there are a number of tetrapods that were placed on for protecting the beach locally about 1978. Waves are breaking at the same time along the beach, not showing a peeling phenomenon. This fact demonstrates that no longshore sediment transport

exists along the beach that has been well-formed as static stable coral-sand beach. In Photo. 2 (b), a tombolo is formed behind the headland 2 of offshore breakwater type, and is connected with the beach shown in Photo. 2 (a) by forming a stable coral-sand



(a) Taken in the north direction.



(b) Taken in the south direction.

Photo. 2 A static stable coral-sand beach is being formed between headlands 1 and 2 in the Kuta beach taken in 1989.

beach. We conclude, therefore, that further improvement are necessary in constructing headlands, but such a static stable beach has been well-formed between the headlands 1 and 2, and that, as shown in Figure 11, the adjacent beach is also well-formed by the headland 3, tending to connect with the natural northern one. We further conclude that, when well-designed headlands are constructed at the most suitable locations for the boundary conditions for shoreline change, a series of static stable coral-sand beaches can be formed in the large coastal behavior.

## CONCLUSION

In coral-sand beaches, sediment sources are mainly due to the sea animals production so that a very little amount can maintain the beach. Since no available wave data exist

in the Kuta beach, Bali, the most effective wave for beach change has been discussed in terms of wave transformation on a coral reef. By the use of the most effective wave, we predicted long-term shoreline changes in the large scale coastal behavior, with changing positions for the boundary conditions for shoreline change. We found the most suitable arrangement of headlands as the boundary conditions for stabilizing the entire beach against beach erosion.

On the basis of this findings and theory of the formation of static stable beach, a methodology for coral-sand beach stabilization was proposed. Since parts of the headlands proposed in the methodology were constructed, a stable beach had been well-formed between the headlands. We concluded that the coral-sand beach had almost approached the final shape of static stable one. Therefore, since the application of the proposed methodology has been examined satisfactorily, this methodology can be applied to other coral-sand beaches.

When Professor Y. Tsuchiya, the second author revisited Bali in 1990, however, the coral-sand beach that had been forming so wonderfully was no longer there. Dr. A. R. Syamsudin, the first author and Professor Tsuchiya who were standing on the groin were angered by the reconstruction of this beach with two big groins to make a marine resort, rather than beach preservation.

### Acknowledgments

Throughout this investigation on beach erosion control in Bali, many individuals have helped us for which we wish to thank; in particular, Ir. Rachmat Tirtotjondro, Former Director, Ir. Soelastris Djennoedin, Immediately Past Director, Institute of Hydraulic Engineering (presently, Research Institute for Water Resources Development) and Dr. Badruddin Machbub, Director, Research Institute for Water Resources Development, Agency for Research & Development, Ministry of Public Works of Indonesia, who kindly provided their supervision and cooperation in carrying out this investigation. Thanks are also due to the Ministry of Education, Science & Culture of Japan for its cooperation.

### References

- Battjes, J.A. (1974): Surf similarity, Proc. 14th ICCE, ASCE, Vol. 1, pp. 466-479.
- Hsu, J.R.C., R. Silvester and Y.M. Xia (1989): Static equilibrium bays; New relationships, Jour. Water., Port, Coast. & Ocean Eng., ASCE, Vol. 115, No. 3, pp. 285-298.
- Nelson, R.C. (1994): Depth limit design wave heights in very flat regions, Coastal Engineering, Vol. 23, pp. 43-59.
- Seeling, W.N. (1982): Laboratory study of reef-lagoon system hydraulics, Jour. Water. Port, Coast. & Ocean Eng., ASCE, Vol. 109, No. 4, pp. 380-391.
- Syamsudin, A.R. (1993): Beach Erosion in Coral Reef Beaches and Its Control, PhD Dissertation, Kyoto Univ. 221p.
- Takayama, T., Y. Koyama & O. Kikuchi (1977): Study on the wave transformation on reefs, Technical Report, Port & Harbor Res. Inst., Min. Trans. Japan, No. 278, pp 1-32 (in Japanese).
- Tsuchiya, Y., M. Yahya and A.R. Syamsudin (1976): Field investigations on beach erosion in the Bali coast (1)-Kuta beach-, UNDP, OTC/SF Project, INS-70/527, Inst. Hyd. Eng., Agen. Res. & Dev., Min. Pub. Work. & Pow. Indonesia, 148p.
- Tsuchiya, Y., M. Yahya and A.R. Syamsudin (1979): Beach erosion in Indonesia, Proc. 26th Japanese Coast. Eng. Conf. JSCE, pp. 267-271 (in Japanese).

- Tsuchiya, Y. (1987): Final report on beach erosion control in Bali and West Java, and short course on coastal engineering, Inst. Hyd. Eng., Agen. Res. & Dev., Min. Pub. Work. Indonesia, 52p.
- Tsuchiya, Y., I. Chin and C. Wada (1993): Formation of stable sandy beaches; Theoretical configurations and their applicability, Proc. Japanese Coast. Eng., JSCE, Vol. 40 (1), pp. 371-375.
- Tsuchiya, Y., A.R. Syamsudin and T. Yamashita (1993): Erosion control in coral reef beaches in Bali, Proc. Coast. Eng. JSCE, Vol. 40 (1), pp. 466-470.
- Tsuchiya, Y., T. Yamashita, T. Izumi and K. Tottori (1993): Prediction of large scale coastal behavior-Case study for Joetsu-Ogata coast-, Proc. Coast. Eng. JSCE, Vol. 40 (1), pp. 456-460 (in Japanese).
- Tsuchiya, Y. (1994): Formation of stable sandy beaches and beach erosion control; A methodology for beach erosion control using headlands, Bulletin, Disas. Prev. Res. Inst., Kyoto Univ. Vol. 43, Part 2 (in press).
- Tsukayama, M., E. Nakaza & K. Gakiya (1989): Study on the wave transformation on reefs, Proc. 36th Japanese Conf. Coast. Eng., JSCE, pp. 70-75 (in Japanese).
- Yamashita, T., Y. Tsuchiya, M. Matsuyama and T. Suzuki (1990): Numerical models for beach change, Annuals, Disas. Prev. Res. Inst., Kyoto Univ., No. 33, B-2, pp. 503-542 (in Japanese).



## CHAPTER 195

# Fundamental Characteristics of a New Wave Absorbing System Using Sand Liquefaction

S. Takahashi, S. Yamamoto, and H. Miura\*)

### Abstract

When a sand bed is liquefied due to a high pore pressure gradient, it significantly reduces the height of waves passing over it. This study investigates the fundamental characteristics of a liquefied sand bed including the wave damping effect.

### 1. INTRODUCTION

Two types of sand liquefaction exist. The first is a well-known phenomenon that occurs during an earthquake, namely, the generation of excess pore pressure caused by the shear deformation of sand, while the second is so-called quick sand or boiling of sand, which is generated by the upward pore pressure gradient of seepage flow in sand. A pore pressure gradient can also be generated by waves, and this causes sinking or settlement of sea structures such as block mound breakwaters.

The primary objective of the present study is to elucidate the fundamental features of a liquefied sand bed. One of its most impressive ones is the wave damping effect; i.e., when a sand bed is liquefied, the sand moves due to wave action and consumes wave energy, which results in generating this unique effect.

A series of model experiments were carried out to investigate the fundamental characteristics of liquefied sand and the wave-damping effect, with this report describing the results of the experiments and some theoretical considerations.

---

\*) Port and Harbour Research Institute, 3-1-1 Nagase, Yokosuka, Japan 239, Fax: +81-468-42-7846

## 2. SAND LIQUEFACTION SYSTEM AND EXPERIMENTAL PROCEDURES

### Sand Liquefaction System

Figure 1 shows the newly developed sand liquefaction system which is comprised of a sand bed and horizontal pipes buried at its bottom. Water is pumped into the pipes to increase the pore pressure in the sand bed and cause so-called boiling of the sand. Basically, a kind of sand liquefaction takes place since the sand behaves like a liquid.

When this phenomenon occurs, the shear modulus of the liquefied sand is significantly decreased, and a large movement of sand occurs due to wave action. Consequently, wave energy is consumed by the resultant friction generated between sand particles during their wave-induced movement.

### Experimental Setup

The experiments were conducted in a small wave flume (30 m x 1 m x 0.5 m). Six cylindrical pipes with an inner diameter of 13 mm and a length of 4 m were horizontally installed at the bottom of the sand bed. Holes were drilled in them to supply water into the sand bed. The pore pressure is changed by adjusting the flow valves.

Two sand bed heights of  $h_s = 20$  and 40 cm were tested. During the experiments, we measured pore pressure, flow rate from the pipes, wave height, and sand movement.

Four types of tests were conducted:

- 1) Permeability tests
- 2) Scouring tests
- 3) Block-sinking tests
- 4) Wave damping tests

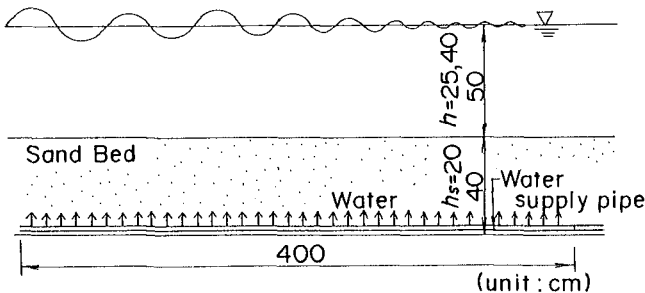


Fig. 1 Diagram of the Wave-Absorbing System

### 3. EXPERIMENTAL RESULTS

#### Hydraulic Gradient and Liquefaction

Figure 2 shows the results of the permeability tests, and also the results of a typical permeability test done by Yoshimi (1975). The x-axis is seepage flow rate, while the y-axis is the hydraulic gradient.

In Yoshimi's ordinary permeability test, the proportionality remains until the hydraulic gradient,  $i$ , reaches the critical hydraulic gradient,  $i_{cr}$ , and then even though the seepage flow rate is increased, the hydraulic gradient slightly decreases. This phenomenon in sand is usually called "boiling" or "quick sand." The proportionality of the seepage flow rate with respect to the hydraulic gradient determines the permeability, which is 0.038 cm/s in Yoshimi's test.

Here, however, the proportionality vanishes when the hydraulic gradient is greater than about 0.5, that is, partial boiling is caused by the nonuniform distribution of seepage flow produced by supplying water through the pipes. In this case, the permeability of the sand bed is 0.14 cm/s.

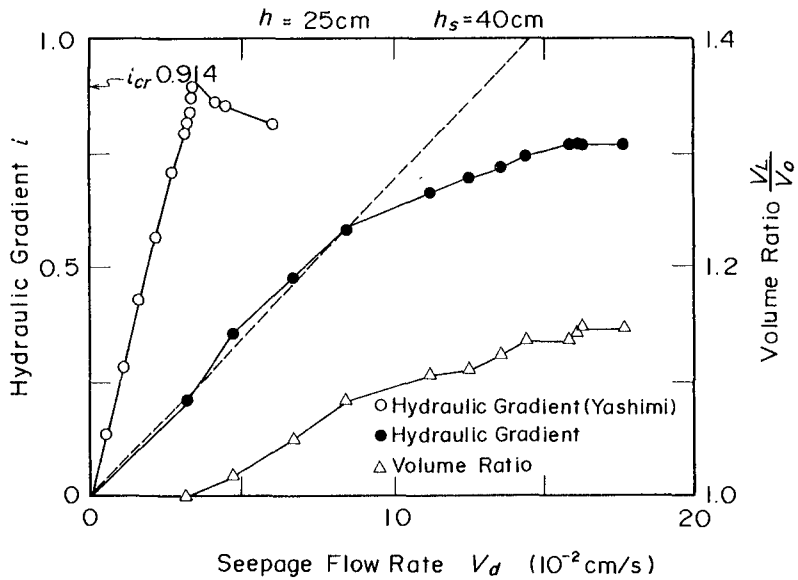


Fig. 2 Results of Permeability Tests

### Ripples and Leveled Sand Surface

A typical feature of a liquefied sand bed is its level surface. It is well known that a sand bed surface normally forms sand ripples due to wave action, whereas a liquefied sand bed always stays level.

Figure 3 shows photographs of these two sand surfaces: ripples in a non-liquefied sand bed and no ripples in a liquefied sand bed. Even if a trench is dug in the liquefied sand surface, it is soon back-filled by the leveling movement.

### Scouring of Sand Bed by Rapid Water Flow

A liquefied sand bed may easily suffer scouring due to rapid water flow over its surface. We therefore directed a water jet at the surface of an ordinary non-liquefied and liquefied sand bed, with Fig. 4 showing the resultant scouring of the liquefied sand bed due to the water jet from the nozzle, shown on the left above the bed. The sand particles are lifted up as indicated. It should be noted that the scoured location is back-filled quickly by the leveling behavior of the liquefied sand, and that the lifting of the sand particles continues.

Sand particles in the non-liquefied sand bed were lifted-up similarly to those in the liquefied sand bed and it becomes small after the sand bed was scoured to a certain depth. This is the significant difference between ordinary and liquefied sand beds.

Our results suggest a difference exists in the scouring mechanism. However, we cannot confirm that a liquefied sand bed suffers scouring more easily in comparison with ordinary beds.

### Sinking of Blocks/Caisson Breakwater

Figure 5 shows a photo of sinking concrete blocks caused by liquefied sand. The blocks appear stable in the upper photo, while in the lower ones, they sink after water is pumped into the pipes.

Figure 6 shows the sinking speed of a concrete block as a function of the hydraulic gradient  $i$  for three water supply methods: constant flow, one-side oscillatory flow, and two-side oscillatory flow. Note that sinking rapidly occurs for each method when the hydraulic gradient is greater than about 0.5.

Sand liquefaction induced by wave action is believed to be a major reason causing the blocks to sink or settle



Fig. 3 Leveling of Sand Surface

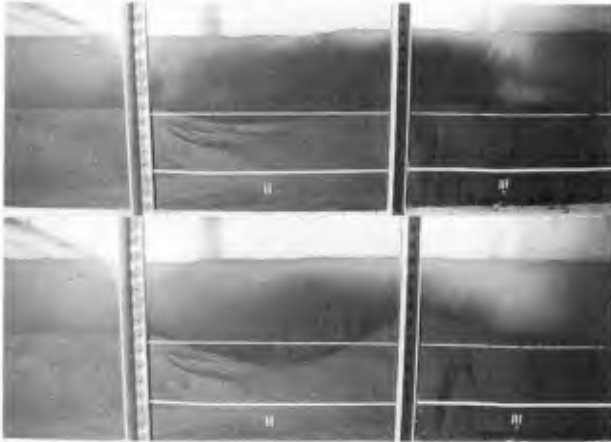


Fig. 4 Scouring of a Liquefied Sand Bed

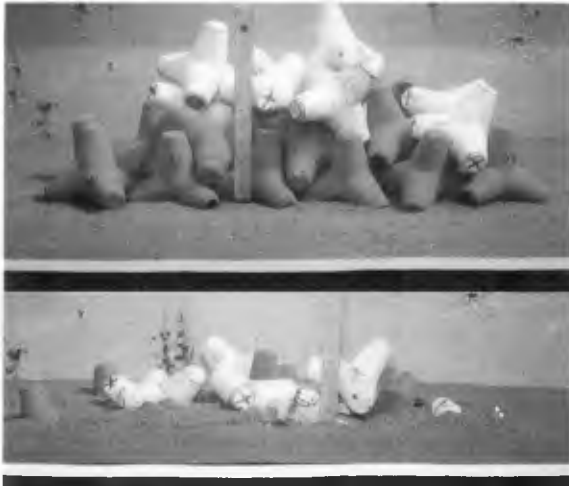


Fig. 5 Sinking of Blocks

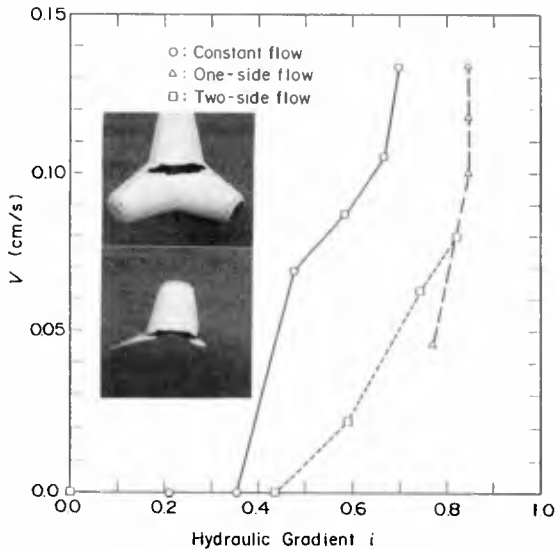


Fig. 6 Sinking Speed of a Concrete Block

(Nago (1981), Maeno (1985), Sakai (1992), Zen (1993), Iwagaki (1993)). It is believed that such sinking happens when the pore pressure gradient due to a wave exceeds the critical hydraulic gradient. However, this is not the case, because sinking occurs even when the hydraulic gradient is around 0.5.

Figure 7 shows the settlement of a caisson breakwater into a sand bed after pore water was supplied from its bottom. Although the caisson was expected to quickly sink due to its heavy weight, instead it remained relatively stable. The sand under the caisson is actually not liquefied, although other parts are. Consequently, the toe of the rubble mound begins sinking first.

Due to the caisson weight, the effective stress of the sand under it increases and prevents liquefaction. Wave-induced liquefaction is usually determined by considering the pore pressure gradient  $dp/dz$ . However, instead of employing this parameter, it is presumably better to apply Mohr-Coulomb failure criteria including the effective stress.

Of particular interest, the toe settlement occurring in the mounds of prototype composite breakwaters is very similar to the photographed settlement behavior. This

phenomenon was considered to be a result of scouring damage due to wave-induced water particle velocity. However, wave-induced liquefaction might be another reason for this type of damage, and therefore, proper countermeasures should be taken to mitigate this effect.

It should also be noted that the rubble mound plays an important role in preventing caisson sinking. Actually, owing to the rubble foundation, prototype caissons of composite breakwaters have never suffered from a failure like that shown in Fig. 7. The importance of the rubble mound foundation should be emphasized in the design of sea structures, however, its function has not been fully clarified.



Fig. 7 Settlement of a Caisson Breakwater

#### 4. WAVE DAMPING DUE TO SAND LIQUEFACTION

##### Wave Damping

Wave damping due to soft clay movement is generally known to be high (Yamamoto and Takahashi, 1985). On the other hand, that due to sand movement is much less because of its high shear modulus, though when liquefaction occurs, the sand becomes soft and induces high damping similar to soft clay.

Typical wave records obtained during model experiments are shown in Fig. 8. The sand bed was 40-cm-thick and regular waves with a 1-s period were applied in 25-cm-deep water. As indicated, these wave records were taken at the offshore side, the center of the sand bed, and harbor side. A record of the oscillations of the sand bed surface is also shown.

Note that wave damping clearly occurs after the water supply is started. The wave at harbor side is very small, and its height is reduced by more than 75%. In this case, the sand surface oscillates with an amplitude that is 6% of the incident wave amplitude, having a phase difference of approximately  $50^\circ$ .

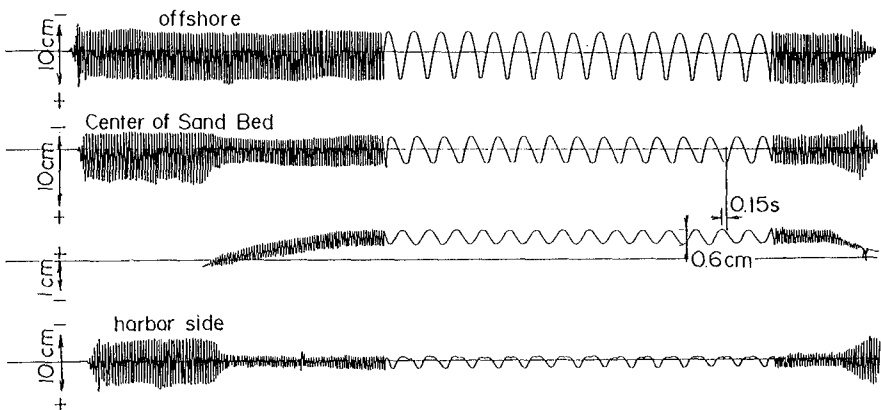


Fig. 8 Typical Wave Damping Record



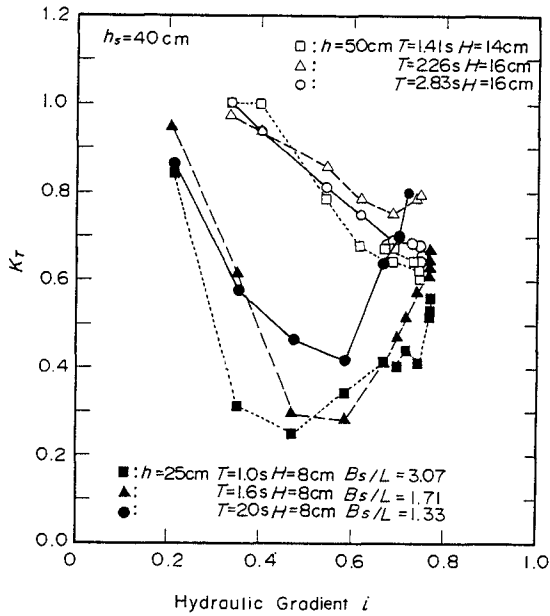


Fig. 9 Wave Transmission Coefficient ( $h_s = 40 \text{ cm}$ )

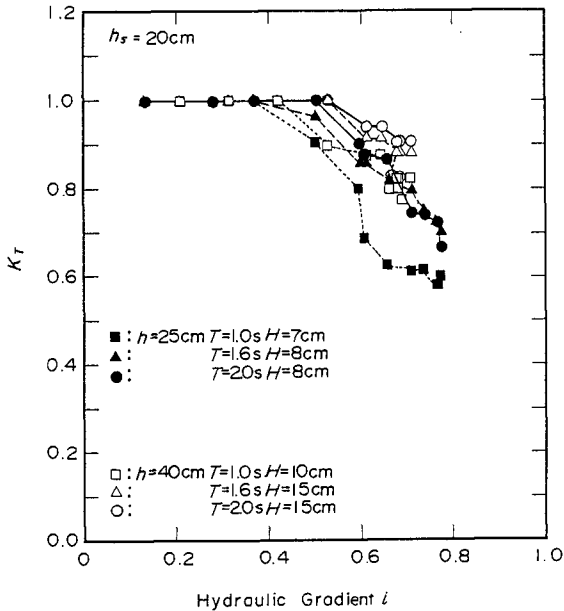


Fig. 10 Wave Transmission Coefficient ( $h_s = 20 \text{ cm}$ )

In Fig. 9, the wave transmission coefficient  $K_t$  is plotted as a function of the hydraulic gradient  $i$  for three wave conditions and two water depths, where  $K_t$  becomes very small when  $i$  is around 0.5 at  $h = 25$  cm. However, when  $h = 50$  cm, it is not so small, i.e., the damping is slight. Figure 10 is a corresponding graph in which the sand thickness  $h_s$  is 20 cm. Note that wave damping is comparatively much less.

These results indicate that wave damping is large when the soil thickness is deep and the water depth is shallow. It is also apparent that wave damping is large when the sand is partially, not fully liquefied.

Wave Action on a Liquefied Sand Bed

Figure 11 shows the half amplitude of pore pressure due to wave action when  $h = 25$  cm and  $h_s = 40$  cm. The pore pressure increases with an increase in the pressure of the water supplied from the bottom of the sand bed. Due to liquefaction, wave pressure penetrates deeper into the soil.

Figure 12 is a graph showing the amplitude of vertical oscillations of the sand, which increases with an increase in the hydraulic gradient, being about 10% that of the wave height at  $i = 0.5$ . Such large movement was not usually expected.

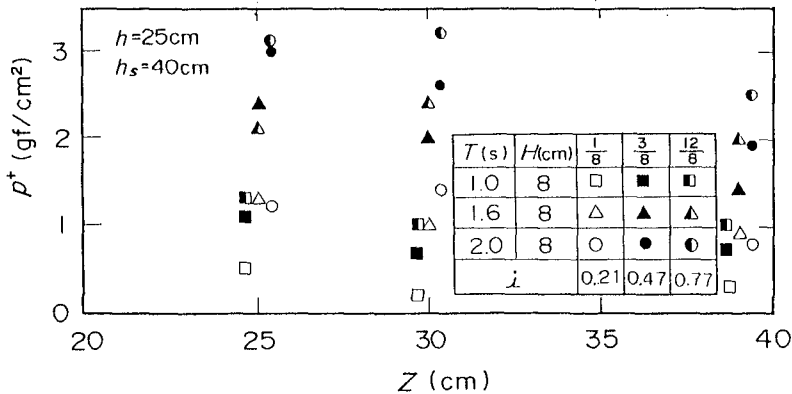


Fig. 11 Amplitude of Wave-Induced Pore Pressure Variation

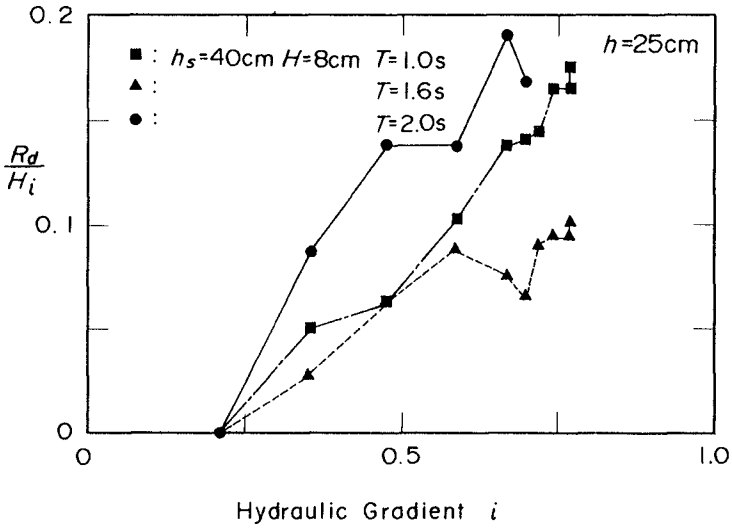


Fig. 12 Amplitude of Sand Movement

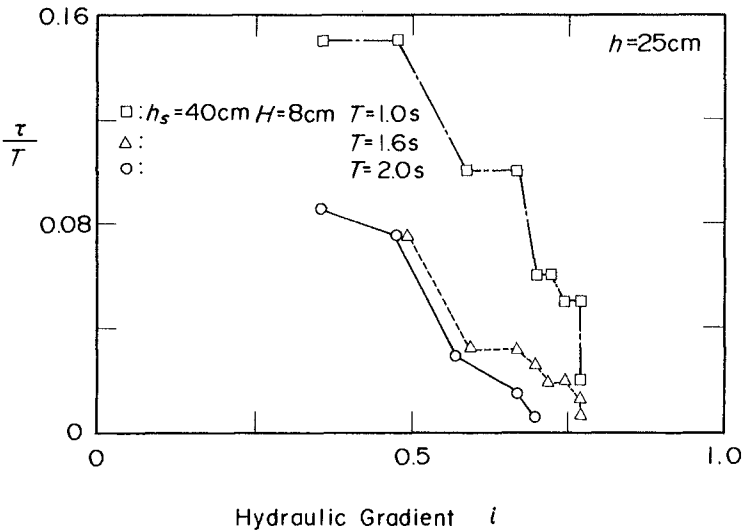


Fig. 13 Phase of Sand Movement

Figure 13 shows the phase of the sand oscillations, which is actually ahead of the wave profile. As the hydraulic gradient increases, the phase difference approaches closer to zero, being about 10% of the wave period when  $i = 0.5$ . Obviously these differences in amplitude and phase are closely related to damping of wave energy in a liquefied sand bed.

As will be discussed, wave damping is large when the sand movement is large and its phase difference is close to  $90^\circ$ . As the wave pressure on the sea bed increases, the sand movement increases and the phase difference approaches close to  $0^\circ$ . However, wave damping reaches maximum at a phase difference of  $90^\circ$ , vice  $0^\circ$ .

## 5. WAVE DAMPING THEORY

### Biot's Equation

Wave damping in a soil bed has been extensively studied. Application of linear wave theory in conjunction with Biot's theory for soil motion (Biot, 1962) is generally considered useful for describing wave damping in a sea bed, even during the occurrence of sand liquefaction.

Figure 14 illustrates the phenomena of wave damping and soil motion, where  $U_z(0)$ , which is expressed as a complex number, is the amplitude of soil oscillations at the surface. In wave damping theory, the amplitude and phase of  $U_z(0)$  determine wave damping.

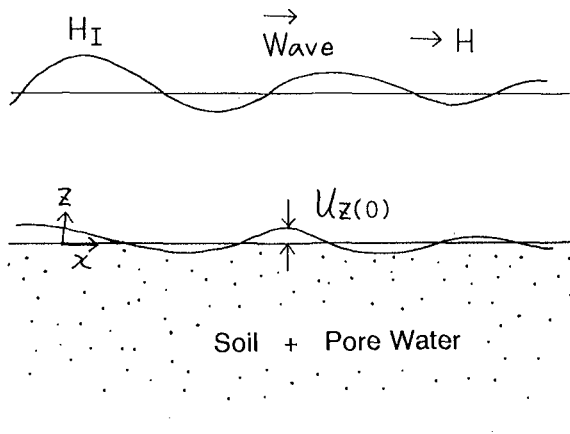


Fig. 14 Wave Damping and Soil Motion

Biot's theory, being widely used to describe a sand bed filled with water, employs the equations of motion of the sand and pore fluid (see Yamamoto and Takahashi, 1985).

#### Linear Wave Damping Coefficient

Wave damping on a sea bed can be defined as follows using the linear wave damping coefficient  $D_f$ :

$$K_t = H/H_I = \text{Exp} (D_f x) \quad (1)$$

where  $K_t$  is wave transmission coefficient,  $H$  the wave height at distance  $x$ , and  $H_I$  the incident wave height.

$D_f$  for an infinitely deep soil bed can be defined by the imaginary part of the complex amplitude of the vertical oscillation of sand at the surface, and therefore, it can be expressed using (see Yamamoto and Takahashi, 1985):

$$D_f = \rho_f g \delta^* / (2G^* \cosh^2 k_0 h (1 + 2 k_0 h / \sinh 2k_0 h)) \quad (2)$$

where  $\rho_f$  is the density of water,  $g$  the acceleration of gravity,  $k_0$  the wave number,  $h$  the water depth,  $G^*$  the representative shear modulus, and  $\delta^*$  the equivalent damping factor.

It should be realized that  $G^*$  and  $\delta^*$  are difficult to evaluate. Using the typical wave record in Fig. 8, for example,  $D_f$  is  $0.35 \text{ m}^{-1}$  and the value of  $G^*/\delta^*$  is  $2700 \text{ N/m}^2$ . If it is assumed that  $\delta^*$  ranges from 0.1 to 100, then  $G^*$ s ranges from 27 to 27,000  $\text{N/m}^2$ . However, this value is quite small, and consequently, these parameters should be investigated further.

## 6. CONCLUDING REMARKS

Our major conclusions are as follows:

1) The fundamental characteristics of a liquefied sand bed were experimentally studied, and it was shown that partial liquefaction occurs when pore water is supplied from pipes located at the bottom of sand bed. It was also found that blocks will sink into a sand bed even when a small hydraulic gradient is present. Effective stress analysis using Mohr-Coulomb failure criteria is considered to be better than pore pressure gradient analysis in determining whether a sinking failure will occur.

2) Wave damping due to a liquefied sand bed can be

significant, even at a hydraulic gradient as low as about 0.5. When the water depth is shallow and the sand bed thickness is deep, then wave damping is large. Wave damping can be expressed by Biot's equation using the linear wave damping coefficient.

Our new wave-absorbing system can be employed as a wave barrier designed to produce a calm sea area, and may be especially suitable for damping waves at a harbor entrance. The necessary electrical power for system operation can be supplied from a land-based power generation station or possibly wave power converters. Further work will be directed at researching practical system application.

### References

- Biot, M., A., (1962) "Mechanics of deformation and acoustic propagation in porous media," *Journal of Applied Physics*, Vol. 33, pp. 1482-1498.
- Iwagaki, Y., Nishiguchi, M., and Okuda, Y. (1993) "Study on vertical displacement of seabed and structure due to water pressure variation (in Japanese)," *Proc. Japanese Conference on Coastal Engineering*, Vol. 40, pp. 591-595.
- Maeno, Y., and Hasegawa, T. (1985) "Evaluation of wave-induced pore pressure in sand layer by wave steepness," *Coastal Engineering in Japan*, JSCE, Vol. 28, pp. 31-44.
- Nago, H. (1981) "Liquefaction of highly saturated sand layer under oscillating water pressure," *Memories of School of Engineering, Okayama Univ.*, Vol. 16, No. 1, pp. 91-104.
- Sakai, T., Hatanaka, K., and Mase, H. (1992) "Wave induced effective stress in seabed and its momentary liquefaction," *Jour. of WW*, Vol. 118(2), ASCE, pp. 202-206.
- Yamamoto, T., and Takahashi S. (1985) "Wave damping by soil motion," *Jour. of WW*, Vol. 111, No. 1, ASCE, pp. 62-77.
- Yamamoto, T., Takahashi, S., and Schuckman, B. (1983) "Physical modeling of sea-seabed interactions," *Jour of EM*, Vol. 109, No. 1, ASCE, pp. 54-72.
- Yoshimi, Y., Kuwahara, F., and Tokimatsu, K. (1975) "One-dimensional volume change characteristics of sand under very low confining stresses," *Proc. of Soil Engineering*, Vol. 15, No. 3, pp. 51-60.
- Zen, K., and Yamazaki, H. (1993) "Wave-induced liquefaction in a permeable seabed," *Rept. of Port and Harbour Res. Inst.*, Vol. 31, No. 5, pp. 155-192.

## CHAPTER 196

### LABORATORY STUDY OF SURF-ZONE TURBULENCE ON A BARRED BEACH

Francis C. K. Ting<sup>1</sup>

#### ABSTRACT

Wave height, wave set-up, undertow, and turbulent velocity on a plane beach and a barred beach were compared in the case of regular waves. The study showed that the presence of an offshore bar altered the turbulent flow in the surf zone by altering the characteristics of the broken waves. It was found that the magnitude of undertow and turbulence intensity were smaller in the inner surf zone on the barred beach. These results suggest that it may be possible to reduce the erosive wave action on beaches by construction of underwater berms in the nearshore zone. Further studies are needed to determine the effects of water depth, berm width and crest elevation on surf-zone turbulence under different wave conditions in order to provide explicit design guidance.

#### INTRODUCTION

This study deals with the characteristics of surf-zone turbulence on a barred beach. The motivation for this work is the effect of offshore bars on beach erosion. It is well known that the dynamic response of a beach under storm wave attack is to sacrifice some beach. Most of the sand removed from the beach are transported offshore and deposited as longshore bars. These bars in turn protect the beach from further erosion. The question which is the basis of this study is how offshore bars protect a beach from erosion. Knowing the how may allow us to develop more effective methods to curb beach erosion. For example, the U.S. Army Corps of Engineers has been using dredged material to construct underwater berms in the nearshore zone (MacLellan 1990, MacLellan and Kraus 1991). Such berms are placed in the form of long linear mounds for the protection of the coastline. It is believed that a berm with sufficient relief will shoal and break the higher erosive waves accompanying storms, forcing the waves to dissipate their energy in the surf zone, and thus reduce the erosive wave action on the beach. In reality, the process is probably more complicated than

---

<sup>1</sup> Oc. Engrg. Program, Dept. of Civ. Engrg., Texas A&M Univ., College Station, TX 77843-3136.

this. Since sediment transport and beach erosion are tied in a fundamental way to the turbulent flow in the surf zone, description of wave characteristics alone will not solve the whole problem. It will be shown that information on flow velocity and turbulence are needed in order to develop explicit design guidance for nearshore berm construction. Moreover, a thorough understanding of mean and turbulent flow characteristics on barred beaches will improve our knowledge of surf-zone dynamics, which is imperative for the development of more reliable coastal models.

There are very few studies which directly address the differences between wave breaking on barred and plane beaches. Smith and Kraus (1991, 1993) studied wave height transformation, reflection, and runup of monochromatic and random waves on barred and plane beach profiles in a wave tank. They found that incident waves with the same characteristics in deep water break differently on barred and plane beaches. For example, some waves that would spill on a plane slope plunge if a bar is present, and some plunging waves on plane slope collapses on a barred profile. Smith and Kraus's study pertained only to macro-features of wave breaking; micro-features of flow velocity and turbulence were not investigated. However, from their description of breaking wave characteristics on plane and barred beaches it may be expected that the presence of offshore bars would alter the turbulent flow in the surf zone by altering the process of wave breaking and turbulence production.

The structure of surf-zone turbulence has a profound influence on sediment transport and beach erosion. Recently, Ting and Kirby (1994) studied the characteristics of mean flow and turbulence in spilling versus plunging breakers. Here, "mean flow" is defined as the organized wave-induced flow which includes the undertow and the orbital wave motion. They found that turbulent kinetic energy was transported seaward under a spilling breaker and landward under a plunging breaker by the mean flow. Considering the common assumption of turbulent energy stirring up sediment and making it available for transport by the mean flow, it may be concluded that the direction of sediment transport would be seaward under spilling breakers and landward under plunging breakers. This is consistent with the field and laboratory observation that spilling breakers tend to result in beach erosion, while plunging breakers produce accretionary beach profiles. It also suggests that the types of beach profiles produced by storm and swell waves are tied in a direct way to the turbulence dynamics in breaking waves, particularly to the relationship between mean flow and turbulent kinetic energy. Because of this, it would be important to compare the mean and turbulent flow characteristics on plane and barred beaches for the same incident wave conditions to determine the effects of offshore bars on the turbulence flow in the surf zone.

In this present study, fluid velocities in a laboratory surf zone were measured using a two-component laser-Doppler anemometer, and surface elevations were measured using a resistance wave gage. Wave height, wave set-up, undertow, and turbulent velocity on a plane beach and a barred beach were compared for the same incident wave conditions. Although experiments were conducted using



both regular and irregular waves, only the results for regular waves are presented here. The structure of turbulent flow in irregular waves will be the subject of a separate paper.

## EXPERIMENTAL PROCEDURE

A schematic diagram of the experimental arrangement is shown in Fig. 1. The experiments were conducted in a two-dimensional wave tank in the Hydromechanics Laboratory at Texas A&M University. The wave tank was 37 m long, 0.91 m wide, and 1.22 m deep with glasswall throughout. It was equipped with a hinged-flap programmable wavemaker. A 1/35 slope false bottom built of marine plywood was installed in this tank to create a plane beach; the slope was sealed to the tank walls with silicone sealant. The coordinate system was chosen with  $x$  measured positive seaward from the shoreline and  $z$  extending positive upward from the still water level. The water depth in the constant-depth section was 45.72 cm. The incident wave height was 12.2 cm and the wave period was 2.0 s. The ratio of deep-water wave height  $H_0$  to deep-water wavelength  $L_0$  was 0.02 based on linear shoaling. The waves broke at a water depth of about 20.0 cm in the form of a spilling breaker. The breaking point was defined as the location where air bubbles began to be entrained in the wave crest.

The barred beach was created by placing a submerged solid triangular-shape object on the sloped false bottom. The geometry of the object was selected based on large wave tank studies and field measurements of bars (see, Larson and Kraus 1989). The dimensions of the bar are shown in Fig. 2; it was 9.6 cm high, 145 cm wide, with a seaward bar angle of  $6^\circ$  and a shoreward bar angle of  $10^\circ$ . The bar was located at the breaking point on the plane beach; the still water depth was 23.1 cm at the seaward toe of the bar, 10.4 cm at the bar crest, and 18.8 cm at the shoreward toe of the bar. In order to determine the incident wave heights it was necessary to measure the reflection coefficients for the plane and barred beaches. Therefore, a wave gage was mounted on an instrument carriage which was moved along the constant-depth section of the wave tank to measure the spatial modulations in wave amplitudes created by the interference of the incident and reflected waves. The reflection coefficient  $K_r$  was determined from the two extreme wave heights  $H_{\max}$  and  $H_{\min}$  of the envelope of amplitudes by  $K_r = (H_{\max} - H_{\min}) / (H_{\max} + H_{\min})$ . It was found that the reflection coefficients for the plane and barred beaches were almost the same and in both cases less than 5%. Hence, the bar did not reduce the wave energy reaching the surf zone. Instead, it caused the waves to plunge into the water ahead, and thus dissipated more energy in the outer surf zone.

Water surface elevations and fluid velocities were measured at three locations in the inner surf zone; their exact locations and water depth are given in Table 1. The following notations are used in this paper;  $\zeta$  is water surface,  $u$  is horizontal velocity,  $w$  is vertical velocity,  $H$  is wave height,  $d$  is still water depth,  $\bar{h}$  is mean water depth, and the superscripts overbar, tilde and acute accent denote time average, phase average and turbulent fluctuation, respectively. Surface elevations were measured using a resistance wave gage. The gage was

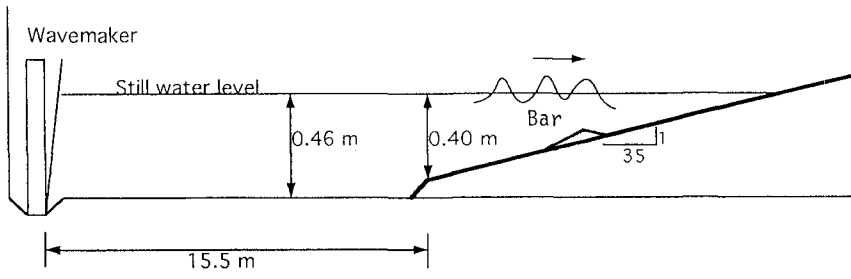


FIG. 1. Schematic Drawing of Wave Tank Arrangement

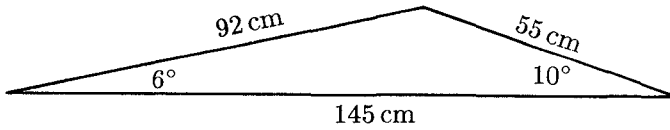


FIG. 2. Schematic Drawing of Bar Profile

Station	$x$ (m)	$d$ (cm)	$H$ (cm)	$\bar{\zeta}$ (cm)	$h$ (cm)	$\frac{H}{h}$
1	4.76	13.62	6.98	0.51	14.13	0.49
2	3.29	9.39	5.23	1.04	10.43	0.50
3	2.21	6.34	3.83	1.32	7.66	0.50

(a) Plane Beach

Station	$x$ (m)	$d$ (cm)	$H$ (cm)	$\bar{\zeta}$ (cm)	$h$ (cm)	$\frac{H}{h}$
1	4.76	13.68	7.79	1.08	14.76	0.53
2	3.29	9.30	4.93	1.44	10.74	0.46
3	2.21	6.28	3.12	1.41	7.69	0.41

(b) Barred Beach

**TABLE 1** Locations of Measurements and Water Depths

calibrated in quiescent water, the calibration curve was found by fitting a fourth order polynomial to 15 data points. Water particle velocities were measured using a two-component laser-Doppler anemometer (LDA). Velocity measurements were conducted mainly in the region below trough level and above the bottom boundary layer. The LDA was a backscatter, three-beam system built by Dantec Electronics. It consisted of a 4 W argon-ion laser (Innova 70-5 from Coherent Inc.), transmitting and receiving optics, traverse mechanism, and one frequency tracker and shifter for each velocity component. It was found that the output voltage from the frequency trackers had a non-negligible long-term fluctuation, which could seriously affect the accuracy of time average velocity measurement such as the undertow. Therefore, the output voltage from the frequency trackers in still water condition was recorded in each experiment and used to correct the measured velocity. The estimated error for the undertow was  $\pm 1.0$  cm/s.

Periodic waves were generated for 15 minutes before data were taken. Thus, the measurements corresponded to a steady-state condition in the wave tank. Data were taken by an IBM compatible 486 computer equipped with a Metra-Byte DASH-16(F) data acquisition board. Sampling frequency was 100 Hz for each channel. The measured velocity was first high-pass filtered at 0.1 Hz to remove any long-term fluctuation due to electronic signal drifting. The orbital wave velocity was obtained by phase averaging the filtered velocity over one hundred and two successive waves. The turbulent velocity was found by subtracting the phase average velocity from the filtered velocity. The frequency tracker had a built-in lock detector to record signal drop-out, which was typically less than 5% in these experiments. Nevertheless, velocity data that were obtained during signal drop-out were not used in computing the mean flow and the turbulent velocity.

## RESULTS

Figs 3(a)–3(c) compare the phase average surface profiles at each station on the plane and barred beaches. The control signal to the wave generator has been used to synchronize the surface profiles in different experiments. Table 1 summarizes the major results including wave height and wave set-up. Visual observations showed that the waves broke in the form of a spilling breaker on the plane beach, whereas they plunged into the water shoreward of the bar on the barred beach. It is seen in Figs. 3(a)–3(c) that the waves on the barred beach lagged behind the waves on the plane beach, which is to be expected. The wave set-up was larger on the barred beach but closer to shore the difference became increasingly smaller. On the plane beach, the wave height to water depth ratio  $H/h$  remained constant through the inner surf zone; the measured value of 0.5 is typical of spilling breakers. The ratio of wave height and water depth was somewhat smaller on the barred beach and continued to decrease shoreward. Perhaps the most important difference is that the broken waves on the plane beach had a “saw-tooth” profile which varied only slowly from one station to another, whereas the broken waves on the barred beach had a

secondary crest and the waves reformed through the surf zone. This behaviour has been observed by Smith and Kraus (1991, 1993), but its significance was not recognized. It is seen that the wave profiles were significantly different on plane and barred beaches. This would have a profound influence on the process of wave breaking, and thus the turbulence dynamics in the surf zone. This is because wave breaking originates from instabilities in the water surface therefore the rate of energy transfer from organized wave motion to turbulent motion (i.e. turbulence production) will be related to the details in the broken waves such as wave height and wave shape. Furthermore, since turbulence transport processes such as turbulent diffusion and viscous dissipation are passive processes which can only proceed at a rate dictated by the behaviour of large-scale structure created by wave breaking we should expect that turbulence dynamics in the surf zone will also depend on the wave characteristics. These ideas will be elucidated further when we examine the structure of undertow and turbulence.

Figs. 4(a)–4(c) plot the variations of undertow with distance from mean water level on the plane and barred beaches. The undertow for the plane beach at stations 1 and 2 were taken from Ting and Kirby (1994), which has virtually the same experimental conditions. It is seen that the magnitude of undertow on the barred beach was generally smaller. This is the result of different wave characteristics on the plane and barred beaches. In these experiments, the wave conditions at each station were recorded using a video camera. The video recording showed that wave breaking in the inner surf zone was less intense on the barred beach. Since the undertow is a return current that is created to balance the water carried shoreward by the surface rollers, we should expect that the magnitude of undertow would be smaller under a weaker breaker. Thus, it appeared that by causing the incident waves to form a plunging breaker, the bar changed the way the broken waves evolved through the surf zone which in turn, altered the turbulent flow.

Figs. 5–7 plot the variations of turbulent velocity with distance from mean water level on the plane and barred beaches. It is seen that the horizontal and vertical components of turbulent velocity decreased with increasing distance from the surface, and the vertical velocity remained smaller than the horizontal velocity; these results are to be expected. The important new result is that these figures clearly show that turbulent velocities in the inner surf zone were considerably smaller on the barred beach. If it is assumed that turbulent velocity fluctuations are responsible for keeping sediment in suspension, and the undertow transports the sediment, then the rates of sediment transport from onshore to offshore would be decreased by the formation of offshore bars. This would have a beneficial effect on the beach profile.

## CONCLUSIONS

To examine the effects of offshore bars on wave and turbulence characteristics in the surf zone laboratory experiments were conducted in which measurements of fluid velocity and surface elevation were made on a plane beach and a barred

beach. Some experimental results for regular waves are reported here. The following main conclusions can be drawn from this study:

1. The broken waves reformed on the barred beach, the wave profiles in the surf zone were significantly altered in comparison to the broken waves on the plane beach.
2. The offshore bar reduced the magnitude of undertow in the inner surf zone.
3. Wave breaking in the inner surf zone was less intense on the barred beach.
4. Turbulent velocity in the inner surf zone was considerably smaller on the barred beach.
5. This study shows that undertow and turbulence intensity differ on plane and barred beaches. This behaviour is related to the effect of the bar on wave breaking. It is further shown that description of turbulent flow characteristics on barred beach profiles is important for providing the data base for developing explicit design guidance for nearshore berm construction.

### ACKNOWLEDGEMENTS

This study was sponsored by the Texas Higher Education Coordinating Board through Grant 999903-261.

### REFERENCES

- Larson, M., and Kraus, N. C. (1989) "SBEACH: Numerical model for simulating storm-induced beach change." *Tech. Report CERC-89-9, U.S. Army Corps of Engrs. Coast. Engrg. Res. Ctr., Vicksburg, Mississippi.*
- McLellan, T. N. (1990) "Nearshore mound construction using dredged material." *J. Coast. Res.*, Special Issue No. 7, 99-107.
- McLellan, T. N., and Kraus, N. C. (1991) "Design guidance for nearshore berm construction." *Proc. Coast. Sediments '91*, ASCE, 2000-2011.
- Smith, E. R., and Kraus, N. C. (1991) "Laboratory Study on wave breaking over bars and artificial reefs." *J. Waterway, Port, Coast., and Oc. Engrg.*, ASCE, 117, 307-323.
- Smith, E. R., and Kraus, N. C. (1993) "Laboratory study of wave transformation on barred beach profiles." *Proc. 23rd Intl. Coast. Engrg. Conf.*, ASCE, 630-643.
- Ting, F. C. K., and Kirby, J. T. (1994) "Observation of undertow and turbulence in a laboratory surf zone." *Coast. Engrg.*, 24, 51-80.

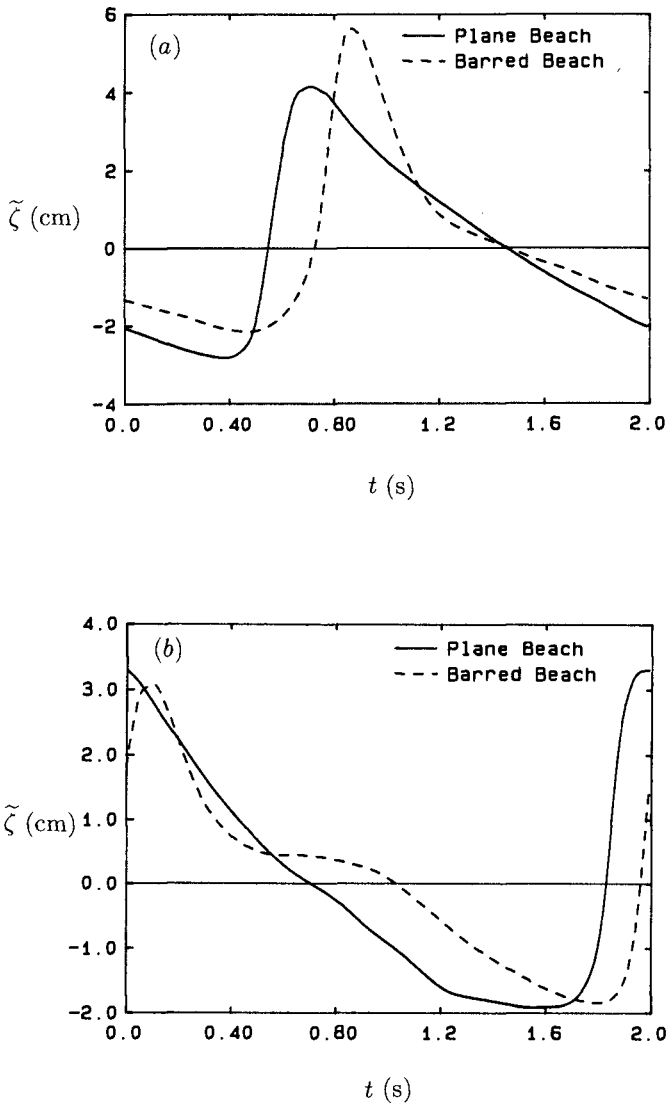


FIG. 3. Phase Average Water Surface Profiles. (a) Station 1, (b) Station 2, (c) Station 3

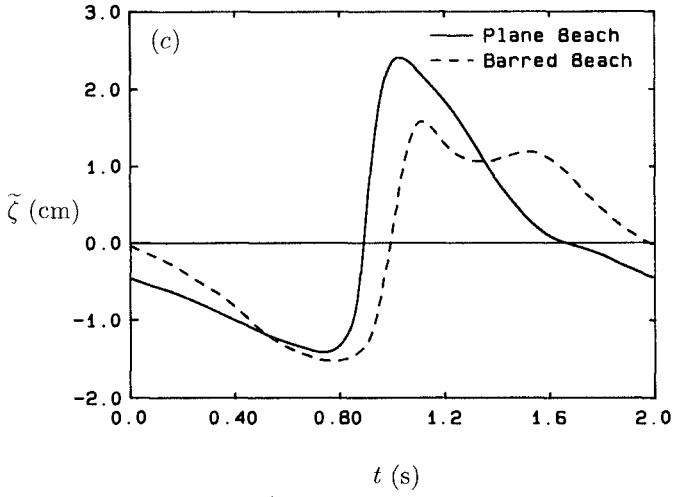


FIG. 3. (Continued)

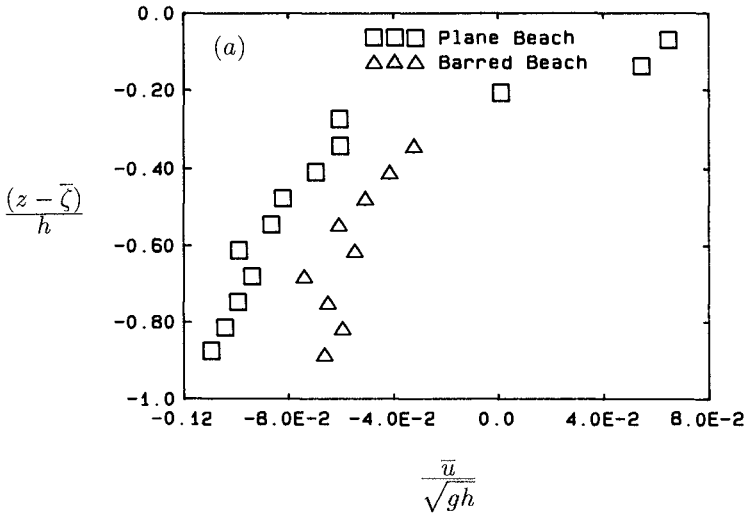


FIG. 4. Variation of Undertow with Depth. (a) Station 1, (b) Station 2, (c) Station 3



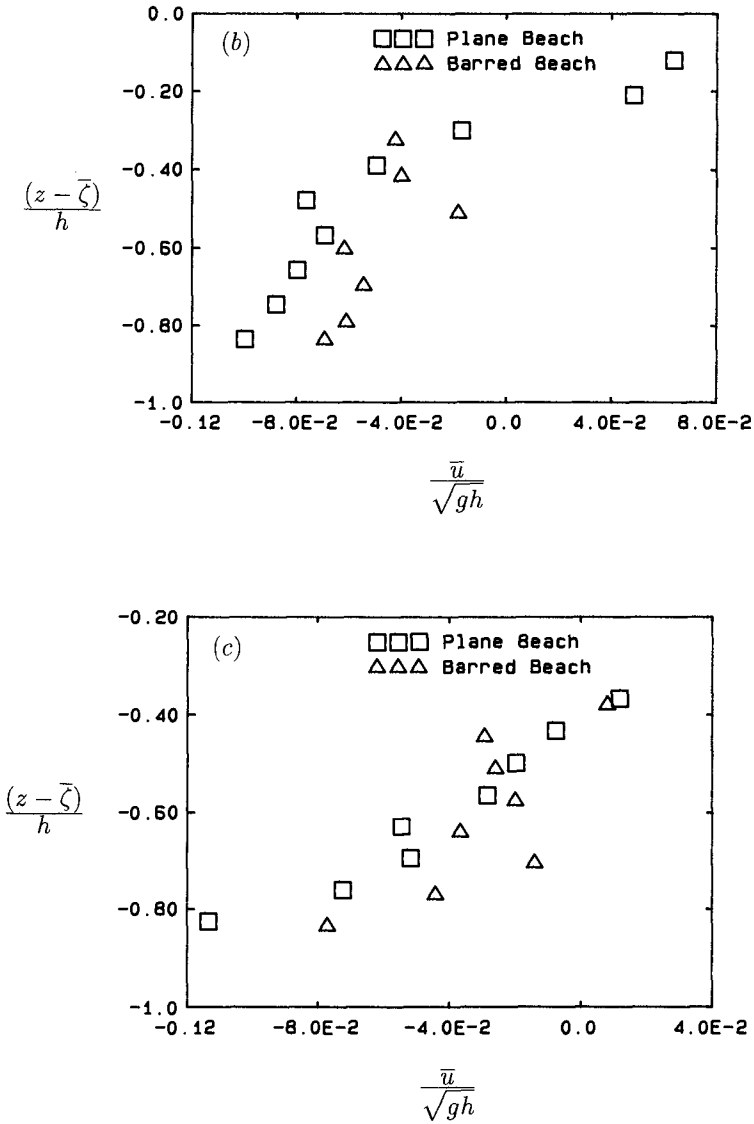


FIG. 4. (Continued)

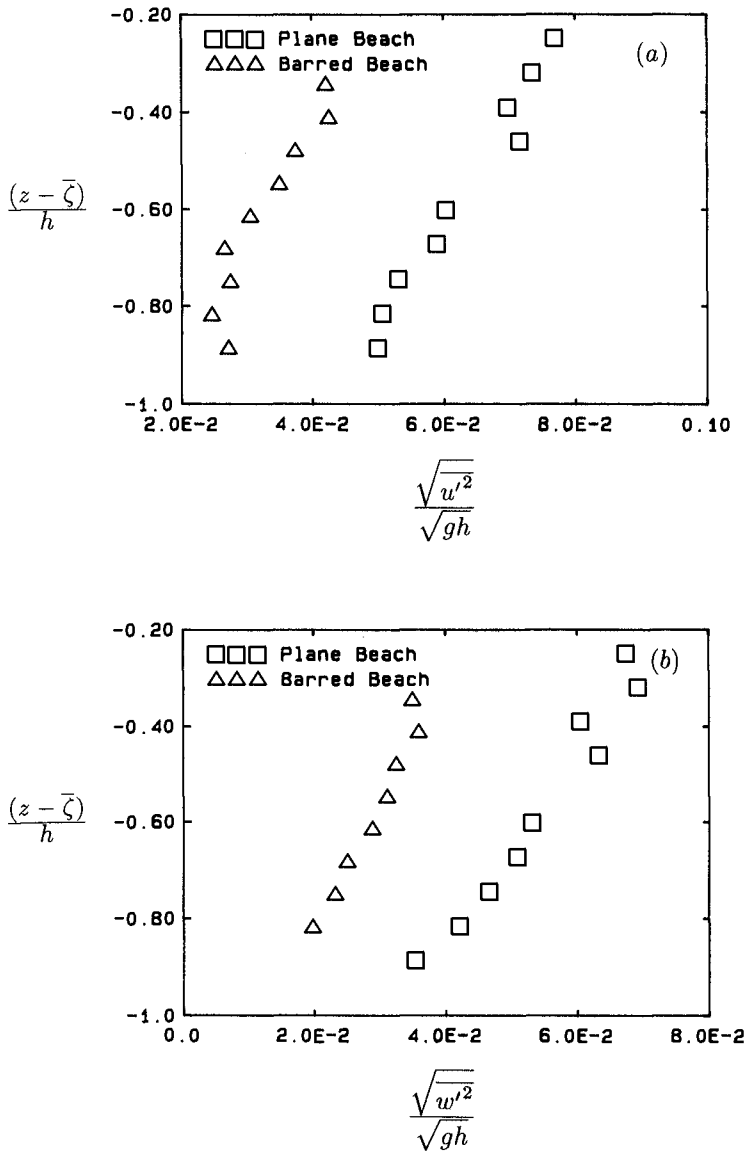


FIG. 5. Variation of Time Average Turbulent Velocity with Depth at Station 1. (a) Horizontal Component, (b) Vertical Component

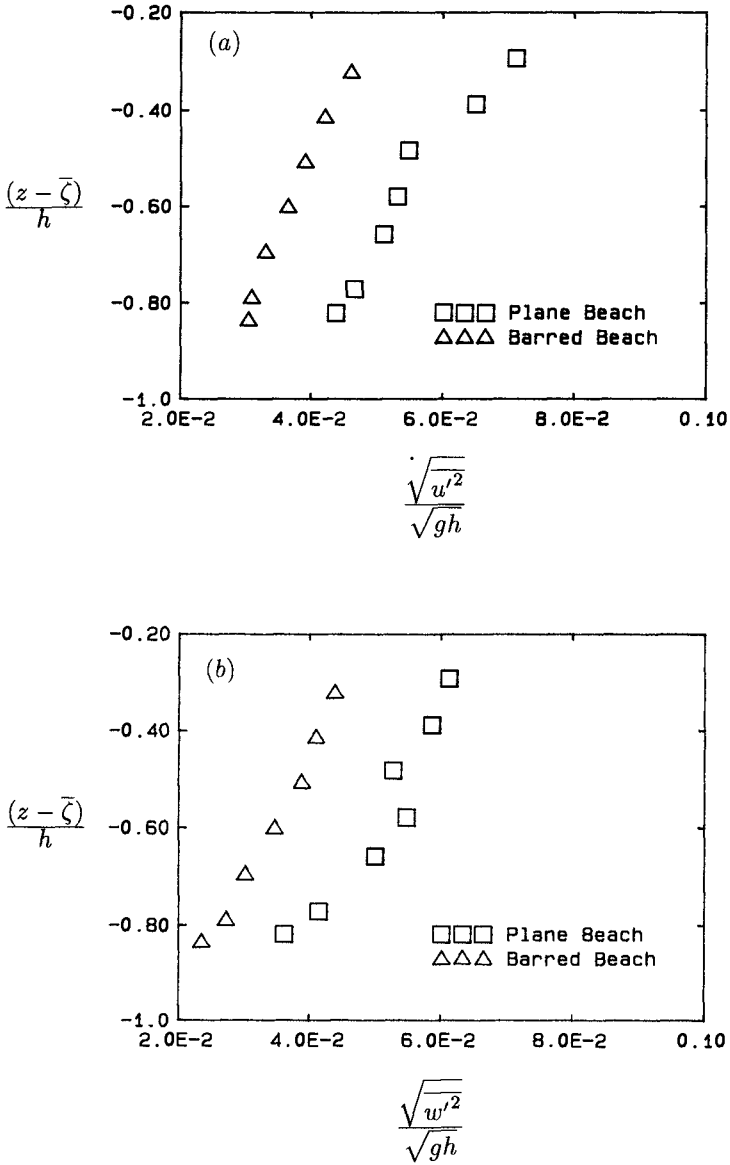


FIG. 6. Variation of Time Average Turbulent Velocity with Depth at Station 2. (a) Horizontal Component, (b) Vertical Component

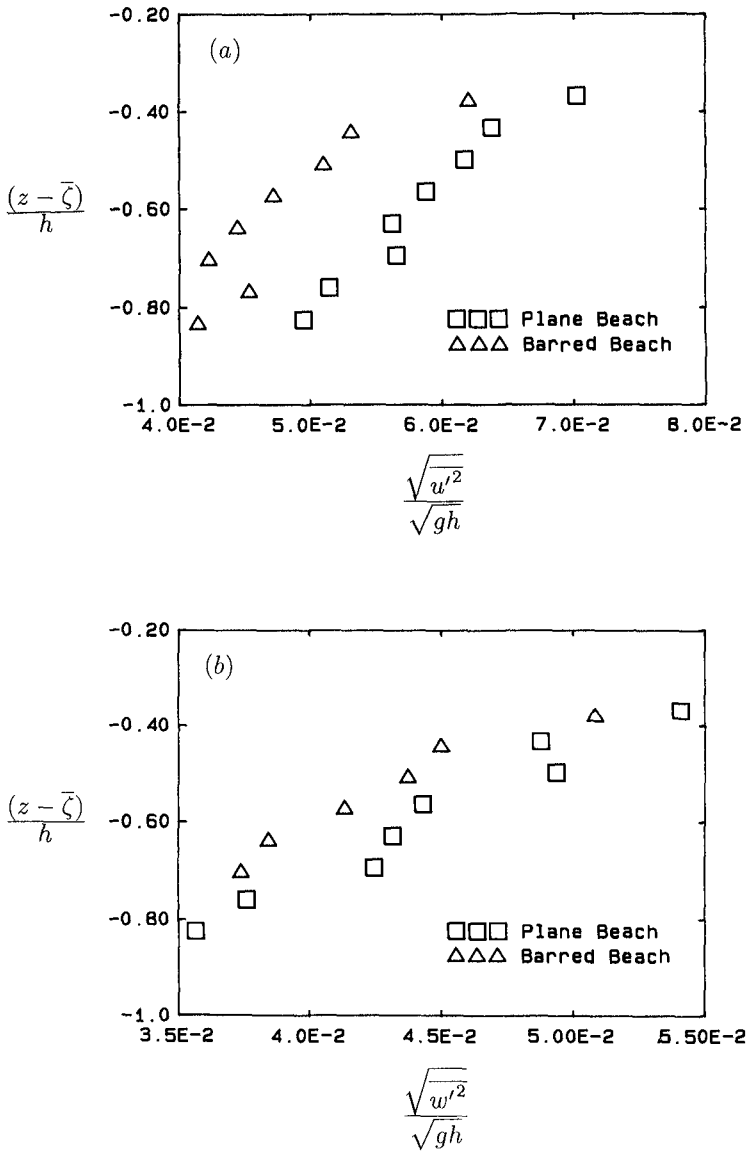


FIG. 7. Variation of Time Average Turbulent Velocity with Depth at Station 3. (a) Horizontal Component, (b) Vertical Component

## CHAPTER 197

### BEACH EROSION AROUND A SAND SPIT –An Example of Mihono-Matsubara Sand Spit–

Takaaki Uda<sup>1</sup> and Koji Yamamoto<sup>2</sup>

#### Abstract

Topographic changes around Mihono-Matsubara Sand Spit were studied based on bottom sounding data and aerial photographs. On the Shizuoka and Shimizu coasts located upcoast of the sand spit, erosion waves are generated due to interruption of longshore sand transport by the construction of coastal structures. The propagating velocity of these erosion waves was found to range from 0.5 to 0.8km/yr. This agrees considerably well with the theoretically estimated value of 0.47km/yr. Comparison of beach profiles showed that the dominant beach changes take place at depths shallower than  $-7\text{m}$ , and this provides the closure depth for profile changes on this coast. The longshore sand transport rate was evaluated to be  $1.3 \times 10^5 \text{m}^3/\text{yr}$  at specific locations on the Shizuoka and Shimizu coasts, and it was found that this transported sand discharges into submarine canyons, forming a steep slope of around  $1/2$ , thus resulting in the net loss of sand from this coast.

#### 1. INTRODUCTION

In general, sand spits form where obliquely incident waves are dominant and a large amount of sediment is supplied from rivers or coastal cliffs to the channel or the bay. Johnson (1919) and Zenkovich (1967) studied the formation process of various kinds of sand spits, focusing on the change in shoreline configuration. In their studies, spit forms were well classified, but the consideration of the relationship between spit formation and ambient bottom profiles, which is of vital importance to wave refraction, was not adequate. From this point of view, Uda and Yamamoto (1986, 1988, 1989, 1991) studied the formation process of sand spits along with the deformation mechanism by comparing data obtained from coasts, lake shores and model experiments with particular emphasis on the relationship between sea bottom topography and sand spit formation.

On the western coasts of Suruga Bay there are several well developed sand spits;

<sup>1</sup>D. Eng., Coastal Eng. Div., Public Works Res. Inst., Ministry of Construction, Ibaraki 305, Japan.

<sup>2</sup>Research Engineer, Ditto.

examples are Mihono-Matsubara Sand Spit and Wadabana Sand Spit on the Suruga coast. Mihono-Matsubara Sand Spit is one of the most famous compound spits, being the largest in Japan, together with the Notsukezaki Spit in eastern Hokkaido. This sand spit was originally formed by northward longshore transport carrying a large amount of sediment supplied from the Abe River. The decrease in sand supply from the river as a result of the excavation of the river bed to obtain construction material caused serious beach erosion around the Abe River mouth after 1965. The area of erosion rapidly expanded northeastward after 1977 and reached further downcoast (Shimizu coast) in 1982 (Toyoshima et al., 1981; Toyoshima, 1984). After 1979 various countermeasures against beach erosion were adopted and related construction work is still underway. No fundamental solution to the erosion problem, however, has yet been obtained. Beach erosion has also in recent years started at the tip of the Mihono-Matsubara Spit. Similar beach changes have been commonly observed at other coasts near sand spits in Japan.

In order to solve the above-mentioned coastal erosion problem, it is necessary to fully understand the topographic characteristics and deformation process of the sand spit. Such beach changes are considered to be different from those of straight coastlines with a gentle bottom slope. From this viewpoint, the present study aims at the investigation of beach erosion and accretion around a sand spit, taking the Shizuoka and Shimizu coasts as typical examples. The results of this case study will be useful when considering measures against beach erosion on other coasts suffering from similar problems. For this purpose, the topographic characteristics and beach deformation around the Mihono-Matsubara Sand Spit are studied using bottom sounding data and aerial photographs (Uda and Yamamoto, 1992).

## 2. TOPOGRAPHIC CHARACTERISTICS AND WAVE CONDITIONS

The Mihono-Matsubara Sand Spit, a typical compound sand spit in Japan, is located on the west coast of Suruga Bay (Fig. 1). Within the study site, the area of about 7km from the Abe River mouth to the Takigahara River mouth is referred to as the Shizuoka coast, and the 10km from the end of the Shizuoka coast to the tip of Mihono-Matsubara Sand Spit as the Shimizu coast. Suruga Bay is very deep, having the Suruga Trough in the center, and the bottom slope on each shore of the bay is steep. Narrow continental shelves develop only near the alluvial fans of the Abe and Ohi Rivers. The continental shelf off the Abe River mouth has a water depth of about 100 m at its offshore end.

The sea bottom topography near Mihono-Matsubara Sand Spit is illustrated in Fig. 2. The bottom slope at the tip of the sand spit is very steep; it falls to -400m with a slope of about 1/5, and several submarine canyons exist very close to the shoreline. Between the base of the sand spit and the Abe River mouth a gentle slope is found between -10m and -30m depths. The shape of bottom contours deeper than -50m is complicated, and several submarine canyons develop. Figure 2 also shows the arrangement of survey lines. Point No. 0 is located at the tip of the spit, No. 175 is at the left bank of the Abe River mouth, and the survey lines are arranged at 100m intervals from east to west. It is seen from the figure that the shoreline configuration is convex seaward between No. 0

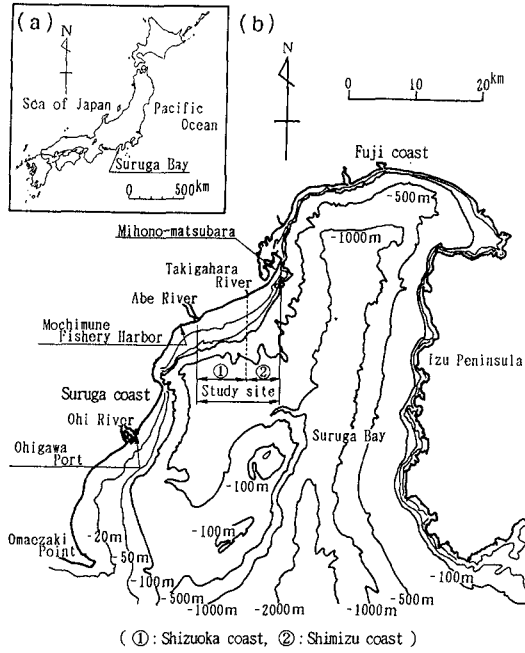


Figure 1. Location of Shizuoka and Shimizu coasts on the western shore of Suruga Bay.

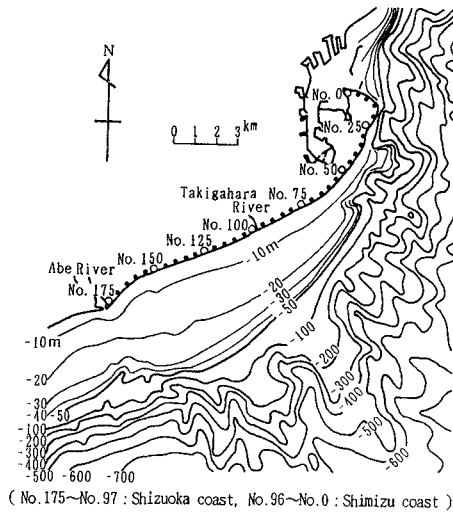


Figure 2. Bottom contours off Shizuoka and Shimizu coasts and alignment of survey lines (No. 0 - No. 175). No. 0 is located at the tip of the sand spit and No. 175 at the left bank of the Abe River mouth.

and No. 75, straight between No. 75 and No. 150, and concave seaward between No. 150 and No. 175.

Since no wave observation is performed off this coast, the distributions of wave directions with the classification of wave height obtained by wave observation off Mochimune Fishery Harbor and Ohigawa Port are shown in Fig. 3. These observatory stations are respectively located about 2.5km WSW and 20km SSW from the Abe River mouth, as shown in Fig. 1. It can be seen from Fig. 3 that the predominant wave direction is SSE at Mochimune Fishery Harbor and SE at Ohigawa Port. The energy-averaged significant wave height estimated from Ohigawa Port data from 1967 to 1979 is 0.82m, the mean period is 9.0s, and the dominant wave direction is SE. The direction of the normal to the coastline on the Shizuoka and Shimizu coasts runs SSE through ESE. Therefore, waves from S to SSE are obliquely incident to the coasts, causing northeastward longshore sand transport. According to foreshore sampling conducted in 1989, beach material has a median diameter in the range of 0.3mm to 20mm and specific gravity between 2.67 and 2.72. As for the tide condition, the mean monthly highest water level is T.P. + 0.806m and the mean monthly lowest water level is T.P. -0.733m, where T.P. is the abbreviation of the Tokyo Peil (mean tide level in Tokyo bay).

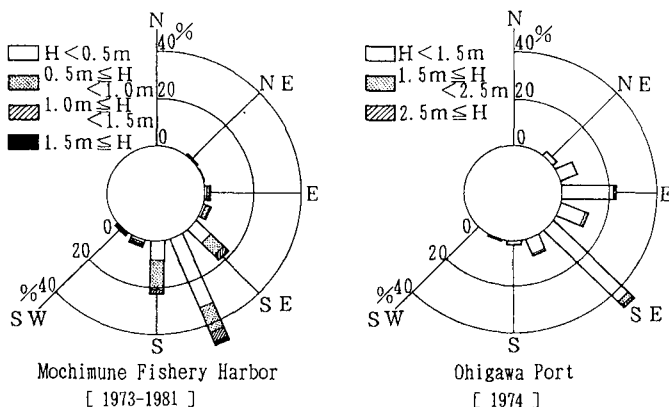


Figure 3. Directional probability of wave occurrence measured off Ohigawa Port and Mochimune Fishery Harbor (For location, see Fig. 1).

### 3. TOPOGRAPHIC CHANGES OF THE COAST

#### 3.1 Long-Term Change in Shoreline Configuration

Long-term change in shoreline position in the study area was investigated by comparing aerial photographs taken in 1948 and 1987 (Fig. 4). Shoreline position was read from the aerial photographs enlarged to the scale of 1/10000. The beach slope near the shoreline is from 1/5 to 1/10, which is steep enough to neglect shoreline change due to change in tide level. On the Shizuoka coast (No. 175 to No. 97) the shoreline retreated



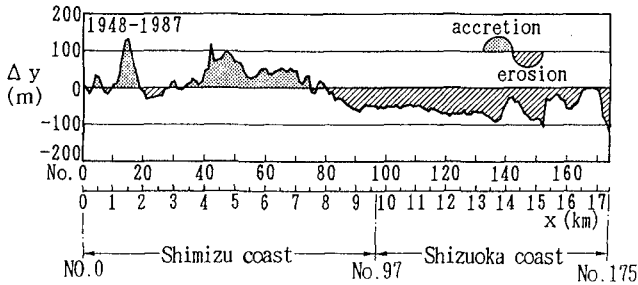


Figure 4. Change in shoreline position between 1948 and 1987 observed from aerial photographs.

approximately 50m on average during the 39 years, while the shoreline apparently advanced on the Shimizu coast located to the east. The shoreline configuration fluctuates considerably between No. 140 and No. 170 because of the accretive effect of the offshore breakwaters built in this area.

The longshore distribution of the annual change in shoreline position determined from soundings off the Shizuoka and Shimizu coasts is shown in Fig. 5, where all soundings were carried out in March unless otherwise indicated in the figure. The longshore distribution of cumulative shoreline change during the entire survey period is also shown at the bottom of the figure. Arrows in the figure indicate the position of the eastern end of the area where wave-dissipating structures were adopted as countermeasures against beach erosion. The area has been extended eastward along the shore from the Abe River mouth.

In 1975, beach erosion began between No. 144 and No. 159. The area where the shoreline retreated moved eastward with time and reached the Shimizu coast in 1983. The mean propagation velocity of the erosion wave, in which the eroded zone propagates downdrift (Inman, 1987), was about 0.8km/yr between 1975 and 1983. In 1988, the eroded area reached the area between No. 59 and No. 80. The propagation velocity of the erosion wave decreased between 1983 and 1988 compared to that between 1975 and 1983, but the area of erosion still extended at a rate of about 0.5km/yr. Inman (1987) suggested that the propagation velocity of the accretion wave, referring to the propagation of the opposite perturbation caused by the sudden release of sand, ranges from 0.5 to 1.5km/yr near Santa Cruz and 0.6 to 1.1km/yr at San Onofre in California. These values are on the same order as in the present study, although the nature of the waves is quite different. It is noted in Fig. 5 that the maximum change in shoreline position at the moving center of mass is around 25m. It should be further noted that, together with the extension of the eroded area, the area covered by the wave-dissipating structures apparently extended. The erosion waves seem to have propagated as a result of the extension of the wave-dissipating measures, but this is not true. In fact, these measures were undertaken at least one year after the onset of beach erosion. This indicates that the countermeasures followed the propagation of the erosion waves.

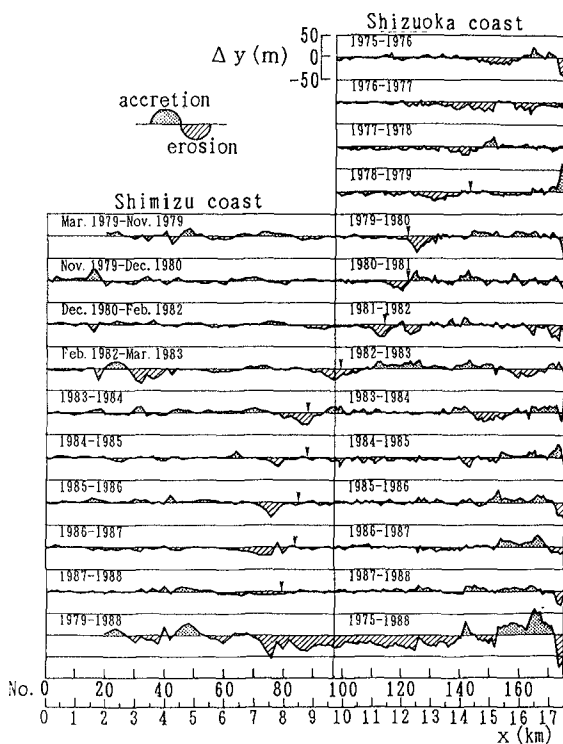


Figure 5. Longshore distribution of annual change in shoreline position between 1975 and 1988 calculated by bottom sounding data. An erosion wave defined by the longshore propagation of the eroded area (shaded zone in the figure) can be observed and its propagation velocity is about 0.8km/yr in the period between 1975 and 1973, and about 0.5km/yr between 1983 and 1988.

### 3.2 Longshore Changes in Sea Bottom Topography

In order to investigate the topographic features of the Shizuoka and Shimizu coasts, the longshore distribution of the offshore distance from the reference point to 0 to  $-10\text{m}$  contour lines was obtained from the bottom sounding data taken in 1988 and is summarized in Fig. 6.

Between No. 75 and No. 175, the intervals between 0 to  $-5\text{m}$  contour lines are considerably narrow, and the bottom slope of this area is 1/10 to 1/15. The intervals between  $-5$  to  $-10\text{m}$  contour lines further offshore are much wider, the bottom slope being gentler at 1/90 to 1/125. The gentle bottom slope in the offshore zone is considered to have formed as a result of erosion of a region shallower than the closure depth for profile changes, which is associated with shoreline recession. On the other hand, the shoreline configuration is very similar to the shape of contour lines up to  $-7\text{m}$ . This suggests that the beach profiles near the shoreline move in parallel and that the profile

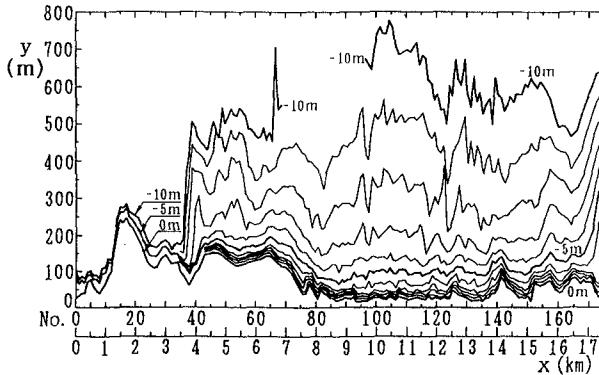


Figure 6. Longshore distribution of offshore distance from a reference point to some contour lines along the study area observed in 1988.

changes are caused by longshore sand transport.

Between No. 35 and No. 75 close to the Mihono-Matsubara Sand Spit, the intervals between 0 to  $-5\text{m}$  contour lines are narrow, similarly to the case of the western coast, and the bottom slope is about  $1/10$ , whereas the intervals between  $-5$  to  $-10\text{m}$  contour lines suddenly decrease from No. 40. The intervals between 0 to  $-10\text{m}$  contour lines at the tip of the Mihono-Matsubara Spit (No. 0 to No. 35) are very short, and the bottom slope is steep at about  $1/5$ .

The comparison of the bottom topography of these three areas with the change in shoreline configuration between 1948 to 1987, as shown in Fig. 4, explains that the topographic features of the sea bottom and the change in shoreline configuration correspond well to each other; that is, a gentle offshore slope is formed between No. 75 and No. 175, where the shoreline retreated in recent years, and a steep slope is formed between No. 10 and No. 20 near the tip of the sand spit, where the shoreline greatly advanced. From these characteristics it should be noted that Fig. 6 shows not only the present topography, but also contains information relating to the topographic changes during beach deformation.

### 3.3 Comparison of Beach Profiles

Two typical profiles along survey line Nos. 122 and 142 on the Shizuoka coast were selected for investigation of long-term profile changes. First, the profile changes at No. 142 are shown in Fig. 7, in which the reference year is selected as 1975. The beach had been severely eroded by 1980 to yield the concave profile upward. Thereafter, sediment accumulated and the beach slope became gentle. Because a group of detached breakwaters was constructed east of this survey line after 1980, eastward longshore sand transport was blocked. This is the cause of accretion on the survey line. Figure 7 indicates that the closure depth for profile changes associated with beach erosion or accretion is about  $-7\text{m}$ .

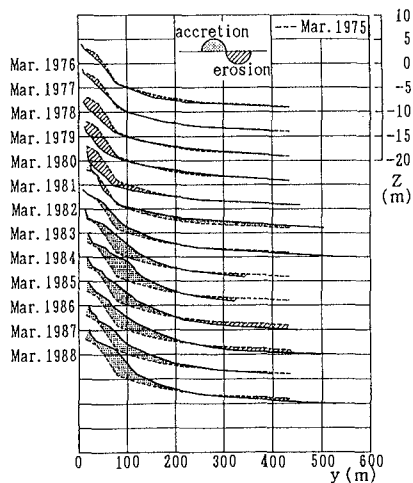


Figure 7. Temporal changes in beach profiles at No. 142. Beach was eroded severely up to 1980, leading to a concave profile near the shoreline, and beach slope became gentle due to sand accumulation.

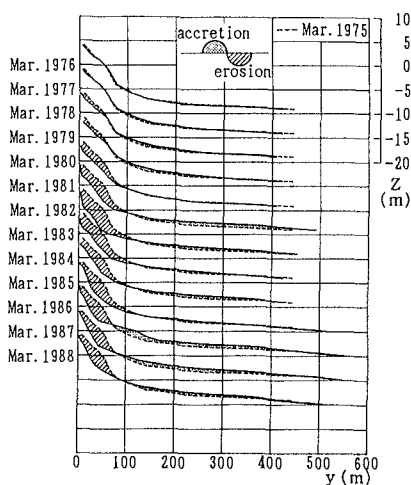


Figure 8. Temporal changes in beach profiles at No. 122. This beach was also eroded severely and a concave beach profile was formed.

The profile change at No. 122 located 2km east of No. 142 is shown in Fig. 8. Along this line, erosion progressed rapidly from 1975 to 1982, and the beach profile became concave upward. It is revealed that the location of the shoreline in 1975 was at a depth of 3~4m in 1982 as a result of the erosion. Two profiles, as mentioned above, show the characteristic features of a very gentle slope existing in the offshore zone. Such a flat bottom was formed by the erosional effect of waves, since the water depth over the slope is almost equal to the closure depth for profile changes. Furthermore, when sand accumulates on the beach, the profile near the shoreline becomes convex; it becomes concave when erosion occurs. This agrees well with the profile characteristics around a sand spit obtained in previous studies by Uda and Yamamoto (1986, 1991).

#### 4. ESTIMATION OF THE LITTORAL TRANSPORT RATE AND PROPAGATION VELOCITY OF EROSION WAVES

Figure 5 reveals considerable advance and retreat of the shoreline position west of No. 42 and wide, gentle offshore slopes were well developed below  $-7\text{m}$ . Thus, in these areas the closure depth for profile change is considered to be approximately constant. At the tip of the sand spit, sand discharges into the deep ocean, and it is difficult to define the closure depth. Eight survey lines were therefore selected between No. 42 and No. 161; variation in cross sectional area,  $\Delta A(\text{m}^2)$ , and the change in shoreline position,  $\Delta y(\text{m})$ , were calculated for each profile. The data were examined by means of regression analysis to obtain the following relationship between  $\Delta A$  and  $\Delta y$  with the

correlation coefficient  $R=0.87$ :

$$\Delta A = 11.0 \Delta y - 19.0 \quad (1)$$

The regression coefficient of  $\Delta A$  and  $\Delta y$  gives the characteristic height of beach change,  $h$ , when topographic change is caused by longshore drift. Figure 9 illustrates the definition of the characteristic height of beach change due to longshore sand transport, where  $h_c$  is the closure depth for profile change and  $h_R$  the wave run-up height. The characteristic height is often used in the one-line model for shoreline change to relate the change in cross-sectional area to the change in shoreline position. The characteristic height for this coast is thus evaluated as  $h=11\text{m}$ .

Based on the above definition, the volume change of the beach can be calculated by multiplying the change in beach area by the characteristic height of beach change. Furthermore, the littoral transport rate can be estimated from the temporal change in sand volume taking into account the continuity condition of littoral transport. With reference to Fig. 5, the littoral transport rate is estimated by selecting the area between No. 70 and No. 85, where the eroded region simply extended from 1984 to 1988 and the area between No. 151 and No. 166, where the accretion progressed in the same period, each area having a length of 1,500m. A great number of wave-dissipating structures were installed west of No. 85, so that sand supply from upcoast is considered to be greatly decreased. On the other hand, between No. 151 and No. 166, the discharge of longshore drift is considered to have been interrupted by the group of detached breakwaters and the jetty of the floodway located at No. 151. Figure 10 shows the cumulative change in beach areas of accretion and erosion since 1984. The area of erosion between No. 70 and No. 85 simply increased with time, and the total increase in four years was  $4.5 \times 10^4 \text{m}^2$ . The rate of increase is therefore  $1.1 \times 10^4 \text{m}^2/\text{yr}$ . Similarly, an increase of  $5.2 \times 10^4 \text{m}^2$  occurred between No. 151 and No. 166, the rate of increase being  $1.3 \times 10^4 \text{m}^2/\text{yr}$ . Here

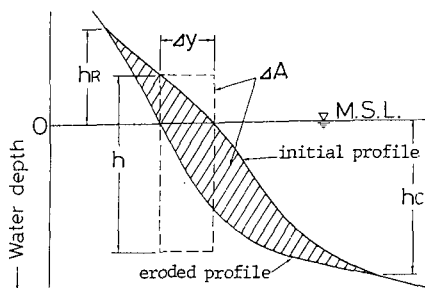


Figure 9. Definition of characteristics height of beach change due to littoral transport ( $\Delta A$ : increase in cross-sectional area,  $\Delta y$ : the change in shoreline position).

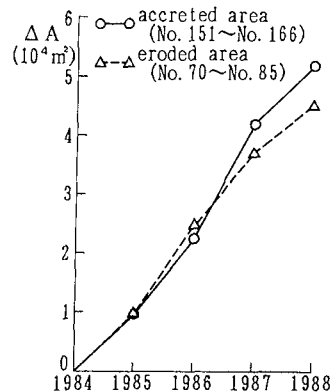


Figure 10. Temporal changes in accreted (No. 151–No. 166) and eroded (No. 70–No. 85) beach areas since 1984.

assumptions that the total amount of sand supplied from upcoast is deposited in the accretion zone and that a constant amount of sand discharges out of the erosion zone without any sand supply were made. The rate of change in Fig. 10 multiplied by the characteristic height of beach change then gives the littoral transport rate. Multiplying by  $h=1$  m determined from Eq.(1), the littoral transport rate across No. 70 is evaluated as  $1.2 \times 10^5 \text{m}^3/\text{yr}$  and across No. 166 as  $1.4 \times 10^5 \text{m}^3/\text{yr}$ , the average being  $1.3 \times 10^5 \text{m}^3/\text{yr}$ . These values are very close, and this indicates that no erosion or accretion occurred as long as continuous longshore drift took place in this range of the coast. This also implies that erosion will begin in the future at the tip of the sand spit because of significant decrease in sand supply.

Inman (1987) defined the propagation velocity of accretion or erosion waves,  $V$ , in terms of the longshore sand transport rate  $Q$  ( $\text{m}^3/\text{yr}$ ) and the volume change  $q$  associated with the moving center of mass as

$$V=Q/q. \quad (2)$$

As mentioned above, here,  $Q = 1.3 \times 10^5 \text{m}^3/\text{yr}$  on average. Furthermore, the relation of  $q = h \Delta y_{\text{max}}$  holds where  $\Delta y_{\text{max}}$  is the maximum shoreline change in terms of the moving center of mass. Substituting  $h=1$  m and  $\Delta y_{\text{max}} = 25$  m as obtained from Fig. 5 into this relation, we obtain  $V=0.47$  km/yr, which is comparable to the measured velocity (0.5–0.8 km/yr). As shown in Fig. 6, between Points No. 150 and No. 100 the foreshore width is so narrow that the maximum shoreline retreat ( $y_{\text{max}}$ ) is reduced owing to the restriction of the sea wall. This may cause a higher velocity of erosion waves. On the other hand, between Points No.100 and No.60 the foreshore width is sufficiently wide, and this is a possible reason for the agreement between measured and calculated velocities. It is finally concluded that the extension of the area of erosion can be explained well by introducing the concept of erosional waves.

## 5. BEACH CHANGES IN VICINITY OF TIP OF SAND SPIT

Figure 11 shows sea bottom contours and alignment of survey lines at 100m intervals around the tip of the Mihono-Matsubara Sand Spit. The origin of the survey lines is set at No. 0 at the tip of the sand spit. Steep submarine canyons develop at locations No. 12 through No. 30, No. 36 through No. 44, and No. 48 through No. 54, as shown in Fig. 11, in strong contrast to the development of a wide continental shelf with a gentle bottom slope west of No. 55.

First, the change in shoreline position between No. 47 and No. 71 is shown in Fig. 12 with reference to the shoreline form in 1988. In 1988 the shoreline extended straight north of No.71, where a coastal revetment had been installed to protect the coastline. The shoreline had started to retreat north of this revetment by 1989. The shoreline retreat takes a maximum value at a location beside this revetment, and it gradually decreases eastward with negligibly small change at No. 58. The shoreline change up to 1990 is similar to that measured to 1989, but the shoreline change increased west of No. 62 with a slight recession of the shoreline between No. 50 and No. 58. It is well known that installation of a coastal revetment and wave-dissipating breakwaters at a site updrift of littoral drift simply causes downcoast erosion, requiring further preventive measures

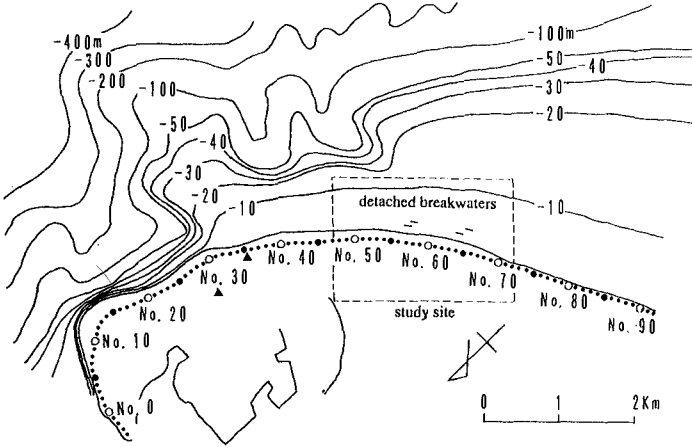


Figure 11. Bottom contours and alignment of survey lines at the tip of the sand spit.

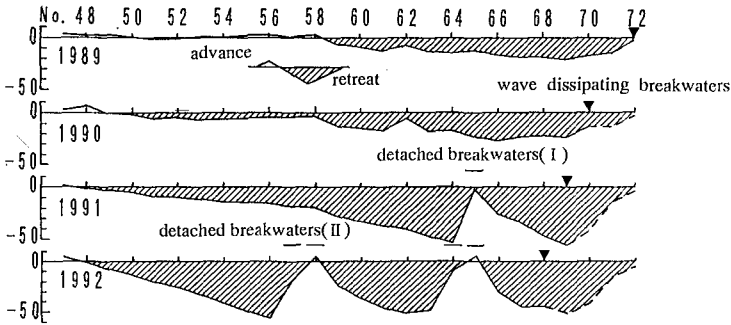


Figure 12. Change in shoreline position between No. 47 and No. 72.

against beach erosion. Recurrence of this process reduces the sandy coastline to an artificial coastline protected by various coastal structures, and the disappearance of natural sandy beaches. On the Shimizu coast, therefore, a method of stabilizing the coastline, in which a set of detached breakwaters is installed in a leap-frog manner at wide intervals, was employed. In 1991 a detached breakwater was installed at No. 65 as part of this plan. Since the detached breakwater blocked northward littoral drift, a step-type shoreline was formed at that location. As expected, downcoast, the shoreline between No. 64 and No. 48 retreated to become triangular. The area of erosion extended eastward about 900m in two years, resulting in the expansion rate of erosion of 0.45 km/yr. This propagation velocity is very close to the value of 0.5 km/yr obtained for the Shizuoka coast between 1983 and 1988, as mentioned earlier. In 1992 two sets of

detached breakwaters with an opening width of 500m were installed. Due to the installation of these detached breakwaters the shoreline between the two sets of detached breakwaters retreated a maximum of about 36m relative to the initial position in 1988, but the recession rate clearly decreased. In contrast the downcoast shoreline retreated in the same manner as the shoreline change observed in 1991.

Here detailed topographic changes around detached breakwaters are investigated. Figure 13 shows the change in sea bottom contours before and after the installation of detached breakwaters. Every contour extended straight alongshore in 1988 before the installation, as shown in Fig. 13(a). The interval between the contours between the shoreline and 4m depth is very narrow, in strong contrast to the gentle slope beyond 5m depth. In 1992 the coastline which was almost straight in the past became step-type form as a result of the installation of detached breakwaters I and II, as shown in Fig. 5(b). Typical topographic features showing the dominance of northward littoral drift can be observed in the vicinity of detached breakwaters I and II. For example, the western shoreline of these detached breakwaters extends straight toward the breakwater, whereas the eastern shoreline has an embayment shape with maximum shoreline retreat at the location beside the detached breakwater.

Mihono-Matsubara Sand Spit protrudes the furthest northeastward at No. 12, as shown in Fig. 11. At this site the sandy beach is very wide, but steep submarine canyons are developed very close to the shoreline. Figure 14 shows the beach profiles measured in 1988 and 1992 along No. 14 through No. 10 in the vicinity of the tip of the spit. At No. 14 sand is deposited up to a depth of 65m to form a steeper slope. A similar feature can be observed at No. 13, showing deposition up to a depth of 65m. The depth of the submarine canyon gradually decreases north of No. 14, and the offshore point of transition of the slope is located at 50m depth at No. 12. Sand is deposited again at No.

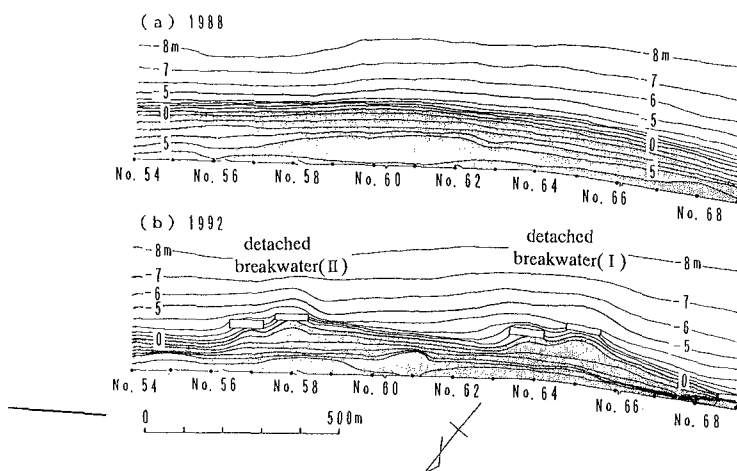


Figure 13. Topographic changes around two sets of detached breakwaters I and II between 1988 and 1992.



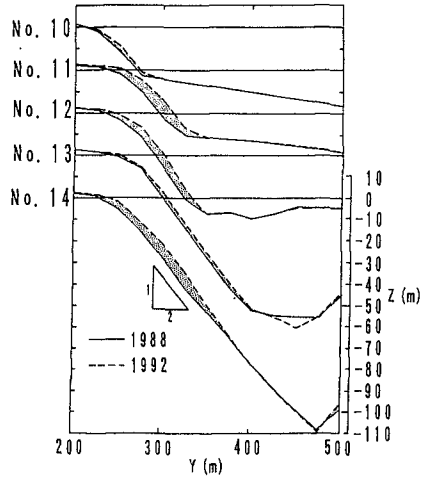


Figure 14. Change in longitudinal profile between 1988 and 1992.

12, while on upward convex profile is maintained. At No. 11 maximum advance of the shoreline position, 16m, is observed.

At No. 10 the point of transition of the slope becomes shallow, 22m depth, compared to the depth at survey lines located south of this line, and sand is deposited only on the steep slope in a zone shallower than 22m depth. It should be noted that sand is deposited up to 70m depth at maximum and 22m depth at minimum in the five beach profiles located in the vicinity of the tip of the sand spit. This is in marked contrast with the fact that the beach was eroded in a region shallower than 7m depth, as mentioned in section 3.2. In the case of beach erosion the shoreline retreats mainly due to the erosion concentrated in a zone shallower than the closure depth of around 7m on this coast, whereas sand discharges into the very deep region, where depth is one order of magnitude greater than the closure depth in the erosion zone, due to the topographic features of the sand spit. This is a very severe problem for this coast, because the total area of accretion becomes much smaller than the area of erosion in comparison to the areal change of the beach, causing net loss in the area of sandy beaches.

Here the change in sand volume of the beaches in accretion and erosion zones is shown in Fig. 15, taking 1988 as the reference year for comparison. As erosion and accretion zones, the area between No. 47 and No. 72 and the area north of No. 47 are selected on the basis of the recent shoreline changes, as shown in Fig. 12. In the erosion zone  $5.4 \times 10^5 \text{m}^3$  of sand was eroded from 1988 to 1992, resulting in an annual decrease rate of sand volume of  $1.35 \times 10^5 \text{m}^3/\text{yr}$ . This is approximately equal to the rate of littoral drift through No. 47, because the coastline west of No. 72 is totally covered by sea walls with concrete armor units at the foot and detached breakwaters, and therefore sand supply from upcoast through No. 72 is assumed to be negligible. This transport rate is very close to the value obtained further upcoast of Shizuoka coast, as discussed in the

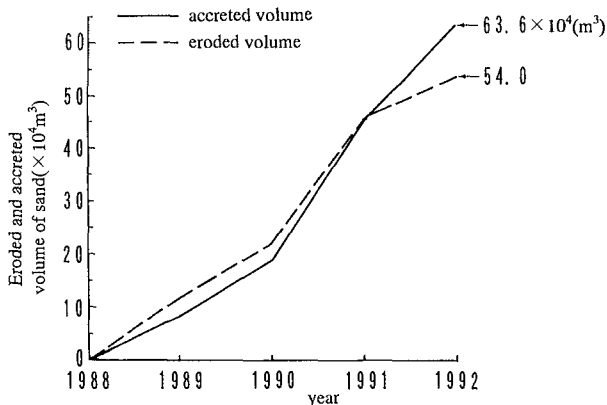


Figure 15. Time change in sand volume in accretion zone north of No. 46 and in erosion zone between No. 47 and No. 72.

previous section.

Total change in accreted sand volume up to 1992 reaches  $6.36 \times 10^5 \text{ m}^3$  which is about 18% greater than total eroded sand volume,  $5.4 \times 10^5 \text{ m}^3$ . However, the correspondence between the two results is considered to be fairly good, taking into account that volumetric calculation in the accretion zone is apt to include large error because of the wide calculation zone and because the sand supply through No. 72 by northward littoral drift is a small but non-negligible value.

## 6. CONCLUSIONS

The principal results of the present study can be summarized as follows.

(1) On the Shizuoka and Shimizu coasts, erosion waves propagated northeastward at a velocity of about 0.8km/yr between 1975 and 1983, and 0.5km/yr between 1983 and 1988. These erosion waves were caused by spatial discontinuity in longshore transport as a result of the installation of various coastal structures. Inman's (1987) method was employed to estimate their propagation velocity as 0.47km/yr, which agrees fairly well with observed values.

(2) A comparison of beach profiles revealed that significant topographic changes occurred in a region shallower than  $-7\text{m}$ , and it was confirmed that this water depth is approximately equivalent to the closure depth for profile changes on this beach. On the other hand, at the tip of the spit, a large amount of sand transported toward the tip of the spit is discharged and deposited up to a depth of 70m, which is one order of magnitude greater than the closure depth of this coast obtained in the erosion zone, forming a very steep slope of 1/2 due to the topographic features of the sand spit. Thus the occurrence of a net loss of sand toward the deep sea is of vital importance for solving beach erosion problems around a sand spit.

(3) The littoral transport rate was evaluated to be  $1.3 \times 10^5 \text{m}^3/\text{yr}$  near No. 70 and No. 166 on the Shizuoka coast from the temporal change in sand volume of the coast. In a recent erosion zone at the tip of the sand spit  $5.4 \times 10^5 \text{m}^3/\text{yr}$  of sand was eroded between 1988 and 1992, resulting in an annual decrease rate of sand volume of  $1.35 \times 10^5 \text{m}^3/\text{yr}$ , which is close to the approximate rate of northward littoral drift through No. 47. Thus the two estimated values are in good agreement.

## ACKNOWLEDGEMENT

The authors would like to express their deepest gratitude to the staff of Shizuoka Civil Engineering Office, Shizuoka Prefectural Government, who provided valuable assistance in collecting various data and information.

## REFERENCES

- Inman, D.L. (1987): Accretion and erosion waves on beaches, *Shore & Beach*, Vol. 55, No. 3, 4, pp. 61-64.
- Johnson, D.W. (1919): *Shore Processes and Shoreline Development*, Wiley, New York, 584p. [Facsimile edition: Hafner, New York (1965)].
- Toyoshima, O., W. Takahashi and I. Suzuki (1981): Characteristics of the beach erosion on Shizuoka coast, *Proc. 28th Japan. Coastal Eng. Conf., JSCE*, pp. 261-265. (in Japanese)
- Toyoshima, O. (1984): Beach erosion prevention works with new blocks, *Proc. 31st Japan. Coastal Eng. Conf., JSCE*, pp. 330-334. (in Japanese)
- Uda, T. and K. Yamamoto (1986): Spit formation in lake and bay, *Trans., Japan. Geomorpho. Union*, Vol.7, pp. 1-22. (in Japanese)
- Uda, T. and K. Yamamoto (1988): Formation process of a sand spit: Comparison of the field data with the model test, *Trans., Japan. Geomorpho. Union*, Vol. 9, pp. 295-307. (in Japanese)
- Uda, T. and K. Yamamoto (1989): Topographic changes of Oyazawa-bana Spit on the north shore of Lake Hinuma: 1983 to 1988, *Trans., Japan. Geomorpho. Union*, Vol. 10, pp. 209-217. (in Japanese)
- Uda, T. and K. Yamamoto (1991): Spit formation in lake and bay, *Coastal Sediments '91*, Vol. 2, pp. 1651-1665.
- Uda, T. and K. Yamamoto (1992): Beach changes around a sand spit - The example of Mihono-Matsubara, *Coastal Eng. in Japan*, Vol. 35, No.1, pp. 111-128.
- Zenkovich, V.P. (1967) : *Processes of Coastal Development*, Oliver & Broyd, Edinburgh, 738p.

## SHORECIRC: A Quasi 3-D Nearshore Model

A.R. Van Dongeren<sup>1</sup>, F.E. Sancho<sup>2</sup>, I.A. Svendsen<sup>3</sup>, and U. Putrevu<sup>4</sup>

**ABSTRACT:** A depth-integrated, short wave-averaged nearshore circulation model is presented, which includes the effects of the 3-D current structure over depth. The model includes the description of time-varying currents such as infra-gravity waves. Two numerical schemes are developed, which will be used for intercomparison in the absence of analytical solutions. An absorbing-generating boundary condition is developed based on the Method of Characteristics in order to allow propagating waves to leave the computational domain with a minimum of reflection while specifying incoming waves at the same boundaries. The model is tested for the time-varying start-up of a longshore current on a cylindrical coast, and the temporal development of both the cross-shore profiles of the longshore current and characteristic samples of the vertical structure of the velocity profiles are given.

### INTRODUCTION

Shoaling, breaking, refraction and randomness of short waves are responsible for larger scale motions such as steady and unsteady currents and low frequency (infragravity) waves. These motions are all described by time-varying nearshore circulation models and can be observed as temporal and spatial variations of the short wave-averaged setup/setdown and longshore and cross-shore currents.

Two classes of models exist to describe these nearshore phenomena: (*i*) models that resolve the instantaneous state of motion, such as models based on the

---

<sup>1</sup>Graduate Student, Center for Applied Coastal Research, University of Delaware, Newark, DE 19716, USA. e-mail: apper@coastal.udel.edu

<sup>2</sup>Graduate Student, Center for Applied Coastal Research, University of Delaware, Newark, DE 19716, USA. e-mail: sancho@coastal.udel.edu

<sup>3</sup>Professor, Center for Applied Coastal Research, University of Delaware, Newark, DE 19716, USA. e-mail: ias@coastal.udel.edu

<sup>4</sup>Research Scientist, NorthWest Research Associates, Inc., Bldg. 7, Suite 220, 300 120th Avenue N.E., Bellevue WA 98009, USA. e-mail: putrevu@calvin.nwra.com

nonlinear shallow water equations or on the Boussinesq-equations and (ii) time-averaged models that calculate large scale motions due to short wave-induced forcing. The latter class can be further subdivided into two categories. Two-dimensional horizontal (2DH) models describe the depth-mean current and the surface elevation. They are based on the turbulence-averaged, depth-integrated, time-averaged Navier-Stokes equations. The second category, 2DV-models, have primarily been used to study the vertical structure of the cross-shore circulation (Svendsen (1984), Dally & Dean (1984), Stive & Wind (1986), Svendsen *et al.* (1987) and Svendsen & Hansen (1988)). Both types of models are an approximation of the fully 3D case, which until now has not been successfully modeled.

Quasi-3D models were developed to combine the effect of the vertical structure with the simplicity of 2DH models. In the approach by De Vriend & Stive (1987), the current is split into primary and secondary flow profiles based on the assumption that the primary velocity profiles are the same in the cross-shore and longshore direction. In a different approach, Svendsen & Lorenz (1989) determined the vertically-varying longshore and cross-shore currents separately under the assumption of weak dependence. They found that the total vertical current profile has a spiral shape (Fig. 1). Svendsen & Putrevu (1990) formulated a steady-state 3D nearshore circulation model using analytical solutions for the 3D current profiles in combination with a numerical solution of the depth-integrated 2D horizontal equations for a long straight coast. Sánchez-Arcilla *et al.* (1990, 1992) presented a similar concept. They split the current velocity into a depth-invariant component and a component with a vertical variation with zero mean flow integrated over the central layer. Putrevu & Svendsen (1992) and Svendsen & Putrevu (1994a) recognized that the current-current and current-wave interactions neglected in previous investigations induce a non-linear dispersion mechanism, which significantly augments the lateral turbulent mixing and explains the apparent difference in magnitude between the vertical and horizontal mixing.

In the present form, SHORECIRC is the time-dependent extension of the model presented by Svendsen & Putrevu (1994a). This comprehensive model is able to describe a number of nearshore phenomena such as surf-beat, edge waves and longshore currents while allowing for alongshore variations in the hydrodynamical conditions. By including finite amplitudes, random wave forcing, and the effects of the 3D current structure, it extends the description of these phenomena beyond the usual analytical solutions. The topography part of the model is presently configured for a cylindrical coast only, but will later be extended to cover arbitrary bottom topography as well. In the present paper we focus on the form of the 2DH equations, the generating-absorbing boundary condition used, and we test the model performance for a time-varying case of the longshore current on a long, straight beach.

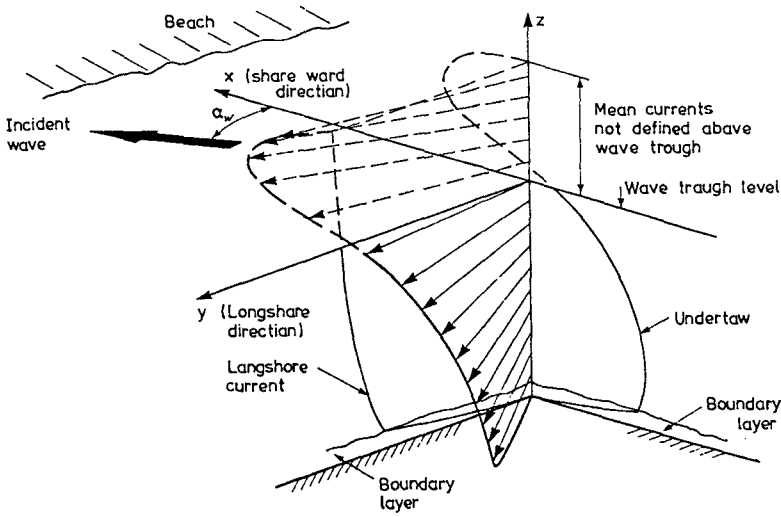


Figure 1: Three-dimensional structure of the current velocities in the surf zone (from Svendsen & Lorenz, 1989).

**GOVERNING EQUATIONS**

The depth-integrated, time-averaged mass and momentum equations read as follows:

$$\frac{\partial \bar{\zeta}}{\partial t} + \frac{\partial}{\partial x_\alpha} \left( \overline{\int_{-h_0}^{\zeta} V_\alpha dz} + Q_{w\alpha} \right) = 0 \tag{1}$$

$$\begin{aligned} &\rho \frac{\partial \bar{Q}_\beta}{\partial t} + \rho \frac{\partial}{\partial x_\alpha} \overline{\int_{-h_0}^{\zeta} V_\alpha V_\beta dz} + \rho \frac{\partial}{\partial x_\alpha} \overline{\int_{\zeta_t}^{\zeta} u_{w\alpha} V_\beta + u_{w\beta} V_\alpha dz} \\ &+ \rho g (\bar{\zeta} + h_0) \frac{\partial \bar{\zeta}}{\partial x_\beta} + \frac{\partial}{\partial x_\alpha} \left( S'_{\alpha\beta} - \overline{\int_{-h_0}^{\zeta} \tau_{\alpha\beta} dz} \right) - \tau_\beta^S + \tau_\beta^B = 0 \end{aligned} \tag{2}$$

where the radiation stress  $S'_{\alpha\beta}$  is given by

$$S'_{\alpha\beta} = \overline{\int_{-h_0}^{\zeta} (\rho u_{w\alpha} u_{w\beta} + \delta_{\alpha\beta} p) dz} - \delta_{\alpha\beta} \frac{1}{2} \rho g h^2 \tag{3}$$

which is equivalent to the definition used by Mei (1983).

In the above,  $V_\alpha$  and  $\bar{\zeta}$  represent the horizontal current velocity and the mean surface elevation, respectively, which is equivalent to the particle velocity

and wave surface elevation if an IG wave is considered.  $u_w$  is the short wave velocity,  $Q_\alpha$  represents the total volume flux and  $Q_w$  is the volume flux due to the short wave motion.  $\zeta_i$  is the elevation of the wave trough,  $\tau_{\alpha\beta}$  is the Reynolds stress,  $h_o$  is the still water depth, while  $\tau_\beta^S$  and  $\tau_\beta^B$  represent the surface (e.g. wind) and the bottom shear stresses, respectively. The overbar denotes short wave averaging and the subscripts  $\alpha$  and  $\beta$  denote the directions in a horizontal Cartesian coordinate system. See Figure 2 for a definition sketch.

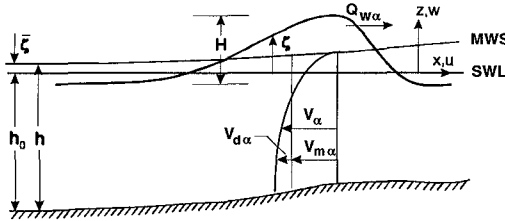


Figure 2: Definition sketch.

The form (2) of the momentum equation is written in terms of  $V_\alpha$  which is the current defined in the traditional way: the net velocity at any point below wave trough level and above the purely oscillatory wave motion (i.e.  $\bar{u}_w = 0$ ). For the general case of depth varying currents it is convenient to split this current into a depth uniform and depth varying component:

$$V_\alpha = V_{m\alpha}(x, y, t) + V_{d\alpha}(x, y, z, t) \tag{4}$$

where

$$V_{m\alpha} = \frac{\bar{Q}_\alpha - Q_{w\alpha}}{h} \tag{5}$$

and

$$Q_{w\alpha} = \int_{-h_0}^{\zeta} u_{w\alpha} dz \tag{6}$$

It may be verified that

$$\int_{-h_0}^{\zeta} V_\alpha dz = \bar{Q}_\alpha - Q_w \quad \text{and} \quad \int_{-h_0}^{\zeta} V_{d\alpha} dz = 0 \tag{7}$$

Then (2) may be written as

$$\begin{aligned} & \rho \frac{\partial \bar{Q}_\beta}{\partial t} + \rho \frac{\partial}{\partial x_\alpha} \left( \frac{\bar{Q}_\alpha \bar{Q}_\beta}{h} \right) + \rho \frac{\partial}{\partial x_\alpha} \int_{-h_0}^{\bar{\zeta}} V_{d\alpha} V_{d\beta} dz \\ & + \rho \frac{\partial}{\partial x_\alpha} \int_{\zeta_t}^{\bar{\zeta}} u_{w\alpha} V_{d\beta} + u_{w\beta} V_{d\alpha} dz + \rho g (\bar{\zeta} + h_0) \frac{\partial \bar{\zeta}}{\partial x_\beta} \\ & + \frac{\partial}{\partial x_\alpha} \left( S_{\alpha\beta} - \int_{-h_0}^{\bar{\zeta}} \tau_{\alpha\beta} dz \right) - \tau_\beta^S + \tau_\beta^B = 0 \end{aligned} \quad (8)$$

where  $S_{\alpha\beta}$  is the radiation stress defined by

$$S_{\alpha\beta} = S'_{\alpha\beta} - \rho \frac{Q_{w\alpha} Q_{w\beta}}{h} \quad (9)$$

which is the definition used by Phillips (1977).

The integrals in (8) represent the effects of the depth-varying currents. The rest of the terms are essentially equivalent to the terms found by Phillips (1977) and Mei (1983).

The equations (1) and (8) are solved by finite differences for the time and space variation of  $\bar{\zeta}$  and  $\bar{Q}_\alpha$  in combination with an analytical solution for the current distribution along the vertical, which is given in terms of eigenfunction expansions. This analytical solution includes integration constants that are in turn determined from the numerical solution of the depth-integrated equation (8). The details of this are left out for reasons of space limitation (Svendsen & Putrevu, 1994b and Putrevu & Svendsen, 1994).

## NUMERICAL SCHEMES

Two numerical schemes have been developed: a second order, explicit predictor-corrector method and a second order, ADI staggered-grid scheme. This allows us to compare the two numerical solutions to each other when an analytical solution for the 2DH current pattern is not readily obtained, for instance in cases of random wave forcing or a complicated bathymetry. Both schemes have inherent advantages and drawbacks. While simpler, the explicit method has a Courant-Friedrichs-Lewy (CFL) limitation on its stability, which sets an upper limit on the time-step allowed. Typically we use a Courant number of 0.35 - 0.7. The ADI method, which has no CFL limit, is both more robust and more complicated for the nonlinear terms. Hence it can be operated at even larger Courant numbers, although it loses accuracy if the Courant number is increased too much.



## ABSORBING-GENERATING BOUNDARY CONDITION

In order to be able to model a limited coastal region in an otherwise large ocean, it is necessary to establish boundary conditions along the open ocean-side boundaries that satisfy two criteria:

1. The region outside the computational domain only influences the motion inside through incident (long) waves and currents, which we know and specify along the open boundaries.
2. (Long) waves propagating out of the computational region must be allowed to propagate freely through the open ocean-side boundaries with minimal reflection.

Thus this boundary condition must be able to generate a specified long wave and simultaneously absorb outgoing waves. Such a generating-absorbing boundary condition is derived below based on the Method of Characteristics (Abbott, 1979; Verboom *et al.*, 1981).

We first notice that the open boundaries are established so that near these boundaries the dominating terms in the continuity and momentum equations are the terms corresponding to the nonlinear shallow water (NSW) equations. Introducing  $\bar{u}_\alpha = \frac{Q_\alpha}{h}$ , where  $h$  denotes total water depth, we can thus write (1) and (8) as

$$\frac{\partial \bar{\zeta}}{\partial t} + \frac{\partial h \bar{u}_\alpha}{\partial x_\alpha} = 0 \quad (10)$$

$$\frac{\partial \bar{u}_\beta}{\partial t} + \bar{u}_\alpha \frac{\partial \bar{u}_\beta}{\partial x_\alpha} = -g \frac{\partial \bar{\zeta}}{\partial x_\beta} + f_\beta \quad (11)$$

where  $f_\beta$  represents forcing terms for the motion which include the radiation stress terms, the  $V_{d\alpha}$ -integrals, the bottom and wind shear stresses and the bottom slope term, all included in the original equations.

In characteristic form these equations can be written as:

$$\frac{\partial \beta^+}{\partial t} = -(\bar{u} + c) \frac{\partial \beta^+}{\partial x} - \bar{v} \frac{\partial \beta^+}{\partial y} - c \frac{\partial \bar{v}}{\partial y} + g \frac{\partial h_o}{\partial x} + F_{\beta^+} \quad (12)$$

$$\frac{\partial \beta^-}{\partial t} = -(\bar{u} - c) \frac{\partial \beta^-}{\partial x} - \bar{v} \frac{\partial \beta^-}{\partial y} + c \frac{\partial \bar{v}}{\partial y} + g \frac{\partial h_o}{\partial x} + F_{\beta^-} \quad (13)$$

$$\frac{\partial \gamma}{\partial t} = -\bar{u} \frac{\partial \gamma}{\partial x} - \bar{v} \frac{\partial \gamma}{\partial y} - g \frac{\partial \bar{\zeta}}{\partial y} + F_\gamma \quad (14)$$

where  $\beta^+$  in (12) is the ingoing Riemann-invariant  $\bar{u} + 2c$  and  $c = \sqrt{g(h_0 + \bar{\zeta})}$ .  $\beta^- = \bar{u} - 2c$  and  $\gamma = \bar{v}$  are the Riemann-invariants of (13) and (14). The forcing terms  $F_{\beta^+}$ ,  $F_{\beta^-}$  and  $F_\gamma$  originate from the  $f$ -terms in (11). Because of these terms, the invariants should actually be called *variables*. It turns out that the  $\gamma$ -equation is the  $y$ -momentum equation itself. See Figure 3 for a definition sketch showing the characteristics. Note that the Riemann-variants  $\beta^+$  and  $\beta^-$  are not related to the subscript  $\beta$  used in (1) through (11).

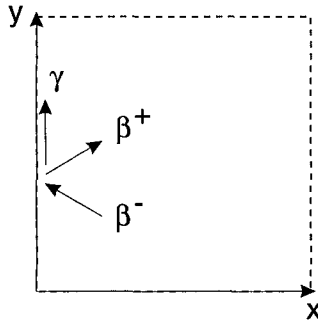


Figure 3: Definition sketch of the characteristics.

From the Riemann variable  $\beta^-$ , which propagates along a trajectory in the negative  $x$ -direction and is updated by (13), we can derive a relationship between the flux of the outgoing wave (subscripted 'r' in the following) and the incoming wave (subscripted 'i'). Assuming linear superposition of these waves

$$\vec{Q} = \vec{Q}_i + \vec{Q}_r \quad (15)$$

and substituting the identities

$$\vec{Q}_i = \vec{c} \zeta_i \quad \vec{Q}_r = -\vec{c} \zeta_r \quad (16)$$

which are valid irrespective of wave theory and only assume constant form, we get

$$|Q_r| (\cos \theta_r + 1) = h_0 \beta^- - |Q_i| (\cos \theta_i - 1) + 2h_0 \sqrt{gh_0} + O\left(\frac{\bar{\zeta}}{h_0}\right)^2 \quad (17)$$

where  $\theta_i$  and  $\theta_r$  are defined as the angles between the normal to the boundary and

the incoming and outgoing waves, respectively. From the  $y$ -momentum equation (14) we then get

$$|Q_r| \sin \theta_r = Q_y - Q_{iy} \quad (18)$$

where  $Q_y = \bar{v}(h_o + \zeta)$ . From (17) and (18) we can find the unknowns  $|Q_r|$  and  $\theta_r$  iteratively. With the incoming wave known through specification, and integrating (13) and (14) in time, the boundary values of total fluxes  $Q_x$  and  $Q_y$ , and the surface elevation  $\bar{\zeta}$ , are determined at the next time step. This boundary condition is essentially a generalized version of the condition derived for the 1-D case by Kobayashi *et al.* (1987).

Two cases have been run to test this absorbing-generating boundary condition. In the first case, linear waves were generated under various angles at the  $x = 0$  and  $y = 0$  boundaries. They were propagated over a flat bottom using the linearized equations and absorbed at the  $x = L_x$  and  $y = L_y$  boundaries. This tests the absorbing capability of the boundary condition. The parameters used were: wavelength  $\lambda = 50 \text{ m}$ , domain lengths  $L_x = L_y = 2\lambda$ ,  $h_o = 1 \text{ m}$ ,  $T = \lambda / \sqrt{g h_o}$ ,  $A = 0.01 \text{ m}$ ,  $\Delta x = \Delta y = \frac{\lambda}{30}$  and  $C_r = 0.6$ . Figs. 4 a-c show the instantaneous water surface for three selected angles  $\theta = 0^\circ, 30^\circ$  and  $75^\circ$ , where  $\theta$  is defined as the angle between the incident wave ray and the  $y$ -axis. Reflections from the boundaries are barely visible.

To calculate the reflection coefficient, a time series was taken at a point on the boundary. Then the domain was extended to be effectively infinite and another time series was taken at the same point. Following Verboom & Slob (1984), the reflection coefficient is then defined as the maximum of the difference of the two time series normalized by the amplitude of the original wave:

$$R = \frac{\max \Delta \zeta(t)}{A} \quad (19)$$

Fig. 4 d shows this reflection coefficient  $R$  (indicated by the dots) as a function of the angle of incidence  $\theta$ .

A comparison is made to the widely-used Sommerfeld radiation condition

$$\left( \frac{\partial}{\partial t} + \frac{c}{\cos \theta_r} \frac{\partial}{\partial x} \right)^n u = 0 \quad (20)$$

where  $n$  indicates the order of the approximation of the boundary condition. For instance, the radiation condition that was introduced by Engquist & Majda (1977) has  $n = 2$ . The theoretical reflection coefficient of this type of condition, which can be calculated as (Higdon, 1986)

$$R = \left| \left( \frac{\cos \theta_r - 1}{\cos \theta_r + 1} \right)^n \right| \quad (21)$$

is shown in Fig. 4d for three values of  $n$ , indicated by the solid lines. The figure shows that the present condition based on the Method of Characteristics has much better absorption capabilities than the Sommerfeld condition. The latter gives large reflection coefficients for large angles and is fully reflecting for waves propagating parallel to the boundary. Note that the reflection, as calculated by (19), includes truncation and other numerical errors, while  $R$ , as calculated by (21), is theoretical only. This probably causes the better performance of the Sommerfeld condition at small angles.

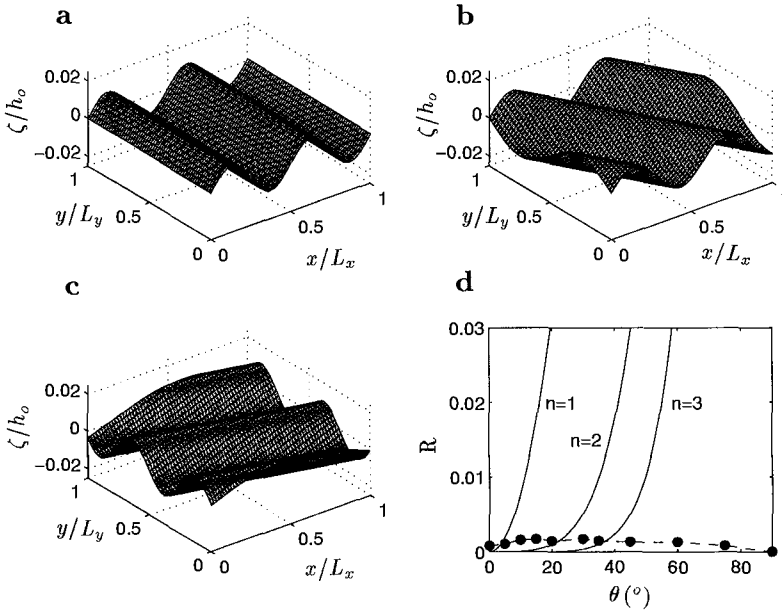


Figure 4: (a) Instantaneous water surface for  $\theta = 0^\circ$ . (b) Same for  $\theta = 30^\circ$ . (c) Same for  $\theta = 75^\circ$ . (d) Reflection coefficients versus angle  $\theta$ , —: Eq. (21),  $\bullet$ : present model.

In a second test, waves are simultaneously generated and absorbed at the  $x = 0$  boundary. From a cold start, waves are generated under an angle of  $0^\circ$  from  $t = 0T - 19T$  and are reflected off a wall at  $x = L_x$ . Parameters used are: wavelength  $\lambda = 50\text{ m}$ , domain lengths  $L_x = 3.3\lambda$  and  $L_y = 0.2\lambda$ ,  $h_0 = 1\text{ m}$ ,  $T = \lambda / \sqrt{g h_0}$ ,  $A = 0.01\text{ m}$ ,  $\Delta x = \Delta y = \frac{\lambda}{60}$  and  $C_r = 0.6$ . Fig. 5a shows the wave propagating in  $+x$ -direction at  $t = 2T$  and Fig. 5b the resulting standing wave. At  $t = 19T$  the incoming wave was turned off instantaneously (causing a minor disturbance wave that is visible in Fig. 5c where a wave propagating in the negative  $x$ -direction is trailed by higher frequency disturbances). The central

part of the time series (taken at  $x = 0$ ,  $y = \frac{L_y}{2}$ ) in Fig. 5d shows the standing wave whose amplitude is equal to the analytical solution within a few percent. It also shows that the transients radiate out with very little reflection. Still-water conditions are reached fairly quickly after the generated waves leave the domain.

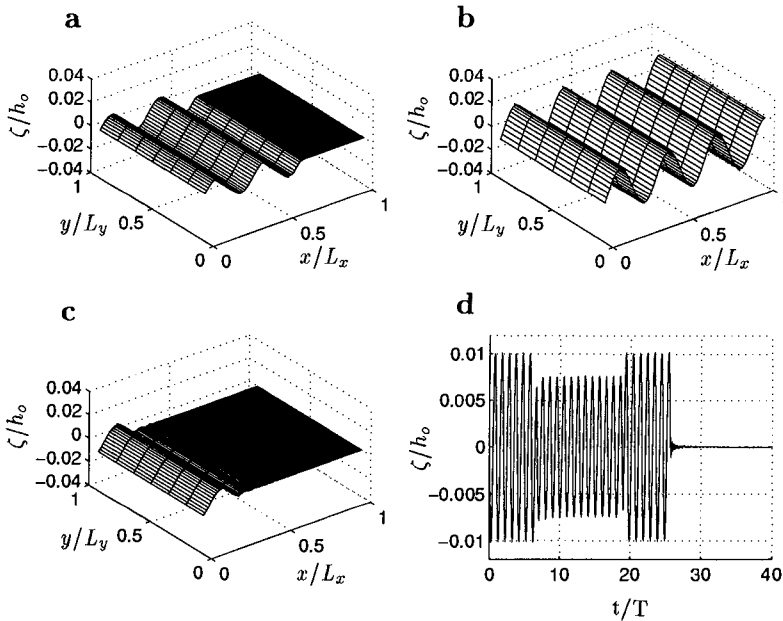


Figure 5: (a) Instantaneous water surface at  $t = 2T$ . (b) Same for  $t = 19T$ . (c) Same for  $t = 25T$ . (d) Time series at  $(x = 0, y = \frac{L_y}{2})$ .

These tests show that the numerical boundaries can be placed close to the regions of interest, which limits the computational time for the model.

### TEST CASE: LONGSHORE CURRENTS

As a formal test of the time-dependent equations (1) and (8), we studied the start-up of a longshore current on a cylindrical coast induced by imposing short wave forcing in a region at rest at  $t = 0$ . The parameters and assumptions used are the same as those in Chapter 4 of Svendsen & Putrevu (1994a), called SP94 in the following, except that here the depth-invariant longshore velocity  $V_0$  (see their (2.6)) is explicitly defined as the depth mean longshore velocity.

Fig. 6a shows the surface elevation versus normalized time for a number of

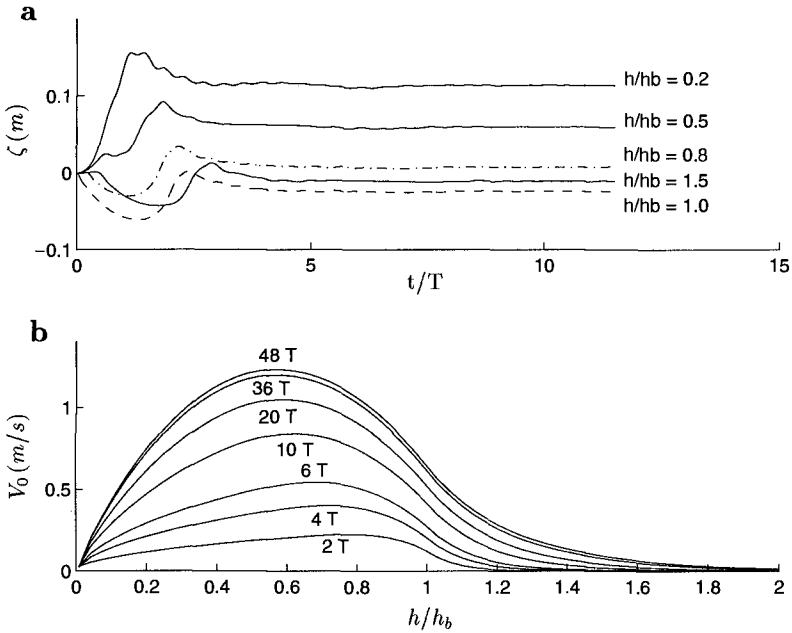


Figure 6: (a) Surface elevation versus time for cross-shore positions indicated in the figure. (b) Cross-shore variations of the longshore current velocities for different time-steps as indicated in the figure.

points in the domain. The normalizing time-scale  $T$  is defined as the ratio of the surf-zone width to the long wave celerity at the breakpoint. It is also seen that the impulsive application of the short wave forcing at  $t = 0$  initiates a surge in the mean surface elevation. After reflection from the beach, it propagates seawards and is absorbed by the ocean-side boundary condition. The steady-state in the set-up is reached in about  $7T$ . The longshore current evolution in Fig. 6 b, however, does not attain steady-state until about  $50T$ , which indicates a difference in time-scales of cross-shore and longshore motion. In fact, the steady-state is only approached asymptotically as the net forcing of bottom friction and the radiation stress decreases to zero. The figure clearly shows that the turbulent and dispersive mixing,  $\nu_{tx}$  and  $D_c$  (defined in SP94 Eq. (2.22)), cause a spreading of momentum (i.e. longshore current velocity) away from the breakpoint but the momentum spreads relatively slowly, in particular outside the surf-zone.

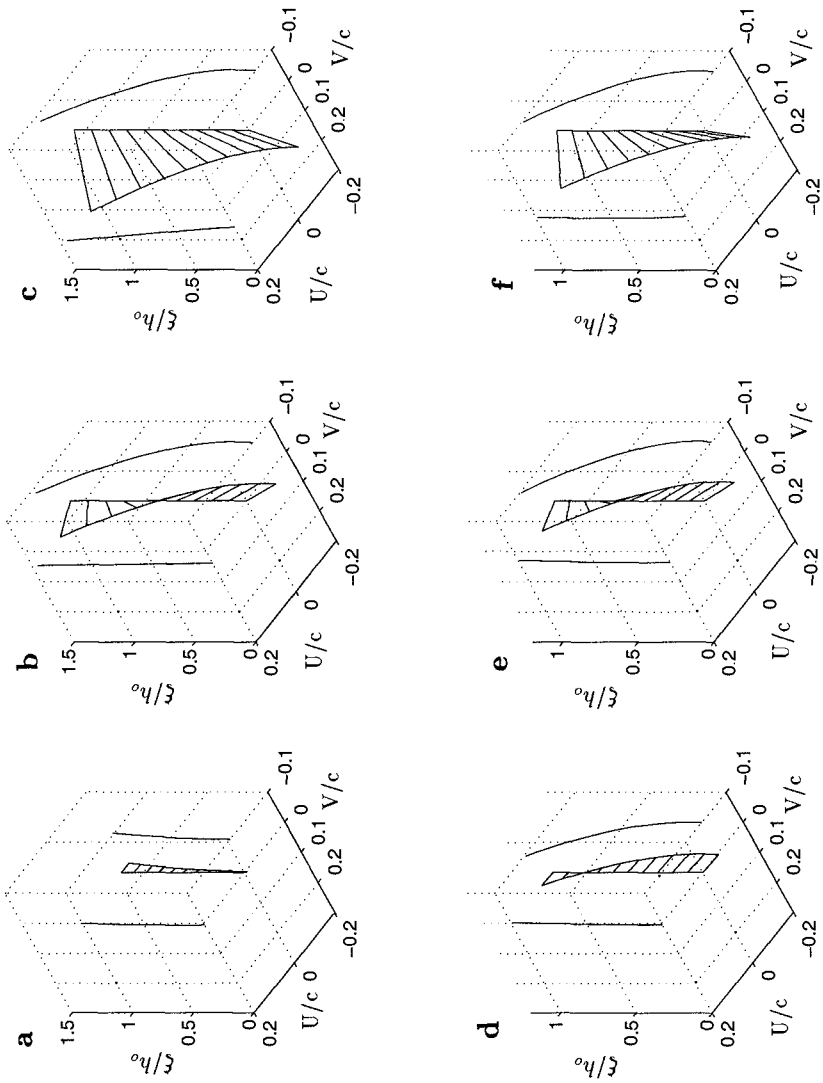


Figure 7: (a) Three-dimensional current spiral for  $\frac{h_0}{h_b} = 0.24$  at  $t = 0.2T$ . (b) Same for  $t = 4T$ . (c) Same for  $t = 48T$ . (d) Three-dimensional current spiral for  $\frac{h_0}{h_b} = 0.98$  at  $t = 0.2T$ . (e) Same for  $t = 4T$ . (f) Same for  $t = 48T$ .

The slow development in the flow implies that the vertical velocity profiles can be considered a quasi-steady response to the instantaneous forcing, including the gradients of the mean water surface. Thus, using SP94's expressions for the undertow and longshore velocity with time-varying coefficients, we can calculate the change in the 3-D current profiles as time progresses. Figs. 7 a-c show three snapshots of the 3-D current spiral for a position close to shore. Figs. 7 d-f show the spirals at the same times for a position in the surf-zone near the breakpoint. The cross-shore and longshore current profiles are also shown as projections. The current velocities,  $U$  and  $V$ , are normalized by the local wave celerity and  $\xi$ , the vertical position above the bed, is normalized by the still water level  $h_o$ . Figs. 7 a and 7 d for  $t = 0.2T$  show that initially the flow is almost entirely in the cross-shore direction. At  $t = 4T$ , the steady-state in the set-up, and consequently in the undertow profile, is not yet reached and the magnitude of the longshore current is increasing rapidly (Figs. 7 b and 7 e). At  $t = 48T$ , both the undertow and the longshore current have reached steady-state (Figs. 7 c and 7 f). Notice that the longshore current profile in Fig. 7 c is pitched forward, whereas the one in Fig. 7 f is tilted back slightly. This is important since the sign of the vertical gradient of  $V$  indicates a sign switch in the dispersive effect, which is known to control the mixing (SP94). We see that the different time scales for the cross- and longshore motion cause the velocity to change quite significantly during the start-up of the longshore current. With time-varying forcing from random waves, the variation will probably be less dramatic. However, the results for the 2DH case with weak wave groups analysed by Svendsen and Putrevu (1994b) suggest that the vertical currents profiles can vary significantly.

For completeness it is mentioned that these computations were performed with a very short coast to ensure that no instabilities in the form of shear waves developed.

## CONCLUSIONS

A time-dependent, short wave-averaged quasi-3D model is presented that governs nearshore circulation processes as well as infra-gravity waves. An absorbing-generating boundary condition has been developed that allows waves to leave the domain with very little reflection while simultaneously specifying an incoming wave. This makes it possible to choose the model boundaries close to the area of interest, thus limiting the computational effort required. The time-dependent model is tested for the start-up of a longshore current on a long straight coast. The vertical velocity profiles are shown to change significantly as the current evolves.

## ACKNOWLEDGMENTS

This work is a result of research sponsored by NOAA Office of Sea Grant, De-



partment of Commerce, under Award. No. NA 16 RG 0162 (Project No. R/OE-15) and by the U.S. Army Research Office, University Research Initiative under Contract No. DAAL03-92-G-0016. F.E. Sancho held a scholarship from the Portuguese Research Council, and his contribution was carried out under the MAST G8 Coastal Morphodynamics Programme, funded by the Commission of European Communities, Directorate General for Science, Research and Development (contract no. MAS2-CT92-0027). U. Putrevu was funded by ONR Coastal Sciences (contract number N00014-94-C0004). The U.S. Government is authorized to produce and distribute reprints for government purposes notwithstanding any copyright notation that may appear herein.

## REFERENCES

- Abbott, M.B. (1979). *Computational Hydraulics. Elements of the Theory of Free Surface Flow.* Pitman Publishing, 324 p.
- Anderson, D.A., J.C. Tannehill and R.H. Pletcher (1984). *Computational fluid mechanics and heat transfer.* Hemisphere Publishing Corp., New York, 599 p.
- Dally, W.R. and R.G. Dean (1984). Suspended sediment transport and beach profile evaluation. *Journal of Waterway, Port, Coastal and Ocean Engineering, ASCE, 110*, pp. 15-33.
- De Vriend, H.J. and M.J.F. Stive (1987). Quasi-3D modelling of nearshore currents. *Coastal Engineering, 11*, pp. 565-601.
- Engquist, B. and A. Majda (1977). Absorbing boundary conditions for the numerical simulation of waves. *Math. Comp., vol. 31, no. 139*, pp. 629-651.
- Higdon, R.L. (1986). Absorbing boundary conditions for difference approximations to the multi-dimensional wave equation. *Math. Comp., vol. 47, no. 176*, pp. 437-459.
- Kobayashi, N., A.K. Otta and I. Roy (1987). Wave reflection and run-up on rough slopes. *Journal of Waterway, Port, Coastal and Ocean Engineering, ASCE, vol. 113, no. 3*, pp. 282-298.
- Mei, C.C. (1983). *The applied dynamics of ocean surface waves.* John Wiley and Sons, New York, 740 pp.
- Phillips, O.M. (1977). *The dynamics of the upper ocean.* Cambridge University Press, 336 pp.
- Putrevu, U. and I.A. Svendsen (1992). A mixing mechanism in the nearshore region. *Proc. of the 23rd International Conference on Coastal Engineering*, pp. 2758-2771.
- Putrevu, U. and I.A. Svendsen (1994). Infragravity velocity profiles in the surf-zone. *Submitted for publication.*

## CHAPTER 199

# A MODEL FOR BREACH GROWTH IN SAND-DIKES

by

Paul J. Visser<sup>1</sup>

### ABSTRACT

A mathematical model for breach growth in sand-dikes and dunes is presented. The model is based on the five-step breach erosion process as observed in several laboratory and field experiments. A simplified Galappatti (1983) pick up mechanism for sand from the bed is combined with Bagnold's (1963) modified (Visser, 1988) energetics-based sand transport conception to describe the breach erosion. The comparison of the model predictions with the data of the Zwin 89 field experiment shows good agreement.

### 1. INTRODUCTION

The Technical Advisory Committee on Water Defences (TAW) in The Netherlands is completing a probabilistic design method for dikes and dunes (hereafter both named dikes). This method will hold a procedure for the design and control of dikes based on a risk-norm (risk of inundation) instead of on a chance-norm (chance of exceeding a certain water level) as in the present deterministic methods, see Kraak et al. (1994). A risk-norm means that the inundation chance is combined with the consequences of flooding (deaths, loss of property and revenues, repair costs, etc.). To determine the consequences of an inundation, it is necessary to predict both the rate and speed of polder flooding, which are especially governed by the flow rate through the breach in the dike. This discharge rate largely depends on the process of breach growth.

The final aim of the investigation is a mathematical model, that describes the breach

---

<sup>1</sup> Delft University of Technology, Department of Civil Engineering,  
P.O. Box 5048, 2600 GA Delft, The Netherlands

growth and the discharge rate through the breach in case of a dike-burst, as function of the parameters involved. These parameters are:

- cross-section of the dike (height, width, angles of the slopes);
- structure of the dike (dike material, revetments, foundation);
- hydraulic conditions (water level against the dike, wave load).

A first version of the model (Visser, 1988) was especially developed for the huge (about 75 m high) sand-dike of a proposed pumped-storage plant in The Netherlands. Visser et al. (1990) extended the model and confronted it with the data of the Zwin 89 field experiment, yielding reasonable agreement for the first stages of the erosion process. This model version was not yet applicable to the last two phases of the breach erosion process (see section 3). If applied, it would fairly overestimate the breach growth in this final phase.

This paper describes a new version of the model. Its improvements with respect to the previous version are:

- inclusion of a description of the breach erosion in phase IV);
- an improved description of the erosion mechanism in phases I, II and III; these improvements refer to both the physics and the mathematical treatment.

Phase V of the breach erosion process is not yet included in the model. This stage is important since it yields the ultimate breach dimensions. Further the model is still restricted to sand-dikes; effects of clay-layers and revetments have to be included in the near future.

## 2. ENTRAINMENT AND TRANSPORT OF SEDIMENT

Fig. 1 shows a typical cross-section of a sand-dike along the breach axis in the initial phase of the breach erosion process. A coordinate system ( $x, z$ ) is adopted with coordinate  $x$  along the inner slope ( $x = 0$  at the top of the dike) and coordinate  $z$  normal to the slope.  $H_w$  is the water level at sea,  $Z_T$  is the height of the top of the dike in the breach (both  $H_w$  and  $Z_T$  are measured above the base of the dike), and

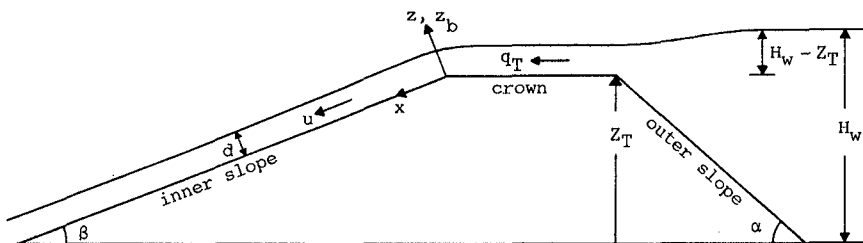


Fig. 1. Typical cross-section of a sand-dike along the breach axis.

the angles of the outer and inner slope are  $\alpha$  and  $\beta$ , respectively.

The entrainment of sand from the horizontal crown of the dike is very small compared with the pick up from the inner slope, see Steetzel and Visser (1992) and Visser (1994). The pick up of sand starts at the upstream end of the inner slope ( $x = 0$ ). For large values of  $u_* / w_s = C_f^{1/2} u / w_s$  (is of order 10 in the present situation, so suspended load transport will dominate bed load transport), the entrainment and subsequent transport of suspended sediment along the inner slope can be approximated according to Galappatti (1983, see also Galappatti and Vreugdenhil, 1985) by:

$$s(x) \approx \frac{x}{l_a} s_s \quad \text{for } 0 \leq x \leq l_a \quad (1)$$

in which  $s(x)$  is the sediment transport (volumes of particles) per unit width along the slope and  $l_a$  is the adaptation length of the suspended load transport:

$$l_a = \frac{ud}{w_s \cos \beta} = \frac{q_T}{w_s \cos \beta} \quad (2)$$

and  $s_s$  is the capacity of the suspended load transport:

$$s_s = \frac{0.01}{(w_s/u)(\cos \beta)^2} \frac{C_f u^3}{g \Delta} \quad [\text{m}^2/\text{s}] \quad (3)$$

where  $u$  is the depth-averaged flow velocity,  $d$  is the water depth (see Fig. 1),  $w_s$  is the fall velocity of sand in water,  $q_T$  is the discharge flow rate per unit width over the top of the dike,  $C_f$  is the friction coefficient for the bed ( $C_f = g/C^2$ , where  $C$  is the Chézy coefficient),  $\Delta = (\rho_s - \rho)/\rho$ ,  $\rho_s$  is the mass density of sand,  $\rho$  is the water mass density and  $g$  is the acceleration of gravity, see Visser (1988). Equation (3) rests on a modified (Visser, 1988) Bagnold (1963) energetics-based sand transport conception for suspended sediment load. The efficiency factor 0.01 is according to Bagnold (1966).

Equation (3) emerges as the best formula out of 15 sand transport formulae in a test with the flume data of Steetzel and Visser (1992) and the data of the Zwin 89 experiment, with Van Rijn's (1984a, 1984b) formulation finishing second best. Most of the other formulae overestimate the measured sediment transport rates significantly, also those formulae which were developed for sand-water mixture flows at high shear stress (for instance Wilson, 1987) and for sediment transport on steep slopes (for instance Rickenmann, 1991). For the moment this conclusion (and the choice for (3)) holds for the first three phases of the breaching process when the flow is supercritical.

### 3. BREACH EROSION PROCESSES

#### 3.1 Discharge rate

The water discharge rate  $q_T$  per unit breach width is described by a weir formula:

$$q_T = m(2/3)^{3/2} g^{1/2} (H_w - Z_T)^{3/2} \quad (4)$$

where  $m$  is the discharge coefficient ( $\approx 1.0$ ). Equation (4) holds as long as the flow in the breach is not affected by the downstream water level, i.e. for phases I through IV (see paragraph 3.2).

#### 3.2 Erosion of inner slope

The equation for the erosion of the inner slope is:

$$(1 - p) \frac{\partial z_b}{\partial t} + \frac{\partial s}{\partial x} = 0 \quad (5)$$

where  $p$  is the bed porosity,  $z_b$  is the position of the inner slope in  $z$ -direction ( $z$  is the coordinate normal to the inner slope, see Fig. 1). Substitution of (1), (2) and (3) into (5) yields:

$$\left| \frac{\partial z_b}{\partial t} \right| = \frac{0.01 C_f}{(1 - p) g \Delta} \left| \frac{\partial}{\partial x} \left[ \frac{x u^4}{q_T \cos \beta} \right] \right| \quad \text{for } 0 \leq x \leq l_a \quad (6)$$

in which it has been assumed that the friction coefficient  $C_f$  is constant.

If  $q_T$  is constant (that is if  $H_w - Z_T = \text{constant}$ , see equation (4)) and assuming  $\cos \beta \approx 1$ , it follows from (6) that:

$$\frac{\partial}{\partial x} \left| \frac{\partial z_b}{\partial t} \right| > 0 \quad \text{for } 0 < x < l_n \quad (7)$$

since the flow velocity  $u$  increases in positive  $x$ -direction for  $0 < x < l_n$ . So the erosion of the inner slope increases along the slope and the inner slope becomes steeper in  $x$ -direction and in time (see Fig. 2).

For  $x = l_n$  the flow velocity  $u$  approaches the normal value for uniform flows:

$$u_n = \frac{(g d_n \sin \beta)^{1/2}}{C_f^{1/2}} = \frac{(g q_T \sin \beta)^{1/3}}{C_f^{1/3}} \quad (8)$$

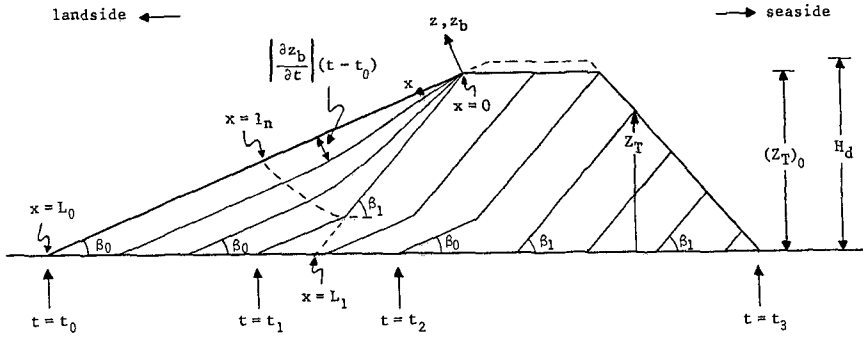


Fig. 2. Erosion of inner slope.

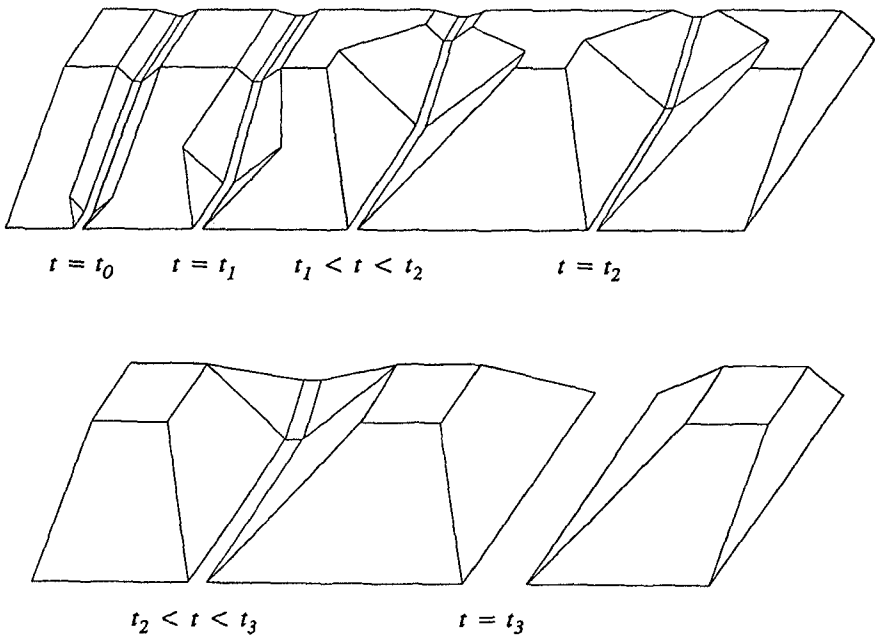


Fig. 3. Process of breach erosion.

Substitution of (1), (2), (3) and (8) into (5) gives:

$$\frac{\partial z_b}{\partial t} = - \frac{0.01}{(1-p)\Delta} \frac{\partial}{\partial x} (x u_n \tan \beta) \quad \text{for } l_n \leq x \leq l_a \quad (9)$$

If  $q_T$  and  $\beta$  are constant then  $u_n$  is constant and (9) becomes:

$$\frac{dz_b}{dt} = - \frac{0.01}{(1-p)\Delta} u_n \tan \beta \quad \text{for } l_n \leq x \leq l_a \quad (10)$$

This means that:

$$\frac{\partial}{\partial x} \left| \frac{dz_b}{dt} \right| = 0 \quad \text{for } l_n \leq x \leq l_a \quad (11)$$

i.e. the erosion of the inner slope is constant for these values of  $x$ , see Fig. 2.

The inner slope becomes steeper for  $0 \leq x < l_n$ . However, the slope angle will not exceed a limit  $\beta_1$ , say  $\beta_1 \approx \phi$  ( $\phi$  is angle of repose). If this limit has been achieved on the entire stretch  $0 \leq x < l_n$  (on  $t = t_1$ ), then the erosion rate becomes constant for  $0 \leq x < l_n$ , as indicated by the lines for  $t \geq t_1$  in Fig. 2.

So, if the breaching process starts at  $t = t_0$  with the flow of water through a small initial channel in the crown and the inner (downstream) slope of the dike, then the following (subsequent) phases can be distinguished in this process (see Figures 2 and 3):

- I. Steepening of the inclination angle ( $\beta$ ) of (the channel in) the inner slope from an initial value  $\beta_0$  up to a critical value  $\beta_1$  at  $t_1$  (see Fig. 1).
- II. Continuation of the erosion of the inner slope resulting in a decrease of the length of the dike-top in the breach for  $t_1 < t < t_2$ ; the inner slope angle remains (in this line of thoughts) at its critical value  $\beta_1$ .
- III. Lowering of the top of the dike in the breach and a subsequent increase of the breach width for  $t_2 \leq t \leq t_3$ .
- IV. After the complete wash-out of the dike in the breach, continuation of the breach growth in both vertical (scour hole) and horizontal direction for  $t_3 < t \leq t_4$ . At  $t_4$  the flow through the breach is critical, i.e. turns from supercritical ( $Fr > 1$  for  $t < t_4$ ) into subcritical ( $Fr < 1$  for  $t > t_4$ ).
- V. Continuation of the increase of the breach width for  $t_4 < t < t_5$ . At  $t_5$  the flow velocities in the breach become so small (incipient motion) that the breach erosion stops.

In phase I the width of the breach remains at its initial small value. At  $t = t_1$  the breach width starts to increase at the downstream side of the crown (so in phase II the breach eats its way into the dike, see Fig. 3). On  $t = t_2$  the width of the breach at the upstream side of the crown also starts to grow. As a first estimation this occurs directly proportional to the breach depth, see Visser (1988). The discharge

rate through the breach starts to increase at  $t = t_2$ . In the period  $t_3 < t \leq t_4$  the scour hole gets its maximal depth. Stages IV and V are the most important stages, since in the period  $t_3 < t < t_5$  most of the water is discharged through the breach and the ultimate dimensions of the breach are determined.

#### 4. MODEL DESCRIPTION

##### 4.1 Steepening of the inner slope (phase I)

The erosion of the inner slope is described by (5) with (1), (2), (3) and an equation for the flow velocity  $u$  follows from (4) and an equation for the non-uniform flow depth along the stretch  $0 < x < l_n$ . Consequently a numerical method is necessary to describe the development of the entire inner slope for  $t_0 < t < t_1$ .

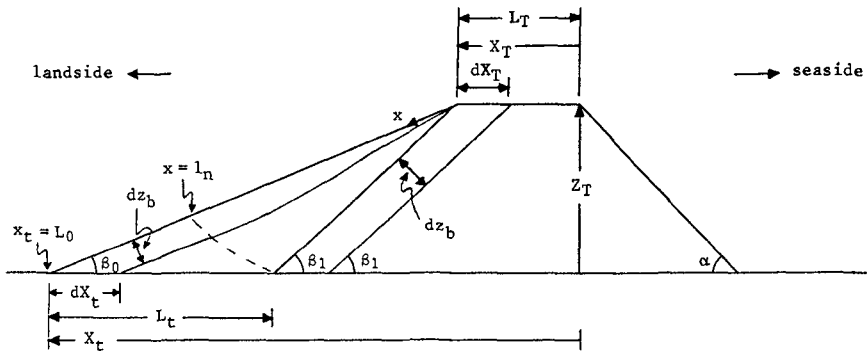


Fig. 4. Horizontal displacements  $dX_t$  and  $dX_T$  due to erosion  $dz_b$  of inner slope.

An analytical solution for stage I is possible along the stretch  $l_n \leq x \leq l_a$ , where equation (10) describes the erosion rate  $dz_b/dt$ . The horizontal displacement  $dX_t$  of the toe of the inner slope can simply be expressed in  $dz_b$  (see Fig. 4):

$$dX_t = \frac{1}{\sin \beta_0} dz_b \quad (12)$$

Substitution of (4), (8), (10),  $\beta = \beta_0$  and  $Z_T = (Z_T)_0$  into (12) yields for  $t_0 \leq t \leq t_1$ :

$$\frac{dX_t}{dt} = -k_0 \sqrt{H_w - (Z_T)_0} \quad \text{for } l_n \leq x_t \leq l_a \quad (13)$$



where  $x_t$  is the  $x$ -coordinate of the toe of the inner slope (see Fig. 4) and:

$$k_0 = \frac{0.0082}{(1-p)\Delta} (m/C_f)^{1/3} g^{1/2} \frac{(\sin \beta_0)^{1/3}}{\cos \beta_0} \tag{14}$$

If  $l_n = L_1$  at  $t = t_1$  then:

$$\int_{t_0}^{t_1} dX_t = -L_t \tag{15}$$

Substitution of (13) into (15) finally yields:

$$t_1 - t_0 = \frac{L_t}{k_0 \sqrt{H_w - (Z_c)_0}} \tag{16}$$

If  $L_1 > l_n(t_1)$  then  $\xi L_t$  as defined in Fig. 5 should replace  $L_t$  in equation (16).

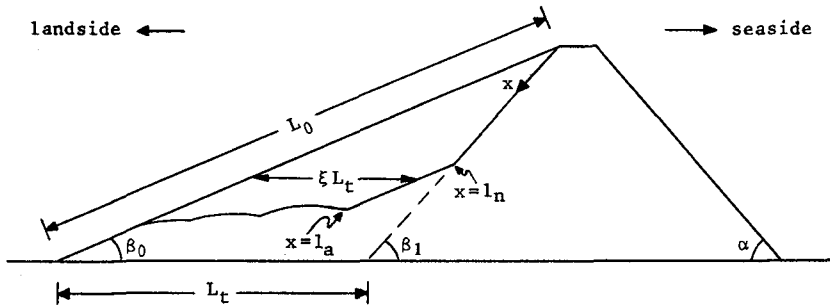


Fig. 5. Erosion of inner slope for relatively high dikes.

#### 4.2 Decrease of crown length (phase II)

At  $t = t_1$  the steepness of the inner slope is at its critical value (angle  $\beta_1$ ). From now on the rate of erosion is constant along the entire stretch  $0 \leq x \leq l_a$ , see Fig. 2. So the erosion of the inner slope for  $t_1 < t < t_2$  is entirely determined by the erosion at the toe of the slope ( $x = L_1$ ) as long as  $L_1 < l_a$ :

$$-L_1(1-p) \frac{dz_b}{dt} = s(L_1) = \frac{L_1}{l_a} s_s(L_1) \quad (17)$$

Generally  $L_1 > l_n$  (see Visser, 1994), so  $u(L_1) = u_n$ . Substituting (2), (3) and (8) with  $\beta = \beta_1$  into (17) yields, in agreement with (10):

$$\frac{dz_b}{dt} = - \frac{0.01}{(1-p)\Delta} u_n \tan \beta_1 \quad \text{for } 0 \leq x \leq L_1 \quad (18)$$

Fig. 4 shows that in the breach the length of the dike-top (initial value  $L_T$ ) decreases for  $t_1 < t < t_2$  due to the erosion of the inner slope. The relation between the decrease of the length of the dike-top ( $dX_T$ ) and the erosion of the inner slope ( $dz_b$ ) is:

$$dX_T = \frac{1}{\sin \beta_1} dz_b \quad (19)$$

Substitution of (4) with  $Z_T = (Z_T)_0$ , (8) with  $\beta = \beta_1$  and (18) into (19) gives:

$$\frac{dX_T}{dt} = -k_1 \sqrt{H_w - (Z_T)_0} \quad \text{for } t_1 < t < t_2 \quad (20)$$

with:

$$k_1 = \frac{0.0082}{(1-p)\Delta} (m/C_f)^{1/3} g^{1/2} \frac{(\sin \beta_1)^{1/3}}{\cos \beta_1} \quad (21)$$

Integration of (20) gives:

$$t_2 - t_1 = \frac{L_T}{k_1 \sqrt{H_w - (Z_T)_0}} \quad (22)$$

Visser (1988) argues that due to the increase of the breach width an extra amount of sand falls into the flow, slowing down the breach erosion in vertical direction (with a factor  $f$  compared with a 2-D situation; to a lesser extent this applies also to phase I). The factor  $f$  will vary from phase to phase. Assuming  $f$  to be constant in each phase, equation (22) becomes for the 3-D situation:

$$t_2 - t_1 = \frac{L_T}{f_1 k_1 \sqrt{H_w - (Z_T)_0}} \quad (23)$$

### 4.3 Decrease of crown level (phase III)

At  $t = t_2$  the top of the dike in the breach starts to drop. The relation between the fall  $dZ_T$  and the rate of erosion  $dz_b$  of the inner slope follows from a simple geometrical consideration (see Fig. 6):

$$dZ_T = \frac{\sin \alpha}{\sin(\alpha + \beta_1)} dz_b \quad (24)$$

Substitution of (4), (8) with  $\beta = \beta_1$  and (18) into (24) yields:

$$\frac{dZ_T}{dt} = -k_2 \sqrt{H_w - Z_T} \quad \text{for } t_2 \leq t \leq t_3 \quad (25)$$

where:

$$k_2 = \frac{\sin \alpha \sin \beta_1}{\sin(\alpha + \beta_1)} k_1 \quad (26)$$

At  $t = t_2$  the width of the breach at the upstream end of the dike-top starts to increase. Visser (1988) argues that the breach width (so also the depth-averaged breach width  $B$ ) increases linearly with the growth of the breach depth  $H_d - Z_T$ :

$$\frac{dB}{dt} = r \frac{d(H_d - Z_T)}{dt} \quad \text{for } t_2 \leq t \leq t_3 \quad (27)$$

where  $r$  is a coefficient with a theoretical value (for sand-dikes) of about 2.2 for the depth-averaged breach width and about 3.8 for the breach width at the top of the dike.

Due to the increase of the breach width an extra amount of sand falls into the flow, slowing down the breach erosion in vertical direction (with a factor  $f_2$  in this stage, see paragraph 4.2). Hence equation (25) becomes:

$$\frac{dZ_T}{dt} = -f_2 k_2 \sqrt{H_w - Z_T} \quad \text{for } t_2 \leq t \leq t_3 \quad (28)$$

in which the factor  $f_2$  is (see Visser, 1988):

$$f_2 = \frac{B + 2q_T/u}{2B} \quad (29)$$

Integration of (28) gives with  $Z_T = 0$  at  $t = t_3$ :

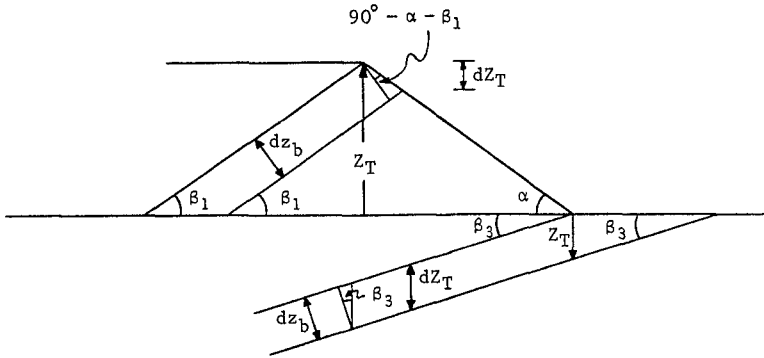


Fig. 6. Relation between  $dZ_T$  and  $dz_b$  in phases III and IV.

$$Z_T(t) = H_w - \left[ \frac{f_2 k_2}{2} (t - t_3) + \sqrt{H_w} \right]^2 \quad \text{for } t_2 \leq t \leq t_3 \quad (30)$$

Substitution of  $Z = (Z_c)_0$  at  $t = t_2$  into (30) gives:

$$t_3 - t_2 = \frac{2}{f_2 k_2} \left[ \sqrt{H_w} - \sqrt{H_w - (Z_T)_0} \right] \quad (31)$$

If the depth of the initial breach  $(H_d - (Z_T)_0)$ , see Fig. 2) is small compared with the dike-height  $H_d$  (so also small compared with  $H_w$ ), then (31) reduces to:

$$t_3 - t_2 = \frac{2}{f_2 k_2} \sqrt{H_w} \quad (32)$$

#### 4.4 Continuation of breach growth (phase IV)

Locally the dike has been completely washed out ( $Z_T = 0$ ) at  $t = t_3$  and the breach continues to grow in both vertical (scour hole:  $Z_T < 0$ ) and horizontal direction for  $t > t_3$ . The equation for the discharge rate  $q_T$  per unit of breach width is for  $t_3 \leq t \leq t_4$ :

$$q_T = m(2/3)^{3/2} g^{1/2} (H_w)^{3/2} \quad (33)$$

The scour hole has an upstream slope ( $\beta_3$ , bed elevation decreasing in flow direction:  $\beta_3$  is not equal to  $\beta_1$ ) and a downstream slope (bed elevation increasing in flow direction). It is assumed that the breach growth in phase IV is determined

by the erosion of the upstream slope of the scour hole. Then equation (10) describes also the erosion in vertical direction in phase IV:

$$\frac{dz_b}{dt} = -\frac{0.01}{(1-p)\Delta} u_n \tan \beta_3 \quad \text{for } l_n \leq x \leq l_a \quad (34)$$

The relation between the increase of the depth of the scour hole  $dZ_T$  and the rate of erosion  $dz_b$  of the upstream slope of the scour hole follows from a simple geometrical consideration (see Fig. 6):

$$dZ_T = \frac{1}{\cos \beta_3} dz_b \quad (35)$$

Substitution of (8) with  $\beta = \beta_3$ , (33) and (34) into (35) and including a factor  $f$  yields:

$$\frac{dZ_T}{dt} = -f_3 k_3 \sqrt{H_w} \quad \text{for } t_3 \leq t \leq t_4 \quad (36)$$

with:

$$k_3 = \frac{0.0082}{(1-p)\Delta} (m/C_f)^{1/3} g^{1/2} \frac{(\sin \beta_3)^{4/3}}{(\cos \beta_3)^2} \quad (37)$$

Integration of (36) gives with  $Z_T = 0$  at  $t = t_3$ :

$$Z_T(t) = -f_3 k_3 \sqrt{H_w} (t - t_3) \quad \text{for } t_3 \leq t \leq t_4 \quad (38)$$

It is assumed that (27) holds also in phase IV; then substitution of (38) into (27) gives the increase of the breach width for  $t_3 \leq t \leq t_4$ . For the initial stage of phase IV this assumption seems reasonable. It is, however, rather obvious that the validity of (38), and consequently also (27), has its limits, otherwise large breach depths are necessary to explain the existence of relatively wide breaches.

One of the aims of a large scale experiment performed October 1994 (Zwin 94 field experiment) has been to solve this uncertainty about the growth of the scour hole and its relation with the increase of the breach width in phase IV. The experimental procedure and results of this field experiment will be presented in a forthcoming publication.

## 5. COMPARISON WITH FIELD DATA

The present breach erosion model is tested to the data of the Zwin 89 experiment. This large scale experiment was performed in the Zwin Channel (an tidal inlet in the south-western part of The Netherlands) in December 1989, see Visser et al. (1990). The dimensions of the sand-dike in the Zwin 89 experiment have been:  $H_d = 2.2$  m,  $L_T \approx 7.5$  m,  $\beta_0 = 18.4^\circ$  and  $\alpha = 39^\circ$ . The 50 m long sand-dike was constructed, exclusively for the experiment, with local sand  $D_{50} \approx 0.22$  mm. A small pilot channel (initial breach), about 9 m long, about 1 m wide and with a depth  $H_d - (Z_c)_0 \approx 0.35$  m was made in the dike-top to ensure breaching near the middle of the Zwin Channel.

The breaching process was both video-taped and photographed. Levelling-staffs in the crown of the dike provided the proper length-scale for the readings from the video-tape and the photographs. The main result of these readings, i.e. the development of the 'depth-averaged' breach width  $B(t)$ , at the downstream end of the crown of the dike, is shown in Fig. 7. These data differ slightly from those in Visser et al. (1990), where breach width  $B(t)$  was given as averaged (both along the breach length and in depth) value of observed breach width.

The comparison of the model prediction with the data of the Zwin 89 experiment

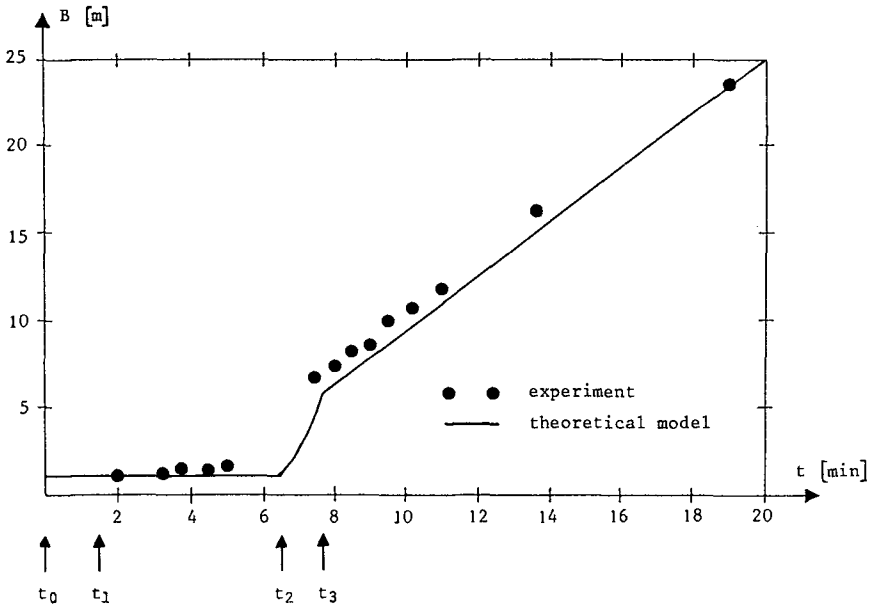


Fig. 7. Comparison of measured (Zwin 89 experiment) and computed breach width  $B(t)$  at the upstream end of the dike-top.

has been done with the following values for the different parameters:  $p = 0.4$ ,  $\Delta = 1.65$ ,  $m = 1.0$ ,  $f_1 = f_2 = f_3 = 0.6$  (estimated with equation (29)),  $C_f = 0.015$ ,  $\beta_1 = 32^\circ$  (see Visser et al., 1990) and  $r = 2.2$  (for depth-averaged breach width). For  $\beta_3$  the value found by Delft Hydraulics (1972) for scour holes has been adopted:  $\beta_3 \approx 12^\circ$  ( $\tan \beta_3 \approx 0.2$ ). This is a very crude assumption since there exists no universal value for this angle.

Setting  $t_0 = 0$ , substitution of these values into (16) with (14) yields  $t_1 = 1.5$  min (in this phase:  $H_w - (Z_T)_0 \approx 0.13$  m), substitution into (22) with (21) gives  $t_2 - t_1 = 5.0$  min (in phase II:  $H_w - (Z_T)_0 \approx 0.17$  m), so  $t_2 = 6.5$  min, and into (31) with (26) gives  $t_3 - t_2 = 1.2$  min (in phase III:  $H_w \approx 2.1$  m), so  $t_3 = 7.7$  min. The increase of the breach width  $B(t)$  is given by (27) with (28) in phase III and by (27) with (36) in phase IV. The result of the model prediction for  $B(t)$  for the Zwin 89 experiment are shown in Fig. 7. The kink for  $t = t_3$  is due to keeping  $\beta$  at  $\beta_1$  for  $t_2 \leq t \leq t_3$  while in reality  $\beta$  will decrease from  $\beta_1$  to  $\beta_3$  in this phase.

The experimental data (flow velocities and water levels measured upstream and downstream from the breach) indicate that  $t_4 \approx 20$  min, see Visser et al. (1990). Hence Fig. 7 shows the development of the breach width  $B(t)$  in phases I through IV.

## 6. DISCUSSION

The agreement between the present breach erosion model and the data of the Zwin 89 experiment is good. It must be emphasized, however, that there still some uncertainties that has to be solved. These uncertainties relate to:

- the development of the scour hole (depth, slope angle  $\beta_3$ ) in phase IV and its effect on the increase of the breach width;
- the magnitude of the factors  $f_1$ ,  $f_2$  and  $f_3$ .

As yet the present version of the model does not describe the breach width in phase V, in which at the end the breach erosion stops and the breach gets its final dimensions.

It is expected that the data of the recent Zwin 94 field experiment (see paragraph 4.4) will significantly contribute to the understanding of the breach erosion process in phases IV and V and to the completion of the breach erosion model in 1995.

## REFERENCES

- Bagnold, R.A., 1963.** Mechanics of marine sedimentation. In *'The Sea: Ideas and Observations'*, 3, Interscience, New York, USA, pp. 507-528.
- Bagnold, R.A., 1966.** An approach to the sediment transport problem from general physics. *Geological Survey Professional Paper 422-1*, U.S. Government Printing Office, Washington, USA.
- Delft Hydraulics, 1972.** Systematic research on two- and three-dimensional scour. *Rep. M648/863* (in Dutch).

- Galappatti, R. (1983).** A depth-integrated model for suspended transport. *Comm. on Hydraulics, Rep. 83-7*, Dept. Civil Eng., Delft Univ. Techn., Delft, The Netherlands.
- Galappatti, R. and Vreugdenhil, C.B., 1985.** A depth-integrated model for suspended sediment transport. *J. Hydr. Res.*, 23, pp. 359-377.
- Kraak, A.W., Bakker, W.T., Van de Graaff, J., Steetzel, H.J. and Visser, P.J., 1994.** Breach-growth research programme and its place in damage assessment for a polder. *Abstracts and Proc. 24th Int. Conf. Coastal Eng.*, Kobe.
- Rickenmann, D. (1991).** Hyperconcentrated flow and sediment transport at steep slopes. *J. Hydr. Eng.*, 117, pp. 1419-1439.
- Van Rijn, L.C. (1984a).** Sediment transport. Part I: bed load transport. *J. Hydr. Eng.*, 110, pp. 1431-1456.
- Van Rijn, L.C. (1984b).** Sediment transport. Part II: suspended load transport. *J. Hydr. Eng.*, 110, pp. 1613-1641.
- Steetzel, H.J. and Visser, P.J., 1992.** Profile development of dunes due to overflow. *Proc. 23rd Int. Conf. Coastal Eng.*, Italy, Venice, pp. 2669-2679.
- Visser, P.J., 1988.** A model for breach growth in a dike-burst. *Proc. 21st Int. Conf. Coastal Eng.*, Malaga, Spain, pp. 1897-1910.
- Visser, P.J., 1994.** Application of sediment transport formulae for sand-dike breach erosion. *Comm. on Hydraulic and Geotechnical Eng., Rep. no. 94-7*, Dep. Civil Eng., Delft Univ. of Technology, Delft, The Netherlands.
- Visser, P.J., Vrijling, J.K. and Verhagen, H.J., 1990.** A field experiment on breach growth in sand-dikes. *Proc. 22nd Int. Conf. Coastal Eng.*, Delft, The Netherlands, pp. 2087-2100.
- Wilson, K.C. (1987).** Analysis of bed-load motion at high shear stress. *J. Hydr. Eng.*, 113, pp. 97-103.



## CHAPTER 200

### SCALING EFFECTS ON BEACH RESPONSE PHYSICAL MODEL

Xu Wang<sup>1</sup>, Li-Hwa Lin<sup>2</sup>, and Hsiang Wang<sup>3</sup>

#### Abstract

A modified modeling law based on the comprehensive work by Wang, *et al.* (1990) has been derived with the assumptions that the suspended sediment transport is the dominant mode under storm wave condition inside the surf zone and the wave breaking index is preserved. This, in essence, adds to the constraint that wave height is properly modelled in accordance to the preservation of breaking index instead of simple vertical geometrical scale. Four different scaling laws including the one proposed presently were examined in the laboratory using 2-D wave tank and 3-D basin models. The model results were compared to prototype data from German large wave tank experiment. The model performances under different scaling laws were evaluated separately in the dune region and bar region of the entire model beach profile. Several statistics, including the errors of sand bar location, bar volume, bar profile, dune erosion volume, and dune profile, between model and prototype, were calculated and the result showed that the newly proposed scaling law presented the best overall model performance among the ones compared.

#### 1. Introduction

Beach and dune erosion as well as the shore profile changes that occur under storm waves and high water level are of basic interests in coastal engineering. And, by all means, physical model has been utilized frequently to improve our understanding of the process of beach and dune erosion and provide useful data for numerical models. Numerous papers have been written proposing various similitude relationships for beach response model study. At present there is no general solution which is also practical. Specific modeling laws are usually only applicable to certain restricted conditions. This paper is aimed at evaluating and improving the scaling law for distorted model guided by the modeling theory and through a series of laboratory

---

<sup>1</sup>Graduate Assistant, <sup>2</sup>Research Scientist, <sup>3</sup>Professor, Coastal and Oceanographic Engineering Department, University of Florida, Gainesville, FL 32611, USA.

experiments carried out at different physical scales with the main assumption that suspended sediment transport is the dominant mode in the surfzone.

## 2. Theoretical Approach

Many different scaling laws of beach response model have been proposed in the past. However, there is no clear indication of which is more appropriate than the others. The approach here is to follow the comprehensive work by Wang, *et al.* (1990) but with consideration of a more general wave breaking criterion to determine the proper wave height scale in model. The approach seems adequate since it shows that the modeling law can be established based on the concept accommodating the sediment transport. The theory applied is simple. Based on the equation balancing the spatial change of sediment transport rate and the temporal change of beach profile, the scaling of sediment transport rate can be shown to be

$$N_q = N_\delta N_\lambda / N_t,$$

where  $N$  indicates the ratio of prototype to model quantities such that  $N_q$  is the scale of volumetric sediment transport rate,  $N_\delta$  and  $N_\lambda$  are the vertical and horizontal length scales, respectively, and  $N_t$  is the morphological time scale. Then, by assuming the suspended load mode predominate the sediment transport, the scale of sediment transport rate can be also expressed in a depth average means as

$$N_q = N_\delta N_u N_c,$$

where  $u$  is the sediment transport velocity, and  $c$  is the sediment concentration. By further assuming that  $N_u$  can be determined in preserving the Froude number  $F = u/\sqrt{gh}$ , where  $h$  is the water depth, and  $N_c$  can be obtained from a perceptive model of sediment concentration under wave motion as

$$c \propto \frac{H f(\xi)}{T SW},$$

where  $H$  and  $T$  denote wave height and wave period, respectively,  $f(\xi)$  is a function of the surfzone parameter  $\xi = \tan \beta / \sqrt{H_o/L_o}$ ,  $\beta$  is the beach slope,  $H_o$  and  $L_o (= gT^2/2\pi)$  are the deepwater wave height and wave length,  $S$  is the submerged specific weight, and  $W$  is the sediment settling velocity, a pair of equations can be established:

$$N_T = N_\lambda N_H^{1/2} / N_\delta, \quad N_t = N_\lambda^2 N_W N_S / (N_\delta^{3/2} N_H^{1/2}),$$

under the condition that surfzone parameter is preserved, or  $N_\xi = 1$ , in model.

As a major difference to the concept utilized by Wang, *et al.* (1990), the wave height scale is now assumed here to be not equal to the vertical scale in general. Clearly, in modeling beach profile change, wave height inside the surf zone should be similar between model and prototype. Of course, by treating wave height as a vertical geometrical scale in essence implicitly assumes that wave height is proportional to the local water depth, i.e.,  $H = \gamma_b h$ , with the  $\gamma_b$  a constant value, which was originally proposed by McCowan (1894) and was widely used as breaking criterion. In this paper, however, a more general wave height scaling law is adopted here:

$$N_H = N_\gamma N_\delta,$$

Table 1: Classification of Beach Profile Modeling Laws.

Author	Geometric Distortion	Hydrodynamic Time Scale( $T$ )	Morphological Time Scale( $t$ )
Vellinga (1982)	$N_\delta = N_W^{0.44} N_\lambda^{0.78}$	$N_T = \sqrt{N_\delta}$	$N_t = N_T$
Hughes (1983)	$N_\delta = N_W^{2/3} N_\lambda^{2/3}$	$N_T = N_\lambda / \sqrt{N_\delta}$	$N_t = N_T$
Wang, <i>et al.</i> (1990)	$N_\delta = N_W^{2/5} N_\lambda^{4/5}$	$N_T = N_\lambda / \sqrt{N_\delta}$	$N_t = \sqrt{N_\delta}$
Wang, <i>et al.</i> (present)	$N_\delta = N_W^{2/5} N_\lambda^{4/5}$ $N_H = N_\delta^2 / N_\lambda$	$N_T = \sqrt{N_\lambda}$	$N_t = N_T$

$N$  =prototype to model scale ratio,  
 $\lambda$  =horizontal length scale,  $\delta$  =vertical length scale,  
 $W$ =sediment fall velocity,  $H$ =incident wave height.

where  $N_\gamma$  represents the scale ratio of the breaking index,  $\gamma_b$ .

A guideline on determining  $N_\gamma$  is proposed by examining the functional form of  $\gamma_b$  as developed by various investigators. The breaking index could be affected by both beach slope and deepwater wave steepness, with the latter likely to be minimal inside the surf zone. A general power law of functional form of  $N_\gamma$  is proposed as

$$N_\gamma = \left[ \frac{N_\delta}{N_\lambda} \right]^k,$$

where the value of  $k$  is likely in the range from 0 to 1. In the case of  $k=0$ , the proposed modeling law reduces to that of Wang's (1990). On the other extreme as  $k=1$ , which states that the scale of breaking index is linearly proportional to the scale of local beach slope, or

$$N_r = N_{\tan\beta} = N_\delta / N_\lambda,$$

assuming  $N_T = N_t$ , i.e., the number of incoming waves per unit time is preserved yields another modeling law as

$$N_T = N_t = N_\lambda^{1/2}, \quad N_H = N_\delta^2 / N_\lambda, \quad N_q = N_\delta N_\lambda^{1/2}, \quad N_\delta = (N_S N_W)^{2/5} N_\lambda^{4/5}.$$

Therefore, the modeling laws derived above and by Wang, *et al.* (1990) represent two limiting conditions of the breaking index scale ratio. Table 1 presents four different modeling laws covering the existing scope of the beach profile modeling law which will be tested against laboratory experiments in this study.

### 3. Laboratory Experiments

In order to verify the scaling laws shown in Table 1, a total of 38 laboratory experiments were conducted, with 25 experiments run in a 30 m long wave tank, 10 experiments completed in a 15 m long tilting flume and three experiments in the 12m wide, 30m long 3-D wave basin. The coarse sand with a median size of 0.2mm has been utilized in both wave tank and tilting flume for the distorted model ( $N_\delta \neq N_\lambda$ )

study. Three different horizontal length scales of  $N_\lambda=20, 30,$  and  $40,$  were selected for the experiments as compared to the prototype data from the German large wave tank experiments, which was also known as the GWK experiment (Dette and Uliczka, 1986). The prototype sand has a median size of  $0.33\text{mm}.$  Accordingly, the corresponding sediment settling velocity scale can be approximated by  $N_W=2,$  and the vertical length scales corresponding to  $N_\lambda=20, 30,$  and  $40,$  can be roughly determined to be equal to  $N_\delta=14.5, 20.0,$  and  $25.2,$  respectively, in the models.

As special cases, fine sand with median size equal to  $0.09\text{mm}$  was also replaced in the same  $30\text{m}$  long wave tank for the undistorted model experiments. For this sand,  $N_W = 6,$  as compared with the prototype sand. Three length scales of  $N_\lambda = N_\delta=20, 30,$  and  $40,$  were again selected for the experiments of undistorted model study. The scaling effects were then tested for all the models of different length scales by using different wave periods and wave heights in individual experiments. Three 3-D wave basin experiments were also conducted as to repeat some 2-D wave tank experiments under the same test conditions to examine the three dimensional effects. All the experimental cases tested in this study are summarized in Table 2.

#### 4. Results

The model performance from the experiments was monitored by surveys of model beach profile at different times. In the 2-D wave tank and wave flume experiments, only the center profile is surveyed. In the 3-D wave basin experiments, five profiles, which were evenly spaced across the basin, were surveyed. All the surveys were carried out at times of  $0\text{min}, 5\text{min}, 10\text{min}, 20\text{min}, 40\text{min},$  and  $80\text{min},$  in model. Since the data set is too voluminous to be included in this paper, only reduced information related to the specific study subject is presented. The test results were compared with the GWK prototype data as for evaluating the scaling laws. Of course, the modelled beach should behave closely to the prototype at the points when model wave height and wave period were scaled by a proper modeling law. Figure 1 presents a few typical model and prototype profiles, all shown in the prototype scale, at the final stage of the experiments. The examination of scaling effects will be carried out only for the cases of the distorted model in which the model behavior resembles more to the prototype. For the undistorted model study (Tests A22 to A26), the experiment results were not encouraging, which generally show small scattered bars and insignificant dune erosion as compared to the prototype. The reason is probably due to the fact that wave energy dissipates more quickly over the flatter bed of fine sand in the undistorted model. An example showing the undistorted model profile from Test A22 in the final model stage is presented in Figure 1.

##### 4.1 Evaluation of Scaling Effects

The evaluation of scaling law is performed by investigating the model beach profile changes in separate dune and bar regions instead of the entire profile. The dune region is defined as from the landward end of the profile to the seaward end of the first slope in initial profile and the bar region is defined as from the beginning of the second slope to the seaward end of profile. Figure 2 shows a schematic of the defined dune and bar regions. The scaling effects were evaluated in the dune region

Table 2: Summary of Experimental Cases.

Test Facility	Test ID#	Wave period (sec)	Wave height (cm)	Water depth (cm)	Grain size (mm)	Horizontal scale, $N_\lambda$	Vertical scale, $N_\delta$
Wave Tank (2-D)	A1	1.00	11.50	52.0	0.20	20.0	14.46
	A2	1.14	10.50	34.6			
	A3	1.20	11.25	52.0			
	A4	1.20	12.75	52.0			
	A5	1.33	10.00	52.0			
	A6	1.33	11.00	35.3			
	A7	1.33	11.25	35.3			
	A8	1.33	12.00	52.0			
	A9	1.33	12.75	52.0			
	A10	1.33	13.00	52.0			
	A11	1.33	17.50	52.0			
	A12	1.45	10.50	52.0			
	A13	1.45	13.50	52.0			
	A14	1.45	18.00	52.0			
	A16	1.33	10.00	40.0	0.20	30.0	20.0
	A17	1.15	9.50				
	A18	1.00	9.50				
	A19	0.80	5.50	40.0	0.20	40.0	25.2
	A20	1.00	9.00				
	A21	1.15	9.50				
	A22	1.34	7.50	40.0	0.09	20.0	20.0
	A23	1.34	7.50			30.0	30.0
	A24	1.10	5.00			30.0	30.0
	A25	1.10	5.00			40.0	40.0
	A26	1.05	3.75			40.0	40.0
Wave Flume (2-D)	T1	1.30	11.50	35.3	0.21	20.0	14.46
	T2	1.30	11.50				
	T3	1.30	12.00				
	T4	1.30	12.50				
	T5	1.30	12.50				
	T6	1.30	13.00				
	T7	1.30	13.00				
	T8	1.30	15.00				
	T9	1.30	16.50				
	T10	1.65	16.50				
Wave Basin (3-D)	B1	1.14	10.50	35.3	0.20	20.0	17.1
	B2	1.14	10.50				14.6
	B3	1.33	12.50				14.6

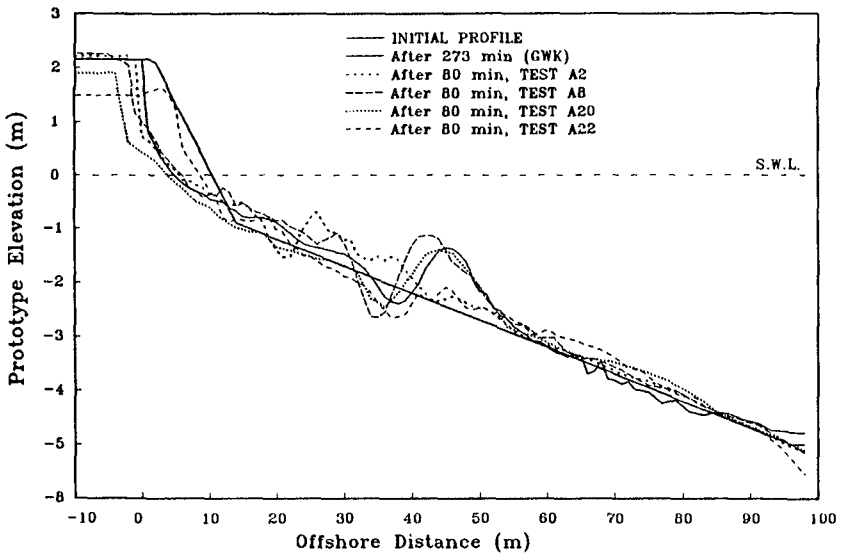


Fig.1: Comparison of model and prototype profiles in equilibrium state.

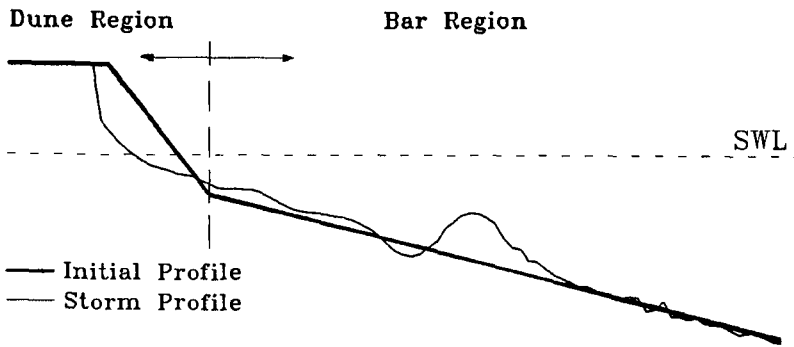


Fig.2: A schematic of dune and bar profile regions.

by calculating the error of dune erosion volume and the RMS error of dune profile as compared to the prototype. In the model bar region, the errors of bar crest location and bar volume, and RMS error of bar profile were calculated as compared to the prototype. The RMS error of the modelled beach profile is defined as

$$\epsilon = \left[ \frac{1}{n} \sum_{i=1}^n (h_{M,i} - h_{P,i})^2 \right]^{1/2},$$

where  $h_M$  and  $h_P$  are the corresponding profile elevations obtained from model and prototype, respectively. Other errors, including the errors of dune erosion volume, bar location and bar volume, are defined in the dimensionless form as

$$\frac{A_M - A_P}{A_P},$$

where  $A_M$  and  $A_P$ , respectively, are the model and prototype quantities used in the calculation of errors. Figures 3 to 7 show these errors computed and compared against model wave height for different model wave periods from all tested cases with  $N_\lambda = 20$  and  $N_\delta = 14.5$ . These errors were computed based on the survey of model profile at the model time of 40min and the final survey of prototype profile at the prototype time of 273min. This model profile from the survey at the model time of 40min is deemed to correspond to the final prototype profile upon the basis of correct morphological time scale. In Figure 3, a somewhat positive linear relationship between model wave height and error of dune erosion volume is observed. This indicates that greater dune erosion in model is likely to occur under larger waves. However, the effect of wave period upon dune erosion in model is less clear revealing a rather weak relationship between the two. The same patterns are also seen in Figures 5 and 6 for the errors of bar volume and bar location. That is, larger bar volume and further seaward bar location in model are likely to occur in the case of higher waves. In Figures 4 and 7, the RMS errors of modelled profile from the prototype in the dune and bar regions, respectively, were compared against model wave height for different wave periods. In these figures, it is seen that the effect of wave height to the RMS errors is less significant. However, the effect of wave period becomes important since a proper model wave period can result a consistent small RMS error which indicates a better fit of modelled profile to the prototype.

Based on the result of errors compared in Figures 3 to 7, it is clear that a proper modeling law should yield smallest absolute value of errors. That is, the zero crossings appeared in Figures 3, 5, and 6, and the least RMS errors in Figures 4 and 7 should correspond to the best modeling law. In order to examine the performance of the four modeling laws presented in Table 1, the errors corresponding to these modeling laws were also identified and marked in these Figures. Clearly, the modeling law derived in the paper presents the best model result in both dune and bar regions as compared to the prototype.

#### 4.2 Evaluation of Morphological Time Scale

The morphological time scale of a modeling law was evaluated by comparing dune and bar profile properties in model and prototype at different time intervals.

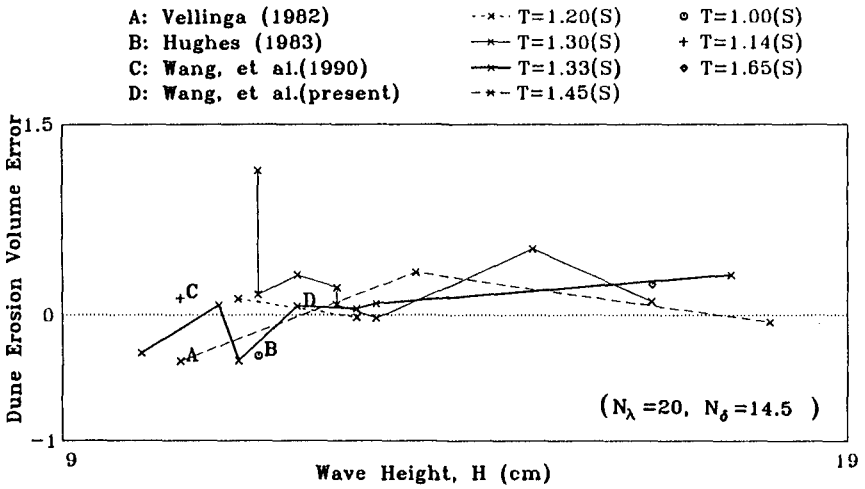


Fig.3: Comparison of error of dune erosion volume.

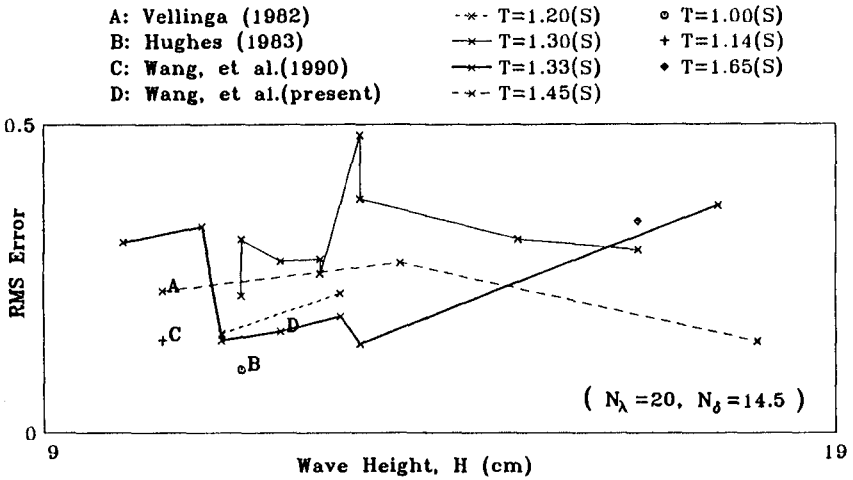


Fig.4: Comparison of RMS error of dune profile.



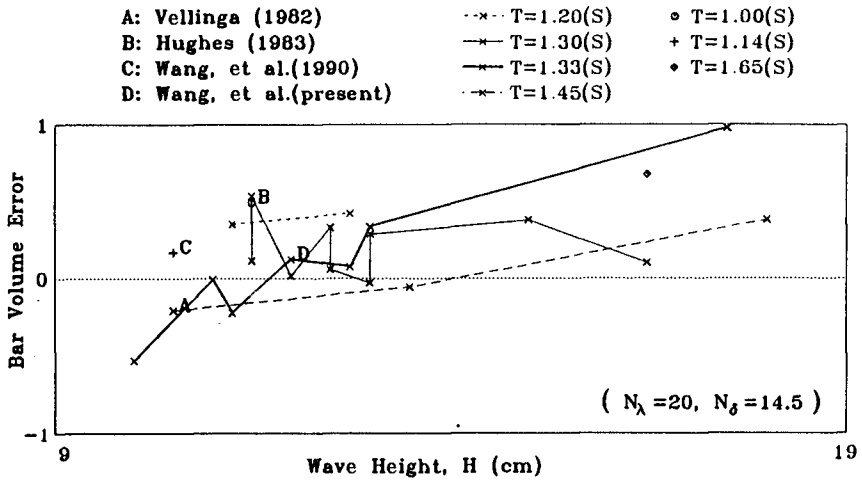


Fig.5: Comparison of error of bar volume.

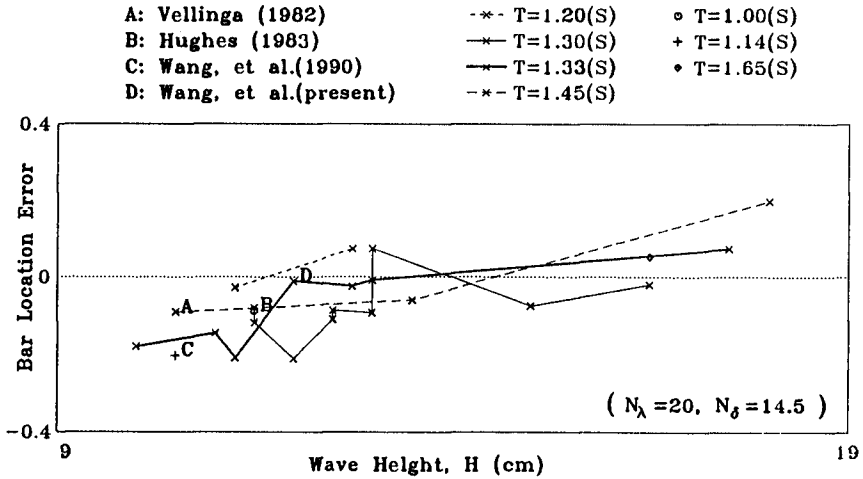


Fig.6: Comparison of error of bar crest location.

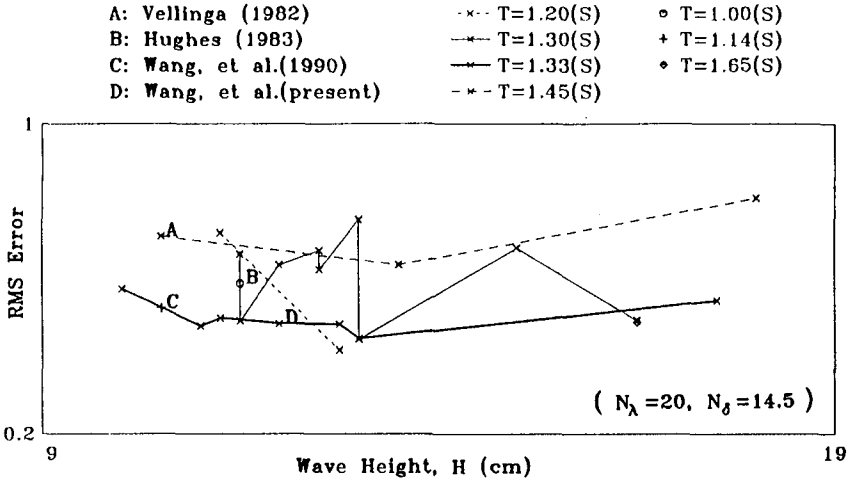


Fig.7: Comparison of RMS error of bar profile.

The modelled beach profile results from three experiments, each presented the best fit model profiles to the final prototype data from three different horizontal scale groups, were selected for this evaluation. The three experiments are Test B3 ( $N_\lambda = 20$ ) from the 3-D wave basin experiment, and Tests A18 ( $N_\lambda = 30$ ) and A20 ( $N_\lambda = 40$ ) from the 2-D wave tank experiment. The 3-D model profiles used in the evaluation are those averaged from the survey of five profiles across the basin to eliminate the minor 3-D effect in model. Based on these experimental data and prototype data, three different morphological time scaling laws as of Hughes (1983), Wang, *et al.* (1990) and the present one shown in Table 1 were compared in terms of the temporal changes of dune erosion volume, RMS elevation difference to initial dune profile, bar volume and bar location, and RMS elevation difference to initial bar profile. The RMS elevation difference to initial profile is defined as

$$e = \left[ \frac{1}{n} \sum_{i=1}^n (h_{S,i} - h_{I,i})^2 \right]^{1/2},$$

where  $h_I$  and  $h_S$ , respectively, are the profile elevations from the initial survey and one following survey at a later time. The results of comparison of these errors computed for the three morphological time scaling laws are shown in Figures 8 to 12.

Figure 8 presents the result of time changes of dune erosion volume for all three scaling laws compared. The comparison shows good model result from the 3-D wave basin experiment for  $N_\lambda=20$  but not the 2-D experiment for  $N_\lambda = 30$  and 40. The reason is probably due to poor compaction and dry condition of sand in the dune region in the 2-D experiment. It appears that none of the model results as well as the prototype have reached equilibrium at the end of the run. For the RMS elevation difference to initial dune profile, all three modeling laws appeared to perform reasonably well in Figure 9 as the scaled model values clustered in a narrow range around the prototype result. For the temporal changes of bar crest location, all

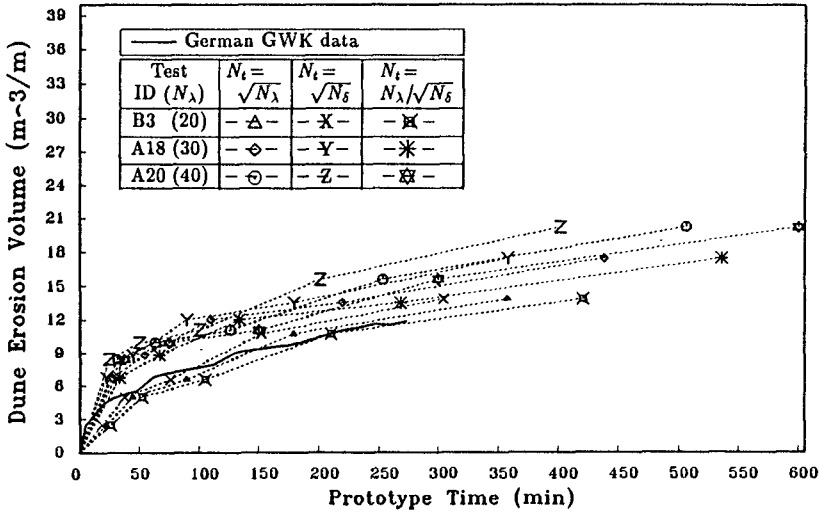


Fig.8: Comparison of temporal changes of dune erosion volume.

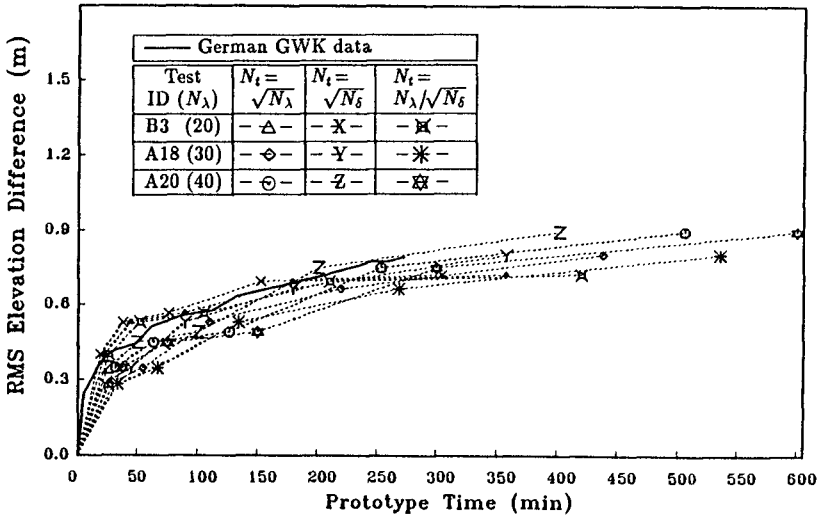


Fig.9: Comparison of RMS elevation difference of dune profile.

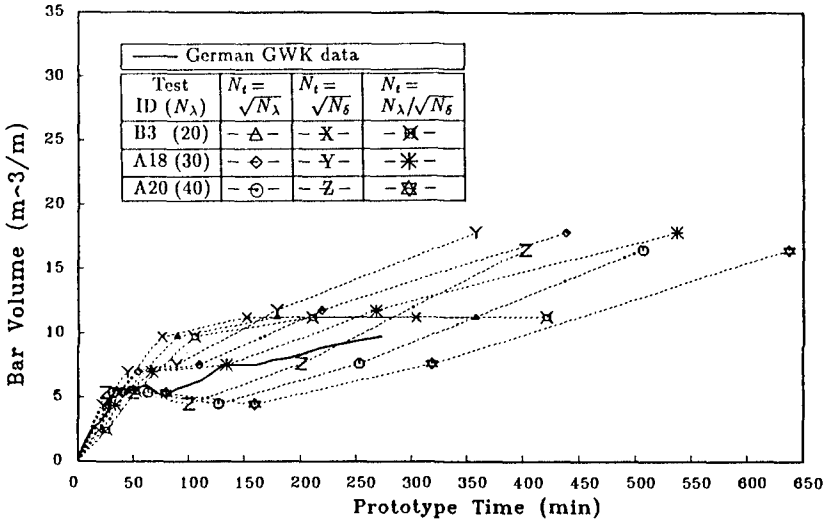


Fig.10: Comparison of temporal changes of bar volume.

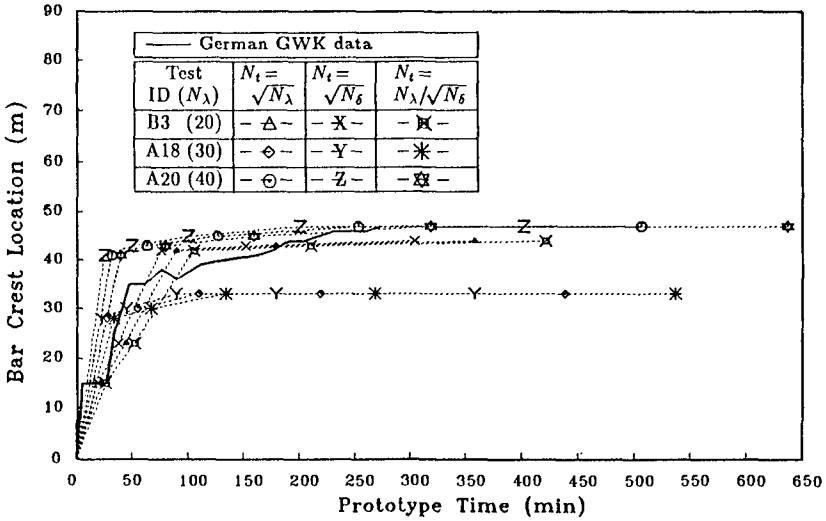


Fig.11: Comparison of temporal changes of bar crest location.

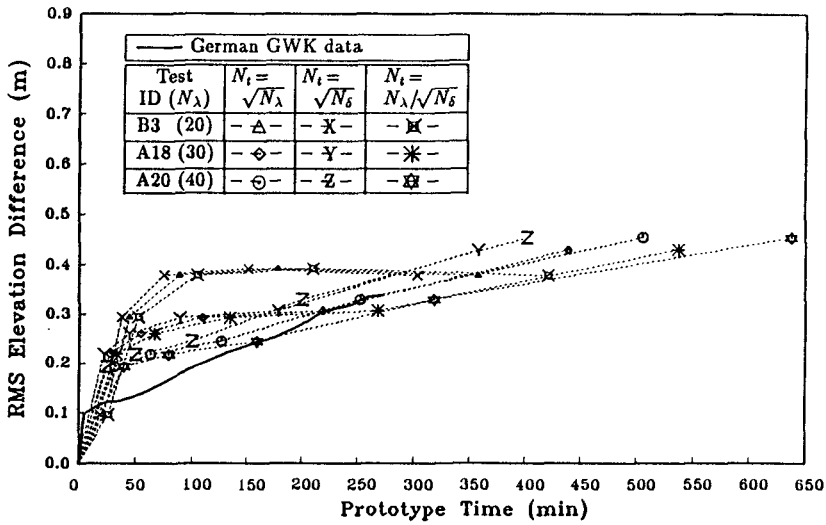


Fig.12: Comparison of RMS elevation difference of bar profile.

three modeling laws appeared to give reasonable results for the data compared to the prototype with the exception of those from Test A18. For the bar volume and RMS elevation difference of bar profile, the modeling law derived in the paper apparently showed the best fit to the prototype data than the other two modeling laws compared. Table 3 presents a summary of the model length and time scales computed based on the four modeling laws and those estimated from the best experimental results for the case of  $N_\lambda = 20$  and  $N_W = 2$ . Certainly, the newly derived modeling law shows overall better performance than the others compared.

5. Summary and Conclusions

A new modeling law for distorted beach model was derived by modifying the one proposed by Wang, *et al.* (1990). The new modeling law preserves not only the sediment transport velocity parameter and surf zone parameter but also the wave breaking index in model. This, in essence, adds to the constraint that wave height may need to be modelled differently from the simple vertical geometrical scale.

In order to investigate the scaling effects, a total of 38 beach model experiments were conducted in the 2-D wave tank and wave flume, and 3-D wave basin. The scaling effects were studied by varying the wave height and wave period in individual experiments and the model results were compared to the prototype data from German GWK experiment. Three different horizontal length scales,  $N_\lambda = 20, 30,$  and  $40,$  were selected in the model experiments. Two different sands, with median sizes equal to  $0.09\text{mm}$  and  $0.2\text{mm},$  respectively, were used in model for undistorted and distorted model studies. The prototype sand has a median size of  $0.33\text{mm}.$

Besides the investigation of scaling effects, four different scaling laws including the new one derived in the paper were also tested against the laboratory model results. The evaluation of scaling laws was carried out by examining the changes of modelled

Table 3. Comparison of Model Performance ( $N_\lambda = 20$ ,  $N_W = 2$ ).

Author	$N_\delta$	$N_H$	$N_T$	$N_t$
Vellinga (1982)	14.5	14.5	3.8	3.8
Hughes (1983)	14.5	14.5	5.3	5.3
Wang, <i>et al.</i> (1990)	14.5	14.5	5.3	3.8
Wang, <i>et al.</i> (present)	14.5	10.5	4.5	4.5

Experimental data	$N_\delta$	$N_H$	$N_T$	$N_t$
Bar location	14.5	11.7	4.5	4.5
Bar volume change	14.5	12.7	4.5	4.5
Dune volume change	14.5	12.4	4.5	4.5

beach profile properties in the separate dune and bar profile regions. Several test parameters, including the errors of dune erosion volume and RMS error of dune profile, bar volume and bar location, and RMS error of bar profile, were utilized to evaluate the model behavior as compared to the prototype. The major conclusions are listed below:

1. Based on the comparison of errors of the model dune erosion volume near the final model stage, greater dune erosion in model is found to occur under larger waves. And, this result is generally not influenced by varying the wave period in model. As comparing the errors of bar volume and bar location, more bar volume and further seaward bar location are found to occur also in the case of larger waves. The smaller absolute value of these errors corresponds to the better cases with the model behavior similar to the prototype. In terms of the RMS errors of modelled beach profile computed in the dune and bar regions, it is seen that the effect of wave height to the RMS errors is less significant. However, the factor of wave period becomes important since a proper model wave period can result a consistent small RMS error which indicates a better fit of modelled profile to the prototype. Accordingly, by applying these results to evaluate the four modeling laws presented in Table 1, the one derived in the present paper appears to have the overall better performance than the other modeling laws.

2. The evaluation of three different morphological time scaling laws, as of Hughes (1983), Wang, *et al.* (1990) and the present one shown in Table 1, by comparing dune and bar profile properties in model and prototype at different times shows that there is less clear which one performs better than the others. In general, all three time scaling laws yield good result to the temporal changes of dune erosion volume and dune profile in model. In terms of bar volume and bar location, the beach model responses seem to develop the bar a little too fast and too large in the initial model stage. However, the results show good agreement to the prototype near the final model stage. It appears that none of the model and prototype profile have reached the equilibrium state at the end of the run.

3. Overall evaluation of the four modeling laws compared in this study shows that the one derived in the present paper performs better than the other three modeling laws. The new modeling law assumes that the fluid motion time scale is the same as the morphological time scale and is equal to square root of the horizontal length scale. The consequences are interesting that both the number of incoming waves per unit time and the deepwater wave length are preserved in model. On the other hand, the new modeling law requires to model the wave height differently from the simple vertical geometrical scale. According to the new modeling law, wave height higher than that from the vertical length scale ratio is needed as to preserve the wave breaking index in the distorted model.

4. The experiments of undistorted model using fine sand of median size of 0.09mm was not successful. The expected bar and dune profile could not be obtained in model. The reason is probably due to the fact that wave energy dissipates more quickly over the flatter bed of fine sand in the undistorted model.

5. The experiments supported the validity of applying distorted model for the prediction of beach and dune erosion in the nearshore zone. However, the present study focuses only on the modeling effects of storm profile. It is necessary to also test the modeling law upon the beach accretion.

#### Acknowledgment

This study is funded by the U.S. Department of Commerce, National Oceanic and Atmospheric Administration, National Sea Grant office under Project # R/C-5-33 with the Florida Sea Grant College Program.

#### REFERENCES

1. Dette, H. H. and Uliczka, K. 1986. "Prototype and Model Evolution of Beach Profile," Proc. Symposium on Scale Effects in Modeling Sediment Transport Phenomena, Toronto, Canada.
2. Hughes, S. A. 1983. "Movable-Bed Modeling Law for Coastal Dune Erosion," Journal of WPCOE, ASCE, New York, Vol. 109, No. 2.
3. McCowan, J. 1894. "On the Highest Wave of Permanent Type. Phil. Mag., Series 5, 38.
4. Vellinga, P. 1982. "Beach and Dune Erosion During Storm Surges," Journal of Coastal Engineering, Vol. 6.
5. Wang, H., Toue, T. and Dette, H. H. 1990. "Movable Bed Modeling Criteria for Beach Profile Response," Chapter 195, Proc. of 22nd ICCE, ASCE, Delft, The Netherlands.

## CHAPTER 201

# A NUMERICAL MODEL OF BEACH CHANGE DUE TO SHEET-FLOW

Akira Watanabe<sup>1</sup>, Kazuhiko Shiba<sup>2</sup> and Masahiko Isobe<sup>3</sup>

### ABSTRACT

First a discussion is made on the relation between the time-average of a Boussinesq-type equation and the mean flow equation. Then nonlinear wave transformation on a sloping bed is computed by a set of Boussinesq equations including a breaker-induced energy dissipation term. Comparisons are made between the computations and laboratory measurements for cross-shore distributions of the wave height and mean water elevation, and for time-histories of the near-bottom velocity near and after breaking. Undertow current velocity in the nearshore zone is calculated by a semi-empirical formula and is also compared with measurement data. A beach profile change model is set up by combining the Boussinesq-type equations, a sediment transport rate formula for the sheet-flow proposed by Dibajnia and Watanabe, which incorporates the asymmetric orbital velocity due to wave nonlinearity as well as the undertow current, and a sediment mass conservation equation proposed by Watanabe *et al.*, which includes the effect of local bottom slope. The validity of the model is examined through the comparisons of the computed transport rate distributions and beach profiles with the laboratory data obtained in large wave flume experiments.

### INTRODUCTION

Prediction of beach processes is generally inevitable to develop or protect coastal zones properly. Short-term beach topography changes have usually been predicted in Japan by the numerical model proposed by Watanabe *et al.* (1986) or its improved versions. In this model, however, since the wave computation is performed with linear time-dependent mild slope equations involving breaker-induced energy dissipation, the calculations of the nearshore currents and the mean water elevation should be carried out only through the evaluation of radiation stresses, and hence the wave-current interaction can be treated by the iteration of the computations of waves and of currents. In addition, the effect of

---

<sup>1</sup> Dept. of Civil Eng., Univ. of Tokyo, Hongo-7, Bunkyo-ku, Tokyo, 113 Japan.

<sup>2</sup> Tokyo Electric Power Co., Ltd.

<sup>3</sup> Dept. of Civil Eng., Univ. of Tokyo.



wave nonlinearity on the sediment transport rate has been incorporated on the basis of the simplified semi-empirical formulas.

Dibajnia *et al.* (1992) have performed the prediction of beach profile change applying the formula by Dibajnia and Watanabe (1992) for the sheet-flow transport rate under nonlinear waves. However, since they have employed the linear wave model for the wave computation, a sort of inconsistency has been existing from a theoretical viewpoint.

Prediction of beach profile change under sheet-flow condition is important, because significant short-term beach deformation is caused by large waves, under which the sheet-flow sediment transport is usually predominant. In addition, under such conditions, one cannot discard the asymmetry of near-bottom orbital motion and the presence of undertow particularly in the surf zone. This paper presents a numerical model of beach profile change based on a sheet-flow transport rate formula mentioned above and on Boussinesq-type wave equations, incorporating the effects of asymmetric velocity and the undertow. Comparisons will be made between the numerical computations and measurements.

## BOUSSINESQ EQUATION AND NEARSHORE CURRENT EQUATION

Boussinesq-type equations include nonlinear terms to the order of  $O(a^2)$ , where  $a$  is the wave amplitude. Since nearshore currents (wave-induced mean flow) and wave setup/down are the phenomena of the order of  $O(a^2)$ , they will be evaluated with a Boussinesq-type equation. In this section, we will show that the time-average of the Boussinesq equation that involves vertical velocity distributions becomes equivalent to the governing equation for the nearshore currents, and that thus the concurrent computation of waves and currents becomes possible.

Abbott (1979) has presented the Boussinesq equation involving vertical velocity distributions as follows:

$$\begin{aligned} \frac{\partial \rho u_\alpha}{\partial t} + \frac{\partial}{\partial x_\beta}(\rho u_\alpha u_\beta) + \frac{\partial}{\partial z}(\rho w u_\alpha) + \rho g \frac{\partial \eta}{\partial x_\alpha} \\ = -\rho \frac{\partial^3 \eta}{\partial x_\alpha \partial t^2} \left\{ \frac{(h + \eta)^2 - (h + z)^2}{2(h + \eta)} \right\} \end{aligned} \quad (1)$$

where  $h$  is the still water depth,  $\eta$  the instantaneous surface displacement,  $u$  the horizontal velocity,  $w$  the vertical velocity,  $t$  the time, and  $x$  and  $z$  are the horizontal and vertical coordinates, respectively. The subscripts  $\alpha$  and  $\beta$  take a value of 1 or 2, and the summation convention is adopted.

Boundary conditions on the free surface and the seabed are as follows:

$$\frac{\partial \eta}{\partial t} - w + u_\alpha \frac{\partial \eta}{\partial x_\alpha} = 0 \quad (z = \eta) \quad (2)$$

$$w + u_\alpha \frac{\partial h}{\partial x_\alpha} = 0 \quad (z = -h) \quad (3)$$

Integrating Eq. (1) from the bottom to the free surface and using the boundary conditions, we obtain

$$\begin{aligned} \frac{\partial}{\partial t} \int_{-h}^{\eta} \rho u_{\alpha} dz + \frac{\partial}{\partial x_{\beta}} \int_{-h}^{\eta} \rho u_{\alpha} u_{\beta} dz + \rho g(h + \eta) \frac{\partial \eta}{\partial x_{\alpha}} \\ = -\rho \frac{\partial^3 \eta}{\partial x_{\alpha} \partial t^2} \frac{(h + \eta)^2}{3} \end{aligned} \quad (4)$$

Here we will decompose the horizontal velocity  $u_{\alpha}$  into the time-average (steady) component  $U_{\alpha}$  and the periodic (wave) component  $u'_{\alpha}$ :

$$u_{\alpha} = U_{\alpha} + u'_{\alpha} \quad (5)$$

and define three kinds of mass transport as follows:

$$\overline{\int_{-h}^{\eta} \rho u'_{\alpha} dz} = M'_{\alpha} \quad (6)$$

$$\overline{\int_{-h}^{\eta} \rho U_{\alpha} dz} = \rho U_{\alpha}(h + \bar{\eta}) = M_{\alpha} \quad (7)$$

$$\overline{\int_{-h}^{\eta} \rho u_{\alpha} dz} = \tilde{M}_{\alpha} = M_{\alpha} + M'_{\alpha} = \rho \tilde{U}_{\alpha}(h + \bar{\eta}) \quad (8)$$

where  $\bar{\eta}$  is the mean water displacement,  $M'_{\alpha}$  and  $M_{\alpha}$  are the mass transport due to the orbital velocity and to the mean flow, respectively, and  $\tilde{M}_{\alpha}$  is their summation.

Substitution of Eqs. (6) to (8) into the time-average of Eq. (4) yields

$$\begin{aligned} \frac{\partial \tilde{M}_{\alpha}}{\partial t} + \frac{\partial}{\partial x_{\beta}} \left\{ \tilde{U}_{\beta} \tilde{M}_{\alpha} + \overline{\int_{-h}^{\eta} \rho u'_{\alpha} u'_{\beta} dz} - \frac{M'_{\alpha} M'_{\beta}}{\rho(h + \bar{\eta})} \right\} \\ + \rho g(h + \bar{\eta}) \frac{\partial \bar{\eta}}{\partial x_{\alpha}} = -\rho \frac{\partial^3 \bar{\eta}}{\partial x_{\alpha} \partial t^2} \frac{(h + \bar{\eta})^2}{3} \end{aligned} \quad (9)$$

On the other hand, Eq. (10) gives the governing equation for the nearshore current and the mean water elevation, in which the bottom friction and lateral mixing terms are neglected.

$$\frac{\partial \tilde{M}_{\alpha}}{\partial t} + \frac{\partial}{\partial x_{\beta}} [\tilde{U}_{\beta} \tilde{M}_{\alpha} + S_{\alpha\beta}] + \rho g(h + \bar{\eta}) \frac{\partial \bar{\eta}}{\partial x_{\alpha}} = 0 \quad (10)$$

where  $S_{\alpha\beta}$  is the radiation stress expressed as:

$$S_{\alpha\beta} = \overline{\int_{-h}^{\eta} (\rho u'_{\alpha} u'_{\beta} + p \delta_{\alpha\beta}) dz} - \frac{1}{2} \rho g(h + \bar{\eta})^2 \delta_{\alpha\beta} - \frac{M'_{\alpha} M'_{\beta}}{\rho(h + \bar{\eta})} \quad (11)$$

Comparing Eqs. (9) and (10), we can readily find that their differences exist only in the radiation stress term and on the right hand side. Since the Boussinesq equation holds for shallow water waves, we apply a long wave approximation to the pressure  $p$  in Eq. (11). Abbott (1979) has obtained the following relation for the pressure, in the process of his derivation of Eq. (1):

$$\frac{p(z)}{\rho} = g(\eta - z) + \frac{\partial^2 \eta}{\partial t^2} \frac{(h + \eta)^2 - (h + z)^2}{2(h + \eta)} \quad (12)$$

Substitution of Eq. (12) into Eq. (11) and some manipulations make Eq. (10) become identical to Eq. (9).

It has thus been shown that, as far as the long wave approximation holds good, the time-average of the Boussinesq equation becomes equivalent to the mean flow equation. In other words, solving the Boussinesq equation, we can compute not only the wave field but also the nearshore current and mean water level field, which are obtained by taking the time-average of the solutions for the velocity  $u_\alpha$  and for the surface displacement  $\eta$ , respectively. This means that the wave-current interaction is automatically incorporated in computations.

### COMPUTATION OF WAVES AND MEAN WATER ELEVATION

A set of one-dimensional Boussinesq equations involving a breaker-induced energy dissipation term is expressed in terms of the surface displacement  $\eta$  and the flow rate  $Q$  as follows:

$$\frac{\partial \eta}{\partial t} + \frac{\partial Q}{\partial x} = 0 \quad (13)$$

$$\frac{\partial Q}{\partial t} + \frac{\partial}{\partial x} \left( \frac{Q^2}{D} \right) + gD \frac{\partial \eta}{\partial x} - \frac{h^2}{3} \frac{\partial^3 Q}{\partial t \partial x^2} + M_D = 0 \quad (14)$$

where

$$D = h + \eta, \quad Q = \int_{-h}^{\eta} u \, dz,$$

$u$  is the horizontal velocity and  $M_D$  corresponds to the breaker-induced energy dissipation and is given by (Sato and Suzuki, 1990)

$$M_D = \frac{gD}{\sigma^2} f_D \frac{\partial^2 Q}{\partial x^2} \quad (15)$$

The quantity  $\sigma$  is the angular frequency, and  $f_D$  is the energy dissipation coefficient expressed as (Watanabe & Dibajnia, 1987):

$$f_D = \alpha_D \tan \beta \sqrt{\frac{g}{h}} \sqrt{\frac{\hat{Q} - Q_r}{Q_s - Q_r}} \quad (16)$$

in which the coefficient  $\alpha_D = 2.5$ ,  $\tan \beta$  is the bottom slope around the breaking point,  $\hat{Q}$  is the amplitude of  $Q$ , and  $Q_s$  and  $Q_r$  correspond to  $\hat{Q}$  in the dissipation zone on a uniform slope and in the recovery zone in the constant depth water, respectively, given by

$$Q_s = \gamma_s C h \quad (17)$$

$$Q_r = \gamma_r C h \quad (18)$$

$$\gamma_s = 0.4 (0.57 + 5.3 \tan \beta) \quad (19)$$

$$\gamma_r = 0.4 \left( \frac{a}{h} \right)_B \quad (20)$$

where  $C$  is the wave celerity, and  $(a/h)_B$  is the ratio of the wave amplitude to the water depth at a breaking point.

In order to avoid re-reflection of outgoing waves (reflected from the slope or structures, if any), we should impose such a condition that they can freely pass through the offshore boundary of a computation domain. For this, we express the flow rate  $Q$  on the offshore boundary as the summation of that of the incident waves  $Q_{in}$  and of the outgoing waves  $Q_{out}$ :

$$Q = Q_{in} + Q_{out} \quad (21)$$

The corresponding horizontal velocities are expressed, under the long wave approximation, as:

$$\bar{u}_{in} = \sqrt{g/h} \eta_{in}, \quad \bar{u}_{out} = -\sqrt{g/h} \eta_{out} \quad (22)$$

Using  $Q = \bar{u}(h + \eta)$  and neglecting terms with  $\eta^2$ , we obtain the following relation from Eq. (21):

$$Q = 2C \eta_{in} - C \eta \quad (23)$$

On the other hand, we impose the condition given by Eq. (24) on the shoreward boundary, where  $r$  is the reflection coefficient.

$$Q = (1 - r) \cdot C \eta \quad (24)$$

Using these boundary conditions, numerical computations for Eqs. (13) and (14) will be conducted by the finite difference method with the central difference-staggered mesh scheme.

Computations of wave transformation on a slope have been made and the results have been compared with experimental data obtained by Sato *et al.* (1987). In the experiment, the water surface displacement and the near-bottom orbital velocity were recorded under the conditions that the bottom slope was 1/20 and the incident wave height and period were 6.1cm and 1.18s.

Figures 1 and 2, respectively, compare the cross-shore distributions of the wave height and the mean water surface elevation between the computations and the measurements. Agreement is very good for the wave height even near the breaking point. The mean water level  $\bar{\eta}$  that has been computed by taking the

time average of  $\eta$ , without the computation of the radiation stress, also shows a fairly good agreement with the measurements.

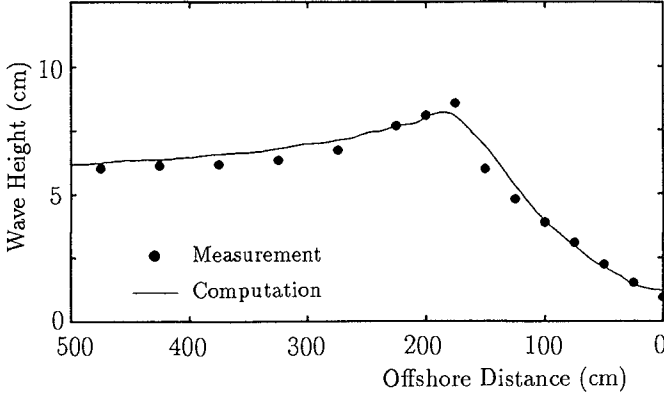


Fig. 1 Comparison of cross-shore distributions of wave height.

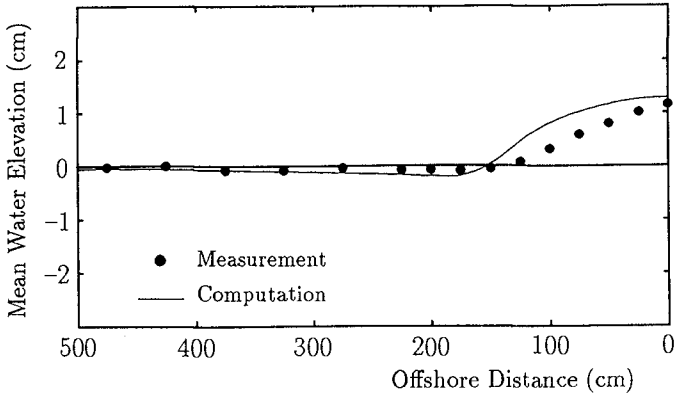


Fig. 2 Comparison of cross-shore distributions of mean water surface elevation.

### CALCULATION OF NEAR-BOTTOM ORBITAL VELOCITY

The orbital velocities were measured at several points 5mm in height above the bottom. By considering the finite water depths in the region, the near-bottom

orbital velocity  $u_b$  has been computed as a function of time at each location by the following equation:

$$u_b = \frac{Q}{h + \eta} \cdot \frac{\cosh(2\pi z'/L)}{\cosh(2\pi h/L)} \tag{25}$$

where  $z'$  is the height of a point above the bottom, and  $L$  is the local wavelength. Figures 3 (a), (b) and (c) show the comparisons of  $u_b$  between the computations and the measurements, for three locations: (a) outside the surf zone, (b) near the breaking point, and (c) in the surf zone.

In previous computations of the orbital velocities based on the small-amplitude wave theory, the method proposed by Isobe and Horikawa (1981) has given fairly good estimates up to the neighborhood of breaking points, but it has failed to evaluate them in the surf zone after breaking. As shown in Figs. 3 (a) to (c), the present model can directly reproduce the near-bottom orbital velocities with a remarkably high accuracy. The above comparisons are for a case of plunging breaker, and it has been found that the present wave model works for cases of spilling breaker as well.

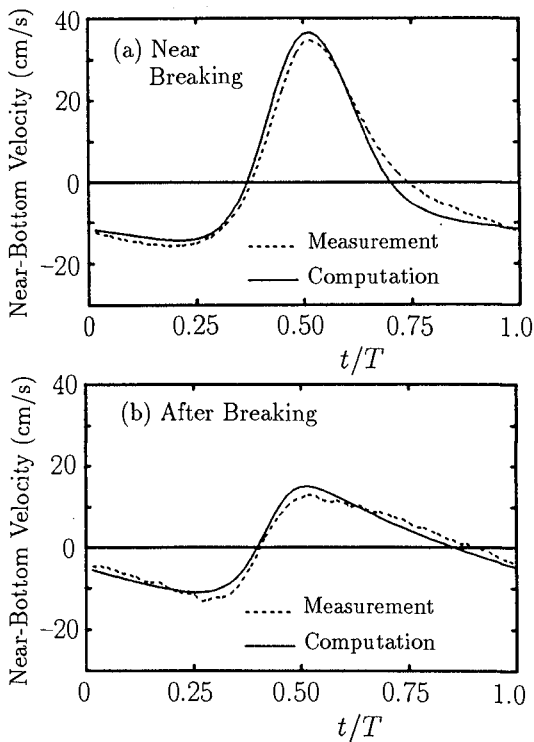


Fig. 3 Comparisons of near-bottom orbital velocities.

## EVALUATION OF UNDERTOW VELOCITY

In the surf zone, the undertow (return flow near the bed) usually develops to compensate the shoreward mass transport accompanying the breakers. Since the concentration of suspended sediment is very high near the bottom, the effect of the undertow on the sediment transport should inevitably be taken into consideration. However, highly reliable models have not yet been established for the prediction of the undertow velocity under general conditions.

In the present study, following Dibajnia *et al.* (1992), we have evaluated the cross-shore distribution of steady flow velocity  $U$  due to the undertow by decomposing it into three components: the return flow velocity  $U_B$  caused by wave breaking, the seaward velocity  $U_W$  compensating the mass transport, and the Eulerian mass transport velocity  $U_E$  at the outer edge of the bottom boundary layer. According to previous studies, the undertow velocity becomes nearly zero near the breaking point. Hence, for simplicity, as a parameter representing the degree of intensity of the breaker-induced large vortex, we have introduced the following function  $K_U$ , whose value is zero before the plunging point  $x \leq X_p$ , being unity after the large vortex development point  $X_i$  and changing linearly between these two points, *i.e.*,

$$K_U = \begin{cases} 0 & (x \leq X_p) \\ \frac{X_p - x}{X_p - X_i} & (X_p < x \leq X_i) \\ 1 & (X_i < x) \end{cases} \quad (26)$$

Then the resultant total undertow velocity  $U$  has been calculated by

$$U = K_U (U_B + U_W + U_E) \quad (27)$$

The first component  $U_B$  has been estimated by the following formula proposed by Sato *et al.* (1987):

$$U_B = -A \frac{H^2}{h \cdot T} \quad (28)$$

where  $H$  and  $h$  are the local wave height and water depth, respectively, and  $A$  is a dimensionless coefficient of the order of unity. In the present study, we have used  $A = 1$ .

Figure 4 shows the comparison of the undertow velocity between the computation and the measurements, indicating a considerably good agreement. However, this only demonstrates the validity of the present method, Eqs. (26) to (28), for a constant slope bed in a wave flume, and its applicability to more general conditions (prototype scale and complicated bottom topography) is still questionable.

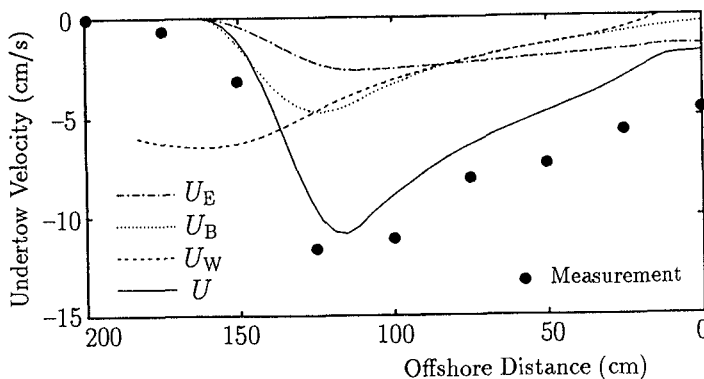


Fig. 4 Comparisons of cross-shore distributions of undertow velocity.

**COMPUTATION OF SEDIMENT TRANSPORT RATE AND BEACH PROFILE CHANGE**

Dibajnia and Watanabe (1992) have proposed a sheet-flow sand transport rate formula based on extensive laboratory data obtained in oscillatory flow tank experiments, considering the entrainment and settling processes of suspended sediment during the two successive half wave periods. According to this formula, the net rate of sheet flow transport  $q_{net}$  can be calculated as a function of the root-mean-square amplitudes,  $u_c$  and  $u_t$  and the time durations,  $T_c$  and  $T_t$ , of the onshore and offshore velocity, respectively, and the grain diameter  $d$ , settling velocity  $w_0$ , and porosity  $\lambda_v$  of the sediment, as follows:

$$q_{net} = \text{sign}(\Gamma) \cdot 0.001|\Gamma|^{0.55} \cdot w_0 d / (1 - \lambda_v) \tag{29}$$

$$\Gamma = \frac{u_c T_c (\Omega_c^3 + \Omega'_c{}^3) - u_t T_t (\Omega_t^3 + \Omega'_t{}^3)}{(u_c + u_t) T} \tag{30}$$

where  $\Omega_c$ ,  $\Omega'_c$ ,  $\Omega_t$  and  $\Omega'_t$  are functions of  $u_c$ ,  $u_t$ ,  $T_c$ ,  $T_t$ ,  $d$ ,  $w_0$  and the specific density of the sediment (For details, see Dibajnia and Watanabe, 1992).

Dibajnia, Shimizu and Watanabe (1992) have presented a numerical model for a profile change of a sheet flow predominant beach using the above transport rate formula and the linear time-dependent mild slope equations. In the present study, we have incorporated the effect of wave nonlinearity in the prediction of beach profile change by combining the wave model based on the Boussinesq equation and the undertow model mentioned above as well as the sediment transport rate formula, Eq. (29). The change of a beach profile has been computed from the cross-shore distribution of  $q_{net}$  by the sediment mass conservation equation including the effect of the local bottom slope (Watanabe *et al.*, 1984):

$$\frac{\partial z_b}{\partial t} = -\frac{\partial h}{\partial t} = -\frac{\partial}{\partial x} \left( q_{net} - \epsilon_s |q_{net}| \frac{\partial z_b}{\partial x} \right) \tag{31}$$



where  $z_b$  is the bottom elevation, and a value of 2.0 has been used for the coefficient  $\epsilon_s$ .

In order to examine the validity of the model, we have performed comparisons of the computations with the measurements obtained by Shimizu *et al.* (1985) in their large scale experiments. Table 1 indicates the experimental conditions for the adopted three cases, in which  $d_{50}$  is the median diameter of the sand,  $\tan \beta$  is the initial beach slope,  $T$  and  $H_0$  are the period and height of incident waves.

Table 1 Experimental conditions.

Case	$d_{50}$ (mm)	$\tan \beta$	$T$ (s)	$H_0$ (m)	Breaker type
3-2	0.27	1/20.0	6.0	1.05	Plunging
3-4	0.27	1/20.0	3.1	1.54	Spilling
4-2	0.27	1/33.3	4.5	0.97	Plunging

Although the measurements were made for a total time duration of 30 hours, the computations have been conducted for a duration of 5 or 7 hours only, because the accuracy of the undertow computation may become unsatisfactory as the beach profiles get complicated with time. Figures 5, 6 and 7 show the comparisons between the computations and the measurements of Cases 3-2, 3-4 and 4-2, respectively, for the wave height distributions, the net rates of the sediment transport, and the beach profiles.

These figures demonstrate considerably good agreement between the computations and the measurements, indicating the overall validity of the present model that includes the nonlinear wave equation, the formulas for the near-bottom orbital velocity and for the undertow velocity, and the sheet flow transport rate formula.

## CONCLUDING REMARKS

This paper has presented a numerical model for beach profile change, which incorporates the asymmetric orbital velocity due to wave nonlinearity as well as the undertow current. By using the Boussinesq equation, the iteration of computations for the waves and for the mean flow and mean water level has become unnecessary, and the computational accuracy of the near-bottom orbital velocities has been highly improved. A beach profile change model has been established by the combination of the wave model based on the Boussinesq equation and the sediment transport rate formula for the sheet flow proposed by Dibajnia and Watanabe (1992). An overall validity of the present numerical model has been examined through the comparisons of the computed sediment transport rate distributions and beach profiles with the laboratory data obtained in large wave flume experiments by Shimizu *et al.* (1985). A better method will be required for the prediction of the undertow velocity distribution under general conditions so as to make the present model more practical and useful.

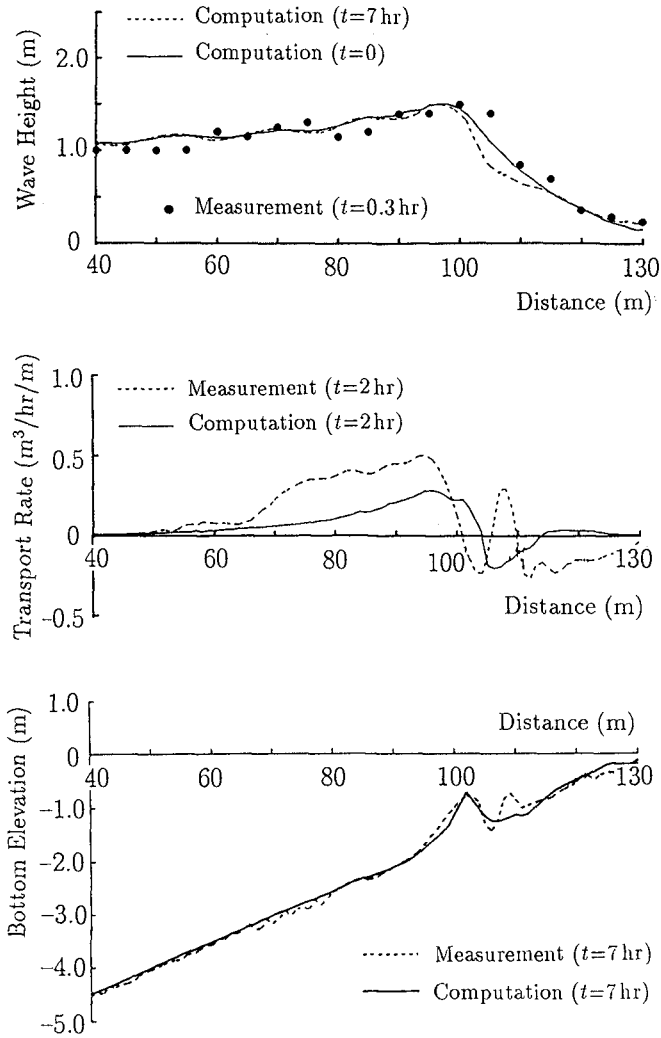


Fig. 5 Comparisons of wave height, net transport rate and beach profile. ( $d_{50} = 0.27mm$ ,  $\tan \beta = 1/20$ ,  $H_0 = 1.05m$ ,  $T = 6.0s$ , Plunging breaker)

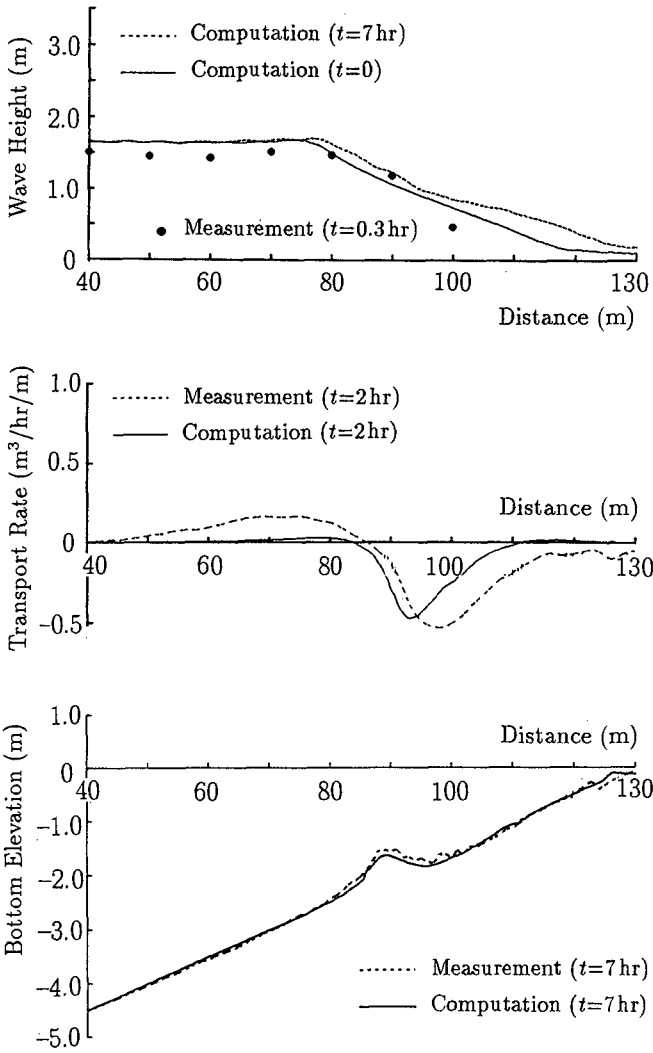


Fig. 6 Comparisons of wave height, net transport rate and beach profile. ( $d_{50} = 0.27mm$ ,  $\tan \beta = 1/20.0$ ,  $H_0 = 1.54m$ ,  $T = 3.1s$ , Spilling breaker)

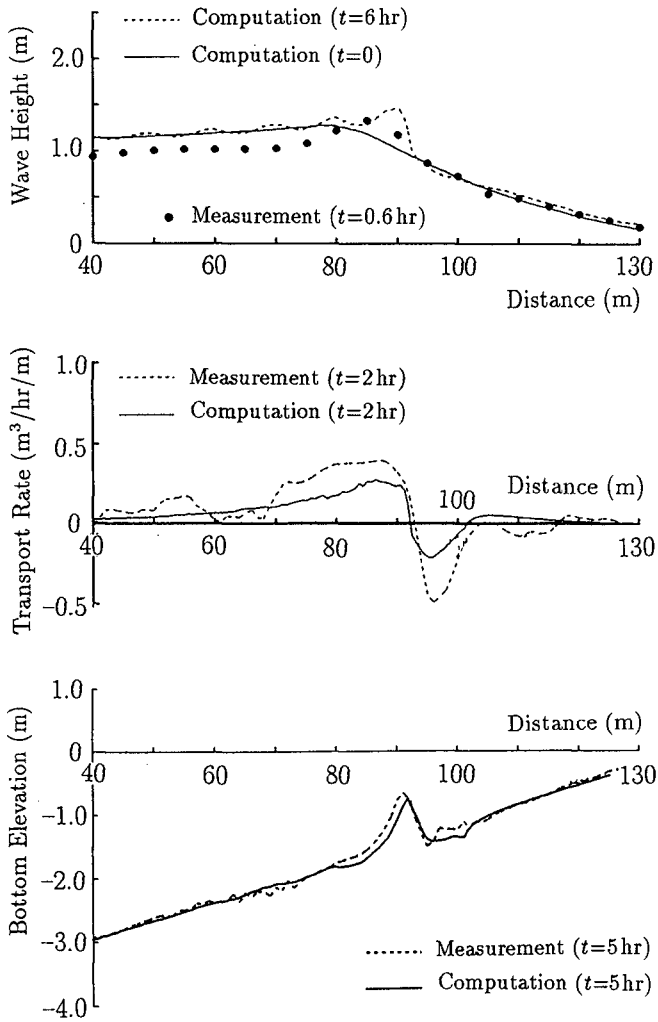


Fig. 7 Comparisons of wave height, net transport rate and beach profile. ( $d_{50} = 0.27\text{mm}$ ,  $\tan \beta = 1/33.3$ ,  $H_0 = 0.97\text{m}$ ,  $T = 4.5\text{s}$ , Plunging breaker)

**REFERENCES**

- Abbot, M.B. (1979): Elements of the Theory of Free Surface Flow, Computational Hydraulics, pp. 51-55.
- Dibajnia, M., T. Shimizu and A. Watanabe (1992): Profile change of a sheet flow dominated beach, Proc. Japanese Conf. on Coastal Eng., JSCE, Vol. 39, pp. 301-305. (in Japanese)
- Dibajnia, M. and A. Watanabe (1992): Sheet flow under nonlinear waves and currents, Proc. 23rd Coastal Eng. Conf., ASCE., pp. 2015-2028.
- Isobe, M. and K. Horikawa (1981): Change in velocity field in and near the surf zone, Proc. 28th Japanese Conf. on Coastal Eng., JSCE, pp. 5-9. (in Japanese)
- Sato, S., M. Fukuhama and K. Horikawa (1987): Experimental study on breaking and near-bottom velocities under irregular waves on a sloping beach, Proc. 34th Japanese Conf. on Coastal Eng., JSCE, pp. 36-40. (in Japanese)
- Sato, S. and H. Suzuki (1990): Estimation method for near-bottom orbital velocities in the surf zone, Proc. 37th Japanese Conf. on Coastal Eng., JSCE, pp. 51-55. (in Japanese)
- Shimizu, T., S. Saito, K. Maruyama, H. Hasegawa and R. Kajima (1985): Modeling of cross-shore sediment transport rate distributions in a large wave flume, Report of Central Res. Inst. for Electric Power Industry, Rep. No. 384028, 60 p. (in Japanese)
- Watanabe, A. and M. Dibajnia (1988): A numerical model of wave deformation in surf zone, Proc. 21st Coastal Eng. Conf., ASCE, pp. 578-587.
- Watanabe, A. and M. Dibajnia (1988): Mathematical modeling of nearshore waves, cross-shore sediment transport and beach profile change, Proc. Symp. on Mathematical Modelling of Sediment Transport in the Coastal Zone, IAHR, pp. 166-174.
- Watanabe, A., K. Maruyama, T. Shimizu and T. Sakakiyama (1986): Numerical prediction model of three-dimensional beach deformation around a structure, Coastal Eng. in Japan, JSCE, Vol. 29, pp. 179-194.

## Field Tests of Radiation-Stress Estimators of Longshore Sediment-Transport

Thomas E. White <sup>1</sup>

### Abstract

Surfzone measurements of longshore sediment-transport with optical backscatter sensors and current meters are compared to transport estimates from offshore wave data. Several methods from the Shore Protection Manual for computing longshore sediment transport from waves are compared and correlated. Some formulas work well some of the time. Circumstances of which equations perform well/poorly under which conditions are specified, and reasons for poor performances are speculated upon. Advice is given for placement of wave gages and methods of analysis, which would increase the probability of obtaining good estimates of longshore sediment transport from directional wave data.

### Introduction

Comprehensive arrays of 43 sensors were deployed to measure waves, currents, tides, and sediment transport at a long straight beach with gently-sloping plane parallel contours near a river outlet, Colorado River, Texas. (See inset map in Figure 1.)

Several state-of-the-art instruments were deployed: a trawler resistant Directional Wave Gage (DWG), a puv gage of colocated pressure and current sensors, Optical Backscatter Sensors for suspended-sediment concentrations, electromagnetic current meters for velocities, a new cable with internally imbedded pressure sensors for surfzone waves, and Acoustic Doppler Current Profilers for inlet currents and sediment flux.

This project of monitoring the behavior of the jetty system had several objectives, only one of which was estimation of longshore sediment transport from the offshore wave gages, the topic of this paper. Table 1 lists the major objectives (hypotheses) of the monitoring project and the means by which various functions

---

<sup>1</sup>Coastal Engineering Research Center, USAE Waterways Experiment Station, Attn: CEWES-CD-P, 3909 Halls Ferry Road, Vicksburg, MS 39180-6199, USA

of the sediment transport ( $Q$  in volumetric terms) would be used to test the hypotheses. In addition to the engineering objectives in Table 1, there were several science objectives as well. The surfzone data are being used to test suspended-load transport theories at a point, in order to find the best ones to use in CERC's numerical models. This paper will describe only the results of the final objective: using the offshore wave data to predict longshore transport.

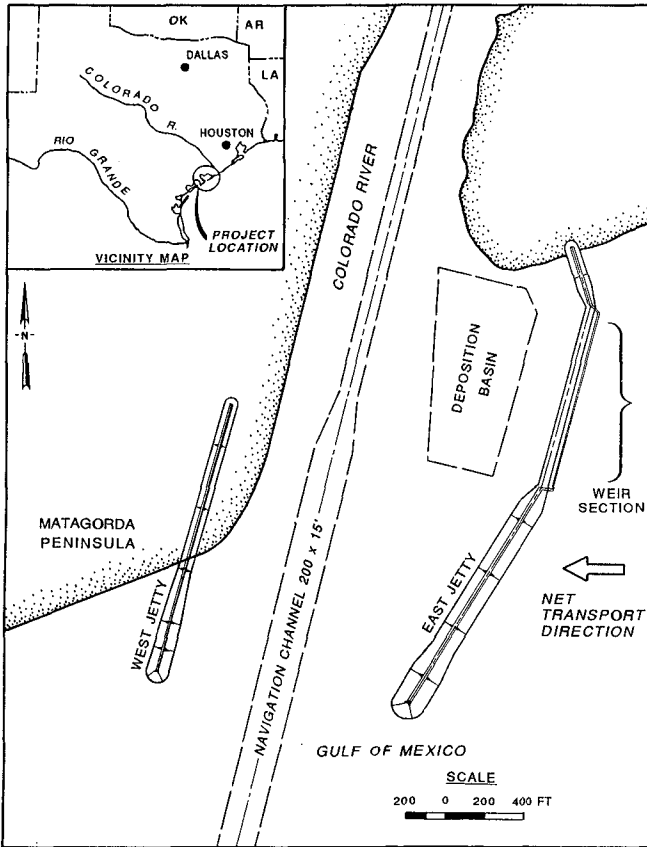


Figure 1. Colorado River location map (inset) and river mouth plan view. The weir section is underwater and allows some sediment to pass.

The purpose of this paper is to compare longshore sediment transport, as determined from both shoaled radiation stress and from transport measurements in the surfzone. For this reason, two sets of measurements were necessary: the offshore directional wave field and the sediment transport in the surfzone.

# MCCP Colorado River, Texas

## HYPOTHESES ..... METHODS

### 1. Weir-Jetty System Hypotheses:

- Weir-trapping efficiency is high ..... Compute  $\frac{Q_{trapped}}{Q_i}$  (Impoundment/Transport)
- Weir length should be 1000 feet ..... Compute minimum of  $Q(x)$
- Weir is in proper cross-shore location ..... Compute  $\frac{\partial Q}{\partial x}$
- Impoundment area is large enough ..... Compute  $\int Q dt$
- Anticipated dredging frequency is reduced by design ..... Compute Required Dredging Frequency =  $\frac{Q_{trapped}}{V_{trap}}$
- Weir should be east of inlet .....  $Q_+ \gg Q_-$
- Jetty length should be 1500 feet ..... Bypassing efficiency =  $1 - \frac{Q(x_{inlet})}{Q_{TOTAL}}$

### 2. Sediment-Transport Hypotheses:

- $I = KECn \sin(\alpha) \cos(\alpha)$  ..... Compute Correlation Coefficient (absolute) and Confidence Interval (relative)
- $K = 0.7$  ..... Compute ratio of Predicted to Predictor
- Offshore wave gage predicts I ..... Correlations of  $S_{xy}$  and measured I



## Radiation Stress Method

The offshore wave field was measured at 10m depth at approximately 3.2km offshore. As seen in Figure 2, the topography is quite linear (plane parallel contours) with very gentle slopes. When designing this project, it was hoped that if shoaled wave energy could be used to predict transport, the method ought to work better here than at many other sites, because of the gentle topography. Of course, it's always better to measure the waves close to where the data are needed (in this case, the breakpoint). But a very shallow gage deployment would have been unlikely to remain stationary over a long period, due to the stresses and topographic changes which are relatively large at 3m depth compared to 10m. Also the area is heavily trawled for shrimp, so gages were deemed more likely to survive in the area of offshore towers, which is where the gages were placed.

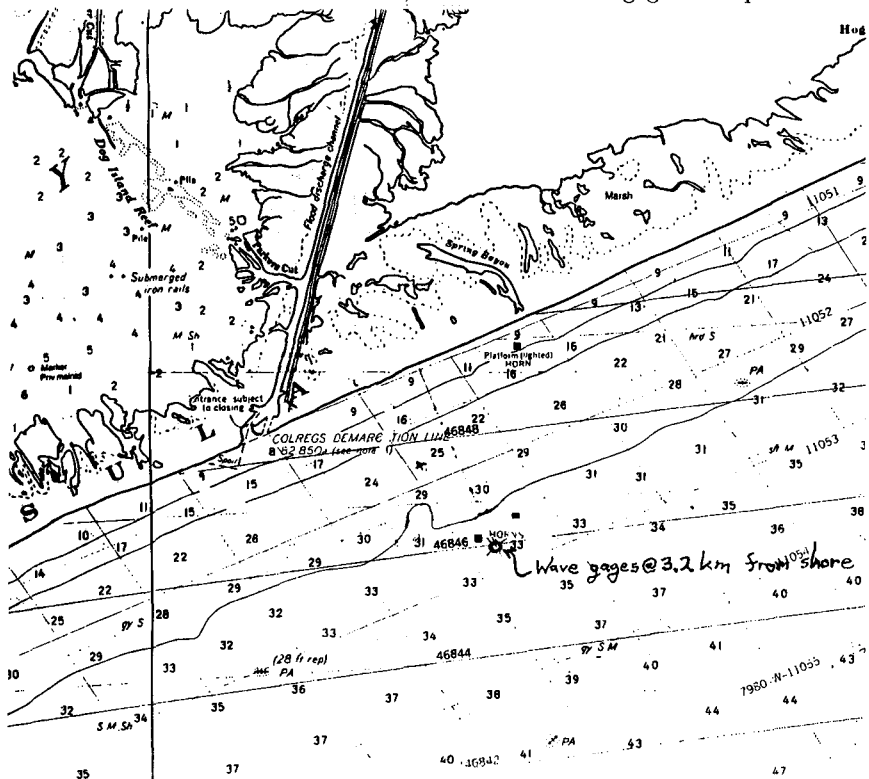


Figure 2. Topographic map of the region offshore of the jetties, with wave gage site marked at 3.2km offshore and 10m depth (from NOAA/NOS Chart #11316, dated 31 May 1980).

The total-load alongshore sediment flux is determined by shoaling the ra-

radiation stress measured at offshore directional wave gages. The offshore directional wave field was measured by both "puv" collocated pressure and current sensors and by a new three-pressure-sensor Directional Wave Gage (Howell, 1992). For both sensor types, the measured wave data were first surface-corrected with the standard  $\cosh k(z+h)/\cosh kh$  factor and then used to compute energy/frequency/direction spectra with the standard methods of Longuet-Higgins, Cartwright, and Smith (1963).

Once the direction/energy spectra are determined, they are used to estimate longshore sediment transport through the radiation-stress concept:

$$I_l = K C S_{xy} \quad (1)$$

where  $I_l$  is the immersed-weight longshore sediment flux,  $K$  is a coefficient (not necessarily constant, White and Inman, 1989),  $C$  is the wave phase speed, and  $S_{xy}$  is the longshore component of the cross-shore momentum flux, as determined from:

$$S_{xy} = E n \sin \alpha \cos \alpha \quad (2)$$

where  $E$  is the wave energy,  $n$  the ratio of group to phase speeds, and  $\alpha$  is the angle of wave approach relative to beach normal.

The energy was then shoaled over the topography using the most common technique of placing the energy summed over the spectrum into the peak band. Using Snell's Law, the direction of propagation was then altered at each 3m horizontal progression of the energy along the beach-profile rangeline between the gage and the breakpoint.

The procedure given above, using equations (1) and (2) and then shoaling the energy to the breakpoint, is equivalent to the "exact" method listed in the Shore Protection Manual (1984) as its Equation 4-40 (although the listed requirement for *deep* water wave angle, rather than the angle at the location where transport is desired, is apparently a mistake.) In addition to this exact method and three other functionally equivalent forms listed as equations 41, 42, and 43 in the Manual, there are four approximate methods for computing volumetric transport  $Q$ . These can be translated to immersed-weight transport  $I$  that we use, under the assumptions of constant densities, constant void ratios, and standard sand densities and voids, via  $I[N/s] = Q[yd^3/yr]/4356$ .

$$Q = 0.884 \rho g^{3/2} H_{sb}^{5/2} \sin 2\alpha_b \quad (3)$$

$$Q = 0.05 \rho g^{3/2} H_{so}^{5/2} (\cos \alpha_o)^{1/4} \sin 2\alpha_o \quad (4)$$

$$Q = 0.00996 \rho g^2 T H_{so}^2 \sin \alpha_b \cos \alpha_o \quad (5)$$

$$Q = 1.572 \rho g (H_{sb}^3/T) \sin \alpha_o \quad (6)$$

where  $\rho$  is fluid density,  $g$  gravity,  $H_s$  significant wave height,  $\alpha$  wave angle,  $T$  wave period,  $o$  the deep-water value, and  $b$  the breakpoint value. We also employed these four methods to compute longshore transport, using shoaled values (at "b") when the equations called for them. These four methods and the exact method were all compared to the sediment transport measured *directly* in the surfzone.

## Direct Method

The surfzone transport was measured by cross-shore integration of the point measurements from three synoptic multi-sensor platform arrays of Optical Backscatter Sensors (OBSs) (Downing, Sternberg, and Lister, 1981) and Electromagnetic Current Meters (ECMs), sonars, and pressure sensors. Figure 3 shows a plan view of the site with various platforms of gages drawn in the general areas where they were deployed.

### MCCP COLORADO RIVER, TEXAS

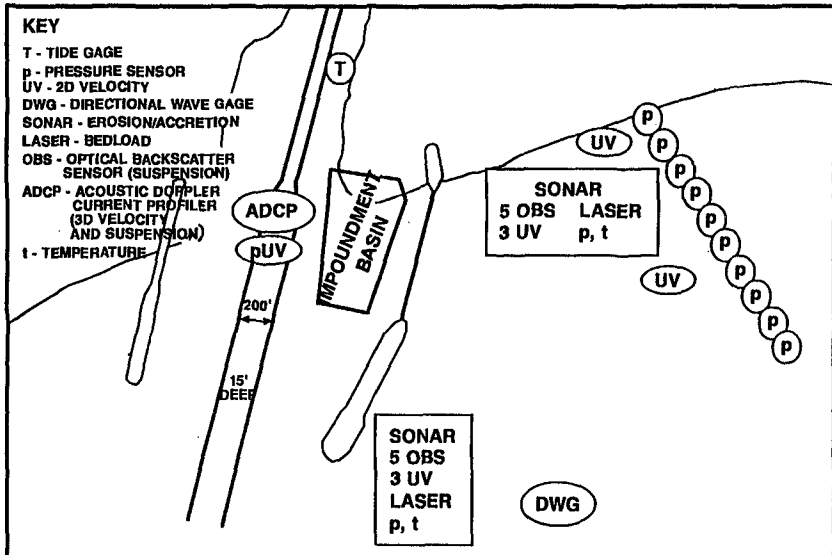


Figure 3. Areas of deployment of each gage type. Gage platforms are not to scale, but for visualization are drawn very large relative to the jetties. The lasers were replaced by micro-OBS gages for bedload.

The sediment concentration was measured with OBS2 optical backscatter sensors, which were each calibrated in a flow tank over a wide range of transport values. The sand from the site was sampled prior to each experiment and generally had a median size of 130 microns, with a size distribution that was always single-peaked. The sand from the site was used in the laboratory to calibrate the sensors over a wide range of transport values (from 1 to 300 grams per liter), both prior to and after each of the three experiments.

The currents were measured with standard 1-inch diameter Marsh-McBirney electromagnetic probes, calibrated just prior to use. Pressure sensors were used to determine the range of vertical integration for each platform, and also to determine when uppermost sensors were out of the water and thus not to be used.

The longshore sediment transport is the direct integration of the product of these two types of calibrated-sensor outputs, as measured in the surfzone:

$$I_l = (\rho_s - \rho)gN_o \int_0^{X_b} \int_0^n v(x, z)c(x, z)dzdx \tag{7}$$

where  $\rho_s$  is the sediment density,  $\rho$  the fluid density,  $g$  the acceleration of gravity,  $N_o$  the solids density (one minus porosity),  $v$  the longshore fluid velocity,  $c$  the sediment concentration, and the integral is taken over both the vertical surf depth and the cross-shore surfzone width.

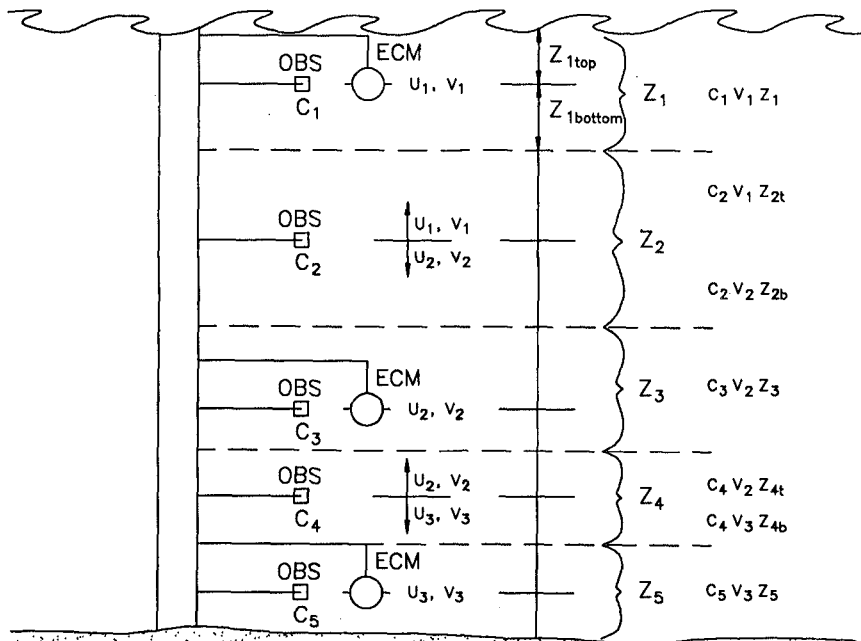


Figure 4. Regions of vertical integration of local sediment transport. Mid-points (dashed lines) between each gage of each type (both ElectroMagnetic Current meters and Optical Backscatter Sensors) separate each region.  $c$  = concentration,  $v$  = longshore velocity,  $z$  = vertical distance.

The above integration is first accomplished in the vertical at each platform location by vertically integrating the values of concentration  $c$ , longshore velocity  $v$ , and vertical range  $z$ , as shown in Figure 4. It is important to note that the vertical integration is performed at each time step of 0.2 seconds, and is thus unaffected by phenomena with longer time periods, such as bursts of sediment out of the boundary layer. Each sensor measures at one instant, and all the

instantaneous products of  $c$ ,  $v$ , and  $z$  are vertically summed before moving to the next 0.2s time step.

The direct measurements are also being used to test theories of suspended-load and total-load sediment transport, which will be done in other publications. These theories of sediment transport relate fluid forcing of waves or velocities to sediment flux on a "local" or point basis. The theories are tested by comparing the predicted transport from the theories with the measured surfzone transport.

## Results

The longshore transport rates from the exact method, the four approximate methods, and the direct method were all computed for the one-week experiments, during which the surfzone platforms were deployed. The rates are listed in the following two tables for the June 1991 and January 1992 experiments. Note the considerable difference in transport values between the different methods. Individual estimates often differ as to the *direction* of transport. It is obvious that the different methods cannot be relied upon to produce comparable results for any specific set of wave conditions. But this is not generally what coastal engineers want to know. The more pertinent question is whether on a long-term basis (years), the wave-based methods can produce comparable transports to the real (measured) rates. The accumulation of the transport over months and years is the sand next to jetties, in navigation channels, or in impoundment basins, such as in Figure 1. Means of coping with this integral of the transport over time are what must be engineered.

Correlations over the 26 time periods in Table 2 and the 24 time periods in Table 3 were computed between the radiation-stress methods and the measured transport. Simple linear regression of the form  $y = mx + b$  was used, where  $x$  are the radiation-stress methods, and  $y$  the measured values. Standard deviations were computed using N weighting, and thus the correlations are simply  $r = m\sigma_x/\sigma_y$ . Negative values represent anti-correlation. The  $r^2$  values are the fraction of the total variance in the data explained by the method.

All the results of this paper are summed up in Table 4. One can reach different conclusions as to the effectiveness of a particular method, depending on which data set one examines. The July 1991 data show that *all* radiation-stress methods poorly predict measured rates. (The  $r^2$  values are quite small.)

On the other hand, the January 1992 data show that all but one method do very well. All but one of the  $r^2$  values are very high. For the method that did poorly, there are a couple possible explanations. It is the easiest method to use, because it does not require shoaling the wave data, but uses only deep-water values and ignores the topography. Another possible explanation, as noted in the table's footnote, is that conservative data-acceptance criteria were applied, whereas all the other methods used all measured data.

In the methods that did well (explained a high fraction of the variance, as

indicated by  $r^2$ ), note that some represent *anti*-correlations, meaning they indicate the right variation, but the wrong longshore direction. In the preparation of this paper, considerable time was spent trying to find any errors in sign. But the signs reported in the table appear to be correct. In fact, it is easy to see by examining individual spectra, that the signs of the correlations are valid. For example, note the reversal in sign between Eq 4-47 and the other methods, for the very large transport rate during a storm, on 18 Jan 1992 (the bottom line in Table 3.) That method agrees with the measured transport direction, whereas the others do not. However, all agree that transport was very large. Thus the correlations agree with conclusions that can be reached by looking at individual data points in Tables 2 and 3.

The bottom half of Table 4 correlates the exact method with one of the approximate methods. Since we are no longer comparing to the measured transport, this allows us to use *all* the offshore wave data, increasing by two orders of magnitude the number of data points (and the sampling of different wave climates throughout the year.) In contrast to the short experiments, these large data sets *consistently* show the same results, no matter which year's data are applied. For the years shown, the  $r^2$  is always about 0.40, so each method contains 40% of the variance of the other method. This low value is not encouraging, since it is the hope of engineers using the Shore Protection Manual that they will obtain roughly the same results, regardless of which method they use.

Modifications to the SPM transport equations may be extracted from Table 4. The slope  $m$  would be a modification to the coefficient  $K$  (Eq. 1) via  $K = 0.7 m$  (since 0.7 was our  $K$  value used in this rms-wave-height data set). For example, Eq. 6 performs well in the Jan 92 data set, so a new  $K$  could be  $K = 0.7 m = 0.7(0.6668) = 0.47$ , *provided* a  $y$ -intercept were also added to the equation. So one might compute  $I$  from the original formula, and then  $I_{new} = mI_{old} + b$ , and in our example  $b$  is negative.

## Conclusions

**The method of computing radiation stress** is clearly of first-order importance, as illustrated by the discrepancy in output from the five methods examined.

**Predicting transport by shoaling the radiation stress** sometimes works very well in predicting transport, and at other times does quite poorly. The possible reasons for this are numerous, and we can only speculate. The wave gage could have been malfunctioning during one of the experiments. But since there are means for testing the reasonableness of the data, it is more likely that sometimes there are processes operating in the surfzone not represented by offshore waves, but at other times these processes are small (e.g., wind, river flow rates, river silt load, etc.).

**Not shoaling the energy over the topography** (just using the deep-water values directly) may worsen the predictive capabilities. Evidence the poor performance of Eq 4-45 (our Eq 4).

**To obtain accurate estimates** of sediment transport, one must do something more than place wave gages offshore. Measuring the transport directly is preferred, but this is tedious and expensive. The different methods of measuring a transport rate, such as tracers, electronic sensors, or extensive beach profiling, all have the same order of magnitude in cost. Spending time and money on means to reliably obtain directional wave data very close to the breakpoint would seem a worthwhile effort. The shoaling process is likely to represent a large portion of the accumulated error in the radiation-stress method.

**Individual transport estimates cannot be reliably performed.** Although certain methods produce reliable results *over many occurrences*, use of an individual wave spectrum to estimate sediment transport can result in huge error, frequently even predicting the wrong direction of longshore transport.

In another study, the main factor not included in the SPM equations that was found to improve *local* estimates of transport, was inclusion of a sediment threshold-of-motion criterion (White, 1987; White, 1989). "Local" refers to predictions and measurements at essentially one point in the horizontal, as opposed to the "global" methods tested in this paper. In comparing predictions of different local transport theories with transport measured by sand tracer, it was found that agreement on direction of transport improved from 70% to 100% of the experiments, once a threshold criterion was added to the theory. It would be interesting to see if this were also true of the "global" equations tested in this paper.

Table 2: Measured and Computed Longshore Transport Rates: July 1991

All transport values are total  $I_l$  in Newtons per second.

Positive transport is upcoast (roughly ENE) on heading 65 degrees geographic.

Date and Time	Measured	Exact SPM	Approximate SPM Methods			
	Longshore	Method	SPM	SPM	SPM	SPM
	Surfzone Transport Eq. (3)	SPM Eq 4-40 (Eqs 1,2)	SPM Eq 4-44 (our Eq 3)	SPM Eq 4-45** (our Eq 4)	SPM Eq 4-46 (our Eq 5)	SPM Eq 4-47 (our Eq 6)
7/16/91 1100	91.5	-87.602	-597.910	-184.696	-402.412	-352.414
7/16/91 1400	17.4	5.557	-56.196	7.908	25.528	9.355
7/16/91 1700	-24.7	519.603	-24799.531	0.000	2386.853	-9238.986
7/17/91 0800	-9.0	3193.869	-79733.180	16971.643	14671.381	80159.672
7/17/91 1100	-8.7	-1490.971	75106.180	0.000	-6848.935	255138.078
7/17/91 1400	-5.8	2272.286	-88223.719	0.000	10437.991	-58378.953
7/18/91 0800	77.9	17.452	-168.193	0.000	55.347	-28.154
7/18/91 1100	91.2	-5.039	-369.507	0.000	-16.030	29.335
7/18/91 1400	14.6	-45.809	-93.181	0.000	-144.886	63.901
7/18/91 1700	18.8	-14.103	80.534	-28.691	-44.555	-26.928
7/18/91 2000	16.9	105.486	-680.172	135.104	332.024	1095.635
7/19/91 0800	281.2	-37.843	-47.146	-12.202	-119.570	-41.433
7/19/91 1100	267.7	-17.466	178.226	-44.099	-55.244	-49.373
7/19/91 1400	189.3	-40.244	-56.797	-110.643	-127.448	-220.015
7/20/91 0800	7.1	45.239	34.388	2.880	182.178	5.852
7/20/91 1100	34.7	-115.315	155.732	-20.051	-384.388	-52.606
7/20/91 1400	-140.9	-28.258	-76.787	-32.335	-89.106	-82.062
7/20/91 1700	392.8	37.447	-96.373	0.000	118.169	-56.893
7/21/91 0800	-187.7	-78.058	2.156	-2.934	-452.588	-7.262
7/21/91 0800*	-88.7	-78.058	2.156	-2.934	-452.588	-7.262
7/21/91 1100	11.8	-18.194	-20.979	-27.497	-57.423	-104.496
7/21/91 1100*	-97.7	-18.194	-20.979	-27.497	-57.423	-104.496
7/21/91 1100*	-171.0	-18.194	-20.979	-27.497	-57.423	-104.496
7/21/91 1700	-48.8	-17.595	99.275	0.000	-55.483	218.513
7/21/91 1700*	-36.5	-17.595	99.275	0.000	-55.483	218.513
7/22/91 0500	-143.4	-14.858	80.358	0.000	-46.850	169.555

\*: Some days had multiple estimates of measured transport that corresponded to one offshore spectrum.

\*\* : For low waves and very large wave angles, King set transport to zero in his method using Eq 4 (SPM Eq 4-45).

The computed transports are reported with far more significant digits than the method justifies, in order to retain digits until the rounding of the final result.



Table 3: Measured and Computed Longshore Transport Rates: January 1992

All transport values are total  $I_l$  in Newtons per second.

Positive transport is upcoast (roughly ENE) on heading 65 degrees geographic.

Date and Time	Measured Longshore Surfzone Transport Eq. (3)	Exact SPM		Approximate SPM Methods			
		Method SPM Eq 4-40 (Eqs 1,2)	SPM Eq 4-44 (our Eq 3)	SPM Eq 4-45** (our Eq 4)	SPM Eq 4-46 (our Eq 5)	SPM Eq 4-47 (our Eq 6)	
1/10/92 1500	-675.0	-0.000	-0.000	0.000	-0.000	-0.000	
1/10/92 1800	-733.5	0.082	0.020	0.000	0.613	-0.001	
1/11/92 0900	-297.0	0.329	0.111	0.000	2.453	-0.004	
1/11/92 1800	-189.0	0.072	-0.011	0.000	0.486	0.001	
1/11/92 1800*	-436.5	0.072	-0.011	0.000	0.486	0.001	
1/11/92 1800*	-423.0	0.072	-0.011	0.000	0.486	0.001	
1/12/92 1200	-2116.0	-0.000	0.000	0.000	0.000	0.000	
1/13/92 1200	166.5	-0.000	0.000	0.000	0.000	0.000	
1/13/92 1500	188.7	0.069	-0.004	0.000	0.586	-0.001	
1/14/92 0900	0.0	-0.000	0.000	0.000	0.000	0.000	
1/14/92 1200	0.0	-0.000	0.000	0.000	0.000	0.000	
1/14/92 1500	0.0	0.044	0.020	0.000	0.260	-0.001	
1/14/92 1800	0.0	-0.000	0.000	0.000	0.000	0.000	
1/15/92 0900	0.0	0.082	0.011	0.000	0.613	0.000	
1/16/92 1500	31.5	60.529	73.570	0.000	279.402	-102.966	
1/16/92 1800	115.5	26.672	-157.781	36.289	123.713	20.788	
1/17/92 1200	-472.5	30.006	-112.689	39.340	135.807	60.029	
1/17/92 1200*	-337.5	30.006	-112.689	39.340	135.807	60.029	
1/17/92 1200*	-891.0	30.006	-112.689	39.340	135.807	60.029	
1/17/92 1500	-1251.0	205.225	-446.378	388.386	947.329	2530.908	
1/17/92 1500*	-990.0	205.225	-446.378	388.386	947.329	2530.908	
1/17/92 1800	-1125.0	517.482	783.706	1252.541	2411.821	2213.608	
1/18/92 0900	-9976.0	1020.884	11451.572	0.000	4597.314	-12620.669	
1/18/92 0900*	-9444.8	1020.884	11451.572	0.000	4597.314	-12620.669	

\*: Some days had multiple estimates of measured transport that corresponded to one offshore spectrum.

\*\* : For low waves and very large wave angles, King set transport to zero in his method using Eq 4 (SPM Eq 4-45).

The computed transports are reported with far more significant digits than the method justifies, in order to retain digits until the rounding of the final result.

Table 4: Correlation of Radiation-Stress and Direct Transport Methods

Method being correlated with measured transport	$\mu$ Mean (N/s)	$\sigma$ Standard Deviation	m Slope of Regression	b Inter- cept (N/s)	r Corr. Coef.	$r^2$
July 1991 (number of spectra, n = 26)						
Measured transport	21.156	136.057				
Exact Eqs 1,2 predict	155.905	815.274	-0.0064684	22.164	-0.03876	0.00150
Approximate methods:						
Eq 3 predicts	-4585.514	27631.621	0.0001806	21.984	0.03667	0.00134
Eq 4 predicts	638.325	3267.050	-0.0019586	22.406	-0.04703	0.00221
Eq 5 predicts	720.832	3742.993	-0.0013555	22.133	-0.03729	0.00139
Eq 6 predicts	10317.407	52714.162	-0.0001128	22.320	-0.04372	0.00191
January 1992 (number of spectra, n = 24)						
Measured transport	-1202.3	2622.1				
Exact Eqs 1,2 predict	131.156	290.880	-8.4357	-95.919	-0.9358	0.8757
Approximate methods:						
Eq 3 predicts	935.915	3191.167	-0.8049	-451.961	-0.9797	0.9597
Eq 4 predicts	90.984	264.404	0.1688	-1217.674	0.0170	0.0003
Eq 5 predicts	596.568	1314.813	-1.8587	-93.502	-0.9320	0.8686
Eq 6 predicts	-744.500	3688.519	0.6668	-705.921	0.9328	0.8702
All days Dec 90 thru July 91, 8 times per day (number of spectra, n = 1823)						
Exact Eqs 1,2:	-108.054	615.681				
Approx. Eq 4:	-135.514	1224.382				
Exact Eqs 1,2 predict results of approximate Eq 4			1.2017	14.8267	0.6043	0.3652
All days Jan 92 thru Dec 92, 8 times per day (number of spectra, n = 2009)						
Exact Eqs 1,2:	-41.7032	216.9353				
Approx. Eq 4:	-75.7956	304.8631				
Exact Eqs 1,2 predict results of approximate Eq 4			0.9434	-0.4755	0.6743	0.4547

For low waves and very large wave angles, King set transport to zero in his method using Eq 4 (SPM 4-45).

The computed transports are reported with far more significant digits than the method justifies, in order to retain digits until the rounding of the final result.

## Acknowledgments

The considerable efforts in obtaining the large field data set at Colorado River were performed by the capable staff of the Prototype Measurement and Analysis Branch of CERC, including Bill Grogg, Doug Lee, Rhonda Lofton, Bill Kucharski, Chuck Mayers, Debbie Shafer, and Kerry Taylor. The data-collection systems were designed and built by Ralph Ankeny, Bill Grogg, Gary Howell, and J. Rosati. The analysis of the surfzone time-series data and computation of measured transport were completed by Joon Rhee. The computations of transport potential using deep-water methods (SPM Eq. 4-45) were provided by David King. All other transport computations, including the extensive work in shoaling the wave data, were performed by Rhonda Lofton. Without her considerable efforts in data analysis, this paper would not have been possible.

The tests described and the resulting data presented herein, unless otherwise noted, were obtained from research conducted under Monitoring Completed Coastal Projects (Colorado River, Texas), Coastal Research (Field Tests of Sediment-Transport Theories), and Coastal Inlets Research Programs of the US Army Corps of Engineers at the Waterways Experiment Station. Permission was granted by the Chief of Engineers to publish the conference Abstract. Clearance for the full paper was requested, but has not been received as of the submission date. Thus this paper should be considered a private submission.

## References

- Downing, J.P., R.W. Sternberg, and C.R.B. Lister (1981). New instrumentation for the investigation of sediment suspension processes in the shallow marine environment. *Marine Geology*, v 42, p 19-34.
- Howell, G.L. (1992). A new nearshore directional wave gage. *Proc. 23rd ICCE, Venice*, ASCE, p 295-307.
- Longuet-Higgins, M.S., D.E. Cartwright, and N.D. Smith (1963). Observations of the directional spectrum of sea waves using the motions of a floating buoy. *Ocean Wave Spectra*, Prentice-Hall, Inc., Englewood Cliffs, NJ, p 111-136.
- Shore Protection Manual (1984). US Army Corps of Engineers' Coastal Engineering Research Center, US Govt Printing Office, 2 vols.
- White, T.E. (1987). Nearshore sand transport. *University of California*, Ph.D. dissertation, 210 pp.
- White, T.E. (1989). "Using sediment-threshold theories in waves and currents," *Sediment Transport Modeling Proc.*, Inter. Symposium of HY Div, ASCE, p 248-253.
- White, T.E. and D.L. Inman (1989). Measuring longshore transport with tracers. Ch 13 in R.J. Seymour, Ed., *Nearshore Sediment Transport*, Plenum Pub., New York, p 287-312.

## CHAPTER 203

### Suspended Sediment Concentration Profiles under Non-breaking and Breaking Waves

Rattanapitikon Winyu and Tomoya Shibayama <sup>1</sup>

#### Abstract

Simple formulas to predict time-averaged suspended sediment concentration are formulated using steady diffusion equation. Empirical formulas are developed to compute reference concentration (boundary condition) and diffusion coefficient. For suspended sediment concentration in the field, the same formulas with regular wave condition can be applied by using root mean square wave height and average wave period. Total 139 data sets are used for calibration of empirical formulas and 175 data sets are used for verification.

#### Introduction

The need for reliable prediction of sediment transport and beach profile change is increasing due to an increasing of human activity on the coast. In order to predict the suspended sediment transport rate, it is necessary to predict the vertical distribution of sediment concentration and fluid velocity accurately. This study focuses an attention on the sediment concentration distribution. Sediment concentration is important not only for computing sediment transport rate but also for significant effect on the water quality for domestic and industrial use. From the last few decades, a number of models and experimental investigation have been performed to draw a clearer picture of suspended sediment concentration. Considerable amount of knowledge has been accumulated so far. However, it has not reached a satisfactory level. This is resulted from the unclear knowledge of movable sand layer and diffusion coefficient. At the present stage of knowledge, any type of model must be based on empirical or semi-empirical formula calibrated from the experimental results. For the prac-

---

<sup>1</sup>Dept. of Civil Eng., Yokohama National University, Hodogaya-ku, Yokohama 240, Japan

tical purposes, simple formulas may be more suitable than the complex ones (if it yields the accuracy in the acceptable range).

Based on wide range of wave and sediment conditions, Shibayama and Winyu (1993) proposed simple formulas to predict time-averaged concentration profiles under both non-breaking and breaking waves. The present study mainly focusses on the application and verification of the formulas. The measured surf zone concentration profile in prototype scale wave flume of Kajima et al. (1983) and in the field of Nielsen (1984) are used in this study. For some background information, a brief introduction of the formulas is also presented.

### Governing Equation

The vertical distribution of suspended sediment is calculated by the diffusion equation. By considering time averaged value of concentration and neglecting convection and horizontal diffusion, the diffusion equation can be written as:

$$cw_s + \epsilon_s \frac{\partial c}{\partial z} = 0 \quad (1)$$

where  $c$  is the time averaged sediment concentration;  $w_s$  is the falling velocity;  $\epsilon_s$  is the diffusion coefficient; and  $z$  is the vertical coordinate. To solve the diffusion equation, concentration at reference level should be given as a boundary condition, and the diffusion coefficient should also be known.

### Reference Concentration under Non-breaking and Breaking Waves

The reference concentration is defined at the level where the concentration can be measured without disturbance to the bed formation. The formula for predicting reference concentration is derived by applying transport rate formula of Watanabe (1982) and dimensional analysis (for more details, see Shibayama and Winyu, 1993). Total thirteen sources of published experimental results, totally 139 experiments, are used to calibrate the formulas. Table 3.1 shows the experiments which are used in formula calibration. As a result, the formula for computing reference concentration is given as:

$$c_r = \frac{10 (\psi - 0.05)\nu}{3 r \sqrt{(s-1)gd}} \quad (2)$$

where  $c_r$  is the reference concentration at  $z = r$ ;  $r$  is the reference level; The reference level is equal to half of ripple height above the ripple crest for vortex ripple case and equal to a hundred times of sand diameter above the mean bed for flat bed (i.e., breaking wave case);  $\psi$  is the grain Shield parameter;  $s$  is the relative density of sediment;  $d$  is the sand diameter and  $\nu$  is the fluid kinematic viscosity. The comparison between measured and computed reference concentration,  $c_r$ , is shown in Fig. 1. Figure 1 shows that about 80 percent of the predicted ones are within factor two.

Table 1: Experiments for suspended sediment concentration study.

No	Sources	Total No.	Legend	Wave condition
1	Bosman and Steetzel (1986)	3	B	regular, non-breaking
2	Deigaard et al. (1986)	6	G	regular, breaking
3	Dette and Uliczka (1986)	8	D	regular, breaking
	Dette and Uliczka (1986)	3	U	irregular, breaking
4	Hayakawa et al. (1983)	4	Y	regular, non-breaking
5	Horikawa et al. (1982)	7	H	regular, non-breaking
6	Irie et al. (1985)	27	I	regular, non-breaking
7	Nakato et al. (1977)	3	N	regular, non-breaking
8	Nielsen (1979)	44	P	regular, non-breaking
9	Sato et al. (1990)	14	T	regular, breaking
10	Sawamoto et al. (1981)	4	S	regular, non-breaking
11	Skafel and Krishnappan (1984)	8	K	regular, non-breaking
12	Sleath (1982)	4	L	regular, non-breaking
13	Vongvisessomjai (1986)	4	V	regular, non-breaking

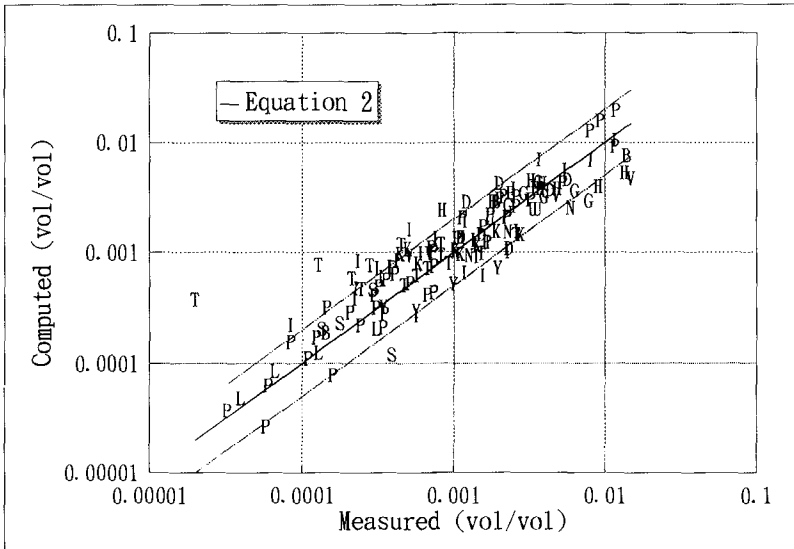


Figure 1: Comparison between measured and computed reference concentration under non-breaking and breaking waves,  $c_r$ , (legend see Table 1).

### Concentration Profiles under Non-breaking Waves

Under non-breaking waves, high concentration areas of suspended sand are usually confined within the thin layer above the bottom, the thickness of which is usually about three ripple-heights or a few hundred times of grain diameter above the bed in laboratory tests and field measurements. Most of the previous experimental results show that if very small concentrations are neglected, the time averaged concentration profile fits well with the exponential form which is derived from steady diffusion equation (Eq. 1) under the assumption that the diffusion coefficient,  $\epsilon_s$ , is independent of vertical coordinate,  $z$ . After the integration of Eq. 1, the analytical solution is expressed as:

$$c(z) = c_r \exp\{-w_s(z - r)/\epsilon_s\} \quad (3)$$

Equation 3 shows that the relation between  $\ln(c)$  and  $z$  is the straight line with the gradient of  $-w_s/\epsilon_s$ .

At present, the knowledge of diffusion coefficient,  $\epsilon_s$ , is very limited, an application of empirical formula cannot be avoided. The difficulty of this approach is to find out the way to relate the diffusion coefficient with flow and sediment properties. From the previous empirical formulas of Sleath (1982), Skafel and Krishnappan (1986), and Nielsen (1988), we may assume that the diffusion coefficient  $\epsilon_s$  is a function of the following quantities:

$$\epsilon_s = f(u_b, A_b, \nu, w_s, d, s, f_w, \eta) \quad (4)$$

where  $f$  is the function;  $u_b$  is maximum orbital velocity;  $A_b$  is the orbital amplitude;  $f_w$  is the wave friction factor;  $\eta$  is the ripple height.

Experimental data of non-breaking wave cases, which shown in Table 1 (totally 108 cases), are used to calibrate the empirical formula. From dimensional analysis, using the experimental data of non-breaking wave cases in Table 1, the following formula is fitted well with the measured ones (see Fig. 2).

$$\epsilon_s = 0.21 u_* A_b \left(\frac{w_s}{u_*}\right)^2 \left(\frac{\eta}{d}\right)^{0.5} d_*^{-1.5} \quad (5)$$

where  $u_*$  is the maximum bed shear velocity; and  $d_* = d(sg/\nu^2)^{1/3}$  is the particle parameter. Eq. 5 is kept in the dimensionless form as in the analysis. Since  $u_*$  can be canceled out,  $\epsilon_s$  is not reverse proportional to  $u_*$ .

Figure 2 shows that about 80 percent of predicted diffusion coefficient,  $\epsilon_s$ , are within factor 1.5. Examples of measured and computed concentration profiles under non-breaking waves are shown in Fig. 3.

It should be mentioned that the exponential form of suspended concentration profile is valid within the thin layer (about few hundred times of sand diameter above the bed). As a results, Eq. 3 can be used to predict only the high concentration near the bed.

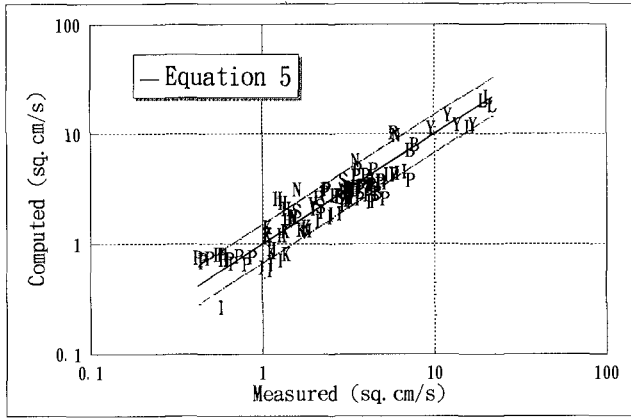


Figure 2: Comparison between measured and computed diffusion coefficient for non-breaking wave cases (legend see Table 1).

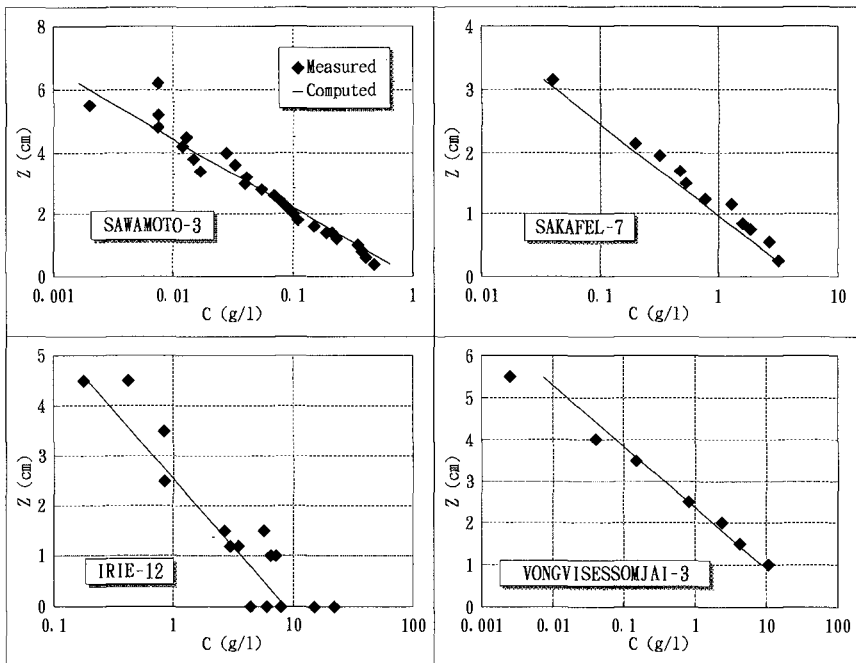


Figure 3: Examples of measured and computed concentration profiles under non-breaking waves of each data source.



### Concentration Profiles under Breaking Waves

The turbulence generated by the breaking waves causes a significant increase in the amount of suspended sediments compare to non-breaking waves of the same wave conditions and water depth. Moreover, the effect of turbulence due to breaking waves changes the shape of concentration profile (see Nielsen, 1978, Fig. 5) and the exponential form of concentration profile is not found. Thus, in breaking wave cases, we can not assume that the diffusion coefficient is constant as we assumed in non-breaking wave cases.

According to the experimental results, Okayasu (1989) suggested the linear distribution of eddy viscosity,  $\epsilon$ , as the function of the rate of energy dissipation due to wave breaking,  $D_B$ . By assuming diffusion coefficient proportional to the eddy viscosity of the flow and incorporating the diffusion coefficient caused by shear in wave field, the total diffusion coefficient,  $\epsilon_{sb}$ , is expressed as:

$$\epsilon_{sb} = [k_a u_* + k_b (D_B / \rho)^{1/3}] z \quad (6)$$

where  $k_a$  and  $k_b$  are the constants and  $D_B$  is the rate of energy dissipation. From the bore model, we can set  $D_B = \rho H^3 g / (4Th)$ .

After integration of the diffusion equation (Eq. 1), the analytical solution of concentration profile can be written in the following form:

$$c(z) = c_r \left( \frac{r}{z} \right)^M \quad (7)$$

$$M = \frac{w}{[k_a u_* + k_b (D_B / \rho)^{1/3}]} \quad (8)$$

From the best-fit technique, using breaking wave data in Table 1 (totally 29 data sets), the following constant parameters are recommended.

$$k_a = 0.04, \\ k_b = \begin{cases} 0.144 & \text{spilling breaker,} \\ 0.216 & \text{spilling-plunging transition breaker,} \\ 0.450 & \text{plunging breaker.} \end{cases}$$

Figure 4 shows the measured and computed parameter  $M$ . Examples of measured and computed concentration profiles under breaking waves are shown in Fig. 5.

It should be noted that Eq. 6 is valid if the turbulent due to the breaking waves can uplift the sediment throughout the water depth. Equation 5 should be used with care for coarse sand (i.e.,  $d > 0.55$  mm) and certainly it can not be used in gravel bed material. Also it can not be used to compute concentration at the bed ( $z = 0$ ).

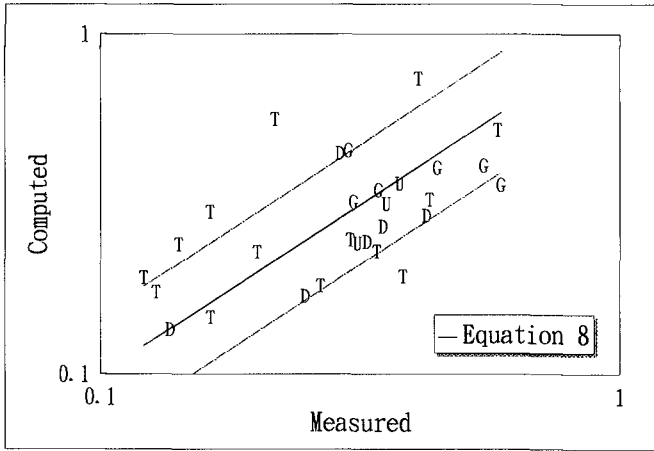


Figure 4: Comparison between measured and computed parameter  $M$  (legend see Table 1).

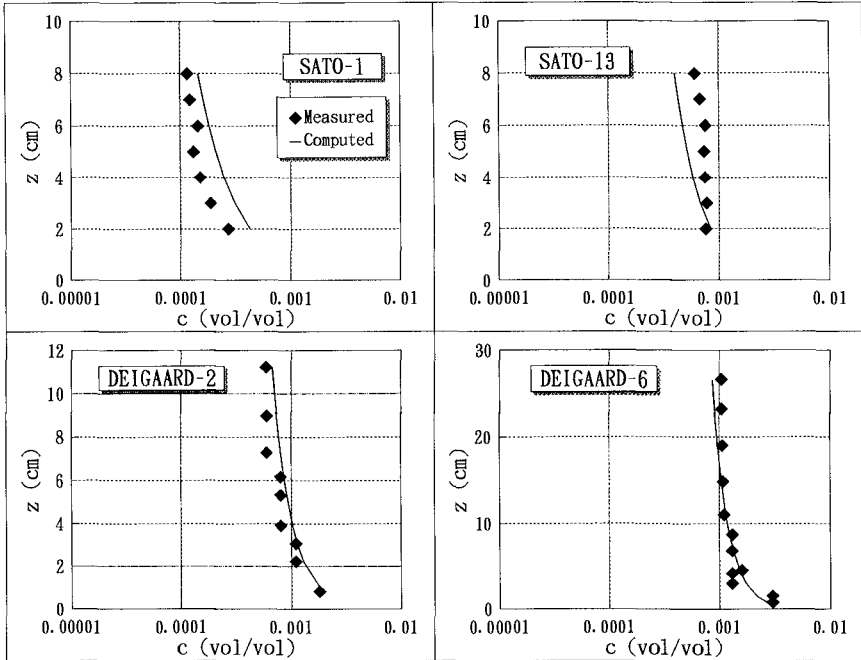


Figure 5: Predicted concentration profiles under breaking waves in comparison with the laboratory data of Deigaard et al. (1986), Sato et al. (1990).

### Verification with Prototype Scale Measurements

In order to confirm an empirical formula, wide ranges of experimental results are necessary in the calibration or verification. The objective of this section is to modify and examine the validity of the Shibayama and Winyu (1993) formulas by using the measured surf zone suspended concentration of a prototype scale wave flume which were performed by Kajima et al. of Central Research Institute of Electric Power Industry (CRIEPI) in 1983. The CRIEPI experiments were carry out under regular wave motion in a large wave flume (205 m long, 3.4 m wide, and 6 m deep). The CRIEPI experimental conditions that used in this section are shown in Table 2. The suspended concentrations were measured, by suction type concentration meter, at various sections along the flume. However, not many points were measured in the vertical direction of each section. Also lowest measuring level is not very near to the movable bed. This may because of the difficulty to measure the concentration very near to the bed accurately. The data may difficult to be used in formula calibration but can be used for formula verification.

The proposed formula assumed that  $\epsilon_{sb} \propto (D_B/\rho)^{1/3}$  and  $D_B$  is computed from the bore model which valid only inside the surf zone (full developed surface roller). Therefore if we use bore model to compute the rate of energy dissipation,  $D_B$ , near the recovery zone where the surface roller is not fully developed, the predicted  $\epsilon_{sb}$  is expected to be over-estimated and also it will yield the over-estimation of suspended concentration at the level above the reference level. To avoid this problem, energy dissipation may be computed from the measured wave height transformation, based on linear wave theory, as:

$$D_B = -\frac{\partial(Ec_g)}{\partial x} \quad (9)$$

where  $E = \rho g H^2/8$  is the wave energy;  $c_g$  is the group velocity; and  $x$  is the horizontal coordinate in wave direction.

Question may be asked that whether energy dissipation computed from bore model and from Eq. 9 are the same or not (in the case of no reformation zone). For verification, measured wave height transformation inside the surf zone (no reformation zone) of Hansen and Svendsen (1984), Okayasu et al. (1988), Sato et al. (1988 and 1989) are used. Figure 6 shows that energy dissipation computed from bore model and Eq. 9 give approximately the same results. Therefore the energy dissipation rate computed from the measured wave height, based on linear wave theory, will be used in the following analysis. However, due to the fluctuation of measured wave heights, the computed energy dissipation rates in some points are negative. So, in the present study, the fluctuated wave heights are smoothed before using for computing energy dissipation rates from linear wave theory.

For diffusion coefficient caused by breaking waves inside the transition zone, the eddy viscosity (or diffusion coefficient) at the breaking point cannot be

incorporated with the same manner as in the inner zone (Okayasu, 1989). From the analysis of undertow data of Nadaoka et al. (1982) and Okayasu (1988) (based on eddy viscosity model), the coefficient of turbulent eddy viscosity,  $K$ , increases linearly from 0.3 at the breaking point to 1 at the transition point. By assuming no vortex ripple occur in the surf zone, the final formula for computing sediment concentration profile can be expressed as:

$$c(z) = \frac{10}{3} \frac{(\psi - 0.05)\nu}{100d\sqrt{(s-1)gd}} \left( \frac{100d}{z} \right)^{w/[0.04u_* + 0.144K(D_B/\rho)^{1/3}]} \quad (10)$$

where  $K$  is the coefficient varies linearly from 0.3 at breaking point to 1 at transition point;  $D_B$  is the energy dissipation computed from measured wave height based on linear wave theory (Eq. 9).

The verification results for all of the measuring points, totally 149 sets, 645 points, are shown in Fig. 7. The examples of topography, wave height and concentration profile variations along the cross-shore direction are shown in Figs. 8-11. Fig. 7 shows that about 80 percent of predicted concentrations are within the factor 3, which can be considered to be well estimation in the field of sediment concentration profile. Since the accuracy of computed reference concentration is within the factor 2 (see reference concentration section), about 2/3 of error in Fig. 7 is expected to be caused by the formula that used for computing reference concentration. The left 1/3 is expected to cause by the formula for computing the distribution of concentration (parameter  $M$ ). Based on the above consideration, for excellent prediction of concentration profiles, the formula for computing reference concentration should be the main target of improvement for the next step.

Table 2: Experimental conditions and number of data sets for verification.

Case	$d_{50}$ (cm)	$m_b$	$T$ (s)	$H_i$ (cm)	$h_i$ (cm)	No. of data set
3.1	0.027	5/100	9.1	107.0	450.0	10
3.2	0.027	5/100	6.0	105.0	450.0	11
3.3	0.027	5/100	12.0	81.0	450.0	11
3.4	0.027	5/100	3.1	154.0	450.0	13
4.1	0.027	3/100	3.5	31.0	350.0	7
4.2	0.027	3/100	4.5	97.0	400.0	9
4.3	0.027	3/100	3.1	151.0	400.0	26
5.2	0.027	2/100	3.1	74.0	350.0	25
6.1	0.027	10/100	5.0	166.0	400.0	27
6.2	0.027	10/100	7.5	112.0	450.0	10

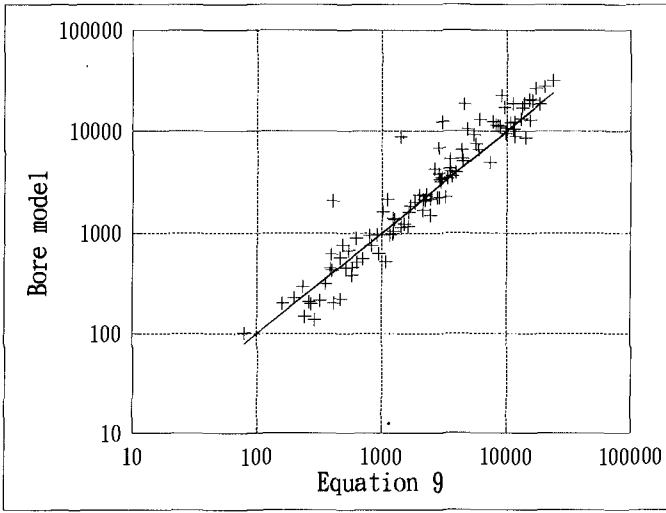


Figure 6: Comparison between computed enegy dissipation from bore model and Eq. 9 (laboratory data from Hansen and Svendsen, 1984; Okayasu et al., 1988; and Sato et al. 1988 and 1989).

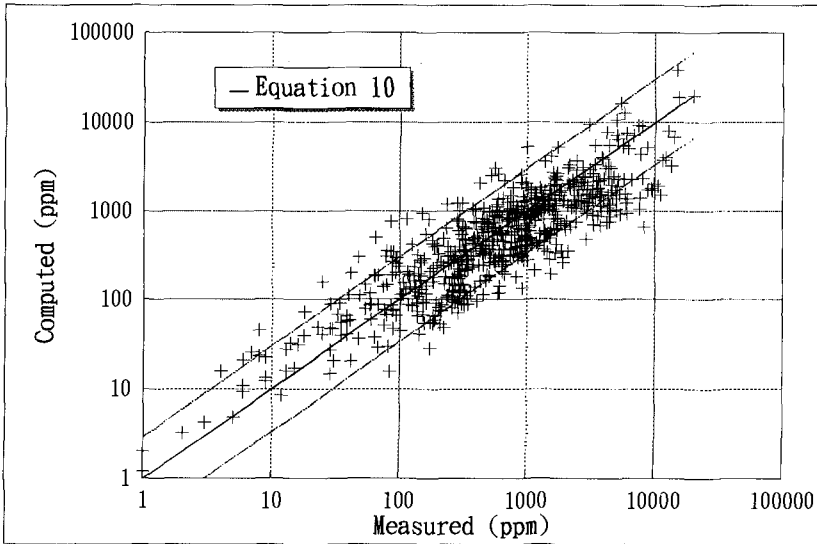


Figure 7: Computed and measured concentration for all of the measuring points (laboratory data from Kajima et al., 1983).

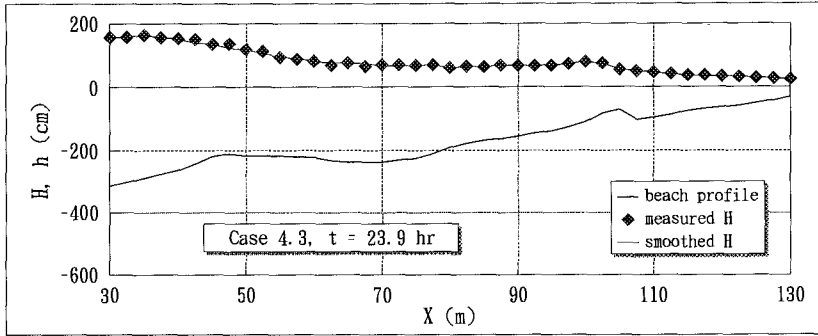


Figure 8: Measured bottom topography and wave height variation (laboratory data from Kajima et al., 1983, case 4.3, time = 23.9 hr).

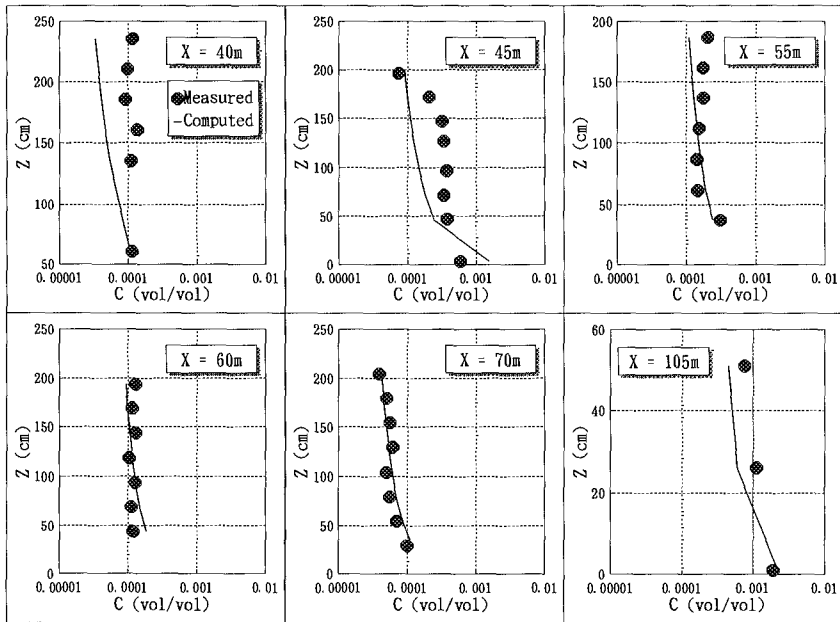


Figure 9: Computed and measured concentration profiles (laboratory data from Kajima et al., 1983, case 4.3, time = 23.9 hr).

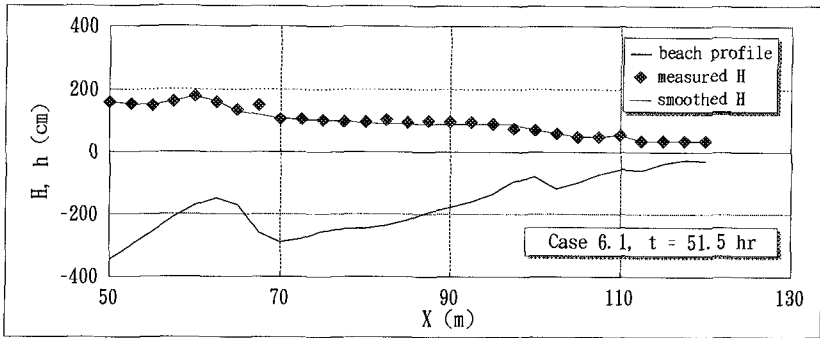


Figure 10: Measured bottom topography and wave height variation (laboratory data from Kajima et al., 1983, case 6.1, time = 51.5 hr).

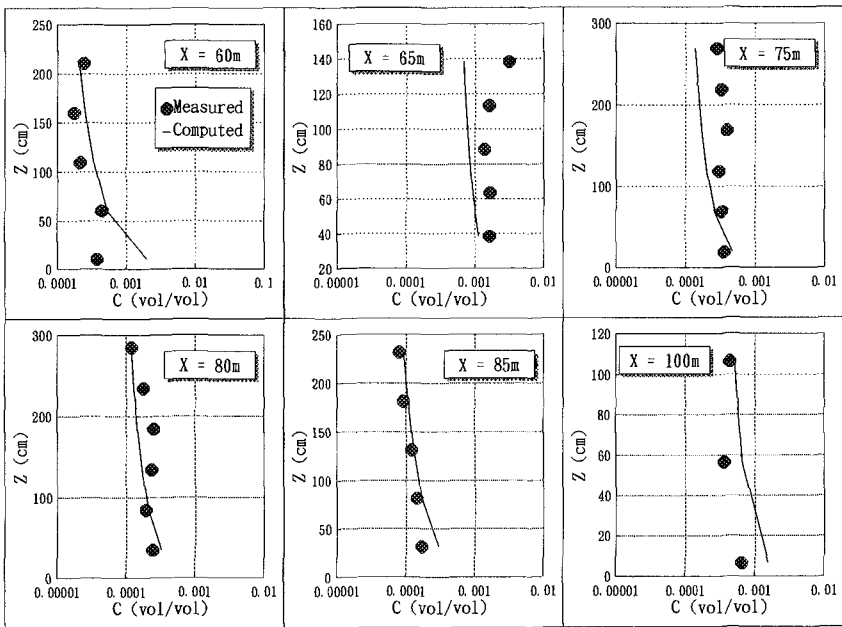


Figure 11: Computed and measured concentration profiles (laboratory data from Kajima et al., 1983, case 6.1, time = 51.5 hr).

### Verification with Field Measurements

Although, the Shibayama and Winyu (1993) formula is developed from the data measured in laboratory, it may also be used to predict the sediment concentration in the natural beach. The objective of this section is to apply Shibayama and Winyu (1993) formula to predict surf zone sediment concentration in the natural beach. Nielsen (1984) measured sediment concentration and hydraulic properties on several beaches and locations in Australia. Total 26 concentration profiles are measured under breaking wave conditions. For each measuring location, 7 elevations suction type is used to measure sediment concentration and the sampling time is about 3 minutes. The selected working depth is about 1.5 m and the measurement started from about 1 cm above the bed. For more details of measured concentration, hydrodynamic and sediment data, please see Nielsen (1984).

By assuming all of the measured locations are within the inner surf zone and there is no vortex ripple, the formula for predicting sediment concentration profiles can be expressed as:

$$c(z) = \frac{10}{3} \frac{(\psi - 0.05)\nu}{(100d)\sqrt{(s-1)gd}} \left( \frac{100d}{z} \right)^{w/[0.04u_* + 0.144\{H^3g/(4Th)\}^{1/3}]} \quad (11)$$

where all variables are calculated based on linear wave theory.

To compute concentration profiles, under irregular wave, from Eq. 11, representative wave height and wave period should be specified. By trial and error of various representative wave height and wave period, root mean square wave height (assuming Rayleigh distribution) and average wave period gives a good prediction on concentration profiles. The comparison between measured and computed sediment concentration for all of the measuring points (26 data sets) is shown in Fig. 12. Examples of predicted concentration profiles are shown in Fig. 13. Fig. 12 shows that about 70 percent of predicted concentrations are within the factor 3, which can be considered reasonably well estimation for the field measurements. However, the number of experimental results may not enough to confirm the ability of the present formula. In the further study, more field experimental results are required to check the ability of present formula.

### Conclusion

Empirical formula of Shibayama and Winyu (1993) has been applied to compute surf zone concentration profiles in prototype scale wave flume experiments of Kajima et al. (1983) and in the field experiments of Nielsen (1984). The computed results show reasonable agreement with the experimental results.



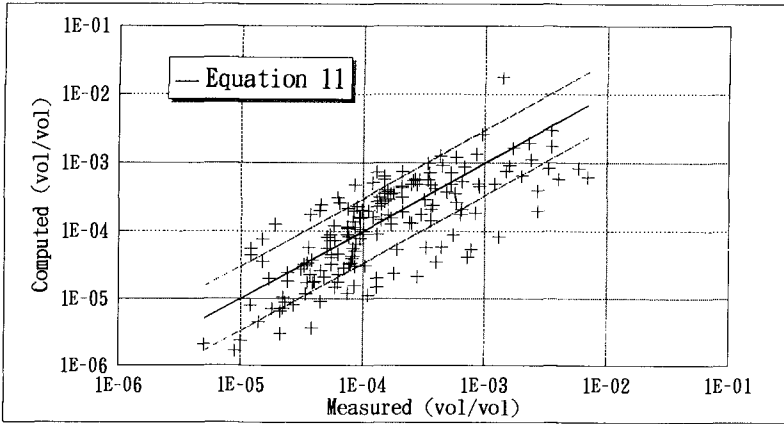


Figure 12: Computed and measured concentration for all of the measuring points (field data from Nielsen, 1984).

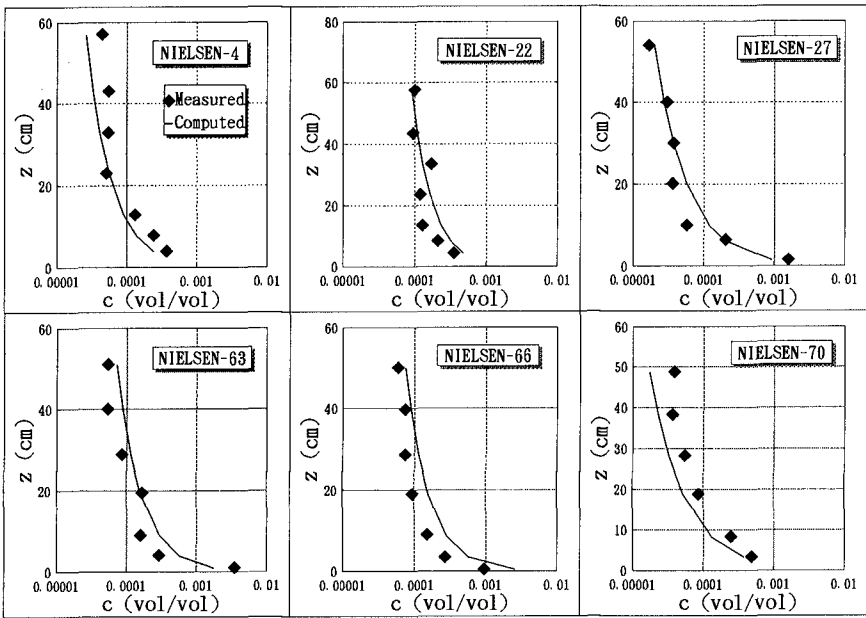


Figure 13: Examples of computed concentration profiles (field data from Nielsen, 1984).

References

- Hansen, J. Buhr and Svendsen I.A. (1984): "A theoretical and experimental study of undertow." *Proc. 19th Coastal Engineering Conf., ASCE*, pp. 2246-2262.
- Kajima, R., Shimizu, T., Maruyama, K., and Saito, S. (1983): "On-offshore sediment transport experiment by using large scale wave flume." Collected data No. 1-8, Central Research Institute of Electric Power Industry, Japan (in Japanese).
- Nadaoka, K, Kondoh, T., and Tanaka, N. (1982): "The structure of velocity field within the surf zone reveal by means of laser-doppler anemometry." *Report of The Port and Harbour Research Institute*, Vol. 21, No. 2, pp. 50-102 (in Japanese).
- Nielsen, P., Svendsen, I. A., Staub, C. (1978): "Onshore-offshore sediment movement on a beach." *Proc. 16th Coastal Engineering Conf., ASCE*, pp. 1475-1492.
- Nielsen, P. (1984): "Field measurements of time-averaged suspended sediment concentrations under waves." *Coastal Engineering*, No. 8, pp. 51-72.
- Okayasu, A., Shibayama, T., and Horikawa, K. (1988): "Vertical variation of undertow in the surf zone." *Proc. 21st Coastal Engineering Conf., ASCE*, pp. 478-491.
- Okayasu, A. (1989): "*Characteristics of Turbulence Structure and Undertow in Surf Zone.*" Dr. Eng. Dissertation, Univ. of Tokyo, Japan.
- Sato, S., Fukuhama, M., and Horikawa, K (1988): "Measurements of near-bottom velocities in random waves on a constant slope." *Coastal Eng. in Japan., JSCE*, Vol. 31, No. 2, pp. 219-229.
- Sato, S., Isayama, T., and Shibayama, T (1989): "Long-wave component in near-bottom velocities under random waves on a gentle slope." *Coastal Eng. in Japan., JSCE*, Vol. 32, No. 2, pp. 149-159.
- Shibayama, T., and Winyu, R. (1993): "Vertical distribution of suspended sediment concentration in and outside surf zone." *Coastal Eng. in Japan., JSCE*, Vol. 36, No. 1, pp. 49-65.

## CHAPTER 204

### Mass Transport and Orbital Velocities with LAGRANGEian Frame of Reference

Stefan Woltering<sup>1</sup> and Karl-Friedrich Daemrich<sup>2</sup>

#### Abstract

Measurements of surface elevations and horizontal orbital velocities in regular waves and two component wave groups were performed to prove the experimental validity of periodic wave theories for regular waves, and empirical engineering methods for calculations in irregular waves. Besides the traditional wave theories a LAGRANGEian approach was introduced. With this LAGRANGEian method for waves of finite height, based on the geometry of orbital paths given by STOKES wave theories, it is possible to extend the region of validity of STOKES theories over a wider range of wave parameter. The use of a superposition method with LAGRANGEian approach and the application to two component wave groups, results in the appearance of non linear interaction components in surface elevations and horizontal orbital velocities, which are in fair agreement as well with a 2nd order approach for irregular wave surface elevation as with the measurements of surface elevation and horizontal orbital velocities.

#### Introduction

Orbital velocities and mass transport velocities are important e.g. for the prediction of forces on coastal structures and the verification of transport models in the near shore region. Traditional wave theories (e.g. STOKES, DSFT-Dean Stream Function Theory etc.) and empirical calculation methods (e.g. modified potential theories) are used for theoretical treatment of regular waves and as a basis for simulation methods for irregular waves (e.g. linear superposition). A point of controversy is the selection of calculation methods to give best results and how to interpret mass transport velocity measurements, especially in wave flumes. Measurements of orbital velocities and mass transport velocities in a wave flume are compared with DSFT and calculations based on STOKES wave theories in different ways of interpretation. A LAGRANGEian approach is introduced by the authors.

---

<sup>1,2</sup> both University Hannover, SFB 205, Franzius Institut, Nienburger Straße 4,  
30167 Hannover, Germany.

Experimental Set-up

The research program was carried out in the Large Wave Flume (Großer Wellenkanal - GWK, University Hannover / Technical University Braunschweig - Length 324m, width 5m, water depth up to 5m) and the Wave Flume "Schneiderberg" (WKS - Length 120m, width 2m, water depth up to 1,2m) of the Franzius-Institute / University Hannover. The investigations were concentrated on waves in intermediate water depth. The measurements were taken with electromagnetic type velocity probes located in fixed positions below the still water level, and also with a velocity probe fixed to a Movable Instrument Carriage (MIC). The MIC follows the water surface with the velocity probe in a constant position below the moving surface. The waves were generated with a piston type wave maker using modified higher order control signals to reduce free parasitic wave components.

The LAGRANGEian approach

For simplicity the introduced LAGRANGEian approach is explained using the linear description of orbital paths. Figure 1 shows a principal sketch for the LAGRANGEian approach surface elevation. Figure 2 gives a detailed information concerning wave kinematics calculation for a fixed probe position below the deepest wave trough. During the calculation process the centre of the orbital path of the respective water particle will be determined for every time step  $\Delta t$  by linear iteration, using the formulas for  $\eta$  and  $\zeta$  given by the respective order of the theory (Equations 1, 2 for linear wave theory).

$$\zeta(x_0, z_0, t) = -\frac{H}{2} \cdot \frac{\cosh 2\pi(z_0 + d) / L}{\sinh 2\pi d / L} \cdot \sin 2\pi \left( \frac{x_0}{L} - \frac{t}{T} \right) \quad (1)$$

$$\eta(x_0, z_0, t) = \frac{H}{2} \cdot \frac{\sinh 2\pi(z_0 + d) / L}{\sinh 2\pi d / L} \cdot \cos 2\pi \left( \frac{x_0}{L} - \frac{t}{T} \right) \quad (2)$$

where  $\zeta(x, t)$  = horizontal location of water particle;  
 $\eta(x, t)$  = vertical location of water particle;  $L$  = wave length;  
 $H$  = wave height;  $x_0, z_0$  = still water position;  $T$  = wave period

The surface elevation results from the particle motion of the most upper water particles. The LAGRANGEian surface elevation for first order particle motion and deep water conditions contains higher harmonic components, which are nearly in the same magnitude, as calculated with STOKES higher order theories. For more shallower water STOKES higher order descriptions of orbital paths are used for the LAGRANGEian method. The calculation procedure is the same as outlined before. As the surface elevation results directly from the water particle movement, the kinematic free surface boundary condition is satisfied.

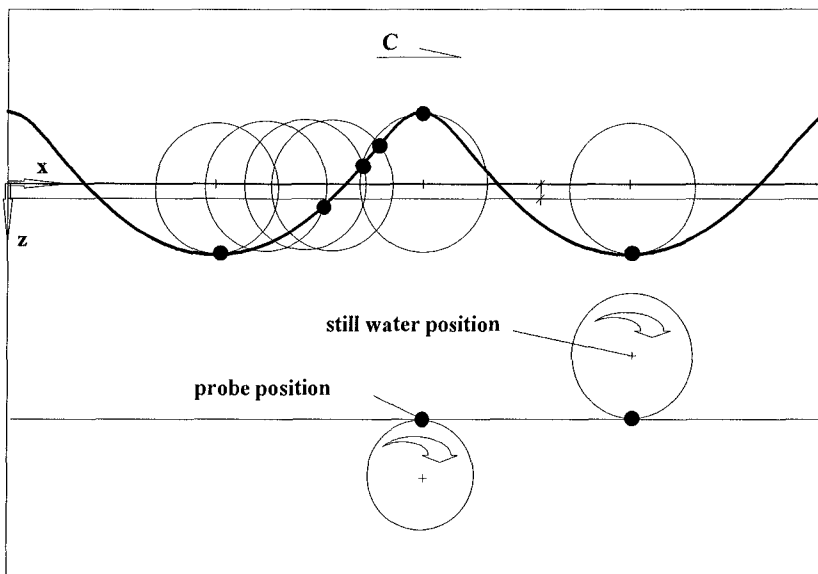


Figure 1. Principle sketch of LAGRANGEian surface elevation

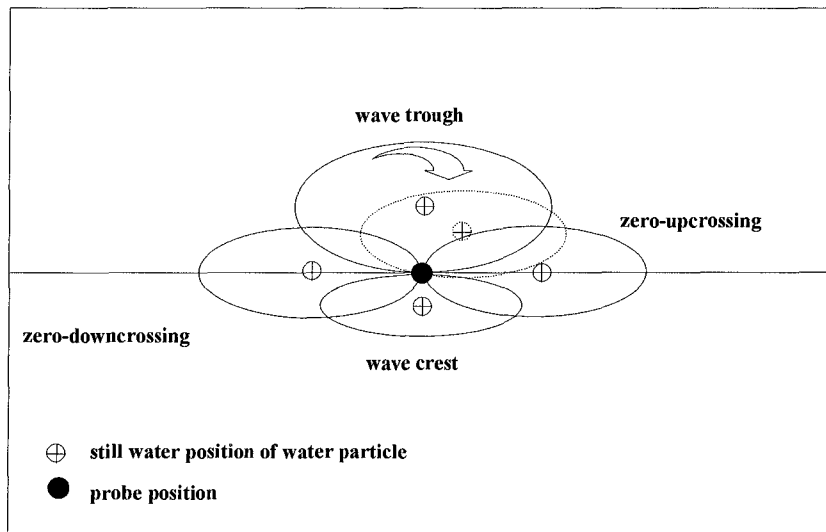


Figure 2. Principle sketch of LAGRANGEian method for the calculation of orbital velocities

The orbital velocity is calculated for the actual position of a water particle along its orbital path at the location of the probe for each time step. The velocity below wave crest results from the smaller orbit below the velocity probe, the velocity below wave trough relates to the wider orbital path above the probe position, and in the same way for all time steps between crest and trough. Figure 3 shows the time series of horizontal orbital velocity for a theoretical calculated example of 1st order LAGRANGEian approach in comparison to linear wave theory. Figure 4 is the amplitude spectrum for the difference curve of the both methods.

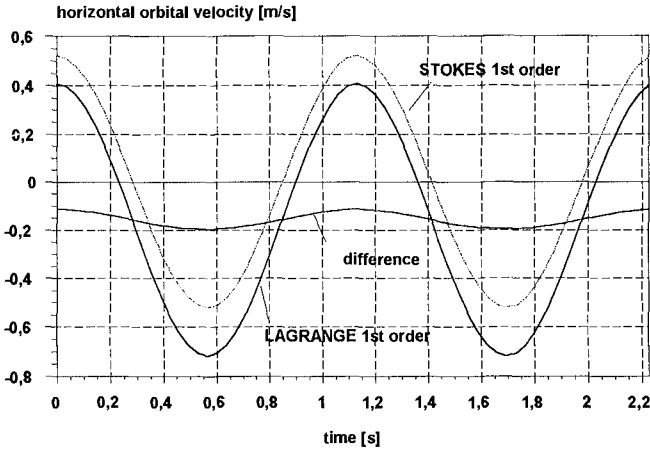


Figure 3. Time series of horizontal orbital velocity  
( $T=1.13s$ ,  $H=0.35m$ ,  $d=1.00m$ ,  $z=-0.20m$ )

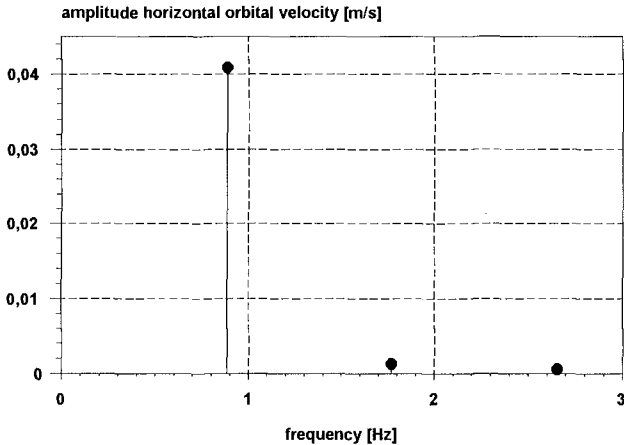


Figure 4. Fourier transformation of difference time series

The Fourier analysis of the theoretical time-series (e.g. motion on orbital paths according to linear theory) results in higher harmonic components and shows a slight decrease of the basic component. In addition a negative dc-value (mean velocity) for the horizontal orbital velocity appears. This negative mean velocity is not to be interpreted as a constant velocity in the opposite direction of wave travel. The LAGRANGEian time series has to be corrected to zero mean, which is in fact the superposition of the mass transport velocity. This again gives a clear argument, that linear wave theory already contains mass transport.

The LAGRANGEian approach can be transferred to irregular waves, by using the superposition method for the particle motion on orbital paths of the linear components of a spectrum, however, effects of mass transport and back flow have to be determined separately. Figure 5 shows an amplitude spectrum of a wave group for a theoretical calculated deep water example.

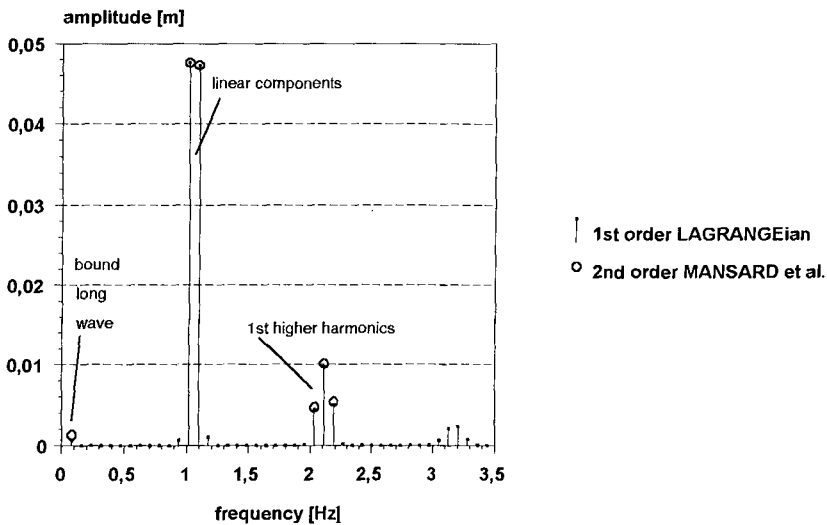


Figure 5. Amplitude spectrum of surface elevation  
 1st order LAGRANGEian approach - 2nd order MANSARD et al. (1986)  
 ( $f_1=1.01\text{Hz}$ ,  $f_2=1.09\text{Hz}$ ,  $H_1=H_2=0.1\text{m}$ ,  $d=1.00\text{m}$ )

The components of the wave group spectrum according to 2nd order are in the same magnitude for both methods, and for the 1st order LAGRANGEian approach in addition components higher than 2nd order are clearly visible. This non-linear interactions are automatically appearing using the described superposition method for the orbital motion of the two linear components of the surface elevation spectrum. The formulation of  $\eta$  and  $\zeta$  for the two linear components is simply added during the iteration procedure.

Figure 6 shows a comparison of super harmonics by the LAGRANGEian approach with the transfer function  $G^{+nm}h$  for the 2nd order frequencies of the linear components as given by MANSARD et al. (1986). In deep water a 1st order LAGRANGEian approach gives same results as 2nd order theory. For more shallow water a 2nd order description of particle motion is needed for the LAGRANGEian approach to achieve fair agreement with MANSARD's approach.

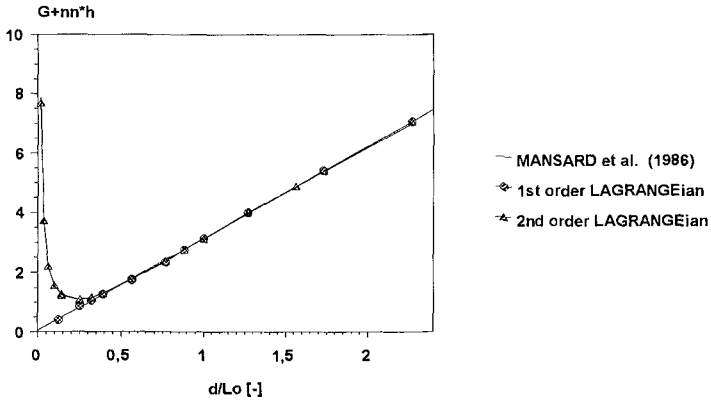


Figure 6. Comparison of 2nd order MANSARD et al. (1986) with LAGRANGEian approach for  $f_n+f_n$  and  $f_m+f_m$

Figure 7 shows the transfer function  $G^{+nm}h$  for the higher harmonic component at frequency  $f_m+f_n$ .

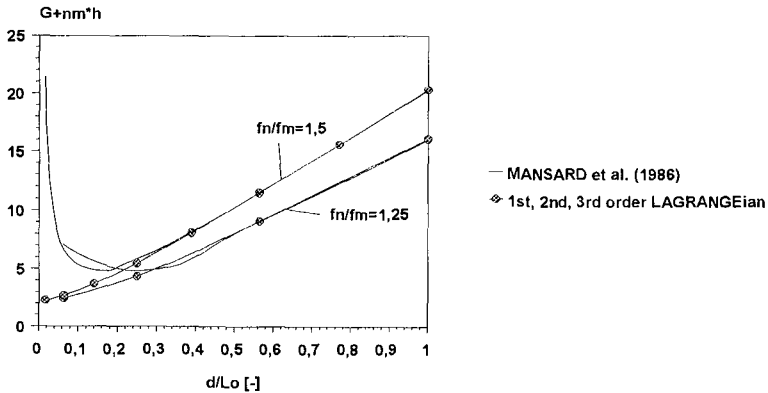


Figure 7. Comparison of 2nd order MANSARD et al. (1986) with LAGRANGEian approach for  $f_m+f_n$



The value of the transfer function depends on the relative spacing of the linear components in frequency domain  $f_n/f_m$ . For deep water the 1st order LAGRANGEian approach shows fair agreement with the 2nd order theory of MANSARD et al. (1986). In more shallower water the LAGRANGEian approach of higher order is not able to calculate the  $f_m+f_n$  higher harmonic amplitude in that order of magnitude, however, differences between LAGRANGEian approach and Mansard's approach are not to big for intermediate water depth. In addition it has not yet been defined clearly to what extend a 2nd order theory is suitable to shallower water conditions. As shown in Fig. 5 LAGRANGEian approach results are of higher than 2nd order.

#### Comparison with measurements

Figure 8 shows measured mean velocities and mass transport velocities for one example of regular waves plotted as depth distribution. For the fixed measurements a fair agreement with the EULERian backflow considered as constant over depth can be seen. The analysis is done in a time window without reflecting waves. The mean velocities from the movable probe can be interpreted neither as backflow nor as real mass transport velocity according to STOKES 2nd order theory. Only by a LAGRANGEian analysis of the data, a fair agreement of the data with real mass transport velocity, superposed by a backflow to a zero-net mass transport in the closed wave channel, can be achieved.

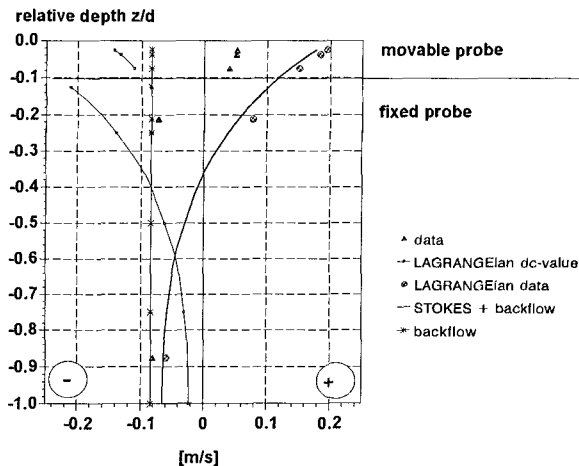


Figure 8. Measured and calculated mass transport velocity and backflow ( $T=3.20s$ ,  $H=1.20m$ ,  $d=4.00m$ )

The constant EULERian backflow is considered in all theoretical calculations. It is known, that the constant profile of the backflow is only an approximate value, which neglects any influence of viscosity in the boundary layer. The analysis of the data shows that variations of the backflow profile due to the influence of viscosity appear, however, outside the time window chosen for velocity analysis.

Figure 9 shows measured surface elevations in comparison to 5th order DSFT and 3rd order LAGRANGEian approach for a wave in intermediate water depth with  $d/L = 0.1$ . Small differences are appearing in the crest region, which can be related mainly to a not quite perfect wave generation. It can be assumed, that a certain amount of free wave is superposed on the stable wave, however, both theories show a good overall agreement with the measured time series.

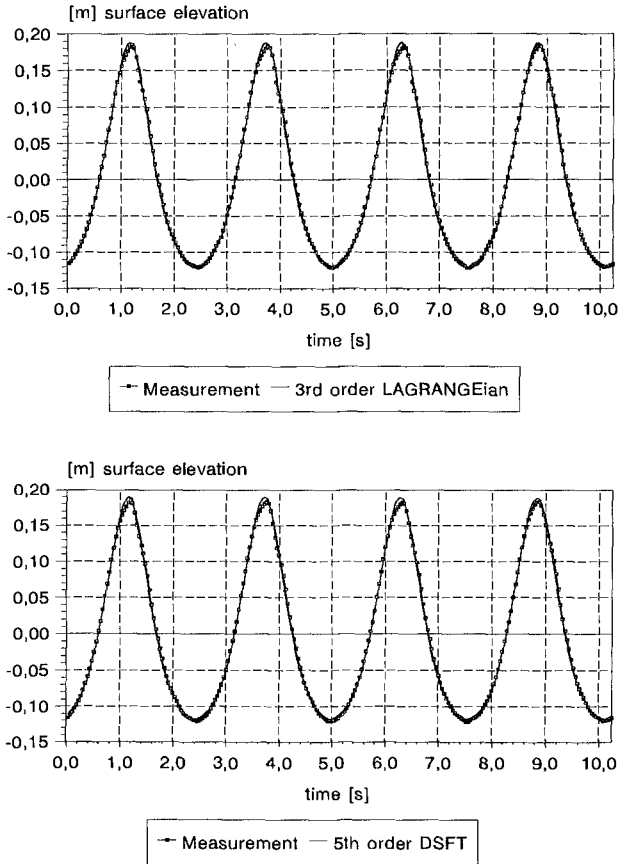


Figure 9. Comparison of measured and calculated surface elevation (T=2.56s, H=0.30m, d=1.00m)

Figure 10 shows comparison of measured and calculated horizontal orbital velocities below the wave crest for the above shown wave case.

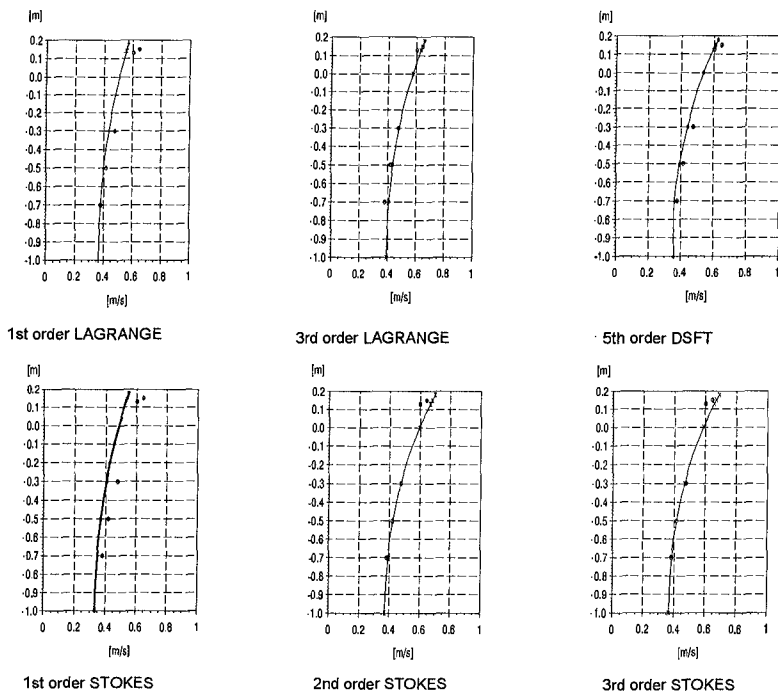


Figure 10. Horizontal orbital velocities below the wave crest  
( $T=2.56s$ ,  $H=0.30m$ ,  $d=1.00m$ )

1st order LAGRANGEian approach and 1st order STOKES theory show a clear underestimation of the measured velocities near the wave crest. Velocities below the deepest wave trough are well predicted using 1st order LAGRANGEian approach. As outlined before, the surface elevation was in fair agreement with 3rd order LAGRANGEian approach and 5th order DSFT, and as the surface elevation is a result of the particle movement on their respective orbits, it is consequent to use this higher order theories also for velocity prediction. Comparison of the data with this approaches show good agreement. 2nd and 3rd order STOKES theory used in EULERian way tend to overpredict the near crest velocities slightly.

The same tendencies also hold for the horizontal orbital velocity below the wave trough, as can be seen in Figure 11. The 3rd order LAGRANGEian approach and the 5th order DSFT fit the measurements, 2nd and 3rd order STOKES theory calculate too high negative velocities, as well as 1st order LAGRANGEian approach and linear wave theory.

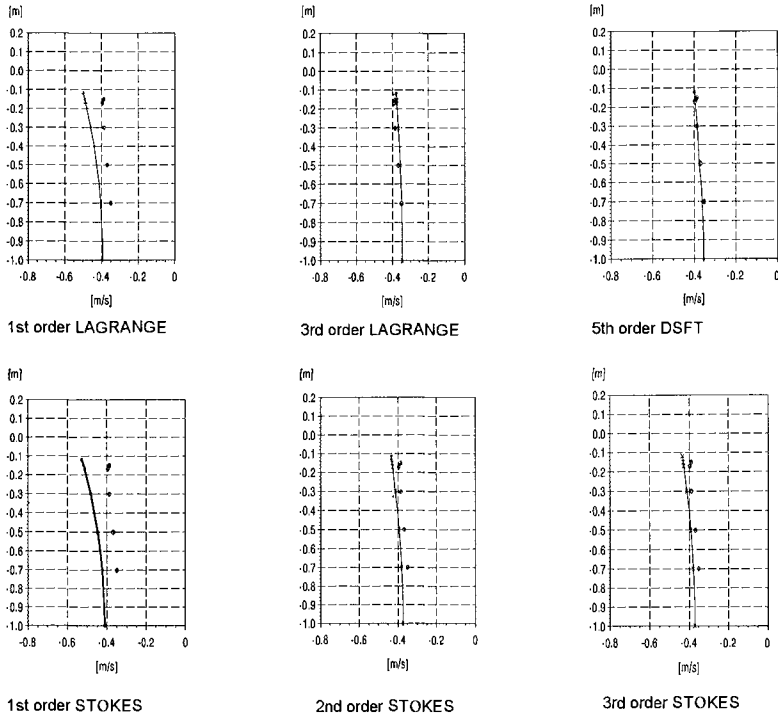


Figure 11. Horizontal orbital velocities below the wave trough (T=2,56s, H=0.30m, d=1.00m)

Results of measurements of horizontal orbital velocities in wave groups and comparison with various engineering methods and with LAGRANGEian approach are shown in Figures 12 to 15. Two wave groups with wave parameter listed in table 1 are considered for this paper.

	$f_m$ [Hz]	$f_n$ [Hz]	$H_m$ [m]	$H_n$ [m]	$d$ [m]
group 1	0,78	0,86	0,07	0,07	1,00
group 2	0,78	0,86	0,12	0,03	1,00

Table 1. Wave parameter of the wave groups

Figure 12 shows a comparison of measured horizontal orbital velocities with the theory as scatter plots for wave group 1. The measurement is done below the deepest wave trough at  $z=-0.10m$  with a fixed velocity probe. The Linear Transfer Function Method (LTFM) shows the known tendency of overprediction of the crest velocities.

WHEELER's stretching method gives slightly better results below the wave crest, but there is a small tendency of underprediction of the velocities below the wave troughs. The complementary method shows similar tendencies as the LTFM. The stretching after DEAN and LO (1986) under predicts the crest velocities as well as the velocities below the wave troughs. DONELAN's superposition method (1992) shows good results, and finally a 2nd order LAGRANGEian approach fits the measurement best.

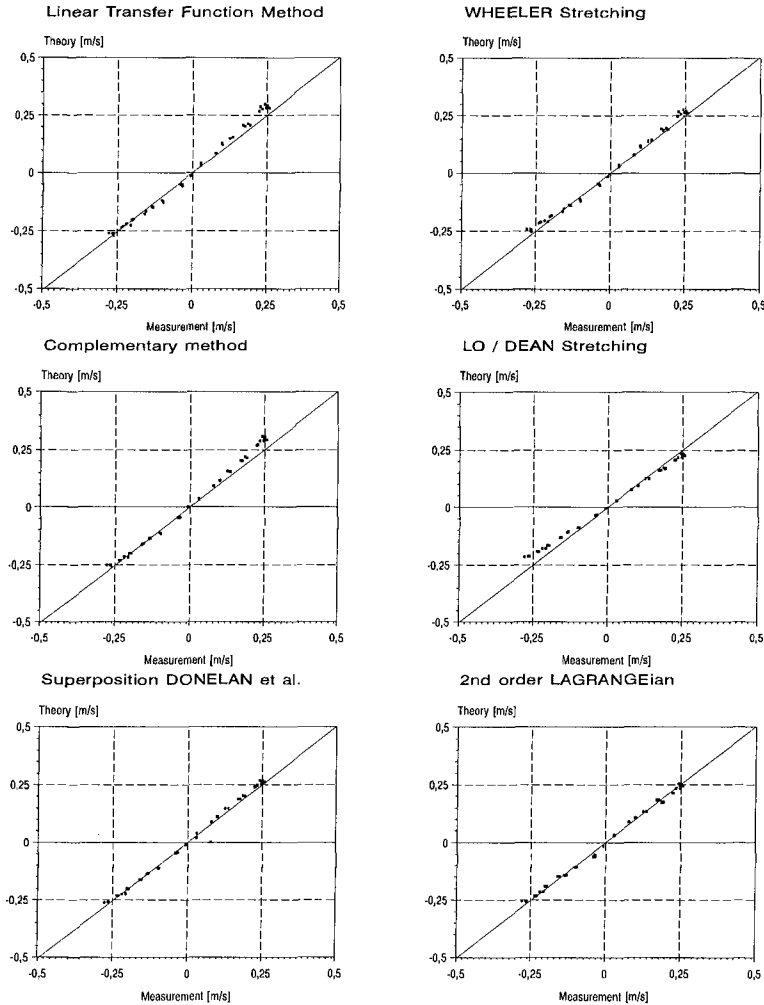


Figure 12. Comparison of measured and calculated horizontal orbital velocity at  $z=-0.10\text{m}$  for wave group 1

The tendencies outlined before also hold for wave group 2 in figure 13, however, there are stronger deviations in the results of LTFM and DONELAN's superposition method.

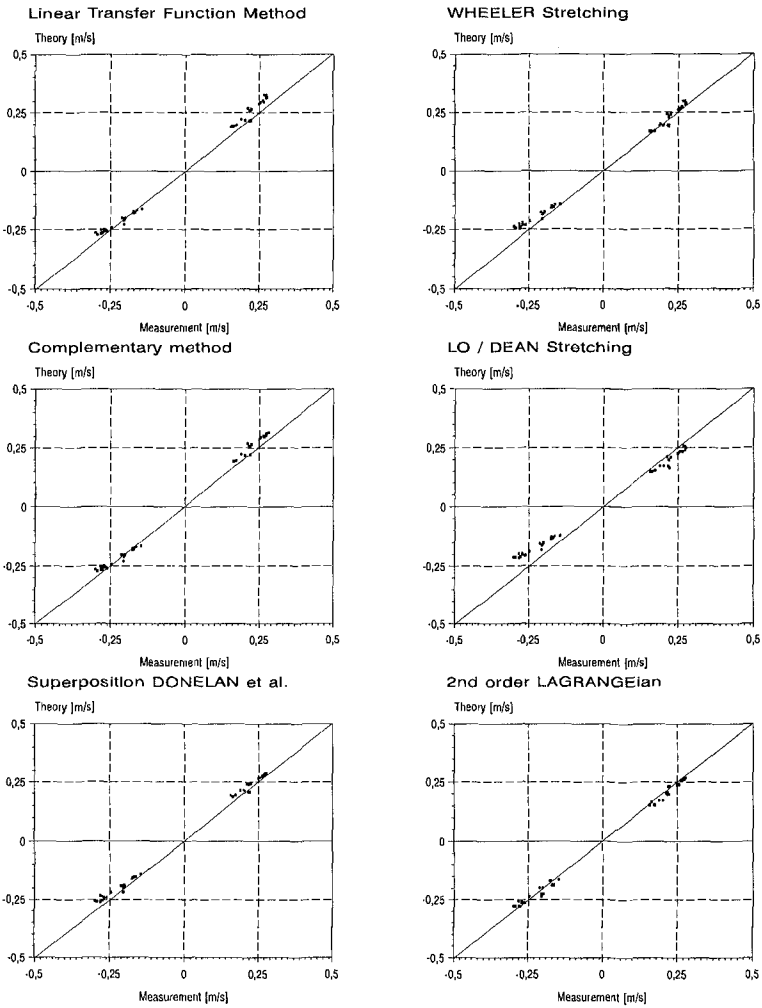


Figure 13. Comparison of measured and calculated horizontal orbital velocity at  $z=-0,10\text{m}$  for wave group 2

The reason for the mentioned tendencies becomes more clear looking to the comparison of the calculated and measured velocity components in frequency domain.

Figure 14 gives the measured and calculated values according to 2nd order theory for wave group 1. LTFM calculates too high basic components of the horizontal orbital velocity as well as too high 2nd order super harmonics. WHEELER's stretching counteracts this concerning the linear components, the higher harmonic components, however, are over predicted. DONELAN's superposition method calculates too high linear velocity components, the super harmonics are better predicted than by the two before mentioned methods. Finally, the 2nd order LAGRANGEian approach gives fairly good results concerning the linear components and also concerning the higher harmonic components of the horizontal velocity, which in this example are relatively small. For the velocity at frequency component  $f_n - f_m$  it can be stated, that, except DONELAN's superposition method, all methods calculate the velocity in the same magnitude and in disagreement with the measurement. This will not be discussed in detail, since this is state the of actual research work. It is assumed, that the misinterpretation of the bound long velocity component belongs to interaction of mass transport velocity and back-flow in the wave channel and the resulting free long wave. The analysis of the data shows, that the deviations between the theoretically calculated and measured long wave velocity is not the reason for the before mentioned tendencies.

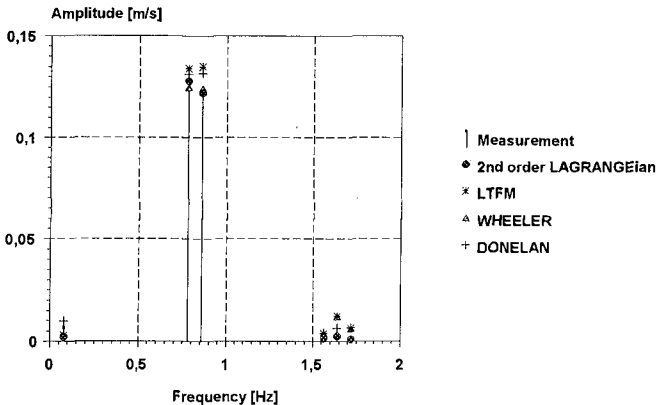


Figure 14. Amplitude spectrum of measured and calculated horizontal orbital velocity according to 2nd order for wave group 1,  $z=-0.10\text{m}$

A main reason for the failure of the engineering methods in prediction of orbital velocities in irregular waves is the misinterpretation of the higher harmonic components. In figure 15 measured and calculated profiles of the horizontal orbital velocity below the highest wave crest and the deepest wave trough are plotted for both wave groups. The overprediction of the higher order velocity components using the higher order components of the surface elevation as linear input for the LTFM, increases rapidly above still water level. Complementary method and also DONELAN's superposition method counteracts this tendency, but clear deviations are visible. Only LAGRANGEian approach, which uses the basic components of the surface elevation as input, fits the measurement near the surface. The opposite tendency of underpre-

diction of the trough velocities is for all methods the same. LAGRANGEian approach is in fair agreement with the measured values.

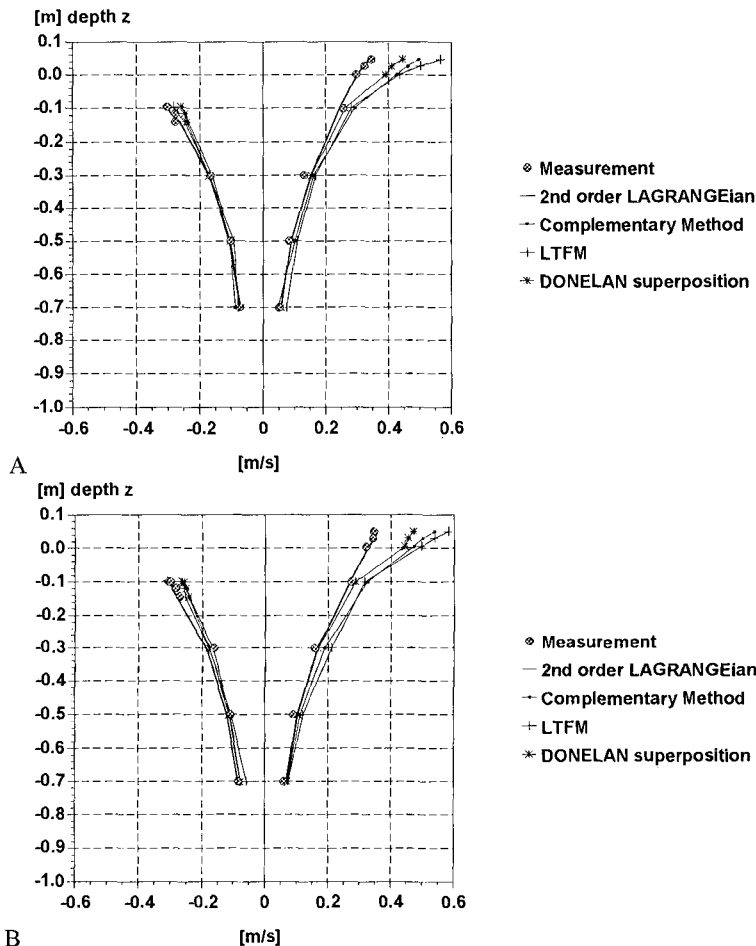


Figure 15. Measured and calculated horizontal orbital velocities below the highest wave crest and below the deepest wave trough (A : wave group 1 | B : wave group 2)

Conclusions

Measurements of surface elevations and horizontal orbital velocities in regular waves and in two component wave groups are compared with various calculation methods. A LAGRANGEian approach, which bases on the geometry of orbital paths given by STOKES 1st, 2nd and 3rd order theory was introduced by the authors.



Following conclusions can be achieved after presentation and discussion of the results:

- The periodic wave theories of the respective order show good agreement with measured regular wave kinematics as well as with regular wave surface elevations.
- The introduced LAGRANGEian approach gives good results concerning surface elevations and orbital velocities and needs a lower order for calculation than other periodic wave theories.
- Using LAGRANGEian approach on the basis of STOKES wave theories, the application range of the STOKES theory can be extended over a wider range of wave parameter.
- Stretching techniques and engineering methods on the basis of linear wave theory seem to be not the right physical tool for the calculation of wave kinematics in irregular waves. The main reason for the failure of these methods is the linear treatment of the super harmonics of the surface elevation.
- Using a superposition method with the LAGRANGEian approach, nonlinearities are automatically appearing. Especially in deep water a 1st order LAGRANGEian approach allows to calculate higher order irregular wave kinematics as well as higher order irregular surface elevations in a mathematical and physical conclusive way.

#### Acknowledgement

The investigation described in this paper was carried out as part of the research programme of the Sonderforschungsbereich 205 (SFB 205) at the FRANZIUS-Institute for Hydraulic Research and Coastal Engineering, University of Hannover. The authors gratefully acknowledge the Deutsche Forschungsgemeinschaft (DFG) for their financial support throughout the investigations.

#### References

- Wheeler, J.D., 1969. "Method for Calculating Forces produced by Irregular Waves", *Offshore Technology Conference (OTC)*, Pre-prints 1970, Vol. 1, pp. I-71 / I-82.
- Daemrich, K.-F., Eggert, W.D., and Cordes H., 1982. "Investigations on Orbital Velocities and Pressures in Irregular Waves", *Proceedings 18th ICCE*, Cape Town,
- Mansard, E.P.D., Sand, S.E., 1983. "Reproduction of higher harmonics in irregular waves", *Ocean Engineering*, Vol.13, No.1.
- Dean, R.G., Lo, J.-M., 1986. "Evolution and Development of Water Wave Theories for Engineering Application", *Proceedings 20th ICCE*, Taipei, pp. 522-536
- Daemrich, K.-F., and Göttschenberg, A., 1986. "Near-Surface Orbital Velocities in Irregular Waves", *Proceedings 20th ICCE*, Taipei, pp. 97-108.
- Donelan, M.A., Ancil, F., Doering, J.C., 1992. "A Simple Method for calculating the velocity field beneath irregular waves", *Coastal Engineering*, Vol. 16, pp. 399-424
- Woltering, S., and Daemrich, K.-F., 1994 a. "Large Scale Measurements of Near Surface Orbital Velocities in Laboratory Waves by Using a Surface Following Device", *Proceedings of Coastal Dynamics '94*, Barcelona, Spain
- Woltering S., and Daemrich, K.-F., 1994 b. "Regular Wave Investigations of Wave Kinematics with LAGRANGEian approach", *Proceedings of International Symposium on Waves - Physical and Numerical Modelling*, Vancouver, Canada

## CHAPTER 205

### CROSS-SHORE PROFILE MODELLING UNDER RANDOM WAVES

Yongjun WU<sup>1</sup>, Hans-H. DETTE<sup>2</sup> and Hsiang WANG<sup>3</sup>

#### Abstract

This paper presents part of the test results conducted in the Large Wave Flume (LWF) for 2D beach profile response under random wave input as well the numerical modelling effort to simulate the laboratory data. The tests were conducted with various input wave spectra, initial profiles and for both erosional and accretional cases. The numerical model is a 2DV(two dimensional vertical) beach profile model. It couples a sediment transport model with a random wave model. The sediment model is a modified version of the SBEACH model developed by Larson and Kraus (1989) for regular waves. The input wave condition is a time-series of irregular waves simulated from a given wave height probability density function, here selected as the Rayleigh distribution. The final profile is then computed from the cumulative changes due to each randomly occurring individual wave.

#### Introduction

In the last few decades, many studies have been carried out for modelling beach profile evolution under storm wave conditions. Most of these efforts, whether physical or numerical, have been for regular waves and for beaches under the state of erosion. It is only natural to extend the effort for cases of random waves. Therefore, since 1987, a systematic series of experiments were carried out in the Large Wave Flume (LWF) located in Hannover, Germany to study the beach response under random wave inputs. The tests were conducted for various types of input wave spectra, with different initial slopes and for both accretional and erosional conditions. In a parallel effort, attempts were made to simulate the laboratory results with numerical model. The numerical model is largely built upon existing modeling techniques.

---

<sup>1</sup>Assistant Scientist, <sup>2</sup>Academic Director, Hydrodynamics and Coastal Engineering Department, Leichrweiss- Institute for Hydraulics, Technical Uni. Braunschweig, 38106, Braunschweig, Germany

<sup>3</sup>Professor, Coastal & Oceanographic Engr. Dept., Uni. of Florida, Gainesville, FL. 32611, USA

Two different approaches have evolved in the past decades for beach evolution modelling. One approach is to establish the mechanics of sediment mobilization and transport first on micro-scale; transport models are then constructed at integrated temporal and spatial scales. This approach is referred to as mechanics approach or fine-scale approach. This type of model could yield better temporal and spatial resolution but may not be practical for long term or large spatial scale simulation. The other approach avoids the details of the mechanics of sediment transport and simply attempts to relate sediment transport to flow properties on a macro scale. The commonly inferred flow properties are temporal and spatially averaged wave energy, wave energy flux or rate of wave energy dissipation. Sediment transport models of this kind ignore the details and bypass the basic sediment mechanics; they are, more or less, heuristic and mainly based upon physical reasoning and/or empirical evidence. This approach is referred to as heuristic approach or macro-scale approach. Since models of the latter type deal with integrated flow properties they are usually more suitable for long term simulation. At present, most of the workable models are of the latter type. And, as mentioned they are mostly restricted to 2D, regular wave input and erosional case. In principle, extending these models for irregular wave application presents no fundamental difficulty, although different approaches can be taken. Indeed, various efforts have been made towards this extension. One of the major handicaps has been the lack of adequate data for calibration and verification.

One of the objectives of the present study is to develop and test a 2DV numerical model that simulates the changes of cross-shore profile under random wave action. The model like most of its kind is composed of a sediment transport model driven by a hydrodynamic model. The beach profile change is then computed by use of conservation of sediment mass. The model is intended for engineering application. The aim is to keep the basic characteristics of the model simple, but still reliable and realistic. Generality and mathematical rigor are, at times, compromised.

### **Laboratory Measurements and Results**

The experiments were carried out in the LWF located in the University of Hannover, which is 320 m long, 5 m wide and 7 m deep and is capable of generating waves up to 2 m high. Beach profile response tests under random waves inputs were carried out in four test series in 1986/87, 90, 91 and 93, respectively. The 1986/87 test was concentrated on dune erosion under regular and irregular waves. The same initial profile were exposed to both regular waves and irregular waves with height of 1.5 m and period of 6 sec. In 1990 and 1991, the main concern of the experiments was to measure the energy dissipation and the sediment transport with an initial equilibrium profile. In 1993, experiments were carried out to study both erosional profile evolution under short waves and accretionary profile evolution under long waves. The effect of water level variations due to tide effect was also examined. The test conditions are given in Table 1.

Table 1 GWK TEST SCHEDULE

Spectrum type	Initial Profile	$H_s$ (m)	$T_p$ (sec)	Water Depth,	Duration (hr)	Response Type
JONSWAP (1987)	$m=1:20$ , $D_{50}=0.33$ (mm)	1.5	6	5 m	9.8	Erosion
PM(1990)	$h=Ax^{2/3}$ , $A=0.08$ $D_{50}=0.22$	0.8	6 - 8	2 m	9.0	Equilibrium
TMA (1991)	$h=Ax^{2/3}$ ; $A=0.08$ $D_{50}=0.33$	0.9-1.04	6 - 8	2.5 m	9.6	Equilibrium
TMA (1993)	Uniform slope $m=1:30$ $D_{50}=0.22$	1.2	5-10	4.5 m	23.5 (no tide) 84.0 (with tide)	Erosion and Accretion

Detailed results can be found in Wu (1994). Only a selected sets of results from 1993 tests were given here. The 1993 test was a long sequential experiment of 3 phases. Phase I was regular waves of erosional(short wave period)-accretional(long wave period)-erosional(short wave period) sequence. It was followed by Phase II test of irregular wave input with short period waves followed by long period wavesl. Phase III has the longest test period with irregular wave input coupled with water level variations, consisting of 45 hrs of short period wave test followed by 39 hrs of long period wave. The test conditions are summarized in Table 2.

Table 2 Summary of Test Conditions, 1993

## PHASE I. REGULAR WAVE

H=1.2 M; T=5 SEC	H=1.2 M; T=10 SEC	H=1.2 M; T=5 SEC
17 HRS	15.75 HRS	7.33 HRS

## PHASE II. IRREGULAR WAVE, NO TIDE

$H_s=1.2$ M; $T_p=5$ SEC	$H_s=1.2$ M; $T_p=10$ SEC
13 HRS	10.5 HRS

PHASE III. IRREGUAR WAVE, WITH TIDE	
$H_s=1.1 \text{ M}; T_p=5 \text{ SEC}$	$T_s=1.1 \text{ M}; T_p=10 \text{ SEC}$
45 HRS	39 HRS

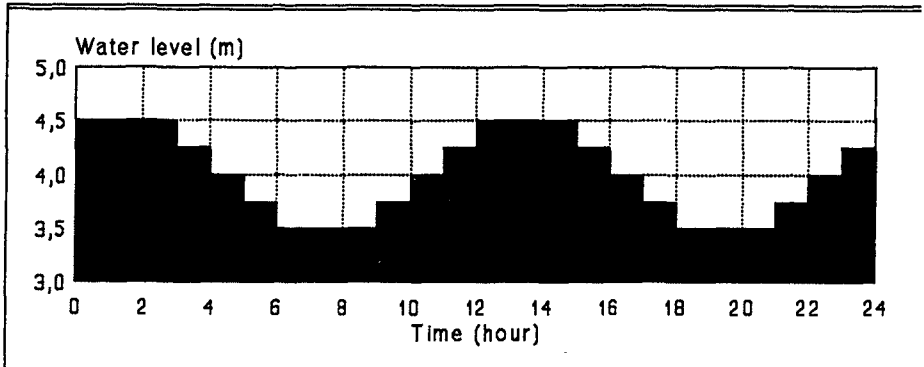


Figure 1 shows the end profiles of Phase I tests. In the first 17 hrs. of phase I-1, the 5 sec waves built a bar 0.75 m high. Then under 15.75 hrs. action of 10 sec waves in phase I-2, the bar moved about 3 m in onshore direction. In the next 17 hrs. of short waves, an the bar moved offshore again and a smaller inner bar was developed. The change in the dune region took place mainly in the 2 short-wave phases.

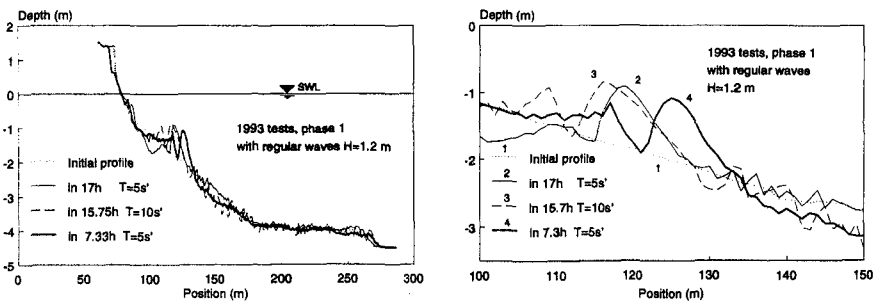


Figure 1. Profile Evolutions in Phase I test, 1993

Figure 2 shows the end profiles of Phase II tests. It is quite apparent that the initial bar-trough profile was smoothed into a foreshore tarrace during the short period wave test. In the subsequent long-period wave test, onshore sediment motion was observed. Different from the regular wave case, the bar was much lower and broader. The bed changes in the inner surf zone were also more rigious and rapid. The results of Phase III test are given in Fig. 3. In this Phase, water surface variations due to tide (12-hr period) were also simulated in addition to the irregular wave input.

During the short-period wave test, the variation of water depth appeared to aid in offshore sediment movement causing the bar to move further offshore. In the subsequent long-period wave test, the development of the profile was very gradual as the bar was flattened and moved inshore.

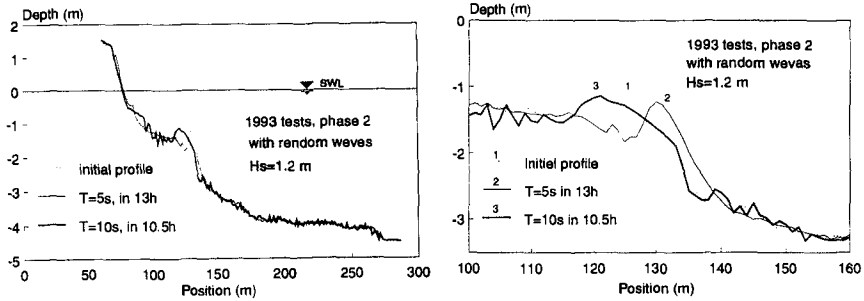


Figure 2. Profile Evolutions in Phase II test

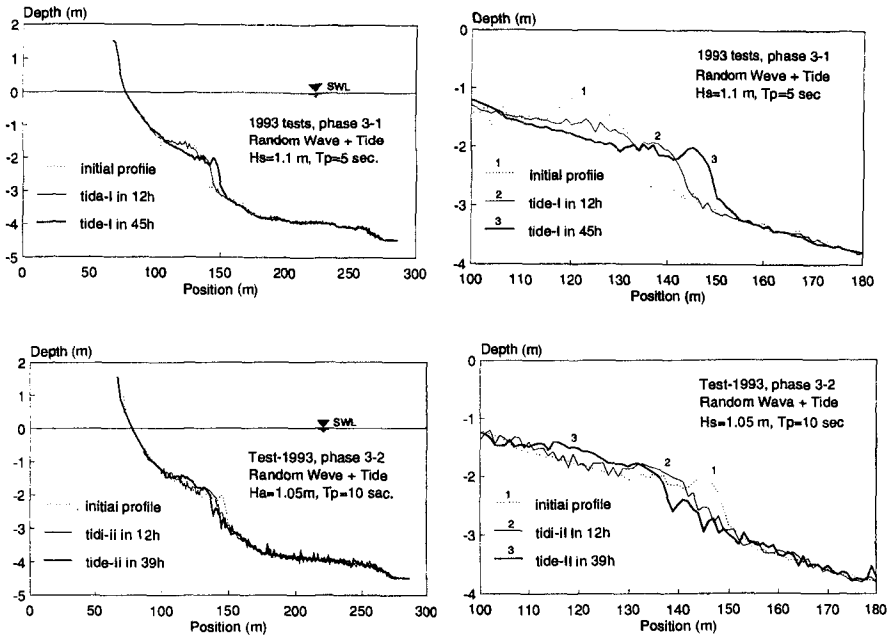


Figure 3. Profile Evolutions in Phase III test

## Numerical Modelling With Random Waves

The profile response model consists of two major parts: the wave input model and the sediment transport model. Conceptually, the randomness should be entered in both parts. At present the randomness can be incorporated in the input wave only.

### (1) Random Wave Model

There appear to be three basic approaches for treatment of random wave transformation in shoaling water and through the surf zone: They are: (1). Using a deepwater random wave time series as input and transforming each individual wave in the series as if it were a regular wave component with a distinct wave amplitude and period. (2). Carrying out a spectral transformation first from deepwater into shallow water. A time series is then created from the shallow water spectrum for further shoaling and surf zone transformation of each individual wave. The first step is equivalent to transformation of Fourier components under the constraint of energy conservation. Numerous numerical models can be used to accomplish this transformation. (3). Conducting a "parametric" type transformation of deepwater random wave directly into surf zone. The surf zone wave properties are then expressed as significant wave parameters and, sometimes, with associated distribution functions. Each approach presented above can be considered for random wave input information. Approach (1) and (2) are conceptually the same except that another layer of model is required in (2) to carry out shallow water wave transformation. The third approach yields local wave information inside the surf zone but it is difficult to reconstruct a continuous spatial variations of each wave which is required in some of the sediment transport models.

The wave model used here was based on approach (1) for its directness. The essential assumptions are: shoaling and breaking are not affected by wave-wave interaction, reflection is weak and the waves are unidirectional. The method is called as the "time dependent discrete pdf method". As an initial attempt the input wave is assumed to be uni-directional and narrow-banded in wave period with the deepwater wave heights following Rayleigh distribution.

First, a random wave height series is generated by the Monte-Carlo method. If  $\rho$  is a uniformly distributed random number with a value between zero and one, the Rayleigh distributed wave height corresponding to this level of probability is given ;

$$H_p = H_{rms} \sqrt{\ln(1/\rho)} \quad (1)$$

in which  $H_p$  is the wave height that is exceeded by  $\rho N$  waves,  $\ln$  is natural logarithm and  $H_{rms}$  is root-mean-square wave height. The  $H_{rms}$  value is the only required input.

Each wave height from this random series is treated as a regular wave in one profile simulation time-step and is transformed through the computational space by the wave

decay models of Dally et al. (1984). The number of waves used in one simulation run is determined by comparing the simulated wave height distribution with the target Rayleigh distribution. Since Rayleigh distribution has no upper bound, the function must be truncated in high wave end (for example, cutoff at  $H/H_{rms}=2.5$  or 2.0) to avoid unrealistically high waves. To save computational time, the distribution is also truncated at the low wave end to cutoff small waves that make no contribution to sediment transport. Figure 4 shows an example of the simulated time series and the comparison of the wave height histogram from 500 waves with the target Rayleigh distribution. Numerical experiments showed that approximately 100 waves are needed to produce a reasonable Rayleigh distribution and 500 waves will produce a very good one.

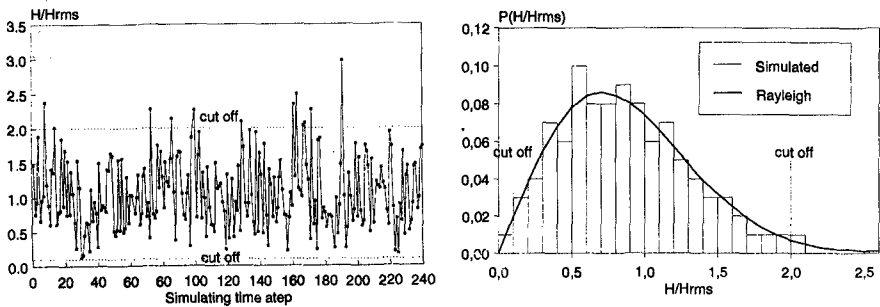


Figure 4 Example of Simulated Random Waves from Rayleigh Distribution

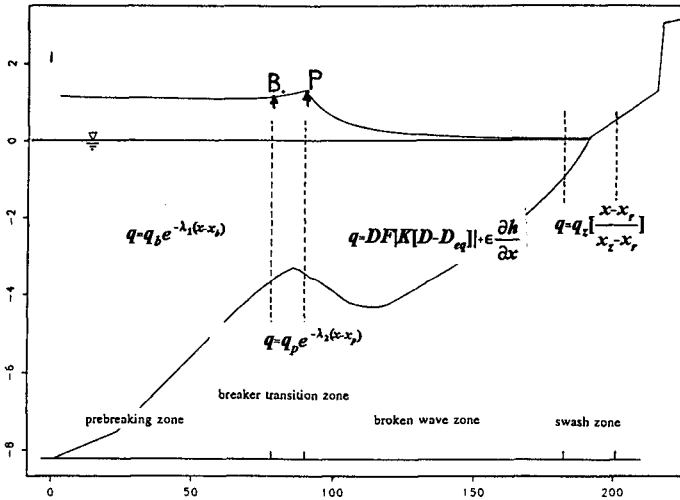
## (2) Sediment Model

The selected sediment transport model is one of the macro-scale type which is based on the energy dissipation concept as used by Moore (1982), Kriebel and Dean (1985) and Larson and Kraus (1989). The reason for selecting this type is that the numerical results from the SBEACH model (Larson & Kraus, 1989) appear to yield the best overall agreement with our own laboratory experiments for regular waves. Their model is modified for random wave inputs.

The SBEACH model is expressly developed to incorporate the offshore bar formation and movement produced by storm waves and water levels. Bar formation and movement produced by breaking waves are satisfactorily simulated. In essence, the model is an extension of Kriebel and Dean's approach. The sediment transport model is patterned after Kriebel and Dean but empirically adjusted from large wave tank test results to insure bar formation and movement. The sediment transport is partially restricted to the equilibrium beach profile in the inshore zone of profile evolution. The sediment transport formulae proposed in this model is one of the possibilities of extending Dean's equilibrium beach profile concept to bar-berm profiles. The basic formation is delineated in the following schematicst:



**Schematics of Sediment Transport Model**

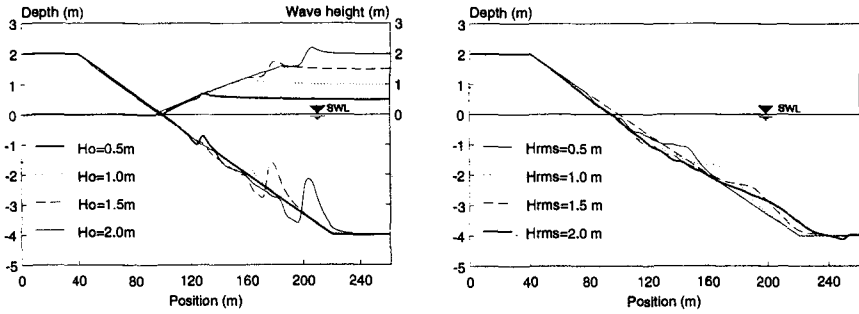


This scheme is almost the same as the SBEACH with the exceptions that most of the coefficients have been adjusted. Also, the definition of the swash zone in the original model is defined in terms of controlling depth whereas in the present model it is defined in terms of percentage of the total surf width to produce more realistic nearshore profile. For detail see Wu (1994).

**Model Sensitivity and Stability**

Systematic sensitivity analysis to assess the influence of model parameters and empirical coefficients has been performed, with both regular wave and random wave. This allows us to examine the physical implications of the model parameters and their effects. It is also serves to explore the applicability of the model beyond the range for which it was calibrated.

Related to time scale of simulation, with increase of total simulating time in both regular and random wave cases, the change of profile will reach quasi equilibrium form. Regular waves are not sensitive to the size of time step,  $dt$ , which regulate the number of iterations. But for random waves, the time step (used  $dt: 5T_p - 80T_p$ ,  $T_p$ : peak period) must be small enough to include a sufficient number of sample waves (at least 100 waves) to represent the Rayleigh distribution. Model sensitivity to wave height  $H_o$  or  $H_b$ , wave period  $T$  or  $T_p$ , change of water level, and breaker index were analyzed. The profile evolution is significantly affected by the change of wave height, **Fig. 5**, but it is not sensitive to the wave period. Under given wave condition, beach erosion always increases with increasing water level as the surf zone moves inshore with increasing water level, **Fig. 6**. The influence of sediment transport model



(a) Regular Waves

(b) Irregular Waves

Fig. 5. Effects of Wave Height on Profile response

parameters, i.e. the sediment diameter  $D_{50}$ , fall velocity  $w$  and coefficient of equilibrium beach profile  $A$  were evaluated. As expected, a finer sand will produce flatter beach slope and coarse sand a steep profile. The influence of the coefficient of sediment transport rate  $K$  only affects the rate of transport but has very little effect on the final profile.

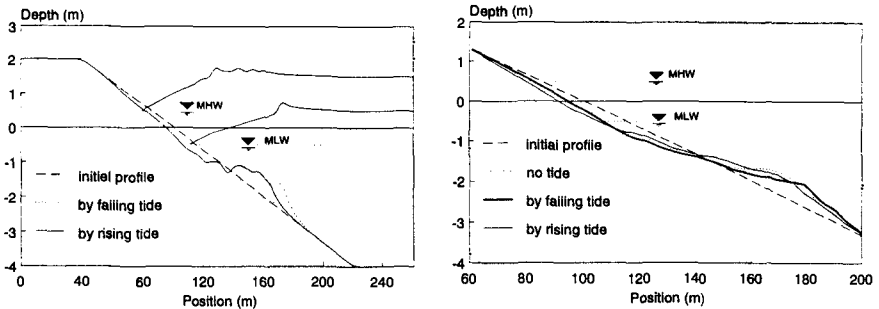


Figure 6. Effect of Water Level Changes on Profile Response

**Comparison Between Numerical and Experimental Results**

The model simulations are compared with limited cases of experimental results from the Large Wave Flume. Fig. 7 shows the comparison between the numerical simulation and the experiments of 1987. As can be seen, the step-type profile is fairly well represented so is the transport rate. In the 1990 and 91 experiments, the initial profile was shaped in accordance to an equilibrium form (Dean, 1977) with  $A=0.07$ . Both numerical and experiment results showed only small changes. The results

indicate that the method is capable of simulating equilibrium profile shapes under random wave conditions.

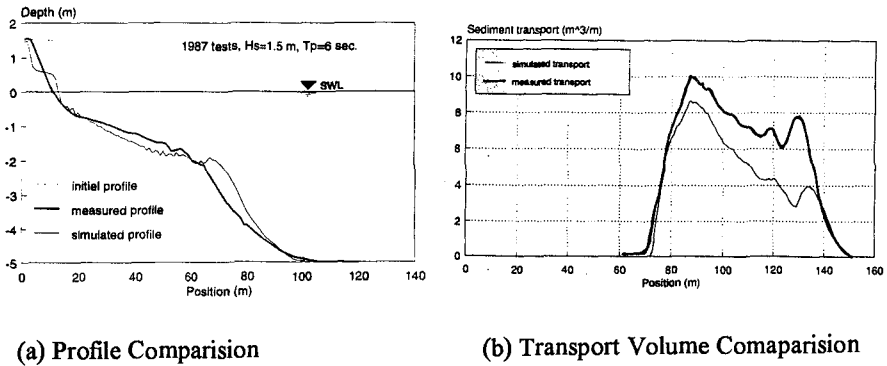


Figure 7. Model Simulations, 1987 Random Wave Test

**Figure 8** shows the comparison of numerical simulation with the experimental result of tests in 1993. The model simulation for phase I test is shown in **Fig. 8a**. The test consisted of a combined erosional cycle with an accretional cycle with regular wave input. It is evident that the numerical model was not successful for the accretional cycle. In the phase II test of irregular waves, the numerical model was reasonably successful for the erosional cycle as shown in **Fig. 8b**. The surf zone became broader, the bar decreased and its position moved in onshore direction. Near the shore line, the dune erosion is somewhat over estimated by the model. Again, the simulation was unsuccessful in the accretional cycle (not shown). In test phase III-1, random waves of 5 sec period were run with change of water level. The model simulation was successful for this erosional cycle. The measured final profile was well represented by the simulated one and it approached to an equilibrium form, **Fig 8c**. In the phase III-2, longer waves were run, which produced onshore sediment movement. The model, again, failed to simulate this case partly because the onshore-offshore criterion used in the model by Larson and Kraus (1989) suggests offshore transport for  $H_{1/3} = 1.1$  m and  $T_p = 10$  sec whereas in the experiment the sediment was clearly onshore. The criteria from Dean (1973), Hattori and Kawamata (1980) also indicate offshore sediment transport; only the criterion from Sunamura and Horikawa (1975) indicate onshore sediment transport. For the specific case simulated, one actually found that the absolute magnitude of transport volume measured in the laboratory was about the same order as that predicted by the numerical model, **Fig. 8d**.

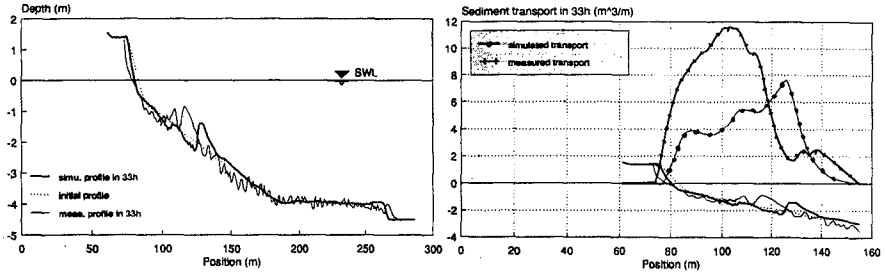


Figure 8a Numerical Simulation for Phase I, 1993

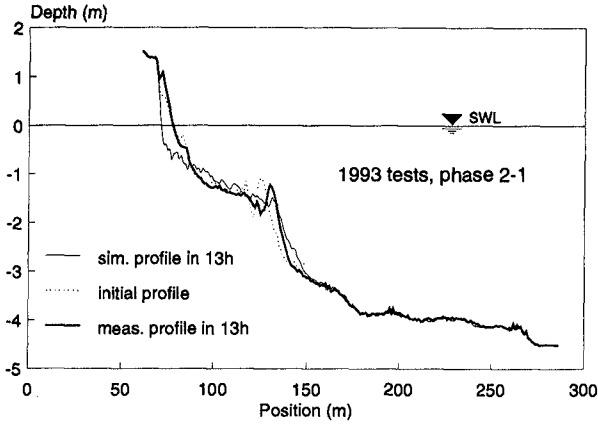


Figure 8b. Numerical Simulation for Phase II-1, 1993

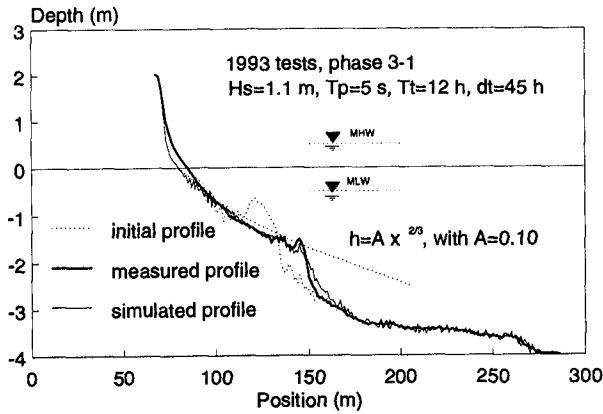


Figure 8c. Numerical Simulations for Phase III-1, 1993

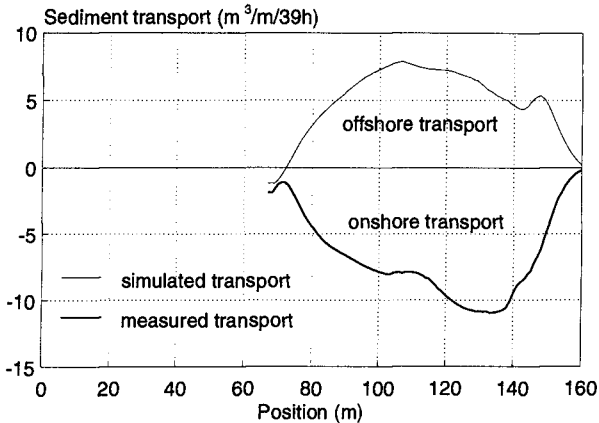


Figure 8d. Rate of Transport Simulated in Phase III-2, 1993

### Conclusions

A systematic series of experiments have been carried out in the LWF to study the beach profile response under random wave conditions. A 2DV numerical model was also developed based on the SBEACH model. The study was aimed at documenting the laboratory observation as well as evaluating numerical modelling capabilities. It was found that:

Under erosional condition, berm profiles were generated under random wave instead of the bar profile under regular waves.

Beach recovery was difficult without water level changes and random wave input.

Beach profiles appeared to be able to reach quasi-equilibrium under both erosional and accretional cases and for both regular and irregular waves of constant conditions. At times, the profile appeared to have reached an equilibrium only to become active again due to unknown causes; it will then reach an equilibrium the second time which was usually more stable.

The numerical model adequately predicted the proper shapes of the profile for both regular and irregular waves under erosional condition in both profile shape and rate of erosion. The model as presented in the present study responds well to changes in water level and is numerically stable. The original SBEACH model, at occasions, becomes unstable. The numerical model as presented was not capable of reproducing the profile under accretional condition.

The current erosional and accretional criteria as proposed by various authors should be re-examined.

Further development of the profile model is required, possibly by (1) extending the model for simulation of beach accretion or combined beach erosion-accretion; (2) extending the present "discrete pdf" to a joint wave height and period distribution to accommodate the broad banded random sea; (3) taking the nonlinear wave transformation into account.

### Acknowledgement

This work was carried out as part of the G8 Coastal Morphodynamics research program. It was funded partly by the Commission of European Communities, Directorate General for Science, Research and Development, under contract no. MAS2-CT92-0027, partly by the German Ministry of Research and Technology (BMFT).

### References

- Battjes, J.A., Janssen, J.P.F.M., 1978. Energy Loss and Setup due to Breaking of Random Waves. Proc. 16th Coastal Eng. Conf., pp569-587.
- Dally, W.R. 1992. Random breaking waves: field verification of a wave by wave algorithm for engineering application. Coastal Engineering, Vol. 16 No. 4, pp369.
- Detle, H.H., Rahlf, H., Wu, Y. and Peters, K., 1992d. Wave Measurements Across the Surf Zone at Equilibrium Beach Profile - Prototype Experiments (1990/1991) with Monochromatic Waves and Wave Spectra. Leichtweiss-Institut, Report no. 762.
- Detle. H.H. and Uliczka, K., 1987. Prototype Investigation on the Time-Dependent Dune Recession and Beach Erosion. Proc. of Coastal Sediments'87, ASCE, pp.1430-1444.
- Kraus, N.C. and Larson, M., 1991. NMLONG: Numerical Model for simulating the Longshore Current. Report 1 of a series, Technical Report CERC-89-7.
- Larson, M., and Kraus, N.C., 1989. SBEACH: Numerical Model for Simulating Storm-induced Beach Change. Report 1, Technical Report CERC-89-9
- Thornton, E.B. and Guza, R.T., 1983. Transformation of Wave height Distribution. J. of Geophy. Research. Vol. 88, No. C10. pp. 5529-5938
- Wu, Y., 1994. Simulation of Cross Shore Beach Profile Modelling Under Random Waves. Die nachstehende Arbeit wird veroffentlicht in: Mitteilungen aus dem Leichtweiss-Institut for Wasserbau der Technischen Universitat Braunschweig -ISSN 0343-1223.

## CHAPTER 206

# MULTIPLE BAR FORMATION BY BREAKER-INDUCED VORTICES: A LABORATORY APPROACH

Da Ping Zhang<sup>1\*</sup> and Tsuguo Sunamura<sup>1</sup>

**ABSTRACT:** Using a two-dimensional wave flume and a two-video-camera system, mechanism and process of multiple bar formation were investigated in the light of breaker-induced vortices. A fixed-bed experiment revealed that (1) the vortex formed at the wave break point can be classified into three: oblique, A-type horizontal, and B-type horizontal vortices; (2) the vortex formed in the surf zone is always oblique; and (3) the location of a vortex reaching bottom can be described by wave properties and the bottom slope, and its water depth can be expressed by breaker height alone. A movable-bed experiment indicated that bars are initiated by the vortices reaching bottom in the surf zone; the number of bars formed coincides with the number of such vortices. Suspension of the bottom sediment due to vortex action and the mean-drift-velocity pattern can play an important role in multiple bar formation; mechanism for break-point bar formation is "convergence", while that for inner bar formation is "congestion". Two major modes for the development of multiple bars were found: simultaneous and successive: these depend on the interaction of vortex action and topography in the surf zone. Multiple-bar features such as trough spacing and crest depth could be explained from vortex features found through the fixed-bed experiment.

## INTRODUCTION

Major hypotheses regarding multiple bar formation are: the wave breaking hypothesis (e.g., O'Brien, 1968; Dhyr-Nielsen and Sorensen, 1970; Exon, 1975; Dolan and Dean, 1985; Sunamura and Takeda, 1993), and standing wave hypothesis (e.g., Suhayda, 1974; Short, 1975; Bowen, 1980; Katoh, 1984; Aagaard, 1991). In both hypotheses, no clear explanation on multiple bar formation has been provided

---

<sup>1</sup> Institute of Geoscience, University of Tsukuba, Ibaraki 305, Japan.

\* Present Address: Coastal Engineering Division, Public Works Research Institute, Ministry of Construction, Ibaraki 305, Japan.

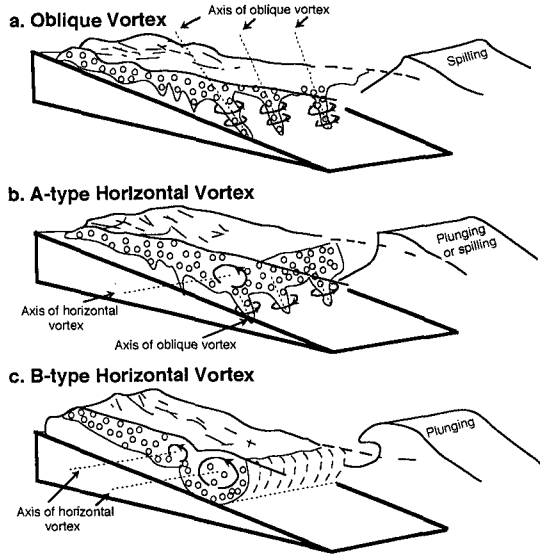


**Fig. 1 Three vortex types**

based on sediment dynamics.

With the recent progress of measuring techniques of flow velocity, studies from a micro-scopic point of view have been conducted with the purpose of elucidating the nearshore hydrodynamics. Nadaoka et al. (1987, 1988) found the presence of "oblique vortex" in the surf zone under spilling breaker conditions, and reconfirmed that this oblique vortex induced sediment suspension in the surf zone. Although they have not noted the interaction of the oblique vortex and bar formation, it is suggested that such sediment suspension could influence the net sediment movement in the surf zone resulting possible bar formation.

This study, conducted in the laboratory from the standpoint of the breaking-wave hypothesis, attempts to investigate the possibility of vortices induced by breaking waves to form multiple bars.

**FIXED-BED EXPERIMENT ON BREAKER-INDUCED VORTICES REACHING BOTTOM**

In order to examine the characteristics of vortices produced by breaking waves, an experiment was conducted setting up a 1/10 or 1/20 uniform steel bottom in a wave flume (12 m long, 0.2 m wide, and 0.4 m deep) equipped with a regular-wave generator. The period of waves ranged from 0.6 to 2.4 sec and the height of



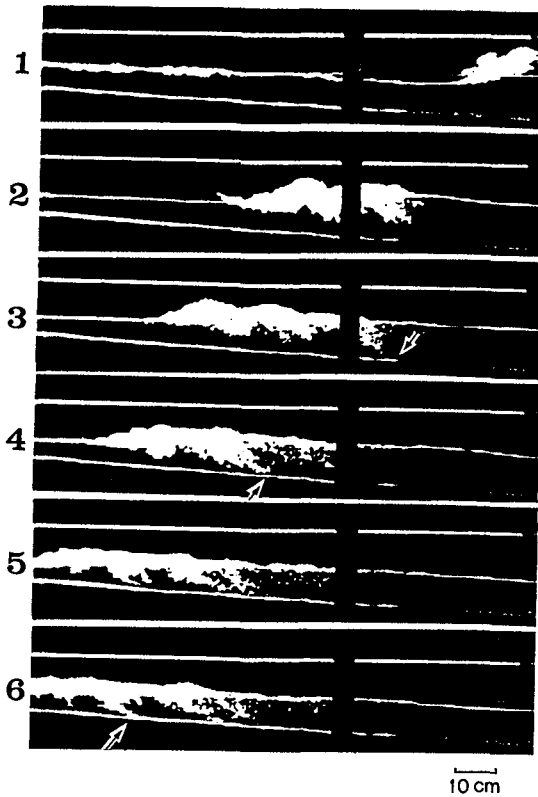


**Fig. 2 Development of triple vortices reaching bottom**  
 $(H_b=11\text{cm}, T=1.2\text{s}, \tan \beta =1/20)$

breaking waves from 5.0 to 14 cm. To examine the characteristics of vortices developed in the whole surf zone, two video cameras were set up beside the flume. One was placed normal to the side of a glass window of the flume, and the other was installed with an angle of 30 degrees at the offshore side of the wave break point. The three-dimensional characteristics of vortices were examined on reproduced video pictures using both breaker-induced air bubbles and neutrally buoyant particles (1.2mm in diameter) as tracers.

Vortices formed just after wave breaking are classified into three types according to the direction of vortex axis: oblique vortex and two types of horizontal vortex, i.e., A-type and B-type horizontal vortices (Zhang and Sunamura, 1990). The oblique vortex is like a tornado that has an obliquely stretched axis of rotation (Fig. 1a). The B-type horizontal vortex looks a cultivator that has a horizontal axis of rotation (Fig. 1c). The A-type horizontal vortex is a hybrid between horizontal and

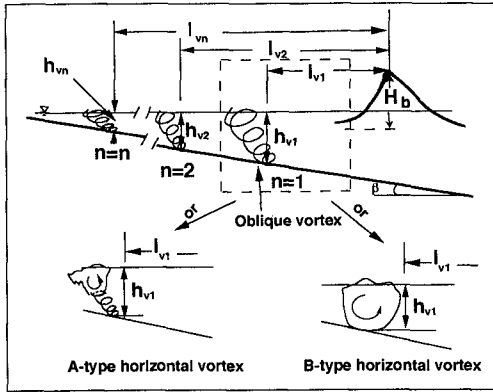


**Fig. 3** Definition sketch of location of vortices reaching bottom

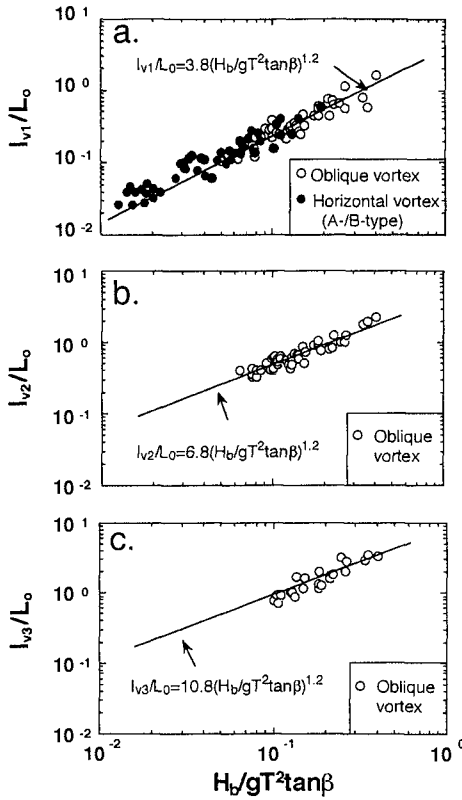


**Fig. 4** Relationship between  $H_b/gT^2 \tan \beta$  and  $l_{vn}/L_0$

oblique vortices (Fig. 1b). Namely, the horizontal vortex forms first in the upper part of water column and then it changes to the oblique vortex. Considering that a vortex which is stretched to reach bottom play a very important role in sediment motion and resulting topographic change, we focused on this kind of vortices.

The experiment showed that the vortices reaching bottom are not only formed at the wave break point, but also in the whole surf zone depending on experimental conditions. Figure 2 is an example of a sequence of video-pictures that show developmental processes of the triple vortices reaching bottom. The time between one stage to the next is 0.3 sec. The first oblique vortex develops at Stage 2 just after wave breaking (spilling breaker) and it touches the bottom as indicated by the arrow at Stage 3. As the bore propagates, the second oblique vortex develops inshore and reaches bottom at Stage 4, and finally the third oblique vortex reaching bottom forms further inshore at Stage 6 as indicated by the arrow. The vortex strength tends to decrease with increasing distance from the wave break point.

Results obtained through the present experiment indicate that the first vortex, i.e., the vortex formed just after wave breaking, is an oblique vortex or an A-type or a B-type horizontal vortex depending on experimental conditions, but the vortex or vortices in the surf zone are always oblique. It was also observed in this experiment that the vortices not reaching bottom appeared when the breaker height was extremely small.

The location and water depth when the first vortex touches the bottom were almost constant with time, whereas those of vortices reaching bottom in the surf zone slightly fluctuated with waves. Average location and depth were measured by reproducing video-pictures for six consecutive waves.

The average horizontal distance from the break point to the location of the vortex reaching bottom, counting from the first vortex ( $n=1$ ), is denoted as  $l_{vn}$  (Fig. 3). Data were analyzed using three dimensionless quantities,  $l_{vn}/L_o$ ,  $H_b/gT^2$ , and  $\tan \beta$ , where  $L_o$  is the deep-water wavelength,  $H_b$  is the breaker height,  $T$  is the wave period, and  $\tan \beta$  is the bottom slope. These three quantities are the same that Sunamura (1985) used to analyze the data of the location of the deepest penetration of breaker-produced bubbles in the surf zone.

Figure 4 shows the result of analysis. From the equation written beside the straight line in each graph, it is anticipated that the location of the  $n$ -th vortex can be described by

$$l_{vn}/L_o = A(H_b/gT^2 \tan \beta)^{1.2} \quad (1)$$

where  $A$  is a dimensionless coefficient that varies with the value of  $n$  as shown in Fig. 4. To obtain the relationship between  $A$  and  $n$ ,  $A$  is plotted against  $n$  in Fig. 5; the line in this figure can be expressed by

$$A = 3.98 n^{0.86} \quad (2)$$

One obtains the following relation:

$$l_{vn}/L_o = 3.98 n^{0.86} (H_b/gT^2 \tan \beta)^{1.2} \quad (3)$$

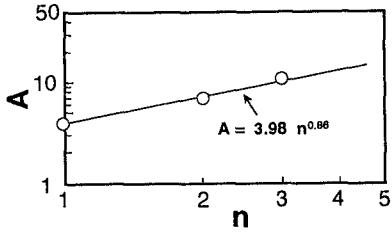


Fig. 5 Relationship between  $A$  and  $n$

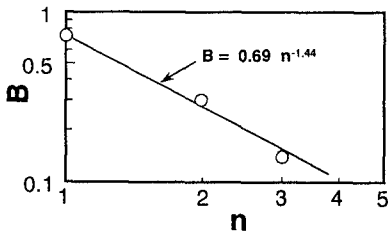


Fig. 7 Relationship between  $B$  and  $n$

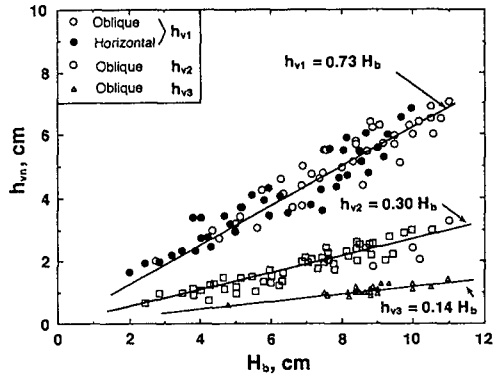


Fig. 6 Relationship between breaker height and water depth for vortex reaching bottom

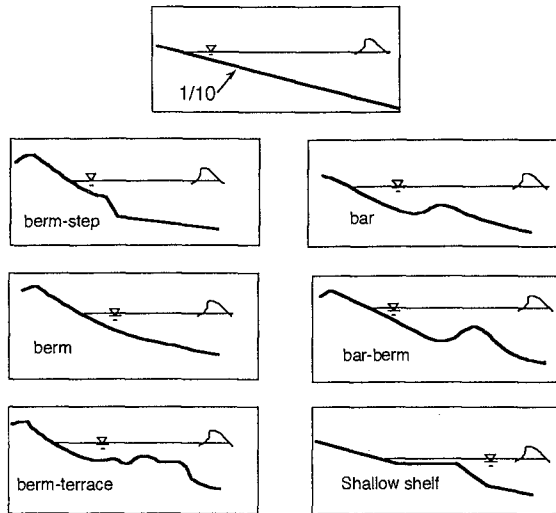


Fig. 8 1/10 uniform and six non-uniform beach profiles used as the initial boundary condition for movable-bed experiment

This equation allows us to predict the position of multiple vortices which can touch the bottom.

Denoting the water depth of the  $n$ -th vortex reaching bottom as  $h_{vn}$  (Fig. 3), Fig. 6 shows the relationship between breaker height and water depth of 1st, 2nd, and 3rd vortices. It is easily anticipated from the equations in this figure that the case of the  $n$ -th vortex can be described by

$$h_{vn} = B H_b \quad (4)$$

The values of  $B$  are plotted against  $n$  in Fig. 7, and the line in this figure is given by

$$B = 0.69 n^{-1.44} \quad (5)$$

The following relation can be written:

$$h_{vn} = 0.69 n^{-1.44} H_b \quad (6)$$

Prediction of the water depth of multiple vortices reaching bottom is possible by the use of this equation.

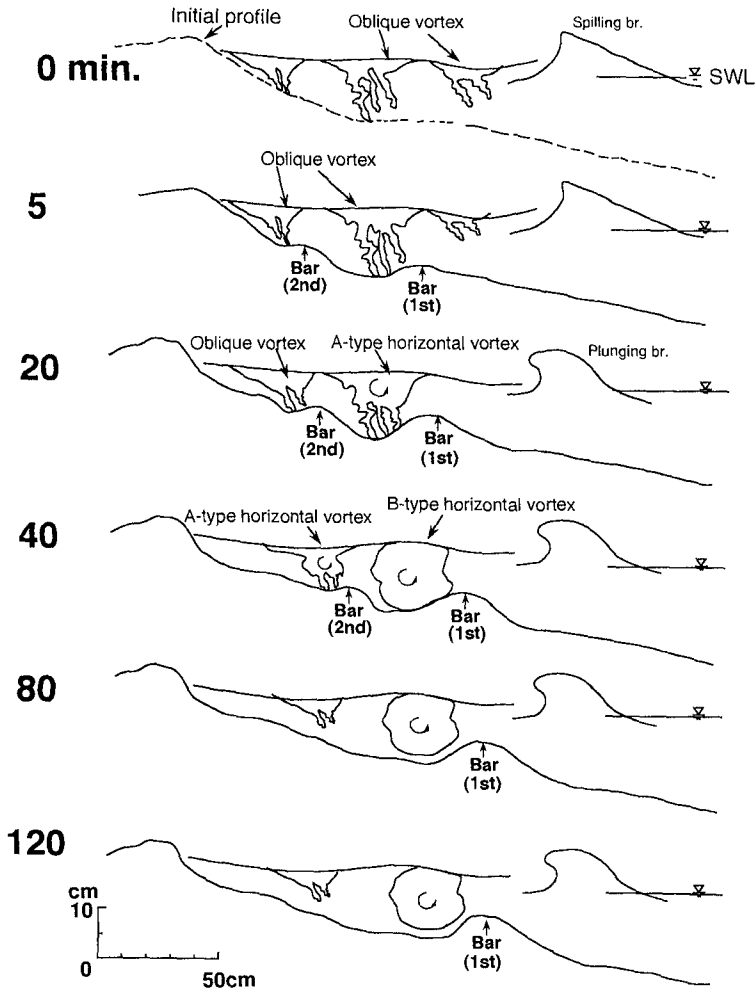
### MOVABLE-BED EXPERIMENT ON BAR FORMATION DUE TO BREAKER-INDUCED VORTICES REACHING BOTTOM

An experiment was conducted using 1/10 uniform beach profile and six kinds of non-uniform profiles as the initial boundary condition set up in the same wave flume as used before. Figure 8 is a schematic illustration of the seven initial beach profiles, of which "1/10" and "shallow shelf" were artificial and the remaining five were formed by waves (Zhang, 1994). To examine the vortex characteristics and vortex-topography interaction, the two-video camera system was again used. Changing the combination of these initial beach slopes, the grain size of beach material (0.22, 0.69, 1.3, and 2.4 mm), wave period (0.7, 0.8, 0.9, and 1.0 sec), and breaker height (5.0~10cm), 61 experiment runs were conducted. As the breaker height, the value measured at the initial stage where no significant topographic change occurred was adopted in this study. Waves continued to act until no significant development of the break-point bar occurred. This stage is defined as the equilibrium; the time required for it ranged from thirty minutes to two hours depending on experiment runs. The beach topography was measured at the center of the flume by an automatic profiler every five minutes as a general rule.

The result showed that multiple bars were formed depending on the experiment conditions. It was found that (1) the bar formation is closely associated with the action of vortices reaching bottom, (2) the number of bars formed coincides with that of such vortices, and (3) the shape of initial morphology greatly affects the mode of multiple bar formation. Two major modes will be illustrated below.

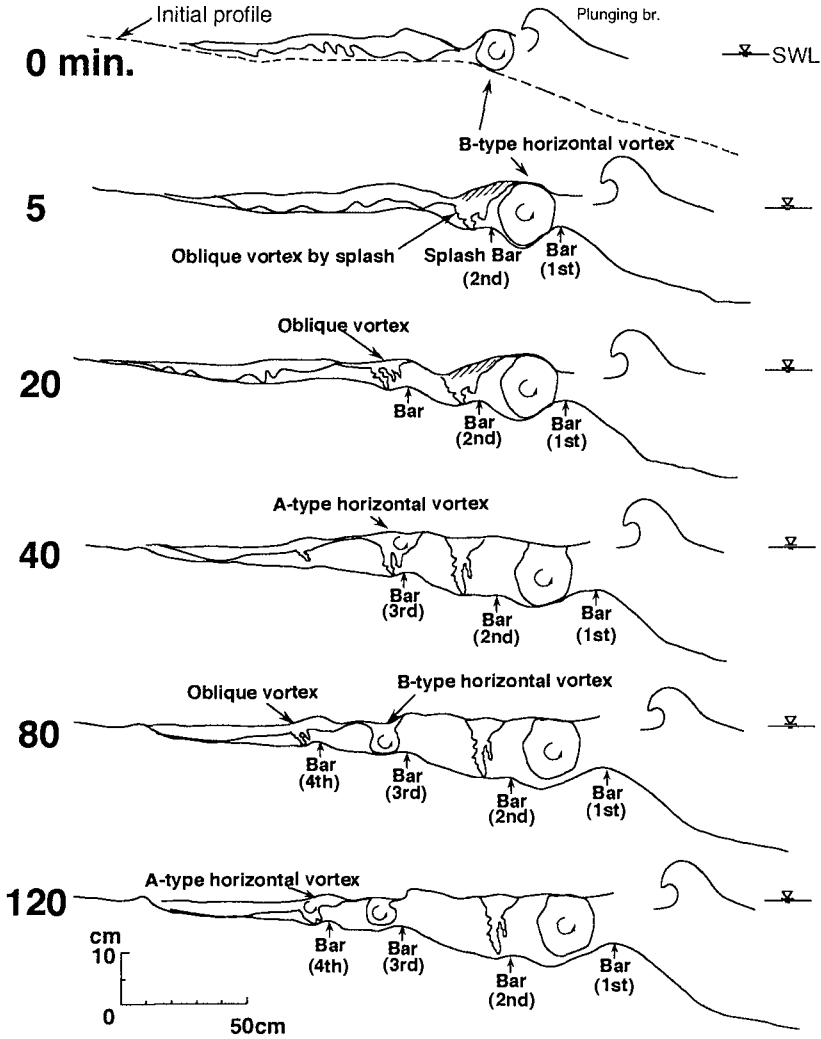
#### Simultaneous and Successive Modes for Multiple Bar Formation

Figure 9 shows an example of simultaneous mode of double bars. The initial morphology was a berm profile. During the first 5-minute wave action, two bars started to form at the same time by two oblique vortices reaching bottom,



**Fig. 9 An example of simultaneous development of double bars**

respectively. The breaker-point bar, located offshore, grew to a large bar; then the breaker type changed from spilling to plunging, which resulted in the change of vortex type from the oblique vortex to the A-type and finally to the B-type horizontal after 40-minute wave action. At the same time, the vortex type near the inner bar changed from the oblique to the A-type horizontal vortex. After 80 minutes, the breaker-point bar attained the equilibrium with the B-type horizontal vortex having no significant force to further scouring of the trough, because the trough was too deep for the vortex to reach bottom any more. The inner bar disappeared after 80



**Fig. 10** An example of successive development of quadruple bars

minutes due probably to the decrease in force of the inshore vortex, which has already changed from the A-type to the oblique vortex at the stage of 80 minutes. In the present experiment, this type of bar development, i.e., simultaneous occurrence of bars, was observed in the cases in which the initial morphology was a berm or a berm-step. Simultaneous occurrence of multiple vortices acting on the bottom is

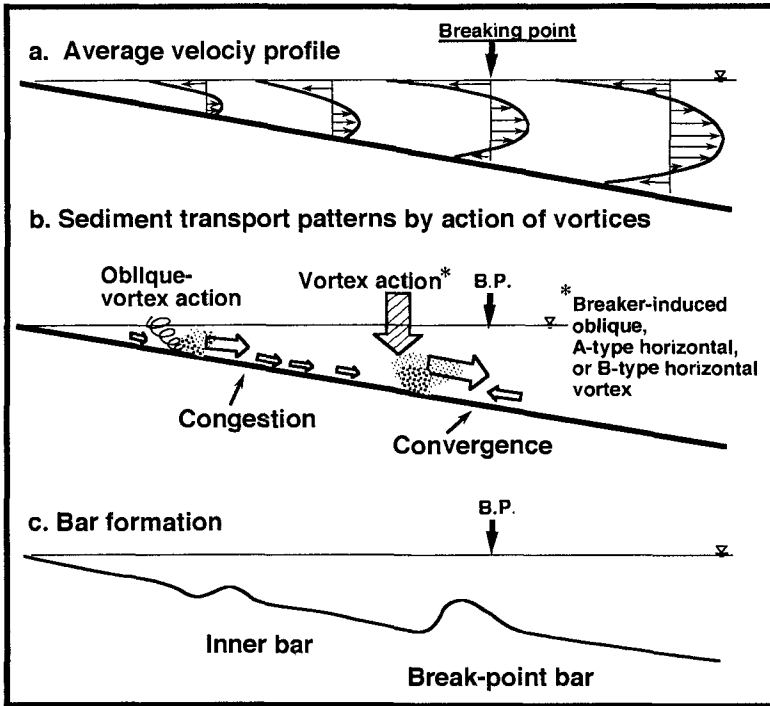


**Fig. 11** Formative processes of inner and break-point bars at the initial stage. (a) Average drift velocity profile in the surf zone; (b) different patterns of sediment transport by the action of vortices; and (c) formation of inner and break-point bars

necessary for simultaneous bar development.

Figure 10 shows an example of successive development of four bars. The initial morphology had a profile of a shallow shelf. During the first 5 minutes, the break-point bar was formed by the B-type horizontal vortex due to plunging breakers, and the second bar was formed inshore almost simultaneously by the action of oblique vortex produced by the strong shear flow of rushing bores induced by splash of the plunging breakers. At 20 minutes, the third bar appeared by the action of oblique vortex occurred further inshore. At 40 minutes this oblique vortex changed to the A-type horizontal vortex, which finally changed to the B-type horizontal vortex at 80 minutes. At the same time the second breakers were observed above the third bar. At this stage, the fourth bar was formed most landward by the oblique vortex. Finally, the equilibrium state of four bars was achieved when most vortices did not touch the bottom. This type of bar growth was observed in the cases in which the initial morphology was a shallow shelf.



As illustrated in Fig. 10, the multiple bars are formed successively from the wave break point to the inshore zone due to the coupling between the vortex action and nearshore topography. As the third bar clearly indicates, the order of change in vortex type occurring there is from oblique to A-type and finally to B-type horizontal vortices due to the interaction between bar growth and change in breaker type.

The present experiment showed that the second bar, as shown in this case (Fig. 10), was initiated by the vortex action induced by splash of plunging breakers, and it was always located deeper than and closer to the first bar. This type of bar is called a "splash inner bar" in this paper. A splash inner bar often occurred when plunging breakers acted on the beach.

### **Difference in Formative Processes Between Inner and Break-point Bars**

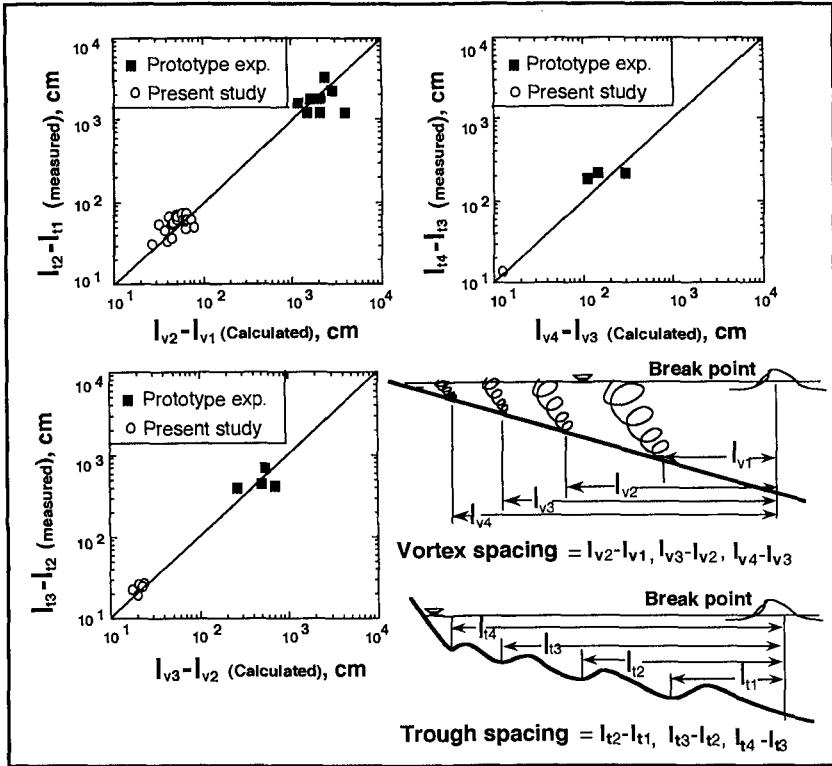
Figure 11a shows the average drift velocity profile in the surf zone induced by spilling breakers which may form bars; this result is obtained from the result of float observation in this study and supplemented by the results of studies by Pae and Iwagaki (1984), Svendsen (1984), and Wang et al. (1984). The average velocity is found to direct onshore in the upper layer of water column, and offshore in the middle to bottom layers within the surf zone, where the middle layer has higher offshore velocity than the bottom. The onshore velocity occurs near the bottom in the offshore zone including the break point.

Figure 11b shows two modes of net sediment transport under the action of vortices. One is the "congestion" in the surf zone. Sediment particles lifted by the vortex occurring inshore are more rapidly transported by the higher offshore velocity, whereas the sediment particles located adjacent to the vortex but not lifted by the action of the vortex are transported by the lower offshore velocity without suspension. The difference in sediment particle velocities directed offshore causes congestion. The other mode of sediment transport is the "convergence" near the wave break point. Sediment particles suspended by the action of the breaker-induced vortex are transported offshore by offshore-directed drift velocity, whereas sediment particles rested on the bottom seaward of the break point may be transported onshore by the onshore-directed drift velocity near the bottom. Convergence of transported sediments occurs immediately seaward of the place where the vortex acts on the bottom.

Figure 11c illustrates the inner bar formation by congestion, and the break-point bar formation by convergence. Sediment grain size that controls the height of suspension is also important in multiple bar formation. Sediment particles suspended by the surf-zone vortex would be transported to the break point to form the break-point bar, if the fall velocity of the sediment is too low to settle down immediately seaward of the vortex. In this case no inner bars would form.

### **RELATIONSHIPS BETWEEN CHARACTERISTICS OF MULTIPLE VORTICES AND MULTIPLE BAR FEATURES**

Figure 12 shows the relationship between vortex spacing (defined in this figure) calculated using Eq. (3) and the observed trough spacing using bar-profile data of small-scale experiments (the present experiment and Yokotsuka, 1985) and



**Fig. 12 Comparison of calculated vortex spacings and measured bar-trough spacings**

the existing prototype experiments (Sunamura and Maruyama, 1987; Kraus and Larson, 1988), except the "splash inner bar". This figure illustrates that the calculated value of vortex spacing is almost equal to the observed value of trough spacing. In the calculation using Eq. (3), a problem is how to evaluate  $\tan \beta$  for the case of non-uniform beach profiles. Considering that the wave breaking is crucial for multiple bar formation, the average beach slope shoreward of the wave break point,  $i$ , was used for  $\tan \beta$ . The average slope  $i$  is defined as

$$i = 2h/l \tag{7}$$

where  $h$  and  $l$  are the average water depth and the width of the surf zone (from the wave break point to the still-water line), respectively. The average depth  $h$  is given by

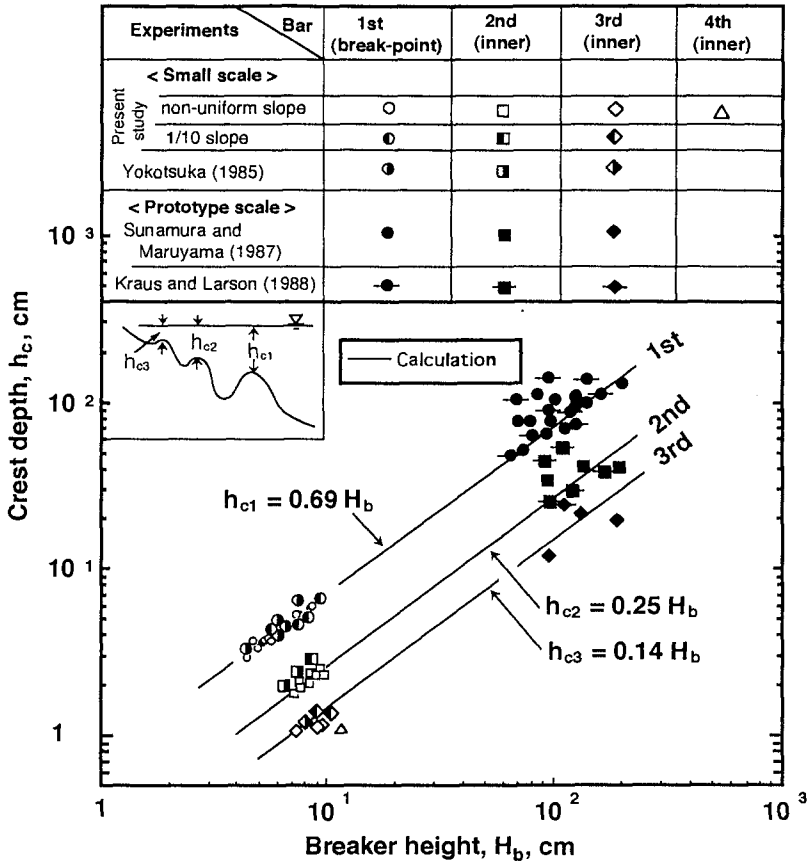


Fig. 13 Relationship between bar-crest depth and breaker height

$$h = \frac{1}{l} \int_0^l h(x) dx = S/l \tag{8}$$

where  $S$  is the cross-sectional area of the surf zone. From Eqs. (7) and (8), we have

$$i = 2S / l^2 \tag{9}$$

The relationship between the breaker height and the water depth at the crest of

n-th bar is shown in Fig. 13, using data of the above-mentioned small-scale and prototype experiments; data of the "splash inner bar" were again excluded. It was found that the water depth of bar crest is independent of time and is almost equal to the water depth where the vortex reaches bottom at the initial stage (Zhang, 1994). Assuming that the water depth of vortex reaching bottom is equal to the water depth of bar crest, the following equation is obtained from Eq. (6):

$$h_{cn} = 0.69 n^{-1.44} H_b \quad (10)$$

where  $h_{cn}$  is the water depth of n-th bar crest. The straight lines in this figure are the result of calculation by use of this equation substituting  $n=1, 2,$  and  $3$ . It is seen that calculation and experiment are in fairly good agreement.

## CONCLUSIONS

- (1) Bars are only formed by the vortices reaching bottom; the number of bars formed coincides with the number of vortices reaching bottom. The occurrence of vortices reaching bottom in the surf zone is crucial for the multiple bar formation.
- (2) Average drift velocity and sediment suspension due to vortex action can play an important role in bar formation. The mechanism for break-point bar formation is "convergence"; however, that for inner bar formation is "congestion"(Fig. 11).
- (3) Multiple-bar features such as trough spacing and crest depth can be explained from vortex features found through a fixed-bed experiment (Figs. 12 and 13).

## ACKNOWLEDGMENTS

Part of this study was made under the Grant-in-Aid for Scientific Research from Ministry of Education, Science and Culture to TS (B-04452329).

## REFERENCE

- Aagaard, T. 1991. "Multiple-bar morphodynamics and its relations to low-frequency edge wave," *J. Coastal Res.*, 7, pp. 801-813.
- Bowen, A. J. 1980. "Simple models of nearshore sedimentation: beach profiles and longshore bars," In: *The Coastline of Canada*, edited by S. B., McCann, Geological Survey of Canada, Paper 80-10, pp. 1-11.
- Dhyr-Nielsen, M. and Sorensen, T. 1970. "Sand Transport Phenomena on Coasts with bars," *Proc. 12th Conf. Coast Eng., Am. Soc. Civil Eng.*, pp. 855-866.
- Dolan, T. J. and Dean, R. G. 1985. "Multiple longshore sand bars in the upper Chesapeake bay," *Estuarine Coastal Shelf Science*, 21, pp. 727-743.
- Exon, N. F. 1975. "An extensive offshore sand bar field in the western Baltic Sea," *Marine Geology*, 18, pp. 197-212.
- Kraus N. C. and Larson, M. 1988. "Beach profile change measured in the tank for large waves 1956-1957 and 1962," *Coastal Engineering Research Center, Technical Report 88-6*, 39 p.
- Nadaoka, K., Ueno, S., and Igarashi, T. 1987. "Characteristics of bottom velocity and sediment suspension in the surf zone," *Proc. 34th Japan. Conf. Coastal Eng.*, pp. 256-260 (in Japanese).
- Nadaoka, K., Hino, M., and Koyano, Y. 1989. "Structure of the turbulent flow field

- under breaking waves in the surf zone," *J. Fluid Mech.*, 204, pp. 359-389.
- O'Brien, M. 1968. "Multiple bar systems in Chesapeake Bay," MA. Thesis, College of William and Mary, Williamsburg, Virginia, 56 p.
- Pae, W. G. and Iwagaki, Y. 1984. "Mechanism of beach profile deformation due to on-offshore sand drift," *Proc. 19th Conf. Coastal Eng., Am. Soc. Civil Eng.*, pp. 2124-2139.
- Short, A. D. 1975. "Multiple offshore bars and standing waves," *J. Geophys. Res.*, 80, pp. 3838-3840.
- Suhayda, J. N. 1974. "Standing waves on beaches," *J. Geophys. Res.* 79, pp. 3065-3071.
- Sunamura, T. 1985. "Predictive relationships for position and size of longshore bars," *Proc. 32nd Japan. Conf. Coastal Eng., JSCE*, pp. 331-335 (in Japanese).
- Sunamura, T. and Maruyama, K. 1987. "Wave induced geomorphic response of eroding beaches with special reference to seaward migrating bars," *Proc. Coastal Sediments '87, Am. Soc. Civil Eng.*, pp. 788-801.
- Sunamura, T. and Takeda, I. 1993. "Bar migration and shoreline change: predictive relations," *J. Coastal Res.*, SI, 15, pp. 125-140.
- Svendsen, I. A. 1984. "Mass flux and undertow in a surf zone," *Coastal Eng.*, 8, pp. 347-365.
- Wang, H., Sunamura, T. and Hwang, P. A. 1982. "Drift velocity at the wave breaking point," *Coastal Eng.*, 6, pp. 121-150.
- Yokotsuka, Y. 1985. "A wave-tank study on topographical change of sandy beaches," Unpublished BSc Thesis, Institute of Geoscience, University of Tsukuba, 51 p. (in Japanese with English abstract).
- Zhang, D.P., 1994. Wave flume experiments on the formation of longshore bars produced by breaking waves, *Sci. Rept., Univ. Tsukuba, Sect. A, Vol. 15*, pp.71-127.
- Zhang, D. P. and Sunamura, T. 1990. "Conditions for the occurrence of vortices induced by breaking waves," *Coastal Eng. Japan*, 33, pp. 145-155.

## CHAPTER 207

### IDENTIFICATION OF SOME RELEVANT PROCESSES IN COASTAL MORPHOLOGICAL MODELLING

Hakeem Johnson<sup>1</sup>, I. Brøker<sup>1</sup>, J.A. Zyserman<sup>1</sup>

**ABSTRACT:** This paper presents a coastal morphology modelling system based on an explicit forward time integration scheme for the morphological evolution involving the following stages: a) Initialisation, b) Sediment transport computation using a deterministic sediment transport model, c) Wave computation using an arbitrary wave model, d) Hydrodynamic computation assuming a mobile bed evolving at  $\partial z/\partial t$ , with optional use of a module to determine the apparent roughness in combined wave-current motion and e) Bed level update scheme using an improved second order Lax Wendroff scheme. A series of numerical tests is performed with the aim of evaluating the effect of space-varying hydraulic roughness in combined waves and current, choice of wave modelling approach and of directionality of the waves on the morphological evolution. A detached breakwater is used as test case.

#### INTRODUCTION

The numerical modelling of morphological evolution in coastal areas has experienced an important development in recent years and is becoming a feasible alternative to physical modelling. The morphological modelling system considered here

---

<sup>1</sup>) Danish Hydraulic Institute, Agern Allé 5, DK 2970 Hørsholm, Denmark

consists of a wave module, a depth-integrated hydrodynamic module (in which the two horizontal dimensions are taken into account), a quasi-3D sediment transport module (Deigaard et al., 1986) and a modified second order Lax-Wendroff scheme for updating the bed level. A module for accounting for the effect of wave-related bed roughness on the current (Fredsoe, 1984) is also included in the modelling system. In the morphological model, the way in which the different modules are coupled is user-specified; for example, the influence of currents on wave refraction (influence of current module on wave module) may be accounted for or not; the same applies to the influence of waves on the apparent bed resistance for currents (influence of wave module on current module).

While the flow of information among the different modules and the inherent stability of such a modelling system have been discussed in detail (de Vriend, 1987 and de Vriend et al., 1993), an assessment of the influence of relevant parameters related to practical aspects of morphological modelling is still lacking. A series of numerical tests has therefore been devised in order to identify relevant parameters from the point of view of coastal area morphological modelling. The following aspects have been considered:

- The type of wave model used to simulate the propagation and transformation of the nearshore wave field
- The influence of directional spreading of the waves
- The influence of accounting for the apparent (wave-related) bed roughness on the current field, and consequently on the sediment transport field and the rates of bed level change.

The use of the model complex in practical engineering situations is further illustrated by investigating the morphological evolution behind a detached breakwater using different layouts and wave parameters.

## DESCRIPTION OF THE MODELLING COMPLEX

The modelling of the morphological response in the coastal zone, both on a natural coast and a coast influenced by structures, requires in principle simultaneous simulation of waves, currents and sediment transport, as the bathymetry develops.

Considering the various time scales which are involved, an explicit approach has been developed with sequential calculations of waves, currents, sediment transport and rates of bed level changes. The first version of the present model was described in Andersen, et al. (1988).

A block flow chart, showing the morphological modelling scheme, is illustrated in Figure 1. This figure is explained as follows: Given the initial bathymetry and

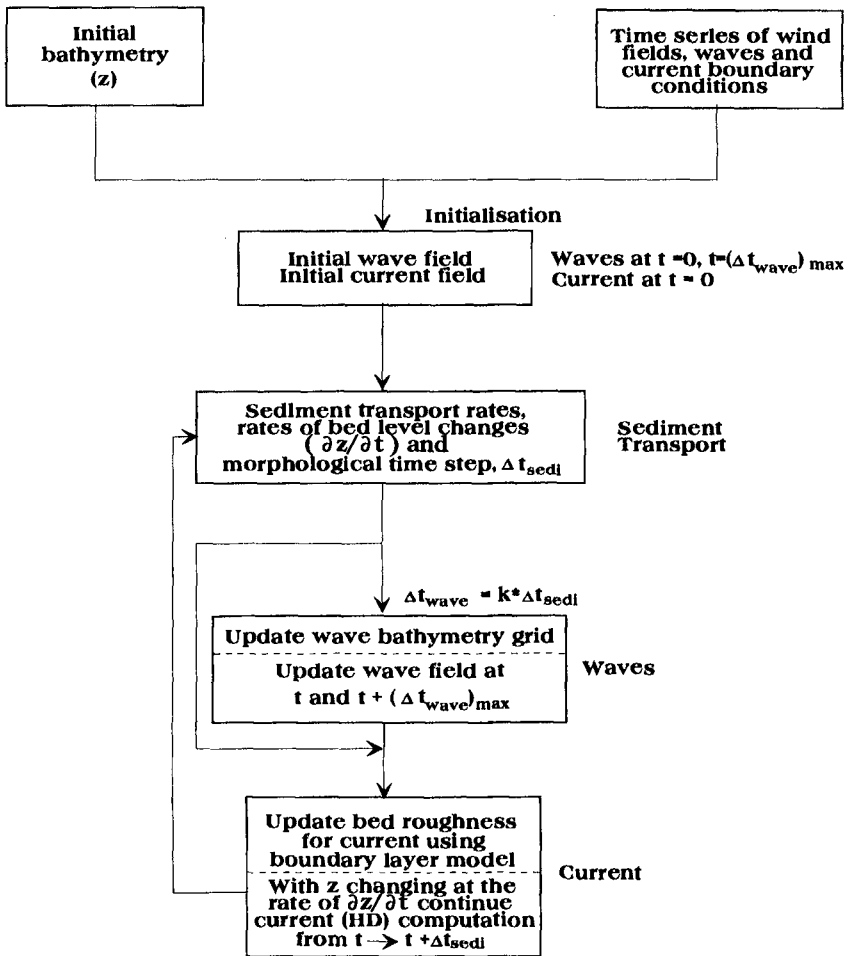


Figure 1. Block flow chart for morphological model.

time series of boundary wave and current conditions, the initial wave and current fields are first computed before entering the morphological loop. Then the loop is entered and the sediment transport, the rates of bed level changes  $\partial z/\partial t$  and the allowable maximum morphological time step,  $\Delta t_{\text{sedi}}$  (based on the stability condition for the bed update scheme) are computed. Next the wave field is updated



if necessary (since this is done every  $k$ -th update of the sediment transport field, where  $k$  is an integer  $\geq 1$ ). Next the bed resistance map is updated taking into account the apparent roughness in combined wave-current motion using a boundary layer model, and lastly the hydrodynamic calculation is continued from present time,  $T$ , to  $T+DT_{\text{sedi}}$ , where the sediment transport field is updated. Using the calculated  $\partial z/\partial t$ , the bed level is gradually updated during the hydrodynamic computation. The whole process is then repeated in a cyclical loop until the prescribed length of simulation is completed.

In the sections below, the modules in the modelling complex are described.

### Wave Models

The wave models presently built into the morphological complex are: an elliptic mild slope model, MIKE 21 EMS, a parabolic mild slope model, MIKE 21 PMS and a spectral nearshore wind wave model, MIKE 21 NSW.

MIKE 21 EMS is a linear refraction-diffraction wave model including back-scattering and wave breaking. The model solves the mild slope equation (Berkhoff, 1972), and includes a general formulation of radiation stresses which applies in crossing wave trains and in areas of strong diffraction. Of the three models, this is the most accurate for monochromatic linear waves under the test conditions chosen and is selected as our reference model. However, it is the one with the largest computational requirements.

MIKE 21 PMS is based on a simplification of the mild slope equation assuming wave propagation in one predominant direction ( $x$ -dir), neglecting diffraction in this direction and back-scattering in the opposite direction. Using the approach of Kirby (1986), this model is made to allow large-angle (up to 60 deg.) propagation to the  $x$ -dir. Furthermore, MIKE 21 PMS includes the effect of a frequency spectrum and directional spreading. The model is extremely cost-efficient and requires a very low computational effort, being approximately 50 times faster than the elliptic mild slope model for the same setup.

MIKE 21 NSW is a stationary directionally decoupled parametric model based on the wave action conservation equations as formulated by Holthuijsen et al. (1989). It describes the propagation, growth and decay of short-period waves in nearshore areas. The model takes into account the effects of refraction and shoaling due to varying depth as well as wind generation, energy dissipation due to bottom friction and wave-breaking plus the effect of current on these phenomena. Although this model does not include diffraction (an important effect behind the breakwater), it is nevertheless included in the analysis to illustrate the relative importance of this limitation.

In the three wave models, wave-breaking is formulated using the theory of Battjes and Janssen (1978).

#### Flow Model

The hydrodynamic module in the morphological modelling complex is MIKE 21 HD, which solves the vertically integrated equations of conservation of mass and momentum in two horizontal dimensions. The rate of bed level changes  $\partial z/\partial t$  has been included in the equation for conservation of water mass. The methods of solution are described in Abbott et al. (1973, 1981, 1988).

The hydrodynamic model is capable of operating with a space- and time-varying hydraulic roughness. The theory of Fredsøe (1984) for the apparent roughness in combined waves and currents has been implemented. The apparent roughness is updated every morphological time step.

The hydrodynamic model uses fluxes or levels as boundary conditions. In cases where the boundaries cut through the surf zone, the conditions are found from the radiation stress gradients assuming quasi-stationary flow.

#### Sediment Transport Model

A deterministic intra-wave period model for non-cohesive sediment is applied. A detailed description is given in Deigaard et al. (1986) It is noted that the model covers the range from pure current to combined current and waves (breaking or non-breaking). It is a basic assumption in the present model complex that the transport capacity is a function of the local conditions only, ie. no time and space lag effects are included.

#### The Bed Level Changes $\partial z/\partial t$

The rates of bed level change are described by the equation of continuity:

$$\frac{\partial z}{\partial t} + \frac{1}{1-n} \frac{\partial q_x}{\partial x} + \frac{1}{1-n} \frac{\partial q_y}{\partial y} = 0$$

where  $x$ ,  $y$  and  $z$  are horizontal and vertical space coordinates, respectively;  $t$  is time,  $n$  is porosity and  $q_x$ ,  $q_y$  are sediment transport rates in  $x$ - and  $y$ -directions. A second-order accurate explicit finite-difference method is applied. The truncation errors are eliminated by applying a modified Lax Wendroff scheme, see Abbott (1978). The solution is kept stable by adjusting the morphological timestep so that the maximum Courant number, reflecting migration rates of bed forms, is  $\leq 1$ .

## THE CHOICE OF WAVE MODEL

The most appropriate wave model must be chosen depending on the dominating phenomena in the area to be studied using the morphological model. Morphological modelling requires many repetitive calculations of the wave field. Consequently, there is a need for finding the optimal balance between accuracy and computational effort.

The problem has been investigated by calculation of the initial wave, current and sediment transport fields behind an offshore breakwater for normally incoming waves with the three wave models available in the morphological complex: the elliptic mild slope model, EMS, the parabolic mild slope model, PMS, and the spectral wind wave model, NSW.

The phenomena shoaling, depth refraction and breaking are all well described by the three models. Diffraction is best described by the elliptic model, approximately by the parabolic model and not at all in the spectral wind wave model. To compensate for the lack of wave energy penetration behind the breakwater in the case of the spectral wave model, this model was run with directional spreading of the incoming waves.

The studied configuration is a 300 m long shore-parallel breakwater located 280 m from the shoreline on a plane sandy beach with a slope of 1:50. The wave height ( $H_{\text{RMS}}$ ) and period are 2m and 8s, respectively, at 10 m water depth. The sediment is sand with a median grain size of 0.25 mm and a gradation  $\sigma_g$  corresponding to  $(d_{84}/d_{16})^{1/2} = 1.1$ .

A grid spacing of 5m was used in the EMS and PMS models. Furthermore, the front face of the breakwater is assumed to have zero reflection in the EMS model. This is achieved by placing a 5-line sponge layer inside the breakwater. The incident wave field is assumed to be monochromatic and unidirectional in the EMS and PMS models. For the NSW model, the grid spacing was chosen as  $DX=2\text{m}$ ,  $DY=10\text{m}$  and a  $\cos^2$  directional spreading function was used. The bed roughness in the wave models was chosen as 1.5mm.

The radiation stresses from the wave models are interpolated to a square grid with  $DX=DY=10\text{m}$  used for the hydrodynamic simulations. The hydrodynamic time step is 6 s and a bed roughness corresponding to a Manning number (in the Strickler sense) of 32 is used.

Figure 2 shows the contours of wave heights, wave-induced currents and sediment transport vectors from the three models.

Although the NSW model does not include diffraction, some wave energy can be observed behind the breakwater due to the use of a broad-banded ( $\cos^2$ ) directional

spectrum. However, the computed NSW wave heights in the diffraction zone are much smaller than corresponding EMS waves, while the PMS wave heights are generally closer to the EMS waves.

All three models drive two eddies between the breakwater and the shoreline. The maximum current speed in the EMS model is slightly greater than 1m/s, which is nearly the same as obtained with the PMS model. However, the current speeds are generally lower for the NSW model, the maximum in this case being about 0.8m/s. The difference in wave-induced currents between NSW and the others is partly due to directional spreading in NSW: the directional spreading results in a smoothing of the radiation stress field, and hence in a reduction of the radiation stress gradients.

The combined wave and current fields are used for calculating the sediment transport rates. As can be expected from a comparison of the waves and current fields, the sediment transport rates computed using the NSW model are about a factor 3 smaller than those calculated using the EMS model. In contrast, the PMS model results are generally much closer to the EMS values, except for the alternating high and low transport rates computed close to the shoreline behind the breakwater which arise from alternating bands of high and low wave heights (constructive/destructive interference) which are well described by the EMS model, but only partially modelled in the PMS model.

It is concluded that the PMS model is an optimal choice for computing the sediment transport field and hence the morphology response behind the offshore breakwater, since it gives comparable results to the EMS model at a much lower cost.

The NSW model is found to be unsuitable for computing sediment transport rates for the test setup selected in which diffraction is an important phenomenon.

## EFFECTS OF DIRECTIONAL SPREADING

The effects of directional spreading of the waves on the flow field and on the sediment transport field have been investigated with a similar setup as used for the discussion of types of wave model. The parabolic mild slope model has been applied and the direction of the waves at 10m depth is  $10^\circ$ . Furthermore, the distance from the shoreline to the breakwater is now 200m. Simulations have been made with unidirectional waves and with directional spreading. Five (5) directional components have been used to resolve the directional energy spectrum which at 10m water depth is described as  $\cos^5(\theta - \theta_{\text{mean}})$ .

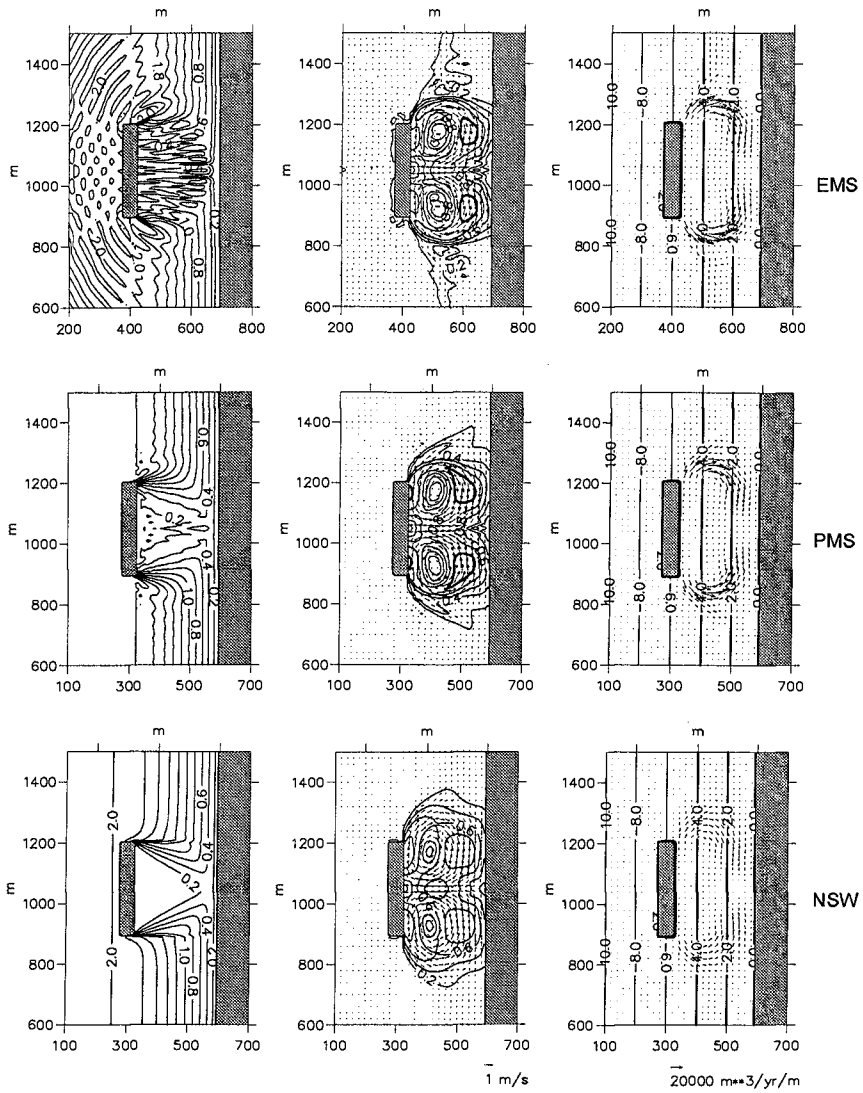


Figure 2. Contours of wave heights (a), current speeds (b) and sediment transport field (c).

The calculated initial wave, current and sediment transport fields are shown in Figure 3.

The comparison of the two wave heights fields shows an increase of  $H_{RMS}$  behind the breakwater in the case of directional waves compared to unidirectional waves. The longshore currents and the littoral drift are both decreased along the open coast due to the directional spreading. However, the sediment transport into the area behind the breakwater has increased with the directional spreading, both from 'updrift' and from 'downdrift'. This is also seen from the comparison of longshore sediment transport shoreward of the breakwater.

The different changes in the transport along the open coast and behind the breakwater indicate that the directional spreading also influences the morphological response.

### EFFECT OF APPARENT ROUGHNESS

The effect of the apparent hydrodynamic roughness due to the presence of a turbulent wave boundary layer on the morphological evolution is evaluated by comparison of initial current and transport fields calculated using a constant hydraulic roughness,  $k_N = 0.625$  mm (grain roughness) and an apparent roughness,  $k_w$ , respectively.  $k_w$  is calculated according to Fredsøe (1984). The data for these tests is as follows: length of the breakwater is 100 m, distance from shoreline is 200m, beach slope is 1:50 out to 10m depth, grain size ( $d_{50}$ ) is 0.25, gradation ( $\sigma_g$ ) is 1.1, wave height  $H_{RMS}$ , direction, period (at 10 m depth) are respectively 2.0 m,  $10^\circ$  and 8s. The waves are unidirectional and the model used is MIKE 21 PMS.

The two sets of results are compared in Figure 4. The presence of the wave boundary layer increased the hydraulic roughness by a factor of 5 to 10 in the area most relevant with respect to sediment transport. This leads to reduction of current speeds with a factor of about 0.6 and reduction of the sediment transport with a factor of 0.3 - 0.5.

From the comparison of littoral drift shoreward of the breakwater shown in Figure 4, it appears that apart from an obvious difference in time scale of the morphological response the non-linearities will lead to a different erosion/deposition pattern when the space-varying roughness is included.

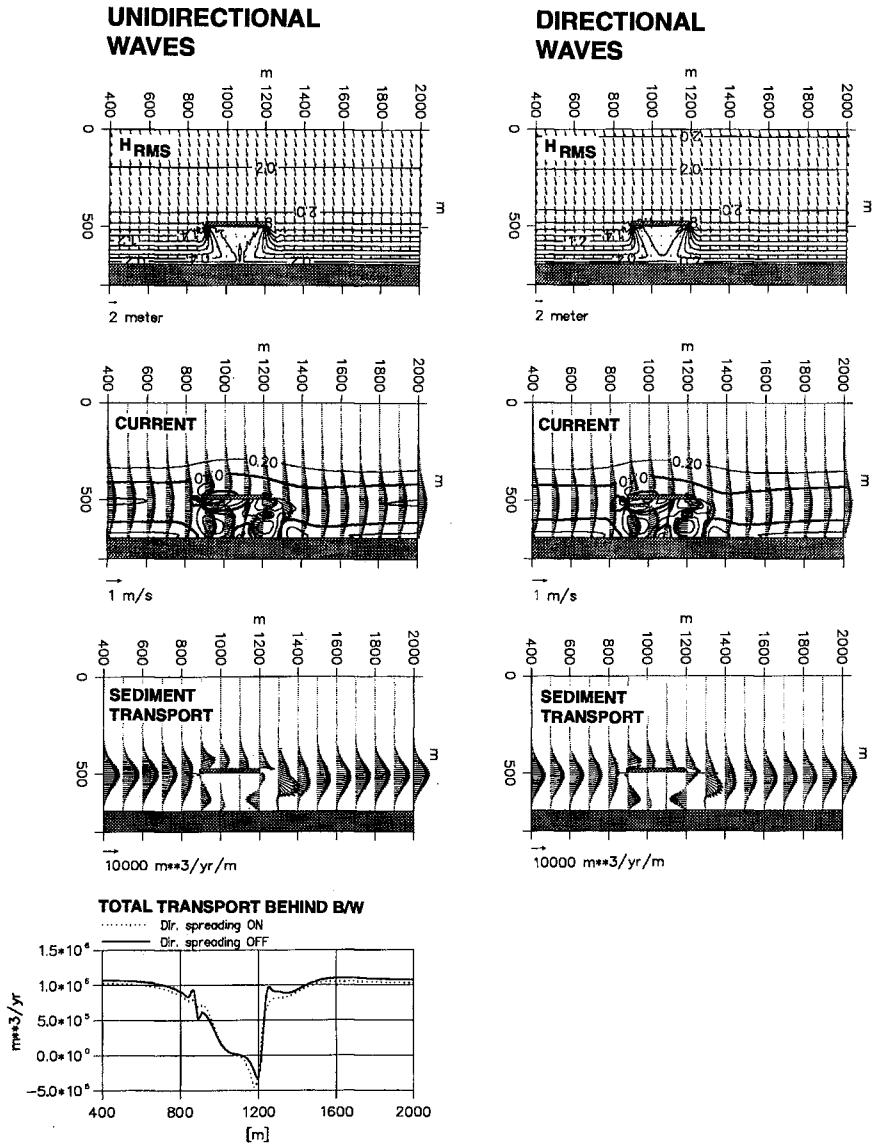


Figure 3. Wave, current and sediment transport fields for unidirectional and directional waves. Comparison of longshore sediment transport.

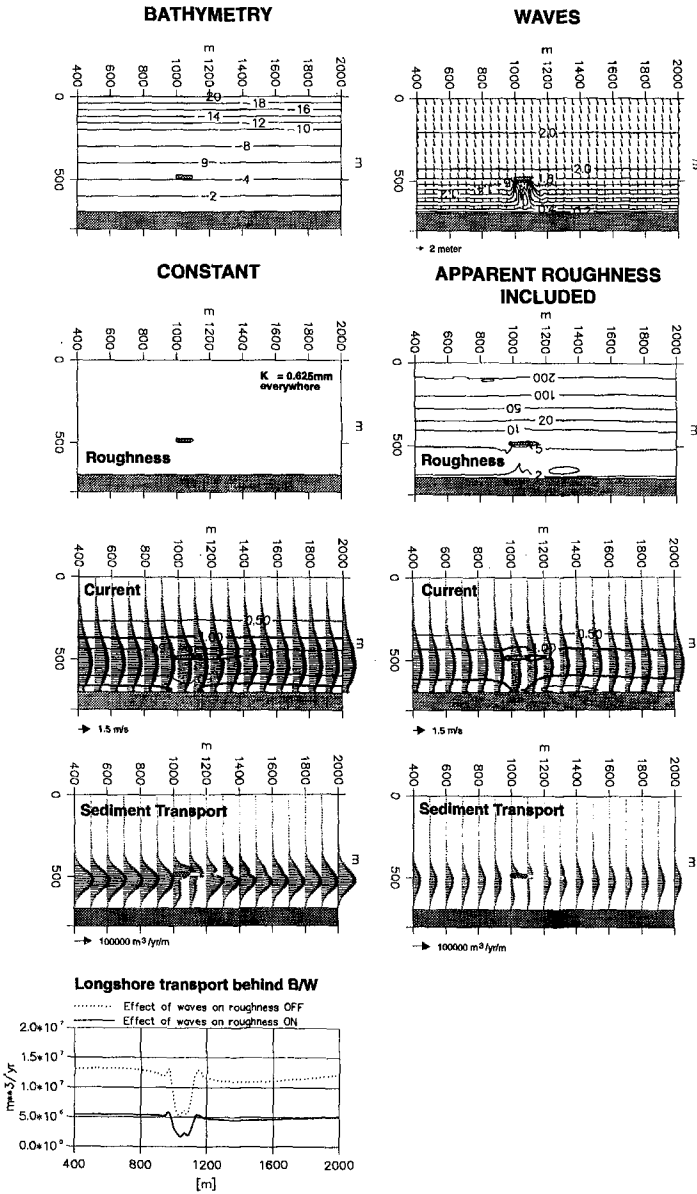


Figure 4. Roughness distribution and current- and sediment transport fields for constant and wave-enhanced roughness. Comparison of longshore sediment transport.



## ON THE EFFECTS OF SHORE-PARALLEL BREAKWATERS

The overall purpose of discussing morphological models is to produce tools to guide and support the design of coastal structures.

Although the present modelling complex does not include all relevant processes, a first attempt at a systematic study of the effects of shore-parallel breakwaters on sandy beaches has been initiated.

The initial conditions for all the presented simulations are a plane beach with a slope of 1:50 extending out to a depth of 10 m. The coastline is a fixed boundary which cannot be eroded. The incoming waves have been kept constant in time along the offshore boundary. The morphological evolution has been simulated for different dimensions of the breakwater and different incoming waves. The applied model setup is as previously described. The wave module applied is MIKE 21 PMS and the waves have been taken as unidirectional.

In Figure 5, the bed contours after a certain period of time are shown for varying angle of the incoming waves, varying wave height, varying distance from the shore to the breakwater and varying length of the breakwater. For the four different comparisons all other parameters are kept constant. (Note that in Figure 5, areas between the 0.5m contour and the shoreline are black. This is only to make the illustration clear).

The simulations indicate that localised scour occurs around the heads of the breakwater and a double or single-peaked salient forms behind the breakwater.

With increasing angle of the incoming waves the pattern changes from being localised redistribution of sediment to a trap for the littoral drift followed by downdrift erosion.

The salient peak 'updrift' decreases, while the 'downdrift' peak increases and is shifted further downdrift with increasing angle.

Sand ridges oriented at an obtuse angle to the shoreline are also seen for the simulations with large angle of incidence. The reason for the occurrence of this ridges is still under investigation.

As the distance of the breakwater to the shoreline decreases, there is a reduction of the scour around the breakwater heads and a greater tendency of tombolo formation.

With decreasing wave height, the surf zone becomes narrower, accompanied with a decreasing total littoral drift and a slower overall morphological response. However, it is noted that the deposition close to the shoreline is slightly increased for

the smaller waves due to the fact that the trapped littoral transport in this case is trapped in the very narrow surf zone close to the shore, as opposed to being distributed over a wide surf zone as for the high waves.

The length of the breakwater and the distance from shore both influence the development of the salient, and determine whether it is single or double-peaked.

These first results are only indicative and future long simulations and detailed quantitative analysis are expected to contribute considerably to the established knowledge of design of breakwaters.

### **CLOSING REMARKS**

The effects of a number of relevant processes in coastal morphological modelling have been investigated in this paper. The processes considered are: (1) the choice of wave model, (2) effect of directional spreading, and (3) the influence of wave boundary layer on the hydraulic roughness used in flow modelling. It is concluded that the above processes influence the results of the morphological modelling.

Using the presented model complex, the morphological response of a single detached breakwater subject to different wave conditions was investigated. A qualitative description of the effects of various layouts and wave conditions is also presented. The occurrence of sand ridges downdrift of the breakwater for large angle of wave incidence is noted, however this subject is still under investigation.

Overall, these first results are indicative and future work is expected to contribute considerably to the established knowledge on morphological modelling and the design of offshore breakwaters.

### **ACKNOWLEDGEMENT**

This work has been carried out as a part of the G8 Coastal Morphodynamics research programme. It was funded jointly by the Danish Technical Research Council (STVF) within the frame of the 'Marin Teknik' programme and the Commission of the European Communities, Directorate General for Science, Research and Development, under contract no. MAS2-CT92-0027.

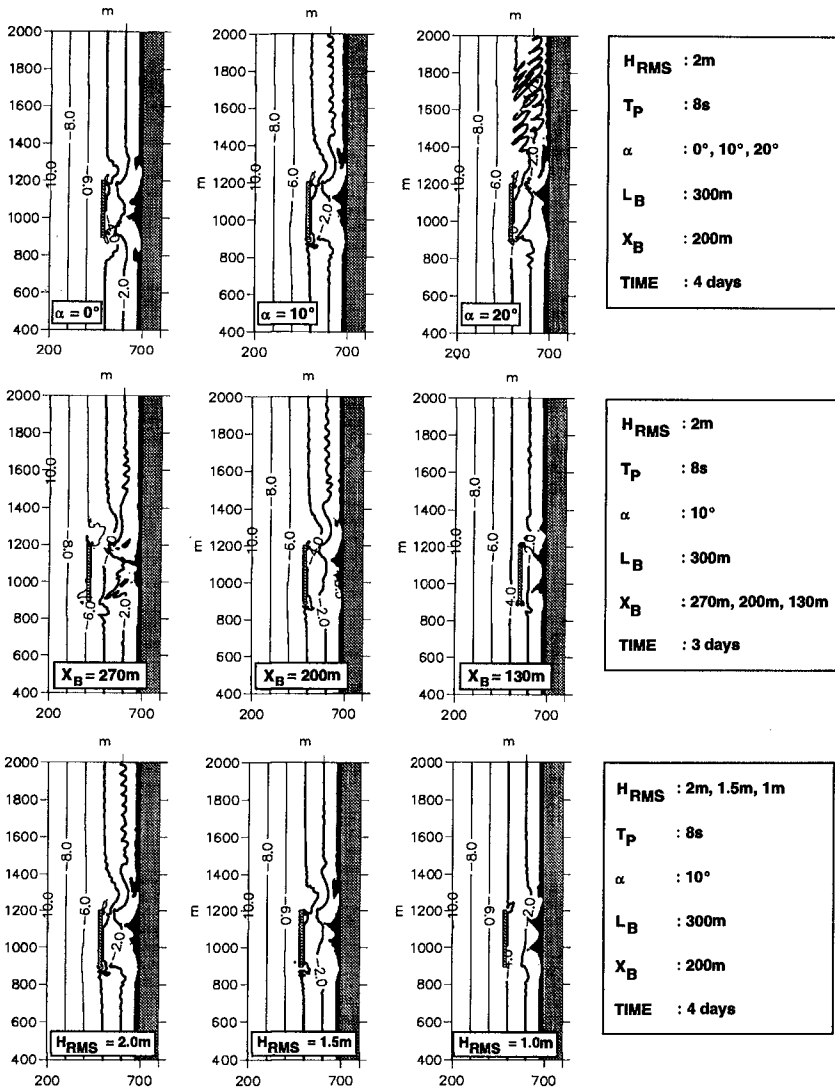


Figure 5. Simulated bathymetries for different combination of breakwater design and wave parameters. Common parameters: initial bed slope 1:50, medium grain size 0.25 mm,  $\sigma_g = 1.1$ .

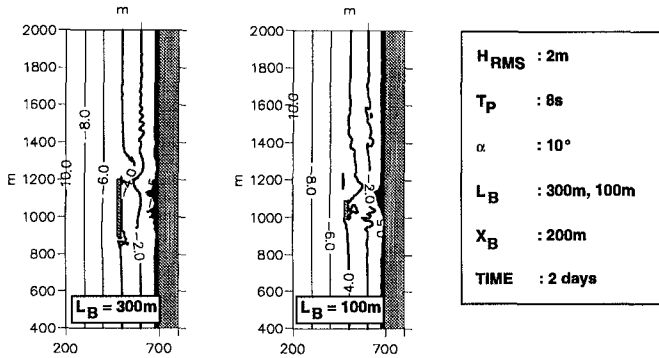


Figure 5 cont'd.

## REFERENCES

- Abbott, M.B. (1979): 'Computational Hydraulics, Elements of the Theory of Free Surface Flows', Pitman Publishing, London.
- Abbott, M.B., H. Shoaling & I.R. Warren (1988): 'Auto-dispersion processes in numerical models', *Computer Modelling in Ocean Engineering, Venice, 1988, Balkema*, pp. 723-727.
- Abbott, M.B., A. McCowan & I.R. Warren (1981) 'Numerical Modelling of Free-surface flows that are Two-dimensional in Plan', *Transport Models for Inland and Coastal Waters, Academic Press*, 1981, pp. 222-283.
- Abbott, M.B., A. Damsgaard & G.S. Rodenhuis (1973) 'System 21, Jupiter, A Design System for Two-dimensional Nearly Horizontal Flows', *Journal of Hydraulic Research*, Vol. 11, 1973, pp. 1-28.
- Andersen, O.H., I.B. Hedegaard, R. Deigaard, P. Girolamo and P. Madsen (1988): 'Model for Morphological Changes Under Waves and Current', *Proc. IAHR Symp. on Math. Modelling of Sediment Transport in the Coastal Zone, Copenhagen*.
- Battjes J.A., Janssen J.P.F.M.(1978) 'Energy loss and set-up due to breaking in random waves' *Proceedings of the 16th International Conference on Coastal Eng.* pp 569-587, ASCE.
- Berkhoff, J.C.W. (1972): 'Computation of combined refraction-diffraction', *Proc. 13th Coastal Engrg. Conf.*, Vancouver pp. 471-490.
- Deigaard R., J. Fredsøe, I. Brøker Hedegaard (1986) 'Suspended sediment in the surf zone', *Journal of the Waterway, Port, Coastal and Ocean Eng.* ASCE, Vol 112, No. 1, pp. 115-128.
- De Vriend, H.J. (1987): 'Analysis of 2DH morphological evolutions in shallow water'. *Jour. Geoph. Res.*, Vol. 92, No. C4, pp 3877-3893.
- De Vriend, H.J., J.A. Zyserman, J. Nicholson, J.A. Roelvink, Ph. Pêchon and H.N. Southgate (1993): 'Medium-term 2DH coastal area modelling', *Special Issue Coastal Engineering*, pp. 193-224.
- Fredsøe J. (1984) 'The turbulent boundary layer in combined wave-current motion', *J. of Hydraulic Eng.* ASCE Vol. 11, pp. 1103-1120.
- Holthuijsen, L.H., N. Booij and T.H.C. Herbers (1989): 'A prediction model for stationary, short-crested waves in shallow water with ambient current', *Coastal Engrg.* Vol. 13, pp. 23-54.
- Kirby, J.T. (1986): 'Rational approximations in the parabolic equation method for water waves' *Coastal Engrg.* Vol. 10, pp. 355-378.
- Madsen, P.A. and J. Larsen (1987): 'An efficient finite difference approach to the mild-slope equation', *Coastal Engrg.* Vol. 11, pp. 329-351.

## CHAPTER 208

### Experimental Shoreface Nourishment, Terschelling (NL)

J.P.M. Mulder<sup>1</sup>, J. van de Kreeke<sup>2</sup>, P. van Vessem<sup>1</sup>

#### Abstract

An experimental shoreface nourishment was implemented at Terschelling, the Netherlands in 1993. The effectiveness of this nourishment will be evaluated in the framework of an EU sponsored project NourTEC.

The design of the Terschelling nourishment including the objectives and alternatives, are described in detail. Preliminary monitoring results lead to a cautious optimism with regard to the performance of the nourishment.

#### NourTEC: evaluation of innovative nourishment techniques

Full scale experiments with alternative coastal nourishment techniques, including shoreface nourishments, are being carried out in three countries around the North Sea: at the island Terschelling in the Netherlands, at the island Norderney in Germany and at the closed barrier coast near Torsminde Tange in Denmark (Fig. 1; Table 1). A comparative analysis of all these experiments is planned within the project NourTEC.

---

<sup>1</sup> Rijkswaterstaat, National Institute for Coastal and Marine Management (RIKZ), P.O. Box 20907, The Hague, The Netherlands

<sup>2</sup> Rijkswaterstaat, National Institute for Coastal and Marine Management (RIKZ), *visiting from:* Rosenstiel School of Marine and Atmospheric Science, University of Miami, 4600 Rickenbacker Causeway, Miami, Florida, USA

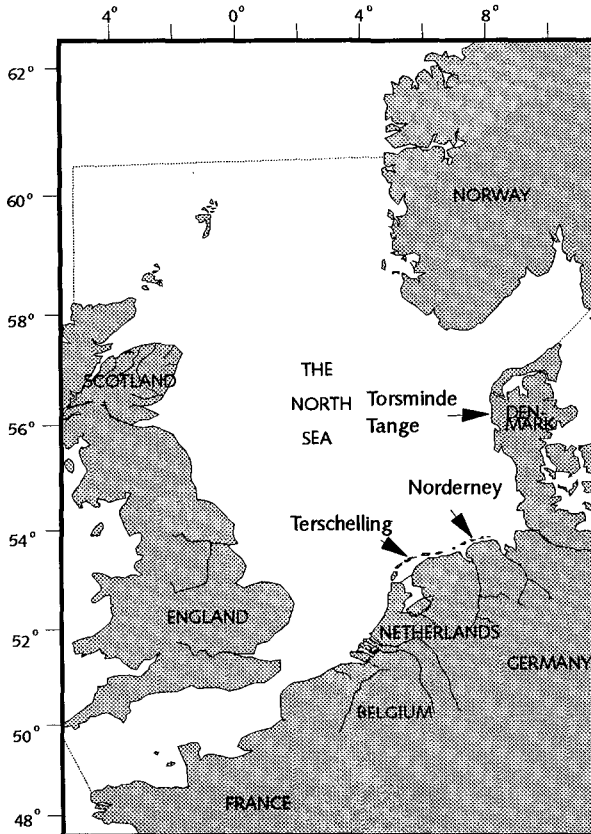


Fig. 1 Location of the three NOURTEC test sites

NOURTEC locations	nourishment type	total amount ( Mm <sup>3</sup> )	averaged volume ( m <sup>3</sup> /m )	year
Terschelling (Netherlands)	- shoreface	2	450	1993
Norderney (Germany)	- combined shoreface- and beach	0.45	250	1992
Torsminde Tange (Denmark)	- shoreface	0.25	250	1993
	- beach	0.25	250	1993

Table 1 Characteristics of nourishment experiments in the NOURTEC project

In particular, Nourtec aims at generalized conclusions on the design, the effectiveness and the feasibility of shoreface nourishment techniques in different coastal environments.

In general, shoreface nourishments can be used to attain one, or a combination, of the following design objectives (i) coastline stabilization, (ii) coastal protection, (iii) creating or maintaining a recreational beach. Although each of the Nourtec nourishment experiments has a specific design objective - i.e. coastal protection for Torsminde and Norderney and coastline stabilization for Terschelling - within the framework of Nourtec each will be evaluated for all of the above design objectives. The final report is due in 1996.

Each nourishment experiment is accompanied by an extensive monitoring program including frequent bathymetric surveys and monitoring of the offshore wave climate and nearshore tidal current field. In addition to this special process-oriented field programs are carried out (Hoekstra et al., 1994; Kroon et al., 1995).

This paper will focus on the design of the Terschelling nourishment (Nourtec, 1994) and some initial results of the monitoring program.

### Coastal defense policy in the Netherlands

About three-quarters of the Dutch coast consists of dunes and beaches. Together they offer a natural, sandy defence to the North Sea. Under the influence of nature, this barrier is constantly changing; advancing at one location, receding at another. In 1990 the Government and Parliament of the Netherlands instituted a new national coastal defence policy: dynamic preservation of the 1990 coastline. This policy is based on the concept of a standard or reference coastline, the so-called basal coastline (BKL). Whenever the actual coast line tends to move to a position landward of the basal coastline, the beaches will be restored.

The main method in the Netherlands, to preserve the 1990 coastline is beach nourishment. On a yearly basis 5 to 7 million m<sup>3</sup> of sand is added to the (dry) beaches.

### Definition of coastline

To arrive at a uniform measure for the overall change in a cross-shore profile, a critical region 0 - indicated by the hatched area in Fig. 2 - is defined. In the vertical direction the critical region extends between the elevation of the dune foot and a depth corresponding to twice the vertical distance between Mean

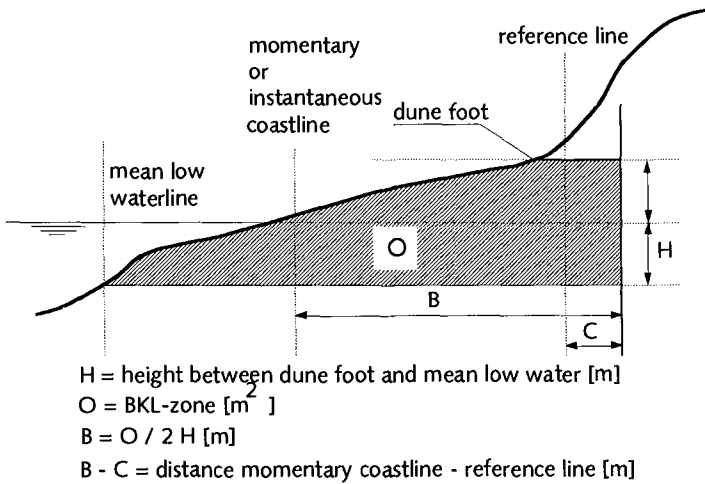


Fig. 2 Definition sketch of the BKL zone and the Momentary Coastline

Low Water (MLW) and the elevation of the dune foot. In the landward direction the critical region is bounded by a vertical line. The location of this line is sufficiently landward so that erosion is not encountered. This critical region is called the BKL - zone.

Making use of the concept of the BKL - zone, the momentary coastline is defined as a line located at a horizontal distance  $B$  seaward of the dune foot. The magnitude of  $B$  follows from  $B = O / (2H)$ . Note that in general the momentary coastline does not coincide with MLW. To document the position of the coastline, once a year cross-shore profiles spaced 200 - 250 m apart are measured along the entire Dutch coast. For each cross-shore profile, the values of  $O$  and  $B$  are calculated and the position of the coast line is referenced to fixed survey monuments.

To account for yearly fluctuations, a transient coastline (TKL) is defined. The TKL for a given year follows from the linear trend of the momentary coastline during the preceding ten years. As an example, in Fig. 4 the TKL for 1992 is indicated, based on coast line data over the period 1982 - 1991.

The TKL for 1990 was defined as the basal coastline.

#### Coastline retreat at Terschelling

The project site is located on the central part of the island of Terschelling; see Fig. 3. As an example of



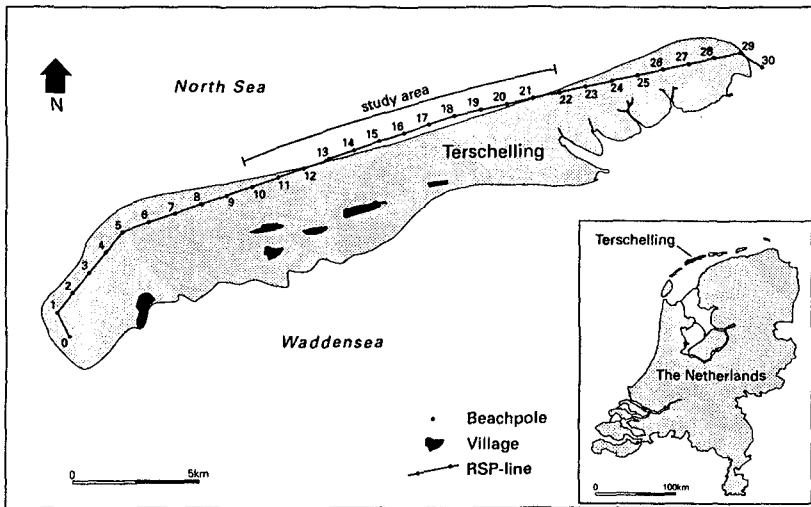


Fig. 3 Location of nourishment at Terschelling; the numbers correspond with km-positions of the cross-sectional profiles along the coast

coastline retreat the position of the coastline over the period 1965 to 1991 at km 16.00 is plotted in Figure 4. In the same figure the position of the basal coastline (BKL) and the transient coast line (TKL) for 1992 are presented. The transient coast line suggests that at km 16.00, the TKL 92 will soon retreat to a position landward of the BKL. Calculations showed that for 68 % of the profiles between km 13.70 and 17.80 the TKL 92 had already crossed the BKL. On this basis it was decided that for this stretch of the Terschelling coast the coast line had to be restored by means of a nourishment. Because of the west to east direction of the littoral drift, the project area was extended to km 18.20.

To calculate the amount of sand required to assure that the TKL for the next ten years remains landward of the BKL, the erosion rates were determined from the trend lines of the various profiles. Erosion rates for the project area range between 1- 5 m /year. This corresponds to a loss of approximately 110 thousand cubic meters per year. If this trends continues, 1.10 million cubic meters of sand will have been removed out of the BKL-zone in the next ten years.

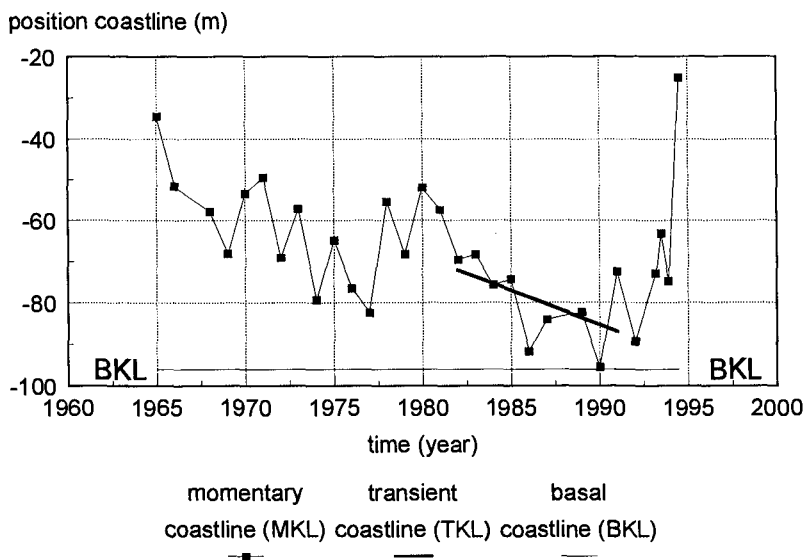


Fig. 4 Coast line development at km 16.00; indicated are the Transient Coastline (TKL) for 1992 derived from the period 1982 - 1991, and the Basal Coastline (BKL). Note the remarkable positive trend after the nourishment (Nov 1993 - June 1994).

### Design objectives

The design objectives are to return the TKL to a position seaward of the BKL and to assure that the TKL will not retreat landward of the BKL during the next ten years. Maintaining a sufficiently wide recreational beach and protecting the low-lying polderland landward of the dunes from storm surge are not acute problems and therefore are not part of the design objectives.

### Pertinent physical parameters

At the location of the project, the width of the surf zone ranges between 1600 m and 2000 m. The morphology is characterised by three long-shore bars. Typically, the distance between the bar crests, measured in the cross-shore direction, varies between 100 m and 400 m. The vertical distance between trough and landward crest can be as large as 4 m. Using bathymetric data of the past 26 years, Ruessink (1992) showed that bars tend to originate between the high water and low water line, migrate in an offshore direction and fade out at a depth of 8-11 m below MSL or about 2000 m offshore; see Fig. 5.

The total sequence takes approximately 10-15 years. Although less pronounced than the offshore directed movement, there is also a long-shore movement of the bars. The area is in general very dynamic with a considerable transport of sediment.

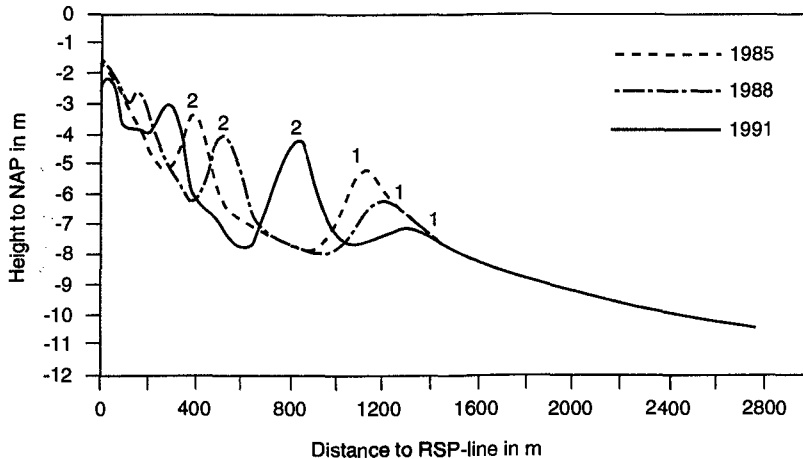


Fig. 5 Typical example of migration of longshore bars

The wave climate at the project site is characterised by an annual average significant wave height of 1.2 to 1.5 m. Tides are semi-diurnal with neap tidal range of 1.5 m and a spring tidal range of 2.1 m. The amplitude of the tidal current at the nourishment site is estimated at 0.4 m/sec. There are indications that the residual current is from west to east. The sand present in the nourishment area has a median grainsize of 155 - 165  $\mu\text{m}$ .

### Principles of shoreface nourishment

Shoreface nourishment involves placement of sand on the shoreface rather than on the beach. The principle of the shoreface nourishment is based on the observation that erosion of the shoreface leads eventually to erosion of the beach and the dunes. Conversely, it is expected that nourishment of the shoreface might stop or retard the erosion of the beach.

There are two types of shoreface nourishments: a stable berm and a feeder berm. A stable berm is constructed in deeper water. It's function is to attenuate storm waves and to reduce the wave energy expanded on the beach. For Terschelling this is not a viable design alternative because there is no initial

contribution of sand to the BKL-zone, implying that the TKL will remain landward of the BKL, and subsequent transport of sand to the BKL-zone is, by definition, not expected. A feeder or nearshore berm is constructed in relatively shallow water and therefore part of it could be in the BKL - zone. It serves as a dissipator of incident wave energy and is expected to gradually provide additional sand to the BKL-zone.

Both types of shoreface nourishments have been constructed since 1935. Only the more recent projects were accompanied by monitoring programs. With regard to the feeder berm projects the monitoring results showed a gradual movement of sand in the landward direction and consequently a movement of the coastline in the seaward direction. In addition, the following general conclusions can be reached:

- the estimated cost of a shoreface nourishment is half of that of a beach nourishment;
- sand should be placed as high as possible in the profile to assure landward transport, a depth of less than 10 m is recommended;
- the length of the nourishment in the along-shore direction should be several times the average local wavelength to minimize the potential for wave focusing.

Obviously, more monitoring is needed to verify performance and to quantify the physical benefits of shoreface nourishments.

Roelvink (1989) carried out a desk study to determine the effect of a shoreface nourishment on the coast. In particular he focused on

- depth of placement
- volume of the nourishment
- influence of sea level rise.

He defined the effectiveness of the shoreface nourishment as the increase in volume of a specified part of the cross - shore profile, for example the BKL - zone, expressed as a percentage of the nourished volume. The autonomous development of the profile is not taken into account.

The main conclusions of Roelvink's study are that

- shoreface nourishments become more effective when placed close to shore; for the Dutch coast nourishments placed landward of MSL -7 m have a definitely favourable effect on the beaches; the nourishment has little or no effect when placed seaward of MSL - 10 m;
- the volume of a specific part of the beach profile and therefore the effectiveness increases linear with the volume of the nourishment;
- the effectiveness is little influenced by an

increase in the rate of sea level rise. Parameter values used in the calculations by Roelvink pertain to the Dutch coast. Conclusions are valid within this parameter range and should not be extended beyond this range.

Partly in response to Roelvink's study, Hillen et al. (1991) carried out a feasibility study for shoreface nourishment including methods of construction and cost. One of their conclusions was that for nourished volumes of 1-10 million cubic meter, distances to the borrow area of 15-20 km and a nourishment depth of less than MSL -7 m, only nourishments carried out by small to medium size split barge hopper dredges lead to a price per cubic meter of sand that is substantial lower (50 %) than that of a beach nourishment. Furthermore, using the results of Roelvink they calculated how much sand is expected to be in the BKL-zone as a function of time and depth of placement. The results showed that a shoreface nourishment placed between MSL -5 m and MSL -7 m has an effectiveness of 35% to 60 % after 5 years. It was concluded that, compared to a beach nourishment (effectiveness estimated at 90 %), twice the volume of sand is needed for a shoreface nourishment to arrive at the same volume of sand in the BKL-zone after 5 years. In view of the 50 % reduction in the price of a cubic meter of sand in place, it follows that the total cost of a beach nourishment and a shoreface nourishment, which would guarantee the same volume of sand in the BKL - zone after 5 years, are about the same.

Hillen et al. (1992) emphasize that estimates of cost and effectiveness of the shoreface nourishments used in their study are conservative; this to not create false expectations. However it seems clear that the method has potential, and ultimately could lead to substantial savings considering the annual budget of 60 million Dutch guilders (28 million Ecu) spent in The Netherlands to combat erosion. In view of this it was decided for Terschelling to select the option of a shoreface (feeder berm) nourishment.

#### Design of the shoreface nourishment

Further specification of the feeder berm design was largely based on experience with earlier nourishments and on theoretical results. Unfortunately, state-of-the-art models turned out to be of limited use as a design tool. For the shoreface nourishment to meet the design objectives stated above, a total of (2 \* 1.10 million = ) 2.20 million cubic meter of sand is required. Sand should be placed as high as possible in the profile. However an upper limit of MSL - 5 m was imposed by the smallest

available hopper dredge. This depth is still available within the BKL - zone which extends to NAP - 5.24 m at the project site. This allowed at least a fraction of the sand to be placed initially in the BKL - zone.

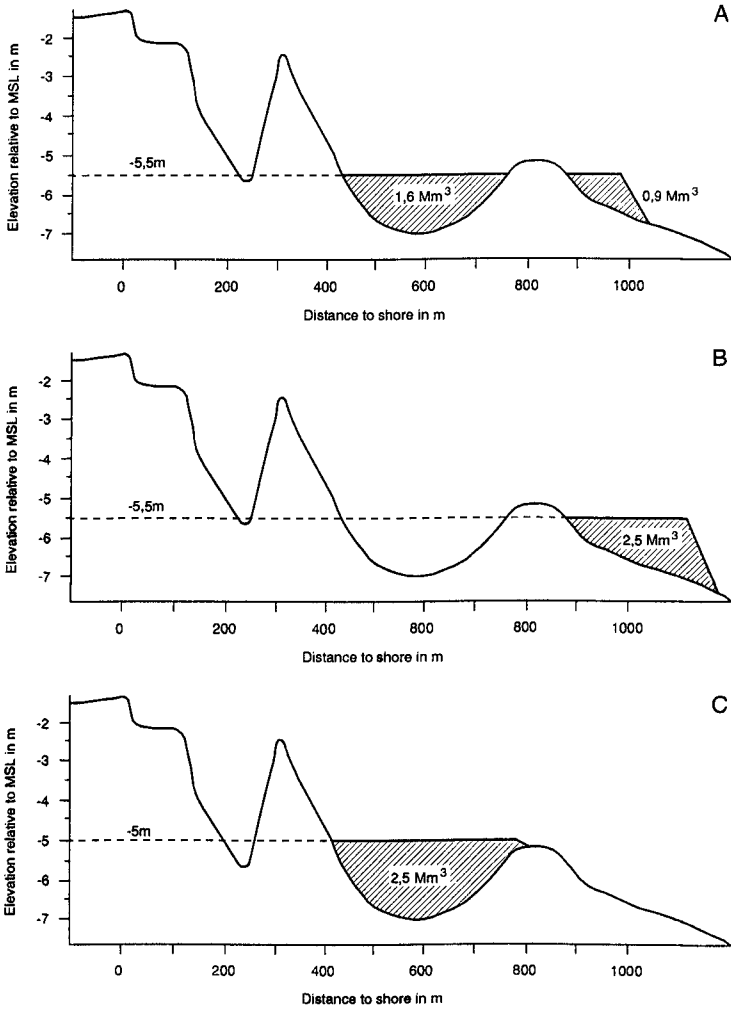


Fig. 6 Design alternatives for a shoreface nourishment at Terschelling

Three possible designs for a shoreface (feeder berm) nourishment were considered; see Fig. 6. To reiterate, the design objectives or functional requirements to be

met by each of the designs were

- After placement of the sand the TKL should be seaward of the BKL everywhere at the project site;
- The TKL should not retreat landward of the BKL during the next ten years.

Furthermore the design should allow adequate monitoring (this in view of the experimental character of the nourishment). The optimum design is the one that meets the functional requirements at a minimum total cost.

Calculations with a 3-LINE model (Bakker, 1995), which included the actual geometry with the three bars, suggested that nourishment seaward of the outer bar, as in designs A and B, could not sufficiently compensate for the landward movement of the coastline of about 1-5 m per year during the next ten years. The nourished volume seaward of the outer bar would act as a breakwater, however, with little effect on the natural erosion of the coast. For design C, the model indicated that the nourishment would prevent the TKL from retreating behind the BKL in the next ten years. It should be emphasized however, that the calculations were of an exploratory nature.

For designs A and B sand loss during dumping could be substantial due to the relatively large depth and tidal current speed. For design C, losses during construction were expected to be minor due to the placement of the sand between two bars. Consequently, the cost per cubic meter sand in the profile was expected to be lowest for design C. In design C a substantial fraction of the sediment is initially placed in the BKL-zone. From a monitoring point of view both designs B and C were acceptable. Design A was less attractive because it consists essentially of two parts.

It follows that design C is the only design that meets all design criteria and it has the lowest cost. Therefore, this design was selected as the final design. Because of financial constraints the total volume of sand was somewhat reduced to 2 million cubic meters. The nourishment stretched between km 13.6 and km 18.2; see Fig. 3. Originally a volume of 0.3 million cubic meter was placed in the BKL zone.

The type of sand to be selected for the nourishment should closely resemble the native sand to avoid additional complications and to facilitate interpretation of the behaviour of the shoreface nourishment. If it is different, the sand should preferably be coarser than the native sand. This will lead to less loss of sediment during and immediately after placement and will lead to an extended life span of the nourishment. Borrowing of sand in the Dutch territorial waters is limited to the

zone offshore of the 20 m isobath. A good source of sand resembling the native sand was found 10 km of the project site at the 22 m depth contour with a median grain size in the range of 183 - 212  $\mu\text{m}$ .

The nourishment was implemented using three suction split hull hopper dredges with hopper capacities ranging between 1200 and 2100 cubm. The draft of the vessels ranged between 4.50 to 5.30 m. To provide access to the project site, an entrance channel was dredged through the most seaward bar at km 16.30. The channel depth was 6.50 m below NAP. The nourishment area was divided into 9 dump sections each with a width of approximately 500 m. The dumping started simultaneously at the west and east side of the project area. Depending on the direction of the tidal current, the dredges placed the sand in the outermost east or west section. At the end of the construction the entrance channel was closed. For execution of the project an accurate electronic positioning system was used. Total construction time was 6 months (May - November 1993). Due to an unexpectedly high frequency of unfavourable swell conditions hindering manoeuvring of the dredges between the bars, the total operation took 65 instead of the planned 36 weeks of shipping time.

The contractor was reimbursed based on results of bathymetric surveys rather than volumes of sand transported by the hopper dredges. It appeared that the transported volumes were about 30% larger than the bathymetrically observed volumes.

### Monitoring results

Since the completion of the nourishment in November 1993, bathymetric surveys have been carried out at regular intervals. Based on these surveys the position of the coastline was calculated for various cross-sections. As an example, for km 16.00 the positions of the coastline since the nourishment have been added to Fig. 4. Between the nourishment and the last survey during June 1994 the coastline has advanced by 50 m. In Fig. 7, the change in volume of the BKL-zone since the start of the nourishment in May 1993 is indicated. As per June 1994, the volume in the project area (between km 13.60 and km 18.20) has increased by 0.9 million cubic meter. Originally only 0.3 million cubic meter of sand was placed in the BKL zone. The additional 0.6 million cubic meter was transported landward by wave action, leading to cautious optimism with regard to the performance of the shoreface nourishment.



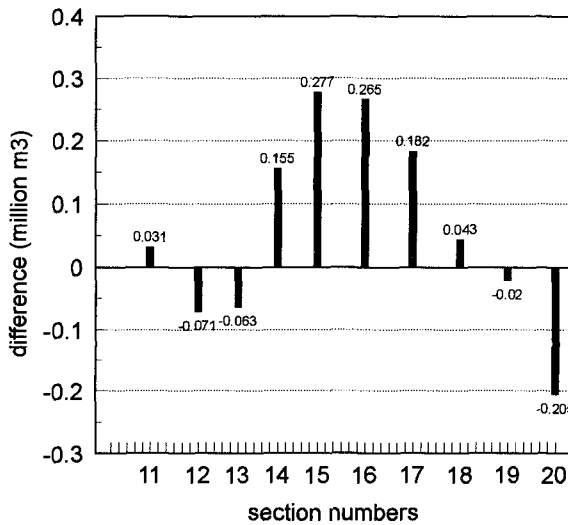


Fig. 7 Volume changes in the BKL zone after implementation of the shoreface nourishment over the period May 19, 1993 to June 20, 1994.

#### Acknowledgements

NOURTEC is a joint Dutch-German-Danish effort co-sponsored by the Commission of the European Communities under the Marine Science and Technology Programme (MAST-II), contract number MAS2-CT93-0049. Partners on the Dutch side are Rijkswaterstaat - National Institute for Coastal and Marine Management (RIKZ) and Utrecht University - Institute for Marine and Atmospheric Sciences (IMAU), on the German side the Coastal Research Station Norderney and on the Danish side the Danish Coastal Authority.

In the Netherlands the fruitful co-operation is acknowledged with the Rijkswaterstaat Directorates Noord Nederland and Noord Holland. Special thanks are due to mr. Edwin Biegel who was largely responsible for the analysis of the bathymetric monitoring data and for illustrating this contribution.

#### References

- Bakker, W.T., N.F. Kersting and H.D. Niemeyer, 1995, Prediction or Evaluation Sandsupply by Line-Models, Proceedings 24th International Conference on Coastal Engineering 1994, Kobe, Japan

- Hillen, R., P. van Vessem and J. van der Gouwe, 1991,  
Shoreface nourishment, a feasible alternative to  
beach nourishment ? (in Dutch) Report GWWS-91.012,  
Rijkswaterstaat, Dienst Getijdewateren, The Hague ,  
48 pp.
- Hoekstra P., K.T. Houwman, A. Kroon, P. van Vessem and  
B.G. Ruessink, 1994,  
The NOURTEC experiment of Terschelling: process-  
oriented monitoring of a shoreface nourishment  
(1993-1996), Proceedings Coastal Dynamics '94  
Conference, Barcelona February 21-25, 1994, ASCE,  
New York (in press)
- Kroon A., P. Hoekstra, J.P.M. Mulder, D. Roelvink, K.T.  
Houwman and B.G. Ruessink, 1995,  
Process-oriented monitoring of a shoreface  
nourishment; NOURTEC experiment at Terschelling, the  
Netherlands, Proceedings 24th International  
Conference on Coastal Engineering, Kobe, Japan
- NOURTEC, 1994,  
Design report of the three NOURTEC sites, NOURTEC  
report no. 1, RWS-RIKZ The Hague, pp.62
- Roelvink, J.A., 1989,  
Shoreface nourishments (in Dutch), Technical Report  
14, Kustverdediging na 1990, Rijkswaterstaat, The  
Hague
- Ruessink B.G., 1992,  
The nearshore morphology of Terschelling (1965-  
1991). Report R 92-11, Institute of Marine and  
Atmospheric Research Utrecht, Utrecht University,  
Utrecht



# **PART V**

## **Coastal, Estuarine and Environmental Problems**



## CHAPTER 209

### IMPORTANCE OF PERMEABILITY IN THE SEDIMENTATION CONSOLIDATION PROCESS

A. Alexis<sup>1</sup>, P. Thomas<sup>1</sup>

#### ABSTRACT

This paper first presents a literature review of permeability laws. A link between hydraulics and geotechnics formulations is pointed out. Second, reduced permeability expressions are discussed from experimental data available in literature. An extended exponential expression of reduced permeability is proposed.

#### 1. INTRODUCTION

In coastal engineering, sedimentary transports and harbour silting are governed by the sedimentation-consolidation process.

The current modellings are based on:

- hydraulics laws for very low concentration soils (less than 100 g/l) applicable to sedimentation and using the settling velocity

- soil mechanics laws for high concentration soils (greater than 500g/l) applicable to consolidation and using permeability and effective stress.

Sedimentation-consolidation process is complex. Its settling velocity parametrisation has important limits, because of the lack of distinction between effective stress and permeability influences, and also because of the lack of account of consolidation.

On the other hand, we observe that the flow law is at the core of the confrontation between hydraulics and geotechnics approaches.

It is interesting to use an important flow law parameter : the permeability.

So, the topic of this paper is the analysis and the suitability of the permeability concept with the sedimentation-consolidation process.

We will select a main parameter which will allow us to use sedimentation and consolidation results.

---

<sup>1</sup>Civil Engineering Laboratory E.C.N.I.U.T. St NAZAIRE BP 420, F 44606 St-NAZAIRE CEDEX (FRANCE)



So, permeability is infinite and we can see, here, the great interest of a parametrisation by means of reduced permeability which remains finite.

So, we obtain a link between geotechnics and hydraulics, that is between consolidation and sedimentation, by means of reduced permeability.

Most representative theories for modelling sedimentation-consolidation process are Richardson's law and Kozeny's law.

First, the empirical Richardson's law corresponds to the beginning of the phase called hindered settling.

The settling velocity is linked to Stokes' velocity  $v_o$  and porosity  $n$ , which is a function of void ratio ( $n=e/(1+e)$ ):

$$v_s = v_o \cdot n^{4,65}$$

In this case, we deduced reduced permeability  $k_r$  as a power law of porosity :

$$k_r = k_{ro} \cdot n^{4,65}$$

Second, Kozeny's law corresponds to a porous media.

Permeability is a function of specific area  $a$ , viscosity and porosity :

$$k = \frac{\gamma_w}{h_k a} \cdot \frac{n^3}{2 \eta (1-n)^2}$$

It appears the Kozeny's constant  $h_k$ , which depends on grain shape and tortuosity of the flow between grains.

Usually,  $h_k$  equals 4.5.

For spheric grains, we obtain a formulation of reduced permeability with porosity :

$$k_r = \frac{\gamma_w d^2}{36 h_k \eta} \cdot \frac{n^3}{1-n}$$

Using Stokes' reduced permeability, we deduce a new relation between reduced permeability and porosity :

$$k_r = \frac{k_{ro}}{9} \cdot \frac{n^3}{1-n}$$

So, we can compare these 2 theories by means of the formulation of reduced permeability in function of porosity.

So, the reduced permeability  $k_r$  is the basic parameter which enables the link between hydraulics and geotechnics.

We compare the results of Kozeny's law and Richardson's law (fig.1)

It appears differences for values of porosity higher than 90% in the extremal condition of very low

concentration  $k_r$  remains finite for Richardson's law while  $k_r$  is infinite for Kozeny's law.

For porosities lower than 90%, the 2 curves are rather close.

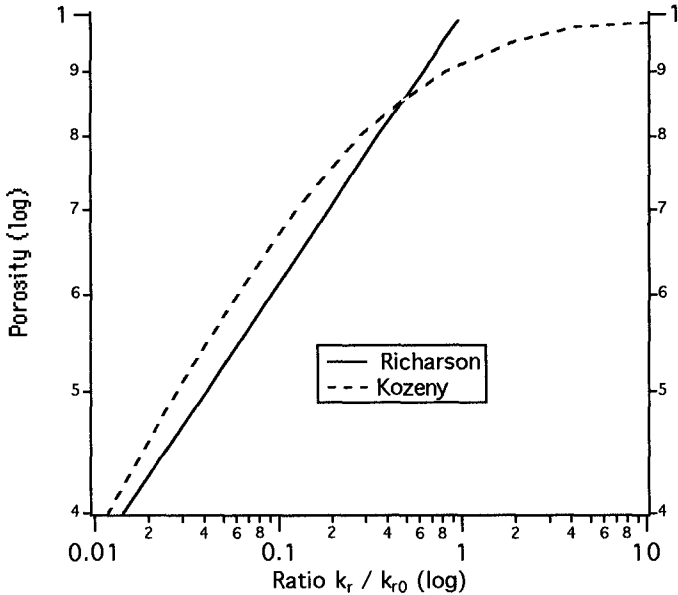


Fig.1 Comparison of Kozeny's and Richardson's laws

So, for the middle concentrated mixtures which are the most interesting, we can consider that the hydraulics analysis of Richardson and the geotechnics analysis of Kozeny give quite similar results.

**3. INVENTORY OF EXPERIMENTAL LAWS AND CHOICE**

The experimental flow laws are numerous in litterature, as every experimenter, according to his speciality and the range of his measurements , looks for a particular shape , both simple and representative which is able to synthesize his values.

So, there is a lot of permeability laws with a lot of parameters.

We propose a methodology consisting in choosing main parameters, such as reduced permeability  $k_r$ , permeability  $k$  and void ratio  $e$  and then in translating settling velocity, porosity and concentration in terms of  $k_r$ ,  $k$  and  $e$ , and at last in gathering different laws to show the links and particular cases.



For this specific work, we are going to propose an original tree-shaped diagram (fig.2) showing the links between the different types of laws.

We are also going to propose new generic laws.

Two main families of experimental laws can be distinguished :

- power laws for reduced permeability in the upper part of this scheme.

- and logarithmic laws for permeability in the lower part of this scheme.

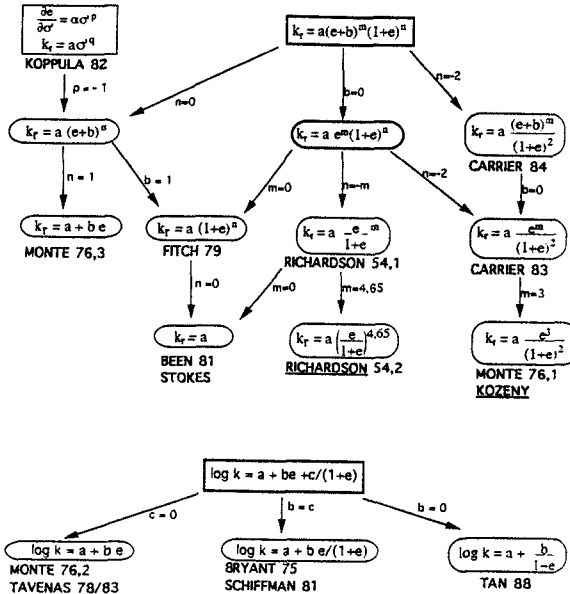


Fig.2: Synthetic arborescent scheme of reduced permeability laws

The name of each parametric constant  $a$ ,  $b$ ,  $m$ ,  $n$ , is only generic, for instance we have always named  $a$  the first parametric constant.

Each law is presented with his author and the year of its publication.

For gathering all this laws, we propose new generic laws (in bold). These new generic laws allow a general linkage between all the experimental laws.

In our representation, each stage corresponds to a number of parametric constant. So, we presents 16 laws with 1, 2, 3 or 4 parametric constants.

Once mathematical shapes are compared, we also compare the representative curve of these laws (Fig. 3).

For that, we choose an experimental data set with values of void ratio between 1 and 6 (these values are issued from experiments on clay ey-silt by YONG, 1982).

We study the 10 previous laws with 1 or 2 parameters.

For each law, we obtain the value of each parameter by means of a best fit method of regression on these experimental data.

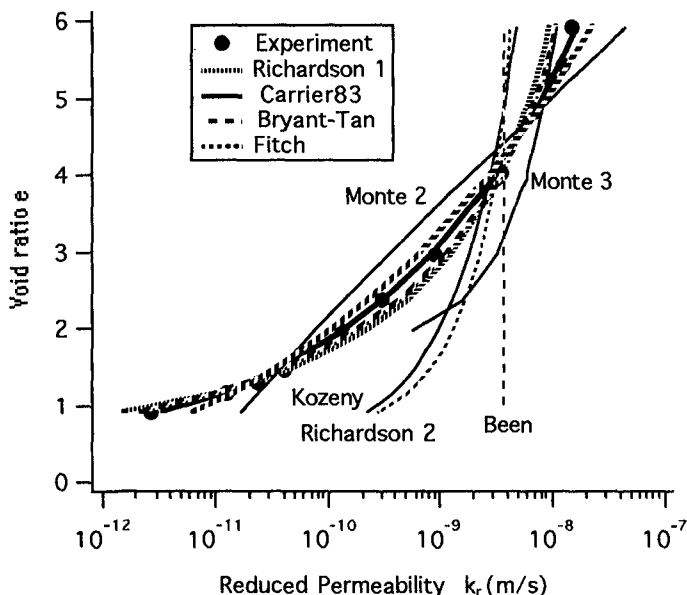


Fig.3: Comparison of reduced permeability laws

In fig.3, experimental values are represented by dots, and each curve corresponds to 1 law.

Corresponding to Stokes'law, BEEN's law is not representative for our problem, neither Richardson 2, Kozeny, Monte 3 laws

We remark that TAN and BRYANT laws give the same curve.

Among these 10 laws, we have written, in the legend, five laws which seem to be representative.

Among these 5 best laws, Carrier's and Richardson 1's laws are the only ones that give a permeability zero where void ratio is zero.

So, we will choose these 2 most representative laws.

To conclude this comparison of curves, we can use 3 criterions :

- representativity
- adequacy with extremal conditions of Stokes with infinite value of void ratio, that is initial sedimentation.
- adequacy with extremal conditions of zero value of void ratio and permeability, that is final consolidation.

Carrier's law seems to be the most representative, but the law of Richardson 1 with 2 parameters has a better adequacy with the extremal condition of Stokes.

CRITERIONS	CARRIER'S LAW	RICHARDSON 1'S LAW
REPRESENTATIVITY	++	+
STOKES EXTREME (e infinite)	-	++
$k_r = 0$ (e=0)	++	++

Tab. 1 : Synthesis of comparison of curves.

#### 4. VALIDATION

The previous comparison allowed a first sorting of the laws of reduced permeability. These selected laws have to be validated over a much wider range. The bibliographic study reveals a lack of experimental data covering this range (down to a concentration of 50 g/l).

So, we are going to exploit a very large range of cohesive sediment data from different authors, for values of void ratio between 1 and 50 (concentrations between 1300g/l and 50g/l).

The conversion law of settling velocity into reduced permeability during pure sedimentation is :

$$v_s = \frac{\gamma'_s}{\gamma_w} k_r = 1.65 k_r$$

$$(\gamma_s = 26.5 \text{ kN/m}^3)$$

Figure 4 represents the reduced permeability data in function of void ratio.

Toorman's tests were expressed in terms of settling velocity, they have been continued until the beginning of consolidation, where the relation  $v_s$  equals  $1.65 k_r$  is not valid.

So, the previous conversion implies a left shift for the lowest dots of each set.

The regularity of the evolution confirms the concept of continuous process of sedimentation-consolidation.

So, we will keep 2 sets of experimentation data (set1 = Toorman 1 + Pane 1, Set 2 : Toorman 2 + Yong).

Previous figure (fig.4) was interesting but we have no continuous wide-distributed set of measurements.

In order to validate the laws in a wide field, we propose now to synthetise the 2 previous sets of experimentations.

By means of these coherent data sets, we will compare for each set :

- 3 theory-based laws (Richardson 1 and 2 and Kozeny)
  - and 2 selected laws (Richardson 1 and Carrier)
- Dots are experimental data of set 1 for figure 5 and set 2 for figure 6.

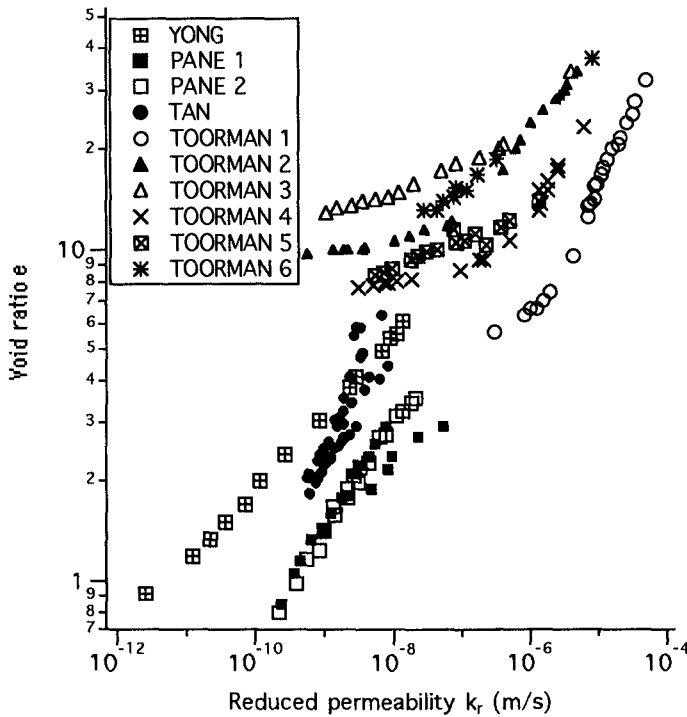


Fig.4: Evolution of experimental reduced permeability with void ratio

These 2 figures show again clearly that the one parameter laws (Richardson 2 and Kozeny) are not convenient.

The curve of Richardson 1 law (here with a power about 20) is not enough representative.

Carrier's law is well representative, and its shape is quasi-linear on this graph.

So, we propose a more simple power-typed law, for the whole range of void ratio between 1 and 50 (or concentration between 50 and 1 300 grains per liter) :

$$k_r = a e^b$$

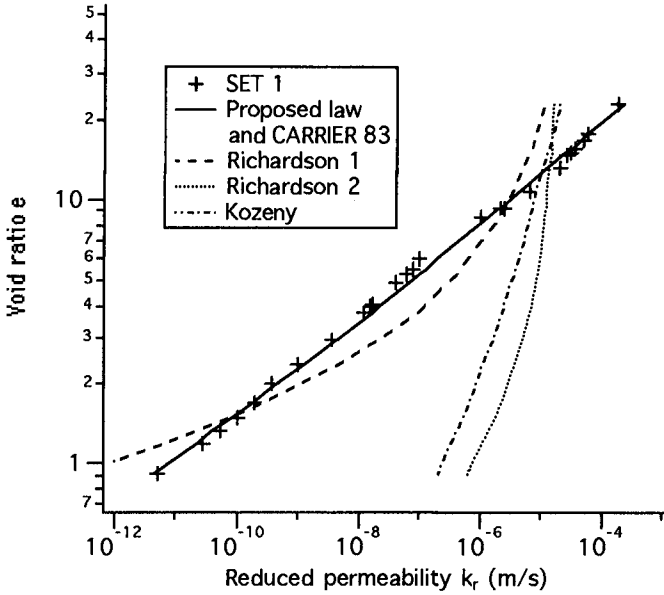


Fig.5: Proposed law and other laws of reduced permeability with Set 1.

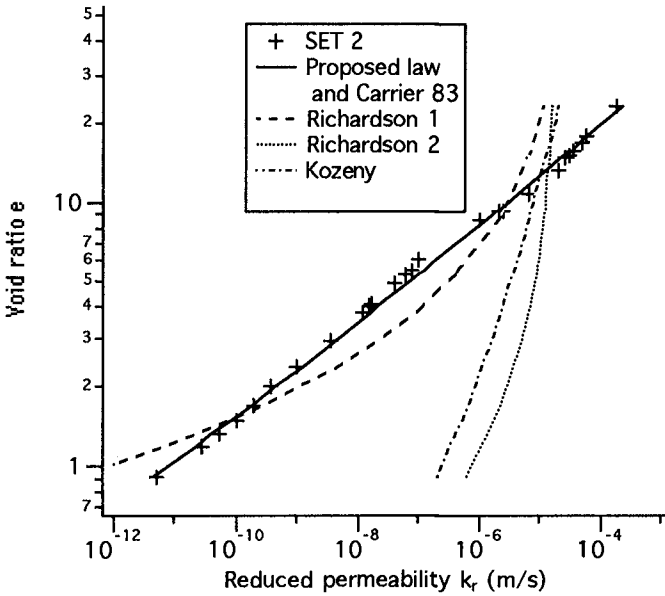


Fig.6: Proposed law and other laws of reduced permeability with Set 2.

## 5. CONCLUSION

The flow law is essential for the modelling of the sedimentation-consolidation process. We have shown the interest of the reduced permeability which links hydraulics and geotechnics.

We have described and compared theory-based laws. We have proposed a tree-shaped synthesis scheme which allows a gathering of laws, which are various as for their origins as for their shapes, and we have proposed new generic laws.

We have achieved a first selection of laws by means of one data set issued from bibliography in which void ratio is between 1 and 6. We have selected two laws, close to the theoretical ones by their shapes.

Then, we have validated by means of extended data sets in which void ratio is between 1 and 50. The position of the dots tends to confirm the continuity of the sedimentation-consolidation process. We have suggested to express the reduced permeability as an exponential law of the void ratio. We have thus extended the validity range of the reduced permeability concept and the concentration field of the modelling.

## 6. ACKNOWLEDGEMENTS

The present research on consolidation is undertaken as part of the MAST European program Coastal Morphodynamics (contract n°035).

## 7 - REFERENCES

- ALEXIS, A., P. BASSOULET, P. LE HIR & C. TEISSON (1992). Consolidation of soft marine soils: unifying theories, numerical modelling and in situ experiments. Proc. of the 23rd International Conference on Coastal Engineering ICCE'92, Venice, Italy. ASCE, Ed. B.L. Edge, 2949-2961.
- ALEXIS, A., P. THOMAS, S. GALLOIS (1993). Tassement des sédiments cohésifs, Contrat Européen MAST. IUT St Nazaire, France, Jan. 1993, pp 134.
- BEEN, K., and SILLS G.C. (1981). Self-weight consolidation of soft soils: an experimental and theoretical. Geotechnique 31, n°4, p. 519,535.
- BRYANT, W.R., HOTTMAN, W. and TRABANT, P. (1975). Permeability of unconsolidated and consolidated marine sediments, Gulf of Mexico. Marine Geotechnology, vol 1. p.1,14
- CARRIER, W.D.III, BROMWELL, L.G. and SOMOGYI, F. (1983). Design capacity of slurried mineral waste ponds J Geotech Engng Div Am Soc Civ Engrs 109 GT5. p.699,716

- CARRIER, W.D.III and BECKMAN, J.F. (1984). Correlations between index tests and the properties of remoulded clays *Geotechnique* 34, N°2. p. 211,228
- FITCH, B. (1979). Sedimentation of flocculent suspensions: State of the art. *AICHE, J.* 25 (6). p.913,930
- KOPPULA, S.D. (1970). The consolidation of soil in two dimensions and with moving boundaries. Ph D dissertation, Department of Civil Engineering, University of Alberta, E 281.
- MONTE, J.L. and KRIZEK, R.J. (1976). One-dimensional mathematical model for large-strain consolidation *Geotechnique*, vol 26, n°3. p. 495,510
- PANE, V., CROCE, P., ZNIDARCIC, D., KO, H.Y., OLSEN, H.W. and SCHIFFMAN, R.L. (1982). Effects of consolidation on permeability measurements for soft clays. *Geotechnique* v33: p. 67,72
- RICHARDSON, J.F. and ZAKI, W.N. (1954). Sedimentation and fluidization (Part I). *Transactions of the Institution of Chemical Engineers* 32. p.35,53
- SCHIFFMAN, R.L. and CARGILL, K.W. (1981). Finite strain consolidation of sedimenting clay deposits. *Proc 10th Int Conf Soil Mech and Found Engrg, Stockholm*, vol 1. p.239,242
- TAN, S.A., TAN, T.S., TING, L.C, YONG, K.Y., KARUNARATNE, G.P. and LEE, S.L. (1988). Determination of consolidation properties for very soft clay. *Geotech. Testing J*, v11 n°14: p. 233,240
- TAVENAS, F., BRUCY, M., MAGNAN, J.P., LA ROCHELLE, P. and ROY, M. (1978). Analyse critique de la théorie de consolidation unidimensionnelle de Terzaghi. *Revue française de géotechnique* 7. p.29,43
- TOORMAN, E.A. (1992). Modelling of fluid mud flow and consolidation. PhD thesis. Civil Eng. Dept., K.U. Leuven.
- YONG, R.L., SIU, S.K.H. and SHEERAN, D.E.(1983). On the stability and settling of suspended solids in settling ponds (Part I). Piece-wise linear consolidation analysis of sediment layer. *Canadian Geotechnical Journal*. 20: p. 817,826

## CHAPTER 210

### WAVE-CURRENT INTERACTION WITH MUD BED

Nguyen Ngoc An<sup>1</sup>  
Tomoya Shibayama<sup>2</sup>

#### ABSTRACT

A series of wave flume experiments for wave-current-mud system has been performed. The results reveal that the rate of wave attenuation increases in the opposing currents and decreases in the following currents. The results are the same with the waves on the fixed bed. Another important result is that the mud mass transport velocity increases in the opposing currents and decreases in the following currents. The visco-elastic-plastic model which was proposed by Shibayama and An (1993) for wave-mud interaction has further been extended to the wave-current-mud system by taking a wave deformation effect into considerations. The extended model succeeds in predicting the laboratory results. The model shows that due to pressure gradient in wave propagating direction, the largest mud mass transport velocity occurs in the strongest opposing current and the smallest one in the strongest following current.

#### INTRODUCTION

The wave-current interaction is a phenomenon of considerably practical interest. Also waves traveling on mud bed is another important phenomenon because these results in high wave attenuation (Gade, 1958 and Tubman and Suhayda, 1976) and large mud mass transport (Sterling and Strohbeck, 1973).

---

<sup>1</sup> D. Eng., Department of Civil Engineering, HCMC University of Technology

<sup>2</sup> D. Eng., Associate Professor, Department of Civil Engineering, Yokohama National University



The wave-current interactions on fixed bed have been studied through both laboratory experiments and mathematical analyses (Brevik and Aas, 1980, Thomas, 1981, etc.). And it is known that currents introduced into wave field make change of wavelength and wave height. The wave-current interactions on the mud bed have not yet been studied well, and therefore their effects on the mud mass transport velocity and the wave attenuation remain unclarified. In order to evaluate wave attenuation rate under this condition, Nakano et al. (1989) tried to include current effect to their multi-layered viscous fluid model (Tsuruya et al., 1987). But the results are not well compared with their own laboratory data.

These interactions among wave, current and mud will be investigated through both laboratory experiments and the numerical model in the present study.

## **THEORETICAL CONSIDERATIONS**

It is understood that the pressure gradient of water waves is much more important than shear stress at the interface between the water layer and the mud layer in creating movement of mud in the mud bed. In the mathematical formulation, it is assumed that the wave attenuation process will take place after waves are deformed due to the currents. This means that the mud bed responds only to the deformed waves resulting by the wave-current interaction. This assumption will be later justified with the laboratory experiments. It is also assumed that the current itself has no effect on the mud mass transport in the bed layer. The experimental results of Otsubo and Muraoka (1986a) can be used to justify the latter assumption. It was found that when currents flow over mud bed, sediments are transported only in the water layer by the current if they are suspended or if the bed surface is massively destroyed. No mass transport in the mud layer was reported. In the followings, two models which describe the two processes will be present.

### **Model of Wave Deformation due to Current**

In this process, no energy loss is taken into account while formulating the model of wave deformation due to the currents. Two main parameters of deformed waves are the wave height and the wavelength. The accuracy in

predicting the wavelength variation using the dispersion relation has been verified (Thomas, 1981). The accuracy in predicting the wave height variation, however, depends on the nature of currents. Several models are available. Longuet-Higgins and Stewart (1961,1964) assumed that the current was irrotational and its profile was uniform over depth. Jonsson et al. (1978) solved for rotational currents by assuming current with constant vorticity. Thomas (1981) numerically solved for more general case by considering current to be a function of elevation from bottom. In a simple case where the depth-averaged velocity was used, he found that the model well predicted the wavelength and wave height variations.

Under steady condition following Thomas (1981) for the simple case, the conservation equation for wave action is (Bretherton and Garrett, 1969; Whitham, 1974; Brevik and Aas, 1980)

$$\frac{E}{\sigma}(U + C_{gr}) = \text{const.} \quad (1)$$

where  $E$  is the wave energy,  $\sigma$  is the relative angular frequency defined by  $\sigma = \omega - kU$ ,  $\omega$  is the absolute angular frequency,  $U$  is the mean depth-averaged current velocity,  $k$  is the wave number, and  $C_{gr}$  is the group wave velocity. Because the wave energy is proportional to the square of wave height,  $H$ , Eq. (1) can be rewritten as:

$$\frac{H^2}{\sigma}(U + C_{gr}) = \text{const.} \quad (2)$$

The wavelength variation is obtained from the usual irrotational dispersion relation as follows:

$$(\omega - kU)^2 - gk \tanh kd_i = 0 \quad (3)$$

where  $d_i$  is the water depth. Following Thomas (1981), in order to use Eqs. (2) and (3), it is necessary to specify a reference level to define the constant in Eq. (2). The reasonable choice of reference level is the values with no current. This introduces the quantities  $H_0$  and  $L_0$ , corresponding to the wave height and the wavelength respectively when no current exists.

### **Model of Wave-Current Interaction on the Mud Bed**

The model of wave-mud interaction which was developed by Shibayama and An (1993) is used. In this process, the model of wave-mud system is extended

to the wave-current-mud system by taking the wave deformation effect into consideration. For example, the free surface displacement is given by  $\eta_1(x,t) = a_1 \cdot \exp[i(kx - \sigma t)]$ , where  $a_1$  is the deformed wave amplitude due to the current and determined by Eq. (2).

The rheological equation and the governing equations are modified here while making use of new parameters.

(1) Rheological equations are the followings:

$$\sigma'_{ij} = 2\mu_e e'_{ij} \tag{4}$$

$$\text{where } \mu_e = \begin{cases} \mu_1 + \frac{iG}{\omega} & \left( \frac{1}{2} \sigma'_{ij} \sigma'_{ij} \leq \tau_y^2 \right) \\ \mu_2 + \frac{\tau_y}{\sqrt{4|\Pi_e|}} & \left( \frac{1}{2} \sigma'_{ij} \sigma'_{ij} > \tau_y^2 \right) \end{cases} \tag{5}$$

and  $\sigma'_{ij}$  and  $e'_{ij}$  are stress and strain tensors, the prime indicates the deviator of these two tensors, the dot indicates derivative with time.

(2) Governing equations are the followings:

$$\frac{\partial \hat{u}_j}{\partial x} + \frac{\partial \hat{w}_j}{\partial z} = 0 \tag{6}$$

$$\frac{\partial \hat{u}_j}{\partial t} = -\frac{1}{\rho_j} \frac{\partial \hat{p}_j}{\partial x} + \nu_{e,j} \left( \frac{\partial^2 \hat{u}_j}{\partial x^2} + \frac{\partial^2 \hat{u}_j}{\partial z^2} \right) \tag{7}$$

$$\frac{\partial \hat{w}_j}{\partial t} = -\frac{1}{\rho_j} \frac{\partial \hat{p}_j}{\partial z} + \nu_{e,j} \left( \frac{\partial^2 \hat{w}_j}{\partial x^2} + \frac{\partial^2 \hat{w}_j}{\partial z^2} \right) \tag{8}$$

where  $\hat{u}$  and  $\hat{w}$  are the horizontal and vertical components of orbital velocities,  $\nu_{e,j}$  is the kinematic viscosity of mud and  $\hat{p}$  is the dynamic pressure.

(3) The solutions are put to be the following forms:

$$\hat{u}_j(x,z,t) = u_j(z) \exp[i(kx - \sigma t)] \tag{9}$$

$$\hat{w}_j(x,z,t) = w_j(z) \exp[i(kx - \sigma t)] \tag{10}$$

$$\hat{p}_j(x,z,t) = p_j(z) \exp[i(kx - \sigma t)] \tag{11}$$

## EXPERIMENTAL SET-UP AND METHODOLOGY

### Set-up

The experiments were carried out in a flume at the Department of Civil Engineering of Yokohama National University, Japan. The length of the flume was 17m, the width was 0.6m and the total depth was 0.55m. The still water depth was 30cm during experiment on the fixed bed and 26.3 cm on the mud layer of 8cm. Figure 1 shows the experimental set-up with the mud bed.

### Instrumentation

Wave heights were measured by means of electric capacitance wave gauges. Two sensors with distance of 50cm were installed at the movable carriage to measure water elevations at every half meter along the flume. The signals from the sensors were amplified and digitally recorded for 1030 records at the frequency of 20Hz. Using the technique introduced by Goda and Suzuki (1976), the incident and reflected waves were estimated.

Horizontal component fluid velocities were measured with a Fiber-Laser Velocimeter. Steady current velocity at one point was taken as an average value of all data recorded in certain duration.

Table 1: Wave damping coefficients in wave-current condition.

Run No.	$T$ (s)	$H$ (cm)	$U$ (cm/s)	$d_t$ (cm)	$k_i$ (1/m)	Remarks
W1	1.01	3.49	0.00	30.0	0.0036	fixed bed
WC2	1.01	2.98	-16.00	30.0	0.0085	fixed bed
WC1	1.01	2.98	-7.34	30.0	0.0044	fixed bed
W2	1.01	2.98	0.00	30.0	0.0036	fixed bed
WC3	1.01	2.98	5.58	30.0	0.0039	fixed bed
WC4	1.01	2.98	16.65	30.0	0.0027	fixed bed
WC5	1.01	4.48	-19.11	26.3	0.1032	mud bed
WC6	1.01	4.48	-9.00	26.3	0.0840	mud bed
WW7	1.01	4.48	0.00	26.3	0.0718	mud bed
WC8	1.01	4.48	8.10	26.3	0.0624	mud bed
WC9	1.01	4.48	18.64	26.3	0.0543	mud bed

Mud mass transport velocities were measured from movement of colored mud used as a tracer. The technique introduced by Sakakiyama and Bijker (1989) was adopted.

### **Experimental conditions**

Table 1 shows the experimental conditions of waves and currents. The mixture of 158% water content of commercial kaolinite and fresh water was used for the bed material when the experiments on the mud bed were conducted.

## **RESULTS**

### **Wave height variation due to current**

(1) Measurement of wave heights on fixed and mud beds.

Firstly, the reference values of wave amplitude were measured. A problem arose when the location for references was selected to ensure the condition of Eq. (2). On the fixed bed, there is no problem since the wave attenuation is expected to be small. On the mud bed, however the wave attenuation rate is rather high. In this experiment, the location for references  $x=0$ , was chosen at front edge of the mud layer. This selection was based on the assumption that the high wave attenuation is supposed to start when the waves come to the mud bed.

Currents were generated and the velocity profiles were measured. These currents were superimposed with progressive waves produced by the wave generator. The input data of wave period  $T$ , wave height  $H$ , and water depth  $d_1$  were the same for all runs. The actual wave amplitudes were then measured at  $x=0$  for various current velocities. The measured values of  $H$  and the corresponding predicted value of  $L$  are listed in Table 2, where the subscript 0 here indicates the condition without current generation.

(2) Results.

The experimental results on the wave height variation are shown in Table 2. Figures 2 and 3 show the wave height variation for various current speeds on the fixed bed and on the mud bed, respectively. It was seen that the strongest opposing currents yielded the biggest wave heights on both the fixed and mud beds.

Table 2: Wave height variation due to currents.

Run No.	$U$ (cm/s)	$H$ (cm) Measured	$H$ (cm) Predicted	$H/H_0$ Measured	$H/H_0$ Predicted	$L_0$ (cm)
WC2	-16.0	3.72	3.88	1.25	1.30	113
WC1	-7.34	3.23	3.32	1.08	1.11	128
W2	0.00	2.98	2.98	1.00	1.00	139
WC3	5.58	2.78	2.79	0.93	0.93	147
WC4	16.65	2.66	2.48	0.89	0.83	162
WC5	-19.1	6.00	6.21	1.34	1.39	104
WC6	-9.00	4.91	5.11	1.10	1.14	121
WW7	0.00	4.48	4.48	1.00	1.00	134
WC8	8.10	4.07	4.07	0.91	0.91	145
WC9	18.64	3.64	3.66	0.81	0.82	159

The comparisons of the measured and predicted wave heights are showed in Table 2 and in Figs. 2 and 3. Good agreements are seen. The assumption in which the mud bed responds only to deformed wave are therefore justified.

#### Wave attenuation due to interaction with current

To estimate the wave attenuation quantitatively, a first approximation is to assume an exponential decay law of wave height:

$$H = H_{x=0} \exp(-kx) \quad (12)$$

where  $H_{x=0}$  is the initial wave height at  $x=0$ ,  $H$  is the wave height at  $x$  and  $k$ , is the wave attenuation rate (or wave damping coefficient). This approximation is similarly supported by theoretical and experimental investigations of Keulegan (1950) and Iwasaki and Sato (1972). Although, this is only a first approximation, it turned out to be well fitted in representing present laboratory data both on the fixed and mud beds.

#### (1) Wave attenuation on the fixed bed by current interaction.

Although the present work mainly deals with the mud bed, one test with fixed bed was first conducted. The purposes of this test were given as follows. The first purpose was to check the wave attenuation rate with the ones obtained in previous works. The second one was to estimate a magnitude of wave attenuation rate from which the effects of currents and the effects of mud bed can be easily distinguished in the later experiments over the mud bed.

The experimental results on the wave attenuation rate,  $k_i$ , for the case  $T=1.01$ s and  $H_0/L_0=0.021$ , are shown in Fig. 4 and in Table 1 for several values of current speed. The values of  $k_i$  were determined on the basis of regression analysis. The vertical line lengths represent standard deviations. The small standard deviations mean that the reliability is high in evaluating the wave attenuations.

There is a clear tendency in which  $k_i$  is the greatest in the strongest opposing currents and decreases slowly with the following currents. As long as the bottom boundary layer is laminar, the increase of wave number will result in the increase of energy dissipation rate. The opposing currents made the wavelength shorter. The wave number therefore increased and the higher wave attenuation rates were seen. On the other hand, the following currents made the wavelength longer. The wave number, therefore, decreased and the lower wave attenuation rates were seen.

It should be noted that the values of  $k_i$ , around  $0.004 \text{ m}^{-1}$ , obtained in the present experiment are close to the theoretical value about  $0.002 \text{ m}^{-1}$  given by Hunt (1952). These values are, however, relatively small compared to the ones of  $0.02 \text{ m}^{-1}$  obtained by Iwasaki and Sato (1972) and of  $0.01 \text{ m}^{-1}$  by Brevik (1980). The reason for this difference can be explained as follows. The incident wave heights were used in the present work to analyse wave attenuation. The closeness of present values to the theoretical ones is reasonable as long as only progressive waves are concerned.

The results of runs W1 and W2 given in Table 1 show that the same wave attenuation rates were obtained with different wave heights. Examination of the wave conditions in these tests indicated that the bottom boundary layers were laminar because the maximum Reynolds number of 3215 in the tests was smaller than the critical one of  $1.26 \times 10^4$  (Jonsson, 1966). The wave attenuation rates should, therefore, be same because they do not depend on the initial wave heights as long as the bottom boundary layers are laminar (Ippen, 1966).

## (2) Wave attenuation on the mud bed due to interaction with current.

The effect of currents on the wave attenuation is again considered in this part.

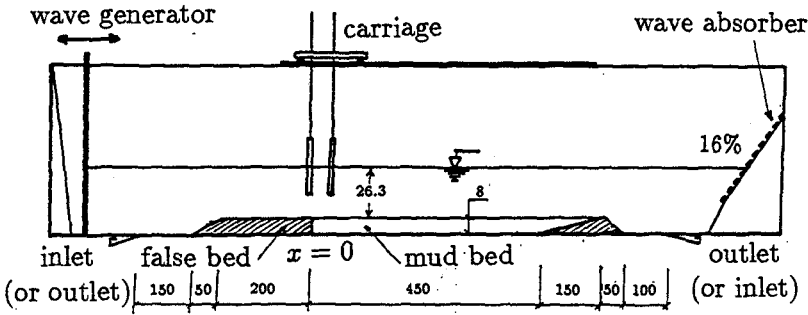


Figure 1: Sketch of experimental set-up.

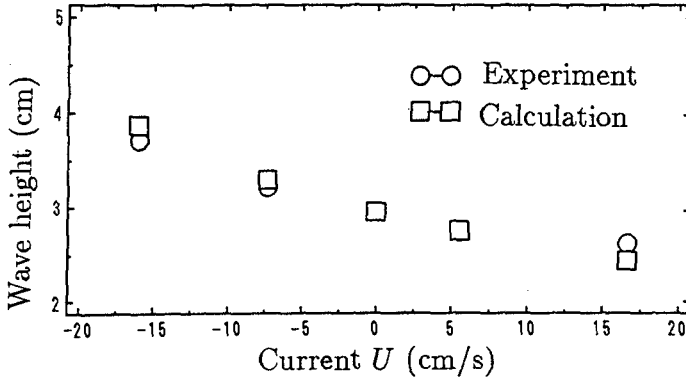


Figure 2: Wave height variation due to currents on the fixed bed.

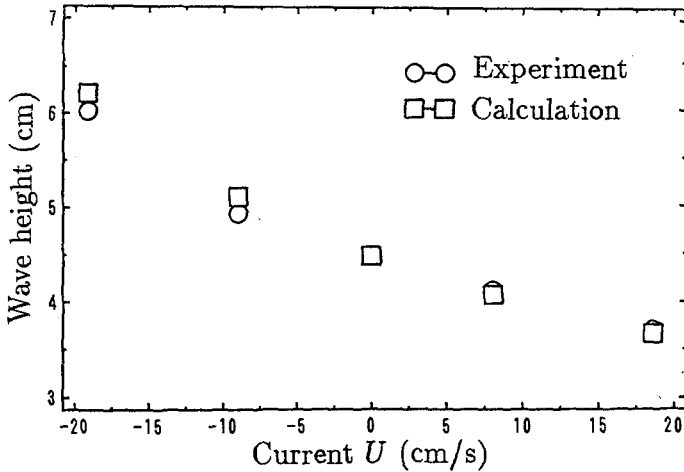


Figure 3: Wave height variation due to currents on the mud bed.



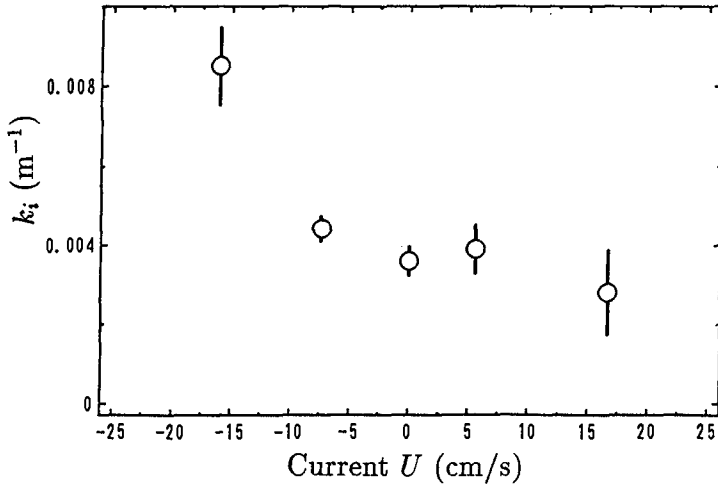


Figure 4: Effect of currents on wave attenuation on the fixed bed.

The experiments were carried out on the mud bed. Similarly, the experimental results of  $k_i$ , for the case  $T=1.01s$  and  $H_0/L_0=0.013$ , are shown in Fig. 5 and Table 1 for several values of current velocity. The wave attenuation rate is the highest in the strongest opposing currents and decreases in the following currents, in the same manner with the waves on the fixed bed. Although the same tendency of wave attenuation are found for waves on the fixed bed and the mud bed, the magnitudes of wave attenuation for waves on the mud bed are one order of magnitude greater than the ones for waves on the fixed bed. It was confirmed again that the mud bed enhances wave attenuation.

These laboratory results are now utilized to verify the numerical model. The comparison between the laboratory data and the computed ones are shown in Fig. 5. The model predicts the highest wave attenuation rate in the strongest opposing currents and the lowest wave attenuation rate in the fastest following currents, in the same manner with the wave attenuation which varied with the current speeds observed in the experiments. In terms of the absolute magnitudes, the model also predicts well the wave attenuations in all cases of various current speeds except in the case of strongest opposing current where the model gives underestimation. The strongly nonlinear wave pattern in the strongest opposing current might be the reason for this underestimation because the model is based on the linear waves.

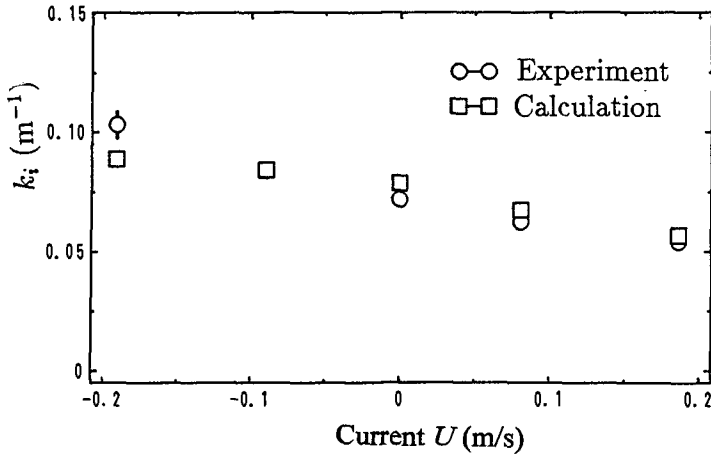


Figure 5: Effect of currents on wave attenuation on the mud bed.

### Mud mass transport velocity under wave-current interaction

#### (1) Measurements.

The mud mass transport velocity is the average velocity obtained from the measured displacement over the duration of experiment. The duration time, therefore, was a decisive factor in determining the mud mass transport velocity. A long duration would render the mud surface slope tilted at the onshore end and less mud mass transport might be resulted. On the other hand, if a very short duration was applied, the effect of inertial force and thixotropy effect would become profound. By trial and by carefully observing the formation of mud surface slope, the proper duration was selected to be from 65 s to 75 s. For each run, the mud mass transport was measured at the location of 1.0 m downstream of the front edge of the mud layer.

#### (2) Mud mass transport velocity.

A series of five runs with various current speeds was performed in order to analyse the effect of currents on the mud mass transport velocity.

Before comparisons are made between the calculated results with the laboratory data some parameters used in calculation are explained here. The parameters  $\mu_1$  and  $G$  were given by Shibayama and An (1993). The values of  $\mu_2 = 4.5 \text{ N s/m}^2$  and  $\tau_y = 17.0 \text{ N/m}^2$  are chosen by being fitted to mud mass transport velocity and wave attenuation rate in the case of no current, and then

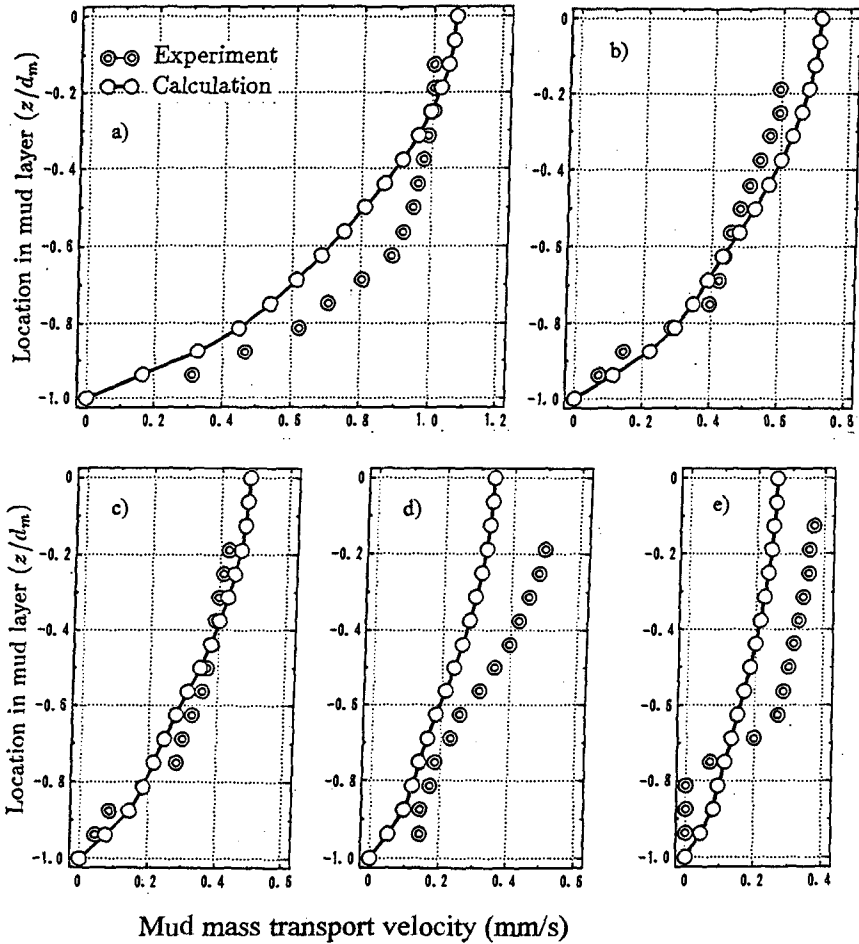


Figure 6: The comparison between the experimental and calculated results on mud mass transport velocity. a) Run WC5: $T=1.01s$ ,  $U=-19.1 \text{ cm.s}^{-1}$ , b) Run WC6: $T=1.01s$ ,  $U=-9.0 \text{ cm.s}^{-1}$ , c) Run WW7: $T=1.01s$ ,  $U=0$ , d) Run WC8: $T=1.01s$ ,  $U=+8.1 \text{ cm.s}^{-1}$ , e) Run WC9: $T=1.01s$ ,  $U=+18.6 \text{ cm.s}^{-1}$ .

applied them for other calculations with currents.

The results of mud mass transport velocity at  $x=1.0\text{m}$  in five runs are shown in the Fig. 6. There is a trend that the mud mass transport velocity is biggest in the strongest opposing current and decreases with increasing current in the positive direction. This trend can also be predicted by the numerical model. The good agreement between the experimental results and the computed ones confirms that the numerical model on the wave-mud interaction can further be extended to predict the wave-current-mud interaction by taking wave deformation effect into consideration. The effect of currents on mud transport can be explained by the wave deformation due to current as follows. In the opposing currents, the water pressure gradient at the water-mud interface becomes great as the wave height increases and the wavelength decreases, and this change causes to yield large mud transport. In the following currents, the pressure gradient becomes small as the wave height decreases and the wavelength increases and this results small mud transport.

## CONCLUSIONS

From the present study, some conclusions on the wave-current-mud interaction are drawn as follows.

- (1) Usage of the incident wave height improves the reliability of analysis of wave attenuations significantly.
- (2) Wave attenuation increases in the opposing currents and decreases in the following currents on both the fixed and mud bed.
- (3) Wave height variation due to wave-current interactions on the mud bed can be predicted well by a simple model of irrotational slowly-varying current.
- (4) The mud mass transport velocity increases in the opposing currents and decreases in the following currents.
- (5) The numerical model for the wave-mud interaction has further been extended for the wave-current-mud interactions by taking a wave deformation effect into consideration. The extended model succeeded in predicting the

laboratory results that the largest mud mass transport velocity and highest rate of wave attenuation occur in the strongest opposing current and the smallest and lowest ones in the fastest following current.

## ACKNOWLEDGMENTS

The research reported in this paper is supported in part by the Grant-in-Aid for Scientific Research from the Japanese Ministry of Education, Science and Culture (No. 03650417) and by the research support of Penta-Ocean Construction Co. Ltd.

## REFERENCES

- Bretherton, F.P. and Garrett, C.J.R. (1969): Wavetrains in inhomogeneous moving media, *Proc. R. Soc. London, Ser. A*, 302, pp. 529-554.
- Brevik, I. and Aas, B. (1980): Flume experiment on waves and currents I. rippled bed, *Coastal Engineering*, 3, 1980, pp. 149-177.
- Brevik, I. (1980): Flume experiment on waves and currents II. smooth bed, *Coastal Engineering*, 4, 1980, pp. 89-110.
- Gade, H.G. (1958): Effects of a nonrigid, impermeable bottom on plane surface waves in shallow water, *Jour. Marine Research*, Vol. 16, No. 2, pp. 61-82.
- Goda, Y. and Suzuki, Y. (1976): Estimation of incident and reflected waves in random wave experiments, *Proc. 15th Conf. on Coastal Eng., ASCE*, 1976, pp. 828-845.
- Hunt, J.N. (1952): Viscous damping of waves over an inclined bed in a channel of finite width, *La Houille Blanche*, Dec., pp. 836-842.
- Ippen, A.T. (1966): *Estuary and coastline hydrodynamics*, Mc Graw-Hill Book Co., Inc., New York, USA.
- Iwasaki, T. and Sato, M. (1972): Dissipation of wave energy due to opposing current, *Proc. 13th Conf. on Coastal Eng., ASCE*, 1972, Vol. 1, pp. 605-622.
- Jonsson, I.G. and Thomas, G.P. (1978): Wave action and set-down for waves on a shear current, *Jour. Fluid Mech.*, Vol. 87, pp. 401-416.

Keulegan, G.H. (1950): Wave motion, chap. 11 of Engineering Hydraulics, John Wiley and Sons, Newyork, 1950.

Longuet-Higgins, M.S. and Stewart, R.W. (1961): The change in amplitude of short gravity waves on steady non-uniform currents, Jour. Fluid Mech., Vol. 10, pp. 529-549.

Longuet-Higgins, M.S. and Stewart, R.W. (1964): Radiation stress in waves, a physical discussion with applications, Deep-Sea Res., Vol. 11, pp. 529-562.

Nakano, S., Ito, N. and Fujihira, Y. (1989): Interaction between surface waves and soft mud in an uniform current, Proc. Coastal Eng., JSCE, Vol. 30, pp. 339-343 (in Japanese).

Otsubo, K. And Muraoka, K. (1986 a): Resuspension of cohesive Sediment by currents, Proc. 3<sup>rd</sup> International Symp. on River Sedimentation, Vol. III, 1986, pp. 1680 - 1689.

Sakakiyama, T. and Bijker, E.W. (1989): Mass transport velocity in mud layer due to progressive wave, Jour. Waterway, Port, Coastal and Ocean Eng., ASCE, Vol. 115, No. 5, pp. 614-633.

Shibayama, T. and An, N.N. (1993): A visco-elastic-plastic model for wave-mud interaction. Jour. of Coastal Engineering in Japan, Vol. 36, No. 1, pp. 67-89.

Sterling, G.H. and Strohbeck, E.E. (1973): The failure of the South Pass 70 "B" platform in hurricanes Camille, Proc. 5th Conf. on Offshore Technology, Houston, Texas, 1973, pp. 719-730.

Thomas, G.P. (1981): Wave-current interactions: an experimental and numerical study. Part 1. Linear waves, Jour. Fluid Mech., Vol. 110, pp. 457-474.

Tsuruya, H., Nakano, S. and Takahama, J. (1987): Interaction between surface waves and a multi-layered mud bed, Rep. Port and Harbour Res. Inst., Ministry of Transport, Japan, Vol. 26, No. 5, pp. 141-173.

Tubman, M.W. and Suhayda, J.N. (1976): Wave action and bottom movements in fine sediments. Proc. 15th Conf. on Coastal Eng., ASCE, 1976, pp. 1168-1183.

Whitham, G.B. (1974): Linear and nonlinear waves, A Wiley-Interscience Publication, John Wiley & Sons, New York, 636pp.

## CHAPTER 211

### On Residual Transport in Shallow Tidal Basins <sup>1</sup>

Andrea Balzano <sup>2</sup>

#### Abstract

In the paper the influence of some physical and numerical effects on computations of residual transport in shallow tidal basins is analysed. Investigations deal with: i) the Coriolis acceleration, ii) the specification of the tidal forcing, iii) the diffusion coefficient, iv) a time weight in a standard implicit numerical scheme. The analysis has been carried out by means of intratidal mathematical models with reference to three schematic basins, with the tide being the only forcing of the system. These are typical conditions in which critical environmental events like anoxia occur. Usual assumptions in mathematical modeling of 2D flows in shallow basins regarding the above effects are tested both in the short and long term. The different importance of that effects depending on both the time scale of processes and the basin morphology is shown. Results are presented in terms of turbulence-time-averaged circulation patterns, Lagrangian residual circulation patterns, distributions of relative differences induced in the latter by including or not the investigated effects, and convection-dispersion of a passive solute.

#### 1. Introduction

Environmental modelling of a tidal basin generally requires long-term hydrodynamic and transport simulations. For such a task, either *intratidal* and *intertidal* mathematical models could be seen as proper tools from a cost-benefit point of view, depending on the actual time extent of the simulations required for the specific problem to be solved (weeks, months, years, etc.). However, whatever the model used, one is essentially interested in the net (residual, *intertidal*) transport over a time extent of the order of the period of a representative tidal component - typically, 12-24 hours - rather than in a detailed description of the motions occurring at a smaller (*intratidal*) time scale.

It is well known that residual transport is strongly influenced by the nonlinearities acting in water motion (Van de Kreeke, 1976; Zimmermann, 1979)

---

<sup>1</sup>Research carried out with the financial support of Sardinia Regional Authorities.

<sup>2</sup>Research Engineer, CRS4, Centro di Ricerca, Sviluppo e Studi Superiori in Sardegna - Centre for Advanced Studies, Research and Development in Sardinia, Via Nazario Sauro 10, 09123 Cagliari, Italy, E-mail: balzano@crs4.it.

and usually at least one order of magnitude smaller than the tidal excursion. Thus, typical schematizations that are commonly accepted - and acceptable, indeed - when dealing with turbulence-time-averaged quantities could no longer be so when, based on the relevant, intratidal, velocity fields, computations of residual fields are to be performed. This, as long as results may be seriously influenced by effects - either physical or numerical - that are minor factors at smaller time scales.

Many studies about residual circulation can be mentioned, concerning fields of quite different characteristics: harbours (Falconer, 1985), estuaries (Cheng and Casulli, 1982), open sea (Maier-Reimer, 1977). A great deal of research work has been done on Mediterranean lagoons, even with environmental safeguard purposes (O' Kane et al., 1990; Avanzi e Fiorillo, 1983; Cioffi e Gallerano, 1990; Dejak et al., 1990; Cioffi et al., 1994; Defina e D'Alpaos, 1994). Indeed, such water bodies are particularly liable to environmental hazards due to their relatively weak refreshment capability. However, fewer studies of their long term dynamics by field-verified mathematical models exist.

As a preliminary step to the implementation of a water quality forecasting system for eutrophic water bodies in the island of Sardinia, the influence of some of the above mentioned effects on residual transport has been analysed by means of intratidal mathematical models. Since the system is to be applied primarily to relatively small and shallow lagoons, the analysis has been carried out on schematic tidal basins whose geo-morphological characteristics resemble those of such natural water bodies. However, several mediterranean tidal basins match these general features as well. The present investigation is then to be seen as a specific contribution, strictly significant for the particular class of water bodies mentioned above.

Moreover, at this stage particular environmental conditions are considered like those eventually determining anoxia in the water body. These are essentially high temperature and the absence of wind, the latter being of major importance for the setup of residual circulations. Results are then to be intended as realistic for time extents not longer than, say, one month, in the summer season.

## 2. Description of numerical experiments

In the numerical experiments the three prototypes shown in fig. (1) have been considered, namely: (a) a completely flat, 1 m deep, basin with a 400 m long by 800 m wide inlet, whose axis coincides with the symmetry axis of the basin, sided by two expansions whose dimensions are 4000 x 4000 m; (b) a similar basin, in which the central, 800 m wide, strip is occupied by a 5 m deep channel; (c) a basin in which the depth varies gradually from 5 m in the central strip to 1 m at the lateral borders of the expansions. The tidal range at the entrance of the inlet is assumed of the order of 1 m; a latitude of 45° is considered. For the three prototypes and for the various effects investigated, comparisons have been made between either the two-dimensional, depth averaged, Lagrangian residual circulation fields and the results of a stochastic convection-dispersion model based on the random-walk technique.

The influence of the following factors on residual transport has been investigated: i) the Coriolis acceleration; ii) the specification of the tidal forcing at the basin inlet; iii) the diffusion coefficient,  $K$ , in the equation of motion; iv) the time weight,  $\alpha$ , of the finite difference implicit scheme for both the divergence of fluxes in the equation of continuity and the gradient of the free surface elevation in the equation of motion.



For the computations of the intratidal velocity fields a 2D finite difference, Eulerian-Lagrangian, hydrodynamic model was employed. This is based on the usual shallow water equations

$$\frac{\partial \eta}{\partial t} + \frac{\partial U}{\partial x} + \frac{\partial V}{\partial y} = 0$$

$$\frac{\partial U}{\partial t} + \frac{\partial(uU)}{\partial x} + \frac{\partial(vU)}{\partial y} + gh \frac{\partial \eta}{\partial x} - K \nabla^2 U - \frac{\tau_{sx}}{\rho} + g \frac{\sqrt{U^2 + V^2}}{k_s^2 h^{7/3}} U - fV = 0 \quad (1)$$

$$\frac{\partial V}{\partial t} + \frac{\partial(uV)}{\partial x} + \frac{\partial(vV)}{\partial y} + gh \frac{\partial \eta}{\partial y} - K \nabla^2 V - \frac{\tau_{sy}}{\rho} + g \frac{\sqrt{U^2 + V^2}}{k_s^2 h^{7/3}} V + fU = 0$$

where  $x, y$  are the cartesian coordinates in the horizontal plane;  $t$ , the elapsing time;  $u, v$  and  $U, V$ , respectively the mean velocity and unit width discharge components in the  $x$  and  $y$  directions;  $g$ , gravity acceleration;  $\eta$ , free surface elevation above a datum;  $h$ , total depth;  $K$ , the horizontal diffusion coefficient;  $\tau_{sx}$  and  $\tau_{sy}$ , respectively the  $x$  and  $y$  components of the surface stress;  $\rho$ , the density of water;  $k_s$ , the Strickler roughness coefficient ;  $f = 2\omega \sin \varphi$ , the Coriolis parameter;  $\omega$ , the angular speed of the earth's rotation;  $\varphi$ , latitude.

A fourth order Lagrangian method for the treatment of the convective terms and a real bidimensional solution of propagation ensures the correct representation of the velocity fields even in the presence of a dramatically irregular bathymetry (Benqué et al., 1982; Balzano, 1993). Lagrangian residual velocity fields were computed on the basis of the following definition (Cheng and Casulli, 1982)

$$\mathbf{v}_{lr}(\mathbf{x}_o, t_o) = \frac{1}{T} \int_{t_o}^{t_o+T} \mathbf{v}[y(\mathbf{x}_o, t), t] dt \quad (2)$$

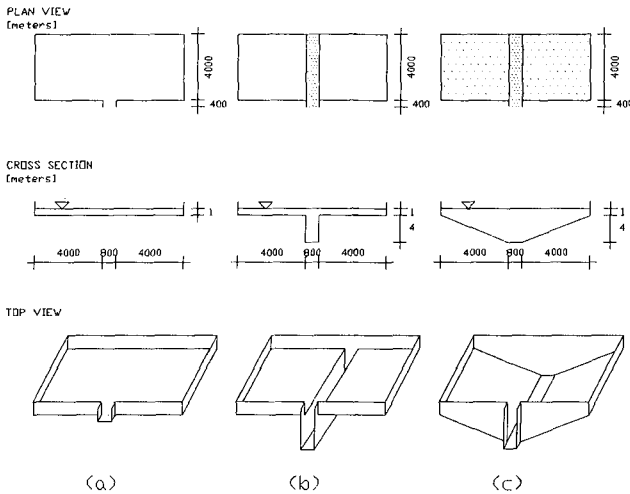


Figure 1: Schematic test basins

where  $\mathbf{v}_{lr} \equiv (u_{lr}, v_{lr})$  is the Lagrangian residual velocity computed in the point of coordinates  $\mathbf{x}_o$  for the tidal phase  $t_o$ ;  $T$  is the tidal period;  $\mathbf{v}(\mathbf{x}, t) \equiv (u, v)$  the eulerian velocity;  $\mathbf{y}(\mathbf{x}_o, t)$  the coordinates of the trajectory of a passive tracer released in the point  $\mathbf{x}_o$  at time  $t_o$ . In the numerical integration (2), the time step was assumed as  $\Delta t = \min \left\{ \frac{\Delta x/n}{u}, \frac{\Delta y/n}{v} \right\}$ , with  $n = 5 \div 10$  and  $\Delta t \leq 10 \div 30$  s. Numerical convergence of the residual velocity fields required time steps down to  $60 \div 120$  s in the hydrodynamic model, corresponding to values of the Courant number  $Cr=0.7 \div 3$ . Incidentally, it is remarked that this suggests the feasibility of resorting to explicit or ADI models for this kind of problems. This, particularly in the case that developments on parallel computers are foreseen to achieve higher computational speed.

In the stochastic transport model a mass of passive solute is represented as a "cloud" of mutually independent particles, subject to the resultant of the deterministic mean flow velocity and random fluctuations (Ghoniem and Sherman, 1985; Maier-Reimer and Sundermann, 1982)). Gaussian random displacements, uncorrelated in the directions normal and tangent to the trajectory were assumed. These are computed on the basis of the relevant longitudinal and transverse components of the dispersion tensor,  $K_l$  and  $K_t$ , as given by Elder formulas, i.e.  $K_l = 5.93 u^*h$ ,  $K_t = 0.23 u^*h$ , where  $u^*$  is the shear velocity. Thus, also dispersion due to vertical shear is represented. Computed values of the above diffusion coefficients are in agreement with those obtained by others with subgrid scale energy techniques for similar water bodies (Pfeiffer et al., 1988).

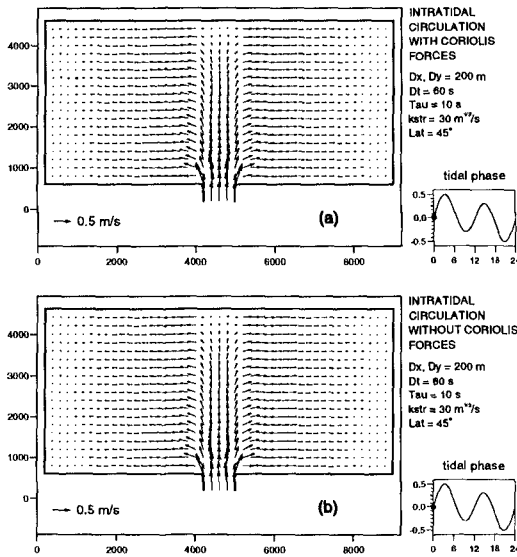


Figure 2: Intratidal circulation velocity field in a flat, 1 m deep, tidal basin with a central, 5 m deep, channel, computed (a) with and (b) without the Coriolis forces

3. Results

3.1 Coriolis acceleration

Classical order of magnitude analysis of the governing equations shows that Coriolis forces are negligible compared to convective terms whenever the Rossby number,  $Ro = \frac{v^*}{2\omega L^*}$ , is large,  $v^*$  and  $L^*$  being a characteristic velocity and length (Pedlosky, 1987). Moreover, they can be small compared to bottom friction in the presence of relatively small water depth and large bottom roughness. As a matter of fact, Coriolis forces are usually regarded as a minor factor in lagoons on the basis of the above arguments (Morandi Cecchi, 1989) and therefore neglected in real case studies (Chignoli e Rabagliati, 1977; Volpi e Sguazzero, 1977; Umgiesser et al., 1988, 1993; Rosso et al., 1993; Cioffi et al., 1994). If only intratidal fields are required, for a number of practical applications it can be agreed upon this choice. As an example, in fig. (2) the instantaneous (i.e. turbulence-time-averaged) velocity fields at mean flood tide in the basin with channel, computed (a) with and (b) without the Coriolis terms included, are shown. For a significant comparison Strickler roughness coefficients down to  $k=30 \text{ m}^{1/3}\text{s}^{-1}$  were assumed in the computations. Indeed, this value corresponds to a rather rough bottom and results from calibrations of models with field data (Umgiesser et al., 1988). In order to avoid problems arising when a uniform level is directly imposed in the presence of the Coriolis forces (Cheng e Walters, 1982), the same symmetrical time series of discharges has been imposed at the inlet as common boundary condition. This was deduced from preliminary computations with the Coriolis terms not included, for a reference mixed tide of 1 m of range. This is composed of a semidiurnal component of amplitude  $a_s = 0.4 \text{ m}$  and a diurnal component  $a_d = 0.141 \text{ m}$  with the same phase.

Clearly, hardly significant differences can be perceived between the two patterns, even in details. Even though differences are more evident near the high and low tide, nonetheless it is agreeable that a reliable description of the instantaneous circulations can be obtained without the inclusion of the Coriolis terms. However, residual velocity fields based on intratidal fields computed including or not the Coriolis terms show significant differences for all the three prototypes, particularly for the flat and the channeled basin. In the former (see fig. (3)), quite different locations of the centers of the macro-vortexes can be observed, while in the latter (see fig. (4)) a large zone of close recirculation is not reproduced without the inclusion of the Coriolis terms. This occurs also in the third basin, but with narrower recirculating eddies. It is to be noted that not only the test basins are given a remarkable roughness, but also they are much smaller than the real water bodies for which Coriolis effect was assumed as negligible in the references previously quoted, i.e. the Venice lagoon ( $550 \text{ km}^2$ ).

A quantitative analysis has been carried out, resulting in curves of the cumulative frequencies,  $F(S)$ , of the relative differences,  $S$ , between the values of the residual velocity components in the grid nodes as computed in the two cases. These are plotted for various tidal phases, to which Lagrangian residual quantities are sensitive (phase 0 = flood, mean tide). Also, these curves are plotted for different threshold values,  $\Theta$ , of the velocity components in order to point out whether large relative differences affect even the greatest velocity components in the residual field. In symbols:

$$S_w(\Theta) = \left| \frac{w_{i,j}^a - w_{i,j}^b}{w_{i,j}^a} \right| \quad \text{with} \quad w_{i,j}^a \geq \Theta \text{ OR } w_{i,j}^b \geq \Theta ; \quad w = u_r, v_r$$

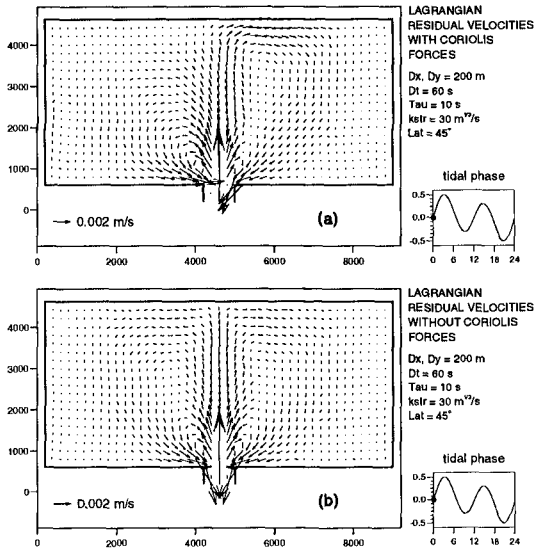


Figure 3: Lagrangian residual circulations in a flat, 1 m deep, tidal basin computed (a) with and (b) without the Coriolis forces

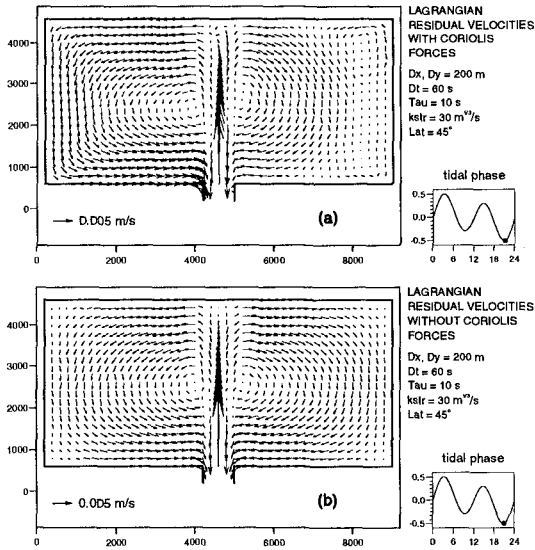


Figure 4: Lagrangian residual circulations in a flat, 1 m deep, tidal basin with a central, 5 m deep, channel, computed (a) with and (b) without the Coriolis forces

In fig. (5a-c) such curves computed for the three basins in the cases that Coriolis forces were included or not are shown. For instance, for the flat basin (fig. (5c)) it is seen that not only the about 1100÷1350 values of residual velocity components greater than 0.0001 m/s – whatever the tidal phase – but also the 26 values greater than 0.002 m/s – for the 0/8 tidal phase – still exhibit significant relative differences, i.e. even greater than 100%. More impressive

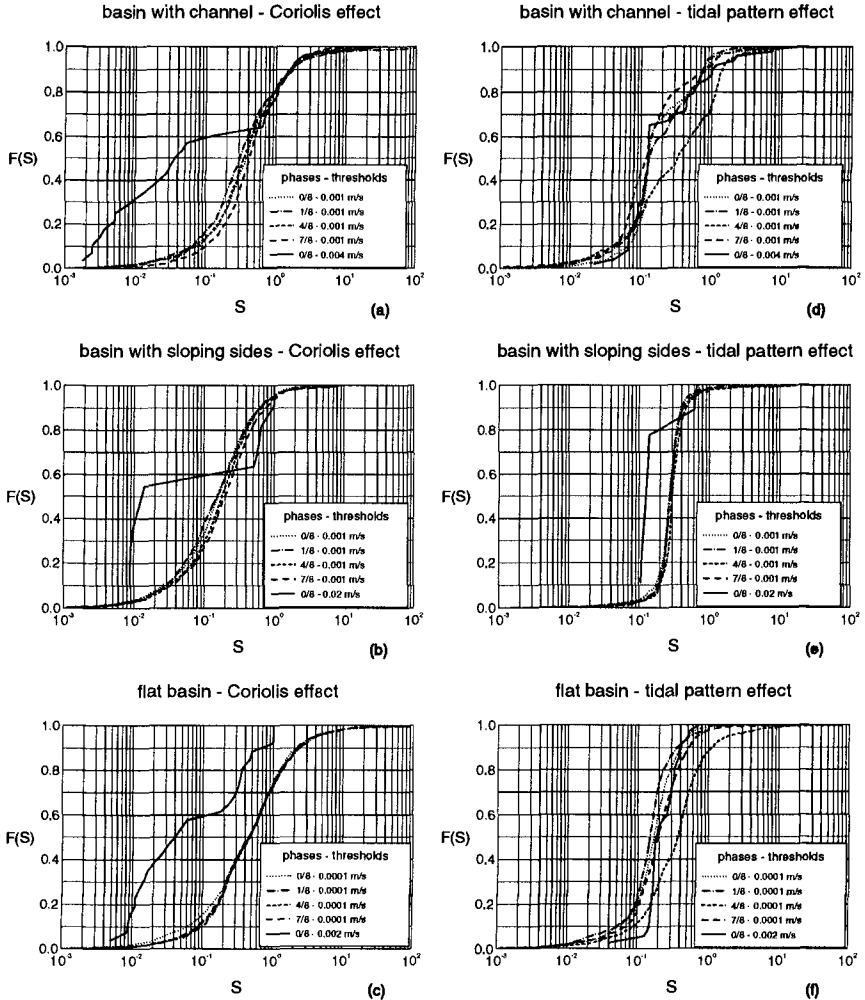


Figure 5: Curves of the cumulative frequencies,  $F(S)$ , of the relative differences,  $S$ , between residual velocities components computed for the three test basins (a-c) with the mixed tide including or not the Coriolis terms and (d-f) with the Coriolis terms considering the semidiurnal or the mixed tide

results obtained with the stochastic transport model will be shown further on, together with analogous results from analysis of the effect of the tidal pattern.

### 3.2 Specification of tidal wave at open boundaries

The second comparison has been carried out between the specification of a semidiurnal and a mixed tide (see fig. (6c,b)) as boundary condition of the hydrodynamic model. Indeed, the latter is the basic pattern of a possibly more complicated real tide like that shown in fig. (6a). This general behaviour can be observed at Mediterranean coasts, as well as at many other sites in the world. However, in literature cases can be mentioned in which, given a real irregular pattern, the semidiurnal one is assumed either, generically, for the sake of simplicity or since it is assumed that very refined results should not be expected when a necessarily rough specification is given as to any other parameter or forcing – typical is the case of wind – included in the model (Cheng and Casulli, 1982). It seems then useful to elucidate what the consequences of this choice might be if a less rough description of residual circulation is desired in the case that no other important external forcing is acting on the field. As mentioned earlier, this is not an unacceptible abstraction since these are exactly the conditions in which, e.g. anoxia phenomena occur in an eutrophic water body. However, the present investigation is, in turn, somewhat simplified in that the tidal amplitude variability in the syzygial period is not taken into account. The present investigation may then be regarded as a first attempt to define a suitable representative tidal pattern to be used in practical applications to approximate the real behaviour in the intertidal approach.

The mixed tide to be approximated is the one already mentioned in section 3.1 and shown in fig. (6b). At first, results obtained with tides of equal amplitude  $a = 0.5$  m (fig. (6c)) have been compared. Then, tentative alternative specifications of the semidiurnal tide have been tried, namely: i) the single semidiurnal component extracted from the mixed tide ( $a = a_s = 0.4$  m); ii) the semidiurnal tide whose mean energy equals that of the mixed tide ( $a = \sqrt{a_s^2 + a_d^2} = 0.424$  m), mean tidal energy over the period,  $T$ , being defined as

$$E = \frac{1}{T} \int_T \eta^2 dt$$

In no case significant improvements were obtained as to the similarity of numerical results. In fig. (5d-f) the curves of cumulated frequencies of relative

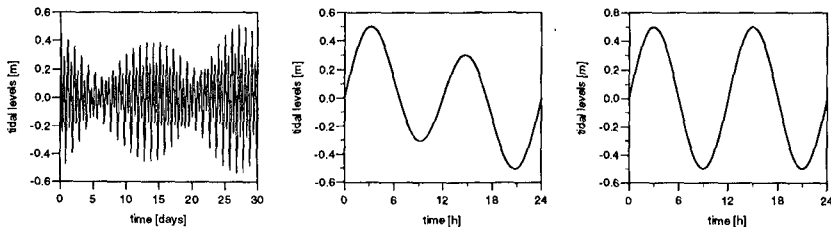


Figure 6: Simplification of tidal patterns: (a) typical real behaviour of a Mediterranean tide, (b) mixed pattern, (c) semidiurnal pattern

differences computed for the three basins for the comparison to the semidiurnal tide of equal range are shown.

### 3.3 Simulations of convection-dispersion

Numerical simulations of convection-dispersion of a passive solute released in various points of the basins confirmed the significance of the previously mentioned differences.

In the flat basin the spreading of the tracers is very weak and regular. Indeed, according to the simple gaussian model of dispersion (Adams and Baptista, 1987), the second central moment of the mass distribution

$$D_{sq}^2 = \frac{1}{N} \sum_{i=1}^N (x_i - x_c)^2 + (y_i - y_c)^2$$

where  $x_i$ ,  $y_i$  are the coordinates of the  $i$ -th particle of the ensemble of  $N$  particles, and  $x_c$ ,  $y_c$  are the coordinates of the center of mass, was found to be fairly linearly proportional to the elapsed time for a specified tidal phase, at least after a sufficiently long time from the release. This is shown in fig. (7) for the release point No. 1 of fig. (8), in the presence of both mixed tide and Coriolis forces. Although the alternate stretching and contracting behaviour of the cloud is governed essentially by the mean velocity gradients, the order of magnitude of the ratio  $D_{sq}^2/2t$  is as that of the intratidal diffusion coefficients considered in the simulation of random fluctuations.

Under the above conditions of regularity of diffusion, exclusive reference can be made to the position of the center of mass for the comparison of the effects of the tidal pattern and the Coriolis forces. Results are shown in fig. (8) for three points of release of the mass of solute and for the four possible combinations of the above factors. Trajectories followed by the centers of mass over a time extent of 20 days are plotted with a time step equal to the period of the relevant tidal pattern, so that tidal excursion is not resolved. It is apparent that

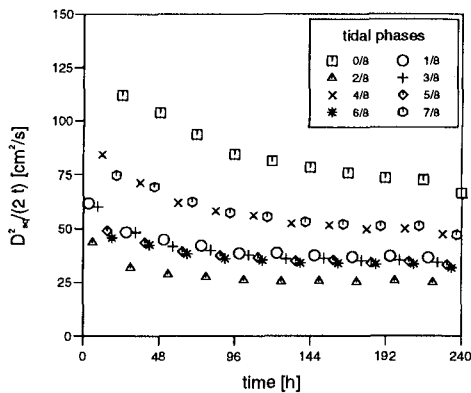


Figure 7: Ratios  $D_{sq}^2/(2t)$  computed at fixed tidal phases for a cloud of passive solute transported in the flat basin under the effect of both the mixed tide and the Coriolis forces - release point No. 1 of fig. (8)

neglecting of the Coriolis forces leads to a much more unrealistic simulation of the transport phenomenon compared to the approximation of the mixed tide by the semidiurnal one.

In the channeled basin, depending on the location of the release point, intratidal dispersion can be completely dominated by the spread induced by noticeable mean velocity gradients. Indeed, in that zones intratidal dispersion is only responsible for the initial, near field, displacement from which the second factor leads to a spread of a greater order of magnitude. In fig. (9a-f) the displacements of clouds of solute after four days from the release in two points of the basin are shown. Depending on the location of the point of release, a different relative importance of the Coriolis forces and the tidal pattern in the convection-dispersion process can be perceived. In particular, near the shore, just like in the flat basin, considering the Coriolis forces is much more important than exactly specifying the tidal pattern. However, in the proximity of the channel both factors must be properly represented for a correct reproduction of the dispersion process.

It is apparent that the reason of this behaviour is to be found in the major role played by the channel in the whole dynamics of the water body, it being able to produce a circulation that is one order of magnitude stronger than in the flat basin. Apparently, the Coriolis forces act more as a direct driving factor of the circulation in the flat areas of both basins. Instead, in the areas influenced by the channel their role is mainly that of inducing different interactions between the expansions and the channel itself, whose presence, along with the associated strong velocity gradients, is indeed responsible of the important convection and dispersion at the intertidal scale. If boundary conditions like the tidal wave are changed, then the low hydraulic conductivity of the flat areas - in particular, of the inlet - causes the effects of the changes to be damped as well. Instead, the major conductivity of the channel causes the features of an important driving mechanism, and so the resulting features of circulation, to be remarkably modified too.

The basin with sloping sides behaves essentially like the channeled one, as far as analogous conditions at the inlet are involved. This is shown in fig. (10a-f) for the same points and initial tidal phases of release as for the channeled basin. In particular, for the release in the proximity of the channel, while considering the mixed pattern makes only a small part of the particles to be out of the domain after four days, none of them remains within it if the semidiurnal tide is considered, regardless of the inclusion of the Coriolis terms.

### 3.4 Diffusion coefficient and numerical time weight

Let us consider the following simplified form of the x-momentum equation drawn from system (1):

$$\frac{\partial U}{\partial t} + gh \frac{\partial \eta}{\partial x} + \gamma U = 0 \quad (3)$$

where  $\gamma U$  is the linearised bottom friction term. This can be discretised on a fully staggered, Arakawa-C grid as

$$\frac{U_{i+1/2,j}^{n+1} - U_{i+1/2,j}^n}{\Delta t} + \alpha \left( gh_{i+1/2,j}^{n+1} \frac{\eta_{i+1,j}^{n+1} - \eta_{i,j}^{n+1}}{\Delta x} \right) \quad (4)$$



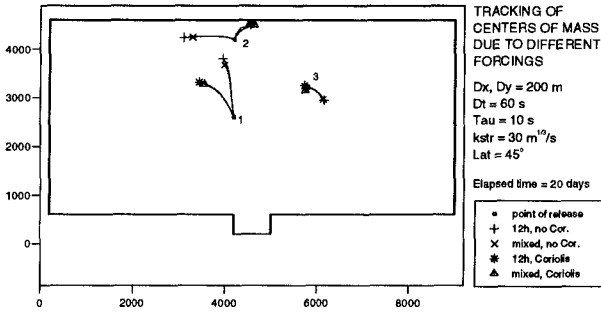


Figure 8: Pathlines of the centers of mass of clouds of a passive solute dispersing in a flat, 1 m deep, tidal basin under different forcing conditions

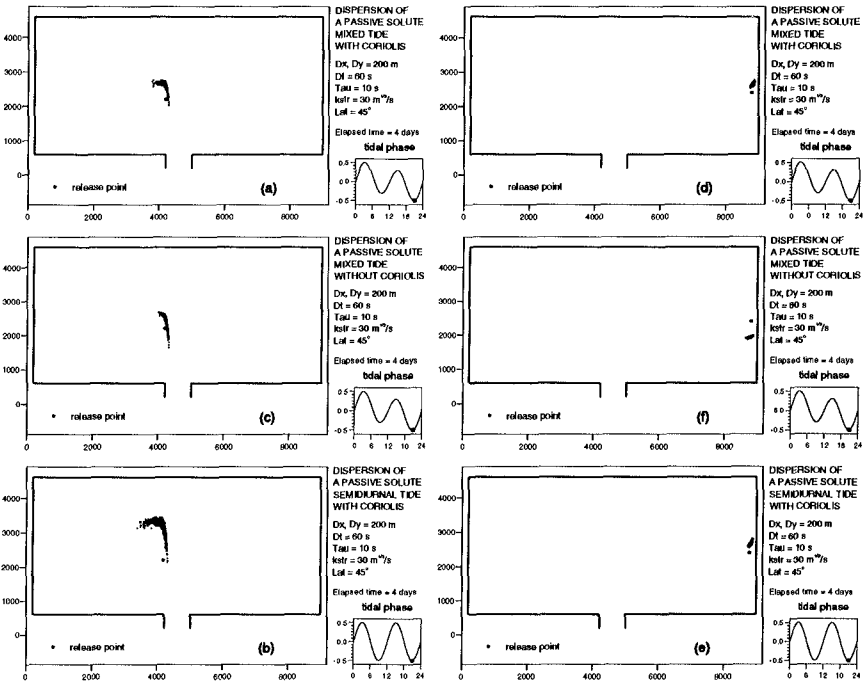


Figure 9: Advection-dispersion of a passive solute in a flat, 1 m deep, tidal basin with a central, 5 m deep channel, four days after release in two points, computed for a mixed tide (a,d) with and (b,e) without the Coriolis forces, and (c,f) for a semidiurnal tide of equal range with the Coriolis forces

$$+ (1 - \alpha) \left( g \bar{h}_{i+1/2,j}^n \frac{\eta_{i+1,j}^n - \eta_{i,j}^n}{\Delta x} \right) + \gamma U_{i+1/2,j}^{n+1} = 0$$

where  $\alpha = 0.5 \div 1$  is required for a stable discretization. Analysis of the relevant truncation error shows that using scheme (4) in numerical computations equals solving

$$\frac{\partial U}{\partial t} + gh \frac{\partial \eta}{\partial x} + \gamma U = - \left[ \left( \frac{1}{2} - \alpha \right) \frac{\partial^2 U}{\partial t^2} + (1 - \alpha) \gamma \frac{\partial U}{\partial t} \right] \Delta t + O(\Delta t^2, \Delta x^2, \Delta y^2)$$

regardless of the method used for the linearisation of the barotropic pressure gradient. This holds also for a fully non-conservative analog of equation (3), involving velocity components alone. In the absence of bottom friction, the scheme can be made of second order in time by letting  $\alpha = 0.5$ , while values greater than 0.5 provide a damping effect (Casulli and Cattani, 1993). Since this effect, even though not remarkable, is nonetheless clearly perceivable at the intratidal time scale, a check on its importance at the intertidal scale has been done.

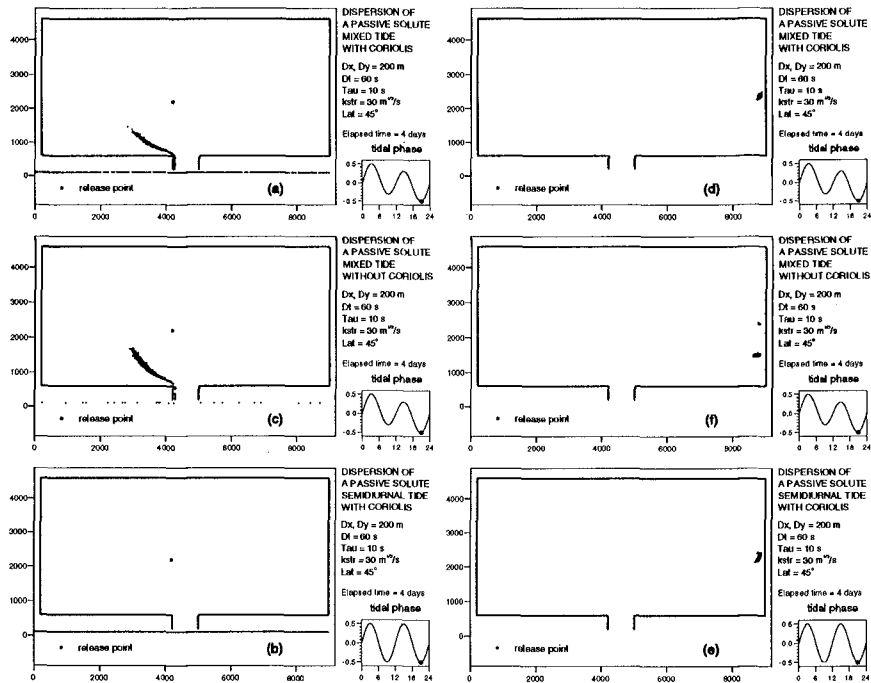


Figure 10: Advection-dispersion of a passive solute in a tidal basin with a central, 5 m deep, strip and sloping sides, four days after release in two points, computed for a mixed tide (a,d) with and (b,e) without the Coriolis forces, and (c,f) for a semidiurnal tide of equal range with the Coriolis forces

The effect of diffusion terms in equations (1) is also often considered negligible in current simulations in lagoons, provided that sufficiently small space and time scales are considered in the computations (Pfeiffer et al., 1988; Rosso et al., 1993; Umgiesser et al., 1993).

As far as regards the parameter,  $\alpha$ , and the diffusion coefficient,  $K$ , comparisons have been carried out, for the channeled basin only, between results obtained in a reference case (the above mixed tide of 1 m of range,  $K=0$ ,  $\alpha=0.5$ , i.e. Crank-Nicholson scheme), and two cases differing respectively by  $K=1 \text{ m}^2/\text{s}$  and  $\alpha=1$  (fully implicit scheme). These values represent a strictly upper limit value for the latter parameter and a reasonable one, though roughly estimated, for the former, depending on the characteristics of both the basin and the motion. In fig. (11a,b) the relevant curves of relative differences are shown. Though the channeled basin was expected to be, among the three, the most sensitive to changes in the above mentioned parameters, results are apparently much less significant compared to the cases of Coriolis forces and tide specification.

4. Conclusions

Some features of long term transport in shallow and relatively small lagoons under a relatively weak tidal forcing alone have been analysed. Results are then applicable to Mediterranean tidal basins in the absence of wind, i.e. in conditions like those eventually leading to anoxia in the water body.

It has been shown that the usual assumption of neglecting Coriolis forces in this kind of basins is acceptable only for the purpose of determining the general characteristics of intratidal circulation. Indeed, this factor proved essential to the correct simulation of long term transport in all the three prototypes considered. Potentially dangerous mistakes of practical interest in applications have been shown. A mixed tidal pattern proved well approximated by a semidiurnal one of equal range in a flat basin in which the tidal range is substantially damped at the inlet, as well as in the peripheral, shallower areas of basins in which propagation of the tidal wave is allowed to a larger extent. In the latter, a more realistic tidal pattern is required for a correct simulation of convection-dispersion in areas

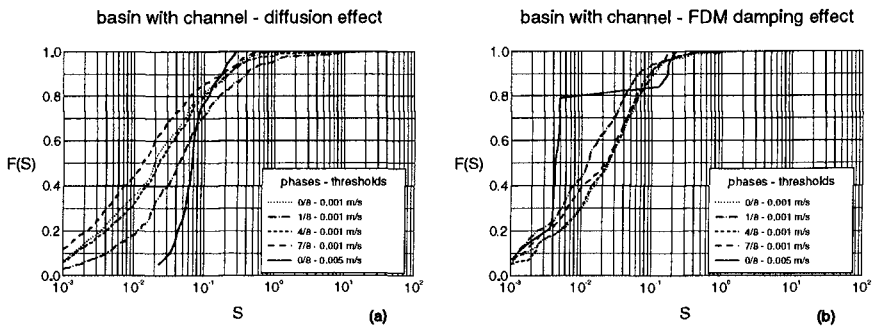


Figure 11: Curves of the cumulative frequencies,  $F(S)$ , of the relative differences,  $S$ , between residual velocities components computed for the basin with channel with the mixed tide and Coriolis forces (a) including or not the diffusion terms with  $K = 1 \text{ m}^2/\text{s}$  and (b) selecting  $\alpha = 0.5$  and  $\alpha = 1$  in the numerical discretization (4) of the propagation terms

characterized by relatively strong velocity gradients in the hydrodynamic field.

Though numerical results should always be regarded with caution even when an accurate check is done on numerical convergence and a robust and accurate model is employed, particularly in the presence of a highly irregular bathymetry (D'Alpaos et al., 1992), nonetheless it seems that, if not exactly the numerical entity of the mentioned differences, at least the remarkable differences shown as to the circulation patterns should be regarded as really meaningful.

On the basis of the above results, it seems that a representation of the long term transport due to a real tide of variable amplitude in the syzygial cycle in terms of residual fields for semidiurnal tides of correspondingly varying amplitudes can be tried for basins like the flat one considered in this study.

On the other hand, residual circulation seems to be less sensitive even to reasonably high values of the diffusion coefficient, which, however, could not be assigned an accurate value at the start of the art. Even less significant is the effect of the numerical time weight  $\alpha$ , of a standard implicit discretization scheme for spatial derivatives, whose smoothing effect when equal one is not so much important on tidal waves compared to short and high-frequency ones.

#### Appendix. - References

- Adams, E.E., and Baptista, A.M., (1987). Ocean Dispersion Modelling. In *Enciclopedia of Fluid Mechanics, Gulf Publishing Company, v. 6*, 865-895.
- Avanzi, C., and Fiorillo, G., (1983). Modello di dispersione bidimensionale intermareale della laguna di Venezia. Pub. 352 Ist. di Idraulica Univ. di Padova.
- Balzano, A., (1993). Sulla modellazione matematica di onde lunghe mediante metodi euleriano-lagrangiani bidimensionali. *PhD Thesis*, Milano.
- Benqué, J.P., Cunge, J.A., Feuillet, J., Hauguel, A. and Holly, F.M. Jr, (1982). New Method for Tidal Current Computation. *Journal of Waterways, Port, Coastal and Ocean Division, A.S.C.E., v. 108*, 396-417.
- Casulli, V., and Cattani, E., (1993). Stability, Accuracy and Efficiency of a Semi-Implicit Method for Three-Dimensional Shallow Water Flow. *Computer and Mathematics with Applications*.
- Cheng, R.T. and Casulli, V., (1982). On Lagrangian Residual Currents With Application in South San Francisco Bay. *Water Res. Research, 18, 6*, 1652-1662.
- Cheng, R.T. and Walters, R.A., (1982). Modelling of Estuarine Hydrodynamics and Field Data Requirements. In: *Finite Elements in Fluids, Ed. Gallagher et al. 4, John Wiley, New York*, 89-108.
- Chignoli, C., and Rabagliati, R., (1977). A Two-Dimensional Model for the Lagoon of Venice: Acqua Alta and Modular Sluices. *Proc. XVII IAHR Congress, v. 3, Baden Baden, FRG*, 393-399.
- Cioffi, F., and Gallerano, F., (1990). Effetti dei ricambi idrici forzati sul contenimento delle crisi anossiche nella laguna di Orbetello *Atti del XXII Convegno di Idraulica e Costruzioni Idrauliche, Cosenza*, 149-162
- Cioffi, F., Di Eugenio, A., and Gallerano, F., (1994). Simulation model for forecasting anoxic crisis in lagoons. *Proc. of Conference on Computer Techniques in Environmental Studies, San Francisco*, 107-120
- D'Alpaos, L., Defina, A. and Zovatto, L., (1992). Correnti residue fisiche e numeriche in un bacino a marea indagata con schemi di calcolo bidimensionali. *Atti del 29° Convegno di Idraulica e Costruzioni Idrauliche, D.139, Firenze*.

- Defina, A., and D'Alpaos, L., (1994). Una breve nota sui coefficienti di dispersione intermareale. *Atti del XXIV Convegno di Idraulica e Costruzioni Idrauliche, Napoli, Italy*, T1 49-56
- Dejak, C., Franco, D., Pastres, R., and Pecenic, G., (1990). A 3-D Eutrophication-diffusion Model of the Venice Lagoon: Some Applications. In: *Coastal and Estuarine Studies, Vol. 38, R.T. Cheng Ed., Residual Currents and Long-term Transport, Springer Verlag New York.*, 526-538.
- Falconer, R.A., (1985). Residual Currents in Port Talbot Harbour: A Mathematical Model Study. *Proc. Inst. Civ. Engrs., London, Part 2, 79, Mar.*.
- Ghoniem, A.F., and Sherman, F.S., (1985). Grid Free Simulation of Diffusion Using Random Walk Methods. *Journal of Computational Physics, 61*, 1-37
- Maier-Reimer, E., (1977). Residual Circulation in the North Sea Due to the M2-Tide and Mean Annual Wind Stress. *Deutsche Hydrographische. Zeitschrift, 30*, 69-80.
- Maier-Reimer, E., and Sundermann, J., (1982). On Tracer Methods in Computational Hydrodynamics. In: *Engineering Applications of Computational Hydraulics, Eds. Abbott, M.B. and Cunge, J.A., vol. 1, Pitman Publ. Inc.*, 198-219.
- Morandi Cecchi, M., (1989). Study of the behaviour of Oscillatory Waves in a Lagoon. *Int. Journal of Numerical Methods for Engineers, v.27*, 103-112.
- O'Kane, J.P., Suppo, M., Todini, E., Turner, J., (1990). Project for Optimal Management of the Goro Lagoon by Means of a Three-Dimensional Hydrodynamical-Diffusive Model. In: *Computational Methods in Surface Hydrology, Brebbia, C.A. et al. Eds., Venice, Italy*, 139-147.
- Pedlosky, J., (1987). Geophysical Fluid Dynamics. *Springer Verlag New York*.
- Pfeiffer, K.D., Duwe, K.C., and Sundermann, J., (1988). A High-Resolving Eulerian Current and Lagrangian Transport Model of the Lagoon Valle Vallona. In: *Computer Modelling in Ocean Engineering, Schrefler, B.A. and Zienkiewicz, O.C. Eds., Balkema, Rotterdam Brookfield, Netherland*, 393-400.
- Rosso, M., Fettweis, M., and Yu, C.S., (1991). Tidal Flow Simulation in the Lagoon of Venice. *Proc. II International Conference on Computer Methods and Water Resources, Marrakesh, Morocco*.
- Umgiesser, G., Sundermann, J. and Runca, B., (1988). A Semi-Implicit Finite Element Model for the Lagoon of Venice. In: *Computer Modelling in Ocean Engineering, Schrefler, B.A. and Zienkiewicz, O.C. Eds., Balkema, Rotterdam, Netherland*, 71-79.
- Umgiesser, G. and Bergamasco, A., (1993). A Staggered Finite Element Model of the Venice Lagoon. In: *Proc. VIII International Conference on "Finite Elements in Fluids", Barcelona, Spain*.
- Van de Kreeke, J., (1976). Tide-Induced Mass Transport; a Flushing Mechanism for Shallow Lagoons. *Journal of Hydr. Res., v. 14, n° 1*.
- Volpi, G., Sguazzerio, P., (1977). La propagazione della marea nella laguna di Venezia: un modello di simulazione ed il suo impiego nella regolazione delle bocche di porto. *Rivista Italiana di Geofisica, v. IV (1,2)*.
- Zimmermann, J.T.F., (1979). On the Euler-Lagrange Transformation and the Stokes' Drift in the Presence of Oscillatory and Residual Currents. *Deep Sea Research, 26 A*, 505-520.

## CHAPTER 212

### THE EXTENT OF INLET IMPACTS UPON ADJACENT SHORELINES

Kevin R. Bodge, Ph.D., Member ASCE<sup>1</sup>

#### Abstract

*The erosional impacts of improved inlets upon adjacent shorelines may be best estimated by first computing the volume of material removed from the littoral system and then examining the adjacent shorelines to identify the length along which this volumetric impact has been manifest. This contrasts with the traditional approach whereby erosion is identified along a finite reach of shoreline and attempts are then made to link the erosion to a plausible cause. The length and volume of inlet-related erosion at two inlets considered herein are significantly greater than that traditionally ascribed to the inlets. Both feature near-field and far-field downdrift erosion signatures separated by stable shoreline.*

#### INTRODUCTION

Improved ocean inlets are becoming increasingly recognized for their role in effecting beach erosion along adjacent shorelines. Such inlets include those which have been created or stabilized by dredging and/or by structures for purposes of navigation, water quality, flood control, etc. The total extent of these projects' influence upon the adjacent shorelines is not presently certain and is the subject of considerable debate. In the United States, perhaps the first examination of the topic was prepared for the U. S. Army Chief of Engineers in 1938 (Blackman, 1938). More recent discussions include those of Dean and O'Brien (1987), Fields *et al.* (1989), Work and Dean (1990), Bodge (1993), Bruun (1994), among others.

This paper considers the proposition that the littoral impact of inlets (and similar coastal perturbations) may be much greater than previously suspected. The reasons for this could be that (1) the littoral impacts are more closely related to interruptions of the gross transport rates (rather than the net transport rates), and (2) that the traditional identification of downdrift shoreline change may be a poor indicator of an inlets' total volumetric impact. Because the paper examines the degree to which man-made coastal projects impact the shoreline's littoral drift regime, its applicability need not be limited to ocean inlets. That is, the principles considered herein should be applicable to coastal perturbations in general which act as a sediment sink; e.g., marinas, breakwaters, long groins, nearshore dredging, etc.

#### GENERAL CONSIDERATIONS OF INLET IMPACTS

**The Influence of Gross vs. Net Transport.** An inlet's littoral impact is often expressed in term of its "interruption of the *net* littoral drift." While this is a useful

---

<sup>1</sup> Senior Engineer, Olsen Associates, Inc. 4438 Herschel St., Jacksonville, Florida 32210 U.S.A. (904) 387-6114; Telefax (904) 384-7368.

concept to help explain inlet impacts to laymen, it is a significant simplification of littoral processes -- and risks marked underestimation of an inlet's actual impacts.

For example, it is known that a perturbation (such as a groin) placed along a beach with large gross transport but negligible net transport will, indeed, induce changes to the adjacent shorelines. The degree to which the beach will be erosional or accretional on each side may depend upon the state of the transport regime or the overall supply of sediment at the time the perturbation is introduced. Thus it is recognized that the *gross* components of transport may be central in characterizing the response of shorelines to perturbations. This idea is not new (Galvin, 1990, among others), but perhaps is increasingly overlooked.

An improved inlet represents such a shoreline perturbation, and in particular, is often a sediment sink in response to gross transport processes (e.g., Bruun and Battjes, 1963; Dean and Walton, 1975; Walton and Adams, 1976). Consider, for example, a shoreline with component drift rates of +100 and -20 units, yielding a net drift rate of +80 units, along which is constructed a stabilized inlet (Figure 1). If all or part of the transport directed toward the inlet on its downdrift side leaks into the entrance channel, then the net downdrift erosion stress could be as much as 100 units instead of 80. Similarly, if all or part of the transport directed toward the updrift side is sunk to the channel or permanently impounded, there will be up to 20 units of localized erosion well updrift of the inlet. The total potential erosional impact would thus be 120 units (the gross transport rate), not 80 units (the net transport rate).

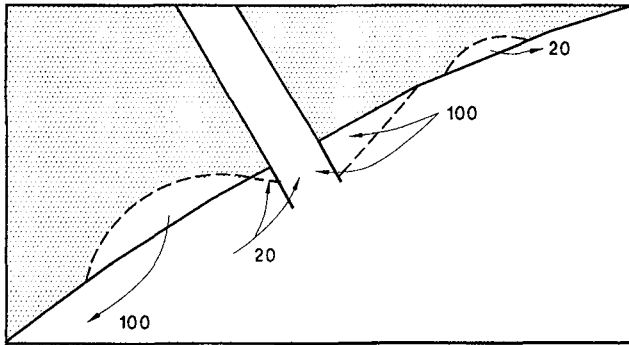


**Figure 1:** Potential effect of an inlet upon a shoreline with gross transport rate components of 100 and 20 units. By introducing the inlet, the potential downdrift and updrift erosional impacts are 100 units and 20 units, respectively. Consideration of only the net drift rate leads to the erroneous conclusion that erosional impacts are limited to 80 units on the downdrift side.

**Mechanisms of Inlet Impacts.** The general mechanisms by which inlets impact the adjacent shorelines are known: Material is removed from the littoral system by impoundment against the inlet's terminal structures and by transport through, over and around leaky terminal structures (i.e., jetties which are too short, porous, or low). That

material which is transported past the structures is then deposited into tidal shoals or along the channel seabed. Dredging and subsequent offshore disposal further removes some of this material from the system. Even recent efforts to restore the suitable dredged material to the system are not 100% effective because the beach material which deposits in the channel often mixes with ambient silts and clays -- making the material unsuitable for nearshore recovery (i.e., beach or nearshore berm disposal).

The volumetric sum of these components (impoundment, shoal formation, and dredge disposal out of the system), measured relative to natural conditions, represents the inlet's littoral impact. Through consideration of the conservation of mass, this must also represent the total erosional impact of the inlet upon the adjacent beaches.

**Approach.** A reasonable approach to estimate an inlet's littoral impacts may therefore be to *first* identify the volume of sand removed from the system by the inlet, and *then* examine the adjacent shorelines to identify the extent of the shoreline along which this volume has been realized. This approach contrasts with that conventionally employed to determine inlet impacts; i.e., where one first estimates volumetric erosion along a finite length of beach and then attempts to link the erosion to a plausible cause.

#### APPLICATION: PORT CANAVERAL, FLORIDA

As an example of the approach outlined above, the case of Port Canaveral, Florida, will be considered. Port Canaveral is located on the Atlantic coastline of the southeastern United States in the state of Florida (Figure 2). The port's inlet is presently

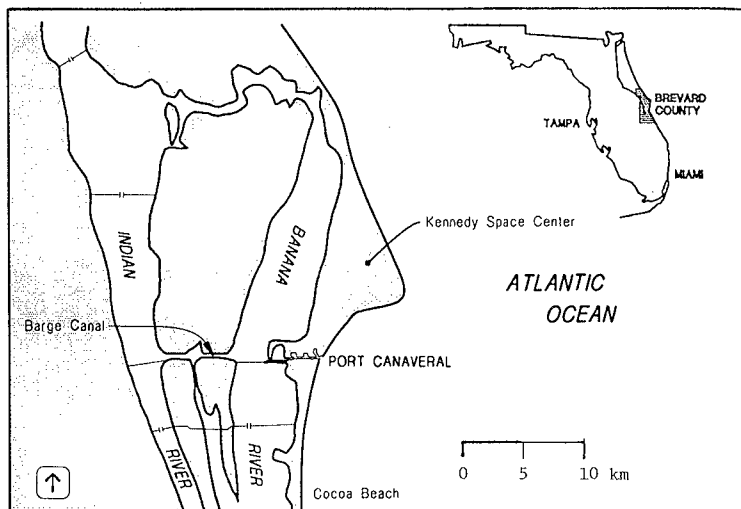


Figure 2: Location map of Port Canaveral, Florida.



maintained to a depth of -14 m MLW. Dual rock jetties which extend about 275 m and 70 m seaward of the pre-inlet MHWL bound the channel entrance to the north and south, respectively. There are no tidal shoals associated with the inlet because the port has always been hydraulically isolated from inland waters by a navigation lock or berm, and the inlet's tidal currents are weak. The dominant drift direction is southerly.

The inlet was artificially established by dredging through a sandy barrier island in 1950-52. The pre-inlet shoreline was regular, though arcuate, and accretive. Subsequent to the inlet construction, the shorelines north and south of the new inlet rapidly advanced and eroded, respectively. Despite the placement of almost 1.8 MCM of beach fill in the mid-1970's, the present shorelines north and south of the inlet are offset by over 280 m.

**Updrift Impoundment.** The volume of sand impounded by the inlet's north jetty was estimated by comparing historical shoreline records prior to and after construction. The shoreline changes were converted to volumetric changes through an approximate, fixed multiplier of  $8.23 \text{ m}^3$  per m of change per m of shorefront. (This is a conservative value; i.e., it may underestimate the volume change. Comparison of the limited profile data historically collected along this beach suggested a value 20% greater than  $8.23 \text{ m}^3/\text{m}/\text{m}$ .) The computed volume changes were then expressed as *cumulative* volume change updrift of the inlet -- annualized over the years between shoreline surveys (Figure 3a).

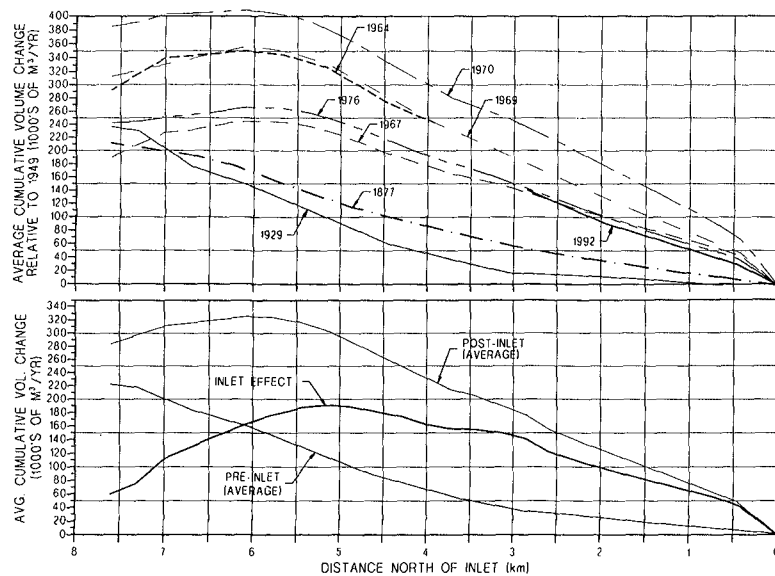


**Figure 3:** Cumulative annualized volume changes updrift of Port Canaveral developed from (a) discrete shoreline change records and (b) the average signals of the pre- and post-inlet shoreline change records. The difference between the pre- and post-inlet signals is the inlet effect.

The volume change data expressed in this way clearly fell into two groups corresponding to pre- and post-inlet conditions, respectively. The average of the cumulative curves in each of the two groups was computed to yield the approximate pre- and post-inlet rates of updrift volume change as a function of distance from the inlet. The difference between these two averages represents the net updrift effect of the inlet (Figure 3b). The updrift extent of the impoundment signal -- suggested by the maxima in the curve -- is noted about 3.3 to 5.0 km updrift of the inlet. The magnitude of the impoundment signal over this distance is about 152,500 m<sup>3</sup>/yr ( $\pm 37,500$  m<sup>3</sup>/yr). Over the first 40 years since the inlet was constructed, this represents about 6.1 ( $\pm 1.5$ ) million cubic meters (MCM) of impoundment.

**Dredging.** Only a portion of the sand which is transported toward the north jetty is impounded. The jetty is low and porous, and is now too short relative to the accreted shoreline. The south jetty is likewise low and porous. Sand which is transported over, through and around the jetties deposits in four well-defined, consistent shoals at the landward and seaward ends of the structures. Diving, core-boring, and dredging inspection reveals that these shoals are composed of sand from the adjacent beaches. From "condition" surveys of the inlet entrance collected quarterly over the past few years, these shoals re-appear after dredging at a combined, average annual rate of about 150,000 m<sup>3</sup>/yr. Over a 40 year period, this amounts to 6.0 MCM. The latter value agrees well with independent estimates of the sand volume thought to have been dredged from the inlet. Specifically, dredging records and geotechnical data (which reveal a consistent lower depth to the local surficial sand lens) suggest that about 6.0 MCM of the 38 MCM of material dredged from the inlet over its first 40 years was beach-quality sand which was removed for purposes of maintenance and placed in deep water, offshore.

Over the inlet's first 40 years since construction, then, about 6.1 ( $\pm 1.5$ ) MCM of sand have been impounded by the north jetty beyond pre-inlet trends, and about 6.0 MCM have been dredged and disposed of out of the littoral system. The total, about 12.1 ( $\pm 1.5$ ) MCM, represents the inlet's littoral impact to the beaches over 40 years.

**Impact to Shorelines.** It has been historically assumed that the inlet's effects extended only about 3 km downdrift -- an area over which the post-inlet shoreline has been severely erosive (Figure 4). South of this distance (for a length of about 4 km), the shoreline has been stable to accretional. It is important to note, however, that the rate of accretion along this reach has been less than in pre-inlet conditions, and the beach south of this area has exhibited erosion.

Erosion along the downdrift 3 km of shoreline was estimated in a similar manner as for the impoundment signal on the updrift side of the inlet. Historical shoreline change data were converted to volumetric equivalents (using a multiplier of about 5.8 m<sup>3</sup>/m/m based upon typical profile comparisons), and expressed as average annual, cumulative volume change downdrift of the inlet. The effects of two beach fills during 1972-1975 were approximately removed by subtracting the placed volume from the post-fill data along the placement area. Like the updrift volume changes, the results fall into two groups corresponding to pre- and post-inlet timeframes (Figure 5a). The difference between the average of the two groups yields the inlet's effect (Figure 5b).

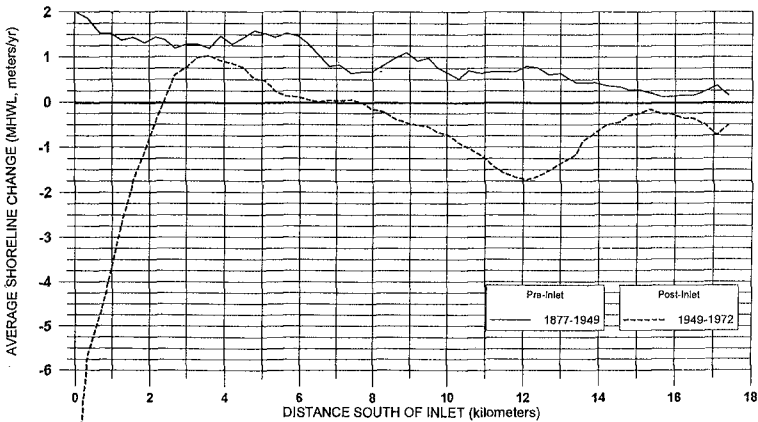


**Figure 4:** Historical shoreline changes south (downdrift) of Port Canaveral Entrance for pre- and post inlet conditions.

The inlet's primary erosive effect is evident within about 3.3 km south of the inlet (i.e., the point at which the cumulative volume change curve "levels out" in Figure 5b). Over this reach, the inlet's effect has been equivalent to about 75,000 m<sup>3</sup>/yr of erosion, on average. Over the first 40 years since the inlet's construction, this represents about 3.0 MCM of erosion. The inlet's total littoral impact, however, is computed as about 12.1 ( $\pm 1.5$ ) MCM -- which leaves another 9.1 ( $\pm 1.5$ ) MCM of impact unaccounted for. It is possible, but not certain, that 1.3 MCM of inlet-related impact may be associated with erosion north of the inlet's impoundment fillet. Such updrift erosion is predicted by the sediment budget (see below). Impacts further updrift are improbable; therefore, by deduction, the inlet's remaining 7.8 ( $\pm 1.5$ ) MCM of erosional impacts are likely associated with the beaches beyond 3.3 km south of the inlet. The inlet's total downdrift impact is thus estimated as about 10.8 ( $\pm 1.5$ ) MCM (Figure 6).

Cumulative volume changes along the beach downdrift of the inlet were computed beginning at the inlet for pre- and post-inlet conditions (Figure 7). An erosional volume of 10.8 MCM, accounting for pre-inlet processes is noted between 31 and 42 km south of the inlet. The  $\pm 1.5$  MCM uncertainty in the volume impact increases this range to between 22 and 53 km. Recent independent estimates of beach nourishment requirements within 42 km south of the inlet total 5.6 to 8.8 MCY (USACE 1992; Coastal Tech. Corp. 1992). Another 2.8 MCM of beach fill have already been placed herealong during the period of study. When this 2.8 MCM is added to the existing requirements, the total restoration requirement is 8.4 to 11.6 MCM. These values corroborate the author's findings; i.e., that the inlet's total downdrift impact, based upon a sediment budget, is 10.8 ( $\pm 1.5$ ) MCM.

**Sediment Budget.** The sediment budget developed for the inlet in pre- and post-project (existing) conditions is illustrated in Figure 8. The results are based solely

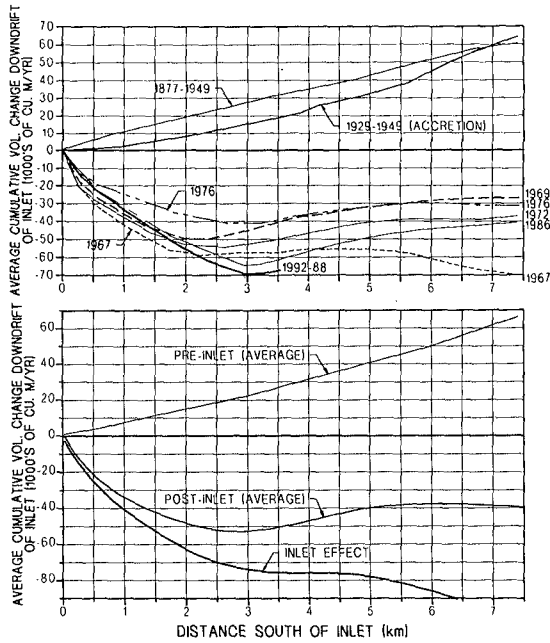


Figure 5: Cumulative annualized volume changes downdrift of Port Canaveral developed from (a) discrete shoreline change records and (b) the average signals of the pre- and post-inlet shoreline change records. The difference between the pre- and post-inlet signals is the inlet effect.

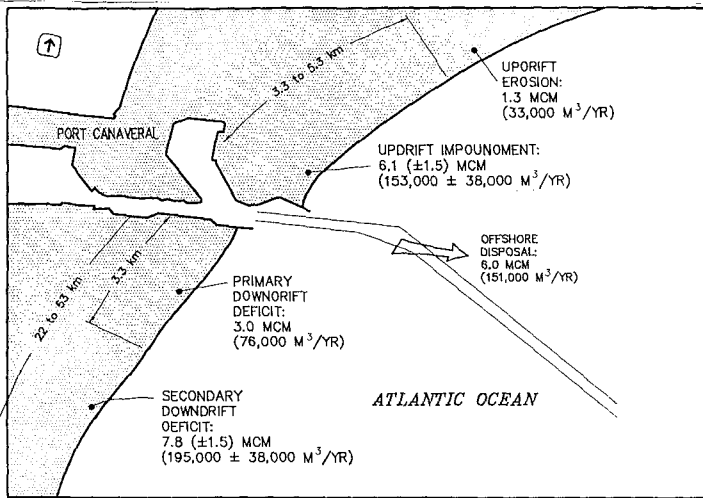
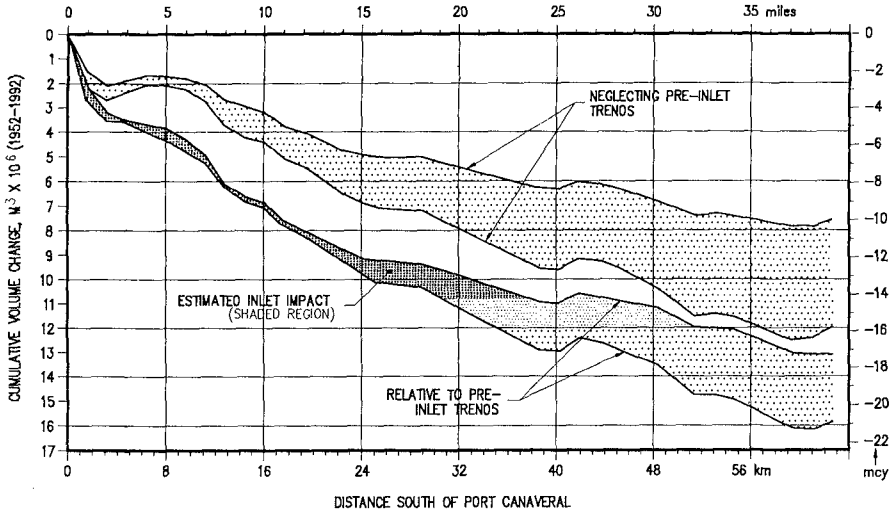
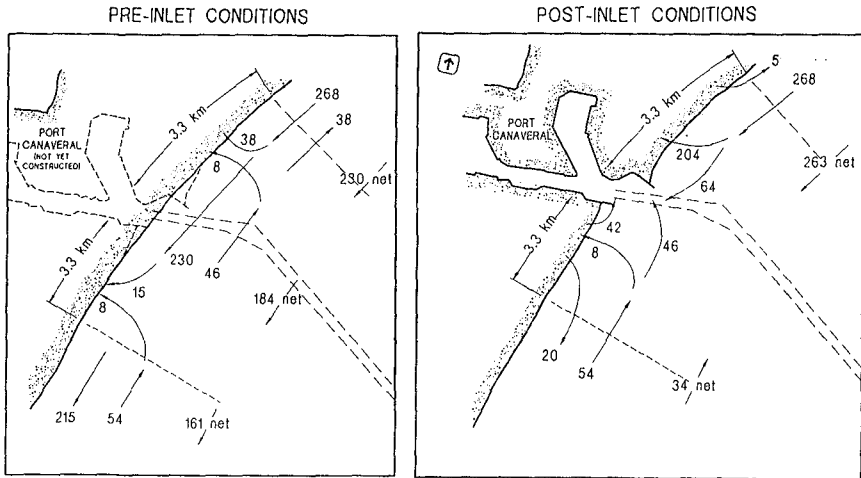


Figure 6: Overview of volumetric impacts attributed to Port Canaveral over the 40 years since the inlet's construction.



**Figure 7:** Cumulative change in beach volume estimated as a function of downdrift distance from Port Canaveral Entrance. The upper pair of curves refers to "observed" changes since the inlet's construction. The lower pair refers to changes since the inlet's construction -- relative to the local pre-inlet accretional trend. The range between the curves in each pair reflects error bars associated with transforming shoreline change data to volumetric estimates.



**Figure 8:** Gross sediment budget computed for Port Canaveral Entrance. The arrows and values represent longshore sediment transport rate in thousands of cubic meters per year.

upon interpretation of (i) measured shoreline changes north and south of the inlet, (ii) maintenance dredging records, and (iii) assumed values of the gross southerly and northerly transport rates incident to the inlet. The selection of the latter values was guided by refraction and GENESIS modelling results, and early studies of shoaling at the newly cut inlet (USACE 1961, 1992).

The pre-project, net littoral drift rate across the inlet entrance is estimated to have been 184,000 m<sup>3</sup>/yr to the south. From the sediment budget, however, the inlet's net impact is estimated to be 302,500 m<sup>3</sup>/yr. The 64% difference in these values is attributable to the sink effect of the inlet. Along the south beach in particular, the sand which chronically leaks through the south jetty (about 88,000 m<sup>3</sup>/yr) is lost from the beach and is no longer available for southerly transport during the predominant wave climate. At Port Canaveral, the result is an apparent *reversal* in the net transport direction downdrift of the inlet. This example illustrates the potential underestimates of inlet impact when *net* transport rates are considered in lieu of *gross* transport rates.

#### APPLICATION: SOUTH LAKE WORTH INLET, FLORIDA

South Lake Worth Inlet, Florida, is another example of a case where traditional examination of the downdrift erosion signature fails to reveal the extent of the inlet's littoral impacts. The inlet is located along the Atlantic coastline of Florida, about 150 km south of Port Canaveral, in Palm Beach County. The inlet was artificially cut through a sandy barrier island in 1927 for the purposes of improving water quality within the southern half of Lake Worth. Dual jetties stabilize the entrance channel, which reduces to 41 m width and 3 meters depth at its smallest point. The net littoral drift is southerly-directed. Despite the operation of a sand bypassing plant at the inlet's north jetty (which discharges sand to the downdrift shoreline south of the inlet), the beach to the south of the inlet has exhibited chronic erosion. The shoreline within about 2 km south of the inlet has been authorized as the site of a Federal shore protection (beach restoration) project.

**Sediment Budget.** The major sediment transport paths at the the inlet were identified as shown in Figure 9. The net volume of sand reaching the inlet's north shoreline ( $Q_1$ ) is impounded at the north beach ( $Q_2$ ), lost to the ebb shoal or offshore ( $Q_3$ ), lost to the inlet interior ( $Q_4$ ), naturally bypassed via the inlet's bar ( $Q_5$ ), and/or mechanically bypassed ( $Q_6$ ). The net volume of sand which is transported away from the inlet's south shoreline ( $Q_9$ ) includes sand which is naturally and artificially bypassed ( $Q_5$  and  $Q_6$ ), placed upon the south beach from interior dredging ( $Q_7$ ), and/or eroded from the south shoreline within about 2 km of the inlet ( $Q_8$ ). That is,

$$Q_1 = Q_2 + Q_3 + Q_4 + Q_5 + Q_6 \quad (1)$$

$$Q_9 = Q_5 + Q_6 + Q_7 + Q_8 \quad (2)$$

Estimates of six of the nine components in Eqs. 1 and 2 were developed for a number of time intervals using available data, including shoreline change records,

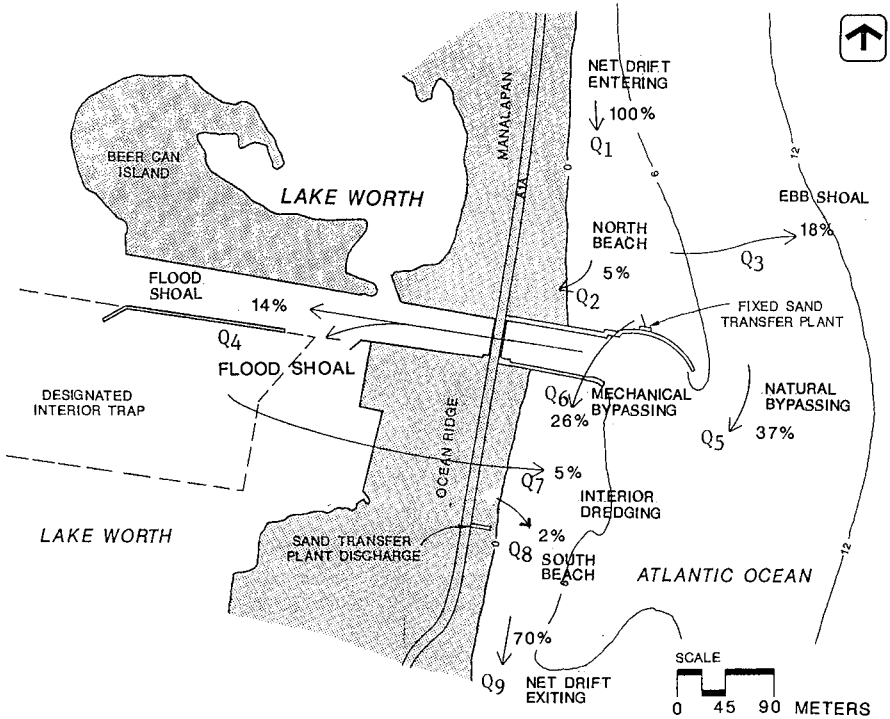


**Figure 9:** Net sediment transport components identified for South Lake Worth Inlet.

surveys of the ebb and flood tidal shoals, aerial photography, sand bypassing and dredging records. Using the values for these components, estimates of the natural bar bypassing rate ( $Q_5$ ) and the net drift rate leaving the inlet area ( $Q_9$ ) were computed from Eqs. 1 and 2 for net littoral drift rates incident to the inlet ( $Q_1$ ) ranging from 135,000 to 173,000  $m^3/yr$ . In this way, it was estimated that over the period 1927-90 (the first 63 years since the inlet's construction), about 28% to 36% of the incident net drift was bypassed mechanically ( $Q_6$  and  $Q_7$ ) while about 37% of the incident net drift was bypassed naturally ( $Q_5$ ). (See Figure 9.) Thus, only about 65% to 73% of the net drift incident to the inlet's north beach has been transported across the inlet to the beaches south of the inlet -- implying that the inlet has removed a volume of sand from the area's littoral system equal to about 27% to 35% of the incident net drift rate. This material has been diverted to interior shoals (much of which was dredged and used for upland fill along Lake Worth's shoreline), and the formation of an ebb shoal/bypassing bar platform and updrift impoundment fillit.

Considering the incident net drift rate to be on the order of 154,000  $m^3/yr$  (Watts, 1953; Bruun et al., 1966), the inlet is therefore estimated to have diverted as much as 2.6 to 3.4 MCM of sand from the littoral system over its first 63 years. On the

other hand, shoreline change records (including those which were incorporated to the sediment budget analysis) suggest that the shoreline within about 2 km south of the inlet has eroded by only about 2% of the net drift rate incident to the inlet's north side -- or about 0.2 MCM over the inlet's first 63 years.

**Obfuscation of Downdrift Impact.** In the case of South Lake Worth Inlet, the downdrift erosion signature along the 2-km (+/-) reach of coastline thought to be most severely impacted by the inlet potentially underestimates the inlet's littoral impact by a factor of 16. The reason may be related to the significant degree to which the downdrift shoreline has been artificially manipulated through armoring (seawalls), the construction of groins, and the placement of sand (sand bypassing). In such cases, the shoreline's response to erosional stress may be extraordinarily obscured.

By simple inspection of the nautical charts and historical aerial photography, there can be no doubt that the construction of South Lake Worth Inlet has removed from the littoral system far more than the 0.2 MCM of sand indicated by the immediate downdrift shoreline. The erosional stress that the inlet placed upon the shorelines (coupled with imprudent development in some cases) resulted in significant shoreline armoring adjacent to the inlet. This armoring limits the erosional signal of the beach, and/or precludes its identification from shoreline change data (which describe shoreline positions, not beach volumes). Reliance only upon the "near-field" downdrift shoreline history to deduce inlet-related impacts can result in significant underestimation of the inlet's impacts in those cases where the shoreline has been artificially manipulated. Additionally, in those cases where the adjacent shoreline(s) has (have) been stabilized against erosion, the inlet's erosional impacts must -- by deduction -- extend particularly far afield.

## DOWNDRIFT EXTENT OF INLET-RELATED EROSION

**Theoretical Considerations.** In the two example applications presented above, it was noted that the inlets' littoral impacts may extend far from the inlets, despite their young age. In both cases, however, the apparent *limit* of the erosion was traditionally thought to be about 2 km or less downdrift of the inlets; i.e., on the order of about 10 jetty lengths downdrift. Pelnard-Considére (1956) presented now-classical solutions for shoreline change adjacent to a sediment-trapping structure. At the time at which the structure becomes filled to capacity and begins to bypass sand, according to his solution, the shoreline recession ( $y$ ) at a distance ( $x$ ) downdrift of the structure is

$$\frac{y}{Y} = [\exp(-u^2) - \sqrt{\pi} u \operatorname{erfc}(u)] \quad (3)$$

where

$$u = \frac{x}{Y} \frac{1}{\sqrt{\pi}} \tan(\alpha_p) \quad (4)$$



where  $Y$  is the structure length, and  $\alpha_b$  is the wave breaking angle (assumed to be quasi-steady). Both  $y$  and  $Y$  are measured relative to the no-structure shoreline. Figure 10 presents solutions to Eq. 3 for various values of the wave breaking angle. For typical angles on the order of 4 to 8 degrees, shoreline recession on the order of 5% of the structure's length might be anticipated between 15 and 30 jetty lengths downdrift.

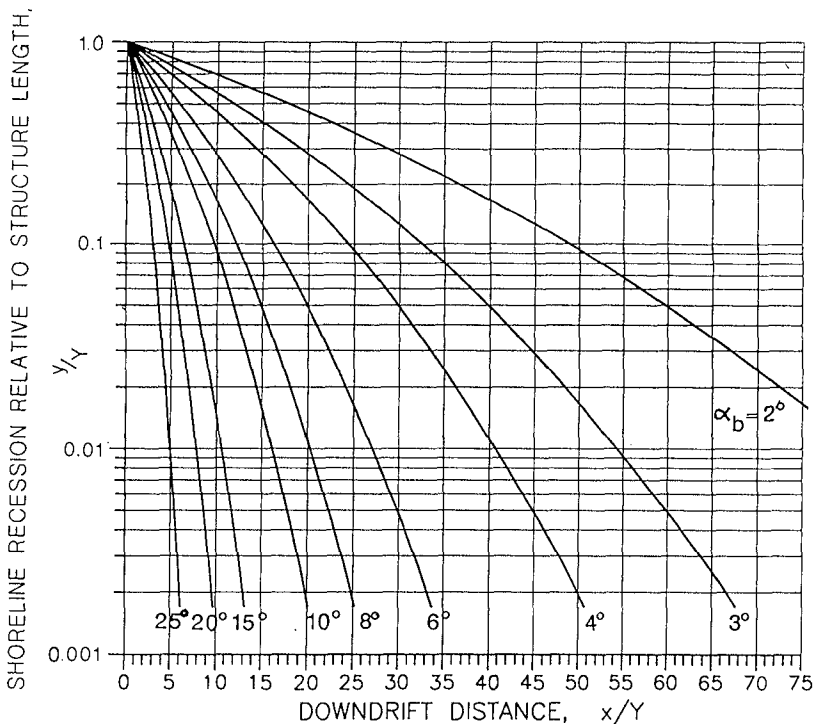


**Figure 10:** Shoreline recession predicted from Eq. 3 as a function of structure length and distance downdrift of the structure. The condition corresponds to the time at which sand begins to bypass the structure.

In the case of Port Canaveral, the average-annual breaking wave angle south of the inlet (as computed from hindcast data refracted to shore) is about 4 degrees. Taking  $Y = 275$  m (the length of the north jetty measured from the pre-inlet shoreline), downdrift recession on the order of 5 m over the inlet's history is predicted to occur about 37 jetty lengths downdrift, or about 10 km. (Recession less than about 5 m over 40 years is generally perceived as negligible in this locality.) When one considers that the updrift impoundment represents only half of the inlet's estimated impacts (the other half is dredging related), then the appropriately predicted distance may be twice as great -- or about 20 km. This length agrees in general magnitude with that estimated by the method presented in this paper. In any case, it is considerably greater than the 3 km shoreline reach along which the inlet's erosion is traditionally attributed.

In the case of South Lake Worth Inlet, the lineal extent of the inlet's impacts to the adjacent shorelines is not entirely clear. Considering that the estimated volumetric impact is 2.6 to 3.4 MCM over 63 years, and that typical observed erosion rates in the area are on the order of 0.5 m/yr or less (or about 2.75 m<sup>3</sup>/m/m/yr), the length of effected shoreline may be on the order of 15 to 20 km. The actual length is probably much greater -- and/or perhaps the volume of sand removed by the inlet has never been fully mitigated by erosion of the adjacent beaches -- because long reaches of the adjacent shorelines are armored by seawalls which significantly reduce observed shoreline and volumetric erosion of the beach.

**"Near-field" and "Far-field" Impacts.** The primary reason that the inlet impact associated with Port Canaveral was considered as only 3 km was that the shoreline south thereof (for a distance of a few km) appears stable to accretional. Indeed, this shoreline remained accretional after inlet construction -- but the rate of accretion was about two-thirds less than pre-inlet rates. Bodge (1994) demonstrates through a large-scale sediment budget that it is possible to have net shoreline accretion in the midst of an otherwise erosive regime downdrift of the Port Canaveral inlet. In any case, the overall picture is one of a severe "near-field" erosion wave within a few km of the inlet and a less dramatic "far-field" erosion wave separated from the former by a relatively short reach of stability or accretion. Bruun (1994) discusses numerous examples of this phenomenon and examines possible migration rates of these two erosion features downdrift of inlets. Bruun concludes that the "downdrift shoreline development at a littoral drift barrier may in general, but not always, be described by a short (local) as well as a long distance effect which both move downdrift at various rates, the long distance movement being 2-3 times faster than the short distance, or about 0.5 km/yr versus 1 to 1.5 km/yr.... The short distance effect is a coastal geomorphological feature, the long distance a materials deficit feature."

The appearance of the stable area between the near- and far-field erosion areas may be due to localized shoreline stability (rock outcrops, etc.), local refraction effects (such as those related to the ebb shoal across the inlet mouth), or far-field refraction effects. Local refraction effects and the shoreline attachment of the inlet's bypassing bar are responsible for a short reach of stability/accretion at South Lake Worth Inlet (Bodge, Olsen and Savage, 1990). Far-field refraction effects -- induced by Bull Shoals south of Cape Canaveral -- are apparently responsible for the reach of stability south of Port Canaveral Entrance (Bodge, 1994).

## CONCLUSION

The erosional effects of improved inlets upon adjacent shorelines may be best estimated by first computing the volume of material removed from the littoral system (beyond that which would have been removed naturally in the absence of the improvements) via consideration of the inlet-related (1) impoundment fillets, (2) flood and ebb shoal development, and (3) disposal of maintenance dredged, beach-type material outside of the littoral system. One next examines cumulative beach volume changes along the adjacent shorelines -- beginning at the inlet -- to determine the up- and downdrift-extent along which the inlet's volumetric impacts may be manifest. This fundamental approach contrasts with that conventionally employed to determine inlet

impacts; i.e., where one first estimates volumetric erosion along a finite length of beach and then attempts to link the erosion to a plausible cause. The latter approach is shown to be potentially deficient because (1) the length of the downdrift shoreline classically selected for examination may be much shorter than the actual length which has been affected by the inlet, and (2) downdrift shoreline changes may obfuscate erosion impacts via the effects of coastal armoring, beach reclamation, and other works which have been undertaken in defense against erosion.

The mechanisms by which the inlet's littoral impacts occur illustrate the behavior of many improved inlets as a sediment sink – and the importance of adequate terminal structures to limit sink behavior. It is likewise illustrated that an inlet's impacts are not necessarily limited to interruption of the *net* littoral drift rate, but can extend to the area's *gross* drift rate.

The methodology presented above for deducing inlet-related impacts should also be important to the development of regional sediment budgets. In such regional budgets, the volume of sand removed from the littoral system by an inlet must be accounted for as a deficit within the system as a whole. Barring changes in the wave climate or the natural expansion or appearance of an external sand source, this effect must be manifest as (1) a volumetric erosion of the adjacent beaches, and/or (2) a decrease in the littoral drift rate which reaches the adjacent, downdrift inlets.

For the two example cases presented, the extent of the inlet's littoral impacts is considerably greater (by a factor of 15 to 20) than has been traditionally thought. For the first 40 years after construction of Port Canaveral entrance, the downdrift impact of the inlet is estimated to be 12.1 ( $\pm$  1.5) MCM -- affecting between 31 and 42 km ( $\pm$ 10 km) of shoreline south of the inlet. Traditionally, the effect has been thought to be limited to about 3 km of shoreline, along which only 4 MCM of erosion is detectable. Likewise, for the first 63 years after construction of South Lake Worth Inlet, the inlet's impact is estimated as 2.6 to 3.4 MCM as compared to only 0.2 MCM of impact which is detected from shoreline changes observed along the first 2 km (approx.) south of the inlet. Both inlets feature "near-field" and "far-field" erosion signatures -- separated by a relatively short reach of stable to accretional shoreline. For the two cases examined, the appearance of the latter is related to local and offshore wave refraction effects respectively induced by inlet-related and non-inlet related bathymetries.

## REFERENCES

- Blackman, B., 1938. "Report on Jetties", Shore Protection Board, Office of the Chief of Engineers, Washington D.C., August 15, 1938; 130 pp.
- Bodge, K. R., 1994. "Port Canaveral Inlet Management Plan", Olsen Associates, Inc., 4438 Herschel St., Jacksonville, FL; 335 pp.
- Bodge, K. R., 1993. "Gross Transport Effects and Sand Management Strategy at Inlets", Journal of Coastal Research, Special Issue 18, Fall 1993; 111-124.

- Bodge, K.R., Olsen, E.J. and Savage, R., 1990. "South Lake Worth Inlet Sand Management Plan. Olsen Assoc., Inc., 4438 Herschel St., Jacksonville, FL.
- Bruun, P., 1994. "The Development of Downdrift Erosion", Proc., International Coastal Symposium, Hornafjörður, Iceland; June 20-24, 1994.
- Bruun, P. and Battjes, J.A., 1963. "Tidal Inlets and Littoral Drift", Proc., Int'l. Assn. for Hydraulic Research, 4(1.17), 123-36.
- Coastal Technology Corp., 1992. "Brevard County, Coastal Engineering Analysis; Phase II", Coastal Tech. Corp., 800 20th Place, No. 6, Vero Beach, FL.
- Dean, R.G. and O'Brien, M.P., 1987. "Florida's Inlets: Shoreline Effects and Recommended Action", Univ. of Florida Coastal and Oceanographic Engineering Department, 2 reports.
- Dean, R.G. and Walton, T., 1975. "Sediment Transport Processes in the Vicinity of Inlets with Special Reference to Sand Trapping." *In*: L.E. Cronin (ed.), Estuarine Research. New York: Academic Press, pp. 129-150.
- Fields, M.L., Marino, J.N. and Weishar, L.L., 1989. "Effect of Florida Tidal Inlets on Adjacent Shorelines", Proc., Florida Shore and Beach Preservation Assn., Annual Meeting; FSBPA, Tallahassee, FL; 383-391.
- Galvin, C., 1990. "Importance of Longshore Transport", Shore and Beach, January 1990.
- Pelnard-Considere, R., 1956. "Essai de theorie de l'Evolution des Formes en Plage de Sable et de Galets", 4th Journees de l'Hydraulique, les energies de la Mer, Question III, Parrot No. 1, pp. 289-298.
- USACE, 1961. "Survey Review Report on Canaveral Harbor, FL." Serial No. 106. U.S. Army Corps of Engineers, Jacksonville District. Jacksonville, FL. Became U.S. Senate Doc. 140/87/2 in 1962.
- USACE, 1992. "Canaveral Harbor, Florida; Sand Bypass System." General Re-Evaluation Report with Environmental Assessment. U.S. Army Corps of Engineers, Jacksonville District. Jacksonville, FL.
- Walton, T. and Adams, W., 1976. "Capacity of Inlet Outer Bars to Store Sand", Proc., Fifteenth Int'l. Conf. on Coastal Engineering (Honolulu, HI), ASCE; 1919-1937.
- Watts, G.M., 1953. "Study of Sand Movement at South Lake Worth Inlet, Florida", U. S. Army Beach Erosion Board, Tech. Mem. No. 42, Washington, D.C.
- Work, P. and Dean, R.G., 1990. "Shoreline Changes Adjacent to Florida's East Coast Tidal Inlets", University of Florida, Coastal and Oceanographic Eng. Dept., UFL/COEL 90/018; 98 pp.

## CHAPTER 213

### The Spreading of Dredging Spoils During Construction of the Denmark-Sweden Link

Ida Brøker<sup>1</sup>, John Johnsen<sup>1</sup>, Morten Lintrup<sup>1</sup>,  
Anders Jensen<sup>1</sup>, and Jacob Steen Møller<sup>1</sup>

#### Abstract

An overview of the model complex, including a combined Lagrangian and Eulerian approach to simulation of sediment transport, developed to study spreading of dredging spoils in connection with off-shore earth works necessary for construction of the Denmark-Sweden Link is provided; - together with in-depth descriptions of two particular work topics: (a) Model representation of flow friction to allow application of an inherently depth-integrated model system to a partially stratified environment, and (b) overall design of the model complex to make it fit as a versatile tool at several stages of this large project.

#### Introduction (Location and Scope)

In connection with the planned Link between the Danish capital Copenhagen and Malmoe in Sweden along the Drogden Sill, see Figure 1, dredging of clay and chalk is necessary for flow compensation as well as for direct construction purposes since it is required that the net water and salinity exchange through the Sound must not be affected. The dredging results in release of substantial amounts of fine material within an area, which is both environmentally perceptible and hydraulically complicated since the sill in combination with an approximately 25 PSU longitudinal salinity difference between Kattegat to the north and the Baltic to the south induces a mobile and variable mixing front over a fairly stable salinity interface normally extending southwards only to Drogden Sill.

The model setup and calibration have been supported by laboratory and field experiments. The model complex is verified by comparison with data from test dredgings totalling 64,000 m<sup>3</sup> of moraine clay and chalk, of which 8,200 m<sup>3</sup> were spilled. During these tests spill percentages and variability for different types

---

<sup>1</sup>Danish Hydraulic Institute, Agern Allé 5, DK-2970 Hørsholm, Denmark.

of operations were specifically evaluated. The actual dredgings are expected to approach 7 mill.  $m^3$  after early planning had indicated dredging requirements to be twice that amount.

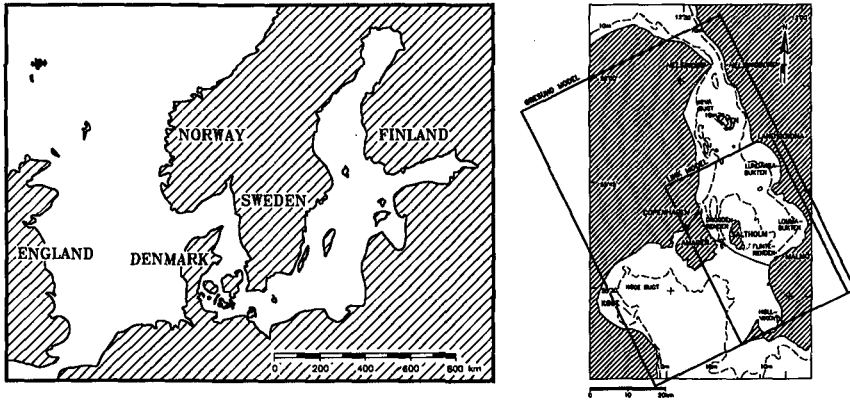


Figure 1. Location Map (left) and Model Areas (right).  
The large area indicates extent of main model. The small area corresponds to a fine resolution model used in calibration/verification of material specific parameters.

The scope of the present study was to establish a numerical model complex for simulating the spreading of fines, notably determining shading effects associated with dredging plumes and the eventual fate of spilled material. This should be done so as to facilitate subsequent planning of actual dredging operations as well as to prepare a tool useful in the implementation of an actual dredging spill control strategy.

Administrative objectives as well as legal requirements for dredging operations primarily focus on instantaneous spill rates, specified by area and season. These limitations have been derived from maximum acceptable concentrations by inverse interpretation of results obtained with the model complex described in this paper. An effective dredging period of almost 4 years is anticipated.

Overall, an upper limit to the average spill rate of 5% (implying a total spill of up to 350,000  $m^3$ ) will be imposed. A dredging control strategy should aim at monitoring during the entire operation that actual spill rates allow compliance with this target. Since economical dredging practice dictates operating with a variable spill rate, this implies comparison of measured spill to an *a priori* planned and contractually agreed spill budget.

### Background, Physical Processes and Model Complex Overview

The seabottom material along the planned link consists of hard chalk (limestone), partly overlaid by moraine clay. Construction works include dredging operations for a submerged tunnel along half the crossing length, foundation of bridge piers (approx. tot. 4.5 mill. m<sup>3</sup>) and compensation dredging to maintain the present water and salinity exchange through the Sound (approx. 2.3 mill. m<sup>3</sup>).

The spreading of fine particulates from dredging spoils is a function of currents, wave action and sediment properties. Immediately after the release spreading takes the form of narrow plumes which can be observed far away from the source due to generally appreciable current speeds. Parts of the material settles and deposits on the bottom where a consolidation process takes place.

The settling velocity - which is one of the most important parameters - depends on the material in question, salinity, temperature and biological activity due to flocculation. However, preliminary simulation results indicated application of straight values of 0.00018 m/s (moraine clay) and 0.00021 m/s (chalk/limestone) to be satisfactory in this case.

If bed shear stresses are increased above a critical value, resuspension takes place. This resuspension is a function of the degree of consolidation, see Mehta et al. (1989), whose formulation has generally been followed in the modelling.

All relevant processes are represented in a comprehensive setup of numerical models, comprising (H=Horizontal):

- 2-D(H) hydrodynamic model
- 2-D(H) discrete spectral wind wave model
- Particle model (random walk (x,y,z)-tracer technique) for the initial spreading around the source
- 2-D(H) advection-dispersion model for spreading in the far field

Furthermore, these models have been linked to an associated ecological model, describing growth and distribution of benthic vegetation notably eelgrass, *Zostera marina*. The ecological model is also an integrated part of the EIA (Environmental Impact Assessment) and anticipated dredging control procedures, and it is reported elsewhere, Bach et al. (1991).

The source/sink term in the advection-dispersion model represents the link between transporting agents and in-the-bottom processes. A multi-layer representation of shear strength of the bed and consolidation in the bed are included.

The study concept has been to apply nested far-field and near-field models (two, with resolutions of 500 m and 100 m, termed ØRESUND and LINK modelling areas, respectively, see Figure 1) and to couple wave, current and sediment models as shown in Figure 2. Sediment models must be run separately for both moraine clay and chalk, and result fields added, as needed.

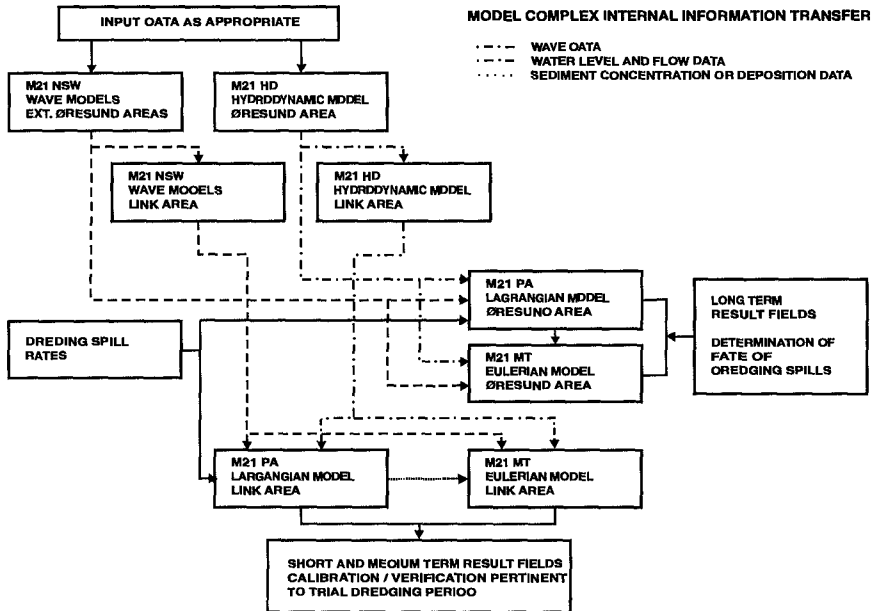


Figure 2. Sediment Spreading Model Complex. Overview emphasizing internal structure and input/output of data on transport/deposition rates.

The two nested models have to some extent served different objectives. The finer model has been sufficiently detailed to allow model calibration and verification to test data from field experiments covering a three months period with respect to material specific parameters; - whereas the coarser model has proved useful for repeated, several-year-long simulations covering a larger area in support of operations planning.

Two coupled sediment models have been applied; the first having a Lagrangian modelling approach. In addition to savings in execution time and computer storage, two main advantages are achieved over traditional, direct Eulerian modelling:

Numerical dispersion due to "poor" resolution is avoided even though a relatively coarse grid is maintained for the current, i.e. model concentra-



tions of suspended matter reach realistic high values very close to the source. This is important for subsequent modelling of eelgrass growth.

Most dredging spoils are released near the surface, ie. the areal spread and time lag before it is justified to assume a standard vertical concentration profile is considerable. This adaptation takes place within the Lagrangian model.

After a certain period the sediment is then transferred to an advection-dispersion model comprising a more refined description of bed consolidation and resuspension effects. The transfer period is basically a matter of technical judgment and compromise; here values in the range 3-6 hours have been found to work satisfactorily.

The *sediment transport module* needs input of settling velocity of flocs depending on degree of flocculation, whereas the *bottom process module* needs input of critical bed shear stresses for erosion and deposition for description of reentrainment and erosion and parameters for description of the consolidation process. Parameters in the sediment transport and bottom process modules are derived from laboratory and field experiments.

In-situ settling experiments using an Owen settling tube to determine settling rates were carried out. In the laboratory the resuspension as a function of shear stress and degree of consolidation were investigated in an annular flume. Consolidation rates were studied in the annular flume and in settling tubes.

Flow conditions in the laboratory are stationary and the biological activities are minimized. Those experiments have therefore been supplemented with field experiments where a test area ( $20 \times 10 \times 0.25 \text{ m}^3$ ) was constructed in the Sound close to the Link alignment. The test area was covered by chalk similar to the finest fractions ( $<63\mu$ ) of dredging spoils. All experiments and the sediment model calibration process including actual selections of parameters are described in detail in Johnsen et al. (1994).

The wave climate in Øresund has been demonstrated to be effectively fetch-limited and dominated by locally generated waves. As a result, conditions are generally mild with waves in the range  $H_s=0.2$  to  $0.6 \text{ m}$ . This has justified a simplified wave modelling approach based on a number (36) of stationary simulated wave fields (12 wind directions times wind speeds 5, 10, and 15 m/s), from between which instantaneous wave fields as input to sediment models were interpolated using measured wind conditions.

The flow is modelled dynamically with bathymetry, bed resistance, eddy viscosity, wind and boundary water levels as the main defining input. The latter are derived from four water level stations - two each north and south of the Sound;

two lying on the Danish and two on the Swedish side. An entire year of registered currents at two stations were available for verification of the flow model. A detailed description of the bed resistance input is provided in the following section.

In Figure 3 is shown an example comparison of plumes observed, respectively simulated on basis of the combined wave, current and sediment models.

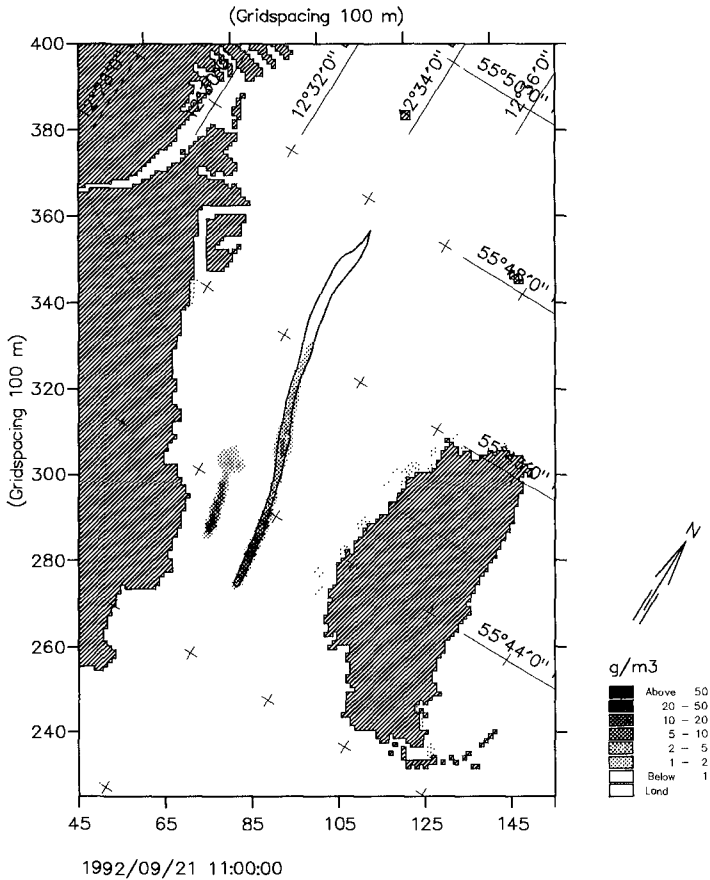


Figure 3. Comparison of Observed and Simulated Plumes for Model Verification (example)

The verified model has been run for a full year, Sept. '92 - Aug. '93, to simulate the fate of spoils from the test dredgings. That same year has then been designated as design period for subsequent EIA-studies.

With respect to spoils from test dredgings it appears that final deposition areas are mainly along the Danish coastline, and there is only a minor difference between spreading of moraine clay and chalk because settling characteristics are very similar and both types of spoil consolidate relatively quickly after deposition. It is estimated that 90% of moraine clay and 80% of chalk spoils are deposited within the Sound, the majority less than 20 km from the spill site.

### Model Representation of Flow Friction

In order to use the DHI MIKE 21 hydraulic modelling system - which assumes a "homogenous" (one-layered) current regime - to simulate the normally stratified environment in the Sound north of Drogden sill, a correction procedure has been developed and applied to the flow friction; expressed in the model in terms of a Chezy no.,  $C$ , which is reciprocally defined in relation to current velocities.

For homogenous flow a logarithmic velocity profile is assumed. When the water column is stratified, the velocity profile will be contorted and for identical head losses result in a higher water discharge. In other words, stratification may be seen as a lubricant for the current. The principal differences between homogenous and stratified (two-layered) current regimes may be visualized as in Figure 4.

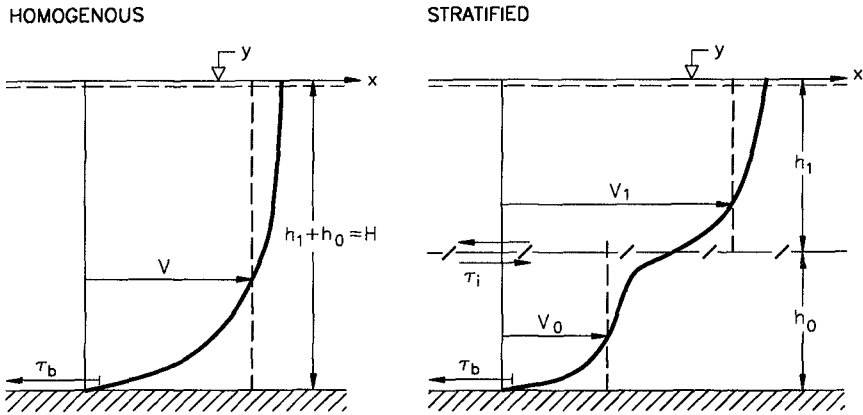


Figure 4. Definition sketch for homogenous (left) and two-layered (right) current regimes

The reduced energy loss caused by the stratification can be incorporated in a homogenous one-layer calculation by introducing an *equivalent (reduced) bottom friction*. This is done on the assumption that the current is dominated by barotropic effects, ie. pressure gradients caused by water level differences are (much) more significant than those caused by density gradients in the flow momentum equation. Then, the momentum equations may be written as:

$$gh_1 I = \frac{\tau_i}{\rho_R}$$

$$gh_0 I = \frac{\tau_b}{\rho_R} - \frac{\tau_i}{\rho_R}$$

where  $g$  ( $9.81 \text{ m/s}^2$ ) is gravity,  $h$  (m) is the thickness of a layer (index 1 is for the upper layer, and 0 for the lower),  $I$  is the energy gradient,  $\tau$  ( $\text{N/m}^2$ ) is the friction (index b is for the bottom, and i for the interface), and  $\rho_R$  ( $1010 \text{ kg/m}^3$ ) is a reference density. Shear stresses are determined by

$$\frac{\tau_i}{\rho_R} = (1-c) \frac{f_i}{2} \frac{1}{4} (V_1 - V_0)^2 + c \frac{f_b}{2} V_1^2$$

$$\frac{\tau_b}{\rho_R} = (1-c) \frac{f_b}{2} V_0^2 + c \frac{f_b}{2} V_1^2$$

where  $f$  is the friction factor, and  $V$  (m/s) is the mean velocity in a layer. The factor  $c$  has been introduced to the equations in order to transfer bottom shear stress directly to the surface layer when bottom layer thickness,  $h_0 = H - h_1$ , decreases to a value comparable to the equivalent bottom roughness,  $k$ :

$$c = \frac{h_1}{H} \exp \frac{-(H-h_1)}{\alpha k}$$

The equivalent bottom roughness is typically 0.3 m in the Sound. The  $h_0/k$  aspect ratio,  $\alpha$ , has been roughly estimated as  $\alpha=2$ . It is noted that the equations lead to the traditional one-layer formulation when the thickness of either of the two layers approaches zero.

Dividing the momentum equations, an equation regarding the ratio of the upper and lower layer velocities,  $V_1/V_0$ , is obtained: The ratio shows a higher velocity in the upper layer than in the lower as shown in Figure 4 and measured

in Øresund. In the velocity ratio equation, the ratio between the friction factors,  $f_t/f_b$ , is present. This ratio is evaluated to be 1/3.

Adding the momentum equations it is seen that the total pressure is balanced by the bottom friction, which in the considered case is a function of both the lower and upper layer velocity (the right side of next equation). To model the two layer system as a one-layer system we need to relate the bottom friction to the depth mean velocity by defining an equivalent bottom friction factor ( $f_e$ ):

$$\frac{f_e}{2} \cdot \left( \frac{h_0 V_0 + h_1 V_1}{h_0 + h_1} \right)^2 = \frac{f_b}{2} \left( (1-c) V_0^2 + c V_1^2 \right)$$

Thus, by applying the equivalent bottom friction factor in the flow simulations the correct depth mean velocity is obtained.

The relation between a friction factor and its corresponding Chezy no,  $C$ , is taken as:

$$C = \left( \frac{2g}{f} \right)^{1/2} \Leftrightarrow \frac{f}{2} = \frac{g}{C^2}$$

Following calibration of the model a constant "homogenous" reference Chezy no.,  $C_b$  of 35 m<sup>1/2</sup>/s has been used, corresponding to  $f_b=0.016$ . By applying an equivalent Chezy no.  $C_{eq}$  instead of  $C_b$  for calculations north of Drogden Sill the lubricating effect of stratification on current has been accounted for in the modelling. In Figure 5 is seen how the equivalent Chezy no. (corresponding to a reference Chezy no. of 35 m<sup>1/2</sup>/s) varies with the position of the interface for different total water depths. The importance of the stratification as a lubricant is evident from the figure.

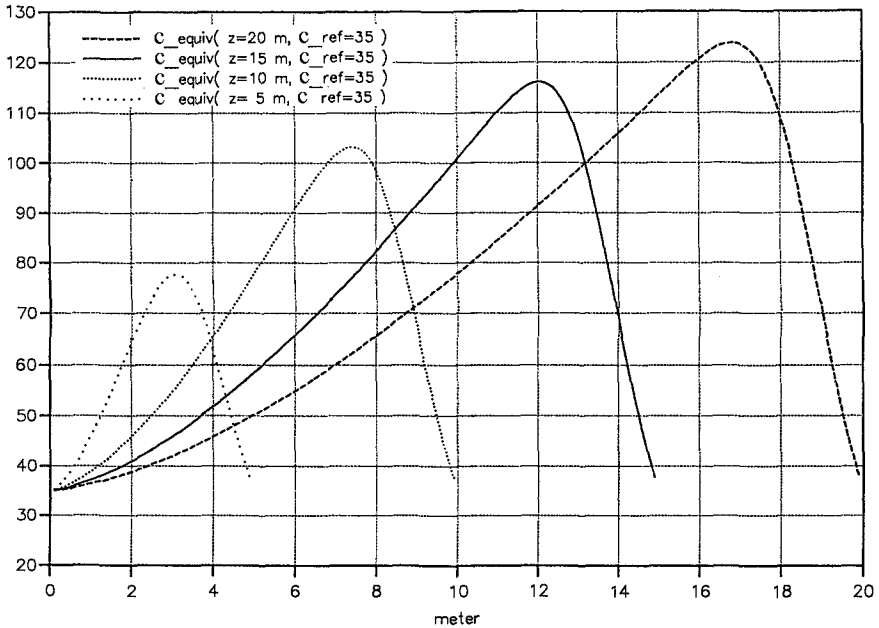


Figure 5. Equivalent Chezy no. as a function of interface depth for total depths 5, 10, 15, and 20 m.

### Model Complex Applications with Example Results

In this section it is demonstrated how the developed model complex has been and continues to be a useful tool in several, at least three, cases (a)-(c), stages of the project planning and execution.

Particularly, it is noted how the modelling complex may provide results with a statistical character since it is comprehensive, yet operationally manageable for extensive and/or repetitive calculations. Thus the complex is especially likely to be useful in connection with criteria, objectives, requirements etc. that are cast in statistical terms.

Additionally, it is noted that results may be obtained by inverse as well as direct interpretation of results.

**(a)** A number of relatively short simulations were made corresponding to four typical key dredging and deposition activities, two different dredging (spill)

intensities, and two types of hydrographic conditions, summer calm and autumn variable (incl. storm) conditions.

Results from these simulations were compared to conservatively estimated empirical tolerances with respect to bathing water quality, eider and swan forage (1), mussel beds (2), mussel larvae settling (3), and herring migration (4). Tolerances were expressed as concentration maximum exceedance time (1), max. weekly sedimentation (2), sedimentation rate max. exceedance time (3), and max. concentration (4), - all concerning specific areas and seasons. From the comparison a number of restrictions on dredging activities expressed as maximum spill rates (kg/s) were identified, and in some cases it was demonstrated that conflicts were unlikely to occur.

In Figure 6 is shown an example result field of calculated  $6 \text{ g/m}^3$  concentration percentage exceedance time pertaining to herring migration tolerance.

**(b)** Based on experiences from (a) above a complete realistic dredging scenario was worked out for EIA purposes assuming that two backhoe dredgers and one cutter suction dredger will be employed. This preliminary scenario consists of 26 individual dredging (and deposition) activities and spans the period October '95 to April '99. Scenario resolution is daily production rates.

By recursive application of the design year period EIA background simulations for the entire dredging operation could be made. The associated ecological (eelgrass) module was similarly applied.

The model complex has been further refined for this application to include movable sources along piece-wise linear transects in the sediment modules.

As an example and to illustrate the areal impact of the entire operation is shown in Figure 7 the calculated distribution of net accumulation after four years. It is noted that expected maximum accumulation is just over  $5000 \text{ g/m}^2$ .

Presently, EIA is an ongoing process actively in support of project planning and development rather than just a passive instrument for legal acceptance.

**(c)** It is anticipated that the model complex will be applied also at later stages in connection with implementation of control procedures for actual dredging operations, but the exact role(s) and extent of its use remains to be defined.

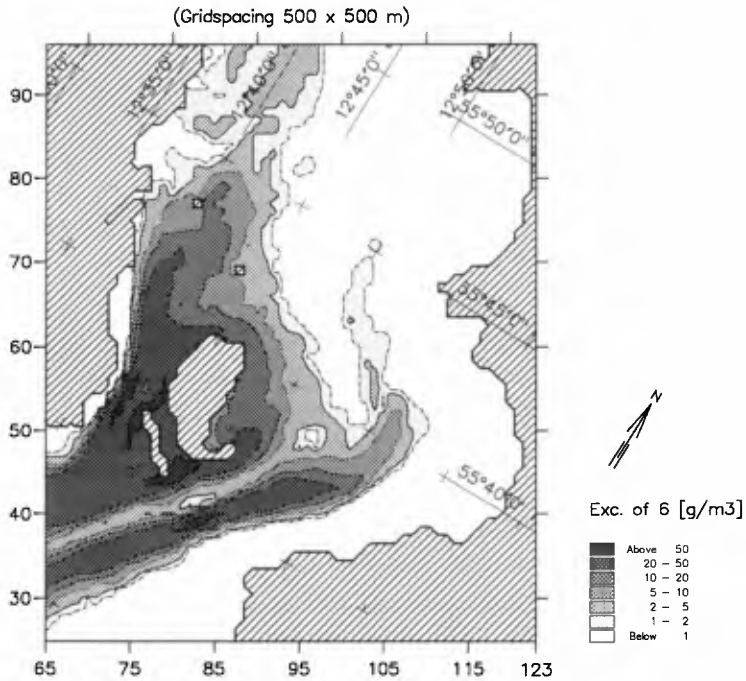


Figure 6. Example results pertaining to Migration of Herring. Depth averaged concentration of 6 g/m<sup>3</sup>, Percentage Exceedance Time.

### Conclusion

A general and figurative outline of the entire complex developed for modelling of spreading of dredging spoils during construction of the Denmark-Sweden Link, - mainly composed of already existing individual modules, - but with some customizations to fit special requirements and make it a versatile tool in connection with several project stages, - has been given.



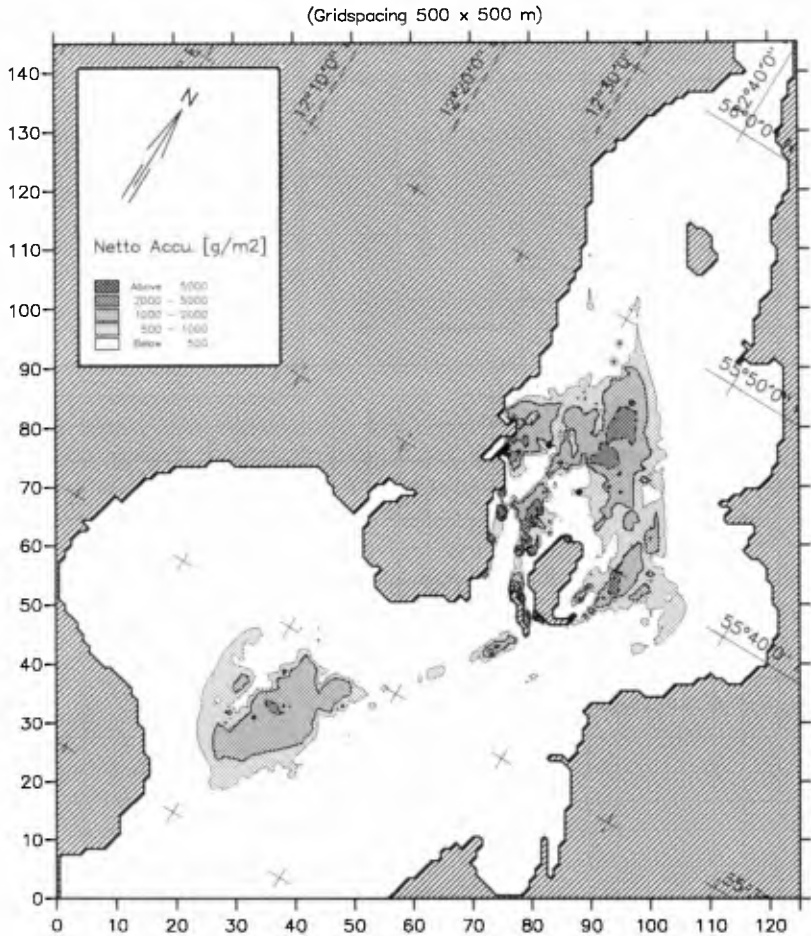


Figure 7. Calculated Net Accumulation from Entire Dredging Operation, 951001-990930.

The main innovation is the use of a relatively fast and practical Lagrangian (random walk particle tracer) sediment model to describe spreading very close to the source, rather than an Eulerian (2-D advection-dispersion) model, which becomes very unwieldy when a high resolution is required.

It has been demonstrated how - given the right circumstances - a depth-integrated hydraulic model system may be adapted for application to a stratified

environment by the introduction of an equivalent (reduced) bottom friction calculation.

Furthermore it has been demonstrated how overall design of the model complex is made to fit requirements for EIA-purposes as well as anticipated procedures for control of dredging spill compliance with strict administrative and legal requirements.

More generally, the model complex allows generation and presentation of results in a statistical form. Thus, whenever biological criteria, administrative objectives, legal requirements, etc. are cast in statistical terms the complex is likely to be a useful tool.

### Acknowledgments

The Sound model complex was implemented under contract to the Øresundsconsortium. The cohesive sediment models were developed as part of the G8 Coastal Morphodynamics programme (contract no. MAS2-CT-92-0027).

### References

- Bach, H., E.K. Rasmussen & H.H. Riber (1991). Use of an Ecological Model in Assessing the Impact from Sediment Spill on Benthic Vegetation. Proceedings of the 12'th Baltic Marine Biologists Symposium held in Helsingør, Denmark, 25-30 August.
- Johnsen, John, A. C. Ellegaard, and A. Jensen, (1994). Calibration data for modelling of spreading of fines from dredging operations during construction of the Øresund Link. Australian Journal of Marine & Freshwater Research.
- Mehta, A.J., Hayer, E.J., Parker W.R., Krone R.B., and Teeter, A.M., (1989). Cohesive Sediment Transport, I: Process Description. J. Hydraul. Eng., Vol. 115, No. 8, pp. 1076-1093.
- Møller, Jacob Steen, I. Brøker, and R. Warren, (1994 A). Engineering design for minimum impact on ecology. Proceedings for COEI/CWR Joint International Symposium on 'Ecology and Engineering'. Malaysia.
- Møller, Jacob Steen, I. Brøker, and J. Krogsgaard Jensen, (1994 B). The environmental aspects of the Denmark-Sweden Link. Proc. 1st International Symposium in Habitat Hydraulics in Trondheim, Norway. August 18-20, 1994.

## CHAPTER 214

### EXPERIMENTAL STUDIES ON THE EFFECT OF THE DREDGING ON CHANG-HWA RECLAMATION AREA, TAIWAN

Tai-Wen Hsu<sup>1</sup> and Hsien-Kuo Chang<sup>2</sup>

#### ABSTRACT

The effects of offshore dredging at Chang-Hwa reclamation area, Taiwan, are investigated by using movable bed model tests. A practical scale relation for the design of movable bed model is presented. It takes the advantage to give more flexibility for the selection of model sediment. The scale relations of wave conditions in the model test are obtained based on the similitude of two parameters: wave steepness and mobility number. Time scale of sea bottom changes is determined by longshore sediment transport rate. Experimental results show that the proposed scale relations are able to reproduce beach changes in nature. Topographical changes before and after dredging are predicted in model tests. Special attention was made to study the location of erosion and accretion of sea bed configuration owing to offshore dredging.

#### INTRODUCTION

In recent years the utilization of coastal zone has been increased for human activities due to the growth of economics and population and the limited land. The land reclamation project was steadily executed at Chang-Hwa Coast, located on the west coast of central Taiwan (see Fig. 1), to obtain an industrial area. The method of dredging from offshore sea bed is considered as one of the sources of sand supply for

---

1 Associate Professor, Dept. of Hydraulic and Ocean Engineering, National Cheng Kung University, Tainan, Taiwan, 70101.

2 Associate Researcher, Tainan Hydraulics Lab., National Cheng Kung University, Tainan, Taiwan, 70101.

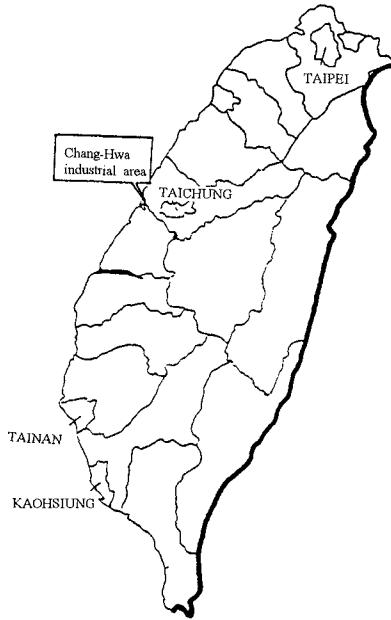


Figure 1 Geographical location of Chang-Hwa industrial area in Taiwan

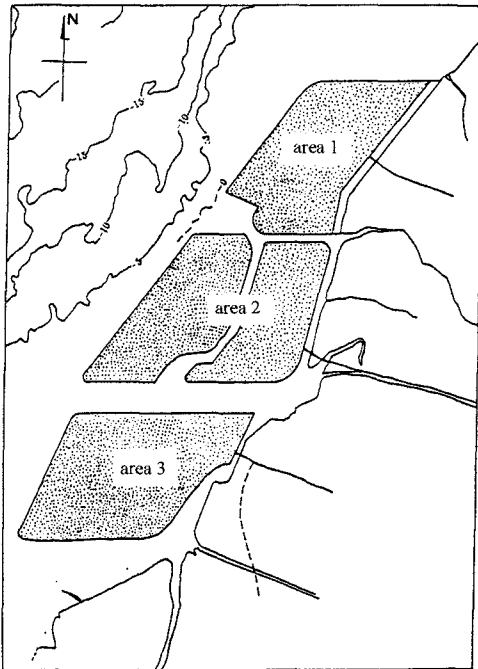


Figure 2 Schematic diagram of Chang-Hwa reclamation area

reclamation. The reclamation regions at Chang-Hwa Coast shown in Fig. 2 covers a length of 12 kilometers from north to south and extends 3.5 to 4.5 kilometers offshore. The planned layout is divided into three districts (Fig. 2) with a total area of 3643 hectares to accommodate heavy industries such as machinery, steel, power and petrochemistry. Generally the topographical changes in the coastal region tend to reach a dynamic equilibrium for a long term period without significant interference. However, a new sea bottom formed after dredging may lead to changes of coastal process and result in beach erosion. An assessment of coastal environment impact for this project becomes important in engineering practice.

It is recognized that field survey, physical hydraulic model and numerical modeling are three dominant methods to solve coastal problems. Among them, the physical hydraulic model is an alternate means of replacing governing equation with complicated initial and boundary conditions and permit examination in controlled conditions of coastal processes and effects due to gravity waves and other environmental forces.

Satisfactory reproduction of sandy shore and nearshore regions in a movable bed model can provide a valuable tool to the coastal engineering. Design and operation of moving bed models are a difficult task involving complex considerations of hydraulics and sedimentation. The aim of this paper is to investigate the effects of offshore dredging on reclamation area by movable bed tests. A practical scale relation for the design of movable bed model is presented. Predictions of topographical changes after dredging and countermeasures against beach erosion are discussed.

## MODEL SIMULATION

### **1. Scale Relationships**

A practical scale relationship for the design of movable bed test is proposed to reproduce physical features of sediment transports in prototype. Two parameters of wave steepness and mobility number were selected as the important factors of beach changes:

$$\left( \frac{H_0}{L_0} \right)_m = \left( \frac{H_0}{L_0} \right)_p \quad (1)$$

$$\left( \frac{U_*^2}{\gamma' g D_{50}} \right)_m = \left( \frac{U_*^2}{\gamma' g D_{50}} \right)_p \quad (2)$$

where  $H_0$  and  $L_0$  are the wave height and wave number in deep water, respectively.  $U_*$  is the bottom friction velocity,  $\gamma'$  the submerged specific gravity of sediment,  $g$  the

gravitational acceleration, and  $D_{50}$  the median diameter of sand grain. The subscript m and p represent physical quantities of model type and prototype, respectively.

According to the former scale laws [3,4,6,7], the sediment in the model can not be chosen freely that makes the scale laws inapplicable in most of cases. The present scale give more flexibility for the selection of model sediment.

Based on the similitude of Eqs. (1) and (2), the scale relations for wave height and wave period are found as follows

$$N_{H_0} = \left( N_v^{1/2} N_{D_{50}}^{1/2} N_f^{-1/2} N_v^{2/3} \right)^{6/7} \quad (3)$$

$$N_T = \left( N_v^{1/2} N_{D_{50}}^{1/2} N_f^{-1/2} N_v^{2/3} \right)^{3/7} \quad (4)$$

where N denotes the ratio of parameter of model to prototype,  $N_v$  is the vertical scale, f the friction factor.  $N_f=10.4$  was adopted in the present study. The conversion of wave height and wave period between the model and nature was obtained on the basis of Eqs. (3) and (4).

Tidal variation should be considered in model test because it causes sediment movement significantly in Chang-Hwa area. This area has a maximum tidal change of 4.5m and its temporal variation has been modeled. The similitude of Froude number was applied for simulating tidal variations:

$$N_{Fr} = \frac{N_u}{\sqrt{gN_v}} = 1 \quad (5)$$

in which u indicates tidal velocity. From Eq. (5) the tidal period scale ratio is obtained

$$N_{td} = N_h^{1/2} \quad (6)$$

The equation of sediment conservation is

$$\frac{\partial h}{\partial t} = \frac{1}{1-\lambda} \frac{\partial q_y}{\partial y} \quad (7)$$

where h is the water depth, t the time,  $\lambda$  the sediment porosity,  $q_y$  the littoral transport per unit width. It is assumed that both model and prototype have the same value of  $\lambda$ , then Eq. (7) is reduced to

$$N_t = N_v N_h N_{q_y}^{-1} \quad (8)$$

in which  $N_h$  is the horizontal length scale and  $N_{qy}$  is the littoral transport scale. The time scale for sediment transport is obtained from Eq. (8) based on littoral sediment transport formula proposed by Le Mehaute[6]:

$$N_t = N_h^2 N_v^{-1} N_\gamma^{1/2} N_{D_{50}}^{-1/2} \quad (9)$$

Its inappropriate for apply Eq. (9) for the case of a topographical changes induced by typhoon waves. Hughes [3] suggests an empirical relation of time scale

$$N_t = N_v^{1/2} \quad (10)$$

## 2. Preliminary tests of the distorted ratio

The distorted ratio was determined by the preliminary tests performed in a  $60\text{m} \times 1\text{m} \times 1.2$  wave flume. Three selected beach slopes  $\tan\beta=1/30$ ,  $1/40$ , and  $1/50$  were placed with fine sand of  $0.12\text{mm}$  median diameter under the action of monsoon and typhoon wave conditions. The vertical scale is calculated on the basis of the distorted ratio and horizontal scale. These geometric scales were chosen in order to let model be similar to the prototype in sea bed changes.

Fig. 3 shows the time history of standard deviation of beach profile changes for different beach slopes and wave steepnesses  $H_0/L_0$ . It is seen that the minimum standard deviations are occurred  $\tan\beta=1/50$  for all  $H_0/L_0$  on the exception of  $H_0/L_0=0.047$ . Since the averaged beach slope in the prototype is  $1/300$ , this implies that the proper distorted ratio is 6.

Based on scale ratios mentioned above, all physical quantities are calculated and listed in Table 1. Table 2 gives the time scale of topographical changes during monsoon and typhoon .

## MODEL TESTS

Planar movable bed model tests were conducted in a wave basin of  $50\text{m} \times 16\text{m} \times 0.8\text{m}$ . Four wavemakers wave been installed in the basin to generate regular waves from deep water. The board of each wavemaker is  $4\text{m}$  in length and is motivated by a  $20\text{HP}$  motor. A total number of wave conditions have been tested for sea bottom changes under the conditions of (1) the present condition; (2) dredging at  $-15\text{m}$  water depth; (3) countermeasures for shore protection after dredging. These test cases are presented in Table 3.

Coal ash was used as bed material which has a median diameter of  $0.12\text{mm}$ , with a submerged specific gravity of  $1.02$ . The field sand has a median diameter of  $0.24\text{mm}$  with a submerged specific gravity of  $1.65$ . All relative physical quantities in model and prototype are given in Table 1.

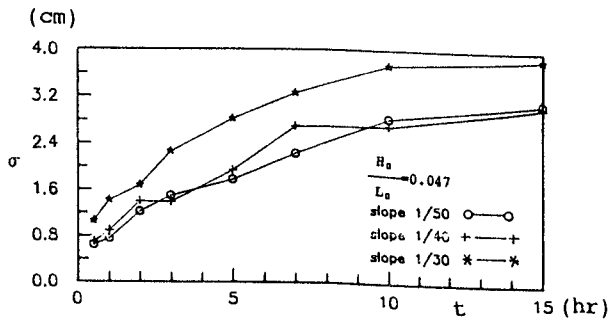
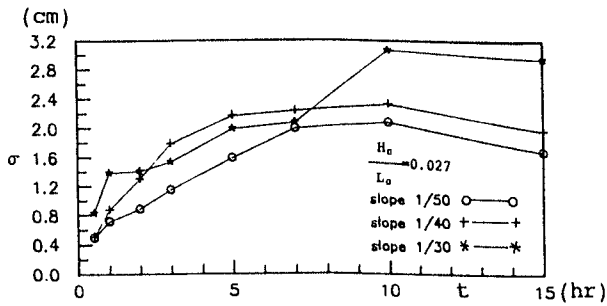
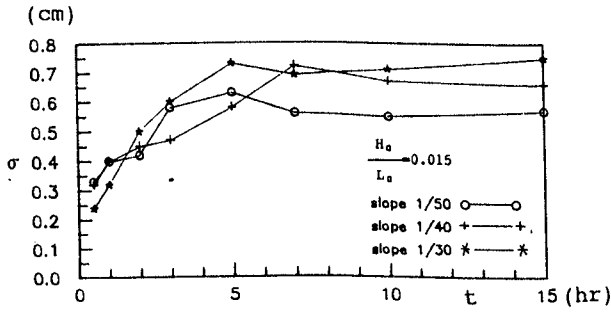


Figure 3 Time history of beach profile changes



Table 1. Physical quantities in model and prototype

physical quantity	scale	prototype		model
horizontal length	1/600	24.0km		40m
vertical length	$\frac{1}{100}$	water depth	+3m~-2.0m	+3cm~-2.0cm
		tidal level	+2.38m - -2.13m	+2.86cm~-2.56cm
wave height	$\frac{1}{74.3}$	monsoon wave	2.60m	3.35cm
		typhoon wave	4.50m	6.90cm
wave period	$\frac{1}{8.62}$	monsoon wave	7.76sec	0.90sec
		typhoon wave	11.20sec	1.38sec
Tidal period	$\frac{1}{10}$	12.42hr		1.242hr
submerged specific gravity	$\frac{1}{1.62}$	1.65		1.02
median diameter	$\frac{1}{2}$	0.24mm		0.12mm

Table 2. Time scale of topographical changes

quantities wave	scale	prototype	model
monsoon wave	1/5267.4	0.6 year	1.0 hr
typhoon wave	1/10	10 hr	1.0 hr

Sea bottom topography was measured at 30 minutes time interval by five point gauges set up on a moving vehicle. Ten traps were buried at the middle position of the model to measure littoral transport across surf zone. Fig. 4 depicts the distribution of littoral transport from laboratory observations. The summation of all traps gives the total longshore sediment transport. Fig. 5 presents temporal variations of longshore sediment transport. We notice that longshore sediment transport tends to become a constant value after 3 hours.

## RESULTS AND DISCUSSION

### **1. Sea bed changes under present conditions**

Using the time scale obtained in the previous section, the monsoon and typhoon waves were respectively generated for 10 hours in the model for the equivalent of 6 years and 10 hours in the nature. The topographical changes under the action of monsoon and typhoon waves in NNE direction are shown in Fig. 6 and Fig. 7. In both cases, the region of the existence of longshore current caused sea bed changes owing to limited sand supply from upstream. Erosion of the sea bottom occurs around seawall of each reclamation area. A remarkable recession of the shoreline appears at area 1 .

### **2. Sea bed changes after dredging**

The industrial area shown in Fig. 8 and Fig. 9 was reclaimed by sand materials. The method of dredging from offshore sea bottom at -15m water depth is considered as one of the sources of sandy supply for reclamation. It extends to 1.5km offshore and the water depth becomes -16m at the dredging area. All sides of industrial area were protected by seawalls to prevent beach erosion from wave attack.

From Fig. 8, we can see that severe erosion takes place along new seawalls. The wave conditions are the same with those without dredging. The figures show the wave energy is not attenuated due to a deeper bathymetry. The interaction between incoming waves and reflected waves forms a very complicated distribution of longshore sediment transport. In Fig. 9, it is evident that on-offshore sediment is dominated for topographical changes. Most of sands were carried offshore and deposit at deep water.

Table 3. Cases of planar movable bed tests

Case No.	wave condition	Case No.	Wave condition	construction	sand supply
	NNE		SW		
R1	$H_0=3.35$ cm $T=0.90$ sec $t=10$ hr	R9	$H_0=3.35$ cm $T=0.90$ sec $t=10$ hr	present seawall	longshore sediments
R2	$H_0=3.35$ cm $T=0.90$ sec $t=10$ hr	R10	$H_0=3.35$ cm $T=0.94$ sec $t=10$ hr	present seawall	longshore sediments
R3	$H_0=3.35$ cm $T=0.94$ sec $t=10$ hr	R11	$H_0=3.35$ cm $T=0.94$ sec $t=10$ hr	new seawall	longshore sediments
R4	$H_0=6.90$ cm $T=1.38$ sec $t=10$ hr	R12	$H_0=3.35$ cm $T=0.94$ sec $t=10$ hr	new seawall	longshore sediments
R5	$H_0=3.35$ cm $T=1.38$ sec $t=10$ hr	R13	$H_0=3.35$ cm $T=1.38$ sec $t=10$ hr	new seawall groins	longshore sediments
R6	$H_0=6.90$ cm $T=1.38$ sec $t=10$ hr	R14	$H_0=6.90$ cm $T=1.38$ sec $t=10$ hr	new seawall groins	longshore sediments
R7	$H_0=3.35$ cm $T=0.90$ sec $t=10$ hr			new seawall	longshore sediments river
R8	$H_0=3.35$ cm $T=0.90$ sec $t=10$ hr			new seawall groins	longshore sediments river

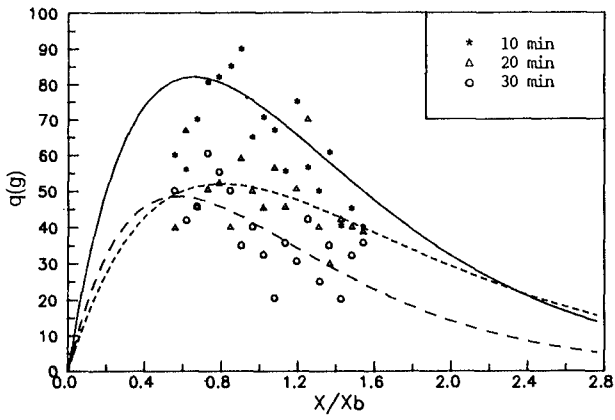


Figure 4 Distribution of longshore sediment transport

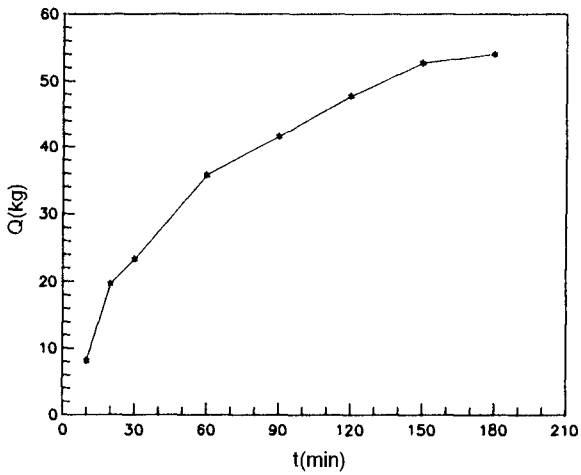


Figure 5 Temporal variation of total longshore sediment transport

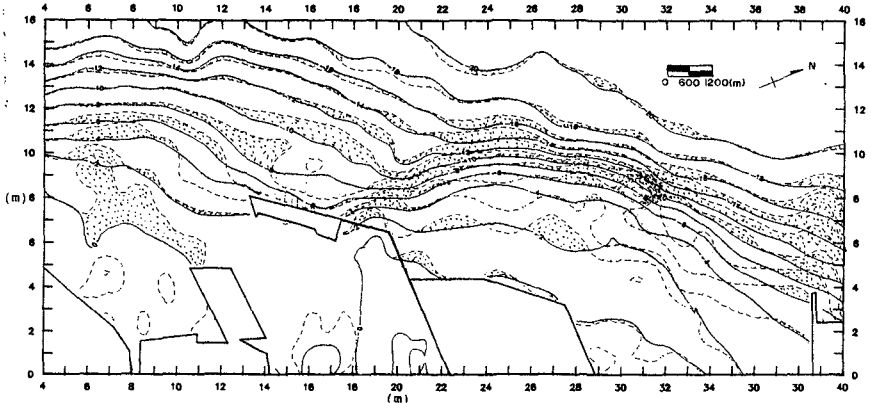


Figure 6 Sea bed changes due to monsoon wave action (the present condition)

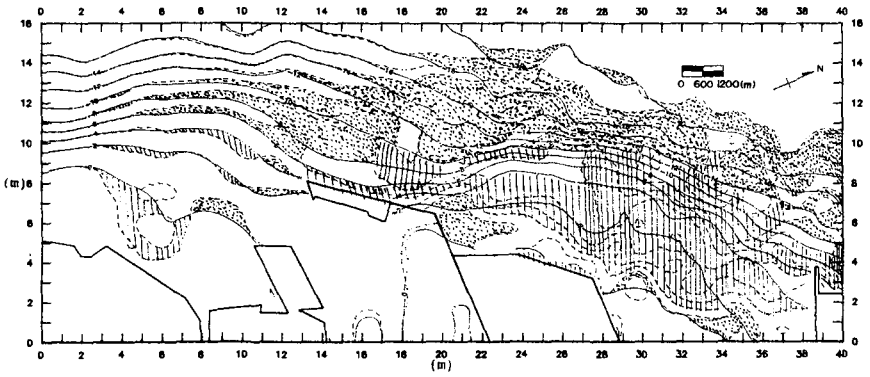
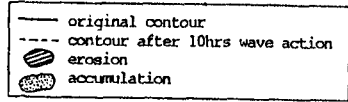
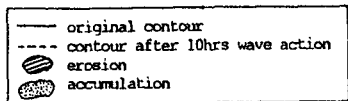


Figure 7 Sea bed changes due to storm wave action (the present condition)



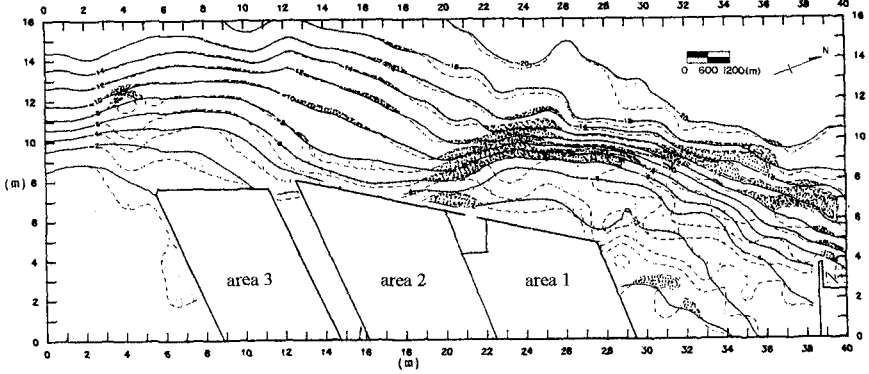


Figure 8 Sea bed changes due to monsoon wave action (new reclamation area after dredging)

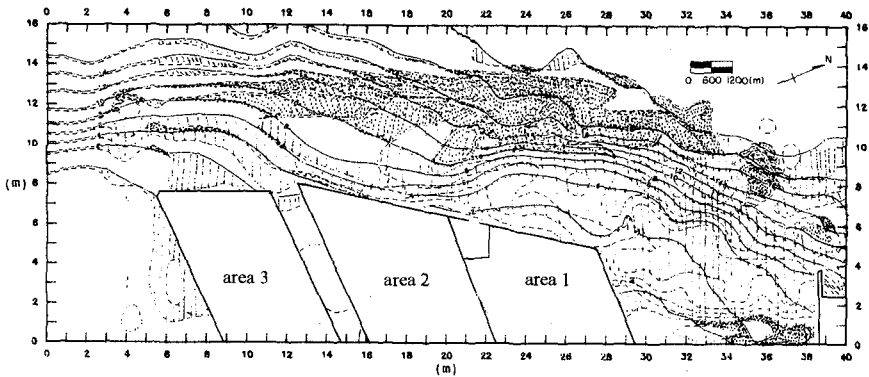
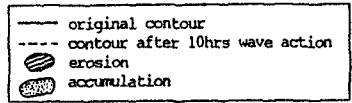
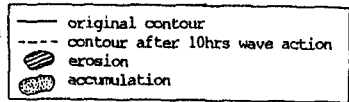


Figure 9 Sea bed changes due to storm wave action (new reclamation area after dredging)



### 3. New reclamation area protected by groins

Model tests reveal that erosion occurs along the segment of coast from area 1 to area 2. Accretion takes place in the north of Koshui river (area 3). The most important effect due to dredging can be found as shoreline recession and beach erosion in the vicinity of seawalls. To decrease the influence of dredging, the erosion of reclamation area was designed to be protected by groins. The groins in the model were made of small armour units as shown in Fig. 10 and Fig. 11.

The topographical changes for the case of monsoon and typhoon wave attack are illustrated in Fig. 10 and Fig. 11. The wave conditions in these cases are the same as the previous cases. It is noted that the system of groins almost protected the shore from erosion and accordingly the accretion around the shoreline where erosion occurred was stopped.

## CONCLUSIONS

The effects of dredging on Chang-Hwa reclamation area have been studied by movable bed model tests. The scale relations of wave conditions in the model design are obtained based on the similitude of wave steepness and mobility number. Time scale of topographical changes is determined by longshore sediment transport rate. The present scale law provides a useful tool in practical applications. It takes the advantage to give more flexibility for selection of model sediment.

Several test cases have been carried out including (1) tests for determination of time scale; (2) tests for sea bottom changes under present conditions; (3) tests for sea bottom changes after dredging at -15m water depth; and (4) tests of countermeasures for shore protection after dredging. The most important influence on the position of erosion has been found. The method of construction of groins was considered to decrease beach erosion. It is shown that the proposed groins protect the shore from erosion quite well.

## REFERENCE

1. Kuo, C.T., Lai, C.J., and Hsieh, C.H., 1983. Report of Chang-Hwa Project (2): The evaluation of the breakwater to the sand drafts obstruction, Bulletin No.4, Hydr. and Ocean Engrg., Tainan, Taiwan.(in Chinese)
2. Tainan Hydraulics Laboratory, 1992. Field investigation and model test for the reclamation of Chang-Hwa industrial area, Bulletin No.128, Vol.1, Tainan, Taiwan.(in Chinese)
3. Hughes, S.A., 1983. Movable-bed modeling law for coastal dune erosion, J. Waterway, Port, Coastal and Ocean Engrg., 109(2), 164-179..
4. Ito, M. and Tsuchiya, Y., 1984. Scale-model relationship of beach profile, Proc. 19th International Conf. on Coastal Engrg., Houston, 1386-1402.

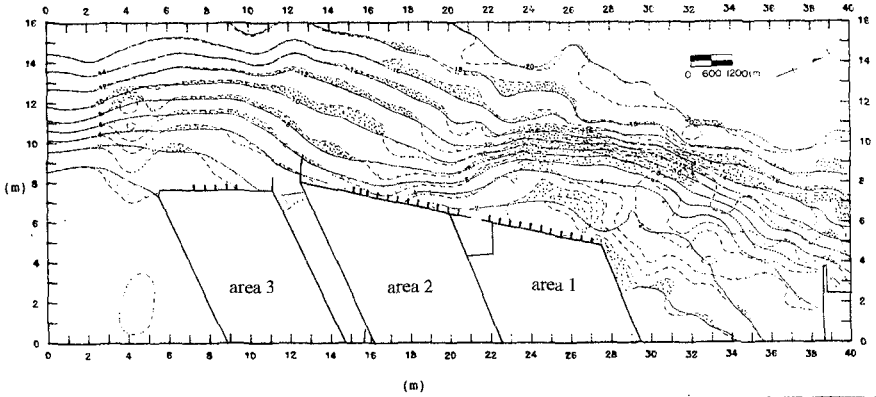


Figure 10 Sea bed changes due to monsoon wave action  
(new reclamation area protected by groins)

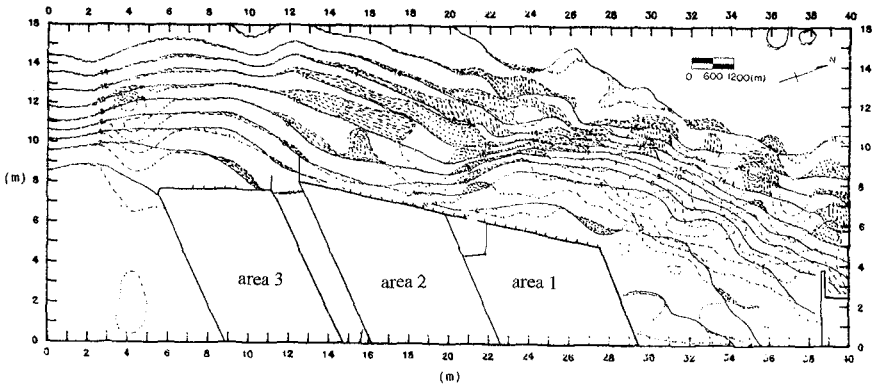
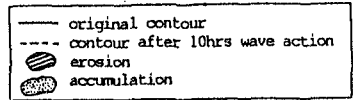
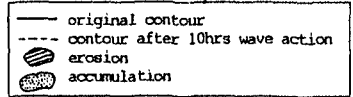


Figure 11 Sea bed changes due to storm wave action  
(new reclamation area protected by groins)





5. Kuo, C.T. and Lai C.C., 1981. Report on the experimental studies on the topographical changes caused by Chang-Hwa reclamation area, Technical report of Dept. of Hydraulics and Ocean Engrg., National Cheng Kung Univ.(in Chinese)
6. LeMehaute, B., 1970. A comparison of fluvial and coastal similitude, Proc. 12th Coastal Engrg. Conf., 1077-1096.
7. Noda, E.K., 1970. Coastal movable bed model relationship, Report No. Tc-191, Tetra Tech. Inc., Passerine, California.

## CHAPTER 215

### OSCILLATIONS INDUCED BY IRREGULAR WAVES IN HARBOURS

C.R. Chou \*, W.Y. Han \*\*

#### ABSTRACT

An approach for predicting the harbour oscillations induced by unidirectional irregular waves in a harbour of arbitrary shape and variable water depth is presented. Effects of partial reflection along harbour and breakwater boundaries were considered by involving an energy dissipation coefficient in boundary conditions. Numerical results on wave heights within a rectangular harbour were presented and a realistic harbour geometry was selected for trial computations. The results of the computations were verified through hydraulic model experiments.

#### 1. INTRODUCTION

One of the major objectives in harbour engineering is the maintenance of a relatively undisturbed water surface within regions of interest. The most effective way to achieve this is to reserve some area in a harbour for natural dissipation. However, almost all the harbours, especially the fishery harbours, in Taiwan have insufficient space to allow for wave energy dissipation. An alternative way is to dispose the vertical dissipating quays in harbours, as many examples are found both in Taiwan and in Japan. However, the choice

---

\* Professor, Dept. of Harbour and River Eng., National Taiwan Ocean Univ.,  
Taiwan, R.O.C.

\*\* Graduate student, ditto.

of the most suitable location and length of the dissipating structure in a harbour is rather problematic. To solve this problem, engineers have usually relied on model experiments in the past, but numerical methods have also been developed. With the increasing speed of performance and lowering cost for acquisition of modern computers, numerical analyses seem to provide a potentially more economical alternative than model experiments.

Many investigators have studied various aspect of the harbour oscillation problem. Miles and Munk(1961) used a point source method to analyze harbour oscillations associated with radiation effects that expand from harbour entrance to offshore. They found the phenomenon of harbour paradox. Ippen and Goda(1963) used Fourier tranformation to analyze a rectangular basin with impermeable veritical wall. Hwang and Tuck (1970) used a boundary integral method which involves the distribution of wave sources along the harbour boundary to calculate oscillations in harbours of constant depth and arbitrary shape. Lee(1971) applied Weber's solution to solve Helmholtz equation and analyzed harbour oscillation of arbitrary shape with constant water depth. Chou and Lin (1986) used a boundary element method to analyze wave-induced oscillations in a harbour of arbitrary shape, together with rigid quays in variable water depth.

The above studies, however, suffer a deficiency, in other words, they are applicable to complete reflection at the harbour boundaries. In fact, reflecting boundaries are not always fully reflecting. In order to treat this problem, Chou and Lin (1989) applied a boundary element method involving an energy dissipating coefficient  $\alpha(= \sqrt{1 - Kr^2})$  based on the theory of energy conservation in arbitrary reflecting boundary to analyze oscillations in a harbour of arbitrary shapes with constant water depth. Chou and Han (1993) also applied a boundary element method to analyze oscillations in a harbour of arbitrary shapes with variable water depth.

All of the above studies can be applied only to small amplitude waves. However, waves in seas are one of the most complex and changeable phenomena in nature. In this paper, an extended model for unidirectional irregular waves will be presented. For verification, model experiments were carried out and compared with numerical predictions.

2. THEORETICAL ANALYSIS

2.1 Regular Wave

Fig.1 schematically shows a harbour configuration under consideration. A Cartesian coordinate system is employed, the origin of which is located at  $o$  with the  $z$ -axis vertically upwards. As shown in the figure, the flow field is divided into two regions by a pseudo-boundary surface  $\Gamma_1$ : Region I is an open sea region with constant depth, and Region II is a harbour basin bounded by  $\Gamma_1$  and the harbour and breakwater boundaries, with variable water depth.

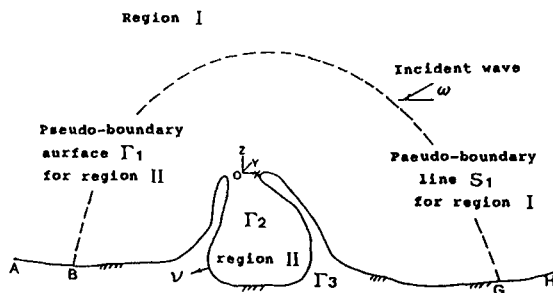


Fig. 1 Definition sketch

Usual assumptions of the fluid being inviscid and incompressible and the flow being irrotational are adopted here. We consider linear waves, having angular frequency  $\sigma (= 2\pi/T, T$  is the wave period) and amplitude  $\zeta_0$  incident from the open sea at an angle of  $\omega$  against the  $x$ -axis. Fluid motions in both the regions will then have velocity potentials as follows:

$$\Phi(x, y, z; t) = \frac{g\zeta_0}{\sigma} \cdot \phi(x, y, z) \cdot \exp(-i\sigma t) \tag{1}$$

where  $g$  is the gravitational acceleration, and  $\phi(x, y, z)$  must satisfy the Laplace equation  $\nabla^2 \phi = 0$

Applying Green's law(Chou and Han(1993)), the potential function for any point in Region I can be calculated from the following integral equation:

$$cf^*(x, y) = \int_{s_1} \left[ \left( \frac{i}{4} H_0^{(1)}(kr) \right) \frac{\partial}{\partial \nu} f^*(\xi, \eta) - f^*(\xi, \eta) \frac{\partial}{\partial \nu} \left( \frac{i}{4} H_0^{(1)}(kr) \right) \right] ds \tag{2}$$

where  $f^*(\xi, \eta)$  is the potential function specified by the geometric condition of the boundaries in Region I,  $\partial f^*(\xi, \eta)/\partial \nu$  is its normal derivative with  $\nu$  the

local normal coordinate to the boundary taken outwards.  $H_0^{(1)}(kr)$  is the zeroth order Hankel function of the first kind, and  $r = [(x - \xi)^2 + (y - \eta)^2]^{1/2}$  is the distance between a point under consideration and the boundary. The factor  $c$  equals to unity within the boundary, but will have a value of  $1/2$  on boundaries.

In the numerical analysis, the boundary  $S_1$ , where  $c=1/2$ , is discretized into  $M$  segments, each having a constant element. Equation (2) is then rewritten in a matrix form as

$$\{F^*\} = [K^*]\{\bar{F}^*\} \quad (3)$$

where  $\{F^*\}$  and  $\{\bar{F}^*\}$  are the potential function and its normal derivative on the pseudo-boundary  $S_1$ , and  $[K^*]$  is a coefficient matrix related to the geometric location of  $S_1$ .

According to Green's second identity law, velocity potential  $\phi(x, y, z)$  at any point within Region II can be determined as

$$c\phi(x, y, z) = \int \left[ \frac{\partial\phi(\xi, \eta, \zeta)}{\partial\nu} \left(\frac{1}{4\pi r}\right) - \phi(\xi, \eta, \zeta) \frac{\partial}{\partial\nu} \left(\frac{1}{4\pi r}\right) \right] dA \quad (4)$$

where  $r = [(x - \xi)^2 + (y - \eta)^2 + (z - \zeta)^2]^{1/2}$ . As before,  $c$  is unity for points inside the region and is equal to  $1/2$  on smooth boundaries.

To proceed with numerical calculation, surfaces of the boundaries  $\Gamma_1$  through  $\Gamma_4$  are divided into  $N_1$  to  $N_4$  discrete segments with constant elements.

For the case that  $c=1/2$ , Eq.(4) is readily expressed as

$$\{\phi\} = [K]\{\bar{\phi}\} \quad (5)$$

where  $\{\phi\}$  and  $\{\bar{\phi}\}$  are the potential function and its normal derivative on the boundaries  $\Gamma_1$  through  $\Gamma_4$ .  $[K]$  is a coefficient matrix related to the geometry of the boundaries.

The boundary conditions required for the case under consideration are summarized as follows:

(i) The free surface condition:

For constant air pressure, the kinematic boundary condition for the free water surface is expressed as:

$$\bar{\phi} = \frac{\sigma^2}{g} \cdot \phi \quad , \quad z = 0 \tag{6}$$

(ii) Boundary condition on impermeable sea bed:

For an impermeable sea floor, the flow is zero in the normal direction:

$$\bar{\phi} = 0 \tag{7}$$

(iii) Boundary condition on the pseudo-boundary at open sea:

The requirement of continuity for mass and energy fluxes between Region I and Region II at the pseudo-boundary  $\Gamma_1$  leads to the expression:

$$\bar{\phi}_0(\xi, \eta, z) = \bar{\phi}(\xi, \eta, z) \tag{8}$$

$$\phi_0(\xi, \eta, z) = \phi(\xi, \eta, z) \tag{9}$$

(iv) Boundary condition on a quay or breakwater

Assume the boundaries of the quays or breakwaters  $\Gamma_3$  are impermeable and have an arbitrary coefficient of reflection  $K_r$ . Since waves are reflected only partially, based on the theory of energy conservation, these constructions can therefore be treated, conceptually, as having a energy dissipating coefficient  $\alpha$  indicated by Chou and Lin(1989) reads

$$\alpha = \sqrt{1 - K_r^2} \tag{10}$$

The boundary condition on  $\Gamma_3$  can be expressed conveniently as:

$$\bar{\phi}(\xi, \eta, \zeta) = ik\alpha\phi(\xi, \eta, \zeta) \tag{11}$$

Substitution of Eqs.(6),(8),(9) and (11) into Eq.(5), a little algebra lead to

$$\begin{bmatrix} [K_{11} - CRK^*Q] & \frac{\sigma^2}{g} K_{12} & ik\alpha K_{13} \\ K_{21} & \frac{\sigma^2}{g} K_{22} - I & ik\alpha K_{23} \\ K_{31} & \frac{\sigma^2}{g} K_{32} & ik\alpha K_{33} - I \end{bmatrix} \begin{bmatrix} \bar{\phi}_1 \\ \phi_2 \\ \phi_3 \end{bmatrix} = \begin{bmatrix} R[F^o - K^*\bar{F}^o] \\ 0 \\ 0 \end{bmatrix} \tag{12}$$

where  $C = k/(N_0 \sinh kh)$ ,  $\{F^o\}$  and  $\{\bar{F}^o\}$  are the potential function and its normal derivative of the incident wave, [R] and [Q] are coefficient matrices given by Chou and Han (1993).

By solving the above equation, the potential functions on boundaries  $\Gamma_2$  are obtained. The wave height ratio,  $K_d$ , defined as the ratio of the wave height in Region II to the incident wave height, can be calculated from

$$K_d = |\phi_2| \quad (13)$$

## 2.2 Irregular Wave

The approach for the oscillations of unidirectional irregular waves in the harbour of arbitrary shape with dissipating quays is based on the spectral resolution method (Nagai (1972)), where each component wave is known. Assuming that incident component waves are small amplitude waves, the oscillations of these regular waves can be obtained by numerical method in section 2.1, then the water surface oscillations for irregular waves can be obtained through linear superposition method.

In this paper, the Bretschneider spectrum (Bretschneider(1968)) was used. In order to simplify the process of numerical analysis, the incident spectrum was transformed into dimensionless type as follows:

$$S^*(f^*) = af^{*-5} \exp[-(bf^{*-4})] \quad (14)$$

$$a = b/4$$

$$b = 0.675/0.9^4 = 1.0288$$

To obtain the component waves, the dimensionless spectrum is discretized into  $m$  parts, each with the same energy  $\Delta E$  (each part under the spectrum having the same area), then, the representative frequencies  $f_{cn}^*$  of each component wave can be written as

$$f_{cn}^* = \sqrt{\frac{8am\sqrt{\pi}}{\sqrt{b}} \left[ \operatorname{erf} \left( \sqrt{2 \ln \left( \frac{m}{n-1} \right)} \right) - \operatorname{erf} \left( \sqrt{2 \ln \left( \frac{m}{n} \right)} \right) \right]} \quad (15)$$

where  $a$  and  $b$  are the coefficients of the dimensionless Bretschneider spectrum;  $n=1,2,\dots,m$ ; and  $\operatorname{erf}(x)$  is the error function given as

$$\operatorname{erf}(x) = \int_0^x \frac{\exp(-z^2/2)}{\sqrt{2\pi}} dz \quad (16)$$

2.3 Wave height ratio  $K_D$  and period ratio  $K_T$  due to irregular waves

From section 2.1, the wave height ratio  $K_d$  due to regular component waves can be obtained, then the wave height ratio  $K_D$  and period ratio  $K_T$  due to irregular waves can be obtained by following equations.

$$K_D = \frac{H_{1/3}}{(H_{1/3})_o} = 4.0 \sqrt{\int_0^\infty S_D^*(f^*) df^*} \tag{17}$$

$$K_T = \frac{T_{1/3}}{(T_{1/3})_o} = \sqrt[3]{\pi b} \sqrt{\frac{\int_0^\infty S_D^*(f^*) df^*}{\int_0^\infty f^{*2} S_D^*(f^*) df^*}} \tag{18}$$

$$S_D^*(f^*) = K_d^2 S^*(f^*) \tag{19}$$

where  $S_D^*(f^*)$  is the spectrum in the harbour induced by the incident spectrum  $S^*(f^*)$ , subscript "o" means the values in off-shore.

3. DETERMINATION OF THE REFLECTION COEFFICIENT

To proceed with the analysis numerically, the energy dissipation coefficient  $\alpha$  in Eq.(11) must be determined. In other words, the reflection coefficient of the dissipating structure in Eq.(10) must be found empirically. This was done in a 2-D wave flume, shown schematically in Fig.2. The reflection coefficients can be obtained as shown in Fig.3, where the dotted curve shows the best fit of the experimental data in a least squares sense. Reflection coefficients for different frequencies determined from this empirical function were used in the subsequent calculations.

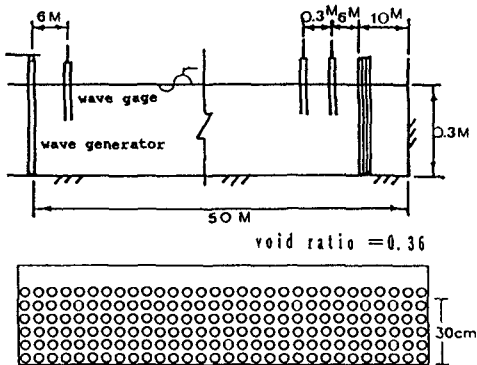


Fig. 2 Setup of 2-D wave flume & dissipating quay

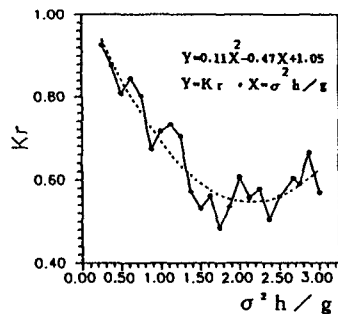


Fig. 3 The reflection coefficient of dissipating quay



4. EXAMPLE

Table 1. Cases of square basin

	S1	S2	S3	remarks
case I	x	x	x	x:impermeable quay
case II	o	o	o	o:dissipating quay
case III	x	o	x	
case IV	o	x	o	

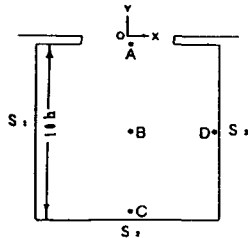


Fig. 4 Definition sketch for square harbour

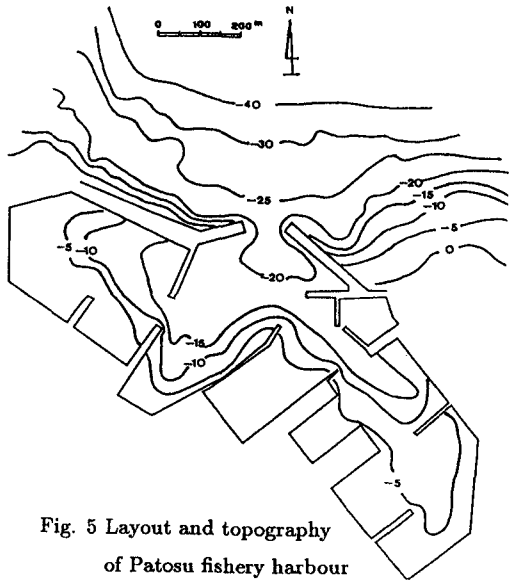


Fig. 5 Layout and topography of Patosu fishery harbour

Calculations were first carried out for a square basin with a width equal to  $10h$ , ( $h$  is the water depth of the open sea) and an opening width  $b=5h$  at the center of the basin, as shown in Fig.4. The same dissipating quays as those in the two-dimensional wave flume experiment were assumed and uniform water depths in both the Regions I and II.

In the numerical analysis, the surfaces of the boundaries are divided into 1056 discrete areas with constant element ( $N_1=104, N_2=720, N_3=52, N_4=180, M=2$ ). Waves propagating perpendicular toward the harbor entrance were used. Distributions of wave heights for dimensionless frequencies  $\sigma_{1/3}^2 h/g = 1.206$  ( $T_{1/3} = 1.0$  second) was determined. Table 1 shows the conditions used for the calculation.

Computations were also performed for an example of the Patosu fishery harbour built 3 years ago in the northern part of Taiwan. The layout and topography of the harbour are given in Fig.5. Quays and breakwaters of this fishery harbour are dissipating structures (PERFORCELL), whose reflection coefficient is estimated approximately at 0.75, the energy dissipation coefficient being 0.661. In the numerical computation, water depth larger than 40

m was regarded as constant, and the boundary surfaces were divided into 1988 discrete segments with constant elements ( $N_1=152, N_2=1329, N_3=176, N_4=331$  and  $M=2$ ). Distributions of wave heights were calculated for incident waves propagating from  $23.5^\circ$  north-northeast ( $\omega = 66.5^\circ$ ) toward the harbour entrance with dimensionless frequencies of  $\sigma_{1/3}^2 h/g = 1.611$  ( $T_{1/3} = 1.0$  second).

In the numerical analysis, the dimensionless spectrum is discretized into 12 segments ( $m=12$ ), then the representative frequency  $f_{cn}^*$  of each component wave can be calculated by Eq.15, and the wave height ratio  $K_D$  and period ratio  $K_T$  can be obtained by Eq.17 to 18.

## 5. LABORATORY EXPERIMENT

Experiments were carried out in a 3-D wave basin. The wave basin is 30 m long, 24 m wide and 1 m deep. The programmable wave generator is capable of generating regular and irregular waves. Water depth was kept to be 0.3m throughout the experiments. Water surface displacements were measured with capacitance-type wave gauges.

## 6. RESULTS AND DISCUSSION

Fig.6 shows the wave height distributions for irregular waves obtained both by the present numerical method and experiments for case I and case II of square basin with significant wave period  $(T_{1/3})_0 = 1.0$  second. From these figures, a general increase of wave height in case I due to reflection effects and decrease of that in case II due to the effects of disposing dissipating quays were found. The tendencies of wave height distributions predicted by the present numerical model are confirmed by the experiments.

Fig.7 shows the period distributions  $K_T$  for irregular waves obtained both by the present numerical method and experiments for case I and case II of square basin with significant wave period  $(T_{1/3})_0 = 1.0$  second. The spatial variation of  $K_T$  is increasing in the range of 20% in the square basin, and the spatial similarity between numerical solutions and experimental results are reasonable.

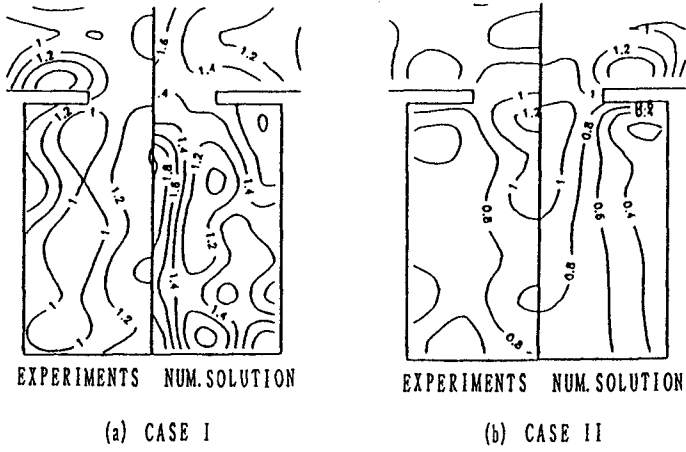


Fig.6 Wave height distributions  $K_D$  for irregular wave  
 $(\sigma_{1/3})^2 h/g=1.206$ ,  $t=1.0$  sec,  $h=30$  cm,  $\omega = 90^\circ$

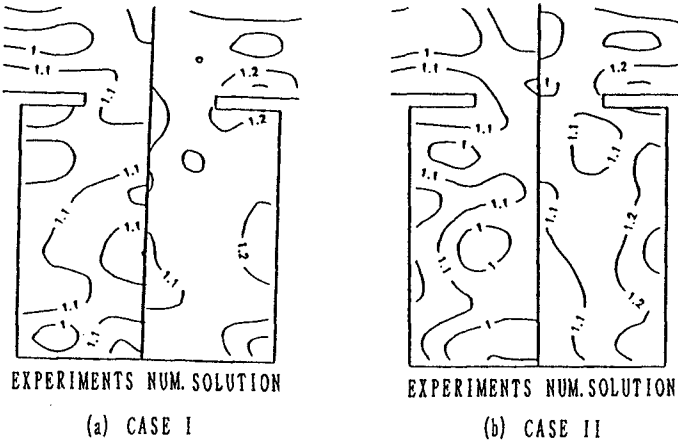


Fig.7 Wave height distributions  $K_T$  for irregular wave  
 $(\sigma_{1/3})^2 h/g=1.206$ ,  $t=1.0$  sec,  $h=30$  cm,  $\omega = 90^\circ$

Fig.8 shows the comparison of wave height distributions in square basin by numerical model to regular waves with period  $T=1.0$  second and to irregular waves with significant period  $(T_{1/3})_0 = 1.0$  second for case I to IV respectively. For both regular and irregular waves, the oscillations in case II to IV is apparently reduced because of disposing dissipating quays. Compared the difference of wave height distributions induced by regular and irregular waves, it can be found that the wave height distributions induced by irregular waves are, in general, more stable than those induced by regular waves. The wave motions by irregular waves generally consist with those existing in nature sea-water surface.

Fig.9 shows the distribution of wave height  $K_D$  for irregular wave obtained by the numerical method and experiments for the Patosu fishery harbour with  $\alpha = 0.661$ , wave direction of  $23.5^\circ$  north-northeast and wave period  $(T_{1/3})_0 = 1.0$  second. Compared the difference of these figures with Fig.10, the same phenomena in square basin mentioned above that the wave height distributions induced by irregular waves are more stable than those induced by regular waves was found. The spatial similarity between numerical solutions and experimental results are reasonable too.

Fig.10 shows the period distributions  $K_T$  for irregular waves obtained both by the present numerical method and experiments for the Patosu fishery harbour with significant wave period  $(T_{1/3})_0 = 1.0$  second. The spatial variation of  $K_T$  is increasing in the range of 20% in the numerical results. Because the wave heights in the inner region of the harbour are too small to measured, the significant wave period in that region can not be obtained in the laboratory.

## 7. CONCLUSION

The effects of dissipative quays and/or breakwaters are modeled using a coefficient for energy dissipation in the boundary condition. Comparisons of calculated and measured results for both a square basin and a real harbour are shown. From the examples presented above show that the spatial similarity between numerical solutions and experimental results are reasonable. It is conjectured that, given the correct coefficient, the most suitable position for dissipating quays in a harbour could be estimated by the present method.

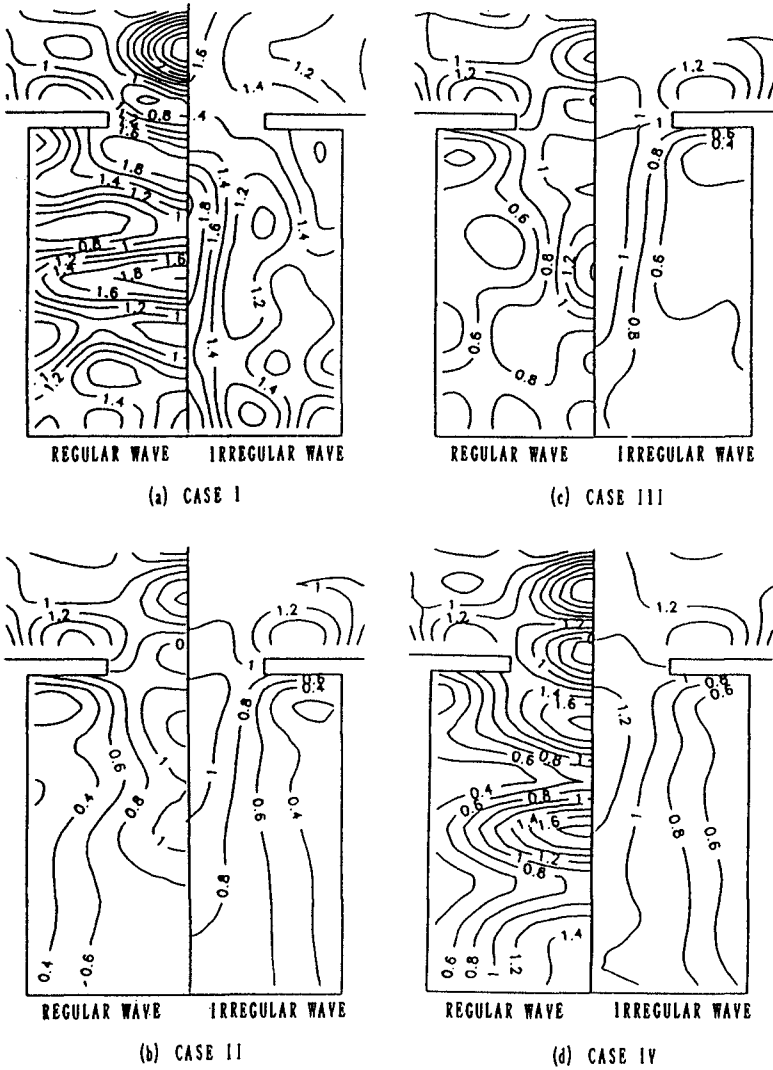


Fig.8 Wave height distributions for regular wave ( $T=1.0$  sec.)  
and irregular wave ( $T_{1/3}=1.0$  sec.)

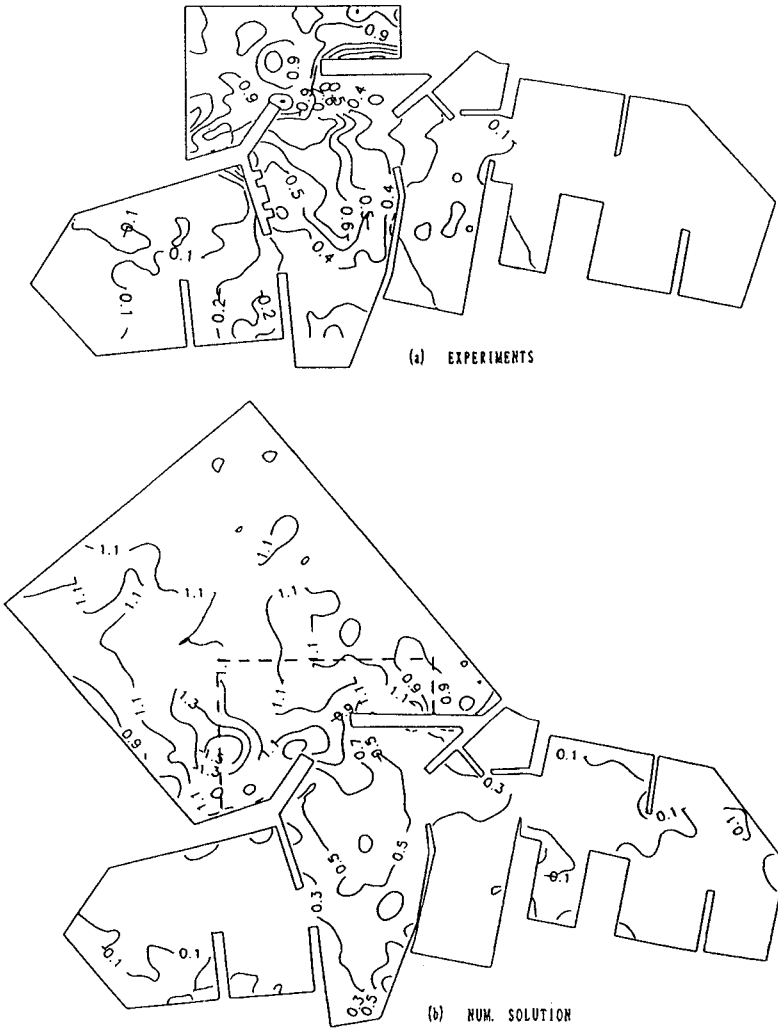


Fig.9 Wave height distributions  $K_D$  for irregular wave in Patosu fishery harbour, ( $T_{1/3}=1.0$  sec.)

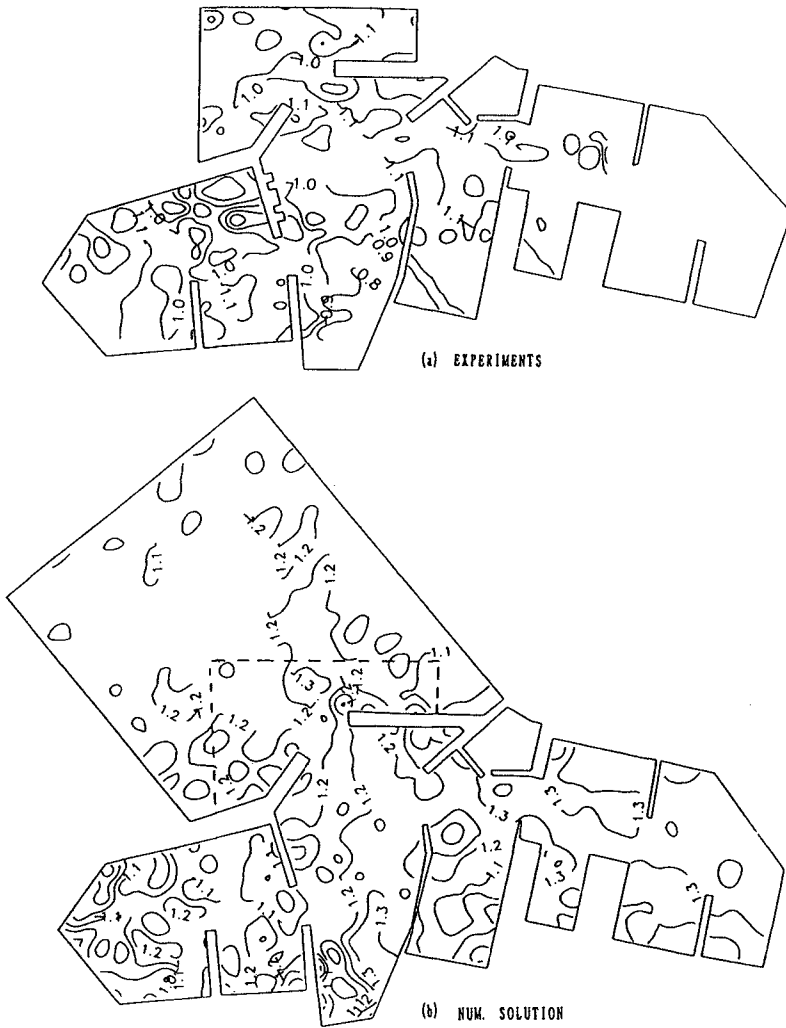


Fig.10 Wave period distributions  $K_T$  for irregular wave in Patosu fishery harbour, ( $T_{1/3}=1.0$  sec.)

Though only the Bretschneider spectrum as incident wave spectrum was used in this paper, other spectrums such as Pierson Moskowitz spectrum or JONSWAP spectrum can be applied by this method also.

It is thus concluded that the present numerical method can be used to study problems related with harbour oscillations.

#### ACKNOWLEDGEMENTS

This work is sponsored by the National Science Council of the Republic of China under the grant No. NSC 81-0209-E-019-3, the advice and financial support of the National Science Council are gratefully acknowledged.

#### REFERENCE

- Miles, J. and Munk, W. (1961): Harbors paradox; *J. Waterways and Harbors Division, ASCE*, Vol. 87, No. WW3, pp. 111-130.
- Ippen, A. T. and Goda, Y. (1963): Wave-induced oscillations in harbors: the solution for a rectangular harbor connected to the open-sea; *Report No. 59, Hydrodynamics Lab., M.I.T.*
- Bretschneider, C. L. (1968): Significant waves and wave spectrum, *Ocean Industry*.
- Hwang, L. S. and Tuck, E. O. (1970): On the oscillations of harbors of arbitrary shape. *J. Fluid Mech.*, 42.
- Lee, J. J. (1971): Wave-induced oscillations in harbors of arbitrary geometry; *J. Fluid Mech.*, Vol. 45, pp. 375-394.
- Nagai, K. (1972): Diffraction of the irregular sea due to breakwaters, *Coastal Engineering in Japan*, JSCE. 15
- Chou, C. R. and Lin, J. G. (1986): Numerical analysis for harbor oscillation of arbitrary shape in uneven sea bed by BEM; *8th Conf. on Ocean Engng., R.O.C.*, pp. 111-130. (in Chinese)
- Chou, C. R. and Lin, J. G. (1989): Numerical analysis for harbor oscillation with wave absorber; *11th Conf. on Ocean Engng., R.O.C.*, pp. 365-381. (in Chinese)
- Chou, C. R. and Han, W. Y. (1993): Wave-induced oscillations in harbours with dissipating quays; *Journal of Coastal Engineering in Japan*, Vol. 36, No. 1, pp. 1-23.



## CHAPTER 216

### Mechanism and estimation of sedimentation in Bangkok Bar Channel

Ichiro DEGUCHI<sup>1)</sup>, Toru SAWARAGI<sup>2)</sup>, Masanobu ONO<sup>3)</sup>  
and Sucharit KOONTANAKULVONG<sup>4)</sup>

#### ABSTRACT

Mechanism of sedimentation in Bangkok Bar Channel in Thailand is investigated by using the periodically measured water depth around channel, dredged volume and the relation between discharged sediment concentration and discharged velocity measured at the river mouth of Chao Praya. Simple numerical simulations for predicting sedimentation volume in the channel are also carried out. The results show that both discharged sediment from the river and sedimentation around Bangkok Bar caused by waves and current play an important role in the sedimentation in the channel.

#### Introduction

The city of Bangkok has been developed along the Chao Praya River. The Bangkok Harbor plays very important role in economic and social activities of Thailand. Bangkok Bar Channel is a unique approach channel to Bangkok Harbor that is the representative river port constructed along the river mouth of the Chao Praya, Thailand. Various facilities are scattered along the both sides of the river between the river mouth and the bridge located about 50km upward (see Fig.1). Due to the heavy sedimentation discharge from the river and severe sedimentation around the bar, the channel is barely maintained its fair way through the continuous dredging of about 5million m<sup>3</sup>/year.

Some reports have already been published about the sedimentation of the channel by NEDECO(1963), Port Authority of Thailand and so on. They reported many important and interesting phenomena and fact about hydraulics of the river mouth and characteristics of the bed material

The aim of this study is to investigate the mechanism of sedimentation in Bangkok Bar Channel and to estimate the volume of sedimentation in the channel through the statistical analysis of measured time history of river discharge, dredged volume and bottom profiles during August 1989 and August 1991 together with the results mentioned in the above-mentioned reports. In 1992, we also carried out field measurements of velocity and silt concentration at river mouth.

1),2) and 3) Associ. Prof., Prof and Research Associ., Dept. of Civil Engineering, OSAKA University, Yamadaoka, Suita, Osaka 565, Japan 4) Associ. Prof., Dept. of Water Resources Engineering, CHULALONGKORN University

For the estimation of siltation volume in the channel, we conducted some numerical simulation of non-equilibrium sediment concentration caused by waves and current that crossed the channel. It is generally recognized that there are two modes of silt transport that is transport by mud flow and that by suspension. Here, we only evaluate the sedimentation volume in latter mode.

### Outline of Bangkok Bar Channel

The construction of the channel began in 1951 and was completed in 1954. The volume of capital dredging was about 16million  $m^3$ . The length of the channel is 18km and the channel crosses Bangkok Bar, the depth of which is less than 2m at low tide. Figure 1 shows a plane view of the Bangkok Bar Channel. A mean depth of the channel is about -8.5m under the mean sea level and the width of the channel varies from 100m (at straight part) to 200m (at the bend).

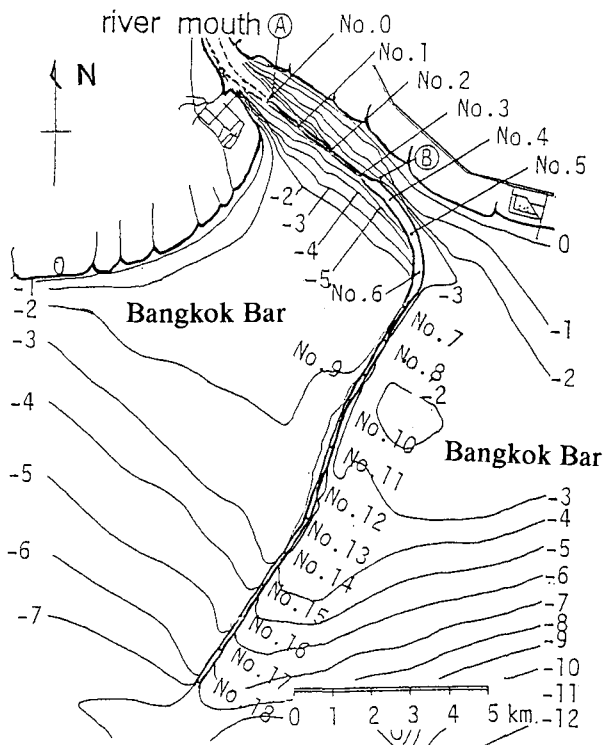


Fig.1 Plane view of Bangkok Bar Channel

There is a couple of possible causes for the sedimentation around the channel, such as sedimentation of discharged silt from the river, sedimentation caused by waves and tidal current, that caused by waves and wave-induced current around the

bank, and so on. There are also some mode of sediment transport, such as suspended sediment transport, bed load transport, mud flow, and so on. Among them, we firstly evaluated the volume of discharge sediment from the river based on the depth averaged discharge velocity and siltation concentration measured in May and in August 1991. Then, the amount of sedimentation due to suspension around the Bangkok Bar caused by waves and tidal current was predicted through the numerical simulation.

### Characteristics of River discharge and Monsoon

Sedimentation around the channel seems to deeply depend on the river discharge and wind waves generated by monsoon. In usual, the maximum discharge is more than  $3000\text{m}^3/\text{s}$  that took place at rate September to October that will be shown in Fig.5(b) later. However, in the objective period (from August, 1989 to August, 1991), the discharge was far less than the usual year as will be shown in Fig.6(b).

Figure 2 is the time series of wind direction and wind velocity measured at the Bangkok during objective period.

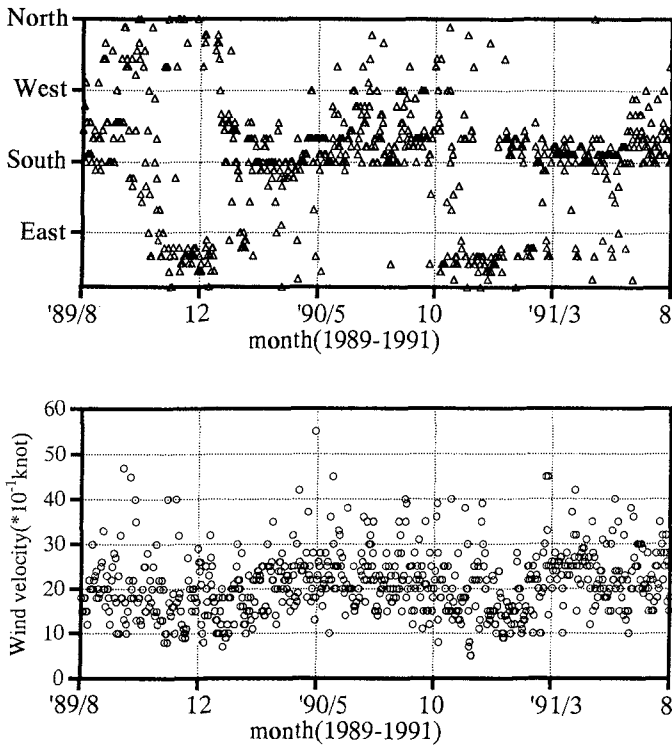


Fig. 2 Time series of wind direction and velocity during objective period

NE monsoon and SW monsoon seasons usually begin at November and May, respectively. In the objective period, each monsoon seasons began first than usual. The mean wind velocity is about 0.5m/s to 3.0m/s and a little bit strong wind blows in SW monsoon season.

The direction that brings significant wind waves is from south to south-west. From May to July in 1990, both discharged flow from the river and wind waves caused by the monsoon might affect sedimentation in the channel. Only the discharged flow was the sedimentation agency in channel from October to December in 1989 and only waves and tidal current caused sedimentation in the channel from May to July in 1991.

#### Sedimentation volume in the channel

Sedimentation volume in the channel was estimated from measured channel topography and records of dredged volume. Sounding of the channel has been carrying out by Port Authority of Thailand twice a month at distances of 200m in the offshore (transversal) direction and 5m in the longitudinal direction. We express the measured depth in the following way:

$$h(x, y, t) = h(i\Delta x, j\Delta y, k\Delta t) \quad (1)$$

$x$  : transversal direction,  $\Delta x = 200m, 1 \leq i \leq 91$

$y$  : longitudinal direction,  $\Delta y = 5m, 1 \leq j \leq 61$

$\Delta t = month/2$

Sedimentation volume was calculated by the following relation:

$$\Delta V(i, j, k) = \{h(i, j, k) - h(i, j, k + 1)\} \Delta x \Delta y \quad (2)$$

We define the total sedimentation volume  $\Delta TV$  as a sum of  $\Delta V$  and dredged volume  $\Delta V_d$ . We obtained there data through the courtesy of the Port Authority of Thailand.

The characteristics of the time and spatial variation of the sedimentation volume is investigated by comparing the time histories of river discharge and wind data.

Figure 3 illustrates the temporal and spatial distribution of the total siltation volume of the channel. The vertical axis is the distance from the river mouth and the horizontal axis is the month.

It can be seen that dark parts centered around 3 to 8km from the river mouth. This section of the channel corresponds to the bending part. Especially, from August to October and April to July, large volume of sediment deposited. These two duration corresponds to the two peaks of river discharge (see Fig.6(b)). However, there are another dark parts in the bend during February and August in 1991 (south-west monsoon season) when there was only small river discharge.

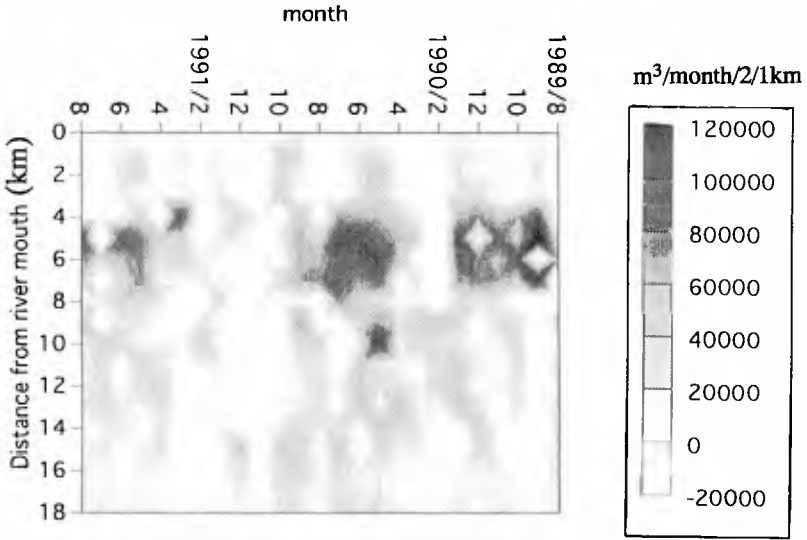


Fig.3 Temporal and spatial distribution of the total sedimentation volume

Figure 4 illustrates the variance of the change in water depth  $\Delta h_{vr}(i,j)$  that means the magnitude of the topographic change in the channel.

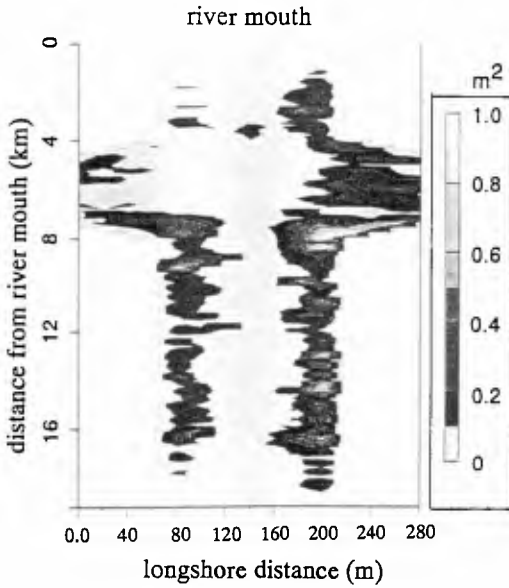


Fig.4 Variance in water depth around the channel

The variance is calculated by Eq.(3).

$$\Delta h_{vr}(i, j) = \sum_k \{h(i, j, k) - \overline{h(i, j)}\}^2 / 25 \quad (3)$$

where  $h(i, j)$  is the averaged water depth during the objective period.

The vertical axis is again the distance from the river mouth and the horizontal axis is the longshore distance. It is found that change in water depth is large in the bend and the slope of the channel where the non-equilibrium property of suspended sediment is strong.

Figure 5 shows the comparison of the averaged river discharge and the averaged total siltation during 1957 and 1963. The averaged total siltation volume is calculated in upper section (from 0km to 6km from the river mouth), middle section (from 6km to 12km from the river mouth) and lower section (from 12km to 18km from the river mouth) separately in the following way and are shown by a solid line, a dotted line and a broken line, respectively.

$$\Delta TV_l(k) = \sum_{i=(l-1)*30}^{l*30-1} \sum_j \Delta TV(i, j, k), \quad (4)$$

$l=1$ : upper section,  $2$ : middle section,  $3$ : lower section

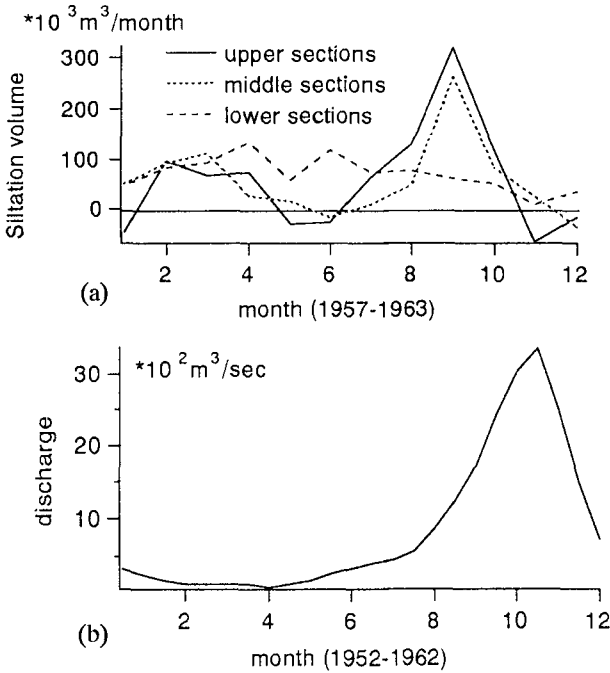


Fig. 5 Comparison of the seasonal changes of averaged total sedimentation volume and river discharge

River discharge has a peak at middle of October and the total siltation in the upper and the middle sections have peaks at middle of September that correspond to the peak of river discharge. They also indicate large values during February and April when the river discharge becomes minimum. The total siltation in the lower sections dose not show any significant seasonal change.

From these results, we can judge that sedimentation in the upper and the middle sections is mainly caused by river discharge and in the lower sections river discharge has little influence. Waves and current also play an important role in sedimentation in dry SW monsoon season in the upper and middle sections and in the lower sections they become unique agitation and transporting agency of bed material to deposit in the channel.

Figure 6 shows the comparison of time histories of the total siltation and river discharge during August 1989 and August 1991. In this duration there are three peaks in river discharge and again there are increases in the total siltation in the upper and the middle sections. However, the correspondence is not so clear as the former figure due to the scattering of the data because these are the raw and unsmoothed data.

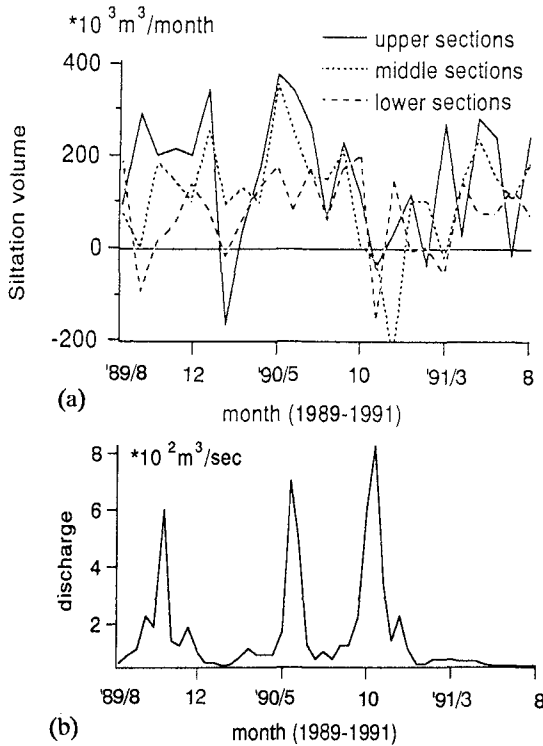


Fig.6 Comparison of time histories of total siltation volume and river discharge during the objective period

Estimation of sedimentation volume discharged from the river

We carried out field measurement of discharged velocity and silt concentration in May and August 1992 at two point near the river mouth. Here, we roughly estimated the siltation volume using the measured results. Figure 7 illustrates the relation between the mean discharged velocity and mean silt concentration presented in the report of NEDECO (1963). The open circles in the figure are the result of our measurements.

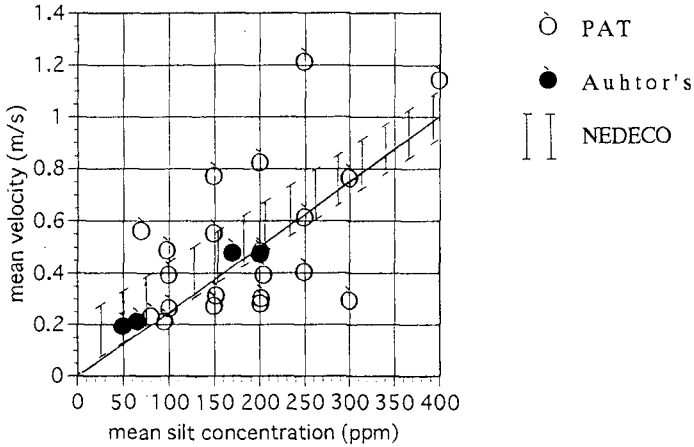


Fig.7 Relation between depth averaged discharge velocity and silt concentration at the river mouth

As you know well, the mean silt concentrations in the beginning of the discharge and in the descending period of the discharge are not the same. Generally it is lower in the later period. However, we assume that the mean silt concentration is a unique function of the mean velocity. Then we have the relation between them from the figure in the following form:

$$C[ppm] = 400U[m/s] \tag{5}$$

Let the discharged volume and sectional area of the flow at the river mouth be  $Q$  and  $A$ , then the discharged silt volume  $Q_s$  is expressed as:

$$Q_s = AUC = 400Q^2/A * 10^{-6} [m^3/s] \tag{6}$$

Further we assume that the time history of the river discharge is expressed by the triangle with the peak value of  $3000m^3/s$  and continues for two months as shown in Fig.8 and the sectional area of the river mouth be  $2000m^2$ . Then the total siltation volume discharged from the river is calculated by the integration

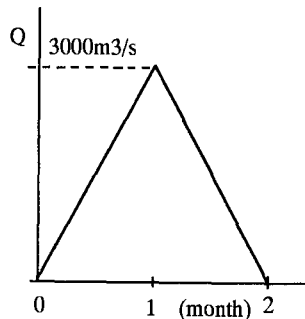


Fig.8 Assumed hydrograph



$$Q_{total} = \int_0^{two-month} Q_s dt \quad (7)$$

that gives  $1.6 \cdot 10^6 m^3/year$ . The value is about a half of the annual averaged total annual siltation volume.

**Estimation of sedimentation volume caused by waves and tidal current**

In this section, siltation volume due to waves and current, an another sedimentation agency in the channel is evaluated by a simple numerical simulation.

For the sake of simplicity, and to grasp the rough figure of the sedimentation in the channel, we assume that the waves and current cross the channel at right angle as shown in the lower figure. X-axis is taken in the direction of wave propagation and we simulate the flow and sedimentation in 2-D phenomena (see Fig.9).

In such case, sever sedimentation will take place due to the non-equilibrium suspended sediment transport caused by the existence of channel. In the numerical simulation, we have to reproduce the non-equilibrium state of the suspended sediment concentration adequately.

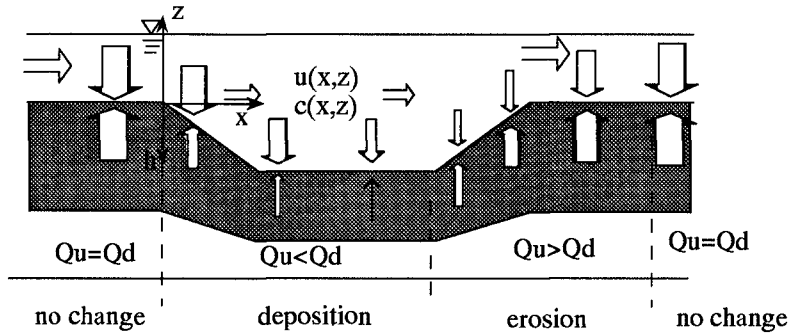


Fig.9 Coordinate system

A governing equation of suspended sediment concentration  $c$  is an advection-diffusion equation that is expressed by Eq.(8).

$$\frac{\partial c}{\partial t} + u \frac{\partial c}{\partial x} - W_f \frac{\partial c}{\partial z} = \epsilon_x \frac{\partial^2 c}{\partial x^2} + \epsilon_z \frac{\partial^2 c}{\partial z^2} \quad (8)$$

where  $u$  is the mean current velocity that has a vertical distribution,  $\epsilon_x$  and  $\epsilon_z$  are the diffusion coefficients in  $x$  and  $z$  direction and  $W_f$  is the settling velocity of bed material.

It has been recognized that it is generally difficult to numerically solve the advection-diffusion equation with high accuracy because it contains two mathematically and physically different terms, i.e., advection term and diffusion term. Recently, highly accurate numerical procedures for solving the advection-diffusion equation have been developed by Komatsu et.al.(1985) that is called a split operator approach.

We applied two procedures to simulate non-equilibrium suspended sediment concentration. Eq.(8) is solved by using a split-operator approach in Method-1 and in Method-2, an advection-dispersion equation Eq.(9) instead of Eq.(8) is solved to obtain sediment concentration. Equation (9) is derived by taking depth average of Eq.(8).

$$\frac{\partial C}{\partial t} + U \frac{\partial C}{\partial x} + V \frac{\partial C}{\partial y} = \kappa_x \frac{\partial^2 C}{\partial x^2} + \kappa_y \frac{\partial^2 C}{\partial y^2} + \Delta Q_s \quad (9)$$

$$\Delta Q_s = \left\{ C_0 u^* (1 - W_f / u^*) - W_f C \right\} / h \quad (10)$$

$$\gamma = 1, \quad u^* / W_f \leq 1, \gamma = 0, \quad u^* / W_f > 1$$

where  $U$  and  $V$  are the depth averaged mean current velocity in  $x$  and  $y$  directions,  $C$  is the depth averaged concentration of suspended sediment,  $\kappa_x$  and  $\kappa_y$  are the dispersion coefficients in  $x$  and  $y$  directions,  $u^*$  is the bottom shear velocity caused by waves and current  $C_0$  is the reference concentration at the bottom and  $h$  is the water depth.

In Method-1, the advection-diffusion equation is split into the advection and the diffusion equations Eqs.(11) and (12).

$$\frac{\partial c}{\partial t} + u \frac{\partial c}{\partial x} - W_f \frac{\partial c}{\partial z} = 0 \quad (11)$$

$$\frac{\partial c}{\partial t} = \varepsilon_x \frac{\partial^2 c}{\partial x^2} + \varepsilon_z \frac{\partial^2 c}{\partial z^2} \quad (12)$$

These two equations are transformed to a pair of finite difference equations by using 6-point and 5-point methods, respectively. The difference equations are calculated iteratively at grid points. The boundary condition for concentration is given at the upstream end and at the bottom.

After obtaining the steady solution, we can evaluate suspended sediment flux (Eq.(13)) and the rate of topographic change by Eq.(14).

$$q_s(x, z) = \int c(x, z) u(x, z) dz \quad (13)$$

$$\frac{\partial h(x, t)}{\partial t} = \frac{1}{1 - \lambda} \frac{\partial q_s(x, t)}{\partial x} \quad (14)$$

In Method-2, a depth averaged advection-dispersion equation (Eq.(9)) is solved by using an Alternating Direction Implicit method. The boundary condition for the depth averaged concentration is given at the upstream end and at the bottom. The change in water depth is calculated by using vertical sediment flux  $\Delta Q_s$  as follows:

$$\frac{\partial h}{\partial t} = \frac{-\Delta Q_s}{1 - \lambda} \quad (13)$$

We have already developed this method for the simulation of topographic change in coastal region. We apply the procedure to calculate topographic change of channel section. About 20 times as much as CPU time is required in Method-1 when compared with that required in Method-2.

We carried out numerical simulations of channel topography change of two cases as shown in Fig.10. In both cases, the depth of the fairway was 8.5m. The depth at the channel approach was 3m in Case-1 and 5m in Case-2. The non-equilibrium property of suspended sediment is stronger in Case-1 than in Case-2.

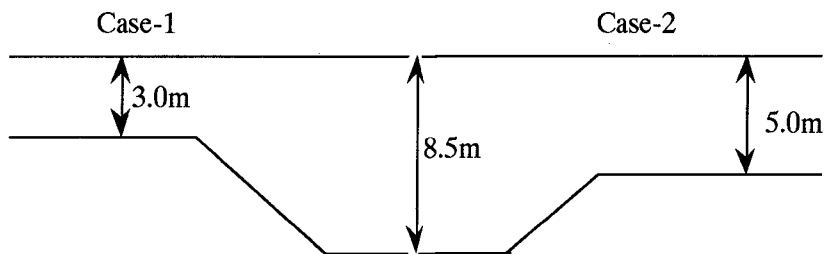


Fig.10 Channel section of numerical simulation

Height and period of incident waves were 1.5m and 6s. According to the report of the Port Authority of Thailand, waves of such magnitude would occur more than 30hrs per year. The mean current velocity was determined to be 0.3m/s that was a mean tidal current that crosses the channel. The settling velocity of bed material was 0.12cm/s that included the effect of flocculation (NEDECO, 1963).

In the numerical simulation, we first calculated waves and current based on equations of wave energy conservation and depth averaged momentum conservation where the bottom shear stress were evaluated from the turbulent boundary layer equation (Deguchi, 1995). In Method-1, the vertical distribution of mean current was determined from the depth averaged mean current velocity by using the kinematic eddy viscosity as a function of bottom shear velocity.

Figure 11 illustrates flow charts of both methods. We used the same value as the kinematic eddy viscosity for the diffusion coefficient in Method-1. The dispersion coefficient in Method-2 was given as a function of the product of the bottom shear velocity and the water depth.

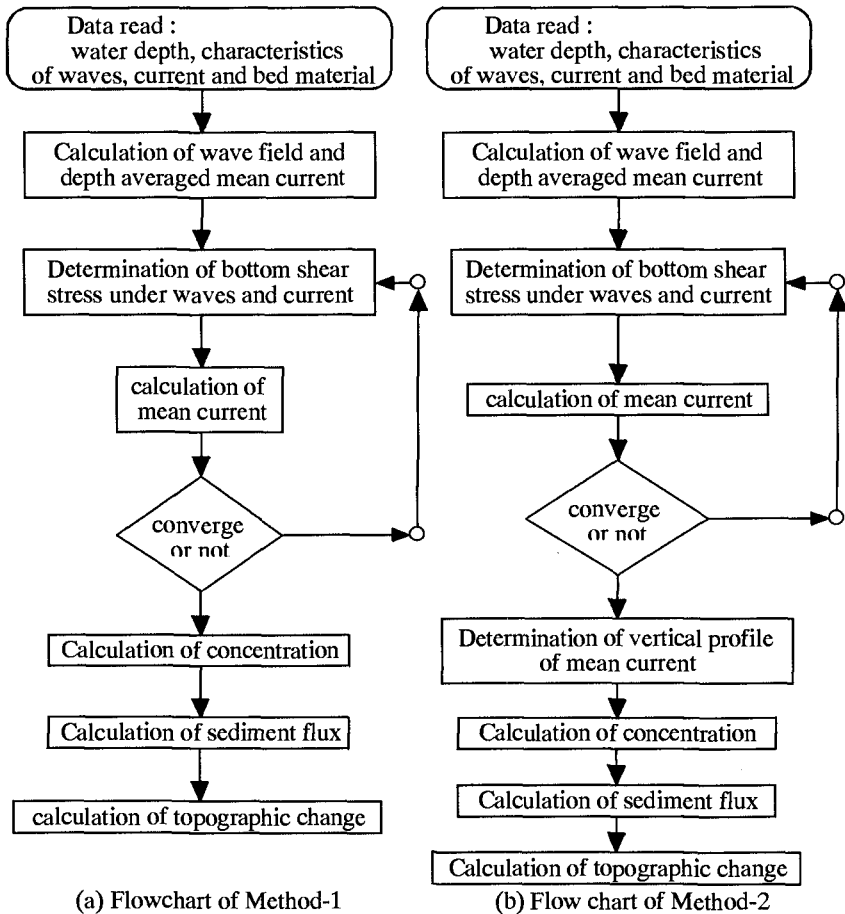


Fig.11 Flow chart of numerical simulation

Figure 12 shows the comparison of predicted changes in water depth at two representative channel sections by two methods. Although there are significant difference between the simulated results by the two methods, we can judge that we can not neglect the effect of the waves and current in the sedimentation in channel. In Case-1 (Fig.(a)), the predicted decrease in water depth in channel by Method-1 is larger than 20cm per one hour. On the other hand, the decrease of the depth in Case-2 (Fig.(b)) is only 6cm per hour in average.

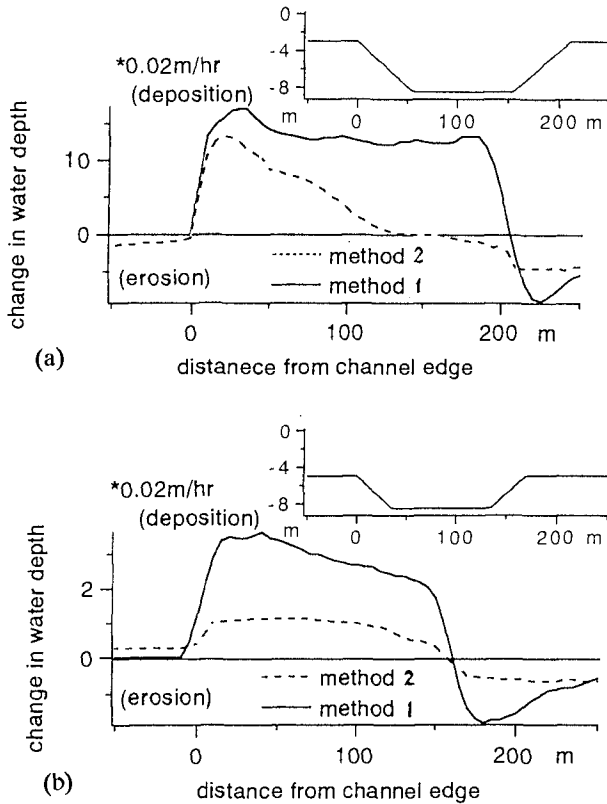


Fig.12 Change in water depth across channel  
 ((a):Case-1, (b):Case-2)

According to the calculated change in water depth by Method 2, volumetric change per unit length per one hour of the channel is about  $17\text{m}^3/\text{m}/\text{hour}$  that will be about  $500\text{m}^3/\text{m}/\text{year}$ . When we assume that this amount of siltation take place along the middle sections 6km (From No.6 to No.12) where the depth of approach is about 3m, the total amount of sedimentation will be  $3 \times 10^6\text{m}^3/\text{year}$  that is the same order of the siltation volume due to river discharge.

From these results the amount of sedimentation caused by waves and current is estimated to be about  $3 \times 10^6\text{m}^3/\text{year}$  that is the same order of the sedimentation volume discharged from the river.

### Conclusions

Through the statistical analysis of the topographic change in the channel, it is found that sedimentation in the upper and the middle sections of the Bangkok Bar Channel is mainly caused by the river discharge. In the lower sections, the river discharge has little influence. Waves and tidal current also play an important role in sedimentation in the middle and lower sections and they become a unique agitation and transporting agency of bed material to deposit in the channel of lower sections.

From the results of simplified numerical simulation of the sedimentation in the channel, we can judge that the order of the amount of sedimentation caused by waves and current in the middle sections is almost the same as that brought about by the river discharge.

### References

- Deguchi I, 1995, Waves, wave-induced currents and sediment transport, in "Coastal Engineering-Waves Beaches and Wave-Structure Interactions-", Ed., T. Sawaragi, Elsevier Science B.V. (in printing).
- Komatsu, T., Holly, F.M.Jr., Nakashiki, N. and Ohguchi, K., 1985, Numerical calculation of pollutant transport in one and two dimensionals, JHHE, Vol.3, No.2, pp.15-30.
- NEDECO, 1963, A study on the siltation of the Bangkok Port Channel, 474p.
- Sawaragi, T., I. Deguchi, M. Ono and K.S. Bae (1991), Numerical simulation for shoaling process of navigation channel, Int'l. Sympo. on Natural Disaster Reduction and Civil Engineering, JSCE, pp.117-126.

## CHAPTER 217

### Turbidity and Suspended Sediment Associated With Beach Nourishment Dredging

Daniel M. Hanes<sup>1</sup>, Member A.S.C.E

#### Abstract

A field observation program was carried out to measure natural and man-induced fluctuations in suspended sediment and turbidity in connections with a beach nourishment project. The project was carried out at Longboat Key, on the west coast of Florida. The analysis of the manual turbidity, sedimentation, and wave data revealed several significant facts concerning the differences between the hard bottom sites and control sites and the interactive dynamics between these three phenomena. The sedimentation measurements indicate that the sand sedimentation rates are highly variable, particularly with time. In contrast, the fines sedimentation rates are relatively less variable with respect to both location and time. It is evident from the examination of the sedimentation data that the sand sedimentation rates at the hard bottom sites were approximately 2.5 times higher than those of the control sites. The statistical analysis indicated that there is less than a 10% probability that this difference is due to chance. In contrast, there were no significant differences in fines sedimentation rates between the hard bottom and control sites. The manual turbidity measurements indicate high variability in space and time. Based on approximately 15 measurement dates, following nourishment the hard bottom sites experienced approximately 50% less turbidity than the control sites. The variations in sand sedimentation rates are believed to be directly related to the hydrodynamic forces resulting primarily from waves. The wave height was approximately 33 % greater at the hard bottom sites.

#### Introduction

Turbidity, a measure of light scattering due to particles or impurities suspended in solution, is important to underwater visibility and light transmission.

-----  
<sup>1</sup> Associate Professor of Coastal and Oceanographic Engineering, University of Florida, P.O. Box 116590, Gainesville, FL 32611-6590, USA.  
email: hanes@coed.coastal.ufl.edu.

Periods of high turbidity significantly stress some underwater communities such as coral. Suspended sediment contributes to turbidity and independently stresses corals through the deposition of sediment. Turbidity and suspended sediment concentration vary substantially in the nearshore region under natural conditions. Natural variations in these quantities may be significantly enhanced by engineering activities such as beach nourishment dredging.

A field observation program was carried out to measure natural and man-induced fluctuations in suspended sediment and turbidity in connections with a beach nourishment project. A large scale beach nourishment project was carried out at Longboat Key, Florida, during the period of observations. Sedimentation, turbidity, and wave climate were measured over a two year period. Figure 1 is a time line of these activities.

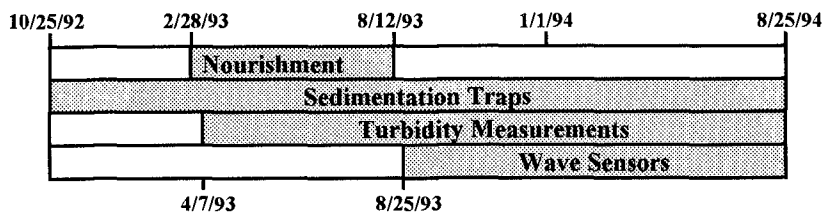


Figure 1: Time Line of Nourishment and Monitoring Activities

The monitoring locations (see Figure 2) include four stations at hard bottom study sites along Longboat Key and three control stations on adjacent Siesta Key, Anna Maria Island and Long Key. Table 1 provides the names, locations and mean lower low water depths of each site during the period of wave measurements. Sedimentation rates and turbidity measurements were obtained at all seven sites. Wave sensors were deployed at the Long Key and Siesta Key control sites and the Longboat Key #34 and Longboat Key #2 hard bottom sites.

Table 1: Monitoring Locations

Site	Latitude	Longitude	Depth
Siesta Key - SK	27°15'40" N	82°33'09" W	4.6 m
Longboat Key #6 - LBK6	27°23'21" N	82°38'43" W	4.5 m
Longboat Key #2 - LBK2	27°23'38" N	82°38'57" W	5.6 m
Longboat Key #43 - LBK43	27°25'28" N	82°40'34" W	4.6 m
Longboat Key #34 - LBK34	27°25'19" N	82°40'42" W	5.3 m
Anna Maria Island - AM	27°30'47" N	82°43'33" W	4.6 m
Long Key - LK	27°42'27" N	82°44'39" W	4.5 m



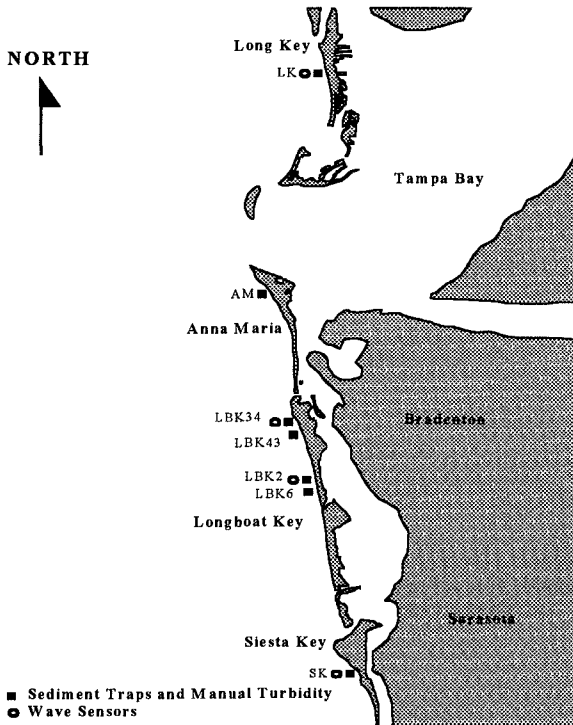


**Figure 2:** Location Map of Monitoring Sites

### Sedimentation Monitoring

Sediment traps are deployed in order to measure the relative amounts of sand sized sediments and fine sediments suspended in the water column. The sediment trap used in this study is shown in Figure 3. The traps function by capturing suspended sediment which have sunk into the trap opening due to the tendency for sediment to settle downward due to gravity. Once inside the trap, sediments are presumably not resuspended or eroded. Thus the measured sedimentation rates are actually a measure of the product of the concentration of suspended sediments and the settling velocity of the sediments. The sedimentation rates are not a measure of deposition rates upon the bed. In fact, high sedimentation rates can sometimes indicate low deposition rates, because the sediment is suspended above the bed and advected away by currents.

After the initial deployment in October, 1992, field trips to retrieve the samples were scheduled for the first week of January, 1993 and approximately every four weeks thereafter during nourishment. After the completion of nourishment, field trips were scheduled at a maximum of every six weeks.

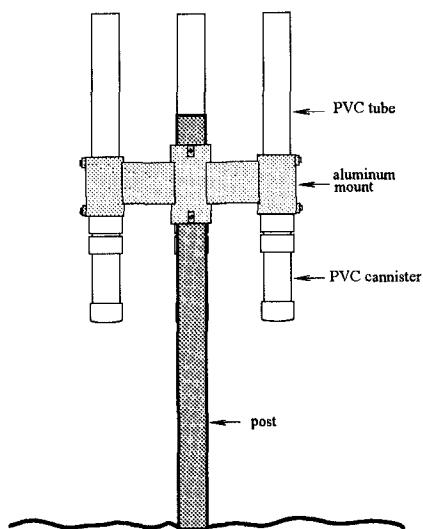


**Figure 3:** Sediment Trap and Mounting  
 deployment) were then averaged to provide the best estimate of the sedimentation rate for that site during the measurement period.

Each sample was separated into sub-samples of sand and fines by wet sieving with a 63 micron sieve. These sub-samples were then dried at 110° C and weighed to determine dry weight of the sand and fines portion. Finally, the samples were ashed at 500 ° C for two hours and re-weighed to determine the weight of organic matter. Sedimentation rates, given in milligrams per centimeters squared per day, were calculated by dividing mass by the area of trap entrance and Julian days between deployment and retrieval. The sedimentation rates for multiple traps at each station (for each

Table 2 shows the average sand sedimentation rates of the four hard bottom sites off Longboat Key and of the three control sites for each deployment. Of the nearly 350 sedimentation samples, there were three cases in which one of the three sediment traps was significantly different from the other two traps at the same location. For these cases the deviant measurement was discarded. The bottom row is the average of all of the hard bottom samples and all of the control samples over all deployments.

**Table 2:** Average Sand Sedimentation Rates (mg/cm<sup>2</sup>/day)  
 Hard Bottom Sites vs. Control Sites  
 (Continued on next page)

DATE		SITE	
Installation	Retrieval	Hard Bottom	Control
10/26/92	1/2/93	3.8	1.8
1/2/93	2/6/93	1.3	1.0
3/6/93	4/7/93	485.2	148.4
4/7/93	5/1/93	8.5	6.2
5/1/93	5/29/93	1.3	0.9
5/29/93	6/26/93	6.3	1.2

6/26/93	7/14/93	7.0	2.2
7/14/93	8/25/93	1.6	3.0
8/25/93	9/29/93	1.7	1.7
9/29/93	11/10/93	67.1	47.0
11/10/93	12/22/93	19.1	13.7
12/22/93	2/16/94	131.4	58.5
2/16/94	3/22/94	189.5	50.4
3/22/94	4/30/94	7.0	2.4
4/30/94	6/12/94	1.0	1.5
6/12/94	7/18/94	3.5	2.8
7/18/94	8/25/94	38.5	4.7
<b>OVERALL AVERAGES</b>		47.5	20.4

Table 3 provides the average fines sedimentation rates for the four hard bottom sites and the three control sites.

**Table 3: Average Fines Sedimentation Rates (mg/cm<sup>2</sup>/day)  
Hard Bottom Sites vs. Control Sites**

DATE		SITE	
Installation	Retrieval	Hard Bottom	Control
10/26/92	1/2/93	16.1	18.3
1/2/93	2/6/93	23.2	35.1
3/6/93	4/7/93	66.6	58.9
4/7/93	5/1/93	27.3	27.3
5/1/93	5/29/93	18.6	10.7
5/29/93	6/26/93	8.5	5.7
6/26/93	7/14/93	12.1	9.4
7/14/93	8/25/93	9.6	7.9
8/25/93	9/29/93	8.3	7.6
9/29/93	11/10/93	30.8	22.8
11/10/93	12/22/93	34.1	31.7
12/22/93	2/16/94	41.2	31.8
2/16/94	3/22/94	43.5	30.5
3/22/94	4/30/94	16.8	16.4
4/30/94	6/12/94	6.8	12.5
6/12/94	7/18/94	7.9	11.4
7/18/94	8/25/94	14.8	11.7
<b>OVERALL AVERAGES</b>		21.4	20.6

The sand sedimentation rate data is punctuated by high sedimentation rates for the deployment retrieval dates of 4/7/93, 11/10/93, 12/22/93, 2/16/94, 3/22/94 and 8/25/94. These coincide with periods of high waves, as is discussed further in the wave data analysis. There is a pronounced difference in sand sedimentation between the hard bottom and the control sites. It seems evident that the sedimentation rate is much higher for the sites at Longboat Key. This result is partially explained by the spatial variations in wave climate, which is presented later.

In contrast, the difference in fines sedimentation rates between hard bottom and control sites is small. These data reflect high values for the deployments retrieval dates of 4/7/93, 11/10/93, 12/22/93, 2/16/94, and 3/22/94. However, the increase in fines sedimentation rates during these times was not as dramatic as for sand sedimentation. The sedimentation rates for the fine material is essentially similar at all study locations, particularly relative to the enormous variations measured for the sand sedimentation rates. The overall mean and standard deviation of the fines sedimentation rate are 21.1 and 15.9 mg/cm<sup>2</sup>/day, respectively. The means of each site are well within one standard deviation of the overall mean.

The sedimentation rates can be compared before, during, and after nourishment. Because the nourishment project occurred over a period of approximately 6 months, the beach upland of each hard bottom site was nourished at different times as the project progressed along the coast. Rather than subjectively determining "before, during, and after" dates for each site, we choose rather to apply the same dates to all sites, as described in the introduction to this report. This allows for the grouping of hard bottom sites and control sites, as will be statistically justified in the following section on statistical analysis. Table 4 gives the average sand and fines sedimentation rates for hard bottom (HB) and control sites (Con) before, during and after nourishment. These values are given in mg/cm<sup>2</sup>/day. The average value of the ratio HB/Con is also given. The hard bottom sites have sand sedimentation rates which are approximately 2.5 times the control sites, but the fines sedimentation differ only slightly at the hard bottom and control sites.

	Sand Sedimentation Rates			Fines Sedimentation Rates		
	HB	Control	HB/Con	HB	Control	HB/Con
Before	2.5	1.8	1.7	19.6	18.3	0.8
During	85.0	27.0	2.5	23.8	20.0	1.3
After	51.0	20.3	2.5	22.7	19.6	1.1

**Table 4:** Average sedimentation rates before nourishment (1/2/93 and 2/6/93 retrieval dates), during nourishment (4/7/93 to 8/25/93 retrieval dates) and after 9/29/93 to 8/25/94 retrieval dates). Values are given in mg/cm<sup>2</sup>/day.

In summary, the study period was characterized by moderate sedimentation through the first nine months with the notable exception of the hundred year storm in March, 1993. In contrast, sedimentation in the Fall/Winter of 1993/1994 and again in Summer of 1994 were marked by significant activity, especially at the hard bottom sites. There is a notably greater sand sedimentation rate for the hard bottom sites. Finally, the data shows that fines sedimentation rates are less variable than sand sedimentation rates.

A statistical analysis of these data indicate that there were no significant differences within the hard bottom sites and also no significant differences within the control sites. The sites were therefore combined into two categories: hard bottom and control. These data were then paired for comparison during the nourishment project and following the nourishment project. The comparison was made using the Binomial Sign test. The Sign test provides the probability that the number of positive differences is greater (or less) than random chance (50 % of the values). For the sand sedimentation rates measured during the nourishment project, the results of the Sign test indicate  $P=0.094$ . For the sand sedimentation rates measured after the nourishment, the results of the Sign test indicate  $P=0.087$ . There is less than a 10% probability that the differences between the hard bottom and control sites in sand sedimentation rate both during and following nourishment occurred by chance.

### Manual Turbidity Monitoring

Manual measurements of turbidity were obtained through the use of SCUBA divers during each field trip. Divers obtained a water sample near the surface, mid-depth, and near the bottom of the water column. The surface and bottom samples were generally obtained approximately two feet from the surface or bottom. The water samples were then sub-sampled on board the boat and inserted into an H-F Scientific Model DRT-15C portable turbidimeter for reading.

Table 5 shows the average manual turbidity readings for hard bottom and control sites and presents the ratio of hard bottom to control turbidities (HB/Con) for the nourishment and post nourishment periods.

**Table 5: Manual Turbidity Readings (NTU), During and After Nourishment**

	level	Hard Bottom	Control	HB/Con
During Nourishment	surf.	4.6	2.9	1.6
	mid	5.8	4.0	1.5
	bot.	7.5	5.5	1.4
After Nourishment	surf.	2.8	4.4	.64
	mid	3.2	5.5	.58
	bot.	4.4	9.2	.48

On the whole, the manual turbidity readings are relatively low compared to the 29 NTU standard. It must be noted here that the turbidity values represent discrete readings and that this sampling cannot be considered random. The manual turbidity samples were taken only when weather permitted. Obviously weather is a very significant forcing mechanism for turbidity. Thus, in all likelihood, these values underestimate actual time-average turbidity levels.

Table 5 clearly illustrates three facts. First, the turbidity at the hard bottom sites was larger than at the control sites during nourishment. Secondly, the turbidity at the hard bottom sites decreased significantly after nourishment. Finally, the turbidity of the hard bottom sites is significantly less than the control sites after the nourishment. These average values are based on seventeen sampling dates.

### Wave Sensors

Two instrument package designs were deployed for the turbidity and wave climate monitoring. These packages are referred to as system I and system II. Both systems were self contained, with on-board power and data storage capabilities. The waves were measured using Transmetric pressure sensors.

System I consisted of two model 1 Optical Backscatterance Sensor (OBS), a pressure transducer, and a Marsh McBirney Electromagnetic current meter. This package was used almost exclusively at the Longboat Key #2 hard bottom site. The system I samples at one hertz for 1024 seconds every two hours. The 12V power source required renewal approximately every month. A spare system I was employed until it was damaged in the field during the fifth deployment. The system II package consisted of one model 3 OBS and a pressure transducer. These packages were deployed at the Long Key, Siesta Key, and the Longboat Key #34 hard bottom sites. System II samples turbidity and waves at one hertz for 512 seconds every two hours. The 1Mb RAM is filled approximately every month but the 12 V power source lasted approximately three months. Therefore, the initial plan was to download the data in the field every deployment and perform complete maintenance, which included battery change, every three months. A spare system II was also employed as a backup. The field configuration of the system II package is presented in Figure 4.

All of the instruments required calibration for interpretation. The calibrations of the pressure sensor and current meter are straight forward, and were performed in some cases by the instrument manufacturer. In some cases we also calibrated these instruments at the Coastal Engineering Laboratory at The University of Florida. Turbidity is measured in Nephelometric Turbidity Units (NTU's). Calibration is accomplished using formazin in the laboratory. For the manual turbidity measurements, a HF Scientific model DRT 15C portable turbidimeter is utilized. The OBS calibration is somewhat more problematic. We calibrated the sensors in

the laboratory using a formazin solution. Formazin is the turbidity standard accepted by National Institute of Standards Technology. Each time the OBS are removed from the water for cleaning (approximately once per month), they are recalibrated. However, upon deployment in the field, these calibrations were not always accurate.

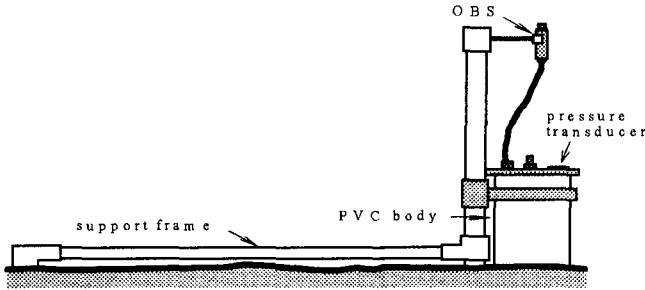


**Figure 4:** System II Package Field Configuration

The instrument deployment began August 25, 1993 and the preliminary plan was to schedule deployments every month thereafter. However, due to severe biofouling and unforeseen package damage, the deployments were interspersed as conditions demanded. A time line of the wave data coverage for the monitoring project is given in Figure 5. Lapses in coverage were largely due to equipment damage and maintenance.

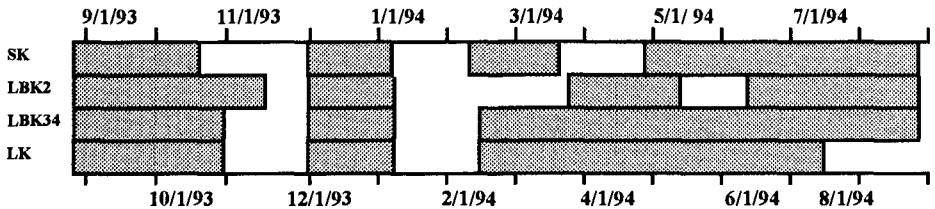


**Figure 5:** Time Line of Wave Data Coverage

Figure 5 points to two main lapses in wave data coverage. These interruptions occurred from 11/1/93 to 12/1/93 and from 1/11/94 to 2/16/94. The first incident was due to the unexpected severity of the biofouling of the OBS's. The packages were taken back to the coastal lab for maintenance, data offload and recalibration. System I packages suffered extensive damage in the field during the fifth and eighth deployment due to crab traps. The crab traps and buoy lines tended to collect around the instrument package, often becoming entangled in it, and extensive damage was incurred as the crab fishermen retrieved the traps. One system

I package was damaged beyond repair. Each of the sensors on the package was sheared off. In the case of the second system I package, the repairs required almost two months of work. The spare system II was utilized in its place at the Longboat Key #2 site. Even after the repairs to the system I package, the current meter was no longer functioning and much of the OBS signal was unsatisfactory.

As can be seen, maintaining the instrument packages in the field proved to be very demanding. This can be attributed to severe biofouling and field damage to the packages. The biofouling on the face of the OBS was more troublesome than anticipated. It served to block out the OBS signal after a few days in some cases.

The performance of the OBS's was dismal and our painstaking efforts to correct the problem were generally ineffective. Biofouling was anticipated before the initial package deployment and the OBS face was painted with an anti-biofoulant. The OBS were subsequently painted whenever the packages were removed from the field. It was evident that the severity of the fouling was grossly underestimated. As a result, we attached commercially available caustic hoods to the OBS. The manufacturer of these hoods claimed that they would keep OBS's clean of growth and fouling for 2 to 3 months at the project site. Although the hoods did somewhat decrease the amount of fouling, the effect of the hoods were not significant enough to improve the OBS signal. Our next plan of attack was to simply remove the packages more frequently to repaint the OBS face. The system II packages were eventually removed monthly for this purpose. Unfortunately, this provided disappointing results as well. Eventually, we tried underwater field cleaning of the OBS face biweekly. We found that we were not able to obtain valid turbidity data for more than a maximum of seven days after the OBS faces were painted with anti-biofoulant and for more than three days after cleaning with a nonscouring pad in the field. Although this seemed unproductive, we had no recourse. This presented an opportunity to increase the frequency of manual turbidity readings, which were gaining in importance due to the ineffectiveness of the OBS's. By the eighth deployment, we designed and implemented an 'OBS wipe' instrument which was mounted to the OBS to mechanically clean the face of the OBS every hour. Once again, this proved ineffective. Our final decision was to discard the OBS data.

The average values of the depth ( $D_{av}$ ), significant wave height ( $H_{m0}$ ) and peak period ( $T_p$ ), as well as the number of days of wave data coverage within the period are summarized in Table 6. For purposes of comparison, the averages in Table 6 were calculated to correspond to the sedimentation data periods. These values represent the averages of the available wave data within these periods. The average values in the last row and column are weighted to reflect the varying days of coverage within periods and monitoring sites.



**Table 6:** Deployment Averaged Wave Data

Date			SITE			
Start	End		LK	LBK34	LBK2	SK
8/25/93	9/29/93	Dav, m	4.27	5.55	5.60	4.59
		Hmo, m	0.16	0.26	0.26	0.21
		Tp, s	5.65	4.97	5.02	5.27
		Days	35	34	36	36
9/29/93	11/10/93	Dav, m	4.53	5.38	5.52	4.65
		Hmo, m	0.21	0.30	0.30	0.19
		Tp, s	5.02	5.47	5.59	5.44
		Days	32	32	40	23
11/10/93	12/22/93	Dav, m	4.51	5.29	5.89	5.00
		Hmo, m	0.26	0.35	0.32	0.29
		Tp, s	5.13	5.92	6.02	5.83
		Days	22	21	30	21
12/22/93	2/16/94	Dav, m	4.38	5.02	5.84	4.87
		Hmo, m	0.32	0.40	0.49	0.34
		Tp, s	6.47	6.55	6.33	6.74
		Days	21	20	20	24
2/16/94	3/22/94	Dav, m	4.67	5.64		4.47
		Hmo, m	0.26	0.32		0.26
		Tp, s	5.46	5.73		6.10
		Days	36	33		34
3/22/94	4/30/94	Dav, m		5.16	5.75	4.59
		Hmo, m		0.24	0.25	0.21
		Tp, s		5.20	5.02	5.11
		Days		38	38	34
4/30/94	6/12/94	Dav, m	4.41	5.17	5.35	4.67
		Hmo, m	0.15	0.18	0.15	0.16
		Tp, s	3.84	4.50	3.03	4.32
		Days	42	41	13	42
6/12/94	7/18/94	Dav, m	4.85	5.23	5.44	4.80
		Hmo, m	0.21	0.27	0.28	0.25
		Tp, s	4.70	4.34	4.18	4.03
		Days	31	34	34	34
7/18/94	8/25/94	Dav, m		5.36	5.54	4.28
		Hmo, m		0.30	0.33	0.23
		Tp, s		5.07	5.13	5.51
		Days		38	39	40
Average		Dav, m	4.52	5.32	5.62	4.63
	Hmo, m	.21	.28	.30	.23	
	Tp, s	5.07	5.19	5.14	5.27	
	Days	33	34	34	34	

### Discussion

The relatively higher sand sedimentation rates measured at the hard bottom sites relative to the control sites can be explained by examining the wave conditions at the sites. Table 7 compares the average wave characteristics between the hard bottom and control sites. It is evident from this table that the hard bottom sites have experienced larger waves than the control sites.

**Table 7: Average Wave Data Characteristics**

Characteristic	Hard Bottom	Control
Average Depth, $D_{av}$	5.47 m	4.58 m
Significant Wave Height, $H_{mo}$	.29 m	.22 m
Peak Period, $T_p$	5.17 s	5.17 s

In addition to time average data, an examination of discrete storm events provides valuable insight. An examination of the five largest, measured, storm events is presented in Table 8. The maximum significant wave height ( $H_{mo(max)}$ ) and maximum peak period ( $T_{p(max)}$ ) for the storm events are given for each of the sites. The largest waves of our monitoring were recorded at LBK2 and LBK34 from 1/3/94 and to 1/5/94. The most recent storm event beginning on 8/13 and subsiding on 8/18/94 was tropical storm Beryl.

**Table 8: Maximum Height and Period for Five Storm Events**

Event Date		SK	LBK2	LBK34	LK
10/29/93 to	$H_{mo(max)}$		1.78 m	1.99 m	1.42 m
11/1/93	$T_{p(max)}$		10.7 s	10.7 s	10.7 s
12/14/93 to	$H_{mo(max)}$	1.28 m	1.40 m	1.43 m	1.11 m
12/17/93	$T_{p(max)}$	9.1 s	9.8 s	9.1 s	9.1 s
1/03/94 to	$H_{mo(max)}$	1.84 m	2.23 m	2.15 m	1.62 m
1/05/94	$T_{p(max)}$	10.7 s	11.6 s	12.8 s	10.7 s
3/1/94 to	$H_{mo(max)}$	1.43 m		1.63 m	1.61 m
3/5/94	$T_{p(max)}$	10.7 s		10.7 s	10.7 s
8/13/94 to	$H_{mo(max)}$	1.26 m	1.51 m	1.72 m	
8/18/94	$T_{p(max)}$	8.0 s	7.5 s	8.0 s	

Table 8 illustrates two important facts. First, this data shows that in every case, the hard bottom sites recorded larger maximum significant wave heights for these storm events. Secondly, these five storm events occurred during the periods of highest sand sedimentation rates.

In order to demonstrate the relationship between significant wave height and sand sedimentation rate, Figure 6 displays the deployment averaged measurements for both the hard bottom sites and the control sites. Plotted on a log-log scale, Figure 6 shows that the sand sedimentation rate is an increasing function of the significant wave height. Furthermore, the hard bottom sites and the control sites plot with approximately the same trend. This supports the conclusion that the difference in sand sedimentation rate is largely due to the differences in significant wave height.

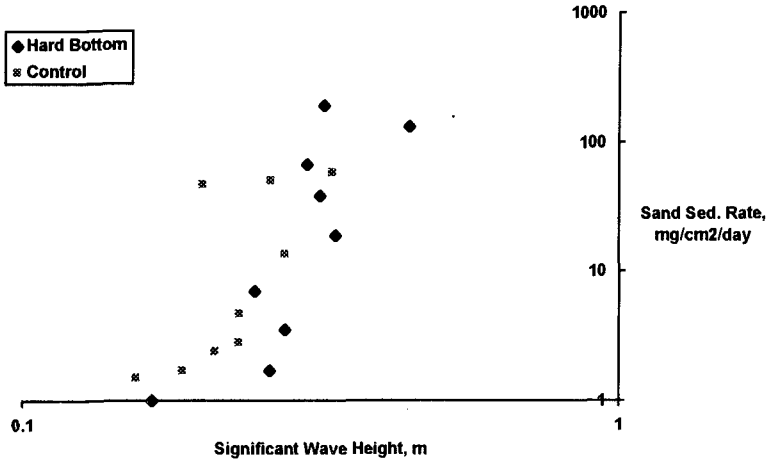


Figure 6: Log-Log plot of sand sedimentation rate versus significant wave height.

### Conclusions

The analysis of the manual turbidity, sedimentation, and wave data revealed several significant facts concerning the differences between the hard bottom sites and control sites and the interactive dynamics between these three phenomena.

The manual turbidity measurements indicate high variability in space and time, and were probably under-sampled and biased toward low wave conditions. During the monitoring period, turbidities exceeding 29 NTU were measured only at sporadic locations on 11/10/93, 12/22/93 and 2/16/94. Based upon three measurement dates, the manual turbidity measurements during the nourishment indicate that the hard bottom sites experienced approximately 50% higher turbidity than the control sites. However, based on approximately 15 measurement dates, following nourishment the hard bottom sites experienced approximately 50% less

turbidity than the control sites. Statistical analysis confirmed that the lower turbidity at the hard bottom sites relative to the control sites following nourishment is statistically significant at the 0.05 probability level.

The sedimentation measurements indicate that the sand sedimentation rates are highly variable, particularly with time. In contrast, the fines sedimentation rates are relatively less variable with respect to both location and time. It is evident from the examination of the sedimentation data that the sand sedimentation rates at the hard bottom sites were approximately 2.5 times higher than those of the control sites. The statistical analysis indicated that there is less than a 10% probability that this difference is due to chance. In contrast, there were no significant differences in fines sedimentation rates between the hard bottom and control sites.

The variations in sand sedimentation rates are believed to be directly related to the hydrodynamic forces resulting primarily from waves. During periods that included large waves, correspondingly large sand sedimentation rates were measured. Wave forcing also partially explains the trend for higher sand sedimentation rates at the hard bottom sites relative to the control sites. The wave height was approximately 33 % greater at the hard bottom sites. This higher wave height results in the wave energy being approximately 75% higher at the hard bottom sites relative to the control sites. The increased wave energy at the hard bottom site is probably the reason for the relatively higher sand sedimentation rates. Because a high sedimentation rate is an indication of high concentration of suspended sediment, these findings indicate that sand deposited at the hard bottom sites is most likely resuspended into the water column during periods of large waves.

#### Acknowledgments

The assistance of Darwin Stubbs with both the field work and the data analysis is greatly appreciated.

## CHAPTER 218

### SOIL MECHANICS OF SHIP BEACHING

N.-E. Ottesen Hansen<sup>1</sup>, B.C. Simonsen<sup>2</sup>, and M.J. Sterndorff<sup>3</sup>

#### Abstract

When a ship hits a soil or gravel slope it will create a large transient pore pressure in the soil which will force the ship bow upwards. At the same time the pore water will cause ruptures in the soil which influences the lifting forces on the ship bow. Methods of analysis are presented for the pore water build up, the soils rupture and the resulting reactions on the ship bow for frictional soils. Soil slopes with low permeability (sand in connection with a scour protection) generates large reactions on an impacting ship with the result that the ship will ride up on the surface of the slope and be brought to a stop by friction . Soil slopes with high permeabilities as pebbles or quarry run generate smaller reactions, and the ship will plow itself into the slope. It will then be stopped by a combination of friction and passive soils pressure. The analytical results are compared with test results made in a hydraulic laboratory and by full scale testing in nature of a ship sailed into a beach. Good agreement was found between the theoretical findings and the test results.

#### Introduction

In many places structures are placed adjacent to heavily trafficked navigation channels. The ship traffic is supposed to stay in the main navigation channel. Some ships, however, do loose their way or their steering and may ram the structure. One method to protect against the impact is to surround the structures with works built in fill materials. An example of this is the protective works for the side span

---

<sup>1</sup> Ph.D. Director, LICEngineering A/S, Ehlersvej 24, DK-2900 Hellerup, Denmark.

<sup>2</sup> Ph.D. Student, Technical University of Denmark, Department of Ocean Engineering, Bygn. 101 E, DK-2800 Lyngby, Denmark.

<sup>3</sup> Ph.D. Chief Engineer, Danish Hydraulic Institute, Agern Allé 5, DK-2970 Hørsholm. Denmark.

piers of the Great Belt suspension bridge in Denmark. They are designed to stop all ships with a displacement greater than 4000 tonnes before they reach the bridge foundations, figure 1. The impact of smaller ships can be sustained by the bridge piers themselves.

Such protective works will have the effect that they either force the ship to ride up the slope and absorb the energy of the ship by friction or they will absorb the ship impact inside the soil skeleton as passive soil pressure. An accurate calculation of the stopping length of the ship will therefore be important. Typical marine structures to protect are bridge foundations or immersed tunnel elements.

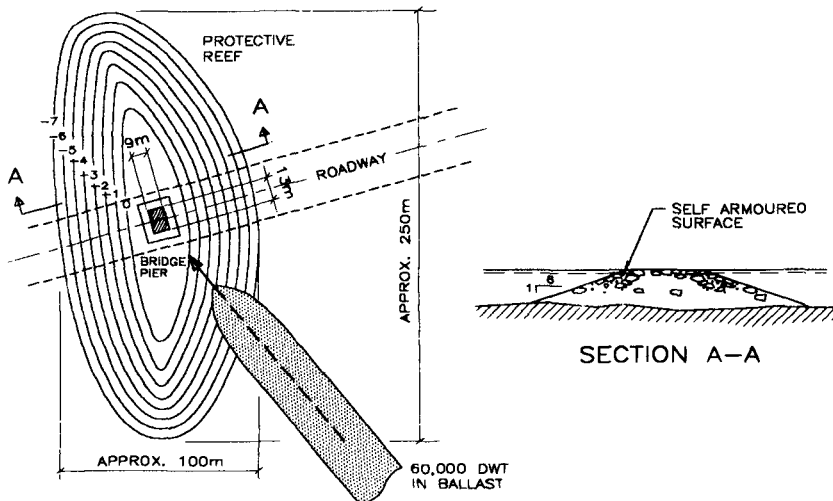


Figure 1. Protective work for one side span foundation of the Great Belt suspension bridge, Denmark.

### Mechanics of Ship Grounding

The stopping force acting on a beaching ship is the result of ruptures in the soil at the areas of contact between bow and soil. The mechanics of this rupture is complicated. This is illustrated by an example where a ship with cylinder bow with vertical sides is rammed horizontally into a submerged slope of sand of 1:6, Figure 2. The bow has a semi-circular shape with a radius of  $r = 378$  mm. The bottom is flat. The sand is very uniform in gradation with a mean diameter of 0.125 mm, permeability coefficient  $9 \cdot 10^{-5}$  m/s and frictional angle of  $39^\circ$ . The ship is rammed with constant velocity and it is locked in the horizontal position such that it cannot heave or pitch.

In figure 2 the horizontal forces and vertical forces for different impact velocities are presented as a function of horizontal position for a ship with cylindrical bow rammed into a slope of 1:6. The soil reaction is shown for tests in both dry sand and submerged slopes of different impact velocities.

The horizontal resisting force and the lifting force as the bow depends on the velocity. The force is 10-20 times larger than the resisting force for the identical tests performed out of water where the bow is rammed into the same slope of dry sand, figure 2.

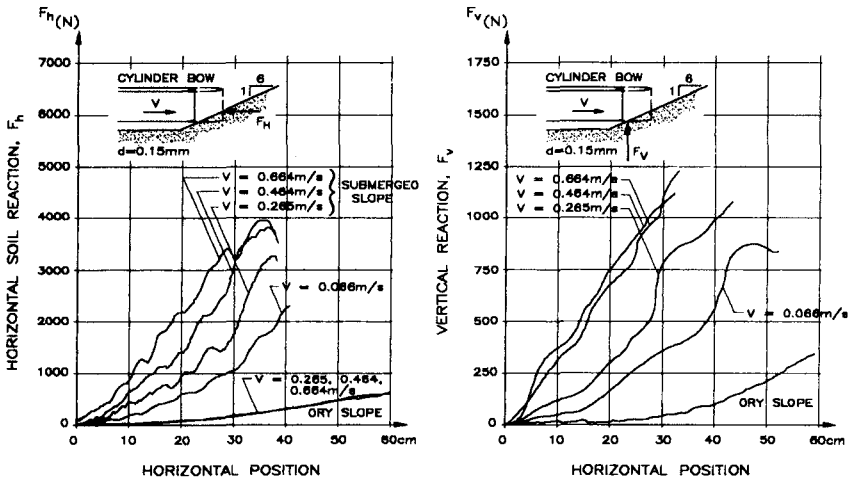


Figure 2. Force on ship bow.

Therefore the porewater flow generated by the bow during the impact must have great influence on the behaviour of the ship. The porewater flow creates strong effective stresses in the soil which act on the hull both as normal stresses and as tangential stresses. It is then the question of how these effective stresses are generated. There seem to be two possible mechanisms to choose:

1. At the rupture the sand will dilatate and thereby create a large suction in the pore water in the rupture zones. This suction will result in a just as large effective stresses in the grain skeleton.
2. At the impact the sand will be compressed and pore water will be squeezed out in the compression zone creating an additional pore water flow. This pore water flow will build up large effective stresses in areas of the grain skeleton.

In other areas liquified zones will be formed.

Which of the two mechanisms are correct can be decided by investigating the vertical lift on the ship bow. This lift must partly be caused by friction on the front and partly of the pore water pressure at the bottom of the model ship. From figure 2 it can be seen that there is a relatively large lift on the bow. Consequently there must be an excess pore pressure underneath the bow. This indicates that the impact follows the mechanism, 2, where the sand skeleton is compressed and the pore water squeezed out.

The pressure generated by the porewater has further been demonstrated by establishing a vertical downwards directed pore water flow through the sand (originally made to compact the laboratory sand), figure 3. This drainage will reduce the initial pore pressure with depth. Figure 3 shows the difference between the lift on the ship bow with and without the additional vertical pore water flow. The important finding is that even though the initial pressure underneath the bottom of the model ship is reduced, still a lift is generated. This proves that excess pore pressures are generated by the impact.

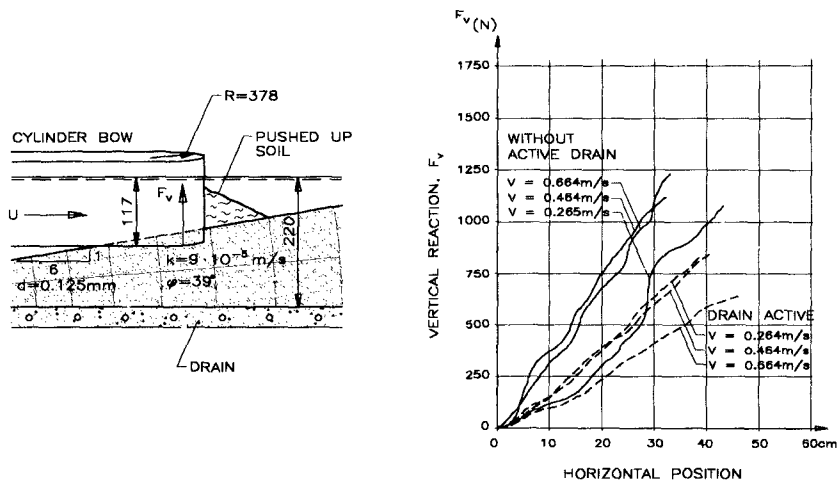


Figure 3. Variation in lifting force for various drainage conditions in the soil.

### Method of Analysis

The analysis of the soils forces acting on an impacting ship must be made with some simplifications in order to obtain a result.



Ships with bulb- and V bows have a narrow keel such that the foot print into the slope becomes oblong, figure 4. Hence the soils resistance can locally be calculated by two-dimensional methods.

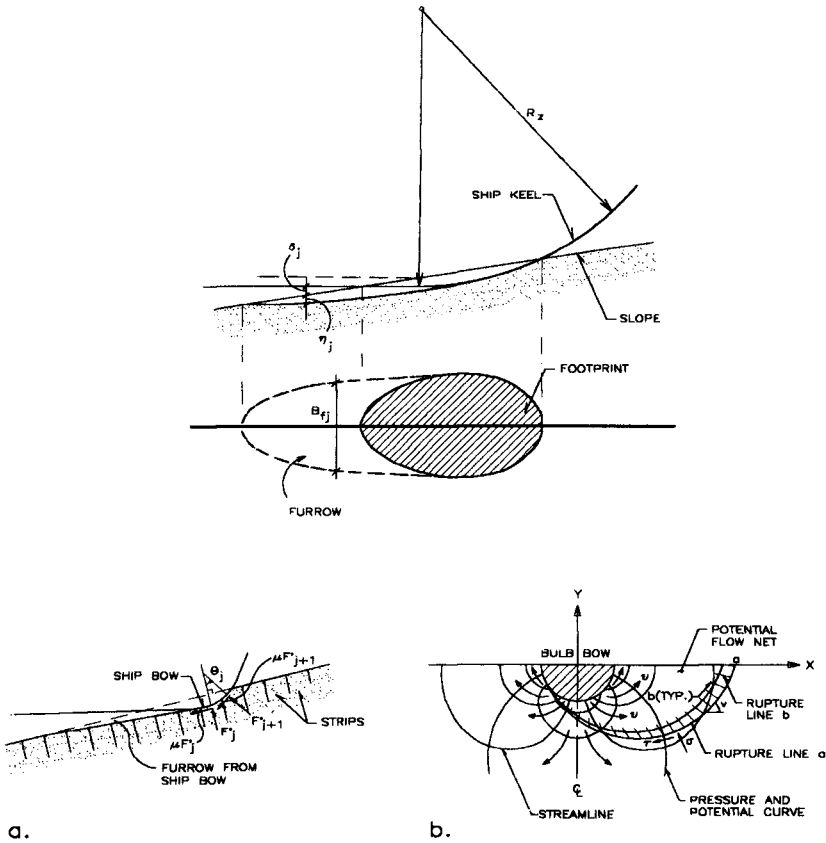


Figure 4. Principle of strip calculation model.

- a) The division of the slope into elements.
- b) Soils movement and porewater flow lateral to ship movement in a strip.

The slope is divided into a series of strips. Within these strips the soil deformation and porewater movement are calculated using a two-dimensional solution, figure 4. Using this reference frame the deformation of the slope can be described in detail and it is possible to determine which strips are in contact with the bow, furrow geometry etc.

The total soil reaction is found by summing up the soil reaction force from

each of the soil strips in contact with the bow. This provides a normal force perpendicular to the slope and a frictional force parallel with the slope. They can be used for the equations of motion of a beaching ship. The ratio between the frictional force and the normal force is defined as the effective frictional coefficient.

Thus the system is reduced to a two-dimensional system which is easier to analyse.

The cylinder bow mentioned as an example in the preceding paragraphs can be approximated with strips along the periphery of the bow in the vertical plane.

### Basic Assumptions

In order to explore the impact on the soil the basic one-dimensional case of the cylinder bow is considered

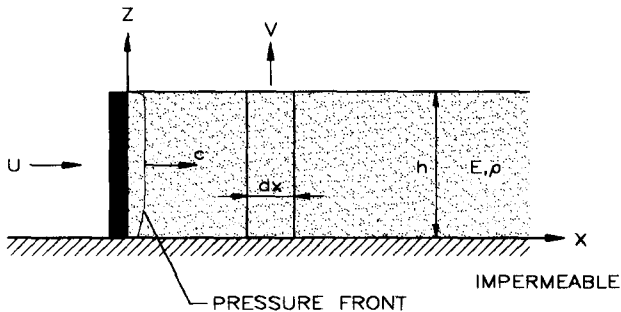


Figure 5. Basic case of impact of cylinder bow.

For an impulsively started motion at  $t = 0$  to  $U$ , a pressure wave with celerity,  $c$ , is sent out. Joukowski's law then gives for the horizontal force,  $F_H$

$$F_H \sim \rho c U h \quad , \quad c \approx \sqrt{\frac{E}{\rho}}$$

$\rho$  is the density of saturated soil and  $E$  the Young's modulus of dry sand. The ratio between effective stresses from pore water flow and inertia force are decided by the soil permeability,  $k$  and given by

$$\frac{\rho_w g h U}{\rho k c^2}$$

This means that the forces from the pore water for normal sand dominates over the inertial forces.

From the expression for  $F_H$  it can be seen that the stresses at the impact in this example will be very high ( $\sim 100 \text{ kN/m}^2 - 500 \text{ kN/m}^2$ ). This is extremely high. So high that a soil rupture must occur. The rupture force will depend on how large vertical stresses can be generated by friction against the ship hull.

Hence in the following the inertia forces can be neglected, and calculations can be treated as a quasi steady soil rupture problem even though it is an impact problem.

### Equilibrium Equations for an Element of saturated Soil in Rupture

In order to analyse the rupture problem, the approximation of using a series of circles as rupture lines is used. The rupture figure are then kinematically allowable and will produce stresses which are slightly higher then the correct stresses. The method is an adaption of the equilibrium method of Brinch Hansen, 1953.

The stress conditions for soil elements in a circular rupture line are shown in figure 6. There is a flow of pore flow through the element which generates tangential and radial pressure gradients

The shear stress,  $\tau_r$ , along the circular rupture line in frictional soil is given by the Kötter equation, Brinch Hansen, 1953:

$$\frac{\partial \tau_r}{\partial v} + 2 \tan \varphi \tau_r + \gamma' r \sin(v + \varphi) \sin(\varphi) - \sin^2(\varphi) r \frac{\partial p_p}{\partial r} + \sin(\varphi) \cos(\varphi) \frac{\partial p_p}{\partial v} = 0$$

$r, v$  are the polar coordinates and  $\gamma'$  is the submerged weight of the soil.  $\varphi$  is the frictional angle of sand.  $P_p$  is the pore water pressure.

The normal stress,  $\sigma_r$ , is found from the Coulomb relationship

$$\tau_{rv} = \tan \phi \sigma_r$$

With the known boundary conditions and pore water pressure field,  $p_p$ , this equation can be integrated to give the effective shear stress,  $\tau_{rv}$ , along the considered rupture line.

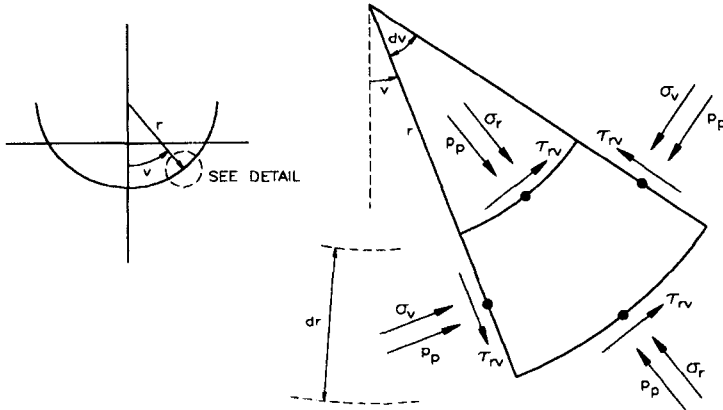


Figure 6. Effective stresses and pore water pressures on a soil element in a circular rupture line.

### Soil Reaction on a Strip of the Bow

To demonstrate how the soil reaction is calculated, one strip on the slope (see figure 4) is considered. Normal velocity and acceleration of the bow at the considered strip is  $u_b$  and  $\dot{u}_b$ , respectively, figure 7a.

The first simplification of the problem shown in figure 7a is achieved by assuming that the penetrating bow can be modelled by a plate of width  $B$  corresponding to the immediate width of the bow in the plane of the slope, figure 7a,b.

Initially the grain skeleton is compressed elastically and a pore water flow is generated. When the force reaches a certain level soil rupture will develop. During beaching of a ship the deformations of the soil are sufficiently large to develop complete rupture.

The geometry of the rupture body can be approximated by a circular arc with its center placed off the surface of the soil in  $(x,y) = (a,b)$ , figure 7. This is the most simple approximation. A better approximation would be to use a number of

consecutive circles. For an impact problem this additional accuracy is not warranted. The procedure is now to choose  $a, b$ , and the unknown force on the bow,  $F$ , such that the rupture body is in both horizontal, vertical and moment equilibrium.

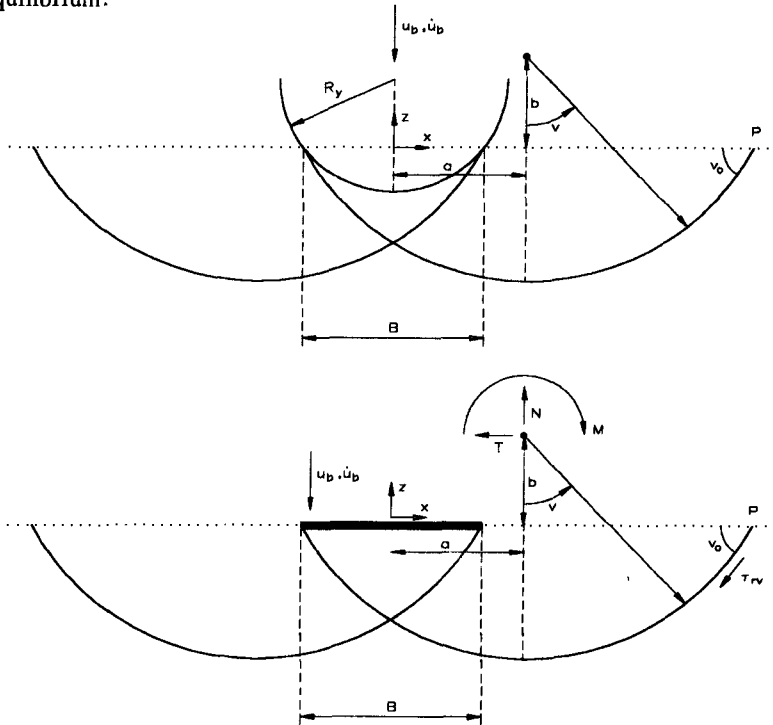


Figure 7. Assumed circular rupture below a bow penetrating saturated soil. Equivalence between bow and flat plate.

The total loads,  $T$ ,  $N$  and  $M$ , on a given rupture body are the resultants of the effective stresses,  $\tau_{rv}$ ,  $\sigma_r$  in the rupture line, the pore water pressure,  $p_p$ , along the edge of the rupture body, the submerged weight of the soil in the rupture body and the load from the bow,  $F$

The effective stresses,  $\tau_{rv}$ ,  $\sigma_v$  and  $\sigma_r$  in the rupture line can be calculated from the Kötter equation, if the pore water pressure,  $p_p$ , and the boundary conditions for  $\tau_{rv}$  are known.

In the general case the pore water pressure cannot be found without considering the kinematics of the grains. However, in this case of modest penetration of a bow it can be assumed that the displacements of the grains are small compared with that of the pore water. The pressure field,  $p_p$ , can then be

found by use of Darcy's law and the of continuity equation for water.

The solution can be written, Lamb, 1932

$$\frac{P_p(x,z)}{\gamma'' \frac{B}{z}} = z' \sqrt{z'^2 + \frac{1}{2}(1-x'^2-z'^2)} + \sqrt{z'^2 + \frac{1}{4}(1-x'^2-z'^2)^2}$$

$$\gamma'' = \frac{\rho g u_b}{k} + \frac{(1+e)}{e} \dot{u}_b$$

$$x' = \frac{x}{B/2} = \frac{a}{B/2} + \frac{r}{B/2} \sin \nu, \quad z' = \frac{z}{B/2} = \frac{b}{B/2} + \frac{r}{B/2} \cos \nu$$

in which  $\rho_w$  is the density of the pore water,  $g$  the gravity acceleration,  $e$  the void ratio, and  $k$  the permeability coefficient.

Inserting these equations into the Kötter equation the variation of  $\tau_{rv}$  along the rupture line is expressed in terms of the non-dimensional parameters.

$$\frac{\gamma'}{\gamma''}, \frac{r}{B/2}, \frac{a}{B/2}, \frac{b}{B/2}, \nu, \varphi$$

The boundary conditions for  $\tau_{rv}$  and the angle,  $\nu_0$ , of the rupture line at point P are, figure 7

$$\tau_{rv}(P) = 0$$

$$\nu_0 = \pi/2 - \varphi/2$$

Using the approximation of a circular rupture there will not be sufficient degrees of freedom to satisfy all boundary conditions. However, the second condition can be neglected without losing too much accuracy, Brinch Hansen, 1966.

If boundary condition for the shear stress is used in the solution of the Kötter equation negative effective stresses will occur in an area around P. They cannot exist. Therefore there is liquefaction in this area and no contribution to the resistance. Therefore the boundary condition is  $\tau_{rv} = 0$  from P to the point in the

rupture line where the shear stress can grow towards positive values, see for instance figure 9. This point is characterized by

$$\frac{\partial \tau_r}{\partial v} = 0$$

The effective stresses and the porewater pressure acting on a given rupture body at a given value of  $\gamma'/\gamma''$  can be calculated. The resulting values of  $\gamma'/\gamma''$ , a,b,F are the ones which result in equilibrium for both horizontal and vertical forces and for the moment. The results of the analysis are presented in figure 8 in which the force F on the plate is expressed as a function of  $\gamma'/\gamma''$  for soils with a frictional angle of  $\phi = 32^\circ$ .

Typical values for the parameters in  $\gamma'/\gamma''$  are  $\rho_w = 10^3 \text{ kg/m}^3$ ,  $\gamma' = 10^4 \text{ N/m}^3$ ,  $u_b = 1 \text{ m/s}$ ,  $k = 10^{-4} \text{ m/s}$ ,  $\dot{u}_b = 0 \text{ m/s}^2$  giving a typical value of  $\gamma'/\gamma''$

$$\gamma'/\gamma'' = \frac{k}{u_b} = 10^{-4}$$

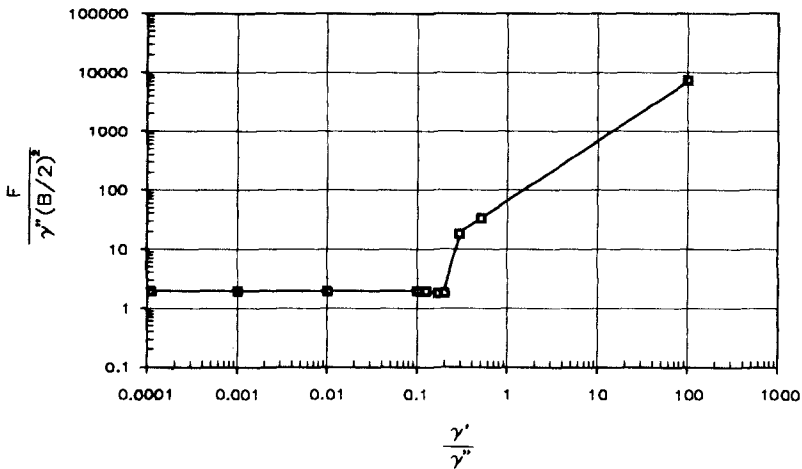


Figure 8. Non-dimensional rupture load for different values of  $\gamma'/\gamma''$  for  $\phi = 32^\circ$ .

For values of  $\gamma'/\gamma''$  below 0.1 the nondimensional total force, F, is seen to be approximately constant

$$\frac{F}{\gamma''(B/2)^2} \approx 2$$

Thus for  $\gamma'/\gamma'' < 0.1$  the model does not predict an upper level for the soil reaction - it is simply proportional to

$$\gamma'' \left( \frac{B}{2} \right)^2$$

The pore water pressure gives a vertical reaction which is included in the above total force. The pore water contribution,  $F_{pw}$ , is

$$\frac{F_{pw}}{\gamma'' (B/2)^2} = \frac{\pi}{2} \approx 1.57$$

Therefore in this example of  $\phi = 32^\circ$ , the effective stresses between plate and soil only account for approximately 20% of the total load for small values of  $\gamma'/\gamma''$ .

Figure 9 shows the rupture body and the effective stresses on the rupture body for  $\gamma'/\gamma'' < 0.01$ .

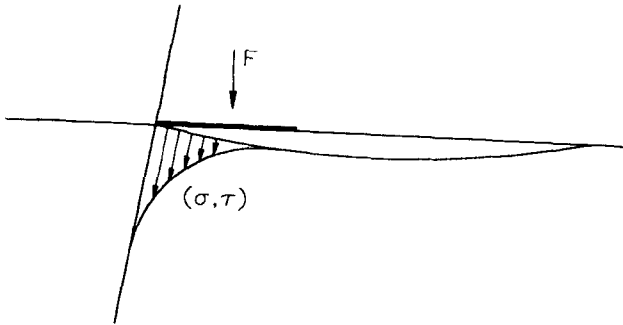


Figure 9. Rupture body and effective stresses in the rupture line for small values of  $\gamma'/\gamma''$  ( $\gamma'/\gamma'' < 0.01$ ).

For such small values of  $\gamma'/\gamma''$  the rupture load is carried by very large effective stresses directly below the bow, figure 9.

Knowing the effective soils normal force,  $F$ , on the bow at the considered strip, the tangential force,  $T$ , is simply taken as



$$T = \mu \cdot (F - F_{pw})$$

$\mu$  is usually set to 0.38.

Knowing the soil reaction in each strip in contact with the bow, the total soil reaction is found by summing up forces vectorially. Inserting this expression into the equation of motion for the ship, the beaching course can be calculated.

For V-bows similar expressions can be developed. Instead of using a flat plate-approximation, a wedge approximation is used.

### COMPARISON WITH TESTS

The results of the soil reactions have been compared with both laboratory tests and with full scale tests. Parameters such as apparent coefficient of friction and calculated and measured stopping lengths were compared.

The laboratory tests were performed with a ship model corresponding to a 20,000 DWT ship in scale 1:60. The ship was forced into a sand slope inclined 1:6. Both fine and coarse sand were considered. Various bow types were considered.

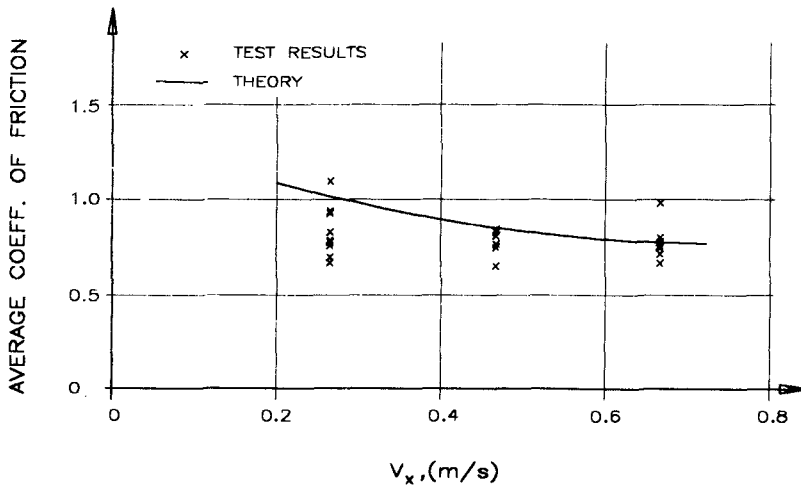


Figure 10. Comparison between theory and test results for effective coefficient of friction.

The measured effective coefficients of friction were compared with the corresponding calculated values, figure 10. This effective coefficient of friction is the ratio between the tangential and normal components of the soil and pore water reaction.

It is interesting to note that the effective coefficient of friction is in the order of 0.6 - 1.0 whereas the coefficient of friction between fill and ship plating is 0.38 (for the effective soils stresses).

The full scale tests were performed with a condemned 300 DWT fishing vessel which was rammed into an island built of the same materials as will be used for the protective works of the Great Belt suspension bridge. The vessel had a V-bow. The tests were made with velocities up to 10 knots. The stopping length and ship motions were recorded. Further, the foot prints in the slope were surveyed. The tests were repeated for various impact energies and various slopes.

Figure 11 shows a comparison between the calculated and the measured stopping length.

It is seen that the agreement is satisfactory. The measured furrow depths on the in-situ tests further show good agreement with the calculated furrow depth.

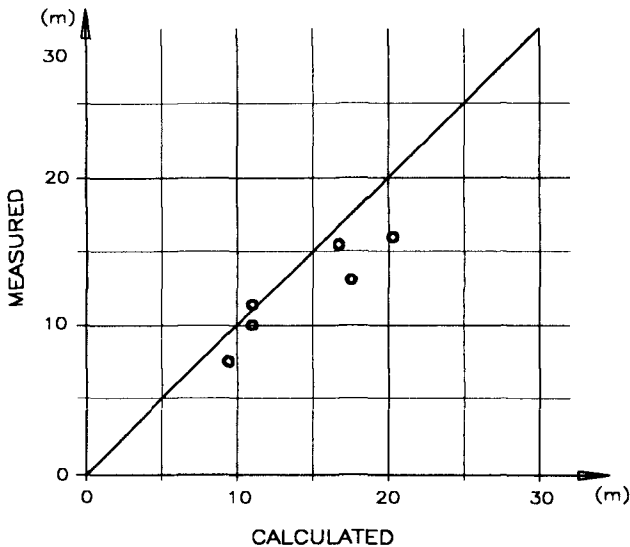


Figure 11. Measured stopping length depicted as function of calculated stopping length for a 300 DWT fishing vessel rammed into sand

slopes varying between 1:6 and 1:11.

### ACKNOWLEDGEMENTS

The authors wish to express their gratitude to the Great Belt Link Company for permission to publish the test results.

### REFERENCES

Brinck-Kjær, O., F.P. Brodersen and A. Hasle Nielsen, 1983. Modelling of Ship Collisions against Protected Structures. Proc. IABSE Colloquium on Ship Collision with Bridges and Offshore Structures. Copenhagen, 1983. IABSE Reports, Vol. 41, pp. 147-164.

Denver, H., Geotechnical Model Tests for the Design of Protective Island. Proc. IABSE Colloquium on Ship Collisions with Bridges and Offshore Structures. Copenhagen, 1983, IABSE Reports, Vol. 42. pp. 353-360.

Hansen, J. Brinch, 1953. Earth Pressure Calculation, The Danish Technical Press, Copenhagen 1953.

Hansen, J. Brinch, 1966. Comparisons of Methods for Stability Analysis, Bulletin No. 21, The Danish Geotechnical Institute, 1966.

Huther, M. and J.C. Letourneur, 1980. Estimation of the Contact Length after Grounding on a soft Shore. Bulletin Technique du Bureau Veritas, Feb. 1980.

Lamb, H. 1932, Hydrodynamics, Cambridge University Press, Cambridge. 6. Edition. 1932.

Ottesen Hansen, N.-E., B.C. Simonsen and M.J. Sterndorff, 1994. The Ship Impact Protection of the Great Belt Suspension Bridge. Proc. of the Third Symposium on Strait Crossings, Ålesund, Norway, 12-15 June 1994.

Ottesen Hansen, N.-E., J.R. Thomsen, Leif Sjøgren and M.J. Sterndorff, 1994. Artificial Islands as Protection against Ship Impact. Proceedings of ISOPE 94, Kobe, Japan.

Pedersen, P.T., S. Valsgård, D. Olsen and S. Spangenberg, 1993. Ship Impacts, Bow Collisions. Int. J. Impact Engng. Vol. 13. No. 2, pp. 163-187, 1993.

Simonsen, B.C., 1993. The Mechanics of Ship Grounding. (in Danish). Department of Ocean Engineering. Technical University of Denmark, 1993.

## CHAPTER 219

# THE DILUTION PROCESSES OF ALTERNATIVE HORIZONTAL BUOYANT JETS IN WAVE MOTIONS

Hwung, Hwung-Hweng<sup>1</sup>, Jih-Ming Chyan<sup>2</sup>, Chen-Yue Chang<sup>3</sup>, and Yih-Far Chen<sup>4</sup>

### Abstract

To investigate the angle effects on the initial mixing processes of the buoyant jet under wave action, the flow visualization and concentration measurements based on laser-induced fluorescence are employed in this study. The dilution improvement of the effluent in the co-wave and opposing-wave is mainly caused by the velocity gradient increasing due to the opposite wave flow and the wave tractive mechanisms resulted from the onshore and offshore wave motion. When orthogonally discharged into wave motions, the effluent is increasingly diluted by the formation of wake vortex and trajectory deflection curved by the wave flow. From the quantitative measurement of tracer concentration, the dimensionless dilution rate shows a function linearly increasing with the dimensionless wave parameter whose coefficient in the orthogonal discharge is above 33% higher than the other two cases. For practical design, it suggests that the orientation of the nozzle should be orthogonal to the propagation of principal wave motion.

### Introduction

Ocean outfall has been a feasible alternative of sewage disposal to diminish water pollution problems in most coastal cities. The primary parameter in practical design is the initial dilution rate which should meet the environmental legislation for public health and biological considerations. For the engineers, a simple but accurate method in initial dilution predictions of jet flow discharged into the ocean has been longing for decades. In the past, most relevant researches were theoretically and experimentally conducted in stagnant fluid. However, domestic sewage in the initial mixing processes is affected by oceanographic influences such as currents, density gradients, natural convective processes and wave action. Among these factors, the interaction of jet flow with surface waves is a very fascinating phenomenon in hydrodynamics and also important in the practical design of ocean outfalls.

The subjects concerning the kinematic and dynamic behaviours of jet flow under wave actions were not initiated until Shuto & Ti (1974). It shows that the dilution

---

<sup>1</sup> Professor, Dept. of Hydraulic and Ocean Engineering. — Director of Tainan Hydraulics Laboratory, National Cheng Kung University, Taiwan, R.O.C.

<sup>2</sup> Associate Researcher of Tainan Hydraulics Laboratory,

<sup>3</sup> Master, Dept. of Hydraulic and Ocean Engineering,

<sup>4</sup> Ph.D. Candidate, Dept. of Hydraulic & Ocean Engineering, Assistant Researcher of Tainan Hydraulics Laboratory.

rate of buoyant plumes in long waves is proportional to the ratio of the discharge velocity to a characteristic horizontal velocity of wave motion, and inversely proportional to the square of the ratio of the water depth to the nozzle diameter. Based on limited experimental results, Ger (1979) suggests that the axial dilution in shallow water waves linearly increase with the dimensionless horizontal distance when it is less than 12. Sharp & Power (1985) observed the dispersion patterns in short waves and long waves respectively, and qualitatively concluded that the short wave would change the jet flow when approaching the surface. The mixing pattern in long waves was obviously affected as soon as the effluent left the nozzle. The above investigations support insufficient information needed in the practical design since most ocean outfalls locate in the intermediate water depth. From the experimental and computational results of Chin (1987) and Chin (1988), the ratio of the initial dilution rate in intermediate water waves and in still water is shown to be linearly increasing with the ratio of  $L_q/Z_m$ .  $L_q$  is the spatial scale where the nozzle geometry influences the jet behaviour and  $Z_m$  is the length scale required for the wave-induced momentum to be on the same order of the jet momentum. Because of experimental wave conditions being similar to the field situations, the prediction equation proposed is more practicable for the design engineers.

Under the consideration of practicality, however, the interaction mechanisms between the jet flow and surface waves has not been thoroughly understood in the past. Hwung & Chyan (1990) and Chyan & Hwung (1993) investigate a pure momentum jet vertically discharged from the bottom of wave flume and identify the interaction mechanisms, *i.e.*, *jet deflection, wake vortex structure and wave tractive mechanism*, which are responsible for the increase of initial dilution. It also concluded that the jet has a higher dilution ratio when orthogonal to the propagation direction of surface waves. The interaction angle between jets and waves should be an important factor influencing the interaction mechanisms that occur and the sewage dispersion that improves. The purpose of this paper is to investigate discharging angle effects on the mechanisms and the initial dilution of horizontal buoyant jets interacting with surface waves. Avoiding the interference from the direct sampling instruments, the qualitative and quantitative experiments are conducted by an optical method based on laser-induced fluorescence.

### Theoretic Considerations

The dilution rate of jet effluents in wave motion is function of the control parameters of the buoyant jets and surface wave, respectively, which includes the factors of the kinematic and dynamic behaviours of buoyant jets such as momentum flux,  $M = QV_o$ ; buoyancy flux,  $B = Qg_o$  (effective gravity,  $g_o = \frac{\Delta\rho_o}{\rho_o}g$ ); volume flux,  $Q = \pi/4D^2V_o$ ; and discharging depth,  $H$ . In the mentioned parameters,  $\Delta\rho_o$  denotes the initial density differences between the effluent and the ambient and  $\rho_o$  represents the initial density

of the effluent. The parameter groups describing the motion of surface waves are water depth,  $h$ ; wave amplitude,  $a$ ; wave period,  $T$ ; and gravity,  $g$ . There are two more variables describing the relative spatial relationship between the buoyant jet and the surface wave, which are the discharging angle relative to the horizontal plane,  $\theta_1$ ; and the discharging angle relative to the the direction of wave propagation,  $\theta_2$ . From these control parameters, the characteristics of dilution rate is, then, described as

$$S = f(M, B, Q, H, h, a, T, g, \theta_1, \theta_2) \quad (1)$$

Chin (1987) suggests that the dominant mechanisms influencing the dilution of the effluent may be more easily characterized by formulating the dimensional variables in terms of length scales. As proposed by Fischer *et. al.* (1979), the definitions of appropriate length scales are

$$L_q = \frac{Q}{M^{1/2}} = (A)^{1/2} \quad (2)$$

$$L_m = \frac{M^{3/4}}{B^{1/2}} \quad (3)$$

$$Z_m = \frac{M^{1/2}}{U_{max}} \quad (4)$$

where  $L_m$  is the length scale beyond which the buoyancy dominates the plume flow;  $A$  denotes the area of the nozzle cross section; and  $U_{max}$  is the amplitude of the horizontal wave particle velocity. From the small amplitude wave theory,  $U_{max}$  is defined by

$$U_{max} = -\frac{agk}{\sigma \cosh kh} \quad (5)$$

$\sigma = \frac{2\pi}{T}$  and  $k = \frac{2\pi}{L}$  are the angular frequency and the wave number, respectively. From the Buckingham  $\pi$  theorem and Eq.(2)~Eq.(4), non-dimensionalizing Eq. (1) with the dilution rate of buoyant jets in still water,  $S_o$ , yields

$$\frac{S}{S_o} = f\left(\frac{H}{L_m}, \frac{L_m}{L_q}, \frac{Z_m}{L}, \frac{h}{L}, \theta_1, \theta_2\right) \quad (6)$$

which contains the non-dimensional variable groups characterizing the dilution enhancement of the effluent under wave action. In most practical conditions,  $H \gg L_m \gg L_q$ , which indicates that the effluent will be plume-like very quickly after leaving the nozzle. According to the observations of Sharp & Power (1985) and Chyan & Hwung (1993), no strong interaction between the jet flow and wave motion occurs when the axial jet momentum being weak. In fact,  $H/L_m$  and  $L_m/L_q$  are important dimensionless

parameters influencing  $S_o$ , however, they become minor in the dilution improvement effect of wave motion on buoyant jets when  $H \gg L_m \gg L_q$ . In the present study,  $\theta_1=0$  and Eq. (6) can be simplified as

$$\frac{S}{S_o} = f\left(\frac{Z_m}{L_q}, \frac{h}{L}, \theta_2\right) \quad (7)$$

Chin (1987) suggests that the relative depth,  $h/L$ , does not play a significant role in the dilution enhancement. From Eq. (5),  $Z_m/L_q$  is not independent of  $h/L$ , then, the effect of the latter in the dilution enhancement is implicitly involved in the former. From the experiments conducted by Chin (1987), the relation of Eq. (7) is demonstrated to be a linear function

$$\frac{S}{S_o} = 1 + C_s \frac{L_q}{Z_m} \quad (8)$$

where  $C_s$  is a coefficient depending on the interaction angle between the buoyant jet and surface wave. From the quantitative measurement,  $C_s$  can be determined to evaluate the characteristics of the angle effect.

### Experimental Setup

The nature of surface waves is an unsteady kinematical phenomenon. Optical method based on laser-induced fluorescence (LIF) is employed to carry out the flow visualization and the concentration measurements. The technique of LIF avoids distorting the interaction flow of jets and surface waves, and is sensitive up to tracer concentration of 0.19 pb. The experiments are conducted in a wave tank of  $12m \times 0.5m \times 0.6m$ . A piston type wave maker is installed on one end of the wave flume and a wave absorber locates on the other side to diminish the wave energy. Supplied by a constant head assembly, the effluents mixed with tracer is discharged by a nozzle of diameter of 0.33 cm at middle part of wave flume. Three discharge angles of jet flow relative to the propagating wave direction, *i.e.*,  $0^\circ$  (co-wave),  $180^\circ$  (opposing wave),  $90^\circ$  (orthogonal discharge), are selected to investigate the angle effects on the initial dilution processes. In case of orthogonal discharge, the nozzle is located nearby the side wall and otherwise in the centerline of the flume.

### Flow Visualization—

Drexhage (1973) found that the dye, Rhodamin 6G ( $C_{28}H_{31}ClN_2O_3$ ), could emit yellow fluorescence (wavelength=570 nm) when stimulated by an Argon-ion laser (wavelength = 514.5 nm). If the effluent contains with fluorescent dye, the flow pattern and vortex structures of the jet flow under wave action could be visualized by a sheet of laser light. The installation of flow visualization is shown in Fig. 1 where the laser beam is

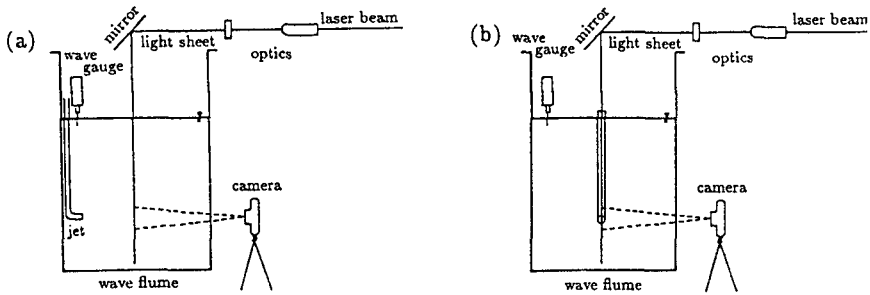


Fig. 1 Experimental layout of flow visualization for cases of (a) orthogonal discharge  
(b) co-wave or opposing-wave

transformed to a light sheet by an optical system. In order to understand the flow pattern related to the wave phase, signals from the wave gauge and the electrical shutter of the camera are simultaneously collected by the data acquisition system. As shown in Table 1, three cases (Case 1 ~ Case 3) with a lower Reynolds number ( $Re = 772$ ,  $F_d = 7.05$ ) is employed to clearly visualize the vortex structures. Especially, there is no buoyancy in Case 2 because of the necessity for the observation of wake vortex formed in the interaction process. Strong density difference will seriously distort the image. If the location of laser light sheet is in the zone of flow establishment, pure momentum jet can be employed to simulate the interaction of buoyant jet with surface waves since the momentum force rather than the buoyant force is the dominant force of the flow field.

#### Quantitative Measurements—

The principle of LIF is also applicable to the quantitative measurements. According to the Lambert–Buoguer–Beer law in Yoe & Koch (1957), the fluorescent intensity,  $F$ , can be described by the Taylor series,

$$F = K_1 I_o \left[ 2.3ecd - \frac{(-2.3ecd)^2}{2!} - \frac{(-2.3ecd)^3}{3!} - \dots - \frac{(-2.3ecd)^n}{n!} \right] \quad (9)$$

where  $K_1$ =proportional coefficient;  $I_o$ =intensity of incident laser beam;  $e$ =molar extinction coefficient;  $c$ =tracer concentration; and  $d$ =length of test section. If the tracer concentration is low enough to the have the higher order terms neglected in the equation, the intensity of fluorescence with fixed  $K_1$ ,  $I_o$ ,  $e$  and  $d$  will be a linear function of tracer concentration. A calibration process is able to quantify this characteristic function which, in the following quantitative measurements, transforms the voltage signals from photo-detector into concentration data. Fig. 2 shows an example of calibration



Table 1 Experimental conditions

Case	$\Delta\rho$ $\sigma$	$D$ <i>cm</i>	$Q$ <i>cm<sup>3</sup>/s</i>	$h$ <i>cm</i>	$H$ <i>cm</i>	$T$ <i>sec</i>	$2a$ <i>cm</i>	$h/L$	$L_q/Z_m$
1	30	0.33	1.9	40	36	1.20	5.80	0.207	0.1187
2	0	0.33	1.9	35	22	1.00	4.00	0.273	0.0527
3	30	0.33	1.9	35	22	1.00	4.00	0.273	0.0527
4	30	0.33	7.7	40	36	0.83	5.32	0.378	0.0527
5	30	0.33	7.7	40	36	0.93	4.83	0.309	0.0626
6	30	0.33	7.7	40	36	1.20	4.66	0.207	0.0892
7	40	0.33	7.1	40	36	0.89	6.51	0.334	0.0827
8	40	0.33	7.1	40	36	1.10	5.72	0.235	0.1060
9	40	0.33	7.1	40	36	1.35	5.70	0.175	0.1210
10	40	0.33	7.1	40	36	1.38	5.48	0.170	0.1182
11	40	0.33	7.1	40	36	1.24	6.85	0.197	0.1356
12	40	0.33	7.1	40	36	1.11	6.01	0.232	0.1049
13	40	0.33	7.1	40	36	1.00	7.45	0.273	0.1122
14	40	0.33	7.1	40	36	0.89	6.35	0.334	0.0753
15	40	0.33	7.1	40	36	0.84	5.87	0.370	0.0589
16	40	0.33	7.1	40	36	1.12	6.30	0.229	0.1099
17	40	0.33	7.1	40	36	0.83	7.25	0.378	0.0723
18	40	0.33	7.1	40	36	0.89	8.09	0.334	0.0957
19	40	0.33	7.1	40	36	1.00	7.04	0.278	0.1060
20	40	0.33	7.1	40	36	1.25	5.64	0.195	0.1120
21	40	0.33	7.1	40	36	1.32	5.95	0.181	0.1329
22	40	0.33	7.1	40	36	0.90	6.39	0.327	0.0834
23	40	0.33	7.1	40	36	1.09	4.99	0.238	0.0914
24	40	0.33	7.1	40	36	1.00	4.83	0.273	0.0779
25	40	0.33	7.1	40	36	0.92	4.16	0.315	0.0575
26	40	0.33	7.1	40	36	0.92	4.75	0.315	0.0656
27	40	0.33	7.1	40	36	1.00	7.57	0.273	0.1220
28	40	0.33	7.1	40	36	1.09	5.55	0.240	0.1014

curves. Three cases, such as pure water ( $\rho = 998\text{kg/m}^3$ ,  $20^\circ\text{C}$ ); water-alcohol mixture (1:5.33); and pure alcohol (95%,  $\rho = 808\text{kg/m}^3$ ,  $20^\circ\text{C}$ ), are employed to investigate the effect of compositions. It shows that the slopes are the same except the intercept caused by different system error. Before conducting the concentration measurement in a new test point, the background level of tracer concentration has to be determined to rid data of system error. The correlation coefficient of each calibration curve is larger than 0.999 and the standard deviation is lower than 0.1 ppb.

Most ocean outfalls usually locate in the intermediate water depth where the depth-to-wavelength ratio,  $h/L$ , ranges from 0.05 to 0.5. On the consideration of prac-

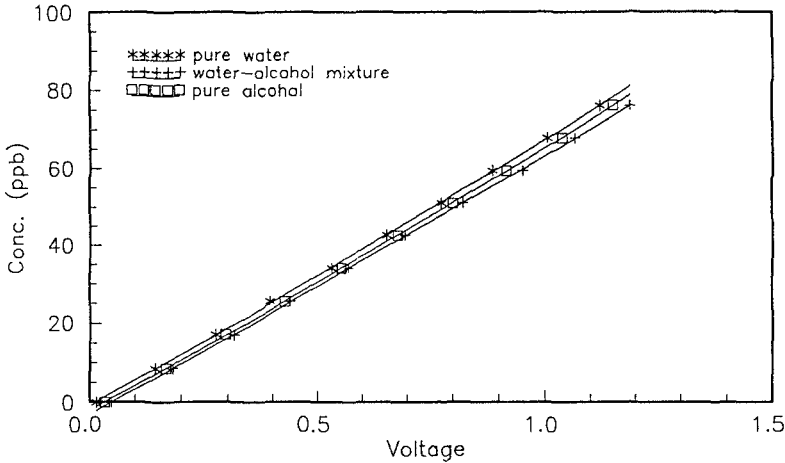


Fig. 2 Calibration curves of different compositions

tical applications, all of experimental conditions are in this range as shown in Table 1. Suitable *Reynolds No.* ( $Re > 2450$ ) and *Froude No.* ( $18.9 < F_d < 23$ ) are also selected to keep the simulated flow pattern similar to that of the diffusers. According to Chin (1987), the blocking layer of a buoyant jet with a poor dispersive ability is about 10% of the discharge depth. The measuring plane including 5 ~ 7 points locates 5 cm under the still water surface. The water surface variations induced by surface waves may block the fluorescence emitted from the measuring point while moving toward a higher test level. With the appropriate experimental conditions, the quantitative measurements of a buoyant jet under the action of surface waves can be proceeded. The data acquisition system collects signals from photo-detector and wave gauge in a sampling rate of 100 Hz and sampling duration of 60 sec. The initial dilution of different interaction cases can be determined from the experimental data, therefore, quantitative assessment of angle effects can be obtained and applied in the practical design of ocean outfalls.

## Results and Discussions

### Flow Visualization—

The flow visualization results of buoyant jet in co-wave are shown in Photo 1 where the flow pattern in still water is also pictured in Photo 1(a) for comparison. The trajectory in still water near the nozzle remains horizontal in the momentum-dominant domain, however, it gradually bends as the buoyant force getting stronger. During the ascending period, the effluent mixes with the ambient water and the boundary



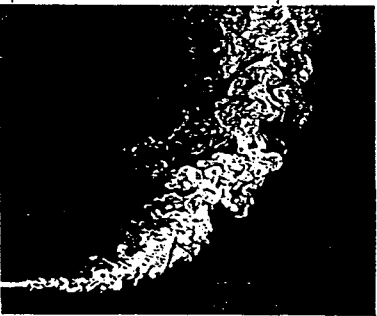
(a)



(b)



(c)



(d)



(e)

Photo 1 Flow of buoyant jets in co-wave (Case 1), (a) still water,  $t/T =$  (b) 0, (c) 0.25, (d) 0.49, (e) 0.73.

spreads simultaneously. Obviously, the vortex resulted from the velocity gradient plays an important role in lateral mass transfer and concentration dilution. Concerning the buoyant jet in wave motion, it is classified according to the temporal duration of wave crest and wave trough. The effluent experiences a co-stream flow induced by wave motion in the former while it interacts with an opposing flow in the latter. In case of wave-induced opposing flow, as shown in Photo 1(b), it is interesting to observe that the spreading rate of jet boundary in the neighborhood of the nozzle is larger than that in still water. The horizontal distance from the nozzle to the location where the plume ascending completely upward is shorter in Photo 1(b) than that in Photo 1(a). It shows that the effluent interacts with an opposing and inclining flow induced by wave motion. A greater velocity gradient and the opposing flow explain the formation of an increasing spreading rate and shorter excursion distance. There are many slender and inclining strips of jet fluid near the nozzle. According to Chyan & Hwung (1993), this structure is closely connected to the wake vortex. Due to the buoyancy and the upward wave flow being the same direction, the former will accelerate the formation of wake vortex even if the latter is small. As shown in Photo 1(e) where the opposing wave flow still influencing the effluents, there doesn't exhibit similar structures. It is because that the buoyant force prohibits the formation of wake vortex. From the above discussion, it explains the reason that, as shown in Photo 1(b) ~ Photo 1(e), the slender strips of the effluent always occur in the offshore side of the buoyant jet. This mechanism also changes the symmetry of profile distribution of the buoyant jet. However, these phenomena imply the mechanisms responsible for the increase of dilution rate.

On the phase of wave crest ( $t/T = 0.25$ ), as shown in Photo 1(c), the wave flow near the nozzle is parallel to the jet flow. It results in a smaller velocity gradient which depressing the formation of vortex and spreading rate. When  $t/T = 0.49$ , the inclining flow contains an upward velocity component, it will be against the ascending tendency of the effluent. As shown in Photo 1(d), there is a region where the trajectory is almost horizontal. Compared to the buoyant jet of the same trajectory characteristics in still water, the length scale in horizontal direction is longer and the spreading rate is smaller. From the observation of the effluent influenced by the co-stream of wave motion, the wave flow during the phase of wave crest seems to diminish the dispersion ability of the buoyant jet. In fact, there is an additional mechanism of dilution improvement during the interaction of co-stream and opposing flow on the effluent. As mentioned in the above discussion, the excursion distance will be shortened by the opposing and upward wave flow and stretched by the co-stream and downward wave flow. When the velocity of buoyant jet being too low to interact with surface waves, the plume will merely oscillate with wave motions which can not change the relative position within the effluent. Sharp & Power (1985) and Chyan & Hwung (1993) had observed the same phenomena. The effluent plumes ascending in the stretched excursion of wave

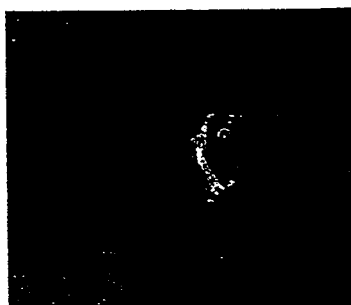
crest phase will enclose a large volume of ambient water with the following plume in the shortened excursions of wave trough. Therefore, a few patches of fresh water can be found in the ascending effluent plume as shown in Photo 1(b) ~ Photo 1(e). This additional mechanism provides a new chance of dilution and is similar to the wave tractive mechanism found by Chyan & Hwung (1993).

The flow visualization results of buoyant jet oppositely discharged into the wave motion would not be discussed herein since it shows a qualitatively similar result obtained in the co-wave case. Photo 2 depicts the formation cycle of wake vortex on the plane 1.1 cm away from the nozzle in the orthogonal discharge case. Within the momentum dominating domain of buoyant jets, it is acceptable to employ a pure momentum jet to simulate the momentum interaction of buoyant jets with surface waves for observing the inside structures of wave vortex. As shown in Photo 2(a) ( $t/T = 0$ ), the appearance of the effluent has been upwardly distorted into a horseshoe by the cross-flow induced by waves. The vertical velocity of intermediate wave is usually smaller than the horizontal velocity. During the wave phase of  $t/T = 0$  and  $t/T = 0.5$  when the vertical velocity dominates, the vortex induced by wave motion can not develop completely. A pair of counter-rotating vortex are not formed until the cross-flow of wave motion is large enough, as shown in Photo 2(b). As shown in Photo 2(a) ~ 2(f), the axes of vortex pair also rotates clockwise as the wave flow vector does except that the vortex around the phase of  $t/T = 0$  or  $t/T = 0.5$  is relatively immature. The formation of wake vortex certainly increases the dilution rate due to additional forced entrainment.

In order to investigate the buoyancy effect on the wake vortex formation, the flow visualization experiments of Photo 2 repeat again except the substitute of the pure momentum jet with a buoyant jet. The experimental results are shown in Photo 3 whose images are obscured by the density gradient. From the appearance of the flow structures, the wake vortex can still be found in Photo 3(c). The interacted structures are more sophisticated than that of the momentum interaction as depicted in Photo 2. A curved vortex tail following the wake vortex is observed and it mainly results from the vortex occurred before the test section. From the above observations, it suggests that the buoyancy effect will enhance the unsteadiness of the jet flow. The dispersion area of the effluent is enlarged by this effect, which implies the increase of dilution rate. In fact, the flow field of buoyant jet orthogonally discharged into the wave motion is a very complex but interesting flow phenomenon. In addition to the formation of wake vortex, the jet trajectory deflects in a status of 3-dimensional while a 2-dimensional deflection was observed by Chyan & Hwung (1993). Generally, the jet is onshore and offshore deflected in wave phase of  $t/T = 0.25$  and  $t/T = 0.75$ . In phase of  $t/T = 0$ , the ascending process of the effluent occurs earlier because of the upward vertical wave velocity while the horizontal domain of the trajectory will be stretched in phase of



(a)



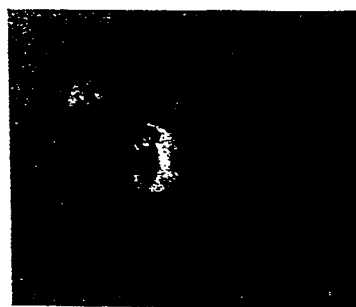
(b)



(c)



(d)



(e)



(f)

Photo 2 Formation cycle of wake vortex in orthogonal interaction (Case 2)  
 $t/T =$  (a) 0, (b) 0.21, (c) 0.30, (d) 0.44, (e) 0.65, (f) 0.81.

$t/T = 0.5$ . Due to the periodic deflection induced by wave motion, the shape of the effluent plume is no longer a circle, however, the mixing area of the effluent will be increased by the deflection mechanism and wake vortex structures.

From the above discussions, it suggests that the mechanisms improving the dilution rate of the buoyant jet in cases of co-wave and opposing wave result in the velocity gradient increase and wave tractive mechanism. The deflection mechanism and wake vortex structure play an important role in the enhancement of dilution rate when the buoyant jet orthogonally discharged into the wave motion. Concerning the contribution of these mechanisms to the dilution increases, it can only be evaluated by the quantitative measurements which will be discussed in the following.

#### Dilution Measurements—

From the elaborate measurements of  $S$  and  $S_o$ , the data obtained was processed according to Eq. (8) and the results of interaction angles,  $0^\circ$ ,  $180^\circ$ , and  $90^\circ$ , are shown in Fig.3. The regression relationships of  $S/S_o$  and  $L_q/Z_m$  are linear as proposed by Eq. (8) which are

$$\text{co-wave} \quad : \quad \frac{S}{S_o} = 1 + 4.21 \frac{L_q}{Z_m} \quad (10)$$

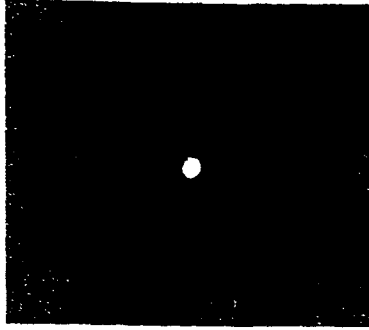
$$\text{opposing-wave} \quad : \quad \frac{S}{S_o} = 1 + 4.16 \frac{L_q}{Z_m} \quad (11)$$

$$\text{orthogonal discharge} \quad : \quad \frac{S}{S_o} = 1 + 5.55 \frac{L_q}{Z_m} \quad (12)$$

with the correlation coefficients being 0.90, 0.93, and 0.91, respectively, while the standard deviations are 0.10, 0.08, and 0.10. Positive slopes indicate the wave action increasing the dispersion of the effluent. From the flow visualization identifying the similar interaction mechanisms in cases of co-wave and opposing wave, it results in the coefficient,  $C_s$ , almost equivalent in both cases. As shown in Fig. 3, Chin (1987) suggests a higher estimate of  $C_s = 6.15$  which may be because of the sampling method and the calibration relation. The mechanisms, *i.e. wave deflection and wake vortex*, formed in the orthogonal discharge obviously play a more effective role in the dilution enhancement. In coastal water, the propagation of surface waves is not unidirectional so that the orientation of the diffusers can only be designed to be orthogonal to the principal direction which will provide the highest initial dilution. To estimate the dilution rate increased by wave action, the data obtained in different interaction angles is collected in Fig. 4 which shows  $C_s = 4.87$ .

#### Conclusion

The mechanisms improving the initial dilution processes of jet flow in co-wave and opposing wave are identified as the velocity gradient increase induced by the opposite



(a)



(b)



(c)



(d)



(e)

Photo 3 Buoyancy effect on the formation of wave vortex (Case 3), (a) still water,  $t/T =$  (b) 0.08, (c) 0.27, (d) 0.42, (e) 0.88.



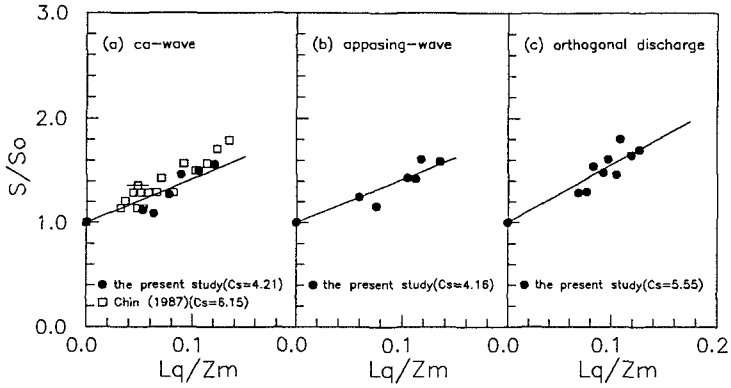


Fig. 3 Angle effects on initial dilution rate of jet-wave interaction  $\theta_2 =$  (a)  $0^\circ$ , (b)  $180^\circ$ , (c)  $90^\circ$

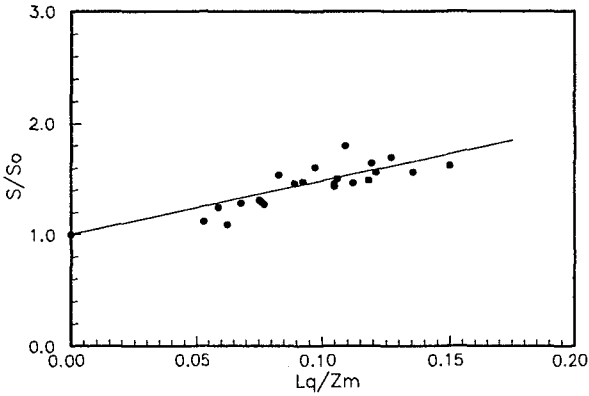


Fig. 4 Estimate of initial dilution increase

wave flow and the wave tractive mechanism stemmed from the onshore and offshore wave flow. When orthogonally discharged into wave motion, the effluent is affected by different interaction mechanisms, such as wake vortex and wave deflection. The concentration measurements show that the increase of the initial dilution is comparable in cases of co-wave and opposing wave. However, a higher increasing tendency is found in the orthogonal discharge whose  $C_s$  is 33% larger than that of the other cases. It

implies that the orthogonal discharge is a more effective orientation in the enhancement of mixing efficiency. Considering the field situation in coastal water, an average value of  $C_s = 4.87$  is suggested to estimate the dilution rate increase of the buoyant jet under the wave action.

### Reference

1. Chin, D.A. (1987), Influence of surface waves on outfall dilution, *J. of Hydraulic Eng.*, Vol. 113, No. 8, pp.1006-1017.
2. Chin, D.A. (1988), Model of buoyant-jet-surface-wave interaction, *J. of Waterway, Port, Coastal, and Ocean Eng.*, Vol. 114, No. 3, pp.331-345.
3. Chyan, J.M. & Hwung, H.H. (1993), On the interaction of a turbulent jet with waves, *J. Hydraulic Research*, Vol. 31, No. 6, pp. 191-810.
4. Drexhage, K.H. (1973), Structures and properties of laser dyes, *Topics in Applied Physics*, Springer, Vol. 1, pp. 145-193.
5. Fischer, H.B., List, E.J., Koh, R.C.Y. Imberger, J. & Brooks, N.H. (1979), *Mixing in inland and coastal waters*, Academic Press, New York, N.Y., U.S.A.
6. Ger, A.M. (1979), Wave effects on submerged buoyant jets, *Proc. Hydraulic Eng. in Water Resources Development and Management*, IAHR, pp. 295-300.
7. Hwung, H.H. & Chyan, J.M. (1990), The vortex structures of round jets in water waves, *Proc. Int'l. Conf. on Physical Modeling of Transport and Dispersion in conjunction with the GARBIS H. KEULEGAN Centennial Symp.*, IAHR, pp.10A.19-10A.24.
8. Sharp, J.J. & Power, K.C. (1985), The local effect of wave action on submerged effluent discharge, *Canadian Coastal Eng.*, pp.1-10.
9. Shuto, N. & Ti, L.H. (1974), Wave effects on buoyant plumes, *Proc. 8th Cong.*, IAHR, pp.295-300.
10. Yeo, J.H. & Koch, H.J. (1957), *Trace analysis , Fluorometer*, John Wiley & Sons. Inc.

## CHAPTER 220

### STUDY ON THE BEHAVIORS OF COHESIVE SEDIMENT IN THE YANGTZE ESTUARY

Xiaochuan Zeng<sup>1</sup>, Yixin Yan<sup>2</sup>, Kai Yen<sup>2</sup>

#### Abstract

In order to study the deposition and erosion behaviors of the cohesive sediment in the navigation channel through the bar of the Yangtze Estuary, a series of experiments have been made with a standard settling tube and Ubbelodhe viscometer. The tests show that the flocculation and rheological behaviors of the cohesive sediment differ from the clay mineral contained in the fine sediments. Different clay mineral aggregates or flocs have their apparent volume due to the thin layer of water surrounding the aggregates or water entrained in the flocs. The Bingham relative viscosity and yield stress are obtained:  $\mu_r = (1 - KC_v)^{-2.5}$ ,  $\tau_y = 0.13K \exp(7kc_v)$ . The suspended load transport rate and depositional behavior of the cohesive sediment have been studied with rotating annular channel. It is shown that there is a certain silt carrying capacity for a certain flow condition. The equilibrium silt concentration can be expressed:  $C_{\infty q} = A(\tau_b - \tau_1)$  and the concentration-time relation is  $C = C_{\infty q} + (C_0 - C_{\infty q}) \exp(-\alpha \omega t / 2H)$ . Using the above formulas and tidal velocity analysis the yearly average dredging amount in the the navigation channel can be calculated.

#### Introduction

The Yangtze River is the largest river of China. It carries annually  $924 \times 10^9 \text{ m}^3$  of runoff and  $470 \times 10^6 \text{ t}$  of sediment

- 
1. Instructor, Hohai University, Nanning 210024, China
  2. Professor, Hohai University, Nanning 210024, China

into the sea. The yearly average suspended concentration is  $0.544 \text{ kg/m}^3$ . The grain size of suspended load is generally greater than  $5 \phi$ , 30% of which are clay particles. Most of the sediment is deposited on the estuarine area, causing shoaling of navigation waterway, thus greatly affecting the traffic capability of port Shanghai and other port along the lower reaches of the River. The grain size of the materials deposited in the navigation channel is of the same order magnitude as that of suspended sediment (Chang Zhizhong, 1981). Extensive dredging has to be carried out to maintain the required water depth of the navigation channels, particularly the approach channel to the sea. Therefore regulation works have to be carried out in combination with dredging to cope with such adverse situation. For this purpose study was made, among others, on the behaviors of cohesive sediment of the Estuary, which is necessary for the planning and design of the regulation works, as well as for the disposal of the dredged materials in the dredging operation. The deposition and erosion of the cohesive sediment of the navigation channel in the Yangtze Estuary is affected by various factors, such as tidal current, runoff, wave, salinity, pH value etc.. The floc size and floc strength of cohesive sediment are important factors affecting deposition and erosion. In this paper the rheological behaviors of the cohesive sediment are studied from the test results with Ubbelodhe viscometer for different clay mineral composition and mediums. Transportation and deposition tests for Yangtze Estuary clay were conducted in the annular rotating channel. For deposition the concentration versus time relationship is obtained and could be used for calculating dredging amount in the navigation channel.

#### Experimental Study on the Rheological Behavior of Cohesive Sediment

On silty coast and estuaries the fine sediment usually consists of mixture of clay, silt, fine sand and occasionally some organic matters. Previously it was taken that there is no difference in behaviors between the clay minerals and the primary minerals except their grain size. In reality, the clay particles of the cohesive sediment carry electric charge which causes flocculation and deflocculation of the sediment. Size distribution analysis with a setup of settling tube is shown in Table 1. Different clay mineral particles have

different ratio of width to thickness and the flocculation sized of different clay mineral varies appreciably from each other in different mediums, but for fine silt particles of quartz there is no significant difference in the flocculation size  $d_{50}$  in different mediums. For example, kaolinite can be flocculated in distilled water but montmorillonite cannot.

Table 1.  $d_{50}$  of quartz, kaolinite and montmorillonite in different mediums

Minerals  Mediums	Non clayey sediment	Clay minerals		Remarks
	Quartz silt	Montmoril- lonite	Kaolinite	
Distilled water	0.010	0.0024	0.038	1. Unit : mm 2. Quantity of [NaPO <sub>3</sub> ] <sub>6</sub> added: 0.5N. l.c.c. / g.
Water with salinity 10‰	0.015	0.027	0.040	
Distilled water+[NaPO <sub>3</sub> ] <sub>6</sub>	0.011	0.0021	0.0032	

The modes of particle (aggregate) association are of great importance to the essential behaviors of the flocs, such as settling, shearing, swelling etc., and are affected by factors such as pH value, concentration of electrolyte and sediment as well as composition of mineral etc. . Under normal conditions edge to face association is the principal mode of association, which leads to voluminous card-house structures and entrains a large amount of water. The aggregates or flocs will increase their apparent volume due to the thin layer of water surrounding the aggregates or water entrained in the flocs. The degree of association will change with different mediums. Along coast of China, the major clay minerals are illite, kaolinite, montmorillonite and in the Yangtze Estuary the clay mineral consists mainly of illite. The optimum salinity for flocculation is about 10~15‰. With this salinity the apparent volume and settling velocity of the flocs attain a maximum.

In order to investigate the erosion of sediment and movement of fluid mud, the rheological behavior tests of cohesive sediment are conducted with Ubbelodhe viscometer for different clay mineral suspension and mediums (Yen, Kai, et al, 1989), as shown in Fig. 1. It is clear that for the same

concentration the relative viscosity of montmorillonite suspension is larger than that of kaolinite suspension with salinity of 10%. For the same clay mineral, the relative viscosity in salinity medium is larger than that of suspension with peptizer. The degree of volume expansion K, which can be

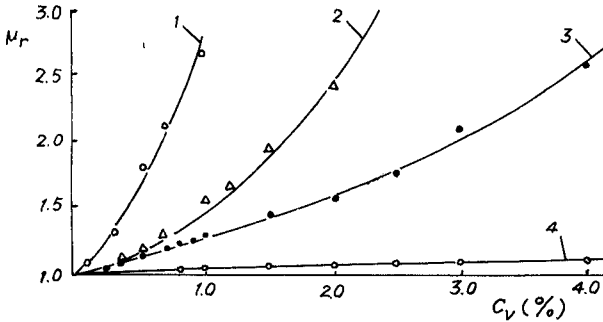


Fig. 1  $\mu_r$ - $C_v$  curves of montmorillonite and kaolinite suspended in different mediums: 1-montmorillonite suspension with salinity of 10 %. 2-montmorillonite suspension with peptizer. 3-kaolinite suspension with salinity of 10%. 4-kaolinite suspension with peptizer.

expressed by the ratio of the volumes after and before expansion, may be obtained from the formula

$$\mu_r = (1 - KC_v)^{-2.5} \quad (1)$$

In this formula  $\mu_r$  is the relative viscosity coefficient and  $C_v$  the volumetric concentration. The volume expansion K for different clay mineral and mediums are given in Table 2.

Table 2 Value K obtained by Ubbelodbe viscometer

Minerals	Saline water with salinity 10%	Distilled water + peptizer of $[\text{NaPO}_3]_s$	Remarks
Montmorillonite	37.0	15.3	Quantity of $[\text{NaPO}_3]_s$ added: 0.5N, 0.5c.c./g
Kaolinite	7.8	1.5	

The Bingham yield stress is a measure of the number and the strength of the links in card-house (Van Olphen, 1977). The magnitude of Bingham yield stress is closely related to the size of flocs and to volume of the entrained water in the

flocs, as shown in Fig. 2. When peptizer is added into the suspension, the card-house structures are completely dissociated, and the Bingham yield stress will tend to disappear. The formula of Bingham yield stress for Yangtze Estuary clay is:

$$\tau_y = 0.13K \exp(7KC_v) \quad (2)$$

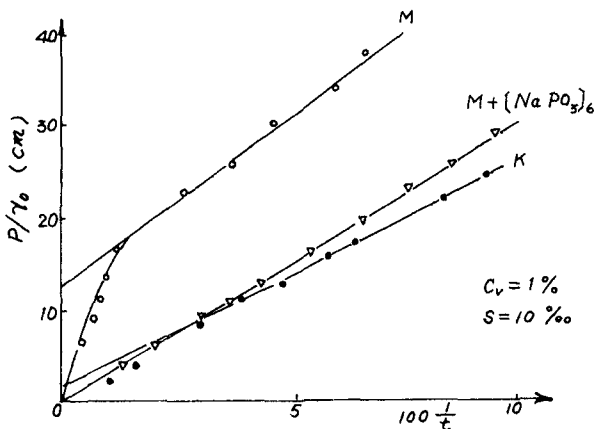


Fig. 2 Equivalent yield stress of montmorillonite and kaolinite suspension

For the Yangtze Estuary clay, which consists mainly of illite, the values of volume expansion K in Equ. (1) and Equ. (2) are given in Table 3.

Table 3. Value d in Different Salinity Mediums

Salinity	2%	5%	10%	20%	25%
n	5.9	6.3	5.0	6.0	5.6

Comparison of  $\mu_r$  values between experimental and calculated by Equ(1) is shown in Fig. 3 and comparison of Bingham yield stress between experimental and calculated by Equ. (2) is shown in Fig. 4. It shows that Equ. (1) and Equ. (2) conform with experimental data.

All the above tests show that the composition of clay minerals is of great importance to the essential properties of flocs.

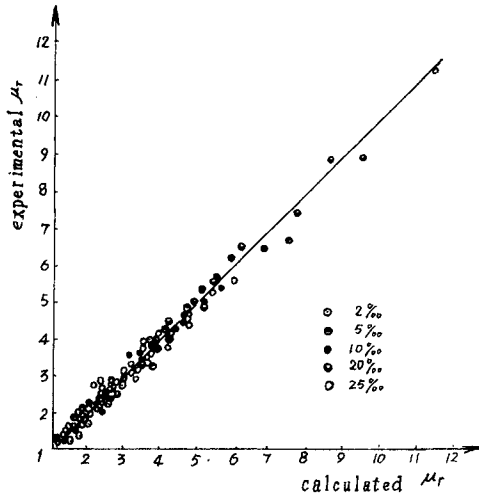


Fig. 3 Comparison between experimental and calculated  $\mu_r$  values

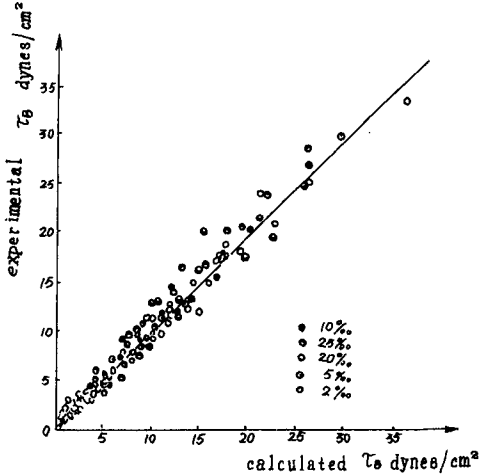


Fig. 4 Comparison between experimental and calculated Bingham yield stress

### Deposition Behavior of Cohesive Sediment

A series of deposition tests with different clay mineral composition and the Yangtze Estuary clay in sea water were conducted in an annular rotating channel to study the relation between the deposition behavior of cohesive sediment and the bed shear stress (Zeng Xiaochuan, 1985). Fig. 5 shows the results of test for kaolinite. It can be seen that there is a critical critical shear stress  $\tau_1$  below which the flocs of the



cohesive sediment will be all deposited on the channel bed, and when the bed shear stress  $\tau_b$  is greater than the critical shear stress  $\tau_1$ , the suspended sediment will attain a state of equilibrium with concentration  $C_{eq}$ . The relation between equilibrium concentration  $C_{eq}$  and bottom shear stress  $\tau_b$  for different initial concentration  $C_0$  can be divided into single-valued stage (along  $\tau_1$ ) and the multi-valued stage (on the right of  $\tau_1$ ) respectively. At the single valued stage  $C_{eq}$  versus  $\tau_b$  is independent on the initial concentration  $C_0$ . That is, there is a certain silt carrying capacity for a certain flow condition. At this stage  $C_{eq}$  varies with  $\tau_b$  in a straight line relation. For a give water depth it can be written

$$C_{eq} = A(\tau_b - \tau_1) \quad (3)$$

where  $A$  is a coefficient and  $\tau_1$  the critical shear stress, both depend on the salinity of water and kind of clay mineral. On the right of curve  $\tau_1P$ , the values of  $C_{eq}$  vary with initial concentration  $C_0$  for a constant flow condition. At this stage there is no marked siltation on the bed. On the bare fiber glass channel bed there could be no exchange between bed load and suspended load. When a large amount of sediment is deposited on the bed, free exchange between suspended load and bed load occurs, thus obtaining the relation as shown by the curve  $\tau_1P$ .

For clay suspension in the Yangtze Estuary, equilibrium  $C_{eq}$  versus differential motor speed  $\Delta n$  between ring and channel is shown in Fig. 6. This could also be seen from Equ. (3). The values  $A$  and  $\tau_1$  in different salinity mediums are shown in Table 4. Making use of equation (3), we analysed sediment

Table 4. Value  $A$  and  $\tau_1$  in Different Salinity Mediums

Salinity	$A$	$\tau_1$ (dyne/cm <sup>2</sup> )
5%	11.28	0.72
10%	10.67	0.90
20%	10.99	0.76
30%	10.79	0.82

concentration data (average over semitidal period) in Yangtze Estuary during spring or neap tide in both high flow and low flow seasons. Both laboratory test and field data show that equation (3) well describes the relationship between suspension concentration and bed shear stress.

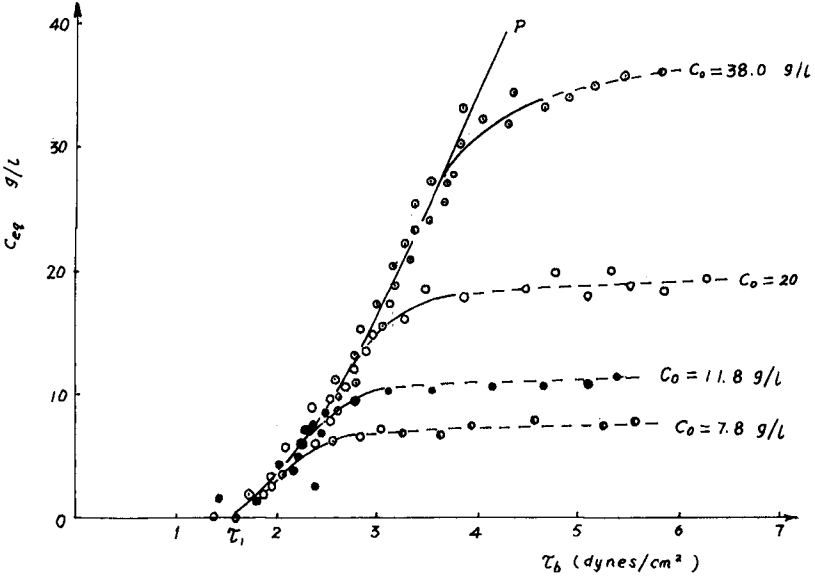


Fig. 5 Equilibrium concentration  $C_{eq}$  versus bed shear stress  $\tau_b$  for kaolinite

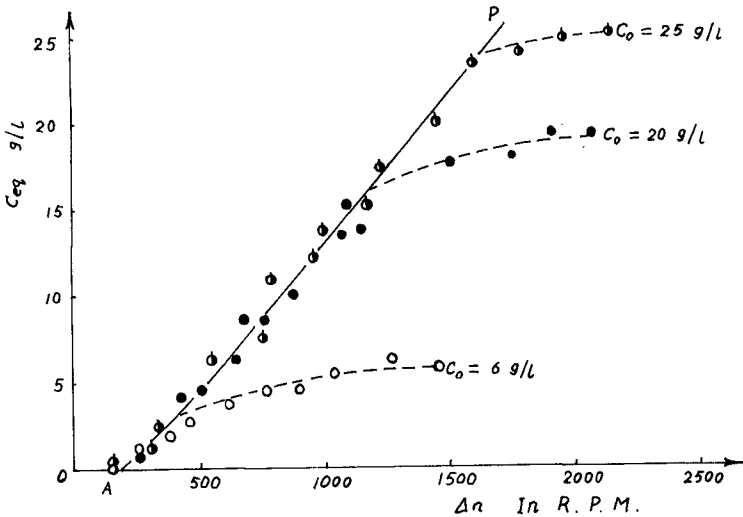


Fig. 6  $C_{eq}$  versus differential motor speed  $\Delta n$  between ring and channel for Yangtze Estuary Clay

No matter at which stage, the vertical concentration distribution can be expressed by the diffusion equation (Ren, Ru-shu et al, 1987), from which the settling velocity can be calculated. The curve  $\omega_s$  versus  $\tau_b$  can be expressed by equation

$$\omega_s = \omega_o \exp [-b(\tau_b - \tau_1)] \tag{4}$$

$\omega_o$  and  $b$  depend on salinity and depth of water and kind of clay mineral. It can be seen that the settling velocity of the flocs decreases exponentially with increase of the bed shear stress, indicating that cohesive sediment is very sensitive to the dynamic actions of flow, as shown in Fig 7. For Yangtze Estuary clay, the settling velocity in turbulent flow is much smaller than that in still water and reduces with increasing bed shear stress, the values  $\omega_o$  and  $b$  in different salinity water are shown in Table 5.

Table 5 Value  $\omega_o$  and  $b$  in Different Salinity Mediums

Salinity	$\omega_o$	$b$
5‰	$2.17 \times 10^{-2}$	0.63
10‰	$3.64 \times 10^{-2}$	0.90
20‰	$3.45 \times 10^{-2}$	0.76
30‰	$1.13 \times 10^{-2}$	0.46

In order to forecast the dredging amount in navigation channel, which is needed for the planning of regulation works and determining the required capacity of dredging equipment, the depositional behavior of the cohesive sediment in turbulent flow was studied in the annular rotating channel. For a given flow condition, the sediment movement equation can be written as:

$$\frac{\partial(AC)}{\partial(QC)} + \frac{\partial t}{\partial x} + \alpha \beta \omega (C - C_{eq}) = 0 \tag{5}$$

where  $A$  is cross-sectional area,  $Q$  is discharge,  $B$  is channel width, and  $\alpha$  is the probability of sediment siltation. For the annular rotating channel,  $x = \bar{v}t$ , where  $\bar{v}$  is mean velocity, then Equ. (5) can be written as:

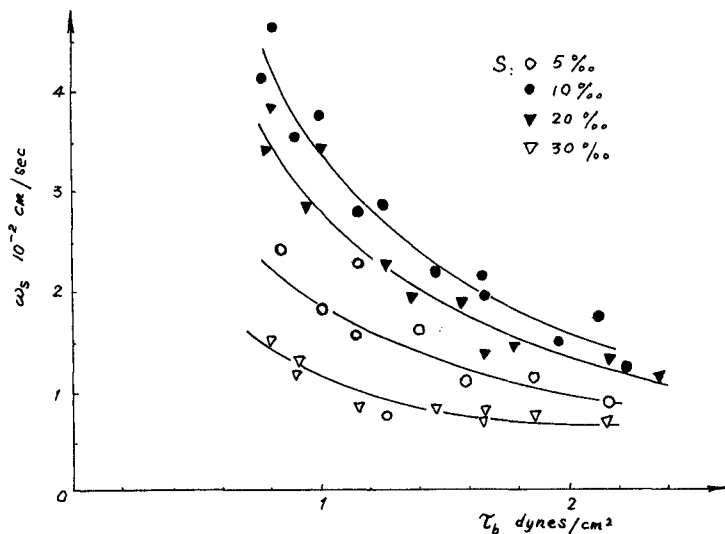


Fig. 7  $\omega_s$  versus bed shear stress  $\tau_b$  (lower layer)

$$2 \frac{\partial(HC)}{\partial t} + \alpha \omega (C - C_{eq}) = 0 \tag{6}$$

where H is the water depth, we have

$$C = C_{eq} + (C_0 - C_{eq}) \exp(-\alpha \omega t / 2H) \tag{7}$$

where  $C_{eq}$  can  $\omega$  could be calculated by Equ. (3) and Equ. (4). Equ. (7) conforms well to the experimental data.

The siltation thickness p in the navigation channel for steady flow can be obtained from:

$$P = \frac{H}{r_0} (C_0 - C_{eq}) (1 - \exp(-\alpha \omega T_d / 2H)) \tag{8}$$

where  $r_0$  is the dry specific weight of deposited sediment,  $T_d$  is the time of current passing through the channel.

For unsteady flow, the thickness p of deposited sediment can be written as:

$$P = \beta \frac{H}{r_0} (C_0 - C_{eq}) (1 - \exp(-\alpha \omega T_d / 2H)) \tag{9}$$

where  $\beta$  is a coefficient.

### Conclusions

a. The mineral composition and its content are of great importance to the hydrodynamic behaviors of fine cohesive sediment.

b. The transportation of cohesive sediment can generally be divided into three stages. At single valued stage  $C_{eq}$  is independent of  $C_0$ .

c. The vertical concentration distribution of sediment can be expressed by diffusion equation. The settling velocity in turbulent flow is smaller than that in still water.

d. The relation of suspension concentration versus time in turbulent flow can be obtained from tests with an annular rotating channel, formula (7) could be used for calculating the yearly dredging amount.

Apart from the factors mentioned above, there are also many other factors affecting the hydrodynamic behavior of cohesive sediment.

### REFEREBCE

1. Chang Zhizhong, (1981) "The Sedimentary Characteristics of south Channel of the Yangtze Estuary", Navigation Channel Improvement of the Yangtze Estuary, Vol. 1, pp.49-59. (in Chinese).
2. Ren, Rushu and Xiaochuan Zeng (1987). The sdttling velocity and rheological behavior of cohesive sediment in Yangtze Estuary. Proc. of 2nd Chinese-German Symposium on Hydrology and Coastal Engineering, vol. 2.
3. Van Olphen, h. (1977) An Intraduction to Clay Colloid Chemistry, A wiley-Interscience Publication, New York.
4. Yen, Kai, Rushu Ren and Xiaochuan Zeng (1989). Some sediment problems of silty coast and esdstuary. Proc. of 4th International Symposium on River Sedimentation, Beijing, China.
5. Zeng, Xiaochuan (1985). A preliminary study on the dynamic behavior of cohesive sediment. Master thesis, Hohai University (in Chinese).

## CHAPTER 221

### Dispersion of pollution in a Wave Environment.

R. Koole<sup>1</sup> & C. Swan<sup>2</sup>.

#### Abstract.

This paper concerns the wave-induced mixing of a discharged contaminant, and presents the results of a two-part laboratory investigation in which both a two-dimensional and a three-dimensional jet were discharged beneath a series of progressive gravity waves. In each case the measured data is compared to an identical discharge in a quiescent ambient. This comparison suggests that the oscillatory wave motion generates a region of intense fluid mixing which cannot be predicted by the existing integral solutions. Comparisons with a Lagrangian model, first proposed by Chin (1988), highlights the importance of the "apparent" mixing associated with the wave-induced deflection of the jet-axis. This provides a convincing explanation for both the non-Gaussian distributions observed by Sharp (1986), and the multi-stage structure of the centre-line decay (Chyan et al., 1991). Furthermore, quantitative comparisons with the Lagrangian model suggest that in addition to the wave-induced deflection, the oscillatory motion produces a significant increase in the rate at which ambient fluid is entrained into the emerging jet.

#### 1. Introduction.

The design of coastal outfalls, and in particular the estimate of pollutant concentrations, is usually based upon a simplified steady state or quasi-steady state analysis. In the near-field region, close to the outlet orifice, the velocity and concentration profiles are typically described by some form of integral solution based upon the concentration of mass, momentum and, where appropriate, species concentration. Although these solutions were originally developed for buoyant

---

<sup>1</sup> Research assistant & <sup>2</sup> Lecturer. Department of Civil Engineering, Imperial College of Science Technology and Medicine, London, United Kingdom. SW7 2BU.

discharges in a quiescent ambient (Morton et al., 1956), subsequent research has shown that they may also be applied to a range of quasi-steady flows. This extension of the existing theory is, however, only valid if the unsteadiness of the ambient fluid has a time-scale which is significantly larger than the time-scales of the turbulent fluctuations within the emerging jet. As a result, a quasi-steady solution (based upon a modified integral solution) may be used to describe the discharge of pollution in a tidal flow, but should not be used to model the near-field mixing which arises when pollution is discharged into a wave environment. In this latter case the typical wave periods are similar to the eddy time-scales (of the order of seconds), and consequently there may be significant coupling between the turbulent fluctuations and the unsteadiness of the surrounding flow.

Indeed, previous qualitative studies (Shuto and Ti (1974), Ger (1979), Sharp (1986) and Chyan et al. (1991)) suggest that the oscillatory motion associated with the propagation of the surface gravity waves has a significant effect upon the local mixing characteristics. In particular, the wave motion appears to produce a large increase in the dilution immediately downstream of the discharge orifice. This region, which is usually referred to as the "zone of flow establishment", is characterised in a quiescent ambient by a gradual transition from a top-hat velocity profile at the exit to an approximately Gaussian distribution further downstream. This latter state marks the beginning of the so-called "zone of established flow" within which the integral solutions are valid. Recent quantitative measurements presented by Chyan and Hwung (1994) and Koole and Swan (1994) have shown that the "zone of flow establishment" is considerably shortened by the wave motion; and that a region of intense fluid mixing arises, the characteristics of which cannot be predicted by the existing integral solutions.

For example, there is both qualitative (Sharp, 1986) and quantitative evidence (Chyan and Hwung, 1994) to suggest that in some circumstances the radial distribution of both the axial velocity and the "pollutant" concentrations are no longer Gaussian. These observations are interpreted as providing evidence for a new wave-induced mixing mechanism (referred to as the "wave tractive mechanism") which involves the "entrapment" of large volumes of uncontaminated (ambient) fluid into the central area of the jet. Furthermore, Chyan and Hwung (1994) conclude that the axial variation in both the centre-line velocities and the concentrations no longer follow a typical exponential decay. Indeed, they provide evidence of a multi-stage decay in which three specific mechanisms of wave-induced mixing are identified.

The present paper will consider the nature of the mixing processes within the near-field region, and will, in particular, examine the occurrence of non-Gaussian distributions within the "zone of established flow". Section 2 commences with a brief outline of the experimental apparatus in which two widely differing discharges were considered. The first concerns a two-dimensional, non-buoyant, jet discharged in a horizontal plane; while the second concerns a three-dimensional, buoyant (thermal) discharge orientated in a vertical plane. In both cases two sets of measurements were undertaken so that the mixing and dilution of the jet in a wave environment can be

directly compared with an identical discharge in a quiescent ambient. In section 3 the velocity and temperature data are compared with both the existing integral solutions and a simplified Lagrangian model. This latter solution was first proposed by Chin (1988) and further developed by Koole and Swan (1994). Evidence to support the various wave-induced mixing mechanisms is examined, as is the multi-stage structure of the centre-line decay. Finally, some conclusions regarding the effectiveness of the additional wave-induced mixing are made, and the practical implications for outfall design assessed.

## 2. Experimental apparatus.

### Case 1: Two-dimensional, non-buoyant jet.

The first experimental study was undertaken within a narrow wave flume located in the Civil Engineering Department's hydraulics laboratory at Imperial College. This facility has good optical access, and is equipped with a numerically controlled random wave paddle located at one end of the wave flume. A large block of poly-ether foam is positioned at the opposite end to provide passive wave absorption. Typical reflection coefficients within this facility are less than 3%. The tank is 25m long, 0.3m wide, and has a working depth of 0.7m. The two-dimensional jet was introduced through a horizontal slot ( $D=1\text{cm}$ ) located at mid-depth at the downstream end of the wave flume (figure 1a). The present results correspond to an exit velocity of 0.75m/s, and include measurements undertaken within a quiescent ambient and beneath a progressive regular wave train in which the wave amplitude was 30mm, and the wave period 1.04s.

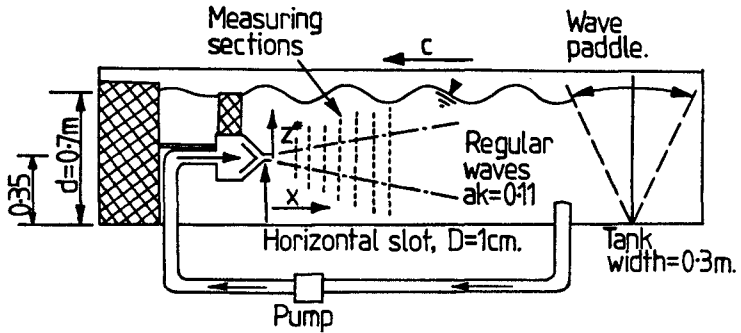
The resulting flow field was measured using a two component laser Doppler anemometer in a forward scatter configuration. A 35mW helium-neon laser was used to create a three beam arrangement with cross polarisation. This apparatus allows the simultaneous measurement of two velocity components within a measuring volume which was estimated to be  $0.5\text{mm}^3$ . After seeding the flow with milk (added in the ratio of approximately 100ppm), a data rate in excess of 2kHz was achieved so that the velocity components could be sampled at 500Hz with a measuring accuracy of  $\pm 2\%$ . Further details of these experimental observations are given by Koole and Swan (1994).

### Case 2: Three-dimensional, buoyant jet.

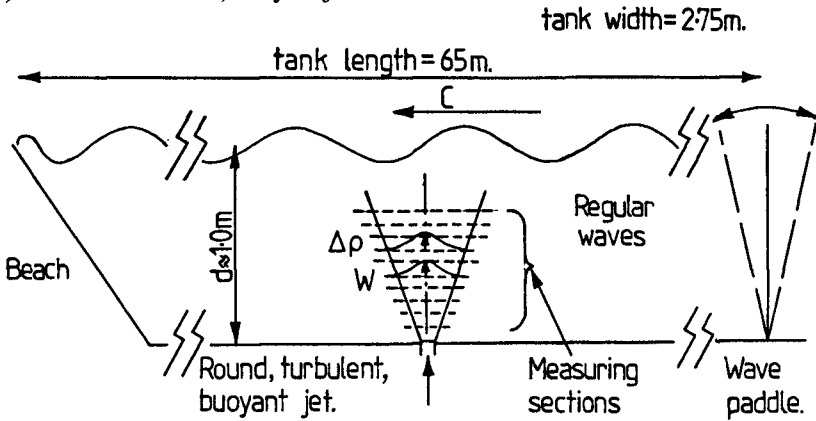
The second set of measurements were undertaken in a larger wave flume which is also located in the hydraulics laboratory at Imperial College. This facility is 65m long, 2.75m wide, and is also equipped with a numerically controlled random wave paddle. At the downstream end of this flume the wave energy is dissipated on a 1:20 sloping beach. Under the present test conditions (see below) this produced a reflection coefficient of 4%. The "pollutant" was introduced in the form of a hot water discharge, through a 1cm diameter nozzle located on the bed of the wave flume. The initial jet was orientated in a vertical direction, and was positioned along the centre-line of the wave flume some 25m downstream of the wave paddle (figure 1b).



## 1(a). Two-dimensional, non-buoyant jet.



## 1(b). Three-dimensional, buoyant jet.



Figures 1a-1b. Experimental apparatus.

Although a wide range of test conditions were investigated, the present paper is only concerned with one specific data set in which the discharged "pollutant" was  $35^{\circ}\text{C}$  above the temperature of the ambient fluid. The results presented in section 3 correspond to an exit velocity of  $0.55\text{m/s}$ . Once again, measurements were undertaken in a quiescent ambient, and beneath a progressive wave train in which the wave amplitude was  $30\text{mm}$  and the wave period was  $1.0\text{s}$ . Due to the restricted access and the physical dimensions of this facility a second laser Doppler anemometer was used to measure the velocity field. This system is based upon a  $10\text{mW}$  helium-neon laser which is used to create a two beam arrangement from which one component of the flow field could be determined. The beams were passed down a fibre-optic cable, and emerged through a converging lens to focus  $60\text{mm}$  from the fibre head. The intersection of the beams was observed in a back-scattered configuration. With careful seeding of the flow (using Trimiron Supersilk, MP-1005) an accuracy and data rate

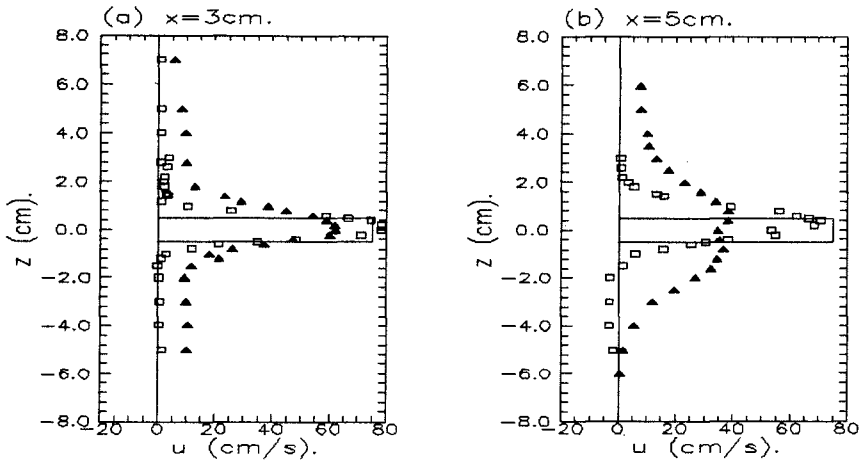
similar to that noted above were achieved. The temperature variations within the developing plume were measured using an array of 8 K-type thermocouples. These were manufactured at Imperial College using teflon coated wire with a diameter of 3 microns. Calibration tests indicated that these probes have an accuracy of  $\pm 0.05^\circ\text{C}$  with a response time of 0.05s. This was sufficient to measure the temperature fluctuations within a wave cycle, and to assess the mixing and dilution of the jet at differing wave phases.

### 3. Measured data.

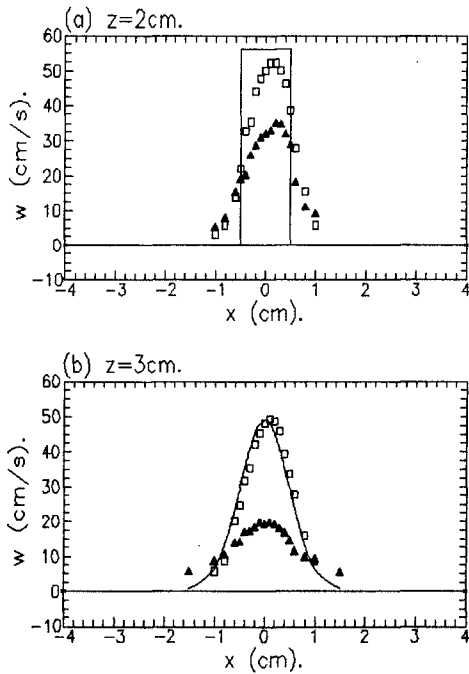
The axial velocity measured within the "zone of flow establishment" in Case 1 (described above) is shown on figures 2a-2b. In each of these figures, and many of the subsequent figures, two data sets are presented. The first, indicated by the open squares, corresponds to a discharge in a quiescent ambient; while the second, indicated by the solid triangles, corresponds to a discharge in the relevant wave conditions. Within the "zone of flow establishment" the mean jet velocity ( $U$ ) in Case 1 is significantly larger than the wave-induced fluid motion ( $u,v$ ), and thus there is little wave-induced displacement of the jet-axis. The experimental data presented on figures 2a-2b suggest that there is significant mixing of the jet immediately downstream of the nozzle, and that the "zone of flow establishment" (or the region over which a Gaussian distribution evolves) is significantly shortened. A similar pattern is observed in figures 3a-3b which describe the evolution of the three-dimensional discharge outlined in Case 2.

Figures 4a-4b concern Case 1, and present the variation in the axial velocity within the "zone of established flow" ( $x > 5\text{cm}$ ). It is within this region that the integral solutions discussed previously are applicable. However, since the mean jet velocity is now of a similar magnitude to the wave-induced velocity (ie  $U/v_{\text{max}} \approx 1$ ), the jet will undergo considerable lateral displacement. As a result the laboratory data, which corresponds to measurements undertaken at a number of points fixed in space and time-averaged over an integer number of wave periods (typically 40), will reflect both the dilution of the jet and its lateral displacement. In consequence, the velocity data gathered in a wave environment are very different from the integral solutions (indicated by a solid line on figures 4a-4b), whereas the measurements undertaken in a quiescent ambient are in good agreement with the existing theory. A similar sequence of results also arises in Case 2. In figures 5a-5b the average temperature profiles are presented within the so-called plume region (ie. that region of the flow where the buoyancy effects are important). Once again the influence of the wave motion is clearly apparent.

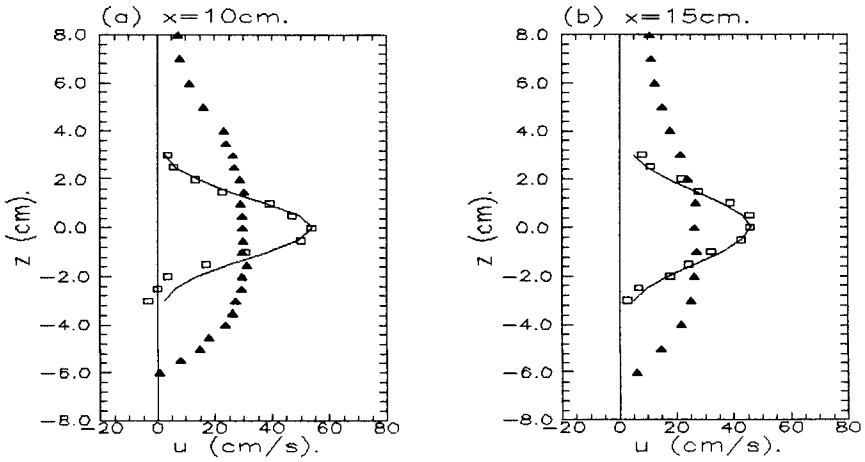
These results suggest that in both Case 1 and Case 2 the standard integral solutions are unable to describe the time-averaged laboratory data if the pollutant is discharged in a wave environment. However, the extent to which this change is due to the lateral displacement of the jet or the occurrence of additional wave-induced mixing remains unclear.



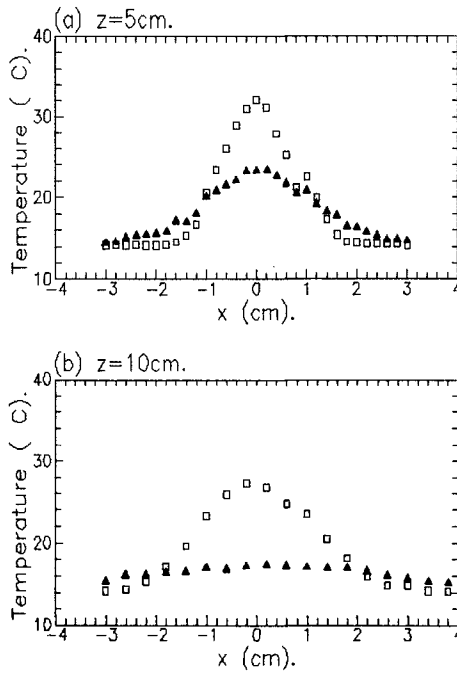
Figures 2a-2b. Case 1: axial velocity within the "zone of flow establishment".  
□ Discharge in quiescent ambient, ▲ Discharge in waves.



Figures 3a-3b. Case 2: axial velocity within the jet region.  
□ Discharge in quiescent ambient, ▲ Discharge in waves.



Figures 4a-4b. Case 1: axial velocity within the "zone of established flow".  
 □ Discharge in quiescent ambient, ▲ Discharge in waves.



Figures 5a-5b. Case 2: temperature profiles within the plume region.  
 □ Discharge in quiescent ambient, ▲ Discharge in waves.

#### 4. Discussion of Results.

To examine the relative importance of the jet displacement a simplified Lagrangian model similar to that proposed by Chin (1988) was adopted. This solution considers a succession of fluid elements discharged at regular intervals throughout a wave cycle. Each element is tracked, in both space and time, and the entrainment characteristics are based upon the velocity of the jet relative to the surrounding fluid. The conservation equations appropriate to Case 1 are given by:

$$\frac{\partial}{\partial \xi} \int_{-\infty}^{+\infty} U(\xi, \eta) \cos(\gamma) \partial \eta - 2\alpha U(\xi, 0) \cos(\gamma) + \beta |U(\xi, 0) \sin(\gamma)| \quad (1)$$

$$\frac{\partial}{\partial \xi} \int_{-\infty}^{+\infty} [U(\xi, \eta) \cos(\gamma)]^2 \partial \eta - 0 \quad (2)$$

where  $(\xi, \eta)$  represent the local cartesian co-ordinates in which the  $\eta=0$  corresponds to the instantaneous jet-axis,  $U$  is the velocity of the fluid element relative to the surrounding flow (figure 1a), and  $\gamma$  is the angle between  $U$  and the jet-axis. In Case 2 the conservation equations (including a heat flux relation) are best expressed in local polar co-ordinates  $(\xi, r)$ , where the  $\eta=0$  once again represents the instantaneous jet-axis:

$$\begin{aligned} \frac{\partial}{\partial \xi} \int_0^{\infty} 2\pi r \rho(\xi, r) W(\xi, r) \cos(\gamma) \partial r - 2\pi b \rho_0 \alpha W(\xi, 0) \cos(\gamma) \\ + 2b \rho_0 \beta |W(\xi, 0) \sin(\gamma)| \end{aligned} \quad (3)$$

$$\frac{\partial}{\partial \xi} \int_0^{\infty} 2\pi r [W(\xi, r) \cos(\gamma)]^2 \rho(\xi, r) \partial r - \int_0^{\infty} 2\pi r [\rho_0 - \rho(\xi, r)] g \cos(\gamma) \partial r \quad (4)$$

$$\frac{\partial}{\partial \xi} \int_0^{\infty} 2\pi r [W(\xi, r) \cos(\gamma)] T(\xi, r) \partial r - 0 \quad (5)$$

In this case  $W$  represents the velocity of the fluid element relative to the surrounding flow (figure 1b),  $\rho(\xi, r)$  is the variable density within the jet,  $T(\xi, r)$  is the corresponding temperature, and the subscript 0 refers to the ambient conditions within the surrounding fluid. In both cases (equations 1 and 3)  $\alpha$  defines the coefficient of radial entrainment which is based upon the velocity component in-line with the instantaneous jet-axis ( $U \cos(\gamma)$  or  $W \cos(\gamma)$ ). In contrast,  $\beta$  is the coefficient of forced entrainment which defines the proportion of the laterally impinging flow ( $U \sin(\gamma)$  or

$W\sin(\gamma)$  which is entrained.

Having identified an appropriate set of initial conditions, and made an assumption regarding the radial distribution of the velocity, density, and temperature, the conservation equations may be integrated to yield a Lagrangian solution for one fluid element released at a given phase of the wave cycle. If these calculations are repeated for a succession of fluid elements released at small increments of the phase angle, the resulting data may be time-averaged in the spatial domain to give a solution which is consistent with the laboratory measurements outlined above.

If the Lagrangian solution is based upon the entrainment coefficients appropriate to discharges in a quiescent ambient (ie.  $\alpha=0.052$ ,  $\beta=0$ ) a comparison with the existing integral solutions highlights the importance of the wave-induced displacement of the jet-axis. Calculations of this type suggest that there is significant wave-induced mixing. However, the reduction in the time-averaged velocities and/or concentrations does not in this case represent a "real" mixing process, but merely reflects the fact that under certain wave conditions the "pollutant" discharge only occupies some spatial locations for a small fraction of the wave cycle. Nevertheless, these results are important since they provide a qualitative explanation for two important features of the flow field which have been misinterpreted by previous researchers.

**(a) The occurrence of non-Gaussian distributions.**

Previous studies by Sharp (1986) and Chyan and Hwung (1994) have commented on the occurrence of "flat-topped" and, in particular, "bi-peaked" velocity and concentration profiles. These distributions have also been noted in the present study as indicated by the temperature data (Case 2) presented on figure 6. However, previous researchers have sought to explain this effect via an additional wave-induced mixing mechanism (referred to as an "enclosing mechanism") which involves the "entrapment" of ambient fluid within the interior of the jet. In contrast, the present calculations suggest that these non-Gaussian distributions may be directly explained by the lateral displacement of the jet and the time-averaged analysis of the data.

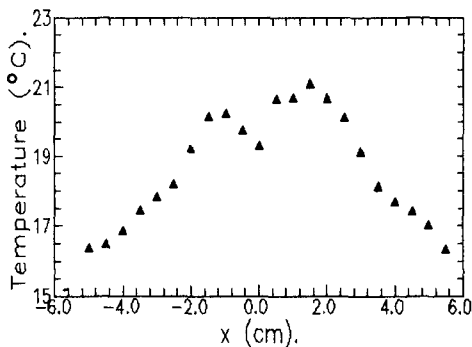


Figure 6. Radial variation in temperature data.

For example, if the length scale ( $l$ ) of the wave-induced displacement is large in comparison to the width ( $b$ ), the characteristics of the wave motion are such that the "residence-time" of the jet at any one spatial location increases with distance from the time-averaged centre-line. This may be demonstrated by considering the displacement of a Gaussian distribution at equal intervals throughout a wave cycle (Case 2 on figure 7a). This indicates that since the wave-induced horizontal velocity reduces to zero (as part of the cyclic reversal) at the extremities of the lateral displacement, the jet spends a larger proportion of one wave period at these locations. This, combined with the method of time-averaging in a fixed spatial domain (or, indeed, data collection from a probe fixed in space), produces a bi-peaked velocity and concentration profile (figure 7b). Furthermore, if the ratio of  $l/b$  is varied, then other non-Gaussian profiles such as the flat-topped velocity distributions shown on figure 7c may be explained.

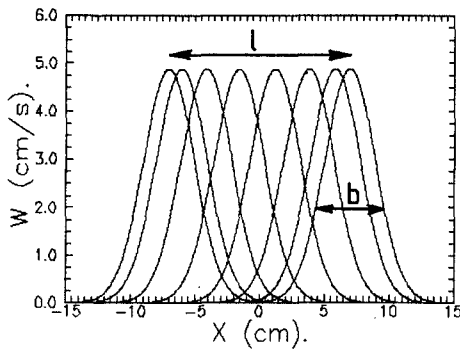
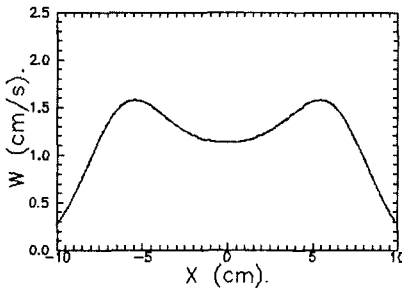
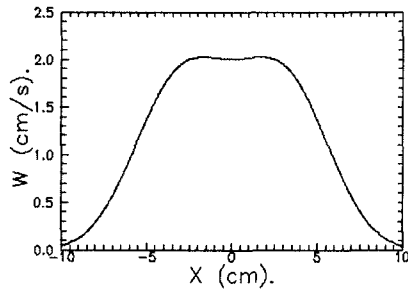


Figure 7a. Lateral displacement of a Gaussian distribution.

(b)  $l > b$ .



(c)  $l > b$ .



Figures 7b-7c. Time-averaged radial distributions.

**(b) The structure of the centre-line decay.**

If the time-averaged velocity and concentration data is measured along the mean jet-axis a decay curve similar to that indicated by the data points in figure 8 (Case 2) results. Once again, this pattern has been observed by previous researchers including Chyan et al (1991) and Chyan and Hwang (1994). Indeed, measurements of this type have been used to classify a three stage decay in which (with increasing distance from the nozzle) the so-called "deflection region" is characterised by a rapid dilution; the "transition region" by a steady or small rise; and the "developed region" by a gradual decay. Unfortunately, the nature of the mixing mechanisms within these layers remains unclear. In particular, no previous explanation has been offered for the increase in both the axial velocity and the pollutant concentrations with increasing distance from the nozzle (ie. within the "transition region").

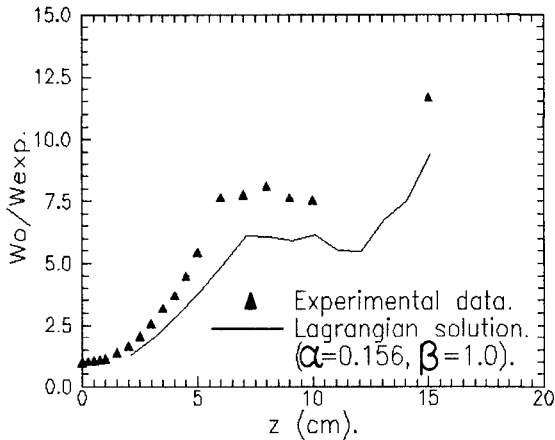


Figure 8. Decay of centre-line velocity (Case 2).

However, it is difficult to envisage how the dilution of the jet could in some way reduce (ie. for the fluid to effectively become un-mixed). As a result, a more probable explanation lies in a reduction in the "apparent" dilution. In other words, at some height above the nozzle, the wave-induced displacement of the jet-axis is reduced. The Lagrangian solution outlined above predicts exactly this effect. Figure 9 describes the trajectory of successive fluid elements released at equal intervals throughout a wave period. In this case, it is clear that the maximum lateral displacement of the fluid elements, and hence the maximum "apparent" dilution, occurs at a height of 12cm above the nozzle. Beyond this point the displacement first reduces and then increases. The present calculations suggest that this intermediate stage will produce an increase in both the predicted time-averaged velocity and concentration. Indeed, the solid curve indicated on figure 8 corresponds to the present Lagrangian solution. This appears to be in good qualitative agreement with the experimental data. In particular, it provides a convincing explanation for the multi-stage structure of the centre-line decay.



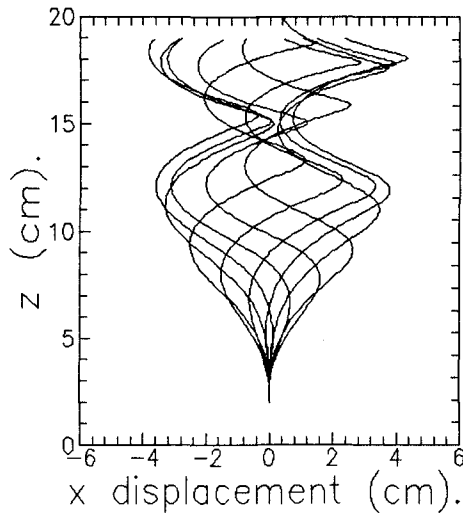


Figure 9. Trajectory of fluid elements (Case 2).

Unfortunately, good quantitative comparisons with the experimental data are, as yet, difficult to achieve because of the uncertainty in the entrainment coefficients ( $\alpha$  and  $\beta$ ). For example, the Lagrangian solution presented on figure 8 was based upon a three-fold increase in the coefficient of radial entrainment ( $\alpha=0.156$ ). This suggests that in addition to the so-called "apparent" mixing (associated with the displacement of the fluid elements), the wave motion also produces a "real" increase in the dilution of the discharged pollutant. This point is further emphasised in figures 10a-10b. Figure 10a describes the mean centre-line velocity (Case 1), and compares the data with a number of potential solutions. The uppermost curve (indicated by a dashed line) represents an integral solution based upon the standard entrainment coefficients ( $\alpha=0.052$  and  $\beta=0$ ); while the second curve corresponds to a Lagrangian solution in which the forced entrainment is maximised ( $\beta=1.0$ ), but the coefficient of radial entrainment remains unchanged ( $\alpha=0.052$ ). The difference between these curves indicates the cumulative effect of the forced entrainment and "apparent" mixing. However, neither curve provides a good description of the experimental data. Indeed, a sensitivity study conducted by Koole and Swan (1994) showed that the best fit to the measured data was achieved by altering the initial conditions to shorten the "zone of flow establishment", and increasing the coefficient of radial entrainment to  $\alpha=0.156$ . This solution is presented on figure 10b. However, the present study (including the data presented on figure 8) suggests that these values ( $\alpha=0.156$  and  $\beta=1.0$ ) are not universally applicable. Indeed, the entrainment coefficients appear to be critically dependent upon the flow conditions at the discharge orifice. In particular, the relative balance between the momentum flux of the jet and that of the wave-induced motion at the discharge orifice appears to be very important.

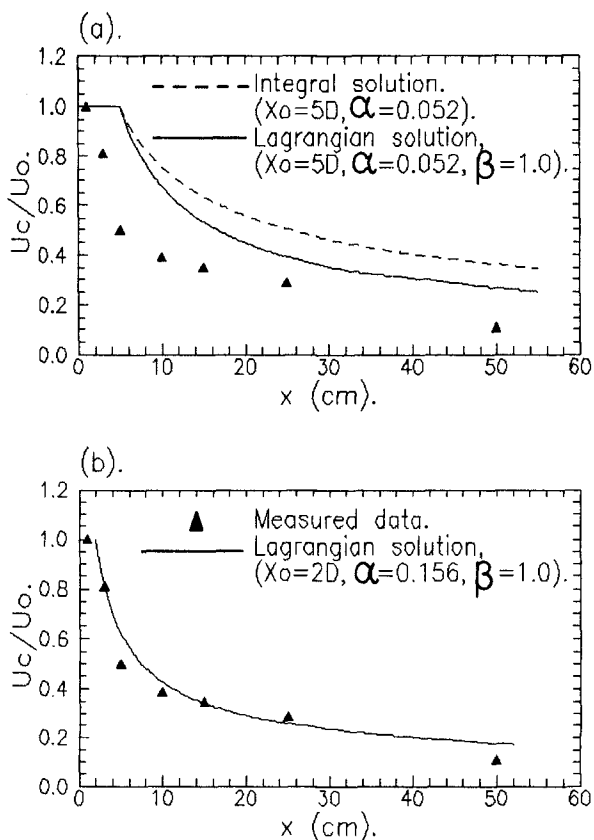


Figure 10a-10b. Non-dimensional centre-line velocity (Case 1).

## 5. Concluding remarks.

The present paper has presented the results of a two-part experimental study in which a two-dimensional non-buoyant jet (orientated in a horizontal direction), and a three-dimensional buoyant jet (orientated in a vertical direction) were discharged beneath a progressive regular wave train. In both cases the mean flow characteristics (including the temperature distribution in Case 2) were compared with an identical discharge in a quiescent ambient. These comparisons confirm that the oscillating wave kinematics have a significant effect upon the near-field mixing and dilution. In particular, the experimental data suggests that a region of intense fluid mixing arises immediately downstream of the discharge orifice, and that this results in a significant shortening of the "zone of flow establishment". This occurrence cannot be predicted by the existing integral solutions which form the basis of present near-field design

calculations.

In contrast, a Lagrangian solution similar to that proposed by Chin (1988) provides a good qualitative description of the experimental data. In particular, it highlights the importance of the "apparent" mixing associated with the wave-induced displacement of the instantaneous jet-axis, and provides a plausible explanation for the non-Gaussian distributions of both the axial velocity and temperature. Indeed, it also explains the non-exponential decay of the mean centre-line characteristics. In particular, the apparent increase in both the velocity and concentration observed by previous authors (notable Chyan and Hwung, 1994) may be explained by the lateral displacement of the jet, and the time-averaged analysis of the laboratory data. Unfortunately, quantitative comparisons between the laboratory data and the Lagrangian solution are, as yet, difficult to achieve because of the uncertainty in the entrainment coefficients ( $\alpha$  and  $\beta$ ). However, the measurements suggest that in addition to the "apparent" mixing the wave motion also produces a significant increase in the rate at which ambient fluid is entrained into the jet. In the two-dimensional case a three-fold increase in the radial entrainment coefficient was recorded. However, comparisons with the three-dimensional data suggest that this increase is insufficient to predict the measured dilution. Indeed, it seems very unlikely that one universal entrainment coefficient will be applicable to all cases of wave-induced mixing.

Finally, although the present paper has only considered wave effects within the near-field region, one should not lose sight of the fact that these solutions provide the "initial" conditions for the random walk formulations used to calculate the dispersion of pollution in the far-field. As a result, the wave-induced mixing identified in the present paper may potentially have a significant effect upon the concentration contours predicted in the far-field.

### **Acknowledgements.**

The authors gratefully acknowledge the financial support provided by the Engineering and Physical Sciences Research Council (EPSRC) under grant number GR/H/18999.

### **References.**

- Chin, D.A., 1988. Model of buoyant-jet surface-wave interaction. *J. Waterway, Port, Coastal and Ocean Engng*, ASCE, 114:331-345.
- Chyan, J.M., Hwung, H.H. & Chang, Y.H., 1991. Wave effects on the mean flow characteristics of turbulent round jets. In: J.H.W. Lee and Y.K. Cheung (Editors), *Environmental Hydraulics*. Balkema, Rotterdam, The Netherlands. 1:109-114.

Chyan, J.M. & Hwang, H.H. 1994. On the interaction of a turbulent jet with waves. *J. Hyd. Res.* 31 (6): 791-810.

Ger, A.M., 1979. Wave effects on submerged buoyant jets. *Proc. 8th Congress, Int. Ass. for Hyd. Res., New Delhi, India C:295-300.*

Koole, R. & Swan, C. 1994. Measurements of a 2-D non-buoyant jet in a wave environment. *Coastal Engineering*, 24:151-169.

Morton, B.R., Taylor, G.I. & Turner, J.S., 1956. Turbulent gravitational convection from maintained and instantaneous sources. *Proc. Roy. Soc., Series A*, 234:1-23.

Sharp, J.J., 1986. The effects of waves on buoyant jets. *Proc. Instn. Civ. Engrs., Part 2*, 81:471-475.

Shuto, N. & Ti, L.H., 1974. Wave effects on buoyant plumes. *Proc. 14th Inter. Conf. Coastal Eng.*, 2199-2209.

## CHAPTER 222

### Model of Bivalve On/offshore Movement by Waves

Hisami Kuwahara<sup>1</sup>

Junya Higano<sup>2</sup>

#### Abstract

This study aimed to develop a numerical method of calculating bivalve movement by waves, and to consider the validity of this model with comparison between the calculated distribution of bivalves and real sampled data.

The distribution of bivalves calculated by this numerical method coincided well with the real sampled data. This numerical method can predict the difference of distribution according to shell length, specific gravity of bivalve, shape of bivalves and so on. Thus, this method will be able to explain the mechanism of zonation of bivalves.

#### Introduction

It has been generally thought that the fishing productivity is low for sandy beach facing the open sea. However, only a few studies about the fishing productivity of sandy beaches have been performed in Japan because of severe sea conditions such as the surf zone. Therefore, almost no technology exists to develop the sandy beaches as fishing grounds.

Many bivalves live in the dissipative exposed sandy beach. These include species commercially important as fishery resources, for example, *Meretrix lamarckii*, *Gomphina melanaegis*, *Pseudocardium sachalinensis* and so on. We believe that the movement of bivalves by waves is closely related to the formation of grounds for their fishing. Therefore, it is very important to study the movement of bivalves for the development of fishing grounds.

On the other hand, recently, the development of

---

<sup>1</sup>Abashiri Fishery Experiment Station, Hokkaido Government, 31, Masuura, Abashiri, Hokkaido, 099-31, Japan.

<sup>2</sup>Natl. Research Inst. of Fishery Engineering, Ebidai, Hasaki-machi, Kashima-gun, Ibaraki Pref., 314-04, Japan.

waterfronts has attracted our attention in Japan and many kinds of artificial facilities have been constructed. Those facilities change the physical environment around them, such as wave velocity, wave direction and so on. It means that bivalves incur risks of being moved to other places where the environment is undesirable for them. We need to predict how such facilities will affect the movement of bivalves, if we are afraid of destruction of the coastal ecosystem.

The study on the movement of bivalves by waves is important not only for the improvement of fishing ground but also for environmental conservation of the sandy coastal zone.

Since 1986, we have studied the relationship between the beach profile and the distribution of bivalves in the surf zone utilizing the pier of the Hasaki Oceanographic Research Facility (HORF) of the Port and Harbor Research Institute. From numerous investigations, we found the following:

1. Passive movement by waves is more important for the distribution of bivalves than their own motility.
2. The distribution of bivalves is related to physical conditions, such as waves, the beach profile, the bivalve and so on.

Therefore, it is considered possible to analyze the mechanism of bivalve movement numerically, based on civil engineering methods.

From these points of view, this paper proposes a numerical method that predicts the movement of bivalves by waves. The wave field is calculated with a time-dependent mild slope equation. The bivalve model is expressed by specific gravity, shell length, coefficient of mass force and drag force and so on. The moving distance is calculated for bivalves at any place and time. After that, we consider the validity of the numerical method with comparison between the calculated distribution of model bivalves and the real sampled data at HORF. The field survey of distribution of bivalves has been carried out by both the National Research Institute of Fishery Engineering and the Port and Harbor Research Institute.

### Numerical Method

This numerical method consists of three calculation steps as follows:

- 1) of the wave field.
- 2) of the distance a bivalve is moved by one wave.
- 3) of the distance a bivalve is moved by cyclic waves.

Through these steps, we can predict the moving distance is calculated for bivalves at any place and time.

### Wave Field

We calculated the wave field in the on/offshore including the surf zone at an optional beach profile with the time-dependent mild slope equations as follows (Watanabe and Maruyama, 1984).

$$\frac{\partial Q_x}{\partial t} + c^2 \frac{\partial \zeta}{\partial x} + f_b Q_x = 0 \quad (1)$$

$$\frac{\partial \zeta}{\partial t} + \frac{1}{n} \frac{\partial (n Q_x)}{\partial x} = 0 \quad (2)$$

where  $Q_x$  denotes  $\int u dz$  ( $u$ : horizontal component of wave orbital wave,  $z$ : vertical coordinate),  $\zeta$ : water surface elevation,  $c$ : wave celerity,  $n$ :  $1/2(1+2kh/\sinh 2kh)$ ,  $k$ : wave number,  $h$ : water depth,  $f_b$ : damping coefficient by wave breaking,  $x$ : horizontal coordinate,  $t$ : time.

The determination of wave breaking point depends on the ratio of orbital velocity and celerity of the wave (Isobe, 1986).

The wave orbital velocity on the seabed is shown as follows. This equation is given by the small amplitude theory.

$$u_{bv} = k Q_x \sin(\sigma t + \epsilon_x) / \sinh(kh) \quad (3)$$

where  $\epsilon_x$  denotes phase difference,  $\sigma$ : angular frequency ( $= 2\pi/T$ ,  $T$ : wave period).

In the surf zone, the flow in the offshore direction, the undertow, occurs when the breaking waves generate mass flux in the onshore direction. Eq.(4) denotes the undertow velocity calculated by Sato et al.(1987). It is assumed that the distribution of undertow is the largest value at the making point of bore and decreases linearly from this point to 10 times breaking water depth in the offshore direction. Eq.(5) shows the distance between the wave breaking point and the making point of bore (Okayasu et al., 1990). Eqs.(4) and (5) are experimentally obtained.

$$U_{br} = A \frac{H^2}{hT} \quad (4)$$

$$l_t = \left( \frac{1}{5 \tan \beta} + 4 \right) h_b \tag{5}$$

where A denotes experimental constant, H: wave height,  $h_b$ : breaking water depth,  $\beta$ : beach slope near breaking point. In this calculation step, we aim to calculate the wave and flow on seabed which acts on the bivalve.

Bivalve Movement by One Wave

Figure 1 shows the bivalve movement model. For bivalves with shell length D on the seabed with slope  $\beta$ , the bivalves move at velocity  $u_s$  due to the wave bottom velocity  $u_b$ . It is assumed that bivalves are passively moved by waves and move on the surface of the bottom by sliding. The components of forces acting on the bivalve are also shown in Figure 1.

- 1) the force caused by the pressure gradient of waves:  $mdu_b/dt$
- 2) the mass force caused by the relative movement between bivalve and fluid:  $C_M m (du_b/dt - du_s/dt)$
- 3) the drag force caused by the relative velocity:  $1/2 C_D \rho_w A (u_b - u_s) |u_b - u_s|$
- 4) the component of gravity parallel to the seabed surface:  $g(M-m) \sin \beta$
- 5) the frictional resistance force caused by sliding of the bivalve on the seabed:  $-\mu_f g(M-m) \cos \beta u_s / |u_s|$ .

where M denotes mass of bivalve ( $1/6 \pi \rho_s D^3$ ,  $\rho_s$ : specific gravity of bivalve), m: mass of water ( $1/6 \pi \rho_w D^3$ ,  $\rho_w$ : specific gravity of water),  $C_M, C_D$ : coefficient of apparent mass force and drag force respectively, A: area of the bivalve that projects,  $\mu_f$ : the frictional resistance coefficient. However,  $\mu_f$  in this numerical method is

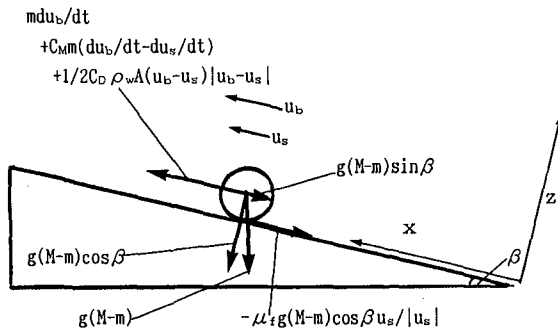


Figure 1. Bivalve Movement Model By Wave.



defined as the coefficient of the degree of movement, which includes the effect of burrowing, rough ripple and so on. Thus, we assumed that the bivalve was moved by the balance of these forces.

The resulting equations of motion of bivalve by wave are shown as follows. These equations are able to express Lagrangian analysis of bivalve movement, when the orbital velocity on the seabed is precisely given at the moved position of bivalve.

$$\frac{dX(t)}{dt} = u_s(t) \quad (6)$$

$$\begin{aligned} M \frac{du_s(t)}{dt} = & m \frac{du_b(X, t)}{dt} + C_d m \frac{d(u_s(t) - u_b(X, t))}{dt} \\ & + \frac{1}{2} C_D A \rho_w |u_b(X, t) - u_s(t)| (u_b(X, t) - u_s(t)) \\ & - (M - m) g \sin \beta - \mu_f g (M - m) \cos \beta \frac{u_s(t)}{|u_s(t)|} \end{aligned} \quad (7)$$

The bivalve starts to move when the total of the drag force and the mass force exceeds the total of the gravity and the frictional resistance force. The bivalve stops when the velocity of the bivalve becomes zero. In addition, the frictional resistance coefficient used is the static one when the bivalve stops and is the dynamic one when the bivalve moves. These equations are calculated by the Runge-Kutter-Gill method. In this calculation step, the distance the bivalve is moved by one wave is calculated at each position of the whole beach.

#### Bivalve Movement by Cyclic Waves

The number of cyclic waves and the position and the number of bivalve individuals are given. The bivalve movement by the cyclic waves is able to be calculated by piling the moving distance by one wave which is given at the previous calculation step.

#### Method of Field Survey & Conditions of Numerical Calculation

The investigation was carried out at the HORF research pier. This pier is on the Hasaki coast in Ibaragi Prefecture, Japan (Figure 2). The total HORF length is 427m and the deck width is 2.5m. This pier juts out into the surf zone. The distribution of bivalves has been investigated at intervals of 10m along HORF once a month since 1986 by means of the Smith-McIntyre grab (22×22cm). This investigation

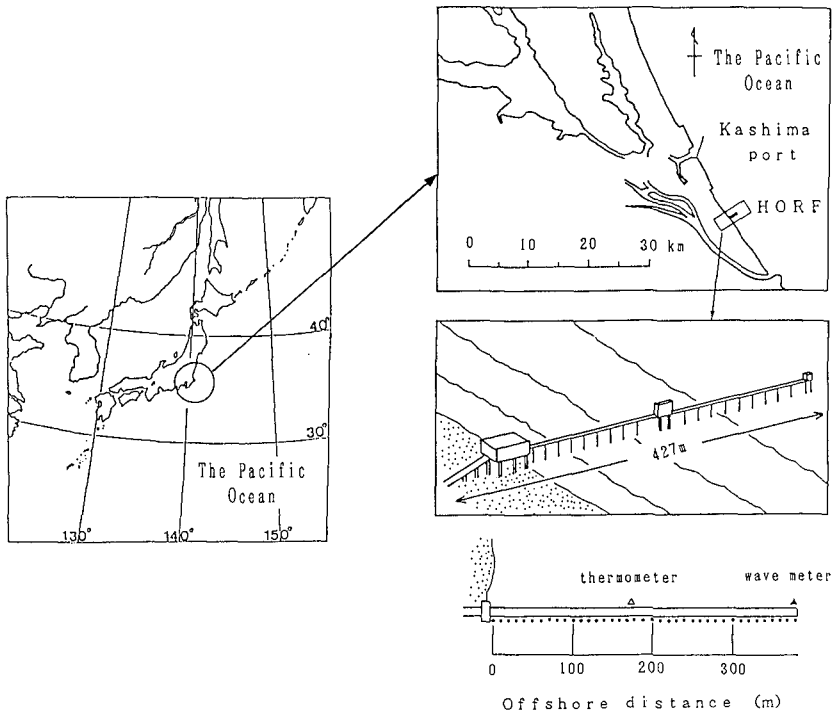


Figure 2. Study Site of Field Survey. The coast consists of exposed sandy shores facing the Pacific Ocean. Location of Hasaki Oceanographical Research Facility (HORF), water temperature meter, wave gages and sampling stations of bottom sediments(\*) are shown.

method and results were described in detail by Higano et al. (1993a).

The following conditions were used in the numerical calculation. The beach profile used the field data at HORF and the tidal level used the value of the observation at 15:00, June 23, 1987. The physical characteristics of waves and bivalves were used the following values.

$H_0=1.5\text{m}$ ,  $T=7.0\text{sec}$

$D=20\text{mm}$ ,  $\rho_s=1.8$ ,  $C_M=0.5$ ,  $C_D=0.5$ ,  $\mu_{fs}=1.0$ ,  $\mu_{fd}=0.5$

The specific gravities  $\rho_s$  of *Macra crossei*, *M. lamarckii* and *G. melanaegis* are 1.3, 1.6, and 1.8, respectively (Higano et al., 1993b).

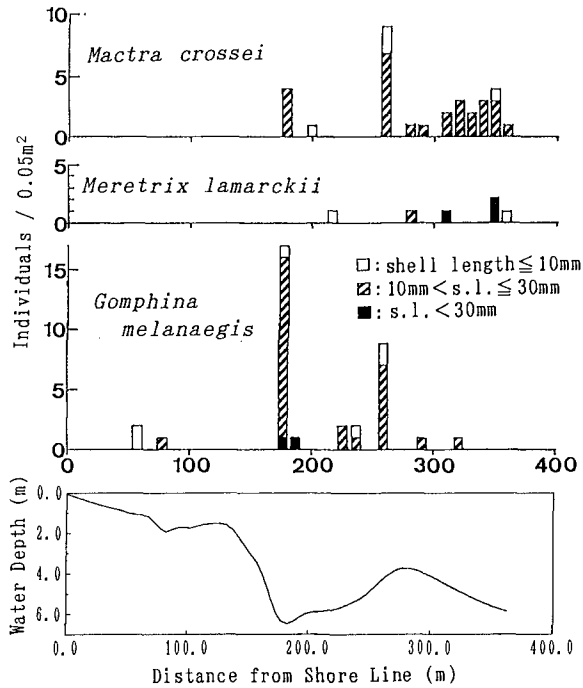


Figure 3. Beach Profile and Distribution Density of Bivalves (columns) at HORF on June 23, 1987.

## Results and Discussion

### Results of Field Survey (June 23, 1987)

Figure 3 shows the distributions of three bivalve species and the beach profile at HORF, on June 23, 1987. The beach profile indicated the trough largely scoured by a storm a few days previously. The onshore side of the trough became remarkably steep. *G. melanaeigis* were accumulated extremely densely at 180m from the shoreline. *M. lamarckii* tended to distribute on the offshore side of the bar. *M. crossei* distributed mainly on the zone farthest offshore.

Photograph 1 shows the bivalves sampled in this field: *G. melanaeigis*, *M. lamarckii* and *M. crossei*, in order from left. These physical characteristics (for example, specific gravity, shape, roughness of bivalve surface and so on) are varied. It is considered that the physical differences of bivalves form the zonation of bivalves as shown in Figure 3.



Photo 1. Bivalves Sampled at HORF. ( Left: G. melanaegis, Center: M. lamarckii, right: M. crosseii )

#### Results of Numerical Calculation

Figure 4 shows the results of calculation of the wave field. The offshore wave is assumed to have  $H_0$  of 1.5m and  $T$  of 7.0sec.

Figures 4 (a), (b) and (c) show the distributions of the wave height, the wave orbital velocity on the seabed and the undertow velocity, respectively. These horizontal axes show the distance from the shoreline.

The wave breaking occurred at 157m from the shoreline. The wave height, wave orbital velocity and undertow velocity were maximum near the breaking point and were damped drastically at the onshore side of the trough.

We exerted the wave orbital velocity and undertow velocity on the model bivalve and calculated the bivalve movement. Figure 5 shows the bivalve's movement by waves. The model bivalve assumed the physical characteristics of G. melanaegis. Figure 5 (a) shows the distribution of the distance moved by one wave. The vertical axis shows the moving distances of bivalves, which are taken to be positive in the onshore direction and negative in the offshore direction. Figure 5 (b) shows the movement of bivalves by the cyclic wave. The vertical axis is the passage of time. Each model bivalve was placed on the seabed at intervals of 10m along the on/offshore line in the initial condition.

Although bivalves on the offshore side of the bar and on the onshore side from 100m showed almost no movement, they moved in the onshore direction from the top of the bar to the bottom of trough and in the offshore direction on the

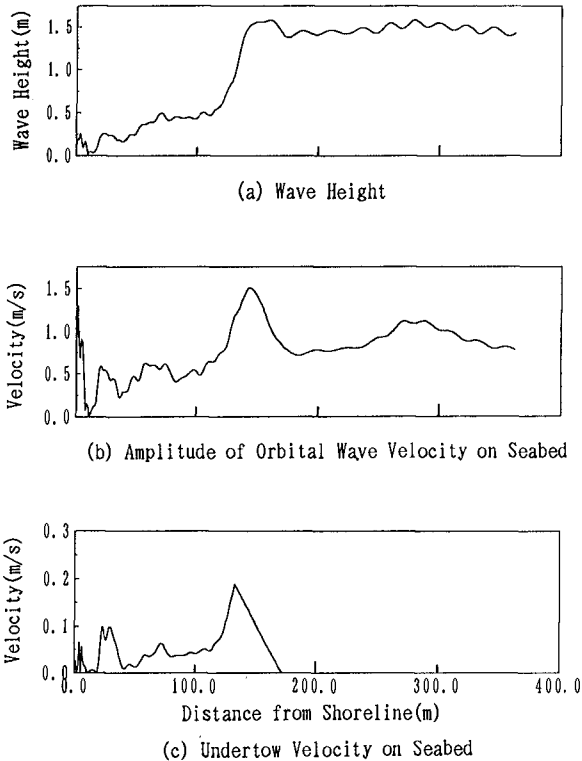


Figure 4. Results of calculation of Wave Field. ( The beach profile is shown in Figure 3. The offshore wave are  $H_0=1.5\text{m}$  and  $T=7.0\text{sec}$ . )

onshore side of the trough. Bivalves were extremely densely accumulated at 180m by cyclic waves, which is the bottom of trough. This tendency was the same as the field survey in Figure 3.

After that, we varied the physical characteristics of the waves and the bivalves and tried to calculate model bivalve distributions. Figure 6 shows the results of calculated distribution of the model bivalves. Figures 6 (a), (b) and (c) show the effect of wave characteristics, shell length and specific gravity of the bivalve, respectively. Individual bivalves were counted in each section at an interval of 10m. The distributions after 10,000sec were shown.

In Figure 6 (a), although bivalves hardly moved when the wave height was 0.5m and the wave period was 5.0sec, they

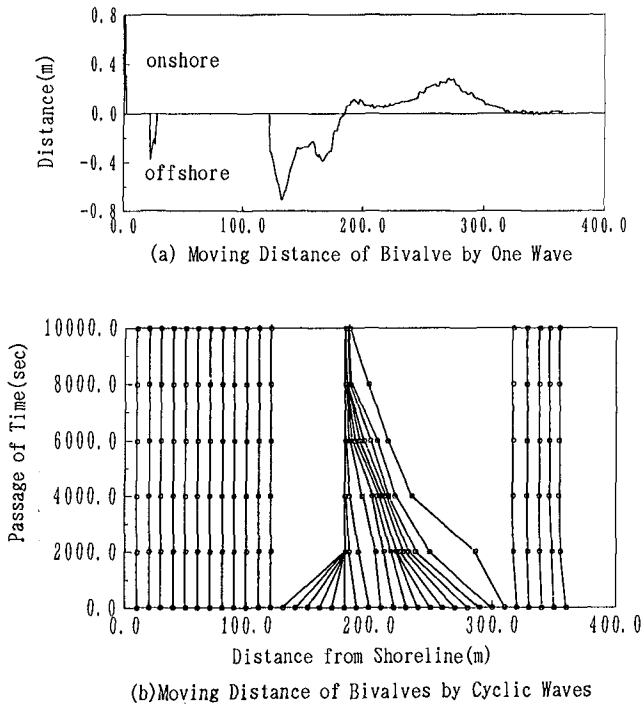


Figure 5. Bivalves Movement by Waves. The model bivalves assumed the *G. melanaegis*. (  $D=20\text{mm}$ ,  $\rho_s=1.8$ ,  $C_M=0.5$ ,  $C_D=0.5$ ,  $\mu_{fs}=1.0$ ,  $\mu_{fd}=0.5$  )

accumulated in the trough when the wave height was 1.5m and the period was 7.0sec and on the top of the bar when the wave height was 2.5m and the period was 9.0sec. In Figure 6 (b), the model bivalves with shell length 5mm accumulated at 150m and 170m. Those of shell length 20mm accumulated at 180m. However, those of shell length 40mm hardly moved. In Figure 6 (c), the distribution of model bivalves of specific gravity 1.6 had the same tendency as those of specific gravity 1.8. These model bivalves accumulated at 180m. The model bivalves of specific gravity 1.3 accumulated at 150m and 170m. These calculated results coincide well with the real sampled data for *G. melanaegis* of 10 to 30mm in diameter accumulated at the bottom of trough. But this calculated result cannot explain *M. crossei* in the offshore side of the bar. The reason why the results don't coincide may be that the initial distribution of bivalve at the real beach was different from that of the numerical study.

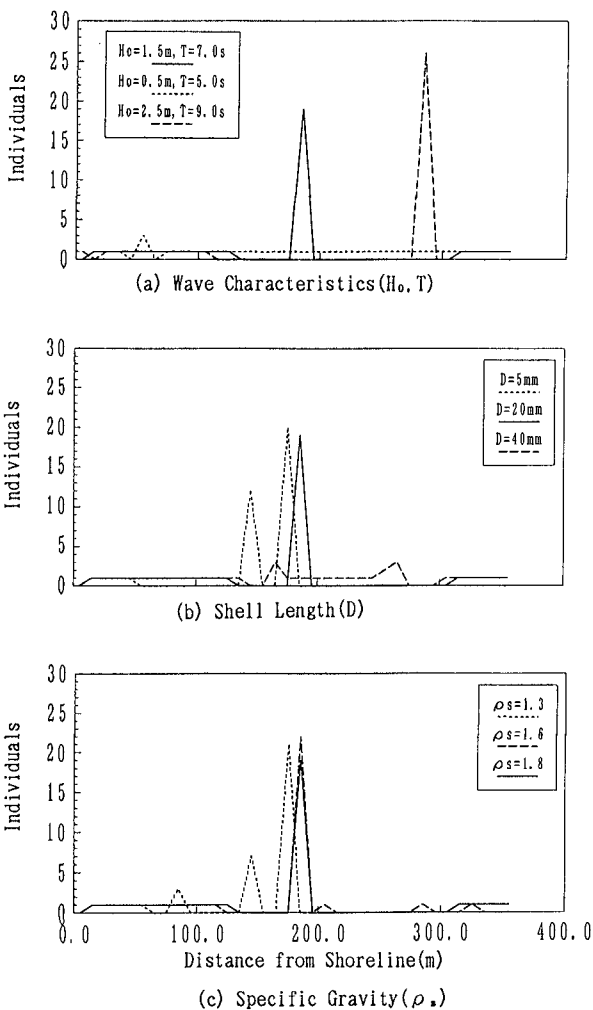


Figure 6. Relation between Distributions of Model Bivalve and Physical Characteristics of Waves and Bivalves.

### Conclusion

In this study, we developed the numerical method of calculating bivalve movement by waves, and we considered the validity of this model with comparison between the calculated distribution of bivalves and the real sampled

data at HORF.

As a result, the following main findings were obtained from this study:

- 1) This numerical method can predict the difference of distribution given the shell length, the specific gravity and so on. Thus, this method will be able to explain the mechanism of zonation of bivalves.
- 2) This numerical method explains the tendency which the bivalves accumulate in the trough. The result coincides well with the real accumulation of G. melanaegis.
- 3) But, this numerical method cannot explain the accumulation of M. crosseii on the offshore side of the bar.
- 4) The bivalves throughout the area start to move and accumulate remarkably when the waves become severe.

As mentioned above, we found that this numerical method was useful in predicting the bivalves' movement by wave. We are conducting experimental study with the 2-dimensional wave tank. We are trying to give this numerical method more precision. This numerical prediction method will be able easily to be applied to bivalves' horizontal movement by waves. With this numerical method, we hope to contribute to the development of fishing grounds and the conservation of coastal zones.

#### Acknowledgements

The authors wish to thank Dr. T. Yamashita (Hokkaido Univ.), Dr. N. Mimura (Ibaraki Univ.) and Dr. Y. Nakamura (Hokkaido National Fishery Research Institute) for many helpful comments.

#### References

- Isobe, M. (1987). Parabolic equation model for transformation of irregular waves due to refraction, diffraction and breaking, Coastal Eng. Japan, Vol.30, No.1, pp.33-47.
- Okayasu, A., M., Isobe and A., Watanabe (1990). Experimental study on making point of bore wave breaking, Proc. 44th Annual Conf. for Civil Eng., JSCE, II, pp.614-615. (in Japanese)
- Kuwahara, H. and J. Higano (1994). Analysis method on-offshore movement of bivalves by waves, Bull.N.R.I.F.E. 15, pp.25- 40 (in Japanese).
- Kuwahara H., Higano J, Nakamura Y. and N, Mimura (1994). Study on mechanism of bivalve movement by waves and validity of numerical method, Proc.41th Japanese conf. on Coastal Eng., JSCE pp.376-380 (in Japanese).
- Higano J., K. Kimoto and Y. Yasunaga, (1993a). The change of beach profile and the distribution of sandy beach



- bivalves at Kashima-nada I. report of the result in 1987. Tech.Rept N.R.I.F.E. Aquacul.& Fish. Port. 14, pp.1-16 (in Japanese).
- Higano J., K.Kimoto, and Y.Yasunaga(1993b). Influence on the relation between burrowing behavior and physical environment regarding the distribution of sandy beach bivalves Meretrix lamarckii and Gomphina melanaegis. Bull.N.R.I.F.E. 14, pp.65-87(in Japanese).
- Sato S., M.Fukuhara and K.Horikawa(1987). Laboratory study on near-bottom velocity due to irregular wave, Proc.34th Japanese conf.on Coastal Eng., JSCE, pp.36-40 (in Japanese).
- Watanabe A. and Maruyama Y.(1984). Numerical analysis of combined refraction, diffraction and breaking, Proc. 31st Japanese Conf.on Coastal Eng., JSCE, pp.103-107 (in Japanese).

## CHAPTER 223

### INITIAL GAP IN BREAKOUT OF HALF-BURIED SUBMARINE PIPE DUE TO WAVE ACTION

Adrian W.K. Law<sup>1</sup> and Mostafa A. Foda<sup>2</sup>

#### ABSTRACT

An analytical formulation is presented for the analysis of the breakout of a half-buried submarine pipe due to wave action. The formulation accounts for the contact between the pipe and the soil due to the horizontal hydrodynamic force. An asymmetric gap geometry is described that incorporates a second order expansion in the gap opening due to the pipe rise. Results with this formulation demonstrate the existence of an initial gap of the order 1 mm in the breakout experiments. With this initial gap, the gap flux dominated the influx of water into the gap from the beginning of the breakout process.

#### 1.0 INTRODUCTION

Breakout of a partially buried pipe under severe wave action is one of the possible mechanisms for the pipe to detach from the sea bed (Foda, 1985). The configuration is schematically sketched in Figure 1. Experiments were performed by the authors to investigate the breakout of a half-buried pipe in the laboratory, and the results were previously reported in Foda et al. (1990).

---

<sup>1</sup> Bechtel Corporation, 50 Beale St., P.O. Box 193965, San Francisco, CA 94119, USA

<sup>2</sup> Hydraulic and Coastal Engineering Division, Department of Civil Engineering, University of California at Berkeley, Berkeley, CA 94720, USA

The bulk of the Foda et al. (1990)'s paper dealt with the analysis of the pressure and displacement measurements from the breakout tests. An uniform lift analytical model using the poro-rigid bed assumption was also presented in that paper. This uniform lift model is based on the consideration of the action of the net lift force on the pipe. This net lift force induces an uniform liftoff of the pipe in the vertical direction, thus creating a symmetric gap geometry as well as symmetric gap suction pressures about the vertical axis of the semi-circular trench. However, further considerations of the effect of the oscillatory horizontal hydrodynamic force reveal that this uniform liftoff conceptualization may not be fully representative of the physical breakout process. These considerations are discussed in the followings.

Through analysis of the measurements on the hydrodynamic forces and the resultant forces by the gap suction pressures, we demonstrated in Foda et al. (1990) that the pipe was always in contact with the soil. In essence the pipe was bouncing back and forth against the sides of the soil's semi-circular interface. In doing so, the gap distribution would become asymmetric with respect to the vertical axis. There would be some finite opening on one end of the semi-circular trench whereas on the other end the gap would be closed by the contact between the pipe and the soil. This asymmetric gap distribution, however, is not reflected in the symmetric gap assumption in the uniform lift model.

The asymmetric gap distribution also poses differences in the pressure boundary conditions on both ends. On the opening edge the gap pressure is subjected to the positive pressure buildup due to the stagnation point in front of the pipe, whereas on the other side the contact between the pipe and the soil isolates the suction pressures inside the gap to the ambient pressure above. The situation in terms of the pressure boundary conditions is thus closer to the tilted lift case than the uniform lift case in Mei et al. (1985). With the differences in the gap pressure distribution about the vertical axis, the resulting horizontal force will be reinforcing the horizontal hydrodynamic force in the first harmonic. This is indeed what was observed in our analysis of the laboratory measurements on the horizontal force balance. The above discussion demonstrates that an asymmetric gap model can better represent the physical situation than the uniform lift model.

With these considerations, we set out to develop an asymmetric gap formulation that incorporates the effect of the oscillatory horizontal hydrodynamic force. Subsequently, based on this formulation, we will address the existence of some initial gap opening in the beginning of the breakout process. However a brief summary of the laboratory experiments is first presented in the next section.

## **2.0 EXPERIMENTAL SETUP**

The experimental setup consisted of a 0.22 m diameter PVC pipe half-buried in a sand basin inside a wave flume under 0.61 m water depth. The sand was a well-sorted medium sand with  $d_{50}$  of 0.32 mm and with permeability approximately equal to  $0.85 \times 10^{-11}$  m. The half-buried pipe was subjected to monochromatic waves of approximately 3 second wave period and 0.15 m wave height until breakout from the sea bed occurred.

Submerged weight of the pipe was used as a control parameter to generate different net lift forces on the pipe thus producing different breakout times. The vertical displacement of the pipe was monitored using a hermetically sealed sensor installed inside the pipe. Pressures around the pipe were also recorded. Additional descriptions of the experimental setup can be found in Foda et al. (1990).

A typical vertical movement history of the half-buried pipe in the experiments is shown in Figure 2. As can be observed in the figure, after the half-buried pipe was exposed to the monochromatic waves, the pipe started to rise with a steady but very slow rate (of the order of 2.5 mm/min in the experiments). No significant soil erosion around the pipe was observed. Minor oscillatory motion of the pipe was also recorded superimposing on the net vertical movement. The net rising rate gradually increased near the breakout time. Subsequently, at the breakout time a sudden and rapid release of the pipe from the sea bed occurred.

## **3.0 PORO-RIGID MODEL WITH ASYMMETRICAL GAP DISTRIBUTION**

In this section, an analytical formulation is presented for the analysis of the breakout of a half-buried pipe from sea bed due to wave action. First, the movement of the pipe during one wave cycle is examined as shown in Figure 3. The pipe oscillates horizontally with respect to the underlying trench due to the wave-induced horizontal force. This horizontal oscillatory motion of the pipe produces a mirror image setting between the two halves of a wave period. With this mirror image and in a quasi-steady manner, it is postulated that the situation can be analyzed as if the pipe is subjected to a steady lift force  $F_L$  and an unidirectional steady horizontal force  $F_h$  (Figure 4) of the following magnitudes based on the Morrison equation:

$$\text{horizontal} \quad F_h = \frac{2}{T} \int_0^{T/2} \rho \left[ C_M \frac{\pi D^2}{4} \frac{\partial u}{\partial t} + \frac{1}{2} C_D D u |u| \right] dt \quad (1a)$$

vertical 
$$F_L = \frac{1}{T} \int_0^T \frac{1}{2} \rho C_L D u^2 dt \quad (1b)$$

where  $T$  is the wave period,  $\rho$  the water density,  $D$  the pipe diameter,  $u$  the wave-induced horizontal velocity at the mud line, and  $C_L$ ,  $C_M$  and  $C_D$  the lift, added mass and drag coefficients for a half-buried pipe respectively. In our experiments the value of  $C_L$  was measured to be 2.55.

At this point, to facilitate further analysis we introduce a conformal mapping to transform the geometry of the seabed to a full half plane without indentation:

$$\zeta = \frac{1}{2} - \frac{1}{2D} \left( z + \frac{D^2}{4z} \right) \quad (2)$$

where  $z = (x,y)$  = the physical plane with coordinate orientation as shown in Figure 4;  $\zeta = (\xi,\eta)$  = the mapped domain. From a geometrical standpoint, the asymmetric gap induces by the rise of the pipe while maintaining contact with the soil can be approximated as:

$$\Delta(\theta, t) = \Delta_o(t) \left( \sin \theta - \frac{\delta}{2} \cos \theta (1 - \cos \theta) \right); \quad \delta = \frac{\Delta_o(t)}{R} \quad (3)$$

where  $\Delta$  is the gap thickness,  $\Delta_o$  the midgap thickness, and  $R$  the pipe radius. The gap distribution is shown in Figure 5. The asymmetry of the gap is thus only in the second order, or  $O(\delta^2)$ . However this second order asymmetry properly accounts for the expansion in the gap opening due to the pipe rise, and thus is necessary for computing the growth of the gap flux which is the supply of ambient water through the gap opening at  $\xi = 1$ . In the mapped plane, this gap distribution becomes:

$$\Delta(\xi, t) = \Delta_o(t) f(\xi); \quad f(\xi) = \left( 2\sqrt{\xi - \xi^2} + \delta(t)\xi(2\xi - 1) \right) \quad (4)$$

We will now follow the poro-rigid bed approach in Mei et al. (1985) to formulate the governing equation for the flow inside the gap between the pipe and the soil. In this approach, the soil is assumed to be poro-rigid and Darcy's law is assumed for the pore water flow. Lubrication theory is used to analyze the flow along the gap between the pipe and the soil. Following the analysis of Mei et al. (1985) and with an further assumption of a no-slip boundary condition at the surface of the porous bed, we obtain the following water budget equation for the expanding gap:

$$\xi D \frac{d\Delta_o}{dt} = \frac{k}{\mu\pi} \int_0^1 \frac{p}{\eta - \xi} d\xi + \frac{\partial p}{\partial \xi} \frac{\Delta^3 \sqrt{\xi - \xi^2}}{6\mu D} \quad (5)$$

where  $\mu$  is the viscosity,  $k$  the intrinsic permeability of the porous bed, and  $p$  the dynamic pressure in the gap. Taking  $\xi = 1$ , the left-hand side of Eq. 5 then represents the first order, or  $O(\delta)$ , expansion rate of the gap volume. The first term on the right-hand side gives the contribution to such expansion from the pumping of pore water into the gap, which is given in terms of a Cauchy principle-value integral. The last term of Eq. 5 gives the gap flux. It should be noted that the gap flux term will not vanish at  $\xi = 1$  despite its appearance. This is because both  $\Delta(\xi = 1)$  and  $\left. \frac{\partial p}{\partial \xi} \sqrt{\xi - \xi}^2 \right|_{\xi=1}$  have finite non-zero values at this edge of the semi-circular trench where the ambient water is drawn into the gap.

Next, the balance of forces before the breakout is considered. With the asymmetric gap distribution, the resultant force from the gap suction pressures in the horizontal direction will be reinforcing the horizontal hydrodynamic force. Together they will then be resisted by a reaction force from the soil. In the vertical direction, the balance of forces yields:

$$F + D \int_0^1 p \, d\xi = 0 \quad (6)$$

where  $F$  is the net lift force = time-averaged hydrodynamic lift  $F_L$  minus the pipe submerged weight  $F_s$ . The horizontal force balance in the first harmonic and the vertical force balance in the zero harmonic were both observed in the experimental results.

At this point, we need to address the pressure boundary condition at the gap opening  $\xi = 1$ . Due to Bernoulli's effect, there will be positive pressure buildup with the stagnation point in front of the pipe. This positive pressure can be calculated in a quasi-steady manner as:

$$p_o = \frac{1}{T} \int_0^T \frac{1}{2} \rho u^2 dt = \quad (7)$$

The formulation of the asymmetric gap model is now completed. We will further convert the governing equations into nondimensional form by introducing the following variables:

$$P = \frac{pD}{F}; \quad \sigma = (Dk)^{-1/3} \Delta_o; \quad \tau = \frac{Fk^{2/3}}{\mu D^{7/3}} t \quad (8)$$

The two governing equations, Eqs. 5 and 6, become:

$$\xi \frac{d\sigma}{d\tau} = \frac{1}{\pi} \int_0^1 \frac{P}{\eta - \xi} d\xi + \sigma^3 \frac{\partial P}{\partial \xi} \frac{\sqrt{\xi - \xi^2}}{6} f^3(\xi) \quad (9)$$

$$\int_0^1 P d\xi = -1 \quad (10)$$

Eqs. 9 and 10 permit numerical computation in a manner as suggested in Mei et al. (1985). However it should be emphasized that closely spaced numerical grid will be required near  $\xi=1$ . This is to avoid introducing arbitrary large opening for the computation of the gap flux in the numerical algorithm. For example, following the mid-point computation approach in Mei et al. (1985) with  $N+1$  nodes (resolution  $\varepsilon = N^{-1}$ ), the volume of the gap flux in Eq. 9 will be computed as  $\frac{P_{at\xi=1} - P_{at\xi=1-\varepsilon}}{6\sqrt{\varepsilon}/2} \sigma^3 (\sqrt{2\varepsilon} + \delta)^3$ . Since this flux term should be proportional to  $\sigma^3 \delta^3$ , it is thus required that  $\varepsilon < \frac{\delta^2}{2}$ . Typically  $\delta \sim O(10^{-2})$  when the gap flux becomes significant, and thus the requirement would then be  $\varepsilon \sim O(10^{-4})$  or  $N \sim O(10^4)$ . This is a stringent requirement since the computation will then involve finding the inverse of a large  $N \times N$  matrix, a task that is both time-consuming and error-prone.

Note that if indeed the finite gap opening at the edge of the trench is due only to the second order expansion due to the pipe rise, it would be more appropriate to use another time scale,  $T_b = \frac{\mu D^{8/3}}{Fk^{5/6}}$ , based on the balance of terms in Eq. 5 at  $\xi = 1$  of  $\frac{D^2 \delta}{T_b} \sim \frac{kF}{\mu D} \sim \frac{FD \delta^6}{\mu}$ . However whether the gap opening is realistically second order in nature will be discussed in the following section on the existence of an initial gap.

#### **4.0 INITIAL GAP**

As shown in Figure 2, the pipe typically rose with a net constant rate during the initial stage in the breakout process. These initial rates of rise,  $R \frac{d\delta}{dt}$ , were of the order of 2.5 mm/min (0.04 mm/s) in the laboratory experiments. The gap volume expansion due to this vertical rise of the pipe should be balanced by the combined pore water and gap fluxes. In the following section we will discuss the implication of these measured rates on the initial gap geometry base on the derived governing equations.

Numerical computation using Eqs. 9 and 10 without the gap flux term shows that the initial rate of rise,  $\frac{d\sigma}{d\tau}$ , due to the pore water flux alone is approximately 0.85. This is slower than the corresponding rate with the uniform lift model which can be determined analytically to be equal to  $8/\pi$  (see Mei et al. (1985)) but in the same order of magnitude.

With  $D = 0.22\text{m}$  and  $k = 0.85 \times 10^{-11} \text{ m}^2$  in our experiments, the non-dimensional length scale will then be  $(Dk)^{1/3} = 0.12 \text{ mm}$ . The breakout time scale,  $T_b$ , was of the order of  $O(10^2)$  in the breakout tests. The measure rate of rise of approximately  $0.04 \text{ mm/s}$  thus represents a nondimensional rate of rise of around 30. This measured rate is an order of magnitude higher than the predicted rate supported by the pore water flux. Despite the fact that there were possible variations in some of the experimental parameters such as the soil permeability, the differences were judged to be too large to be explained by these variations. Clearly this points to the existence of an initial gap in the beginning of the breakout process. In addition, it also shows that in our experiments the pore water flux, though always important in relieving the negative pressures near the contact ( $\theta \cong 0$ ) where the gap width is always small, was insignificant in terms of expanding the gap volume and allowing the pipe to rise.

Physically, this initial gap can be due to the imperfect contact between the pipe and the soil. Another mechanism of generating this initial gap in the soil region around the two ends of the semi-circular trench would be through plastic deformations. In the first half of the wave cycle, one end of the soil trench will be compressed as the horizontal force and the resultant force from the gap pressures together push the pipe against the soil. This compression will subsequently be released in the second half of the wave cycle when the pipe moves to rest against the opposite side. It is possible that the soil skeleton in these areas is weakened by the periodic compression and relaxation, allowing plastic deformations to take place.

We will first use a scaling analysis to examine the magnitude of this initial gap. Let  $\bar{\Delta}$  be a characteristic length scale for the initial gap. Comparing the two terms in the RHS of Eq. 5 for  $\xi = 1$  suggests that the balance between the pore water and the gap fluxes will be of the order of  $O\left(\frac{kD}{\bar{\Delta}^3}\right)$ . This implies that  $\bar{\Delta}$  should be much larger than  $\sqrt[3]{kD}$ , or  $0.1 \text{ mm}$  in this case.

The initial gap geometry in reality can be very complicated, and will also depend to some extent on the processes how the pipe was half-buried. To get an general assessment on the order of magnitude of the initial gap in our experiments, we assume a simple constant gap geometry as follows:



$$\Delta = \Delta_i \quad \text{for} \quad 0 < \theta \leq \pi \quad (11)$$

where  $\Delta_i$  represents an initial constant gap. Ignoring the pore water flux term, Eq. 5 can be simplified in the physical plane to be:

$$R^2(1 - \cos \theta) \frac{d\delta}{dt} = \frac{\Delta_i^3}{12\mu R} \frac{\partial p}{\partial \theta} \quad (12)$$

Substituting the constant gap geometry into Eq. 12 and integrating yield:

$$p = p_o - \frac{12\mu R}{\Delta_i^3} \frac{d\delta}{dt} (\pi - \theta + \sin \theta) \quad (13)$$

Finally, substituting Eq. 13 into 6 in the physical plane, the initial rate of rise can then be estimated as:

$$R \frac{d\delta}{dt} = \frac{(F + 2p_o R)\Delta_i^3}{18\pi \mu R^3} \quad (14)$$

With  $R = 0.11$  m,  $\mu = 10^{-3}$  kg/ms,  $p_o \sim O\left(\frac{F}{R}\right)$  and  $F \sim O(10)$  in our experiments, the measured initial rate of rise of the order of 0.04 mm/s would represent an initial gap  $\Delta_i$  of the order of 1 mm in the beginning of the breakout process.

## 5.0 CONCLUSION

An asymmetric gap model is presented for the analysis of the breakout of a half-buried pipe from sea bed due to wave action. The model accounts for the contact between the pipe and the soil due to the horizontal hydrodynamic force. An asymmetric gap geometry is described that incorporates the second order expansion in the gap opening due to the pipe rise. Quasi-steady vertical force balance is assumed. The resultant horizontal force from the distribution of the gap pressures reinforces the horizontal hydrodynamic force in the first harmonic which is consistent with the experimental observations. Calculations with this asymmetric gap model demonstrate the existence of an initial gap of the order of 1 mm between the pipe and the soil in the breakout experiments. This initial gap is postulated to be due to imperfect contact between the pipe and the soil and possible plastic soil deformations due to periodic compression and relaxation of the soil skeleton around the pipe. With this initial gap, the gap flux is found to dominate the influx of water from the beginning of the breakout process. The pore water flux, though important in relieving the negative pressures near the

contact where the gap width is always small, was insignificant in terms of expanding the gap volume and allowing the pipe to rise. The role of the initial gap and the soil deformation around the pipe to the breakout process will be further examined in the future.

### **ACKNOWLEDGMENT**

This work is a result of research sponsored in part by NOAA, National Sea Grant College Program, Department of Commerce, under grant number NA85AA-D-SG140, project number R/OD-2, through the California Sea Grant College Program, and in part by the California State Resources Agency.

### **REFERENCES**

- Foda, M.A. (1985). Pipeline breakout from seafloor under wave action. *Appl. Oc. Res.*, 7(2), pp79-84.
- Foda, M.A., Chang, J.Y.H. & Law, A.W.K. (1990). Wave-induced breakout of half-buried marine pipes. *J. Waterways, Port, Coast. and Oc. Div., ASCE*, 116(2), pp267-286.
- Mei, C.C., Yeung R.W. & Liu, K.F. (1985). Lifting of a large object from a porous seabed. *J. Fluid Mech.*, Vol. 152, pp 203-215.

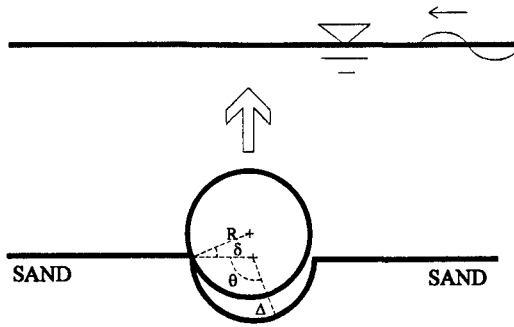


Figure 1. Configuration of the breakout of a half-buried pipe from sea bed due to wave action.

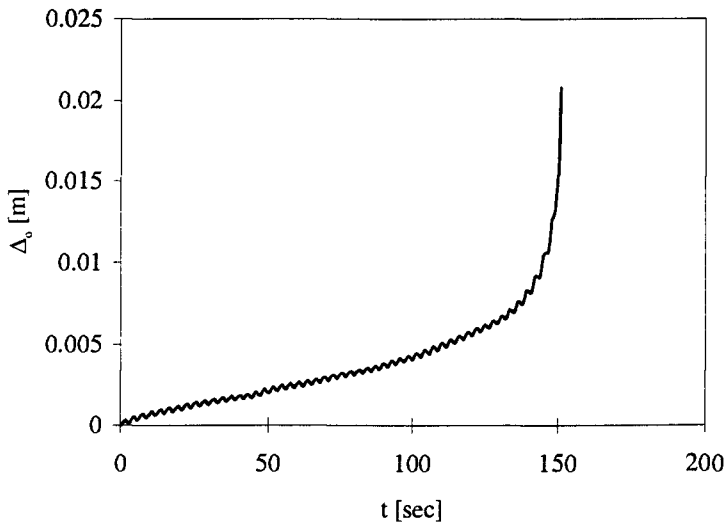


Figure 2. Measured vertical displacement history in Experiment F4.

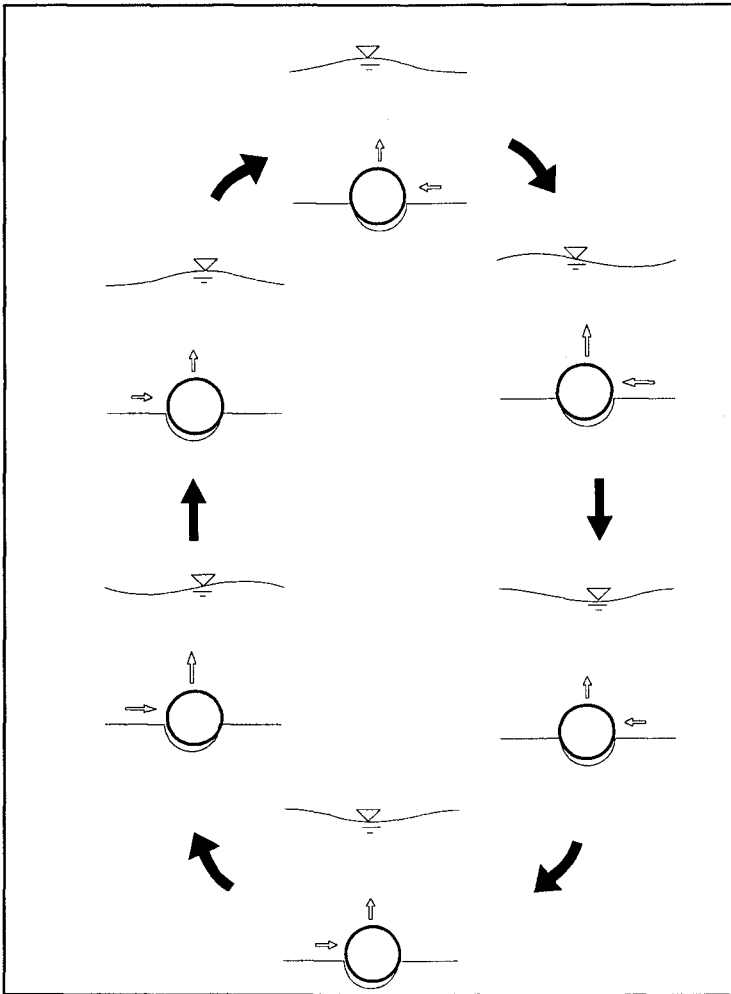


Figure 3. Movement of the pipe during one wave cycle.

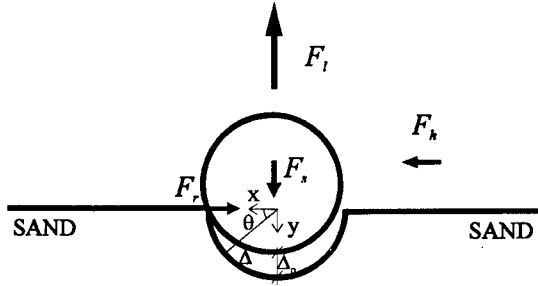


Figure 4. Conceptual model for the quasi-steady analysis of the breakout of a half-buried pipe from sea bed due to wave action.

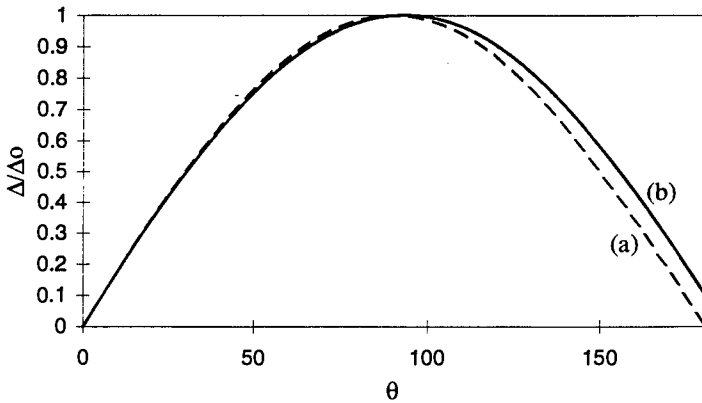


Figure 5. Geometry for (a) a symmetric gap  $\Delta = \Delta_0 \sin \theta$  and (b) an asymmetric gap  $\Delta = \Delta_0 (\sin \theta - \delta \cos \theta (1 + \cos \theta)/2)$  with  $\delta = 0.1$ .

## CHAPTER 224

# ANALYTICAL SOLUTION FOR THE WAVE-INDUCED EXCESS PORE-PRESSURE IN A FINITE-THICKNESS SEABED LAYER

Waldemar MAGDA \*

### ABSTRACT

This paper presents the analytical solution to the wave-induced excess pore-pressure oscillations in permeable seabed sediments, derived for the case of limited thickness of the seabed layer. In order to show the utility of the analytical solution, a wide parameter study has been performed with a special emphasis to the relative compressibility of the two-phase (soil skeleton – pore-fluid) medium. The results of example computations are discussed with respect to the accuracy of the ‘finite-thickness’ analytical solution for the pore-pressure.

### INTRODUCTION

The excess pore-pressure oscillations in permeable seabed sediments, induced by regular surface waves, have been the subject of several investigations and theoretical considerations over the last 40 years.

For many purposes in soil mechanics, it is permissible to uncouple the soil and fluid parts of any analysis in order to treat them separately. However, it may also be desirable on occasion to analyse the true coupled performance of a composite continuum, in which the two phases interact. Examples of practical importance would involve external loads which vary in time, and structure-foundation interaction analyses where the generation of foundation pore-pressure is completely dependent upon the relative stiffness of the components of the system. That is, a stiff or inhomogeneous structure causes different pore-pressures from a flexible or homogeneous one.

---

\* *Ph.D., Research Engr.*

*University of Hannover, Sonderforschungsbereich 205, Appelstr. 9 A, 3000 Hannover 1, Germany (on leave from the Marine Civil Engineering Department, Hydro-engineering Faculty, Technical University of Gdańsk, Poland)*

In many practical problems appeared in the coastal engineering, there are many subsoil stratifications and hydro-engineering structures that can be treated as vertically two-dimensional. Assuming also that the seabed is loaded by harmonic waves characterized by long crests parallel to each other, then as a result the seabed is deformed under plain strain conditions. Under these conditions, the following two equations, describing elastic deformations, together with the 'storage' equation constitute the coupled problem and can be written as:

$$G \left( \frac{\partial^2 u_x}{\partial x^2} + \frac{\partial^2 u_x}{\partial z^2} \right) + \frac{G}{1-2\mu} \frac{\partial}{\partial x} \left( \frac{\partial u_x}{\partial x} + \frac{\partial u_z}{\partial z} \right) = \frac{\partial p}{\partial x} \quad (1a)$$

$$G \left( \frac{\partial^2 u_z}{\partial x^2} + \frac{\partial^2 u_z}{\partial z^2} \right) + \frac{G}{1-2\mu} \frac{\partial}{\partial z} \left( \frac{\partial u_x}{\partial x} + \frac{\partial u_z}{\partial z} \right) = \frac{\partial p}{\partial z} \quad (1b)$$

$$\frac{k_x}{k_z} \frac{\partial^2 p}{\partial x^2} + \frac{\partial^2 p}{\partial z^2} - \frac{\gamma n \beta'}{k_z} \frac{\partial p}{\partial t} = \frac{\gamma}{k_z} \left( \frac{\partial u_x}{\partial x} + \frac{\partial u_z}{\partial z} \right) \quad (1c)$$

where:  $p$  is the wave-induced excess pore-pressure,  $u_x$  and  $u_z$  are the horizontal and vertical displacements of soil skeleton, respectively,  $G$  is the shear modulus of the soil skeleton,  $\mu$  is the Poisson's ratio,  $k_x$  and  $k_z$  are the coefficients of permeability of soil in horizontal and vertical direction, respectively,  $\gamma$  is the unit weight of the pore-fluid,  $\beta'$  is the compressibility of the pore-fluid,  $n$  is the porosity of soil,  $x$  and  $z$  are the horizontal and vertical coordinates of the Cartesian system, respectively.

The problem described in Eqs. (1a) to (1c) is very often called as a 'storage' problem because the third is based on the 'storage' equation given by Verruijt (1969), as the governing equation for flow of a compressible fluid in a homogeneous compressible porous medium.

The earlier simplified theoretical solutions give only approximated values for the pore-pressure response. Others, more advanced theories (*e.g.*: Madsen, 1978; Yamamoto *et al.*, 1978; Okusa, 1985) seem to be enough developed in order, at least, to describe the governing problem by introducing additional, meaningful parameters giving thereby a possibility of wide analyses of real soil-water conditions. All these three theories have the same physical background and they differ from each other in the applied method of deriving the particular solution. Okusa (1985), as a first one, discussed also the problem of phase-lag (time-shift) phenomenon existing in a gas-laden sediment for the wave-induced pore-pressure and stresses. The theoretical values calculated from the 'storage' theory lie far away from the 'potential' solution, originally presented by Putnam (1949) and based on the assumptions of incompressible pore-fluid and soil skeleton. These rigorous assumptions differ strongly from the realistic conditions of the soil and pore-fluid two-phase medium. The differences between the 'storage' solution and the 'consolidation' solution proposed by Moshagen & Tørum (1975) and assuming compressibility only for the pore-fluid, are not so drastic

but they might become meaningful especially when a relatively compressible soil (*e.g.*, loose sand) is concerned.

### 'FINITE-THICKNESS' ANALYTICAL SOLUTION

The solutions obtained from the 'potential' problem and 'consolidation' problem approximate roughly the pore-pressure response. Both of these solutions can be used in a feasibility study. More precise information on the pore-pressure attenuation and phase-lag distribution with depth can be obtained at the preliminary or detailed design level where the both components of two-phase system (*i.e.*, soil skeleton and pore-fluid) are considered to be compressible.

The appropriate analytical solutions for the pore-pressure response in case of a homogeneous, poro-elastic, semi-infinite seabed were derived by many authors (*e.g.*: Madsen, 1978; Yamamoto *et al.*, 1978; Okusa, 1985) and obtained in terms of the pore-pressure and effective stresses in seabed sediments. Analytical solutions of the 'potential' and 'consolidation' equation for the case of limited thickness of the seabed layer are also well known (*e.g.*, Moshagen & Tørum, 1975). Using the general solution presented by Madsen (1978), Magda (1989, 1992) derived a particular solution for the wave-induced excess pore-pressure under the assumption of a finite thickness of the seabed layer. A 'finite thickness solution' has a very important bearing on further analysis and verification of laboratory test results but would also have a wide application to several engineering problems where natural soil-water conditions exist.

#### Boundary conditions

The boundary conditions at the surface of the seabed require that both the vertical wave-induced effective stress  $\sigma_z$  and the wave-induced shear stress  $\tau$  are zero, and additionally, the pore-pressure  $p$  at the seabed surface is induced by the hydrodynamic bottom pressure. Therefore, one has to fulfil the following boundary conditions at the surface of the seabed ( $z = 0$ ):

$$p = P_0 \exp[i(ax - \omega t)] \quad (2a)$$

$$\sigma_z = 0 \quad (2b)$$

$$\tau = 0 \quad (2c)$$

Field investigations frequently prove the existence of a limited thickness of permeable and isotropic seabed layer or layers with different properties in the upper boundary of seabed. In such cases, the soil profile may look like a sand layer, possibly with permeable sub-layers, a few metres thick overlaying an impermeable clay stratum.



If a finite, permeable layer overlaying a stiff and impermeable base is considered the boundary conditions at the bottom of permeable seabed layer ( $z = -d$ ) have to be specified. And thus,

$$u_z = 0 \quad (2d)$$

$$\frac{\partial p}{\partial z} = 0 \quad (2e)$$

$$u_x = 0 \quad \text{completely rough base} \quad (2f)$$

$$\tau = 0 \quad \text{perfectly smooth base} \quad (2g)$$

where:  $p$  is the wave-induced excess pore-pressure,  $\sigma_z$  is the wave-induced effective vertical stress,  $\tau$  is the wave-induced shear stress,  $u_x$  and  $u_z$  are the horizontal and vertical displacements of the soil skeleton, respectively,  $z$  is the vertical coordinate of the Cartesian system, and  $d$  is the thickness of a permeable seabed layer.

### Finite thickness solution

Below, a solutions for the instantaneous wave-induced excess pore-pressure in the seabed sediments is presented whereas the problem is considered in terms of the wave response of a single layer resting on a stiff impermeable base. The solution derived in order to obtain the response of a single layer, can be successfully used for the case of a multi-layered seabed; however, the number of mathematical manipulations will increase substantially.

Taking the general solution for the wave response together with the boundary conditions for a finite layer overlaying a perfectly smooth, stiff and impermeable base, a set of six linear and complex-valued equations is obtained. This system of equations can be solved either in its complex form or in form of real values; this would induce however twelve equations involved in the solution procedure.

An implementation of the six boundary conditions leads to a system of six coupled linear equations. Because of rather lengthy form of each of 36 constant coefficients accompanied by unknowns  $Y_{1,\dots,6}$ , the calculation procedure has been programmed. The matrix representation of the equation system is as follows:

$$[\mathbf{D}]\{\mathbf{Y}\} = [\mathbf{B}] \quad (3)$$

where each of these three matrices can be written as:

$$\mathbf{D} = \begin{bmatrix} D_1^{(1)} & D_2^{(1)} & D_3^{(1)} & D_4^{(1)} & D_5^{(1)} & D_6^{(1)} \\ D_1^{(2)} & D_2^{(2)} & D_3^{(2)} & D_4^{(2)} & D_5^{(2)} & D_6^{(2)} \\ D_1^{(3)} & D_2^{(3)} & D_3^{(3)} & D_4^{(3)} & D_5^{(3)} & D_6^{(3)} \\ D_1^{(4)} & D_2^{(4)} & D_3^{(4)} & D_4^{(4)} & D_5^{(4)} & D_6^{(4)} \\ D_1^{(5)} & D_2^{(5)} & D_3^{(5)} & D_4^{(5)} & D_5^{(5)} & D_6^{(5)} \\ D_1^{(6)} & D_2^{(6)} & D_3^{(6)} & D_4^{(6)} & D_5^{(6)} & D_6^{(6)} \end{bmatrix} \tag{4}$$

$$\mathbf{Y} = \begin{Bmatrix} Y_1 \\ Y_2 \\ Y_3 \\ Y_4 \\ Y_5 \\ Y_6 \end{Bmatrix}, \quad \mathbf{B} = \begin{bmatrix} 0 \\ 0 \\ 0 \\ 0 \\ -P_0 \\ 0 \end{bmatrix} \tag{5,6}$$

Matrix **D** contains constant coefficients accompanied by proper unknowns in equations of the boundary value problem. And thus,  $D_j^{(i)}$  represents a set of constant coefficients related to  $j$ -th unknown in  $i$ -th equation. There are six equations where  $i$ -equation ( $i = 1, \dots, 6$ ) relates to the boundary condition (Eqs. 2f, 2d, 2b, 2c, 2a, and 2e, respectively). Matrix **Y** represents unknowns  $Y_j$  ( $j = 1, \dots, 6$ ), and matrix **B** is composed of free term in each expression for the boundary condition problem. The 36 coefficients of matrix **D** can be computed using the following relationships (Magda, 1992):

$$D_1^{(1)} = \exp(-ad) \tag{7.1a}$$

$$D_2^{(1)} = -d \exp(-ad) \tag{7.1b}$$

$$D_3^{(1)} = \exp(ad) \tag{7.1c}$$

$$D_4^{(1)} = -d \exp(ad) \tag{7.1d}$$

$$D_5^{(1)} = \exp(-\bar{k}ad) \tag{7.1e}$$

$$D_6^{(1)} = \exp(\bar{k}ad) \tag{7.1f}$$

$$D_1^{(2)} = \left( a^3 - X_2a + X_3 \frac{1}{a} \right) \exp(-ad) \tag{7.2a}$$

$$D_2^{(2)} = \left( 3a^2 - a^3d - X_2 + X_2ad - X_3 \frac{ad+1}{a^2} \right) \exp(-ad) \tag{7.2b}$$

$$D_3^{(2)} = -D_1^{(2)} \exp(2ad) \tag{7.2c}$$

$$D_4^{(2)} = \left( 3a^2 + a^3d - X_2 - X_2ad + X_3 \frac{ad-1}{a^2} \right) \exp(ad) \tag{7.2d}$$

$$D_5^{(2)} = \left( \bar{k}^3 a^3 - X_2 \bar{k}a + X_3 \frac{1}{\bar{k}a} \right) \exp(-\bar{k}ad) \tag{7.2e}$$

$$D_6^{(2)} = -D_5^{(2)} \exp(2\bar{k}ad) \quad (7.2f)$$

$$D_1^{(3)} = X_1 a^4 - X_1 X_2 a^2 + X_1 X_3 + X_5 ia \quad (7.3a)$$

$$D_2^{(3)} = 4X_1 a^3 - 2X_1 X_2 a \quad (7.3b)$$

$$D_3^{(3)} = D_1^{(3)} \quad (7.3c)$$

$$D_4^{(3)} = -D_2^{(3)} \quad (7.3d)$$

$$D_5^{(3)} = X_1 \bar{k}^4 a^4 - X_1 X_2 \bar{k}^2 a^2 + X_1 X_3 + X_5 ia \quad (7.3e)$$

$$D_6^{(3)} = D_5^{(3)} \quad (7.3f)$$

$$D_1^{(4)} = a + X_1 ia^4 - X_1 X_2 ia^2 + X_1 X_3 i \quad (7.4a)$$

$$D_2^{(4)} = 1 + 3X_1 ia^3 - X_1 X_2 ia - X_1 X_3 i \frac{1}{a} \quad (7.4b)$$

$$D_3^{(4)} = -D_1^{(4)} \quad (7.4c)$$

$$D_4^{(4)} = D_2^{(4)} \quad (7.4d)$$

$$D_5^{(4)} = \bar{k}a + X_1 \bar{k}^3 ia^4 - X_1 X_2 \bar{k} ia^2 + X_1 X_3 \frac{i}{\bar{k}} \quad (7.4e)$$

$$D_6^{(4)} = -D_5^{(4)} \quad (7.4f)$$

$$D_1^{(5)} = X_7(a^4 - X_2 a^2 + X_3) + X_4 ia + X_6 \frac{a}{i} \quad (7.5a)$$

$$D_2^{(5)} = 2X_7 a(2a^2 - X_2) + 2X_6 \frac{1}{i} \quad (7.5b)$$

$$D_3^{(5)} = D_1^{(5)} \quad (7.5c)$$

$$D_4^{(5)} = -D_2^{(5)} \quad (7.5d)$$

$$D_5^{(5)} = X_7(\bar{k}^4 a^4 - X_2 \bar{k}^2 a^2 + X_3) + X_4 ia + X_6 \frac{\bar{k}^2 a}{i} \quad (7.5e)$$

$$D_6^{(5)} = D_5^{(5)} \quad (7.5f)$$

$$D_1^{(6)} = D_1^{(5)} a \exp(-ad) \quad (7.6a)$$

$$D_2^{(6)} = (D' + D'') \exp(-ad) \quad (7.6b)$$

$$D_3^{(6)} = -D_1^{(5)} a \exp(ad) \quad (7.6c)$$

$$D_4^{(6)} = (D' - D'') \exp(ad) \quad (7.6d)$$

$$D_5^{(6)} = D_5^{(5)} \bar{k} a \exp(-\bar{k}ad) \quad (7.6e)$$

$$D_6^{(6)} = -D_5^{(5)} \bar{k} a \exp(\bar{k}ad) \quad (7.6f)$$

The above presented set of coefficients is derived to solve the pore-pressure problem with the assumption of rough basement under the permeable seabed layer. Principally, the same procedure is applied for a finite layer overlaying a completely smooth base. The only difference is that the boundary condition (2f) has to be replaced by the relation (2g) which is foreseen for the smooth base condition. It means that the sub-set of constant coefficients  $D_j^{(6)}$  is built up using constant coefficients of Eq. (2g). All the elements in the other two matrices (i.e.,  $\mathbf{X}$  and  $\mathbf{B}$ ) stay unchanged. Equations (7.6a) to (7.6f) were derived for the case of perfectly rough basement. If a perfectly smooth basement is assumed Eqs. (7.6a) to (7.6f) have to be replaced by the following set of equations in the computational procedure, respectively:

$$D_1^{(7)} = X_6(a + X_1ia^4 - X_1X_2ia^2 + X_1X_3i) \exp(-ad) \tag{7.7a}$$

$$D_2^{(7)} = X_6 \left[ 1 - d + 3X_1ia^3 - X_1dia^4 - X_1X_2ia + X_1X_2dia^2 - X_1X_3 \frac{i(ad + 1)}{a} \right] \exp(-ad) \tag{7.7b}$$

$$D_3^{(7)} = -D_1^{(7)} \exp(2ad) \tag{7.7c}$$

$$D_4^{(7)} = X_6 \left[ 1 + d + 3X_1ia^3 + X_1dia^4 - X_1X_2ia - X_1X_2dia^2 + X_1X_3 \frac{i(ad - 1)}{a} \right] \exp(ad) \tag{7.7d}$$

$$D_5^{(7)} = X_6(\bar{k}a + X_1i\bar{k}^3a^4 - X_1X_2i\bar{k}a^2 + X_1X_3\frac{i}{a}) \exp(-\bar{k}ad) \tag{7.7e}$$

$$D_6^{(7)} = -D_5^{(7)} \exp(2\bar{k}ah) \tag{7.7f}$$

where:

$$D' = X_7(5a^4 - 3X_2a^2 + X_3) + X_1X_3X_6 + X_4ia + 3X_6\frac{a}{i} \tag{8a}$$

$$D'' = -X_7ad(a^4 - X_2a^2 + X_3) + X_1X_3X_6 - X_4ia^2d - X_6\frac{a^2d}{i} \tag{8b}$$

$$X_1 = \frac{2(1 - \mu)k_z}{a\omega\gamma \left( n\beta + \frac{1 - 2\mu}{G} \right) + i(k_z - k_z)a^3} \tag{8c}$$

$$X_2 = a^2 + \frac{[k_z(1 - 2\mu) + k_z]a^2 - i\omega\gamma n\beta(1 - 2\mu)}{2k_z(1 - \mu)} \tag{8d}$$

$$X_3 = a^2 \left( a^2 \frac{k_z}{k_z} - \kappa^2 \right) \tag{8e}$$

$$X_4 = -\frac{(1-\mu)E}{(1+\mu)(1-2\mu)} \quad (8f)$$

$$X_5 = \frac{\mu}{1-\mu} \quad (8g)$$

$$X_6 = -G \quad (8h)$$

$$X_7 = X_1(X_4X_5 + X_6) \quad (8i)$$

Solution of the coupled linear equations' system [Eq. (3)], obtained in terms of coefficients  $Y_1, \dots, 6$ , constitutes simultaneously an explicite solution to the pore-pressure (and also to the wave-induced effective stresses and strains) within the seabed layer of finite thickness. The pore-pressure solution can be written as:

$$p = -\left(\sigma_z + \frac{1}{ia} \frac{\partial \tau}{\partial z}\right) \quad (9)$$

where:

$$\sigma_z = X_4(T_1 + X_5T_2) \exp[i(ax - \omega t)] \quad (10)$$

$$\begin{aligned} \frac{\partial \tau}{\partial z} = & X_6[2Y_2a \exp(az) + (Y_1 + Y_2z)a^2 \exp(az) \\ & - 2Y_4a \exp(-az) + (Y_3 + Y_4z)a^2 \exp(-az) \\ & + Y_5\bar{k}^2a^2 \exp(\bar{k}az) + Y_6\bar{k}^2a^2 \exp(-\bar{k}az) \\ & + T_2ia] \exp[i(ax - \omega t)] \end{aligned} \quad (11)$$

$$\begin{aligned} T_1 = & ia[(Y_1 + Y_2z)a^2 \exp(az) + (Y_3 + Y_4z)a^2 \exp(-az) \\ & + Y_5\bar{k}^2a^2 \exp(\bar{k}az) + Y_6\bar{k}^2a^2 \exp(-\bar{k}az)] \end{aligned} \quad (12)$$

$$\begin{aligned} T_2 = & X_1\{4Y_2a^3 \exp(az) + (Y_1 + Y_2z)a^4 \exp(az) \\ & - 4Y_4a^3 \exp(-az) + (Y_3 + Y_4z)a^4 \exp(-az) \\ & + Y_5\bar{k}^4a^4 \exp(\bar{k}az) + Y_6\bar{k}^4a^4 \exp(-\bar{k}az) \\ & - X_2[2Y_2a \exp(az) + (Y_1 + Y_2z)a^2 \exp(az) \\ & - 2Y_4a \exp(-az) + (Y_3 + Y_4z)a^2 \exp(-az) \\ & + Y_5\bar{k}^2a^2 \exp(\bar{k}az) + Y_6\bar{k}^2a^2 \exp(-\bar{k}az)] \\ & + X_3[(Y_1 + Y_2z) \exp(az) + (Y_3 + Y_4z) \exp(-az) \\ & + Y_5 \exp(\bar{k}az) + Y_6 \exp(-\bar{k}az)]\} \end{aligned} \quad (13)$$

in which:

$$\bar{k} = \sqrt{\frac{k_x}{k_z} - \frac{\kappa^2}{a^2}} \quad (14)$$

and

$$\kappa^2 = i \frac{\omega \gamma \{n\beta' + (1 - 2\mu)/(2(1 - \mu)G)\}}{k_z} \quad (15)$$

where, additionally to the formerly described parameters:  $a$  is the wave number,  $\omega$  is the wave angular frequency, and  $i$  is the imaginary unit.

Having the formula for the pore-pressure  $p$  distribution with depth  $z$ , which is written in a complex-number form, the formulae describing the amplitude,  $|p|$ , and the phase-lag,  $\delta$ , of the pore-pressure oscillated in seabed sediments, with respect to the phase of bottom pressure oscillations, can be easily obtained.

### RESULTS OF EXAMPLE CALCULATIONS

In order to perform illustrative calculations the following input data were used:

- coefficient of isotropic permeability:  $k_x = k_z = 0.0001$  m/s
- porosity of soil:  $n = 0.4$  (loose sand),  $n = 0.36$  (dense sand)
- Poisson's ratio:  $\mu = 0.3$
- Young's modulus of soil:  $E = 10^4$  kN/m<sup>2</sup> (loose sand), and  $E = 10^5$  kN/m<sup>2</sup> (dense sand)
- degree of saturation: from  $S = 1.00$  (fully saturated soil conditions) to  $S = 0.95$  (unsaturated soil conditions)
- seabed layer of finite thickness:  $d = 0.5$  m (smooth or rough basement)
  - wave period:  $T = 6$  s
  - water depth:  $h = 4.5$  m

Using the analytically derived finite-thickness layer solution (Magda, 1989, 1992), two different boundary conditions assumed at the bottom of the permeable seabed layer [Eqs. (2f) and (2g)] were introduced in order to simulate either rough ( $u_x = 0$ , *i.e.* no movement of the soil skeleton) or smooth ( $\tau = 0$ , *i.e.* no friction and free movement) surface of a rigid and impermeable basement underneath the permeable seabed layer.

The results of pore-pressure response in a permeable seabed layer of finite thickness, overlaying either a smooth or rough impermeable stiff base, are given in Fig. 1 (the solid-line denotes the rough base condition and the dashed-line denotes the smooth base condition) in terms of the pore-pressure amplitude and phase-lag as functions of depth in the seabed. Different soil saturation conditions ( $S = 0.95 - 1.00$ ) as well as different compressibilities of soil skeleton, *i.e.*:  $E = 10^5$  kN/m<sup>2</sup> for dense or semi-dense sandy sediments (see Fig. 1), and

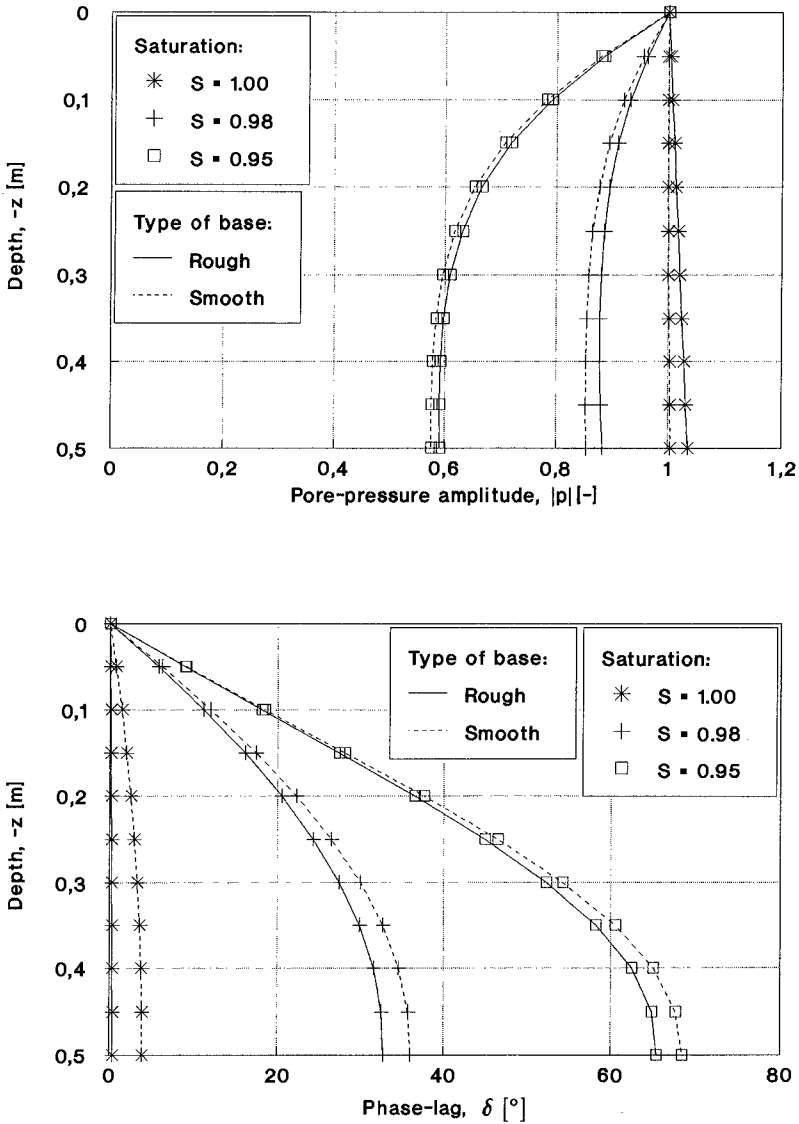


**Figure 1.** Pore-pressure amplitude and phase-lag distribution with depth for different saturation conditions and type of impermeable basement (finite-thickness-layer solution,  $E = 10^5 \text{ kN/m}^2$  – dense sandy sediments)

$E = 10^4 \text{ kN/m}^2$  for loose sandy sediments (the results are not presented here in graphical form) were introduced into computations.

In case of dense sandy sediments (Fig. 1), the difference between the rough and smooth base is relatively small. The influence of introduction of the smooth base is magnified when loose sandy sediments are considered. In both cases (*i.e.*, loose and dense sediments) the smooth base condition makes the pore-pressure attenuation as well as the phase-lag larger with respect to the rough base condition. Although the pore-pressure gradient is more inconvenient (more dangerous for the stability of seabed sediments) when the smooth base is assumed, although the rough base condition seems to be more natural.

Performing comparative calculations and wide parameter studies, it was found that fully saturated soil conditions ( $S = 1.00$ ) and a finite thickness of the seabed layer cause some unexpected disturbances in the pore-pressure distribution with depth, namely, the pore-pressure value at the impermeable base exceeds the value of inducing hydrodynamic pressure at the seabed surface (see Fig. 1) which normally – from the physical point of view – should not appear. This phenomenon can be explained if the value of relative compressibility of both components in the two-phase system (*i.e.*, soil skeleton and pore-fluid) as well as the boundary condition choice are investigated carefully.

It is believed that the discrepancy between the calculated and logically expected (*i.e.*, a vertical-profile distribution with depth) values of the pore-pressure amplitude might be caused by:

- ill-conditioned coefficient matrix  $\mathbf{D}$  (numerical problem), or
- unrealistic boundary conditions assumed at the surface of seabed sediments (boundary-condition problem), or
- interaction of both of them (mixed problem).

In order to get more detailed insight into the problem, some additional computations were performed where the influence of different extreme values of the relative compressibilities of the two-phase medium was studied (Figs. 2 and 3).

The ratio between the absolute smallest and largest values in the coefficient matrix  $\mathbf{D}$  differs in order between  $10^{14}$  and  $10^{22}$ , in the case analysed and presented in Fig. 3. On the other hand, it is commonly known that the matrices like this one are ill-conditioned and can very often cause some serious numerical problems.

In direct methods of solution, roundoff errors accumulate, and they are magnified to the extend that the governing matrix is close to singular (Press *et al.*, 1989). In spite of the Gaussian elimination method, the following three methods, dealing with sets of equations that are either singular or else numerically very close to singular, were applied:

- LU decomposition,
- iterative improvement of a solution,
- singular value decomposition (SVD).



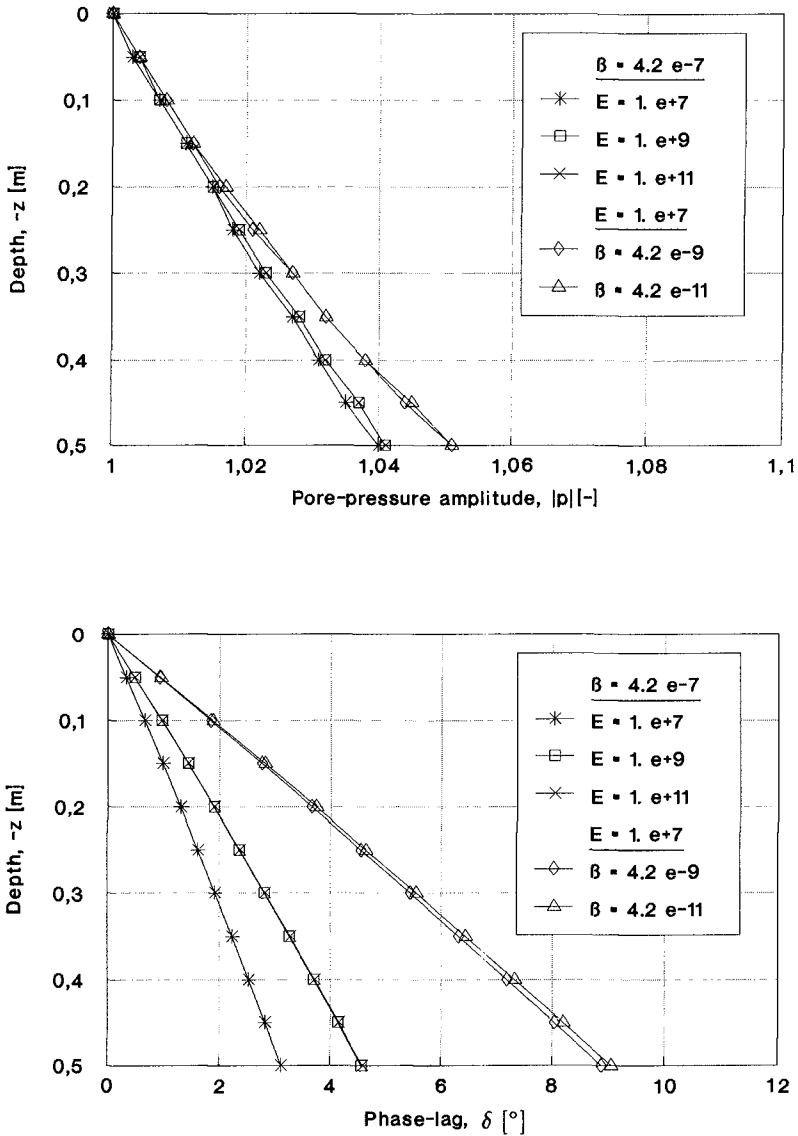


**Figure 2.** Test on numerical accuracy – pore-pressure amplitude and phase-lag distribution with depth for fully saturated soil conditions ( $S = 1.00$ ) (finite-thickness-layer solution, rough basement,  $\beta' E = 4.2 \times 10^0 (2)(4)$  and  $\beta' = 4.2 \times 10^{-7} \text{ m}^2/\text{kN}$  or  $E = 10^7 \text{ kN/m}^2$ )

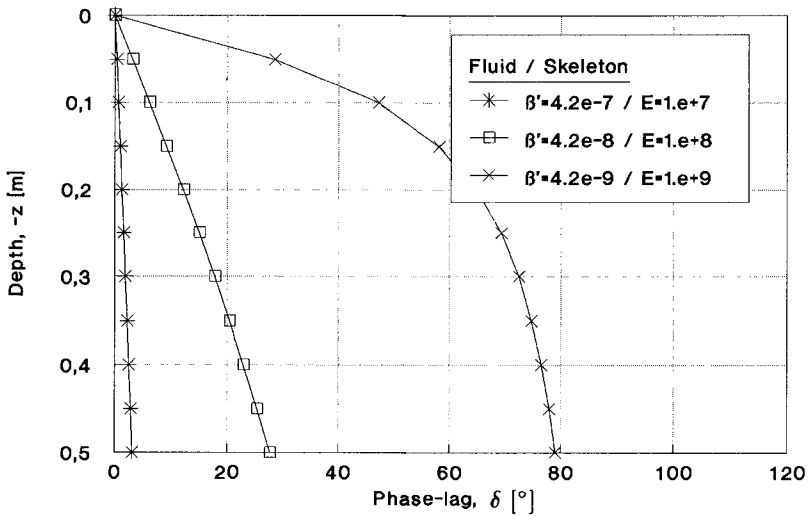
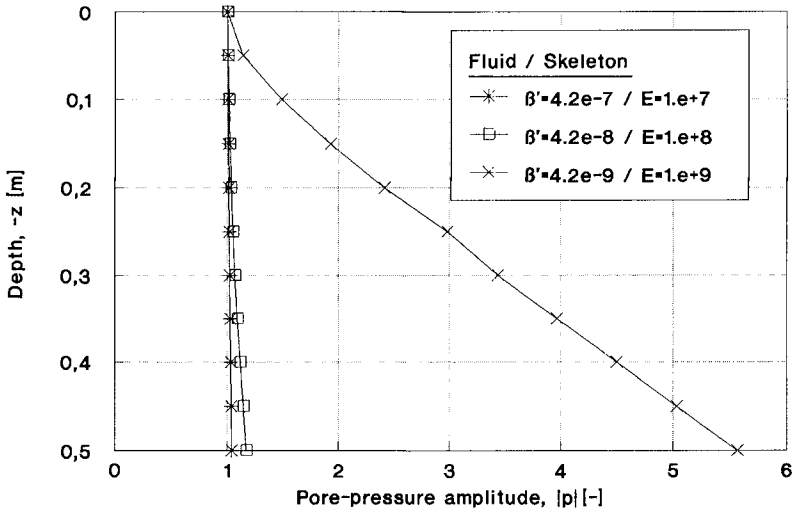


**Figure 3.** Test on numerical accuracy – pore-pressure amplitude and phase-lag distribution with depth for fully saturated soil conditions ( $S = 1.00$ ) (finite-thickness-layer solution, rough basement,  $\beta^i E = 4.2$  (const) and  $\beta^i = 4.2 \times 10^{-7(-9)(-11)} \text{ m}^2/\text{kN}$ )

Although performing all computations in a double-precision mode, neither of these methods could avoid the numerical problems discovered in Fig. 1, confirmed in Fig. 2 and strong emphasized in Fig. 3.

Figure 2 illustrates that by assuming a constant value of one of the compressibility parameters (*i.e.*, the compressibility of pore-fluid  $\beta' = 4.2 \times 10^{-7} \text{ m}^2/\text{kN}$  or Young's modulus of soil skeleton  $E = 10^7 \text{ kN/m}^2$ ) and enlarging a value of the second one, the numerical problems do not lead to a dramatical increase of both the pore-pressure amplitude and the phase-lag, which show to be coherent and vary: amplitude – from 1.04 to 1.05, phase-lag – from  $3^\circ$  to  $9^\circ$ , computed at the bottom of seabed layer. A simultaneous increase of both the compressibility parameters (see Fig. 3), however, brings both the pore-pressure amplitude and the phase-lag onto an enormous and unrealistic level (amplitude – from 1.04 to 5.5, phase-lag – from  $3^\circ$  to  $80^\circ$ , computed at the bottom of seabed layer).

## CONCLUSIONS

Taking into account the results of the above presented analysis, it is a rather lucky coincidence that the realistic values of compressibility of the pore-pressure and soil skeleton are:  $\beta' \geq 4.2 \times 10^{-7} \text{ m}^2/\text{kN}$  and  $E \leq 10^5 \text{ kN/m}^2$ , respectively. These conditions guarantee that the order of maximum ratio between the absolute smallest and largest value in the coefficient matrix  $\mathbf{D}$  will be always less than  $ca 10^{14}$ . Only by a near-incompressible system (*i.e.*,  $\beta' = 4.2 \times 10^{-7} \text{ m}^2/\text{kN}$  for fully saturated soil conditions  $S = 1.00$ , and  $E = 10^5 \text{ kN/m}^2$ ) some numerical problems are expected as indicated in Fig. 1. It was shown, however, that even in this case, the difference between the computed pore-pressure amplitude and the logically expected values (*i.e.*, a vertical-profile distribution with depth) have no practical meaning and can be neglected.

There is, however, another method that helps to solve the governing problem, correctly, omitting simultaneously the above mentioned numerical problems when solving the system of coupled linear equations. This method, based on a finite-element approximation of one-dimensional model for wave-induced excess pore-pressures and displacements in the soil skeleton, allows to omit a bit artificial boundary conditions (*i.e.*,  $\sigma_z = 0$  and  $\tau = 0$ ) assumed at the seabed surface, and gives more realistic picture of the pore-pressure field in permeable seabed sediments. The results of such a numerical analysis was published by Magda (1991, 1992).

The preparation of all elements [Eqs. (7.1a) to (7.6f)] from the coefficient matrix  $\mathbf{D}$  in the analytical solution requires much more mathematical operations with relatively small and large values before the equations system is solved. This complicated and superfluous procedure is omitted in the finite-element solution where the elements of coefficient matrix are computed using less mathematical operations.

## ACKNOWLEDGEMENTS

This study has been financially supported by grants from the German Research Foundation (DFG) directed to the Special Collaborative Programme – 205 “Coastal Engineering” (Sonderforschungsbereich – 205 “Küsteningenieurwesen”) at the University of Hannover as well as Grant No. 772629102 “Wave-induced excess pore-pressure oscillations in seabed sediments – computational methods for evaluating the hydrodynamic loadings acting on a submarine buried pipeline” at the Technical University of Gdańsk (Marine Civil Engineering Department).

## REFERENCES

- Madsen, O.S.** (1978). Wave-induced pore pressures and effective stresses in a porous bed. *Géotechnique*, 28, No. 4, pp. 377-393.
- Magda, W.** (1989). Wave-induced pore water pressure generation in a sand bed. *Internal Report No. 1, SFB-205 'Küsteningenieurwesen', TP A13*, University of Hannover, pp. 1-94.
- Magda, W.** (1991). A finite-element approximation of the one-dimensional model for wave-induced pore-water pressure and displacements within the seabed. *Internal Report No. 8, SFB-205 'Küsteningenieurwesen', TP A13*, University of Hannover, pp. 1-89.
- Magda, W.** (1992). *Wave-Induced Pore-Pressure Oscillations in Sandy Seabed Sediments*. Ph.D. Thesis, Technical University of Gdańsk, pp. 1-160.
- Magda, W.** (1992). Finite-element approximation of one-dimensional model for wave-induced pore pressure and displacements within seabed sediments. *Archives of Hydroengineering*, Vol. XXXIX, No. 3, pp. 58-77.
- Moshagen, H., Tørum, A.** (1975). Wave-induced pressures in permeable seabeds. *Proc. ASCE. Journal of Waterways, Harbors and Coastal Engineering Division*, Vol. 101, No. WW1, Proc. Paper 11099, pp. 49-57.
- Okusa, S.** (1985). Wave-induced stresses in unsaturated submarine sediments. *Géotechnique*, 35, No. 4, pp. 517-532.
- Press, W.H., Flannery, B.P., Teukolsky, S.A., Vetterling, W.T.** (1989). *Numerical Recipes. The Art of Scientific Computing*. Cambridge University Press.
- Putnam, J.A.** (1949). Loss of wave energy due to percolation in a permeable sea bottom. *Transactions American Geophysical Union*, Vol. 30, No. 3, pp. 349-356.
- Verruijt, A.** (1969). *Elastic storage of aquifers*. Chap. 8 in: *Flow through porous media*. De Wiest (ed.), Accademic Press, London, pp. 331-376.
- Yamamoto, T., Koning, H.L., Sellmeijer, H., Hijum, E.** (1978). On the response of a poro-elastic bed to water waves. *Journal of Fluid Mechanics*, Vol. 87, Part 1, pp. 193-206.

## CHAPTER 225

# Response Characteristics of River Mouth Topography in Wide Time Scale Range

A. Mano<sup>1</sup>, M. Sawamoto<sup>1</sup> and M. Nagao<sup>2</sup>

### Abstract

Based on the observations, response characteristics of sand barrier and flood terrace for the Abukuma River mouth are analyzed in wide time scale range spanned from several hours to half century. We propose some measures representing magnitude of the deformation and the external forces to find quantitative relationship between them. The analyses deal with breaching in the flood process, development of the sand barrier, alternation of the barrier side, and the formation and decay of flood terrace, together with their time scales. There will be also shown interaction between the barrier and the terrace.

### 1 Introduction

The final goal in the study of river mouth topography is to predict it in the near and far future, and to make control, if necessary, for the flood passage, voyage, or coastal sedimentation. Stable prediction generally requires both qualitative analyses and quantitative evaluation of long-term history.

The complexity of the topographical deformation in the river mouth area would be produced by complication of the external forces, i.e. duality of river flow and waves, and their fluctuating characteristics, and by influences from the topography itself and man-made structures, which are also changing.

The key to resolve these entangling situation is time scale of each process. Sawamoto and Shuto(1988) have found various time scales on the topographical change around the Abukuma River mouth based on the observations. The time scales range from several hours of flood process to half century of the alternation of the sand barrier side. This paper develops their findings by collecting further observation data on both the deformation and the external forces, and

---

<sup>1</sup>Department of Civil Engineering, Tohoku University, Sendai 980-77, Japan

<sup>2</sup>Department of Civil Engineering, Ashikaga Institute of Technology, Ashikaga 326, Japan

by connecting them. To perform the analyses, we introduce some new measures representing their magnitude, that enables some quantitative evaluations.

Further new findings is the existence of the interaction between the sand barrier and the terrace, especially in the stage when the deformation of the terrace is proceeded. This is added to patterns of the deformation.

At the end of this paper, will be presented a diagram summarizing each deformation stage and time scale.

## 2 Outline of the river and data collection

The Abukuma River is the first class river, with the catchment area of 5,400 km<sup>2</sup> and the main channel length of 239 km, managed by the Ministry of Construction in Japan. The river has a mouth opened eastwards to flow into the Pacific Ocean (Fig. 1). At the mouth, the annual mean discharge of the river is about 120-180 m<sup>3</sup>/s, which is comparable with the mean tidal discharge in the half cycle of 50 - 130 m<sup>3</sup>/s. Therefore, the channel at the mouth is usually maintained by both the river and tidal flow. The incident waves, there, having dominant direction, ESE, produce littoral drift from the south to the north macroscopically.

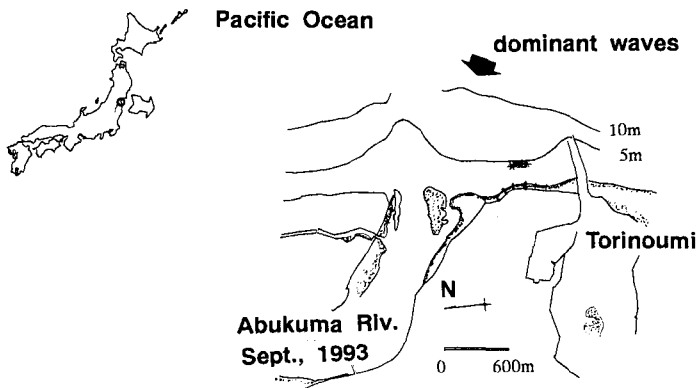


Fig. 1: Geography around the Abukuma River mouth.

There are some man-made structures near the mouth. The large saline barrier called Abukuma Ohzeki, which locates 10 km up the river mouth and was constructed in 1982, prevents the sediment transport for usual flow, that is, except floods. Training jetties have been established, not at the Abukuma river mouth, but at the entrance of Torinoumi lagoon which is an old mouth of the river. They were in construction in 1954 - 1980 to be lengthened to about 400 m. In order to prevent erosion between the entrance and the mouth, a detached break-water and groins were set up in 1986 - 1992 and 1974 - 1976 respectively. The effect of these coastal structures on the river

Table 1: Observation circumstance

contents	organization	start	period
topographical survey	Geograph. Survey Inst.	1907	
depth sounding	Min. Construction	1940	1 year
river discharge	Min. Construction	1941	1 hour
aerial photograph	Geograph. Survey Inst.	1947	1 month -
	U.S. military etc.		3 years.
waves(Sendai Harb.)	Min. Transport	1979	2 hours
barrier shoreline	Tohoku University	1984	1 - 2 weeks(usual) continuous(1985 flood)
barrier elevation	Tohoku University	1989	1 - 2 weeks

mouth topography is not so clear, because the river has function as a sediment source also.

The circumstance of observations is given in the Table 1. Depth sounding, river discharge, and aerial photograph have half century's history, while our observations for the sand barrier are relatively new, but the period of the observations covers short to middle term change. Especially, the flood process in 1985 was recorded on the video tape. The aerial photographs have been taken by the U.S. military, and the Geographical Survey Institute and Tohoku Regional Construction Bureau, the Ministry of Construction.

The discharge is observed at Iwanuma, located 7.8 km up the mouth. Since the floods are most influential on the response among the river flow, we have collected hydrographs of major floods, as well as daily mean discharge in the long period. They are utilized in the examination of the new measure. The maximum flood in the peak discharge occurred in 1986. Its flush and the recovery process have been observed by ourself as well.

The wave observation is performed off the Sendai Harbour locating about 26 km NNE of the mouth and has relatively short history corresponding to the construction of the harbour.

### 3 Response of sand barrier

#### 3.1 long-term change

The history of sand barrier in the long time span is shown in Fig. 2 which is edited from the aerial photographs. The oldest plate of 1947 indicates the barrier in the right side, which is dominant due to the macroscopically prevailing direction of the littoral drift. The shoreline position of the barrier is more seaward than recent one is.

Then, switch of the side to the left is recognized in the plate of 1969 and this side continues until the plate of 1979, with the thickness getting very thin. Again, the barrier in the right side appears in the plate of 1984 to last up to now. The recent two plates of 1992 and 1993 show quite different shape of the barrier from

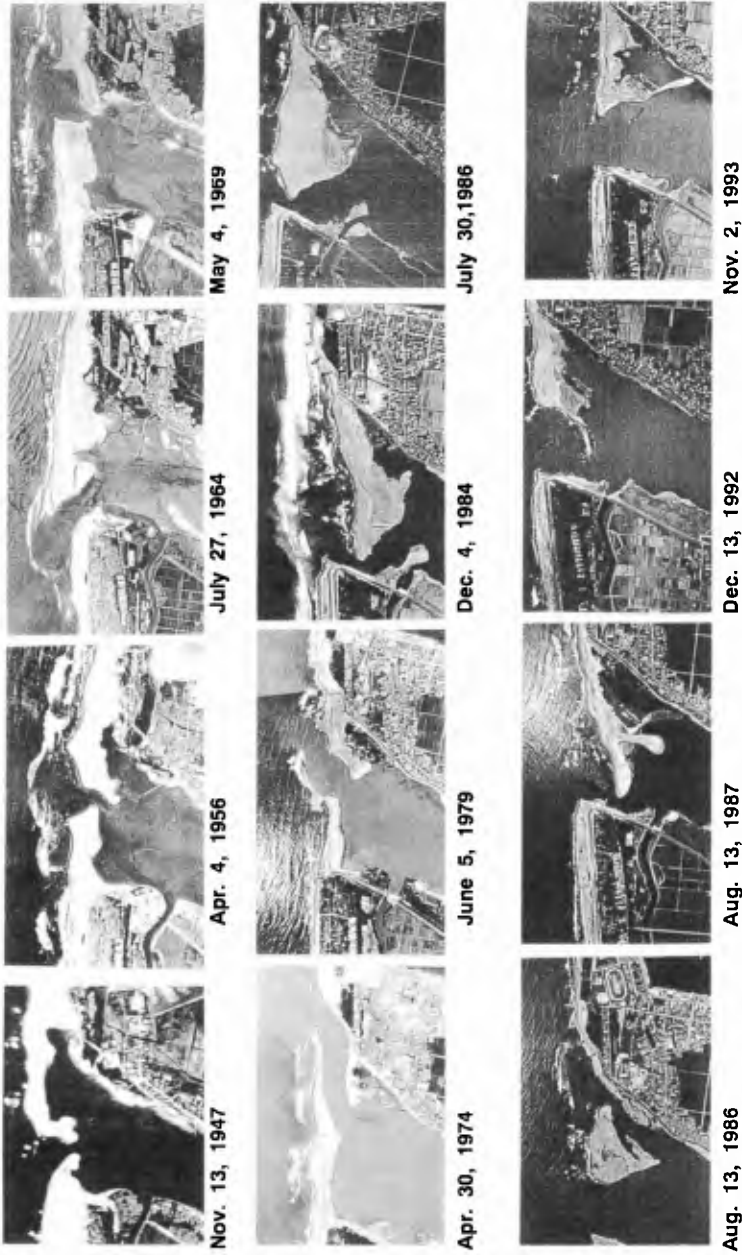


Fig. 2: History of the sand barrier. The photographs of 1947 and 1956 were taken by the U.S. military; 1964, 1969, 1974, 1979, and 1984 by the Geographical Survey Institute; 1986, 1987, 1992, and 1993 by Tohoku Regional Construction Bureau.



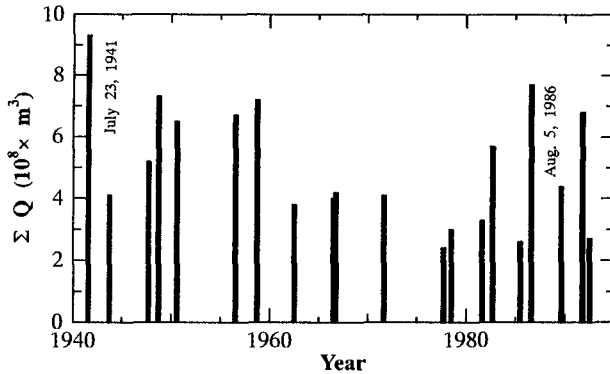


Fig. 3: History of the floods.

any other one. This will be analyzed in Section 5.

Here, let us focus on the long term change, that is the alternation of the side. This is corresponding to the activity of the floods. Figure 3 shows the whole history of the major floods observed. The ordinate indicates the total discharge, integrated in one flood, which is a new measure and will be discussed in the next subsection.

Long-term fluctuation exists, that is, in 1940s and 1950s there occurred many floods in huge magnitude, which caused serious disasters. The flood in 1941 is the biggest in the total discharge. In the following two decades; 1960s and 1970s, the flood activity calmed down and then in 1980s and 1990s floods are again active. The flood in 1986 is another representative having the biggest peak discharge in the history. The time scale of the long-term fluctuation is about half century.

The alternation of the side to the left would be triggered by the overhang of the right side barrier in 1964, because this is unstable for the flood passage. Backwater induced by the resistance of the overhang would cause the overflow somewhere around the lower part of the barrier to make a new channel there. The channel at the mouth is usually maintained strait by the flush due to floods in appropriate period. The calmness of the flood activity in 1960s promotes the overhang. Once the side is changed to the left, the supply of the littoral drift to the barrier is prevented by the flow in the channel. Hence the barrier becomes thin, that is corresponding the barrier shape in 1960s and 1970s. Although thin barrier is unstable for the flood passage, the left side barrier continued until 1979, that is more than 10 years. This continuation is also assisted by the calmness of the flood in this period.

Therefore the long-term deformation of the side alternation synchronizes with the fluctuation of the flood activity, through the mechanism provoked by the calmness in the flood intensity.

3.2 short-term change

The opposite extreme in the time scale range would be flood process. The breaching of sand barrier during the flood of 1985 was recorded by the video tape and analyzed by Sawamoto et al.(1988). Here we will examine about the measure of the flood relating with the breach. Figure 4, showing the change of the minimum channel width at the mouth , $B$ , during the flood, indicates that significant change occurs even after the peak of the discharge has passed. Therefore the terminal channel width  $B_T$  after one flood passage should be related to the quantity representing the whole flood.

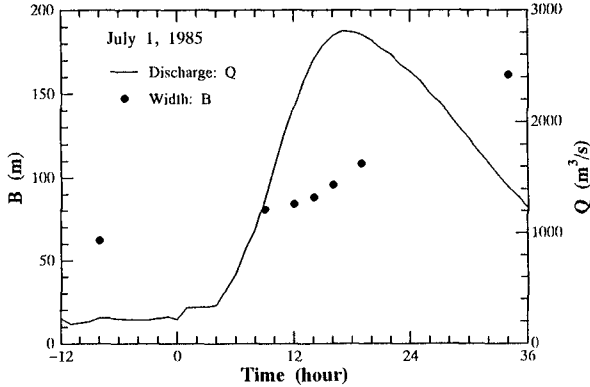


Fig. 4: Breaching process.

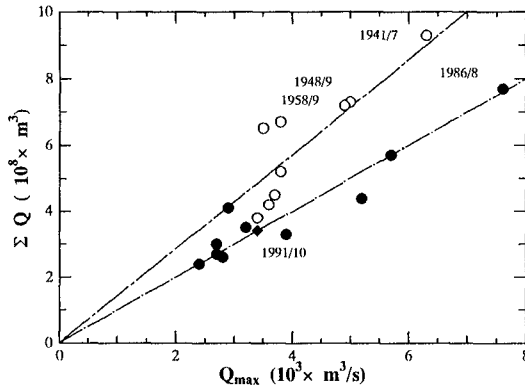


Fig. 5: Runoff characteristics.

Another examination is about the relationship between the peak discharge,  $Q_{max}$ , and the total discharge(Fig. 5). In a short period, these two quantities are on one linear relationship, but in the long time span the gradient apparently

changes. The border of the change is in 1960s and 1970s, which are not clear because of the absence of the huge floods in the period. The change would be resulted from the channel improvement of the Abukuma River after the serious disasters in 1940s and 1950s. Decrease of the gradient corresponds to decrease of the resistance in the channel. The flood in October, 1991 has special hydrograph with two peaks which are produced by the twin typhoons. Filled diamond in Fig.5 is the plot of half of the total discharge for this flood. This is still on the recent relationship.

Since the total discharge is a simple and invariant quantity including the information of the whole flood, we adopt it as a measure of magnitude of the flood relating with the breach. The dependence of the terminal width on the total discharge is given by the linear relationship(see Fig.6). The flood in 1991 is also included in this figure and on the relationship. The flood in 1992 is the exception, that is, the channel was widened for relatively small amount of total discharge. Although the thin barrier at the tip(see Fig.2)is the direct cause, it will be shown later that the influence of the deformation of the flood terrace with different time scale is more original cause.

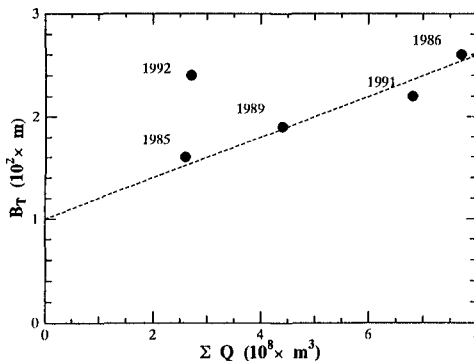


Fig. 6: Terminal channel width after the flood passage.

### 3.3 middle-term change

The breaching follows the recovery process of the sand barrier. The change of the channel width and the area of the sand barrier are plotted in Fig. 7, where the region accounting the area is defined in the left plate. After the flood, the littoral drift is spent to fill up the channel deepened by the flood. Therefore the change of the width is not evident. Then, the channel width starts to decrease rapidly to reach the stationary value of 50 - 60 m. The time scale of the decrease is 4 to 12 months depending on the scale of breaching. The stationary state is maintained by the dynamic equilibrium between the traction by the flow and deposition by waves, that is shown by Aota and Shuto (1980).

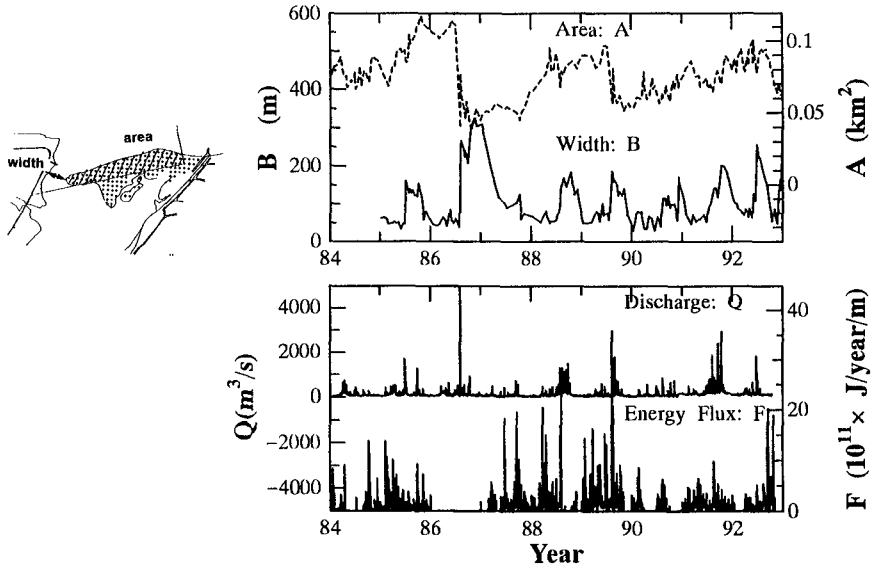


Fig. 7: Middle-term deformation of sand barrier.

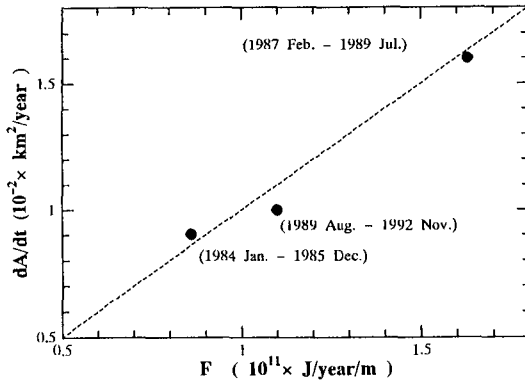


Fig. 8: Barrier development rate.

Even though the equilibrium at the channel is reached, the shape of the sand barrier is still thin. The thickening process of the barrier continues, which is indicated by the increase of the area. In this figure the daily mean discharge of the river and the wave energy flux are also shown. The flux is calculated by the equation;

$$F = \frac{1}{32\pi} \rho g^2 H^2 T \cos \theta$$

where,  $H$  and  $T$  are the wave height and period, respectively,  $\theta$  is the wave direction measured clockwise with the origin at the direction normal to the macroscopic coastline. These three quantities are all measured off Sendai Harbour. This figure shows the response characteristic that the channel width decreases sensitively for even minor flood, but the change of the area is more gradual. Hence, we evaluate the mean increase rate of the area in the three regions bounded by the major floods in 1986 and 1989 to correlate with the energy flux ( Fig. 8).

It is shown that the increase rate of the area,  $dA/dt$ , is directly proportional to the wave energy flux,  $F$ . This relation gives the time scale of the recovery of the sand barrier. Since the flood in 1986 flushed the area  $0.01 \text{ km}^2$  out of  $0.11 \text{ km}^2$ , the recovery would require 7 years for the energy flux of the ordinal sea condition,  $1.0 \times 10^{11} \text{ J/year/m}$ , that is  $3.2 \text{ kW/m}$ .

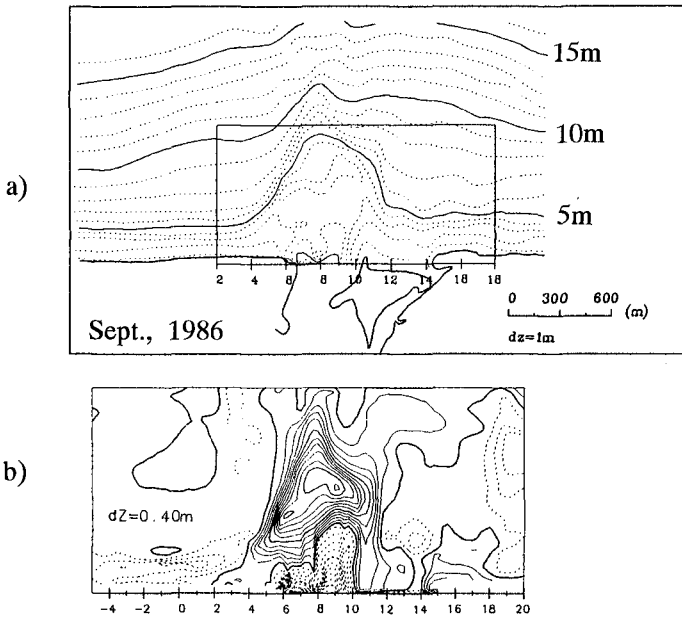


Fig. 9: Formation of flood terrace in 1986.

#### 4 Formation and decay of flood terrace

Figure 9 a) shows the flood terrace produced by the flood in 1986 and b) the distribution of deposition (solid line) and erosion (dashed line) obtained by taking difference of the two bathymetry charts sounded before and after the flood in the interval of six month. The terrace is about 4 m in depth and very flat. The maximum deposition is 4 m in height and locates the distance 800 m offshore of the shoreline. The channel at the mouth, the sand barrier, and its front area were

eroded by the flood. The volume of the erosion estimated to be about 60 % of that of the deposition by Mano et al.(1993). Hence, the rest would be due to the transport in the river. For any kind of sediment, the formation of flood terrace requires work transporting a large quantity of sediment by the long distance from the mouth.

Here we adopt the total kinetic energy in one flood at the mouth, *T.K.E.* as a measure of the flood magnitude relating to the terrace formation. The assumptions introduced to compute the quantity are; 1) the flood flow is critical at the mouth, 2) the channel width changes, linearly in terms of time, from the initial width to the terminal width. Where for the floods before 1982, we used 50 m and the terminal value shown in Fig. 6. as these width respectively. The energy is written as follows;

$$T.K.E. = \int \rho g^{2/3} \frac{Q^{5/3}}{2B^{2/3}} dt$$

where,  $\rho$  is density of water,  $g$  gravitational acceleration,  $Q$  the discharge,  $B$  the channel width. The integration is taken over one flood. While the measure on the terrace formation is also necessary. Since we can not extract precise information from the old bathymetry chart, we define  $L_5$  as the longest distance from the macroscopic shoreline near the mouth to the contour line of 5 meter depth. The changes of these two measures in half century time span are well corresponding (Fig.10). The threshold of the external force for the big terrace formation would be given by the value,  $1.3 \times 10^{13} J$ . The figure shows that major floods are of 1941, 1948, 1858, and 1986. In the case of 1986 flood, sediment near the mouth also contributed to the terrace formation.

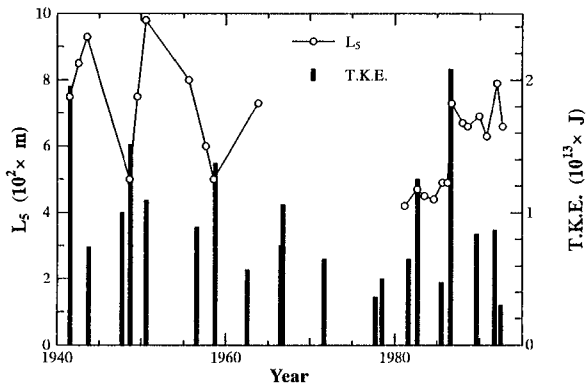


Fig. 10: Terrace formation and T.K.E.

The bathymetry chart sounded just before the 1986 flood still shows small terrace. From the interval of major floods, the time scale of disappearance of the big terrace would be given by more than 27 years.

## 5 Interaction

The last two plates in Fig. 2 show the recent sand barrier. The formation of big arc at the barrier tip in the plate of December, 1992 shows the wave direction approximately normal to the shoreline, which is different from the offshore wave direction. The effect of wave refraction becomes important. Although there exist some small arcs at the tip before, they would not be influential. The wave direction at the arc in 1992 prevents the development of the barrier toward the tip to result in the thin tip and to change the response characteristics of terminal width in Fig. 6. The plate of November, 1993 shows more advanced stage. Two strait shoreline facing the sea and river would be formed by waves refracted near the mouth. In this stage, the channel width is kept open.

The characteristics of the wave refraction is shown in Fig. 11. Wave rays, given by the numerical integration of the ray equation, see, for example, Mei(1983),pp. 66, are plotted for the bathymetry of 1993. The wave condition is for the dominant wave; direction of ESE and period of 8 s.

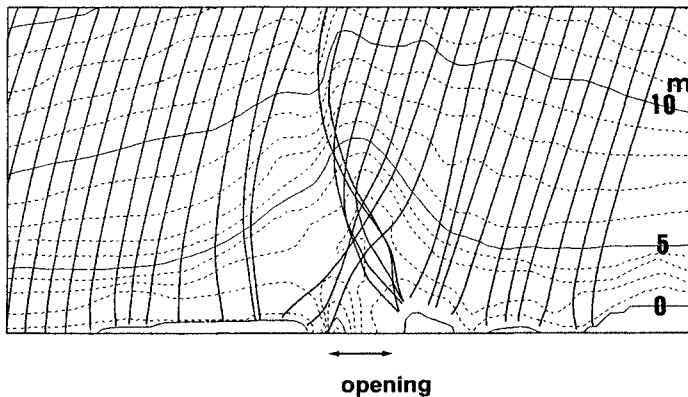


Fig. 11: Refraction characteristics.

The caustic is stably formed at the hollow on the flood terrace for the various offshore directions and the periods. The wave rays refracted at the hollow approach the barrier from ENE, that is, two dominant wave directions exist at the sand barrier. As stated above, these waves change significantly the barrier shape and various response characteristics.

This hollow would be formed by the river flow, mainly by the passage of floods after 1986. The time scale on the hollow formation is about 6 years.

## 6 Concluding remarks

We have shown various deformation of the river mouth topography and its time scales, and their interactions. Figure 12 shows the summarizing diagram mainly for the right side barrier. The lines with arrow indicate the direction of the change with the cause, which is distinguished by the type of lines. The right direction

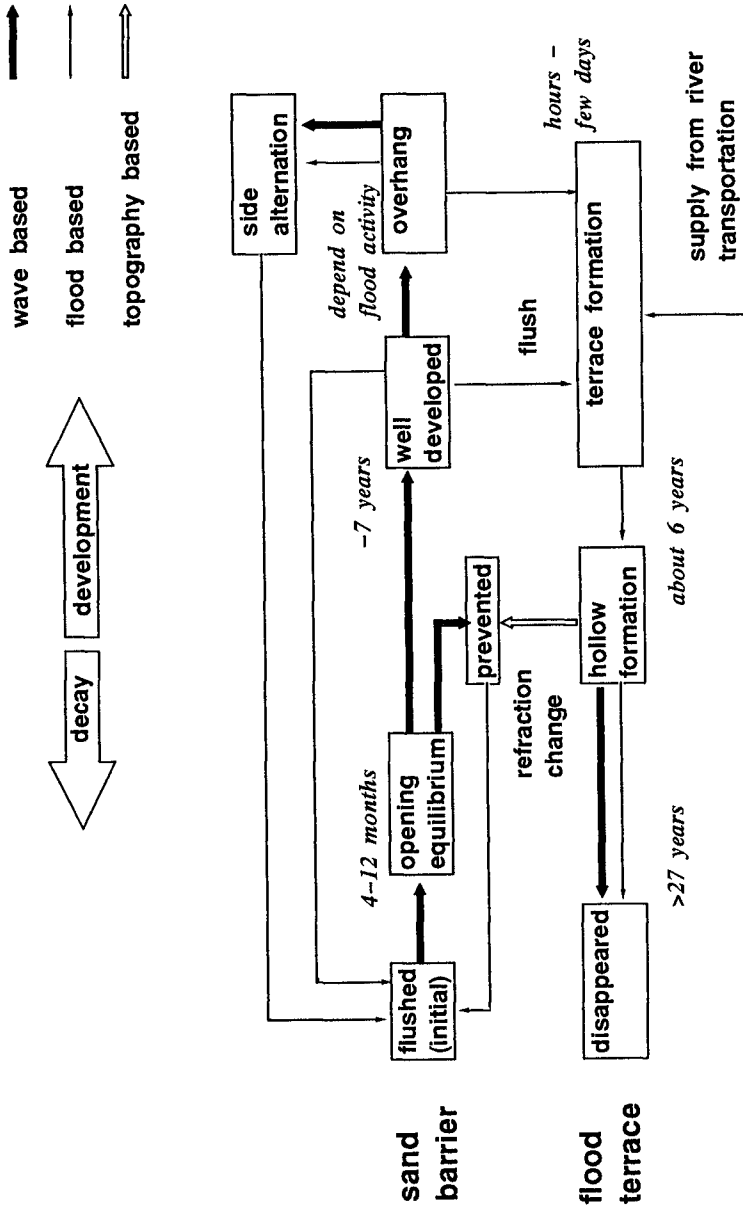


Fig. 12: Deformation stage and time scale.



corresponds to development and vice versa. Each box shows the stage of the deformation. The italic numbers are time scales based on the recent observations. The initial condition of the sand barrier is flushed state by the flood. Then it changes into equilibrium at the opening channel, well developed state, and overhang, depending on the flood activity. Although the main cause for the terrace formation is flood, sediment at the barrier contributes as well. Once the hollow is formed, it changes the refraction characteristics to prevent the development of the barrier. Depending on the timing, the barrier may not reach the equilibrium.

### Acknowledgement

The authors wish to express their gratitude to the Ministry of Construction and the Ministry of Transport for allowing to access the observed data. They also wish to express their thanks to the River Environment Fund by the Foundation of River & Watershed Environment Management and to Tohoku Regional construction Bureau, the Ministry of Construction for the sponsorship to this study. Acknowledgement also is due to the Ogawa Memorial Fund for the financial support for the publication.

### References

1. Aota, S and N. Shuto (1980):A model of the change of the sectional area at the river mouth, *Proc. Hydraulic Eng., JSCE, Vol. 24*, pp.203-208, (in Japanese).
2. Mano, A, M. Sawamoto, M. Nagao and K. Togashi(1993):Deformation characteristic of the Abukuma River mouth,*Proc. Coastal Engineering, JSCE, Vol.40*, pp.486-490 (in Japanese).
3. Mei,C.C(1983):*The Applied Dynamics of Ocean Surface Waves*, John Wiley & Sons, 740p.
4. Sawamoto, M. and N. Shuto(1988):Topography change due to floods and recovery process at the Abukuma river mouth. *Coastal Eng. in Japan, Vol. 30, No. 2*, pp.99-117.

## CHAPTER 226

### Half-Life Period of Sedimentation - Model Test on a Scale 1:1

Helmut Manzenrieder<sup>1</sup>

#### Abstract

In the framework of an extension plan for a large cargo handling berth, it is necessary for one alternative to build an artificial approach. The bottom of this dredged channel will lie approx. 6 m under the natural seabed level. The run of the axis is unfavourable since it is perpendicular to strong tidal currents which reach 2 m/s in the 705 cycles per year. In a model test, re-sedimentation for a volume of approx. 210,000 m<sup>3</sup> was observed indirectly in the standard procedure with repeated measurements by echo sounding as well as with a direct method using a sand-surface-meter combined with wind, tide, current and wave measurements.

#### History

The most important entrepot for energy in the Federal Republic of Germany is Wilhelmshaven. Its recent but nevertheless highly varied history began late - in 1853 - when a large Prussian naval port was established, the tradition of which continues up to the present time. In the year 1889, King William I of Prussia named the town after himself, i.e. Wilhelmshaven. Starting in 1957, the settlement of various oil companies and chemical concerns with their respective cargo handling installations including four large piers (Fig. 1) was influenced by the favourable natural conditions along the shore, especially water depth. Although no maintenance dredging had been carried out for a period of more than 10 years (1944 - 1957), a navigational depth of 11 m was still encountered. This can be attributed to the natural scouring force of the tidal current.

With the constantly increasing size of oil tankers, the navigation channel has been further deepened over several stages. The present target depth is between 18.5 and 20.0 m below chart datum so that fully laden tankers of 250,000 D.W.T. can put in at Wilhelmshaven under the right tidal conditions. The deep water region of

---

<sup>1</sup> Consulting Engineering Office Dr. Manzenrieder and Partner, Brookweg 29, D-26127 Oldenburg, Germany

Wilhelmshaven is located on the Jade which is a large arm of the sea on the coastline on the south side of the North Sea. The bay (555 km<sup>2</sup>) has very little fresh water flow, so most of the deterministic and stochastic parts of the energy in the regime are transferred only from the North Sea into the Jade which differs from the situation in a typical river estuary.

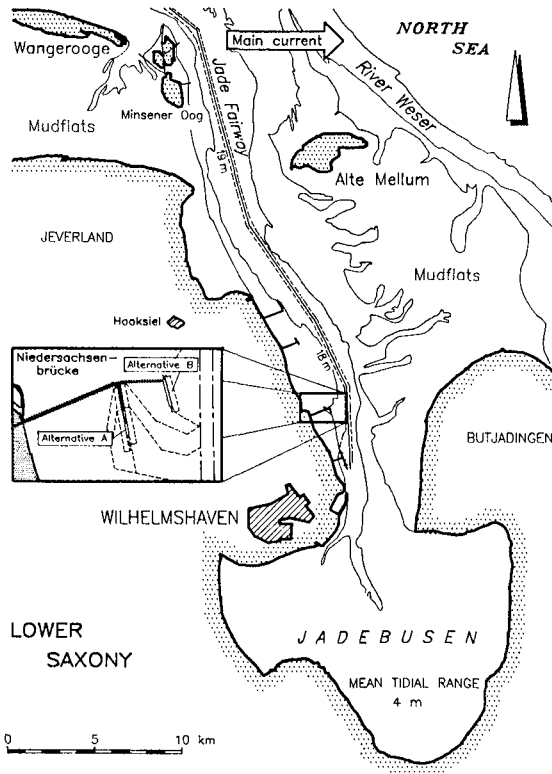


Figure 1. The Jade with the fairway and four cargo handling berths

Situation and Methods

The regular semi-diurnal tidal range of close to 4 m reaches its maximum all along the German coast. During one tide, approx. 1 billion cubic meters of salt water move into and out of the Jade, 705 times a year. As a rough estimate, approx. 6 million cubic meters of solid material is carried into the regime during this period. This process in combination with the artificial water depth in the fairway is the reason for recurrent dredging activities of up to 10 million cubic meters per year. In the framework of a current extension plan for a large cargo handling berth (called

"Niedersachsenbrücke") on the inner part of the Jade, there are two alternatives. For one alternative it is necessary to build an artificial approach between the berth and the navigation channel (see Fig. 1). The bottom of this dredged channel with a length of approx. 1 km will lie 6 - 7 m below the natural seabed level (12 - 13 m). The run of the axis is unfavourable since it is perpendicular to strong tidal currents which reach 2 m/s and have a high suspension load.

In view of this background, the simple but also substantial question for a cost-benefit calculation is the amount of maintenance dredging that will be needed to equal the sedimentation rate for a defined span of time in such an underwater depression. Also, because of the increasing importance of environmental aspects concerning the disposal of the material, a most critical point in design is the estimation of quantity in maintenance dredging which can be summarized in the question: *How many m<sup>3</sup> should be expected per year?*

Since we intuitively feel that the quantity of maintenance dredging will be related to the channel geometry, a prediction of this maintenance dredging will be necessary in order to complete the evaluation of particular alternatives. On the other hand, the prediction of such sedimentation is an extremely complex problem in itself and the classical sediment transport formulas will not be sufficient for predicting the bottom changes in a marine approach channel. In the example (Fig. 2), the deepening from 9.8 to 11.3 m is the reason for an increased shoaling rate of more than 200 %. However, a few untested methodologies for predicting channel shoaling do exist (SPM/I 1984, Galvin 1983, Bijker, Massie 1986).

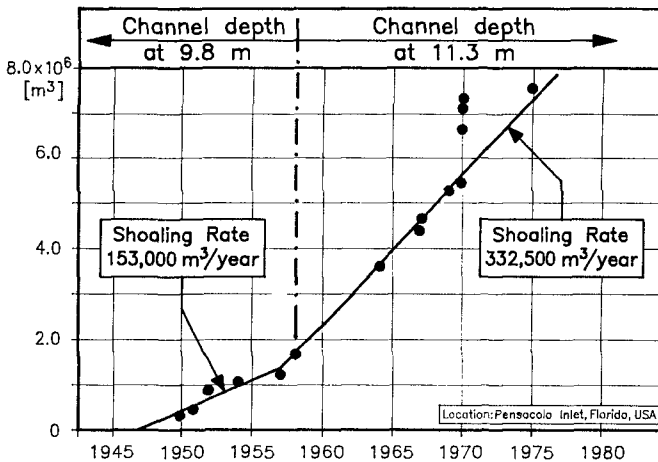


Figure 2. Mass dredging curve (from CERC, 1984)

The quality of powerful numerical models for such sophisticated questions are at a research level and far from adequate for forecasting engineering practice. The condition is much the same for simple models, for example, combining suspension

load and sink velocity. To meet the requirements, valid data on the physical processes in the specific area will be needed as input for calibration and checkup.

For the assessment of the different alternatives, the potential of sedimentation in the area is important. For the evaluation of these values, different methods are used (Basinski, 1989):

- Contained water samples
- Pumping samples in vertical profiles
- Turbidity profiles
- Stationary traps on the bottom
- Sand gauges (Sand-Surface-Meter)
- **In-situ model test on a scale 1:1**

One important result during regular tides was the quantity of sediment in suspension which was measured at approx. 15 t per hour and unit meter or about 100,000 t in the channel during the flood and ebb tide current. The local flow and wavefield has a rather high influence on this transport capacity.

#### Results of the Model Test in a Scale 1 : 1

In the framework of the investigation, a model test was set up at this stage since there was an independent requirement for a volume of approx. 210,000 m<sup>3</sup> of sand on land. After checking the physical parameters of the sandy soil ( $d_{50} = 0.25$  mm and  $d_{60}/d_{10} = 2.3$ ), a large underwater depression was dredged in the center of the designed approach with a maximum depth of approx. 22 m below chart datum (Fig. 3).

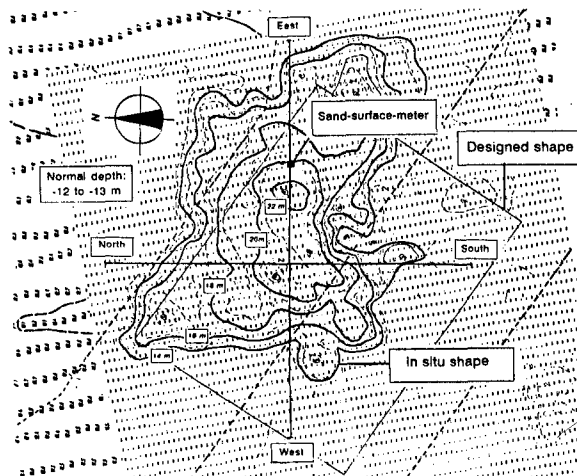


Figure 3. Test dredging - in situ shape in the initial stage

Subsequently, re-sedimentation was observed indirectly by the standard procedure with repeated measuring by echo sounding as well as with a direct method using a so-called Sand-Surface-Meter (SSM) in the deep center area of the dredged structure over a two month period (Manzenrieder, Witte 1986, Erlingsson 1990). Re-sedimentation and/or rearrangement within the structure started already during the dredging activities. The results of repeated precise echo sounding give information on the development in quantity over a period of one year. In table 1, all numerical values are listed.

Table 1: Re-sedimentation in an artificial depression  
(<sup>a</sup> Days after the end of-dredging )

Sounding No.	Sounding Date	Duration of Sedimentaion <sup>a</sup>	Max. Depth	Artificial Volume
0	31.01.1991	-	13,0 m	0 %
1	09.02.1991	2	22,5 m	100 %
2	12.02.1991	5	22,3 m	98 %
3	21.02.1991	14	22,0 m	95 %
4	05.03.1991	26	21,8 m	93 %
5	04.04.1991	56	20,9 m	83 %
6	03.05.1991	85	20,2 m	76 %
7	05.06.1991	118	19,2 m	65 %
8	10.07.1991	153	18,2 m	55 %
9	11.09.1991	216	17,8 m	51 %
10*	13.11.1991	279	17,8 m	51 %
11*	16.01.1992	343	16,9 m	41 %

\* Uncertainty in the echo sounding execution

In Fig. 4, the development of the bottom shape which was taken by echo sounding is given up to sounding No. 9. The right-angled axis is shown in Fig. 3. The tidal currents cross the depression in the North-South direction with velocities up to 2 m/s. In Fig. 5, the remaining value at the end of the dredging period is assigned to time. The analysis of the information from the soundings indicate an average sedimentation rate of 2.4 cm per day.

To get more detailed information on the processes in the dredged structure, a Sand-Surface-Meter (SSM) was installed in the center area of the depression. Modern instruments such as this were used in addition to the classical areal sounding method which of course only give continuous data on the relative bottom position for a single point but during all sea conditions (Manzenrieder, Snippe 1991). The necessity for this instrument is shown in Fig. 6.

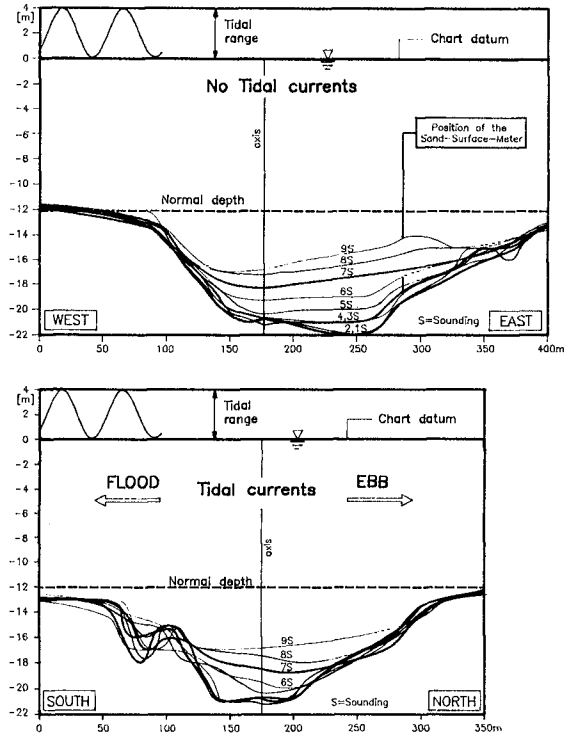


Figure 4. Cross-sections in the center area

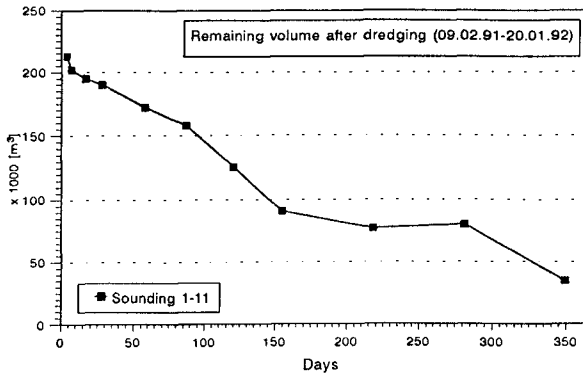


Figure 5. Re-sedimentation in the depression

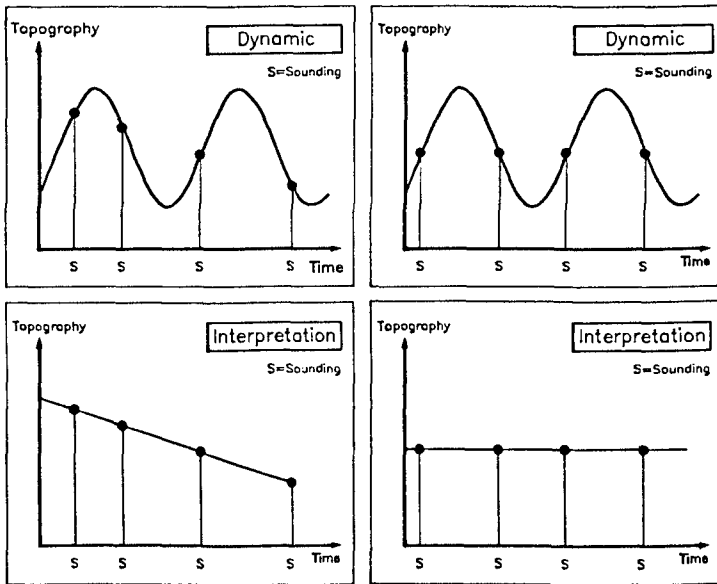


Figure 6. Uncertainty in the Interpretation of Soundings

In Fig. 7, a sketch of such specific measurements under water should give an impression how such devices give a sort of microscopical view of the complex processes. The newest generation of these instruments is also qualified to observe transport processes above the bottom (bed load). In its application for observing sedimentation in the introduced dredging contour, the constant time interval was 60 minutes, the range of measuring 1.5 m and it was supported by diver inspections. One system exchange was necessary. For a period of approx. two months, digital information was collected continuously and the original results are displayed in Fig. 8. Sedimentation in the first two weeks was almost linear. After that, some discontinuous steps were measured. Between the following linear gradients, two periods without significant sedimentation are conspicuous. The average sedimentation rate over the two month period was calculated at 4.1 cm/day.

Combined with wind, tide, current and wave measurements, direct observation of the boundary layer especially provided deeper insights (Fig. 9). During a strong gale of up to Bft No. 8, the sedimentation rate increased to 18 cm/day. After the event there was a period without significant sedimentation. This remarkable process during a higher energy level in the watercolumn is an indication for the sedimentation potential on the bottom which is mobilized during such periods in the form of a suspended charge. Afterwards, the bottom in general showed an over-proportional absorption capacity before reaching standard conditions of "normal" sedimentation.



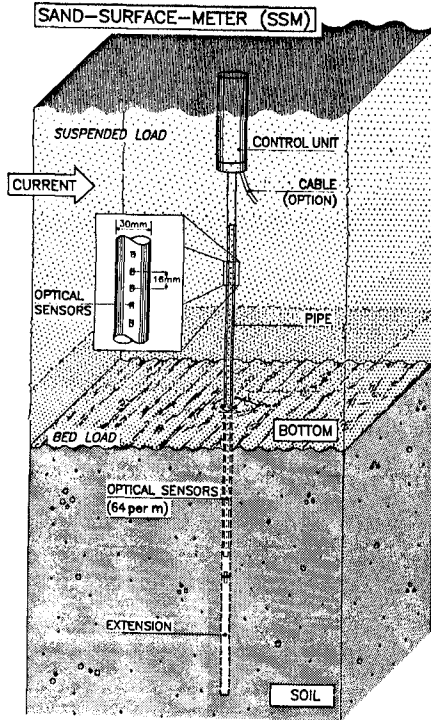


Figure 7. Field Measurements with a Sand-Surface-Meter (schematic)

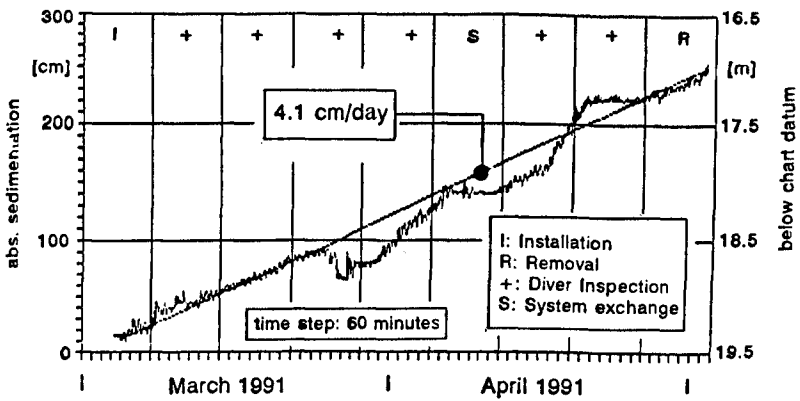


Figure 8. Sedimentation in the Center Area (Continuous Observation with Sand-Surface-Meter)

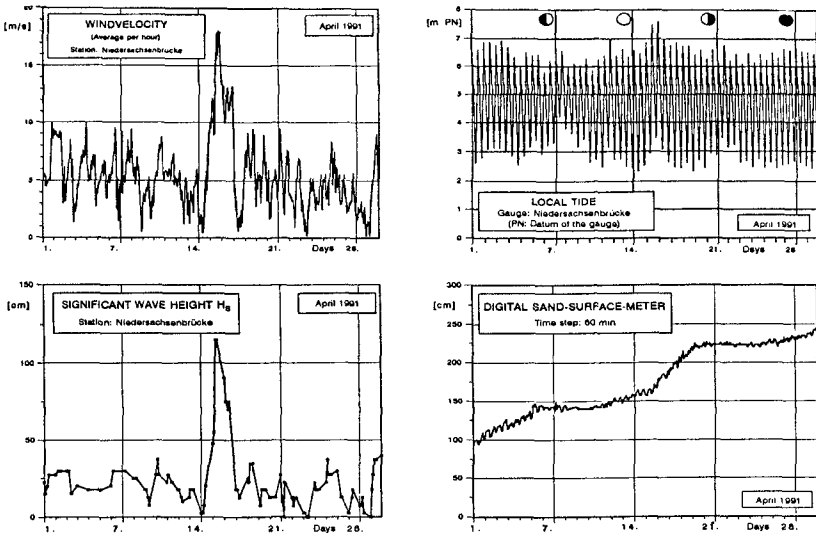


Figure 9. Assignment for the Sedimentation Processes

Theoretical Approach

All present observations and the results of investigations on erosion of beach nourishments (Führböter 1974, 1991) support a non-linear nature for the material on the balance sheet. Führböter based his approach on the assumption that the local, long term wave climate is constant and mentioned the same exponential law known in nuclear physics using the definition of a half-life period. In relation to the erosion processes close to the surface, sedimentation in artificial underwater structures (e.g. channels) is influenced by water depth. Especially due to this hydraulic filter in deeper regions, the assumption of a more constant local transport regime could be supported. Taking a sediment-laden current crossing a channel into consideration, the abrupt change in hydraulic conditions will cause time dependent morphological changes in the channel. The supposed function over time is given schematically in Fig. 10.

Under the assumptions stated above for an analytical expression of the sedimentation processes, the dredged volume  $V$  below the natural horizon at time  $t$  is the initial information. In the next time step  $\Delta t$ , this artificial volume will be reduced due to sedimentation by an amount of  $\Delta V$ .

$$- \frac{\Delta V}{\Delta t} = \lambda V \text{ or } \Delta V = - \lambda V \cdot \Delta t \tag{1}$$

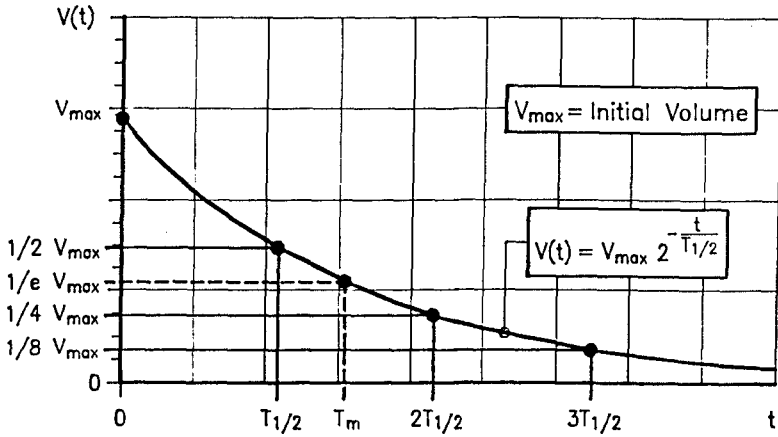


Figure 10. Sedimentation in an Artificial Underwater Depression (schematic)

The negative sign deals with the sedimentation tendency. Very little knowledge is available on the range of sedimentation parameter  $\lambda$ . One step for the evaluation of this value is a part of this paper.

In equation (1), the assumption is included that volume  $V$  is constant during time-step  $\Delta t$ , so that the relation will be stabilized with increasing time between each sample (sounding). The transition for the gradient of the secant  $\Delta V, \Delta t$  to the differential form (gradient of the tangent) follows at

$$dV = -\lambda V dt \text{ or } \frac{dV}{V} = -\lambda dt \tag{2}$$

After the integration of eq. 2, the description for the sedimentation during any time is given. The integral for the time 0 with an initial volume  $V(0) = V_{max}$  to time  $t$  with the remaining volume  $V(t)$  has the form

$$\int_{V_{max}}^{V(t)} \frac{dV(t)}{V(t)} = -\lambda \int_0^t dt \tag{3}$$

with the solution

$$\ln V(t) - \ln V_{max} = -\lambda t \text{ or } \frac{V(t)}{V_{max}} = e^{-\lambda t} \tag{4}$$

The sedimentation coefficient  $\lambda$  will be written in the following form

$$\lambda = - \frac{\ln V(t) - \ln V_{max}}{t} \tag{5}$$

the derivative trend with respect to time is

$$V(t) = V_{\max} e^{-\lambda t} \quad (6)$$

Equation 6 is in relation to the basic equation for radioactive decay, so this could be used as a basic sedimentation equation in artificial depressions. The evaluation of sedimentation factor  $\lambda$  as the central input parameter is based on experimental investigations. In contrast with nuclear physics, no universal indications are available. The lack of qualified instrumentation for such measurements is only one reason for this limitation. Following the analogy for the sedimentation factor  $\lambda$ , the half-life period  $T_{1/2}$  could be used with the definition:

The half-life period  $T_{1/2}$  of an artificial depression is the time for a 50% reduction of the (dredged) volume due to re-sedimentation.

When describing the relation between the half-life period  $T_{1/2}$  and the sedimentation factor  $\lambda$  the remaining volume in the depression  $V(t_1)$  at the time  $t_1$  could be used

$$V(t_1) = V_{\max} e^{-\lambda t_1} \quad (7)$$

After expiration of the time  $T_{1/2}$ , that means the total time  $t_1 + T_{1/2}$  bisected by the artificial volume

$$\frac{1}{2} V(t_1) = V_{\max} e^{-\lambda(t_1 + T_{1/2})} \quad (8)$$

Using both equations above, it follows that

$$e^{-\lambda t_1} = 2 e^{-\lambda(t_1 + T_{1/2})} \quad (9)$$

and

$$-\lambda t_1 = \ln 2 - \lambda(t_1 + T_{1/2}) \quad (10)$$

or

$$T_{1/2} = \frac{\ln 2}{\lambda} = \frac{0,693}{\lambda} \quad (11)$$

The half-life period  $T_{1/2}$  is consequently a characteristic value which is independent from the previous sedimentation period. This is important when applying in practical applications. It is common to use the half-life period in a mathematically more simple form

$$e^{\frac{t \ln 2}{T_{1/2}}} = 2^{-\frac{t}{T_{1/2}}} \quad (12)$$

with the relation for  $\lambda$  the volume  $V(t)$  is indicated

$$V(t) = V_{\max} \cdot e^{-\frac{\ln 2}{T_{1/2}} t} \quad (13)$$

or

$$V(t) = V_{\max} \cdot 2^{-\frac{t}{T_{1/2}}} \quad (14)$$

Another important characteristic value for the behaviour of an artificial structure underneath a stable bottom is the average lifetime  $T_m$ .

By adjusting the assessed values, the average stability of the dredged volume defined as the area between the axis  $V(t)$ ,  $t$  and the function of sedimentation (eq. 5), it follows that

$$V(t) = V_{\max} e^{-\lambda t}$$

and from this

$$T_m = \frac{1}{V_{\max}} \int_0^{\infty} V_{\max} e^{-\lambda t} dt = \int_0^{\infty} e^{-\lambda t} dt = \left| -\frac{1}{\lambda} e^{-\lambda t} \right|_0^{\infty} = \frac{1}{\lambda} \quad (15)$$

With this, the average stability  $T_m$  for the structure result from the reciprocal value of the sedimentation factor  $\lambda$ . A more subordinated value in this context could be the remaining volume after expiration of the average lifetime:

$$V(T_m) = V_{\max} e^{-\lambda T_m} = V_{\max} e^{-1} = \frac{1}{e} V_{\max} \quad (16)$$

For practical applications, for example maintenance dredging, it is important to predict the time for determining re-sedimentation. Using the results above, this time could be calculated with the knowledge of the sedimentation factor  $\lambda$  respectively the half-life period  $T_{1/2}$ . If the required part of sedimentation is expressed with the factor  $p$  as percentage of the initial volume, it follows from eq. 6

$$V(t_p) = V_{\max} e^{-\lambda t_p}$$

with

$$V(t_p) = \frac{p}{100} V_{\max} \quad (17)$$

or

$$\frac{p}{100} V_{\max} = V_{\max} e^{-\lambda t_p} \tag{18}$$

and from this

$$\ln \frac{p}{100} = -\lambda t_p \tag{19}$$

the required time  $t_p$  as a function of  $\lambda$

$$t_p = -\ln \frac{p}{100} \frac{1}{\lambda} \tag{20}$$

or as a function of the half-live period  $T_{1/2}$

$$t_p = -\ln \frac{p}{100} \frac{T_{1/2}}{\ln 2} \tag{21}$$

Application

Using the information gained by repeated soundings which were a part of the observations made during re-sedimentation in the introduced test dredging, a first application of the theoretical considerations was made. The results are concentrated in table 2.

From equation 5, the respective sediment factor  $\lambda$  is calculated (column 4)

$$\lambda = -\frac{\ln V(t) - \ln V_{\max}}{t}$$

After the solution for  $\lambda$ , the half-life period is known as  $T_{1/2}$  from equation 11. Furthermore, the average lifetime  $T_m$  of the structure is one result. As one example in the last column shows, time  $t_p$  describes the span of time in which the artificial structure is refilled up to  $p = 10\%$  of the initial volume. The initial dredging volume  $V_{\max}$  was approx. 210,000 m<sup>3</sup> and the total observation time approx. one year (341 days).

Conclusion

Test dredging in connection with the design of an artificial approach and various observations provided the following main results:

- In general, re-sedimentation of the approx. 210,000 m<sup>3</sup> artificial underwater depression took on an exponential form over a one year period.
- Differences between sedimentation in a crater-shaped underwater structure and a channel as a negative line source exist but are highly influenced by the axis orientation in relation to the efficient current system.
- Based on the repeated measurements with echo sounding, the average sedimentation rate was calculated at 2.4 cm per day. To maintain a constant

depth as substantial as the one demanded for operating conditions, this value which in total equals approx. 9 m of sedimentation per year is important.

Table 2: Test dredging in the artificial approach - Niedersachsenbrücke -

V	ln V	t	$\lambda$	$T_{1/2}$	$T_m$	$t_p$ (p=10%)
[m <sup>3</sup> ]	-	[days]	[1/days]	[days]	[days]	[days]
212,650	12.267	0	-	-	-	-
201,900	12.216	3	0.017	41	59	136
194,530	12.178	12	0.0074	94	135	312
190,140	12.156	24	0.0046	151	217	502
171,780	12.054	54	0.0039	178	256	591
157,900	11.97	83	0.0036	193	278	641
126,200	11.746	116	0.0045	154	222	512
90,760	11.416	151	0.0058	120	172	399
76,530	11.245	214	0.0048	144	208	478
80,390*	11.295	269	0.0036	193	278	641
35,410*	10.475	314	0.0053	131	189	435
Mean value			0.0061	140	201	465
Weighted Average			0.0046	152	220	508

\* Uncertainty in the echo sounding execution

- Due to the basic physical limitations of the echo sounding principle on such sloped bottoms, a precise determination of the underwater geometry is not possible (slope error, etc.). Normally, the slope given is too small.
- The average of the directly measured sedimentation rate over a two month period in the center area was determined at 4.1 cm/day by a linear gradient. Using this higher value, 15 m of sedimentation in one year must be calculated for dredging and disposal.
- During a strong gale of up to Bft No. 8, the sedimentation rate increased to 18 cm/day. After the event, there was a period without significant sedimentation which seemed remarkable.
- With respect to the area of the approach (~ 450,000 m<sup>2</sup>), the definition of the actual sedimentation rate will influence the choice of alternatives.
- In theory, the mathematical consequence is that continuous maintenance dredging in the horizon of the nautical depth will minimize the total quantity. Due to meteorological and hydrological as well as practical aspects, limitations must be considered.

- The need for repeated maintenance dredging in artificial coastal areas is determined by the number of stochastic meteorological events.
- When predicting sedimentation rates over a longer period, it is remarkable that single meteorological events do not necessarily increase the average value. This could be of importance for numerical simulation as well.
- After two years, no indication of the artificial depression could be determined by echo sounding.

### References

- Basinski, T. (1989). Field studies on sand movement in coastal zone. Polska Akademia Nauk, No. 16
- Erlingsson, U (1990). Sediment transport monitoring. Dept. of Physical Geography Uppsala, Sweden, UNGI Rapport 76
- Galvin, C (1983). Shoaling with bypassing for channels at tidal inlets, Proceedings of the 18th Int. Conference on Coastal Eng., pp. 1496-1513
- Führböter, A. (1974). A refraction groyne built by sand. Proceedings of the 14th Int. Conference on Coastal Eng., Vol. II, Chapter 85
- Führböter, A. (1991). Artificial nourishment with refresher intervals a theoretical analysis. Die Küste, No. 52, page 241 - 254 (in German)
- Manzenrieder, H. and Witte, H.-H. (1986). Observation of dynamic changes on the seabed - procedures, limitations and new methods. Leichtweiß-Institute T.U. Braunschweig, No. 93, page 329 - 378 (in German)
- Manzenrieder, H., Snippe, B. (1991). Continuous observation at the tidal bottom by using a Sand-Surface-Meter. Die Küste, No. 52, page 255 - 263 (in German)
- Massie, W.W. (ed.) (1986). Coastal Engineering, TH Delft, Volume II
- SPM/I (1984). Shore Protection Manual. Coastal Engineering Research Center, Volume I



## CHAPTER 227

### Risk assessment for coastal and tidal defence schemes

Meadowcroft IC<sup>1</sup>, von Lany PH<sup>2</sup>, Allsop, NWH<sup>3</sup> and Reeve DE<sup>2</sup>

#### ABSTRACT

This paper describes risk assessment techniques developed in a research project carried out for the UK National Rivers Authority (NRA) (Meadowcroft and Reeve, 1993). The main aim is to develop probabilistic design and analysis methods to assess the risks of failure for new and existing sea and tidal defence schemes. The flood risk takes account of the failure probability and the consequences of failure. There is a contrast between conservative design criteria that attempt to minimise failure rates, and risk-based design criteria that offer a more cost-effective solution despite a possible increase in failure frequency. The procedures are intended to be used in the design of new schemes, for assessment of existing defences and prioritisation of maintenance and refurbishment.

#### 1. INTRODUCTION

The paper outlines new procedures under development for the National Rivers Authority to assess risks of failure for new and existing sea and tidal defence schemes. The project includes assessment of areas at risk of flooding, but this paper concentrates mainly on risk assessment and probabilistic analysis of structures. The research is being used to formulate procedure for assessment of flood risk. The key elements of the procedures are:

- A tiered classification system;
- Modular procedures allowing more or less complex methods to be applied as appropriate;
- Risk defined as a combination of the probability and consequence of flooding;
- Screening tests using existing data such as that held in the National Sea Defence Survey (NSDS) to identify defences at greatest risk;
- Identification of principal failure modes and more detailed analysis of these using probabilistic methods;
- Advice on methods for flood area mapping and data collection as a means of

---

<sup>1</sup>HR Wallingford, Howbery Park, Wallingford, Oxon, OX10 8BA, UK

<sup>2</sup>Sir William Halcrow and Partners Ltd, Burderop Park, Swindon, Wiltshire, SN4 0QD, UK

<sup>3</sup>HR Wallingford, Howbery Park, Wallingford, Oxon; Professor (Associate) University of Sheffield

assessing the consequences of failure.

The paper firstly describes the overall structure of the procedures, and then examines in more detail the role of probabilistic methods in assessing flood risk.

**2. STRUCTURE CLASSIFICATION AND FAILURE MODES**

One of the first tasks of the research was to develop an appropriate classification system for structures. The classification system is hierarchical, based on three levels:

- Level 1: generic type eg narrow embankment with sloping face
- Level 2: general form of construction eg vertical wall with crest and back slope unprotected
- Level 3: detail of individual components eg revetment type

The advantage of this approach is that failure mechanisms at different levels of detail can be assigned to each level of the classification. The structure classification is used to guide preliminary assessment at the screening stage. The structure type affects its vulnerability to different failure mechanisms. Part of the structure classification system is

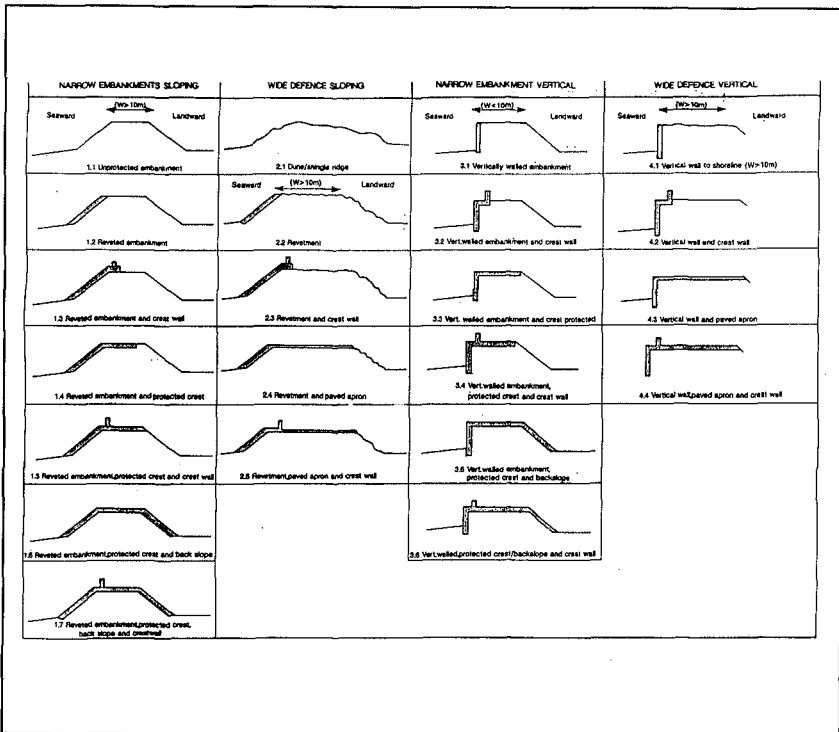


**Figure 1 Structure classification scheme. The structure type can be used as a guide to the most likely failure mechanisms, and to identify appropriate response functions.**

shown in Figure 1.

An example of the linkage between structure classification and response function is the selection of an appropriate method for calculating wave overtopping. Potential consequences of overtopping include flooding, danger to the public and damage to defence structures. Numerous methods are available depending on the geometry of the structure.

Four categories of structure each requiring different methods are detailed:

- i) For sloping seawalls, the actual overtopping,  $Q_{act}$ , may be calculated using an equation developed from the method by Owen (1980)

$$Q_{act} = A\theta \left( \frac{-B R_c J_r}{T_m \sqrt{gH_s}} \right) T_m g H_s \quad (m^3/s/mrun)$$

A and B can be obtained from standard tables

r is the effective roughness of the seawall slope, established from site visit or from table 3, Owen (1980)

$R_c$  is the freeboard (crest level minus water level)

- ii) For sloping seawalls with wave return walls, the method derived by Owen & Steele (1991) is appropriate. This extends from the method for sloping sea walls, with the freeboard being considered as the distance from SWL to the top of the wave wall, as opposed to the top of the seawall. It should be noted that this method was derived for recurved wave return walls and will therefore give a value which is less than the actual overtopping discharge for vertical wave return walls which experience a greater degree of overtopping.
- iii) Overtopping for vertical walls is calculated using standard graphs and the expression (Goda, 1971)

$$Q_{act} = Q \cdot (2gH_s^3)^{0.5}$$

- iv) For vertical seawalls with wave return walls, no defined method was found. It was concluded that the seawall and the wave wall should be considered as a single defence, taking the structure height as the height of the two defences combined. The method for standard vertical walls can then be applied.

Table 1 illustrates a simple look-up procedure to link seawall type, profile classification and calculation method. Profile references refer to the structure types identified in Figure 1.

A wide range of other failure mechanisms have been identified and appropriate response functions recommended (eg Allsop 1993).

Structure type	Profiles	Method
Sloping seawall	1.1, 1.2, 2.1, 2.2	(i)
Sloping seawall with wave return wall on crest	1.3, 1.5, 1.7, 2.3, 2.5	(ii)
Vertical seawall	3.1, 3.3, 3.5, 4.1, 4.3	(iii)
Vertical seawall with wave return wall	3.2, 3.4, 3.6, 4.2, 4.4 (assuming height of structure to be sum of seawall and wave return wall heights)	(iv)

**Table 1 Overtopping calculation method depending on structure classification**

A survey of flood defence failures has been undertaken as part of the project. This has shown that, while there have been a numerous reported flood events due to defence failures, information about failures of defences is normally very limited in scope, and is rarely sufficient for identifying the precise sequence of mechanisms leading to a failure. One may gain more useful information from studying rates of damage and deterioration, where the condition of the defence may indicate potential failure mechanisms.

#### Damage cause by burrowing animals

According to anecdotal and documented information from NRA staff, a particular area of concern is the damage caused by burrowing animals such as rabbits and badgers. The main problems are the serious structural damage caused, including voids and passages through embankments, the difficulty in carrying out effective repair, short of re-building the affected part of the embankment, and the likelihood of re-infestation. The number of rabbits, in particular, can be particularly difficult to control. In one severe case, over 1000 rabbits are reported to have been killed over a few months, but the embankment continues to be colonised. Conservation interests can have a great influence on the measures taken. There are, for example, controls on the disturbance of badger setts.

The project has found very little information on the effect of animal burrows on embankment safety and flood risk, either in terms of animal behaviour or from the point of view of hydraulic and geotechnical impacts. Research is at present underway to fill some of these gaps, but in the meantime, approximate methods such as assuming a reduced effective crest level can be used. Site investigation is also important, from recording the number of burrows, and their positions, to mapping the internal structure of voids caused by animals. Non-destructive investigation techniques may have potential to investigate the size, extent and location of burrows and other voids.

### 3. RISK ASSESSMENT METHODS

There are several different definitions of 'risk', but for our purposes, risk is defined as the combination of the probability or frequency of occurrence of a defined hazard, and the magnitude of the consequences. The method of combination is generally to multiply the probability and consequences. This gives a measure of the expected value of the consequence incurred in the time period being considered. Risk as defined is thus closely related to the assessment of benefits which is commonly carried out as part of the project appraisal process.

Even within the relatively narrow topic of flood risk, there are a number of aspects of risk likely to be of interest to user of the procedures:

- The danger to the public from flooding, expressed in terms of number of injuries or deaths, and associated frequency
- The probability of death or injury to individuals
- The frequency of flooding at different locations in the potential flood area taking account of all the possible causes of flooding and all possible failure mechanisms. This information can be shown as frequency contours.
- The depth and duration of flooding.
- The degree of risk inherent in each defence structure ie the expected annual consequences of failure of the structure
- 'What if' scenarios, ie flood outlines conditional upon some prescribed defence failure

A general procedure for risk assessment is illustrated in Figure 2, which illustrates the process of hazard identification, and assessing the probabilities and consequences of failure.

Although the concept of risk is straightforward, the implementation is complicated because a full risk assessment must consider *all* hazards which could result in damage or loss. Clearly some hazards will make an insignificant contribution compared to others, but in principal all hazards must be identified and studied as far as necessary to establish what degree of risk they pose. Similarly, even a relatively simple structure will have a number of potential failure mechanisms, and it will not usually be known with certainty which are the most likely to contribute most to the risk.

The procedure illustrated in Figure 2 should therefore be repeated for different hazards, and for different failure mechanisms. This would result in a large amount of work which would prevent the wide application of detailed risk assessment. This explains the need for simplified procedures to screen out 'low risk' structure and to identify those in need of the most detailed analysis.

The project has identified failure modes, defined as a number of individual mechanisms. Failure mechanisms are described using a nested system to reflect the level of detail of the classification system. At Level 1, the failure mechanisms are simply breaching and overtopping/overflow. At Level 2, we identify mechanisms affecting the main parts of the structure such as the seaward face, crest, and landward face. Level 3 considers failure of individual structure elements such as

breakage of revetment units.

One of the early findings of this work was that, whilst conventional fault trees and event trees as used in the electronics and chemical industries may be suitable for systems of binary components that either fail or do not fail, they are not sufficient on their own for failure of sea walls and related structures. These exhibit complex failure modes with interactions between different damage mechanisms. For example, overtopping and geotechnical slope failure of the landward face of an embankment may not, individually, pose a high risk, but the damage due to the geotechnical failure will make erosion due to overtopping much more likely: the mechanisms interact. Furthermore, the quantity of water overtopping may be very important in determining the area flooded and hence the consequence: one cannot talk only of 'failure' and 'no failure' for this type of risk assessment, since a spectrum of outcomes can result.

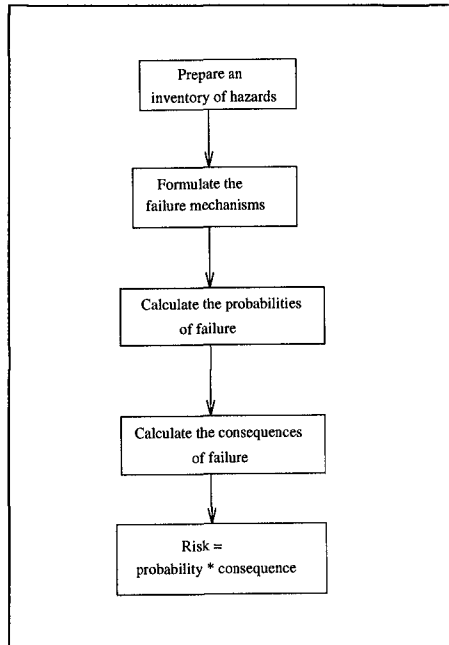


**Figure 2 Overall procedure for risk assessment (from CUR/TAW, 1990)**

The project considers a number of practical techniques for dealing with a broader range of mechanisms needed for an assessment of a sea defence system. One particular method makes use of 'event chains' leading from a particular trigger event (ie storm), through failure mechanisms to set a of consequences. For each consequence, a probability of occurrence is calculated, conditional upon the initial event. It is necessary to incorporate connections between some event chains, to account for the physical dependence noted above.

An advantage of the method is that it provides a framework which can be applied at several levels of complexity, providing a modular approach at each level of detail appropriate to the degree of risk and data availability. This tiered approach is illustrated in Figure 3. The first steps make use of data already held by the NRA as part of the National Sea Defence Survey (NSDS). This has created a set of data about sea defences in England and Wales, including information such as the length and position of defences, and an assessment of their condition and effectiveness. The survey includes classification of the area of the potential flood area and the land use within that area. Thus the NSDS provides an important starting point for assessing risk. Automated screening tests have been developed using this data, and the indicative or relative risk is also based partly on NSDS data. More detailed assessment of risk requires additional site-specific data.

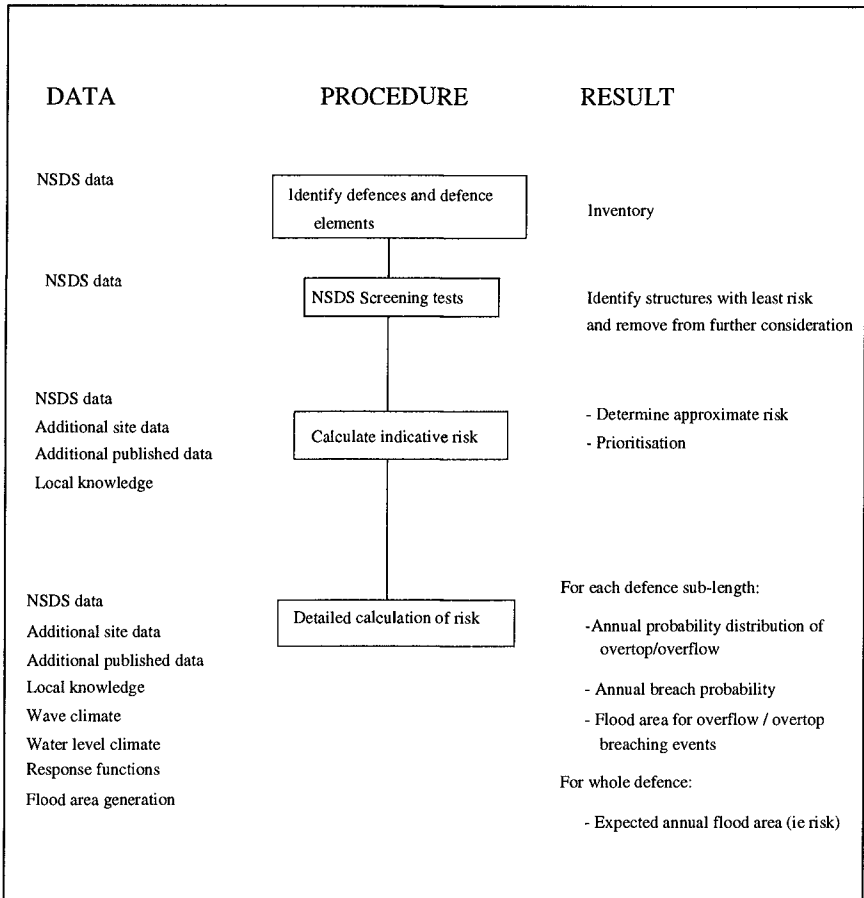


**Figure 3 Tiered assessment procedure showing level of data, analysis and results at each stage**

#### 4. PROBABILISTIC METHODS

Probabilistic methods are used to account for uncertainty in data values or in response functions. The main sources of uncertainty are:

- Identification of hazards
- Identification of failure processes / failure modes
- Development of damage leading to failure, time effects
- Data on load parameters, lack of data or errors in data
- Long term changes including climate changes
- Stochastic nature of loading, even if statistics are well known
- Structure geometry and material properties
- Responses: form of functions and empirical coefficients

- Thresholds for failure

Probabilistic methods can be applied to account for many of these uncertainties to give an estimate of the response which is consistent with our level of knowledge or ignorance. This estimate will generally be in the form of a probability distribution, although if a threshold for failure is defined, the result may be in the form of a failure probability. Of course, the exact *actual* or realised failure probability of a particular structure will only be known in the future, and it will have a value of either 0.0 or 1.0, but random variations in loads, and uncertainties in strengths and response functions prohibit us from predicting failure or otherwise exactly. We can only hope to estimate a probability of failure based on current knowledge.

Probabilistic methods enable uncertainties in strength and loading variables to be propagated through the risk assessment procedure. The final risk assessment therefore takes account of lack of precise knowledge of the structure properties, the environmental loading, and the response function. Probabilistic methods provide a basis for accounting for the effects of uncertainty in a structured and systematic manner. These can have significant cost and benefit implications. Probabilistic methods may be subjective, based on engineering opinion, or objective, based on Monte-Carlo sampling or analytical methods.

Development and application of probabilistic methods for structural design and analysis is described in more detail elsewhere (CIRI, 1977, Thoft-Christensen & Baker 1982). Application of a range of methods to coastal structures is described by Meadowcroft & Allsop (1994).

The simplest analytical methods (known as Level II, first order mean value methods) are in fact closely related to sensitivity tests: the key advantage is that they account for the variability in input parameters as well as the sensitivity of the response to the inputs, and probabilistic methods take account of the combined effects of variability of all relevant parameters.

Several examples are now given which illustrate the data required and results obtained from probabilistic methods.

#### Example 1: Level III (Monte Carlo sampling) prediction of damage to a rock armour structure

This simplified example demonstrates clearly the influence of variability in input parameters on the resulting prediction. The response function is the Van der Meer (1988) equation to predict the degree of damage,  $S$ , to rock armour under plunging waves as a function of structure and load parameters. In this case, the occurrence of the design storm is presumed, so the variability results from uncertainty in structure parameters such as rock armour size, and from errors in estimating the design wave height. There is also some uncertainty in the values of the empirical parameters  $a$  and  $b$  in the response equation: these can be treated like any other probabilistic input parameter.



Input parameter	Distribution	Standard deviation (coefficient)	Mean
Significant wave height $H_s$ (m)	Normal	10%	3.0 (depth limited to 0.55h)
Slope angle ( $^\circ$ )	None	-	0.5
Rock density ( $\text{kgm}^{-3}$ )	Normal	5%	2650
Nominal rock diameter $D_{n50}$ (m)	Normal	5%	1.3
Permeability parameter P	None	-	0.1
Wave steepness $s_m$	Normal	10%	0.05 (truncated at 0.07)
van der Meer parameter a	Normal	10%	6.2
van der Meer parameter b	Normal	10%	0.18

**Table 2** Input distributions for calculating probability distribution of damage

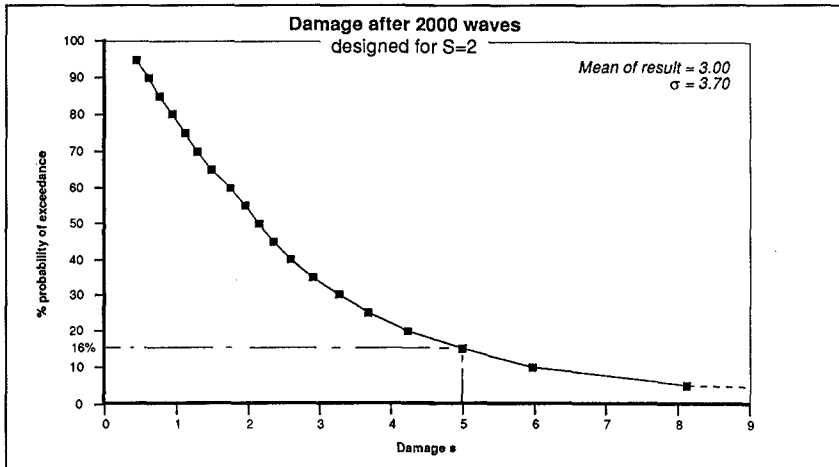


**Figure 4** Probability distribution for damage to rock armour structure

The resulting probability distribution (Figure 4) shows predicted damage for a structure designed for minor damage ( $S=2$ ). Reliability of the structure against other damage levels can be assessed. The probability of the damage exceeding 5, for example, is about 16%, and for  $S=8$ , corresponding to severe damage, about 3%.

Example 2 Level II assessment of damage due to overtopping

The amount of wave overtopping is a principal indicator of damage and failure of coastal structures. It is therefore important to be able to calculate the probability that a structure will fail to meet acceptable criteria for overtopping. These include the ultimate limit state (ULS) corresponding to damage which may lead to complete collapse and breach, and serviceability limit state (SLS) corresponding to failure to meet a service criteria such as danger to the public.

Level II methods are used to produce analytical approximations to the probability of failure. They are based on partial differentiation of the response function with respect to each of the probabilistic input variables.

The simulations shown below were carried out using a Level II probabilistic method, the Approximate Full Distribution Approach (AFDA). This is a relatively sophisticated technique that enables the use of input probability distributions which are non-normal, and uses iteration to converge on a more accurate solution than the mean value approach. Results in Table 3 show the impact of raising the crest of a structure on the annual probability of failure due to excessive wave overtopping. These results are illustrated in Figure 5, together with the annual probability of exceedance of a serviceability criteria.

Crest Level (mAD)	Annual probability of severe damage due to overtopping (ULS)
14.0	0.72
16.0	0.28
18.0	0.08
20.0	0.03

**Table 2** Example of results of probabilistic analysis of a seawall to establish annual probability of severe damage at an ultimate limit state, ULS.

A key advantage of the full distribution method is its ability to cope with non-normal distributions. In this example, the significant wave height and still water level were both specified using Weibull distributions. Use of distributions fitted to all data rather than to annual maxima or other selected data enables two or more time-varying load variables to be combined simply. It is not necessary to consider the reduced probability of an extreme value of one variable occurring at the same time as the extreme value of another. In this case waves and water levels are independent although techniques are available to incorporate correlation into Level II methods.

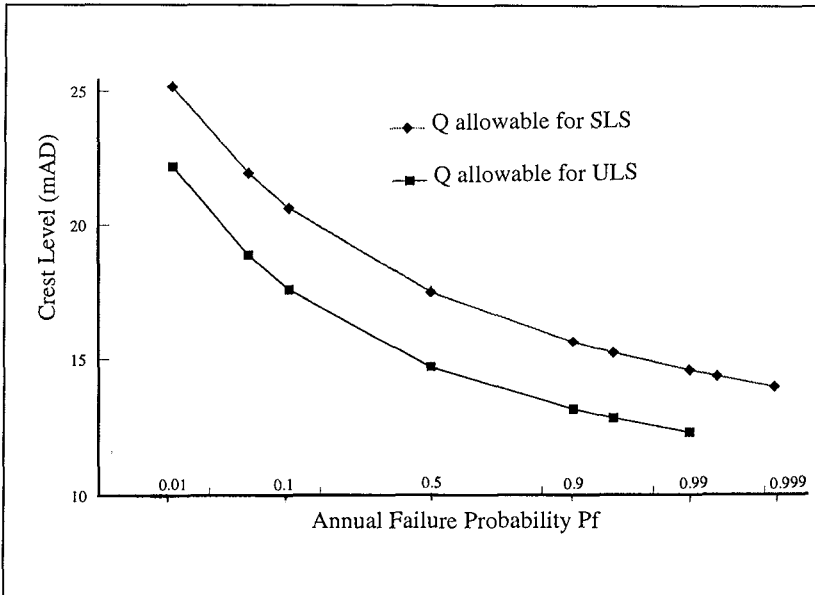


**Figure 5 Probabilistic analysis of overtopping: annual failure probability for serviceability and ultimate limit states**

### Example 3 Probabilistic assessment of slope stability

This example illustrates the use of the Level II method in conjunction with a numerical model of slope stability. The advantage of this approach over the Level III method is that it is not necessary to carry out many repeat simulations to build up the resulting probability distribution. This can be particularly onerous when predictions are made using a computationally-intensive numerical model.

The method relies on carrying out a small number of model runs to enable numerical, rather than analytical differentiation of the response with respect to each probabilistic input variable. In this way a fundamentally deterministic model is used to produce probabilistic results by appropriate selection of input data and suitable analysis of the results.

The model in this case was SLOPE, part of the Oasys suite of geotechnical programs. This was used to analyse a circular slip surface on the landward face of an earth embankment (Figure 6). The model gives the factor of safety  $F$ , which is essentially the restoring moment divided by the disturbing moment. Thus a value of  $F$  less than 1 indicates failure of the slope.

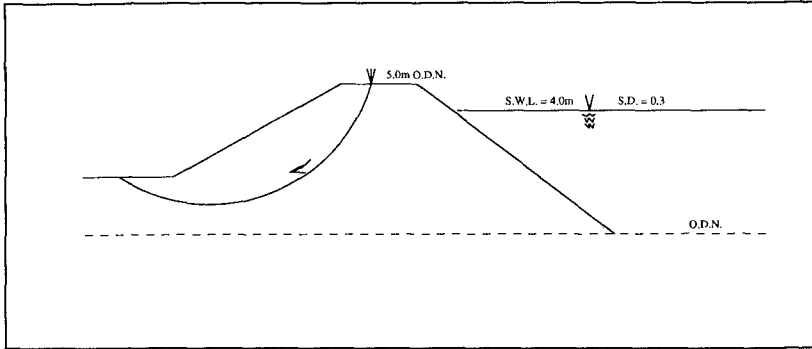


Figure 6 Circular slip failure mechanism for an earth embankment.

Input parameter	Distribution	Standard deviation (coefficient)	Mean
Cohesion $c'$ ( $\text{kNm}^{-2}$ )	Normal	29%	9.0
Angle of friction $\phi'$ ( $^\circ$ )	Normal	16%	31
Dry density $\gamma$ ( $\text{kNm}^{-3}$ )	Normal	2.5%	16
Phreatic surface $R_u$	Normal	8%	0.50

Table 4 Data used for Level II slope stability prediction

Probabilistic data is given in Table 4. All data was assumed to be normally distributed. The factor of safety calculated from the mean values was 1.6, but given the prescribed variability in soil properties, the probability that the factor of safety is less than 1.0 is 0.03, or 3%.

5. CONCLUSIONS

The risk assessment procedures outlined here encompass a broad range of activities, including identification of hazards and key failure modes, classification of structures, assessment of hydraulic loading conditions, probability of failure due to the principal failure modes and modelling consequences in terms of flooded areas.

In view of the number of defences to be assessed, we have adopted a tiered approach for classification and analysis: the early stages are characterised by approximate screening procedures, with more detailed assessment on selected defences thought to be at highest risk.

The results of this project will substantially improve the methods available to analyse the risks of failure for existing flood defence schemes, and to design new schemes to agreed risk levels. The procedures will provide a consistent, rigorous framework for comparative assessment of a wide range of flood defences in tidal and coastal

regions.

## 6. ACKNOWLEDGEMENTS

The research on which this paper is based has been supported by the UK National Rivers Authority (NRA) R&D Commission C - Flood Defence. Additional information has also been used from research at HR Wallingford supported by the Department of the Environment (DoE) under research contract PECD 7/6/248. The views expressed here are those of the authors and not necessarily those of the NRA or DoE.

## REFERENCES

- Allsop N.W.H. "Formulae for rubble mound breakwater failure modes" Final report of PIANC, PTC II, Working group 12, Sub-group A, PIANC, April 1993.
- CIRIA (1977) "Rationalisation of safety and serviceability factors in structural design" Report 63.
- CUR/TAW (1990) "Probabilistic design of flood defences" Centre for civil engineering research and codes / Technical advisory committee on water defences. Report 141.
- Goda Y (1971) "Expected rate of irregular wave overtopping of seawalls" Coastal engineering in Japan, Vol 14.
- Meadowcroft IC and Allsop NWH (1994) "Probabilistic assessment of coastal structures and breakwaters". HR Wallingford Report IT392.
- Owen M.W. (1980) "Design of seawalls allowing for wave overtopping" Report EX 924, HR Wallingford, June 1980.
- Owen MW and Steele AAJ (1991) "Effectiveness of recurved wave return walls" HR Report SR261
- Thoft-Christensen P and Baker MJ (1982) "Structural reliability theory and its applications". Springer-Verlag.
- Van der Meer JW (1988) "Rock slopes and gravel beaches under wave attack", PhD thesis Delft University of Technology, April 1988. (Available as Delft Hydraulics Communication 396)

## CHAPTER 228

### Water oxygenation in the vicinity of coastal structures due to wave breaking

C. I. Moutzouris<sup>1</sup> and E. I. Daniil<sup>2</sup>

#### Abstract

Experiments on oxygenation due to breaking waves on a uniformly sloping beach and on an S - type breakwater were performed. The water was chemically deoxygenated and dissolved oxygen (D.O.) concentration was followed over time in characteristic locations. Experimental data showed that the transfer velocity increased with increasing wave height for waves of the same frequency. Experiments with waves of the same wave height but increasing wave frequency showed also an increase in transfer velocity. The breakwater data give lower transfer velocities as compared to the sloping beach data for the same wave characteristics.

The one - dimensional transport equation was used for the determination of the transfer coefficients. Analysis of the data indicated that the transfer coefficients varied almost linearly with the vertical wave velocity at the water surface. A rather good linear correlation was obtained for the breaking wave data on the sloping beach, with much higher slope as compared to the case of non-breaking waves.

#### Introduction

Air/water gas transfer for water bodies is one of the main sources of dissolved oxygen (D.O.), an often used water quality index. It also acts as a sink of carbon dioxide and other greenhouse gases and has a significant role in global biogeochemical cycles of atmospheric compounds. Finally, air/water gas transfer is an important parameter in the design of hydraulic structures, as in the case of stepped chute spillways (Chanson, 1994), and can be used beneficially, as in the case of the SEPA (sidestream elevated pool aeration) project of the Metropolitan Water Reclamation District of Greater Chicago, that was awarded the 1994 Outstanding Civil Engineering Achievement Award (Civil Engineering, 1994).

Research on oxygenation dates back to 1925 (Streeter and Phelps, 1925, Streeter, 1926), when river pollution problems started to appear. Gradually,

---

<sup>1</sup> Professor, <sup>2</sup> Researcher

Laboratory of Harbor Works, Civil Engineering Department, National Technical University of Athens, 5 Iroon Polytechniou, 157 73 Zografou, Athens, GREECE, Tel. - 30 - 1 - 77 83 866, Fax. - 30 - 1 - 77 59 565

interest spread to other water bodies (e.g. lakes and oceans) and other gases, such as carbon dioxide and methane (Brutsaert and Jirka, 1984, Wilhelms and Gulliver, 1991). Although air/water gas transfer is controlled by the interaction of the air/water boundary layer, the wave field is a parameter that has rarely been included in the predictive equations so far. However, its effect has often been noted qualitatively. Experiments on the effect of waves on gas transfer have been reported by Hosoi et al (1977), Hosoi and Murakami (1986), Jähne et al (1985,1987), Daniil and Gulliver (1991) and Wanninkhof and Bliven (1991). For lakes and oceans the transfer coefficient is usually correlated to the wind velocity. It should be noted though, that laboratory data and field data give different correlations and do not compare favorably (Liss, 1983, Daniil, 1988). It is generally recognized that the presence of waves increases the penetration of gases into the water. Gas concentrations in the water mass are found to be higher when waves are present, due to the action of a steering mechanism on the interface. Therefore, waves may be considered to have a positive effect on the oxygenation of water bodies. In the experiments of Hosoi et al (1977) D.O. was measured in one location of the flume only and neither the effect of horizontal diffusion nor the uniformity of D.O. concentration across the flume was investigated. Hosoi and Murakami (1986) measured the D.O. distribution across the flume. They concluded that oxygenation due to non-breaking waves was negligible and assumed that the whole flume is oxygenated through the breaking wave zone. This assumption yields much higher transfer coefficients than what would have been obtained if oxygenation through the remaining free surface had also been taken into account.

Wave breaking is a highly turbulent physical mechanism, that essentially creates a two phase flow, which facilitates the transfer of gases considerably. Therefore, it is believed that breaking waves have a further positive effect on the oxygenation of water masses. Until now the effect of wave breaking in water oxygenation has been described mostly qualitatively. Hosoi et al (1990) performed a number of experiments on reaeration due to wave breaking at coastal structures and proposed an equation indicating that the reaeration coefficient is correlated with the dissipated energy. They also note that in their experiments aeration increased with the height of incident waves and with the width of the breakwater. Moreover, impermeable sloping seawalls were more effective in promoting aeration than other structures.

A research program has started at the Laboratory of Harbour Works, Civil Engineering Department, National Technical University of Athens (NTUA) in order to investigate and quantify the effect of breaking waves on oxygenation. Oxygenation due to breaking waves is studied experimentally in a wave flume with a uniformly sloping beach (Daniil and Moutzouris, 1993, 1994a, b) and with an S-type breakwater. The influence of increasing wave frequency and wave height on the oxygen transfer coefficient is discussed.

### **Experimental Procedure**

Experiments on the transfer of oxygen under breaking waves were conducted in a wave flume of the Laboratory of Harbour Works, NTUA. The dimensions of the flume are 27.40 (length) x 0.60 (width) x 1.53m (height). A smooth sloping beach with a uniform slope of 1 (vertical) : 2.3 (horizontal) was

placed at the one extremity of the flume (Fig. 1). The water was chemically deoxygenated. Details for the experimental setup have been presented previously (Daniil and Moutzouris, 1993, 1994 a, b).

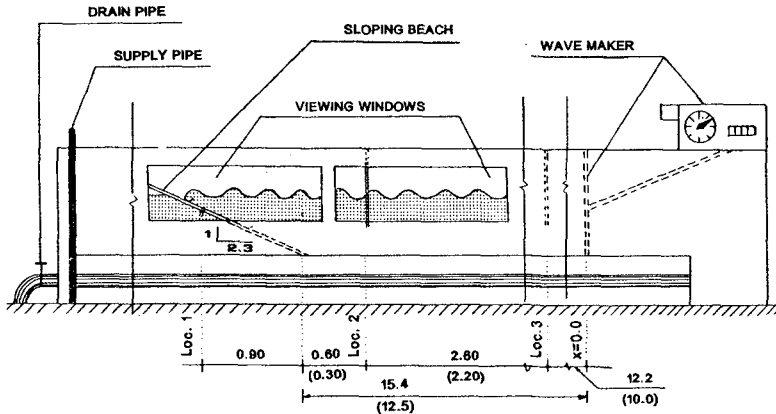


Fig. 1. Longitudinal view of the wave channel with the smooth sloping beach.

Additional experiments were performed with an S - type rubble mound breakwater with a slope of 1 (vertical) : 1.5 (horizontal) located 15.0 m from the wave maker (Fig. 2).

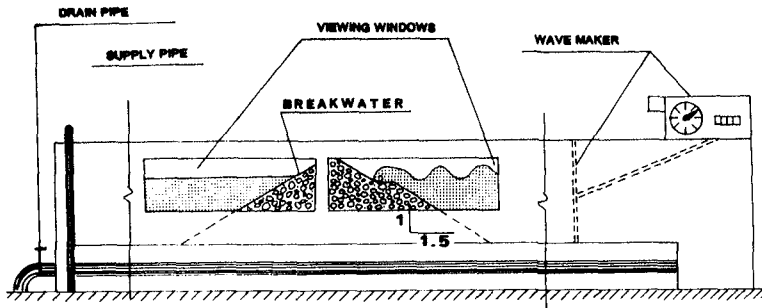


Fig. 2. Longitudinal view of the wave channel with the rubble mound breakwater.



Monochromatic waves were created by a wave generator of the piston type. The waves propagated along the flume and broke over the sloping beach or the breakwater. For the sloping beach experiments D.O. concentration in the water body was followed over time in three locations along the flume. Wave heights tested ranged from 5.6 to 15 cm and wave periods from 0.75 to 1.60 sec. For the breakwater experiments D.O. concentrations were measured in front and behind the structure. Wave heights tested ranged from 5.6 to 28.0 cm and wave periods from 0.75 to 1.60 sec. The water depth was 0.60 m for all experiments with the exception of experiment K6 that had a water depth of 0.83 m. Experimental conditions are shown in Table 1 for both sets of experiments.

**Table 1 - Experimental conditions for experiments with the sloping beach and the breakwater**

Exp. No.	Wave Period T (sec)	Wave Height H (cm)	Wave Length L (m)	Water Temp. $\theta$ ( $^{\circ}$ C)	Atmosp. Pressure (mm Hg)
<b>Sloping beach data</b>					
A3	1.60	9.9	3.27	23.5	750
A2	1.45	7.6	2.85	24.0	750
B7	1.45	9.1	2.85	10.5	750
B6	1.45	12.0	2.85	9.6	749
B9	1.45	14.9	2.85	10.6	753
A4	0.75	5.6	0.88	21.5	750
A5	0.75	7.1	0.88	23.6	750
B8	0.75	7.3	0.88	7.5	759
<b>Breakwater data</b>					
K2a	1.60	9.9	3.27	14.9	747
K3	1.45	12.0	2.85	23.8	747
K6	1.45	28.0	3.07	12.7	757.5
K2b	0.75	5.6	0.88	14.7	747
K1	0.75	7.1	0.88	12.7	749

#### Data Acquired

Fig. 3 shows D.O. - time histories as obtained from experiments B9, B6 and B7 with waves of the same frequency ( $T=1.45$ sec), but different wave height

( $H = 14.9, 12.0, 9.1$  cm) in the presence of the sloping beach. It is concluded that the transfer velocity increases as the wave height increases. Moreover, D.O. concentration becomes more uniformly distributed seawards of the breaker zone as the wave height increases, due to increase of horizontal dispersion. Similar comparison of D.O. - time histories for experiments with waves of almost the same height, but differing frequency shows that the transfer velocity increases, as the wave frequency increases.

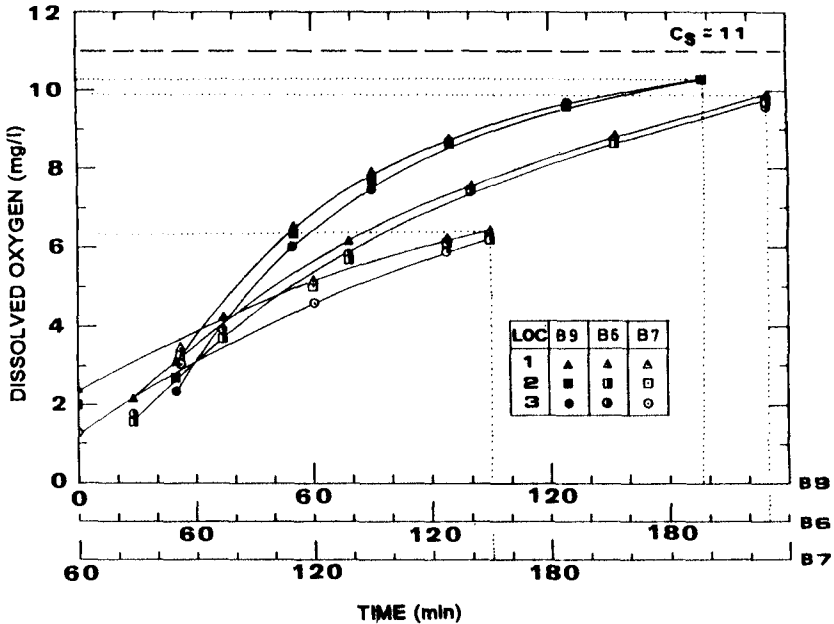


**Fig. 3.** Comparison of D.O. - time histories for waves of the same frequency but different wave height breaking on a sloping beach (after Daniil and Moutzouris, 1993)

D.O.- time histories in the presence of (i) a sloping beach and (ii) a breakwater are presented in Fig. 4. Concentrations are found to be lower in front of the breakwater than along the sloping beach, due to a more moderate wave breaking in the former case. D.O. concentrations are found to be very low behind the structure and to increase in time due to transport of oxygen through the body of the breakwater. The saturation concentration,  $C_s$ , is also noted for the two cases ( $C_s = 8.4$  mg/l for the sloping beach and  $C_s = 9.86$  mg/l for the breakwater).

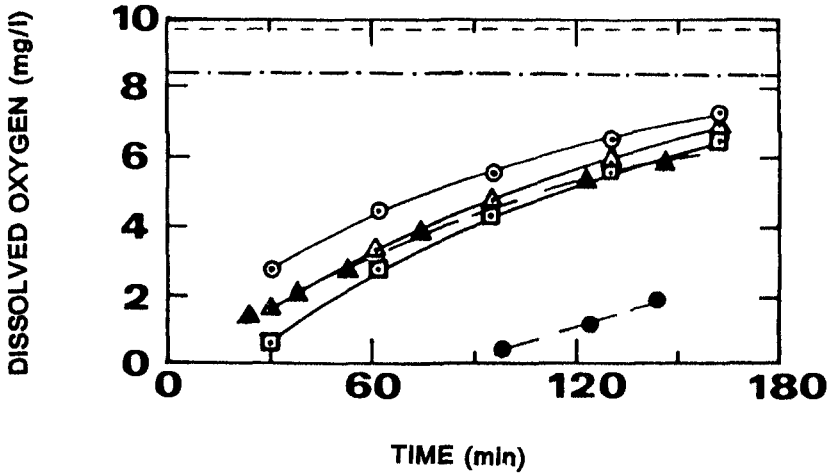


Fig. 4. D.O. - time histories for waves (incipient wave:  $H=7.1$  cm,  $T=0.75$  sec) breaking (i) on a sloping beach (open symbols) and (ii) on a breakwater (solid triangles refer to the concentration in front and solid circles to the concentration behind the breakwater).

#### Data Analysis

The one-dimensional transport equation was used for the analysis of the data. Data from locations where the composite effect of the horizontal transport was assumed to be negligible were used for determining the oxygen transfer coefficient. The transfer coefficient is determined from the following equation, using linear regression and the measured D.O. concentrations:

$$\ln (C_s - C) = -K_L (A/V) t + \ln (C_s - C_0) \quad (1)$$

where  $C$ ,  $C_0$  and  $C_s$  are the average, initial and saturation D.O. concentrations, respectively.  $K_L$  is the oxygen transfer coefficient,  $t$  is time,  $A$  is the projected free surface area on the horizontal plane and  $V$  is the aerated volume extending from the free surface to the bottom of the channel.

The coefficients  $K_L$  obtained from the above procedure, along with the wave parameters used in the correlations presented in the following sections, are listed in Table 2. The transfer coefficients were translated to 20° C according to the equation given by Daniil and Gulliver (1988):

$$(K_{L20}/K_L) = (Sc/Sc_{20})^{1/2} = (v/v_{20}) [293/(\theta+273)]^{1/2} (\rho/\rho_{20})^{1/2} \quad (2)$$

where  $Sc = v/D$  is the Schmidt number ( $Sc_{20} = 546$ ),  $v$  is the kinematic viscosity of water,  $D$  is the molecular diffusivity of oxygen in the water,  $\theta$  is the water temperature in degrees Celsius and  $\rho$  is the water density. The subscript 20 denotes the value of the corresponding parameter at 20° C. The water properties were determined by the relations given by Heggen (1983).  $H$ ,  $L$  and  $f$  are the wave height, length and frequency, respectively.

**Table 2.** Oxygen Transfer Coefficients and wave parameters used in the correlations for breaking waves on a sloping beach and on a rubble mound breakwater

Exp. No.	Satur. Conc. $C_s$ (mg/l)	Schmidt number $Sc$ (-)	$Hf \times 100$ (m/sec)	Transfer Coeff. $K_{L20} \times 10^5$ (m/sec)	Transfer Coeff. $K_L \times 10^5$ (m/sec)	Transfer Coeff. $K_L Sc^{1/2} \times 10^4$ (m/sec)
<b>Sloping beach data</b>						
A3	8.4	458	6.19	2.7	2.9	6.2
A2	8.3	446	5.24	5.0	5.5	11.6
B7	11.0	918	6.28	8.3	6.4	19.4
B6	11.2	967	8.28	15.0	11.3	35.1
B9	11.0	912	10.28	22.0	17.0	51.3
A4	8.7	506	7.47	5.1	5.3	11.9
A5	8.4	455	9.47	9.0	9.9	21.1
B8	12.0	1096	9.73	15.0	10.6	35.1
<b>Breakwater data</b>						
K2a	9.9	716	6.19	3.2	3.7	8.6
K3	8.3	450	8.28	6.9	6.3	14.6
K6	10.6	809	19.3	23.3	28.4	66.3
K2b	9.9	716	7.47	3.6	4.1	9.6
K1	9.9	701	9.47	6.3	7.1	16.7

The oxygen transfer coefficients  $K_L$ , as determined from the above analysis, are compared to the relation obtained for non-breaking waves by Daniil and Gulliver (1991). The two authors related the transfer coefficient to

the vertical wave velocity at the water surface and used a renewal model to express the average renewal rate as a function of a wave Reynolds number. They derived the following equation:

$$K_L Sc^{1/2} = 0.0159 H f \quad (3)$$

For breaking waves on a sloping beach from the present experiments the following equation was fitted to the data:

$$K_L Sc^{1/2} = 0.066 H f - 2.80 \times 10^{-3} \quad (\text{m/s}) \quad (4)$$

Equation (4) holds for  $H f > 0.056$  m/s, which was approximately the low limit of the present experiments, and expresses the general trend of the oxygen transfer coefficient for breaking waves. It is felt that a further expansion is needed to include a parameter describing the non-linearity of the breaking.

A comparison of the results obtained (see Fig. 5) shows that oxygenation in front of a breakwater is less significant than in the presence of a sloping beach, due to a less intense penetration mechanism. Breakwaters are causing wave reflection, which reduces the degree of wave breaking.

Equations (3) and (4) are compared to the experimental data in Fig. 5.

### Discussion

The experiments reported in the present paper demonstrate the importance of breaking waves in nearshore oxygenation. The oxygen transfer coefficient was described through a surface renewal model. The average surface renewal rate was correlated to the wave characteristics and the oxygen transfer coefficient was found to be proportional to the maximum vertical wave velocity at the water surface. The correlation for the breaking wave data on a sloping beach gave a much higher slope than that for non-breaking waves. Breakwater data give lower transfer coefficients compared to the sloping beach data, but higher than the non breaking waves for the same wave characteristics. The obtained relation for the sloping beach data needs to be extended in order to incorporate breaking wave parameters.

The experimental results presented here were obtained using tap water. They could be translated to seawater if the corresponding Schmidt number and the saturation concentration for seawater were introduced. Nevertheless, it is noted here that experiments by Downing and Truesdale (1955) on the effect of wind using seawater and distilled water had shown no significant difference.

Undoubtedly, the results are influenced by the scale of the experiments conducted. Scale effects are believed to be significant. For this reason, the research program of the Laboratory of Harbour Works, NTUA, was recently enlarged with further experiments executed in the large wind-wave facility of Delft Hydraulics, The Netherlands. The experiments were financed by the European Community Large Installations Program (LIP). A preliminary analysis of the experimental data collected clearly shows that oxygenation rates are considerably reduced, as a result of the larger dimensions (Tsoukala and Moutzouris, 1994, personal comm.).

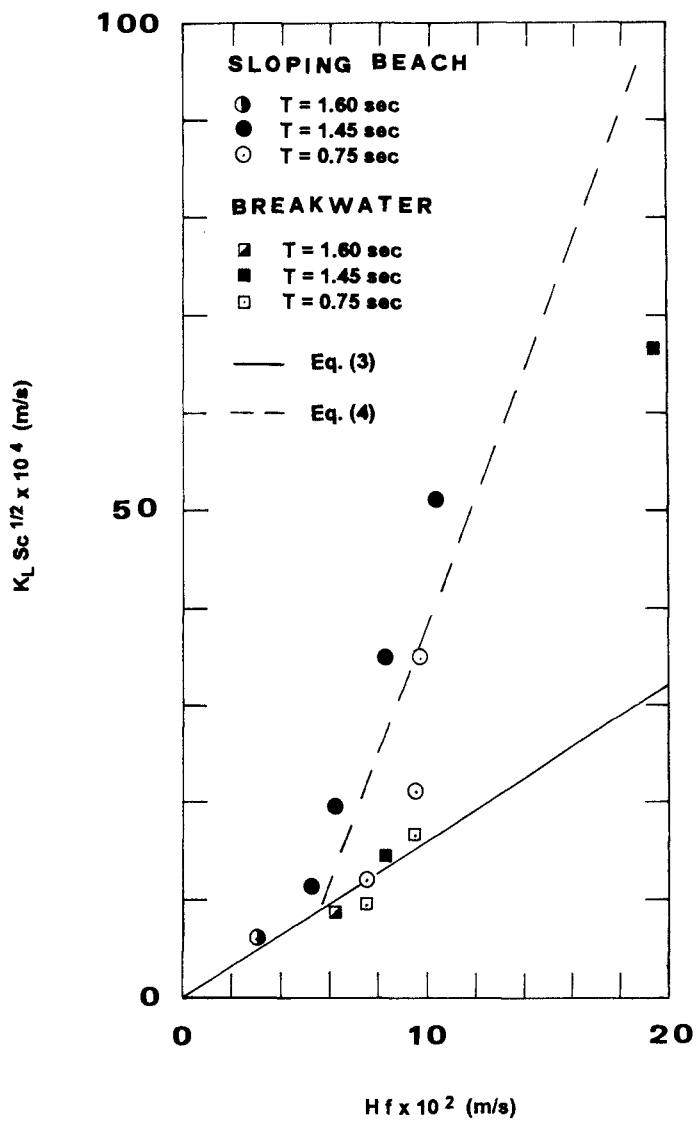


Fig. 5. Variation of the transfer coefficients with the wave parameter  $H_f$ .

A first conclusion from the present experiments is that incorporating wave characteristics in water quality models can improve the design of nearshore sewage outfalls, taking advantage of the "self-cleaning" capacity of the water body. Coasts in which wave breaking is a dominant mechanism present considerable advantages from the point of view of oxygenation of the effluent by physical mechanisms. Disposing the effluent near the breaking wave zone can possibly be combined with reduced treatment, thus leading to a more economic design.

A second conclusion is that coastal structures, such as breakwaters, reduce the oxygenation rate of seawater, due to increased wave reflection. This could have some negative influence on the fauna, although the beneficial effect of rubble-mound structures to the number of fish population and the types of species developed in the area is by now well documented.

### References

- Brutsaert, W. and G. H. Jirka, eds. (1984) "Gas Transfer at Water Surfaces", Reidel Publishing Co.
- Chanson, H. (1994) "State of the art of the hydraulic design of stepped chute spillways", *International Journal on Hydropower and Dams*, Vol. 1(4), PP. 33-42.
- Civil Engineering (1994) "Chicago's Waterfalls", *ASCE*, Vol. 64(7), pp. 36-39.
- Daniil, E. I. (1988), "The Effect of Waves on Air-Water Gas Transfer", Doctoral Dissertation, University of Minnesota, Minneapolis, MN
- Daniil, E. I. and J. S. Gulliver (1988) "Temperature dependence of the liquid film coefficient for gas transfer", *ASCE, J. Environmental Engineering*, 114(5), pp. 1224-1229.
- Daniil, E. I. and J. S. Gulliver (1991) "The Influence of Waves on Air-Water Gas Transfer" .*ASCE, J. Environmental Eng.*, 117(5), pp. 522-540.
- Daniil, E. I. and C. I. Moutzouris (1993) "Oxygenation experiments in the wave breaking zone", *ASCE, Hydraulics '93*, pp. 2008 - 2013.
- Daniil, E. I. and C. I. Moutzouris (1994a) "Gas transfer experiments with breaking waves" in Galileo. Disturbing the Universe. *The Air - Sea Interface*, M. A. Donelan, W. H. Hui and W. J. Plant, eds., The University of Toronto Press, Toronto.
- Daniil, E. I. and C. I. Moutzouris (1994b) "Oxygenation on a sloping beach under breaking waves", *Mitteilungen des Franzius - Instituts für Wasserbau und Künsteningenieurwesen der Universität Hannover* (in press).
- Downing, A. L. and G. A. Truesdale (1955) "Some factors affecting the rate of solution of oxygen in water", *J. Appl. Chemistry*, 5, 570 - 581.
- Heggen, R. J., (1983), "Thermal Dependent Physical Properties of Water," *Jour. of Hydraulic Eng.*, ASCE, 109(2), pp. 298-302
- Hosoi, M. A., A. Ishida and K. Imoto (1977) "Study on reaeration by waves", *Coastal Engineering in Japan*, 20, pp. 121-127.
- Hosoi, Y. and H. Murakami (1986) "Effect of waves on dissolved oxygen and organic matter", *20th Coastal Eng. Conference*, Proc. CERC, ASCE, Taipei, pp. 2498-2512.

- Hosoi, Y., H. Murakami and H. Mitsui (1990) "Reaeration due to wave breaking at coastal structures", *Coastal Engineering in Japan*, Vol. 33(1) pp. 89 - 100.
- Jähne, B., T. Wais, L. Mémery, G. Cauliez, L. Mérlivat, K. O. Münnich and M. Coantic (1985) "He and Rn Gas Exchange Experiments in the Large Wind -Wave Facility of IMST", *Jour. Geophys. Research*, 90(C6), pp. 11989-11997.
- Jähne, B., K. O. Münnich, R. Böisinger, A. Dutzi, W. Huber and P. Libner (1987) "On the parameters influencing air-water gas exchange", *Jour. Geophys. Research*, 92(C2), pp. 1937-1949.
- Liss, P. S., "Gas Transfer: Experiments and Geochemical Implication"(1983), In *Air-Sea Exchange of Gases and Particles*, P. S. Liss and W. G. N. Slinn (eds.), pp. 241-298
- Streeter, H. W., (1926), "The Rate of Atmospheric Reaeration of Sewage Polluted Streams", *ASCE Transactions*, Vol.89, pp. 1351-1364.
- Streeter, H. W. and E. B. Phelps (1925), "A Study of the Pollution and Natural Purification of the Ohio River", Washington, U. S. Public Health Service, *Public Health Bulletin.*, 146, 75p.
- Tsoukala, V. and C. I. Moutzouris (1994), personal communication.
- Wilhelms, S. C. and J. S. Gulliver, eds.(1991) "*Air Water Mass Transfer*", ASCE, New York.



## CHAPTER 229

### Environmental Assessment of Hypothetical Large-Scale Reclamation in Osaka Bay, Japan

Keiji Nakatsuji<sup>1</sup>, Toshiaki Sueyoshi<sup>2</sup>, Kohji Muraoka<sup>1</sup>

#### ABSTRACT

In urban coastal areas in Japan, large-scale reclamation projects have recently increased, which have caused drastic changes in topographical features of the coastline. In Osaka Bay, the sea area of 5,200 ha have been reclaimed in the past 40 years and many development projects are under construction. As a natural consequence, the sea water has been polluted due to poor exchange of water with outer oceans and the load of nutritious substances discharged from rivers; hence, algal blooms occur independent of season and anoxia appears near the sea especially in summer. A 3-D baroclinic flow model is proposed to predict the tidally-interacting estuarine circulation and residual baroclinic currents in Osaka Bay and to evaluate the effects of hypothetical large-scale reclamation on the estuarine system.

#### INTRODUCTION

Osaka Bay is one of semi-enclosed urban coastal seas in Japan. High density populated and industrialized cities such as Osaka and Kobe are located at the head of Osaka Bay. The GNP (Gross National Product) of Osaka Prefecture approximately corresponds to that of Australia, in addition, the total amount of GNP of Osaka, Kobe and Kyoto does to that of Canada. Area of Osaka Bay is only 1400 km<sup>2</sup> and its mean depth is 28 m. In the past 40 years the coastal area of 5,200 ha have been reclaimed for satisfying the economical and industrial demand, and lots of development projects are under construction including a 511 ha for newly-built Kansai International Airport Island. As a result, the sea water has been polluted due to poor exchange of water with outer oceans and the load of nutritious substances from rivers; hence, algal blooms near the sea surface and anoxia near the sea bottom have

-----  
1 Dept. Civil Eng., Osaka University, Osaka 565, Japan.

2 Former student, Osaka University, Osaka 565, Japan

had adverse effects on fishery and recreation. Such a tendency, however, will have to continue because of the limited land and increasing volume of industrial and domestic waste products in the countries of their limited territory like Japan. Strategies for optimum environmental conservation must be examined in order to achieve integrated and multiple utilization of coastal seas in a sustainable manner.

Figure 1 shows a drastic change in topographical features of the coastline in Osaka Bay due to reclamation. The area of total reclaimed land is only 4 % against the total area of Osaka Bay at the present time. It, however, corresponds to 76 % as compared with the area of coastal waters shallower than 10 m depths. Such coastal area is of great importance for the special nursery of the fish and shellfish. Figure 2 shows the variation of shellfish catch with a cumulative area of reclaimed coastal area. It indicates that the reclamation causes strong damage to fishery.

Authors(1992) had already examined the impact assessment of large-scale reclamation on the tidal flow system and water quality transfer by the depth-integrated, two-dimensional finite element method. In the present study, since the density-induced current system is found to be of great importance, a three-dimensional baroclinic flow model is proposed to predict residual baroclinic currents and a tidal front observed in Osaka Bay and to evaluate the effects of hypothetical large-scale reclamation on the estuarine system.

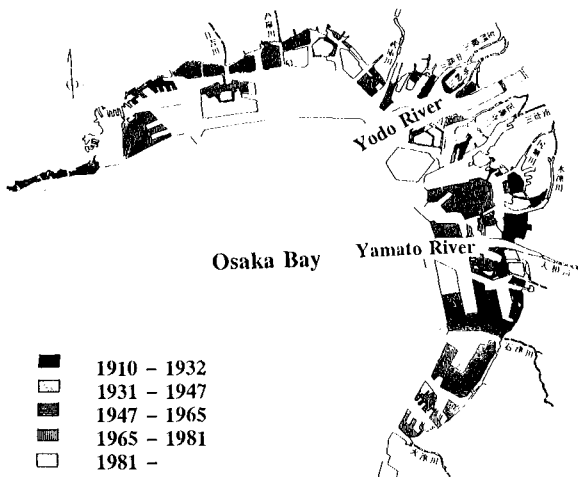


Figure 1. Change of shoreline due to reclamation projects in Osaka Bay.

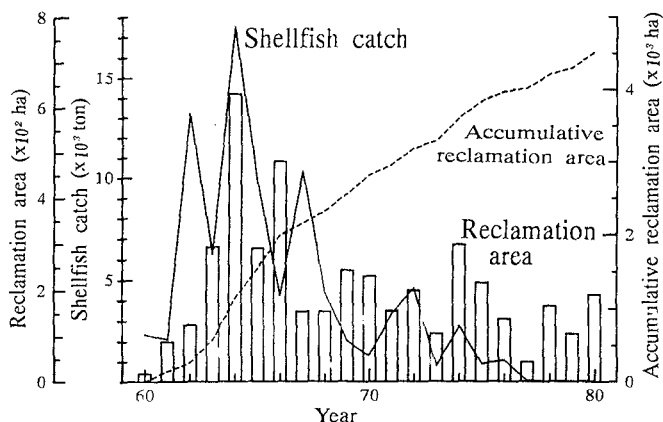


Figure 2. Variation of shellfish catch and cumulative area of reclamation.

### MODEL DESCRIPTION

The computation solves the primitive equations of the ocean, governing the conservation of volume, momentum in three dimensions and density-difference simplified by the Boussinesq assumption and hydrostatic equilibrium.

$$\frac{\partial U}{\partial x} + \frac{\partial V}{\partial y} + \frac{\partial W}{\partial z} = 0 \quad (1)$$

$$\frac{DU}{Dt} - fV = -\frac{1}{\rho} \frac{\partial P}{\partial x} + \frac{\partial}{\partial x_i} (\epsilon_i \frac{\partial U}{\partial x_i}) \quad (2)$$

$$\frac{DV}{Dt} + fU = -\frac{1}{\rho} \frac{\partial P}{\partial y} + \frac{\partial}{\partial x_i} (\epsilon_i \frac{\partial V}{\partial x_i}) \quad (3)$$

$$0 = -g - \frac{1}{\rho} \frac{\partial P}{\partial z} \quad (4)$$

$$\frac{D\Delta\rho}{Dt} = \frac{\partial}{\partial x_i} (K_i \frac{\partial \Delta\rho}{\partial x_i}) \quad (5)$$

where  $(U, V, W)$  are velocities in the  $x, y$  and  $z$  directions,  $\zeta$  is the water elevation,  $P$  is the pressure,  $\Delta\rho (= \rho_s - \rho)$  is the density difference from the sea water density ( $\rho_s$ ),  $D/Dt$  is a nonlinear operation such that  $DA/Dt = \partial A/\partial t + \partial(UA)/\partial x + \partial(VA)/\partial y + \partial(WA)/\partial z$ ,  $\epsilon_i$  and  $K_i$  are the

eddy viscosity and diffusivity coefficients respectively in each direction, and  $f$  is the Coriolis parameter ( $0.8296 \times 10^{-4} \text{ s}^{-1}$ ). The pressure is obtained by integrating the vertical momentum equation (4) from the water surface ( $z = -\zeta$ ) to any depth. Therefore, the pressure gradient  $\partial P / \partial x_i$  can be expressed as a sum of the water surface gradient  $\partial \zeta / \partial x_i$  (barotropic mode) and the density gradient  $\partial \Delta \rho / \partial x_i$  (baroclinic mode).

A first-order closure scheme is used to account for the eddy viscosity and diffusivity coefficients. A small horizontal eddy viscosity or diffusivity ( $20 \text{ m}^2/\text{s}$ ) is used in all model runs. On the other hand, the vertical eddy viscosity coefficient are affected by the reduction of turbulence due to stable stratification. On the basis of the study of three-dimensional buoyant surface discharges by Murota et al. (1989), the Webb formula (1970) and Munk and Anderson's formula (1948) are adopted for  $\epsilon_z$  and  $K_z$ , with a neutral value of  $\epsilon_{z_0} = 0.005 \text{ m}^2/\text{s}$ . Both empirical formulae are functions of the gradient Richardson number,  $Ri \equiv g(\partial \rho / \partial z) / (\partial U / \partial z)^2$  as follows;

$$\epsilon_z / \epsilon_{z_0} = (1 + 5.2 Ri)^{-1} \quad (6)$$

$$K_z / \epsilon_z = (1 + 10/3 \cdot Ri)^{-3/2} / (1 + 10 \cdot Ri)^{-1/2} \quad (7)$$

In the computation of tidal flow, however, turbulence energy in straits becomes unrealistically large. Hence, the values of  $200 \text{ m}^2/\text{s}$  and  $0.05 \text{ m}^2/\text{s}$  are used near the straits for horizontal and vertical eddy coefficients, respectively.

Boundary conditions are the following. The model basin is initially filled with saline sea water of  $1022 \text{ kg/m}^3$ . Freshwater of zero salinity then flows near the surface from rivers located in the estuary head. The model ocean is everywhere bounded by solid vertical walls except the river mouth and the open seas.

Vertical walls are assumed impenetrative and slip, so that for solid boundary

$$\rho \epsilon_h \partial(U, V) / \partial x_h = \tau_h, \quad K_h \partial \Delta \rho / \partial x_h = 0, \quad V_n = 0 \quad \text{and} \quad \partial \Delta \rho / \partial x_n = 0 \quad (8)$$

where 'h' mean the normal and tangential components to the boundary and  $\tau_h$  means the shear stress along the boundary.

At the river mouth, the time-variation of river discharges is given according to the observed hydrographs and the water elevation is assumed to be zero, so that

$$Q = Q(t), \quad \Delta \rho = 0.0, \quad \partial \zeta / \partial x_n = 0 \quad \text{at river mouth} \quad (9)$$

The open sea boundaries are

$$\partial(U, V) / \partial x_n = \partial \Delta \rho / \partial x_n = \zeta = 0 \quad (10)$$

When a tidal flow is taken into account, the time variation of tidal elevation is added on the basis of harmonic analysis of observed tidal elevation,

$$\partial(U, V) / \partial x_n = \partial \Delta \rho / \partial x_n = 0 \quad \text{and} \quad \zeta = \zeta(t) \quad (11)$$

On the free surface ( $z = -\zeta$ ), fluxes of momentum and density are zero, so

$$\partial(U, V, \Delta \rho) / \partial z = 0 \quad \text{at} \quad z = -\zeta \quad (12)$$

On the ocean bottom ( $z = H$ ), the momentum flux is balanced by a bottom stress  $\tau_z$ , while the density flux and the vertical velocity are zero, so that

$$\rho \varepsilon_z \partial(U, V) / \partial z = \tau_z, \quad \partial \Delta \rho / \partial z = W = 0 \quad \text{at} \quad z = H \quad (13)$$

### OUTLINE OF 3-D BAROCLINIC FLOW COMPUTATION

The algorithm and computational scheme was written in the authors' published paper. (See Murota, et al.(1988))

The computational domain as shown in Fig. 3 covers Osaka Bay and surrounding coastal seas, Sea of Harima and Ki-i Channel, in order to evaluate the amount of flowing through Akashi and Kitan Straits as precisely as possible. The model's resolution is 1 km in the horizontal plane with seven vertical layers having thickness of 2, 4, 6, 8, 10, 15 and 15 m. The time increment is 30 seconds.

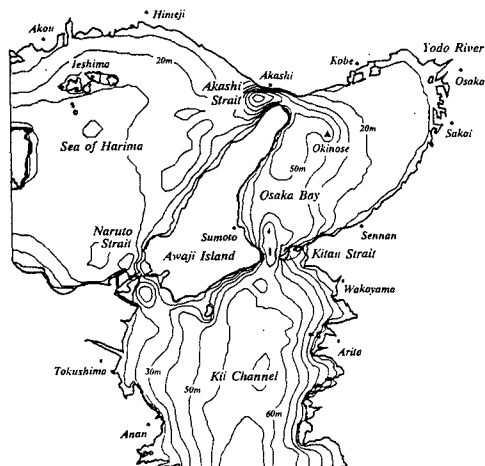


Figure 3. Topological features of Osaka Bay and computation domain

A semi-diurnal tide is represented by a sine-wave curve with a 12 hours cycle at two open boundaries. The amplitude and phase of tide are 36-39 cm and  $330^\circ$  at the boundary in Sea of Harima, and 46 cm and  $174^\circ$  at the boundary in Ki-i Channel according to the field surveys of the Ministry of Transportation. For the density-driven current, the average discharge and the density of the Yodo River was set to  $205 \text{ m}^3/\text{s}$  and  $0.997 \text{ kg}/\text{m}^3$  respectively. Another buoyancy flux is the thermal flux at the sea surface of  $29.7 \text{ cal}/\text{s}/\text{m}^2$  in summer, which was also taken into account.

### TIDAL FLOW PATTERN AND TIDAL FRONT IN OSAKA BAY

The computation results to be discussed here are that on the 36th tidal cycle, in which the change in the flow and density distributions over time is almost equivalent to those of the previous tidal cycle. Figure 4 shows the velocity and the density fields of the surface layer (1 m deep from the surface) when the eastward or westward flow through Akashi Strait reaches its maximum. The contours of density field are marked at every 10% of the density difference between the river water and sea water where  $\sigma_t = 23$ . When the eastward flow at Akashi Strait is at its maximum, the flow into Osaka Bay spreads in a jet-like form toward the southeast. The flow makes its way in clockwise circular arcs along a 20 m-deep contour line toward the Kitan Strait, off the coast of Sennan. Meanwhile the discharge from the Yodo River spreads southwest,

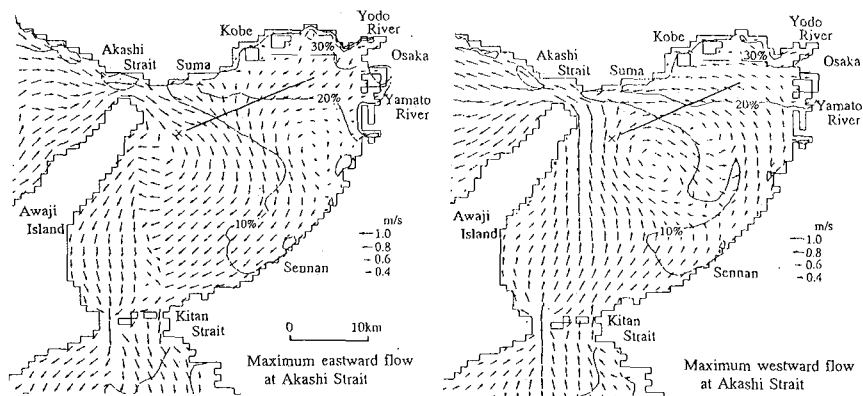


Figure 4. Surface flow vectors and density distribution at the maximum eastward and westward flow through the Akashi Strait.

running southward to cross the 20% density contour line at a right angle. The jet-like tidal flow from the Akashi Strait combines with this river discharge at the 20 m-deep point and continues southward.

When the westward flow is at its maximum, the water flow can roughly be divided into two: one running from the Kitan Strait northward along the east coast of Awaji Island, and the other that flows northward, off the coast of Sennan. Water from the Yodo River is carried by the tidal flow toward Kobe, a part of which flows into the Akashi Strait. The other part of the flow mixes with the circulation flow near Okino-se (indicated by X in Fig. 4). It is worth noting that the southeastward flow at Okino-se due to the eastward tidal flow persists even when the tidal flow direction changes. Between this southeastward flow and the flow in the inner bay, a discontinuous flow is observed. If the density distribution in Fig. 4 is represented in finer colour lines, the discontinuous boundary can be shown to be bands of different densities. That is a tidal front.

Figure 5 shows the density distribution at the cross-section of the tidal front, which is indicated by the solid line in Fig. 4. The horizontal 0 point corresponds to the 20 m-deep sea bed. The direction toward the inner bay (toward Osaka) is positive, and the direction toward the outer bay (toward Awaji Island) is negative. In the inner bay, approximately 5 m-thick stratification with  $\sigma_t = 22$  or lower is observed. The stratification is stable, rarely affected by the change in the tidal flow. The area where the sea bed is deeper than 20 m ( $x < 0$ ) is exposed to stronger tidal flows and, as a result, vertical mixing occurs. In this area  $\sigma_t$  is 22.5 or higher. Between these two areas, where  $\sigma_t$  is more than 20 and less than 22, density contours are almost perpendicular to the water surface.

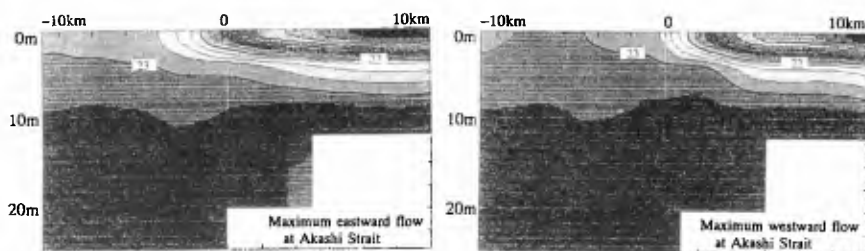


Figure 5. Density distribution at the section across tidal front at the maximum eastward and westward flow through the Akashi Strait.

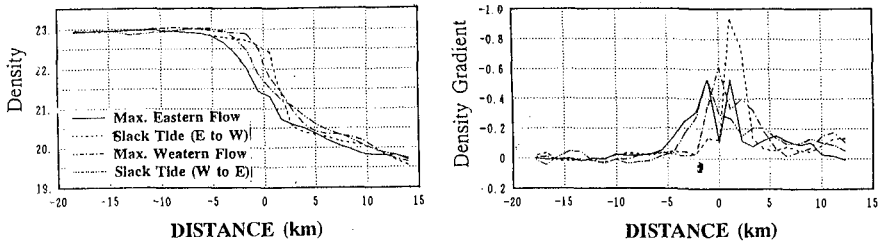


Figure 6. Surface density and its gradient distributions at the section across tidal front every three hours.

Figure 6 shows the horizontal distributions of surface density and its gradient every three hours. The gradient indicates the sharpness of the front. This figure shows that the tidal front on the cross section develops along the line connecting 20 m depth points. The density changes by  $\sigma_t = 2$  over 7 km on this plane. The density gradient is the greatest when the eastward tidal flow through Akashi Strait reverses westward. At this time the front is 2 km wide and  $\sigma_t$  rises from the head to the center of the bay by  $\sigma_t = 2$ . It is because the eastward flow through Akashi Strait spreads deep into the head of bay. Field data obtained by Yanagi and Takahashi (1988) indicated the density change of  $\sigma_t = 3$  over 5 km width of the tidal front. From these comparison, the computation results overestimate a little larger than observation ones.

### RESIDUAL BAROCLINIC CURRENT SYSTEM

Figure 7 shows the residual current distribution in the first (-1 m) and third layers (-9 m). The residual current is calculated by integrating the flow velocity over one tidal cycle, that is, 12 hours. The residual current in the surface layer consists mainly of the Okino-se Circulation and the east-coast residual current offshore of Sennan. The figure especially at the surface shows higher velocities than the tidally-induced circulation. The remnants of the density-driven current generated by the inflow of the Yodo River spread only slightly from the river mouth to Suma. This density-driven current is caught by the edge of the Okino-se circulation, and as a result, it enhances the Okino-se circulation and the east coast residual current in their surface layers. In the third layer, where the influence of density-driven



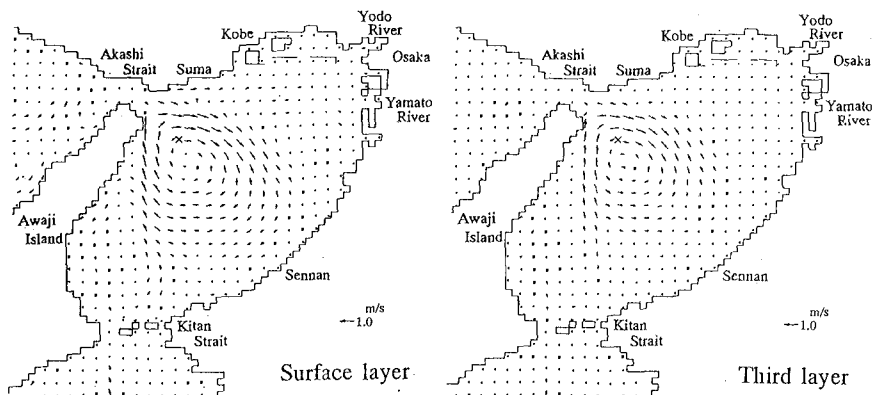


Figure 7. Residual baroclinic currents at the surface layer (-1 m) and the third layer (-9 m).

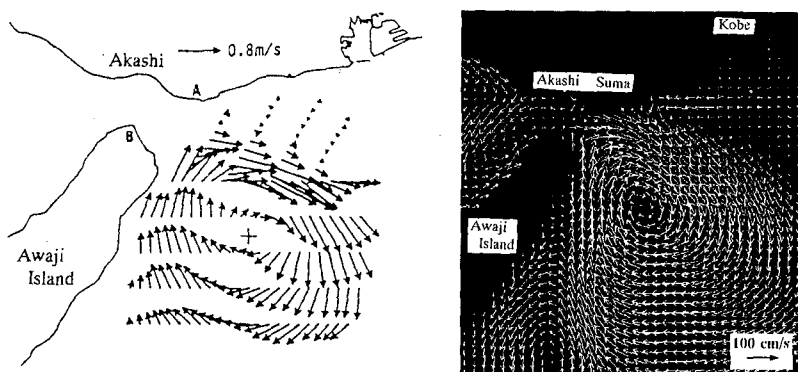


Figure 8. Observed residual current at 10 m depth corresponding to Okino-se Circulation and computed one at surface layer of 1 m depth.

current is less, there is a weak flow in the inner bay toward the Yodo River. Since the Okino-se circulation covers the surface to the bottom layers, they are assumed to be the remnants of the tidally-induced residual current. The strength of Okino-se circulation, therefore, changes depending on the tidal amplitude, but not on river discharges. According to the harmonic analysis of the time series of computed velocity fluctuation, it is found that the residual current component is possible to be larger than the tidal flow. (Nakatsuji et al.; 1994)

Figure 8 shows the comparison between residual current observed using four ADCP by Fujiwara et al.(1994) and computed one. Both results are substantial agreement with each other.

In order to understand the role of the residual current system on turbulent transport process, the numerical experiment was conducted that the four markers placed at the water surface near the Akashi Strait and inside Osaka Bay are traced by Lagrangian diffusion analysis based on Monte Carlo method. In this experiment, the spreading particles are assumed to move only at a surface layer.

If the particles are transformed by a tidal flow, they naturally return to their original points after one tidal cycle because the tidal flow behaves a periodic movement. As shown in Fig. 9, however, the computed tracers are far from their original positions and they remain in the center of Osaka Bay taking the shape of oval. After two tidal cycles, 24 hours, similar tendency can be observed. It suggests that the residual current system play a more important role on the transport process than the periodic tidal flow. Therefore, tracers are distributed with surrounding the Okino-se Circulation as a circle.

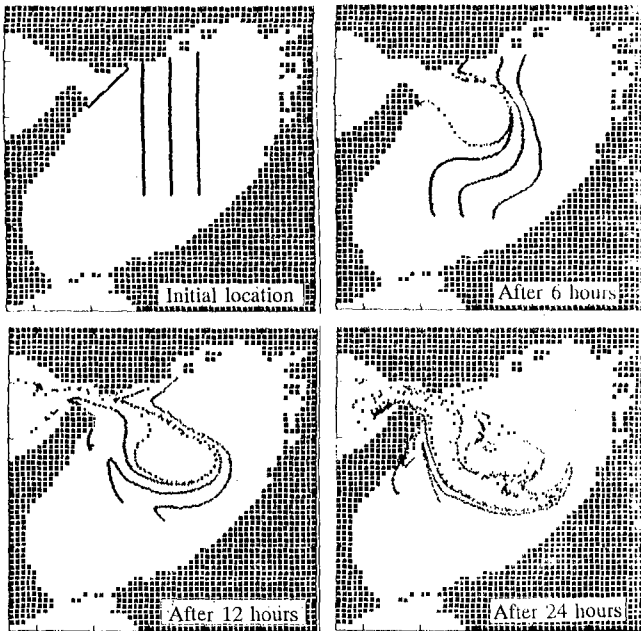


Figure 9. Computed trajectories of floating markers transported by the residual current system.

### IMPACT ASSESSMENT OF HYPOTHETICAL LARGE-SCALE RECLAMATION

For examining the effects of hypothetical large scale reclamation on the flow movement and water quality transport, two simple reclamation topographies are assumed. They are the reclamation of coastal waters shallow than 15 m and 18 m. The decreasing rates in area and volume correspond to 26 % and 11 % for the reclamation shallow than 15 m depth, and 36 % and 20 % for that shallow than 18 m depth. It is of importance that the impact assessment must be established from the view point of long-term and circumstance of whole coastal seas. According to the above-mentioned discussion, the 'Okino-se Circulation' and the 'tidal front' can be adopted as the physical indexes for assessment.

#### *Effects on Okino-se Circulation*

Figure 10 shows the distribution of residual baroclinic current at the surface layer supposing the hypothetical reclamation could be constructed. The outer boundary in the west side is adjacent to the line connecting 20 m depth points, where the velocity of residual current becomes smaller in the rate of 10 % as compared with that in the case of present topography. And, no particular difference between the cases of 15 m or 18 m reclamation. Since the Okino-se Circulation occurs at all depths in all cases, it is a tidally-induced residual current; hence, it is a matter of course that the effects of reclamation inside the head of bay has not strongly affected on the Okino-se Circulation developed near the Akashi Strait.

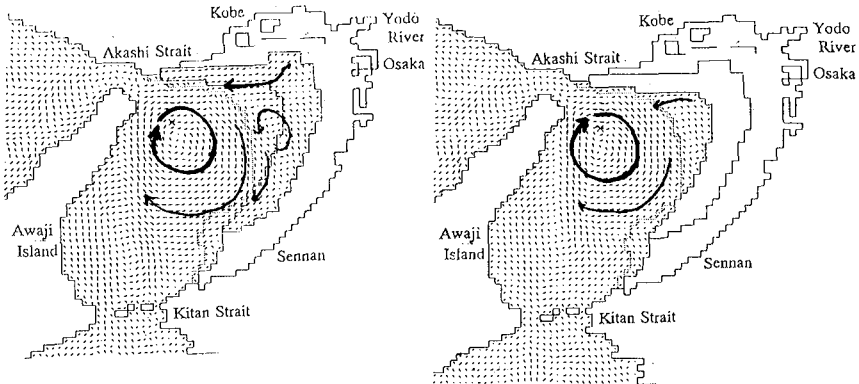


Figure 10. Residual baroclinic current at the surface layer in hypothetical reclamation of 15 m and 18 m depth.

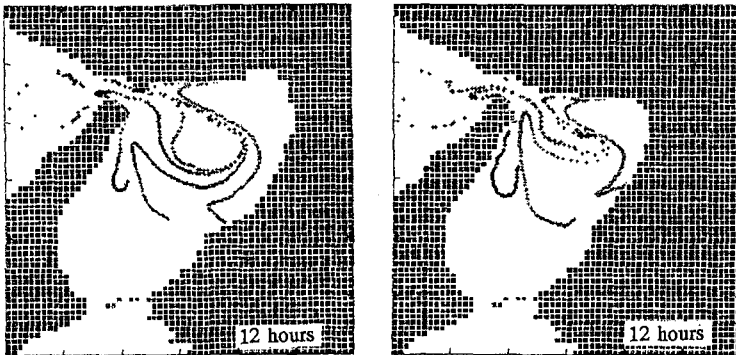


Figure 11. Computed trajectories of floating markers after one tidal cycle in reclamation of 15 m and 18 m depth.

Figure 11 shows the computed trajectories of four markers after one tidal cycle. As compared with Fig. 9, there is a little difference in the computed trajectories between the present topography and the reclamation of coastal seas shallower than 15 m. However, in the case of reclamation of 18 m depth, continuous ring-shaped markers are distorted to be pushed into the head of bay.

#### *Effects on Tidal Front and Density Field*

Accompanied with the reclamation in shallow coastal seas, the volume of river water has direct effects on the stratification in the eastern bay or mixing process. For example, the computation indicates that the thickness of stratified and upper layer in the head of Osaka Bay becomes 8 m. Its thickness is twice as large as that observed in the present topography.

Figures 12 and 13 show the comparison of density and its horizontal gradient at the sea surface across the tidal front along the solid line shown in Fig. 4. The axis of abscissas is the same as Fig. 5. The '0' point corresponds to the sea bed of 20 m depth. The positive value in the abscissas axis means the direction of eastern bay. The maximum value of density gradient and its horizontal point indicate the strength and location of the tidal front, respectively. The maximum value and its location are almost the same between the present topography and the reclamation of 15 m depth. In addition, the density in the eastern sea ( $x > 0$ ) is mixed to gradually change in the range of  $\sigma_t = 19$  to 23 for the present topography and  $\sigma_t = 18$  to 22 for the reclamation of 15 m depth.

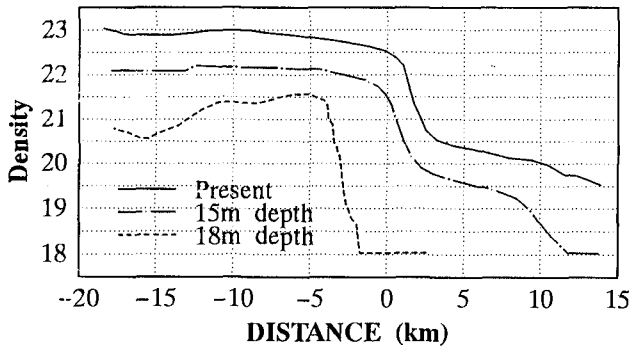


Figure 12. Distribution of surface density at the section across the tidal front against two reclamation cases.

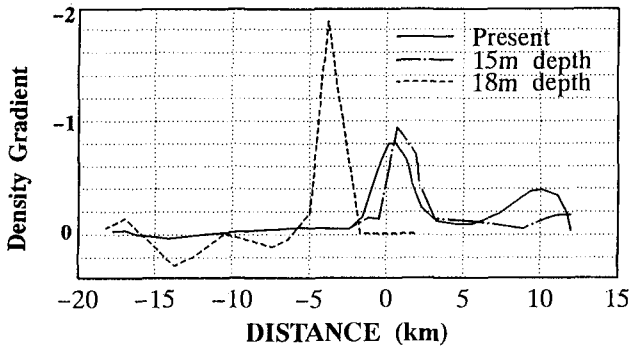


Figure 13. Change of location and intensity of tidal front depending on the gradient of density at the surface layer (-3 m).

On the other hand, in the case of reclamation of 18 m depth, the volume corresponding to about 20 % of whole Osaka Bay is lost; so that mixing between river water and sea water becomes decreased and remained in the head of bay. As a result, there is  $\sigma_t = 18$  in the eastern sea, while  $\sigma_t = 22.5$  in the western sea. A tidal front, therefore, develops in the narrow band of only 2.5 km. The maximum density gradient, namely the strength of tidal front, is twice as large as other cases. The location moves about 5 km in the western direction.

## CONCLUSION

Through numerical experiments using a three-dimensional baroclinic flow model, the physical processes governing the flow movement and long-term mass transport processes in Osaka Bay, one of typical semi-enclosed coastal seas, are discussed. On the basis of discussion and the comparison of computation results with field observations, the 'Okino-se Circulation' and 'tidal front' are selected as the standards for examination of the impact assessment of hypothetical large scale reclamation in Osaka Bay. The computation results become clear from the physical viewpoint that the reclamation of coastal seas shallow than 15 m depth has not so strong effects on the flow movement and mass transfer processes, but that the reclamation of 18 m depth considerably affects them.

## ACKNOWLEDGEMENT

Authors are indebted to Dr Tateki Fujiwara, Associate Professor of Department of Fishery, Kyoto University for providing useful discussion on residual current system in Osaka Bay.

## REFERENCES

- Fujiwara, T., Sawada, Y., Nakatsuji, K. and Kuramoto, S. (1994). "Water exchange time and flow characteristics of the upper water in the easter Osaka Bay - Anticyclonic circulation in the head of the estuary." *Research Note on Coastal Seas, Oceanographical Society of Japan*, 31(2), 227-238. (in Japanese)
- Murota, A., Nakatsuji, K. and Huh, H.Y. (1988). "A numerical study of three-dimensional buoyant surface jet." *Proc. 6th APD-IAHR Congress*, 3, 57-64.
- Murota, A., Nakatsuji, K. and Huh, T.Y.. (1989). "A three-dimensional computer simulation model of river plume." *Refined Flow Modelling and Turbulence Measurements*, Ed. Y. Iwasa et al., University Academic Press, 539-547.
- Munk, W.H. and Anderson, E.R. (1970). "Notes on a theory of the thermocline," *J. Marine Res.*, 7, 276-295.
- Nakatsuji, K., J.Y. Huh and A. Murota (1991): "Numerical experiments of three-dimensional buoyant surface discharges," *Proc. JSCE*, 434/II-16, 29-36. (in Japanese)
- Nakatsuji, K., Karino, H., Kurita, H. and Muraoka, K. (1992). "Impact of Large-Scale Reclamaton on Tidal Current System and Water Quality Structure in Osaka Bay." *Hydraulic and Environmental Modelling : Coastal Waters*, Ed. R.A. Falconer et al., Ashgate, 43-53.

- Nakatsuji, K., Sueyoshi, T. and Fujiwara, T. (1994). "An estuarine system in semi-enclosed Osaka Bay." *Flux Change in Estuaries*, Ed. K. Dyer, Olsen and Olsen, 79-84.
- Webb, W.K. (1970). "Profile relationships, the log-linear range and extension to strong stability." *Quarterly J. Royal Meteorological Soc.*, 6, 67-90.
- Yanagi, T. and Takahashi, T. (1988). "A tidal front influenced by river discharges.", *Dynamics Atmosphere and Ocean*, 12, 191-206.

## CHAPTER 230

### FLOOD AND EROSION CONTROL IN THE CONTEXT OF SEA-LEVEL RISE

E. Bart Peerbolte<sup>1)</sup> and Herman G. Wind<sup>2)</sup>

#### ABSTRACT

Low-lying countries such as the Netherlands are very vulnerable to climatic changes, which are likely to cause an increase in sea-level rise. The most obvious threat is permanent inundation of unprotected low areas. However, such a 'final' situation will be preceded by a period of increasing episodic flooding and coastal erosion. Sea-level rise causes *safety* against flooding and erosion to reduce which should be accounted for in long-term coastal zone management plans. The question is to what extent such increases are tolerable and what can we do about it. This problem concerns the levels of safety which are desired, also in coastal areas which are already protected from flooding: is there a surplus of safety so that no intervention is required, or does the coastal defence system need to be adapted? The relevance of this question lies not perse in the threat of sea-level rise: the same question may be raised in the case of developing coastal areas, where economic values at stake increase: such developments cause a relative weakening of the flood defence system: the desired safety standards increase so that the existing defence system may not meet any longer the changed demand for flood protection and is to be adapted.

The above problem description was the background of a number of studies in the Netherlands to assess the impacts of a possible climatic change and to evaluate potential counter measures. A model has been developed for quick analysis of combinations of scenarios for climate change and potential counter measures. This paper describes the limitations of Cost Benefit Analysis as a tool for the appraisal of flood alleviation in view of the inaccuracies in investment costs and material flood damages.

---

1) Harbours, Coasts and Offshore Technology, Delft Hydraulics

2) University of Twente



## INTRODUCTION

The decision problem many coastal managers are facing concerns coastal protection. Intuitively, or explicitly by spelling out all possible advantages and disadvantages of possible protection options, the coastal manager puts the decision problem in a cost-benefit framework. In general, such a framework is not necessarily confined to monetary values only, also values in other units may play a role. Often a multi-criteria evaluation method is applied to evaluate all effects of the various options being compared.

However, the manager will tend to limit the amount of different units of expression in his decision framework, mostly he will try to monetize the effects in terms of benefits and costs, simply because he needs (monetary) budgets to implement any preferred policy. Therefore, the most appealing framework for the coastal manager is Cost-Benefit Analysis. Intangible effects and other, often external, effects which cannot be expressed in terms of money, are accounted for then as PM issues and are subject to, for example, environmental impact procedures. In this paper we point that there are practical problems when applying Cost-Benefit Analysis for the appraisal of flood protection and coastal defence systems, also in the case that only concrete monetized material benefits and costs are considered. These problems are due to the uncertainties in the various components, i.e. the various types of flood damages and cost estimates related to flood protection and erosion control.

## FRAMEWORK OF ANALYSIS

When applying the method of Cost-Benefit Analysis (CBA), there are some issues which need to be addressed, viz.

- *valuation*: how to value the different measures and effects in monetary terms;
- *time*: how to account for future costs and benefits;
- *scale*: how to determine the scale the effects are to be looked at (accounting stance).

Suppose we know how to handle these issues, the decision to invest in coastal protection, as far as monetary effects is concerned, is not difficult if the costs  $C$  of a scheme and the benefits  $B$  differ significantly, i.e. if  $C \ll B$  or  $C \gg B$ . If  $B \approx C$  a closer inspection of the uncertainties in the cost and benefits is required.

When appraising a coastal defence system it is generally tried to maximize the net benefits  $Z$  over the analysis period:

$$Z = W - C_I - C_F \quad (1)$$

where  $W$  represents the income in the endangered area,  $C_I$  the investment cost and  $C_F$  the flood (or erosion) damages.

In most cases the costs and benefits are uncertain and unequally distributed over time. Figure 1 shows an example of two investments in flood defence between which the flood damage and benefits are constant, as determined by constant hydraulic forcing. Economic development or natural phenomena like sea-level rise may cause the cost and benefit streams to change over time.

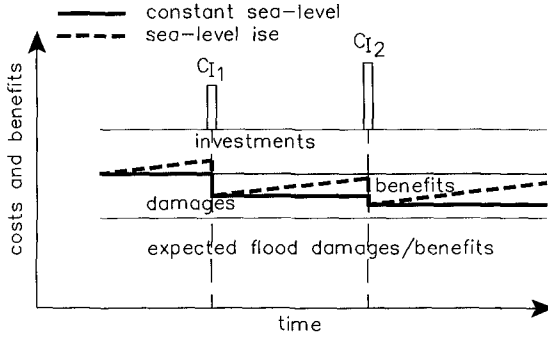


Figure 1 Costs and Benefits of flood protection

We suppose there is a number of  $K$  intervals, starting in the first year and with an investment  $C_{I_k}$  on the start of each interval  $k$ . Further each interval  $k$  ends on time  $p_k$ . The expected present value of the total investment cost  $C_{I_{tot}}$  is written as

$$E\{C_{I_{tot}}\} = \sum_{k=1}^K E\{C_{I_k} \cdot \alpha^{p_{k-1}+1}\}$$

where  $\alpha = \exp(-i)$  with  $i$  as the discounting factor.

In each investment interval flood and erosion damage may occur, and benefits due to flood protection. These damages and benefits are determined by the pattern of storm surges impacting on the structures, the structures themselves, and the topography and objects in the protected area. We need to capitalise these cost and benefit streams as follows in order to get the expected total damage to be put in the Cost-Benefit Analysis:

$$E\{C_{F_{tot}}\} = \sum_{k=1}^K \sum_{j=p_{k-1}+1}^{p_k} E\{C_{F_{k,j}}\} \alpha^j \tag{2}$$

and

$$E\{B_{tot}\} = \sum_{k=1}^K \sum_{j=p_{k-1}+1}^{p_k} E\{B_{k,j}\} \alpha^j \tag{3}$$

In principle, the expected benefits and costs can be compared now:

$$E\{B_{tot}\} < ? > E\{C_{I_{tot}}\} + E\{C_{F_{tot}}\}$$

Looking more in detail in the cost of flooding, we can schematize the cost of flood damage by

$$C_F = V \cdot F_p \cdot (1 + F_s) \quad (4)$$

where  $V$  represents the value of one or more flooded objects, and  $F_p$  and  $F_s$  damage factors, pertaining to primary and secondary (multiplier effects) flood damage.

The occurrence of flood damage is uncertain, depending on storm surge attacks, and the value of objects is often uncertain and can be estimated only from available statistical data on land-use and economics. Furthermore, the value of objects will change over time, due to development of activities in the flood-protected coastal zone. We suppose a growth factor of  $(1+g)$ . In order to project the time streams of costs and benefits in a reference year, we discount the benefits and costs, with a discounting factor  $i$ . Further the damage factors  $F_p$  and  $F_s$  are also uncertain variables. The expected value of the total flood discounted damage, in time interval  $k$  [ $p_{k-1}+1, p_k$ ] is written as:

$$E\{C_{F_{tot,k}}\} = E\left\{\sum_{j=p_{k-1}+1}^{p_k} V_j \cdot \alpha^j \cdot F_{p_j} (1 + F_{s_j})\right\} \quad (5)$$

where  $V_j$ ,  $F_{p_j}$  and  $F_{s_j}$  are uncertain variables. Further  $\alpha = e^{(-i+g)}$ .

By definition, and taking continuous functions for the uncertain variables,

$$E\{C_{F_{tot,k}}\} = \sum_{j=p_{k-1}+1}^{p_k} \int \int \int v_j \cdot \alpha^j \cdot f_{p_j}(1 + f_{s_j}) \cdot \prod(v_j, f_{p_j}, f_{s_j}) dv_j df_{p_j} df_{s_j} \quad (6)$$

Supposing  $V_j$ ,  $F_{p_j}$  and  $F_{s_j}$  are independent, we find

$$E\{C_{F_{tot,k}}\} = \sum_{j=p_{k-1}+1}^{p_k} \int \int \int v_j \cdot \alpha^j \cdot f_{p_j}(1 + f_{s_j}) \cdot \prod(v_j) \prod(f_{p_j}) \prod(f_{s_j}) dv_j df_{p_j} df_{s_j} \quad (7)$$

which leads to

$$\begin{aligned}
 E\{C_{F_{tot}k}\} &= \sum_{j=p_{k-1}+1}^{P_k} E\{V_j\} \alpha^j E\{F_{P_j}\} E\{1+F_{S_j}\} \\
 &= \frac{\alpha}{(1-\alpha)} (\alpha^{P_{k-1}} - \alpha^{P_k}) E\{V_j\} E\{F_{P_j}\} E\{1+F_{S_j}\}
 \end{aligned}
 \tag{8}$$

Similarly, the expected value of the total benefits incurred by the construction of a coastal protection system is written as

$$\begin{aligned}
 E\{B_{tot k}\} &= E\left\{ \sum_{j=p_{k-1}+1}^{P_k} B_j \alpha^j \right\} \\
 &= \sum_{j=p_{k-1}+1}^{P_k} E\{B_j\} \alpha^j \\
 &= \frac{\alpha}{(1-\alpha)} (\alpha^{P_{k-1}} - \alpha^{P_k}) E\{B_j\}
 \end{aligned}
 \tag{9}$$

The investments  $C_I$  are composed by the initial cost  $C_{IM}$  resulting from mobilisation and demobilisation, and the variable cost  $C'_{IV}$  depending on the "amount" of construction works, which is derived from the amount  $Q$  and the unit cost  $C_{IV}$ :

$$C_I = C_{IM} + Q \cdot C_{IV}
 \tag{10}$$

The expected value of the capitalized total construction cost is written as

$$E\{C_{I_{tot}}\} = \sum_{k=1}^K E\{C_{IM_k} + Q_k \cdot C_{IV_k}\} \alpha^{P_{k-1}+1}
 \tag{11}$$

Equations (9), (10) and (11) provide the framework for the evaluation of the difference between the benefits and costs resulting from coastal protection measures. The distributions of the various variables should be known to assess the reliability of the indicators, such as benefit-cost ratio, resulting from the CBA.

## UNCERTAINTIES

### Flood and erosion damages

The most violent case of coastal flooding in the Netherlands was the well-known February Storm Surge Flood in 1953. The impacts have been analysed in detail in governmental reports, consultancy reports and publications resulting in an idea about the uncertainty in flood damages. Further, in the case of riverine floodings, the Flood Hazard Research Institute in UK has collected a lot of material on flood damages [Penning-Rowse & Chatterton, 1977]. Also in France systematic research

damages [Penning-Rowsell & Chatterton, 1977]. Also in France systematic research is being carried out in the field of flood appraisal, focusing on the effect of flood warning systems [Torterotot, 1993]. In the Netherlands recently a major project has been carried out to assess the consequences of the December 1993 floods of the Meuse River, and to analyse the best options for structural and non-structural measures [Delft Hydraulics, 1994].

From analysis of the published data on flood damages due to the 1953 storm surge flood [CBS, 1953; TNO, 1982; TNO, 1989] it becomes apparent that there is quite some uncertainty about the size of flood losses [Peerbolte, 1993], this is confirmed by studies for other countries [Penning-Rowsell & Chatterton, 1977; Torterotot, 1993; Klaus & Schmidtke, 1990]. We conclude that the alleged accuracy in the assessment of direct material flood losses, in comparison with the assessment of losses to immaterial values is often overemphasized; even in the former category accuracy is not expected to be less than 40%. We will illustrate this figure by looking at the various damages resulting from the 1953 flood in the Netherlands.

The 1953 storm surge flood in the South-West of the Netherlands killed 1835 people and caused substantial damages, between 5 and 8 billion Dutch guilders on the current price level. The number of damaged houses and farms amounted to about 55,000, spreaded in a flooded area of more than 200,000 ha. Figure 2 shows the flooded areas. In the following some damage categories are described.

The cost of rehabilitation of agricultural land amounted to about DFL 6000 per ha (present prices) and was fairly constant across the flooded areas which is very substantial, in some cases 30 to 50% of the land price. The most important component is the repair and cleaning of ditches, drainage provisions, etcetera. However, it depends very much on the scale of the inundation and the violence of the flood. More recent minor floods in the Netherlands did not result in such high levels of damage to agricultural land.

Other damages to agricultural objects concern greenhouses in horticulture, plants and orchards, cattle, inventories, products and stocks of raw materials. Comparing observed, often estimated damages, with the values of the concerned objects, we observe a large variability in damage factors which supports the hypothesis that no fixed, overall valid values exist (Figure 3). It is seen from the graph that damage to greenhouses and inventories (agricultural equipment, vehicles, tractors) varies between 10 and 20%, to plants and orchards between 20 and 40%, and to stocks of products and raw materials, between 40 and 80%, a very large variability. Finally, the damage resulting from drowned cattle amounts to about 20% of the stock present in the affected area.

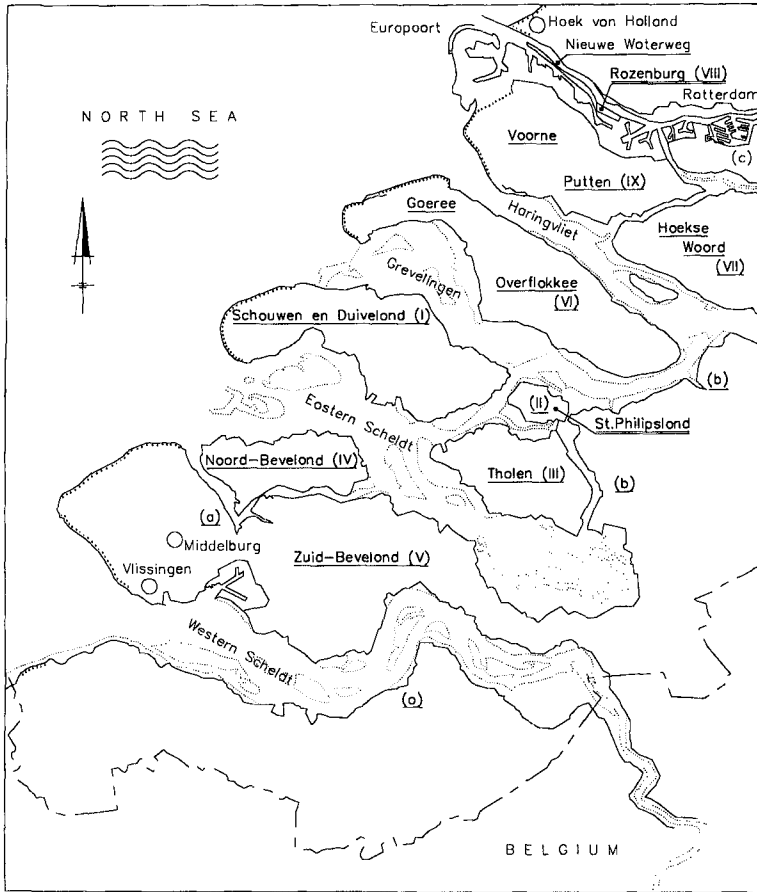


Figure 2 Areas flooded in 1953

Another picture is shown in the damages to the sector of industry, trade and banking, which is situated in the more populated areas. The core flooding areas which have been hit the most show damage factors for buildings and inventories of between 30 and 40%, and even up to 70% for stocks. The damage factors in the other core flooding areas and the surrounding areas are relatively constant with values between 10 and 20% for buildings and inventories, and between 20 and 40% for stocks (Figure 3).

The damage factor to motor vehicles amounts to about 10 or 20% of the replacement values, with the exception of some core flooding areas where the damage factors reach values of up to 40%.

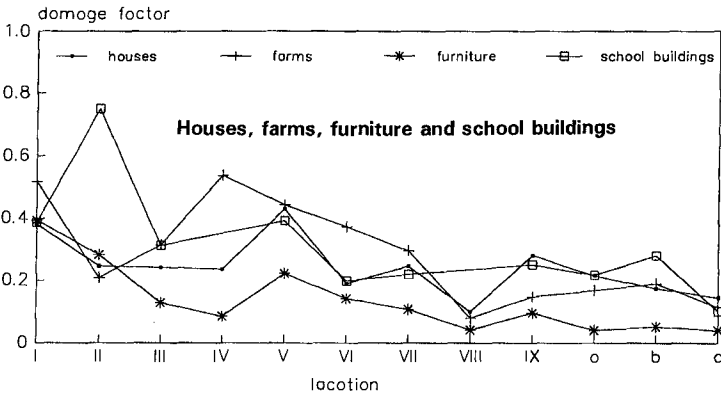
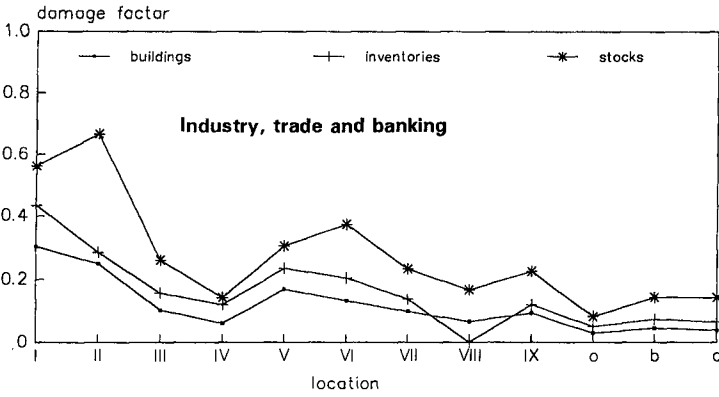
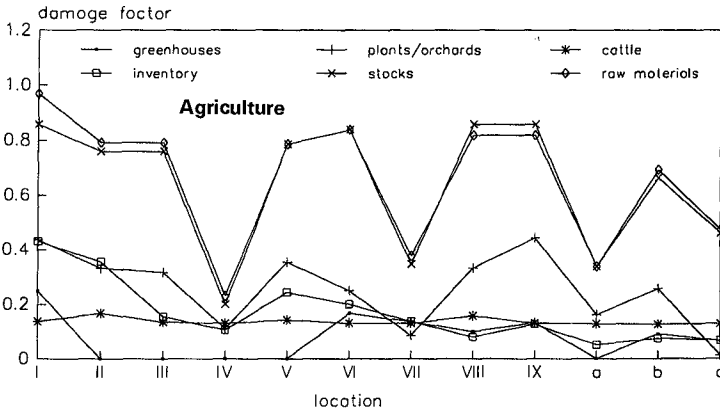


Figure 3 Damage factors in flooded areas

Damage to residential houses and farms, and the private belongings of the inhabitants, such as furniture, represents an important damage category. In addition, damage to public buildings such as schools will generally contribute substantially to the flood damage. The graph in Figure 3 shows that in the core flooding area the damage factor for houses and farms varies between 20 and 40%. Damages to furniture are more or less limited to 10%. Beyond the core area, in areas a, b and c, a damage factor of about 20% results.

The number of objects affected by the flooding is large, as mentioned earlier, so we may expect a fairly reliable result of the above survey. The crucial factor in the damage assessment has been the social survey; the structure and accuracy of this survey have eventually determined the accuracy of the resulting damage factors. Because of the large number of observations it is expected that the influence of subjectivity is averaged out and that there exists really a variability in resulting damage factors of the order as concluded above. The resulting figures give insight into this variability. Such variations can be explained by different factors such as i) inundation depth, ii) flow velocities, varying especially near a breach in the dike, iii) the time available to take preparatory measures and to evacuate, iv) the water quality and v) the weather conditions [TNO, 1982].

### THE INFLUENCE OF FLOODING DEPTH

Earlier analysis of the influence of the flood depth on the damage factor resulted in the graph shown on Figure 4. In the TNO report by Duiser [TNO, 1982] it is stressed that the scatter in data is wide, although the dependency of the damage factor on flood depth is obvious. From analysis of different damage categories it appears that furniture, buildings in industry, trade and banking and inventory in agriculture have, again roughly, the same damage factors as houses and farm buildings. Stocks and inventories in industry and trade tend to a somewhat higher damage factor. In Figure 4 the damage factor is plotted as a function of the different damage categories.

A later literature survey [TNO, 1989] has not resulted in new data on coastal flooding; all found studies considered concern riverine flooding. As regards flood damages to houses this study also confirms that a high variability in data exists.



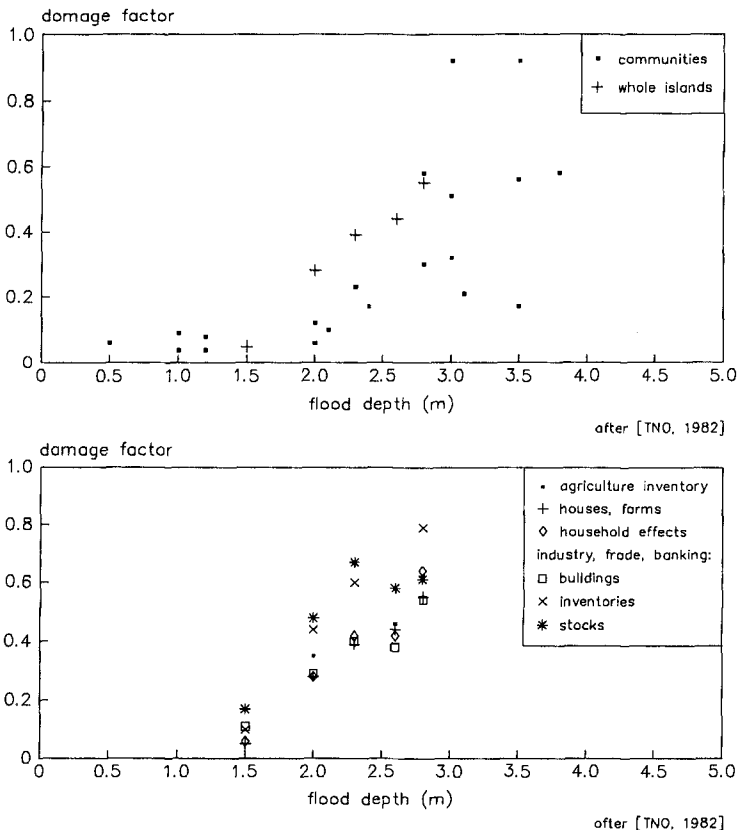


Figure 4 Damage-depth relationship

**CONCLUSIONS ON FLOOD DAMAGES**

Although major efforts have been undertaken to assess as precisely as possible the damages in real flood cases, a large variability in reported damage remains, partly due to a real variability in damages, for example caused by variations in flooding depth, duration and quality of buildings, but also partly due to differences in assessments. Whereas the 1953 damage data have been drawn from social surveys, focused on houses and household contents, the 1987-update of FHRC points to significant differences between perceived damages and real economic losses. Whilst the dependency on flooding depth may be obvious, as for example the work by TNO shows, a major scatter in data still exists, apparently because a lot of other parameters play a role in flood damages. For example, major influence on the variability

of damage factors is attributed to the effectivity of hazard warning systems and flood preparedness compared with physical parameters like flooding depth, flow velocities and flood duration.

Uncertainty in extreme water levels obviously adds to the uncertainty of flood damages. If the probability of exceedance of a certain design water level lies between  $3 \cdot 10^{-5}$  and  $2 \cdot 10^{-4}$ , the resulting expected damages may vary by 100% if the damage factors are uncertain and range between 20 and 40%, as has been shown above. So the strength of the flood protection system cannot be unambiguously defined in a CBA framework, and we should have insight in the distributions of the relevant uncertain parameters.

## SAFETY AND INVESTMENTS

Investments in dike-raising depend on a number of factors, which can be divided in two classes. First the required dimensions and strength of the dike are important factors. Secondly, the location of the dike determines the cost to a large extent. Dike sections in habitated areas are normally more complicated and hence costly to construct compared to dike sections in rural areas.

In the case of the Netherlands dike-raising is required when safety standards are no longer met. These standards are expressed in terms of water level exceedance probabilities as follows:

$$UF = 10^{-\frac{FB}{D}} \quad (12)$$

where  $UF$  represents the unsafety factor, determined by the decimating height  $D$  and the freeboard of the dike  $FB$ , being the difference between the actual crest level and the required level according to the safety standard. From analysis of the situation in the Netherlands it is concluded that the relative inaccuracy in  $UF$  may vary between 25 and 100% for dikes in coastal and deltaic areas, and even more than 100% in riverine areas Peerbolte, 1993].

Dike-raising  $p$  which is carried out as a response to a rise in sea-level of  $S_1$ , a rise in storm surge set-up of  $S_2$  and increases  $S_3$  in river discharges is related to these climate factors as follows [Peerbolte et al, 1991]:

$$p = \alpha S_1 + \beta S_2 + \gamma S_3 + 0.6\mu (S_1 + S_2 - \epsilon S_1) \quad (13)$$

The parameters  $\alpha$ ,  $\beta$  and  $\gamma$  reflect the propagation of sea-level changes and changes in river peak flow levels in the study area. Basically such parameters can be determined rather accurately. Wave run-up is accounted for by the parameter  $\mu$ , and depends on the design wave and structural properties. Also this parameter is relative

accurate. The morphological response of the sea-bed is represented by  $\epsilon$ . If  $\epsilon$  is equal to 0 (i.e. the sea-bed does not raise due to sea-level rise), its accuracy is not important, compared to the other parameters because it does not contribute to the required dike-raising. If sufficient sediment is supplied and if there is no human interference, it is generally expected that the sea-bed follows sea-level rise. In that case  $\epsilon$  is equal to 1 and only increase in storm surges may cause additional wave impacts leading to higher required dike-raising. In such cases the accuracy of  $\epsilon$  is important: 20 to 40% of the accuracy in required dike-raising is due to the accuracy of  $\epsilon$ . The fact that  $\epsilon$  is an important parameter in coastal areas is illustrated by the reduction in required dike-raising: if  $\epsilon$  is equal to 1, the required dike-raising is 25% less than in the case of  $\epsilon = 0$ , i.e. no sea-bed response to sea-level rise.

Finally we make a remark on the cost of dike-raising. From analysis by the Dutch Public Works Department it is concluded that the estimates of the cost of dike-raising vary between 10 and 40%. Figure 5 shows the total cost of dike-raising of all primary dikes (3400 km) in the Netherlands.

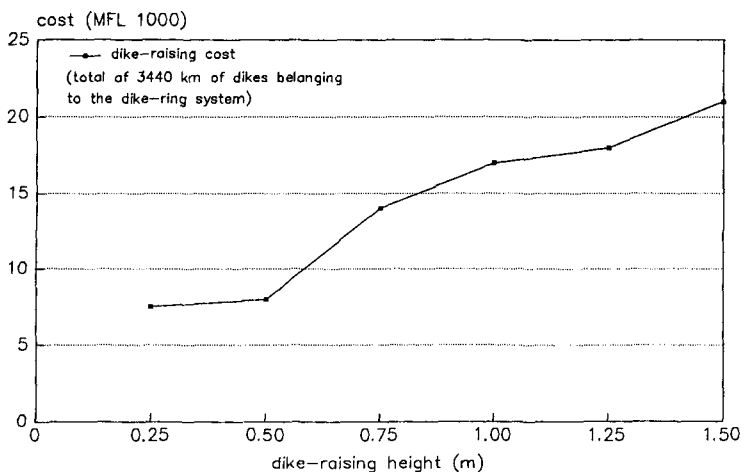


Figure 5 Cost vs. dike-raising of 3440 km primary flood dikes

## THE NETHERLANDS

The studies carried out so far have produced the computational models to evaluate the costs and benefits of flood protection and erosion control in a deterministic way. These models relates investments to flood protection measures on the one hand, and the expected flood damages to the protection level on the other hand, and provide the information to optimize the investments in dike-raising (Figure 6). Full description of the various underlying models can be found in [Peerbolte, 1993].

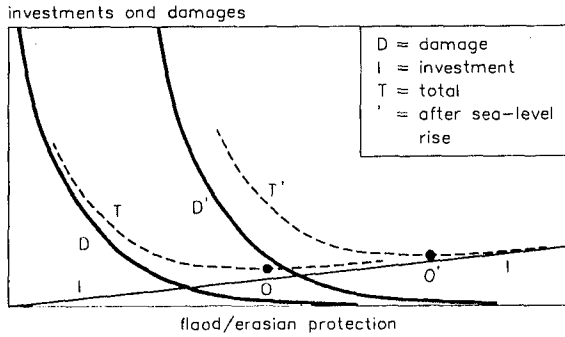


Figure 6 Principle of the shift in the optimal level of protection

Two aspects can be considered when evaluating these models: a) the cost of flood protection and coastal defence related to the protected tangible and intangible values, and b) the point of time at which the current dike-raising strategy, based on a rise of sea-level of 0.2m per century, should be reconsidered in order to maintain the present safety standards. As far as the cost of flood protection related to protected values is considered, in the Netherlands the benefits from flood protection obviously by far outweigh the necessary investments to maintain the established safety levels (see Figure 7). The optimal investment level (Figure 6) would be obtained if the dikes are raised with at least 1 metre [Peerbolte, 1993].

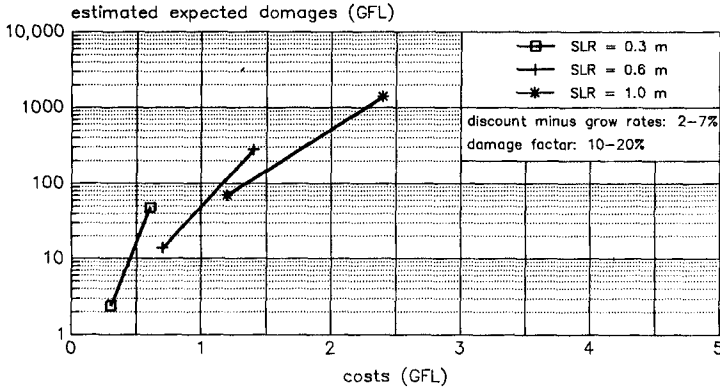


Figure 7 Estimated benefits and costs for different sea-level rise scenarios

As far as point b) is concerned, the conclusion is that it seems to be justified to reconsider this dike-raising strategy after 30 to 40 years, and to intensify dike-raising if the data point to a higher rate of sea-level rise. If, within this period of time a more serious scenario is seen to be inevitable, there is still time to switch to a dike-raising strategy matching these new predictions. This follows from computations of the unsafety factor and dike-raising cost, and the sensitivity thereof, for a number of sea-level rise scenarios. However, it should be kept in mind that the constraint on the system consisted of prescribed safety levels in terms of water level exceedance frequencies. These standard safety levels have been based on economic analysis by Van Dantzig [Delta Committee, 1962].

The above conclusions are based on modelling the different natural subsystems in the Netherlands, i.e. the coastal system, the estuarine systems in the North (Wadden Sea) and the South (Delta area), the lower and upper river systems, and the flood protected land itself, the analysis concentrated on the cost of dike-raising given a set of climate scenarios. The main conclusion regarding dike-raising is that there is no reason now to anticipate more severe scenarios than the present value of 0.2 m sea-level rise. With this scenario an average additional cost of roughly MFL 60 per year may be expected after about 60 years from now.

Vrijling has presented the formulation of a probabilistic optimization model on the basis of the problem definition by Van Dantzig whereby risk is defined as the product of uncertain flood levels and deterministic economic damages [Vrijling, 1993]. The above main conclusion regarding dike-raising is confirmed by the results of this probabilistic approach by Vrijlink.

## DISCUSSION

One of the arguments against CBA is that this method cannot account for intangible values like human life and distress. The present study shows that also uncertainties in the "concrete" material damages form an important drawback for a practical application of CBA in flood defence appraisal. The assessment of these damages involves a great deal of uncertainty. It is therefore recommended to estimate the distributions of the various uncertain economic parameters as well, such as the parameters related to construction cost and protected values, in order to be able to apply a more comprehensive probabilistic model than a model with only water levels as stochastic variable. It may even be considered to apply only the values protected as guiding parameter, without including a damage factor, and to choose (political choice) a fraction of the established values for investment in flood alleviation schemes.

## REFERENCES

- Baarse, G., Peerbolte, E.B., Van Deursen, W.P.A., Meyer, Th.J.G.P., De Vrees, L.P.M. and Vrijhof, H. (1992); *Analysis of Vulnerability to the Impacts of Sea Level Rise; a Case Study for the Netherlands*. Project report, May 1992. Resource Analysis, Delft Hydraulics and Tidal Waters Division of Rijkswaterstaat.
- CBS (1953); Gegevens betreffende de materiële schade, veroorzaakt door de overstromingen in Februari 1953 (in Dutch). In: *Statistische en econometrische onderzoekingen*. Nieuwe reeks, Jaargang 8, no. 2, 2e kwartaal 1953. Centraal Bureau voor de Statistiek. Uitgeversmaatschappij W. de Haan N.V., Utrecht.
- Delft Hydraulics (1994); *Onderzoek Watersnood Maas* (in Dutch). Report for a national committee, "Committee Meuse Flood", on the evaluation of the December 1993 floods in the Netherlands of the river Meuse.
- Delta Committee (1962); *Final Report*. Contribution of Mathematical Centre on Storm Surges and Tides, authors: D. van Dantzig, J. Hemelrijk, J. Kriens and H.A. Lauwerier. State Printing and Publishing Office, The Hague.
- Klaus, Joachim, and Reinhard F. Schmidtke (1990); *Bewertungsgutachten für Deichbauvorhaben an der Festlandküste - Mdellgebiet Wesermarsch* (in German). Research report for the Ministry of Agriculture and Forestry, Bonn.
- Peerbolte, E.B., Baarse, G., de Ronde, J.G. and de Vrees, L. (1991); *Impact of Sea Level Rise on Society, A case study for the Netherlands*. Final Report, H750, Rijkswaterstaat and Delft Hydraulics, The Netherlands.
- Peerbolte, E.B. (1993); *Sea-level rise and Safety - A consideration of safety impacts in low-lying coastal areas with particular reference to the Netherlands*. Thesis University of Twente, University for Technical and Social Sciences. ISBN 90-9006337-4, c/o Delft Hydraulics, The Netherlands.
- Penning-Rowsell, E.C. and Chatterton, J.B. (1977); *The benefits of flood alleviation: a manual of assessment techniques*. Farnborough, Saxon House/Gower, UK.
- Penning-Rowsell and Peerbolte (1994); 'Concepts, Policies and Research' in: Penning-Rowsell and Fordham (1994); *Floods Across Europe - Flood Hazard Assessment, Modelling and Management*. Middlesex University Press, London.
- TNO (1982); *Een verkennend onderzoek naar methoden ter bepaling van de inundatieschade bij dijkdoorbraak* (in Dutch). Organisatie voor Toegepast-Natuurwetenschappelijk Onderzoek (TNO), Ref. Nr. 82-0644, Dossierrn. 8727-70114. Author: J.A. Duiser. 's-Gravenhage.
- TNO (1989); *Inundatieschade, een vergelijking op basis van literatuur* (in Dutch). Organisatie voor Toegepast Natuurwetenschappelijk Onderzoek, TNO-bouw, Report BI-89-224. Author P.H. Waarts. Apeldoorn, The Netherlands.
- Torterotot, J.P. (1993); *Le cout des dommages dus aux inondations: estimation et analyse des incertitudes*. Doctoral thesis, Ecole Nationale des Ponts et Chaussees, Paris.
- Vrijling, Jan K.; 'Sea Level Rise: A Probabilistic Design Problem'. In: Duckstein, L. and Parent, E. (1993); *Engineering Risk in Natural Resources Management*. Kluwer.

## CHAPTER 231

### OFFSHORE BREAKWATERS VERSUS BEACH NOURISHMENTS A COMPARISON

M. Pluijm<sup>1</sup>, J.C. van der Lem<sup>2</sup>, A.W. Kraak<sup>3</sup>, J.H.W. de Ruig<sup>4</sup>

#### ABSTRACT

In the last decades two methods of coastal protection have become increasingly popular for the protection of sandy shores: beach nourishments and offshore breakwaters. In The Netherlands the first of both is well known and applied regularly. The second method has not been applied yet. With the increasing cost for beach nourishment and the apparent succes of offshore breakwater systems abroad, a study has been executed to the technical and economic feasibility of offshore breakwater systems in The Netherlands compared to the present strategy of beach nourishments. This paper highlights the results of this feasibility study.

#### INTRODUCTION

Protection of eroding sandy beaches can be done in many ways, each with its individual advantages and disadvantages. One of the things learned from the past is that dynamic coastal systems preferably should be kept dynamic. Including rigid structures in such environments often generate more problems than they solve. A demonstration of the new approach is the increase in application of beach nourishments as a shore erosion control measure.

---

<sup>1</sup> Head of Marine Department, Frederic R. Harris B.V., Badhuisweg 11, P.O. Box 87875, 2508 DG, The Hague, The Netherlands

<sup>2</sup> Senior Coastal Engineer, Frederic R. Harris B.V., Badhuisweg 11, P.O. Box 87875, 2508 DG, The Hague, The Netherlands

<sup>3</sup> Project Engineer, Rijkswaterstaat, Road and Hydraulic Engineering Division, P.O. Box 5044, 2600 GA Delft, The Netherlands

<sup>4</sup> Project Engineer, Rijkswaterstaat, National Institute for Coastal and Marine Management, P.O. Box 20907, 2500 EX The Hague, The Netherlands

A disadvantage of this method is the certainty that, at sites with structural erosion, the nourishment will be eroded in due course and will have to be repeated. Apart from expensive, to outsiders this gives the impression that money is thrown into the water. In order to reduce the number of maintenance nourishments (increase the timespan between two nourishments) one could therefore decide to protect the beaches with structures of some kind.

One of the successful methods, in certain cases, to achieve such protection is the application of offshore breakwaters. By interfering in the near shore sediment transport processes, offshore breakwaters influence the development of the coastline. It has been shown in numerous projects that offshore breakwaters have beneficial effects on beaches and can be used in combination with nourishments or even when nourishments are not applied.

For the Dutch coast where offshore breakwaters are not (yet) applied, but with a number of sites where beach nourishments are repetitively executed, it has been investigated whether application of offshore breakwaters will result in technically and economically feasible alternatives to singular beach nourishments.

## THE DUTCH COAST

Although The Netherlands is well known to many people for its dikes and the Deltaworks, most people do not know that the majority of the Dutch coastline does not consist of dikes. Of the approximately 350 km of coastline (Figure 1), 254 km (72%) consists of dunes, 38 km (11%) of beach flats, 34 km (10%) of seadikes and 27 km (7%) of seawalls, boulevards and the like. This makes it clear that the major part of the Dutch coastal protection effort is put into the protection and maintenance of dunes and beaches.

Fortunately the shape of and the conditions along the Dutch coast are such that only at a limited number of sites structural erosion takes place. With the increase in pumping capacity of dredgers since the 1950's and the success of the strategy, beach nourishments have been applied in increasing numbers (Figure 1, Roelse 1990). The total volume of sand applied in nourishments has increased significantly over the years. Starting with some 1.5 million m<sup>3</sup>/year in the 1950's the volume increased to

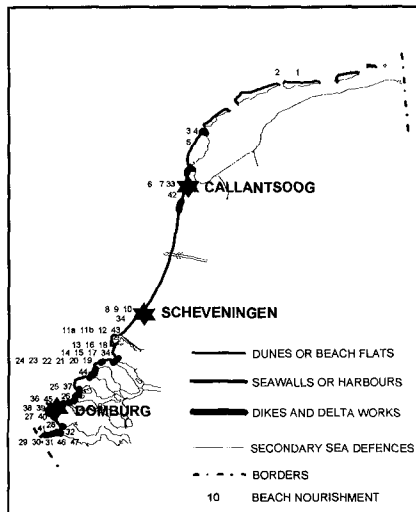


Figure 1 The Dutch coast



about 3 million m<sup>3</sup>/year in the 1970's and 1980's. Currently this figure has increased even further to about 5-7 million m<sup>3</sup>/year. The total budget currently made available by the Dutch government for beach nourishments is Dfl. 60 million per year (Hillen 1993).

In view of this budget it is not surprising that questions have been raised whether the applied beach nourishment strategy has not become too expensive and whether cheaper methods (or reduction methods) would not result in a reduction of total maintenance cost.

## SHORE PROTECTION METHODS

With the majority of the Dutch coast consisting of sand, it is not surprising that beach erosion problems are not new to the Dutch coastalmanagement organizations. In fact, at most of the locations along the Dutch coast where structural beach erosion takes place, shore protection measures have already been taken. In most cases these consist of groynes and at some places also dunefoot protection is applied. Some of these groyne systems have been set-up more than a century ago (the construction of the oldest systems has been initiated more than 200 years ago) and because of this, a lot of applied experience has been gained. Experience has shown that the effects of groyne systems along the Dutch coast are small (Verhagen 1990). Only at sites where tidal gullies run near the coast or for sites where a strong predominant oblique wave direction is present, groyne systems have some effect. For sites with a large variation in wave direction and hence a small nett littoral drift, the groyne systems hardly show a beneficial effect.

In view of this, new groyne systems were not proposed to reduce erosion of executed beach nourishments. Instead, because of experience gained abroad, offshore breakwaters were proposed as a seemingly attractive alternative for coastal protection of the Dutch coast. Questions to be answered in order to decide whether offshore breakwaters would be technically and economically feasible are:

Technically:            does an offshore breakwater system help to reduce repetitive nourishments and how much is the reduction?

Economically:        Will the cost for shore protection (including construction and maintenance of the offshore breakwater, remaining beach nourishment cost etc.) be less than the current practice of beach nourishments only?

The answer to these questions depends on many things and not the least on site conditions. With the numerous locations in The Netherlands where nourishments have been and are executed, it was decided not to relate the research to one site, but to three sites, each of which with its own specific site conditions.

## SITE SELECTION

After evaluation of potential sites, the three sites selected for further analyses were:

**CALLANTSOOG:** The beach and dunes near Callantssoog (Figure 1) are subject to structural erosion in the order of 1 to 2 m per year. The beach and dunes are relatively narrow and safety against flooding is the main argument for execution of regular beach nourishments (1976/ '77, '79/80, '86 and '91). The shore is protected with groynes, but is not intersected by breakwaters, rivers or others.

**SCHEVENINGEN:** The regularly (1969, '75, '85, '91) nourished beach at Scheveningen (Figure 1) is backed by a vertical seawall and is located just north of Scheveningen harbour. The shore is protected by groynes (constructed before construction of the harbour) and the coastline is intercepted by two short breakwaters (Figure 2). The vertical seawall prevents the construction of a mass sand storage in the form of dunes and consequently beach acts as the only sand buffer. Quick erosion of this beach during extreme events, the lee side effect of the harbour moles and the lack of natural regeneration are the major arguments why regularly beach nourishments have to be executed.

**DOMBURG:** The coastline at Domburg (Figure 1) is subject to structural erosion in the order of 4 m per year. Typical of the site is the presence of a vast system of sand banks in the nearshore area, albeit that a tidal channel runs between this sandbank system and the coast. A system of pile rows is aimed at keeping the tidal current away from the shore. For northwesterly storms the coastline is very sensitive to erosion. Any loss of sand in the tidal gully is a permanent loss. As a result the coast near Domburg has been nourished in 1986, '89, '90 and '92.

## OFFSHORE BREAKWATERS IN DUTCH COASTAL WATERS

What distinguishes the site conditions in Dutch waters from many of the other locations in the world where offshore breakwaters are applied, are two main items. First the tidal motion. The tidal range for the three sites varies between approx. 3.90 m (Domburg) and 1.50 m (Callantssoog). Consequently under normal tidal conditions the influence of an offshore breakwater is influenced by the water level and tidal current. The second is the influence of storms. Because of the funnel shape of the North Sea, northwesterly storms can generate considerable increases in water level (storm surge). With the majority of the land area behind the dunes well below mean sea level (MSL), the design storm surge level (in combination with waves) for which the sea defences should maintain safety is in the order of +5.50 m above MSL (1 in 10,000 years risk of flooding).

In order to keep the offshore breakwater system economically feasible it is clear that the breakwaters should be kept small. Hence under extreme conditions as indicated

above, the breakwaters will be submerged and their influence consequently reduced. On the other hand, for low water level conditions it is likely that the offshore breakwater system will emerge above still water level. These conditions impose special requirements in the design of the offshore breakwater system. Combinations of different water levels and wave height and consequently different loading conditions (submerged, emerged yet overtopping) must be taken into account in the design of the breakwaters.

Although for the cross sectional design of an offshore breakwater system numerous alternatives can be thought off, the combination of conditions indicated above imposes the requirement that a proper breakwater system must be designed for a wide range of different conditions (water levels, waves, currents). In addition, it is required that the costs for breakwater construction and maintenance are kept small. This led to the conclusion that a rubble mound breakwater type was to be preferred. Design rules would be available for all different loading combinations, construction and maintenance cost assessment would be easy and general experience with this type of breakwater is good.

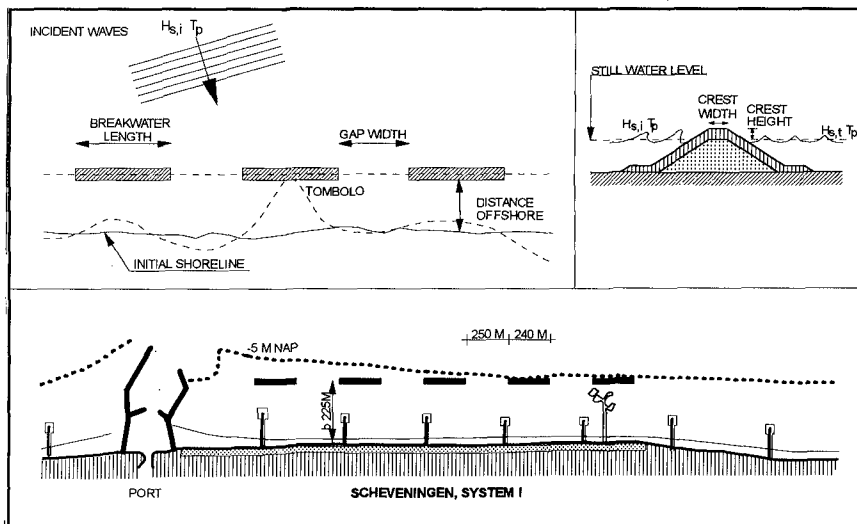


Figure 2 Offshore breakwaters at Scheveningen

## PLAN VIEW AND CROSS SECTION OF OFFSHORE BREAKWATERS

Although a lot has been published on the application of offshore breakwaters (Dally and Pope 1986, Rosati 1990) and the physics by which offshore breakwaters function becomes more and more understood, accurate and straight forward design methodologies are not available.

The initial lay-out design of the offshore breakwater systems therefore has been based on rules from practice (Rosati 1990) relating dimensions as breakwater length, gap width, distance offshore etc. (figure 2). In this initial design stage it has been adopted as design requirement that tombolo formation (such large accretion of the beach that the accreted sand reaches the lee slope of the offshore breakwater - figure 2) should not develop. This requirement is invoked by the expectation that tombolo formation will result in blocking of longshore sediment transport and consequently causing large lee side erosion.

The combined effect of water level and wave height imposes special requirements on the cross sectional design of the rubble mound breakwaters. Especially the height of the crest relative to still water level and the width of the crest influence the overtopping (and thus the wave attack on beach and dune) as well as the wave loads on the breakwater itself.

Cross sectional design, offshore distance, breakwater length and gap width finally will determine the total volume of the breakwater construction materials. To keep the cost of the breakwater systems small, it was chosen to locate the breakwaters as near to the coast as possible (minimum depth) but far enough to prevent tombolo formation. For the Scheveningen site this resulted in the breakwater scheme of Figure 2. For the Domburg and Callantsoog site the proposed breakwater schemes were more or less similar.

The cross sectional design was chosen to be trapezoidal with side slopes of 1 in 1.5. This will result in a minimum rubble mound breakwater which will remain stable with a reasonable rock size as armouring. The height of the breakwater is dominant for the overtopping and the weight of the armour to be used. The higher the breakwater, the less the transmission and overtopping but the heavier the armour unit to be applied and visa versa. Eventually for Scheveningen it was decided to put the crest level of the offshore breakwater system at approximately +1.25 m MSL, just above mean high water of spring tides. Under these conditions the impact of the breakwaters on wave transmission is maximised, but this will reduce with increasing water levels. At extreme high water levels the breakwaters will be submerged and be subject to reduced wave forces despite the higher waves associated with the storm surges and deeper water. Finally under normal daily wind and wave conditions the breakwater system will be visible, not unimportant for the increasing pleasure craft navigation along the Dutch coast.

## **QUALITATIVE DESCRIPTION OF THE IMPACT OF OFFSHORE BREAKWATERS ON THE DUTCH COAST**

Before trying to estimate the magnitude of the effects of offshore breakwaters on the Dutch coast, it is first of all important to identify the processes involved. By understanding the processes involved, mathematical approximation of these processes

may be used to indicate the magnitude of the impact of offshore breakwaters. As implicitly indicated in the previous, a differentiation should be made between normal conditions (without storm surges) and extreme events (including storm surges). The influence of offshore breakwaters under these two conditions will be quite different.

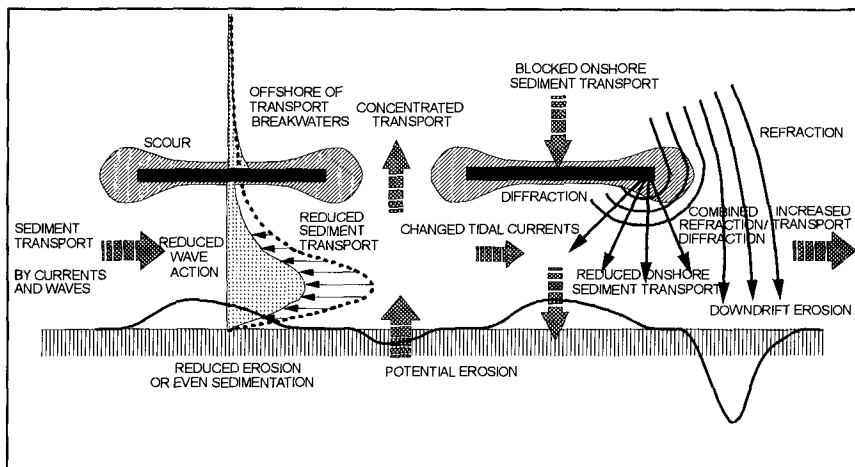


**Figure 3** Offshore breakwaters: physical processes under normal conditions

### Normal Conditions

Under normal conditions the morphological processes at the coast under influence of waves and tidal currents result in predominant longshore sediment transport. The application of offshore breakwaters is under these conditions aimed at reducing the longshore sediment transport behind the breakwaters, by shielding the coast from predominant wave attack. Assuming that this can be accomplished, the result will be a reduced erosion behind the breakwaters or even sedimentation (Figure 3).

The offshore breakwater system will have a limited length and consequently will end somewhere. In the Dutch case, with a net longshore sediment transport in northerly direction, a reduction in sediment transport behind the offshore breakwaters is likely to result in erosion on the northside of a breakwater system (lee side erosion). This lee side erosion is an important phenomena which counter effects the positive effect of beach accretion behind offshore breakwaters. In the overall (economic) evaluation this lee side erosion and consequent additional beach nourishments should be taken into account.

Although longshore sediment transport will be dominant under normal conditions, the cross shore transport will also be influenced by offshore breakwaters. An important aspect in this cross shore transport under normal and fair weather conditions is the

transport of sediment towards the coast. Being primarily a bedload transport offshore breakwaters will block the onshore transport and prevent the natural rehabilitation of eroded beaches.

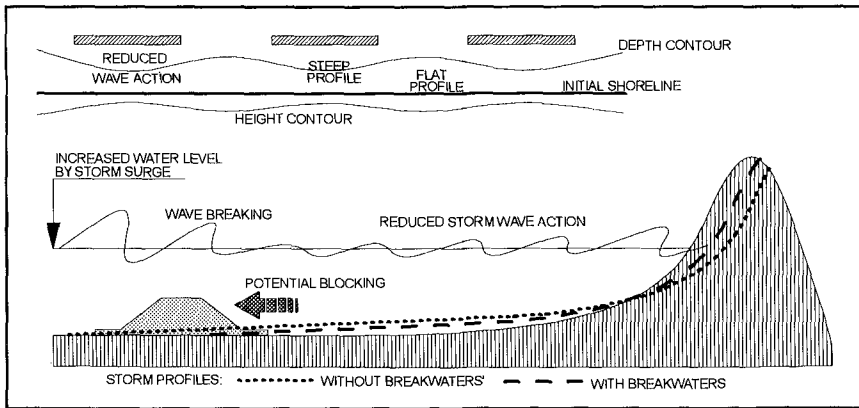


**Figure 4** Offshore breakwaters: physical processes under extreme conditions

#### Extreme Conditions

Under extreme conditions, the breakwaters may be submerged and wave conditions will be severe (Figure 4). Without offshore breakwaters under such conditions erosion of beaches and dunes can be expected. However, even though the offshore breakwaters are submerged, the crest level is still so high that the breakwaters will influence the wave conditions. Reduced wave conditions will result in reduced erosion of beach and dunes. Depending on the distance of the offshore breakwaters relative to the coastline, the resulting cross sectional storm profile of dune and beach may reach as far as the breakwaters. The breakwaters then could perform a containment function.

As indicated previously, a disadvantage of offshore breakwaters is that they not only prevent natural rehabilitation of the beach (and the dunes) from the seaward side of the breakwaters towards the coast, but also due to the reduced wave conditions behind the breakwaters from the landward side.

#### QUANTITATIVE DESCRIPTION OF THE IMPACT OF OFFSHORE BREAKWATERS ON THE DUTCH COAST

A quantitative assessment of the influence of all these processes on the coastline clearly will be difficult let alone inaccurate. This difficulty finds its origin in the complexity of the hydraulics and the coastal morphology processes. The current and

wave field between the breakwaters will have a strong two-dimensional effect. Generated bed shear stresses, radiation stresses etc. also will vary significantly in a horizontal plane. Gradients will not only occur parallel to the coast, but also perpendicular to the coast. Currently available coastline models are often one line models in which the complex water/sediment/structure interaction has to be included in a simple way. Usually only the sheltering of wave action is included in the model (Delft Hydraulics 1992, Hanson 1989). Changes of tidal current conditions are usually not included. In view of this it was concluded that the available one-line models are still limited in predicting shoreline changes with sufficient detail and reliability to support the design of offshore breakwater systems. Especially in feasibility studies where eventually costs will have to be implemented, a proper assessment of remaining nourishments volumes may be the key element of the outcome of the study.

A quantitative assessment of the influence of offshore breakwaters under extreme conditions may be made, assuming that under extreme conditions primarily cross sectional profile changes occur. With the breakwaters under water, the wave height still will be reduced and a reduction in cross sectional erosion may be expected. The effects of offshore breakwater on erosion profile development has been studied using two cross sectional erosion models (RWS-DWW 1992). The results of this study indicated that by applying offshore breakwaters, under extreme conditions a reduction in cross sectional erosion is achieved up to a maximum of 30%.

In view of the previous it appears to be impossible to conclude whether offshore breakwaters in The Netherlands would be economically feasible, not knowing the beneficial and negative effects of these breakwaters on the protected and adjacent coastline. One way to overcome this is to make the economic evaluation based on an assumed beneficial effect.

## **CROSS SECTIONAL DESIGN OF OFFSHORE BREAKWATERS**

As indicated previously, the offshore breakwaters have been designed as rubble mound breakwaters. The influence of water level and wave conditions have been taken into account in the design of the breakwaters, as well as the effect of wave breaking on the wave height and the wave height distribution.

A requirement in the breakwater design is the flexibility of the breakwaters. Further the breakwaters should not be sensitive to damage (maintenance) nor for excessive damage (collapse). To fulfil these requirements, the breakwaters have been designed out of one grade of (main) armour, without filter layers and core. Only a filterlayer/bottom protection is provided (Figure 5). The advantage of such design is that even with large damage, filterlayers and core can not be eroded since these are not applied. The porosity of the structure is high, which allows the application of relatively small main armour units. Major damage most likely will manifest itself in

the form of lowering of the crest. This will reduce the effect of the breakwaters on the wave conditions and thus on the coast. However, because of the single grade of main armour it would be relatively easy to increase the height again. Similarly because of the single grade main armour, extension or shortening the offshore breakwaters would be relatively simple.

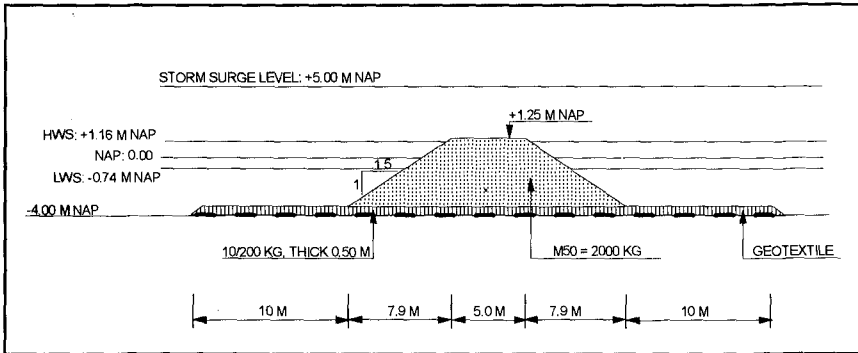


**Figure 5** Scheveningen: typical offshore breakwater cross section

In the design of the breakwaters, the combination of design conditions required the breakwaters to be designed as overtopping breakwater and as submerged (reef) breakwaters. Applying appropriate design rules (CUR/CIRIA 1991) the cross sectional design for the Scheveningen site is presented in Figure 5. Similar designs were developed for the Domburg and Callantsoog site. Based on this type of cross section a cost estimate for the construction of the breakwater system was established.

## ECONOMIC EVALUATION

In the economic evaluation of the feasibility of offshore breakwaters in The Netherlands three main items have to be taken into account:

1. What are the present costs for coastline maintenance, i.e. without offshore breakwaters?
2. What are the future costs for coastline maintenance, i.e. with offshore breakwaters?
3. What are the costs for the construction of the breakwaters?

The evaluation will be illustrated for the Scheveningen location. For the other locations a similar approach has been followed.



#### Present costs for coastline maintenance.

The size of maintenance beach nourishments as executed in the past years approximates 70,000 m<sup>3</sup>/yr. Adopting a unit rate of Dfl 10.00 per m<sup>3</sup>, the yearly cost for beach nourishments for the situation without offshore breakwaters would be Dfl 700,000. With the length of the nourished beach being in the order of 2000 m, the yearly costs amount Dfl. 350.00 per linear meter of coast. These costs refer to the nourishments only. (The total yearly maintenance costs of the coastline are much higher, taking into account the costs for maintenance of the groynes, the seawall, the dunes etc. For these costs a total of Dfl 150.00 per linear meter should be added.)

#### Future cost for coastline maintenance.

The future cost for coastline maintenance depends on the effectiveness of the offshore breakwaters to reduce the costs for beach nourishments. Most optimistically would be a situation that the offshore breakwaters just counter effect the erosion (no remaining nourishments). Most pessimistically would be a situation that still additional nourishments would be required, varying from 0% (no additional nourishments) to more then 100% (more than currently required). The latter situation would develop, if behind the breakwaters sedimentation would take place and in the lee side of the breakwater system the nett sediment transport is generated again. With the nourishment cost at Dfl 350.00 per linear meter of coast per year, the future cost for nourishment may range between Dfl 0.00 and more than Dfl 350.00 depending the effectiveness of the offshore breakwater system.

#### Cost for breakwater construction

The capital costs for the breakwater cross section presented in Figure 5 is estimated at Dfl 15,000.00 per linear meter of breakwater. The cost per linear meter of coast is a function of the breakwater length and the gap width between the breakwaters. For the Scheveningen site a gap width - breakwater length ratio of 250/240 (system I) and 60/120 (system II) has been used. In the first case the capital costs are approx. Dfl 7,350.00 per linear meter of coast and in the second case approx. Dfl. 10,000.00 per linear meter of coast.

#### Comparison

The final comparison is based on a nett present value calculation for the shore protection with and without offshore breakwaters. In this calculation, the effect of the offshore breakwater on the coast is expressed in percentage of remaining nourishment (0% = no more nourishments, 100% = unchanged nourishment volume). The interest rate has been taken at 5% and the calculation period at 30

years. At the end of the calculation period, the breakwater rest value is assessed at 40% of the initial construction cost. Maintenance for the breakwater is 2% per year. The results for Scheveningen are presented in Figure 6. This figure indicates that both offshore breakwaters schemes proposed for Scheveningen are more expensive than beach nourishments only, given the adopted unit rates for breakwater construction material, sand etc.

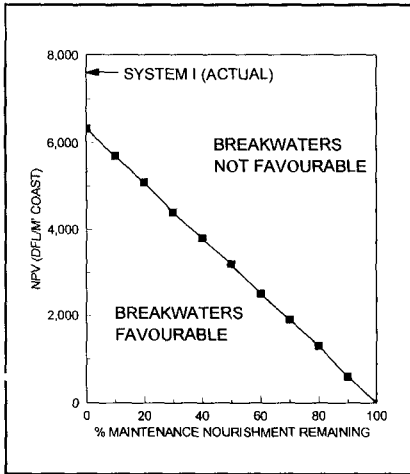


**Figure 6** Scheveningen: NPV comparison for two systems

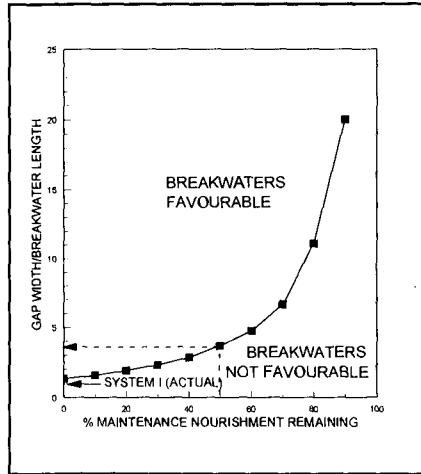


**Figure 7** Scheveningen: break even NPV

Using the same nett present value approach, Figure 7 indicates what the cost for offshore breakwaters per linear meter of coast may be, assuming the magnitude of the remaining beach nourishments, to reach a break even point with beach nourishments only. The figure indicates that if the effect of the offshore breakwater scheme is small (large remaining nourishments) the breakwater construction cost should be small. If the effect is large (small remaining nourishments) the breakwater construction costs may be higher.

Given these break even construction cost and the construction cost per linear meter of breakwater (based on Figure 5), the gap width/breakwater length ratio can be determined to reach the break even point for an assumed effect of the offshore breakwaters on the nourishment (Figure 8). This figure indicates that a reduction of the maintenance nourishment to 50% of the present nourishments should be achieved with a gap width/breakwater length ratio of approximately 4. With the large gaps thus resulting between the breakwaters it is assessed that this can not be achieved.

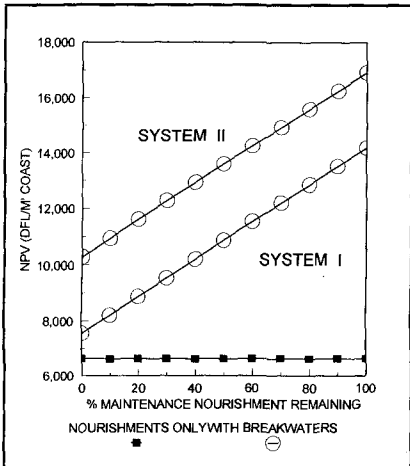


**Figure 8** Scheveningen: break even gap width/breakwater length ratio

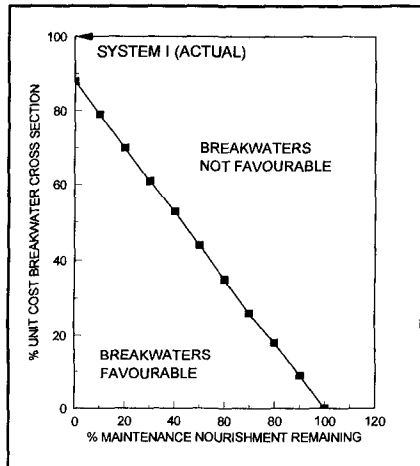


**Figure 9** Scheveningen: break even relative cross sectional costs

Alternatively, knowing the break even costs for the offshore breakwater scheme, the average unit rate for the breakwater construction material has been determined. Using the cross sectional profile of Figure 5 and a gap width/breakwater length of 1 the average rates are indicated in Figure 9. It should be noted that the average cost for the breakwater according Figure 5 is approximately Dfl 187.00 per m<sup>3</sup>. The results indicate that if the effect of the offshore breakwater is large, the breakwaters can be constructed of a more expensive material (rock). When the assumed effect of the breakwaters is small, the breakwaters should be constructed of a cheap material (sand). However in the last situation, the offshore breakwaters are not breakwaters any more but offshore sandbanks. Under these situation the morphological processes will be quite different compared to statically stable offshore breakwaters.

**EVALUATION**

Often Coastal Zone Management organizations resent the application of repetitive beach nourishment as shore protection methodology. This aversion initially is generated by the idea that over the years, regular beach nourishments will cost a large amount of money. For this reason one tends to take protective measures to reduces the losses or even completely stop the erosion of the coast.

The qualitative evaluation of offshore breakwater schemes executed in this study indicates that for ongoing sandy coasts the erosion at the down drift side of the offshore breakwater scheme forms an important aspect and an argument to expect

that even after construction of offshore breakwaters, maintenance nourishments will still be required to counter measure this.

In cases where offshore breakwaters are applied and large storm set-up occur, erosion of beach and dunes still can be expected, although the magnitude of the erosion will be reduced. Hence in cases where single storms may have a large impact, offshore breakwaters will have a mitigating influence on the effect of each single event.

The quantitative assessment of the effect of offshore breakwater schemes on the coastline, especially for a hydro-morphological system including currents and waves, still appears to be complex. One-line coastline models available to the Consultant insufficiently represented this complex hydro-morphological system to supply reliable results to support the outcome of this study.

In that respect initial results of 2-dimensional modelling of offshore breakwater schemes show promising results. It is expected that in the future this will allow for more physically correct modelling and be the basis for a reliable assessment of the quantitative effect of breakwaters on the coast.

Because of the latter limitation, the economical feasibility study of the application of offshore breakwater in Dutch coastal waters has been based on an assumed beneficial effect. Rubble mound offshore breakwater do not show to be economically feasible with the unit rates for sand and breakwater construction materials as applicable in The Netherlands. Offshore breakwaters may become economically attractive when the construction cost is reduced. This may be achieved by alternative breakwater designs, but this has not been executed in this study.

Finally, one could argue whether other arguments can be raised to construct offshore breakwaters despite the higher cost. Assuming some beneficial effect of the offshore breakwater scheme, the average interval between consecutive maintenance nourishments will increase, giving to the public the impression that "less money is thrown into the water". Secondly, taking into account that the beneficial effect of an offshore breakwater scheme is partly counter affected by erosion at the down drift side of the breakwater scheme, offshore breakwater may be used to "shift" the problem. This can be applied to shift the nourishment activity to less frequently used beaches.

## REFERENCES

- ROELSE, P. (1990) Beach and dune nourishment in The Netherlands. Proc. 22nd Int. Coastal Eng. Conference, Delft, The Netherlands
- HILLEN, R. and HAAN, Tj. de (1993) Coastlines of the southern North Sea, ASCE.

VERHAGEN, H.J. (1990) Coastal protection after 1990, Technical report 12: groynes and pile rows, Ministry of Transport and Public Works and Watermanagement (Rijkswaterstaat), Road and Hydraulic Engineering Division, The Netherlands (in Dutch)

DALLY, W.R. and POPE, J. (1986) Detached breakwaters for shore protection, WES, CERC, Vicksburg, USA

ROSATI, J.D. (1990) Functional design of breakwaters for shore protection: empirical methods, WES, CERC, Vicksburg, USA

HANSON, H (1989) Genesis: generalized model for simulating shoreline change, WES, CERC, USA.

DELFT HYDRAULICS (1992), Unibest-CL: a software suite for simulation of sediment transport processes and related morphodynamics of beach profiles and coastline evolution, Delft Hydraulics, The Netherlands

RWS-DWW (1992) Comparative calculations with DUROSTA and DUINAF to determine beach and dune erosion for situations with and without offshore breakwaters, Rijkswaterstaat, Road- and Hydraulic Engineering Department (DWW), The Netherlands (in Dutch).

## CHAPTER 232

### Morphological modelling of Keta Lagoon case

J.A. Roelvink<sup>1,2</sup>, D.J.R. Walstra<sup>1</sup> and Z. Chen<sup>1</sup>

<sup>1</sup>DELFT HYDRAULICS p.o. box 152, 8300 AD Emmeloord, The Netherlands.

<sup>2</sup>Netherlands Centre for Coastal Research, Delft University of Technology, Faculty of Civil Engineering, p.o. box 5048, 2600 GA Delft, The Netherlands

#### **Abstract**

DELFT HYDRAULICS' morphological model system is applied to the case of Keta Lagoon, Ghana; the results are compared with a physical model test carried out by DELFT HYDRAULICS in 1982.

#### **1. Introduction**

Predictions of morphological evolution in a coastal area are of importance in many engineering applications. Such predictions have often been made by carrying out physical model tests, which are usually very expensive and time-consuming, and which may suffer from scale effects. Nowadays, mathematical models offer a relatively cheap and efficient way for morphological predictions. However, validation of such models requires much attention.

The objective of this study is to test the coastal area model developed at DELFT HYDRAULICS against the measurements from physical model tests and to produce results for comparison with other models.

The study is part of the "G8 Coastal Morphodynamics" research programme, which is funded partly by the Commission of the European Communities in the framework of the Marine Science and Technology Programme (MAST), under contract no. MAS2-CT92-0027. For more background information see De Vriend et al. 1992). Details of the present study are described in Walstra (1994).

#### **2. Morphological model system**

The morphological model system to be tested here is a subset of DELFT HYDRAULICS' system DELFT3D, which has recently been developed in order to allow a flexible integration of the models for currents, waves, sediment transport, bottom

changes, water quality and ecology. The morphological system contains the first four models and a control model. This control model allows the user to prescribe any combination of processes and arranges the time-progress of each model and possible iterations between models. The models relevant to morphological simulations are outlined below:

#### *Waves*

Stationary multi-directional (short-crested) wave model HISWA (Holthuijsen et al., 1989).

#### *Hydrodynamics*

2D or 3D flow model TRISULA based on the shallow water equations, including effects of tides, wind, density currents, waves, spiral motion and turbulence models up to  $k-\epsilon$ ; for morphodynamic computations, a quasi-3D option to account for wave-driven cross-shore currents is available.

#### *Sediment transport*

New model TRANSP, including a sub-model TRSTOT, bed-load and suspended load transport according to several formulae, and TRSSUS, a quasi-three-dimensional advection-diffusion solver for suspended sediment, including temporal and spatial lag effects.

#### *Bottom change*

New model BOTTOM, which contains several explicit schemes of Lax-Wendroff type for updating the bathymetry based on the sediment transport field. Options for fixed or automatic time-stepping, fixed layers, various boundary conditions.

The first combination used in this study is similar to that used in the earlier MaST intercomparisons, viz. 2DH currents, multi-directional wave propagation and Bijker transport model.

The flow diagram for the combination of models applied in this study is given in Figure 1. Starting from an initial bathymetry, a number of wave computations covering a tidal cycle are carried out, followed by a run of the flow model which includes tidal and wave forcing. The wave and current computations can be iterated to account for full wave-current interaction. Sediment transport computations are carried out for a number of steps within the tide. The transports are averaged over the tidal cycle and the bathymetry is updated based on the residual transport pattern. A very important branch in this scheme is denoted B. Here, the discharge pattern is kept constant and (small) bottom changes are assumed to affect the current velocity only locally: at a constant discharge rate, the current velocity increases if the depth decreases. This is a reasonable assumption as long as the bottom changes are small and leads to an enormous reduction in computational cost. Typically, 20-40 so-called continuity correction steps can be taken in between full hydrodynamic runs (branch A).

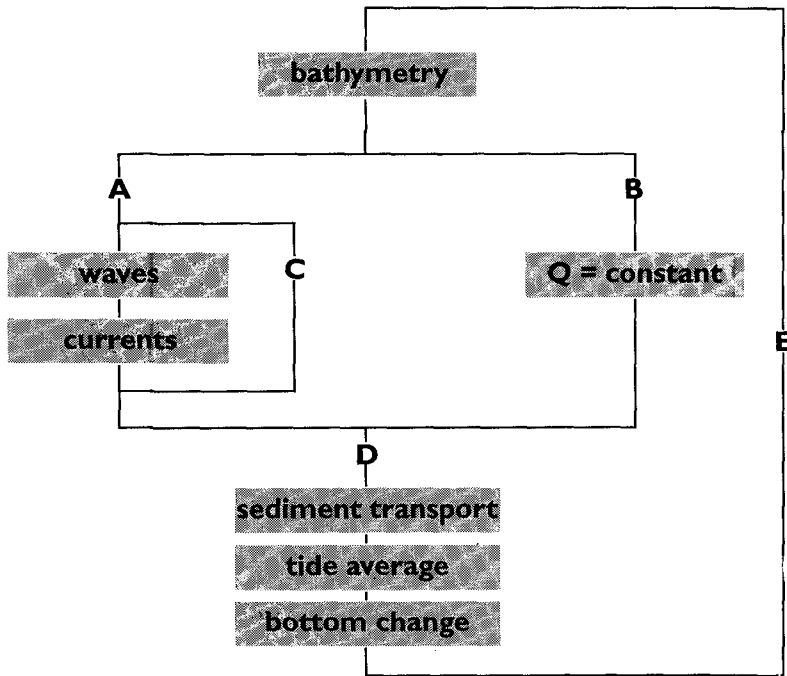


Figure 1. Flow diagram of morphological model system.

### 3. Test case

The town of Keta is situated in the south-east of Ghana, near the delta of the Volta River, and was built on a narrow sand ridge between the Gulf of Guinea and the Keta Lagoon. In past years Keta Town has suffered much from erosion, which attacked the heart of the town and destroyed a great number of houses.

Beside the great threat from the sea the main problem for the inhabitants of Keta is the lack of land at a sufficiently high level to enable them to construct their houses safe from the lagoon floods. The Keta Lagoon, with an area of 300 square kilometres, collects the run-off from a large catchment area. From the lagoon the excess water may find its way to the sea through a long winding channel towards the mouth of the Volta River. Most of it however evaporates during the dry season. In very wet years, the lagoon water level becomes so high that houses and crops on the lagoon side of the sand ridge are inundated. In the years 1963 and 1968 the situation was considered dangerous and a small cut was made in the



sand ridge. In both cases the excess water was discharged successfully into the sea, forming however, a tidal inlet of considerable capacity by scouring due to high lagoon levels (see Fig. 2). Consequently, traffic to and from Keta was interrupted.

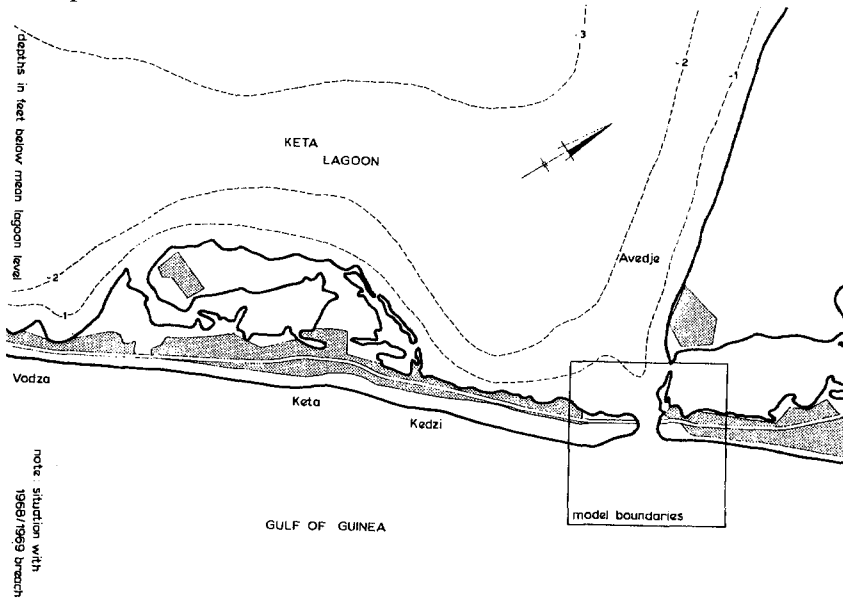


Figure 2. Situation at Keta (with 1968/1969 breach)

#### 4. Physical model study

A physical (movable-bed) model study was carried out at DELFT HYDRAULICS in 1982 (Delft Hydraulics Laboratory, 1982). The aim of this physical model study was to investigate the possible stabilization of the lagoon outfall and to determine the most favourable layout of the outfall structure. The model has been calibrated by reproducing the conditions which occurred in 1963 and 1969.

In the model, a dyke was built separating the lagoon from the sea. At the sea-side, a uniform beach profile was applied. The bottom of the lagoon was horizontal. The sea and the lagoon were connected by a straight channel.

At the sea boundary, irregular waves were generated by means of a paddle-type wave generator at an angle of  $15^\circ$  to the coastline. In addition to the waves, two phases of steady current were generated with a water circulating system, representing an ebb and a flood respectively.

In the tests, measurements were made of the initial and final bed topography. A summary of the parameters used in the physical model is given below.

Physical model description	
Model scales	horizontal 36 vertical 28
Model size	30 m by 30 m
Bathymetry	beach profile: 1:15, depth 0 m to 0.125 m 1:45, depth .125 m to .28 m inlet channel: depth 0.19 m, width 2.4 m, 1:4 slopes lagoon: flat, depth 0.07 m
Waves	irregular wave height $H_s=0.07$ m, $T_p=1.5$ s, $15^\circ$ to coastline
Currents	ebb/flood, cycle time 2 hr 30 min. additional littoral drift (magnitude unknown)
Sediment	$D_{50}=0.21$ mm, $D_{35}=0.19$ mm
Test duration	75 hr
Measurements	bottom topography with intervals 1 m by 0.25 m no wave measurements no current measurements
Programs	Two sets of tests with different tidal discharges through the channel. Test case used here T0-3

### 5. Set-up of the numerical model

Since it is difficult to exactly reconstruct the physical model in the numerical model, a different approach was chosen: given the same prototype data that were used to schematise the physical model, a new schematisation was made for the numerical model. Prototype scale was used for the numerical model. It covers an area of 1500 m longshore by 1100 m cross-shore. A rectangular grid was used, initially with a uniform grid size of 15 m by 15 m and approximately 6500 active points. The first computations showed that the resolution at the channel entrance was rather poor with this grid, and consequently a variable grid size was applied, with cell widths ranging from 30 m in the lagoon and deep water to 5 m near the entrance. The bathymetry was obtained by scaling the physical model back to

prototype scale. Prototype scale significant wave height is 1.96 m, peak period is 8 s.

A tidal movement was assumed at the sea boundary, which is perpendicular to the coastline with a tidal range of 0.98 m. The tidal movement was described with the water level variation at the sea boundary. For simplicity, a sinusoidal variation was assumed with a period of 12 hr 30 min. The tidal data are primarily based on the field observations (mean tide). In the physical model, the tidal movement was schematized into an ebb and a flood phase each lasting for 1 hr. Inside the lagoon, the water level variations are very small (0.03 to 0.06 m) according to the field observations. Thus at the lagoon boundary (western, northern and eastern sides), the water level is assumed to be constant. i.e. at Mean Sea Level. Both lateral boundaries are prescribed as current boundaries. The current is the computed longshore current on a uniform beach, with a varying water level. All boundary conditions

The bed material chosen for the model has a uniform size distribution at all locations in the model. The characteristics of the material are:  $D_{50} = 0.54$  mm (with fall velocity of 0.0785 m/s),  $D_{35} = 0.30$  mm. A uniform roughness height of 0.1 m is assumed; the enhancement of bottom friction by waves is modelled using the Bijker approach.

Other characteristics are:  $g=9.81$  m/s<sup>2</sup>, density of sea water 1030 kg/m<sup>3</sup>, turbulent viscosity 2 m<sup>2</sup>/s and no Coriolis force.

## 6. Results

Figure 2 shows the initial bathymetry. The beach has a bed slope of 2% and connects the sea side area with an area of uniform water depth of 8 meter. The channel has a width of approximately 130 meters, the length of the channel is 250 meter and its depth is 5.4 meters below MSL. The sand ridge has a maximum height of 3.60 m above MSL.

Per hydrodynamic run, three wave computations were carried out to represent the tidal variation (LW, MSL and HW). after which the current model was run for 1.5 tidal cycle. Here, the wave forces were obtained by linear interpolation. Comparison with results for more wave runs per tide showed no significant differences.

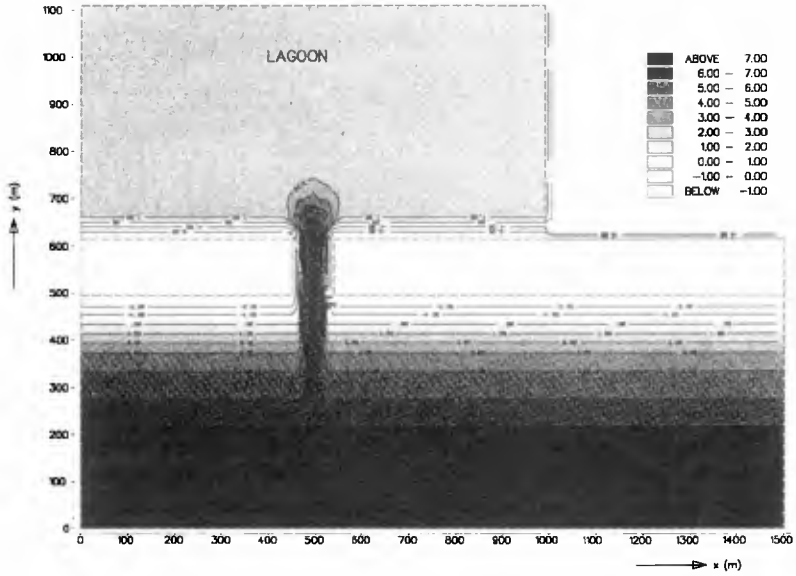


Figure 3. Initial bathymetry in numerical model.

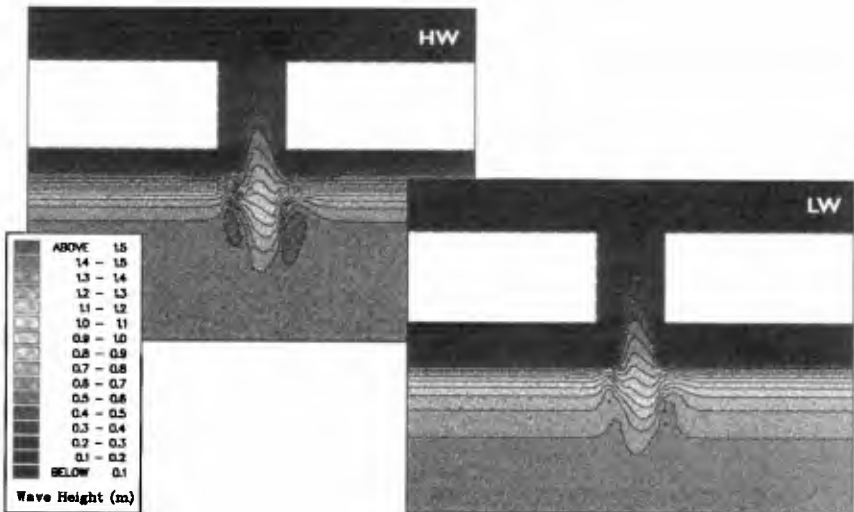


Figure 4. Wave height patterns near the entrance, High Water and Low Water.

In Figure 4, the initial Hrms wave height patterns for high water (HW) and low water (LW) are shown. The main effect of the water level variation is a horizontal shifting of the pattern. The effect of the current on the wave height pattern was investigated in trial runs and found to be significant. However, in order to reduce the complexity of the morphodynamic problem, this aspect was not taken into account further.

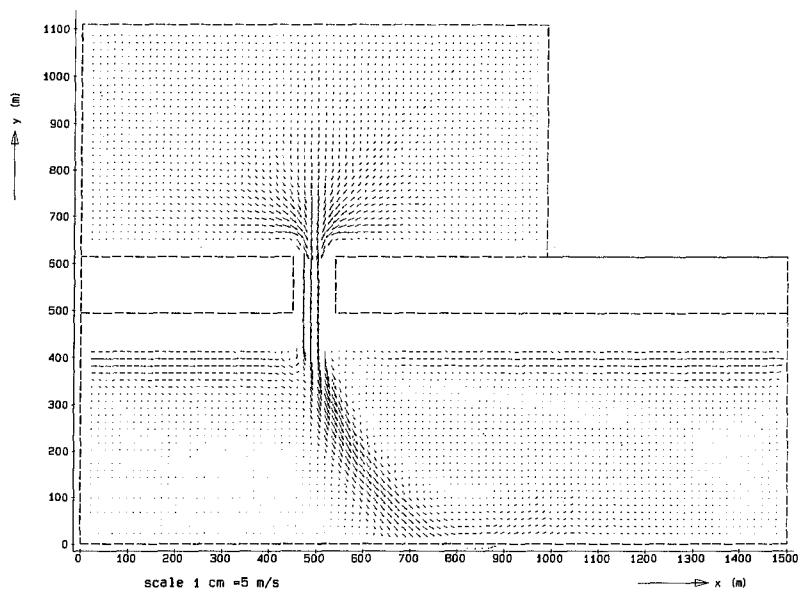


Figure 5. Current pattern at LW.

From trial runs without tidal variation it was clear that the wave-induced set-up forces a nett discharge into the lagoon. Though this may happen initially, in reality the lagoon will fill up until an equilibrium is reached. Through iteration the correct water level increase in the lagoon was found to be 0.091 m; with this mean level inside, the nett discharge through the channel was very close to zero. The boundary conditions in the lagoon were adjusted accordingly.

In Figures 5, 6 and 7 the current pattern is shown at LW, MSL and HW respectively. In all three cases the wave-driven longshore current is evident. During LW there is a strong ebb current which is forced sideways by the longshore current. The MSL phase shows mainly the longshore current and local effects of the channel. During flood, the longshore current accelerates towards the channel on the upstream side, whereas it is suppressed on the downstream side.

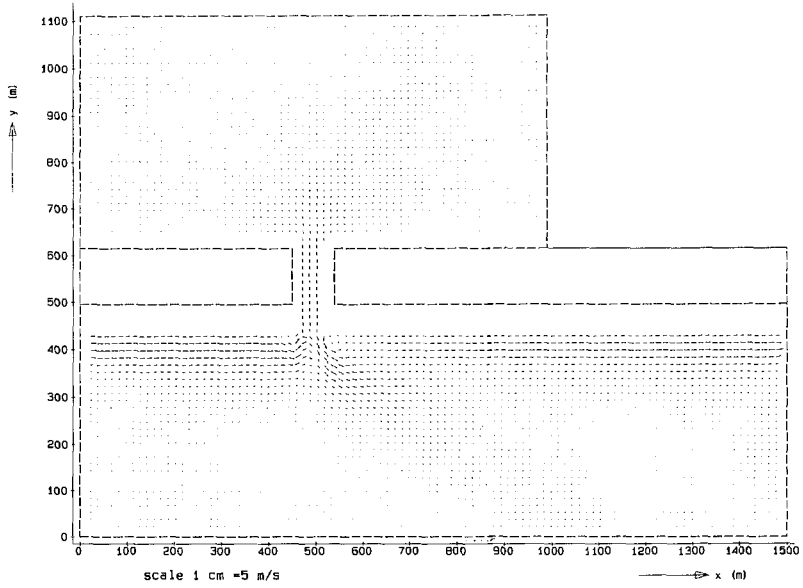


Figure 6. Current pattern at MSL.

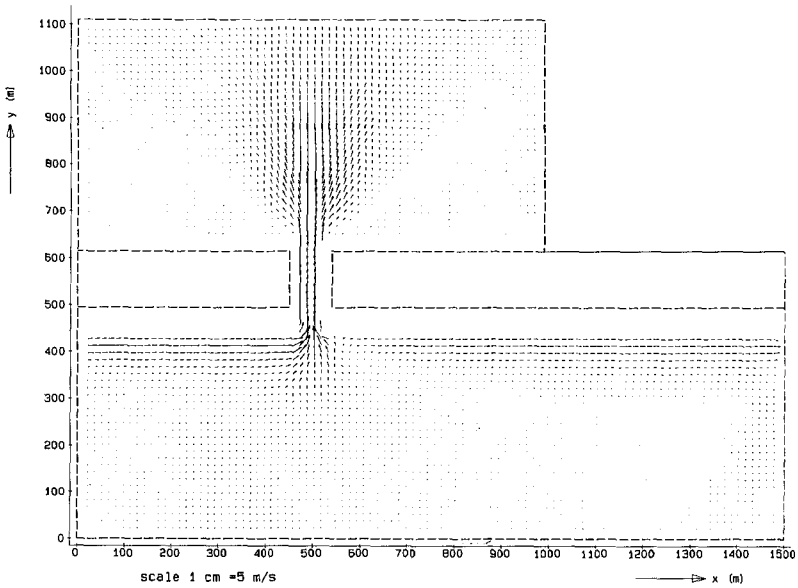


Figure 7. Current pattern at HW.

The above results were obtained for the original coarse grid and showed a rather poor resolution at the entrance of the channel. For further computations, a much finer grid was applied, as is shown in Figure 8 for the velocity at MSL.

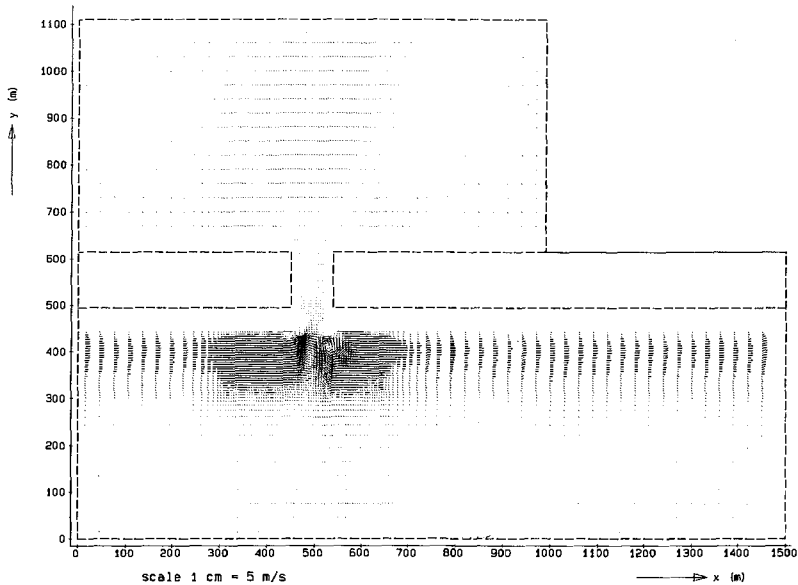


Figure 8. Current pattern at MSL, locally refined grid.

Sediment transport computations were carried out at 15 min. intervals; the sediment transports were averaged over a tidal cycle.

Morphodynamic computations were made using the tide-averaged transport patterns, since the morphological time scale of interest was much larger than the tidal period. However, for numerical reasons, a morphological time step in the order of 0.5-1.0 hour was used in the run presented here. The time step was computed automatically based on a Courant number criterion. Twenty steps using continuity correction were taken before each full hydrodynamic update. Results indicate that the number of intermediate steps may be increased further, since no shocks are evident in the time-evolution of the bottom.

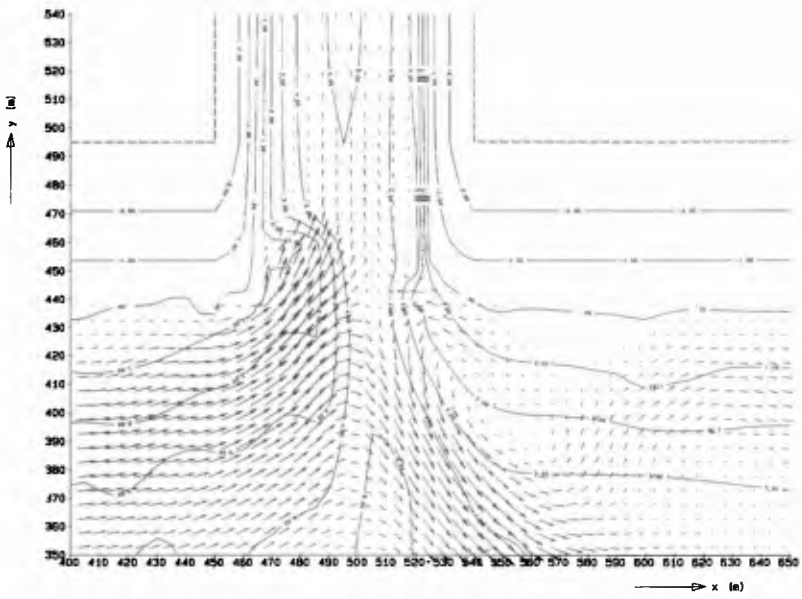


Figure 9. Tide-averaged sediment transport on updated bathymetry after 5 tides. Detail near entrance.

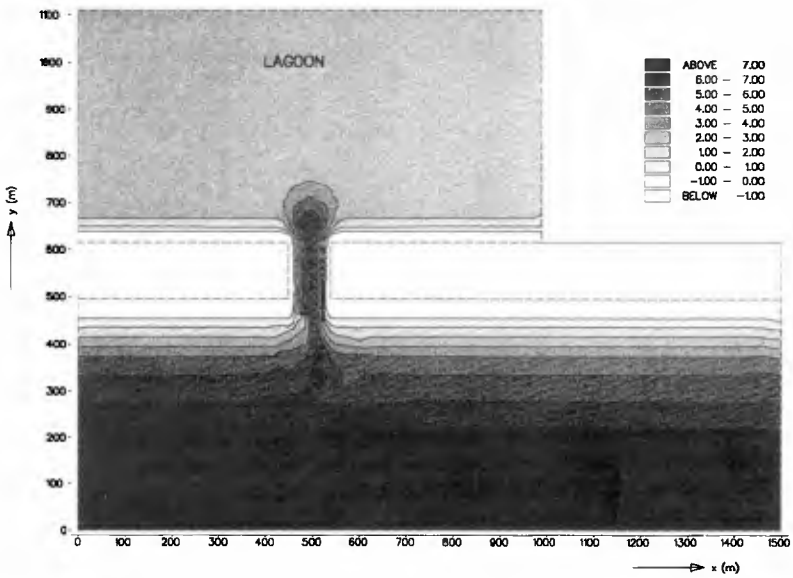


Figure 10. Computed bathymetry after 5 tides.



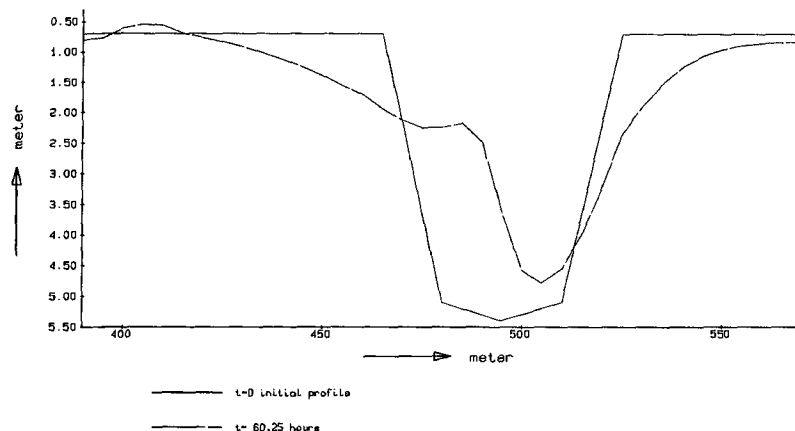


Figure 11. Development of longshore profile at  $Y = 420$  m

In Figure 10, the computed bathymetry after 5 tides is shown. Clearly, the channel moves sideways due to the longshore current. The upstream part of the channel is accreting, whereas the downstream part erodes. This is further illustrated by Figure 11, which shows the evolution of the longshore profile at  $Y = 420$  m.

In Figure 12, the computed bed level changes are shown. For comparison, the bed level changes obtained in the physical model test are shown in Figure 13. In view of many uncertainties related to the actual conditions in the physical model and in view of scale effects, a quantitative comparison is not possible. However, a qualitative assessment can be made.

The accretion on the upstream (left-hand) part of the channel is reproduced in the numerical model. Also, the erosion on the downstream (right-hand) side and the deposition due to the ebb current are represented in the model.

The morphological development in the physical model has progressed much further than that in the numerical model. The time span modelled in the physical model is meant to represent approx. half a year, whereas the numerical model has not progressed beyond some days. The reasons for this will be discussed in the next Section.

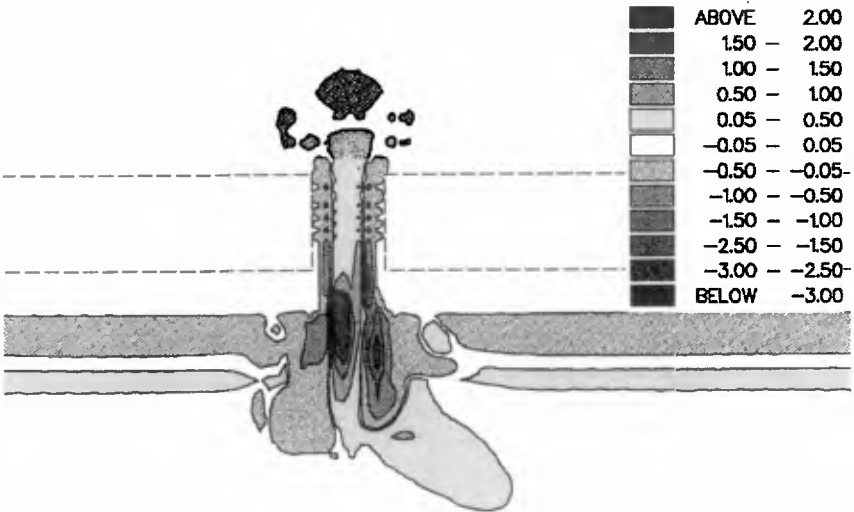


Figure 12. Computed bed level changes after 5 tides.

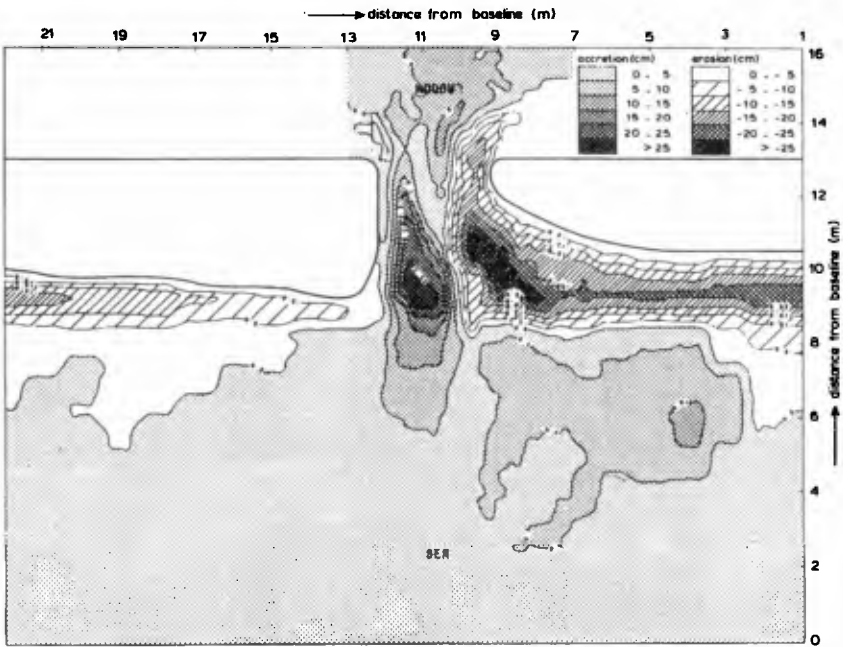


Figure 13. Bed level changes measured in physical model.

## 7. Discussion

The results presented so far are encouraging in the sense that important aspects of a complex morphodynamic system can be represented in a computer model. Problems of informatics and numerical stability have been dealt with to the point where we can again focus on the physical aspects.

An important phenomenon which has to be represented is the erosion of the dry beach. The model has to be able to deal with this in order to be able to describe the actual migration of the inlet. To achieve this, an "avalanching" mechanism must be included in some way. Here a problem to be solved is the fact that the very steep slopes that occur in reality cannot be modelled even in a very fine grid such as was applied here. A more general "slope term" may be the solution. Experiments using such a slope term have not yet yielded the desired effect in this case.

Another important aspect is wave-current interaction. Up till now, we have only applied the wave effect on the current in these computations; the current refraction effect is important in this case and will be further investigated.

The effect of waves on the current profile (undertow) and on the bed load transport (wave asymmetry effects) is significant, since a considerable part of the erosion in the physical model is due to cross-shore transport. A quasi-3D approach has been implemented and is currently under investigation.

Once a workable mechanism for eroding the dry beach has been established, the problems of running the model over longer time-scales will be reduced, and making predictions on a time-scale of interest to engineers will be quite feasible.

## References

- Delft Hydraulics Laboratory (1982).** Outfall Keta Lagoon; Report on model investigation, M 1613, Delft, February 1982.
- Holthuijsen, L.H., N. Booij and T.H.C. Herbers (1989).** A prediction model for stationary, short-crested waves in shallow water with ambient currents. Coastal Engineering, Vol. 13, pp. 23-54, Elsevier.
- De Vriend, H.J., J. Zyserman, J. Nicholson, J.A. Roelvink, P. Péchon and H.N. Southgate (1993).** Medium-term 2DH coastal area modelling. Coastal Engineering, 21 (1993) pp. 193-224, Elsevier.
- Walstra, D.J.R. (1994).** Keta Lagoon Study; validation of the program DELFT2D-MOR. DELFT HYDRAULICS report H1684, October 1994.

## CHAPTER 233

### Cost-benefit analysis of Shore Protection Investments

Luis Felipe Vila Ruiz<sup>(1)</sup>  
Fernando Bernaldo de Quirós<sup>(2)</sup>

#### Subject 2: Coastal processes: Shore protection

##### 0.- Abstract

The paper describes the methodology established in Spain to assess shore protection investments. The method consists of two phases: a pre-assessment based on physical and economic indicators and an assessment in which the financial, economic and social appraisals are estimated using cost-benefit analysis techniques.

The paper also contains the preparatory works to create a data-base necessary to establish a demand-modelling.

##### 1.- Introduction

The Spanish coastline is 7,883 km long, and stretches along 10 of the country's 17 Autonomous Communities. 4,990 km correspond to the Peninsula and 2,893 km to the Balearic and Canary archipelagos and to Ceuta and Melilla.

The 478 coastal towns have a permanent population of 14 million inhabitants, approximately 35% of the population of Spain, in a 36,252 km<sup>2</sup> area, 7.2% of the total area. This means that in the coastal towns, population density is 5 times greater than the national average.

---

<sup>(1)</sup> Asesor del Director General de Costas. Ministerio de Obras Públicas, Transportes y Medio Ambiente. P<sup>o</sup> Castellana, 67 - 28046 Madrid (España)

<sup>(2)</sup> Presidente de TEMA GRUPO CONSULTOR,S.A. Avda. de América, n<sup>o</sup> 37, 1<sup>a</sup> planta - 28002 Madrid (España).

It is estimated that international tourism will bring 60,000,000 visitors and about 40,000,000 tourists to Spain in 1994. The majority of this tourism (over 80%) is conventional sun and beach tourism. If national tourism is added to this conventional international tourism, the conclusion is, that in the peak period, population density in the coastal areas is 1,000 inhabit/km<sup>2</sup>, about 12.5 times the national average.

Tourist production in Spain comprises between 8% and 9% of the GNP.

Various reasons, among them town-planning pressure from fixed population settlements and the need to provide the coastal area with sufficient tourist capacity, have meant that between 1960 and 1980 the Spanish coast has rapidly deteriorated.

This deterioration and greater awareness of the population to environmental issues has created a desire to change the existing situation, by establishing a shore protection policy and regeneration of the already deteriorated shore, so that current and future generations will benefit, (sustainable development) and so that the quality of the environment is improved.

This desire for a change has been reflected in various actions.

- More and more shore investments, which have gone up from 225 million pesetas in 1979 to 19,766 million pesetas in 1993. (FIGURE 1)
- The enactment of a new Coast Law in 1988, which in the explanatory preamble stated: "Apart from a clash of interests on many occasions for land and sea public property, the overriding idea of this law is twofold: To guarantee its public character and conserve its natural characteristics by reconciling development demands with protection requirements."
- Preparation of an analysis, planning and appraisal method on shore investments from 1987.
- Writing of a 1993-1997 Coast plan.

The basic aim of the present document, is to describe the studies which the National Coast Office has conducted in recent years to rationalise planning and shore investment appraisal, so that, as mentioned earlier, sustainable development is maintained and shore protection and cost-effectiveness of investments is ensured.

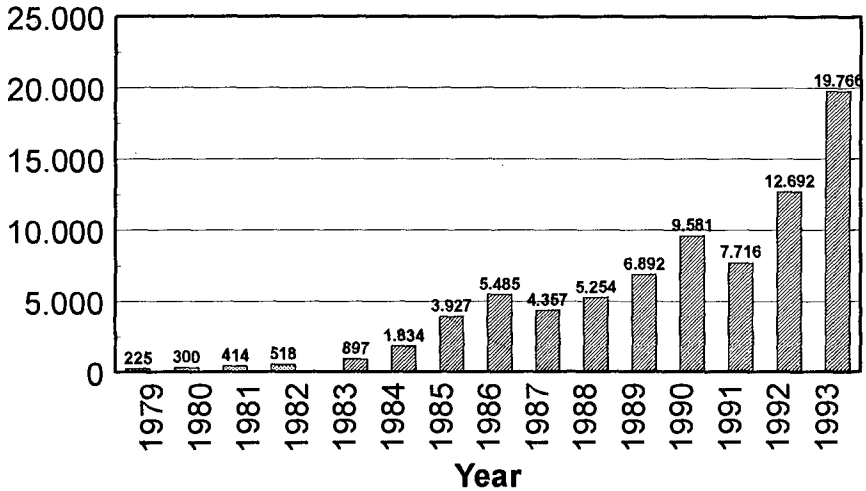
**Millions of pesetas**

Figure 1. Investment evolution at the coast

## 2.- Description of the Cost-Benefit Analysis Method of Shore Protection and Utilisation

There were various reasons for establishing a method for appraising shore investments, in line with other public sector investments.

- A sharp rise in shore investments from 1983.
- Achievement of a rational and uniform method for comparing and selecting shore investments, since the financing of these investments compete with others also within the realms of the Budget.
- Correct sizing of the investments to be undertaken and determination of their order of priority, according to the benefit expected.
- Promotion of natural resources development in the shore environment, deteriorated in some areas, as a major factor in the economic development of the adjoining areas.

- Protection of the coastal environment and its regeneration in deteriorated areas.

This method has been developed in various studies, some theoretical, and others practical, with the compilation of basic information. The main studies are summarised below.

### 2.1.- The Manual on investment appraisal

In 1987, the first study was prepared "**Study on the appraisal of the social and economic effect of investments**". This study, theoretical in nature, began with a bibliographical search and it showed that there were hardly any records on this type of work. **Using the scant references found and the basic principles of optimal resource allocation, the fundamental guidelines were drawn up for a shore appraisal investment methodology.**

In 1989, and taking as the starting point the results from the previous study, a "**Manual on shore investment appraisal**" was written.

In this Manual three types of appraisals were established:

- **Financial appraisal:** It quantifies the effects of shore investments on public sector revenue and expenditure, as promoting the area of public land and sea property.

The most relevant items of cost and revenue are considered to be:

- On the cost side, are land cost, investment cost and variations in conservation and operating costs between situations "with and without" investment.
- On the revenue side, are the variations which occur with the collection of taxes for economic activity between the two aforementioned situations, as well as the variation in revenue from the Administration's operating of public services.

In order to calculate revenue and expenditure variations, it is necessary to **estimate the number of users** of coastal facilities, **using mathematical models to forecast demand**, and **average expenditure per user** on the various facilities.

In the financial appraisal, costs and revenue are assessed at market prices. Comparison of revenue and cost flows, for the time interval under analysis, means that traditional cost-effective investment appraisal indicators can be established, using the updating technique: **updated net benefit, cost-benefit ratio,**

internal rate of return, etc.

- **Economic appraisal:** Generally, in this appraisal the viewpoint adopted is that of the community. Therefore, the main effects under consideration are:

- As benefits, **variation of user and business surpluses between the situations "with and without"**. The main components of user surplus are the variations in the level of satisfaction as a result of the variation in quality and capacity of the beach (or the coast, in general) installations and facilities, variation in security and possible improvement in accessibility.

The business surplus is calculated for all the agents concerned and, in particular, for building Companies in the investment execution phase, and for service-lending Companies and owners of property or premises revalued by the investment, in the operating phase.

Cost components are basically the same as the financial appraisal components, although it has to be borne in mind that in the economic appraisal resource prices must be assessed in terms of opportunity cost, **or in terms of the highest value than at the moment of analysis which could result from alternative use** of these resources. This requires the corresponding adjustments of market prices and, in particular, removal of taxes which are only transfers between economic agents.

As for the financial appraisal, the habitual cost-effective indicators can be obtained in the economic appraisal.

- **Social appraisal:** This appraisal aims to measure what each investment project contributes to the general social aims. The most important of these aims are the following:

- Generation of employment, both in the investment execution phase and the operating phase.

- Redistribution of income. This effect can be considered as giving a greater weight to the benefits perceived or the costs borne by the lowest income groups, establishing weighting coefficients for different income levels.

- Protection and environmental improvement. The following can be considered:

- .. quantifying possible harmful effects of investment by the cost of the measures essential for avoiding them,



- .. estimating the cost of other alternative and essential actions for achieving the same beneficial effects on the environment which, in this instance, stem from the shore investments under analysis, or
- .. giving a monetary reference value to the property to be protected or improved (for example, monetary value attributable to a hectare of dunes or marshes).

## 2.2.- Database of beach supply and demand

The systematic application of an investment appraisal process on shore protection and utilisation requires, as has already been stated, other information such us:

- calculation of the demand for coastal installations and facilities and
- estimation of user unit expenditure.

This information is absolutely essential for investment in beaches.

For this reason, when the Method and Manual on shore investment appraisal had been prepared, a **Plan for recording data and surveys was established, with the intention of achieving a time series which** would facilitate the aforementioned estimates for different situations.

This campaign for recording data has been developed during 1990, 1992, 1993 and 1994 and a computing device has been designed for the inclusion and processing of annual data in order to have a sufficiently reliable chronological sequence.

The information collected every year is basically threefold:

- **Number of beach users.** Counts are done on a sample of beaches on working days, Saturdays and holidays, chosen randomly during the summer months (normally July, August and September).
- **Characteristics and user behaviour patterns.** Surveys are conducted, during the summer months, to a sample of users, who are asked for details on: nationality, length of stay, type of accommodation, length of time and means of transport from the summer abode to the beach, frequency of beach use, rating of beach quality, income group, amount spent on the main items (accommodation, beach services, transport, etc).
- **Data on beach supply.** These data refer to:

- Natural characteristics of the beach and its surroundings: beach plan, length, width, area, slope, sand type, quality of the water, rainfall, average temperature, wind system, sunshine hours, etc.
- Beach installations: Showers, changing rooms, WCs, sunbeds, parasols, promenade, car parks, etc.
- Town facilities: Town plan, hotel and other accommodation capacity, restaurants, bars, scenic view and surroundings, entertainment and recreation facilities, etc.

### 2.3.- Modelling of user demand

The models which have been used to explain the current demand for beach use and, mainly, to estimate future users for various beach characteristics and facilities include three types of variables:

- **Variables representing beach characteristics.**
- **Variables measuring potential users.**
- **Friction variables**, linked to the cost and the time it takes to get from the summer abode to the beach.

a) As regards the variables **representing beach characteristics**, on the one hand, ratings have been included on the beaches from the surveys to users and on the other hand, general beach characteristics have been included. The latter could possibly affect rating: length, width, promenade length, sand quality, number of showers, WCs, parasols, changing rooms, etc.

To avoid constantly having to conduct surveys to users on beach rating, for every possible investment study, and since it is impossible to conduct surveys on hypothetical future situations of the beach in question, preparation of a mathematical model beforehand has been considered instrumental for rating the beach. The dependent variable has been taken as the rating given by users to the beaches under study and independent variables as the general beach characteristics mentioned above.

After various trials and errors, the adjusted model corresponded to the formula:

$$R = e^{1,4973} \times Wid^{0,016928} \times Prom^{0,010299} \times Nat^{0,3083} \times WC^{0,008848}$$

where:

R = beach rating

Wid = average width of the beach, in metres

Prom = quotient of the length of the promenade by the length of the beach

Nat = sand nature and quality (1, 2 or 3)

WC = no. of WCs per km of beach, with a correlation coefficient  $r = 0.82$

b) Consideration of **variables representing potential users** has meant it has been advisable to conduct two model demand groups:

- for permanent resident demand, the representative variable has been taken as the population of adjoining towns,
- for tourist demand, the variable of hotel and other accommodation beds on offer multiplied by the occupation rate has been considered.

c) **Inclusion of variables representing the cost of accessibility to the beach, as a dissuasive factor** forces the models to be adjusted in line with the resident population, or the variable of hotel and other accommodation beds multiplied by the occupation rate, according to distance intervals, giving each interval an average value.

Bearing in mind these considerations, the adjusted models correspond to the formulae:

- For resident users:

$$U = 0,9385 \times P^{0,7531} \times R^{1,19506} \times D^{-0,51139}$$

- For habitual non-resident tourists:

$$U = 1,5018 \times P_t^{0,25030} \times R^{3,82106} \times D^{-0,47245}$$

In these formulae,

U = no. of users on an average day of the season considered.

P = resident population, in the distance interval of D average value.

D = average value of each distance interval considered, in metres.

R = beach rating, according to the model mentioned in section a).

P<sub>t</sub> = hotel and other accommodation places multiplied by the occupation rate.

The correlation coefficients are low in both cases,  $r = 0.64$  for residents and  $r = 0.58$  for tourists. Better results can be obtained by breaking down the models into: months, beach type, working days, Saturdays or holidays, etc. However, not enough data on the chronological sequence available meant these breakdowns could not be done in 1992 when these models were adjusted. Currently, we have the 1993 data and, shortly, we shall be having the 1994 data, then it will be possible to readjust and break down the models.

In addition to this readjustment, the models need to be made more sophisticated, so that it is possible to determine where new users have come from for the additional demand in response to improved beach characteristics and services. User type distinction is as follows:

- "Generated" users, that is to say, who previously did not use any other beach.
- "Captivated" users from another overcrowded national beach.
- "Captivated" users from a non-overcrowded national beach.
- "Captivated" users from other foreign beaches.

In fact, this distinction is vital, for financial, economic and social appraisals. It can be done, either by breaking down the models further into generated or captivated user type, or by developing a global model for analysing user deviation among the group of competing beaches. This is a line of research to pursue, coupled with extension of the supply and demand Database chronological sequence.

#### 2.4.- The determination of planning indicators

Application of the appraisal method established in this Manual, on the one hand, is aimed mainly at beach investments and, on the other hand, requires a technical project of the actions to be conducted and a relatively laborious appraisal process, especially while there is no database for a sufficient number of years.

**All this implies costs and analysis time which would be unjustified if, in the end, the investment were not considered to be financially, economically or socially profitable.** This risk will tend to be even greater where the most obvious cost effectiveness investments have already been made.

Therefore, a study is currently being developed for designing a set of indicators with the following aims:

- to have a rapid appraisal tool in keeping with the Manual, although less polished,

- to compare "grosso modo" alternative actions,
- to establish acceptable investment ceilings for various types of actions,
- to establish criteria and prepare indicators for measuring variation in user "satisfaction", as a result of various actions on the coast,
- to include measures of the effects on protection and improvement of the environment,
- to establish indicators not only for beach actions but for the rest of the shore.

With this in mind, a preliminary list of types of actions has been prepared for: beach regeneration, building of promenades, building of paths for coastal areas difficult to get to, protection of wall enclosures, protection and regeneration of dunes, building of seawalks, protection of cliffs, installation of recreation areas, preparation of areas for shallow or underwater fishing, water sports facilities, etc.

**For each of these actions, the basic and ancillary aims pursued will be established and depending on these aims, the indicators for measuring their level of achievement will be prepared.**

Since the study is still in the execution phase, it is not possible, for the time being, to advance any results. However, the intention is to establish a double entry matrix for action and aim typology, and the indicators to be calculated are defined in each intersected box in order to measure physical or monetary contribution of each type of action to each specific aim. **Considerable effort is being given to defining the aims precisely so that it is possible to quantify the level of achievement.**

For monetary indicators, average unit values will be established for each type of action and effect which can be assessed in monetary terms.

**It is thought that the preliminary appraisal process should be completed by applying a multicriteria appraisal method in order to achieve an operating synthesis.**

#### 2.5.- Theoretical scheme of the shore action planning process

Bearing in mind the studies conducted, experience obtained and the works in progress, a theoretical scheme of the shore action investment planning process could be the one represented in the following chart. **(FIGURE 2)**

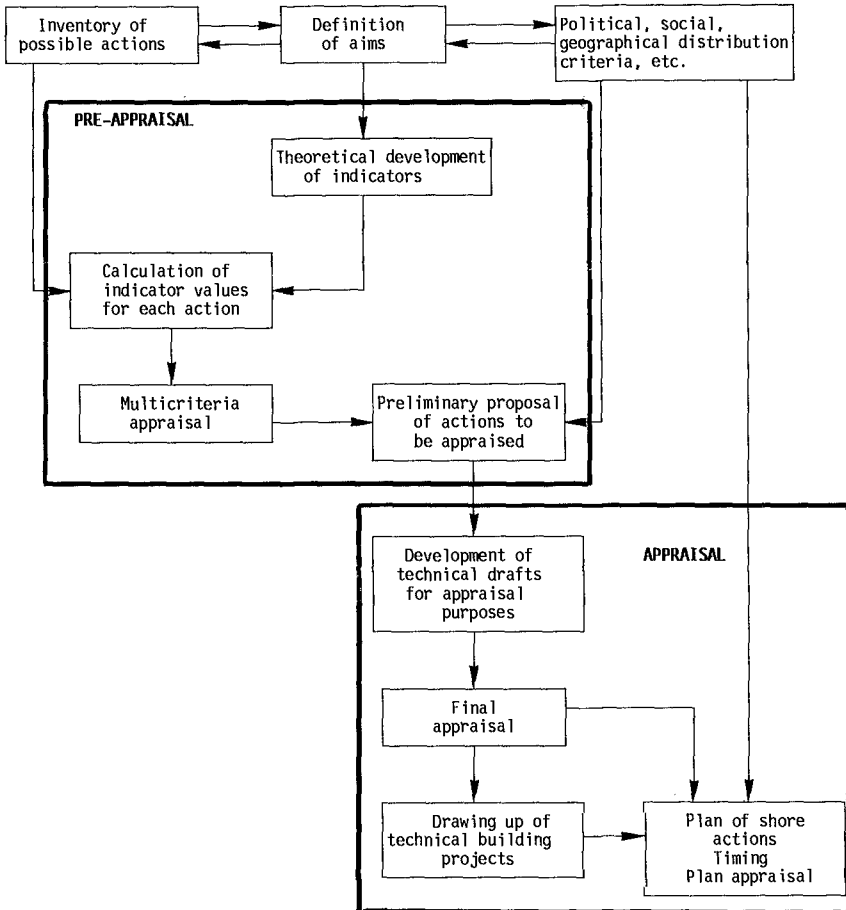


Figure 2

This chart illustrates that, beginning with political criteria and aims and knowledge of the shore, a relatively extensive inventory of possible shore actions can be established.

A pre-appraisal process is applied to this inventory, based on the establishment of indicators, and definitions of actions from a previous study. As a result of this pre-appraisal, a set of actions, probably viable from a technical and economical point of view, are selected and these are thoroughly analysed and appraised and the other remaining actions are discarded.

In the final appraisal phase, those actions selected in the first instance are defined more precisely by preparing the corresponding preliminary project and, the appraisal is made using the information in this preliminary project and the appraisal method in the Manual on shore investments is followed. The corresponding building projects are drawn up for the actions selected in the second phase and the execution of these projects are scheduled depending on their order of priority.

### 3.- Some actions implemented and Cost-Effective values obtained

Below are some examples of actions which have been implemented or are in progress, and the basic features of these actions and the cost-effective values obtained.

#### - Regeneration of the Pedralejo beach (Málaga)

Located in a modest district in the east of Málaga, with houses close to the sea. The beach has been regenerated with two free-standing breakwaters, two breakwaters in a Y shape and a breakwater with a flap to the west, and sand has been brought in. The already existing small fishing houses have been considerably revalued.

**Investment:** 489 million pesetas (M pt), at market prices

**Financial appraisal:** Updated net profit UNP = 71 M pt.

**Cost-Benefit Ratio** C/B = 1.15    **Internal Rate of Return** IRR = 7.37%

**Economic appraisal:** UNP = 1,322 Mpt    C/B = 3.7    IRR = 42.7%

**Social appraisal:** UNP = 1,496 Mpt    C/B = 4.06    IRR = 50.30%

#### - Regeneration of the Maresme: Premiá del Mar-Mongat (Barcelona)

The beach has virtually disappeared with the building of the Port of Arenys del Mar. Regeneration of the beach, about 7 km long, has consisted of building a breakwater and bringing in about two million m<sup>3</sup> of sand.

**Investment:** 972 million pesetas (M pt), at market prices

**Financial appraisal:** Updated net profit UNP = 238 M pt.

**Cost-Benefit Ratio** C/B = 1.25    **Internal rate of return** IRR = 8.63%

**Economic appraisal:** UNP = 2,314 Mpt    C/B = 3.38    IRR = 29.01%

**Social appraisal:** UNP = 2,678 Mpt    C/B = 3.75    IRR = 33.45%

- **Regeneration of Magalluf beach (Balears)**

Located at the western end of the bay of Palma de Mallorca, with an impressive hotel infrastructure, which causes massive overcrowding on this narrow stretch of beach.

136,000 m<sup>3</sup> of sand were brought in to a cove between two projections and naturally protected from the force of the waves by an existing island.

**Investment:** 176 million pesetas (Mpt), at market prices

**Financial appraisal:** Updated net profit UNP = 3656 Mpt.

**Cost-Benefit Ratio** C/B = 21.78 Internal Rate of Return IRR = 122.02%

**Economic appraisal:** UNP = 8,442 Mpt C/B = 48.97 IRR = 248.1%

**Social appraisal:** UNP = 7,991 Mpt C/B = 46.41 IRR = 241.7%

- **Regeneration of La Laja beach (Las Palmas de Gran Canaria)**

The aim of this regeneration is to provide Las Palmas with a beach for decongestion of Las Canteras beach. This has consisted of building two dikes, tipping 400,000 m<sup>3</sup> of sand, remodelling a promenade for cars and building a complex with cafeteria and public conveniences.

**Investment:** 835 million pesetas (Mpt), at market prices

**Financial appraisal:** Updated net profit UNP = -848 Mpt.

**Cost-Benefit Ratio** C/B = -0.02 Internal rate of return IRR = -11.04%

**Economic appraisal:** UNP = -272 Mpt C/B = 0.67 IRR = 1.53%

**Social appraisal:** UNP = 37.2 Mpt C/B = 1,04 IRR = 6.59%

- **Regeneration of the Gross beach in San Sebastián (Guipúzcoa)**

The aim is to provide the Gross district in San Sebastián with a stable beach, even at high tide, in order to reduce overcrowding on La Concha and Ondarreta beaches. Actions have consisted of prolonging the channelling of the River Urumea, the tipping 1,100,000 m<sup>3</sup> of sand and building a promenade and beach services. The regenerated length is about 900 m.

**Investment:** 2,773 million pesetas (Mpt), at market prices

**Financial appraisal:** Updated net profit UNP = 684 Mpt.

**Cost-Benefit Ratio** C/B = 1.25 Internal rate of return IRR = 9.03%

**Economic appraisal:** UNP = 4,833Mpt C/B = 2.74 IRR = 27.45%

**Social appraisal:** UNP = 4,833Mpt C/B = 2.74 IRR = 27.45%



- **Regeneration of the stretch of the shore Peñíscola-Benicarló**

This has consisted of extending the current 1,800 m of beach next to the town of Peñíscola towards the north, as far as Benicarló. It is about 6 km long and about 70 m wide. Planned actions are: reinforcement of the coastline, building a promenade, detour of the road towards the interior and tipping of sand.

**Investment:** 3,391 million pesetas (Mpt), at market prices

**Financial appraisal:** Updated net profit UNP = 4,572

**Cost-Benefit Ratio** C/B = 2.35 Internal Rate of Return IRR = 17.46%

**Economic appraisal:** UNP = 13,399 C/B = 4.95 IRR = 37.85%

**Social appraisal:** UNP = 16,160 C/B = 5.77 IRR = 43.59%

## CHAPTER 234

### Parametrization for conceptual morphodynamic models of Wadden Sea areas

Ernst Schroeder<sup>1</sup>, Roland Goldenbogen<sup>1</sup> and Hans Kunz<sup>2</sup>

#### Abstract

Climate changes could lead to remarkable changes of boundary conditions with respect to the interactions between hydrodynamics and morphology. This would impact especially coastal areas with movable beds like the Wadden Sea of the Southern North Sea. Therefore applicable tools for a prediction of morphodynamical development due to changing conditions are demanded. The German-Dutch research project "*Morphological development of the Wadden Sea region with special emphasis of the impact of an increasing relative sea level rise - WADE*" deals with the described problem by developing suitable conceptual morphodynamic models. An essential part of these models is parametrization. Empirical investigations were carried out for different tidal basins of the German Wadden Sea leading to parameters which describe and quantify the interactions between hydrological impacts and morphological responses. The gained results had been applied to a case study based on an empirical model.

#### Introduction

The German Wadden Sea consists of barrier islands, tidal basins and salt marshes which is important with respect to several ecological and economical aspects. Viewing the ecology, it is a consistent system of highly specialized flora and fauna. Beyond the actual geographical extension it is a remarkable resting- and

---

<sup>1</sup>Research engineer, Dipl.-Ing.

<sup>2</sup>Director, Dr.-Ing.

Coastal Research Station (CRS) of the Lower Saxonian Central State Board for Ecology, An der Mühle 5, D-26548 Norderney/Germany

breeding-ground for migrating birds. Economically it represents a main component of the coastal defence system by which the islands and the low lying parts of the marshland are protected. The Wadden Sea is also used for fishery and recreational means.

The goal of the investigations is to answer the critical question how tidal basins (tidal flat areas) will be influenced by changing hydrological and morphological boundary conditions and whether they will be able to keep pace with an accelerated relative sea level rise.

Therefore, a converted version of the model by Van Dongeren & de Vriend (1994) has been applied to predict the longterm behaviour of tidal basins. This empirical conceptual morphodynamical model needs parametrizations of the hydrographical and the morphological boundary conditions and their physical interactions. The paper deals with these parametrizations (tidal basins in total and as hierarchically systems of subareas) by empirical functions which are based on statistical analyses.

### Investigation area

The investigations have been carried out for two study areas along the German coast of the North Sea: The "East Frisian Wadden Sea" and the "Bay of Dithmarschen".

The East Frisian Wadden Sea extends about 80 km from the west (Osterems) to the east (Harle) see Fig. 1.

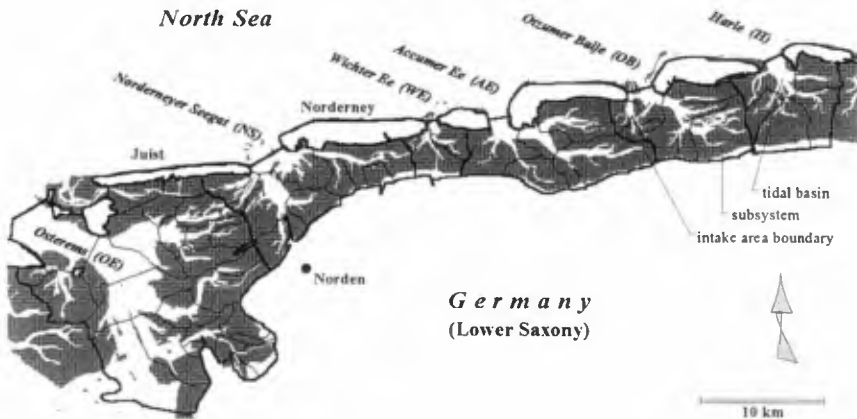


Fig. 1 East Frisian Wadden Sea with islands, tidal inlets, basins and subsystem-areas (1990)

It covers an area of about 800 km<sup>2</sup> between the mainland and its barrier islands. The East Frisian Wadden Sea contains 6 tidal inlets with the connected tidal basins. Each basin (intertidal catchment area) is divided into several "hierarchical subsystems", limited by the area boundaries.

The Bay of Dithmarschen is located in front of "Schleswig-Holstein". It is an open single tidal basin (Fig. 2). In 1972 and 1978 parts of the bay had been reclaimed: by the enclosure in 1972 about 11.5 km<sup>2</sup> in the southern part and in 1978 about 21.5 km<sup>2</sup> in the northern part. Before 1972 the area covers about 200 km<sup>2</sup>; it has been divided into "subsystems" - see Fig. 2.

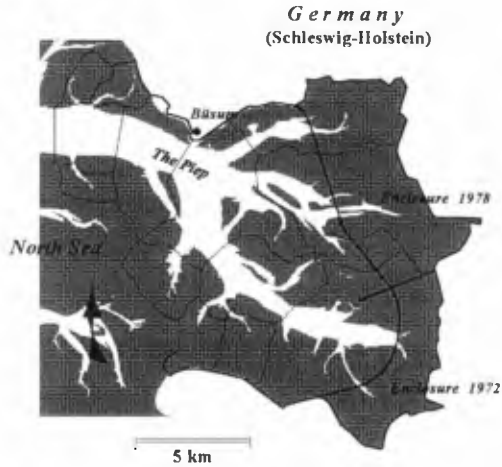


Fig. 2 Bay of Dithmarschen with hierarchical subsystems (1969)

Both investigation areas are characterized by semidiurnal tides propagating east- respectively northwards along the coast. According to Hayes (1975) the areas can be classified as tide-dominated and high-mesotidal (the medium tidal range for the East Frisian-area is about 2.50 m; that for the Dithmarschen-bay is about 3.30 m). The significant mean wave heights (offshore) induced by the predominant wind out of the western sector are in the range of 1.0 m. Fresh water run off or discharges by sluices are negligible.

#### Data sets

The basis-data for the investigations of the East Frisian Wadden Sea are the three topography surveys from 1960, 1975 and 1990. The calculations for the Bay of Dithmarschen are based on 9 surveys carried out between 1942 and 1990. The density of data is very high and detailed.

The investigations have been executed by using a Geographic Information System (GIS, ArcInfo by ESRI<sup>TM</sup>) (Liebig, 1993). The topographical data of the study areas

were implemented by digitizing maps. All parameters have been calculated with this database as geometrical quantities.

### Parametrization

Within the scope of these investigations the parametrizations for the tidal basins and the subsystems were restricted to areas, volumes and a *characteristic height* describing the geometrical structure inside a tidal basin. In a further step it is desirable to include a parameter which describe the impact of the wave climate.

The extension of the areas for parametrization have been fixed by the intersecting lines between the actual topography and horizontal reference levels. The reference levels have been defined as horizontal planes. Exemplary calculations showed, that the error between horizontal and inclined planes are less than 1%. The reference levels are the mean high water (MHW), mean low water (MLW) and the German ordnance-datum (NN) which approximately corresponds with the MSL for the German Bight. The mean values have been calculated over the last five years before the survey. Missing data have been completed by using correlations between adjacent gauges.

With respect to the hierarchy of the subsystem structure the investigated functions were also checked for small areas. In general the scattering increases with decreasing size of the area. When subsystems are located close to the coastline, than the characteristics (tide- or wave-dominated) can be affected by tides or waves. The characteristics of subsystems may be influenced by anthropogenic changes of the boundaries, especially by land reclamation means - see Bay of Dithmarschen.

The spatial dimension (6 & 1 tidal inlets) allows complementary investigations to verify different relationships.

The "basic parameters" (O'Brien, 1931) are:

$A_b$	basin area
$A_c$	cross sectional area
$V_T$	mean tidal prism.

Additional geometric parameters describing the morphological structure of the Wadden Sea areas are (Renger, 1976):

$A_i$	intertidal area (MLW - MHW)
-------	-----------------------------

and (Dieckmann, 1985; Wieland et al., 1987):

- $l_i$  characteristic level of the intertidal area  
 $V_i$  intertidal sediment volume.

The last three parameters have been proven as valid to balance the morphological dynamics or the changing sediment volumes inside a tidal basin.

The validity of the functions for areas smaller than  $A_{b \text{ MHW}} = 10 \text{ km}^2$  is questionable as a result of local influences. Moreover the nonlinear functions needs a threshold value to estimate physical suggestive results. Also in this context the threshold value should be greater than  $A_{b \text{ MHW}} = 10^7 \text{ m}^2$  and  $V_T = 10^7 \text{ m}^3$  respectively.

General aspects and relations based on the parameter basin area  $A_b$

Amongst the basin area  $A_b$ , the mean tidal prism  $V_T$  is the main parameter which influences the shape and structure of the tidal inlet or the morphology respectively. Figure 3 displays the comparison between those data sets for tidal basins along the North Sea coast and the US-coast.

Results of investigations based on historic data which go back to the seventeens century are published by Niemeyer (1993).

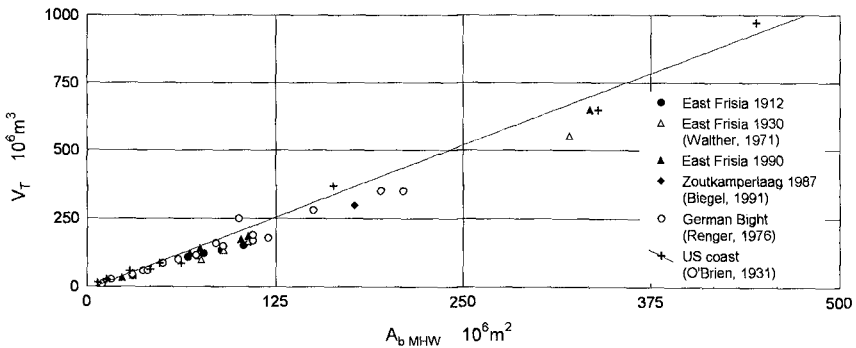


Fig. 3 Basin area  $A_b$  versus tidal prism  $V_T$  - Comparison of data for the North Sea- and the US-Coast

Consistent data based on GIS-proceeding have been elaborated for a period of about 30 years for the East Frisian Wadden Sea and 50 years for the Bay of Dithmarschen. Figure 4a shows the data for the East Frisian

Wadden Sea with linear regression functions. It shows a tendency of increasing tidal prisms with time. This is possibly a result of changing tide levels (Fig. 6).

The quality of the results gained by statistical investigations are clearly explained by the data set of 1975: The scatter plot of  $A_b$  versus  $V_T$  in logarithmic scale displays a good fitting of the linear function (Fig. 5). The comparison of observed versus predicted values showed a satisfactory accordance not only for the tidal basins, but also for the small subareas.

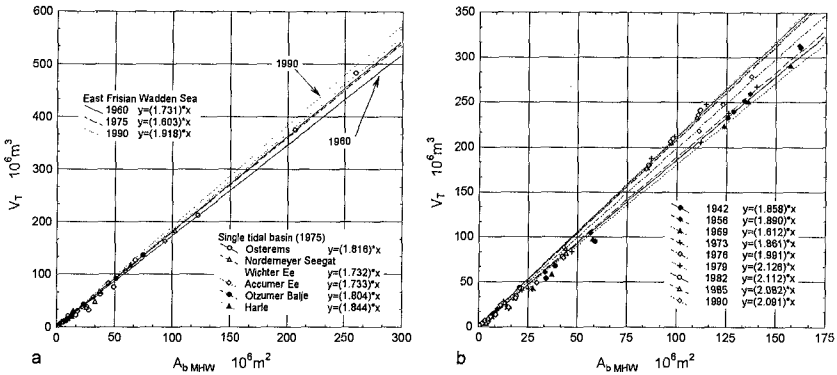


Fig. 4 Basin area  $A_b$  versus tidal prism  $V_T$  - East Frisian Wadden Sea (a) and Bay of Dithmarschen (b)

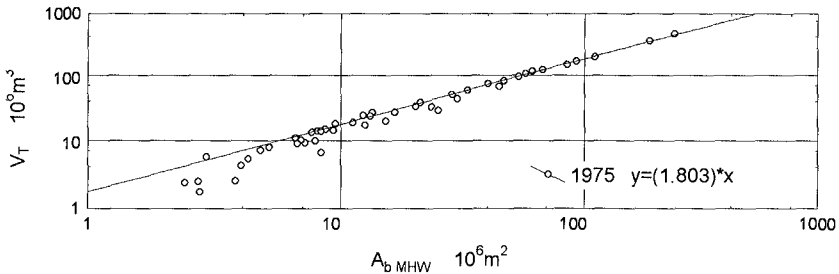


Fig. 5 Basin area  $A_b$  versus mean tidal prism  $V_T$  - East Frisian Wadden Sea (logarithmic scale)

The comparability of tidal basins of the East Frisian Wadden Sea has been investigated. The result is a concentrated bunch of functions that have no orderly sequence in regard to the location along the coast (Fig. 4a).

However, the fitted regression functions of the coefficients show a slight increase along the coast from west to east (Fig. 6).

Similar results are yielded by the investigations for the Bay of Dithmarschen (Fig. 4b). The coefficients are slightly higher than those of the East Frisian Wadden Sea. The mean value comes to 1.855 for the period between 1942 and 1969. On account of the reclamation in 1972, it would be expected that the function of 1973 would shift. But the decreasing MHW (0.05 m) and MLW (0.03 m) compensates this effect. The counterrotating effect occurred in 1976 as a result of the increasing tidal level and tidal prism.

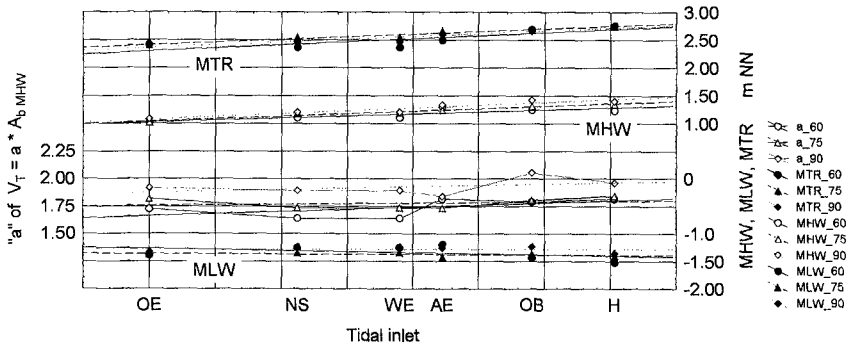


Fig. 6 Coefficient "a" of  $V_T = a \cdot A_b$  MHW, MHW, MLW and MTR for locations of the East Frisian Wadden Sea

The data of the second reclamation in 1978 display a consistent outcome. The mean value comes to 2.095 for the period between 1982 and 1990. A weak tendency of a decreasing tidal prism and basin area is noticeable. The difference between the coefficients of 1973 ( $a = 1.862$ ) and 1990 ( $a = 2.091$ ) corresponds with an increasing tidal prism of about 12 %. The comparison between the East Frisian Wadden Sea and the Bay of Dithmarschen yield a greater tidal prism (3 to 9 %) relatively to the basin area for the Bay of Dithmarschen.

The second parameter which is used in modelling is the intertidal area  $A_i$ . The intertidal area is defined as the vertical projection of the topography within the limits defined by the MHW and MLW (Renger, 1976). The investigation of the relationships  $A_b$  versus  $A_i$  led to nonlinear functions. In contrast to the previous findings, the data do not show a continuous shifting (Fig. 7a). Because of the slight differences of the results for the distinguished time-periods, it is reasonable to calculate a mean function for the whole period; the result is:

$$A_{i \text{ MLW}} = 13.172 A_{b \text{ MHW}}^{0.837}.$$



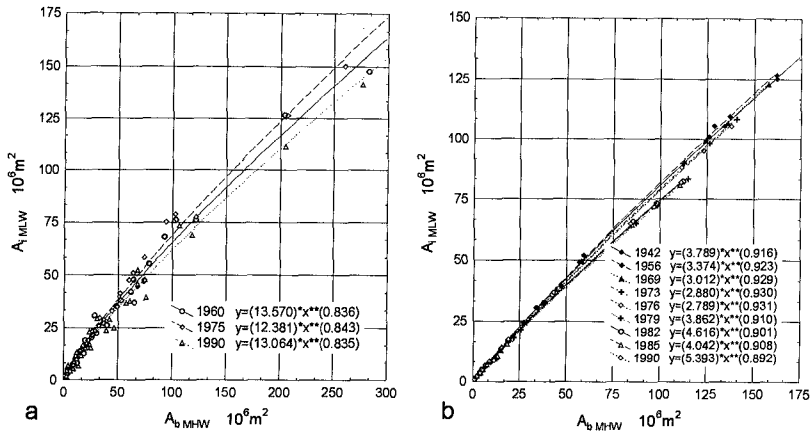


Fig. 7 Basin area  $A_b$  MHW versus intertidal area  $A_i$  MLW - East Frisian Wadden Sea (a), Bay of Dithmarschen (b)

The data of the Bay of Dithmarschen display a similar image (the data are divided into two groups). There is no significant deviation due to the first reclamation in 1972. As a result of the second reclamation in 1978 there is a distinct shifting visible. The data from 1979 to 1990 tend to a backwards directed development due to a decreasing basin area  $A_b$  and an increasing intertidal area  $A_i$ . This led to the expectation that the mean function of the period 1942 to 1969 describes an equilibrium state (Fig. 7b):

$$A_i \text{ MLW} = 3.372 A_b \text{ MHW}^{0.923}.$$

Furthermore the relation of the intertidal area versus the basin area indicates a greater share of the intertidal area for the Bay of Dithmarschen than for the East Frisian Wadden Sea. The amount of this difference depends on the size of the basin area; for  $A_b = 100 \text{ km}^2$  the difference of  $A_i$  is 25 %.

The intertidal volume  $V_i$ , describing the sediment volume, is defined as the volume between MHW and MLW according to Wieland et al. (1987). This is the range which is mainly influenced by the tidal prism. The investigation shows two groups of data. One includes the data of the years 1960 and 1975. The regression functions are nearly coincident. The other one is the function of 1990, which is substantially different (Fig. 8a). The intertidal volume  $V_i$  decreased significantly compared to 1960 and 1975 as a result of a raise of MHW and MLW in

combination with changes of the topography (erosion). The function which describes the equilibrium state can be calculated with the data of 1960 and 1975. This leads to:

$$V_i \text{ MLW} = 32.99 A_b \text{ MHW}^{0.790} .$$

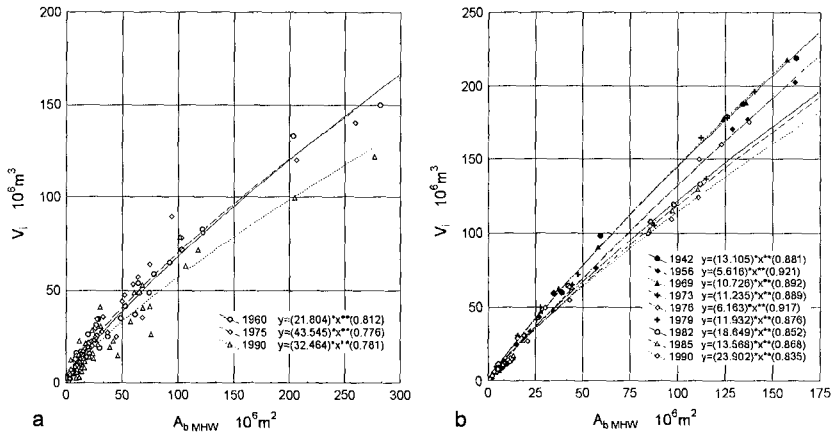


Fig. 8 Basin area  $A_b$  MHW versus intertidal volume  $V_i$  - East Frisian Wadden Sea (a), Bay of Dithmarschen (b)

The evaluation for the Bay of Dithmarschen shows three different relationships (Fig. 8b). The relations shown in the upper part enclose the years 1942, 1969 and 1973. The survey of 1973 had been carried out one year after the first enclosure. The middle part shows the functions of 1956 and 1976. The contradictory developments of both groups are mainly affected by changing water levels and are not the consequences of erosion or sedimentary effects. In the bottom-group of relationships, the scattering is very small; the tendency of decreasing intertidal volume results also in the growth of the MLW. The general tendency of decreasing tidal volumes relative to the basin areas results in the enclosure of the high lying supratidal areas in front of the coast. Based on 1942 and 1969 the equilibrium function is:

$$V_i \text{ MLW} = 11.96 A_b \text{ MHW}^{0.886} .$$

For investigations based on the relationship between basin area  $A_b$  versus cross sectional area  $A_c$  it is important, that the lowest scattering was found by using  $A_c$  related to the reference level NN (area between NN and the contour line).  $A_c$  was determined at the location with the strongest constriction of the streamlines. The

analysis led to linear functions (Fig. 9a). Based on all three data sets together, the mean function of the East Frisian Wadden Sea has been found as:

$$A_{c\ NN} = 0.000165 A_{b\ MHW}$$

The data of the Bay of Dithmarschen display the distinguished "influenced" and "noninfluenced areas" as a result of the enclosure works (Fig. 9b). The equilibrium function was calculated with the data of the last survey before enclosure (1969):

$$A_{c\ NN} = 0.000123 A_{b\ MHW}$$

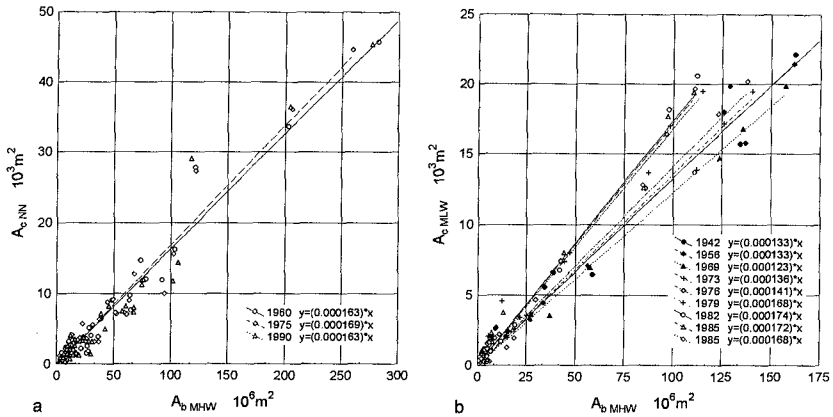


Fig. 9 Basin area  $A_{b\ MHW}$  versus cross sectional area  $A_{c\ NN}$  - East Frisian Wadden Sea (a), Bay of Dithmarschen (b)

In order to describe the development of the height of intertidal areas or the volumes respectively, the characteristic level  $l_i$  (Dieckmann, 1985) has been investigated. Herewith it is possible to verify the progress of erosion or sedimentation for stages of dynamic equilibrium. The parameter  $l_i$  is defined as the level where the intertidal area  $A_i$  is half exposed and half submerged. This led to a characteristic level between MHW and MLW. The scatter plot of  $l_i$  versus  $A_{b\ MHW}$  shows an asymptotic behaviour with increasing  $A_{b\ MHW}$  (Fig. 10 and 11). The graphs contain the empirical function which represent the lower and upper limit of  $l_i$ . Deviations of  $l_i$  indicate a nonequilibrium stage of the subsystem or the impact of local influences by the different boundary conditions that lead to variations between the subsystem and its total tidal basin.

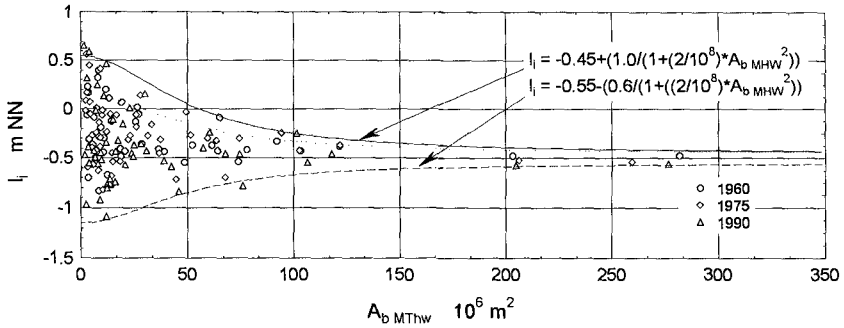


Fig. 10 Basin area  $A_b$  MTHW versus intertidal level  $l_i$  of the East Frisian Wadden Sea

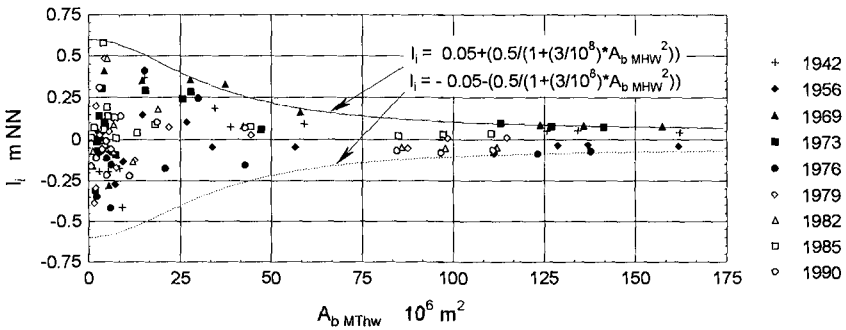


Fig. 11 Basin area  $A_b$  MTHW versus intertidal level  $l_i$  of the Bay of Dithmarschen

Relations based on the parameter mean tidal prism  $V_T$

The mean tidal prism  $V_T$  has been defined as the volume between MHW and MLW. The analysis of the relationship between  $V_T$  and  $A_i$  led to the same behaviour as explained before (Fig. 12a and b). Remarkable is the overlapping bunches of functions for both investigation areas. This is possibly a result of the parameter  $V_T$  which implicitly includes the tidal range as one of the main boundary condition for the classification of tidal inlets (Hayes, 1975). The derivation of an equilibrium relationship are based on the years 1960 and 1975 for the East Frisian Wadden Sea and on 1942 and 1969 for the Bay of Dithmarschen. The relations are:

$$A_{i \text{ MLW}} = 15.50 V_T^{0.805} \quad (\text{East Frisian Wadden Sea})$$

$$A_{i \text{ MLW}} = 9.199 V_T^{0.841} \quad (\text{Bay of Dithmarschen}).$$

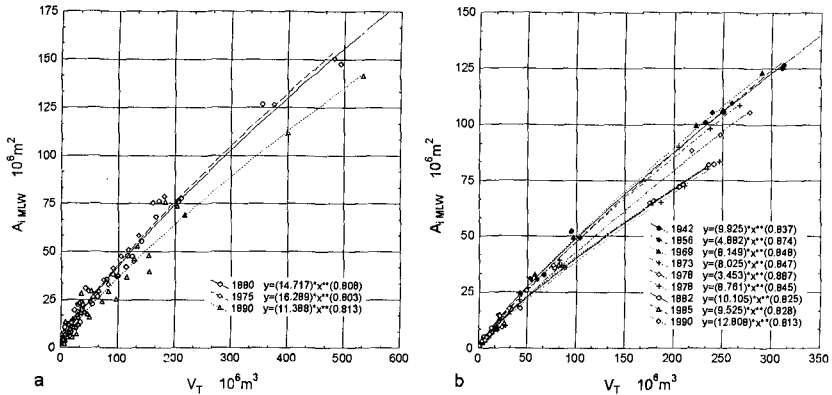


Fig. 12 Mean tidal prism  $V_T$  versus intertidal area  $A_{i, MLW}$  - East Frisian Wadden Sea (a), Bay of Dithmarschen (b)

Furthermore the relation tidal prism  $V_T$  versus intertidal volume  $V_i$  indicates the same grouping of influenced and noninfluenced surveys (Fig. 13a and b). The equilibrium functions are:

$$V_{i, MLW} = 36.83 V_T^{0.761} \quad (\text{East Frisian Wadden Sea})$$

$$V_{i, MLW} = 28.97 V_T^{0.812} \quad (\text{Bay of Dithmarschen}).$$

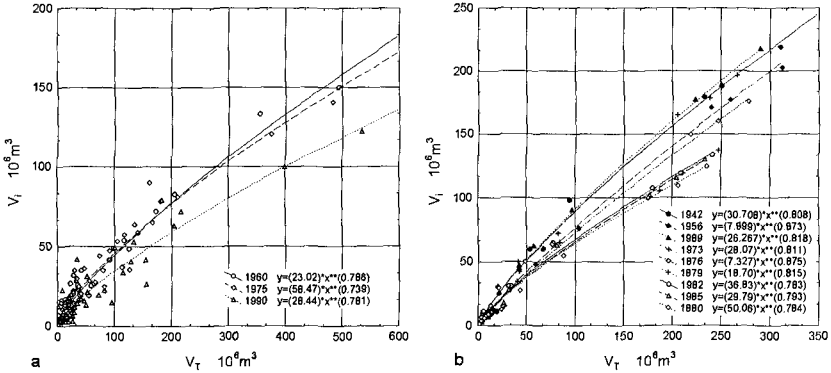


Fig. 13 Mean tidal prism  $V_T$  versus intertidal area  $V_{i, MLW}$  - East Frisian Wadden Sea (a), Bay of Dithmarschen (b)

It appears that the overall aspect about the amount of the intertidal volume relative to the size of basin area and tidal prism is greater for the Bay of Dithmarschen than for the tidal basin of the East Frisian Wadden Sea. The small differences during 1979 up to 1990

seems to tend to a new relationship as a result of changing geometrical boundary conditions.

### Example of application

The described functions (parameters) were applied in a conceptual morphodynamic model for large scale morphological changes of hierarchically structured channel-basin-systems in tide-dominated coastal areas. This model is based on Van Dongeren & de Vriend (1994). The model reproduces erosion and sedimentation due to changes of tidal parameters by moving sand volumes within a hierarchically system composed of channels and connected subareas (Goldenbogen, 1994). It has been applied for the Bay of Dithmarschen by using some of the above presented parametrizations (Schroeder, 1994):

$$A_i \text{ MLW} = 3.372 A_b \text{ MHW}^{0.923}$$

$$A_c \text{ NN} = 0.000123 A_b \text{ MHW}$$

$$l_i = 0.05 + 0.5 / ( 1 + ( 3 * 10^{-8} A_b \text{ MHW} )^2 ).$$

The simulation cover a period of 20 years. Figure 14 shows the results at the location southern of Büsum (see Fig. 2). Two superimposed effects have been calculated: a rise of the relative sea level (0.005 m/a) and the enclosures in 1972 and 1978.

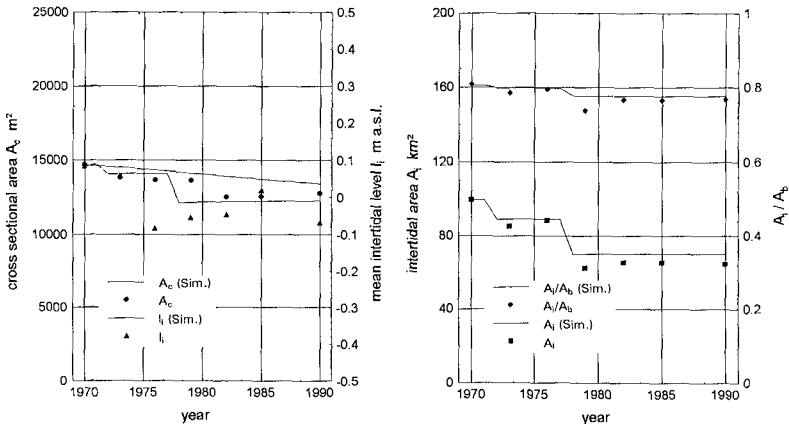


Fig. 14 Comparison of model results and field data

On account of the small amount of the assumed relative sea level rise this influence does not become noticeable. The enclosures is reproduced by the model in a realistic manner. With the exception of the cross

sectional area  $A_c$ , which has been simulated by a continued process, all the other parameters show a discontinually pattern as impact of the enclosure (immediately reduction of predominant highly situated areas in front of the coastline). A new equilibrium stage requires an increase of the intertidal area  $A_i$  over time, as it, for example, has been after the first enclosure of the Bay of Dithmarschen in 1972.

The model does not consider influences of changing wave climate or the geometric shape of the basin. This require further adaptations of the equilibrium functions.

### Conclusions

The results of investigations for two different tide-dominated Wadden Sea areas of the Southern North Sea (open bay and bays sheltered by barrier islands) demonstrate, that a reliable parametrization of the interactions between hydrological impacts and morphologically responses is possible. This result is proven as well for tidal basins as for distinguished subareas of different size and location. However, the validity of functions for tidal areas smaller than  $A_b$  MHW = 10 km<sup>2</sup> is questionable. The proven empirical functions had been applied to a conceptional morphodynamic model. The results showed that empirical morphodynamical modelling is a suitable tool to reproduce transitional morphological stages leading from a former to a new equilibrium fixed by changed boundary conditions. The method can lead to a profound forecasting of the development of Wadden Sea areas in medium time scales, needed for decisions on engineering and ecological purposes.

### Acknowledgement

The presented results have been elaborated by the Coastal Research Station, Norderney of the Lower Saxonian Central State Board of Ecology within the framework of the Dutch/German-research-program WADE. The German part is supported by the Federal Ministry of Research and Technology (BMFT), Bonn and is scientifically joined by the Kuratorium für Forschung im Küsteningenieurwesen (KFKI), Kiel.

### References

**Biegel, E.J. (1991):** Fase Rapport ISOS\*2, Fase 1: inventarisatie, bewerkingen analyse, Rijksuniversiteit Utrecht, Vakgr. Fys. Geogr., Den Haag, 16-12-1991.

**Dieckmann, R. (1985):** Geomorphologie, Stabilitäts- und Langzeitverhalten von Watteinzugsgebieten der Deutschen Bucht, Mitteilungen des Franzius-Instituts der Universität Hannover, Vol. 60, pp. 133-361.

**Goldenbogen, R. (1994):** Erste Ergebnisse empirischer Modellierung der Morphodynamik eines Watteinzugsgebietes am Beispiel der Dithmarscher Bucht, Die Küste, H. 56, KFKI.

**Hayes, M.O. (1975):** Morphology and sand accumulation in estuaries, in: L.E. Cronin: Estuarine Research, Vol. 2., Academic Press, New York, pp. 3-22.

**Liebig, W. (1993):** GIS-applications to Wadden Sea areas. Proc. of the Int. Coastal Congress ICC - Kiel '92, Verlag Peter Lang, Frankfurt am Main, pp. 550-558.

**Niemeyer, H.D. (1993):** Long-term morphodynamical behaviour of the East Frisian islands and coast, in: List, J.H., ed., Large Scale Coastal Behavior '93, U.S. Geological Survey, Openfile report 93-381, pp. 145-148.

**O'Brien, M.P. (1931):** Estuary tidal prisms related to entrance areas, ASCE, Civ. Eng., Vol. 1, No. 8.

**Renger, E. (1976):** Quantitative Analyse der Morphologie von Watteinzugsgebieten und Tidebecken, Mitteilungen des Franzius-Instituts der Universität Hannover, Vol. 43, pp. 1-160.

**Schroeder, E. (1994):** Parametrisierungen morphodynamischer Strukturen von Watteinzugsgebieten für empirisch-konzeptionelle Modellierungen, Die Küste, H. 56, KFKI.

**Van Dongeren, A.R. and De Vriend, H.J. (1994):** A model of morphological behaviour of tidal basins, Coastal engineering Vol. 22, Elsevier Science B.V., The Netherlands, pp. 287-310.

**Walther, F. (1972):** Zusammenhänge zwischen der Größe der Ostfriesischen Seegaten mit ihren Wattgebieten sowie mit Watten und Strömungen. Jber. 1971, Forsch.-Stelle f. Insel- u. Küstenschutz, Vol. 23, pp. 7-32.

**Wieland, P., Thies, E. and Bergheim, V. (1987):** Bilanz hydrologischer und morphologischer Untersuchungen in der Dithmarscher Bucht, Büsumer Gewässerkundliche Berichte, H. 54, ALW Heide, Dez. Gewässerk., Büsum.



## MUD TRANSPORT AND MUDDY BOTTOM DEFORMATION BY WAVES

Daoxian SHEN\* Masahiko ISOBE† and Akira WATANABE†

### ABSTRACT

The present study focuses on numerical simulation of wave height decay and muddy bottom deformation under wave action. Experiments have been performed to determine the vertical distribution of the water content ratio of mud. Using the experimental results, a simulation model has been set up to estimate change in the water content ratio in the mud bed. Also, a simple one-dimensional numerical model has been developed to predict the muddy bottom deformation under waves as well as the wave height decay. Wave flume experiments have been carried out and the changes in the bottom topography and wave height have been compared with the calculations.

KEYWORDS: Change in water content ratio, Wave height decay, Mud transport, Muddy bottom deformation.

## 1 Introduction

Along muddy coasts fine grained, cohesive sediment is consistently present in the nearshore waters and around the shoreline. These muddy bed sediments may have a significant effect on the hydrodynamic processes. Prediction of mud transport and resultant bathymetric change due to waves are essential in order to take effective countermeasures against erosion and siltation and to plan rational new works in coastal regions. Although many studies on mud transport under waves and on wave dissipation due to mud motion have been conducted (Gade, 1958; Dalrymple and Liu, 1978; Mei and Liu, 1987; Shibayama, 1993), only few attempts have been reported so far on the prediction of topography change on soft mud beaches.

The establishment of topographical change models for muddy beaches seems to be difficult for three reasons. First, the transport of fine-grained cohesive sediment is quite different from that of coarse-grained sediment. The cohesiveness

---

\*Engineer, Coastal Engineering Consultants Co., Ltd., Tamura Bldg. 3F, Hongo 5-23-13, Bunkyo-ku, Tokyo, 113 Japan

†Professor, Department of Civil Engineering, University of Tokyo, Hongo 7-3-1, Bunkyo-ku, Tokyo, 113 Japan

of soft mud makes its motion under the action of waves and currents more complicated than that of non-cohesive sediment. Second, the vertical structure of the concentration depends on both wave conditions and mud properties. Third, it is difficult to formulate a relationship for the local transport rate under the waves. It may be stated that our knowledge of mud transport processes has not yet reached a level where we can deal with these problems effectively.

On the other hand, the interaction between propagating ocean waves and a stable seabed or consolidated soil has received an extensive attention in the field of offshore and foundation engineering (Yamamoto, 1978; Zen and Yamazaki, 1991). However, their interest is either in the wave-induced liquefaction in a porous seabed or on the problem of unfavorable pore pressure, which could make the seabed or an offshore structure unstable.

The present study focuses on the numerical simulation of wave height decay and muddy bottom deformation under wave action. First, the vertical distribution of the water content ratio of mud was investigated experimentally, and numerical simulations on the change in the water content ratio in the mud layer were made. Then, a simple one-dimensional numerical model was developed to predict the muddy bottom deformation under waves as well as the wave height decay. Wave flume experiments were carried out and the measured changes in the bottom topography and wave height were compared with the calculations.

## 2 Vertical distribution of water content ratio in mud layer

### 2.1 Experiments

The water content ratio of soft mud strongly affects its rheological properties and the vertical distribution of the water content ratio is significant for estimating mud motion. In order to clarify the effects of wave action on the change in the water content ratio in mud layers, two groups of experiments have been performed using commercial kaolinite; one for static water loading and the other for regular wave loading.

In the first group of experiments, a plastic square tank with a side length of 45cm and a plastic circular bucket with a radius of 38cm were used. The depths of the newly mixed mud in the tank and the bucket were set to about 14.4cm and 12.1cm, respectively, above which water was poured to 30cm and 26cm depth in order to allow comparison with the other group of experiments.

During the experiments the vertical distribution of the water content ratio of the soft mud was measured for about 220 hours and the results from one test is shown in Fig. 1. Meanwhile, the settlement of the mud layers in the containers were also observed, and the results were displayed in Fig. 3.

Figure 1 indicates that the change in the water content ratio by mud consolidation is large near the fixed bed and small in the surface layer.

The other group of experiments on the effects of wave action were performed

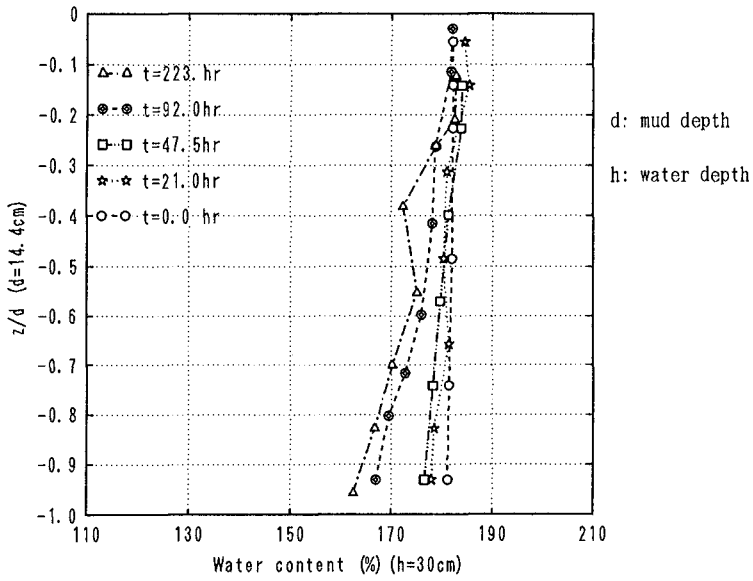


Figure 1: Change in water content ratio in still water

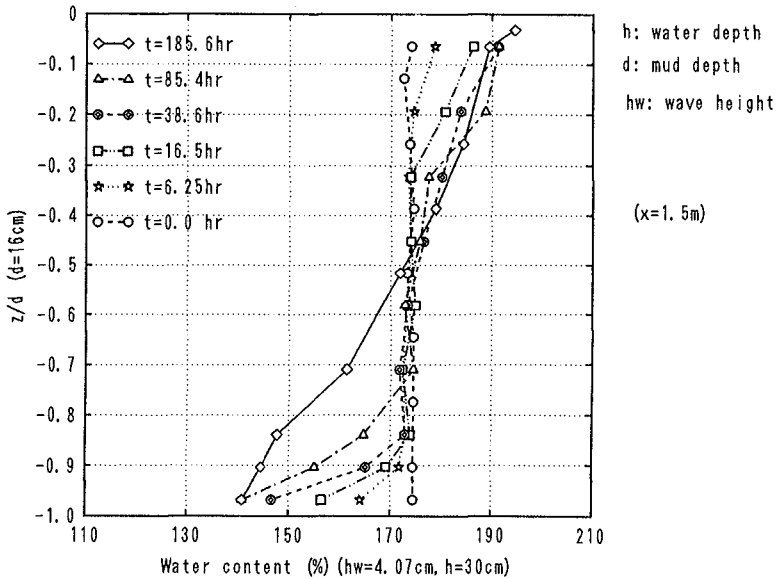


Figure 2: Change in water content ratio under waves (WE93A.15)

Table 1: Experimental conditions on change in water content ratio

Run	Mud depth (cm)	Period (s)	Water content (%)	Wave height (cm)
WE92E	16.4*(8,8.4)	1.02	(182, 120)	5.52
WE93A	16.0	1.02	175	5.20
WE93C	12.0	1.02	175	6.00

\* two-layered bottom with a 8.0cm newly mixed upper layer and a 8.4cm consolidating lower layer

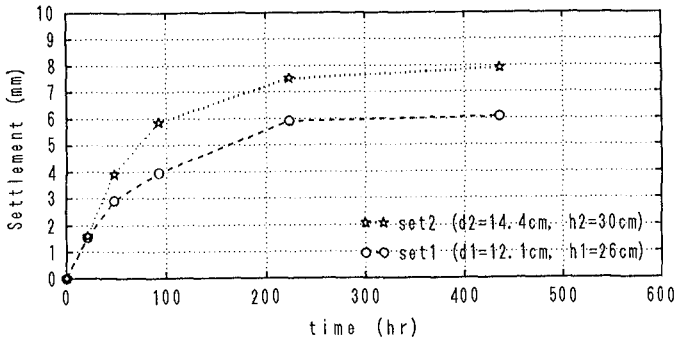
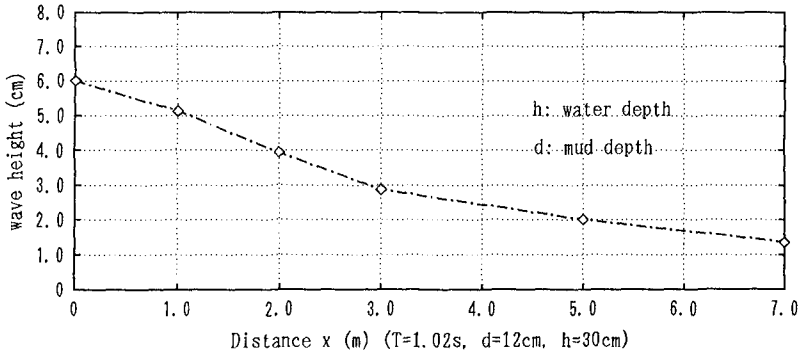


Figure 3: Settlement of mud layer in still water

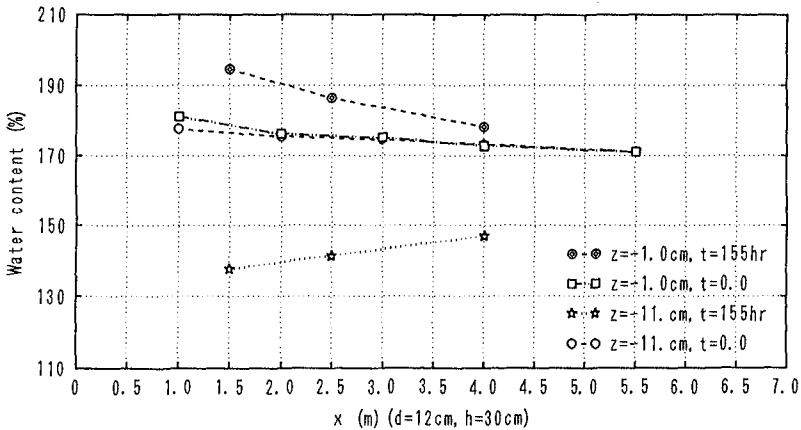
in a large wave flume shown in Fig. 8, and the experimental conditions are summarized in Table 1. The water content ratio was measured at a few sections in the flume together with the distribution of the wave height and one typical example of the change in water content ratio is plotted in Fig. 2. This figure shows that the water content ratio in the surface layer increases with time due to the mud loosening whereas it decreases near the bottom because of the mud densification.

From the two groups of the experimental results, it can be seen that the change in the water content ratio of soft mud is caused by both wave action and self-weight. However, the roles of these two mechanisms are quite different. Gravity and static water only consolidate soft mud to consolidate whereas wave force can cause both "liquefaction" in the surface layer and densification in the lower layer of mud. Moreover, the densification produced by waves is much faster than that by static water and gravity. In addition, the position of the demarcation point of liquefaction and consolidation at a fixed section changes with the state of the mud consolidation.

The change in the water content ratio depends on both wave and mud layer properties. The influence of wave height on the change in the water content ratio has also been investigated experimentally, and the results are shown in



(a) Distribution of wave height measured in the x-direction(WE93C)



(b) Distr. of water content ratio measured in the x-direction(WE93C)

Figure 4: Influence of wave height on the change in water content ratio

Fig. 4. Figure 4b plots the distribution of the water content ratio measured in the on-offshore direction, and Fig. 4a depicts the corresponding wave height at the beginning of the experiment. The figure implies that a larger wave height produces a larger change in water content ratio.

**2.2 Simulation of the change in water content ratio**

The above experimental results suggest that wave action affects soft mud both through densification in the lower layer and liquefaction in the surface layer. Enlightened by the experimental investigation we first consider the two processes of mud consolidation and liquefaction separately, and then combine their effects on the change in the water content ratio linearly. We assume that mud densification which results in the decrease of the water content ratio is induced only by

the mud self-weight and the positive dynamic pressure or compressive stress, and reversely, that mud liquefaction which leads to the increase of the water content ratio is produced only by the negative dynamic pressure or tensile stress. Thus, the process of liquefaction is treated as the complete reversal of consolidation.

To describe the densification of the mud layer, the one-dimensional consolidation equation in soil dynamics is applied, and for general case written by,

$$\frac{\partial e}{\partial t} - \frac{\partial e}{\partial z} \left[ g(e) \frac{\partial e}{\partial z} \right] - f(e) \frac{\partial e}{\partial z} = 0 \quad (1)$$

where the parameters  $g(e)$  and  $f(e)$  depend upon the wave properties as well as the mud characteristics. As a first step, those parameters are estimated using the following formulas which are based on limited experimental results, trial computations, and dimensional analysis,

$$g_c = \frac{k_c(e)}{\rho(1+e)} \frac{dp_m}{de} \left\{ 1 + \alpha_c \left( \frac{H_w}{L} \right)^{m_1} \left( \frac{H_w}{\sqrt{hd}} \right)^{m_2} \frac{k_c(e) - k_l(e)}{k_c(e) + k_l(e)} \right\} \quad (2)$$

$$f_c = \frac{\rho_m - \rho}{\rho} \frac{d}{de} \left\{ \frac{k_c(e)}{1+e} \left[ 1 + \frac{k_c(e) - k_l(e)}{k_c(e) + k_l(e)} \right] \right\} \quad (3)$$

In the above equations  $e$  denotes the void ratio,  $k_c$  and  $k_l$  indicate the permeability in the conditions of compressibility and dilatation of mud,  $\rho_m$  and  $\rho$  are the densities of the mud and the sea water,  $p_m$  is the amplitude of the pore pressure,  $d$  the mud depth,  $H_w$  the wave height,  $L$  the wavelength, and  $h$  the water depth. The variables  $\alpha_c$ ,  $m_1$ , and  $m_2$  are constants.

Following Been and Sills (1981), the governing equation can be solved with the appropriate boundary and initial conditions.

Next, we consider the loosening of mud under waves which is tentatively called "liquefaction" in the present study. Because the process of liquefaction is regarded as the reversal of consolidation, all of the assumptions and equations mentioned above can be applied to calculate liquefaction. The parameters  $g(e)$  and  $f(e)$  are expressed as follows,

$$g_l = \frac{k_l(e)}{\rho(1+e)} \frac{dp_m}{de} \left[ \alpha_l \left( \frac{H_w}{L} \right)^{m_3} \left( \frac{H_w}{\sqrt{hd}} \right)^{m_4} \frac{k_c(e) - k_l(e)}{k_c(e) + k_l(e)} \right] \quad (4)$$

$$f_l = \frac{\rho_m - \rho}{\rho} \frac{d}{de} \left[ \frac{k_c(e)}{1+e} \cdot \frac{k_c(e) - k_l(e)}{k_c(e) + k_l(e)} \right] \quad (5)$$

where  $\alpha_l$ ,  $m_3$  and  $m_4$  are constants.

Finally, the vertical distribution of the water content ratio under waves and gravity can be estimated by combining linearly the effect of consolidation and liquefaction. The depth of the liquefied mud layer is also determined through this combination.

As an example, Fig. 5 compares the calculated and measured vertical distribution of the water content ratio of mud under waves, and the values of the main

Table 2: Computational parameter values for the experiment

$k_c(e)/[\rho_f(1+e)]$	$k_l(e)/[\rho_f(1+e)]$	$g_c$	$g_l$	$dp_m/de$
$4.0 \times 10^{-11}$	$3.0 \times 10^{-11}$	$7.2 \times 10^{-9}$	$1.9 \times 10^{-9}$	18.0

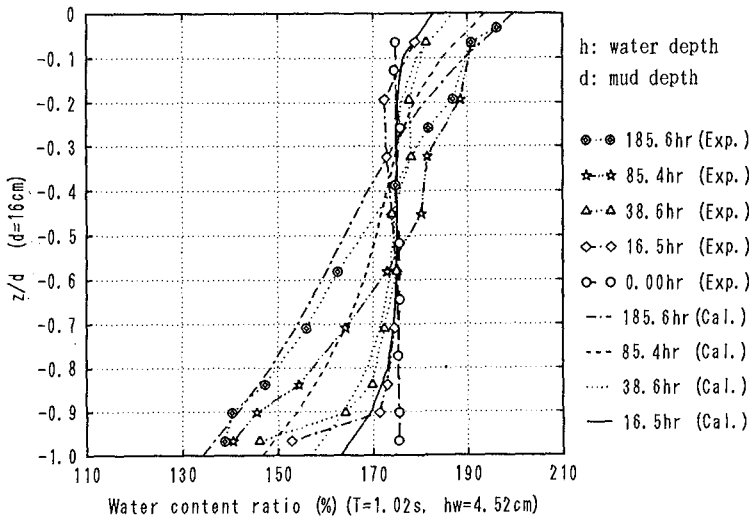


Figure 5: Comparison of the calculated and measured distribution of the water content ratio(WE93A.10)

parameters used in the computation are listed in Table 2. These values were determined by numerical experimentation. As can be seen from the figure, the calculated and measured shape of the vertical distribution agree well, but the magnitudes in the surface layer and near the fixed bed differ. This difference may partially be due to the neglect the nonlinear terms in the consolidation equations, and partially because of other model simplifications.

In summary, the simple model is applicable for predicting the vertical distribution of the water content ratio in the mud layer under wave action, keeping in mind the range of values employed in the experiment.

### 3 Muddy bottom deformation due to waves

#### 3.1 Development of a topographical change model

Following the general structure of numerical models of sandy topography evolution, a one-dimensional numerical model of muddy bottom deformation is developed with a model structure as shown in Fig. 6. This model consists of three submodels for calculating 1) the vertical distribution of the water content ratio in the mud layer, 2) the wave deformation and mud motion, and 3) the mud transport rate and bathymetric change.

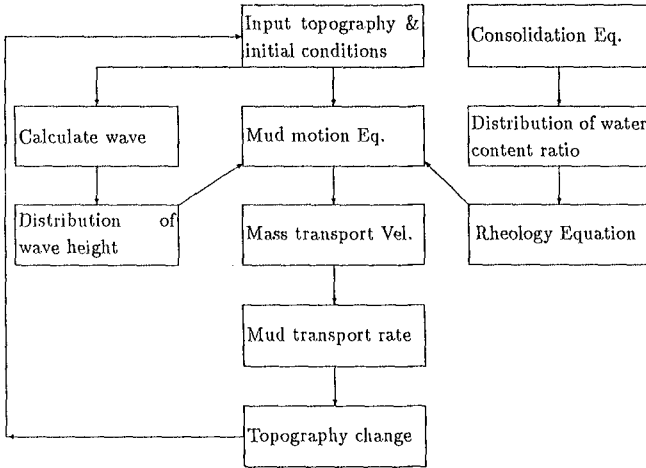


Figure 6: Structure of the numerical model of bottom change

First, let us discuss the calculation of the wave field. The mild-slope equation with the energy dissipation term is adopted to calculate the wave field,

$$\nabla \cdot (cc_g \nabla \phi) + (\sigma^2 \frac{c_g}{c} + i\sigma f_D)\phi = 0 \tag{6}$$

where  $\phi(x, y)$  is the velocity potential on the mean free surface assumed to be

$$\Phi(x, y, z, t) = \phi(x, y) \frac{\cosh k(z+h)}{\cosh kh} e^{-i\sigma t} \tag{7}$$

and  $c$  and  $c_g$  denote the wave velocity and the group velocity, respectively,  $\sigma$  is the angular frequency, and  $k$  the wave number. The energy dissipation coefficient  $f_D$  varies both with the spatial coordinate and time and is defined as

$$f_D = \frac{\epsilon_D}{E} \tag{8}$$

where  $E$  is the wave energy intensity, and  $\epsilon_D$  denotes the rate of energy dissipation per unit area estimated from the mud motion as,

$$\epsilon_D = \int_0^d \overline{\tau \frac{\partial u}{\partial z}} dz \tag{9}$$

where  $\tau$  is the shear stress in the mud layer and  $u$  the local velocity. The symbol  $\overline{\quad}$  denotes the average over one wave period and  $d$  the fluidized mud depth.

For the two-dimensional case with a constant water depth the equation (6) becomes

$$\frac{d^2 \phi}{dx^2} + \bar{k}^2 \phi = 0 \tag{10}$$



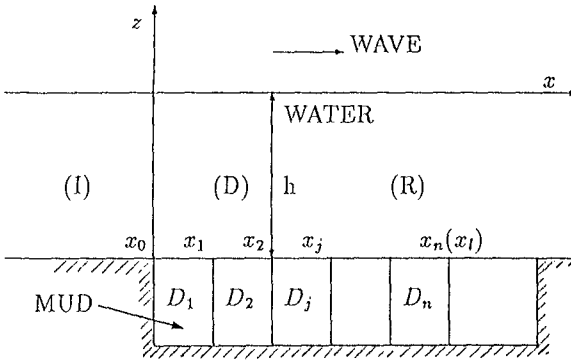


Figure 7: Definition sketch and coordinate system (Dissipation Area  $0 < x < x_l$ )

where

$$\bar{k}^2 = k^2 \left( 1 + \frac{icf_D}{c_g\sigma} \right) \tag{11}$$

One case of wave propagation over a muddy bed in a wave flume is discussed here. As shown in Fig. 7, the wave field is divided into three regions. The damping region occupies (D)  $0 < x < x_l$  and the flow domain extends to infinity ( $x \rightarrow \pm\infty$ ). Wave breaking is assumed not to appear in the regions studied. In regions (I) and (R), there are no energy dissipation,  $f_D = 0$ , and the solutions to Eq. (10) is

$$\phi_I = -\frac{igH_w}{2\sigma} (e^{ikx} + K_R e^{-ikx}) \quad x < 0 \tag{12}$$

$$\phi_R = -\frac{igH_w}{2\sigma} K_T e^{ikx} \quad x > x_l \tag{13}$$

where  $|K_R|$  and  $|K_T|$  represent the reflection and transmission coefficients, respectively. The damping region (D) is furthermore divided into  $n$  subregions because the dissipation coefficient varies with both the spatial coordinate and time, and the velocity potential in the  $j$ -th subregion is

$$\phi_{D_j} = -\frac{igH_w}{2\sigma} (B_j e^{i\bar{k}_j x_j} + F_j e^{-i\bar{k}_j x_j}) \quad x_{j-1} < x < x_j \tag{14}$$

where  $B_j$  and  $F_j$  are unknown constants to be determined and  $j = 1, 2, \dots, n$ .

By using the continuity conditions for  $\phi$  and its normal derivative, the unknown variables can be determined numerically from the following system of equations,

$$\phi_{D_j} = \phi_{D_{j+1}} \quad \text{at} \quad x = x_j \tag{15}$$

$$\frac{d\phi_{D_j}}{dx} = \frac{d\phi_{D_{j+1}}}{dx} \quad \text{at} \quad x = x_j \tag{16}$$

where  $j = 0, 1, 2, \dots, n$

For the simplest case  $n = 1$ , Liu *et al.* (1986) obtained an analytical solution for the equations given by

$$F = \frac{2 \left( \frac{\bar{k}}{k} - 1 \right)}{\left( \frac{\bar{k}}{k} + 1 \right)^2 \exp(-2i\bar{k}x_l) - \left( \frac{\bar{k}}{k} - 1 \right)^2} \quad (17)$$

$$B = \frac{2 - F \left( 1 - \frac{\bar{k}}{k} \right)}{1 + \frac{\bar{k}}{k}} \quad (18)$$

$$K_R = \frac{2 \left( 1 + \frac{F\bar{k}}{k} \right) - \left( 1 + \frac{\bar{k}}{k} \right)}{1 + \frac{\bar{k}}{k}} \quad (19)$$

$$K_T = \frac{2 - F \left( 1 - \frac{\bar{k}}{k} \right)}{1 + \frac{\bar{k}}{k}} \exp\{i(\bar{k} - k)x_l\} + F \exp\{-i(\bar{k} + k)x_l\} \quad (20)$$

Next, we turn to the simulation of the mud motion. The interaction between the waves and a muddy bottom is very complicated mainly because of the complex characteristics of mud, especially its rheological properties. We have derived an empirical rheological equation based on another set of experiments (Shen *et al.*, 1993a), and it reads

$$\tau = G\epsilon - \tau_G \tanh(\alpha_G \epsilon) + \mu\gamma + \tau_0 \tanh(\alpha_\mu \gamma) \quad (21)$$

where  $\tau$  is the shear stress,  $\epsilon$  the shear strain,  $\gamma$  the shear rate, and  $G$ ,  $\tau_G$ ,  $\alpha_G$ ,  $\mu$ ,  $\tau_0$  and  $\alpha_\mu$  are constants, of which  $G$  and  $\mu$  represent the elasticity and viscosity, respectively. Most of the constant parameters can be determined by rheological experiments and expressed as functions of the water content ratio.

It has been recognized that the interaction between the waves and the muddy bed will result in bottom deformation which produces a mild slope at the mud surface. The local mild slope strongly affects the mud motion in turn. Including the effect of the mild surface slope, the one-dimensional linearized equation of mud motion is modified as

$$\rho_m \frac{\partial u}{\partial t} = -\frac{\partial p}{\partial x} + \frac{\partial \tau}{\partial z} - (\rho_s - \rho)g \sin\theta \quad (22)$$

where  $\rho_m$ ,  $\rho_s$  and  $\rho$  denote the densities of the mud at any elevation, the mud at the surface layer and the water, respectively,  $\theta$  represents the surface slope angle of the mud layer,  $u$  is the velocity of mud particles,  $p$  the dynamic pressure which is calculated from the solution of the mild-slope equation, and  $\tau$  the shear stress evaluated by the proposed rheological relationship (21).

Numerical calculations have been carried out to solve the empirical rheological equation of soft mud, the mild-slope equation with the wave energy dissipation term, and the modified equation of mud motion.

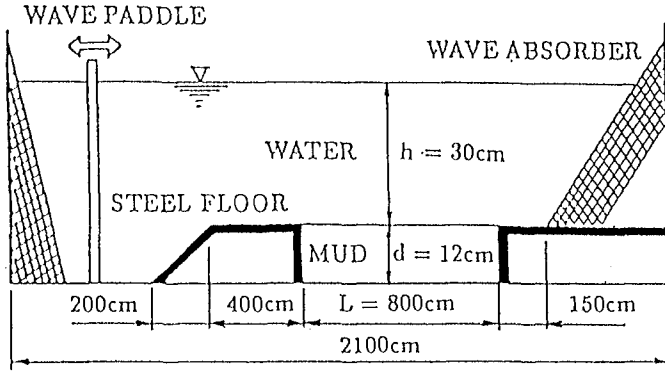


Figure 8: Experimental set-up

After obtaining the wave height change and the local velocity of the mud particles, the mass transport velocity can readily be estimated from the following formula used by Huynh *et al.* (1991)

$$U_L = U_E + \overline{\frac{\partial u}{\partial x} \int u dt} + \overline{\frac{\partial u}{\partial z} \int w dt} = U_E + U_S \quad (23)$$

where  $U_E$  represents the Eulerian average velocity and  $U_S$  the Stokes drift. For the one-dimensional case, they are evaluated by

$$U_S = \overline{\left( -\frac{1}{c} \frac{\partial u}{\partial t} - u \frac{f_D}{2c_g} \right) \int u dt} \quad (24)$$

$$\mu' \frac{\partial^2 U_E}{\partial z^2} = -\frac{f_D}{c_g} \rho_m u^2. \quad (25)$$

where  $\mu'$  denotes the equivalent viscosity of mud.

Furthermore, the change in the local bottom elevation is computed by solving the conservation equation for sediment modified by Watanabe *et al.* (1984),

$$\frac{\partial z_b}{\partial t} = -\frac{\partial}{\partial x} (q_x - \epsilon_m |q_x| \frac{\partial z_b}{\partial x}) \quad (26)$$

where  $z_b$  denotes the change in the local elevation of the mud surface,  $\epsilon_m$  is a positive constant which is determined empirically, and  $q_x$  is the sediment transport rate per unit width estimated by

$$q_x(x) = \int_0^d U_L dz \quad (27)$$

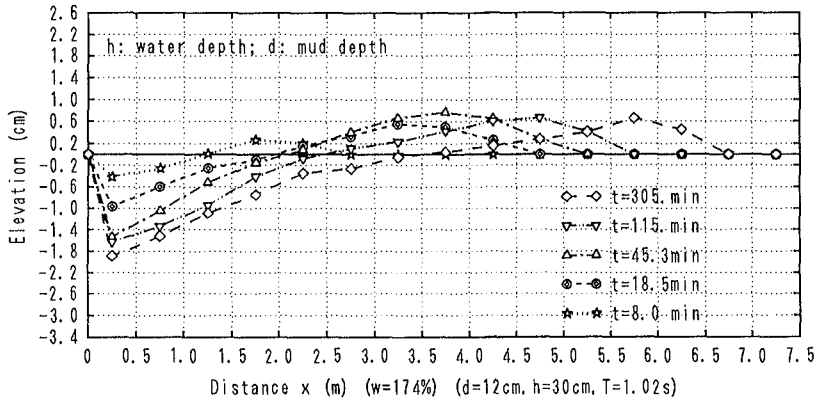


Figure 9: Change in the local elevation of the mud layer

### 3.2 Experiments and comparisons with calculations

Laboratory experiments were performed in a wave flume 21m long and 0.8m wide (Fig. 8) to verify the developed one-dimensional numerical model. The completely mixed commercial kaolinite (water content ratio: 174%) was placed in the middle of the flume. The depths of the mud and water layer were set to 12cm and 30cm, respectively. During the experiment for a few hours, measurements were made on the distribution of the wave height along the direction of wave propagation, the water content ratio of the mud layer, the concentration of the suspended mud, and the change in the local bottom elevations.

The measurements of the change in the local bottom elevation were not easily performed because (i) the suspension of the mud layer makes the water layer translucent or opaque and (ii) the mud layer is too soft to resist loading. Therefore, some instruments which works very well in sand are invalid for mud. Based on trial and error, a set of height gauge reequipped and a set of elevation meter newly made were used simultaneously to measure the change in the local elevation of the mud bottom and to correct the measured values.

As an example, Fig. 9 shows the experimental results in terms of the measured elevation change. From these results, some understanding of and conclusions on the topography change can be obtained as summarized in the following:

a) The eroded volume is a little larger than the deposited volume for a short time interval, and the difference increases with the loading time due to both the mud suspension and the settlement of the mud layer.

b) The peak of the deposited area moves slowly with the loading time in the direction of wave propagation. An erosion trough was always produced in the offshore direction. In addition, the mud surface slopes have a tendency to become smaller and smaller with the loading time.

c) The wave has a larger damping ratio for the newly mixed soft mud, and the

Table 3: Computational conditions and main parameter values

Run	Mud depth (cm)	Period (s)	Water content (%)	Wave height (cm)
WE93B	12.0	1.02	175.4	4.95
$\rho_m$ (kg/m <sup>3</sup> )	$\rho_s$ (kg/m <sup>3</sup> )	$\tau_0$ (N/m <sup>2</sup> )	$\mu$ (Ns/m <sup>2</sup> )	G (N/m <sup>2</sup> )
1300	1270	7.0	4.8	55

damping ratio will decrease with the loading time due to mud consolidation. It seems reasonable to conclude that only a fluidized mud layer plays a role in the wave dissipation. If the mud is completely consolidated, it may not absorb wave energy. In fact, this conclusion has also been arrived at through other experiments not discussed here.

Next, we attempt to apply the one-dimensional model for a simple case of mud motion in the flume. Some additional simplifications and assumptions are added here on the basis of the experimental results. Because the change in the water content ratio of the mud layer is very small for a relatively short time interval, as a first step, we neglect this change. Moreover, we suppose that mud consolidation for a relatively short time interval has so little effect on the rheology relationships that the influence can be ignored. The settlement of the mud layer and the transport of suspended mud are also omitted. In addition, the vertical two-dimensional mud motion near the starting point of the flume ( $x = 0$ ) is simplified as one-dimensional by a so-called equivalent transforming of the local velocity of mud particles (Shen, 1993b).

Figure 10 compares the calculated and measured bottom change in the flume. The computational conditions and the main parameter values are listed in Table 3. It is seen that the calculated results of the bottom change have a similar tendency to the measured. However, at the right-hand side of the flume (downstream), the experimental results show that the mud motion stops at a certain position whereas the calculations can not simulate this phenomenon.

This discrepancy can be explained as follows. In the present one-dimensional model, an empirical rheology equation is utilized that implies mud will move under waves no matter how small the wave height is. In fact, the cohesive mud has a yield value that must be exceeded before the mud has a possibility to start moving. In addition, the simplifications and assumptions introduced in the present model have an effect on the prediction accuracy.

Figure 11 shows a comparison of the measured and calculated wave height distribution at the initial stage of an experiment, indicating a good agreement between them.

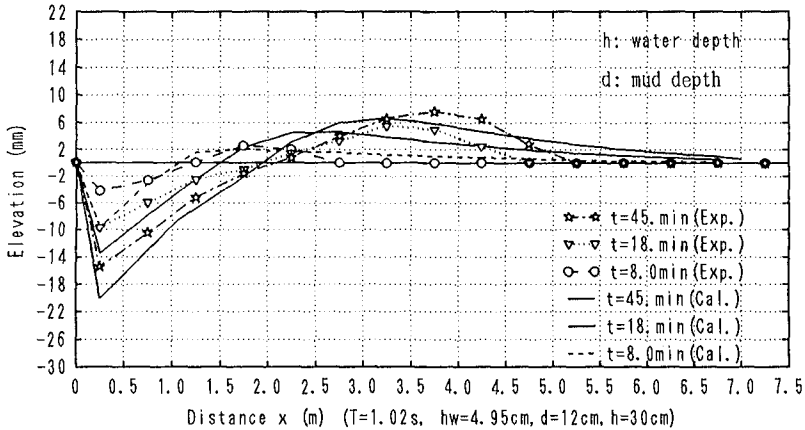


Figure 10: Comparison of measured and calculated bottom topography change in the flume

## 4 Conclusions

The present study focuses on investigating the vertical distributions of the water content ratio in a mud layer and numerical simulation of muddy bottom deformation and wave height decay.

The results of the first two groups of experiments have revealed that the change of the water content ratio is caused by both the wave action and the gravity of mud. However, the effects of wave action and gravity are quite different. The gravity only causes soft mud to consolidate, whereas the wave action can induce both the loosening in the surface layer and the consolidation in the lower layer of the mud. Numerical estimation of the change of the water content ratio in the muddy bed by the proposed simulation model has shown a similar tendency in the in the calculations as for the measurements.

A simple one-dimensional numerical model has been developed to predict the muddy bottom deformation under waves as well as the wave height decay. In conclusion, the one-dimensional model has been verified by the flume experiments to be applicable to predict the experimental phenomena, although its applicability is dependent on the accuracy of the rheological equation of mud.

## Acknowledgement

The authors would like to express their appreciation to Prof. I. Towhata of Tokyo Univ., Japan, T. Shibayama of National Yokohama Univ., Japan, and M. Larson of Univ. of Lund, Sweden, for their helpful discussion. The present study was financially supported by the Grant-in-Aid for Scientific Research, Japanese

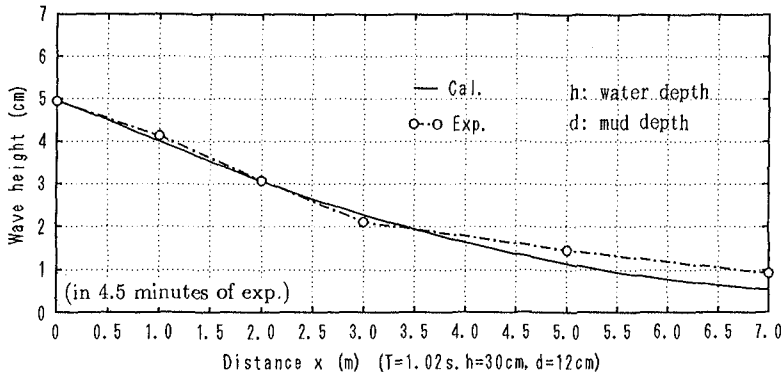


Figure 11: Comparison of measured and calculated wave height distribution

Ministry of Education, Science and Culture.

## References

- [1] Been, K. & Sills, G.C.(1981): Self-weight consolidation of soft soils: an experimental and theoretical study, *Géotechnique* 31, No. 4, pp. 519-535.
- [2] Darymple, R.A. and Liu, P.L.-F.(1978): Waves over soft muds: a two-layer fluid model, *J. Physical Oceanogr.*, Vol. 8, pp. 1121-1131.
- [3] Gade, H.G (1958): Effect of nonrigid, impermeable bottom on plane surface waves in shallow water, *J. Marine Res.*, Vol. 16, No. 2, pp. 61-82.
- [4] Huynh, T.N., M. Isobe and A. Watanabe(1991): Study on the mud mass transport under waves on basis of the rheology properties of mud, *Proc. Japanese Conf. on Coastal Eng.*, Vol. 38, pp. 466-470 (in Japanese).
- [5] Mei, C.C. and K.F. Liu(1987): A Bingham-plastic model for a muddy seabed under long waves, *J. Geophys. Res.*, Vol. 92, No. 13, pp. 14581-14594.
- [6] Liu, L.-F., *et al.* (1986): Wave reflection from energy dissipation region, *J. Waterway, Port, Coastal and Ocean Eng.*, Vol. 112, No. 6, pp. 632-644.
- [7] Shen, D.X., M. Isobe and A. Watanabe (1993a): Mud mass transport under waves based on an empirical rheology model, *Proc. of 25th IAHR*, Vol. 4, pp. 120-127.
- [8] Shen, D.-X.(1993b): Study on mud mass transport and topography change of muddy bottom due to waves, *Doctoral dissertation of Tokyo University*, 165pp.
- [9] Shibayama, T. and An, N.N.(1993): A visco-elastic-plastic model for wave-mud interaction, *Coastal Eng. in Japan*, vol. 36, No. 1, JSCE, pp. 67-89.
- [10] Watanabe A., *et al.* (1984): Three-dimensional numerical model of beach deformation with the onshore structures, *Proc. Japanese Conf. on Coastal Eng.*, Vol. 31, pp. 406-410 (in Japanese).
- [11] Yamamoto, T., H.S.L. Koning and E. Van Hijum(1978): On the response of a pore-elastic bed to water waves, *J. Fluid Mech.*, Vol. 87, Part 1, pp. 193-206.
- [12] Zen, K. *et al.* (1990): Oscillatory pore pressure and liquefaction in seabed induced by ocean waves, *J. of Soils and Foundations*, JSCE, Vol. 30, No. 4, pp. 147-161.

## CHAPTER 236

### WAVE-INDUCED SEDIMENT RESUSPENSION AND MIXING IN SHALLOW WATERS

Y. Peter Sheng<sup>1</sup>, M. ASCE, Xinjian Chen<sup>2</sup>, and Eduardo A. Yassuda<sup>2</sup>

#### ABSTRACT

A field and modeling study on the resuspension and vertical mixing of sediments in Tampa Bay, a large shallow estuary, and Lake Okeechobee, a large shallow lake in Florida, U.S.A. has been studied. The study was aimed to obtain a quantitative understanding of the fundamental processes controlling resuspension and vertical mixing of sediments in the water column and to develop models for simulating resuspension and mixing of sediments in shallow waters. For the field study, field data (including wind, wave, currents, suspended sediments and water quality parameters) were collected from Tampa Bay and Lake Okeechobee during several episodic events. These data were then used for the development of a one-dimensional water column model of hydrodynamics, sediment dynamics and water quality dynamics. Results of the study indicate that during episodic events, bottom stresses induced by the wind waves are very effective in causing significant resuspension of sediments and nutrients from the bottom of shallow estuaries and lakes. Vertical turbulent mixing due to wind-driven and tidal currents, however, are more effective in distributing suspended sediments through the water column.

#### INTRODUCTION

A field and modeling study on the resuspension and vertical mixing of sediments has been conducted in a large shallow estuary (Tampa Bay in Figure 1) and a large shallow lake (Lake Okeechobee in Figure 2) in Florida. The primary objectives of the study are: (i) to quantify the fundamental processes controlling resuspension and vertical mixing of sediments in the water column, (ii) to compare the

---

<sup>1</sup> Professor, <sup>2</sup> Graduate Student, Coastal & Oceanographic Eng. Dept., University of Florida, Gainesville, Florida 32611-6590, U.S.A.



processes controlling resuspension and vertical mixing of sediments in the shallow estuary to those in the shallow lake, (iii) to develop models for simulating resuspension and mixing of sediments in shallow waters, and (iv) to quantify the effects of sediment resuspension and vertical mixing on contaminant transport in shallow waters.

To accomplish the objectives of the study, field experiments and numerical simulations were conducted. Because of scaling problems in laboratory simulation of field processes, only limited laboratory experiments were conducted.

### FIELD EXPERIMENTS

Field studies were conducted in Tampa Bay (Sheng et al., 1993a) and Lake Okeechobee (Sheng et al., 1993b) during episodic events in 1992 and 1993. For example, a no-name storm passed the Tampa Bay area in February 1992. A front passed Lake Okeechobee in January 1993. A "Storm of the Century" passed Tampa Bay in March 1993. To obtain data during the storms, instrument platforms (Figure 3) were deployed in the water bodies prior to the storms. For example, platforms were deployed at Site A and Site B (Figure 1) in Tampa Bay during 1993, while platform was deployed at Site A in Tampa Bay during 1992. Platform was deployed in Lake Okeechobee at Site L002 during 1993.

On each platform, instruments were mounted to measure wind (anemometer), wave (underwater pressure gauge), current (2-3 Marsh McBirney EM current meters), water level (vented pressure gauge), salinity and temperature (2-3 SeaBird CTD sensors), and suspended sediment concentration (2-3 OBS sensors). In addition, various instruments were mounted to measure such water quality data including dissolved oxygen concentration, pH, and concentration of various nitrogen and phosphorus species. With the exception of instruments for measuring nutrient concentrations, most instruments can be connected to a data logger to collect continuous data with 2-Hz sampling frequency over several (e.g., 5-7) days using battery power. 15-minute averaged data are also recorded. However, since the storms usually last less than 1-2 days, it is extremely difficult for the instruments to "capture" the storms. The instrument platforms usually have to be deployed in the water body 1-2 weeks prior to the arrival of a forecasted storm, activated 1-2 days before the storm, and retrieved a few days after the storm. The collection of nutrient data is particularly difficult since it requires immediate filtering of water samples at the data site.

The field data were used to provide information on the dominant forcing mechanisms for sediment resuspension/erosion and vertical mixing. In particular, statistical analysis was performed to determine the dominant frequencies and correlations of various physical parameters. In addition to the data analyses, numerical models were used to assist the interpretation of field data and to quantify

the various processes.

### NUMERICAL MODELING

Three-dimensional numerical models of sediment transport have been developed by Sheng (1986) and Sheng et al. (1991). In this study, since the focus is on the fundamental processes in the vertical water and sediment columns, a vertical one-dimensional numerical model was used. Basically, the vertical 1-D model developed by Sheng and Villaret (1989) and Sheng et al. (1989) was significantly modified to simulate the current, turbulence, and sediment dynamics in the water column. Basically, the one-dimensional model includes a hydrodynamic component and a sediment component. The hydrodynamic component of the 1-D model computes the horizontal velocities forced by wind, wave, and pressure gradients (associated with tidal circulation and baroclinic circulation). In order to simulate the vertical turbulent mixing throughout the water column, we developed a procedure which determines the horizontal pressure gradients (associated with tidal, wind-driven and density-driven circulations) in the water column by assimilating the measured 15-minute averaged currents into 1-D model simulation which uses a relatively large time step (e.g., 15 minutes). These slowly varying pressure gradients are then combined with the fast-varying wave-induced pressure gradients to drive the water column in the 1-D model simulation which uses a very small time step (about 1/100 of the wind wave period). These model simulations produce accurate vertical turbulent mixing and bottom shear stress under combined current-wave motion without resorting to ad-hoc wave-averaging procedure.

The sediment component of the 1-D model includes the following processes: vertical turbulent mixing, gravitational settling, resuspension/erosion, deposition and a fluid mud layer at the bottom. One important feature of the present 1-D model is that simultaneous deposition and resuspension/erosion are allowed, while the critical stress for deposition is generally several times larger than the critical stress for erosion. The resuspension/erosion rate of sediments is modeled as a linear function of the excess bottom shear stress (Sheng et al., 1989), while the deposition rate is computed by combining the deposition velocity formula of Sheng (1986) with the deposition probability of Krone (1993).

The 1-D models were used to simulate the measured suspended sediment data and to determine the resuspension/erosion rate during the storm events. The 1-D models were also used to test various hypotheses concerning dominant processes for sediment resuspension/erosion and mixing. A sensitivity study was also conducted to examine the effects of various model parameters on model results. Resuspension/erosion rates determined by the 1-D models were used in a three-dimensional model of sediment transport to simulate the long-term sediment transport in the estuary and the lake.

## RESULTS

Using the field data measured at 2 Hz sampling frequency, analysis was performed to determine the dominant forcing for sediment resuspension. For both the estuary and the lake, wind wave was found to be the dominant mechanism for sediment resuspension. In both the tidal estuary and the lake, currents played little role in causing sediment resuspension, but are primarily responsible for the vertical mixing of sediments.

For example, Figure 4 shows the wind speed and direction in Tampa Bay during a storm event (Julian day 30 to 40) in 1992. Figure 5 shows the measured horizontal North-South velocities and suspended sediment concentration at two vertical levels at Station A in Tampa Bay during Julian day 35.6 to 36.6, 1992. Because of the strong wind from the south on Julian day 36, significant wave-induced bottom stress caused resuspension of sediments. As shown in Figure 5, suspended sediment concentration increased from 10 mg/l to more than 40 mg/l in less than 2 hours. The simulated horizontal velocities and suspended sediment concentration at Station A as shown in Figure 6 compare very well with the measured data.

The sediments in the vicinity of Station A in Tampa Bay are composed primarily of silt with a small amount of clay. The resuspension of sediments led to release of ammonium adsorbed on the sediments into the water column. The one-dimensional model was used to simulate the currents, suspended sediment concentration, and ammonium concentration in the water column during the episodic event. Model results also suggest that fully turbulent boundary layer only exists during part of a tidal cycle. Thus, the presence of viscous sublayer should be incorporated into the model for accurate estimation of bottom stress and vertical mixing.

Three-dimensional flow fields in Tampa Bay have been simulated using a three-dimensional curvilinear-grid hydrodynamics model CH3D (Sheng 1989), which is capable of resolving the complex shoreline and navigation channel in Tampa Bay. As shown in Figure 7, the vertically-averaged currents in Tampa Bay during a typical flood tide are generally less than 50 cm/sec. During storm conditions, however, currents could be stronger and contribute to resuspension of sediments.

The resuspension event in Lake Okeechobee showed different behavior since the bottom sediments are consisted primarily of cohesive mud particles and flocs. Wind wave is also the driving force for resuspension of sediments. However, suspended sediment concentration can reach 100-2000 mg/l, depending on the location in water column. Near the bottom, there exists a very thin "lutocline" where sharp suspended sediment concentration gradient is found. The thickness of the lutocline varies significantly with time, as a result of variations in hydrodynamic forcing. As an example, results of a three-day simulation and field data at the Center-Lake Station C are shown in Figure 8. Erosion/resuspension and deposition

of fine sediments were described by relationships similar to those used in the Tampa Bay model. Flocculation apparently had a more significant effect on the gravitational settling of sediments in Lake Okeechobee than in Tampa Bay. Resuspension of sediments led to the subsequent release of phosphorus into the water column (Sheng 1993).

## DISCUSSIONS

The study demonstrated the significance of wind wave in causing resuspension of sediments and contaminants in shallow estuaries and lakes. The effect of wave groups on sediment resuspension was found to be insignificant. Wind-driven currents and tidal currents are generally insufficient to cause sediment resuspension, but are more effective in causing vertical mixing of suspended sediments. The process-based one-dimensional models were able to successfully simulate the mean flow, turbulent mixing, and suspended sediment dynamics in Tampa Bay and Lake Okeechobee. Model simulations showed that flocculation and lutocline dynamics are important processes in Lake Okeechobee but not in Tampa Bay.

## ACKNOWLEDGEMENT

The study was supported by the Florida Sea Grant and the South Florida Water Management District. Mr. Sidney Schofield and others of the Coastal & Oceanographic Engineering Department, and staff of the South Florida Water Management District contributed to the field experiments. Pittsburgh Supercomputing Center and Florida State Supercomputing Center provided some computer time.

## REFERENCES

- Krone, R.B., 1993: "Sediment Revisited," In (A.J. Mehta, Ed.), *Coastal and Estuarine Studies 42: Nearshore and Estuarine Cohesive Sediment Transport*. American Geophysical Union, Washington, DC, pp. 108-125.
- Sheng, Y.P., 1986: "Modeling Bottom Boundary Layers and Cohesive Sediment Dynamics," in *Estuarine Cohesive Sediment Dynamics*, Springer-Verlag, pp. 360-400, 1986.
- Sheng, Y.P., 1989: "Evolution of a Three-Dimensional Curvilinear-Grid Hydrodynamic Model for Estuaries, Lakes and Coastal Waters: CH3D," *Estuarine and Coastal Modeling* (M.L. Spaulding, Ed.), ASCE, pp. 40-49.
- Sheng, Y.P., 1993: "Hydrodynamics, Sediment Transport and Their Effects on Phosphorus Dynamics in Lake Okeechobee," in *Nearshore, Estuarine and Coastal Sediment Transport* (A.J. Mehta, Ed.). *Coastal and Estuarine Studies*, 42, American

Geophysical Union, pp. 558-571.

- Sheng, Y.P. and C. Villaret, 1989: "Modeling the Effect of Suspended Sediment Stratification on Bottom Exchange Processes," *Journal of Geophysical Research*, **94:C10**, pp. 14429-14444, 1989.
- Sheng, Y.P., V. Cook, S. Peene, D. Eliason, S. Schofield, K.M. Ahn, and P.F. Wang, 1989: "A Field and Modeling Study of Fine Sediment Transport in Shallow Waters," in *Estuarine and Coastal Modeling* (M.L. Spaulding, Ed.), ASCE, pp. 113-112.
- Sheng, Y.P., D.E. Eliason, X.-J. Chen, and J.-K. Choi, 1991: "A Three-Dimensional Numerical Model of Hydrodynamics and Sediment Transport in Lakes and Estuaries: Theory, Model Development, and Documentation," *Final Report for Environmental Research Laboratory*, U.S.E.P.A., Athens, GA.
- Sheng, Y.P., X.-J. Chen, E. Yassuda, K.R. Reddy, and M.M. Fisher, 1993a: "Quantifying Sediment Resuspension Flux of Nutrients and Contaminants in Estuaries due to Episodic Events," *Final Report to Florida Sea Grant*, Coastal & Oceanographic Engineering Department, University of Florida, Gainesville, Florida 32611.
- Sheng, Y.P., X.-J. Chen, S. Schofield, and E. Yassuda, 1993b: "Hydrodynamics and Sediment and Phosphorus Dynamics in Lake Okechobee During an Episodic Event," *Final Report to South Florida Water Management District*, Coastal & Oceanographic Engineering Department, University of Florida, Gainesville, Florida 32611.

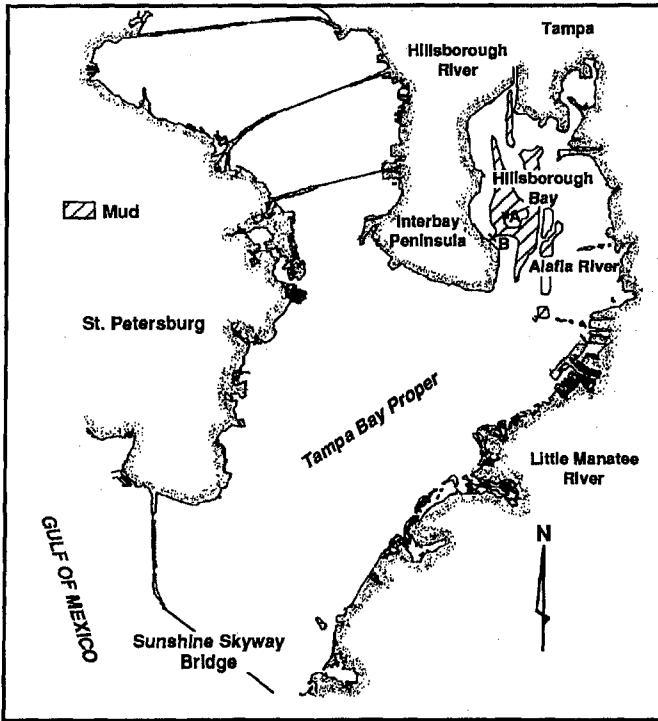


Figure 1. Map of Tampa Bay, Florida Showing Field Stations A and B (from Sheng et al. 1993a).

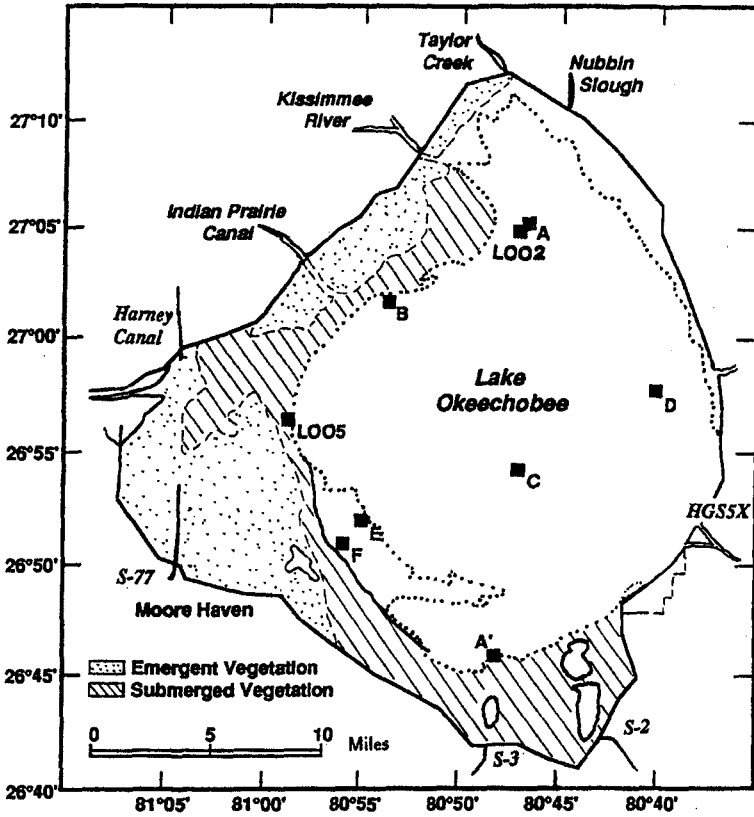
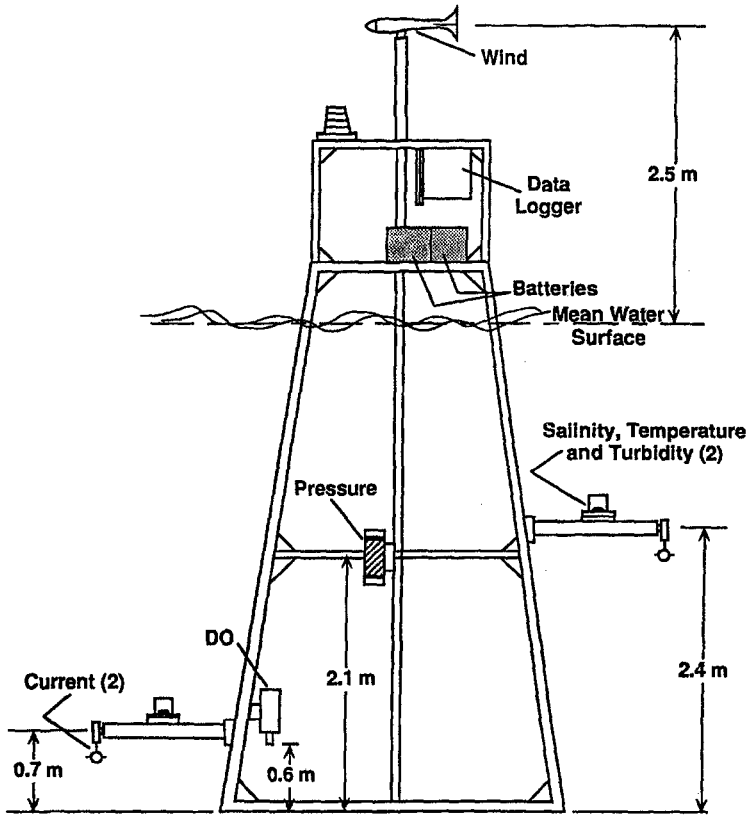
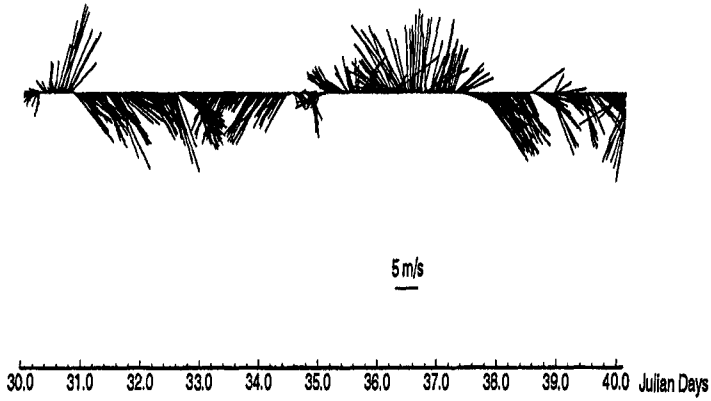


Figure 2. Map of Lake Okeechobee, Florida Showing Locations of Field Stations (from Sheng et al. 1993b).



**Figure 3.** Instrument Platform and Some Hydrodynamic Instruments Used for the Tampa Bay and Lake Okeechobee Studies. Water Quality Instruments Are Not Shown.





**Figure 4.** Stick Diagram of Wind Speed and Direction in Tamapa Bay During Julian Day 30 to 40, 1992.

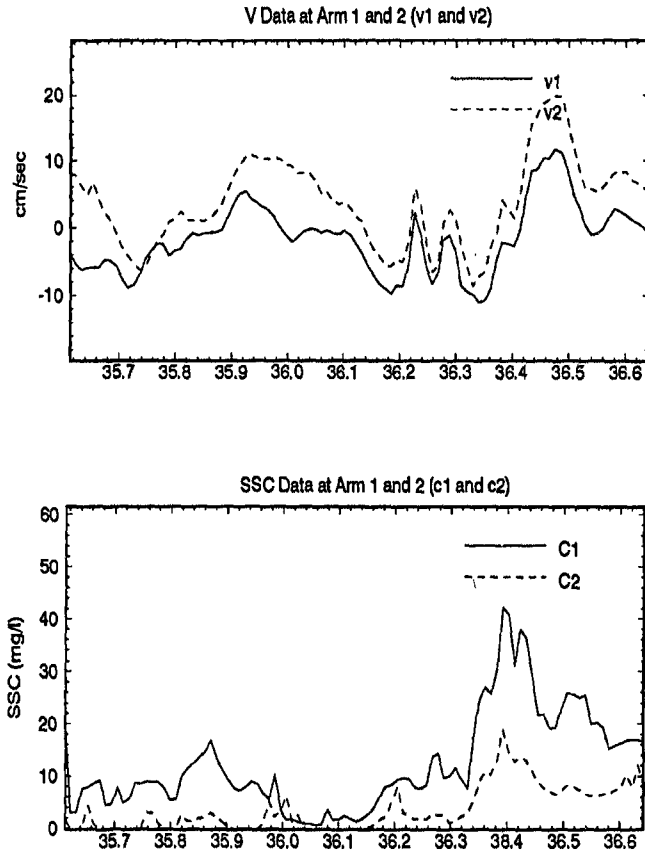


**Figure 5.** Measured North-South Velocity and Suspended Sediment Concentration at the Near-Surface (C1) and Near-Bottom (C2) Arms at Station A in Tampa Bay During A 1992 Storm between Julian Day 35.6 and 36.6.

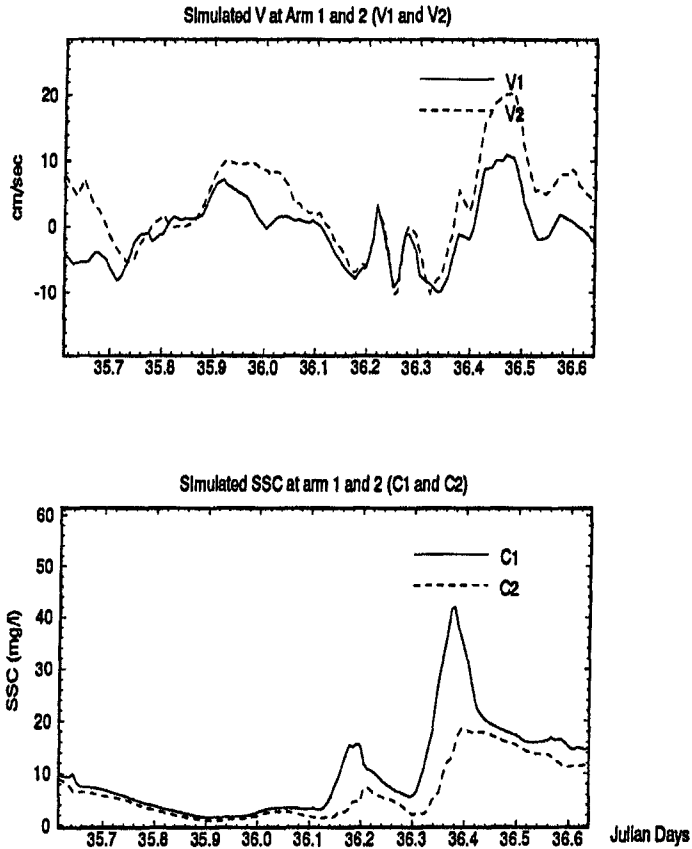


**Figure 6.** Simulated North-South Velocity and Suspended Sediment Concentration at the Near-Surface (C1) and Near-Bottom (C2) Arms at Station A in Tampa Bay During a 1992 Storm between Julian Day 35.6 and 36.6.

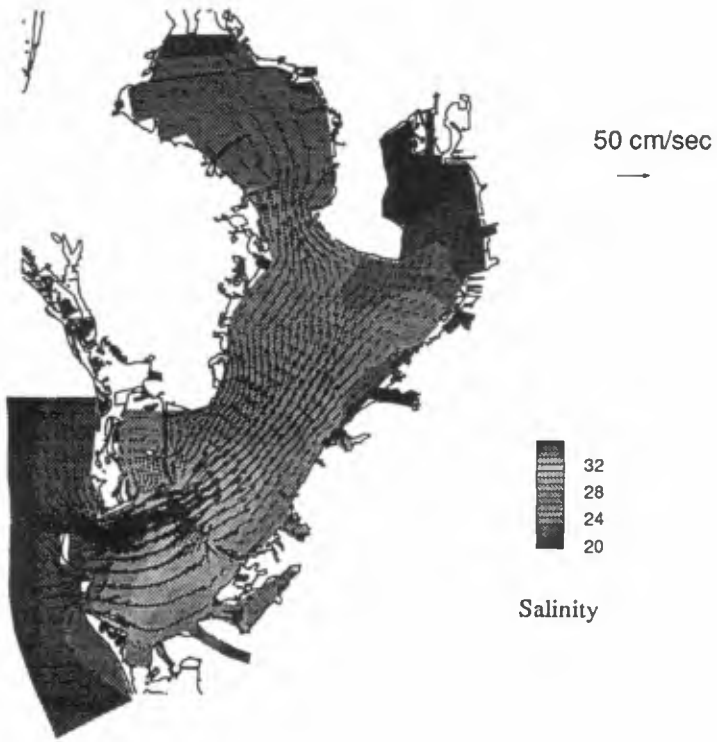


**Figure 7.** Simulated Tide- and Density-Driven Vertically-Averaged Currents and Near-Surface Salinity During a Typical Flood Tide in Tampa Bay. Results Obtained With a 3-D Curvilinear-Grid Hydrodynamics Model CH3D.

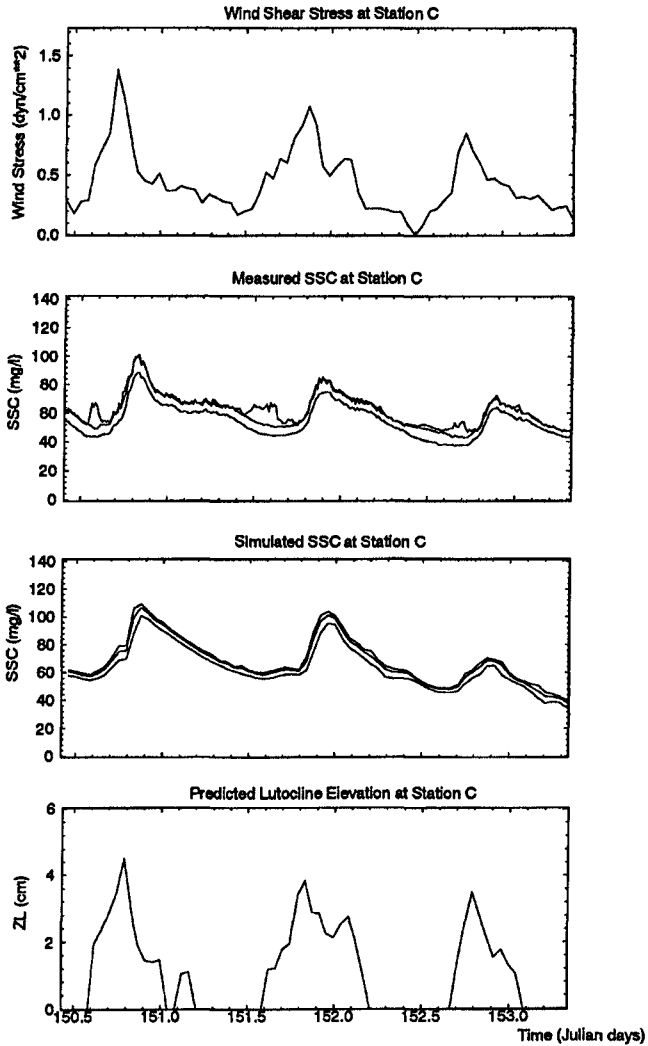


**Figure 8.** Wind Stress, Measured Suspended Sediment Concentration at 3 Depths, Simulated Suspended Concentration at 3 Depths, and Simulated Lutocline Thickness at Station C in Lake Okeechobee During a 3-Day Event in Spring 1989.

## CHAPTER 237

### A NUMERICAL MODEL FOR BEACH DEFORMATION AROUND RIVER MOUTH DUE TO WAVES AND CURRENTS

by

Tomoya Shibayama\* and Akiko Yamada\*\*

#### Abstract

A numerical model is proposed for beach deformation under wave and current in river mouth area. The model includes three major driving forces for sediment transport which are wave, wave-induced current and river discharge. Interaction of wave and current is also included. Laboratory experiments are performed to be compared with numerical results. Wave field, current field and beach deformation are compared between laboratory and numerical results and good agreements are obtained.

#### 1. Introduction

In asian coastal region, we have many problems for the maintenance of waterway which connects big river port with open ocean. The examples are Chao Phraya river in Thailand or Mekong river in Vietnam. In the present paper, sedimentation and beach processes will be considered in river mouth area in order to minimize maintenance costs for these large rivers. A new numerical model is proposed for the simulation of beach processes in this area under waves, wave induced current and river discharges. Laboratory experiments are also performed to understand the physical mechanism of sediment transport and the results are used to examine the numerical model.

---

\* Associate Professor, Dept. of Civil Eng., Yokohama National University, Hodogaya-ku, Yokohama 240 Japan

\*\* Engineer, Penta-Ocean Construction Co., Ltd.

## 2. Numerical Model

A numerical model is developed to predict bottom topography changes around river mouth. The model is composed of three sub-models which are wave model, current model and beach deformation model. The wave field is calculated by using mild slope equation with including wave-current interaction effect (Ohnaka and Watanabe, 1990). The breaking point is determined by the comparison of wave phase velocity and water particle velocity. Near-bottom velocity variations and the distribution of radiation stress are evaluated by using the calculated wave field. The current field associated with sand movement is calculated including wave induced current calculated from distribution of radiation stress, and river discharge. The river current is introduced into the model as boundary conditions which are given as water level and depth-averaged current velocity at river area. Since we included wave-current interaction, it is necessary to calculate by iteration process in order to get converged solutions for wave calculation and current calculation.

Bed load transport rate is calculated from bottom shear stress caused by wave orbital motion, wave induced nearshore current and river current. The bottom friction factor is calculated from wave-current friction factor of Tanaka and Shuto (1980). Sand transport formula of Watanabe et al., (1986) is used to calculate bed load. Suspended sand discharge from the river and suspended sand due to wave breaking are also included in the model. The suspended sand flux from river is calculated from the following formula which is derived from Brown type formula.

$$q = A \frac{q_b}{1 - \lambda} \dots \dots \dots (1)$$

where

$$\frac{q_b}{u_* d} = 10 \left( \frac{u_*^2}{sgd} \right)^2 \dots \dots \dots (2)$$

and  $u_*$  : bottom shear velocity,  $\lambda$  : porosity,  $s$  : sand specific gravity in water and  $d$  : sand diameter. The value  $A$  is a empirical constant and set to be  $5 \times 10^{-4}$  for the present calculations.

The suspended sand is produced in river mouth and wave breaking area. The suspended sand concentration in wave breaking are given according to the result of Nielsen (1986). The suspended sand is transported by river current and wave-induced current and deposit to the bottom with sediment fall velocity (Numano et al., 1989).

Table 1: Laboratory Conditions

Case	Wave Period (s)	Deep Water Wave Height (cm)	Flow Velocity in River Mouth (cm/s)	River Discharge (cm <sup>3</sup> /s)
1	1.34	3.41	20.0	222
2	1.39	6.09	20.0	222
3	1.38	2.75	18.5	421

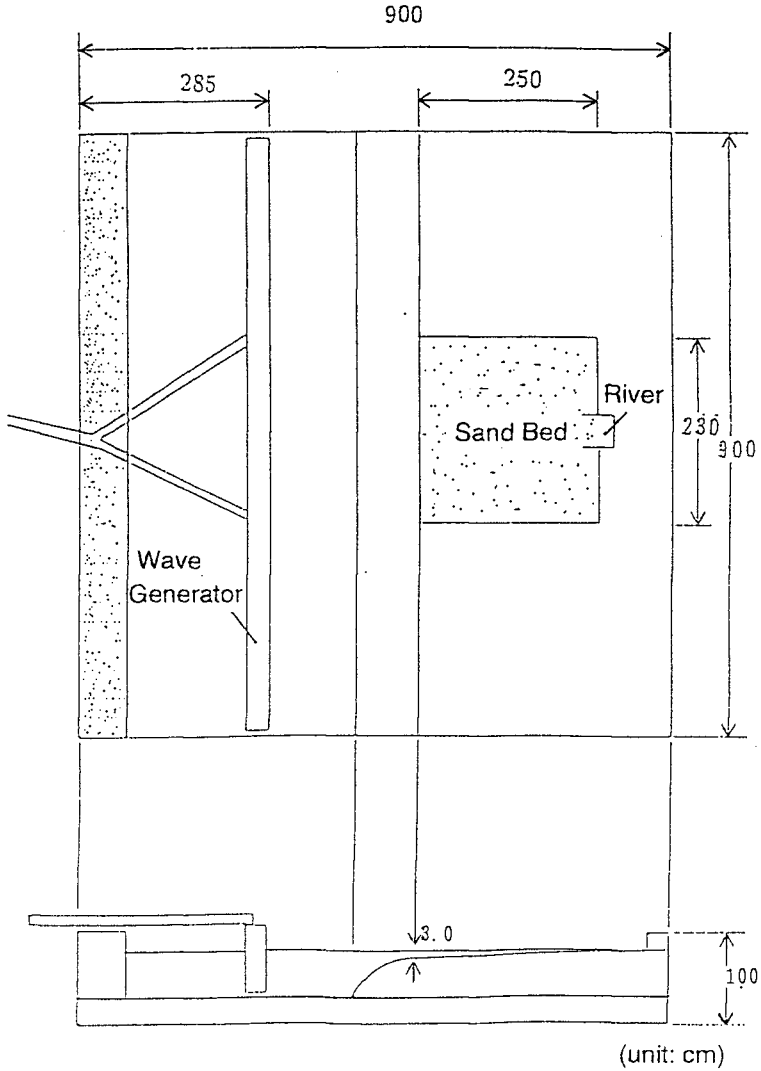


Figure 1: Laboratory Set-up



The calculated results of wave field, current field and bottom topography changes will be compared with laboratory results in order to examine the accuracy of numerical model.

### **3. Laboratory Experiment**

Laboratory experiments are performed in a wave basin designed to facilitate the understanding of the mechanism of sand movement as well as the behavior of wave and current field around river mouth. Well-sorted sand (median diameter 0.15 mm) are laid in the wave basin to make an 2.5 times 2.3 meter test bed with the initial slope of 1/20. A river mouth with water discharge was installed at upper end of the test bed. Figure 1 shows the laboratory set up. The distribution of wave height and the variation of near-bottom velocities in the test section are measured in details by using capacitant wave gages or an ultra-sonic velocity meter respectively for three conditions of monochromatic waves and river discharges.

The laboratory conditions are listed in Table 1. These conditions corresponds to the following situations: (1)effect of river discharge and effect of wave to sand transport are almost equivalent (case 1), (2)wave effect is greater than river discharge effect (case 2) and (3)river discharge effect is greater than wave effect (case 3). The changes of bottom topography during each experimental run are measured. In these three cases, bar or terrace are formed in front of river mouth and this may cause interruption of waterway.

### **4. Comparison of numerical results and laboratory results**

Figure 2 shows distributions of nearshore current for case 3. In the figure, calculated and measured velocities are shown. Here, the calculated values are depth-averaged values and the measured values are in the vicinity of bottom. The measured values may include the effect of undertow. As a result of interaction process, the calculated current field becomes asymmetric in terms of river mouth and this agrees with laboratory phenomena.

Figure 3 shows the comparison of wave field. The top figures show the two dimensional distributions of calculated wave fields by the numerical model. The bottom figures show the corresponding two-dimensional distributions of measured wave fields in the laboratory experiment. The middle figures show comparison of calculated and measured values in on-offshore distribution in front of river mouth. There are under-estimations of wave height in wave breaking area and over-estimations in the surf zone. This means the physical process

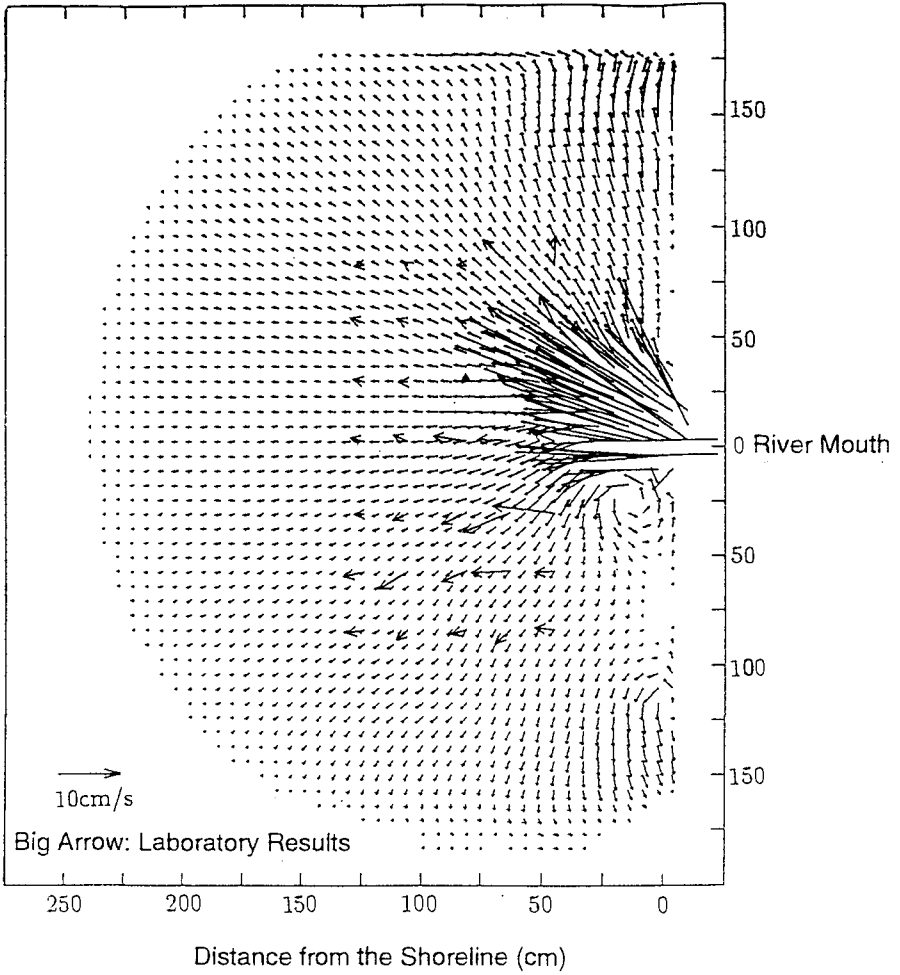


Figure 2: Measured and calculated current field (Case 3)

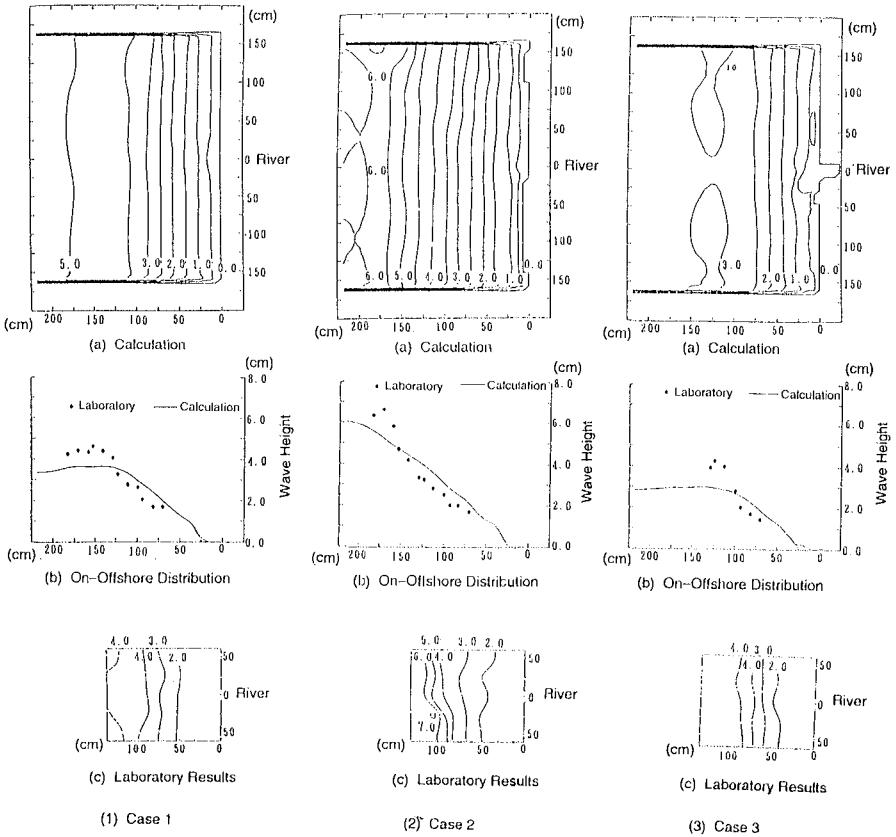


Figure 3: Comparisons of wave field  
(a)calculated wave field,  
(b)comparison of on-offshore distribution and  
(c)measured wave field in laboratory



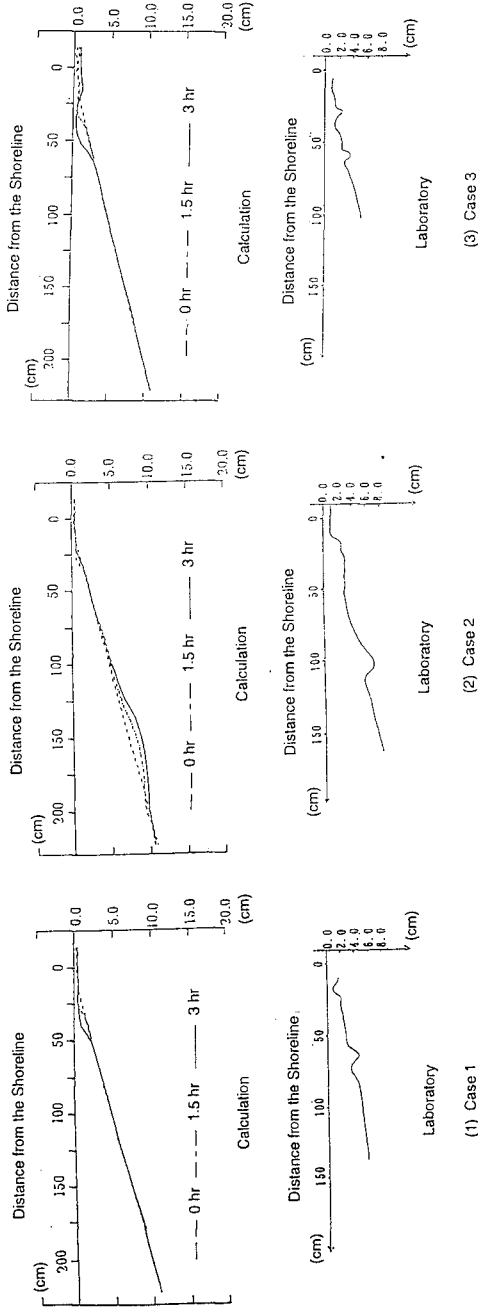


Figure 5: Cross-sectional change of beach topography in front of river mouth

of interaction between wave and current in wave breaking area is not fully included in the numerical model.

Figure 4 is the comparison between calculated beach topography in the numerical model and measured topography in the laboratory experiment. The measured area in the wave basin is limited because of limited area of movable sand bed area. In case 3, terrace formation in front of river mouth is well estimated by the numerical model. In cases 1 and 2, bar formation in offshore area is clearly observed in laboratory but is not so clear in numerical model.

Figure 5 shows cross-sectional change of beach topography in front of river mouth. In case 3, we can observe the formation and offshore directed movement of terrace. In the calculation, the terrace gradually developed in front of river mouth.

From these figures, we can judge that the present numerical model, which includes wave-current interaction, bed load and suspended load due to wave breaking and river discharge, is useful to predict laboratory results of beach changes in the vicinity of river mouth areas.

## 5. Conclusion

A numerical model is developed for prediction of beach profile change in river mouth area. The model is compared with laboratory results. From the comparison, we can conclude that the model is not satisfactory but promising for the future development. The possible modifications are (1)more precise evaluation of wave field, (2)including the effect of vertical distribution of current field and (3)more precise evaluation of diffusion and dispersion process of suspended sand.

## REFERENCES

Nielsen P. (1986):Suspended sediment concentrations under waves. Coastal Eng., Vol.10, pp. 23 -31.

Numano, Y., S. Sato and T. Shibayama (1989): A simulation model of beach deformation including the effect of dispersion of suspended sand and undertow, Proc. of Coastal Eng., JSCE, Vol. 36, pp. 394 - 398 (in Japanese).

Ohnaka, S. and A. Watanabe(1990): Modeling of wave-current interaction and beach changes, Proc. of 22nd Coastal Eng. Conf., ASCE, pp.2443 - 2456.

Tanaka, H. and N. Shuto (1981): Friction coefficient for a wave-current coexistent field, Coastal Eng. in Japan, JSCE, Vol. 21, 105-128.

Watanabe, A., K. Maruyama, T. Shimizu and T. Sakakiyama (1986): Numerical prediction model of three dimensional beach deformation around a structure, Coastal Eng. in Japan, Vol. 29, pp. 179 -194.

## CHAPTER 238

### Development of a Numerical Simulation Method for Predicting the Settling Behavior and Deposition Configuration of Soil Dumped into Waters

Kazuki Oda<sup>1</sup> and Takaaki Shigematsu<sup>1</sup>

#### **Abstract**

A numerical simulation method, which combines the Marker And Cell method and the Discrete Element Method, for analyzing the settling behavior and deposition configuration of the particles dumped into waters is described. Some calculated results are compared with the experimental ones, and what the settling behavior of the particles and the deposition configuration on the water bottom depend on is discussed.

#### **1. Introduction**

In recent years in Japan, large-scale man-made islands such as offshore ports and airports in coastal areas have been increasing in number. They are constructed in general by reclamation with a large volume of soil dumped from a split-hull barge. Hence, from the view point of both the construction management and environmental conservation, it has become very important to predict accurately the settling behavior and deposition configuration of soil. While there are a few studies ( Oda, 1989 ; Matsumi, 1992) which treated these problems, their studies can not predict them accurately because in which the interaction of an ambient fluid motion and a particle motion is not taken into consideration in theoretical analyses.

In the present study, a new numerical simulation method for predicting more accurately the settling behavior and deposition configuration of soil particles

---

<sup>1</sup>Dept. of Civil Engrg. Osaka City Univ. 3-3-138, Sugimoto, Sumiyoshi-ku, Osaka, 558



dumped into waters is developed, and what the settling behavior and deposition configuration depend on is discussed.

## 2. Simulation Method

The developed numerical simulation method consists of two phases; one is for analyzing the motion of each particle and the other is for analyzing the ambient fluid motion. In this paper the two dimensional calculation procedure will be presented( Oda, 1991 ).

### 2.1 Calculation of Particle Behavior

The motion of each particle is calculated by using the Discrete Element Method (the DEM) (Cundall, 1974) which is considered to be useful in analyzing the dynamic behavior of granular assembly.

The momentum and rotational momentum equations of particle  $i$  are written

$$(m_i + m'_i)\dot{u}_{pi} = \sum_j [F_x]_{ij} + f_x \quad (1)$$

$$(m_i + m'_i)\dot{w}_{pi} = \sum_j [F_z]_{ij} + f_z \quad (2)$$

$$(I_i + I'_i)\dot{\omega}_{pi} = \sum_j [M]_{ij} \quad (3)$$

where  $m_i$  and  $m'_i$  are the mass and added mass of particle  $i$  respectively,  $I_i$  and  $I'_i$  are the inertia and added inertia moment,  $u_{pi}$ ,  $w_{pi}$  are the horizontal and vertical velocity component of the particle,  $\omega_{pi}$  is the rotational angular velocity of the particle,  $[F_x]_{ij}$  and  $[F_z]_{ij}$  are the horizontal and vertical component of the force exerted between the particles  $i$  and  $j$  by their contact,  $[M]_{ij}$  is the rotational moment resulted from the contact with the particles  $i$  and  $j$ ,  $f_x$  and  $f_z$  are the fluid forces, "." represents the derivative by time, and  $\sum_j$  represents the sum with respect to every particle which contacts with particle  $i$ .

The forces  $[F_x]_{ij}$ ,  $[F_z]_{ij}$  and moment  $[M]_{ij}$  are calculated by

$$[F_x]_{ij} = -[f_n]_{ij} \sin \alpha_{ij} + [f_s]_{ij} \cos \alpha_{ij} \quad (4)$$

$$[F_z]_{ij} = -[f_n]_{ij} \cos \alpha_{ij} - [f_s]_{ij} \sin \alpha_{ij} + V_i \rho_p g \quad (5)$$

$$[M]_{ij} = -\frac{d_i}{2} [f_s]_{ij} \quad (6)$$

where  $\rho_p$  is the particle density,  $V_i$  is the particle volume,  $g$  is the acceleration due to the gravity,  $d_i$  is the diameter of particles  $i$ ,  $\alpha_{ij}$  is the angle between  $x$  axis and the segment of line which connects the center of particles  $i$  and  $j$ .  $[f_n]$  and  $[f_s]$  are the normal and tangential forces caused from their contact between the particles  $i$  and  $j$ , which are represented

$$[f_n]_{ij} = K_n \delta_n + \eta_n \delta_n / \Delta t_{DEM} \tag{7}$$

$$[f_s]_{ij} = K_s \delta_s + \eta_s \delta_s / \Delta t_{DEM} \tag{8}$$

where  $K$  is the spring constant,  $\eta$  is the damping coefficient,  $\delta$  is the relative displacement between the particles  $i$  and  $j$  during the time interval  $\Delta t_{DEM}$ , and the subscripts  $n$  and  $s$  represent the normal and tangential direction.

With the assumption that taking only the drag forces as fluid forces into consideration, the fluid forces acting on the particle  $i$  are written

$$f_x = -\frac{1}{2} C_D A_i \rho_f (u_p - u_f) \sqrt{(u_p - u_f)^2 + (w_p - w_f)^2} \tag{9}$$

$$f_z = -\frac{1}{2} C_D A_i \rho_f (w_p - w_f) \sqrt{(u_p - u_f)^2 + (w_p - w_f)^2} - \rho_f g V_i \tag{10}$$

$$C_D = \frac{24}{Re} + C_{D0}, \quad C_{D0} = 2.0 \tag{11}$$

$$Re = \frac{d_i \sqrt{(u_p - u_f)^2 + (w_p - w_f)^2}}{\nu} \tag{12}$$

where  $\rho_f$  is the fluid density,  $A_i$  is the cross sectional area,  $\nu$  is the coefficient of kinematic viscosity.

The interaction between particles and fluids is taken into account by calculating the drag force by using the relative particle velocity to the fluid given by Eq.(11).

The each particle acceleration at given time is calculated by solving Eqs.(1)~(3) explicitly, subsequently the velocity and location of each particle are determined.

### 2.2 Calculation of fluid motion

No calculation method will be presently available to analyze the ambient fluid motion caused by settling of a particle cloud. Edge and Dysart(1972) developed a model with the assumption that dumped material may behave as a dense liquid moving in waters. In the present method, an ambient fluid motion driven by a particle motion is analyzed by means of the MAC method under the assumption that the differences of the density of liquid-solid fluid which contains the particles may cause the motion of fluid.

The equation of continuity and momentum are respectively

$$\frac{\partial u_f}{\partial x} + \frac{\partial w_f}{\partial z} = 0 \tag{13}$$

$$\frac{\partial u_f}{\partial t} + u_f \frac{\partial u_f}{\partial x} + w_f \frac{\partial u_f}{\partial z} = -\frac{1}{\rho_f} \frac{\partial p}{\partial x} + \varepsilon_x \frac{\partial^2 u_f}{\partial x^2} + \varepsilon_z \frac{\partial^2 u_f}{\partial z^2} \tag{14}$$

$$\frac{\partial w_f}{\partial t} + u_f \frac{\partial w_f}{\partial x} + w_f \frac{\partial w_f}{\partial z} = -\frac{1}{\rho_f} \frac{\partial p}{\partial z} + \frac{\rho}{\rho_f} g + \varepsilon_x \frac{\partial^2 w_f}{\partial x^2} + \varepsilon_z \frac{\partial^2 w_f}{\partial z^2} \quad (15)$$

where  $\rho$  is the density of liquid–solid fluid which is evaluated as the mean density of liquid and particles, of which locations are determined by the DEM at some given time, in each numerical cell and  $\varepsilon$  is the coefficient of kinematic eddy viscosity which is calculated as follows

$$\varepsilon = 4 + 0.26v_0 + 32 \times 10^{-3}v_0^2 \quad (16)$$

where  $v_0$  is the fluid velocity component. This equation comes from the experimental observation by the ocean and meteorological agency in Nagasaki.

### 3. Calculation Condition

Some vertically two dimensional numerical simulations are performed in order to obtain the settling and dispersion behavior of particles dumped into waters from the water surface. The bottom of a container for dumping of particles is fixed on the water surface. After particles are arranged with short distances between other particles in the container, only the motion of each particle is calculated by using only the DEM until every particle stops to become stable in the condition of keeping the container bottom closed. Then the container bottom is opened, the motion of the particles and fluid are calculated.

According to making reference Kiyama (1983)  $10^{-6}$  sec is used for  $\Delta t_{DEM}$ . The value of the constants in the mathematical models are summarized in Table.1.

The calculation domain is taken between -50cm and +50cm in the horizontal direction for the MAC method and the cell size is taken constant:  $\Delta x = 2.5$ cm. The movements of particles and ambient flows are analyzed for the different water depths from 10cm to 100cm . The number of interior cells in the vertical direction is constant 40. The time step used in calculation is  $\Delta t_{MAC} = 10^{-5}$  sec.

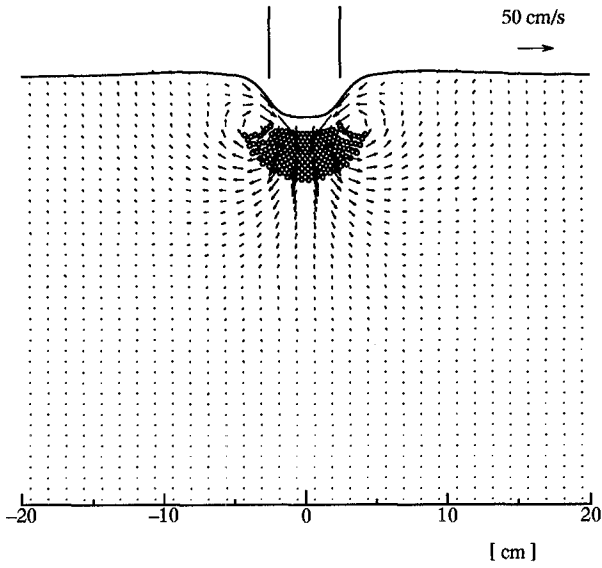
## 4. Calculated Results

### 4.1 Comparison with the experimental results

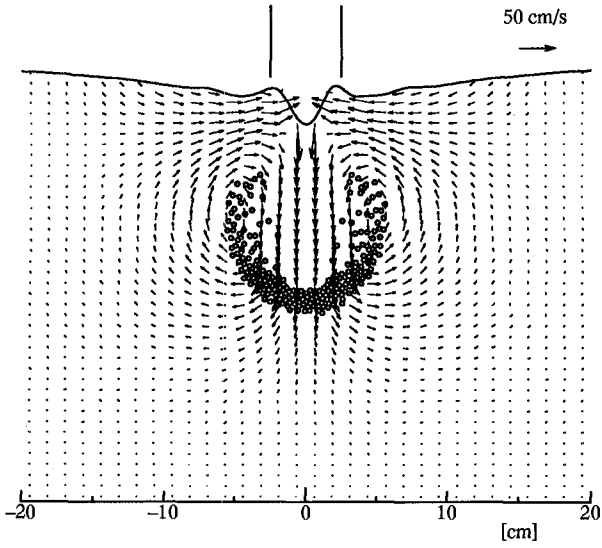
Fig.1 shows the calculated results of the settling and dispersion behavior of the particles with  $d=0.3$  cm diameter, of which the volume is  $20 \text{ cm}^3/\text{cm}$ , and the

Table 1. Values of the Constants in the Mathematical Model

Spring Constant	$K_n/\rho_p g = 4.23 \times 10^4 \text{ (cm)}$ $K_s/\rho_p g = 1.05 \times 10^4 \text{ (cm)}$
Dumping Coefficient	$\eta_n/\rho_p g = 2.47 \text{ (cm} \cdot \text{s)}$ $\eta_s/\rho_p g = 1.24 \text{ (cm} \cdot \text{s)}$
Friction Coefficient	$\tan \mu = 30^\circ$



(a)  $t = 0.2$  sec



(b)  $t = 0.4$  sec

Fig. 1. Calculated results

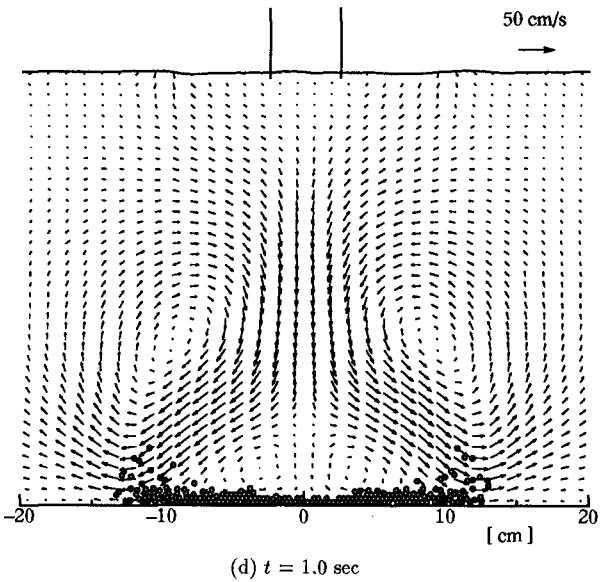
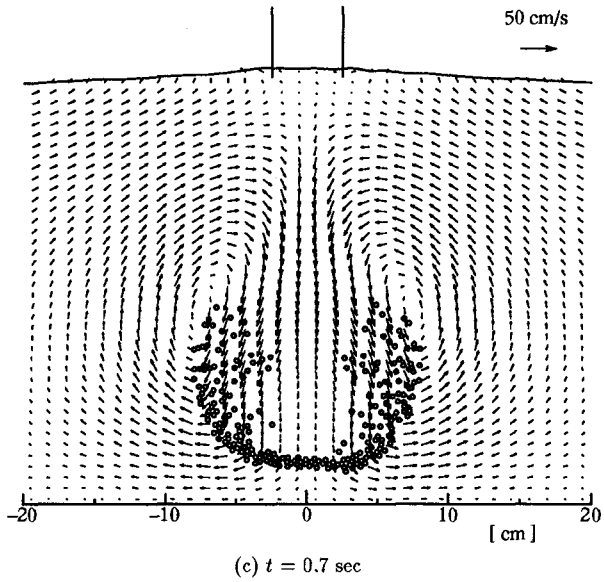


Fig. 1. Calculated results

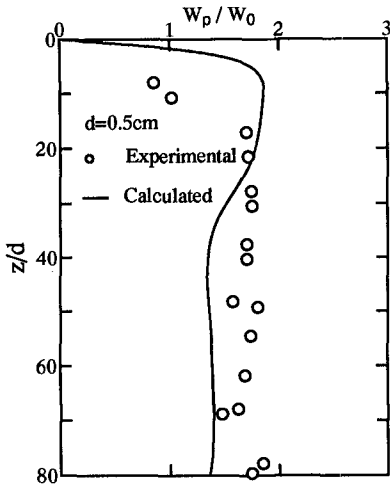


Fig. 2. Settling velocity of a particle cluster

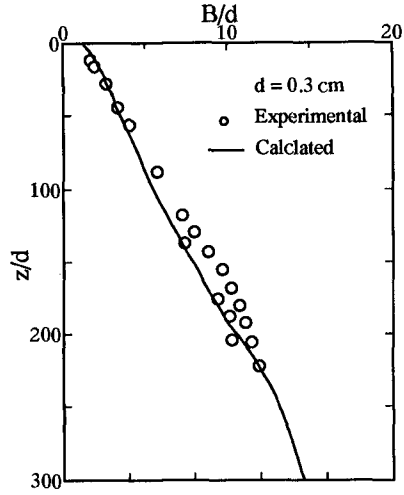


Fig. 3. Dispersion width of a particle cluster

movements of the ambient fluid flow at the specific time after dumping under the condition of water depth  $h=30$  cm and instantaneous opening of the container bottom of which width  $b_0$  is 5cm. From Fig.1, it may be seen that the particles are settling as a cluster rather than individually. These calculated results show a similar tendency to the experimental ones by Murota et al.(1988).

Fig.2 shows the comparison of the calculated results with the experimental ones on the settling velocity of the particle cluster. The settling velocity  $W_p$  is normalized by  $W_0 = \sqrt{(\rho_p/\rho_f - 1)gd}$ . Similarly the comparison of the calculated results with the experimental ones on the dispersion width  $B$  of the cluster in settling is shown in Fig.3. From Figs.2 and 3, it would be said that the present method can predict reasonably well the settling and dispersion behavior of particles.

#### 4.2 Deposition configurations and water depth

The distributions of the relative number of particles passing through per unit width of the horizontal plane at  $z/h = 0.2, 0.4, 0.6, 0.8$  and  $1.0$  in the case of  $h=10, 30, 50$  and  $100$  cm are shown in Fig.4. It should be noted that the distribution of relative number at  $z/h=1.0$  displays the deposition configuration of particles at rest on the water bottom. It is found in Fig.4(b) that for  $h=30\text{cm}$  the distribution has two peaks at  $z/h=0.4$  and the distance between two peaks becomes wider as the particles settling deeper. The deposition configuration on the bottom seems to be a mountain with two peaks. It can be seen in Fig.4 (c) that with settling of

particles two peaks are separated farther, those heights become smaller and the final deposition configuration becomes flatter. For  $h=100\text{cm}$ , the distribution seems to be almost uniform at  $z/h=0.6$  and subsequently the width and the height of the distribution become much wider and lower. These tendencies coincide with Mutoh's experimental results (1974).

Based on the experimental observation, he presumed that an increase in the horizontal fluid velocity near the bottom with the water depth induced an increase in the horizontal velocity of the particles near the bottom. But from the present calculated results it would be considered that the deposition configuration of the particles significantly depends on the dispersion behavior of the particles in the process of settling.

### 4.3 Settling behavior of particles and opening angular velocity of the container

Fig.5 shows the calculated results of the variation of space positions of particles and fluid velocity field at the moment of the contact of their lowest part with the water bottom with the opening angular velocity of the container bottom for  $h=30\text{cm}$ . From the calculated result for  $\omega = 30 \text{ deg./s}$ , each particle seems to be settling individually with characteristic of a single particle. But the particles for  $\omega=60 \text{ deg./s}$  would be settling as a cluster as shown in Fig.5(b). The cluster of the particles for  $\omega=90 \text{ deg./s}$  becomes larger than one for  $\omega=60\text{deg./s}$ .

The same calculations for  $h=10$  and  $50 \text{ cm}$  were performed. Based on those results for  $h=10\text{cm}$ , we could not see any longer the cluster of particles in settling even in the case of  $\omega=90 \text{ deg./s}$ . But for  $h=50\text{cm}$  the clusters could be seen in every case of  $\omega=30, 60, 90 \text{ deg./s}$  and became larger with an increase of the opening angular velocity of the container bottom. It is found, therefore, that the settling behavior of particles gets to depend more and more on the opening angular velocity of the container with in increase of the water depth.

### 4.4 Deposition configuration and opening angular velocity of the container

The deposition configurations under the condition of the particle volume  $V_0=20 \text{ cm}^3/\text{cm}$ , particle diameter  $d=0.3 \text{ cm}$ , the container width  $b_0=5\text{cm}$ ,  $\omega=30, 60, 90 \text{ deg./s}$ , and  $h= 10, 30, 50 \text{ cm}$  are calculated. From the calculated results as shown in Fig.6, it is found that the opening angular velocity of the container bottom does not effect on the deposition configurations in the case of  $h=10$  and  $30 \text{ cm}$ , but that for  $h=50\text{cm}$  the deposition width and height become wider and lower with an increase of the opening angular velocity. When the particles are dumped into waters with some opening angular velocity of the container bottom,

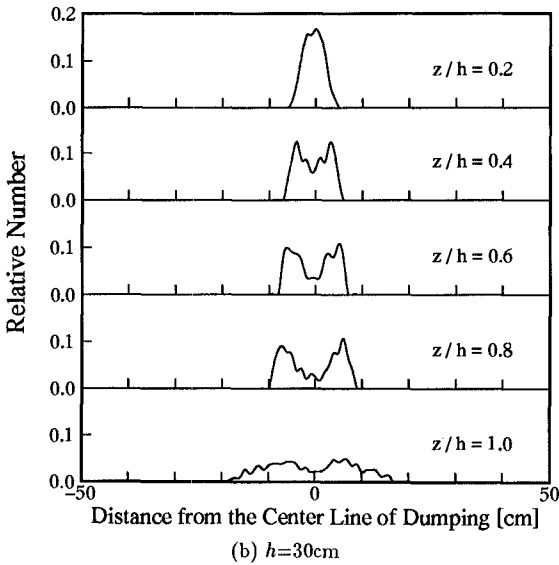
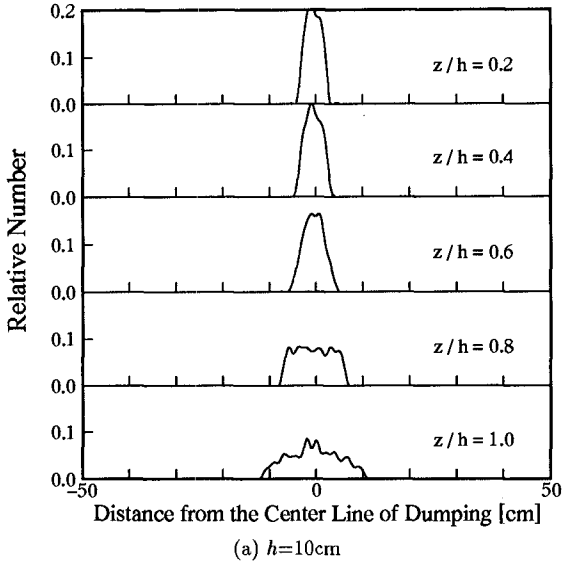


Fig. 4. Distribution of Relative Number of Particles Passing through the Horizontal Plane



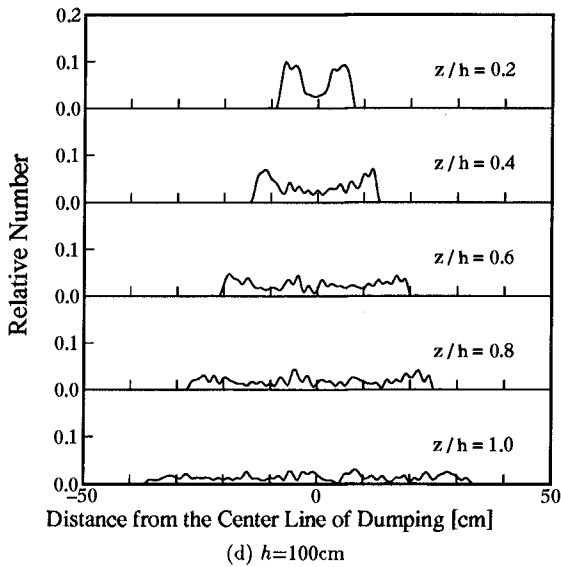
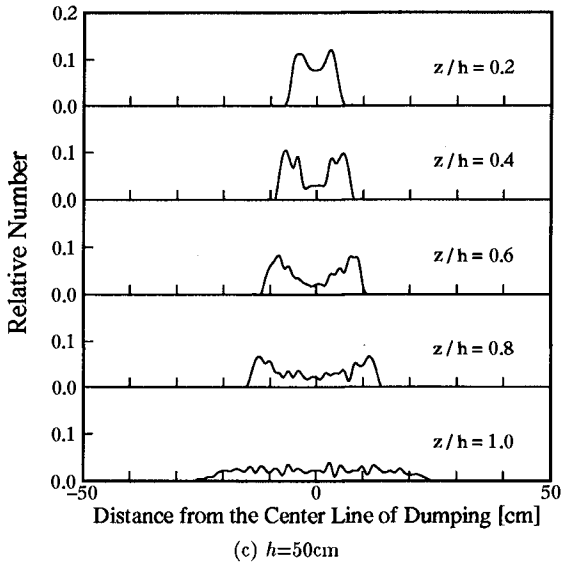
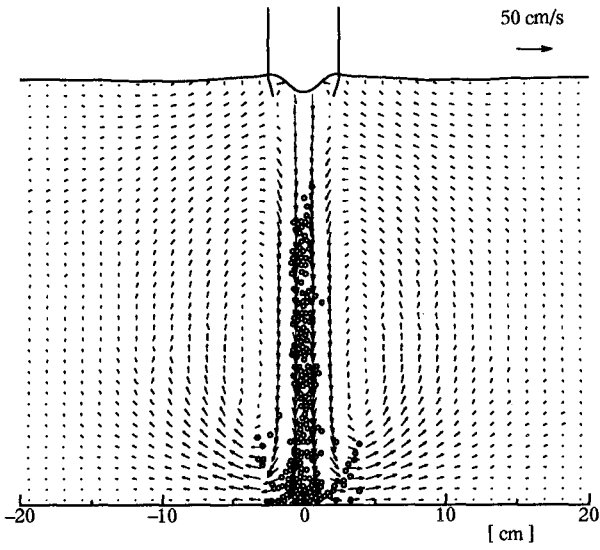
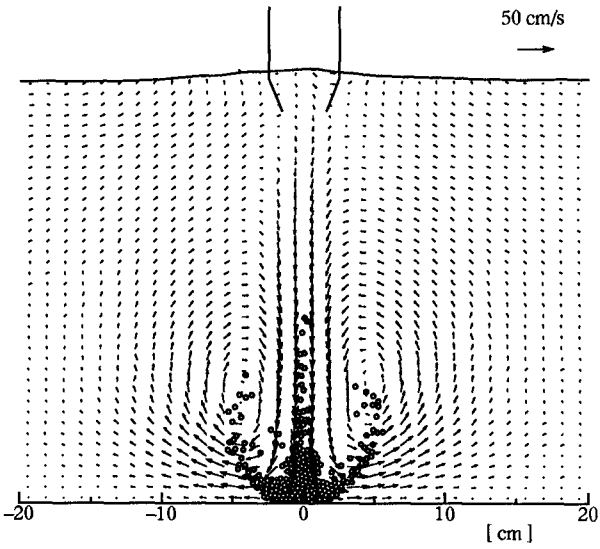


Fig. 4. Distribution of Relative Number of Particles Passing through the Horizontal Plane



(a)  $\omega=30$  deg./s



(b)  $\omega=60$  deg./s

Fig. 5. Calculated results

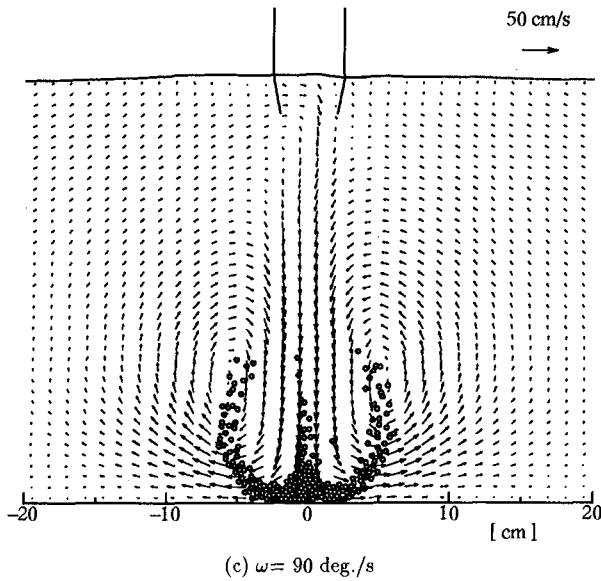


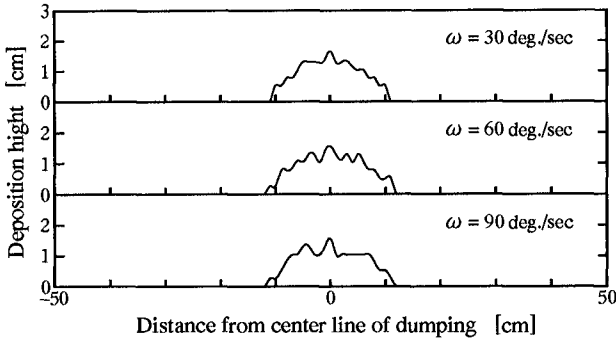
Fig. 5. Calculated results

the particles settle as a cluster on condition that the water depth and opening angular velocity are larger and the particle cluster grows larger with an increase of the water depth as described in section 4.3. Hence, it would be thought that the growth of the cluster of particles in settling effects on the deposition configuration.

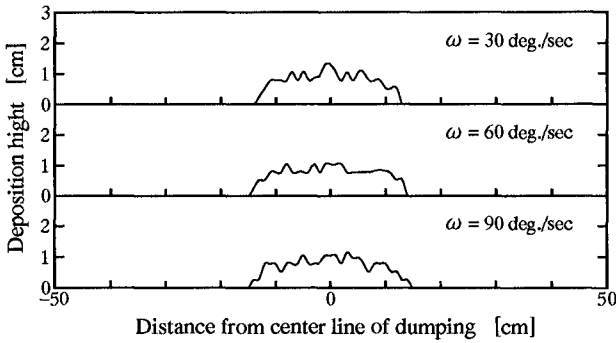
#### 4.5 Effect of the container width and the volume of dumped particles on dispersion width

The calculated results concerning the effect of the container width on a dispersion configuration when the volume of dumped particles is constant  $V_0 = 20 \text{ cm}^3/\text{cm}$  and the water depth is  $h = 30 \text{ cm}$ , are shown in Fig.7. The dispersion widths of particles in settling for  $b_0 = 2.5$  and  $5.0 \text{ cm}$  are almost the same and the deposition widths in both cases are also almost the same. But the dispersion and deposition widths for  $b_0 = 10 \text{ cm}$  are different from those for other cases.

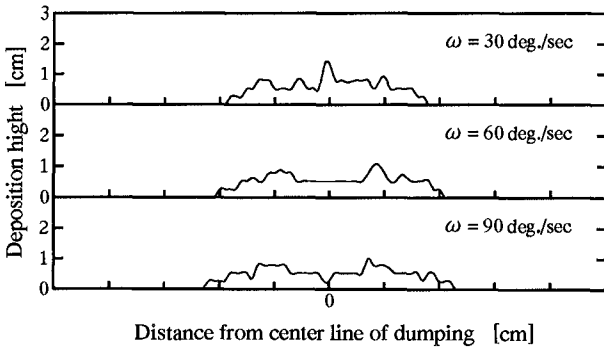
Fig.8 shows the calculated results concerning the effect of the dumped volume  $V_0$  on the dispersion width under the condition that the container width is



(a)  $h = 10$  cm



(b)  $h = 30$  cm



(c)  $h = 50$  cm

Fig. 6. Variation of the deposition configuration with the opening angular velocity of container bottom

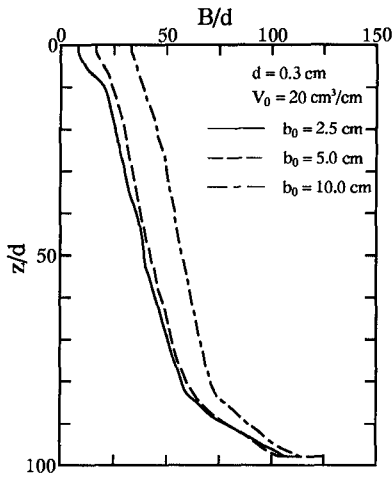


Fig. 7. Variation of dispersion width with container width

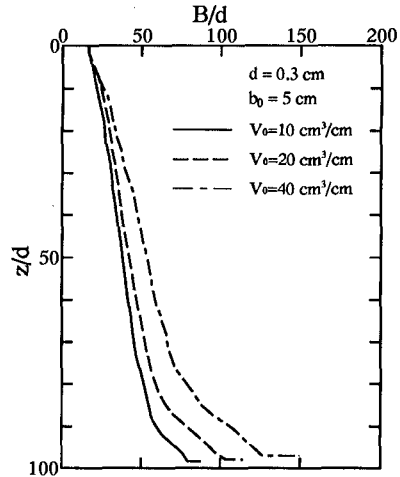


Fig. 8. Variation of dispersion width with the volume of particles

constant  $b_0=5.0\text{cm}$  and the water depth is  $h=30\text{ cm}$ . The dispersion width in settling and the deposition width on the water bottom become wider with an increase of the volume of dumped particles. Moreover what is evident comparing Fig.7 with Fig.8 is that the deposition width depends on the volume of dumped particles much more than the container width under the present calculation condition.

## 5. Conclusions

A calculation method for analyzing simultaneously the settling and dispersion behavior of particles and ambient fluid motion simultaneously was developed. It was founded that the calculated results of those behavior by the present method were reasonably good agreement with the experimental ones. Moreover the deposition configurations were calculated under the condition of the various water depths, container width, volume of dumped particles, and opening angular velocity of the container. The obtained results are summarized as follows :

- (1) The dispersion width of the settling particles and deposition width on the water bottom become wider with an increase of the volume of dumped particles.
- (2) The deposition width depends on the volume of dumped particles rather than the container width.

- (3) The deposition configuration depends on the water depth and it is influenced by the dispersion behavior of settling particles.
- (4) The increase of the opening angular velocity makes the deposition width wider in deeper water but it has few effect on the deposition configuration in shallower water.

## References

- [1] Cundall, P.A. (1974) : Rational Design of Tunnel Supports – A Computer Model for Rock Mass Behavior Using Interactive Graphics for the Input and Output of Geometrical Data, Technical Report MRD-2-74, Missouri River Division, U.S. Army Corps of Engineers.
- [2] Edge, B.L. and B.C. Dysart (1972) : “Transport mechanisms governing sludges and other materials barged to sea. ” Civil Engineering and Environmental Systems Engineering, Clemson University.
- [3] Oda K., T. Higuchi and K. Iwata (1989) : “Studies on Deposition–Mound Configurations of Quarry Stones Discharged from a Split–Hull Barge”, Proc. of Coastal Engineering, JSCE Vol.36, pp.814–818, (in Japanese).
- [4] Oda K., T. Shigematsu and K. Ujimoto (1991) : “Descent and Dispersion Analysis of Dumped Particles in Waters by Means of a Combined–DEM–MAC method”, Liquid–Solid Flows –1991, pp.159–163.
- [5] Matsumi Y. and A. Kimura (1992) : “Hydraulic Approach to Determining Optimum Interval of Discharge Sites of Barge in Constructing Rubble Foundation of Deep Water Breakwater”, 23rd Inter. Conf. on Coastal Engrg. ASCE, pp.3149–3162.
- [6] Kiyama H. and H. Fujiyama (1983) : “Application of Cundall’s Discrete Block Method to Gravity Flow Analysis of Rock–like Granular Materials”, Proc. of Japan Society of Civil Engineers, No.333, pp.137–146. (in Japanese)
- [7] Mutoh A., S. Yoshii and T. Ishida (1974) : “Sand Heap Undulation on the Sea Bed by the Bottom–Dumped Barge for Large Scale Land Reclamation”, Mitsubishi Heavy Industry Technical Review, Vol.11, No.1, pp.92–104.
- [8] Murota A., K. Nakatsuji, M. Tamai and H. Machida (1988) : “Formation of solid–and–fluid buoyancy cloud in reclining works”, Proc. of the 35th Japanese Conference on Coastal Engineering pp.777–781.

## CHAPTER 239

### Plane Design of "SPAC"; Countermeasure against Seabed Scour due to Submerged Discharge and Large Waves

Takao Shimizu<sup>1</sup>, Masaaki Ikeno<sup>1</sup>, Hisayoshi Ujiie<sup>2</sup> and  
Kazuaki Yamauchi<sup>3</sup>

#### Abstract

Discussion is carried out on stability of submerged outlet structures of thermal power plants sited on sandy ocean beaches. The authors conceived the new scouring protection "SPAC" constructed by riprapping of the seabed just in front of the outlet. In this study, the authors investigated the plane design of the SPAC by means of 1/25 scale physical model. First of all, properties of seabed scour due to submerged discharge and monochromatic or multi-directional waves were examined. Secondly, the spreading process of the SPAC was investigated, and the necessary width of the SPAC was evaluated based on width of discharged current, and on the drift of discharged current effected by longshore current due to oblique incidence of waves. Finally, the physical model was verified by comparison with field data.

#### Introduction

In front of an outlet of a power plant sited on a sandy open beach, seabed scour due to submerged discharge and large waves causes instability of coastal structures

---

<sup>1</sup>Research Engineer, Central Research Institute of Electric Power Industry, Japan Society of Civil Engineers, 1646 Abiko, Abiko City, Japan 270-11

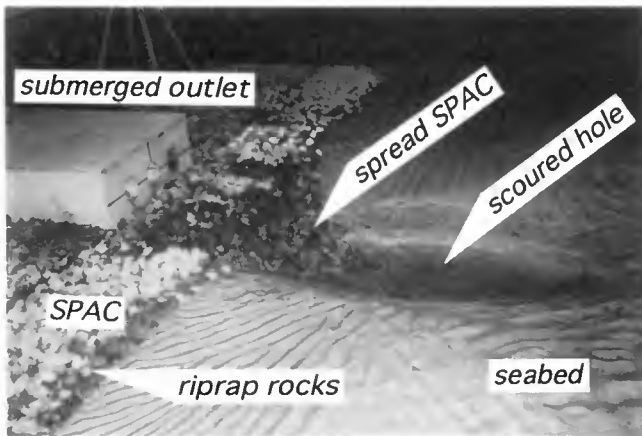
<sup>2</sup>Manager, Tohoku Electric Co., Ltd., Japan Society of Civil Engineers, 7-2-1 Nakayama, Aobaku, Sendai City, Japan 981

<sup>3</sup>Research Engineer, Tohoku Electric Co., Ltd., Japan Society of Civil Engineers, 7-2-1 Nakayama, Aobaku, Sendai City, Japan 981

such as discharge outlets.

Shimizu et al.(1991) proposed a new countermeasure called "SPAC"(Spreading Armor Coat). The SPAC is constructed by replacing seabed sand in front of an outlet with riprap rocks. During the seabed scouring due to current and waves, riprap rocks spread on the slope of the scoured hole forming an armor coat as shown in Poto 1. The SPAC thus protects the base of the outlet structure.

The process of cross sectional design of the SPAC shown in Fig.1 is as follows,(Shimizu et al.,1993).



Photograph 1. SPAC; Spreading Armor Coat

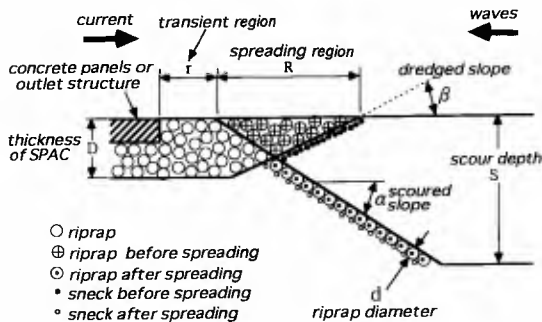


Figure 1. Cross Section of SPAC



1) Riprap diameter  $d$  is determined by the following equation, (Hasegawa, 1993) that gives riprap weight  $W$  that is stable against waves.

$$W = \gamma_r U_b^6 g^{-3} F_{rc}^{-6} (s_r - 1)^{-3} \quad (1)$$

where  $\gamma_r$  and  $s_r$  are respectively weight per unit volume and specific gravity of riprap rocks,  $U_b$  is bottom velocity,  $g$  is gravity acceleration. The value of the experimental constant  $F_{rc}$  is equal to 1.42.

2) Scour depth  $S$  is evaluated by the numerical simulation model, (Ushijima et al., 1992), not by a physical model experiment including scale effect.

3) Length  $R$  of the spreading region of SPAC is given by the following equations assuming that SPAC spreads as a single layer armor coat.

$$\text{if } S \leq 0.5 \delta \lambda^{-1} D^2 d^{-1} + D,$$

$$R = (\lambda^2 d^2 + 2 \delta \lambda S d)^{0.5} - \lambda d \quad (2)$$

$$\text{if } S > 0.5 \delta \lambda^{-1} D^2 d^{-1} + D,$$

$$R = 0.5 \delta D + \lambda d D^{-1} (S - D) \quad (3)$$

where  $D$  is the thickness of the SPAC,  $\delta = \cot \alpha + \cot \beta$ ,  $\lambda = \text{cosec} \alpha$ ,  $\alpha$  is the angle of repose of the scoured slope,  $\beta$  is the dredged slope angle. The value of  $\alpha$  was equal to 20 degree according to the experimental results.

4) Snecks should be inserted under the front edge of the SPAC in order to prevent sands from being sucked out through the void of riprap rocks after spreading. For the size of sneck, 1/3 of riprap diameter is recommended. For the amount of snecks, 15% of the riprap rocks of the spreading region is recommended.

In 1992, a SPAC works was carried out at Noshiro Power Station (Tohoku Electric Power Co.) facing the Japan Sea. In this study, the plane design of the SPAC is investigated to rationalize this countermeasure, by means of a 1/25 scale physical model simulating the sea condition in front of Noshiro Power Station.

#### SCHEME OF PLANE DESIGN

The process of plane design of the SPAC shown in Fig.2 is as follows.

1) Width  $B_f$  of scour is evaluated from the width of

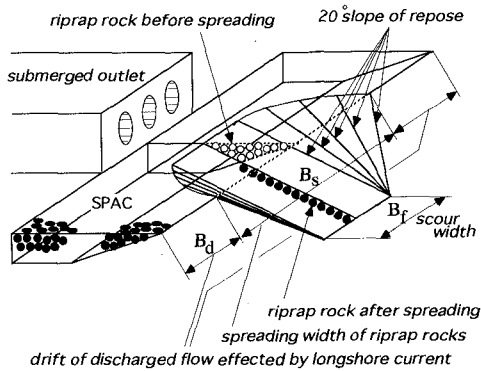


Figure 2. Definition Sketch for Plane Design Parameters of SPAC

the discharged current at the front edge of the SPAC.

2) Width  $B_s$  of the spreading region of the SPAC is evaluated from  $B_f$ .

3) Drift  $B_d$  of discharged current is evaluated from the velocity of longshore current due to oblique wave incidence.

4) The required width  $B$  of the SPAC is evaluated from  $B_s$  and  $B_d$ .

#### PHYSICAL MODEL EXPERIMENTS

In the multi-directional wave basin shown in Fig.3, we made seabed model with a 0.3m water depth, a sea-wall model covered with model armor units, a submerged outlet model consisting of three assembled pipes, and a discharge channel model.

Experimental cases and conditions are shown in Table 1. In the cases A1, A2 and A3, we compared the process of seabed scour due to submerged discharge alone, discharged flow plus multi-directional waves, and discharged flow plus the highest one-tenth monochromatic waves. In the cases B1 and B2, we colored and numbered some of the riprap rocks in both cases, short SPAC ( $R+r$  is small) and long SPAC ( $R+r$  is large), and tracked the spreading process of the rocks. The riprap diameter was 3cm. In the cases C1 and C2, we investigated the drift of the discharged flow effected by the longshore current due to oblique wave incidence. Finally, in the cases D1 and D2, an attempt was made to verify this experimental result by field data.

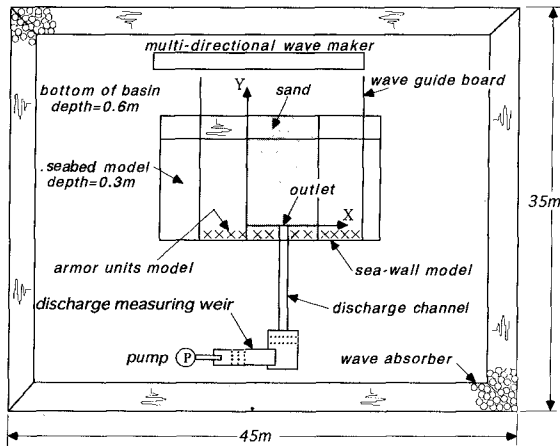


Figure 3. Arrangement of Physical Model Experiment

Table 1. Experimental Cases and Conditions

Case	Seabed	Discharge	Waves
A1	flat sand bed grain size is 0.2mm	3 pipes $\phi = 10.7\text{cm}$ velocity is 1m/s	no wave
A2	ditto	ditto	multi-directional waves $H_{1/3} = 16.5\text{cm}$ $H_{1/10} = 21\text{cm}$ $T_{1/3} = 2.4\text{s}$
A3	ditto	ditto	monochromatic waves $H = 21\text{cm}$ $T = 2.4\text{s}$
B1	flat sand bed protected by SPAC $R+r = 60\text{cm}$	ditto	ditto
B2	ditto except $R+r = 150\text{cm}$	ditto	ditto
C1	1/50 slope solid bed	ditto	oblique incident monochromatic waves $H = 22.1\text{cm}$ $T = 2\text{s}$ offshore wave angle is $30^\circ$
C2	ditto	ditto	ditto except $H = 28.4\text{cm}$
D1	model of Noshiro P.S.	ditto except single pipe	multi-directional waves $H_{1/3} = 16\text{cm}$ $T_{1/3} = 2\text{s}$
D2	ditto	ditto	ditto except no wave in first 80hr.

PROPERTY OF SCOUR DUE TO CURRENT AND WAVES

Fig.4 shows the seabed scour due to submerged discharge and waves in the cases A1, A2 and A3. The scoured hole due to discharge alone is longer along the line of discharged flow, and the maximum scour depth appears farther from the outlet than in other cases. The scoured hole due to discharged flow plus multi-directional waves is shallower, but the maximum depth appears nearer to the outlet. The scoured hole due to discharged flow plus monochromatic waves is the deepest and this condition is the most severe with regard to the stability of the outlet structure. We therefore adopted the last condition to the design of the SPAC.

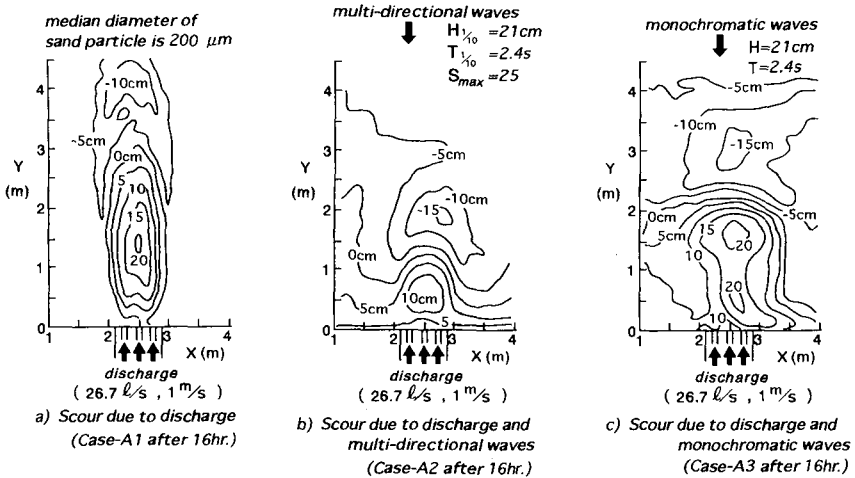


Figure 4. Seabed Scour due to Submerged Discharge and Waves

SPREADING WIDTH OF "SPAC"

Fig.5 shows the seabed scour in front of the SPAC in the cases B1 and B2. The foot of the outlet structure was successfully protected in both cases.

Fig.6 shows the spread profile of the SPAC in the cases B1 and B2. The spread profiles are well predicted by the previously mentioned equations (2) and (3), except that the predicted lengths of the spreading region of the SPAC are slightly longer than the experimental results.

Fig.7 shows the velocity distribution and half-value width of velocity of discharged current flowing against waves propagation in the early stage of Case A3. If the width of discharged current is represented by half-value width, it also represents almost 1/8-value width of sand transport rate distribution, because the sand transport rate is approximately proportional to the cube of the flow velocity. So, it was decided that half-value width  $B_f$  adequately represents the scour width.

Fig 8 shows the relationship between half-value width of discharged current velocity and offshore distance from the outlet in the case A3. The half-value width of discharged current is almost linearly proportional to the distance from the outlet.

Fig.9 shows the spread pattern of the SPAC for cases B1 and B2. The open circle at the end of the pin shaped mark shows the final position of spreading rock, and the other end shows the initial position of the rock. The closed circle shows unspread rock. The riprap rocks spreaded toward the center of the scoured hole, that is, the toe of the spreading SPAC. The spreading area of riprap rocks is perfectly covered by a spreading slope of half-value width  $B_f$  at the center part and a pair of fan shaped transient slopes at both ends. Width  $B_s$  of the spreading region of SPAC is the distance between both intersections of the fans and the initial front end of the SPAC.

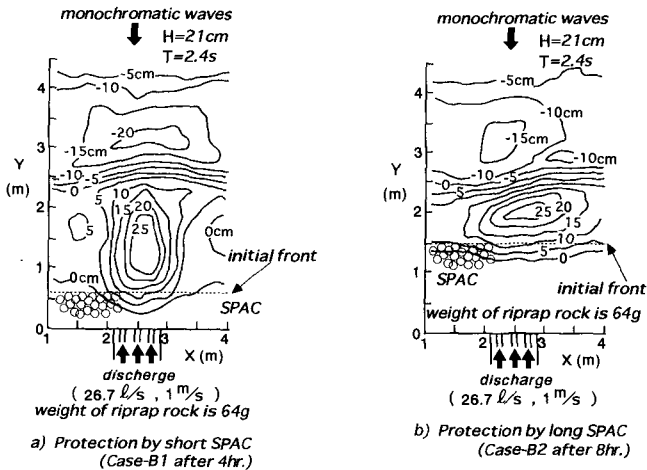


Figure 5. Protection by the SPAC and Seabed Scours in front of the SPAC

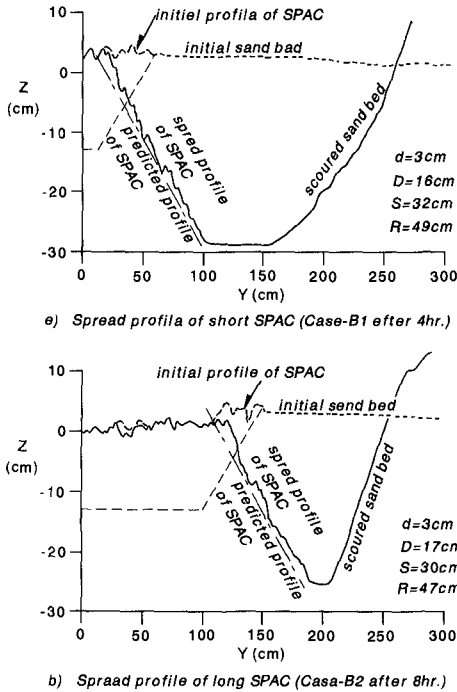


Figure 6. Spread Profile of SPAC

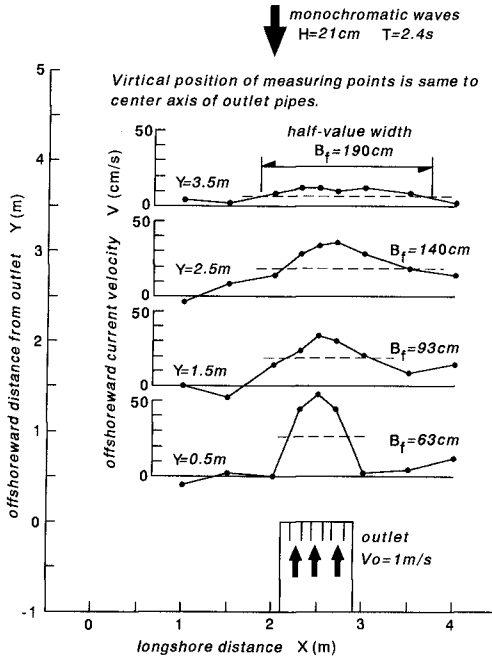


Figure 7. Velocity Distribution of Discharged Current Flowing against Wave Propagation

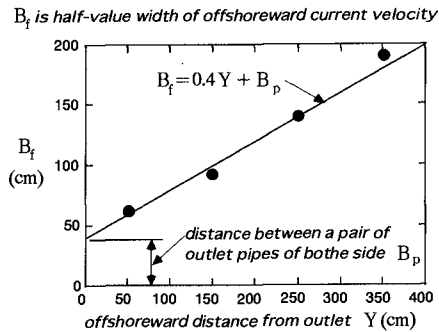
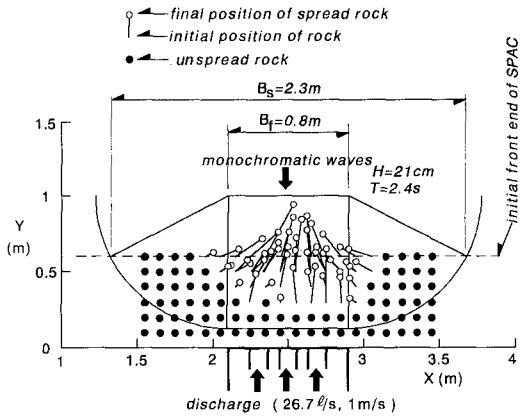
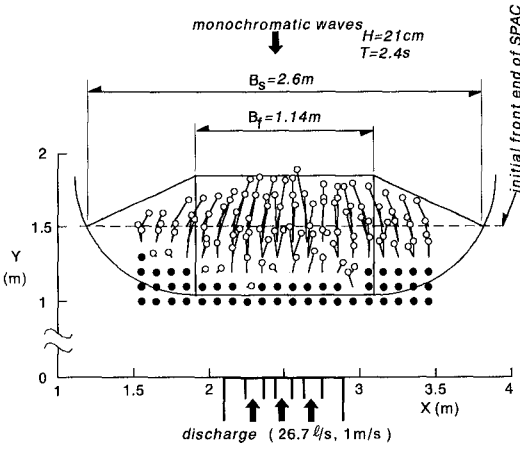


Figure 8. Half-value Width of Offshoreward Current Velocity



a) Spread pattern of short SPAC (Case-B1 after 4hr.)



b) Spread pattern of long SPAC (Case-B2 after 8hr.)

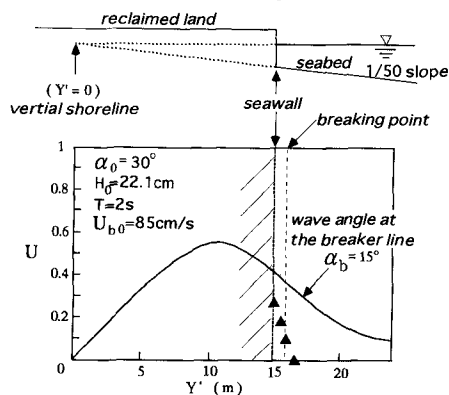
Figure 9. Spread Pattern of SPAC



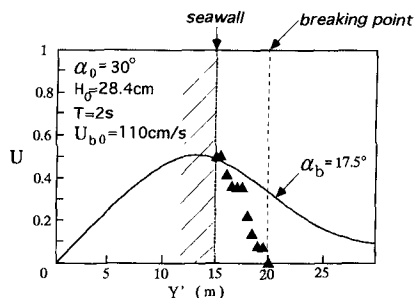
DRIFT OF DISCHARGED CURRENT

Fig.10 shows cross-shore distribution of longshore current velocity due to obliquely incident waves for cases C1 and C2, without discharge from the outlet.  $U$  on the vertical axis shows longshore current velocity normalized by analytical velocity  $U_{b0}$  at the breaking point, neglecting horizontal eddy viscosity. Closed triangles indicate longshore current velocity in front of reclaimed land in the experiment.  $Y'$  on the horizontal axis shows offshore distance from virtual shoreline under the condition of no reclaimed land. Smooth curves show velocity distribution of longshore current along a uniform slope beach after Kraus and Sasaki(1979). Longshore current velocity just in front of the seawall of the reclaimed land is nearly equal to or less than the velocity of longshore current along the beach.

$U$  is longshore current velocity normalized by analytical velocity  $U_{b0}$  at breaking point neglecting horizontal diffusion.



a) Longshore current due to small waves (Case-C1)



b) Longshore current due to large waves (Case-C2)

Figure 10. Longshore Current due to Oblique Incident Waves in front of Reclaimed Land

Fig.11 shows the drift of discharged current effected by longshore current for case C2. Vectors are flow velocity in the experiment. The curve from the outlet to the right is the trajectory of discharged current calculated by the following equation, (Katano et al.,1976).

$$(B_d / B_p) = 0.26 (u / V_0)^3 (Y / B_p)^4 \quad (4)$$

where  $B_d$  is the drift of discharged current,  $B_p$  is the width of the outlet,  $u$  is the longshore current velocity,  $V_0$  is the discharged velocity, and  $Y$  is the offshore distance from the outlet. The drift of discharged flow was well traced by the above equation.

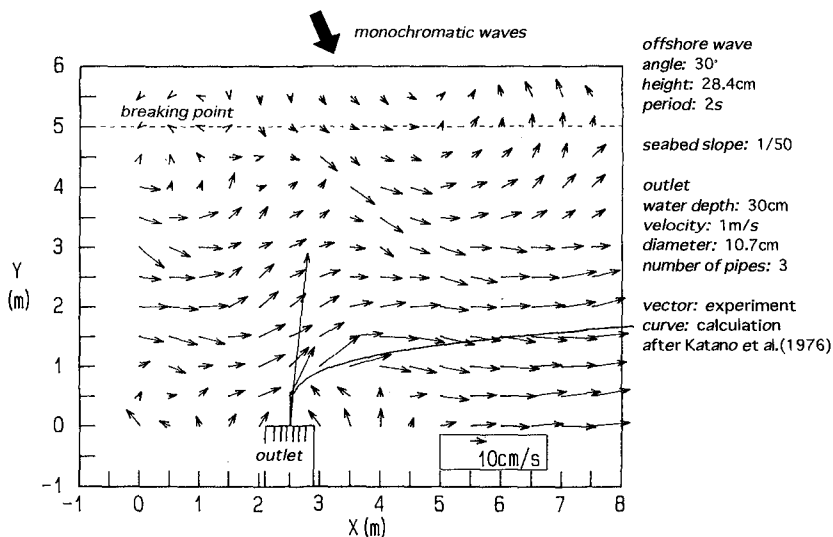


Figure 11. Drift of Discharged Flow Effected by Longshore Current

VERIFICATION by FIELD DATA

Fig.12 shows the field data of waves and warmed water discharge observed at Noshiro Power Station from July 1992 to May 1993. In this period, the unit No.1 of the power plant was under trial running. We adopted a 4m height and 10s period significant wave, and 27.8m<sup>3</sup>/s discharge as the experimental condition for comparison with the field data.

Fig.13 shows the comparison between field scour and simulated scour on 1/25 scale model in the cases D1 and D2. Maximum scour depth 125cm in the field was well simulated as 5cm scour depth in each case of the 1/25 scale models. Scour width in the field was also well simulated in the case D1. The on-offshore length of the scoured hole in the model was smaller than for the field scour. A model scour occurs nearer the outlet structure than for the field scour.

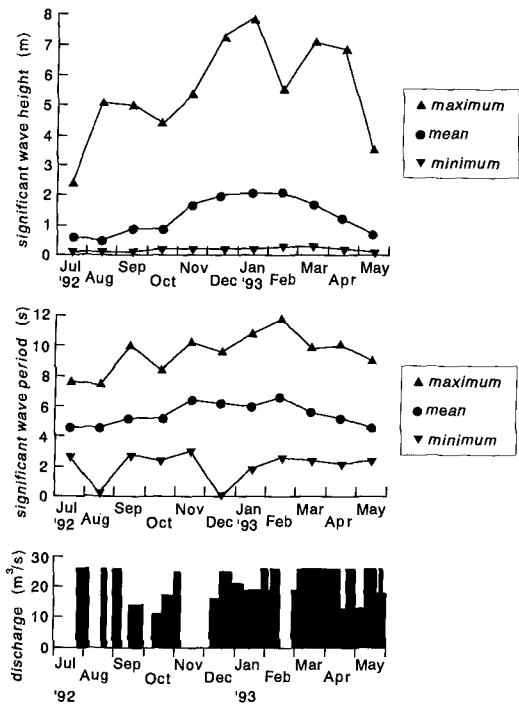
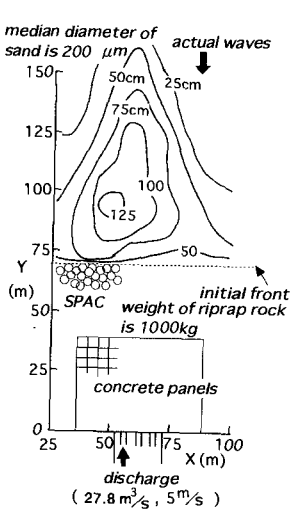
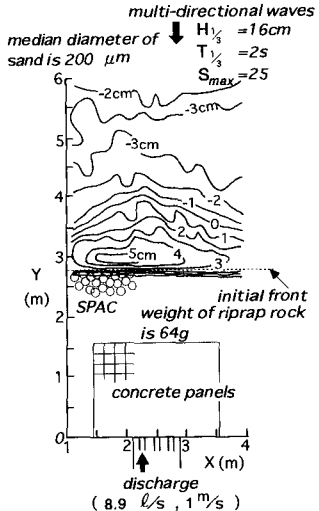


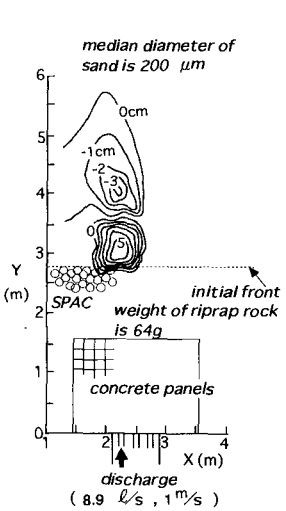
Figure 12. Field Data of Waves and Thermal Discharge Observed at Noshiro Power Station



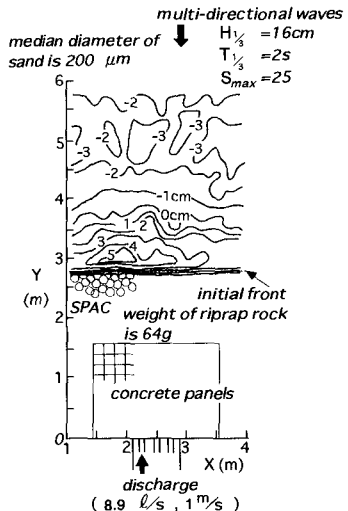
a) Observed scour at Noshiro Power Station (after one winter)



b) Simulated scour due to discharge and multi-directional waves (Case-D1 after 8hr.)



c) Simulated scour due to discharge (Case-D2 after 80hr.)



d) Simulated scour due to discharge and additional multi-directional waves (Case-D2 after extra 8hr.)

Figure 13. Comparison between Field Scour and Simulated Scours in 1/25 Scale Physical Model

CONCLUSIONS

(1) The SPAC design is sufficiently safe for the condition of discharged flow and highest one-tenth monochromatic waves.

(2) The width of the SPAC can be determined by both the spreading width of riprap rocks and the drift of discharged flow effected by a longshore current.

(3) The spreading width of the riprap rocks can be determined by assuming a scouring width as the half-value width of the discharged current velocity distribution, and by turning the 20 degree slope around toes at both ridges.

(4) The drift of the discharged flow effected by a longshore current is determined by using a formula based on a longshore current distribution caused by oblique incident waves, and by using a trajectory formula of jet injected into the current orthogonally.

(5) It was verified by the field data that the design method of the SPAC based on the physical model was within the safety margins required for the stability of the outlet structure.

REFERENCES

- Hasegawa, H. (1993): Demonstration study of artificial beach formation technology using SEASUP concrete revetment with a gentle slope, *Report of Central Research Institute of Electric Power Industry*, No. U93033, p.66 (in Japanese).
- Kraus, N.C. and T. Sasaki (1979): Effects of wave angle and lateral mixing on the longshore current, *Coastal Engineering in Japan*, Vol. 22, pp. 59-74.
- Shimizu, T., A. Sasaki and H. Ujiie (1991): The new counter-measure SPAC against seabed scour due to submerged discharge and large waves, *Proc. of Civil Eng. in the Ocean*, Vol. 7, pp. 301-306 (in Japanese).
- Shimizu, T., M. Ikeno, H. Ujiie and A. Sasaki (1993): Using "SPAC" artificial armor coat to protect seabed against scour due to submerged discharge and large waves, *Proc. of XXV Cong. of Int. Asso. for Hydraulic Res.*, Vol. IV, pp. 151-158.
- Ushijima, S., T. Shimizu, A. Sasaki and Y. Takizawa (1992): Prediction method for local scour by warmed cooling-water jets, *Journal of Hydraulic Eng.*, Vol. 118, No. 8, pp. 1164-1183.

## CHAPTER 240

### MODELLING AND ANALYSIS TECHNIQUES TO AID MINING OPERATIONS ON THE NAMIBIAN COASTLINE

G G SMITH<sup>1</sup>, G P MOCKE<sup>1</sup> and D H SWART<sup>2</sup>

#### ABSTRACT

The extraction of diamondiferous ore deposits along the coastal strip of southern Namibia has called for novel mining techniques. Quantitative analysis of coastal processes incorporating the prediction of short and long term shoreline response has proved particularly useful in optimizing such techniques. Further attention has been given to assessing the impact of mining operations on the nearshore ecosystem through comprehensive monitoring and modelling analyses.

#### 1 INTRODUCTION

Diamond mining operations in the southern coastal region of Namibia involve temporary coastal protection and beach reclamation schemes as well as the projected discharge of mine overburden material into the nearshore zone. In the extreme south of Namibia, near the town of Oranjemund (Figure 1), NAMDEB construct sand seawalls to protect mining operations. These seawalls have been successfully used to reclaim precious mining terrain in a highly dynamic wave climate (Moller and Swart, 1988). The continuation of these reclamation efforts over an area where reduced quantities of seawall replenishment material is available has however called for optimization. In this regard the construction of massive groynes for enhancing shoreline progradation has been investigated.

A proposed initiative incorporates the use of a dredger so as to mine the overburden of a coastal region. As a result of the dredging, some 26 million m<sup>3</sup> of sediment will be discharged onto the neighbouring beach. The accretion resulting from this nourishment will effectively reclaim land and provide a protective beach which reduces water seepage during final mining operations. Coastline modelling has

---

<sup>1</sup> Research Engineers, Ematek, CSIR

<sup>2</sup> Director, Ematek, CSIR, P O Box 320, Stellenbosch, 7600, South Africa

proved extremely useful in the planning and assessment of this mining initiative.

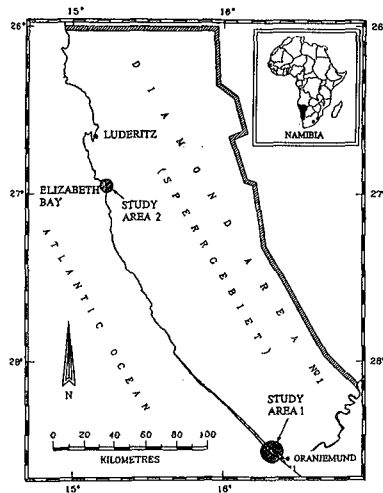


Figure 1: Location map indicating the diamond mining region within Namibia

Further north at Elizabeth Bay (Figure 1), NAMDEB mining operations involve the separation of undersized sediments from the diamondiferous ore. This fraction, comprising some 75% of the total excavated quantity of 20 million  $m^3$ , is discharged onto the beach in the adjacent sheltered bay. Due to the proximity of lobster and other biological communities, the necessity for assessing the environmental impact of such operations beyond the confines of the bay was identified. A comprehensive ongoing monitoring program, incorporating environmental measurements and predictive coastline and circulation modelling, was initiated for this purpose before commencement of mining operations.

## 2. ORANJEMUND

### 2.1 Environmental Conditions

The dynamic wave climate at Oranjemund, as derived from local Waverider buoy recordings has an average significant wave height of 2,2 m (average wave period is 12 seconds). Storms occur frequently, with significant wave heights over 4 m occurring about 25 times (average duration ~ 11,8 hours) per year. The predominant wave direction ranges between  $180^\circ$  and  $200^\circ$ .

The coastline is relatively straight, and lacking features such as headlands, is unprotected from wave attack. Vertical profile excursions of up to 4 m reflect the dynamic environment, where a sand grain size of approximately  $D_{50} = 500 \mu m$  occurs on the steep beach face.

Longshore sediment transport calculations as determined via a wave refraction study indicate a northward transport rate of 1,4 Mm<sup>3</sup>/yr. This rate was further verified via one-line modelling simulations (CSIR, 1979; CSIR, 1994a).

## 2.2 Seawall Mining Operations

Several attempts have previously been made to protect the coastal mining operation from wave action and to increase the mining area by mining closer to the waterline. One such attempt involved the placing of cobbles on the seaward face of a sand seawall, however the cobbles were removed and strewn across the beach. Various geofabric options such as covering the sand seawall with tarpaulins and protecting the seawall toe with cloth bags were also unsuccessful. In addition, short groynes were made from metal frames and filled in with boulders. However these structures did not penetrate sufficiently into the surf zone to interrupt the longshore sediment transport to cause accretion. Sheet piles were also used for a time, which allowed the mining of bedrock some 25 m closer to the sea. It was intended to re-use the piles as mining operations proceeded along the coast. However the percentage of sheetpiles which could be re-used was lower than predicted and the method was therefore found to be uneconomical. A further attempt involved the use of interlocking concrete blocks. These were interlocked laterally, but could slide downwards as sand was scoured from beneath them. This system was destroyed during the larger storms, however and took 8 to 10 days to re-establish. Since this system was also uneconomical, it was stopped. The most recent such initiative involved the use of flexible mattress, which failed principally due to toe scour.

The most successful of the protective structures has simply been a massive sand seawall (Figure 2), which has been practical to construct from the sand overburden material, and which is stripped almost to bedrock at a depth of some 20 m in places. Constant sand nourishment to the eroding seaward face of the seawall, which is 300 m to 800 m in length, ensures its structural integrity. At one stage of the mining operation, advantage was taken of the abundant sand overburden by advancing the seawall up to 300 m seaward. This ambitious scheme involved the placing of massive quantities of sediment on the seawall.

An interesting aspect of the study is that although a total of 12.7 million m<sup>3</sup> is used for the construction and maintenance of seawalls during the 5 year period, records show that at most 8 million m<sup>3</sup> of this amount was obtained from the mine. Thus a deficit of some 4.7 million m<sup>3</sup> exists. It is assumed that much of this material was rehandled, i.e. the material fed onto the wall is eroded and subsequently deposited to the north, where it is re-excavated and again fed to the wall.





Figure 2: Seawalls protecting the adjacent mining operations

Constant erosion from the seawall of average length 600 m occurred as it advanced northwards. Thus the quicker mining operations advanced, the less the total amount of material needed for the seawall. This is borne out by the optimization curve shown in Figure 3 which is constructed from data obtained during the mining operation. A regression analysis yields the equation of the curve:

$$V = 1450000R^{-0.963}$$

where:  $V$  = Volume of material used per metre length of the wall (in  $m^3$ ).  
 $R$  = Rate of northwards advance of the wall (in  $m/year$ ).

As can be seen from the curve, a rate of advance of less than about 500  $m/year$  is detrimental since it requires in considerable maintenance. High advance rates are, however, constrained by available resources and the necessity to maintain long seawall sections.

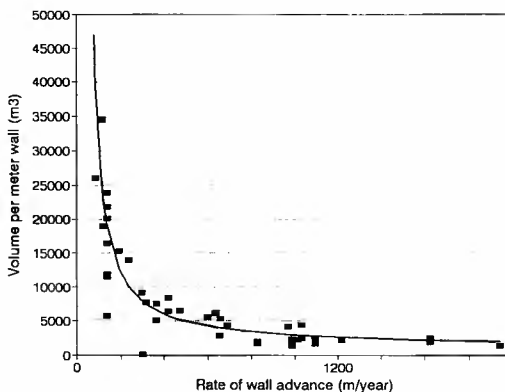


Figure 3: The relationship between rate of wall advance and sediment volume placed on the wall.

Further support for mining operations has been provided through an early warning system for wave attack. With the dominant incident southerly wave conditions at the site a remote link to waveriders to the south provides up to 12 hours of advance warning of extreme events.

### 2.3 Groyne "sand trap"

A unique initiative to capitalize on the high longshore transport rate, which is enhanced by the above-mentioned nourishment, is to construct groynes and thereby facilitate land reclamation updrift. A site favourable for both mining reasons and for groyne construction (i.e. foundations on a rocky outcrop) was selected, and one-dimensional coastline model simulations formed the basis of a detailed feasibility study.

Figure 4 shows the calibration of the one-line UNIBEST model for a 2 year period, over a 10 km coastline extent width. The relevant sediment sources are input to the model. This includes the beach nourishment as supplied to seawalls in the region, which varies between 60 000 m<sup>3</sup> and 270 000 m<sup>3</sup> at various locations along the coast. In addition, the point discharge of sediment from a processing plant is included (as indicated in the figure). This amounts to about 1.7 million m<sup>3</sup> of material; however this is somewhat finer material than that discharged to the seawalls.

As seen in Figure 4, the measured shoreline after 2 years is reasonably well predicted, taking into consideration that the measured beach cusps are not simulated by the model. In particular, the coastline accretion near the discharge point as well as a prominent coastline inflection point are well simulated.

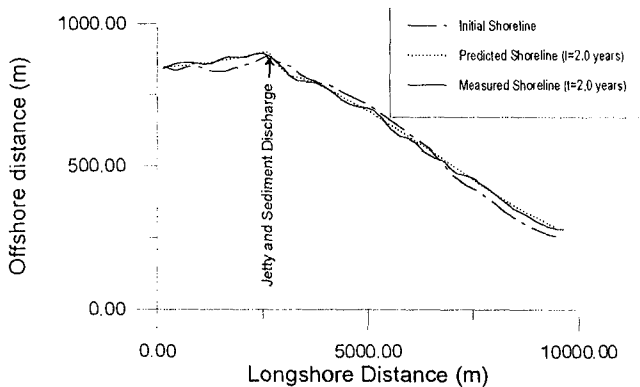


Figure 4: Coastline calibration prior to groyne accretion predictions

On this basis the coastline evolution due to groyne lengths of 150 m, 200 m and 300 m was assessed. For each case, two scenarios were considered. The first assumed a large sand seawall which is built so that it extends 40 m beyond the coastline. This calls for considerable input of sediment to maintain wall integrity

with estimates from a modelling exercise indicating this to be from 540 000 m<sup>3</sup>/year to 740 000 m<sup>3</sup>/year. The second scenario assumed a protective sand wall (termed a "beachwall") constructed about 40 m above mean sea level. The anticipated maintenance quantity for this wall involves between 105 000 m<sup>3</sup>/year and 144 000 m<sup>3</sup>/year.

Table 1 illustrates the accreted areas obtained for each of these scenarios. Between 10% and 20% extra area is gained through the inclusion of seawalls. This is due to the land reclamation facilitated by the seawalls *per se*, as well as the extra sediment input which accretes at the groyne. The benefit of a longer groyne is obvious. As may be observed the accretion from a 300 m groyne is more than double that of the 150 m structure for the beachwall case.

**Table 1: Accreted areas**

Groyne length	Beachwall (m <sup>2</sup> )	Seawall (m <sup>2</sup> )
150 m	151 400	181 800
200 m	222 400	248 700
300 m	363 100	297 400

A conceptual structural design of the groyne was carried out in parallel with this study. There was a number of unique constraints associated with the design; namely security limitations restricting the hire of plant, unsuitable armour rock material in the region and a groyne lifespan limited to about 6 years. Concrete armour and Caisson-type structures were found to be the most suitable under the above constraints.

#### 2.4 Dredge Discharge

A proposed initiative is the removal of some 26 million m<sup>3</sup> of sand overburden via dredging. This material extends to a depth of -26 m MSL globally and has a sand composition which is roughly similar to the beach sediment. It is intended to discharge this volume of material, after screening for diamond extraction, onto the beach, where the coast has already accreted by some 300 m due to sediment from discharge at an adjacent processing plant. Considering the prevailing dynamic wave climate and sediment composition, high offshore losses of sediment from the discharge can be expected.

Primary objectives of the study are to assess shoreline changes for input to seepage rate calculations as well as to co-ordinate the discharge in order to maximise accretion of the coastline during the final stages of mining. The reason for this is to minimise seepage from the sea into the deep mining area which is totally dewatered at this final stage. In addition the mining region must be protected from wave attack

which could lead to flooding of the working area.

The calibration of the one-dimensional coastline model is illustrated in Figure 5, in which historical coastlines were obtained from a topographical map, aerial photographs and a recent beach survey. The simulation is run from the initial shoreline of 1971. As can be seen, each of the measured shorelines is reasonably well predicted by the model. Of particular interest is the period between 1979 and 1986, during which a decrease in the discharge rate led to the retreat of the coastline.

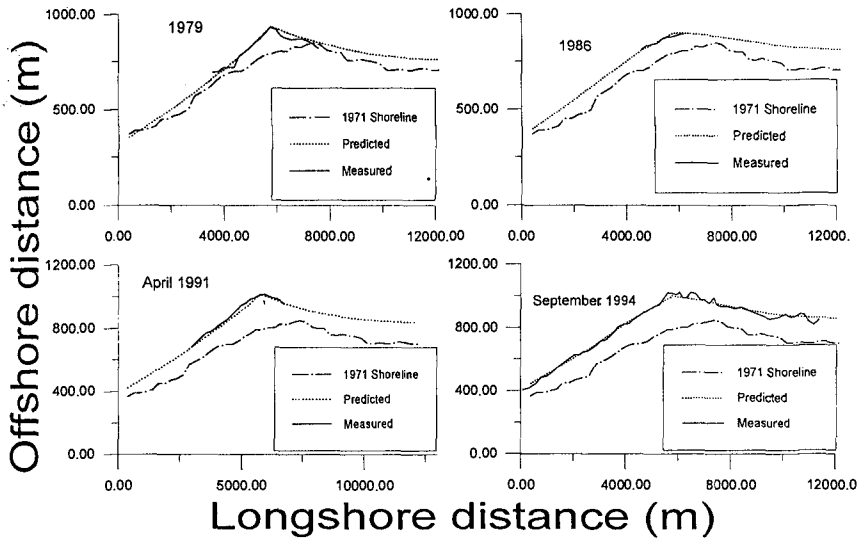


Figure 5: Calibration of the coastline model - dredge region

Further verification of the model was conducted by modelling a 20 km stretch of coast (Figure 6). In this simulation all of the major sediment inputs to the system were included as they occurred over the 23.4 year period. As seen, the model is fairly well validated against the measured coastline. The exception is in region of +5000 m, where unusually large accretion occurred.

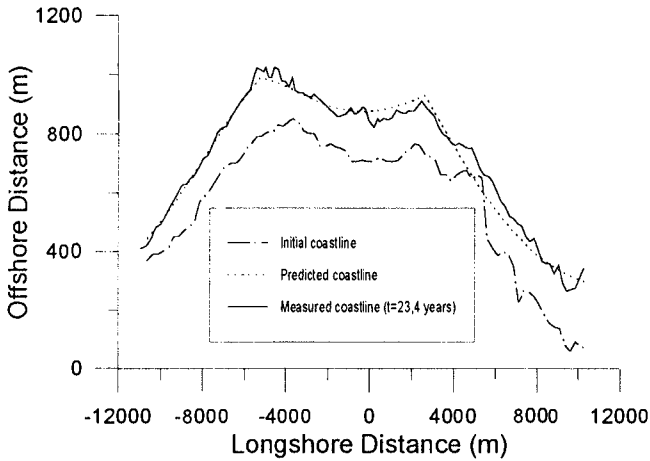


Figure 6: Calibration of the coastline model - extended region

With the validity of the model verified, various scenarios were explored. Figure 7 illustrates the accretion resulting from an optimised strategy from 4 discharge points. As seen, the accretion fillet at the completion of the discharge is centered opposite the final region of dredging. With the intention being to mine the region subsequently; the predictions of 0.5 and 1.0 year later show that the accreted coastline is still centered around the appropriate region in spite of considerable erosion.

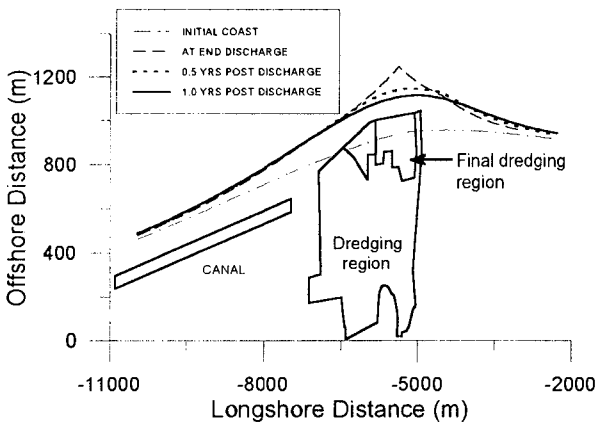


Figure 7: Coastline evolution in response to the optimised discharge strategy

**3. ELIZABETH BAY**

As schematized in Figure 8 some 75% of the mined ore deposit is discharged onto the beach within Elizabeth Bay. Although expected impacts on the sandy beach system within the bay have been deemed to be inconsequential, concerns have been

expressed regarding potential impacts on lobsters and other biological communities beyond the confines of the bay. The primary sediment input into the bay is at the eastern boundary, with a prominent sink the indicated aeolian dune corridor. The bay is relatively protected from incident waves, which are from a dominant southerly direction.

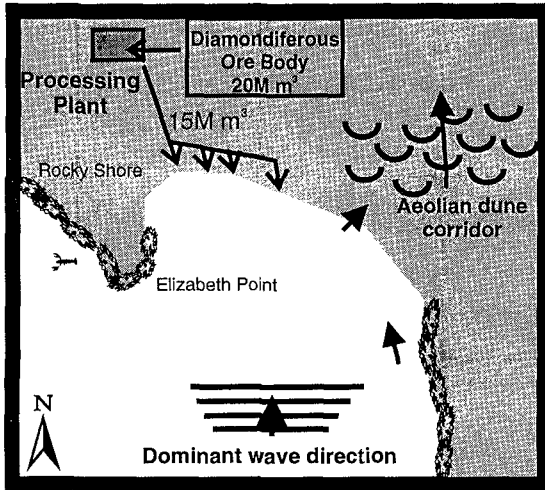


Figure 8: Schematisation of the sediment transport processes at Elizabeth Bay

### 3.1 Monitoring Programme

In anticipation of the commencement of mining operations at Elizabeth Bay in July 1991 a comprehensive monitoring programme was initiated the previous year. Data emanating from regular monitoring is supplemented by recordings made during the course of an earlier impact assessment (CSIR, 1988) as well as two field measurement campaigns (CSIR, 1992).

The principal components of the monitoring programme comprise aerial photography (including control sites), plant discharge (rates and granulometry), nearshore bathymetry, beach surveys, nearshore and beach observations (pro forma), wind recordings (two weather stations) and a bio-sampling transect.

### 3.2 Data Analysis

#### 3.2.1 Morphological response

Beach and nearshore bathymetric surveys recorded prior to mining operations constitute an effective baseline for assessing the impacts of discharge operations. The minimal changes apparent in these pre-mining surveys attest to a state of morphodynamic equilibrium within the bay.

For approximately the first 18 months of discharge operations an average monthly volume of the order 130 000 m<sup>3</sup> of sediment was discharged to the beach. This discharge, which was somewhat higher than originally anticipated, was concentrated at the outlet DP1 shown in Figure 9. Following a reduction in processing volumes, monthly rates have reduced to approximately 50% of the above figure since early 1993. Discharge was further extended to the more easterly outlets shown in Figure 9.

As further illustrated in the figure, shoreline response to the initial concentrated discharge is characterised by a local protrusion. A reduced and more distributed discharge thereafter, however, results in more even alongshore progradation.

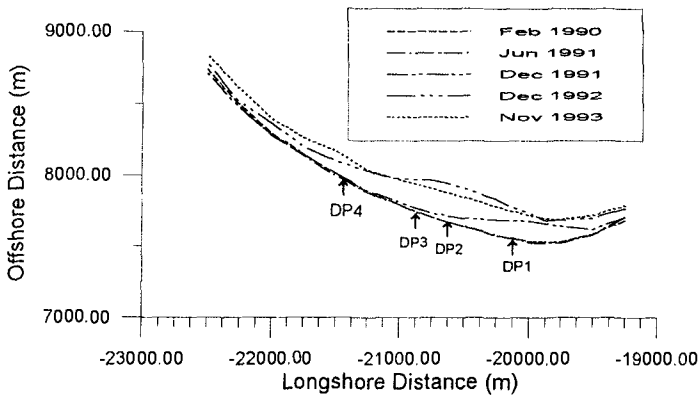


Figure 9: Coastline evolution at Elizabeth Bay and principal discharge stations

The measured cross-shore profile response at a location near the area of maximum discharge is depicted in Figure 10. Within the context of an original impact assessment (CSIR, 1988) the SEAGAR2 cross-shore profile model was employed for determining equilibrium profile response due to the discharge. The significantly steeper measured profile reflects only limited alongshore and cross-shore redistribution of beach material.

With an average  $D_{50}$  grain size in the range 0,25 mm - 0,4 mm the discharge fraction is somewhat coarser than the native material ( $D_{50} \sim 0,15$  mm). In the medium term an equilibrium profile somewhat steeper than the native state will therefore result. As anticipated in the original impact assessment, this will have an initial negative impact on the intertidal biotic community.

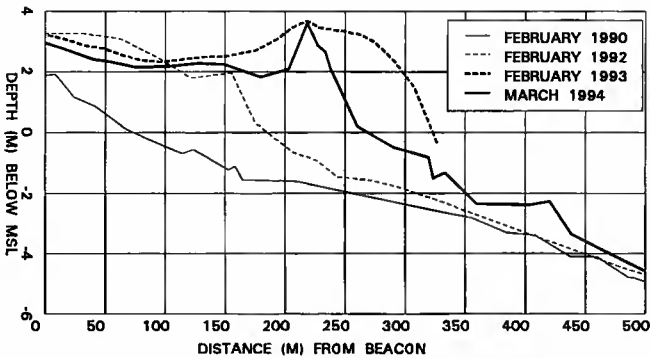


Figure 10: Cross-shore profiles measured at Elizabeth Bay

The difference chart comparing the pre-mining February 1990 bathymetric survey to that of March 1994 illustrates how morphological changes have been confined to the nearshore area. Although the most significant variability occurs at the western end of the bay near the discharge point, some seawards movement of material is evident near the eastern extent of the survey area. As will be discussed in 3.2.2 this area is coincident with a flow convergence zone and associated rip-current.

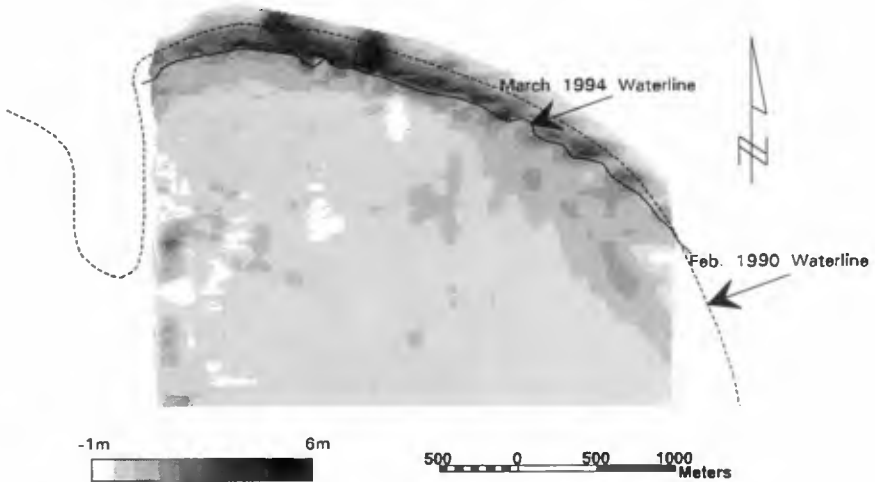


Figure 11: Bathymetric difference chart (February 1990 - March 1994)

**3.2.2 Sediment budget**

Schematized in Figure 8 are the primary constituent components of the sediment budget at the study site. A theoretical analysis incorporating wave refraction modelling predicted an influx into the bay of the order 0,25 Mm<sup>3</sup>/yr. This longshore transport rate may be seen to be substantially less than further south at Oranjemund,



which is a far more exposed section of coast. It further reflects the influence of aeolian sediment pathways feeding the Namib desert, of which the study site constitutes a prominent component. Field and theoretical barchan dune movement studies have estimated an annual transport in the range  $0,15 \text{ Mm}^3$  to  $0,3 \text{ Mm}^3$ . With a negligible flux of sediment around the prominent Elizabeth Point at the western boundary, it is likely that the influx into the bay and the aeolian sink are in approximate natural balance.

A summation of volume charges computed from beach survey measurements accounts for roughly 70% of the total  $3,1 \text{ Mm}^3$  discharged to January 1994. The 30% discrepancy with the discharge quantity is primarily attributable to the restriction of volume calculations to the limiting depth of surveys, which is of the order of 1 m below MSL. Other factors are bulking errors and increased aeolian losses due to an enlarged deflation zone following beach progradation. A further factor, discussed below, is the offshore transport of suspended fines. With up to 8% of the discharge material having a diameter less than 0,1 mm it likely an appreciable proportion of the pumped discharge is lost in this manner. A reliable summation of these variable contributions appears to account for the discrepancy.

#### *Turbid plumes*



An ubiquitous feature of the study coastline is the apparition of turbid plumes. Aerial photographic and on site monitoring has highlighted an increase in extent and frequency of such plumes since the commencement of mining operations. Such plumes are, however, primarily manifested within the confines of the bay. During the course of two field exercises (CSIR, 1992) under contrasting wind and wave conditions plume related parameters such as temperatures, salinities, currents and suspended matter characteristics were measured. In Figure 12 is schematized recordings of particle inorganic matter (PIM) concentrations over the study domain. Although elevated near the discharge area concentrations are considered to be within the range of naturally occurring turbidity ( $\sim 5 \text{ mg/l}$ ).

Figure 12: Particle inorganic matter distribution on 18 May 1992

### 3.3 Predictive Modelling

#### 3.3.1 Plume dynamics

The two dimensional hydrodynamic TIDEFLOW model was used to simulate tidal and wind driven circulation in the study area. Such a model, which was calibrated against drogue measurements, was considered to be appropriate due to the vertically well mixed state of the bay as recorded during the dominant strong wind conditions. The computed hydrodynamic flow field was coupled with the PLUME dispersion model for the prediction of turbid plume response within the bay. Measured concentrations were used for validation of this model. In Figure 13(a) is shown the simulated plume response under the dominant southerly wind conditions. Although relatively high concentrations are evident in the vicinity of the discharge area, values beyond the bay confines are minimal. Somewhat higher values in the vicinity of the point are evident for the infrequent NE wind conditions (Figure 13(b)), however, values remain within the range of naturally occurring turbidity. Scenario modelling showed increased movement of turbid water beyond bay confines in the event of a prograded coastline, however, this was remedied by moving the discharge points further east.

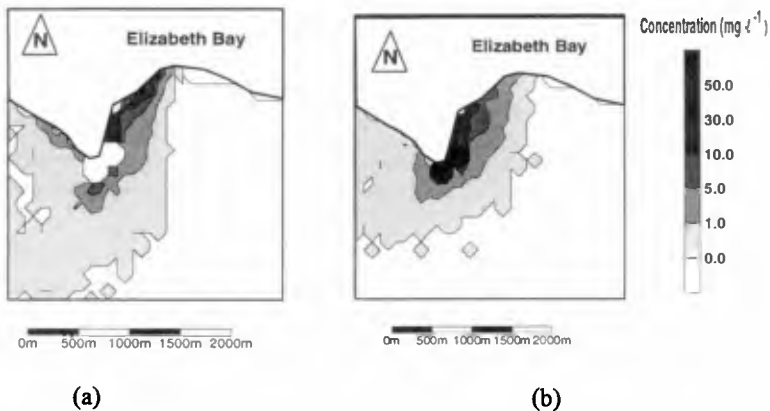


Figure 13: Modelled plume response after 48 hours for (a) a southerly and (b) north-easterly wind of 10 m/s

#### 3.3 Shoreline Response

Shoreline response to projected discharge was modelled, with reference made to the sediment budget discussed in Section 3.2.2 for definition of appropriate boundary conditions. The dominant contributions in this regard are an equivalent sediment influx and sink of the order 0,25 Mm<sup>3</sup>/yr at the eastern boundary and aeolian corridor respectively. Reference was made to the measured and equilibrium profile characteristics for the definition of short and longterm effective depths for the model.

As illustrated in Figure 14, the model is reasonably well validated against measured shoreline changes to date. Projecting the model to variable discharge scenarios, Figure 15 shows the engerated promontory developed by a concentrated discharge. A preliminary analysis of 2-D wave driven currents demonstrate the susceptibility to rip-current generation of such a prominent coastline feature. As is also shown in Figure 15, a distributed discharge strategy results in a more even progradation due to enhanced alongshore spreading of material.

Such an evolution will mitigate against prominent rip-current features, which may enhance seawards movement of different sediment size fractions.

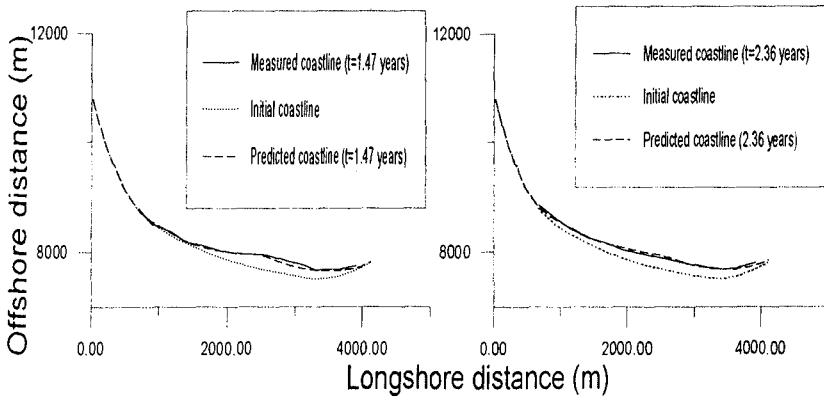


Figure 14: Calibration of the shoreline model at Elizabeth Bay

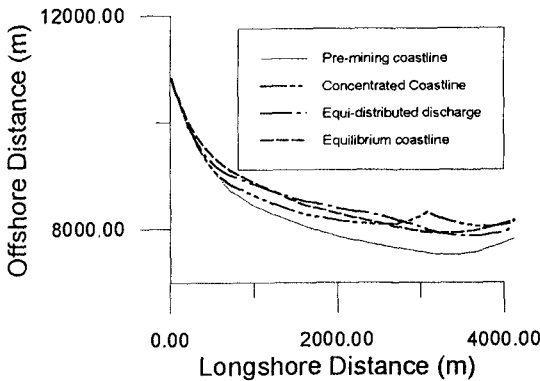


Figure 15: Discharge scenario simulations at Elizabeth Bay

## CONCLUSIONS

The comprehensive monitoring and analysis of environmental data has provided a critical underpinning element to coastal mining operations in Namibia. Assessments of the morphological response to variable mining strategies, which have led to the optimization of mining techniques, have been greatly facilitated by predictive modelling methods. Such methods, validated against available monitoring data, have further proved vital in assessing the potential impacts of such operations on adjacent eco-systems. In this regard, a controlled discharge strategy is not expected to pose a threat to biological communities beyond the confines of the bay.

## REFERENCES

- CSIR (1979). Oranjemund Beach Study. CSIR Report C/SEA 7935, Stellenbosch, South Africa.
- CSIR (1988). Elizabeth Bay production facility. Environmental Impact Study. CSIR Report EMAS-C 8887/2. Stellenbosch.
- CSIR (1990). Oranjemund Inshore Mining Project: Extension of Seawall North of No. 3 Plant. CSIR Report EMA-C 90137.
- CSIR (1992). The composition and dynamics of turbid seawater at Elizabeth Bay. CSIR Report EMAS-C 93004.
- CSIR (1993). Inshore Mining Project 1992 review report. CSIR Report EMAS-C 93034. Stellenbosch.
- CSIR Elizabeth Bay Monitoring Project; 1993. Review. CSIR Report EMAS-C 94059.
- Moller, J. P. and Swart, D. H. (1988). Extreme erosion event on an artificial beach. Proc of the 21st Coastal Eng. Conf., ASCE, pp 1882-1896
- Swart, D. H. (1981). Effect of Richards Bay Harbour Development on the adjacent coastline. 25th Congress. PIANC. Edinburgh, Section II, Vol. 5, pp889-917.

## CHAPTER 241

### Engineering Approach to Coastal Flow Slides

Theo P. Stoutjesdijk<sup>1</sup>, Maarten B. de Groot<sup>1</sup>,  
Jaap Lindenberg<sup>2</sup>

#### Abstract

Flow slides can play an important role in the stability of coastal foreshores and structures, in harbour design, in dredging activities and placing of hydraulic fill structures. In the south western part of the Netherlands the phenomenon is of major concern for the protection against flooding by means of dikes. More than 1100 slides have been registered since the year 1800. In the paper the practical experience and the knowledge obtained from experiments and fundamental research is briefly summarized. An engineering approach to coastal flow slides that combines the Dutch experience with flow slides with results of fundamental research of the past 10 years, is described.

#### Introduction

It is now 45 years ago that Koppejan et al [1948] first published on the subject of coastal flow slides in the Netherlands. The major concern at that time was that parts of the sandy foreshore in the Dutch province of Zeeland, sometimes including parts of the dike or the entire dike body, suddenly liquefied and disappeared into deeper water. Figure 1 is an example of such an event along the shore of the Eastern Scheldt basin. These events were called flow slides, as the loosely packed sand, apparently without reason, lost its

-----  
<sup>1</sup>Delft Geotechnics, P.O.Box 69, 2600 AB Delft, The Netherlands

<sup>2</sup>Ministry of Transport and Public Works, Department of Road and Hydraulic Engineering, P.O.Box 5044, 2600 GA Delft, The Netherlands

stability and moved like a highly concentrated sand-water mixture. The major slides involved a tremendous quantity of sand, leaving behind very gentle final slopes.

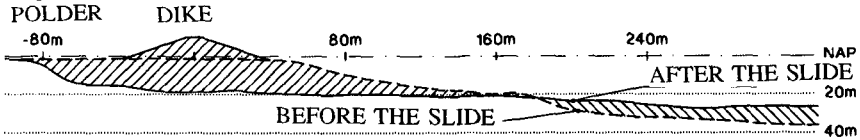


Figure 1 Example of an actual flow slide along the shore of the Eastern Scheldt basin (Leendert Abrahampolder)

Flow slides can play an important role in the stability of coastal foreshores and structures, in harbour design, in dredging activities and placing of hydraulic fill structures. This paper deals with practical aspects of the phenomenon of flow slides. In many situations the chance that a flow slide will occur is negligible, but at the same time there is a need for practical tools to judge this risk. An engineering approach to coastal flow slides is presented that combines the Dutch experience with flow slides with results of fundamental research of the past 10 years.

## Description of flow slides

A flow slide can be described as an instability that occurs in a fairly gentle underwater slope consisting of loose sand, causing liquefied sand to flow out into an even more gentle slope. A flow slide may occur after a change in slope geometry, for example steepening and/or deepening of the channel as a result of scour. A rather small, but quick change in load may trigger the sudden liquefaction of a vast amount of sand, which subsequently flows down the slope (Kramer 1988). In many cases the triggering mechanism is not known. It is thought flow slides can be triggered by almost any small change in soil stresses, caused by for instance seepage due to tidal water level variation, vibrations, ship waves, and so on. Consequently, if the conditions in the subsoil required for liquefaction are present, it is of no great importance what exactly initiates a flow slide.

Flow slides also occur in other parts of the world, for instance along the banks of the Mississippi river (Torrey, 1994), along the slopes of artificial sand islands in the Beaufort Sea (Sladen et alii 1985). The risk of flow slides is also present during dredging works in loose sand, unless special preventive measures are taken.

If a loosely packed sand is loaded by applying a small shear stress the sand will tend to reduce in volume. If the pores between the grains are water saturated either water will have to flow out of the pores, or the water will have to be elastically compressed to effect this change in volume. If no water can flow out (undrained conditions) an excess pore pressure will be the result.

Excess pore pressure reduces the effective pressure, and with that, the shear strength of the soil. If the sand is present in an underwater slope this can result in slope failure. This slope failure may take the form of a small slip failure but if conditions are unfavourable enough this may develop into a full size flow slide. In our opinion, liquefaction often first starts near the toe of the slope. A sudden loss of stability at the toe leads to a retrogressive failure of the entire slope.

### **Dutch experience**

Flow slides are encountered in many parts of the world. The Dutch experience is largely limited to the estuaries in the South Western part of the Netherlands, and in some cases in harbours or sand gain pits elsewhere. Since 1800 records of flow slides and slip failures along the shores of the Province of Zeeland have been kept (Wilderom, 1979). Between 1881 and 1946 229 flow slides were registered, resulting in a total area lost of 660 acres and a displaced volume of 25 million m<sup>3</sup> (Koppejan et al, 1948). The material displaced during one single slide can amount up to 5 million m<sup>3</sup> and a recession of the shore line up to 400 m. On several occasions stretches of dike of several hundreds metres width were lost. Of a total of 1129 slides that have been registered between 1800 and 1979 a number of 200 were sufficiently documented to make further analysis possible. This has led to practical criteria for the occurrence of flow slides under Dutch circumstances. Among these conditions is the assumption that flow slides are mostly found in young holocene marine sediments. Local experience shows that older holocene deposits and pleistocene deposits are less susceptible to flow slides. This empirical rule may be subject to local conditions. In Zeeland the pleistocene deposits are often densely packed. The older holocene deposits can be deposited more slowly than the younger holocene deposits, resulting in a denser package of the material. In case of the older deposits also bonding effects may play a role. There may also be an influence of difference in stress history between the deposits. These factors can be different for other locations however.

One of the most important geometrical factors is the initial slope along the channel. Figure 2 shows the average slope inclination before the occurrence of more than 100 field flow slides (squares) as a function of total slope height or channel depth. Much scatter is found and a useful tendency can not be deduced from this graph. A reasonable explanation is that the scatter is primarily caused by differences in local circumstances among which different sand properties and different in-situ densities. Apart from that, the average slope angle is probably not the best measure for evaluating the flow slide susceptibility. It stands to reason that the inclination of the steepest part of the slope may be a better measure.

In Figure 3 therefore, instead of the average slope, the inclination of the steepest part of the slope is shown, again as a function of slope height for the more than 100 locations where flow slides occurred in the past. The idea is that

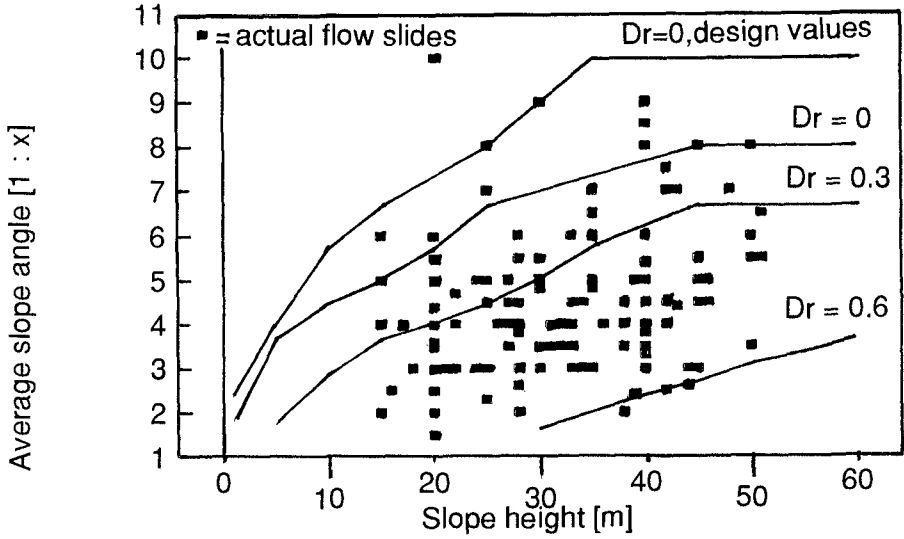


Figure 2 Actual flow slides compared to model results: Average slope angle before the slide as a function of slope height

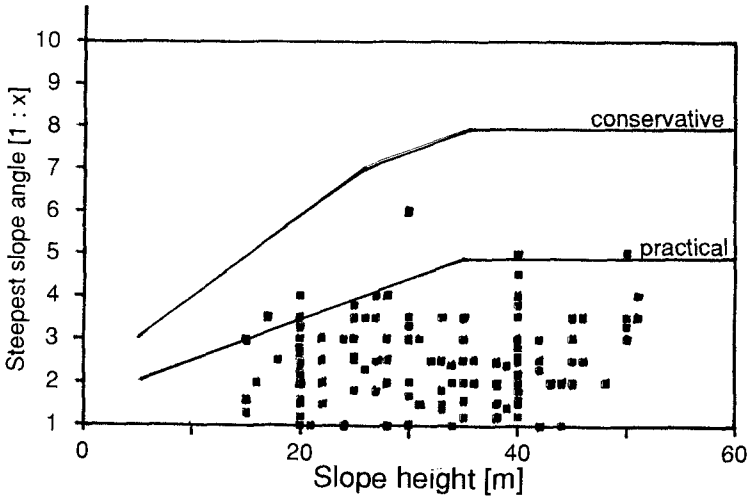


Figure 3 Actual flow slides compared to model results: Slope angle of steepest part of the slope as a function of slope height



steepening due to scour will be most dangerous in the steepest part of the slope. The height of the steepest part varies between a few metres to about 30 m. Although a somewhat better result is found, the scatter remains rather dominant. Practical criteria for the initial slope inclination at which flow slides may take place, derived from the geometrical information gathered in Fig. 2 and 3, will be very uncertain if applied to a specific location and a large safety margin should be included. On the other hand the available data of flow slides in the field makes it possible to get a rough impression of the flow slide probability. Therefore the total number of slides within the period of the last 100 years combined with the total stretch of dikes and foreshore principally vulnerable for flow slides and the geometric data of the flow slide records are analysed thoroughly. Moreover the average chance that not only the foreshore is affected, but also dike failure takes place, in relation to the locally present foreshore length can be assessed too by using the available information concerning final slopes after occurrence of the slides. Although very useful in Dutch engineering practice, again this statistic result has to be treated very carefully if applied to a specific site where local geotechnical information is absent.

### **Measures against flow slides**

In past centuries no measures against the effects of flow slides along the foreshore were taken. The occurrence of dike falls was simply taken for granted. Secondary dikes were built behind the sea dike to keep the area of inundation limited. Since 1880, due to increased application of stone protection, in more and more stretches the recession of the shore line has been stopped. The number of flow slides and slip failures has reduced accordingly. The effectivity of shore protection in regard to the prevention of flow slides is not due to a reduction of flow slide susceptibility of the sand. Instead, fixing the foreshore makes steeper slopes impossible. The observations that flow slide occurrence was stopped after slope fixation confirmed the theory that in addition to sand properties and actual slope steepness, also change in geometry (e.g. steepening of the slope) is an important conditional factor for the occurrence of flow slides.

Another method, consisting of the application of groynes to arrive at a system of 'fixed points', was less successful. Although the objective of keeping the tidal channel away from the dike could be realized by this system, local scour caused slides near the tip of the groynes, causing the system to fail.

The risk of flow slides can be reduced by densification. Experiments using different densification techniques have been carried out in the Netherlands. The success of different techniques depends on material properties such as the amount of fines. Also, densification has to be possible up to a certain depth to be effective. In the Netherlands, one example of large scale densification is known. The subsoil of the Storm Surge Barrier in the Eastern Scheldt was densified, using a specially developed densification ship, the

Nautilus. With large vibratory needles, densification up to a depth of 30 metres could be realised. In most cases however, densification is not economically feasible.

## Experiments

Flow slides are seldomly witnessed, and then of course only surface events can be seen. Witness reports of flow slides indicate that the process can take several hours, during which at the surface sandmasses of one metre thick by several metres width slide down into the water. The retrogression speed is several metres per hour. There are also indications that under water the flow of sand and water is much quicker, in the order of metres per second. A fine opportunity to study flow slides were large scale tests on hydraulic fill in 1988 (Bezuijen and Mastbergen, 1988). During the test series sand bodies were constructed with varying deposition rates in a test flume of 2,5 m height. Especially the tests with fine sand ( $D_{50}$  of 135  $\mu\text{m}$ ) showed that flow slides were of major influence on the final slope angle. Tests with a coarser sand ( $D_{50}$  of 225  $\mu\text{m}$ ) showed considerably less flow slide susceptibility, resulting in steeper slope angles. Another remarkable result of these tests was the fact that slope height was very important. The sand body could develop to a height of 1 to 1,5 m before a flow slide took place, after which the same cycle started again. Pore pressure measurements showed that liquefaction occurred very sudden: pore pressures rose from zero to values indicating almost complete liquefaction within 0,1 seconds. After that the actual slide and the dissipation of pore pressures could last approximately one minute. The sand body of course was of limited dimensions, which can implicate that with increasing dimensions also the time scale in which events take place will be larger.

Other interesting large scale experiments were carried out between 1973 and 1976 (Kroezen et al, 1982). During these tests a loosely packed and water saturated sand body of 2.5 m high, 3 m wide and 25 m long was forced to liquefy at the fairly steep slope at one end of the mass consisting of fine sand. After that a retrogressive failure mechanism could be witnessed that displaced with a horizontal speed of 0.5 to 1.5 m per second through the sand body. In some tests the retrogressive failure almost reached the other end of the facility at 25 m distance of the location where the mechanism was initiated. Very gentle final slopes were found (up to 1 to 25). During the passage of the failure front excess pore pressures almost equal to the initial effective stress in the sand were measured, indicating that full liquefaction had taken place.

## Research

In 1981 fundamental research was started. By that time liquefaction could be understood in terms of critical density, as defined by the results of drained and undrained triaxial tests on soil samples (Lindenberg and Koning,

1981). Since then progress has been made in two aspects. First, it has been attempted successfully to describe the constitutive behaviour of loosely packed sands, based on the results of drained triaxial tests. On the one hand there is contraction, caused by shear stress, which results in excess pore pressure if no drainage can take place. Excess pore pressure in its turn leads to decompression. These two volumetric aspects can be measured separately in drained triaxial tests. If the behaviour of the soil is undrained, such as is the case in liquefaction problems, the tendency to contract and the tendency to increase in volume due to excess pore pressure have to compensate each other. Models that take these aspects in regard have proven to be successful in describing the response and failure of loosely packed sand in triaxial tests.

In underwater slopes in nature, shear stress is related to the foreshore geometry. Slope height and slope angle have influence on in-situ stresses. A research programme was started in 1985 to study the influence of slope geometry. A mathematical model has been developed in which the effects of sand properties and geometry characteristics were combined. The in-situ stresses for a given geometry are given by analytical formulae, obtained by generalizing the results of Finite Element computations.

These in-situ stresses are introduced in the liquefaction model together with the basic relevant constitutive behaviour of the sand as a function of sand density.

The model itself verifies for 500 points in the sand mass the so called instability criterion during an incremental slope steepening under undrained conditions (Stoutjesdijk, 1993):

$$d\gamma = 1/\lambda \cdot d\tau_{xy}$$

- $\lambda$  = stability factor
- $d\gamma$  = incremental change in shear strain
- $d\tau_{xy}$  = incremental change in shear stress

$\lambda$  is in fact the eigenvalue of a matrix system comprising the entire system of stress strain relations for the sand for given sand density.

Instability occurs if  $\lambda < 0$ . It means that an increase in shear strain can only be attended by a decrease in shear stress. Because slope steepening is generally accompanied by shear stress increase, the condition  $\lambda < 0$  in fact indicates that large shear deformation will take place. The instability condition has been assumed identical to liquefaction.

Because the stress state as well as the sand behaviour varies from point to point, and with slope angle and slope height, instability will start in one point in the sand mass for a certain slope angle. The corresponding slope is the critical slope inclination for the considered foreshore. As the slope steepening in the calculation proceeds, the unstable zone will grow. An extensive series of calculations has shown that the most critical zone in most cases is located next to or just below the toe of the slope. In Figure 4 the result of a calculation is shown. The figure shows several contourlines. Inside each area, defined by a

contourline, instability has occurred during the calculation for a certain slope angle. The most inner contourline gives the critical slope inclination, in this case 1 : 4.5 ( $\tan\alpha = 0.222$ ). The critical zone, as can be seen in Figure 4, is situated near the toe of the slope at some depth beneath the toe.

In the liquefaction model only two slope shapes can be introduced and the sand properties refer to one sand density for the entire mass. For practical purposes the properties of the most susceptible layer will be introduced in the model. This sandlayer only has to be considered critical when the calculated unstable zone has reached the layer boundary. The corresponding slope inclination is the critical inclination for that most sensitive layer. In case a second layer could be susceptible too, the calculation has to be repeated with the sand properties for that layer. In this way the stability of a foreshore can be assessed.

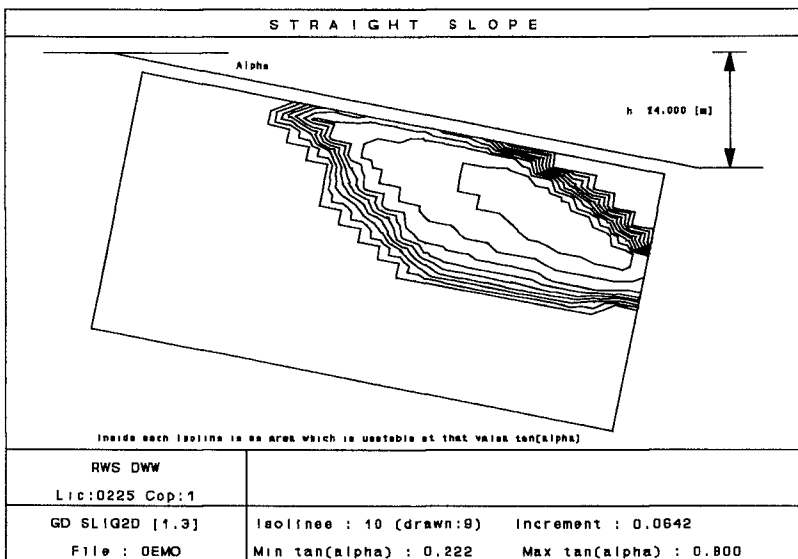


Figure 4 Example of a calculation result with the model. Note the situation of the critical zone inside the inner contourline.

### Verification

The research results have lead to a model for the prediction of flow slides. In the model slope height, slope angle and (material behaviour as a function of) relative density are the most important factors. The model has been verified on a number of flow slides, that have taken place in the past. Also the trend following from some 150 actual flow slides as shown in Fig. 2 and Fig. 3

can be compared with the results of model calculations. Average values for the input parameters have been used. Calculations were made for several slope heights and several relative densities. Relative density is defined here as  $Dr = (n_{max} - n)/(n_{max} - n_{min})$ , in which  $n$ ,  $n_{max}$  and  $n_{min}$  are the in-situ density, the maximum density and the minimum density. Fig. 2 and 3 show that most actual slides can be represented by relative densities between 0 and 0.6. Another important trend is the influence of the slope height or channel depth. The calculation results in Fig. 2 and 3 indicate that a flow slide may occur at a much more gentle slope in case of deeper channels. This effect is the logical consequence of the basic stress strain relations for sand, found from triaxial tests in the laboratory and introduced in the model.

## Practical approach

To make a prediction of the flow slide susceptibility for any particular situation with the flow slide model it is necessary to perform in-situ borings, in-situ density measurements, triaxial tests, calculations and analysis. For many practical applications this may either take too much time or may be too expensive. A set of calculations has been performed, based on Dutch sands and applicable to comparable situations only (similar material, tidal range 3 to 5 m). Unfavourable assumptions have been used to be on the safe side. The result is shown in Fig. 2 as the line marked "Dr=0, design values". In many cases information on local circumstances may lead to a less conservative result.

It is possible to derive an impression concerning the type of material and the in-situ density from cone penetration tests (CPT's). Probably, because of the relatively static character of this test, the CPT yields a better impression of in-situ density than more dynamic tests such as the widely used Standard Penetration Test (SPT's). A second advantage of the CPT is that a continuous image of the subsoil is obtained.

If the investigation is further pursued, then an extensive programme of field tests, laboratory tests and calculations has to be performed. Because of the size and the cost of these activities, it has to be considered whether or not the chance that the investigation will lead to limitation of preventive measures is present. The investigation consists of electrical density measurements, borings, sieve curve analysis, determination of maximum and minimum densities, triaxial testing and calculations with the flow slide model. This entire programme is necessary because the flow slide susceptibility of one particular situation can only be determined if detailed information on in-situ density and behaviour of the material of the site is available.

Uncertainties are introduced with each step of the procedure. These uncertainties can be quantified by assuming that each relevant parameter has a stochastic character, which can be described with the expectancy value, a standard deviation and a statistical distribution. Uncertainties concerning the calculation models can be implemented too. As described before, the liquefaction calculation model yields the eigenvalue  $\lambda$ . This  $\lambda$  can be conceived

as a function of the stochastic variables so that  $\lambda$  may be used as the reliability function in a probabilistic analysis. The probability analysis yields two results:

- the probability of the occurrence of a flow slide
- the contribution to the uncertainty of each of the parameters to the total failure probability.

The latter result enables the designer to decide whether additional investigations may help to increase the reliability of the assessment of potential flow slides. In this way, the design cycle of modelling and determining input parameters can be optimized.

## References

Bezuijen, A. and Mastbergen, D.R. (1988). "On the Construction of Sand Fill Dams. Part 2: Soil Mechanical Aspects." *Mod. of Soil-Water Interactions, Delft*.

Koppejan, A. W., Wamelen, van B.M. and Weinberg, L.J.H. (1948). "Coastal Flow Slides in the Dutch Province of Zeeland." *Proc. 2nd I.C.S.M.F.E., Rotterdam*.

Kramer, S.L. (1988). "Triggering of liquefaction flow slides in coastal soil deposits." *Engineering Geology, 26, 17-31*.

Kroezen, M., Vellinga, P., Lindenberg, J. and Burger, A.M. (1982). "Geotechnical and hydraulic aspects with regard to seabed and slope stability." *Proc. 2nd Canadian Conf. on Marine Geotechnical Engineering, Halifax, Canada, June 7-11, 1982*.

Lindenberg, J. and Koning, H.L. (1981). "Critical Density of Sand." *Geotechnique 31, No. 2, 231-245*.

Sladen, J. A., D'Hollander, R.D., Krahn, J. and Mitchell, D.E. (1985). "Back analysis of the Nerlerk berm liquefaction slides." *Canadian Geotechn. J., 22, 579-588*.

Stoutjesdijk, T. P. (1993). "Liquefaction study Eastern Scheldt foreshore." *Proc. Third Int. Conf. on Case Histories in Geot. Eng., St. Louis, Missouri, June 1-4, 1993, 643 - 648*.

Torrey III, V. H. (1993). "Flow Slides in Mississippi Riverbanks". *Preprints International Riprap Workshop 1993, 1008-1031*.

Wilderom, M. H. (1979). "Results of investigation of the foreshores along the waters of Zeeland (in Dutch)." *Rijkswaterstaat, Research Dept. Vlissingen, Nr. 75.2*.

## CHAPTER 242

### EROSION OF LAYERED SAND-MUD BEDS IN UNIFORM FLOW

Hilde Torfs<sup>1</sup>

#### Abstract

In a laboratory flume the formation and erosion of stratified sand-mud beds in uniform flow was studied. The experiments showed that depending on the initial conditions of suspended sediment concentration and mixture composition, consecutive inputs of a mud/sand suspension will lead to the formation of a layered sediment bed. Peaks in the measured density profiles show the different layers and indicate a possible segregation of the sand due to differential settling. During the erosion of the stratified bed, the sediments are eroded layer by layer. This results in a sequence of suspended load (fines) and bed load (sand) transport phases.

#### Introduction

The sediments in estuaries and coastal areas are generally a mixture of sand and mud. Due to tidal action the sediments are periodically suspended and afterwards, during slack water, deposited. This sequence of erosion and deposition results in many cases in a layered bed structure, because the sand fraction settles faster. In the Scheldt Estuary layers of a few millimetres up to two centimetres thick are found (Bastin 1974). Also for the Humber Estuary and the Severn Estuary sediment laminations are reported (Williamson 1991). Understanding the erosion of such sediment bottoms is important for the control of navigation channels, dredging activities and pollution as well as for the modelling of sediment transport in estuaries and coastal seas.

---

<sup>1</sup>Research assistant for the Belgian Fund for Collective Fundamental Research F.K.F.O., Hydraulics Laboratory, Katholieke Universiteit Leuven, de Croylaan 2, B-3001 Heverlee, Belgium

To study the fundamental aspects of the erosion of layered sand-mud beds, laboratory experiments in uniform flow were carried out. During these tests the whole erosion process was followed starting from the formation of the bed out of a suspension and looking at the layer thickness and the density profiles, over the incipient motion phase until the different modes of erosion of the stratified, mixed bed.

### Experimental Procedure

The laboratory set up consists of a 9 m long flume with a rectangular cross section of 40 cm wide. The total length of the flume is divided into 4 different regions: a 4 m upstream inflow region with fixed bed, a 3 m long glass wall measuring section with the sediment bed, a sediment trap and a 1.5 m downstream outflow region with fixed bottom. A settling tank (1 m high) can be mounted on top of the flume, above the measuring section.

The tank is filled with salt water ( $3 \text{ kg/m}^3$ ). To simulate a tidal cycle, at regular time intervals - twice a day - a slurry of mud mixed with sand is pumped into the settling tank. The slurry density results in suspended sediment concentrations in the settling tank of a few grams per litre, too low for hindered settling to occur but about the order of magnitude of the near bed sediment concentration after a heavy erosion event. This filling procedure is repeated until, after deposition of all the layers, a bed thickness of  $\pm 8 \text{ cm}$  is reached. For each layer the same amount of mass (same initial density and volume) is added. Exactly the same is done in a 0.1 m diameter perspex settling column of the same height. In the column the layer thickness can be read and density profiles can be measured using a gamma-densimeter. In this way both measurements are done without destruction of the sediment bed in the flume. Details on the experimental procedures can be found in Torfs (1994).

After the formation of the bed, the erosion experiment can start. The discharge in the flume is stepwise increased until the start of the erosion process is observed. The water levels upstream and downstream of the measuring section (sediment bed), the discharge and the cumulative weight of the bed load in the sediment trap are recorded continuously. At 15 minute time intervals samples of the suspended load are taken upstream and downstream of the sediment bed. With these data erosion rates and bed shear stresses can be calculated (Torfs 1994).

The sediments used in the experiments are mixtures of natural mud, dredged from the Scheldt river near Antwerp, and a uniform fine sand. In some preliminary tests, however, kaolinite and a montmorillonite pottery clay were used as cohesive fraction. Two types of natural Scheldt mud are used. Mud2 is a subtidal mud, with a sand content of about 15 %. Mud3 comes from an intertidal flat, the sand content was much higher, about 38 %. Mud3 was heavily contaminated with oil. Table 1 gives an overview of the mixtures used in the experiments.



**Table 1:** Used mud/sand mixtures.

Name of the mixture	Sand content	Initial density (kg/m <sup>3</sup> )	Number of layers	Mud type
J1	24.6	1006	4	Mud2
J2	18.1	1005	3	Mud2
J3	20.7	1005	3	Mud2
J4	26.6	1005	3	Mud2
J5	28.7	1005	3	Mud2
J6	40.8	1006	5	Mud3
J7	46.2	1006	5	Mud3
J8	53.1	1006	5	Mud3

### Measured Density Profiles

The different layers in the bed can be visually observed and measured in the transparent settling column. The stratification is also present in the density profiles measured using the gamma-densimeter. Fig. 1 is a typical example of a density profile for experiment J5. The profile shows density peaks indicating the layer interfaces. Part of the sand seems to be accumulated at the bottom of each layer and some of that sand probably intruded in the previous layer. In any case the peaks show that in the small time in between two inputs, the previous layer (with low densities at the top) already developed enough structural strength to carry the next denser layer. The presence of a high density sand layer depends on different factors (Toorman et al 1993 and Williamson et al 1992): the percentage of sand in the mixture (a slurry can only contain a certain amount of sand within its matrix), the density of the mixture (for higher initial densities hindered settling occurs preventing the sand of falling through the mud), the type of cohesive sediment and the supply rate. Another example of a measured density profile is presented in Fig. 2 for experiment J6, using Mud3. Also in this case the layered bed structure is clear.

Looking at the shape of the measured density profiles, there is a clear difference between the experiments with Mud2 (Fig. 1) and the experiments with Mud3 (Fig. 2). In both sets of density profiles some sort of segregation is visible. The density profiles from Mud2 mixtures however show a pronounced high density peak at the bottom of each layer and then a fairly uniform zone of constant density (around 1.06 kg/dm<sup>3</sup>). At the top of each layer some sort of low density peak can be seen as well. A similar feature

has been reported by Edge et al (1989). For Mud3 the density is decreasing throughout the whole layer. This could indicate that in this case sand is also withheld within the mud matrix and that there is a smooth evolution of sand content over the layer thickness. Mud3 already contained a high sand content, it could be that this sand is held within the mud and that only the additional sand falls through. Mud2 has a low natural sand content and here more (all?) sand falls through. Williamson et al (1992) showed that segregation increased with increasing sand content. They found for their experiments a sand content of about 47 % as maximum limit of sand held within the matrix. Above the limit segregation occurs. In the experiments of Huysentruyt (1994) on Mud2 the segregation limit was less than 10 % sand added (i.e. about 25 % total sand content). This agrees well with these tests: the sand content in the Mud2 mixtures was around 25 % and always segregation occurred.

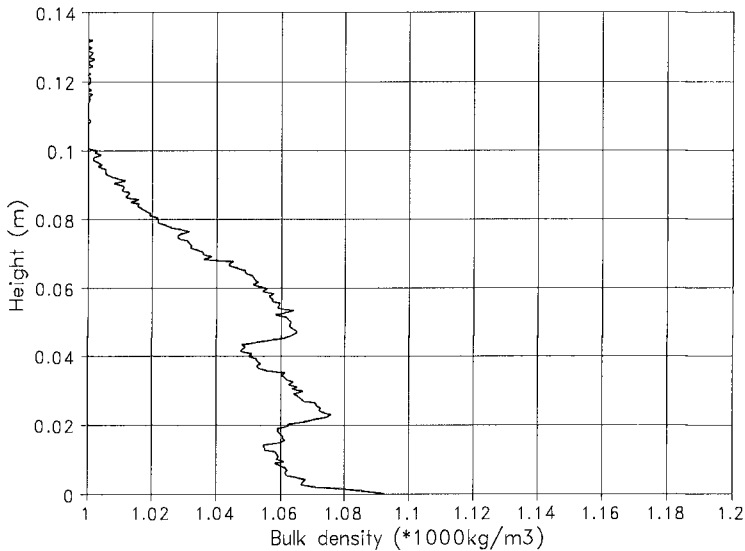


**Fig. 1:** Density profile for experiment J5.

A comparison of all the density profiles shows higher peak densities in the case of Mud3 mixtures. For those mixtures the density in a layer varies between 1.08 and 1.14 kg/dm<sup>3</sup>. For Mud2 (with a lower sand content) the density in a layer goes from 1.05 to 1.12 kg/dm<sup>3</sup>. Williamson et al (1992) stated that an increase in the sand content leads not only to a higher segregation but also to a greater and faster consolidation and thus to higher densities. The higher permeability of the sand layer enhances the drainage of the pore water.

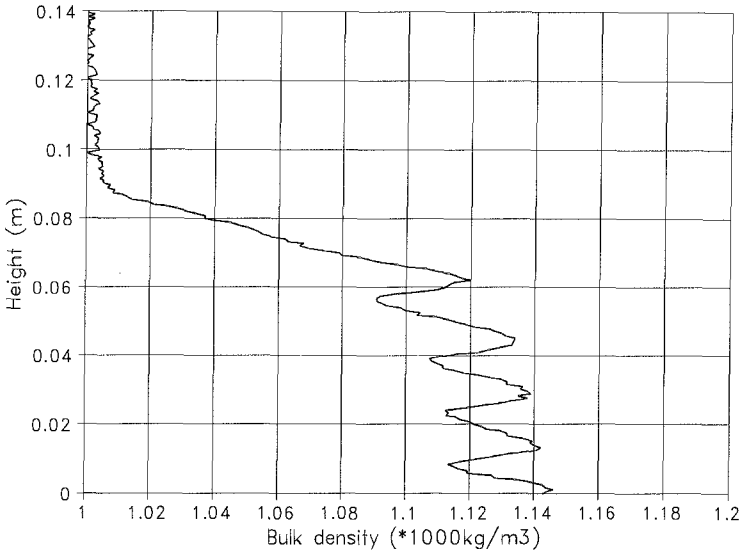


**Fig. 2:** Density profile for experiment J6.

Also the layer thickness is influenced by the sand content of the sediment mixture. Fig. 3 gives the average layer thickness for each experiment, including the preliminary tests, as a function of sand content. A general decreasing trend over all experiments is visible. But also the type of sediments can be partly responsible for that. If only the data for Mud2 are considered, a decrease of layer thickness with increasing sand content is noticed but the decrease seems to be much less pronounced. An extensive set of consolidation experiments with amongst others Mud2 by Huysentruyt (1994) showed that the settling behaviour is only affected by the addition of sand up to a certain maximum percentage of sand added. In the case of Mud2 an addition of 10 % and more sand does not change the settling behaviour any more. Segregation takes place and the thickness and density peak of the bottom layer remain the same. An addition of 10 % sand means a total sand content of about 25 %, the results of Fig. 3 again confirm this limit.

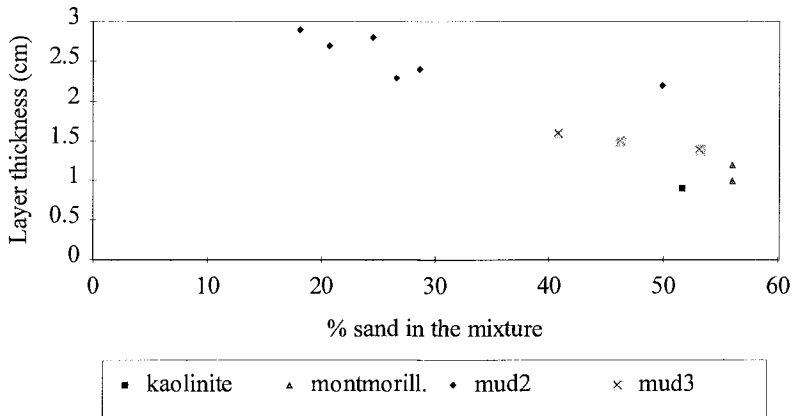
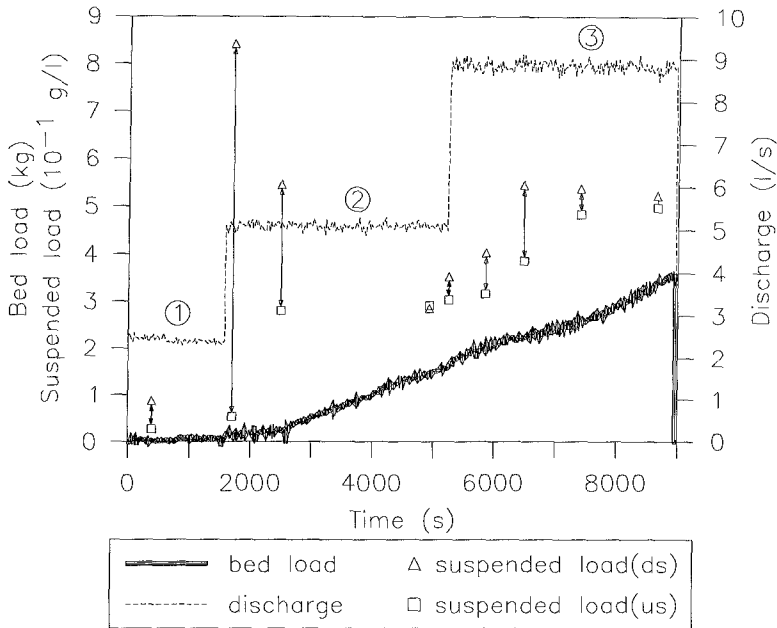


Fig. 3: Mean layer thickness as a function of sand content.

### Results of the Erosion Experiments

Fig. 4 gives an overview of an erosion experiment. The discharge in the flume is slowly increased, step by step. During the first step a thin film (only fine material) is lifted of the bed surface and goes into suspension. On the surface longitudinal fine lines appear. Increasing the discharge (step 2, Fig. 4), the erosion of the first layer (mainly mud) starts. The suspension concentration increases suddenly (suspended load downstream minus suspended load upstream = eroded material). At the beginning of this step, no bed load erosion occurs (slope of cumulated bed load in Fig. 4 is zero). After a while, the mud erosion decreases. Two different factors can cause this decrease. Due to the increasing bed density with depth, also the erosion resistance of the surface material increases during the erosion. Depending on the magnitude of the applied bed shear stress as compared to the erosion resistance, the erosion can eventually stop. Another possibility is that a sand layer is reached. That is the explanation in this case. The sediments in this layer are transported mainly as bed load. Hence, the slope of the curve of the measured bed load increases, whereas the difference between suspended load concentrations measured upstream and downstream decreases. Also the formation of sand ripples on the bed can be observed. These bed forms move towards the downstream end of the flume. Increasing the discharge (step 3, Fig. 4) increases the bed load transport of the sand until all the bed forms reach the downstream reservoir. Meanwhile at the upstream end of the sediment bed, the next mud layer becomes available and goes into suspension. The bed load decreases... For all experiments on layered sediment beds a similar sequence of suspended load and bed load transport is encountered, indicating a layer by layer erosion of the bed.



**Fig. 4:** Overview of an erosion experiment.  
(us = upstream, ds = downstream)

Although the bed densities are very low, between 1.06 and 1.15 kg/dm<sup>3</sup>, the experiments learned that the sediment bed has a significant erosion resistance. It is not clear if this is partly caused by the presence of sand in the matrix. Using an empirical formula (Eq. 1) presented by Delo in 1988,

$$\tau_{cr} = 0.0012\rho_d^{1.2} \quad (1)$$

with  $\tau_{cr}$  the critical shear stress for erosion in Pa and  $\rho_d$  representing the dry density in g/l, the calculated critical shear stresses for the surface layer lie between 0.1 and 0.2 Pa.

An important aim of this study was to look at the influence of the sand content on the erosional behaviour. For the determination of the erosion resistance, in general a higher sand content in the mixture means a faster consolidation and hence, higher bed densities that will lead to an increased erosion resistance. Of course also the type of sediment is important. During the erosion process, the presence of an important amount of sand in the sediment bed causes bed load transport. Depending on the amount of sand

in the mixture and the importance of the segregation, the bed load transport can be very significant and therefore, cannot be neglected in transport modelling.

### Conclusions

Sediment layering is known in many environments ranging from the tidal reaches of rivers to the deep sea. Energy variations are the main cause for the development of layers. During a period of high energy (flood) sediment is transported either as bed load or suspended load. As the energy level decreases first the coarse and then the finer sediments settle. Laboratory experiments have shown the formation of a layered bed as a function of mud type and sand content. The presence of sand enhances the consolidation, decreases the layer thickness and increases the bed densities.

Erosion of these layered sediment beds leads to a sequence of suspended load and bed load transport phases. The sand content normally increases erosion resistance of the deposited sediment bed by enhancing the consolidation and by increasing the bed density. The presence of a significant amount of sand in the sediment bed increases the importance of the bed load transport in the total erosion and sediment transport process.

### Acknowledgment

This work was carried out as part of the G8 Coastal Morphodynamics programme. It was partly funded by the Commission of the European Communities, Directorate General for Science, Research and Development, under contract no. MAS2-CT-92-0027.

### References

- Bastin, A. (1974) Regionale sedimentologie en morfologie van de Zuidelijke Noordzee en van het Schelde estuarium. *Phd thesis, Katholieke Univeriteit Leuven, Faculteit der Wetenschappen* (in dutch).
- Delo, E.A. (1988) Estuarine Muds Manual. *Hydraulics Research Wallingford Report No. SR 164*.
- Edge, M.J. and Sills, G.C. (1989) The development of layered sediment beds in the laboratory as an illustration of possible field processes. *Quarterly Journal of Engineering Geology, Vol. 22*, pp. 271-279.
- Huysentruyt, H. (1994) Experiments on consolidation of natural mud. Effect of composition, mixtures with sand and layering. *4th Nearshore and Estuarine Cohesive Sediment Transport Conference INTERCOH'94*, Wallingford (poster session).

Toorman, E.A. and Berlamont, J.E. (1993) Settling and consolidation of mixtures of cohesive and non-cohesive sediments. *Advances in Hydro-Science and Engineering, Vol. 1*, Sam S.Y. Wang (ed.), pp. 606-613.

Torfs H. (1994) Erosion of sand/mud layers in uniform flow. *Progress report 1994*, Mast2 G8M, Project 4: Cohesive Sediments.

Williamson, H.J. (1991) Tidal transport of mud/sand mixtures, Sediment distributions - A literature review. *HR Wallingford, Report SR 286*.

Williamson, H.J. and Ockenden, M.C. (1992) Tidal transport of mud/sand mixtures, laboratory tests. *HR Wallingford, Report SR 257*.

## CHAPTER 243

### Standing wave induced soil response in a porous seabed

Ching-Piao Tsai\* and Tsong-Lin Lee\*\*

#### ABSTRACT

This paper presents the experimental results of the pore water pressures within the soil under the action of standing waves. Both the spatial and time variation of pore pressures are generally well agreement between the theory and the experiment. The experiments also show some nonlinear phenomenon of the pore pressures within the soil.

#### INTRODUCTION

When incident waves arrive to a breakwater they will be reflected, then normally or obliquely standing waves are formed in front of the structure. The forces of standing waves play a very important role for designing the coastal structures. There were a lot of theories concerning this subject. It was known from the previous reports (Smith and Gordon, 1983; Silvester and Hsu, 1989) that some breakwaters have failed possibly due to soil instability and trench scouring, rather than structural causes. The investigations of the soil response in front of such a structure under the action of waves are thus become important.

As gravity waves exert cyclic pressures on a sedimentary seabed, they penetrate into the porous medium and induce pore pressure within the soil column. The soil will lose its strength in bearing any load if the induced pore pressures

---

\* Associate Professor, Department of Civil Engineering, National Chung-Hsing University, Taichung 402, Taiwan, R.O.C.

\*\* Senior Graduate Student, Department of Civil Engineering, National Chung-Hsing University, Taichung 402, Taiwan, R.O.C.



become excessive in the soil skeleton. A number of theories have been developed for the wave-induced pore pressure in the porous medium, such as Yamamoto et al. (1978), Madsen (1978), Mei and Foda (1981) and Okusa (1985). There were many previous works investigated the wave-induced pore pressures in the laboratory as well as prototype conditions. However, only the case of the progressive wave was considered.

For the cases in front of a breakwater, Hsu et al. (1993) has developed a general three-dimensional solution of the soil response induced by the short-crested wave system. Tsai (1995) extended to the case of partially reflected waves and evaluated the potential liquefaction under the action of such a wave system. Their solutions can be reduced to the case of two-dimensional standing wave that the incident-wave is normally to a vertical wall. Mase et al. (1994) proposed a numerical model for calculating the soil response under the action of standing waves. This paper shows the experimental results of the standing wave induced pore pressure in the sand bed in front of a breakwater.

## EXPERIMENTS

The measurements of pore pressures within the sand bed due to the action of standing waves were conducted in a wave flume. The experimental set-up is shown in Fig. 1. The dimension of the wave flume is 2 m in width, by 2 m in height and by 100 m in length. Sand soil of medium firmness was filled 50 cm in depth and 2 m in length in front of the wall.

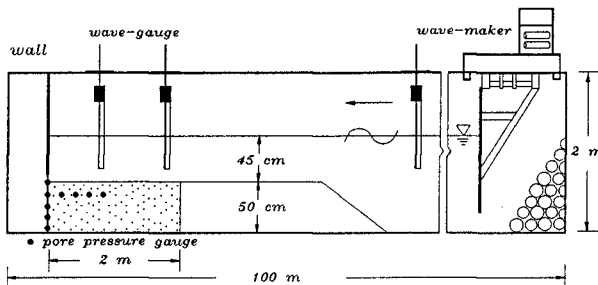


Fig. 1 Sketch of the experimental set-up.

The physical properties of the sand are measured: the specific gravity of soil  $G_s$  is 2.64, the mean grain size  $D_{50} = 0.187$  mm, the uniformity coefficient  $D_{60}/D_{10} = 1.8$ , the specific gravity is 2.64, permeability is  $1.2 \times 10^{-4}$  cm/sec, the water content  $w$  is 0.23, the porosity  $n = 0.38$  and the void ratio  $e$  is 0.62. Then the degree of saturation of the soil is 98% which is calculated from the formula  $S_r = wG_s/e$ .

The water depth  $d$  above the mudline is 45 cm. The wave periods  $T$  generated in the experiment are varied from 1.0 to 3.0 seconds. The wave heights of incident waves are ranged from 4 cm to 16 cm, from which the sand drifting is not obviously observed.

Under the position of anti-nodal point of the standing wave, the time variation of pore pressures at various distances from the mudline were measured by five pore-water pressure transducers. Also five transducers were placed horizontally below the mudline to measure the spatial variations of pore pressures.

## RESULTS AND DISCUSSION

The solution of pore pressures of the standing wave can be reduced from the three-dimensional solutions given by Tsai (1995), from which the solution of the two-dimensional standing wave are given by

$$P = \frac{p_o}{1 - 2\mu} \{ (1 - 2\mu - \lambda) C_1 e^{kz} + (1 - \mu) \frac{(\delta^2 - k^2)}{k} C_2 e^{\delta z} \} \cos kx e^{-i\omega t} \quad (1)$$

in which  $P$  is the wave-induced pore pressure in excess of the hydrostatic condition,  $k$  is the wave number,  $\omega$  is the wave frequency,  $t$  is the time; the  $x$ -direction is measured normal to the wall, and the  $z$ -axis is positive upward from the mudline. The parameter  $\mu$  is the Poisson's ratio of soil. The parameters  $\delta$  and  $\lambda$  are coupled with soil properties and wave conditions, they are given by

$$\delta^2 = k^2 \left[ \frac{K_x}{K_z} \right] - \frac{i\omega\gamma_w}{K_z} \left[ n\beta + \frac{1 - 2\mu}{2G(1 - \mu)} \right] \quad (2)$$

$$\lambda = (1 - 2\mu) \left\{ k^2 \left( 1 - \frac{K_x}{K_z} \right) + \frac{i\omega\gamma_w n\beta}{K_z} \right\} \left\{ k^2 \left( 1 - \frac{K_x}{K_z} \right) + \frac{i\omega\gamma_w}{K_z} \left[ n\beta + \frac{1 - 2\mu}{2G} \right] \right\}^{-1} \quad (3)$$

respectively, in which  $K_x$  and  $K_z$  are the coefficients of soil permeability in the  $x$ - and  $z$ -directions,  $\gamma_w$  is the unit weight of the pore water,  $n$  is the soil porosity and  $G$

is the shear modulus. While  $\beta$  is the compressibility of the pore fluid which can be related to the apparent bulk modulus of the pore water  $K'$  and the degree of saturation  $S_r$  (Verruijt, 1969), such that

$$\beta = \frac{1}{K'} = \frac{1}{K} + \frac{1 - S_r}{P_{w0}} \quad (4)$$

where  $K$  is the true bulk modulus of elasticity of water and  $P_{w0}$  is the absolute pore-water pressure. Coefficients  $C_1$  and  $C_2$  in the equation (1) can be determined from

$$C_1 = \frac{\delta - \delta\mu + k\mu}{\delta - \delta\mu + k\mu + k\lambda} \quad (5)$$

$$C_2 = \frac{k\lambda}{(\delta - k)(\delta - \delta\mu + k\mu + k\lambda)} \quad (6)$$

The above solutions are based on the assumptions that (i) The porous bed is homogenous, unsaturated, hydraulically anisotropic and of infinite thickness, and (ii) The soil skeleton and the pore fluid are compressible.

For comparisons of theory and experiment, some values of parameters are needed besides the physical properties of the sand stated above. These are the stiffness of soil,  $G\beta$ , in which  $G$  is the shear modulus of soil and  $\beta$  is the compressibility of the pore water, and the Poisson's ratio of soil,  $\mu$ . The value of  $\beta$  can be determined from the relationship of the apparent bulk modulus of the pore water and the degree of saturation  $S_r$  (see Yamamoto et al., 1978), from which it is given by  $\beta = 3.7 \times 10^{-6} \text{ N/m}^2$  for this study. From the best fit made by the series experimental data, it is adopted reasonably by  $G\beta = 5$  and  $\mu = 0.3$  for the soil of medium firmness. The permeability of soil in the experiment is considered as hydraulically isotropic, i.e.  $K_x = K_z = 1.2 \times 10^{-4} \text{ cm/sec}$ .

Unlike those of progressive waves, the pore pressures under the action of standing waves are spatial and time variations which are shown in Fig. 2 for both theoretical and experimental results measured below the mudline  $z = -10 \text{ cm}$ . The maximum pore pressure occurs at the position under the anti-nodal point of the standing wave ( $kx = 0$ ), while the almost zero value is at the nodal point ( $kx = \pi/2$ ). The pore pressures, under the position of the anti-nodal point, at various depths from the mudline are depicted in Fig. 3. It is found that the pore pressure decreases and a time-phase delay appears as the depth increases. It is noted that there is no

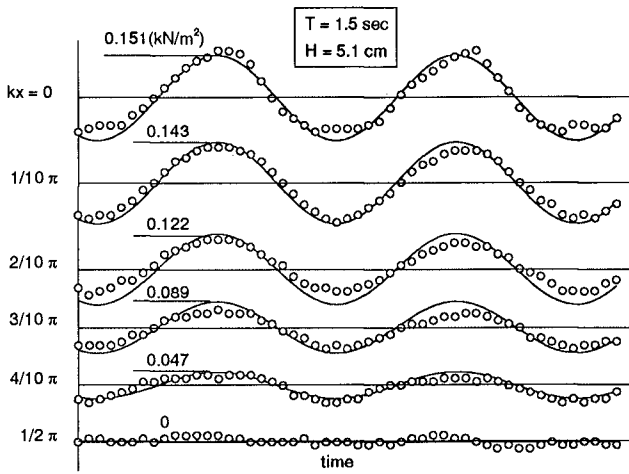


Fig. 2 Spatial and time variations of pore pressures below the mudline  $z = -10$  cm.

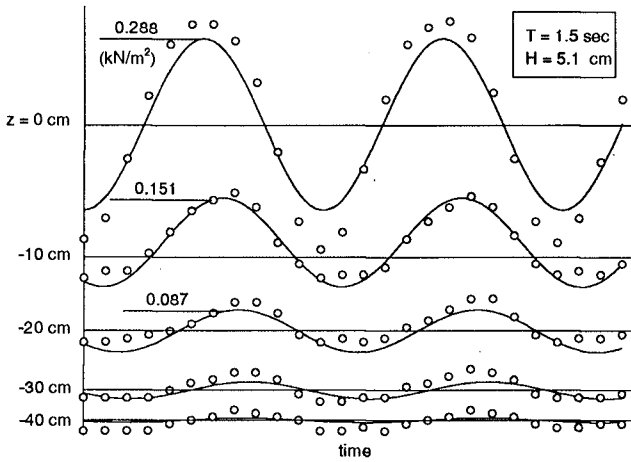


Fig. 3 Time variations of pore pressures at various depths, at  $kx = 0$ .

phase lag in the saturated soil theoretically, because the coefficient of  $C_2$  in equation (1) is zero.

The depth profiles of pore pressures ratio  $P/P_0$  are given in Fig. 4, in which  $P$  is the measured amplitude and  $P_0$  is the amplitude of bottom pressure of the incident wave estimated by linear wave theory. It is seen from the theoretical curves that the fully saturated condition ( $G\beta = 0$ ) gives the larger values than those of partially saturated soil. The measured amplitudes at the mudline are smaller than the theoretical values, as the larger wave height actions. In contrary, the measured values near bottom are slightly larger than those of theory. The former may be caused by the energy damping from water column through the porous bed, while the latter is due to the effect of finite thickness of soil in experiments as opposed to infinite thickness of the theory. Nevertheless, the experiments are good in agreement with the theory over all.

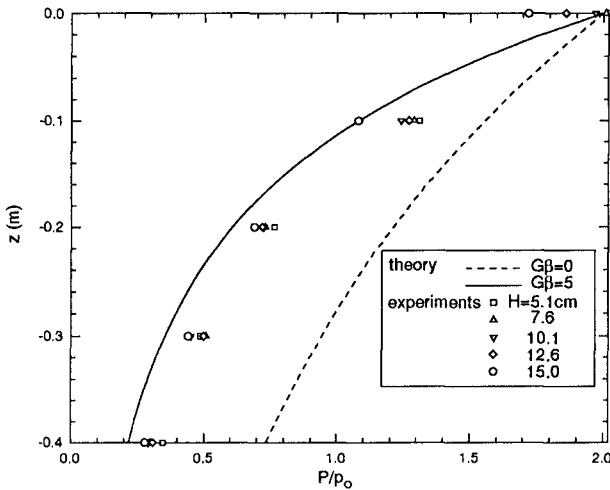


Fig. 4 The depth profiles of pore pressures ratio  $P/P_0$ , at  $kx = 0$ .

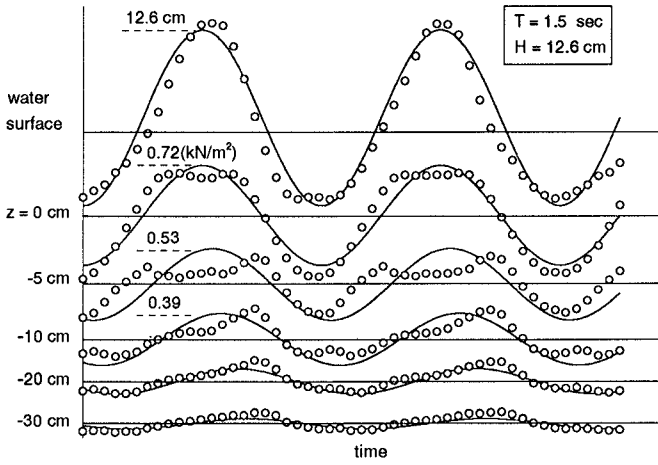


Fig. 5 Double humps of time variations of pore pressures, at  $kx = 0$ .

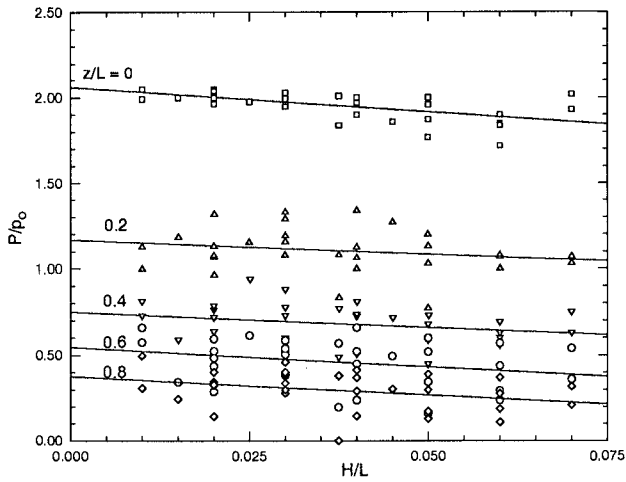


Fig. 6 Effect of the wave steepness on the pore pressures ratio  $P/P_0$ , at  $kx = 0$ .

It was known that the double humps appear in the time-history of pressures of nonlinear standing waves. This nonlinear phenomenon also influences the pore pressures within the soil column, which is shown in Fig. 5. Due to the effect of phase lag, the double humps become asymmetric as depth increases. However, it is obviously seen that the nonlinear effect can not be observed in the linear theory.

The pressure ratio  $P/P_0$  at the mudline and within the soil skeleton is independent on wave steepness theoretically. Nevertheless, it can be seen in Fig. 6 that the pressure ratio slightly decreases as the wave steepness increases, although the plotted points are scatter over a range.

## CONCLUSIONS

1. Standing waves are not only important for their forces on a maritime structure, but they have been received attention for their conducive scouring in front of a breakwater.
2. This study presented the experimental results of pore pressures under the action of standing waves.
3. In general, the spatial and time variations of pore pressures induced by the standing waves are well agreement between the experiment and theory.
4. It was found that some nonlinear characteristics of pore pressures exists for the larger wave cases.

## REFERENCES

- Hsu, J.R.C., Jeng, D.S. and Tsai, C.P. (1993). Short-crested wave induced soil response in a porous seabed of infinite thickness. *Intl. J. Num. and Anal. Meth. in Geomech.*, 17(8), 553-576.
- Madsen, O.S. (1978). Wave-induced pore pressures and effective stresses in a porous bed. *Géotechnique*, 28(4), 377-393.
- Mase, H., Sakai, T. and Sakamoto, M. (1994). Wave-induced porewater pressure and effective stresses around breakwater. *Ocean Engineering*, 21(4), 361-379.
- Mei, C.C. and Foda, A. (1981). Wave-induced responses in a fluid-filled poro-elastic solid with a free surface - a boundary layer theory. *Geophys. J. R. Astr. Soc.*, 66, 597-631.
- Okusa, S. (1985). Wave-induced stresses in unsaturated submarine sediments. *Géotechnique*, 35(4), 517-532.

- Silvester, R. and Hsu, J.R.C. (1989). Sines revisited. *J. Waterway, Harbor and Coastal Eng.*, ASCE, 115(3), 327-344.
- Smith, A.W. and Gordon, A.O. (1983). Large breakwater toe failures. *J. Waterway, Harbor and Coastal Eng.*, ASCE, 109(2), 253-255.
- Tsai, C.P. (1995). Wave-induced liquefaction potential in a porous seabed in front of a breakwater. *Ocean Eng.*, 22(1), 1-18.
- Yamamoto, T., Koning, H.L., Sellmeijer, H. and van Hijum, E. (1978). On the response of a poro-elastic bed to water waves. *J. Fluid Mech.*, 87(1), 193-206.



## CHAPTER 244

### EROSION CONTROL BY CONSIDERING LARGE SCALE COASTAL BEHAVIOR

Yoshito Tsuchiya<sup>1</sup>, M. ASCE, Takao Yamashita<sup>2</sup> and Tatsuhisa Izumi<sup>3</sup>

#### Abstract

Due to the construction of Naoetsu harbor, severe beach erosion has taken place on the Joetsu-Ogata coast facing the Japan Sea. To establish a principal methodology for beach stabilization, large scale coastal behavior first is investigated by constructing a long-term shoreline change model in which the representative monsoon wave is introduced. Comparison of hindcast and actual long-term shoreline change shows that the proposed model can predict long-term shoreline change. Shoreline change after the construction of Naoetsu harbor also was predicted under the condition that natural sandy beaches had been retained. Results show that shoreline retreat is severe near the harbor and extends to the central part of the coast. To determine the most suitable location for headlands to be used for stabilizing the coast, long-term shoreline changes were calculated under the condition that a headland is given at several locations. We conclude that in principle when the boundary condition for shoreline change by headland is given near the Shinbori River, a sandy beach tends to have stable large scale coastal behavior during long-term shoreline change. We propose a principal methodology for beach stabilization, part of which is being used in current construction.

#### INTRODUCTION

When planning erosion control works for sandy beaches, investigation of their coastal behavior from the long-term and large-scale view points is extremely important. Local and temporal measures alter sandy beaches, sometimes destroying them. This is what coastal engineers have learned from their experiences during the past several decades in Japan. Many attempts have been made to control beach erosion throughout the world, but in the long term none have succeeded in stabilizing sandy beaches that are being eroded. Almost all the common countermeasures are of little use for stabilization as they cause beach profiles

---

<sup>1</sup>Professor Emeritus, Kyoto University & Professor, Meijo University, Tenpaku-ku, Nagoya 467, Japan

<sup>2</sup>Instructor, Disaster Prevention Research Institute, Kyoto University, Uji, Kyoto 611, Japan

<sup>3</sup>Director, Niigata Port Construction Bureau, Niigata Prefecture, Niigata 950, Japan

gradually to become steep. This study treats beach erosion control on the Joetsu-Ogata coast, facing the Japan Sea, to show a principal methodology for sandy beach stabilization in which the large scale behavior of a sandy beach under continuous development is considered (Tsuchiya, Yamashita, Izumi and Tottori, 1993).

In 1967, the Disaster Prevention Research Institute, Kyoto University established a wave observatory on this coast for the investigation of the beach erosion mechanism and its control. A T-shaped observation pier that extends 260m offshore was constructed. The coast (shown in Figure 1) is a slightly concave sandy beach about 25 km long and is bounded by the Gotsu and Yoneyamazaki headlands respectively on its west and east ends. It has been an erosive beach since the construction of Naoetsu Harbor on the right side of the mouth of the Seki River in 1961. The history of the construction of coastal structures is shown briefly in the figure, and shoreline changes measured on aerial photographs also are shown. Severe beach erosion began

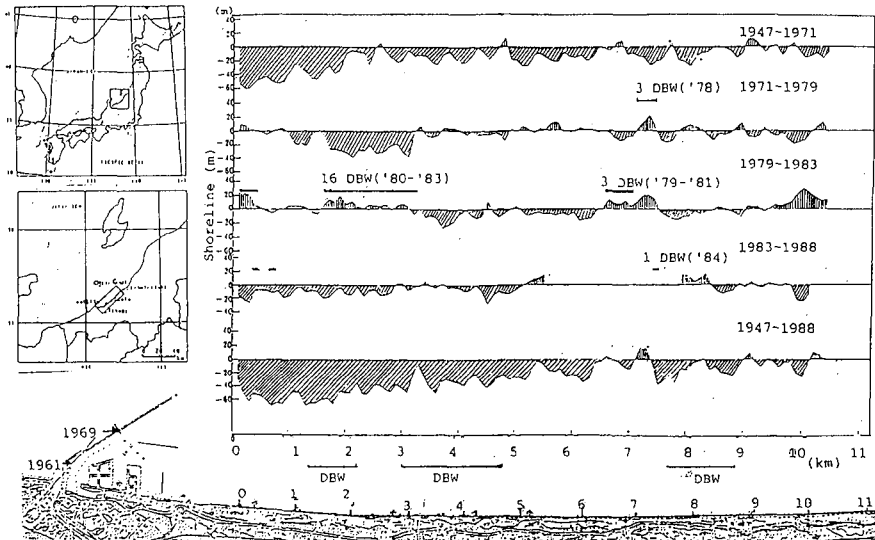


Figure 1. Location of the Joetsu-Ogata coast and the history of the construction of coastal structures in relation to shoreline change.

near the east end of the harbor due to the lack of longshore sediment transport and has propagated eastward in relation to the extension of the breakwaters in the harbor. The countermeasures taken have been sea dikes with armor blocks, offshore breakwaters and, recently, mild-slope revetments. Beach erosion has continued to take place, resulting in steep beach profiles, and little can be expected of these countermeasures in terms of beach stabilization.

The erosive process along this coast is investigated in terms of large scale coastal behavior. A long-term shoreline change prediction model is established by introducing the representative monsoon wave and qualifying the alongshore distribution of the longshore sediment transport rate. The hindcast result is compared with actual shoreline change from 1910 to 1961, before beach erosion took place. Calculations of wave and nearshore current fields are used to estimate the alongshore distribution of longshore sediment transport in relation to the extending breakwaters. The rates of longshore sediment transport are compared with those estimated from bottom topography changes. Numerical predictions of long-term shoreline change show the most suitable locations for the headlands to be constructed for beach

stabilization of large scale coastal behavior. Based on these findings, as well as on the theoretical background of the formation of stable sandy beaches, we propose a principal methodology for beach stabilization in relation to change in longshore sediment transport rates.

## HINDCAST OF SHORELINE CHANGE BEFORE CONSTRUCTION OF NAOETSU HARBOR

### Bottom topography for the computational domain

The oldest shoreline recorded by the Geographical Survey of Japan is shown in a topographical map issued in 1910. The biggest coastal structure in the area, at present, Naoetsu Harbor, was constructed in 1961. The coast, at least before 1961, probably behaved naturally, having had no artificial impact on it. Hindcasting the shoreline changes for the period 1910 to 1961 (before harbor construction), should provide important information about such natural external forces that act on long-term beach change as storm wave conditions and the magnitude of sediment input from rivers. The bottom topography for the computational domain was reproduced by connecting two maps, a marine chart and a topographical map issued in 1910, on the assumption that beach topography shallower than a 20m water depth can be replaced by the equilibrium beach profile proposed by Dean (1981);

$$h = Ay^{2/3} \quad (1)$$

where  $h$  is the water depth,  $y$  the distance taken offshore from the shoreline, and  $A$  the model constant which may be related to the beach sediment diameter. The bottom topography for the computational domain was obtained. The model constant varies alongshore. Nearly the same tendency for the alongshore distributions and maximum exists for both the model constant and sediment diameter near the observation pier.

### The long-term shoreline change prediction model

**(1) Shoreline change prediction model** A one-line shoreline change prediction model can be used. An outline of the model we used (Yamashita, Tsuchiya, Matsuyama & Suzuki, 1990) is explained. The equation of continuity for shoreline change is given by

$$\frac{\partial y_0}{\partial t} + \frac{1}{(1-\lambda)} \frac{\partial Q_x}{\partial x} = \frac{Q_R(t)}{h_c B} \delta(x-x_0) \quad (2)$$

where  $y_0$  is the shoreline change from the datum line,  $t$  the time,  $x$  the alongshore distance from the origin,  $h_c$  the critical depth for beach change,  $\lambda$  the porosity of beach sediment,  $Q_x$  the total rate of longshore sediment transport,  $B$  the width of the river mouth, and  $Q_R(t)$  the sediment input from the river as the beach sediment source. Practically, the CERC formula for the total rate of longshore sediment transport can be used;

$$Q_x = \frac{a\rho g^2}{64\pi} H_0^2 T K_R^2 \sin 2\alpha_{BS} \quad (\text{m}^3/\text{yr}) \quad (3)$$

where  $H_0$  is the deep water wave height,  $T$  the wave period,  $\alpha_{BS}$  the breaker angle to the shoreline,  $K_R$  the refraction coefficient,  $\rho$  the density of water,  $g$  the gravitational acceleration, and  $a = 1.26 \times 10^7$  an empirical constant that may be changeable in relation to sediment properties but is assumed to be constant in this

shoreline change prediction. Introduction of the geometrical relation in shoreline change and combing (3) and (2) yields

$$\left. \begin{aligned} \frac{\partial Q_x}{\partial t} &= \frac{\partial Q_x / \partial \alpha_{BS}}{(1 - \lambda) \{1 + (\partial y_0 / \partial x)^2\}} h_k \frac{\partial^2 Q_x}{\partial x^2} + A_R \\ A_R &= \frac{\partial}{\partial x} \left[ \frac{Q_R(t)}{h_k B} \delta(x - x_0) \right] \end{aligned} \right\} \quad (4)$$

where  $\alpha_{BD}$  is the breaker angle to the initial shoreline. This diffusion type equation can be solved under the given initial shoreline and boundary conditions by an implicit method to obtain the total rate of longshore sediment transport  $Q_x$ . By its use shoreline change can be obtained by solving (2). In practice, when boundary conditions are given at both ends where no longshore sediment transport exists, forward and backward differentials must be applied alternatively to solve this equation numerically.

**(2) The representative waves and their transformation** In long-term shoreline change prediction two methods have been used to estimate the most effective wave or the representative wave in shoreline change: a time series of waves to be obtained by long-term wave data, and a certain representative wave for shoreline change. In the second method, in practice the single representative wave is estimated by use of the annual total rate of wave power proportional to the longshore sediment transport rate which can be evaluated by long-term wave data. As the representative wave condition has been evaluated from the annual total rate of wave power under deep water wave conditions, relatively small waves have been estimated. It is questionable whether such waves actually cause shoreline change. In this paper, therefore, in relation to the monsoon wave sequences in the Japan Sea, we assume the representative waves shown in Table 1 where the 1st, 2nd and 3rd waves

Table 1. Representative waves proposed in relation to monsoon wave sequences and their properties.

Representative Waves	Wave Direction	Wave Period in sec	Wave Height in m
1st	NW5°W	6	2
2nd	NW	7	3
3rd	NW 10°N	8	2

respectively correspond to the monsoon wave sequences, generating and developing wind wave stages, and decaying swell stage.

At Naoetsu Harbor, wave observation has been carried out over a long period. From the collected data the annual averaged duration of waves higher than 2 m in terms of significant wave height was evaluated as 264 hr/yr. We assume that monsoon waves with a duration of 24 hr strike the coast 11 times a year. A representative monsoon wave is defined as a sequence of three successive representative waves each having a duration of 8 hr.

Using three representative waves, we could calculate their transformation. In the wave refraction diagrams shown in Figure 2(b) small black points indicate the breaking points. The breaker angles are so small that accurate calculation is needed to evaluate them. Figure 3 shows the alongshore distributions of breaker height and

and angle for the three representative waves, the dotted lines indicating smoothed breaker heights. Breaker height varies remarkably alongshore around the Gotsu headland, Naoetsu Harbor (the Seki River), and the Kakizaki River, in particular for the second representative wave. This is because of wave refraction by the localbottom topography. Note, however, that no remarkable alongshore variations

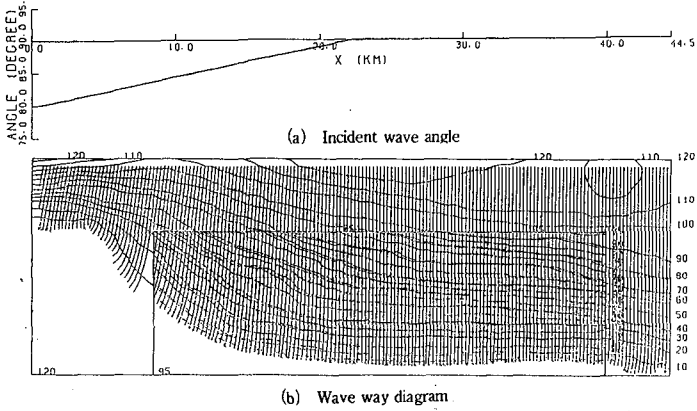
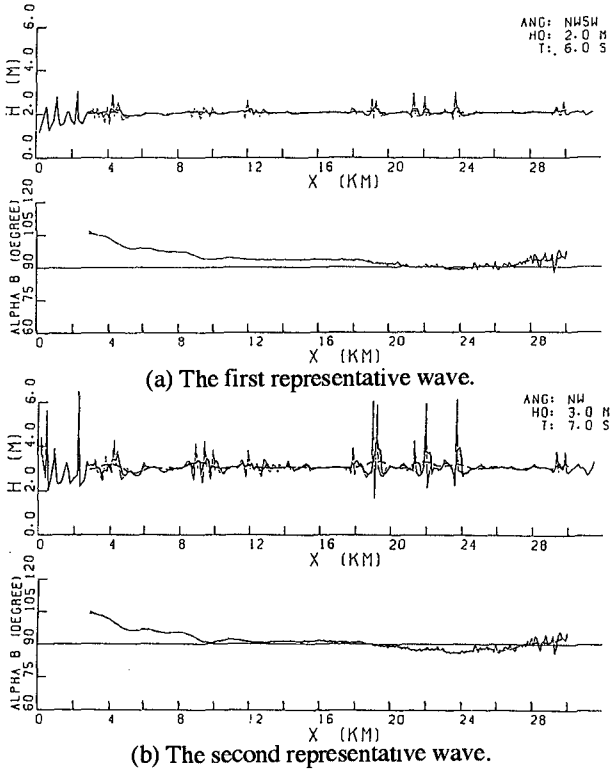
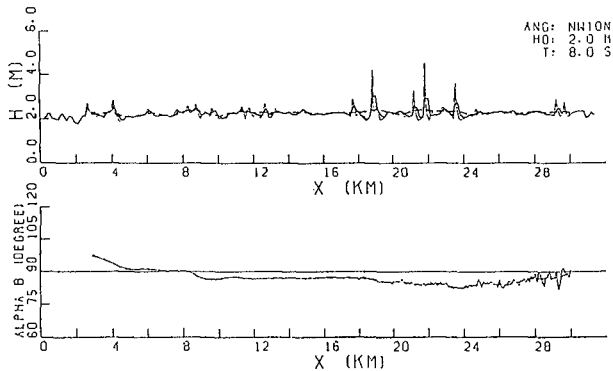


Figure 2. Wave ray diagrams and incident angle of the representative wave.





(c) The third representative wave.

Figure 3. Alongshore distributions of breaker height and angle for three representative waves.

take place, but there is a distinct change in breaker angle that is positive in the east direction west of the center of the coast but negative east of the center. This tendency is a direct reflection of longshore sediment transport along the coast, resulting in the formation of a coast bounded by the Gotsu and Yoneyamazaki headlands in relation to the sediment sources from the Seki and Kakizaki Rivers.

**(3) The boundary conditions** As stated earlier, the two main sediment sources are the Seki and Kakizaki rivers. The rates of sediment input from these rivers have been estimated, but it is not known what rate contributes to the sediment source. When sediment sources are given as point sources, a sharp river delta may develop which may not contribute to long-term shoreline change because the sediment input from the rivers is due to flooding in summer, whereas in the other seasons, sediment deposited near the rivers' mouths is transported by waves both as longshore and offshore sediment transport. In long-term shoreline prediction, the period of flooding that results in sediment input from the rivers actually is very short compared with shoreline evolution. Therefore we here have estimated the incident wave angle by changing the incident wave angle in deep water along the coast so that long-term shoreline changes could be calculated under the third representative wave condition, in which the wave height and wave period are 0.7 m and 8 sec, until we could successfully hindcast the actual shoreline on the Joetsu-Ogata coast. The final estimate of the incident wave angle is shown in Figure 2(a), the upper part showing the estimated incident wave angle and the lower part its wave ray diagram. As shown in Figure 1, an island (Sado Island) lies several tens of kilometers offshore. Waves are formed due to wave dispersion and diffraction by this island.

This may result in the change in the incident wave angle as discussed above. In the long-term shoreline change prediction, the boundary conditions are

1) At the Gotsu headland on a rocky shore, no longshore sediment transport is assumed to occur. Actually, a small sea cliff has supplied a small amount of sediment to the coast, but currently no sediment input is assumed.

2) At the Yoneyamazaki headland on a rocky shore bounded by small sandy beaches an offshore bottom topography composed of fine sand is assumed where there is longshore sediment transport.

3) As previously stated, the Seki and Kakizaki Rivers discharge at the coast, providing the sediment sources. Their annual sediment rates respectively are assumed to be 10,000 to 100,000 m<sup>3</sup>/yr and 5,000 m<sup>3</sup>/yr.

Based on these boundary conditions for shoreline change, long-term shoreline

change is hindcast in two steps:

- 1) First step: No sediment sources from the rivers are assumed. No longshore sediment transport is assumed at the Gotsu headland, but is assumed around the Yoneyamazaki headland.
- 2) Second step: The sediment sources from the rivers are added to the first step to evaluate the effect of the rivers on shoreline change.

### Hindcast long-term shoreline change and the representative monsoon wave

The shoreline changes hindcast are compared with those measured in 1910 and 1961 when there was a natural sandy beach along the coast before construction of Naoetsu Harbor. On the basis of the results of this comparison we propose the representative monsoon wave for the long-term shoreline change prediction model.

(1) **In the case of the first step** Using three representative waves, we hindcast long-term shoreline changes for 51 years. Figures 4, 5 and 6 show the respective shoreline changes hindcast by the first, second and third representative waves, the changes being shown for intervals of 10 years. In these figures, the upper part shows the alongshore distribution of the longshore sediment transport rate, the direction of

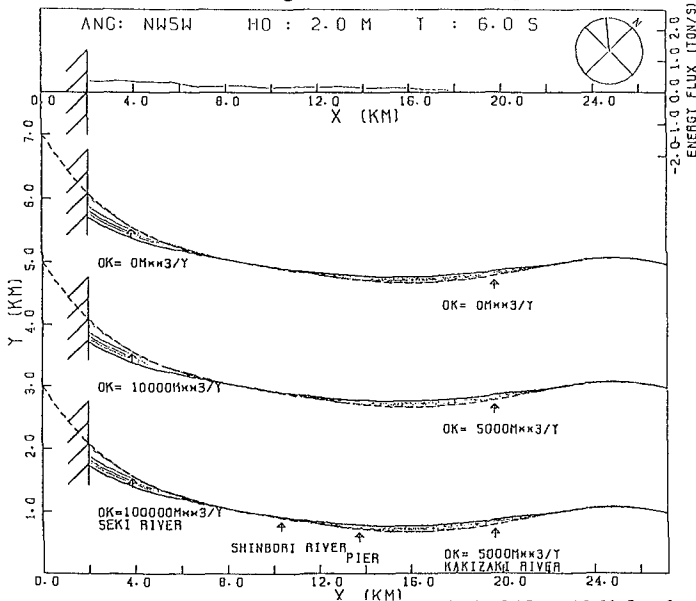


Figure 4. Hindcast shoreline changes in the period 1910 to 1961 for the first representative wave.

which is taken as positive in the easterly direction. The three respective lower parts indicate shoreline changes in the first and second steps, the sediment sources being given. In the cases of the first and second representative waves, the shoreline retreats near the Gotsu headland, whereas accretion takes place along the central part of the coast and little change occurs near the Yoneyamazaki headland. In contrast, in the case of the third representative wave, shoreline accretion takes place near the Gotsu headland and the central part of the shoreline due to westerly longshore sediment transport. Figure 7 shows the alongshore distributions of the longshore sediment

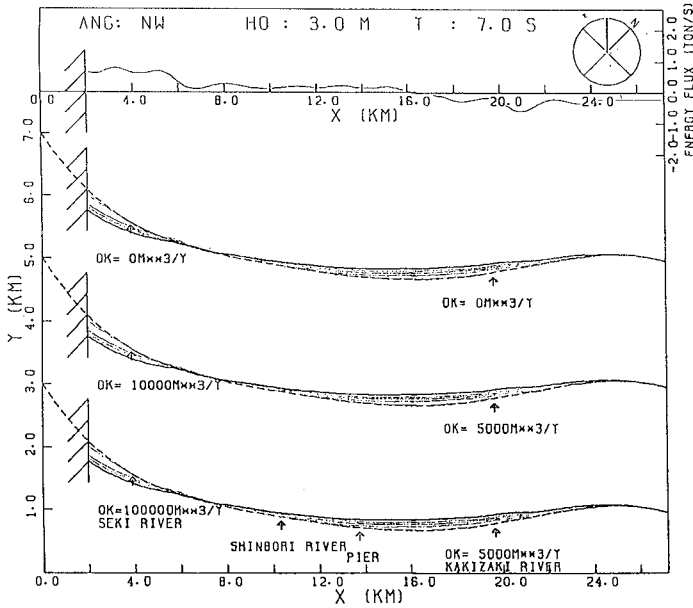


Figure 5. Hindcast shoreline changes in the period 1910 to 1961 for the second representative wave.

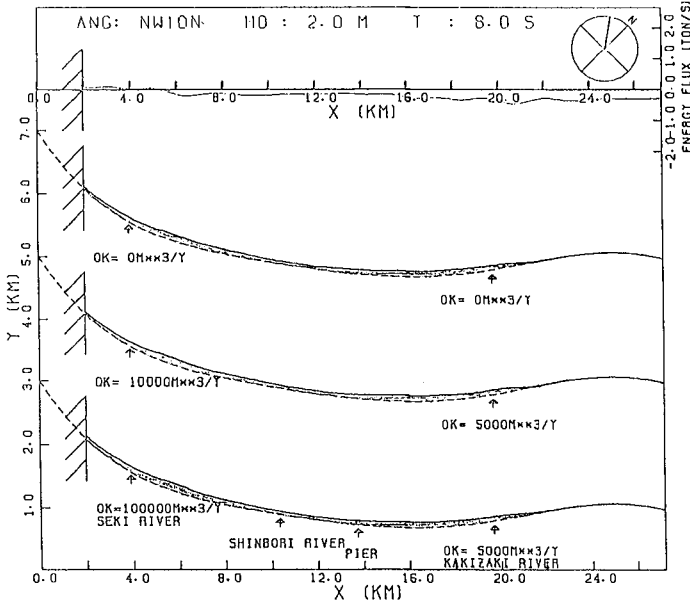


Figure 6. Hindcast shoreline changes in the period between 1910 to 1961 for the third representative wave.

transport rates for the initial shoreline condition and the three representative waves,



in which the dotted curve indicates the annual averaged rate of longshore sediment transport. This varies alongshore in relation to variations in breaker height (Figure 3), but shows the same tendency for alongshore distribution as the breaker angle shown in Figure 3. The first and second representative waves show the same tendency, but the third differs.

**(2) In the case of the second step** In Figures 4, 5 and 6, the shoreline changes predicted for the second step are shown. In these predictions, the sediment sources

are 1) 10,000 m<sup>3</sup>/yr and 5,000 m<sup>3</sup>/yr; 2) 100,000 m<sup>3</sup>/yr and 5,000 m<sup>3</sup>/yr. The sediment sources influence shoreline accretion in the central part of the coast and tend to decrease shoreline retreat near the Gotsu headland. For shoreline change, the alongshore changes in longshore sediment transport rate are given in Figure 7. This shows that the alongshore distributions change slightly near the river mouths, but here was remarkably little influence on shoreline changes by the sediment sources for period of about half a century.

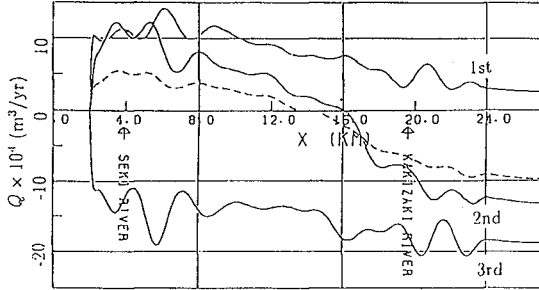
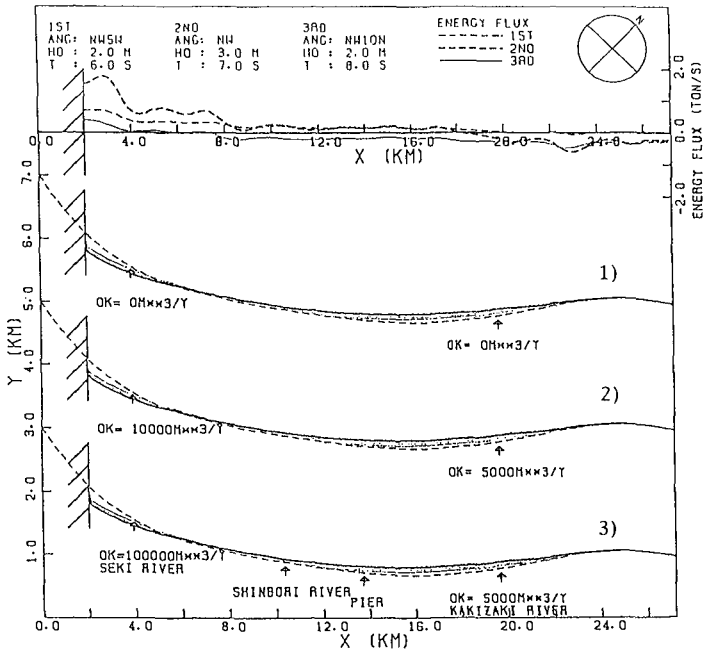


Figure 7. Alongshore distributions of longshore sediment transport rates for the three representative waves and the annual averaged one when the sediment sources are 100,000 m<sup>3</sup>/yr and 5,000 m<sup>3</sup>/yr.

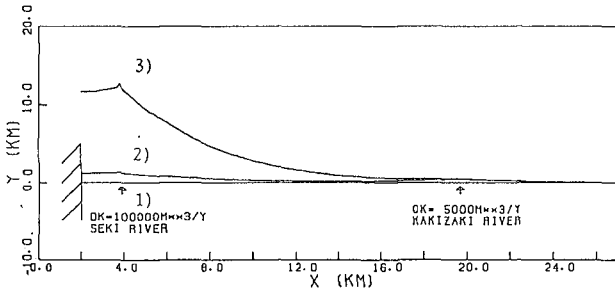
**(3) The representative monsoon wave and predicted long-term shoreline change**

As to the sequence of wind waves and swells generated by a monsoon, we have assumed that the representative monsoon wave is composed of first, second, and third representative waves each with a duration of 8 hours and that these repeat 11 times a year. Using the representative monsoon wave, we hindcast the change in the initial 1910 shoreline for 51 years, and compared it with the actual recorded shoreline change. In Figure 8 (a) the upper most part shows the alongshore distributions of the longshore sediment transport rates produced by the representative waves, and the lower three parts respectively indicate the comparison under the given conditions that 1) no sediment sources are given, 2) 10,000 m<sup>3</sup>/yr and 5,000 m<sup>3</sup>/yr are given from the rivers, and 3) 100,000 m<sup>3</sup>/yr and 5,000 m<sup>3</sup>/yr are given. Figure 8 (b) shows the detailed expression of shoreline changes produced by the sediment sources. The alongshore distribution of longshore sediment transport by the representative monsoon wave is shown by the dotted curve in Figure 7. The annual averaged total rate of longshore sediment transport reaches a maximum near Naetsu Harbor and amounts to about 50,000 m<sup>3</sup>/yr; nearly equal to the value estimated from the bottom topography change. In the alongshore distribution, it is positive and decreases gradually in the easterly direction on the central part of the coast, but changes to the westerly direction along the east part. This tendency demonstrates that the central part of the coast is depositional in long-term beach evolution and that easterly and westerly longshore sediment transport exists in relation to the breaker angle of the incident waves. The offshore bottom topography measured in the central part also is depositional.

From this comparison, we conclude that the long-term shoreline change calculated shows some shoreline retreat near the Gotsu headland and shoreline accretion along the central part of the coast, but it is in good agreement with the actual long-term shoreline change over 51 years. We therefore conclude that our proposed long-term



(a) Long-term shoreline changes hindcast for 51 years.



(b) Detailed expression of shoreline change under the given sediment sources.

Figure 8. Comparison of long-term shoreline changes hindcast by the representative monsoon wave with actual shoreline change from 1910 to 1961.

shoreline prediction model, in which the representative monsoon wave is introduced, is applicable for future long-term shoreline change prediction as large scale coastal behavior.

### PREDICTION OF SHORELINE CHANGE AFTER CONSTRUCTION OF NAOETSU HARBOR

#### Changes in the sedimentation system and longshore sediment transport rates

(1) Calculation of the wave and nearshore current fields As stated previously, Naoetsu Harbor was developed in 1961 with extending western breakwaters. Its

construction has changed the sedimentation system, resulting in severe beach erosion the area of which has expanded easterly in relation to the extension of the breakwaters. To establish a principal methodology for beach stabilization, we predicted changes in wave and nearshore current fields numerically in order to evaluate changes in the longshore sediment transport and shoreline along the coast. In considering large scale coastal behavior, long-term shoreline change along the

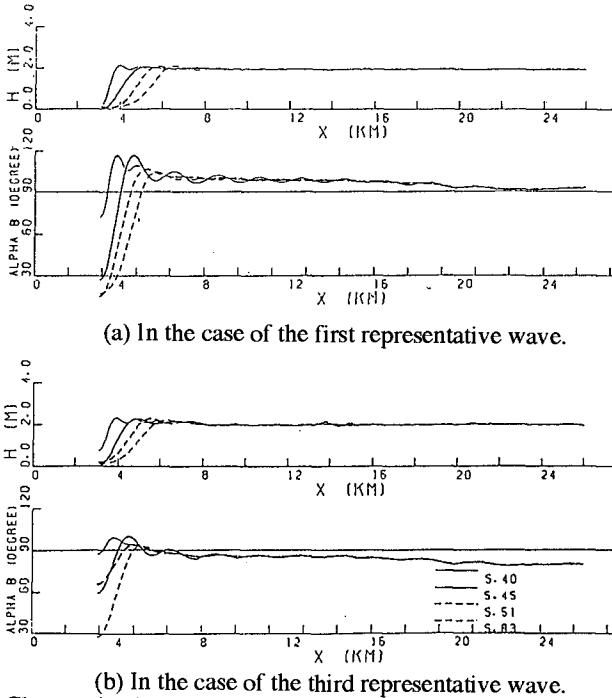


Figure 9. Changes in alongshore distributions of breaker height and angle in relation to the extension of western breakwaters in Naoetsu Harbor.

coast is predicted on the assumption that sandy beaches have remained when shoreline retreat has taken place. Various numerical simulation models of waves and nearshore currents have been proposed in terms of the so-called mild-slope equation and nearshore current equations. In relation to the extension of the western breakwaters, we calculated changes in the wave and nearshore current fields due to the construction of these breakwaters using a numerical model (Yamashita, Tsuchiya, Matsuyama & Suzuki, 1990).

**(2) Changes in the wave and nearshore current fields** Figure 9 shows changes in the alongshore distribution of breaker height and angle after the construction of Naoetsu harbor, S. 40, S. 45, S. 51 and S. 63 respectively indicating 1965, 1970, 1976 and 1988. The wave and nearshore fields have changed in the area where breakwater influence is marked. In the nearshore current field, some circulation has formed within the area, resulting in the westerly movement of longshore sediment (For more detail consideration, see Tsuchiya, Yamashita, Izumi and Tottori, 1993).

**(3) Alongshore distributions of longshore sediment transport rates** Using the wave characteristics for 1988, we calculated the alongshore distribution of longshore

sediment transport rates by (3), as shown in Figure 10 where the solid curves marked 1st, 2nd and 3rd were reduced by the first, second and third representative waves, and the dotted curve indicates the annual averaged total rate of longshore sediment transport. The total rate of transport is reduced near the harbor due to the effect of the break-

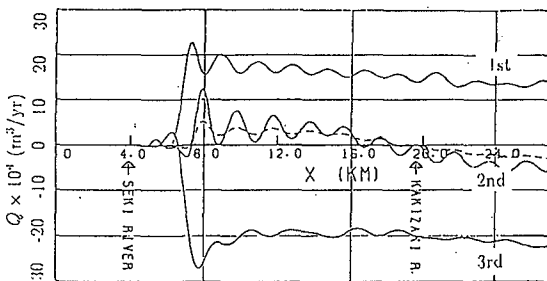


Figure 10. Alongshore distributions of longshore sediment transport rates for three representative waves and the annual averaged one after the construction of Naoetsu Harbor.

waters. A comparison of this figure with Figures 7 and 10 shows that longshore sediment transport has been reduced in the area near the harbor and that its direction is positive along the part of the coast west of the central area, but negative in the eastern part. Note that the location in which the direction of the annual averaged longshore sediment transport changes from easterly to westerly has become more easterly. We therefore conclude that construction of the large harbor has changed the sedimentation system and affected large coastal behavior.

**The mechanism of beach erosion and long-term shoreline change prediction**

As previously shown, the alongshore distribution of the longshore sediment transport rate has changed after the western breakwaters were built. It is of prime importance for the principal methodology of beach stabilization to show how this influences long-term shoreline change as large scale coastal behavior. In the numerical prediction of long-term shoreline change, we assume that natural sandy beaches have remained even after shoreline retreat has taken place.

Using the long-term shoreline change prediction model and the representative monsoon wave, we predicted numerically the shoreline change from 1961 for one hundred years, under the boundary conditions that at Naoetsu Harbor no longshore sediment is given and that longshore sediment transport exists at the Yoneyamazaki headland. Figure 11 shows the predicted shoreline change along the coast, the dotted curve indicating the initial shoreline, and the solid curves shoreline change at

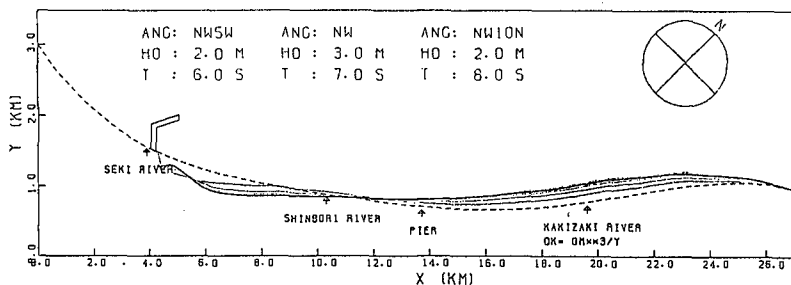


Figure 11. Long-term shoreline change predicted for 100 years after the construction (1961) of Naoetsu Harbor.

intervals of 20 years. The prediction includes the influence of building the west breakwater shown in Figure 9. Due to the direct effect of the breakwater, severe shoreline retreat takes place down the coast from the harbor. A cusped foreland is formed inside the harbor due to changes in the wave and nearshore current fields. In contrast, in the central part near the Kakizaki River shoreline accretion takes place. This long-term shoreline change should be considered as one type of large scale coastal behavior for a coast bounded by two headlands. It should be mentioned that the depositional area is wider than the eroded area due to the westerly longshore sediment transport passing the Yoneyamazaki headland. If the total amount of longshore sediment transport from the headland is assumed to be reduced, the accretional area may become narrower. Note, however, that this tendency for shoreline accretion corresponds to the present bottom topography change. Actually, the various countermeasures have been taken along this coast have resulted in the retardation of shoreline retreat, but produced a steep beach profile.

### THE METHODOLOGY FOR BEACH STABILIZATION

#### Long-term shoreline change with boundary conditions

On the basis that long-term shoreline change is large scale coastal behavior, a principal methodology for beach stabilization must be established because a large coastal construction, Naetsu Harbor, has created a man-made boundary condition that is so effective for shoreline change that we must look for a methodology for stabilizing the whole coast.

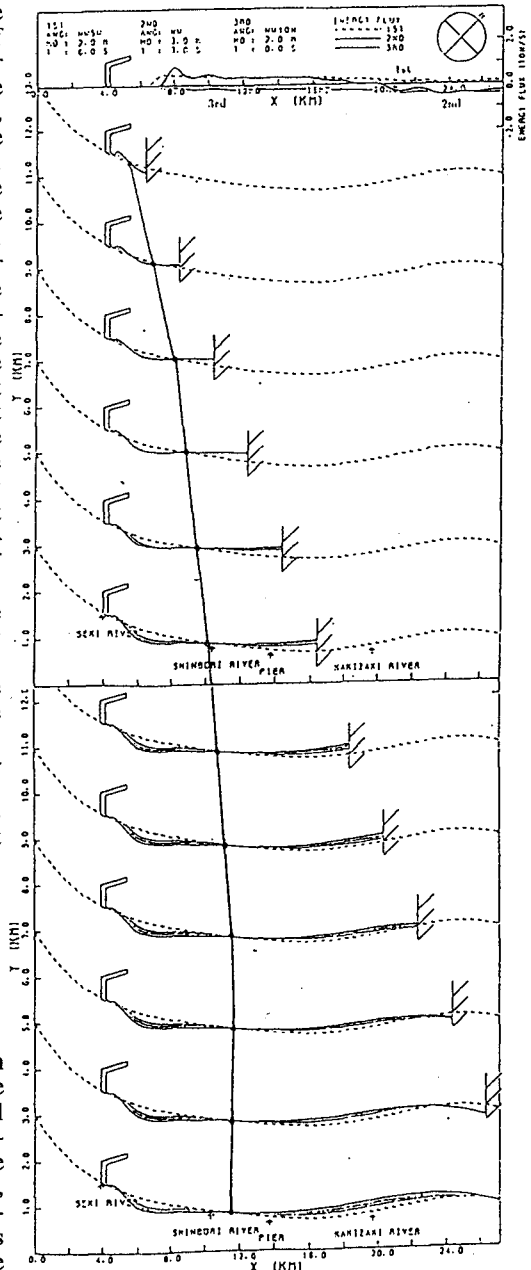


Figure 12. One-hundred years of shoreline evolution with change in the location of the boundary condition.

Therefore, we predict long-term shoreline change for another condition that counters the man-made boundary condition of the breakwater. The new boundary condition is given at a location where longshore sediment transport is completely stopped, but no wave diffraction is introduced. As previously, we predicted the shoreline changes shown in Figure 12 where the upper and lower figures are the cases for the boundary conditions located 2 to 12km and 14 to 24km from the Gotsu headland. In this figure, the solid curves show the shoreline change for one hundred years at intervals of 20 years. Shoreline change is subject to the location of the boundary condition, but the nodal point for shoreline change clearly exists near the Shinbori drainage river and remains at the same location with change in the position of the boundary condition. This is a most important factor in shoreline change as large scale coastal behavior for stabilization of the coast against the man-made boundary condition.

### A principal methodology for beach stabilization

Generally, beach erosion takes place locally due to various causes of erosion, but it is more pervasive down coast. When countermeasures were taken to prevent further erosion at that location, more severe erosion took place down coast. To stabilize the coast against erosion, we must therefore first consider what will happen along the entire coastal area due to erosion as large coastal behavior. Second, we must investigate whether the coast can be stabilized by some boundary conditions for beach change. Once a possible boundary condition for stabilizing the coast in the large coastal behavior, based on the theoretical background of the formation of stable sandy beaches (Tsuchiya, Chin and Wada, 1993, and Tsuchiya, 1994) is found, a principal methodology for beach stabilization can be established.

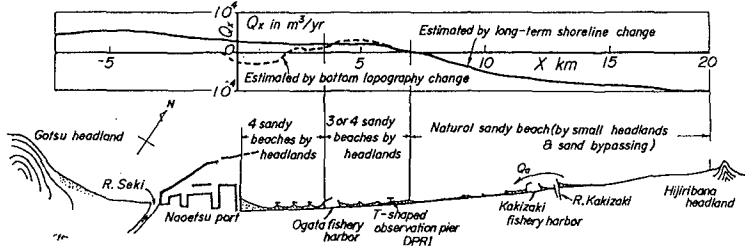


Figure 13. The methodology for beach stabilization proposed for the Joetsu-Ogata coast where two west headlands are under construction.

As stated, there is the possibility of stabilizing the coast against beach erosion by constructing a boundary condition for shoreline change at the nodal point for shoreline change. However, how this boundary condition is to be constructed must be considered. We can not construct a mathematical headland that has no wave diffraction and deflection. It must be a headland that reflects natural headlands or small islands that produce as little wave diffraction and deflection as possible. Therefore, when a headland is constructed, another boundary condition is needed to compensate for its direct influence in order to stabilize the down coast for making stable sandy beaches form. Based on the boundary condition found from viewing long-term shoreline change as large scale coastal behavior, we propose the methodology for beach stabilization shown in Figure 13, in which the upper part shows the alongshore distribution of the longshore sediment transport rate estimated by numerical calculation (solid curve) and from the bottom topography change (dotted curve). The lower part shows the proposed series of headlands used as boundary conditions for shoreline change. It should be noted that the direction of the longshore sediment transport rate has changed from easterly to westerly due to

changes in the wave and nearshore current fields (Tsuchiya, Yamashita, Izumi and Murakami, 1994). These two west headlands shown in the figure are now under construction.

## CONCLUSION

In establishing a methodology for beach stabilization, two principal roles must be taken into account: 1) Beach erosion must be considered over the entire coastal area as large scale coastal behavior and possible measures for stabilizing the coast from erosion found. 2) Based on the theoretical background of the formation of stable sandy beaches, a principal methodology for beach stabilization must be established. Beach erosion on the Joetsu-Ogata coast and its stabilization have been investigated in terms of these roles. The main conclusions are

(1) By introducing the representative monsoon wave, a prediction model for long-term shoreline change could be proposed using the so-called one-line model. This model was applied to hindcast long-term shoreline change on the Joetsu-Ogata coast, which is bounded by two headlands, for the 51 years before the construction of Naoetsu Harbor. The results agree well with the actual shoreline changes that are part of the large scale coastal behavior.

(2) On the assumptions that a natural sandy beach has remained during shoreline evolution and that the direct influence of building a harbor breakwater is introduced, we predicted long-term shoreline change for 100 years after the construction of the harbor. Severe shoreline retreat takes place along the west part of the coast, but shoreline accretion occurs along the east part. This tendency is very similar to the current bottom topography change.

(3) We have also predicted long-term shoreline changes with a given boundary condition for shoreline change. We found the most suitable location for the boundary condition to be the nodal point for shoreline change. Based on the large scale shoreline change and the theoretical background of the formation of stable sandy beaches, a principal methodology for beach stabilization has been proposed that uses a series of headlands.

## References

- Dean, R. (1991): Equilibrium beach profiles: Characteristics and applications, *Jour. Coastal Research*, Vol. 7, No. 1, pp. 53-84.
- Tsuchiya, Y. (1994): Formation of stable sandy beaches and beach erosion control; A methodology for beach erosion control using headlands, *Bulletin, Disas. Prev. Res. Inst., Kyoto Univ.*, Vol. 42, Part 2 (in press).
- Tsuchiya, Y., I. Chin and C. Wada (1993): Formation of stable sandy beaches; Theoretical configurations and their applicability, *Proc. Coastal Engineering, JSCE*, Vol. 40, pp. 371-375 (in Japanese).
- Tsuchiya, Y., T. Yamashita, T. Izumi and K. Tottori (1993): Prediction of large scale coastal behavior-Case study for Joetsu-Ogata coast-, *Proc. Coastal Eng., JSCE*, Vol. 36, pp. 456-460 (in Japanese).
- Yamashita, T., Y. Tsuchiya, M. Matsuyama and T. Suzuki (1990): Numerical models for beach change, *Annuals, Disas. Prev. Res. Inst., Kyoto Univ.*, No. 33, B-2, pp. 503-542 (in Japanese).
- Yamashita, T., Y. Tsuchiya and K. Murakami (1994): Beach processes of Ogata coast and change in fishery production rate, *Proc. Coastal Engineering, JSCE*, Vol. 41, pp. 371-375 (in Japanese).

## CHAPTER 245

### SHORELINE EROSION DUE TO OFFSHORE TIN MINING

By Suphat Vongvisessomjai<sup>1</sup>, Member, ASCE

#### ABSTRACT

Phuket is a well-known island resort on the west coast of the peninsula of Thailand and it is rich in tin deposits. Tourist and tin mining are conflicting especially in Bang Tao Bay. Before offshore tin mining in the bay, the bathymetry is quite simple/natural and the bay is almost in equilibrium with offshore sand movement by storm waves and onshore sand movement by swell. After tin mining in 1987, people in Villages 4 and 5 sent a petition to district and city officers from May to June 1988 to the effect that offshore tin mining in the bay had caused beach erosion and road damage, and that the dredger owner should be responsible for the cost of repairs. The sounding map makes in this study reveals that deep holes are created by dredgers, those nearshore are found to interrupt the cyclic changes and sand movement on the beach that results in a permanent loss of sand into the dredged holes and causes shoreline erosion; the maximum erosion in the middle of the bay is 40 meters in the 3 years from 1987 to 1990. A field test during May to June 1991 confirms that the high rate of shoreline erosion is consistent with that found in large wave tank experiments. Offshore tin or sand mining should not be made in shallow water where sand is mobile. If offshore mining were allowed nearshore, conditions should be imposed so that the bathymetry in the vicinity of the offshore mining should not change significantly.

#### INTRODUCTION

Phuket is a well-known island resort on the west coast of the peninsula of Thailand as shown in Fig.1. In general, tin mining is not presently allowed in most of the beach resorts of the island except in Bang Tao Bay where two concessions were granted for offshore tin mining in the belief that the dredged materials, after the sorting out for tin by the dredgers, would be replaced in the dredged holes, which would not change the bathymetry much.

---

<sup>1</sup> Professor, School of Civil Engineering, Asian Institute of Technology, P.O. Box 2754, Bangkok 10501, Thailand.



The study area in the vicinity of the Dusit Laguna beach of the Bang Tao Bay on the west coast of Phuket island is shown in Fig. 1. The bay is attacked by waves during the southwest monsoon from May to September. Predominant waves attacking the bay are mainly from the west and they cause onshore-offshore transport with not so much alongshore transport. During the northeast monsoon, the wind blows from land to sea over the bay; therefore, there is negligible wave action in the bay. In addition to these monsoons, the bay is occasionally attacked by cyclonic waves prevailing in the Andaman Sea. The bathymetry of Bang Tao Bay before offshore tin mining is quite natural as shown in Fig. 1c.

From May to June 1988, at the beginning of southwest monsoon, severe waves caused erosion of the shoreline and road damage in the Bang Tao Bay. People in Villages 4 and 5 sent a petition to district and city officers to the effect that offshore tin mining in the bay was the cause of beach erosion and road damage and that the dredger owner should be responsible for the cost of repairs. On October 15, 1988 the Minister of Industry visited the site and asked the Mineral Resources Department to order the dredger to dredge beyond 500 meters from the shoreline. The Mineral Resources Department (1990) studied the cause of erosion of the Bang Tao Bay with the assistance of the Committee for Co-ordination of Joint Prospecting for Mineral Resources in Asian Offshore Areas (CCOP) and concluded that (i) severe waves caused erosion of all beaches on the west coast of Phuket in 1988 and (ii) the instability of the BangTao shoreline due to previous tin mining on land might be the cause of erosion. Due to the limited time of the study, no reason for erosion caused by offshore tin mining could be found, however the search would be studied further.

The causes of the shoreline erosion can be initially listed as follows:

1. Storm waves with high wave steepness generated by cyclones or southwest monsoon move sand on the beach offshore.
2. Alongshore currents generated by inclined breaking waves move sands alongshore and deposit it somewhere.
3. Offshore tin mining close to the beach creates holes which draw beach sand.

The objectives of this study are as follows:

1. To make field surveys to collect relevant data and to monitor dredger activity.
2. To find out the causes of beach erosion.
3. To recommend remedial measures to conserve the beach resorts from erosion.

Steps to solve the problem are as follows: a review of the literature is made first on the effects of the offshore dredged holes on shoreline erosion. The most important part of this study is the field survey which is then described, while field data and their interpretation are finally presented.

## REVIEW OF LITERATURE

There are limited reports on the effects of offshore dredged holes on shoreline erosion; the followings are some examples.

**Motyka and Willis (1974)** presented the preliminary results of a study of the beach erosion by wave refraction over offshore dredged holes. A mathematical model was used of an idealized sand beach, typical of those on the English Channel and the North Sea coasts of Great Britain. Depth and side slopes of dredged area and original water depth before dredging were varied. Beach erosion increased with increasing hole depth and with depth. At present, dredging was not allowed shoreward of the 18 m depth contour on sediment supply considerations. Their results suggested that for the North Sea and the English Channel coasts, the effects of wave refraction also point to an 18 m minimum depth. This is approximately half the wavelength of the most common wave period, and a fifth of the length of the extreme wave period; hence it might be possible to extrapolate these results to other areas on a wavelength basis. Beach erosion due to holes in water depths greater than half the length of "normal" waves, or a fifth of the length of extreme waves, was negligible. They concluded that results were conservative, that the study was predicting larger amounts of erosion than would occur in nature. This was due to the fact that erosion was caused by differences in sediment transport along the beach, and the assumption in the refraction calculation that wave energy could not propagate along the wave front tended to exaggerate these difference.

**Price, Motyka and Jaffrey (1978)** dealt with the licensing procedure of dredging and assessed how dredging might affect the coastline. They provided some guidelines on the monitoring of shoreline erosion due to dredging:

(1) Beach drawdown - This usually occurs during storms due to the action of high steep waves. Beach material is eroded from the upper foreshore and moved seawards. However, during periods of calmer weather the material is returned to the beach by long low swell. If the dredged area is too near the coastline then this dynamic equilibrium can be upset, in that material may be transported from the upper portion of the beach into the dredged hole and erosion of the foreshore may result. The active zone of offshore-onshore movements extends to a certain depth of water and a certain distance from the shore. Thus, with respect to beach drawdown, there are two criteria - a minimum depth of water and a minimum offshore distance.

(2) Interception of sediment - If the beach is being fed from offshore by current and wave action then dredging may trap a proportion of this material and interrupt the supply to the shore. It is very important, therefore, that dredging should be excluded from any deposits which are moving actively. The threshold of movement of sediments. The dredged trenches above a certain depth within the active zone of littoral movement may interrupt the beach littoral system in that they serve as a trap to littoral sediment that would travel either onshore or alongshore.

(3) Dredging area included offshore banks - Offshore banks help to protect the coastline from wave attack either by dissipating wave energy as a result of bed friction, by partial breaking of the waves, by refraction or by any combination of these three. A permanent lowering of the crest of the bank due to dredging can result in changes of the wave refraction pattern and hence changes in the net angle of wave attack at the shoreline. Thus, under certain circumstances, dredging from offshore banks can alter the rate of littoral drift and hence affect the stability of the shoreline.

(4) The effect of changes in wave refraction - As waves approach the shore, they travel with a group velocity that is dependent upon their period and upon the depth of water. If the water depth increases locally, e.g., over a dredged hole, the velocity and wavelength change. The local increase in wave celerity due to the increase water depth causes changes in the angle of wave approach to the beach. Such changes result in a variation in the rate of littoral drift along the shoreline and can cause either accretion or erosion.

**Kojima, Ijima and Nakamuta (1986)** carried out comprehensive coastal engineering studies over four years in order to evaluate the impact of offshore dredging on shorelines as well as the adjacent seabed along the Genkai Sea, Japan. The results (data presented) indicated a possible relationship between sand mining and the shoreline changes. Although the available data were not sufficient to establish a direct cause-and-effect relationship between offshore mining and beach instability, the correlation was sufficient to serve as a warning of a potentially serious problem. Moreover, dredged holes above the water depth of about 30 meters were found to be refilled with sand which would be mainly transported from the onshore side, thereby interrupting the beach littoral system by trapping sand which might travel in the on-offshore or alongshore direction and causing a steeper beach slope in the long run. It was advisable, therefore, that the indiscriminate removal of sand from seabed be avoided at such water depth of 35 meters. Thus, offshore mining that would minimize interruption of beach littoral system should be operated below a depth of 35 meters in the study area.

**Uda, Agemori and Chujo (1986)** investigated the conditions of the dredging of the offshore bed on the Kochi Coast, facing Tosa Bay, Japan. Aerial

photographs and the sounding data of the coast were analyzed to obtain the beach changes accompanied by the formation of the dredged hole. The flood of the Niyodo river brought large amount of sediment to the coast; the sediment outflow from the river fell into the dredged hole by eastward littoral drift. The hole was refilled slowly from the west side by the littoral drift directing eastward. An abrupt change of the topography due to the onshore-offshore sand transport did not happen as the dredged hole was filled by river sediment carried by the flood and littoral current.

**Larson, Kraus and Sunamura (1988)** developed a numerical model for simulating beach profile change in the surf zone produced by wave-induced cross-shore sand transport. Model development was founded on two data sets from large wave tank experiments performed by the U.S. Army Corps of Engineers in the years 1956-1957 and 1962 while the second data set was from experiments performed at the Central Research Institute of Electric Power Industry in Japan.

Storm waves with high wave steepness erode the beach producing offshore bars while swells with low wave steepness accrete the beach bringing back bar material onto the beach; the cyclic changes of beach are shown in Fig.2. When storm waves attack a beach for a sufficiently long time, its beach profile would approach an equilibrium. In other words, when sand moves offshore the offshore bar simultaneously increases in volume to approach an equilibrium size as shown in Fig. 3. Their chronological changes of beach profiles for 2 cases are shown in Fig.4. At the beginning of an attack by storm waves, the beaches change rather quickly but they change rather slowly when they approach the equilibrium. Correlation analysis involving wave and beach profile parameters showed that equilibrium bar volume was most closely related to wave height  $H_o$  and sand fall velocity  $w$  (or grain size). A large wave height implied a larger bar volume, and a higher fall velocity (or larger grain size) produced a small bar volume. A regression relationship was derived relating the non-dimensional equilibrium bar volume  $V_{eq}/L_o^2$  to the quantities  $H_o/(wT)$  and  $H_o/L_o$  according to

$$\frac{V_{eq}}{L_o^2} = 0.028 \left( \frac{H_o}{wT} \right)^{1.32} \left( \frac{H_o}{L_o} \right)^{1.05} \quad (1)$$

where deepwater wavelength  $L_o = gT^2/(2\pi)$  and  $T$  = wave period.

Note that the active zone of sand movement is confined mainly in the surfzone where waves are broken due to their instability in shallow water when the water depth is about equal to the wave height. Therefore, the higher wave would create a wider surfzone and would result in much more active sand transport.

**Dette and Uiczka (1987)** investigated dune recession and beach erosion at prototype scale in the big wave flume in Hannover, Germany. Results on time

-dependent erosion volume and recession of dune were presented for “**dune without foreshore**” and “**dune with foreshore**” in Figs.5 and 6. The simulated wave had a significant height of 1.5 m and peak period of 6 sec at 5 m depth of water, while the sand used had a median diameter of 0.33 mm. In the presence of the foreshore, compared to the profile development due to regular waves, the recession of the dune’s edge was only about one-third of that recession measured for dune without the foreshore. The bar location was about 10 m further seaward. Hence, the breaking occurred further away from the dune’s face and a wider surf zone provided additional dissipation of wave energy.

## FIELD SURVEY AND RESULTS

### Program of Field Survey

Field data on wave climate, alongshore current, wind and resulting beach erosion were collected to obtain pertinent information on morphological changes and offshore dredging effects on the shoreline. The characteristics and behavior of the beach were monitored by field measurements of beach shape and profile, soundings and bed material sampling. Locations of dredgers operating in the bay were measured daily by reading the angles of the dredger at two observation locations onshore.

Three soundings have been made for an area of 2.5 km alongshore by 1.5 km offshore, the first at the end of October 1990 before the arrival of dredgers; the second at the end of April 1991 by the end of dredging; and lastly at the end of October 1991 after the attacks of southwest monsoon waves. The first and the last soundings were accompanied by beach profile measurement and beach material samplings.

Waves and winds were measured at two locations about 300 m offshore, together with alongshore current at one hour intervals during the daytime.

### Topographical Change

From the above three soundings maps surveyed in October 1990, and April and October 1991, the following topographical changes could be seen.

(1) Shoreline erosion - Comparing contour lines of soundings in 1990 with those in 1987 for the shorelines, it was found that severe erosion occurred between DL3 and DL5. Average erosion rate from 1987-1990 was about 7 meters per year with the maximum of about 13 meters per year in the vicinity of Inlet 2.

(2) Creation of deep holes nearshore - It can be seen from Fig.7 of the sounding of the Bang Tao Bay in October 1990, that many deep holes were created by dredgers operating nearshore from 1987 to 1990 as compared with the natural bathymetry before offshore tin mining, shown in Fig.1c. These nearshore deep holes interrupted the cyclic changes of the beach in terms of erosion by storm waves and subsequent accretion by swells (Fig.2) and, therefore, resulted in a permanent loss of sands from the erosion of beach into the

dredged holes. It can be seen from the beach profiles at DL1, DL2, DL3 and DL4, plotted in Figs.8 (a), (b), (c) and (d) respectively, that deep holes existed at an offshore distance of about 300 meters, while the beach profiles at DL5 and DL6 in Figs.8(e) and (f) respectively are more natural, namely without deep holes nearshore. The onshore sides of these nearshore deep holes in the active zone of sediment movement by wave action; the mobile sediment will fall down the steep slopes of the deep holes especially the deep hole A4 at DL4. Comparing these beach profiles with those in Fig.6, it can be seen that profile DL4 is similar to that of dune without foreshore while profiles DL5 and DL6 are similar to that dune with foreshore. Therefore, nearshore deep holes changed the natural beach of dune with foreshore to dune without foreshore which experienced a much higher rate of erosion.

(3) Field test of shoreline erosion - In order to obtain an order of magnitude estimate of shoreline erosion, a test was made by dumping about 6,000 m<sup>3</sup> of sand on the beach for alongshore distance of 300 m. The beach-fill was agitated by the southwest storm waves on June 2-4, 1991 and approximately half of the filled sand was eroded while the remaining half was eroded during June 5-13, 1991. Practically, no erosion occurred on May 15 to June 1, 1991. According to the wave data collected during May 18 - June 13, 1991, wave heights were the largest on June 2 - 4 and 9 - 13 with a range of 1.0 - 2.5 m while the wave period was about 6.4 sec. During the period of June 5 - 8, wave heights were around 0.8 - 1.4 m with a wave period of 8.1 sec. The wave condition was calmer from May 18 - June 1 with wave height of 0.4 - 0.9 m and period of 8.2 sec. Slope of beach at the upper section is steeper compared to that of the offshore side in the mid tidal zone. When waves attacked upper section of the beach at high tide the erosion rate was higher. The average erosion volume per meter of beach was 20m<sup>3</sup>/m.

### Field Conditions

Winds and waves change from year to year. However, their trends or orders of magnitude are common. The most probable of commonly recorded waves measured in this study during the southwest monsoon by Vongvisessomjai and Huq in 1991, as compared with those measured earlier in 1980 shown in brackets (Gayman, 1983) are as follows:

Month	Wave Height (m)		Period (sec)	
	1991	(1980)	1991	(1980)
May	0.3-0.5	(0.0-0.5)	7.0	(4.5)
June	0.5-1.5	(0.5-1.0)	7.0	(6.5)
July	0.5-1.5	(0.5-1.0)	7.0	(6.5)
August	0.5-1.5	(0.5-1.0)	7.0	(6.5)

The above wave characteristics could serve as commonly recorded waves on the west coast of Phuket during the southwest monsoon.

The southwest monsoon waves are mainly from the southwest or west or northwest. As they propagate into shallow water and break near the shoreline, their crestlines are almost parallel or make some small angles with respect to the shoreline. Therefore, they generate no alongshore current or alongshore current towards the north/south direction. The magnitudes of alongshore current measured in this study are about 0.15 - 0.20 m/sec. with a north or south direction in May, a predominantly north direction in June and a predominantly south direction in July and August 1991.

The erosion volume  $V_{eq}$  of the equilibrium profile (Eq.1) depends on deepwater wave height and fall velocity (or grain size). A larger wave height implies a larger erosion volume, and a higher fall velocity (or larger grain size) produces a smaller erosion volume. Using typical median diameters of 0.5 and 0.2 mm, wave period of 6.5 sec and wave heights of 0.5 - 2.0 m, the computed erosion volumes  $V_{eq}$  are listed below:

$d_{50}$ (mm) (1)	$H_o$ (m) (2)	T(sec) (3)	$L_o$ (m) (4)	w(m/s) (5)	$H_o/L_o$ (6)	$H_o/(wT)$ (7)	$V_{eq}$ (m <sup>3</sup> /m) (8)
0.5	0.5	6.5	66	0.074	0.008	1.01	1
	1.0				0.015	2.08	4
	1.5				0.023	3.12	10
	2.0				0.030	4.16	20
0.2	0.5	6.5	66	0.027	0.008	2.85	3
	1.0				0.015	5.70	15
	1.5				0.023	8.55	39
	2.0				0.030	11.40	77

The erosion volumes of fine sand ( $d_{50}=0.2$  mm) are about four times those of coarse sand ( $d_{50} = 0.5$  mm). These computed erosion volumes agree well with those tested in the field of shoreline erosion of 20m<sup>3</sup>/m.

### RECOMMENDATION

1. Offshore tin mining or sand mining should not be made on the west coast of Phuket in shallower water than 15 meters based on wave conditions and sand characteristics at the site compared with those of England and Japan of 18 and 35 meters respectively.

2. If offshore tin mining were allowed nearshore in shallower water than 15 meters, conditions should be imposed so that the bathymetry in the vicinity of offshore mining should not change significantly.

3. Beach nourishment should be made around Inlet 2 in order to restore the beach of Dusit Laguna; structural control of shoreline erosion would not be effective here due to the presence of nearshore deep holes.

## REFERENCES

- Dette, H. and Uliczka, K. (1987). "Prototype Investigation on Time-Dependent Dune Recession and Beach Erosion", Coastal Sediments'87, Vol. II, pp. 1430-1443.
- Gayman, W. (1983). "An Investigation of Turbidity Control Methods for Use on Tin Dredges Operating off the West Coast of Thailand", Report No. ROAP/THA/83/1, UNEP, Regional Office for Asian and Pacific, Bangkok, Thailand.
- Kojima, H., Ijima, T. and Nakamura, T. (1986). "Impact of Offshore Dredging on Beaches", International Conference on Coastal Engineering, pp. 1281-1295.
- Larson, M., Kraus, N.C. and Sunamura, T. (1988). "Beach Profile Change: Morphology, Transport Rate and Numerical Simulation", International Conference on Coastal Engineering, pp. 1295-1309.
- Mineral Resources Department (1990). "Study on Cause of Erosion of Bang Tao Bay, Phuket" (in Thai).
- Motyka, J.M. and Willis, D.H. (1974). "The Effect of Wave Refraction over Dredged Holes", International Conference on Coastal Engineering, pp. 615-625.
- Price, W.A., Motyka, J.M. and Jaffrey, L.J. (1978). "The Effect of Offshore Dredging on Coastlines", International Conference on Coastal Engineering, pp. 1347-1358.
- Sallenger, A.H. Jr., Holman, R.A. and Birkemeier, W.A. (1985). "Storm-Induced Response of Nearshore-Bar System", Marine Geology, Vol.64, pp. 237-257.
- Vongvisessomjai, S. and Huq, Md. Anisul (1991). "Shoreline Erosion Study of Bang Tao Bay", Research Report No.245, Asian Institute of Technology, 104 pp.



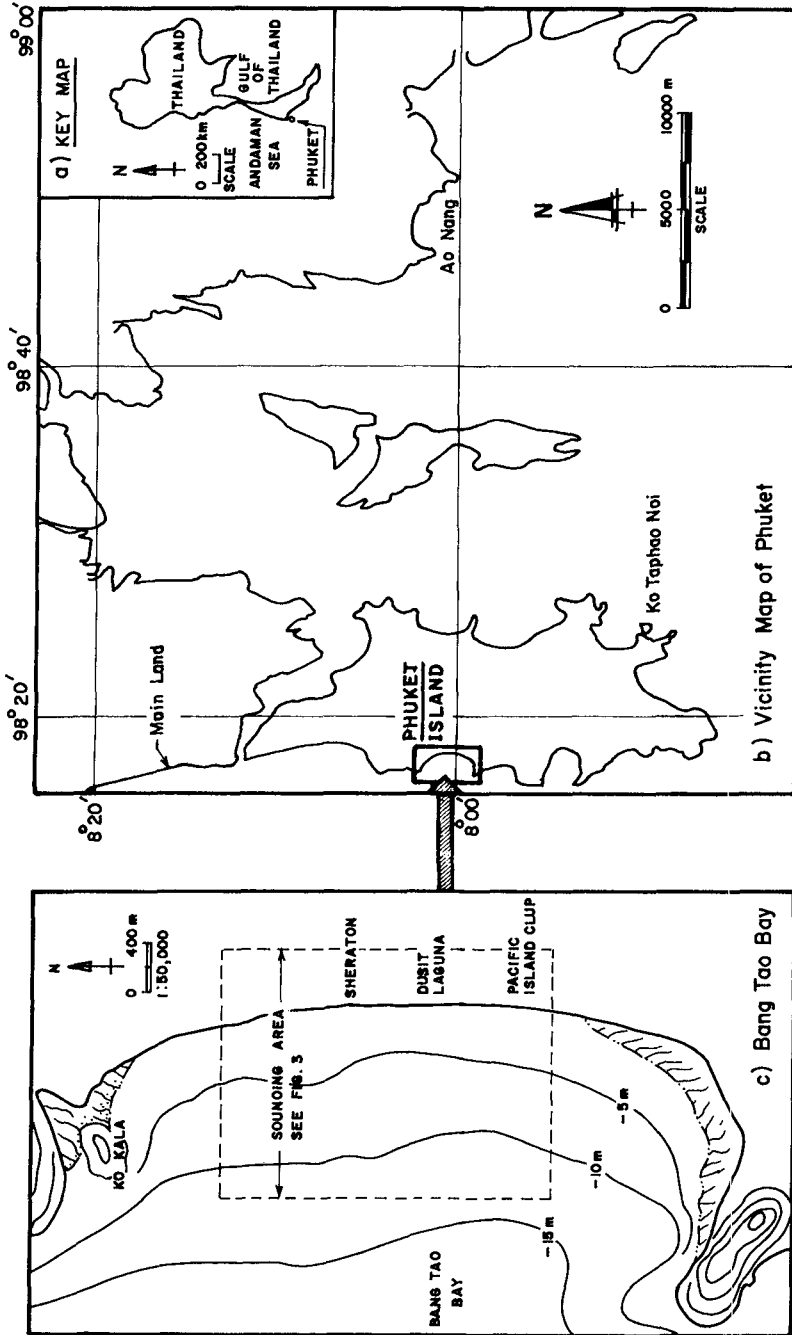
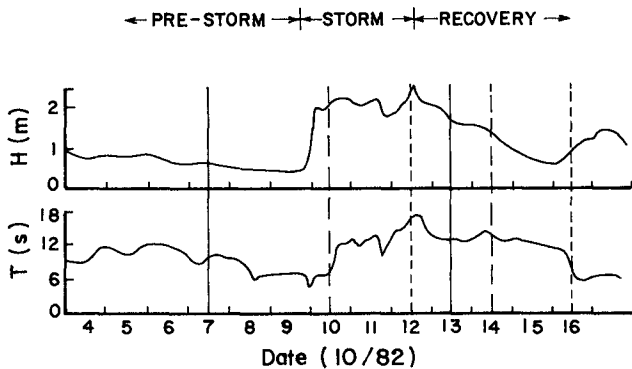
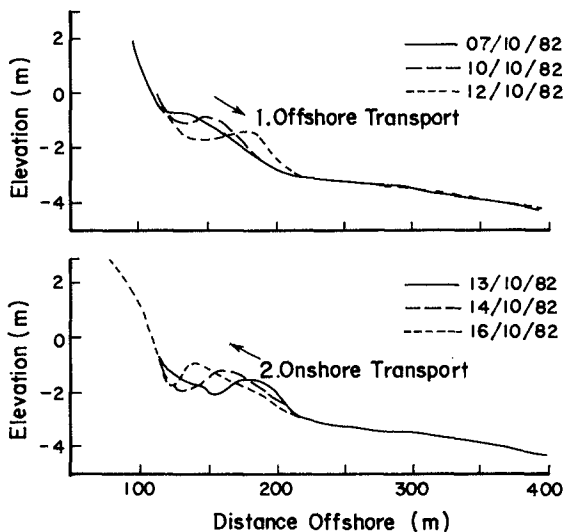


FIG. 1 - a) Key Map and b) Vicinity Map of Phuket as well as c) Bang Tao Bay and its Bathymetry before Offshore Tin Mining



(a) Significant Wave Height and Period



(b) Beach Profiles

FIG. 2 - Actual Offshore and Onshore Transports at Duck, North Carolina (Sallenger et al., 1985)

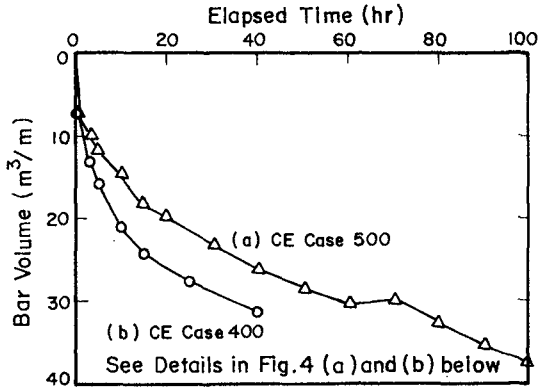


FIG.3 - Growth of Bar Volume with Elapsed Time (Larson et al., 1988)

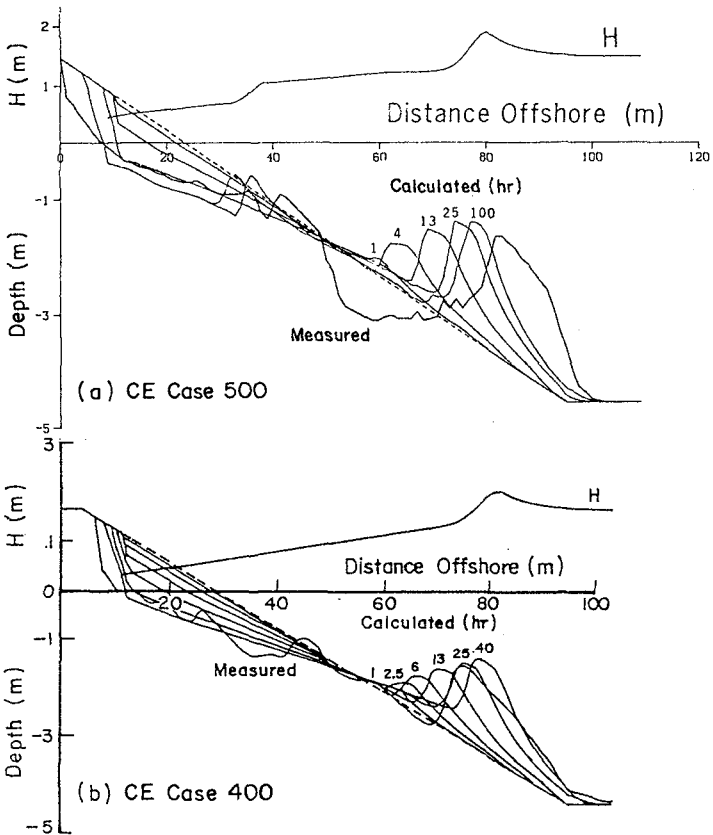


FIG.4 - Chronological Changes of Beach Profiles (Larson et al., 1988)

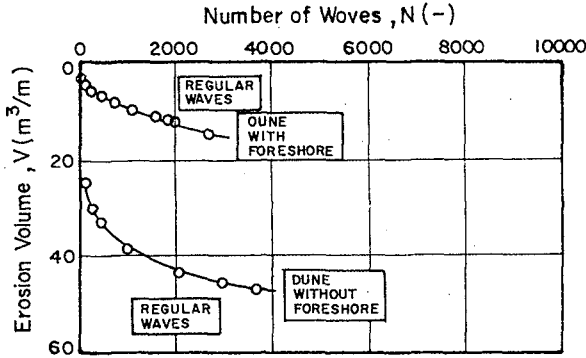


FIG. 5 - Erosion Volume with Elapsed Time of Beach Profiles of Dune with and without Foreshore (Dette and Uliczka , 1987 )

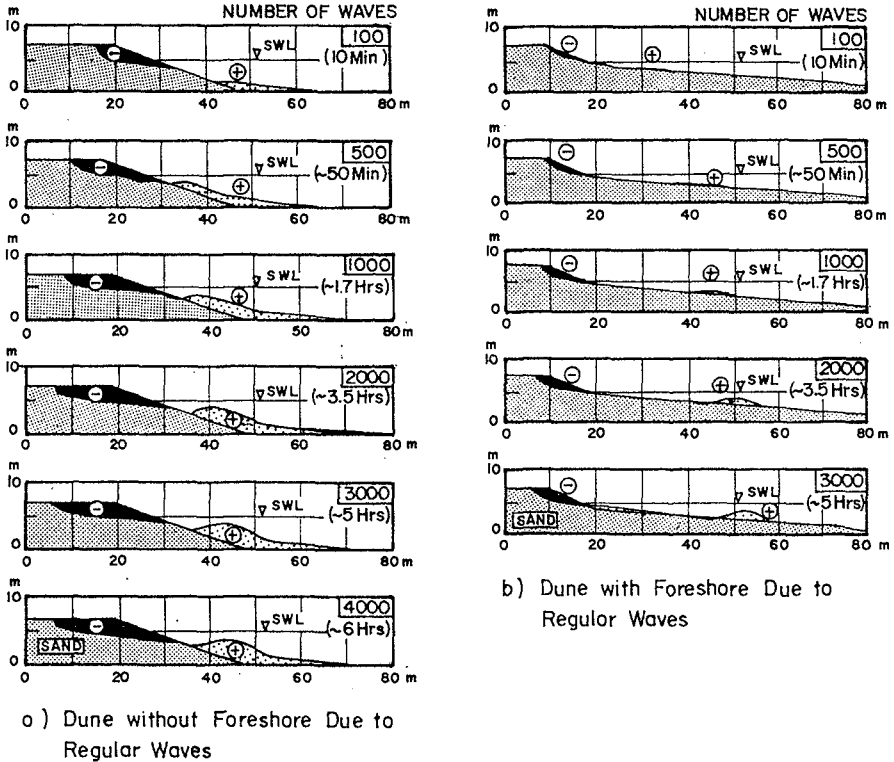


FIG. 6 - Time - Dependant Development of Dune and Beach Profile (Dette and Ulicka , 1987)

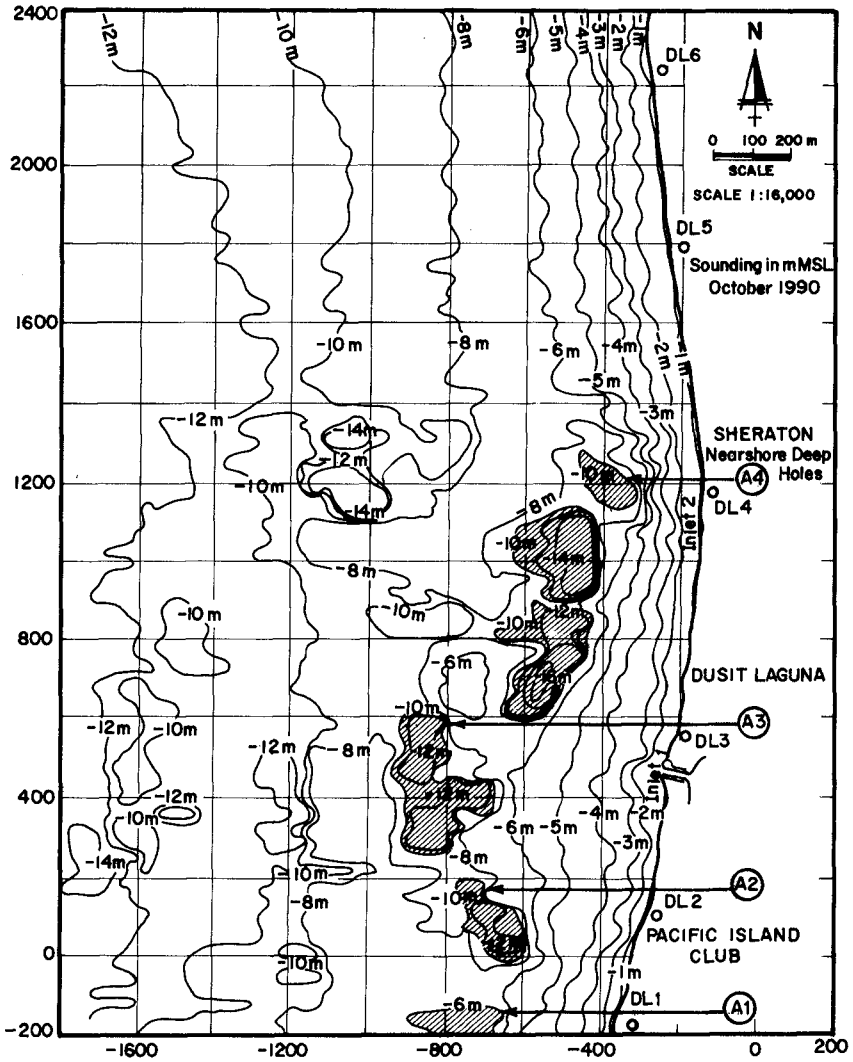


FIG. 7 - Sounding Map in October 1990 Showing Nearshore Deep Holes A1 to A4

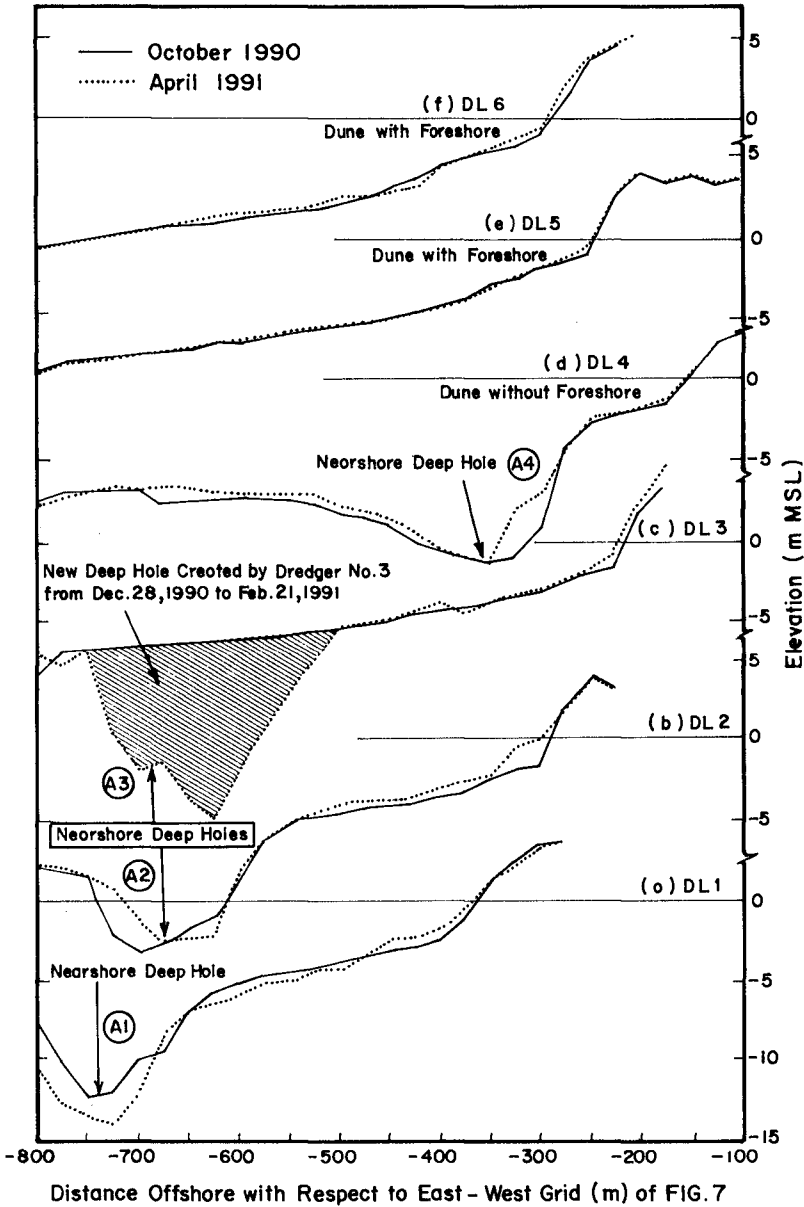


FIG. 8 - Beach Profiles at DL 1 to DL 6

## CHAPTER 246

### Behaviors of Fluid Mud under Oscillatory Flow

Hiroyuki Yamanishi<sup>1</sup> and Tetsuya Kusuda<sup>2</sup>

#### *Abstract*

Characteristics of settling velocity of fine particles and movements and the mechanism of maintenance of the fluid mud layer under oscillatory flow are investigated to control the transport flux of suspended solids in estuaries and the coastal zone. Settling velocity of fine particles under oscillatory flow is reduced as a function of only the local concentration. Motion of fluid mud depends on shear stress acting on the interface between the overlying water layer and the fluid mud layer and the horizontal pressure gradient. Especially, the horizontal pressure gradient causes a phase lag between the overlying water layer and the fluid mud movements. Velocity profiles calculated by a linearized model agree well with the measured velocity profiles in spite of assuming the kinematic viscosity in the fluid mud layer to be homogeneous. The apparent viscosity in the fluid mud layer is approximately 200 times as large as that of pure water.

#### **1.Introduction**

The water layer on mud bed under waves and currents is generally divided into two parts; one is the overlying water layer which is comparatively dilute in concentration and the other is the fluid mud layer which is high in concentration. Moving fluid mud under waves and currents maintains a loose state without consolidation on the bottom. Concentrations of the fluid mud layer are 1 order to 2 orders of magnitude higher than those of the overlying water layer. The flux of suspended solids transported in the fluid mud layer is larger than that in the overlying water layer, though the transport rate of suspension in the fluid mud layer is smaller than that by advection in the overlying layer.

A series of field measurements on shoaling of Kumamoto Port, located in the west side of Kyushu Island, were carried out to confirm effects of submerged mounds against siltation (Tsuruya *et al.*, 1990). Three trenches were set inside the navigation pass of Kumamoto Port under construction. One was surrounded by a

---

<sup>1</sup>Research Associate, Dept. of Civil Eng., Kyushu University, 6-10-1 Hakozaki, Higashi-ku, Fukuoka, 812 JAPAN.

<sup>2</sup>Professor, Dept. of Civil Eng., Kyushu University.

type of submerged mound, but the others were not. Although there was little difference of deposition amounts between them under normal conditions, heavy depositions were observed in the no submerged mound trenches under some severe conditions. From these temporal variations of the depositional amounts inside these three trenches during about a year, the submerged mounds were found effective against siltation. These facts also indicate that fluid mud moves along the sea bed under waves. Results of the field measurements made by Odd and Owen(1972) and Smith and Kirby(1989) also suggest the existence of a high concentration layer near the bottom. Therefore, studies on behaviors of fluid mud under currents and waves are of importance for siltation. Furthermore, so far, as is known, little work has been done on the mechanism of maintenance of fluid mud layers under waves and currents.

The purposes of this study are to explain the formation process of the fluid mud layers, the vertical transport process between suspended solids and fluid mud, the mechanism of maintenance of the fluid mud layers, settling velocity of particles, viscosity in fluid mud, the role of pressure gradient within fluid mud layers, and modeling of the fluid mud movement under oscillatory flow. These results will give useful suggestion on what maintains the fluid mud layer under oscillatory flow and the control of shoaling.

## 2.Theoretical Analysis

A fluid mud layer, according to Ross and Mehta(1989) and our experimental results, consists of both mobile and stationary fluid mud layers. Fluid mud moves as not solid but viscous fluid because the fluid mud layer is high in concentration. Around the upper interface between the overlying water and the fluid mud, a zone of high concentration gradient exists, which is referred to as "lutocline." Based on these facts, in order to accurately formulate the equations of motion of the layer, a multi-layered fluid model was used(Yamanishi and Kusuda, 1991). The model, however, could not show any phase lag of movement between both layers. In this study, in order to explain the causes of the phase lag, a simple linearized and horizontally uniform model was applied. As a model, a simplified vertical structure is adopted as illustrated in Fig.1, where the x axis is taken at the interface. Since the motions of the fluid mud are subjected to both shear stress acted on the interface and the horizontal pressure gradient,  $\partial p/\partial x$ , in the fluid mud, the motions of the fluid mud are modeled by superposing two motions induced by these two forces. The

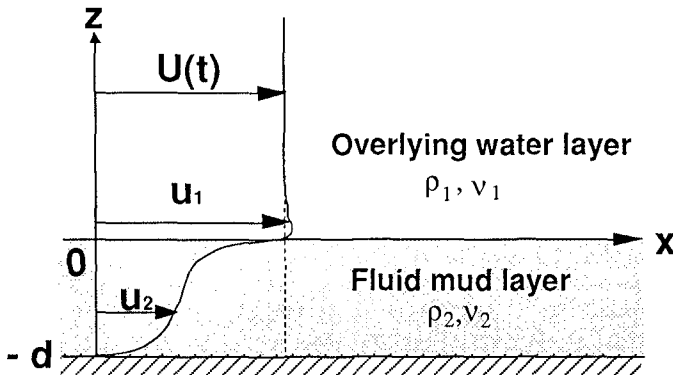


Fig.1 Definition sketch for fluid mud model



following assumptions are made owing to model the motions of fluid mud under oscillatory flow:

- (a) Each layer moves only to the horizontal direction;
- (b) Velocity  $U$  in the overlying water is a function of time  $t$  only;
- (c) The advective terms in the equations of motion are negligible small;
- (d) The pressure amplitude is uniform in the vertical direction; and
- (e) The kinematic viscosity in each layer is homogeneous.

Under the above assumptions, the linearized equations of motions of the fluid mud and overlying water become as follows:

**Overlying water layer(  $z \geq 0$  ):**

$$\left\{ \begin{array}{l} \frac{\partial U}{\partial t} = -\frac{1}{\rho_1} \frac{\partial p}{\partial x} \dots (1) \\ \frac{\partial u_1}{\partial t} = -\frac{1}{\rho_1} \frac{\partial p}{\partial x} + \nu_1 \frac{\partial^2 u_1}{\partial z^2} \dots (2) \end{array} \right.$$

**Fluid mud layer(  $-d \leq z < 0$  ):**

$$\frac{\partial u_2}{\partial t} = -\frac{1}{\rho_2} \frac{\partial p}{\partial x} + \nu_2 \frac{\partial^2 u_2}{\partial z^2} \dots (3)$$

where,  $u_j$ ,  $p_j$ ,  $\nu_j$  and  $\rho_j$  are the horizontal velocity, the pressure, the kinematic viscosity and the layer-averaged density, respectively. The subscript  $j$  indicates each layer, so that  $j=1$  for the overlying water layer and  $j=2$  for the fluid mud layer.

In order to analytically solve Eqs.(1)~(3), some solutions described by using the complex representation are supposed as the following equations:

$$U = -i \widehat{U} e^{i\omega t} \dots (4)$$

$$\tilde{u} = -i \widehat{\tilde{u}} e^{i\omega t} \dots (5)$$

$$u_2 = -i \widehat{u_2} e^{i\omega t} \dots (6)$$

$$\widehat{U} = a\omega \dots (7)$$

$$\partial p / \partial x = -\widehat{p}_x e^{i\omega t} \dots (8)$$

$$\widehat{p}^* = \rho_1 a \omega^2 \dots (9)$$

where,  $\widetilde{u} = u_1 - U$ ,  $a$  is the amplitude,  $\omega$  is the frequency ( $\omega = 2\pi/T$ ,  $T$ ; period),  $t$  is the time,  $\widehat{\phantom{x}}$  indicates the amplitude, and  $i$  is the imaginary unit ( $i^2 = -1$ ).

The boundary conditions necessary to solve them are as follows:

$$u_1 = U(t), \text{ for } z \rightarrow \infty \dots (10)$$

$$u_1 = u_2, \text{ at } z = 0 \dots (11)$$

$$-\rho_1 \nu_1 \frac{\partial u_1}{\partial z} = -\rho_2 \nu_2 \frac{\partial u_2}{\partial z}, \text{ at } z = 0 \dots (12)$$

$$u_2 = 0, \text{ at } z = -d \dots (13)$$

The velocity  $U(t)$  in the overlying water is regarded as a function of time  $t$  only. These boundary conditions satisfy the continuity of the velocities and stresses across  $z=0$  and the non-slip condition at  $z=-d$ .

The analytical solutions of  $u_1$  and  $u_2$  which satisfy the above boundary conditions are as follows:

$$\left\{ \begin{array}{l} u_1 = -i \left\{ (1 - e^{-\lambda_1 z}) \widehat{U} + e^{-\lambda_1 z} \widehat{u}_i \right\} e^{i\omega t} \dots (14) \end{array} \right.$$

$$\left\{ \begin{array}{l} u_2 = -i \left[ \left\{ 1 + \frac{\sinh \lambda_2 z}{\sinh \lambda_2 d} - \frac{\sinh \lambda_2 (z+d)}{\sinh \lambda_2 d} \right\} \cdot \frac{\widehat{p}}{\rho_2 \omega} + \frac{\sinh \lambda_2 (z+d)}{\sinh \lambda_2 d} \widehat{u}_i \right] e^{i\omega t} \dots (15) \end{array} \right.$$

where,

$$\widehat{u}_i = \frac{\rho_1 \nu_1 \lambda_1 \widehat{U} + \rho_2 \nu_2 \lambda_2 \frac{1 - \cosh \lambda_2 d}{\sinh \lambda_2 d} \cdot \frac{\widehat{p}}{\rho_2 \omega}}{\rho_1 \nu_1 \lambda_1 - \rho_2 \nu_2 \lambda_2 \frac{\cosh \lambda_2 d}{\sinh \lambda_2 d}} \dots (16)$$

$$\lambda_1 = (1 + i) \sqrt{\frac{\omega}{2 \nu_1}} \dots (17)$$

$$\lambda_2 = (1 + i)\sqrt{\frac{\omega}{2\nu_2}} \dots (18)$$

From results of the simulations, validity of the model is examined with respect to behaviors of fluid mud and the phase lag.

### 3.Experiments

**Figure 2** shows a U-shape oscillating water tunnel used in this study. This water tunnel does not allow the horizontal transport of fluid mud even for a long time experiment. Mud used was obtained at the Ariake Bay where the maximum tidal range is 5m. This fluid mud was directly sampled from the surface of stationary mud at an ebb tide. The mud consists of clay(55.6%), silt(41.7%) and sand(2.7%) as an average. Its mean diameter and density were  $4.0\mu\text{m}$  and  $2540\text{kg/m}^3$ , respectively.

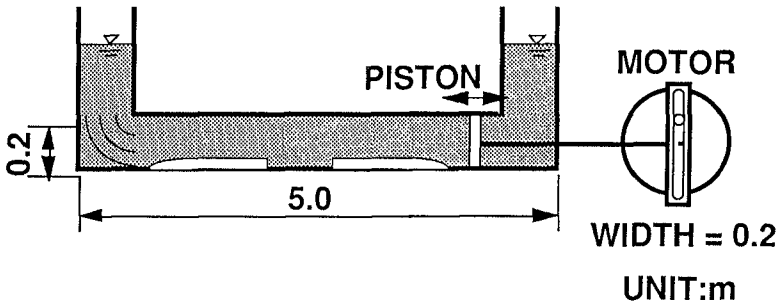


**Fig.2** U-shape oscillating water tunnel

After pouring a mud-seawater mixture with a certain concentration into the tunnel, experiments were immediately started. During the experiments, suspension in the tunnel was sampled through pipes at several points toward the vertical direction at a prescribed time interval, and concentrations of suspended solids were measured with membrane filter. The motion of fluid mud was monitored by a video camera with a closed-up lens and motor-driven camera with extension rings. Pressure in the fluid mud layer was also measured to understand pressure effects.

### 4.Results and Discussion

#### **(1)Settling velocity of particles**

**Figure 3** indicates some temporal changes of the interface in height. In addition, its change under a quiescent state is plotted on it. These plots indicate that the fluid mud exits as suspension on the bottom. The settling velocity of the interface decreases gradually because of the decrease in the apparent velocity of particles. This settling of particles is determined by the local concentration  $C$  only. In this case, the equation governing the vertical mass concentration is:

$$\frac{\partial C}{\partial t} - \frac{\partial F_a}{\partial z} = 0 \dots (19)$$

$$F_a = w_s C - F_e = w_{as} C \dots (20)$$

Here,  $C$  is the local concentration,  $F_a$  is the apparent settling flux,  $w_s$  is the settling velocity,  $F_e$  is the vertical solids flux and  $w_{as}$  is the apparent settling velocity. The z-axis is taken to be upward from the bottom. The apparent settling velocity can be calculated by using the following equation on the basis of the concentration profiles under a quiescent state and oscillatory flow:

$$\overline{w_{as} C} |_{z=h} = - \frac{\partial}{\partial t} \int_0^h C dz \dots (21)$$

in which,  $\overline{w_{as}}$  and  $\overline{C}$  are the average apparent settling velocity and the average

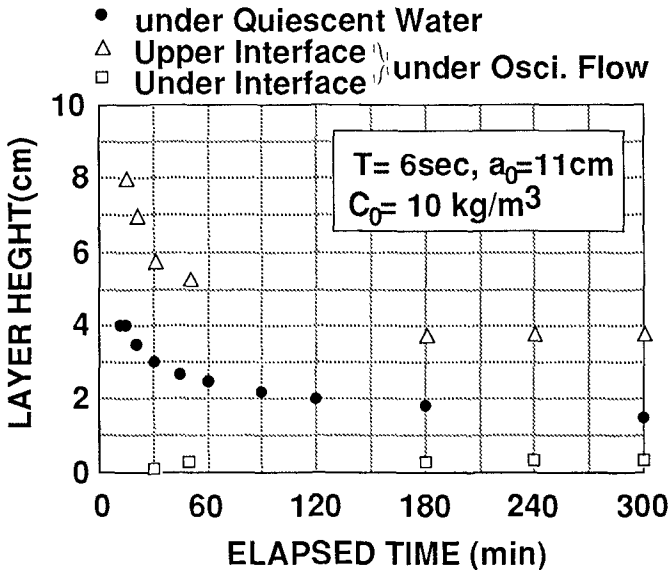


Fig.3 Temporal changes of the interface in height

concentration at a certain height ,  $h$ .

If  $F_e$  in Eq. (20) is equal to zero, the settling velocity  $w_s$  under a quiescent state is obtained. Figure 4 depicts the settling velocity  $w_s$  and the settling flux  $w_s C$  under a quiescent state. If the settling velocity  $w_s$  is assumed to be a function of only the

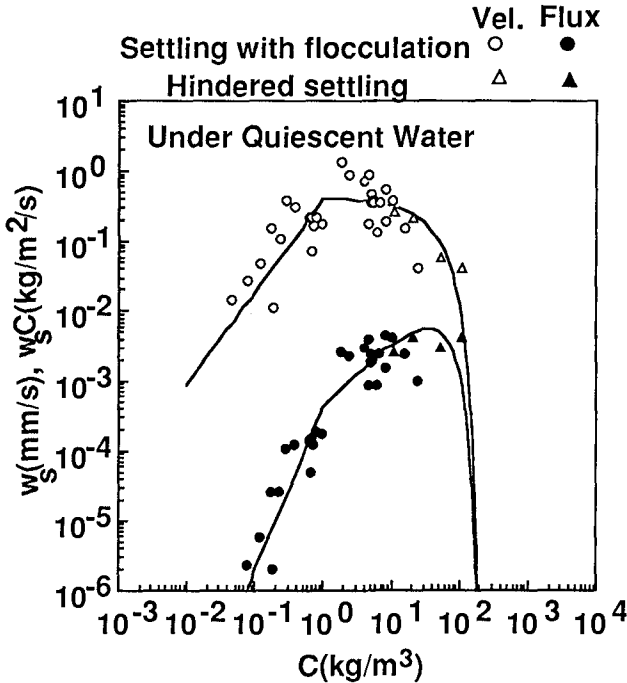


Fig.4 Settling velocity under a quiescent water

local concentration as the formers (ex., Smith and Kirby 1989), the following best fit relation between the settling velocity and the concentration under a quiescent state is derived from Fig.4.

$$\left. \begin{aligned}
 w_s &= 0.4 C^{4/3} \text{ (mm/s)} & C \leq 1 \text{ (kg/m}^3\text{)} \\
 &= 0.4 & 1 < C \leq 2 \\
 &= 0.42 (1 - 0.005 C)^5 & C > 2
 \end{aligned} \right\} \dots (22)$$

Similarly, Fig.5 shows the apparent settling velocity  $w_{as}$  and the flux  $w_{as}C$  calculated by Eq.(21). In order to compare the apparent settling velocity  $w_{as}$  under oscillatory flow with the settling velocity  $w_s$  under a quiescent state. Eq.(22) is also drawn in the same figure. The apparent settling velocity  $w_{as}$  is evidently smaller than  $w_s$  and the observed values scatter. This results from that the settling velocity is subject to shear rate and floc size in addition to local concentration of suspended solids. Furthermore, it is possible to describe the changes in height of fluid mud layers by using the method of Kynch(1952). Toorman and Berlamont(1992) adopted this method in order to unify a hindered settling model and a soil mechanics model by estimating apparent settling velocity under a quiescent state. However, these results can not directly explain the mechanism which maintains a fluid mud layer under

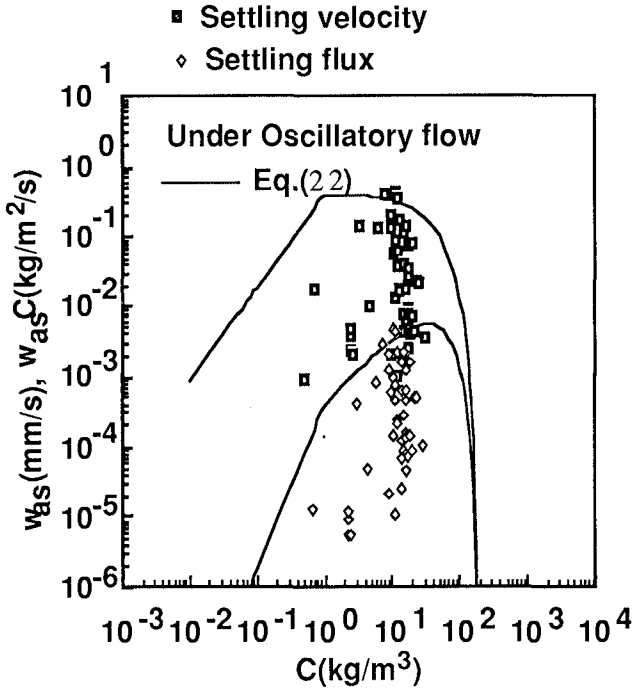


Fig.5 Settling velocity under oscillatory flow

oscillatory flow. Consequently, the maintenance mechanism of fluid mud layers is considered due to the balance between settling flux by gravity and upward flux produced by mixing. If each term could be estimated on the basis of the results, the maintenance mechanism of the fluid mud layer would become clear, and the temporal changes in height of fluid mud layer by using the mass conservation equation could be solved at the same time. This problem seems to be worthwhile for further research work.

**(2) Kinematic viscosity in fluid mud**

Some results simulated by the linearized model are shown in Figs.6 and 7. Figure 7 is velocity profiles measured and calculated at different times. The calculated conditions are taken as the period  $T=3\text{sec}$ , the horizontal amplitude  $=5\text{cm}$ , the apparent kinematic viscosity  $\nu_2=2 \times 10^{-4}\text{m}^2/\text{s}$  and the fluid mud layer thickness  $d=2.1\text{cm}$  in order to compare with the experimental data. It is also important to consider the wall effect. Here, the results have been corrected by assuming an oscillating Poiseuille flow.

Assuming the kinematic viscosity in the fluid mud layer to be uniform as a Newtonian fluid, these results agree well with the measured values. The viscosity in the fluid mud layer used for the calculation notices about 200 times as large as that of pure water. There is an Einstein equation applicable to a dilute suspension but not for dense suspension. Furthermore, the present theoretical analyses for the viscosity of

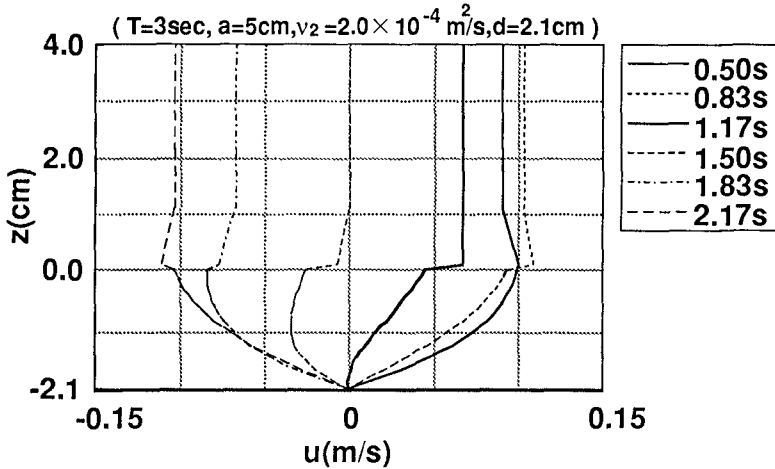


Fig.6 Analytical solutions

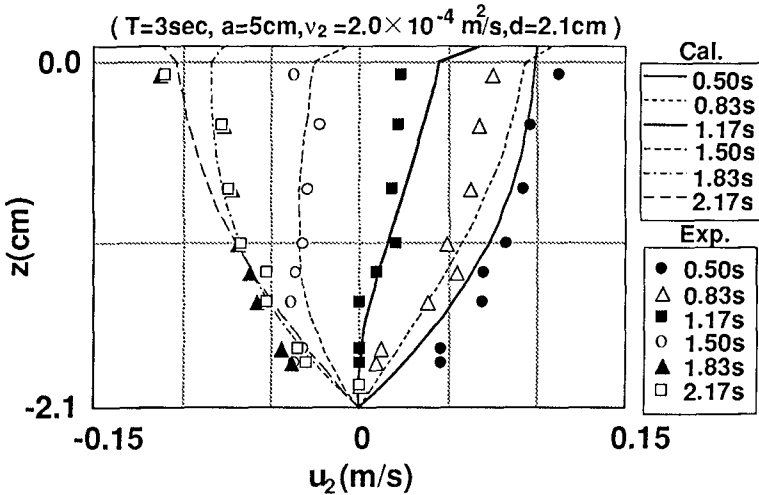


Fig.7 Calculated velocity profiles compared with measurements in the fluid mud

suspension are insufficient for engineering purposes, yet. In general, the viscosity (or kinematic viscosity) is a function of void fraction and shear rate. Here, based on the constitutive equation (Eq.(23)) obtained experimentally by Kusuda *et al.* (1994), the apparent viscosity in the fluid mud was evaluated.

$$\mu_a = \mu_w (6.1 D^{0.66} + 1) \times \left\{ 3.8 \times 10^3 \left( \frac{\rho_2 - \rho_w}{\rho_2 - \rho_w} \right)^{1.7} + 1 \right\} \text{ (Pa} \cdot \text{s)} \dots (23)$$

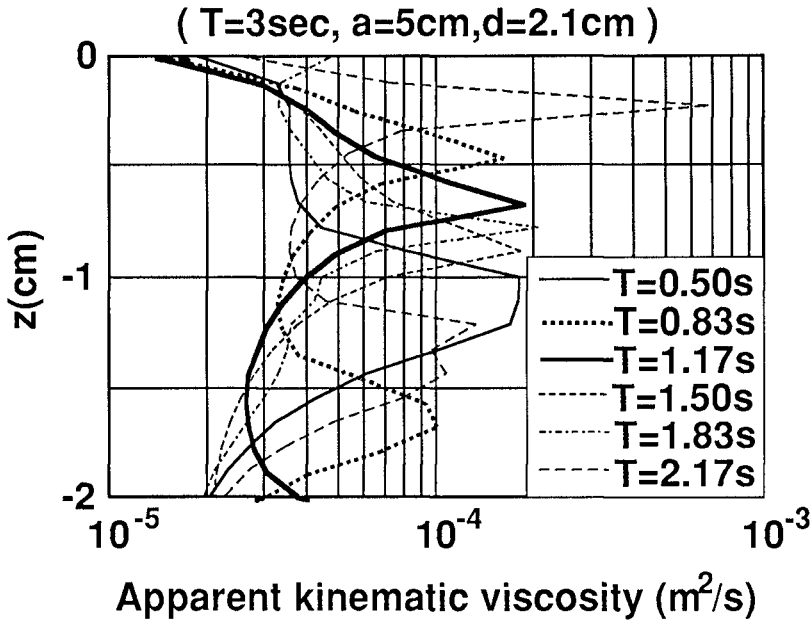


Fig.8 Apparent kinematic viscosity profiles in the fluid mud

in which,  $\mu_a$  is the apparent viscosity,  $\mu_w$  is the viscosity of water,  $D$  is the shear rate,  $\rho_s$  is the particle density and  $\rho_w$  is the water density. After the flow field was calculated by Eqs.(1) and (2) and the following equation (Eq.(24)), the apparent viscosity was estimated.

$$\rho_2 \frac{\partial u_2}{\partial t} = - \frac{\partial p}{\partial x} + \frac{\partial}{\partial z} \left( \mu_a \frac{\partial u_2}{\partial z} \right) \dots (24)$$

Calculation was repeated until the apparent viscosity calculated by Eq.(23) converges.

Figure 8 expresses a result of the apparent kinematic viscosity obtained by Eq.(23). The apparent viscosity is also about 10 to 100 times as large as that of pure water. Because a power exponent function of shear rate is involved in Eq.(23), the apparent kinematic viscosity at a small shear rate in Fig.8 becomes extremely large. In order to obtain the apparent viscosity with high precision, the fluid mud should be regarded as an elastic or a visco-elastic fluid at small shear rates or considered the change in apparent density under oscillating shear stress.

**(3)Phase lag between overlying water and fluid mud**

Figures 6 and 7 also indicate the phase lag between the overlying water layer and the fluid mud layer velocities. This implies that the motion of fluid mud is different from that of viscous fluid under shear flow. So that, the motions of fluid mud



(  $T=3\text{sec}$ ,  $a=5\text{cm}$ ,  $v_2 = 2.0 \times 10^{-4} \text{ m}^2/\text{s}$ ,  $d=2.1 \text{ cm}$  )

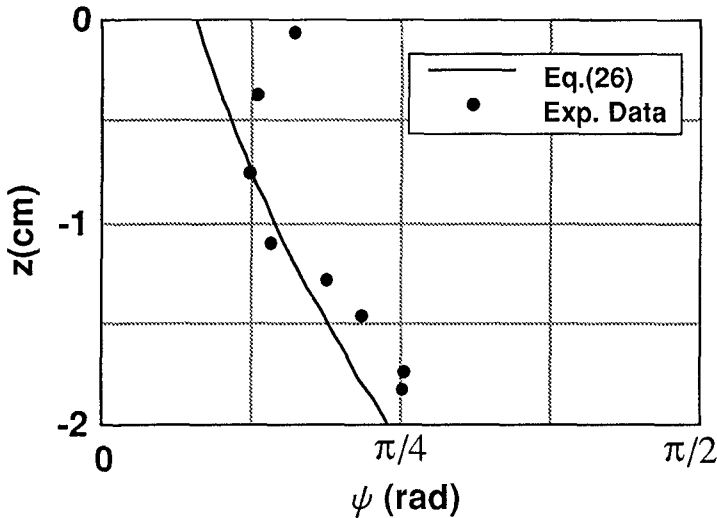


Fig.9 Observed and calculated phase lag profiles

layer are governed by both horizontal pressure gradient and shear stress acted on the interface between the overlying water and the fluid mud layers. Especially, the horizontal pressure gradient causes a phase lag between them. Therefore, when velocity in the fluid mud decreases under a positive pressure gradient, it becomes slower to lose the kinematic energy by high viscosity in the fluid mud. As a result, the fluid mud may move opposite against the overlying water. This phase lag may be derived from Eq.(6). Therefore, as  $\hat{u}_2$  is a complex velocity amplitude, it is transformed by the following equation;

$$\begin{aligned}
 u_2 &= -i\hat{u}_2 e^{i\omega t} \\
 &= -i(\hat{u}_R + i\hat{u}_I) e^{i\omega t} \\
 &= -i\sqrt{\hat{u}_R^2 + \hat{u}_I^2} e^{i(\omega t + \psi)} \dots (25)
 \end{aligned}$$

$$\psi = \tan^{-1}\left(\frac{\hat{u}_I}{\hat{u}_R}\right) \dots (26)$$

where,  $\hat{u}_R$  and  $\hat{u}_I$  indicate the real part and the imaginary part of  $\hat{u}_2$ , respectively.

Figure 9 compares the experimental results with the calculated ones. There is slight difference between the measured and the calculated values, but the analytical solutions approximately explain the experimental results. This simple model proposed here describes well the phase lag at the fluid layer movements. In these ex-

periments, the phase lag ranged from  $\pi/12$  to  $\pi/4$ .

## 5. Conclusions

The summary of the results is as follows:

- (1) Settling velocity was shown as a function of only the concentration of suspended solids;
- (2) The maintenance mechanism of fluid mud layers is due to the balance between the settling flux by the gravity and the upward flux produced by mixing in the fluid mud layer;
- (3) The viscosity in the fluid mud layer is approximately 100 times as large as that of pure water.
- (4) The motion of the upper layer in the fluid mud depends on shear stress acted on the interface between the upper water layer and fluid mud layer. The motion of the lower layer in the fluid mud layer is mainly governed by horizontal pressure gradient. This causes a phase lag between the upper layer and the fluid mud movements.
- (5) The fluid mud layer moves in advance, compared to the overlying water layer and in this experiments the maximum phase lag was  $\pi/4$ .

## Acknowledgement

This study was supported in part by a Grant in Aid for Fundamental Scientific Research and scholarship of the Nakamura Foundation.

## References

- Einstein, A. (1906). A new determination of molecular dimensions, *Ann., Phys.*, 19, 289-306.
- Kinch, G.J.(1952). A theory of sedimentation, *Transactions Faraday Society*, 48, 166-176.
- Kusuda, T., Watanabe, R. and Yamanishi, H.(1994). Mass fluxes in fluid mud layers on an inclined bed, *Proceedings of 4th Nearshore and estuarine cohesive sediment transport conference*.
- Odd, N. V. M. and Owen, M. W. (1972). A two-layer model of mud transport in the Thames Estuary, *Proc. the Inst. of Civil Eng., Paper 7517s*, 175-205.
- Ross, M. A. and Mehta, A. J. (1989). On the mechanics of lutoclines and fluid mud, *Jour. Coast. Res. Special Issue, No.5*, 51-62.
- Smith, T. J. and Kirby, R. (1989). Generation, stabilization and dissipation of layered fine sediment suspensions, *Jour. Coast. Res. Special Issue, No.5*, 63-73.
- Toorman, E.A. and Berlamont, J.E. (1992). Mathematical modeling of cohesive sediment settling and consolidation, *Nearshore and Estuarine Cohesive Sediment Transport, edited by Mehta, Vol.42*, 168-184.
- Tsuruya, H., Murakami, K. and Irie, I. (1990). Mathematical modeling of mud transport in ports with a multi-layered model - Application to kumamoto port -, *Report of the Port and Harbor, Res., Inst., Vol.29*, No.1, 3-51
- Yamanishi, H. and Kusuda, T. (1991). Formation and stabilization of fluid mud layer under oscillatory flow, *Proc. Coastal Eng. Conf., JSCE*, 39, 286-290. (in Japanese)

## CHAPTER 247

### FORMATION OF HABITATS FOR BIVALVES BY PORT AND HARBOR STRUCTURES

K.Yano<sup>1</sup>, S.Akeda<sup>2</sup>, Y.Miyamoto<sup>3</sup> and S.Kuwabara<sup>4</sup>

#### ABSTRACT

Impacts of the construction of large-scale port and harbor at open sandy beach on inhabitation of the Japanese surf clam (*Spisula sachalinensis*) have been studied. It has been found that the populations of the Japanese surf clam has been increasing with the extension of the breakwater since the start of the construction of Ishikari Bay New Port in 1972. A series of numerical simulation was carried out to estimate the changes over time in the currents distribution around Ishikari Bay New Port associated with the construction of the breakwater for each construction phase. The change in dominant areas of the Japanese surf clam in the harbor over the years is explained by patterns of nearshore currents around the port. The construction of Ishikari Bay New Port resulted in the formation of a new fishing ground of the Japanese surf clam and an increase in the populations of the clams.

---

1 Head of Fisheries Engineering Section, Civil Engineering Research Institute, Hokkaido Development Bureau, 1-3 Hiragishi, Toyohira, Sapporo, Hokkaido, 062 Japan.

2 Assistant Head, ditto.

3 Deputy Director-General, Kushiro Development and Construction Department, Hokkaido Development Bureau.

4 Chief of Environmental and Hydraulic Section, North Japan Port Consultants Co., Ltd.

**INTRODUCTION**

In recent years, demand has been increasing for port and harbor construction to co-exist with nature and preserve the environment. It is becoming more important to examine the effect of the construction of port and harbor facilities on the accumulation and propagation of fish, shellfish and reef resources.

Figure 1 shows the relationship between the length of the breakwater extended and catches of Japanese surf clams (*Spisula sachalinensis*) around the Tomakomai Port located on southwest Hokkaido's Pacific coast. The Japanese surf clam catch in Tomakomai city began increasing gradually in 1985 and has increased sharply since 1987. The catch of this clam in Tomakomai in 1990 was 15% of the total catch in Hokkaido. This increase in the amount of the yearly total in Tomakomai is considered to be an effect of the Tomakomai east and west port facilities. Especially, the construction of the East Port District is assumed to have been playing a particularly important role.

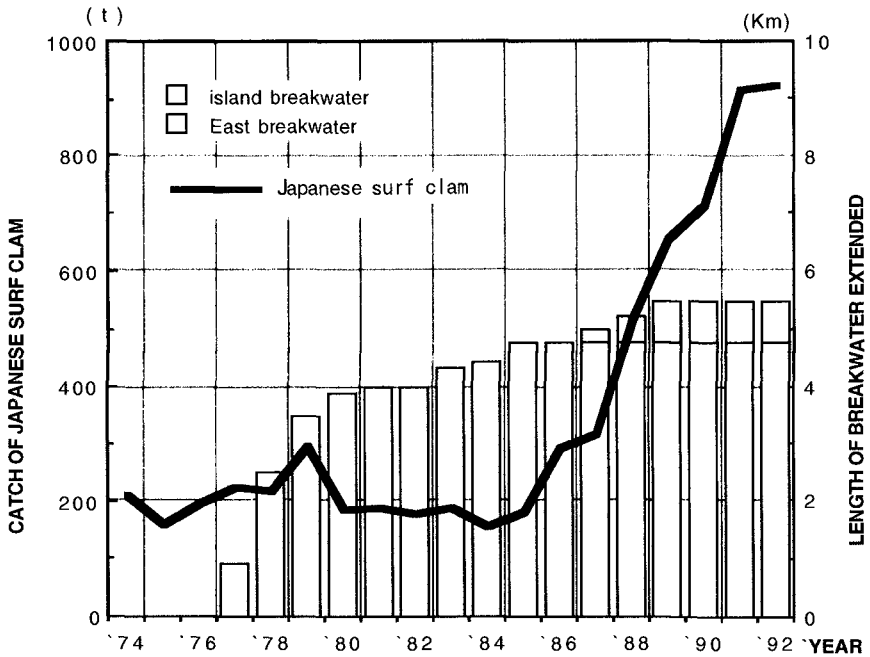


Figure 1: Catches of Japanese surf clams and the breakwater extension at Tomakomai Port (East Port District)

These effects of the port and harbor structures on inhabitation of fishery resources has received much attention from fishermen. The Hokkaido Development Bureau has been conducting studies on the functions of fishery harmony provided by port facilities such as breakwaters. Based on the results of these studies, the present paper describes resource-culturing effects on the Japanese surf clam by the port and harbor construction of Ishikari Bay New Port, whose construction began in 1972.

#### THE ECOLOGY AND FISHERY OF JAPANESE SURF CLAM

Sasaki (1992) reported the ecological characteristics of Japanese surf clam. The Japanese surf clam (Figure 2) is a large bivalve inhabiting in sandy, shallow zones along the wide coastal range of Tohoku and Hokkaido. It has been an important fisheries resource. In general, Japanese surf clams spawn in June and July in Ishikari. When the larvae have grown to about 0.2 to 0.3 mm in shell length, they shift to a benthic life after having drifted in the water for about one month. There is a considerable decrease after the clams shift to a benthic life, particularly marked soon after this shift. Less than 1% of those who start a benthic life reach the age of two years. The major factors for the decrease of juvenile and mature clams are being washed ashore by action of large waves (Figure 3) and natural mortality.

For the clams to mature and grow to a size that contributes to the reproduction of the resource, it takes about 4 years in southern Hokkaido and 5 years in Ishikari Bay and eastern Hokkaido. Most of the individuals with a shell length of more than 7.5 cm are mature. Hokkaido bans catching clams smaller than 7.5 cm.

#### CONSTRUCTION IN ISHIKARI BAY NEW PORT AND CHANGES IN CATCHES OF THE SURF CLAMS

Ishikari Bay New Port is located about in the center of the sandy shore and 7 km southwest of the mouth of Ishikari River in Hokkaido (Fig.4). The bottom slope is very gradual, and the average gradient from the shoreline to the depth of 50 m is about 1/500. The progress of the construction of the port between 1972 and 1992 is shown in the Figure. The entire current of Ishikari Bay moves north in summer and weakens in winter. At present, most of the north, island and east breakwaters, the eastern and central areas and the central channel are complete. The construction of the western area is under way.

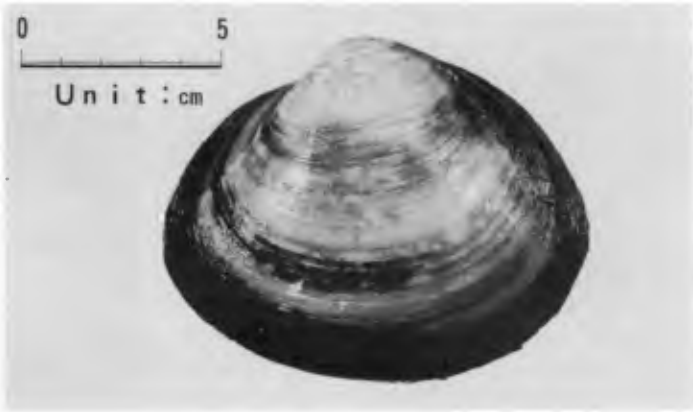


Figure 2: Japanese surf clam (mature size)



Figure 3: Bivalves washed ashore

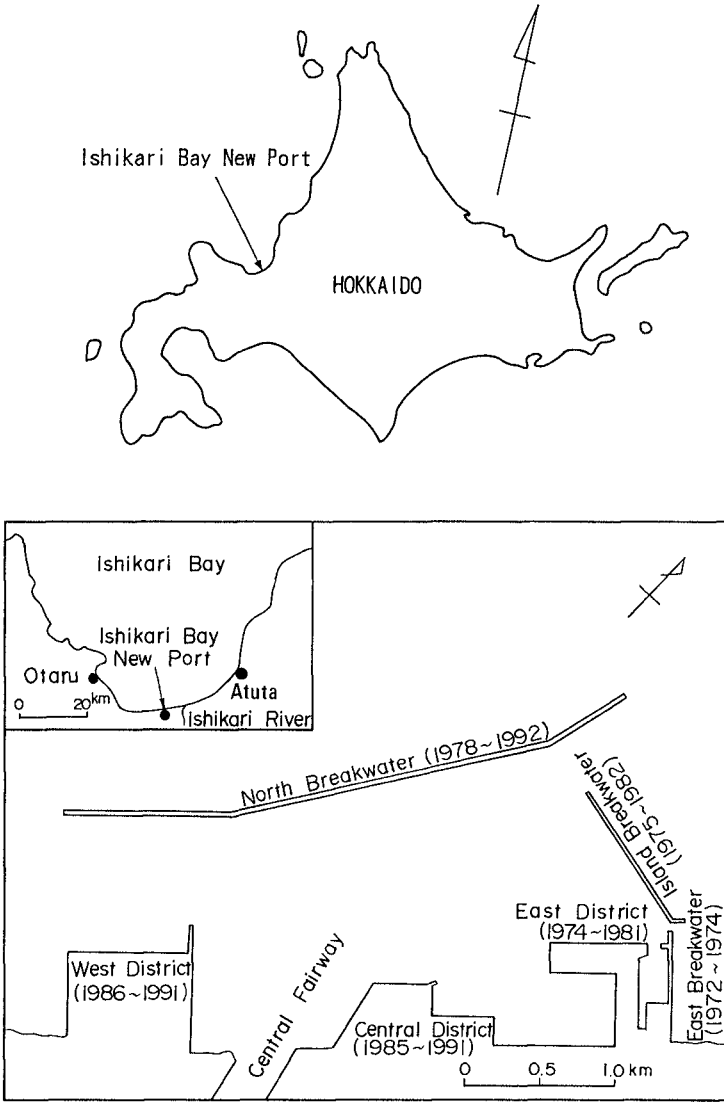


Figure 4: Location map and progress of the construction of Ishikari Bay New Port

To understand the influence of the extension of the breakwater in Ishikari Bay New Port on catches of Japanese surf clams, the relationship between the length of the breakwater extended and catches of Japanese surf clams in the town of Ishikari is shown in Fig. 5. As the figure shows, a sharp increase in the catch of the clams coincided with construction of the breakwaters. Considering the fact that 4- to 5-year-old clams are caught, the remarkable increase in that period seems to be related to the east breakwater built in 1972 to 1974. The catch has not been increasing since 1980 because they restricted the catch in order to preserve the resources. Furthermore, a drastic catch decrease in 1982 and 1983 can be attributed to extreme storm waves that occurred in December 1981, with the maximum wave height at 9.8 meters with a wave period of 10.1 seconds. A strict regulation on clam fishing was enforced after 1983 led to an increase in the catches in 1987. This increase trend continues today.

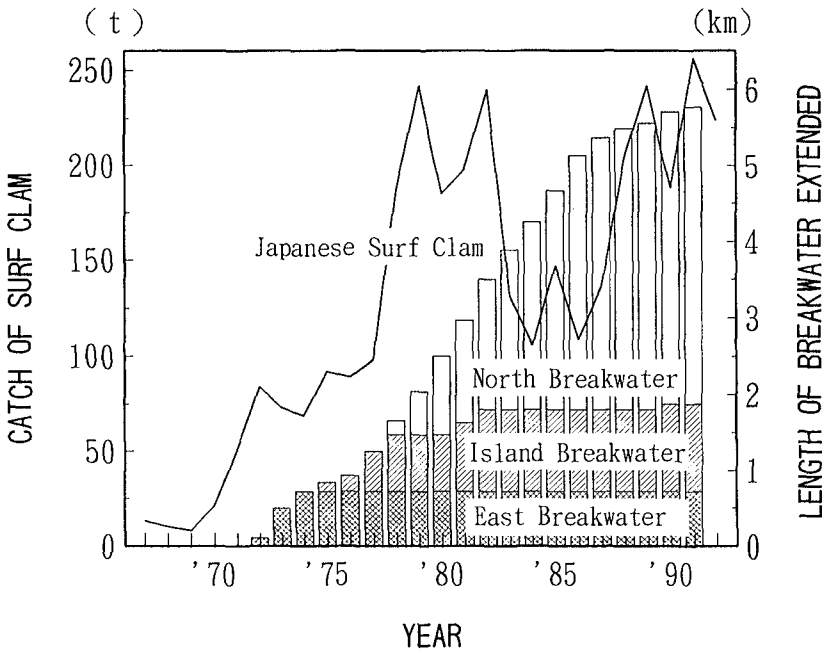


Figure 5: Catches of Japanese surf clams and breakwater extension at Ishikari Bay New Port (data of catches from Hokkaido Government)



COMPARISON OF THE POPULATIONS OF THE CLAM IN AREAS SURROUNDING ISHIKARI BAY NEW PORT

Figure 6 shows the changes over time in the density of mature Japanese surf clams (the number of mature clams per  $100 \text{ m}^2$ ) in the Ishikari, Otaru and Atsuta areas, which was estimated from surveys on populations. As evident from the figure, the Otaru area had the highest density of mature clams for the decade after 1975, while the clam density in the Ishikari area was about half that of in Otaru. The major factor in this difference was probably that the median grain size of the sediment in Otaru was about  $0.2 \text{ mm}$ , which is suitable for the Japanese surf clam, while the diameter increased northward from Ishikari to Atsuta and these areas were not suitable habitats for the Japanese surf clam.

After 1985, changes in oceanographic conditions resulting from the construction of Ishikari Bay New Port, the accumulation of drifting larvae, the promotion of the settlement of immature clams and the fishing regulation were thought to have had a combined effect toward increasing the density of mature clams in the Ishikari Bay western area, including the Otaru area. The density of mature clams in the Ishikari area increased to almost the same level as in the Otaru area. On the other hand, the construction of Ishikari Bay New Port did not so contribute to the Atsuta area, an area influenced by the Ishikari River, and there was little change over time in the density.

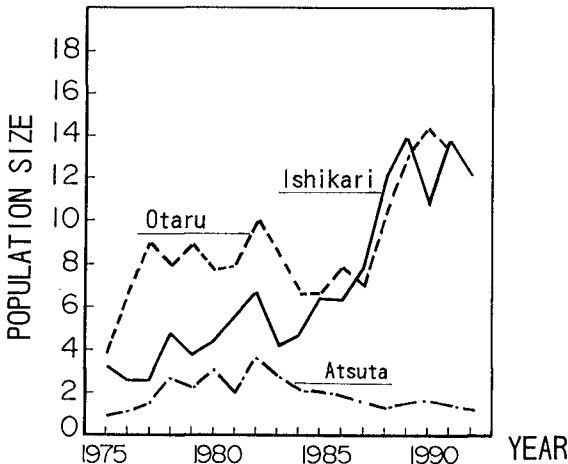


Figure 6: Change of regional population size of Japanese surf clam (data from Hokkaido Government)

CHANGES IN HABITATS OF THE JAPANESE SURF CLAMS

In order to clarify the effect of breakwaters on the formation of habitats for the surf clams, we calculated the nearshore current around Ishikari Bay New Port for 1979, 1984, 1989, and 1992, and examined the relationship between the pattern of nearshore current and the distribution of mature Japanese surf clams associated with the construction of port and harbor facilities. The nearshore current model using an energy balance equation was used to calculate the currents. The direction of waves, wave height and wave period used in the calculation are NW, 1.6 m and 6.0 seconds, respectively. Figure 7 diagrams changes in the dominant areas of Japanese surf clams around Ishikari Bay New Port, based on the existing references obtainable from fishermen's associations and on inquiries to fishermen. The nearshore currents calculated at different stages of the construction of the breakwaters are also indicated in the figure.

When one compares the phase of construction of the port and harbor facilities with changes in the distribution of Japanese surf clams, it seems that as construction in the eastern area (the east and island breakwaters) was completed and construction started on the north breakwater and moved to the central area, the central channel and to the western area, the distribution of the mature clams tended to shift from the eastern sea area to the west. It is clear from Figure 7 that the stagnant and eddy-current areas were created by the construction of port and harbor facilities, and mature Japanese surf clams were distributed in the areas.

In addition, in the beginning, the mature clams were distributed in the harbor where the water became calm due to the breakwater construction. However, as the water became even calmer, the diameter of sediment grains became finer, and became muddy, thus becoming unsuitable as a habitat for the Japanese surf clam. It was no longer a major distribution area of the mature Japanese surf clam after 1985 when Ishikari Bay New Port went into operation. Based on these facts, it is presumed that the distribution of mature Japanese surf clams changes along with the changes in stagnant and eddy-current areas caused by the construction of breakwaters; the distribution is concentrated in areas which are relatively calm in the beginning, and shifts along with the changes in the sediment and feeding environment.

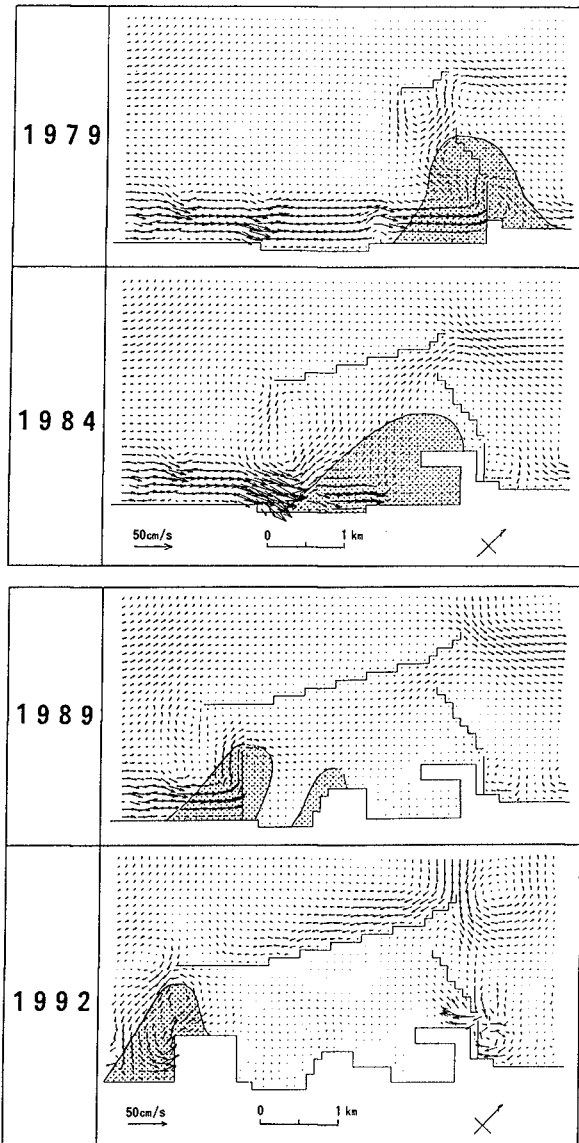


Figure 7: Change in calculated velocity field of nearshore current and dominant areas of highly dense distributions of mature Japanese surf clams

DOMINANT AREAS OF HIGHLY DENSE DISTRIBUTIONS OF JUVENILE SHELL

Figure 8 shows the distribution of juvenile Japanese surf clams in and around Ishikari Bay New Port in 1992 (Ohsaki et al., 1993). As indicated before, the eddy-current areas correspond to those of the areas of highly dense distribution of the juvenile shells. This was probably because the eddy-current areas formed by the near shore currents accumulated the planktonic larvae of the Japanese surf clams, or because they prevented the dispersal of the larvae to elsewhere. This, in turn, resulted in an increase in the number of juvenile shells settling on the sea bottom. Figure 9 shows change in the distribution of juvenile shells. The drastic decrease in March 1985 can be attributed to extreme storm waves that occurred in January 1985, with significant wave height at 4.9 meters with wave period at 9.9 seconds. In spite of these dispersion, the dominant areas of clams were unchanged.

Hydraulic experiments have confirmed that Japanese surf clams with shell lengths of 10-50 mm began to drift or to move as a result of overturning at a current velocity of 29-50 cm/s, and that about 10% died after having been vibrated in the sand for 24 hours (Watanabe, 1982, 1983). These are the reasons Japanese surf clams, which inhabit the wave breaking zone where the velocity of the nearshore current becomes greater, tend to be reduced due to being washed ashore. On the other hand, the eddy-current area formed around the breakwater can act as a relatively calm area in relation to waves coming from a certain direction. Therefore the eddy-current area is assumed to contribute to the survival of the Japanese surf clam when storm wave attack the coast.

SUMMARY

In this report, it is investigated the impact of the construction of the large-scale port and harbor at the open sandy beach on the Japanese surf clam. The principal results are as follows:

(1) Planktonic larvae of Japanese surf clams accumulated in the stagnant and eddy-current areas created by the breakwaters; this promoted the settlement of juvenile shells.

(2) Mature Japanese surf clams were found distributed around the stagnant and eddy-current areas, which were areas of relative calmness, and which were formed in association with the extension of the breakwaters.

(3) The construction of Ishikari Bay New Port resulted

in the formation of a new fishing ground of the Japanese surf clam and an increase in the populations of the clams.

#### REFERENCES

- Ohsaki, H., et al. (1993): 1992's dominant year class of Japanese Surf Clam in Ishikari Bay, *Hokusuishi Dayori* 21, Hokkaido Central Fisheries Experimental Station, (in Japanese).
- Hokkaido Development Bureau (1988): Research for Promotion of the Development of Shallow Fishing Grounds with Utilization of Coastal Structures, 1983-1987, (in Japanese).
- Hokkaido Government: Current Situation of Hokkaido Fisheries, (in Japanese).
- Sasaki, K (1993): Ecology and Stock Property of Japanese Surf Clam, *A Library of the Fisheries Research* 42, Japan Fisheries Resource Conservation Association, (in Japanese).
- Watanabe, E (1982): Experimental Study on the Decrease of Surf Clam under Wave Action, *Monthly Report of The Civil Engineering Research Institute* No. 351, (in Japanese).
- Watanabe, E (1983): Experimental Study on the Decrease of Surf Clam Babies under Wave Action and Burying Condition in the Sand, *Monthly Report of The Civil Engineering Research Institute* No. 359, (in Japanese).

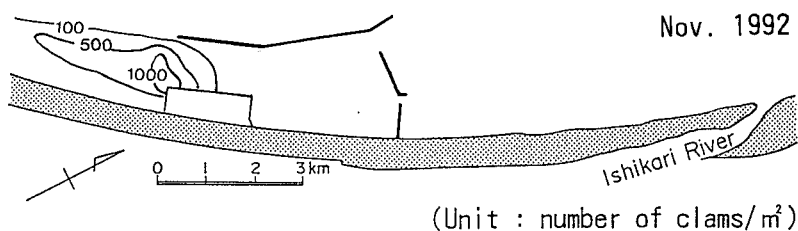


Figure 8: Distribution of juvenile Japanese surf clams in and around Ishikari Bay New Port (modified from Ohsaki, H., et al., 1993)

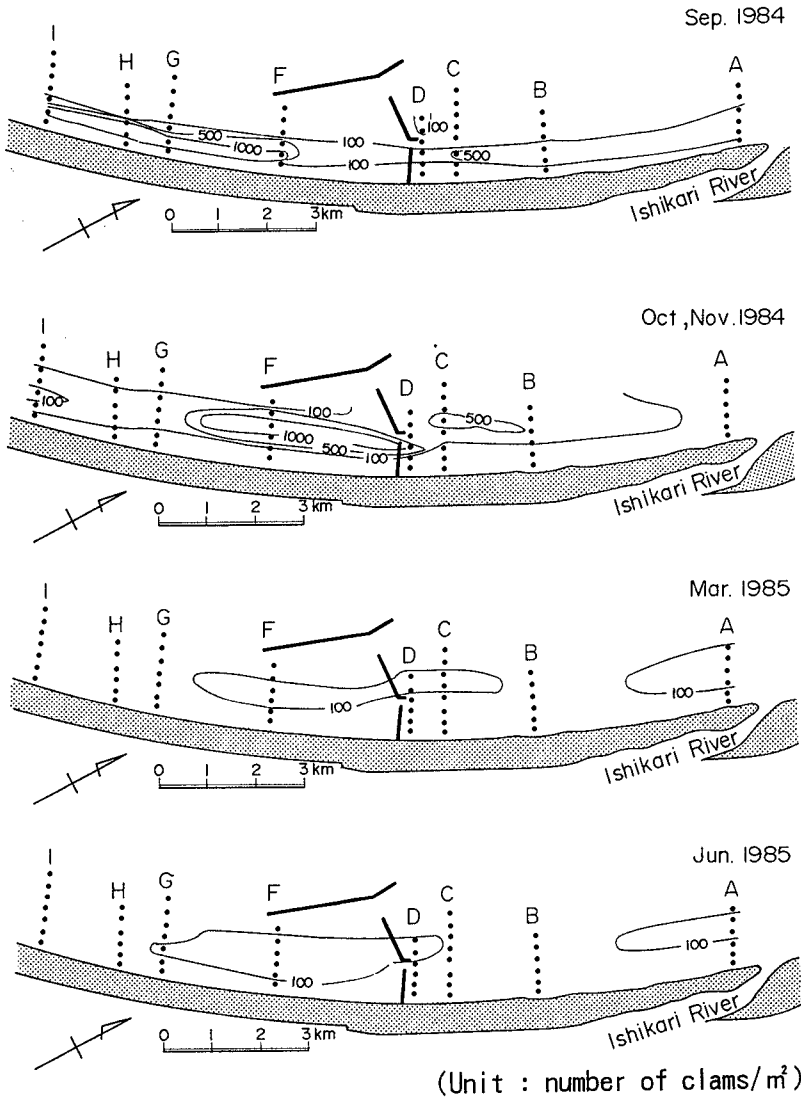


Figure 9: Change in density of juvenile Japanese surf clams in and around Ishikari Bay New Port (modified from Hokkaido Development Bureau, 1988)

## CHAPTER 248

### USE OF THREE-DIMENSIONAL HYDRODYNAMICS MODEL FOR TIDAL INLETS STUDIES

E.A. Yassuda<sup>1</sup> and Y.P. Sheng<sup>2</sup>, M.ASCE

#### ABSTRACT

This study utilizes a multi-dimensional hydrodynamics model originally developed by Sheng (1989) and later modified by Sheng *et.al* (1992) to first quantify the flow field in Little Sarasota Bay in Florida, USA with a closed (present condition) and an opened (proposed condition) Midnight Pass, and then to produce a closure curve of the Midnight Pass. This study demonstrates that robust multi-dimensional hydrodynamics models can be used to provide more quantitative analysis of tidal inlet stability.

#### INTRODUCTION

Tidal inlets connect various bays and lagoons to coastal oceans. As such, tidal inlets can have significant effects on circulation and transport in the bays/lagoons as well as longshore sediment transport in the coastal oceans. For example, tidal inlets can affect the location of nodal zones and flushing of materials into and out of the bays/lagoons (e.g. Sheng *et.al.*, 1992). Tidal inlets can also affect longshore sediment transport by causing erosion on the downstream side of the inlet while causing deposition on the upstream side of the inlet (Dean and Dalrymple, 1994).

Tidal inlets, however are not very stable and often require dredging to keep them open. Since the closing and opening of tidal inlets can significantly affect the circulation and transport within bays/lagoons, it is essential to be able to predict the stability of tidal inlets. Escoffier (1940) performed a simple analysis to study the stability of a tidal inlet. van de Kreeke (1985) analyzed the stability of multiple inlet

---

<sup>1</sup> Graduate Student, <sup>2</sup> Professor, Coastal & Oceanographic Eng. Dept.,  
University of Florida, Gainesville, Florida 32611, USA.

system. Basically, for a single inlet system, one needs to calculate a "closure curve" that relates the cross-sectional area of an inlet with the maximum current in the inlet for given tidal conditions, inlet length and inlet shape. The next step is to compute an equilibrium velocity or bottom stress at which the sediment transport capacity of the inlet currents is just sufficient to remove the sediment deposited in the inlet. Van de Kreeke (1992) pointed out that to determine the exact closure curve for a real inlet, it requires a full-fledged multi-dimensional model for the hydrodynamics of the inlet and the bay.

This study is an extension of a project funded by the Sarasota Bay National Estuary Program. The primary objective of the project was to quantify the circulation and transport in the Sarasota Bay system, located in the southwest coast of Florida, USA (Figure 1). The Sarasota Bay project consists of a field study and a modeling study. For the field study, the University of Florida collected continuous data of surface elevation, current, salinity, water temperature, turbidity, and wind at five stations during two months in 1991, and two months in 1992. For the modeling study, the three-dimensional circulation model CH3D, originally developed by Sheng (1989), was applied, improved, calibrated and verified.

The estuarine system shown in Figure 1 is actually formed by two interconnected sub-systems: the Tampa Bay system, which is a classical coastal plain estuary, with a manmade navigation channel, and the Sarasota Bay system, which is a multiple-inlet shallow coastal lagoon. In the southern part, the Little Sarasota Bay has an average depth of less than 2 meters and a manmade IntraCoastal Waterway (ICW) which bisects the length of the bay. In Little Sarasota Bay, a tidal inlet, Midnight Pass, has been closed since 1983, and much has been discussed about the feasibility and potential environmental implications of its proposed opening.

Based on the field data collected in 1990 and 1991, the CH3D model has been applied and verified for the Sarasota Bay and Tampa Bay system. There is generally a good agreement between model results and field data, with the errors on the order of 5-10% for surface elevation and 10-20% for currents (Sheng and Peene, 1992; Sheng *et al.*, 1992; Sheng *et al.*, 1994a). The effect of the Midnight Pass on the circulation and tidal flushing inside the Little Sarasota Bay was studied by Sheng *et al.* (1992).

This study utilizes the CH3D model to first quantify the flow field in Little Sarasota Bay with a closed (present condition) and an opened (proposed condition) Midnight Pass, and then to produce a closure curve of the Midnight Pass in its proposed opened conditions.

## METHODOLOGY

To study the stability of a tidal inlet, one can use the simple analysis of



Escoffier (1940), O'Brien and Dean (1972) or, in the case of multiple inlets, the analysis of van de Kreeke (1985). All these methods are based on the Keulegan repletion coefficient, which is strictly applicable to the case of uniform water level over the entire bay, an inlet flow depending exclusively on the head difference between the bay and the ocean, and a friction term represented by the Manning's coefficient (Figure 2). According to Escoffier (1940), the following limitations should be considered in applying this analysis:

- "The available values for Manning's  $n$  are based on observations made in uniform prismatic channels and their reliability in nonuniform channels such as those usually found in inlets is uncertain;
- Little is known about the loss of head that takes place due to the contraction and expansion of the currents passing through the inlet; and
- The formula is for steady state flow and ignores the temporal acceleration."

In addition, the simple analysis ignores the nonlinear effects associated with complex geometries inside the bay.

To improve estimates of the simple analysis, an approach which does not contain any of the above assumptions should be used. For this study, the CH3D model was used to quantify the detailed flow pattern in the vicinity of the Midnight Pass. To determine the closure curve of the Midnight Pass, the bottom shear stress within the opened Midnight Pass was simulated using both the 3-D version and the 2-D vertically integrated version of CH3D.

CH3D is a three-dimensional hydrodynamic model which can use non-orthogonal boundary-fitted grid as well as orthogonal or Cartesian grids. This feature allows the model to better represent the small scale processes in bays/lagoons with complex geometries. The vertical turbulent eddy coefficients are computed from a simplified second-order closure model, and the horizontal turbulent eddy coefficients are assumed to be constant, which vary with grid size and horizontal current.

In order to make the stability analysis more quantitative, it is necessary to characterize the capacity of an inlet to transport sediments in terms of the bottom shear stress. In the three-dimensional model CH3D (Sheng, 1989), the bottom shear stress is obtained from the near bottom velocity within a logarithmic boundary layer, according to:

$$(\tau_x, \tau_y) = \left[ \frac{\kappa}{\log(z_1/z_0)} \right]^2 \cdot \sqrt{u^2 + v^2} \Big|_{z_1} \cdot (u, v) \Big|_{z_1} \quad (1)$$

where,  $(\tau_x, \tau_y)$  are components of bottom shear stress,  $\kappa$  is the von Karman constant,  $z_1$  is the reference height,  $z_0$  is the bottom roughness height, and  $(u, v)$  are the horizontal velocity components at  $z_1$  within the bottom boundary layer. The only empirical coefficient,  $z_0$  appears in the logarithmic denominator, thus making it less sensitive.

In the 2-D vertically-integrated model, the bottom shear stress is obtained from the vertically-averaged velocity components  $(U, V)$ , according to:

$$(\tau_x, \tau_y) = \frac{g}{H C_c^2} \sqrt{U^2 + V^2} (U, V) \quad (2)$$

where  $g$  is gravitational acceleration,  $H$  is total water depth, and  $C_c$  is the Chezy coefficient.

In the simple analysis, the repletion coefficient relates the inlet cross-sectional area to tidal forcing and bottom friction, according to (Keulegan, 1967):

$$K = \frac{T}{2\pi a_0} \frac{A_c}{A_B} \frac{\sqrt{2ga_0}}{\sqrt{K_{en} + K_{ex} + \frac{fl}{4R}}} \quad (3)$$

where  $T$  is the tidal period,  $a_0$  is the tidal amplitude,  $A_c$  is the inlet cross-sectional area,  $A_B$  is the bay surface area,  $K_{en}$  is the friction loss at the entrance,  $K_{ex}$  is the friction loss at the exit,  $f$  is the Darcy-Weisbach friction coefficient,  $l$  is the inlet length, and  $R$  is the hydraulic radius of the inlet.

## RESULTS FOR AN IDEALIZED INLET-BAY SYSTEM

Before performing the analysis of inlet stability in Midnight Pass, the 2-D results of CH3D were compared with the simple method for the case where the simplified assumptions were valid. A Cartesian grid with 40 by 30 cells was used, with a uniform grid spacing of 250 m. The tidal forcing along the boundary was represented by a sinusoidal wave with an amplitude of 46 cm and a period of 12 hours. The depth in the offshore region and inside the bay was assumed to be a constant 2 m. The inlet cross-sectional area was varied by keeping the width constant and varying the depth from 50 cm to 2 m.

Figure 3 shows the ebb flow in the idealized bay in a five day simulation for

the case of an inlet with 1.5 m depth. Repeating this simulation for different inlet configurations, it was possible to construct two closure curves for the hypothetical inlet, one for each inlet width, and then to compare these results versus the curves obtained from the simple analysis (Figure 4). The closure curves present the maximum ebb velocity (in cm/s) as a function of the inlet cross-sectional area (in  $m^2$ ), for a given tidal forcing and Manning's coefficient. These curves clearly demonstrate the concept of critical cross-sectional area at which the velocity attains its maximum. The dots represent the 2-D model results and the solid lines represent the results of simple analysis. In the second plot, a different closure curve was obtained due to a different width of the inlet, which affects the hydraulic radius. Different values of hydraulic radius corresponding to rectangular, trapezoidal and parabolic cross-sections were used, but the simple analysis does not seem to be sensitive to different shapes in cross-section.

Results of the 2-D model and the simple analysis shows some discrepancies, particularly in terms of the critical cross-sectional area. The discrepancies can be attributed to the high sensitivity of the simple analysis to the Manning's coefficient. In this case, even the 2-D model requires significant calibration. Although the 3-D version of CH3D also contains some model coefficients, these coefficients are less empirical, and the bottom friction formulation shown by Equation (1) is much more robust than the Chezy-Manning formulation shown by Equation (2).

#### APPLICATION TO MIDNIGHT PASS, FLORIDA

The CH3D model was sufficiently calibrated and validated with data from Tampa Bay and Sarasota Bay (Sheng and Peene, 1992, Sheng *et al.*, 1992). For this study, the 2-D and 3-D versions of CH3D were used to compute the detailed flow within the Midnight Pass under various hydrodynamic forcing conditions, and various configurations of the Midnight Pass. The closure curve obtained from the 3-D model runs and the simple analysis is shown in Figure 5, wherein the dots represent the CH3D results while the solid lines were obtained from the simple analysis using different Manning's coefficients. The simple analysis is highly sensitive to the Manning's coefficient, thus producing a wide range of values of maximum velocity.

CH3D was used to simulate three scenarios: the first scenario (solid circle) represents the bay prior to the dredging of the IntraCoastal Waterway (ICW); the second one (square) represents the bay with the ICW and a shallow inlet (1.5 m deep); the third one (triangle) represents the bay with the ICW and a deeper inlet (3 m deep); and the fourth one (circle) represents the bay with the ICW and a much wider inlet. Results shown in Figure 5 indicate that the ICW made the Midnight Pass less stable. Figures 6,7 and 8 show the residual flow fields obtained from the 30 day simulations corresponding to each of the three scenarios.

Figure 9 shows the stability curve expressed in terms of the bottom shear

stress, the cross-sectional area of the Pass, and the equilibrium bottom shear stress of Bruun (1978). This shows that the inlet is only marginally stable even for the case without the ICW.

## DISCUSSION

Due to its importance to human activities, tidal inlets have been a subject of coastal engineering studies for many years. Studies have showed that physical processes in tidal inlets are quite complex and much scientific study is needed to improve the empirical engineering analysis. This study demonstrates that multidimensional numerical hydrodynamics model can be used as a comprehensive tool to provide more accurate analysis and guidance to further understanding of the physical processes involved.

Our modeling study showed that the IntraCoastal Waterway (ICW) probably made the Midnight Pass more unstable, although the Pass was only marginally stable for a long time prior to its closure. This is consistent with the earlier suggestions by Davis *et al.* (1987) and Dean (1992), which did not provide a quantitative analysis.

To determine if the Pass should be opened, a more comprehensive and quantitative study is needed. The CH3D model can be used to simulate the circulation and inlet stability under a variety of hydrodynamic conditions and inlet configurations. Additional parameters such as water quality dynamics and sediment can be considered by using a coupled hydrodynamics-sediment-water quality model being developed (e.g., Sheng *et al.* 1994b).

## ACKNOWLEDGEMENT

The authors wish to express their gratitude for support of the Sarasota Bay National Estuary Program and valuable discussions with R.G. Dean, D. Tomasko, and J. van de Kreeke.

## REFERENCES

- Bruun, P., 1978: *Stability of Tidal Inlets*, Elsevier, Amsterdam. 510 pp.
- Davis, R.A., Jr., A.C. Hine, and M.J. Bland, 1987: "Midnight Pass, Florida: Inlet Instability Due to Man-Related Activities in Little Sarasota Bay", in *Coastal Sediments 1987*, pp. 2062-2077.
- Dean, R.G., 1992: "Inlet and Shorelines", in *Framework for Action, Sarasota Bay*. Sarasota Bay National Estuary Program, U.S. Environmental Protection Agency, pp. V.28-V.32.

- Dean and Dalrymple, 1994: "Coastal Processes with Emphasis on Engineering Applications", class notes for *Littoral Processes* course, Coastal & Ocean. Eng. Dept., University of Florida.
- Escoffier, F.F., 1940: "The Stability of Tidal Inlets", *Shore and Beach*, **8**, 4, 114-115.
- Keulegan, G.H., 1967: "Tidal Flow in Entrances. Water-level Fluctuations of Basins in Communication with Seas", *U.S. Army Corps of Engineers Tech. Bull.* 14, 87 pp.
- O'Brien M.P., R.G. Dean, 1972: "Hydraulics and Sedimentary Stability of Coastal Inlets", in *Proceedings of the 13th International Conference on Coastal Engineering*, Vancouver, Canada. ASCE.
- Sheng, Y.P., 1989: "Evolution of a Three-Dimensional Curvilinear-Grid Hydrodynamic Model for Estuaries, Lakes, and Coastal Waters: CH3D", in *Estuarine and Coastal Modeling* (M.S. Spaulding, ed.). American Society of Civil Engineers, pp. 40-49.
- Sheng, Y.P. and S.J. Peene, 1992: "Circulation and Its Effects on Water Quality in Sarasota Bay", in *Framework for Action, Sarasota Bay*. Sarasota Bay National Estuary Program, U.S. Environmental Protection Agency, pp. V.2-V.18.
- Sheng, Y.P., S.J. Peene and E.A. Yassuda, 1992: "Circulation and Transport in Sarasota Bay, Florida: The Effect of Tidal Inlets on Estuarine Circulation and Flushing Quality", in *Proceedings of 6th International Symposium on Physics on Estuarine and Coastal Seas*, Margaret River, W. Australia, American Geophysical Union.
- Sheng, Y.P., X.-J. Chen and E.A. Yassuda, 1994: "Measurement and Modeling of Wave-Induced Sediment Resuspension and Mixing", in *Proceedings of the 24th International Conference on Coastal Engineering*, Kobe, Japan. ASCE.
- Sheng, Y.P., E.A. Yassuda and C. Yang, 1994: "Effect of Nitrogen Load Reduction on the Water Quality and Seagrass Dynamics of Roberts Bay", Ongoing Study for the Sarasota Bay National Estuary Program.
- van de Kreeke, J., 1985: "Stability of Tidal Inlets - Pass Cavallo, Texas". *Estuar. Coastal Shelf Sci.*, 21, pp. 33-43.
- van de Kreeke, J., 1992: "Stability of Tidal Inlets; Escoffier's Analysis". *Shore and Beach*, pp. 9-12.

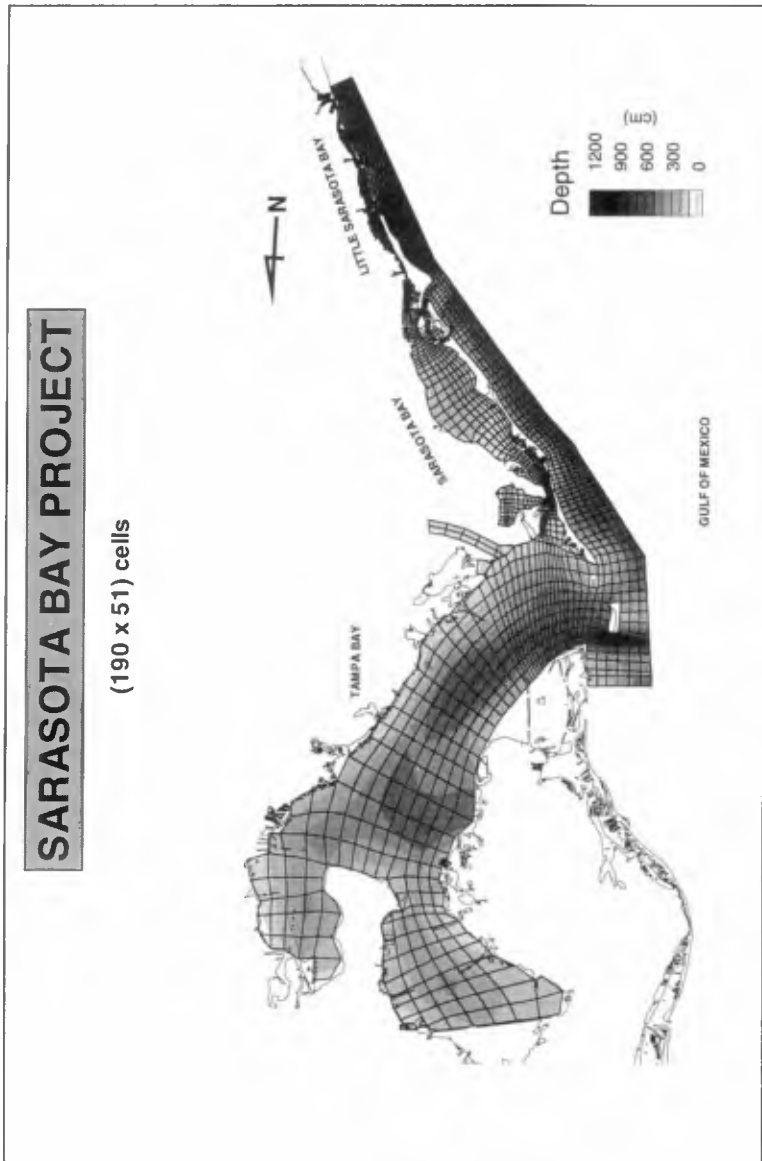


**Figure 1 - Sarasota Bay and Tampa Bay Systems**

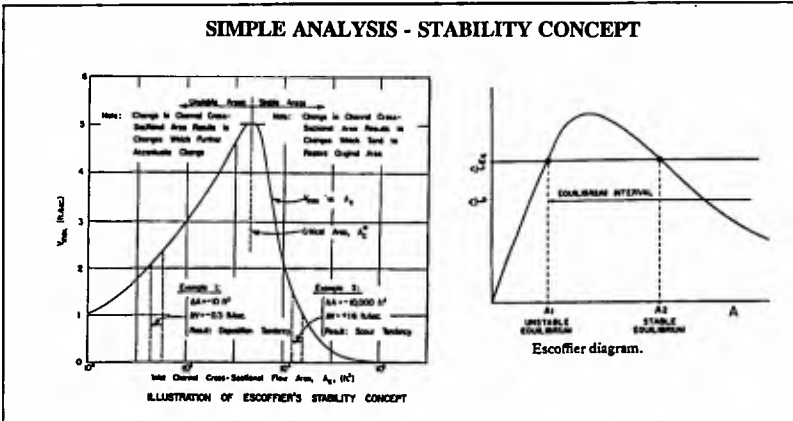


Figure 2 - Closure curves based on the analysis of (a) O'Brien and Dean (1972) and (b) van de Kreeke (1985).

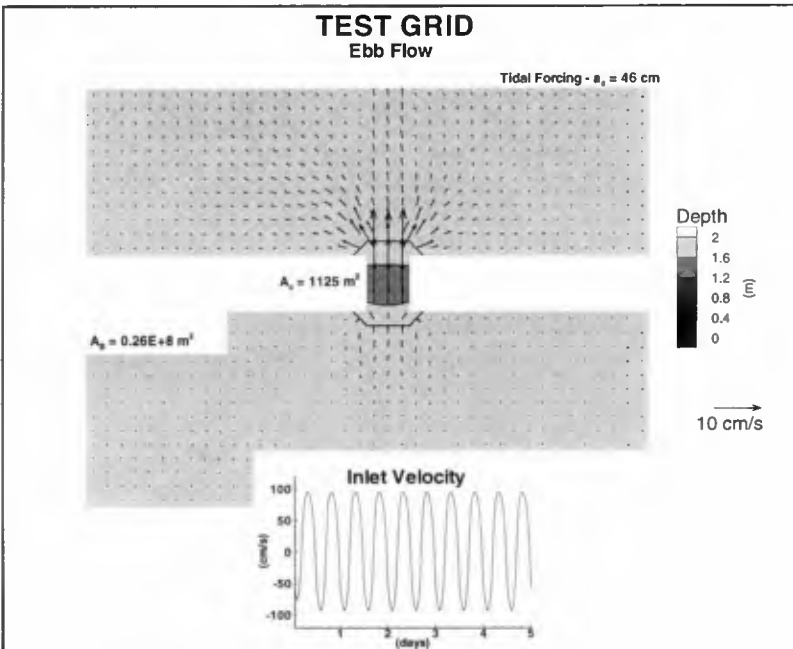
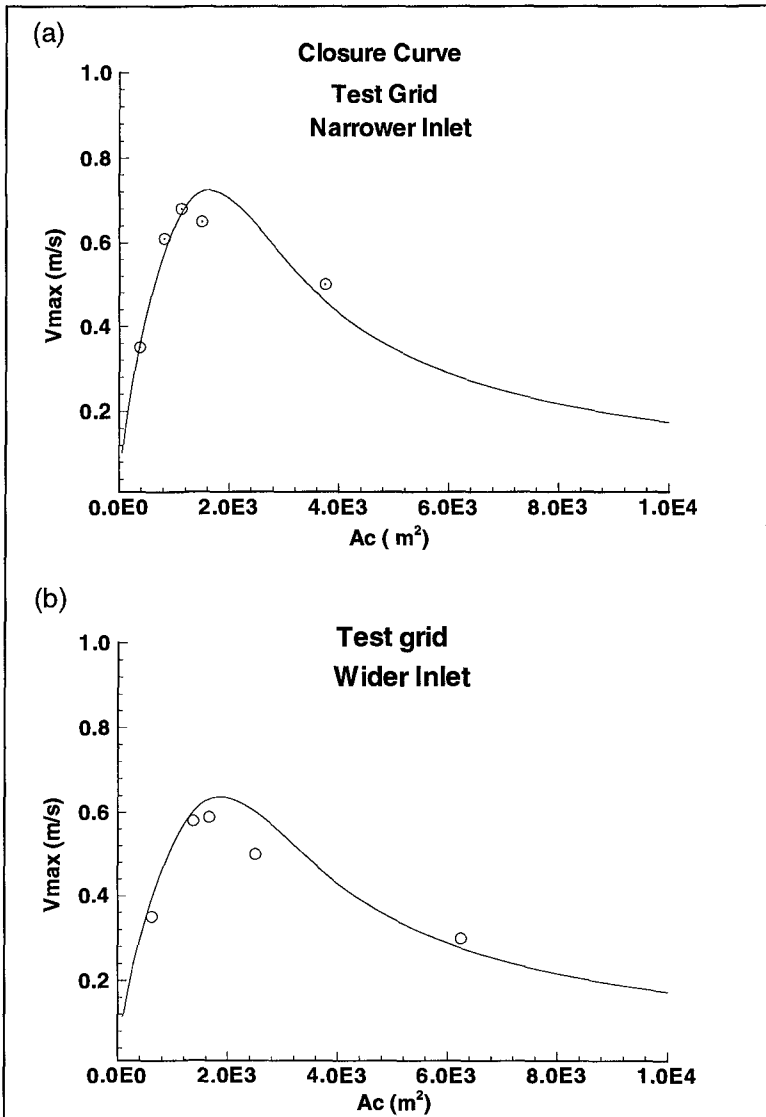
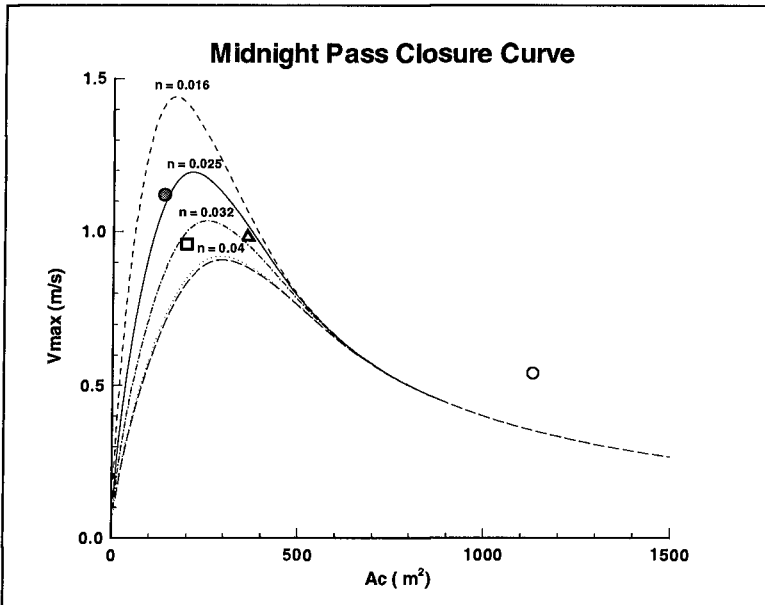


Figure 3 - Vertically-averaged ebb flow in idealized basin with 40x30 points, a grid spacing of 250m, and a depth of 2m.



**Figure 4** - Comparison between results of vertically-integrated CH3D (circles) and simple analysis (solid lines) in an idealized basin with (a) a narrower inlet and (b) a wider inlet.





**Figure 5** - Comparison between results of CH3D and the simple analysis in the Midnight Pass - Little Sarasota Bay.

- |                |   |
|----------------|---|
| Solid circle:  | Bay prior to intracoastal waterway dredging, narrow inlet, 1.5m deep; |
| Open square:   | Bay with the intracoastal waterway, narrow inlet, 1.5m deep;          |
| Open triangle: | Bay with the intracoastal waterway, narrow inlet, 3.0m deep;          |
| Open circle:   | Bay with the intracoastal waterway, wider inlet, 3.0m deep.           |

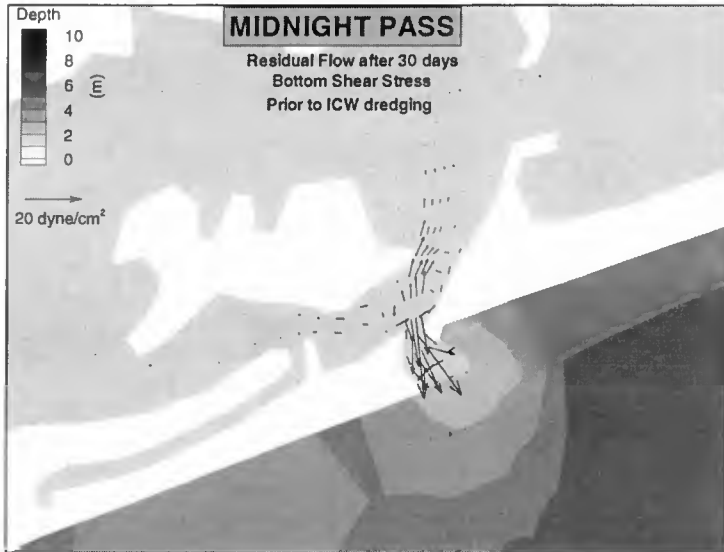


**Figure 6** - Residual bottom shear stress over a 30 day simulation without intracoastal waterway but with a narrow inlet.



**Figure 7** - Residual bottom shear stress over a 30 day simulation with intracoastal waterway and a narrow inlet.

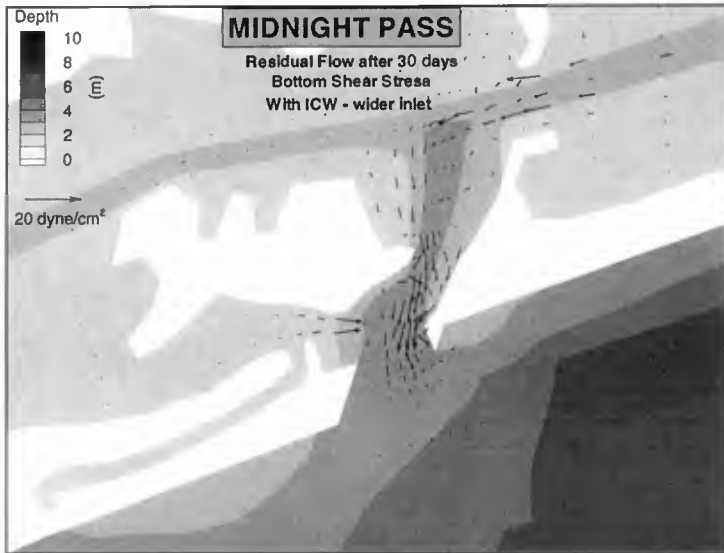


**Figure 8** - Residual bottom shear stress over a 30 day simulation with intracoastal waterway and a wider inlet.

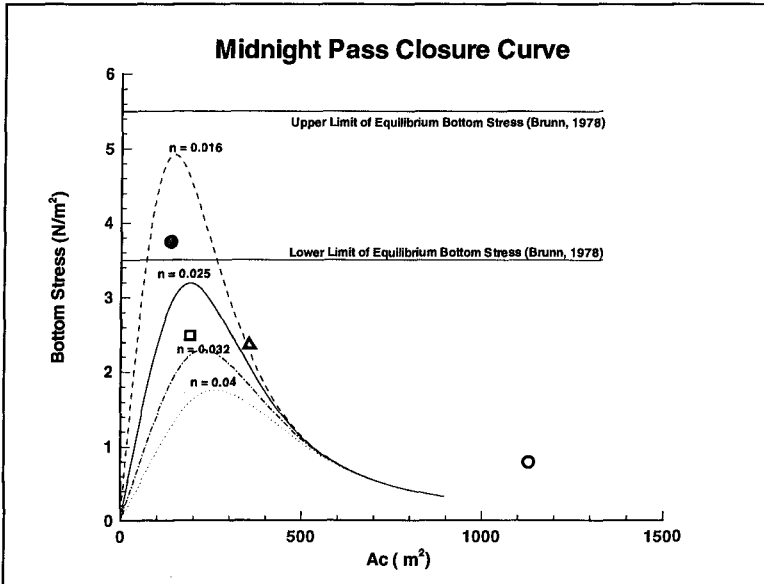


**Figure 9** - Comparison between results of CH3D and simple analysis in the Midnight Pass - Little Sarasota Bay, with Bruun's equilibrium bottom shear stress added.

- Solid circle: Bay prior to intracoastal waterway dredging, narrow inlet, 1.5m deep;
- Open square: Bay with the intracoastal waterway, narrow inlet, 1.5m deep;
- Open triangle: Bay with the intracoastal waterway, narrow inlet, 3.0m deep;
- Open circle: Bay with the intracoastal waterway, wider inlet, 3.0m deep.

## CHAPTER 249

### Study of Upwelling Phenomena of Anoxic Water 'A-oshio'

Jong Seong Yoon<sup>1</sup>, Keiji Nakatsuji<sup>2</sup>, Kouji Muraoka<sup>2</sup>

#### ABSTRACT

The field data analyses and both two dimensional hydraulic and numerical experiments were performed to understand the physical features of the 'A-oshio' appearance in Tokyo Bay. Lots of field observations show that the 'A-oshio' phenomenon may be intimately related with the upwelling of the anoxic water in the bottom layer under the wind blowing towards off-shore for more than a couple of days. Therefore, the two-dimensional hydraulic and numerical experiments are performed for clarifying the wind-induced upwelling and mixing processes in a two-layered stratified flow system with a downstream open boundary, which is exposed to wind stresses at the water surface. In these experiments, the upwelling phenomena are found to occur only in the range of  $Ri_x \times (2h_1/L) \leq 12.0$ . The numerical experiments are quantitatively confirmed to show a good agreement with the results of field observation and hydraulic experiments.

#### INTRODUCTION

Recently, unique phenomena have been frequently observed in the head of Tokyo Bay in Japan during late summer to autumn. The color of surface water changes to milky-blue or milky-green when the northeast wind blows during a couple of days. Fisheries have been damaged by lots of perish of fishes and shellfishes. Such phenomena are called 'A-oshio' regarding to the color of water. 'A-o' means blue and 'shio' does a tide in Japanese.

According to lots of field observations, an 'A-oshio' phenomenon is considered to be accompanied by the upwelling of anoxic bottom water. When an off-shore wind blows, the surface water is transported towards off-shore induced

1 CTI Engineering Co., Ltd, Osaka City, Osaka 540, Japan  
2 Dept. Civil Engng., Osaka University, Osaka 565, Japan

by wind-driven surface stress ; hence, the bottom water moves upwards along a sea bed to make compensation for the transported surface water. The color of 'A-oshio' water is considered to be changed by the oxidation of sulfide included in the upwelled bottom water which becomes anoxic during summer under no vertical mixing due to the strong stratification and the biological activities. The 'A-oshio' phenomenon, therefore, is fundamentally different from 'Akashio' (a red tide in Japanese), which is biologically induced by the excess propagation of plankton. The 'A-oshio' phenomena, therefore, can be treated as the upwelling of anoxic bottom water from the physical view point and the oxidation from the chemical one.

Even though many field observations have carried out, the detailed mechanism of 'A-oshio' appearance has been left unsolved. The reason is that only several points-measurements are not sufficient to obtain the understanding of overall physical features. The present paper, therefore, is to examine the physical mechanism regarding to 'A-oshio' appearance.

First of all, the field data obtained in Tokyo Bay are analyzed to understand the physical characteristics during the 'A-oshio' appearance. Secondly, two-dimensional hydraulic and numerical experiments are carried out to clarify the interface movement and the upwelling phenomena in a two-layered stratified flow system exposed to wind stresses at the surface. A downstream condition is set to be opened in the similar sense as semi-enclosed coastal seas or small bays. There is few experiments with such a condition, although many experiments in an enclosed flume have been done for simulating the mixing processes occurred in the lakes or reservoir. The mixing process is unsteady and rapidly changed; hence the measurements in hydraulic experiments are too difficult. Therefore, the two dimensional numerical experiment with  $\kappa$ - $\epsilon$  turbulence model and non-hydrostatic assumption is also performed to support the physical understanding of 'A-oshio' in the quantitative sense.

## FIELD OBSERVATION ABOUT 'A-OSHIO' IN TOKYO BAY

### Previous Study About 'A-oshio' Phenomenon

Tokyo Bay is one of the highly eutrophicated bays in Japan. The topographical feature of Tokyo Bay is shown in Fig. 1. It has an area of  $1200 \text{ km}^2$ , and the average depth is about 17 m. The ratio of area less than 10 m depth against a total area is about 30%. The numbers of No.1 to No.13 as shown in Tokyo Bay indicate the location of observation stations conducted by The Environment Agency.

The bay is surrounded by metropolitan cities including Tokyo and many industrial factories where more than 24

million peoples live. A large amount of nutrients and organic matter have been drained into the bay. It is known that the eutrophic status of the bay is hypertrophic condition, and algal blooms have been occurred through a year. It makes the color of surface water change to reddish-brown, that is a red tide ('Akashio' in Japanese). The 'Akashio' recently tends to occur independent of season and worldwide coastal seas, especially in the urban coastal seas.

A shaded area shown in Fig.1 indicates the coastal waters where the 'A-oshio' has often appeared. In summer, an amount of discharged river water and the heat transfer through the sea surface make the stratification strength, which results in damping the vertical transfer of momentum and eutrophicated matters. The bottom water, hence, becomes anoxic due to the precipitation and the decomposition of organic matters produced by algal blooms and the hydrogen sulfide occurs in the bottom layer (Kakino (1986)).

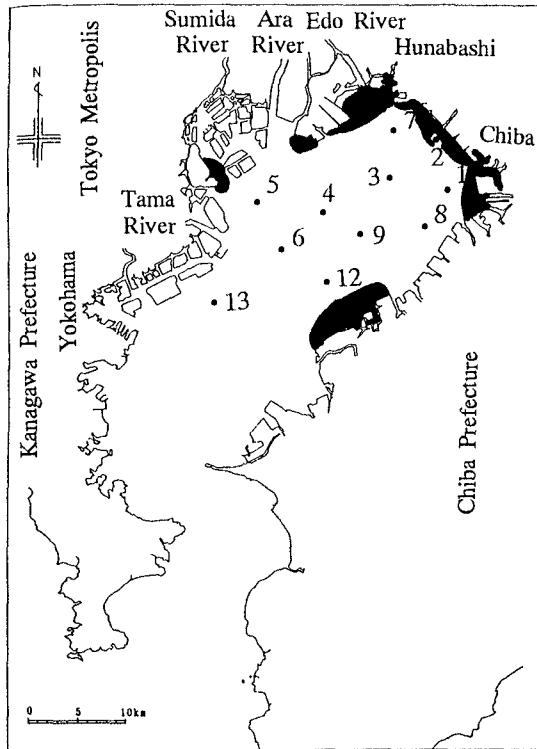


Figure 1. Topological feature of Tokyo Bay and observation stations. A shaded area indicates the coastal waters where 'A-oshio' has often appeared.



Figure 2 shows a photograph of the 'A-oshio' appearance observed on 8th September, 1988 in Hunabashi Port, which is located at the head of Tokyo Bay as shown in Fig. 1.

Table 1 shows the time variation of 'A-oshio' appearance, the perish of shellfishes and the production of a short-necked clam reported by Kakino(1986). For example, late in September 1985, 30,000 ton of short-necked clam perished which brought the economical damages about 3.6 billion yen for fisheries.

Tominaga et al. (1988) reported the presence of colloidal particles of sulfur in the boundary layer between surface oxygen-sufficient water and anoxic bottom water at the head of Tokyo Bay.



Figure 2. 'A-oshio' appeared in Funabashi Port located in the head of Tokyo Bay. This photograph was taken from air on 8th September, 1988.

### Oceanographical and Meteorological Features of 'A-oshio'

The Environment Agency has conducted field measurements for 7 years from 1988 in order to clarify the mechanism of 'Aoshio' from the multi-view points such as physical, chemical, biological and ecological aspects. During the field observations from 22th July to 11th August, 1992, 'A-oshio' appeared during 3rd August to 6th August.

Figure 3 shows the time variation of wind velocity and direction observed by the Chiba Meteorological Observatory. It is of great interest that before the 'A-oshio' appearance the southwest (on-shore) wind stronger than 5

Table 1. Field data of 'A-oshio', perish of shellfishes and the year production of clam (Kakino; 1986)

Year	Month, Day	Appearance of Aoshio etc.	Influence to the Shellfish	Production of Clam (ton)
1975	late in September	Aoshio (middle or large scale)	partly perish of clam	22,099
1976				7,238
1977	8.10~8.16	Aoshio(large scale)	perish of clam	12,843
1978	7.8~7.10	Aoshio(middle scale)	mass perish of clam	8,620
1979	6.13 7.16~7.17 8.14 9.30	Aoshio(small scale) Aoshio(middle scale) Aoshio(middle scale) Aoshio(middle scale)	negligible negligible negligible negligible	2,610
1980	8.2~8.5 8.26 9.9 9.19 9.25	Aoshio(large scale) Aoshio(small scale) Aoshio(small scale) Aoshio(small scale) Aoshio(small scale)	negligible negligible negligible a few perish of clam negligible	6,979
1981	late in July	anoxic water	perish of clam	5,907
1982	7.27~7.29 bearly in August	Aoshio(large scale) turbid water	a few perish of clam perish of clam	3,843
1983	6.8 6.18	Aoshio(small scale) Aoshio(small scale)	negligible negligible	2,972
1984				7,349
1985	6. 8.20 late in September	Aoshio(small scale) Aoshio(middle scale) Aoshio(large scale)	negligible negligible mass perish of clam (secondly water depravation)	

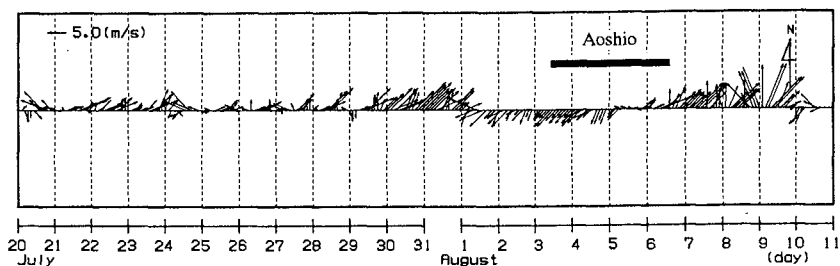


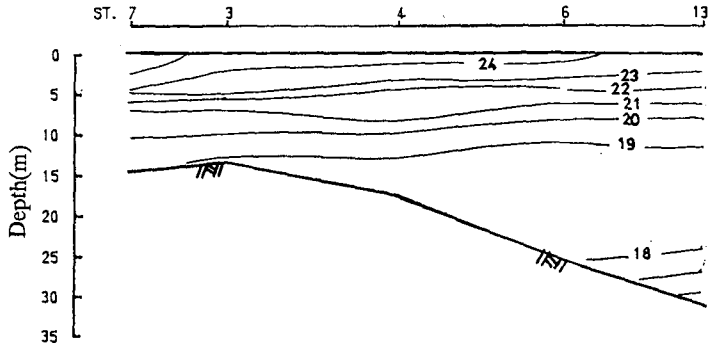
Figure 3. Time variation of wind velocity and direction at the Chiba Meteorological Observatory

m/s kept blowing from 30th July to 1st August, and in succession the northeast (off-shore) wind blew. The northeast or east northeast wind stronger than 5 m/s kept blowing from 1st August. The former event may play a role to make the stratification strengthen. Other observations show that there is heavy rainfall before the 'A-oshio' appearance. The authors point out that such events of south-west wind blowing or lots of rainfall are of fundamental importance in considering the mechanism of 'A-oshio' appearance. Namely, strong stratification is a necessary condition for 'A-oshio' appearance.

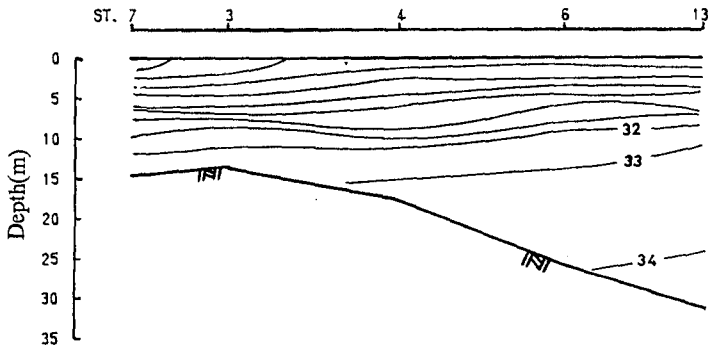
Figures 4 and 5 show the distributions of water temperature, salinity and dissolved oxygen (DO) along the vertical section from the stations No.7 to No.13, the location of which is shown in Fig.1. The measurements were conducted on 22th July and 4th August. The thermal stratification remarkably develops depending on heat flux through water surface in summer. The contours of temperature and salinity show a layered structure of 24 °C to 18 °C and of 26 ‰ to 34 ‰, respectively. The difference in water temperature between the upper and the lower layers is about 6 °C on 22th July. The contour lines of DO also show horizontal in the upper layer and the anoxic water less than 5 mg/l exists deeper than 5 m depth on 22th July. The contours of 0 and 1 mg/l DO, however, indicate no stratification but a curious tendency. It may be induced by the error in measurement at station No.6. It is found from these distributions except the profile of DO that the strong stratification develops on 22th July.

On the other hand, on 4th August, the contours of 22 °C temperature, 31.5 ‰ salinity and 4 mg/l DO are upwelled to attain to water surface near No. 7 station. It is worth noting that the counter lines of 2 and 3 mg/l DO tend to deepen gradually in the off-shore direction. Such a tendency is physically reasonable. If a wind blows off-shore in the long term, the water surface tends to lean upward in the same direction as wind-blowing, namely in the offshore direction in this case. And, the stratified interface leans downward in the offshore direction according to the balance of pressure. The 0 and 1 mg/l DO contour lines is upwelled to -6 m depth at the station No. 7. As compared with Figs. 4 and 5, it is clarified that the upwelling of the hypolimnetic anoxic water was caused by the northeast wind blowing continuously for four days from 1st August.

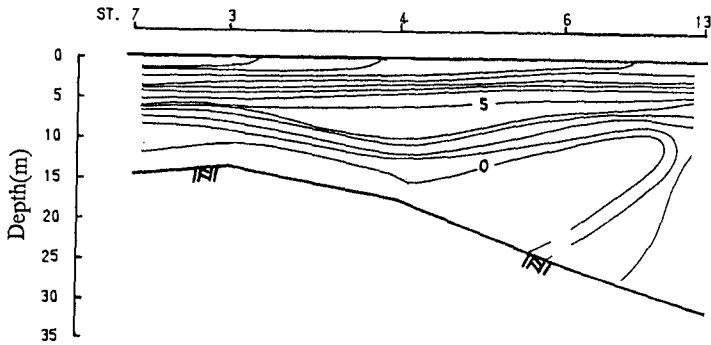
Joh (1989) pointed out that the formation of the anoxic water mass correlates well with the temperature difference between the surface and the bottom layers based on field data obtained in Osaka Bay. The same tendency was confirmed in Tokyo Bay by The Environment Agency (1991). It indicates that the stratification affects not only the upwelling phenomena but also the generation of anoxic water.



(a) Water Temperature (°C)

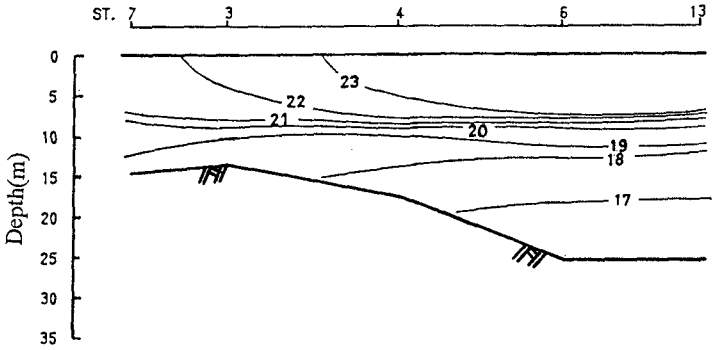


(b) Salinity (‰)

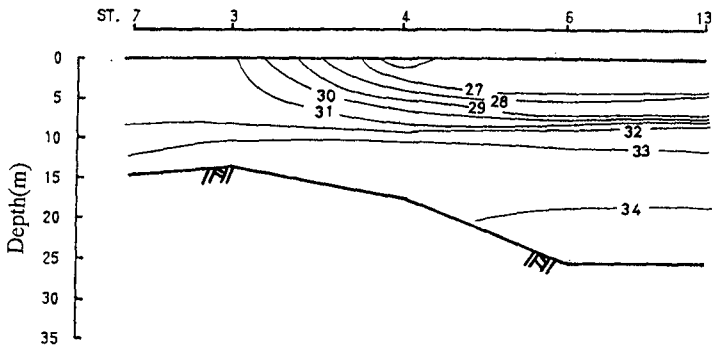


(c) DO (mg/l)

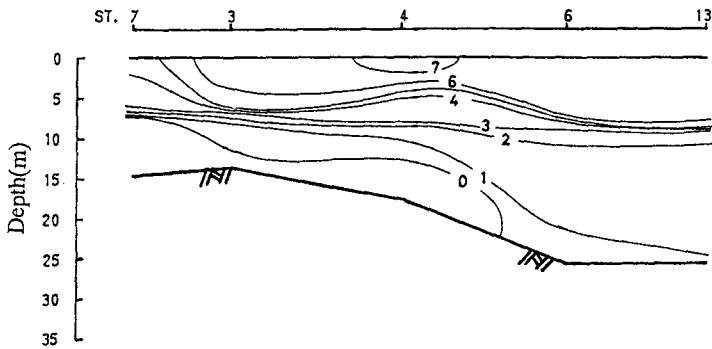
Figure 4. Distributions of water temperature(°C), salinity (‰) and DO(mg/l) on 22th July, 1992 along the vertical section from St.7 to St.13 as shown in Fig. 1



(a) Water Temperature ( $^{\circ}\text{C}$ )



(b) Salinity ( $\%$ )



(c) DO ( $\text{mg}/\ell$ )

Figure 5. Distributions of water temperature( $^{\circ}\text{C}$ ), salinity ( $\%$ ) and DO ( $\text{mg}/\ell$ ) on 4th August, 1992 along the vertical section from St.7 to St.13 as shown in Fig. 1

Based on the above-discussed field observations, a conceptual sketch of 'A-oshio' appearance can be drawn as Fig. 6.

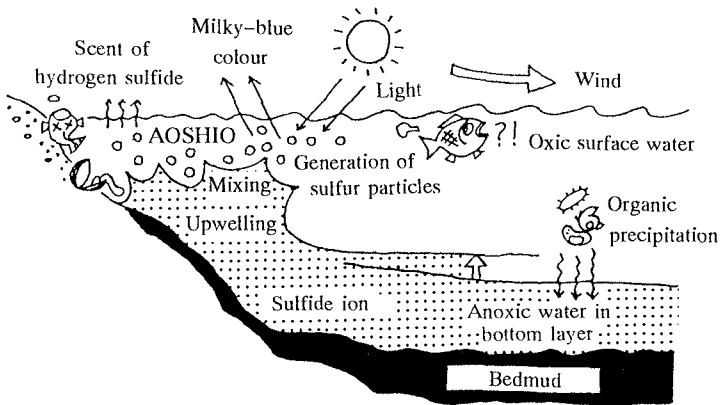


Figure 6. Conceptual sketch of 'A-oshio' appearance

## TWO DIMENSIONAL HYDRAULIC AND NUMERICAL EXPERIMENTS

Both hydraulic and numerical experiments are carried out in the present study. It is because only the hydraulic experiments are too difficult to quantitatively understand the unsteady phenomena such as the flow movement and strong mixing processes at the stratified interface.

### Setup of Hydraulic Experiments

The experimental facility is shown in Fig. 7. It is composed of a main test flume (an acrylic flume of 600 cm length, 15 cm width and 30 cm depth), a wind tunnel (6 shuttlecock of 100 cm and the maximum rotation of 1500 rpm) and a large tank (300 cm length, 200 cm width and 25 cm depth) connecting with the downstream end of the test flume. The experiments were conducted in a stratified flow system with two layers of fresh water and salt water. The degree of stratification depends on the density of salt water. The initial thickness of the upper layer was always kept to be 10 cm. Mean velocities in the upper layer were measured using a LDV (Laser Doppler Velocimetry) and the analyses of tracer trajectories. Two 35 mm cameras and a video camera were used to observe the movement of the stratified interface and its mixing process. The density profiles were measured using a salinometer.

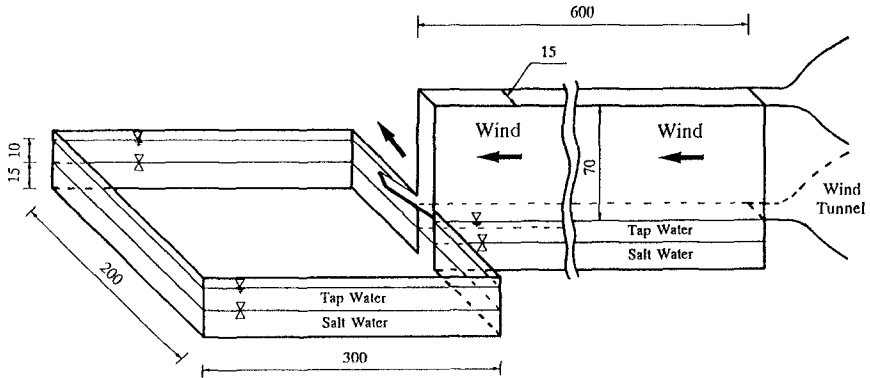


Figure 7. Experimental facility of two-layer stratified flow system with wind tunnel

### Setup of Numerical Experiments

A two-dimensional numerical experiment was also performed under the same physical conditions as hydraulic experiments. The governing equations were composed of the continuity equation, the longitudinal and vertical momentum equations and the diffusion equation of density. The non-hydrostatic model of SIMPLE method (Patankar, 1980) was used. The  $k-\epsilon$  model was used to represent turbulent transfer of momentum and scalar quantities. The standard values were used for the unknown constant values including the  $k-\epsilon$  equation. The resolution was 7.5 cm and 1 cm in the longitudinal and vertical directions, respectively. The hydraulic conditions are as follows; the friction velocity due to the wind stress at the water surface  $u_* = 6.5$  cm/s, the upper layer depth  $h_1 = 10$  cm, and the range of  $Ri_* = 23-1090$  and  $Ri_* \times (2h_1/L) = 0.76 \sim 36.3$  depending on the density difference, in which  $L$  is the length of flume, in other words, the distance of the wind blowing.

### EXPERIMENTAL RESULTS AND DISCUSSION

Spigel and Imberger (1980) proposed that the mixed-layer dynamics in lakes or reservoirs could be classified into four regimes in terms of Wedderburn number defined as  $We = Ri_* \times (2h_1/L)$ . It means the product of the Richardson number and the aspect ratio of the two-layered stratified flow system. Furthermore, Thompson and Imberger (1980) indicated on the basis of numerical experiments that the stratified interface could be upwelled to attain the water surface in the case of the Wedderburn numbers 'We' less than 3 or 4. Since the present experiment with an open downstream condition is a little different from the

experiment of Imberger et al.,  $Ri_* \times (2h_1/L)$  is used as the dimensionless parameter.

The time variation of observed density interface is shown in Fig. 8 in the case of  $Ri_* \times (2h_1/L) = 36.3$  and 12.0. The observation points are the upstream, the center and the downstream of hydraulic flume. In these figures, the axis of ordinates indicates the water depth, while the axis of abscissas does the passing time after the wind blowing starts. That is, the water depth  $h_1 = -10$  cm indicates the initial position of the interface. The middle layer is defined as the water mass mixed with fresh water and salt water, which usually lies upon the density interface. In the case of  $Ri_* \times (2h_1/L) = 36.3$ , the stratification due to density difference is so completely superior to the wind shear during the experiments that the vertical mixing and the variation of the density interface hardly occur during the wind blowing. On the other hand, in the case of  $Ri_* \times (2h_1/L) = 12.0$ , it is observed that the mixed layer at the upstream end upwells after about 70 seconds, and the density interface does after 110 seconds.

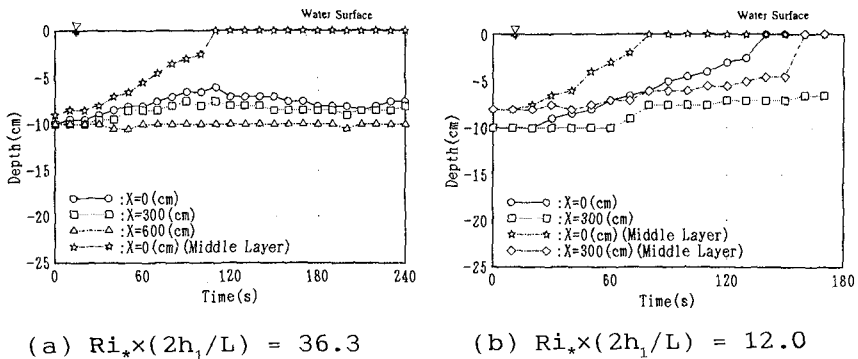
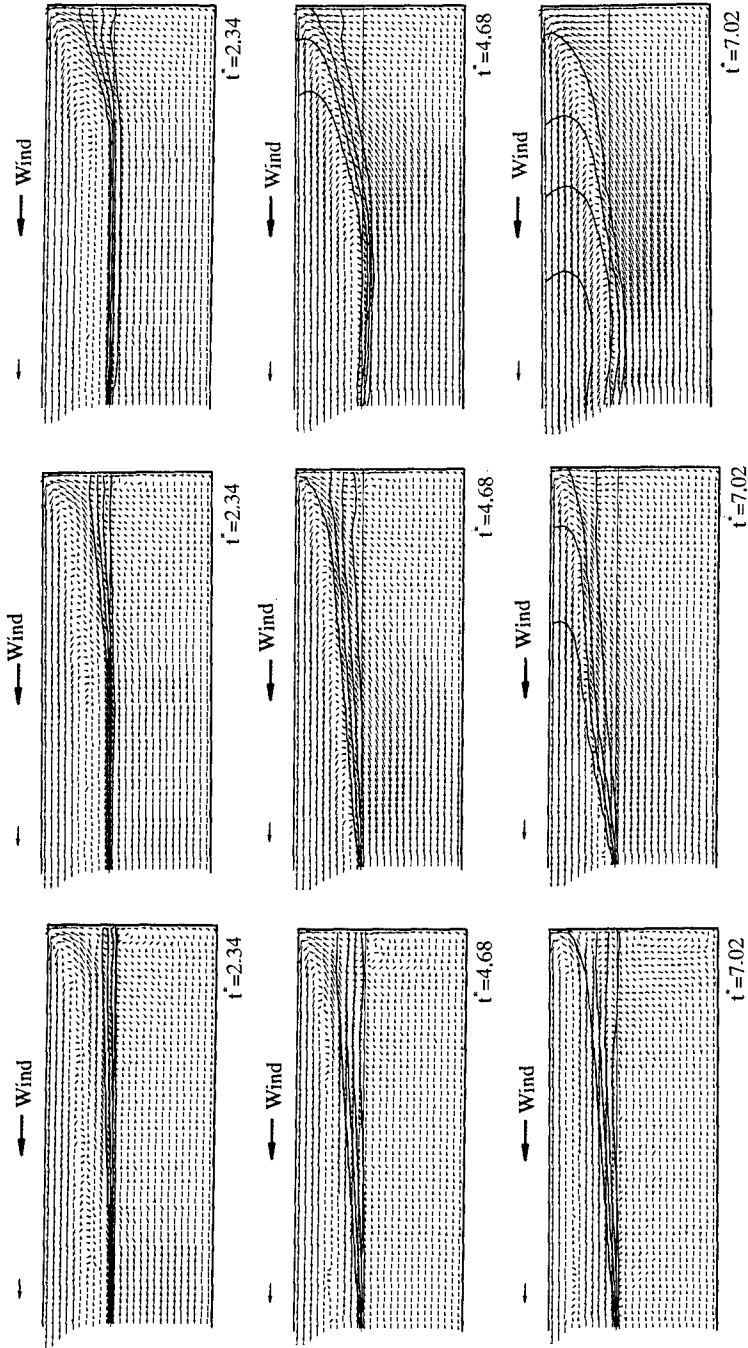


Figure 8. Time variation of density interface during wind blowing

Figure 9 shows the time variation of velocity and density difference fields obtained by numerical experiments in the flume with the open downstream condition. The values of  $Ri_* \times (2h_1/L)$  are 36.3, 12.0 and 3.1. And the value of  $t^*$  shown in the figures is the dimensionless passing time after the wind blowing, which is defined as  $t^* = tu_* / h_1$ . The density difference between fresh water and salt water are plotted every 20% from 10% by the contour lines.

It was confirmed by authors' experiments (1994) with a closed downstream condition that the results of numerical experiments are in a good agreement with those of hydraulic experiments. In the case of an open downstream bound-





(a)  $Ri_* \times (2h_1/L) = 36.3$

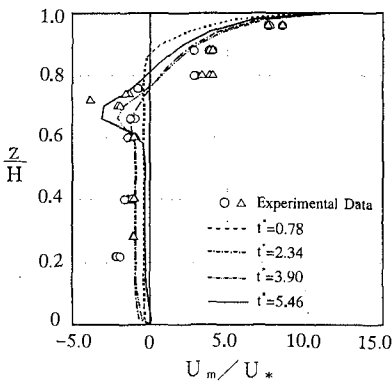
(b)  $Ri_* \times (2h_1/L) = 12.0$

(c)  $Ri_* \times (2h_1/L) = 3.1$

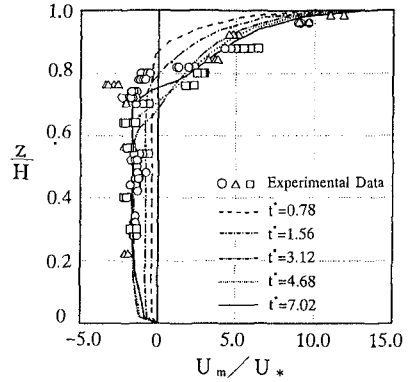
Figure 9. Effects of stratification on the distributions of velocity and density difference fields in a two-layered stratified flume with an open downstream condition

any condition, vertical circulation in the upper layer of the flume is not observed. The density interface upwells at the upstream side and the mixing occurs in the same manner as the closed flume experiments in cases of larger Wedderburn number. (See; Yoon et al.(1993)) On the basis of both hydraulic and numerical experiments, it is found that the upwelling of density interface at the upstream end occurs in the range of  $Ri_* \times (2h_1/L)$  less than 12.0. The deepening of density interface is observed only for the case of weakly stratification,  $Ri_* \times (2h_1/L) = 3.1$ . In the present computation, the vertical position of stratified interface is postulated to be fixed as  $h_1 = -10$  cm and the gradients of all hydraulic variables are constant at the downstream condition. Therefore, when the entrained volume into the upper layer is not balanced with the compensated one, which is inflowed in the lower layer from the connected large tank, the stratified interface is possible to deepen with time. It is not sure whether the deepening phenomena is caused by the postulated downstream condition or not, but it may be one of the reason of the deepening.

Figure 10 shows the comparison of computed vertical profiles of mean velocity with observed ones in the case of  $Ri_* \times (2h_1/L) = 36.3$  and 12.0. The computed mean velocity gives a good agreement with measured ones at the middle section of the flume. It may be suggested from this figure that the upper layer flows in the same direction as the wind blowing, while the lower layer flows in the reverse direction in order to compensate the entrained volume of the lower layer to the upper layer.



(a)  $Ri_* \times (2h_1/L) = 36.3$



(b)  $Ri_* \times (2h_1/L) = 12.0$

Figure 10. Comparison of computed vertical velocity profiles with observed ones

APPLICATION TO NUMERICAL EXPERIMENTS TO TOKYO BAY

It is easy on the basis of above discussion to evaluate whether the 'A-oshio' appears or not in the head of Tokyo Bay by the calculation of  $Ri_* \times (2h_1/L)$  based on field data obtained. Table 2 shows the observed hydraulic values during 'A-oshio' appearance in Tokyo Bay.  $\Delta\rho$  means the difference in density between the upper and the lower layers,  $h_1$ ; thickness of the upper layer,  $W_{10}$ ; wind velocity at 10m upper from water surface,  $L$ ; longitudinal length of Tokyo Bay and  $T_m$ ; the calculated time for upwelling of density interface to water surface.

According to Table 2, it is confirmed that the 'A-oshio' phenomena, namely the upwelling of anoxic water in the lower layer, would occur in the range of  $Ri_* \times (2h_1/L)$  less than 10.0 in the limits of obtained field data. The values are within the computation criterion value of  $Ri_* \times (2h_1/L) = 12.0$ . As shown in Table 2, the condition of 'A-oshio' appearance is that the wind of mean velocity over 4 m/s blows continuously for more than two or three days. It shows a good agreement with the previously observed results during 'Aoshio' appearance, too.

Table 2. The values of  $Ri_* \times (2h_1/L)$  during 'A-oshio' appearance in Tokyo Bay

Observed Date	$\Delta\rho$ ( $\text{kg/m}^3$ )	$h_1$ (m)	$W_{10}$ (m/s)	$Ri_*$	$\frac{2h_1 Ri_*}{L}$	$T_m$ (hr)
16-17, July, 1979	4.0	10.0	3.3	25,000	10.0	49.3
20-21, Aug, 1985	10.0	7.5	4.2	28,940	8.7	31.3
5-6, June, 1986	4.0	7.5	3.0	22,680	6.8	38.4

Where,  $\Delta\rho$ : difference of density between upper layer and lower one,  $h_1$ : depth of upper layer,  $Ri_*$ : Richardson number,  $L$ : longitudinal length of Tokyo Bay,  $T_m$ : time for upwelling of density interface to water surface

CONCLUSIONS

The data analyses of many field observations and the two dimensional hydraulic and numerical experiments were conducted in order to make clear the hydraulic conditions of 'A-oshio' appearance in Tokyo Bay. The following conclusions can be obtained.

- (1) 'A-oshio' phenomena can be treated as the upwelling phenomena of the anoxic water in the bottom layer under the wind blowing towards offshore for more than a couple of days based on lots of field observations.
- (2) In the two dimensional hydraulic and numerical experiments, the upwelling phenomena are found to occur only in the range of  $Ri_* \times (2h_1/L) < 12.0$ .
- (3) The results of numerical experiments are also confirmed to agree well with those of hydraulic experiments.

## REFERENCES

- 1) The Environmental Agency (1991) : The annual observation report on generation mechanism of Aoshio.
- 2) Joh, H. (1989) : Oxygen-deficient water in Osaka Bay, Vol.26, No.2, pp.87-98. (in Japanese)
- 3) Kakino, J. (1986) : The examples of the perish of shellfishes in the head of Tokyo Bay, Fisheries Engineering, Vol.23, pp.41-47. (in Japanese)
- 4) Patankar, S.V. (1980) : Numerical heat transfer and fluid flow, McGraw-Hill Book Com..
- 5) Spigel, R.H. and J. Imberger (1980) : The classification of mixed-layer dynamics in lakes of small to medium size, J. Phys. Oceanogr., Vol.10, pp.11043-1121.
- 6) Thomson, R.O.R.Y. and J. Imberger : Response of a numerical model of a stratified lake to wind stress, Proc. Int. Symp. Stratified Flow, 2nd, pp.562-570.
- 7) Tominaga, M., A. Kimura, T. Samukawa, K.Ohta, S. Matsuo, M. Yamamoto, H. Kitamura and I. Kon (1988) : Pollution Control, Vol.23, pp.285-294. (in Japanese)
- 8) Yoon, J.S., K. Nakatsuji and K. Muraoka (1993) : A study on the wind-driven density flow in the stratified water body of open downstream boundary, Proc. Coastal Eng. JSCE, Vol.40, pp.241-245. (in Japanese)
- 9) Yoon, J.S., K. Nakatsuji and K. Muraoka (1994) : What is 'A-oshio'? - Physical Processes of Upwelling Phenomena of Anoxic Water, Proc. Techno-Ocean '94, pp.517-522.

## CHAPTER 250

# Sea Level Rise and Coast Evolution in Poland

Ryszard B. ZEIDLER<sup>1</sup>

### Abstract

*Trends established for ten Polish tide gauge stations show the annual mean sea level (AMSL) growth rate from 0.8 to 2.9 mm per year in recent 35 years, and a linear trend computed for the years 1901–1990 yields some  $1.2\text{--}1.6 \pm 0.2$  mm/yr. Annual SL maxima (ASLM) trends are about one-half of the ASLM trends. Positive 6-hr SL increments  $\Delta h$  from storm events show a growing trend associated with 'storminess'.*

*In the 'retreat' option for Polish coast, the impact zones between contour lines 0–0.3 m, 0.3–1 m, and 1–2.5 m cover respectively 845, 883 and 476 km<sup>2</sup>, thus 2204 km<sup>2</sup> in total, in addition to 30 km<sup>2</sup> of beaches and dunes likely to dissappear for ASLR2. Described by Zeidler (1992) are various 'full protection' techniques adopted.*

*The Baltic atmospheric circulation is found to change as to direction but not as to wind speed. Subsequent (Fig. 9) insignificant changes in the net sediment transport, in the order of 15% per century are noted. Hence the coast evolution due to climatic changes in wind circulation patterns seems less important than the anticipated sea level rise induced changes.*

### 1 INTRODUCTION

The Baltic Sea forms Poland's borders along 500 km. It is a shallow, almost land-locked sea. Its salinity is low, barely 7-8 ppt in the Polish coastal zone.

The Polish coast consists of two basic types — sandy dunes (including barrier beaches) and cliffs. The former stretch along most of the coast while cliffs occupy slightly above 80 km. Coastal barriers between the sea and lakes are well developed in the central and eastern parts of the coast. The Hel Peninsula is a unique spit system separating the Gulf of Gdańsk from open sea. Because of its intensive erosion and multifarious importance, it has become a subject of concern to both Polish and international authorities.

The present climate of both Poland and its coast is believed to undergo perceptible change due to global warming. However, as for many other areas, the possible changes in precipitation, evaporation, transpiration, and their uncountable outcomes over the Baltic Sea and its drainage area, are all not amenable to

---

<sup>1</sup>Professor, Polish Academy of Sciences' Institute of Hydro-Engineering *IBW PAN* 7 Koscierska, 80-953 Gdansk, Poland

ready prediction. Global circulation models (GCM) are not yet powerful enough to yield a reliable prediction of climate change in regions such as Poland's coastal zone. Yet one can focus attention on the most likely and conspicuous outcome of such change, the sea level rise.

At the same time, some research programmes under way in Poland and the Baltic area (cf. Miętus 1993, 1994) are centered around changes in regional atmospheric circulation, thus adding to identification of hazardous meteorological and hydrologic processes in the Polish Baltic coast zone and coupling of atmospheric circulation and sea level. The two aspects of climate change, i.e. sea level rise and wind patterns are dealt with in this paper, in linkage with coast evolution.

The warming of climate in southern Poland is seen in Figure 1 while changes perceptible in seawater are noted in Figure 2.

## 2 ACCELERATED SEA LEVEL RISE (ASLR)

### 2.1 *Annual Mean and Maximum Sea Level in Poland*

Recent examination of trends and statistical distributions in sea level datasets, revised and updated for the Polish coast, has partly confirmed some earlier conclusions drawn for mean sea level and exposed new findings for extremum sea levels. The trends have been established for ten Polish tide gauge stations, which show the mean sea level growth rate from 0.8 (Kołobrzeg) to 2.9 (Gdańsk) mm per year in last 35 years, with acceleration in recent years (Zeidler et al. 1994). A linear trend for the years 1901–1990 has not been rejected statistically at the 0.05 significance level, and has been found to be smaller than the above figures for 35 years (i.e. some  $1.2\text{--}1.6 \pm 0.2$  mm per year).

### 2.2 *Storminess and Wave Climate*

Annual sea level maxima (ASLM) add to the present knowledge of the Polish Baltic hydrology. Inherent trends and periodicities have been examined (cf. Zeidler et al. 1994). The ASLM trends have been found to approach 0.53 mm/yr at Swinoujście, 0.7 mm/yr at Kołobrzeg and 1.73 mm/yr in Gdańsk, thus about one-half of the mean-sea level trend. Hamming windowing displayed significant periodicities about 8, 5–6 and 3 years. Bartlett testing confirmed the data independence for Gdańsk but not for the other stations. Seasonal occurrence of the maxima is obvious — 74% of all ASLM occurred between November and February, these months encompassing all ASLM with 10% exceedance and 91% of 25% exceedance (remaining 9% in October and March).

Another interesting research objective attacked now consists in description of the correlation matrices for joint sea level and wave height events under storm conditions observed and hindcast along the Polish Baltic. This programme is hoped to be fruitful both scientifically and practically (design of coastal and maritime structures basing on more than just one storm parameter such as sea level).

For the identification of both 'regular' and extreme storm-induced sea level changes as well as definition of hazardous sea states it is worthwhile to examine short-term increments of SL and count them in some statistically representative classes in order to see if those numbers change in longer time scales, which would point to the presence of what could be labelled a 'storminess change'. This has been done under the programme indicated in the acknowledgements, and

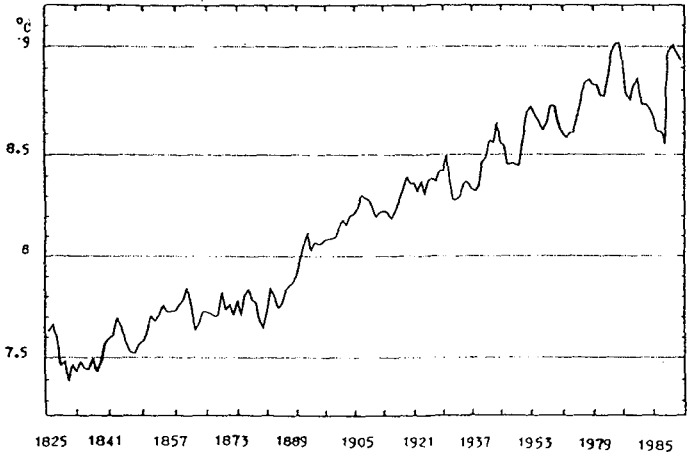


Figure 1. Air temperature in Cracow (20-year moving average)

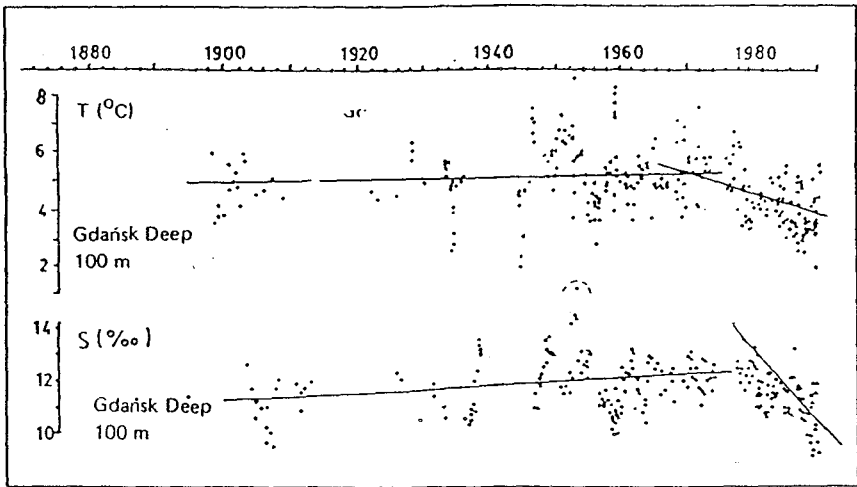


Figure 2. Water temperature and salinity variation in the Baltic Sea as exposed by Piechura in 1993.

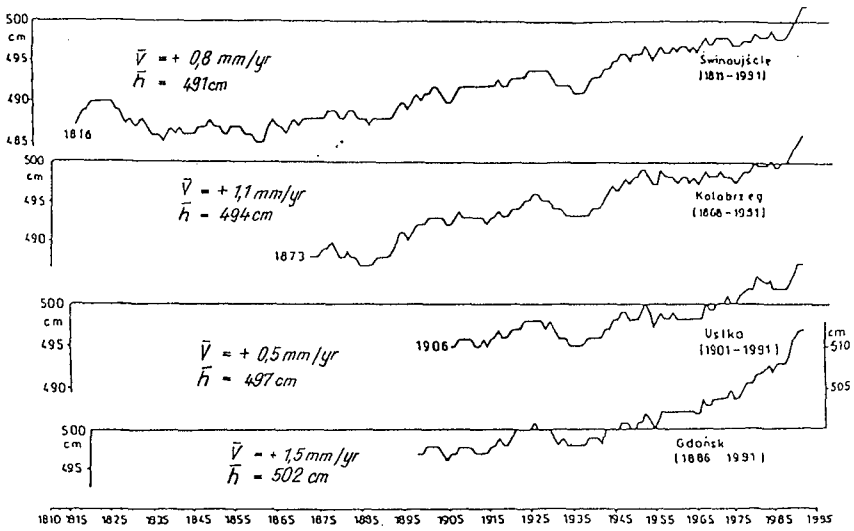


Figure 3. 11-yr moving-average mean SL at the most reliable Polish tide gauge stations (cf. Zeidler et al. 1994).

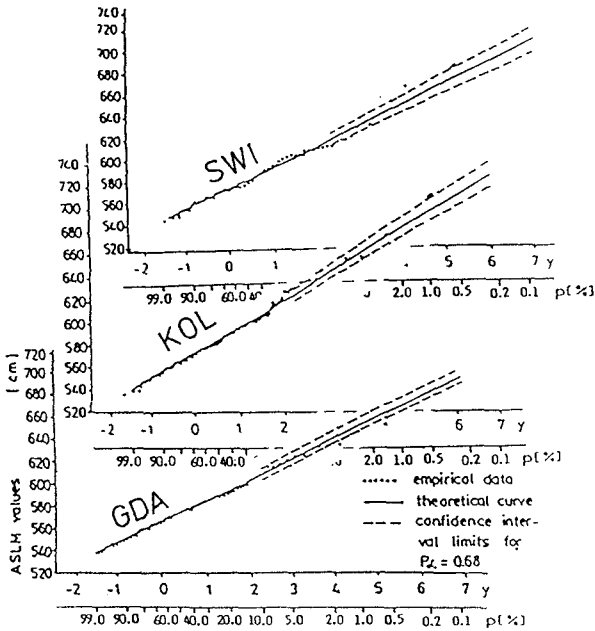


Figure 4. ASLM exceedance curves fitting the Gumbel distribution for three Polish tide gauge stations; (A) Świnoujście; (B) Kołobrzeg; (C) Gdańsk; cf. Zeidler et al. (1994).



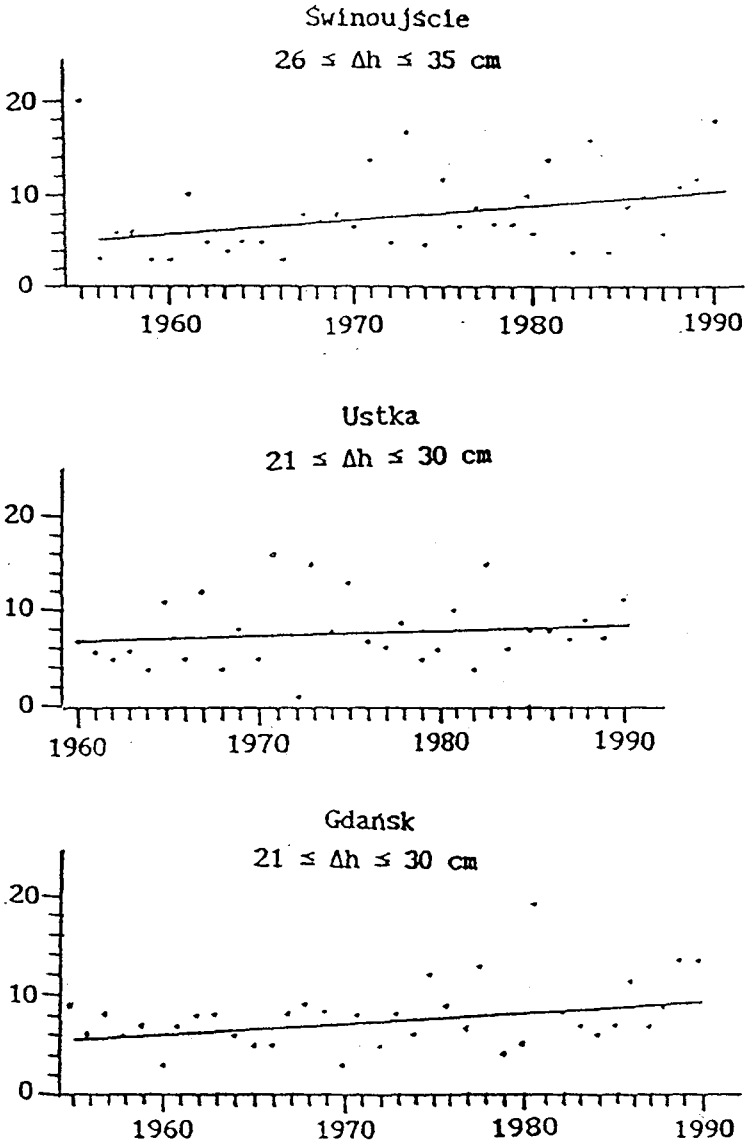


Figure 5. Trends in annual occurrence numbers for 6-hr sea level increments  $\Delta h$  for three Polish stations.

the basic findings are illustrated in Figure 5. For the three stations analyzed, the positive 6-hr SL increments were found from time series extending over some forty-odd years. As they had to be statistically meaningful, the increments  $\Delta h$  were arranged in three classes (slightly different for every station), and the central class data are presented in Figure 5. It is seen that the occurrence numbers of  $\Delta h$  show a growing trend.

The above conclusion agrees with similar findings for the occurrences of annual crossings of some sea levels regarded as 'warning' and 'emergency' levels (roughly 60 and 80 cm above MSL in Poland, respectively). Those occurrence numbers, too, have been observed to grow over decades. To further investigate this issue, statistical series have been found under our programme for both  $\Delta h$  and sea level alone. Similar behaviour and agreement of the two families with Pearson type III exceedance functions, above some thresholds of 70 cm for SL and 25 cm for  $\Delta h$ , is notable. This proves that sea levels above 70 cm (or 570 as a standard format of reference in Poland) can indeed be identified with a short-term rise in SL (recall that  $\Delta h$  classes in our analysis have been only positive). Then the statistical distributions of high sea levels are representative of hazardous situations associated mostly with growth of the sea level, not incidental fall.

### 3 POLAND'S VULNERABILITY TO ASLR

#### 3.1 General

Of the three response strategies suggested by IPCC we selected only two, i.e. 'retreat' and 'full protection' ('adaptation' was largely neglected).

The Polish 'Study Area' has been defined as the area within which the physical effects of the accelerated sea level rise (ASLR) over the next century could be felt. The inland boundary of the study area was chosen as the +2.5 m contour.

Out of the total length of the Polish coastline, the 'open sea' coast is almost exactly 500 km (of which 72 km on both sides of the Hel Peninsula), while the banks of the Szczecin Bay measure about 240 km, and those of the Vistula Bay about 100 km.

Because of their distinct features, distinguished have been four major Areas: the Odra Estuary (Area 1), western dunes and barrier beaches (Area 2), central-east dunes and barrier beaches with the Hel Peninsula (Area 3), and the Vistula Delta (Area 4). Area 1 includes the agglomeration of Szczecin (and Świnoujście), while Area 4 encompasses the three-city complex of Gdańsk, Gdynia and Sopot, together with Elbląg.

The division into three impact zones permitted a convenient distinction through the study area cross-section within which flooding probabilities could be assessed: (I) between 0.0 m and +0.3 m MSL contours; (II) between +0.3 m and +1.0 m MSL; (III) between +1.0 m and +2.5 m MSL.

The data collected from maps, reports, computations, studies and other sources (e.g. land-use, socio-economic etc) were entered pertaining to each of the impact zones separately in working tables. Flooded areas (i.e. areas 'lost') could then be readily deduced as zone I at ASLR1 (30 cm/100 yrs) and zones I+II at ASLR2 (1 cm/yr), while the area at risk was defined as II+III at ASLR1 and III at ASLR2.

For the purposes of assessment, the following habitats have been distinguished: coastal waters, beaches and dunes, forests, lagoons and barrier lakes,

rivers and estuaries, and swamps/bogs. Coastal forests display the highest biodiversity among all coastal habitats.

### 3.2 *The Extent of Vulnerability for the 'No Measures' Option*

The extent of inundation and population hazards in our study area are visible in Tables 1 and 2.

The impact zones between contour lines 0–0.3 m, 0.3–1 m, and 1–2.5 m cover respectively 845, 883 and 476 km<sup>2</sup>, thus 2204 km<sup>2</sup> in total, in addition to 30 km<sup>2</sup> of beaches and dunes likely to disappear as a result of ASLR2 (and some 10 km<sup>2</sup> due to ASLR1).

The principal ASLR impact in the Odra estuary will consist in inundation extending at ASLR2 up to River Rurzyca (KM 695). Polder dykes have crests about 1.5–2 m above MWL. At higher stages most polder dykes will be overtopped. The inundated polders will include those of Miedzyodrże (between East and West Odra), around the Szczecin Bay, Swina and Dziwna. Equally endangered by flooding are urban areas of Szczecin (primarily Dąbie district), Świnoujście, Trzebież and other towns. Indirect effects encompass damage to sewerage and other infrastructure. Parts of the Ports of Szczecin, Świnoujście and Police are also vulnerable. The impact zones I and II within Area 1 measure in total 163.8 and 496.6 km<sup>2</sup>, respectively.

All Polish coastal polders, arranged in eight complexes of 243 polders measuring 183,557 hectares will be at stake.

In Areas 2 and 3, narrow coastal barriers between the sea and low-lying lakes (much as lagoons or embayments in other area) could erode, making inland areas widely accessible to sea water. The higher levels attained by storm surges in ASLR scenarios will destroy foredunes and erode barrier islands and spits. The lowered barriers will then be susceptible to storm washover. The lakes will grow more saline.

Stowiński National Park and Łeba dune field, a memorable natural landscape, special enough to be included on UNESCO's list of the world's Biosphere Reserves, are endangered as well. The Hel Peninsula, a quite unique spit formation separating the Gulf of Gdańsk is most vulnerable, and will become a smaller island if no measures are applied.

Gdańsk, Szczecin, Świnoujście and Gdynia ports are all flooded and at risk, though to different degree. For instance, the industry of Gdańsk (ports included) occupies 430 and 330 hectares in impact zones I+II and III, respectively. In addition, Gdańsk is now a lively industrial, scientific and cultural centre of northern Poland. The endangered urban areas of Gdańsk cover 450 and 680 ha in the same zones. Full prevention measures should be taken to avoid any loss of this valuable and historical piece of our study area.

One should point out the importance of ports and several shipyards in Gdańsk, Gdynia and Szczecin, the industrial hinterland, such as oil refinery linked to oil terminal in Gdańsk in Area 4 and the Lower Odra power plant and the large chemical plant and port at Police in Area 1, the architecture, historical, and cultural values of old cities, primarily Gdańsk in Area 4, and numerous roads and railways, in addition to other infrastructure.

The Vistula Delta covers an area of 2,320 km<sup>2</sup> with major cities of Gdańsk, Elbląg and Malbork. Its polder area occupies 180,000 hectares (2% of the land area of Poland). Most of its depressions and low land will be damaged. The dikes already built will be too low for the new hydrological conditions, especially ASLR2. They have been designed to stay under water not longer than a couple

Table 1. Distribution of Land-Use Categories in Impact Zones I, II and III; area in hectares, length in kilometres.

Impact Zone I — 0.0–0.3 m.										
Area	AH	AL	AO	F	W	U	I	R	NR	RD/LR/TL/RL/NT/B
1	90	11,955	2,635	1415	30	40				30/25/41/1/1/1
2		30	400						430	
3		130	40							
4	64,870	130	1,685		352	130	150			291/108/302/29/6/
Tot	64,960	12,245	4,760	1,415	382	170	150		430	321/133/343/29/6/
Total Impact Zone I Surface Area = 84,512 ha										
Impact Zones I + II — 0.0–1.0 m										
1	297	34,338	5,435	7,290	550	640	505	35		70/89/74/15/1/1/17
2		11,100	995	2,745	110	90			465	27/11/30/1/1/4
3		11,531	118	24	17	5	8	12		6/8/7/2/1/1
4	86,910	1,930	2,265	1,260	2,590	705	430	95	275	428/179/415/61/65/26
Tot	87,207	58,899	8,813	11,319	3,267	1,440	943	142	740	531/287/525/79/66/47
Total Impact Zones I+II Surface Area = 172,770 ha										
Impact Zone III — 1.0–2.5 m										
1		7,935	145	1,690			300			36/9/35/6/2/4
2		5,380		2,315	370					36/7/5/3/1/1
3		3,210		330	155	85		730		28/10/7/11/1/1/1
4	21,520	200		795	1,215	815	370			97/12/60/8/9/1/1
Tot	21,520	16,725	145	5,130	1,740	900	670	730		197/38/107/ 28/11/5
Total Impact Zone III Surface Area = 47,560 ha										

NOTES: The land-use category 'Industry' (I) includes 'Ports' here (!)

(RD) road; (LR) local road; (TL) power transmission line; (RL) railway; (NT) narrow-track rail; (B) bridges (# !!).

Table 2. Population of the Study Area.

Area	Zone	Urban	Rural	Total
1	I (0–0.3 m)	1,630	3450	5,080
	II (0.3–1.0 m)	21,080	9,630	30,710
	III (1–2.5 m)	28,960	2,940	31,900
2	I	0	270	270
	II	1,210	4,580	5,790
	III	870	2,880	3,750
3	I	0	110	110
	II	740	9,310	10,050
	III	1,550	2,490	4,040
4	I	9,590	25,810	35,400
	II	40,980	17,650	58,630
	III	36,080	13,030	49,110
Total		142,690	92,150	234,840

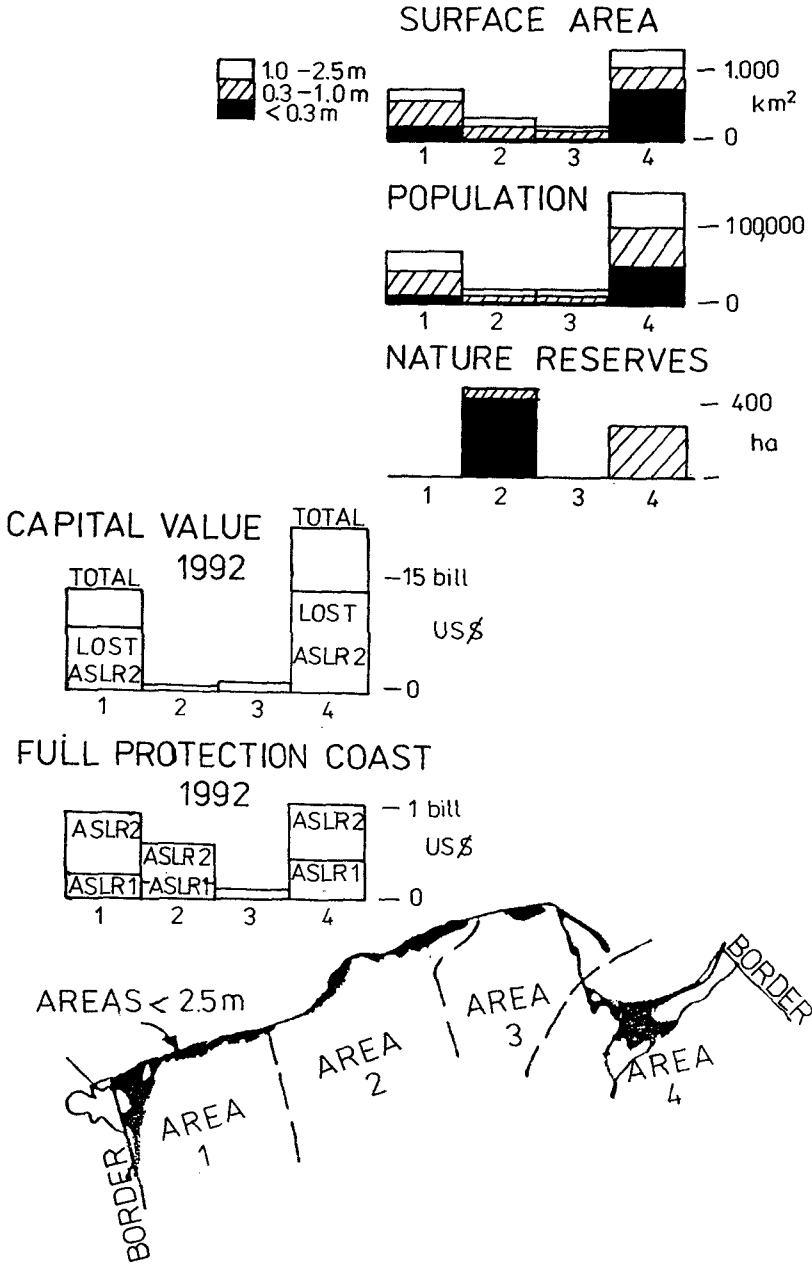


Figure 6. Poland's study areas, lost values in retreat and costs of both retreat and 'full protection

of days. In summary, the area losses under ASLR1 and ASLR2 are very heavy — 672 km<sup>2</sup> (80% of all Area 1–4) and 948 km<sup>2</sup> (55%) respectively. The length of roads flooded is 400 km and 564 km in the two cases, in addition to 35 and 126 km of railways, 300 and 415 km of primary power lines, and 26 bridges.

Enhanced shoreline erosion and shore retreat has been analysed by the use of field data, Bruun computations and numerical models. All results point to a figure exceeding 150 m of shoreline and dune retreat in the course of 100 years of ASLR2 scenario. The counterpart for ASLR1 can be estimated at 50 m per 100 years.

Hence the impact zones between contour lines 0–0.3 m, 0.3–1 m, and 1–2.5 m cover respectively 845, 883 and 476 km<sup>2</sup>, thus 2204 km<sup>2</sup> in total, in addition to 30 km<sup>2</sup> of beaches and dunes likely to disappear as a result of ASLR2 (and some 10 km<sup>2</sup> due to ASLR1).

### 5.3 Outline of the Full Protection Option

Described by Zeidler (1992) are various protection techniques adopted. From that variety of possible coastal defence measures we have chosen dykes, sea-walls, offshore breakwaters, artificial beach nourishment and land elevation, in addition to local land abandonment. Many structures are new, and some existing structures are proposed for reconstruction and adaptation to new ASLR conditions.

*Inter alia*, full protection of the Odra estuary means preservation of the polders on peripheries of the estuary. (107 and 280 km of new dykes must be constructed in Area 4 under ASLR1 and ASLR2, respectively; the lengths of adapted dykes are 243 and 324 km). In Areas 2 & 3, new polders require new facilities such as pump stations, drainage and other infrastructure. In our concept of Hel Peninsula protection we rely mostly on artificial nourishment. In Area 4, it seems imperative to keep the present agricultural use of the Vistula Delta (much as the lower Odra Valley), especially in the polder areas.

Hence full protection of Zulawy polders at ASLR2 requires a bulk adaptation of the existing dykes and the construction of some new dykes and storm and flood prevention facilities. At ASLR2, one should construct 52 km of new dykes and adapt 647 km of those presently in use. Under ASLR1, the respective numbers are 13 and 600 km.

The adaptation should encompass river dykes on Zulawy, frontline dykes on the Vistula Bay, lower dykes around Lake Drużno, and river dykes along Rivers Szkarpa and Nogat, and Kanal Jagiellonski, which make up the navigation route between Gdańsk and Elbląg. The Vistula dykes should be adapted on some 35 km from the mouth upstream. Other rivers will require new dykes, in addition to the adapted ones.

The storm barrier at the entrance of River Tuga should be virtually redesigned in view of ASLR2, and other river gates must be considered to keep storm surges away from the delta.

Additional protection should also be secured on polders around the Vistula Bay (at Krynica Morska, Przebrno, Kadyny, Tolkmicko and Pasłęka).

An outline of the damage and cost incurred over the four Study Areas of Poland's coast in the case of the two response strategies is given in Figure 6 for the sake of better illustration of the notions and quantities in the description above.

It is worthwhile to note that the cost of protection, although high in absolute terms and demanding as to huge investments, is roughly tenfold lower than the value of the property lost, not to mention the fringe losses.

## 4 POLISH COAST EVOLUTION

### 4.1 *Historical Lessons*

The vulnerability assessment for Poland was basically aimed at quantification of the losses and protection measures due to flooding and inundation, as beach erosion contributed marginally to the overall damage. Lessons of such flooding were learned in the past, as illustrated in Figure 7 for the Vistula Delta ('Żuławy'). The mouth and branches of the Vistula River were migrating in the past, with obvious bearing on the overall shore evolution. Long-term evolution of 'open sea' was also recorded. Depicted in Figure 8 is an example of cliff retreat encountered in Poland over roughly 700 years. The factors controlling long-term changes are currently analyzed and modelling approaches are now endeavoured at IBW PAN.

Routine topographic and bathymetric data have been collected at the *IBW PAN* Coastal Research Facility situated on the Polish coast of the Baltic Sea some 80 km from Gdańsk. Along with parameters of wind, waves, currents and other hydrologic factors, topographic features have been measured since 1983 on a 2.7-km beach and nearshore zone extending some 800 m from shoreline. The beach profiles have been arranged every 100 m. The first systematic and mutually compatible records of beach and shore topography date back to 1964, and echosoundings plus tachimetry are continued every four weeks.

In addition to Lubiatowo, a few other sites have also been made available to *IBW PAN* staff, such as Bulgarian Black Sea or Senegalese coast off St. Louis, not to mention the cartographic material for Poland's coastal units such as Hel Peninsula. Hence we have insight into a considerable bulk of a reliable field database stretching over a reasonably long span of time. This data set encompasses mostly sandy beaches, and partly cohesive beds. It has been used for various research purposes. At present we focus attention on its use to model the large-scale coastal behaviour (Pruszek & Zeidler 1993).

### 4.2 *Gross Forecast of Coast Evolution*

It has been mentioned that the present attempt of the forecast of coast evolution due to climate change is largely confined to two factors: sea level rise and atmospheric circulation. So far they are treated separately: ASLR in VA and wind change via the chain of effects schematized in Figure 9. Both factors will hopefully be combined in a joint algorithm taking into account a variety of interactions.

At present we adhere to the recent findings that the atmospheric circulation over the Baltic Sea changes as to direction but not as to wind speed (Miętus 1994). The prevailing wind direction tends to follow more and more closely the major axis of the sea. Hence it is assumed that the south-westerly winds blowing along the Polish coast for most time now become more westerly, at the cost of the southerly ones. In the analysis it is taken for granted that among the major eight directional sectors the southern ones are reduced at a rate of 2.5% per 50 years while their northern counterparts gain the same, and the same is repeated in the west-east direction, at the cost of the easterly winds.

The procedure illustrated in Figure 9 reflects the natural and common logics: from wind to sediment transport. From statistical yearly distributions of wind speed and direction for the intervening Baltic fetches one computes waves by a spectral method, uses a Battjes-Jansen procedure for irregular wave trans-





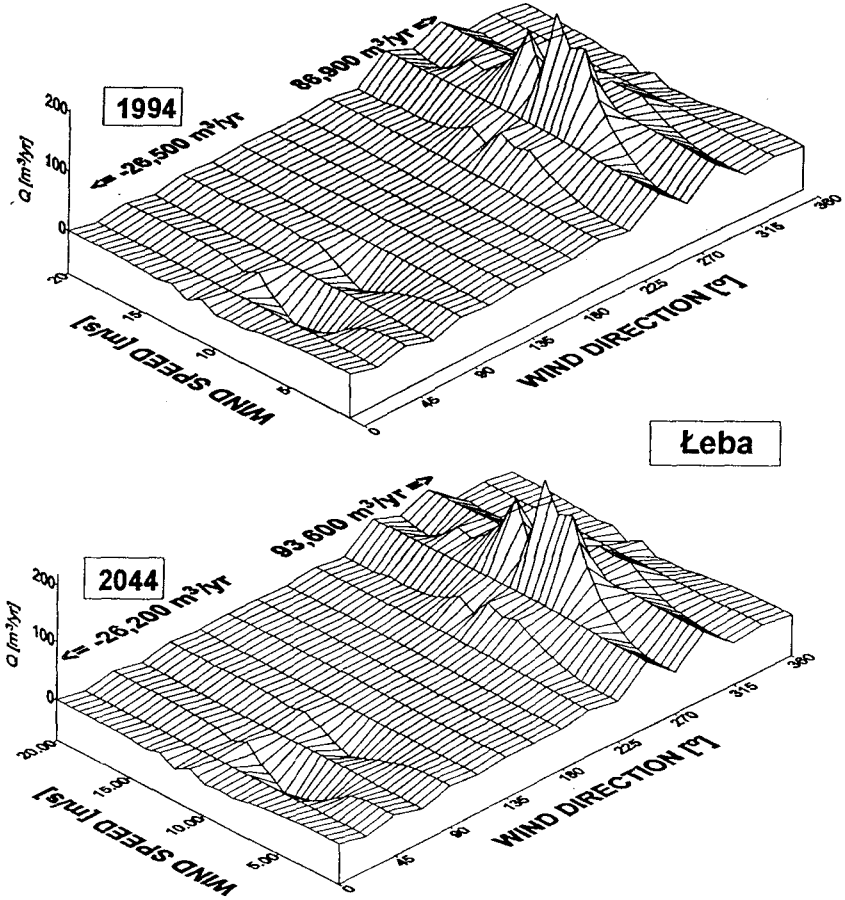
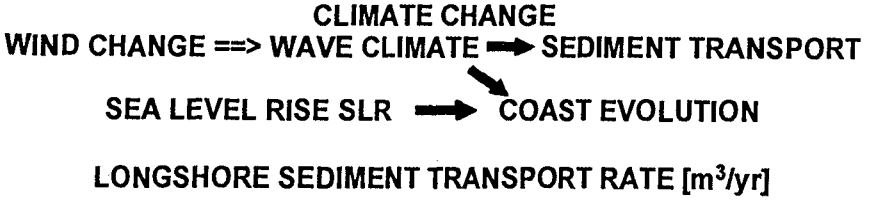


Figure 9. Two-dimensional (wind speed-direction) distributions of sediment transport rates across the entire shore profile at Leba (east-central Polish coast) in the years 1994 and 2044.

formation in the shoaling zone, employs the IBW PAN method for prediction of wave-induced currents, and computes the sediment transport rates basing on the modified Bijker method.

## 5 CLOSURE

The transition from sediment transport rate to shore evolution is being implemented by simple tools basing on one-line theory, apparently sufficient for this type of gross estimates. At present it is somehow striking to note fairly insignificant changes in the net sediment transport, in the order of 15% per century. It may then be concluded on a very tentative basis that the coast evolution due to climatic changes in wind circulation patterns are less important than the anticipated sea level rise induced changes.

## LITERATURE

- Miętus, M. 1993. Local circulation index over southern Baltic compared to wind, temperature and sea level at the Polish coast. *Contemporary Climatic Changes. Proceed. CCC '93 Conference* 223–231. Szczecin University.
- Miętus M. 1994. Vector of geostrophic wind in the Baltic Sea region as index of local circulation and its relation with hydro-meteorological characteristics along the Polish coast. *Proceed. European Workshop on Climate Variations Majvik*. (May 15–17; in press).
- Pruszek Z. (1993), The analysis of beach profile changes using Dean's method and empirical orthogonal functions. *Jour. of Coastal Eng.*, 19: 245–261.
- Pruszek Z. & R.B.Zeidler 1992. Beach changes and sediment movement in the surf zone. *Proceed. 23rd ICCE*, Venice, ASCE, pp. 2370–2382.
- Pruszek Z. & R.B.Zeidler 1993. Modelling Large-Scale Coast Evolution. *Proceed. 5th German-Polish Seminar on Coastal and Estuary Dynamics; Schriften GKSS Geesthacht* 5: 121–140.
- Wróblewski A. 1993. Analysis and long-term sea level forecast at the Polish Baltic Sea coast. Part I. Annual sea level maxima. *Oceanologia* 33.
- Zeidler R.B. 1990. Shore evolution due to waves and sea level changes. *Hydrot. Trans.* 53: 41–62.
- Zeidler R.B. 1992. *Assessment of the Vulnerability of Poland's Coastal Areas to Sea Level Rise*. H\*T\*S Gdańsk. ISBN 83-85708-01-4.
- Zeidler R.B. 1994. Polish Baltic coast: changes, hazards and management. *Geographia Polonica* 62: 81–98.
- Zeidler, R.B., A. Wróblewski, M. Miętus, Z. Dziadziuszko & J. Cyberski 1994. Wind, wave, and storm surge regime at the Polish Baltic coast. *IGU Symposium Polish Coast '94 — Present, Past and Future*. Gdynia.

## Acknowledgements

This paper results from the scientific projects 6 P202–004-04 KBN and US Country Study SE13, which is hereby gratefully acknowledged. The author expresses his particular gratitude to the sponsors under the latter programme, who enabled him to participate in the 24th ICCE conference in Kobe.



# **PART VI**

## **Case Studies**



## CHAPTER 251

### FORMATION OF DYNAMICALLY STABLE SANDY BEACHES ON THE AMANOHASHIDATE COAST BY SAND BYPASSING

Ikuro Chin<sup>1</sup>, Minoru Yamada<sup>2</sup> and Yoshito Tsuchiya<sup>3</sup>, M.ASCE

#### Abstract

Due to the construction of fishery harbors up coast, severe beach erosion has taken place on the Amanohashidate Coast of Japan, a typical sand spit, resulting in such a reduction of the sand spit that countermeasures have had to be taken. The sand bypass method recently has been used to stabilize the sandy beaches on this spit. Annual change in the configuration of a sandy beach formed between groins first is considered in relation to erosion countermeasures and the sand volume bypassed. We found that the sandy beaches along the Amanohashidate Coast are being formed with little fluctuation at what approaches the stable condition. On the basis of the theoretical background of the formation of stable sandy beaches (Tsuchiya et al.,1993; Tsuchiya,1994), a satisfactory comparison of the actual and theoretical shoreline configurations was made.

Next, alongshore change in the longshore sediment transport rate was investigated in relation to the sand volume nourished and bypassed. We found that when the sandy beaches formed between groins have nearly reached the stable condition, the relation between the longshore sediment transport rate and wave energy power results in an estimated necessary sand volume to be bypassed of  $5,000\text{m}^3/\text{yr}$ . We conclude that in the case of the Amanohashidate Coast, the use of sand bypassing could well form a series of dynamically stable sandy beaches between groins, the sand volume required for bypassing being only  $5,000\text{m}^3/\text{yr}$ .

---

<sup>1</sup> Director, Hydraulic Engineering Division, NEWJEC Inc., Chuo-ku, Osaka 542, Japan

<sup>2</sup> Director, Fukuchiyama Construction Office, Kyoto Prefecture, Fukuchiyama, Kyoto 620, Japan

<sup>3</sup> Professor Emeritus, Kyoto University & Professor, Meijo University, Tenpaku-ku, Nagoya 467, Japan

INTRODUCTION

Results of the most recent survey of the actual state of coastal erosion in Japan show that beach erosion on shorelines forming part of a sand spit has taken place due to the construction of coastal structures that interrupt longshore sediment transport (Uda,1992). Beach erosion also is reported to be actively advancing in many countries of the world (Tsuchiya, 1982). Silvester(1993) has published a geomorphological review that shows that the formation and deformation of sand spits play an important part in the formation and development of barrier beaches. He defines the mode of spit construction and the erosive conditions, and suggests an approach to the control of beach erosion on a sand spit coast.

As seen in Figure 1, the Amanohashidate Coast is a typical sand spit that extends in the direction of the predominant longshore sediment transport in Miyazu Bay.

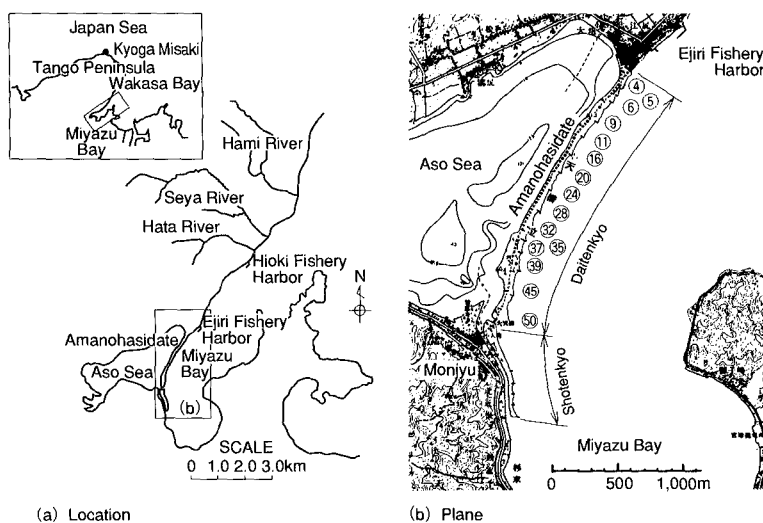


Figure 1. Location and plane figure of the Amanohashidate Coast.

Therefore, if longshore sediment transport is interrupted at an updrift point, beach erosion is inevitable and will take place immediately on the downdrift side of the coast in terms of the continuity of sediment transport. In fact, soon after the construction of breakwaters in both the Ejiri and Hioki fishery harbors upcoast, the natural sandy beaches of Amanohashidate began to be eroded, and groins were erected to protect the shoreline. Recently, beach nourishment and sand bypassing have been applied for the first time in Japan (Yajima,1982; Kuroda,1985). As a result, beautiful sandy beaches have been reformed, as shown in Figure 2. These sandy beaches appear gradually to be approaching dynamic stability. Bypassing the amount of sediment necessary to maintain dynamically stable sandy beaches

therefore may aid in protecting this shoreline, a significant reason for the application of this method.

We here describe the annual change in the shoreline position of sandy beaches formed between groins in relation to changes in the volume of sediment used for beach nourishment and for sand bypassing. The processes by which sandy beaches between groins reach stability are investigated in relation to the theoretical background of the formation of stable sandy beaches reported by Tsuchiya, Chin and Wada(1993) and Tsuchiya(1994) in order to determine the minimum amount of sand to be bypassed.

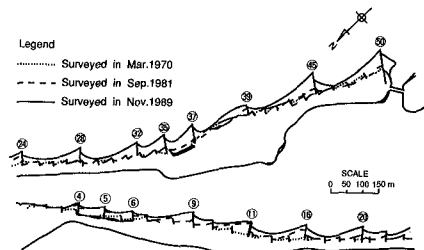


Figure 2. Formation of a series of sandy beaches between groins on the Amanohashidate Coast.

## APPLICATION OF THE SAND BYPASS METHOD

Three types of countermeasures against beach erosion have been taken on this coast: groins, beach nourishment, and sand bypassing. At present, these three measures used in combination prevent beach erosion, and have re-established sandy beaches. Small and large groins first were constructed about 1955 and functioned for about 25 years; but, they did not prove very effective because the sandy beaches continued to erode, and the sand spit has gradually been reduced. From 1979 to 1985 beach nourishment was carried out and resulted in a shoreline advance of about 20m, sand being deposited on the upstream coast of the large groins and transported sand being accreted along the front edge of the groins. Thus, over the Daitenkyo area of the spit (Figure 1), continuity of sand transport has nearly been accomplished (Kyoto Prefecture, 1987). Since 1985, a so-called "conveyer belt" of sand transport (Bascom, 1970), has been formed, which has increased the feasibility of using sand bypassing. After tests, sand bypassing has been done on a large scale. As of 1992, the total volume of sand nourished and bypassed for a 9-year period was about 120,000m<sup>3</sup>.

## REFRACTION CHARACTERISTICS OF WAVES INCIDENT TO SANDY BEACHES

Past wave data recorded for Miyazu Bay, shows there is a relation between the waves in Miyazu Bay and those in the open sea (Kyoga-Misaki). Of the open sea wave characteristics, the wave periods are of very wide range (significant wave

period  $T_{1/3}=5\text{--}12$  sec), and swells are frequent in the monsoon (Kyoto Prefecture, 1987). These waves pass in through the wave window in Miyazu Bay. In terms of this wave window, however, the relation between waves in the open sea and those in the bay has not yet been determined; therefore, the representative waves coming onto the Amanohashidate Coast can not be specified. In terms of wave refraction and the wave window, we first determine the conditions of the waves incident to the coast that control beach change, then using the specified representative waves, we calculate the wave refraction to obtain the breaker characteristics.

### Observation of incident breaking wave rays by aerial photography

As shown in Figure 1(a), the wave window for the Amanohashidate Coast is very narrow; therefore, limited waves come in to the beach. To predict the breaker characteristics along the beach, detailed calculation of wave transformation is necessary, therefore an aerial observation of the incident waves was conducted (Figure 3). The wave rays calculated by the wave ray method and the wave crest lines observed are approximately orthogonal at the breaking points. This indicates that the calculated wave rays are of sufficient accuracy. The observed wave period is nearly equal to 8.0sec, and wave period at Kyoga Misaki, when the photographs were taken, also was 8.0sec. Waves with the direction of  $N48^\circ E$  off Wakasa Bay were incident at that time, and they were directly incident because the angle of direction is within the range of the wave window of Miyazu Bay.

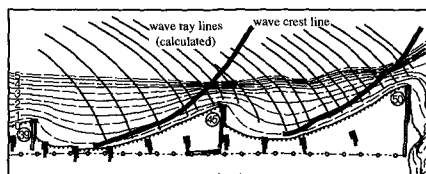


Figure 3. Wave crest lines taken from aerial photographs.

### Calculation of wave transformation

As to the wave conditions in the deep sea off Wakasa Bay, the incident waves are subjected to angles of direction from N to  $N48^\circ E$ . For the refraction calculations, taking into account the wave window of Miyazu Bay as well as the plane topography, the wave periods used are: a) 10–12 sec, the periods of relatively long waves coming with the swell into the bay for N to  $N35^\circ E$  with the passage of the winter monsoon and b) 6–8 sec, the periods of the wind waves for  $N35^\circ E$  to  $N48^\circ E$ . Results calculated using the detailed bottom topography of the coast, including Miyazu Bay, show that waves from  $N45^\circ E$  to  $N48^\circ E$ , which are within the range of the wave window of Miyazu Bay, come directly in; that the most effective are the waves from  $N45^\circ E$  to  $N48^\circ E$  with a wave period of 8sec and those from  $N40^\circ E$  to  $N45^\circ E$  with the same wave period; and that they are incident to the beach at nearly the same angle. The estimated breaker angles of the incident waves correlate



well with the breaker heights along the beach for a representative wave height of 1.0m offshore of the Amanohashidate Coast.

**ANNUAL CHANGE IN THE SANDY BEACH CONFIGURATION**

Because sediment movement results in beach change, it is important to understand sediment characteristics, in particular the grain size distribution on the beach. Figure 4 shows the median grain size,  $d_{50}$ , of the shoreline sediments, indicating that on the whole the beaches along this coast consist of fine sediments. The alongshore distribution of grain size can be regarded as almost uniform on the coast in the case of the representative season (winter); but, the grain size ranges from  $d_{50}=0.1\sim 0.2\text{mm}$  for the very fine sand of Daitenkryo beach to  $d_{50}=0.2\sim 0.5\text{mm}$  for the somewhat coarse sand of Shotenkryo beach.

Furthermore, as concerns the sediments in the mouth of the rivers flowing into the area upcoast, which are regarded as the source of littoral sediments, their grain sizes, are somewhat coarser than those on the Amanohashidate Coast. Hence, the source sediment can be said to have been transported downstream by the longshore current, producing a fine grain size that is almost the same as that of the sediments brought to the Amanohashidate Coast by longshore sediment transport.

Groins serve as natural headlands that function to control changes in the sandy beach configuration between groins, thereby approaching the condition of beach stability. Using the definition of stable sandy beaches shown in Figure 5 (Tsuchiya,1991), the annual change in sandy beach configuration is obtained in relation to the

annual changes in the sand volume nourished and bypassed. Moreover, the morphological characteristics of stable beaches are obtained. Figures 6 and 7 respectively show the annual changes in shoreline positions and in the sand volume deposited between representative groins.

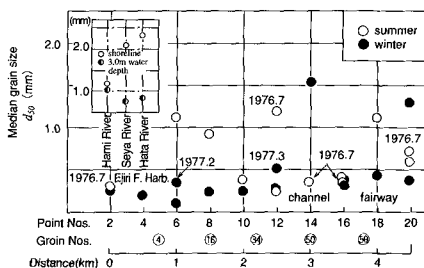


Figure 4. Alongshore distribution of grain size  $d_{50}$  along the shoreline and at river mouths.

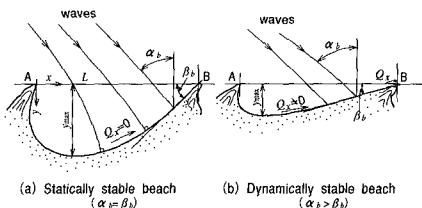


Figure 5. Two kinds of beach form.

Shoreline changes are expressed by the changes in the maximum indentation ratio of the bay ( $y_{max}/L$ ) together with the position. After 1986, little change took place (Figure 6) and the tendency is to approach equilibrium at each headland. In Figure 7, in which the sand volume deposited between groins is plotted as a deviation from the beach formation of 1980~1981, almost the same tendency is shown, although there is some fluctuation. Until 1986, when beach nourishment was actively carried out, the outcome shows large fluctuation. In this case, bottom soundings were made at 10~20m intervals along the shoreline, the level staff method being used for all sections with a water depth shallower than 4.0m.

To show the relationship between the sand volume nourished and deposited in greater detail, the ratio of these values is plotted annually in Figure 8. A ratio of less than 1.0 means that the sand volume deposited is less than that directly nourished, whereas for a ratio of more than 1.0 it is greater. In both cases, with some variation, since 1986 the ratios have been almost constant. The uppermost headland group, Nos.4 and 5 (represented by the star), corresponds to the former case in which almost all the sand nourished is transported as longshore downdrift. That is, under the stationary condition, beaches already have sufficient sand volume, what is called "a feeling of fullness". If an excess volume of sand is supplied to such a beach, the

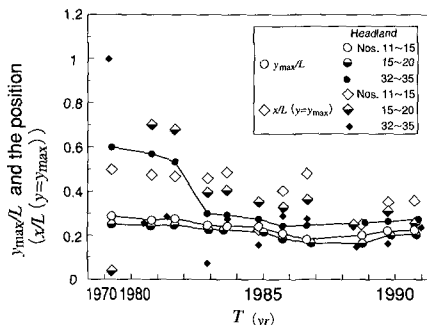


Figure 6. Annual change in the maximum indentation rate and the position.

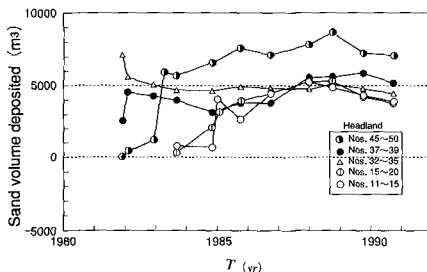


Figure 7. Annual change in the sand volume deposited at groins.

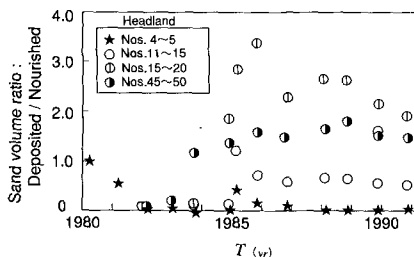


Figure 8. Annual change in the ratio of the sand volume deposited to that nourished.

longshore sand transport rate on the downdrift side of the beach may increase. In the latter case of a ratio of more than 1.0, sand transport coming from the updrift side is trapped between the groins, and the beach is nourished naturally under the function of the headland and the action of natural forces even when a lesser volume of sand is nourished directly. This is distinctly seen on headlands Nos.15 and 20.

Figure 9 shows the relation between  $y_{max}/L$  and the sand volume deposited to that nourished for the sandy beaches between the headlands. Changes in all three elements are shown for the headlands selected (only the sand volumes nourished are shown for the other headlands), the numbers indicating the years when the beach sand was nourished. This figure shows changes in  $y_{max}/L$  and the sand volume deposited on the downdrift side of the beach, due to sand fill on the updrift beach: a) the sand volume nourished on the updrift side intricately related to the increase in the sand volume deposited on the downdrift side, and b) the larger the sand volume deposited on a beach, the lower the indentation rate; i.e., the shoreline position advances.

Changes in indentation,  $b/L$ , averaged spatially are shown in Figure 10. The ratio of  $b/L$  decreases as the sand volume deposited increases and generally the shoreline position advances, whereas the ratio tends to be constant once the volume of sediment exceeds a certain limit. Figure 11 shows the annual changes in the shoreline angle,  $\beta$ , on

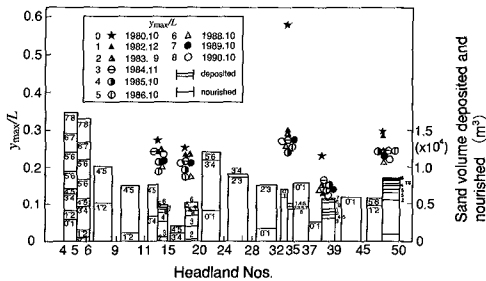


Figure 9. Annual change in the maximum indentation rate and sand volume deposited.

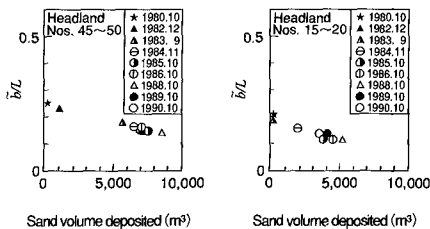


Figure 10. Relation between the mean indentation rate and the sand volume deposited.

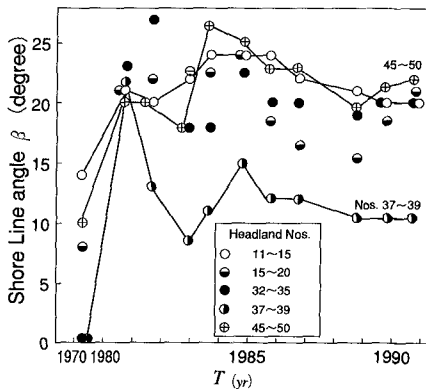


Figure 11. Annual change in the shoreline angle ( $\beta$ ) of the sandy beaches.

the beach immediately on the updrift side of the headland, which depend on the shoreline position and sand volume deposited. Because angle  $\beta$  has remained almost constant since 1986, the beaches have tended to approach the steady state condition with only slight fluctuations.

The most interesting finding here is that there has been no orderly formation of stable sandy beaches from the updrift side. The position of the beaches on the sand spit and the function of the sedimentation between groins, as well as the effects of artificial sand nourishment, may produce a time lag spatially in the formation of stable sandy beaches.

Finally, the maximum indentations  $y_{max}/L$  are compared to the results for morphological characteristics of dynamically stable beaches given in Figure 12. The data representing the relation between  $y_{max}/L$  and shoreline angle  $\beta$  are in good agreement with the lines found by Tsuchiya (1987), further evidence that the sandy beaches between the groins on the Amanohashidate Coast have, to a high degree, already are in dynamically stable conditions.

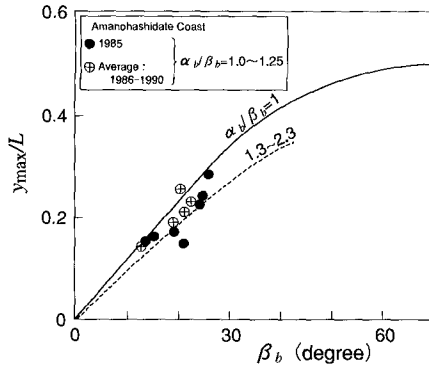


Figure 12. Relation between the maximum indentation rate on and shoreline angle ( $\beta$ ) of sandy beaches.

**SHORELINE CONFIGURATION AND THE FORMATION OF DYNAMICALLY STABLE SANDY BEACHES**

On the basis of the results found for annual changes in the plane form of the actual shoreline, the beach process of approaching the dynamically stable condition was considered in terms of the theoretical background of stable sandy beaches (Tsuchiya, Chin and Wada,1992; and Tsuchiya,1994). Figure 13 gives a comparison of the actual and theoretical shoreline configurations (theoretical ones, dotted curve) to show whether the sandy beaches have achieved or are approaching stability. The parameters used for the theoretical calculations were estimated from the representative wave breaker characteristics obtained by calculating the wave transformation and from the actual nearshore configuration characteristics obtained in survey of October 1991. These are shown in Table 1. As

Table 1. Values of incident waves and beach forms.

Symbols headland Nos.	$\alpha_b$ (deg)	$\beta_b$ (deg)	$\alpha_b/\beta_b$	$L$ (m)	$h_b$ (m)	$L/h_b$	$y_{max}/L$	$x/L$	$m$
50	26.4	22.0	1.20	218	1.55	141	0.22	0.30	1/21
39	13.7	13.0	1.05	176	1.44	122	0.14	0.31	1/24
35	25.0	24.0	1.04	84	1.10	76	0.27	0.14	1/20
20	20.8	20.0	1.04	174	1.14	153	0.21	0.26	1/20
15	20.8	20.0	1.04	178	1.07	166	0.21	0.30	1/19

$\alpha_b$  : Incidence angle,  $\beta_b$  : Shoreline angle,  $L$  : Groin space  
 $h_b$  : Breaking water depth,  $y_{max}$  : Maximum indentation distance  
 $x$  : Position where  $y_{max}$  observed,  $m$  : Mean sea bottom slope

indicated by the actual shorelines in Figure 13, the annual sand nourishment and sand bypassing done since 1980, sedimentation between the groins has increased annually, resulting in shoreline advance. In December 1984, the shorelines adjacent to the just updrift sides of the groins reached the tips of the groins. Since then, the shorelines generally have shown an annual advance and have tended to be in the steady state, even though locally there has been some fluctuation.

As to the process of approaching and forming nearly stable beaches, a) the observed shoreline forms are asymptotically approaching the theoretical forms and b) on the whole the two are equivalent, although some differences in local configurations exist because the diffraction effect of the waves due to the presence of the groins was not introduced to the theory. On the basis of all these findings, we conclude that the sandy beaches that presently exist on the Amanohashidate Coast have been steadily approaching the dynamically stable condition.

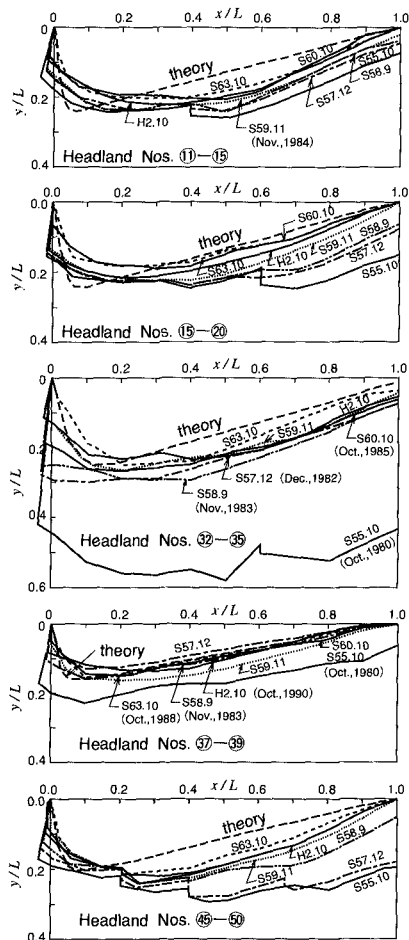


Figure 13. Comparisons between observed shoreline forms of sandy beaches between groins and theoretical ones.

## ESTIMATION OF LONGSHORE SEDIMENT TRANSPORT RATE

The longshore sediment transport rate,  $Q_x$ , is calculated using the continuity equation for beach change, on the basis of the detailed survey results for beach deformation. Up to 1986 the effect of sand nourishment on the time and spatial fluctuations of  $Q_x$  is large. Results after 1986, which show less fluctuation, were adopted.

Figure 14 shows the alongshore changes in the longshore sediment transport rate under the beach process of approaching a stable sandy beach. The annual sand volume bypassed averages about 5,700m<sup>3</sup>, with little annual fluctuation. There are three types of the alongshore change of  $Q_x$ :  $\partial Q_x/\partial x > 0$ ,  $\partial Q_x/\partial x < 0$ , and a combination of both. The following correspondence exists for these changes, where  $x$  is the coordinate taken to be positive on the downdrift side: first, for periods ② and ③ shown in the figure, there is alongshore change from  $\partial Q_x/\partial x < 0$  to  $\partial Q_x/\partial x > 0$ . In period ② the rate  $Q_x$  decreases toward the downdrift side on the sandy beaches, indicative that on the whole drift sand is deposited on the beaches. On the downdrift groin of No.50, the rate is only 1,000m<sup>3</sup>/yr. In period ③, the rate  $Q_x$  increases on all the beaches, and is 12,000m<sup>3</sup>/yr on No.50. This is because the sand volume deposited during period ② and that bypassed at the beginning of period ③ are both transported as longshore drift sand. In period ④, the regions  $\partial Q_x/\partial x < 0$ ,  $\partial Q_x/\partial x > 0$ , and  $\partial Q_x/\partial x = 0$  appear on the beaches. Note that the fluctuations of  $Q_x$  in alongshore change are greatly reduced as compared to those in periods ② and ③ and, on the average, the rate  $Q_x$  being equilibrated with the sand volume bypassed at any point on the beaches. This indicates that for almost stable beaches even if an unequilibrium occurs in the longshore sediment transport rate, the beaches probably function by themselves, thereby reducing the differences in the rate. That is, a series of groins are considered to serve as headlands that directly control drift sand accretion and erosion in turn and that function organically in the general stabilization of the sandy beaches.

As the alongshore gradient of the longshore sediment transport rate should be related to the magnitude of the topographical beach changes, the alongshore changes in beach sand volume are shown in Figure 15. Although the magnitude of fluctuation differs according to the groin, in general a longshore sediment transport rate with a range of approximately 10<sup>3</sup>-10<sup>4</sup>m<sup>3</sup>/yr responds to fluctuation in the sand volume between groins with an annual

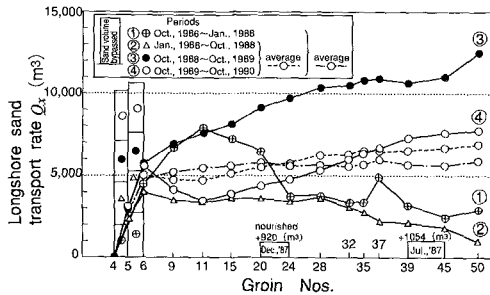


Figure 14. Alongshore change in the longshore sand transport rate.

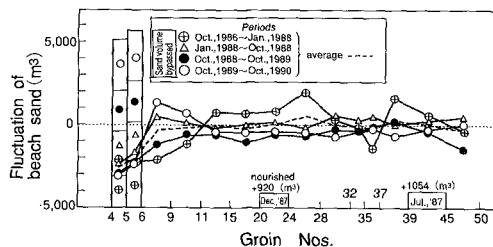


Figure 15. Alongshore change in the beach sand fluctuation rate.

maximum of  $\pm 1,000\text{m}^3$ . Even though such fluctuations are observed, the annual averaged longshore sediment transport rate (indicated by the broken line in Figure 13) is about  $5,300\text{m}^3/\text{yr}$ , and as uniformly plotted alongshore agrees very well with the sand volume bypassed. From this, we assume that at present the sediment transport system in the Daitenkyo area functions very satisfactorily for the formation of dynamically stable beaches.

To establish both only beach stabilization and the applicability of the sand bypass method using groins, it is necessary to determine the longshore sediment transport rate and to recognize the alongshore change in the course of beach erosion under the continuity of sediment transport. The beach process before 1976 should provide useful information. Figure 16 shows the alongshore change of the annually averaged longshore sediment transport rate, as derived by the procedure described previously that is based on change in the beach sand volume surveyed. The drift sand treated here could not, however, necessarily be specified longshore sediment transport because the entire sand volume carried away from the eroding beaches is taken into account; therefore, offshore sediment transport may be included to some extent in the data given in the figure. We estimate that the sediment transport rate has been as much as  $20,000\text{m}^3/\text{yr}$  on the average, even after small groins were constructed; but, once small and large groins were placed in combination, the rate was reduced to approximately  $10,000\text{m}^3/\text{yr}$ . The value of the spatial gradient of the longshore sediment transport rate is positive everywhere, and it is almost constant, whereas its magnitude tends to be reduced, which corresponds to the progress made in the countermeasures taken against beach erosion. This means that in general sandy beaches in the area of concern, continued to erode and be weakened. These facts led to the very important finding that generally sand bypassing decreases the longshore sediment transport rate to about  $5,000\text{m}^3/\text{yr}$  (as stated above) and that sandy beaches become well stabilized through the alongshore balance of the sediment transport rate.

Taking into account that longshore sediment transport depends substantially on the breaker angle  $\alpha_b$ , the facts discussed above suggest the following: the breaker angle formed before the use of sand bypassing was comparatively large because the beaches had been severely eroded and had a poor-looking, saw-tooth like profile; whereas, after sand bypassing the shorelines have advanced, drift sand has accumulated, and the beaches have become dissipative so that sandy beaches have formed well, decreasing the angle  $\alpha_b$ ; i.e., sandy beaches between groins have

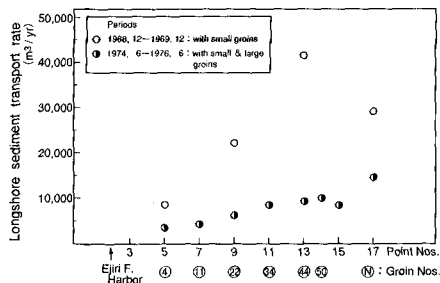


Figure 16. Alongshore change in the longshore sediment transport rate before sand nourishment and bypassing.

oriented their shorelines as parallel to the breaking wave crest as possible, reducing sediment transport. Therefore, in regard to future beach maintenance by means of sand bypassing the following must be considered: Approximately  $5,000\text{m}^3/\text{yr}$  of bypassed sand is considered sufficient to maintain the dynamically stable sandy beaches that presently exist. With regard to appropriate sand volume control, increases and fluctuations in sand drift and beach sand caused by an excess volume of bypassed sand should be avoided. Minimization of the sand volume to be bypassed and fluctuations in the sediment transport rate must also be further considered. To what extent these amounts can be minimized remains to be determined.

## CONCLUSIONS

The main conclusions of our study are

- (1) Sandy beaches that have formed between groins on the Amanohashidate Coast because of the use of sand bypassing have already come very close to being dynamically stable beaches.
- (2) This has been confirmed because in terms of the theoretical background of the formation of stable sandy beaches, the actual shoreline forms surveyed have converged into a steady state with decreasing fluctuations, and the shoreline formation process in general has been asymptotically approaching the theoretical results.
- (3) These phenomena and the relation between the longshore sediment transport rate during the formation of stable sandy beaches and the corresponding magnitude of the sand volume fluctuation, provided appropriate maintenance is not neglected, show that the necessary sand volume to be bypassed is only  $5,000\text{m}^3/\text{yr}$ .
- (4) One criterion of the sand bypassing method therefore, the sand volume bypassed, can be precisely controlled through the formation of dynamically stable sandy beaches.

## ACKNOWLEDGMENTS

We are grateful to Professor Yuichi Iwagaki, Meijyo University, for his valuable suggestions about this research. We also are grateful to the Ministry of Transport for its cooperation in the implementation of this research and for permission to using part of the findings from its surveys of erosion control and shore protection on the Amanohashidate Coast.

## REFERENCES

Kyoto Prefecture, Port and Harbor Bureau (1987). "Survey report for erosion control



on the Amanohashidate Coast in Miyazu Bay." ,1-70 (in Japanese).

Kuroda, H. (1985). "Regenerating Amanohashidate, survey report on the sand bypassing method." Disaster Prevention in Ports and Harbors, No.78, 17-26 (in Japanese).

Silvester, R. and J.R.C.Hsu (1993). *Coastal Stabilization*, PTR Prentice-Hall, New Jersey.

Tsuchiya, Y. (1982). "The rate of longshore sediment transport and beach erosion control." Proc. 18th ICCE, ASCE, Vol.2, 1326-1334.

Tsuchiya, Y. (1987). "Beach erosion control." Proc. JSCE, No.387, II-8, 11-23 (in Japanese).

Tsuchiya, Y. (1991). "Beach stabilizing methods; theory and practices." Jour. JSCE, March, 15-17 (in Japanese).

Tsuchiya, Y., I. Chin and C. Wada (1993). "Formation of stable sandy beaches; theoretical configuration and applicability." Proc. Coast. Eng., JSCE, Vol.40, 371-375 (in Japanese).

Tsuchiya, Y. (1994). "Formation of stable sandy beaches and beach erosion control; a methodology for beach erosion control using headlands." Bulletin, Disas. Prev. Res. Inst., Kyoto Univ., Vol., Part2 (in press).

Uda, T. (1992). "Beach erosion caused by a breakdown in the continuity of longshore sediment transport." Jour. JSCE, Vol.77-9, 84-86 (in Japanese).

Yajima, M., A. Uezono, T. Yanai and F. Yamada (1982). "Application of the sand bypassing method on the Amanohashidate Coast." Proc. 29th Conf. Coast. Eng., JSCE, 304-308 (in Japanese).

Bascom, W. (1970). *Waves and Beaches*, (Science Study Series 32, Doubleday, Garden City, New York.), Translated by K.Yoshida and T.Uchio (Japanese Title: *Kaiyo no Kagaku*), Kawade-Shobo, Tokyo, (in Japanese).

## CHAPTER 252

# **The Reconstruction of Folly Beach**

by

Billy L. Edge<sup>1</sup>, Millard Dowd<sup>2</sup>, Robert G. Dean<sup>3</sup> and Patrick Johnson<sup>4</sup>

### **ABSTRACT**

*Folly Beach is an island, nearly 10 km long, south of the entrance to Charleston Harbor. A large beach nourishment plan was planned and conducted to counter the large erosion rates the Island has suffered for several decades. Because of the limitation on operations dictated by the turtle nesting season in the local area, it was required that all construction be completed in one season and extending from November 1 until May 15, 1993. During the construction of the Project, which included 1,908,000 m<sup>3</sup> of material, two very significant winter storms caused some loss of material to the offshore and some damage to the pipeline system. The majority of the material moved by the storm has either migrated back onto the beach or stabilized in a lower part of the subaqueous profile. The success of the first phase of construction of this 50 year project is in many ways attributed to the excellent working relationship between the City of Folly Beach, the Charleston District of the Corps of Engineers and the contractor. The long term success of the project will depend upon the frequency and severity of the storms which attack the project.*

### **BEACH NOURISHMENT AS AN EROSION CONTROL MEASURE**

There have been many designs and attempts to halt erosion along the coast of the United States as well as other nations. In many instances the attempts have been ill conceived and did not perform as expected. One of the most successful approaches to dealing with eroding areas is to provide solutions which are in harmony with nature. The

<sup>1</sup> W.H. Bauer Professor of Dredging Engineering, Civil Engineering Department, Texas A&M University, College Station, TX 77843-3136. (Formerly, President of Edge & Associates, Inc., Charleston, SC).

<sup>2</sup> Coastal Engineer, U.S. Army Engineer District, Charleston, P.O. Box 919, Charleston, SC 29402-0919.

<sup>3</sup> Professor and Head, Department of Coastal and Oceanographic Engineering, University of Florida, Gainesville, FL 32611.

<sup>4</sup> Project Manager, T.L. James & Company, Inc., Kenner, LA.

best solution known today for many of the severely eroding beaches is the addition of sand into the natural littoral system. Although this has been accomplished in rare circumstances by hauling sand from inland borrow pits, the most common methods employ dredging from riverine sources, inlets or from offshore sources. Normally these projects require not only initial reconstruction but periodic renourishment at five to eight year intervals.

According to the Corps of Engineers (1994), the total cost for beach nourishment over the 44 year period of record in 1993 dollars has been \$1,150,000,000 or \$26,100,000 per year. The federal share of beach nourishment costs has been approximately 60 per cent. This report estimates that over the next 54 years, another \$505,000,000, in 1993 dollars, will be spent on future renourishment of these projects. Moreover if all of the other 26 shore protection and beach restoration projects which are awaiting authorization, construction or funding are approved then the total annual construction costs in 1993 dollars would be approximately \$34,000,000. Currently, the United States spends considerably less on beach protection and nourishment than does Germany, Japan, The Netherlands or Spain. The amount invested by the United States in relation to the economic value of the beaches, rated in terms of the income from travel and tourism, is significantly less than that of the countries listed above.

The most well known and successful beach nourishment project in the United States is the Dade County Beach Project near Miami, Florida, where seven million cubic meters of sand were placed. There have been many other projects with nearly equal success save for the stability offered by the magnitude of the nourishment project. A recently completed project at Folly Beach, South Carolina is a good example of a long term erosional beach where the reconstruction of the beach by dredging in the back river has helped stabilize the beach, bolstered the local economy and helped the local environment.

### ***FOLLY BEACH***

Folly Beach is a barrier island near Charleston, South Carolina. The nearly 10 km long island has experienced large rates of erosion of approximately 1.4 m per year for over 100 years. The Island, as shown in Figure 1, is south of the entrance to Charleston Harbor with its deepened channel and jetties extending nearly 6 km seaward.

The Corps of Engineers (1987) estimated that as a result of the completion of the jetties a net southerly alongshore drift of approximately 122,00 to 152,000 m<sup>3</sup>/year has been permanently blocked. They showed that in response to the channel stabilization begun in 1878, the offshore shoals have lost 199,000,000 m<sup>3</sup> of sand resulting in an increase of the wave energy of 100%. A further evaluation of the relationship of the erosion on Folly Island to the navigation project is given in Edge and Dean (1991). The barrier island provides significant public access with two county parks, 50 public accesses with dune walk overs, a fishing pier and both onstreet and public parking lots. The construction of the beach nourishment project was based on cost sharing of 85% Federal and 15% local participation. The local sponsor is the City of Folly Beach. As local sponsor, the City of Folly Beach was involved in the plan formulation, project

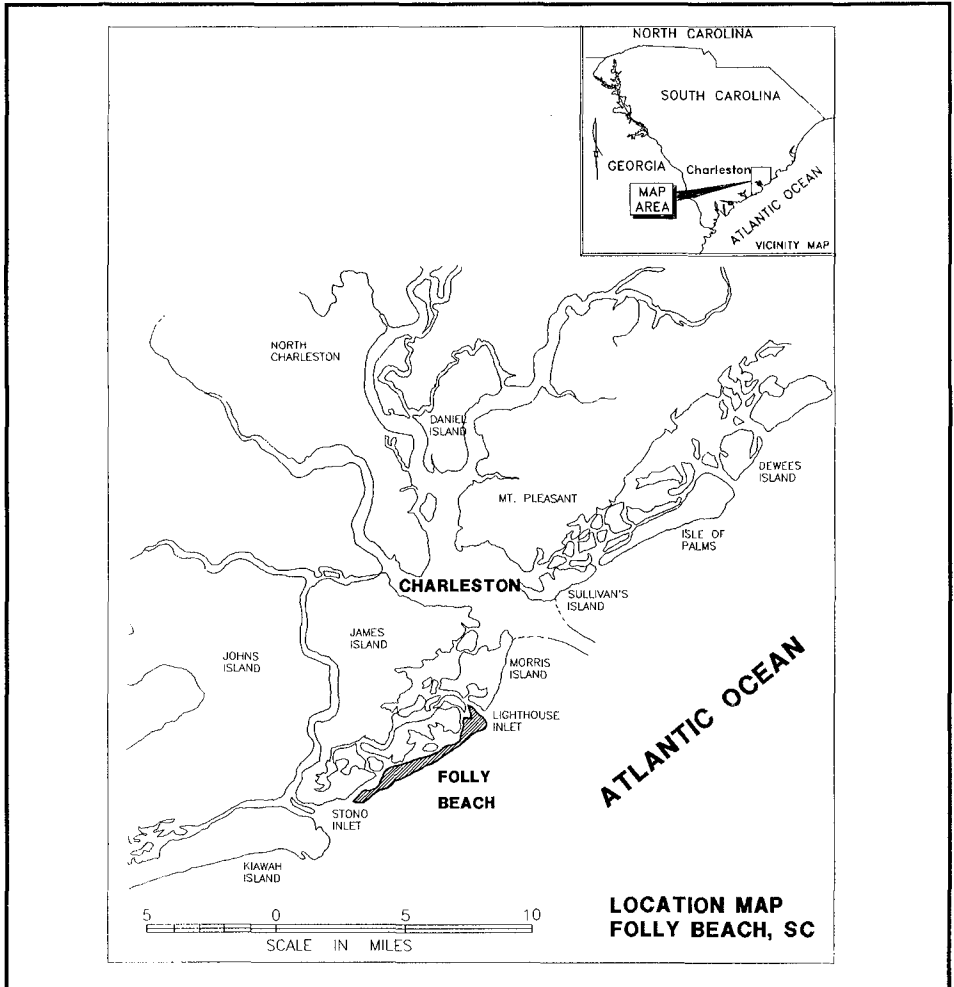


Figure 1. Location map of Folly Beach, South Carolina and the nearby jetties for Charleston Harbor

review and approvals and the City provided all lands, easements and rights of ways for the project. The City is responsible for maintenance of the project and providing the local share for all future renourishment requirements.

### *THE NOURISHMENT PLAN*

The United States Congress authorized a beach erosion project at Folly Beach in 1979. The project was restudied pursuant to Section 501 of the 1986 Water Resources Development Act. In 1988 a Section 111 report was completed which found that 57

percent of the erosion was directly attributable to the Federal navigation project at Charleston harbor. An economic re-evaluation was completed in 1988 and again in 1989 after Hurricane Hugo; the final project was then developed.

The final project design provided for the initial reconstruction of approximately 8.6 km of shoreline and periodic renourishment for a period of 50 years. The plan called for the initial placement of 1,908,000 m<sup>3</sup> of material which would be obtained from the Folly River landward of the Island at the southern end. The design placement quantities ranged from 175 m<sup>3</sup>/m to 250 m<sup>3</sup>/m (70 yd<sup>3</sup>/ft to 100 yd<sup>3</sup>/ft .) The construction section included a storm berm at 2.7 m above MSL with a width of 4.6 m sloping down on a 1:10 grade to a berm at elevation 2.1 m which extended seaward from 18 to 40 m. The native beach sand had a mean grain size from 0.12 to 0.21 mm with a composite of 0.17 mm. Early measurements of the borrow site showed a composite mean grain size, of 0.15 mm.

Final engineering plans were based upon the results of SBEACH and GENESIS simulations performed by the Coastal Engineering Research Center (U.S. Army Corps of Engineers, 1991). Two important results of the model studies indicated that (a) in the area of most severe erosion nine existing groins should be rebuilt to slow the unusually high erosion rate and (b) the project would require renourishment approximately every 5 to 8 years.

### ***CONSTRUCTION***

Because of the requirements that all construction be completed in one season between November 1 and May 15, the number of potential contractors who could meet these special requirements was limited. The limitation on operations was dictated by the turtle nesting season in the local area. Moreover, because of environmental concerns and the location of the borrow area, the contractor would have to pump up to a distance of approximately 12.5 km. There were only three contractors which bid on the project. In the Fall of 1993, a separate contract was let for grassing the dune at a cost of approximately \$260,000. Engineering, land acquisition, environmental studies and other miscellaneous costs were estimated at \$3,227,650. The 50-year cost of the project is estimated to be \$115,000,000. During the initial construction, several winter storms occurred but two were significant and caused production to cease. Both storms caused major relocation of up to 6 km of pipeline and claims for loss of material and time. The second storm on March 12 - 14, 1993, was called the "Storm of the Century." That storm created hurricane force winds along much of the Atlantic seaboard.

### **THE SOLICITATION**

As previously noted, the most limiting factor facing the potential contractor was the requirement that the total beach fill placement and groin construction be completed by May 15, 1993. This date represented the beginning of the nesting and hatching season of the Loggerhead Turtle. This requirement forced construction to be performed in the winter months thereby ensuring the most extreme weather conditions under which to

do the dredging and other construction. The third factor was the entire issue of dredge pipeline; the length of line required to effect placement of the fill; the limited space available for maneuvering with and storage of more than 9.1 km of shorepipe; and requirements for transporting the shorepipe to the site by truck due to bathymetric conditions surrounding the shoreline of the island and the lack of commercial dockage available.

The bid opening was held on November 9, 1992, one month after the solicitation. A comparison of the bid amounts submitted by each contractor for the major features of the contract is shown in Table 1.

**Table 1. Folly Beach Contract Bids**

Item	Bidder 1		T. L. James & Co.		Bidder 3	
	Unit price	Total \$US	Unit price	Total \$US	Unit Price	Total \$US
Mob & demob for dredging		1,038,500		1,500,000		800,000
Mob & demob for beach fill placement, groin demolition & new groin construction		100,000		13,050		16,000
Beach fill (m <sup>3</sup> )	4.47	8,550,000	2.52	4,825,000	3.33	6,375,000
Groin demolition		15,000		18,000		21,000
Foundation blanket stone (ton)	35	164,500	56	263,200	45.35	213,145
Placement of existing armor stone		100,000		177,500		128,000
Steel sheet piling						
install sheet piling (m)	164	1,145,000	161	1,122,100	192	1,339,650
splicing	400	2,000	500	2,500	600	3,000
cutting	125	625	150	750	175	875
Geotextile installation (m <sup>2</sup> )	1.5	10,500	1.75	12,250	2	14,000
Tilling (acre)	500	66,500	850	113,050	650	86,450
Mob & demob for drill rig for borings		2,500		3,000		3,500
Borings - drilling, sampling & testing	2,000	50,000	2,450	61,250	3,300	82,500
<b>TOTAL</b>		<b>\$11,245,125</b>		<b>\$8,111,650</b>		<b>\$9,083,120</b>

### THE CONSTRUCTION PLAN

Concerns were expressed relating to the issue of quantity, delivery, storage, and placement of the various types of pipeline necessary to transport the material from the borrow area to the beach. The lack of any moorage deep enough to serve a fully loaded pipe barge and the spatial constraints that existed on the island adjacent to the beach

would force the Contractor to haul the 650 pieces of 15 m shorepipe to several small pipe laydown areas strategically placed along the beach. Unloading equipment capable of handling these pipes in such constrained conditions had not been included in the estimate, creating an unforeseen cost. Also the designated pipeline route from the borrow site to the beach required that over 600 m of shore pipeline be located in extremely shallow water through an existing marsh to a shore connection.

The hydraulic cutterhead dredge, *Tom James*, was used for the project. At the center of the pumping system of the *Tom James* is a 16 cylinder Enterprise diesel delivering up to 6000 shaft hp to a centrifugal pump. The pump has a 91 cm suction and a 76 cm discharge and could house impellers ranging from 210 to 240 cm. Based on hydraulic models of the dredge and booster system it was empirically determined and endorsed by historical performance that a 213 cm impeller could be used. The dredge had been dredging at depths of up to 15 m on the Mobile River and was equipped with a 30 m ladder. Based on the vertical limit of dredging allowed within the borrow area at Folly Beach, the decision was made to replace this ladder with the 20m ladder available in Houma, LA. Both ladders supported the 1800 hp ladder pump used to improve the pumping capacity of the main pump. The dredge was returned to the Houma Yard and the short ladder was installed in Mobile. On Dec. 18, 1992, refitted for the Folly Beach, the dredge and attendant plant, along with 700 m of floating pipeline began towing, via the Gulf Intracoastal Waterway, to Folly Beach.

The dredge arrived on site on December 30, 1992, and began preparations to begin dredging. The Plan of Operation submitted to the Corps indicated that dredging would begin at Station 0+00 proceeding in a northerly direction. The dredge was to make two 60 m cuts from Station 0+00 to Station 52+00, three 60 m cuts from Station 52+00 to Station 78+00, and four 60 m cuts from Station 78+00 to the limit of borrow at Station 115+00. (Note that stationing is in the original units of feet as specified in the contract plans.) As also dictated by the contract, the borrow site was to be excavated to a maximum depth of 5.5 m MLW in the first two designated reaches and 6.1 m MLW in the last reach.

A 3050 m submerged line was installed from the borrow area to the south end of the island where it connected with 9750 m of shorepipe. A shore connection was made at Station 91+00S. Starting at this location and pumping northerly conserved 500 m between Station 91+00S and the south limit of work at 107+00S to be used to prevent a shutdown in the event of damage to the pipeline on the beach or the installation of the booster. The flow from the 76 cm ID discharge pipes was trained by a 330 m levee located along the approximate break point of the berm. The trained flow of the effluent slurry served to maximize the retention of material, thereby increasing the efficiency of the dredging process while simultaneously minimizing the loss of the material placed in the surf zone. Stationing of the project and the location of the borrow area are shown in Figure 2.

Equipment for the beach fill operations was hauled by truck to the project. In accordance with the proposed plan of operations three bulldozers, two Caterpillar D6H LGP and a Cat D6D LGP were used to manage and dress the fill. Two Caterpillar 518S





Corps chose to control the quantity of required fill at any given point along the beach. Although design templates for various portions of the project were included in the project plans, these templates were not the conventional static geometry. The templates were instead, dynamic, holding constant the total number of cubic meters of fill for each linear meter of advance; adjustments in the width of the berm were made to compensate for changes in the required quantity. This approach, while rendering a more finite and predictable final fill quantity, substantially complicated both the placement of the fill and the computation of the pre- and post dredging volumes.

Specifications required that both pre and post dredging surveys be taken in the form of cross sections at a frequency of 30 m intervals, normal to the project baseline, with no more than 7.5 m between individual measurements. These cross sections were taken within five days prior to the time of placement of the fill and as soon as practical after the placement of the fill. The cross sections were taken by conventional leveling techniques beginning 15m landward of the project baseline and extending seaward until the -1.0 m NGVD<sup>5</sup> contour was reached.

Seaward from the -1.0 m contour to a point 460 m distant from the project baseline, cross sections were taken with echo sounding instrument. This task was complicated substantially as a result of the vertical oscillations of the survey vessel between the crests and troughs of the waves. Under these conditions conventional hydrographic survey procedures for correcting data for the effects of tide and draft would yield grossly unreliable and nonrepeatable measurements. The Contractor used a "surf boat" for data collection. The surf boat system consisted of a 6m, broad beam skiff equipped with a Del Norte DMU 547 Microwave Positioning System for horizontal positioning, an Odum Echotrac 3100 semi-portable fathometer using a dual frequency 24/208 Khz transducer for vertical measurement, and a 486DX laptop computer installed with data collection software developed by the Contractor.

The unique feature in the surf boat system was the method by which compensation for heave was made. A Spectra-physics Laserplane<sup>TM</sup> plane laser was placed above a point of known elevation, NGVD datum, and an height of instrument taken from the point to the infrared light beam. As a data collection event occurred, a differential measurement between the bottom of the receiver mast and the point at which the receiver mast was intersected by the beam was recorded. This differential measurement combined with the known distance from the bottom of the mast to the face of the transducer and the depth measurement, defined the vertical component of the measurement as an elevation relating to project datum.

### **DEMOLITION AND CONSTRUCTION OF GROINS**

Prior to construction, the remains of nine timber groins existed just north of the Holiday Inn site from project Station 1+50N to 49+60N. The nine groins were from 100-150 m in length with a total of 100 m required to be moved. The removal of these groins and any other remains of old structures immediately adjacent was necessary for

---

<sup>5</sup> NGVD represents approximately mean sea level.

driving new sheetpiles to replace the wooden groins. The removal of these structures required the handling of old creosote pilings.

The new groin design consisted of steel sheet pilings driven into the ground at  $\pm 0.3$  cm vertical tolerance. The soils adjacent to the sheet piling were to be stabilized using a layer of geotextile covered by a layer of blanket stone and subsequent layer of armor stone. Much of the existing armor stone surrounding the existing timber groins was recovered and reused. The stones were laid so that they would interlock creating a surface less susceptible to movement by wave action. Lastly, a steel reinforced concrete cap was installed on top of the steel sheet pilings.

A vibratory hammer was used to drive the sheet pilings. The pile driving was vertically controlled by the use of a teflon-coated dual template allowing 6 m sections of piling to be driven at one time. When pile driving on an individual groin structure was completed, forming and pouring of the concrete cap was done. Finally the placement of the geotextile and stone work was performed using a 690LDC and a 890JD John Deere trackhoe and two John Deere 544 front end loaders. In addition to the problem of limited workspace and times available for working, the tidal and wave action created erosion problems adjacent to the groins far in excess of what the contractor expected for this type of construction.

#### **DREDGING AND PLACEMENT OF BEACH FILL**

In addition to the hydraulic dredge, *Tom James*, provision was made in the estimate to allow for the use of the *Atlas Booster* should the required line lengths on the north end of the project hinder production to such a level so as to jeopardize completion before the May 15 deadline. A comprehensive selection of peripheral equipment comprising the attendant plant was also delivered. Two 900 hp tenders and a smaller 600 hp tug were used to move and position the dredge within the borrow area, handle pipelines, and shift swing anchors as advance in the cut dictated. Also accompanying the dredge were two "skadgit" stiff leg derricks, a 10,000 lb. crane, and numerous barges employed in fuel and water storage, raw materials supply, welding, and pipe barges.

The dredge was placed in the southwest portion of the borrow area and was hooked onto the shortest length of pipeline for the project. A wye valve was placed at the end of the shore connection. This wye valve allowed the fill to proceed either north or south as needed. On January 12, 1993, the dredge began pumping material from the borrow site and placing it on the beach at Station 91+15S and advancing in a northerly direction. The dredge was positioned at Station 57+00 in the borrow area and began pumping through 2865 m of pipeline with a velocity of 3.4 m/s. Dredge positioning was performed by the Del Norte DMU 547 Microwave positioning system.

The dredge was equipped with a six blade serrated cutter ideal for the sandy conditions encountered in the borrow area. Although borings taken prior to dredging indicated that sufficient material of acceptable quality was available within the borrow area, as the dredge moved north several areas yielded high shell content. These shell deposits had a negative effect on production. Adjustments were made in dredge position as these areas were encountered.

Near the end of February, the contractor realized that using the *Tom James* alone to complete the project would jeopardize the timely completion of the contract. The decision was made to use the 3600 hp *Atlas Booster*. Arrangements were made and the booster was towed to the site. As pipe line length approached 7600 m, production continued to drop off at a progressively greater rate. On April 19, 1992, the booster was installed at a point 1220 m down line of the dredge. Though not immediate, the result was impressive. The production rate is shown in Figure 3. The upper line represents gross output at the borrow site and the lower line represents the net output on the beach. The booster pump was placed on line when the line reached about 7,300 m (24,000 ft). Small mechanical repairs and adjustments to the new hydraulic system improved the production from 1140 m<sup>3</sup>/hr. to 2430 m<sup>3</sup>/hr. This system was maintained until the terminus of the project, Station 175+00N, was reached on April 17, 1992. Once pumping was completed to the northern limits of the project, the pipeline was pulled back to refill the area between the newly constructed groins. Also remaining to be pumped was the 500m south of the initial starting point at Station 91+00S. On April 29, 1993, the dredging was completed and demobilization from the site was begun.

Dredge production on the project was estimated at 1,300 m<sup>3</sup>/hr yielding 26,000 m<sup>3</sup> for each day of operation. The dredge operated a total of 72 days without a booster and twenty-nine days with the booster pump in operation. In the final analysis, the dredge pumped on the project 101 days for the original contract amount plus an additional 126,160 m<sup>3</sup>. This represents a daily production of 20,300 m<sup>3</sup>. Approximately 2.7M m<sup>3</sup> of borrow material was removed to place 2.0M m<sup>3</sup> of material on the beach. This represents an overfill ratio of 1.4.

The distribution of non effective time during production is given in Figure 4. It is obvious that a large amount of non-productive time was created by adding or moving beach pipelines and pipelines to the dredge. Weather was not a significant factor as was originally considered and did not cause appreciable down time.

As the end of the project approached preparations were made to commence tilling in areas where the fill had a compaction of greater than 500 psi. The compaction measurements were taken with a cone penetrometer between the seaward side of the storm berm at elevation 2.7 m NGVD and the high tide line. A total of five tests were taken at 61 m intervals for each 305m acceptance reach within five days of the placement of the fill. Areas not meeting the criteria defined above were required to be tilled to a depth of 0.9 m. On April 22, 1992, tilling of areas determined to be deficient commenced using a D8D equipped with a clearing rake. The tines on the rake were marked with paint at .9m to guide the operator. On May 8, 1993 tilling was completed.

### **STORMS DURING CONSTRUCTION**

After eighteen days of continuous production, a major winter storm occurred on 5-7 February 1993. The storm surge reached 1.5 m NGVD with waves of 1.5 to 2.4 m (Ebersole, Nielans and Dowd, 1995). The storm caused severe damage on property in the community and did considerable damage to the fill being placed on the beach. The fill operations were approaching the seawall fronting the Holiday Inn in the vicinity of

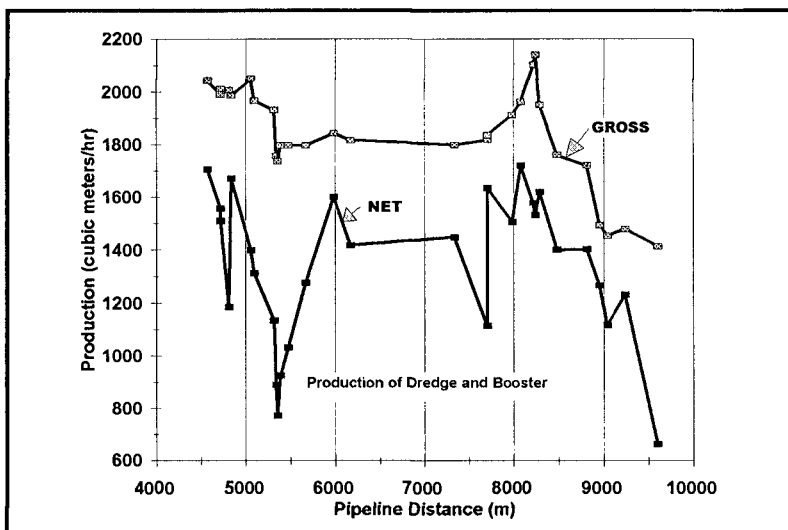


Figure 3. Production rate of *Tom James* versus length of pipeline.

Station 12+00S when the storm commenced. Contract specifications required that only 114 m<sup>3</sup>/m be placed against the concrete seawall in front of the Holiday Inn in an area of severe erosion. The resultant narrow berm width provided insufficient space to operate the equipment necessary to accomplish the fill operation. These contradicting requirements, one contractual and one practical, required that placement of a quantity of material far in excess of the design fill in order to create a berm with adequate width to facilitate the continued operation of the tractors.

As the storm built to full intensity, the waves began to severely erode the newly placed fill. By the next day conditions had worsened. The dredge continued to pump; however, the purpose was no longer to fill to required line and grade but to maintain the integrity of the pipeline. As the storm intensity increased these efforts were proven to be ineffective. In the afternoon of February 6 the shorepipe, now resting on bare rock, was broken apart by the pounding surf. Damage to the beach between Stations 11+50S and 6+50S was extensive. Pieces of 15 m shorepipe, dislocated and tossed in the surf, were strewn about on the beach. The portions of the pipeline not broken apart, once straight, now meandered up the beach. Shore crews recovered the loose pieces of pipeline and, at the direction of the Corps of Engineers removed the pipeline back to Station 11+50 and began refilling the area.

A second major storm occurred on March 3 and 4 with a maximum storm surge of 1.4 m NGVD and waves of 1.5 to 2.1 m. This storm created additional losses with most located at the seawall in front of the Holiday Inn. The third and strongest storm occurred on March 12-14 with wind gusts up to 35 m/s (Ebersole, Neilans and Dowd, 1995). This storm, called the "Storm of the Century," caused a storm surge of 1.4 m

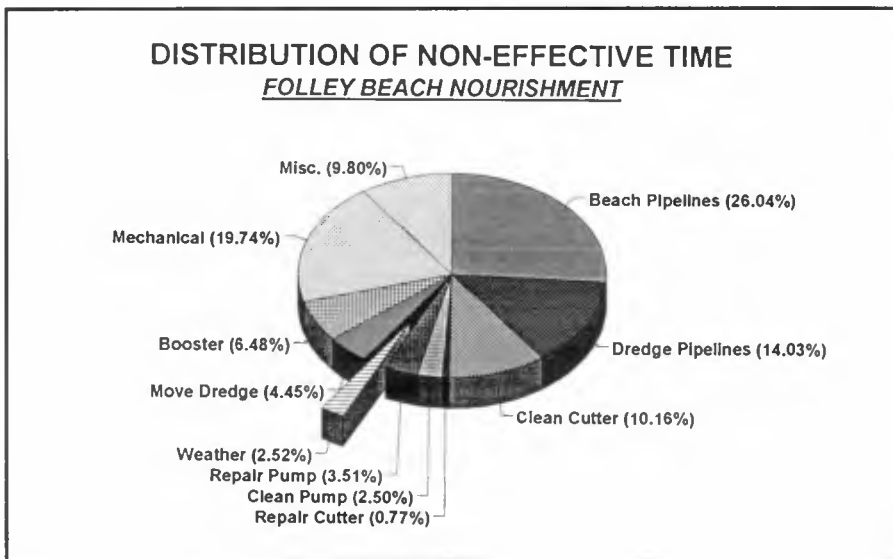


Figure 5. Distribution of non-effective time for *Tom James* during construction

above NGVD with large waves. The contractor continued pumping throughout the storm to keep the pipeline full of water. There was much erosion of the placed material because of this storm.

The last storm resulted in the loss of 25,000 m<sup>3</sup> of material as well as the destruction and/or replacement of 200 m of pipeline. In addition to these losses the contractor also requested fair compensation for the additional 156,000 m<sup>3</sup> of fill required to create an adequate berm for sustaining the fill process.

### ***MONITORING***

As noted previously, surveys were conducted within one week prior to placement and immediately after the profile was constructed. Thus the total sand placed and remaining in the section out to -9 m NGVD was captured. Following the first and third winter storms, surveys were completed which showed the loss of some material and the redistribution of other material. After project completion, semiannual surveys have been conducted across the profile at 31 stations to closure depth. These surveys are part of the statewide monitoring program.

Figure 5 shows a comparison of the volume of sand which was placed on the beach with the design quantities specified in the construction plans. Note that the plans only allowed 114 m<sup>3</sup>/m (45 yd<sup>3</sup>/ft) at the seawall fronting the Holiday Inn in the center of the City. The Holiday Inn property had an existing seawall jutting seaward of the adjacent properties and the design was selected to only provide as much sand as necessary to carry the dredge pipe on the ocean side of the wall. Moreover, the project design

considered that the primary objective was shoreline protection and the seawall at the Holiday Inn did not require any additional protection by the new beach. The Holiday Inn is located approximately between stations 15+00S and 5+00N. Center Street in the City of Folly Beach was used for the 0+00 in the construction stationing. The quality of the material obtained from the borrow area was compared with the native beach material and it was determined that the borrow material when placed on the beach had a  $d_{50}$  equal to or greater than the native beach material at the time it was sampled.

### BEACH RESPONSE

The most obvious change in the beach profile since construction has been by the waves in the two large winter storms between the end of construction and January 1994. These storms caused the movement of sand from the dry sand beach to the offshore area. Surveys show that the sand did not disappear; where the contractor placed 225 m<sup>3</sup>/m of sand initially, 225 m<sup>3</sup>/m of sand remained in the section although some of it did move to between 1 and 4 m below mean sea level. This adjustment of the beach fill generally occurs more slowly over a period of 12 to 18 months with the resulting dry sand beach being about 45% as wide as the newly placed sand after the adjustment period. It is expected however, and the early data indicated this to be true, that the profile will

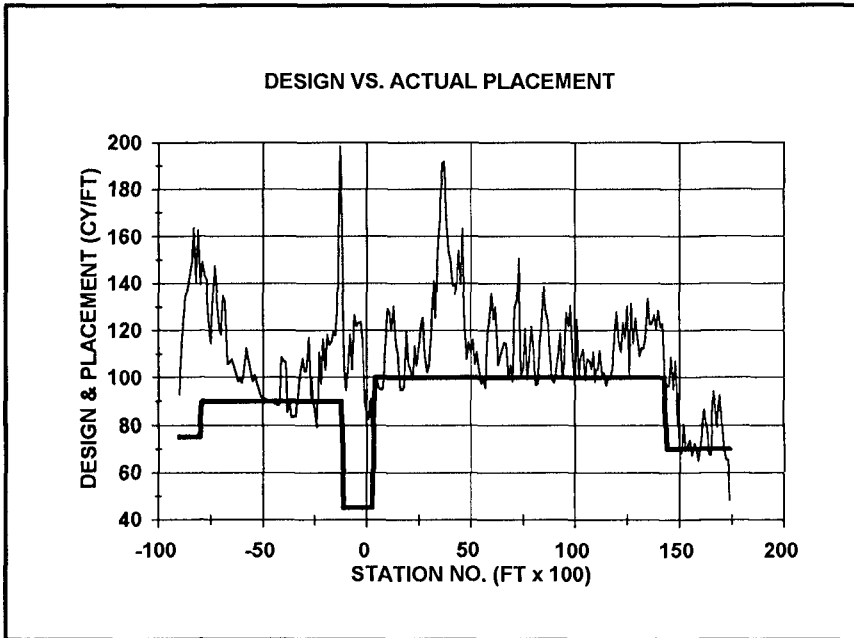


Figure 5. Comparison of the design (dark line) and the actual placement quantities.

continue to recover until by the end of the 1994 summer season it should have nearly 45% of the predicted initial equilibrium profile. As the beach fill ages there will be long-shore movement of the material as well. In fact the surveys and observations of 1994 indicate a movement of the material in the area of the "washout" to the northeast and somewhat to the southwest. As of July 1994, 95% of the placed material was accounted for within the limits of project construction according to Ebersole, Neilans and Dowd (1995).

Figure 7 is represents the movement of the mean high water line over the period of July 1993 until January 1994. Note that the stationing is taken from the most south-westerly end of the project. In the figure "HI" represents the location of the Holiday Inn. This figure shows the relationship of the shoreline position to the project baseline so the results of position are all relative to the baseline. It is interesting to note that there has been recession of the mean high-water line in general all along the beach and that two areas have particular features. The first area is the Holiday Inn area where after the first winter storm, the shoreline moved landward as far as the seawall where it cannot approach the baseline any closer. The second area of interest is at the "washout" where the sand moved both offshore and probably alongshore to the northeast between the first and second surveys.

Figure 8 shows the same information in the form of shoreline advance/erosion over the period of record. Although the general trend is toward erosion it must be remembered that these surveys only show the response of the summer post nourished beach to the winter storm season. As noted previously, the beach is adjusting and "hot spots" are appearing as the sediment moves alongshore and equilibrates by moving out into the equilibrium profile further from the baseline. Surveys are being taken quarterly to track the movement of the sediment. The quarterly surveys are being correlated with tide and wave records.

### ***PERFORMANCE PREDICTION***

The performance of a beach nourishment project is dependent upon the quality and quantity of sand placed, presence of stabilization structures, project length, the wave climate that tends to spread out the sand along the beach and the background erosion rate, which in this case, is primarily due to the interruption of the longshore sediment transport by the Charleston Entrance jetties and navigational channel. Project performance may be considered in terms of: (1) the equilibrium beach profile formed and the associated dry beach width, and (2) the spreading out of the sand in the longshore direction. Based on equilibrium beach profile concepts, the equilibrium additional dry beach width would be less than 10 m compared to 22 m if the native and borrow sand sizes had been equal. Considering a representative wave height of 0.9 m, based on the Wave Information Study (Hubertz, et al., 1993), the time required for the project to lose 50% of the material placed is approximately 4 years. Of course, the losses near the ends of the project at any one time will be much greater than the average. The monitoring results will be compared to the predicted profiles after the first annual surveys are completed.

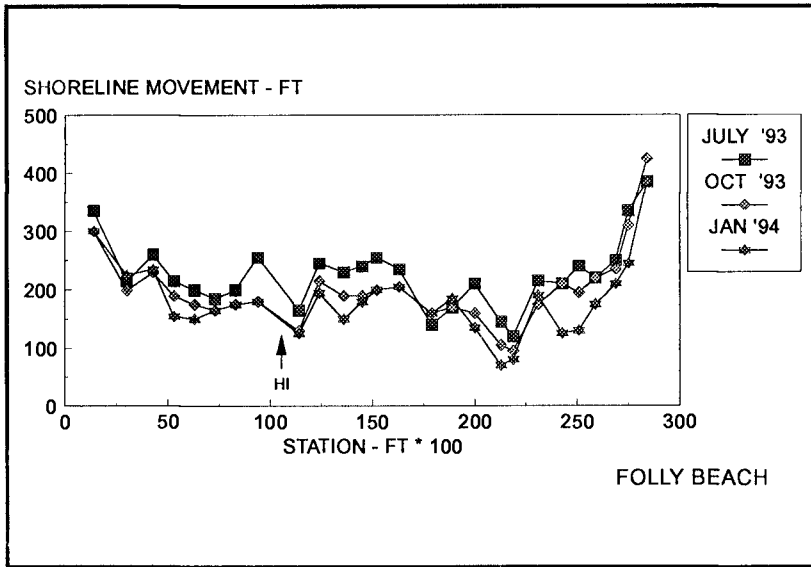


Figure 7. Shoreline position relative to the project baseline showing response to winter storms.

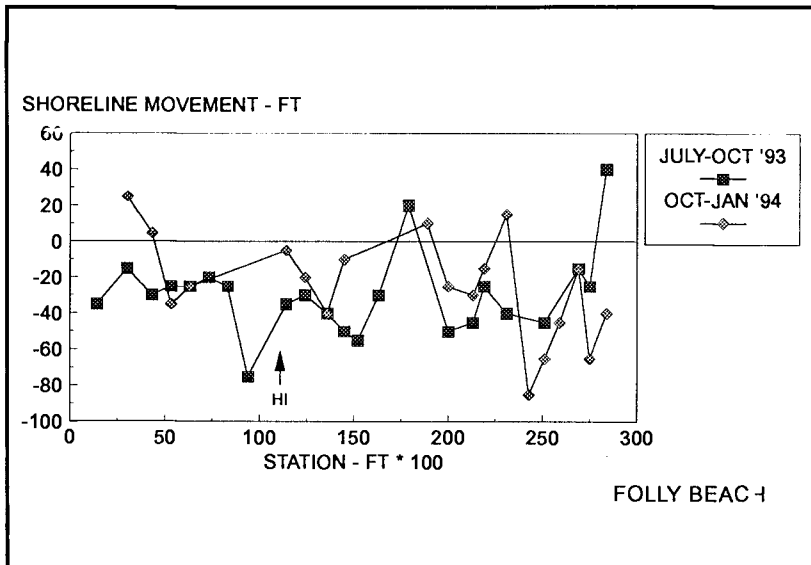


Figure 8. Change in shoreline position between the periods of July-Oct '93 and Oct-Jan '94.



### ***SUMMARY***

The reconstruction of Folly Beach is an example of the success of a dredging - beach nourishment - project which was successfully completed within the environmental constraints of winter conditions, very short time windows, and large pumping requirements. The success of the project is in many ways attributed to the excellent working relationship between the City of Folly Beach, the Charleston District of the Corps of Engineers and the personnel of T. L. James & Company. The long term success of the project will depend upon the frequency and severity of the storms which attack the project.

### ***REFERENCES***

Ebersole, B.A., P.J. Neilans and M. Dowd, 1995, "Beach Fill Performance at Folly Beach, South Carolina, and Evaluation of Design Methods," unpublished report furnished to the Charleston District for the Coastal Engineering Research Center, Vicksburg, MS.

Edge, B.L. and Robert G. Dean, 1991, "Folly Beach Erosion: Relationship to the Charleston Harbor Entrance," report prepared by Edge & Associates, Inc., for Charleston County.

Edge, B.L., P.M. Johnson and C.W. Grainger, 1994, "Renourishment at Folly Beach, SC," *Proceedings of 27th WEDA Conference*, Center for Dredging Studies, College Station, TX.

Hubertz, J. M., R. M. Brooks, W. A. Brandon, and B. A. Tracy, 1993, "Hind-cast Wave Information for the US Atlantic Coast," Coastal Engineering Research Center, WIS Report No. 30, Waterways Experiment Station, Vicksburg, MS.

U.S. Army Corps of Engineers, 1994, "Shoreline Protection and Beach Erosion Control Study, Phase I: Cost Comparison of Shoreline Protection Projects of the U.S. Army Corps of Engineers," U.S. Army Corps of Engineers, Washington, D.C.

U.S. Army Corps of Engineers, 1987, "Evaluation of the Impact of the Charleston Harbor Jetties on Folly Island, South Carolina," Coastal Engineering Research Center, Vicksburg, MS.

U.S. Army Corps of Engineers, 1991, "General Design Memorandum: Folly Beach, South Carolina, Shore Protection Project," Vol. I and II. U.S. Army Corps of Engineers, Charleston District, Charleston, SC.

## CHAPTER 253

### **The Complementary Interaction between Beach Nourishment and Harbour Management : Four Cases in Spain**

**Gregorio Gómez-Pina (\*) & Jose L.Ramírez(\*\*)**

#### **ABSTRACT**

This paper describes several results on beach nourishment and harbour management interaction, within the authors' area of responsibility. These positive results show the socio-economic benefits which can be achieved through effectively combining harbour and coastal requirements.

#### **1.- INTRODUCTION.**

Although harbour works have sometimes produced negative effects on the coast, there can be works which, by combining harbour and coastal requirements satisfactorily, could improve the scenario which exists in some coastal areas adjacent to the harbour. In particular, harbour dredged material, if adequate, should be used for beach nourishment and/or littoral drift restoration. Also, Coastal & Harbour Authorities should work in coordination from the initial stages of the projects where a combined design could satisfy the objectives of both parties.

#### **2.- OBJECTIVE.**

The main objective of this paper is to describe several positive results of beach nourishment and harbour management interaction, which have been achieved within the authors' technical area of responsibility, at the Spanish Coast Directorate (MOPTMA). These cases have been chosen to demonstrate the socio economic benefits which can be achieved through effectively combining harbour and coastal requirements.

---

(\*) Civil Engineer, MSc Ocean Engineering, Coastal Project Manager, Area I, General Directorate of Coasts; Address : Dirección General de Costas, Ministerio de Obras Públicas, Transportes y Medio Ambiente (MOPTMA), Paseo de la Castellana 67, 28071 Madrid, Spain.

(\*\*) Technical Civil Engineer, Projects & Works Division, Area I; Same Address.

Although at the time of writing the first abstract our intention was to describe four Spanish cases, we have added one more case which we found interesting within the scope of this paper. The main points of this paper are the following : I.- Effects of Harbour Works on the Coast. (Some examples of "uncoordinated works"). II.- Positive Results of Coordinated Works. III.-Conclusions and Recommendations.

### **3.- EFFECTS OF HARBOUR WORKS ON THE COAST.**

(Some examples of "uncoordinated works").

Before showing the positive results of coordinated works (which is the main object of this paper), we would like to show, as an example, some pictures related to what we could call "uncoordinated works" in Spain. The negative effects on the coast produced by the construction of harbour breakwaters are classic topics in Coastal Engineering and can be found all over the world.

Typical negative effects which the presence of harbours cause on the coasts could be the following: A) Littoral Drift Interruption B) Beach Change Induced by a Harbour and C) Effect of Wave Reflection on the Coast Induced by a Harbour Breakwater. Fig.1 depicts a view of Almerimar Marina, located in the Almerian coast. Note the interruption of the littoral drift and the improper design of the marina entrance.



Fig 1. A View of the Effect Caused by the Littoral Drift Interruption.  
(Almerimar Marina, Almerian Coast)

Fig.2 shows the destruction of the seafront due to the coastline erosion caused by the negative effect produced on coast by the construction of the aforementioned marina.



Fig.2.- Erosion Caused by Littoral Drift Interruption.

In Fig.3 the siltation at the entrance channel is clearly indicated "on site" by the length of the first author's kayak paddle.



Fig.3.- Siltation at the Marina Entrance Channel.

#### **4.- SOME POSITIVE RESULTS OF COORDINATED WORKS**

A summary of the cases of positive results of coordinated works is shown below:

##### **A.-DREDGING WORKS**

- 1.- HARBOUR ENTRANCE CHANNEL DREDGING AND URBAN BEACH NOURISHMENT (Cádiz Harbour and Urban Beaches)
- 2.- HARBOUR ENTRANCE CHANNEL DREDGING AND LITORAL DRIFT RESTORATION (Huelva Harbour-Playa de Castilla Beach)

##### **B.- COMBINED HARBOUR/BEACH DESIGN**

- 1.- A DESIGN WHICH COMBINES A SHELTERED INNER HARBOUR BASIN AND A NEW URBAN BEACH (Algeciras Harbour-La Línea Beach)
- 2.- A DESIGN WHICH COMBINES AN EXISTING INNER MARINA BREAKWATER AND A NEW URBAN BEACH (Gijón Marina-Levante Beach)
- 3.- CREATION OF BOTH BEACH AND HARBOUR (Luanco Beach and Harbour)

The first point deals with harbour dredging and how the dredged material was used : urban beach nourishment and littoral drift restoration.

In the second point Coastal & Harbour Authorities coordinated the combined design of harbour and coastal works.

## **5.- DREDGING WORKS**

### **5.1.- GENERAL**

Traditionally the dredging of a harbour channel was a matter which concerned only Harbour Engineers. The different phases of the dredging projects were mainly carried out focussing on harbour engineering requirements.

Years ago, the question of whether or not the sand in a harbour channel could be suitable for a possible beach nourishment or for a littoral drift restoration project was not a concern of the Port Authority.

In other words : the countless millions of cubic meters of sand regularly wasted in dredging operations might have been more suitably used in beach nourishment or littoral drift restoration projects if Maritime Civil Engineers at that time had been more aware of the importance of combining both harbour and beach considerations.

Speaking in general terms, harbours need more water depth for their extensions and the coastline will benefit with beach nourishment. To obtain a real benefit, dredged materials should accomplish the following requirements :

a.- Dredged Material Quality.

b.- No Negative Effect on the Coast.

c.- Proper Attention to Archeological Artifacts (if applicable).

Harbour and coastal engineers should "coordinate" their works from the initial stages of the project.

Multidisciplinary teams (marine biologists, geologists and archeologists, as well as environmental and landscape specialists) should participate during the different phases of the projects.

## **5.2.- HARBOUR ENTRANCE CHANNEL DREDGING AND URBAN BEACH NOURISHMENT: CADIZ HARBOUR AND URBAN BEACHES.**

The need to dredge the entrance channel in Cádiz Harbour, together with the loss of dry beach width, at the popular urban beach of La Victoria under normal daily high tide conditions, prompted the Spanish Directorate of Ports and Coasts to plan a joint project looking at both harbour and beach requirements.

Furthermore, two other very popular urban beaches, Santa María del Mar (adjacent to La Victoria Beach) and La Caleta, were nourished. It should be noted that this was the first time in Spain that a dredging project of such importance (more than 6 million m<sup>3</sup>) was planned fulfilling both harbour and coastal engineering needs.

Due to the great historical importance of Cádiz bay, archaeological works were also carried out by specialists during different phases of the project, recovering more than 5.000 artifacts, mainly coins.

The sand volumes needed for the nourishment of the aforementioned beaches were (1.730.000 m<sup>3</sup> in project). The total project budget was 3.900 Mill. Pts.

In order to identify suitable borrow areas for beach nourishment, specific survey, geophysical, vibrocoring and biological studies were undertaken by the Coastal Project Division of the Spanish Ministry of Public Works and Transportation (MOPTMA). Also, specialists carried out submarine prospects to investigate the existence of valuable archeological deposits.

Owing to the location of La Victoria beach and Cádiz Harbour, it was necessary to lay a 90 cm diameter pipeline from the La Cabezuela inner quay, where a barge was loading sand from the dredge, to the beginning of La Victoria beach. The sand by-passing works had to pass over the main motorway and a train line to reach the beach, using approximately 5 kilometers of pipeline.

Two modern trailing hopper dredgers ( ANTIGOON AND HAM 310) were used, the former performing 90% of the work. The average sand nourishment ratio was 45.000 m<sup>3</sup>/day. The fact that only 0.75% of the volume was refused for beach nourishment indicated the efficiency of the preliminary studies and dredging operations.

The selective channel dredging plan obtained from vibrocoring studies enabled the coastal project engineers to use different grain size diameters depending on wave exposure location :  $0.2 < D_{50} < 0.30$  mm, for most of the beach and  $0.30 < 50 < 0.30$  mm, for the relatively more exposed Northerly final part of the beach.

The initial colour of the sand (apparently very dark) changed very quickly into the same nice colour as the native sand, as soon as the dumped sand dried and oxidized, as was expected. Otherwise, the beach nourishment project would not have been a succes popularly speaking.

A three year field monitoring program is being carried out to obtain a better understanding of the La Victoria beach behaviour, with respect to the littoral processes and coastline kinetics. This will aid coastal managers to adopt effective coastal management strategies regarding beach stability.

The following picture depicts an aerial view of La Victoria Beach under daily high tide conditions. Notice the occupation of the former dune by high buildings and the seafront as well as waves impinging upon the vertical face of the sea-front.



Fig.4.- A detail of the La Victoria Beach under Daily Tide Conditions Prior to Beach Nourishment.



The following pictures show the general dredging plan for beach nourishment, as well as a detail of the beach width (Notice the blocks used to protect the seafront from waves under daily high tide conditions).

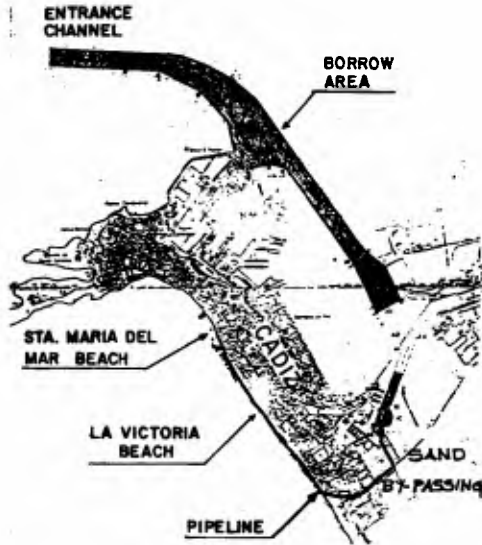


Fig 5.- General Dredging Plan for Beach Nourishment.



Fig 6.- La Victoria Beach after Beach Nourishment.

### **5.3.- HARBOUR ENTRANCE CHANNEL DREDGING AND LITORAL DRIFT RESTORATION ( Huelva Harbour-Playa de Castilla Beach).**

The Huelva Harbour Authorities have recently carried out a project to dredge the main harbour entrance channel. Approximately 5 million cubic meters of sand could be adequate for beach nourishment. Presently Coastal Authorities are studying the feasibility to build a submerged bar at -4 m. water depth to restore the littoral drift interrupted, among other causes, by the Huelva Harbour breakwater. These works will enhance a previous littoral drift restoration project carried out at the adjacent beach, Playa de Castilla (Refer.1, 2 & 3), where 1.5 million cubic meters of sand were supplied to form a protruding area, aimed at restoring the net littoral drift balance. The following picture depicts the erosion existing at the end of Playa de Castilla, in Matalascañas Beach. It should be noticed that this erosion is also caused by the former construction of a seafront and buildings on the dune.



Fig.7.- Erosion at the End of Playa de Castilla (Matalascañas Beach)

## **6.- COMBINED HARBOUR AND BEACH DESIGN**

### **6.1.- A DESIGN WHICH COMBINES A SHELTERED INNER HARBOUR BASIN AND A NEW URBAN BEACH.** **(Algeciras Harbour and La Línea Beach).**

The need to provide a sheltered inner basin in Algeciras Harbour was combined with the creation of an urban beach in great demand by the La Línea city's population. The following picture shows an aerial view of the works.



Fig.8.- A view of La Línea Beach Restoration.

### **6.2.-A DESIGN WHICH COMBINES A SHELTERED INNER HARBOUR MARINA AND A NEW URBAN BEACH (Gijón Marina-Levante Beach).**

An urban beach and seafront were designed taking advantage of one of the marina's existing breakwater (Fig.9). Navigational and sedimentation problems at the marina entrance channel were two important problems taken into consideration, as well as the overall integration of the beach design into the existing urban development. In this case the Gijón Harbour Authorities were responsible of the whole project and work. The technical staff of the Coastal Authorities cooperated during different stages of the project.

The geophysical studies carried out by coastal specialists were used by the Gijón Harbour technical staff to determine the potencial sand reserve areas, after undergoing vibrocoring and biological studies. These latter studies were very beneficial to Coastal Authorities to plan future beach nourishment projects along the Asturian coastline, and in particular for the next case of Luanco Beach.

The project consisted of the construction of two breakwaters and the dumping of 380,000 m<sup>3</sup> of sea bottom sand. It was necessary to dredge 17,000 m<sup>3</sup> of rock, as well as to demolish 32,000 m<sup>3</sup> of an existing seawall protruding into the sea. The project cost was 1,000.000.000 pts. The projected magnitudes obtained for the new beach are the following : HTWL beach : 60,000 m<sup>2</sup>; (3 m<sup>2</sup> /p); 20,000 people; M.T.W.L. beach : 100,00 m<sup>2</sup> ; (3 m<sup>2</sup> /p) 33,000 people. Breakwaters'length: 400 m; Seafront length: 800 m.



Fig.9.- A Composite Aerial View of Gijón Marina & Levante Beach

Next figure shows aerial views just after project completion.



Fig.10.- Aerial Views after Project Completion.

### **6.3.- CREATION OF BOTH BEACH AND HARBOUR** **(Luanco Beach and Harbour).**

This final case is the creation of both beach and harbour in Luanco (Asturias). The harbour has been designed by the Asturian Ports Division and presently there are local discussions about the feasibility of its construction. Since the construction of a lateral groin was considered necessary to create a new beach, the design of the beach was carried out taking into account the geometry of the future harbour. A relatively low-crested groin was designed in order to achieve the minimum visual impact. The section of this groin could be enlarged as a part of the outer harbour breakwater. Fig 11 is an aerial view of Luanco; note the scarce existing beach. The cost of the beach restoration has been 120 million pts. A sea front has also been designed to restore and integrate the maritime facade. Both projects are expected to be completed by the summer of 1995.

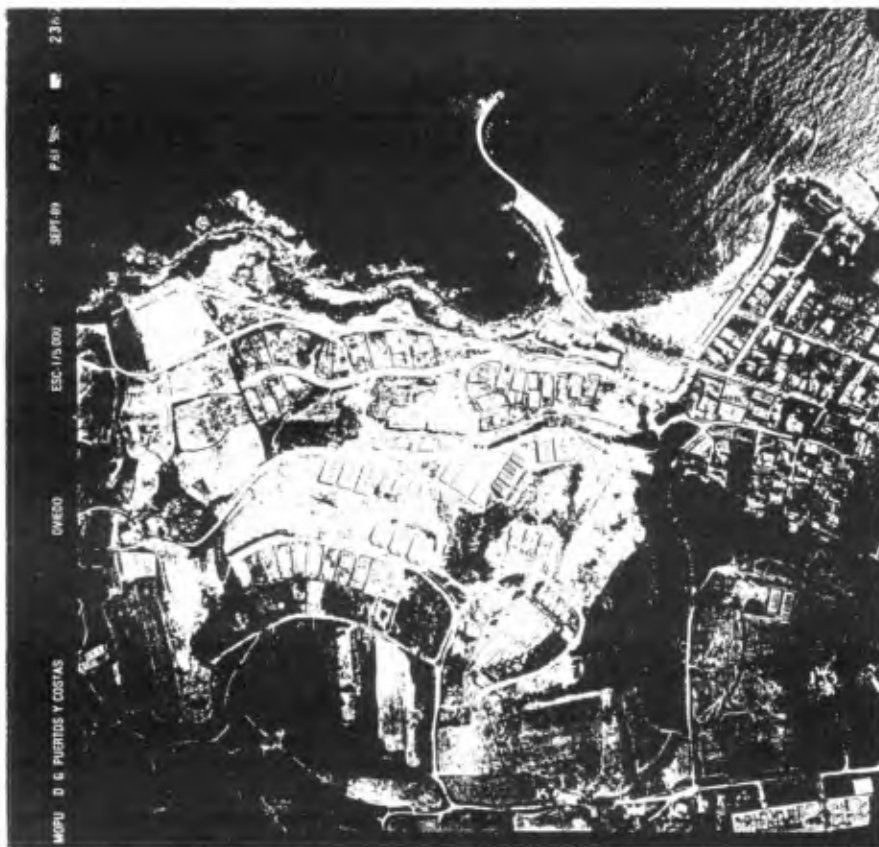


Fig.11.- An Aerial View of Luanco (Asturias).

Fig.12 schematizes the combined beach & harbour design.

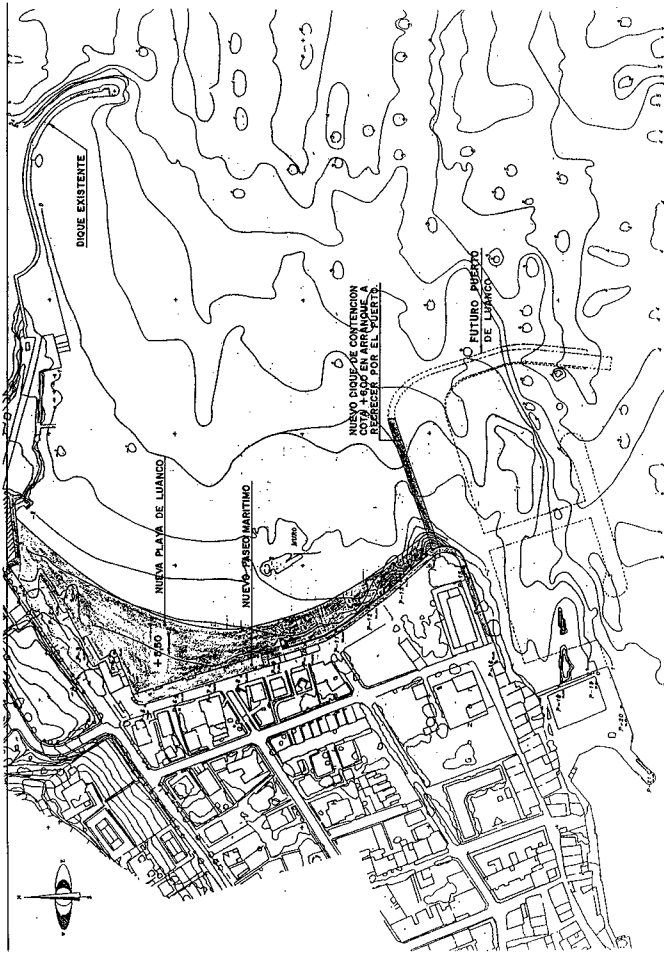


Fig.12.- Projected Luanco Beach .

## **7.- CONCLUSIONS AND RECOMENDATIONS**

A.- Although it is known that harbour works frequently have produced negative effects on the coast, there can also be works that combined harbour and coastal requirements satisfactorily. This could improve the scenario existing in some coastal areas adjacent to the harbour.

B.- The harbour and coastal technical staff should coordinate the works from the initial stages of the project, taking into account other multidisciplinary teams such as marine biologists, geologists and archeologists, as well as environmental and landscape specialists.

C.- The existence of strong legislation which protects the litoral, such as the actual Spanish Shore Act, that prohibits the use of sand for purposes other than beach nourishment, make it possible to succesfully accomplish the works described in this paper.

## **8.- ACKNOWLEDGEMENTS.**

We are grateful to the many people and multidisciplinary teams who have participated in all the projects described herein.

Without the interest and involvement of the Harbour and Coastal Authorities of Cádiz, Huelva, Algeciras and Gijón, these coordinated projects could not ever have been accomplished.

## **9.- REFERENCES.**

1.- **Fernández, J., Gómez-Pina G., and Muñoz, A.**, 1990 "Sand Bypassing to Playa Castilla, Huelva, Spain", Proc .22nd International Conference on Coastal Engineering, ASCE, pp 3183-3193.

2.- **Fernández, J., Gómez-Pina G., Cuenca G., and Ramírez J.**, 1992, "A Field Experiment on a Nourished Beach", Proc. 23rd International Conference on Coastal Engineering, ASCE, pp 2043-2056.

3.- **Losada, M., Medina, R., and González M.**, 1992, " Análisis de los Datos Obtenidos del Estudio de la Evolución de La Playa de Castilla durante el Periodo Junio 1990/Junio 1992", Informe de la Fundación Torres Quevedo (Universidad de Cantabria) para la Dirección General de Costas.



## CHAPTER 254

### Wave Impacts on the Eastern Scheldt Barrier Evaluation of 5 Years Field Measurements

Leo Klatter<sup>1</sup>, Hans Janssen<sup>2</sup>, Michiel Dijkman<sup>1</sup>

#### Abstract

During the past five years an extensive program of field measurements has been carried out to evaluate the effects of wave impacts on the Eastern Scheldt Barrier in the Netherlands, under operational conditions. High impact pressures were measured. The evaluation of the measurements shows that these high pressures affect only a small area simultaneously.

#### Introduction

The Eastern Scheldt Barrier is located in the southwest part of the Netherlands. The barrier has been built across three main channels in the mouth of the Eastern Scheldt, respectively one kilometer, one kilometer and two kilometers wide. The actual barrier consists of 62 basic sections that are 45 meters wide (see figure 1). The sand bed is covered by a filtermat. On this mat concrete piers are placed. The flow opening is formed by two concrete beams. A steel gate, driven by hydraulic cylinders, can close the opening. On top of the piers a motorway bridge is located. The piers and sill beams are packed in by a rubble sill structure. All structural elements, piers, beams and gates, were prefabricated at a dry construction site and have been placed in open sea with heavy floating equipment. The barrier has been completed in 1986. Until 1994 11 storm closures were performed.

-----  
<sup>1</sup>Rijkswaterstaat, Construction Division, Hydraulic Department,

P.o. box 20.000, 3502 LA Utrecht, The Netherlands

<sup>2</sup>Rijkswaterstaat, Road and Hydraulic Engineering Division,

P.o. box 5044, 2600 GA Delft, The Netherlands

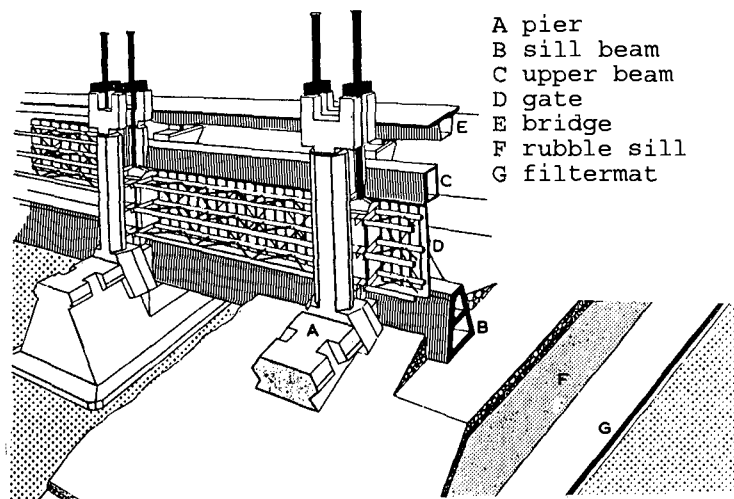


Figure 1: Elements in the Eastern Scheldt Barrier

### Wave Impacts

Under storm conditions the barrier is subject to wave attack from the North Sea. During the more severe storm surges the gates of the barrier will be closed. These gates are subject to wave impacts during the closure operation of the barrier, when the girders of the gates, which are located at the North Sea side of the barrier, cross the water level. After the gates have been closed the front and top side of the upper beam are subjected to wave slamming. Wave impacts on the bottom of the beam occur, when the gates are open, under moderate storm conditions and with more severe conditions just before the gates start closing.

The design impact forces for the gates and the upper beam were determined from extensive scale model tests. For the design computations the wave impacts were schematized to a triangular pressure diagram, as shown in figure 2. The rise time and decline time have average values of respectively 0.05 s and 0.10 s. The peak pressure varies from 0.45 Bar to 0.65 Bar (1 Bar = 100 kN/m<sup>2</sup>) depending on the wave conditions and the location in the barrier.

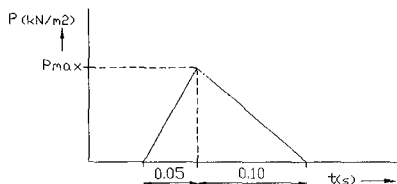


Figure 2. Schematized Impact Pressure

### Monitoring Program on Wave Impacts

In an early stage of the design of the barrier it was decided to set up a monitoring program to evaluate the hydraulic aspects of the barrier. This program consisted of field measurements of hydraulic loads on the barrier and the response of the structure (Klatter, 1990). In this program the wave impacts on the barrier were included. For the monitoring program on wave impacts a selection was made on the most critical items of the design. Critical, because the construction was very sensitive to a certain aspect or because the design technique was uncertain. For the monitoring program wave impacts on the main girders and supports of the gate and against the bottom of the upper beam were selected as critical items for the design (see figure 3).

Wave impacts on the girders of the gates generated such large impact pressures that the design of the gate had to be adapted several times to reduce these pressures. These aspects were therefore included in the monitoring program. The girders were instrumented in two locations: one at the center part of a top girder, the other at the end of a bottom girder near the joint with the support.

For the upper beam wave impacts against the bottom of the beam were regarded to be critical, because the relatively light weight prestressed concrete beam could be lifted from its supports.

For the monitoring of the wave impacts, one gate and one upper beam were instrumented with accelerometers, pressure gauges, a water level gauge and force gauges. Details of the instrumentation are given in tables 1, 2 and 3, and in figures 4 and 5.

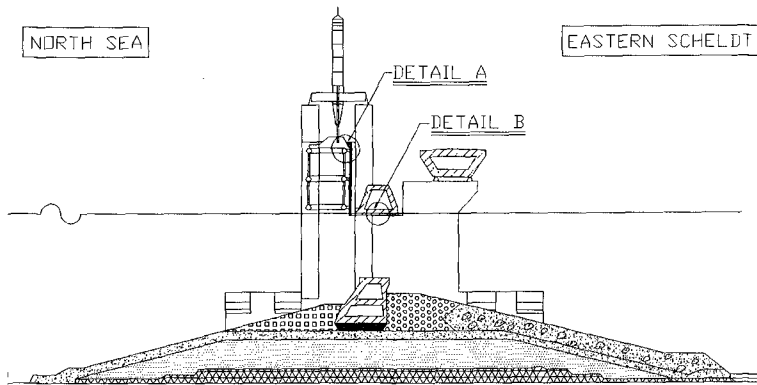


Figure 3. Locations for Wave Impact Monitoring

DETAIL A

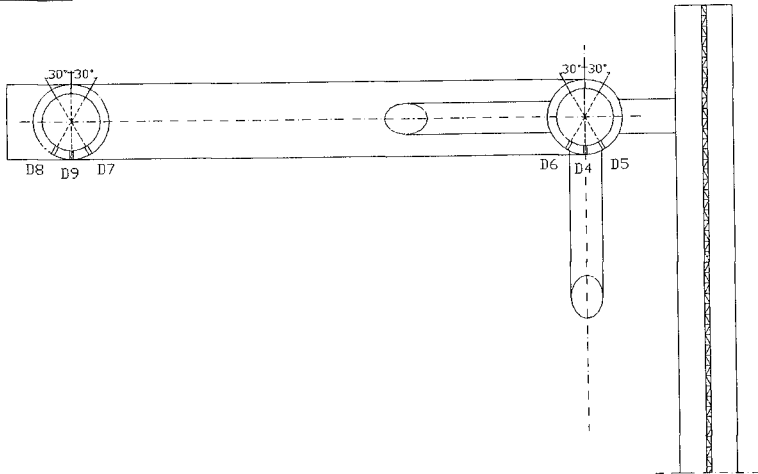


Figure 4. Locations Pressure Gauges Gate Girders

DETAIL E (bottom view)

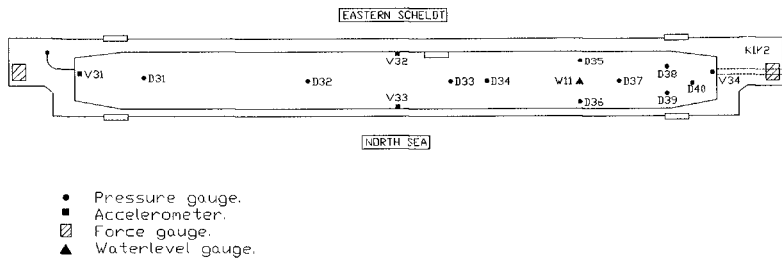


Figure 5. Instrumentation Upper Beam

sensor type	number	range	sample frequency
accelerometer	2	$\pm 250 \text{ m/s}^2$	1000 Hz
pressure gauge	6	3 Bar	1000 Hz
water level gauge	2	4 m	10 Hz

Table 1. Instrumentation Top Girder

sensor type	number	range	sample frequency
accelerometer	2	$\pm 500 \text{ m/s}^2$	1000 Hz
pressure gauge	5	6 Bar	1000 Hz
water level gauge	2	6 m	10 Hz

Table 2. Instrumentation Bottom Girder

sensor type	number	range	sample frequency
accelerometer	4	$\pm 25 \text{ m/s}^2$	100 Hz
pressure gauge	10	2 Bar	1000 Hz
force gauge	2	$\pm 10 \text{ MN}$	100 Hz
water level gauge	1	1.6 m	10 Hz

Table 3. Instrumentation Upper Beam

The water levels are measured on both sides of the barrier and the wave spectra are measured by a directional wave buoy, located approximately 500 m seaward of the barrier. The measurements were concentrated in measurement campaigns during storm closures of the barrier.

### Results

The measurements of wave impacts on the top girders of the gate were performed during the closure operations of the gates, when the girders cross the water level. Under these conditions 10 successful measurement series were obtained. From these series the most severe impacts were selected for further analysis.

Date	Time	$H_s$	D4	D5	D6	D7	D8	D9
		m	Bar	Bar	Bar	Bar	Bar	Bar
27-feb-90	14:33:59.5	2,15	0,72	0,38	0,39		0,21	0,21
27-feb-90	14:35:47	2,15	0,24	0,05	0,43	0,16	0,05	1,17
27-feb-90	14:36:25	2,20	0,81	0,66	0,46	0,11	0,19	0,01
27-feb-90	14:36:29.5	2,20	2,27	0,14	0,44	0,10		
27-feb-90	14:36:43.5	2,20	1,10	0,18	0,53	0,58	0,01	0,08
27-feb-90	14:43:47	2,20	2,17	0,33	0,18		0,11	0,12
14-feb-89	06:28:59.5	1,80	0,28	0,12	0,09		0,26	0,53

Table 4. Maximum Impact Pressures Gate Girder

The measured maximum impact pressures are presented in table 4, for impacts with a maximum pressure over 0.50 Bar on one or more of the sensors.

The maximum impact pressure registered is 2.27 Bar with a significant wave height of 2.20 m. The time history of this impact is given in figure 6. In figure 7 the peak is given in more detail.

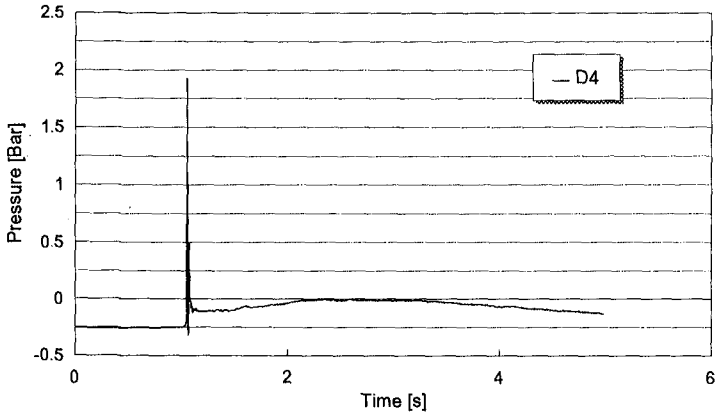


Figure 6. Registration Maximum Pressure

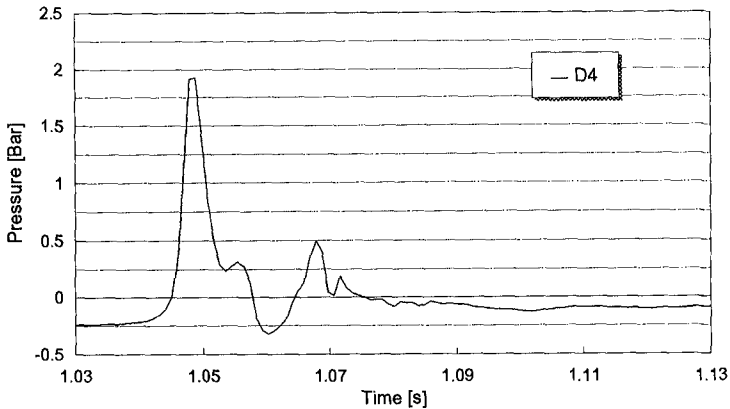


Figure 7. Pressure Peak (Detail)

The measurements of wave impacts on joints of the bottom girder and the support show relatively moderate impact pressures. The instrumentation is located close to the edge of the gate. The gate edge crosses the water level during the closure of the barrier at the first phase of a storm surge. At this time the water flows into the Eastern Scheldt. The closure causes a translation wave that accelerates the rise of the water level at the North Sea side. The result is that the instrumented section crosses the water level so rapidly that hardly any wave impacts occur. The maximum recorded impact pressure is 0.37 Bar.

The wave impacts measurements against the bottom of the upper beam start with an outside water level 1 meter below the bottom level of the beam and end with the start of the closure of the gates. Under these conditions 14 successful measurement series were obtained. From these series the most severe impacts were selected for further analysis. A problem for the analysis is that only 4 of the 10 pressure gauges functioned during all measurement campaigns. The maximum pressures recorded with these remaining gauges are presented in table 5, for the (7) most severe impacts registered.

Date	Time	H <sub>g</sub>	D35	D36	D37	D39
		m	Bar	Bar	Bar	Bar
14-feb-89	05:06:17	1,45	0,31	0,59	0,07	
14-feb-89	05:09:47	1,45	0,27	0,52	0,04	
14-feb-89	05:30:37	1,50	0,14	0,29	0,20	0,22
14-feb-89	05:31:19.5	1,50	0,03	0,09	0,30	
14-feb-89	13:03:42.5	1,15	0,15	0,30	0,38	0,62
14-feb-89	13:13:50	1,05	0,29	0,17	0,25	0,29
14-feb-89	13:22:51	1,00	0,52	0,28	0,34	0,14

Table 5. Maximum Impact Pressures Upper Beam

To illustrate the wave impact on the upper beam and the response of the beam the time series of two pressure gauges (D35 and D36) of the impact recorded at 14<sup>th</sup> February 1989 at 13:13:50 are presented in figure 8. This figure shows a sharply peaked impact which first hits the North Sea side of the beam bottom and moves to the Eastern Scheldt side in the wave direction.

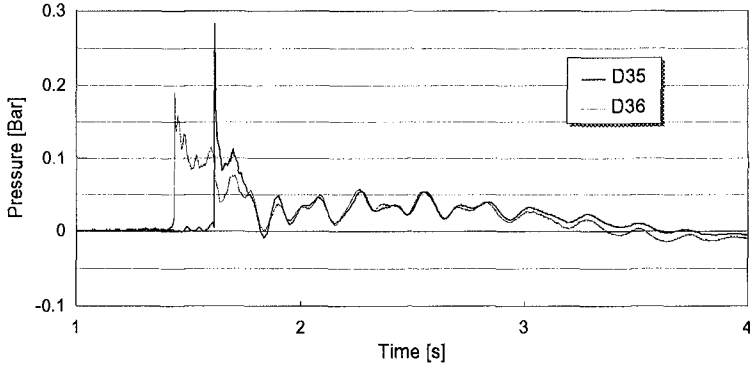


Figure 8. Registration Impact pressures Upper Beam

The response of the beam is illustrated by the acceleration registered at V33, presented in figure 9 (see figure 5 for the instrumentation). The response starts at the first hit of the beam. After the impact the beam vibrates in its natural frequency of approximately 5 Hz.

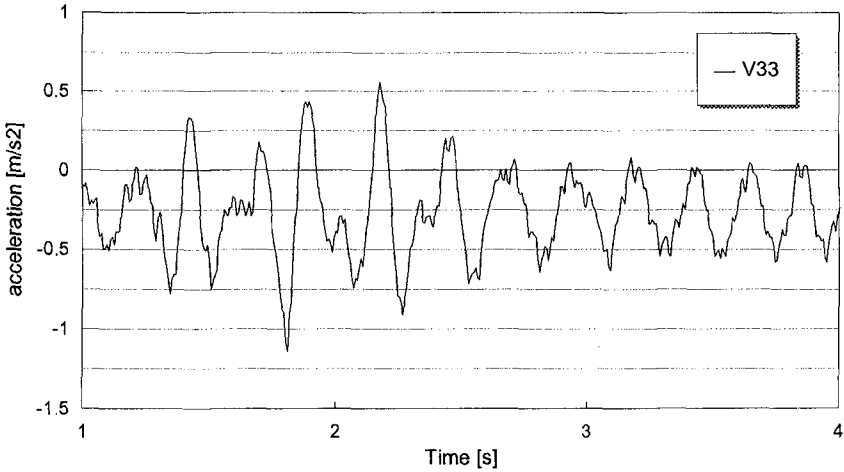


Figure 9. Registration Acceleration Upper Beam



The response of the support force to the impact is presented in figure 10. Note that the short wave impact (with a amplitude of 675 kN) is small in comparison with stationary support force (of approximately 6000 kN).

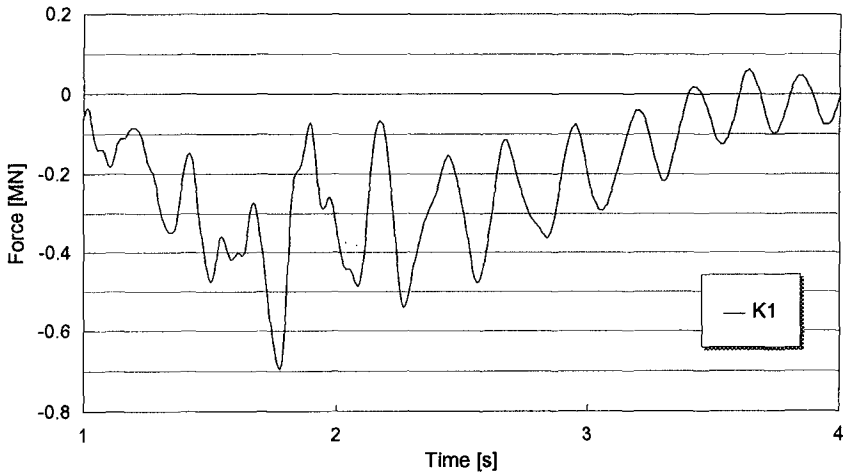


Figure 10. Registration Support Force Upper Beam

### Discussion of the Results

In the field measurements high impact pressures were recorded ( $> 2$  Bar). The frequency of exceedance of the maximum impact pressure on the gate girders and the upper beam is estimated between 1% and 0.1%, based on the total number of waves recorded during the measurements. These maximum pressures are higher than the design values (0.45 - 0.65 Bar). The design values were determined for larger impact areas, however. The measured peak pressures are representative for only a small area related to the dimensions of the sensors (diameter approximately 1 cm). The maximum pressures measured in the field show a very large spatial variation. Because of this variation, the impact pressure, averaged over a larger area, will be relatively small; smaller than the design values.

An other item of discussion is the type of wave impact. From the model tests impacts were expected with a sharp pressure peak and little air content. The impacts registered in the field show even sharper peaks and there is hardly any sign of the high frequency oscillations, that indicate air intrusion (compare Hattori 1990). The observed oscillations, see for example figure 8, are

related to the vibration of the structural elements itself. The pressure peaks were analyzed in more detail. The rise time was in the order of 0.01 s and the decline time in the order of 0.02 s, see figure 7.

A quantitative comparison of the results of the field measurements with the scale model tests appeared to be quite difficult for different reasons. In the field measurements local pressures were measured, while in most of the model tests impact forces, averaged over a larger area, were measured directly. Because the spatial variation is much greater than expected, the average impact force in the field can not be computed accurately from the individual pressure registrations. This effect is intensified by the failure of a number of the pressure sensors. Another handicap for the comparison of the field results with the model results are the instationary boundary conditions in the field measurements.

### Conclusions

Wave impacts with high pressures were recorded during the field measurements. The wave impacts show sharp pressure peaks. The impact pressures show a large spatial variation. The impact pressure, averaged over a larger area, is relatively small.

The type of impact observed in the field is comparable with the type of impact, that was expected from the model tests. The spatial variation observed in the field measurements is much greater than expected from the model tests. The two-dimensional and stationar character of the model tests differs from the three-dimensional instationary field conditions.

Finally some general conclusions on field measurements of wave impacts can be given:

- This sort of monitoring programs are long term projects. It appeared to be very difficult to manage this type of projects in a constantly changing organisation with shifting priorities and budgets.
- The measurements are performed with relatively moderate boundary conditions. One has to keep this in mind with te selection of the phenomena to be measured.
- The measurements are not repeatable.

## References

Klatter H.E., Konter J.L.M., Jongeling T.H.G., "Monitoring Hydraulic Loads on the Eastern Scheldt Storm Surge Barrier", 22th International Conference on Coastal Engineering, Delft 1990.

Hattori M, Arami, A, "Impact Breaking Wave Pressures on Vertical Walls", 23rd International Conference on Coastal Engineering, Venice 1992.

## CHAPTER 255

### Salinity and Water Levels in the Weser Estuary during the last hundred years - Anthropogenic influences on the Coastal Environment

H. Kunz<sup>1</sup>

#### Abstract

Today the Weser Estuary (Unterweser) is one of the most regulated rivers in Europe. It connects the harbour of Bremen with the Southern North Sea (German Bight) and is used by ocean-going ships. The first substantial deepening was done during the last decade of the 19th century. As the vessels became larger, the river has been deepened and widened for several times. The sequence of engineering works changed drastically the hydrological, morphological and ecological conditions within the Unterweser. The tidal water levels and the salinity had been measured since the beginning as part of an extended interdisciplinary monitoring program providing sound data over one century. These data are a valuable base to investigate the impact of the regulation works on the natural ecosystems of the coastal environment and on demands of the society, such as flood protection, irrigation, drainage. New questions arise from the vision, that impacts might be amplified by global climate changes.

#### Channelization of the Unterweser-estuary

The Unterweser-estuary is an important link for the merchandise town Bremen to the deep water of the North Sea (Fig. 1). The depth of the Unterweser decreased after the middle ages. To ensure the competitiveness of the Bremen-harbour, several attempts to deepen the river had been made since the 18th century. However, they were of limited success - KELLER (1901), ROHDE (1970). The first substantial step towards channalization was executed

-----  
<sup>1</sup>Coastal Research Station (CRS) of the Lower Saxonian Central State Board for Ecology, An der Mühle 5, 26548 Norderney/Germany, Director of CRS, Dr.-Ing.

between 1883 and 1895 after the plans of FRANZIUS (1888) by concentrating the tidal currents in a dredged channel (tidedependent draft of 5.0 m), which had been stabilized by embankments, groynes, training walls. In principal, similar techniques were applied during the following construction periods to reach drafts of 7.0 m (1913/16 and 1921/24); of 8.0 m (1925/29, with an extension to 1939); 8.7 m (1953/59) and of 10,5 m (1973/79), which is called 9.0 m -correction due to the sea-chart-zero as the new reference datum-level - WETZEL (1987).

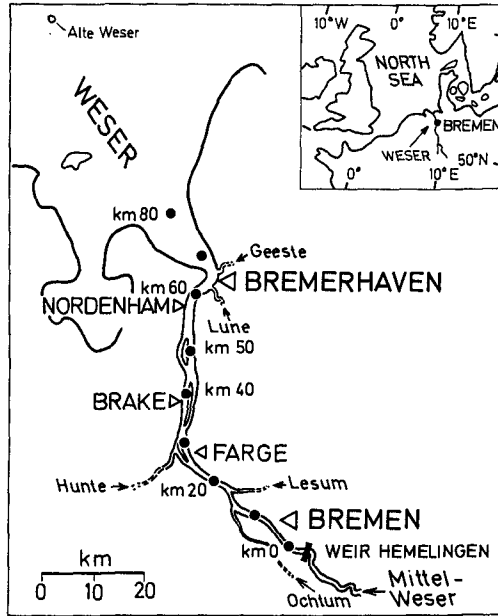


Fig. 1 Location map of the Weser Estuary (Unterweser)

After the first correction it was necessary to limit the tidal influenced part of the river by a weir in Bremen-Hemelingen, stopping erosion and groundwater intrusion (1906/11).

The time scale of the channelization is displayed on Fig. 2, righthand picture. The development of the channel-bottom depth relative to the German datum (NN, which is approximately equal to mean sea level) over time is shown on the picture below, lefthand.

The correction works changed the morphology drastically and influenced the hydrological and ecological conditions substantially. Fig. 3 gives an example on the development of the cross-section in the Bremen-area. The river surface, as well as the riparian area between Bremen und Bremerhaven, were reduced by the sequence of works to about one third and about 60 % of the eulittoral embankments of the navigable channel were covered by various packing material; most of the highly valuable backwaters and flats were lost (BUSCH et al. 1989).

Additionally dykes were displaced towards the river and storm surge barriers were installed in tributaries.

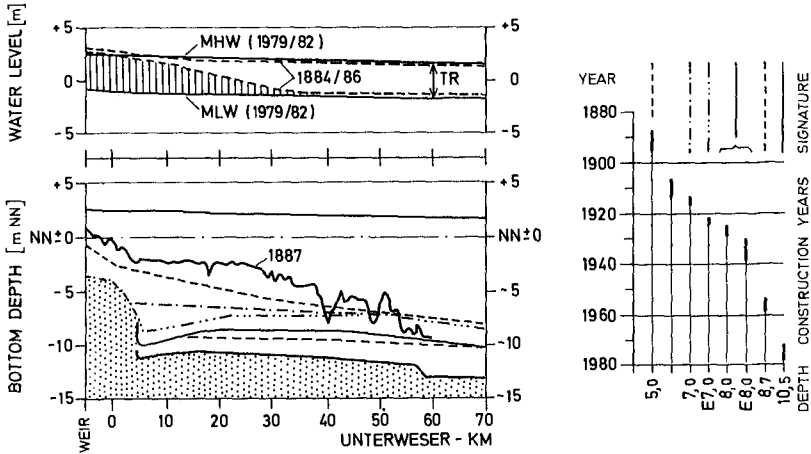


Fig. 2 Channelization of the Unterweser over 100 years. Right: time scale for construction periods. Left, below: bottom depth of the channel. Left, top: high & low water (MHW, MLW), tidal range (TR)

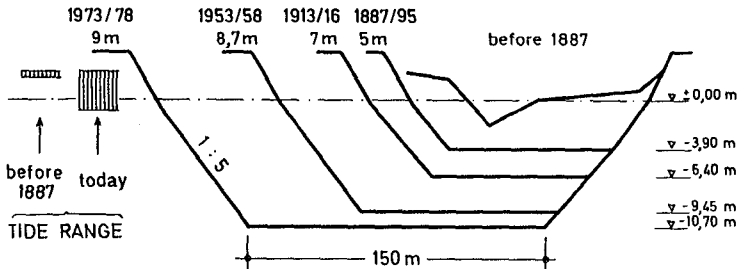


Fig. 3 Cross-sections (Unterweser-km 11, Bremen-Hasenbüren) before 1887 and as designed later

Hydrology

The water levels in the Unterweser are influenced by tides (propagating from the German Bight to the weir in Bremen) and freshwater run off (discharge measured at the gauge of Intschede, upstream the weir). General information on these input-data are displayed on Fig. 4: the tides (HW, LW) are semidiurnal (M2 + S2); the high values for the run off (HQ) occur mainly in spring, the low values (LQ) in late summer or autumn.

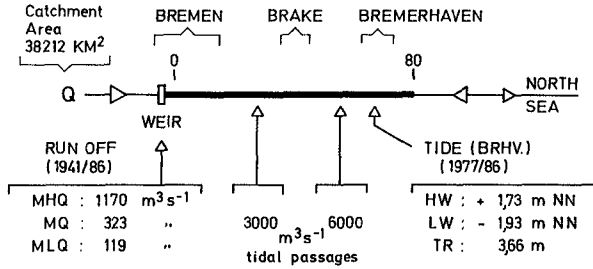


Fig. 4 Hydrological data for the Unterweser

The tidal curves on Fig. 5 provide information, how nowadays the tide propagates into the estuary. A comparison with Fig. 2, lefthand on top, shows how water levels and tidal range have changed with respect to the situation before the first regulation. The low water level (MLW) has been lowered in the upper part of the Unterweser, while the high water level (MHW) remained comparably unaffected. Thus the tidal range increased in Bremen from almost zero to about 4.0 meter. A more detailed picture is given by the graphs on Fig. 6.

The first construction periods, including the 8.0 m-correction, had the main impact on the changes of the water levels. The influence of the first correction had

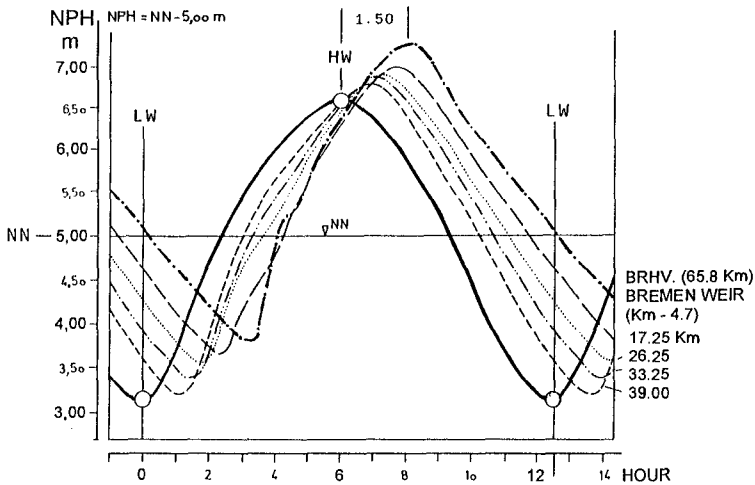


Fig. 5 Tides in the Unterweser (Bremerhaven to Bremen) for averaged conditions. Data: Federal Water and Shipping Authority Aurich, Bremen, Bremerhaven

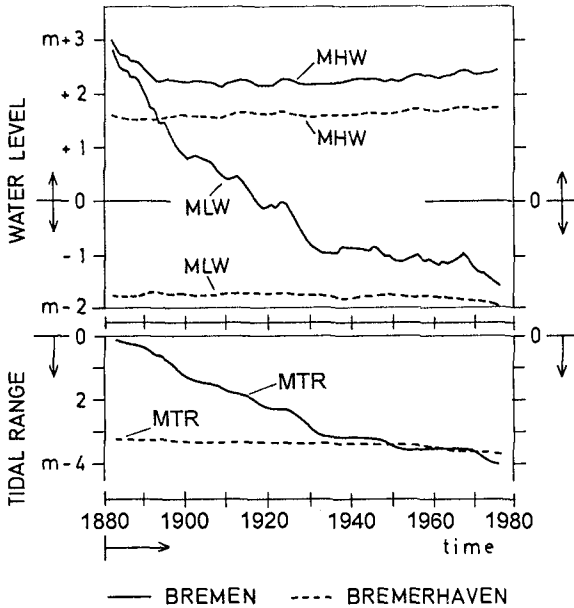


Fig. 6 Development of mean high water (MHW), mean low water (MLW), mean tidal range (MTR) over 100 years in the Unterweser at Bremen and Bremerhaven

been underestimated with an error of prediction up to almost 1.5 m. The impact of the 8.0 m-correction (water level-difference) reached up to about 0.75 m (WALTHER, 1954). An extended discussion concerning the impacts of the distinguished Unterweser-corrections on tides, water levels, tidal range is published by WALTHER (1954), STRÖHMER (1963) and is documented in unpublished reports (WSV 1957/85) of the Federal Water and Shipping Authority. The impact of the regulation works on extrem high water levels during storm floods is overlapped and hidden by the predominant anthropogenic influences caused by the coastal protection means, such as diking (in former days often combined with land reclamation) and storm surge barrages.

Monitoring programs

There had been many objections against the first large Unterweser-regulation proposed by FRANZIUS. An important group were the farmers who especially worried about higher water levels, more salinity and their correlated effects. Thus an extended monitoring program was established and executed over about one hundred years



with only one large gap caused by the second world war. Additionally, money was paid to compensate in advance parts the presumed disadvantages (PLATE, 1951). These were about the same actions as they are nowadays required in Germany for the environmental impact assessment and common to promote the implementation of projects: it was a progressive and really successful approach. A substantial part of the program focused on the water quality of the Unterweser-estuary, especially concerning the salinity. Fig. 7, left shows the location where samples were taken; information on the observation-periods are added. The measured data (once a week at high water) were supplemented by a large number of special investigations related to space (e.g. verticals, cross-sections, longitudinal profiles) and time (e.g. tide circles, periods with special hydrological conditions) - WSV (1957/85).

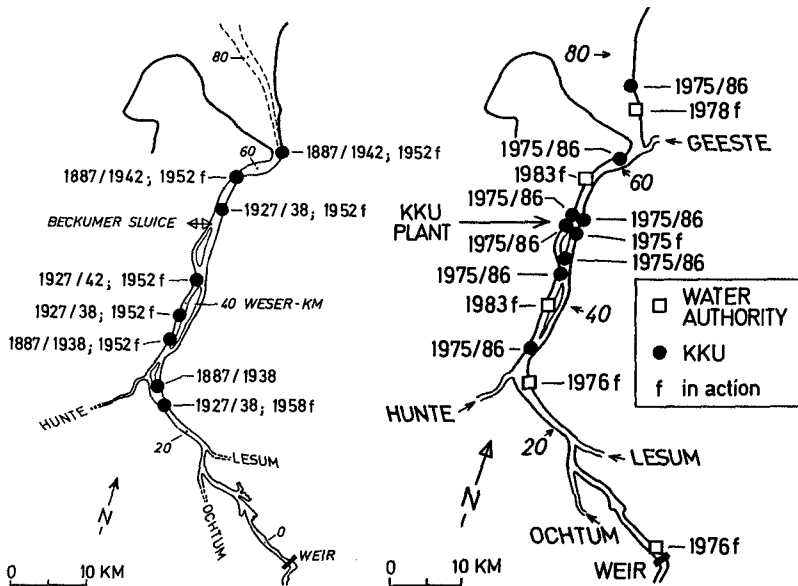


Fig. 7 Location of the Unterweser-Stations.  
Left: weekly sampling. Right: permanent recording

A system of permanent working stations had been installed since 1975. Fig. 7, right distinguishes stations which were established by Water Authorities and those, which were specifically established to control the KKU-nuclear power plant KUNZ (1979). These stations are interlinked with measurements, which are regularly done by fast running boats (KUNZ et al. 1984).

The Unterweser is classified as a well mixed estuary; it has been proven, that the data gained by the stations in one measuring point can approximate the average situation of the cross-section sufficiently well with respect to the aims of the long term and large scale monitoring programs - e.g. WSV (1957/85), BARG (1979). However, interpretations of the data are limited to the fixed targets.

Salinity

The salinity in the Unterweser-estuary is mainly caused by the intrusion of saltwater from the sea and is additionally affected by the salt which discharge factories into the upper parts of the Weser - e.g. Lüneburg et al. (1975), Arge Weser (1982). The distribution of salinity in the estuary is influenced by the tidal motion and the fresh water run off ( $Q_0$ ). This is shown in principal on Fig. 8. The graphs are simplifications for a defined phases of the tide ( $K_f$ ,  $K_e$ ).

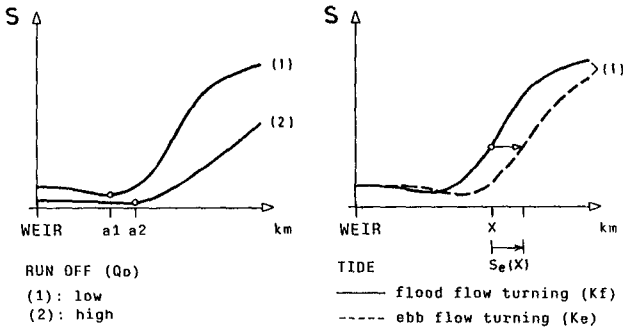


Fig. 8 Distribution of salinity in the brackish area of an estuary. Left: impact of run off (discharge  $Q_0$ ). Right: influence of the tidal motion ( $K_f$ ,  $K_e$ )

The changing of salinity over time (tidal cycles) is shown on Fig. 9, left (salinity is proportional to the displayed conductivity  $L_f$ ) for different areas (location of the stations see Fig. 7, right) of the Unterweser. The tide-phase-time of the flow turnings (flood, ebb) are indicated as  $K_f$ ,  $K_e$ . The distribution of the conductivity (longitudinal profiles) for the phases  $K_f$  and  $K_e$  can be drawn from the  $L_f$ -values of the five stations. The result is shown on the righthand picture.

Longitudinal profiles for the phase  $K_f$  have been measured by sensors which were installed in fast running boats. Results provides Fig. 10, left: areas in which the measured curves fit in dependency of the significant

fresh water run off ( $Q_0/10$  after BARG, 1979). The profiles on the right picture have been derived from all measured profiles. The large impact of the run off value on the salinity is obvious. Comparable results have been published by BARG (1979) with salinity-data (NaCl) of the KGU-stations.

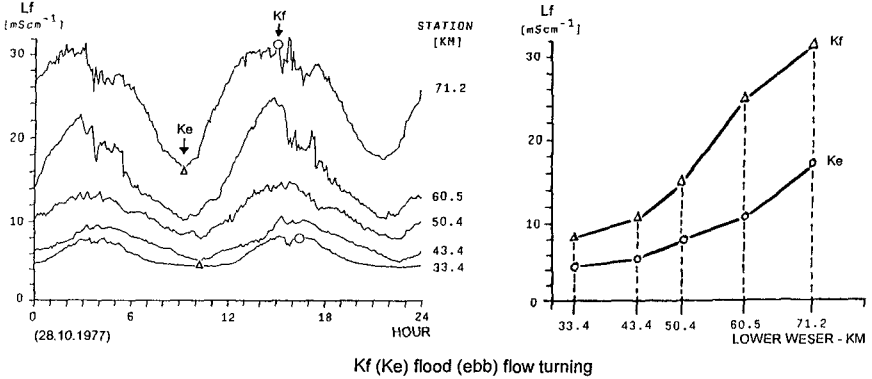


Fig. 9 Left: Conductivity ( $L_f$ ) over time for different measurement stations in the Unterweser. Right: Conversion of the  $L_f$ -data into longitudinal  $L_f$ -profiles for the tide phases Kf and Ke (KUNZ 1979)

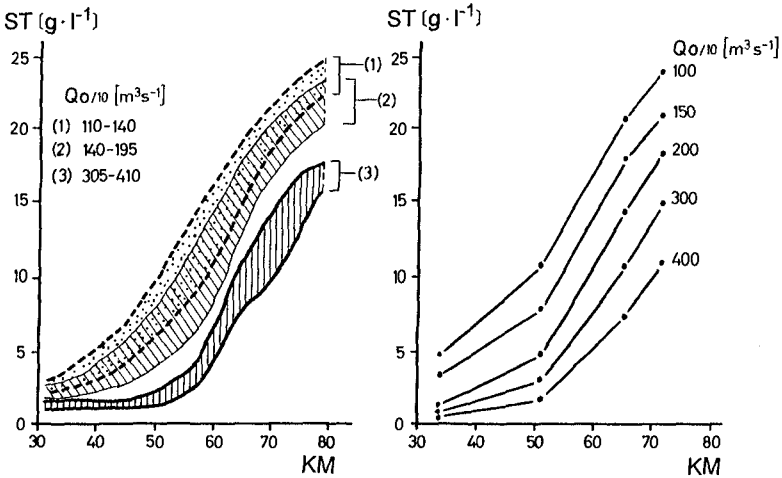


Fig. 10 Longitudinal profiles for Total Salinity (ST) as function of ( $Q_0/10$ ). Left: envelopes for groups of measured profiles. Right: ST-functions ( $Q_0/10$  is parameter) calculated with measured profiles

Investigations concerning the influence of the Unterweser-regulation works on the salinity-distribution in the brackish area of the Unterweser have been based on the long term data of the sampling stations. Longitudinal profiles for the phase Kf were constructed with these data, as demonstrated in principal by Fig. 9, right; e.g. STRÖHMER (1963), PLATE (1951), GRABEMANN et al. (1983) and nonpublished reports WSV (1957/85). An example is given by Fig. 11, where salinity-data (NaCl) for the time-period 1890 to 1975, selected for the mean run off (MQ), had been converted into longitudinal profiles. The data for the period from 1890 to 1932 are combined in the picture to the left: no significant influence of the regulation works. The interpretation of the righthand picture (1931 to 1975) is more difficult. GRABEMANN et al. (1983) tried to separate the natural from the man induced fluctuations and came up with the result, that the influences of the natural long-term changes (trends of relative sea level rise, characteristics of the tides - e.g. JENSEN et al. (1993)) - dominate the other impacts. This corresponds to results achieved by HN-models.

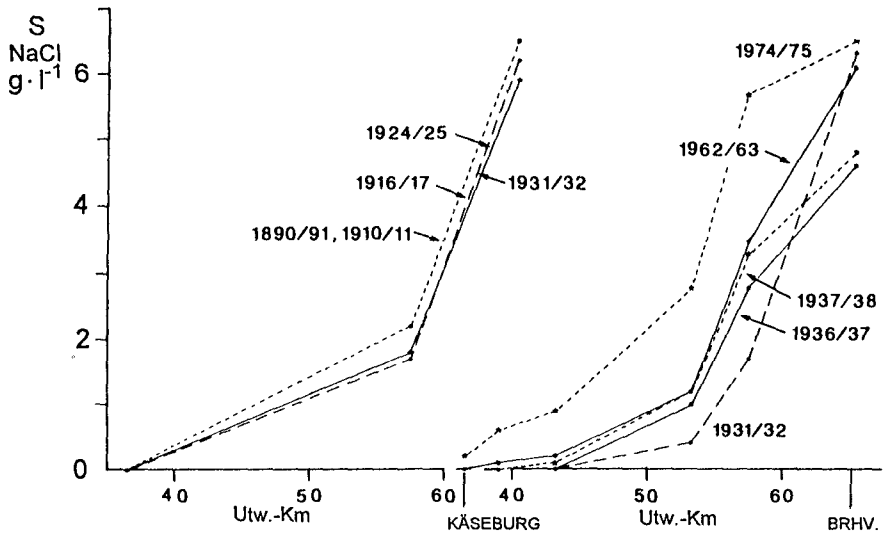
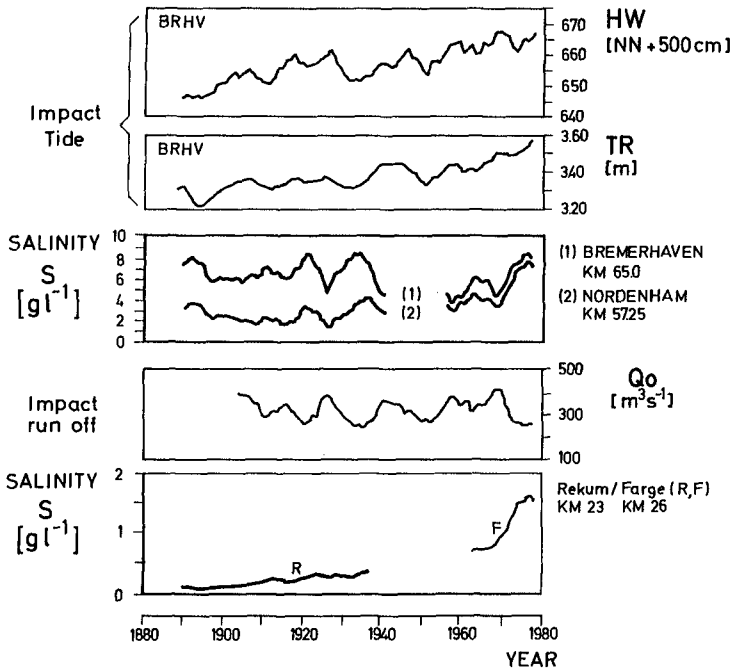


Fig. 11 Development of the NaCl-Distribution (profiles) in the Unterweser between Käseburg/km 36,5 and Bremerhaven/km 65.8 for mean Run Off (MQ), 1890 to 1975 - GRABEMANN et al.(1983), Shipping Authority Bremen/Aurich

The development of the salinity  $S$  ( $\text{NaCl}$ ) over time is shown by Fig. 12 to 14 for selected stations. The Fig. 12 combines  $\text{NaCl}$  values (Station Bremerhaven (Brhv.), Nordenham, Rekum/Farge) with information on the main impact parameters: tides (HW, TR) and run off (discharge  $Q_0$ ). The increase of salinity in the Bremen-area (Rekum/Farge) is caused by industrial salt-discharges into upstream parts of the river in combination with the  $Q_0$ -parameter - ARGE WESER (1982). The salinity-graphs for Bremerhaven and Nordenham show similar downs and ups related to  $Q_0$ ; there seems to be a trend towards increasing values and a steepening of the gradient since about 1970. This is most likely induced by changed hydrological conditions and not by the sequence of correction-works - e.g. BARG (1979), GRABEMANN et al. (1983), WETZEL (1987), WSA BRHV (1991).



DATA : STRÖHMER (1970), GRABEMANN et.al.(1983), WSV (1957/85)

Fig. 12 Development of the Salinity  $S$  in the Unterweser (Bremerhaven, Nordenham, Rekum/Farge) and of hydrological Data: High Water (HW) & Tidal Range (TR) at Bremerhaven (BRHV); Run Off ( $Q_0$ ) for Intschede, (all values as five yearly running means)

Fig. 13 displays for the station Nordenham (km 57,25) how the salinity has been controlled by the fresh water discharge ( $Q_0$ ). The diverting graphs before 1906 may be related to the first correction. However, that's not conclusive. From 1955 onwards different behavior is obvious, which presumably is caused by the increased tidal range, as mentioned before.

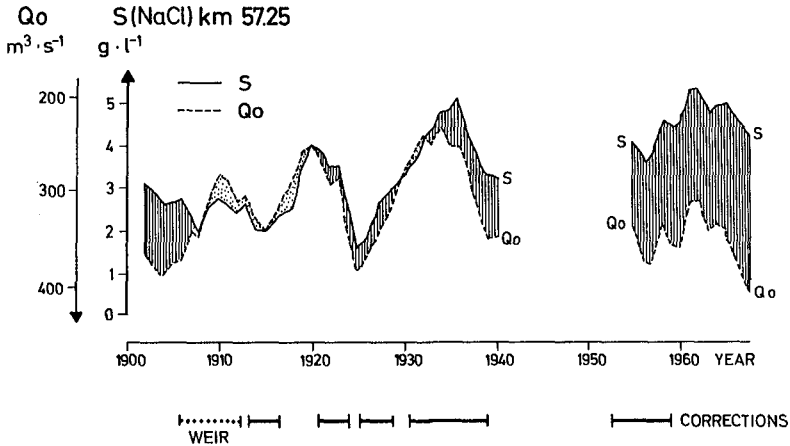


Fig. 13 Combination of Salinity S (NaCl) for Nordenham (km 57.25) with the Run Off ( $Q_0$ ) at Intschede-gauge after STRÖHMER (1970)

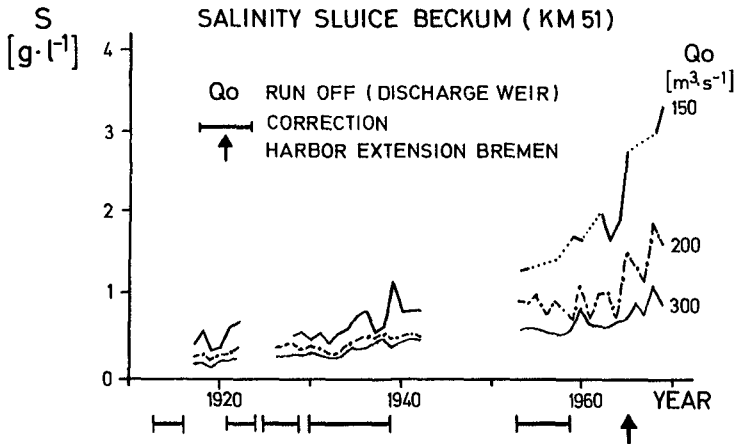


Fig. 14 Development of the Salinity S at the Beckum-slucice (km 51) for  $Q_0 = 150, 200, 300 \text{ m}^3/\text{s}$  since 1917. PLATE (1951), WSV (1957/85)

Since the content of salinity in the Unterweser-estuary is important for irrigation means (e.g. drinking water for cattle), the samples had also been taken in the Beckum-sluiice (intake for irrigation water) at km 51 - e.g. PLATE (1951), WALTHER (1954). The development of the NaCl over time with respect to distinguished run off-values ( $Q_0 = 150, 200, 300 \text{ m}^2/\text{s}$ ) is shown on Fig. 14. The salinity has increased and led to problems during periods of low run off ( $Q_0$ ), especially since the fifties as a result of the mentioned effects.

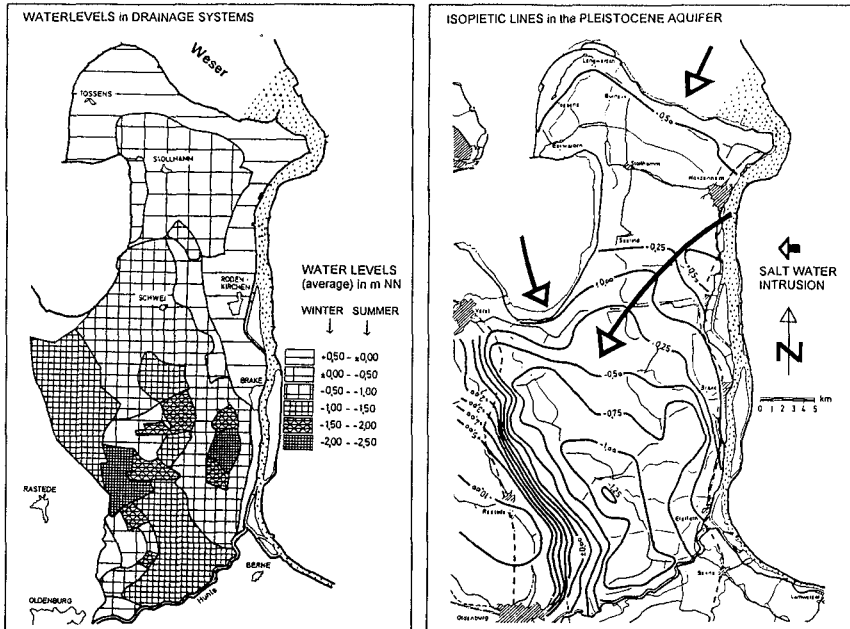


Fig. 15 Saltwater intrusion from the Unterweser into the aquifer of the lowlands. Left: Water level in the drainage system (ditches). Right: Isopiestic lines in the pleistocene aquifer and direction of the anthropogenic induced salt water intrusion - KUNZ (1993)

#### Effects on groundwater

The intrusion of saltwater out of the Unterweser into the groundwater (holocene and pleistocene) of the low lying areas is influenced by the regulation works. This question has become more important, as extensive

drainage systems were installed. Nowadays the water levels in the drainage ditches are far below the mean water level of the Unterweser (about NN), as to be recognized from Fig. 15, left. Consequently the isopiestic lines of the pleistocene groundwater has been changed and the intrusion of salinity out of the Unterweser can increase - Fig. 15, right. This impacts the holocene cover layers by vertical directed flows. The main driving force in the synergism of the addressed impacts is the drainage; the effects of the Unterweser-regulation works are comparatively small - KUNZ (1993).

### Conclusions and final remarks

For almost 100 years regular water samples were collected at several stations along the Unterweser-estuary on a scheme which remained unaltered. The combination with the tide gauge data provide an unique data set on salinity and water levels. This is a remarkable achievement of the Federal Water and Shipping Agencies and their scientific staff, who devoted time and effort into this admirable task. Today this valuable data set is of more than local interest. The traditional sampling scheme has been supplemented by extensive measurement programs and numerical modelling throughout the last decades. However, many controversially discussed questions concerning developments and impacts were only to be answered by referring to the long term data. This is an example which should encourage society to require appropriate long term monitoring programs being obligatory for every human activity that has substantial impact on the environment. The modern tools, such as modelling, information systems etc. should not lead to the believing, that we can do without providing sustainable field data-records on the anthropogenic changings of our environment to the next generations.

### References

- ARGE WESER (1982): Weserlastplan 1982; Arbeitsgemeinschaft der Länder zur Reinhaltung der Weser, Bremen.
- BARG, G. (1979): Untersuchungen über Salzgehaltsverteilungen in Brackwassergebieten von Tideflüssen am Beispiel der Unterweser; Mitteilg. des Franzius-Instituts, vol. 49, University of Hannover.
- BUSCH, D., M. SCHIRMER, B. SCHUCHARD, P. ULLRICH (1989): Historical changes of the River Weser; in: Historical change of large alluvial rivers-Western Europe (ed.: G.E. Petts); John Wiley & Sons Ltd., Chichester.



FRANZIUS, L. (1888): Die Korrektion der Unterweser; Bremen.

GRABEMANN, J., G. KRAUSE, G. SIEDLER (1983): Langzeitige Änderung des Salzgehaltes in der Unterweser; Dt. hydrogr. Z., vol. 36.

JENSEN, J., J.L.A. HOFSTEDE, H. KUNZ, J. DE RONDE, P.F. HEINEN, W. SIEFERT (1993): Long term water observations and variations; in: Coastlines of the Southern North Sea (ed. R. Hillen, H.J. Verhagen), CZ '93, ASCE, New York.

KELLER, H. (1901): Weser und Ems. Ihre Stromgebiete und ihre wichtigsten Nebenflüsse; Berlin.

KUNZ, H. (1979): Das automatische Meßsystem für die Beweissicherung WASSER beim Kernkraftwerk Unterweser; Mitteilg. d. Franzius-Instituts, vol. 49, University of Hannover.

KUNZ, H. (1993): Impact of drainage on the ground water of inner tidal regions; Congress on Irrigation and drainage - Water Management in the next Century, ICID & CIID, vol. 1-c, New Dehli.

KUNZ, H., M. GRODD, C. KRAUSE (1984): Wasser-güte-Längsprofile der Unterweser (1982 bis 1984) aufgenommen mit der Bakensand des WWA Brake; report, published by Wasserwirtschaftsamt Brake.

LÜNEBURG, H., K. SCHAUMANN, S. WELLERSHAUS (1975): Physiographie des Weser-Ästuars (Deutsche Bucht); Veröff. Inst. Meeresforsch., vol.15, Bremerhaven.

PLATE, H. (1951): Die Salzgehaltsverhältnisse im Brackwassergebiet der Unterweser; Neues Arch. f. Nds., vol.25.

ROHDE, H. (1970): Die Entwicklung der Wasserstraßen im Bereich der deutschen Nordseeküste; Die Küste, vol. 20.

STRÖHMER, P. (1963): Die Abflußkennwerte der Unterweser und ihre Veränderung seit 1840; Mitteilg. des Franzius-Instituts, vol. 22, University of Hannover.

STRÖHMER, P. (1970): Sonderuntersuchungen zum Salzgehalt der Unterweser, Gewässerkundl. Grundlagensammlung; report (unpubl.), Wasser- und Schifffahrtsdirektion, Bremen.

WALTHER, F. (1954): Veränderungen der Wasserstände und Gezeiten in der Unterweser als Folge des Ausbaues; Hansa, vol. 21/22.

WETZEL, D. (1987): Der Ausbau des Weserfahrwassers von 1921 bis heute; Jahrbuch d. Hafenbautechnischen Gesellschaft, vol. 42, Springer-press, Berlin.

WSA BRHV (1991): Zur Lage der oberen Brackwassergrenze; report 1991/3 (unpubl.), Wasser- u. Schifffahrtsamt, Bremerhaven.

WSV (1957/85): Jährliche und zusammenfassende Berichte über die Sonderuntersuchungen zum Salzgehalt in der Unterweser; Die Entwicklung der Salzgehaltsverhältnisse in der Unterweser seit Beginn des Ausbaus; div. reports (unpubl.) Federal Water & Shipping Agencies WSD Aurich/WSD Bremen.

## CHAPTER 256

### REVIEW OF SOME 30 YEARS BEACH REPLENISHMENT EXPERIENCE AT DUNGENESS NUCLEAR POWER STATION, UK

By Dr Roger Maddrell<sup>1</sup>, Bill Osmond<sup>2</sup> and Bin Li<sup>1</sup>

#### INTRODUCTION

Dungeness was formed initially as a shingle bar across a bay that existed between Winchelsea and Hythe at the end of the last glaciation (see Figure 1). The bar was the early coast and caused the landward accumulation of estuarine deposits, which now form the marshes. Shingle continued to accumulation on the seaward side to form the Ness. The present alongshore drift, resulting from refraction and diffraction of the dominate southwest waves, moves shingle eastward, eroding the southern coast and causing accretion along the eastern side (see Figure 2). The past morphology of the Ness, first described by Lewis, 1932, can be seen clearly from the shingle ridges, which represent old coastlines.

In the late 1950's the then Central Electric Generating Board (CEGB) chose the Ness as a nuclear power station site. Studies at that time by Sir William Halcrow & Partners (Halcrow) established that the rate of erosion of the southern shore was of the order of 1.1m annually, but near the point of the Ness, where the Station was to be sited, could be up to 1.5m annually, with an annual rate of drift of about 125,000m<sup>3</sup>. Various schemes for protecting the Station frontages from erosion, and thus flooding, were examined (Halcrow, 1963) and one of recycling shingle from the accreting east face of the Ness

---

<sup>1</sup> Sir William Halcrow & Partners Ltd, Burderop Park, Swindon, Wiltshire SN4 0QD, UK

<sup>2</sup> Nuclear Electric plc, Dungeness 'B' Station, Dungeness, Kent, UK

was recommended. The proposed volume of gravel initially was 15,000m<sup>3</sup> annually, but rising to 20,000m<sup>3</sup> with the construction of the second station.

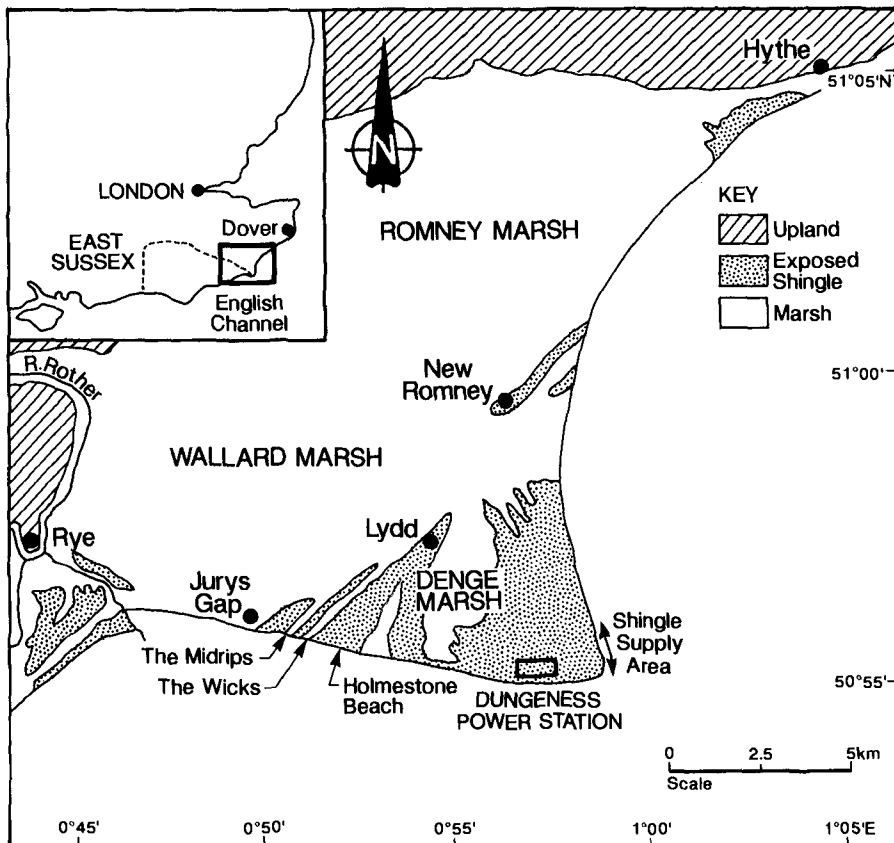


Figure 1 : Site Area

Beach feeding has been continuous since 1965, concentrating mainly at the western, updrift, end of the site. As the updrift coast eroded, the recharge area became more and more out of regime, requiring additional shingle to hold it. Recent studies recommended that a policy of coastal retreat or coastal set back should be implemented. This has resulted in a considerable saving to the amount of gravel required for beach feeding and a

reduction in the impact of winning material from the supply area.

### **EVOLUTION OF DUNGENESS**

The post-glacial marsh and shingle deposits attain a thickness of some 30m and are derived from a combination of terrestrial and marine sources (Long, 1994). Between 4000 and 2000 BP sea-level was relatively stable at about -2.5m OD, but during the last 2000 years it rose by about 2.5m. There has also been considerable subsidence, which in the last 4000 years has been between 1-2mm per year (Shennan 1989; Long and Shennan, 1993). The net relative sea level rise is predicted to be about 0.4m by the year 2050 (Maddrell and Burren, 1990).

Shingle probably entered Romney Bay by 5300-6000 BP, although radiocarbon-dated shells collected from -34m OD beneath the Station are only 3000-2000 years old (Greensmith and Gutmanis, 1990), which suggests that the shingle in this area is considerably younger than 2000 years old. The shingle is driven in a west to east direction by the dominant SW waves and the chronological development of the Ness can be seen in the remaining ridge pattern (see Figure 2). However, the dating is tentative as the time of shingle deposition can only be established where the shingle is underlain by organic sediments, which can themselves be dated by radiocarbon or where shoreline positions can be estimated from historical and archaeological sources. Unfortunately, the former condition is rarely met, while the latter provides only an approximate chronology, which tends to be restricted to the last 1500 years. Lewis and Balchin's 750? shoreline (see Figure 2) was based on Ward's 1931 interpretation of two Saxon Charters, which indicate the approximate position of the coast at this time. The 1600 shoreline is based on M Pokers' 1617 map of Romney Marsh, which is one of the earliest relatively accurate maps, while the 1800 shoreline is obtained from the 1794 Ordnance Survey. The 1990 BP coast is from recent radiocarbon dating.

There are three areas of low-lying marsh deposits to the west of the Station eg The Midrips, which have been interpreted as evidence for 'several oscillations of level from the late Neolithic times to the Bronze Age' (Lewis and Balchin 1940). There are also raised ridge levels north of the Station, which are taken as evidence of more severe climatic conditions during the Middle Ages.

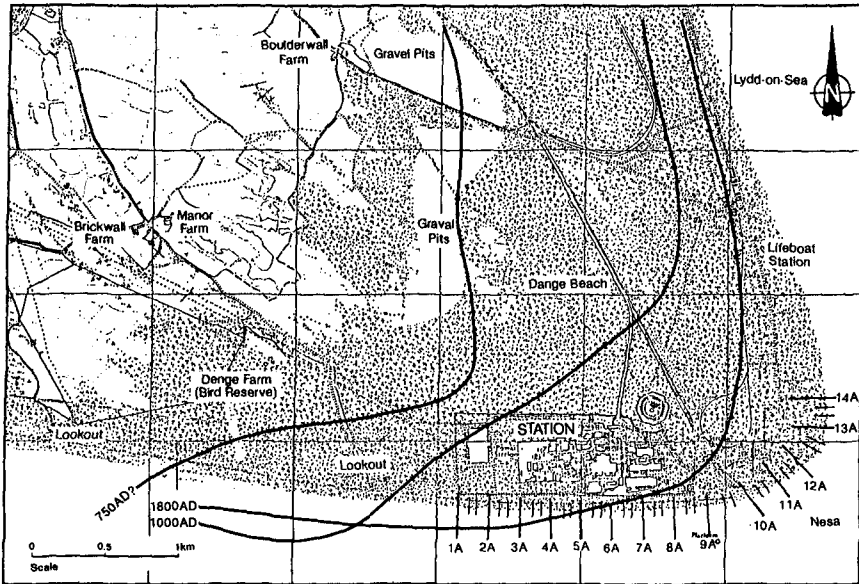


**Figure 2 : Historical Coastline at Dungeness and the survey lines at the Station**

The Ness is a continually evolving feature, as can be seen on Figure 2, with shingle erosion on its southern face and deposition on the east. The siting of the Station at the tip of the Ness close to the south coast, while morphologically controversial, was mainly because of the close proximity of deep water (-30m OD) adjacent to the Ness.

**BEACH FEEDING**

**General**

Southeast England is subsiding which, when combined with the rise in mean sea level, has meant a requirement for an increased level of coast protection for the southern

eroding face of the Ness in front of the Station. Inundation was seen during construction in 1960 and 1961 and more recently in local areas adjacent to the site in 1983, 1984, 1989, 1990 and 1992. The need for flood protection is reflected in the increase in recharge volume, which increased from some 15,000m<sup>3</sup> at the beginning to some 70,000 m<sup>3</sup> in 1992. Breastwork and two local groynes were constructed for emergency protection, but are now buried.

The volumes of beach feed material required has been established by surveying specific sections of the beach at the end of the winter, with the recommended shingle being placed on the beach over the following winter period. Initially this was done by ground surveys, but in recent years has been done by photogrammetry.

The idea of recycling shingle for use as beach protection was unique at the time and has been the subject of regular review. The most recent review indicated that not only was this the most effective method of protection (costing less than the interest payment of a more formal method of protection), but was also environmentally friendly.

The southern coast of Dungeness is being held at two points, the Station and at Jurys Gap, some 8km to the west (see Figure 1). An erosive bay has formed between these two stable points, decreasing the alongshore supply of shingle to the Station frontage over the years. Thus, the main point of beach feed, which lies at the western end of the station, was becoming more and more exposed as the up drift coast has receded and the natural supply of shingle dwindles. Consequently, in recent years the amount of beach feed required was in excess of 50,000m<sup>3</sup> annually.

The beach feeding scheme has operated for 28 years during which time Halcrow have produced annual reports describing the work done during the previous season and recommending the quantities and positions for shingle feeding during the forthcoming season. Until 1972 the amount lost during the year was replaced at locations which had suffered the greatest erosion and was distributed in roughly equal proportions at a series of points. After 1972 it was realised that a more efficient method of protecting the beach would be to place most of the recharge at the western end, allowing natural movement to distribute the shingle over the frontage.

The levels along each of the cross-sections are now established on the 42 sections, which are at 100m intervals, by photogrammetric methods. It is considered that the 1:5000 scale of photography normally used allows individual beach levels to be determined to an accuracy of within approximately  $\pm 0.20$  metres (assuming no errors in the control grid). There are 14 sections each with three sub-sections (see Figure 2), 9 in front of the station and 5 downdrift in the supply area. One of the major advantages of the beach feeding scheme has been its flexibility and the ability to respond quickly to potential problems and periods of intensive storms. Figure 3 shows the gross losses, the quantities of material deposited and the volume changes each year since beach feeding began in 1965. The total volume of shingle between profiles 1A and 9A has increased by some 102,394m<sup>3</sup> between 1965 and 1993/94, resulting from an average annual recharge of about 30,000m<sup>3</sup>, with an average annual gross loss of about 26,500m<sup>3</sup>. The records clearly demonstrate that the beach feeding successful stabilised the beach and that the build up of the profiles have been sufficient of balance the increased losses in extreme years. A typical profile of the build up of shingle over the years can be seen on Figure 4.

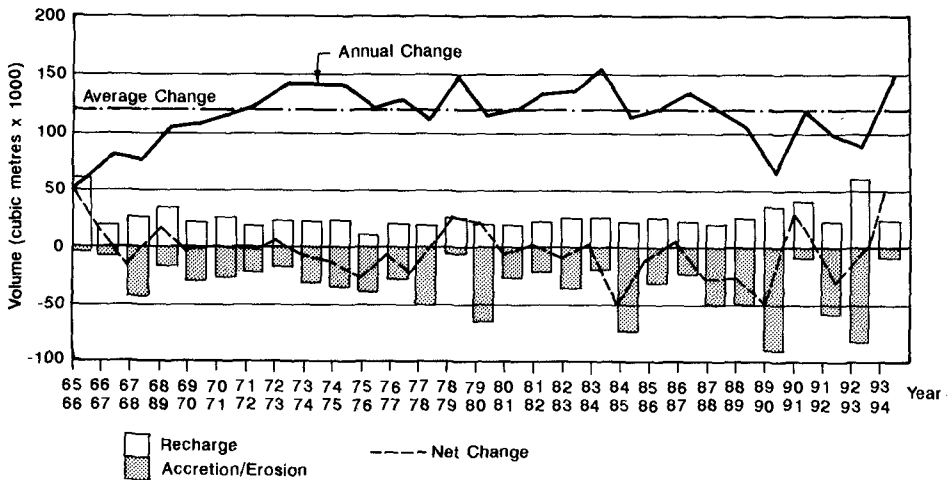


Figure 3: Volume changes from 1965 to 1994



The beach feeding programme has been effective in preventing flooding and damage to the Station. Prior to 1983 there appear to be no records of serious flooding, apart from during construction, but there has been flooding adjacent to the site on:

- 28th January - 1st February 1983
- February 1984
- November 1984
- Winter 1989-1990
- February/March 1990
- August 1992

This increase in the potential flood risk may be related to an increase in wave energy during the period (see Figure 5) and has led to a change in the "emergency" and "normal" profiles. These profiles for sections 1A to 9A were conceived nearly 30 years ago. The original concept was that the "normal" profile should be the minimum cross-section of beach to be maintained, where the "emergency" profile represented conditions which could lead to major overtopping of the beach and flooding, hence requiring "emergency" works. The levels were increased last year to take account of the impact of a tsunami wave, which has a 1 in 10,000 year return period.

### **Past Investigations**

In an effort to reduce the annual costs associated with the beach feeding programme, and any adverse environmental impacts, Halcrow have for many years attempted to relate beach loss to local meteorological conditions. It was originally hoped that this would allow predictions of required recharge volumes to be made without the expense of conducting an annual aerial survey. While this would never totally replace the need for surveys, it would allow their frequency to be reduced to say once every two or three years.

The 1969/70 Halcrow report described an early attempt to relate the incident energy flux to the quantity of shingle moved, but this proved unsuccessful because only four years of records were available. The 1978/79 study the

correlated the observed shingle loss and wind gusts which exceeded 47 knots ie storm conditions. This proved to be reasonably successful, but in the early 1980's it was proved less so. One of the difficulties in trying to establish any correlation stems from the fact that the average annual gross loss, represents a fairly thin layer over the surface of the total shingle volume of approximately 1.25 million m<sup>3</sup> contained within the survey section limits ie the losses are only approximately 2% of the total. Furthermore, the computations do not allow for irregularities in the beach profiles between the measured cross-sections which are at 100m centres. The gross loss has to be determined by the difference of these total volumes, over successive years, so that small errors in the determination of the total volume have a significant effect on the calculation of the gross loss for any one year. It was concluded that no simple relationship exists between beach losses and non-directional wind intensity.

#### **Analysis of Beach Erosion**

It was originally predicted in 1963 that the natural supply of littoral material from the west of the station, which was about 120,000m<sup>3</sup> would slowly reduce with time, requiring a commensurate increase in beach feeding. This effect results from the gradual formation of a shallow bay between the stabilized sections of the coast at Jury's Gap and the Station. This was confirmed by beach plan shape modelling, which shows the yearly gross shingle loss along the Station is rising, on average, by some 880m<sup>3</sup>/year. The previous analysis of the seven year rolling means in 1984 showed the annual rate to be 540m<sup>3</sup>.

The cumulative average annual gross loss of beach material upto 1992 was 29,490m<sup>3</sup>. However, the average over the past five years has been 42,000m<sup>3</sup>. In the previous five years it was 30,000m<sup>3</sup> ie 1983 to 1987, 25,000m<sup>3</sup>/year from 1978 to 1983, and 24,000m<sup>3</sup>/year for 1973 to 1978.

#### **Wave Data**

Offshore wave data were derived using a parametric wave model based on wind measurements between 1971 and 1990. Such models are limited to hindcasting of locally generated waves within defined fetches. To determine the importance of swell, wave data were obtained from the British Meteorological Office's wave model for the years 1989 to 1992. The swell wave portion of the wave spectrum,

coming up the Channel from the Atlantic was found to be 25%.

Section 7A (see Figure 2)

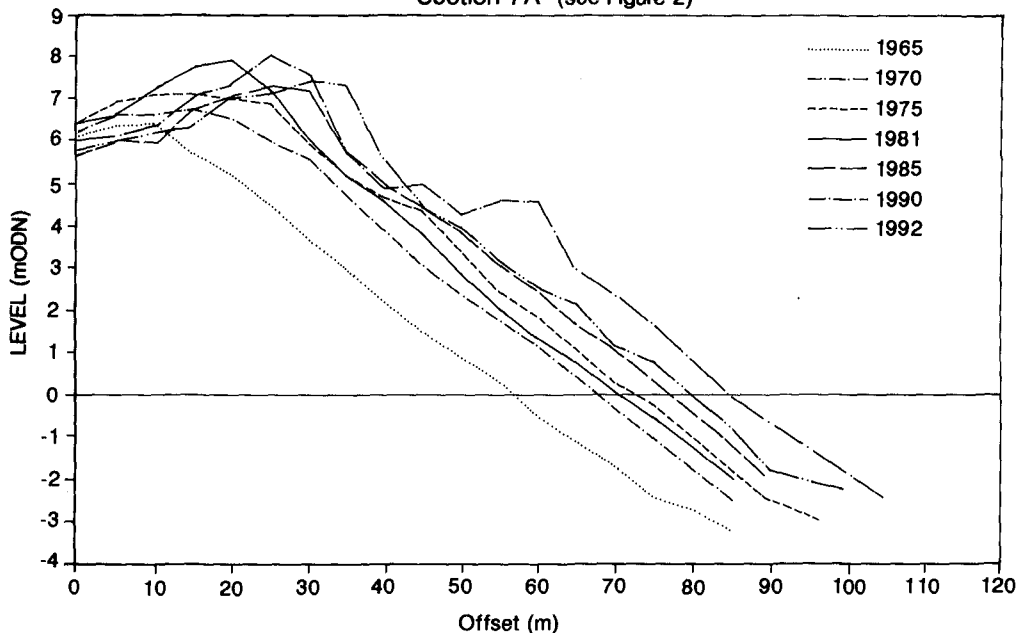


**Figure 4: Beach Movement 1965-1992**

The available wind wave data were statistically analysed to produce seasonal, directional, yearly and average values of wave energy, with only the last four years including swell waves. Values of alongshore energy were derived for each year and used to produce a trend analysis as shown in Figure 5. Despite the wide scatter of data there is clearly an increasing trend in longshore wave energy. The gradient of the graph is approximately 16 KN/year.

The increase in wave energy may in part account for the increased rate of annual shingle loss also shown in Figure 5. For example, equating the long term average gross beach erosion to the long term average alongshore drift gives a figure of approximately 500m<sup>3</sup>/year increase in beach erosion, which can be directly attributed to an overall increase in wave energy. Subtracting this figure from the

880m<sup>3</sup>/year derived from the trend analysis of gross erosion gives a figure of 380m<sup>3</sup>/year, which may be attributed to the changes in alongshore drift at Station.

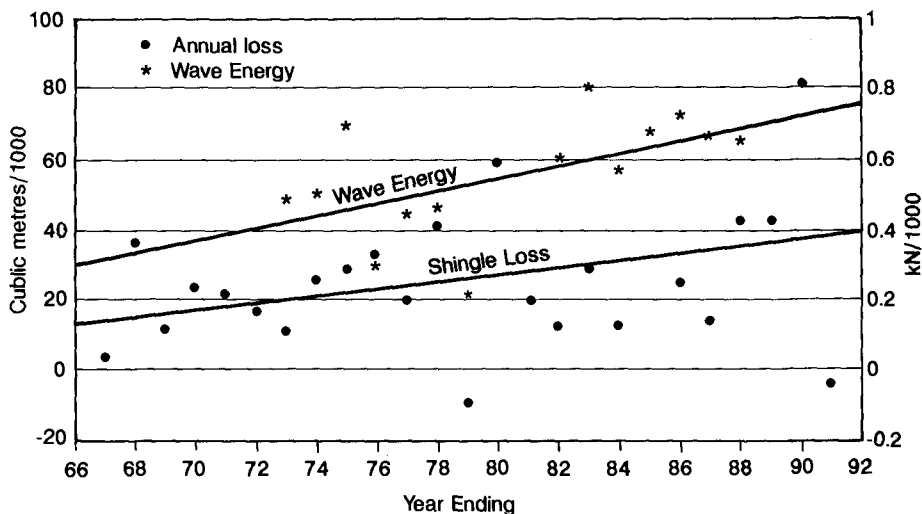


**Figure 5: Annual Shingle Losses and Wave Energy**

While the trend lines show a clear correlation between increasing beach loss and wave energy, the comparison of individual years shows large deviations and therefore little predictive capability based on annual results. Figure 5 shows alongshore wave energy plotted against beach loss for the years 1989-1990, 1990-1991, 1991-1992 and 1992-1993. While there is a good fit for some years, the energy available for 1989-1990 underpredicts the beach loss. However, the winter of 1989-90 was marked by a series of four gales, some with hurricane force winds, all of which coincided with spring tides which weakened the beaches. Had not the gales of 1989-90 occurred on spring tides, the measured gross loss of material at the Station would have been much less. Thus, a simple analysis of alongshore energy will tend to underpredict beach losses for those years affected by extreme water levels.

The past studies have shown that while there was a reasonable relationship between wave energy and the littoral transport, it was not a simple one. Predictions can vary depending on the coincidence of high wave energy

and surges during the period and the predicted and actual volume, could vary by as much as a factor of 2.

#### **ALONGSHORE TRANSPORT**

The present alongshore shingle transport rate of about 90,000m<sup>3</sup> was established using an existing beach plan shape model. Studies were also carried out using electronic pebbles to monitor shingle movement during the storms and the transport rates of different sizes of shingle. These 'smart' pebbles show, rather surprisingly, that the larger shingle travelled at a faster rate possibly because of the greater area of exposure of the larger shingle in a mixed grading. Studies of the grain size of material on the beach also showed significant changes both in relation to storm and the size of the feed material.

#### **BEACH PLAN SHAPE MODELLING**

There is sufficient gravel accreting on the eastern coast of the Ness which can be used to improve and strengthen the beach at the Station. However, it was realised that taking increasing amounts of gravel could adversely affect the downdrift coastline, especially as it is the source area for beach feeding elsewhere. Consequently, there was a review of the beach feeding, which included, in particular, a sediment transport model in order to predict the drift rates and future changes in coastal morphology.

Three schemes were adopted for examination during the model study, namely:

- Scheme 1 - supply beach feed at Section 1A (see Figure 2) to maintain the existing beach line. This corresponds to the present beach feeding policy.
- Scheme 2 - supply beach feed at Section 4A (see Figure 2) to maintain the existing beach line east of it. Beach sections to the west of Section 4A are allowed to evolve naturally.
- Scheme 3 - Construct a long strong point at Section 9A (see Figure 2),

at the downdrift end of the site and use accumulated material to maintain the beach east of Section 1A as in Scheme 1.

The model was run to simulate fifty years operation of each of the above schemes. The feed quantities envisaged for each scheme are shown on Table 1.

Year	Scheme 1 Feed at Section 1	Scheme 2 Feed at Section 4	Yearly Saving in m <sup>3</sup>
1	40,000	13,172	26,828
5	41,000	18,494	22,506
10	41,119	23,816	17,303
20	42,548	28,902	13,646
50	46,627	35,970	10,657

**Table 1 Predicted Feed Quantities (m<sup>3</sup>/year)**

As can be seen, Scheme 2 shows considerable savings over Scheme 1.

#### **ECONOMICS OF BEACH FEEDING AND ALTERNATIVES**

The economics of beach feeding at the Station were last examined in detail in 1983 in connection with studies for a proposed new station. As discussed earlier, in the last five years beach recharge quantities have increased significantly, and it was considered necessary to reassess the economics of the present operations compared with alternative forms of coastal protection.

From the earlier beach recharge quantities and trends, it was concluded that the base estimate for quantities should be 40,000m<sup>3</sup>/year ie the situation before managed coastal retreat or set back, using upper and lower bound figures of 125m<sup>3</sup>/year and 500m<sup>3</sup>/year for the rate of increase of beach recharge.

The above figures were used to calculate the Net Present Value (NPV) of the following cost of beach recharge discounted over a period of 50 years:

Initial Recharge	Rate of Increase	NPV in £
40,000m <sup>3</sup> /yr	125m <sup>3</sup> /yr	3,033,471
40,000m <sup>3</sup> /yr	500m <sup>3</sup> /yr	3,469,502

The alternative forms of coastal protection considered in the 1983 review of coastal protection included:

- beach feeding
- several forms of groyne and breastwork
- artificial headlands and an initial beach fillings
- an armoured revetment

The comparison of various options was based on Net Present Values for 35 year and 105 year life spans. These are summarised in Table 2.

SCHEME		Net Present Value £ X 10 <sup>6</sup>	
		35 Year Life	105 Year Life
1	Beach Feeding	2.1	2.7
2	Timber Groynes and Breastwork	4.8	5.7
3	Mass Concrete Groynes and Timber Breastwork	5.7	6.5
4	Armabrade Steel Sheet Piled Groynes and Timber Breastwork	8.2	9.4
5	Two Strongpoints and Initial Feeding	4.3 plus cost of lee scour	4.3 plus cost of lee scour
6	Revetment of Armour Units	15.3	15.3

**Table 2 Net Present Values of Coastal Protection Schemes at Dungeness, 1983 Prices.**

These costs clearly demonstrate that the existing practice of beach feeding is the most economic form of coastal protection. The present policy of managed retreat or set back enhances the benefits.

## CONCLUSIONS

### Review of Beach Feeding

- The beach feeding campaign has been effective in preventing flooding and damage to the Station.
- It is the most cost effective method of protection.

### Beach Movement and Meteorological Conditions

- An analysis of wave data derived from wind hindcasting showed a recent increase in wave energy and a clear correlation between increasing wave energy and increasing beach loss. However, the comparison with values for individual years did not show a good correlation with measured beach losses and wave energy. The inclusion of swell waves provides a more reliable predictive method for calculating beach losses in all but the most extreme years.
- In the past five years beach feed quantities have increased dramatically. Recent studies have concluded that there has been an increase in the number of severe storms affecting Wales and Southern England, although this does not form part of a clear statistical trend. Moreover, these recent storms would not have appeared to be so unusual had not the 1970's and early 1980's been so mild.

### Economics of Beach Feeding and Alternative

- A net present value of beach feeding for the 1992-1993 season over a lifespan of fifty years was established using an updated base estimate of the annual beach feed quantity and the future annual increases.



- Beach feeding, ignoring the benefits of coastal retreat, is still significantly cheaper than the other forms of coastal protection.

#### Coastal Retreat

- The concept of coastal retreat has lived upto its expeditions, significantly reducing the quantities of shingle required, thus reducing costs and any adverse environmental and geomorphological impacts that might stem from shingle extraction from the supply area.

**REFERENCES**

- Greensmith, J T, and Gutmanis, J C, 1990. Aspects of the late Holocene depositional history of the Dungeness area, Kent. Proceedings of the Geologists' Association, 101, 164-74.
- Sir William Halcrow & Partners, 1963, Report on Coast Protection.
- Lewis, W V, 1932. The formation of Dungeness foreland. Geographical Journal, 80, 309-24.
- Lewis, W V and Balchin, W G V, 1940. Past sea-levels at Dungeness. Geographical Journal, 96, 258-85.
- Long, A and Shennan, I, 1993. Holocene sea-level and crustal movements in southeast and northeast England, UK. Quaternary Proceedings, 3, 15-19.
- Long, A, 1994. Evolution of the south shore of Dungeness, Report for the Romney Marsh Research Trust.
- Maddrell, R J and Burren, K: "Predicted sea level changes and their Impact on coastal works worldwide", 3rd Australian Port and Harbour Engineering Conference, 1990.
- Shennan, I, 1989. Holocene crustal movements and sea-level changes in Great Britain, Journal of Quaternary Science, 4, 77-89.
- Ward, G, 1931. Saxon Lydd. Archaeologia Cantiana, 43, 39-47.

## CHAPTER 257

### PROJECT, WORKS AND MONITORING AT BARCELONA OLYMPIC BEACHES

Carlos Peña (\*) & Manuel F. Covarsl(\*)

#### 1.- INTRODUCTION.

Barcelona is the second city in Spain(2.3 million inhabitants) after Madrid (4 million) and is also the city that held the last Olympic Games in July 1992.

It is the third segment of a physiographic unit beginning at Tordera River Delta and ending at the port of Barcelona.(A description of the whole physiographic unit can be found in ref. 1 by Carlos Peña 1992).

But in the last decades it became one of the ugliest and most degraded part of the coast of Spain. Everybody considered most of the sea-front side as the rubbish dump where everybody could get rid of everything.

In addition to this, there was some groins constructed to assure the discharge of Barcelona sewage draining system.(Nowadays there are still from time to time, rain water discharges there).

#### 2.- THE SCHEME.

The first important decision to be taken when the recovery of this part of the city was decided was to choose between the simple sand nourishment or the stabilization of the coast line with rigid structures.

The previously existing groins have conditioned the solution to recover the beaches of Barcelona sea-front. If these groins were not there as an unavoidable condition the solution probably was a simple and periodic sand nourishment since in the vicinity of Barcelona many millions cubic meters of coarse sand are available at less than 30 m. depth water.

---

(\*) Civil Engineers, General Directorate of Coasts;

Address : Dirección General de Costas, Ministerio de Obras Públicas, Transportes y Medio Ambiente (MOPTMA), Paseo de la Castellana 67, 28071 Madrid, Spain.

But since it was necessary to keep and improve the discharge capacity of the draining system of Barcelona, the solution finally adopted was to rigidize the coast and to build pocket beaches between every couple of groins.

A schematic plan of the whole project in front of the Olympic Village can be seen in fig.1 and a part of it in fig.2.

### **3.- THE WORKS**

The landscape has deeply changed; a marina has been constructed as part of the Olympic Games infrastructure, beaches can be found instead of previous rubbish tips, and the groins have been rebuilt in order to assure the stability of the beaches.

Fig. 13 shows an aerial view of the whole area in 1993 after the works have been completed.

As a whole, 1,485,476 m<sup>3</sup> of sand have been pumped to the beaches and most of the groins have a submerged part in order to stabilize the sand without horizon visual intrusion, supporting the submerged part of the sand profiles at the southern part of every pocket beach of this project.

As we can see later this part of the project only partially did work properly.

An important element is the submerged groin of fig.3a and fig.3b. It was designed with a double purpose: The first one is to act on the incident waves in order to make them refract in the same way as an emerged breakwater would do. The second one is to support the submerged profile of the Somorrostro Beach.

It was built with the crown at mean sea water level to in order to keep the horizon line free of visual intrusion as much as possible.

In order to precisely design this part of the project so that to keep the energy transmission coefficient below 0.1 and to test its stability, a lot of experiments were carried out at the Centro de Estudios y Experimentación de Puertos y Costas (CEPYC-CEDEX, ref.2). As a result, the groin has the crown 34 m. wide at mean sea water level.

The coast line was predicted using only very simple numerical models (logarithmic spiral of Carlos Garau - ref.3 - and the theory of pocket beaches of Silvester - ref.4 -), and available visual wave data records. We all were well aware that, since these visual wave data are not very accurate, some errors could be done in the project as a whole.

Works have been completed just before the Olympic Games (July-1992), and since then the whole project is being monitored.

### **4.- THE MONITORING**

The monitoring has been focussed and divided in three different parts:

### a) Topography

The cartography and drawing of the sea-land line has been done in June and February of 1993 and April and June of 1994.

Some of the results of this topographic work are shown in fig. 4 and 7 , where also the coast line of 1987 previous to the project and the so called theoretical line have been drawn. This last line has been obtained by means of Garau logarithmic spiral theory and proves to be good enough to predict future coast lines when complete, accurate and reliable wave climate are not available.

### b) Bathimetric surveys

Bathimetric surveys of the whole area have been carried out just after the works have been completed in June 1992 and September 1993.

The lower part of fig.10 shows the measured profiles obtained at the key plan of the same fig.10. The profile of July 87 previous to the works is also included.

It is clear that these three profiles should fit below 7 or 8 m. depth but it can be seen that they do not fit even below 10 or 12 m. depth. Therefore some error (systematic or not) must have been introduced. This kind of trouble is very common in making bathimetries all over the world and as a matter of fact, this kind of surveys are useless for scientific purposes. Further investigations, research and experimentation should be done in order to improve bathimetric technic. Anyway, if we correct all the profiles forcing them to fit below 10 m. depth, (upper part of fig. 10)we can draw the map of erosion and deposition areas, and we can find out a slight trend in the sand to move to the South, except in Nova Icaria Beach which is fully stabilized by the submerged groin (fig.8) and Somorrostro Beach which shows a trend to tilt towards the Port's mouth (fig. 5).

### c) Tracers

The very same sand of the beach colored with rhodamine, uvitex and auramine was used to trace the movements of the sand. Two hundred points were sampled twice in 1993 to find out the movements of six different tracers. The results of two of them are shown in figures 6 and 9 showing the same general trend found out in the bathymetric surveys but with another very important conclusion: The submerged breakwaters and groins are not impermeable to movements of sand grains although we are not able to quantify the amount of sand that traversed them.

## **5.- CONCLUSIONS**

1) The logarithmic spiral theory of Carlos Garau and Silvester is a very useful tool to predict the coast line changes.

2) Further research should be carried out to make available better bathimetric technic.

3) Tracers are a very useful tool to find out the general trends of sand movements.

4) As far as Barcelona beaches is concerned we can conclude that the project as a whole is working well but a few small corrections should be introduced because:

a)The equilibrium shape of the pocket beaches seem to be slightly tilting to the south.

b)The submerged breakwaters and groins are not completely impermeable to sand movements.

c)The Somorrostro Beach is slightly tilting to the Port's mouth.

## **REFERENCES**

1) Peña C. et alt - Projects, works and monitoring at Barcelona Coast. - Coastal Engineering 1992 - Proceedings of the twenty-third International conference.

2)Gomez-Pina G. - Experiments on coastal protection submerged breakwaters:a way to look at the results.- Coastal Engineering 1992. Proceedings of the twenty-third International conference.

3)Garau C. - Conditions for Beach Stability - Revista de Obras Publicas.January 1981 (in Spanish)

4)Silvester R. - Coastal Engineering,2 - Chapter 2 (Elsevier Scientific Publishing Company 1974).

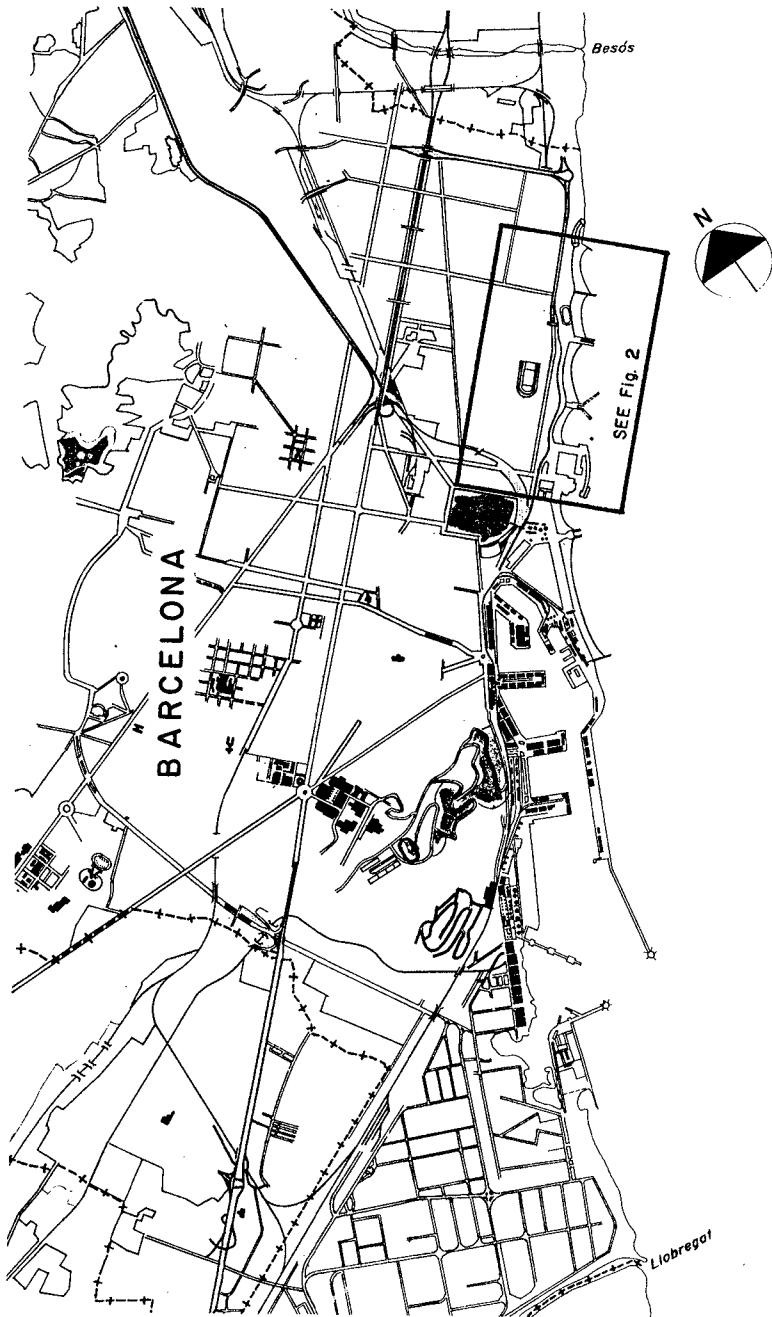


Fig. 1 GENERAL PLAN OF BARCELONA SEA-FRONT RECOVERY PROJECT.

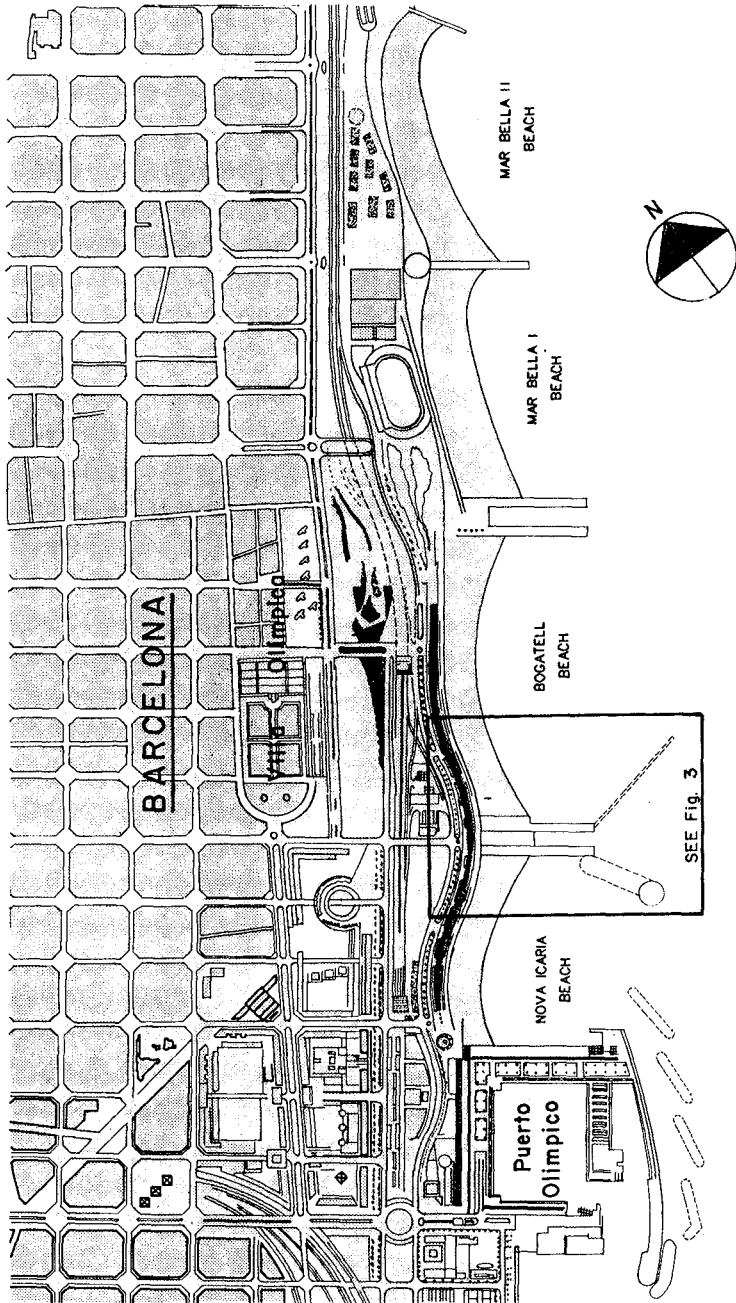


Fig. 2 PARTIAL PLAN OF THE BEACHES.



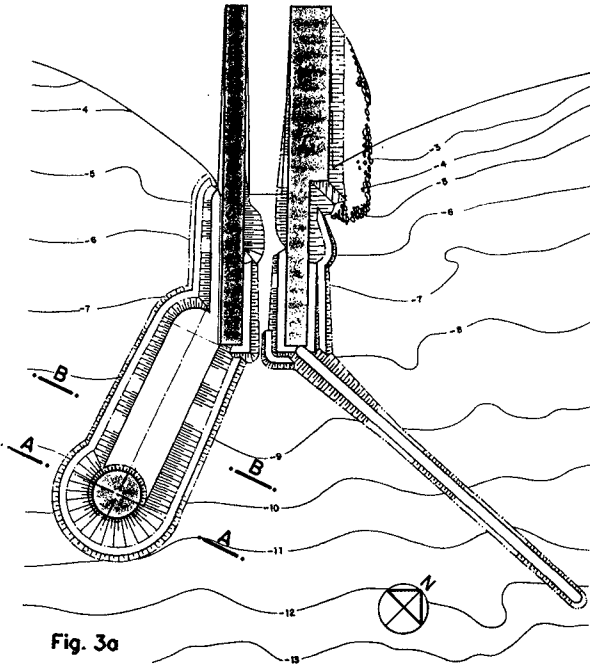
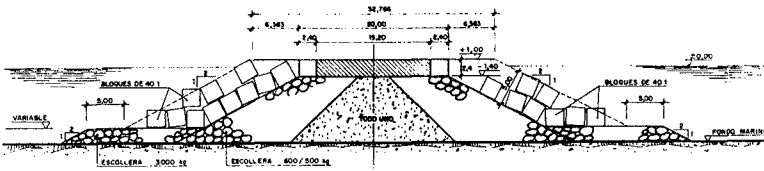
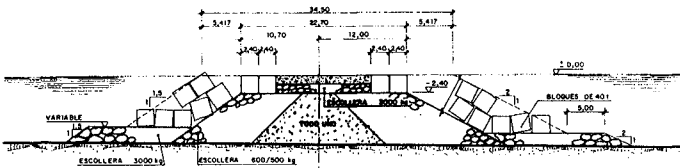


Fig. 3a



SECCION A-A



SECCION B-B

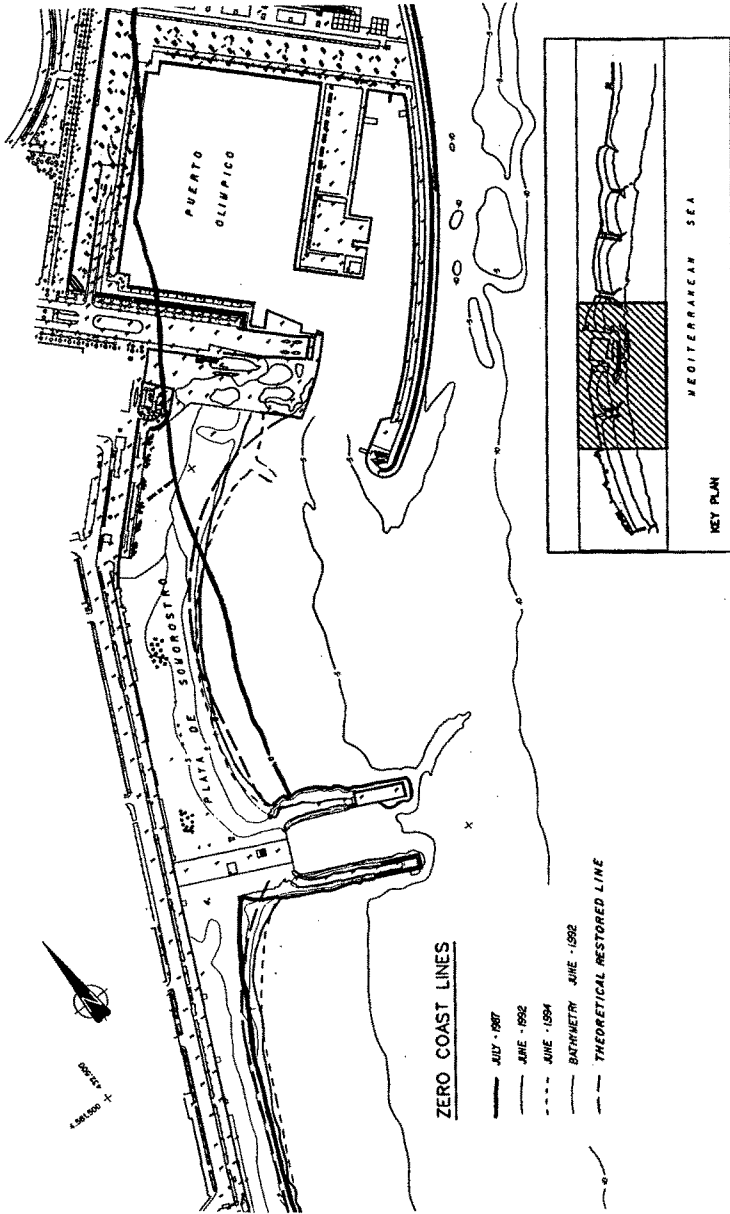


Fig. 4 THE SHORELINE OF BEACH ( Playa de Somorrostro ) HAS EXPERIENCED VERY BIG CHANGES SINCE JULY 1987. THE SO CALLED THEORETICAL LINE IS OBTAINED WITH CARLOS GARAU'S SPIRAL.

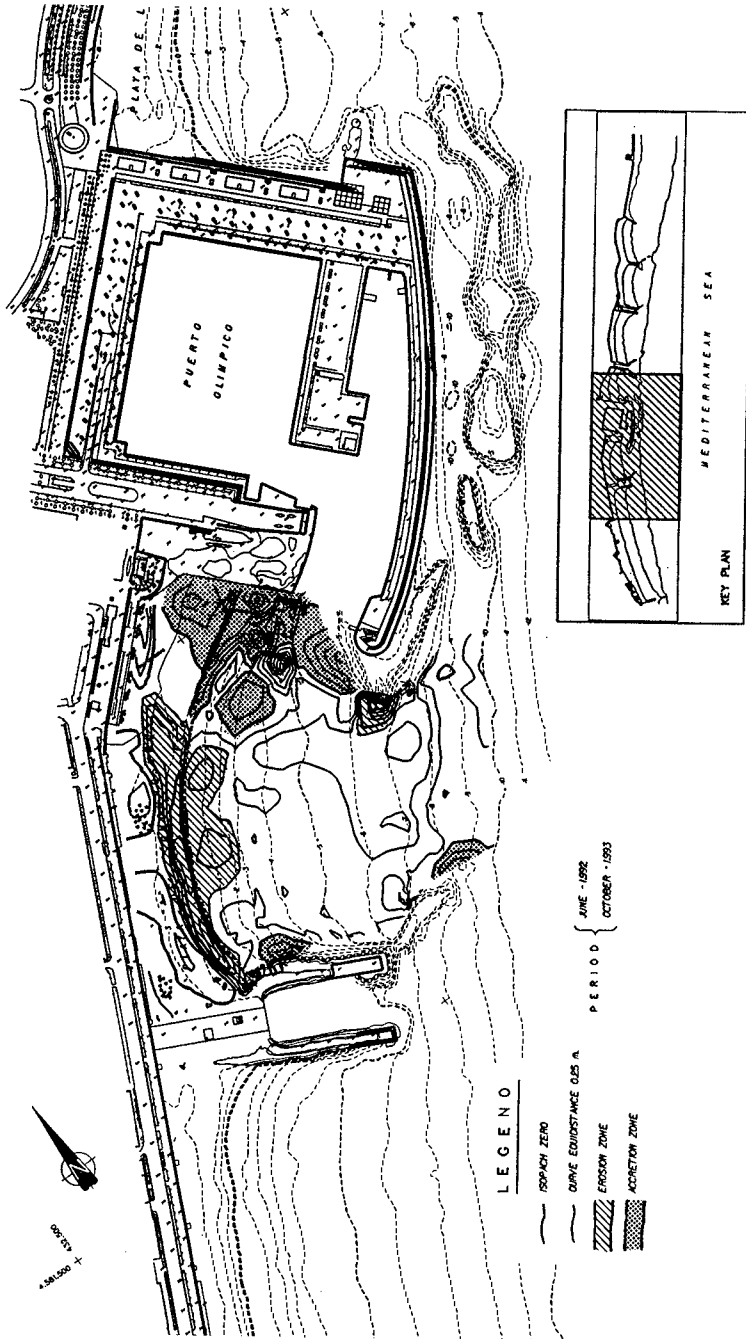


Fig. 5 THIS FIGURE SHOWS THE AREAS OF SEDIMENTATION AND EROSION IN SOMORROSTRO BEACH.

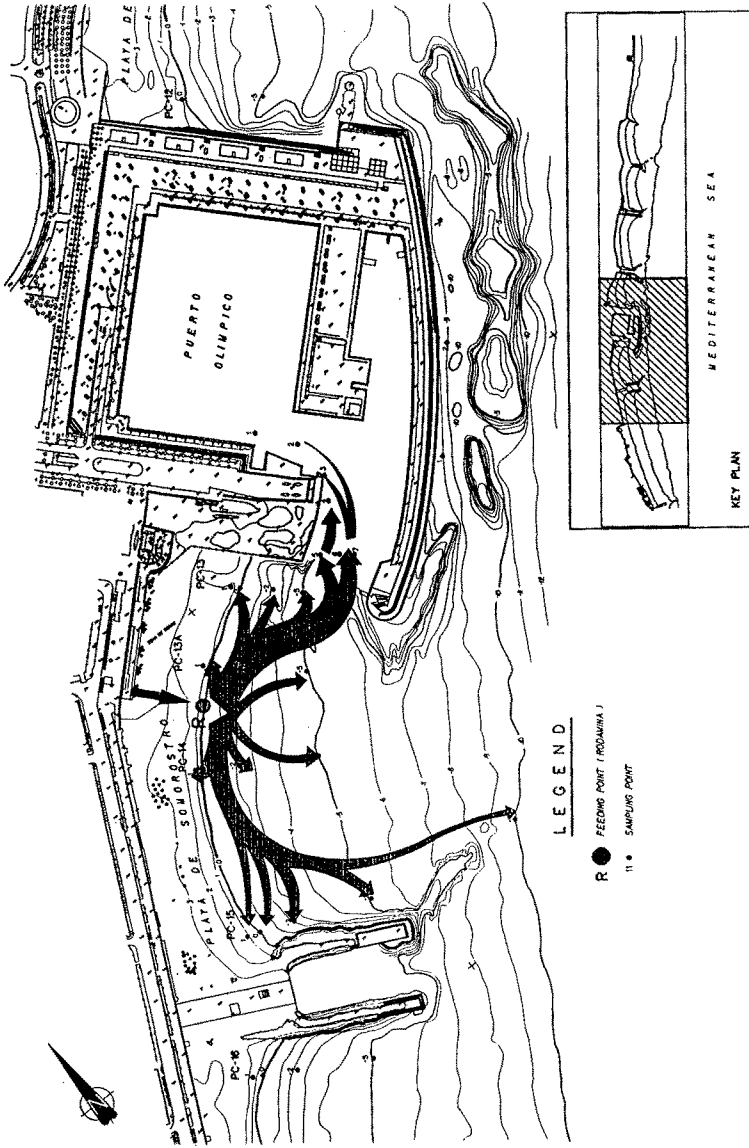


Fig. 6 TRACERS FEEDED IN R AND SAMPLED IN MANY POINTS SHOW THEY TEND TO MOVE MAINLY TOWARDS THE PORT-MOUTH.

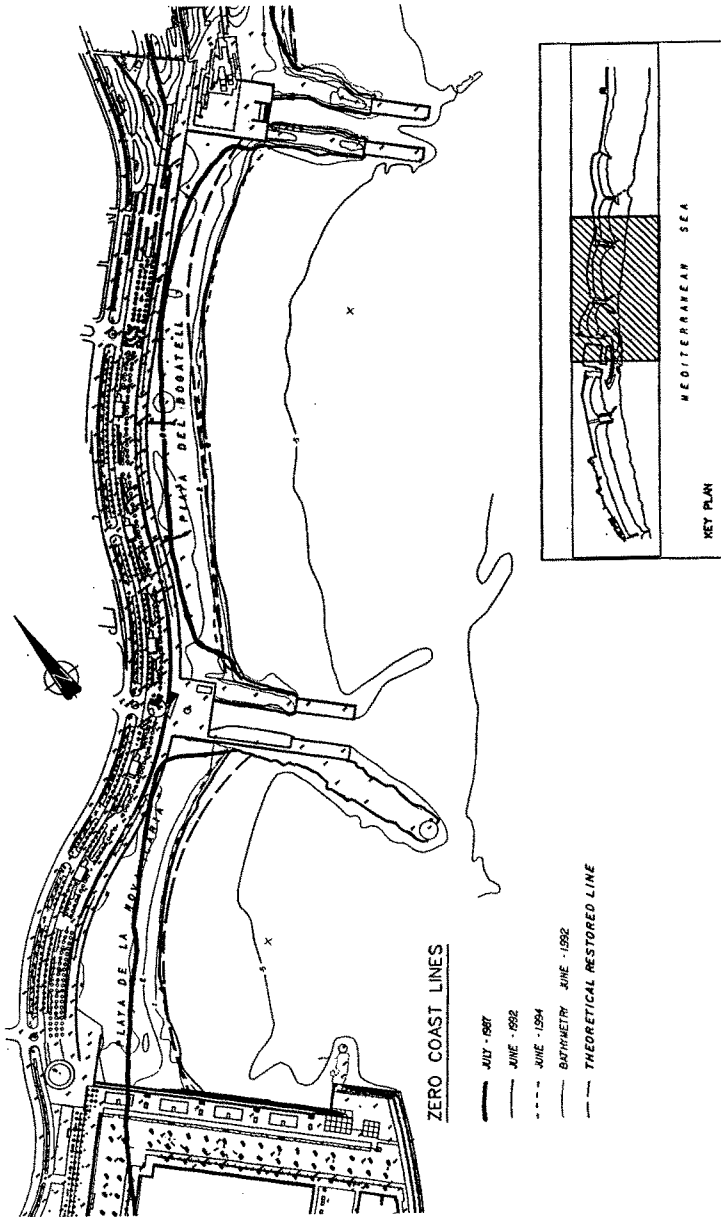


Fig. 7 AT THE NORTHERN PART OF THE PORT THE COASTAL LINE ADVANCED ABOUT TWENTY METERS AFTER THE WORKS.

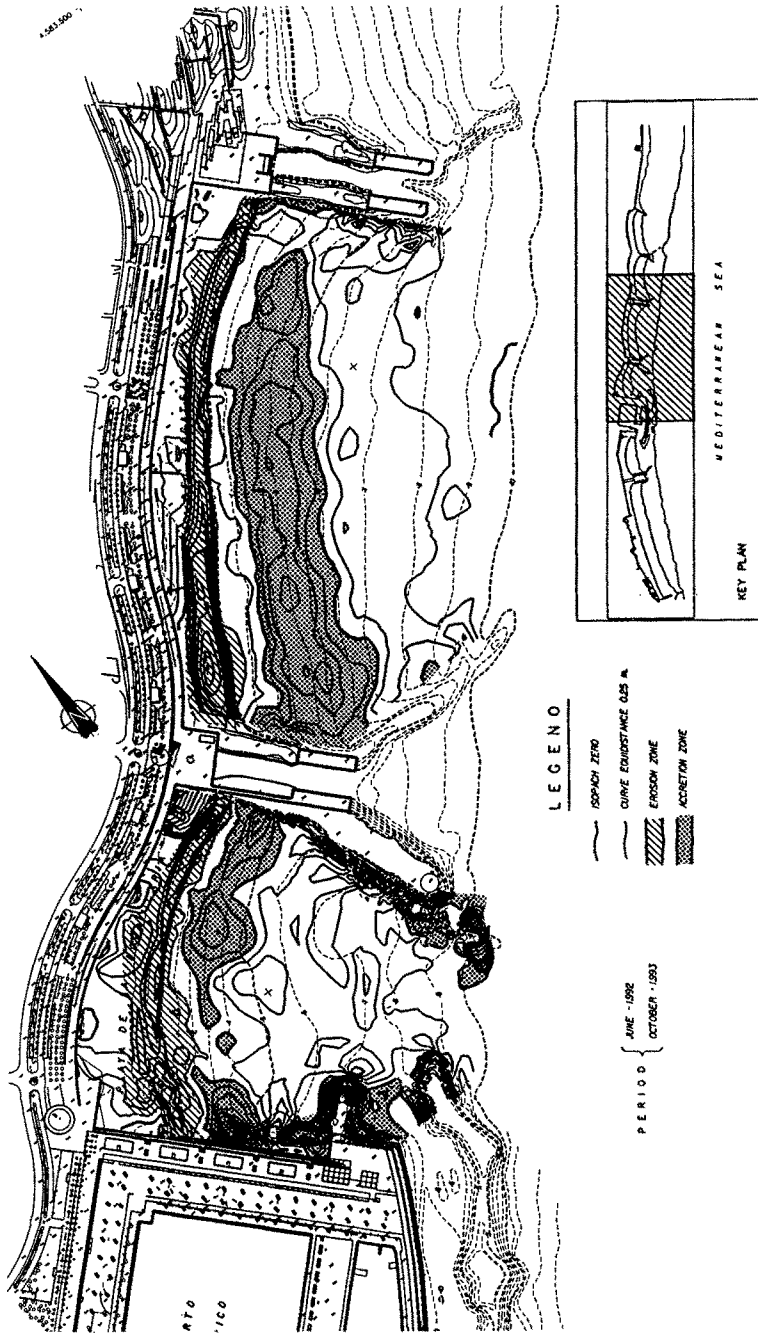
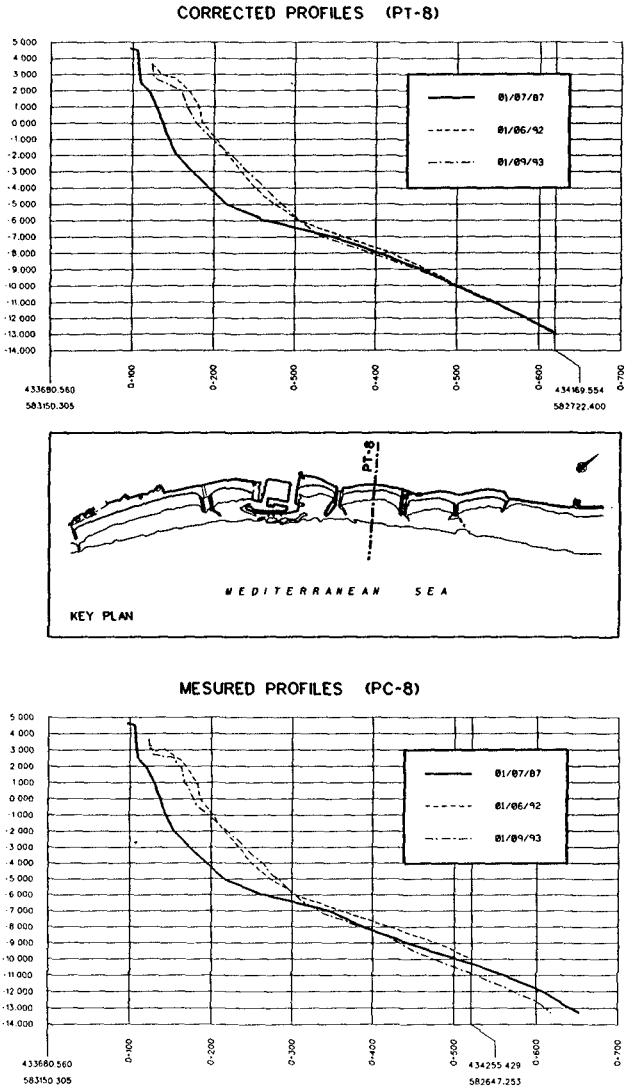


Fig. 8 DARK ZONES ARE DEPOSITION AREAS SINCE JUNE-1992. THEY SHOW A GENERAL TENDENCY TO MOVE SLITLY TO THE SOUTH.





**Fig. 10** THE LOWER FIGURE SHOWS MEASURED PROFILES IN 87, 92 AND 93 BATHIMETRIES. THEY DO NOT FIT EVEN BELOW 10 METERS DEPTH. THE UPPER PROFILES SHOW THE CORRECTED ONE'S.





**Fig. 11** A GENERAL AERIAL VIEW OF BARCELONA'S OLYMPIC BEACHES. FROM THE LOWER PART OF THE PHOTO TO THE END WE CAN SEE SOMORROSTRO BEACH, THE OLYMPIC MARINA, NOVA ICARIA BEACH, BOGATELL BEACH, MAR BELLA I AND MAR BELLA II BEACH.

## CHAPTER 258

### SANTA CRISTINA BEACH NOURISHMENT WORKS AND MONITORING PROGRAM

E. TOBA, G. GOMEZ-PINA and J. ALVAREZ 1

#### ABSTRACT

The purpose of this paper is to analyze the suitability of the solution adopted to restore Santa Cristina beach in La Coruña (Spain). The solution, which did not include any structures such as groins, consisted of adding 450.000 M3. of sand dredged from the sea bottom.

Also, a monitoring program was carried out for two years in order to implement appropriate coastal management strategies.

#### 1.- INTRODUCTION

##### 1.1 Morphological Description and Historic Evolution.

Santa Cristina beach lies at the southern end of the La Coruña estuary ("Ría"), approximately 6 Kilometers from the estuary's entrance, forming a classic spit configuration which includes in its interior the Burgo Estuary as well.

The beach has a semi-circular shape and is approximately 1.000 meters in length.

Santa Cristina and Bastiaqueiro Grande beach, which is located to the East of Santa Cristina beach and separated from it by Fiaiteira Point, comprise the bottom of the La Coruña Estuary.

-----  
1.- EDUARDO TOBA BLANCO, GREGORIO GOMEZ-PINA AND JOSE ALVAREZ ALVARADO.

MINISTRY OF PUBLIC WORKS, TRANSPORTS AND ENVIRONMENT, SPAIN.

Manuel Murguía, 6

LA CORUÑA-15011-SPAIN

From East to West, the beach is bounded landward by:

- a pier abutting against a vertical wall 80 meters long
- a vertical wall, approximately 150 meters long, built upon rocks (where "Casa Sara" was formerly located)
- rubble-mound protection, 700 meters in length,  $\cot\alpha=1.5$  and above the Highest Tidal Level (HTL)
- beach and dune, 300 meters in length.
- El Burgo Estuary rivermouth, bordered on its Western end by a cliff and Oza Point, known as the "El Pasaje" zone.

Urban development of the spit, in addition to the effect of the coastal defense works and sand mining in the past, caused the near destruction of almost one Kilometer of dry beach.

Santa Cristina Beach before urban development of the spit (see figure 1 and 2)



FIG. 1 SANTA CRISTINA BEACH. 1.940 (PHOTO: BLANCO)



FIG.2 SANTA CRISTINA BEACH. 1.950 (PHOTO: BLANCO)

### 1.2 Previous Analysis

Two preliminary studies were performed to evaluate the feasibility of the nourishment project: one by the CEPYC, and the second by Professor Losada, University of Cantabria.

The studies treated the variations of the tidal prisms or river flow of the El Burgo Estuary, incident waves variations, changes to the terms of the global balance of sediments equations, and the deterioration of the land areas adjoining the beach.

The following conclusions were reached:

- During the period studied, the beach would have lost approximately one million cubic meters (600.000 M<sup>3</sup> between the highest high tide and lowest low tide, and 400.000 M<sup>3</sup> between the lowest low tide and the bathymetric 5, which would not have undergone any significant changes in its position.

- The loss would occur in the Eastern zone of the beach.
- The tidal shoal was shifted approximately 100 meters to the West, but keeping its morphology.
- The principal cause of the changes was sand mining carried out during the last century.
- Construction of the Barrié de la Maza Dike has not caused important changes to the beach's contour.
- Construction of the Paseo Marítimo protective breakwater has caused the dismantling of 400 meters of dry beach, although the volume of sand affected by this disappearance is small, approximately 150.000 M3.

Figures 3, 4, 5 and 6, illustrates the shoreline evolution.



FIG. 3 LA CORUÑA ESTUARY 17 TH CENTURY

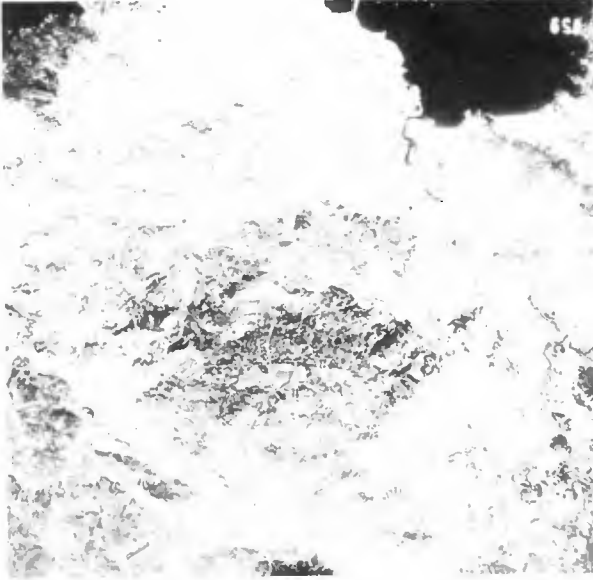


FIG. 4 LA CORUÑA ESTUARY - AERIAL PHOTO 1.945



FIG. 5 SANTA CRISTINA BEACH BEFORE NOURISHMENT WORKS.  
AERIAL PHOTO 1.990

After studying the effect of the newly constructed Oza Dock on Santa Cristina beach, it was concluded that it would be feasible to restore the spit to its original position, by means of adding approximately 450.000 M3 of sand dredged from the sea bottom. This figure is similar to the one reached by the CEPYC. (See fig. 7 and 8)



FIG. 6 SANTA CRISTINA BEACH BEFORE NOURISHMENT WORKS

## 2. HYDRODINAMIC CONDITIONS

- Wave regime

- Return Period (years)	Hs (m)
15	9,5
50	10,7
100	11,3
150	12,1

- Tidal range, 4M

- Wave diffraction effect (outer breakwater and the new inner quay of Oza)

- Effect of tide currents

- Annual maximum discharge (instantaneous) 15,9 M3/sg

- Annual average discharge 1,8 M3/sg

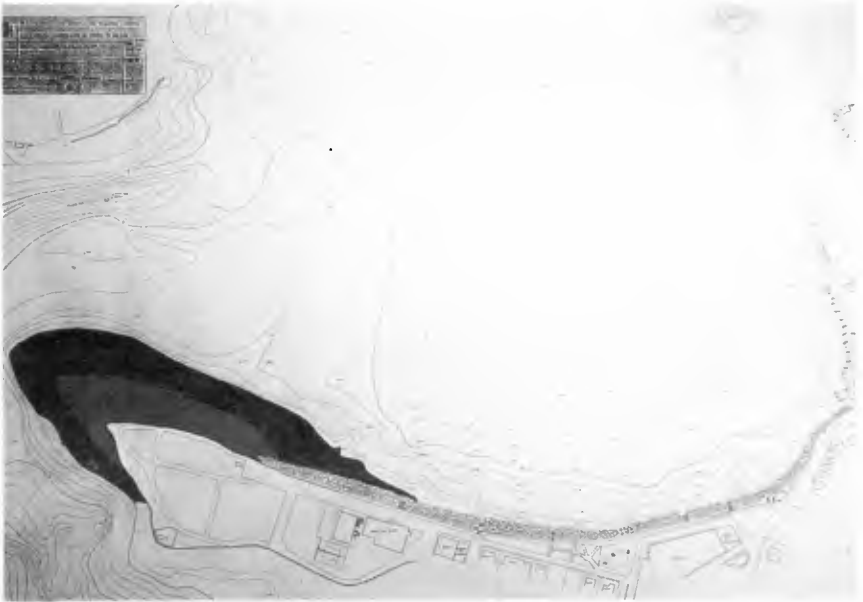


FIG. 7 SANTA CRISTINA BEACH BEFORE NOURISHMENT WORKS

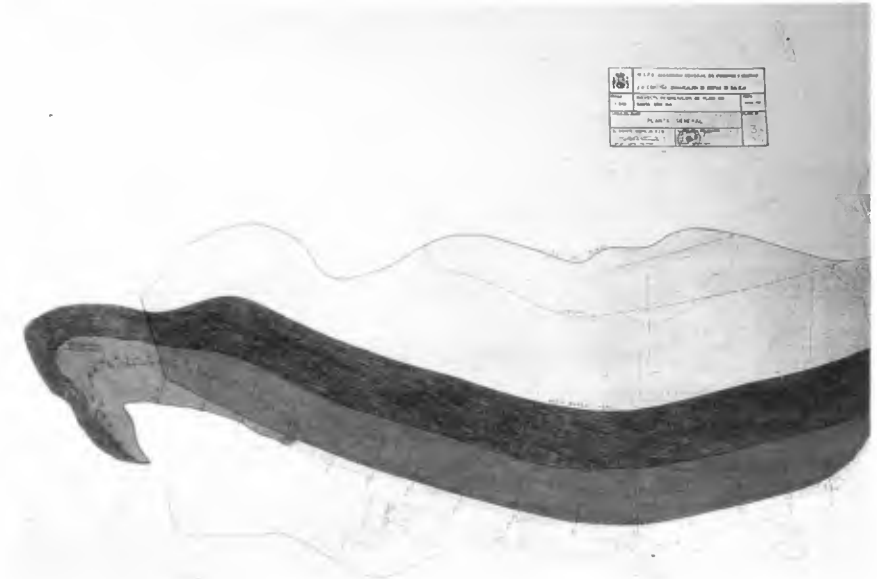


FIG. 8 SANTA CRISTINA BEACH AFTER NOURISHMENT WORKS FORECAST.



### 3. SEDIMENTOLOGICAL CHARACTERISTICS

#### - NATIVE SAND

D50= 0,18 mm at -1.0 meter water depth

D50= 0,15 mm at -5.0 meter water depth

#### BORROWED SAND

450.000 m<sup>3</sup> of sand from the sea bottom was added which is D50 = 0,45 mm at -5.0 meter water depth. (FIG.9)

Furthermore, the rubble mound defending the sea front was modified to satisfy aesthetic and social considerations. The city's population can now enjoy sitting on the stepped sea front which has become a popular meeting point at night for the city's teenagers.



FIG. 9 SANTA CRISTINA BEACH AFTER NORISHMENT WORKS

4. MONITORING

4.1 Bathymetric Procedure Utilized

To eliminate possible errors in the oceanographic devices normally used, as well as the influence of the tides, it was decided to gather data as if treating a classic leveling situation on land, that is to say, obviating the sea.

Once the data information was known, it was analyzed by computer to obtain level curves, volumes, etc.

Presently, bathymetric and granulometric works are performed every three months to monitor its evolution for the purpose of identifying areas where accretion and erosion occur. (Fig. 10)

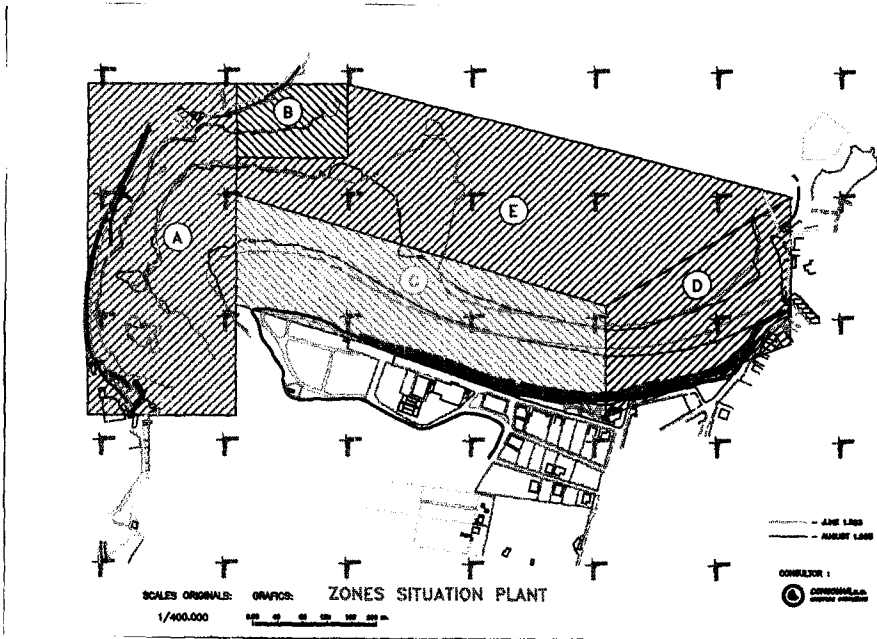


FIG. 10 ZONES SITUATION PLANT

#### 4.2 Elements Studied

The following elements have been studied:

- evolution of the beach's high and low tide lines
- beach transects and channel
- comparison between the areas of erosion and accretion
- volumetric changes of the eroded and accreted areas

#### 5. BEACH EVOLUTION/DEVELOPMENT

The beach has a 900 m.l. coastline which is exposed directly to waves. (See figure 11)  
 The eroded area (600 meters in length) is situated between the transversal outlines 1 and 4 in the East zone and reflects a typical spiral form due to the diffraction process. In this area, the beach is at  $30^\circ$  angle with respect to the alignment of the spit, as indicated in the outlines 5, 6 and 7, whose bathymetrics are noticeably parallel to the Paseo Marítimo and have experienced no changes during the entire process. Therefore, we can emphasize that this alignment corresponds to the beach's geomorphological equilibrium position.

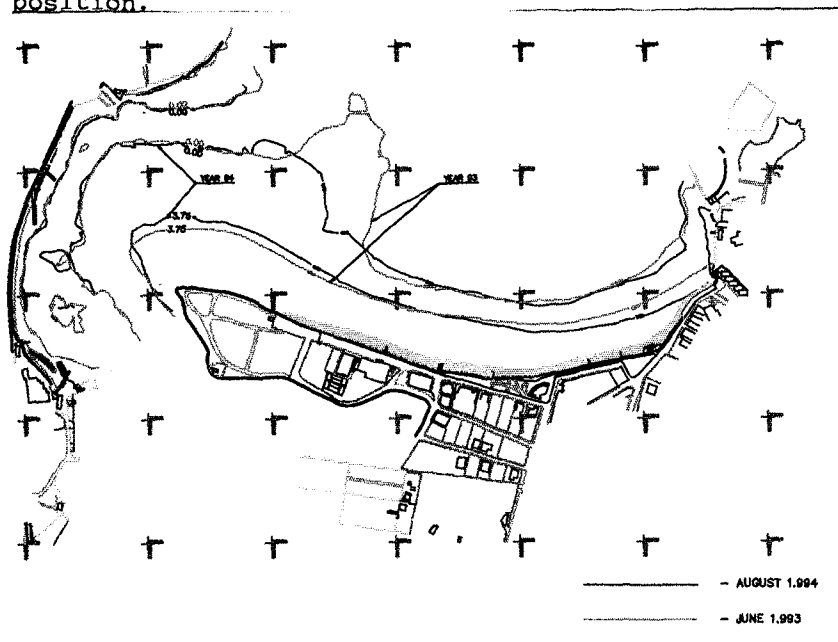


FIG. 11 BEACH EVOLUTION/DEVELOPMENT JUNE 1.993-AUGUST 1.994.

Figure 12 shows the isopachetes curves in the period june 1.993 - august 1.994

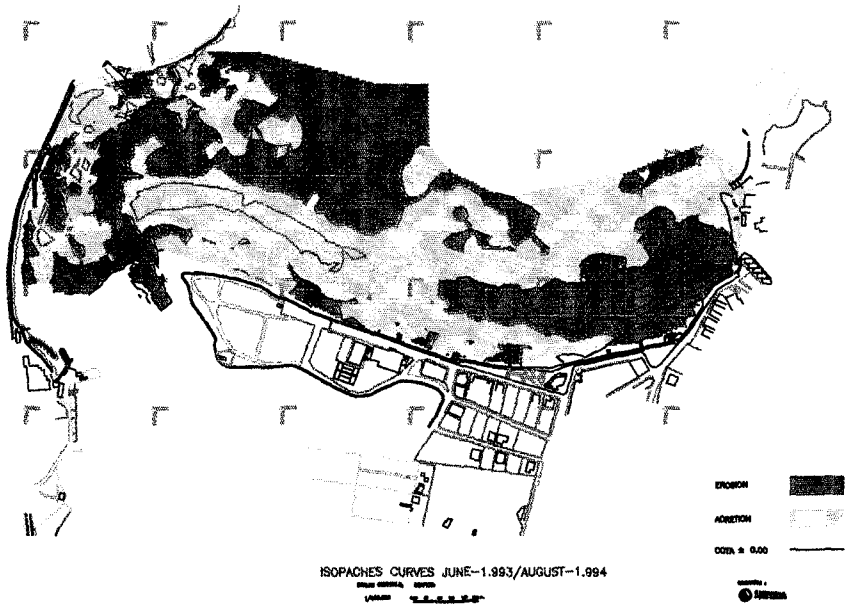


FIG. 12 ISOPACHES CURVES JUNE 1.993 - AUGUST 1.994

The sediment drift movements are showed in figures 13 and 14.

The sand eroded at the beach's Eastern zone is carried and deposited to the Western zone (spit) where significant growth is noted both in surface and elevation as a result of receiving 52.000 M3 continuously in two years (actual monitoring period).

The beach area submerged under the low tide has lost 17.000 M3 due to erosion in the last year. This sand has shifted to the spit's mouth (extreme West) and to the left bank of the river mouth.

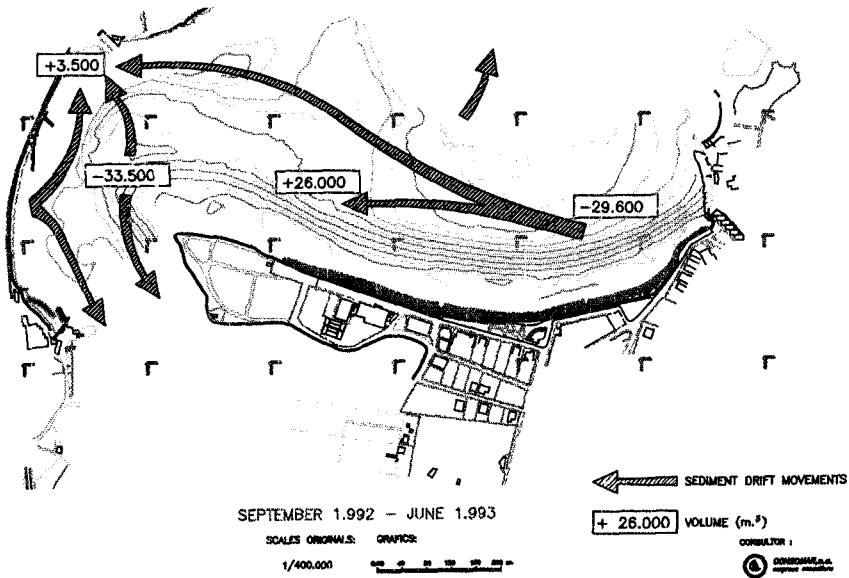


FIG. 13 SEDIMENT DRIFT MOVEMENTS SEPTEMBER 1.992 - JUNE 1.993

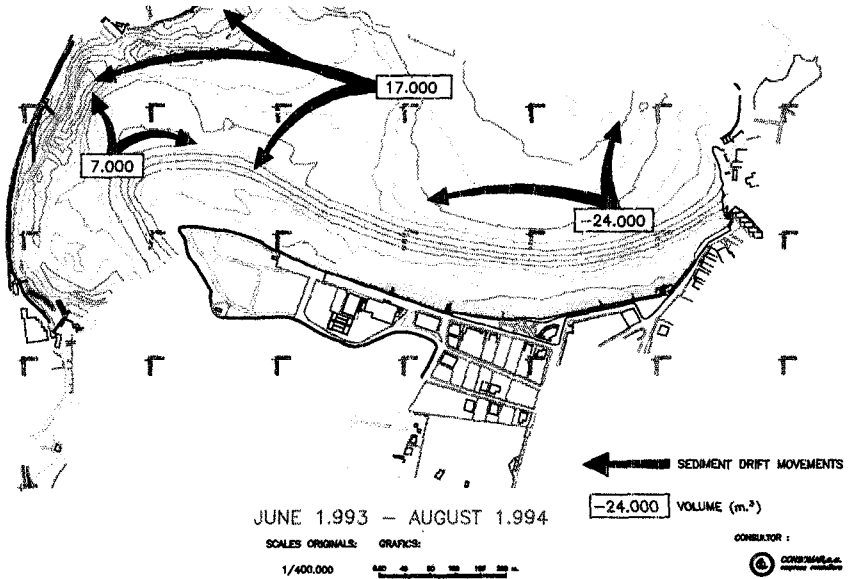


FIG 14 SEDIMENT DRIFT MOVEMENTS JUNE 1.993 - AUGUST 1.994

One of the causes of this phenomenon could be the diffractive effect produced by the new Oza breakwater, which was constructed after the beach's nourishment works had been completed, and whose effects (already predicted in the previously mentioned studies) were as follows:

1. Wave height will be reduced at every point on the beach: approximately 50% reduction in the Western half of the beach and 20% reduction in the Eastern half.

No significant change to the wave's transversal gradient will be noted, except in the beach's extreme Western sector.

2. The wave's angle of incidence will not change in the Eastern half of the beach and in the Western half, will be modified approximately 15°, reaching maximum values of 30° in the extreme Western sector of the beach.

Based on data gathered during the monitoring period, the following points can be made:

a) Coastline retreat (outline 2) "East zone" has been:

	Elevation +0,00	Elevation +3,75
Period Sept. 92 to June 93:	-28,00	-28,00
Period June 93 to Aug.94:	-10,00	-21,00
	-----	-----
TOTAL	-38,00	-49,00

b) Coastline advancement (outline 8) "West zone" has been:

	Elevation +0,00	Elevation +3,75
Period Sept. 92 to June 93:	-2,00	+36,00
Period June 93 to Aug.94:	+13,00	+18,00
	-----	-----
TOTAL	+11,00	+54,00

The results of the profiles evolution are showed in figures 15 and 16.

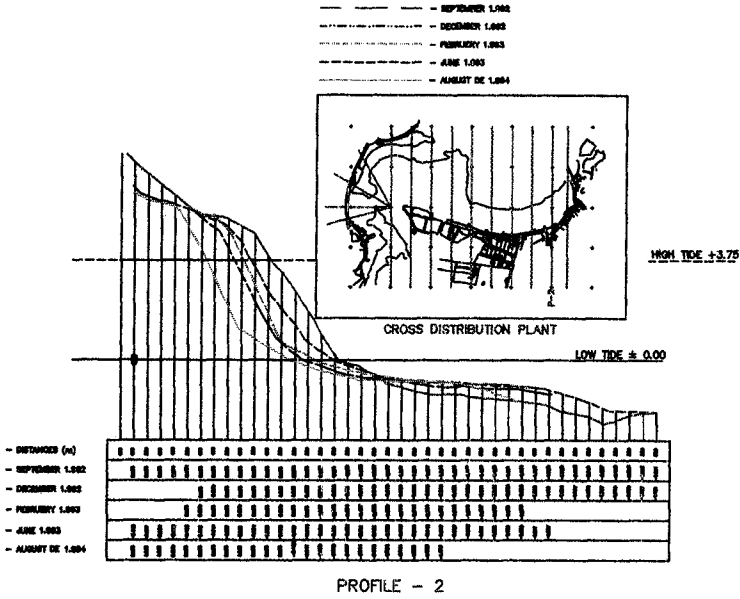


FIG. 15 PROFILE - 2

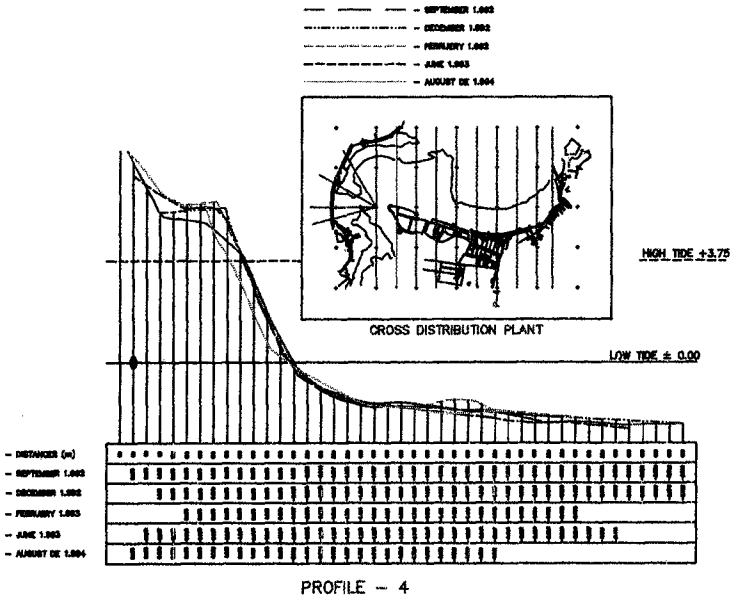


FIG. 16 PROFILE - 4

## 6. CONCLUSIONS

1<sup>a</sup> The evolution of the beach in the two annual periods studied are similar.

2<sup>a</sup> The east side is being wearing away continually. The semi-circular shape of the beach is identical to an spiral. Typical shape of beaches that are resting on by the balancing diffraction's surge.

3<sup>a</sup> The central area remains in balance and there-is no significant change.

4<sup>a</sup> The west side (arrow) wins an amount of sediments. Coming mainly from the east side. The arrow go forward parallel to itself and in the direction of the flow of the mouth of the Mero river, being more noticeable the advance in the high tide than in the low tide.

5<sup>a</sup> The element of control studied shows and equilibrate sedimentary balance between erosion and accretion.



## CHAPTER 259

### DESIGN AND CONSTRUCTION OF AN EXTENDED BERM BREAKWATER AT PORT OF HAINA, DOMINICAN REPUBLIC

David W. Yang<sup>1</sup>, Mark H. Lindo<sup>2</sup>, Edward J. Schmeltz<sup>3</sup>  
Joaquin Fernandez<sup>4</sup>, Daniel Gomez<sup>5</sup>

#### ABSTRACT

This paper presents the design, model test, and construction to rehabilitate a deteriorated rubblemond breakwater at Port of Haina, south shore of Dominican Republic (Figure 1). The original structure, 350 meter east breakwater and 250 meter west breakwater of rock and concrete block construction, was badly damaged during the storms in 1979 as shown in Figures 2 and 3. After numerous temporary repairs and studies, a rehabilitation design plan was approved. Construction started in June 1993 and is expected to complete by the end of 1995.

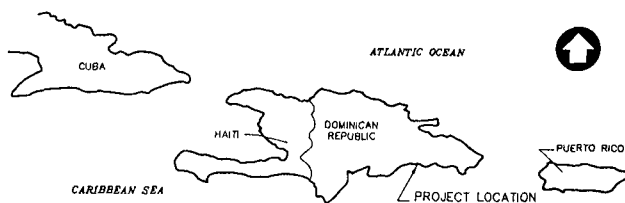


Figure 1 Location Map

- 
1. Manager, Coastal Eng. Dept. Frederic R Harris, Inc. New York, NY 10017
  2. Head, Eng. Dept. Van Oord ACZ, Marine Contractors, The Netherlands
  3. Senior Vice President, Frederic R Harris, Inc.
  4. Resident Engineer, Frederic R Harris, Inc. Santo Domingo, Dominican Republic
  5. Special Assistant to Minister of Public Works, Dominican Republic

## INTRODUCTION

The Port of Haina, a fully developed port complex with a wide spectrum of cargo handling capabilities, is located on the southern coast of the Dominican Republic at the mouth of the Haina River. The harbor is protected against incoming waves by two breakwaters (Figure 2). During the fall of 1979, the site was affected by two hurricanes, Frederick and David, which resulted in considerable damage to the breakwaters. 110 meters of the east breakwater and 65 meters of the west breakwater were essentially destroyed (Figure 3). Since that time, progressive deterioration of the structures warrants a full rehabilitation of the breakwaters. Frederic R. Harris, Inc. was appointed by the Ministry of Public Works of the Dominican Republic to supervise the design review and construction inspection of the breakwaters.

The original contract plan was prepared by TAMS in 1989. During the bid process, the Government of Dominican Republic invites contractors to propose alternative designs leading to lower construction cost and equal or better stability. The winning bid, presented by Conde and Van Oord ACZ (Reference 1), proposed an alternative design featuring extended berm and low, wide crest. This "Extended Berm Breakwater" is different from the conventional "Berm Breakwater" in design concept proposed by Baird et al (Reference 2).



Figure 2 Site Photo

This breakwater design underwent extensive three-dimensional hydraulic model test conducted by Delft Hydraulics and was certified by Danish Hydraulic Institute. The alternative berm breakwater was approved by the Government of Dominican Republic and is being constructed since June 1993.

The construction site is subject to an 8.2 meter significant design wave height with 14 second wave period. The toe of breakwater is located in up to 15 meter water depth. Due to the large design wave, the conventional design by TAMS called for an 80 ton concrete block armor unit. The alternative breakwater by Van Oord ACZ adopted an extended berm design with typical berm width of 20 meter and a wider crest width at 20 meter.

The concept of an extended berm is to pre-break the incident wave further out at the berm elevation. The armor stability is greatly enhanced due to wave breaking on a level surface instead on a slope. The runup height is also reduced by the extended berm. Due to the higher armor stability and lower runup, the alternative berm breakwater is able to adopt a smaller concrete armor unit (40 ton vs 80 ton) and a lower crest elevation (5.0 meter vs 8.2 meter) as shown in Figure 4.

Approximately 30% cost savings are accomplished due to reduced armor and stone sizes and quantities and cheaper handling and transportation costs. By reducing the size of concrete cube, reinforcement is no longer required which simplifies the casting process and increases the production rate.

#### DESIGN CONCEPT

The basic design concept is to respect the geometry and alignment of the existing destroyed breakwater as much as possible in order to reduce excavation and dredging in the old remains. Adopting such a design approach results in non-standard breakwater cross-sections for which no standard design rules have been developed yet. Similar concepts have proven to be economical in other breakwater rehabilitation projects such as Tripoli breakwaters, Libya; Arzew breakwater, Algeria; Ashdod, Israel and Sines, Portugal. In the first two projects a horizontal berm, similar as for Haina had been applied. For Ashdod a dynamic berm has been applied, for Sines a stepped sloping profile was used.

Prior to the development of an alternative design, the causes of damage, state of the damaged breakwaters

and the re-design prepared by TAMS have been studied carefully, as well as the constructibility of the designs. The following discuss background, design approach, and special features of the alternative berm breakwater.



Figure 3 Existing Condition

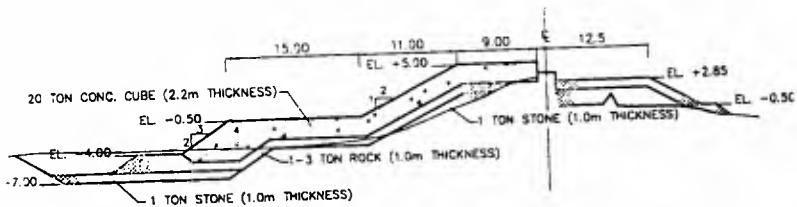


Figure 4 Typical Section

## Background

The existing breakwaters has been severely damaged by tropical hurricanes passing through the site. The condition of the breakwaters is described as severely damaged armor layers, displacement of concrete caps at the east head section, settlement and severe deterioration of concrete cap walls, and severe damage to the harbor side armor due to overtopping waves. Due to these instabilities the existing profiles, especially the east breakwater, show a flattened shape.

The head of the main breakwater (East Breakwater) situated at approximately -10 meter is located at the edge of a reef running down to approximately -40 meter on a slope of 1V:3H. This means that severe plunging almost deep water waves are directly hitting the breakwater head. The boundary and design conditions are summarized as follows:

Water Level Tides are small in the area and due to the large foreshore depth, the effect of wind setup can be neglected. The maximum still water level fluctuations to be considered are between + and -0.50 meter.

Currents Tidal currents are small in the region and are generally less than 1 meter/second.

Waves The maximum significant wave height offshore Port of Haina at a water depth of 40 meter is 8.7 meter, which is equivalent to a 250 year event. The corresponding wave period is about 16 second. The critical design wave direction is south-east.

Subsoil Conditions The subsoil conditions along the breakwater are characterized as cemented sand varying between dense and very dense.

## Design Criteria

The following design criteria have been adopted for the alternative design:

- During the maximum design wave condition ( $H_s=8.7m$ ) only small damage and displacements to the primary armor is accepted, after which the breakwater must remain able to fulfil its function.
- Hydraulic (dynamic) stable, damage criterium of the rock toe due to severe wave conditions is acceptable as long as it remains to fulfil its function of supporting the armor cubes.

- Displacement of armor units into the entrance channel is not allowed.
- For the underlayers and core material the filter requirements should be met such that no material can wash through the upper- and armor layers.
- No breakage of armor units due to severe wave attack is acceptable, so that the use of special shaped armor units (Dolosse, Tetrapods) will not be considered.
- Wave overtopping during moderate storms (recurrence interval of less than 10 years) must be negligible.

### **Extended Berm Breakwater Design**

Since the critical wave direction is from the southeast, the east breakwater was redesigned with a complete new concept of extended berm principle which would reduce the crest height and armor size while at the same time achieving more protection on wave overtopping and wave transmission. The berm has been designed along the following principles based on experiences on the previous designs such as Tripoli and Arzew and previous model tests:

- The horizontal berm elevation will be constant along the length of breakwater except for the head, where it will be raised in such a way that the amount of excavation of the old breakwater can be reduced to a minimum.
- The width of the berm may vary along the breakwater depending on the local water depth in such a way that the requirements for stability and overtopping are met along the total length of the breakwater.
- The armoring of berm consists of concrete cubes with varying weight, depending on the local wave attack, in such a way that the requirements for stability are met.
- The existing crest base will be improved in such a way that the breakwater will be accessible for trucks and/or cars.

After having developed this basic concept of berm breakwater it has been tested and optimized to an acceptable level of confidence in the 3-dimensional model of Delft Hydraulics Laboratory which tests have been inspected and evaluated by the Danish Hydraulic Institute.

### Geometrical Design

In general the berm level is -0.5 meter MSL, however, at the head section the elevation of the berm has been raised to +3.2 meter MSL, in order to reduce the amount of the excavation of the breakwater remains to a minimum. The width of the crest (approximately 70 meter) is such that wave overtopping over the head will still be negligible. The berm width is 25 meter in the deep sections but at shallow sections the berm width has been reduced to 10 meter for economic reasons. The width of the head section is approximately 70 meter.

Depending on the local wave attack the main armoring varies from 20 tons to 40 tons concrete cubes. The 40 tons concrete cubes are used for the most severely attacked sections, in a double layer for the 1:1.5 side slope of the head and in the transition from head to trunk and in a single layer for the toe of the head and the outer part of the crest of the transition. The 20 tons concrete cubes are used for the less severely attacked sections, such as the crest and the rear of the head, the rear and inner part of the crest of the transition, and the front and rear of the outer trunk section.

The toe of the armor layers is constructed in an excavated trench to ensure stability of the cubes at the toe and to support and protect the cubes on the slope against sliding during wave action. The trenched depth at the toe vary from -5.0 meter at the head to -3.0 meter at the trunk.

### MODEL TESTS

A three dimensional model investigations was carried out at Delft Hydraulics in a wave basin on a linear scale of 1:47. Three test series each consisting of 5 runs of 4 hours prototype were performed applying irregular waves of the JONSWAP type. Due to the exposed position of the west breakwater head particular attention was focused on this part. Especially the breakwater toe was in some occasions directly attacked by the impact of breaking waves. On those locations the toe had to be excavated into the seabed in order to avoid failure of the toe and thus to avoid consequential damage to the armor layer on the 1V:1.5H slope which was supported by the toe. Due to these measures the overall stability remained satisfactory in all test runs up to the maximum significant wave height of 8.7 meter. The following describe more details of the model test.





### Model Scales

Tests have been performed, using a linear scale factor of  $n = 47$ . As gravity forces are predominant in case surface water waves are to be modeled, the Froude number  $v/\sqrt{gD}$  should be identical in model and nature. From this the scales follow for:

$$\begin{aligned} \text{velocity } n_v &= n \\ \text{time } n_t &= n \\ \text{mass } n_m &= n^3 \\ \text{mass density } n &= 1 \end{aligned}$$

For dynamic similarity in rubble-mound stability models the scale factor of the Reynolds number  $vD/\nu$  should also be 1. From these two equations  $n_{\text{Froude}} = n_{\text{Reynolds}} = 1$  it follows that  $n = n^{1.5}$ . Since in all tests water was used and thus  $n = 1$ , perfect dynamic similarity can not be obtained. However by selecting a linear scale factor of sufficient size the effects of viscous forces are minimized.

### Test Program

A total of 3 tests has been performed. Each test consists of 5 runs of 4 hours each. In the first test the amount of excavation was reduced as much as possible by using a conventional toe of 3-6 ton rock on the original seabed level. This test was not satisfactory regarding design conditions. Especially the toe of the head section showed considerable damage, resulting in a great number of displaced cubes. Besides the armor layer of 3-6 ton rock on the rear of the trunk did not remain stable.

To improve the stability, the toe structure and the rear of trunk were changed in the second test. In the second test the toe structure consists of a single layer of 40 ton cubes having a width of 4 blocks, while the top of the toe structure was at the original seabed level. The slope of the rear of the trunk was changed from 1:1.5 to 1:2. The armor layer of the 3-6 ton rock was replaced by 20 ton cubes. The second test was satisfactory.

For the third test the width of the 40 ton toe was reduced to 3 blocks, which also increased the distance from the toe to the steep foreshore. The third test was satisfactory except for the 40 ton blocks were displaced into the entrance channel, for which the second test the toe was stable. Therefore it can be stated that using the positive results of test 2 and test 3 will result in

a satisfactory design. The layout and cross sections of this recommended design are shown in Figures 6 and 7.

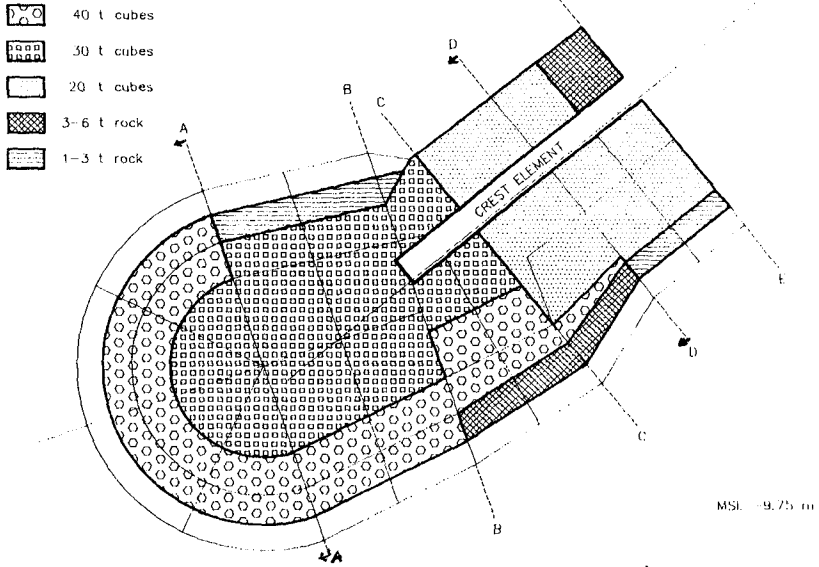


Figure 6 Layout of Recommended Design

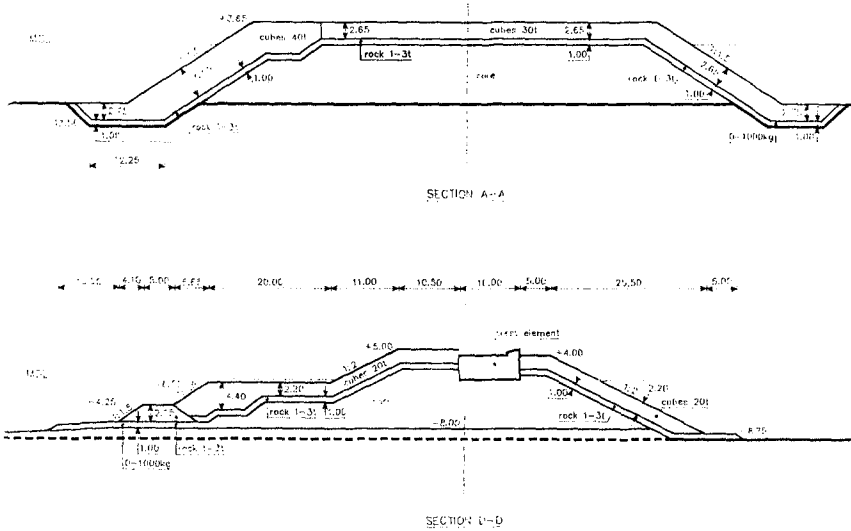


Figure 7 Typical Section of Recommended Design

## CONSTRUCTION

Construction of the breakwater began in June, 1993 with an estimated 18 month construction period. Special features of the construction work include the following:

### **Large quantities of concrete blocks**

Approximately 2,000 units of 40 ton and 6,000 units of 20 ton concrete blocks are used. Due to the large quantity, an on-site mixing plant is set up to deliver mixed concrete with trucks to the casting yard. Due to the limit of space, concrete units are stacked 3 units high. Each casted unit is inspected visually for cracks, spalling and defects. The rejected units are used at non-critical area or substitute for rock armor. The armors are not reinforced. Photos 1 and 2 presents the production of concrete blocks.

### **Quarry Production**

A large quantity of rocks has to be produced and delivered on site to keep up with the pace of construction. The approximate quantities of rock include:

0 - 1 ton of core stone:	101,600 Cubic Meter
1 - 3 ton of underlayer:	65,200 Cubic Meter
3 - 6 ton armor:	10,100 Cubic Meter

The quarry is located approximately 10 kilometer from site. The local quarry are predominantly limestone with good quality and durability in sea water. The average density of stone is 170 pounds per cubic foot. All rocks delivered to site are inspected for integrity and size, rejected armor are broken and used for underlayer or core material. Photo 3 shows typical rock armor used for west breakwater.

### **Toe Excavation and Concrete Block Placement**

Since deep trench has to be excavated for toe, underwater camera and diver are used to ensure the proper construction of the toe. Concrete blocks are placed randomly with specified density. The blocks are casted with slots on both sides and lifted with a special grip developed by the contractor as shown in Photos 4 and 5.

### **Dredging and Excavation**

Approximately 74,000 cubic meters of material are dredged at the toe, channel, and existing breakwater. During

construction of west breakwater, an extra 13,000 cubic meter of soft silt layer at the head and partial trunk section has to be dredged with hydraulic pump to ensure a firm foundation.

### ONCLUSIONS

The alternative design of berm breakwater is able to employ a smaller concrete block and a less toe trenching requirement. The design was aided with a physical model test and has been proved to be effective at various construction sites. Although several design changes were made, the construction is proceeding well and is expected to complete in 1996.

### REFERENCES

1. Van Oord ACZ, Marine Contractors, 2 Jan Blankenweg, P.O. Box 458, 4200 AL Gorinchem-Holland.
2. Baird, W.F. and Hall, K.R., "The Design of Breakwaters Using Quarried Stones", 19th International Conference on Coastal Engineering, Houston, Texas, 1984, pp.1024-1031.



Photo 1 Concrete Plant



**Photo 2 Block Production**



**Photo 3 Block Handling**



Photo 4 Block Placement



Photo 5 Rock Armor

## CHAPTER 260

### Rehabilitation of the West Breakwater - Port of Sines, Portugal

O.T. Magoon, J.R. Weggel, W.F. Baird, B.L. Edge, R.W. Whalin, D.D. Davidson, & E. Mansard

American Society of Civil Engineers, Waterways, Port Coastal & Ocean Division,  
Rubble Mound Structures Committee  
P.O. Box 279, Middletown, CA 95461, USA

#### Introduction

In 1978, construction of what is now termed the "West Breakwater" at the Port of Sines, Portugal, was nearing completion when it suffered severe damage from a large storm having significant wave heights estimated at nine meters. In February 1979, a subsequent storm with significant waves near the design height of eleven meters virtually destroyed the breakwater. The breakwater, armored with 40 ton dolosse, was approximately 1.7 km long and extended generally southward from the mainland to provide the primary wave protection for the Port of Sines as shown in Figure 1.

Sines is about 120 km south of Lisbon. Water depths of 50 meters exist close to shore at this site making it a viable site for a deep water port. The site is exposed to waves approaching generally from the west to northwest. The spring-tide range is about 3.6 meters. Cargo entering the port includes oil and coal (Dias & Toppler 1993). Petrochemicals and refined petroleum products are exported. Tankers off load their oil at berths 2 and 3 located immediately leeward of the west breakwater shown in Figure 2. With a water depth of 28 meters, berth 2 accommodates tankers up to 350,000 dwt. Berth 1 in the original design could have accommodated tankers up to 500,000 dwt, however, the severe storm damage to the breakwater and a reassessment of port development vis-a-vis changes in the world's tanker fleet resulted in abandoning berth 1. In addition to providing berths itself, the west breakwater shelters a number of other facilities within the harbor complex including the refined products loading berths, coal terminal, break bulk and the proposed container cargoes.

#### Emergency Repairs

In August 1979, following the damaging storms, emergency repairs were started on the west breakwater so that port operations could continue while final rehabilitation plans for the breakwater were developed. Emergency repairs to a 500 meter-long section of the west

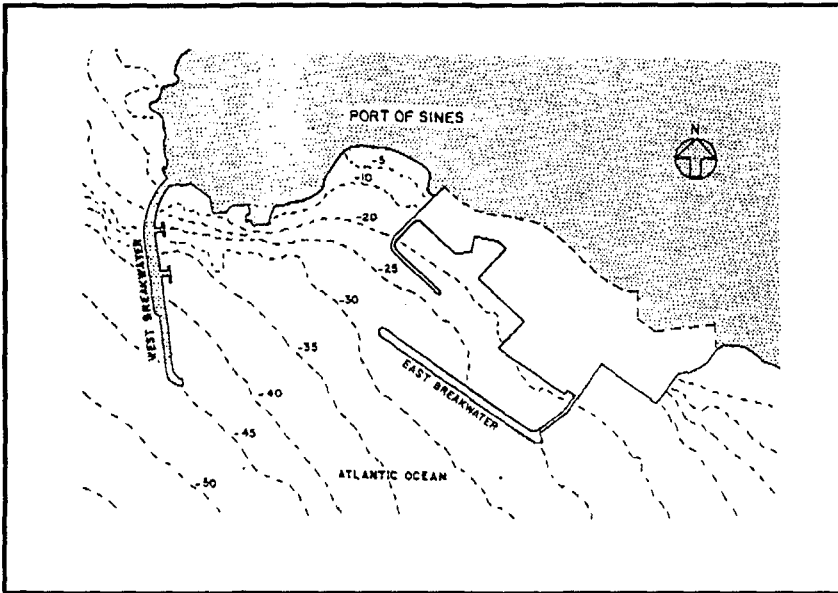


Figure 1. Final Port Master Plan 1985, Sines, Portugal (After Dias and Toppler, 1993)

breakwater were completed in May 1981. Repairs to the breakwater included the placement of 40 ton dolosse from the landward end of the breakwater out to berth 3 and the placement of 90 ton "Antifer" cubes between berth 3 and berth 2 on a slope flatter than that of the original breakwater.

Subsequent to construction, hydraulic model tests of the emergency repairs were made in 1981 at a 1:12 scale (the results of these tests are summarized by Mol, et al., 1983). Generally, the model tests showed that no modifications to the armor adopted for the emergency repairs were necessary. The gaps between the armor blocks and the parapet could be filled to reduce wave impact pressures. The tests also showed that the pipelines on the west breakwater needed protection from overtopping and that improvements to the breakwater from its landward root to berth 3 were necessary.

These results were preliminary to the design of the definitive breakwater rehabilitation, however, the emergency repairs undertaken between 1979 and 1981 imposed some constraints on the final rehabilitation. (Ligteringen, van der Meer and Rita, 1993)

### The Final Design

Additional studies were undertaken for the final breakwater rehabilitation including a reassessment of the wave climate at Sines based on hindcasts for the period 1956-1980 and for 20 major storms, numerical and physical model refraction analyses, additional hydraulic model stability tests -- including some with instrumented armor blocks to measure armor block



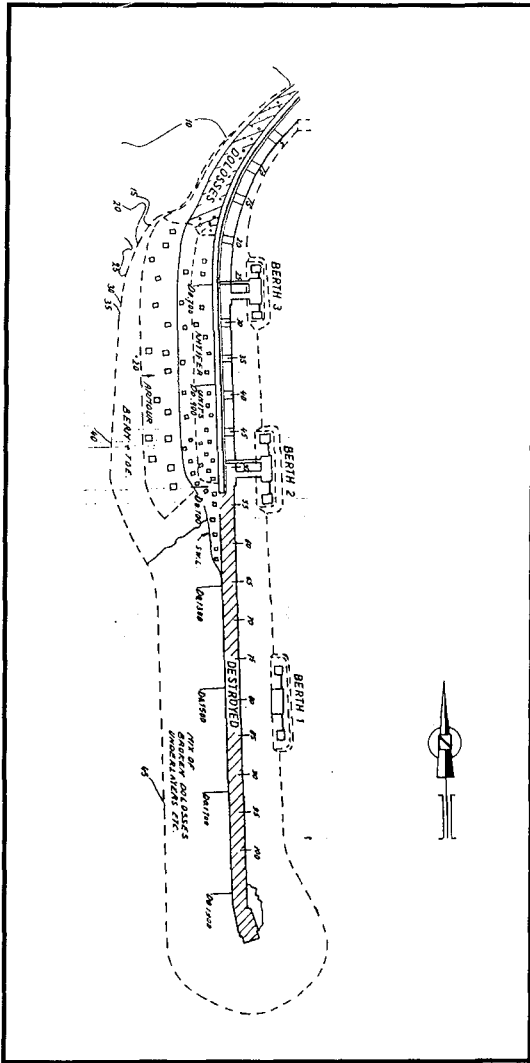


Figure 2. Sines West Breakwater Following Emergency Repairs, April 1981 (After Ligteringen, van der Meer and Rita, 1993)

hydraulic model tests.

The probability that minor damage (2%-3%) would occur at least once during the project's lifetime was 40% and the probability of major damage at least once was 15%. Therefore, based on previous tests of armor unit breakage, a velocity of 3 meters/sec was adopted as the impact velocity causing breakage to the breakwater. (Ligteringen, Ramos, van der Meer and Rita, 1993)

accelerations, prototype- scale Antifer cube impact tests to assess the conditions under which the cubes might break, geotechnical modeling and a study to establish the optimum length of the rebuilt breakwater and its effect on port operations.

The wave height distribution adopted for the design condition has a significant height with a return period of 100 years of  $H_s = 14$  meters. A 50 year return period of  $H_s = 13$  meters, and a 10 year return periods of  $H_s = 11$  meters. While refraction coefficients as high as 1.1 were found for some incident wave periods and directions, no increase in wave height due to refraction was assumed for the design. Design criteria adopted for the outer section of the breakwater trunk (between berths 2 and 3) allow 2% to 3% armor damage by the 100 year event ( $H_s = 14$  meters), based on a project lifetime of 50 years, and 10% damage by the 300 year event ( $H_s = 15.5$  meters). These levels of damage were those established in the earlier



The outer end of the breakwater, beyond berth 2, underwent continued deterioration following the 1978-1979 storms and the design of the new rebuilt breakwater head would have to include some of the remaining debris. See Figure 4. Some of the debris was removed by blasting and excavating, but most of the debris formed the new base of the breakwater head. An optimization study led to the decision to rebuild 500 meters of the outer portion of the west breakwater -- out to the location of the former berth 1, rather than just 300 meters as had originally been planned. This new, round head was armored with 105 ton Antifer cubes having the same dimensions as the 90 ton cubes. Concrete with a density of 3.1 ton/m<sup>3</sup> was used to produce the heavier cubes. The final design, which uses three layers of high density Antifer cubes over the entire breakwater head section, was not model tested.

### Monitoring Program

An extensive monitoring program is currently underway which measures waves, currents, tides, wind, etc., and their effect on the breakwater cross sections (Pita, et al., 1993). Periodic visual and photographic inspections are made from the top of the west breakwater and by boat. These inspections are made monthly between the months of October through April and in the mid-summer -- for a total of 8 inspections per year. In early spring, a yearly inspection is made by scuba divers to determine underwater conditions. Additional data includes: yearly hydrographic surveys, aerial photography/photogrammetry and topographic of the breakwater's cross section. Additionally, special surveys are conducted after storms with significant wave heights greater than 5 to 8 meters. A storm with a 5 meter wave height triggers a visual inspection of the breakwater, while a storm with 8 meter waves triggers a complete set of visual topographic, hydrographic, and photographic measurements.

This paper is the result of a Seminar on the reconstruction of the Sines West Breakwater in Portugal organized by the ASCE Rubble Mound Structures Committee and hosted by the Sines Port Authority, 17-18 September 1993. The complete text of the papers presented at the Seminar and referenced in this paper were published by the American Society of Civil Engineers in New York, NY. The Rubble Mound Structures Committee gratefully acknowledges the extraordinary efforts and the friendly spirit of cooperation of the Administracao do Porto de Sines in making this information available to the Civil Engineering Profession.

Rubble Mound Structures Committee Members who participated in the Sines West Breakwater Seminar and inspection were: Orville Magoon, J.R. Weggel, W.F. Baird, B.L. Edge, E. Mansard and R. W. Whalin.

### REFERENCES

Condotte, d'Aqua, (1993), "Rehabilitacao do Molhe Oeste do Porto de Sines," *Porto de Sines, Seminario Molhe Oeste*, 17-18 September, 1993, Sines, Portugal.

Dias, M.D.C., and J.F. Toppler (1993), "Brief History of the Port of Sines and General Presentation of the West Breakwater," *Porto de Sines, Seminario Molhe Oeste*, 17-18 September 1993, Sines, Portugal.

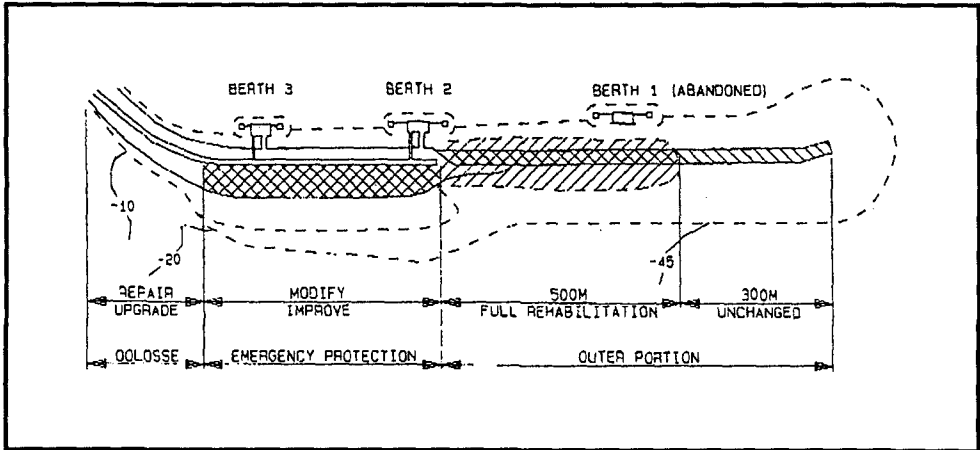


Figure 4. Sines West Breakwater After Complete Rehabilitation  
(After Dias and Toppler, 1993)

Ligteringen, H., F. Silveira Ramos, J.W. van der Meer, and M. Rita (1993), "West Breakwater Sines -- Definitive Rehabilitation, General Concept," *Porto de Sines, Seminario Molhe Oeste*, 17-18 September 1993, Sines, Portugal.

Ligteringen, H., J.W. van der Meer, and M. Rita (1993), "Sines West Breakwater -- Emergency Repair, Hydraulic Studies," *Porto de Sines, Seminario Molhe Oeste*, 17-18 September 1993, Sines, Portugal.

Mol, A., H. Ligteringen, R. L. Groeneveld and C.R.A.M. Pita (1983), "West Breakwater Sines -- Study of Armour Stability," *Proceedings of the ASCE Special Conference: Coastal Structures '83*, Arlington, VA, March 1983.

Pita, C., F. Abecasis, and A. Fernandes (1993), "Sines Breakwater Monitoring Program," *Porto de Sines, Seminario Molhe Oeste*, 17-18 September 1993, Sines, Portugal.



## SUBJECT INDEX

Page number refers to first page of paper

- Aeration, 1895  
Aerial photographs, 1998  
Air entrainment, 1496  
Airport runways, 2683  
Aquatic plants, 142  
Armor units, 918, 958, 986, 1001, 1061,  
1090, 1143, 1157, 1227, 1388, 1412,  
1426, 1439, 1511, 1541, 1568, 1625,  
1641, 1713  
Artificial islands, 1568  
  
Barrier islands, 181, 2222, 2417, 2886,  
3251, 3491  
Bathymetry, 871  
Beach erosion, 315, 609, 1197, 1880,  
1934, 2070, 2252, 2340, 2380, 2434,  
2449, 2571, 2683, 2726, 2943, 3208,  
3393, 3478, 3491  
Beach nourishment, 1359, 1797, 1934,  
2100, 2222, 2395, 2668, 2886, 3016,  
3208, 3491, 3507, 3548, 3564, 3579  
Beaches, 540, 1157, 1782, 1812, 1880,  
2115, 2325, 2395, 2449, 3167, 3378  
Bed load, 3360  
Bed load movement, 2513  
Bed ripples, 635, 1975, 2013, 2043, 2070,  
2140  
Bed roughness, 300  
Bedforms, 2185  
Benefit cost analysis, 3237  
Berm, 1075, 1343, 1625, 2252, 2712,  
3594  
Blocks, 932  
Boundary conditions, 272, 442, 594, 886,  
1770  
Boundary element method, 871, 1241,  
1700  
Boundary layer, 594, 1827  
Boundary layer flow, 384, 2527  
Breaking waves, 219, 330, 399, 412, 511,  
525, 594, 609, 1101, 1255, 1312,  
1496, 1553, 1672, 1739, 1895, 1961,  
2252, 2282, 2365, 2461, 2503, 2557,  
2583, 2813, 2856, 3167  
Breakwaters, 272, 525, 791, 1016, 1030,  
1046, 1101, 1255, 1269, 1298, 1343,  
1359, 1373, 1397, 1412, 1426, 1439,  
1454, 1580, 1595, 1625, 1657, 1700,  
1754, 1880, 2583, 2653, 2668, 2871,  
3167, 3208, 3420, 3564, 3608  
Buoyant jets, 3045  
Buried pipes, 1553, 2571, 3099  
  
Caissons, 1030, 1046, 1255, 1298, 1373,  
1580  
Calibration, 207  
Case reports, 3491, 3507, 3564, 3579,  
3594  
Channel bends, 128  
Channels, waterways, 128, 3002, 3060,  
3139, 3533  
Circular channels, 1373  
Climatic changes, 3193, 3251, 3462  
Coastal engineering, 1, 1837  
Coastal management, 3579  
Coastal morphology, 142, 1782, 1797,  
1837, 1906, 2100, 2207, 2222, 2252,  
2340, 2417, 2513, 2871, 3126, 3223,  
3251  
Coastal processes, 57, 2380, 2406, 3237,  
3335  
Coastal structures, 511, 2476, 3154, 3167,  
3522, 3564  
Cohesionless sediment, 2043, 2406  
Cohesive sediment, 2004, 2058, 3060  
Collisions, 3030  
Comparative studies, 3208  
Composite structures, 1030  
Computer analysis, 1090  
Computer models, 2311  
Concrete, 1426, 1641  
Concrete blocks, 1269  
Conical bodies, 1595  
Consolidation, soils, 2004, 2902  
Construction, 3594  
Coral reefs, 609  
Cost effectiveness, 1412  
Cross sections, 1130  
Currents, 113, 384, 565, 624, 1484, 2476,  
2503  
Cylinders, 973, 1115, 1212

**Volume 1 1-1196**

**Volume 2 1197-2416**

**Volume 3 2417-3614**

- Dam breaches, 2755
- Damage assessment, 2197
- Damage estimation, 1412
- Damage patterns, 1001, 1090, 1157, 1657
- Deep water, 12, 412, 455, 579, 973, 1343, 3608
- Deltas, 2542
- Design, 1327, 1359
- Digital mapping, 1998
- Dikes, 1075, 1169, 2197, 2639, 2755, 3350
- Dilution, 3045
- Discrete elements, 192
- Dispersion, 3071
- Displacements, 1255, 1625
- Distribution, 3086
- Distribution patterns, 192
- Dolos, 958, 1388, 1426, 1511, 1641
- Drainage systems, 1568, 2571
- Dredge spoil, 2928, 3305, 3507, 3579
- Dredging, 2972, 3002, 3016, 3060, 3139, 3393, 3533
- Dunes, 1934, 2028, 2197, 2434, 2488, 2755, 2770
  
- Earthquakes, 886
- Eddy viscosity, 384
- Embankments, 1130
- Energy dissipation, 635, 1454, 2557
- Energy losses, 761
- Entrainment, 3071
- Entropy, 232, 340
- Environmental impacts, 3178
- Erosion, 2058, 2170, 2488, 2542, 2639, 3360
- Erosion control, 1880, 1934, 2070, 2155, 2683, 2712, 3193, 3208, 3378, 3491
- Estuaries, 2004, 3060, 3178, 3281, 3408, 3533
  
- Failure modes, 1388, 1713
- Failures, 1526, 1657, 1754, 3350
- Field investigations, 540, 719, 1946, 2028, 2513, 3522
- Field tests, 665, 689, 945, 1269, 2115, 2610, 2799
- Filters, digital, 168
- Finite element method, 746, 871, 1388
- Fish habitats, 3420
- Fisheries, 1484, 3447, 3478
  
- Flocculation, 3060
- Flood control, 3126, 3193
- Flooding, 2197, 2755, 3154
- Flow characteristics, 27
- Flow measurement, 1975
- Flow patterns, 1770
- Flow rates, 98, 1975, 2058, 2085
- Flow simulation, 2140
- Flow visualization, 861, 3045
- Fluid flow, 98
- Fluid-structure interaction, 1115
- Flumes, 86, 1641, 1880, 2843, 2913
- Free surfaces, 86
- Frequency analysis, 12
- Frequency response, 207
- Friction, 1983
- Friction factor, 565, 986
  
- Geomorphology, 1837
- Global warming, 3462
- Grasses, 2639
- Gravel, 1880
- Gravity waves, 86, 579, 635, 1919, 3071
- Greens function, 442
- Groins, structures, 1157, 1327, 1782, 2668, 3564
  
- Harbor engineering, 791, 806
- Harbor structures, 3507
- Harbors, 871, 2987
- Hydraulic models, 1001, 1182, 1197, 1269, 2987, 3447
- Hydraulic performance, 918, 1373
- Hydraulic properties, 1454
- Hydraulic roughness, 2871
- Hydraulics, 2902
- Hydrodynamic pressure, 973, 1484
- Hydrodynamics, 861, 1849, 1919, 2282, 2340, 2741, 3099, 3432
- Hydrologic aspects, 3251
  
- Impact loads, 958, 3522
- Impulsive loads, 1580
- Indonesia, 609, 821
- Inlets, waterways, 2943, 3432
- Instrumentation, 42
  
- Japan, 1, 247, 674, 886, 1016, 1046
- Jetties, 2799

- Kinematics, 540  
 Laboratory tests, 42, 98, 128, 168, 650,  
     689, 776, 1075, 1101, 1143, 1157,  
     1212, 1241, 1284, 1610, 1641, 1782,  
     1946, 2115, 2325, 2449, 2461, 2476,  
     2488, 2843, 2856, 3295  
 Lagoons, 2928, 3223  
 Lagrangian functions, 2828  
 Lakes, 2380, 3281  
 Land reclamation, 2972, 3178, 3305  
 Landslides, 821  
 Layered soils, 3360  
 Lift, 1115, 3099  
 Linear analysis, 285  
 Liquefaction, 2698, 3350  
 Littoral currents, 27, 1895, 1919, 1983,  
     2237, 2267, 2282, 2297, 2503, 2741  
 Littoral deposits, 1327  
 Littoral drift, 2513, 2595, 2625, 2726,  
     2799, 2943, 2972, 3478, 3507  
 Long waves, 455, 791, 847, 886, 1961  
  
 Marshes, 3548  
 Mass transport, 86, 2828, 2913  
 Mathematical models, 1241, 1727, 2125,  
     2197, 2350, 2755, 2928, 3223  
 Measuring instruments, 42, 207  
 Meteorological data, 79  
 Mining, 3335, 3393  
 Mixing, 3071, 3281  
 Model accuracy, 57, 2595  
 Model analysis, 57  
 Model studies, 1880, 2770  
 Model tests, 1030, 1061, 1182, 1197, 1298  
 Model verification, 901, 1961, 2595, 2610,  
     2785, 3223  
 Monitoring, 1511, 1812, 2100, 2222,  
     2799, 2886, 3522, 3579  
 Monsoons, 3378  
 Mooring, 791, 847  
 Movable bed models, 300, 1782, 1906,  
     2972  
 Mud, 2004, 2913, 3266, 3360, 3408  
  
 Navier-Stokes equations, 511, 1739, 2297  
 Navigation, 3139, 3533  
 Nearshore circulation, 68, 207, 272, 330,  
     1895, 2237, 2267, 2340, 2365, 2461,  
     2583, 2610, 2741, 3420  
  
 Netherlands, 2886, 3193, 3208, 3350  
 Nonlinear analysis, 157, 285, 427, 467,  
     1961  
 Normal stress, 986  
 North Sea, 261, 1359, 1797  
 Numerical calculations, 427  
 Numerical models, 27, 79, 113, 157, 192,  
     272, 442, 467, 511, 689, 746, 776,  
     806, 821, 871, 886, 1016, 1672, 1700,  
     1739, 1880, 1919, 1946, 1983, 2043,  
     2070, 2140, 2155, 2237, 2311, 2434,  
     2503, 2542, 2557, 2610, 2653, 2741,  
     2785, 2843, 2871, 3086, 3295, 3305,  
     3420  
  
 Ocean mining, 3393  
 Ocean waves, 232, 340, 806, 1526  
 Offshore engineering, 2928  
 Offshore structures, 1115  
 Oscillations, 847, 1255, 2987  
 Oscillatory flow, 1541, 1553, 1975, 1983,  
     3408  
 Outfall sewers, 1553, 3045, 3071, 3564  
 Overtopping, 511, 918, 1016, 1030, 1046,  
     1130, 1182, 1373, 1568, 1687, 1700,  
     2028, 2639, 3154  
 Oxygen content, 3447  
 Oxygenation, 3167  
  
 Particle motion, 2406  
 Permeability, 1101  
 Perturbation, 746, 973, 1469  
 Photogrammetry, 1998  
 Photographic analysis, 1511  
 Plates, 1312, 1454  
 Plunging flow, 1739  
 Polders, 2197  
 Pollution, 3071  
 Pore pressure, 932, 1727, 2698, 3111  
 Pore water pressure, 3030, 3369  
 Porous media, 635, 1770  
 Porous media flow, 1739  
 Ports, 1197, 3608  
 Portugal, 3608  
 Pressure distribution, 1770  
 Probabilistic methods, 1754, 3154  
 Probability density functions, 482  
 Probability distribution, 247, 356, 482,  
     497  
 Progressive waves, 86



- Prototypes, 1016  
 Public safety, 1016, 1046  
 Random waves, 192, 272, 285, 300, 370, 412, 427, 482, 553, 565, 579, 704, 719, 1130, 1157, 1610, 2125, 2252, 2843  
 Recreation, 2395  
 Recreational facilities, 2668  
 Reefs, 1484  
 Regression models, 247  
 Rehabilitation, 3594, 3608  
 Research, 1  
 Residence time, 553  
 Residual strength, 2639  
 Return flow, 1101  
 Revetments, 932, 1001, 1269, 1687  
 Rip currents, 2583  
 Riprap, 3320  
 Risk analysis, 3154  
 Rivers, 3002, 3126, 3295  
 Rotational flow, 861  
 Rubble-mound breakwaters, 918, 958, 986, 1001, 1061, 1090, 1182, 1227, 1397, 1511, 1526, 1610, 1713, 1727, 3594  
 Salinity, 2928, 3533  
 Sand, 3360  
 Sand transport, 2557  
 Sandbars, 157, 1837, 1865, 2222, 2311, 2325, 2571, 2712, 2770, 2856, 3126, 3548  
 Scale effect, 1143, 2668, 2770  
 Scour, 1284, 1595, 3320  
 Scouring, 1212  
 Sea cliffs, 2170  
 Sea floor, 3111, 3139, 3320, 3369  
 Sea level, 2115, 2311, 2340, 3193, 3462  
 Sea state, 247  
 Sea walls, 1046, 1130, 1169, 1496, 1568, 1672, 1812, 3154, 3335  
 Sediment concentration, 1827, 2085, 2125, 2476, 2813  
 Sediment deposits, 2185, 3305  
 Sediment transport, 27, 98, 142, 300, 370, 525, 1212, 1327, 1770, 1827, 1837, 1849, 1865, 1906, 1919, 1946, 1975, 2028, 2043, 2070, 2125, 2140, 2185, 2282, 2406, 2503, 2513, 2527, 2595, 2625, 2770, 2785, 2799, 2843, 2871, 2902, 2928, 2928, 2972, 3295, 3360, 3478  
 Sedimentation, 2004, 3002, 3139  
 Sensors, 2185, 2799  
 Settling velocity, 3408  
 Shallow water, 261, 330, 370, 455, 467, 482, 665, 704, 731, 761, 1212, 1343, 1849, 2350, 2928, 3281  
 Shape, 1343, 1388, 1439, 1625  
 Shear stress, 98, 565, 594, 986, 1595, 2058  
 Shear waves, 1919  
 Shellfish, 3086, 3420  
 Ship motion, 791, 847, 871  
 Ships, 3030  
 Shoaling, 12, 467, 594, 2365  
 Shock, 1075  
 Shore protection, 142, 3237, 3335  
 Shoreline changes, 1327, 1782, 1812, 1837, 1906, 1946, 1998, 2380, 2610, 2625, 2653, 2683, 2726, 2755, 2785, 2813, 2943, 3178, 3295, 3335, 3378, 3393, 3462, 3478  
 Silts, 2902, 3060  
 Simulation models, 821, 3266  
 Sliding, 1580  
 Slope stability, 1553  
 Slopes, 315, 746, 1075, 1568, 1865, 2325, 2350, 3167  
 Soil mechanics, 2902, 3030  
 Soil permeability, 2902, 3111  
 South Africa, 1511  
 Spatial distribution, 579, 674  
 Spectral analysis, 12, 68, 384, 731  
 Spits, coastal, 2380, 2726, 3478  
 Stability, 918, 932, 1061, 1143, 1227, 1397, 1426, 1439  
 Stability analysis, 1865  
 Standing waves, 3369  
 State-of-the-art reviews, 1, 832  
 Statistical analysis, 674  
 Statistical data, 832  
 Statistics, 79  
 Stones, 1553, 1625  
 Storm surges, 901, 2170, 2434  
 Storms, 79, 261, 1526, 1849, 1934, 2843, 3491, 3608  
 Stratification, 3360  
 Stratified flow, 3447

- Strength, 1388  
Stress distribution, 1713  
Structural response, 832, 1412, 1641  
Structural strength, 958  
Submerged discharge, 3320  
Subsidence, 1541  
Surf beat, 399, 689, 1961  
Surf zone, 98, 315, 399, 553, 1895, 1934, 2085, 2155, 2237, 2267, 2282, 2350, 2503, 2513, 2542, 2712, 2813, 2856  
Surface roughness, 1169  
Surface waves, 467, 635, 3111  
Suspended load, 3360  
Suspended sediments, 1827, 1849, 1865, 2013, 2043, 2085, 2125, 2406, 2476, 2527, 2770, 2813, 3002, 3016, 3281  
Suspended solids, 3408  
  
Tensile stress, 1713  
Three-dimensional flow, 370  
Three-dimensional models, 871, 901, 1227, 2267, 2297, 2340, 2461, 2741, 3432  
Tidal currents, 2282, 3281  
Tidal hydraulics, 861  
Tidal marshes, 3251  
Tidal waters, 181, 2417, 3533  
Tides, 3462  
Time dependence, 272, 285, 553, 635  
Tin, 3393  
Tombolo, 1197, 2653  
Topography, 272, 746, 1212, 1865, 1946, 2325, 2557, 2610, 3126  
Transport rate, 2785, 2828, 2913, 2972  
Tsunamis, 821, 886  
Turbidity, 3016  
Turbulence, 98, 861, 901, 2712, 3281  
Turbulent boundary layers, 300, 384  
Turtles, 3491  
Two-dimensional analysis, 3447  
Two-dimensional flow, 27  
Two-dimensional models, 1030, 2155  
Typhoons, 1, 219, 674, 2434  
  
Ultrasonic testing, 624  
Undertow, 330, 399, 2125, 2610, 2712, 2785  
Uplift pressure, 932, 1298  
  
Velocity profile, 86  
Vertical cylinders, 1284, 1469, 1595  
Vibration, 1115  
Vibration analysis, 455  
Viscoelasticity, 2913  
Viscoplasticity, 2913  
Viscosity, 3408  
Vortices, 113, 525, 1115, 1975, 2140, 2856  
  
Water content, 3266  
Water depth, 261, 1343  
Water flow, 1373  
Water level fluctuations, 2170  
Water levels, 2365, 3533  
Water pollution, 3178  
Water pressure, 1541  
Water quality, 2395  
Water surface profiles, 455, 624, 704, 1469  
Water table, 2115, 2449, 2571  
Water waves, 455  
Waterfront facilities, 901  
Wave action, 315, 918, 1001, 1061, 1212, 1227, 1269, 1739, 1934, 2013, 2058, 2639, 2698, 2712, 3016, 3045, 3099, 3266, 3522  
Wave attenuation, 1312, 2913  
Wave climatology, 181, 247, 1526, 2311  
Wave crest, 356, 497, 540  
Wave damping, 142, 609  
Wave diffraction, 128, 285, 442, 973  
Wave energy, 609, 761, 791, 806, 1454, 2698  
Wave forces, 330, 1046, 1075, 1115, 1298, 1312, 1439, 1469, 1484, 1496, 1580, 1754  
Wave generation, 68, 168, 650, 704, 776  
Wave groups, 689, 776, 832, 847, 945, 1526, 1568, 1827, 1961, 2828  
Wave height, 79, 181, 192, 247, 261, 356, 370, 399, 412, 497, 579, 609, 674, 746, 1016, 1101, 1182, 1241, 1397, 1657, 1754, 2155, 2207, 2311, 2350, 2365, 2488, 2698, 2828, 2987, 3266, 3608  
Wave measurement, 42, 57, 207, 232, 624, 731, 776, 806, 832, 1610, 1906, 2207  
Wave pressure, 1312, 1541  
Wave propagation, 157, 168, 181, 232, 665, 1241

- Wave reflection, 128, 168, 442, 719, 945,  
1241, 1610, 2434
- Wave refraction, 68, 285, 442
- Wave runup, 27, 315, 399, 553, 689, 761,  
776, 821, 886, 1169, 1687, 1727,  
2115, 2155, 2170, 2207, 2325, 2488,  
2557, 2571, 2583
- Wave spectra, 12, 42, 68, 232, 340, 370,  
384, 467, 482, 497, 624, 665, 719,  
731, 806, 2843
- Wave tanks, 128, 650, 1469, 1880, 1906,  
2207, 2449
- Wave velocity, 427, 525, 540, 565, 986,  
1046, 1454, 2527
- Waves, 113, 2476
- Wind, 57
- Wind direction, 79, 3447
- Wind speed, 79, 261, 330, 1687
- Wind waves, 12, 68, 181, 232, 330, 665,  
731, 761, 901, 945, 2350

## AUTHOR INDEX

Page number refers to first page of paper

- Ahn, K., 482  
Akeda, S., 3420  
Alexis, A., 2902  
Alexis, Alain, 2004  
Allsop, N. W. H., 918, 1130, 1157, 3154  
Alvarez, J., 3579  
An, Nguyen Ngoc, 2913  
Andrassy, Christopher J., 2100  
Anglin, C. D., 2380  
Aono, Toshio, 12  
Asai, Tadashi, 232, 847  
Asano, Toshiyuki, 27  
Aydin, Ismail, 1770
- Badiei, Peyman, 1782  
Baird, W. F., 3608  
Bakker, Willem T., 1797  
Bakker, Wim T., 2197  
Balzano, Andrea, 2928  
Barnes, T. C. D., 776  
Barthel, Volker, 791  
Basco, David R., 1812  
Battjes, J. A., 157  
Bedford, K., 1827  
Beji, Serdar, 427  
Bellomo, Doug, 1812  
Benoit, Michel, 42, 1610  
Bergmann, Hendrik, 553, 1075  
Bertotti, Luciana, 57, 79  
Besley, P., 918  
Bezuijen, Adam, 932  
Blomgren, Sten H., 1327  
Boccotti, Paolo, 945  
Bodge, Kevin R., 2943  
Booij, N., 68, 261  
Bouws, E., 261  
Brandt, Günther, 181  
Briggs, Michael J., 806  
Brøker, I., 2871  
Brøker, Ida, 2958  
Bruce, T., 1975  
Burcharth, Hans F., 958
- Caballería, Miquel, 1983  
Carnero, Ovidio Varela, 1657  
Cavaleri, Luigi, 57, 79  
Chacaltana, J. T. Aquije, 973  
Chang, C., 1700  
Chang, Chen-Yue, 3045
- Chang, Hsien-Kuo, 2972  
Chaplin, John R., 1115  
Chen, Xinjian, 3281  
Chen, Yih-Far, 3045  
Chen, Z., 3223  
Chilo, Bruno, 1090  
Chin, Ikuo, 3478  
Chisholm, T. A., 1849  
Chou, C. R., 2987  
Christensen, E. Damgaard, 1865  
Christensen, Erik Damgaard, 1919  
Christensen, Morten, 168  
Christiansen, N., 1595  
Chyan, Jih-Ming, 3045  
Ciešlikiewicz, Witold, 86  
Coates, T. T., 1880  
Collado, F. R., 2542  
Cornett, Andrew, 986  
Cornett, Andrew M., 1001  
Coussirat, M. G., 2542  
Covarsi, Manuel F., 3564  
Cox, Daniel T., 98  
Cummins, I., 113
- da Silva, A. F. Teles, 973  
Daemrich, Karl-Friedrich, 2828  
Dally, William R., 1895  
Dalrymple, Robert A., 128  
Damgaard, Jesper Svarrer, 1919  
d'Angremond, K., 1713, 1754  
Daniil, E. I., 3167  
Davidson, D. D., 3608  
Davies, Michael H., 1001  
de Gerloni, M., 1030  
De Groot, M. B., 1727  
de Groot, Maarten B., 3350  
de Quirós, Fernando Bernaldo, 3237  
de Ronde, J. G., 261  
de Ronde, John G., 761  
de Ruig, J. H. W., 3208  
de Vriend, Huib J., 594  
Dean, Robert G., 1906, 2449, 3491  
Deguchi, Ichiro, 370, 2476, 3002  
Deigaard, R., 1865, 2043  
Deigaard, Rolf, 1919, 2583  
Dette, Hans H., 1934  
Dette, Hans-H., 2843  
Dette, Hans-Henning, 553  
Dibajnia, Mohammad, 1946

- Dijkman, Michiel, 3522  
 Dodd, N., 1880  
 Dodd, Nicholas, 1961  
 Dowd, Millard, 3491  
 Drago, Michele, 540  
 Dubi, Alfonso, 142  
  
 Earnshaw, H. C., 1975  
 Easson, W. J., 1975  
 Easson, William J., 525  
 Edge, B. L., 3608  
 Edge, Billy, 1687  
 Edge, Billy L., 3491  
 Eldeberky, Y., 157, 261  
 Endo, Taiji, 2395  
 Endoh, Kimihiko, 1016, 1046  
  
 Falqués, Albert, 1983  
 Ferier, P. G. P., 261  
 Fernandez, Joaquin, 3594  
 Fisher, John S., 1998, 2488  
 Foda, Mostafa A., 3099  
 Fontijn, Henri L., 1553  
 Franco, C., 918  
 Franco, L., 1030  
 Fredsøe, J., 1595, 1865, 2043  
 Fredsøe, Jørgen, 1919  
 Frigaard, Peter, 168  
 Fujima, Koji, 1115  
 Fukushima, Masahiro, 2571  
 Furuta, Goichi, 861  
  
 Gal, J. Andorka, 261  
 Galland, J.-C., 1061  
 Gallois, Stéphane, 2004  
 Gärtner, Joachim, 181  
 Giménez, Marcos H., 192  
 Glaser, Detlef, 181  
 Goda, Yoshimi, 1241  
 Goldenbogen, Roland, 3251  
 Gomez, Daniel, 3594  
 Gomez-Pina, G., 3579  
 Gómez-Pina, Gregorio, 3507  
 Goto, Chiaki, 12  
 Gotoh, H., 1541  
 Gotoh, Hitoshi, 2013  
 Gracia, V., 2542  
 Grass, Tony J., 565  
 Greated, C. A., 1975  
 Greated, Clive A., 540  
  
 Grote, Wout V., 1553  
 Grüne, Joachim, 181, 1075  
 Gudmestad, Ove T., 86  
 Guiducci, F., 1343, 1625  
 Guiducci, Franco, 1090  
  
 Hamilton, David G., 1782  
 Han, W. Y., 2987  
 Hancock, Mark W., 2028  
 Hanes, Daniel M., 3016  
 Hansen, E. A., 2043  
 Hansen, N.-E. Ottesen, 3030  
 Hansen, S. B., 1595  
 Hanslow, David J., 207, 2115  
 Hanson, Hans, 1327  
 Hanzawa, Minoru, 1143  
 Hara, Koji, 2461  
 Hardaway, C. Scott, 2653  
 Harkins, Gordon S., 806  
 Harris, J. M., 300  
 Harshinie, Karunarathna G., 689  
 Hashida, Misao, 219  
 Hashimoto, Noriaki, 232, 624, 847  
 Hashimoto, O., 1197  
 Hashimoto, Seiya, 2070  
 Hata, Sadakatsu, 2571  
 Hatada, Yoshio, 247, 674  
 Hattori, Masataro, 1101  
 Hattori, Takeshi, 704  
 Hayashi, Kenjirou, 1115  
 Hazelton, John M., 1812  
 Herbert, D. M., 1130  
 Hibbert, Kevin, 207  
 Higaki, Futoshi, 1115  
 Higano, Junya, 3086  
 Hoekstra, Piet, 2222  
 Holthuijsen, L. H., 68, 261  
 Holtzhausen, A., 1511  
 Holtzhausen, A. H., 1388  
 Hosoi, Yoshihiko, 1454  
 Houwing, Erik-Jan, 2058  
 Houwman, Klaas, 2222  
 Hsu, Tai-Wen, 2972  
 Hujii, Atsushi, 1046  
 Hwang, Kyu-Nam, 2488  
 Hwung-Hweng, Hwung, 3045  
  
 Ikeno, Masaaki, 3320  
 Imamura, Fumihiko, 821, 886  
 Iranzo, Vicente, 1983

- Iric, Isao, 2070  
 Ishii, Toshimasa, 272  
 Isobe, Masahiho, 719  
 Isobe, Masahiko, 272, 285, 2785, 3266  
 Ito, Kazunori, 847  
 Ito, Masahiro, 1143  
 Ito, Yoshiki, 624  
 Itoh, Sadahiko, 1454  
 Iwagaki, Yuichi, 1, 1143  
 Iwata, Koichiro, 1212, 1439  
 Izumi, Tatsuhisa, 3378
- Jaffe, Bruce E., 2085  
 Janssen, Hans, 3522  
 Jenscn, Anders, 2958  
 Jensen, Frerk, 181  
 Johnsen, John, 2958  
 Johnson, Hakeem, 2871  
 Johnson, Patrick, 3491  
 Jones, R. J., 918, 1157  
 Juang, Jea-Tzyy, 1169  
 Juhl, J., 1754  
 Juhl, Jørgen, 1182
- Kabling, Michael B., 2557  
 Kaczmarek, L. M., 300  
 Kaihatsu, Sumio, 1269  
 Kaiser, Ralf, 181  
 Kamata, A., 1197  
 Kamphuis, J. William, 1782  
 Kana, Timothy W., 2100  
 Kang, Hong-Yoon, 2115  
 Karjadi, Entin A., 2155  
 Katoh, Kazumasa, 315  
 Katopodi, Irene, 2125, 2527  
 Kawaguchi, T., 1197  
 Kawata, Yoshiaki, 330  
 Kersting, Nico F., 1797  
 Kheyruri, Z., 1727  
 Kim, Chang-Je, 1212  
 Kim, Hyeon-Ju, 1526  
 Kim, Hyoseob, 2140  
 Kim, Kyu Han, 2476  
 Kim, Taerim, 340  
 Kimura, A., 497  
 Kimura, Akira, 356  
 Kimura, Katsutoshi, 1227  
 Kirby, James T., 128  
 Kitou, Nikos, 2125  
 Kittitanasuan, Wudhipong, 1241
- Kiyokawa, Tetsushi, 650  
 Klammer, P., 1255  
 Klammer, Peter, 1298  
 Klatter, Leo, 3522  
 Kobayashi, Akio, 847  
 Kobayashi, Masonori, 1269  
 Kobayashi, Nobuhisa, 98, 1373, 2028, 2155  
 Kobayashi, Tomonao, 861, 1284  
 Koelewijn, Ria, 2527  
 Kohlhase, Søren, 1298  
 Kojima, Haruyuki, 1312  
 Komar, P. D., 2170  
 Koole, R., 3071  
 Koontanakulvong, Sucharit, 3002  
 Kortenhaus, Andreas, 1298  
 Kos'Yan, R. D., 2185  
 Kraak, A. W., 3208  
 Kraak, Aric, W., 2197  
 Kraus, Nicholas C., 1327  
 Kriebel, D. L., 2325  
 Kriebel, David L., 2207  
 Kroon, Aart, 2222  
 Kung, Chen-Shan, 1837  
 Kunisu, Hiroshi, 1568  
 Kunz, H., 3533  
 Kunz, Hans, 3251  
 Kuriyama, Yoshiaki, 2237  
 Kusuda, Tetsuya, 3408  
 Kuwabara, S., 3420  
 Kuwahara, Hisami, 3086  
 Kwon, J. G., 370
- Lamberti, A., 1343, 1625  
 Larson, Magnus, 2252  
 Larsonneur, Claude, 2282  
 Laustrup, Christian, 1359  
 Law, Adrian W. K., 3099  
 Lee, Dal Soo, 1373  
 Lee, J., 1827  
 Lee, J. J., 1700  
 Lee, Jung Lyul, 2267  
 Lee, Tsong-Lin, 3369  
 Levoy, Franck, 2282  
 Li, Bin, 2297, 3548  
 Liberatore, Gianfranco, 525  
 Lin, Li-Hwa, 340, 2770  
 Lindenberg, Jaap, 3350  
 Lindo, Mark H., 3594  
 Lintrup, Morten, 2928

- Liu, Shuxue, 731  
 Liu, Zhou, 958  
 Longo, Sandro, 2527  
 Luger, S., 1511  
 Luger, S. A., 1388  
  
 MacDonald, N. J., 2311  
 Maddrell, Roger, 3548  
 Maddrell, Roger J., 2297  
 Madsen, Holger Toxvig, 1359  
 Madsen, O. S., 1849  
 Madsen, Ole Secher, 384  
 Madsen, P. A., 399  
 Madsen, Per A., 2583  
 Magda, Waldemar, 3111  
 Magoon, O. T., 3608  
 Mano, A., 3126  
 Mansard, E., 3608  
 Mansard, E. P. D., 832, 1397  
 Mansard, Etienne, 791, 986  
 Mansard, Etienne P. D., 1001  
 Manzenrieder, Helmut, 3139  
 Mase, Hajime, 635  
 Matsumi, Y., 1397  
 Matsumoto, Akira, 442  
 Matsunaga, Nobuhiro, 219  
 Matsuoka, Michio, 442  
 Matsutomi, Hideo, 886  
 Mayer, R. H., 2325  
 Mayerle, Roberto, 2340  
 McDougal, W. G., 2170  
 Meadowcroft, I. C., 3154  
 Medina, Josep R., 192, 1412  
 Melby, Jeffrey A., 1426, 1641  
 Memos, Constantine D., 2350  
 Miura, H., 2698  
 Miyaike, Yoshihito, 1212  
 Miyamoto, Y., 3420  
 Mizui, Hiroyuki, 219  
 Mizumoto, T., 1197  
 Mizutani, Norimi, 1439  
 Mocke, G. P., 2365, 3335  
 Møller, Jacob Steen, 2958  
 Monfort, Olivier, 2282  
 Mori, Nobuhito, 412  
 Moutzouris, C. I., 3167  
 Mulder, J. P. M., 2886  
 Murakami, Hiroshi, 1143  
 Murakami, Hitoshi, 1454  
 Murakami, Keisuke, 1469, 2070  
  
 Muraoka, Kohji, 3178  
 Muraoka, Kouji, 3447  
  
 Nadaoka, Kazuo, 427, 650  
 Nagai, Toshihiko, 232, 624, 847  
 Nagao, M., 3126  
 Nairn, R. B., 2380  
 Nakagawa, Hiroji, 2013  
 Nakagawa, Yasuyuki, 427  
 Nakamura, Satoshi, 2070  
 Nakamura, Tetuya, 1312  
 Nakatsuji, Keiji, 3178, 3447  
 Nemoto, Kenji, 1143  
 Nielsen, Peter, 207, 2115, 2406  
 Niemeyer, Hanz D., 181, 1797, 2417  
 Nishi, Ryuichiro, 2434  
 Nishida, H., 1484  
 Nishihira, F., 1484  
 Nishimura, Hitoshi, 442  
 Nishimura, Tsukasa, 861  
 Nochino, Masao, 455  
 Nwogu, Okey, 467  
  
 Ochi, M. K., 482  
 O'Connor, B. A., 300, 2311  
 O'Connor, Brian A., 2140  
 Oda, Kazuki, 3305  
 Oda, Kenji, 1284  
 Oh, Tae-Myoung, 1906, 2449  
 Ohhama, Hoiku, 2395  
 Ohta, T., 497  
 Ohta, Takao, 356  
 Ohyama, Takumi, 650, 871  
 Okayasu, Akio, 98, 2461  
 O'Neil, S., 1827  
 Ono, Masanobu, 2476, 3002  
 Ono, Nobuyuki, 2070  
 Oshiro, Shinichi, 609  
 Osiecki, Daniel A., 1895  
 Osmond, Bill, 3548  
 Oumeraci, H., 1255, 1672  
 Oumeraci, Hocine, 1298  
 Overton, Margery F., 1998, 2488  
 Owen, M. W., 1130  
  
 Park, Woo Sun, 1373  
 Partenscky, H.-W., 1255, 1672  
 Péchon, Philippe, 2503  
 Peerbolte, E. Bart, 3193  
 Peña, Carlos, 3564

- Peña-Santana, Patricia G., 2395  
 Peregrine, D. H., 776, 1496  
 Perrier, G., 2043  
 Petit, H. A. H., 511, 1739  
 Petti, Marco, 525, 540  
 Phelp, D., 1511  
 Phelp, D. T., 1388  
 Pluijm, M., 3208  
 Podymov, I. S., 2185  
 Presti, A. Lo, 2625  
 Prieto, J., 2542  
 Pruszek, Zbigniew, 2513  
 Putrevu, U., 2741
- Quinn, Paul A., 525, 540
- Ramadan, Khaled A. H., 2527  
 Ramírez, Jose L., 3507  
 Raudkivi, Arved J., 1934  
 Reeve, D. E., 3154  
 Ribberink, Jan S., 2527  
 Ris, R. C., 68  
 Rodriguez, A., 2542  
 Roelvink, J. A., 3223  
 Rousset, Hélène, 2282  
 Rubin, David M., 2085  
 Ruessink, Gerben, 2222  
 Rufin, Teofilo Monge, Jr., 1439  
 Ruggiero, P., 2170  
 Ruiz, Luis Felipe Vila, 3237  
 Rutledge, J., 1397  
 Ryu, Cheong-Ro, 1526
- Sakai, Hiroyuki, 1101  
 Sakai, T., 1541  
 Saleh, Wameidh M., 565  
 Sallenger, Asbury, Jr., 2085  
 Sánchez-Arcilla, A., 2542, 2625  
 Sánchez-Carratalá, Carlos R., 192  
 Sancho, F. E., 2741  
 Sand, S. E., 832  
 Sasaki, Hiroshi, 624  
 Sato, Michio, 2434, 2571  
 Sato, Shinji, 2557  
 Sawamoto, M., 3126  
 Sawamura, Yoshiyuki, 1454  
 Sawaragi, Toru, 2476, 3002  
 Schäffer, H. A., 399  
 Schäffer, Hemming A., 2583  
 Schiereck, Gerrit J., 1553
- Schmeltz, Edward J., 3594  
 Schoonees, J. S., 2595, 2668  
 Schroeder, Ernst, 3251  
 Schröter, Andreas, 2340  
 Schüttrumpf, Holger, 553  
 Scott, R. D., 2380  
 Seijffert, J. W. W., 2639  
 Sekimoto, Tsunehiro, 1568  
 Shen, Daoxian, 3266  
 Sheng, Y. P., 3432  
 Sheng, Y. Peter, 3281  
 Shiba, Kazuhiko, 2785  
 Shibata, Takao, 847  
 Shibayama, Tomoya, 2461, 2813, 2913,  
 3295  
 Shigematsu, Takaaki, 3305  
 Shih, S.-M., 2170  
 Shim, Youngbo, 2140  
 Shimizu, Takao, 3320  
 Shimizu, Takuzo, 1946, 2610  
 Shimosako, Kenichiro, 1580  
 Shinoda, Seirou, 704  
 Shiraishi, Naofumi, 2395  
 Shuto, Nobuo, 821, 886  
 Sierra, J. P., 2625  
 Sigemura, Toshiyuki, 1115  
 Simons, Richard R., 565  
 Simonsen, B. C., 3030  
 Sistermans, Paul G. J., 1553  
 Sloth, Peter, 1182  
 Smit, F., 2365  
 Smith, G. G., 3335  
 Smith, G. M., 2639  
 Sørensen, O. R., 399  
 Sørensen, Ole R., 2583  
 Stansberg, Carl Trygve, 579  
 Steetzel, Henk J., 2197  
 Sterndorff, M. J., 3030  
 Stive, Marcel J. F., 594, 761  
 Stive, Marcer, 1837  
 Stoutjesdijk, Theo P., 3350  
 Sueyoshi, Toshiaki, 3178  
 Sugihara, Yuji, 219  
 Suh, Kyung Duck, 2653  
 Sulaiman, Dede M., 609  
 Sumcr, B. M., 1595  
 Sunamura, Tsuguo, 2856  
 Svendsen, I. A., 2741  
 Swan, C., 113, 3071  
 Swart, D. H., 2668, 3335



- Syamsudin, Abdul R., 2683
- Tada, A., 1484
- Takahashi, S., 2698
- Takahashi, Shigeo, 1016, 1046, 1227, 1580
- Takahashi, Tomoharu, 624
- Takahashi, Tomoyuki, 821, 886
- Takayama, Tomotsuka, 624
- Takeba, Ken, 635
- Tamashita, Takao, 901
- Tanaka, Masahiro, 650
- Tanimoto, Katsutoshi, 689, 1227, 1580
- Tehrani, Mehrdad M., 565
- Teisson, Charles, 42, 1610, 2503
- Theron, A. K., 2595
- Thomas, P., 2902
- Thomas, Pierre, 2004
- Tillotson, K. J., 2170
- Ting, Francis C. K., 2712
- Toba, E., 3579
- Tobikik, Isao, 847
- Togashi, Hiroyoshi, 746
- Tolman, H. L., 261
- Tomasicchio, G. R., 1343, 1625
- Toms, Geffery, 1837
- Tonder, A. van, 1388, 1511
- Tönjes, P., 511, 1739
- Tøorum, Alf, 142
- Topliss, M. E., 1496
- Torfs, Hilde, 3360
- Toue, Takao, 847
- Tsai, Ching-Piao, 3369
- Tsuchida, Mitsuru, 871
- Tsuchiya, Toshito, 609
- Tsuchiya, Yoshito, 2683, 3378, 3478
- Tsujimoto, Tetsuro, 2013
- Tsuru, Masahito, 2610
- Tsutsui, Shigeaki, 609
- Turk, George F., 1426, 1641
- Uda, Takaaki, 2726
- Ujiiie, Hisayoshi, 3320
- Valdecantos, Vicente Negro, 1657
- van de Graaff, Jan, 2197
- van de Kreeke, J., 2886
- van den Bosch, P., 511, 1739
- van der Lem, J. C., 3208
- van der Meer, J. W., 1030, 1713, 1754,
- 2639
- Van Dongeren, A. R., 2741
- Van Evra, R., 1827
- van Gent, M. R. A., 511, 1727, 1739
- van Nes, C. P., 1713
- van Rijn, Leo C., 2058
- van Vessem, P., 2886
- van Vledder, Gerbrant Ph., 761
- Verhagen, L. A., 665
- Villaret, C., 2043
- Visser, Paul J., 2197, 2755
- von Lany, P. H., 3154
- Vongvisessomjai, Suphat, 3393
- Walstra, D. J. R., 3223
- Wang, Hsiang, 340, 2267, 2434, 2770, 2843
- Wang, Xu, 2770
- Ward, Donald L., 1687
- Watanabe, Akira, 272, 719, 1946, 2610, 2785, 3266
- Watson, G., 776
- Weggel, J. R., 3608
- Whalin, R. W., 3608
- White, Thomas E., 2799
- Wibncr, Christopher G., 1687
- Williams, Greg, 1812
- Wind, Herman G., 3193
- Winyu, Rattanapitikon, 2813
- Woltering, Stefan, 2828
- Wright, L. D., 1849
- Wu, N. T., 1672
- Wu, Yongjun, 2843
- Yamada, Akiko, 3295
- Yamada, Minoru, 3478
- Yamaguchi, Masataka, 247, 674
- Yamamoto, Koji, 2726
- Yamamoto, Masato, 1143
- Yamamoto, S., 2698
- Yamamoto, T., 1541
- Yamamoto, Yoshimichi, 689
- Yamanishi, Hiroyuki, 3408
- Yamashita, Takao, 609, 2683, 3378
- Yamauchi, Kazuaki, 3320
- Yamazaki, H., 1727
- Yamazaki, Tsuyoshi, 1568
- Yan, Yixin, 3060
- Yang, David W., 3594
- Yano, K., 3420

- Yassuda, E. A., 3432  
Yassuda, Eduardo A., 3281  
Yasuda, Takashi, 412, 704  
Yen, Kai, 3060  
Yokoki, Hiromune, 719  
Yoon, Jong Seong, 3447  
Yoshida, Akinori, 1312, 1469  
Yoshioka, Hiroshi, 609, 901  
Young, I. R., 665  
Ysuchiya, Yoshito, 901  
Yu, Hong-Sun, 1212  
Yu, Xiping, 746  
Yu, Yuxiu, 731  
Zeidler, Ryszard B., 2513, 3462  
Zeng, Xiaochuan, 3060  
Zhang, Da Ping, 2856  
Zhang, Jun, 1687  
Zhuang, F., 1700  
Zielke, Werner, 2340  
Zou, Zhili, 1961  
Zuzek, P. J., 2380  
Zyserman, J. A., 2871